

On the Cathodic Reduction of Manganese Dioxide in Alkaline Electrolyte

G. S. Bell and R. Huber

Development Laboratories, Varta Pertrix-Union G.m.b.H., Ellwangen (Jagst), Western Germany

ABSTRACT

The equilibrium potentials of several varieties of manganese dioxide at various stages of reduction have been measured and an interpretation offered in terms of the phase changes involved. An explanation of the lattice collapse observed in γ - MnO_2 has been suggested.

The theoretical treatment of the thermodynamics of oxide electrodes recently published by Vetter (1) has suggested a novel approach to the study of the manganese dioxide electrode. In alkaline electrolyte it would appear to be a reasonable assumption that sections 3, 4, and 5 of Vetter's publication are applicable since the solubility of the oxide (hydroxide) is known to be very small. Consequently, any change of phase occurring during reduction can be deduced from the shape of the emf/ MnO_x curve, and related to the crystal structure determined by x-ray analysis of the solid reduction products. This technique has previously been applied by Bode and co-workers (2) to the chemical reduction of manganese dioxide with hydrazine over a limited range.

Experimental Technique

Bobbins used in the production of standard D size alkaline manganese dioxide cells were pressed and wrapped in alkali-resistant filter paper. Each bobbin was placed concentrically to an over-dimensioned cylindrical zinc anode in a discharge vessel containing approximately 250 ml of electrolyte and sealed off from the air by a film of transformer oil. The electrolyte composition was 46% KOH pellets (86% KOH), 7.5% ZnO, and 46.5% distilled water. The mix contained 85 parts by weight of oxide, 10 parts of graphite, and 5 parts of acetylene carbon black and was moistened with 12 parts of electrolyte of the same composition as previously described. All cells were allowed to stand 2 or 3 days before commencing discharge over 100 ohms for 100 hr per week at room temperature ($22^\circ \pm 2^\circ\text{C}$).

During discharge cell voltage readings were taken at intervals not exceeding 24 hr using a standard laboratory voltmeter (resistance 10 kohm/v) and at suitable intervals cells were removed from discharge and allowed to stand until the ocv remained constant. The recuperation period was in all cases protracted to at least six weeks although during the early part of the discharge a constant potential was achieved after approximately 1 week. The constant ocv was measured with a potentiometer and recorded. At frequent intervals during the experiment the electrolyte was changed, care being taken to avoid contamination of the electrodes with the oil, and since no change in cell voltage was observed it can be taken that the zinc potential remained

substantially constant. After the ocv had been determined, the bobbin was immersed in running water, broken down to powder, and left for at least 48 hr until the last traces of alkali had been removed. The powdered product was then dried in air at 105°C and a Debye-Scherrer x-ray powder photograph made using standard techniques (Fe $K\alpha$ radiation).

To assist in the thermodynamic interpretation of the results, the potential of the zinc anode was measured against a hydrogen electrode ($P_{\text{H}_2} = 1 \text{ atm}$) in the same electrolyte used for the discharge.

Three types of manganese dioxide have been studied: (a) γ - MnO_2 , a Japanese product obtained from the electrolytic oxidation of Mn^{2+} in hot, acid solution; (b) β - MnO_2 , a naturally occurring pyrolusite from the Caucasus containing 10-15% of foreign matter (largely alkaline earth silicates and some iron and nickel); and (c) an oxide of indeterminate structure obtained as a by-product in the saccharin industry.

Results

The cell voltage has been plotted against x in MnO_x for the three types of oxide in Fig. 1-3. The value of x was determined from the ampere hours taken from the cell and from the initial analytically determined O:Mn ratio (1.98 for γ - MnO_2 and 2.0 for β - MnO_2). In each figure, two points A and B are indicated. Beyond point A cementation of the

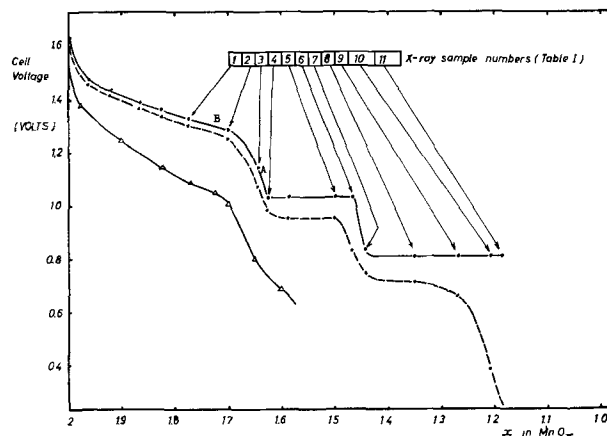


Fig. 1. γ - MnO_2 : \circ , open circuit voltage after recuperation; \bullet , closed circuit voltage 100 ohms/100 hr/week; \triangle , closed circuit voltage 5 ohms continuous (for comparison).

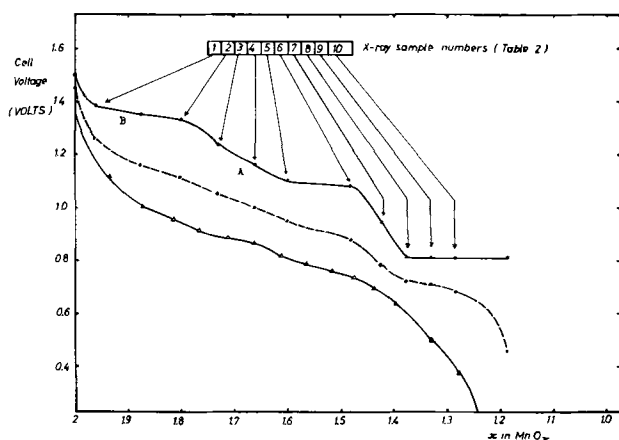


Fig. 2. β - MnO_2 : \circ , open circuit voltage after recuperation; \bullet , closed circuit voltage 100 ohms/100 hr/week; Δ , closed circuit voltage 10 ohms continuous (for comparison).

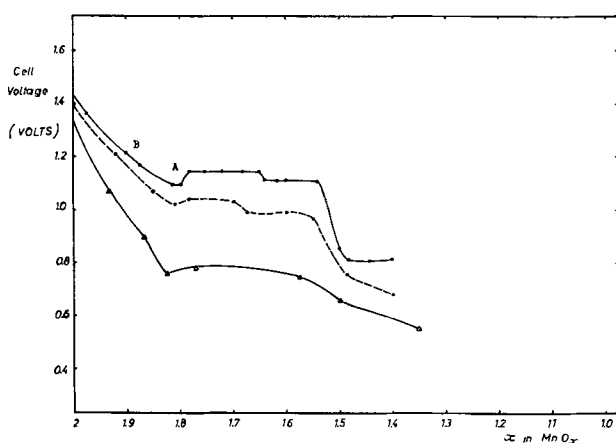


Fig. 3. By-product oxide: \circ , open circuit voltage after recuperation; \bullet , closed circuit voltage 100 ohms/100 hr/week; Δ , closed circuit voltage 10 ohms continuous (for comparison).

bobbin had occurred to such a degree that difficulty was experienced in breaking it down for the washing operation. At point B a reddish-violet color appeared in the separator paper. Both cementation and color persisted to the end of the discharge, although slightly less intense below $\text{MnO}_{1.5}$. In all experiments, a considerable increase in volume of the bobbin was observed. At no time in any experiment did any coloration or precipitate develop in the electrolyte. However, traces of dissolved manganese were found in the later stages of discharge, especially in the case of the oxide obtained as a by-product.

During the preparation of the mix containing the product (c) a considerable increase in temperature was noted on addition of the electrolyte. The chemical reaction thus indicated is now the subject of a separate investigation and the results of x-ray analysis will not be presented here, but the emf/ MnO_x curve shown in Fig. 3 warrants interest despite the uncertainty which must be attached to its interpretation.

The results of the analysis of the Debye-Scherrer photographs for γ and β - MnO_2 are presented in Tables I and II, respectively. The new lines appearing at each stage of discharge have been grouped together, and in each table comparative figures for possible reduction products are quoted for easy ref-

erence. Only d values have been given since no conclusion depending on the intensity have been drawn.

Several determinations of the zinc anode potential against hydrogen at 1 atm in the same electrolyte yielded results varying between -0.442v and -0.450v . A representative value of -0.445v has been taken for the thermodynamic treatment.

Discussion of Experimental Results

In considering the x-ray data presented here it should be noted that our observed δ values are 0.3-0.6 degrees smaller than those reported by Gattow (3). Further, we have preferred the older notation in which electrolytic oxide is designated γ - MnO_2 . The newer notation (η) and the differentiation into the many sub-varieties as proposed by Glemser and Gattow have not been applied.

According to Vetter's thermodynamic treatment, a potential varying with composition indicates homogeneous phase reduction. When the potential remains constant over a given range of composition, a heterogeneous, two-phase system is indicated. These criteria are applicable only when the rate of solution of the oxide (hydroxide) is so low that the equilibrium between the oxide and/or hydroxide ions in the solid phase and in the electrolyte is not disturbed and second when equilibrium between two heterogeneous solid phases can be established. In the following it is assumed that these restricting conditions are fulfilled.

γ - MnO_2 (Fig. 1 and Table I): Neglecting the initial rapid fall in potential down to approximately $\text{MnO}_{1.95}$, the following division can be made:

- (i) MnO_2 - $\text{MnO}_{1.7}$ Homogeneous phase reduction
- (ii) $\text{MnO}_{1.7}$ - $\text{MnO}_{1.47}$ Heterogeneous system
- (iii) Below $\text{MnO}_{1.47}$ Heterogeneous system

Examination of the x-ray data reveals that many new lines have appeared in the mix as compared with the original γ - MnO_2 . All these lines may be allocated to Ramsdellite and/or α - MnOOH (Grou-tite) and since no reduction has taken place at this point, this observation provides interesting corroboration of the generic relationship between Ramsdellite, γ - MnO_2 , and α - MnOOH of the type first proposed by Bystrom (4) and more recently by Bode (5). By some mechanism, probably penetration of cations into the defective γ -lattice, a pattern is obtained more typical of the parent Ramsdellite structure. In cells 1, 2, and 3 the lattice dilation reported by Brenet (6) is clearly recognized and the α - MnOOH structure is developing progressively. The appearance of the violet color at this stage of the reaction is feasibly due to a true Mn^{3+} complex. At cell 4 cementation of the bobbin has occurred, suggesting recrystallization, and in the x-ray diagram many new lines typical of a γ - Mn_2O_3 structure have appeared.

It seems logical therefore to regard the first heterogeneous system (ii) above as a mixture of $\text{MnO}_{1.7}$ and $\text{MnO}_{1.47}$ oxides, the former having the rhombic Grou-tite structure (and also therefore probably hydrated) and the latter the tetragonal γ - Mn_2O_3 structure. Between $\text{MnO}_{1.7}$ and $\text{MnO}_{1.625}$ and also between $\text{MnO}_{1.47}$ and $\text{MnO}_{1.43}$ the de-creas-

Table II. X-ray analysis (d values in Å) β - MnO_2 and reduction products

Oxide	Cell number										Reference data*			
	1	2	3	4	5	6	7	8	9	10	A	B	C	D
3.30	3.31	3.31					3.30		3.31		3.35	3.39	3.40	
3.07	3.10	3.12	3.12								3.11			
2.38	2.40	2.40	2.40	2.40	2.40						2.41	2.42		
2.17	2.21	2.19	2.18	2.19	2.18	2.19					2.20	2.18		
2.10	2.11	2.11	2.11								2.11			
1.95	1.97	1.98									1.96			
1.62	1.62	1.62	1.62	1.61	1.61	1.62	1.62	1.62	1.62	1.62	1.62	1.63	1.61	1.67
1.55	1.56	1.55	1.55	1.57	1.57	1.57	1.57	1.57	1.57	1.57	1.56		1.58	1.58
1.43	1.44	1.43	1.43	1.43	1.43	1.43	1.43	1.44	1.43	1.44	1.44		1.44	1.45
1.39	1.39										1.39			
1.30	1.30	1.31	1.31		1.31	1.32	1.32		1.31	1.32		1.32	1.32	
1.25	1.26				1.26	1.26	1.26	1.26	1.26	1.26			1.24	1.23
1.20	1.21					1.20							1.20	
1.16	1.16	1.16	1.15	1.15	1.15	1.16	1.16	1.16	1.16	1.16	1.16	1.15		1.17
1.12	1.12					1.12	1.12	1.12	1.12	1.12	1.12	1.13	1.13	
1.10	1.10					1.11					1.10			
1.06	1.06	1.06				1.06	1.06	1.06	1.06	1.06	1.06		1.05	
1.04	1.04						1.03							
1.00	1.00													
	4.09	4.03									4.09			
	1.82		1.80			1.81	1.80				1.79	1.79	1.82	1.82
	1.51			1.50	1.51	1.52		1.51				1.49	1.47	
	1.18		1.18					1.18				1.18	1.18	
	1.08							1.09	1.09	1.09		1.08	1.09	
		7.12	7.32	7.05										
		1.02				1.01	1.01	1.01	1.01	1.01		1.02		
		0.99				0.99	0.99	0.99	0.99	0.99		0.99		
			2.28		2.26		2.28					2.26		
			1.76	1.76	1.77	1.78	1.77	1.77	1.78	1.77		1.77	1.78	
			1.37		1.37	1.38	1.38	1.38	1.37	1.38	1.37		1.34	1.38
				2.99	3.01	3.05	3.02	3.04	3.04	3.05			3.09	
				2.64	2.67	2.72	2.71	2.71	2.69	2.73	2.66	2.63		
				2.46	2.46	2.48	2.46	2.47	2.47	2.48	2.54	2.52	2.46	2.46
						2.43								
					2.86	2.87	2.86	2.87	2.86	2.87			2.88	2.84
					1.07	1.08	1.08	1.07	1.07	1.08		1.08	1.07	
						4.94	4.86	4.86	4.74	4.90			4.72	
						2.32	2.32	2.32		2.32				2.34
						1.73	1.74		1.73		1.71	1.70	1.68	
						1.53	1.52	1.53	1.52	1.53			1.54	1.55
							1.14							
								4.59		4.66				
											[3.44]	[1.66]	[2.04]	
													[1.55]	

* A, β - MnO_2 ; B, γ - MnOOH ; C, γ - Mn_2O_3 ; D, $\text{Mn}(\text{OH})_2$. Reflections characteristic of graphite are not shown.

oxide surface. In any case we have found no evidence of the formation of $\text{Mn}(\text{OH})_2$ early in the discharge. Cahoon's hypothetical Mn_4O_7 corresponds approximately with the lower limit of the homogeneous phase.

Vosburgh and De Lap (8) found that over a limited range the cathode potential is a linear function of the oxide composition, but make no reference to the occurrence of constant potential.

Brenet (9) has reported the formation of Mn_2O_3 first and later MnOOH in the usual $\text{NH}_4\text{Cl}/\text{ZnCl}_2$ system. This is incompatible with our observations.

The slope of the potential curve in Fig. 1 down to $\text{MnO}_{1.7}$ corresponds quite well with that found by Bode *et al.* (2), but the general level of our curve is about 215 mv lower. Further, these authors did

not observe the sharp change in slope at about $\text{MnO}_{1.7}$ such as reported here. There is however little room for doubt that this significant change is characteristic of γ - MnO_2 in alkaline solution since it has been confirmed on samples from four other sources in similar experiments.

β - MnO_2 (Fig. 2 and Table II): The reduction of β - MnO_2 may be differentiated as follows:

- (i) MnO_2 - $\text{MnO}_{1.96}$ Homogeneous phase reduction
- (ii) $\text{MnO}_{1.96}$ - $\text{MnO}_{1.8}$ Heterogeneous system
- (iii) $\text{MnO}_{1.8}$ - $\text{MnO}_{1.6}$ Homogeneous phase reduction
- (iv) $\text{MnO}_{1.6}$ - $\text{MnO}_{1.48}$ Heterogeneous system
- (v) Below $\text{MnO}_{1.48}$ Heterogeneous system

The x-ray evidence shows the development of the monoclinic γ - MnOOH structure early in the

discharge and later, below MnO_{1.6}, the typical tetragonal γ -Mn₂O₃ structure. Some evidence of Mn(OH)₂ is found beyond MnO_{1.375}. Several points are worthy of comment. In the first heterogeneous region (ii above) the potential is not constant, varying 50 mv from beginning to end. This result requires further investigation and possibly indicates a failure of equilibrium between the solid phases to be established. The homogeneous region (iii above) is most unexpected in view of Bode *et al.* (2). The transition region between MnO_{1.48} and MnO_{1.375} appears to cover a wide range but since the experimental points are relatively widely spaced, a more restricted region corresponding to that found for γ -MnO₂ would not violate the present experimental evidence. The potential of the last heterogeneous region corresponds exactly with that found for γ -MnO₂, and this suggests that the phases involved are the same for both types of manganese dioxide.

There is very little published work with which the above results can be compared. Brenet's findings have been confirmed, but there is a very significant difference from Bode *et al.* (2). It would not appear unreasonable to suppose that the phase breadth of a hydrated oxide is at least partly determined by the composition of the liquid phase with which it is in contact and this may be a prime factor in accounting for the discrepancy.

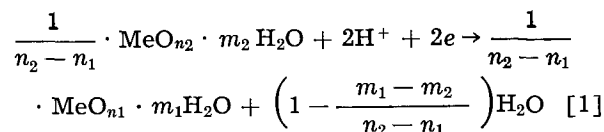
By-product oxide (Fig. 3): As previously stated, little discussion of the potential curve can be attempted but attention is drawn to the characteristic increase of potential immediately below MnO_{1.8}. A possible explanation of this peculiarity may be that the homogeneous phase extends into a region of instability due to the retarded development of nuclei necessary for the crystallization of the new heterogeneous phase.

Lattice dilation and collapse in γ -MnO₂.—Analytical data for most commercially available γ -MnO₂ varieties (electrolytic oxides) approximate the formula MnO₂ · 1/5 H₂O. Reduction in homogeneous phase implies assimilation of protons into the crystal lattice as OH⁻ ions. This process continues, accompanied by dilation of the lattice, until, as in these experiments, a limiting composition represented by a product lower in O and higher in H₂O is reached. It is postulated that the lattice is saturated at this point and that further reduction to MnO_{<1.7} > 1/2 H₂O produces instability in the phase and leads to recrystallization as an anhydrous oxide in the tetragonal γ -Mn₂O₃ phase. Examination of light-drain discharge curves for standard Leclanché-type dry cells containing γ -MnO₂ shows that here also there is a significant fall in voltage after the critical composition has been passed.

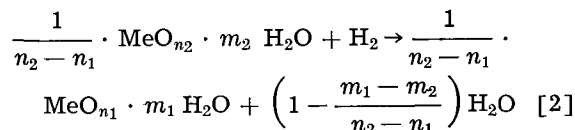
Thermodynamic considerations.—Before discussing the thermodynamic implications of the results presented here, a word of comment regarding Vetter's theoretical treatment may not be out of place. Vetter relates the potential of an oxide electrode to the change in free enthalpy, $\Delta G(n)$, of the reaction in which the oxide is formed from the parent metal and water. This has the practical advantage that $\Delta G(n)$ is easily calculated provided that the free

enthalpy of formation of the oxide from the elements is known. It would, however, appear advantageous to describe the oxide electrode as a modified oxygen electrode. This is achieved as follows:

The electrode reaction is



Coupled with a hydrogen electrode, the cell reaction is



and if the hydrogen electrode is operating with $p_{\text{H}_2} = 1$ atm the change in free enthalpy $\Delta G(R)$ is given by

$$\Delta G(R) = \frac{1}{n_2 - n_1} \left[\Delta G_o \left(\frac{n_1}{m_1} \right) - \Delta G_o \left(\frac{n_2}{m_2} \right) \right] + \left(1 - \frac{m_1 - m_2}{n_2 - n_1}\right) \Delta G_o(\text{H}_2\text{O}) \quad [3]$$

where the ΔG_o 's are the standard free enthalpies of formation from the elements.

$$\text{Now } \Delta G_o \left(\frac{n}{m} \right) = \Delta G_o(n) + m \Delta G_o(\text{H}_2\text{O}) + \Delta G_o(h)$$

where $\Delta G_o(h)$ is the free enthalpy change in the reaction



Substituting in Eq. [3]

$$\Delta G(R) = \frac{1}{n_2 - n_1} [\Delta G_o(n_1) - \Delta G_o(n_2) + \Delta G_o(h_1) - \Delta G_o(h_2) + (m_1 - m_2) \Delta G_o(\text{H}_2\text{O})] + \left(1 - \frac{m_1 - m_2}{n_2 - n_1}\right) \Delta G_o(\text{H}_2\text{O}) \quad [5]$$

and writing

$$\begin{aligned} \delta_n &= n_2 - n_1 \\ \delta \Delta G_o(n) &= \Delta G_o(n_2) - \Delta G_o(n_1) \\ \delta \Delta G_o(h) &= \Delta G_o(h_2) - \Delta G_o(h_1) \end{aligned}$$

$$\Delta G(R) = \frac{1}{\delta_n} [-\delta \Delta G_o(n) - \delta \Delta G_o(h)] + \Delta G_o(\text{H}_2\text{O}) \quad [6]$$

$$\text{and since } E = \frac{-\Delta G(R)}{nF}$$

and taking the hydrogen electrode with $p_{\text{H}_2} = 1$ atm and in the same solution (same pH), the cell voltage becomes

$$E = 1.23 + \left[\frac{\delta \Delta G_o(n) + \delta \Delta G_o(h)}{2 \cdot \delta_n \cdot F} \right] \quad [7]$$

For a heterogeneous system, δ_n , $\delta \Delta G_o(n)$, and $\delta \Delta G_o(h)$ have definite characteristic values and the cell voltage, *i.e.*, the oxide electrode potential against hydrogen in the same solution, can be found from Eq. [7].

When the electrode reaction occurs in homogeneous phase, $(n_2 - n_1)$ can be taken infinitely small and in the limit, as $\delta n \rightarrow 0$

$$E_{\delta n \rightarrow 0} = 1.23 + \frac{1}{2F} \cdot \left[\frac{d\Delta G_o(n)}{dn} + \frac{d\Delta G_o(h)}{dn} \right] \quad [8]$$

For practical applications it is often convenient to write Eq. [7] in the equivalent form (obtainable directly from Eq. [3])

$$E = 1.23 \left(1 + \frac{\delta m}{\delta n} \right) + \frac{\delta \Delta G_o \left(\frac{n}{m} \right)}{2\delta n F} \quad [9]$$

where $\delta m = m_2 - m_1$.

Turning now to the experimental results presented here, an attempt has been made to evaluate the free enthalpy of formation from the elements of all the phases involved in the reduction of γ -MnO₂. The cell voltages (converted to cathode potentials and corrected to the hydrogen scale by subtraction of 445 mv) and the Latimer value for Mn(OH)₂, -146.9 kcal/mole, have been used as a basis. For the homogeneous phase the relationship between the electrode potential and MnO_x has been approximated to a straight line. Using Eq. [7], [8], and [9] where applicable, the following free enthalpies of formation have been estimated

MnO _{1.47}	ΔG_o : -108.9 kcal/formula wt
MnO _{1.7} · 1/2 H ₂ O	ΔG_o : -145.0 kcal/formula wt
γ -MnO ₂ · 1/5 H ₂ O	ΔG_o : -131.9 kcal/formula wt

Approximating $\Delta G_o(h)$ for the hydrated oxides to $-56.7 - 3.4 = -60.1$ kcal/mole H₂O [as is the case for Mn(OH)₂] the corresponding free enthalpies for the anhydrous oxides are

MnO _{1.7}	ΔG_o : -115 kcal/formula wt
γ -MnO ₂	ΔG_o : -119.9 kcal/formula wt

Although these values cannot be credited with any great degree of accuracy, the calculations serve as

an illustration of the utility of Vetter's thermodynamics in the interpretation of oxide electrodes.

Conclusion

Vetter's theory of oxide electrodes and the concept of phase breadth have been applied in the interpretation of the emf characteristics of several varieties of manganese dioxide. Further study is required to clarify and confirm the chemical composition of the individual phases involved and in particular, the relationship to electrolyte composition. The investigation of the oxide obtained as a by-product is proceeding. A phase analysis of mixtures of several varieties of manganese dioxide, as commonly used in dry cell technology, is projected.

Acknowledgments

Thanks are due to the directors of Varta-A.G. for permission to publish and to Professor H. Bode (Varta-A.G.) and Professor K. J. Vetter (Fritz Haber Institute, Berlin) for much stimulating discussion during the course of the investigation. In particular it is a pleasure to acknowledge the assistance of Dr. Sterr (Varta-A.G.) who prepared and evaluated all the Debye-Scherrer photographs.

Manuscript received Feb. 15, 1963.

Any discussion of this paper will appear in a Discussion Section to be published in the December 1964 JOURNAL.

REFERENCES

1. K. J. Vetter, *Z. Elektrochem.*, **66**, 577 (1962).
2. H. Bode, A. Schmier, and D. Berndt, *ibid.*, **66**, 586 (1962).
3. G. Gattow, *Batterien*, **15**, 201 (1961); **16**, 322 (1962).
4. A. M. Bystrom, *Acta Chem. Scand.*, **3**, 163 (1949).
5. H. Bode, *Angew. Chem.*, **73**, 553 (1961).
6. J. P. Brenet, 8th C.I.T.C.E., Madrid, 1956, Butterworths Scientific Publ. 7.4, 394.
7. N. C. Cahoon and M. P. Korver, *This Journal*, **106**, 745 (1959).
8. W. C. Vosburgh and J. De Lap, *ibid.*, **107**, 255 (1960).
9. S. Ghosh and J. P. Brenet, *Electrochim. Acta*, **7**, 449 (1962).

A High-Rate, High-Energy Thermal Battery System

Sidney M. Selis, John P. Wondowski,¹ and Richard F. Justus

Research Laboratories, General Motors Corporation, Warren, Michigan

ABSTRACT

The system is Ca/KCl-LiCl-AgCl-K₂CrO₄/Ag. The products at the anode are calcium oxide and chromium(III) oxide in a film which does not polarize the electrode because the latter is covered with a fluid calcium-lithium alloy formed *in situ*. The cathode process is the reduction of silver ion to silver metal; silver chloride is regenerated by the oxidation of the metal by chromate ion. Cells have been built within rectangular silver containers (which are also the positive electrodes), and they have been discharged at several constant currents. For a $\pm 10\%$ voltage tolerance, energy outputs of 3.0 to 8.0 watt-min/cm³ have been obtained for the 2.1- to the 13.4-min rates, respectively.

Over the past decade military and civilian needs have been expressed for batteries of increased energy output per unit weight and volume. It seems that the thermal battery is a satisfactory approach to meeting some of these requirements. A thermal

battery is comprised of cells with an electrolyte having a high melting point. When activated by sufficient heat to melt the electrolyte, the cells are ready to deliver power.

First of all, one can expect the very favorable electrode kinetics, that is, small charge transfer polarizations with large current densities, that are

¹ Present address: Hightstown Laboratories, National Lead Company, Hightstown, New Jersey.

the consequence of using elevated cell temperatures. Furthermore, high voltages can be realized with stable, nonaqueous electrolytes, and zero-current values of 2.7-2.8v have been measured in the present work.

There are some other interesting advantages to thermal batteries. The cells would be under an inert atmosphere in hermetically sealed containers, and they would be completely latent for indefinitely long periods of time at temperatures up to the melting point of the electrolyte.

The range of ambient temperatures is often specified as -55° to $+75^{\circ}\text{C}$, and it would be very difficult to arrange for the same aqueous battery structure to be usable at the two extremes. The properties of the molten salt system would be not nearly so responsive to differences in temperature.

It is not in the province of this paper to discuss how thermal cells may be heated to accomplish activation. However, cell designs up to this time have been based on very small electrolyte thicknesses (less than a millimeter) so that the cells could be rapidly activated. Such small anode-to-cathode distances have limited the choice of cathode reactants to insoluble materials or certain dissolved oxyanions so that short-circuiting dendrites would not form (1, 2). But with these positive electrode materials, full advantage is not taken of the fastest electrochemical processes, and in exchange for very rapid activation, high-rate output of thermal batteries has not been very large.

In the present work, physical arrangement was not limited to very thin cells. It is expected that activation will be a longer process with larger amounts of electrolyte, but that there will be a wider choice of electrochemical systems. This paper introduces one of these and discusses it from both the basic and applied points of view.

Experimental

Chemicals and special cell materials.—All inorganic salts were of reagent grade and were not further purified. The kaolin powder used to retain the catholyte had been washed and ignited prior to being packaged. The calcium metal sheet was 3.2 mm in thickness; it was obtained from the Fielding Chemical Company. Semi-quantitative spectrochemical analysis showed magnesium to be the main impurity but in amounts of less than 0.1 mole %.

The surface of the calcium metal was bluish-gray in color, presumably coated with calcium oxide and calcium nitride. Even if the surface was initially cleaned, it would become oxidized again by the time the electrode was immersed in the electrolyte according to the procedure given below, and in fact, abrading the metal made no difference in electrode performance.

The silver sheet was 0.13 mm in thickness and was 99.9 wt % pure. Before use it was rubbed with fine emery paper and then rinsed with distilled water and dried with absorbent paper. The lead wires and strips directly connected to the calcium and silver sheet electrodes were either of this grade of silver

or else of dead-soft commercially pure nickel (99+ %).

The silver cans were electroformed on aluminum blocks that had been "flashed" with copper. The last steps in removing the aluminum were to soak the cans in dilute hydrochloric acid, rinse them thoroughly with distilled water, and allow them to dry in the air. They were not treated beyond this. Spectrochemical analysis showed the main impurity to be less than 0.1 mole % of copper.

Certain insulating materials were used to make counterelectrodes and cells. The counterelectrodes were covered with asbestos paper that had been heated in a burner flame or with glass cloth that had been heated by the manufacturer to remove the sizing. Some of the insulation in the can cells was a nonwoven fabric of polycyclized acrylonitrile obtained from the Kendall Company. Prior to its use in cells, it was heated in a burner flame to remove the binder.

Procedure for single electrode studies.—Figure 1 shows the construction of cells that were used for single electrode studies. The container was a 38 x 300-mm Pyrex test tube. The rubber stopper was bored for the four 8-mm Pyrex tubes.

The silver or the calcium measurement electrodes under study, as well as the silver counterelectrodes used only for passing current through the cells, were 25 mm in width and 32 mm in height. Across the tops of the calcium electrodes were spot-welded strips of soft nickel ribbon 3 mm wide. To each of these had been soldered two leads of 16 B & S gauge silver wire. (These wires could be directly attached to the silver electrodes by soldering.) The leads from the measurement electrodes were passed through the bores of two-hole ceramic tubing which had been fired at 600°C . This ceramic tubing was then pushed through lengths of 8-mm Pyrex tubes. The assemblies were completed by applying de Khotinsky cement to the tops of the Pyrex and ceramic tubes and to the wires. With this arrangement the

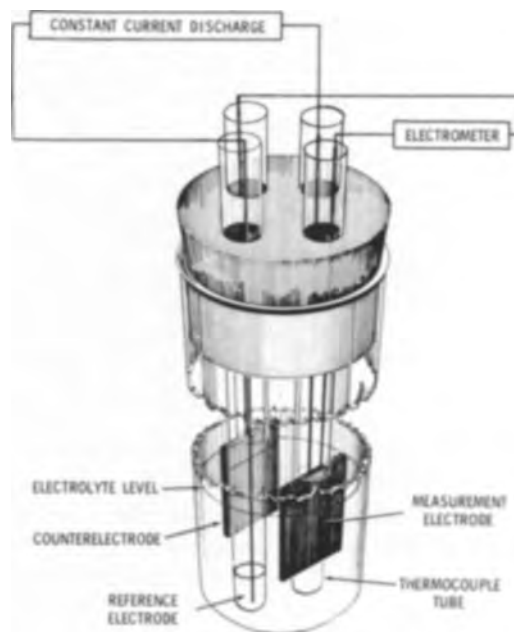


Fig. 1. Cell arrangement for single electrode measurements

potential readings do not include the IR drop through the leads. This was an especially important matter when studying the calcium electrode, because one did not always know whether the formation of calcium oxide under the nickel strip did not result in a high resistance. The resistance would not necessarily be of either basic or practical significance since it might be diminished by using special assembly techniques.

For the counterelectrodes the use of ceramic tubing was obviated because there was only one lead which was cemented to the Pyrex tube at the top. The counterelectrode was covered with asbestos paper or glass cloth. This prevented short-circuits due to silver dendrites or the liquid calcium-lithium alloy that will be mentioned later.

The Ag/KCl-AgCl/glass reference electrodes were made by packing into an 8-mm Pyrex tube, closed at one end, a mixture containing 30 mole % of potassium chloride and 70 mole % of silver chloride. This mixture was found to be completely liquid at temperatures above 325°C and could be easily melted by holding the tube in a burner flame. When it was molten a length of silver wire was pushed down the tube to the bottom so that it made contact with the KCl-AgCl mixture. The electrode was then allowed to cool. The fourth piece of 8-mm tubing was sealed at one end and served to protect the chromel-alumel thermocouple. The four tubes were then pushed through the rubber stopper as shown in Fig. 1.

The reference was always Ag/KCl-AgCl/glass, but several different electrolytes were used in the main body of the cell in conjunction with the measurement and counterelectrodes. The following procedure was consistent for all of these. The electrolyte components were weighed out rapidly (to avoid excessive absorption of water) and introduced into a cell test tube. The weight of electrolyte was 80g in each case, and the molten salts occupied about 50 cm³. The tube, covered with a watch glass, was then lowered into a cylindrical furnace heated to the experiment temperature.

Next, the electrode assembly was lowered into the cell and held so that the bottoms of the electrodes were about 20 mm above the electrolyte surface. They were kept in this position for about 10 min so that they would be heated to the experiment temperature. While this preheating continued the electrical connections were made as shown in Fig. 1.

A Keithley Model 220 electrometer was connected between the reference electrode and one lead of the measurement electrode. This multirange meter was employed for convenience rather than for its high input impedance. Actually the resistance of the reference electrode is sufficiently low so that a null-balancing potentiometer can be used. The second lead from the measurement electrode and the lead from the counterelectrode were connected to the constant-current discharge apparatus.

When the experiment temperature was reached the electrodes were lowered into the electrolyte. This could be done with the load switch open or closed so that one could read zero-current potentials for a while or else activate the electrode under constant-current load. The current was controlled manually,

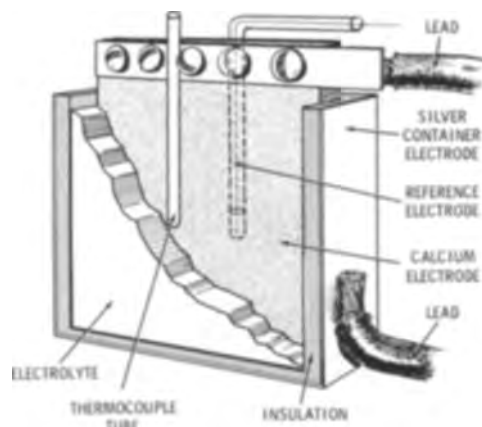


Fig. 2. Rectangular can cell with reference electrode and thermocouple.

and there was a supporting storage battery in the circuit. Results of some discharges are given below, and the current density is based on the apparent area of both sides of the electrodes even though one was faced away from the counterelectrode. The dimensions of the electrodes immersed in the electrolyte were 2.5 x 2.5 cm, and the largest current density used with these cells was 1.50 amp/cm².

Procedure for rectangular can cells.—Figure 2 is a diagram of an assembled cell. The silver cans were the containers and, at the same time, the positive electrodes. Their inside dimensions were 8.90 x 8.90 x 1.60 cm, but they were used to a depth of only 8.3 cm, and the effective cell volume was 118 cm³. A heavy lead was silver-soldered to an outside edge of the can as shown in the diagram. Either two lengths of 3-mm Pyrex rod or a strip of the polycyclized acrylonitrile fabric was then laid on the bottom of the can.

More than one electrolyte composition was used with these rectangular cells, but the following procedure was the same with each of them. The can was set in a furnace heated to 450°C, and 150g of electrolyte salts were added. The unfused chemicals have a much larger bulk than does the liquid, and it was often necessary to add some of the salts, allow them to melt, and then add the remainder.

In the meantime the anode was prepared. From the calcium sheet a rectangle with a width of 8.30 cm and a height of 11.0 cm was cut. Across the top, five holes were drilled and tapped. A narrow strip of silver, to which a heavy lead had been attached with silver solder, was then fastened to the anode with silver-plated steel ¼ in.-20 bolts. It was found that the resistance at this connection did become large after a week, due to oxidation of the calcium between the electrode and the bolts, but the technique was certainly satisfactory if the cell was to be discharged within two or three days. It should be noted that such an effect does not constitute a fundamental difficulty in making these thermal cells because it can be overcome with special techniques.

Also attached to the calcium electrode were pieces of polycyclized acrylonitrile fabric on the edges as well as a 4-mm Pyrex thermocouple protection tube and a 4-mm tube containing KCl-AgCl for the reference electrode shown in Fig. 2. These tubes also

served to keep the anode away from the can, and the fabric and the tubes were tied in place with glass cloth ribbons.

When the electrolyte had melted, the anode assembly was pushed down into place. The cell was immediately placed between blocks of steel, 10 by 10 by 3 cm, cooled to 0°C so as to freeze the electrolyte and deactivate the cell. It was then put in a desiccator charged with calcium sulfate and kept there no more than two days before it was discharged.

The cell was activated by putting it between similar steel blocks in a furnace heated to the proper temperature. At this time the chromel-alumel thermocouple and the silver reference electrode wire were also inserted. Changes in voltage as a function of time and temperature are shown in Fig. 6. When the cell finally reached the experiment temperature the load was applied, and discharge was made at constant current controlled by a servo-mechanism. The largest current used was 100 amp, corresponding to an anode current density of 0.86 amp/cm².

Chemical analyses.—After electrochemical measurements were completed on a can cell it was removed from the furnace and the anode was withdrawn. The coating on the electrode was scraped away and submitted to x-ray powder diffraction analysis. The removal was strictly by mechanical means, no water being used.

The molten electrolyte had been poured into a beaker where it froze. The coating material and the electrolyte salts were both examined for silver chloride and chromate ion. The coating scraped from the anode and the residue within the can were leached with distilled water, and the electrolyte salts were concurrently treated in the same way. Several quantities of water were used, and when the liquid finally remained essentially colorless, the washings from the coating and the electrolyte were combined and filtered and diluted to a known volume (2,000 ml).

To determine the total amount of chromate ion from a given cell, a 50-ml aliquot of the solution was acidified with sulfuric acid, and an excess of ferrous ammonium sulfate was added to it, the excess being determined by titration with decinormal permanganate solution. To determine the silver chloride, the water-insoluble part of the cell residue was leached for several days in concentrated ammonium hydroxide solution. The entire solution was filtered and made acid with hydrochloric acid solution. Silver chloride was precipitated and collected in a filter crucible, washed, dried, and weighed. The cell residue was checked for silver chloride that had not been removed. It was leached a second time with ammonium hydroxide, followed by acidification with the hydrochloric acid.

Results and Discussion

An electrode with a very cathodic potential is silver, silver chloride. Moreover, the melting point of the metal is sufficiently high so that it will be physically stable in a thermal cell, and silver chloride should not unduly raise the liquidus temperature of an alkali metal chloride electrolyte. This Ag, AgCl pair might provide a very fast, simple electron

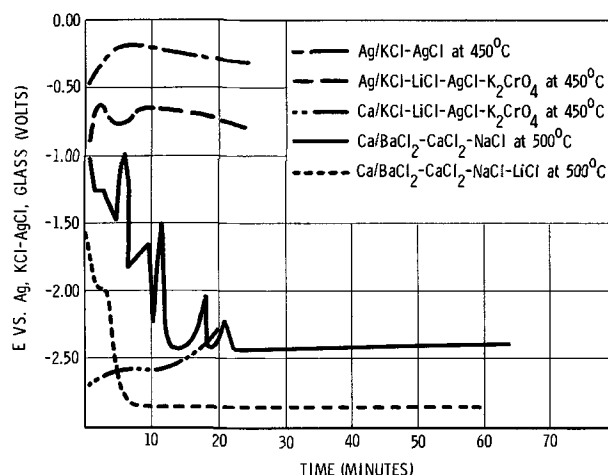


Fig. 3. Calcium and silver potentials in molten chloride electrolytes in test tube cells. Current density, 1.50 amp/cm²; temperatures as shown.

transfer process. Calcium was chosen as the negative electrode metal. Potentials as low as -3.0v have been measured with respect to the silver, KCl-AgCl, glass reference, and, in fact, calcium has been used successfully in other thermal battery systems (3). The following paragraphs discuss experiments with electrodes in molten salt electrolytes, and then data are given for a successful primary cell system.

Silver electrode studies.—The first experiments on positive electrodes were with silver metal immersed in pure silver chloride or in the KCl-AgCl mixture; these are liquid at relatively low temperatures, 455° and 325°C, respectively. The kinetics are excellent for both of these couples acting as cathodes in the arrangement shown in Fig. 1. With a current density of 1.50 amp/cm², the potential rose for 6 or 7 min, and 20 min after the maximum was reached, it had dropped by no more than a tenth of a volt as shown by Fig. 3 for Ag/KCl-AgCl.

Neither silver chloride nor KCl-AgCl can be used as the electrolyte, however. The fact was demonstrated by measuring calcium potentials in these melts. The calcium reduces silver ion and metallic silver coats the anode; the potentials are then the same as that of silver metal. Another serious problem was the formation of silver dendrites which grew out from the cathode and tended to make short-circuits with the negative electrode. This happened even if no current was passed through the electrode.

The next step was to try to exclude the silver chloride from the main electrolyte and to confine it to the cathode. This cathode was made by coating the silver sheet with a kaolin matrix containing the KCl-AgCl mixture. The main electrolyte was the ternary eutectic mixture of barium, calcium, and sodium chlorides (14.5 mole % BaCl₂, 47.0 mole % CaCl₂, 38.5 mole % NaCl) which has a melting point of 450°C (4). This cathode was used as a counterelectrode in the arrangement shown in Fig. 1; the temperatures were 500° and 550°C. Now the coating of the calcium with silver was postponed for a few moments until the silver chloride had migrated into the main electrolyte, but a sudden rise of the anode potential did occur eventually as did the dendrite formation.

Later on in this paper it will be seen that the eutectic mixture of potassium and lithium chlorides (40.0 mole % KCl and 60.0 mole % LiCl; melting point, 354°C) was found to be the basis of a satisfactory electrolyte with the calcium electrode. At this point, however, it will be discussed in terms of the silver electrode. The actual composition to be considered is 33.3 mole % KCl, 50.1 mole % LiCl, 10.0 mole % AgCl, and 6.65 mole % potassium chromate; it is found to be completely liquid at temperatures above 440°C.

Figure 3 shows the discharge performance of the positive electrode Ag/KCl-LiCl-AgCl-K₂CrO₄ at the apparent current density of 1.50 amp/cm²; this behavior is reasonably consistent in the temperature range of 450°-550°C, and potential is almost as high as with the KCl-AgCl electrolyte. As with KCl-AgCl there is an initial rise in potential, apparently due to local resistive heating and concomitant depolarization. Then as dendrites are formed, the actual current density is reduced, and this may explain the temporary rise in potential occurring 7 min after activation. Potential falls again due to polarization. Dendrites do not cause short circuits when the electrolyte is KCl-LiCl-AgCl-K₂CrO₄; the reason for this is given below.

The arrangement shown in Fig. 1 represents an electrode in a great excess of electrolyte, and therefore, discharge at a high current density can continue for long periods of time. This could not be the situation with cells built into rectangular silver cans as shown in Fig. 2 where only a limited amount of active material could be included in the relatively small volume of electrolyte.

However, a wholly unexpected effect is observed based on the results in Fig. 4 which are the polarizations (including IR terms) of the electrodes in the silver can cell discharged at 100 amp. The positive electrode polarizes by no more than 0.15v even after 6 min. But the 29.4g of silver chloride included in the 150g of electrolyte is stoichiometrically equivalent to only 3.30 min at 100 amp.

There is only one other oxidizing agent in the system, and the rest of the observed capacity can only

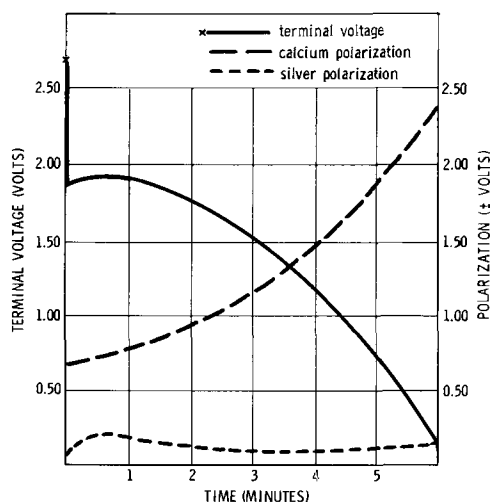
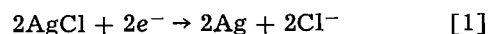


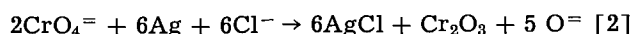
Fig. 4. Cell voltage and electrode polarizations during discharge of a rectangular can cell at 100 amp; temperature, 500°C.

be accounted for in terms of the reduction of chromate ion. But if this is the situation, then there might be no reason for including silver chloride; chromate ion alone could conceivably be the reducible species at the cathode. Accordingly, some cells were prepared in which the electrolyte was simply 6.65 mole % of potassium chromate and 93.4 mole % of the KCl-LiCl mixture. The cells were heated until the zero-current voltage was fully developed and the 100-amp load was applied. The positive electrode immediately polarized by 6v, just as if there was no reactive species at the cathode.

Based on these observations the authors offer the following hypothesis. The over-all process at the cathode is as shown by Eq. [1]. Silver chloride is part of the initial electrolyte



composition, but it is also formed by way of reaction [2] which replaces



the silver ion that was used galvanically at the positive electrode or that was reduced nongalvanically by calcium metal. Little or nothing is known concerning the standard free energies of chromate ion and oxide ion in the molten chloride electrolyte, and for this reason, the thermodynamics cannot be discussed on a quantitative basis. The equilibrium point of reaction [2], however, will certainly be displaced to the right because stable and insoluble calcium and chromium oxides are formed, thus decreasing the activity of oxide ion in the electrolyte.

In an earlier paper one of the present authors discussed a similar concept for thermal cell chemistry (5). The cathode half-cell was Ni/KCl-LiCl-K₂CrO₄, and it was postulated that nickel is oxidized by chromate ion to a nickel oxide. It is the latter species which is reduced galvanically. This same idea of pre-oxidation of the cathode metal is introduced here except that stronger evidence is available. That is, it is evident that discharge continues well beyond the stoichiometric limit based on the amount of silver chloride initially included.

As with the earlier example of pre-formation of a nickel oxide, the process shown as Eq. [2] does not keep pace with reaction [1] operating at high currents; this is evident from Fig. 5 which shows how the silver chloride content decreased with coulombic passage at the 100-amp rate. Zero passage on this plot corresponds to that time when the cell was fully activated but the load not yet applied. At this moment there were 0.131 equivalent of silver chloride and 0.355 equivalent of chromate ion present. That is to say, 0.074 equivalent of silver chloride and 0.053 equivalent of chromate ion had been used nongalvanically. Furthermore, another tenth of an equivalent of oxidizing agents had been expended nongalvanically before discharge was finished as signalled by the complete usage of silver ion and chromate ion concurrent with essentially zero and rapidly decreasing cell voltage. As is shown in Fig. 5, discharge was finished when 0.40 faraday had been passed; with a current of 100 amp this required 6.43 min.

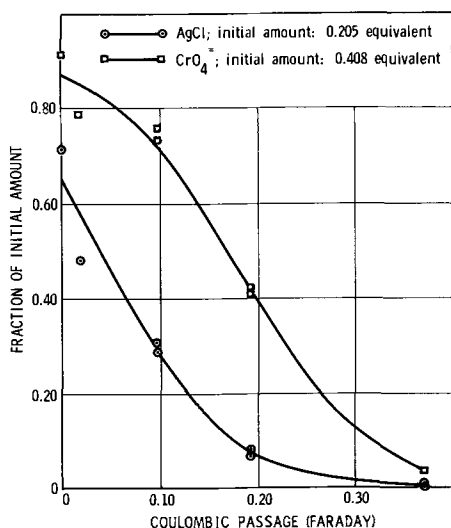


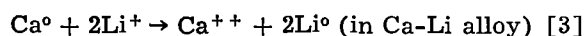
Fig. 5. AgCl and chromate ion content as a function of coulombic passage during discharge of a rectangular can cell at 100 amp; temperature, 500°C.

On the basis of the above results the silver electrode seems very satisfactory as part of a high-rate, high-output battery system. The negative half-cell can now be considered.

Calcium electrode studies.—In order to obtain the greatest energy output per unit weight and volume, there should be little or no nongalvanic side reactions. For the best kinetic performance the electrode probably should be of the first kind. That is, calcium metal should be in equilibrium with calcium ions dissolved in the electrolyte, and as with the cathode, there should be a simple electron transfer process.

The use of calcium immersed in BaCl₂-NaCl-CaCl₂ was an attempt at this. Neither barium nor sodium ion is reduced by calcium metal, and the half-cell would indeed seem to be a reversible electrode of the first kind. The steady-state potential is very anodic as seen in Fig. 3. But as shown in this figure, a long time is required for the development of this potential under load. The reason is that metallic calcium is subject to air oxidation and becomes coated with a layer of calcium oxide and nitride, and this delays equilibration with the electrolyte. The other difficulty with this half-cell has already been mentioned. When silver chloride enters the electrolyte, silver ion is reduced to silver metal on the calcium surface, and the potential of the anode rises to that of silver.

The next step was to include 10 mole % of lithium chloride in the electrolyte. Now the calcium undergoes a side reaction as shown by Eq. [3]. Lithium ion is reduced to the metal which forms a liquid



alloy with calcium. It has already been shown how this continually renewed, fluid metal surface can prevent the electrode from ever becoming polarized or passive due to a solid oxide layer (6).

Although this addition of lithium ion did ameliorate electrode behavior, the improvement was not sufficient. Potentials under load were more anodic, but activation of the electrode still required several

minutes. Moreover, the presence of small amounts of silver ion still caused the potential to rise nearly to the value for silver.

Finally, lithium chloride was included in large amounts. The electrolyte was now the KCl-LiCl eutectic mixture which is 40.0 mole % of KCl and 60.0 mole % of LiCl, melting at 354°C. In this electrolyte, reaction [3] takes place rapidly and extensively, and one now encounters a problem concerning dimensional stability of the negative electrode. There is no difficulty at all, however, in the activation of the electrode. A very anodic potential is measured immediately on immersion of the heated electrode; it is $-3.01 \pm 0.05\text{v vs. Ag, KCl-AgCl, glass}$ at 1.50 amp/cm².

The next thing learned was that the calcium potential remains sufficiently negative with silver chloride present. Calcium appeared to be a suitable electrode even with 10 mole % of silver chloride in the electrolyte. The potential was as low as -2.71v , and the initial rise with a current density of 1.50 amp/cm² was no more than a tenth of a volt.

The calcium electrode is less anodic with silver ion in the electrolyte as compared with its behavior in the eutectic mixture of potassium and lithium chlorides. Even so, the formation of liquid calcium-lithium alloy is still extensive in the electrolyte KCl-LiCl-AgCl, and, as pointed out above, this is fortunate and is probably the reason why calcium can be used as a negative electrode in the first place. But improved physical stability was needed. The approach used in this work to make the calcium electrode more stable from the dimensional standpoint was to include in the electrolyte a species which is an oxidizing agent and, at the same time, a source of oxide ion. Several of these, including permanganate, metavanadate, and nitrate ions, were tried, but chromate ion was the most satisfactory in terms of giving an electrode with a very stable and anodic potential and having a long discharge life. A suitable concentration of chromate ion was 6.65 mole %.

The principle underlying the use of this oxidizing agent is that calcium is made somewhat less reactive and reduces lithium ion and silver ion not as rapidly and thus becomes a practical electrode for a high-energy battery system. The insoluble and protective coating developed on the discharged calcium electrode was analyzed by x-ray powder diffraction measurement as noted above. Calcium oxide was found as was chromium (III) oxide. These two phases are stable in the range of experiment temperatures, and there is no basis for postulating any other phases.

There is a physical advantage and a disadvantage to this film. It does block the silver dendrites and short-circuits are thereby avoided. On the other hand, it retards the movement of electrolyte to the electrode surface and so deprives the calcium of oxide ion. This is a mass transport polarization, but it would also be the cause of internal resistance near the negative electrode.

As is shown by Fig. 3, the behavior of the electrode Ca/KCl-LiCl-AgCl-K₂CrO₄ is very satisfactory, at least with a large excess of electrolyte. The potential is very anodic (-2.59v) under a discharge

load of 1.50 amp/cm², and if the period of discharge seems short (approximately 11 min), it should be remembered that thermal batteries have not been used for times much longer than 5 min. It may be noted that the temperature for this discharge as shown in Fig. 3 is 450°C, although behavior was consistently good in the region 450°-550°C.

It has been shown that the anode half-cell mentioned in the previous paragraph, as well as the cathode half-cell Ag/KCl-LiCl-AgCl-K₂CrO₄, are apparently satisfactory for use in a primary battery, at least when separately examined in test tubes containing an excess of electrolyte. Next in order was to demonstrate their usefulness in a primary cell with a somewhat practical geometry.

Cell studies with rectangular cans.—As described earlier in this paper, a can cell was connected in the constant-current discharge circuit and then placed between the steel blocks in the furnace. The recorder was started at this time, and the trace is shown in Fig. 6. The initially measured voltage was zero due to the very high resistance of the electrolyte prior to its melting while the input impedance of the controller-recorder unit was only 1500 ohms.

After a few seconds the voltage began to rise. As shown in Fig. 6, the temperature was still not much above room temperature, and the recorded voltage was apparently due to dissolution of electrolyte salts in the water contained by the hygroscopic lithium chloride;² this solution would result in a lowering of the internal resistance of the cell. As seen in the figure, about two minutes were required for this "early voltage" to be developed, and it persisted for about 80 sec or until the temperature reached 220°C.³ At this point the water had apparently boiled away, and since the salts had not yet started to melt, cell resistance was again high and voltage declined to about 1.33v.

Ninety seconds later the temperature reached 320°C, and the salts began to melt. The voltage changed abruptly, and within a few seconds it rose to 2.55v and then slowly increased to 2.70v. The load

² It should be pointed out that good technological practice would include using a low-humidity room to minimize this absorbed water and thereby to avoid the "early voltage" and also to lessen attack of the calcium metal.

³ The temperature scale in Fig. 6 is only approximate. It is shown to be linear up to 400°C, and of course, this is not justified. However, it represents a precision which is within the limits of measurement error.

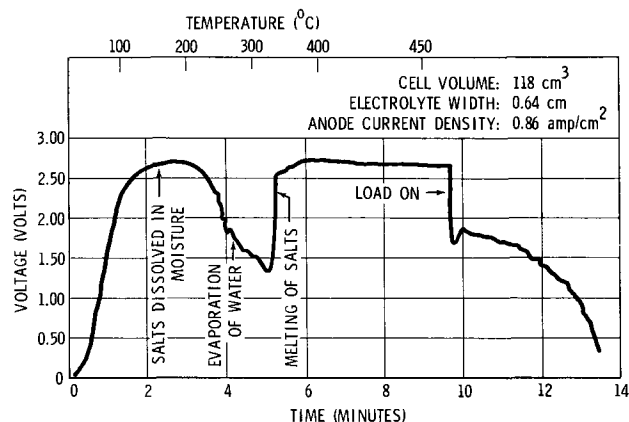


Fig. 6. Activation and discharge of a rectangular can cell at 100 amp; temperature, 450°C.

Table 1. Rectangular can cell performance at 450°C

Current (amp)	E (Peak) (v)	±5% Variation		±10% Variation		Energy (watt-min/cm ³)
		\bar{E} (v)	Time (min)	\bar{E} (v)	Time (min)	
30	2.35	2.24	11.0	2.14	13.4	7.99
50	2.18	2.08	3.44	1.98	5.19	4.70
72	2.04	1.94	2.38	1.85	3.38	4.01
100	1.80	1.71	1.69	1.64	2.13	2.96

was not yet applied. Another four minutes were allowed for the temperature to approach closely or to reach 450°C. When the 100-amp load was finally applied the voltage suddenly fell to 1.62v (a large part of this initial decrease may be due to IR drop). There was then a temporary rise to 1.85v. It is assumed that this rise was due to increased silver electrode area from dendrite formation as well as internal heating which resulted in a depolarization of both electrodes.

Discharge was continued at constant current until the terminal voltage had fallen to 0.5v or somewhat less. Voltage was recorded as a function of time, and the typical numbers in Table I were either read directly or else were immediately derived. Four values of current were used. Peak voltage was read. For the determination of cell life or discharge time it was considered that voltage might be held to within 5% ($\bar{E} \pm 0.05\bar{E}$) or to within 10% ($\bar{E} \pm 0.10\bar{E}$) of a mean value. That is to say, a battery in practical application would certainly not be useful after its voltage had fallen to a relatively low point; in fact, the limits quoted above are realistic. Peak voltage can be taken as the upper limit, and mean voltage can be determined from peak voltage by dividing the latter by 1.05 or 1.10. The lower limit of voltage is then 0.95 or 0.90 of mean voltage, and on this basis one could mark the beginning and end of effective discharge and obtain the discharge times. Table I also gives values for the energy output per unit volume based on voltage held to within 10% of a mean value. This was obtained by measuring the area under the voltage-time curve for the discharge period as defined above. This area (in volt-minutes) was then multiplied by the current and divided by the cell volume (118 cm³).

It is clear that the specific energy outputs in Table I are not realistic for a practical thermal battery. This is because no volume has been allowed for the heating mechanism nor for thermal insulation. It would be difficult to estimate these, and, similarly, no attempt has been made to estimate the weights of cells and batteries. On the basis of the can cells alone, however, energy output is certainly very impressive compared with the capabilities of commercial batteries, and with heating and insulation contributing additional weight and volume, energy output would still be exceptionally high.

Acknowledgment

The authors express their appreciation to Miss Gladys Sobieska for her assistance in the preparation of the manuscript.

Manuscript received May 20, 1963; revised manuscript received Aug. 2, 1963. This paper was presented at the Boston Meeting, Sept. 16-20, 1962.

Any discussion of this paper will appear in a Discussion Section to be published in the December 1964 JOURNAL.

REFERENCES

1. E. S. McKee, "Thermal Cells," Proc. 10th Ann. Battery Res. and Dev. Conf., Power Sources Div., Signal Corps Engineering Labs., Fort Monmouth, N. J. (1956).
2. S. M. Selis, L. P. McGinnis, E. S. McKee, and J. T. Smith, *This Journal*, **110**, 469 (1963).
3. R. B. Goodrich and R. C. Evans, *ibid.*, **99**, 207C (1952).
4. A. G. Bergman and S. P. Pavlenko, *Compt. rend. acad. sci., U.R.S.S.*, **27**, 972 (1940).
5. S. M. Selis and L. P. McGinnis, *This Journal*, **106**, 900 (1959).
6. S. M. Selis and L. P. McGinnis, *ibid.*, **108**, 191 (1961).

Effect of Velocity and Oxygen on Corrosion of Iron in Sulfuric Acid

Z. A. Foroulis and H. H. Uhlig

Corrosion Laboratory, Massachusetts Institute of Technology, Cambridge, Massachusetts

ABSTRACT

Corrosion rates were determined for 0.009% C iron, and 0.24% C and 1.05% C steel in 0.33N H₂SO₄ at velocities up to 4000 rpm (3.5 m/sec). In acid deaerated with nitrogen, the corrosion rate of 0.009% C iron was constant, and no effect of velocity was found. In aerated stagnant acid, the rate was lower than in deaerated acid and increased markedly with velocity. Corrosion rates of carbon steels, on the other hand, at first decreased with velocity, reaching a minimum which occurred at higher velocities the higher the carbon content. Beyond the minimum, corrosion increased linearly with velocity. These results are explained by an initial inhibiting effect of oxygen on the corrosion rate. Polarization measurements confirm that small amounts of oxygen increase anodic polarization probably by adsorption on anodic sites. Higher concentrations of oxygen cause depolarization of cathodic areas accompanied by an increase of corrosion. In absence of oxygen, velocity is without effect because the reaction is controlled by activation polarization accompanying hydrogen evolution, and this is not sensitive to velocity. Ferric ion also can act as inhibitor or depolarizer depending on surface concentration.

An understanding of the effect of velocity on corrosion is useful to establish mechanism of reaction, particularly when the effect is not solely one of diffusion control. Although the relation of velocity to corrosion of iron has been reported by others, some details of previous observations are not yet adequately explained, such as occurrence of a minimum in corrosion as velocity increases. A possible explanation became apparent to us during the course of studies on another subject by A. P. Bond of this laboratory, who found that zone-refined iron corrodes in 1N H₂SO₄ at lower rates when the acid is aerated [415 mg/dm²/day (mdd)] than when deaerated (680 mdd) employing purified hydrogen. This is opposite to any effect which might have been predicted based on oxygen as a cathodic depolarizer. Bond also found the same inhibiting effect of oxygen employing various pure cobalt-iron alloys immersed in 1N H₂SO₄ (1). Since the effect of increasing velocity is to bring increasing amounts of oxygen to the metal surface blanketed with H₂ bubbles, it follows that the inhibiting effect of oxygen described above should also be found in corrosion experiments conducted at variable velocity. This is the basis of the present investigation.

The effect of velocity on corrosion of iron in 0.01-0.2N aerated H₂SO₄ using rotating disks was reported in 1922 by Friend and Dennett (2). They found that

dissolution increased linearly with rotational speed up to 4000 rpm. Whitman *et al* (3) criticized the work of Friend and Dennett and carried out, in greater detail, extensive experiments in aerated and O₂- or N₂-saturated sulfuric acid of various concentrations (0.0043-5N). They found in aerated acid of all but the lowest concentration that corrosion of mild steel first decreased as velocity increased, passed through a minimum, and then increased linearly with speed of rotation. The same effect was reported for N₂-saturated acid, although the corrosion rate was less and the minimum was less pronounced. They explained the minimum as being caused by smaller H₂ bubble formation during rotation, the energy required for forming small bubbles being greater than for large bubbles characteristic of stagnant solutions. At still higher velocities, depolarization by O₂ predominated. Wormwell (4) investigated the effect of velocity on corrosion of mild steel in 0.5N NaCl, finding only an increase with speed of rotation. In this solution, H₂ evolution did not occur, the corrosion rate being controlled by O₂ depolarization alone.

Experimental Detail

The present study employed a cylindrical specimen of iron or steel (1.6-1.8 cm diam, 5 cm long) attached to a carefully balanced rotating shaft, and immersed in 1.5 liters of 0.33N H₂SO₄. The experi-

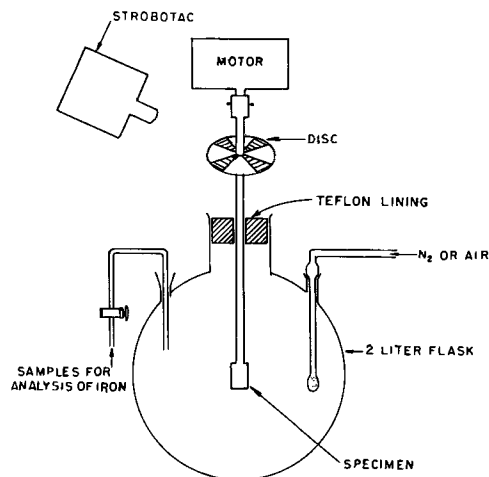


Fig. 1. Vessel for corrosion rate measurements of rotating specimen

mental arrangement is shown in Fig. 1. The speed of the motor reaching 5800 rpm was controlled by means of a variable transformer. The precise speed was measured using electronically pulsed stroboscopic light (General Radio "Strobotac"). For low speeds (less than 600 rpm), a reduction gear was required. The specimen was threaded into the end of the main steel shaft which in turn was attached to the motor or the reduction gear. The bottom portion of the specimen, as well as the sides of the shaft, were coated with three layers of methyl methacrylate resin, with 2 hr drying time between each coat. Only the sides of the specimen, therefore, were corroded during the experiment. The specimen was abraded with No. 120 followed by No. 600 emery paper; then pickled for 2 min in 1:1 HCl, washed with tap and distilled water, and immediately introduced into the test acid. The corrosion rate was followed by analyzing successive portions of the acid for iron, using the orthophenanthroline colorimetric method (5). Gas saturation of the acid was accomplished by previously passing purified gas through sintered glass bubblers for 8 hr at 150 ml/min in the case of nitrogen, and 1 hr in the case of air. Nitrogen was purified by passing it over hot copper turnings at 400°C using glass tubing from purifier to cell. All the apparatus was contained in a constant temperature room maintained at $25^\circ \pm 0.5^\circ\text{C}$. Tests were of 5 hr duration.

Polarization measurements were carried out at 25°C in a three compartment cell, the middle compartment of which contained 2 liters of 0.33N H_2SO_4 . A Luggin capillary containing the same acid con-

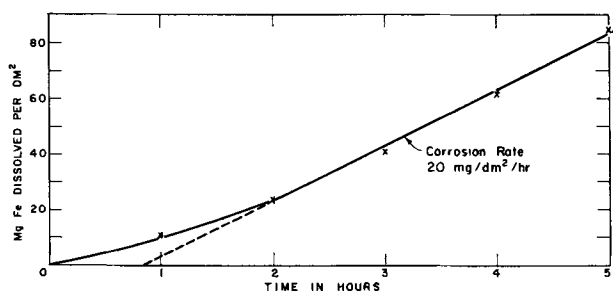


Fig. 2. Typical weight loss-time plot, 0.009% C iron in deaerated 0.33N H_2SO_4 , 600 rpm.

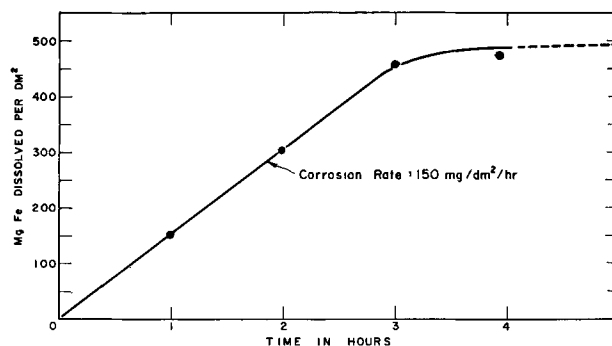


Fig. 3. Dissolution of 0.24% C steel in aerated 0.33N H_2SO_4 , at 4000 rpm.

nected to a salt bridge and to an Ag-AgCl, 0.1N KCl reference electrode. The electrolyte was deaerated with nitrogen as previously described, or with nitrogen-oxygen mixtures the proportions of which were determined by flowmeters connected to a manifold. The acid was pre-electrolyzed for 3-hr employing several milliamperes. Specimens for potential measurements were prepared from relatively pure iron containing 0.009% C (Ferrovac). For corrosion tests, specimens included 0.009% C iron and also two commercial steels containing 0.24% C and 1.05% C, respectively.

Results

Weight losses of 0.009% C iron rotating at 600 rpm as a function of time in deaerated 0.33N H_2SO_4 are shown in Fig. 2. An induction time of about 2 hr precedes a constant corrosion rate of 20 mg/dm²/hr. For 0.24% C steel in aerated acid at 4000 rpm, the rate was typically higher, being constant at first, then falling to lower values after a few hours (Fig. 3). (The point at 5 hr below that at 4 hr is accounted for by experimental error.) It was found that the falling off in rate occurred after a certain amount of iron had accumulated in the acid, averaging about 70 mg/liter. The final rate, where such accumulation occurred, was considerably less than the initial rate. This decrease was caused by ferric ion, as was demonstrated by comparing the initial steady-state corrosion rate of a steel rotating at 4000 rpm in aerated acid to the corresponding rate in the same acid to which 72 mg Fe^{+++} /liter were added in the form of $\text{Fe}_2(\text{SO}_4)_3 \cdot 9\text{H}_2\text{O}$. The striking difference in rates confirms that ferric ion under conditions of high velocity acts as inhibitor (Fig. 4) despite the usual role of Fe^{+++} as a depolarizer and accelerator

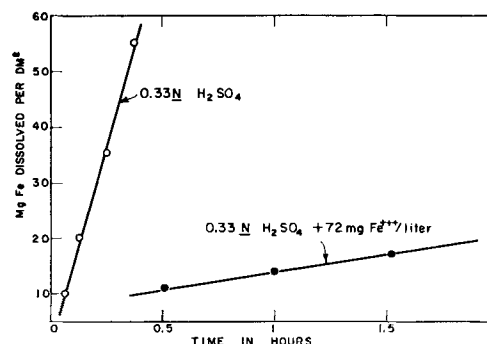


Fig. 4. Effect of Fe^{+++} on corrosion of 0.24% C steel in aerated 0.33N H_2SO_4 , 4000 rpm.

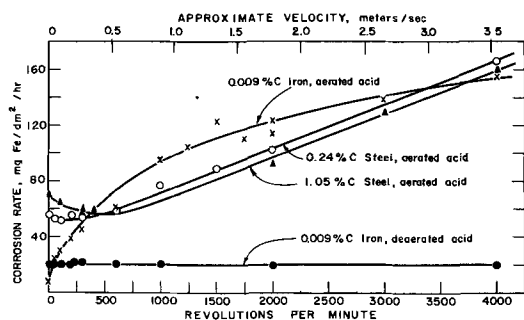


Fig. 5. Effect of velocity on corrosion rate in 0.33N H_2SO_4

of corrosion. Potential measurements of a similar steel specimen at 4000 rpm in aerated acid showed that the potential became more noble or more cathodic by 20 mv within about the same time (3.5 hr) as the corrosion rate underwent a change to lower values.

The effect of velocity on the steady state corrosion rate of 0.009% C iron in deaerated and aerated 0.33N H_2SO_4 is shown in Fig. 5. Data are also included for 0.24% C and 1.05% C steels in aerated acid. It is important to note that in deaerated acid, the corrosion rate remains constant at 20 mg/dm²/hr and is independent of velocity. In aerated stagnant acid, omitting bubbling of air to avoid stirring the acid, the rate is lower (7 mg/dm²/hr) than in deaerated acid with or without stirring, confirming earlier results of Bond on the inhibiting effect of O_2 for pure iron exposed to acid. For 0.24% C steel, the corrosion rate at zero velocity is higher by reason of increased carbon content. The rate in this instance starting at 55 mg/dm²/hr reaches a minimum at 125 rpm (51 mg/dm²/hr), then increases linearly with velocity beyond 500 rpm. The 1.05% C steel corrodes at a still higher rate at zero velocity (70 mg/dm²/hr), reaches a minimum rate (55 mg/dm²/hr) at 600 rpm, and then increases linearly with velocity.

Discussion

In deaerated acid, low-carbon iron corrodes at the same rate under either stagnant or high-velocity conditions. This might be expected if one considers that the corrosion rate is controlled by rate of H^+ discharge (cathodic control). The rate of H^+ discharge, in turn, at current densities below values of significant concentration polarization is known to be unaffected by relative motion of metal and electrolyte (activation polarization). Whitman *et al.*, on the other hand, found a minimum in N_2 -deaerated 0.33N H_2SO_4 at about 250 rpm or 0.25 m/sec (0.7 ft/sec). This result is probably explained by traces of O_2 entering the acid during the corrosion tests and acting as inhibitor in the lower velocity range. Contamination by oxygen in their experiments is not surprising considering use of pyrogallol at room temperature to purify N_2 , and use of watch glasses over open beakers to exclude atmospheric oxygen. The present experiments, on the other hand, were conducted with rigid exclusion of oxygen. In some experiments, the specimen was pickled in the test flask and the deaerated acid introduced using N_2 pressure without the specimen coming into contact

with air. This procedure avoided introduction of O_2 or Fe^{+++} into the acid by the specimen itself.

Figure 5 shows that, in aerated acid, velocity very much accelerates corrosion, as previous investigators also reported. It is at first surprising that 0.009% C iron between 300 and 3500 rpm should corrode at a higher rate than the carbon steels. In stagnant solution, the effect of increasing carbon in steels is known to accelerate corrosion, and the present data confirm this relationship. The inverse relationship under intermediate velocity conditions is unexpected and is probably caused by the essentially smooth, clean surface of 0.009% C iron maintained throughout the test, whereas for the higher carbon steels a visible rough black film is formed, composed of amorphous carbon mixed with cementite (6). The clean surface allowed ready depolarization by O_2 , compared to the carbon film which acted as a barrier for diffusion of O_2 . At still higher velocities, the barrier film either eroded away or its presence interfered less with diffusion to or from the metal surface. The results for low carbon iron plotted on a log-log plot are linear with a slope of 0.5. On the other hand, the rough surface of the carbon steels accounted for greater turbulence of the acid and showed a linear dependence of corrosion rate on velocity in the high velocity region. An effect of surface roughness in this same direction was reported by Makrides and Hackerman (7), who measured as a function of velocity the dissolution rate of mild steel in 2N HCl containing various depolarizers.

An unmistakable inhibiting effect of oxygen is shown by the lower corrosion rate of 0.009% C iron in aerated compared to deaerated acid at zero velocity (Fig. 5). An inhibiting effect of oxygen is also the cause of minima in the corrosion rate for carbon steels as velocity increases. The higher rate of hydrogen evolution for these steels at zero velocity prevents oxygen from reaching the metal surface, but as velocity increases, the hydrogen is swept away and above a specific range of velocities oxygen reaches the surface in sufficient concentration to act first as inhibitor and later as depolarizer. The higher the carbon content the higher is the corrosion rate and H_2 evolution, and hence the higher must be the velocity at which the inhibiting effect of oxygen is observed. For 0.009% C iron the minimum occurs below velocities generated by gas bubbles; for 0.24% C steel the minimum comes at about 125 rpm (0.1 m/sec); for 1.05% C steel, it comes at 600 rpm (0.5 m/sec). Analogously, the minimum in corrosion occurs at higher velocities as the acid concentration increases, as shown by data of Whitman *et al.* The minimum in their data for 0.12% C steel occurs at 250 rpm (0.25 m/sec) in air-exposed 0.33N H_2SO_4 ; at 1200 rpm (1.2 m/sec) in 1.58N H_2SO_4 ; at 1625 rpm (1.6 m/sec) in 2.87N acid; and at 2800 rpm (2.8 m/sec) in 5N acid.

Although a small amount of dissolved oxygen inhibits the corrosion rate of iron or steel in sulfuric acid, in higher concentrations it accelerates attack. Apparently, an oxidizing agent like Fe^{+++} can also act as inhibitor (Fig. 4) or depolarizer. The inhibiting effect of Fe^{+++} was missed by Makrides (8) who studied potentials and polarization of iron in

H_2SO_4 . Gatos (9) reported that Fe^{+++} added to stagnant 1N H_2SO_4 began to lose its accelerating effect on dissolution of 0.29% C steel above 0.47 g-ions Fe^{+++} /liter (26 g/liter) and that at about 4 g-ions/liter (223 g/liter), the dissolution rate was the same as if the acid did not contain Fe^{+++} . Although in stagnant 1N acid high concentrations of Fe^{+++} are apparently required to reverse the effect of depolarization, at 4000 rpm only 0.07g Fe^{+++} /liter in 0.33N H_2SO_4 induces marked inhibition. Gatos speculated that high concentrations of Fe^{+++} increase polarization of the anodic sites.

Our polarization measurements using 0.009% C iron showed that traces of oxygen at the metal surface decrease cathodic polarization; however, the same traces of oxygen increase anodic polarization (Fig. 6). Consequently, it is reasonable to conclude that increase of anodic polarization accounts for inhibition of the corrosion rate by either oxygen or Fe^{+++} . These effects, including a shift of corrosion potential in the more noble direction, are shown by the schematic polarization curve of Fig. 7.

In Fig. 6, polarization data required at least 15 min for each point in order to reach steady state values. This time accounted for an accumulation of Fe^{+++} in the acid, which in turn brought a discontinuity in the cathodic polarization curve at a limiting current density contributed by diffusion of both O_2 and Fe^{+++} . If dissolved O_2 alone had been operative, the O_2 concentration at the discontinuity corresponding to 0.1 ma/cm² would have been more than 10 times the critical ratio of 0.04 for volume O_2 /volume N_2 that was observed.

The mechanism accounting for increase in anodic polarization of iron in sulfuric acid by traces of O_2 is probably related to adsorption of O_2 on the iron

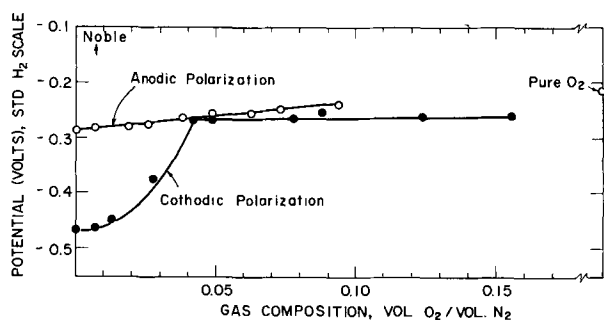


Fig. 6. Effect of increasing dissolved oxygen on polarization of 0.009% C iron in 0.33N H_2SO_4 at constant current density of 0.1 ma/cm².

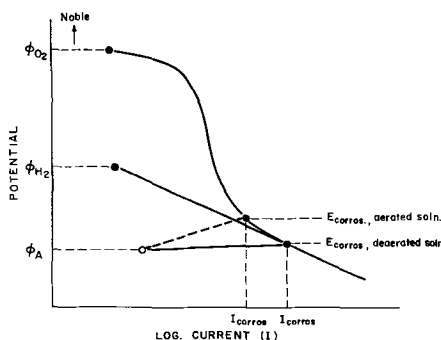


Fig. 7. Schematic polarization curves for iron showing how aeration of acid can decrease the corrosion rate.

surface. From the independence of corrosion rate of pure iron in deaerated acids on pH (10, 11), it follows that the amount of adsorbed H on iron probably increases as H^+ concentration increases, thereby restricting residual anodic areas and increasing anodic polarization. Under this condition, the corrosion rate remains almost constant, despite increased acidity (pH 1 to 4). Traces of O_2 may then increase anodic polarization still further by preferentially adsorbing on anodic sites and restricting the residual anodic area. This occurs whether or not the iron is pure, provided O_2 can reach the metal surface in spite of H_2 evolution. Only at higher concentrations of O_2 does depolarization at cathodic sites occur by reaction of oxygen with hydrogen adsorbed on the metal surface. When depolarization occurs, the anode area increases, O_2 is no longer available in sufficient concentration to adsorb on all anodic sites, and, as a result, the corrosion rate increases.

The same general effects occur in neutral or alkaline media except that adsorption of H at cathodic sites is less pronounced than in acids, there is consequently diminished reaction between H and depolarizer, and adsorption of O_2 at anodic sites is favored. This situation leads to passivity and to a marked reduction in corrosion, the necessary partial pressure of O_2 to induce passivity being lower the more alkaline the solution. Oxygen, therefore, apparently increases anodic polarization of iron over a wide range of pH. It also, of course, acts as depolarizer, and the particular role that predominates in any given circumstance determines whether O_2 is an inhibitor or an accelerator of corrosion. In chloride media, competitive adsorption excludes O_2 at anodic sites, and O_2 acts mainly as depolarizer. Hence, in chloride media, e.g., as illustrated by Wormwell's experiment (4), velocity only increases corrosion. In absence of passivity-destroying Cl^- in near-neutral water, velocity first increases corrosion because of depolarization, then reduces it (12) as O_2 concentration at the iron surface reaches a value sufficient to increase anodic polarization. Ferric salts in stagnant H_2SO_4 apparently act like dissolved O_2 in neutral H_2O in that with first additions depolarization predominates, and at higher concentrations inhibition becomes apparent. It is likely that Fe^{+++} adsorbs on anodic sites analogous to adsorbed O whenever the concentration of Fe^{+++} at the metal surface reaches a sufficient value. High velocity helps assure an adequate surface concentration reaching through an ever present barrier layer of ferrous salt solution.

Acknowledgment

This research was supported by a fellowship grant established by the Shell Oil Company Foundation, Inc., to whom the authors express their appreciation.

Manuscript received March 8, 1963. This paper was presented at the Boston Meeting, Sept. 16-20, 1962.

Any discussion of this paper will appear in a Discussion Section to be published in the December 1964 JOURNAL.

REFERENCES

1. A. P. Bond, Sc.D. Thesis, Department of Metallurgy, M.I.T. (1958).

2. J. Friend and J. Dennett, *J. Chem. Soc. (London)*, **121**, 41 (1922).
3. W. Whitman, R. Russell, C. Welling, and J. Cochran, *Ind. Eng. Chem.*, **15**, 672 (1923).
4. F. Wormwell, *J. Iron and Steel Inst.*, **154**, 219P (1946).
5. E. B. Sandell, "Colorimetric Determination of Traces of Metals," p. 374, Interscience Publishers, Inc., New York (1950).
6. E. Heyn and O. Bauer, *J. Iron and Steel Inst.*, **79**, 109 (1909).
7. A. Makrides and N. Hackerman, *This Journal*, **105**, 156 (1958).
8. A. Makrides, *ibid.*, **107**, 869 (1960).
9. H. Gatos, *ibid.*, **103**, 286 (1956).
10. M. Stern, *ibid.*, **102**, 609 (1955).
11. K. Bonhoeffer and K. Heusler, *Z. Physik. Chem. N.F.*, **8**, 390 (1956).
12. R. Russell, E. Chappell, and A. White, *Ind. Eng. Chem.*, **19**, 65 (1927).

Pitting and Uniform Corrosion of Aluminum by pH 3.5 Citrate Buffer Solution

E. L. Koehler and S. Evans¹

Central Research and Engineering Division, Continental Can Company, Inc., Chicago, Illinois

ABSTRACT

Corrosion of 3003 aluminum in citrate buffer solution in the presence of air may be by pitting or by uniform attack. Polarization data indicate that uniform attack is controlled by the rate of chemical dissolution of the oxide film. There is a simultaneous thickening of the film by a tarnishing-type reaction at the same rate to maintain the film at constant thickness. Values of $\Delta D/\Delta E$ determined from polarization data at constant potential were indicated to be the same for a film being formed principally by the tarnishing mechanism as for a film being formed entirely by anodic action. It was found possible to determine whether or not pitting was occurring from anodic polarization data.

In an earlier paper, the use of polarization methods in determining the corrosion rates of aluminum in anaerobic acid and food media was investigated (1). Corrosion here was uniform and was strictly of the hydrogen-evolution type. Metal destruction was of no consequence, the only concern being hydrogen evolution which, in can applications, may cause the ends of the can to bulge. Even a small amount of metal destruction is of concern, however, when corrosion is localized, leading to eventual perforation of the container or vessel. It was the purpose of this work to investigate by polarization methods pitting and uniform corrosion of 3003 aluminum within the pH range of acid foods when air is present.

Experimental

Experimental methods employed were much the same as those described in earlier work, except that for tests in the presence of air the test medium was flushed with air prior to use and the top of the test cell was open to the air (1, 2). Identical specimens were sealed to opposite ends of the "T" cells with microcrystalline wax, the assembly being held together with a clamp. The test medium used was an unstirred pH 3.5 citrate buffer solution, 0.05M in total citrate. In preparing the solution, reagent-grade citric acid and sodium citrate were used. The water was deionized and distilled from an alkaline permanganate solution. Anaerobic solutions were de-aerated by flushing for 3 hr with oxygen-free hydrogen. Any oxygen which might remain after this treatment disappears in the cells by reaction with the specimens. In some cases reagent-grade sodium chloride was added. The temperature was

37.8°C (100°F). Weight loss rates were determined by simultaneously setting up a number of test cells and discontinuing the individual cells after varying time intervals. A potentiostatic device was used to obtain polarization data. In recording polarization curves, the potential vs. saturated calomel was continuously changed at a preselected linear rate. This is called a potentiodynamic polarization curve. Except where otherwise specified, the rate was 50 mv/min. The reference electrode was in a plane midway between the two specimens. The specimen at the opposite end of the cell served as the auxiliary electrode. The potential drop due to resistance of the electrolyte was not significant in most cases. Where required, it was compensated for. The aluminum was annealed 3003 sheet, normally containing manganese, 1.0-1.5%; silicon, 0.6% max; iron, 0.07% max; copper, 0.20% max; zinc, 0.10% max; all others, 0.15% max. Specimens were cleaned with carbon tetrachloride but not abraded or polished prior to use.

Results and Discussion

Figure 1 shows weight loss curves for 3003 aluminum in pH 3.5 citrate buffer solution. The lower two curves, representing the anaerobic condition, give the equivalent of weight loss as determined by hydrogen evolution measurement. The rate of hydrogen evolution under such conditions is equivalent to the rate of weight loss (1). This figure represents data for one series of tests. In a second series of tests the data were essentially the same, except that the rate of weight loss for the top curve, with the 0.2% NaCl addition, was somewhat lower.

Addition of sodium chloride caused a slight increase in the anaerobic corrosion rate. With air pres-

¹ Present address: Rocketdyne, A Division of North American Aviation, Inc., Canoga Park, California.

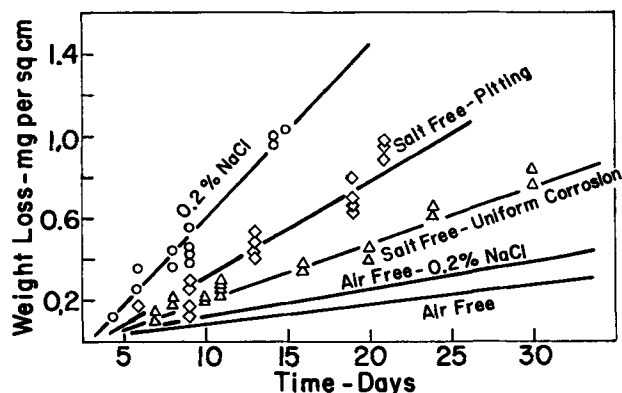


Fig. 1. Weight loss curves for 3003 aluminum in pH 3.5 citrate buffer at 37.8°C.

ent and no chloride, the data had to be separated into two groups: one in which the specimens were pitting, and one in which there was uniform corrosion. Insofar as we are aware, all these specimens and test cells were treated identically. Pitting here was always preceded by a period of uniform corrosion. With specimens corresponding to the "salt-free, pitting" points in Fig. 1, pitting developed usually in about two to three days. In some cases pitting started after longer times, *i.e.*, 9 days, 15 days, etc. It was possible to determine at any specific time, from anodic polarization data, whether pitting was occurring. With air present and with the 0.2% NaCl addition, the specimens always pitted. Table I gives current equivalents for the corrosion rates of Fig. 1.

Thickening and Dissolution of Films on Uniformly Corroding Specimens

Aluminum tends to thicken its oxide film on anodic polarization preferentially to any alternate anodic process (3). Electrolytes in which the rate of dissolution of the oxide is relatively high, like sulfuric acid, produce a porous oxide film. Electrolytes in which the film is insoluble produce a nonporous film of high resistance. The growth of an insoluble film at constant potential causes a continuous decrease in ionic current and the equivalent rate of film growth to zero as a limiting value. The present case is viewed as being intermediate, *i.e.*, the electrolyte dissolves the film at a low, but appreciable, rate. Decrease in current at constant potential for the case of an electrolyte which dissolves the film at a low rate is shown schematically in Fig. 2. Assuming that there is no non-ionic current in the film, the measured current, i , will be equivalent to the rate of film formation. The rate of film formation decreases with time until a steady state is attained in which the rate

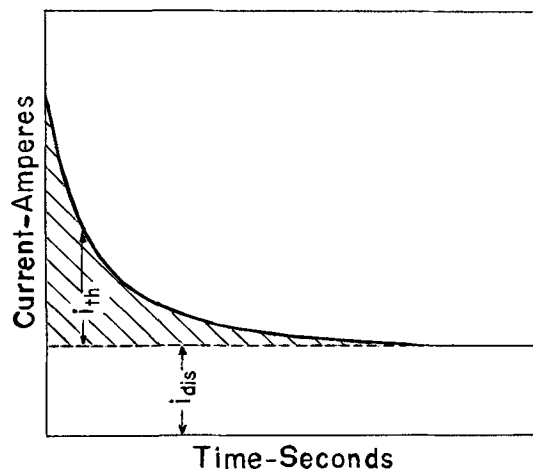


Fig. 2. Schematic representation of decrease in current during thickening of film at constant potential under conditions in which non-ionic current is zero, with small constant rate of dissolution of film in electrolyte. i_{th} is the net rate of film thickening; i_{dis} is the rate of film dissolution; shaded area is the coulombic equivalent of net increase in film thickness.

of film formation is equal to the rate of film dissolution, or $i = i_{dis}$. At such time, the net rate of film thickening, $i_{th} = i - i_{dis}$, is equal to zero. Such a film will not thicken indefinitely at constant potential, but will approach a definite limit. The shaded area under the curve represents the coulombic equivalent of the net increase in film thickness.

At low fields non-ionic current is normally high compared to the ionic current. This non-ionic current usually causes oxygen evolution once the potential has reached values where this is possible (3). The rate of film dissolution, i_{dis} , does not change with potential. Evidence to be presented below indicates that in the absence of any applied potential the film thickens by a tarnishing-type mechanism, at a rate equal to i_{dis} . Oxygen reduction rather than oxygen evolution occurs on such a corroding specimen. This tarnishing-type corrosion involves a flow of non-ionic current in the reverse direction (4, 5). With a very small applied anodic potential on the corroding specimen the film will thicken by a combination of anodic (applied) and tarnishing-type (local) actions. There is a range of potentials, intermediate to those at which reduction of oxygen and those at which evolution of oxygen occurs, in which there is neither significant reduction nor evolution of oxygen. In this range the non-ionic current should equal zero, and unit current efficiency would be expected. Arguments have been presented to support the claim of unit current efficiency below the reversible oxygen evolution potential for zirconium (6, 7).

Results of anodic polarization at potentiostatically controlled potentials for specimens uniformly corroding with air present are summarized in Table II. Typical curves are shown in Fig. 3. Such data were obtained after the tests had been set up for three or more days so as to obtain a steady condition of corrosion of the aluminum in the test medium. Polarizations represented are millivolts anodic to the steady-state corrosion potential of the aluminum specimen, as measured with the saturated calomel electrode immediately prior to the polarization. For

Table I. Corrosion rates of 3003 aluminum in pH 3.5 citrate buffer solution at 37.8°C

	Corrosion rate	
	mg/day cm ²	μa/cm ²
Anaerobic	0.010	1.2
Anaerobic, 0.2% NaCl	0.014	1.7
No salt, air present, uniform corrosion	0.029	3.6
No salt, air present, pitting	0.047	5.9
0.2% NaCl added, air present	0.090	11.2

Table II. Summary of results for anodic polarization at constant potential, uniformly corroding specimens, air present

Polarization, mv	Limiting current, $\mu\text{a}/\text{cm}^2$	Steady-state local action current, $\mu\text{a}/\text{cm}^2$	$\frac{\int_0^\infty (i - i_{lim}) dt}{E - E_{corr}}$ mc/v cm^2
0		3.6	
25	0.8	2.8	8.2
80	1.6	2.0	7.5
110	2.4	1.2	9.3
160	2.7	0.9	8.3
185	3.1	0.5	8.2
210	3.6	0	8.6
270	3.7		7.7
300	3.5		7.5
360	3.7		8.2
580	4.3		(7.5)*

* Approximate, peak current off of recorder scale.

polarizations sufficiently great to render local action negligible, 210 mv or greater, the limiting current attains a value of $3.6 \mu\text{a}/\text{cm}^2$. Since all the current through the film is ionic, this represents the rate of dissolution of the oxide film in the medium, i_{dis} . The somewhat high value of limiting current for the greatest polarization represented may include some portion of non-ionic current, representing formation of oxygen.

It should be noted that the $3.6 \mu\text{a}/\text{cm}^2$ value for equivalent rate of dissolution of the oxide is identical to the rate of corrosion of the uniformly corroding specimens as represented in Table I. This strongly suggests that such uniform corrosion of aluminum is controlled by the rate of dissolution of the oxide film in the medium, the film being formed by a tarnishing-type mechanism at the same rate as which it dissolves. This conclusion is the same as that reached by Troutner for the uniform corrosion of aluminum in the temperature range of $90^\circ\text{--}250^\circ\text{C}$ on the basis of experimental evidence of a different type (8).

For polarizations of less than 210 mv there is significant reduction of oxygen on the surface (local action). Since the rate of oxide dissolution is not affected by potential, the difference between the rate of oxide dissolution ($3.6 \mu\text{a}/\text{cm}^2$) and the indicated

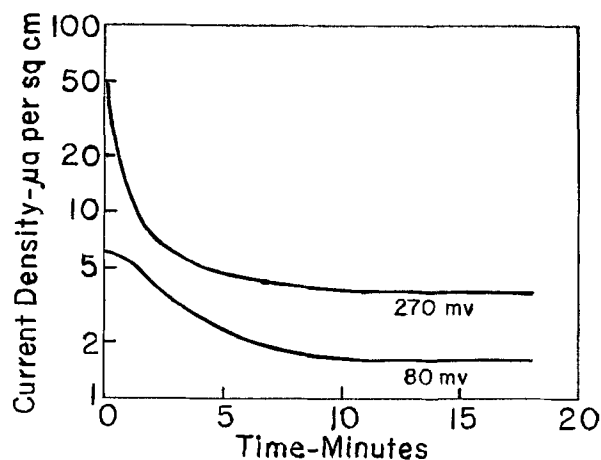


Fig. 3. Representative curves of current vs. time during thickening of film. Uniformly corroding specimens, pH 3.5 citrate buffer solution in presence of air, specimens anodically polarized at indicated potentials relative to steady-state corrosion potential of specimen.

limiting current represents the rate of oxygen reduction on the specimen at steady state. These values are given in the column headed "Steady-state local action current."

The last column gives the amount of the measured current utilized in increasing the net thickness of the film per volt of applied potential. This quantity was found to be constant over the range of potentials investigated, without regard to whether the film was being formed by anodic action alone or by a combination of anodic and tarnishing-type actions. Specifically

$$\frac{\int_0^\infty (i - i_{lim}) dt}{E - E_{corr}} = 8.2 \text{ millicoulombs}/\text{cm}^2/\text{v} \quad [1]$$

where i is the measured current, i_{lim} is the limiting current, t the time elapsed, E the potential of the specimen, and E_{corr} the corrosion potential of the specimen as measured immediately prior to polarization. Net increase in film thickness per volt is

$$\frac{\Delta D}{\Delta E} = \frac{\int_0^\infty (i - i_{lim}) dt}{E - E_{corr}} + \frac{\int_0^\infty (i_{la} - i_{la}^0) dt}{E - E_{corr}} \quad [2]$$

where i_{la} is the local action current and i_{la}^0 is the local action current at steady state. For polarizations at potentials where local action is negligible, $i_{lim} = i_{dis}$, and

$$\frac{\Delta D}{\Delta E} = \frac{\int_0^\infty (i - i_{dis}) dt}{E - E_{corr}} = 8.2 \text{ mc}/\text{v cm}^2 \quad [3]$$

as has been indicated in Fig. 2. The simplest explanation for the behavior at polarizations of less than 210 mv, where local action is not negligible, is that the rate of reduction of oxygen on the specimen is constant for any given potential during film thickening ($i_{la} = i_{la}^0$), making the second term in [2] equal to zero, and giving

$$\frac{\Delta D}{\Delta E} = \frac{\int_0^\infty (i - i_{lim}) dt}{E - E_{corr}} = 8.2 \text{ mc}/\text{v cm}^2 \quad [4]$$

Further, the free energy change of the tarnishing reaction produces a potential across the film which is additive to the applied potential (9), $\Delta D/\Delta E$ being the same for the tarnishing reaction as for anodic film formation.

Assuming a density of $3.1 \text{ g}/\text{cm}^3$ for the oxide, $8.2 \text{ mc}/\text{v cm}^2$ corresponds to a value of $\Delta D/\Delta E$ of $47/\sigma \text{ \AA}/\text{v}$ where σ is the surface roughness factor of the corroding specimen. Determinations made by other investigators for films formed in a variety of electrolytes at higher potentials are in the range of $15 \text{ \AA}/\text{v}$ (3). This would lead to a surface roughness factor of about 3.1 for the corroding specimen, assuming that the nature of the film formed is the same.

Anodic Polarization Curve As Indicator of Pitting

In potentiodynamic anodic polarization curves on such specimens the current density approaches a limiting value. This limiting value is dependent on the rate of change of potential with respect to time in the determination of the curve. For a curve determined sufficiently slowly, less than $5 \text{ mv}/\text{min}$, the limiting value is the expected $3.6 \mu\text{a}/\text{cm}^2$. For

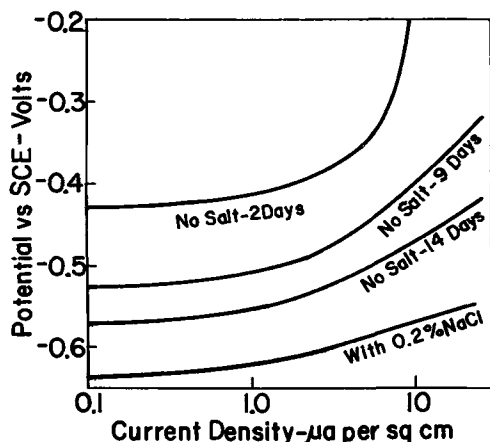


Fig. 4. Anodic polarization curves at 50 mv/min rate of change of potential with respect to time, air present. Top curve, uniformly corroding specimen; middle two curves, same specimen, later, now pitting; bottom curve, pitting, sodium chloride present.

a curve determined at a rate of 50 mv/min, our usual rate, a limiting value of about $9 \mu\text{a}/\text{cm}^2$ is obtained. The same type of potentiodynamic anodic polarization curve is not obtained for a specimen which is pitting. It was found by making visual examination of specimens that use of anodic polarization curves constitutes a reliable and sensitive method for detecting pitting on aluminum. The top three curves in Fig. 4 are anodic polarization curves taken at various times for a test cell with air present and no salt. At two days, this specimen was not pitting; by the ninth day, the specimen was pitting, as evidenced by the fact that the anodic polarization curve was not of the limiting-current type. It is to be noted that the corrosion potential shifts in the active direction with the development of pits. However, measurement of the corrosion potential does not constitute a reliable method for determining whether or not the specimen is pitting. Plotted on the same coordinates is the anodic polarization curve for a pitting specimen with salt in solution.

Cathodic Polarization

Figure 5 shows a typical potentiodynamic cathodic polarization curve for a uniformly corroding specimen with air present and no salt. A limiting diffusion current for oxygen was always observed. Note that the current first goes up to $10 \mu\text{a}/\text{cm}^2$, then cuts back to $6.5 \mu\text{a}/\text{cm}^2$, at which level there is a short vertical section before the transition to the Tafel-type hydrogen evolution curve. In this curve, $6.5 \mu\text{a}/\text{cm}^2$ was considered to be the limiting diffusion current density. Average current density equivalent of limiting diffusion for all specimens tested was $6.8 \mu\text{a}/\text{cm}^2$. The maximum in the curve is associated with the initially higher concentration of oxygen at the surface prior to establishment of the concentration gradient typical of limiting diffusion. This is not a particularly steady system. Curves determined at 25 mv/min instead of 50 mv/min apparently had lower maxima, but there was frequently some evidence of irregularity in the curve. A curve determined at 5 mv/min was so irregular that no interpretation could be attempted. By running a polarization curve at 50 mv/min to -0.650v and holding

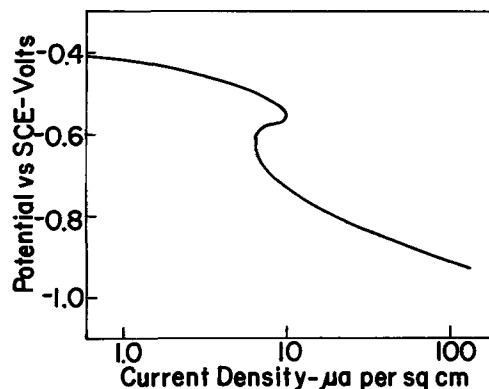


Fig. 5. Cathodic polarization curve at 50 mv/min for uniformly corroding specimen, air present.

at this level, the current cycled in a period of about 9-11 min about a mean in the range of $6.8 \mu\text{a}/\text{cm}^2$. Shaking the cell sharply increased the current, which subsequently leveled off again at $6.8 \mu\text{a}/\text{cm}^2$.

A vertical section in the cathodic polarization curve at limiting diffusion implies that either the anodic partial reaction at this point is negligible, or the anodic partial reaction is independent of potential (vertical anodic partial reaction curve). It is indicated from the anodic polarization data presented above that the steady-state anodic partial reaction curve is vertical for potentials more noble than the corrosion potential. However, there cannot be a vertical anodic curve in the range of potentials where the limiting diffusion current of oxygen is approached, since decrease in the oxygen concentration at the film/electrolyte interface sharply decreases the potential across the film and the rate of film formation. It is indicated, therefore, that the anodic partial reaction at this point is negligible and that $6.8 \mu\text{a}/\text{cm}^2$ approximates the limiting diffusion current for oxygen to the specimen. Since this is close to the $5.9 \mu\text{a}/\text{cm}^2$ equivalent corrosion rate of a specimen which is pitting in the solution with no salt present, it is suggested that the corrosion rate of such pitting specimens is at the equivalent of the limiting diffusion current of oxygen to the specimen.

A variety of cathodic polarization curves between two forms was obtained for pitting corrosion with no salt present. The two types encountered are shown in Fig. 6. In one case there is no perceptible

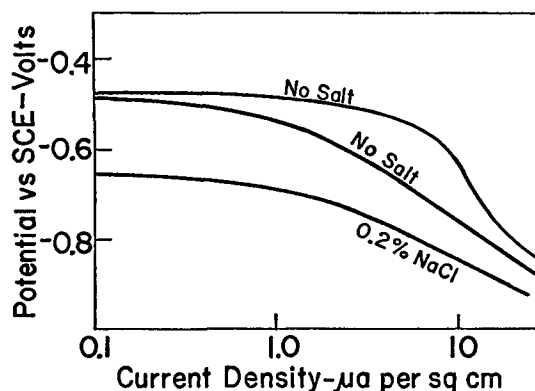


Fig. 6. Cathodic polarization curves at 50 mv/min for pitting specimens. With no salt the curves varied in form, as indicated.

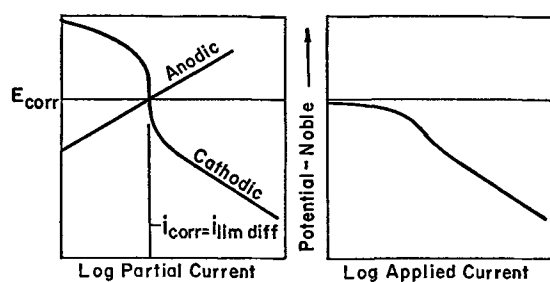


Fig. 7. Analysis of cathodic polarization curve for pitting specimen with no NaCl. Right panel, cathodic polarization curve for specimen; left panel, anodic and cathodic partial reaction curves.

inflection caused by a limiting diffusion current of oxygen; in the other case there is a pronounced inflection. The analysis of this situation is given in Fig. 7. For the particular anodic and cathodic partial reaction curves presented, there is a slight inflection in the resultant cathodic polarization curve for the specimen. However, since the current to the specimen is the sum of the partial reaction currents (the cathodic currents being taken as positive and the anodic currents, negative), it may be readily seen that a variety of cathodic polarization curves would be expected for specimens corroding at the limiting diffusion current of oxygen, dependent on variations in the anodic partial reaction curve. These results, therefore, are in confirmation of the suggestion that such corrosion is controlled by the limiting rate of diffusion of oxygen to the specimen.

Also shown in Fig. 6 is a cathodic polarization curve for a specimen which is pitting with salt present. This type of cathodic polarization curve was always obtained in this instance; there was never any indication of an inflection due to limiting diffusion current of oxygen. Since corrosion is above the limiting diffusion current of oxygen, hydrogen evolution occurs simultaneously. Extrapolating the Tafel portion of such a curve back to the corrosion potential gives the current equivalent of the hydrogen evolution rate on the corroding specimen. Within the limits of reproducibility of the data, adding this figure to the limiting diffusion current of oxygen gives a value which is consistent with the observed rate of weight loss of such specimens.

It has been pointed out that pitting corrosion cannot be completely described by the usual steady-state polarization curves employed in corrosion studies (10). Representation of a continuous cathodic partial reaction curve for a specimen pitting

with salt present is not strictly valid. It has been observed many times, and confirmed here, that hydrogen is evolved from the pits, which do not even exist at more noble potentials (11). The cathodic partial reaction curve cannot, therefore, be continuous in a rigorous sense, since it is evident that the cathodes are not independent of the anodic processes occurring on the specimen. It further seems evident that the anodes are not independent of the cathodic processes occurring. A pit on aluminum is an electrochemically generated device, and a certain minimum of current is required to sustain an active pit. Below this level, the acid which keeps the pit active will diffuse away and the pit will cease to exist. Even for local action within a pit, however, there is an evident electrochemical relationship between the oxidation and reduction processes locally occurring. Specimens pitting in the salt-containing medium had more active potentials than those without salt. There were many more pits with the salt, but the current per pit was about $4-5 \mu\text{a}$ without salt and about $1\frac{1}{2} \mu\text{a}$ with the salt. Specimens perforated much more rapidly in the cells without the NaCl addition. Edeleanu and Evans have stated that, due to local action with hydrogen evolution in the pits, the anodic surface never becomes film-free and that local action thus slows down attack (11). However this may be, it appears that the evolution of hydrogen in the pit does slow down attack.

Manuscript received May 24, 1963. This paper was presented at the Detroit Meeting, Oct. 1-5, 1961.

Any discussion of this paper will appear in a Discussion Section to be published in the December 1964 JOURNAL.

REFERENCES

1. S. Evans and E. L. Koehler, *This Journal*, **108**, 509 (1961).
2. E. L. Koehler, *Corrosion*, **17**, 93t, (1961).
3. L. Young, "Anodic Oxide Films," Academic Press, New York (1961).
4. C. Wagner, *Z. Physik Chem.*, **21B**, 25 (1933).
5. T. P. Hoar and L. E. Price, *Trans. Faraday Soc.*, **34**, 867 (1938).
6. G. B. Adams, Jr., P. van Rysselberghe, and M. Maraghini, *This Journal*, **102**, 502 (1955).
7. G. B. Adams, Jr., T. S. Lee, S. M. Dragonov, and P. van Rysselberghe, *ibid.*, **105**, 660 (1958).
8. V. H. Troutner, *Corrosion*, **15**, 9t (1959).
9. D. A. Vermilyea, *This Journal*, **101**, 389 (1954).
10. N. D. Greene and M. G. Fontana, *Corrosion*, **15**, 25t (1959).
11. C. Edeleanu and U. R. Evans, *Trans. Faraday Soc.*, **47**, 1121 (1951).

On the Etching of II-VI and III-V Compounds

G. A. Wolff,¹ J. J. Frawley,² and J. R. Hietanen¹

Solid State Research and Electronics Division, The Harshaw Chemical Company, Cleveland, Ohio

ABSTRACT

Etch pit shape and orientation as obtained from microscope and electron microscope investigations are related to light-figure reflection patterns. The usefulness of the light-figure technique is demonstrated using II-VI and III-V compounds as examples.

Chemical and physical etching studies have proved to be of importance in many investigations of crystals. The determination of crystallographic orientation, the type and number of dislocations, and the polarity of crystals without a center of symmetry are common examples.³ Less known is the application of mechanical and chemical etching leading to the determination of chemical bonding on clean surfaces and on surfaces containing absorbed atoms (2, 3).

Etched surfaces are generally investigated by microscope or by goniometric inspection. The light-figure, although it provides in many cases more useful information as far as angular and structural data are concerned, is less frequently utilized. The visual microscopic and electron microscopic investigations reveal the shape and topography of the etched surfaces rather than their more intricate morphology features such as the etch pit, growth, and solution form. Complete and detailed information on the morphology of crystals can be obtained by conventional but sometimes tedious goniometry. The light-figure technique supplies this information in a more elegant and rapid manner (4). This method has not been commonly applied, however. A possible reason for this is that, in addition to crystallographic factors, kinetical factors also determine the type of light-figure observed. This often renders the light-figure reflection more complex and difficult to interpret. For the useful application of this method, therefore, an understanding of the influence of these factors is necessary. A description and explanation of their influence is given below. The investigation of the etching of the II-VI and III-V compounds will demonstrate an application of the light-figure technique and its evaluation.⁴

Crystal Etching and Light-Figure Reflections

In general, the bottom or concave part of an etch pit and the convex parts of a growing crystal are finally bounded by flat planes when the etch or growth process has proceeded a sufficient time. On the other hand, the rims or convex parts of the etch pits and the concave or hidden parts of the growing crystal will assume curved shapes. The curved portions of a crystal will more often than not be curved

cylindrically, *i.e.*, curved parallel to a crystallographic direction or zone (6). In the corresponding light-figure, *i.e.*, in the projected figure resulting from the reflection of parallel light impinging on the crystal surface, crystallographic planes will appear as intense spot reflections or as the intersection of lines. These, in turn, represent light reflections from at least two sets of vicinal planes tilted along specific zonal directions. In some cases reflection spots appear alone. This occurs when the surface is composed entirely of macroscopic flat planes. These points are illustrated in Fig. 1.

In some cases the etching can be partly nonpreferential. In this case certain portions of the crystal surface appear polished. These portions of the surface are generally curved to various degrees and at times contain nearly flat areas which are for the most part crystallographically insignificant. Their

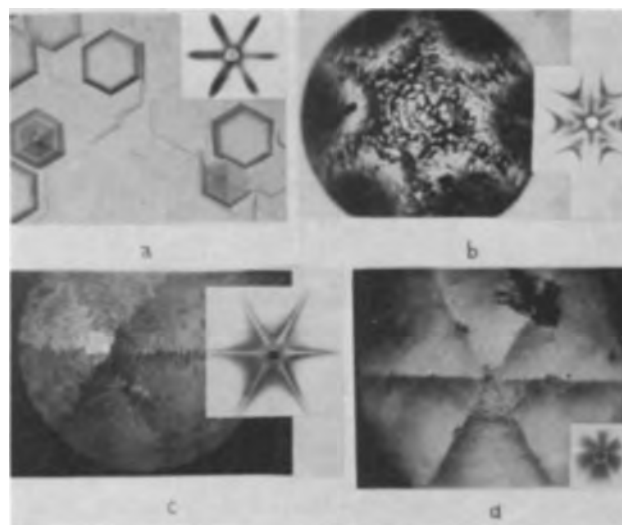


Fig. 1. Photomicrographs and light-figure patterns of concave and convex etching of CdS. (a) Light-figure patterns of this type are associated with concave etching. The central spot is the reflection from the flat bottomed pits. Each spoke results from the reflection of light from vicinal planes tilted about one zonal axis. Pits with pointed bottoms contain dislocations. (b) Light-figure patterns of this type are associated with a combination of concave and convex etching. The central star-like reflection is the result of concave etching. The extra features of the pattern appear as convex etching increases. (c) Light-figure patterns of this type are associated with nearly total convex etching. Ridges are now discernible; some concave etching is still evidenced by their broken appearance. (d) Light-figure patterns of this type are associated with total convex etching. Ridges appear unbroken. Reflection comes from relatively smooth areas between ridges. The (00,1) plane shown was identified by x-ray as the "cationic" plane (with R.F. Belt).

¹ Present address: Erie Technological Products Inc., Erie, Pa.

² Present address: Rensselaer Polytechnic Institute, Troy, N. Y.

³ For information on this subject consult review, and related articles in ref (1).

⁴ On related investigation consult ref. (5).

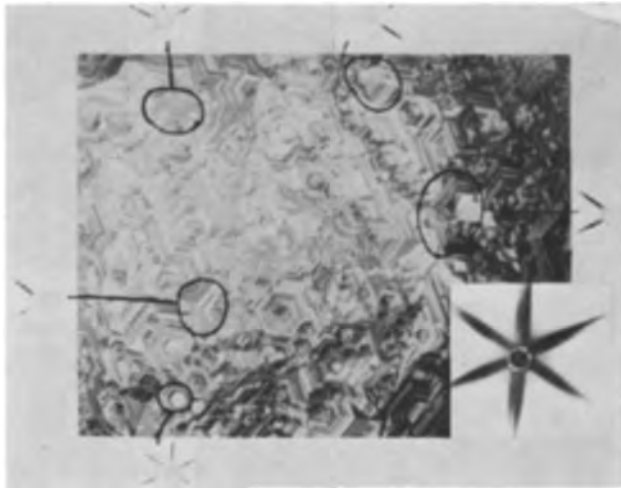


Fig. 2. Photomicrograph of $(00\cdot1)$ of CdS etched in HNO_3 . Broad light-figure pattern results from the reflection of a large diameter light beam. This pattern is composed of a combination of reflections from small areas within certain portions of the beam. The narrower light-figure line reflections are associated with the respective marked areas of the surface of the photomicrograph.

existence depends largely on the kinetic factors of dissolution rates and only to a minor degree on crystallographic considerations. Therefore, care must be taken during light-figure examinations of crystals to distinguish between preferentially and nonpreferentially etched regions of a crystal.

The light-figure technique of examining crystals has many useful applications. By using light beams of sufficiently small diameters, polycrystalline samples can be scanned and the orientation of various grains of the sample determined. For samples con-

taining small crystal grains larger than about 50μ , light-figure studies can be accomplished using a properly constructed microscope. The determination of the effect of grain orientation on grain boundaries is also possible by this technique. The same applies to twin boundary and other surface topography studies (see Fig. 2).

Etching of II-VI Compounds, Wurtzite Structure

As has been previously stated, the usefulness of this method lies in the fact that the light-figure reflection pattern if correctly interpreted, *i.e.*, if reduced to zones and planes, can be directly transformed to the stereographic projection of an ideal solution or etch pit form from which, in turn, the



Fig. 4. Negative crystal etch form of CdS (cavity etching). Compare with form in Fig. 5. Etched by flowing concentrated HNO_3 into crystal cavity via two horizontal (inlet and outlet) holes with masked walls; surface protected with nonreactive Apiezon wax.

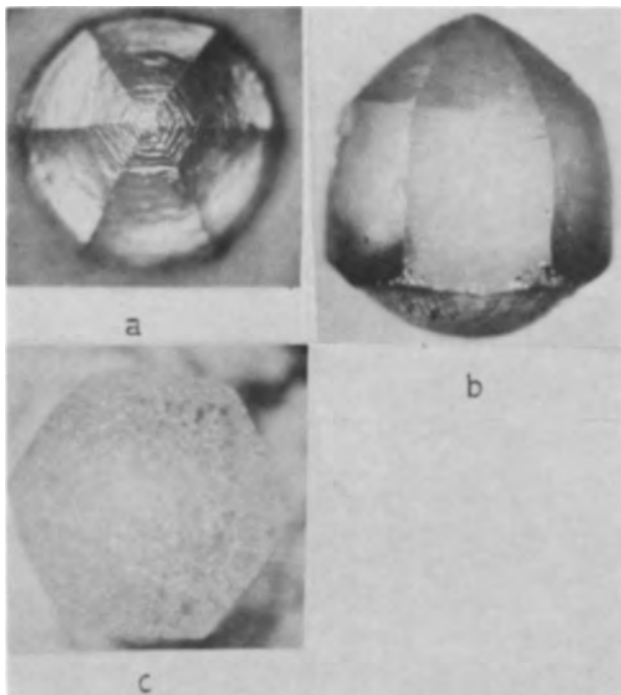


Fig. 3. Solution form photomicrograph of CdS. (Etched 1 min in concentrated HNO_3). Compare with form in Fig. 5. (a) Cadmium side. Point of intersection of six ridges represents $(00\cdot1)$. Ridges are zones of slowest attack during dissolution. Each point of the ridge represents a vicinal plane tilted in one direction for all other planes of that zone. (b) Side view. Intersection of horizontal and vertical ridges represent $(10\cdot\bar{1})$. (c) Sulfur side.

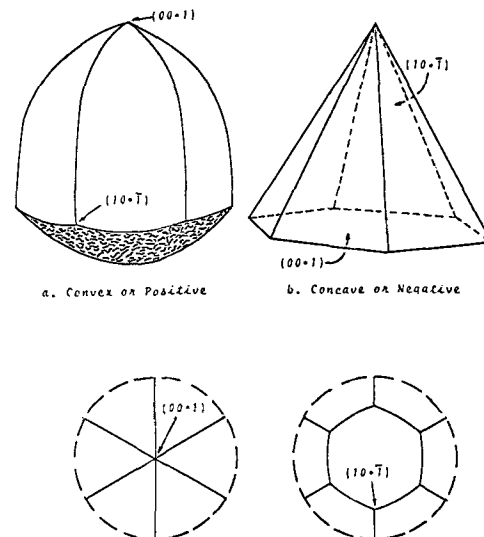


Fig. 5. Schematic drawing of the solution and etch pit form of CdS and their associated stereographic projection. The partial light-figure pattern of the solution form is given in Fig. 1d; that of the etch-pit form is given in Fig. 1a. A complete light-figure of the etch-pit form exactly corresponds to the stereographic projection.

respective ideal growth or equilibrium form can be deduced. This type of a correlation is demonstrated in Fig. 3-6 using CdS as an example.

The etch pit and solution form of CdS etched in HCl and HNO₃ can be matched with the equilibrium form where $\gamma \leq 1/3$ in Fig. 7a. Vapor and vacuum etch patterns of CdS reveal (see Fig. 7), however, patterns that more nearly match the conditions $1 > \gamma > 1/3$ in Fig. 7a or $3 > \beta > 1$ in Fig. 7b. This is also true for the observed vapor phase growth form (see Fig. 8). The differences in the observed forms are explained on the basis of bonding changes that occur at the surface in the various etchants. These changes at the surface may involve surface deformation by atomic displacement, foreign atom adsorption, or the formation of bond chains from bond arrays by the strengthening of bonds when electronic charge separation within these arrays or ionic character is introduced (7). The evidence available is not sufficient to distinguish completely between the various possibilities. Vapor growth forms of crystals, however, are closely related to ideal equilibrium forms; differences in the two being associated with surface deformation or the effects of second or more distant neighbors. Vacuum solution or thermal etch pit forms yield, in a first approximation, the same results in regard to the existence of strong bonding arrays ("bond

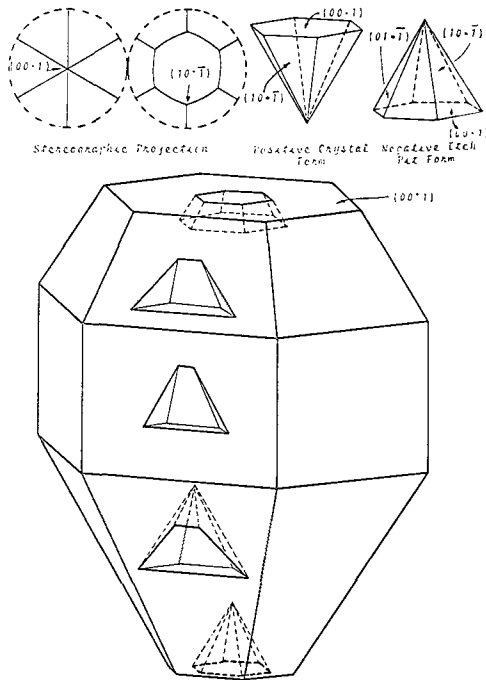


Fig. 6. Schematic drawing of the etch-pit form intersecting various surfaces of an arbitrary chosen CdS polyhedron of wurtzite structure. The ideal positive growth form and its supplement, the negative crystal cavity etch (pit) form, and the stereographic projection are also given. The pits shown intersecting the various surfaces are ideal. Only those concave pit-edges are stable which correspond to strong bond chains. Stable edges are denoted in the stereographic projection by lines between points of intersection; e.g., all edges of the pit intersecting (00·1) are stable, while all edges of the pit intersecting (00·1̄) are unstable. Stable and unstable edges for pits intersecting other faces can, in a like manner, be determined with the use of the stereographic projection shown. Unstable edges will "wash away" leaving undefined pits if all edges are unstable, as on (00·1̄) or poorly defined pits if some but not all the edges are stable, as on (10·1), (10·0), and (10·1̄).

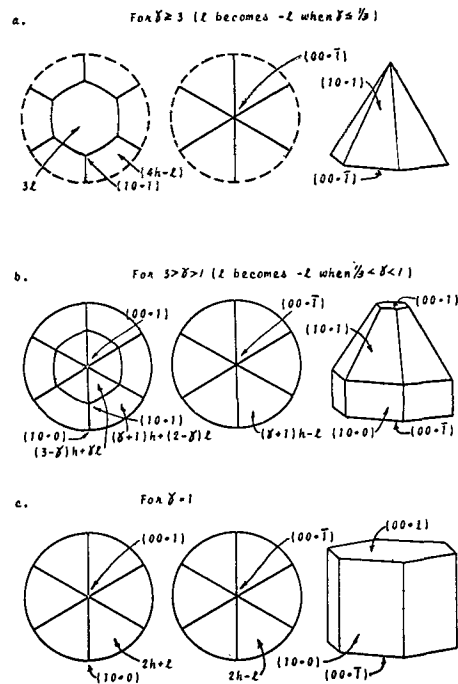


Fig. 7(a). Stereographic and parallel perspective projections of crystal forms of wurtzite structure for various ratios γ of cation to anion contribution to the surface (or interface) free energy. These structures are calculated by the methods given in ref. (7) for first nearest neighbor interactions only. β is assumed to be unity [see Fig. 7(b)].

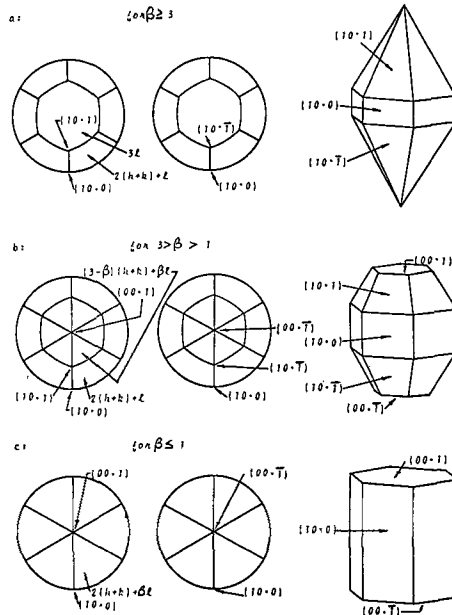


Fig. 7(b) Stereographic and parallel perspective projections of crystal forms of wurtzite structure for various ratios of c-directional to a-directional contribution to the surface (or interface) free strength of "c-bond" energy. $\beta = \frac{\text{strength of "c-bond"}}{\text{strength of "a-bond"}}$, when $\gamma = 1$.

chains") in crystals. Differences between vapor growth and vacuum solution or thermal etch pit forms are explained on the basis of a difference in the preferred reaction paths of the two processes. (The respective reaction paths in either case can be treated as quasi-equilibria. This type of a treatment is permissible in crystal surface kinetics.) Differences between the aforementioned forms and forms resulting from dissolution pro-

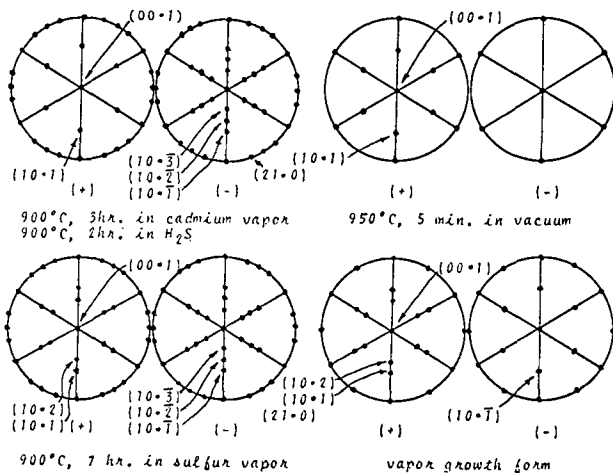


Fig. 8. Light-figure patterns of vapor phase grown CdS crystals. The polarity was measured vs. piezoelectric (8) and by x-ray techniques (9).

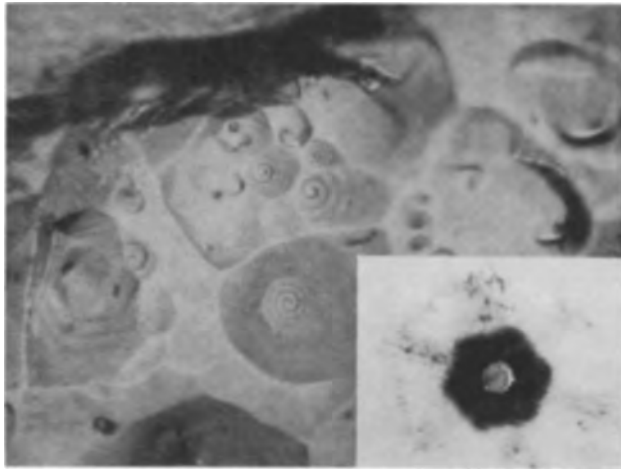


Fig. 9. Screw dislocations on $(00\bar{1})$ revealed by a concentrated HNO_3 etchant containing silver ions. Associated light figure pattern at lower right.

cesses occurring in foreign media, e.g., in acid solutions, result from the absorption of foreign atoms into surface sites in such a way that new strong bonding arrays are created. The solution and etch pit forms of CdS etched in HCl and HNO_3 can be explained by the creation of strong bonding arrays resulting from the adsorption of, for example, water or halide anions on cadmium atoms of positive charge. In this case well developed etch pits of hexagonal shape appear on the "cationic" $(00\bar{1})$ plane. If on the other hand, silver cations are applied in the etching process, etch pits are produced on the "anionic" $(000\bar{1})$ plane through the cation adsorption on the negative sulfur surface atoms (Fig. 9).

The growth and etch habits of other II-VI compounds yield similar results. A number of other wurtzite-type II-VI compounds etched in various hydrogen halide acids are shown in Fig. 10. The similarity between the etch pit habit of the various materials and that of CdS is obvious. With the exception of ZnO the cation plane remains stable while the anion plane disappears. This is in accord with the different etching behavior of antipole planes observed by many investigators on II-VI and III-V compounds. Here again, the vapor and vacuum etch

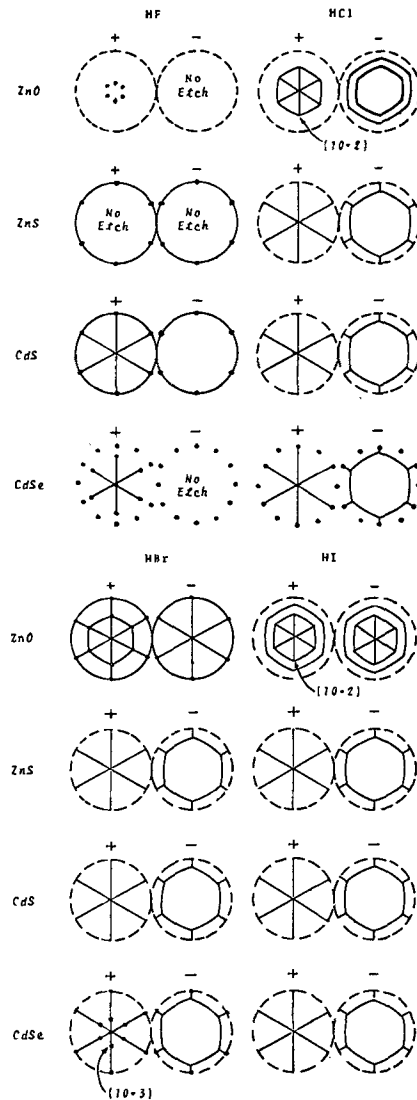


Fig. 10. Light-figure patterns of wurtzite type crystals etched in hydrogen halide acids. $(00\bar{1})$ is specular, $(00\bar{1})$ is matte. Polarity was measured by piezoelectric techniques. ZnO was Li-doped semiconducting.

forms and the vapor growth forms, while different from each other (Fig. 11) are also different from the acid etch forms. In addition, the vacuum etch forms of CdSe changes at different temperatures, indicating a change in controlling process or reaction paths with temperatures. This type of change can be explained by the presence of selenium chains, the length of which vary with temperature, adsorbed on the crystal surface. In the two cases different species of selenium molecules and their relative concentration radically changes the reaction process.

Etching of II-VI and III-V Compounds, Sphalerite Structure

The same type of an analysis can be carried out for sphalerite type structures of the groups II-VI and III-V compounds. The theoretical equilibrium forms are given in Fig. 12. The pit shapes to be expected on various surfaces of a sphalerite type crystal are given in Fig. 13 for the cases $\gamma \geq 3$ and $3 > \gamma > 1$. Some of the etch forms for sphalerite type II-VI compounds are given in Fig. 14. Here again, however, the experimental data are not suffi-

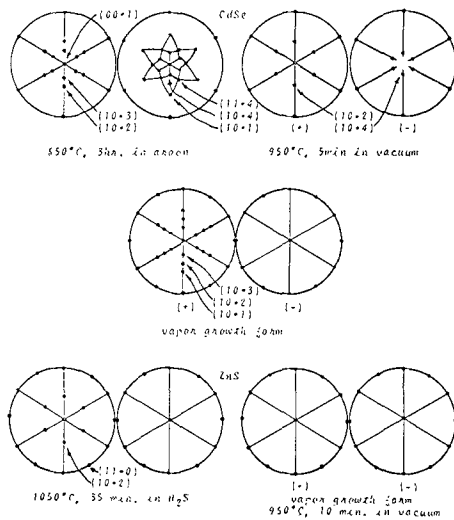


Fig. 11. Light-figure patterns of vapor and vacuum etched and growth form crystals of some wurtzite type crystals. Polarity was measured by matching the observed pattern with hydrogen halide etch patterns on the same crystal.

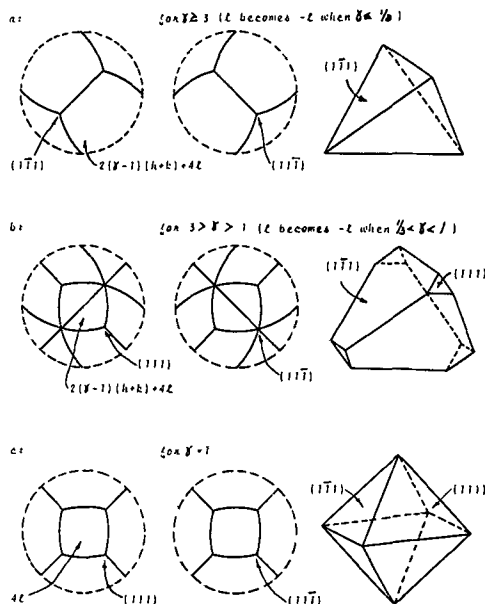


Fig. 12. Stereographic and parallel perspective projections of sphalerite type materials for various ratios γ of cation to anion contribution to the surface (or interfacial) free energy. These structures are calculated by the method given in ref. (7) for first nearest neighbor interactions only.

cient for a complete analysis to be performed. Most of the general conclusions made for wurtzite-type structures are directly applicable, however.

Acknowledgment

Thanks are due to Messrs. W. E. McCallum, Jr., and F. D. Gage for their assistance in this work; to Mr. R. D. Bradford for his efforts in development of the light-figure microscope. The authors also would like to thank Dr. D. C. Reynolds of the Aeronautical Research Laboratory, Wright Air Development Center, USAF, Ohio, for his personal interest in this work.

This paper was supported in part by the Air Force Research Division, Air Research and Development Command, United States Air Force, under Contract AF33(657)-7916.

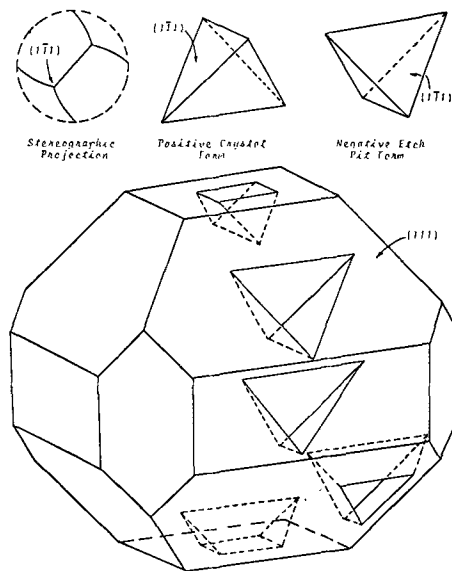


Fig. 13(a). Schematic drawing of the etch-pit form intersecting various surfaces of an arbitrarily shaped sphalerite type crystal. $\gamma \cong 3$. Etch pits on $(\bar{1}\bar{1}\bar{1})$ are stable.

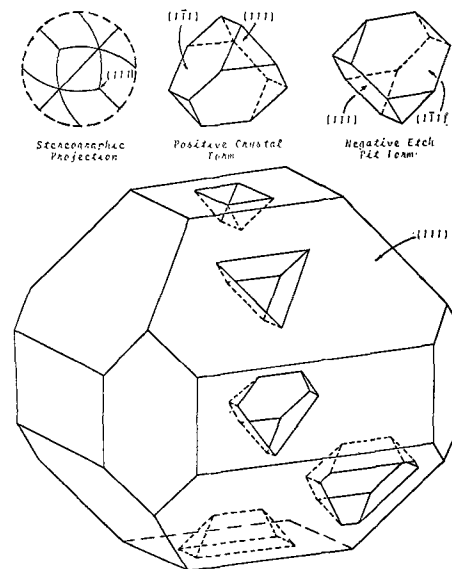


Fig. 13(b). $3 > \gamma > 1$. The explanation as given in the caption of Fig. 6. holds here. Etch pits on both tetrahedral planes are stable.

Manuscript received May 1, 1963. This paper was presented at the Boston Meeting, Sept. 16-20, 1962.

Any discussion of this paper will appear in a Discussion Section to be published in the December 1964 JOURNAL.

REFERENCES

- H. C. Gatos, in "The Surface Chemistry of Metals and Semiconductors," p. 381, H. C. Gatos, Editor, John Wiley & Sons, New York (1960); J. W. Faust, Jr., in "Methods of Experimental Physics," Vol. 6, p. 147, "Solid State Physics," K. Lark-Horovitz and V. A. Johnson, Editors, Academic Press, New York (1959).
- G. A. Wolff and J. D. Broder, *Acta Cryst.*, **10**, 848 (1957); **12**, 313 (1959); G. A. Wolff, in "Compound Semiconductors," Vol. 1, p. 34, R. K. Willardson and H. L. Goering, Editors, Reinhold Publishing Corp., New York (1962).
- W. B. Pearson and G. A. Wolff, *Discussions, Faraday Soc.*, **28**, 143 (1959).
- G. A. Wolff, J. M. Wilbur, Jr., and J. C. Clark, *Z. Elektrochem.*, **61**, 101 (1957).

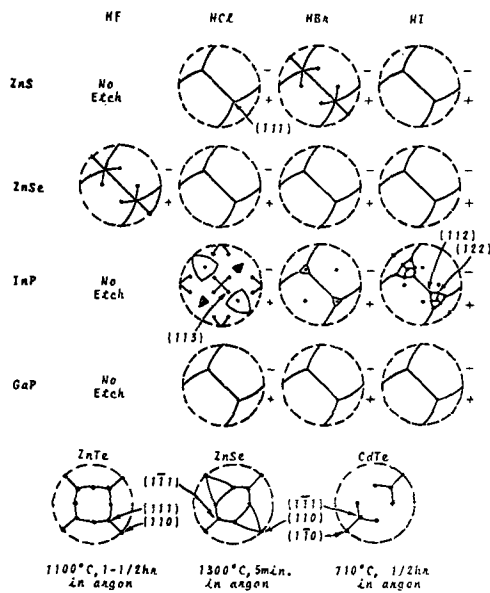


Fig. 14. Light-figure patterns of sphalerite type crystals etched in hydrogen halide acids. The last three stereograms denote the thermal etch patterns of ZnTe, ZnSe, and CdTe, respectively. Polarity was measured by piezoelectric techniques; this is indicated by + and - signs the same as in Fig. 8 and 10. The sign denotes the electric charge on the respective tetrahedral plane which appears on expansion of the crystal in the $[111]$ -direction. (111) is specular; $(\bar{1}\bar{1}\bar{1})$ is matte.

5. S. B. Austerman, D. A. Berlincourt, and H. H. A. Krueger, *J. Appl. Phys.*, **34**, 339 (1963); J. W. Faust, Jr., and A. Sagar, *ibid.*, **32**, 331 (1960);

- H. C. Gatos and M. C. Lavine, *This Journal*, **107**, 427 (1960); *J. Appl. Phys.*, **31**, 743 (1960); M. Inoue, I. Teramoto, and S. Takayanagi, *ibid.*, **33**, 2578 (1962); M. C. Lavine, H. C. Gatos, and M. C. Finn, *This Journal*, **108**, 974 (1961); A. N. Mariano and R. E. Hanneman, *J. Appl. Phys.*, **34**, 384 (1963); J. C. Monier and R. Kern, *Compt. rend.*, **241**, 69 (1955); *Bull. soc. franc. Mineral. Crist.*, **79**, 495 (1956); E. P. Warekois, M. C. Lavine, A. N. Mariano, and H. C. Gatos, *J. Appl. Phys.*, **33**, 690 (1962); E. P. Warekois and P. H. Metzger, *ibid.*, **30**, 960 (1959); J. G. White and W. C. Roth, *ibid.*, **30**, 946 (1959); G. A. Wolff, U. S. Army Signal Res. & Dev. Lab., Exploratory Res. Div. E, Publication No. 5910 (1959); *This Journal*, **106**, 207C (1959); G. A. Wolff and J. R. Hietanen, in Contract AF 33(616)-7528 Reports, Third Quarterly Progress Report, pp. 51-59, (1961), Fifth Quarterly Progress Report, pp. 68-80 (1961), ASD-TDR-62-69, Vol. I, pp. 40-53 (1962), ASD-TDR-62-69, Vol. II, pp. 48-61 (1962), in Contract AF33(657)-9975 Reports, Second Quarterly Report pp. 32-37 (1963), in Contract AF33(657)-7916 Reports, Third Quarterly Report pp. 4-15 (1963); *Proc. International Symposium on Condensation and Evaporation of Solids*, Dayton, Ohio, Sept. 1962; R. Zare, W. R. Cook, and L. R. Shiozawa, *Nature*, **189**, 217 (1961).
6. J. G. Gualtieri, M. J. Katz, and G. A. Wolff, *Z. Krist.*, **114**, 9 (1960).
7. G. A. Wolff and J. G. Gualtieri, *Amer. Mineral.*, **47**, 562 (1962); G. A. Wolff, *Z. Phys. Chem.*, **31**, 1 (1962).
8. D. C. Reynolds and S. J. Czyzak, *J. Appl. Phys.*, **31**, 94 (1960).
9. R. F. Belt, ASD-TDR-62-69, Vol. II, pp. 58-61, (1962).

Charge Storage Effects in Tantalum Oxide Films

Rudolf Dreiner

Research Laboratory, Sprague Electric Company, North Adams, Massachusetts

ABSTRACT

The phenomenon of the residual discharge current following an inverse time law, $i_{\text{res}} \propto b/t$, was confirmed for tantalum electrolytic capacitors. It was shown that the coefficient b was independent of charging fields up to $2/3$ of the formation field and that the residual current increased with temperature. The activation energy was 2.5 kcal/mole. Furthermore, it was shown that, if the external resistor was removed and the cell was left with open terminals, the internal residual current continued to flow until the build-up field modified the flow. If the oxide film were illuminated during discharging, two different photoeffects were recorded: the transient effects due to wavelengths of $320 \text{ m}\mu$ to about $600 \text{ m}\mu$ and the stationary photocurrent mostly due to wavelengths shorter than $300 \text{ m}\mu$.

Several models are discussed which lead to an inverse time law. Preference was given to the idea that a net positive space charge arises within the oxide during charging; that this space charge causes two internal fields of opposite directions and that the residual discharge current is the difference of two currents flowing in the opposing fields, thus neutralizing the space charge. Irradiation during charging and discharging affected the positive transient effect and the space charge field.

The phenomena of residual effects, specifically the residual discharge current and the residual voltage, are common to many types of capacitors. The residual discharge current is the current in excess of the ideal RC discharge current which is released from a charged capacitor undergoing a discharge through an external resistor. The residual or open

circuit voltage is the potential which appears across the terminals of a capacitor if the capacitor has been charged, discharged, and then left with open terminals. Guenterschulze and Betz (1) have described these effects and more recently Lehovec and Reinheimer (2) reported more extensive data on the residual discharge current emerging from an

anodic oxide film on aluminum if this oxide film were first subjected to an anodic potential and then discharged.

In the following, results will be presented which were obtained from investigations on capacitors of the system Ta/Ta₂O₅/aqueous electrolyte/Pt. Particular interest is paid to the residual discharge current and the influence that illumination of the oxide film has on the residual discharge current.

Experimental

Samples of high purity (Fansteel, impurities <0.1%) tantalum foil (10 mils thick; area ≈ 18 cm²) were degreased, chemically polished for 15 sec in a solution consisting of 5 parts concentrated H₂SO₄, 2 parts concentrated HNO₃ and 2 parts 48% HF, leached in boiling deionized water for 10 min, and then vacuum annealed ($\approx 10^{-4}$ Torr) at 2100°C for 30 min. Anodization occurred in 0.1% H₂SO₄ solution at about 34°C. Up to the final formation potential, a constant current of 2 ma/cm² flowed. Then the sample was connected to a constant voltage supply, and the anodization continued for a total time of 1 hr. At the end of this time current densities were ~ 5 μ a/cm² for anodizations to 150v and ~ 0.5 μ a/cm² for anodizations to 9.5v.

Each sample was assembled into a cell containing an electrolyte of 0.1% H₂SO₄ solution. A Pt sheet (~ 100 cm²) made the electrical contact to the electrolyte. The current was measured and recorded by a Keithley 610A electrometer in combination with an Esterline-Angus recorder. The cell and the leads were shielded to avoid pick-up of stray signals.

For the investigation of the effect of light on the residual discharge current a different sample configuration was used. A Ta disk (Fansteel, impurities <0.1%) was, after degreasing, anodized to 150v at about 95°C. Then the disk was potted in epoxy resin leaving one circular face of 2.83 cm² uncovered. This face was mechanically polished (0.3 μ finish), carefully rinsed in deionized water, and anodized for 1 hr to 150v. The current densities at the end of formation were about 35 μ a/cm². The formation solution was either 1 ml of 85% H₃PO₄ diluted to 1 liter or 1% Na₂SO₄.

In Fig. 1 the experimental set-up for the photo-investigations is shown. A Pt ring, immersed in the electrolyte, provided the electrical contact. The cell

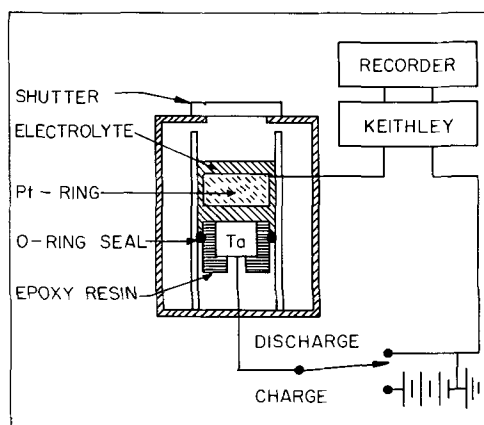


Fig. 1. Experimental arrangement for photo-investigations

was mounted in a dark box (which also served as an electrical shield) to prevent any light from falling on the oxide film. However, a shutter arrangement was provided on the box to permit a controlled irradiation of the oxide layer. The use of the anodized Ta disk had the advantage that the whole oxide film could be directly illuminated from one light source.

The oxide film was illuminated with a high pressure mercury arc having a total light intensity of about 13 to 14w. A heat absorbing glass between the light source and the cell prevented any significant temperature rise inside of the cell. The distance between the oxide film and the arc was about 6 in., and the light had to pass through the electrolyte, the height of which was about $\frac{1}{2}$ in. Except where it is specifically mentioned, the full spectrum of the mercury lamp was used.

Results

Investigations of the residual discharge current.—A capacitor with a Ta foil anodized to 150v was always charged for 30 min and then discharged. When the discharge currents were too small to be measured as a potential drop across 10^6 ohm, higher resistors were applied. It was made certain, however, that the residual discharge current did not depend on the external resistor up to 10^8 ohm. Thus the current is driven by a constant current source. It is seen in Fig. 2 that the recorded discharge current very quickly deviated from the ideal RC-decay and approached a straight line in a log-log plot. For this straight line an empirical relation for the residual current was given by Lehocvec and Reinheimer (2).

$$i_{\text{res}} = \frac{b \cdot V_{\text{ch}} \cdot C}{t^n} \quad [1]$$

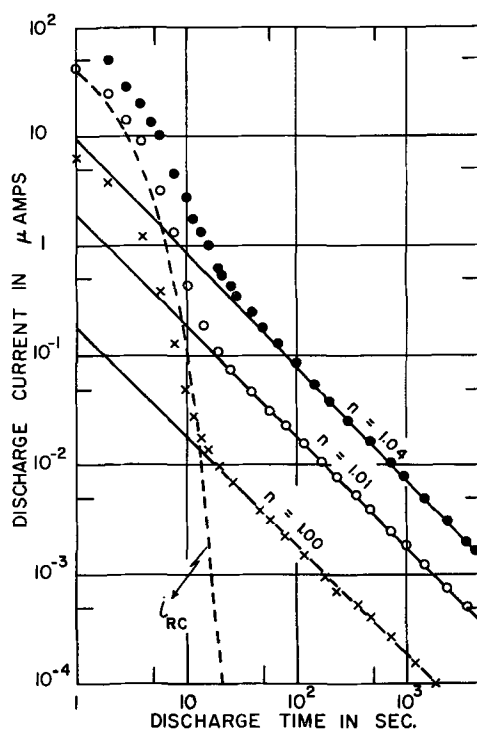


Fig. 2. Discharge currents as a function of time; formation potential 150v; charging potentials, \bullet 143v, \circ 70v, \times 10v; capacitance at 120 cps, 1.63 μ F.

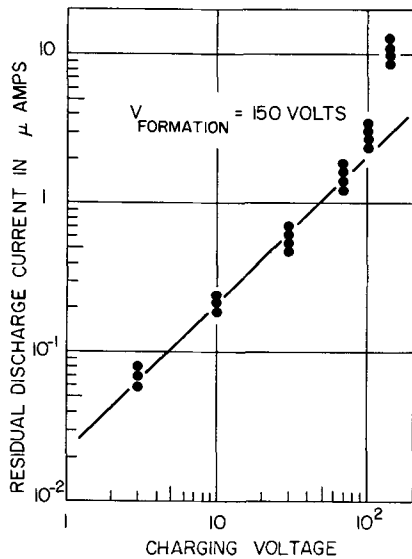


Fig. 3. Residual discharge currents at a discharge time of 1 sec as a function of the charging field; the charging voltage is proportional to the charging field for a constant oxide thickness.

V_{ch} is the charging voltage, C the capacitance at audio frequency, and t is the time. The coefficient b is, as later shown, independent of charging field and film thickness. From numerous runs n values close to unity were obtained, ($0.93 < n < 1.07$). Within these limits n was found to be independent of charging fields. The lowest charging voltage was 3v and the highest 143v. By extending the straight lines in Fig. 2 the values of the residual discharge time of 1 sec were determined. These values should change linearly with the charging field if coefficient b is independent of the field. In Fig. 3 the residual discharge currents at 1 sec are plotted vs. the charging voltage which is directly proportional to the field for a constant oxide thickness. The scattering of the points was rather random and no connection with the history of the cell was apparent. For fields lower than about two-thirds of the formation field a straight line is obtained, the slope of which corresponds to a b of 0.014 (b is unitless for $n = 1$).

Guenterschulze and Betz reported the value 0.32 $\mu\text{a sec/cm}^2$ for the relation

$$a = \frac{i_{res} \cdot t \cdot V_{Form}}{A \cdot V_{ch}}$$

where i_{res} is the residual current, t is the time from the start of discharging, V_{Form} is the formation voltage, V_{ch} is the charging voltage, and A is the area in cm^2 of the capacitor. This is essentially the same relation as Eq. [1] with the reciprocal of the capacitance proportional to the formation potential. In their experiment the Ta/Ta₂O₅ electrolytic capacitor was charged to the formation voltage ($V_{ch} = V_{Form} = 106\text{v}$). Here the corresponding value for a is 0.19 $\mu\text{a sec/cm}^2$ for the linear part of Fig. 3 and 0.7 $\mu\text{a sec/cm}^2$ for $V_{ch} = 143\text{v}$.

The residual discharge current at discharge time $t = 1$ sec was independent of the oxide thickness for constant charging fields (charging field about 1/2 of the formation field), Fig. 4. Therefore, with the reciprocal of the capacitance proportional to the

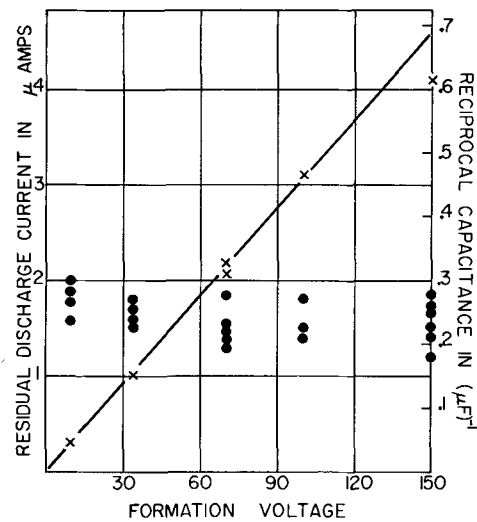


Fig. 4. • Residual discharge currents at a discharge time of 1 sec as a function of the oxide thickness for a constant charging field of about 1/2 of the formation field. X Reciprocal capacitance as a function of the oxide thickness.

thickness of the oxide (or the formation potential) and from Eq. [1], it follows that the coefficient b is independent of the oxide thickness for constant charging fields for the range investigated here. The reciprocal capacitance values of the samples measured at 120 cps are given in Fig. 4.

With a capacitor formed to 150v and charged to 70v for 30 min the temperature dependence of the residual discharge current at $t = 1$ sec was determined for the range from +50° to -57°C. The electrolyte was a solution of about 40% H₂SO₄. The data fitted a straight line in a plot of $\log i_{res}$ vs. $1/T$, Fig. 5, and the slope corresponded to an activation energy of 2.5 kcal/mole. The almost identical results shown at room temperature in Fig. 3 and 5 proved that the concentration of the electrolyte did not affect the residual discharge current.

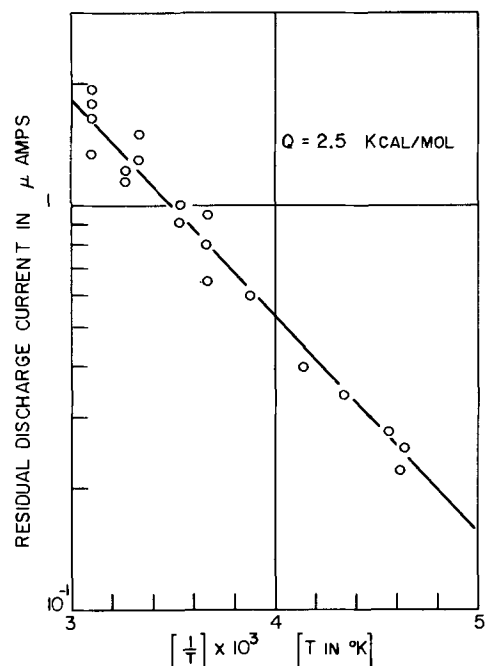


Fig. 5. Temperature dependence of the residual discharge current at a discharge time of 1 sec.

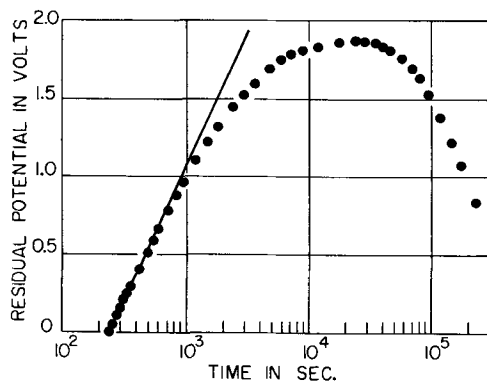


Fig. 6. Open circuit voltage build-up and decay

After an electrolytic capacitor has been charged and discharged, a residual voltage of anodic polarity will build up when the capacitor is left with open terminals. This effect, the residual voltage build-up, is reported by Guenterschulze and Betz (1), by van Geel and Pistorius (3), and by Lehovc and Reinheimer (2). The last authors (2) pointed out that the build-up of the residual voltage and the residual discharge current are caused by the same effect, the motion of charges in the oxide film. With $C(dV/dt) = i$, and relation [1], the residual voltage build-up should, therefore, be proportional to $\ln t$. This was confirmed, Fig. 6, for the initial build-up to about 1v, but after that the data deviated from a straight line very probably due to the change of the internal charge motion by the increasing field across the plates. (Experimental conditions: $V_{\text{Form}} = 150\text{v}$, $V_{\text{ch}} = 70\text{v}$, charging time 30 min, discharge time 4 min, and $R_{\text{series}} = 10^6$ ohms). From the slope of the straight line in Fig. 6, a b value was calculated which was only slightly less (1.04×10^{-2}) than the value obtained from the residual discharge current (1.14×10^{-2}).

Equation [1] was confirmed for capacitors with an anodized disk as anode. Exponent n stayed within the limits previously mentioned. The average b was 0.022, with extreme values of 0.028 and 0.018, and within this range the b values obtained after longer charging times were the higher ones (charging times: 1 min, 10 min, 30 min, 60 min, 920 min).

Investigations of photoeffects.—The initial inves-

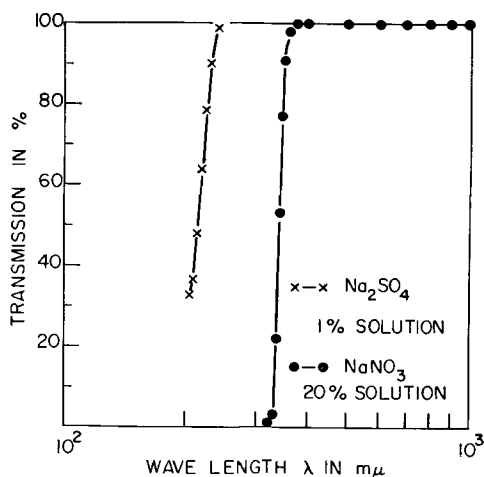


Fig. 7. Transmittance of electrolytes vs. wavelength

tigations were done with cells containing a 20% NaNO_3 solution as electrolyte. The transmission spectrum of this solution is plotted in Fig. 7. In the range investigated, this electrolyte completely absorbed wavelengths from 205 to 310 $\text{m}\mu$ and transmitted from 375 to 1000 $\text{m}\mu$.

The charging voltage was usually 50v applied for 30 min and it was assumed that this is sufficiently low to exclude ionic current during the charging cycle. On discharging through a series resistance of 10^7 ohms, the residual discharge current (straight line) was approached within a time of 30 to 50 sec. To permit the determination of the constants of relation [1] more accurately, the discharge time was always extended to 180 sec or more before the illumination of the oxide.

The effect of illumination on the discharge current is shown in Fig. 8, where the results of the following procedure are plotted: the capacitor discharged for 180 sec in the dark, then the oxide was irradiated for 120 sec and then darkened again for 120 sec; this was repeated. With the start of the first illumination the discharge current decreased (negative effect) briefly and then increased substantially (positive effect) to a maximum and declined. With the illumination shut off, the discharge current responded with a second positive surge (positive aftereffect) and then approached the extrapolated dark residual discharge current. It was observed with the sequence of the illumination cycles that the first negative effect increased strongly, that the positive effect decreased almost to zero with respect to the calculated dark residual discharge current, and that the positive aftereffect became only slightly smaller.

Young (4) has mentioned similar behavior of the total current but this was observed under different conditions. With the tantalum negative with respect to the electrolyte, he observed the following: "With

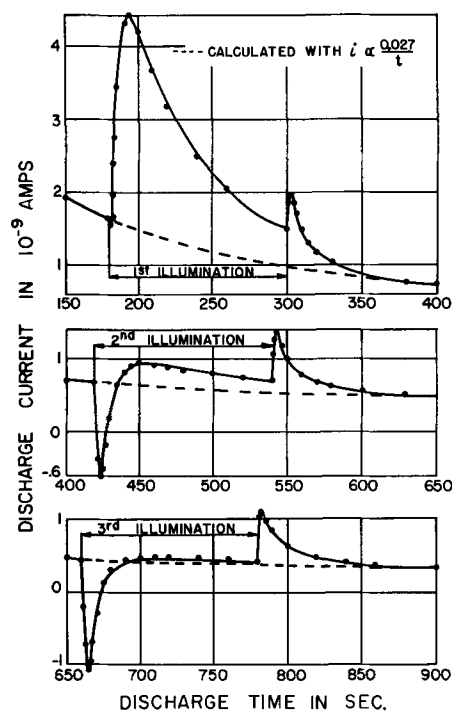


Fig. 8. Photoresponse of Ta_2O_5 with repeated short illuminations

the start of the illumination, a short positive surge was followed by a steady negative photocurrent; on cutting off the light, a negative surge occurred and the dark current became less negative than before illumination."

If the illumination was continued (and not interrupted as shown in Fig. 8), the total current declined, changed polarity, and finally leveled off at a constant photocurrent. When the illumination was shut off, a rapid polarity change occurred and the positive aftereffect was observed from which the current decayed to the residual discharge curve calculated with Eq. [1].

A second illumination which started after the oxide had remained in the dark for 1 hr did not cause the strong positive surge as observed with the first illumination. Only a strong negative transient effect was recorded. At the end of the irradiation almost the same positive aftereffect occurred. It was found that the strong positive effect could only be observed once during a particular discharging. After a new charging, however, the positive effect could be observed again on irradiating the oxide during the discharge. It is apparent that tantalum oxide exhibits two types of photoeffects: the transient effects and a steady photocurrent.

As a next step, the oxide film was illuminated during charging. The irradiation during charging was always done for 5 min after charging for 20 min in the dark. After illumination the charging was continued for 5 min in the dark for a total charging time of 30 min.

Illumination during charging affected the dark residual discharge current and the photoeffects. On discharging, higher residual currents were recorded; however, relation [1] remained valid. The b values were observed up to 0.04. The exponent n stayed the same.

The influence on the photoeffects was as follows: the negative effect at the start of illumination was suppressed, the positive effect appeared much stronger, and the positive aftereffect did not change considerably. Charges corresponding to the area between the positive surge and the calculated residual current from the time 180 to 300 sec amounted to 0.4 μ coulombs when the oxide was illuminated during charging and to 0.08 μ coulombs when the film remained in the dark during the chargings. ($Q = CV \approx 11.5 \mu$ coulombs.)

With the data graphed in Fig. 9 both effects are shown, the increase in the residual discharge current and the changes in the photoeffects. In addition, the influence of continued illumination is demonstrated and the results did not differ from those obtained after the capacitor had been charged in the dark as previously described. The constant negative photocurrent was the same in both cases.

The duration of illumination during charging and the time interval between the end of irradiation and the start of discharging affected the dark residual discharge current and the positive transient effect. Longer illumination, but the same dark period prior to discharging, increased the dark residual discharge current and the positive transient effect. Higher values also were observed when the interval between

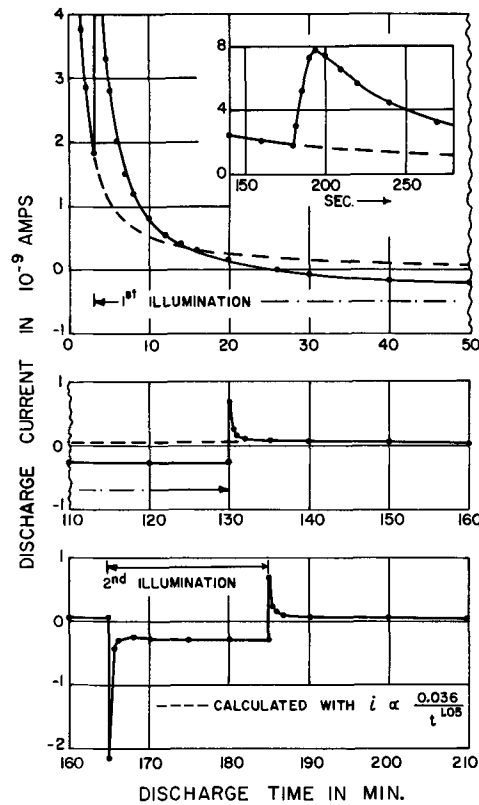


Fig. 9. Transient and stationary photocurrents from Ta₂O₅; oxide film was illuminated for 5 min during charging.

the end of illumination and the discharge was shorter. The time period from the start of discharge to the beginning of illumination influenced only the positive transient effect after the oxide had been irradiated during charging. A decline was observed as the initial dark period was extended.

van Geel, Pistorius, and Winkel (5) found the

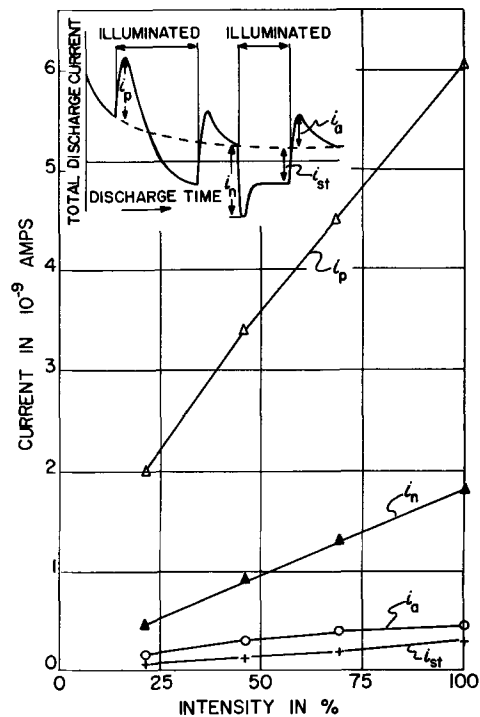


Fig. 10. Transient and stationary photocurrents as a function of irradiation intensity.

photocurrent to be proportional to the intensity of irradiation. Here this was confirmed for the stationary effect and, as seen from Fig. 10, the transient effects also depended almost linearly on the intensity. In these experiments the intensities were changed by putting wire meshes between the light source and the oxide.

So far, all of the experiments were done with a 20% NaNO_3 solution as the electrolyte. This solution had a sharp absorption edge at about $330 \text{ m}\mu$, Fig. 7. It was surprising to find photoeffects through this filter since the tantalum oxide is reported to be only sensitive to light having wavelengths shorter than $300 \text{ m}\mu$ (4-6). To be able to determine a spectral distribution of the photoeffects, the electrolyte was changed to 1% Na_2SO_4 solution which was transmittant in the u.v. region, Fig. 7. In Fig. 11, the transmission of the Corning Filters which were used and the photoeffects obtained with filtered light are plotted. The few points at about $250 \text{ m}\mu$ in the transmission *vs.* wavelength graph are calculated transmission values for a tantalum oxide film of 3000\AA thickness. The absorption coefficients used were those reported by Bray, Jacobs, and Young (7).

With filter 2403 in the light beam no photoeffect was observed. The other results indicated that the transient photoeffects are associated with wavelengths longer than $300 \text{ m}\mu$ and the stationary photo-

current is mostly related to wavelengths shorter than $300 \text{ m}\mu$.

Discussion

It was shown, Fig. 6, that the residual voltage build-up and the residual discharge current are due to the same cause. First explanations of these dielectric aftereffects used the Maxwell-Wagner model (8,9). According to this theory, the capacitor consists of two or more layers of different conductivities and dielectric constants. During charging, a space charge will build up in the boundary layer and these charges will either flow as an additional discharge current or, with the terminals of the capacitor open, will cause a residual potential.

Guenthereschulze and Betz (10) related the residual effects to space charges. van Geel and Pistorius (3) reported that the displacement of Al^{+++} ions in Al_2O_3 during charging and their subsequent return to equilibrium condition after the capacitor had been discharged and left with open terminals accounted very well for the build-up of the open circuit potential. Consequently, the same charge motion should generate the residual discharge current.

A theory of ion displacement and, in addition, the orientation of dipoles by the external field with the assumption of a relaxation time distribution has been used (11) to explain the dependencies of capacitance and equivalent series resistance on the frequency. A rather simple equivalent circuit, a pure capacitance in parallel with an RC combination which can be considered as the storage mechanism, will discharge according to an inverse time law provided the time constant of the storage mechanism changes linearly with time (12).

Here it is thought that the displacement of ions is not the dominant cause of the residual discharge current since the activation energy, Fig. 5, is rather low for ionic motion. Further supporting evidence is the fact that the dark residual discharge current can be enhanced by irradiation of the oxide during low field chargings (field 1/3 of formation field or less). The wavelength of the light was about $330 \text{ m}\mu$ and longer, and therefore, the photoenergy should be insufficient to move ions.

Since the exponent n remained unity or very close to unity, the irradiation of the oxide film during charging could change two factors in relation [1], the coefficient b and the capacitance C . An increase of either of these would yield more discharge current. Vermilyea (13) and Bray, Jacobs, and Young (7) found that the capacitance decreased when the irradiation was done at the formation field. However, higher capacitances were observed after illumination with a field across the oxide which was less than the formation field (but still higher than 40% of the formation field).

During this work no increase in capacitance or observable interference color change was noted when the oxide was irradiated for periods up to 1 hr with u.v. light at fields 1/3 of the formation field or less. Even after illuminating the oxide for 1000 min at these low fields, the capacitance had only gained 2-4%. Capacitance measurements under bias (1/3 of formation field or less) were made and the values

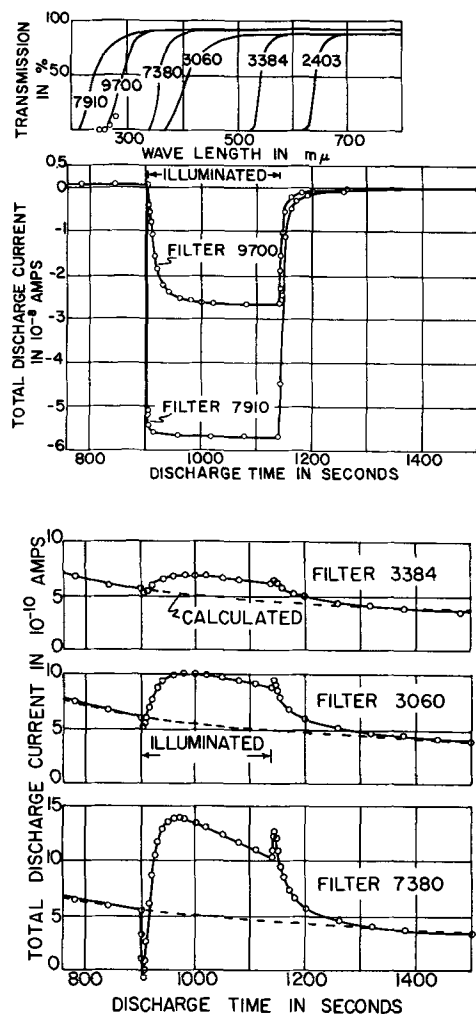


Fig. 11. Photoresponse of Ta_2O_5 to light of different frequencies

prior to an illumination of 5 min and shortly afterwards were the same. These results indicated that the capacitance either did not change at all or changed very little due to illumination during charging at such low fields, and, therefore, the larger residual discharge current was caused by an increased space charge rather than by an increased capacitance. This conclusion is in agreement with the work of Baer (14) who showed that, if a Ta_2O_5 film was illuminated during the anodic charging, more space charges were released on discharging than if the charging were done in the dark.

The residual discharge current could also be due to the release of electronic carriers from traps of different activation energies. This leads to a one over time dependency as derived by Randall and Wilkins (15) in their report about the decay of phosphorescence.

If a net space charge arises in the oxide film during charging, then on discharging the capacitor the space charge will result in two fields of opposite direction in the oxide layer. Lehovc (16) expressed the idea that the observed residual current is the net of two opposing internal currents. Schmidt *et al.* (17) described how a net space charge may arise. To account for the observed data, the authors (17) stated that under an anodic formation field, induced emission of trapped electrons will create net positive charges in the oxide. With a smaller field across the film, the net positive charge will be close to the oxide electrolyte interface since some electrons will enter from the metal and will be trapped, thus reducing the space charge near the metal. Evidence of two fields due to a net space charge is reported by Spear (18), who concluded from electron bombardment effects in thin dielectric layers that somewhere within the dielectric the space charge field changes sign.

The net positive space charge has to be neutralized by carriers injected into the oxide from both interfaces. Electrons entering the oxide from the metal constitute a current in the "forward direction" and electrons coming from the electrolyte are flowing in the blocking direction. Therefore, it is thought that the first possibility is the dominant one. The observed activation energy, Fig. 5, is here connected to the barrier opposing the flow of electrons from the metal into the oxide. The flow of electronic carriers across the interface will be affected by the structure of the interfacial layer and by the field across it. It is known from the work of Vermilyea (19) and Young (20) that different pretreatments of the metal can result in thin films of different compositions and properties at the metal-oxide interface. This might explain the difference between the b values obtained from runs with foils ($b = 0.014$) and disks ($b = 0.022$). The foils were chemically polished and vacuum annealed and the disks were mechanically polished before anodization. Lehovc (2) derived that an injection results also in an inverse time relation if the rate of injection of charges is proportional to an exponential function of the field ($\exp a F$) and the field is proportional to the space charge. If the internal field distribution due to a net positive space charge would be such that the injection

across the oxide-electrolyte interface would be larger than the injection from the metal, a cathodic polarity (Pt-counterelectrode high) of the residual effects should be observed. Furthermore, if the injection from the electrolyte would reduce the adjacent field to the level where no injection or very little takes place, the current from the metal into the oxide should become the dominant one and the polarity of the residual effects should again be anodic. These assumptions would explain the recorded polarities of the open-circuit voltage after a disk capacitor (formed to 150v) had been charged cathodically to 0.76v and then discharged for several minutes. The residual voltage rose first to a maximum cathodic potential, then changed polarity and the Ta became the high terminal again. Prior to these tests the cell was shorted for more than a week to make the influence of the last anodic charging as small as possible.

The effect of light is expected to be two-fold; first to generate additional carriers, and second to modify the internal fields by redistribution of charges due to the flow of photoelectrically released carriers. The low-energy light affected the space charge and by that the internal field when the oxide was irradiated during charging (higher b value in Fig. 9). However, from Fig. 9, it is also seen that even after illuminating the oxide for about 160 min the residual discharge current returned to the level which would have been reached without irradiation. Therefore, the low energy light applied during the discharge did not apparently modify the space charge or the internal fields as it did in connection with the charging field during the anodic charging. Ultra-violet light, however, affected the internal fields as seen from Fig. 11, where in the run denoted with Filter 7910 the current did not rapidly return, if it returned at all, to the expected dark level.

More evidence was obtained from the following experiments; a disk formed with 2 ma/cm² to 100v (formation continued to 1 hr total at constant voltage of 100v) in 0.1 H₂SO₄ at 33°C was charged to 33v (10⁶ ohms in series) for 30 min, then discharged for an appropriate time through 10⁵ ohms and 10⁶ ohms to determine the constant b of relation [1] and then shorted, 1 ohm in series, for a total of 120 min. After this, the b value was calculated from the initial slope of the residual voltage build-up. Both values agreed very well ($b \approx 0.020$) provided the oxide stayed in the dark during the whole short-circuit period. However, if the oxide was irradiated with the full spectrum of the mercury lamp for 10 min ($t = 5$ min to $t = 15$ min) during the 120 min short-circuit period, a lower $b \approx 0.012$ was obtained from the slope of the initial open-circuit voltage build-up.

A few points in the transmission *vs.* wavelength graph of Fig. 11 indicate that the tantalum oxide is probably transparent for low energy light. Therefore, a large part of the longer wavelength light will readily penetrate to the metal and could cause photo-emission from the metal into the oxide. This additional current should be a function of the field across the interface. It was observed that the positive transient effect decreased when the period from the start of the discharge to the beginning of the illumina-

nation increased. This should have been expected since the field across the metal oxide interface decreases with the short circuit time.

Photoemission from the metal into the oxide would so far only explain an increase of the residual discharge current. If, however, carrier flow from the metal into the oxide would modify the field across the interface so that photoemission ceases, photocurrent due to excitation within the oxide could become the dominant one. Here, the steady negative photocurrent is connected to the absorption of light within the oxide. However, after the irradiation terminated, the residual discharge current returned to the level which it would have reached without illumination, Fig. 9, and from this fact it was previously concluded that the low energy light did not affect the internal fields. The modification of the field across the metal oxide interface, therefore, can only be temporary, as long as the light is acting.

A photoresponse of different polarity was also observed by Lucovsky *et al.* (21). The samples used in their investigations consisted of semi-transparent electrodes of Al or Ta, which were oxidized thermally in the case of Al and anodically in the case of Ta. Irradiation of the oxide through the evaporated metal counterelectrode (also semi-transparent) made the Al or Ta electrode always the negative terminal of the photoresponse. However, the polarity depended upon the wavelength when the light entered the oxide through the Al or Ta electrode. For wavelengths longer than about $340\text{ m}\mu$ the electrode was the positive terminal and for wavelengths less than $340\text{ m}\mu$ the negative terminal of the photopotential across the film. In their explanation, the authors assumed a nonuniform potential distribution in the insulator and compared the magnitude of volume excitation in the oxide film with the amount of photoemission out of the metal into the insulator. The latter was taken as the dominant effect when the electrode acquired a positive potential due to low energy light entering through the Al-electrode.

A clear model which accounts in a consistent way for all of the observed phenomena cannot be presented. Further investigations of the open-circuit voltage which is, as shown, interconnected with the

residual discharge current will hopefully yield more clarifications and the results will subsequently be submitted for publication.

Acknowledgment

The author is greatly indebted to Dr. K. Lehovec for helpful advice. Valuable discussions with Dr. D. Smyth, Dr. G. Shirn, and J. R. Schimmel are gratefully acknowledged.

Manuscript received April 15, 1963; revised manuscript received ca. Aug. 1, 1963. This paper was presented at the Indianapolis Meeting, April 30-May 3, 1961.

Any discussion of this paper will appear in a Discussion Section to be published in the December 1964 JOURNAL.

REFERENCES

1. A. Guenthereschulze and H. Betz, *Electrolyt-Kondensatoren*, Technischer Verlag H. Cram Berlin W35 2.Auflage (1952).
2. K. Lehovec and H. Reinheimer, "Conduction, Storage and Photoelectric Phenomena in Anodic Oxide Films," Electrochemical Society Meeting, Chicago, May 1960.
3. W. Ch. van Geel and C. A. Pistorius, *Philips Research Rept.*, **11**, 471 (1956).
4. L. Young, *Trans. Faraday Soc.*, **50**, 164 (1954).
5. W. Ch. van Geel, C. A. Pistorius, and P. Winkel, *Philips Research Repts.*, **13**, 265 (1958).
6. L. Apker and E. A. Taft, *Phys. Rev.*, **88**, 58 (1952).
7. A. R. Bray, P. W. M. Jacobs, and L. Young, *J. Nuclear Materials*, **1**, 356 (1959).
8. H. Schering, "Die Isolierstoffe der Elektrotechnik," J. Springer, Berlin (1924).
9. A. R. von Hippel, "Dielectrics and Waves," p. 228, John Wiley & Sons, New York (1959).
10. A. Guenthereschulze and H. Betz, *Z. Phys.*, **91**, 70 (1934).
11. P. Winkel and D. C. de Groot, *Philips Research Repts.*, **13**, 489 (1958).
12. G. Shirn, Private communication.
13. D. A. Vermilyea, *This Journal*, **104**, 212 (1957).
14. W. Baer, *Z. Phys.*, **155**, 658 (1940).
15. J. T. Randall and M. H. F. Wilkins, *Proc. Royal Soc.*, **A184**, 390 (1945).
16. K. Lehovec, Private communication.
17. P. F. Schmidt, F. Huber, and R. F. Schwartz, *J. Phys. Chem. Solids*, **15**, 270 (1960).
18. W. E. Spear, *Proc. Phys. Soc.*, **68**, 991 (1955).
19. D. A. Vermilyea, *This Journal*, **103**, 690 (1956).
20. L. Young, *Trans. Faraday Soc.*, **53**, 841 (1957).
21. G. Lucovsky, C. T. Repper, and M. E. Lasser, *Bull. Am. Phys. Soc.*, **7**, 399 (1962).

Addendum to

"The Formation of Metal Oxide Films Using Gaseous and Solid Electrolytes"

(December 1963 Journal, Vol. 110, pp. 1240-1245)

It should be noted that the results obtained in the gas anodization experiments referred to in the above paper cannot be explained by formation of polymerized pump oil as has been suggested to us on several occasions. The reasons for this are: (i) A number of metals show no growth of barrier film (*i.e.*, Au Sn In Cu) under the same conditions where reproducible oxides are grown on aluminum. (ii) In the case of aluminum the thickness of oxide varies between 20 \AA and thousands of angstroms in

the same time of exposure to the discharge depending on whether an electrical contact is made to the sample or not. (iii) The vacuum system used for these experiments was pumped with an "Octoil" filled diffusion pump. Polymerization of pump oil certainly occurs in vacuum systems containing silicone oils and greases in the presence of a gaseous discharge. Hence it is of prime importance to ensure that no such oils are present during gas anodization experiments.

John L. Miles

The Electrodeposition of Nickel-Iron-Phosphorus Thin Films for Computer Memory Use

W. O. Freitag, J. S. Mathias, and G. DiGuilio

UNIVAC, Division of Sperry Rand Corporation, Research and Engineering Center, Blue Bell, Pennsylvania

ABSTRACT

Thin films of a ternary Ni-Fe-P alloy suitable for use in computer memories have been electrodeposited from a sulfate bath containing sodium hypophosphite. Glass coated with conductive vacuum evaporated layers of chromium and gold was used as a substrate. Essentially nonmagnetostrictive films, 1200Å thick and 3 x 3 in. in area, with coercivities of 2 oe and anisotropy fields of 3.5 oe were prepared reproducibly. The effects of hypophosphite ion in the plating solution on the deposit composition, cathode potentials, and magnetic properties of the films are discussed.

The electrodeposition of thin ferromagnetic films has in recent years become a subject of intense interest to research workers involved in the study of materials for computer memories (1-3). Binary alloy films having a composition of 81% Ni and 19% Fe have shown the most promise for high speed magnetic film memories since these films exhibit negligible magnetostrictive effects. Wolf has studied binary nickel-iron films (2,3) as well as ternary alloy films of nickel, iron, and cobalt (4) and has determined the dependence of the magnetic properties of these films as a function of composition and thickness. Mathias (1) has recently studied ternary alloy films of nickel, iron, and phosphorus and has shown that the presence of a nonmetallic constituent in the magnetic alloy does not have an adverse effect on the magnetic properties of the films. The data presented here are an extension of this work and deal with the magnetic properties of ternary alloy films of nickel, iron, and phosphorus as a function of their composition and thickness.

Experimental

Plating cell.—The plating cell consists of a rectangular lucite vessel which has fittings to hold the anode and cathode rigidly. The cell is surrounded by a large coil which provides a uniform vertical magnetic field of 30 oe during electrodeposition of the film. The cell and the coil rest on a set of leveling screws which permit exact alignment of the magnetic field direction with the desired direction of easy axis of the magnetic film deposited on the cathode. The substrates used as cathodes were made from No. 2 Corning Micro-Sheet glass that had been coated with vacuum evaporated layers of chromium and gold. These substrates were approximately 8 mils thick, 3 in. high and 3 in. wide. The thickness of the evaporated gold layer was about 800Å. The substrates were mounted in a removable cathode holder which permitted reproducible alignment with the direction of the applied magnetic field. A high purity rolled nickel sheet was used as the anode.

Electrolyte.—The electrolyte was an aqueous solution of nickel and iron sulfates. The nickel sul-

fate concentration was maintained constant at 0.8M and the iron sulfate concentration was varied to alter the composition of the alloy deposit. Addition of sodium hypophosphite to the electrolyte provided a convenient method of introducing phosphorus into the deposit. The standard nickel plating additives such as boric acid, sodium lauryl sulfate, and saccharin were also present in the electrolyte. The pH of the electrolyte was maintained at 2.2. Plating of the film was carried out at room temperature at a current density of 6 ma/cm². The electrolyte was not agitated during the plating cycle.

Under these conditions, plating rates for Ni-Fe films averaged 16.6Å/sec; for Ni-Fe-P films, about 18.0 Å/sec. It is of interest to note that plots of thickness *vs.* plating time were straight lines which passed through zero thickness at about 5 sec.

Analytical.—Deposits were analyzed by dissolving a film of known area in 1:4 nitric acid and diluting to volume. Nickel, iron, and phosphorus were determined by standard colorimetric procedures using separate aliquots; nickel by the pink nickelic dimethylglyoxime in alkaline solution; iron by the red orthophenanthroline complex after nitrate removal; and phosphorus by the molybdenum blue method. All colorimetric comparisons were made with a Beckman DU spectrophotometer using calibration curves prepared from pure metal and sodium hydrogen phosphate standards. Nickel and iron determinations are accurate to 1% or better, phosphorus 10% or better, of the reported percentage composition value.

Film thicknesses were estimated by converting the weight per unit area found for each component to an individual thickness value using the density of the pure material. The sum of these thicknesses was reported and is believed accurate within ±10%.

Magnetic measurements.—The magnetic parameters of primary interest in this study were the coercive force (H_c), the anisotropy field (H_k) and the switching time (T_s). A detailed description of the equipment used to determine these parameters has been previously reported (1). The values of H_c and H_k for 3 x 3 in. films and for ¼ x ¼ in. squares cut

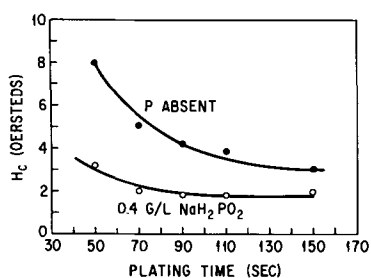


Fig. 1. Coercivity vs. plating time (thickness) for films plated from a solution before (closed circles) and after (open circles) the addition of sodium hypophosphite.

from them were determined to a precision of $\pm 5\%$ or better on 60 cycle hysteresographs. Arrays of 50 mil spots etched from films on 3×3 in. substrates were evaluated on a 1000 cycle hysteresograph. Magnetostriction coefficients were determined by measuring the change in the anisotropy field (H_k) when the film was bent into a known arc in a 60 cycle hysteresograph. Switching time measurements were made on a strip transmission line switching apparatus with a pulse rise time of 0.6 nanosecond and a pulse length of 400 nanoseconds.

Results and Discussion

Magnetic Properties of Ni-Fe-P Films

It has been shown previously (1) that increasing the concentration of the hypophosphite ion in the plating bath from 0 to 0.4 g/liter results in a decrease in the coercive force and anisotropy field of magnetic films having a thickness of 1200Å.

Since the coercive force is also a function of thickness, the values of coercive force for films having different thicknesses were determined. Figure 1 shows a typical plot of coercive force as a function of plating time (thickness) for films plated from a solution before and after the addition of sodium hypophosphite. It will be noticed that in both cases the coercive force decreases with increasing thickness but that this decrease is less marked for the films that contained phosphorus.

Since the average film composition as well as the thickness changes with plating time, these curves do not truly indicate the relationship between H_c of the film and its thickness. The hypophosphite ion, as will be shown later, tends to decrease the variations of the ratio of nickel and iron in the film and probably accounts for the smaller change in the coercive force of Ni-Fe-P films with increasing thickness.

Ternary films of Ni-Fe-P also have a much smaller switching constant than the binary 81-19 Ni-Fe films. This is shown in Fig. 2 where the reciprocal of the switching time of the magnetic films (180° switching mode) is plotted against the drive field at fixed values of the transverse field for a typical electrodeposited permalloy films and a typical electrodeposited film of Ni-Fe containing 2% P.

The permalloy film ($H_c = 1.9$, $H_k = 3.3$ oe) had a switching coefficient of 0.06 oe- μ sec; the value for the Ni-Fe-P film ($H_c = 1.4$, $H_k = 2.9$ oe) was 0.006 oe- μ sec.

It is believed that this improvement in the switching constant is a result of the greater uniformity of

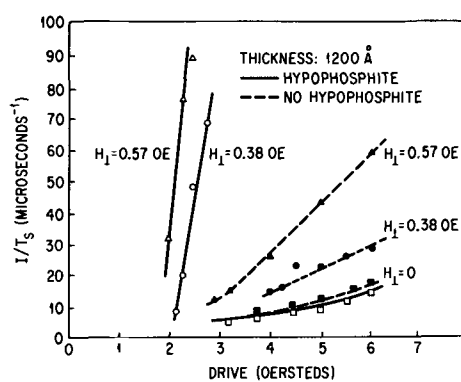


Fig. 2. Reciprocal of switching time, $1/T_s$, vs. drive field plots for comparable binary Ni-Fe (dashed lines; H_c , 1.9; H_k , 3.3) and ternary Ni-Fe-P film (solid lines; H_c , 1.4; H_k , 2.9).

composition of the ternary film of Ni-Fe-P. Examination of the domain wall movement during switching of Ni-Fe films using the Kerr-Magneto-optical technique has shown that the domains' motion tends to be blocked in certain areas. This may be the result of the film having areas of higher H_c or higher H_k . The Ni-Fe-P films on the other hand exhibit a smooth and very fast transition from one state to the other as the drive field is increased.

The magnetic properties of films having approximately the same relative nickel and iron content and the same thickness, but differing in their phosphorus content are compared in Table I. Composition is expressed as Ni-Fe atomic ratio, and phosphorus content in per cent by weight. When 1 to 2% by weight phosphorus is present in the films, appreciably lower values of H_c and better anisotropy characteristics are obtained. At higher phosphorus

Table I. Effect of phosphorus content of electroplated Fe-Ni alloys on magnetic properties

Thickness, Å	Film composition		Magnetic properties	
	Atomic ratio, Ni:Fe	P content, % by wt	H_c , oe	H_k , oe
1200	1.9	—	8.5	i
1200	2.1	2.1	3.1	7.5
1300	2.5	—	6.1	i
1300	2.4	1.2	4.4	5.0
1100	3.8	—	5.1	4.5
1000	3.7	2.7	4.0	5.0
1200	4.3	—	5.1	i
1100	4.5	1.3	2.8	3.9
1400	4.3	1.7	2.1	4.5
1300	4.2	3.1	7.5	i
1800	4.3	—	3.9	3.3
1900	4.3	1.4	2.0	5.7
1600	4.9	—	4.0	3.3
1800	4.6	1.4	2.0	4.5
2700	5.3	—	2.7	3.1
3200	5.2	1.4	1.2	4.0
2600	5.4	—	3.6	3.1
3000	5.6	1.4	1.5	4.6
1100	6.4	—	6.2	i
1150	6.9	1.1	2.6	2.6
1300	6.0	4.2	n	n

i = "semi-isotropic;" n = no magnetic output at 10 oe drive.

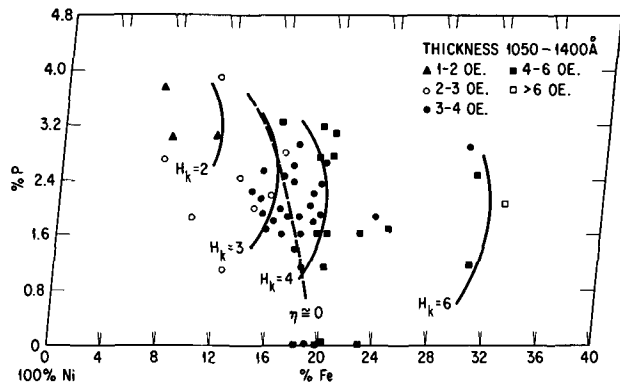


Fig. 3. Map of H_k vs. film composition for Ni-Fe-P films approximately 1200Å in thickness. The low iron-low phosphorus corner of the ternary composition diagram is represented with the scale of the phosphorus content exaggerated. The dashed line shows locus of nonmagnetostrictive compositions.

contents, the magnetic properties deteriorate. The term "semi-isotropic" used in Table I was applied to films with ill-defined anisotropies. These films were characterized by considerable hysteresis in the hard direction, the B-H loops being open, but not square. Films for which H_k values are given were square in the easy direction and showed little or no hysteresis in the hard direction except at higher drive fields.

The variation of H_k with film composition for films in the thickness range 1100-1400Å is shown in Fig. 3. The low iron-low phosphorus corner of the Ni-Fe-P ternary composition diagram is represented with the scale of phosphorus content exaggerated. The various ranges of H_k values for a collection of films in the thickness range of 1100-1400Å are mapped out roughly by the solid curved lines. The spread of the data reflects uncertainties in the analytical results and variations of thickness within the 1100-1400Å range. Still, a relatively smooth increase in H_k is observed as the iron content is increased. There also appears to be a rather definite maximum phosphorus concentration range for useful films of this thickness. Above this range "semi-isotropic" films or films having no magnetic response in drive fields of 10 oe were obtained. The higher iron regions were not explored.

Also indicated on Fig. 3 by means of the dashed line is the locus of compositions having little or no detectable magnetostriction. The Ni-Fe atomic ratio corresponding to zero magnetostriction increases from approximately 4.0 in the absence of phosphorus, to about 5.5 at 3.2 wt % P. This is in contrast to the behavior of Ni-Fe-Co films (4) where the Ni-Fe ratio corresponding to zero magnetostriction has been shown to be nearly constant for cobalt additions up to 65% by weight.

Effect of Plating Parameters on Film Composition

The instantaneous composition of an alloy deposit will change if changes occur in the relative concentrations of the ions in the cathode double layer. Such concentration changes may be quite pronounced during the first moments of deposition until deposition and diffusion rates come into balance and a

steady state is reached, whereupon some equilibrium composition is deposited. Thus a composition gradient is formed across the thickness of the deposit, and if the time required to establish the deposition of the equilibrium composition is an appreciable portion of the entire plating time, the average composition of the total deposit becomes a function of the plating time.

This effect has been discussed with respect to binary Ni-Fe films by Cockett and Spencer-Timms (5). The first portions of the depositing films are relatively more iron-rich than those portions deposited later.

The effect of such a concentration gradient on the magnetic properties of the films is not clear. Several methods for minimizing such gradients have been suggested, however, including agitation of the plating bath (1), use of pulsed currents (5) and operation under constant cathode potential conditions rather than constant current density (6, 7). At lower current densities (3 ma/cm²), Wolf (2) observes little or no variations in average composition in the 500-5000Å thickness range.

In the presence of hypophosphite, however, the severity of the concentration gradient across the thickness of the deposit is greatly reduced. Figure 4 shows the average iron concentration of films plated for varying lengths of time from the same solution before and after the addition of hypophosphite. The high iron concentration of the initial deposit is markedly suppressed by the hypophosphite. While a concentration gradient still exists, it is far less steep than that which is obtained under these conditions in the absence of phosphorus.

It is also to be noted in Fig. 4 that the over-all iron concentration of the deposit is reduced by the presence of hypophosphite. This is true for all solution compositions tested. In Fig. 5, the composition of the electrolyte is related to the composition of the deposit at a constant deposit thickness of 1000Å. The lower curve shows the relation between the amount of ferrous sulfate in the solution (nickel sulfate hexahydrate concentration is constant at 220 g/liter), and the Ni-Fe atomic ratio in the deposit in the absence of hypophosphite. The upper

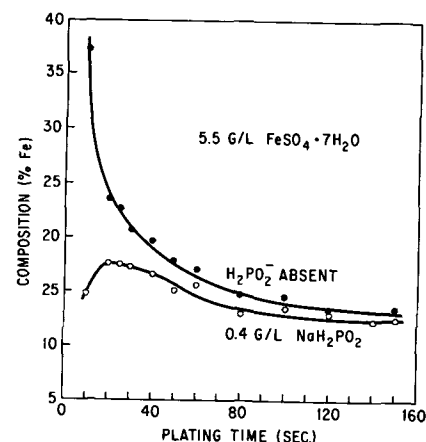


Fig. 4. Iron content of films vs. plating time showing the effect of the addition of sodium hypophosphite to the plating solution. Current density was 6 ma/cm². Films 1000Å in thickness are obtained in approximately 65 sec.

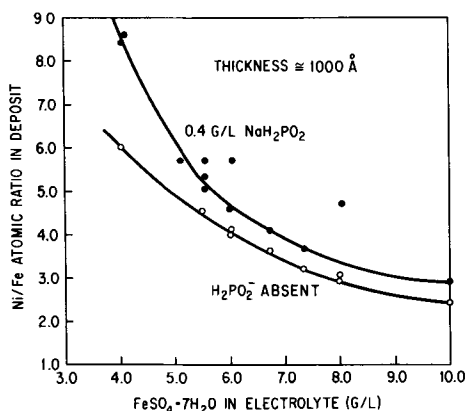


Fig. 5. Composition of 1000Å deposits vs. electrolyte composition in the presence and absence of sodium hypophosphite. The nickel sulfate concentration in the electrolyte was held constant at approximately 0.8M.

curve shows the shift in this relation when hypophosphite is added.

To determine whether the action of hypophosphite was primarily one of suppression of the rate of iron discharge or enhancement of the deposition rate of nickel, the current-voltage characteristics of the plating system were measured. The curves shown in Fig. 6 and 7 were traced out by an X-Y recorder. The voltage applied to the plating cell was increased from zero at a rate of about 1v per 5 sec while recording the cell current against the potential of a sealed fiber type calomel cell placed close to a pre-plated cathode. The repeatability was good; successive traces were essentially superimposed (within 10 mv). The traces for a typical plating solution are shown in Fig. 6. Curve 1 was obtained before the

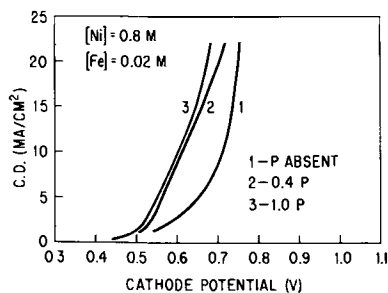


Fig. 6. Current density vs. cathode potential traces for a typical plating solution containing 0, 0.4, and 1.0 g/liter sodium hypophosphite.

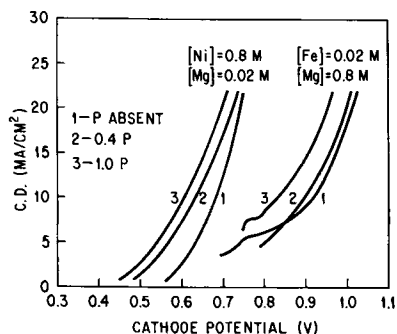


Fig. 7. Current density vs. cathode potential traces for plating solutions where iron sulfate (left hand curves) or nickel sulfate (right hand curves) was replaced by an equivalent amount of magnesium sulfate, each at three different sodium hypophosphite concentrations.

addition of sodium hypophosphite, and curves 2 and 3 were obtained after the addition of 0.4 g/liter and 1.0 g/liter sodium hypophosphite, respectively. It may be observed that hypophosphite ion not only depolarizes the alloy deposition, but changes the shape of the curve as well.

Similar experiments were carried out using electrolytes containing only nickel, or only iron. A nickel test solution was made up to the same composition as the alloy plating bath except that the iron sulfate was replaced by an equivalent amount of magnesium sulfate. This was done to maintain the over-all ionic strength of the test solution approximately the same as that of a regular plating bath. An iron test solution was prepared in an analogous way. The cathode polarization curves for these solutions are shown in Fig. 7. At current densities above 8 ma/cm² both metals are depolarized by large amounts (1 g/liter) of hypophosphite, but in the usual operating range (6 ma/cm² and 0.4 g/liter NaH₂PO₂) the deposition of nickel is depolarized by about 70 mv, while that of iron is only very slightly affected. Thus there is a net effect favoring the deposition of nickel.

The changes in instantaneous alloy film composition during deposition under constant current conditions suggest that corresponding changes in cathode potential occur. That this is indeed the case is shown in Fig. 8 where the variations of cathode potential with time are traced for two different current densities (upper curves, 10 ma/cm²; lower curves 6 ma/cm²) each at three different hypophosphite concentrations. A more uniform cathode potential is observed during film deposition from solution containing hypophosphite.

The lowering of the cathode polarization effected by the hypophosphite ion is again illustrated in Fig. 8. Since the amount of hydrogen which is codeposited with the alloy should be reduced at the lower operating potential, one might expect an increase in current efficiency as a result of adding hypophosphite. In the absence of phosphorus, current efficiencies are about 75-80%; when hypophosphite is added efficiencies are increased to about 85-90%. The amount of codeposited hydrogen was not

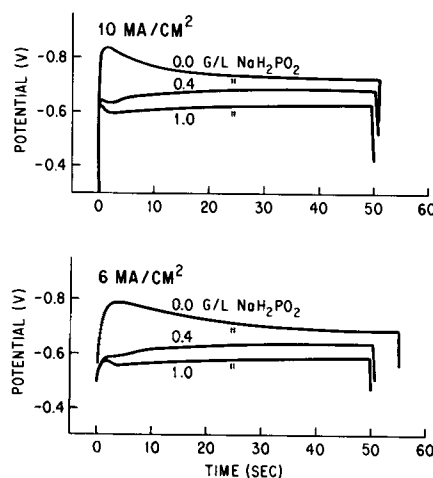


Fig. 8. Cathode potential vs. time curves for alloy deposition from a typical plating solution showing the effect of sodium hypophosphite concentration.

measured, however, so that it is not certain whether the apparent efficiency increase is due to reduced potentials or to some additional nickel deposition by the electroless mechanism.

Summary

It has been shown that the addition of hypophosphite ion to a nickel-iron sulfate plating system results in the deposition of magnetic films with properties superior to those deposited from solutions not containing the hypophosphite ion. Optimum magnetic properties are obtained with an average phosphorus content of 1 to 2% by weight. This plating system provides sufficient control to produce films suitable for computer memory use.

In addition to introducing phosphorus into the nickel-iron alloy, the presence of sodium hypophosphite in the nickel-iron sulfate electrolyte reduces fluctuations in cathode potential during deposition and produces deposits with more uniform compositional cross-sections. At the preferred current density of 6 ma/cm² hypophosphite increases

the relative amount of nickel in the deposit by depolarizing nickel deposition while hardly affecting iron deposition.

Manuscript received April 1, 1963; revised manuscript received July 18, 1963. This paper was presented at the Boston Meeting, Sept. 16-20, 1962.

Any discussion of this paper will appear in a Discussion Section to be published in the December 1964 JOURNAL.

REFERENCES

1. "The Preparation and Characteristics of Thin Ferromagnetic Films," Final Report, Contract AF 19(604)-4978, UNIVAC, Division of Sperry Rand Corporation, Philadelphia, 1961; see also Final Engineering Report, Contract AF 19(604)-2659, UNIVAC, Division of Sperry Rand Corporation, Philadelphia, 1958.
2. I. W. Wolf, *This Journal*, **108**, 959 (1961).
3. I. W. Wolf, *J. Applied Phys.*, **33**, 1152S (1961).
4. I. W. Wolf, Symposium on Magnetic and Electric Properties of Thin Layers, Leuven, Belgium, 1961.
5. G. H. Cockett and E. S. Spencer-Timms, *This Journal*, **108**, 906 (1961).
6. F. H. Edelman, *ibid.*, **109**, 440 (1962).
7. British Pat. 859,725, (1961), J. H. Stephen to United Kingdom Atomic Energy Authority.

Quasistatic Flux Reversal Characteristics of Electrodeposited Thin Permalloy Films

R. D. Fisher, H. E. Austen, and H. E. Haber

The National Cash Register Company, Dayton, Ohio

ABSTRACT

The rotational switching behavior of electrodeposited thin films is shown to be similar to that reported for vacuum deposited thin films. The influence of the Hc/Hk ratio (0.30-1.1), dispersion (5°-13°) of the easy axis, thickness (500Å-2800Å), and the angle of the applied field to the easy axis were determined on (i) the magnetization path during flux reversal, and (ii) the wall motion and rotational thresholds. The rotational thresholds were compared to the Stoner-Wohlfarth curve for simple coherent rotation. The separation of the rotational and wall motion thresholds appears to be thickness dependent.

Vacuum deposited magnetic films have been extensively studied in regard to preparation techniques and to the physics of the flux reversal process. Electrodeposition represents an alternate technique for obtaining magnetic thin films. Electrodeposited films with a relatively low maximum dispersion and hysteresis characteristics similar to those of vacuum deposited films have been reported (1, 2).

We have evaluated the quasistatic flux reversal characteristics of electrodeposited permalloy (81% Ni-19% Fe) thin films with a uniaxial anisotropy. The flux reversal process was evaluated with regard to the path of the magnetization and to the wall motion and rotational thresholds. The rotational thresholds were compared to the Stoner-Wohlfarth model (3) for simple coherent rotation.

Experimental

Test equipment.—The drive fields were produced by two Helmholtz coils at right angles. Another Helmholtz coil (rotatable) was used for earth's field

cancelation. Two identical coils (100 turns each) were used for flux pick-up and cancelation. The canceling coil could be rotated about the vertical and horizontal axes so that simultaneous cancelation was obtained for both driving coils. The sample could be rotated within the pick-up coil over a measured arc of about 160°. In the case of determining the magnetization path, the flux pick-up was amplified (Tektronix 122), integrated, reamplified (Tektronix 122), and fed into one input of a type H preamplifier. In the case of the threshold measurements, the pick-up was amplified (Tektronix 122) and fed into a Tektronix type H preamplifier. A type B preamplifier was used for the drive field. A Tektronix 536 oscilloscope was used for all measurements.

Method of determining flux path.—The selected sample was placed on the rotatable table within the pick-up coil and adjusted to the desired angle with respect to the drive field (5 oe, a.c.). A photograph was taken of the hysteresis characteristics at this angle of drive field (*x* component of the flux or mag-

netization). Since the pick-up coil and cancelling coils could not be rotated, the sample was rotated 90° and the drive field switched to the other Helmholtz coil. A photograph was then taken of the hysteresis characteristics at this position (y component of the flux or magnetization). These x and y components of the magnetization determined from the photographs of the hysteresis characteristics at equivalent drive fields were vectorially plotted to trace the magnetization path from 0° to 360° .

Method of determining wall motion and rotational thresholds.—The wall motion and rotational thresholds were determined from the 60 cycle differential loop, i.e., the dM/dt vs. H_a (applied field) trace, by using a 5 oe a-c (60 cycle) field in the easy direction and d-c bias fields of $0.4 H_k$ to $1.5 H_k$ in the hard direction. The wall motion and rotational thresholds were obtained as the value of the field at the midpoint of the observed domain wall and rotational switching traces.

Hysteresis parameters.—The measured hysteresis parameters were (i) the coercive force in the easy direction, H_c ; (ii) the anisotropy field, i.e., the field required to saturate in the hard direction, H_k ; and (iii) the maximum and quartile dispersion, α_m and α_q . The dispersion angles were measured in the manner described by Crowther (5). The coercive force of the deposits in the easy direction varied from 1.0 to 3.0 oe and the anisotropy field value was varied from 3.0 to 6.0 oe. The maximum dispersion angle ranged from 5° to 13° and the quartile dispersion varied from 1° to 3° .

Electrodeposition conditions.—Films were electrodeposited onto a circular cathode in the presence of a magnetic field. The diameter of the cathode was 1.37 cm and the thickness of the deposits was varied from approximately 500 to 2800 Å. This large ratio of spot diameter to thickness minimizes the magnitude of demagnetizing fields in the plane of the film. The composition of all deposits was approximately 81% Ni-19% Fe. The films lacked any appreciable strain sensitivity in the easy and hard directions. The thickness was determined from the known geometry and the theoretical flux density for permalloy (81% Ni-19% Fe). Thick deposits (4000 Å) were made to check the thickness calculations based on geometry and flux density by weight-density calculations. Thicknesses calculated by these methods agreed within 5%. The electrolyte used was similar to that described by Wolf (1). However, a platinum anode was used rather than a Fe-Ni anode and fresh solutions were used to obtain each deposit. The current density was 6 ma/cm². Solutions were prepared using reagent grade chemicals and triple distilled water. The electrolyte was used at room temperature without agitation.

Experimental Results and Discussion

Films with varying H_c/H_k ratios from 0.30 to 1.1 and maximum dispersion in the range of 5° to 13° were evaluated as to the path of the magnetization at applied field angles to the easy direction of 30° , 60° , and 75° . Typical flux paths are shown in Fig. 1. These results show that two mechanisms of flux reversal clearly occur, as evidenced by the variation

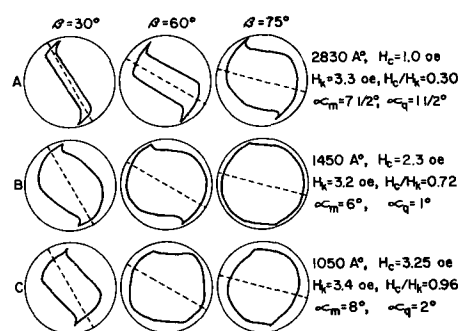


Fig. 1. Flux paths of electrodeposited films at applied field angles of 30° , 60° , and 75° .

in path: a coherent rotation as shown by the circular path, and an incoherent or wall motion reversal process as evidenced by the linear path. The linear path obviously cannot be a single domain process since the resultant magnetization vector magnitude is considerably less than the saturation magnetization value indicated by the outer complete circle. The linear path is very likely due to wall motion since observation of the dM/dt vs. H_a curve in this region shows considerable Barkhausen jumps in all cases. When the a-c field is applied at an angle of 30° to the easy axis, very little flux change occurs perpendicular to the easy axis for samples with an H_c/H_k ratio less than 0.5 (e.g., Fig. 1A). In fact, flux reversal for these samples is almost completely by wall motion processes. However, a sample with an H_c/H_k ratio greater than 0.5 indicates some rotational behavior over an angle of approximately 45° (e.g., Fig. 1B and C), but considerable eccentricity is shown in the path.

At increasing applied field angles (60° and 75°) to the easy axis, samples with an H_c/H_k ratio less than 0.5 show improved rotational characteristics as indicated by the partially curved path but again considerable eccentricity occurs (Fig. 1A). Samples with an H_c/H_k ratio greater than 0.5 show considerable rotation over angles as large as 75° and 85° (Fig. 1B and C) and little eccentricity in the curved path which is especially obvious in Fig. 1B and C. However, a complete coherent rotational switch was never observed and some wall motion always followed the rotational switch to complete the flux reversal. Thus, only a partial rotation of the magnetization occurs. These results are similar to those of vacuum deposited films (4). The extent of coherent rotation increases with an increase in H_c/H_k ratio. This can be seen from the two samples with the same dispersion but different H_c/H_k ratios. This is especially apparent at applied field angles of 75° to the easy axis. Thus, increasing the H_c/H_k ratio increases the minimum angle for rotation.

Assuming the applicability of the Stoner-Wohlfarth theory for simple coherent rotation an equation can be derived relating the applied field, at angle β with the easy axis, and the angle θ through which the magnetization has been rotated away from the easy axis by the applied field, as shown below

$$h_a = Ha/Hk = \frac{\sin 2\theta}{2 \sin (\beta - \theta)}$$

For any given β , the magnetization will rotate until a maximum energy position is reached and will then rotate coherently to a position between H_a and the easy axis without further applied field. However, this will occur only if the ratio of H_c to H_k is greater than some minimal value, e.g., if the component of H_a along the easy axis exceeds H_c before the angle of maximum energy for rotation is reached then a domain wall switch will occur. A domain wall switch obviously occurs for the sample shown in Fig. 1A for which the H_c/H_k ratio is below the minimal value but for samples shown in Fig. 1B and C, the H_c/H_k ratio is above the minimum value for rotation. In all samples the domain wall switch is at an angle to the easy axis, since the magnetization will rotate until the easy axis component of the field is approximately equal to the coercive force. As the crystallites begin to switch the intensity of magnetization decreases. The path will then show a curving away or eccentricity to the circular path (see Fig. 1). Those crystallites which have already switched will aid the applied field by magnetostatic interaction, and a domain wall switch should occur at a lower applied field than expected on the basis of zero dispersion. However, after the switch, the direction and magnitude of the magnetization will be nearly the same as it would be with zero dispersion. This accounts for the domain wall switch occurring at various angles with the easy axis as observed experimentally. The angle is dependent on the maximum dispersion and on the H_c/H_k ratio (Fig. 1).

To obtain additional information concerning the wall motion and rotational characteristics of electrodeposited films, the dependence of the wall motion

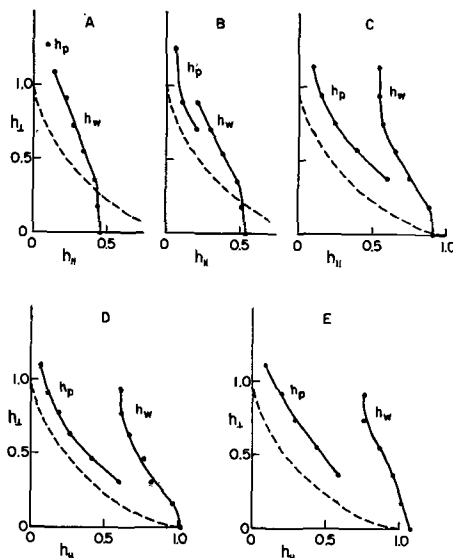


Fig. 2. Wall motion and rotational thresholds of electrodeposited thin films. (A) Thickness, 1600Å; H_c , 1.6 oe; H_k , 3.48 oe; H_c/H_k , 0.46; α_{\max} , 12°; α_q , 3°. (B) Thickness, 1410Å; H_c , 1.9 oe; H_k , 3.54 oe; H_c/H_k , 0.54; α_{\max} , 10°; α_q , 2°. (C) Thickness, 730Å; H_c , 3.1 oe; H_k , 3.36 oe; H_c/H_k , 0.92; α_{\max} , 5°; α_q , 1°. (D) Thickness, 635Å; H_c , 4.1 oe; H_k , 4.04 oe; H_c/H_k , 1.02; α_{\max} , 10.5°; α_q , 2°. (E) Thickness, 518Å; H_c , 3.7 oe; H_k , 3.44 oe; H_c/H_k , 1.08; α_{\max} , 13°; α_q , 5°. h_w is wall motion and h_p is rotational thresholds. - - - is Stoner-Wohlfarth curve.

and rotational thresholds on the angle of the applied field was evaluated. The rotational thresholds were then compared to the Stoner-Wohlfarth equation ($H_T/H_K = H_L/H_K \tan \theta + \sin \theta$) (4). The data were obtained from the differential curves (dM/dt vs. H_a) by using an a-c field of 5 oe in the easy direction and various d-c bias fields (0.4 H_k to 1.5 H_k) in the hard direction. Field values at the mid points of the domain wall (h_w) and rotational switching traces (h_p) were taken as the threshold field values. These threshold values were then plotted vs. the magnitude of the d-c bias field. All values were normalized to H_k .

In all cases the rotational thresholds were greater than those predicted by simple coherent rotational switching. Thus, for a given angle of applied field (formed by applying fields in the hard direction at a given easy direction field) higher field values than predicted are required for rotation. All samples which showed both rotational and wall motion thresholds could be considered inverted above a certain angle of applied field. This is to say that the rotational threshold is less than the wall motion threshold (inverted). These results can be seen in Fig. 2 and are similar to those reported for vacuum deposited films by Methfessel *et al.* (5). By extrapolating the experimental rotational thresholds to intersect the experimental wall motion threshold the theoretical minimum angle of applied field (β) for a rotational switch can be obtained. This minimum angle can then be plotted vs. the H_c/H_k ratio as shown in Fig. 3. The curve shows that the theoretical minimum angle of the applied field for a rotational switch is a function of the H_c/H_k ratio. Experimentally a H_c/H_k ratio of 0.4 requires an applied field angle of 68° to the easy axis to produce a rotational switch but a H_c/H_k ratio of 1.0 requires approximately a 5° applied field angle to the easy axis to produce a rotational switch. This observation agrees with a coherent rotational switching behavior (6). The lower the H_c/H_k ratio, the higher the bias field required to obtain a rotational switch.

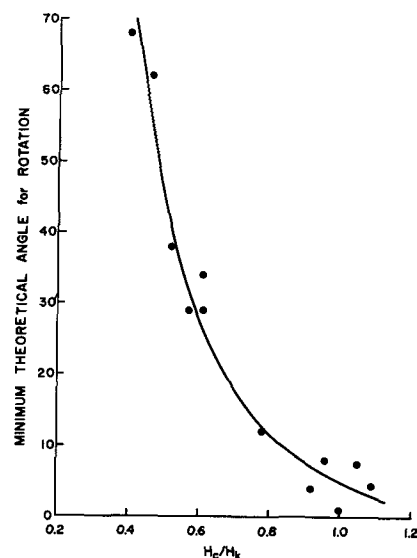


Fig. 3. Theoretical minimum angle of applied field for rotational switching as a function of the H_c/H_k ratio.

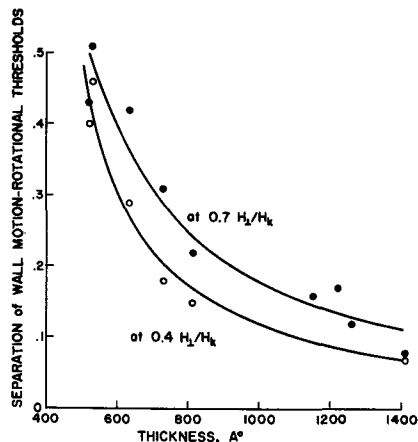


Fig. 4. Separation between rotational and wall motion thresholds at a fixed bias field.

The separation between the wall motion and rotational thresholds (Δh_{11}) at a fixed d-c bias field appears to be primarily dependent on the thickness of the film. There does not appear to be any direct correlation of wall motion and rotational threshold separation with maximum dispersion or H_c/H_k ratio. A plot of wall motion and rotation threshold separation (Δh_{11}) vs. thickness is shown in Fig. 4 at d-c bias fields of $0.4 H_{\perp}/H_k$ and at $0.7 H_{\perp}/H_k$. These results show that the maximum separation occurs as the thickness is decreased over the range of thickness measured (500-1400Å). The effect of thickness on the separation (Δh_{11}) may be associated with the type of wall formation. The wall motion threshold may decrease with increasing thickness due to a change from Neel to Cross-Tie to Bloch wall formation. Thus a Bloch wall would have a lower wall motion threshold than a Neel wall.

Conclusions

Electrodeposited films show a partial rotational switching behavior similar to that reported for vacuum deposited films as evidenced by (i) a circular flux path, and (ii) rotational thresholds. The H_c/H_k ratio determines the minimum angle between the easy axis and the applied field for coherent rotational switching. Increasing dispersion at a fixed H_c/H_k ratio reduces the wall motion threshold. The wall motion and rotational threshold separation is primarily dependent on thickness. Magnetization path and threshold measurements clearly show that two mechanisms of switching occur during flux reversal, a rotational switch followed by a wall motion switch as the magnetization moves through the hard direction.

Acknowledgment

The authors would like to express appreciation to Thomas S. Crowther for helpful comments on this manuscript.

Manuscript received May 13, 1963. This paper was presented at the Pittsburgh Meeting, April 15-18, 1963.

Any discussion of this paper will appear in a Discussion Section to be published in the December 1964 JOURNAL.

REFERENCES

1. I. W. Wolf, *This Journal*, **108**, 959 (1961).
2. R. D. Fisher and H. E. Haber, *Letters J. Appl. Phys.*, Vol. 2, No. 1, p. 11 (1963).
3. E. C. Stoner and E. P. Wohlfarth, *Phil. Trans. Roy. Soc. (London)*, **A240**, 599 (1948).
4. T. S. Crowther, Lincoln Lab Report 51-2, February 1959.
5. S. Methfessel, S. Middelhoek, and H. Thomas, *J. Appl. Phys.*, **32**, 1959 (1961).
6. S. Middelhoek, *I.B.M. Journal*, p. 394 (October 1962).

Chemical Deposition of Thin Films of Lead Selenide

Ralph A. Zingaro and Dean O. Skovlin

Department of Chemistry, Agricultural and Mechanical College of Texas, College Station, Texas

ABSTRACT

A method has been developed which yields chemically deposited thin films of lead selenide on a glass surface. These are uniform in appearance and electrical resistance [$1-4 \text{ meg}/(0.635 \text{ cm})^2$]. The coating solution is made up of a lead citrate complex and dimethylselenourea with sodium sulfite present as an antioxidant. All of the parameters involved in the coating process were studied, including the pretreatment of the glass surface, and the optimum conditions for the coating reaction are described.

The method of preparing thin films of lead chalcogenides by homogeneous precipitation from solution has received relatively little attention. The method is of considerable interest because it readily lends itself to large-scale production techniques.

The chemical deposition of lead sulfide films was described by Hauser (1) in 1910. This method involves the reaction of dilute solutions of thiourea with lead acetate. Almost all subsequent investigations dealing with the chemical deposition of lead sulfide essentially have employed modifications of Hauser's method. The principle variations have in-

volved changes in the concentrations of the lead acetate and thiourea solutions used, the temperature of deposition, and the use of surface seeding nuclei as a means of improving the properties of the films. An exception to the lead acetate-thiourea reaction is the method described by Wilman (2). In this case hydrogen sulfide is passed over an acidic solution of lead acetate and a floating film of lead sulfide is formed.

Pick (3) has discussed the factors which influence film formation in homogeneous precipitation reactions. These include the rate of diffusion of colloidal particles to the glass surface and the influence of

crystallization nuclei which can be formed by the addition of metal ions whose sulfides are extremely insoluble such as silver, mercury, platinum, and gold. The mechanism of precipitation of lead sulfide out of alkaline lead-thiourea solutions in terms of a thiourea-lead hydroxide complex has been discussed by Kicinski (4).

The chemical deposition of thin films of lead selenide has been only scantily investigated. This has been due, in large part, to the instability of the organic selenium bearing compounds which have been used as precipitants.

Wilman (2) has described the formation of a thin mirror of lead selenide on the surface of lead acetate solutions acidified with acetic acid over which hydrogen selenide was passed. The surface mirror of lead selenide was carefully floated on the surface of a nickel gauze, washed, and dried *in vacuo*.

A method described by Milner and Watts (5) involves the reaction of lead acetate with selenourea in aqueous solution. Prior to carrying out this reaction, a very thin film of lead sulfide is deposited on the surface to be coated. This fine deposit furnishes the nuclei which act as a seeding layer for the growth of microcrystalline lead selenide. The lead sulfide layer is prepared by immersion, for a short time, of the surface to be coated in a bath of lead acetate and thiourea which is made increasingly alkaline. After removal of this solution, lead selenide is then deposited on the seeded surface by the reaction of a solution of selenourea and lead acetate. The reaction is very slow and about an hour is required for the deposition of a sufficiently thick layer of lead selenide. These investigators give no information regarding the conditions of the reaction, the stability of the selenourea solution, or the concentration of reagents used.

The present work describes a method which utilizes dimethylselenourea (DMS) as the precipitant and utilizes citrate ion to control the lead ion concentration. Details on various phases of the homogeneous precipitation of lead selenide are described, and lead selenide mirrors of reproducible physical and electrical properties can be formed easily.

Experimental

Selection of reagents.—Selenourea is difficult to prepare and quite unstable. Therefore, its derivative, N,N-dimethylselenourea was used. Its preparation is easily accomplished (6). On exposure to air and light DMS deposits red, colloidal selenium. Storage in a dry nitrogen atmosphere in a light-tight container inhibits such decomposition indefinitely.

Stabilization of aqueous DMS solutions.—In order to inhibit the decomposition of DMS from its aqueous solutions, a variety of antioxidants were investigated. These included ascorbic acid, sodium sulfite, sodium thiosulfate, hydroquinone, formaldehyde, and displacement of dissolved oxygen by saturation of the solution with nitrogen gas. First evidence of selenium deposition from 0.1M aqueous solutions of DMS in the absence of any inhibitors was observed after 3 min. Formaldehyde actually appears to catalyze the oxidation; selenium decomposition in such solution was observed to occur less than 30 sec after

mixing. Some of the other antioxidants extended the inhibition period by 2 to 17 min. Maximum inhibition was observed with ascorbic acid and sodium sulfite; the first evidence of selenium decomposition using these reagents at 0.1M concentration was in excess of 72 hr. Sodium sulfite was the antioxidant selected because in subsequent evaluation it was found to yield mirrors of a much more homogeneous quality.

Complexing of the lead ion.—Because of the ready precipitation of lead hydroxide, especially at higher pH's, studies of the reaction in alkaline solution could be carried out only in a medium in which the lead ion concentration was reduced to a level so low that the solubility product for lead hydroxide was not exceeded. As a result, various complexing ions, such as oxalate, tartrate, and citrate, were investigated as complexing agents. Of these, only citrate was found to be effective; the other two formed precipitates insoluble in an excess of the ions.

The use of excess citrate reduces the concentration of lead ion and permits an increase in pH with still further reduction in the free lead ion concentration. This will be discussed subsequently.

Effect of pH on mirror formation.—Lead-citrate solutions were prepared from 5.0 ml lead nitrate (0.1M) and 2.5 ml sodium citrate (0.8M). Ammonium hydroxide (7.5M) was added stepwise, and the pH of the solution was measured at each step with a model H-2 Beckman pH meter.

To determine the optimum pH for the deposition of lead selenide mirrors, various lead-citrate solutions containing varying amounts of ammonium hydroxide were prepared as described and tested. In each case, 5.0 ml of DMS (0.1M), containing sodium sulfite (0.01M) as the antioxidant, was added to the ammoniacal lead-citrate solution and the speed of the reaction and nature of the lead selenide mirror formed were noted.

The best films were produced from solutions having a pH of 9.8. Smooth, even mirrors were deposited after 30 min of reaction. The reaction in the solution having a pH of 9.5 was too slow; a thin, uneven film was produced after 1 hr of reaction. Gross precipitation occurred in the solution of pH 10.1, with the formation of a thin, uneven mirror. A pH of 9.8 was selected and used in all further experiments.

Effect of aging on the stability of DMS-sulfite solutions.—It was observed, when using sodium sulfite as the antioxidant, that the deposition reaction did not always proceed at the same rate. Not only did the pre-mirroring time vary but also the amount of mirror deposition. This effect was found to be due to the time elapsed between the preparation and use of the DMS-sulfite solutions. Freshly prepared solutions gave a very slow reaction, whereas older solutions reacted more rapidly.

A study of the effect of aging on the speed of the reaction was made by following the light transmission of the lead selenide suspension using a Cenco-Sheard-Sanford Photometer, Type B2. The deposition reaction was studied using various samples of the DMS-sulfite solutions of the same concentration, but for which different intervals of time have elapsed between the time of preparation and the

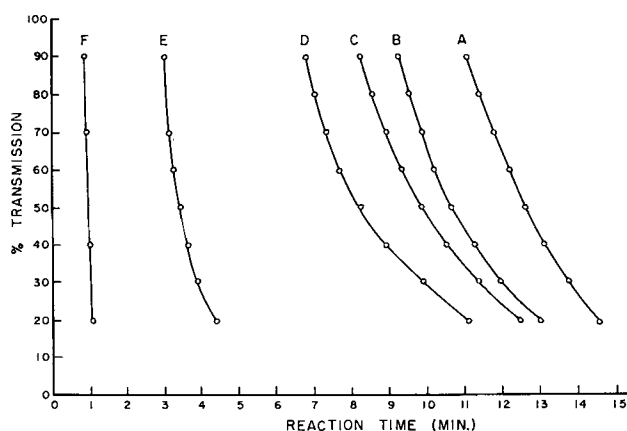


Fig. 1. Effect of aging of the DMS-sulfite solution on the rate of precipitation of lead selenide. Pre-reaction aging time: A, 6 min; B, 1 hr; C, 2 hr; D, 4 hr; E, 6 hr; F, 21 hr.

reaction with lead-citrate solution. The transmission of white light by the solution was observed as a function of total reaction time. The photometer was opened to its maximum slit width and no filter was used. The time plotted as the abscissa in Fig. 1 is that required for the needle to move from the position of extreme deflection to the per cent transmission noted. It can be seen that the effect of aging of the DMS-sulfite solutions on the rate of formation of lead selenide is critical. Readings below 40% transmission are of limited value because of the formation of a thin reflecting film of lead selenide on the reaction tube surface.

In Fig. 2 the reaction time of the homogeneous precipitation is plotted *vs.* the aging time of the DMS-sulfite solution. In this case, the time required for the solution to reach 90% transmission was chosen as a standard so that mirror formation would not interfere. This plot shows that, for DMS-sulfite solutions more than 10 hr old, aging is only of secondary importance.

Conditions for reproducibility of PbSe deposition.

—One of the basic objectives of this investigation was to establish a reproducible set of conditions for

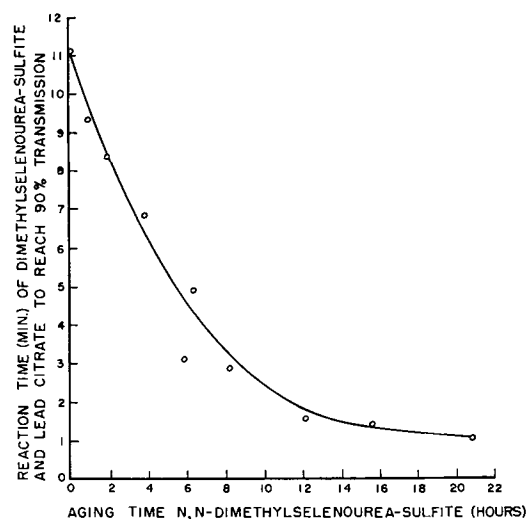


Fig. 2. Effect of aging of the DMS-sulfite solution on the rate of lead selenide precipitation; the ordinate is the time required for a lead citrate-DMS, sulfite mixture to reduce a beam of light of equal intensity to 90 per cent of its initial intensity.

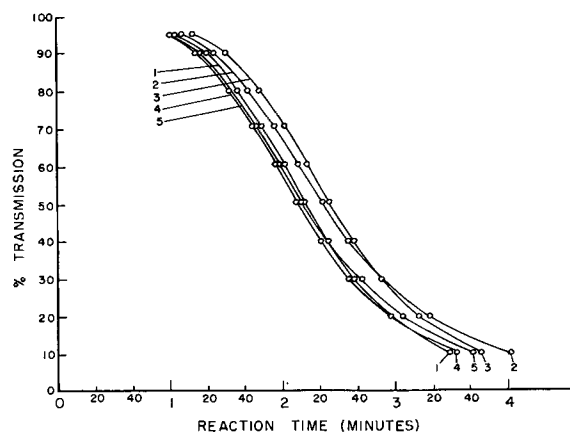


Fig. 3. Reproducibility of homogeneous lead selenide precipitation. Ideally, the five curves would be entirely superimposed. Solution aging time, 1 hr.

the preparation of lead selenide mirrors. One of the parameters studied was the reproducibility of the pre-mirroring reaction. This was evaluated by studying photometrically the reaction time for a number of solutions having what was considered to be optimum composition. The solutions were made up as follows: lead solution: 2.5 ml sodium citrate (0.4M), 5.0 ml lead nitrate (0.1M), 0.4 ml ammonium hydroxide (7.5M); DMS solution: 5.0 ml DMS (0.1M) in sodium sulfite (0.01M, 0.0755 g); aging time, 5.0 min.

Solutions were prepared in a constant temperature bath (25°C) and remained in the bath until placed in the photometer. A red filter was used, and the photometer was adjusted to 100% transmission with the lead-citrate solution after which the DMS-sulfite was added and the stop watch energized. The data as plotted in Fig. 3 show that a highly reproducible pre-mirroring reaction can be achieved. In view of the fact that all samples were probably not heated uniformly and the many other variables that could be introduced, the reproducibility achieved is excellent.

Study of film resistance as a function of DMS-sulfite aging.—Solutions at optimum coating composition (see previous section) were brought to constant temperature (25°C), a glass slide (treated as described subsequently) was placed in the lead solution, and the DMS-sulfite solution was added. The test tube was gently swirled to insure complete mixing of the solution and then placed in the 25° bath. The reaction was permitted to proceed for 30.0 min. After this time the solution was removed from the constant temperature bath, poured out, and the test tube containing the glass slide rinsed with distilled water. The slide was then rinsed separately and dried in 110° oven for 10 min. The resistances were measured after the preparation of electrode surfaces as described in the next section.

Preparation of electrodes.—While being coated with lead selenide, the slide rested in the coating bath at an angle of approximately 60° (cylindrical flat-bottomed vessels of proper diameter should be used as coating containers so that the slide can rest at approximately this angle). Thus, the surface of the slide facing the bottom of the tube could be

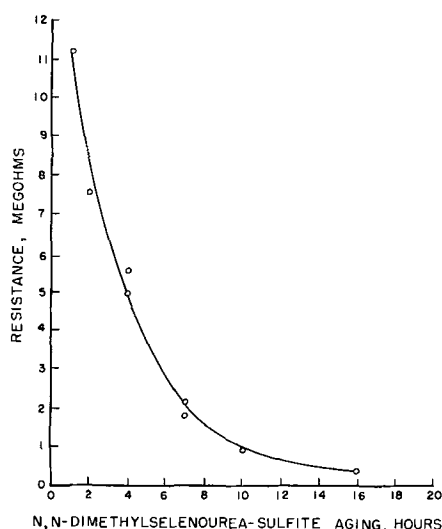


Fig. 4. Resistivity of chemically deposited lead selenide films on glass as a function of the aging time of the DMS-sulfite solution.

coated by adsorption of lead selenide particles while the upper side could be coated by sedimentation as well. The film on the under side of the slide was used for resistance measurements. This side was easily distinguished for it possessed a very bright, even, reflecting surface while the upper side was dull and sooty in appearance.

The lead selenide on the backside of the slide was removed by rubbing with a cotton swab moistened in 10% nitric acid, and the film along the edges was removed by rubbing with emery cloth. Aquadag electrodes were then painted at the edges of the lead selenide surface while masking the center portion with smooth paper strip exactly 0.635 cm in width. The resistance of films prepared in the manner described in the section immediately preceding, but in which DMS-sulfite solutions had aged from 2-16 hr is shown in Fig. 4. The shape of this curve closely resembles that of Fig. 2. Again it is shown that after 10 hr the age of the DMS-sulfite is no longer a critical factor.

Pretreatment of the glass surface.—Pick (3) observed that the condition of the glass surface profoundly affected the quality of lead sulfide mirror deposition. Seeding nuclei play a very important role in determining both the type and amount of mirror deposited.

As a means of obtaining a more uniform and reproducible deposition, three methods of introducing seeding nuclei on the glass surface were used: bathing the slide in a colloidal solution, introduction of a cation which forms an insoluble selenide in the reaction medium, and precoating the glass surface with a very light film of lead selenide.

Prior to mirroring, the slides were placed in colloidal solutions of silver iodide (7), gold (8), and lead sulfide (9) for 10 min. The slides were then transferred directly to the lead-citrate solution. Mirrors were then obtained in exactly the same manner as described using DMS-sulfite solutions that were aged for 1.0 hr in all cases. This type of pretreatment in silver iodide and lead sulfide sols adversely affected the quality of the mirror deposit. In all cases

very thin and uneven mirrors were formed. Pre-immersion in the colloidal gold suspension produced an extremely uniform film, but it was very thin.

Lead-citrate solutions were prepared that were $10^{-4}M$ in silver or copper(II) ion concentration. Mirrors were then prepared in exactly the same way as above, using DMS-sulfite solutions aged for 1.0 hr. After 30.0 min, the mirror prepared in presence of the silver ion had peeled completely. After 66.0 min, the mirror prepared in the presence of Cu(II) ion was very thin, uneven, and spotty.

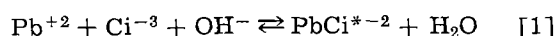
Mirrors formed in the presence of 10^{-5} and $10^{-6}M$ silver ion did not peel after a 30.0-min deposition and were very even. Resistances of the films prepared from lead solutions containing 10^{-5} and $10^{-6}M$ silver ion had resistances of 11 and 21 megohms, respectively. A film formed under like conditions but with silver ion absent had a resistance of 37 megohms.

Glass slides were placed in the 7.9 ml standard lead citrate solution and 5.0 ml DMS-sulfite (aging time, 5.0 min) was then added. The reaction was allowed to proceed at 25° for 7.0 min. The reaction was stopped by pouring off the solution and rinsing the test tube containing the slide with distilled water. The slide, after rinsing, was coated with a very light film of lead selenide. The lightly coated slide was then placed in another standard lead citrate solution and 5.0 ml of a second DMS-sulfite solution (aging time, 16.0 hr) was then added. After 30.0 min at 25° the reaction was stopped. The slide was rinsed and dried at 110° for 10 min. The slides were prepared for resistance measurements as described previously. Resistances obtained on sixteen slides prepared in this manner were as follows: 3.0, 4.0, 1.8*, 0.7*, 1.1, 2.0, 2.2, 1.9, 2.8, 3.2, 2.0*, 1.4*, 2.2, 4.0, 3.8, and 3.7 meg/(0.635 cm)², where the figures marked with an asterisk indicate that the lead selenide film had peeled. This method produced slides with considerable less variation in resistance and of greater uniformity and adhesion than with any other set of conditions investigated.

It was noted, when precoated slides were used, that lead selenide particles started to grow at the under surface of the slide almost immediately after the coating solutions were mixed. The attraction of colloidal lead selenide for the treated surface was such that the coating on the slide appeared opaque before any mirroring took place on the untreated walls of the container.

Discussion

The rate of homogeneous precipitation of lead selenide in the system just described will be determined largely by the lead ion concentration. The lead ion concentration will, at the pH employed in the reaction, be governed by the following equilibrium (10)

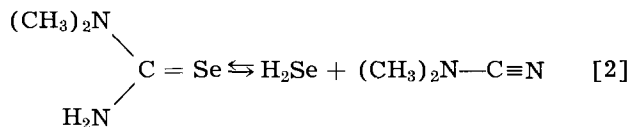


where the Ci^* is the completely ionized tetravalent citrate ion. The use of sodium plumbite, whose formation requires a very large excess of hydroxyl ion, was found to be quite undesirable since it leads to a gross, bulk, precipitation of lead selenide. This

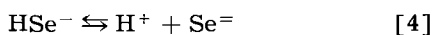
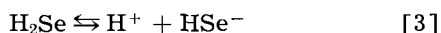
may be due also to the instability of DMS in highly alkaline solutions.

The most probable mechanism by which DMS oxidizes is the following:

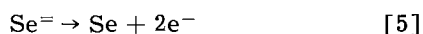
1. Equilibrium with hydrogen selenide



2. Ionization of H_2Se

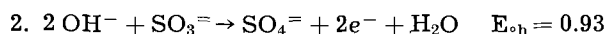
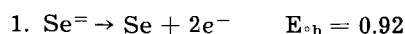


3. Oxidation of selenide ion



This mechanism gains support from the following observations:

First, a solution of DMS and lead ion (pH 6) alone will produce lead selenide only very slowly (of the order of several days). If ammonium hydroxide is introduced, the rapid formation of lead selenide takes place. The concentration of selenide ion will be increased as the pH is increased due to the shift of the equilibrium described in Eq. [3] and [4] to the right. The formation of colloidal selenium [5] is inhibited by the presence of a reducing agent (sodium sulfite or ascorbic acid). A consideration of the following oxidation potentials (11) explains this inhibitory action:



At unit activity sulfite ion is only a very slightly better reducing agent than selenide ion in alkaline solution. However, in the solutions used in this investigation, the concentration of selenide ion is very small compared to the sulfite ion concentration and this would favor oxidation of the sulfite in preference to the selenide. Also, it should be noted that metallic selenium can react with sodium sulfite to form sodium selenosulfate, Na_2SeSO_3 (12). This was demonstrated by the reaction of 0.1g sodium sulfite with 25 ml of a DMS (0.1M) solution that had undergone considerable decomposition. Within 5 min the red, colloidal selenium had disappeared and a colorless solution was formed. Hence, sulfite may not only function as an oxidizing inhibitor, itself forming sulfate, but can also react with the selenium that may be initially present to form selenosulfate ion and thus prevent the deposition of red, colloidal selenium. It is assumed that ascorbic acid functions only to prevent the oxidation of the selenide ion for it will not remove colloidal selenium from decomposed DMS.

If the formation of lead selenide is ionic in nature, the rate of this reaction will be proportional to the concentrations of the lead and selenide ions. These concentrations must be maintained at very low values, since the solubility product of lead selenide is 10^{-38} (13).

Let us now consider the mechanism by which the antioxidants inhibit the formation of lead selenide. The reaction between alkaline lead citrate and DMS was much more rapid in the absence of a reducing agent. Assuming that the reaction involves the combination of the ions, the question arises as to how sulfite ion could reduce the selenide or lead ion concentrations. The lead ion concentration would be reduced if undissociated molecules of lead sulfite were formed in solution. The formation of a lead sulfite complex is not probable (14). An alternative could involve the formation of a complex between sulfite ion and DMS. This would reduce the selenide ion concentration by complexing the DMS thus inhibiting both the decomposition and the deposition reactions. The variation in behavior of DMS-sulfite solutions as a result of aging is most probably due to the reduction in sulfite concentration as it is oxidized to sulfate. To illustrate this, 0.006g of solid sodium sulfite was added to an aged solution of DMS-sulfite (16 hr). The resulting reaction with lead ion was the same as that observed for a fresh DMS-sulfite solution, the inhibitory effect being completely restored.

The ability of seeding nuclei to enhance the formation of colloidal gold has been discussed by Weiser (15). Pick (3) has described the use of seeding nuclei in the deposition of lead sulfide films and proposes the following mechanism to explain their effect.

First, seeding nuclei are adsorbed on the surface on which the lead sulfide is to be deposited. These nuclei then serve as the base to which lead sulfide particles are attracted and become more adherent to the surface. Pick points out that the seeding effect is greatest when the seeding nuclei and the material to be deposited is isomorphous.

In the deposition of lead selenide it was found that precoating the glass slides with colloidal solutions of gold, lead iodide, or lead sulfide did not improve mirror formation and actually produced mirrors of poorer quality. Apparently the solutions containing these sols interfered with the lead selenide deposition probably by producing an undesirable surface condition on the glass. In contrast, the presence of silver ion in the deposition reaction resulted in a more rapid mirror deposition. In this case the formation of silver selenide did improve the quality of the mirror.

The most desirable rate of deposition and the best reproducibility in resistance as well as maximum uniformity and homogeneity in mirror quality were obtained when the slides were precoated with colloidal lead selenide. This treatment apparently furnished a bed of nuclei which attracted and held lead selenide particles to the surface during the actual deposition reaction.

Manuscript received May 7, 1963.

Any discussion of this paper will appear in a Discussion Section to be published in the December 1964 JOURNAL.

REFERENCES

1. O. Hauser and E. Biesalski, *Chem.-Ztg.*, **34**, 1079 (1910).
2. H. Wilman, *Proc. Phys. Soc.*, **60**, 117 (1948).
3. H. Pick, *Z. Physik*, **126**, 12 (1949).

4. F. Kicinski, *Chem. & Ind.*, **1948**, 54.
5. C. J. Milner and B. N. Watts, *Nature*, **163**, 322 (1949).
6. R. A. Zingaro, F. C. Bennett, Jr., and G. W. Hammar, *J. Org. Chem.*, **18**, 292 (1953).
7. H. B. Weiser, "Inorganic Colloid Chemistry," Vol. 3, p. 113, John Wiley & Sons, Inc., New York (1938).
8. H. B. Weiser, *ibid.*, Vol. I, p. 32 (1933).
9. J. Brooks, *J. Phys. Chem.*, **32**, 1717 (1928).
10. M. Bobtelsky and B. Graus, *J. Am. Chem. Soc.*, **75**, 4172 (1953).
11. W. M. Latimer, "Oxidation Potentials," p. 74, Prentice Hall Inc., New York, N. Y. (1952).
12. California Research Corp., Brit. 631,464, Nov. 3, (1949).
13. W. M. Latimer, "Oxidation Potentials," p. 155, Prentice Hall Inc., New York (1952).
14. N. V. Sidgwick, "Chemistry of the Elements and Their Compounds," Vol. I, p. 626, University Press, London (1951).
15. H. W. Weiser, "Inorganic Colloid Chemistry," Vol. I, p. 35, John Wiley & Sons, Inc., New York (1933).

Luminescent Behavior of the Rare Earths in Yttrium Oxide and Related Hosts

K. A. Wickersheim¹ and R. A. Lefever²

General Telephone and Electronics Laboratories, Inc., Palo Alto, California

ABSTRACT

The absorption, excitation, and fluorescence spectra of $\text{Y}_2\text{O}_3:\text{Eu}$ are presented and interpreted. The high luminescent efficiency of this material and its unusual performance at elevated temperatures are discussed. The comparative behavior of other rare earths in yttrium oxide and of the rare earths in certain other oxides of yttrium and lanthanum are also discussed briefly.

Increased interest in the rare earths as fluorescent ions has resulted from solid state laser studies. The sharpness of the rare earth emission lines and the long fluorescence life times are particularly attractive in this application. As a result of this specialized interest in rare earth luminescence for laser applications, optically perfect and physically hardy crystals of materials not previously employed as hosts for the rare earths are currently of considerable interest.

For several years we have pursued an exploratory program concerned with the growth and properties of single crystal metal oxides. Given the problem of designing an optimum laser material, we decided to ignore at the outset the constraint imposed by the current availability of crystals and to first select or design a material which met the more fundamental requirements. Thus we looked for oxides (either simple or complex) having desirable optical and mechanical properties, which would accept the trivalent rare earths without problems of ion size or charge. At the same time, we looked for hosts with rare earth sites of exceptionally low symmetry in the hope of increasing the probability of radiative transitions (within the 4f-electron shell) through destruction of parity forbiddenness. It was also hoped that hosts would be found where competing (e.g., nonradiative) relaxation processes would be minimized, although (except for selection of materials with low frequency lattice vibrations) we knew of no direct means of controlling this parameter. Of the oxides considered, compounds having the yttrium oxide structure appeared best to meet the majority of the specified requirements.³ We had

already completed preliminary studies on the growth (2) and optical properties (3) of this material and felt that it offered promising possibilities.

A fortuitous aspect of the resulting work with rare earths in yttrium oxide was the discovery of strong, broad absorption bands which could be utilized for excitation of certain of the ions. Although these bands occur in the ultraviolet, they are in some instances well located for efficient excitation by conventional ultraviolet sources.

General considerations.—The sharp-line emission and absorption spectra of the rare earth ions in solids have intrigued spectroscopists for years.⁴ Out of the detailed studies of these spectra has come a rather complete understanding of the f-electron energy levels of the majority of the trivalent rare earths, including, in many instances, their detailed dependence on crystalline environment. Somewhat less well understood are the rules governing intensities of transitions between f-electron levels. Still less well understood are the nature of the more highly excited states of these ions in solids, the nature of the various energy transfer mechanisms utilized in the excitation of fluorescence, and the details of processes involved in nonradiative relaxation.

In the free ion, electric dipole transitions between f-electron levels are strictly forbidden by parity considerations. However, such transitions (as well as occasional magnetic dipole transitions) are observed to occur weakly in solids. This is interpreted in terms of either static or dynamic breakdown of parity. Nonradiative processes, which compete with the radiative processes in determining fluorescent efficiency, depend on the frequency of available lattice vibrations and the effectiveness of their coup-

¹ Present address: Departments of Materials Science and Electrical Engineering, Stanford University, Stanford, California.

² Present address: Sandia Laboratory, Albuquerque, New Mexico.

³ For crystallographic data, see ref. (1).

⁴ The literature on this subject is extensive. For a general discussion, giving reference to the majority of the principal contributors to the field, see ref. (4), especially pp. 453-476.

ling with the rare earth electrons. Thus, site symmetry and the lattice vibration spectrum play inter-related roles in determining the intensities of emission and absorption in rare earth-containing compounds.

In addition to the better understood properties of the rare earths, certain empirical relationships have been noted. For example, a general decrease in fluorescent efficiency occurs as one proceeds away from the center of the rare earth sequence (5). Thus, assuming equivalent excitation, gadolinium (which emits in the ultraviolet) is the most intensely fluorescent ion, europium and terbium are the next brightest emitters, dysprosium and samarium are next, and so on. This effect is in part associated with the size of the energy gap to be bridged. As the size of the gap decreases, competing nonradiative processes increase in relative importance. In addition, there is some indication that coupling of the f-electrons to the crystal lattice increases as one proceeds outward in the sequence from gadolinium.

A large fraction of the early spectroscopic work was done on concentrated rare earth salts, which were normally hydrated and in which the rare earth ion frequently occupied a site of relatively high symmetry. Low fluorescence intensities were generally observed, probably as a result of a combination of factors, including high site symmetry, the presence of high frequency vibrations associated with the waters of hydration, and concentration quenching. The results of these early studies, leading to the opinion that rare earth fluorescence is relatively inefficient, have generally been accepted as applicable to all rare earth-containing systems. As a result of the assumption of low fluorescent efficiency combined with relatively high materials costs, the rare earths have heretofore been considered commercially only for special-purpose (luminescent) applications.

Experimental

A flame fusion process for the growth of single crystals of yttrium oxide and related materials has been presented elsewhere (2). Except for the introduction of the desired rare earth dopants, single crystals used in the present study were grown by the techniques already described. Single crystals were used for absorption measurements, for certain of the excitation and fluorescence measurements and for all of the laser experiments. The results of the laser studies are described elsewhere (6).

Many of the measurements (particularly of excitation and fluorescence) were made with powder samples. The powders were prepared either by flame sintering of mechanically mixed oxides or by coprecipitation of the constituents as oxalates followed by ignition to the oxide. For rapid surveying of various compositions, the use of powder samples was especially convenient.

For brevity and because of the qualitative nature of many of the observations, the experiments will not be described in detail. The basic instruments used, either singly or in combination, were a Cary Model 14 spectrophotometer, a Leiss double mono-

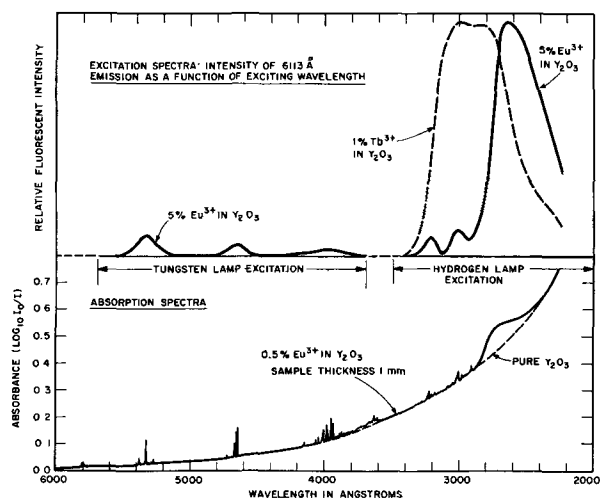


Fig. 1. Absorption and excitation spectra of $Y_2O_3:Eu$. For comparison, the absorption of pure Y_2O_3 and the main excitation peak of $Y_2O_3:Tb$ are also shown. No corrections were made in the absorption spectra for reflection losses, nor in the excitation spectra for spectral distribution of sources.

chrometer, and a Bausch and Lomb Dual Grating spectrograph, together with auxiliary excitation and detection systems. Our measurements have since been repeated more quantitatively by others, and their techniques, results and further discoveries will be reported separately.

Results and Discussion

Yttrium oxide.—The optical properties of yttrium oxide can be thought of as intrinsic, defect-induced and/or impurity-induced. We will consider here the visible and ultraviolet characteristics of yttrium oxide, the infrared properties having been discussed separately (3).

Yttrium oxide exhibits a band edge in the vicinity of 2000Å (see Fig. 1), the exact position of the edge being a function of sample purity. The crystal is essentially transparent from this edge well into the infrared. Increasing reflection losses, caused by the rapidly rising index of refraction as the band edge is approached, produce the apparent gradual decrease in sample transmission indicated in Fig. 1.

Even in the highest purity,⁵ yttrium oxide exhibits a bluish-white luminescence. This broad emission, present as a weak background in rare earth activated samples (see Fig. 2), appears to be defect-

⁵ For example, 99.999 + % pure yttrium oxide, Lindsay Code 1117.

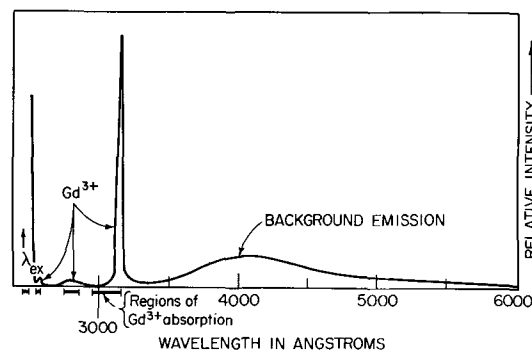


Fig. 2. Emission from $Y_2O_3:Gd$ (1%) with background emission also shown. Excitation at 2480Å. Principal Gd emission peak occurs at 3150Å. For optimum Gd concentration, the height of this peak is about twice that shown.

induced. The intensity of this emission can be enhanced by increasing the firing temperature (above that required for complete reaction) during the preparation of powder samples. Increasing the firing temperature would be expected to increase the number of defects (probably in the form of oxygen vacancies) in the final product. The observations of color center phenomena in single crystals of yttrium oxide at low temperatures give further evidence of a defect structure. At liquid nitrogen temperatures yttrium oxide crystals take on a bluish cast upon intense ultraviolet excitation. On warming the discolored crystals bleach and simultaneously thermoluminesce via the bluish-white emission described above and (in rare earth doped crystals) via rare earth luminescence as well.

Rare earths in yttrium oxide.—The rare earths introduce their own characteristic emission and absorption lines into the spectrum of yttrium oxide. These lines are for the most part sharp (see Fig. 1 and 2), falling into groups which can be identified by reference to earlier work on the corresponding rare earths in other compounds. These lines represent transitions between 4f-electron levels. In addition to the sharp lines, strong, broad absorption bands are observed in the ultraviolet for a few of the rare earths in yttrium oxide (for example, Eu^{3+} and Tb^{3+}) with occasional broad emission bands (notably for Ce^{3+} and Yb^{3+}) being observed as well.

The origin of the broad bands has not been well established. They may represent $4f \rightleftharpoons 5d$ transitions⁶ or charge transfer bands. For our purposes, the important point is that the total absorption in the broad bands is much greater than that in the sharp lines and the efficiency of excitation of fluorescence via the broad bands is correspondingly greater. For Gd^{3+} , traditionally the strongest fluorescer, no broad band is found (on the long wavelength side of the band edge of the crystal) and photoexcitation in this region has to be carried out via the sharp $f \rightarrow f$ absorptions. For Eu^{3+} and Tb^{3+} , broad excitation bands not only exist but are well placed (in yttrium oxide) relative to the ultraviolet emission of a mercury discharge (see Fig. 1). The efficiency of excitation of $Y_2O_3:Eu$ by the 2537Å line from a low pressure mercury discharge is sufficiently great to arouse interest in this material for both lamp phosphor and laser applications.

Whereas the efficiency of photoexcitation depends critically on the existence and proper placement of excitation bands of a given rare earth (in yttrium oxide) relative to the frequency of the exciting radiation, excitation at energies above the band edge (e.g., by x-rays) is more uniformly effective in exciting rare earth fluorescence. Under x-ray excitation, Eu^{3+} and Tb^{3+} are again the brightest visible (red and green, respectively) emitters, but the other rare earths are also strongly excited in contrast with

⁶ This is the interpretation given, for example, by Feoflov (7) for the broad ultraviolet absorption band found for Yb^{3+} in CaF_2 . This interpretation requires that the 5d levels of the rare earths be drastically depressed in the solid state relative to free ion values. This may result from mixing of the d-orbitals with p-orbitals of the neighboring oxygen ions. If such mixing is involved, the broad absorption bands would be more correctly thought of as a cross between interconfigurational transitions and charge transfer bands. In any event, the transitions should not be parity forbidden and should, therefore, be considerably more intense than the $f \rightarrow f$ transitions (as observed).

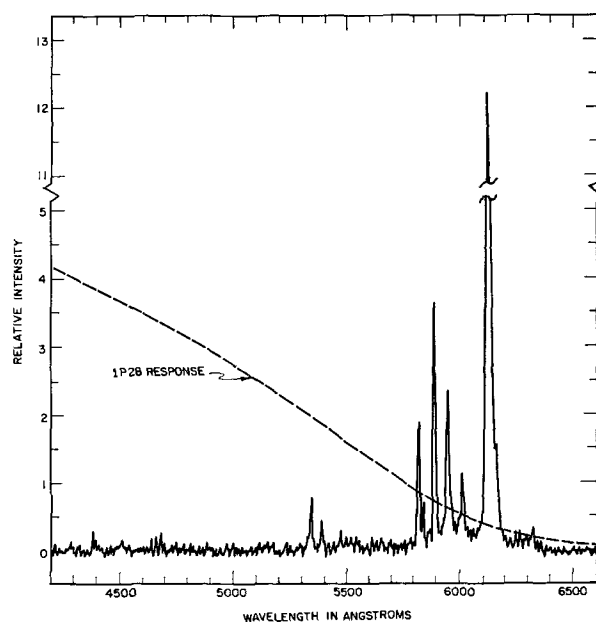


Fig. 3. $Y_2O_3:Eu$ (5%) emission spectrum. Not shown are lines of moderate strength just beyond 7000Å, see ref. (6). Peak intensities should be corrected for the response of the 1P28 photomultiplier (dashed curve).

their relatively poor performance under mercury excitation.

$Y_2O_3:Eu$.—Europium is the most effective of the trivalent rare earths as an yttrium oxide activator. As shown in Fig. 3, the emission is concentrated for the most part in one line at 6113Å.

Certain of the emission characteristics of $Y_2O_3:Eu$ are peculiar to the europium ion itself, although the striking fluorescence efficiency of this compound relative to other europium-activated materials indicates that the environment of the ion is important as well. Figure 4 shows the energy level scheme

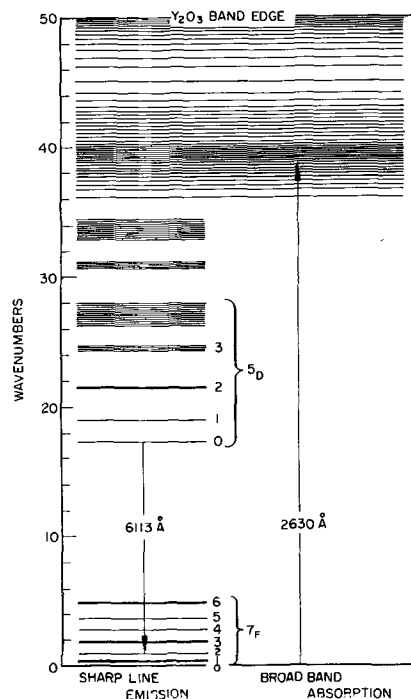


Fig. 4. Energy level diagram for $Y_2O_3:Eu$, showing sharp (Eu^{3+} f-electron) levels and broad bands. Principal excitation and emission wavelengths are indicated.

(minus detailed crystal field splittings) for $Y_2O_3:Eu$. It should be noted that the ground state and the principal metastable state are both $J=0$ levels, not easily perturbed by changes in the crystal field. Neither state has a magnetic moment so that magnetic interactions between an excited europium ion and nearby ground state ions are negligible. For these reasons neither thermal quenching nor concentration quenching of fluorescence is expected to be pronounced.

The principal emission from $Y_2O_3:Eu$, regardless of means of excitation, is a transition from the 5D_0 state to one of the 7F_2 levels. In the majority of Eu^{3+} -containing compounds, the strongest transitions occur either in the $^5D_0 \rightarrow ^7F_1$ group or in the $^5D_0 \rightarrow ^7F_2$ group, with some instances where lines from both groups appear with nearly equal strength. Transitions to other 7F levels and from other 5D levels are observed but with much lower intensity (see Fig. 3). Excitation of the Eu^{3+} fluorescence can occur by absorption to one of the excited f-levels (above 5D_0), by excitation in the 2630Å excitation band (discussed earlier) or by excitation at (or above) the band edge of the host. Population of the 5D_0 state occurs by cascading (through various f-electron states) largely by means of nonradiative processes. A confirmation of this picture is provided by the behavior of the fluorescence as the temperature is lowered. At liquid nitrogen temperatures bottlenecks develop between adjacent 5D levels. Fluorescence from 5D_1 and 5D_2 levels becomes correspondingly stronger while the $^5D_0 \rightarrow ^7F_2$ lines weaken perceptibly.

At room temperature, the lifetime of the 5D_0 state is approximately 900 μ sec. A weak phosphorescence having a much longer decay time (on the order of seconds) is also observed.

The fluorescent efficiency of $Y_2O_3:Eu$ remains high even at elevated temperatures. The fluorescent output (under high pressure mercury excitation) actually increases with temperature (see Fig. 5) up to 650°C and does not diminish again to the room temperature level until a temperature of 850°C is reached. The increase in fluorescence with temperature is caused in part by a pronounced shift of the

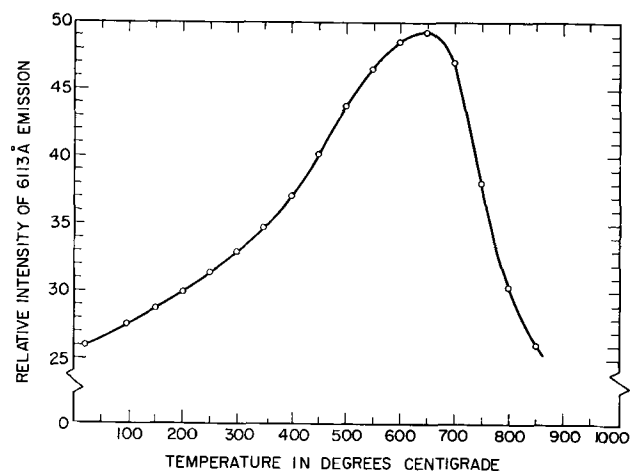


Fig. 5. Intensity of the 6113Å emission from $Y_2O_3:Eu$ (5%) under constant high pressure mercury excitation as a function of sample temperature.

principal excitation band of $Y_2O_3:Eu$ to longer wavelengths, the shift producing a better wavelength match with the high pressure mercury radiation. The point being made here is that pronounced quenching is only observed at unusually high temperature.

As expected on the basis of the introductory considerations, the optimum europium concentration is high, in excess of 5 mole % (regardless of means of excitation) with strong luminescence observed for concentrations as high as 20 mole %.

Although purity does not generally seem to be a problem, certain rare earths are known to be capable of quenching the europium fluorescence (8). In the present studies, dysprosium (present in lower purity grades of yttrium oxide) was particularly effective in reducing the fluorescent intensity. For this reason, we have generally worked with relatively high purity yttrium oxide.

The rare earth-yttrium oxide phosphors are chemically stable and can be heated to fusion without producing a noticeable change in performance. In fact, many of the earliest samples were prepared from crystals grown by flame fusion.

Europium in other oxide hosts.—A number of trivalent oxides are isostructural with yttrium oxide. These include Mn_2O_3 , In_2O_3 , Sc_2O_3 , and the majority of the rare earth oxides at room temperature. Of these compounds, only In_2O_3 , Sc_2O_3 , and Gd_2O_3 exhibit the characteristic europium fluorescence when doped with europium, and of these materials only $Gd_2O_3:Eu$ is comparable with $Y_2O_3:Eu$ in brightness. Measurements made by the Sylvania Laboratories have shown that $Gd_2O_3:Eu$ (in the cubic phase) is actually superior to $Y_2O_3:Eu$ under low pressure mercury excitation.

We examined a number of simple (divalent and trivalent) metal oxides as hosts for europium, but found none which were equal to $Y_2O_3:Eu$ and $Gd_2O_3:Eu$ in luminescence efficiency under low pressure mercury vapor excitation. However, $La_2O_3:Eu$, which has the A-type hexagonal rare earth oxide structure (9), is superior under high pressure mercury excitation. (This compound is stable in an inert atmosphere, but hydrolyses rapidly in air, losing its luminescence in the process.) $La_2O_3:Eu$ does not exhibit the outstanding high temperature performance of $Y_2O_3:Eu$.

A variety of mixed oxides of the trivalent metals were examined as hosts. Several compounds were formed which exhibited color and performance similar to $Y_2O_3:Eu$ and $Gd_2O_3:Eu$, though brightness was not as great.

In the general survey of hosts, characteristic differences in the performance of Eu^{3+} in yttrium and lanthanum compounds were noted. Yttrium compounds often showed good performance under low pressure mercury radiation and good performance at high temperatures. Lanthanum compounds generally performed better under high pressure mercury excitation and always showed poor performance at high temperatures. The same differences had already been noted for the simple oxides activated with europium.

The similarities in luminescent performance (despite effects produced by structural differences) that we observed among the various lanthanum compounds as contrasted with the behavior of the various yttrium compounds suggest that site size and details of bonding may be as important as site symmetry in determining the character of rare earth luminescence. Van Uitert, Linares, Soden, and Ballman (10) have suggested that the mixing of f-electron and valence electron wave functions and the subsequent overlap of these wave functions with the p-orbitals of neighboring oxygens could play an important role in the quenching of rare earth fluorescence in the oxides. Although this point was made with specific reference to concentration quenching, the same mechanism could (depending on the degree of oxygen overlap) generally control the relative importance of all nonradiative relaxation processes. Thus, the characteristic difference in the thermal quenching behavior of europium luminescence in lanthanum and yttrium compounds might reflect characteristic variations in such a mechanism.

Excitation characteristics are likely to be even more dependent on details of bonding. If, for example, the principal excitation bands of europium (and certain other rare earths) are charge transfer bands or excitations to mixed d-electron ligand orbital states, the frequencies of these bands will certainly depend on proximity and arrangement of oxygen neighbors. Thus, europium in yttrium compounds might characteristically have its excitation bands at higher energies (shorter wavelengths) than in lanthanum compounds.

Concluding Remarks

We have used $Y_2O_3:Eu$ and $Gd_2O_3:Eu$ as examples of a new class of potential phosphor materials. Actually, the behavior of these europium-activated compounds is not typical of the entire class. Of the remaining rare earth activators, only terbium shows much chance of being sufficiently efficient to be useful in (visible) photoluminescent applications. $Y_2O_3:Gd$ should be a very efficient phosphor but its emission is at short wavelengths ($\approx 3150\text{\AA}$) and, because of the absence of strong excitation bands, performance is not expected to be good under mercury excitation. Cerium and ytterbium have some possibilities as ultraviolet emitters (via broad band transitions), but their performance in Y_2O_3 has not been investigated in detail. Clearly, many (perhaps most) of the rare earths have potential as laser activators in yttrium oxide.

While much has been made of the brightness of $Y_2O_3:Eu$, little mention has been made, except with respect to laser performance, of the sharp line character of the emission. Advantages and disadvantages of this feature of the europium (and other rare earth) emission suggest themselves and any practical phosphor application will have to take into account the monochromaticity of the emission.

We should remark that Van Uitert *et al.* (10) have also reported extensive studies of rare earth fluorescence in the garnets and orthoaluminates. Likewise Rosenberger (11) has examined the fluorescence of erbium in yttrium oxide and lanthanum oxide using crystals grown by flame fusion.

Acknowledgments

We wish to acknowledge the help of many people: N. C. Chang, who in the course of laser studies took many of the excitation and emission spectra; K. H. Butler of the Sylvania Lighting Division Laboratories, who provided encouragement and advice during early stages of the investigation and who has since, with R. W. Mooney of Sylvania's Chemical and Metallurgical Division, undertaken more detailed and quantitative studies of the materials described herein; R. L. White, for support and for many helpful discussions; L. E. Sobon and F. A. Rogers, for assistance with sample preparation; and W. F. Marshall and W. H. Semorile, for technical assistance.

REFERENCES

1. L. Pauling, *Z. Krist.*, **75**, 128 (1930).
2. R. A. Lefever and G. W. Clark, *Rev. Sci. Instruments*, **33**, 769 (1962); R. A. Lefever, *ibid.*, **33**, 1470 (1962).
3. K. A. Wickersheim and R. A. Lefever, *J. Optical Soc. Am.*, **51**, 1147 (1961).
4. D. S. McClure, "Solid State Physics," vol. 9, pp. 400-525, Academic Press, New York (1959).
5. G. H. Dieke and L. A. Hall, *J. Chem. Phys.*, **27**, 465 (1957).
6. N. C. Chang, K. A. Wickersheim, R. A. Lefever, and R. L. White, Post-deadline paper R-15 presented at the Meeting of the American Physical Society, Stanford, California, December 27, 1962. N. C. Chang, To be published.
7. P. O. Feofilov, *Opt. i Spekt.*, **5**, 216 (1958).
8. L. G. Van Uitert and S. Iida, *J. Chem. Phys.*, **37**, 986 (1962).
9. R. S. Roth and S. J. Schneider, *J. Research Nat. Bur. Standards*, **64A**, 311 (1960).
10. L. G. Van Uitert, R. C. Linares, R. R. Soden, and A. A. Ballman, *J. Chem. Phys.*, **36**, 702 (1962).
11. D. Rosenberger, *Z. Physik*, **167**, 349, 360 (1962).

Iron Activated ZnS Phosphors

P. M. Jaffe¹

Research Department, Lamp Division, Westinghouse Electric Corporation, Bloomfield, New Jersey

and E. Banks²

Department of Chemistry, Polytechnic Institute of Brooklyn, Brooklyn, New York

ABSTRACT

Iron can serve as an activator in ZnS phosphors, giving a 660 m μ -peaked red emission. Previous difficulties with the preparation of reproducible samples are overcome with the use of Cl, Br, I, Al, Ga, or In coactivators. The red emission is always accompanied by a 460 m μ blue emission attributed to Cu impurity and/or (more likely) to Zn vacancies. Detailed luminescence characteristics of ZnS:Fe,I phosphors under ultraviolet (u.v.) and EL excitation are presented. A model of the Fe center showing the transitions leading to luminescence and killing, which may occur in the same center, is given.

The killing effect of iron, cobalt, and nickel on the luminescence of ZnS phosphors is well known. Less known are their intensification effects (1-4). In several cases both killing and intensification are present simultaneously depending on the particular combination and concentration of activator [Cu, Au (2, 3) or Ag (4)] and killer. In addition to killer and intensifier action, there are also reports of iron (4-7), cobalt (4, 8), and nickel (4) acting as true activators, *i.e.*, originators of luminescence, having red and near and far infrared emission, respectively.

Because these phosphors have weak emissions and are difficult to reproduce no previous detailed study has been reported. In the case of ZnS:Fe phosphors, it has been found that the use of coactivators (Cl, Br, I, Al, Ga, or In) resulted in reproducible samples. This, coupled with the use of modern instruments, allows a study of the ZnS:Fe system to be made.

The Fe activated phosphors were studied under cathode-ray, u.v. (365 m μ) and a-c field (EL) excitation, but the cathodoluminescence will not be reported here since it was similar to the photoluminescence.

Phosphor Preparation

Phosphors were prepared from RCA ZnS(33Z19). Iron, Cu (when used to make EL phosphors) and halogens were added from stock solutions of the nitrate, sulfate, and ammonium salts, respectively. Al was added as a solution of NH₄Al(SO₄)₂, and Ga and In were added as the sesquisulfides.^{3,4} After addition of the appropriate amounts of the components, the raw mixes were slurried and dried at 110°C. The dried powders were remixed and placed in a loosely capped silica test tube which was then put into a larger silica firing tube having one end closed and a gas inlet and outlet at the other end.

¹ Present address: General Precision, Inc., Aerospace Research Center, Little Falls, New Jersey.

² Consultant, Research Department, Lamp Division, Westinghouse Electric Corp., Bloomfield, New Jersey.

³ Kindly supplied by A. Wachtel of these laboratories.

⁴ Iodine was the coactivator used in most of the experimental work since it resulted in the brightest samples. Experiments with the other coactivators were limited to checking brightness and emission color.

Prior to firing, 5 weight per cent (w/o) of purified sulfur⁵ was added to each sample. The sulfur aids in removing oxygen from the phosphor; this is more important with EL phosphors, but the addition was made to all samples for the sake of consistency. Similar results were obtained with and without the addition of sulfur. The samples were fired for 1 hr at 950°C in a flowing nitrogen atmosphere. After firing, the samples were treated with boiling deionized water to disintegrate the lightly sintered powder, rinsed with alcohol and dried at 110°C. The wash water from the I-coactivated phosphors was tested for iron and iodine, with negative results. The phosphors containing Cu were also washed in a NaCN-NaOH solution to remove free copper sulfides. All the phosphors prepared here were essentially cubic as indicated by their x-ray patterns.

Representative samples containing variable additions of Fe and iodine were analyzed for their residual Fe and iodine content as follows: The samples were dissolved in 4N HNO₃. Iron was determined in one portion by preparing the orthoferrous phenanthroline complex and comparing the colors photometrically against standards. No loss of any initially added Fe was found. It was found, however, that the finished phosphors contained an additional 1-5 ppm iron. Part of this came from the raw materials and part from the post-preparative handling. The additional Fe was confirmed by spectroscopic analysis. Since the exact amount of Fe present in the unfired samples was not known, and since the presence of the "impurity" Fe has little effect on the results and conclusions, all Fe concentrations will be reported as the amounts added to the raw mix. The iodine in another portion of the solution⁶ was found by adding silver nitrate, and determining the iodine concentration by turbidimetric comparison with standards, with an accuracy of $\pm 75\%$. Over the range of iodine concentration added to the phosphor

⁵ Obtained from the General Chemical Div., Allied Chemical and Dye Corp., New York, N. Y.

⁶ Tests showed that in this concentration range no iodine was lost during dissolution of the sample.

raw mix, the iodine content was approximately 0.013 atomic per cent (a/o) and is apparently independent of the amount added to the raw mix.

Experimental Results

Role of coactivator.—From the results of earlier workers it was known that luminescence due to iron could only be obtained with iron concentrations of about 0.001–0.01%⁷ (4, 5, 7, 9). In the present investigation, the preparation of ZnS samples containing 0.01Fe or 0.03Fe, 0.3Cu by firing in N₂ resulted in nonluminescent samples.⁸ Addition of a coactivator such as halide (Cl, Br, or I) or a trivalent cation such as Al, Ga, or In (at least to the ZnS:Fe,Cu phosphors) resulted in luminescence. (The samples with the trivalent cations were fired in H₂S to ensure sulfide formation.) The phosphors containing the cation coactivators had weak red plus blue luminescence for field or u.v. excitation. In addition, there was very weak emission due to the Ga and In.

One role of a coactivator is that of a charge compensator (10). With I coactivation, there could be two possible ways for compensation to occur if iron has a valence other than two. The iodine can be located interstitially if iron is 3+, which seems rather unlikely due to the large size of the I⁻ ion. Alternately, iron as Fe⁺ could be compensated by I⁻ located substitutionally for S²⁻. This latter possibility is very doubtful since Fe⁺ would be unstable. It is therefore believed that iodine is not present as a charge compensator for iron. However, Fe³⁺ could also be charge compensated by a monovalent cation such as Li, Na, or K according to scheme: Fe³⁺ + M⁺ replacing 2Zn²⁺. Samples were prepared containing 0.01Fe and 0.01M, where M was Li, Na, or K (added as the carbonate and fired in H₂S). These samples were nonluminescent under u.v. or cathode-ray excitation.

From these results it appears that a coactivator must be present for red emission to occur and that apparently Fe is divalent. Concurrently with the red emission there is always blue emission.

Photoluminescence

Reflectance spectra.—Reflectance spectra were taken with a Beckman Model DU spectrophotometer with diffuse reflectance and photomultiplier attachments. The standard technique for powder samples was used. For measurements below 400 mμ, a Corning No. 5840 filter was placed in front of the photomultiplier to eliminate emission from the sample.

Reflectance spectra were measured for a series of phosphors in which the iron additions were varied over the range of 0–1%. The absorption [= (100-% reflectance)] characteristics of this series are shown in Fig. 1. The absorption edge was around 340 mμ (3.65 ev) which agreed with the results reported in the literature (11). Increasing the iron additions resulted in an over-all increase in absorption plus the appearance of three new absorption bands. These

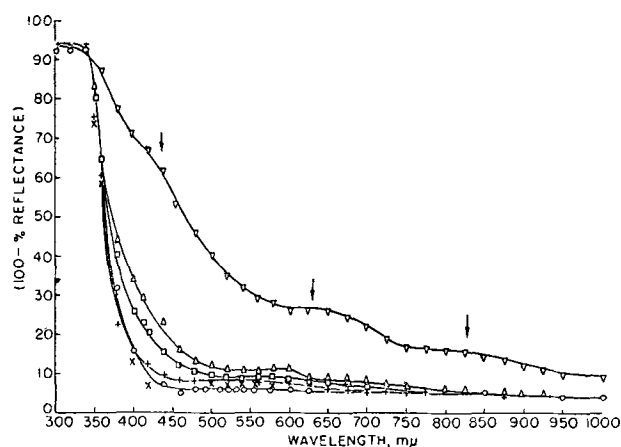


Fig. 1. Absorption spectra of ZnS:xFe, 1.0I as a function of the Fe concentration. x, 0 and 0.001 Fe; +, 0.05 Fe; o, 0.01 Fe; □, 0.05 Fe; Δ, 0.1 Fe; ▽, 1.0 Fe.

bands peaked around 425 mμ (2.9 ev), 600–650 mμ (2.1–1.9 ev) and 825 mμ (1.5 ev).

Fine structure in the absorption spectra was looked for by taking absorption data at much smaller wavelength intervals, 20Å, but none was found. This is quite different from ZnS:Mn phosphors which do show fine structure consisting of four small absorption bands located between 390 and 500 mμ (12).

Absorption spectra for ZnS:Fe samples containing the monovalent cations lithium, sodium, or potassium were identical with those of phosphors containing no coactivators. The presence of the monovalent cation apparently had no effect on the oxidation state of iron, since a change in the oxidation state of Fe would be expected to result in some change in the absorption spectra.

Excitation spectra.—Excitation spectra for the red and blue emissions were obtained with the aid of a 500 mm Bausch and Lomb grating monochromator equipped with a grating drive. The exciting source was a stabilized 100w xenon lamp. The phosphors were deposited from an alcohol suspension on the composite blue or red filters. The red filter was Corning No. 2404 plus Baird V-3-507 interference filter, and the blue one was Corning No. 5543 + Wratten No. 47. The red filter combination passes a line around 658 mμ. The photocurrent was recorded on a Model AW Esterline-Angus recorder. All spectra are given relative to a 0.2% fluorescein solution which has unit quantum efficiency over the range 250–500 mμ (13).

The excitation spectra were measured for three different iron additions: 0, 0.001 and 0.1%. The excitation spectra of the blue emission show a strong peak at 340 mμ (3.65 ev) with a shoulder on the long wavelength side which indicated a second peak around 375 mμ (3.33 ev). Addition of 0.001% Fe resulted in a large decrease in the intensity of the blue excitation band while a further Fe increase decreased the intensity of the excitation band almost to zero. For the red emission, all three samples showed a primary excitation peak at 340 mμ with a secondary peak (shoulder) near 375 mμ. The intensity of the primary peak increased by approximately a factor of 2 as the Fe addition was increased from 0 to 0.001%, but the secondary peak was only

⁷ All activator and coactivator concentrations are in atom per cent.

⁸ All samples without copper were examined under 365 mμ u.v. and representative samples were also examined under cathode-ray excitation. The samples with copper were examined for electroluminescence.

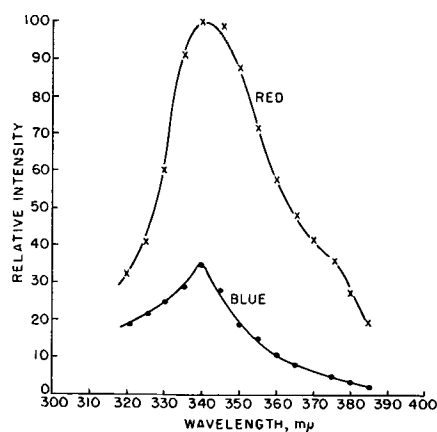


Fig. 2. Excitation spectra of the red and blue emissions from ZnS:0.001Fe, 1.0I .

slightly affected. Increasing the Fe addition to 0.01% resulted in a decrease of the primary peak and a proportionate decrease in the secondary peak (by a factor of 1.7-1.8). Figure 2 shows the excitation spectra of the red and blue emissions from the phosphor with 0.001 Fe.

Irradiation into the three iron absorption bands at 405, 600-650, and 821 $m\mu$, did not result in any detectable luminescence in the visible region of the spectrum.

Emission spectra.—Spectral distributions were taken with a Gaertner constant deviation spectrometer which had been fitted with a prism drive. The photomultiplier output, after amplification by a Keithley Model 210 Electrometer, was recorded on an Esterline-Angus Model AW recorder. All distributions were corrected for spectral sensitivity of the detector and dispersion of the prism. Excitation was by 365 $m\mu$ radiation obtained from a 400w high-pressure mercury lamp equipped with Corning No. 9863 plus No. 5860 filters. This lamp and filter combination was used in most of the measurements involving 365 $m\mu$ excitation.

The effect of increasing iron additions on the emission spectra was examined over the range of 0-0.01% Fe; at higher iron concentrations, the intensity was too low for measurement. No effect on

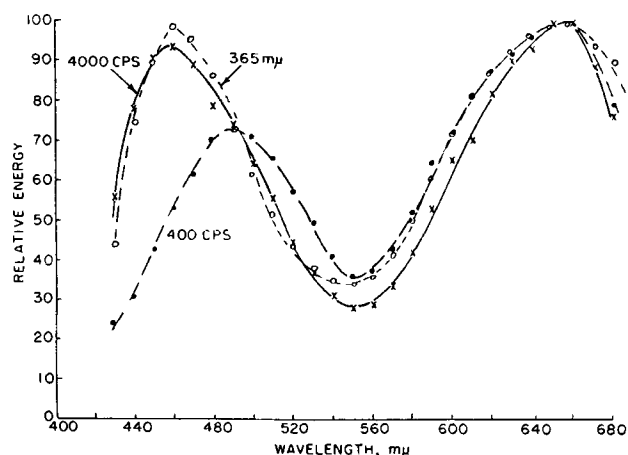


Fig. 3. Photoluminescent emission spectrum from ZnS:0.005Fe, 1.0I and electroluminescent emission spectra of $\text{ZnS:0.01Fe, 0.3Cu, 0.7I}$. Excitation by 365 $m\mu$ ultraviolet and by 400 and 4000 cps, respectively.

the peak positions of the blue and red emission bands was found, only an alteration of their peak heights. The emission spectrum from ZnS:0.005Fe, I is shown in Fig. 3.

Fluorescence intensity as a function of Fe and I additions.—The effects of Fe and I variations on the intensity of the ZnS:Fe, I luminescence were measured with a 1P22 photomultiplier and a Keithley Electrometer.

The concentration of Fe added to the raw mix was varied over the range 0-0.01% for iodine additions of 0.01, 0.1, 1, and 10%. The results are shown in Fig. 4; also shown is the corresponding EL behavior for ZnS:xFe, 0.3Cu, I . Increasing the Fe addition from 0 to 0.001% results in an increase in the red emission. In the range 0.001-0.007% Fe the behavior of the red emission varies depending on the I addition

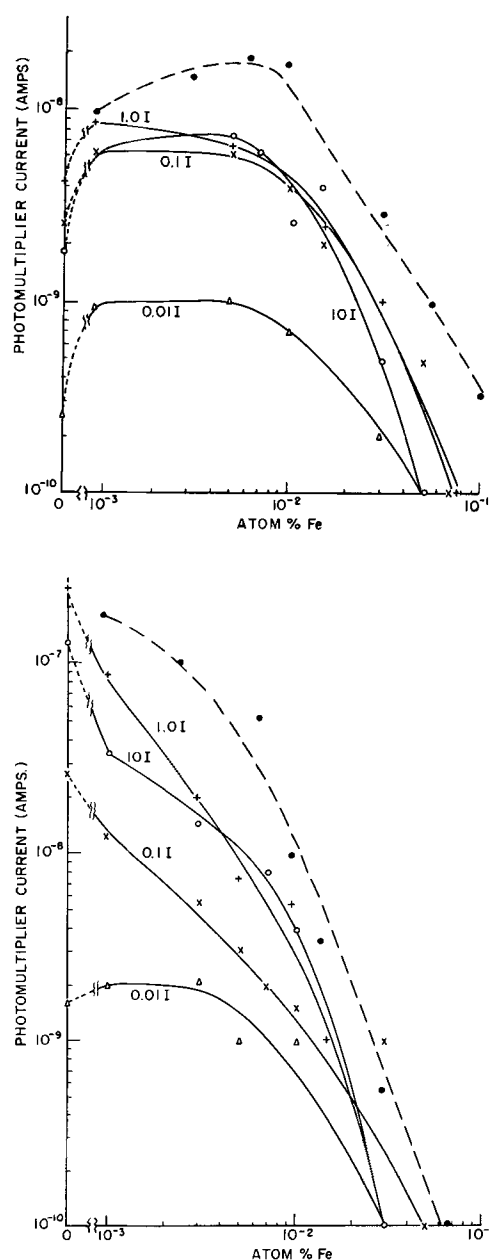


Fig. 4. Intensity of the (A, top) red emission and (B, bottom) blue emission from ZnS:xFe, I and $\text{ZnS:Fe, 0.3Cu, 0.7I}$ as a function of the amount of Fe added to the phosphor raw mix. Excitation by 365 $m\mu$ ultraviolet and 2000 cps, 1200v rms, respectively; —, photoluminescence; - - -, electroluminescence.

(Fig. 4A) which shows that there is a variation of the residual I concentration, at least within the limits of the I analysis of $\pm 75\%$. For increasing concentrations above 0.007% there is a progressive decrease in the red luminescence. The samples are essentially quenched for iron additions between 0.05–0.08%. For the blue emission, with all but the lowest iodine addition of 0.01%, increasing amounts of iron resulted in a rapid decrease in intensity with complete quenching at Fe additions of 0.03–0.05% (Fig. 4B). In samples containing 0.01% iodine, the blue emission had essentially constant intensity for increasing Fe additions from 0.001 to 0.003%, and then decreased rapidly with further increases in iron.

Temperature dependence of fluorescence.—Based on a method proposed first by Mott and Gurney (14) and further developed by Klasens (15), the energy difference between the top of the filled band and the ground-state level of an excited center (in the Schön-Klasens model) may be calculated from the variation of the emission intensity with temperature during excitation. The basis of this method was the assumption that the cause of the decrease of luminescence at high temperatures is filling of excited centers by the raising of electrons from the valence band to the excited center.

According to Klasens' formulation the temperature dependence of the emission is expressed by the equation

$$L/L_0 = 1/[1 + A \exp(-E_q/kt)] \quad [1]$$

where L is luminescence intensity at temperature $T^\circ K$, L_0 is a constant which varies from sample to sample and may correspond to the intensity of the maximum observed emission, A is a constant, k is Boltzmann's constant, and E_q is the thermal quenching energy. This equation can be applied to both the red and blue emissions.

Temperature dependence measurements of the red and blue emissions were made on a series of phosphors having increasing additions of iron. The iron additions used and the temperature breakpoints, T_b , are listed in Table I.

A typical temperature dependence curve is shown in Fig. 5. There are several things to be noted in these curves: (a) the blue emission starts to increase with increasing temperature at a lower temperature than the red emission; (b) the red emission starts to increase rapidly near the temperature at which the blue emission has its maximum; (c) the blue emission has decreased considerably at the temperature at which the red emission has its maximum.

Table I. Apparent thermal quenching energies, E_q , and temperature breakpoints, T_b , as a function of Fe additions

ZnS:xFe, 1I	Blue		Red	
	E_q , ev	T_b , °C	E_q , ev	T_b , °C
x = 0	0.40 ± 0.02	-16	0.38 ± 0.02	+46
0.001	0.41	-28	0.41	+42
0.003	0.36	-30	0.31	+20
0.005	0.27	-30	0.27	+8
0.01	0.25	-39	0.27	+10

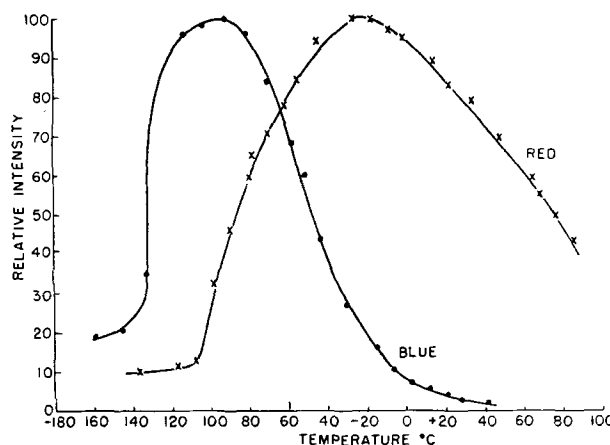


Fig. 5. Temperature dependence of the red and blue emissions from ZnS:0.001Fe, 1.01. 365 mμ excitation.

Using Klasens' equation, the apparent thermal quenching energies for the red and blue emissions from the ZnS:Fe,I phosphors were calculated. These are also listed in Table I. For both emissions E_q decreased with increasing iron additions.⁹ For a given phosphor, E_q had the same value for both emissions. The temperature breakpoints of the two emissions moved to lower temperatures as the iron additions increased; this had also been observed by Klasens (15) for ZnS:Ag,Ni phosphors. The red Fe emission appeared to shift slightly faster than the blue emission. The exact behavior of the temperature breakpoint for the high iron additions is not known, owing to possible thermoluminescence contributions in the region of the lower T_b 's.

Excitation-intensity dependence of fluorescence.—The intensity of the red and blue emissions as a function of increasing iron additions was measured over two decades of excitation intensity. The phosphors were mounted on an optical bench and the distance from the sample to the lamp varied by predetermined amounts to give the required excitation intensity.

The intensity of both emissions followed the equation $L = aI^n$ where a and n are constants and I is the intensity of the exciting source. It was found that n has the same value for both emissions (1.2) and is independent of the Fe concentration.

Thermoluminescence (glow curves).—The introduction of Fe into ZnS:I phosphors results in the appearance of several glow peaks, the most pronounced being at -100 , -75 , -40 , and $+25^\circ C$ which are attributed to Fe; there is also a strong peak at $-140^\circ C$ which is apparently due to halogen (16). Increasing the Fe addition to 0.01% initially increased the $-75^\circ C$ peak relative to the other peaks. A further increase in Fe resulted in a rapid decrease of the $-75^\circ C$ peak relative to the $-140^\circ C$ peak; at 0.05% Fe only the $-140^\circ C$ peak remained but of very low intensity. Somewhat similar behavior for ZnS:Cu,Ni has been reported by Hoogenstraaten (17).

Glow curves of the red and blue emission from a ZnS:0.001Fe,I sample were measured and found to be essentially the same (Fig. 6).

⁹ Klasens has observed similar behavior in ZnS:Ag,Ni phosphors (15).

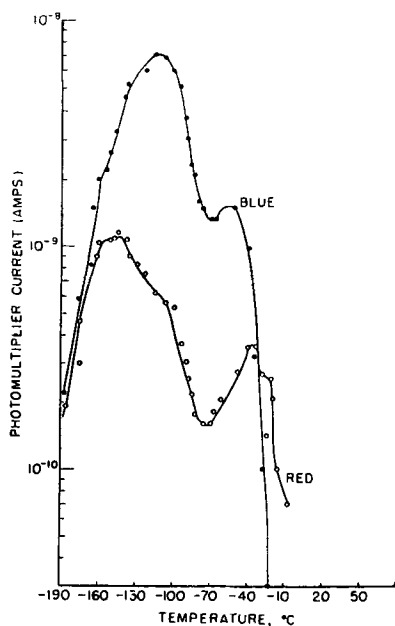


Fig. 6. Glow curves from ZnS:0.001Fe,1.01 for observation of the red and blue emissions. 365 m μ excitation. Heating rate was 10°C/min.

Decay of phosphorescence.—The phosphorescence decay of the red and blue emissions as a function of the Fe concentration was measured. The photocurrent from the detector was amplified by a Keithley Model 210 Electrometer and the output fed into a Sanborn Model 128 recorder. The sample was first allowed to reach equilibrium under excitation; then the exciting source was cut off by a fast-acting shutter.

The blue emission always built up and decayed faster than the red emission. Analysis of the decay curves showed that the red emission consisted of two components, an initial fast decay which was exponential and a slower decay which followed a power law of the type $L \sim L_0 t^{-n}$. The blue emission, except from samples having no added Fe, decayed according to an exponential law. The blue emission from the samples containing no added Fe had both the initial exponential decay and the slower power-law tail. The values of n (exponent in the power law decay) and τ (the life-time) are: red $\tau = 0.13 \pm 0.02$, $n = 1.0 \pm 0.05$; blue $\tau = 0.05 \pm 0.01$, $n = 1.35$.

Photoconductivity.—Photoconductivity was measured in a demountable cell having one electrode transparent¹⁰ and the other aluminum; the cell spacing was 3 mils. The phosphor was mixed with castor oil in the weight ratio 1.5:1. Two 45v batteries in series were placed across the cell; the transparent electrode was always kept at the same polarity. The photocurrent was measured with a Keithley Model 200A Electrometer. The exciting source was a 100w Hg lamp. Various combinations of filters were used to isolate bands at 365, 405, 658, and 821 m μ , corresponding to the observed absorption peaks.

Photoconductivity was sought in samples having increasing additions of iron. Excitation by 365 m μ

¹⁰ Made from tin oxide-coated glass having a resistance of 100 ohms.

Table II. Light-to-dark-current ratio, γ , of ZnS:xFe,11 as a function of the excitation wavelength

Fe concentration	γ for irradiation by			
	365 m μ	405 m μ	658 m μ	821 m μ
x = 0	2.6	2.78	1.00	1.00
0.001	2.3	1.65	1.00	1.00
0.01	1.55	1.03	1.00	1.00
0.03	1.46	1.05	1.00	1.00

resulted in weak photoconductivity. Increasing the iron concentration resulted in a decrease in the photoconductivity.

The reflectance spectra for ZnS:Fe,I discussed previously showed the presence of three new absorption bands which are apparently due to iron (Fig. 1). The same samples used in the previous photoconductivity measurements were irradiated with radiation lying near the three absorption peaks. The results are shown in Table II which gives the light-to-dark current ratio, γ , as a function of the exciting wavelength. Only radiation lying in the short wavelength absorption band resulted in photoconductivity. This photoconductivity also decreased with increasing iron additions.

Bube (18) has reported that self-activated ZnS has very little photoconductivity at wavelengths greater than 390 m μ while ZnS containing Cu is quite photoconductive under excitation by radiation up to 500 m μ . The ZnS phosphors prepared here are known to contain trace amounts of Cu (~ 1 ppm) so that in all probability the photoconductivity obtained by 405 m μ irradiation is due to the presence of the Cu impurity.

Electroluminescence

Experimental results.—The EL characteristics were measured using castor oil as the dielectric, a Hewlett-Packard Model 200 wide range oscillator, a Lafayette Model PE75 100w amplifier, and a UTC Model CVP5 audio transformer. The voltage across the cell was measured with an RCA Senior Volt-Ohmyst which had been calibrated against an electrostatic voltmeter. The intensity of the EL was measured with a Photo Research Corporation Spectra Spot Brightness Meter using the built-in filters. EL waveforms were observed on a dual beam oscilloscope.

Emission spectra.—The emission spectra of ZnS:0.01Fe,0.3Cu,0.7I were obtained at 400 and 4000 cps, Fig. 3. Both spectra contained a short and long wavelength band. Increasing the frequency made the short wavelength band (peak) shift from 490 to 458 m μ . The peak wavelength of the red emission was unaffected by a change in frequency and was at the same wavelength as that obtained with u.v. excitation.

EL intensity as a function of Fe additions.—The influence of increasing Fe additions, at constant Cu (0.3%) and I (0.7%), on the red and blue EL was determined at 2000 cps, 1200v rms. Results were similar to those obtained with 365 m μ excitation (Fig. 4).

Voltage dependence.—The voltage dependencies of the red and blue EL were determined at 2000

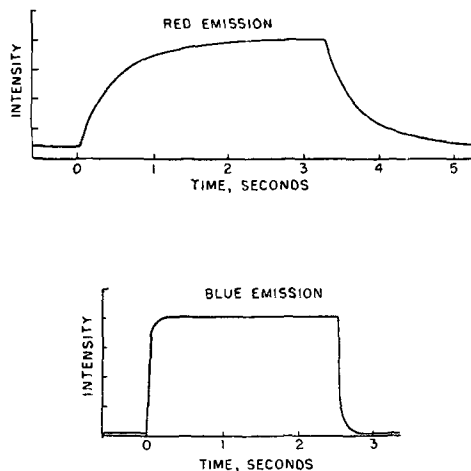


Fig. 7. Build-up and decay of the red and blue electroluminescence of ZnS:0.1Fe, 0.3Cu, 1.0I.

cps as a function of increasing iron additions. Both emissions were found to follow the well known equation (19) $L = L_0 \exp [-(V_0/V)^{1/2}]$ where L is EL intensity at voltage V , L_0 is the EL at infinite voltage, and V_0 is a constant, approximately 5.3×10^4 for both the red and blue emissions.

Frequency dependence.—The frequency dependences of the red and blue emissions were determined between 100 and 10,000 cps at a constant voltage of 100v rms. The emission increases with increasing frequency from 100 to 1000 cps, and begins to approach saturation for higher frequencies. The slopes n of the curves (for a log-log plot of EL vs. frequency) for the red and blue emissions as a function of the iron additions are constants and independent of the Fe concentration: red $n = 0.72$; blue $n = 1.16$. No variation in slope as a function of frequency was observed, in contrast to Goldberg's results for ZnS:Cu phosphors containing cobalt or nickel (7).

Build-up and decay.—The build-up and decay of the red and blue EL were measured for one sample, ZnS:0.01Fe,0.3Cu,0.7I, at 400 cps, 450v rms. They were similar to those obtained with ZnS:Fe,I excited by $365 \text{ m}\mu \text{ u.v.}$, i.e., the blue emission builds up and decays faster than the red emission (Fig. 7). The decay of both emissions was primarily exponential with $\tau = 0.05$ sec for the blue emission and $\tau = 0.49$ sec for the red emission. The time constant of the blue EL was essentially the same as that obtained with the blue photoluminescence, but the time constant of the red EL was approximately four times larger than that for the red photoluminescence.

Waveforms.—The effect of increasing Fe concentration on the waveforms of the red and blue emission from ZnS: x Fe,0.3Cu,0.7I was examined over the range 0.01 to 0.12% Fe at 400 cps, 400v rms (Fig. 8). The EL waveforms, except for the blue emission from high Fe samples, consisted of a primary and a secondary wave per half-cycle of the applied field; the minima of the waveforms are above the zero base line. These two components are generally called the a-c and d-c components of the emission, respectively (20).

The waveforms of the red and blue emissions from the sample containing the lowest iron concentration (0.01%) showed strong primary peaks. The sec-

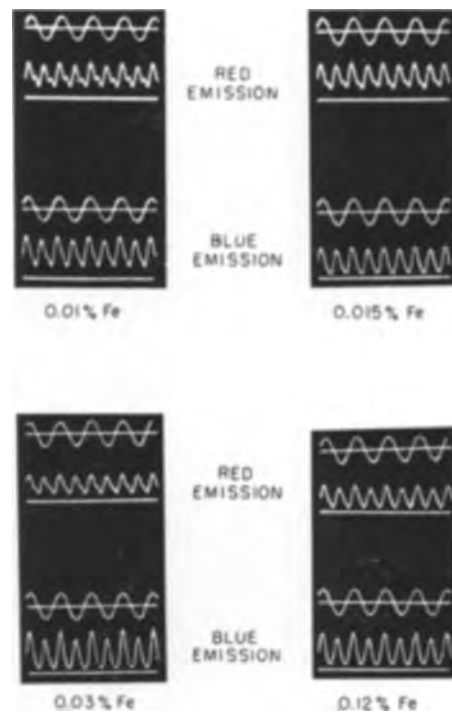


Fig. 8. Electroluminescence waveforms of the red and blue emissions from ZnS: x Fe,0.3Cu,0.7I. Excitation at 400 cps, 400v rms. In each picture the top set of curves is for red emission, bottom for blue. Top curve of each trace is waveform of applied field, lower curve the corresponding emission waveform. Horizontal traces are zero base lines, i.e., no field.

ondary peak of the red emission was well developed, but that of the blue emission was barely perceptible. There was a strong d-c level for both emissions. Increasing the Fe concentration caused a progressive decrease in the d-c level of both emissions, with the d-c level of the blue emission decreasing faster. Increasing iron content also caused a progressive decrease in the amplitude of the primary and secondary waves, again with the blue decreasing faster. The secondary wave of the blue emission completely disappeared for iron concentrations above 0.015%, but for the red emission it was still discernible in the phosphor containing the highest iron concentration, 0.12%.

The effect of increasing the frequency, at constant voltage, on the behavior of the waveforms of the blue and red emissions was also examined. Figure 9 shows the waveforms for the sample with 0.01% Fe at 100, 300, and 3000 cps at a constant voltage of 150v rms; the behavior of the other samples was similar. At 100 cps, the amplitude of the primary wave was much larger than that of the secondary wave for both emissions. Increasing the frequency caused a small progressive increase in the amplitude of the blue secondary wave relative to the primary. However, the primary blue wave was still the predominant one even at 3000 cps. The situation was reversed in the case of the red emission. Here, an increase in frequency to 300 cps resulted in a large increase in the secondary wave, the amplitude of the two waves being approximately the same. A further frequency increase, to 3000 cps, made the secondary wave larger than the primary. For both emissions there was an increase in the d-c level with

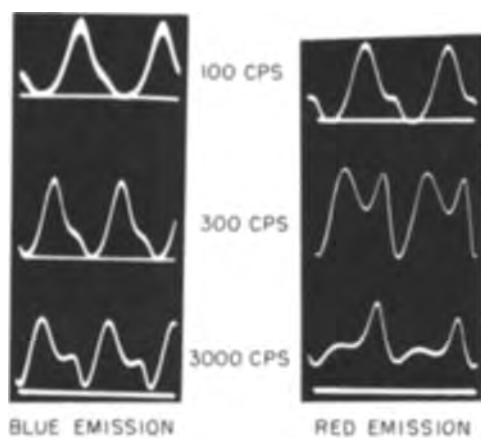


Fig. 9. Effect of increasing frequency on the electroluminescence waveforms of the red and blue emissions from $\text{ZnS:0.01Fe,0.3Cu,0.7I}$. Data taken at 150v rms.

increasing frequency, the increase for the red emission being larger.

Discussion and Conclusions

Identity of the red emission.—Because of the similarity of the emission peaks of the ZnS:Cu “red” and the ZnS:Fe red phosphors, there was some question whether these were really different emissions. It is possible that Fe can intensify the Cu emission (due to the trace Cu impurity, ~ 1 ppm, in the ZnS:Fe phosphors). However, comparison of the optical properties (21-23) of the two phosphors shows them to be different systems. For example:

(a) The “red” Cu emission has the same temperature dependence as the blue “self-activated” or blue Cu emission and is almost completely quenched at about 40°C while the Fe red emission is quenched well above 100°C .

(b) The Cu “red” emission band is much wider than the Fe band. Because of its larger width the Cu emission looks orange, while the Fe emission looks red, in spite of the fact that the two emissions peak at the same wavelength.

(c) The Cu “red” emission is destroyed if a coactivator is present, but the Fe red appears only if there is a coactivator.

(d) There is no quenching or stimulation of the Fe red on irradiation with infrared, but the Cu “red” emission is stimulated by infrared.

(e) The ZnS:Fe phosphors always have two emission bands but ZnS:Cu phosphors can be prepared showing only the Cu “red” emission.

General.—The luminescence characteristics of iodine coactivated ZnS:Fe phosphors are similar regardless of whether the excitation is by u.v. or alternating electric fields. This means that the luminescent centers in the EL phosphors (coactivated ZnS:Fe,Cu) are similar to those in the photoluminescent phosphors (coactivated ZnS:Fe) and that the transitions leading to luminescence are also similar, only the excitation mechanism differing. Therefore, data obtained by these two modes of excitation may be used to elucidate the nature of the iron centers and the transitions involved in luminescence and quenching.

The introduction of iron into ZnS containing a halide or a trivalent cation, *i.e.*, Al, Ga, or In, gives rise to the appearance of a new red emission which is due to iron. Unless there is a coactivator present there is no luminescence (red or blue).

The need for a coactivator in ZnS:Fe or ZnS:Fe,Cu in order for the red luminescence to occur is surprising. Iron is apparently divalent in ZnS up to its limit of solubility (24). Further, Title (25) using electron spin resonance techniques, found that iron is divalent in the unexcited phosphor but is trivalent during excitation.¹¹ Therefore, there is no need for a coactivator on departure from bivalency for iron to be incorporated into ZnS . It is significant that when these ions are present, there is also a blue emission in addition to the red emission. Many of the luminescent characteristics of the two emissions are similar, indicating that there is a relationship between these emissions. For example:

(a) The excitation spectra of the red and blue emissions are essentially the same.

(b) The thermal quenching energies, E_q , of the red and blue photoluminescence are the same for a given iron concentration and decrease similarly as iron is added. The temperature breakpoints, T_b , also decrease in a similar manner with increasing additions of Fe.

(c) The slope of the curves of the red and blue emission intensities as a function of the u.v. exciting intensity or the strength and frequency of the applied electric field are the same for a given mode of excitation.

(d) The glow peaks of the red and blue emissions are almost identical.

Further indication of a relationship between the two emissions can be seen in Fig. 5, which gives the temperature dependence of the red and blue emissions. The red emission intensity begins to increase at the temperature at which the blue emission starts to decrease. Klasens (26) and Tolstoi (8) have found that this behavior generally occurs for emissions that are related. From the data shown in Fig. 5, the apparent activation energy for the rise of the red emission was calculated and found to be the same as the thermal quenching energy of the blue emission; this is the same sort of relationship found by Tolstoi for the red and blue emissions from ZnS:Co (8). However, the results with the ZnS:Fe,I phosphor are somewhat open to question since not all the points on the rising red curve fit the equation. A similar relationship between the fall and rise of the blue and orange emissions in ZnS:Mn has also been observed (27).

The need for a coactivator and the similarity in luminescence characteristics can be explained if the assumption is made that, regardless of the mode of excitation, the blue centers (“self” or Cu) are initially excited, followed by a transfer of energy from these centers to the iron centers, which may then emit. This transfer of energy may occur by a resonance transfer process or by the transfer of charge (28).¹² In view of Title’s results on the valence

¹¹ Actually only 30% of the iron becomes trivalent in Title’s samples.

¹² We are ruling out cascade and exciton transfer.

change of iron from 2+ to 3+ on excitation (25), it appears most likely that the energy transfer occurs by movement of charge, which would also result in photoconductivity. However, there still may be some energy transfer by a resonance mechanism, as indicated by the similarity of the thermal quenching energies of the red and blue emissions, a fact that cannot be explained by a charge transfer process. In the discussion to follow it will be assumed that the predominant mechanism is that of charge transfer.

If Fe is divalent in the unexcited phosphor, and if charge transfer does occur, then there would be a valence change of the Fe^{2+} center since an electron is removed from this center; i.e., the Fe^{2+} center captures a hole. The capture of an electron from the conduction band by the Fe^{3+} center resulting in an excited Fe^{2+} center (Fe^{2+*}), and its subsequent return to the ground state returns the Fe^{2+*} center to the 2+ ground state. The photoconductivity that is observed is thus due to the movement of both electrons and holes. This change in valence of the Fe centers indicates the location of this center with regard to the band gap. If the Fe center were located in the valence band as postulated for Mn (12), there would be no valence change on excitation (29).¹³ A valence change can only occur if the center is located in the forbidden energy gap (29).

In addition to the iron luminescence center there are killer centers, apparently also due to iron. This is indicated by the behavior of the luminescence as a function of the iron concentration: the blue emission decreases rapidly with increasing Fe while the behavior of the red emission for iron concentrations below 0.007% is rather unusual. With activators such as silver, copper, or manganese, a progressive increase in the concentration results in a progressive increase in the emission intensity to a maximum, followed by a decrease in the intensity for further increases in the activator concentration. This decrease in intensity is called "concentration quenching" and occurs at concentrations that are higher than the 0.007% Fe concentration required for quenching of the iron emission. For silver, copper, or manganese the approximate concentrations resulting in maximum luminescence are (30): Ag = 0.03-0.1%, Cu = 0.05-0.1%, and Mn ~ 2%. Apparently in the region of low iron concentration there are two simultaneous effects occurring, red luminescence and killing. This dual behavior of the "killer" has been observed by Arpiarian (3) and Gergely (4). If the iron center has a very high capture cross section for electrons and holes, then the quenching of the blue emission can be explained, but one would not expect quenching of the red emission at such low iron concentrations. Instead, the quenching should occur at higher iron concentrations, of the order of 1%, as it does with Mn, i.e., "normal" concentration quenching (12).

The model shown in Fig. 10 illustrates the transitions that are assumed to occur in excitation, luminescence and killing. The same iron ion can act both

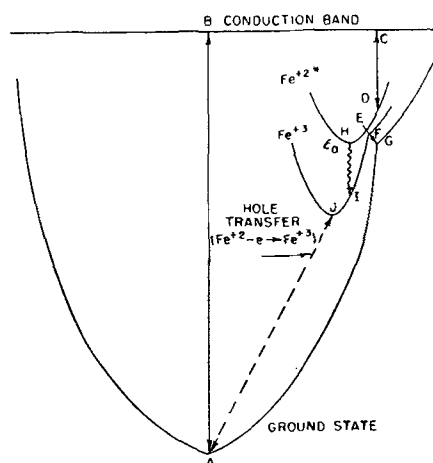


Fig. 10 Configurational coordinate model (schematic) of ZnS:Fe, coactivator, showing transitions leading to both luminescence and killing which may occur in the same center.

as a luminescent center and as a killer center. Transition AB corresponds to excitation of an electron from the ground state (valence band, or "self-activated" or blue Cu center) to the conduction band. Transition AJ results in the transfer of a hole from the ground state (valence band or blue center) to an Fe^{2+} center, resulting in an Fe^{3+} center. The Fe^{3+} center has a positive charge relative to the lattice and so can trap an electron from the conduction band forming an excited Fe^{2+} state, transition CD. The electron may be returned to the conduction band, transition d.c., or the center may rearrange itself to its equilibrium position by losing some of the energy (as phonons) imparted to it by the capture of the excited electron, i.e., the electron moves from D to H. Luminescence occurs when the electron makes the transition HI. As the excited electron moves to its equilibrium position in the excited level of Fe^{2+} , it may make transition EFG which returns it to the Fe^{2+} ground state without the emission of visible radiation.

If ρ_e is the probability that the excited electron will make transition HI resulting in luminescence and ρ_k the probability that the electron will make the radiationless transition EFG, then the probability of the electron returning to its ground state is $\rho = \rho_e + \rho_k = 1$. From the behavior of the red iron emission as a function of increasing iron additions (Fig. 4A and B) and the temperature dependence of the fluorescence (Fig. 5), it appears that ρ_k is a function of, and increases with, increasing iron concentration and ambient temperature. These relationships together with the well known Schön-Klasens model are sufficient to explain most of the experimental data.

The iron luminescence center is apparently of the "Mn" type in that luminescence transitions occur within the center, that is, from an excited state of the Fe^{2+} ion to the ground state; i.e., among the 3d electrons. Evidence for these transitions comes from the electroluminescence emission spectra as a function of frequency. Increasing the applied frequency from 400 to 4000 cps results in a shift of the short wavelength emission toward shorter wavelengths, but the iron emission is invariant. This in-

¹³ We have assumed here that the Fe center is similar to a Mn center in that luminescence involves transitions from an excited state of the center to the ground state. That this is the case will be shown later.

variance with a change in frequency also occurs with ZnS:Cu,Mn phosphors whose emission is known to involve transitions between the excited and ground states of the Mn ion (12, 30, 31).

The effect of iron on the blue emission can readily be understood in terms of the model presented in Fig. 10.¹⁴ Excitation of the phosphor by 365 m μ u.v. excites an electron from a blue (Cu or self-activated) center to the conduction band, the hole remaining in the activator center. While the electrons are in the conduction band, the holes in the blue centers may be filled by electrons from the valence band if the necessary (thermal) energy is available. If this happens, the hole may move through the valence band and be trapped by another blue center or by a red center. Which center traps the hole is determined by the ratio of the capture cross sections of the two centers. The electron in the conduction band may return to a blue center, giving rise to blue emission, or be captured by another Fe³⁺ center.¹⁵ Since the blue emission decreases rapidly with increasing Fe concentration, it is apparent that the Fe center has the larger hole capture cross section.

The thermal quenching energies, E_q , of the red and blue emissions from a phosphor with a given iron concentration are the same, decreasing with increasing Fe. The temperature breakpoint, T_b , of the blue emission is lower than that of the red, and increasing iron additions cause a progressive decrease in T_b for both emissions. These results can be explained as follows: At a low temperature the holes are localized in the blue centers, except for statistical "leakage," so that the luminescence is predominantly blue. As the temperature increases the intensity of the blue emission increases to a maximum while the red emission is still weak. This increase in the intensity of the blue emission occurs because electrons, that were in shallow traps and thus removed from the luminescence process, are being returned to the conduction band, from which they return to the blue centers. However, above a certain temperature, T_1 , holes start to leave the blue centers and are transferred to the red centers because of their greater capture cross-section; red emission commences and the blue emission starts to decrease. As the temperature increases, more and more holes are transferred to the red centers. This transfer is at the expense of the blue emission and depends on the temperature in an exponential manner, $\exp(-E_q/kT)$, as discussed by Klasens (15). Tolstoi has found this to be the case in ZnS:Co phosphors (8). Finally, at a temperature T_2 almost all the holes from the blue centers are transferred to the red centers, and the blue center is essentially quenched. At a still higher temperature, T_3 , the red emission also starts to decrease because the Fe quenching mechanism, which is simultaneously operative and increases exponentially with temperature, becomes the dominant mechanism. An ex-

planation is still lacking for the red and blue emissions having the same thermal quenching energies unless we assume that there is resonance transfer of energy from blue to red centers as mentioned earlier.

The apparent decrease in thermal quenching energy, E_q , with increasing Fe additions can be explained in one of the following ways: If E_q represents the energy necessary to raise an electron from the valence band to an excited blue center, then a decrease in E_q with increasing Fe could mean a decrease in the distance between the blue center and the top of the valence band. If this were due to a movement of the blue level toward the valence band, there should be a change in the wavelength of the blue and/or red emission peak by an amount equal to the change in E_q . The maximum change in E_q is about 0.15 eV, Table I, which should shift the blue emission from 460 to 440 m μ and the red emission from 600 to 620 m μ . These shifts are not observed. A decrease in height of the blue level with no emission shift could occur if the band gap were decreasing while maintaining the separation between the conduction band and the blue level. However, no such shift in band gap is observed. The most likely reason for the variation of E_q with iron concentration is that the constant A in Eq. [1] is not a constant but is a function of the Fe concentration. For this reason, the values of E_q calculated from the equation have been called "apparent thermal quenching energies."

Thermoluminescence measurements show that Fe introduces several new glow peaks into the phosphors. No identification of the trapping levels leading to these glow peaks has been made. Electrons released from these traps return to both red and blue centers, presumably via the conduction band, as shown by the similarity of the glow curves made through red and blue filters (Fig. 6).

Generally, the transition of an electron from an excited state of a transition metal ion to its ground state (or the reverse), as in the case of manganese, is considered to be "forbidden" (12, 14, 30). That this is the case for the ZnS:Fe,I and ZnS:Fe,Cu,I phosphors is indicated by the relatively long lifetimes, τ , of the red EL and photoluminescence, 0.49 and 0.13 sec, respectively.

In the voltage dependence of the red and blue EL V_0 is the same for both emissions as discussed earlier. This behavior is expected if energy transfer occurs. Similar behavior has been observed at low fields for ZnS:Cu,Mn (32).

A possible explanation for the variation of the brightness waves as a function of the Fe content is that on reversal of the field, electrons which had been swept away from the ionized centers in the previous half-cycle now return; the (primary) electrons that were free or in shallow traps first, followed by those (secondary) which had either been released from deeper traps or had been retrapped, thus leading to primary and secondary waveforms, respectively. The returning electrons are divided up between the blue and red centers, leading to primary and secondary output waveforms for the

¹⁴ Assuming that charge transfer is the predominant process.

¹⁵ Whether the electron trapped by the Fe center makes a radiative or radiationless transition depends on the respective probabilities ρ_e and ρ_k as discussed previously.

two emissions;¹⁶ it should be noted that these waveforms are in phase with each other. Since the secondary waves are due to delayed return of the secondary electrons, a decrease in the number of trapped and retrapped electrons will result in a decrease in the amplitude of both output waveforms but will affect the secondary waves more strongly. It was shown earlier that iron results in "leaky traps" whose number increases with increasing Fe concentration, i.e., there is a decrease in the concentration of effective traps. The decrease in the d-c emission component is also due to the return of electrons to the ground state via radiationless transitions in the iron centers.¹⁷ An explanation for the effect of frequency on the brightness waves of the red and blue emissions is lacking.

Acknowledgment

The authors would like to thank Mr. G. T. Scanlon for his aid in various aspects of this work and Dr. H. F. Ivey for his continued interest in this project. Thanks are also due to Dr. C. K. Lui-Wei for the x-ray measurements and Mr. E. Gritz for the Fe analysis. The support of a portion of this work by the Westinghouse Lamp Division is gratefully acknowledged. Portions of this work were supported by the U.S. Air Force, Wright-Patterson Air Force Base, Ohio, under Contract No. AF33(616)-7350.

Manuscript received July 29, 1963. This paper is from a Dissertation submitted by P. M. Jaffe in partial fulfillment of the requirements for the degree of Ph.D. at the Polytechnic Institute of Brooklyn. Copies may be obtained from University Microfilms, Ann Arbor, Mich., No. 62-5626.

Any discussion of this paper will appear in a Discussion Section to be published in the December 1964 JOURNAL.

REFERENCES

1. L. Levy and D. West, *Trans. Faraday Soc.*, "Luminescence Discussion" (1938).

¹⁶ Only a portion of the electrons trapped by the Fe center makes radiative transitions as discussed earlier.

¹⁷ We are following Thornton's ideas here on the cause of the d-c level (33).

2. N. Arpiarian, *J. Phys. Radium*, **17**, 674 (1956).
3. N. Arpiarian, *Compt. rend.*, **230**, 1948 (1950).
4. G. Gergely, *J. Phys. Radium*, **17**, 679 (1956).
5. A. A. Bundel, A. I. Rusanowa, and E. V. Yakovheva, *Bull. Acad. Sci. U.R.S.S., Ser. phys.*, **9**, 543 (1945).
6. N. T. Melamed, *This Journal*, **97**, 33 (1950).
7. P. Goldberg, *ibid.*, **106**, 948 (1959).
8. N. A. Tolstoi, *Optics and Spectroscopy*, **3**, 73 (1957).
9. A. A. Bundel and A. Rusanowa, *Bull. Acad. Sci. U.R.S.S., Ser. phys.*, **13**, 173 (1949).
10. F. A. Kröger and J. Dikhoff, *Physica*, **16**, 297 (1950).
11. J. Gisolf, W. de Groot, and F. A. Kröger, *ibid.*, **8**, 805 (1941).
12. F. A. Kröger, Thesis, University of Amsterdam, July 1940.
13. J. F. Hammann, *Z. angew. Phys.*, **10**, 187 (1958).
14. N. Mott and R. Gurney, "Electronic Process in Ionic Crystals," 2nd Edition Clarendon Press, Oxford (1950).
15. H. A. Kläsens, *Nature*, **158**, 306 (1946).
16. P. M. Jaffe, *This Journal*, **108**, 711 (1961).
17. W. Hoogenstraaten, Thesis, University of Amsterdam, February 1958.
18. R. Bube, *Phys. Rev.*, **90**, 70 (1953).
19. P. Zalm, G. Diemer, and H. A. Kläsens, *Philips Res. Repts.*, **10**, 205 (1955).
20. W. W. Piper and F. E. Williams, *Phys. Rev.*, **81**, 151 (1952).
21. H. C. Froelich, *This Journal*, **100**, 280 (1953).
22. M. H. Aven and R. M. Potter, *ibid.*, **105**, 135 (1958).
23. W. Van Gool and A. P. Cleiren, *ibid.*, **106**, 672 (1959).
24. G. Kullerud, *Saertrykk and Norsk Geol. Tids.*, **32**, 61 (1953).
25. R. Title, *Bull. Am. Phys. Soc., Series 2*, **7**, 88 (1962).
26. H. A. Kläsens, *This Journal*, **100**, 72 (1953).
27. V. L. Levshin and V. F. Tunitskaya, *Optics and Spectroscopy*, **9**, 118 (1960).
28. C. C. Klick and J. H. Schulman in "Solid State Physics," Vol. 5, F. Seitz and D. Turnbull, Editors, Academic Press, New York (1957).
29. J. G. Van Santen, Private communication.
30. H. W. Leverenz, "Luminescence of Solids," John Wiley & Sons, New York (1950).
31. P. Zalm, G. Diemer, and H. A. Kläsens, *Philips Res. Repts.*, **9**, 81 (1954).
32. J. Mattler and T. Ceva, International Conference on Luminescence, New York University, Oct. 9-13, 1961.
33. W. A. Thornton, *Phys. Rev.*, **102**, 38 (1956).

Studies of the InSb Crystal-Melt Interface

N. Albon

Battelle Memorial Institute, Columbus, Ohio

ABSTRACT

The InSb interface was studied by microscopical examination of crystals decanted from the melt. Crystals which had been allowed to approach equilibrium at a curved isotherm showed facets on which the features could be correlated with crystal growth mechanisms. On the curved areas of the interface, lines having a regular spacing were observed, which previously have been assumed to be growth steps. The lines were shown to be grooves without a definite crystallographic orientation and evidence against their origin during the crystal growth process was obtained.

When crystals of InSb are grown from a melt containing Se or Te the existence of facets at the growth interface results in a high concentration of impurity locally in the crystals (1-3). This effect

results from adsorption of the impurity on the growing crystal and differences between the topography and growth kinetics of the facets and the remainder of the growth surface.

This type of problem was discussed theoretically by Cabrera and Vermilyea (4). Application of their theory requires, however, a detailed knowledge of the growth surface and of the behavior of growth steps.

The methods of direct observation of growth steps which have been applied to this problem in other crystal growth systems cannot be applied directly to the growth of indium antimonide from the melt. Another method of approach was used to study the surface of growing indium antimonide crystals. This provides information which can be used as a guide for application of the Cabrera-Vermilyea theory, although it is lacking in the detailed results required for precise calculations.

Considerable experimental difficulties arise in attempting to examine a crystal/melt interface in an opaque system. Many such systems have been studied by the procedure of decanting excess melt. Fine detail such as growth steps may be obscured by a residual film of the melt which freezes on the surface. When studying crystals growing from a highly concentrated transparent medium, Albon and Dunning (5) found that steps observed on growing crystals were obscured on removal unless special procedures were adopted. However, the properties of the InSb melt are more favorable, and a thinner adhering layer would be expected. Allred and Bate (3) had observed well-defined, evenly spaced lines on the growth surfaces of decanted indium antimonide crystals which were assumed to be growth steps. The experimental approach adopted in the present work was to grow crystals under conditions such that the surface topography would be known and to examine these crystals after decanting from the melt. For example, crystals were allowed to equilibrate in a thermal gradient so that they were neither growing or melting before being removed from the melt. The starting material was high-purity InSb (extrinsic carrier concentration less than 10^{16} cm^{-3}), and undoped melts were employed.

Experimental Procedure

The apparatus employed was similar to that normally used for the Czochralski process with a graphite crucible having a thermocouple for observing temperature changes placed on the axis close to the bottom of the melt, which was approximately $\frac{1}{2}$ in. deep. The crucible was heated by RF power, using a separate thermocouple for control.

The procedure was to insert a seed, approximately 5 mm in diameter, into the melt. After wetting the seed the temperature was reduced slowly without rotating or pulling the seed. When the crystal had grown to a convenient size (1-3 cm in diameter) a constant temperature was maintained for 2-31 min. The crystal then was rapidly pulled from the melt for examination of the growth surface. Both manual and mechanical lifting were employed, with no detectable change in the features being noted.

The growth surface was assumed to represent the shape of the melting point isotherm when sufficient time had been allowed for equilibrium. When a seed of 5 mm diameter was used, the isotherms were roughly hemispherical and centered on the point

where the seed touched the surface. Thermal gradients in the melt were measured in this way by observing the final positions of a solid/liquid interface at different temperature settings. These gradients varied from about $10^\circ\text{C}/\text{cm}$ to $100^\circ\text{C}/\text{cm}$, depending on such factors as the distance of the interface from the seed and the cross sectional area of the seed.

Growth interfaces on crystals growing in the usual manner by pulling (without rotation) were also examined. These crystals were pulled clear of the melt while growing.

Experimental Observations

Crystal shape.—Under the conditions used, when the temperature is held at a constant value, the rate of growth of the crystal diminishes as its interface approaches the melting point isotherm. In areas where the interface is not a close-packed plane, growth can proceed to within a few interatomic distances from the isotherm, giving a macroscopically smooth hemispherical shape. On close-packed planes, facets form inasmuch as growth may stop before the isotherm is reached. The supercooling at the facet center, when this occurs, will depend on the growth mechanism.

Both curved areas and facets of 111 and $\bar{1}\bar{1}\bar{1}$ orientation were visible on all crystals grown. The facet size and supercooling at the facet center varied considerably, supercooling being calculated from facet diameter and thermal gradient, with the maximum value of supercooling observed for a smooth facet being 0.4°C . This variation in calculated supercooling indicates that growth on the facets under these conditions is not dependent on a surface nucleation process. Etching experiments revealed dislocations at facet boundaries, and facet size appeared to be determined by the distribution of screw dislocations. As growth of the crystal proceeds, the facet area diminishes until there are no longer any dislocations terminating within the facet, when growth will cease. Determination of the critical supercooling for surface nucleation on a facet, which may be possible by this procedure, thus requires a crystal of low dislocation content.

Surface features on facets.—When the system was held at constant temperature for a long period before removing the crystal, any facets present were

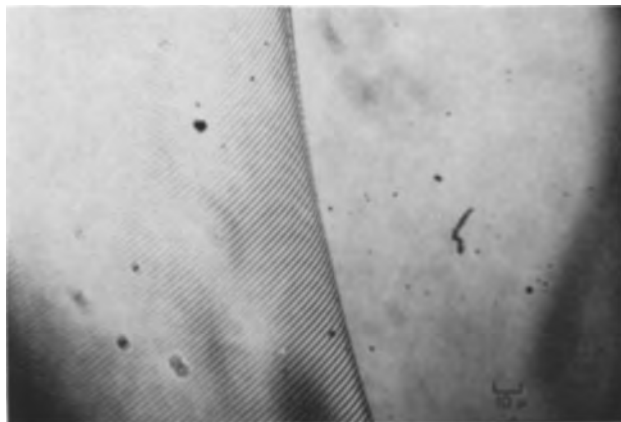


Fig. 1. Smooth facet and grooves on curved interface. Magnification X600.

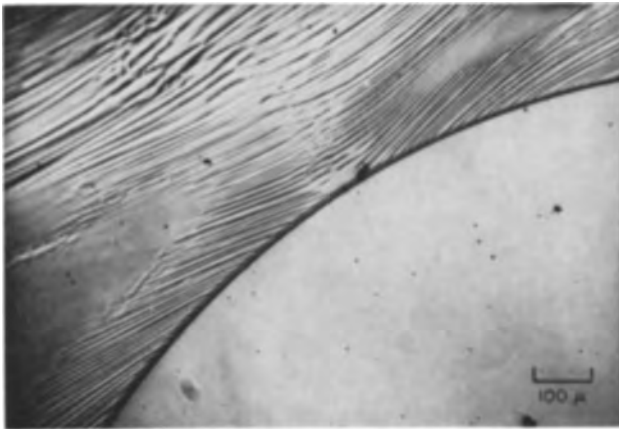


Fig. 2. Facet and groove intersection pattern on curved interface. Magnification X150.

expected to be completely smooth with steps having grown out. The experimental results confirmed this and indicated that any surface film adhering to the facet as a result of the decanting process is without surface structure. Smooth facets were consistently observed on crystals which had been left to equilibrate for 30 min and portions of such facets are visible on Fig. 1 and 2.

Crystals removed after having equilibrated for shorter times (2-20 min) showed facets on which steps were visible. The observations described in the preceding paragraph indicate that these are true growth steps, although they may have been modified during decanting.

The spacing and regularity of these steps varied considerably even between faces growing on the same crystal. Groups of steps of even height and spacing were frequently observed. Step-height measurements indicated average values of 300\AA . On a few crystals, step sources could be identified as dislocations. These sources included incoherent twin boundaries and jogs on twin lines. A regular step pattern on a facet is shown on Fig. 3 and also on Fig. 4.

Surface features on curved areas.—The areas where the surface is not a close-packed plane should reach the melting point isotherm rapidly, as only a low supercooling is required for growth, and produce a smooth surface. The experimental observa-

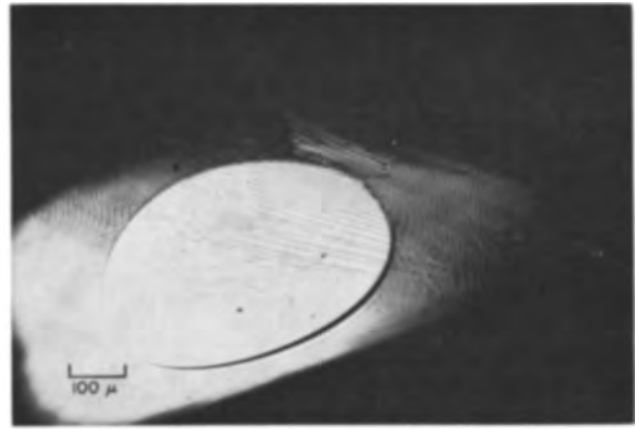


Fig. 4. Facet and also smooth and striated curved interface areas. Magnification X150.

tions made were that some of the curved areas were smooth, but adjacent areas were covered by grooves or striations of remarkably even spacing. The characteristic appearance observed on all crystals examined is illustrated by Fig. 4 which shows an unusually small facet. Both smooth and striated areas are visible and these usually appeared in the same relation to a facet. A line intersection pattern always associated with the facet can be seen in Fig. 4 and also in Fig. 2.

Examination with an interference microscope shows that the lines are grooves about 0.2μ deep. The spacing between grooves is $2-3\mu$ and the shape of the surface except for the grooves is identical with the shape in the smooth areas. As the figures readily show, the grooves are not steps parallel to the facet and do not seem to be oriented with respect to any low index surface.

A probable explanation of these features is that they are formed during the process of removal from the melt. This leaves open the questions of how such a regular structure is produced, why it does not appear on the facets, and why it appears on some parts of the curved areas and not on other parts of equivalent orientation. Possibly a critical thickness of surface film which freezes shortly after decanting is necessary for the structure to form.

The formation of the grooved structure by a growth process seems unlikely under the experi-

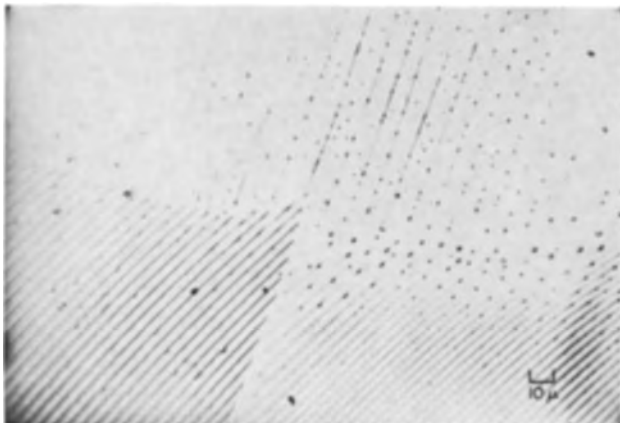


Fig. 3. Steps on facet (upper half of photograph). Magnification X600.



Fig. 5. Features characteristic of a facet and of a curved interface during growth of an InSb crystal. Magnification X150.

mental conditions. Rates of growth and concentrations of impurities are quite different from those required to form structures by segregation processes. However, when steps are present on the facets, these often seem to join with the grooves without any discontinuity. This is illustrated in Fig. 3 and 5.

Surface features on growing crystals.—Examination of growth surfaces on a crystal which was decanted while being pulled (without rotation) in the usual manner revealed features which were quite similar to those already described. More bunching and irregularity of the lines was apparent, as is shown on Fig. 5.

Conical growth hillock.—On the curved region of the growth surface a few small features of distinctive appearance were observed on every sample examined. Examples are shown on Fig. 6. There is a small facet and two black dots of unequal size joined by a line. At lower magnification, termination of a group of the grooves in this area is apparent. These features have some similarity to conical hillocks observed on gallium arsenide and other materials of similar structure (7). The appearance and mode of preparation indicate that these hillocks differ considerably from those observed by Haneman (8).

Discussion

A number of features have been observed on decanted interfaces of indium antimonide. Similar features have been reported on metals during electropolishing (9) and crystal growth (10). In the latter case, the possible formation of such structures

by the adhering film was discussed. A thin film of melt which remains on the crystal surface after decanting may modify the existing surface when it solidifies.

When fine parallel evenly spaced lines are visible on surfaces prepared by similar methods, they usually have been interpreted as growth steps (11). The experiments described here show that such features are visible on crystals which were not growing when decanted. Some modification of the appearance was noted on crystals growing when decanted. Our observations support the view that a surface film is retained on the crystal surface and that this gives rise to an appearance similar to a crystal growth surface. Caution in the interpretation of structures on decanted interfaces is necessary. The way in which such a regular structure is formed remains unexplained. Possibly an instability arises in the molten surface film, and this may occur because of the changes in contact angle, resulting from surface tension, between liquid and solid indium antimonide in the vicinity of the melting point.

For the reasons given in the section on Experimental Observations, the observations made on facets indicate that at low supercooling, growth is proceeding by the screw dislocation mechanism. Although the supercooling required for growth of a facet by a surface nucleation process was not measured, it was established to be larger than 0.4°C . Growth on the facets was shown to proceed by the movement of multiple steps. However, a quantitative application of the theory of Cabrera and Vermilyea (4) requires more information on the spacing and heights of steps on the surface.

Acknowledgments

The author is indebted to S. E. Miller for making available the seed crystals used in these studies, and to A. C. Beer and R. C. Himes for helpful comments on the manuscript.

Manuscript received Jan. 14, 1963. This paper was presented in part at the Boston Meeting, Sept. 16-20, 1962. The research was supported by the Air Force Office of Scientific Research under Contract No. AF 49(638)-959.

Any discussion of this paper will appear in a Discussion Section to be published in the December 1964 JOURNAL.

REFERENCES

1. K. F. Hulme and J. B. Mullin, *Phil. Mag.*, **4**, 1286 (1959).
2. J. B. Mullin and K. F. Hulme, *J. Phys. Chem. Solids*, **17**, 1 (1960).
3. W. P. Allred and R. T. Bate, *This Journal*, **108**, 258 (1961).
4. N. Cabrera and D. A. Vermilyea, "Growth and Perfection of Crystals," p. 393, John Wiley & Sons, New York (1958).
5. N. Albon, *Acta Cryst.*, **15**, 474 (1962).
6. N. Albon and W. J. Dunning, *ibid.*, **13**, 495 (1960).
7. S. E. Miller and N. Albon, To be published. Preliminary details were given at the meeting of the Electrochemical Society Boston, Sept. 16-20, 1962, Abstract No. 86.
8. D. Haneman, *J. Appl. Phys.*, **31**, 217 (1960).
9. K. F. Hulme, *Acta Met.*, **3**, 572 (1955).
10. A. Hellowell and P. M. Herbert, *Proc. Roy. Soc.*, **A269** (1962).
11. R. Illingworth, *Phil. Mag.*, **8**, 631 (1963).

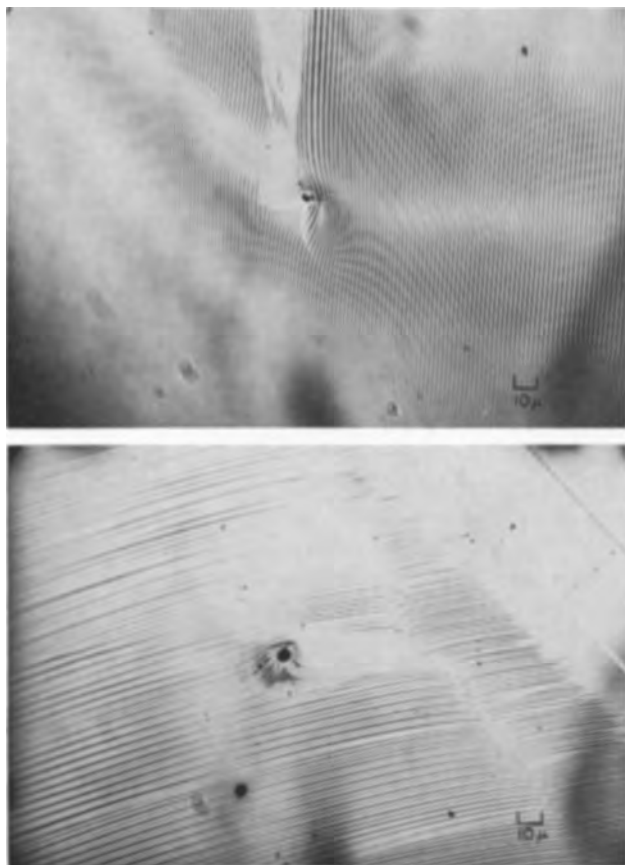


Fig. 6. Small protuberances on InSb growth interfaces as observed on two different crystals. (a) Top; (b) bottom. Magnification X600.

Impurity Content of Germanium Crystallized from the Liquid Ternary Alloy Ge-In-Sb

K. Lehovc and A. Slobodskoy

Sprague Electric Company, North Adams, Massachusetts

ABSTRACT

The compositions of the liquid ternary alloys Ge-In-Sb, which coexist with either solid germanium or solid indium antimonide, are calculated with emphasis on indium-rich alloys. Activity coefficients for the three components in the liquid ternary systems are derived by assuming that the integral molar excess free energy for the ternary system is a linear combination of those for the three binary systems, which are taken from data of Thurmond and Kowalchik for Ge-In and Ge-Sb and of Schottky and Bever for In-Sb. Data of Glasow and Tschishewskaya on the solubilities of Ge in liquid InSb are discussed. Using the activity coefficients of indium and antimony in the ternary liquid alloy in conjunction with the mass action law for the transfer of neutral impurities into the germanium, and expressing the heat energy change by the distribution coefficients of impurities in the binary alloys Ge-In and Ge-Sb at the melting point of the germanium, the concentrations of neutral antimony and neutral indium in the crystallized germanium are calculated. The total concentrations of antimony and indium are then obtained by taking into account the ionization equilibrium in the semiconductor. The ionization equilibrium in a semiconductor containing two kinds of impurities is discussed in the appendix from a more general viewpoint considering impurities of equal and of opposite types and degenerate and nondegenerate conditions, assuming, however, that the impurities have energy levels which coincide with the boundaries of the forbidden band. The solid solubilities of antimony and indium in germanium crystallized from a liquid ternary alloy measured recently by Zemskov *et al.* differ significantly from the experimental data for binary systems by Thurmond and Kowalchik and by Trumbore and from our calculated data for the ternary system.

The importance of certain impurities for the electric properties of semiconductors is well-known. There exists a great deal of empirical information on solidus and liquidus lines of binary semiconductor-impurity systems particularly for the semiconductors germanium and silicon (1, 5). More recently, ternary systems involving a semiconductor and two types of impurities have become of interest, *e.g.*, an important process to prepare transistor structures, the so-called post-alloy diffusion process (6, 7), utilizes a region in a semiconductor containing two types of impurities promoting p- and n-conductivities. The two types of impurities are incorporated into the semiconductor by crystallization of the semiconductor from a ternary liquid alloy containing the two impurity elements. In this paper the composition of the solid and liquid phases at crystallization is analyzed theoretically for the case Ge-In-Sb, assuming quasi-thermal equilibrium conditions.

In the section on Crystallization of Germanium from a Liquid Alloy Ge-In-Sb the chemical interaction of the three components in the liquid ternary alloy is discussed in terms of activity coefficients, derived approximately from data of the three binary systems. Using these activity coefficients, the alloy composition coexisting at a given temperature with either solid germanium or else solid indium antimonide will be calculated.

In the section on Concentrations of Antimony and of Indium in the Crystallized Germanium the concentrations of neutral impurities in the crystallized germanium are calculated, following the procedure used previously by one of us (8) for binary semiconductor-impurity systems with miscibility gap in the solid phase. Then the total concentrations of indium and antimony in the semiconductor are calculated from that of neutral impurities by taking into account the ionization equilibrium in the semiconductor. The procedure is similar to that of Reiss and co-workers (9) for the cases of Ge containing Ga and Li, and Si containing B and Li. However, while Reiss *et al.* derive the added lithium concentration in terms of the total p-type impurity concentration (Ga or B) already present in the crystal, for our purpose the total impurity concentrations must be expressed in terms of the neutral impurity concentrations. An appendix contains the derivation of the pertinent equations as well as the discussion of the ionization equilibrium from a more general viewpoint, including the cases of degeneracy and nondegeneracy, and of the presence of two kinds of impurities of the same conductivity type as well as of opposite conductivity types.

Crystallization of Germanium from a Liquid Alloy Ge-In-Sb

The composition of the liquid alloy Ge-In-Sb will be characterized by the mole fractions of its

components, x_{Ge} , x_{In} and x_{Sb} , of which only two are independent in view of the identity

$$x_{\text{Ge}} + x_{\text{In}} + x_{\text{Sb}} = 1 \quad [1]$$

We shall be concerned particularly with indium-rich liquid alloys since these are of practical interest in making some types of transistors (6, 7). In a certain temperature range solid germanium may crystallize if x_{Ge} is sufficiently large, and solid InSb may crystallize from an indium-rich melt if x_{Sb} is sufficiently large. We need not be concerned about the crystallization of solid antimony since we shall not be interested in the Sb-rich corner of the ternary system. When crystallizing a small portion of a ternary melt into solid germanium, the ratio

$$r = x_{\text{Sb}}/x_{\text{In}} \quad [2]$$

in the liquid phase remains constant (neglecting the traces of In and Sb incorporated in the solid Ge). Thus it is practical to introduce x_{Ge} and r as the independent parameters, from which

$$x_{\text{In}} = (1-x_{\text{Ge}})/(1+r) \quad [3]$$

and

$$x_{\text{Sb}} = (1-x_{\text{Ge}})/(1+1/r) \quad [4]$$

Next we shall discuss the temperature T at which the composition (x_{Ge} , r) coexists with solid germanium. Considering that (i) the partial vapor pressures of germanium above solid germanium and above the coexisting liquid alloy are the same, $P_{\text{Ge}}^{\text{l}} = P_{\text{Ge}}^{\text{s}}$, (ii) the partial vapor pressure above solid germanium is practically not influenced by traces of indium and antimony, (iii) the vapor pressures above pure liquid ($P_{\text{Ge}}^{\text{l},0}$) and pure solid germanium differ by an exponential factor involving the heat of fusion of germanium $\Delta H_{\text{F}}^{\text{Ge}}$ (we neglect differences in specific heats) and are equal at the melting point of pure germanium, T_{M}^{Ge} , and finally (iv) the definition of the activity coefficient, γ_{Ge} , by

$$P_{\text{Ge}}^{\text{l}} = \gamma_{\text{Ge}} x_{\text{Ge}} P_{\text{Ge}}^{\text{l},0} \quad [5]$$

we obtain the well-known equation

$$\gamma_{\text{Ge}} x_{\text{Ge}} = \exp \left[-\frac{\Delta H_{\text{F}}^{\text{Ge}}}{R} \left(\frac{1}{T} - \frac{1}{T_{\text{M}}^{\text{Ge}}} \right) \right] \quad [6]$$

Given γ_{Ge} as a function of x_{Ge} , r , and T , for each composition (x_{Ge} , r) we may calculate from [6] the temperature T at which the liquid alloy is coexisting with solid germanium.

The dependence of the activity coefficient γ_{Ge} (and of the corresponding coefficients γ_{Sb} and γ_{In}) on composition and on temperature will be estimated as follows: Assuming that the three binary systems can be characterized by the following simple expression for the integral molar excess free energies

$$F_{12}^{\text{E}} = A_{12}x_1x_2; F_{13}^{\text{E}} = A_{13}x_1x_3; F_{23}^{\text{E}} = A_{23}x_2x_3 \quad [7]$$

we may approximate the integral molar excess free energy of the ternary system by (10-12)

$$F^{\text{E}} = A_{12}x_1x_2 + A_{13}x_1x_3 + A_{23}x_2x_3 \quad [8]$$

The partial molar excess free energy F_1^{E} is obtained in a well-known manner (13)

$$F_1^{\text{E}} = F^{\text{E}} + (1-x_1) \left(\frac{\partial F^{\text{E}}}{\partial x_1} \right)_{x_2/x_3 = \text{constant}} \\ = A_{12}x_2(1-x_1) + A_{13}x_3(1-x_1) - A_{23}x_2x_3 \quad [9]$$

and is related to the activity coefficient by

$$\gamma_1 = \exp (F_1^{\text{E}}/RT) \quad [10]$$

The coefficients A_{12} (Ge-In) and A_{13} (Ge-Sb) were taken from an interpretation of the liquidus lines of these binary systems by Thurmond and Kowalchik (1), who find that

$$A_{12} = a_{12} + b_{12}T \quad [11]$$

$$A_{13} = a_{13} + b_{13}T \quad [12]$$

with $a_{12} = 1570$ cal/mole, $b_{12} = -0.56$ cal/mole $^{\circ}\text{K}$, $a_{13} = 2540$ cal/mole, and $b_{13} = -1.98$ cal/mole $^{\circ}\text{K}$. Values of A_{12} and A_{13} at several temperatures are listed in Table I. Note that A_{12} (Ge-In) depends comparatively little on temperature, while A_{13} (Ge-Sb) shows a significant temperature dependence. For an interpretation of this temperature dependence the reader is referred to Thurmond and Kowalchik (1). Empirical data on the eutectic temperature and composition of the Ge-Sb binary system agree well with data obtained from the numerical values above (1). Empirical data (5) of the Ge-rich solidus of the binary systems Ge-In and Ge-Sb agree well with γ_{Sb} and γ_{In} as derived above (8).

Schottky and Bever (2) have analyzed the liquidus of the In-Sb binary system by a method of Wagner (14) and find over a wide temperature range $A_{23} = a_{23} = -3960$ cal/mole. As expected from the partially ionic interaction between In and Sb, the value of a_{23} is negative. Accordingly, the activity coefficients of indium and antimony become substantially smaller than unity in a liquid alloy rich in the other element. On the other hand the values A_{12} and A_{13} are positive indicating repulsive type of interaction between Ge and In or Sb. Accordingly, the activity coefficient of Ge in ternary alloys Ge-In-Sb may exceed unity considerably.

Introducing [11] and [12] into [10] with [9], one obtains

$$\gamma_{\text{Ge}} = \exp \{ [(1-x_{\text{Ge}})^2/RT] [a_{12} + a_{13}r - a_{23}r/(1+r) + T(b_{12} + b_{13}r)/(1+r)] \} \quad [13]$$

The liquidus compositions coexisting with solid germanium at temperatures of 600 $^{\circ}\text{K}$, 700 $^{\circ}\text{K}$, 800 $^{\circ}\text{K}$, 900 $^{\circ}\text{K}$, and 1000 $^{\circ}\text{K}$ were calculated by Eq. [6] with [13] using $\Delta H_{\text{F}}^{\text{Ge}} = 8100$ cal/mole, $T_{\text{M}}^{\text{Ge}} = 1210^{\circ}\text{K}$ and $R = 2$ cal/mole $^{\circ}\text{K}$, and are shown as nearly

Table I. Coefficients A_{12} for Ge-In and A_{13} for Ge-Sb as functions of temperature

T, $^{\circ}\text{K}$	A_{12} , cal/mole	A_{13} , cal/mole
600	1234	1452
700	1178	1254
800	1122	1056
900	1066	858
1000	1010	660

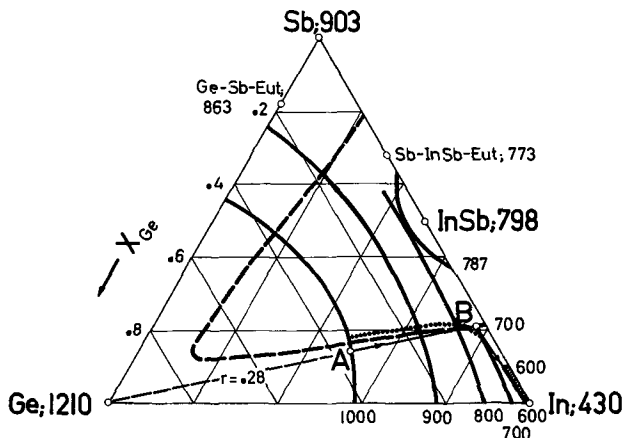


Fig. 1. Ternary phase diagram Ge-In-Sb showing: 1. the lines where the liquid alloy coexists with solid germanium at the temperatures (in °K) indicated along the Ge-In-side; 2. the lines where the liquid alloy is coexisting with solid indium antimonide at 787°K, 700°K, and 600°K. The dashed part of the line at 700°K is hypothetical since liquid alloy cannot exist due to formation of solid germanium. At 600°K the figure shows only the section of the line which limits the region (shaded area) where liquid alloy can occur at 600°K. The dotted line separates the regions of crystallization of n-type and p-type germanium. The line $r = 0.28$ from point A to B is an example of an alloying cycle to germanium, discussed in the text.

solid lines in the ternary phase diagram of Fig. 1. The intersections of these lines with the sides Ge-In ($x_{Sb} = 0$) and Ge-Sb ($x_{In} = 0$) are the liquidus compositions of the binary systems Ge-In and Ge-Sb, respectively. The intersections of these lines with the line $x_{In} = x_{Sb}$ indicate the solubilities of germanium in liquid indium antimonide. There is good agreement of our calculated lines with the liquidus compositions of the binary systems Ge-In and Ge-Sb, since we have used the empirical coefficients A_{12} and A_{13} derived by Thurmond and Kowalchik (1) from these liquidus compositions.

On the other hand, there are substantial discrepancies between the calculated solubilities of germanium in liquid indium antimonide and the empirical values of Glasow and Tschishewskaya (3). These authors have interpreted their experimental data, curve 1 of Fig. 2, in terms of the activity coefficient of germanium in a binary system consisting of germanium and of indium antimonide. Curve 2 is the ideal liquidus of a binary germanium system, which differs considerably from the empirical data. Curve 3 is the ideal liquidus of the ternary system Ge-In-Sb, which agrees much better with the observed liquidus than curve 2. The deviations between the ideal liquidus of the ternary system and the empirical data are such that in Fig. 2 the ideal curve is too high near the melting point of germanium and too low at lower temperatures. The latter could be attributed to an activity coefficient $\gamma_{Ge} > 1$. The discrepancy near the melting point is not understood at present since, according to Raoult's law, $\gamma_{Ge} \rightarrow 1$ for $x_{Ge} \rightarrow 1$. The discrepancy may thus point to a systematic error in the empirical data, these data indicating a solubility of germanium, which is too high at a given temperature. If this were the case along the entire curve the discrepancy between the empirical data and the liquidus

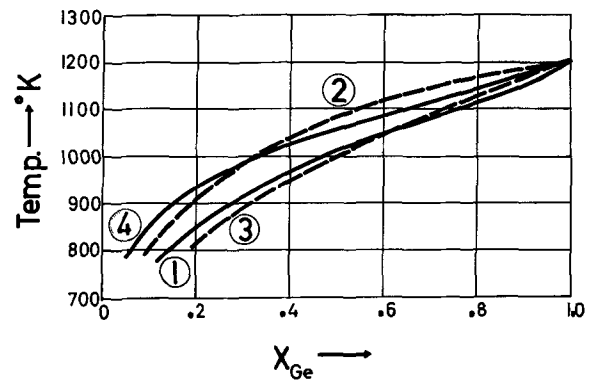


Fig. 2. Solubility of germanium in liquid InSb expressed in mole fraction of germanium, $x_{Ge}^{(T)}$, in the ternary system Ge-In-Sb. [(T) for "ternary" and (B) for "binary".] 1. Empirical data by Glasow and Tschishewskaya (3). 2. Ideal liquidus of a binary system (Eq. [6]) with

$$\gamma_{Ge} = 1, x_{Ge} = x_{Ge}^{(B)} = \frac{2x_{Ge}^{(T)}}{1+x_{Ge}^{(T)}}.$$

3. Ideal liquidus of a ternary system (Eq. [6]) with

$$\gamma_{Ge} = 1, x_{Ge} = x_{Ge}^{(T)}.$$

4. Actual liquidus of a ternary system (Eq. [6] with [13]).

curve 4 in Fig. 2, which was calculated by [6] with [13] and $\tau = 1$, would be decreased.

Figure 3 shows the activity coefficient of germanium in the liquid alloy calculated by Eq. [13] for various ratios r , and for temperatures at which solid germanium coexists with the alloys of composition x_{Ge} , r . Since in Fig. 1 the lines for crystallization of germanium at constant temperature are almost parallel to the lines of constant x_{Ge} near $x_{In} \approx x_{Sb}$, the curves γ_{Ge} at $x_{Ge} = \text{constant}$ coincide with curves γ_{Ge} at constant T in the vicinity of $r = 1$. Note that the activity coefficient of germanium reaches values large compared to unity at small germanium concentrations and thus plays an important role in Eq. [6]. For $x_{Ge} > 0.6$ the activity coefficient of germanium becomes almost independent of r , approaching unity. The temperature of coexistence with solid germanium depends then only

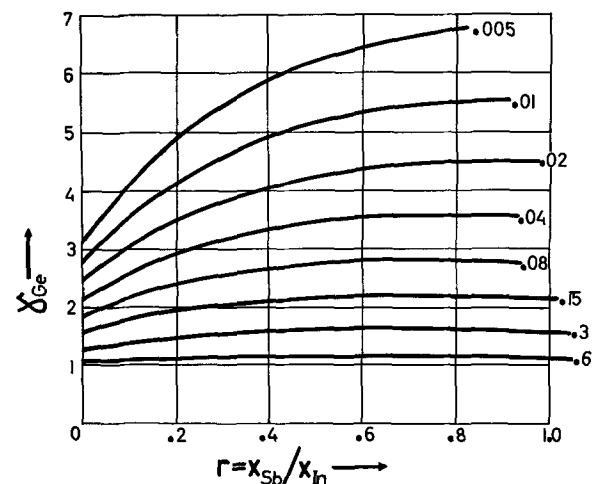


Fig. 3. Activity coefficient of germanium in the liquid ternary alloy as function of the Sb:In ratio, r , and of the germanium mole fraction, x_{Ge} , (indicated along the curves), and at the temperature at which the liquid alloy is coexisting with solid germanium.

on x_{Ge} , but not on r , and the lines of constant temperature coincide closely with the straight lines $x_{Ge} = \text{constant}$ in Fig. 1. The maximum change in crystallization temperature along a line $x_{Ge} = \text{constant}$ occurs near $r \approx 1$, where γ_{Ge} has its maximum. This temperature change can be estimated by comparing the liquidus temperature of the germanium-indium binary system with that of curve 4 in Fig. 2, pertaining to the same value of x_{Ge} .

At a given temperature the range of composition of the liquid ternary alloy can be limited not only by crystallization of solid germanium but also by crystallization of solid indium antimonide. Solid indium antimonide coexists with the ternary liquid alloy at temperatures and compositions related by

$$4\gamma_{In}\gamma_{Sb}x_{In}x_{Sb} = \exp \left[\frac{A_{InSb}}{2RT_M^{InSb}} - \frac{2\Delta H_F^{InSb}}{R} \left(\frac{1}{T} - \frac{1}{T_M^{InSb}} \right) \right] \quad [14]$$

where A_{InSb} is the excess heat of solution of solid InSb in the liquid alloy, ΔH_F^{InSb} the heat of fusion of InSb and T_M^{InSb} the melting point of indium antimonide. Equation [14] arises from the ideal liquidus of the binary system In-Sb by multiplying the left side by the product of the activity coefficients $(\gamma_{In}\gamma_{Sb})_{T,x_{In},x_{Sb}}$ and the right side by

$$(\gamma_{In}\gamma_{Sb})_{T=T_M^{InSb}; x_{In}=x_{Sb}=1/2} = \exp \left(\frac{A_{InSb}}{2RT_M^{InSb}} \right)$$

as found from [8], [9], and [10] for $\gamma_3 = \gamma_{Sb}$ and $\gamma_2 = \gamma_{In}$. Using the values $\Delta H_F^{InSb} = 6100$ cal/mole, $T_M^{InSb} = 798^\circ\text{K}$ and $A_{InSb} = -3960$ cal/mole in Eq. [14] for $x_{Ge} = 0$, the empirical liquidus of the indium-antimony system (15) is well reproduced by Eq. [14] in the range $x_{In} > 0.5$.

Lines (or sections thereof) indicating compositions of the liquid ternary alloy, coexisting with solid indium antimonide are plotted in the phase diagram, Fig. 1, for $T = 600^\circ\text{K}$, 700°K , and 787°K . These lines intersect with the In-Sb side of the phase triangle at the compositions of the In-Sb liquidus. We are primarily interested in the shape of these lines in the region of small germanium concentrations. For an ideal case (activity coefficients of unity), such a line would be given by $x_{In} \cdot x_{Sb} = f(T)$, i.e., the compositions of the ideal ternary liquidus coexisting with solid indium antimonide at a given temperature should lie on a hyperbola. However, the strong deviations from ideality in the In-Sb system reflect in activity coefficients for Sb and In which differ strongly from unity. Their dependences on concentration have a significant influence on the shape of the liquidus lines coexisting with solid indium antimonide. The importance of the activity coefficients in Eq. [14] can be appreciated from Fig. 4, where γ_{Sb} and γ_{In} are plotted pertaining to temperatures of 600°K - 1000°K and compositions of the liquid alloy coexisting with solid germanium at these temperatures. Note that these activity coefficients are generally smaller than unity and that γ_{Sb} becomes quite small for Sb-poor alloys.

The lines of the liquid alloy coexisting with solid germanium and with solid indium antimonide, per-

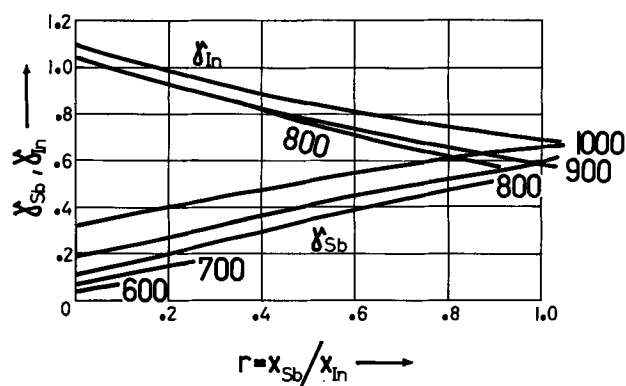


Fig. 4. Activity coefficients of indium, γ_{In} , and of antimony, γ_{Sb} , for liquid Ge-In-Sb alloys coexisting with solid germanium as functions of the Sb:In ratio and of the temperature in $^\circ\text{K}$ indicated along the curves.

taining to the same temperature T , intersect for $T \leq 787^\circ\text{K}$. Thus for $T \leq 787^\circ\text{K}$ (and of course $T > T_M^{In}$) the line pertaining to coexistence with solid indium antimonide at the same temperature is the boundary of a region of liquid ternary alloy, which extends from the indium corner of the phase diagram. For $T = 600^\circ\text{K}$ this region has been indicated by the shaded area. The corner of the region marks a composition where the liquid ternary alloy is coexisting with both solid germanium and solid indium antimonide. The highest temperature where this is possible is 787°K and the composition of the liquid alloy is then $x_{Ge} = 0.05$; $x_{In} = 0.475$; $x_{Sb} = 0.475$. This alloy may be considered as the eutectic of the pseudobinary system Ge-InSb.

Let us consider the crystallization from a Ge-In-Sb alloy on cooling. Suppose we have an alloy of the composition indicated by point A in the ternary diagram, Fig. 1, at a given temperature exceeding 1000°K . On cooling solid germanium will crystallize at 1000°K since the composition chosen lies on the line where solid germanium is coexisting with liquid alloy at 1000°K . Since germanium is removed by crystallization from the liquid alloy but practically all indium and antimony remain in the liquid phase,¹ the composition of the liquid phase shifts along the line of constant r indicated by an arrow. This line prolonged beyond the point A would go through the Ge corner and is the locus of all alloys of $r = 0.28$. When cooled to 900°K , the composition of the liquid alloy is $x_{Ge} = 0.17$; $x_{In} = 0.65$; $x_{Sb} = 0.18$. On further cooling a temperature is reached where not only solid germanium but also indium antimonide crystallize. In the example chosen, this occurs at 700°K and at the composition B. When cooling further, the composition of the liquid alloy changes by simultaneous crystallization of germanium and of indium antimonide along the line marked by an arrow and leading toward the indium corner of the phase diagram. The line in question connects the points where the liquid alloy is coexisting with both solid germanium and solid indium antimonide.

In the cooling range where only solid germanium

¹ The traces of In and Sb, which are incorporated with the solid germanium, are not significant for the composition of the liquid phase.

crystallizes, the thickness Z of the crystallized layer at a temperature T is given by

$$Z = \frac{L_0}{AN_{Ge}} \frac{1 - x_{Ge}/x^0_{Ge}}{1 - x_{Ge}} \quad [15]$$

where x^0_{Ge} is the initial mole fraction of germanium in the liquid alloy, x_{Ge} that after crystallization of the layer of thickness Z and area A ; L_0 is the number of germanium atoms in the initial liquid alloy and, N_{Ge} is the number of atoms per unit volume in the crystallized germanium.

Concentrations of Antimony and of Indium in the Crystallized Germanium

By applying the mass action law to the transfer of neutral antimony from the liquid alloy into the semiconductor, one obtains

$$C^{x_{Sb}} = \gamma_{Sb} x_{Sb} N_V \Gamma^{Sb} \exp(-U^{Sb}/RT) \quad [16]$$

where U^{Sb} is the energy (heat content change) required to transfer one mole of impurities from the liquid alloy into the germanium crystal and Γ^{Sb} is the ratio of the partition sums of antimony in the solid semiconductor and in the liquid alloy which will be approximated by the corresponding expression for pure solid antimony and pure liquid antimony

$$\Gamma^{Sb} = \exp\left(-\frac{\Delta H_F^{Sb}}{RT_M^{Sb}}\right) \quad [17]$$

The energy U^{Sb} can be expressed (8) in terms of the segregation coefficient, K_M^{Sb} , of antimony at the melting point of germanium and of the electric parameters n_i (intrinsic carrier concentration) and N_c (partition sum for electrons in the conduction band) of the semiconductor

$$U^{Sb} = RT_M^{Ge} \ln \left[\left(1 + \frac{1}{2} \frac{N_c}{n_i}\right) \gamma_{Sb} \Gamma^{Sb} / K_M \right]_{T_M^{Ge}} \quad [18]$$

In the case of p-type impurities, such as indium, N_c must be replaced by N_v , the partition sum for holes in the valence band.

Table II contains values of Γ and U for several important doping impurities in germanium and silicon calculated by Eq. [17] and [18] using empirical data of the distribution coefficients, activity coefficients, and the electric parameters n_i , N_c , N_v , discussed elsewhere (8).

Table II. Activity coefficients of impurities, γ , for binary semiconductor impurity systems at the melting point, T_M^S , of the semiconductor; partition sum ratios, Γ , (Eq. [17]); and heat content changes, U , (Eq. [18]) for several impurities in germanium and silicon

Impurity	γ	Γ	U , cal/mole
Germanium			
As	0.79	0.048	4,510
Al	0.53	0.25	3,510
Ga	0.94	0.11	2,510
Sb	1.1	0.073	10,960
In	1.46	0.40	16,820
Silicon			
As	3.9	0.048	4,180
Al	0.54	0.25	17,650
Ga	0.7	0.11	14,120
Sb	6.0	0.073	15,680

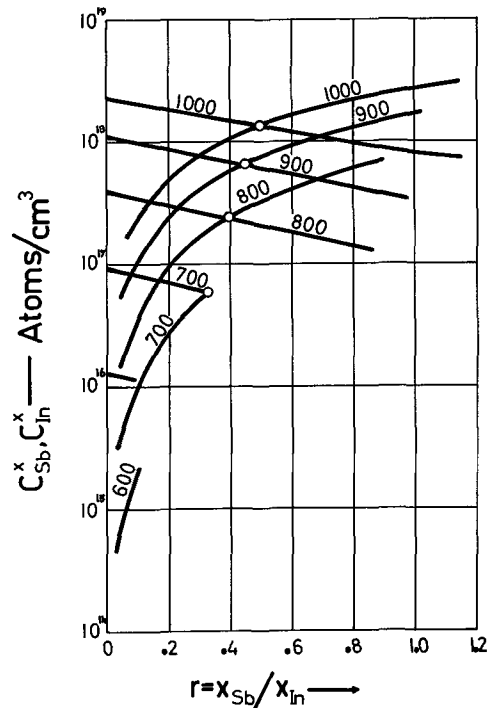


Fig. 5. Concentrations of neutral antimony and of neutral indium in germanium crystallized at the temperatures indicated along the curves (in °K) from a ternary alloy Ge-In-Sb of the Sb:In ratio shown as abscissa. $C^{x_{Sb}}$ are the rising curves and $C^{x_{In}}$ are the descending curves.

The concentrations of neutral indium and antimony have been calculated by Eq. [16] utilizing the activation energies, U , and the values of Γ of Table II, the composition of the liquid alloy coexisting with solid germanium (Fig. 1) and the activity coefficients of indium and antimony in the liquid alloy at the crystallization temperature from Fig. 4.

Figure 5 shows that the concentration of neutral indium in the crystallized germanium decreases with increasing concentration of antimony in the liquid alloy. There are two causes for this decrease: (i) increasing antimony concentration in the liquid alloy decreases its indium concentration at a fixed crystallization temperature (cp. Eq. 3), and (ii) increasing antimony concentration decreases the activity coefficient of indium in the liquid alloy. The same is true, of course, for the concentration of neutral antimony in germanium as function of the indium concentration in the liquid alloy.

The total impurity concentrations (neutral and ionized impurities) are obtained from those of the neutral impurities by taking into account the ionization equilibrium in the semiconductor. Pertinent equations will be derived in the appendix from a general viewpoint considering impurities of the same and of opposite conductivity types, and non-degenerate as well as degenerate conditions.

In the present case, where we deal with impurities of opposite conductivity types and with nongenerate conditions, it will be shown in the appendix that

$$C_{Sb} = C^{x_{Sb}} \left\{ 1 + \frac{1}{2} \exp(G/2) \left[\frac{C^{x_{In}} + 2N_c \exp(-G)}{C^{x_{Sb}} + 2N_v \exp(-G)} \right]^{1/2} \right\} \quad [19]$$

$$C_{\text{In}} = C_{\text{In}}^x$$

$$\left\{ 1 + \frac{1}{2} \exp(G/2) \left[\frac{C_{\text{Sb}}^x + 2N_v \exp(-G)}{C_{\text{In}}^x + 2N_c \exp(-G)} \right]^{1/2} \right\} \quad [20]$$

G designating the forbidden band gap divided by kT , which is related to n_i by

$$n_i^2 = N_c N_v \exp(-G) \quad [21]$$

The "1" in Eq. [19] and [20] is found to be small compared to the other expression in the parenthesis indicating that $C_{\text{Sb}} \gg C_{\text{Sb}}^x$ and $C_{\text{In}} \gg C_{\text{In}}^x$. Thus the concentration of antimony is increased due to the effect of the indium on the ionization equilibrium by about the factor $\sqrt{1 + C_{\text{In}}^x/2N_c \exp(-B)}$, and that of indium due to the presence of antimony by about the factor $\sqrt{1 + C_{\text{Sb}}^x/2N_v \exp(-B)}$. Numerical values for $2N_c \exp(-B)$ and $2N_v \exp(-B)$ have been listed in Table III and can be compared with the concentrations of neutral antimony and indium plotted in Fig. 4. For the range of composition and temperature covered by the data of Fig. 4, it is found that the increase in the antimony concentration resulting from the effect of the indium on the ionization equilibrium is appreciable in all cases, ranging from about a factor 2 at 600°K and small antimony concentration to about 1.5 at 1000°K and small antimony concentration, and decreasing only slightly with increasing antimony concentration. The effect of the antimony on the indium concentration by means of the ionization equilibrium is less pronounced since Fig. 4 covers mainly indium-rich, antimony-poor alloys; i.e. small r . However, the effect of antimony on the indium concentration due to the ionization equilibrium is by no means negligible for $r > 0.2$.

The total concentrations of indium and of antimony in the crystallized germanium have been calculated by Eq. [19] and [20] using the concentrations of neutral impurities shown in Fig. 5, and the numerical values of the electric parameters, n_i , N_c , and N_v as used in ref. (8), which come from a review paper by Conwell (16). Figure 6 shows C_{Sb} and C_{In} at several crystallization temperatures as a function of the ratio $r = x_{\text{Sb}}/x_{\text{In}}$. Note that with increasing r at a given crystallization temperature the crystallized germanium changes from p-type to n-type. The compositions of the liquid alloy at which this transition occurs, i.e. at which the germanium is compensated, have been marked by the dotted line in Fig. 1. At 600°K the Sb:In ratio required for crystallization of n-type germanium is not accessible because of formation of solid indium antimonide. Using the liquid alloy of $r = 0.28$, p-type germanium would

Table III. Numerical values of certain parameters occurring in the Eq. [19] and [20]

Temp, °K	$2N_c \exp(-B)$	$2N_v \exp(-B)$
600	$4.05 \times 10^{15} \text{ cm}^{-3}$	$2.23 \times 10^{15} \text{ cm}^{-3}$
700	2.50×10^{16}	1.37×10^{16}
800	1.44×10^{17}	7.97×10^{16}
900	6.23×10^{17}	3.44×10^{17}
1000	2.02×10^{18}	1.11×10^{18}

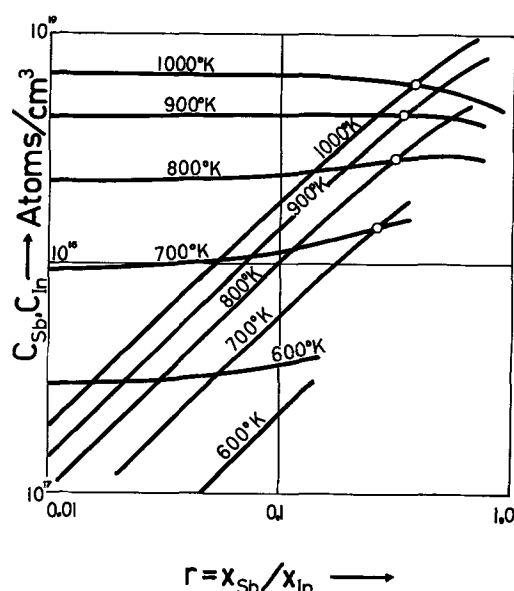


Fig. 6. Total concentrations of antimony, C_{Sb} , and of indium, C_{In} , in germanium crystallized at the temperatures indicated along the curves (in °K) from a ternary alloy Ge-In-Sb of the Sb:In ratio shown as abscissa. C_{Sb} are the curves which rise almost linearly with r . The intersection points of the two families of curves correspond to impurity-compensated germanium.

crystallize above 750°K and n-type germanium below 750°K. For $T > 800^\circ\text{K}$ the values of r corresponding to compensation are close to $r \approx 0.3$ which is the ratio of Sb to In if the segregation coefficients at the melting point of Ge for the binary systems Sb-Ge and In-Ge would apply to the ternary system at various temperatures, and if there would not be any interaction between Sb and In. This surprising agreement is a consequence of compensation of the effects resulting from the activity coefficients and from the ionization equilibrium.

The p-type conduction of the germanium crystallized at a given temperature depends on the Sb-concentration in the liquid alloy for the following reason: (a) Increasing x_{Sb} decreases x_{In} at a given T . (b) Increasing x_{Sb} decreases γ_{In} . (c) Presence of Sb in the germanium increases the ratio $C_{\text{In}}/C_{\text{In}}^x$. (d) Presence of Sb in the germanium partially compensates the presence of In with respect to conductivity.

The relations (a), (b), and (d) tend to suppress the p-type conductivity while the relation (c) enhances the p-type conductivity. The influence of the relations (a) and (b) is clearly recognizable in Fig. 5 regarding the concentration C_{In}^x . Figure 6 shows that the influence of the relations (a), (b), and (c) on the total indium concentration just about compensates at 900°K for $x_{\text{Sb}}/x_{\text{In}} \lesssim 0.5$ and at 1000°K for $x_{\text{Sb}}/x_{\text{In}} \lesssim 0.2$. At 800°K, 700°K, and at 600°K the influence (c) dominates over (a) and (b) already at comparatively small ratios $x_{\text{Sb}}/x_{\text{In}}$.

The concentration of antimony increases almost linearly with $x_{\text{Sb}}/x_{\text{In}}$ for any temperature between 600°K and 1000°K up to the ratio $x_{\text{Sb}}/x_{\text{In}}$ where change from p-type to n-type occurs. The concentration of indium in germanium in the limit of zero antimony agrees fairly well with experimental data by Lee (17) as discussed in ref. (8).

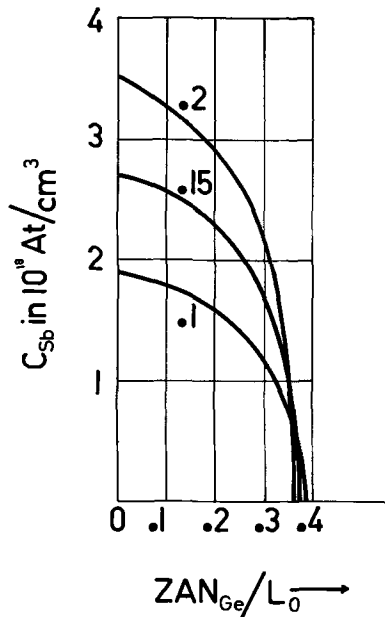


Fig. 7. Distribution of antimony in germanium crystallized from a saturated ternary alloy Ge-Sb-In when cooling from 1000°K, for the Sb/In-ratios $r = 0.2, 0.15,$ and 0.1 . The abscissa is the position in the crystallized layer expressed in dimensionless units by multiplying with the area (A), the concentrations of atoms in solid germanium (N_{Ge}) and dividing by the number of Ge atoms in the liquid alloy at the start of crystallization (L_0).

For the post alloy diffusion process (6,7), it is important to control the distribution of antimony in the recrystallized germanium as the initial condition for a subsequent diffusion. Of particular importance is the total concentration of antimony per unit area in the recrystallized layer

$$N_{Sb}/A = \int_0^{L_0/A N_{Ge}} C_{Sb} dZ \quad [22]$$

which can be calculated for various alloy cycles by combination of Eq. [15], Fig. 1 to provide $T(x_{Ge})$, and Fig. 6 to provide $C_{Sb}(T)$. Examples are found in Fig. 7.

In producing the emitter region of a transistor by an alloying process it is customary to add small amounts of Al and Ga to In in order to increase the p-type conductivity of the crystallized germanium, i.e., using a quaternary system,² e.g., Ge-In-Ga-Sb. The substitution of less than 1% of Ga for part of the In will not affect the activity coefficient of antimony significantly, or the temperature of coexistence with solid germanium. However, if the concentration of gallium in the solid germanium exceeds that of indium the concentration of antimony would be affected because of the ionization equilibrium.

Comparison with Experimental Data of Zemskov et al. (4)

Zemskov et al. (4) have determined the concentrations of antimony and of indium in germanium crystallized from liquid ternary alloys of the compositions $x_{Ge} = 0.867, 0.71,$ and 0.412 , and various antimony to indium ratios r . The antimony content was determined by using the isotope Sb^{124} and the indium content was then derived using Hall effect data at room temperature. The crystallization temperatures

² In some cases Pb is added.

and the solidus concentrations of Zemskov et al. (4) for the two binary systems Ge-In ($r = 0$) and Ge-Sb ($r = \infty$) differ considerably from the data of Thurmond and Kowalchik (1) and of Trumbore (5). The discrepancy in the solidus concentrations cannot be explained by the discrepancy in the liquidus temperatures and is particularly strong for Ge-Sb at $x_{Ge} = 0.412$ and for Ge-In at $x_{Ge} = 0.867$, where solidus concentrations of Zemskov (4) are higher by a factor 2.5 and 2, respectively, than Trumbore's values. The germanium compositions investigated corresponded to crystallization temperatures of 1143°K, 1085°K, and 945°K, respectively. While these temperatures differ significantly from the temperatures for the binary systems of equal germanium concentrations according to Thurmond and Kowalchik (1), this discrepancy is not important for the following discussion. The two higher temperatures are in the range beyond the curves plotted in Fig. 6, but we may infer from the trend of the curves that no maximum of C_{In} with increasing r is expected. This is in contrast to Zemskov et al., who observe a maximum by a factor 1.2 (at $x_{Ge} = 0.867$) and 2 (at $x_{Ge} = 0.71$) higher than C_{In} at $r = 0$. At the composition $x_{Ge} = 0.412$, there is a significant change in the crystallization temperature with composition r (compare the curvature of the line $T = 1000^\circ K$ in Fig. 1, showing the change of composition x_{Ge} with r at a constant crystallization temperature). By using the data of Thurmond and Kowalchik (1) and of Fig. 2, curve 3, we find that $T_{r=1} - T_{r=0} = 52^\circ K$ at $x_{Ge} = 0.412$. Thus the indium concentration in solid germanium as a function of r at $x_{Ge} = 0.412$ would not correspond to a constant temperature curve, but should change from the curve $T = 978^\circ K$ to $T = 1030^\circ K$ in Fig. 6 in the range between $r = 0$ and $r = 1$. While this might lead to a shallow maximum of C_{In} , this maximum would certainly not be as pronounced as the factor 3 observed by Zemskov et al. The shape of the curves in Fig. 6 arises in part from the deviations from ideal behavior as expressed by activity coefficients differing from unity and in part from the ionization equilibrium. If we would have used activity coefficients of unity throughout, taking only into consideration the ionization equilibrium, curves would have been obtained which still would not exhibit the pronounced maximum of C_{In} with r observed by Zemskov et al. (5). It is interesting to note that compensation, $C_{Sb} = C_{In}$, is found to occur by Zemskov et al. at $r \approx 0.3$, for the two higher germanium concentrations, roughly in agreement with Fig. 6. However, at the lowest germanium concentration compensation is found at $r \approx 0.1$, while we would expect it still around $r \approx 0.3$.

Since the ionization equilibrium cannot account for the observations of Zemskov et al., formation of neutral InSb molecules in the solid germanium has been considered by us as a tentative explanation. The maximum concentration of these molecules may be expected to occur at the ratio $r = 1$, corresponding to the maximum of $C_{In}^x \cdot C_{Sb}^x \approx x_{In} \cdot x_{Sb}$ (ignoring effects arising from the activity coefficients as second order ones). However, the maximum of C_{In} as found by Zemskov et al. (4) occurs at $r \approx 0.3, 0.3,$

and 0.1, respectively, for the three germanium concentrations. Thus the data of Zemskov *et al.* cannot be explained by means of the ionization equilibrium or by means of neutral (InSb) molecules. It appears desirable to examine additional experimental data, particularly in view of the serious discrepancies with existing experimental data (1, 5) on the binary systems.

Summary and Conclusion

The concentrations of two electrically active impurities (indium and antimony) in a semiconductor (germanium) have been discussed, which arise under thermal equilibrium conditions of doping assuming that the two impurity types interact in the semiconductor only through their combined influence on the ionization equilibrium. For convenience it has been assumed that the impurities have energy levels coinciding practically with the bottom of the conduction band or the top of the valence band, respectively. The case where the semiconductor is crystallized from a ternary melt has been investigated in detail taking into account the interaction of the semiconductor element with the two impurity elements in the liquid phase by activity coefficients which were obtained approximately from a linear combination of integral molar excess free energies of the three binary liquid phases.

The concentrations of the liquid ternary Ge-In-Sb alloy coexisting with (a) solid germanium, or (b) solid indium antimonide have been derived, and the concentrations of indium and antimony in solid germanium crystallized from alloys of composition (a) have been computed. There are ranges of concentrations and temperatures where p-type and others where n-type germanium crystallizes. Under certain conditions InSb crystallizes simultaneously with germanium.

Our computed data agree well with the liquidus of the three binary systems Ge-In, Ge-Sb, and In-Sb (for $x_{\text{In}} \gtrsim 0.5$) due to the choice of the energies involved in the activity coefficients.

The solubility of germanium in liquid indium antimonide was measured by Glasow and Tschishewskaya (3). Treating this as an ideal ternary system, fair agreement with the empirical data is achieved except near the melting point of Ge, where a systematic error in the empirical data is indicated since Raoult's law is violated. Incorporating our activity coefficients the agreement is generally not improved, the correction being of the correct sign but too large.

The experimental solidus data by Zemskov *et al.* (4) exhibit serious discrepancies with experimental data (1, 5) for the two binary systems Ge-In and Ge-Sb. For the ternary systems, Zemskov *et al.* find a prominent maximum of C_{In} at a finite antimony concentration. The maximum is much higher than accounted for by the ionization equilibrium. Formation of neutral (InSb) clusters is not a satisfactory explanation because the maximum occurs at much smaller r -values than the $r \approx 1$ expected for clustering.

While the quantitative values computed in this paper may require some modification in the light

of new empirical data, it is believed that the qualitative features present a valuable survey of the problems and possibilities encountered in crystallizing a semiconductor from a liquid ternary system containing two impurity elements, and that precise data of this kind should prove valuable for certain industrial transistor processes (6, 7).

In our considerations the chemical interaction of the two impurity types in the solid, consisting of formation of molecules, has been neglected. This interaction need not concern us here if these molecules are inactive as donors or acceptors of conduction electrons. The "total" impurity concentrations as used in this paper are then the concentrations of neutral and ionized single impurities excluding molecules. However, the degree of association of molecules will generally vary with temperature, so that the concentration of impurity molecules at the crystallization temperature T_1 will not be equal to that at the temperature T_2 ($<T_1$) where electric measurements are performed. In this sense the molecule formation may become significant for the electric properties of the semiconductor. For further discussion see Reiss and co-workers (9).

Acknowledgment

The authors would like to thank Professor C. Wagner, Goettingen, Germany, for helpful discussions, and Mr. K. Schoeni, Sprague Electric Company, for computing some of the numerical data.

Manuscript received April 23, 1963; revised manuscript received Aug. 8, 1963. This paper was presented at the Pittsburgh Meeting, April 15-18, 1963.

Any discussion of this paper will appear in a Discussion Section to be published in the December 1964 JOURNAL.

REFERENCES

1. C. D. Thurmond and M. Kowalchik, *Bell System Tech. J.*, **39**, 169 (1960).
2. W. F. Schottky and M. B. Bever, *Acta Met.*, **6**, 320 (1958).
3. W. M. Glasow and S. N. Tschishewskaya, *Doklady Akad. Nauk. SSSR*, **129**, 869 (1959).
4. V. S. Zemskov, A. D. Suckova, and B. G. Zhurkin, *Zhur. Phys. Chem. USSR*, **36**, 1914 (1962).
5. F. A. Trumbore, *Bell System Tech. J.*, **39**, 205 (1960).
6. J. R. A. Beale, *Proc. Phys. Soc. London*, **70B**, 1087 (1957).
7. J. S. Lamming, *J. Electronics and Control*, **4**, 227 (1958).
8. K. Lehovec, *J. Phys. Chem. Solids*, **23**, 695 (1962).
9. H. Reiss, C. S. Fuller, and F. J. Morin, *Bell System Tech. J.*, **35**, 535 (1956).
10. K. Wohl, *Trans. Am. Inst. Chem. Engrs.*, **42**, 215 (1946).
11. M. Benedict, C. A. Johnson, E. Solomon, and L. C. Rubin, *ibid.*, **41**, 371 (1945).
12. G. Kortum and H. Buchholz-Meisenheimer, "Die Theorie der Destillation und Extraktion von Flüssigkeiten," p. 176, Springer, Berlin (1952).
13. C. Wagner, "Thermodynamics of Alloys," p. 17, Addison-Wesley Press, Cambridge, Mass. (1952).
14. C. Wagner, *Acta Met.*, **6**, 309 (1958).
15. T. S. Liu and E. A. Peretti, *Trans. Am. Soc. Metals*, **44**, 539 (1952).
16. E. Conwell, *Proc. IRE*, **46**, 1281 (1958).
17. M. A. Lee, *Solid-State Electron.*, **1**, 194 (1960).

APPENDIX

Ionization equilibrium of two impurities in a semiconductor.—When considering the crystallization of

germanium from a liquid ternary alloy, the total concentration of neither impurity type can be considered as given a priori, but the concentrations of the neutral impurities are fixed by mass action laws (section on Concentrations of Antimony and Indium in the Crystallized Germanium). Therefore, we require the total concentration of either type of impurity in terms of the neutral concentrations of the impurities, i.e., the ionization equilibrium.

Let us designate the two types of impurities by "C" (donors) and "W" (donors or acceptors). C and W will be used for the concentrations of these impurities.

The ionization equilibrium is fully characterized by the Fermi level, which is determined by the zero space charge condition in the bulk of a homogeneously doped semiconductor

$$C^+ \pm W^\pm + p - n = 0 \quad [\text{I}]$$

where C^+ , W^\pm are the concentrations of ionized impurities and p , n are the hole and electron concentrations in the semiconductor. Expressing the four terms in Eq. [I] by the Fermi energy, E_F , assuming for the moment nondegenerate electron and hole assemblies, and identifying the energy levels of the impurities with the boundaries of the conduction (E_c) and valence (E_v) bands one obtains

$$C^+ = \frac{C}{1 + 2 \exp \eta^+} \quad [\text{II}]$$

$$W^+ = \frac{W}{1 + 2 \exp \eta^\pm} \quad [\text{III}]$$

$$p = N_v \exp \eta^- \quad [\text{IV}]$$

$$n = N_c \exp \eta^+ \quad [\text{V}]$$

$$\eta^+ = (E_F - E_c)/kT \quad [\text{VI}]$$

and

$$\eta^- = (E_v - E_F)/kT \quad [\text{VII}]$$

Using these equations the concentrations of ionized impurities expressed in terms of concentrations of non-ionized impurities ($C^x = C - C^+$ etc) become

$$C^+ = C^x/2 \exp \eta^+ \quad [\text{VIII}]$$

$$W^+ = W^x/2 \exp \eta^\pm \quad [\text{IX}]$$

Introducing the Eq. [IV], [V], [VIII], and [IX] into Eq. [I] and considering that

$$-\eta^+ - \eta^- = (E_c - E_v)/kT = G \quad [\text{X}]$$

we obtain in the case that "C" and "W" are donors

$$\exp \eta^+ = \sqrt{[C^x + W^x + 2N_v \exp (-G)]/2N_c} \quad [\text{XI}]$$

$$C = C^x \{1 + \sqrt{N_c/[2(C^x + W^x + 2N_v \exp (-G))]} \} \quad [\text{XII}]$$

$$W = W^x \{1 + \sqrt{N_c/[2(C^x + W^x + 2N_v \exp (-G))]} \} \quad [\text{XIII}]$$

while in the case that "C" are donors, "W" are acceptors $\exp \eta^+ = \exp (-G/2)$

$$\sqrt{[C^x + 2N_v \exp (-G)]/[W^x + 2N_c \exp (-G)]} \quad [\text{XIV}]$$

and Eq. [19] and [20] of the text.

Presence of impurities of the same type decreases the total impurity concentration, while presence of impurities of the opposite type increases the total impurity concentration.

Our considerations were limited so far to the case of nondegenerate electron or hole assemblies by the use of Eq. [IV] and [V]. The case of a degenerate electron (or else hole) assembly will be discussed now briefly using the function $f(C/N_c, n_i/N_c)$ of ref. (8).

In the case that both "C" and "W" impurities are of the same type (e.g., donors) with energy levels at the boundary of the band, one has

$$\frac{C^x}{C} = \frac{W^x}{W} = \frac{f[(W + C)/N_c, n_i/N_c]}{(W + C)/N_c} \quad [\text{XV}]$$

and therefore

$$\frac{C(W)}{C(O)} = \frac{f[C(O)/N_c, n_i/N_c]}{f[(W + C)/N_c, n_i/N_c]} \frac{(W + C)}{C(O)} \quad [\text{XVI}]$$

If the "C" and "W" impurities are of opposite types and if $C \ll W$, the ionization equilibrium of the "C" impurities expressed in terms of the ionization equilibrium of the dominant "W" impurities is

$$C^x/C = 4(W/W^x - 1) n_i^2/(N_c N_v) \quad [\text{XVII}]$$

This equation was obtained by elimination of $\exp \eta^+$, $\exp \eta^-$ from the Eq. [II], [III], and [VIII], which are all valid for degenerate and nondegenerate conditions, by considering that $C^x/C \ll 1$ if the Fermi level is determined by the dominant "W" impurities, and by using Eq. [21] of the text.

Expressing the ionization equilibrium of the "W" impurities by the f -function, mentioned previously, one obtains

$$\frac{C(W)}{C(O)} = \left\{ \frac{N_v N_c}{4n_i^2} \left[\frac{W/N_v}{f(W/N_v, n_i/N_v)} - 1 \right]^{-1} \right\} \frac{f[C(O)/N_c, n_i/N_c]}{C(O)/N_c} \quad [\text{XVIII}]$$

The term in parenthesis is $C(W)/C^x$, which has been assumed to be large compared to unity. The other factor on the right is $C^x/C(O)$. The concentration $C(O)$ can be calculated by the equations of ref. (8) for solid-gas and solid-liquid equilibria. Using the multiplication factors [XVI] or [XVIII], respectively, the concentration of "C" impurities in presence of prevalent "W" impurities can be derived.

Polarographic Studies in Acetonitrile and Dimethylformamide

VIII. Behavior of Benzyl Halides and Related Compounds

S. Wawzonek, R. C. Duty, and J. H. Wagenknecht

Department of Chemistry, State University of Iowa, Iowa City, Iowa

ABSTRACT

Polarographic studies of benzyl chloride, benzyl bromide, benzyl iodide, benzylmercuric iodide, dibenzylmercury, mercuric iodide, ethyl chloroacetate, and ethyl bromoacetate have been made in acetonitrile and dimethylformamide containing tetrabutylammonium salts. Benzyl chloride and ethyl chloroacetate were found to undergo a facile displacement reaction with bromide ion. Benzyl chloride and bromide react with iodide ion to form benzyl iodide which reacts rapidly with mercury and forms benzylmercuric iodide. The latter compound, on standing, slowly forms mercuric iodide.

Large-scale electrolytic reduction with uncontrolled potential of benzyl chloride in the absence and presence of carbon dioxide gave toluene. The semi-controlled potential electrolytic reduction of benzyl chloride in the presence of carbon dioxide gave phenylacetic acid.

The unusual polarographic behavior reported for the reduction of benzyl halides in aqueous medium (1) in which monovalent negative ions and free radicals are postulated as intermediates suggested a further study of these compounds in dimethylformamide and acetonitrile. Previous work (2) in these solvents had indicated that stable carbanions and anion free radicals are formed in the reduction of certain unsaturated hydrocarbons. Data obtained for the halides in these solvents would therefore aid in the formulation of a reduction mechanism.

Experimental

The solutions were studied in cylindrically shaped cells fitted with side arms for the anode connection and for the admission of nitrogen. The anode was a pool of mercury, and measurements were made in a water thermostat at $25^\circ \pm 0.1^\circ$.

The electrolytic cell was similar to the cell used in previous studies (2). The bath temperature of the cell was maintained at 0° .

The Sargent Model XII polarograph was used to obtain the polarograms. The polarograph had a current-scale calibration of $0.005714 \mu\text{a}/\text{mm}$ at a sensitivity of one. The gas chromatograph was a Perkin-Elmer Model 154 and used helium as the carrier gas.

Three dropping mercury electrodes were used in this study, and all the data listed in the table are for capillary one unless stated otherwise in the table. Capillaries one and two operated with a mercury head of 48 cm, and capillary three operated with a mercury head of 54 cm. Capillaries one, two, and three had a drop time of 3.82 sec, 4.12 sec, and 3.30 sec, respectively, and had $m^{2/3} t^{1/6}$ values of $1.91 \text{ mg}^{2/3} \text{ sec}^{-1/2}$, $1.88 \text{ mg}^{2/3} \text{ sec}^{-1/2}$, and $1.95 \text{ mg}^{2/3} \text{ sec}^{-1/2}$, respectively.

The acetonitrile and dimethylformamide were purified by the methods given in an earlier paper (3). Tetrabutylammonium bromide, tetrabutylammonium iodide (3), benzyl bromide (4), benzyl-

mercuric chloride (5), and dibenzylmercury (6) were prepared by methods given in the literature. Benzyl iodide was prepared from benzyl chloride by a modification of the directions of Kumpf (7). Sodium iodide and acetone were substituted for potassium iodide and alcohol. Benzyl chloride, ethyl chloroacetate, and ethyl bromoacetate were purified by distillation. Reagent grade mercuric iodide was used without further purification.

Benzylmercuric iodide.—A solution of sodium iodide (7.8g) in acetone (25 ml) was shaken with a solution of benzylmercuric chloride (17g) in acetone (150 ml) for 1 hr. The resulting suspension was filtered, and the filtrate was evaporated to dryness. Extraction with ether gave a quantitative yield of benzylmercuric iodide. Recrystallization from ethanol after treating with decolorizing carbon gave benzylmercuric iodide melting at 115° - 117° . The literature (8) reports a melting point of 117° .

Electrolysis of Benzyl Chloride

A solution of 350 ml of dimethylformamide containing 22.6g of tetrabutylammonium iodide and 10 ml of benzyl chloride was electrolyzed in an H-cell (2) containing a mercury pool cathode (45 cm^2) and a platinum screen anode. Both anode and cathode compartments were fitted with glass exit tubes. Gases given off during the electrolysis were passed through a dry ice trap, a 10% hydrochloric acid solution and ascarite and anhydrous tubes and then collected over water.

Direct current using a line voltage of 85v was passed through the cell after degassing with purified nitrogen for 2 hr. The current started at 0.3 amp and fell to less than 0.15 amp after 24 hr.

Approximately 600 ml of nitrogen was passed through the system after completion of the electrolysis and combined with the gases formed during the electrolysis. The gas mixture was transferred to 100 ml serum bottles and capped with a combination rubber and steel stopper. The contents were ana-

lyzed by vapor phase chromatography using an activated charcoal column at 28° and carbon monoxide and methane were found in a ratio of 25:1. Other gases present in smaller amounts were *n*-butane and the butenes (traces) and were determined on a di-2-ethylhexyl sebacate column at 33°.

The hydrochloric acid trap contained no dimethylamine.

The catholyte and anolyte were combined, and a small sample was analyzed by the v.p.c. method using a Silicone oil D.C. 200 column at 123°, and contained toluene; the yield was 75%. Distillation of the anolyte and catholyte under reduced pressure (5 mm), and collection of the volatile materials in a dry ice trap was followed by v.p.c. analysis using a tetramethylene glycol dimethyl ether column at 63°. Compounds identified were *n*-butane, butenes, isopentane, and toluene. The ratio of *n*-butane to the butene was approximately 8:1, and the ratio of *n*-butane to isopentane corresponded approximately to 7:1. No dimethylamine was found in this distillate.

A similar reduction when carried out while carbon dioxide was passed through during the electrolysis gave no phenylacetic acid.

Modification of the last electrolysis by using a voltage of 13v and a solution of dimethylformamide (250 ml) containing 0.15M tetrabutylammonium bromide and benzyl chloride (10 ml) gave a current of 0.035 amp. This current remained constant for 48 hr. The resulting solution was stripped of dimethylformamide under reduced pressure (2 mm), and the residue was treated with dilute aqueous potassium hydroxide. Extraction of this solution with ether was followed by acidification of the aqueous layer. The acidified solution on extraction with ether gave phenylacetic acid (0.1g). Identification was made by comparing the infrared spectrum and NMR spectrum with those of an authentic sample.

Results

The polarographic data for the reduction of various benzyl halides in dimethylformamide (DMF)

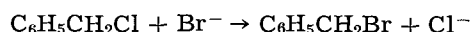
and acetonitrile are listed in Table I. Data are also listed for ethyl chloroacetate and ethyl bromoacetate since these compounds represent halogen compounds of comparable reactivity to that of the benzyl halides.

To elucidate the mechanism of reduction of benzyl iodide, the behavior of benzylmercuric iodide, dibenzylmercury and mercuric iodide was also studied and the results are given in Table I. The polarographic curves for benzylmercuric iodide and mercuric iodide in acetonitrile containing tetrabutylammonium iodide changed with time and are shown in Fig. 2-5.

To determine the mechanism of reduction of benzyl chloride and the stability of the benzyl anion, large scale electrolytic reductions were carried out in the presence and absence of carbon dioxide. Gases collected in the latter were examined by vapor phase chromatography to determine how the solvent, dimethylformamide, was involved in the electrode reaction.

Discussion of Results

Examination of the results in Table I indicates that the polarographic behavior of benzyl chloride depends on the supporting electrolyte employed. In solutions containing tetrabutylammonium bromide benzyl chloride gives two waves whose heights change with time; the first wave grows at the expense of the second wave. The half-wave potential of the first wave approximates that found for benzyl bromide and would point to the formation of benzyl bromide from benzyl chloride.



A similar behavior was found to occur with ethyl chloroacetate in bromide solution. The first wave had approximately the same half-wave potential as that found for ethyl bromoacetate. No dip in the diffusion current was observed in agreement with the work in aqueous and methanolic medium (1). Both waves based on the diffusion current constant (I_d)

Table I. Polarographic behavior of benzyl halides and related compounds in dimethylformamide and acetonitrile containing 0.175M tetrabutylammonium salts

Compound ^{a, b}	Salt	Solvent	$E_{1/2}$	(vs. Hg pool)	I_d^c	$E_{1/2}$ (vs. Hg pool)	I_d^c
$\text{C}_6\text{H}_5\text{CH}_2\text{Cl}$	Br	DMF	-0.84		0.50	-1.82	2.17 ^d
$\text{C}_6\text{H}_5\text{CH}_2\text{Br}$	Br	DMF	-0.83		2.58 ^e		
$\text{C}_6\text{H}_5\text{CH}_2\text{Cl}$	Br	CH_3CN	-0.83		1.58	-1.88	3.10
$\text{C}_6\text{H}_5\text{CH}_2\text{Br}$	Br	CH_3CN	-0.84		4.18		
$\text{ClCH}_2\text{COOC}_2\text{H}_5^f, g$	Br	CH_3CN	-0.39		0.83	-1.74	2.38
$\text{BrCH}_2\text{COOC}_2\text{H}_5$	Br	CH_3CN	-0.43		3.70		
$\text{C}_6\text{H}_5\text{CH}_2\text{I}^h$	Br	CH_3CN	-0.24		18.1		
$\text{C}_6\text{H}_5\text{CH}_2\text{Cl}$	I	CH_3CN	-0.12	(-1.04) ^k	2.99	-1.89	3.22 ^d
$\text{C}_6\text{H}_5\text{CH}_2\text{Br}^g, i$	I	CH_3CN	-0.19	(-0.87) ^k	20.0		
$\text{C}_6\text{H}_5\text{CH}_2\text{I}^j$	I	CH_3CN	-0.27	(-0.92) ^k	18.7		
$\text{C}_6\text{H}_5\text{CH}_2\text{HgI}^g$	I	CH_3CN	-0.31	(-0.92) ^k	17.8		
$(\text{C}_6\text{H}_5\text{CH}_2)_2\text{Hg}^i$	I	CH_3CN	-1.64		4.78		
HgI_2	I	CH_3CN	-0.06	(-0.19) ^k	20.0		

^a The concentration is 0.001M unless otherwise noted.

^b The solution was deoxygenated for 1 hr unless otherwise noted.

^c $I_d = \frac{i_d}{Cm^{2/3}t^{1/6}}$

^d Capillary 2.

^e Capillary 3.

^f Concentration $2.56 \times 10^{-3}M$.

^g The solution was deoxygenated for 30 min.

^h The solution was deoxygenated for 60 min prior to the addition of benzyl iodide and an additional 10 min following the addition.

ⁱ Concentration $5 \times 10^{-4}M$.

^j Deoxygenated for 12 min.

^k Voltage at which the wave dropped to normal.

for the benzyl halides would correspond to a reduction of these compounds to toluene. The reduction is irreversible since a slope analysis of the benzyl bromide wave gave a value of 0.11.

A similar displacement reaction with iodide ion occurs for benzyl chloride and benzyl bromide in solutions containing tetrabutylammonium iodide; the reaction with benzyl chloride is, however, much slower since a wave for benzyl chloride appears at -1.89v . Benzyl iodide once formed, reacts rapidly with mercury and forms benzylmercuric iodide since the waves obtained for these two compounds are quite similar (Fig. 1 and 2). The slight difference is probably caused by the formation of some mercuric iodide in the reaction of benzyl iodide with mercury. This formation of a benzylmercuric derivative would occur more rapidly in aqueous medium because of the higher dielectric constant and may be responsible for the observation that benzyl bromide and benzyl iodide are reduced at the same point (1).

The curve found for benzylmercuric iodide is unusual in appearance; a broad maximum is obtained which then drops to the reduction wave (Fig. 2). This maximum changes with time and splits into two maxima (Fig. 3 and 4); the maximum in the

zero volt region resembles the maximum found for mercuric iodide (Fig. 5).

The change in the polarographic curve with time would suggest that the following reaction may be occurring

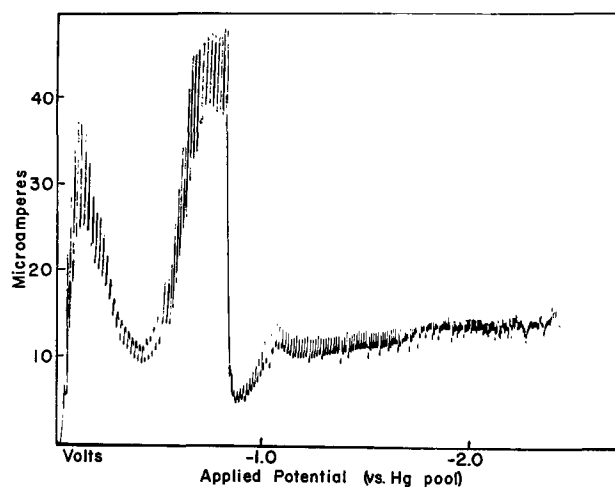


Fig. 3. Polarogram of 10^{-3}M benzylmercuric iodide in acetonitrile containing 0.175M tetrabutylammonium iodide after 3 hr.

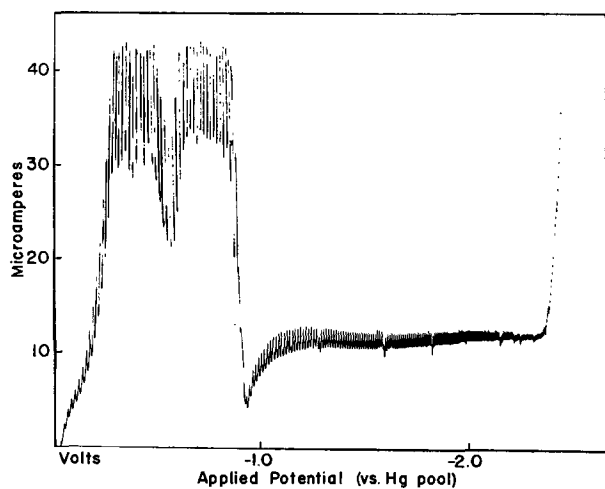


Fig. 1. Polarogram of 10^{-3}M benzyl iodide in acetonitrile containing 0.175M tetrabutylammonium iodide after 12 min.

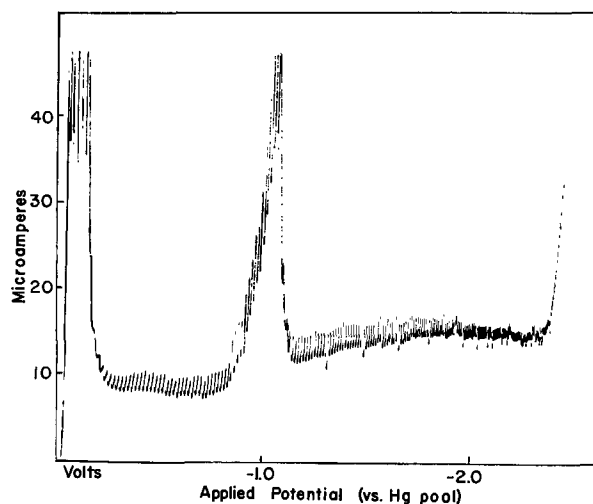


Fig. 4. Polarogram of 10^{-3}M benzylmercuric iodide in acetonitrile containing 0.175M tetrabutylammonium iodide after 72 hr.

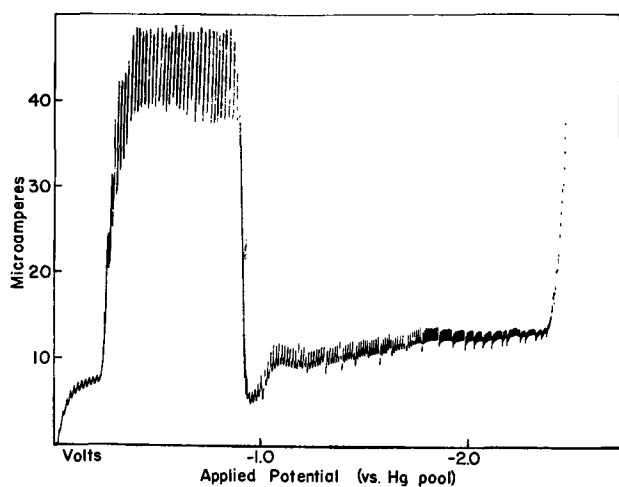


Fig. 2. Polarogram of 10^{-3}M benzylmercuric iodide in acetonitrile containing 0.175M tetrabutylammonium iodide after 1 hr.

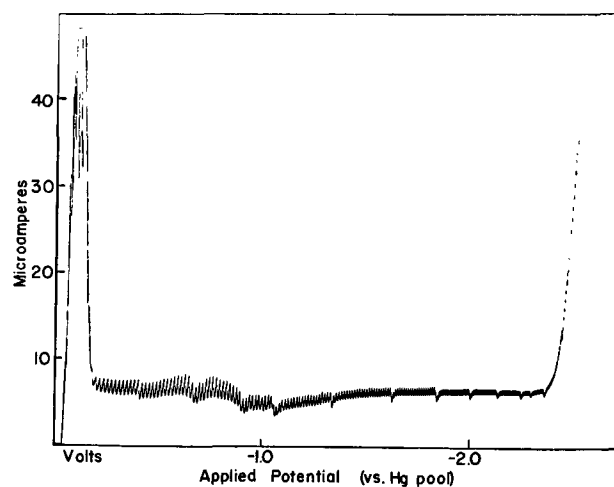
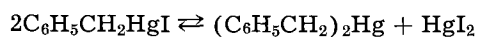
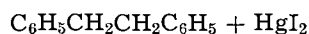
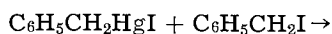
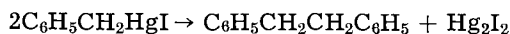


Fig. 5. Polarogram of 10^{-3}M mercuric iodide in acetonitrile containing 0.175M tetrabutylammonium iodide after 90 min.



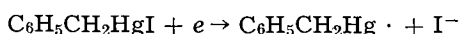
The wave ($I_d = 1.06$, Fig. 3), occurring at the point where dibenzylmercury is reduced (-1.70v) indicates that this reaction occurs to the extent of about 40%. The reversibility of this system was demonstrated by starting with equimolar concentrations of dibenzylmercury and mercuric iodide in dimethylformamide and studying the reaction polarographically. After 5 hr the curve approximated the curve shown for benzylmercuric iodide after 3 hr (Fig. 3).

Other possibilities for the production of mercuric iodide are shown below and were checked by allowing a solution of benzyl bromide,



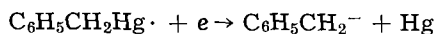
tetrabutylammonium iodide, and mercury in acetonitrile to stand for two days and checking the products by gas chromatography. The poor yield of bibenzyl obtained eliminated this reaction as a major contributor. The above reaction or a Wurtz type condensation may be the source of the bibenzyl reported in the large scale electrolytic reduction of benzyl bromide in 50% methanol (1).

The possibility exists that the reduction of benzylmercuric iodide occurs in a manner similar to that observed for phenylmercuric halides in aqueous media (9). The first wave would involve the following reaction

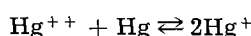


Superimposed on this wave is a maximum brought about possibly by the adsorption of the reduction product on the surface of the drop. This phenomenon apparently has little effect on the electrocapillary curve in this solvent since the curve is the same as that found for a solution without the benzylmercuric iodide.

The second wave which occurs after the drop of the maximum would correspond to the further reduction of the intermediate.



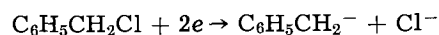
Both reduction steps are modified with time by the mercuric iodide and dibenzylmercury present. Mercuric iodide not only gives a maximum in its reduction but also modifies and shifts the maximum for the benzylmercuric iodide to more negative potentials. The wave for mercuric iodide is no doubt caused by the reduction of mercurous ions formed by the equilibrium (10)



Large scale electrolytic reduction with uncontrolled potential of benzyl chloride in dimethylformamide containing tetrabutylammonium iodide gave toluene as the principal product. The same type of reduction in the presence of carbon dioxide gave toluene as the main product and no phenylacetic acid.

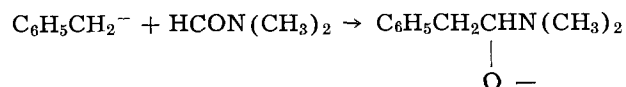
Reduction with a controlled potential was difficult to carry out since it was not possible to find a stable reference electrode. Silver-silver halides dissolved slowly in dimethylformamide. By using a lower applied potential it was possible to obtain semicontrolled conditions. Under such conditions the reduction of benzyl chloride in dimethylformamide containing tetrabutylammonium bromide gave in the presence of carbon dioxide a small yield of phenylacetic acid.

The above results confirm the two-electron reduction of benzyl chloride to a benzyl carbanion



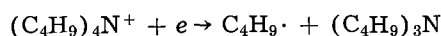
The carbon dioxide converts the carbanion to the acid isolated.

In the absence of carbon dioxide the benzyl-carbanion would be expected to add to dimethylformamide and form an intermediate which

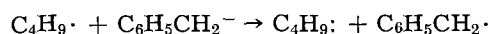


should yield phenylacetaldehyde on hydrolysis. An electrolysis carried out under such conditions was tried but no aldehyde was isolated probably because of the sensitivity of this compound to condensations.

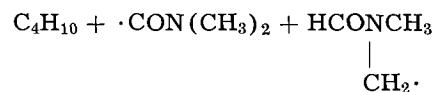
When uncontrolled potentials are used, deposition of the supporting electrolyte occurs and produces butyl radicals which can either react with the



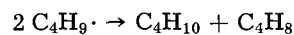
benzyl carbanion



abstract hydrogen from the solvent



or disproportionates.



The benzyl radical thus produced can abstract hydrogen from the solvent and form toluene. The latter compound could also be formed by the reaction of the benzyl carbanion with traces of moisture in the dimethylformamide.

The possibility of a reaction between the benzyl carbanion and the supporting electrolyte mentioned earlier (11) cannot be eliminated as a source of toluene.

The butyl carbanion generated in the above reaction probably adds to the dimethylformamide. No effort was made to isolate this product.

Abstraction of hydrogen from the solvent by butyl radicals is apparently one of the main reactions since the ratio of butane to butenes found was 8:1.

The carbon monoxide and methane produced probably comes from the dimethylcarbamoyl radical. In earlier work (2) the methane was erroneously identified as hydrogen. The radicals produced from dimethylformamide and peroxides are re-

ported to dimerize (12) and to react with fragments of the peroxide (13). No mention of the formation of carbon monoxide is made in any of these studies.

Decomposition of dibenzoyl peroxide in dimethylformamide carried out in this laboratory gave a small amount of carbon monoxide in the gaseous products. These results suggest that the dimethylcarbamoyl radical decomposes into carbon monoxide and the dimethylamino free radical. The latter may be the source of the methane found since this gas is reported to be found in the photolysis of dimethylamine (14).

Manuscript received June 10, 1963. This paper is based on the Ph.D. thesis of R. C. Duty (February 1961) and J. H. Wagenknecht (February 1964) and was presented at the Detroit Meeting, Oct. 1-5, 1961. The research was supported in part by the Office of Ordnance Research under Contract DA-11-022-ORD-1868.

Any discussion of this paper will appear in a Discussion Section to be published in the December 1964 JOURNAL.

REFERENCES

1. L. W. Marple, L. E. I. Hummelstedt, and L. B. Rogers, *This Journal* **107**, 437 (1960).
2. S. Wawzonek, E. W. Blaha, R. Berkey, and M. E. Runner, *ibid.*, **102**, 235 (1955).
3. S. Wawzonek and R. C. Duty, *ibid.*, **108**, 1135 (1961).
4. J. F. Norris, *J. Am. Chem. Soc.*, **38**, 639 (1920).
5. M. S. Kharasch, H. Pines, and J. H. Levine, *J. Org. Chem.*, **3**, 351 (1938).
6. J. L. Maynard, *J. Am. Chem. Soc.*, **54**, 2118 (1932).
7. G. Kumpf, *Ann.*, **224**, 96 (1884).
8. J. L. Maynard, *J. Am. Chem. Soc.*, **54**, 2108 (1932).
9. R. E. Benesch and R. Benesch, *J. Phys. Chem.*, **56**, 648 (1952).
10. I. M. Kolthoff and C. S. Miller, *J. Am. Chem. Soc.*, **63**, 2732 (1941).
11. S. Wawzonek and R. C. Duty, *Rev. Polarog. (Kyoto)*, **11**, 1 (1963).
12. L. Friedman, *Tetrahedron Letters*, **1961**, 238.
13. C. H. Bamford and E. F. T. White, *J. Chem. Soc.*, **1959**, 1860.
14. C. H. Bamford, *ibid.*, **1939**, 17.

The Crystal Structure and Polarity of Beryllium Oxide

Deane K. Smith, Herbert W. Newkirk, and J. S. Kahn

Lawrence Radiation Laboratory, University of California, Livermore, California

ABSTRACT

New x-ray intensity data from synthetic beryllium oxide crystals have verified the distorted wurtzite-type structure previously reported by Jeffrey, Parry, and Mozzi. The oxygen z parameter obtained from the refinement is 0.3786 ± 0.0005 compared to 0.375 for the undistorted structure. The resulting structure has a Be-O bond distance of $1.659 \pm 0.003 \text{ \AA}$ parallel to the c -axis and three distances of $1.645 \pm 0.003 \text{ \AA}$ completing the tetrahedral coordination. The difference of 0.014 \AA appears statistically significant and indicates that the long bond has slightly more ionic character than the other three. Measurement of the signs of the piezoelectric and pyroelectric charge and the shape and rate of etch pit formation were correlated with the internal crystal structure to identify the crystallographic polarity. On crystals showing a hemimorphic habit, consisting principally of a hemipyramid, a prism and a dominant pedion, the dominant pedion has been shown to be terminated by oxygen atoms. In oxidizing etching media the $\{00\bar{1}\}$ surfaces are much more reactive than the $\{00.1\}$ surfaces. The differences in surface reactivity are consistent with a modified version of the Warekoi-Gatos hybrid orbital bonding model for $A_{III}-B_V$ and $A_{II}-B_{VI}$ compounds. A discussion is presented relating the crystalline structure of beryllium oxide to its mechanical properties and mechanism of crystal growth.

The successful application of beryllium oxide as a moderator in high-temperature, gas-cooled nuclear reactors has stimulated considerable research into the properties of this compound (1, 2). An accurate knowledge of the structure, bonding relationships, and polarity in beryllium oxide would prove invaluable in interpreting results from crystal growth studies and electrical, mechanical, and optical property measurements.

The present study was undertaken to verify the reported structure of beryllium oxide, in particular, to verify the inequality of the symmetrically non-equivalent bonds reported by Jeffrey, Parry, and Mozzi (3), and to relate the crystallographic polarity to the measurements of polar properties such as the piezoelectric and pyroelectric effects, crystal morphology, growth phenomena, and surface effects.

Crystal Structure of Beryllium Oxide

Previous work.—Beryllium oxide is one of several binary compounds crystallizing with the wurtzite- or zincite-type (hexagonal ZnS or ZnO) structure. The structural arrangement of wurtzite was originally determined by Bragg (4), and was shown to be related to the structure of sphalerite, cubic ZnS (5). McKeehan (6) first reported the isostructural relationship of the natural mineral bromellite, BeO, to zincite. Aminoff (7) made a more thorough investigation of bromellite to differentiate between the structure reported by McKeehan and NaCl-type structure reported by Gerlach (8). Using single-crystal x-ray data, Aminoff showed that the intensity measurements agreed closely with intensities calculated for the wurtzite-type structure. The most recent structure determination on beryllium oxide,

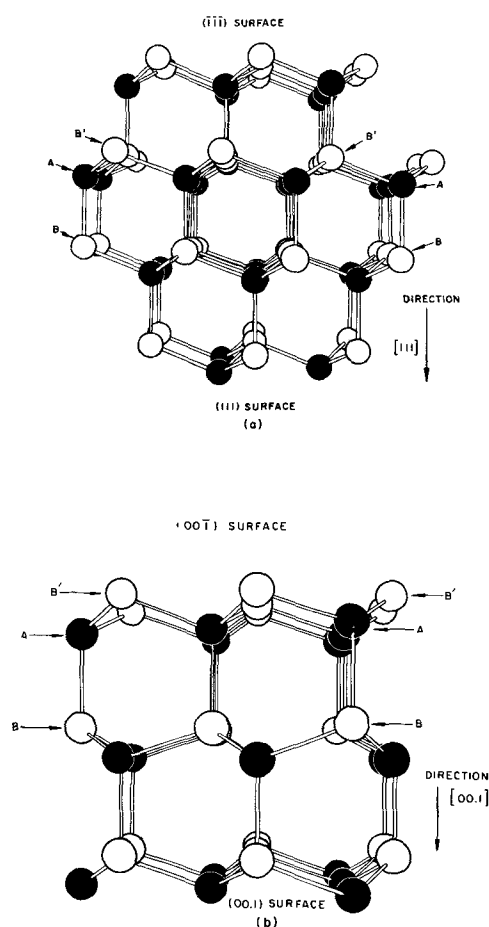


Fig. 1. Models of the zinc blende (a) and the wurtzite (b) structures. The white spheres are nonmetal atoms and the black spheres metal atoms. The corresponding cubic and hexagonal symmetries are clearly illustrated.

made by Jeffrey, Parry, and Mozzi (3), indicated that the ideal tetrahedral configuration was probably distorted so that the bond lengths were not all equal.

General features of the wurtzite-type structure.—The relationship of the wurtzite-type structure to the cubic sphalerite-type structure is illustrated in Fig. 1 and can be described in many ways; it is probably clearest to depict both structures as two separate, identical, and interpenetrating arrays of metal and nonmetal atoms. In the wurtzite-type structures each array is hexagonal close-packed with the metal atom array shifted along the c -axis with respect to the nonmetal array so that the atoms of one array fit into the tetrahedral interstices of the other array. The sphalerite-type structures may be described in the same manner except that the arrays are cubic close-packed. Both structures are non-centrosymmetric. In the wurtzite-type structures, the tetrahedra of one atom type all point in the same direction along the c -axis. The tetrahedra of the other atom type point in the opposite direction. In the sphalerite-type compounds the four 3-fold axes are polar. In each structure the outermost atom layer in the basal surface consists of either all metal atoms or all nonmetal atoms. This condition results from the fact that the $\{00.1\}$ surfaces in the wurtz-

ite-type structure and the $\{111\}$ surfaces in the sphalerite-type structure can be created only by cuts between planes where adjacent atoms are singly bonded across the cut (such as between AA and BB in Fig. 1). A cut between AA-B'B' would create an unstable surface configuration containing atoms singly bonded to the structure and three dangling or disconnected bonds (9-11). These crystal faces are not necessarily planar, but any steps that exist must be diatomic or some multiple of two atoms. These relations give rise to properties in these compounds which depend on vectorial differences, i.e., piezoelectricity, pyroelectricity, and chemical etching.

If the wurtzite-type structures were made up of undistorted, hexagonal close-packed spheres, the c/a ratio would be 1.633. Actually, very few of the compounds have ratios which are close to this value. Among the $A_{II}-B_{VI}$ and $A_{III}-B_V$ compounds, only ZnS has a ratio greater than 1.633; all the other known wurtzite-type structures have ratios less than the "ideal." Beryllium oxide has a ratio of 1.622. Previous workers have not been able to correlate the departures from the 1.633 ratio with any characteristic of the elements. However, when the compound exists in both the sphalerite and wurtzite-type modifications, the hexagonal c/a is close to 1.633.

The crystal symmetry of the wurtzite structures is $C_{6v}^4-P6_3$ mc. There are two molecules per unit cell. All the ions are on sites $2b$), $1/3, 2/3, z$ and $2/3, 1/3, 1/2 + z$. The z parameter is not fixed for either atom, so it is customary to define z as zero for one of the atoms. In the ideal wurtzite-type structure, the z parameter of the other atom would then be 0.375 if the atom is to be at the center of the coordination tetrahedron. Very few of these compounds have had their structures worked out with sufficient accuracy to determine departures from the 0.375 position. It was for this reason that Jeffrey *et al.* (3) undertook to refine the crystal structures of AlN and BeO. They found that in these structures, in which the c/a ratios are 1.600 and 1.622, respectively, the z parameter is greater than 0.375. They were able to show that the parameter was somewhat larger than would be predicted by assuming all four bond lengths equal in the distorted tetrahedral configuration determined from the c/a ratio. Their values are 0.378 for BeO as compared to a predicted 0.375 and 0.385 (as compared to 0.380) for AlN. Thus they found the interatomic distances parallel to the c -axis are longer than the other three. In BeO the difference was reported to be only 0.008Å. Whether or not this difference is truly significant was not determined by Jeffrey *et al.*, but they noted its analog to the deviations found in AlN.

Redetermination of structure.—It was considered worthwhile to re-examine the structure reported by Jeffrey *et al.*, because new intensity data using the high-quality synthetic single crystals of BeO now available might yield more information on the significance of the difference in bond distances. The crystal used in this investigation was grown by a hydrothermal technique similar to that used to grow ZnO crystals (12). The major impurities shown by spectrochemical analysis were silicon, 100 ppm; iron,

Table I. X-ray and optical properties of beryllium oxide

Crystal symmetry	P6 ₃ mc
Morphological point group	6mm (dihexagonal-pyramidal)
Cell constants	
a_0	$2.6979 \pm 0.0002\text{\AA}^*$
c_0	$4.3772 \pm 0.0002\text{\AA}^*$
Molecules per unit cell	2
Theoretical density	3.0100 g/cc*
Optical sign	Positive
Indices of refraction n_e	1.719
n_o	1.733
Birefringence ($n_o - n_e$)	0.014

* Bellamy, Baker, and Lively (13).

10 ppm; and boron, 7 ppm. Morphological forms which are present on the crystal were identified by two-circle goniometric measurements (discussed in a later section) and include the prism {10.0} and the pyramid {10.1}. Neither form is perfectly developed and other forms may also be present. The base pedion, {00.1}, is not developed because the crystal was attached at this point. The crystal is dominated by the prism and is 0.10 mm in diameter by 0.38 mm in length.

A resumé of the x-ray cell data and optical properties of BeO crystals is given in Table I. The cell dimensions are those reported by Bellamy, Baker, and Lively (13).

The x-ray intensities were measured using a General Electric single-crystal orienter and Zr-filtered MoK α ($\lambda = 0.7107\text{\AA}$) radiation. Each reflection was counted for a fixed time interval of 40 sec with the crystal stationary. The position of the peak was checked before most measurements to be sure the calculated position corresponded to the intensity maximum. Except for a few low-order reflections, the differences were less than 0.02° on all settings.¹ Measurable intensities were obtained for all non-extinct reflections with $(\sin \theta)/\lambda$ less than 1.40\AA^{-1} . A total of 244 reflections were measured, giving duplicate values for all intensities except the 00.1's and the hh.l's. Background was measured as a function of 2θ at several χ settings. The intensities were corrected for background and the Lorentz and polarization effects but not for absorption. For BeO, $\mu = 3.24\text{ cm}^{-1}$; thus μr for this crystal varies from 0.32 to 1.21. This absorption was considered small enough to ignore, although slightly more accurate data would be obtained by making the correction. All 244 measurements were considered as independent reflections during the subsequent least-squares refinements.

Because the structure was already well established, the only calculations considered necessary to refine estimates of the z parameter were those involving a least-squares analysis. Two routines were used, a recent version in FORTRAN language (14) of the Bushing and Levy (15) program, and a program written by Gantzel, Sparks, and Trueblood (16), henceforth referred to as ORLS and LALS, respectively. The first refinements were made using

¹ All settings for the single-crystal orienter were calculated using the cell constants reported by Bellamy, Baker, and Lively. Other reported cells were tried, but the high angle settings showed larger setting errors and were thus discarded.

isotropic atomic temperature factors and $z = 0.375$. The ORLS routine yielded $z = 0.3786$, $B_{\text{Be}} = 0.613\text{\AA}^{-2}$, $B_{\text{O}} = 0.477\text{\AA}^{-2}$, and $R = \Sigma||F_o| - |F_c||/\Sigma|F_o| = 0.043$. The values obtained from the LALS routine are $z = 0.3788$, $B_{\text{Be}} = 0.526\text{\AA}^{-2}$, $B_{\text{O}} = 0.398\text{\AA}^{-2}$, and $R = 0.046$. Although the temperature factors are not in close agreement, the z parameter agreement is very good. If the final parameters from the ORLS calculation are used in an LALS refinement, the program still refines to the same parameters with the R -factor showing a corresponding increase from 0.042 to 0.046. The differences in the temperature factors are somewhat surprising, considering the fact that the same data are used for both routines. One difference between the programs is in the interpolation technique for determining the atomic scattering factor from the input f -curves. It is observed that the calculated structure factors for identical reflections are not the same for each routine using the identical input data. Any systematic deviation in atomic scattering factors would be compensated by changes in the scale factor and temperature factors. Differences in the scale factors were also obtained. The divergent results of the two programs may be due to the interpolated scattering factors or to other differences or errors existing in the routines. The observed structure factors are compared with the values calculated by the ORLS routine in Table II.

Further refinements were carried out using anisotropic temperature factors. The ORLS routine uses $T = \exp [-(h^2B_{11} + k^2B_{22} + l^2B_{33} + 2hkB_{12} + 2hlB_{13} + 2klB_{23})]$ as the temperature factor expression. The LALS routine does not contain the factor 2 associated with the cross terms. The refinements were carried out

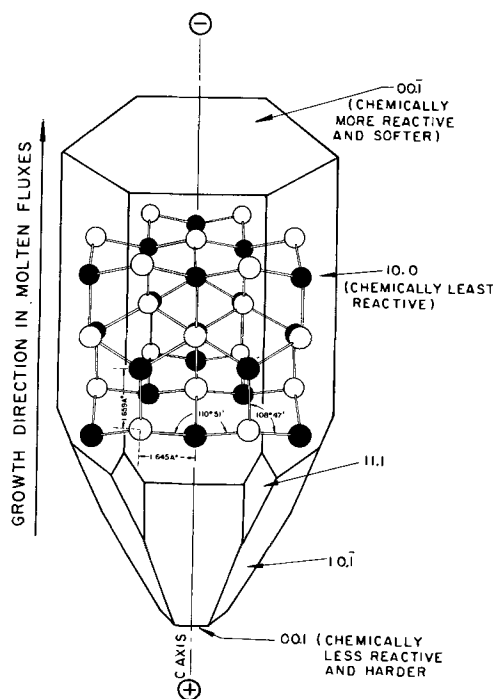


Fig. 2. Relationship between the internal crystal structure and the crystal morphology and properties. The principal faces observed on BeO crystals are shown. White spheres are oxygen atoms and black spheres are beryllium atoms.

Table II. Observed and calculated structure factors for BeO

h	k	l	F _o	√(A ² +B ²)	h	k	l	F _o	√(A ² +B ²)	h	k	l	F _o	√(A ² +B ²)	h	k	l	F _o	√(A ² +B ²)	h	k	l	F _o	√(A ² +B ²)
0	0	4	2.35	2.30	0	2	9	0.97	1.01	0	5	5	1.37	1.38	3	1	4	0.58	0.56	3	2	3	1.98	2.02
0	0	6	3.12	3.04	2	0	9	0.97	1.01	5	0	5	1.37	1.38	1	3	4	0.56	0.56	2	3	3	1.92	2.02
0	0	8	2.98	2.82	0	2	10	0.76	0.69	0	5	6	0.57	0.57	3	1	5	2.15	2.19	3	2	4	0.53	0.52
0	0	10	1.76	1.60	2	0	10	0.73	0.69	5	0	6	0.60	0.57	1	3	5	2.15	2.19	2	3	4	0.53	0.52
0	0	12	0.88	0.81	0	2	11	1.13	1.02	0	5	7	0.79	0.78	3	1	6	0.84	0.86	3	2	5	1.83	1.72
0	1	0	7.50	7.38	2	0	11	1.12	1.02	5	0	7	0.77	0.78	1	3	6	0.86	0.86	2	3	5	1.82	1.72
1	0	0	7.33	7.38	0	3	0	5.18	4.86	0	6	0	1.63	1.44	3	1	7	1.03	1.12	3	2	6	0.74	0.71
0	1	1	6.54	6.72	3	0	0	5.06	4.86	6	0	0	1.62	1.44	1	3	7	1.12	1.12	2	3	6	0.70	0.71
1	0	1	6.56	6.72	0	3	2	3.14	3.35	0	6	2	1.17	1.13	3	1	8	0.88	0.84	3	2	7	0.97	0.93
0	1	2	4.46	4.15	3	0	2	3.18	3.35	6	0	2	1.18	1.13	1	3	8	0.86	0.84	2	3	7	0.91	0.93
1	0	2	4.37	4.15	0	3	4	1.09	1.18	0	6	4	0.72	0.73	3	1	9	0.83	0.79	3	2	8	0.74	0.67
0	1	3	6.58	6.60	3	0	4	1.06	1.18	6	0	4	0.76	0.73	1	3	9	0.85	0.79	2	3	8	0.71	0.67
1	0	3	6.47	6.60	0	3	6	1.88	1.99	1	1	2	5.95	5.80	1	3	10	0.57	0.51	3	2	9	0.67	0.68
0	1	4	0.98	0.95	3	0	6	1.89	1.99	1	1	4	1.41	1.46	4	1	0	2.42	2.29	2	3	9	0.63	0.68
1	0	4	0.96	0.95	0	3	8	1.91	1.96	1	1	6	2.55	2.58	1	4	0	2.42	2.59	4	2	0	1.00	0.98
0	1	5	4.01	4.19	3	0	8	1.86	1.96	1	1	8	2.47	2.47	4	1	2	1.87	1.91	2	4	0	0.98	0.98
1	0	5	3.95	4.19	0	3	10	1.24	1.16	1	1	10	1.46	1.43	1	4	2	1.86	1.91	4	2	1	0.98	0.98
0	1	6	1.32	1.43	3	0	10	1.19	1.16	1	2	0	2.92	2.84	4	1	4	0.98	1.01	2	4	1	0.95	0.98
1	0	6	1.30	1.43	3	1	10	0.56	0.51	2	1	0	3.00	2.84	1	4	4	1.01	1.01	4	2	2	0.75	0.75
0	1	7	1.46	1.62	0	4	0	1.67	1.63	1	2	1	2.17	2.11	4	1	6	1.38	1.32	2	4	2	0.79	0.75
1	0	7	1.50	1.62	4	0	0	1.68	1.63	2	1	1	2.23	2.11	1	4	6	1.38	1.32	4	2	3	1.44	1.44
0	1	8	1.35	1.35	0	4	1	1.28	1.35	1	2	2	1.95	1.92	4	1	8	1.33	1.26	2	4	3	1.40	1.44
1	0	8	1.35	1.35	4	0	1	1.28	1.35	2	1	2	1.99	1.92	1	4	8	1.37	1.26	4	2	4	0.44	0.43
0	1	9	1.00	1.08	0	4	2	1.09	1.17	1	2	3	3.59	3.69	5	1	0	0.85	0.88	2	4	4	0.44	0.43
1	0	9	0.97	1.08	4	0	2	1.09	1.17	2	1	3	3.48	3.69	1	5	0	0.86	0.88	4	2	5	1.34	1.23
0	1	10	0.80	0.77	0	4	3	2.16	2.30	2	1	4	0.58	0.61	5	1	1	0.85	0.89	2	4	5	1.26	1.23
1	0	10	0.84	0.77	4	0	3	2.20	2.30	1	2	4	0.62	0.61	1	5	1	0.93	0.89	4	2	6	0.56	0.52
0	1	11	1.22	1.13	0	4	4	0.56	0.54	2	1	5	2.68	2.91	5	1	2	0.68	0.67	2	4	6	0.57	0.52
1	0	11	1.19	1.13	4	0	4	0.53	0.54	1	2	5	2.75	2.91	1	5	2	0.69	0.67	4	2	7	0.68	0.72
0	1	12	0.45	0.40	0	4	5	1.87	1.93	2	1	6	1.06	1.08	5	1	3	1.31	1.28	2	4	7	0.67	0.72
1	0	12	0.45	0.40	4	0	5	1.84	1.93	1	2	6	1.03	1.08	1	5	3	1.35	1.28	5	2	0	1.32	1.29
0	2	0	4.28	3.92	0	4	6	0.80	0.78	2	1	7	1.27	1.33	5	1	4	0.42	0.41	2	5	0	1.36	1.29
2	0	0	4.18	3.92	4	0	6	0.81	0.78	1	2	7	1.29	1.33	1	5	4	0.47	0.41	5	2	2	1.05	1.03
0	2	1	3.28	3.07	0	4	7	1.01	1.02	2	1	8	1.05	1.05	5	1	5	1.15	1.10	2	5	2	1.06	1.03
2	0	1	3.31	3.07	4	0	7	0.99	1.02	2	2	8	1.06	1.05	1	5	5	1.20	1.10	3	3	0	2.03	2.03
0	2	2	2.66	2.55	0	4	8	0.82	0.75	2	1	9	0.91	0.93	5	1	6	0.48	0.48	3	3	2	1.57	1.55
2	0	2	2.63	2.55	4	0	8	0.79	0.75	1	2	9	0.91	0.93	1	5	6	0.49	0.48	3	3	4	0.89	0.88
0	2	3	4.91	4.64	0	4	9	0.75	0.73	2	1	10	0.68	0.62	2	2	0	3.83	4.01	3	3	6	1.17	1.08
2	0	3	4.67	4.64	4	0	9	0.75	0.73	1	2	10	0.69	0.62	2	2	2	2.72	2.83	4	3	0	0.71	0.69
0	2	4	0.71	0.68	0	5	0	1.19	1.10	1	2	11	0.95	0.93	2	2	4	1.11	1.13	3	4	0	0.72	0.69
2	0	4	0.71	0.68	5	0	0	1.15	1.10	2	1	11	0.97	0.93	2	2	6	1.72	1.78	4	3	1	0.79	0.76
0	2	5	3.37	3.42	0	5	1	1.07	1.06	3	1	0	1.76	1.90	2	2	8	1.82	1.76	3	4	1	0.81	0.76
2	0	5	3.40	3.42	5	0	1	1.02	1.06	1	3	0	1.82	1.90	2	2	10	1.09	1.06	4	3	2	0.59	0.55
0	2	6	1.24	1.23	0	5	2	0.83	0.83	3	1	1	1.44	1.51	3	2	0	1.35	1.41	3	4	2	0.59	0.55
2	0	6	1.25	1.23	5	0	2	0.79	0.83	1	3	1	1.47	1.51	2	3	0	1.31	1.41	4	3	3	1.10	1.03
0	2	7	1.42	1.46	0	5	3	1.55	1.60	3	1	2	1.23	1.35	3	2	1	1.19	1.24	3	4	3	1.07	1.03
2	0	7	1.37	1.46	5	0	3	1.60	1.60	1	3	2	1.31	1.35	2	3	1	1.16	1.24	4	3	4	0.38	0.36
0	2	8	1.19	1.19	0	5	4	0.48	0.47	3	1	3	2.44	2.64	2	3	2	0.99	1.03	3	4	4	0.38	0.36
2	0	8	1.22	1.19	5	0	4	0.46	0.47	1	3	3	2.50	2.64	3	2	2	1.00	1.03					

using 1/6 of an atom distributed over each of the twelve general positions. Table III shows the final parameters determined from these refinements. The bond distances and angles in the structure are shown in Fig. 2. Although both z parameters are essentially identical within the limits of error, the temperature parameters again do not show good agreement.

Accuracy of the structure determination.—The question of the deviation from equal bond lengths in the coordination tetrahedra for beryllium oxide is still not unequivocally resolved. A difference of 0.014 Å has been found in this study. To evaluate the significance of this difference, it is necessary to consider the relationship of the measured z parameter to the z parameter predicted assuming all bond lengths to be equal. This comparison is required because the bond lengths are both dependent on the single position parameter. The value of z found in this study is 0.3786 ± 0.0005 . If the bonds were of equal lengths the value of z would be 0.3765. The difference between the z parameters is 0.0021. When this difference of 0.0021 is compared with the standard deviation of the measured z , which is 0.0005, a significant difference of four standard deviations is observed. A more intuitive argument for real differences may be made using the parallelism of the results of this study with the work of Jeffrey *et al.* (3). The z parameter of 0.379 is identical within one standard deviation to their value of 0.378. It is important to remember that the structure of alu-

Table III. Crystal structure parameters of beryllium oxide

	Be		O	
	ORLS	LALS	ORLS	LALS
Coordinates				
x	0.333	0.333	0.333	0.333
y	0.667	0.667	0.667	0.667
z	0.000	0.000	0.3786 ± 0.05	0.3789
Temperature factors				
B_{11}	$0.024_3 \pm 1_9$	0.0227	$0.020_2 \pm 0_6$	0.0186
B_{22}	0.024 ₃	0.0227	0.020 ₂	0.0186
B_{33}	$0.009_1 \pm 0_6$	0.0077	$0.005_6 \pm 0_2$	0.005 ₀
B_{12}^*	0.012 ₁	0.0227	0.010 ₁	0.0186
B_{13}	0.000	0.000	0.000	0.000
B_{23}	0.000	0.000	0.000	0.000

R (ORLS) = 0.042; R (LALS) = 0.046.
Bond distances and bond angles: Be—O (|| to c), 1.659 Å; Be—O', 1.645 Å; O—Be—O', 108°47'; O'—Be—O', 110°51'.
* For ORLS, $B_{12} = 1/2B_{11}$; for LALS, $B_{12} = B_{11}$. See text.

minum nitride also shows deviations in the bond lengths which are in the same direction as in beryllium oxide.

The anisotropy of thermal vibration of the beryllium and oxygen atoms is also of interest. Using the parameters obtained from the ORLS routine, the anisotropy of the beryllium atom appears to be real, but small, when compared with the standard deviation (reported in Table III). On the other hand, the anisotropy of the oxygen atom is negligible. However, the disagreement between the thermal parameters obtained from the ORLS and LALS routines indicates that the precision is somewhat



Fig. 3. A synthetically grown beryllium oxide crystal (dihexagonal hemimorphic class). The habit is apparent: hexagonal prism elongated along the *c*-axis. The presence of the hemipyramid indicates the lack of a center of symmetry. The small hemipyramid at the center of the large negative basal complex is the visible portion of another crystal having reversed polarity but in optical continuity with the crystal surrounding it (25X).

questionable. Consequently the question of anisotropy of thermal motion is still open to discussion.

Polarity of Beryllium Oxide

Crystal morphology.—Natural bromellite and synthetically grown crystals of beryllium oxide crystallize in the dihexagonal hemimorphic class, 6 mm. The habit of the natural crystals is prismatic with one end terminated by a large pedion and the other end by a hemipyramid modified by a small pedion. The habit of the synthetic crystals is varied and depends on many factors (12). Prismatic, hemipyramidal, and tabular habits have been observed, depending on the flux or the growth technique. Figure 3 shows the hemimorphic habit of a crystal grown in a lithium molybdate flux. The presence of the hemipyramid indicates the lack of a center of symmetry and demonstrates that the opposite pedion faces are crystallographically different.

The identification of the crystal faces was made by measuring the interfacial angles using a two-circle optical goniometer. To determine the Miller indices these angles were compared with angles calculated from the cell constants determined by x-ray methods. In general, the crystals are bounded by the second-order prism $\{10.0\}$, the positive hemipyramid $\{10.1\}$, and the negative pedion $\{00.\bar{1}\}$. These forms are in agreement with those reported for natural crystals (7). The minor forms corresponding to $\{00.1\}$, $\{10.\bar{1}\}$, and $\{11.\bar{1}\}$ are also observed to be present. Several other forms in which the faces are not planar are common. The positive and negative nomenclature agrees with the crystallographic polarity determined in this work.

Polarity identification.—In some noncentrosymmetric crystals the polarity can be uniquely determined and the kinds of atoms in the idealized sur-

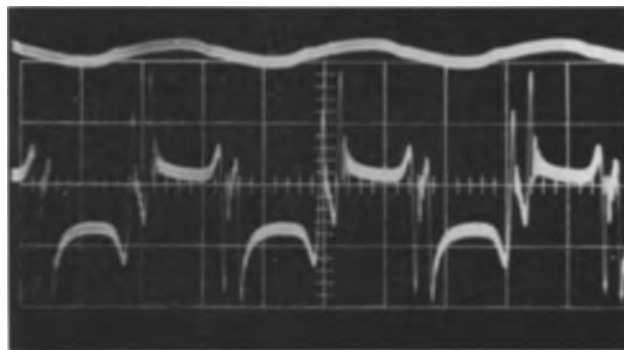


Fig. 4. A double exposure, showing no piezoelectric resonance (upper trace), and one of many piezoelectric resonances (lower trace) exhibited by a single crystal of beryllium oxide. The resonance above occurred at a frequency of 2.22 megacycles and was the strongest one observed in this crystal. In both exposures the vertical sensitivity was 1 mv/cm and the sweep speed was 5 msec/cm.

face layers identified (17, 18). One technique (19, 20) is to determine the variation in the x-ray peak intensity of a reflection using wavelengths close to the absorption edge of one of the atoms present. In the case of beryllium oxide, however, the *K* absorption edge for beryllium atoms lies at 110.68Å and for oxygen atoms at 23.301Å. These wavelengths would be difficult to generate and sustain in any apparatus currently available. An alternate technique is to determine the sign of the charge developed under stress on the pedion faces by sensitive electrical methods utilizing the piezoelectric and pyroelectric effects and to relate the sign to displacements of the crystal structure. Supporting evidence can be obtained from etching studies. The crystal morphology will then serve as a useful criterion for future determinations of the polarity. All findings should be consistent with the results obtained for zinc oxide, cadmium sulfide, and cadmium selenide, whose absolute identifications have been obtained by Warekois *et al.* (17) and Mariano and Hanneman (18).

Piezoelectric effect.—The piezoelectric effect was determined on flux-grown crystals 3-6 mm in length along the *c*-axis. The crystals examined had either a prismatic or pyramidal habit. A typical spectrochemical analysis of these crystals showed the impurities and their concentrations to be: lithium, 0-400 ppm; molybdenum, 0-500 ppm; boron, 0-15 ppm; iron, 0-55 ppm; and silicon, 0-25 ppm.

Figure 4 shows one of the piezoelectric resonances exhibited by a synthetically grown crystal and demonstrates the lack of a center of symmetry in the crystal structure. The resonance was determined using a differential transmission type of detector (21). This resonance, measured parallel to the *c*-axis, occurred at a frequency of 2.22 megacycles and was the strongest one observed in this crystal.

The sign of the polarization charge on the basal faces developed under stress was determined using a static method. The equipment consisted of two silver electrodes, connected in series with a sensitive electrometer. The electrode assembly permitted a known load to be applied slowly to the crystal placed between them. A dozen crystals were tested by applying a compressive stress parallel to the

c-axis.² In all cases, the negative end of the crystal had the better developed pyramidal faces.

In order to relate the sign of the polarization charges to the atoms in the surface layers, the dynamics of the direct piezoelectric effect must be correctly understood. If a compressive stress is applied parallel to the c-axis, then the tetrahedral configuration about an atom will be distorted. The bonds not parallel to the c-axis are easily bent, whereas the bonds parallel to the c-axis are not easily compressed. The result is that the hexagonal close-packed array of metal atoms is shifted with respect to the similar array of nonmetal atoms, although neither array is significantly distorted. The centers of the charge distributions, which were coincident before stress, are separated so that a momentary electric field is developed within the crystal parallel to the c-axis. The direction of the field causes charges to develop on the parallel basal surfaces which are opposite in sign to the type of atom on that surface. The piezoelectric polarization is weak because of steric hindrance arising from the close packing of atoms due to the relative atomic radii. Thus the polarity can be established by determining the sign of the charges which appear on the basal pedions.

The relationship between the relative positions of the beryllium and oxygen atoms of the crystal structure and the crystal morphology is shown in Fig. 2. Thus the pedion opposite the hemipyramid is the oxygen surface. These results are analogous to the results obtained on ZnO by Hutson (22).

Pyroelectric effect.—The pyroelectric effect was observed on the same crystals used in the piezoelectric tests. The equipment consisted of a silver electrode system, which permitted the crystal to expand freely, and a thermocouple for measuring temperature. The assembly could be conveniently raised or lowered into a Dewar flask filled with liquid nitrogen. Measurements were made parallel to the c-axis with the crystal connected in series with a sensitive electrometer.³

In all cases, the end of the crystal with the better developed pyramidal faces became positive on cooling and negative on heating. Accordingly, the pyroelectric coefficient is negative, since an increase in temperature causes a pyroelectric polarization in that direction which was adopted as positive for the crystal.

In contrast to the piezoelectric effect, the pyroelectric effect is difficult to relate to the crystal structure. Besides causing a primary charge separation, any change in temperature in an unconstrained crystal causes a deformation of the structure. This

deformation develops a secondary polarization due to the piezoelectric effect. Consequently, the observed effect is the sum of the primary and secondary contributions. In practice the secondary effect is usually numerically greater than the primary effect, and in many cases the latter is too small to be observed. Unless the elastic and piezoelectric constants are precisely known (23), the primary and secondary effects are difficult to separate.

Although the pyroelectric effects cannot at present be separated in beryllium oxide, a qualitative analysis can be made of the effect of temperature on the crystal structure and the effect on charge distributions. The thermal expansion is anisotropic with the a-axis expanding at a faster rate than the c-axis on heating (24). Consequently, on cooling, the more rapid contraction of the a-axis will cause distortions of the structure toward the "ideal" wurtzite structure. Whether the pyroelectric effect developed would be predominantly primary or secondary is not clear, but the charge separation would be opposite to that observed when a crystal is stressed compressively along the c-axis as in the piezoelectric measurements. Warming the crystal would reverse the charge separation. These predicted signs are in agreement with the observations.

Etching studies.—The distinction of the A and B surfaces⁴ is based either on differences in rate of attack involved in etch pit formation or in the density of etch figures. Crystals placed in boiling 85% orthophosphoric acid developed etch figures which allowed the surfaces to be unambiguously distinguished. Etching of the crystals was also obtained using either steam at 1500°C or hydrofluoric acid fumes, but rates were difficult to control.

Tests were made on single crystals grown from flux or by hydrothermal methods. The crystals were ground, polished, and then etched for varying periods of time from a few seconds to 10 min. The crystals were examined microscopically before and after etching.

The dissolution rate of the A surface (*i.e.*, the beryllium surface as identified by the piezoelectric and pyroelectric effect) was observed to be much slower than that of the B surface (oxygen surface), although the difference was not measured quantitatively. The prism faces, which we will call C surfaces, appeared to be attacked at the slowest rate. This anisotropic etching behavior undoubtedly accounts for the observed variation in etching ratio of individual crystals in polycrystalline BeO compacts. Figure 5 shows the microstructure of the A and B surfaces after etching. The A surface etches nonuniformly, producing well-formed hexagonal etch figures only after 10 min. The hexagonal outline parallels the prism cross section. The B surface, on the other hand, etches more rapidly and uniformly with characteristic hexagonal etch figures developing after only 10 sec. The etch figures on the C surfaces are irregular triangles with

² Separate experiments were carried out to determine the piezoelectric constant for the crystals. Polarization charges developed by slowly lifting a known weight from a compressed hexagonal platelet were collected on a low-loss capacitor connected in parallel with the crystal, and the voltage on the capacitor was read by means of a vibrating-reed electrometer. The measured charge was then used to calculate the piezoelectric strain constant in the usual way. The average value for five crystals was determined to be $d_{33} = +0.623 \times 10^{-12}$ coulomb/newton (at 24°C).

³ Separate experiments were carried out to determine the pyroelectric coefficient for the crystals. Polarization charges from a hexagonal platelet were collected on a low-loss capacitor connected in parallel with the crystal, and the voltage on the capacitor was determined using a vibrating-reed electrometer. The measured charge and dimensions of the crystal were used to calculate the pyroelectric coefficient in the usual way. The average pyroelectric coefficient $(\partial P/\partial \theta)_T$ for five crystals was determined to be -3.55×10^{-12} coulomb/cm² - °C (-183° to +24°C).

⁴ It is customary to designate the Group II atoms (beryllium) as A atoms, and the {00.1} surfaces terminating with A atoms as A surfaces. Similarly the Group VI atoms (oxygen) are designated as B atoms, and the {00.1} surfaces terminating with B atoms as B surfaces.

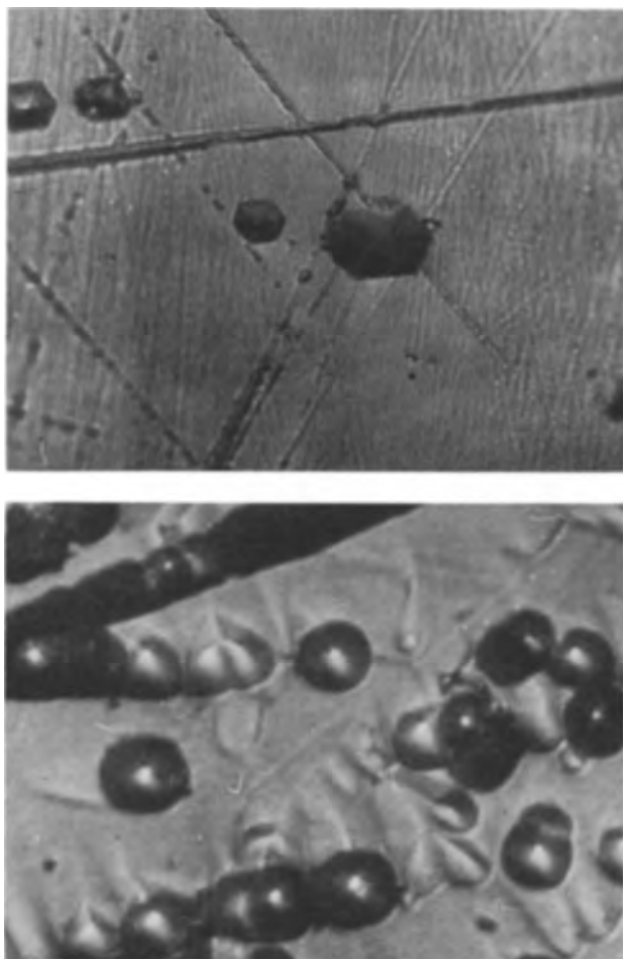


Fig. 5. The A (beryllium) (top) and B (oxygen) (bottom) surface of a beryllium oxide crystal etched in boiling phosphoric acid solution. The beryllium surface (A) is less reactive and develops regular hexagonal etch figures only after 10 min. The oxygen surface (B) develops characteristic etch figures after a 10-sec etch. After 10 min, the surface is nondescript, flat, and grainy. The well-defined etch figures reflect the six-fold symmetry on the $\{00.1\}$ surface (900X).

bases normal to the *c*-axis, and the apex pointing toward the positive end of the crystal. These results are analogous to results obtained on ZnO by Mariano and Hanneman (18).

Discussion

The variation in bond lengths present in the beryllium oxide structure and the determination of several of its polar properties raise several questions, three of the more important being:

1. What relationship exists between the inequality of the symmetrically nonequivalent bonds and the degree of ionic and covalent character of the bonding?
2. Can a plausible bonding model be devised that explains the difference in surface reactivity?
3. Can such a model be used to predict other asymmetric properties?

Unfortunately, the available data are too limited to permit the development of quantitative answers to these questions. However, it is possible to discuss these questions qualitatively, considering some of the data obtained in this study and other recent research.

Bond length and bond character.—The crystal structure refinement has increased the certainty of differences in the symmetrically nonequivalent Be-O distances (3). The symmetry of the wurtzite structure, unlike its cubic counterpart, does not require the interatomic distances to be all equal and the coordination tetrahedra to be regular. However, the equality and regularity could still exist if all the bonds were of equal character. The fact that neither condition is true for beryllium oxide suggests that the degree of ionic and covalent character for nonequivalent bonds is different; the departure from the undistorted wurtzite structure is an indication of this difference.

For the purpose of this discussion 100% covalent character is defined as the state wherein the eight valence electrons are shared equally by both atom types. The formal representation for complete covalency is therefore $(\text{Be}^{-2}, \text{O}^{+2})$. Measures of the degrees of ionic character of the bonds in beryllium oxide can be estimated in several ways. Preliminary optical measurements indicate the band gap to be around 14.5 eV (25). A value of this magnitude is normally associated with materials having a high degree of ionic character to their bonding. Electronegativity differences using empirical relationships (26-28) predict the degree of covalency to be 46 to 63%, depending on which empirical relation is used. Nuclear quadrupole resonance was used by Hon (29) to give an estimate of 50%. The validity of this estimate was questioned by Hon, because the assumptions used to obtain some of the necessary values were considered doubtful. The results were best interpreted as indicating only that beryllium oxide has more covalent than ionic character. Another prediction can be made using Pauling's (30) covalent tetrahedral and ionic radii. These radii are 1.54 Å for covalent tetrahedral coordination and 1.71 Å for ionic bonding. The measured distances for beryllium oxide fall about midway between these values, suggesting a 40-60% ionic character.

These estimates have not considered the possibility of differences in degree of ionic character of different bonds. The fact that the bond lengths show a 0.014 Å difference indicates that the ionic character of the bonds is not the same. If Pauling's values are used as an indication of the slope of the line relating bond distance to ionic character, the difference of 0.014 Å found in the present study corresponds to a difference of 8-10% in ionic character. The 50% covalent character indicated by the above work on BeO would then correspond to the electrically neutral condition. The neutral condition of a III-V compound is at 25% covalency. Thus the ionic field around any particular atom site is effectively screened by its nearest neighbors, and long-range ionic effects are probably quite small. Jeffrey *et al.* have pointed out that in wurtzite-type structures there is one second nearest neighbor at $(5/8)c$, whereas the nine next nearest are at $(\sqrt{33}/8)c$. They attribute some of the distortion of the structure to the long-range ionic effect of this second nearest neighbor. If, however, the sites were effectively neutral, this long range effect would be

negligible. Considering this fact, the bond distances are most likely an indication that the ionic character of the nonequivalent bonds differs significantly from bond to bond.

The longer bond in the BeO structure is parallel to the *c*-axis (as shown in Fig. 2), and its length indicates that it is 8-10% more ionic than the other three bonds. No hypothesis is presently available which will account for these differences. However, it is interesting to see their effect on the surface bonding model proposed (17, 31) to explain the differences in relative surface reactivity of III-V and II-VI compounds with the sphalerite and wurtzite structure.

Bonding model.—There are essentially two fundamental approaches to understanding the nature of the polar surfaces. One is the quantum mechanical or statistical treatment and the other the atomistic or chemical bonding concept. At the present time, the quantum mechanical studies are in a state of development and can be employed only in a few special cases to interpret surface behavior (32). In our present state of knowledge it is more meaningful to consider the surface atoms as individual entities bonded to the crystal framework, but with fewer bonds than atoms in the interior. Surface atom rearrangements and adsorbed impurities cannot be ignored but for the present argument are considered to be of second order importance.

Applying the Gatos and Warekois surface bonding model to beryllium oxide and considering the modification indicated by the present structure determination, it can be seen that the surface atoms are triply bonded, and the bulk atoms are tetrahedrally bonded. The three symmetrically equivalent bonds resonate between covalent and coordinate covalent bond types so that the average covalency is near 50%. The fourth bond also resonates with the other three, but the average covalent character would be 8-10% less: Referring to Fig. 1, and considering a cut made perpendicular to the [00.1] direction between planes AA and BB, it will be seen that only one bond per unit cell is broken. Making the cut between planes AA and B'B' involves breaking of three bonds, a process requiring more energy. The B surface will then have two electrons per atom in the cut bonding orbital (Fig. 6), whereas the A surface has no electrons which are available for bonding. The more rapid dissolution observed on the oxygen surface suggests control by surface electrons and is in agreement with this model. Conversely, the unfilled orbitals should make beryllium atoms relatively unreactive toward electrophilic reagents, and this has been observed in the present etching studies. It would be instructive to verify the electrical behavior attributable to the acceptor and donor properties of the A and B surfaces by measuring surface conductivity, photoconductivity, surface recombination velocity, and thermionic or photoelectric emission.

Other asymmetric properties.—The predicted asymmetry in the electrophilic nature of the A and B surfaces should create rather interesting structural modifications. For example, oxygen surface atoms would have a sufficient number of electrons

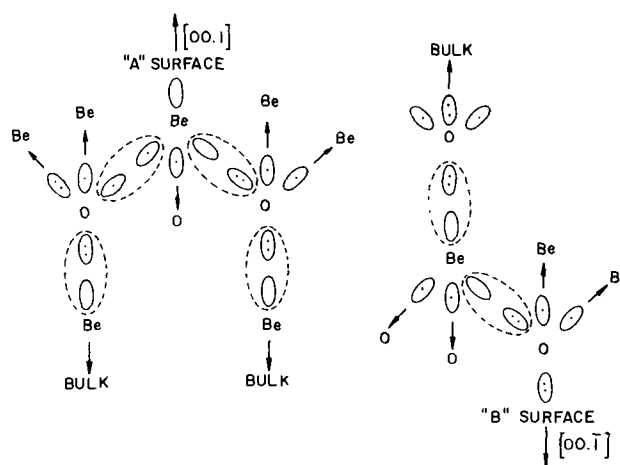


Fig. 6. Schematic representation of the electronic configuration on the A and B surfaces in beryllium oxide. The beryllium atoms in the A surface layer are pictured as being electron deficient and acting as electron acceptors, whereas oxygen atoms in the B surface layer have an excess of electrons and act as electron donors. Adsorbed impurities and surface rearrangements are considered to be second-order effects.

to retain their sp^3 hybridized configuration, much as nitrogen does in the ammonia molecule or phosphorus in the phosphine molecule. Only minor deviations from the tetrahedral coordination are to be expected. Conversely, beryllium surface atoms would have only two L-shell electrons to form the four tetrahedral orbitals, and sp^3 type hybridization could not be maintained. Consequently, the three bonds to the crystal framework must be distorted to satisfy a lower order hybrid, probably a planar sp^2 type. The bonds cannot become completely coplanar, however, for two reasons: (i) the tetrahedral configuration of the bonds underneath the surface layers, and (ii) steric effects related to the repulsion of neighboring oxygen atoms. The over-all result is a strained structure with the positive surface under compression, and the bonding configuration between the sp^3 and sp^2 types. Thus, if the structural strain is great enough and the BeO thin enough, an observable bending of the crystal should occur. Such spontaneous elastic bending of thin wafers has not been observed as yet in BeO, but has been reported in InSb (33), the A surface being convex. The total energy associated with the bending distortion of the A surface in beryllium oxide could undoubtedly be calculated if one knew the elastic strain energy per mole of surface atoms and the energy required to rearrange surface atoms or create defect structures. Unfortunately, these data are not available, but it is not unreasonable to assume that the energy is a substantial fraction of the normal tetrahedral single-bond energy of 36 kcal/mole.

The deviation of the *c/a* ratio from the "ideal" wurtzite value of 1.633 may be an indication that the bulk structure retains some of the predicted strain energy. One would expect this strain energy to be highest at the positive surface and decay exponentially within the crystal. The bulk strain energy would not be zero because of the tendency of the cations to form planar sp^2 hybrids, and of the anions to form tetrahedral sp^3 hybrids in the

manner already discussed. Thus the distortion in the observed crystal structure would be a balancing of these tendencies into a state of minimum free energy. The variable z parameter in the crystal structures of beryllium oxide and aluminum nitride shifts more rapidly from the ideal value of 0.375 than would be predicted considering only the c/a ratio. Whether these deviations are true for other wurtzite-type compounds remains to be seen. Certainly, all configurations of free molecules tend toward a condition of maximum symmetry and consequently minimum free energy. Any deviation from regularity leads to an increase in energy due to the development of strained bonds. If this hypothesis is to be applied to the distortions in wurtzite compounds, zinc oxide, with $c/a = 1.600$, should show more strain than beryllium oxide. The effect of atomic radius and charge complicates the problem, however, and the hypothesis may require modification before it can be applied to all the wurtzite compounds.

The structural changes and the stored elastic energy discussed above would be expected to create pronounced differences in the structural (mechanical) properties between the beryllium and oxygen surfaces and in the mechanism of crystal growth on these surfaces. Although our data are by no means conclusive, findings to date are consistent with this prediction: For example, differences in hardness were found on the opposite pedions using a Knoop diamond indenter; the *A* surface is 15% harder than the *B* surface. The effect is apparently not limited to beryllium oxide, since hardness asymmetry has been observed in zinc oxide (34).

Although hardness has not been analyzed with respect to the tensor properties of a crystal, some aspects are already clear. The observed differential hardness is the sum of the crystal or bulk structure and surface contributions. The crystal structure contribution is related to the elasticity, a fourth-rank tensor, and is thus centrosymmetric. Any differential hardness observed on opposite faces must have its origin in additional properties of the crystal structure, such as a gradient in dislocation density, or strains in the surface layers. The plastic deformation accompanying a hardness measurement is undoubtedly a complex process involving the generation, motion, and interaction of dislocations largely controlled by internal electric fields set up as a consequence of thermal and electrostrictive effects. Although we do not have a verification of the one-to-one correspondence of dislocations and etch pits, we have observed differences in etch figure density on the *A* and *B* surfaces. This finding suggests a dislocation density gradient which is compatible with predictable deformation systems and crystal symmetry. For example, consideration of an idealized model of the beryllium oxide structure shows that slip is most probable on $\{10.1\}$ -type planes and in the $\{11.0\}$ (close-packed) direction. The dislocation axis in this structure is parallel to the $\{10.1\}$ and forms a 60° angle with the Burger's vector. Thus, edge dislocations can intersect both the beryllium and oxygen surface. Elec-

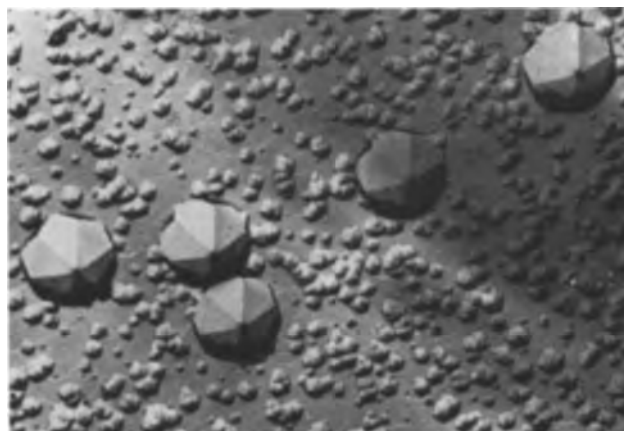


Fig. 7. An electron micrograph of a positive replica of the *A* surface in beryllium oxide. The crystal was etched for 2 min in boiling HF vapor. The etch figures are believed to correspond to a line of 60° edge dislocation terminating at the basal surface (10,000X).

tron microscopy examination of basal faces (Fig. 7) has revealed etch pits arranged in what appear to be networks of dislocation half-loops which are tilted at 60° from the surface. Thus, a possible explanation for the observed asymmetry in hardness arises: edge dislocations terminating at the *A* surface are locked or pinned because of the strains set up as a consequence of the departure from sp^3 hybridization of the atoms. Conversely, edge dislocations terminating at the unstrained *B* surface are not locked or pinned and are free to move.

Finally, some observations on the growth of BeO crystals in various environments as they relate to polar symmetry are worth mentioning. Crystals grown by hydrothermal techniques or by vapor deposition-decomposition are always untwinned and found to be attached to the substrate at the negative end. Conversely, crystals grown in molten fluxes are attached to a substrate at the positive end and are twinned. Figure 3 illustrates a typical example of a hemimorphic or polar twin, which is quite common in prismatic crystals grown from the flux. A small hemipyramid appears within the center of the large negative basal pedion. Etching studies and hardness measurements reveal that this pyramid has reverse polarity with respect to the crystal surrounding it. In reality, this small hemipyramid is a core in optical continuity with the crystal within which it is situated.

Conclusions

1. The symmetrically nonequivalent Be-O bonds in beryllium oxide have been shown to have different ratios of ionic to covalent character. No satisfactory model has been proposed which can account for the differences in bond length and bond character. However, the inequality does indicate that the bonds normal to the basal surfaces are more ionic than the other three bonds. This result is not incompatible with the hybrid orbital bond model used to explain relative surface reactivities. Accurate structural data on other wurtzite compounds to determine if unequal bonding is common in these materials will be necessary before a satisfactory theory can be devised.

2. Crystal morphology is a useful criterion for determining crystallographic polarity in beryllium oxide.

3. The chemical reactivity of opposite polar surfaces in beryllium oxide can be related to the surface bonding configuration of the beryllium and oxygen atoms, as described by the hybrid orbital model. However, to support this model, the electrophilic nature of opposite polar surfaces in beryllium oxide needs to be extensively investigated.

4. The differences in hardness and crystal growth on opposite polar surfaces and deviations from the "ideal" c/a ratio are a reflection of the strains in the surface layers as well as in the bulk lattice. These findings are consistent with proposed hybrid orbital bonding model. However, critical experimental tests of this model are still lacking.

5. The present studies have revealed only a few of the important roles played by crystalline structure and crystallographic polarity in surface phenomena and crystal growth.

Acknowledgments

The authors wish to acknowledge the very helpful suggestions and comments from their colleagues Carl Cline, Van Frechette, Ivan Cutler, and Frank Abell. This work was performed under the auspices of the U. S. Atomic Energy Commission.

The authors would like to thank Dr. S. B. Austerman of Atomics International, Canoga Park, Calif., for a preprint of, "Polar Properties of BeO Single Crystals," written with D. A. Berlincourt and H. H. A. Krueger of the Clevite Corporation, Cleveland, Ohio. Austerman's results verify etching observations of the authors. The calculated constants of Austerman *et al.* were $\Delta P = -0.075\mu$ coulombs/cm²; $(\partial P/\partial\theta)_T = -3.4 \times 10^{-10}$ coulombs/cm² - °C; and $d_{33} = +0.24 \times 10^{-12}$ coulombs/newton $\pm \sim 25\%$.

Manuscript received Feb, 7, 1963; revised manuscript received Sept. 16, 1963.

Any discussion of this paper will appear in a Discussion Section to be published in the December 1964 JOURNAL.

REFERENCES

1. A. Rothman, Lawrence Radiation Laboratory (Livermore) Rept. UCRL-6502-T, June 28, 1961 (Unclassified).
2. S. Carniglia, *J. Nucl. Mater.*, **4**, 165 (1961).
3. G. A. Jeffrey, G. S. Parry, and R. L. Mozzi, *J. Chem. Phys.*, **25**, 1024 (1956).
4. W. L. Bragg, *Phil. Mag.*, **34**, 647 (1920).
5. W. L. Bragg, *Proc. Roy. Soc. London*, **A89**, 468 (1913).
6. H. McKeehan, *Proc. Natl. Acad. Sci. U.S.*, **8**, 270 (1922).
7. G. Aminoff, *Z. Krist.*, **62**, 113 (1925).
8. W. Gerlach, *Z. Physik*, **9**, 184 (1922).
9. M. C. Lavine, A. J. Rosenberg, and H. C. Gatos, *J. Appl. Phys.*, **29**, 1131 (1958).
10. J. D. Venables and R. M. Braudy, *ibid.*, **29**, 1025 (1958).
11. P. Haasen, *Acta. Met.*, **5**, 598 (1957).
12. H. W. Newkirk and D. K. Smith, Lawrence Radiation Lab. (Livermore) Rept. UCRL-7466 Aug. 12, 1963 (Unclassified).
13. B. Bellamy, T. W. Baker, and D. T. Livey, Atomic Energy Research Establishment, Harwell, Berk., England, *AERE-R-3744*, July, 1961 (Unclassified).
14. K. O. Martin, W. R. Busing, and H. A. Levy, Oak Ridge National Laboratory, Oak Ridge, Tennessee Preliminary Report 1962 (Unclassified).
15. W. R. Busing and H. A. Levy, Oak Ridge National Laboratory, Oak Ridge, Tennessee ORNL-59-4-37, May 1959 (Unclassified).
16. P. K. Gantzel, R. A. Sparks, and K. N. Trueblood, Program number 317, Amer. Crystallographic Assn. Program Listing, Second Edition, Nov. 1961.
17. E. P. Warekois, M. C. Lavine, A. N. Mariano, and H. C. Gatos, *J. Appl. Phys.*, **33**, 690 (1962).
18. A. N. Mariano and R. E. Hanneman, *J. Appl. Phys.*, **34**, 384 (1963).
19. R. W. James, "Optical Principles of the Diffraction of X-Rays," G. Bell and Sons, Ltd., London (1958).
20. H. Cole and N. R. Stemple, *J. Appl. Phys.*, **33**, 2227 (1962).
21. R. J. Blume, *Rev. Sci. Instr.*, **34**, 598 (1961).
22. A. R. Hutson, Bell Telephone Laboratories, Private communication, September 21, 1962.
23. W. G. Cady, "Piezoelectricity," McGraw-Hill Book Co., New York (1946).
24. C. G. Grain and W. J. Campbell, U. S. Bureau of Mines, RI 5982 (1962).
25. W. Barr and R. Morrow, University of California Radiation Laboratory, Private communication, October 10, 1961.
26. N. R. Hannay and C. P. Smyth, *J. Am. Chem. Soc.*, **68**, 171 (1946).
27. L. Pauling, "The Nature of the Chemical Bond," 2nd ed., p. 74, Cornell University Press, Ithaca, New York (1948).
28. H. O. Pritchard and H. A. Skinner, *Chem. Rev.*, **55**, 745 (1955).
29. J. F. Hon, *Phys. Rev.*, **124**, 1368 (1961).
30. L. Pauling, *op. cit.*, p. 246.
31. H. C. Gatos and M. C. Lavine, *This Journal*, **107**, 427 (1960).
32. H. J. Juretschke in "The Surface Chemistry of Metals and Semiconductors," H. C. Gatos, Editor, John Wiley & Sons, New York (1960).
33. R. E. Hanneman, M. C. Finn, and H. C. Gatos, Lincoln Lab., Massachusetts Institute of Technology, Lexington, Mass., Private communication. To be published in the *J. Phys. Chem. Solids*.
34. C. Cline and J. S. Kahn, *This Journal*, **110**, 773 (1963).

Equilibrium Pressures of Oxygen over Mn_2O_3 - Mn_3O_4 at Various Temperatures

Earl M. Otto

National Bureau of Standards, Washington, D. C.

ABSTRACT

The equilibrium represented by the equation $6\text{Mn}_2\text{O}_3(\text{c}) = 4\text{Mn}_3\text{O}_4(\text{c}, \alpha) + \text{O}_2$ has been studied by measuring the equilibrium pressures of oxygen over Mn_2O_3 - Mn_3O_4 . From the data obtained in the 1132°-1247°K range studied ΔH° and ΔS° were calculated for the reaction at 1200°K to be 41.2 ± 1.2 kcal and 32.9 ± 1.0 cal/deg, respectively. These constants can be used in the equation

$$-4.5758 \log p\text{O}_2 (\text{atm}) = 41,200/T - 32.9$$

to relate $\log p\text{O}_2$ and temperature of the system in the above-mentioned range with no appreciable additional error. A slight extrapolation showed $p\text{O}_2 = 1$ atm at 1252°K. The above ΔH and ΔS values were converted to 298.15°K and compared with those in the literature. A new entropy $S^\circ_{298} = 36.8$ cal/deg for Mn_3O_4 and a new heat of formation $\Delta H^\circ_{298} = -228.7$ kcal for Mn_2O_3 are indicated from analysis of data in the literature and the present data. This value of entropy of Mn_3O_4 is higher by 1.3 cal/deg (roughly $R \ln 2$) than the value taken from the literature.

Though the chemical literature has numerous references to the dissociation of manganese dioxide to form manganic oxide, confusing and contradictory as some of them are, relatively few give original observations on the further dissociation of the manganic oxide to form manganous-manganic oxide. Meyer and Rötgers (1) observed the temperatures to which Mn_2O_3 had to be heated to cause it to lose weight in air and oxygen gas, respectively, the atmospheric pressure not being stated. Honda and Sone (2) detected a change in the magnetic susceptibility of the Mn_2O_3 at a definite temperature and they assumed this temperature marked the change from Mn_2O_3 to Mn_3O_4 . Saito (3) using a thermal balance and increasing the temperature of the specimen 1-2° per minute reports the temperature at which Mn_2O_3 starts to lose weight. The atmosphere is not described. Simon and Feher (4) heated Mn_2O_3 , possibly in a closed system, and report the temperature when oxygen reached 10 mm pressure. They present a graph showing a plot of X in MnO_X against temperature. Krüll (5), by using a manometer to indicate any development of a difference in pressure between the atmospheres over Mn_2O_3 and an inert material heated to the same temperature, found, by frequently bleeding off the evolved oxygen, the temperature to which the two substances had to be heated for the oxygen evolution to become complete. This was the temperature at which no Mn_2O_3 remained. Ulich and Siemonsen (6) determined heats of reaction and from these heats and other thermodynamic data calculated oxygen pressures at various temperatures. Tatievskaya *et al.* (7) experimentally determined for Mn_2O_3 , from the dissociation and oxidation approaches, the equilibrium pressures at low temperatures (up to 1100°K). Also they calculated pressure-temperature equi-

librium values from heats of formation and entropies. McMurdie (8), conducting a differential thermal analysis of MnCO_3 in air, gives as the dissociation temperature of Mn_2O_3 the temperature at which there was a break in the curve. Probably the three best values for pressure-temperature equilibria were reported by Hahn and Muan (9). Their experimental procedure consisted in passing a gas of known oxygen content over heated samples of Mn_2O_3 and Mn_3O_4 . After a suitable time the samples were quenched and the phases present determined by x-ray methods. The temperature at which no phase change in either sample was noted was taken as the equilibrium temperature. Their second method involved a thermal balance.

Pertinent thermodynamic constants of Mn_2O_3 and Mn_3O_4 , with or without reference to calculated pressure-temperature equilibria, have been reported by Brewer (10), Coughlin (11), Vlasor (12), Dushman (13), and others.

The references given above show that there is a lack of precise experimental data giving actual pressure-temperature relationships at equilibrium. It was the object of this investigation to study these relationships carefully.

Experimental

Mn_2O_3 , obtained by heating pyrolusite (99.5% MnO_2) at about 660°C in an atmosphere of air, was found at 885°C to be 100% converted to Mn_3O_4 . Cooling the product slowly in air to room temperature resulted in a mixture of 34% Mn_3O_4 and 66% Mn_2O_3 , while cooling quickly in air gave 95% Mn_3O_4 and 5% Mn_2O_3 . (Calculations were based solely on weight changes.) Hence the dissociation of Mn_2O_3 to form Mn_3O_4 and oxygen appears to be readily reversible.

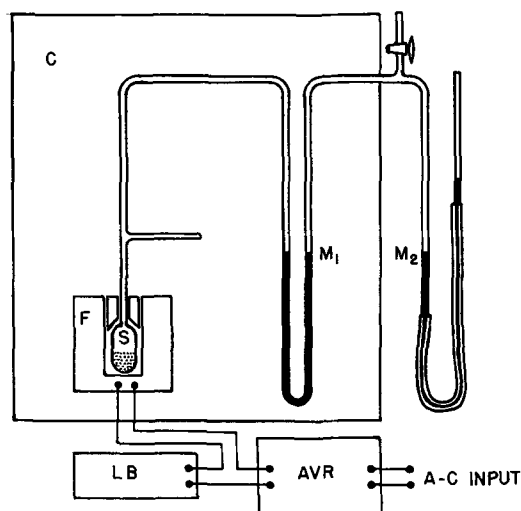


Fig. 1. Diagrammatic sketch of apparatus. C, Temperature controlled cabinet; S, Vycor tube containing sample; M_1 and M_2 , manometers, M_2 serves as leveling device; AVR, automatic voltage regulator; LB, lamp bank; F, furnace.

The apparatus used in two much more precise experiments is shown in diagrammatic form in Fig. 1. The MnO_2 sample (S) was heated to $750^\circ C$ and the system evacuated and closed. The closed system consisted of a Vycor bulb (containing the oxide) connected by a graded seal to small diameter Pyrex tubing leading to a manometer (M_1). To extend the versatility of the apparatus a second manometer (M_2) comprising two straight glass tubes joined by transparent plastic tubing, was attached through a tee-tube to the first manometer. The tee-tube allowed adjustment of the pressure of the air confined between the two manometers thereby making it possible to have a constant volume in the closed system and possible to cause major pressure changes of oxygen pressure over the manganese oxide. Another tee-tube was used in the apparatus, this second one being between the graded seal and the first manometer in order to permit evacuation of or have more oxygen added to the system. The entire apparatus, with the exception of the second manometer, was kept in a thermostated cabinet (C) while the second manometer and the cabinet were in a temperature controlled room.

The furnace (F) was heated to a controlled temperature by maintaining a fixed voltage $\pm 0.05v$ across the heating element of the furnace. This was accomplished by connecting the output of an automatic voltage regulator (AVR) to the heating element in series with a lamp bank (LB). The resulting temperatures remained constant to within $\pm 0.5^\circ C$. Oxygen pressure readings were taken to within ± 0.2 mm mercury. During the investigation twenty-one different pressure-temperature equilibria were observed.

Figure 2 shows by the left ordinate the oxygen pressures at equilibrium, obtained at various temperatures. The plotted points (lettered for run No. 1 and numbered for run No. 2) allow one to observe the nondependence of an equilibrium on the preceding equilibrium. Figure 3 is a plot of oxygen pressure against time for a part of one of the two precise experiments. The temperature was

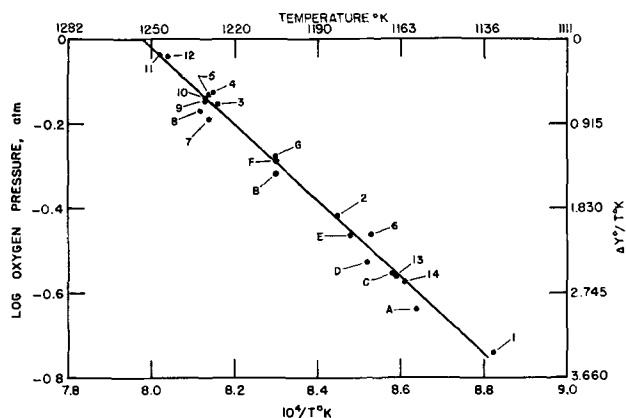


Fig. 2. Dissociation of Mn_2O_3 . Pressure-temperature relationship. Equilibrium points shown chronologically, by letters for run No. 1 and by numbers for run No. 2. Lines for $\log pO_2$ vs. $1/T$ and for Y°/T vs. $1/T$ are indistinguishable on the graph.

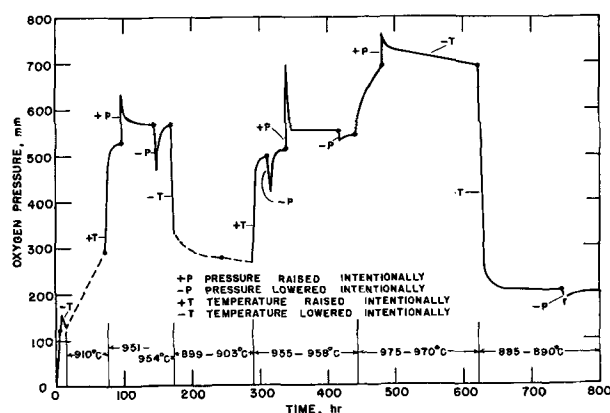


Fig. 3. Dissociation of Mn_2O_3 . Pressure-time relationship, showing effect of varying temperature and pressure intentionally.

altered, three times up and four times down. In addition the pressure was changed by suddenly altering the mercury level in the first manometer, four times to a lower and three times to a higher pressure. Sufficient readings were taken while equilibrium was being re-established to show that the dissociation of Mn_2O_3 definitely is reversible. After sudden changes in pressure the equilibria could again be established in 2-10 hr, apparently a little more rapidly after decreasing the pressure than increasing it. Sudden changes in temperature were obviously impossible but required 2-4 hr. However, raising the temperature disturbed the equilibrium for about 20 hr and lowering it for about 100 hr. Hence, in the reversible reaction $6Mn_2O_3 \rightleftharpoons 4Mn_3O_4 + O_2$ the dissociation is faster than the combination, while equilibrium is being established.

Treatment of Data

The temperature and pressure data obtained in the two runs are given in columns two and three of Table I. In the range of pressures (0.18 to 0.92 atm) the fugacity of oxygen differs from the pressure by less than 0.05%, and hence the actual pressures may be used to obtain the free energy by the relation: $\Delta F^\circ = -RT \ln pO_2$ for the reaction: $6Mn_2O_3(c) \rightarrow 4Mn_3O_4(c,\alpha) + O_2(g)$.

From the plot (Fig. 2) of $\log pO_2$ vs. $1/T$ an approximate value of ΔH° may be calculated from the slope of the straight line fitted to the points and

Table I. Temperature and pressure data

	T, °K	pO ₂ , atm	-4.5758 log p	"Correction" C	ΔY°/T, cal/deg
A	1158.15	0.2303	+2.9181	-0.0059	+2.9122
B	1205.15	0.4776	1.4686	-0.0004	1.4682
C	1165.15	0.2789	2.5375	-0.0041	2.5334
D	1174.15	0.2974	2.4099	-0.0023	2.4076
E	1179.15	0.3447	2.1166	-0.0015	2.1151
F	1205.15	0.5145	1.3206	-0.0004	1.3202
G	1205.15	0.5289	1.2658	-0.0004	1.2654
1	1132.15	0.1816	3.3902	-0.0159	3.3743
2	1183.15	0.3842	1.9010	-0.0011	1.8999
3	1225.15	0.6987	0.7125	-0.0022	0.7103
4	1227.15	0.7513	0.5683	-0.0026	0.5657
5	1228.15	0.7487	0.5751	-0.0028	0.5723
6	1172.15	0.3671	1.9915	-0.0027	1.9888
7	1228.15	0.6553	0.8399	-0.0028	0.8371
8	1231.15	0.6776	0.7735	-0.0035	0.7700
9	1230.15	0.7263	0.6355	-0.0032	0.6323
10	1230.15	0.7158	0.6645	-0.0032	0.6613
11	1247.15	0.9184	0.1692	-0.0071	0.1621
12	1243.15	0.9132	0.1804	-0.0060	0.1744
13	1164.15	0.2737	2.5750	-0.0044	2.5706
14	1162.15	0.2671	2.6235	-0.0048	2.6187

it will apply strictly for some temperature T_{av} near the mean temperature of the experiments. The entropy change $\Delta S^\circ_{T_{av}}$ may be obtained from the intercept at $1/T = 0$ or by the relation $\Delta S^\circ_{T_{av}} = (\Delta H^\circ_{T_{av}} - \Delta F^\circ_{T_{av}})/T_{av}$. However, since C°_p is available for the substances in the above reaction at the temperatures of the experiments, the following method suggested by Prosen (14) can be used to convert the data to yield a theoretically straight line plot of $\Delta Y^\circ/T$ vs. $1/T$, where this line is the tangent to the $\Delta F^\circ/T$ curve at a selected temperature. Furthermore, the slope and intercept of this line give ΔH° and ΔS° at this specific temperature. The temperature selected was 1200°K. The C°_p value for the reaction, obtained from data given by Kelley (15), is $\Delta C^\circ_p = -2.66 - 6.00 \times 10^{-3}T + 10.18 \times 10^5/T^2$.

From the relations

$$\Delta Y^\circ/T = (\Delta H^\circ_{1200}/T) - \Delta S^\circ_{1200}$$

and

$$\Delta Y^\circ/T = -4.5758 \log pO_2 + C$$

where the correction

$$C = -\Delta(H^\circ_T - H^\circ_{1200})/T + \Delta(S^\circ_T - S^\circ_{1200}) \\ = -1/T \int \Delta C^\circ_p dT + \int (\Delta C^\circ_p/T) dT$$

one obtains the corrections to be applied to $-4.5758 \log pO_2$ to obtain $\Delta Y^\circ/T$. For the 1200°K region the correction is given by

$$C = 10.2135 - 0.003T - 8,360.33/T + 5.09 \times 10^5/T^2 \\ - 2.66 \ln T/1200$$

In column 5 of Table I the corrections are listed and in column 6, $\Delta Y^\circ/T$ for each equilibrium observation. Since the corrections shown in the table are small, the straight line derived by the method of least squares, relating $\Delta Y^\circ/T$ to $1/T$, coincides in Fig. 2 with the line obtained for $\log pO_2$ vs. $1/T$.

The constants of this straight line $\Delta Y^\circ/T = (\Delta H^\circ_{1200}/T) - \Delta S^\circ_{1200}$, become

$$\Delta H^\circ_{1200} = 41.2 \pm 1.2 \text{ kcal}^1$$

and

$$\Delta S^\circ_{1200} = 32.9 \pm 1.0 \text{ cal/deg}$$

The uncertainties given above are the standard deviations obtained by the method of least squares.

If one adds to these constants 5.185 kcal, ($H_{1200} - H_{298}$), and 4.75 cal/deg, ($S_{1200} - S_{298}$), calculated from the tabulated heat content and entropy data given by Kelley (15) for the substances involved, the resultant constants become

$$\Delta H^\circ_{298} = 46.4 \pm 1.2 \text{ kcal}$$

and

$$\Delta S^\circ_{298} = 37.7 \pm 1.0 \text{ cal/deg}$$

The above values may now be compared with those given in the literature. From the data tabulated by Rossini *et al.* (16) 67.0 kcal is calculated for ΔH°_{298} for the reaction. The heat of formation of Mn_2O_3 is very uncertain. From the heat of formation of Mn_3O_4 taken to be correct as -331.4 kcal, and the new heat of reaction given above, the heat of formation of Mn_2O_3 ($\Delta H^\circ_{f_{298}}$) is calculated to be -228.7 ± 0.2 kcal. This value is in fair agreement with the -229.2 kcal given by Brewer (10) and Coughlin (11) and the -228.4 kcal estimated by Mah (17). However, these values differ widely from the -232.1 kcal given by Rossini *et al.* (16).

The new entropy value of ΔS°_{298} may also be compared with that given in the literature. Glassner (18) gives the entropies at 298° for $Mn_2O_3(c)$, $Mn_3O_4(c, \alpha)$, and $O_2(g)$ as 26.4, 35.5, and 49.0 cal/deg mole, respectively. These yield 32.6 cal/deg for the dissociation reaction, which is 5.1 cal/deg lower than the value resulting from the present study. There is little doubt of the correctness of the entropy of oxygen. The entropy of $Mn_2O_3(c)$ given above was determined recently by King (19) and is considered reliable, though the rather long extrapolation from 51° to 0°K introduces some uncertainty. On the other hand the entropy of $Mn_3O_4(c, \alpha)$ was determined by Millar (20) in 1928 and the measurements go down only to 70°K. Also Kelley and Moore (21) have shown the measurements of Millar contain some errors. Thus, the errors can reasonably be ascribed to an error in the entropy of $Mn_3O_4(c, \alpha)$. When one fourth of the 5.1 cal/deg error is added to the old value of 35.5 cal/deg the new value is 36.8 cal/deg for $Mn_3O_4(c, \alpha)$.

It should be noted that the heat capacity curve obtained by Todd and Bonnickson (22) for MnO shows a hump at 118°K with an entropy content of 0.9 cal/deg; the curve by Kelley and Moore (21) for MnO_2 shows a hump at 92°K with an entropy content of 1.1 cal/deg; and the curve by Orr (23) for Mn_2O_3 shows a hump at 79°K with an entropy content of 1.2 cal/deg. All of these oxides show a hump with an entropy content approaching $R \ln 2$ (1.38 cal/deg). Millar's curve for Mn_3O_4 shows no hump down to 70°K. It is interesting to suppose

¹ One thermochemical calorie equals 4.1840 absolute joules.

Table II. Types of investigations of Mn_2O_3 - Mn_3O_4 - O_2 reaction

Reference	Type of investigation	Range of pO_2 or temperature	pO_2 , atm	Temperature, °K
Meyer and Rötgers (1)	Thermogravimetry	0.2 and 1.0 atm	1.0	1363
Honda and Soné (2)	Magnetic susceptibility	Assume 1 atm air	0.2	1200
Saito (3)	Thermogravimetry	Assume 1 atm air	0.2	1123
Simon and Feher (4)	O_2 pressure measured	To 1573°K	0.013	1143
Krüll (5)	Thermogravimetry	1173°-1223°K	Unknown	<1223
Ulich and Siemonsen (6)	Calorimetry only	—	—	—
Tatievskaya (7)	O_2 pressure measured	1000°-1100°K	0.05	1100
Brenet (24)	Thermogravimetry	To about 1300°K	Unknown	1143
Kulp and Perfetti (25)	Differential thermal analysis	To about 1300°K	0.2	1278
Hahn and Muan (9)	X-rays, thermogravimetry	0.2, 0.46, and 1.0 atm	1.0 ₀	1241
Grasselly and Klivényi (26)	Heat, then chem. analysis	733°-1323°K	0.2	1153
Földvari-Vogl and Koblenz (27)	Differential thermal analysis	373°-1273°K	0.2	>1223
McMurdie (8)	Differential thermal analysis	373°-1573°K	0.2	1243
Present work	O_2 pressure measured	0.2-1 atm	1.00 ₀	1252
Brewer, Glassner (10, 18)	Collation and computation		1	1620*

* In private communication to the author Dr. Brewer states the temperature should read 1350°K.

that the 1.3 cal/deg error in Millar's value is due to the fact that he did not carry his experiments to low enough temperatures where a hump possibly exists.

Table II lists various types of investigations pertaining to the Mn_2O_3 - Mn_3O_4 - O_2 reaction reported in the literature, showing the recorded temperatures and pressures. It is to be observed that temperatures required to produce a given pressure such as 1 atm, are, with the exception of the one given by Hahn and Muan (9), much higher than those obtained in the present study. There might have been even closer agreement with Hahn and Muan, if these investigators had noted precise oxygen pressures. (Apparently they released effluent gases to the air at the prevailing atmospheric pressures.) Also the MnO_2 specimens used may have been of a different allotropic form and the nature of the resulting Mn_2O_3 may have differed somewhat, even though the alpha form would have been the stable one in both investigations.

Figures 4 and 5 show the pressure-temperature relationship derived from the present investigation (curve 1) and extended by the use of the heat

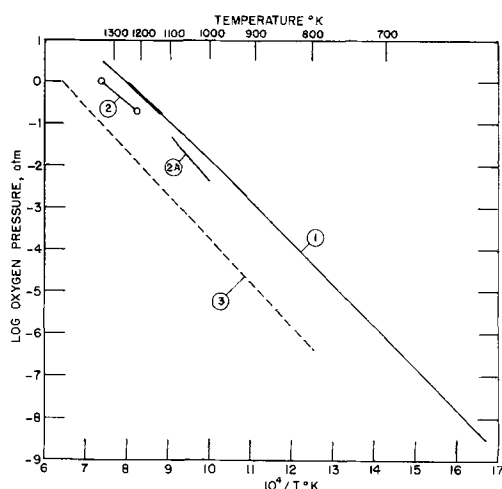


Fig. 4. Dissociation of Mn_2O_3 . Pressure-temperature relationship. Curve 1, Present work, (heavy line is for the range of present experimental investigation); curve 2, Meyer and Rötgers; curve 2A, Tatievskaya; curve 3, Coughlin and Dushman.

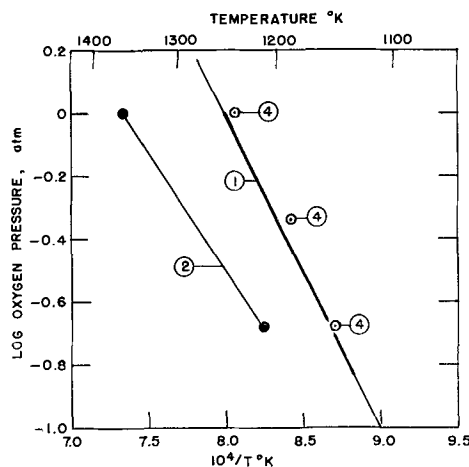


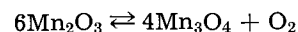
Fig. 5. Dissociation of Mn_2O_3 . Pressure-temperature relationship. Range 0.1 to 1 atm. Curve 1, Present work; curve 2, Meyer and Rötgers; points 4, Hahn and Muan.

content and entropy data (15). Also shown are the experimental points due to Meyer and Rötgers (1), Hahn and Muan (9), and Tatievskaya *et al.* (7). The dotted line represents the pressure-temperature relation derived from the older data Coughlin (11) gave.

Conclusions

A method has been developed for the precise and very dependable control of temperature of a furnace and for the precise measurement of oxygen pressure in a closed system.

It has been learned in the study of the dissociation of Mn_2O_3 that a true equilibrium can be obtained. Thus the equation is



A disturbance of the equilibrium by a change of temperature of the oxide or a change of oxygen pressure shifts the equilibrium to absorb the stress. The reverse action has been found to be much slower than the forward.

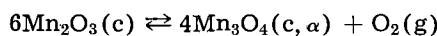
At an oxygen pressure of 1.000 atm the equilibrium temperature is 979°C (1252°K), while in air at 1.000 atm it is 871°C (1144°K).

Based on the present data and the data in the literature, the following thermodynamic constants

are considered to be the most reliable ones available at present

	$S^{\circ}_{298.15}$, cal/deg	$\Delta H_f^{\circ}_{298.15}$, kcal
$Mn_2O_3(c)$	26.4 (19)	-228.7
$Mn_3O_4(c, \alpha)$	36.8	-331.4 (16)
O_2	49.0 (16)	0

For the reaction:



$$\Delta H^{\circ}_{298.15} = 46.4 \text{ kcal}$$

$$\Delta S^{\circ}_{298.15} = 37.7 \text{ cal/deg}$$

$$\Delta F^{\circ}_{298.15} = 35.2 \text{ kcal}$$

Acknowledgment

Mr. E. J. Prosen of the National Bureau of Standards has contributed very greatly to this paper and the author wishes to express deep gratitude on his part. Mr. Prosen studied at great length the new data presented in this paper and treated them to yield thermodynamic constants. These constants he has compared with the best previously accepted values. Much of the section on Treatment of Data was composed by him. The author wishes to express his gratitude also to Dr. W. J. Hamer under whose direction this work was conducted and who exhibited keen interest from the inception of the study to its conclusion.

Manuscript received April 26, 1963.

Any discussion of this paper will appear in a Discussion Section to be published in the December 1964 JOURNAL.

REFERENCES

- R. J. Meyer and K. Rötgers, *Z. anorg. Chem.*, **57**, 104 (1908).
- K. Honda and T. Sone, *Science Repts. Tohoku Imp. Univ.*, **3**, 139 (1914).
- H. Saito, *ibid.*, **16**, 37 (1927).
- A. Simon and F. Feher, *Z. Elektrochem.*, **38**, 137 (1932).
- V. F. Krüll, *Z. anorg. Chem.*, **208**, 134 (1932).
- H. Ulich and H. Siemonsen, *Arch. Eisenhuttentw.*, **14**, 27 (1940).
- E. P. Tatievskaya, G. I. Chufarov, and V. K. Antonov, *Izvest. Akad. Nauk. S.S.S.R.*, 371 (1948).
- H. F. McMurdie, *J. Research, Natl. Bur. Standards*, **41**, 589 (1948).
- W. C. Hahn, Jr. and A. Muan, *Am. J. Sci.*, **258**, 66 (1960).
- L. Brewer, *Chem. Reviews*, **52**, 1 (1953).
- J. P. Coughlin, *U. S. Bur. Mines Bull.*, 542 (1954).
- V. G. Vlasor, *Trudy Ural, Politeckh. Inst.*, **49**, 145 (1954).
- S. Dushman, "Scientific Foundations of Vacuum Techniques," p. 742, 2nd Edition, John Wiley & Sons, New York (1962).
- E. J. Prosen, To be published.
- K. K. Kelley, *U. S. Bur. Mines Bull.*, 584 (1960).
- F. D. Rossini, *U. S. Natl. Bur. Standards Circular* 500 (1952).
- A. D. Mah, *U. S. Bur. Mines Repts Invest.* 5600 (1960).
- A. Glassner, *U. S. Argonne Nat. Lab., ANL* 5750 (1957).
- E. G. King, *J. Am. Chem. Soc.*, **76**, 3289 (1954).
- R. W. Millar, *ibid.*, **50**, 1875 (1928).
- K. K. Kelley and G. E. Moore, *ibid.*, **65**, 782 (1943).
- S. S. Todd and K. R. Bonickson, *ibid.*, **72**, 3894 (1951).
- R. L. Orr, *ibid.*, **76**, 857 (1954).
- J. Brenet, *Compt. rend.*, **240**, 1210 (1955).
- L. Kulp and J. Perfetti, *Mineralog. Mag.*, **29**, 239 (1952).
- G. Grasselly and E. Klivenyi, *Acta Univ. Szege-diensis Acta Mineral. Petrog.*, **9**, 15 (1956).
- M. Földvari-Vogl and V. Koblencz, *ibid.*, **9**, 7 (1956).

The Effect of Internal Oxidation on the Plastic Deformation of Silver-Aluminum Single Crystals

M. J. Marcinkowski and Dorothy F. Wriedt

Edgar C. Bain Laboratory for Fundamental Research,
United States Steel Corporation Research Center, Monroeville, Pennsylvania

ABSTRACT

The critical resolved shear stresses for slip and twinning have been obtained for a series of internally oxidized Ag-Al single crystals containing from 0 to 1.35 a/o Al. It was found that both these stresses increased with Al additions. The stress for slip, however, increased at a much more rapid rate, so that twinning was often the preferred mode of deformation at the higher Al concentrations. Using the model of Wriedt and Darken for the oxide particles, a theory has been developed which is in principle the same as that proposed by Kelly and Nicholson. Specifically it involves the cutting of the oxide particles by a highly flexible dislocation line. This theory leads to an equation of the type

$$\tau = \tau_{Ag} + (\tau_{ox} - \tau_{Ag})f_{A,Al}^{1/2}$$

The present experimental results are in satisfactory agreement with this relation. Also implicit in the above equation is that τ is independent of either the size or dispersion of the oxide particles for a fixed Al concentration, which is also in agreement with experimental results.

The strengthening of metals by internal oxidation was first demonstrated by Meijering and Druyvesteyn (1) and by Meijering (2) in 1947. In brief,

this technique consists of choosing a metal such as Ag, Cu, or Ni in which oxygen diffuses very rapidly, and which has very little affinity for oxygen. A

per cent or more of a second element such as Al, Si, Mg, Mn, or Ti for which oxygen has a strong affinity is added; the alloy is annealed in oxygen or air at a suitable temperature. Since oxygen diffuses much more rapidly than the solute element, a fine stable dispersion of oxide particles is formed, which imparts a marked strengthening to the base metal. Martin and Smith (3) have shown that a large increase in creep resistance is obtained after oxidizing polycrystalline Cu-Al and Cu-Si alloys. These same investigators (4) have also studied the effect of internal oxidation on the fatigue properties of similar Cu alloys. In addition, Gregory and Smith (5) have carried out a study of the tensile properties of polycrystalline Ag-Al and Ag-Si alloys which were oxidized at various temperatures in order to produce various degrees of oxide dispersion.

Whereas polycrystalline specimens, because of intercrystalline brittleness, show little or no ductility, depending on the solute concentration and the oxidizing temperature (1, 2, 5), single crystals have been reported to be completely ductile (1, 2). However, no detailed investigation has been made of the plastic behavior of internally oxidized single crystals. The purpose of the present investigation, therefore, was to undertake such a study. The metal chosen was silver containing various amounts of Al as solute. This choice was made because Ag_2O is unstable above $190^\circ C$ at atmospheric pressure, while the oxide of Al is one of the most stable known. Furthermore, silver, which is one of the softest of metals, is hardened by a dispersion of Al_2O_3 , which is one of the hardest substances known, so that the strengthening effect should be optimized in this alloy. A detailed investigation of the manner in which the amount and dispersion of the oxide particles can be varied as a function of Al concentration and oxidizing temperature has been made by Wriedt and Darken (6), portions of which have been presented in Darken's 1961 Campbell Memorial Lecture (7). These results will be drawn on extensively in the present study.

The format followed in this paper is to discuss first the experimental results in a very general way. The latter portion of the paper then attempts to reconcile these results with the present theories of dispersion strengthening, along with some new ones which have evolved from the present investigation.

Experimental Procedure

The materials used in the present investigation were 99.9999% Cominco Ag and 99.99% Alcoa research Al. All melting was carried out in molds fabricated from National Carbon Company's ultra high purity graphite grade AGKSP spectroscopic rod in a horizontal zone purification unit under an atmosphere of purified hydrogen. Before alloying, the Ag was first degassed by passing a molten zone through it at a rate of 20 in./hr to remove traces of dissolved oxygen.

Because of the large disparity in the densities of Ag and Al, and since homogeneity was a prime requisite in the present investigation, the following elaborate procedure was carried out in order to in-

sure a uniform distribution of solute element. A master alloy containing the desired amount of Al was first prepared from a portion of the degassed Ag bar. This master alloy was rolled to the same length as the unalloyed Ag bar and placed on top of it; the two were then zone leveled at a rate of 12 in./hr in both the forward and reverse directions. The resulting ingot was cold rolled into a sheet 0.080 in. thick and cut into a rectangular bar shaped at one end with a nucleation point which was separated from the main portion of the bar by a small constriction. This bar was placed in an identically shaped split graphite mold for the crystal growing pass during which a horizontal zone was passed through it starting from the point end at a rate of $\frac{1}{2}$ in./hr. Although suitable crystals could be obtained in this way, more than half the attempts proved unsuccessful mainly because of the profuse formation of growth twins and/or a lineage structure. Rectangular crystals 3 in. long by $\frac{3}{8}$ in. wide were cut from the larger crystal. Analysis of the material adjacent to both ends of each four specimens gave the average Al concentrations shown in Table I where the corresponding variations from end to end are also included. The composition variation over the $1\frac{1}{4}$ in. gauge length was of course much smaller. The oxidizing treatment for each of the specimens as well as the atom ratio of O to Al resulting from each of these anneals are also given in Table I. The difference in the oxidizing anneals is not considered to be significant since Wriedt and Darken (6) have shown that both the hardness and yield strength of internally oxidized polycrystalline alloys are practically independent of the oxidizing temperature. In order to remove any possible steep gradients in oxide concentration existing at the surfaces of the specimen, 0.020 in. of metal were removed from each face. Flat tensile specimens with a cross section of 0.040 x 0.250 in. and a gauge length of $1\frac{1}{4}$ in. were then prepared. In order to eliminate any deformation during the fabrication of the specimens, all cutting and planing operations were carried out with a Servomet electric spark cutting machine. The samples were finally electropolished in a 9% KCN electrolyte. All five specimens were pulled at room temperature in an Instron tensile testing machine with the cross head speed set at 0.02 in./min. The flat smooth ends of the specimen were adequately held between flat grips to which was cemented No. 240 emery cloth. Even at loads of up to 1000 lb (five times the maximum load encountered in this investigation) no slipping in the grips was detected.

Experimental Results and General Discussion

The initial tensile axis orientations of the five single crystals used in the present investigation are shown by the symbols with the identification 1 in the unit stereographic triangle of Fig. 1. On the assumption that slip took place on the primary system (111)[$\bar{1}01$], the stress-strain curves for each specimen were plotted as shown in Fig. 2 by using the relation

$$\tau = \frac{F}{A} \cos \phi \cos \lambda \quad [1]$$

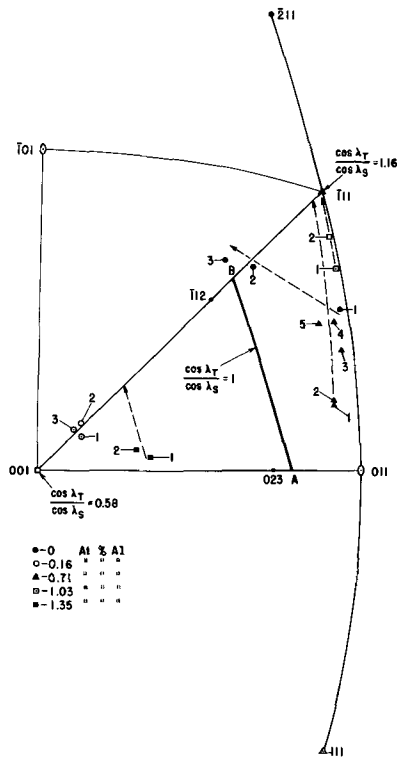


Fig. 1. Points inside unit stereographic triangle show the manner in which the tensile axes of the five single crystals rotated during plastic deformation.

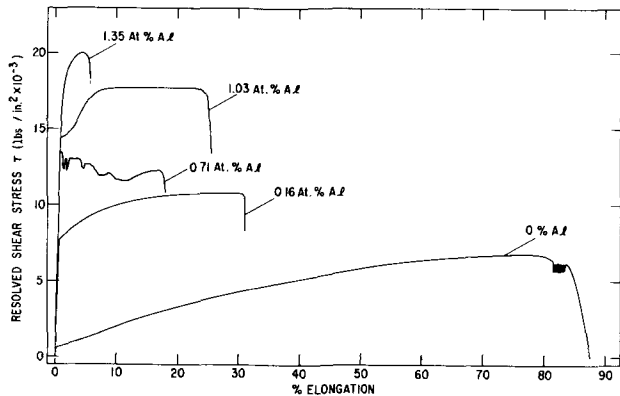


Fig. 2. Stress-strain curves obtained from the five crystals listed in Table I.

where τ is the resolved shear stress, F the applied load along the tensile axis, A the cross-sectional area, ϕ the angle between the tensile axis and slip plane, and λ the angle between the tensile axis and slip direction. Because of the complexity of the deformation with increasing strain, no attempt was made to plot true stress-strain curves in Fig. 2. Specifically τ for all strains is based on the initial values of ϕ , λ , and A , while the strain is shown simply as per cent elongation. The simplification, however, does not affect the qualitative features of these curves.

An analysis of the deformation markings during the early stages of flow show that they were caused by slip on the primary slip planes (111). As expected, the flow stress in general increased because of work hardening in these early stages of deformation. On the other hand, after approximately 8%, 0%, and 82% elongation in the 1.03 atomic per

cent (a/o) Al, 0.71 a/o Al, and 0 a/o Al specimens, respectively, flow continued at a nearly constant stress level until fracture occurred. In the case of the latter two specimens, this stress was not quite constant, but it oscillated between narrow limits giving rise to a serrated plateau. These regions of zero work hardening were all initiated by the formation of very pronounced deformation bands which spread from a single region and increased in thickness with increasing strain as can be seen by the dark bands in Fig. 3a, or else they formed discontinuously from a number of different regions along the specimen gauge length as in Fig. 3b. The fact that repeated polishing and etching failed to remove these markings strongly suggested that they were deformation twins.

Because of the large amount of distortion within the lamellae, it was not possible to obtain a suitable Laue back reflection pattern for positive identification. However, since the twin lamellae were frequently discontinuous and contained portions of un-twinned and relatively undeformed crystal within them, it was possible by using a very fine collimator to obtain a Laue back reflection pattern from these un-twinned regions. As an example, a Laue pattern was obtained from the un-twinned areas 2, 3, 4, and 5 shown at the head of the arrows in Fig. 3a. The tensile axes corresponding to these areas were plotted stereographically in Fig. 1, from which it is seen that the tensile axis rotates toward $[\bar{2}11]$ which is the di-

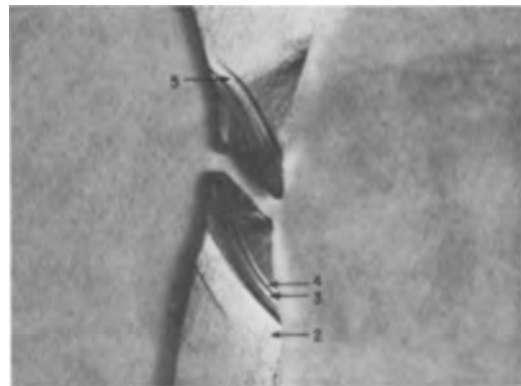


Fig. 3a. Dark region near fracture is a twin band formed during the deformation of an internally oxidized 0.71 a/o Al-Ag alloy. Micrograph taken with oblique illumination at 4.5X.

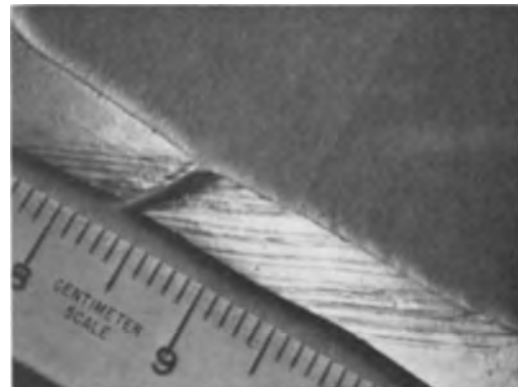


Fig. 3b. Narrow horizontal discontinuous bands along specimen gauge length are twin lamellae which resulted from the plastic deformation of an internally oxidized 1.03 a/o Al-Ag alloy. Micrograph taken with oblique illumination at 4.5X.

rection for twinning. The change of orientation of this axis is proportional to the amount of twinned volume separating the untwinned regions.

In the case where only slip occurred, the slip direction is easily determined from Laue back reflection patterns obtained along the length of the specimen from the least deformed (and thus least rotated) regions near the shoulders of the specimen to the most highly deformed regions in the necked down portions of the crystal. The direction of rotation of the tensile axes for the five specimens obtained in this manner is shown by the dotted lines in the unit stereographic triangle of Fig. 1. Increasing identification numbers in Fig. 1 correspond to regions of increasing rotation along the gauge length. It is apparent that the 0.71 and 1.03 a/o Al specimens deform predominantly by twinning in the $[\bar{2}11]$ direction, while the remaining three crystals deform by slip along $[\bar{1}01]$. Because of the small amount of deformation by slip in the two former specimens their tensile axis rotation toward $[\bar{1}01]$ was not detected. These data along with the slip or twinning planes deduced from the deformation traces on the specimen surface are shown in Table I.

The critical resolved shear stresses for both slip and twinning are shown in Fig. 4. The critical resolved shear stress for twinning was determined as accurately as possible by measuring the cross sectional area as well as the values of ϕ and λ immediately adjacent to the twin lamellae. Although the twinning stress curve in Fig. 4 is based on results obtained from only three crystals, it is believed that the curve indicates the general relation between the twinning stress and the stress required to initiate slip. On the basis of Suzuki and Barrett's (8) extensive investigation of Ag-Au alloys it is also assumed that a critical resolved shear stress for twinning is valid for the present specimens. Blewitt *et al.* (9), on the other hand, because of the wide scatter in their values of the twinning stress for Cu single crystals, have concluded just the opposite. According to Blewitt *et al.* (9), twinning occurs only when the tensile axis of the specimen rotates to the portion of the dodecahedral plane lying between the $[\bar{1}11]$ and $[\bar{1}13]$ directions. The present investigation, how-

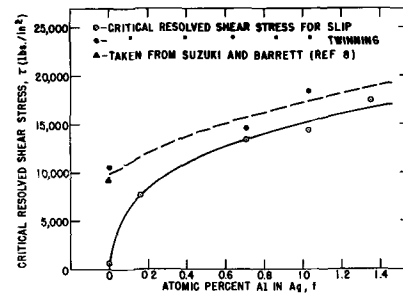


Fig. 4. Critical resolved shear stress for both slip and twinning in internally oxidized Ag-Al alloys as a function of Al concentration.

ever, indicates that twinning occurs only after the crystal has work hardened by slip to the stress level where twinning can occur. Similar arguments have been used by Suzuki and Barrett (8) in their Ag-Au investigation. In Fig. 4 it is seen that the critical resolved shear stress for twinning in pure Ag is 15 times that for slip, while in the case of the internally oxidized 1.35 a/o Al alloy it is only 1.1 times as large. In other words, the critical resolved shear stress for twinning is much less sensitive to the oxide content than is that for slip.

On the basis of the two curves in Fig. 4, it is of interest to analyze the particular orientations in the unit stereographic triangle of Fig. 1 to see if there are any in which one type of deformation is favored over the other. This is best seen as follows. If (111) acts as both the slip and twinning plane, Eq. [1] says that the ratio of the resolved shear stress on this plane between the twinning and slip system is $\cos \lambda_T / \cos \lambda_S$, where λ_T and λ_S are the angles that the twin and slip directions make with the tensile axis of the specimen respectively. It is apparent that when τ_T / τ_S , as determined from Fig. 4, is less than $\cos \lambda_T / \cos \lambda_S$, then twinning will occur without any prior slip. If this condition is not met, then τ_S will increase because of work hardening until the proper ratio is attained, at which point twinning will occur. For reference purposes the line AB in Fig. 1 shows the locus of tensile axis orientations at which $\cos \lambda_T / \cos \lambda_S = 1$, i.e., $\tau_T = \tau_S$. As this line moves toward the left or (001) pole, $\cos \lambda_T / \cos \lambda_S$ approaches 0.579; whereas when it moves toward the right, that is toward the $(\bar{1}11)$ pole, $\cos \lambda_T / \cos \lambda_S$ approaches 1.16. From this analysis it is apparent that pure silver in which $\tau_T / \tau_S = 15$ will never twin at the yield point, but it must first be work hardened to an appropriate stress level by slip, as is apparent from Fig. 1 and 2. In the case of the 0.16 and 1.35 a/o Al specimens, because of the unfavorable position of their tensile axis in the unit stereographic triangle, fracture occurs before this appropriate stress level for twinning is reached. In the case of the 0.71 and 1.03 a/o Al specimens, $\cos \lambda_T / \cos \lambda_S$ is close to that of τ_T / τ_S obtained from Fig. 4, so that the stress level for twinning is reached after little or no work hardening. In the present analysis it has been tacitly assumed that the critical stress for twinning is essentially independent of the degree of work hardening by slip. Although the results of Suzuki and Barrett (8) indicate that this is approximately so, the finding is quite surprising in view of the fact that

Table I. Deformation behavior of internally oxidized Ag-Al alloys as a function of their O/Al ratio

Al, a/o	Oxidizing treatment	O/Al	Slip system*	Slip system*
0		∞	(111) $[\bar{1}01]$ P	($\bar{1}\bar{1}\bar{1}$) $[\bar{1}21]$ K
0.16 \pm 0.02	10 hr at 800°C	1.7	(111) $[\bar{1}01]$ P	None
0.71 \pm 0.04	191 hr at 600°C	1.70	(111) $[\bar{1}01]$ P	(111) $[\bar{2}11]$ P
1.03 \pm 0.10	21 hr at 800°C	1.66	(111) $[\bar{1}01]$ P	(111) $[\bar{2}11]$ P
1.35 \pm 0.04	69 hr at 700°C	1.78	(111) $[\bar{1}01]$ P	None

* The suffixes P and K refer to the primary and conjugate systems, respectively.

Marcinkowski and Lipsitt (10) have shown that as little as 3% plastic deformation at room temperature suppresses twinning completely at -195°C in chromium, a temperature at which it occurs profusely without prior plastic deformation. The fact that twinning in Ag can occur after 82% elongation indicates that there may be a basic difference between the twinning mechanisms in face centered cubic and body centered cubic structures.

In the discussion of deformation by twinning it would seem that specimens with their axes near the [001] pole in the unit stereographic triangle of Fig. 1 would prefer to have $[\bar{1}\bar{1}2]$ as their twinning direction. However, Venables (11) has shown that the stress on the twin system (111) $[\bar{1}\bar{1}2]$ would be such as to produce an extrinsic fault which has a prohibitively high energy.

The stress-strain curve for pure Ag is quite similar to that obtained by Hauser (12). On the other hand, with increasing additions of Al and thus increasing amounts of oxide, the rate of work hardening during the initial stages of deformation (that which occurred by slip) appears to increase.

It is also apparent in Fig. 2 that the amount of elongation before fracture is only 5% for the 1.35 a/o Al specimen. This specimen, however, gave a chisel type fracture; that is, it deformed in a quite ductile manner over a very small localized region. For this reason the over-all ductility was poor. In the case of the three specimens that twinned, fracture occurred entirely within the twin band.

Nature of the Strengthening Mechanism

Thus far the effect of internal oxidation on the strength of Ag-Al alloys has been discussed on a phenomenological basis and no attempt has been made to examine the atomistic picture of the interaction between the oxide particles and dislocations. Before this can be done, it is first necessary to know something about the nature of the oxide particles in the silver matrix. Although Ashby and Smith (13) have reported the oxide in internally oxidized Cu-Al alloys to be of the γ -alumina type, both x-ray and electron diffraction techniques have failed to reveal a crystal structure other than pure Ag in the internally oxidized Ag-Al alloys.

Because of this lack of direct experimental information, only a very general model of the oxide will be postulated. Specifically, the model of Wriedt and Darken (6) will be adopted, in which it is assumed that the oxygen atoms diffuse to the substitutionally dissolved Al atoms and take up the six octahedral interstices surrounding it. An Al atom diffusing to an adjacent substitutional site undergoes

a similar oxidation until a well defined oxide particle is formed. During this process only a relatively small volume change occurs which can be accommodated elastically by the matrix. Also, because of the similarity in size between the silver and aluminum atoms, the atom fraction of Al atoms $f_{A,Al}$ can be assumed equal to the volume fraction of Al atoms $f_{V,Al}$. The diameter of the oxide particles, taken to be spheres, can be found by first assuming a linear relationship between the oxygen-aluminum ratio O/Al and $1/\sqrt[3]{N}$, where N is the number of Al atoms associated with an oxide particle (6). It is also apparent on the basis of the Wriedt-Darken model that, O/Al should have values of 1 and 6 when $1/\sqrt[3]{N}$ takes the values of 0 and 1.0, respectively. Using the relationships described above, values of $1/\sqrt[3]{N}$ can be obtained for the four O/Al ratios as shown in Table II. The volume associated with a given oxide particle is simply $N a_0^3/4$ where a_0 is the edge length of the unit cell of Ag, and the factor of 4 takes care of the fact that there are four atoms in the fcc unit cell. Equating this to the volume of a sphere, $4/3\pi (d/2)^3$ where d is the true diameter of the sphere, the following relation can be obtained

$$d = 6.84 \times 10^{-8} N^{1/3} \quad [2a]$$

The mean diameter \bar{d}_i on the slip plane is given as (14)

$$d_i = \sqrt{2/3} d \quad [2b]$$

Values of d and d_i determined for these equations are listed in Table II. Next, by arranging the circles of diameter d_i on a square mesh of edge length Λ on the slip plane so that Λ is the center to center distance between particles, and assuming that the volume fraction of oxide particles $f_{V,ox} = f_{V,Al} = f_{A,Al}$ is equal to their area fraction on the slip plane, one obtains according to Kelly and Nicholson (14)

$$\Lambda = \sqrt{\frac{\pi}{6}} \left(\frac{d^2}{f_{A,Al}} \right)^{1/2} \quad [3]$$

Values of Λ obtained from the above relation are listed in Table II. It is important to note here that Λ as defined above is essentially the nearest neighbor distance between oxide particles on the slip plane. Also implicit in the above model is that the oxide particles remain coherent with the Ag matrix. This appears reasonable in view of the divergent beam x-ray back reflection patterns obtained by Weissmann and Wriedt (15).

The number of different strengthening mechanisms that have evolved over the past two decades are quite numerous. The theories of Orowan (16),

Table II. Significant parameters associated with the internally oxidized Ag-Al alloys described in Table I which were calculated on the basis of the theoretical model of Wriedt and Darken

Al, a/o	O/Al	$1/\sqrt[3]{N}$	d , cm	d_i , cm	$f_{A,Al}$	Λ , cm	r , cm
0	∞	∞	0	0	0	∞	—
0.16 ± 0.02	1.7	0.142	48.1×10^{-8}	39.2×10^{-8}	0.0016	866×10^{-8}	729×10^{-8}
0.71 ± 0.04	1.70	0.142	48.1×10^{-8}	39.2×10^{-8}	0.0071	412×10^{-8}	417×10^{-8}
1.03 ± 0.10	1.66	0.133	51.4×10^{-8}	41.9×10^{-8}	0.0103	364×10^{-8}	388×10^{-8}
1.35 ± 0.04	1.78	0.157	43.5×10^{-8}	35.4×10^{-8}	0.0135	270×10^{-8}	320×10^{-8}

Fisher, Hart, and Pry (17) as well as the chemical strengthening theory of Kelly and Fine (18) all depend on either Λ or d_i alone. On the other hand, the hardness data of Wriedt and Darken (6, 7) indicate that the strengthening due to internal oxidation in the Ag-Al alloy may not depend on either Λ or d_i alone. There are a number of theories in which the shear stress depends only on the volume fraction of precipitate or in the present case $f_{A,Al}$. The most notable of these is that due to Mott and Nabarro (19-22). However, this theory predicts a linear relation between τ and f , and in view of the results shown in Fig. 4, must be rejected. Based on the experimental observations of Meiklejohn and Skoda (23), Ansell (24) has also developed a theory in which τ is function of only the volume fraction of dispersed second phase particles. However, as pointed out by Kelly and Nicholson (14), there are very strong objections, both experimental and theoretical, associated with these two latter investigations, respectively.

Another theory, and one that possesses considerable merit has been described in detail by Kelly and Nicholson (14). In particular, it involves the cutting of the precipitate particle by the moving dislocation. In this model the lattice friction stress of the particles is assumed to be much larger than that of the matrix. Curiously and erroneously, Kelly and Nicholson (14) begin their derivation by assuming a perfectly rigid dislocation line, where in fact their theory applies only to one which is highly flexible. It will be demonstrated, however, in the following paragraph that in spite of what they say, their theory is indeed valid for a highly flexible dislocation line.

On the basis of what has been said earlier, the oxide particles can be assumed to be perfectly coherent with the matrix and to possess a structure essentially the same as that of the matrix. The Burgers vector of the dislocation within the particle can thus be taken essentially equal to that within the Ag matrix. For illustrative purposes the oxide particle configuration to be expected on the slip plane of the internally oxidized 0.71 ± 0.04 a/o Al-Ag alloy described in Tables I and II is shown in Fig. 5. The figure was constructed to scale using the values of d_i , $f_{A,Al}$, and Λ listed in Table II. In the absence of an externally applied stress, a dislocation segment AB will remain essentially straight and lie in the softer Ag matrix. Under the action of an externally applied shear stress τ which is just below the yield stress, the dislocation line will take the curved shape shown by A'B'. Two factors determine the shape of the line A'B'. The first is that just under the yield stress, the dislocation line must not pass through the particles. Second, under this same stress the radius of curvature of the dislocation line at any point must not be less than

$$r = \frac{\alpha G b}{\tau} \quad [4]$$

where α is on the order of $1/2$, G the shear modulus of Ag is taken to be 2.64×10^{11} dynes/cm², while b the Burgers vector of the dislocation line is $2.93 \times$

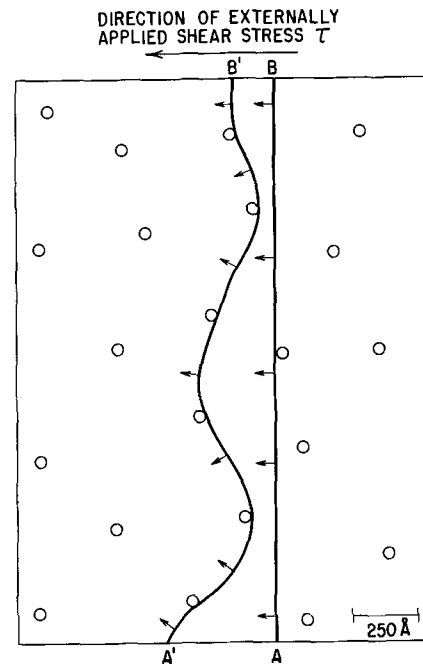


Fig. 5. Schematic illustration showing the response of an initially straight dislocation segment AB lying on the slip plane of an internally oxidized Ag-Al alloy to a shear stress τ whose magnitude is just below that of the yield stress. The above configuration corresponds to the internally oxidized 0.71 ± 0.04 a/o Al.

10^{-8} cm. Using the values of τ for slip shown in Fig. 4, the various values of r calculated from Eq. [4] are listed in Table II. It is apparent from these results that r is on the order of Λ for all of the present alloys, so that the dislocations are highly flexible. This becomes immediately apparent by referring to Fig. 5. On the other hand, the dislocations are not sufficiently flexible to bow out between the particles in the manner predicted by the Orowan theory, since a simple calculation shows that this would give rise to shear stress more than twice that observed in all of the present internally oxidized alloys.

Because of the large value of Λ in the present alloys, the dislocation line can be thought of as connecting nearest neighbor oxide particles, i.e., the value of Λ given by Eq. [3]. The dislocation segment connecting two such neighboring particles will in general be curved and will slice through the particles with little or no help from adjacent segments of the dislocation line. A schematic illustration of the sequence of events whereby an initially straight dislocation line is forced through a pair of neighboring oxide particles is shown in Fig. 6a-6d. If as Kelly and Nicholson (14) had assumed, the dislocation were to move as a rigid straight line, the total works ΔW expended in driving the dislocation through the oxide particles with spacing Λ is given to a good approximation by

$$\begin{aligned} \Delta W &= F \Lambda d_i = F_{Ag} (\Lambda - d_i) d_i + F_{ox} (d_i^2) \\ &= \tau_{Ag} b (\Lambda - d_i) d_i + \tau_{ox} b (d_i^2) = \tau b \Lambda d_i \quad [5] \end{aligned}$$

This relation would be exact for square particles of edge length d_i . The subscripts Ag and ox on F and τ refer to the friction force per unit length and stress acting on the dislocation within the silver matrix and

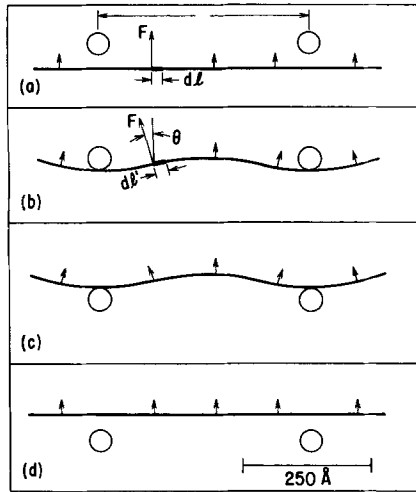


Fig. 6. More detailed schematic illustration of how a generally curved segment of dislocation line such as that shown in Fig. 5 cuts through the oxide particles.

oxide precipitate, respectively. The fact that the dislocation is curved as it moves through the oxide particles has no effect on Eq. [5]. This follows from the realization that only the component of force in the direction of the dislocation motion, $F \cos \theta$ acting on a dislocation segment $dl' = dl/\cos \theta$, does work. Referring to Fig. 6, the total force acting on the curved dislocation segment in the Ag matrix and in the direction of motion of the dislocation line is therefore

$$\int_0^{\Lambda-d_i} F_{Ag} \cos \theta dl' = \int_0^{\Lambda-d_i} F_{Ag} dl = F_{Ag} (\Lambda - d_i) \quad [6]$$

which is the same as that given in Eq. [5] for the straight rigid dislocation line. Since the diameter of the oxide particles is quite small, no change in the shape of the dislocation line is expected to occur between stage (b) and (c) in Fig. 6. After the dislocation segment passes through the particles, it straightens itself more or less, releasing most of its line energy due to curvature, to thermal vibrations within the crystal. In no case does the curvature of the dislocation line enter into the work of driving it through the oxide particles, *i.e.*, sequence (b) and (c) in Fig. 6.

Combining Eq. [2b], [3], and [5] leads to the following relationship

$$\tau = \tau_{Ag} + (\tau_{ox} - \tau_{Ag}) 1.13 f_{A,Al}^{1/2} \quad [7a]$$

The above relation is in principle the same as that obtained by Kelly and Nicholson (14), but expressed in terms of the dislocation friction stresses in both the Ag matrix and the oxide particle, instead of the specific energy γ associated with the sheared precipitate interface. Also if the same mean width of precipitate, $\bar{d} = \pi/\sqrt{6} d/2$ used by Kelly and Nicholson (14) were used in Eq. [5] in place of d_i the factor of 1.13 would be replaced by $1/1.13$. However, in view of the uncertainties associated with the best choice of geometric factors in the present analysis, Eq. [7] can be written for convenience without loss of precision as

$$\tau = \tau_{Ag} + (\tau_{ox} - \tau_{Ag}) f_{A,Al}^{1/2} \quad [7b]$$

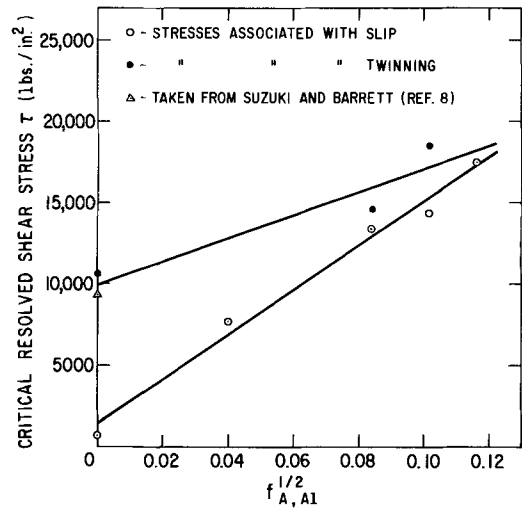


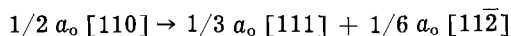
Fig. 7. Critical resolved shear stresses, obtained from Fig. 4, plotted in accordance with the theoretical relation given by Eq. [7b].

Thus according to Eq. [7b], τ should vary with $f_{A,Al}^{1/2}$ and be independent of the state of dispersion of the oxide. This is in agreement with the microhardness data of Wriedt and Darken (6) and Darken (7). The data of Fig. 4 are plotted against $f_{A,Al}^{1/2}$ in Fig. 7. Although there is some scatter in τ , the data fall quite close to a straight line. From the intercept and slope of the line associated with slip in Fig. 7, τ_{Ag} and τ_{ox} are found to be 1500 psi and 138,000 psi, respectively. In view of the high hardness of aluminum oxides in general, the above value for the stress to move a dislocation through the oxide does not appear to be unreasonably large.

Although the flexible dislocation model gives a functional relationship which agrees well with experiment, the lack of detailed knowledge concerning the nature and magnitude of the friction stress within the oxide, precludes further verification of the model. For this reason other dislocation models such as cross slip around the particle cannot be ruled out completely. Preliminary transmission electron microscopy observations on internally oxidizing Ag-Al alloys (7, 25) have shown the presence of large numbers of elongated dislocation loops after deformation which seem to support this model. It is not yet known whether this behavior is characteristic of the oxidized alloys or the Ag itself. A serious difficulty with the cross slip model is that Ag has a relatively low stacking fault energy. The fact that twinning becomes more frequent in the oxidized alloys suggests that twinning dislocations, which cannot cross slip, probably shear the oxide particles. A similar shearing by regular slip dislocations could, therefore, also be expected. If the oxide particles are indeed sheared during plastic deformation, then this should lead to the formation of oxide interfaces in which there are unbonded atoms of Al with O. This feature should manifest itself as an additional weight gain on further oxidation at elevated temperatures.

The final topic of interest in this investigation concerns an analysis of the twinning mechanism. It is generally assumed that the critical stress for twinning τ^T involves the stress necessary to form the first layer of the twin lamella. This layer is simply

a stacking fault formed by the motion of a $1/6 a_0 <112>$ type partial or twinning dislocation in the (111) plane resulting from the following dislocation reaction (26)



Models based on this mechanism have been used by Venables as well as Suzuki and Barrett (8). The simplest model, described above, will be used in the present analysis. In view of the success of the rigid dislocation cutting model in accounting for the variation of the critical resolved shear stresses with oxide content, it is of interest to employ similar reasoning in the case of the twinning stresses. Specifically, the following equation, analogous to Eq. [7b], can be written

$$\tau^T = \tau_{Ag}^T + (\tau_{ox}^T - \tau_{Ag}^T) f_{A,Al}^{1/2} \quad [8]$$

In spite of the fact that critical resolved twinning stresses for only three different Ag-Al alloys were obtained, they have nevertheless been plotted in Fig. 7 in accordance with Eq. [8]. Although these limited data do not provide an accurate test of Eq. [8], it will nevertheless be assumed to be valid. From the intercept and slope of the straight line associated with the twinning mode of deformation in Fig. 7, τ_{Ag}^T and τ_{ox}^T are found to be 10,000 psi and 58,500 psi, respectively. On the basis of the twinning stress model described in the previous paragraph, the following relationships can be obtained.

$$E_F^{Ag} = \tau_{Ag}^T b_{1/6 a_0 <112>} \quad [9a]$$

$$E_F^{ox} = \tau_{ox}^T b_{1/6 a_0 <112>} \quad [9b]$$

where E_F^{Ag} and E_F^{ox} are the stacking fault energies in the silver matrix and the oxide particle, respectively, while $b_{1/6 a_0 <112>} = 1.67 \times 10^{-8}$ cm is the Burgers vector of the $1/6 a_0 <112>$ twinning dislocation in pure silver and is assumed to be the same as that in the oxide particles. On substitution of the appropriate values into Eq. [9a] and [9b], one obtains $E_F^{Ag} \cong 12$ ergs/cm² and $E_F^{ox} \cong 67$ ergs/cm². The above value for silver is only about half the value of 25 ergs/cm² determined by Howie and Swann (27) in thin foils, and may in part be due to the reduction in the externally applied stress by piled-up dislocation groups as suggested by Venables (11). Applying the reasoning to the oxide particles, E_F^{ox} should then be about 134 ergs/cm². This large value of the stacking fault energy in the oxide particles is to be expected in view of their possible ionic structure and will in general lead to an imbalance in the charge distribution across the fault plane. Unfortunately, however, independent measurements of E_F^{ox} are not available with which to obtain further clarification of the validity of Eq. [8].

Summary and Conclusions

1. The critical resolved shear stress for slip in internally oxidized Ag-Al single crystals increases from about 600 psi for pure Ag to 17,500 psi for an internally oxidized alloy containing 1.4 a/o Al. The critical resolved shear stress for twinning is about 10,600 psi for pure Ag and increases to about 18,500 psi for an internally oxidized 1.03 a/o Al alloy.

Thus, the critical resolved shear stresses for slip and twinning become more nearly equal as the Al concentration increases; the preferred mode of deformation depends strongly on orientation. Specifically, twinning is preferred when the specimen tensile axis lies near $<111>$, while slip is the preferred mode of deformation for a tensile axis near $<100>$. In the case of the internally oxidized lower Al concentration alloys, appreciable work hardening by slip must first occur before twinning can take place.

2. Although the inapplicability of all other strengthening mechanisms has not been wholly ruled out, a theory of strengthening based on the model of Kelly and Nicholson (14) which involves cutting of the oxide particles by a highly flexible moving dislocation line has been developed. The model chosen for the oxide has been that first proposed by Wriedt and Darken. The present theory leads to the following equation for deformation by slip

$$\tau = \tau_{Ag} + (\tau_{ox} - \tau_{Ag}) f_{A,Al}^{1/2}$$

where τ_{Ag} and τ_{ox} are the lattice friction stresses in the Ag matrix and oxide particles respectively, while $f_{A,Al}$ is the atomic fraction of Al in the Ag. The reason why $f_{A,Al}$ appears in the above equation is that in the present system it is very nearly equal to the volume fraction of oxide particles. The present results are in satisfactory agreement with the above relation. Also implicit in the above equation is that τ is independent of either the size or dispersion of the oxide particles for a fixed value of $f_{A,Al}$. This agrees with earlier hardness results obtained by Wriedt and Darken (6).

Although the critical resolved shear stress data for twinning were limited in the present investigation, they can also be fitted to an equation of the form given above. In this case, however, τ_{Ag}^T now represents the stress necessary to create a stacking fault within the oxide particle.

Acknowledgment

The authors would like to express their grateful appreciation to the following members of this Laboratory: R. M. Poliak for assistance in testing the single crystals; B. F. Oliver, E. W. Troy, and T. R. Ayers for preparing the single crystals; to A. Szirmai for cutting and polishing the tensile specimens; L. Zwell and E. J. Fasiska for obtaining the Laue x-ray back reflection patterns; D. S. Miller, P. R. Swann, and F. Garofalo for their helpful discussions during the course of this investigation; and finally L. S. Darken who was responsible for initiating this work and who also provided the impetus and motivation for its completion.

Manuscript received April 11, 1963; revised manuscript received Aug. 23, 1963.

Any discussion of this paper will appear in a Discussion Section to be published in the December 1964 JOURNAL.

REFERENCES

1. J. L. Meijering and M. J. Druyvesteyn, *Philips Research Repts.*, **2**, 81, 260 (1947).
2. J. L. Meijering, Report of a Conference on Strength of Solids, held at the H. H. Wills Physical Lab., University of Bristol, July 7-9, 1947, published by the Physical Society, London, p. 140 (1948).

3. J. W. Martin and G. C. Smith, *J. Inst. Metals*, **83**, 417 (1954-1955).
4. J. W. Martin and G. C. Smith, *ibid.*, **83**, 153 (1954-1955).
5. E. Gregory and G. C. Smith, *ibid.*, **85**, 81 (1956-1957).
6. D. F. Wriedt and L. S. Darken, To be published.
7. L. S. Darken, The Edward DeMille Campbell Memorial Lecture for 1961, *Trans. Am. Soc. Metals*, **54**, 599 (1961).
8. H. Suzuki and C. S. Barrett, *Acta Met.*, **6**, 156 (1958).
9. T. H. Blewitt, R. R. Coltman, and J. K. Redman, *J. Appl. Phys.*, **28**, 651 (1957).
10. M. J. Marcinkowski and H. A. Lipsitt, *Acta Met.*, **10**, 95 (1962).
11. J. A. Venables, *Phil. Mag.*, **6**, 379 (1961).
12. J. J. Hauser, *Trans. AIME*, **221**, 305 (1961).
13. M. F. Ashby and G. C. Smith, *Phil. Mag.*, **5**, 298 (1960).
14. A. Kelly and R. B. Nicholson, "Progress in Materials Science," Bruce Chalmers, Editor, Vol. 10, 149, The Macmillan Company, New York (1963).
15. S. Weissmann and D. F. Wriedt, To be published.
16. E. Orowan, Discussion in "Symposium on Internal Stresses," p. 451, Institute of Metals, London (1947).
17. J. C. Fisher, E. W. Hart, and R. H. Pry, *Acta Met.*, **1**, 336 (1953).
18. A. Kelly and M. E. Fine, *Acta Met.*, **5**, 365 (1957).
19. N. F. Mott and F. R. N. Nabarro, *Proc. Phys. Soc., London*, **52**, 86 (1940).
20. N. F. Mott, *J. Inst. Metals*, **62**, 367 (1946).
21. N. F. Mott and F. R. N. Nabarro, "Report of a Conference on Strength of Solids," p. 1, Physical Society, London (1948).
22. N. F. Mott, "Imperfections in Nearly Perfect Crystals," W. Shockley, J. H. Hollomon, R. Maurer, and F. Seitz, Editors, p. 173, John Wiley & Sons, Inc., New York (1952).
23. W. H. Meiklejohn and R. E. Skoda, *Acta Met.*, **8**, 773 (1960).
24. G. S. Ansell, *ibid.*, **9**, 518 (1961).
25. P. R. Swann and D. F. Wriedt, To be published.
26. A. H. Cottrell, "Dislocations and Plastic Flow in Crystals," p. 89, Oxford at the Clarendon Press (1953).
27. A. Howie and P. R. Swann, *Phil. Mag.*, **6**, 1215 (1961).

High-Temperature Electrical Conductivity in the Systems CaO-ZrO₂ and CaO-HfO₂

H. A. Johansen and J. G. Cleary

Research Laboratories, Westinghouse Electric Corporation, Pittsburgh, Pennsylvania

ABSTRACT

The a-c electrical conductivity of CaO-ZrO₂ and CaO-HfO₂ was measured from 800° to 2000°C. The two systems are similar. The conductivity maximum was found near 12 mole % CaO in both zirconia and hafnia.

Earlier published data (1, 2) on the electrical conductivity of the CaO-ZrO₂ system indicated several discrepancies in the behavior of the isotherm at 1000°C. It was the purpose of the present investigation to resolve these differences, to extend the measurements to higher temperatures using highest purity materials, to locate the conductivity maximum as precisely as possible, and to measure and compare the conductivity of the previously unreported system CaO-HfO₂.

Experimental

Material.—The zirconia used was a low-hafnium grade obtained from Numec. Analysis furnished indicated a purity of 99.93% ZrO₂ + HfO₂, and Fe, Cr, and Ti as principal impurities. Hafnium was reported to be 60 ppm. The zirconia was then reacted with high-purity graphite to form ZrC. The ZrC was chlorinated to form anhydrous ZrCl₄, and the chloride dissolved in water to form zirconyl chloride solution. The chloride solution was converted to zirconyl nitrate solution. Zirconium oxide, prepared from the nitrate solution by evaporation to dryness and ignition, showed on analysis 99.985% ZrO₂ + HfO₂, with Cr, Al and Si as principal impurities. Anhydrous-hafnium chloride (U.S. Bureau of Mines) was converted to hafnium nitrate solution. Hafnium oxide prepared from the nitrate solution

showed on analysis 99.98% HfO₂ + ZrO₂, with Fe as principal impurity. Zirconium in the hafnia was reported to be 1-4%. The calcium oxide necessary to make the preparations was added as Fisher Certified calcium carbonate.

Preparation of specimens.—To insure homogeneity, all specimens were prepared by evaporation to dryness, and ignition to 1000°C, of the zirconium or hafnium nitrate solution to known concentration, the necessary quantity of CaCO₃ being first dissolved in the nitrate solution. The powders so obtained were then pressed in carbide dies with no binder, fired in argon atmosphere in a graphite resistor furnace to 1900°C, ground, repressed, and refired as before. This produced cylindrical specimens 1 x 2 cm with densities about 70% of theoretical. A coating of TaSi₂ was applied by plasma jet to the ends to form a low ohmic contact.

X-ray diffraction.—X-ray powder diffraction patterns were obtained for all compositions prepared to determine the phases present and, in the cubic single phase region, to look for evidence of superlattice.

Metallographic.—Metallographic examination of compositions in the monoclinic-cubic, cubic, cubic-orthorhombic, and orthorhombic regions were made for identification of phases.

Electrical conductivity measurements.—Measurements were made from 800° to 2000°C using a

split graphite resistor furnace with argon atmosphere as described in (3).

Results

The System (CaO)_x(ZrO₂)_{1-x}.—The conductivity, σ , may be represented by the relation

$$\sigma = A \exp - \frac{\Delta E}{kT} \quad [1]$$

where A is a pre-exponential term, k is the Boltzmann constant, T is the absolute temperature, and ΔE represents the activation energy for conduction. Typical curves are shown in Fig. 1. For x values higher than 0.6 there was some uncertainty and variation in results due to possible uptake of H₂O or CO₂ by the calcia rich compositions. Such ex-

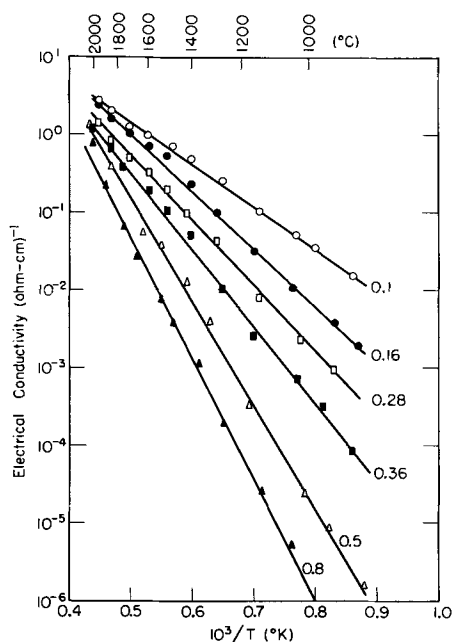


Fig. 1. Typical curves for electrical conductivity of $(\text{CaO})_x(\text{ZrO}_2)_{1-x}$.

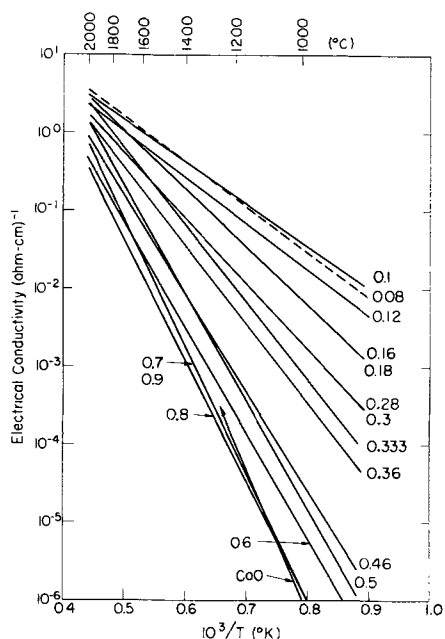


Fig. 2. Summary of electrical conductivity of $(\text{CaO})_x(\text{ZrO}_2)_{1-x}$.

posure of these specimens was minimized, but some slight reaction was probable. Figure 2 shows a summary of the plot of the electrical conductivity vs. the reciprocal absolute temperature for values of x from 0.08 to 1. (The curve for $x = 0.08$ is dashed for clarity.) The highest conductivities are in the region of $x = 0.1$. All other compositions tend toward increasing ΔE 's and lower conductivities with increasing values of x . An activation energy of 3.8 eV was found for ZrO₂, and 1.07 eV for $x = 0.1$; from this minimum, the activation energy increased approximately linearly to 2.78 eV for $x = 0.5$. The lattice parameter for the composition $x = 0.12$ was 5.127Å.

From Fig. 1 it is noted that there is some deviation from the Arrhenius relation for several of the compositions. Replots of these data on a larger scale show no particular trend with composition. Deviations from the Arrhenius relation have been reported by Dixon *et al.* (4) for the compositions $x = 0.18$ and 0.24 and attributed to decomposition of the cubic phase. The deviations in Fig. 1, however, appear at a higher temperature and at lower compositions than in (4). No explanation can be offered for this apparent deviation from the strict Arrhenius relation.

Conductivity isotherms are shown in Fig. 3. Measurement of $x = 0$ (pure ZrO₂) was carried out to about 1600°C. The results below this temperature fall reasonably close to a straight line in an Arrhenius plot. The value for ZrO₂ at 2000° in Fig. 3 is extrapolated from lower temperatures.

The boundaries of the cubic single-phase region have been reported by Duwez, Odell, and Brown (5) to extend from 16 to about 28 mole % CaO; however, the x-ray cubic and metallographic results summarized in Table I indicate that the cubic phase boundaries are near 12 and 22 mole % CaO, respectively.

The System (CaO)_x(HfO₂)_{1-x}.—Figure 4 shows a summary of the plot of the conductivity vs. the reciprocal temperature for values of x from zero to

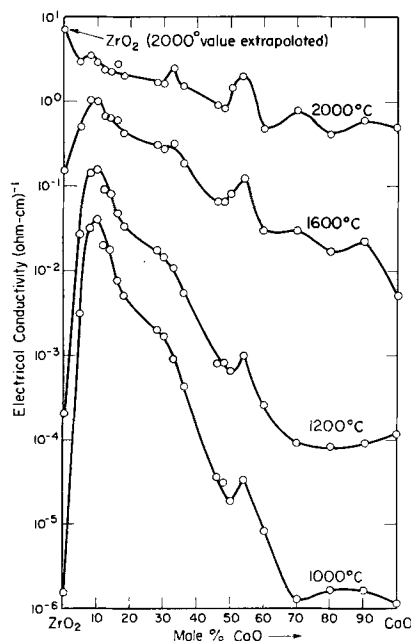


Fig. 3. Conduction isotherms $(\text{CaO})_x(\text{ZrO}_2)_{1-x}$.

Table I. X-ray diffraction and metallographic results for CaO-ZrO₂

Composition mole % CaO	X-ray	Metallographic
5	Monoclinic + cubic	Two phases
8	Monoclinic + cubic	Two phases
10	Cubic + trace monoclinic	Single phase
12.5	Cubic	Single phase
16	Cubic	Single phase
20	Cubic	Single phase
22	Cubic	Single phase
23	Cubic + zirconate	—
25	Cubic + zirconate	Two phases
33.3	Cubic + zirconate	Two phases
50	Zirconate	Single phase

1. (The curves for $x = 0.15, 0.17$, and 0.5 are dashed for clarity.) An activation energy of 2.86 eV was found for HfO₂, and a minimum ΔE of 1.43 eV for $x = 0.12$. The composition $x = 0.12$ gave the conductivity maximum, and the lattice parameter for this composition was 5.112 Å.

Discussion

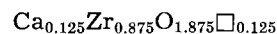
The 33 mole per cent anomaly.—Trombe and Foex (1) found for the system CaO-ZrO₂ a minimum in the conduction at 33 mole % CaO. They suggested that a compound (CaO)(ZrO₂)₂ existed, but no evidence has been found to support this view. Volchenkova and Palguyev (2) repeated the work of Trombe and Foex and showed a smoothly descending curve from their conduction maximum at 15 mole % CaO to the minimum at 50 mole %. In (1), the specimens were prepared by fusion in a solar furnace, and in (2) by heating only to 1500°C. The preparative method in the present work was different again. Initial measurements in the CaO-ZrO₂ systems gave results similar to the results of Trombe and Foex (1), but repeated trials over varying conditions of heating and starting materials showed that the presence, or absence, of the mini-

mum-maximum in the two-phase region was a function of the preparative technique. A possible explanation is that the preparative technique affects the microstructural distribution of two phases of different conductivities.

The conductivity maximum.—The work reported in (1) and (2) showed the conductivity maximum to be near 15 mole % CaO in ZrO₂. As the data show in Fig. 1 and 2, $x = 0.1$ has the highest conductivity and the lowest activation energy, ΔE , for all compositions. The differences in ΔE between $x = 0.08, 0.1$, and 0.12 are probably not significant due to the experimental difficulties, but the values of ΔE are clearly less than for $x = 0.16$. For the (CaO)_x(HfO₂)_{1-x} system, Fig. 4, the maximum is placed at $x = 0.12$, but the differences among $x = 0.08, 0.1$, and 0.15 are slight. For the two systems the conductivity maximum is considered to be probably at the composition $0.1 < x < 0.15$, or $x = 0.125$. Dixon *et al.* (4) reported a maximum in the conductivity of about 0.2 (ohm-cm)⁻¹, and a minimum in the activation energy of 1.06 eV for the composition $x = 0.12$. The corresponding values from our work are 0.06 (ohm-cm)⁻¹ and 1.16 eV. The slightly lower conductivity and higher activation energy for this work probably reflects the higher purity ZrO₂ and the difference in density.

It is generally accepted that the mode of conduction in calcia stabilized zirconia is ionic (6-9) and occurs by oxygen ion migration via anion vacancies in the fluorite lattice.

At the conductivity maximum, $x = 0.125$, we have



where the symbol \square indicates oxygen vacancy. Since this corresponds to 0.5 vacancy per unit cell, or one vacancy every other unit cell, the singularity in the conductivity-composition curves may be connected with a possible ordered structure of vacancies as has previously been suggested (2).

Summary

The electrical conductivity of the systems (CaO)_x(ZrO₂)_{1-x} and (CaO)_x(HfO₂)_{1-x} has been measured from 800° to 2000°C. The two systems are similar. The cubic phase boundaries were found at $x = 0.12$ and $x = 0.22$ for (CaO)_x(ZrO₂)_{1-x}. A previously reported conductivity anomaly in the two-phase region $x = 0.22$ to $x = 0.5$ may be explicable on the basis of the distribution of the two phases and appears to be a function of the method of preparation. The conductivity maxima in both systems are placed at $x = 0.125$ and might be related to an ordered arrangement of anion vacancies.

Manuscript received April 26, 1963; revised manuscript received Aug. 29, 1963. This paper was presented at the Pittsburgh Meeting, April 15-18, 1963.

Any discussion of this paper will appear in a Discussion Section to be published in the December 1964 JOURNAL.

REFERENCES

1. F. Trombe and M. Foex, *Compt. rend.*, **236**, 1783 (1953).
2. Z. Volchenkova and S. Palguyev, *Trans. Inst. Electrochem.*, **1**, 97 (1961).
3. H. Johansen and J. Cleary, *This Journal*, **109**, 1076 (1962).

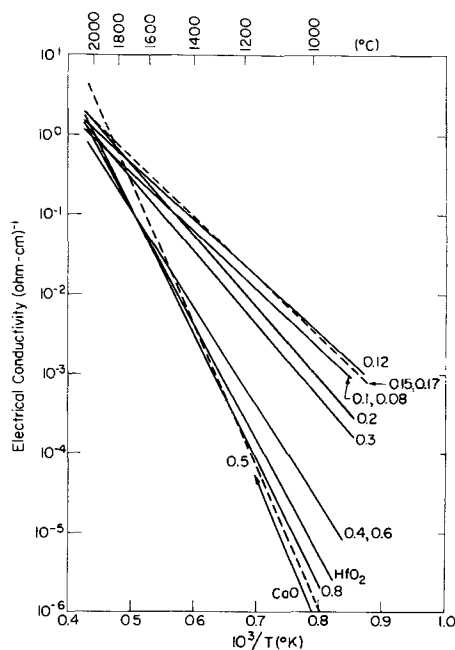


Fig. 4. Electrical conductivity of (CaO)_x(HfO₂)_{1-x}

4. J. Dixon, L. LaGrange, U. Merten, C. Miller, and J. Porter, II, *ibid.*, **110**, 276 (1963).
5. P. Duwez, F. Odell, and F. Brown, Jr., *J. Am. Ceram. Soc.*, **35**, 107 (1952).
6. F. Hund, *Z. Phys. Chem.*, **199**, 142 (1952).
7. K. Kiukkola and C. Wagner, *This Journal*, **104**, 379 (1957).
8. W. Kingery, J. Pappis, M. Doty, and D. Hill, *J. Am. Ceram. Soc.*, **42**, 393 (1959).
9. J. Weissbart and R. Ruka, *This Journal*, **109**, 723 (1962).

Kinetics of Oxidation of Pure Tungsten, 1150°-1615°C

E. A. Gulbransen, K. F. Andrew, and F. A. Brassart

Physical Chemistry Department, Westinghouse Electric Corporation, Pittsburgh, Pennsylvania

ABSTRACT

Weight change and oxygen consumption measurements were used to study the kinetics of oxidation of tungsten from 1150° to 1615°C at oxygen pressures of 2-100 Torr. The data were collected in a static type reaction system. Volatilization of tungsten trioxide above 1100°C changed the nature of the oxidation reaction for temperatures between 1100° and 1250°C. At 1150°C and 76 Torr oxygen pressure, oxide scale formed and some tungsten trioxide volatilized, while at 1250°C and 76 Torr oxygen pressure, all of the oxygen reacted to form volatile tungsten trioxide.

Initial oxidation rates were used to evaluate the effect of temperature and pressure on the kinetics of oxidation. Between 1100° and 1250°C, the initial rates of oxidation were nearly independent of temperature. A rapid increase in the rates of oxidation occurred between 1250° and 1350°C for oxygen pressures above 5 Torr. Above 1350°C the rate data also increased with temperature but to a smaller extent. Due to oxide volatility, oxygen pressure had a major influence on the formation of oxide scale for temperatures between 1000° and 1250°C. Low oxygen pressures favored volatilization of the oxide for a given temperature. Above 1300°C, where oxide scales were absent, the effect of oxygen pressure on the rate of reaction followed the equation

$$dn/dt = KP^{1.1}$$

Here dn/dt is the rate of oxidation, P is the pressure, and K is a constant. Above 1300°C, the rate-controlling process was probably the diffusion of oxygen gas through a barrier layer of tungsten trioxide vapor. Comparison of the rates of oxidation with those for carbon and molybdenum obtained under similar reaction conditions showed tungsten to have the fastest rate of oxidation. This may be related to the nature of the barrier layer of reaction product surrounding the specimen undergoing reaction.

Tungsten and its alloys have many good high-temperature mechanical properties. However, the oxidation resistance of the metal and its alloys is poor. Due to experimental difficulties, few quantitative measurements have been reported on the oxidation rates of tungsten above 1200°C. As a result, it has been difficult to compare the oxidation rates of tungsten with other metals and to develop mechanisms for the high-temperature oxidation reaction.

This paper reports a new study on the kinetics of oxidation of tungsten between 1150° and 1615°C and for oxygen pressures of 2-100 Torr. Special treatment is given to the region of high rates of oxidation between 10^{17} - 10^{19} atoms of tungsten reacting per square centimeter per second. Correlations are made with our earlier studies at lower temperatures and with collision theory calculations.

Literature.—A number of studies have been made on the oxidation of tungsten below 1200°C. These were reviewed in our earlier papers (1, 2) and by Barth and Rengstorff (3).

Langmuir (4) studied the reaction of tungsten with oxygen at pressures of 10^{-1} to 10^{-4} Torr and

at temperatures between 1070° and 2770°K using tungsten filaments heated electrically. A continuous increase in the rate of oxidation was found to the highest temperatures. Below 10^{-3} Torr, a linear variation of the rate of oxidation with pressure was found.

Perkins and Crooks (5) used a modified Langmuir method. Direct electrical heating was used with the rate being determined by direct measure of the surface recession.

Semmel (6) studied the oxidation of tungsten in free flowing air between 982° and 1371°C. Tungsten was found to oxidize following the linear rate law at 1000°C. A transition to parabolic occurred near 1200°C with a decrease in the rate of oxidation. Gulbransen and Andrew (1) made a systematic study of the oxidation of tungsten between 600° and 1300°C. For small size specimens, tungsten trioxide was found to volatilize as fast as it was formed during oxidation at 1200°C and 76 Torr oxygen pressure. The parabolic rate law was applied to most of the data between 600° and 1100°C. Several transitions were observed in the over-all oxidation

rate. Four types of oxidation phenomena were found as the temperature was raised and the pressure changed.

In a recent work, Gulbransen, Andrew, and Brasart (7) extended their oxidation studies on tungsten to 1615°C. Two independent methods were used to monitor the oxidation rate. Four types of oxidation processes were presented.

Experimental

Oxygen reacts with tungsten at high temperature to form solid, liquid, or gaseous tungsten trioxide. To monitor the oxidation reaction it is essential to determine total oxygen used as well as to measure the weight change. Total oxygen used gives the total amount of tungsten reacting while the weight change gives the difference between oxygen forming solid oxide scale and tungsten lost by reaction and evaporation of the oxide.

Balance.—Since large weight changes were observed during oxidation, a low sensitivity gold plated metal beam balance (10) was used. The balance had a beam length of 14.5 cm and a beam weight of 46g. Calibration of the balance showed a sensitivity of 60 μ g for a 0.001 cm deflection at 7.25 cm using a weight of 0.83g. Specimens were suspended using a 2 mil nickel-chromium alloy wire in the cold zone and an 8 mil section of platinum wire in the hot zone of the furnace tube.

Oxygen consumption.—Oxygen consumed in the reaction was determined by measuring the rate at which the pressure of a calibrated 287 cc reservoir decreased as oxygen was leaked through a sensitive leak valve into the reaction system.

Furnace tubes and reaction system.—The balance housing and reaction system are shown in Fig. 1. The furnace tubes were 1 in. diameter high-purity vacuum-tight alumina. The tubes were closed at one end and attached to the vacuum system by means of a flange and rubber O ring.

One major difficulty was found in using ceramic furnace tubes for tungsten oxidation studies. Alu-

mina was found to react with tungsten trioxide vapor above 1500°C as shown by discoloration of the tube and subsequent cracking.

A Kanthal-Super furnace was used to heat the furnace tubes.

Temperature measurement.—Temperatures were measured using Pt-Pt+10% Rh thermocouples. These thermocouples were calibrated at seven temperatures between 400° and 1200°C. Above 1200°C, the emf-temperature curve was deduced from tables and from the calibration values found at lower temperatures. At 1200°C, the error in temperature measurement was $\pm 2^\circ\text{C}$ while at 1600°C the error was probably $\pm 5^\circ\text{C}$.

For the balance experiments, the temperature of the system was measured by a thermocouple placed inside the reaction system near the sample. For very fast reactions where oxygen consumption measurements only were made, the specimens were mounted close to the thermocouple itself. In the former system, comparison was made between temperatures on the specimen and at a point in the furnace tube near the specimen. All temperatures were corrected to the temperature at the specimen. Figure 1 shows the thermocouple arrangement.

Specimens.—Specimens were machined from pure tungsten rod. They weigh about 0.825g and have a surface area of 0.680 cm². These specimens have a dumbbell shape with hemispherical ends. Sharp edges were avoided. The smaller diameter of the dumbbell shaped specimens was used for supporting the specimen by using a loop of platinum wire.

A spectrographic analysis of the tungsten showed the following in parts per million: Si, 1; Ti, <100; Mn, <4; Sb, <10; Fe, 8; Pb, <4; Mg, <1; Al, 1; Ni, 4; Be, <1; Sn, <4; Cu, 1; Ag, <1; Zn, <10; Co, <10; Cr, <5; Ca, 1; B, <4; Nb, <100; Mo, <100; V, <100; Cd, <4. An unreacted specimen is shown in Fig. 3A.

Specimen preparation.—Pure tungsten samples were machined from rods that had previously been centerless ground. After the samples were machined, they were polished through 4/0 polishing paper and washed in petroleum ether and pure ethyl alcohol. When only oxygen consumption measurements were made, the samples were suspended from a glass hook in the top of the balance chamber.

Between successive experiments it was necessary to bake the ceramic tube for about 20 min at the temperature of the next planned experiment or slightly above. This was necessary to avoid reaction between the clean tungsten sample and oxygen released from the tube during the heat-up of the specimen. Absorbed WO₃ vapor was also expelled from the tube walls during this tube pretreatment.

Method.—Experiments were made using the balance in combination with the pressure measuring device. In experiments in which the weight changes were beyond the limits of the balance, the pressure apparatus alone was used.

After the specimen was brought to temperature, pure oxygen was admitted to the system from a precharged reservoir to the desired pressure. Weight changes were observed with a micrometer

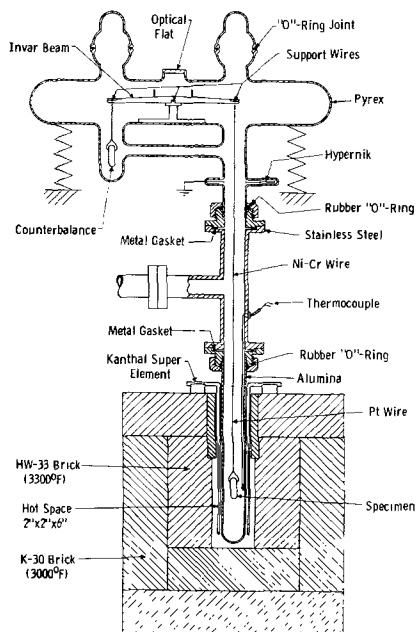


Fig. 1. Reaction system assembly

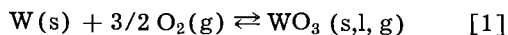
microscope as a function of time. Pressure changes in the reservoir were also noted as a function of time by means of a Wallace and Tiernan pressure gauge. A Granville-Philips leak valve was adjusted manually to maintain a constant pressure in the reaction system.

Results

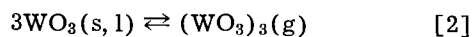
The experimental work is planned to determine: (a) the basic phenomena associated with the oxidation of tungsten between 1150° and 1615°C, (b) effect of time, temperature, and pressure on oxidation rates, (c) absolute values of oxidation rates and how these values compare with the theoretical rate based on collision theory, and (d) the several mechanisms of oxidation at high temperature.

Oxidation at 1150°C and 19 Torr oxygen pressure.—Curves A and B of Fig. 2 show oxygen consumption and weight change measurements. Both curves are in units of milligrams per square centimeter. The data show a linear rate of oxidation after an initial period of slow reaction. The total amount of tungsten reacted can be calculated from the oxygen consumed by using the stoichiometric ratio of W/3 O and the atomic weights of W and O. We are also interested in determining the amount of tungsten volatilized and the amount remaining as oxide scale. To do this we have made the following analyses.

Equation [1] relates the oxygen used to the formation of solid, liquid, or gaseous tungsten trioxide.



The weight change given by the balance readings indicates the difference between the oxide formed and tungsten lost as volatile tungsten trioxide according to the equation



From Eq. [1] and [2] and the laws of stoichiometry we set down the following equations

$$w_O = xw_O + (1-x)w_O \quad [3]$$

$$w_B = xw_O - w_W \quad [4]$$

Here w_O is the weight of oxygen consumed, w_B is the weight change of the balance, w_W is the weight of tungsten volatilized, and x and $(1-x)$ the fractions of oxygen used to form oxide scale and volatile oxide. From the atomic weights of W and O in WO_3 we have

$$w_W = 3.83(1-x)w_O \quad [5]$$

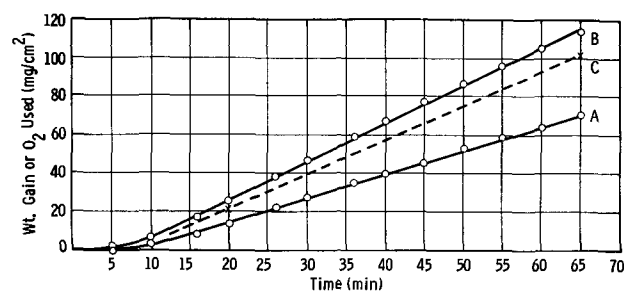


Fig. 2. Oxidation of tungsten, 1150°C, 19 Torr: A, balance; B, O_2 used; C, calculated oxygen in oxide film.

subtracting [4] and [3] and substituting [5] we have

$$w_O - w_B = 4.83(1-x)w_O \quad [6]$$

$$w_W = \frac{3.83}{4.83}(w_O - w_B) \quad [7]$$

Equation [7] can be used to calculate the weight of tungsten volatilized while Eq. [4] and [7] can be used to calculate the weight of oxygen forming oxide scale. Curve C of Fig. 2 shows the weight of oxygen used to form oxide scale for the 1150°C experiment. For this experiment, 90% of the oxygen reacted to form oxide scale. The oxide thickness in Angstroms can be calculated from the net oxygen forming oxide scale in mg/cm^2 by the factor 67,500. This factor is only approximate. The factor assumes a density of 7.16 for tungsten trioxide, a surface roughness ratio of unity, no lower oxides form, cracking does not occur and the surface area remains constant during reaction. From Fig. 2, curve C, a thickness of $6.75 \times 10^6 \text{Å}$ was found for the oxide scale after 65 min of reaction.

The weight of tungsten reacting with oxygen can be calculated by multiplying the weight of oxygen used by the factor 3.83 assuming the oxide is tungsten trioxide. The surface recession in Angstroms is related to the oxygen used in mg/cm^2 by the factor 19,840.

The following conclusions were made on the nature of the oxidation processes on tungsten at 1150°C and 76 Torr oxygen pressure. 1. A nearly linear rate of oxidation was observed. 2. Ten per cent of the oxygen reacts to form volatile tungsten trioxide. 3. Ninety per cent of the oxygen reacts to form oxide scale. The linear rate of oxidation indicates that the oxide scale has no protective properties and that an interface reaction is rate controlling.

Visual observations show the oxide scale to be cracked and unprotective. Figure 3A and 3B shows

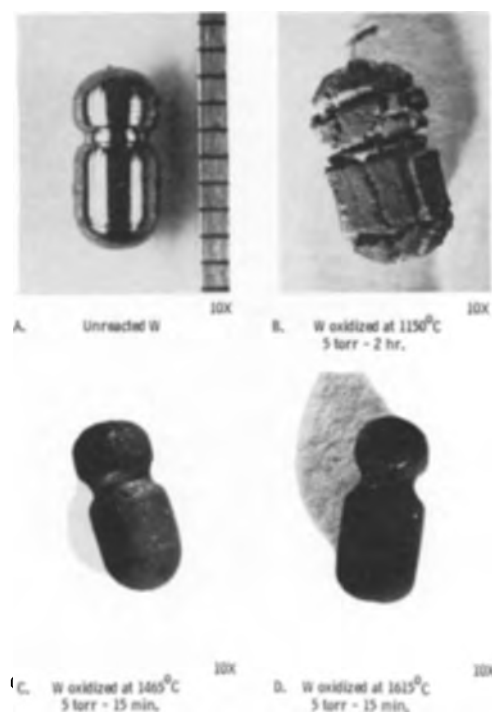


Fig. 3. Photograph of tungsten specimens

photographs of the specimen before and after oxidation. A thick oxide scale with large cracks is formed.

Experiments at 1200°C and 19 Torr oxygen pressure show both oxide scale formation and oxide volatility. The percentage of oxide scale formed is smaller than that found at 1150°C. At 1250°C and 38 Torr oxygen pressure, all of the oxygen reacted to form volatile tungsten trioxide. For pressures in the range of 5-76 Torr the change from oxide scale formation to complete oxide volatility occurs between 1100° and 1300°C.

These results support those reported by Gulbransen and Andrew (1) using small pieces of tungsten wires as specimens.

Oxidation at 1250°C and 38 Torr and 1615°C and 19 Torr.—Figure 4, curves A and B, show oxygen consumption and weight change measurements for the 1250°C oxidation experiment. Curve A shows a nearly linear rate of oxidation; 40 mg/cm² of oxygen were consumed in 12 minutes. Curve B shows no evidence of a positive weight change characteristic of oxide scale formation. Curve A can be used to calculate total W reacting. If the total W reacting equals the experimental weight loss, curve B, then we can conclude that little or no oxide scale is formed and that the volatile oxide is (WO₃)_n. The experimental and calculated curves show good agreement.

For the highest temperatures, the weight loss values were beyond the range of the balance. For these experiments the oxygen consumption curve was used to calculate the weight loss of tungsten during oxidation. Figure 5, the oxidation curve for 1615°C and 19 Torr oxygen pressure, shows a decreasing rate of reaction as a function of time. The decrease is due to a change in surface area as a result of reaction.

Temperature rise of sample.—One of the characteristics of the measurement of fast oxidation rates is the effect of the heat of reaction on the temperature of the specimen. For tungsten, the high heat of formation of WO₃ is partially compensated for by the heat of sublimation of W₃O₉. At 1700°K the net heat of reaction is -154.7 kcal/mole of WO₃. In our earlier paper (7), we have estimated the actual reaction temperature for a typical oxidation at

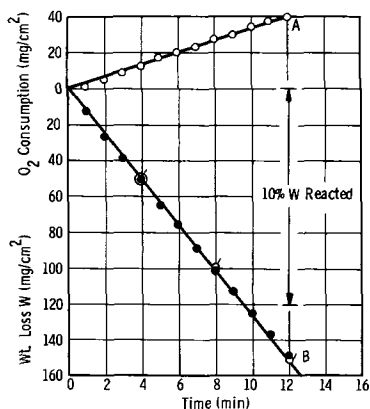


Fig. 4. Oxidation of tungsten, 1250°C, 38 Torr: ○, O₂ consumed (A); ●, weight loss balance (B); ◊, calculated weight loss from O₂ consumed.

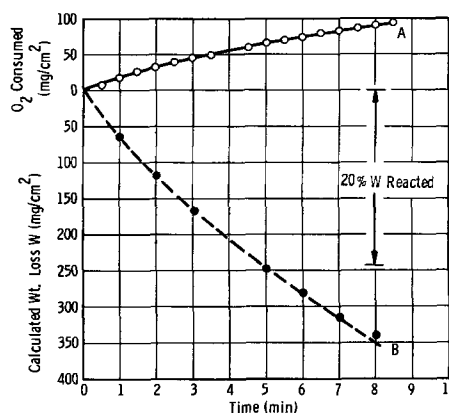


Fig. 5. Oxidation of tungsten, 1615°C, 19 Torr: ○, O₂ consumed (A); ●, calculated weight loss from O₂ consumed (B).

1465°C and 49 Torr oxygen pressure. Given the experimental rate of reaction and the net heat of formation and sublimation, the heat evolved can be calculated. Assuming radiation as the major source of heat loss and an emissivity of 1, a temperature increase of 113°C was calculated. If an emissivity of 0.5 was assumed, a temperature increase of 207°C was estimated.

Experiments with the thermocouple mounted on the specimen showed temperature changes of 15°-20°C. These temperature changes were much less than those calculated. The reasons for this discrepancy were not clear. Experimentally it was difficult to mount the thermocouple so that surface temperature was measured. Temperatures given here are the uncorrected temperatures.

Effect of temperature.—Table I shows the effect of temperature on the oxidation of tungsten at 5, 19, 38, and 100 Torr oxygen pressure. The measurements cover the temperature range of 1150°-1616°C. Due to the rapid reaction rates observed, the longest reaction time was 15 min. Oxidation rates were calculated from large-scale plots of the data at $t = 0$. In a few cases an induction period was noted. For these experiments the maximum rate of reaction was calculated after the induction period. For comparison, we have calculated the initial oxidation rates for oxidations made in the temperature range of 900°-1150°C from data given in our earlier paper (1). These data are based on weight change measurements only. Since oxide volatility occurs for the low-pressure runs, only the high-pressure oxidation experiments will be used when comparisons are made with rate calculations from this study.

All of the rate data in Table I are given in units of atoms of O or W reacting per cm²-sec. Except for the very fast reactions at the highest temperatures, the data were taken with both the balance and the oxygen consumption apparatus. For the fast reactions, only oxygen consumption could be measured and the tungsten weight loss curves were calculated.

Figure 6 shows a log rate vs. $1/T$ plot of the rate data. Some scatter is found in the rate calculations due to experimental difficulties in measuring fast reactions with high heats of reaction. Above 1500°C, the furnace tube can absorb (WO₃)_n vapors at an appreciable rate especially for the low-pressure experiments where gas diffusion is rapid through the

Table I. Summary new and old rate data 900°-1615°C, oxidation of tungsten

Old data (1)					New data				
t, °C	Press, Torr	dO/dt, at./cm ² /sec	Log dO/dt, oxygen	Log dn/dt, tungsten	t, °C	Press, Torr	dO/dt, at./cm ² /sec	Log dO/dt, oxygen	Log dn/dt, tungsten
900	76	3.15 × 10 ¹⁷	17.50	17.02	1050	53	1.27 × 10 ¹⁸	18.10	17.62
950	76	4.98 × 10 ¹⁷	17.70	17.22	1050	39	1.16 × 10 ¹⁸	18.06	17.58
950	36	3.73 × 10 ¹⁷	17.57	17.09	1050	20	9.43 × 10 ¹⁷	17.97	17.49
950	19	2.98 × 10 ¹⁷	17.47	16.99	1050	8.6	4.79 × 10 ¹⁷	17.68	17.20
950	9	2.90 × 10 ¹⁷	17.46	16.98	1100	76	2.01 × 10 ¹⁸	18.30	17.82
950	4	1.96 × 10 ¹⁷	17.29	16.81	1100	39	1.46 × 10 ¹⁸	18.16	17.68
1000	76	8.94 × 10 ¹⁷	17.95	17.47					
1000	9	5.01 × 10 ¹⁷	17.70	17.22					
1050	76	1.73 × 10 ¹⁸	18.24	17.76					
1150	49	1.96 × 10 ¹⁸	18.29	17.81	1365	19	6.0 × 10 ¹⁸	18.78	18.30
1150	38	1.68 × 10 ¹⁸	18.23	17.75	1365	9.5	2.53 × 10 ¹⁸	18.40	17.92
1150	19	1.26 × 10 ¹⁸	18.10	17.62	1365	5	1.28 × 10 ¹⁸	18.11	17.63
1150	9.5	9.73 × 10 ¹⁷	17.99	17.51	1365	2	5.2 × 10 ¹⁷	17.72	17.24
1150	5	7.84 × 10 ¹⁷	17.89	17.41	1400	19	4.9 × 10 ¹⁸	18.69	18.21
1150	2	1.67 × 10 ¹⁷	17.22	16.74	1400	9.5	3.54 × 10 ¹⁸	18.55	18.07
1250	100	3.3 × 10 ¹⁸	18.52	18.04	1465	38	1.87 × 10 ¹⁹	19.27	18.79
1250	38	2.06 × 10 ¹⁸	18.31	17.83	1465	19	7.56 × 10 ¹⁸	18.88	18.40
1250	19	1.31 × 10 ¹⁸	18.12	17.64	1465	9.5	2.65 × 10 ¹⁸	18.42	17.94
1250	9.5	1.06 × 10 ¹⁸	18.03	17.55	1465	5	1.57 × 10 ¹⁸	18.20	17.72
1250	5	8.74 × 10 ¹⁷	17.94	17.46	1465	2	6.9 × 10 ¹⁷	17.84	17.46
1250	2	5.3 × 10 ¹⁷	17.72	17.24	1520	19	8.84 × 10 ¹⁸	18.95	18.47
1300	19	2.75 × 10 ¹⁸	18.44	17.96	1545	5	1.96 × 10 ¹⁸	18.29	17.81
1300	9.5	2.16 × 10 ¹⁸	18.34	17.86	1615	38	1.86 × 10 ¹⁹	19.27	18.79
1365	100	4.15 × 10 ¹⁹	19.62	19.14	1615	19	1.06 × 10 ¹⁹	19.03	18.55
1365	76	1.89 × 10 ¹⁹	19.28	18.84	1615	9.5	9.8 × 10 ¹⁸	18.99	18.51
1365	38	1.05 × 10 ¹⁹	19.02	18.54	1615	5	2.53 × 10 ¹⁸	18.40	17.92
					1615	2	4.12 × 10 ¹⁸	18.62	18.14

oxygen gas. The rate of adsorption of (WO₃)_n vapors can affect the diffusion barrier surrounding the sample increasing the oxidation rate. Experiments at 2 Torr oxygen pressure are not included in Fig. 6.

Curves A, B, C, D, E, and F show the rates at the several pressures. Curves A and B were not extended below 1150°C since weight gain measurements were not giving total oxygen reacted for pressures of 5 and 9.5 Torr. Curves C, D, and E gave more reliable values for total oxygen. Curves C, D, and E show that the two sets of data are in reasonable agreement although flat plate samples of 0.32 and 0.61 cm² area were used in our earlier studies.

Below 1150°C, the oxidation curves followed a modified parabolic rate law and not the linear rate law. The initial oxidation rates were calculated and included for comparison purposes.

Figure 6 shows a complex dependence of the rate of oxidation on temperature. Between 1100° and 1250°C, the rates of oxidation were nearly independent of temperature for all pressures. For pressures of 9.5 Torr and higher, a large increase was found between 1250° and 1350°C. Above 1350°C, a nearly straight line behavior was noted. An empirical heat of activation of 14.3 kcal/mole was estimated from curves A and C.

Visual and light microscopic examination of the specimens confirms the complex nature of the reaction. Figure 3 shows photographs of the unreacted

and oxidized samples. Figure 3B shows a sample of W oxidized at 1150°C and 5 Torr oxygen pressure for 2 hr. The main feature of the reaction is the formation of oxide scale. Large cracks appear in the oxide although the original sample was smooth. Figure 3C and D show photographs of tungsten specimens oxidized at 1465°C and 5 Torr pressure for 15 min and at 1615°C and 5 Torr for 15 min. Oxide free surfaces were observed. The influence of oxide volatility is noted by comparing 3B with 3C and D.

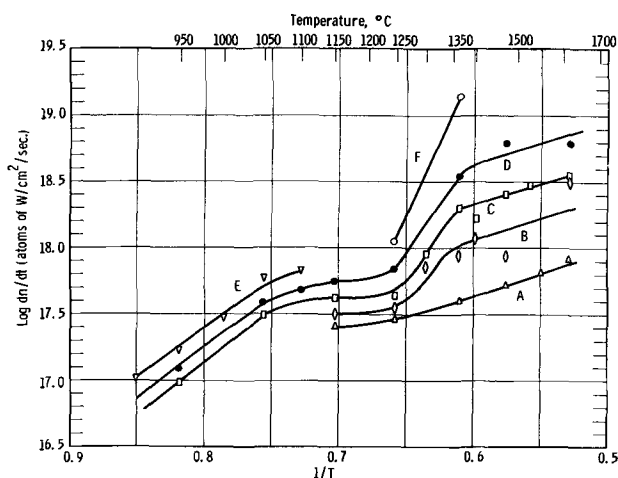


Fig. 6. Log dn/dt vs. 1/T, 900°-1615°C, 5-100 Torr of O₂: A, 5 Torr; B, 9.5 Torr; C, 19 Torr; D, 38 Torr; E, 76 Torr; F, 100 Torr; ΔH 1365-1615 = -14,300 cal/mole.

Effect of pressure.—Pressure has a major influence on the mechanism and the oxidation rate. A summary of the effect of pressure on the initial oxidation rates is shown in Table I.

At 1150°C weight gains were observed for the higher oxygen pressures and weight losses for the lower pressures. Oxidation rates given in Table I are from oxygen consumption measurements.

At 1250°, 1365°, 1465°, and 1615°C all of the experiments show weight loss curves with the rate of weight loss increasing with oxygen pressures.

We conclude from an analysis of the pressure study that at 1150°C and pressures of 19 Torr and higher, oxide scale formed and some tungsten trioxide volatilized, while at 1250°C and 76 Torr oxygen pressures all of the oxygen reacted to form volatile tungsten trioxide.

Figure 7 shows the effect of pressure on the initial reaction rate dn/dt vs. log pressure plot. Three temperatures were considered in Fig. 7: 1365°, 1465°, and 1615°C. The following equation could be derived from the plot

$$dn/dt = K P^{1.1}$$

Here K is a constant dependent on the temperature. For most purposes, we can conclude that the oxidation reaction follows a linear pressure dependence over the temperature range of 1365°-1615°C.

Collision theory calculations.—Collision theory gives the following equation for the number of impacts n of oxygen molecules with a cm^2 surface per sec.

$$n = 3.52 \times 10^{22} P / (MT)^{1/2}$$

Here M is the molecular weight, T the temperature in °K, and P the pressure in Torr. At 1465°C and 19 Torr, $n = 2.83 \times 10^{21}$. Assuming WO_3 as the reaction product and that all oxygen colliding with the surface reacts with no activation energy, we calculate a rate of oxidation of 1.9×10^{21} atoms of tungsten per cm^2 per sec.

The experimental oxidation rate at 1465°C and 19 Torr is 2.5×10^{18} . The percentage of theoretical is 0.13.

Empirical rate equation.—Using the empirically determined activation energy and pressure depend-

Table II. Comparison of oxidation rate with collision theory and empirical rate equation

1465°C, 19 Torr, 0.68 cm^2	
Experimental	$dn/dt = 2.5 \times 10^{18}$ at. W/ cm^2 -sec
Empirical equation	
$\Delta H = -14,300$ cal/mole	
Collision theory	$dn/dt = 2.1 \times 10^{18}$ at. W/ cm^2 -sec
Per cent theory	$dn/dt = 1.9 \times 10^{21}$ at. W/ cm^2 -sec
	0.13

ence, we can derive the following rate equation for the temperature interval of 1350°-1615°C

$$\frac{dn}{dt} = 6.2 \times 10^{18} P^{1.1} e^{-14,300/RT}$$

Here dn/dt is the atoms of W reacting per cm^2 -sec, P is the pressure in Torr, T the absolute temperature in °K, and R the gas constant.

Table II shows a comparison of the experimental oxidation rate with that predicted from collision theory and the empirical rate equation for oxidation at 1465°C and 19 Torr.

Comparison of oxidation rates of tungsten with carbon and molybdenum.—A comparison of these oxidation rates is very interesting since each element forms volatile reaction products above 1300°C. In general, comparisons are difficult to make and to interpret unless the basic mechanisms of reaction are known. In two recent studies, we have determined for both carbon (8) and molybdenum (9) the conditions for chemical-controlled oxidation and gaseous diffusion-controlled oxidation. Adsorption, desorption, and chemical reaction processes have appreciable heats of activation and are termed chemical-controlled processes. Diffusion of oxygen through a barrier layer of volatile reaction products has a small temperature dependence and is termed gaseous diffusion-controlled oxidation. For tungsten, the temperature dependence was greater than that found for molybdenum and carbon. We propose that gaseous diffusion of oxygen through a tungsten trioxide vapor barrier is rate controlling, the increase in rate of oxidation being related to a decrease in the vapor barrier by solution of tungsten trioxide in the ceramic tube.

For molybdenum and carbon, the experimental problems in determining the influence of gaseous diffusion on the rate of oxidation were simple since only volatile reaction products were formed. Also, carbon oxides and molybdenum trioxide did not react with the ceramic tube.

For tungsten, the experimental problems were many. First, gaseous tungsten trioxide reacts with the furnace tube. Second, the temperature range where oxide scales are not formed lies above 1300°C. Third, due to the formation of solid tungsten trioxide the vapor barrier is smaller and higher reaction rates are observed.

The similarity in mechanisms of oxidation above 1300°C can be shown by comparing the rates of oxidation for two oxygen pressures and for two temperatures. Tungsten at 1465°C is compared to molybdenum at 1400°C and carbon at 1500°C for specimen areas of 0.6 to 0.7 cm^2 . The oxidation rates for molybdenum and carbon are in the diffusion-controlled region where temperature has only

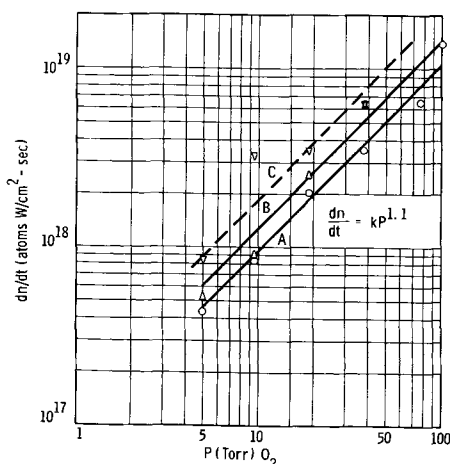


Fig. 7. Effect of pressure on initial rate of oxidation of tungsten. Log-log plot: A, 1365°; B, 1465°; C, 1615°C.

Table III. Comparison absolute values of rates of oxidation of tungsten, molybdenum and carbon at 19 and 38 Torr pressure

Surface area = 0.6 to 0.7 cm²

Element	Temp., °C	Pressure, Torr	Rate dn/dt , atoms/cm ² -sec
Tungsten	1465	19	2.5×10^{18}
Molybdenum (9)	1400	19	2.5×10^{18}
Carbon (8)	1500	19	4.0×10^{17}
Tungsten	1615	38	6.2×10^{18}
Molybdenum (9)	1600	38	2.5×10^{18}
Carbon (8)	1500	38	5.0×10^{17}

a minor effect on the rate of oxidation. At 19 Torr pressure and 1465°C, tungsten and molybdenum oxidize at the same rate and carbon oxidizes at a rate 1/6 as fast. Since the carbon gases are not condensed in the reaction system, the barrier for diffusion of oxygen is greater than that found for the diffusion of oxygen through the reaction products of molybdenum and tungsten which condense in the colder parts of the tube.

The comparison at 38 Torr oxygen pressure and 1615°C shows tungsten oxidizing 2½ times as fast as molybdenum and 12 times faster than carbon. Again, these results can be interpreted in terms of the diffusion of oxygen gas through the gaseous reaction products. The diffusion barrier for oxygen when tungsten is oxidized at 1615°C is small since the alumina tube absorbs WO₃. It is largest for carbon oxidation where completely volatile reaction products are formed.

Comparison of the results of our molybdenum and carbon studies show molybdenum and carbon oxidizing faster than tungsten at low temperature. At high temperature, tungsten presents a special case in which the rate of oxidation is determined by the nature of the reaction system. These data are summarized in Table III.

Discussion and Summary

Summary of kinetic work.—Weight change and oxygen consumption measurements were made on the oxidation of tungsten over the temperature range of 1150° and 1615°C and for pressures of 2-100 Torr of oxygen. These results were correlated with those from earlier studies to aid in interpretation of the oxidation mechanisms. At 1150°C and 76 Torr, oxide scale forms and tungsten trioxide volatilizes during oxidation; while at 1250°C and 76 Torr, only volatile tungsten trioxide is formed. A major change occurs in the mechanism of oxidation.

The effect of time on the total rate of oxidation is nearly linear. Surface area changes and changes in the nature of the barrier layer can result in a falling off from the linear rate law at high temperatures.

The effect of temperature on oxidation rates is complex and is related to the increasing volatility

of tungsten trioxide and to the formation of a barrier layer of gaseous oxides which act to limit diffusion of oxygen to the reaction interface. At the highest temperature, solution of tungsten trioxide in the ceramic tube acts to decrease the barrier layer of oxide.

The effect of pressure on the oxidation reaction also was complex, especially in the transition zone. Pressure was a critical variable in determining the relative role of oxide scale formation and volatility of tungsten trioxide. Above 1350°C, the rate of oxidation followed the 1.1 power of the pressure.

Comparison of the results with collision theory assuming zero activation energy for chemical reaction indicates that 0.13% of the collisions result in the formation of molecules of WO₃ vapor. Comparisons were made also to the oxidation behavior of molybdenum and carbon where volatile reaction products are also formed. At high pressures and above 1350°C, tungsten oxidizes faster than molybdenum due to the unique nature of the reaction products and the reaction system.

Acknowledgment

This research was supported in part by the U.S. Air Force under Contract No. AF33(616)-7888, Aeronautical Systems Division, Wright-Patterson Air Force Base, Ohio.

Manuscript received May 1, 1962; revised manuscript received Jan. 10, 1963. This paper was presented at the Los Angeles Meeting, May 4-10, 1962.

Any discussion of this paper will appear in a Discussion Section to be published in the December 1964 JOURNAL.

REFERENCES

1. E. A. Gulbransen and K. F. Andrew, *This Journal*, **107**, 619 (1960).
2. E. A. Gulbransen and W. S. Wysong, *Trans. AIME*, **175**, 611 (1948).
3. V. D. Barth and G. W. P. Rengstorff, "Oxidation of Tungsten," (DMIC Report 155) AF33(616)-7747, Defense Metals Information Center, Battelle Memorial Institute, Columbus, July 1961.
4. I. Langmuir, *J. Am. Chem. Soc.*, **35**, 105 (1913); *ibid.*, **37**, 1139 (1915).
5. R. A. Perkins and D. D. Crooks, *J. Metals*, **13**, 490 (1961).
6. J. W. Semmel, Jr., "The Oxidation of Tungsten and Molybdenum from 1800 to 2500°F," in "High Temperature Materials," AIME Conference Cleveland, 1957, pp. 510-519, John Wiley & Sons, New York (1959).
7. E. A. Gulbransen, K. F. Andrew, and F. A. Brassart, "Four Types of Oxidation Processes in the Oxidation of Tungsten," Air Force Materials Central and AIME Symposium, Oct. 1962, New York, To be published.
8. E. A. Gulbransen, K. F. Andrew, and F. A. Brassart, *This Journal*, **110**, 476 (1963).
9. E. A. Gulbransen, K. F. Andrew, and F. A. Brassart, *ibid.*, **110**, 952 (1963).
10. E. A. Gulbransen and K. F. Andrew, "Vacuum Microbalance Techniques," Vol. 2, p. 129, Plenum Press, Inc., New York (1962).

Polarization Studies of Molten Carbonate Fuel Cell Electrodes

Isaac Trachtenberg

Texas Instruments Incorporated, Dallas, Texas

ABSTRACT

Polarization measurements have been made on individual electrodes in operating molten carbonate fuel cells by using a third idling electrode. Hydrogen was supplied to the anode and an air-carbon dioxide mixture to the cathode. Overvoltages as a function of time from 10^{-6} to 100 sec after current interruption have been recorded. Analyses of these curves indicate that total electrode polarization is the result of several factors: (a) ohmic polarization caused by electrolyte restrictions between the MgO matrix and the electrode, (b) electrode coverage by reactant and products, (c) concentration gradients of potential determining species in the electrolyte. No activation polarization was observed at either electrode.

Fuel cells employing various eutectics of molten alkali carbonates as the electrolyte have been described previously (1-4). The cells are capable of acceptable performance on a variety of cheap, readily available hydrocarbon or hydrocarbon-derived fuels and air. The work to be presented here is concerned with some of the more fundamental aspects of this fuel cell, establishing the rate-limiting process at the individual electrodes and elucidating the over-all electrode process.

Although hydrogen was used as the fuel in all of the experiments reported here, it rapidly becomes diluted with carbon dioxide. At 600°C the water-gas shift equilibrium is rapidly established and all four components, namely, H_2 , H_2O , CO_2 , and CO , are present. In many instances this is equivalent to the products from steam reforming hydrocarbons.

Operating characteristics of the complete fuel cell were obtained from current-voltage curves such as shown in Fig. 1. Considerable information concerning the complete cell can be obtained from plots of this type. However, this performance is not good enough. Power output needs to be improved. Current densities greater than 200 amp/ft^2 can be obtained but at the expense of considerable electrode polarization. Data of this kind indicate that the cell is polarizing, but they do not say what portion of the observed polarization can be attributed to each

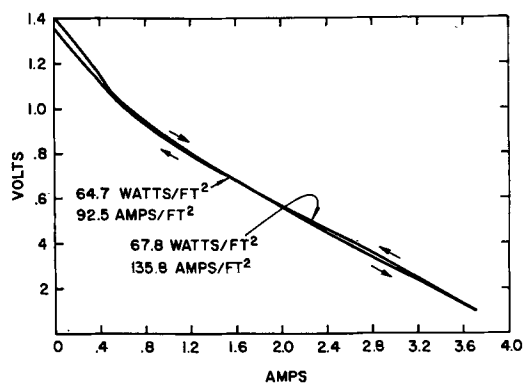


Fig. 1. Operating characteristics of a typical molten carbonate electrolyte fuel cell. Cell No. 289, 5 days operating; temperature, 600°C ; fuel flow, 480 cc/min H_2 .

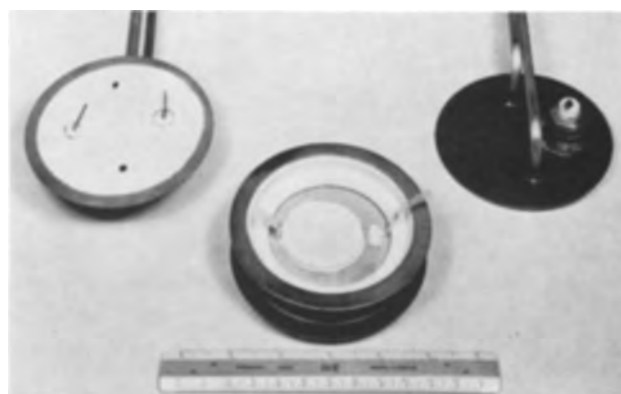


Fig. 2. Cathode chamber of a fuel cell showing third idling electrode.

electrode. Once the extent of the individual electrode polarization is established it is still necessary to find out what causes it and how to avoid it.

Experimental

Figure 2 is an illustration of the cathode chamber of the cell with the third idling electrode. This electrode is used to monitor the performance of the individual anode and cathode in the working fuel cell. The small electrode, 0.5 cm^2 , is a pure silver voltage probe. The large one (15.6 cm^2 or $1/60 \text{ ft}^2$) is the working cathode. Not shown is the anode on the bottom side of the MgO disk. The anode has a geometric configuration identical with the working cathode. The MgO disk is impregnated with the binary LiNaCO_3 eutectic. Electrical connections are made from the electrodes to the various insulated lead-throughs. The only electrical connection within the cell between the three electrodes is through the electrolyte contained in the porous MgO disk. The lids are then welded on to make each chamber gas tight. The cell is placed vertically in a furnace, and the necessary external gas and electrical connections are completed.

All experiments were performed at 600°C with H_2 supplied to the anode and a 4:1 mixture of air: carbon dioxide supplied to the cathode. The electrolyte was a binary eutectic of 50 mole % Li_2CO_3 and 50 mole % Na_2CO_3 (mp $\sim 500^{\circ}\text{C}$) contained within a porous MgO disk.

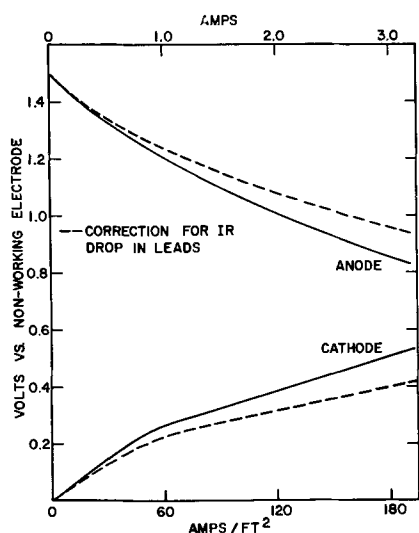


Fig. 3. Current-voltage curves for individual electrodes in a working fuel cell. Dashed line indicates polarization corrected for lead resistance. No. 296, 15th day; 600°C, continuous operation; fuel, H₂; oxidant, air.

Figure 3 is representative of the current-voltage traces obtained for individual electrodes in a complete working cell. A variable transistorized load is placed across the working electrodes and current passed. This current becomes the x-input to a Moseley x-y recorder. The voltage between the non-working electrode and the particular working electrode to be studied becomes the y-input to this recorder. In order to avoid polarization of the non-working electrode the y-axis, or for that matter any voltage measuring device used with this electrode, must have a high input impedance. The complete fuel cell performance may be obtained by subtracting the two curves and an IR correction, where R in this case refers to the true electrolyte resistance. However, in most cases it is easier to repeat the x-y plot using the terminal voltage of the working electrodes as the y-input as illustrated in Fig. 1.

Experiments of this type are very useful. They serve to establish the polarization of the individual electrodes, but for the most part tell very little about the nature of the polarization. Of particular interest are three types of polarization: ohmic, activation, and concentration. These types of polarization may be distinguished on a time interval after removal of the polarizing load. Ohmic polarization disappears immediately for the present investigation in times less than a microsecond. Activation polarization would be decayed in a time interval from 10^{-6} to 10^{-4} sec, about the time required to charge the double layer. Decay of polarization due to concentration effects requires times greater than 10^{-3} sec since appreciable transport of mass (either ions in the electrolyte or molecules in gas phase) must occur. In order to investigate these polarization phenomena a single current interruption technique was used. Essentially this consisted of loading the cell with a fixed load, allowing it to come to equilibrium, and then in less than a microsecond opening this circuit. The voltage of the particular working electrode under investigation *vs.* the nonworking electrode is recorded on film from an oscilloscope

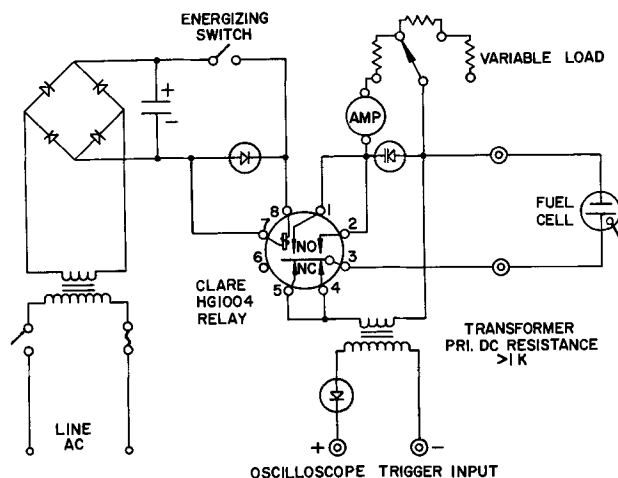


Fig. 4. Interruptor circuit used to obtain voltage-time curve < 1 sec.

sweep. Figure 4 schematically shows the interruptor circuit. The heart of this circuit is the mercury wetted CLARE relay. An interesting feature of this relay is the make before break condition. Typical operation sequence is as follows: the desired load is selected and the relay energized (normally open contacts closed). The cell is allowed to come to equilibrium; usually a few seconds to several minutes are required. The relay is de-energized. The normally closed contact is made 1 msec before the normal open contact opens. A signal is obtained from the normally closed contacts and serves as triggering input to a Tektronix 545A oscilloscope. The scope is set up so that the actual sweep may be delayed from a few microseconds up to several milliseconds. This arrangement is used to obtain time scale on voltage-time records from 5×10^{-7} to 1×10^{-3} sec/cm. When the time scale is longer than 1×10^{-3} sec, no sweep delay is required. Voltage-time curves of more than 1-sec duration were obtained with a fast response recorder and chart speeds up to 12 in./min. In all instances the voltage recorded is that of a working electrode *vs.* the non-working electrode.

Discussion of Results

Figure 5 is an example of the type of data obtained from the oscilloscope traces. One trace is required per decade of time. In other words, to obtain this plot, 5 traces with different time scales were obtained. The only changes made between traces involved the oscilloscope itself (time scale and

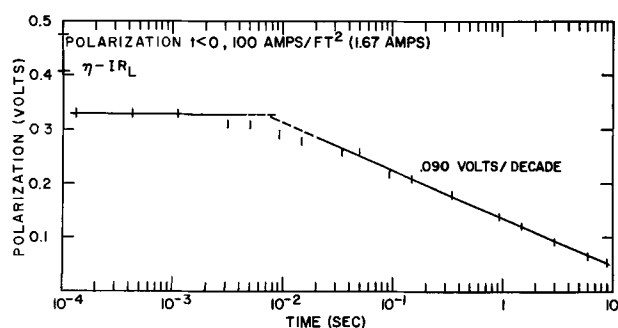


Fig. 5. Polarization-time curve of typical anode after interruption of 1.67 amp. No. 278; anode (H₂); 600°C.

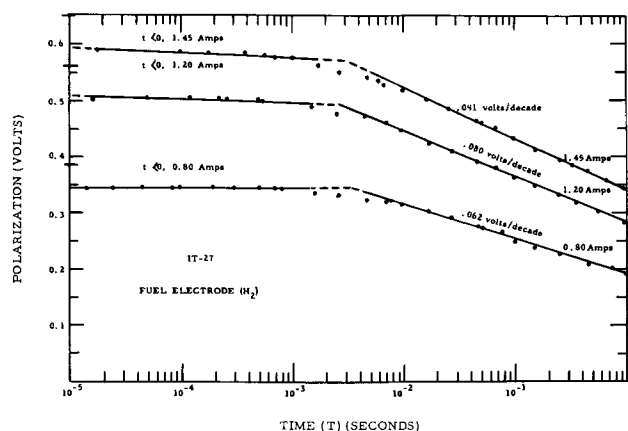


Fig. 6. Polarization-time curves of typical anode for various pre-interruption current.

sweep time delay). Data were taken in the $1 \mu\text{sec}$ range; however, they are somewhat clouded by a ring-back voltage which occurs when the current falls to zero in something like 10^{-7} sec. Data are reported for times from 10^{-4} up to 10 sec after current interruption. The general shape of two straight lines is characteristic of all measurements of this type. The correction for lead resistance is indicated and reduces the total measured polarization. This log relationship continues to be valid until the polarization has decreased essentially to zero (< 20 mv).

Figure 6 illustrates the effect of varying the pre-interruption current. The fuel flow is held constant. The initial overvoltage decay (η_i) is a linear function of current ($\eta_i/I = R_o$). This fact has been checked in a number of fuel electrodes over a current range of two orders of magnitude (0.2-2.0 amp, i.e., 1 amp/ft² to 100 amp/ft²). The intercept of the horizontal line (first few decades of time) with the second line is virtually independent of the current but dependent on fuel flow rate. This same behavior has been observed on a number of different electrodes in the same electrolyte. However, each electrode does have a different dependence on fuel flow rate, and this characteristic of the intercept will occur at different flows for different electrode structures.

Figure 7 illustrates a typical effect of fuel flow rate on the voltage-time curves following current interruption. In this case only the fuel flow rate was

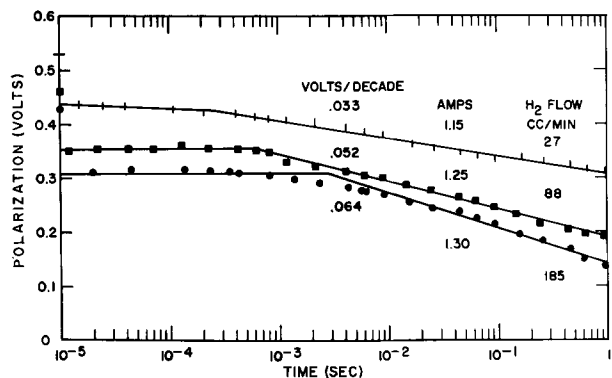


Fig. 7. Polarization-time curves of typical anode for constant load at varying fuel flow rates. No. 266, 600°C, anode.

varied. The load was held constant, but due to increasing polarization with decreasing flow the pre-interruption currents varied slightly. Corrections for the current variation will not alter these results appreciably. There are several interesting observations to be made on these data. The initial polarization decay is independent of fuel flow. The intercept of the characteristic two straight lines moves to shorter times as the flow decreases. This can be attributed to an increased importance of concentrations of products and reactants in the gas phase (presumably electrode coverage) on electrode potential as the flow rate is decreased. The nonexistence of gas leakage effects was established by gas chromatographic analyses of the separate effluent gases. And finally, the slope of the second line increases with fuel flow. At the lowest flow this is particularly true. Times greater than 1 hr are required for the electrode to reach its rest potential. Here again this is due in part to an increased importance of the gas phase concentrations on the electrode potential.

Studies have also been made of air electrodes (cathodes) using this same single current interruptor technique. Figure 8 is an example of a typical voltage-time plot for a cathode. In many respects the behavior is similar to anodes. The major differences are: (A) air electrodes as a rule have larger initial polarization decays which like fuel electrodes are a linear function of the pre-interruption current. There is an ohmic resistance at the electrode-electrolyte interface which is believed to be the result of an electrolyte restriction at that electrode-MgO interface as in the case of the anodes plus an additional ohmic effect because of oxide layers on the electrode; (B) cathodes over the range of flow rates studied are less dependent on gas flows than anodes; (C) cathodes show far less concentration polarization and return quickly to their rest potential.

The lack of dependence on gas flow and the small amount of concentration polarization at the cathode may be explained on the basis that reaction products are not rejected into the gas phase. At this electrode, the product is either $\text{O}^=$ or $\text{CO}_3^=$ and leaves the electrode-electrolyte interface through the electrolyte. There is very little change in electrode coverage by reaction products such as exist at the fuel electrode. The electrode polarization for the most part is an ohmic-type polarization due to the presence of oxide layers on the electrode and

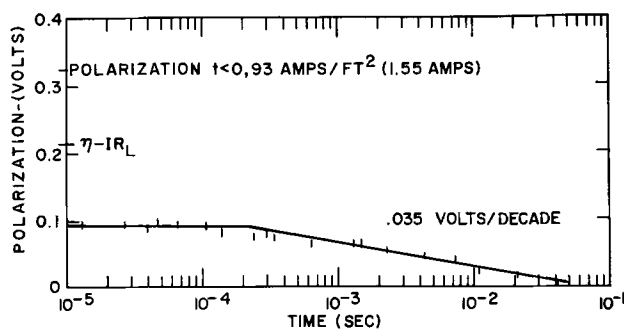


Fig. 8. Polarization-time curve for typical cathode after interruption of 1.55 amp; IT-27, cathode, 600°C.

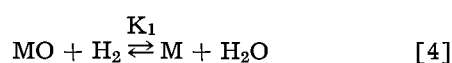
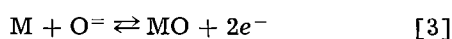
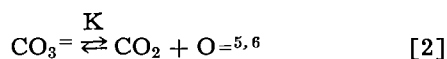
electrolyte restrictions at the electrode-electrolyte interface.

Conclusions

As a result of these experiments and similar ones, a mechanism is proposed for this molten-carbonate electrolyte fuel cell. The potential of the anode may be represented in terms of activities (a_i) as follows:

$$E_A = E^{\circ}_A - \frac{2.3 RT}{n F} \left[\log \frac{a_{H_2O}}{a_{H_2} K_1} + \log \frac{1}{a_{O^=}} \right] \quad [1]$$

where the chemical and electrochemical processes are illustrated as follows



where M is a divalent metal. Since these reactions are taking place at 600°C, the rate should be very rapid and equilibrium conditions maintained.

X-ray information has confirmed the presence of metal oxides on the anode. Examination of the cells operated with N₂ as the anode gas (cells did not operate very long) indicated that considerable amounts of the various base metal M were converted to oxides.

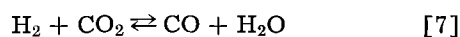
Equation [1] can be further simplified by making the substitution

$$a_{O^=} = \frac{K a_{CO_3^=}}{a_{CO_2}} = \frac{K^1}{a_{CO_2}} \quad [5]$$

Substituting and combining constant terms yields

$$E_A = E^{\circ}_A - \frac{2.3 RT}{n F} \log \left[\frac{a_{H_2O} a_{CO_2}}{a_{H_2}} \right] \quad [6]$$

In evaluating the potential the water-gas shift reaction



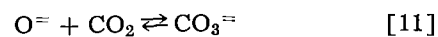
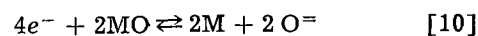
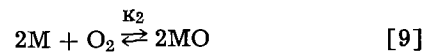
must be considered. At 600°C experiments have demonstrated that this equilibrium in the fuel cell is very rapidly attained. The reactions at the anode as indicated in Eq. [2], [3], and [4] proceed very rapidly, and the electrode-electrolyte interface is in equilibrium at all times independent of current up to 200 amp/ft².

The observed polarization at the anode is the result of an ohmic factor from electrolyte restrictions at the electrode-MgO interface and concentration gradients due to mass transport limitations. An O⁼ concentration may exist in the electrolyte due to a concentration gradient of CO₂.

A similar situation exists at the cathode. The electrode potential may be written as

$$E_C = E^{\circ}_C - \frac{2.3 RT}{n F} \log \left[\frac{(a_{O^=})^2}{a_{O_2} K_2} \right] \quad [8]$$

where the chemical and electrochemical processes may be represented as



Substituting for the $a_{O^=}$ from Eq. [5] in Eq. [8] and combining constants

$$E_C = E^{\circ}_C - \frac{2.3 RT}{n F} \log \left[\frac{1}{a_{O_2} (a_{CO_2})^2} \right] \quad [12]$$

It is assumed that all of the reactions are in equilibrium, since at 600°C the kinetics of these reactions should be very fast. The observed total polarization is due to electrolyte restrictions and a surface oxide layer at the electrode interface which result in ohmic polarization as the major contribution and concentration polarization due to mass transport of O₂ and CO₂ in the gas phase and O⁼ in the electrolyte.

In all of the experiments performed no evidence of activation polarization at current densities up to 200 amp/ft² was observed. The catalysts investigated on the anode were a number of inexpensive metals. The cathodes were sintered silver powder. Electrodes sintered from large particles (3-20 mesh) did not perform well, nor did electrodes prepared from particles through 325 mesh. With the latter the electrode flooded with electrolyte and exhibited greater concentration polarization. The extent of total polarization and the contribution of individual types of polarization for either of the electrodes is dependent on the pore structure and how it controls electrolyte wetting rather than on the electrode material.

Manuscript received April 9, 1963; revised manuscript received Aug. 2, 1963. This paper was presented at the Boston Meeting, Sept. 16-20, 1962.

Any discussion of this paper will appear in a Discussion Section to be published in the December 1964 JOURNAL.

REFERENCES

1. G. H. J. Broers, "High Temperature Galvanic Fuel Cells," Thesis, University of Amsterdam (1958).
2. G. H. J. Broers and J. A. A. Ketelaar in "Fuel Cells," G. J. Young, Editor, pp. 78-93, Reinhold Publishing Co. (1960); H. H. Chambers and A. D. S. Tantrum, *ibid.*, pp. 94-100.
3. M. L. Kronenberg, *This Journal*, **109**, 753 (1962).
4. Y. L. Sandler, *ibid.*, **109**, 1115 (1962).
5. H. Flood, T. Forland, and K. Motzfeldt, *Acta. Chem. Scand.*, **6**, 257, (1952).
6. S. Djordjevic and G. J. Hills, *Trans. Faraday Soc.*, **56**, 269 (1960).

The Effect of Acidity on the Differential Capacity of Polarized Platinum Electrodes

M. C. Banta¹ and Norman Hackerman

Department of Chemistry, The University of Texas, Austin, Texas

ABSTRACT

Differential capacity-potential curves on activated platinum electrodes were obtained in nitrate and chloride solutions of various pH and under conditions of constant ionic strength. The maxima obtained are explained in terms of adsorption-desorption processes. The results suggest that the transition from H_3O^+ discharge to H_2O discharge occurs at a pH of 3-4. Chloride ion inhibits the formation of an oxygen-containing layer on the electrode surface, and this inhibiting effect is greater for low pH and high chloride ion concentration. Some evidence is given which substantiates that the zero point of charge of platinum is at -0.05v on the saturated calomel scale.

There have been many investigations of the interfacial differential capacity (hereafter called "capacity") of polarized platinum electrodes (1-15). The aims of these investigations were widely varied. Some have been concerned primarily with a study of the kinetics of the hydrogen evolution reaction, others with oxygen evolution, and still others with the electrical double layer. An examination of the various results indicates that, in many cases, the capacity varied with time. In addition, the results reported appear to depend markedly on the electrolyte pH. Thus, it appeared expedient to investigate the effect of pH on the capacity of activated platinum electrodes over the entire "ideally polarizable" range of potential under conditions of high purity and constant ionic strength in order to determine how the hydrogen ion activity affects the capacity-potential behavior. For this study, the systems KCl-HCl-KOH and HNO_3 - KNO_3 -KOH were chosen because they can be readily purified and because the effect of the "inert" anion could be investigated.

Experimental

Materials.—The platinum electrodes were prepared by sealing a short length of small diameter platinum wire, supplied by J. Bishop and Company, into a 15 cm length of 6 mm diameter soft glass tubing which had been drawn to a capillary on one end. The exposed end of the wire was heated in a small flame so that the surface tension of the molten metal drew it into a small sphere. This electrode was placed into nearly boiling dichromate cleaning solution for about 10 min, then thoroughly washed in conductivity water, fitted tightly into a standard taper Teflon joint, and introduced into the cell which contained deaerated test solution. Electrodes prepared in this manner appeared bright when viewed under a microscope. A newly prepared electrode was used for each experiment. The area of each electrode was determined by comparison, at a particular potential, of its capacity to the

capacity of a larger platinum wire electrode whose geometric area could be calculated. The particular potential at which the capacity was measured depended on the solution under investigation and the value chosen was one for which the capacity did not change significantly with potential.

All solutions were prepared using water from a Barnstead conductivity still (3×10^6 ohm-cm) and reagent grade HNO_3 , KNO_3 , KCl, and KOH. The KNO_3 and KCl were further purified by two recrystallizations out of conductivity water. Constant boiling HCl was prepared by distillation.

Nitrate solutions of pH 2.1, 3, 11.4, and 12.2 were prepared by dropwise addition of either concentrated HNO_3 or KOH to *N* KNO_3 till the desired pH was reached. The pH 6.55 solution was prepared by adding an appropriate amount of Beckman pH 7 buffer solution concentrate to *N* KNO_3 . For each solution the ionic strength was approximately one.

Chloride solutions of pH 1, 3, 11.4, and 12 were prepared similarly to the nitrate solutions using 6*N* HCl and *N* KCl instead of HNO_3 and KNO_3 . Solutions, 6*N*-0.015*N* HCl, were prepared by dilution of 6*N* HCl with conductivity water.

Cell and method.—The all-Pyrex glass cell contained the test electrode, a saturated calomel reference electrode, and a large platinized platinum auxiliary electrode. This auxiliary electrode served both as a polarizing electrode and a low impedance electrode for the capacity measurements. A stream of Grade A He was passed through the cell solution continuously. The cell was immersed in a grounded, constant temperature water bath which also served as an electrostatic shield.

Differential capacity measurements were made using a series General Radio Model 650 A Impedance bridge accurate to 2%. The alternating voltage across the cell never exceeded 10 mv. Because of the low input voltage to the bridge, two amplifiers and an oscilloscope were required to determine the balance point of the bridge. All circuits were adequately shielded and appropriately grounded.

¹ Present address: Humble Oil & Refining Company, Houston, Texas.

The polarizing voltage was supplied to the test and auxiliary electrodes by a potentiometer connected in series with a microammeter and a choke coil. The coil served to block a.c. from the polarizing circuit.

The potential difference between the test electrode and the saturated calomel electrode was measured with a Keithley electrometer. Therefore, all potentials reported here are with respect to the saturated calomel electrode.

Procedure.—In order to compare the impedance behavior of the systems investigated, it was necessary to adopt some standard procedure for performing the experiments. Of the several procedures which were tried, the following one gave the most reproducible results and it was, therefore, followed through this investigation.

The electrode, after having been carefully cleaned in the manner described above, was placed in the deaerated cell solution and alternately polarized cathodically and anodically in order to expell surface active impurities which may have been adsorbed on the electrode surface. The electrode potential was then adjusted to some value such that an anodic current flowed for several seconds, after which the potential was set to some value for which the electrode was "ideally" polarizable ($i < 0.1 \mu\text{a}$). Capacity data were then taken as rapidly as possible so that the surface active impurities, which experience has shown to be nearly impossible to remove completely, would not have sufficient time to diffuse to the electrode surface, thereby rendering them innocuous. This procedure assumes the condition that the time required to take the capacity data (10-15 sec at each potential) is much less than the time required for surface active impurities to diffuse to the electrode surface. Probably this condition was fulfilled since the capacity did not vary more than about 2-3% in 10 min at each potential and since, in the presence of a surface active substance (9, 32), or for impure solutions (33), the capacity varies rapidly with time during the first 10 min, becoming constant only after 30 min or more. At any rate, data which were reproducible to 3%, except at the maximum occurring at the more active potentials where the reproducibility was 10%, were obtained using this procedure.

Results

The series differential of the electrode impedance, measured at 1000 cps and 23°C, is given as a function of potential for nitrate solutions of various pH in Fig. 1 and 2. Each curve is characterized by a cathodic maximum, occurring at active potentials, and an anodic maximum, occurring at the more noble potentials. For solutions of pH 0, 2.1, 3, 6.55, 11.4, and 12.2, the cathodic maxima occur at -0.17, -0.27, -0.34, -0.50, -0.83, and -0.86v, respectively. For low pH, the capacity rises rapidly with voltage at potentials more active than that at which the cathodic maximum occurs while, for high pH, the capacity continues to decrease at potentials more active than that at which the cathodic maximum occurs. Some current ($\approx 0.1 \mu\text{a}$) indicating the onset of hydrogen evolution, begins

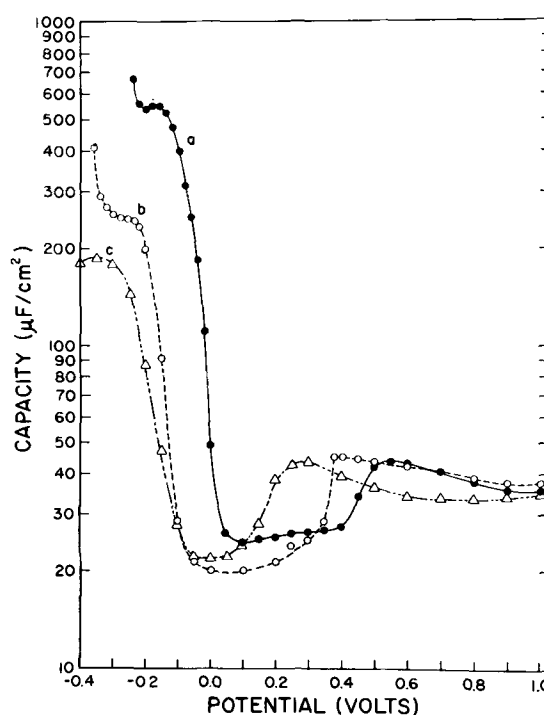


Fig. 1. Differential capacities of activated Pt electrodes in nitrate solutions. Cathodic potential to left. Curve a, pH 0; curve b, pH 2.1; curve c, pH 3.

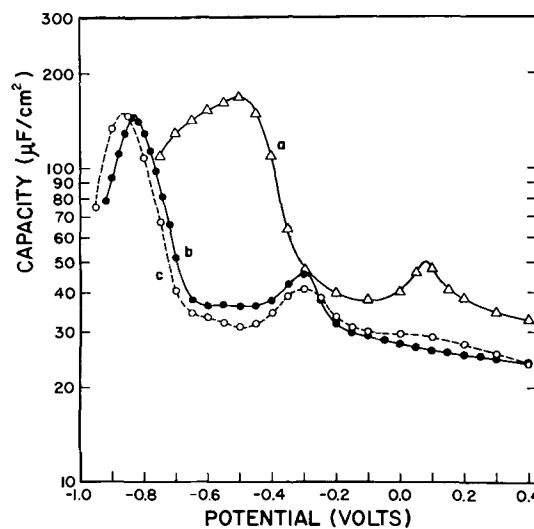


Fig. 2. Differential capacities of activated Pt electrodes in nitrate solutions. Cathodic potentials to left. Curve a, pH 6.55; curve b, pH 11.4; curve c, pH 12.2.

to flow in the polarizing circuit at potentials of about 50 mv more active than that at which the cathodic maximum occurs. The anodic maxima obtained in nitrate of pH 0, 2.1, 3, 6.55, 11.4, and 12.2 occur at 0.55, 0.38, 0.28, 0.08, -0.28, and -0.30v, respectively. For the nitrate solution of pH 0, a slight, but reproducible inflection occurred at -0.05v.

Capacity-potential curves for chloride solutions of various pH are given in Fig. 3, 4, and 5. Results given in Fig. 3 and 4 are for ionic strength of approximately one while the results given in Fig. 5 are for various dilutions of 6N HCl (chloride ion concentration equals hydrogen ion concentration). For pH 0, 1, 3, 11.4, and 12, the cathodic maxima

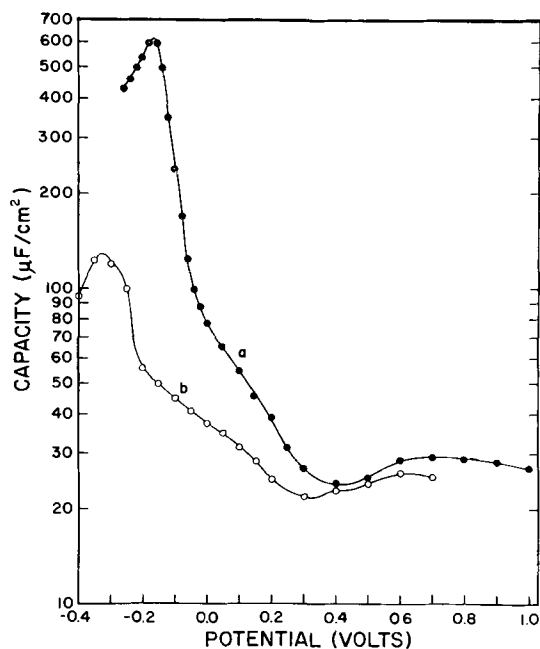


Fig. 3. Differential capacities of activated Pt electrodes in chloride solutions. Cathodic potentials to left. Curve a, pH 1; curve b, pH 3.

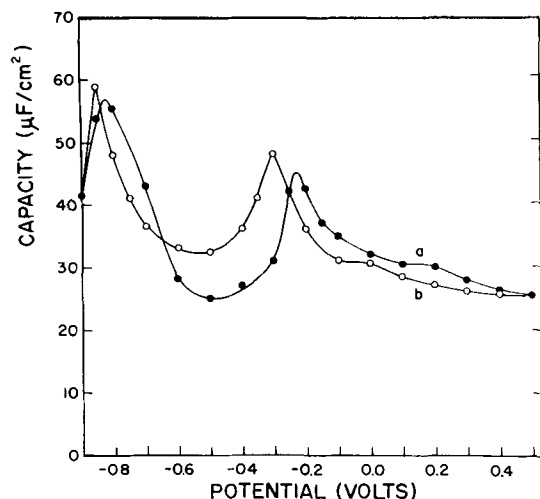


Fig. 4. Differential capacities of activated Pt electrodes in chloride solutions. Cathodic potentials to left. Curve a, pH 11.4; curve b, pH 12.

occur at potentials of -0.12 , -0.17 , -0.33 , -0.82 , and -0.85 v, respectively. There is a maximum which occurs for 1 and 6N HCl at -0.05 v. This maximum does not shift with pH. In addition, for pH 1 and 3, and for 6N HCl, the capacity begins to rise at more noble potentials than for the corresponding nitrate solutions.

The anodic maxima obtained in chloride solutions of pH 11.4 and 12 occur at -0.23 and -0.30 v, respectively. For pH 0, 1, and 3, the anodic maxima are broad and poorly defined. As the chloride and hydrogen ion concentration decrease, the anodic maximum becomes progressively more well defined. The cathodic maximum was not obtained for 0.06 and 0.015N HCl because of the higher solution resistance for these solutions.

The effect of the measuring frequency on the electrode capacity was investigated from 372 to

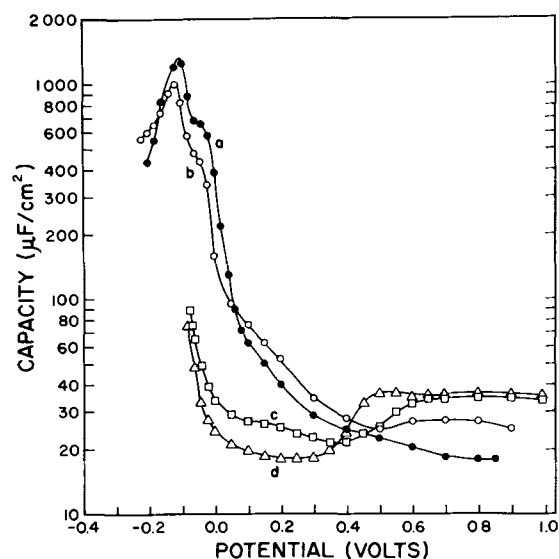


Fig. 5. Differential capacities of activated Pt electrodes in HCl. Cathodic potentials to left. Curve a, 6N; curve b, 1N; curve c, 0.06N; curve d, 0.015N.

1000 cycles/sec for 6N HCl at 23°C. The dispersion was found to be small over this range. The capacities measured at 1000 cps do not differ appreciably from those corresponding to infinite frequency (Fig. 6). The latter were obtained by extrapolation of the reasonably linear plots of electrode capacity vs. the reciprocal of the square root of frequency.

The capacity-potential curves obtained in 6N HCl and 6N H₂SO₄ are given in Fig. 7. The solution temperature was 2°C. The cathodic maxima are similar, and for H₂SO₄ there is an anodic maximum similar to that obtained in nitrate solutions and in HClO₄ (10). The maximum occurring at -0.05 v for 6N HCl also occurs for H₂SO₄.

Discussion

The cathodic maximum can be accounted for as being due to the electrochemical adsorption of hydrogen (1-4) according to either

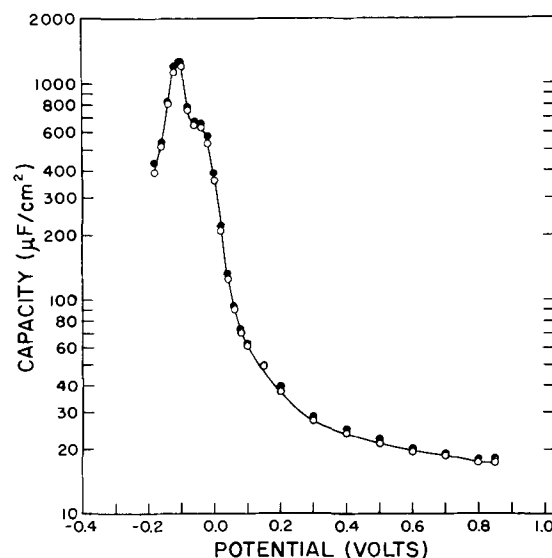


Fig. 6. Differential capacities of activated Pt electrodes in 6N HCl. ● ● ● Frequency of 1000 cycles/sec, ○ ○ ○ extrapolation to infinite frequency. Cathodic potentials to left.

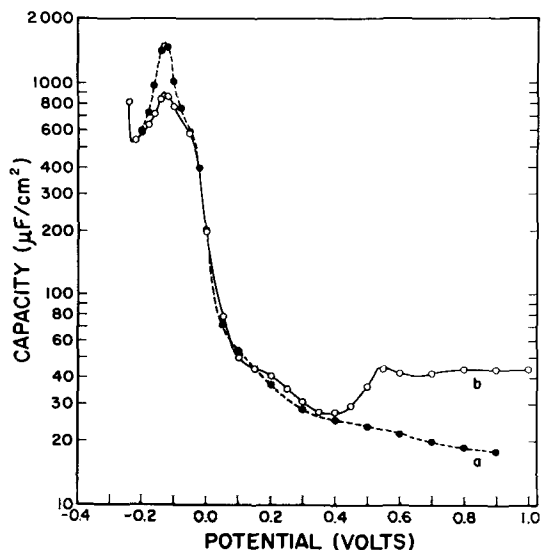
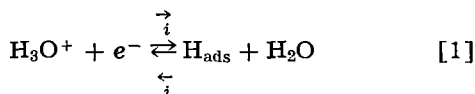
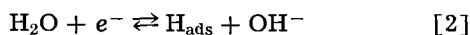


Fig. 7. Differential capacities of activated Pt electrodes. ● ● ● 6N HCl, 2°C; ○ ○ ○ 6N H₂SO₄, 2°C. Cathodic potentials to left.



or



depending on the solution pH.

The impedance associated with either 1 or 2 can be represented as a series combination of the reaction hindrance resistance, θ , the Warburg impedance, W , and the reaction capacity, C_a (16, 17). It has been shown on theoretical grounds that when $\vec{i} = \overset{\leftarrow}{i} = i_0$, a minimum in θ and W , and a maximum in C_a is to be expected provided i_0 is sufficiently large (16). The condition $\vec{i} = \overset{\leftarrow}{i} = i_0$ is expected to occur at some intermediate coverage of the surface with adsorbed hydrogen atoms (18). A maximum in the series differential capacity is to be expected,

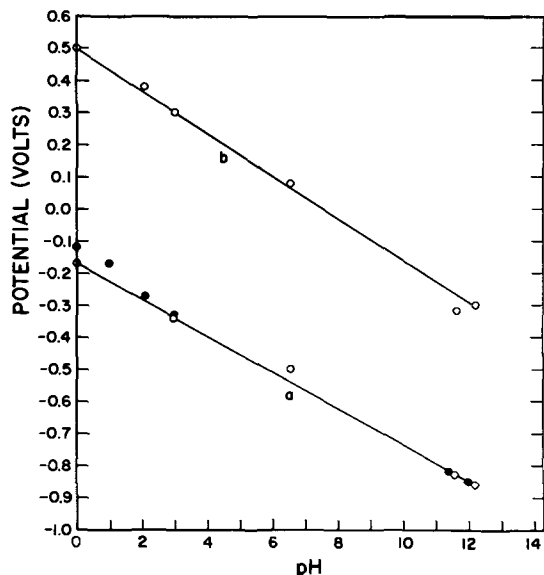


Fig. 8. Relation between pH and the potential of the maximum. Curve a, cathodic maximum; ○ ○ ○ nitrate solutions, ● ● ● chloride solutions. Curve b, anodic maximum for nitrate solutions.

therefore, at some intermediate coverage of the surface with adsorbed hydrogen atoms.

Curve a of Fig. 8 shows the way in which the potential at which the cathodic maximum occurs varies with pH for both chloride and nitrate solutions. The slope of this linear graph is $-2.3 RT/F$. This result is to be expected in view of Eq. [1] and [2] provided the Nernst equation can be applied to this interfacial system and provided the maximum occurs at the same coverage.

In the range $0 \leq \text{pH} \leq 12$, the potential at which the cathodic maximum occurs is 100 mv more noble than the reversible hydrogen evolution potential (rhep) and the rise in capacity, except for acid chloride solutions, indicating the start of the maximum, occurs at a potential 300 mv more noble than the rhep.

Charging curve studies show that for platinum in H₂SO₄ solutions, electrochemical adsorption of hydrogen begins at a potential 300 mv more noble than the rhep and that the coverage is 50-60% complete at a potential 100 mv more noble than the rhep (2, 19, 20).

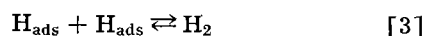
For acid chloride solutions, as well as for 6N HClO₄ (21) and H₂SO₄ solutions, the capacity begins to rise some 500 mv more noble than the potential at which the cathodic maximum occurs. Charging and stripping curve data eliminate the possibility of this rise being due to electrochemical adsorption of H atoms. It can, perhaps, be explained as being due to desorption of specifically adsorbed anions (either Cl⁻, ClO₄⁻, SO₄⁼, or HSO₄⁻) just prior to hydrogen adsorption. There is considerable evidence that Cl⁻ is adsorbed on platinum (9, 22, 23, 34), as well as on Hg (24), and it has recently been found that there is some adsorption of ClO₄⁻ on Hg (25) as well as on Au (26). Alternatively, we may ascribe this early rise in capacity as being due to adsorption of H₃O⁺ ion. According to Frumkin (23, 27, 28), specific adsorption of anions can make the potential at a point near the outer Helmholtz plane more negative and, therefore, promote adsorption of H₃O⁺. In terms of either mechanism, the absence of this region in nitrate solutions can be taken as evidence that NO₃⁻ is not strongly adsorbed.

Breiter (4) pointed out that if the transfer coefficients of the primary discharge reaction ([1] or [2]) are equal to 1/2 and if a Langmuir isotherm is applied, then the rate of 1 or 2 is proportional to the square root of the reaction capacity C_a . In view of this, we can conclude that the discharge reaction is faster for acid chloride solutions than for acid nitrate solutions since the cathodic maximum is considerably higher for chloride than for the nitrate system. This result suggests that chloride ion is adsorbed even during the discharge process since adsorbed chloride is expected to increase the concentration of H₃O⁺ in the double layer (due to a decrease in Frumkin's ψ_1 potential) and, therefore, increase the rate of hydrogen deposition (23, 27-29). In addition, since the cathodic peak heights are approximately constant for $4 \leq \text{pH} \leq 12$, it can be concluded that the transition from reaction [1] to reaction [2] occurs in the pH range of 3-4 pro-

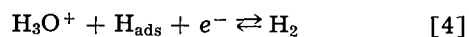
vided the peak height is, as suggested above, a measure of the reaction rate. It is not unreasonable that the transition occurs in somewhat acid solutions since, although the energy of adsorption of H_3O^+ is some 14 kcal less than that of H_2O (30), the concentration of H_2O is of the order of 10^5 higher than the concentration of H_3O^+ .

It is interesting to note that the maximum occurring at -0.05v for solutions of HCl and H_2SO_4 and the slight inflection occurring at -0.05v for N HNO_3 correspond to the zero point of charge on platinum (23). For the case of specifically adsorbed anions, Frumkin's theory predicts that a decrease in the rate of the cathodic process at potentials near the zero point of charge is to be expected over a limited potential range when the surface becomes more negative. Thus, we observe a decrease in capacity (and, therefore, a decrease in reaction rate) at potentials slightly more active than -0.05v followed by an increase in the capacity, in accordance with the theory. These observations, coupled with Frumkin's theory, suggest that the zero point of charge of platinum is at -0.05v and support the hypothesis that SO_4^{2-} (or HSO_4^-) and Cl^- ion are specifically adsorbed on platinum in the potential range under consideration and that NO_3^- ion is not adsorbed.

The rise in capacity for the case of acid solutions at potentials more active than the cathodic maximum can be attributed to the influence of molecular hydrogen on the electrode impedance according to either



or



As the concentration of H_2 builds up at the surface due to either [3] or [4], these reactions become more reversible and a pseudocapacity is expected to arise. The capacity does not rise at corresponding potentials for alkaline solutions suggesting that the reaction producing H_2 is slower and less reversible than the discharge reaction [2]. This is perhaps connected with the hypothesis that hydrogen is more firmly bound to the surface in alkaline solutions, thereby reducing the exchange current for the hydrogen producing reaction (18).

The occurrence of the anodic maximum can be ascribed to desorption of some oxygen-containing species which is present on the surface at potentials more noble than that at which the anodic maximum occurs. This interpretation is based on several experimental observations.

It has been shown by charging curve studies in acid solutions that electrodes pretreated in the same manner as those used here are covered with a monolayer of some oxygen-containing species and that the cathodic removal of this monolayer involves only one electron per surface platinum atom (19, 20). Such studies further show that there is a large hysteresis associated with the electrochemical desorption of this surface layer in that the potential required to remove it is less noble by several hundred millivolts than the potential required for its formation. The electrochemical reduction of this

layer was shown to be relatively fast (12). Capacity measurements made during the desorption process show that there is a capacity maximum in the region of intermediate coverage (10, 19, 20). The present results show a similar capacity behavior.

In curve b of Fig. 8 is a plot of the potential at which the anodic maximum occurs *vs.* the *pH* for nitrate solutions. The slope of this linear graph is $-2.3 RT/F$ which is consistent with a process of reduction of an oxygen layer.

Since the curves obtained in alkaline chloride and nitrate solutions are very similar, it can be concluded that chloride ions are not specifically adsorbed on the surface. This can be reconciled if the zero point of charge on platinum is at -0.05v , as suggested earlier, since, at potentials more noble than this the surface is covered with an oxygen-containing species while at potentials more active than -0.05v the surface bears a negative charge and would not, therefore, favor chloride ion adsorption.

In acid chloride solutions, on the other hand, the anodic maximum is not very well defined. This suggests that chloride ion is adsorbed, thereby inhibiting surface coverage by the oxygen-containing layer. This inhibiting effect is favored by a low *pH* and a high chloride ion concentration. Thus, for 6*N* HCl , the anodic maximum is absent. It becomes more and more well-defined as the *pH* is increased and as the chloride ion concentration is decreased, finally approaching the results obtained in nitrate solutions.

This is consistent with charging curve studies in chloride solutions which indicate that the formation of the oxygen-containing layer is inhibited by specific adsorption of chloride ions and that the concentration of chloride ions necessary to show such an inhibiting effect is of the order of 0.01 to 0.001*N* (21). Corrosion studies (31) on platinum also show that chloride ion inhibits the formation of an oxygen-containing layer, the inhibiting effect being greater for low *pH* and high chloride ion concentration.

The fact that the capacity did not vary significantly with frequency verifies that the electrodes were relatively smooth (16). This result also indicates that the influence of the double layer capacity is negligible in the region of the cathodic maximum which is reasonable in view of the large reaction capacity C_a considered to be in parallel with the double layer capacity.

Summary

Differential capacity curves have been obtained, using a series capacitance bridge, on activated platinum electrodes in molar nitrate and chloride solutions of various *pH*.

The observed maxima in the capacity-potential curves have been interpreted on the basis of adsorption and desorption processes. Thus, a cathodic maximum which shifts 59 *mv/pH* unit was attributed to hydrogen adsorption. From the way in which the peak height varied with *pH*, it was concluded that the transition from H_3O^+ discharge to H_2O discharge occurs at a *pH* of 3-4 and that

hydrogen adsorption begins some 300 mv more noble than the reversible hydrogen electrode potential.

The anodic maximum, which varied with pH in the same way as did the cathodic maximum, was attributed to desorption of some oxygen-containing species, possibly OH⁻, O⁻, or O⁼. This oxygen layer is not very well-defined for solutions of low pH and high chloride ion concentration.

A capacity peak, occurring at -0.05v in acid chloride and sulfate solutions, has been identified with the zero point of charge of platinum. On the basis of this and Frumkin's theory of the effect of specific adsorption of anions on reaction rates, it was concluded that sulfate, perchlorate, and chloride ion are specifically adsorbed on platinum electrodes in acid solution while nitrate ion is not.

Acknowledgment

The authors take this opportunity to express their appreciation for financial support of this program by the Robert A. Welch Foundation of Houston, Texas, and the Office of Naval Research.

Manuscript received April 29, 1963.

Any discussion of this paper will appear in a Discussion Section to be published in the December 1964 JOURNAL.

REFERENCES

1. P. Dolin and B. Ershler, *Acta Physicochim. U.R.S.S.*, **13**, 747 (1940).
2. M. Breiter, "Kinetics of Hydrogen Evolution and Dissolution of Activated Platinum Metals," in "Transaction of the Symposium on Electrode Processes," E. Yeager, Editor, pp. 307-325, John Wiley & Sons, New York (1959).
3. A. Eucken and B. Weblus, *Z. Elektrochem.*, **55**, 114 (1951).
4. M. Breiter, H. Kammermaier, and C. A. Knorr, *ibid.*, **60**, 37 (1956).
5. B. Ershler, *Acta Physicochim. U.R.S.S.*, **7**, 327 (1937).
6. E. D. Robertson, *This Journal*, **100**, 194 (1953).
7. V. L. Kheifets and B. S. Krasikov, *Doklady Akad. Nauk S.S.S.R.*, **94**, 101 (1954).
8. J. N. Sarmousakis and M. J. Prager, *This Journal*, **104**, 454 (1957).
9. P. V. Popat and N. Hackerman, *J. Phys. Chem.*, **62**, 1148 (1958).
10. H. A. Laitinen and C. G. Enke, *This Journal*, **107**, 773 (1960).
11. J. Llopis and F. Colom, "Proceedings of the International Committee on Electrochemical Thermodynamics and Kinetics, Eighth Meeting, 1958," pp. 414-427, Butterworths, London.
12. M. Breiter, *This Journal*, **109**, 425 (1962).
13. A. Ruis, J. Llopis, and F. Colom, "Proceedings of the International Committee of Electrochemical Thermodynamics and Kinetics, Sixth Meeting, 1955," p. 206, Butterworths, London.
14. M. Breiter, *This Journal*, **109**, 42 (1962).
15. M. Breiter, *ibid.*, **109**, 622 (1962).
16. D. C. Grahame, *ibid.*, **99**, 370C (1952).
17. R. Parsons, *Trans. Faraday Soc.*, **56**, 1340 (1960).
18. R. Parsons, *ibid.*, **54**, 1053 (1958).
19. S. Schuldiner and R. M. Roe, *This Journal*, **110**, 332 (1963).
20. C. A. Knorr, Wright Air Development Command Technical Report No. 58-687, 1960.
21. B. Ershler, *Disc. Faraday Soc.*, **1**, 269 (1947).
22. M. Breiter and J. L. Weininger, *This Journal*, **109**, 1135 (1962).
23. A. N. Frumkin, *ibid.*, **107**, 461 (1960).
24. D. C. Grahame, *Chem. Revs.*, **41**, 441 (1947).
25. K. Asada, P. Delahay, and A. K. Sundaram, *J. Am. Chem. Soc.*, **83**, 3396 (1961).
26. G. M. Schmid and N. Hackerman, *This Journal*, **109**, 243 (1962).
27. A. N. Frumkin, *Discussion Faraday Soc.*, **1**, 50 (1947).
28. A. N. Frumkin, "Hydrogen Overvoltage and Adsorption Phenomena: Part I. Mercury," in "Advances in Electrochemistry and Electrochemical Engineering," Vol. I, Paul Delahay, Editor, Interscience Publishers, New York (1961).
29. R. Parsons, "The Structure of the Electrical Double Layer and Its Influence on the Rates of Electrode Reactions," in "Advances in Electrochemistry and Electrochemical Engineering," Vol. 1, Paul Delahay, Editor, Interscience Publishers, New York (1961).
30. R. Parsons and J. O'M. Bockris, *Trans. Faraday Soc.*, **47**, 914 (1951).
31. J. Llopis and A. Sancho, *This Journal*, **108**, 720 (1961).

Technical Notes



An Advanced Electrode Assembly for Electrochemical Measurements in Aqueous Solutions

H. G. Feller and J. Osterwald

Institut für Metallkunde and Institut für Metallhüttenkunde, Technische Universität, Berlin

Stern and Makrides (1) some time ago described an electrode assembly, in which the problem of the isolation of electrical contacts from the test solution is solved in a very advantageous way. Instead of using thermosetting plastics the authors press one face of a cylindrical sample against a Teflon

washer. This assembly however has the disadvantage of exposing surfaces to the solution which are geometrically not equivalent. Thus an ill-defined current density distribution may result. In modifying this basic design Stern and Makrides isolated in some cases the bottom surface of the cylinder by

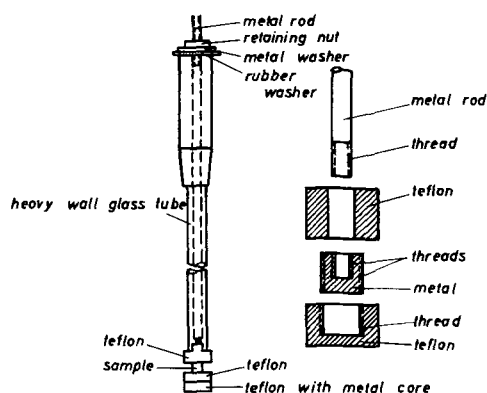


Fig. 1. Electrode assembly

attaching a Teflon washer to the bottom by means of threads.

An advanced assembly, which is described in Fig. 1, combines the advantages of the design of Stern and Makrides with a method of preparing the specimen which can be applied to almost all metals and alloys. A tubular sample is pressed between Teflon washers in such a way that only the cylindrical plane is exposed to the solution. A metal rod with threads on both ends and with good fit goes through the electrode and connects the lower Teflon washer and the retaining nut at the upper part of the glass tube. The lower Teflon washer carries a metal core with threads. In tightening the retaining nut sufficient and continuous pressure is exerted to avoid creepage of electrolyte between Teflon washers and the metal. While pressed between the washers the sample is tilted a little bit and makes good contact with the rod. The measured contact resistance is in the magnitude of milliohm. This electrode is placed in the center of a platinum grid electrode serving as counterelectrode. By enlarging the diameter of the two Teflon washers it is possible to get a uniform current density distribution even in cases where a very low differential polarization resistance of the electrode exists. This assembly has some more advantages: (a) The contact-making rod is often soldered to the sample. This heat-treatment is avoided by this assembly and also by the one Stern and Makrides proposed. (b) The surface of the sample is easily prepared by putting the electrode on a

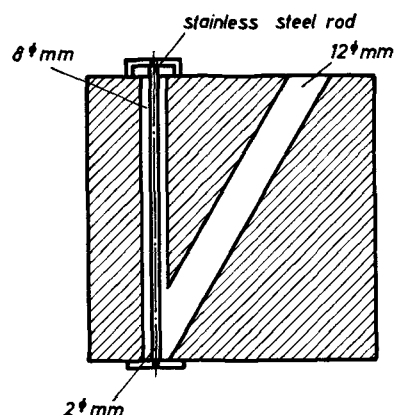


Fig. 2. Bottom casting mold for casting tubes

slightly conical pin of a small lathe and abrading it with emery paper or polishing it by other means while rotating. (c) This assembly can be applied to samples of almost all materials. There is no soldering. Machining and threading can be circumvented as is shown in the next section.

The tubular samples can be made of (a) ductile material by machining on a lathe, (b) hard metal or alloy by machine grinding the cylindrical plane and the face on the lathe, and drilling the hole by the method X-process (2) or other similar means, (c) brittle material by bottom-casting the liquid alloy into a lampblack mold, which carries a lampblack stainless steel rod in the center of the ascending tube (Fig. 2). This method of casting tubes of brittle alloys has been used with considerable success in the case of the γ -Hume-Rothery phase of the copper-zinc-system and in other cases (3). The tubular sample is then machine-ground on a lathe.

Manuscript received June 24, 1963.

Any discussion of this paper will appear in a Discussion Section to be published in the December 1964 JOURNAL.

REFERENCES

1. M. Stern and A. C. Makrides, *This Journal*, **107**, 782 (1960).
2. z. B. Ballhausen, *Werkstattstechnik und Maschinenbau*, **43**, 236 (1953).
3. H. G. Feller, Th. Heumann, and H. Wever: *Z. Naturforschung*, **13a**, 152 (1958).

Use of Low-Temperature Deposited Silicon Dioxide Films As Diffusion Masks in GaAs

S. W. Ing, Jr., and W. Davern

Electronics Laboratory, General Electric Company, Syracuse, New York

It has been shown that the natural oxide of GaAs is porous and cannot be used as a barrier against impurity diffusion (1). Recently Yeh (2) has shown that evaporated silicon suboxide coatings can be used to mask effectively against the diffusion of zinc and cadmium into GaAs. The electrical characteristics of the resulting p-n junctions were not reported.

Because of the unstable nature of silicon suboxide, it cannot serve simultaneously as a device passivation medium and an impurity diffusion mask. This article describes the preparation and use of silicon dioxide films, which are extremely stable and highly impervious to various ambient gases, as diffusion masks for GaAs.

Experimental Methods

The deposition of the silicon dioxide layers was carried out using a recently developed glow discharge technique (3). A suitable organosilicate, such as tetraethylsilicate, was used as the source and was fed into a gas plasma at a pressure of about 100 μ . A high-frequency power source was used to generate the plasma. The organosilicate was dissociated by ion bombardment, and a film of silicon dioxide was deposited on the GaAs substrate which was located in the center of the gas plasma. The bulk substrate temperature during the deposition process was essentially room temperature; the ion bombardment was not intense enough to cause any apparent surface damage to the substrate. The GaAs wafers were chemically etched prior to the deposition, and the deposited oxide films were coherent and adhered well to the GaAs substrate.

Thus far, most of the work has involved diffusion masking against p-type diffusants, namely, Zn, Cd, and Mn. N-type GaAs, with a free electron concentration of 10¹⁶/cm³ was used as the starting material. One face of each wafer was coated with the silicon dioxide film, after which, windows about 1-2 mm square, were cut through the oxide using wax masking and hydrofluoric acid etching techniques.

Diffusion was carried out in an evacuated sealed quartz tube at temperatures ranging between 600° and 800°C. One to two mg of the diffusant source was used and was placed in the same temperature zone as the GaAs wafer. The source materials were Zn, Cd, Mn and a Zn-Ga alloy (1% Zn-99% Ga). After the diffusion step the tube was removed from the hot zone and allowed to cool at room temperature.

The reverse biased characteristics of the planar diodes were measured. Mesas were etched on the reverse sides of the diffused wafers, where there were no oxide masks, and the reverse breakdown voltages of the mesas were measured.

Results and Discussion

The results of the diffusion studies and the diode breakdown voltage measurements are summarized in Table I. Diffusion masking was successfully obtained for the indicated oxide film thicknesses at the temperature range employed. The appearance of the silicon dioxide coatings was not altered in any way after the diffusion process, and their adherence to the GaAs substrates was improved, suggesting that a chemical interaction at the oxide-GaAs interface had taken place during diffusion. This interfacial reaction could also prevent the arsenic from evaporating into the gas phase. The incorporation of gallium and arsenic into the oxide and silicon into the GaAs could be studied, for example, by using the radiotracer technique.

The data of Table I show that Mn has a higher diffusion rate through the SiO₂ layer than either Cd or Zn. Approximate average penetration rates of these metals through the 2000Å thick SiO₂ layer at 700°C are: Zn, 600-670 Å/hr; Cd, 670-1000 Å/hr; and Mn, greater than 1000 Å/hr. The diffusion mechanism, as well as the values for the diffusivities of these metals, through amorphous silica are not

Table I. Diffusion masking in GaAs

SiO ₂ film thickness, Å	Source	T, °C	Diffusion time, hr	Planar V _{BD} , V	Mesa V _{BD} , V
2000	Zn	600	1/6	10	10
2000	Zn	600	2	10	10
2000	Zn	700	2	8	8
2000	Zn	700	3	7.5	6.5
1800	Zn	700	3	Diffused through the oxide	
1800	99% Ga 1% Zn	750	1	45	
2000	Zn	800	1/6	9	8.5
1800	99% Ga 1% Zn	800	1/2	27	
2000	Zn	800	2	Diffused through the oxide	
2000	Cd	700	2	10	14
2000	Cd	700	3	Diffused through the oxide	
1800	Cd	800	1/6	16	
2000	Mn	700	1/6	35	
2000	Mn	700	2	Diffused through the oxide	
1800	Mn	800	1/6	37	

known. However, it is likely that the metal impurity atoms enter the SiO₂ network as ions and that their diffusivities are concentration dependent.

The breakdown voltages of the diffused planar diodes depend largely on the nature of the source. A pure Zn source yielded diodes of somewhat lower breakdown voltages than those obtained using pure Cd sources. A pure Mn source or a diluted Zn source yielded diodes whose breakdown voltages were much higher than those of either pure Zn or Cd.

The cause of the low breakdown voltages cannot be attributed to the oxide masking step since the breakdown voltages for the planar diodes were similar to those of the mesa diodes. Furthermore, the differences between the breakdown voltages of the planar diodes cannot be attributed to any differences in the width of the junction depletion regions, since Kressel and his co-workers (4) have obtained higher breakdown voltages in near abrupt junctions in n-type material that was comparable in donor concentration to the material used in this work.

Microplasma lights were looked for when the diodes were in the avalanche breakdown condition. No lights were visible on those samples which exhibited low breakdown voltages, indicating localized avalanching in the junction region below the surface. However, in those samples which exhibited high breakdown voltages, spots of light were observed around the periphery of the windows. These observations suggest that those diodes that were diffused with high surface concentrations, such as are yielded when a pure Zn or Cd source is used, tend to give p-n junctions that possess a high density of irregularities or spikes which distort the field in the space charge region and cause localized breakdowns when a reverse bias is applied. Junction structures possessing such irregularities could result from the nonuniform surface alloying of the dopant. When Mn or a dilute Zn source was used, vapor pressures and surface concentrations of the metals are much lower at the diffusion temperatures used. The surface concentration of manganese could



Fig. 1. Cross-sectional view of the masked and diffused regions in GaAs, Zn diffused for 2 hr at 700°C with 2000Å thick SiO₂ mask.

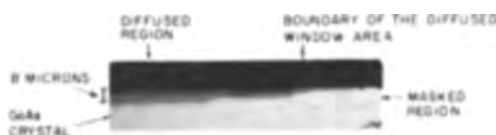


Fig. 2. Cross-sectional view of the masked and diffused regions in GaAs, Zn diffused for 3 hr at 700°C with 2000Å thick SiO₂ mask.

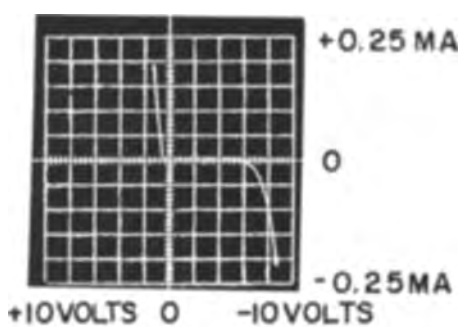


Fig. 3. V-I characteristics of a GaAs planar diode, Zn diffused at 700°C for 2 hr.

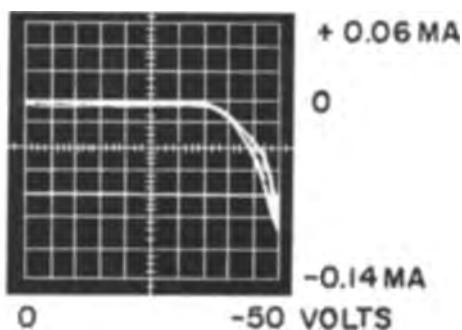


Fig. 4. V-I characteristics of a GaAs planar diode, Mn diffused at 800°C for 10 min.

be limited by its solubility; the Zn surface concentration is limited by its vapor pressure. Under these conditions the distribution of impurities is more uniform across the surface of the wafer and is incorporated into the GaAs surface region, mainly by diffusion, resulting in a much smoother junction plane. The breakdown voltage thus becomes higher and the breakdown starts at the imperfections around the window periphery, at or near the oxide semiconductor interface.

A cross-sectional view of the edge of a diffused window is shown in Fig. 1. It was Zn diffused at 700°C for 2 hr. In the right-hand corner of the photograph, a small protrusion of the junction is visible, which, as stated above, could cause an early localized breakdown. Figure 2 shows a cross-sectional view of another planar diode which was Zn diffused for 3 hr at 700°C. A step in the junction depth, probably caused by the nonuniformity in the concentration of the n-type dopant in the initial material, can be observed at the edge of the window. However, no effect in the breakdown voltage of the diode could be traced to this step.

The forward and the reverse characteristics of a low breakdown voltage diode, and the reverse characteristic of a high breakdown voltage diode are shown in Fig. 3 and 4. The reverse leakage currents of the planar diodes at a bias of 5v were generally less than 0.1 μ a. D-C measurements were made of the reverse V-I characteristics of a few of the planar diodes. At lower biases the reverse currents were apparently generated mainly in the space charge region, since the current is proportional to the voltage raised to a power of 0.5 or slightly less. However, at higher biases, which are still much lower than the breakdown voltage values, excess leakage currents were observed and the currents were proportional to the bias voltage values raised to a power greater than 1 (5, 6).

A few of the planar diodes show reverse leakage currents comparable to the mesa diodes; however, on the average the leakage currents of the planar diodes are higher than the mesa diodes. The reason for this is not known. It is unlikely that the higher reverse currents of the planar diodes are due to any surface damage that might have occurred during the oxide deposition process, since no degradation in the V-I characteristics has been observed on the mesa diodes after being coated with the silicon dioxide films using this new glow discharge technique.

Manuscript received July 8, 1963. This paper was presented at the Pittsburgh Meeting, April 15-18, 1963.

Any discussion of this paper will appear in a Discussion Section to be published in the December 1964 JOURNAL.

REFERENCES

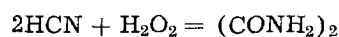
1. H. J. Minden, *This Journal*, **8**, 733 (1962).
2. T. H. Yeh, *ibid.*, **110**, 341 (1963).
3. L. L. Alt, S. W. Ing, Jr., and K. W. Laendle, *ibid.*, **110**, 465 (1963).
4. H. Kressel, A. Blicher, and L. Gibbons, Jr., *Proc. IRE*, **50**, 2493 (1962).
5. A. Goetzberger and W. Shockley, *J. Appl. Phys.*, **31**, 1821 (1960).
6. C. T. Sah, R. N. Noyce, and W. Shockley, *Proc. IRE*, **45**, 1228 (1957).

Preparation of Oxamide from Cyanide by Glow-Discharge Electrolysis

Earl H. Brown, Wendell D. Wilhide, and Kelly L. Elmore

Division of Chemical Development, Tennessee Valley Authority, Wilson Dam, Alabama

The preparation of oxamide from aqueous formamide by glow-discharge electrolysis was described recently (1). The reaction was believed to involve free hydroxyl radicals, and hydrogen peroxide was produced also in the electrolysis, presumably by dimerization of hydroxyl radicals. Hydrogen cyanide reacts with cold, practically neutral aqueous hydrogen peroxide to give oxamide (2); the simplest equation for this reaction is



but the reaction is considerably more complicated. Cyanogen is hydrolyzed to oxamide in slightly alkaline aqueous hydrogen peroxide at room temperature. A study was made of the glow-discharge electrolysis of aqueous cyanide solutions as an alternate method of synthesis of oxamide.

The apparatus was the same as that used in the glow-discharge electrolysis of formamide (1). The two-compartment cell was operated without separation of anode and cathode solutions and was cooled in ice water. Hydrogen cyanide vapor was drawn from an ice-cooled flask into the cell under an operating pressure of 40-100 mm Hg absolute and introduced below the surface of the electrolyte solution in the anode compartment. The discharge between the anode and the solution was maintained for 1 or 2 hr at 0.06 amp with a potential of 450-480v.

In early tests, no oxamide was formed when the electrolyte was 0.8*N* sulfuric acid, sodium sulfate solution with pH 6.3, or phosphate buffer solution with pH 6.7 or 8.6, but oxamide was formed when the electrolyte was a slightly alkaline solution of sodium cyanide.

Results of exploratory tests indicated that the yield of oxamide was affected most by the concentrations of sodium cyanide and sodium hydroxide in the electrolyte, the rate of introduction of hydrogen cyanide, and the pressure in the cell. In a series of runs designed to test the relative importance of these variables, the cell was charged with 75 ml of

electrolyte solution. Hydrogen cyanide vapor was admitted to the anode compartment at a constant rate in the range 0.2-0.8 g/hr with a constant pressure of 40 or 100 mm Hg absolute above the solution. The initial electrolyte solution was 1 or 2*M* in sodium cyanide and 0.04 or 0.11*M* in sodium hydroxide. The glow discharge was maintained with a current of 0.06 amp under a potential of 450v.

Oxamide was produced as a homogeneous, white crystalline powder with the correct optical properties and powder x-ray pattern (3). The product was filtered off, washed with a cold saturated solution of oxamide in water (22 mg/100 ml) and then with ethanol, and sucked dry. There was slight discoloration of the product of runs with high rates of input hydrogen cyanide. Within the ranges studied, the total concentration of sodium in the electrolyte and the pressure in the cell had no significant effect; the pH of the electrolyte appeared to be the controlling variable. Highest electrical efficiencies, 2.3-2.5 equivalents per Faraday (1 mole of oxamide is assumed to represent 2 equivalents), were obtained when hydrogen cyanide was admitted to the cell at a rate (above 0.26g HCN/hr) sufficient to maintain the pH between 9.4 and 10.0. The maximum rate of production of oxamide at 450v and 0.06 amp was 0.24 g/hr. The efficiency, in equivalents per Faraday dropped almost linearly from 2.3 at pH 9.5 to 1.1 at pH 12.0. The highest electrical efficiency was only about 75% of that obtained in the preparation of oxamide by glow-discharge electrolysis of formamide.

Manuscript received April 1, 1963.

Any discussion of this paper will appear in a Discussion Section to be published in the December 1964 JOURNAL.

REFERENCES

1. E. H. Brown, W. D. Wilhide, and K. L. Elmore, *J. Org. Chem.*, **27**, 3698 (1962).
2. Attfield, *J. Chem. Soc.*, **16**, 94 (1863).
3. E. M. Ayerst and J. R. C. Duke, *Acta Cryst.*, **7**, 588 (1954).

Correction

On page 1210 of the December 1963 Journal, in the paper by M. A. Heine and M. J. Pryor "The Distribution of A-C Resistance in Oxide Films on

Aluminum," in Fig. 8 the curve marked \square should read 1.0M.

Investigation of Manganese Dioxides

I. Water Content

Aladar Tvarusko¹

The Carl F. Norberg Research Center, The Electric Storage Battery Company, Yardley, Pennsylvania

ABSTRACT

The water content of natural ores, electrolytic, chemical, and synthetic hydrous MnO₂ samples, equilibrated in an atmosphere of 75% relative humidity, was determined at 110°, 235°, and 400°C. Total water varied from 1% for a highly crystalline β -MnO₂ to 20% for synthetic hydrous MnO₂. The pH of the MnO₂ samples increased with increasing temperature, except for natural ores and their derivatives which showed a decrease in pH at 235°C. The degree of resorption of water vapor was dependent on the drying temperature and decreased with increasing temperature.

The various types of manganese dioxide perform differently in Leclanché dry cells depending on their origin or method of preparation, that is, on their physical and chemical properties. It is recognized in the dry cell industry that MnO₂ of higher water content is more suitable as a depolarizer. Jegge (1) and Sasaki (2) found that the highly hydrated form is more desirable in the dry cell. It is thought that water in any form plays an important role during the discharge of MnO₂ (3), that it helps the proton migration (4, 5), and that the reaction can proceed more readily through the built-in water (6). According to D'Agostino (7), α -MnO₂ has much greater activity and holds water more firmly than the other forms investigated. Drotschmann (8) and Fukuda (9) showed that there is a certain relation between the depolarizing activity and the degree of hydration. Drotschmann (10) claimed that the electron acceptability depends on the degree of hydration in addition to the lattice distortion.

Upon heating MnO₂ the discharge capacity and the water content decrease. According to Vosburgh (11), they are inter-related and influenced furthermore by the structural changes of the MnO₂. This dependence of capacity decrease on the decreasing water content was observed by Sasaki *et al.* (3) and Fukuda (9). Bode *et al.* (6) observed that the equilibrium potential for water-containing β -MnO₂ at various stages of discharge was higher than that of water-free β -MnO₂. The length of the potential plateau was proportional to the water content of the MnO₂.

The status of the water in the manganese dioxide is determined by the magnitude of the force by which the H₂O molecule is bound to the MnO₂ lattice or particle. According to Glemser (12), the greater proportion of the water in manganese dioxide hydrates is loosely bound. Drotschmann (13) classified the forms of water present in MnO₂ as physically retained, sorbed, and constitutional. Bode (14) distinguished between adsorbed and chemically bound water. In the γ -MnO₂ prepared by Srb and Franz (15), chemically bound water was present.

Sasaki *et al.* (2) concluded that the water released below 110°C is purely adherent water, while the weight loss between 110°C and the decomposition temperature represents the combined water. Gruner (16) stated that the water in cryptomelane is of zeolitic nature. However, his own data do not support this fully. According to Fukuda (9), the released water is not zeolitic.

The water molecule in the lattice MnO₂ can be present as H₂O, H₃O⁺, or OH⁻ as described by Glemser *et al.* (17). According to Bode (14), in some synthetic manganese dioxide a proportion of foreign cations can be replaced by H₃O⁺.

It was proposed (6, 11, 16-23) that some of the oxygen ions in the lattice of MnO₂ are replaced by OH⁻. Glemser and his co-workers have definitely established the presence of OH⁻ groups in the lattice of MnO₂ by infrared spectroscopy (24), measurements of proton magnetic resonance (25, 17), and DTA measurements (17, 26, 27). They found that ramsdellite and β -group of MnO₂, however, do not contain OH⁻ groups (26, 27), thus confirming the observations of Brenet *et al.* (28).

The water content depends not only on the origin and type of MnO₂ (29) but also on the parameters of the preparations, for example, for electrolytic γ -MnO₂, on the electrode material (30) and temperature of electrodeposition (27, 31). Gattow (32) describes the difficulty of reproducing the water content.

Besides the thermal measurements, Sasaki *et al.* (33) determined the water content of MnO₂ by the "double resonant circuit method" (34). They found that the dielectric constant of MnO₂ through 100 mesh is directly proportional to the amount of water adsorbed in the particles.

Foote *et al.* (35) found that the surface adsorption of water is markedly reduced only when the temperature is raised above the decomposition temperature. However, Sasaki *et al.* (2) showed that the amount of water re-adsorbed decreased gradually with the increasing temperature of the heat treatment.

The previous studies on the water content of MnO₂ involved various experimental approaches and

¹ Present address: Swiss Federal Institute of Technology, Department of Industrial and Engineering Chemistry, Zurich, Switzerland.

covered only a limited number of types of MnO_2 . It was thought that a more comprehensive study of all available types of MnO_2 , using the same experimental approach, would lead to better understanding of the state of the water in MnO_2 . Such information could be useful for correlation with the physical, electrochemical, and chemical properties.

Experimental

Various types of MnO_2 are used as depolarizers in Leclanché cells or have been evaluated for this purpose. The MnO_2 materials are usually non-stoichiometric and are known in many crystallographic forms with different degrees of crystallinity. Manganese dioxides can also be classified by their origin: natural ores, electrolytic MnO_2 , chemical MnO_2 , and synthetic hydrous MnO_2 . Electrolytic MnO_2 is produced by anodic oxidation of aqueous solution of manganous salts. Chemical MnO_2 is obtained by the decomposition of MnCO_3 at ca. 250°C in the presence of air and moisture. The MnO formed is auto-oxidized in the aforementioned environment of MnO_2 , and the product is acid leached. The synthetic hydrous MnO_2 , the so-called "hydrates," are the by-products of the oxidation of the organic compounds by permanganate. They are amorphous.

The various MnO_2 samples studied are listed in Table I with their crystallographic structures as determined by x-ray diffraction.

There are two highly crystalline β - MnO_2 samples in the natural ore group. Sample L was placed in the hydrate group because of its high water content. It is

not a true hydrate because it has a moderate crystallinity; it is likely an activated ore.

The MnO_2 samples of different origins and processes have been dried to various degrees and may have been stored in an atmosphere of varying relative humidity, and so could have a different amount of adsorbed water and possibly constitutional water. Therefore, it was necessary to equilibrate (standardize) the various MnO_2 samples in an atmosphere of a suitable relative humidity to obtain a common base for their evaluation.

It was found that the water content of various MnO_2 samples will attain an equilibrium value in an atmosphere of 70-80% relative humidity in a relatively short time. Accordingly, the MnO_2 samples to be investigated were standardized in an atmosphere of 75% relative humidity at 20°C (over sulfuric acid of 1.225 density). The depth of the loose powder spread evenly in a Petri dish was maintained about 10 mm because at greater depths it was difficult to reach an equilibrium. After 10 days at 75% R. H. the samples were reweighed and the percentage of weight increase, I_s , due to the adsorption of water vapor was calculated.

It is more or less an accepted practice to dry MnO_2 samples at 110°C to eliminate adsorbed water. The standardized MnO_2 samples were dried in an electric oven in air at $110 \pm 3^\circ\text{C}$ for 16 hr. The MnO_2 samples were allowed to cool in a desiccator over concentrated sulfuric acid and reweighed on an analytical balance. The percentage of the desorbed water of the standardized sample was calculated and is designated as water content, 110°C, in Table I.

Table I. Crystal structure, water vapor uptake, water content, and composition of MnO_2 samples

Name	Crystal type	I_s , %	Water content, % 110°C	Water content of predried sample, % 235°C 406°C		Stand.	x in MnO_x 235°C	400°C
Natural ores								
African, Ghana	$\gamma, T\beta, \alpha$	0.39	0.88	1.4	3.0	1.937	1.956	1.922
Montana	$\gamma, T\beta$	0.86	2.40	2.8	4.2	1.916	1.915	1.841
California	$\gamma, T\beta$	0.55	1.54	1.6	2.6	1.879	1.899	1.838
Moroccan	β	0.26	0.53	0.7	0.7	1.992	1.982	1.980
Mexican	$\beta, T\alpha$	0.76	2.25	2.8	4.0	1.888	1.903	1.801
Greek	γ, T	0.71	2.74	3.8	5.3	1.925	1.929	1.787
Caucasian	β	0.49	1.19	2.0	2.0	1.953	1.958	1.956
Electrolytic MnO_2								
Sample A	$\gamma, T\beta$	0.69	3.82	2.2	4.0	1.932	1.956	1.855
Sample B	$\gamma, T\beta$	0.59	3.56	2.5	4.0	1.924	1.956	1.859
Sample C	$\gamma, T\beta$	0.39	3.35	2.4	4.1	1.988	1.951	1.887
Sample D	$\gamma, T\beta$	0.39	3.44	2.8	4.9	1.982	1.960	1.864
Sample E	$\gamma, T\beta$	0.49	3.33	2.6	4.6	1.956	1.973	1.863
Chemical MnO_2								
Sample F	γ (?)	2.96	5.56	2.0	3.4	1.908	1.910	1.805
Sample G	γ (?)	1.24	5.37	1.9	3.6	1.819	1.831	1.710
Sample H	γ	5.18	5.88	2.2	3.8	1.931	1.935	1.810
Synthetic hydrous MnO_2								
Sample J	amorph.	0.29	15.13	5.7	7.2	1.892	1.846	1.777
Sample K	amorph.	0.68	14.07	7.3	8.9	1.913	1.857	1.788
Sample L	$\gamma, T\alpha, \beta$	0.26	10.01	3.7	5.5	1.844	1.796	1.772
Sample M	amorph.	1.05	15.89	5.1	6.9	1.798	1.680	1.624
Sample N	amorph.	7.31	17.19	7.5	9.7	1.877	1.774	1.610

Note: T, traces of; I_s , percentage of weight increase due to the adsorption of water vapor during standardization; Stand., sample standardized in 75% R. H. at 20°C.

Only MnO_2 samples thus dried were used for the determination of the water content released at higher temperatures. For each determination a new sample was used. The determination of the water content of a solid sample at various temperatures in a tube furnace is an elaborate and lengthy operation. Therefore, a simple, fast, and semi-automatic instrument was chosen and used, the I-R Moisture-matic balance of the Moore-Milford Corporation, Skokie, Illinois, which combines a very efficient source of infrared heat with a motor-driven torsion wire balance.

The procedure for determining the weight loss, that is the water content, consisted of zeroing the balance, weighing-out of the sample *in situ* (approximately 12g), setting the timer and the heater to predetermined values, and positioning the heater assembly over the sample. The weight loss of the sample was automatically recorded on a digital counter to the nearest 0.1% immediately after the short drying time.

Properties of the various MnO_2 samples may be altered by the temperature increase, due to the loss of water and change of chemical composition which are concomitant with a change in the crystal structure. To follow the changes in the properties of the MnO_2 samples, the standardized (Stand) and heat-treated samples were analyzed for available oxygen, for manganese content, and pH, (Tables I and III) After heat treatment, samples were immediately transferred into a desiccator and kept there until the analyses were performed.

The available oxygen was determined by the standard oxalic acid method. The Lingane potentiometric method was used for the determination of manganese content (40). In this, the manganese ion is titrated with a permanganate solution in the presence of sodium pyrophosphate. The x -value in the MnO_x was calculated from these data. The pH of the MnO_2 sample was measured as follows: 10.000g MnO_2 were shaken in a 250 ml Erlenmeyer flask with 200 ml CO_2 -free distilled water. The tightly stoppered flask was placed on a wrist-action shaker for a period of 1 hr at maximum agitation. After allowing 5 min for the MnO_2 to settle, the pH of a portion of the supernatant liquid was measured by a Beckman Model G pH Meter using calomel and glass electrodes. The pH-values observed in this manner are designated as the pH of the MnO_2 samples (Table III).

Results and Discussion

The various MnO_2 samples in every case showed a weight gain, I_s , during the standardization shown in Table I. Weight increases for the various natural ores and electrolytic MnO_2 samples were small and varied only slightly. However, they were not so uniform for the chemical MnO_2 and synthetic hydrous MnO_2 samples. The weight increase due to the ensuing water vapor adsorption was 2-88% of the water content at 110°C. This variation clearly indicates the necessity for standardization of the various MnO_2 samples in an atmosphere of the same relative humidity for their further evaluation to obtain meaningful results. Water adsorbed during the

standardization was retained by the MnO_2 sample in most cases as adsorbed water.

The adsorbed water originally present and that added during the standardization is eliminated when the sample is dried at 110°C. This adsorbed water (water content, 110°C) varies and forms groups according to type of MnO_2 . Natural ores contain the least adsorbed water, but vary significantly depending on where they were mined and what crystal structure type is mainly present in the ore. Moroccan ore (highly crystalline β - MnO_2) has the lowest value of all. Electrolytic MnO_2 samples, having slightly higher and almost uniform adsorbed water contents, are followed by the chemical MnO_2 samples. The synthetic hydrous oxides are all above 10% water content and have a larger variation than the previous two groups.

The weight decrease due to water loss increases with increasing temperature up to a certain temperature, after which decomposition of the MnO_2 takes place. The decomposition temperature depends on the crystal structure of the MnO_2 sample (17, 26-29, 31). Furthermore, the weight decrease due to water loss may depend on the length of the heating time at a given temperature.

The temperature of the sample on the pan of the I-R Moisture-matic balance is influenced by the distance of the heater assembly from the sample and by the control of the heat output of the heating element. A distance of 3.5 cm was chosen, yielding a uniform heat pattern for the sample and adequate temperature range. Since the heat output control was marked in arbitrary units, it was calibrated by using thin-wire copper-constantan and iron-constantan thermocouples, the junctions of which were buried in the MnO_2 sample.

Figure 1 shows the water content of the synthetic hydrous MnO_2 sample J (as received) as a function of heating time at increasing temperatures. This sample was chosen because of its high water content. Readings were taken at 2-min intervals, and the determinations were continued immediately. New

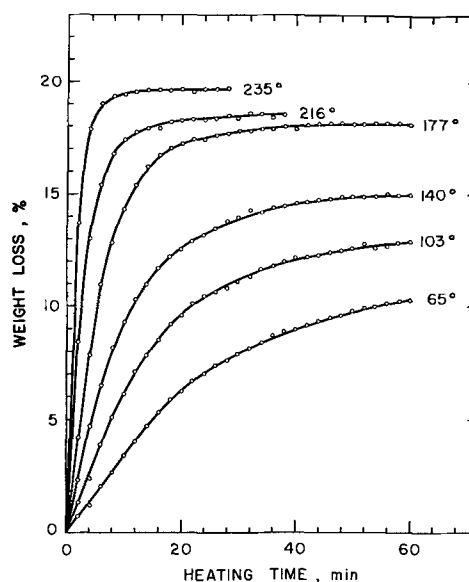


Fig. 1. Weight loss of synthetic hydrous MnO_2 sample J (as received) as a function of heating time at different temperatures.

samples were used for the runs at the various temperatures. It is evident that at low temperatures a long time is needed to obtain a constant value. On increasing the temperature, this time is considerably shortened. The curve for the 140°C temperature reaches a constant value for the water content after a 1-hr periodically interrupted heating period. This value corresponds to the water content obtained by drying the MnO₂ sample at 110°C for 16 hr. When the temperature of the sample on the pan was raised to 177°C, a larger increase of the water content was realized than for the previous equal temperature increase. On further increase of the temperature, the increase of the weight loss due to the eliminated water was small.

Curves, representing the weight loss of the MnO₂ sample at 216° and 235°C, rise rapidly in the beginning and seemingly approach a constant value. The loss does not remain constant but increases slightly with increased heating time. This may indicate a slow decomposition of the sample, a factor which will be discussed later.

In view of the aforementioned observations, the water content of synthetic hydrous MnO₂ sample J (as received) was determined at increasing temperatures (Fig. 2). The duration of the continuous determination was chosen to be 14 min at each temperature to minimize the possible decomposition of MnO₂. The weight decrease due to water loss rose sharply with the increasing temperature, but slowed down around 140°C. On further increase of the temperature, the weight decrease due to the water loss again rose sharply, but slowed down and finally became constant. The accuracy of the determination was at least $\pm 0.2\%$.

Taking into consideration the aforementioned results and the decomposition temperatures of various types of manganese dioxides (26, 28, 29), 235° and 400°C were chosen as temperatures for water content determinations in addition to 110°C. After the activation of the heating element, the temperature

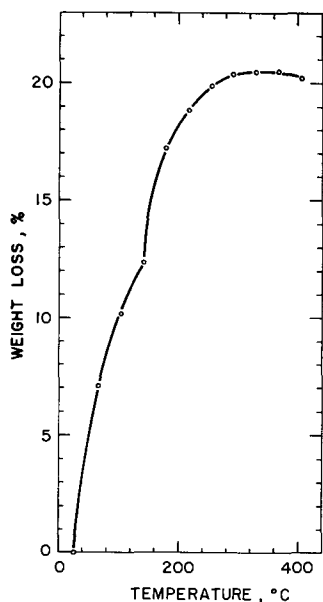


Fig. 2. Weight loss of synthetic hydrous MnO₂ sample J (as received) as a function of temperature.

of the sample rapidly increased and approached a constant value, $235^\circ \pm 5^\circ$ and $400^\circ \pm 5^\circ$, respectively. The time to reach these constant temperatures was 9 min and 4.5 min, respectively. These temperatures remained constant within the $\pm 5^\circ$ C tolerance for the length of the determination (14 min) and could be reproduced repeatedly. The 12-min heating periods were found adequate and chosen for the water content determinations at both temperatures.

Table I shows the water contents of the various MnO₂ samples, predried at 110°, as obtained at 235° and 400°C temperatures. The weight decrease of the predried (110°) MnO₂ sample at 400°C (water content, 400°) is considered as the constitutional water content. The total water content is the sum of the water content, 110°C (weight decrease of the standardized MnO₂ sample at 110°) and constitutional water content.

The amount of the water released at 235°C, and also at the higher temperature (400°), varies with the different groups and also within the group of natural ores and hydrates. The samples of the electrolytic MnO₂ and chemical MnO₂ are more uniform in their water content.

The weight decrease due to the water loss increased further when the temperature was raised to 400°C, for all the samples with the exception of two β -MnO₂ samples, Moroccan and Caucasian ores. The lack of water loss indicates the absence of OH⁻ groups which confirms the results of Gattow *et al.* (26, 27) and Brenet *et al.* (28). They do contain, however, some water which is released at 235°C. It is generally known that the energy required for the destruction of a bond depends on the bond strength between the compound and the species in question, in this case between water and MnO₂ or its microstructure. At 110°C only the adsorbed or physically retained water is released. On increasing the temperature to 235°C, some of the constitutional water is released; this release depends on the type of MnO₂ and seems to increase with the decreasing degree of crystallinity, that is, it is at maximum for amorphous synthetic hydrous MnO₂.

The compositions of the manganese dioxide samples were calculated from the analytical data. The x -value for the MnO_x are shown in Table I. No significant changes can be observed in the x -values for the natural, electrolytic and chemical MnO₂ samples standardized and heated at 235°C. Gattow *et al.* showed that the change of x -value depends on the crystal type of MnO₂ (17, 26, 27); for instance, x -value of most of the γ -MnO₂ samples reached a more-or-less constant value around 250°C, that is, the range in which the β -MnO₂ group exists (27). On increasing the temperature to 400°C, the x -value decreased for all samples, with the exception of the two β -MnO₂ samples. This decrease is due to the decomposition of the MnO₂ sample, *i.e.*, O₂ evolution.

The synthetic hydrous MnO₂ samples, however, showed a gradual decrease of the x -values, *i.e.*, decrease of the oxygen content. Similar MnO₂ samples, designated by Glemser *et al.* (17) as δ -MnO₂, lost O₂ continuously until they reached a minimum x -value at about 250°C.

Table II. Total and corrected constitutional water content of standardized MnO₂ samples

Name	Total water content	Corrected water content	
		Total	Constitutional
Natural ores			
African, Ghana	3.9	3.3	2.4
Montana	6.6	5.2	2.8
California	4.1	3.0	1.5
Moroccan	1.2	1.2	0.7
Mexican	6.2	4.3	2.1
Greek	8.1	5.5	2.7
Caucasian	3.2	3.2	2.0
Electrolytic MnO₂			
Sample A	7.8	5.9	2.1
Sample B	7.6	5.8	2.2
Sample C	7.4	6.2	2.9
Sample D	8.3	6.5	3.1
Sample E	8.0	6.0	2.6
Chemical MnO₂			
Sample F	9.0	7.1	1.5
Sample G	9.0	6.8	1.4
Sample H	9.7	7.4	1.5
Synthetic hydrous MnO₂			
Sample J	22.3	20.2	5.1
Sample K	23.0	20.7	6.6
Sample L	15.5	14.2	5.1
Sample M	22.8	19.6	3.7
Sample N	26.9	22.0	4.8

In view of the analytical results, the weight decreases registered on the digital counter represent not only those due to the water but also include the oxygen loss. Therefore the total water content and the constitutional water content of the standardized samples were corrected for the decrease of x -values. These corrected water contents are shown in Table II. The constitutional water in some cases unavoidably includes the water held by capillary condensation, *i.e.*, the water released by the two β -MnO₂ at 235°C. Furthermore, in the case of the synthetic hydrous MnO₂ samples, some of the more loosely bound constitutional water was released even at 110°C. Natural ores have the lowest total water content, whereas the synthetic hydrous MnO₂ samples have the highest. This may explain the increased capacity of a Leclanché cell with natural ores when a certain part of it is replaced by a synthetic hydrous MnO₂. The influence of the synthetic hydrous MnO₂ on natural ore showed up clearly in the internal resistance behavior of Leclanché cells during discharge (36).

Electrolytic MnO₂ samples have lower total water content than chemical MnO₂ samples, but this is reversed for the constitutional water content. Laurent *et al.* (37) obtained 4.5% for the constitutional water of an electrolytic MnO₂. This is in agreement with the uncorrected constitutional water content of electrolytic MnO₂ samples of this study but is higher than the corrected values. Data of Huber *et al.* (29) for the water content derived at 400°C are in good agreement with some of the corrected constitutional water contents shown in Table II.

When MnO₂ is heated, water and, at higher temperatures, oxygen are released thus changing both the

Table III. pH of the standardized and heat-treated MnO₂ samples

Name	pH		
	Stand.	235°C	400°C
Natural ores			
African, Ghana	6.10	6.24	6.98
Montana	8.24	7.95	8.04
California	6.90	6.72	7.98
Moroccan	8.78	8.47	8.50
Mexican	7.54	7.35	7.60
Greek	8.10	7.85	8.34
Caucasian	8.20	8.25	8.35
Electrolytic MnO₂			
Sample A	5.28	5.62	7.00
Sample B	5.78	7.03	7.40
Sample C	4.92	5.22	6.58
Sample D	5.80	5.90	6.83
Sample E	5.59	6.20	7.00
Chemical MnO₂			
Sample F	5.12	5.50	7.45
Sample G	4.74	5.08	6.35
Sample H	6.45	6.85	7.38
Synthetic hydrous MnO₂			
Sample J	8.21	8.90	9.43
Sample K	9.30	10.42	11.50
Sample L	9.40	8.13	8.28
Sample M	8.83	7.40	7.89
Sample N	5.60	7.40	8.10

surface and bulk properties. If this heat-treated MnO₂ sample is brought in contact with CO₂-free water for a certain length of time, the MnO₂ sample will resorb some, if not all, the lost water. Naturally, a portion of the water adsorbed on MnO₂ can react with the O²⁻ of the MnO₂ forming OH⁻ groups. This in turn will leave an excess of OH ions near the surface of the MnO₂, resulting in an increase in the pH of the distilled water. The pH value of the standardized MnO₂ sample will certainly depend on the impurities present in the MnO₂, *e.g.*, some of the synthetic hydrous MnO₂ samples have a small alkali metal content. This explains the high pH values of the standardized synthetic hydrous MnO₂ samples shown in Table III.

The pH of the supernatant liquid in contact with MnO₂ increased with increasing temperature of the water content determination. This observation was found valid at all temperatures only for electrolytic and chemical MnO₂ samples. The pH increased, however, for all MnO₂ samples tested when the temperature was raised from 235° to 400°C. The pH of CO₂-free distilled water, shaken with natural ores, decreased or remained nearly the same when the temperature of the water content determination was raised to 235°C. In the case of synthetic hydrous MnO₂ samples, only samples L and M resulted in a decreased pH value. One of them (L) is definitely an activated ore, and this may also be true of the other sample (M). This would then indicate that the pH of only the natural ores would decrease when heated to 235°C. The pH change of the two β -MnO₂ samples (Moroccan and Caucasian) with increasing temperature is small to negligible.

Kozawa *et al.* (38) found that, when a heat-treated MnO₂ sample was shaken with an NH₄Cl solution, the pH of the solution increased almost linearly with

the increasing heating temperature above 250°C; below 250°C the pH values did not show a uniform trend. The present data confirm these results (38). Their four samples, however, did not allow them to reach a definite conclusion regarding the behavior of the various samples below 250°C. The results of Kozawa *et al.* (38) and that of the present investigation indicate that the pH increase of the solution shaken with MnO₂ samples increases with the temperature whether salt solution or distilled water is used.

The analytical data and the pH values indicate that the heating of the various MnO₂ samples affected their surface and also bulk properties. These changes should show up also in the resorption of water vapor by the various MnO₂ samples heated to different temperatures. Foote *et al.* (35) claim that the resorption of water is only reduced above the decomposition temperature of the sample, whereas Sasaki *et al.* (2) showed a gradual decrease of the re-adsorbed water with the increasing temperature.

Since the standardization of the MnO₂ samples took place at 20°C in an atmosphere of 75% relative humidity, the same conditions were chosen for the resorption studies. The depth of the evenly spread loose MnO₂ powder in a Petri dish never exceeded 10 mm. In case of greater depths, the resorption took a longer time to be completed. However, the degree of the resorption was the same in both cases, within the experimental error of the procedure. The weight increase due to the resorption of water was measured at intervals on an analytical balance and at least for 10 days. The results were expressed in percentage of the water content of the MnO₂ sample at a particular temperature, taken as 100%.

Figure 3 shows the resorption of water vapor by the Greek ore as a function of time. It can be clearly seen that the amount of the resorbed water decreased with the increasing temperature. The rate of resorption is large in the beginning but decreases with time, finally approaching zero; that is, the resorption becomes small or negligible. The African ore, electrolytic, and chemical MnO₂ samples, together with some of the synthetic hydrous MnO₂ samples, showed similar behavior. However, the curve of the latter samples was different after the initial rapid rise; the extent of the resorption reached the final, nearly constant value within 2%

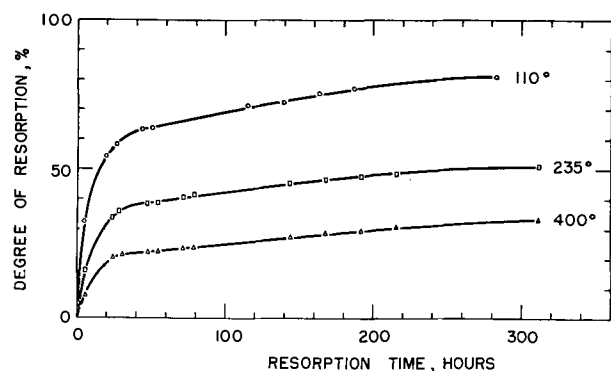


Fig. 3. Degree of resorption of the Greek ore, heated at different temperatures as a function of resorption time.

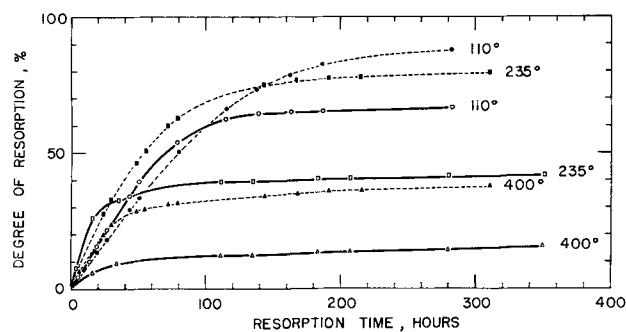


Fig. 4. Degree of resorption of synthetic hydrous MnO₂ sample J (dashed line) and sample O (solid line), heated at different temperatures as a function of resorption time.

after the first 100 hr, in contrast with the curve of Fig. 3.

The synthetic hydrous MnO₂ samples showed two distinctly different behavior patterns illustrated in Fig. 4. The sample represented by solid lines showed a similar behavior to that of Fig. 3. Sample J did not yield the usually larger difference between the 110° and 235°C curves. Furthermore, the resorption curve for 110°C is of different shape. These different resorption curves may indicate the various mechanisms by which the water vapor is resorbed, that is, adsorption of water, capillary condensation or chemical reaction between water and MnO₂.

On the basis of sorption isotherms, Ninagi *et al.* (39) found that capillary condensation takes place to a larger extent in γ -MnO₂, whereas the chemical reaction occurs to a greater degree in α -MnO₂ in accordance with D'Agostino (7).

The fast rise of the resorption curve in the beginning corresponds most probably to a monolayer film of water sorbed or reacted, depending on the degree of crystallinity of the MnO₂. The slowly rising portion of the curve may indicate capillary condensations or a further reaction taking place. The slower rising resorption curves of synthetic hydrous MnO₂ sample J (lower temperatures, Fig. 4) would indicate mixed resorptions taking place simultaneously. For the separation and determination of these various steps, however, the determination of the amount of the resorbed water vapor at a constant relative humidity as a function of time alone is not sufficient.

Acknowledgment

The author is indebted to E. M. Fitchett of Ray-O-Vac Division, Madison, Wisconsin, for the chemical analyses of MnO₂ samples.

Manuscript received Aug. 5, 1963.

Any discussion of this paper will appear in a Discussion Section to be published in the December 1964 JOURNAL.

REFERENCES

1. E. O. Jegge, *Trans. Electrochem. Soc.*, **53**, 71 (1928).
2. K. Sasaki and A. Kozawa, *J. Electrochem. Soc. Japan*, **25**, 115 (1957).
3. K. Sasaki and A. Kozawa, *ibid.*, **25**, 273 (1957).
4. J. Brenet and A. Grund, *Compt. rend.*, **240**, 1210 (1955).
5. A. Kozawa, *This Journal*, **106**, 79 (1959).
6. H. Bode, A. Schmier, and D. Berndt, *Z. Elektrochem.*, **66**, 586 (1962).
7. O. D'Agostino, *Ricerca sci.*, **9**, I, 195 (1938).

8. C. Drotschmann, "Moderne Primärbatterien," pp. 38-9, Nikolaus Branz, Berlin-Schoeneberg (1951).
9. M. Fukuda, *J. Electrochem. Soc. Japan*, **28**, 67 (1960).
10. C. Drotschmann, *Batterien*, **14**, 49 (1960).
11. W. C. Vosburgh, *This Journal*, **106**, 839 (1959).
12. O. Glemser, *Z. Elektrochem.*, **45**, 820 (1939).
13. Ref. (8) p. 121-2.
14. H. Bode, *Angew. Chem.*, **73**, 553 (1960).
15. V. Srb and M. Franz, *Sb. Vysoke Skoly Chem. Technol. v Praze, Oddil Fak. Anorg. Org. Technol.*, **3**, 51 (1959).
16. J. W. Bruner, *Amer. Min.*, **28**, 497 (1943).
17. O. Glemser, G. Gattow, and H. Meisiek, *Z. anorg. u. allgem. Chem.*, **309**, 1 (1961).
18. W. Feitknecht and W. Marti, *Helv. Chim. Acta*, **28**, 129 (1945).
19. A. D. Wadsley and A. Walkley, *Rev. Pur. Appl. Chem. Australia*, **1**, 203 (1951).
20. A. Bystrom and A. M. Bystrom, *Acta Cryst.*, **3**, 146 (1950).
21. J. P. Brenet and A. M. Briot, *Compt. rend.*, **232**, 1300 (1951).
22. A. Kozawa, *This Journal*, **106**, 552 (1959).
23. Yu. Egorov, E. K. Krylov, and E. V. Tkachenko, *Kolloidn. Zh.*, **24**, 159 (1962).
24. O. Glemser and H. Meisiek, *Naturwissenschaften*, **44**, 614 (1957).
25. O. Glemser, *Nature*, **183**, 943 (1959).
26. G. Gattow and O. Glemser, *Z. anorg. u. allgem. Chem.*, **309**, 121 (1961).
27. G. Gattow and O. Glemser, *ibid.*, **309**, 20 (1961).
28. J. P. Brenet, J. P. Gabano, and M. Seigneurin, 16^{ème} Cong. Int. I.U.P.A.C., Paris 1957, pp. 69-80, Editions Sedes, Paris (1958).
29. R. Huber and A. Schmier, *Electrochem. Acta*, **3**, 127 (1960).
30. K. Neumann and W. Fink, *Z. Elektrochem.*, **62**, 114 (1958).
31. V. Srb, *Collection Czechoslov. Chem. Commun.*, **26**, 1231 (1961).
32. G. Gattow, *Batterien*, **15**, 201 (1961).
33. K. Sasaki and K. Kojima, *J. Electrochem. Soc. Japan*, **22**, 567 (1954).
34. Bunjiro Ichijo, *J. Appl. Phys.*, **24**, 307 (1953).
35. H. W. Foote and J. K. Dixon, *J. Am. Chem. Soc.*, **52**, 2170 (1930).
36. A. Tvarusko, *This Journal*, **109**, 557 (1961).
37. J. F. Laurent and B. Morignat, Paper presented at the Third International Battery Symposium, Bournemouth, England, October 1962.
38. A. Kozawa and K. Sasaki, *J. Electrochem. Soc. Japan*, **22**, 569 (1954).
39. S. Ninagi and Y. Miyake, *ibid.*, **30**, 727 (1962).
40. J. J. Lingane and R. Karplus, *Anal. Chem.*, **18**, 191 (1946).

Charging the Silver Oxide Electrode with Periodically Varying Current

I. Brief Increases of Current

Charles P. Wales

United States Naval Research Laboratory, Washington, D. C.

ABSTRACT

Pulses of charge current were added to a constant charge current while a silver electrode was being charged (anodically oxidized) at the 20-hr rate. While charging at the $\text{Ag}_2\text{O}/\text{AgO}$ potential plateau the polarization was lower following a pulse than it was before the pulse. This is believed to be the result of breaking the oxide layer. In 35% KOH the discharge capacity following a charge with pulses reached a maximum that could be considerably greater than the normal capacity. Capacity then decreased as the charge pulse current, pulse length, or pulse frequency increased. In 50% KOH the capacity was always below normal after similar pulses. A commercial silver-zinc secondary cell containing 44% KOH gave intermediate results.

During a study using the current interrupter technique it was noted that the charging potential of a silver electrode often was lower after a period of current pulses than it had been before the pulses. The electrode was being anodically oxidized using a constant charging current at the 24-hr rate. This charging current was stopped occasionally, and then a current lasting about 0.006 sec was pulsed at 60 times/sec, using an anodic pulse current either the same as the charging current had been, or four times as great. While charging at the $\text{Ag}_2\text{O}/\text{AgO}$ potential plateau, several minutes of charging time were required, following a period of pulsing current, before the electrode again reached the potential recorded just previous to the pulse period. The pulse periods had little effect on the subsequent charging potential either early in the charge or later, after oxygen

evolution had been reached. The decreased charging potentials were not an effect of the brief open-circuit periods between the pulses, but were found to be a result of temporarily increasing the charge current to four times its normal value.

These pulse periods had a second effect in addition to the decreased charging potential. A discharge after a charge with pulses of increased charging current was, under certain conditions, up to 50% longer than a discharge following a charge without pulses. It is highly desirable to charge silver electrodes to their full capacity since storage batteries using silver electrodes are costly and are used mainly for purposes requiring an energy source of large capacity but of small size or weight. It was decided, therefore, to investigate in more detail this effect of adding pulses of charge current to the normal charging

current. Periodic open-circuit periods and current reversals during charge are being studied at present and will be the subject of a future paper.

Experimental Procedure

The test cell had a normal capacity of about 1.9 amp-hr and was constructed the same way and used the same size sintered silver electrodes as described earlier (1). Either 35% or 50% KOH was used as the electrolyte at 25°C. The experimental arrangement was similar to that previously reported (2) except that two sources of controlled current were connected in parallel across the cell. The basic current source was held constant during the charge at 100 ma (approximately the 20-hr rate) while the other source supplied a charging pulse current of the same polarity which was added to the basic charge current at controlled intervals of time. Various pulse currents were used at first to see the effect of the pulses on charging potential. These pulse currents ranged from 100 to 9900 ma, giving a total charge current during the pulse of from 2 to 100 times the basic or normal current of 100 ma. Pulse lengths varied from 1 to 60 sec and the interval between pulses was 30 min. After determining that the effect of charge pulses on the following discharge capacity could not be predicted closely from just the potential change during or after a pulse, the pulse current, pulse length, and pulse frequency were kept constant during complete charges using the basic charge current of 100 ma, a pulse current of 100-1900 ma, a pulse length of 2.5-10 sec, and a pulse frequency of 10-60 min.

Pulse charging was also tried on a commercial silver-zinc secondary cell. This cell was rated at 100 amp-hr and contained 44% KOH. It was charged at a basic rate of 5 amp and given additional charge pulses ranging from 5 to 45 amp. The pulses lasted 2-15 sec at intervals of 10 or 30 min.

Results

The effect of added pulses of charge current can be beneficial or harmful to the charge acceptance of a silver electrode in 35% KOH. The discharge capacity following a charge with pulses tended to reach a maximum and then to decrease with increasing pulse current, pulse length, or pulse frequency (Fig. 1). The pulse current had to be decreased to obtain maximum capacity when the pulse length was increased, but this change was not linear since the quantity of pulse electricity needed for obtaining the maximum capacity had also increased. This is shown by the displacement to the right of the maxima of the curves as pulse length increases from 2.5 to 10 sec.

The results given in Fig. 1 were obtained during the first 78 cycles of the silver electrode. In this period there were 13 constant current charges at 100 ma (without pulses) to gas evolution. The majority of the discharges that followed these 13 constant-current charges were within ± 0.1 amp-hr. of the mean capacity of 1.89 amp-hr, and only two exceeded ± 0.2 amp-hr. The standard deviation of the mean was 0.045 amp-hr. Assuming normal dis-

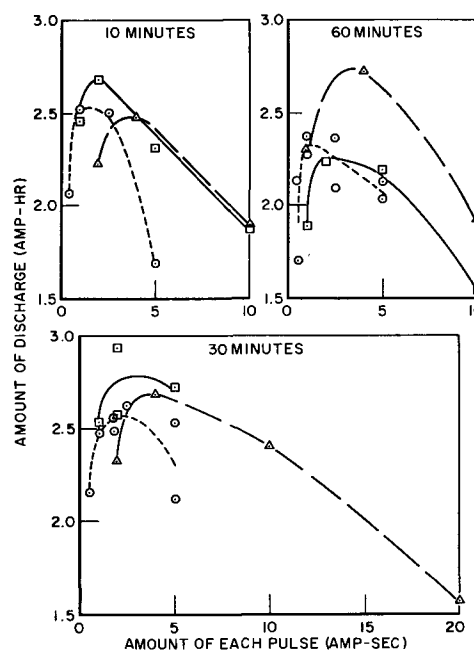


Fig. 1. Capacity of 100 ma discharges of a Ag electrode in 35% KOH at 25°C following 100 ma charges with added pulses of current. Charge current plus pulse current totaled 0.2-2 amp. Each pulse lasted 2.5 sec, \circ ; 5 sec, \square ; or 10 sec, \triangle . Pulses were repeated every 10, 30, or 60 min. Average capacity following charges without pulses was 1.89 amp-hr.

tribution, the true mean should fall within three times the standard deviation of the mean 99.7% of the time, or in the range of 1.76-2.03 amp-hr. There is, therefore, no doubt that increasing the charge current for brief periods of time did affect significantly the amount of charge accepted by the silver electrode. The maximum capacity measured (2.93 amp-hr) was observed following a charge that had the normal 100 ma current increased to 400 ma for 5 sec every 30 min. The average change in discharge capacity was 0.25 amp-hr when 7 of the charges with pulses were repeated. This was within the range of reproducibility of ± 0.2 amp-hr mentioned above.

Capacity tended to be a little higher when the cell was allowed to stand $\frac{1}{2}$ day or longer before recharging than it was when the recharge was begun within a few hours of the discharge. The proportion of discharge that took place at the upper (AgO/Ag₂O) potential plateau gradually decreased as the electrode was given many charge-discharge cycles. The upper and the lower (Ag₂O/Ag) discharge plateaus both increased proportionately following a charge using pulses at the currents that gave the increased capacity. The lower discharge plateau was decreased more than the upper plateau after using pulse currents high enough that they caused the following discharge to be shorter than normal.

A series of charges at the 20-hr rate with added pulses of charge current was tried with a commercial silver-zinc secondary cell that used the same type of sintered silver electrode used in the test cell. Charging potentials were lower after a pulse, but other beneficial results were not appreciable. Most of the discharges had a capacity that did not differ significantly from the average capacity follow-

ing a normal charge at the 20-hr rate. The discharge capacity was less than normal after using relatively long pulses at a high current during a charge; for example, when the normal charge rate of 5 amp was increased to 50 amp for 15 sec every 30 min.

There were three major differences between this commercial silver-zinc cell and the experimental silver cell. The commercial cell used 44% KOH instead of 35% KOH, had the electrodes tightly packed in the cell case, and contained zinc negative plates instead of a silver counter electrode. The zinc plates should not have limited the cell capacity since they had more capacity than the silver plates. Although some zinc may have contaminated the silver plates it was assumed that the presence of zinc was not responsible for the difference in behavior between the cells.

The electrolyte in the experimental cell was changed from 35% KOH to 50% KOH in order to determine the effect of KOH concentration. The normal capacity was only slightly less when using 50% KOH than it had been with 35% KOH. Charges were tried with pulses of 100-900 ma, lasting 2.5 or 5 sec, being added to the normal 100 ma charge current every 10-60 min. In 50% KOH the discharge capacity following a normal 100 ma constant current charge was always larger than the capacity obtained following any of the 22 charges that had pulses of charging current added. Least harmful were pulses at the lowest current, especially if they were only repeated hourly. The detrimental effect of pulses increased as either the pulse length or its frequency increased.

Figures 2 and 3 compare the use of 35% with 50% KOH as the electrolyte. Charge current was increased to 10 times its normal value for 5 sec every 30 min. The capacity following this charge decreased to 76% of the average capacity (based on a normal 100 ma constant current charge) when 50% KOH was used, but the capacity increased to 144% of the average when 35% KOH was used. The pulses had only a slight effect on the subsequent potential at either the first charge plateau or at the gassing or final plateau. In 35% KOH the potentials decreased

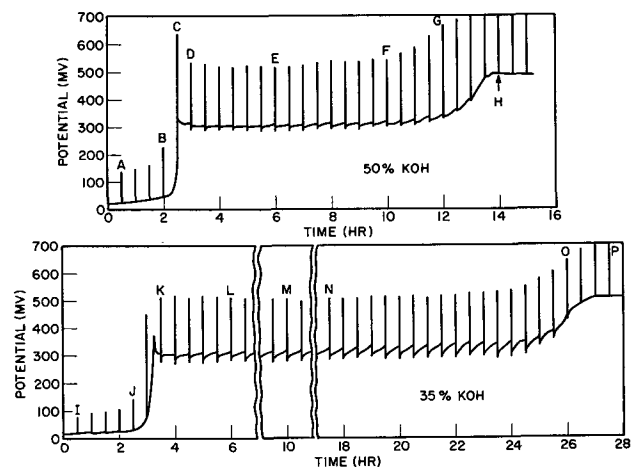


Fig. 2. Charge of the same Ag electrode in 50% and 35% KOH at 25°C. Basic current of 100 ma was increased to 1000 ma for 5 sec every 30 min. Potentials are given with respect to a Ag/Ag₂O reference electrode.

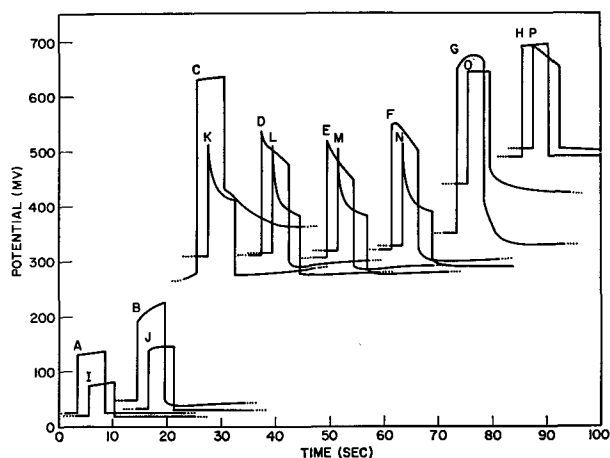


Fig. 3. Potentials during the charges shown in Fig. 2 at the points indicated by the letters in Fig. 2 using an expanded time scale. Potentials are given with respect to a Ag/Ag₂O reference electrode.

more both during pulses and after pulses at the second or Ag₂O/AgO plateau than they did when 50% KOH was used (compare K-N with D-F). The potentials during and after the pulses gradually changed as the charge progressed at the Ag₂O/AgO plateau. The potential after a pulse at this plateau usually dropped to about the same value (dependent on the pulse used) until the charge neared the end of this plateau. Then, although the total potential change was greater, the potential after a pulse did not reach as low a value as it had earlier. When the electrode was given a few charge pulses beginning near the end of the Ag₂O/AgO plateau the discharge capacity in 35% KOH was improved somewhat over the normal capacity, but the improvement was greater when the pulses began at the beginning of the charge.

A comparison of four rates of charging pulses is given in Fig. 4. The potentials following the pulses varied inversely with the pulse current in the cur-

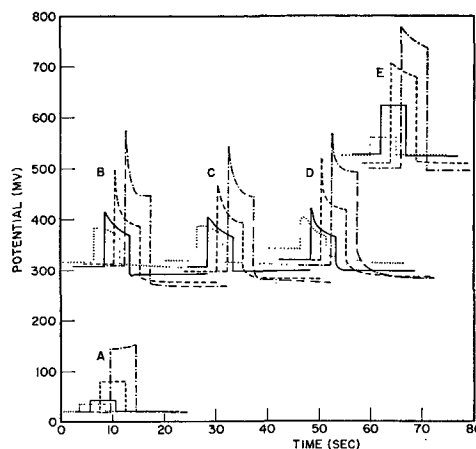


Fig. 4. Potentials observed during 100 ma charges with pulses of a Ag electrode in 35% KOH at 25°C. Pulses lasting 5 sec were repeated every 10 min using the same pulse current. Total current during pulse was 200 ma, dotted line; 400 ma, solid line; 1000 ma, dashed line; 2000 ma, dot and dash alternating line. Potentials are given with respect to a Ag/Ag₂O reference electrode. Electrode was 2% charged at A, had charged 10% at the Ag₂O/AgO plateau at B, was 50% charged at C, was 80% charged at D, and was gassing strongly at E.

rent range shown here. The maximum potential decrease after a pulse was usually observed when the pulse current was 4-20 times the basic 20-hr charge current, with the optimum value of the current dependent on the pulse length. The drop in potential increased with increasing pulse length up to a point, for a particular pulse current. The potentials shown in Fig. 4 were usually still rising when the next pulse was reached (except for the lowest pulse current) due to the pulses being repeated after the relatively short time of 10 min. Since the lowest potentials followed the higher pulse currents, the potentials preceding the pulses were lowest when using high pulse currents. Even though the lowest pulse current had the least effect on the potentials that followed the pulses, the lowest pulse current used for Fig. 4 was more beneficial with respect to discharge capacity than were the two highest currents. This is shown by the solid line and squares in the 10 min section of Fig. 1.

An attempt was made to determine whether an unusually thick Ag_2O layer would inhibit the beneficial effect of charge pulses. A sintered silver electrode was charged using constant current until its potential was rising from the $\text{Ag}/\text{Ag}_2\text{O}$ plateau. The anodization was then continued for 12 days at a constant potential 0.03v below the $\text{Ag}_2\text{O}/\text{AgO}$ equilibrium potential. Approximately 5/6 of the amount of silver that ordinarily oxidized to AgO during a normal charge had been converted to Ag_2O in this time, judging from the amount of current passed. This was about twice the usual amount of Ag_2O . The normal charge current of 100 ma was resumed after the 12 days of constant potential charging. The electrode potential rose immediately to the $\text{Ag}_2\text{O}/\text{AgO}$ plateau. The peak potential at the beginning of the $\text{Ag}_2\text{O}/\text{AgO}$ plateau was not unusually high despite the thicker layer of Ag_2O . After the electrode had charged 0.1 hr at this plateau the current was increased to 4 times its normal value for 5 sec and this was repeated every 30 min during the remainder of the charge. Potential fell in the way already described, beginning with the first pulse of added current. The following discharge was about 25% longer than a normal discharge.

Discussion

It was apparent that polarization decreased during a pulse of increased charge current at the $\text{Ag}_2\text{O}/\text{AgO}$ plateau, since potential dropped during the pulses and since potential after a pulse was lower than before a pulse. The charging potential of a silver electrode at the $\text{Ag}_2\text{O}/\text{AgO}$ plateau is usually considerably above the equilibrium potential, but the potential in the period immediately following a charge pulse at this plateau was about as near to equilibrium as a normal charge is near to equilibrium at the $\text{Ag}/\text{Ag}_2\text{O}$ plateau. The effect of pulses of charge current first became large immediately after the potential peak at the beginning of the $\text{Ag}_2\text{O}/\text{AgO}$ plateau. The potential drop after a pulse continued to be relatively large until the charge reaction changed from the formation of AgO to the evolution of oxygen. This indicated that pulses have their beneficial effect chiefly when the main electrode re-

action is formation of AgO . There is no reason to suppose that any of the proposed higher oxides of silver were formed during the pulses, since high pulse potentials were not necessary for beneficial results (see Fig. 4, dotted lines at B and C).

The film of Ag_2O was many molecules thick on the Ag electrode when the charging potential reached the $\text{Ag}_2\text{O}/\text{AgO}$ plateau. At that time during a normal charge the outer surface of the Ag_2O film oxidized to AgO first in preference to further oxidation of Ag (2, 3). Then, following the initial potential drop after the peak, potential slowly increased as oxidation proceeded deeper into the electrode. There probably was always a very thin layer of Ag_2O between the Ag and the AgO (unless the Ag electrode was being held at a very high anodic potential) since Ag and AgO react readily when in contact to give Ag_2O . An increase in charge current increased the potential of Ag^+ and thus attracted nearby O^{--} more strongly, forming AgO and possibly Ag_2O deep in the film near the Ag instead of nearer to the surface. It is believed that the expansion of the crystal lattice to form AgO next to the base metal broke the film of oxides which covered the electrode and allowed the electrolyte to penetrate nearer to the base metal. Then O^{--} no longer had to move through as thick a layer of AgO as before. Thus polarization was less, following a pulse at the $\text{Ag}_2\text{O}/\text{AgO}$ plateau, than before the pulse occurred.

A pulse of high charging current could only be used for a short period of time before concentration gradients became so large that polarization greatly increased. For this reason pulse charges had a beneficial or harmful effect, depending on the quantity of current used during a pulse (Fig. 1). One indication of the harmful effect of large amounts of pulse current was the smaller drop in potential that followed very high-rate charge pulses. High charging currents are considerably less effective than low ones for oxidizing silver, particularly when using concentrated KOH (2). As a result, long pulses gave less oxidation of the electrode before gas evolution.

Since pulses of charging current had only a small effect at the $\text{Ag}/\text{Ag}_2\text{O}$ plateau but a large one as soon as the $\text{Ag}_2\text{O}/\text{AgO}$ potential plateau was reached, it appears that there was little breaking of the surface film due to formation of Ag_2O . Thickness of the Ag_2O layer was not a factor in pulse effectiveness. The pulses continued to be effective at the $\text{Ag}_2\text{O}/\text{AgO}$ plateau until the AgO film became so thick that the potential necessary for moving the O^{--} through this film reached the oxygen evolution potential, and the main reaction became the production of oxygen.

Charging with pulses would probably have had a different effect if electrodes of pressed Ag_2O or AgO had been used, since these electrodes were reported to react at the grid first instead of at the surface (4, 5). This difference may be due to their relatively high porosity allowing the electrolyte to penetrate to the grid, and in effect moving the solid-liquid interface to the grid.

The difference between the results obtained using 35% and 50% KOH was attributed to increased concentration polarization taking place in the 50%

KOH during a pulse, due to impaired mobility of the OH^- ion (4). This suggested that electrolyte concentration gradients were the limiting factors instead of concentration within the electrode. The superiority of low pulse currents in promoting longer charges was greater than one would expect, judging only by the amount that the potential dropped after the pulses. This may indicate the harmful effect of the concentration polarization which developed at the higher currents. Increasing the pulse frequency had an effect similar to increasing the current.

Normal charges at 100 ma gave a utilization of silver that was generally in the range of 45-53% of the total amount of silver in the electrode, excluding the grid. The maximum utilization measured for charges with added pulses of charging current was 76%, and values from 65% to 70% were obtained frequently when using pulses in 35% KOH. Thus a 30-40% increase in capacity could be obtained

readily by using this method under the proper conditions. A similar increase would be expected in a Ag-Zn storage battery which used a more dilute electrolyte than was used in the Ag-Zn cell tested. A more dilute electrolyte may require changes in the separator material since some types of separator are degraded more rapidly in dilute KOH than in concentrated KOH.

Manuscript received July 2, 1963. This paper was presented at the New York Meeting, Sept. 29-Oct. 3, 1963.

Any discussion of this paper will appear in a Discussion Section to be published in the December 1964 JOURNAL.

REFERENCES

1. C. P. Wales, *This Journal*, **109**, 1119 (1962).
2. C. P. Wales, *ibid.*, **108**, 395 (1961).
3. C. P. Wales and J. Burbank, *ibid.*, **106**, 885 (1959).
4. T. P. Dirkse, *ibid.*, **106**, 920 (1959).
5. T. P. Dirkse, *ibid.*, **107**, 859 (1960).

The Oxidation of Ni-2ThO₂ between 900° and 1400°C

Frederick S. Pettit and Edward J. Felten

*Advanced Materials Research and Development Laboratory, Pratt and Whitney Aircraft,
Division of United Aircraft Corporation, North Haven, Connecticut*

ABSTRACT

The oxidation kinetics of nickel containing 2 volume per cent ThO₂ have been studied between 900° and 1400°C. In this temperature range the oxidation rate obeys the relationship

$$\Delta M/A = k^{0.50}t^{0.55}$$

Metallographic examination of oxidized Ni-2ThO₂ specimens showed the oxide to be composed of a dense outer layer and a porous inner layer. Inert $\alpha\text{-Al}_2\text{O}_3$ markers were found at the boundary between the dense and porous oxide layers. Internal oxidation was also apparent but not to the extent found in pure nickel. X-ray fluorescence analysis showed ThO₂ to be absent in the dense outer oxide but present in the porous inner oxide. Oxidation of Ni-ThO₂ is believed to occur primarily by means of nickel ion diffusion to produce the outer oxide layer and diffusion of oxygen gas to form the inner oxide layer. The oxygen gas required to form the inner oxide layer is produced by decomposition of NiO in the outer oxide layer at the boundary between the inner and outer oxide.

The first commercial dispersion strengthened nickel-base alloy, Ni-2ThO₂, has recently been introduced (1). Dispersion strengthened alloys of the metal-metal oxide type are usually characterized by high temperature stability as expressed by resistance to recrystallization at temperatures near the melting point of the base metal, and flat, stable slopes on the stress-rupture plot. Ni-2ThO₂ is reported to possess these characteristics as well as high thermal conductivity, good ductility and workability, and improved oxidation resistance as compared to wrought nickel.

Ni-2ThO₂ is strengthened by a dispersion of sub-micron thoria particles uniformly distributed throughout the structure. Tests, so far, have shown that its creep and rupture strengths are superior to present day super-alloys in the 1038° to 1093°C temperature range. Because of its stability this

material exhibits usable strength at 1315°C and is currently being considered for applications in the 1093° to 1315°C temperature range.

The purpose of this report is to present our findings on the kinetics and mechanism of oxidation of this alloy. The properties of the Ni-2ThO₂ alloy are compared to those of pure nickel.

Background information.—The nature of the Ni-2ThO₂ alloy suggests that its oxidation mechanism may not differ substantially from that of pure nickel. The alloy contains only a small amount of thoria which under the conditions of the experiments described here can be considered to be inert. While this tends to simplify our system, the oxidation mechanism of pure nickel has not been definitely described.

Based on results obtained by Gulbransen and Andrew (2) as well as Moore (3), for thin films of

Table I. Results from spectroscopic analysis of Ni-2ThO₂

Element	Weight per cent	Element	Weight per cent
Co	0.05-0.15	Zr	ND-0.005
Cu	0.01-0.10	Mo	ND-0.005
Fe	0.005-0.05	Pb	ND-0.01
Mg	P-0.001	Sn	ND-0.01
Mn	P-0.001	Ag	P-0.001
Si	0.001-0.005	Sb	ND-0.01
Ti	0.01-0.05	As	ND-0.01
Al	0.001-0.005	B	ND-0.005
Cr	0.001-0.005	Zn	ND-0.01
Th	1.0-3.0	Ba	ND-0.01
Ni	Remainder	Sr	ND-0.005
V	ND-0.005	Cd	ND-0.01
Ca	P-0.005	W	ND-0.01
Bi	ND-0.01	C	0.001

P = present less than.
ND = not detected (detection limits).

NiO on nickel the oxide layer is sufficiently plastic to maintain contact with the metal and a Wagner mechanism based on nickel ion diffusion applies. For thicker films, Ilchner and Pfeiffer (4), Mrowec and Werber (5) as well as Sartell and Li (6) have found the NiO to consist of two layers. These investigators believe that the external oxide layer grows as a result of outward diffusion of nickel ions while the inner layer forms due to inward diffusion of oxygen; however, there is division of opinion among these investigators with regard to the mechanism of oxygen diffusion.

Experimental Procedures

The Ni-2ThO₂ used in this study was obtained from E. I. du Pont de Nemours and Company. The alloy was analyzed spectroscopically and was found to have a purity in excess of 99.5% as seen in Table I. The pure nickel was obtained from Johnson, Mathey and Company and contained approximately 20 ppm of metallic impurities, iron and silicon being the major impurities.

The oxidation kinetics of Ni-2ThO₂ were studied over the temperature interval from 900° to 1400°C. The data concerning the rate of oxidation of the alloy were determined by the "weight-gain" method which consisted of oxidizing specimens in air for various periods of time and determining the weight gained after cooling to room temperature.

Prior to the oxidation tests all specimens were polished on 600 silicon carbide abrasive paper and then scrubbed in ethylene dichloride. Since the Ni-2ThO₂ was obtained in rod form, the test specimens were cylindrically shaped having a diameter of 0.500 in. and a thickness of about 0.125 in. The surface area of a typical specimen was approximately 3 cm².

Upon conclusion of the weight-gain measurements, the oxidized specimens were examined metallographically. A few marker experiments were also performed in order to determine the mechanism of oxidation. These studies consisted of depositing α -Al₂O₃ in the form of an ethyl alcohol slurry on the surface of the unoxidized specimen and then subsequently locating the position of the α -Al₂O₃ marker in the oxide after the specimen had been heat-treated. The position of the marker in the ox-

ide was ascertained through metallographic examination.

Possible interaction between NiO, formed during oxidation, and ThO₂ was investigated. Blended NiO-ThO₂ mixtures were pressed into pellets and fired at elevated temperatures. The fired specimens were subsequently examined by x-ray diffraction. Specimens of oxide from oxidized Ni-2ThO₂ were also examined by x-ray diffraction.

The composition of the oxide layer as a function of oxide thickness was qualitatively determined by x-ray fluorescence. These measurements consisted of examining the surface of an oxidized specimen by x-ray fluorescence and then repeating the examination after 0.001 in. had been removed from the oxide surface. This procedure was repeated until the oxide had been completely removed. The grinding operation was performed by using a surface grinder which was capable of removing as little as 0.0001 in. of oxide.

Results

Over the temperature interval 900°-1400°C the oxidation kinetics for Ni-2ThO₂ were found to obey the relationship

$$\Delta M/A = k^{0.50}t^{0.55}$$

where $\Delta M/A$ is the weight-increase per unit area, k is the rate constant for the reaction, and t is the time. These results, as seen in Fig. 1, show that the oxidation kinetics follow, at least to a close approximation, a parabolic rate law. This implies that a diffusion process is controlling the oxidation rate, as might be expected, since the oxide formed at elevated temperatures was in all cases tenaciously bonded to the base metal.

The variation of k with reciprocal temperature can be seen in Fig. 2. Since the kinetics were found to approximate the parabolic rate law, the parabolic rate constants obtained by Sartell (6) and by Gulbransen (2) for pure nickel have been included in Fig. 2 for comparison. The rate constant (k) for the oxidation of Ni-2ThO₂ obeys an Arrhenius relationship with an apparent activation energy of

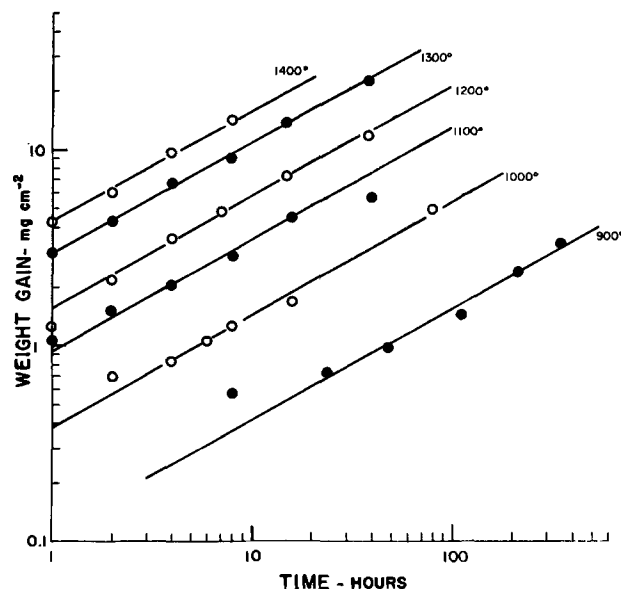


Fig. 1. Oxidation of Ni-2ThO₂ from 900°-1400°C

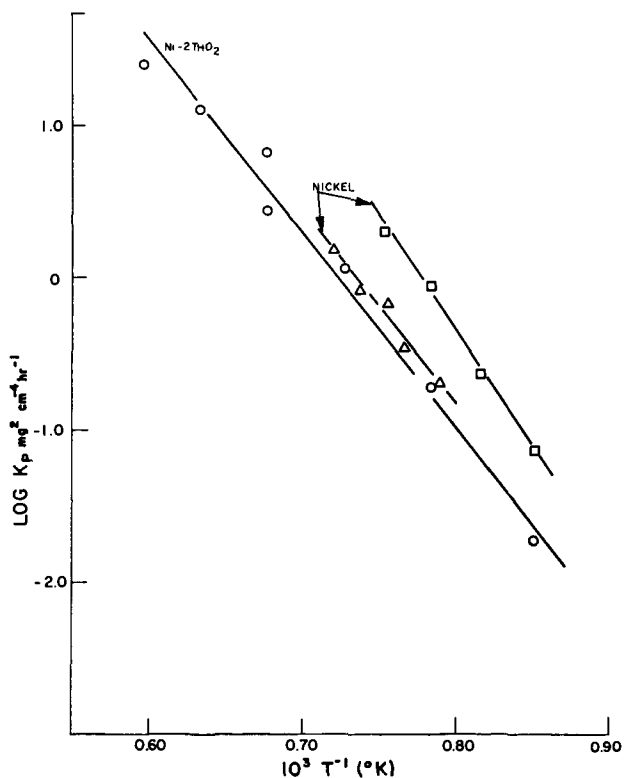


Fig. 2. Arrhenius plot for oxidation of Ni-2ThO₂. Δ , Sartell and Li (P_{O_2} -1 atm); \square , Gulbransen (P_{O_2} -7.6 mm); \circ , present data (air).

56.7 kcal/mole where the statistical probable error is ± 1.2 kcal. Comparison of the results obtained by Sartell on pure nickel with those obtained in this Laboratory for Ni-2ThO₂ indicate that the thoria has not significantly altered the oxidation kinetics. Oxidation experiments on pure nickel showed that the rate of oxidation of pure nickel did not vary appreciably from that of Ni-2ThO₂.

X-ray analysis of the oxide, mechanically removed, showed that it was composed of NiO and ThO₂. This oxide appeared to consist of two distinct layers in most cases. Based on results obtained by Kroger (7), both layers are probably NiO, the inner layer being less cation deficient than the outer layer. Synthetic mixtures of NiO-ThO₂ in molar ratios of 2, 1, and 0.5 were heated for 16 hr at 1400°C with no indication of interaction. On the basis of these results it can be concluded that no intermediate oxide will form, nor will there be any large solubility of one oxide in the other under the conditions of the present experiments.

Metallographic examination of oxidized Ni-2ThO₂ specimens showed that the oxide was composed of two layers. In specimens oxidized for long periods of time or at the more elevated temperatures, the two layers were of distinctly different color. The inner layer was green in color and was very porous. The other layer was blue-black in color and relatively dense, but not pore free. Birks and Rickert (8) observed that the outer blue-black oxide, formed on their nickel specimens, appears green after powdering. Furthermore, even in specimens on which the oxide was distinctly green in color, metallographic examination usually can distinguish the presence of two layers by their relative poros-

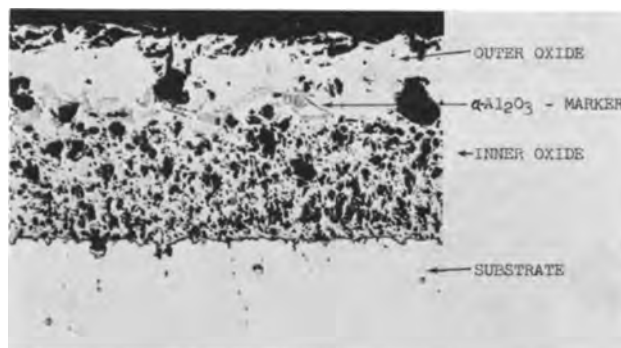


Fig. 3. Ni-2ThO₂ heated for 95 hr at 1200°C (2192°F). An inert marker of α -Al₂O₃ was placed on specimen prior to oxidation and is now located at inner-outer oxide boundary. Magnification 200X.

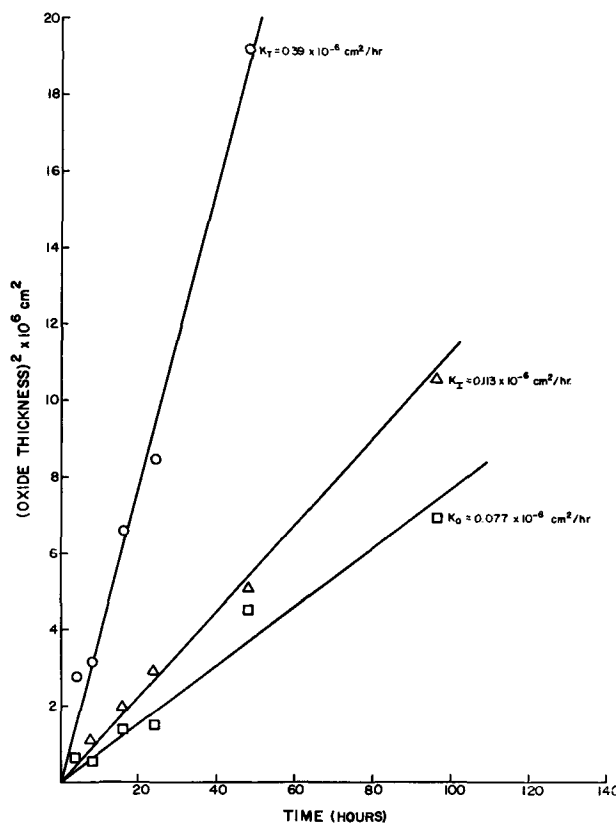


Fig. 4. Relationship of total, outer and inner oxide thickness with time at 1100°C.

ities. In the marker studies the α -Al₂O₃ marker was found at the boundary between the inner and outer oxide as seen in Fig. 3. This indicates that two diffusion processes are operative during oxidation, as previously postulated by a number of investigators (4-6), for the oxidation of nickel.

The thicknesses of the inner and outer oxide layers as well as the total oxide thickness were determined as a function of time for temperatures of 1100°, 1200°, and 1300°C. A plot of oxide thickness, squared, vs. time gives a linear relationship at each of the three temperatures. The data obtained at 1100°C is seen in Fig. 4. Additional data were obtained from single specimens at other temperatures between 1000° and 1400°C, assuming parabolic behavior. As for the weight gain data, the results obtained obey the Arrhenius relationship as seen in Fig. 5. The apparent activation energies for the growth rates of the inner and outer oxide layers

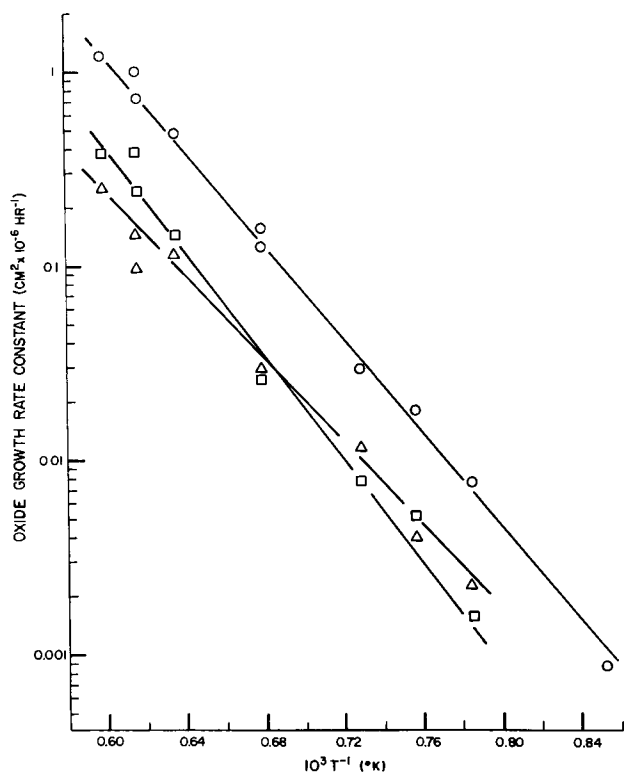


Fig. 5. Arrhenius plot for growth of oxide layers on Ni-2ThO₂. ○, Total oxide; △, inner oxide; □, outer oxide.

and the total oxide along with statistical probable errors are as follows: 48.5 kcal/mole \pm 0.9 kcal inner oxide zone, 59.5 kcal/mole \pm 0.9 kcal outer oxide zone, and 56.7 kcal/mole \pm 2.4 kcal total oxide.

The oxide thickness was usually uniform, but in some instances large clumps of oxide were formed. These clumps extended into the metal and also protruded from the surface. Usually stringers of oxide extended from the clumps deep into the metal substrate. Particles of oxide were also observed elsewhere in the base metal. These particles were sometimes observed along grain boundaries as seen in Fig. 6. The oxide particles could be agglomerated thoria, or NiO formed as a result of internal oxidation. Since pure nickel is susceptible to internal oxidation, the particles are believed to be NiO.

Oxidation studies on pure nickel gave results similar to those for Ni-2ThO₂ oxidized under sim-

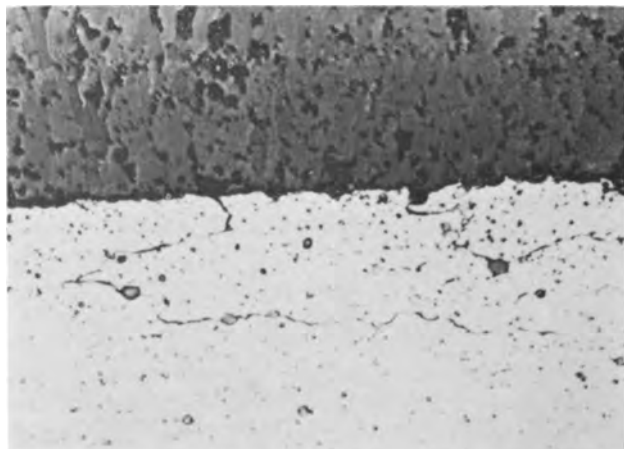


Fig. 6. Ni-2ThO₂ heated 103 hr at 1200°C (2192°F). Note oxide particles within the alloy and their location at grain boundaries. Etchant: 30 lactic acid, 30 HCl, 10 HNO₃. Magnification 500X.

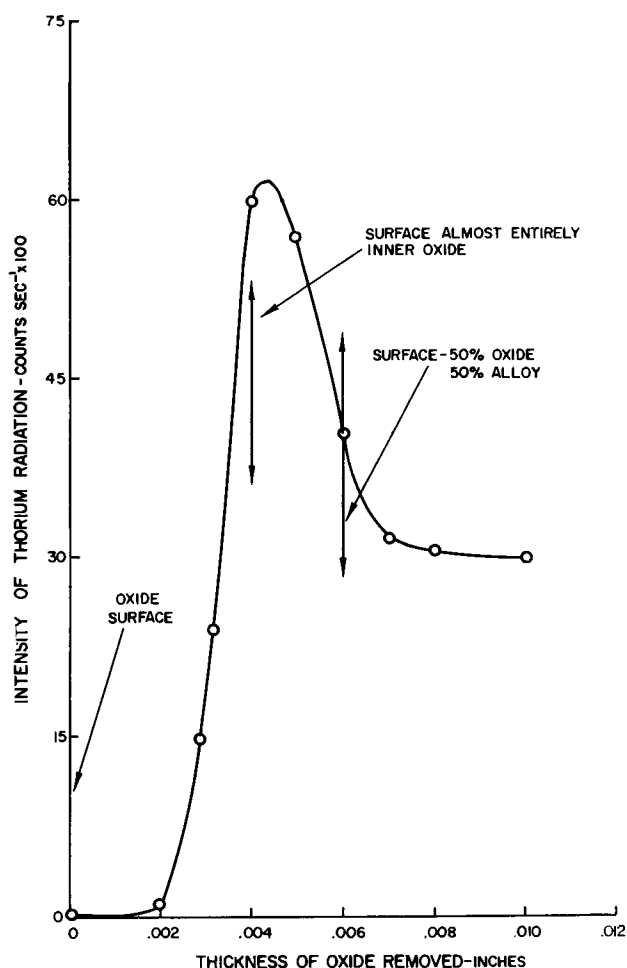


Fig. 7. Thorium content of oxide determined by x-ray fluorescence spectroscopy.

ilar conditions. However, the oxide did not appear to consist of two layers. Moreover a larger amount of internal oxide was observed in these specimens as compared to results obtained for Ni-2ThO₂. The oxide was found to form along grain boundaries and to have a continuity not observed in Ni-2ThO₂.

Results obtained from x-ray fluorescence measurements of oxidized specimens are shown in Fig. 7. It can be seen that the thorium intensity is negligible in the outer oxide and relatively large in the inner oxide. This suggests that the thoria particles are located in the inner oxide layer but not in the outer oxide.

Discussion and Conclusions

As mentioned previously, the presence of approximately parabolic oxidation kinetics indicates that the oxidation of Ni-2ThO₂ is controlled by a diffusion process. An activation energy of 56.7 kcal/mole (see Fig. 1) was observed for this process. The activation energy required for the diffusion of Ni⁺⁺ ions in NiO has been determined by numerous workers (4, 9, 10). Unfortunately, values have been obtained ranging from 42 to 119.5 kcal/mole. Mitoff (11) has surveyed the literature and concluded that the best value for the activation energy required for the diffusion of Ni⁺⁺ ions in NiO is 62 kcal/mole. However, more recent work by Moore (12) indicates that 45.6 kcal/mole may be a better value.

The position of the markers in the oxide indicates that the inner oxide grows inward, and the outer

oxide grows outward. It has also been shown that the thoria particles are found only in the inner oxide. This indicates that the thoria particles behave essentially as inert particles (*i.e.*, as markers). If the thoria particles are assumed to be inert, the formation of a two-layered oxide may be explained by any one of the four following mechanisms:

1. Initially the oxide forms by Ni⁺⁺ ions diffusing outward across the oxide layer. Only one layer of oxide forms. Eventually cracks begin to form in the oxide which permit oxygen to penetrate through the oxide and form an inner zone of oxide. This mechanism has been proposed by Gulbransen (2) to explain the formation of two-zoned oxides on nickel. It is considered unlikely in this case, since no cracking has been observed in oxides formed on Ni-2ThO₂. On the contrary, the oxides have been found to be extremely adherent and protective up to 1400°C. In addition, a change in oxidation rate might be expected following cracking of the oxide initially formed. This was not observed.

2. According to Birchenall (13), an inert particle, be it thoria or an Al₂O₃ marker, can act as a diffusion barrier. Therefore, if an oxide grows by cation diffusion, inert particles will tend to block the diffusion of the cations. As a result of impeding the flow of the cations, the inert particle will become situated on a protruding bit of metal. When this base is undercut by further oxidation, the inert particle will be contained in the oxide. Birchenall has used this mechanism to account for markers contained in sulfides formed on iron. This mechanism is not believed to be applicable to oxidation of Ni-2ThO₂ since it does not yield a distinct boundary between an inner and an outer oxide. Results obtained with Ni-2ThO₂ have shown a distinct boundary exists between the two oxide layers.

3. The inner and outer layers form simultaneously where the outer layer grows by cation diffusion while the inner layer forms as a result of anion diffusion. This mechanism has been proposed by Sartell and Li (6) to explain the formation of two-layered oxides on nickel. It is based on the premise that NiO can exist as an n or p type semiconductor.

4. The outer oxide layer forms by diffusion of Ni⁺⁺ ions outward while the inner layer is produced by diffusion of oxygen gas inward, the oxygen gas being formed by decomposition of NiO in the outer layer at the interface between the inner and outer layers of oxide. This mechanism may be described as follows; a thin layer of oxide forms by diffusion of Ni⁺⁺ ions outward. Insufficient plastic flow in the growing oxide layer together with outward diffusion of nickel leads to progressive loss of contact between the metal and the oxide layer. The outward diffusion of nickel ions is thus restricted and the chemical potential of nickel in the oxide layer is decreased while correspondingly the chemical potential of oxygen increases. Consequently, the NiO adjacent to these points of separation decomposes into Ni⁺⁺ ions and oxygen gas. The Ni⁺⁺ ions resulting from this decomposition process diffuse outward, along with Ni⁺⁺ ions from the metal substrate, to the oxide-gas interface where they take part in reactions leading to the extension of the oxide layer. At the same time

the oxygen gas diffuses to the metal surface where further reaction occurs. Continuation of this process results in the formation of a two-layered oxide. Birks and Rickert (8) have shown indirectly that decomposition of NiO can account for the formation of an inner porous layer on nickel.

The first two growth mechanisms do not appear to apply to the case of Ni-2ThO₂. Of the two remaining mechanisms, the one involving decomposition of the oxide appears more plausible since O'Keefe and Moore (14) have found that the diffusion coefficient of oxygen in NiO between 1000° and 1500°C and at an oxygen pressure of 50 mm Hg, is at least several orders of magnitude less than that of nickel.

The effect of the thoria particles on the oxidation properties of the alloy has not been determined. The present results indicate that thoria may not substantially alter the kinetics. It is possible that the thoria particles do nothing more than inhibit plastic flow in the oxide layer. Maak and Wagner (15) have found that the formation of beryllia during the oxidation of copper-beryllium alloys, inhibits plastic flow in the oxide layer whereby a two-layered oxide is formed.

Acknowledgments

The authors would like to extend their thanks to the people whose assistance proved very valuable during the course of the investigation. They are C. E. Londin, R. G. Babineau, W. P. Shirra, P. G. Sprang, J. C. Cannon, and C. V. Prue. We also wish to thank Professor J. B. Wagner for many helpful discussions. In addition, we wish to thank S. G. Berkley for suggesting the investigation and for obtaining material from Du Pont.

Manuscript received Mar. 8, 1963. This paper was presented at the New York Meeting, Sept. 29-Oct. 3, 1963.

Any discussion of this paper will appear in a Discussion Section to be published in the December 1964 JOURNAL.

REFERENCES

1. F. J. Anders, G. B. Alexander, and W. S. Wartel, *Metal Progress*, **82**, 88 (1962).
2. E. A. Gulbransen and K. F. Andrew, *This Journal*, **104**, 451 (1957).
3. W. J. Moore and M. T. Shim, *J. Chem. Phys.*, **26**, 802 (1957).
4. B. Ilschner and H. Pfeiffer, *Naturwissenschaften*, **40**, 603 (1953).
5. S. Mrowec and T. Werber, *This Journal*, **105**, 363 (1958).
6. J. A. Sartell and C. H. Li, *J. Inst. Metals*, **90**, 92 (1961-1962).
7. E. J. Verwey and F. A. Kroger, *Philips Tech. Rev.*, **13**, 90 (1951).
8. N. Birks and H. Rickert, *J. Inst. Metals*, **91**, 308 (1962-1963).
9. R. Lindner, "Some Problems of Solid State Chemistry," Proc. of the Tenth Solvay Conference, Brussels, p. 459 (1956).
10. R. Lindner and A. Akerstrien, *Disc., Faraday Soc.*, **23**, 133 (1957).
11. S. P. Mitoff, *J. Chem. Phys.*, **35**, 992 (1961).
12. J. Choi and W. J. Moore, *J. Phys. Chem.*, **66**, 1308 (1962).
13. R. A. Meussner and C. E. Birchenall, *Corrosion*, **13**, 677 (1957).
14. M. O'Keefe and W. J. Moore, *J. Phys. Chem.*, **65**, 1438 (1961).
15. F. Maak and C. Wagner, *Werkstoffe u. Korrosion*, **11**, 673 (1960).

High-Temperature Oxidation of Zirconium and Zircaloy-2 in Oxygen and Water Vapor

R. E. Westerman

Chemical Metallurgy Operation, Hanford Laboratories, General Electric Company, Richland, Washington

ABSTRACT

Zirconium and Zircaloy-2 were found to gain more weight in oxygen than in water vapor at low pressures. The pretransition oxidation kinetics of Zircaloy-2 are comparable with those of pure zirconium, both following a cubic rate law. The pretransition oxidation kinetics of Zircaloy-2 are sensitive to water vapor pressure in the range of 5-25 mm, but are not sensitive to oxygen pressure. The post-transition oxidation kinetics of Zircaloy-2 are notably dependent on the pressure of either gas, indicating a gaseous diffusion rate control. Zirconium exhibited no transition in rate from the cubic over the duration of the exposure. It is shown that the rate-controlling mechanism which results in the cubic rate law is not directly dependent on the total thickness of the oxide layer. Activation energies for the rate-controlling mechanism of the cubic rate law lie in the range 50-63 kcal/mole, indicating that similar mechanisms are operative, regardless of material or atmosphere.

The high-temperature oxidation kinetics of zirconium and zirconium alloys in oxygen and water vapor have been the subject of a number of investigations (1-10). The oxidation kinetics can be described by the equation $W^n = kt$, where W is the sample weight gain (or oxygen lost from the test atmosphere) per unit area, t is the time, and k the rate constant. The value of the superscript n will reflect the time dependence, for example, a value of 2 for a parabolic rate or 3 for a cubic rate. The rate constant is usually written $k = Ae^{-\Delta E^*/RT}$, so that the activation energy, ΔE^* , and the frequency factor, A , can be evaluated. Table I gives a summary of the investigations made to date of the high temperature oxidation kinetics of zirconium and zirconium alloys.

Past investigations have yielded inconsistent results. This is not surprising when one considers the different materials, oxidant purities, methods of specimen preparation, and methods of following the oxidation kinetics employed by the various investigators. For example, Stringer (11) shows that the annealing conditions prior to oxidation can influence the oxidation kinetics of titanium. It is likely that

this would also be the case in the oxidation of zirconium.

The majority of the investigators have found that zirconium oxidizes according to a cubic rate law, though Cubicciotti (2), Fassell (7), and Pemsler (9) have reported parabolic oxidation kinetics of zirconium at high temperature. The pressure of the oxygen atmosphere has been found to exert no significant influence, at least at pressures below 800 mm (2, 3).

The Zr-Sn alloys were found to undergo a transition from cubic (or parabolic) to linear kinetics, the time to transition being a function of temperature and tin content. Increasing the tin content decreased the time to transition (3, 5). Pure zirconium does not exhibit a transition in rate, even at long test times at high temperature (3). This is in contrast to results obtained on crystal-bar zirconium in 360°C water, where transition phenomena have been observed at comparatively low weight gains (12).

The present study was undertaken to investigate the following areas of high-temperature oxidation of zirconium and Zircaloy-2:

Table I. Summary of previous investigations

Reference	Material	Temperature range, °C	Oxidant	Rate law	Activation energy, kcal/mole	Method
(1)	Zr	575-950	O ₂ , 1 atm	Cubic	47.2 ± 1	Volumetric
(2)	Zr (high Hf)	600-900	O ₂ , 0.1-20 cm	Parabolic	32	Volumetric
(3)	Zr	400-900	O ₂ , 200 mm	Cubic	42.7 ± 0.7	Volumetric
(4)	Zr	300-600	H ₂ O, 33 mm	Cubic	29.7 ± 0.7	Gravimetric
(5)	Zr + 1.5% Sn	600-800	O ₂ , 1 atm	Cubic	38.4 ± 1.1	Volumetric
		825-900	O ₂ , 1 atm	Cubic	22.6 ± 1.4	Volumetric
	Zr + 2.5% Sn	550-900	O ₂ , 1 atm	Parabolic	32.4 ± 1	Volumetric
(6)	Zr (high Hf)	800	O ₂ , 1 atm	Cubic	—	Gravimetric
(7)	Zr	600-946	O ₂ , 1 atm	Parabolic	30.4	—
(8)	Zircaloy-2	300-850	O ₂ , 0.1 atm	Cubic or	28.6*	Gravimetric
	Zircaloy-3A			Parabolic		

* Evaluated using a parabolic curve fit.

1. Determination and comparison of the oxidation kinetics of zirconium and Zircaloy-2 in equal pressures of high-purity oxygen and water vapor in the temperature range 600°-850°C, using samples carefully pretreated to eliminate as many variables as possible;

2. Effect of oxidant pressure on the oxidation rate of Zircaloy-2 at high temperatures;

3. Post-transition oxidation behavior of Zircaloy-2 in both oxygen and water vapor;

4. Effect of hydrogen overpressure in water vapor on the oxidation and hydrogen pickup of Zircaloy-2 at high temperatures; and

5. Effect of oxygen solution in the metal on the oxidation kinetics.

Materials

The zirconium used in the tests consisted of iodide zirconium rolled into 30-mil strip. The impurity content of the material is given in Table II. The Zircaloy-2 was also used in the form of 30-mil strip. A representative analysis of the ingot is given in Table III.

Research Grade oxygen, supplied by the Matheson Company, was used in the tests requiring an oxygen atmosphere. Maximum and typical impurity limits for this grade of oxygen, as reported by Matheson, are listed in Table IV.

Water vapor atmospheres were obtained by allowing water vapor to equilibrate with distilled water held in a reservoir at a known temperature. The water was thoroughly outgassed by evacuation of the reservoir to prevent contamination of the water vapor by dissolved gases.

The hydrogen employed in the tests was of high purity, produced by the thermal decomposition of UH_3 .

Experimental

Coupons measuring $\frac{1}{2} \times 2$ in. were cut from the strip, degreased, and etched 2 mils/surface in a standard HF- HNO_3 bath. The coupons were then

Table II. Impurity content of zirconium

	ppm
Aluminum	45
Boron	<0.2
Carbon	50
Cobalt	<5
Cadmium	<0.3
Chromium	44
Copper	<25
Iron	225
Hydrogen	3.8
Hafnium	64
Magnesium	<10
Manganese	<10
Molybdenum	25
Nitrogen	19
Nickel	10
Oxygen	130
Lead	<5
Silicon	<40
Tin	<10
Titanium	<20
Tungsten	<25
Vanadium	<5
Zinc	<50

Table III. Composition of Zircaloy-2, lot 1021

	wt %
Tin	1.34
Iron	0.130
Chromium	0.166
Nickel	0.045
Nitrogen	0.0041
Copper	0.0016
Carbon	0.042
Tungsten	0.0018
Aluminum	0.0040
Boron	<0.00005
Cadmium	<0.00005
Cobalt	<0.0005
Hafnium	0.009
Magnesium	<0.001
Manganese	<0.001
Molybdenum	<0.001
Lead	0.006
Silicon	0.003
Titanium	0.001
Vanadium	<0.001

Table IV. Impurity limits on research grade oxygen

Possible impurities	Maximum limits, mole %	Typical analysis, mole %
Carbon dioxide	0.1	0.005
Carbon monoxide	0.01	0.000
Argon	0.01	0.000
Nitrogen	0.05	0.000
Hydrogen	0.01	0.002
Water	0.0002	0.00002

annealed for $\frac{1}{2}$ hr in a vacuum of $<10^{-5}$ mm Hg. The annealing temperature was 900°C for Zircaloy-2 and 840°C for the zirconium. These annealing temperatures were chosen to stabilize the internal structure of the metal at a high temperature in the all-alpha region. All oxidation tests were carried out at temperatures less than the annealing temperature. The sample surfaces after annealing were bright and shiny and were given no further treatment prior to oxidation. The surface roughness factor was assumed to be unity.

Oxidation kinetics of a sample were followed gravimetrically by means of an Ainsworth semi-micro recording balance (model RV-AU-1) which is completely enclosed in the vacuum system. The balance is capable of weighing to $\pm 30 \mu\text{g}$, and its accuracy was confirmed by an independent check against a microbalance of $\pm 20 \mu\text{g}$ precision. A schematic of the balance and associated vacuum system is shown in Fig. 1. Gas turbulence in the balance chamber was found to exert a negligible influence on the recorded weight.

The furnace was controlled to $\pm 5^\circ\text{C}$ with a Brown Pyr-O-Vane controller. The thermocouple-recorder system was checked against the melting points of pure zinc (419°C) and aluminum (660°C) to insure its reliability.

The desired oxidant pressure in the furnace chamber was obtained, in the case of oxygen, through knowledge of the volumes of the reservoir and furnace-balance chamber and application of the $P_1V_1 = P_2V_2$ relationship. The oxygen pressure de-

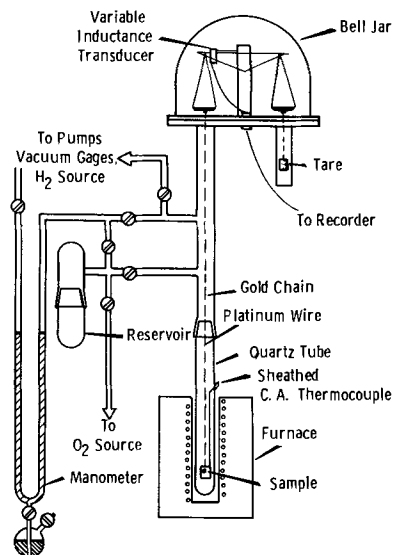


Fig. 1. Schematic diagram of balance and associated vacuum equipment.

creases as the reaction consumes oxygen; however, the pressure drop is only 0.7 mm for a 100 mg/dm² weight gain of a standard coupon.

Three pressures of water vapor were used in the investigation: 5 ± 1 mm, 10 ± 1 mm, and 25 ± 1 mm. The pressure of 5 ± 1 mm was obtained by externally cooling the reservoir to $\sim 0^\circ\text{C}$ with ice. The pressure of 10 ± 1 mm was obtained from room temperature water saturated with K_2CO_3 . The pressure of 25 ± 1 mm was obtained by allowing the reservoir to attain room temperature.

The sample to be oxidized was brought to temperature and held *in vacuo* for 1½ hr before admission of the oxidant. At "zero time" the oxidant was admitted to the furnace chamber, and the weight gain continuously recorded.

Several Zircaloy-2 oxidation tests were run using commercial purity oxygen as the oxidant, and the samples were not preannealed or preheated before admission of the oxygen. Long-term weight gains obtained in this manner were much higher than those reported in the present investigation, for example, 260 mg/dm² at 200 min, 700°C vs. 130 mg/dm² obtained for the same time and temperature in the present study. These results illustrate the importance of the test procedure, and the manner in which it may influence the final results.

Results

Oxidation of Zircaloy-2 in oxygen and water vapor.—The oxidation kinetics of Zircaloy-2 in oxygen and water vapor are shown in Fig. 2 and 3, respectively. The oxidation curves have been transcribed from the balance recorder chart and represent a continuous measurement of the sample weight gain. The oxidation kinetics show a marked similarity, the major difference being a somewhat more rapid oxidation in the pre-transition region in the oxygen atmosphere. The slopes of the curves in the pre-transition region in both atmospheres approximate the value 0.33, indicating adherence to a cubic rate law. In both atmospheres, the minimum time to

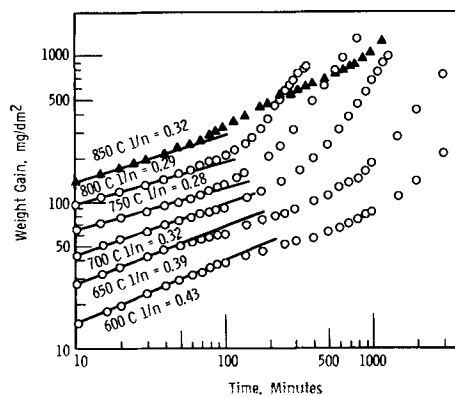


Fig. 2. Oxidation of Zircaloy-2 in high-purity oxygen at 25 mm pressure.

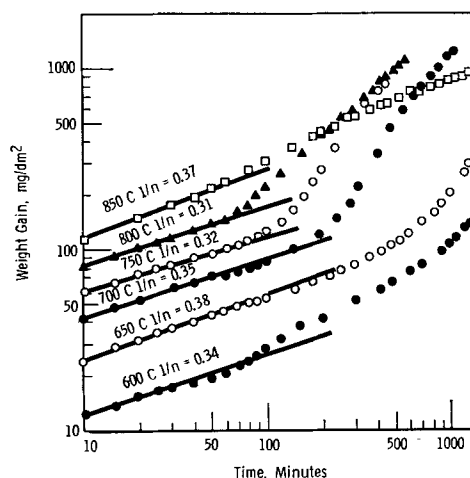


Fig. 3. Oxidation of Zircaloy-2 in water vapor at 25 mm pressure

transition occurs in the range 750°–800°C, in good agreement with previous investigators (5, 8).

In the temperature range 600°–800°C it was found that a final linear rate is attained at a weight gain of about 300 mg/dm². The post-transition weight gains prior to this do not adhere to a linear rate law, but appear to reflect the transition from the over-all cubic to the over-all linear rate. This is sensitive to the specimen geometry, as "transition" first occurs at corners and edges of the specimen. A Zircaloy-2 coupon oxidized at 600°C for 50 hr is shown in Fig. 4. The oxidation kinetics have not yet attained the "final" linear rate, and the geometrical considerations are obvious.

The uniformity of the oxide film in the pre-transition region and in the post-transition region was not determined. In each case, the film was assumed to be of uniform thickness. Only in the region of gradation from the cubic to the linear kinetics is the film actually known to be nonuniform.

Oxidation of Zircaloy-2: pressure dependence.—Increasing the pressure of water vapor in the range 5–25 mm increased both the pre-transition and post-transition oxidation rate of Zircaloy-2 (Fig. 5). The effect on the cubic rate constant is shown in Fig. 6. The limited data preclude a detailed analysis of the reasons for a pressure dependency. The data are presented only for qualitative significance.

Varying the pressure of oxygen over the range 10–100 mm had no effect on the pre-transition oxi-



Fig. 4. Specimen of Zircaloy-2 oxidized for 50 hr at 600°C in 25 mm oxygen. Note the effect of specimen geometry on the oxidation rate. White areas have undergone transition. Magnification approximately 1¼X.

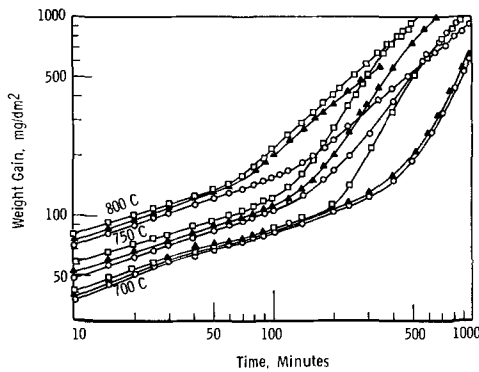


Fig. 5. Pressure dependence of Zircaloy-2 oxidation in water vapor: □, 25 mm pressure; ▲, 10 mm pressure; ○, 5 mm pressure.

oxidation of Zircaloy-2 at 700°C (Fig. 7). The post-transition kinetics showed an increasing oxidation rate with increasing pressure. Insensitivity of pre-transition oxidation to oxygen pressure is in agreement with other investigations (3).

Although the post-transition oxidation rate of Zircaloy-2 is plainly pressure dependent in both water vapor and O₂ atmospheres, no simple mathematical relationship between oxidant pressure and oxidation rate exists. The post-transition oxidation kinetics do indicate that the rate-limiting factor is gaseous diffusion of the oxidant through imperfections in the oxide film.

Oxidation of high-purity zirconium.—The oxidation behavior of high-purity zirconium was investigated in water vapor and oxygen at 25 mm pressure (Fig. 8). No transition in rate occurred, even at long times. Both atmospheres give rise to kinetics which are best fitted by a cubic rate law. As in the case of pre-transition oxidation of Zircaloy-2, the oxidation rates are more rapid in the oxygen atmosphere. The oxide films remained dark and adherent regardless of the temperature or length of the run.

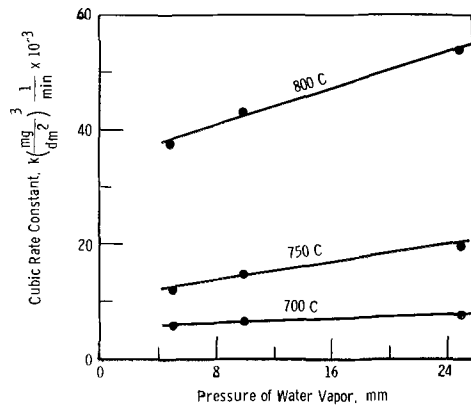


Fig. 6. Oxidation of Zircaloy-2 in water vapor. Variation of cubic rate constant with pressure.

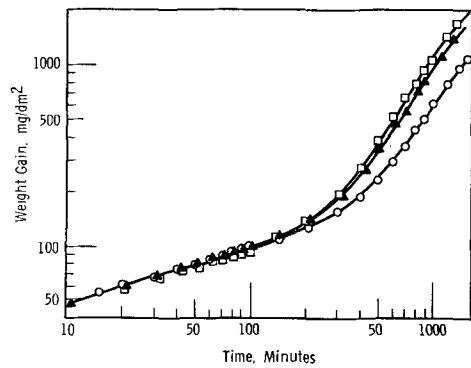


Fig. 7. Oxidation of Zircaloy-2 in high-purity oxygen. Pressure dependence: □, 100 mm pressure; ▲, 50 mm pressure; ○, 10 mm pressure.

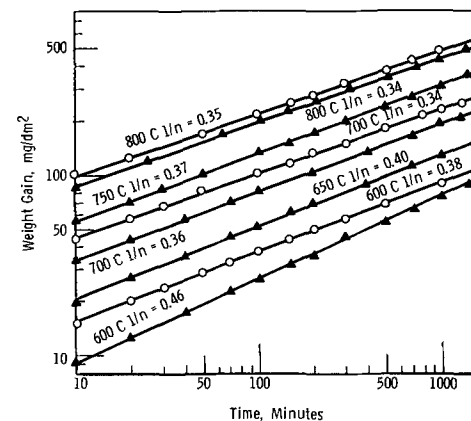


Fig. 8. Oxidation of high-purity zirconium in oxygen and water vapor: ○, O₂, 25 mm pressure; ▲, H₂O vapor, 25 mm pressure.

Effect of hydrogen overpressure on oxidation of Zircaloy-2 in water vapor.—The oxidation kinetics of Zircaloy-2 were determined at 750°C in 10 mm water vapor with zero hydrogen overpressure and 50 mm hydrogen overpressure. Results are shown in Fig. 9. The addition of 50 mm H₂ overpressure causes a rapid increase in the immediate post-transition weight gain, caused by hydrogen pickup, followed by a slowing-down in the final rate. The hydrogen pressure in the system drops as hydrogen is absorbed by the metal, and the amount absorbed can be calculated. Only a small fraction of the hydrogen initially present in the system was absorbed. The final low rate is attributed to the hydrogen acting as a diffusion barrier to the water vapor, causing a gas-

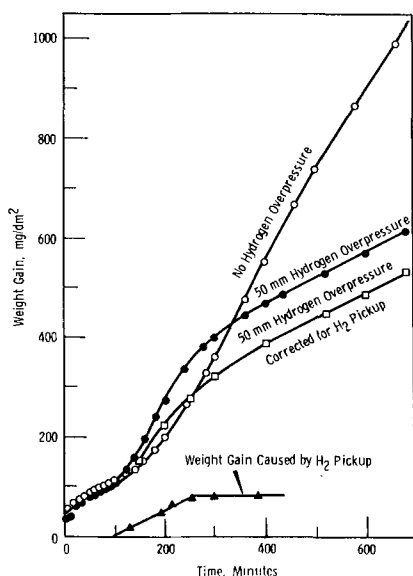


Fig. 9. Oxidation of Zircaloy-2 at 750°C in water vapor at 10 mm

phase diffusion control of the oxidation kinetics. Addition of a 50 mm overpressure of high-purity argon will result in a similar decrease in oxidation rate. It can be shown that the slowness of water vapor diffusion in the tubulation of the vacuum system is exerting the rate-limiting effect.

The transition apparently constitutes a period wherein the metal not only loses its resistance to oxidation but to hydrogen pickup as well, even though water vapor is present in large quantities to inhibit the hydrogen pickup.

Activation energy.—The rate constant may be written

$$k = Ae^{-\Delta E^*/RT}$$

where A is a constant, R a gas constant, T absolute temperature, and ΔE^* activation energy.

A plot of $\log k$ vs. the reciprocal absolute temperature will yield a straight line if the same rate-control mechanism is operative over the temperature range, for a given set of reactants. The slope of the line will yield ΔE^* , the activation energy. The plot of $\log k$ vs. $1/T$ is shown in Fig. 10. The activa-

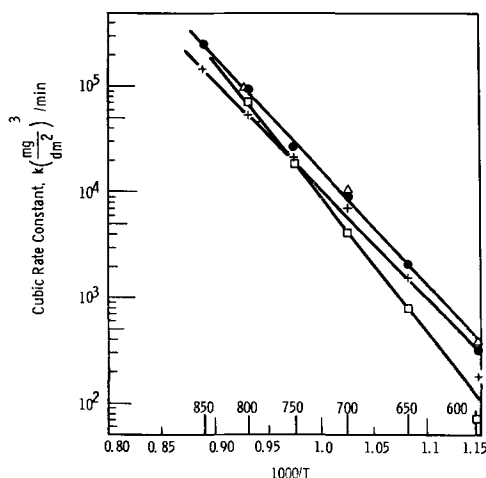


Fig. 10. Rate constant as function of reciprocal temperature: ●, Zircaloy-2 in O₂; △, zirconium in O₂; □, zirconium in H₂O; +, Zircaloy-2 in H₂O.

Table V. Activation energies for zirconium and Zircaloy-2 oxidation in the temperature range 600°-850°C

System	Activation energy, kcal/mole
Zircaloy-2-O ₂	51.3 ± 1.3
Zr-O ₂	51.4 ± 2.5
Zr-H ₂ O	63.4 ± 2.0
Zircaloy-2-H ₂ O	50.7 ± 2.1

tion energies obtained in the present investigation are given in Table V. All rate constants were determined using a cubic rate law fit to the weight gain data. It should be noted that the Arrhenius plot is made on the basis of the rate constant for total weight gain, not on the basis of the rate constant for film growth alone, i.e., the weight of oxygen dissolved in the metal is included.

The similarity of the activation energies obtained for the four systems investigated implies that a similar rate-control mechanism is operative in each case. The activation energies obtained are higher than those obtained by other investigators; only Belle and Mallett (1), Porte *et al.* (3), and Kofstad (21) report comparable activation energies.

Oxide solution during oxidation.—The relative importance of oxygen solution in the metal at various oxidation temperatures was determined so that its over-all effect on the weight gain during oxidation could be evaluated.

The rigorous mathematical determination of the oxygen dissolved in the metal is a complex problem because of the complications introduced by the movement of the metal-oxide interface. However, certain assumptions can be made which simplify the problem and allow a realistic appraisal of the amount of oxygen dissolved as a function of time and temperature.

Consider a zirconium sheet of reasonable thickness held at a constant test temperature. Allow one surface of the sheet to be oxidized in an oxidizing atmosphere of such low pressure that only an infinitesimally thin oxide film is ever allowed to develop. This situation is represented in Fig. 11, where the area under the curve represents the total amount of oxygen diffusing into the metal in a given time. The amount of oxygen which dissolves in the metal under these conditions is the maximum amount which can dissolve under conditions which favor the oxidation of the metal, and the amount may be calculated using the relation given by Crank (13)

$$M_t = 2C_s \left(\frac{Dt}{\pi} \right)^{1/2} \quad [1]$$

where M_t is the total amount of oxygen dissolved

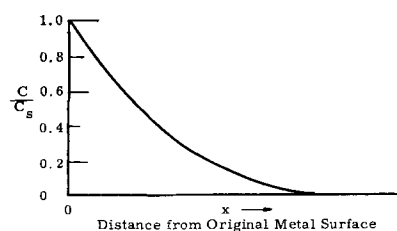


Fig. 11. Oxygen concentration gradient, no oxide film

per unit area in time t , C_s is the terminal solubility of oxygen in zirconium, and D is the diffusivity of oxygen in zirconium at the test temperature. The value used for C_s was 0.45 mg/cm^2 , and the diffusivity was taken as $D = 5.2 \exp(-50,800/RT)$ (14). The diffusivity was assumed to be independent of concentration.

The results of Eq. [1] are strictly valid only if the zirconium medium is semi-infinite and if the initial concentration of oxygen in the zirconium is zero. The 30-mil coupons employed in the test are excellent approximations to semi-infinite media for the times and temperatures employed, and their initial oxygen content is sufficiently low to satisfy the boundary conditions.

The concentration gradient can also be plotted using the same boundary conditions. The most convenient method is use of the tabular data presented by Darken and Gurry (15). The concentration ratio C/C_s is plotted in Fig. 11 as a function of distance from the original metal surface. Here C_s is the terminal solubility of oxygen in zirconium and C is the local concentration. At the metal surface $C = C_s$ and the ratio is equal to 1.

The area under the curve in Fig. 11 represents the maximum amount of oxygen which can be dissolved in the given time because no oxide layer has been allowed to form and consume oxygen-rich metal through inward displacement of the oxide-metal interface.

The minimum amount of oxygen which can dissolve in the metal in the same test time is that which has migrated into the metal beyond the furthest possible inward displacement of the oxide-metal interface. It is estimated in the following manner:

1. The total experimental weight gain is assumed due to formation of ZrO_2 only.

2. The thickness of this layer is calculated.

3. This thickness is superimposed on a plot of the diffusion gradient which would exist if no oxide layer formed (Fig. 11); the resultant plot is shown in Fig. 12. Because of the density difference between zirconium and ZrO_2 , the oxide-gas interface will be to the left of the reference zero of Fig. 12, which represents the original metal surface. The effect of dissolved oxygen on the density of the metal is neglected. Area A, Fig. 12, is a portion of the metal which could dissolve oxygen if no oxide layer has been consumed. Area B represents oxygen which has migrated into the metal beyond the furthest possible inward displacement of the oxide-metal interface and represents, to a first approximation, the minimum dissolved oxygen.

4. The oxygen represented by area B is converted to an equivalent thickness of ZrO_2 and subtracted

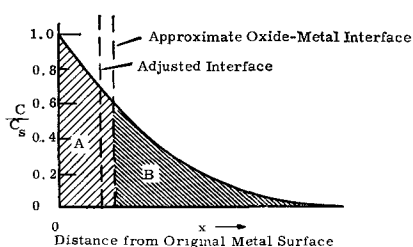


Fig. 12. Hypothetical positions of oxide-metal interface

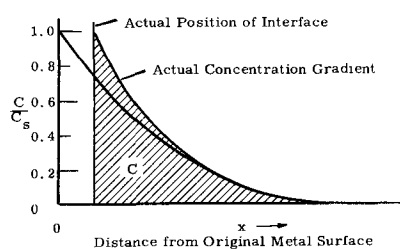


Fig. 13. Actual concentration gradient and interface position

from the original ZrO_2 layer, as it could not have formed ZrO_2 . An adjusted interface is obtained (Fig. 12), which leads to a more accurate determination of the minimum dissolved oxygen, B' . That oxygen represented by the area under the curve to the right of the adjusted interface (Fig. 12) is B' . Repeated approximations are of no value.

5. The minimum dissolved oxygen, B' , is converted to weight of oxygen.

The value of $A + B$ (equal to M_t , the maximum of oxygen which could have dissolved) and B' , the corrected minimum amount of oxygen which could have dissolved, is then simply averaged arithmetically to yield the approximate amount of oxygen dissolved at any time and temperature. Area C in Fig. 13 shows (schematically) the oxygen dissolved in the metal under actual oxidation conditions and represents the quantity being approximated. The position of the actual interface will lie somewhere between the "adjusted interface" of Fig. 12 and the original surface of the metal.

Only M_t and the concentration gradient were evaluated numerically. Values of A , B , and B' were obtained for various times and temperatures by graphical methods. Results of the calculations are shown in Table VI.

The data in Table VI show that the dissolved oxygen becomes a more important contribution to the total weight as the temperature is increased and with increasing time at temperature. Results shown in Table VI are in good agreement with published experimental data (10).

Results given in Table VI are shown graphically in Fig. 14. Curve A represents the experimental weight gain of high-purity zirconium in oxygen at 800°C and 25 mm pressure, and the curve demonstrates close adherence to the cubic rate law. Curve B represents the weight gain of the oxide film alone, that is, Curve A minus the weight of oxygen dissolved in the metal. Note that Curve B no longer adheres to the cubic rate law. The experimental weight gain curves at 700° and 600°C still approx-

Table VI. Oxygen dissolved in zirconium during oxidation

Temperature, $^\circ\text{C}$	Time, min	Maximum O_2 dissolved M_t , mg/dm^2	Minimum O_2 dissolved B' , mg/dm^2	Average, mg/dm^2	% of Total Weight gain*
800	1000	187	124	156	33
800	500	132	90	111	30
800	100	59	29	44	20
700	1000	58	27	43	21
600	1000	12	1.2	6.6	7

* Referred to high-purity zirconium in O_2 , Fig. 8.

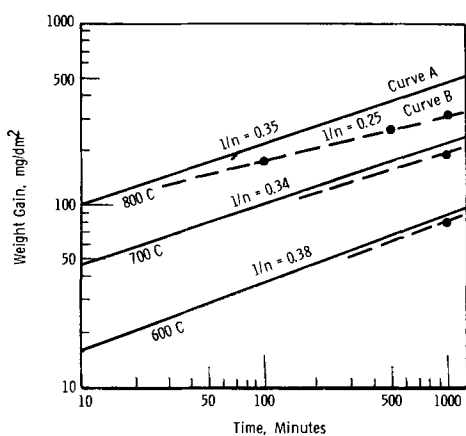


Fig. 14. Oxidation of zirconium in oxygen; total weight gain and weight of oxide film compared: —, total weight gain (experimental), film + dissolved oxygen; — —, weight gain, oxide film only.

imate the cubic rate law, since the amount of oxygen dissolved in the metal at these lower temperatures is less important. From the foregoing observations an interesting conclusion may be drawn: although the oxidation rate falls off with increasing oxide thickness, the rate-determining mechanism in the high-temperature oxidation of zirconium bears no simple mathematical relationship to the total oxide layer thickness.

Porte *et al.* (3) suggest that the cubic rate equation might arise from the simultaneous kinetics of oxide film formation and solution in the metal. However, the present study shows that the cubic law is followed not because of solution effects, but in spite of them. These results are in agreement with those of Sense (16), who has recently utilized approximate solutions to the diffusion equations to conclude, from a mathematical analysis, that the high solubility of oxygen in zirconium is not sufficient to account for a cubic rate law, if the diffusivity of oxygen in the zirconium is independent of concentration.

Conclusions

1. Zirconium and Zircaloy-2 (pre-transition) oxidize in oxygen and water vapor at comparable rates according to the cubic rate law. Zirconium does not exhibit a transition in oxidation kinetics, regardless of temperature or environment in tests of 25 hr duration. A transition is observed for Zircaloy-2 in both oxygen and water vapor, the transition occurring at equivalent times in either atmosphere. Minimum time to transition occurs between 750° and 800°C.

2. Zirconium and Zircaloy-2 exhibit greater oxidation rates in oxygen at 25 mm than in water vapor at the same pressure.

3. The pre-transition oxidation kinetics of Zircaloy-2 are sensitive to water vapor pressure (in the range 5-25 mm), but insensitive to oxygen pressure (in the range 10-100 mm). The oxidation rate at 10 mm oxygen pressure is greater than at 25 mm water vapor pressure.

4. Zircaloy-2 post-transition oxidation kinetics are notably sensitive to the pressure of either oxy-

gen or water vapor, indicating that the oxidation rate is controlled by gaseous diffusion of the oxidant through pores or other defects in the oxide film.

5. A hydrogen overpressure of 50 mm with a water vapor pressure of 10 mm at 750°C is found to result in a rapid hydrogen pickup by the Zircaloy-2 sample at and following transition, indicating access of the atmosphere to the metal surface at transition.

6. Weight gain has a cubic dependence on time in spite of the effects of oxygen solution in the metal, *i.e.*, the film thickness bears no direct relation to the mathematical statement of the rate law. If the film is uniform in thickness and of reasonably uniform structure and composition, there must exist a rate-determining entity which imposes a cubic dependence on time without a direct mathematical dependence on either film thickness or quantity of oxygen dissolved. This conclusion is justification of the Arrhenius plot (Fig. 10), as this rate-determining entity is assumed to limit the total oxygen weight gain, not just that relegated to either the film or the metal (in solution), and it is assumed to impose a cubic time dependence on the total oxygen weight gain.

7. Activation energies for the cubic oxidation kinetics were found to lie in the range 51-63 kcal/mole for the four systems investigated. The similarity of these activation energies implies a similar rate-control mechanism is operative in all cases. As the OH^- ion does not exist in the atmospheres of pure oxygen, the diffusion of $\text{O}^=$ ions would be the rate-determining step in all cases if diffusion of the oxidant through the oxide film exerted the rate control. The activation energies obtained in the present work are considerably higher than those reported for diffusion of oxygen in ZrO_2 : 33,400 cal/mole in single crystals (18) and 29,300 cal/mole in polycrystalline films (10). It is interesting to note the similarity of the oxidation activation energies obtained to those of diffusion of oxygen in the bulk α -phase zirconium: 50,800 cal/mole (14), and 59,700 cal/mole (10). Because gross solution of oxygen in the metal is important (from a weight standpoint) only at high temperatures ($\sim 800^\circ\text{C}$), and then only accounts for a small portion of the total weight gain ($\sim 30\%$ at 1000 min), the high energy of activation cannot be ascribed to large-scale solutions of oxygen and the diffusion control of same. However, it is possible that solution (and diffusion) of the oxygen in the metal might in some obscure way influence the structure of the film or the metal substrate and thereby bring about a rate-control mechanism.

Acknowledgments

The author would like to acknowledge the assistance of W. C. Craven, who helped with the experimental work. Thanks are due A. B. Johnson and R. L. Dillon for contributing many helpful discussions. Work was performed under Contract No. AT(45-1)-1350 between the Atomic Energy Commission and General Electric Company.

Manuscript received Oct. 30, 1962; revised manuscript received July 22, 1963.

Any discussion of this paper will appear in a Discussion Section to be published in the December 1964 JOURNAL.

REFERENCES

1. J. Belle and M. W. Mallett, *This Journal*, **101**, 339 (1954).
2. D. Cubicciotti, *J. Am. Chem. Soc.*, **72**, 4138 (1950).
3. H. A. Porte, J. G. Schnizlein, R. C. Vogel, and D. F. Fischer, *This Journal*, **107**, 506 (1960).
4. M. W. Mallett, W. M. Albrecht, and R. E. Bennett, *ibid.*, **104**, 349 (1957).
5. M. W. Mallett and W. M. Albrecht, *ibid.*, **102**, 407 (1955).
6. K. Østhagen and P. Kofstad, *ibid.*, **109**, 204 (1962).
7. W. M. Fassell, *Progress Report Number III on the High Temperature Oxidation of Metals for June 1 to September 26, 1952*, NP-4246. 1952.
8. E. A. Gulbransen and K. F. Andrew, *Trans. AIME*, **212**, 281 (1958).
9. J. P. Pemsler, Fundamental and Applied Research and Development in Metallurgy, Research on the Mechanism of Zirconium Alloy Corrosion in High Temperature Steam, NMI-1251, October, 1961.
10. J. Debuigne and P. Lehr, "Corrosion Seche du Zirconium non Allie," *Conference sur la Corrosion des Materiaux pour Reacteurs*, Salzburg, June 4-9, 1962, CN-13/45.
11. J. Stringer, *Acta Met.*, **8**, 758 (1960).
12. B. Lustman and F. Kerze, Jr., "The Metallurgy of Zirconium," p. 611, McGraw-Hill Book Co., New York (1955).
13. J. Crank, "The Mathematics of Diffusion," p. 31, Clarendon Press, Oxford (1956).
14. J. P. Pemsler, The Diffusion of Oxygen in Zirconium and Its Relation to Oxidation and Corrosion, NMI-1177 (1957).
15. L. S. Darken and R. W. Gurry, "Physical Chemistry of Metals," p. 444. McGraw-Hill Book Co., New York (1953).
16. K. A. Sense, *This Journal*, **109**, 377 (1962).
17. D. J. Garibotti, H. M. Green, and W. M. Baldwin, Jr., First Technical Progress Report, Case Institute of Technology, USAEC Contract No. AT(11-1)-258, Cleveland, Ohio. March, 1955.
18. D. L. Douglass, "Corrosion Mechanism of Columbium, Zirconium, and Their Alloys, I. Diffusion of Oxygen in Columbium Pentoxide and Zirconium Dioxide," Conference on the Corrosion of Reactor Materials, Salzburg, Austria, CN-13/45, (1962).
19. E. A. Gulbransen and K. F. Andrew, *J. Metals*, **9**, 394 (1957).
20. R. G. Charles, S. Barnartt, and E. A. Gulbransen, *Trans. AIME*, **212**, 101 (1958).
21. P. Kofstad, *Acta. Chem. Scand.*, **12**, 701 (1958).

The Electrochemistry of the Dissolution of Zirconium in Aqueous Solutions of Hydrofluoric Acid

Robert E. Meyer

Chemistry Division, Oak Ridge National Laboratory,¹ Oak Ridge, Tennessee

ABSTRACT

The dissolution of crystal-bar zirconium in aqueous solutions containing HF and H₂SO₄ was investigated by means of electrochemical techniques. Capacities were determined by measuring the initial slope of the voltage-time curve resulting from the application of galvanostatic pulses. Steady-state polarization curves were obtained potentiostatically whenever possible, and galvanostatic polarization curves were determined by a pulse technique. The data are explained by assuming that the dissolution reaction involves the continuous formation and dissolution of a film on the surface of the metal. The conventional anodizing equation describes the formation of the film and the dissolution reaction is controlled by the rate of mass transfer of undissociated HF to the surface of the film.

Of the common aqueous dissolution media, only solutions of HF attack zirconium metal with any degree of rapidity. This reaction has therefore been widely utilized in the processing of zirconium-clad fuel elements for nuclear reactors. Although a large number of investigations of the dissolution of zirconium have been reported, most of them have been carried out from the point of view of chemical processing. Some work on the mechanism of this reaction has been reported, however. Smith and Hill (1) investigated the dissolution of Zr in various aqueous solutions containing HF by measuring the build-up of Zr⁹⁵ in a solution that was circulated past a radioactive Zr electrode. They reported that the rate of dissolution is controlled solely by the rate of mass transfer of undissociated HF to the electrode. Their results also showed that the reac-

tion proceeds with a rate of hydrogen evolution exactly equivalent to the rate of dissolution of the metal.

Dissolution rates in mixtures of HNO₃ and HF were determined by Vander Wall and Whitener (2) by use of a tracer method similar to that of Smith and Hill. According to their results, the reaction is first order with respect to HF and has an activation energy of 6.4 kcal/mole.

Measurements have also been reported by Straumanis, James, and Neiman (3) in HF solutions ranging from 0.01 to 0.5N. They measured rates by determining the rate of evolution of hydrogen with a gas buret. The formation of a black film on the surface of the metal in aqueous solutions containing only HF was reported, and this film was identified by x-ray diffraction as being a zirconium hydride. In solutions containing enough HNO₃, only bright surfaces were observed. They also in-

¹ Operated by the Union Carbide Corporation for the U.S. Atomic Energy Commission.

vestigated the effect of additions of soluble fluorides and found that the electrodes passivated if sufficient fluoride ion was present. The passivating films were identified as fluozirconates, e.g., K_3ZrF_7 . These measurements were extended to solutions of HF above 0.5N by James, Custead, and Straumanis (4), who reported that the reactions are similar to those occurring at the lower concentrations. They suggest that under certain conditions an oxide film may be present on the zirconium, and that in some solutions this film dissolves off with subsequent formation of an hydride film.

Because of the importance of this reaction, it seemed desirable to confirm the above results and to determine what additional information could be obtained by using electrochemical techniques. Preliminary experiments with a number of systems showed that steady-state galvanostatic experiments did not yield easily interpretable results because of drifting, but that potentiostatic and pulse methods could be used with the proper choice of solutions.

Experimental

The experiments required that the cell be constructed of materials that were inert to HF solutions and that would not contaminate the solution. Further, in some experiments, it was desirable that the solution could be changed rapidly without exposing the electrodes to the atmosphere. These requirements were met by two different cells in which only Teflon, platinum, and the electrode were allowed to make contact with the solution. The apparatus used for changing solutions contained six Teflon cups of about 30 ml capacity which were enclosed in a large cylindrical glass container. They were so mounted that any of the cups could be lowered from around the electrode assembly and replaced by any other cup while any desired atmosphere was maintained in the glass container. This cell was used mainly when it was desired to compare the behavior of an electrode in different solutions while maintaining a helium or hydrogen atmosphere about the solution. The other cell was machined from 3-in. diameter Teflon rod, used water-sealed Teflon to Teflon standard taper joints, and had a capacity of 150 ml. Connections to the reference compartment and gas connections were made using Teflon "spaghetti" tubing of various diameters. This tubing was led into the cell by forcing it through holes of slightly smaller diameter drilled either into the cell or into standard taper fittings which were placed on the cell. Such seals, especially when water-sealed, proved very satisfactory.

The zirconium electrodes were cylinders about 1 cm long machined from crystal bar rod either $\frac{1}{8}$ or $\frac{1}{4}$ in. in diameter. They were mounted on the end of a Teflon rod so that one end of the cylindrical electrode was masked from the solution. Electrical contact was made by a stainless steel rod which passed through the axis of the rod and was threaded into the masked end of the electrode. Polarizing currents were passed through a platinum gauze electrode about 1 in. in diameter which

was placed around the zirconium electrode. A 20 gauge platinum wire probe placed a few millimeters from the zirconium electrode served as a reference probe for transient and capacity measurements. For long term measurements, a saturated calomel electrode in a separate compartment was bridged into the cell with the Teflon "spaghetti" tubing. Normally, the bridge and the container in which the reference electrode was immersed were filled with a solution identical to that in use but which did not contain HF. In all experiments, the cells were maintained at 25°C, the 150 ml cell to within $\pm 0.1^\circ$ by a water thermostat and the other cell to within $\pm 1^\circ$ by the room thermostat. The cells were thoroughly cleaned with a 1:1 mixture of concentrated HNO_3 and H_2SO_4 , and rinsed with triply distilled water.

In these experiments, the concentration of HF varied from 0.001 to 0.02N. In some experiments, no additional electrolyte was added, but usually H_2SO_4 , Na_2SO_4 , or both Na_2SO_4 and H_2SO_4 were added. All solutions were prepared from water that was distilled at least twice. One of the distillations was made from alkaline potassium permanganate solution. In some of the experiments, the water was distilled four times, and the solutions were pre-electrolyzed, but no improvements in results were noted. In these experiments, the dissolution of the electrode was rapid enough so that a new surface was continually exposed to the solution.

Potentiostatic current-voltage curves were determined with an electronic potentiostat developed at this laboratory. This potentiostat was able to restore the correct potential in about 5-10 msec after perturbations. Currents from the potentiostat were recorded on a Brown 100 mv recorder coupled with a Hewlett Packard model 425AR D-C microvolt ammeter. The latter instrument measured the potential drop across precision resistors in the potentiostat circuit. Potential differences between the test and reference electrodes were measured with a Keithly 610R electrometer coupled to the Brown recorder.

Galvanostatic pulses for transient and capacity measurements were supplied by a circuit very similar to that described by Vetter and Arnold (5). This circuit used a Clare mercury-wetted-contact relay in conjunction with batteries and appropriate resistors. The 45v necessary to trigger the relay was supplied either by a Tektronix Type 161 pulse generator or a Type 162 wave-form generator. By suitable adjustment of these instruments, one could obtain pulse lengths of from a few milliseconds to 10 sec. Longer pulses were obtained by manual triggering. Depending on the circuit parameters, pulses were obtained that achieved constant current in from less than a microsecond to a few microseconds.

Results

Steady-state polarization.—Steady-state current voltage curves could only be obtained by using the potentiostat on the anodic side of open circuit. Galvanostatic measurements produced only transients which are discussed below. Open circuit po-

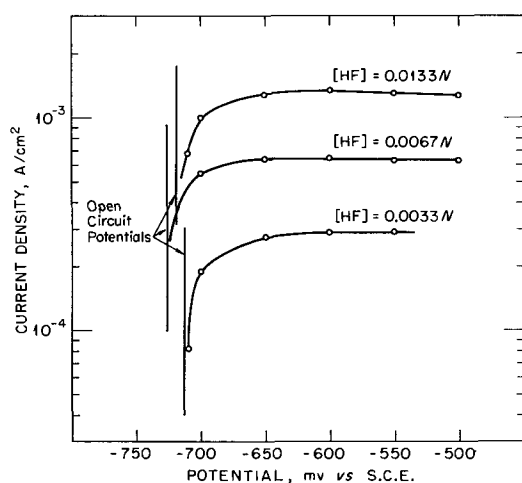


Fig. 1. Anodic polarization of zirconium (potentiostatic) in HF solutions; all solutions 1.8N in H_2SO_4 , 25°C, He atmosphere, stirred.

tentials ranged from -650 to -1000 mv vs. SCE for solutions containing both HF and H_2SO_4 and became more cathodic as the hydrogen ion concentration was reduced. In general, at constant sulfuric acid concentration, the potentials were more negative at the higher concentrations of HF, but there was not sufficient reproducibility of open circuit potentials to establish a quantitative relation. In fact, reversals of this generalization were noted.

In Fig. 1, the results are plotted for potentiostatic determinations of the current-voltage curve on the anodic side of open circuit at various concentrations of HF. Each of these curves shows a constant current plateau characteristic of mass transfer control and attains its plateau within about 100 mv of the open circuit potential as would be expected if the rate were limited by mass transfer also at open circuit. The recorded currents were not actually steady but oscillated about an average value in a manner characteristic of mass transfer. The height of the plateau is approximately proportional to the concentration of HF. In these experiments, slight stirring was achieved by bubbling He into the bottom of the cell. Since the geometry of the cell system was fixed and since the flow rate of the He was maintained constant with a flow meter, the different experiments were conducted under approximately equal mass transfer conditions. From the data shown in Fig. 1, the following equation for the rate of dissolution can be calculated.

$$i = 9.4 \times 10^{-2} [HF] \quad [1]$$

where i is the rate of dissolution in amp/cm² and $[HF]$ is the concentration in moles per liter. In order to show that this current corresponds to the dissolution of zirconium as measured by loss of weight, several experiments were conducted in which the electrodes were held at least 200 mv anodic to the open circuit potential for extended periods of time and the weight loss determined. The results are shown in Table I. The theoretical weight losses were calculated with the reasonable assumption that the equivalent weight is one-fourth the

Table I. Comparison of weight loss measured and weight loss calculated from total charge. All solutions at 25°C, electrodes held potentiostatically at least 200 mv anodic to corrosion potential

Solution composition		Wt. loss meas., mg	Wt. loss calc., mg	% Error
0.005N HF	1N H_2SO_4	1.9	1.90	0
0.005N HF	1N H_2SO_4	2.0	1.40	30
0.005N HF	1N H_2SO_4	2.6	2.53	2.7
0.01N HF	1N H_2SO_4	5.3	4.83	8.9
0.01N HF	2N H_2SO_4	5.45	5.20	4.6
0.0067N HF	1.8N H_2SO_4	7.0	6.60	5.7

atomic weight. The total charge that was passed was determined by graphical integration of the current-time trace recorded from the potentiostat. Stirring conditions and cell geometry were similar to those used in the determinations shown in Fig. 1. As Table I shows, the calculated and measured weight losses agree except that the calculated weight losses are consistently slightly low. The reason for the 30% error in the second experiment is not known.

Weight-loss experiments were also conducted at open circuit, and the results of these experiments are shown in Table II. The first five experiments were conducted under approximately the same conditions as those shown in Fig. 1. The others were done with no stirring at all. The average value of the rate divided by the concentration of HF is 10.4×10^{-2} amp-cm⁻²-mole⁻¹-liter. This can be compared to the value of 9.4×10^{-2} shown in Eq. [1]. The approximate correspondence of these constants shows that the rate at open circuit is about equal to the current on the mass transfer plateau. The average value of the constant for unstirred solutions is 4.11×10^{-2} , which is less than half of the value for stirred solutions. This shows that even the slight stirring employed in the first five experiments had a large effect on the rate.

In a few experiments, sodium sulfate was substituted for the 1N H_2SO_4 , so that the H^+ concen-

Table II. Rates of dissolution of zirconium in solutions of HF by weight loss. All solutions He or H_2 atmosphere and 25°C

Solution composition		Rate in amp/cm ⁻²	Rate + [HF] amp/cm ⁻² M ⁻¹ liter
Stirred solutions			
0.02N HF	1N H_2SO_4	1.95×10^{-3}	9.8×10^{-2}
0.0133N HF	1.8N H_2SO_4	1.56×10^{-3}	11.7×10^{-2}
0.01N HF	1N H_2SO_4	9.55×10^{-4}	9.5×10^{-2}
0.005N HF	1N H_2SO_4	4.96×10^{-4}	9.9×10^{-2}
0.005N HF	1N H_2SO_4	5.60×10^{-4}	11.2×10^{-2}
Average			10.4×10^{-2}
Unstirred solutions			
0.02N HF	1N H_2SO_4	7.90×10^{-4}	3.95×10^{-2}
0.02N HF	1N H_2SO_4	8.60×10^{-4}	4.30×10^{-2}
0.02N HF	1N H_2SO_4	6.50×10^{-4}	3.25×10^{-2}
0.02N HF	1N H_2SO_4	8.25×10^{-4}	4.12×10^{-2}
0.02N HF	1N H_2SO_4	8.16×10^{-4}	4.08×10^{-2}
0.0133N HF*	1M Na_2SO_4	5.90×10^{-4}	5.56×10^{-2}
0.0133N HF*	1M Na_2SO_4	4.90×10^{-4}	4.62×10^{-2}
0.01N HF	1N H_2SO_4	3.68×10^{-4}	3.68×10^{-2}
0.01N HF	1N H_2SO_4	3.44×10^{-4}	3.44×10^{-2}
Average			4.11×10^{-2}

* Concentration of undissociated HF calculated to be 0.0106N assuming $K = 6.9 \times 10^{-4}$.

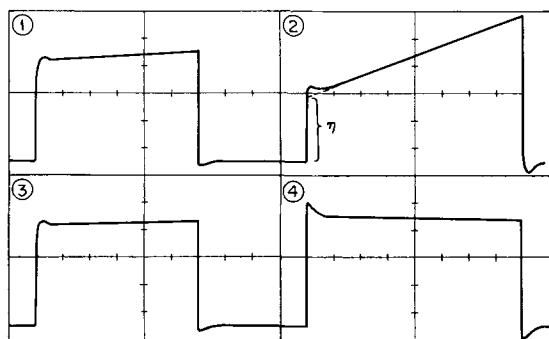


Fig. 2. Oscilloscopic voltage-time traces of galvanostatic pulses applied to zirconium in 0.0133N HF, 1N H₂SO₄ at 25°C and He atmosphere: 1, anodic, 2.1×10^{-4} amp/cm², 10 ms/cm horizontal, 2 mv/cm vertical; 2, anodic, 5.12×10^{-3} amp/cm², 10 ms/cm, 50 mv/cm; 3, cathodic, 2.1×10^{-4} amp/cm², 10 ms/cm, 2 mv/cm; 4, cathodic, 5.12×10^{-3} amp/cm², 10 ms/cm, 20 mv/cm.

tration was much lower and the F⁻ and HF₂⁻ concentrations were much higher. These experiments were done under unstirred conditions and, as shown in Table II, the rate was found to be about the same as rates in H₂SO₄ solutions at the same concentration of HF.

Transient polarization.—Since long term galvanostatic experiments always showed drifting and complicated transient behavior, all constant current experiments were conducted with pulses of about 0.1 sec in duration. The general behavior of the potential as a function of time is shown in Fig. 2. At low current densities, during a pulse of 70 to 80 msec, the potential changes only slightly with time after the slight initial hump. At high cathodic current densities, the potential tends to drop slightly with time. However, at high anodic current densities, the potential rises steeply with time, the slope increasing with increasing current density. A slight peak was frequently observed in the first few milliseconds of the pulse. A value for the polarization ($E - E_{\text{corr}}$) can be obtained by extrapolating the linear section of the potential time curve to

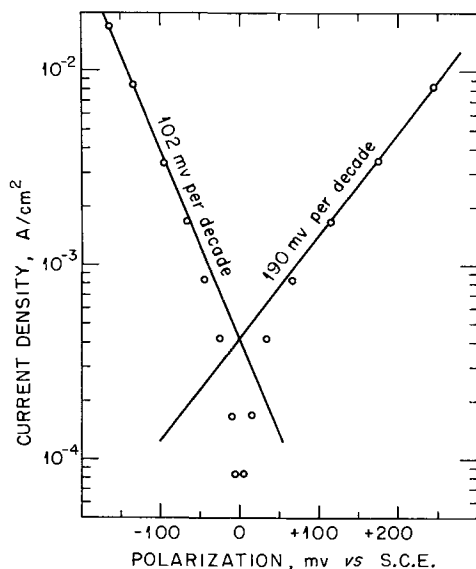


Fig. 3. Transient polarization curve of zirconium. Crystal bar zirconium, 0.005N HF, 1N H₂SO₄, 25°C, He atmosphere.

zero time. If these potential changes are then plotted as log of current vs. polarization, plots such as the one shown in Fig. 3 are obtained. These plots are interpreted as transient current potential curves which relate to the state of the electrode at the onset of polarization and are discussed further below. In the following discussion, these plots must not be confused with steady-state polarization curves, for there is a Tafel region on the anodic side in the transient case and no Tafel region on the anodic side in the steady-state case.

Determinations of the order of the cathodic reaction with respect to hydrogen ion were carried out in experiments in which the concentrations of HF and total sulfate were kept constant and the hydrogen ion concentration varied. An example of such an experiment is shown in Fig. 4. The order of the reduction reaction is equal to the slope of the line obtained by plotting the logarithm of the current vs. the logarithm of the hydrogen ion concentration. In Fig. 5, these lines are plotted for duplicate determinations taken on successive days with the same electrode. The electrode surface was renewed and the solution changed between experiments. The solid lines and the open circles represent the experiment shown in Fig. 4, and the dashed lines and solid points represent the duplicate experiment. The slopes of the solid lines have values slightly greater than 0.8, and the slopes of the dashed lines are about equal to 1.0. The order is therefore taken to be unity. The hydrogen ion concentration was calculated by taking the dissociation quotient of HSO₄⁻ into account.² All three solutions had about the same ionic strength so that the activity coefficients and the dissociation quotient of HSO₄⁻ remained approximately constant.

If it is assumed that mixed-potential theory (7) applies to this system, then the current-voltage

² In this calculation, the strong dependence of the ionization constant of HSO₄⁻ on the ionic strength of the solution must be taken into account. For these solutions, the ionization constant of HSO₄⁻ is about unity, see ref. (6).

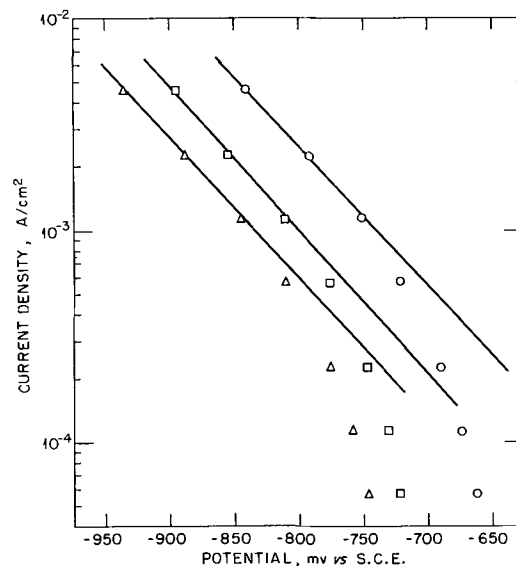


Fig. 4. Cathodic polarization of crystal bar zirconium in solutions of different H⁺ concentration. All solutions 0.01N in HF, 25°C, He atmosphere. Δ , 0.05M H₂SO₄, 0.95M Na₂SO₄; \circ , 0.1M H₂SO₄, 0.9M Na₂SO₄; \square , 0.25M H₂SO₄, 0.75M Na₂SO₄.

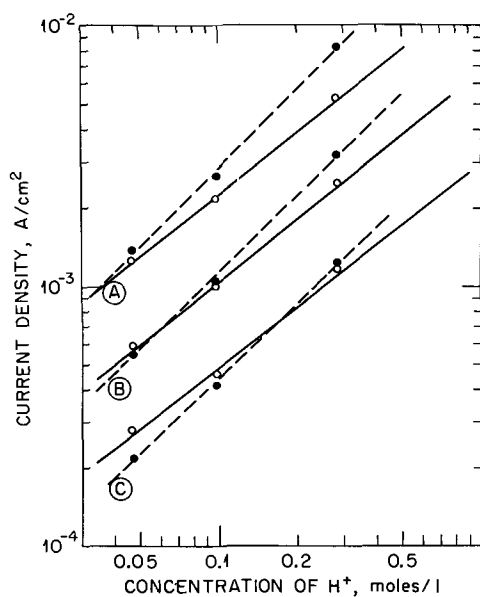


Fig. 5. Determination of order of hydrogen ion reduction. A, -850 vs. SCE; B, -800 vs. SCE; C, -750 vs. SCE. (See text for further explanation.) —○, Experiment No. I; —●, Experiment No. II.

curves for the transient polarization should be given by the following expression

$$i = K_a C_{a,i} \exp(+\alpha_a z_a FE/RT) - K_c C_{c,i} \exp(-\alpha_c z_c FE/RT) \quad [2]$$

where K_a and K_c are constants for the transient anodic and cathodic reactions, respectively, $C_{a,i}$ and $C_{c,i}$ are the concentrations of reactants at the electrode interface, $\alpha_a z_a$ and $\alpha_c z_c$ are the transfer coefficients and charge numbers of the anodic and cathodic reactions, respectively, and the other terms have their usual significance. Table III shows values of $\alpha_a z_a$ and $\alpha_c z_c$ for a number of experiments. It will be noted that $\alpha_c z_c$ tends to be about 0.5 and $\alpha_a z_a$ less than 0.5. It is important to note that the anodic $\alpha_a z_a$ factor becomes smaller, on the average, with decreasing concentration of HF.

Capacity determinations.—Capacities were determined by measuring the initial slopes of the po-

Table III. αz Factors for zirconium in HF solutions at 25°C with He or H₂ atmosphere, all solutions unstirred

Solution composition	$\alpha_c z_c$ Cathodic	$\alpha_a z_a$ Anodic
0.02N HF 1N H ₂ SO ₄	0.51	0.38
0.02N HF 1N H ₂ SO ₄	0.50	0.38
0.02N HF 1N H ₂ SO ₄	0.49	0.46
0.02N HF 1N H ₂ SO ₄	0.60	0.46
0.02N HF 1N H ₂ SO ₄	0.60	0.39
0.02N HF 1N H ₂ SO ₄	0.63	0.33
Average value	0.56	0.40
0.01N HF 1N H ₂ SO ₄	0.54	0.40
0.01N HF 1N H ₂ SO ₄	0.50	0.36
0.01N HF 1N H ₂ SO ₄	0.57	0.24
0.01N HF 1N H ₂ SO ₄	0.54	0.24
Average value	0.54	0.31
0.075N HF 1N H ₂ SO ₄	0.54	0.23
0.005N HF 1N H ₂ SO ₄	0.57	0.21
0.005N HF 1N H ₂ SO ₄	0.54	0.21

Table IV. Capacities of zirconium in various solutions

Solution	Capacity, $\mu\text{F}/\text{cm}^2$
0.01N HF, 1N H ₂ SO ₄	5.3
1N H ₂ SO ₄	3.8
1M Na ₂ SO ₄	3.8
0.01N HF, 1N H ₂ SO ₄	5.5
1N H ₂ SO ₄	3.9
1M Na ₂ SO ₄	3.8
0.001N HF, 1N H ₂ SO ₄	3.4
1N H ₂ SO ₄	3.3
1M Na ₂ SO ₄	3.3

tential time trace (dV/dt) upon application of a galvanostatic current pulse. In general, the currents used in the pulses were kept as large as possible, and the slope was measured during the first 10 to 20 μsec . The capacities per unit area were then calculated from the following equation in the usual way

$$C = i \int \frac{dV}{dt} \quad [3]$$

where i is the current density.

Capacities were measured as a function of the concentration of HF. In three solutions containing 1N H₂SO₄, and HF concentrations of 0.001, 0.005, and 0.01N, the capacities were determined to be 2.15, 4.1, and 5.2 $\mu\text{F}/\text{cm}^2$, respectively. In another experiment, all conditions were duplicated as closely as possible except that galvanostatic pulses were supplied by a fast potentiostat used as a constant current generator (Jaissle Potentiostat, Stuttgart, Germany). Capacities were then measured to be 2.75, 3.7, and 5.1 $\mu\text{F}/\text{cm}^2$. In both experiments, the capacities increased as the HF concentration increased.

Capacities were also measured in experiments in which the electrode was placed first in solutions of HF and 1N H₂SO₄ until a steady-state capacity was achieved. The solution was then quickly changed by means of the cell described in the experimental section to a solution containing only 1N H₂SO₄ and then to another containing only 1M Na₂SO₄. The results of these experiments are shown in Table IV.

In other experiments, capacities were measured as a function of potential. These experiments were carried out by setting the potential with the slow potentiostat described in the experimental section. Plots of capacity vs. potential for various solutions are shown in Fig. 6, where it is shown that the capacity decreases as the potential becomes more anodic.

Effect of fluoride ions.—In order to determine the effect of fluoride ion on the dissolution reaction, progressive amounts of NaF were added to a solution containing 0.0067N HF and 1M Na₂SO₄, in which a zirconium electrode had reached steady-state corrosion behavior. Rates were estimated from measurements of the polarization resistance according to the following equation (8)

$$i = \frac{RT}{F} \times \frac{di}{dE} \Big|_{E \rightarrow E_{\text{corr}}} \times \frac{1}{\alpha_c z_c + \alpha_a z_a} \quad [4]$$

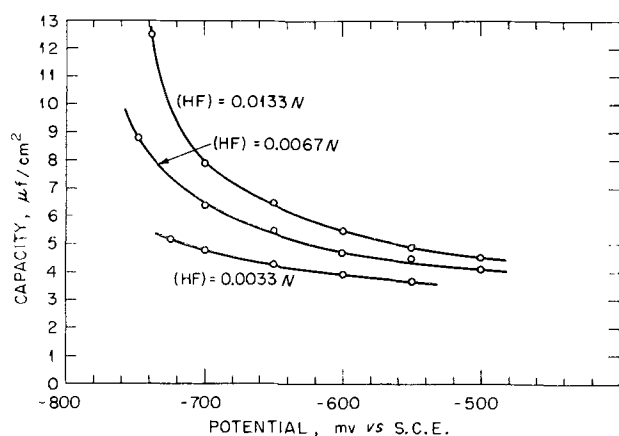


Fig. 6. Variation of capacity of zirconium with potential, 25°C, He atmosphere. All solutions 1.8N in H₂SO₄.

where $(di/dE)_{E \rightarrow E_{corr}}$ is the polarization resistance, i.e., the slope of the transient current-potential curve at the open circuit potential. It was observed that the rates and capacity increased somewhat as the NaF was added. However, examination with a stereo microscope showed that considerable surface roughening had taken place so that it is possible that the current density may not have increased. When the concentration of NaF reached about 0.1M, the potential became more anodic suddenly, and the rate fell several orders of magnitude. Further experiments, in which the electrode was placed into solutions containing 0.0133N HF, 0.1M NaF, and 1M Na₂SO₄ showed no weight loss over a day and a capacity of 1.6 μF/cm². Microscopic examination showed a white crystalline precipitate on the surface. These observations (except for the capacity measurements) are similar to those of Straumanis *et al.* (3), who reported that the film was probably Na₃ZrF₇.

Discussion

The significant observations are the following: (a) A limiting current plateau which is proportional to the concentration of HF is observed when zirconium is polarized anodically with a potentiostat. (b) In solutions containing strong acid, capacity measurements yield values varying from about 1 to 10 μF/cm². (c) The capacity decreases with decreasing concentration of HF, all other factors remaining equal. (d) The capacity decreases as zirconium is polarized anodically. (e) When large anodic galvanostatic currents are applied to the electrode, the potential rises approximately linearly with time. (f) Transient polarization curves (Fig. 3) can be obtained using a galvanostatic pulse technique in solutions containing sufficient strong acid.

It will be shown below that these results can best be explained if it is assumed that the dissolution is a process involving the continuous formation and dissolution of a film and that it is not a process in which bare metal reacts directly with solvent. Furthermore, it is assumed that the dissolution rate is controlled by the rate of mass transfer of undissociated HF to the surface and that the formation of the film is controlled by the usual anodizing equation (9)

$$i_a = K_a \exp \frac{\alpha_f z_f l V F}{d R T} = K_a \exp \frac{\alpha_f z_f l V F / R T}{d_o + K_f \int i_a dt} \quad [5]$$

where K_a is a constant, l is the elementary jump distance, z_f is the charge number of the migrating species, d is the film thickness, d_o is the initial film thickness, K_f is a constant relating charge and film thickness, t is time, and the rest of the terms have their usual significance. The term α_f refers to the fraction of the potential changes that apply to film formation. This model is therefore similar to a model of the corrosion of passive iron which was proposed by Vetter (10).

It seems clear from the data that the reaction at the electrolyte-film interface is controlled by the rate of mass transfer of undissociated HF to the surface of the film in agreement with previous investigations (1-4). The existence of the limiting current plateaus shown in Fig. 1 and the fact that these limiting currents are stirring dependent and show current oscillations typical of mass transfer processes (11) support this conclusion. If the approximate Nernst diffusion layer treatment is assumed to be applicable, then a value for the effective thickness of the diffusion layer can be calculated. The limiting current is then given by the expression

$$i_l = n F A D \frac{C}{\delta} \quad [6]$$

where nF is the amount of charge carried per mole of reactant, A is the area of the electrode, D is the diffusion coefficient of the diffusing substance, C is the bulk concentration of the diffusing species, and δ is the effective thickness of the diffusion layer. With $n = 4$ and $D = 10^{-5}$ cm²/sec, δ can be calculated using the data of Fig. 1 to be 0.04 cm. The diffusion layer is normally taken to be about 10⁻³ cm thick for strongly stirred solutions and about 0.05 cm for natural convection (12). The value 0.04 cm is about right although slightly high for the stirring employed here. If the data for the nonstirred runs were taken, a value of 0.09 cm would be calculated for the diffusion layer as compared to the value 0.05 cm given above.

It is difficult to assess the effect of the F⁻ and HF₂⁻ ions in acid solutions for their concentrations can be increased significantly only in neutral or alkaline solutions, and as shown above the interpretation of results in solutions containing no H₂SO₄ is complicated by surface roughening, formation of fluozirconates, and other effects. It is evident, however, that the fluoride ion alone has no large effect on the rate of dissolution for varying its concentration produces no large effect on the rate.

All the capacity measurements gave values on the order of 1 to 10 μF/cm². If the electrode were film free, we might expect capacity values roughly equal to those on other bare metals, i.e., from 20 to 30 μF/cm² on smooth surfaces and 40 to 50 μF/cm² on these rough surfaces. As shown in Table IV, the capacity of an electrode that had attained a steady-state capacity in 0.001N HF and 1N H₂SO₄ did not change significantly when it was transferred quickly to a solution containing only 1N H₂SO₄ and then to a solution containing only 1M Na₂SO₄. This

experiment indicates that the capacity depends on the properties of the electrode. It is therefore difficult to interpret these small capacity values in any other way than as primarily a film capacity. However, the capacity of an electrode that had attained a capacity of $5.3 \mu\text{F}/\text{cm}^2$ in $0.01N$ HF and $1N$ H_2SO_4 , decreased to about $3.8 \mu\text{F}/\text{cm}^2$ when the electrode was transferred to $1N$ H_2SO_4 and then to $1M$ Na_2SO_4 . In this case, pseudocapacity may contribute to the capacity in the HF solution.

The film thickness may be estimated if the conventional equations describing capacities are assumed to apply to this electrode system. Taking the dielectric constant of the film to be 15, the film thickness for an electrode with a capacity of $5 \mu\text{F}/\text{cm}^2$ would be about 25\AA . Such a thickness could easily be essentially transparent to electrons by a variety of mechanisms (a tunnel effect, *e.g.*). Further, a relatively small potential drop of 250 mv could produce field strengths of 10^6 v/cm, which are sufficiently high so that large anodic currents are attainable with small potential drops.

The increase in measured capacity with increase in concentration of HF can be explained on the basis of the assumptions given above. It is apparent that this observation means that the thickness, which is inversely proportional to the capacity, decreases as the rate increases, since the rate is proportional to the concentration of HF. In order that the system attain a steady state, the rate of film formation must increase as the rate of dissolution increases. This can only be done by increasing the field in the film, either by increasing the potential or by decreasing the film thickness. But the potential cannot become more anodic for this would decrease the rate of the cathodic process which must necessarily be equal to the anodic. Therefore, the film thickness must decrease as the concentration of HF is increased.

Similar considerations apply to the potentiostatic experiments of Fig. 6. Here it is shown that the capacity decreases and therefore that the thickness increases as the potential becomes more anodic. Since the concentration of HF remains constant during the experiment, the steady-state rate must always be the same, and therefore the field in the

film must remain the same. This can only be done if the film thickness increases in proportion to the potential increase.

Some attempts were made to put these considerations on a more quantitative basis. For example, a plot of reciprocal capacity *vs.* potential should be a straight line if it is true that the film thickness increases in proportion to the potential increases. As shown in Fig. 7, this tends to be roughly true if the potential is removed far enough from open circuit. This relation would be expected to be true only if the measured capacity is exactly inversely proportional to the thickness, and this assumption is not likely to be strictly valid. Probably the two most important reasons for this are that the dielectric constant of the film varies with thickness and that other forms of capacity, *e.g.*, pseudocapacity and double layer capacity, may be included in the value of the measured capacity.

The considerations given above also allow some of the features of the transients shown in Fig. 2 to be interpreted. The rates of dissolution encountered in this work are of the order of magnitude of from 10^{-4} to 10^{-3} amp/cm², or in terms of rate of removal of the surface, from 0.3 to $3\text{\AA}/\text{sec}$. Therefore, polarization for durations somewhat more than a second can cause significant changes in film thickness and, if there is any relation between film thickness and the kinetics, transients will be observed. A steady-state thickness of the film is attained whenever the dissolution rate of the film equals the anodic current, i_a , applied to the formation of the film. The current i_a is given by Eq. [5] and is a function of the field strength, V/d . If i_a is greater than the dissolution rate of the film, then the film will thicken, and if i_a is less than the dissolution rate, the HF will decrease the thickness of the film.

If the electrode is polarized cathodically, the potential across the film will be reduced and the field will be decreased. The current i_a will therefore be smaller than the dissolution rate, and the thickness will decrease until the value of V/d is the same as that before polarization. However, on the cathodic side, the potential-time behavior is primarily a function of the behavior of the cathodic reaction which is apparently not a strong function of film thickness. As shown in Fig. 2, the changes of potential with time on the cathodic side are relatively small.

On the anodic side at low currents, steady states can, in principle, be achieved as long as the applied current is not larger than the rate of dissolution. In this case, as the potential becomes more anodic, the cathodic current decreases until the applied current equals the difference between the absolute values of the anodic and cathodic currents. An increase in thickness of the film will occur since the final potential will be more anodic than the original potential. When the applied current exceeds the dissolution rate, then there is no possibility for the applied current to equal the difference of the absolute values of the anodic and cathodic currents, for the steady-state anodic current is limited by the rate of mass transfer of HF to the surface and the

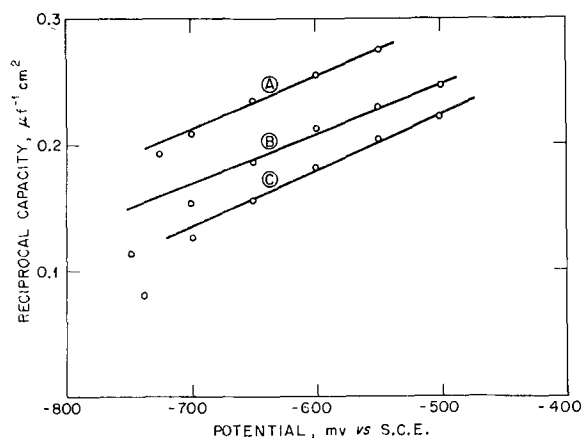


Fig. 7. Reciprocal capacity *vs.* potential for zirconium. A, (HF) = $0.0033N$; B, (HF) = $0.0067N$; C, (HF) = $0.0133N$. All solutions $1.8N$ H_2SO_4 , 25°C , He atmosphere.

cathodic current can, of course, decrease only to zero. If the applied current does exceed the dissolution rate, then the excess charge will go into formation of the film, and the potential will rise with time as in anodizing phenomena. This excess charge is supplied by a current or rate equal to the sum of the applied current and the absolute value of the cathodic current minus the rate at which the film is removed by HF. As shown in Fig. 2, the potential does rise with time at high anodic current densities. Also, the linear sections of the potential-time curves can be extrapolated to zero time to obtain a plot of polarization *vs.* current at constant film thickness, corresponding to the initial state of the electrode.

Further verification of this concept can be obtained by comparing experimentally observed slopes (dV/dt) at the higher current densities with expected slopes. At low current densities, the current applied to the build-up of film is not known accurately since the cathodic current and the dissolution current are not known precisely enough. At high current densities, however, a comparison can be made. In five experiments in 0.01N HF and 1N H₂SO₄ (nonstirred), currents of 1.14×10^{-2} amp/cm² gave slopes of 2.00, 1.97, 2.08, 2.10, and 1.88 v/sec. The rate of dissolution was about 10^{-3} amp/cm² and the cathodic current was negligible at these potentials. The slope may be calculated from Eq. [5] by differentiating *V* with respect to time. If this is done, one obtains the following expression

$$\frac{dV}{dt} = 2.3 \frac{RT}{F} \frac{K_F i \log i / K_a}{\alpha_f z_f l} \quad [7]$$

Adams and van Rysselberghe (13) in an investigation of anodizing phenomena of zirconium obtain the following expression for (dV/dt) in ammonium borate at 20°C

$$\frac{dV}{dt} = 28 i \log \frac{i}{2.9 \times 10^{-11}} \quad [8]$$

where *i* is the current density applied to formation of film. At *i* equal to 1.14×10^{-2} amp/cm², the dissolution rate is about 10^{-3} amp/cm², or the current density applied to the increase in the thickness of the film is about 10^{-2} amp/cm². Substituting this value in Eq. [8], one obtains 2.4 v/sec. This com-

pare favorably with the observed value of about 2 v/sec and indicates that these data are consistent with those of Adams and Van Rysselberghe.

As was shown previously, the $\alpha_a z_a$ factors become larger with increasing HF concentration, all other factors being equal. This is due to the fact that the thickness decreases with increasing HF concentration. A comparison of Eq. [2] and Eq. [5] shows that $\alpha_a z_a$ is actually equal to $\alpha_f z_f l/d$. Therefore, a decrease in the film thickness will increase the value of $\alpha_a z_a$.

It should be possible to obtain rates by extrapolating the Tafel lines obtained from the galvanostatic pulse experiments to the rest potential, for at the rest potential the cathodic current, the rate of film formation, and the rate of dissolution must all be equal. Alternately, one could obtain rates from the polarization resistance according to Eq. [4]. Comparisons of some rates measured by various methods are shown in Table V. Although the rates measured by these electrochemical methods average about 25% lower than the rates determined by weight loss, they are sufficiently close to lend validity to the assumptions used above. As a matter of fact, the rates are consistently low, so that there is probably a reasonably reproducible systematic error in the methods. The proportionality between weight loss rate and the polarization resistance is actually quite good, so that rates could be measured quite accurately by measuring only the polarization resistance and by determining the proportionality constant by several weight loss experiments.

There are a number of reasons why the rates measured by electrochemical methods are lower than those obtained from the actual weight losses. Experimental error, of course, is one possibility. All potentials are measured oscilloscopically, a technique which is not as accurate as most methods of measuring potential, particularly when extrapolations are involved. Another reason is the fact that the electrochemical rates are instantaneous rates while weight loss gives a measure of the average rate. It is conceivable that, since the rates fluctuate due to variations in mass transfer, there are short periods of relatively large rate which would not be likely to show up in the polarization diagram. Lastly, it is quite common that small portions of the metal be-

Table V. Dissolution rates in amp/cm²

Stirred solutions	By wt. loss	By Eq. [4]	By extrapolation of Tafel line
0.02N HF 1N H ₂ SO ₄	1.95×10^{-3}	1.42×10^{-3}	1.3×10^{-3}
0.0133N HF 1.8N H ₂ SO ₄	1.56×10^{-3}	1.12×10^{-3}	1.14×10^{-3}
0.01N HF 1N H ₂ SO ₄	9.55×10^{-4}	6.05×10^{-4}	6.0×10^{-4}
0.005N HF 1N H ₂ SO ₄	4.96×10^{-4}	3.75×10^{-4}	3.7×10^{-4}
0.005N HF 1N H ₂ SO ₄	5.60×10^{-4}	4.00×10^{-4}	5.7×10^{-4}
Unstirred solutions			
0.02N HF 1N H ₂ SO ₄	7.90×10^{-4}	6.68×10^{-4}	6.3×10^{-4}
0.02N HF 1N H ₂ SO ₄	8.60×10^{-4}	6.78×10^{-4}	7.1×10^{-4}
0.02N HF 1N H ₂ SO ₄	6.50×10^{-4}	4.85×10^{-4}	3.9×10^{-4}
0.02N HF 1N H ₂ SO ₄	8.25×10^{-4}	5.72×10^{-4}	5.4×10^{-4}
0.02N HF 1N H ₂ SO ₄	8.16×10^{-4}	5.95×10^{-4}	5.1×10^{-4}
0.01N HF 1N H ₂ SO ₄	3.68×10^{-4}	2.58×10^{-4}	2.9×10^{-4}
0.01N HF 1N H ₂ SO ₄	3.44×10^{-4}	2.73×10^{-4}	2.8×10^{-4}

come detached from the surface during corrosion (chunk effect) and dissolve without being in electrical contact with the electrode.

The small peaks in the initial portion of the transient curves of Fig. 2 are not explained. Possibly they are a result of transient effects in the film. There was no regularity in their relative size and in some experiments they were absent entirely.

As is shown above, the rate of dissolution of the film is controlled by the rate of mass transfer of HF to the surface. It is possible that the HF molecules then become adsorbed on the surface of the film and that a complex containing a zirconium atom and a fluorine atom is formed which then moves into the solution. With the techniques used in this work, there is no way of investigating the kinetics of this surface reaction for the concentration of HF at the film-solution interface is unknown. It is known only that the concentration of HF near the surface is small compared to the bulk concentration because of the fact that the dissolution rate is equal to the limiting rate of mass transfer. Further information concerning this interface reaction could be obtained if the mass transfer conditions were precisely defined so that the rate constants and kinetic orders of the surface reaction could be obtained. Attempts are now being made to define the mass transfer conditions by means of a rotating disk electrode system (14-15).

Ordinarily when zirconium is chemically polished in solutions containing HF, HNO₃ is added to the solution in order to aid in producing smooth, bright surfaces. If the HNO₃ is omitted, there is a tendency toward the formation of roughness and hydride phases on the electrode surface. In this investigation, it was noted that the addition of H₂SO₄ also aided in producing bright, smooth surfaces. It was further noted that the capacity values of electrodes which contained only HF were very high, sometimes more than ten times as high as the capacities of those surfaces formed when H₂SO₄ was present. It would appear from these capacities that there is little or no film present when the HNO₃ or H₂SO₄ is absent and that therefore the role of the strong acid is to promote the formation of a film. It has been reported (16) that the presence of a film resulting from chemically polishing zirconium with a solution containing HF and HNO₃ inhibits the formation of hydrides in a gaseous H₂ atmosphere. Such an effect might be operative in aqueous solutions also. Further, it has been asserted (17) that the presence of a film on an electrode surface leads to the production of smooth surfaces. Thus, the absence of any significant amount of film may explain the observation that in solutions containing only HF, hydride phases and rough surfaces are formed on the electrode.

It can be shown from the kinetic considerations given above, that increasing the hydrogen ion concentration will increase the amount of film in the steady state at constant concentration of HF. In any

solution of fixed concentration of HF, the over-all rate will always be equal to the limiting rate of mass transfer, and these rates must also be equal to the anodic rate (Eq. [5]) and the cathodic rate which is first order with respect to (H⁺). These equalities are expressed by Eq. [9] and [10].

$$i_l = K_a \exp \frac{\alpha_f z_f l V F}{d R T} \quad [9]$$

$$i_l = K_c (H^+) \exp \frac{-\alpha_c z_c V F}{R T} \quad [10]$$

Equations [9] and [10] can be combined to give a quantitative relation between d and H⁺ at constant i_l .

$$d = \frac{\alpha_f z_f l \log [K_c (H^+)] - \alpha_f z_f l \log i_l}{\alpha_c z_c \log (i_l K_a)} \quad [11]$$

This equation shows that the film thickness does increase with increasing hydrogen ion concentration at constant concentration of HF. Equation [11] is valid, of course, only if K_c , K_a , and the other constants are independent of film thickness. This may not be strictly true but is probably approximately true. Thus, the role of the added strong acid in chemical polishing may simply be that of increasing the H⁺ and thus increasing the film thickness.

Manuscript received May 13, 1963; revised manuscript received Sept. 12, 1963.

Any discussion of this paper will appear in a Discussion Section to be published in the December 1964 JOURNAL.

REFERENCES

1. T. Smith and G. R. Hill, *This Journal*, **105**, 117 (1958).
2. E. M. Vander Wall and E. M. Whitener, *Ind. Eng. Chem.*, **51**, 51 (1959).
3. M. E. Straumanis, W. J. James, and A. S. Neiman, *Corrosion*, **15**, 286 (1959).
4. W. J. James, W. G. Custead, and M. E. Straumanis, *J. Phys. Chem.*, **64**, 286 (1960).
5. K. Arnold and K. J. Vetter, *Z. Elektrochem.*, **64**, 407 (1960).
6. M. H. Lietzke and R. W. Stoughton, *J. Phys. Chem.*, **63**, 1188 (1959).
7. C. Wagner and W. Traud, *Z. Elektrochem.*, **44**, 391 (1938).
8. M. Stern and A. L. Geary, *This Journal*, **104**, 56 (1957); F. A. Posey, *ibid.*, **106**, 571 (1959).
9. A. Günterschulze and H. Betz, *Z. Physik*, **91**, 70 (1934); **92**, 367 (1934).
10. K. J. Vetter, *Z. Phys. Chem.*, **202**, 1 (1953); *Z. Elektrochem.*, **58**, 230 (1954).
11. K. J. Vetter, *Elektrochemische Kinetik*, p. 306, Springer-Verlag, Berlin (1961).
12. *Ibid.*, pp. 170-171.
13. G. B. Adams and P. van Rysselberghe, *This Journal*, **102**, 505 (1955).
14. V. G. Levich, "Physico-Chemical Hydrodynamics," Prentice-Hall, Englewood Cliffs, N. J. (1962).
15. D. Jahn and W. Vielstich, *This Journal*, **109**, 849 (1962).
16. E. A. Gulbransen and K. F. Andrew, *ibid.*, **101**, 348 (1954).
17. T. P. Hoar, "The Anodic Behavior of Metals," in "Modern Aspects of Electrochemistry," J. O'M. Bockris, Editor, Vol. II, Butterworths (1959).

Effect of pH, Sulfates, and Chlorides on Behavior of Sodium Chromate and Nitrite as Passivators for Steel

Seigo Matsuda¹ and H. H. Uhlig

Corrosion Laboratory, Massachusetts Institute of Technology, Cambridge, Massachusetts

ABSTRACT

Corrosion rates of iron in chromate and nitrite solutions were measured by a sensitive electric resistance method supplemented by weight loss. The critical concentration below which corrosion increases or pitting occurs is $1 \times 10^{-5} M$ for NaNO_2 and $5 \times 10^{-4} M$ for Na_2CrO_4 . Presence of Cl^- and SO_4^{--} increases these values. Sulfates break down passivity in nitrite solutions more so than do chlorides; the reverse is true of chromate solutions. Minimum concentration of passivator to avoid pitting in presence of Cl^- or SO_4^{--} follows the relation $\log M_s = a + b \log M_p$ where M_s and M_p are molarities of salt and passivator respectively. In chromate solutions in the alkaline range of pH, the corrosion rate is low (0.08 mdd) and no pitting occurs. In the acid range, corrosion remains low to at least pH 2.8 provided HClO_4 is used to adjust pH; when H_2SO_4 is used instead, the corrosion rate increases below pH 5 and pitting begins at pH 3. At temperatures up to 100°C , the steady-state corrosion rates in chromates remain low (<0.1 mdd). An initial higher rate precedes the final lower rate. These relations are explained by passivation through anodic polarization and competitive adsorption of Cl^- or SO_4^{--} with the passivator ion for a site on the passive film. The data support the view that NO_2^- adsorbs more strongly than does CrO_4^{--} .

Based on their reliable performance, chromates and nitrites find widespread practical use as passivators for steel. In the presence of chlorides and sulfates, they sometimes perform less reliably, leading in the extreme to deep pitting of steel, particularly if the concentration of passivator is near or below the critical value. Temperature and pH of the environment may also play a role. Quantitative relations between passivator concentration and factors of the environment have not yet been worked out, although they are important to the proper application of chromates and nitrites for inhibiting steel against both rusting and pitting. The present investigation is concerned with some of the quantitative relations that are needed. These, it is hoped, together with results by others, will supply enough information to provide greater confidence and assurance that a metal system containing any common type water is adequately and continuously protected.

Experimental Methods

Corrosion rates were determined by two methods. The first was a weight loss method employing Armco iron foil (0.023% carbon) 0.0089 cm (0.0035 in.) thick. Specimens of foil, 5 x 10 cm (2 x 4 in.), were formed into spirals of 2 cm diameter. These were hung in duplicate from glass hooks in an all-glass flask as shown in Fig. 1. The specimens were degreased in boiling benzene, annealed for 15 min at 800°C in a helium atmosphere, rapidly cooled in helium, pickled for 3 min in 10% HCl at 70°C , washed in distilled water and dried by immersion first in acetone and then in benzene. After the test, the specimens were cleaned with a soft brush under

water, pickled for 1 min in 10% HCl inhibited with 0.2% ethylquinolinium iodide at 60°C and washed in water, acetone and benzene as above. The blank correction for loss of metal in the latter cleaning operation was 1.5 ± 0.1 mg.

The second was an electric resistance method sensitive to detection of corrosion rates as low as $0.02 \text{ mg/dm}^2/\text{day}$ (mdd) in 5 day tests. This method proved valuable in detecting the very small corrosion losses of steel exposed to chromate- or nitrite-inhibited solutions. It could be used only when the corrosion rates were uniform. The weight loss

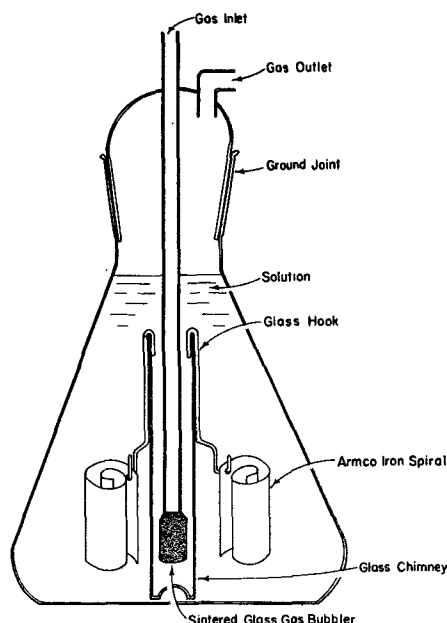


Fig. 1. Cell for weight loss measurements

¹ Present address: ILIKON Corporation, Natick, Massachusetts.

method was used instead when localized corrosion such as pitting corrosion took place.

Specimens for the electric resistance method were machine slit from the same Armco iron foil described above into a band 0.159 cm (0.0625 in.) wide and 366 cm (12 ft) long. The band was formed into a spiral 1 cm in diameter, which was then degreased in boiling benzene and annealed for 15 min at 800°C in a purified helium atmosphere by passing an electric current through the spiral. Helium was purified by passing the gas over copper turnings at 450°C. Temperature was measured using an optical pyrometer. After rapid cooling in helium by switching off the current, 2 Pt wires were spot-welded to each end of the spiral, which in turn connected to silver-soldered copper wires. One pair of wires served as electric current leads, and the other for measuring potential drop across the spiral during flow of current. The wires were protected from contact with aqueous solution by a glass tube, and the spot-welded junctions were covered with stop-off lacquer. At above-room temperatures, epoxy resin was used instead. After the lacquer had thoroughly dried, the spiral was pickled for 3 min in 10% HCl at 70°C, washed in water, and dried by successive immersion in acetone and benzene. Spirals were kept in a desiccator until ready for use.

Figure 2 illustrates the apparatus used for the electric resistance measurements. Glass vessels C_1 , C_2 , C_3 , and C_4 were contained in a water thermostat maintained at $25^\circ \pm 0.01^\circ\text{C}$. The spiral undergoing corrosion was contained in glass vessel C_2 measuring about 7 cm diameter and 40 cm high. A similar vessel labeled C_3 contained an identical Armco iron foil spiral immersed in benzene dried over metallic sodium. Silica gel was added to C_3 to maintain the solvent free of moisture and thereby avoid corrosion. The latter spiral acted as a standard, the change in resistance of which was used to compensate for any slight temperature fluctuations during the test. A standard resistor R_1 of 10 ohms in vessel C_4 was also maintained in dry benzene. The voltage drop across this resistor was a measure of the constant current passing momentarily in series through the two spirals during measurements.

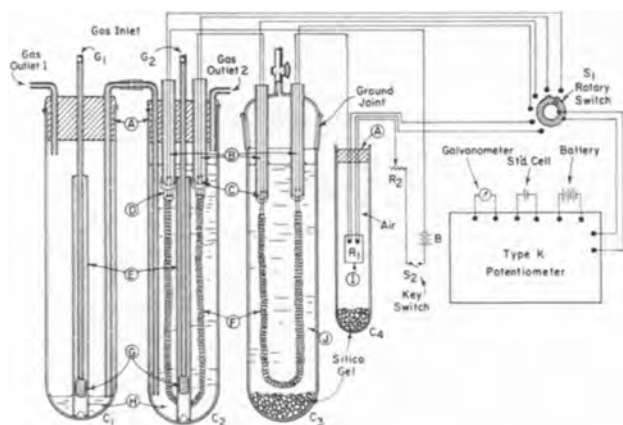


Fig. 2. Apparatus for electric resistance method. A, Rubber stopper; B, copper wire; C, Pt wire; D, stop-off lacquer; E, glass chimney; F, Armco iron spiral ribbon; G, sintered glass; H, solution; I, standard resistance; J, dry benzene.

The procedure was as follows:

1. Fill C_1 with aqueous test solution and either aerate or deaerate solution, as required, for 6 hr or more by passing gas² continuously through the sintered glass bubbler at the bottom of the glass chimney. Insert spiral in C_2 just before test.
2. Transfer solution from C_1 to C_2 by gas pressure. Close gas outlet 1 and open gas outlet 2. Vessel C_2 is previously flushed with the same gas as passes through C_1 . Gas is passed continuously through C_2 during the test, which also stirs the solution.
3. For measurement of corrosion rate, transfer solution temporarily from C_2 to C_1 by closing gas outlet 2 and opening gas outlet 1. In this way, any electrolysis affecting the metallic leads is avoided, and error is avoided caused by electrolyte conductivity during passage of current through the spiral. Pass momentary constant current of about 30 ma through spirals and through R_1 from 6v source using telegraph key. Simultaneously, measure voltage drop across the two spirals and across R_1 . Transfer solution back to C_2 from C_1 .
4. Calculate corrosion rate from the relation

$$\text{mdd} = \frac{9.45 \times 10^6 HW}{t(H+W)} \frac{\Delta R}{R}$$

where H and W , respectively, are the initial thickness and width in centimeters of the Armco iron foil, R is the total resistance of the spiral, and ΔR is the increase in resistance during the time t in hours caused by uniform corrosion of the spiral.

Cleaning the spiral of corrosion products is not necessary. The electrical conductivity of any corrosion product compared to that of metallic iron is so small that corrections are negligible. For example, a film 200Å thick of the good conducting iron oxide Fe_3O_4 ($\rho = 1.06 \times 10^{-2}$ ohm-cm) on the iron foil surface would change the over-all resistance by only 0.00005%. Correspondingly, a corrosion rate of 0.1 mdd for a 5 day test period would produce an increase in resistance equal to 0.013%.

For a few measurements at 40°C, the same apparatus was used. At 100°C, the glass vessel was enclosed by a steam chamber, and a condenser system was employed as shown in Fig. 3. Since the temperature was constant during the time a measurement was made, an identical spiral in an organic solvent could be dispensed with. Absolute temperature was corrected in accord with barometric readings.

Results

Critical concentration.—The effect of passivator concentration on corrosion was determined in aerated solutions ranging from 10^{-5} to $10^{-2}M$ of passivator. For chromate solutions, weight loss measurements were employed for concentrations below $5 \times 10^{-4}M$ and the electric resistance method for higher concentrations. For concentrations below $5 \times 10^{-4}M$, pitting occurred usually at the contact of glass hook with the specimen (crevice corrosion). Above $5 \times 10^{-4}M$, the corrosion rate was higher for

² The gas was air or H_2 . Air was first passed through columns of soda-lime and Ascarite. H_2 was passed over copper turnings at 450°C.

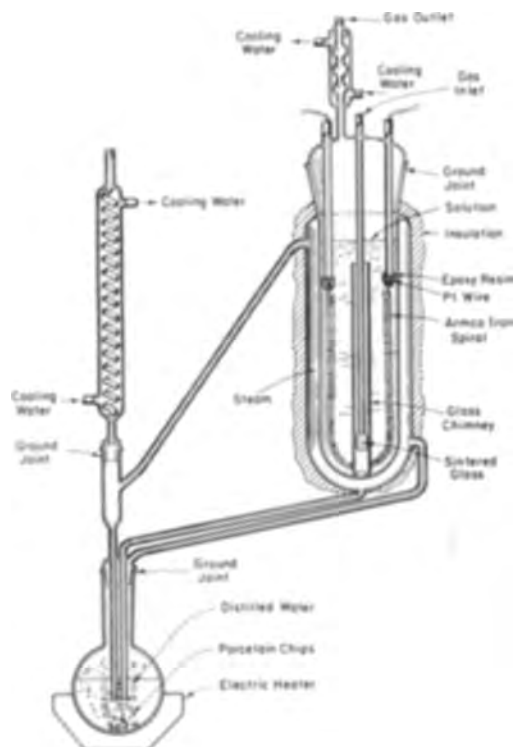


Fig. 3. Electric resistance method for measuring corrosion rates at 100°C.

about the first one or two hours (20 mdd) finally reaching a steady-state value of less than 0.1 mdd (Fig. 4). The critical concentration of $5 \times 10^{-4}M$ is in reasonable agreement with the critical concentrations reported by Robertson (1) ($1 \times 10^{-3}M$), by Pryor and Cohen (2) ($5 \times 10^{-4}M$) and by Powers and Hackerman (3) ($1 \times 10^{-3}M$).

In nitrite solutions, the corrosion rate of iron in 5 day exposure tests was less than the sensitivity of the electric resistance method (about 0.02 mdd) for concentrations as low as $1 \times 10^{-5}M$. Hence, the critical concentration is this value or less. Critical concentrations reported by Robertson (1) ($1 \times 10^{-4}M$) or by Pryor and Cohen (2) ($5 \times 10^{-5}M$) indicate that the critical concentration is lower than for chromate, which the present data confirm.

Addition of 100 ppm Cl^- partially destroyed passivity of specimens in solutions of less than $5 \times 10^{-4}M$ $NaNO_2$, resulting in extensive pitting. In $1 \times 10^{-3}M$ $NaNO_2$, similar addition of 100 ppm Cl^- had no effect.

Aeration or deaeration of the passivator solutions did not substantially affect steady-state corrosion rates. Rates of uniformly passive specimens re-

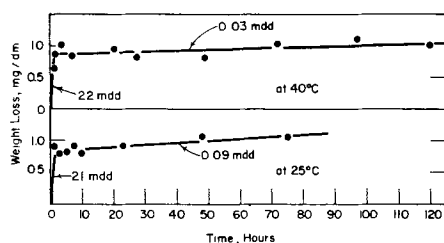


Fig. 4. Weight loss vs. time curve of Armco iron in air-saturated 0.01M Na_2CrO_4 solution at 25° and 40°C by electric resistance method.

mained low for either condition and were below the corrosion rate of iron in deaerated water. For example, the corrosion rate of iron in H_2 -saturated $10^{-2}M$ Na_2CrO_4 averaged less than 0.1 mdd, whereas the corrosion rate in H_2 -saturated distilled H_2O was 0.81 mdd.

Effect of chloride and sulfate ions.—Weight loss measurements and observations of pitting were made using Armco iron foil specimens continuously exposed to air-saturated passivator solutions for a total of 5 days. Solutions contained 10^{-4} to $10^{-2}M$ chromate or 10^{-5} to $10^{-2}M$ nitrite with additions of $NaCl$ or Na_2SO_4 up to about $10^{-2}M$. The results are plotted on a log-log scale in Fig. 5-8, each point representing one or more experiments. In general, a linear relation exists between the log of minimum passivator concentration and log of maximum chloride or sulfate concentration at which pitting does not occur. The critical concentration of chromate discussed earlier is easily discernible as that concentration ($5 \times 10^{-4}M$) below which pitting occurs even if chloride or sulfate concentration is low. The analogous critical concentration of $NaNO_2$ is below $10^{-5}M$.

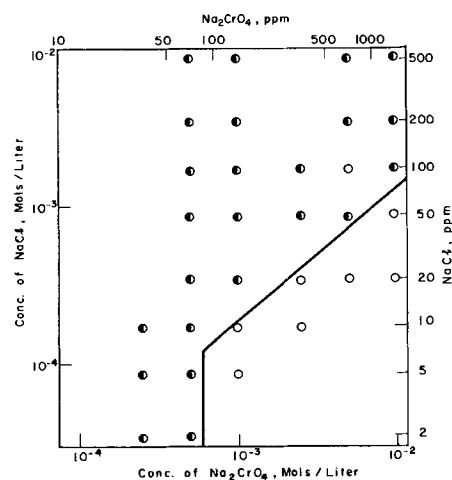


Fig. 5. Effect of $NaCl$ addition on corrosion of iron in air-saturated Na_2CrO_4 solution at 25°C (by weight loss for 5 day immersion). Open circle, No pitting, <1 mdd; half dark circle, some pitting, <10 mdd.

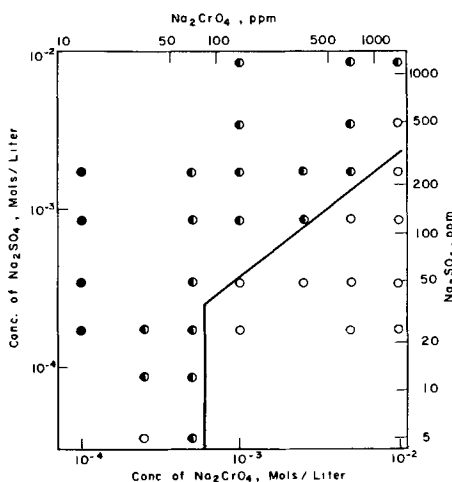


Fig. 6. Effect of Na_2SO_4 addition on corrosion of iron in air-saturated Na_2CrO_4 solution at 25°C (by weight loss for 5 day immersion). Open circle, No pitting, <1 mdd; half dark circle, some pitting, <10 mdd; dark circle, extensive pitting, >10 mdd.

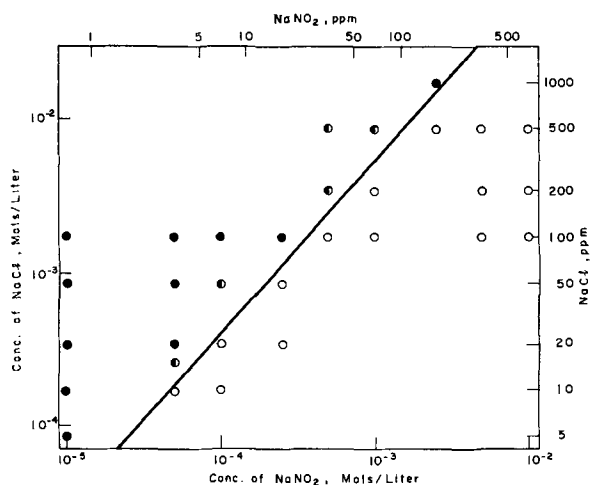


Fig. 7. Effect of NaCl addition on corrosion of iron in air-saturated NaNO_2 solution at 25°C (by weight loss for 5 day immersion). Open circle, No pitting, <1 mdd; half dark circle, some pitting, <10 mdd; dark circle, extensive pitting or general corrosion, >10 mdd.

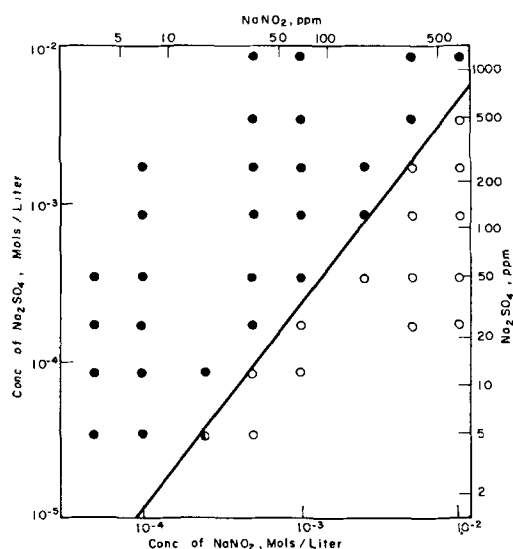


Fig. 8. Effect of Na_2SO_4 addition on corrosion of iron in air-saturated NaNO_2 solution at 25°C (by weight loss for 5 day immersion). Open circle, No pitting, <1 mdd; half dark circle, some pitting, <10 mdd; dark circle, extensive pitting or general attack, >10 mdd.

Although the 5 day exposure period was arbitrary, results obtained within this time apparently apply to longer times as well. A few spot checks for passivator, chloride and sulfate concentrations in which Armco iron foil specimens were immersed for 70 days instead of 5 days followed the prediction of Fig. 5-8. The concentrations chosen were $0.01M$ Na_2CrO_4 containing either 50 ppm NaCl or 243 ppm Na_2SO_4 , and $0.01M$ NaNO_2 containing either 100 ppm NaCl or 243 ppm Na_2SO_4 . No pitting, visible corrosion, or weight loss was found at the end of the 70 days.

The critical concentrations of sulfate and chloride at a specific passivator concentration would, in principle, be expected to hold for indefinite exposure periods provided the passivator concentrations are maintained and the metal surface is clean. Passivator in small amount is reduced and consumed in any metal system on which a passive film is formed.

Table I. Values of constants in $\log M_s = a + b \log M_p$ Expressing critical molarity of salt (M_s) above which increased corrosion and pitting of iron occurs in passivator solutions of molarity (M_p)

Solution	a	b
$\text{Na}_2\text{CrO}_4 + \text{NaCl}$	-1.19	0.85
$\text{Na}_2\text{CrO}_4 + \text{Na}_2\text{SO}_4$	-1.09	0.79
$\text{NaNO}_2 + \text{NaCl}$	1.10	1.13
$\text{NaNO}_2 + \text{Na}_2\text{SO}_4$	0.30	1.31

In presence of organic contamination capable of reacting with the passivator, consumption would be more rapid. Furthermore, in presence of crevices or surface films, and with lack of stirring, eventual breakdown of passivity would be expected at the metal surface shielded from renewed concentration of passivator. A passive-active cell is established, followed by deep pitting of the shielded area. In absence of these situations, however, inhibition of corrosion would continue undiminished.

Referring to Fig. 5-8, the critical concentrations separating increased corrosion and pitting from uniformly passive and nonpitting behavior follow the general relation

$$\log M_s = a + b \log M_p \quad [1]$$

where M_s is molarity of NaCl or Na_2SO_4 , M_p is molarity of passivator, and a and b are constants. Values of a and b as obtained from data of the figures are listed in Table I.

It is obvious from the data that in nitrite solutions, sulfates are more effective than chlorides in breaking down passivity, whereas the reverse is true of chromate solutions. This also has been observed in practice (4). In addition, higher concentrations of chloride or sulfate are required to corrode iron in presence of nitrites compared to chromates. Pitting of iron in chromates appears to be deeper than in nitrites, particularly in presence of sulfates.

Effect of pH on inhibition by chromates.—Nitrites inhibit only above pH 6 because of decomposition into NO and NO_2 in more acid solutions. Chromates, on the other hand, may inhibit over a wider pH range depending on concentration of specific anions that are present. Effect of pH on corrosion rates was measured using the electric resistance method. Solutions of $10^{-2}M$ Na_2CrO_4 were adjusted in pH to alkaline values using NaOH low in carbonates, and to acid values using either H_2SO_4 or HClO_4 . All solutions were deaerated using purified hydrogen. In general, steady-state corrosion rates were preceded by higher corrosion rates lasting 1 to 3 hr. Steady-state values are plotted in Fig. 9. For fully inhibited specimens, measurements of the corresponding low corrosion rates led to some scatter of results, the average rate being 0.08 mdd. In the acid range, inhibition continued in the presence of perchlorate ions to pH 2.85 which was the lowest value included in the tests. In presence of sulfate ion, increase in the corrosion rate began at and below pH 5. Pitting occurred when the sulfate concentration approached the critical value through acid additions to approximately pH 3.

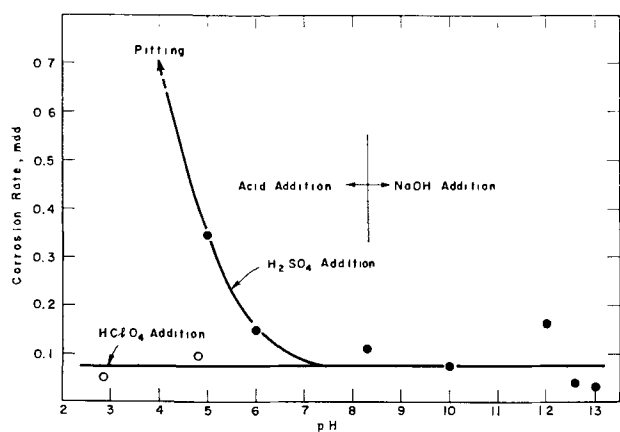


Fig. 9. Steady-state corrosion rate of iron in H_2 -de-aerated $0.01M Na_2CrO_4$ solution at $25^\circ C$ as a function of pH (by electric resistance method).

Effect of temperature.—Measurements were carried out in air-saturated $10^{-2}M Na_2CrO_4$ solutions at 25° , 40° , and $100^\circ C$. Measurements at $100^\circ C$ were complicated by a change in electric resistance of the iron spiral caused by precipitation of iron carbides from supersaturated interstitial carbon in ferrite (quench-aging). Through measuring the resistance of the quenched spiral in dried xylene at $100^\circ C$, it was established that the resistance first increased by 0.35% after approximately the first hour, then decreased to a value 0.18% below the initial value, reaching a steady-state value after 40 hr. These measurements were used to correct changes in resistance during the corrosion tests.

Except for higher initial corrosion rates at higher temperatures, steady-state values were all low and appeared to be as low as or lower than rates at lower temperatures. Too few experiments were done to provide reliable quantitative comparisons in this respect. Steady-state values at all temperatures were less than 0.1 mdd.

Discussion

Based on data from many sources, a reasonable theory of passivation by nitrites or chromates ascribes formation of the passive film to polarization of anodic areas of the metal. At a concentration of chromate or nitrite above the critical value, reduction of NO_2^- or CrO_4^{--} adsorbed at cathodic areas establishes current densities which reach the critical value for anodic passivation (5, 6). Initially, therefore, the rate of reaction between metal and passivator is high until the passive film is established uniformly over the surface. The electric resistance method confirms that a high initial reaction rate takes place. It requires about 1 to 3 hr to reach steady-state conditions. At this stage of events, CrO_4^{--} or NO_2^- ions are adsorbed on the passive film itself and are available by reduction to supply electric current necessary for anodic passivation of any portions of the passive film requiring repair. In presence of Cl^- or SO_4^{--} , necessary repair is more frequent than otherwise and, hence, consumption of passivator ions increases with chloride and sulfate concentration. Increased consumption of passivator under these conditions is well-known in prac-

tice. Should the concentration of disturbing anions reach a critical concentration at which they permanently displace adsorbed passivator ions at local areas and become adsorbed themselves, then the passive film suffers permanent local damage and pitting results. A large cathode area surrounding a small anode area leads to high current densities at the anode.

The relative proportions of passivator or of sulfate or chloride adsorbing on the passive film, according to the above described mechanism, determines whether or not pitting takes place. Which particular species succeeds in the competitive adsorption process depends on relative concentrations of specific ions and their relative affinities for the passive surface. Expressed quantitatively by the Freundlich adsorption isotherm, the amount of substance adsorbed per unit area of passive surface is related to the concentration of anions in solution, where, by Henry's law, "concentration" substitutes for the usual "gas pressure" term. Accordingly

$$a_s = k_1 M_s^{1/n_1} \quad [2]$$

and

$$a_p = k_2 M_p^{1/n_2} \quad [3]$$

where M_s and M_p are molarity of salt and passivator respectively, a_s and a_p are amounts of substance adsorbed per unit area of passive surface, and k and n are constants. The following ratio then holds

$$\frac{a_s}{a_p} = \frac{k_1 M_s^{1/n_1}}{k_2 M_p^{1/n_2}} \quad [4]$$

At a specific critical ratio a_s/a_p , which can be set equal to C , the passive film breaks down locally (first at a particularly vulnerable site). It follows that

$$\log C = \log \frac{k_1}{k_2} + \frac{1}{n_1} \log M_s - \frac{1}{n_2} \log M_p \quad [5]$$

or

$$\log M_s = n_1 \log C - n_1 \log \frac{k_1}{k_2} + \frac{n_1}{n_2} \log M_p \quad [6]$$

Equation [6] has the same form as empirical Eq. [1] where a equals $n_1 \log C - n_1 \log k_1/k_2$ and b equals n_1/n_2 . Values for b should approximate unity if values of n in the Freundlich adsorption isotherm are similar. Empirical values of b in Table I average 1.02 with maximum deviation of 0.29. Values of a in Table I are larger for nitrites than for chromates. According to Eq. [6], assuming C to be approximately constant, k_2 , therefore, must be larger for nitrites than for chromates. This corresponds to greater tendency for NO_2^- to adsorb on the passive film than for CrO_4^{--} . This relation is in fact borne out by the greater concentration of Cl^- and SO_4^{--} necessary to break down passivity of iron in presence of nitrite (Fig. 5-8) and also by the observed lower critical concentration of nitrite ($<1 \times 10^{-5}M$) compared to chromate ($5 \times 10^{-4}M$). In the competitive adsorption of passivator with SO_4^{--} or Cl^- , the greater affinity of NO_2^- for the passive film makes it less sensitive to concentrations of disturbing anions than is the case for chromates.

The effect of pH on corrosion, shown in Fig. 9, is also explained by competitive adsorption. In the acid

region, SO_4^{--} competitively adsorbs with CrO_4^{--} , and the concentration of SO_4^{--} increases as the pH decreases through additions of H_2SO_4 . Higher concentration of SO_4^{--} is accompanied by greater tendency of SO_4^{--} to adsorb, followed by increased corrosive attack. Perchlorate ions, on the other hand, do not tend to adsorb in general, and hence, the passive film is undisturbed even at a pH as low as 2.85. Lack of an effect by HClO_4 additions indicates that the passive film in presence of CrO_4^{--} is inherently insensitive to change in pH between at least 2.8 and 13. The breakdown of passivity in the acid region for chromate-inhibited systems, which is sometimes observed, seems, therefore, to derive from increased anion concentrations such as SO_4^{--} or Cl^- rather than from increased H^+ concentration.

In this connection, there seems to be no marked tendency for OH^- to displace CrO_4^{--} adsorbed on the passive film at pH values as high as 13. Were such competitive adsorption to succeed, one would expect an increase in corrosion rate in the alkaline region, but this is not found. The corrosion rate of iron in deaerated 0.01M Na_2CrO_4 at pH 13 is 0.03 mdd, whereas the corrosion rate in deaerated NaOH of pH 13 equals 0.51 mdd. These results indicate, therefore, that chromates continue to adsorb in the alkaline region up to at least pH 13.

Powers and Hackerman (3) found that iron exposed to $1 \times 10^{-3}\text{M}$ Na_2CrO_4 containing radioactive Cr^{51} at and above pH 11 showed no detectable radioactivity on the metal surface, the specimen being subsequently washed with distilled water. Below pH 11, radioactive Cr was found. This means according to our corrosion rate measurements that reduced CrO_4^{--} products and adsorbed CrO_4^{--} ions were washed off by water in the very alkaline range of pH before residual Cr^{51} on the surface was counted, contrary to the state of affairs below pH 11. This behavior fits the known tendency of OH^- to form soluble complexes with chromium salts.

The above results together with those previously discussed support the view that competitive adsorption determines whether a given concentration of passivator will succeed in inhibiting corrosion in presence of Cl^- or SO_4^{--} . The pH of the solution is not a sensitive factor, discounting effects of anions

which happen to accompany H^+ . On the other hand, pH probably becomes important at the critical concentration of passivator ($5 \times 10^{-4}\text{M}$ for Na_2CrO_4) because of the sensitivity of Flade potential to pH. The corrosion potential of iron in $1 \times 10^{-3}\text{M}$ Na_2CrO_4 , which lies above the critical concentration, we found to be +0.09v on the hydrogen scale. Since the Flade potential of iron in chromates follows the relation $\phi_F(\text{volt}) = 0.54 - 0.059 \text{ pH}$ (6) and the measured pH of $1 \times 10^{-3}\text{M}$ Na_2CrO_4 is 8, the corresponding Flade potential is +0.07v. This value is less noble than the observed corrosion potential and accounts for observed stable passivity. Below the critical concentration, e.g., $1 \times 10^{-4}\text{M}$ Na_2CrO_4 , the corrosion potential on the hydrogen scale is -0.38v. This value lies definitely on the active side of the Flade potential and explains why passivity does not occur at this chromate concentration or below. In presence of Cl^- or SO_4^{--} , however, passivity may break down even if the corrosion potential lies at values noble to the Flade potential. This breakdown occurs because the passivator ion is displaced on the passive metal surface by Cl^- or SO_4^{--} , and also because the passive film itself is displaced at sites where competitive adsorption succeeds. In absence of passive film at such sites, a passive-active cell is set up with pronounced corrosion at the anodes accompanied by pitting.

Acknowledgment

This research was supported jointly by The Shell Oil Companies in the U. S. and by the Office of Naval Research on Contract No. Nonr 1841(09) Nr036-007 to whom the authors express their appreciation.

Manuscript received May 22, 1963. This paper was presented at the Boston Meeting, Sept. 16-20, 1962.

Any discussion of this paper will appear in a Discussion Section to be published in the December 1964 JOURNAL.

REFERENCES

1. W. D. Robertson, *This Journal*, **98**, 94 (1951).
2. M. Pryor and M. Cohen, *ibid.*, **100**, 203 (1953).
3. R. Powers and N. Hackerman, *ibid.*, **100**, 314 (1953).
4. S. Sussman, O. Nowakowski, and J. Constantino, *Ind. Eng. Chem.*, **51**, 581 (1959).
5. M. Stern, *This Journal*, **105**, 638 (1958).
6. H. H. Uhlig and P. King, *ibid.*, **106**, 1 (1959).

The Uptake of Sulfur from Plating Brighteners by Copper and Nickel

John J. Hoekstra¹ and Dan Trivich

Department of Chemistry, Wayne State University, Detroit, Michigan

ABSTRACT

The uptake of radioactive S³⁵ from thiourea by single crystal spheres of copper and nickel was found to increase with increasing concentration of thiourea in the solution, but showed no preference for any crystal face. Allyl sulfonate labelled with S³⁵ was not taken up by nickel under several conditions of simple immersion, but was included under conditions of nickel electrodeposition. Dissolution of the electrodeposits in HCl caused the included sulfur to be evolved as H₂S, as shown by tracer experiments, quantitative analysis, and x-ray diffraction identification.

It is a common practice in the electroplating industry to use various addition agents (1) in metal plating baths to alter the character of the electrodeposits obtained from a given plating bath. One of the most marked changes thus effected by the use of addition agents is the production of mirror like electrodeposits from a plating bath which otherwise produces dull, matte deposits. Although addition agents have been used for at least several decades to produce bright electrodeposits, a completely satisfactory explanation of the mechanism by which the addition agent, or brightener, changes the character of the electrodeposit obtained has not been developed. The present research was undertaken to obtain experimental data which might lead to a better understanding of the mechanism of brightener action. The work to be described consists of two parts: (a) study of the surface reactions of certain brighteners with copper and nickel single-crystal substrates, and (b) study of the fate of the brightener during electrodeposition using sodium allylsulfonate (SAS) (2) in nickel electrodeposition. For most of the work, the respective brighteners were labelled with radioactive S³⁵ for tracer purposes. A previous investigation (3) in this laboratory described some aspects of the interaction of thiourea with single crystals of copper in "adsorption" and electrodeposition.

Experimental Materials

Radioactive brighteners.—(Thiourea).—In the previous study (3) in this laboratory, thiourea-S³⁵ was prepared by the method of Bills and Ronzio (4). Since then, thiourea-S³⁵ has been made available by Tracerlab, Inc., and, as a matter of convenience, this source of thiourea-S³⁵ was used for the present study.

Sodium allyl sulfonate.—The allyl sulfonate was prepared by a micro-adaptation developed in this laboratory of the classic Strecker synthesis (5) for sulfonic acids, which consists of reacting allyl bromide with sodium sulfite. For the synthesis of the labelled allyl sulfonate, sodium sulfite-S³⁵ supplied by Tracerlab, Inc., was used. A pilot run, using iden-

tical amounts of nonradioactive material, was always made concurrently.

In a typical run, 1 mM of sodium sulfite-S³⁵ was placed in a small glass-stoppered reaction tube, followed by 0.55 ml of distilled water and 0.30 ml of freshly distilled (colorless) allyl bromide. The reaction tube was stoppered and then held at 60°C for 30 hr. This was followed by a prolonged ether washing to remove excess allyl bromide. The solution was then treated with three drops of saturated barium hydroxide solution to remove unreacted sulfite or any sulfate ion formed. In this work no detectable precipitate or cloudiness could be observed, indicating the completeness of the reaction. Evaluation of this test showed it to be capable of detecting one part of sulfate or sulfite ion in 2000 parts of sodium allyl sulfonate under these conditions.

The barium was precipitated by saturation of the solution with CO₂ and the barium carbonate was removed by centrifugation. The solutions were transferred to weighing bottles, evaporated to dryness with an infrared lamp, and then weighed to obtain the weight of the products, sodium allyl sulfonate and sodium bromide. The concurrent pilot run was analyzed for sodium bromide by the Volhard method, and the weight of the sodium allyl sulfonate was obtained by difference. The yield of the radioactive run was taken to be that of the parallel pilot run. The yields of final material for many "cold" runs was always close to 97% of theoretical.

The product was characterized by comparison with authentic Eastman Kodak Company product using infrared spectra and microanalysis. Microanalyses of the standard Eastman Kodak sample gave C, 25.34%; H, 3.57%; and S, 22.45% compared with theoretical values of C, 25.00%; H, 3.49%; and S, 22.25%.

In most cases, to avoid further handling, the sodium bromide was not removed from the sample, since bromide has been shown not to interfere in the electrodeposition of bright nickel.

Preparation of single crystal spheres.—Single crystal spheres were machined from copper and nickel single crystal rods by means of a lathe at-

¹ Present address: Dow Chemical Co., Midland, Michigan.

tachment developed here (6). After machining, the spheres were mechanically polished with successively finer metallographic papers through 4/0 grade. This was followed by electropolishing in the appropriate baths until etching showed that all of the worked material had been removed. The copper single crystals were grown in this laboratory by variations of the Bridgman technique; nickel single crystals were obtained from the Virginia Institute for Scientific Research and from Horizons, Inc. The utility of single crystal spheres and the methods of handling them have been established especially by Gwathmey and co-workers (7).

Apparatus—The apparatus developed here for use in the single crystal studies is shown collected in the photograph of Fig. 1. A two-circle goniometer (A) was used to determine the crystallographic orientation of each of the single crystal spheres and also to locate particular crystal faces for observation by radio tracer techniques. The goniometer can be mounted with a Geiger counter-tube housing (B) on a track which serves to locate them in a fixed relation to each other. A small aperture in the nose of the Geiger housing is used to scan a restricted area of interest on a crystal sphere mounted in the goniometer. At (C) is shown a single crystal sphere permanently mounted in a keyed holder which fits into the keyed socket of the goniometer. This holder allows relocation of any chosen crystal face of any particular crystal sphere during a series of experiments. The etch-pit method and stereographic projection techniques as described by Barrett (8) were used to determine the crystallographic orientation of each of the crystals and to locate (100), (110), and (111) faces on them. A jig which is used to mount the crystal spheres in their holders is shown at (D). This jig insures that the center of the mounted crystal sphere will be on a horizontal axis of the goniometer when the holder is inserted in the goniometer socket.

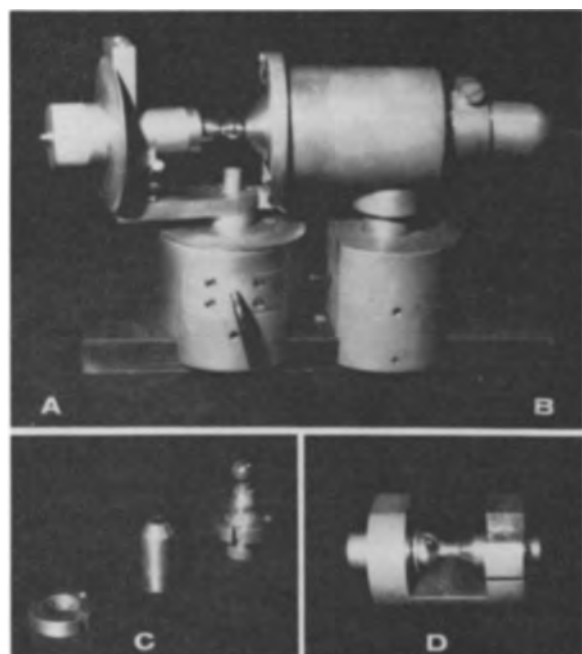


Fig. 1. Two-circle goniometer and associated equipment used for single crystal studies.

Several other techniques and pieces of equipment (not illustrated) have been developed in this laboratory for the study of the single crystal spheres. These include provision for mounting of the goniometer on the track of an x-ray diffraction apparatus, a combination illuminator-telescope for determining orientation by the etch-pit method, and a horizontally mounted metallurgical microscope. Since each of these can be accurately positioned with respect to the goniometer, the system of apparatus allows examination of any chosen spot on a sphere by a variety of techniques.

Surface Reaction Studies

Procedures.—Thiourea on copper.—The experimental studies of the reaction of thiourea on the surfaces of copper crystal spheres were conducted in the following manner. Immediately before each immersion experiment, the crystal to be studied was run through the following cleaning cycle to remove any dust, grease, or radioactivity remaining from a previous experiment: (i) three times through a dilute hydrochloric acid dip and tap water rinse; (ii) cathodic cleaning for 5 min; (iii) tap water rinse. The crystal was then electropolished in 43% H_3PO_4 for 2 min to provide a new experimental surface. After electropolishing, the crystal was rinsed according to a procedure found by Simpson and Hackerman (9) to leave no phosphate ion contamination of the new copper surface. The rinsing procedure was followed by a final 30 sec dip in dilute hydrochloric acid and a 30 sec distilled water rinse. The adhering rinse water was quickly removed by touching the neck of the crystal with a piece of filter paper. The crystal was immediately immersed in the experimental thiourea- S^{35} solution, which was in contact with air.

After immersion for 30 min, the crystal was removed and placed upright in a water vapor saturated atmosphere to drain. This step was taken to avoid concentration changes of the solution on the crystal by evaporation. After draining 15 min, the excess solution was removed from the neck of the crystal with a piece of filter paper, and the crystal was placed in a desiccator to dry.

The crystal was next placed in the goniometer and examined for radioactivity. The activity on three each of the (100), (110), and (111) faces was measured.

Three copper crystals were studied in these experiments; one crystal which would always become pitted during the electropolishing process and two nonpitting crystals. The pits on the one crystal may possibly have been due to crystal faults as microscopic observation showed them to occur in rows near certain crystal directions. The crystals were immersed in aqueous thiourea- S^{35} solutions of the following molarities: 9.66×10^{-4} , 9.66×10^{-5} , 4.33×10^{-5} , 2.17×10^{-5} , 1.95×10^{-5} , 4.33×10^{-6} , and 2.17×10^{-6} .

On nickel.—Two nickel crystal spheres were prepared for the immersion experiments by passing them through a preparative procedure similar to that used for copper. The electropolishing was done in

an $\text{H}_2\text{SO}_4\text{-H}_3\text{PO}_4\text{-HCl}$ solution (10) at 60°C at a current of 5 amp for a $\frac{1}{2}$ -in. diameter crystal.

Two reaction systems were studied with the nickel crystals: exposure to thiourea and exposure to sodium allyl sulfonate. Concentrations of the thiourea- S^{35} solutions studied were 9.66×10^{-4} , 4.83×10^{-5} , and $2.42 \times 10^{-5}\text{M}$.

The nickel-thiourea experiments were conducted in the same manner as the copper-thiourea experiments. The sodium allyl sulfonate- S^{35} solution contained 2g of the brightener per liter since this is a concentration appropriate for bright nickel plating. A number of variations of experimental conditions were used in the study of the nickel-allyl sulfonate system. After the preparative process, separate experiments were performed as follows: (a) immersion of the single crystal sphere in a water solution of SAS; (b) immersion in a water solution of SAS adjusted to pH 2.8; (c) 5 min immersion of the crystal sphere in 6N HCl followed by immersion in SAS solution; (d) 3 min cathodic gassing of the sphere in 6N HCl followed by immersion in SAS solution; (e) 3 min cathodic gassing of the sphere in 6N HCl followed by immersion in SAS solution with a cathodic potential applied just short of that required for visible gas evolution.

Results of the surface reaction experiments.—Copper-thiourea- S^{35} system.—Examination of the copper crystal spheres by means of the goniometer-Geiger counter apparatus showed that radioactive sulfur was present on the crystals following immersion in the radioactive thiourea solutions. The examination did not reveal any statistically significant differences in the amounts of radioactivity present on the (100), (110), or (111) faces of the copper crystals. The graph of Fig. 2 is a log-log plot of the radioactivity, averaged over all three crystals, as a function of the thiourea concentration. The plot has some resemblance to a Freundlich isotherm. The slope of the plot, $n = \Delta \log R / \Delta \log C$, is 0.5 indicating that the measured radioactivity on the crystal surfaces is proportional to the square root of the solution concentration.

Although in the above experiments the behavior of the pitting crystal previously noted was not appreciably different from that of the nonpitting crystals, a very slight modification of the experimental procedure resulted in a detectable difference. If the

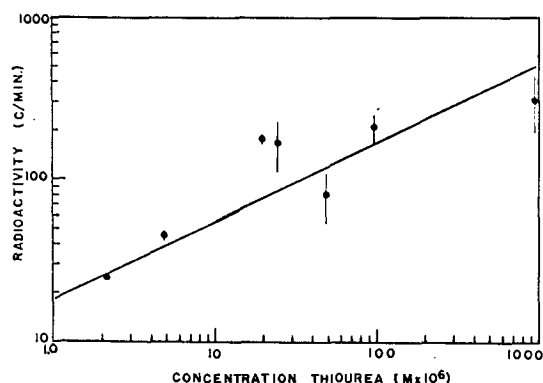


Fig. 2. Amount of S^{35} taken up by single crystal spheres of copper as a function of the thiourea concentration in the solution.

last thirty-second dilute hydrochloric acid dip and thirty-second distilled water rinse were omitted from the preparative procedure, it was found that the pitting crystal would take up radioactivity while the nonpitting crystals would not. For comparison, in an experiment using a $1.65 \times 10^{-5}\text{M}$ thiourea- S^{35} solution, the activity of the pitting crystal averaged 80 cpm while no significant activity could be detected on the nonpitting crystals. This suggests an influence of dislocations which becomes apparent when the crystals have a thin film of oxide.

Nickel-thiourea system.—Results of thiourea- S^{35} experiments with nickel single crystals were similar to those obtained with copper crystals although the amount of radioactivity found on the nickel crystals was much less than that found on the copper crystals for the same thiourea concentration. Again, the experimental data did not indicate any marked differences in the amount of radioactive sulfur found on the different crystal faces.

Nickel-allyl sulfonate systems.—The results of all of the experiments performed with nickel and sodium allyl sulfonate solutions indicate that the allyl sulfonate does not react with the surfaces of the nickel crystals under these nonplating conditions. No appreciable radioactivity was detected on either of the nickel crystals by means of the goniometer-counter apparatus.

Effect of Electrodeposition on Allylsulfonate

Since it was established that the sodium allyl sulfonate was not taken up by nickel under nonplating conditions, and since it is known (11) that bright nickel electrodeposits do contain more sulfur than plain Watts nickel deposits, this suggested that the brightener is taken up by the nickel through an electrochemical process. Therefore further experiments were undertaken to determine the fate of the allyl sulfonate during the course of electrodeposition. These experiments included quantitative determination of the amounts of sulfur taken up as a function of plating time, current density, and brightener concentration, and also experiments designed to characterize the form in which the sulfur was included.

Inclusion of sulfur in nickel electrodeposits.—As a function of plating time.—The basis metal for the electrodeposition was a copper film vacuum evaporated on Lucite reproductions of a $5/16 \times 3/4$ in. section of a $60 \mu\text{in.}$ roughness standard (12). The plating bath was 75 ml of Watts nickel solution (300 g/l $\text{NiSO}_4 \cdot 6\text{H}_2\text{O}$, 60 g/l $\text{NiCl}_2 \cdot 6\text{H}_2\text{O}$, 40 g/l H_3BO_3) containing 0.14g of radioactive sodium allyl sulfonate and 0.01g of nonradioactive sodium allyl sulfonate, giving a concentration of 2 g/l. Separate samples were plated with nickel at 60 amp/ft² (6.5 amp/dm²), 60°C and pH 3, for 5, 10, 15, and 20 min. The relative radioactivity measured with a counter on a $1/8 \times 7/16$ in. area is given as a function of plate thickness in Fig. 3.

Amount of sulfur as a function of concentration and current density.—Samples of bright nickel electrodeposits were obtained by plating on passivated nickel cathodes, 1×3 in.² in area, in Watts baths of

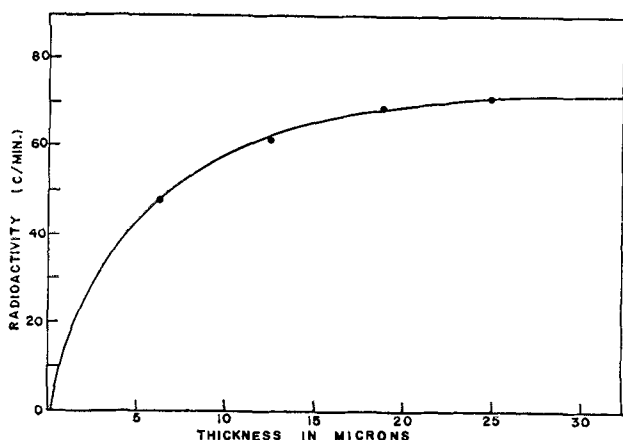


Fig. 3. Amount of radioactivity measured on nickel electrodeposits of various thicknesses plated from a Watts nickel bath containing 2 g/l of sodium allylsulfonate- S^{35} .

800 ml volume containing 2.5 or 7.5 g/l of SAS and at current densities of 30, 60, and 90 amp/ft² and a temperature of 60°C. Bar agitation was used, consisting of 10 cm lineal travel and a period of 3 sec. The pH was adjusted to 2.9-3.0 at the beginning of each plating run and was found never to rise above 3.1-3.2 during the run. Electrodeposits were stripped and analyzed for sulfur by a method (13) suitable for the determination of S in steel. This involved dissolving the sample in concentrated HNO₃ and precipitating the resulting sulfate with barium. Results are given in Table I.

Characterization of brightener degradation products.—Since the sulfur of the SAS was shown to be included in the nickel electrodeposit, it became of interest to inquire as to the form in which the sulfur was included. This inquiry was pursued by a variety of qualitative and quantitative techniques using both radioactive and non-radioactive forms of SAS. **Deposit dissolution studies.**—The following tests and observations were made:

1. A sample of bright nickel electrodeposit plated from a bath containing radioactive SAS was dissolved in concentrated HNO₃ and the resulting solution was found to be radioactive.

2. A similar bright electrodeposit was dissolved in 1:1 HCl. The gases evolved were passed over moist lead acetate paper, which then became black. After complete dissolution of the plate, the solution was boiled to drive off any volatile material. The blackened lead acetate paper was radioactive, while the remaining nickel chloride solution showed no detectable radioactivity.

2A. Control experiments were also performed. In one of these, reagent grade nickel shot was dissolved in 1:1 HCl solution containing dissolved SAS. No volatile sulfur could be detected with the lead

Table I. Percentage of sulfur in nickel electrodeposits as functions of current density and brightener concentration

SAS Conc., g/l	Current density, amp/ft ²		
	30	60	90
	%	%	%
2.5	0.0315	0.0311	0.0304
7.5	0.0457	0.0491	0.0476

acetate paper. In another test, allyl mercaptan was generated by hydrolysis of allyl thiuronium bromide with NaOH solution and gave a yellow color with the lead acetate paper.

3. Larger samples of bright nickel electrodeposits were dissolved in concentrated HNO₃ and analyzed for sulfate. Similar samples were dissolved in HCl, and the evolved gases were caught in ammoniacal hydrogen peroxide solution and analyzed for sulfate. The results were: total sulfur, 0.024%; acid volatile sulfur, 0.0214%, indicating that, within experimental error, practically all of the sulfur in the plate is in a form that is volatile on dissolution of the plate in HCl.

4. Gases evolved from dissolution in HCl were tested with a mass spectrometer, and a peak corresponding to H₂S was found, but mixed with peaks belonging to oxygen, nitrogen, water vapor, and some presumably background hydrocarbon material.

Quantitative characterization.—Since the exploratory tests showed that the sulfur from the SAS eventually showed up as a volatile compound on dissolution of the plate in HCl and strongly suggested that the volatile compound was hydrogen sulfide, further tests were undertaken to confirm this. In one set of experiments, the volatile sulfur compound was precipitated as a mercuric salt (14), the precipitate was dissolved in aqua regia, and the mercury was reprecipitated with authentic hydrogen sulfide. The weight of this final precipitate was compared with the initial mercury precipitate with the unknown sulfur compound. Mercury was chosen because mercuric sulfide can be dried and weighed quantitatively, and the method used is a standard one for mercury determinations. The deviation between the weights of the initial and final precipitates averaged 7% for four determinations. This leads to the fairly safe conclusion that the initial precipitate was HgS, perhaps slightly contaminated with other materials, since any other conceivable sulfur compound such as a mercaptan, would give larger deviations than those observed.

X-ray diffraction tests.—The initial mercury precipitate with the unknown acid-volatile sulfur compound was examined by x-ray diffraction and compared with authentic HgS prepared under similar conditions. Agreement was found between the two patterns, both with respect to the location of the lines and the peak heights. Both patterns agreed also with values published for black cubic HgS (15), as shown in Table II. Thus it can be concluded that the

Table II. X-ray diffraction lines for mercury salt of unknown volatile sulfur compound and for authentic HgS

2θ (deg) for unknown sulfur compound	2θ for authentic HgS	Literature values for HgS		
		d (Å)	I/I ₀	Calc. 2θ
26.6 (100+)	26.5 (100)	3.378	100	26.4
30.9 (38)	30.7 (32)	2.926	34	30.6
44.3 (43)	43.9 (39)	2.068	57	44.0
52.0 (36)	51.9 (28)	1.764	45	51.6

The diffraction angles were read from chart recordings made on the spectrometer goniometer of a Norelco x-ray diffraction unit using the 1.54 Å Cu Kα radiation. The figures in parentheses are estimated peak heights and are not quantitatively comparable because of some line broadening in the unknown. The order of intensities is nevertheless satisfactory.

volatile sulfur compound from the dissolution of the bright nickel electrodeposits in HCl is hydrogen sulfide gas.

Discussion

It is generally believed that adsorption of the addition agents or their products on the surface of the metal electrode is important in bright plating and levelling phenomena. Also it is known (1b) that effective addition agents must possess certain specific structural features. The present experiments with single crystal metal spheres were undertaken in order to detect any possible preferential interaction of certain crystal faces of the metal with the addition agent compounds such as might arise from a match of interatomic spacings in the compound and a particular crystal face. Gwathmey and co-workers have shown a number of cases of such preferential action of certain crystal faces of single crystal metal spheres in oxidation (7f), wetting (7e), catalysis (7a), etc.

Since the present experiments with sulfur-containing compounds did not show the postulated specific interaction with particular crystal faces of the metal, this suggests that the necessity for specific structural features in these addition agent compounds has some purpose other than rendering them susceptible to adsorption. An alternative possible explanation is shown, in the present experiments, by the results obtained with allyl sulfonate. The experiments show that allyl sulfonate is not adsorbed appreciably on nickel in simple immersion, but the tracer sulfur is included in the plate under conditions of nickel electrodeposition and further that the sulfur is included in some electrochemically reduced form, most probably sulfide ion. Thus it appears that effective sulfonate-type addition agents in nickel electrodeposition are those whose structures allow successful electrochemical reduction of the sulfonate radical. A number of authors (1, esp. 1c), have suggested that sulfonates are reduced during nickel electrodeposition and several (1, 16) have postulated the incorporation of the sulfur in the plate in the form of sulfide, but these conclusions were usually inferred from indirect observations. In the case of allyl sulfonate, the present experiments show fairly conclusively that all of the sulfur incorporated in the plate from the brightener is evolved as hydrogen sulfide upon dissolution of the plate. While some, and perhaps all, of the reduction of the sulfonate must occur electrochemically during the electrodeposition of nickel, the possibility exists that a portion of the reduction and perhaps cleavage occurs during the dissolution. Dissolving nickel, hydrogen on nickel, or even active nickel containing hydrogen are quite capable of performing this reduction especially on susceptible sulfur compounds, as shown, for example, by Raney nickel reductions and removal of sulfur containing groups in a variety of organic sulfonic acids (17), sulfoxides, sulfones, and sulfides (18). The question in the case of allyl sulfonate is whether any reduction remains to be done by the dissolution step or whether all of the reduction and cleavage has already been effected during the electrodeposition. Beacom and Riley (19),

who studied by tracer methods the incorporation of both carbon and sulfur from allyl sulfonate in nickel electrodeposits, concluded that some cleavage must occur since they observe the ratio of incorporated carbon to sulfur to depart from a 3 to 1 ratio by more than their experimental error of determination. More direct evidence of the electrochemical reduction of allyl sulfonate has been obtained by Gotthard and Trivich (20) who carried out electrolyses of the compound in $\text{NaHSO}_4\text{-H}_3\text{BO}_3$ solutions in the absence of nickel electrodeposition, but under conditions closely similar to nickel electrodeposition. These authors found the reduction products to consist of sulfite, H_2S , and propylene together with some propane, and further that the ratio of $(\text{SO}_2 + \text{H}_2\text{S})$ to (propylene + propane) was 1:1. From this they concluded that cleavage occurs early in the electrochemical reduction of allyl sulfonate and that the sulfite is further reduced to sulfide. No evidence was found for any mercaptan as an intermediate in the reduction sequence. In the case of aromatic sulfonates as addition agents, DuRose (1c) found the sulfur content of the nickel electrodeposits to be significantly higher than the carbon content, thus supporting the hypothesis of cleavage during electrodeposition. Presumably allyl sulfonate behaves in a similar fashion to the aromatic sulfonates.

It therefore appears that the active principle involved is sulfide ion and that the function of sulfonate type addition agents is to furnish the sulfide in suitably small amounts as needed and where needed to produce the desired effects of bright plating and perhaps levelling.

The inclusion of sulfur in the nickel electrodeposit occurs continuously and fairly uniformly during electrodeposition as shown by Fig. 3 and Table I. The limiting radioactivity reached for thick electrodeposits is due to self-absorption and screening of the deep-lying S^{35} by the overlying electrodeposit. The data of Fig. 3 can be fitted with the theoretical equation for self-absorption, $R = R_\infty(1 - e^{-\mu d})$, in which R is the observed radioactivity at any thickness, d , and R_∞ is the observed radioactivity for infinite thickness. The absorption coefficient, μ , has an average value of $1.7 \times 10^3 \text{ cm}^{-1}$ for the data in Fig. 3. This yields a value of $0.19 \text{ cm}^2/\text{mg}$ for the mass absorption coefficient, μ/ρ , which compares favorably with the average value of $0.22 \text{ cm}^2/\text{mg}$, quoted by Beacom and Riley (19).

The constancy of the sulfur content of the electrodeposits with variation in current density shown in Table I is not in agreement with results of Raub and Wittum (21) on other sulfonates and the results of Beacom and Riley (22) on allyl sulfonate. Probably the difference can be ascribed to differences in diffusion rates and agitation conditions. In the results of this paper, the supply of allyl sulfonate to the electrodes has apparently not reached a limiting diffusion rate, and the incorporation is controlled by the surface electrochemical process which in turn is determined by the current density. Thus an increase in current density which increases the rate of electrodeposition of nickel also increases proportionately the electrochemically produced and included sulfur so that the sulfur to nickel ratio remains constant.

Using another approach, Kardos [quoted in ref. (23)] studied the rate of disappearance of allyl sulfonate from the plating bath, and he concluded that the total rate of consumption gave evidence for diffusion control. However his results are not directly comparable to the results of this paper because of some differences in plating conditions and also because not all of the decomposition products of brighteners are necessarily included in the electrodeposit (23).

The existing data could be interpreted as indicating that only a small amount of cleavage occurs and that a substantial amount of unreduced or partly reduced allyl sulfonate with the allyl radical attached to a sulfur-containing moiety is included in the deposit. However, a more plausible interpretation is that the sulfur is cleaved from the organic radical early in the reduction scheme, as indicated by the electrolytic reduction in $\text{NaHSO}_4\text{-H}_3\text{BO}_3$ solutions (20), and that all of the sulfur included in the nickel deposit is present as simple sulfide, as indicated by total recovery of the sulfur as H_2S in the dissolution with no evidence of the existence of mercaptan. The presence of the carbon in the deposit (19) can then be explained by postulating that the product propylene is strongly adsorbed by nickel. It is known (24) that ethylene and other double-bond containing compounds are strongly adsorbed on nickel. Presumably allyl sulfonate itself is not strongly adsorbed because of the solubilizing action of the sulfonate group but, when this effect is removed, the propylene may be efficiently adsorbed.

In fact, if the postulated reduction scheme (20) for allyl sulfonate is operative in the course of nickel deposition and if the adsorption of the propylene generated at the electrode and the further reduction of the inorganic sulfite and incorporation of sulfide are all efficient processes, one might expect the 3 to 1 carbon-to-sulfur ratio which is shown by the results of Beacom and Riley (19). However, the experimental support for this mechanism is not unequivocal, so that at this point one can only say that the weight of the evidence gives some preference to an early cleavage mechanism with separate incorporation of sulfide and propylene. It is interesting to note in passing that propylene could function as a second-class nickel brightener (1b) so that allyl sulfonate then would constitute a nearly unique example of a brightener combining the functions of both a first-class and second-class brightener. Further, it might be noted that second-class brighteners which presumably do operate primarily by an adsorption mechanism, might be more favorable cases in which to study specificity of interaction with single crystal metal spheres. This is perhaps supported by the fact that the hydrogenation of ethylene proceeds at different rates on nickel films of different crystal orientations (25).²

The case of thiourea as a brightener bears some resemblances and some differences from the case of allyl sulfonate. One difference is that thiourea does

not require an electrochemical process in order for the sulfur to be taken up by the metal. While the present experiments do not establish the form in which the sulfur is taken up, the work of Llopis (26) indicates that copper is attacked chemically by thiourea to form cuprous sulfide. In experiments using both tagged sulfur and carbon, Llopis (27) showed that sulfur is taken up during the electrodeposition of copper, but much less carbon is incorporated so that cleavage of sulfur from the carbon in thiourea is indicated. Also Elze (28) has found sulfide in nickel electrodeposited in the presence of thiourea. Thus it appears that the active principle in the case of thiourea also is sulfide ion. Another difference between allylsulfonate and thiourea is that the amount of sulfur included in the electrodeposit is much greater in the case of thiourea (29) than in the case of allyl sulfonate in the results of this paper.

Since sulfide ion has been singled out as the effective principle in the case of thiourea and sulfonate type addition agents, some remarks are in order as to the manner in which the sulfide is presumed to be effective. In order to avoid the intricacies and speculations which might be associated with a discussion of the details of bright plating, levelling, etc., the discussion can be confined to grain refinement as one aspect of addition agent action. In order to achieve grain refinement, the addition agent must enhance the metal nucleation process or suppress the crystal growth process. It is usual (1a) to class addition agents as inhibitors thus implying a suppression of the growth process. A plausible mechanism by which this inhibition could operate could be described by postulating that the generated sulfide ion moves to crystal growth sites, that is, to kinks on the edges of two-dimensional nuclei or on the edges of screw dislocations, and that the sulfur atoms by occupying these sites would prevent or impede the further addition of metal atoms to the growing crystal. However, Barnes (30) has suggested that sulfide inclusions from thiourea may also enhance the nucleation process so that both possibilities exist to explain the results.

Acknowledgments

The authors are indebted to General Motors Research Laboratories for aid in the form of a fellowship to one of them (J. J. H.). They also wish to thank Mr. J. D. Thomas, of General Motors, and Dr. Henry Brown, of Udyllite Research Corporation, for helpful discussions and Drs. M. R. Wright and N. Vanderkooi for some experimental assistance.

Manuscript received July 1, 1963; revised manuscript received Sept. 13, 1963.

Any discussion of this paper will appear in a Discussion Section to be published in the December 1964 JOURNAL.

REFERENCES

- (a) H. Fischer, "Electrolytische Abscheidung und Elektrokristallisation von Metallen," p. 544, Springer-Verlag, Berlin (1954).
- (b) H. Brown, Extended Abstracts of Symposium on the Effects of Addition Agents in Electrodeposition, Electrochemical Society Meeting, Detroit, October, 1961. Also H. Brown, *Electroplating and Metal Finishing*, 15, 14 (1962).

² Beeck's work, especially that on a series of transition metals, has since been re-interpreted with an emphasis on electronic rather than geometric factors. The experimental fact remains that Beeck observed distinct differences in catalytic efficiency between nickel films of different orientations.

- (c) A. H. DuRose, *Trans. Inst. Met. Finishing*, **38**, 27 (1961).
2. H. Brown, U. S. Pat. 2,466,677, April 12, 1949.
3. B. Ke, J. J. Hoekstra, B. C. Sison, Jr., and D. Trivich, *This Journal*, **106**, 382 (1959).
4. C. W. Bills and A. R. Ronzio, AECU-619 (1949).
5. C. M. Suter, "Organic Chemistry of Sulfur," p. 98, John Wiley & Sons, Inc., New York (1944).
6. B. Ke, J. J. Hoekstra, and D. Trivich, *Rev. Sci. Instr.*, **25**, 1033 (1954).
7. (a) A. T. Gwathmey and A. F. Benton, *J. Phys. Chem.*, **44**, 35 (1940).
 (b) A. T. Gwathmey and A. F. Benton, *Trans. Electrochem. Soc.*, **77**, 211 (1940).
 (c) A. T. Gwathmey and H. Leidheiser, Jr., *This Journal*, **91**, 95 (1947).
 (d) H. Leidheiser, Jr., and A. T. Gwathmey, *ibid.*, **98**, 225 (1951).
 (e) A. T. Gwathmey, H. Leidheiser, Jr., and G. P. Smith, Proceedings Pittsburgh International Conference on Surface Reactions, Corrosion Publishing Co., Pittsburgh (1948).
 (f) A. T. Gwathmey and K. R. Lawless, in "Surface Chemistry of Metals and Semiconductors," H. C. Gatos, Editor, p. 483, John Wiley & Sons, Inc., New York (1959).
8. C. S. Barrett, "Structure of Metals," McGraw-Hill Book Co., New York (1943).
9. N. N. Simpson and N. Hackerman, *This Journal*, **102**, 660 (1955).
10. C. L. Faust and P. D. Miller, U. S. Pat. 2,440,715, May 4, 1948.
11. V. Zentner, A. Brenner, and C. W. Jennings, *Plating*, **39**, 865 (1952).
12. J. D. Thomas, *Proc. Am. Electroplaters' Soc.*, **43**, 60 (1956).
13. I. M. Kolthoff and E. B. Sandell, "Textbook of Quantitative Inorganic Analysis," 3rd ed., p. 685, Macmillan Co., New York (1952).
14. H. H. Willard and H. Diehl, "Advanced Quantitative Analysis," p. 305, D. Van Nostrand Co., Inc., New York (1943).
15. Index to the X-ray Powder Data File, ASTM Special Technical Publication 48-L, American Society for Testing and Materials, Philadelphia (1962), Card No. 6-0261; Swanson *et al.*, NBS Circular 539, IV, 21 (1953).
16. A. V. Pamfilov and O. E. Panchuk, *Ukrain. Khim. Zhur.*, **23**, 391 (1957).
17. E. Schwenk, D. Papa, B. Whitman, and H. Ginsburg, *J. Org. Chem.*, **9**, 1 (1944).
18. R. Mazingo, D. E. Wood, S. A. Harris, and K. Folkers, *J. Am. Chem. Soc.*, **65**, 1013 (1943).
19. S. E. Beacom and B. J. Riley, *This Journal*, **108**, 758 (1961).
20. H. Gotthard and D. Trivich, *Electrochim. Acta*, **7**, 369 (1962).
21. E. Raub and H. Wittum, *Z. Elektrochem.*, **46**, 71 (1940).
22. B. J. Riley and S. E. Beacom, Extended Abstracts of the Symposium on the Effects of Addition Agents in Electrodeposition, Electrochemical Society Meeting, Detroit, October, 1961.
23. O. Kardos and D. G. Foulke, in "Advances in Electrochemistry and Electrochemical Engineering," Vol. 2, C. W. Tobias, Editor, p. 182, Interscience Publishers, New York (1962).
24. O. Beeck *et al.*, *Proc. Roy. Soc.*, **A177**, 62 (1940); *Rev. Mod. Phys.*, **17**, 61 (1945); *Discussions Faraday Soc.*, **8**, 118 (1950).
25. M. McD. Baker and G. I. Jenkins in "Advances in Catalysis," Vol. VII, p. 22, Academic Press, New York (1955).
26. J. Llopis, J. M. Gamboa, L. Arizmendi, and F. Alonso, *This Journal*, **109**, 368 (1962).
27. J. Llopis, J. M. Gamboa, and L. Arizmendi, in "Radioisotopes in Scientific Research," Vol. II, p. 478, (Proc. 1st UNESCO Int. Conf., Paris, 1957), Pergamon Press, New York (1958).
28. J. Elze, in ref. 1 (a), p. 530.
29. S. M. Kochergin and L. L. Honina, *Zhur. Priklad. Khim.*, **36**, 673 (1963).
30. S. C. Barnes, Private communication; cf. G. G. Storey and S. C. Barnes, *J. Inst. Metals*, **90**, 336 (1962); T. B. Vaughan and H. J. Pick, *Electrochim. Acta*, **2**, 179 (1960).

The Effects of Quenching on the Structural, Photo, and Electroluminescent Properties of ZnS:Cu Phosphors

M. J. Presland,¹ R. Marshall,² and J. Franks¹

Research Laboratory, Associated Electrical Industries Limited, Templefields, Harlow, Essex, England

ABSTRACT

Zinc sulfide phosphors containing more than 5.10^{-4} g Cu g⁻¹ ZnS exhibit yellow and red photoluminescence on being quenched in water after firing. Phosphors quenched from above the crystallographic transition temperature remain hexagonal, those quenched from below this temperature are cubic. The phosphors as quenched, are not electroluminescent, but after annealing at low temperatures (e.g., 300°C) the yellow and red emissions disappear and the usual photo and electroluminescent blue and green emissions are obtained, without any detectable changes in crystal structure occurring. Electroluminescence can be induced in the yellow and red phosphors by the deposition of copper on the surface, suggesting that electroluminescence depends more on the presence of a copper rich phase than on the structure. Hexagonal phosphors which are cooled slowly, are converted to the cubic structure. Copper accelerates this process whereas chlorine acts as an inhibitor.

The relationship between the structure of ZnS phosphors and electroluminescence has been the

¹ Present address: Standard Telecommunication Laboratories, Ltd., Harlow, Essex, England.

² Present address: Armour Research Foundation, Chicago, Illinois.

subject of some debate (1) and Ballentyne (2, 3) has recently suggested that cubic-hexagonal disorder is a necessary condition for electroluminescence. If a series of phosphors having concentra-

tions of copper in the range $0-10^{-3}$ g Cu g⁻¹ ZnS are fired at a temperature in the region of the transition point (1024°C), then between the concentrations $10^{-4}-10^{-3}$ g Cu g⁻¹ ZnS, the body color darkens, deep traps as detected by thermoluminescence measurements disappear, the structure becomes mixed cubic-hexagonal, and electroluminescence may be observed. At concentrations less than 10^{-4} g Cu g⁻¹ ZnS the structure becomes totally hexagonal (see comment at the end of the section on X-ray measurements), possibly implying that the presence of copper tends to force the structure cubic as suggested by Aven and Parodi (4). All these structures are observed after the powders have been cooled comparatively slowly. In the present work structures are examined after the powders are quenched from the firing temperature, in an attempt to preserve the structure corresponding to that temperature. In this way a more direct study can be made of the effects of impurities on the structure.

Experimental

Sample preparation.—The raw ZnS powder contained large quantities of sulfate and chloride (luminescent grade ZnS obtained from Derby Luminescents Ltd.). The raw material was extensively washed and then prefired in flowing H₂S for 3 hr at about 800°C. The H₂S was generated in a Kipp's apparatus (FeS), passed through HCl, Ba(OH)₂, and deionized water. After treatment, the chloride content was reduced to 50 ppm and the sulfate to 100 ppm. The only metallic impurity detectable was cadmium (~1 ppm); the limit of detection of copper was 0.1 ppm.

Slurries were prepared in the conventional manner by adding calculated quantities of dopants as solutions to the prefired material. Thus copper was added as CuSO₄ in standard solutions containing 10^{-6} , 10^{-5} , etc. g Cu/ml; aluminum as Al₂(SO₄)₃, and chlorine as KCl. The slurries were dried, ground, and transferred to a silica boat.

The phosphor powders were fired in an atmosphere of argon or hydrogen sulfide, usually for a period of 30 min, in a silica tube which was inserted into a conventional tube furnace.

Some samples were cooled relatively slowly (left in the furnace after switching off, cooling time of about 2 hr), others were cooled more rapidly (by removal of the silica tube with boat enclosed, cooling time approximately 5 min), but the majority were quenched by opening the gas exit joint and tilting the furnace so that the phosphor was plunged directly into a container of de-ionized water (a cooling time of about 1 sec). Although this technique introduced a water contamination risk, other methods such as using sealed containers, or employing liquid nitrogen as the quenching agent, proved to be less efficient as judged by structure differences. Etching away the surfaces did not materially affect the properties of the grains.

After quenching, the phosphors were filtered and dried by vacuum desiccation. (The normal oven drying method has been shown to result in considerable annealing.)

X-ray measurements.—Debye-Scherrer powder photographs were obtained from the samples using a standard powder camera (radius 2.54 cm) and a Hilger microfocuss unit. The samples were not sieved or ground. Both cubic and hexagonal patterns, as well as mixed cubic-hexagonal patterns, were observed depending on the nature and treatment of the samples.

Trace quantities of one or other phase are not detectable by this method. Reference to total cubic or total hexagonal are to be interpreted as meaning that the other phase could not be detected.

Emission measurements.—The fluorescent emission from the samples, under 3650Å radiation from 125w mercury lamp selected by a monochromator, was examined with a Hilger and Watts, Barfit spectrometer. The dispersed emission was detected by a tri-alkali photomultiplier (Type E. M. I. 9558) and the photocurrents, after amplification, were fed to a potentiometric recorder. Direct wavelength-relative intensity recordings were obtained by fitting a simple automatic scan system to the spectrometer; thus the plots give the relative energy per linear increment on the wavelength scale.

Results

Structure

General structure behavior is shown schematically in Fig. 1. The following observations refer to behavior with specific coactivators.

Uncoactivated phosphors ZnS:x.Cu.—Phosphors containing 0, 10^{-6} , 10^{-5} , 10^{-4} , and 10^{-3} g Cu g⁻¹ ZnS, without any deliberately added coactivator, were examined. When fired below 1000°C the structure remained cubic independently of the cooling rate. Above the transition temperature (1024°C) the structure became totally hexagonal within 30 min. All phosphors quenched from 1100°C were totally hexagonal. However, under normal rapid cooling the samples containing 10^{-3} g Cu g⁻¹ ZnS partially reverted to the cubic phase; those containing less copper remained hexagonal. With slow cooling or refiring below 1000°C for about 30 min, the sample containing 10^{-3} g Cu g⁻¹ ZnS became totally cubic; samples containing less copper also

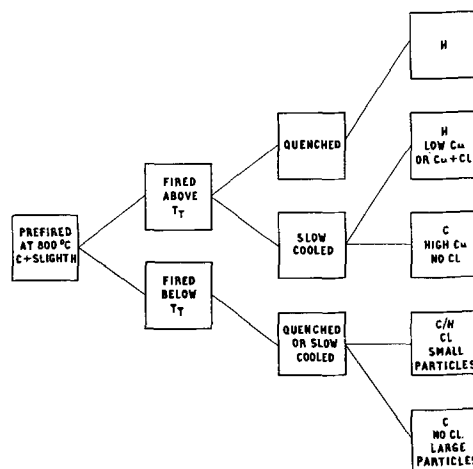


Fig. 1. General structure behavior: T_T, transition temperature 1024°C; H, hexagonal; C, cubic structure.

became cubic but at a much slower rate. The kinetics of this process have not, as yet, been investigated but they are obviously a function of the copper concentration as well as temperature and time.

Aluminum coactivated phosphors ZnS:x.Cu, 10^{-4} Al.—The results are substantially the same as those obtained for the samples without added coactivator. There may be small differences in the rates at which these processes occur, however, these are not obvious from the preliminary studies. The phosphor containing 10^{-3} g Cu and 10^{-4} g Al g^{-1} ZnS is particularly interesting as it exhibits strong electroluminescence when subjected to normal cooling.

Chlorine coactivated phosphors ZnS:x.Cu, 10^{-2} Cl.—As regards structure, chlorine doped phosphors are more difficult to control than those previously described. Experiments indicated that given sufficient time, these phosphors would behave as uncoactivated or aluminum coactivated phosphors, but once the hexagonal phase had been produced, it was extremely difficult to effect a reversion to the cubic phase. Refiring the phosphor ZnS: 10^{-3} Cu, 10^{-2} Cl in argon at 1000°C for 17 hr turned it totally cubic. Lower refiring temperatures or lower copper concentrations in the original phosphor would presumably require very lengthy refiring.

All phosphors containing added chlorine remained hexagonal when fired at 1100°C whether quenched or cooled rapidly.

The tendency for chlorine to force the structure to remain hexagonal contributes to a further complication. If the prefired material contains any hexagonal phase, then this is retained when the phosphor containing chloride is fired at a temperature below the transition point.

The source of the hexagonal phase in the prefired material was traced to the particle size of the raw material. If the powder is fine, then bulk firing is conducive to a partial transition to hexagonal even at 800°C . The reason for this is difficult to ascertain, but it is possibly due to inhomogeneous heat distribution caused by the latent heat of condensation. That it is connected with evaporation and condensation is suggested by the following experiment. If a small sample of the unfired material is spread out thinly in an open boat and a high gas flow-rate is used (factors which tend to prevent recondensation), the hexagonal phase does not appear, but it

does in the same material fired in bulk. Usually the hexagonal phase is only just detectable and disappears when copper is added and firing takes place, but when chlorine is also added it tends to remain unless long firing times are used.

Emission Under U.V. Excitation

A qualitative survey of the emission characteristics of the quenched phosphors was made by spreading the phosphors on a metal foil, heating one end to about 300°C for a few minutes, the other end remaining at about room temperature, and making visual observations. Examples of the changes in emission (after the foil was cooled again to room temperature) in a series of quenched phosphors doped with increasing amounts of copper, subjected to the heating gradient, are shown in Table I. The results shown are for uncoactivated samples but they are also representative of phosphors coactivated with chlorine or aluminum. At concentrations below $\sim 5.10^{-4}$ g Cu g^{-1} ZnS green and blue emissions are obtained which can correspond to the emissions from conventionally prepared phosphors, except that the intensities are reduced. Above a concentration of $\sim 5.10^{-4}$ g Cu g^{-1} ZnS the emission characteristics change drastically, in all cases the quenched phosphors luminesce bright yellow or yellow and red. Table I shows that on heating, the yellow emission turns to red, becomes fainter, disappears and finally becomes bright blue and green as observed along an increasing treatment temperature axis, whether or not the phosphor contains aluminum or chlorine, and independently of structure. According to Henisch (5), bright yellow and red emissions are only observed in the hexagonal phase, but in the high copper content phosphors, the behavior is the same whether the phosphor is prepared at 1000°C and consequently cubic, or whether prepared above the transition point, where the structure is hexagonal. During the low temperature treatment when the emission reverts from yellow, through red, to blue and green, no change in structure is observed.

The body color of the quenched phosphors containing less than the critical amount of copper (*i.e.* $\sim 5.10^{-4}$ g Cu g^{-1} ZnS) is unchanged during the heating treatment, however, as shown in Table I, changes in the emission properties of the high cop-

Table I. Qualitative characteristics of quenched phosphors

Copper content, $g g^{-1}$ ZnS	Body color after quenching	Luminescence after quenching	Effect of annealing gradient			
0	White	Blue	None			
10^{-6}	White	Blue and faint green	None			
10^{-5}	Cream	Blue and green	None			
			• > 300°C Luminescence 20°C			
10^{-4}	Gray	Green and faint blue	Blue	Inert	Green + faint blue Luminescence	
10^{-3}	Yellow-gray	Yellow and some red	Green and blue	Inert	Red	Yellow + some red
			Dark gray	Body color Mid gray		Yellow gray

* No body color changes were observed.

per content phosphors are accompanied by a corresponding darkening of the body color.

The emission spectra of quenched phosphors containing $10^{-3}g \text{ Cu } g^{-1} \text{ ZnS}$ and coactivated with $10^{-2}g \text{ Cl } g^{-1} \text{ ZnS}$ were examined in detail. Four distinct emissions were observed with peaks in the blue ($\sim 4600\text{\AA}$), green ($\sim 5250\text{\AA}$), yellow ($\sim 5700\text{\AA}$), and red ($\sim 6700\text{\AA}$). The wavelengths quoted have been corrected for changes in the spectral response of the detector. Typical records of each emission type are shown in Fig. 2.

Low temperature anneals (e.g., 1 hr at 150°C) are sufficient to cause a rapid decrease of the yellow component (Fig. 3); the red component increases, however, then saturates and finally decreases. Figure 4 shows the latter part of the anneal where the red component is decreasing. The complete behavior of the red emission with various anneal treatments is shown in Fig. 5. The red emission is seen to de-

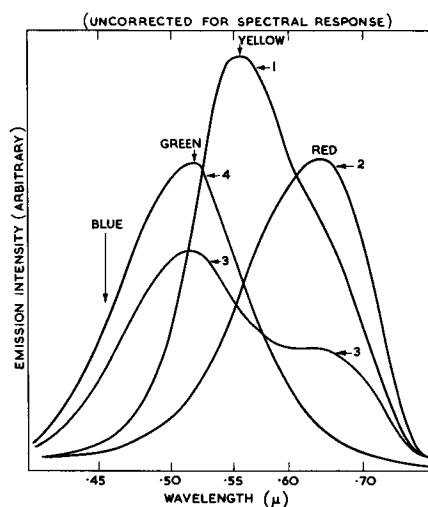


Fig. 2. Quenched ZnS:Cu, Cl phosphors. The four types of emission: 1, unannealed; 2, 60 min anneal; 3, 305 min; 4, 1265 min; temperature, 250°C ; content, $10^{-3} \text{ Cu } 10^{-2} \text{ Cl}$; original powder fired in argon at 1000°C .

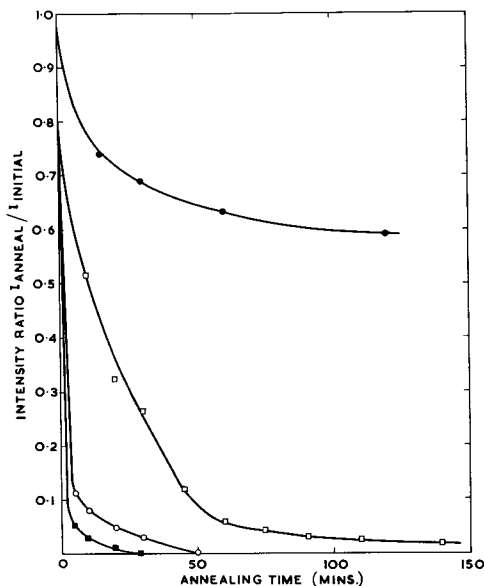


Fig. 3. Annealing effect on the yellow emission. ●, 100°C (the intensity ratio = 0.40 after 2025 min); □, 150°C ; ○, 200°C ; ■, 250°C .

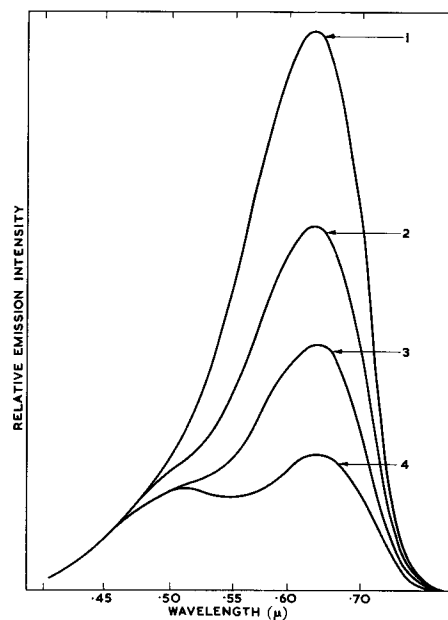


Fig. 4. Quenched ZnS:Cu, Cl phosphors. Annealing of the red center. Anneal temperature, 150°C ; time: 1, 90 min; 2, 110 min; 3, 140 min; 4, 165 min; content, $10^{-3} \text{ Cu } 10^{-3} \text{ Cl}$; original powder fired in argon at 1000°C .

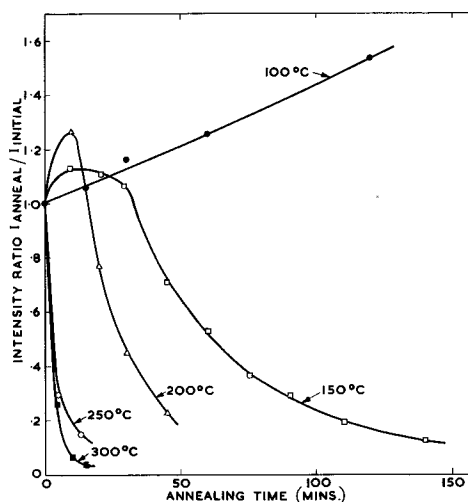


Fig. 5. Annealing effect on the red emission: ●, 100°C ; □, 150°C ; △, 200°C ; ○, 250°C ; ■, 300°C .

crease almost immediately at annealing temperatures above 200°C . After further annealing (e.g., 1 hr at 300°C) green and blue components become visible (Fig. 6). These components similarly saturate and show a tendency to decrease after extended anneals. In this condition the photoluminescence characteristics closely resemble those of the unquenched phosphors. The annealing data were obtained from complete luminescence spectra records for each stage of the anneal program, no wavelength shift of the peaks occurred at any stages in the anneals.

Electroluminescence

No electroluminescence was detected with any phosphors which showed yellow or red photoluminescence. For example a ZnS: $10^{-3} \text{ Cu} : 10^{-4} \text{ Al}$ phosphor, fired in wet H_2S and quenched from 1100°C showed a mixture of red and yellow photoluminescence, total hexagonal structure, but no elec-

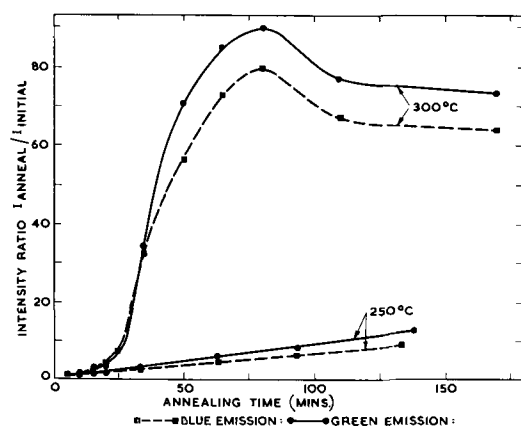


Fig. 6. Effect of annealing on the green and blue emissions

photoluminescence. Refiring at 1000°C turned the phosphor totally cubic. The photoluminescence then showed the usual blue and green components and the electroluminescence was indistinguishable from a phosphor cooled normally from 1100°C .

Annealing the same quenched hexagonal phosphor for 3 hr at 300°C did not affect the structure; the photoluminescence was blue and green and the phosphor was electroluminescent although the emission was somewhat less intense.

Quenched phosphors having red and yellow photoluminescence may be made weakly electroluminescent by the deposition of surface copper at room temperature from solution. Preliminary examination has shown that recombination occurs through the red and yellow centers. These effects are being examined in more detail.

Discussion

The transition temperature of ZnS is 1024°C ; below this temperature the cubic modification is stable and above, the hexagonal form is stable. The results show that this temperature is not significantly affected by the presence of copper, aluminum, or chlorine at the concentrations normally encountered in phosphors. However, it appears that the presence of copper reduced the energy required for the hexagonal-cubic transformation, whereas chlorine increases this energy. Aluminum has no observable effect in this respect.

As regards the photoluminescence characteristics in the quenched phosphors, the red center was first investigated by Froelich (6) and later by several other workers (7-9). A few previous references have also been made to a yellow emission in ZnS:Cu; Froelich observed unresolved red and yellow components (estimated at 5800\AA) and Henderson *et al.* (10) a weak component at about 5810\AA .

It is known that differences in preparation techniques cause some displacement of the emission maxima. The emissions observed in the quenched phosphors at 4600\AA , 5250\AA , 5700\AA are compared with those observed by previous authors in Fig. 7. For clarity and ease of comparison all levels are referred to the conduction band.

The measured blue emission presents some difficulties because Van Gool (8) has recently shown that the copper induced emission is different from

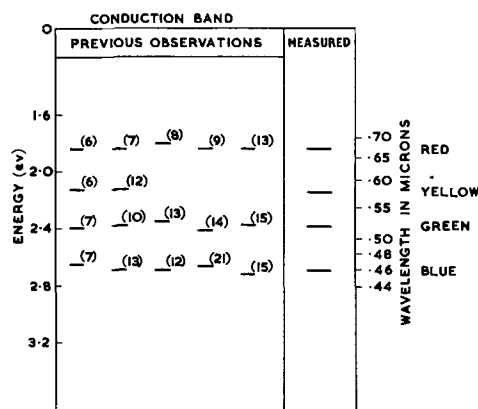


Fig. 7. Comparison of emissions with previous observations

that observed under self-activation only. The large half-width and strong interference from the green component (always present with the blue in the quenched phosphors) makes differentiation of these two types impossible at this stage.

The green emission presents no such difficulty and is undoubtedly the well known emission accompanying the lattice incorporation of copper.

The red and yellow peak positions are in reasonable agreement with previous observations but there is a marked scarcity of data, particularly for the yellow emission, compared to that available on the blue and green emissions so that the comparison is less complete. In general, it may be said that the quenching technique does not radically alter the emission peak positions.

All the previous authors state that the production of the red center, and also the yellow in the case of Froelich (6), is dependent on the total exclusion of oxygenous and halogeneous impurities, and the presence of a sulfur-rich atmosphere during firing. Van Gool and Clieren (8) and Shionoya *et al.* (9) further suggest that the presence of hydrogen is essential. It is also generally agreed that the slightest trace of water vapor in the atmosphere is particularly detrimental. The obvious conclusions from their studies on the more conventional preparation technique is that red or yellow emitting ZnS:Cu phosphors are difficult to produce, scrupulous care being required during firing and subsequent treatment to exclude undesirable impurities.

As described in the section on Sample preparation, however, red and yellow emitting phosphors have been prepared without taking elaborate precautions by the modified quenching technique. In contrast to the reported methods of preparation, high coactivator concentrations (particularly Cl) have been used, and since the phosphors were quenched in a water bath (and several also fired in wet H_2S), water and oxygen contamination were quite possible. It is suggested that the difficulty in preparing yellow and red emitting phosphors stems from the fact that, in such phosphors, a relatively large amount of uncompensated copper must remain incorporated in the lattice. By quenching from high temperatures, it is believed that a copper concentration governed by the high temperature solubility, is frozen in. During annealing and subsequent

destruction of the yellow and red emissions, distinct body color darkening is observed. This may well be caused by copper precipitating and diffusing to the surface resulting in the formation of surface compounds.

The data obtained from the annealing studies could be used to calculate activation energies provided the following assumptions are made. (i) The processes are monomolecular. (ii) Emission intensity is directly proportional to center concentration. The Arrhenius equation becomes

$$\log \frac{I_t}{I_0} = K \exp - \left(\frac{E}{kT} \right) t$$

where I_t is the intensity after an annealing time, t ; I_0 the initial intensity; K the reaction constant; k Boltzmann's constant; E the activation energy.

Plots of $\log I_t/I_0$ against t show that the assumptions are not realized throughout the whole annealing time. The results for the yellow emission are shown in Fig. 8. The fact that straight lines are obtained over certain ranges suggests that the second assumption rather than the first is not fulfilled. From the slopes of the straight line regions at the initial stages, when the red decay has not advanced far, an activation energy of ~ 1 electron volt (ev) is obtained. Similarly the activation energy for the red decay is estimated at 1.2 ev.

Phosphors with high copper content, which are quenched and then annealed until green and blue emission is obtained, exhibit electroluminescence whether totally cubic or totally hexagonal within the limits of detection, contrary to the findings of Ballentyne (2, 3). The presence of an electron-rich phase is evidently necessary, in keeping with his later suggestions (10), since precipitation of a copper-rich phase occurs before the onset of electroluminescence during the annealing process, and since copper needs to be added separately to phosphors in which such precipitation has not occurred (as in quenched yellow and red phosphors to induce electroluminescence). The surface depositions of copper also appear in effect to remove deep traps (the phosphorescence decay time is considerably reduced) and of course causes the phosphor color to darken. These effects are normally observed in ZnS:Cu phosphors exhibiting bright electroluminescence as discussed in the beginning of this paper.

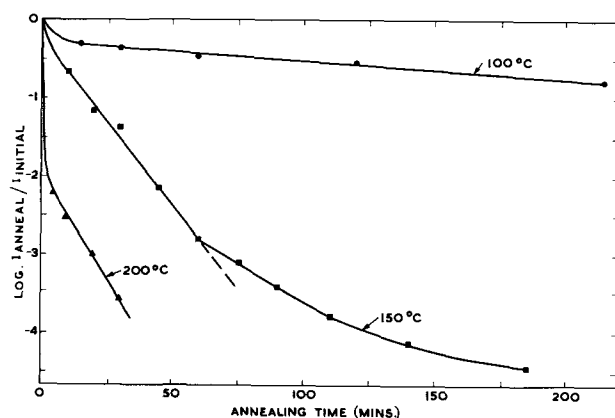


Fig. 8. Yellow emission kinetics

Froelich (6) was able to detect electroluminescence through the yellow and red centers, but his preparation technique could easily have given rise to a copper compound surface layer. It is concluded that the occurrence of electroluminescence is more dependent on the presence of a copper-rich surface phase as suggested by Zalm (11) than on structure.

In accounting for the yellow and red emissions it may be noted that:

(a) In the quenched phosphors, yellow and red emissions only appear when the copper concentration exceeds about $5.10^{-4} \text{g g}^{-1}$ ZnS and this incidentally is also the concentration required for production of bright electroluminescent phosphors.

(b) The presence of a coactivator, under quenching conditions, is only of secondary importance, since the yellow and red emissions are equally well obtained in ZnS:Cu, ZnS:Cu, Al and ZnS:Cu, Cl phosphors.

The problem of associating an emission with a particular defect is formidable. The yellow and red centers may be independent of the blue and green or may be caused by a perturbation of the latter by excess copper in the lattice. In this connection the similarity in energy differences between the yellow and red levels (0.31 ev) and the blue and green levels (0.33 ev) may be significant.

In order to clarify the position, studies of the electroluminescence of the various centers and of infrared quenching effects are being made. Preliminary results show that at low frequencies yellow and red centers exhibit an identical voltage-intensity dependence, from which the existence of a common ground state might be inferred. The 1.3μ quenching band for the green and blue emissions is ineffective for the yellow and red emissions, which could be interpreted as a shifting of the ground state away from the valence band.

Conclusions

The quenching of conventional ZnS freezes in the high temperature equilibrium which is lost by normal cooling methods. The high temperature equilibrium is characterized by the total conversion of cubic to hexagonal structure above the transition point, and the presence of yellow and red luminescent centers, which have previously been produced only under the most stringent conditions.

Slow cooling induces the conversion of the hexagonal structure to cubic. The speed of this transformation is dependent on the presence of impurities such as copper (an accelerator) and chlorine (an inhibitor); aluminum is inactive in this respect.

It has been suggested that the room temperature equilibrium (to which these systems tend in the normal cooling procedure) favors the association of copper centers with native defects or coactivators (or both) producing the familiar green and blue emissions. By quenching at the high temperature a greater lattice solubility is achieved; the perturbing influence of the excess copper may be responsible for the yellow and red emissions. Annealing causes the exsolution of the excess copper after which the normal emissions are obtained,

The occurrence of electroluminescence in these materials is more dependent on the presence of a copper-rich phase than on the structure.

Acknowledgments

We are indebted to Dr. P. D. Fochs for many useful discussions and to Mrs. J. Gazzard for assistance with the x-ray measurements. We also thank Dr. M. E. Haine, Director of the Harlow Research Laboratory of Associated Electrical Industries Ltd., for permission to publish this article.

Manuscript received May 21, 1963.

Any discussion of this paper will appear in a Discussion Section to be published in the December 1964 JOURNAL.

REFERENCES

1. A. H. McKeag and E. G. Steward, *This Journal*, **104**, 41 (1957).
2. D. W. G. Ballentyne, *J. Phys. Chem. Solids*, **10**, 242 (1959).
3. D. W. G. Ballentyne, *This Journal*, **107**, 807 (1960).
4. M. Aven and J. A. Parodi, *J. Phys. Chem. Solids*, **13**, 56 (1960).
5. H. K. Henisch, "Electroluminescence," p. 208, Pergamon Press, London (1962).
6. H. C. Froelich, *This Journal*, **100**, 280 (1953).
7. M. H. Aven and R. M. Potter, *ibid.*, **105**, 134 (1958).
8. W. Van Gool and A. P. D. M. Clieren, *ibid.*, **106**, 672 (1959).
9. S. Shionoya, T. Koda, K. Era, and H. Fujiwara, "Luminescence of Organic and Inorganic Materials," H. P. Kallman and C. M. Spruch, Editors, John Wiley and Sons, London (1962).
10. D. W. G. Ballentyne and B. Ray, *Physica*, **27**, 337 (1961).
11. P. Zalm, *Philips Research Repts.*, **11**, 353 (1956).
12. S. T. Henderson *et al.*, *This Journal*, **106**, 27 (1959).
13. I. Broser and J. Schulz, *ibid.*, **108**, 545 (1961).
14. M. T. Melamed, *J. Phys. Chem. Solids*, **7**, 146 (1958).
15. S. P. Kelley and G. D. Pettit, *Phys. Rev.*, **115**, 526 (1959).

Precipitation of Impurities in Large Single Crystals of CdS

Arthur Dreeben

RCA Laboratories, Radio Corporation of America, Princeton, New Jersey

ABSTRACT

Optical microscopy has been used to examine large single crystals of CdS with and without intentionally added impurities. Inclusions of excess cadmium have been observed in high conductivity, n-type crystals of pure CdS. It has also been demonstrated that extraneous phases precipitate when copper, silver, or gold impurities are present in concentrations as low as $2 \times 10^{-2}\%$. This is also a probable upper limit to the solubility of copper in these crystals. Copper and silver sulfides are distributed as discrete needles or rods at low concentrations, but at higher concentrations, copper forms large disks. These disks may be a more complex phase than a simple sulfide. Gold segregates as hexagonal platelets identified as elemental gold, together with a CdAu phase. These precipitates each have a particular orientation with respect to the c-axis. Dislocations and boundaries have been revealed in many of the crystals by means of decoration effects from the impurities. These results show that caution is required in evaluating properties of cadmium sulfide single crystals which may not be one-phase systems when usual acceptor elements are present.

There have been several reports of p-type conductivity in CdS:Cu crystals believed to be single phase systems (1, 2). Recently in this laboratory, however, absorption data indicated a second phase of Cu₂S in a CdS:Cu crystal with a relatively high, probably p-type conductivity (3). Since Cu₂S itself is a p-type semiconductor (2), the presence of this phase could lead to some ambiguity in deciding the origin of the conductivity in a crystal. This possibility was recognized by Woods and Champion (2) in connection with their measurements. Others have also concluded that some CdS:Cu crystals are two-phase systems, and that the second phase may influence the conductivity (4). Similar phase relationships may be encountered with acceptor elements such as silver or gold which would also be expected to impart p-type conductivity to cadmium sulfide.

In this paper, light microscope and chemical etching methods are used to examine pure CdS crystals, and crystals with copper, silver, or gold impurities with the following results: (a) inclu-

sions have been identified in CdS crystals grown from purified powder; (b) copper, silver, or gold impurities in concentrations as low as $2 \times 10^{-2} \%$ ¹ cause the precipitation of extraneous phases, the features of which depend on the particular impurity and its concentration; and (c) these inclusions and precipitates often segregate along dislocations. Previous microscopic examinations of CdS crystals resulted in descriptions of growth patterns (5, 6), and the identification of dislocations (7, 8) which were believed to have an effect on some electrical properties (8).

Experimental

The crystals described in this paper were grown from the vapor phase by slow motion through a sharp temperature gradient (9, 10) to produce boules as shown in Fig. 1. The acceptors, copper, silver, or gold, introduced as the sulfides, were mixed with the powder charge so that they were incorporated directly in the growing boule. The

¹ All concentrations are expressed as weight per cents in this paper.

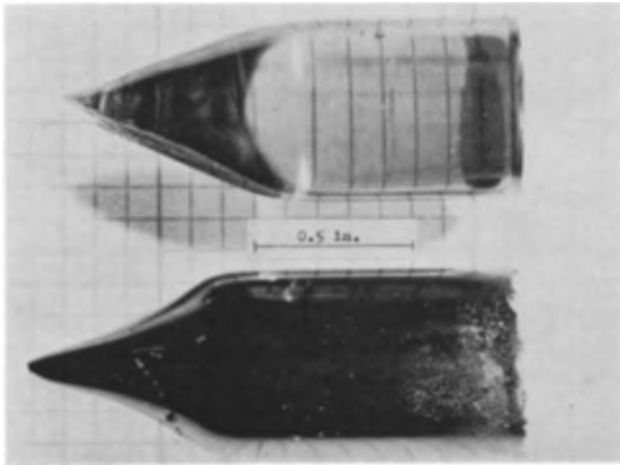


Fig. 1. Pure CdS crystal boule (above), and CdS:Cu boule (below)

ultimate amount in each crystal was determined by chemical analysis. The boules, or large regions of them, were single crystals in which the *c*-axis was not usually coincident with the growth axis. They were oriented by x-ray diffraction methods and mounted so that slices with centimeter dimensions could be cut either parallel or perpendicular to the crystal *c*-axis. Smooth surfaces were produced on the slices by repeated polishing with successively finer aluminum oxide powders. This technique was also used to reduce the thickness of very dark copper or silver doped samples so that details below the surface could be examined under the microscope using transmitted light. Pure and gold doped samples were quite transparent even in thick sections. Surface examinations were conducted by incident and transmitted light microscopy, but the latter was more useful because of the good transparency of the crystals.

Results

Pure CdS crystals.—Examination of a large number of slices from different boules showed that the majority of them contain inclusions. The crystals generally have no other visible distinguishing characteristics throughout their volume. The inclusions are disk-like, but their apparent shape depends on the crystal orientation. For example, when viewed in a direction with the *c*-axis normal to the crystal face, as in Fig. 2, the inclusions ap-

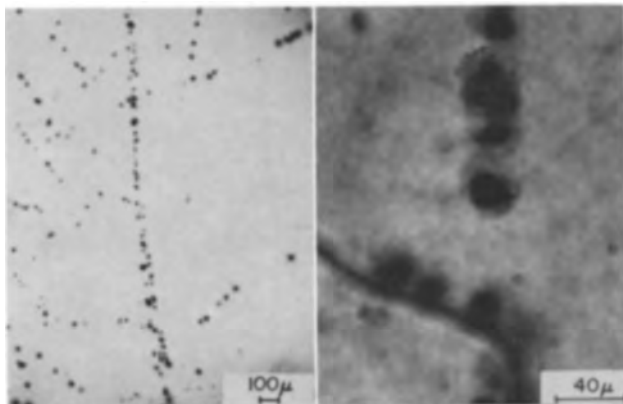


Fig. 2. Photomicrographs of inclusions in pure CdS crystals, *c*-axis normal to face; a, 33X; b, 300X.

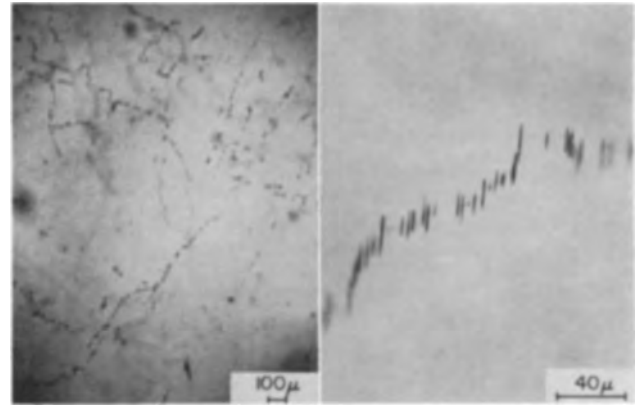


Fig. 3. Photomicrographs of inclusions in pure CdS crystals, *c*-axis parallel to face; a, (left) magnification approximately 33X; b, (right) approximately 300X.

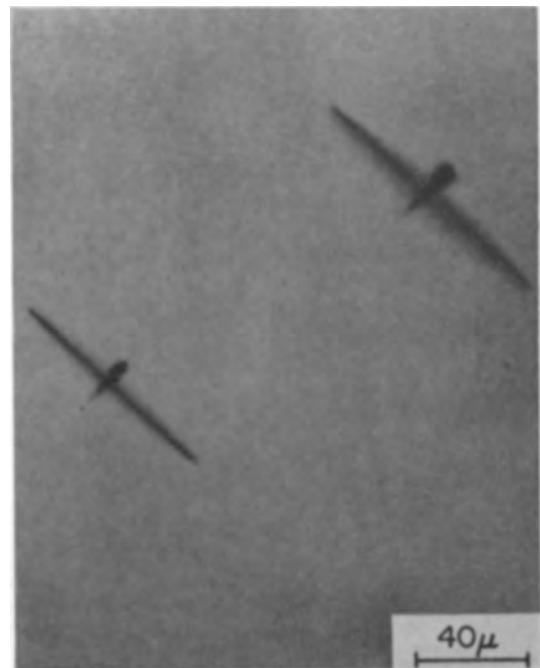


Fig. 4. Photomicrograph of inclusions with central spike in a pure crystal of CdS, *c*-axis parallel to face, 375X.

pear to be essentially circular, consisting of a dark center surrounded by a halo. When, however, the *c*-axis is parallel to the face, as in Fig. 3, the inclusions are seen as thin columns all oriented in the same direction, and with the long side normal to the *c*-axis. Some of these columns have a spike extending through the center as shown in Fig. 4. The disks may be located randomly or in the typical alignment indicative of decorated dislocations. Such an alignment is clearly evident in Fig. 2 and 3.

The inclusions are present throughout the volume of the crystals, and those below the surface may also be brought into sharp focus. When arrays of the inclusions are at or very close to the surface, chemical etching [in this case with a solution described by Woods (8)], produces hexagonal pits which are quite distinct from the general background etch pattern in other regions of the crystal. A typical row of one of the pits, etched repeatedly for various intervals, is shown in Fig. 6. At first, a

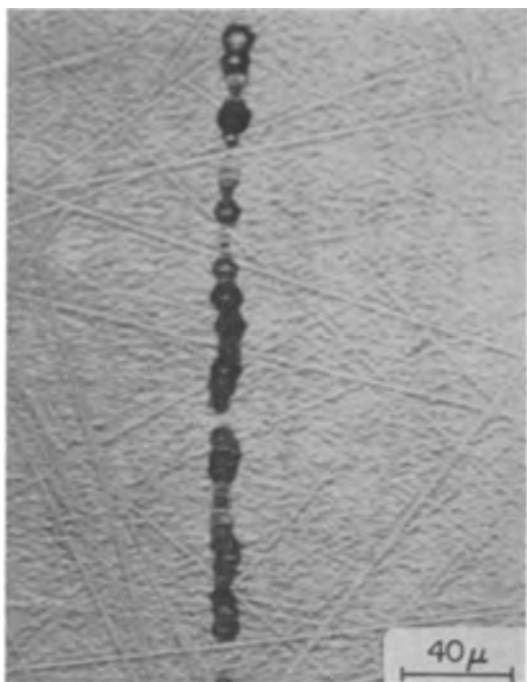


Fig. 5. Photomicrograph of basal plane showing etch pits along a dislocation with inclusions.

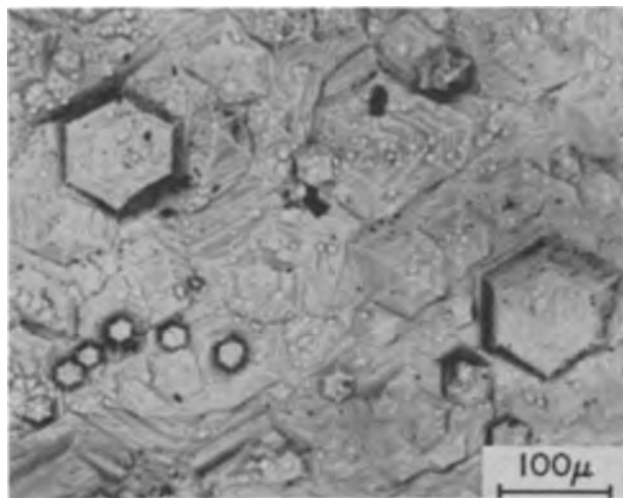


Fig. 7. Photomicrograph of hexagonal etch pits on a basal plane of pure CdS crystal, 150X.

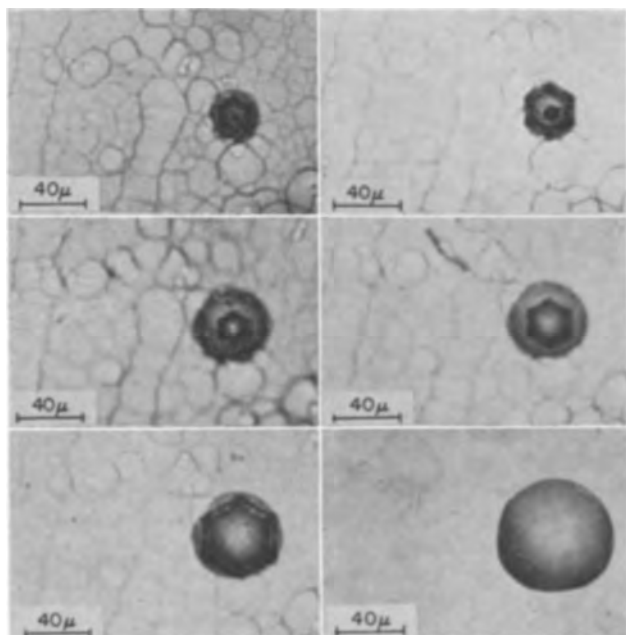


Fig. 6. Photomicrographs of etch pit formation by successive etching of a single inclusion in a basal plane of a pure CdS crystal; a, (top left) "zero" time with additional etches of b, (top right) 45 min; c, (center left) 1.3 hr; d, (center right) 1.5 hr; e, (bottom left) 1.8 hr; and f, (bottom right) 2.7 hr. Magnification approximately 250X.

hexagonal figure forms within the halo and encloses the dark center of the original inclusion (Fig. 6a). As the etching proceeds, the hexagon and the center grow, (Fig. 6b), until the original hexagon disappears at the periphery of the halo, and another hexagon forms at the center, (Fig. 6c). This system then continues to expand, (Fig. 6d and 6e), until ultimately a relatively large void is formed. The typical example shown in Fig. 6f is about 70μ across. Further etching now only enlarges the void. It will be noted that the general background does

not change appreciably as the etching proceeds. However, on the opposite face of the crystal, another type of hexagonal etch pit is observed as shown in Fig. 7. These are not necessarily associated with the inclusions, but seem to be of the type encountered by others on 0001 faces of cadmium sulfide (7, 8).

In view of the earlier finding that as a result of nonstoichiometry, crystals of this type have a high, n-type conductivity (3), it is reasonable to assume that the precipitates are excess cadmium. The dark center may well be a region with the highest cadmium concentration, about which a diffuse concentration gradient is manifested as the observed halo.

A possible alternative explanation may be that the inclusions are foreign impurities. However, spectrographic analysis shows less than 10 ppm of Cu, Al, and Mg, and less than 1 ppm of Ag and Fe. The acceptors, copper and silver, do not account for the observed conductivity of the crystals, and the trace quantities of the remaining impurities seem insufficient to account for the observed number of inclusions.

Crystals of CdS:Cu.—Some optical and electrical properties of these crystals have already been reported (3). As previously noted, these measurements indicated the presence of a Cu_2S phase in the crystals. Examination by x-ray diffraction methods, however, disclosed the presence of only a single phase of hexagonal cadmium sulfide. The following light microscope observations clearly establish that the presence of copper in concentrations lower than were reported in p-type CdS:Cu crystals (1, 2), causes the precipitation of a second phase, several forms of which are shown in Fig. 8 and 9.

One type consists of individual rods having a fairly consistent orientation. With the c-axis normal to the face, as in Fig. 8a, the rods form angles of about 120° with each other. Aligned rows of the rods also appear to meet at a 120° angle to form a network of hexagons, possibly along dislocations (Fig. 8c). Other decorated dislocations can easily be seen in Fig. 8a and 8b, and the depletion of the precipitate along a decorated region is particularly

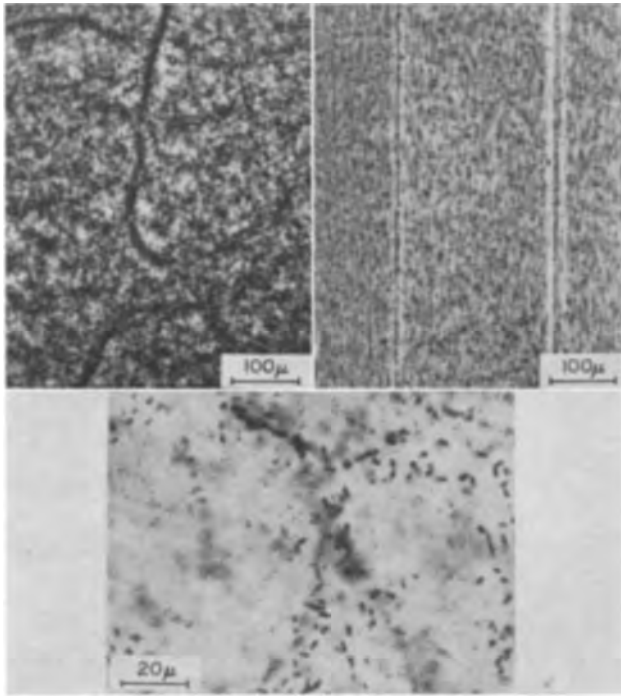


Fig. 8. Photomicrographs of precipitate rods from copper impurity in CdS crystals, c-axis: a, (top left) normal to face showing decorated imperfections; b, (top right) parallel to face showing depletion of Cu at decorated imperfections, 100X; c, (below) normal to face showing hexagonal network of individual rods, 475X.

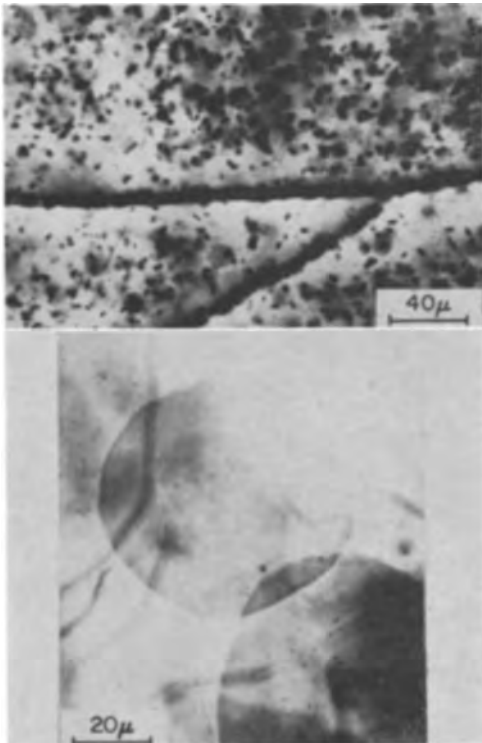


Fig. 9. Photomicrographs of basal plane of CdS:Cu crystal showing: a, (top) decoration of boundaries, approximately 280X; b, (bottom) large precipitate disks, approximately 560X.

evident in Fig. 8b. Note that the alignment of the rods and the direction of the dislocations in this figure are always normal to the c-axis. Somewhat similar decorations consisting of short segments in vapor phase reaction crystals have also been reported by Woods (8).

In Fig. 9a, depletion of the precipitate along decorated, intersecting internal boundaries can be seen. This decoration closely resembles etch pit patterns identified by Woods (8) as low angle boundaries in a highly pure CdS crystal. The precipitate consists of rods, but closer examination also reveals the presence of an additional, circular form, particularly along the boundaries. These circular areas are shown more clearly in Fig. 9b; the particularly large disk in the center is about 65μ across.

These observations suggested that the form as well as the amount of the precipitate in a crystal depends on the copper concentration. It was found that when the amount of copper is below about $2 \times 10^{-2}\%$, no discrete particles are resolved by the light microscope even with a magnification of 1500X. Therefore, $2 \times 10^{-2}\%$ is a probable upper limit to the solubility of copper in these crystals. In some of the otherwise clear samples, however, precipitation was observed along imperfections. The successive changes that occur as a function of the copper concentration are shown in Fig. 10, all views having the crystal c-axis normal to the face.

With $2 \times 10^{-2}\%$ copper, a relatively small number of submicron size particles are distributed throughout the crystal, often in rows denoting dislocations (Fig. 10a). The precipitation at this concentration appears to be imperfection dominated. These particles grow in number and size to form rods (Fig. 10b) which are about 5μ long when the copper concentration is near $2 \times 10^{-1}\%$ (Fig. 10c).

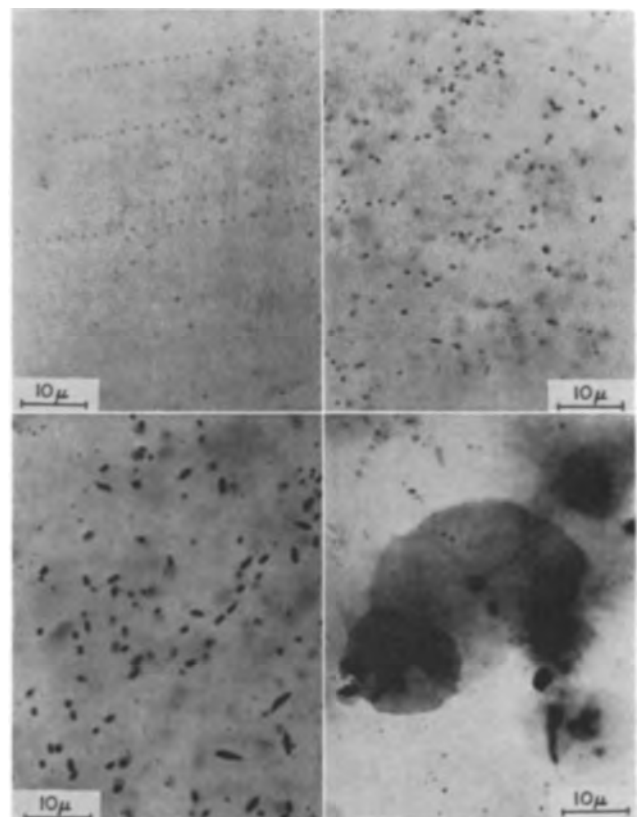


Fig. 10. Photomicrographs showing type and size of precipitates in a basal plane of CdS:Cu crystals as a function of Cu concentration; % Cu in: a, (top left) 0.02; b, (top right) 0.05; c, (bottom left) 0.22; d, (bottom right) 0.88; approximately 1000X.

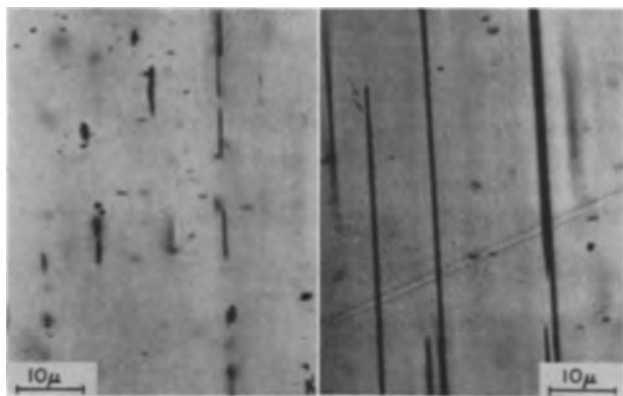


Fig. 11. Photomicrographs of CdS:Cu crystals showing thin cross section of a, (left) small precipitate disks, and b, (right) large disks, c-axis parallel to face; approximately 900X.

Finally when the copper is near 1%, large disks, 30–70 μ in diameter, such as those shown in Fig. 10d or 9b, are present.

The thickness of these disks is very small compared with their diameter. This is seen for some smaller disks in Fig. 11a, and larger ones in 11b. It is interesting to note that even in some very thin samples, these disks are so numerous as to prevent light from being transmitted through them. However, appreciably thicker samples readily transmit the light parallel to the disks through the spaces between them.

Crystals of CdS:Ag.—Some properties of these crystals have already been described (3) and a summary of these includes: (a) a typical CdS optical quenching spectrum terminating in an edge at 1.1 eV; (b) a high dark resistivity and fair photosensitivity; and (c) transmission data consistent with the presence of an Ag₂S phase having a band gap of about 0.9 eV. The presence of a second phase, not detected by x-ray diffraction methods, has now been confirmed by microscopic observation of a precipitate in the crystals. The samples to be described contained 3 or 4 × 10⁻²% silver.

Some features of this precipitate are similar to those just described for copper. For example, segregation occurs in the form of discrete rods which are aligned with their long dimension perpendicular to the direction of the c-axis, (Fig. 12a). When observed with the c-axis perpendicular to the crystal

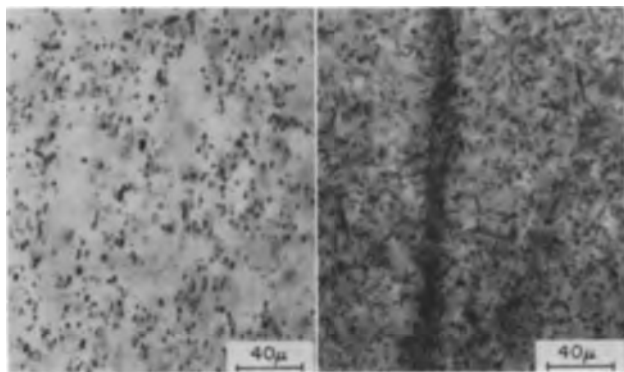


Fig. 12. Photomicrographs of precipitates in CdS:Ag, c-axis: a, (left) parallel to face, 250X; b, (right) normal to face showing orientation of rods and decoration of an imperfection (dark area); approximately 250X.

face, (Fig. 12b) the rods adopt a mutual orientation angle of about 120°. Rows of the inclusions also appear to meet at this angle to form hexagonal networks similar to the example for CdS:Cu shown in Fig. 9c. Preferential segregation at internal boundaries or dislocations, as with copper, is seen for silver in Fig. 12b and 13. It is evident by comparing Fig. 12a and 12b, however, that this precipitate has a less symmetrical cross section than that from copper, (Fig. 8a and 8b). The long dimension has been observed to exceed 50 μ.

Crystals of CdS:Au.—The segregation of gold occurs in the rather striking manner shown in Fig. 14a, which is representative of crystals containing from 4 × 10⁻³ to 5 × 10⁻¹% gold. In contrast to the needles, rods, and disks formed by copper and silver, the gold inclusions are in the form of perfect

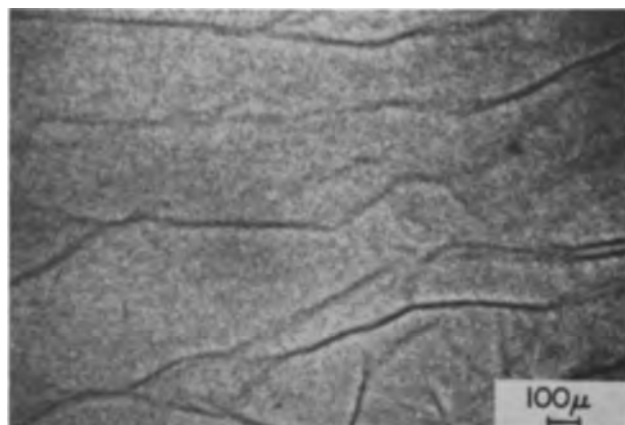


Fig. 13. Photomicrographs of CdS:Ag showing preferential precipitation along dislocations, and depletion in their vicinity, c-axis normal to face; 50X.

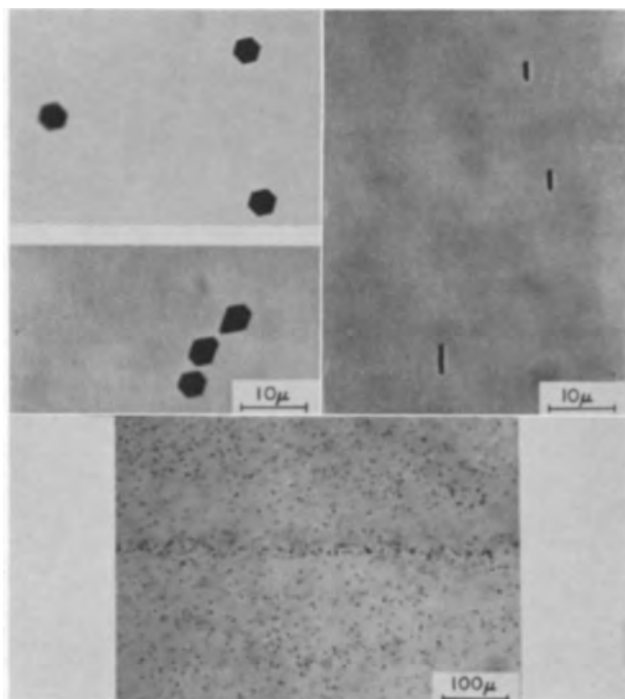


Fig. 14. Photomicrographs of gold particles in CdS:Au crystal: a, (top left) basal plane showing hexagonal platelets, b, (top right) c-axis parallel to face showing edge view of hexagons, approximately 800X; c, (center) c-axis normal to face showing decorated imperfection and distribution of gold particles in crystal, approximately 130X.

and slightly distorted hexagons when viewed along the hexagonal axis. In Fig. 14b, with the crystal face parallel to the c-axis, the particles are revealed as thin platelets perpendicular to the axis. Using lower magnification, individual particles are seen distributed as the second phase throughout the crystal, and also preferentially along a dislocation in Fig. 14c.

Chemical evidence and optical properties under the microscope suggested that the hexagonal platelets were elemental gold. This was confirmed by an electron diffraction examination which also disclosed the presence of another phase indexed as CdAu. The segregation as elemental gold is also consistent with the low decomposition temperatures of the gold sulfides.

In the cases of copper and silver, it has been pointed out that the identification of the precipitates as Cu_2S and Ag_2S , respectively, is consistent with some electrical and optical data (3). However, there is some evidence that other compositions involving these impurities may also be present, particularly at the higher concentrations. For example, one of the CdS:Cu crystals was ground to a powder and washed with an aqueous NaCN solution. This treatment would dissolve any Cu_2S present, yet no copper was found in the wash solution. However, similar treatment of other samples showed that a large proportion of the copper was dissolved by the cyanide. Among the phases to be considered are the three compounds (including Cu_2S) and four phases described in the system Cu_2S -CuS (11). In addition cyanide insoluble phases of the type (Cu,Cd)S have been proposed to account for certain properties of electroluminescent powders (12, 13). The appearance of the different kinds of precipitates in the crystals (needles, rods, and disks) may be associated with the formation of phases of different compositions

Chemical etching.—Some etch figures were described earlier in connection with the pure CdS crystals. The presence of copper, silver, or gold, however, especially at the higher concentrations, seemed to inhibit etching. This may be partially attributed to the formation on the crystal surfaces of insoluble products from the action of the etch solution. It may be noted, however, that a few clear etch figures obtained did not necessarily occur in the vicinity of precipitate particles where stresses might well have caused dislocations. There was also an absence of impurity segregation along some rows of etch pits marking dislocations. This is a likely indication that some dislocations were introduced after crystal growth.

Summary and Conclusions

It has been found that precipitates in cadmium sulfide crystals result from the presence of copper, silver, or gold impurities even at low concentrations in the order of $2 \times 10^{-2}\%$. The nature of the precipitates is a function of the amount and identity of the impurity present. Copper and silver sulfides are distributed as discrete rods or needles at low concentrations, but copper, for example, grows into

relatively large disks when its concentration is approximately 1%. Present observations support the conclusion that $2 \times 10^{-2}\%$ is an upper limit to the solubility of copper in cadmium sulfide crystals. Although phases such as Cu_2S or Ag_2S are likely, compounds and phases of other compositions are also indicated. These results suggest that p-type CdS:Cu crystals reported by others in the past, and assumed to be single phase, may have been more complicated systems.

Gold inclusions distributed in CdS crystals have been identified as elemental gold by means of optical, chemical, and electron diffraction methods. The precipitate crystallizes as hexagonal platelets.

Pure crystals of CdS often have disk-like inclusions distributed throughout their volume. They undergo a characteristic chemical etching which leads to the formation of large voids. The assumption that these inclusions are excess cadmium is consistent with the high conductivity associated with the crystals.

Imperfections, such as dislocations and internal boundaries, have been identified in all of the types of crystals by means of decoration effects from the respective precipitates.

Acknowledgment

The author is indebted to W. M. Anderson for help in the preparation and polishing of the crystals. Electron diffraction data were furnished by M. D. Coutts and W. C. Roth, and x-ray analyses by G. Neighbor. Spectrographic and chemical analyses were performed by H. Whitaker and B. L. Goydish, respectively. Valuable discussions with M. S. Abrahams are gratefully acknowledged.

Manuscript received Aug. 4, 1963. The research reported in this paper was sponsored by the Air Force Cambridge Research Laboratories, Office of Aerospace Research, under Contract No. AF 19(604)-8353.

Any discussion of this paper will appear in a Discussion Section to be published in the December 1964 JOURNAL.

REFERENCES

1. D. C. Reynolds, L. C. Greene, R. G. Wheeler, and R. S. Hogan, *Bull. Am. Phys. Soc.*, Ser. II, **3**, 111, Abstract B4 (1956).
2. J. Woods and J. A. Champion, *J. Electron. Control*, **7**, 243 (1959).
3. R. H. Bube, E. L. Lind, and A. Dreeben, *Phys. Rev.*, **128**, 532 (1962).
4. M. Aven and H. H. Woodbury, Scientific Report No. 2, AFCRL Contract No. AF 19(604)8512, (1962).
5. D. C. Reynolds and L. C. Greene, *J. Appl. Phys.*, **29**, 559 (1958).
6. J. Woods, *Brit. J. Appl. Phys.*, **10**, 529 (1959).
7. D. C. Reynolds and S. J. Czyzak, *J. Appl. Phys.*, **31**, 94 (1960).
8. J. Woods, *Brit. J. Appl. Phys.*, **11**, 296 (1960).
9. W. W. Piper and S. J. Polich, *J. Appl. Phys.*, **32**, 1278 (1961).
10. Scientific Report No. 2, AFCRL Contract No. AF 19(604)8353 (1962).
11. Virginia Ross, *Econ. Geol.*, **49**, 734 (1954).
12. A. Dreeben, Extended Abstract No. 70, Electrochem. Soc. Meeting, Chicago, May 1960; *This Journal*, **110**, 1045 (1963).
13. A. Wachtel, *This Journal*, **107**, 602 (1960).

The Epitaxial Growth of GaP by a Ga₂O Vapor Transport Mechanism

C. J. Frosch

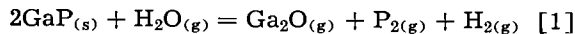
Bell Telephone Laboratories, Incorporated, Murray Hill, New Jersey

ABSTRACT

Single crystals of GaP have been grown from the vapor phase in an open tube process on seeds of either GaP or GaAs. The reaction between H₂O and a GaP source above 700°C in a stream of H₂ provides the vapor phase species which react upon cooling to deposit GaP crystals. Epitaxial layers of GaP have been grown on substrates at temperatures as low as about 700°C, but the growth rates are extremely small. Substrate temperatures of about 1000°-1080°C and source temperatures of 1100°C generally were employed in this investigation to obtain reasonable growth rates for the production of large single crystals. Single crystals of GaAs and solid solutions of GaP_xAs_{1-x} also have been grown by this method. The growth conditions, crystal morphology, crystal properties, doping, and growth from the elements are discussed.

Because of their importance in electronic devices, many investigators are concerned with the development of suitable techniques for growing undoped and doped single crystals of semiconductors from the elements. Crystals of both single and multi-component semiconductors have been grown from the vapor by a halide transport mechanism (1-7). Both sealed and open tube processing procedures have been employed. Single crystals of GaP have been grown in sealed tubes by the reaction of P with Ga₂O (8). This paper describes an open tube carrier gas process for the vapor growth of single crystal GaP by a Ga₂O vapor transport mechanism.

When H₂ containing H₂O vapor is passed over a GaP source at temperatures above 700°C, a deposit of GaP will be formed downstream as the vapor is cooled until a temperature of about 700°C is reached. If a single crystal seed of GaP or GaAs is placed in the region where the GaP deposit occurred, a single crystal layer will be grown. Evidence is presented in another paper (9) which shows that the following reaction is responsible for the volatility of GaP in wet H₂



The reversal of this reaction, when the vapors are cooled, leads to the deposition and crystal growth

of GaP. Single crystal layers of GaAs and GaP_x-As_{1-x} have been grown by the analogous reactions of H₂O vapor with heated sources of GaAs or GaP and GaAs respectively. However, this paper will be concerned largely with the vapor growth of GaP.

The following sections describe in more detail the necessary conditions for crystal growth, the morphology of the growths, rates of growth, some of the electrical and optical properties of the crystals as well as procedures for doping and p-n junction formation.

Apparatus and Experimental Procedure

The apparatus for growing single crystals from the vapor is shown schematically in Fig. 1. It consists essentially of a 25 mm ID fused silica tube extending through two controlled flat temperature zones for the location of a doping impurity at the lower temperature and a polycrystalline source at the upper temperature. The temperatures are controlled to ± 2°C with Pt-10% Pt-Rh thermocouples. The temperature profile should conform approximately to that illustrated in the lower portion of Fig. 1.

GaP source temperatures of 1100°C generally were employed with substrate temperatures from 20° to 100°C lower. This temperature range gives reasonable growth rates for the production of large single crystals without too rapid a deterioration of the fused silica system by devitrification. The appearance of the crystal growth also improves with increasing substrate temperature, presumably because of the higher surface mobility.

The water content in the carrier gas is controlled by bubbling measured fractions of O₂ free H₂ through a fritted glass water bubbler contained in an ice-water bath. A spray trap adjacent to the bubbler within the ice-water bath prevents the entrainment of H₂O droplets by the carrier gas. Saturation of the H₂ with H₂O vapor at 0°C was obtained at the maximum flow rate of 400 cc/min which was passed through the bubbler in this investigation.

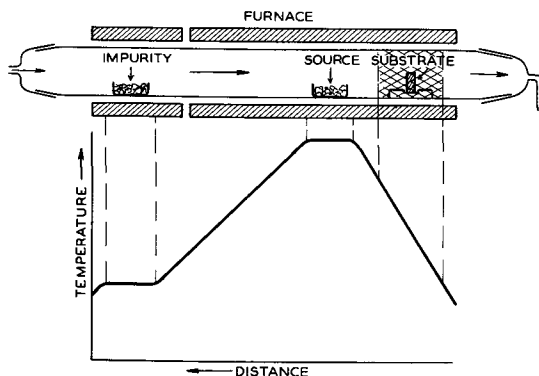


Fig. 1. Apparatus for the vapor growth of GaP and GaAs

When H₂ containing H₂O vapor is passed over an impurity source and then a polycrystalline GaP or GaAs source, as shown in Fig. 1, a doped single crystal layer grows on a single crystal substrate which is located within a predetermined nucleation band. The latter is illustrated by the cross-hatched area which surrounds the substrate.

The source and substrates are located in a separate fused silica tube which is introduced into the furnace tube after the desired flow conditions have been established. This insert tube is convenient for examination of the growth and cleaning after each run. It also prevents nucleation and growth of crystals on the larger furnace tube which often causes fracture of the fused silica when it is cooled.

Materials

The undoped polycrystalline GaP source material was prepared either at this Laboratory or by Merck and Company by a method previously described (10). Undoped boat grown polycrystalline GaAs source material was obtained from Monsanto Chemical Company. Elemental Ga and red P of their highest commercial purity were obtained from The Aluminum Company of America and American Agricultural Chemical Company, respectively.

Boat grown undoped and doped single crystals of GaAs were most frequently used as substrates. These were cut into slices approximately 0.75 mm thick with surface orientations of {100}, {110}, {111} (group III atom surfaces) and $\{\bar{1}\bar{1}\bar{1}\}$ (group V atom surfaces) (11). These slices were lapped and usually diced into 6.3 mm squares before etching (12) to a thickness of about 0.5 mm. However, some of the slices with $\{\bar{1}\bar{1}\bar{1}\}$ surfaces were etched without dicing for large area deposition studies. These slices generally were elliptical in shape with a major axis of about 25 mm and a minor axis of about 15 mm.

Undoped and doped single crystal seeds of GaP were prepared in a similar manner from single crystal floating zone material (10).

Results

Crystal morphology.—Figure 2 illustrates the surface appearance of GaP grown on four different crystal orientations of GaAs seeds. Surfaces of similar appearance are obtained when GaP is grown on GaP and GaAs is grown on GaP or GaAs. All of these layers are found by x-ray analysis to be single crystals with the same orientation as the underlying substrate. The surface appearance illustrated for the four crystal orientations is quite characteristic for growth layers in a thickness range from 0.01 to 0.1 mm.

As will be noted in Fig. 2, the $\{\bar{1}\bar{1}\bar{1}\}$ surface has the best appearance with respect to flatness and uniformity. The growth on the {110} surface is made up of steps or flat planes of different thickness. On the other hand, the growths on the {111} and {100} surfaces show microscopic discontinuities.

The discontinuities evident on the {100} surface are believed to result from nucleation on preferred sites which then grow to form a parallel arrangement of pits of varying dimensions and shapes. The most commonly observed pattern is illustrated in

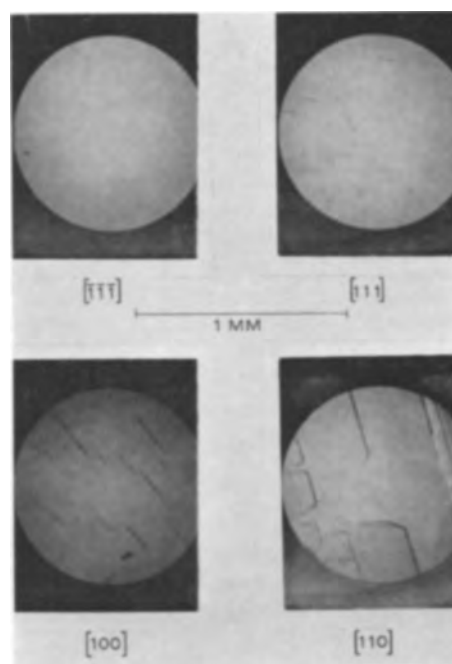


Fig. 2. Effect of substrate orientation on the appearance of vapor grown single crystal GaP.

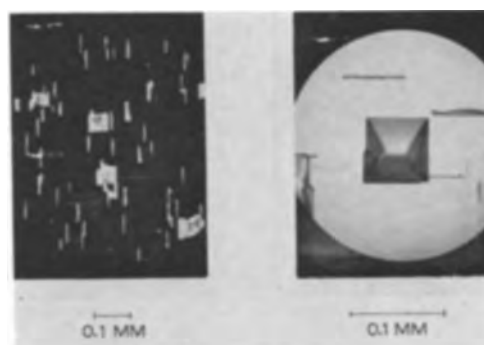


Fig. 3. Rectangular pits in GaP grown from the vapor on a {100} oriented GaAs substrate.

Fig. 3. While these are generally narrow in width as compared to their length, note the shape of the magnified pit with {111} and $\{\bar{1}\bar{1}\bar{1}\}$ oriented walls. Gershenzon (13) has suggested that these pits may originate as the result of nucleation on a pair of screw dislocations. Hence, they would not be expected to appear on other orientations as is in fact found to be true.

The appearance of thick single crystal layers of GaP grown on $\{\bar{1}\bar{1}\bar{1}\}$ oriented GaAs seeds is shown in Fig. 4. These were grown in the same run on 6.3 x 6.3 mm etched slices of GaAs which were located horizontally about 2 cm apart in a 7 mm ID tube. This tube was attached to an 18 mm tube which contained the GaP source at 1100°C. The crystals were grown in about 5 days. The temperatures in Fig. 4 are those at the midpoint of the substrates. For the temperature gradient used, this gives a temperature spread over the substrates of $\pm 5^\circ\text{C}$.

A large area of flat growth on the $\{\bar{1}\bar{1}\bar{1}\}$ surfaces, especially on the upstream sample, is shown in Fig. 4. The $\{\bar{1}\bar{1}\bar{1}\}$ layer is approximately 1.3 mm thick in

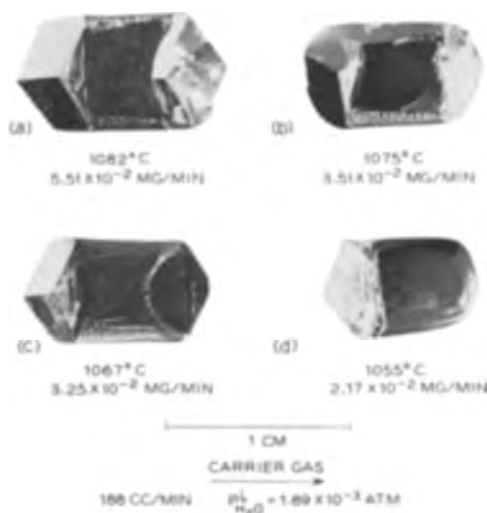


Fig. 4. Appearance of thick single crystal layers of GaP grown from the vapor on $\{111\}$ oriented GaAs substrates.

the first sample, Fig. 4a. Note particularly the well-developed $\{110\}$ faces on the upstream side of the first three samples as well as on the downstream side of the first two samples. The appearance of this well-developed $\{110\}$ face, which was confirmed by x-ray, shows this to be the slowest growth direction. Under the same processing conditions as in Fig. 4a, a larger area GaAs substrate yielded a growth layer thickness of about 1.6 mm with a flat area of 3 cm².

The single crystals of GaP are removed from the GaAs seeds by lapping the underside to expose the substrate. The substrate then is removed by differential etching in cold aqua regia. However, the GaP surface adjacent to the GaAs substrate is found to contain cracks, defects, and a solid-solution transition layer which are essentially removed by lapping off about 0.2 mm. Uniform single crystal slices of GaP up to 25x15x1.0 mm have been prepared by this technique.

Substrate decomposition.—When GaP is grown on GaAs, appreciable decomposition of the substrate occurs especially at the higher temperatures unless the growth rate is sufficiently rapid and the entire surface is covered by the growth. Evidence of substrate decomposition is shown by the rounded surface of the downstream end of the growth sample in Fig. 4d. It also results in the growth of solid solutions of GaP_xAs_{1-x}. Fluorescent x-ray analysis has been made of vapor grown GaP crystals from which the GaAs substrate was removed by differential etching in cold aqua regia. The analysis showed a high As content at the original GaP-GaAs interface which decreased rapidly as material was removed from this surface by etching or lapping. However, As was still detected on the outer surface of a GaP layer over 1 mm thick grown on GaAs. This is not due to self-diffusion but rather to the continued evaporation of As from small exposed areas of the substrate.

Growth rate.—Since growth rate is directly related to the vapor content above saturation at a given substrate temperature, it can be controlled to a

large extent by the source temperature, substrate temperature gradient, water content, and flow rate. However, both GaP and GaAs nucleate and grow on fused silica in the flow system when a definite value of supersaturation is reached for a particular surface condition. Thus the growth rate on a preferred nucleation site such as a single crystal substrate in the gas stream is controlled by this value of supersaturation. It has not been possible to establish a single value of supersaturation before nucleation on fused silica because of the highly variable nature and relatively large area of these surfaces. However, the value of supersaturation before nucleation on the fused silica appears to fall between 2-5% for a large number of runs made during this investigation. Thus an expected range of growth rates can be calculated from the Ga₂O pressure data (9). For example, this gives a growth rate range of 2.40-6.00x10⁻⁷g of GaP per cubic centimeter of carrier gas for a substrate temperature of 1050°C, a source temperature of 1100°C, and a H₂O pressure of 6.01x10⁻³ atm. A single crystal of GaP grown on GaAs under the same conditions at a flow rate of 400 cm³/min increased in weight at a rate of 3.90x10⁻⁷g of GaP per cubic centimeter of carrier gas which falls within the calculated range.

If the value of supersaturation is maintained, the growth rate can be increased by increasing the substrate temperature, source temperature, substrate temperature gradient, water content, and flow rate. However, apparatus limitations and undesirable growth effects limit the choice of process parameters. For example, too high a water content results in nonuniform and often fibrous growth. On the other hand, the appearance of the growth improves with increasing substrate temperature, but this in turn probably increases the concentration of unwanted impurities from the fused silica system. The rapid devitrification of fused silica at high temperatures also restricts the maximum source temperature and hence the maximum flow rate for attaining supersaturation at the lower substrate temperature.

Doping of crystals.—Single crystals of GaP doped n-type with sulphur up to a carrier concentration of 5x10¹⁸ have been grown from the vapor by this process. Attempts to produce single crystals to higher concentrations have not been successful. The doping level is controlled by passing the carrier gas over a temperature controlled S source as shown in Fig. 1. The doping can also be done by adding controlled volumes of H₂S to the H₂ carrier gas. However, side reactions occur which effect the growth habits and alter the conditions required for optimum growth for undoped crystals. For example, the weight loss from a heated GaP source increases with increasing S content in the carrier gas. This is believed due to the formation of a volatile specie such as Ga₂S₂ which has been reported (14). Fairly large, needle-like, transparent, yellow crystals have been grown by passing H₂ containing H₂S over Ga at 1050°C. X-ray analysis has shown these crystals to be hexagonal GaS.

Single crystals of GaP doped p-type with Zn to carrier concentrations of 10¹⁹ have been grown from the vapor. Heated sources of either Zn or ZnO were

used. Side reactions occur which affect the growth habits.

Solid solutions.—Solid solutions of GaP_xAs_{1-x} have been grown from the vapor on GaAs and GaP crystal substrates. Separate sources of GaAs and GaP were heated at 950°C with the GaAs being placed upstream to the GaP. Growth rates from 10⁻⁸ to 10⁻⁹ g/cm³ were obtained with substrate temperatures of 900°C and a wet H₂ flow rate of 100 cm³/min. The substrate squares with 6.3 mm sides were mounted vertically with the growth face perpendicular to the flow direction. Under these conditions a constant composition vapor phase was obtained which deposited a single crystal solid solution layer of GaP_xAs_{1-x}. X-ray diffraction measurements gave $a_0 = 5.54\text{\AA}$ for these layers as compared to $a_0 = 5.654\text{\AA}$ and $a_0 = 5.451\text{\AA}$ for pure GaP and GaAs, respectively. Since GaP_xAs_{1-x} solid solutions follow Vegard's law (15), this would give a value of 44 ± 5 mole % for the GaAs content. These solid solution crystals are a transparent deep red as compared to a transparent amber yellow for pure GaP as would be expected from a reduction in the energy gap. Undoped solid solution layers generally are n-type with N_D—N_A values comparable to the undoped GaP or GaAs layers.

Growth from the elements or oxides.—Single crystals of GaP and GaAs have been grown from the vapor by passing wet H₂ over heated sources of Ga and the Group V elements. The Group V oxides react with the H₂ to provide the necessary H₂O for the Ga₂O transport as well as the Group V element. The H₂ reduces the Ga₂O₃ to Ga₂O plus H₂O. A dual flow system in which the components are brought together in the vapor state has given better control of the process.

Electrical and optical properties of the crystals.—Surface barrier junction capacitance measurements have been made on undoped vapor grown single crystal GaP. In general, these are found to be n-type with N_D—N_A values ranging from about 10¹⁶ to 10¹⁷ atoms/cm³. However, some samples were found to have N_D—N_A values as low as 10¹². The material grown by this process is believed to be compensated. By analogy with GaAs (16), the compensation may be due to oxygen since the process uses a Ga₂O transport mechanism. The compensation may also be due to copper, a deep acceptor, which has been detected (17) in this material. The donor is believed to be silicon.

GaP crystals grown from the vapor on GaAs substrates at temperatures below about 950°C generally do not show the photoluminescence in the visible which frequently is found in boat grown, floating zone, and solution grown material (18). On the other hand, GaP grown from the vapor on GaAs substrates at temperatures above about 950°C generally do show photoluminescence in the visible. However, fairly strong photoluminescent emission in the near-infrared at 0.66, 1.03, 1.30, and 1.66 eV at 80°K is found only in the vapor grown material (17). These emission bands are believed to be associated with Cu (17).

Vapor grown single crystals are more uniformly and less severely strained than the floating zone

material. Moreover, the strains can be removed from the vapor grown material by annealing which is not true for the floating zone crystals.

Junctions.—A detailed discussion of the characteristics of vapor grown GaP junctions is beyond the scope of this paper. These generally are comparable in breakdown characteristics to those produced in equivalent materials by other methods. However, it has been found (18) that junctions prepared wholly by the vapor transport mechanism at substrate temperatures below about 950°C generally do not show the visible electroluminescence which is characteristic of junctions in boat grown and floating zone material. Junctions prepared wholly by the vapor transport mechanism at substrate temperatures above about 950°C generally show visible electroluminescence. On the other hand, diodes prepared by the vapor deposition of doped layers on oppositely doped floating-zone substrates at temperatures above and below 950°C generally are comparable with the corresponding grown junctions.

Vapor grown doped GaP was grown on doped GaAs substrates to give n-n, p-n, and n-p structures for heterojunction measurements. While these all showed junction characteristics, diffusion of the doping impurities during the vapor growth made the exact location of the junction questionable. In addition, the GaP and GaAs were separated by a solid solution transition layer of unknown thickness and composition.

Conclusions

Undoped and doped single crystal layers of GaP and GaAs suitable for material studies and semiconductor devices can be grown in an open tube system by the Ga₂O vapor transport mechanism. Substrate orientations of the {111} face are found to give the best results from the standpoint of uniformity and appearance. Growth rates can be controlled by the source temperature, substrate temperature, temperature gradient, flow rate, and H₂O content in the H₂ carrier gas. The photoluminescent and electroluminescent characteristics of vapor grown crystals at substrate temperatures above 950°C are comparable to those of floating zone and boat grown materials.

Acknowledgment

The author wishes to thank H. G. White and P. W. Foy for some of the measurements and C. D. Thurmond and M. Gershenzon for their helpful suggestions.

Manuscript received June 7, 1963; revised manuscript received Sept. 20, 1963.

Any discussion of this paper will appear in a Discussion Section to be published in the December 1964 JOURNAL.

REFERENCES

1. H. Christensen and G. K. Teal, U. S. Pat. 2,692,839 (1954).
2. G. R. Antell and D. Effer, *This Journal*, **106**, 509 (1959).
3. J. Marinace, *IBM, J. Res.*, **4**, 248 (1960); E. S. Wajda, B. N. Kippenham, and W. H. White, *ibid.*, **4**, 288 (1960).

4. R. L. Newman and N. Goldsmith, *This Journal*, **108**, 1127 (1961).
5. F. A. Pizzarello, *ibid.*, **109**, 226 (1962).
6. N. Holonyak, Jr., D. C. Jillson, and S. F. Bevacqua, A.I.M.E. Tech. Conf., Los Angeles, Aug. 31, 1961.
7. R. R. Moest and B. R. Shupp, *This Journal*, **109**, 1061 (1962).
8. M. Gershenzon and R. M. Mikulyak, *ibid.*, **108**, 548 (1961).
9. C. D. Thurmond and C. J. Frosch, *This Journal*, **111**, 184 (1964).
10. C. J. Frosch and L. Derick, *This Journal*, **108**, 251 (1961).
11. E. P. Warekois and P. H. Metzger, *J. Appl. Phys.*, **30**, 960 (1959).
12. M. V. Sullivan and G. Kolb, *This Journal*, **110**, 585 (1963).
13. M. Gershenzon, Private communication.
14. F. A. Cotton, "Progress in Inorganic Chemistry," Interscience Publishers, Inc., New York, **3**, 113 (1962).
15. H. Flicker and P. K. Herkart, *Bull. Am. Phys. Soc.*, **5**, 407 (1961); Conference Am. Phys. Soc., Chicago, November 25-26, 1960.
16. J. W. Allen, *Nature*, **187**, 403 (1960).
17. M. Gershenzon and R. M. Mikulyak, Abstract No. 27, Paper presented at Electrochemical Society Pittsburgh Meeting (April 1963).
18. M. Gershenzon and R. M. Mikulyak, *Solid-State Electronics*, **5**, 313 (1962).

The Reaction of GaP(s) with H₂O(g) and the Range of Stability of GaP(s) under Pressures of Ga₂O and P₂

C. D. Thurmond and C. J. Frosch

Bell Telephone Laboratories, Incorporated, Murray Hill, New Jersey

ABSTRACT

The reaction of GaP with wet hydrogen has been studied by a vapor transport method. Experimental equilibrium constants in the temperature range of 800°-1100°C have been found to be in satisfactory agreement with the equilibrium constants calculated from the free energies of formation of the reacting components, GaP, H₂O, and Ga₂O. A heat of formation of GaP at 298°K of -42.75 kcal/mole has been obtained from the Knudsen cell measurements of Johnston. A value of S₂₉₈⁰ for GaP of 14.4 cal/deg mole has also been obtained. The range of pressures of Ga₂O and P₂ over which GaP is stable is described. Formation of both Ga₂O₃ and GaPO₄ is considered. Variation in the solubility of oxygen in GaP as a function of the pressures of Ga₂O and P₂ is discussed.

Frosch (1) has grown single crystals of GaP from a vapor phase obtained from the reaction of wet H₂ with a polycrystalline GaP source in the temperature range of 700°-1100°C. The purpose of this paper is to show that the chemical reaction is known that is responsible for the volatility of GaP in wet hydrogen and for the growth of gallium phosphide crystals from the vapor phase. In addition, thermodynamic functions are given for GaP based on the Knudsen cell measurements of Johnston (2).

Wet hydrogen mixtures have been passed over GaP at various flow rates and at temperatures ranging from 800° to 1100°C. From the measurement of sample weight loss, equilibrium constants have been calculated on the assumption that the following reaction was responsible for the volatility of GaP.

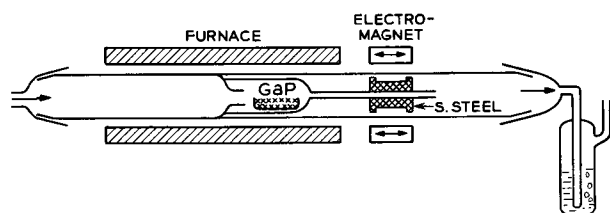
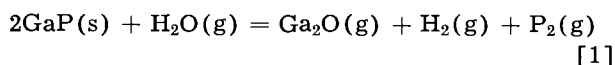


Fig. 1. Schematic drawing of the apparatus used in the volatility measurements.

These equilibrium constants have been compared with equilibrium constants calculated from available free energies of formation of the species involved.

Experimental

The apparatus for measuring volatility is shown schematically in Fig. 1. It consists essentially of a 25 mm ID fused silica tube extending through a 25 cm long flat temperature zone. The temperature zone is controlled to $\pm 1^\circ\text{C}$ with thermocouples and potentiometer controls. A constriction tube approximately 3 mm ID by 13 mm long is ring-sealed inside the furnace tube to reduce back diffusion. This, together with the pusher assembly, provides an enclosure for the sample during a volatility measurement. The pusher assembly consists of a 17 mm ID by 3 cm long tube attached to a 6 mm ID tube. A magnetic stainless steel spool attached to the small tube of the pusher assembly provides the coupling to the movable external electromagnet for movement of the sample during a run. The sample being measured is contained in a fused silica boat approximately 2 cm long by 12 mm wide. An oil bubbler at the exit end of the furnace tube prevents diffusion of air into the system during a run.

The H₂O content of the carrier gas is controlled in the same manner as that previously described for crystal growth (1).

In making a run, a weighed sample is placed in the pusher assembly and inserted into the furnace tube so that the sample is located outside the furnace. During loading and unloading a flow of N₂ rather than H₂ is used to avoid the formation and condensation of H₂O which is difficult to remove from the system. After sealing the oil bubbler to the furnace tube with wax or elastic rubber tape, the system is purged by initiating the desired carrier gas flow. This requires from one to several hours depending on the flow rates being used. The sample then is introduced into the furnace magnetically to the position illustrated in Fig. 1. At the end of the run the sample is withdrawn magnetically to its original position for cooling in the carrier gas before purging in N₂ followed by removal and weighing.

Results

The equilibrium constant for reaction [1] can be calculated from the weight of GaP, W , which saturates a volume of gas, V , at a temperature T . The equilibrium pressure of Ga₂O, $P_{\text{Ga}_2\text{O}}$, will be related to the weight loss, W , by the ideal gas equation

$$P_{\text{Ga}_2\text{O}} = \frac{RT}{2M_{\text{GaP}}} \left(\frac{W}{V} \right)^{\circ} \quad [2]$$

In this equation, M_{GaP} is the molecular weight of GaP, R , the gas constant, $(W/V)^{\circ}$, the weight loss in g/cc at zero flow, and T , the temperature in degrees Kelvin. When the flow rate is measured at 298°K, T , in Eq. [2], is 298°K since the gas phase is ideal. The equilibrium pressure of water, $P_{\text{H}_2\text{O}}$, can be obtained from the requirement that oxygen be conserved and that the partial pressures of H₂O and Ga₂O are small compared to the pressure of hydrogen. Since the H₂ pressure is much larger than all other pressures both before and after reaction, the flow rate of equilibrated gas leaving the reaction zone is the same as the flow rate of the incoming gas heated to the reaction temperature. These conditions lead to the relationship

$$P_{\text{H}_2\text{O}} = P_{\text{H}_2\text{O}}^i - P_{\text{Ga}_2\text{O}} \quad [3]$$

where $P_{\text{H}_2\text{O}}^i$ is the partial pressure of H₂O in the incoming gas stream. The pressures of P₂ and Ga₂O are equal when reaction [1] has proceeded to equilibrium, but are small compared to the hydrogen pressure which is essentially 1 atm. Thus, the equilibrium constant for reaction [1] is given to within a few per cent by the equation

$$K_1 = \frac{(P_{\text{Ga}_2\text{O}})^2}{P_{\text{H}_2\text{O}}^i - P_{\text{Ga}_2\text{O}}} \quad [4]$$

The equilibrium value of the pressure of Ga₂O, $P_{\text{Ga}_2\text{O}}$, has been obtained by extrapolating weight loss measurements as a function of flow rates to zero flow rate. The extrapolation was made in a manner which took into consideration diffusional losses at lower flow rates and undersaturation at higher flow rates.

If reaction [1] comes to equilibrium at the flow rates used, the loss in weight of GaP per unit time, w , will be a linear function of the flow rate, v .

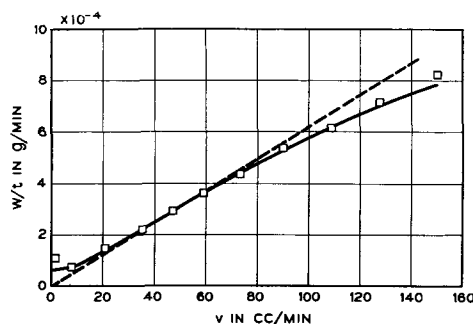


Fig. 2. Linear plot of the weight loss in g/min as a function of H₂ flow rate in cc/min at 1000°C and a $P_{\text{H}_2\text{O}}^i$ pressure of 6.01×10^{-3} atm. The solid line is the calculated curve using Eq. [7] with $\alpha = 280$ cm³/min and $\beta = 10$ cm³/min. The dashed line is for a saturated vapor phase with no diffusional losses.

$$w = \frac{2M_{\text{GaP}}}{RT} P_{\text{Ga}_2\text{O}} v \quad [5]$$

This follows directly from the ideal gas law. At low flow rates, losses will occur from the source by vapor phase diffusion which will produce an increased weight loss. This effect has been considered by Merten (3). According to Merten, an expression of the following form could be expected to account for diffusional losses

$$w = \frac{(W/V)^{\circ}}{1 - e^{-v/\beta}} v \quad [6]$$

where $(W/V)^{\circ} = (2M_{\text{GaP}}/RT) P_{\text{Ga}_2\text{O}}$.

At higher flow rates undersaturation will occur. Frosch and Thurmond (4) have suggested that a term in the numerator of the form $1 - e^{-\alpha/v}$ can be used to approximate this process.

The two processes, diffusional losses and undersaturation, can be included in one expression

$$w = \left(\frac{W}{V} \right)^{\circ} \frac{1 - e^{-\alpha/v}}{1 - e^{-v/\beta}} v \quad [7]$$

We have measured w as a function of v for reaction [1] and find that an expression of the form of [7] is a satisfactory representation of the measurements. This is shown in Fig. 2 for the measurements at 1000°C. The constants α and β were 280 and 10 cm³/min, respectively. Similar measurements were made at 850°C, and the same values of α and β were found to give a satisfactory fit to the experimental results.

The measurements at 1000°C have enabled us to estimate the flow rate range where diffusional losses are not significant and where undersaturation is low. Our experimental measurements have been used to obtain estimates of the equilibrium values of (W/V) by a modified use of Eq. [7]. We have plotted (W/V) which is equivalent to (w/v) , on a semilogarithmic plot, $\log (W/V)$ vs. v . A curve of $\log (1 - e^{-\alpha/v})$ vs. v for which $\alpha = 280$ cm³/min was also plotted on a separate sheet of graph paper. This curve was moved into position over the set of points at each temperature to obtain the value of $(W/V)^{\circ}$. Figure 3 is a semilogarithmic plot which shows all of the experimental data obtained. In each case the curves correspond to a value of α of 280 cm³/min.

Table I. Experimental equilibrium constants for the reaction
 $2\text{GaP(s)} + \text{H}_2\text{O(g)} = \text{Ga}_2\text{O(g)} + \text{H}_2\text{(g)} + \text{P}_2\text{(g)}$

$T, ^\circ\text{K}$	$P_{\text{H}_2\text{O}} \text{ atm}$	$P_{\text{Ga}_2\text{O}} \text{ atm}$	$K_1 \text{ (atm)}^2$
1073	6.01×10^{-3}	9.90×10^{-6}	1.63×10^{-8}
1123	6.01×10^{-3}	5.95×10^{-5}	5.95×10^{-7}
1173	6.01×10^{-3}	1.07×10^{-4}	1.94×10^{-6}
1223	6.01×10^{-3}	2.64×10^{-4}	1.21×10^{-5}
1223	3.09×10^{-3}	1.35×10^{-4}	7.59×10^{-6}
1273	6.01×10^{-3}	7.42×10^{-4}	1.04×10^{-4}
1323	6.01×10^{-3}	1.44×10^{-3}	4.54×10^{-4}
1373	6.01×10^{-3}	2.35×10^{-3}	1.51×10^{-3}

Table I lists the values of $P_{\text{Ga}_2\text{O}}$ calculated from $(W/V)^\circ$ and the equilibrium constants calculated from Eq. [4].

Discussion

Information is available in the literature from which the equilibrium constant for Eq. [1] can be calculated. The agreement between these calculated values and our experimental values is within the uncertainties of the data. This is shown in Fig. 4 where $\log K_1$ is plotted as a function of $1/T$, and the experimental points are compared with the calculated line. The solid line corresponds to a heat content change of 117.4 kcal and an entropy change of 72.8 cal/deg. An estimated uncertainty of 2 kcal in ΔH° and 2 eu in ΔS° lead to the dashed lines shown in Fig. 4.

The calculated equilibrium constants have been obtained from thermodynamic functions for GaP which were based on the measurements of Johnston (2) and from a reevaluated heat of formation for Ga_2O .

Heat and entropy of formation of GaP.—Johnston (2) has recently obtained the pressure of P_2 over GaP from Knudsen cell measurements. The assumption that the principal volatile species over GaP was P_2 is in accord with the equilibrium constants given by Stull and Sinke (5) for the P_2 - P_4 equilibrium. From Johnston's measurements we have obtained a value for $(\Delta H_{\text{GaP}}^\circ)_{298}$ and $(S_{\text{GaP}}^\circ)_{298}$,

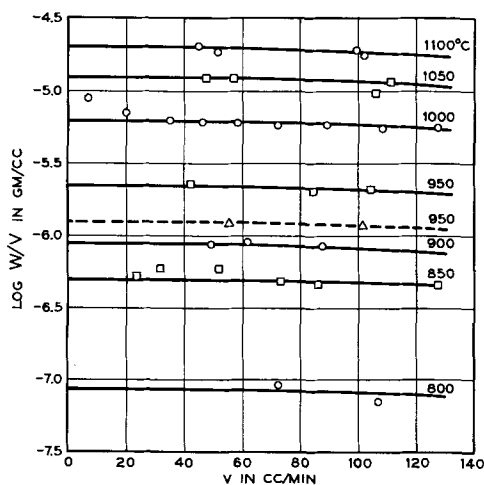


Fig. 3. Semilogarithmic plot of the experimentally determined values of W/V as a function of v showing the extrapolation to zero flow rate. The solid lines and dashed line are for experimental determinations made at a $P_{\text{H}_2\text{O}}$ pressure of 6.01×10^{-3} atm and 3.09×10^{-3} atm, respectively.

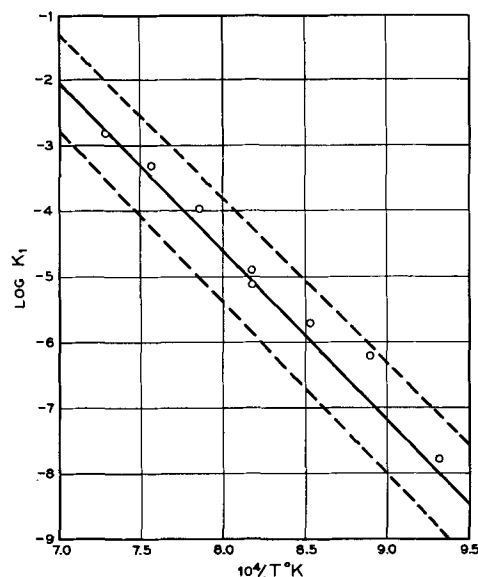
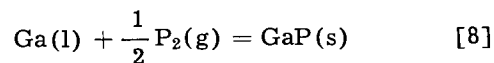


Fig. 4. A $\log K_1$ vs. $1/T$ plot for the experimental data according to Eq. [1]. The solid line is calculated from the available thermodynamic data. The dashed lines represent an uncertainty of 2 kcal in ΔH° and 2 eu in ΔS° .

where the formation reaction is given by the following equation



In the pressure range studied by Johnston, GaP decomposes and two phases are present in his Knudsen cell, *i.e.*, a solid GaP phase and a liquid phase saturated with GaP. The measurements of Rubenstein (7) and Hall (8) show that the Ga rich liquid phase contains less than 1 or 2 at. % of phosphorus in the temperature range studied. Consequently, the liquid phase is essentially pure Ga, and the free energy of formation of GaP can be obtained from the vapor pressure measurements made by Johnston.

The evaluation of the free energy, heat, and entropy of formation of GaP from vapor pressure measurements can best be made if heat capacities are known for the reaction components. The heat capacities of Ga and P_2 are known, but no experimental data are available for the heat capacity of GaP. We have assumed that the heat capacity of GaP is the sum of the heat capacities of germanium (6) and silicon (6)

$$(C_p)_{\text{GaP}} = (C_p)_{\text{Si}} + (C_p)_{\text{Ge}} \quad [9]$$

$$(C_p)_{\text{GaP}} = 11.68 + 1.52 \times 10^{-3}T - \frac{1.60 \times 10^5}{T^2} \quad [10]$$

This estimate is reasonable since the crystal structure of GaP is closely related to that of Ge and Si. In addition it should be noted that the molecular weights of GeSi and GaP are both 101. The heat capacities of Ga and P_2 given by Kelley (6) have been used to obtain ΔC_p . The measurements of Johnston (2) give the free energy of formation of GaP, ΔF_T° , from which the "sigma" function is obtained

$$\Sigma = -\frac{\Delta F_T^\circ}{T} + \frac{1}{T} \int_{298}^T \Delta C_p dT - \int_{298}^T \Delta C_p d \ln T \quad [11]$$

Table II. Heat of formation of GaP at 298°K.
Ga(s) + 1/2 P₂(g) = GaP(s). Data from Johnston (2)

T, °K	$\Delta F^{\circ}_T/T$ cal/deg mole	ΔH°_{298} kcal/mole
1053	-16.62	-42.94
1078	-15.55	-42.88
1109	-14.38	-42.75
1135	-13.20	-42.42
1184	-11.97	-42.86
1234	-10.40	-42.71
1277	-9.30	-42.81

$(\Delta H^{\circ}_{298})_{\text{GaP}} = -42.75 \pm 0.1$ kcal/mole
 $(\Delta S^{\circ}_{298})_{\text{GaP}} = -21.49 \pm 0.1$ cal/deg mole

where Σ is related to the heat and entropy of formation by the following equation.

$$\Sigma = -\frac{\Delta H^{\circ}_{298}}{T} + \Delta S^{\circ}_{298} \quad [12]$$

A plot of Σ vs. $1/T$ should be a straight line of slope $-\Delta H^{\circ}_{298}$ and intercept ΔS°_{298} . An alternative way of showing how well Eq. [12] fits the experimental measurements is to use the best intercept and calculate a value of ΔH°_{298} for each point. Table II gives the values of ΔH°_{298} calculated from each experimental point using a value of the entropy of formation of -21.49 cal/deg.

The heat of formation of GaP(s) of -42.75 kcal corresponds to the heat content change for Eq. [8]. From the heat of vaporization of gallium and the heat of dissociation of P₂ given by Stull and Sinke (5), the heat of atomization of GaP(s) can be calculated. A value of 166.2 kcal is obtained, corresponding to the conversion of GaP(s) to gaseous Ga and P atoms. This number is smaller than the sum of the heats of sublimation of Ge and Si at 298°K by 15%, in accord with the conclusions reached by Goldfinger (9) for other III-V compounds.

The entropy of formation of GaP at 298°K can be used with the known entropies of Ga(l) (5) and P₂(g) (5) to obtain a value of the entropy of GaP(s) at 298°K which is 14.39 cal/deg. Renner (10) has estimated a value of 9.3 cal/deg from a modified Eastman formula, which we believe is too low. An estimate of 12.0 cal/deg is obtained from the sum of the entropies of Si(s) and Ge(s), and an estimate of 15.3 cal/deg comes from the sum of the entropies of Ga(s) and P(s). Goldfinger (9) has quoted a value for the entropy of GaP(s) at 1100°K of 24.3 eu which is to be compared to 30.0 eu obtained from Johnston's data. We believe that the entropy at 298°K of 14.4 cal/deg obtained from Johnston's data is a reasonable value.

Table III. Free energy function for GaP
 $(C_p)_{\text{GaP(s)}} = (C_p)_{\text{Ge(s)}} + (C_p)_{\text{Si(s)}}$

T, °K	$\left(\frac{F^{\circ}_T - H^{\circ}_{298}}{T}\right)_{\text{GaP(s)}}$ cal/deg mole
298	14.39
800	18.51
900	19.41
1000	20.28
1100	21.11
1200	21.91
1300	22.67
1400	23.39
1500	24.08
1600	24.74
1700	25.39

A free energy function table is given in Table III for GaP using a value of S°_{298} of 14.39 cal/deg and Eq. [10] for the heat capacity.

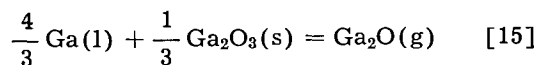
Heat of formation of SiO and Ga₂O.—Cochran and Foster (11) and Frosch and Thurmond (4) have given values for the heat of formation of Ga₂O. Cochran and Foster studied the two reactions



and

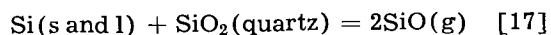
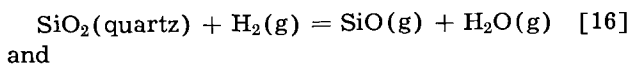


while Frosch and Thurmond studied the reaction



Recently, new experimental data have become available which lead to revised heats of formation for SiO₂ and SiO. These revisions lead to a revision in the heat of formation of Ga₂O as obtained from the reaction described by Eq. [13].

We have obtained a new heat of formation of SiO from the recent measurements Ramstad and Richardson (12) who studied the following reactions



The thermodynamic functions for SiO₂, SiO, Si, H₂O, and H₂ needed in this calculation were obtained from the JANAF Tables (13). The heat of formation of SiO₂ was corrected using the recent value recommended by Good (14) and corroborated by others (15, 16). Since a good value for the entropy of SiO at 298°K is known, 50.55 cal/deg mole (13-17), a value of the entropy of formation is known, $(\Delta S^{\circ}_{298})_{\text{SiO}} = 21.61$ cal/deg mole. Table IV gives the

Table IV. Heat of formation of SiO at 298°K

Equilibrium studied	T, °K	$\Delta F^{\circ}_T/T$ cal/deg	$-(\Delta F^{\circ}_T)_{\text{SiO}}/T$ cal/deg mole	$-(\Delta H^{\circ}_{298})_{\text{SiO}}$ kcal/mole
SiO ₂ (quartz) + H ₂ (g) = SiO(g) + H ₂ O(g)	1700	29.95	34.17	24.00
	1773	26.69	33.20	23.96
	1800	25.63	32.63	23.59
	1873	22.25	31.78	23.52
Si(s and l) + SiO ₂ (quartz) = 2SiO(g)	1509	29.72	36.02	23.73
	1581	25.30	34.98	23.35
	1610	23.77	34.51	23.04
	1673	19.69	34.05	23.28
	1718	17.99	33.03	22.46
	1757	16.40	32.18	21.83

Average $(\Delta H^{\circ}_{298})_{\text{SiO}} = -23.2$ kcal/mole

Table V. Heat of formation of Ga₂O at 298°K

Equilibrium studied	T, °K	$\Delta F^\circ_T/T$ cal/deg	$-\Delta F^\circ_{\text{Ga}_2\text{O}}/T$ cal/deg mole	$-(\Delta H^\circ_{298})_{\text{Ga}_2\text{O}}$ kcal/mole	Avg
SiO ₂ (quartz) + 2Ga(l) = Ga ₂ O(g) + SiO(g) Cochran and Foster (11)	1179	64.25	37.02	24.47	23.0
	1231	59.67	34.74	23.00	
	1280	55.01	33.46	22.42	
	1332	50.31	32.35	22.25	
	1357	47.61	32.42	22.83	
	1383	45.37	32.03	22.76	
MgO(s) + 2Ga(l) = Ga ₂ O(g) + Mg(g) Cochran and Foster (11)	1179	65.86	33.65	20.50	19.7
	1231	60.58	32.60	30.37	
	1280	57.15	30.54	18.77	
	1332	51.73	30.58	19.85	
	1383	48.13	29.30	18.99	
4/3 Ga(l) + 1/3 Ga ₂ O ₃ (s) = Ga ₂ O(g) Frosch and Thurmond (4)	1073	17.41	36.58	21.28	20.7
	1173	12.94	34.32	21.14	
	1223	11.25	32.64	20.25	
	1273	9.17	31.89	20.12	
2GaP(s) + H ₂ O(g) = Ga ₂ O(g) + P ₂ (g) +H ₂ (g)	1073	35.36	38.03	22.84	23.0
	1123	28.38	38.97	25.22	
	1173	25.90	35.93	23.03	
	1223	22.28	34.45	22.52	
	1223	22.52	34.26	22.15	
	1273	17.84	34.30	23.42	
	1323	14.69	33.17	23.09	
	1373	12.36	31.50	21.93	

$$(\Delta H^\circ_{298})_{\text{Ga}_2\text{O}} = -21.5 \pm 1.5 \text{ kcal/mole}$$

pertinent data and the calculated values of ΔH°_{298} . An average value of -23.2 kcal/mole has been taken for the heat of formation of SiO at 298°K. The JANAF Table uses a value of -21.4 kcal/mole.

It is now possible to calculate the heat of formation of Ga₂O from the measurements of Cochran and Foster (11) of the reaction of Ga with SiO₂, Eq. [13]. In addition, we have obtained a heat of formation at 298°K for Ga₂O from reaction [14], reaction [15], and also from reaction [1]. Results of these calculations are given in Table V. It has been assumed that the entropy of Ga₂O at 298°K is 69.54 eu and that the heat capacity of Ga₂O is the same as for CTeS, as recommended by Cochran and Foster (11). The free energy functions given by Stull and Sinke (5) for Ga, Mg, and O₂ were used. The free energy function of Ga₂O₃ given by Cochran and Foster (11) and the ΔH°_{298} for Ga₂O₃ measured by Mah (18) were used. The heat of formation of Ga₂O is found to be -21.5 ± 1.5 kcal/mole. This value is to be compared to -20.4 kcal/mole (SiO₂ reaction) and -19.7 kcal/mole (MgO reaction) given by Cochran and Foster (11) and -20.7 kcal/mole given by Frosch and Thurmond (4).

Reaction of GaP with wet hydrogen.—The relationship between the partial pressure of water vapor in the inflowing hydrogen stream and the equilibrium pressure of Ga₂O is given by Eq. [4]. The equilibrium constants, K_1 , calculated from the thermodynamic functions now available, and plotted in Fig. 4, can be used with Eq. [4] to give $P_{\text{Ga}_2\text{O}}$ and P_{P_2} as a function of $P_{\text{H}_2\text{O}}$. This is shown in Fig. 5 for the seven experimental temperatures used. The experimental points are included. The heavy dashed curves lying between the forked ends give the pressures of Ga₂O and P₂, which are equal, as a function of

the pressure of H₂O in the entering hydrogen stream. At low pressures of H₂O and at high pressures of H₂O new reactions occur which lead to the separate lines at each end of the curves of Fig. 5.

Equation [4] gives the dependence of $P_{\text{Ga}_2\text{O}}$ on $P_{\text{H}_2\text{O}}^i$ over a limited range of $P_{\text{H}_2\text{O}}^i$. When the value of $P_{\text{H}_2\text{O}}^i$ is low enough, the pressures of P₂ and Ga₂O will no longer be equal. Under these conditions

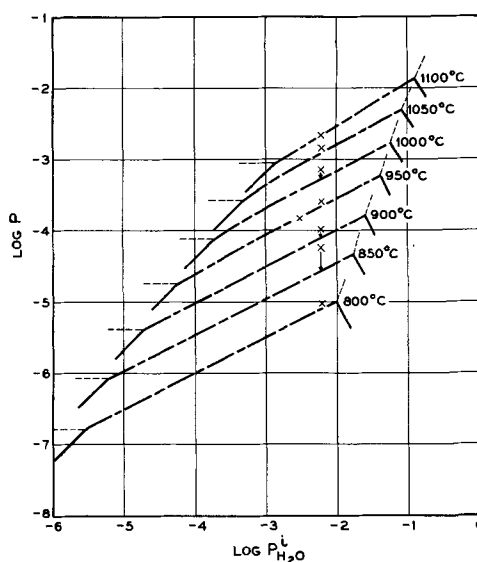


Fig. 5. A log-log plot of $P_{\text{Ga}_2\text{O}}$ and P_{P_2} vs. $P_{\text{H}_2\text{O}}^i$ calculated from available thermodynamic data for each experimental temperature. Experimental points are included. Heavy dashed lines are determined by Eq. [1] in which $P_{\text{Ga}_2\text{O}}$ equals P_{P_2} . At the lower values of $P_{\text{H}_2\text{O}}^i$, lightly dashed lines are the decomposition pressures P_{P_2} from Eq. [8] and the solid lines are the Ga₂O pressures from Eq. [18]. At the higher values of $P_{\text{H}_2\text{O}}^i$, where Ga₂O₃ is present, lightly dashed lines are the P₂ pressures from Eq. [20] and the solid lines are the Ga₂O pressures from Eq. [22].

the pressure of P₂ will be larger than that of Ga₂O and the GaP will decompose. The presence of Ga(l) at equilibrium with GaP(s) will fix the P₂ pressure at GaP decomposition pressure. The reaction responsible for the Ga₂O pressure is shown in the following equation

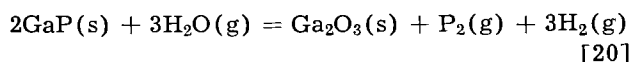


The equilibrium pressure of Ga₂O can be obtained from the equilibrium constant of Eq. [18], K_{18} , and the following equation which follows from the definition of the equilibrium constant.

$$\frac{P_{\text{Ga}_2\text{O}}}{P_{\text{H}_2\text{O}} - P_{\text{Ga}_2\text{O}}} = K_{18} \quad [19]$$

Again, it has been assumed that the pressures of H₂O and Ga₂O are small compared to the pressure of hydrogen, which is 1 atm, and the temperature low enough to insure that the liquid phase is essentially pure Ga. Thus, Eq. [19] describes the dependence of the Ga₂O pressure on the pressure of water in the incoming gas stream until a point is reached where the pressure of Ga₂O is equal to the decomposition pressure of phosphorus over GaP at T .

As the pressure of water is increased, the equilibrium pressures of Ga₂O and P₂ will be equal until a point is reached where Ga₂O₃ is formed. At this point, and beyond, the phosphorus pressure will be determined by the following equilibrium.



The formation of Ga₂O may be accounted for by the reaction given in Eq. [1]. Under the same assumptions used previously, the pressure of P₂ can be shown to be related to the pressure of H₂O in the entering gas stream by the relationship

$$\frac{P_{\text{P}_2}}{(P_{\text{H}_2\text{O}} + 2P_{\text{Ga}_2\text{O}} - 3P_{\text{P}_2})^3} = K_{20} \quad [21]$$

The constant K_{20} is the equilibrium constant for reaction [20]. Since $P_{\text{Ga}_2\text{O}}$ and P_{P_2} are less than $P_{\text{H}_2\text{O}}$, the pressure of P₂ varies approximately as $(P_{\text{H}_2\text{O}})^3$. It also follows that the pressure of Ga₂O varies approximately as $(P_{\text{H}_2\text{O}})^{-2}$.

Range of pressures of Ga₂O and P₂ in equilibrium.

—Equal pressures of Ga₂O and P₂ are generated by the reaction of H₂O with GaP to equilibrium, and the range of these pressures extends from the decomposition pressure of P₂ over GaP to a pressure of Ga₂O and P₂ at which Ga₂O₃ forms. The complete range of pressures possible for Ga₂O and P₂ under conditions of equilibrium with GaP are shown in Fig. 6 for two temperatures, 950° and 1100°C. The dotted line shows the range at each temperature over which Ga₂O and P₂ may have equal pressures, the lower limit being the decomposition pressure of P₂ over GaP and the upper limit the pressure at which Ga₂O₃ forms. At any pressure of P₂ between the decomposition pressure and some very high pressure, where GaP is again unstable, there is an upper limit to the pressure of Ga₂O at which point Ga₂O₃ will form. The following reaction represents this equilibrium.

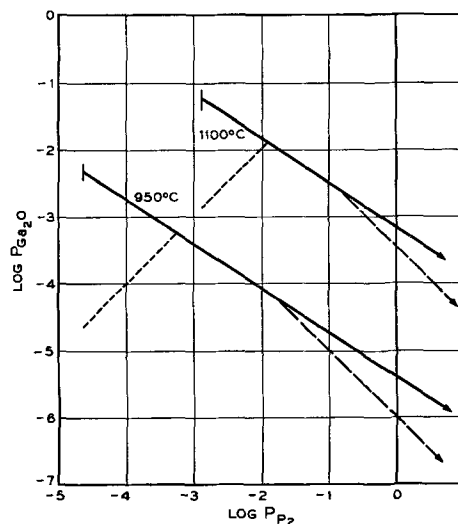
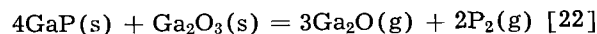
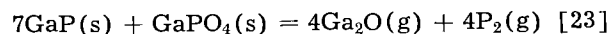


Fig. 6. A log-log plot of the equilibrium pressures of Ga₂O vs. P₂ over GaP in equilibrium with Ga₂O₃. The dashed lines at the lower pressures of P₂ show the range over which $P_{\text{Ga}_2\text{O}}$ and P_{P_2} are equal. The solid lines indicate the pressures of Ga₂O and P₂ where GaP and Ga₂O₃ are at equilibrium. The dashed lines at the higher P₂ pressures indicate the pressures of Ga₂O and P₂ where GaP and GaPO₄ would be at equilibrium.



It can be seen that the pressure of Ga₂O varies as the $-2/3$ power of the pressure of P₂. The solid lines of slope $-2/3$ shown in the log-log plot of Fig. 6 give the pressures of Ga₂O and P₂ at the two indicated temperatures when GaP and Ga₂O₃ are at equilibrium.

The compound GaPO₄ is known to exist (19), but its thermodynamic properties are not known. The stable structure of this compound at temperatures greater than 1000°C or so is cristoballite (19). We have estimated the thermodynamic properties of GaPO₄ by assuming it would have the same properties as the hypothetical mixed oxide crystal GeSiO₄ which would have the same molecular weight and structure as GaPO₄. We can estimate the properties of this mixed oxide by assuming they are the sum of the properties of GeO₂ and SiO₂. The range of conditions over which GaPO₄ and GaP would be in equilibrium can be obtained from the reaction



$$P_{\text{Ga}_2\text{O}}P_{\text{P}_2} = K_{23}^{1/4} \quad [24]$$

The thermodynamic properties of the phase GaPO₄ have been estimated as follows: the heat capacity of GaPO₄ has been assumed to be the sum of the heat capacities of GeO₂ and SiO₂, the entropy at 298°K the sum of the entropies of SiO₂ and GeO₂, and the heat of formation at 298°K the sum of the heat of formation of GeO₂ and SiO₂. These estimates lead to values of the equilibrium constant, K_{24} , of reaction [23]. The dashed lines of Fig. 6 correspond to Eq. [25] at the two temperatures 950° and 1100°C. At pressures of P₂ high enough, the phase GaPO₄ can be expected to form; at lower pressures of P₂ but at high enough pressures of Ga₂O, Ga₂O₃ will be the phase which forms. As long as $P_{\text{Ga}_2\text{O}}$ and

P_{P_2} are below the lines, neither Ga_2O_3 nor $GaPO_4$ will form.

The estimated lines for the GaP-GaPO₄ equilibrium cross the GaP-Ga₂O₃ lines at each temperature at a point where the partial pressure of P₂ is greater than the partial pressure of Ga₂O. According to this estimate, it is concluded that GaPO₄ will not form in the wet hydrogen system where P_{Ga_2O} and P_{P_2} are equal, and Ga₂O₃ will form when high enough values of these pressures are reached.

Vacancy concentrations, stoichiometry, and oxygen solubility.—Nothing is known about the concentrations of vacancies in GaP nor of the solubility of excess Ga or P in GaP other than it is believed that the solubility range is quite narrow. As long as the solubility range is narrow the product of the vacancy concentrations will be constant at any temperature and increase with temperature. Furthermore, the vacancy concentrations are known functions of the partial pressures of the components at any temperature, the Ga vacancy concentration being proportional to the square root of the P₂ pressure and the P vacancy concentration being proportional to the Ga pressure. Nothing can be said about the concentrations of interstitial Ga and P other than the concentration of neutral interstitial Ga will be proportional to the Ga pressure and neutral interstitial P proportional to the square root of the P₂ pressure. From such information the variation in equilibrium vacancy concentrations and interstitial concentrations with P_{P_2} , P_{Ga_2O} , and $P_{H_2O}^i$ can be deduced, but nothing can be said at present of the magnitudes of these concentrations.

Gershenzon (20) has suggested that oxygen is responsible for some of the photoluminescence and electroluminescence seen in GaP crystals and has given experimental evidence that oxygen can be present in GaP crystals at concentrations as high as 10¹⁹ at./cc. The question arises as to the amount of oxygen expected in GaP grown in wet hydrogen. At present this is not known. However, something can be said about the dependence of the oxygen solubility on the pressures of Ga₂O, P₂, and H₂O. It can be shown that the equilibrium concentration of neutral interstitial oxygen atoms will be proportional to the product of the pressures of P₂ and Ga₂O at any temperature, and the highest concentrations of neutral interstitial oxygen atoms will occur when the phase GaPO₄ is in equilibrium with GaP. The concentration of neutral substitutional oxygen atoms will be proportional to the product of the pressure of Ga₂O and the square root of the pressure of P₂. The maximum concentration of substitutional oxygen will occur at the point where GaP is in equilibrium with Ga₂O₃ at the lowest possible P₂ pressure.

When GaP is grown under essentially equilibrium conditions in the wet hydrogen system, the concentration of neutral interstitial oxygen atoms can be shown to be approximately proportional to $P_{H_2O}^i$. The concentration of neutral substitutional oxygen will depend approximately on the 3/4 power of $P_{H_2O}^i$. Thus, the concentration of interstitial oxygen will increase with $P_{H_2O}^i$ somewhat more rapidly

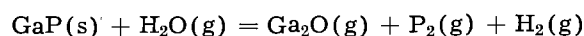
than the concentration of substitutional neutral oxygen.

Conclusions

The agreement between the equilibrium constants of Eq. [1] calculated from the experimental measurements and calculated from the free energies of formation of the compounds involved is taken as evidence that Eq. [1] is the reaction responsible for the volatility of GaP in wet hydrogen. In addition it can be inferred that the reverse of this reaction is responsible for the deposition of GaP from the vapor phase obtained from wet hydrogen passed over GaP at a somewhat higher temperature.

Summary

1. It has been found that GaP reacts with H₂O according to the reaction



2. A value of $(\Delta H_{298}^f)_{GaP(s)}$ of -42.75 kcal/mole has been obtained from the Knudsen cell measurements of Johnston (2) and a value of $(S_{298}^0)_{GaP(s)}$ of 14.4 cal/deg mole.

3. A value of -23.2 kcal/mole has been obtained for the heat of formation of SiO(g) at 298°C from measurements of Ramstad and Richardson (11). This has been used to reevaluate a heat of formation at 298 for Ga₂O.

4. A value of the heat of formation of Ga₂O of -21.5 kcal/mole has been obtained.

5. The variation in the equilibrium pressures of Ga₂O and P₂ over GaP as a result of the reaction of water at various partial pressures in hydrogen has been described.

6. The range of pressures of Ga₂O and P₂ for which GaP is stable has been described. The conditions leading to the formation of Ga₂O₃ have been discussed and the question of the formation of GaPO₄ considered.

7. The questions of vacancy concentrations, stoichiometry and oxygen concentrations have been considered briefly.

Manuscript received June 7, 1963; revised manuscript received Sept. 20, 1963.

Any discussion of this paper will appear in a Discussion Section to be published in the December 1964 JOURNAL.

REFERENCES

1. C. J. Frosch, *This Journal*, **111**, 180 (1964).
2. W. D. Johnston, *ibid.*, **110**, 117 (1963).
3. U. Merten, *J. Phys. Chem.*, **63**, 443 (1959).
4. C. J. Frosch and C. D. Thurmond, *ibid.*, **66**, 877 (1962).
5. D. R. Stull and G. C. Sinke, "Thermodynamic Properties of the Elements," Amer. Chem. Soc., Series (1956).
6. K. K. Kelley, Bull. 582, Bureau of Mines, (1960), U. S. Government Printing Office, Washington, D. C.
7. M. Rubenstein, Electronics Division Abstracts, Vol. 11, No. 1, Abstract No. 65, The Electrochem. Soc. Meeting, Los Angeles, May, 1962.
8. R. N. Hall, *This Journal*, **110**, 385 (1963).
9. P. Goldfinger, "Compound Semiconductors," R. K. Willardson and H. L. Goering, Editors, Vol. 1, Chap. 52, p. 483, Reinhold Publishing Corp., New York (1962).
10. T. Renner, *Solid State Electronics*, **1**, 39 (1960).
11. C. N. Cochran and L. M. Foster, *This Journal*, **109**, 144 (1962).

12. H. F. Ramstad and F. D. Richardson, *J. Metals*, **221**, 1021 (1961).
13. JANAF, Interim Thermochemical Tables, Vol. 2, Thermal Laboratories, Dow Chemical Co.
14. W. D. Good, *J. Phys. Chem.*, **66**, 380 (1962).
15. C. N. Cochran and L. M. Foster, *ibid.*, 380.
16. S. S. Wise, J. L. Margrave, H. M. Feder, and W. N. Hubbard, *ibid.*, 381.
17. L. Brewer and M. S. Chandrasekharaiah, UCRL-8713, June, 1960, Berkeley, Calif.
18. A. Mah, Report of Investigations, 5965, U. S. Department of Interior, Bureau of Mines (1962).
19. E. C. Schafer and R. Roy, *J. Am. Ceram. Soc.*, **39**, 330 (1956).
20. M. Gershenson and R. M. Mikulyak, *Solid State Electronics*, **5**, 313 (1962).

Fluorescent Rare Earths in Semiconducting Thiospinels

Lawrence Suchow and Norman R. Stemple

Thomas J. Watson Research Center, International Business Machines Corporation, Yorktown Heights, New York

ABSTRACT

The system CdS-In₂S₃-Tm₂S₃ has been investigated with the objective of obtaining for physical studies semiconducting crystals with high rare earth content. The new compounds CdR₂S₄ and CdR₂Se₄, where R represents the rare earths of small ionic size, have been found to have the spinel structure. Thulium was chosen as representative of this group of rare earths, and studies have been made largely in the pseudobinary system CdIn₂S₄-CdTm₂S₄, in which complete solid solution was found to occur. Both powder samples and single crystals have been prepared, and their lattice constants and infrared fluorescence measured. The structure of CdTm₂S₄ has been shown to be of the normal spinel type. Weak infrared electroluminescence from single crystals has been observed.

Although rare earth ions in various host lattices are known to exhibit their characteristic fluorescence, there are no known reports of semiconducting host lattices which contain more than about 0.1% rare earth. If such materials were available, and in single crystal form, it might then be possible to demonstrate d-c electroluminescence resulting either from recombination of injected carriers via a rare earth or from optical pumping by photons formed by other recombinations, and electrically-excited laser action might also be found.

In general, the best studied semiconductors are the Group IV elements, the II-VI compounds, and the III-V compounds, all of which have tetrahedral structures, that is, diamond, zincblende, or wurtzite type. On the other hand, binary compounds of the rare earth elements with Group V elements are found to be of the sodium chloride type, in which rare earths are surrounded octahedrally (1), and there are in fact no known compounds with rare earth ions on tetrahedral sites. This very likely explains why, as stated above, there have been no reports of semiconducting host lattices which contain appreciable concentrations of rare earth. Since most of the rare-earth Group V compounds are semiconductors (2), compounds such as the phosphides, arsenides, and antimonides of yttrium, lanthanum, and lutetium (each of which has either completely empty or completely filled 4f orbitals) would be good choices for incorporation of other rare earths via solid solution formation. Unfortunately, the melting points of the rare earth-Group V compounds are extremely high and they tend to decompose prior to melting. Such limitations led to consideration of other more suitable materials. The spinel structure appeared to be a good choice be-

cause octahedral sites are available in addition to tetrahedral sites.

Rare Earth Thio- and Seleno-Spinels

In previously unpublished work by the authors, new compounds, CdR₂S₄ and CdR₂Se₄, in which R represents the rare earths with the higher atomic numbers and smaller ionic sizes, were synthesized and found to have spinel structures. Flahaut, Domange, and Patrie (3) reported synthesis of CdY₂S₄ and looked at its x-ray pattern, but either did not recognize that it had a spinel structure or else did not obtain the same result as that reported here. They did not list the d-spacings and stated simply, "There exists . . . a compound CdY₂S₄ of odd, unidentified structure." The lattice constants of a number of new CdR₂S₄ and CdR₂Se₄ compounds with the spinel structure are listed in Table I along with lattice constants of chemically related new compounds found to have the body-centered cubic Th₃P₄ structure. CdS and Nd₂S₃ did not appear to react with each other to form any new compound or solid solution. Although we have not attempted to prepare all possible compounds of type CdR₂S₄ and CdR₂Se₄, it appears that the rare earths of

Table I. Structures and lattice constants of new ternary rare earth chalcogenides

Compound	Structure-type	Lattice constant, Å
CdY ₂ S ₄	Spinel	11.19 ₆
CdTm ₂ S ₄	Spinel	11.09 ₂
CdY ₂ Se ₄	Spinel	11.65 ₄
CdDy ₂ Se ₄	Spinel	11.65 ₉
CdYb ₂ Se ₄	Spinel	11.53 ₃
CdGd ₂ Se ₄	Th ₃ P ₄	8.72 ₈
EuGd ₂ Se ₄	Th ₃ P ₄	8.86 ₁

small ionic size will yield spinels, those of somewhat larger size the Th_3P_4 structure, and the largest no ternary compounds at all.¹

The following is a description of the method used for synthesis of the ternary compounds discussed in the preceding paragraph. Rare earth sulfides and selenides, R_2S_3 and R_2Se_3 (and EuSe), were first prepared by solid-gas reaction for 5 hr at 1000°C of stoichiometric quantities of Lindsay rare earth metal turnings and sulfur or selenium in sealed evacuated quartz tubes. The ternary compounds were then prepared by solid state reaction for 16 hr at 1100°C in sealed evacuated quartz tubes of stoichiometric mixtures of R_2S_3 or R_2Se_3 with CdS , CdSe , or EuSe .

Advantages of CdIn_2S_4 as a Host Material

Once it was found that the small rare earths would form thiospinels, it was postulated that extensive solid solution between these thiospinels and CdIn_2S_4 would occur because the latter is known to crystallize with the spinel structure, with $a = 10.797\text{\AA}$ (4), a value only several per cent different from those of the cadmium rare earth thiospinels listed in Table I. It is not known whether CdIn_2S_4 is a normal or an inverse spinel because Cd^{2+} and In^{3+} are isoelectronic and therefore will appear much the same to x-rays. However, the rare earth thiospinels were expected to be entirely normal, since the rare earth ions, as stated above, should prefer an octahedral to a tetrahedral site. To check this, structure factors were calculated (with the

¹ R. Penoyer of this laboratory has found that none of the compounds listed in Table I is ferromagnetic down to the temperature of liquid helium.

IBM 7090 computer) for CdTm_2S_4 with both normal and inverse spinel structures assumed, and they were compared with intensities measured with a powder specimen in a standard Norelco diffractometer with filtered Cu radiation. The 21 measured intensities were corrected for Lorentz and polarization factors. For the calculated intensities, appropriate multiplicity terms and an over-all thermal parameter of $B = 0.5$ were included. The sulfur atoms were first placed at the $(\frac{1}{4}, \frac{1}{4}, \frac{1}{4})$ positions [with center of symmetry at $(0, 0, 0)$]. With the use of a least squares refinement program for powder data written by Dr. Y. Okaya of this laboratory, the parameter of the sulfur atom in CdTm_2S_4 and the separate temperature factors were then refined. The final result placed the sulfur atoms in the 32e positions of space group $\text{Fd}3\text{m}$, with $x = 0.257$, and with $B_S = 1.4$, $B_{\text{Tm}} = 0.4$, and $B_{\text{Cd}} = 0.5$. The R factor following this refinement was 5.8%. The complete results are given in Table II and prove that the assumption of the normal spinel is correct. It is assumed as a consequence that in solid solutions of CdIn_2S_4 and CdR_2S_4 the rare earth ion will always be found in an octahedral position regardless of where the In atoms might be.

In addition to the likelihood that the rare earth thiospinels would form solid solutions with CdIn_2S_4 (which would make possible heavy doping of CdIn_2S_4 with rare earth), CdIn_2S_4 appeared to have all the attributes of an ideal host material for the desired product. It is a compound known to be a semiconductor and photoconductor with a band gap variously reported to be 2.18 (5), 2.2 (6), and 2.3 (7) ev. Such a large band gap is desirable so that

Table II. Observed and calculated intensities for $\text{Cd Tm}_2\text{S}_4$

hkl	Observed intensity, I_{obs} .	Calculated intensity, I_{calc} . (normal spinel)	Calculated intensity, I_{calc} . (inverse spinel)	Calculated*** intensity, I_{calc} . (refined normal spinel)
111	0.55	0.48	0.08	0.65
220	1.80	1.86	3.14	1.95
311	9.19*	13.90	14.88	14.04
222	2.27	2.10	1.30	2.31
400	5.93	6.06	3.78	6.09
422	3.63	2.70	4.59	2.75
511, 333	15.49	13.82	14.79	15.49
440	24.14	26.85	27.05	26.90
531	1.82	1.59	0.25	2.10
620	2.27	2.16	3.64	2.13
533	9.37	8.33	8.91	8.54
622	4.96	4.51	2.93	5.60
444	5.36	4.73	2.93	4.53
711, 551	1.70	1.29	0.21	1.82
642	4.20	3.59	6.00	3.86
731, 553	19.92	20.74	22.16	20.22
800	10.09	9.09	9.16	8.84
751, 555	15.86	13.68	14.60	14.77
840	9.49	10.25	6.49	9.32
931	11.35	10.11	10.77	12.24
844	25.67	27.22	27.42	25.69
		R** = 11.6%	R** = 19.5%	R** = 7.8% (R** = 5.8% with 311 excluded)

* 311 reflection was affected greatly by counter saturation and extinction.

** $R = \frac{\sum (F_{\text{obs}}^2 - F_{\text{calc}}^2)}{\sum F_{\text{calc}}^2} \times 100$.

*** $x = 0.257$, $B_S = 1.4$, $B_{\text{Tm}} = 0.4$, $B_{\text{Cd}} = 0.5$.

the rare earth energy levels involved in the emission process can be within the forbidden region of the host material, or at least that the transition energies will be less than the gap width. This means, of course, that any injected electrons and holes will be separated by an energy difference greater than that of the pertinent rare earth levels so that the simple energy requirement is fulfilled. In addition, it is desirable that the rare earth emission be small enough in energy so that other populated centers or host atoms will not be excited and thus act as a source of energy loss. Such a condition is more realizable with wider gap host lattices. CdIn_2S_4 also has the very desirable property of having a melting point below 1100°C . This makes it likely that large single crystals can be grown from the melt, especially if the melting is congruent. In fact, Koelmans and Grimmeiss (8) have reported such growth. In addition, CdIn_2S_4 crystals have reportedly been grown by deposition from vapor by chemical transport reactions (9, 10).

Pseudoternary System $\text{CdS-In}_2\text{S}_3\text{-Tm}_2\text{S}_3$

Thulium was chosen as a suitable representative of the small rare earths for incorporation in the CdIn_2S_4 host. Not only is its ionic size right for CdTm_2S_4 to have the spinel structure, but there have also been studies of its fluorescence and laser action in the infrared. For instance, optical excitation of Tm^{3+} in CaWO_4 at 77°K produces infrared emission ascribed to ${}^3\text{H}_4 \rightarrow {}^3\text{H}_6$ transitions in lines from about 1.73 to 1.94μ , with laser lines at 1.911 and 1.916μ (11). In SrF_2 , the laser line resulting from the same transition is at 1.972μ (11). Although our primary interest was in the pseudobinary system $\text{CdIn}_2\text{S}_4\text{-CdTm}_2\text{S}_4$, studies were also made along the three boundaries of the pseudoternary system $\text{CdS-In}_2\text{S}_3\text{-Tm}_2\text{S}_3$. All preparations were made by reaction for 6 hr at 1150°C in sealed evacuated quartz tubes of proper mixtures of CdS , In_2S_3 , and Tm_2S_3 . The CdS used was General Electric Company luminescent-grade, additionally purified by "baking out" in running vacuum at 750°C for 1 hr. The In_2S_3 , from A. D. Mackay, Inc., was prepared by precipitation from aqueous solution and said to be 99.95% pure. It was also additionally purified, in this case by "baking out" in running vacuum at 500°C for 1 hr. The Tm_2S_3 was prepared as described above.

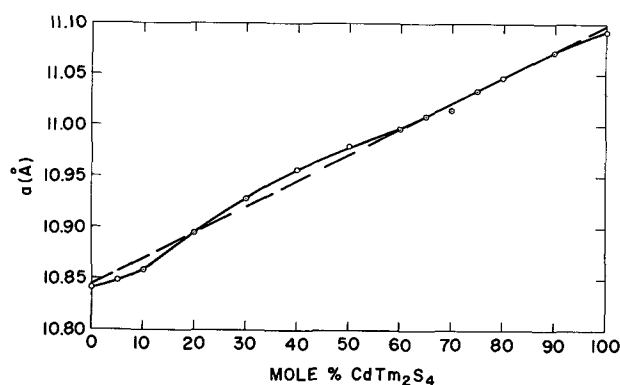


Fig. 1. Lattice constants in the system $\text{CdIn}_2\text{S}_4\text{-CdTm}_2\text{S}_4$. (Solid line is the experimental curve. Dashed line is the best straight line drawn through the same points.)

All preparations were studied by the x-ray diffraction powder method. In the pseudobinary system $\text{CdIn}_2\text{S}_4\text{-CdTm}_2\text{S}_4$, solid solution was found throughout, with slight deviation from Vegard's law (see Fig. 1). The measured lattice constant of CdIn_2S_4 was 10.84_1 , which is slightly different from the value given in ref. 4.

In the $\text{CdS-In}_2\text{S}_3$ system, extensive solid solution was found. $\beta\text{-In}_2\text{S}_3$ was first reported on the basis of powder data to have a disordered defect spinel structure (12), but more recent single crystal work (13) has shown that there is ordering of the vacancies which results in a body-centered tetragonal unit cell, with $a = 7.61$, $c = 32.24\text{Å}$. However, the structure may still be considered as three spinel cells stacked on top of one another with eight In atoms missing. Because of this close structural relationship between In_2S_3 and spinels, there is complete solid solution between CdIn_2S_4 and In_2S_3 . For convenience in presenting results, the lattice constants given in this paper all refer to the simple spinel unit cell. On the $\text{CdS-CdIn}_2\text{S}_4$ end of the $\text{CdS-In}_2\text{S}_3$ line, solid solution was observed to about 46 mole % In_2S_3 -54 mole % CdS . (The lattice constant extrapolation shown in Fig. 2 gave 44.9% In_2S_3 , and application of the "disappearing phase" method, which is probably more accurate, gave 46.6% In_2S_3 .) The $\text{CdS-Tm}_2\text{S}_3$ system appeared to be quite complex and was not thoroughly studied, but the single phase spinel region was found to extend only from about 50 to 55 mole % CdS . In the $\text{In}_2\text{S}_3\text{-Tm}_2\text{S}_3$ system no compound or solid solution was observed in the x-ray studies. (However, fluorescence studies reported below indicate that there is some small solubility.) Perhaps it should be noted here that the x-ray diffraction powder pattern of Tm_2S_3 is quite complex and has not been indexed. The structure is not related to that of spinel or the similar $\beta\text{-In}_2\text{S}_3$.

The data discussed above have been used to construct an approximate pseudoternary phase diagram at room temperature (see Fig. 3). Since only points along the three sides of the diagram and along the $\text{CdIn}_2\text{S}_4\text{-CdTm}_2\text{S}_4$ line have been studied, the diagram is far from complete. However, approximate limits of the single-phase spinel region are shown by dashed lines and the area so enclosed is shaded.

Growth of Single Crystals

Single crystals of CdIn_2S_4 and $\text{CdIn}_{1.8}\text{Tm}_{0.2}\text{S}_4$ were grown from the melt in sealed evacuated quartz tubes with or without graphite liners. In

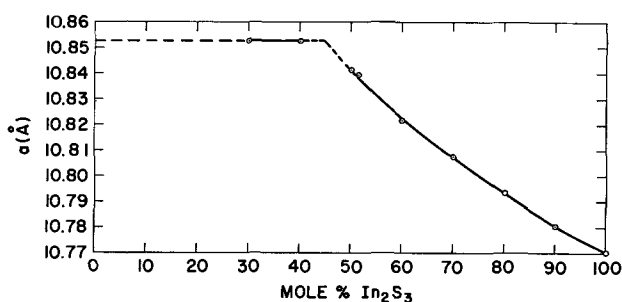


Fig. 2. Lattice constants of the spinel phase in the system $\text{CdS-In}_2\text{S}_3$. The broken portions of the curves are extrapolations.

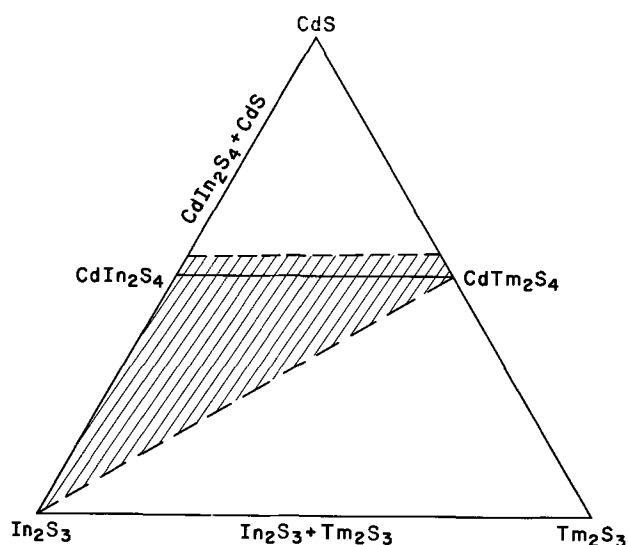


Fig. 3. Partial phase diagram of the pseudoternary system $\text{CdS-In}_2\text{S}_3\text{-Tm}_2\text{S}_3$ at room temperature. Shading delineates approximate area of existence of single-phase spinel.

either case, the container was tapered at the bottom to allow proper nucleation and the tube was moved at 0.13 in./hr through a temperature gradient in a vertical tube furnace whose maximum temperature was 1150°C . The temperature range through which the tube passed included the melting point of CdIn_2S_4 , which M. Berkenblit of this laboratory found by differential thermal analysis to be 1087°C in a sealed system. In_2S_3 crystals with and without Tm_2S_3 additions have also been grown by the same procedure.

When the commercial pure grades of CdS and In_2S_3 described above were used, various problems such as reaction with the quartz container and instability of the crystals were often encountered. However, if the Cd and In sulfides used as starting materials were prepared by slow reaction of semiconductor-grade powdered elements in sealed evacuated quartz tubes, there was little or no reaction with the quartz, and the excellent, large single crystals of doped and undoped CdIn_2S_4 which were obtained were stable. When grown in quartz, the crystals were transparent red, but when grown in graphite liners in quartz tubes, they appeared to be black. The differences between results with purchased and self-prepared starting materials are believed to be due to the presence of oxide or hydroxide in the former.

It was found possible also to grow crystals of CdIn_2S_4 by vapor transport in a temperature gradient in both the presence and the absence of iodine. However, Tm has not been observed to be transported so that the crystals thus formed are undoped.

Fluorescence Studies

The first studies of fluorescence were made on powders prepared by grinding solidified melts (or sintered products where melting points were high) in the system $\text{CdIn}_2\text{S}_4\text{-CdTm}_2\text{S}_4$. These were therefore the same preparations whose lattice constants are given in Fig. 1. Excitation was with a xenon lamp and detection with a lead sulfide photocell. The monochromator used was the Perkin-Elmer

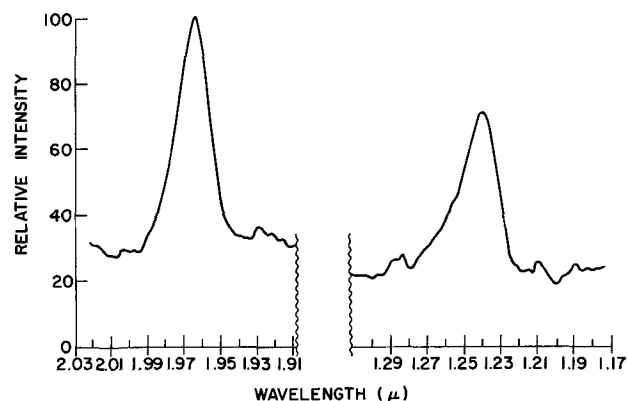


Fig. 4. Emission from thulium in $\text{CdIn}_{1.8}\text{Tm}_{0.2}\text{S}_4$ powder at 6°K (xenon lamp excitation). Also present but not shown is broad emission not due to Tm from about 0.7 to 1μ .

112. Using first a preparation with composition $\text{CdIn}_{1.8}\text{Tm}_{0.2}\text{S}_4$ (i.e., 10 mole % CdTm_2S_4), no emission was found at either room temperature or liquid nitrogen temperature. However, on cooling with liquid helium to 6°K , strong emission was observed in the infrared, with rather sharp peaks at 1.97 and 1.24μ (see Fig. 4). In addition, there is broad emission in the region from about 0.7 to 1μ , but this is present also in undoped CdIn_2S_4 and therefore not due to thulium. The peak at 1.97μ is believed to be due to the same transition ($^3\text{H}_4 \rightarrow ^3\text{H}_6$) as that which produces the laser lines at 1.911 and 1.916μ in $\text{CaWO}_4:\text{Tm}^{3+}$ (11) and at 1.972μ in SrF_2 (11). The peak at 1.24μ is just where one would expect to find the emission due to the $^3\text{H}_5 \rightarrow ^3\text{H}_6$ transition in Tm^{3+} (14). The emission at 1.97μ is seen generally in the preparations in the $\text{CdIn}_2\text{S}_4\text{-CdTm}_2\text{S}_4$ system, but the 1.24μ peak is missing in preparations containing about 20 mole % CdTm_2S_4 or more. Maximum intensity of emission of the 1.97μ peak is observed over the approximate range 7-60 mole % CdTm_2S_4 . CdTm_2S_4 itself still emits at this wavelength, whereas Tm_2S_3 has been found not to emit at all in the infrared. At trace concentrations of CdTm_2S_4 in CdIn_2S_4 , little or no fluorescence is seen.

Fluorescence has also been observed upon xenon lamp excitation of the single crystals described above. For instance, the emission spectrum of the transparent red single crystals obtained from the melt was very similar at 6°K to that of the powder sample but with an additional small peak at 1.87μ . The lattice constants of sections of two of these crystals indicated that the CdTm_2S_4 content was 7 and 16 mole %, respectively, although the starting composition in each case had been 10 mole %. Variation in composition of melt-grown crystals of solid solutions is of course to be expected because of the equilibrium between solid and liquid phases of different and changing compositions.

It has been found in addition that the fluorescence from single crystals may be seen at 77°K as well as at 6°K , although the emission peaks at the higher temperature are much lower, perhaps broader, and shifted to slightly longer wavelengths. The peaks at 1.97 , 1.87 , and 1.24μ are shifted to 1.98 , 1.88 , and 1.26μ , respectively.

Some studies have also been carried out of the fluorescence of In_2S_3 doped with Tm^{3+} . Although, as stated above, x-ray diffraction studies indicate that there is no compound or solid solution formation in the system $\text{In}_2\text{S}_3\text{-Tm}_2\text{S}_3$, the observation of thulium fluorescence in the infrared shows that some Tm does indeed enter the In_2S_3 lattice since Tm_2S_3 itself does not fluoresce. The observed fluorescence is very similar to that in $\text{CdIn}_2\text{S}_4\text{-CdTm}_2\text{S}_4$ preparations but there are differences in detail.

Electroluminescence Studies

The doped and undoped CdIn_2S_4 crystals as grown are n-type and attempts to make them p-type by diffusion of Cu or As have been unsuccessful. Therefore, p-n junctions have not been obtained. However, it has been found that infrared is emitted weakly at liquid nitrogen and liquid helium temperatures from doped crystals to which one electrode of indium and another of 97% In-3% As are soldered. The emission has been observed with both a.c. and d.c., and the intensity is always found to be considerably higher when the electrode containing As is positive. The emission was found to follow the applied field with 60 cycles a.c., and therefore the effects noted could not be due only to overheating of the crystal. With the monochromator, weak broad emission was found from about 0.66 to 0.98 μ . This corresponds to the broad emission found on optical excitation of pure or Tm-doped CdIn_2S_4 . Because the photomultiplier used is not sensitive to the longer wavelength infrared radiation where the emission characteristic of thulium occurs and because a lead sulfide photocell is not sensitive enough, it is not possible to say with the information at hand whether very weak thulium emission is present in the electroluminescence along with the very weak broad emission observed. Since the electroded crystal does not rectify, there is no p-n junction, and it is possible that the infrared emission seen is due to the Destriau effect resulting from field inhomogeneity caused by presence of arsenic on only one side of the crystal.

Concluding Remarks

Many of the chemical and structural problems involved in the design of a rare earth-doped semiconducting thiospinel have been defined and investigated, and it has been shown that the thulium dopant emits in the infrared on optical excitation.

It appears almost certain that the work reported could be duplicated with any of the small radius rare earths in place of thulium.

Although electroluminescence has been observed, it is quite weak and apparently not due to injection of carriers. One of the problems remaining to be solved is how to inject into a crystal electrons and holes which might then have an opportunity to recombine efficiently via thulium atoms or to produce sufficient photons to excite the thulium optically. Preparation of p-type CdIn_2S_4 and p-n junctions may be the key to solution of this problem. With higher efficiency, it would probably also be possible to establish definitely whether the electroluminescence contains any emission characteristic of the thulium.

Acknowledgments

The authors wish to thank Mr. G. D. Pettit for the emission spectra and to acknowledge the capable assistance of Mr. John J. Minchak in most phases of the work.

Manuscript received June 20, 1963. This paper was presented before the New York Meeting, Sept. 29-Oct. 3, 1963.

Any discussion of this paper will appear in a Discussion Section to be published in the December 1964 JOURNAL.

REFERENCES

1. A. Iandelli, "Rare Earth Research," E. V. Kleber, Editor, based on a seminar at Lake Arrowhead, Calif., Oct. 1960, pp. 135-144, Macmillan Co., New York (1961).
2. L. H. Brixner, *J. Inorg. Nucl. Chem.*, **15**, 199 (1960).
3. J. Flahaut, L. Domange, and M. Patrie, *Bull. Soc. Chim. France*, No. 35, 159 (1962).
4. H. Hahn and W. Klingler, *Z. anorg. u. allgem. Chem.*, **263**, 177 (1950).
5. R. H. Bube and W. H. McCarroll, *J. Phys. Chem. Solids*, **10**, 333 (1959).
6. H. Koelmans and H. G. Grimmeiss, *Physica*, **25**, 1287 (1959).
7. J. A. Beun, R. Nitsche, and M. Lichtensteiger, *ibid.*, **26**, 674 (1960).
8. H. Koelmans and H. G. Grimmeiss, *ibid.*, **27**, 606 (1961).
9. R. Nitsche, *J. Phys. Chem. Solids*, **17**, 163 (1960).
10. R. Nitsche, *ibid.*, **21**, 199 (1961).
11. L. F. Johnson, *J. Appl. Phys.*, **34**, 897 (1963).
12. H. Hahn and W. Klingler, *Z. anorg. Chem.*, **260**, 97 (1949).
13. G. S. D. King, *Acta Cryst.*, **15**, 512 (1962).
14. Term assignments are taken from J. B. Gruber and J. G. Conway, *J. Chem. Phys.*, **32**, 1178 (1960).

Chemical Etching of Germanium in Solutions of HF, HNO₃, H₂O, and HC₂H₃O₂

B. Schwartz¹ and H. Robbins²

Hughes Semiconductors, Newport Beach, California

ABSTRACT

A study has been performed on the acid etching of germanium, and the results have been compared with those of a similar study on the acid etching of silicon. The conclusion is reached that subfluorinated compounds of germanium are formed as intermediates in the diffusion-limited composition region. It has also been found that passivating films play an important role in the dissolution of germanium. In addition, the tolerance of the system to dilution with HC₂H₃O₂ is much greater than it is to dilution with H₂O.

Germanium stands directly below silicon in Group IV of the periodic table, and considerable similarity is to be expected between these two elements, in their chemical as well as electrical properties. In accord with this expectation, one finds that both silicon and germanium can be etched by solutions of hydrofluoric and nitric acids (1, 2) or by alkaline peroxide (3, 4). However, there are sufficient differences in the chemistry of these two elements to cause differences in their etching behavior. For example, as expected from the higher heat of formation of SiO₂ than of GeO₂ (52.1 vs. 32.0 kcal/g equivalent), it has been observed by the authors that the heat of reaction of silicon with HF-HNO₃ is approximately twice that of the comparable reaction with germanium. Thus it is not surprising to find that the etching of germanium is, in general, more sluggish than that of silicon and that alkaline solutions without an added oxidant do not attack germanium. An exception to this trend is the fact that HF-H₂O₂ solutions readily dissolve germanium (5, 6), but do not etch silicon at all. In this paper, a comparison of the etching rates of silicon and germanium will show that, although the over-all stoichiometric equations are identical, the actual etching behavior is quite different for the two materials.

The basis of this study was the measurement of the rate of attack by the etchant on 5 ohm-cm, n-type germanium dice by various compositions of etchant from the system HF-HNO₃-H₂O-HC₂H₃O₂, the rate of attack being defined as the total change in die thickness per minute of die immersion in the etchant. Since it was considered probable that the etch rate would be influenced by the crystal orientation, dice were used having the major exposed surfaces of (111), (110), and (100) orientation. For purposes of comparison, the data of Robbins and Schwartz (1, 7, 8) on the etching of (111) oriented, 2.5 ohm-cm, n-type silicon will be used.

Experimental Procedure

The experimental procedure consisted in etching three dice at a time, one from each of the three

¹ Present address: Bell Telephone Laboratories, Inc., Murray Hill, New Jersey.

² Present address: Bell & Howell Research Center, Pasadena, California.

orientations, using slightly different dimensions for the dice as a means of identification. All of the dice were approximately 3 x 10⁻² in. thick and each of the major exposed surfaces was 1.25 x 10⁻², 1.0 x 10⁻², and 1.6 x 10⁻² in.² in area for the (100), (110), and (111) oriented specimens, respectively. Etching was performed in a platinum beaker 1½ in. in diameter and 2½ in. deep suspended in a constant temperature bath thermostated at the required temperature to within ± 0.02°C. The dice were contained in an open mesh platinum basket that was provided with a platinum wire handle for manipulation purposes. Violent agitation of the specimens was produced by rotating the basket back and forth and, at the same time, pumping it up and down in the solution. Quenching was accomplished by rapidly transferring the platinum basket into a separate beaker containing 250 ml of deionized water.

Platinum was chosen as the beaker material because of its resistance to attack by the etchant and because its excellent thermal conductivity made it easier to maintain essentially constant temperature in the solution during the etching period. It had been ascertained in experiments run with both platinum and Teflon beakers that there were no apparent differences in the etch rates that could be attributed to the beaker material.

The etching solutions were made by weighing out the necessary amounts of preanalyzed and adjusted reagents, and the solutions were then stored in polyethylene bottles until used. Twenty ml of etchant were used for each run, and the solution temperature was allowed to equilibrate with the bath before any dice were placed in the solution. Under conditions of maximum germanium dissolution, the amount of material put into solution was approximately 0.1g. This corresponds to a reduction of at most 1% in the HNO₃ concentration and 5% in the HF concentration.³

"Catalysts" were introduced either by bubbling N₂O₄ from a cylinder at the rate of 6 ft³/hr (~ 2.8 liter/min) through the solution for 30 sec or by adding 0.1g of NaNO₂ just prior to introduction of the specimen.

³ This assumes 3Ge + 18HF + 4HNO₃ → 3H₂GeF₆ + 4NO + 8H₂O as the reaction equation. Since some GeF₄ and NO₂ are formed, the depletion of reagents will be even less than is quoted above.

In the case of silicon (1), for the measurements done at 25°C, only one die had been etched at a time in a Teflon beaker containing 10 ml of solution. When the temperature study was made (8), a platinum beaker had been used. Aside from these differences, the experimental procedure had been the same as that outlined above for germanium.

Experimental Results

Since the experimental conditions were selected so that the concentrations of the reactants would remain essentially constant throughout the etching period, it was expected that the etching rate would attain a steady-state value that was independent of the etching time. This behavior had been verified for the etching of silicon (1), and thus it was proper to define an etch rate as the thickness change of the die per unit etching time. However, in spite of all attempts to maintain a constant environment for the germanium specimens during the etching period, it was found that the reaction did not proceed at a constant rate, but was subject to an induction period similar to that observed by Cretella and Gatos (9). In many instances the reaction was abruptly inhibited by some form of passivity. Large errors could thus be introduced in the etch-rate data, and considerably different values could be obtained by averaging the amount of germanium removed over different time intervals, using fresh solution each time. The etch rates were most reproducible in the very high HNO₃ compositions, down to approximately 80 weight per cent (w/o) HNO₃, and over the rest of the composition region the induction period could be minimized by the addition of a small amount of catalyst such as N₂O₄ or NaNO₂, but it could not be entirely eliminated. Figure 1 shows the results of, in one case, etching germanium in a solution pretreated with N₂O₄ and, in the second case, omitting the N₂O₄ pretreatment. It was also observed that the etch rates were more reproducible when the specimen had received a brief pre-etch in the uncatalyzed solution of the composition noted in Fig. 1. This pre-etch was therefore instituted as standard procedure on all dice before

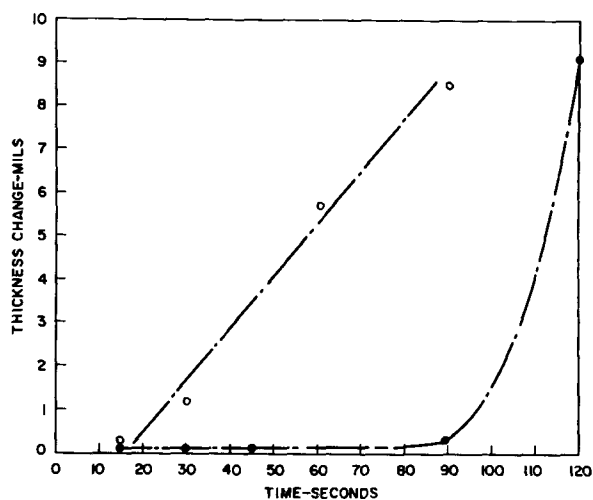


Fig. 1. Thickness change vs. etching time at 25°C for (100) oriented, n-type germanium in 60 w/o HF, 20 w/o HNO₃, and 20 w/o H₂O. Reagents used were 60% HF and 90% HNO₃. ○, Catalyzed with N₂O₄; ●, noncatalyzed.

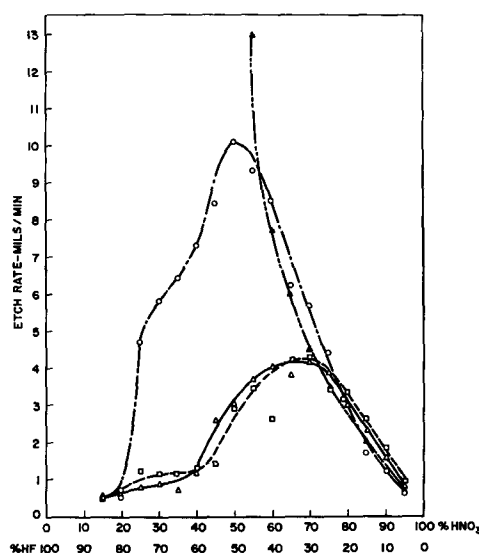


Fig. 2. Etch rate at 25°C vs. weight per cent composition of normalized 49% HF, 70% HNO₃ system with no water added to the system but N₂O₄ catalyzed. Silicon data were obtained using (111) oriented, 2.5 ohm-cm, n-type dice. ○, (100) Ge; □, (110) Ge; △, (111) Ge; ▲, silicon.

any measurement was attempted. Furthermore, by giving the specimens three etches of different duration, 20, 40, and 60 sec, and always using fresh etchant in each case, the linearity of the etch rates with etching time for each solution composition could be verified. This procedure was generally followed, and where an approximate linearity was observed, the 60-sec value was arbitrarily taken as the etch rate. In spite of all these precautions, the induction period was not eliminated completely. Consequently, reproducibility of absolute rate numbers was difficult to achieve, and the experimental error was observed to be greater with germanium than with silicon. However, the relative rates on the different crystal planes were reproducible, and it will be on this fact that most of the discussion will be based. It is interesting to note that the etch rates in the presence of acetic acid were much more reproducible than those where no acetic acid was used.

Effects of Solution Composition and Crystal Orientation

Figure 2 is a comparison of the etch rate of (111) oriented silicon with that of germanium in the three orientations studied. In the case of germanium, N₂O₄ was used, while no additive was present during the etching of silicon.

Let us consider first the high HNO₃ region, from 80 to 95% HNO₃. As the HF content is increased, the germanium etch rates increase in a manner very similar to the etch rates of the silicon system. In addition, it was observed that the absence or presence of catalyst did not influence the etch rates of silicon (1) or germanium to any appreciable extent in this composition region. The etch rates thus seem to be dependent only on the HF concentration. This behavior suggests the same diffusion-governed mechanism for germanium as was determined for silicon (7, 10). However, an examination of the temperature dependence of the etch rates in this composition region (see Fig. 3) gives no simple "activa-

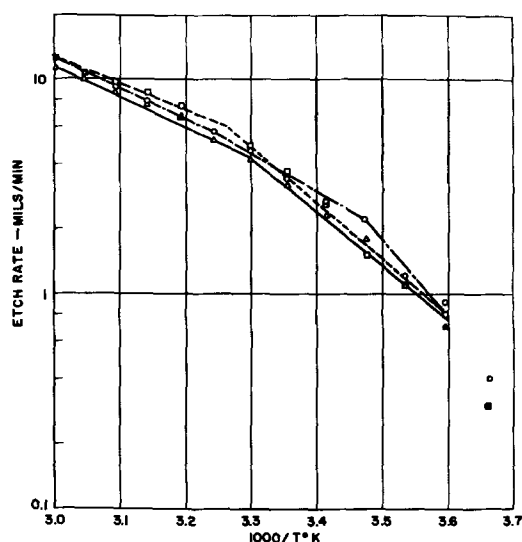


Fig. 3. Influence of temperature on etch rate in 20 w/o HF and 80 w/o HNO₃ with reagents of 49% HF and 70% HNO₃ and N₂O₄ catalysis. Temperature dependences are 7.5 kcal/mole at high temperatures and 11-14 kcal/mole at low temperatures. ○, (100) Ge; □, (110) Ge; △, (111) Ge.

tion energy" consistent with a diffusion mechanism, as is found with silicon. Burgess (11) has determined low diffusion-type temperature dependences for this system in only a very limited composition region of extremely low HF (less than 10%). This is to be compared to silicon, where the diffusion of the complexing agent to the surface as the limiting mechanism has been determined to at least 20% HF (8) and higher (10).

In addition, for silicon no effect of orientation was observable in this composition region (8), whereas the germanium crystal orientation seems to play an important role in the reaction. This is indicated by the data in Table I, where it is shown that at 5, 10, and 15% HF, the rate dependence on the orientation is $R_{(110)} > R_{(111)} > R_{(100)}$. There is also an indication that, even considering the relatively large experimental error, faster etch rates are observed for some germanium planes than for (111) oriented silicon.

In germanium, where induction periods are present to some extent, the error in rate values quoted would be in the direction of a lower value being observed than the actual rate achieved. In spite of this, using the measured values for the (110) plane at the 10 and 15% HF points, it was found that the rates are 40 and 30%, respectively, in excess of the rates for silicon. However, it is necessary to take into account the differences in specific gravity be-

Table I. Comparison of etch rates on different surface orientations in the low HF region

	Ratio of etch rates		
	85% HNO ₃	90% HNO ₃	95% HNO ₃
(110)			
(111)	1.1	1.1	1.1
(110)			
(100)	1.5	1.5	1.5

tween silicon and germanium (2.33 and 5.32 g/cm³) as well as the differences in atomic weight in any direct comparison of etch rates. Considering any given surface area, a 14% deeper penetration into the germanium than into the silicon is required for the removal of equal gram-moles of material. This would account for only 1/2 to 1/3 of the excess value observed, and it is therefore felt that this faster etching of germanium is a real effect which would have to be explained in any proposed model.

Reaction Model

All of the points cited above make it difficult to apply the simple diffusion model proposed for silicon to the case of germanium. However, the etch rates of silicon in this composition region have been rather conclusively demonstrated to be diffusion limited (7, 10). Therefore, since it is improbable that an over-all reaction can proceed at a rate faster than the transport of chemical reactant to the surface, the germanium etch rates must also be limited in some way by the transport of the complexing agent to the surface. One way out of this apparent dilemma is to postulate, first, that in both the silicon and germanium cases all the reactions that take place at the solid surface are faster than the rate at which the rate-limiting reagent reaches the surface and, second, that the types of reaction products formed at the surface of silicon as removable intermediates are different from those formed at the germanium surface. It is suggested that the silicon is leaving the surface in a more highly fluorinated condition than is the germanium. As an example, it might be postulated that compounds of the form GeF₂ or GeOF₂ leave the surface, whereas for silicon the dissolution would occur as SiF₄ or Si₂OF₆ or even Si₂F₆. The analogous chlorides of both germanium and silicon have been isolated and identified, whereas divalent silicon species have been identified only at high temperatures. There is strong evidence that compounds such as SiCl₂ are thermodynamically unstable at room temperature (12, 13). In the compounds postulated for germanium, the ratio Ge:F is 1:2, whereas for silicon the Si:F ratio is 1:3. Therefore, both dissolution rates could still be dependent on the rate at which the complexing agent diffuses to the surface, but the germanium would require less of the incoming complexing species before leaving the site of action than would the silicon. Once in the solution, then, the intermediate compounds further react with the available HF and are converted to the more highly fluorinated forms.

The authors are not implying that one and only one species of reaction product is formed at any given time but that, more than likely, a variety of removable intermediates are being formed in the etching of both germanium and silicon. This model now provides a possible means of explaining orientation influences on the basis of the formation of different concentrations of intermediates on the different faces (5). Also, the temperature effect could be explained as influencing the concentration of the subfluorinated species being generated to give the larger-than-expected temperature dependences.

Verification of this hypothesis will have to await direct experimental evidence for the existence of these intermediates.

The remaining portion of Fig. 2, the composition region from 25 to 75 w/o HNO_3 , will now be considered. The drastic influence of orientation is readily observed in this composition region; Burgess (14) has observed similar effects in his work on etching germanium. At a concentration of about 25% HF the (100) curve separates from the curves of the other two orientations, increasing in an approximately linear fashion, while the (110) and (111) etch rates level off onto a broad, somewhat humped plateau. At a concentration of about 40% HF the germanium (100) curve and silicon curve diverge, with the germanium curve proceeding in its linear ascent while the silicon curve begins a very rapid, exponential type of ascent to a peak etch rate of approximately 78 mils/min at about 65% HF. The exponential increase in the case of silicon has been attributed to the effect of the heat of the reaction, which causes an enhancement of the reaction rate. At low HF concentrations, where the silicon etching system is demonstrably diffusion limited with respect to the complexing agent, the activation energy is low (8) and the heat factor does not exert a very strong influence. At 40% HF, however, the silicon reaction begins to show a larger temperature dependence (10) and, as the HF is further increased and the HNO_3 decreased, the higher "activation energy" shows up as an increased sensitivity of the etch rates to the heat liberated in the reaction. The failure of the germanium etch rates to produce a "thermal runaway" in a similar manner may be partly the result of the lower heat of reaction of germanium, despite the fact that the temperature dependence in this composition region is of the order of 11-14 kcal/mole, as shown in Fig. 4.

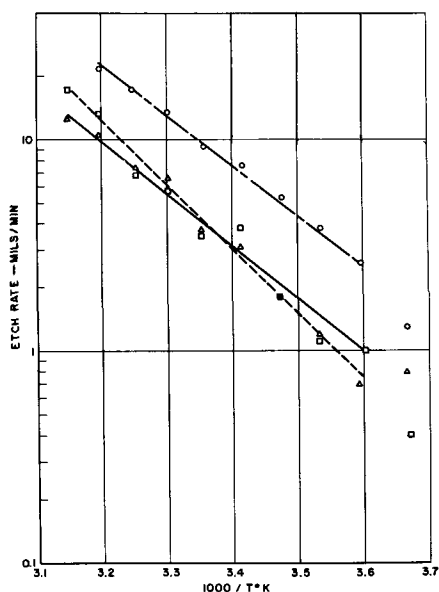


Fig. 4. Influence of temperature on etch rate in 40 w/o HF and 60 w/o HNO_3 , with reagents of 40% HF and 70% HNO_3 and N_2O_4 catalysis. Temperature dependences are 11 kcal/mole for the (100) and (111) and 14 kcal/mole for the (110) orientations. \circ , (100) Ge; \square , (110) Ge; \triangle , (111) Ge.

Influence of Passivating Films

The rate-limiting effect of passive films on the surface of the germanium appears to play a major role in this system. Whereas in the silicon etching system the peak etch rates are thought to be a transition from HF-limited kinetics to HNO_3 -limited kinetics, it is very probable that the leveling off of the (111) and (110) curves is not the result of the lagging of the oxidation step of the reaction. This leveling off takes place at a rather high HNO_3 concentration, and the etch rates have been "catalyzed" with N_2O_4 . If the leveling off of the etch-rate curves for the germanium (111) and (110) surfaces does not reflect a limitation on the part of the oxidant, then it must be concluded that the rate-limiting step involves the complexing of the oxidized germanium or the formation of insoluble reaction products on the surface. Since HF is also readily available for complexing of the oxidized germanium, the difficulty of removal must be ascribed to something related to the "oxide" formed on the surface.

This conclusion is supported by the observation that in these high HF compositions a brown surface coating is formed on the specimens. In moderately high HF this surface coating is a continuous, adherent film,⁴ and in the very high HF region it becomes a powdery crust which can be easily scraped from the surface. Although this surface film may be observed at HF concentrations above 40% on both the (111) surface and the (110) surface, it does not become noticeable on the (100) surface until approximately 60% HF. These are probably the same HF-insoluble "germanium monoxide" films as were observed by Ellis (15), and the leveling off of the etch rates is attributed to the presence of this film. However, the passivity is somehow related to the manner in which the surface film is bonded to the surface, for the passivity does not seem to affect the (100) etch rates over as large a composition range as it does the etch rates of the other two surfaces.

At 50% HF the etch rates of all three oriented germanium surfaces fall off with increasing HF concentration. It is not determinable from the data whether this falling off is caused by a decrease in the nitric acid activity or whether it just reflects an increased passivity of the germanium. From the data of Fig. 5 it is seen that the system behaves erratically in this composition region until a solution temperature of 35°-40°C ($\sim 3.2 \times 10^3/T^\circ\text{K}$) is reached. Above this temperature range the system begins to be more reproducible. It is thought that the extremely erratic behavior around room temperature is the result of induction periods, as observed in Fig. 1. Since N_2O_4 catalysis was used in all of the elevated temperature measurements as well as the room temperature measurements, it is concluded that the simple catalytic influences observed in silicon (1) are being masked by other, stronger influences of a passivating nature.

Lower oxidation states of nitrogen present in the etching solution have been shown to be important as accelerating agents in the oxidation-limited composition region for etching silicon (1). Cretella and

⁴ Electron diffraction examination did not reveal any crystalline structure in this film.

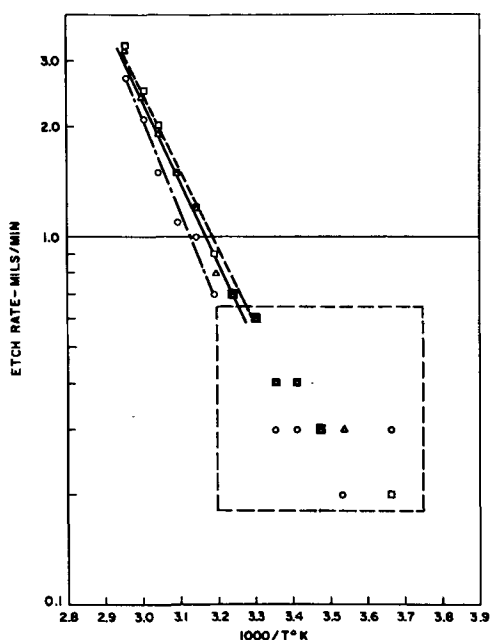


Fig. 5. Influence of temperature on etch rate in 85 w/o HF and 15 w/o HNO_3 , with reagents of 49% HF and 70% HNO_3 and N_2O_4 addition. The temperature dependence is approximately 10 kcal/mole. \circ , (100) Ge; \square , (110) Ge; \triangle , (111) Ge.

Gatos (8) and Miuller *et al.* (3) have also observed the importance of lower oxidation states of nitrogen in the etching of germanium. Table II shows, though, that, as with silicon, the influence of the lower oxidation states of nitrogen is not observed over the entire etching composition region but only in the region where one might expect the oxidation step to be rate limiting. It is also to be noted, as far as reaction rate is concerned, that using bromine as an additive produced essentially the same effect as using NaNO_2 .

Effects of Diluent

Since acid etching solutions for germanium generally contain either added water or added acetic acid, it was considered important to investigate the influence of these diluents on the system. Figure 6 shows the effect of adding water as the diluent. Comparison with silicon shows the peak etch rates of germanium to be about an order of magnitude lower than the peak etch rates of silicon. As was observed with silicon, the tolerance of the germanium system to water as the diluent is very small, and by the time 10% water is present the peak etch rate is

Table II. Comparison of the influence of nitrite and halogen catalysis*

Etchant composition		Etch rate, mils/min		
HF %	HNO_3 %	No catalyst	NaNO_2	Bromine
9	91	1.2	1.4	No measurement made
17	83	2.2	2.2	2.4
26	74	1.9	3.7	3.7
35	65	0.3	5.3	4.0
45	55	0.3	3.1-6.6	No measurement made

* All specimens had (111) orientation and the reagents used were 49.0% HF and 70.0% HNO_3 .

down by a factor of three. In Figure 7 the etch rates of germanium are presented as a function of composition on a triaxial plot. It should be noted that etching still takes place in solutions very high in acetic acid concentration. For this plot 60% HF and 90% HNO_3 solutions have been used as the reference points. Still, it is easily seen that the tolerance of the system for acetic acid as the diluent is much greater, and the gradient in etch rate with amount of acetic acid added is much lower, than with water.

A comparison of the systems HF- HNO_3 - $\text{HC}_2\text{H}_3\text{O}_2$ -Si and HF- HNO_3 - $\text{HC}_2\text{H}_3\text{O}_2$ -Ge reveals an interesting contrast. The silicon system starts out with a much higher etch rate (except in the very high HNO_3 region), which does not fall off much as moderate amounts of acetic acid are added, and which then abruptly decreases almost to the vanishing point on the further addition of a small amount of acetic acid. On the other hand, the etch rates of germanium start out much lower than those of silicon. Using the 10% HF line and proceeding in the direction of increasing $\text{HC}_2\text{H}_3\text{O}_2$, it is observed that the etch rates slowly decrease but remain measurable over the entire composition range. Now, proceeding along the 10% HNO_3 line in the direction of increasing $\text{HC}_2\text{H}_3\text{O}_2$, it can be seen that the etch rates appear

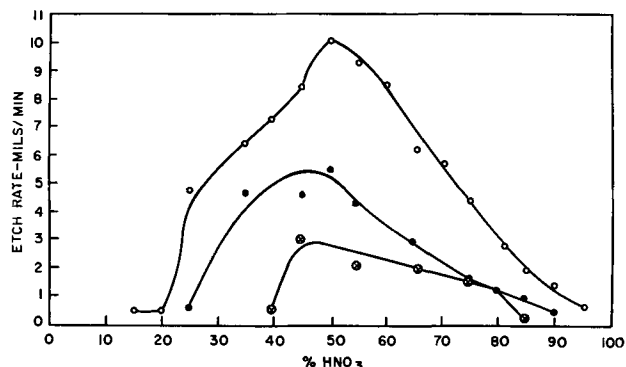


Fig. 6. Influence of water as a diluent on the etch rate of (100) oriented germanium, with 49% HF and 70% HNO_3 as reagents and N_2O_4 as the additive. Added water: open circle, 0%; dark circle, 5%; circle with x, 10%.

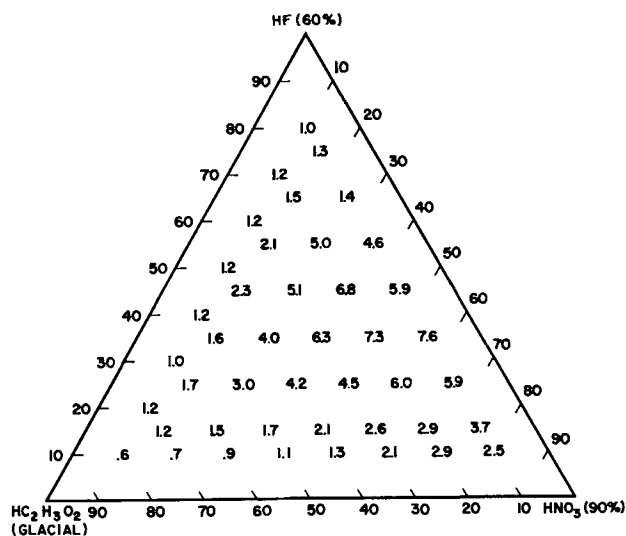


Fig. 7. Etch rate (mils/min) of (111) oriented, n-type germanium at 25°C vs. etchant composition. NaNO_2 was used as a catalyst throughout the entire composition region.

to increase on moderate dilution with acetic acid and then only slowly decrease again as additional acetic acid is added. The critical compositions that are so characteristic of the silicon system are absent in the germanium system. This lack of a critical composition of HNO_3 could be interpreted to mean that the oxidation potential of germanium is much lower than that of silicon. This interpretation would be in accord with the fact that germanium can be etched by aqueous HNO_3 (9) and also by oxygenated water alone (16).

The substitution of $\text{HC}_2\text{H}_3\text{O}_2$, a diluent of lower dielectric constant, for H_2O , a higher dielectric constant material, has the effect of changing the ionization constant of HNO_3 . It is believed that molecular HNO_3 is the important species in the oxidation of the solid germanium; this theory is discussed by the authors in their report on silicon dissolution (7).

Summary

The etching of germanium in the system HF-HNO_3 has been studied. The results indicate that major differences govern the kinetics of the etching of germanium and silicon. Until more is known about the active species in solution, any detailed answers to the problems are speculative. It can be said, though, that the simple diffusion mechanism that has been applied so well to silicon cannot be made to fit in the case of germanium. Other factors, such as dissolution species of low fluoride content, passivating films, etc., have to be considered before the observed phenomena can be explained. In addition, orientation influences on the etching rate have been observed in germanium dissolution which are not operative when silicon is being dissolved. However, the effects of lower oxidation states of nitrogen and dilution with $\text{HC}_2\text{H}_3\text{O}_2$ are the same in the etching of germanium as they are in the etching of silicon.

The reproducibility of results in the germanium system is very poor. Whereas with silicon only

minor difficulty is generally encountered in attempting to reproduce etching results, with germanium such factors as passivating films introduce large errors in any etch rate measurement.

Acknowledgments

The authors would like to express their appreciation to Mr. J. Estlick and Miss J. Werner for making most of the rate measurements. They would also like to thank Dr. O. Haase, of the Bell Telephone Laboratories, for the electron diffraction measurements of the passivating films.

Manuscript received June 6, 1963; revised manuscript received Aug. 20, 1963. This paper was presented at the Houston Meeting, Oct. 9-13 (1960).

Any discussion of this paper will appear in a Discussion Section to be published in the December 1964 JOURNAL.

REFERENCES

1. H. Robbins and B. Schwartz, *This Journal*, **106**, 505 (1959).
2. P. R. Camp, *ibid.*, **102**, 586 (1955).
3. P. Wang, *Sylvania Technologist*, **11**, 50 (1958).
4. R. L. Müller, A. V. Danilov, T. P. Markova, V. N. Mel'nikov, A. B. Nikol'skiĭ, and S. M. Repenskii, *Leningr University, Vestnik, Ser. Fiz. i Khim.*, **15** [1], 80 (1960).
5. J. Bloem and J. C. van Vessem, *This Journal*, **109**, 33 (1962).
6. H. Robbins and B. Schwartz, *ibid.*, **107**, 184C (1960).
7. H. Robbins and B. Schwartz, *ibid.*, **107**, 108 (1960).
8. B. Schwartz and H. Robbins, *ibid.*, **108**, 365 (1961).
9. M. C. Cretella and H. C. Gatos, *ibid.*, **105**, 487 (1958).
10. D. L. Klein and D. J. D'Stefan, *ibid.*, **109**, 37 (1962).
11. T. Burgess, *ibid.*, **109**, 341 (1962).
12. F. A. Cotton and G. Wilkinson, "Advanced Inorganic Chemistry," p. 368, Interscience Publishers, London (1962).
13. P. J. Holmes, "The Electrochemistry of Semiconductors," pp. 212-221, Academic Press, London (1962).
14. T. Burgess, Private communication.
15. R. C. Ellis, *J. Appl. Phys.*, **25**, 1497 (1954).
16. W. W. Harvey and H. C. Gatos, *This Journal*, **105**, 654 (1958).

Epitaxial Growth of Silicon by Vacuum Sublimation

E. Tannenbaum Handelman and E. I. Povilonis

Bell Telephone Laboratories, Incorporated, Murray Hill, New Jersey

ABSTRACT

Silicon has been grown epitaxially on silicon substrates by a process of vacuum sublimation. The important new features of the system are that the reaction chamber contains only silicon and quartz and that the chamber is continuously pumped throughout the process to a pressure of 10^{-9} - 10^{-8} Torr. The physical support for the substrate acts as the source of silicon as well as the source of dopant. In this way a high degree of control of the thickness and resistivity uniformity and reproducibility have been obtained with both n- and p-type epitaxial films on both n- and p-type substrates. Based on the behavior of three source crystals, it is believed that epitaxial layers of any desired resistivity can be grown by given source material of specified purity. The details of the system and an analysis of the results are given. Preliminary results obtained on heterojunctions grown in a similar manner are also reported.

In recent years there have appeared a number of studies of epitaxial growth by evaporation (1-4) or molecular beam (5) techniques. Most of this work involved the evaporation of germanium and

it was generally found that p-type films were produced independent of the conductivity type of the evaporation source. This result was attributed to high densities of structural defects. One investiga-

tor (2) found, however, that although p-type films were produced at relatively poor vacuums (10^{-5} Torr), n-type films could be grown when the background pressure was in the range of 10^{-9} Torr. Since a background pressure of 10^{-5} Torr represents a high level of contamination to a semiconductor (assuming these impurities are incorporated into the growing epitaxial layer) it seems reasonable that the problem is at least partly one of contamination rather than being primarily structural in nature. In view of the obvious inherent advantages of a purely thermal transport process for growing epitaxial layers, this work was undertaken to study such a process under the cleanest conditions obtainable in a practical system. The epitaxial system chosen for study was silicon on silicon. This paper describes the apparatus and procedure designed to meet the above objectives and the results obtained.

Experimental

Description of apparatus.—To obtain an organic-free high vacuum, a pumping station was constructed using a molecular sieve type forepump and a 15 liter/sec ion pump. Bellows type stainless steel valves with CMC-57 O-rings are used, and detachable mountings are sealed with Apiezon W wax. The portion of the system which is heated is constructed entirely of silicon and quartz. A schematic diagram of the apparatus is shown in Fig. 1. The silicon pedestal acts as both the physical support for the substrate and the source of silicon and dopant. The pedestal is $\frac{3}{4}$ in. in diameter and about $1\frac{1}{2}$ in. long. It has a saw cut groove $\frac{1}{4}$ in. deep and an ultrasonically cut ledge 0.02 in. deep designed to hold in place a substrate $\frac{1}{2} \times \frac{1}{2}$ in. The silicon pedestal is heated using a 3 kw, 1.5 mc R.F. generator. With this arrangement, the hottest portion of the system is the silicon source. The geometry and relative mass of the pedestal and substrate are such that the R.F. field is concentrated almost entirely in the silicon pedestal and the substrate is heated primarily by radiation. Temperatures are measured with an optical pyrometer using appropriate corrections for emissivity (6). The ion pump current is used to measure pressure.

Operating procedure.—The substrate is etched in 10:1 HNO_3 :HF and cleaned in hot concentrated HNO_3 followed by several rinses in hot deionized

water. The pedestal is cleaned the same way the first time it is used, but subsequently is not cleaned between successive runs. After assembling and mounting the reaction tube, the system is evacuated to a pressure of less than 1×10^{-8} Torr. The pedestal is preheated with projection lamps enabling direct R.F. coupling to a pedestal of any resistivity. As the pedestal couples with the R.F. field, adsorbed gas from the silicon and the quartz walls is desorbed giving a pressure peak in the 10^{-8} Torr range which decays to less than 1×10^{-8} Torr in less than 1 min. The operating temperature of the pedestal is $1350^\circ\text{--}1380^\circ\text{C}$ (the vapor pressure of silicon is $\sim 10^{-4}$ Torr at this temperature), and the temperature of the substrate is $\sim 1100^\circ\text{C}$. It should be noted that, although the operating temperatures are readily reproduced from run to run, they are not accurately known because the quartz walls become covered with deposited silicon before the temperatures have reached their stable maximum values. Under these conditions, the rate of growth of the silicon on the substrate is of the order of $0.3\mu/\text{min}$. At the end of the run after the pedestal has cooled, the valve to the Vac-Ion pump is closed, and the system is backfilled with nitrogen. Nitrogen is continuously passed through the manifold during the time that the system is open to minimize the adsorption of oxygen and water vapor.

Results

Physical growth characteristics.—With the arrangement shown in Fig. 1, growth of the epitaxial layer occurs only on the side of the substrate facing the pedestal, and, in fact, there is a small loss of silicon from the side facing away from the pedestal. Under the growth conditions outlined in the previous section, a comparison of weight gain with optical thickness measurements indicated an evaporation rate of about $0.02 \mu/\text{min}$ from the back of the substrate. The grown films are always single crystal as checked by a number of techniques including electron diffraction, etching, resistivity measurements, and device characteristics. The microscopic surface features of the epitaxial layers invariably reproduce those of the original substrate surface identically. Across the entire slice, two or three physical holes occasionally may be found in the film.

Films grown at pressures less than 1×10^{-8} Torr are totally free of commonly observed structural defects such as pyramidal peaks and pits, chevrons, etc. However, at higher background pressures crystallite formation can be observed as illustrated in Fig. 2.

Upon etching the epitaxial surface lightly, patterns of stacking faults can be seen under the microscope similar to those observed by others (7, 8). A typical stacking fault pattern is shown in Fig. 3A. The stacking faults are always produced under the operating conditions noted above. Several qualitative experiments were carried out in an attempt to determine the cause of the stacking faults. It was found that preheating the substrate under conditions necessary to produce an atomically clean surface (9) did not eliminate stacking faults even though the substrate surface had been thermally

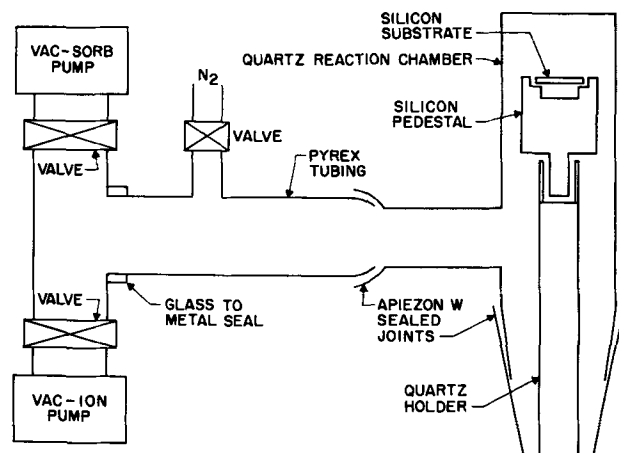


Fig. 1. Schematic diagram of sublimation apparatus

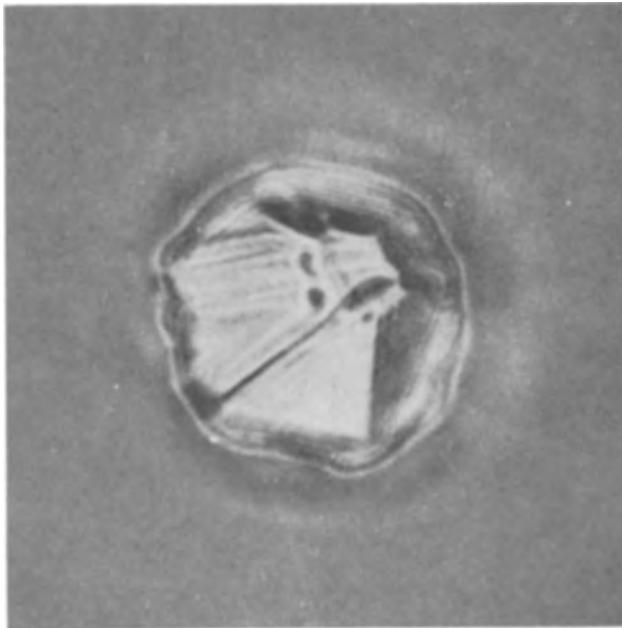


Fig. 2. Crystallite formation in a silicon epitaxial film grown at a pressure of $1 (10^{-7})$ Torr. 500X.

etched prior to growth. The density of stacking faults could, however, be drastically altered by the substrate surface preparation. For example, rinsing the substrate in distilled water instead of deionized water increased the stacking fault density by at least a factor of 100. Growing epitaxial layers on two substrates from different crystals prepared together and located side by side on the pedestal during growth indicated a stacking fault density dependence on the substrate independent of the surface preparation. This effect also appears to be independent of the substrate resistivity and is much smaller than the effect of contamination. A few attempts to eliminate stacking faults by annealing at 1000°C subsequent to growth were unsuccessful. However, the stacking fault etch pattern is virtually eliminated after diffusion. For example, Fig. 3 shows the etch pattern on the same slice before and after diffusion into the epitaxial layer. From these observations, one cannot decide whether annealing is facilitated by the diffusion, whether the faults are being loaded up with diffusant such that preferential etching no longer occurs at these sites, or whether the diffused surface is sufficiently strained to mask the effect of stacking faults. Further work on this phenomenon is in progress.

Thickness uniformity and reproducibility control.—The thickness of the epitaxial layer was measured by interferometry using sodium light on specimens which were angle lapped and stained. Using this technique, the accuracy of measurement is limited to $\pm 0.3\mu$. Measurement of the thickness across a slice $\frac{1}{2}$ in. on a side always showed no variation in thickness within the accuracy of the method. The measurement excludes the two edges of the slice resting on the pedestal where growth occurs at a considerably slower pace. The demarcation of these regions can be seen by eye as sharply defined steps.

To check thickness reproducibility from run to run, a series of twelve runs were carried out with

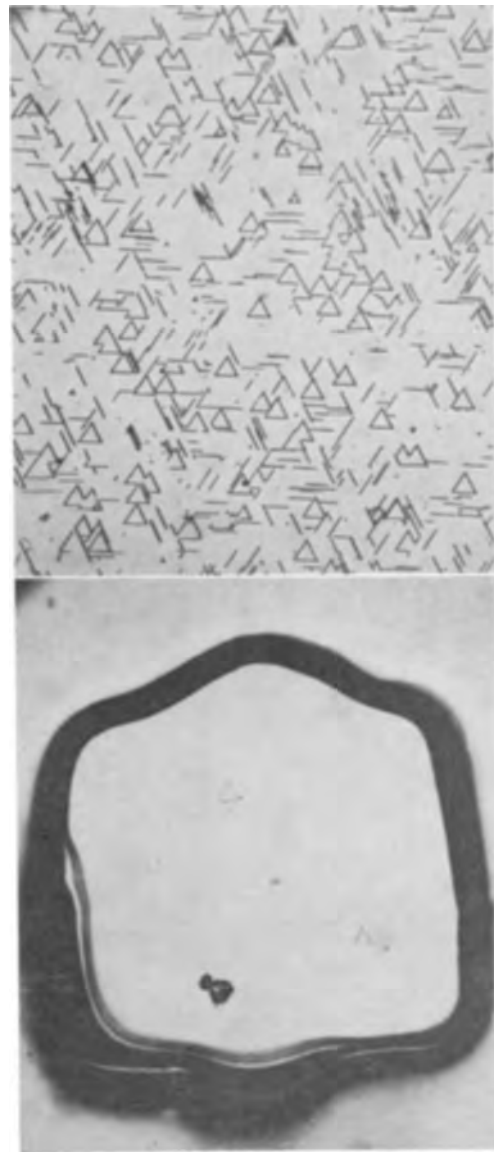


Fig. 3. A (top) Etch pattern in epitaxial silicon before device fabrication, and B (bottom) after device fabrication. Magnification approximately 400X.

all variables controlled as carefully as possible. That is, all runs were done using one pedestal, substrates from one crystal, the same power level of the R.F. generator, etc. The reproducibility of thickness fell within the measurement uncertainty as can be seen from the data given in Table I.

Table I. Thickness reproducibility T substrate $\sim 1050^{\circ}\text{C}$, T pedestal $\sim 1360^{\circ}\text{C}$

Run No.	Time, min	Thickness, μ	Growth rate, μ/min
271	31	6.2	0.200
272	35	6.8	0.194
273	35	6.8	0.194
274	35	6.8	0.194
275	35	6.8	0.194
276	35	6.8	0.194
277	35	6.8	0.194
278	35	6.8	0.194
279	35	6.8	0.194
280	35	6.2	0.188
281	60	11.8	0.196
282	35	7.1	0.200

Dopant transfer.—The conductivity type and resistivity of the epitaxial layer is controlled by the doping of the silicon source. Both p- and n-type films have been grown on both p- and n-type substrates over a range of resistivity. Three pedestals used most extensively were (i) phosphorus doped 3.3-3.9 ohm-cm n-type, (ii) boron doped 0.095-0.11 ohm-cm p-type, (iii) 5000-15,000 ohm-cm p-type. No systematic study of the doping transfer of the phosphorus-doped pedestal was made. However, about a dozen spot checks of resistivity in the course of working with this source all gave grown film resistivities of 4-5 ohm-cm indicating roughly a one to one transfer of dopant.

The behavior of the boron doped pedestal was studied in detail, and the data turned out to be completely self-consistent as well as suggestive of a probable mechanism of dopant transfer. A series of runs was carried out in which the pedestal temperature was 1350°-1380°C, and the substrate temperature was 1050°-1100°C. The substrates were in all cases low resistivity n-type and the grown films p-type. The resistivity was measured by the four-point probe thus giving an average value for the entire film.

The first film grown for 1 hr using the boron doped 0.095-0.11 ohm-cm source had an average resistivity of 0.8 ohm-cm. Successive runs produced progressively lower resistivity films until at the end of 9 hr of heating of the source the resistivity of the grown film fell within the resistivity range of the source. This behavior suggested the establishment of some steady-state distribution of boron at the subliming surface of the source. That is, if one assumes an ideal solid solution of the boron in the silicon then the ratio of boron to silicon being removed from the subliming surface should be related to the partial pressures of the element. If that is the case, then initially there will be a tendency to pile up boron at the surface. This would then account for the high resistivity of the first film grown. Eventually, a steady state will be attained when the pile-up is balanced by the sublimation rate and the back diffusion from the surface of the source into the body. The concentration of boron at the surface of the source as well as the steady-state transfer ratio will be a function of the specific dopant, the relative vapor pressures and sticking coefficients of the dopant and silicon, the diffusion coefficient of the dopant, and the temperature. To test this hypothesis qualitatively, the pedestal was freshly etched, removing the boron enriched surface region, and a second series of runs carried out to observe the change of resistivity with time. The history of the pedestal is summarized in Fig. 4, where the resistivity of the grown film is plotted as a function of the time of heating the pedestal. The length of the horizontal lines indicates the total growth time of the film and the resistivity is an average value over that time. The solid lines trace the initial behavior as discussed earlier, and the dotted lines show the results of the second series of runs after freshly etching the pedestal. The agreement in the behavior of resistiv-

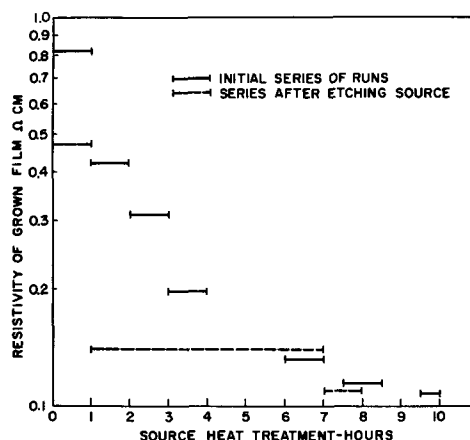


Fig. 4. Resistivity of grown p-type films on n-type substrates as a function of the thermal history of the source. The resistivity is the average through the film obtained by four-point probe measurements. The length of line indicates the growth time of the film. The source crystal was 0.095-0.11 ohm-cm boron doped.

ity with time between the two series is excellent and qualitatively supports the suggested hypothesis.

All the group V n-type dopants would be expected to show the opposite behavior from boron based on this mechanism. That is, all these elements have considerably higher vapor pressures than silicon, so that a leaching of dopant at the subliming surface would be expected rather than a pile up. Thus the first film grown from an n-type source should have a resistivity lower than that of the source with subsequent runs increasing in resistivity and approaching that of the source. If now, one considers a compensated crystal, then the behavior will be the sum of the behavior of the two dopants and hence dependent on the degree of compensation. The problem of compensation for a boron-doped source is very likely of no consequence since compensating n-type impurities are relatively readily removed in zone refining. However, in an n-type crystal, there will undoubtedly be present some level of compensating boron unless special procedures have been used to eliminate the boron in growing the crystal. This is to be expected because the distribution coefficient of boron between liquid and solid in silicon is virtually unity so that the boron is not readily removed by zone refining.

The qualitative behavior of the 5000-15,000 ohm-cm p-type pedestal can be explained by this mechanism assuming some degree of compensation, and considering the doping level of this crystal, the assumption of some compensating impurities is not unreasonable. The pedestal was freshly etched three times in the series of runs, and in each case, the first film grown after etching was n-type; after several hours of heating, the grown film was p-type. The resistivity of the p-films ranged between 26 and 65 ohm-cm. Whether this range of values reflects the background impurity level of the system, the acceptor type dislocation density of the film, or the inherent behavior of the pedestal is not known. Subsequent work with other source crystals has not in all cases yielded consistent values for the steady-state transfer ratios. Although a given crystal will consistently give a reproducible transfer

ratio, the ratio has been found to vary as much as a factor of 10 from one source crystal to another. The variation is believed to be caused by the presence of compensating impurities.

Resistivity control.—After the pedestal has attained the steady-state condition discussed above, the resistivity uniformity of the grown film is exceedingly good both within a given slice and from run to run. The data used to illustrate the resistivity control were gathered in the following way. P-type epitaxial layers were grown on three n-type slices using the 0.095-0.11 ohm-cm p-type source. A narrow strip was cut from each slice for thickness measurements. An array of 0.060 in. diameter mesas

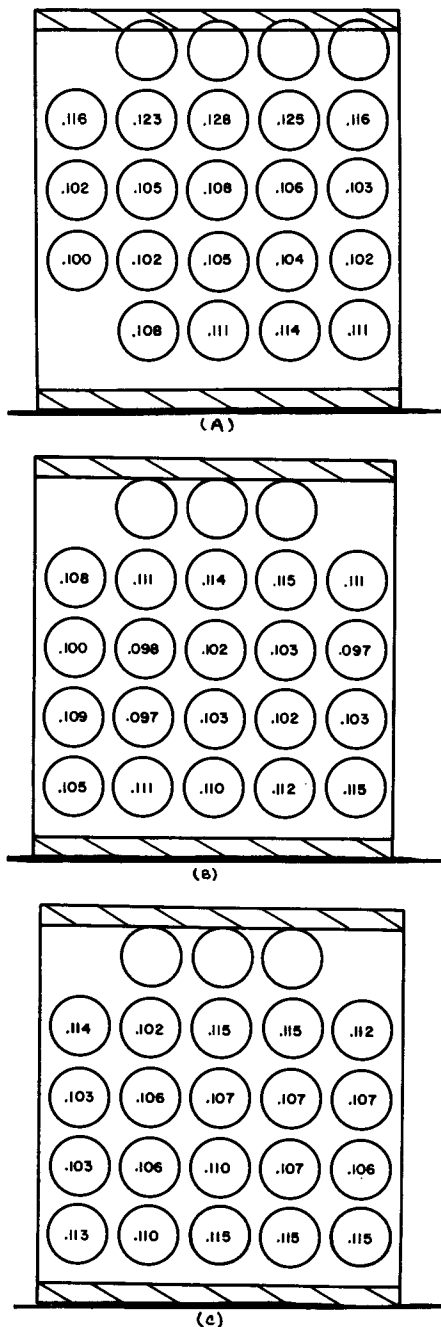


Fig. 5. Resistivity map of p-type film grown on n-type substrate. The circles represent 0.050 in. mesas etched through the grown junction. The slice is 0.5 x 0.5 in. The ruled edges indicate the edges resting on the pedestal during growth. The film thickness of A, B, and C are 19.1, 14.1 and 22.7 μ , respectively. The average resistivities, in the same order, are 0.110, 0.106, and 0.109 ohm-cm.

were etched through the p-n junction on the remainder of each of the slices. Resistivity measurements were then made on each isolated island using a special 4-point probe with 0.010 in. spacing between probe points. Although the probe and bridge used are accurate to better than 1%, the positioning of the probe points on such small mesas is critical, and it was found experimentally that the reproducibility of the measurements was only good to $\pm 5\%$. Thus the precision of the measurements is $\pm 5\%$. About 20 mesas were measured on each slice. The data are presented pictorially in Fig. 5A, 5B, and 5C to show the relative position on the slice of each measurement. The mesas are represented on the scale drawing of the slice by circles, and the numbers within the circles are the individual resistivity measurements. The lined regions indicate the ledges resting on the pedestal during growth.

Examination of the data in detail indicates a consistent trend to a slightly lower resistivity going from the edges resting on the pedestal toward the mid-line of the slice. Although the variation is close to the experimental error of measurement, the trend is so consistent in all three slices that it is very probably real. It is noteworthy that the average resistivity from slice to slice varies less than 3%.

Distribution of dopant in depth.—The distribution of impurities in depth in the film has been found to be constant from the surface of the film down to the outdiffusion tail in the region of the substrate-epitaxy interface. A representative set of measurements is shown in Fig. 6. This epitaxial film was grown on an n+ substrate using the phosphorus doped pedestal. Diodes were made in the film by shallow boron diffusion through a photoresisted oxide mask and the profile determined from capacitance measurements (10).

It can be seen from Fig. 6 that the individual data points fall randomly within $\pm 10\%$ of 1×10^{15} cc $^{-1}$ over the flat portion. The slope and position of the outdiffusion tail was determined from the average of several measurements on thinner films. The uniform distribution in depth found for films grown by the sublimation process is in marked contrast to

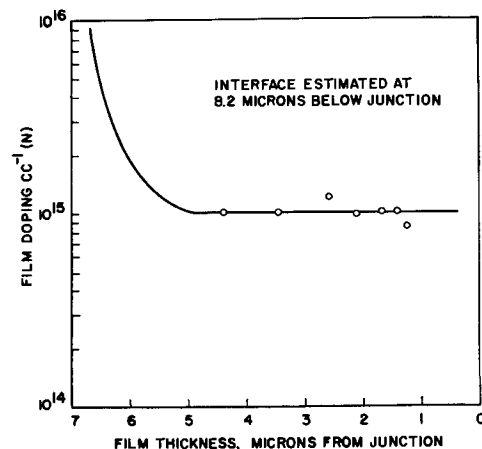


Fig. 6. Doping profile of an N on N $^{+}$ epitaxial layer showing the uniformity of resistivity with depth into the film. The outdiffusion tail was determined from a composite of capacitance measurements on thinner films.

the distributions found in films (10) grown by the hydrogen reduction of SiCl_4 . Analysis of films grown by the latter process showed distributions consisting of three well-defined regions, (i) a region of outdiffusion from the substrate followed by (ii) a region in which the concentration of dopant decayed exponentially to (iii) a region of uniform concentration extending out to the surface. A reverse component in the deposition process was proposed to account for the distributions obtained. The uniform distributions obtained by the sublimation process are ascribed to a much smaller reverse component of the reaction (*i.e.*, thermal etching of the substrate) in the sublimation process as compared with an atmospheric pressure chemical process. The extent of the outdiffusion tail appears to be about the same for both processes.

Heterojunction work.—A few preliminary runs growing silicon on germanium and germanium on silicon have been carried out. The silicon on germanium was grown using the described pedestal design, simply by keeping the pedestal temperature low enough (1050°C) to prevent melting of the germanium substrate (890°C). Under these conditions the vapor pressure of silicon was so low that only about 0.5μ was grown in 6 hr. Examination of the grown film by electron diffraction showed it to be single crystal.

For the case of germanium on silicon, the vapor pressure of germanium in the solid state is too small to make a sublimation technique practical. Thus a silicon pedestal was used as a physical support with a cup arrangement machined in the top to contain the germanium source. The silicon was heavily oxidized ($\sim 10,000\text{\AA}$) to prevent alloying of

the germanium with the silicon. The germanium was heated to about 1050°C and the silicon substrate to about 900°C . The grown film in this case too was found to be single crystal by electron diffraction. Ge on Ge can be grown using the same arrangement, but this has not yet been done. No electrical measurements were attempted on these films. The geometry will have to be altered to give temperature differentials which will give more favorable growth rates before useful films can be produced in this way.

Acknowledgments

The authors would like to thank Mrs. M. H. Read for the electron diffraction results and C. O. Thomas and D. Kahng for the resistivity profile data.

Manuscript received May 29, 1963. This paper was presented at the Boston Meeting, Sept. 16-20, 1962.

Any discussion of this paper will appear in a Discussion Section to be published in the December 1964 JOURNAL.

REFERENCES

1. G. A. Kurov, S. A. Semiletov, and Z. G. Pinsker, *Kristallografiya*, **2**, 59 (1957).
2. I. G. Ptushinskii and I. A. Lupan, *Ukrain. Fiz. Zhur.*, **4** [1], 125 (1959).
3. O. Weinreich, G. Dermit, and C. Tufts, *J. Appl. Phys.*, **32**, 1170 (1961).
4. A. F. Hale and B. D. James, 1960 Electron Devices Meeting, Washington, D. C., Oct. 1960.
5. G. A. Kurov, *Fiz. Tverdoga Tela*, **3**, 1662 (1961).
6. F. G. Allen, *J. Appl. Phys.*, **28**, 1510 (1957).
7. H. J. Queisser, R. H. Finch, and J. Washburn, *ibid.*, **33**, 1536 (1962).
8. G. R. Booker and R. Stickler, *ibid.*, **33**, 3281 (1962).
9. F. G. Allen, J. Eisinger, H. D. Hagstrom, and J. T. Law, *ibid.*, **30**, 1563 (1959).
10. C. O. Thomas, D. Kahng, and R. C. Manz, *This Journal*, **109**, 1055 (1962).

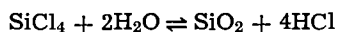
Successive Growth of Si and SiO_2 in Epitaxial Apparatus

W. Steinmaier and J. Bloem

Semiconductor Development Laboratory, N. V. Philips' Gloeilampenfabrieken, Nijmegen, Holland

ABSTRACT

The growth of silicon oxide layers immediately following the deposition of an epitaxial silicon film has been studied, using the reaction



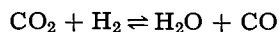
Water vapor or mixtures of CO_2 and H_2 can be used successfully. The formation of amorphous SiO_2 layers on Si substrates, using hydrogen as a carrier gas, proceeds with an activation energy of about 82 kcal/mole. The excess hydrogen plays an important part, as it appears that chemisorption of reduction products of SiCl_4 determines the growth of continuous SiO_2 layers on the substrate.

In planar technology various methods (1-4) exist to provide silicon with thin films of SiO_2 . Atalla *et al.* (1, 2) pointed out that fast surface states can be introduced by both the pre-oxidation treatment and the migration of fast diffusing impurities present in the silicon crystal. As in conventional oxidation methods long times and high temperatures are often required, redistribution of the doping impurities near the SiO_2 -Si-interface may occur.

The method of oxide growing described here is of some technical and academic interest and offers, especially in combination with the epitaxial growth of silicon, advantages as compared with the conventional techniques.

The epitaxial SiCl_4 process uses a mixture of SiCl_4 and H_2 , which is passed over a heated Si substrate. A silicon epitaxial layer is formed by the reduction of SiCl_4 by H_2 (5). Formation of SiO_2 on

the substrate occurs when some water vapor is added to the SiCl₄-H₂ mixture. Instead of water CO₂ can be injected, with the result that water is formed according to the reaction



This reaction occurs at elevated temperatures only, so that the hydrolysis of SiCl₄ is limited to a relatively small reaction zone near the substrate. By choosing the correct range of process parameters it is possible to deposit the SiO₂ as an amorphous continuous film of predetermined thickness on the silicon substrate.

This method is especially attractive in combination with epitaxial growth of Si, as no additional cleaning between epitaxial growth and oxidation is necessary, the mere addition of CO₂ to the gas mixture being sufficient to change the growth of Si into the growth of SiO₂. The growth rate of SiO₂ is normally so high that impurity profiles in the substrate wafer are conserved, and the segregation of donors and acceptors between silicon and silicon oxide is minimized.

Experimental Methods

The apparatus used to perform the experiments was a standard, single slice, vertical reactor using RF heating of a molybdenum susceptor. A quartz glass spacer was placed between susceptor and the silicon substrate (Fig. 1). Temperature differences over the silicon slices were less than 5°C. The silicon tetrachloride saturator was stabilized at 20°C ($\pm 0.02^\circ\text{C}$), part of the total hydrogen flow passing over the liquid to give a SiCl₄ concentration of 1% in the gas phase. CO₂ could be added to the system via flowmeter C. The substrate temperature was measured by means of an optical pyrometer; all temperatures quoted are corrected values.

From 0.007 ohm-cm Sb-doped float zoned Si crystals (111) oriented and optically polished slices were made, 250 μ thick, diameter 20-24 mm. Before growth the slices were cleaned and etched in HF:HNO₃ (1:6), boiled in HNO₃, and rinsed in deionized water. The slices were dried in a stream of warm forming gas and stored under purified forming gas. After placing in the reactor, a 10-min treatment in dry H₂ at 1300°C was used to clean the substrate surface. Subsequently, the slice was brought to the chosen growth temperature, and SiCl₄ was added to the gas stream.

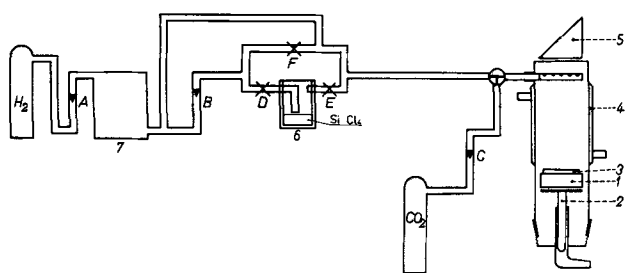
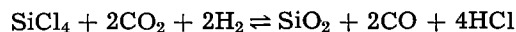


Fig. 1. Schematic diagram of the apparatus: A, B, C, flowmeters; D, E, F, Teflon membrane valves; 1, Mo-susceptor; 2, quartz plateau; 3, silicon wafer; 4, double wall water-cooling; 7, gas purifier.

After formation of a silicon film of the required thickness, CO₂ was added without changing the other process parameters. According to the over-all reaction



the growth of silicon is transferred in this way to the growth of silica on top of the epitaxial layer; the growth of the preceding epitaxial Si layer is not, of course, essential.

The layer thickness of the amorphous SiO₂ layer was evaluated by counting interference rings after local etching with a drop of hydrofluoric acid. For thicknesses greater than 1 μ the measurement was performed by weighing the slice before and after the removal of the entire SiO₂ film.

Experimental Results

In Fig. 2 the growth rate of SiO₂ layers is shown for CO₂ concentrations exceeding the stoichiometric amount needed according to the over-all reaction. With a substrate temperature of 1200°C, a total flow rate of 1 liter/min and a SiCl₄ concentration of 1%, the CO₂ partial pressure was varied between 2 and 12%. The deposition rate increases up to a CO₂ percentage of 4, reaching a saturation value of about 8 μ /hr.

As far as the quality of the dioxide layer is concerned, no pronounced difference was observed throughout this range of CO₂ partial pressures. In all cases the deposited SiO₂ appears to be a flat amorphous film. On the supporting material, however, crystalline SiO₂ needles may appear. Above 8% CO₂ this crystalline appearance vanishes. Increase of the CO₂ percentage above 10% leads to heavy SiO₂ deposits on the reactor walls. Perhaps condensation of water occurs on the water-cooled jacket, causing rapid hydrolysis of the gaseous SiCl₄.

The homogeneity in film thickness does not depend on the CO₂ vapor pressure; differences of 10-15% were commonly present between center and edge.

For CO₂ percentages lower than 2% no homogeneous SiO₂ layers are formed. Using the same experimental parameters as quoted above, for 0.45% CO₂ a crystallographically strongly disturbed Si deposit appears. Increasing the CO₂ content to 0.6% leads to simultaneous growth of Si and SiO₂, and Si islands surrounded by amorphous SiO₂ are observed.

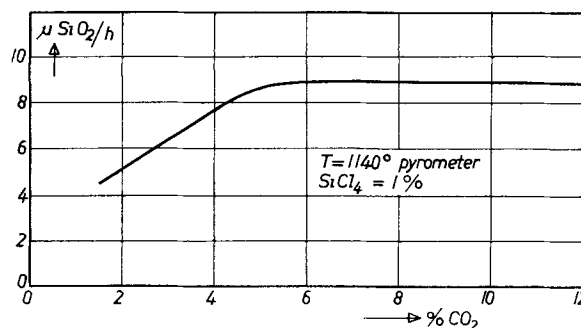


Fig. 2. Growth rate of SiO₂ vs. CO₂ concentration (flow rate 1 liter/min).

For CO_2 concentrations between 1 and 2% the number and size of the Si islands decrease; at 2% finally all the Si is transformed into SiO_2 . In this range also a colorless viscous liquid is formed on the water-cooled reactor wall. At CO_2 percentages greater than 2% this liquid phase disappears in favor of some SiO_2 deposit.

Figure 3 shows the effect of the total flow rate on the deposition rate of SiO_2 for substrate temperatures of 1240° and 1280°C. The SiCl_4 concentration was held at 1% and the CO_2 concentration at 6%, whereas the flow rate was varied between 0.25 and 2.5 liter/min. In this range of flow rates no significant variation in growth rate is observed, indicating that the rate-determining step is not the mass transfer of reactants toward the surface.

This result may be compared with the variation of growth rate with total flow rate found for the deposition of silicon on a silicon substrate (Fig. 4). For low flow rates the growth rate increases linearly, and no temperature dependence is observed. This range is accessible to thermodynamic calculations, assuming an equilibrium in the gas phase near the substrate (6). Higher flow rates lead to a region where mass transfer is no longer rate-limiting; here a strong temperature dependence is found.

In another series of experiments the SiCl_4 and CO_2 concentrations were held at 1 and 8%, respectively, with a total flow rate of 1 liter/min. The substrate temperature was varied between 1000° and 1350°C. In Fig. 5 the logarithm of the growth rate is plotted vs. $1000/T^\circ\text{K}$. From the slope of the experimental line an activation energy of about 82 kcal/mole was calculated.

As far as the structure of the layer is concerned, up to 1300°C the dioxide is deposited as a flat transparent glassy layer. Above 1300°C a dense array of spherically shaped hills of amorphous SiO_2 appears,

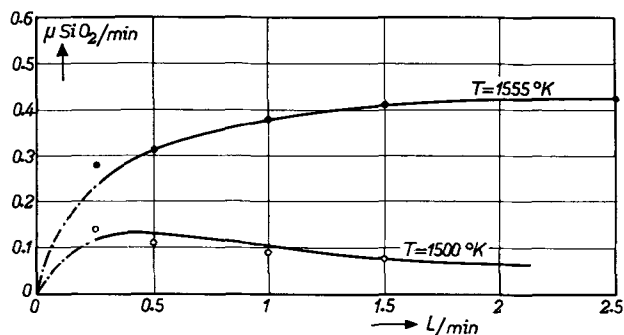


Fig. 3. Growth rate of SiO_2 vs. gas flow rate (1% SiCl_4 , 6% CO_2)

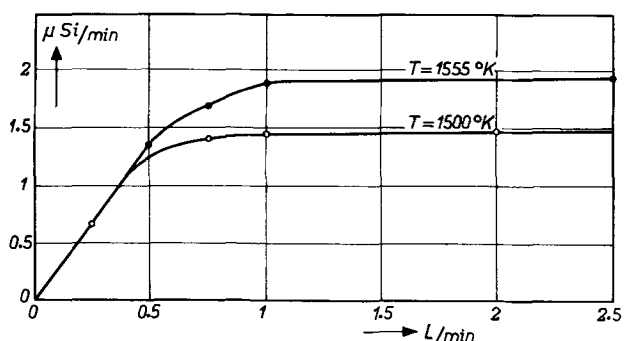


Fig. 4. Growth rate of Si vs. gas flow rate (1% SiCl_4)

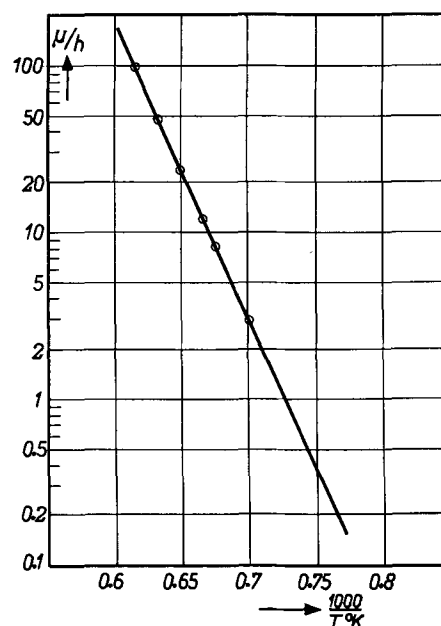


Fig. 5. Growth rate of SiO_2 vs. substrate temperature (1% SiCl_4 , 8% CO_2 , flow rate 1 liter/min).

leading to a dull, nonreflecting surface. This is probably caused by some melting phenomenon. At temperature exceeding 1350°C growth of crystalline SiO_2 is favored, giving porous white films.

To see whether the hydrogen carrier gas plays an active part in the process, first the addition of CO_2 was replaced by the addition of equivalent amounts of water vapor. It was noticed that the results did not differ markedly for both systems. Then hydrogen as a carrier gas was replaced by argon, water being used instead of CO_2 . At a substrate temperature of 1200°C under normal CO_2 - H_2 - SiCl_4 conditions a growth rate of 7 μ /hr was observed.

In contrast to this under modified conditions on the substrate only insignificant deposits were formed; in the reactor tube, however, much more fog was observed than in the case of H_2 - H_2O .

From the fact that in an argon atmosphere practically no deposit is observed although strong SiO_2 formation in the gas phase occurs, it follows that surface reactions involving hydrogen play a predominant part, as they do in epitaxial growth of silicon.

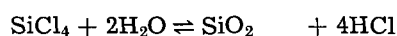
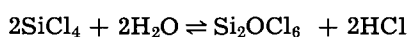
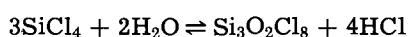
In order to gain further insight into this field, a study was also made of the growth of Si on top of a glassy layer, using 1% SiCl_4 in H_2 . Below a substrate temperature of 1250°C a homogeneous polycrystalline Si layer is formed in this case. Increasing the temperature reduces the growth rate of Si, indicated by the growth of Si islands. Above 1300°C no silicon is deposited at all. Instead an etching of the SiO_2 layer is observed, the etching rate amounting to about 0.1 μ /min, to be compared with a growth rate of Si of about 1 μ /min under the same circumstances but on a silicon substrate.

It may be of some practical importance to remark that directly after the growth of an oxide layer a new epitaxial experiment can be started without cleaning the reaction tube. No adverse influence on layer resistivity or crystal quality is observed.

Discussion

From the experimental evidence it appears that the formation of adherent amorphous dioxide layers is possible if the CO₂ concentration in the gas phase is at least twice the SiCl₄ concentration, and provided an excess of hydrogen is present. The CO₂ can be replaced by water vapor without changing the over-all aspects of the reaction.

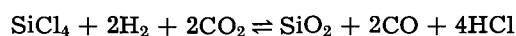
At low water vapor pressures the oxygen content of the deposited silicon increases initially until the formation of a SiO₂-rich second phase is observed, analogous to the considerations of Kaiser and Breslin (7) and Wagner (8). On the reactor walls crystalline SiO₂ is deposited. At low CO₂ or water concentrations viscous liquid deposits are observed as well. Probably these products are formed in the gas phase at sufficiently high temperatures according to



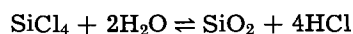
Depending on the relative concentrations of SiCl₄ and H₂O, one of these oxidation products might predominate. For the higher water contents only SiO₂ appears to be formed.

In Fig. 2 and 3 it is shown that the growth rate of SiO₂ is nearly independent of the CO₂ concentration or the total flow rate above a certain level. This, together with the strong temperature dependence of the process (Fig. 4), indicates that variations in layer thickness might be due to small variations in temperature over the substrate.

Another point of interest is the conclusion that mass transfer toward the substrate does not determine the growth rate, while the argon experiments indicate that the formation of SiO₂ on the silicon substrate does not follow the simple course described by the over-all reaction



or



The presence of an excess of hydrogen is necessary, indicating that at least on the substrate the reaction proceeds via an intermediate reaction product of SiCl₄ and H₂.

This indicates an intimate connection between the formation of silicon and silicon dioxide. On the other hand, there are also pronounced differences. Compared with the growth rate of silicon dioxide at a substrate temperature of 1200°C and a SiCl₄ concentration of 1%, the deposition rate of silicon appears to be about a factor of ten higher than the growth rate of the dioxide.

At 1300°C Si is deposited on a silicon substrate with a growth rate of about 1 μ/min. Under the same conditions the deposition of Si on a SiO₂ layer leads to etching of the glassy layer. It is probable

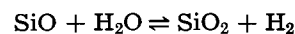
that under these circumstances any silicon nucleating on the SiO₂ surface will react with the silica to form volatile SiO.

As a growth rate of about 1 μ/min is found on a silicon substrate, an etch rate of the same order could be expected on SiO₂. In practice an etch rate of about 0.1 μ/min is found, from which it may be concluded that the rate of nucleation of silicon on the SiO₂ surface will be a factor of ten lower than on a silicon surface.

It may be postulated now that for not too low flow rates, *i.e.*, mass transfer not being the limiting factor, the rate-determining step, both for the growth of Si and SiO₂, could be the chemisorption of a radical, probably from the type SiCl_x.

The difference in deposition rate can then be explained by the different nature of the substrates on which the reaction occurs.

In the presence of a sufficient amount of water vapor the chemisorbed radical on the silica surface is transformed into SiO₂ while SiO formation will be suppressed according to



At water vapor pressures lower than the equilibrium pressure of SiO, etching of SiO₂ occurs if the nucleation rate of Si is lower than the rate of evaporation of SiO.

Conclusion

The method described constitutes a simple means of growing oxide layers on silicon. Employed in connection with the epitaxial growth of silicon, it offers a maximum of simplicity and practical handling. The choice of the right set of process parameters, which may vary in a wide range, guarantees useable qualities for planar devices. This is proved by the manufacture of large quantities of planar diodes from slices provided with grown silicon oxide layers.

Doped oxide layers can be grown by providing the silicon chloride with BBr₃, PCl₃, etc., and may serve as sources for the diffusion of electrical active impurities into silicon.

Manuscript received June 27, 1963. This paper was presented at the New York Meeting, Sept. 29-Oct. 3, 1963.

Any discussion of this paper will appear in a Discussion Section to be published in the December 1964 JOURNAL.

REFERENCES

1. M. M. Atalla, E. Tannenbaum, and E. J. Scheibner, *Bell Syst. Tech. J.*, **38**, 749 (1959).
2. M. M. Atalla and E. Tannenbaum, *ibid.*, **39**, 933 (1960).
3. J. R. Ligenza and W. G. Spitzer, *J. Phys. Chem. Solids*, **14**, 131 (1960).
4. J. R. Ligenza, *This Journal*, **109**, 73 (1962).
5. H. C. Theuerer, *ibid.*, **108**, 649 (1961).
6. W. Steinmaier, *Philips Res. Repts.*, **18**, 75 (1963).
7. W. Kaiser and J. Breslin, *J. Appl. Phys.*, **29**, 1292 (1958).
8. C. Wagner, *ibid.*, **29**, 1295 (1958).

Cross-Substitutional Alloys of InSb

J. C. Woolley¹ and E. W. Williams¹

Physics Department, University of Nottingham, Nottingham, England

ABSTRACT

The paper considers cross-substitutional alloys of InSb produced by replacing In by combinations of (Cd,Sn) or (Zn,Sn) and by replacing Sb by combinations of (Sn,Te), (Sn,Se), or (Ge,Te), so as to keep the ratio of valence electrons to lattice sites equal to four. Limits of solid solution have been determined by x-ray and photomicrograph techniques. All the alloys so produced are degenerate semiconductors of very high carrier concentrations. Values of carrier density and optical energy gap have been determined as a function of composition and the results extrapolated to give data for the conduction band minima in InSb itself. It is found that the $\langle 111 \rangle$ minima lie at 0.47 eV above the valence band maximum and that the (000) minimum will accept 9×10^{18} electrons/cm³ before appreciable number of electrons enter the $\langle 111 \rangle$ minima.

As has been shown by Goodman (1, 2) and others, it is possible to predict new semiconducting materials with zinc blende or the associated chalcopyrite structure by the process of cross-substitution. Effectively this keeps the ratio of valence electrons to lattice sites equal to four. Thus the binary compounds such as GaAs, InSb, etc., may be considered as being cross-substitution products of group IV elements, while further application of this process gives the ternary compounds ZnSnAs₂, CdSnAs₂, etc., from InAs (3-5).

One limitation on the production of new materials by this method is the stability of the resulting compounds. Thus for the heavier compounds, e.g., InSb, the derived ternary compounds are unstable and so are not formed (6). However it is possible in this case to carry out the process to a limited extent, i.e., in the case of InSb to replace only some of the In atoms by combinations of, say, Cd and Sn atoms. The resulting materials can be looked upon as alloys between the A^{III}B^V compound and the derived ternary compound, e.g., InSb-CdSnSb₂, even though the derived ternary is unstable. The only published data on such alloys of InSb is that of Goryunova and Prochukhan (6) who have considered the InSb-CdSnSb₂ system, and from thermal measurements of liquidus and solidus curves have reported a range of solid solution out to 50 mole % CdSnSb₂.²

If alloys of this type showed perfect stoichiometry, they might be expected to show intrinsic semiconductor behavior at relatively low temperatures. This perfect stoichiometry cannot be expected however. Taking InSb-CdSnSb₂ as an example, some solution of Sn in the Sb lattice is to be expected from thermodynamic considerations, leaving excess Cd on the In lattice. Both this Sn and the resulting excess Cd may be expected to act as acceptors giving p type material of high carrier density. Similarly alloys of the type InSb-In₂SnTe would be expected to give n type material of high carrier density.

When the high carrier concentrations are obtained with relatively small amounts of "ternary" material, they can be used to obtain data concerning InSb itself, as has been indicated in the case of similar alloys of the form InSb-In₂Te₃, etc. (7, 8). This is discussed in the concluding section of this paper.

These alloys are also of interest in that it is possible to produce ternary and quaternary derivatives of InSb, for example, where we have an alloy semiconductor in which all of the atoms present have approximately the same mass. Such alloys are of interest when considering transport effect and scattering in alloy semiconductors.

Here we give the results of an investigation of various alloys of InSb in which In is replaced by the combinations (Zn,Sn) and (Cd,Sn) and Sb by (Sn,Te), (Ge,Te), and (Sn,Se), respectively. Standard x-ray powder photograph and photomicrograph methods have been used to determine the range of solid solution in InSb in each case, and measurements have been made at room temperature of Hall coefficient and optical energy gap.

Experimental Procedure

Preparation of alloys.—The InSb was synthesized from the elements which were 99.999% pure and then the InSb was zone refined. The best sections of the zone refined ingots ($n < 2 \times 10^{16}$ /cm³ and $\mu_n > 50,000$ cm²/V sec) were kept for the preparation of alloy specimens used in the electrical and optical work, and the less pure parts of the ingots were used for the x-ray work. For the preparation of most of the alloys, a material equivalent to the appropriate ternary "compound" (e.g., In₂SnTe) was made by melting together the necessary weights of the elements concerned and quenching the ingot produced. Required weights of this material and of InSb were melted together, quenched, and then annealed at an appropriate temperature (see below). As a check on this method, a few alloys were synthesized by melting together the required weights of the various elements concerned. The two methods

¹ Present address: Department of Physics, University of Ottawa, Ottawa, Ontario, Canada.

² In calculating mole % in the systems discussed here, InSb has been treated as In₂Sb₂, e.g., the above figure of 50 mole % indicates In₂Sb₂·CdSnSb₂.

were found to give the same results for alloys of a given composition.

For the x-ray work, the alloys were initially water quenched from the melt at 800°C and powdered, x-ray powder photographs being obtained with 9 cm cameras. The powdered specimens then were compressed and annealed in vacuo, the volume of the quartz ampoule used being as small as possible to reduce loss of components to the vapor phase to a negligible amount. The annealing was continued until equilibrium conditions were attained as indicated by further x-ray examination. A suitable temperature and the required period of annealing had to be determined by trial and error, and the values for the various cases concerned are given below. The alloys used for the photomicrographs were prepared as above, quenched in water and, when necessary, annealed in the solid form under the appropriate conditions. The specimens were then set in an epoxy resin, ground down, and polished with 0.3 μ alumina. Finally they were immersed for up to 20 sec in Wolsky etch (7 parts conc. HCl, 8 parts glacial acetic, 1 part conc. HNO₃) at 35°C and then washed in alcohol.

The specimens for the electrical and optical work were also quenched from the melt and then annealed. For all alloys considered, the x-ray work showed that an annealing temperature of 400°C was suitable. To determine the period of annealing for these solid ingots, the variation of Hall coefficient with time of annealing was determined for one typical specimen in each alloy system, and the time found to give a reasonably constant value of Hall coefficient.

Physical measurements.—The alloys of interest were those containing small amounts of "ternary compound" and so the optical and electrical measurements were in most cases made on single phase alloys containing less than 5 mole % "ternary compound." For the electrical specimens of alloys not containing tellurium or containing less than 1 mole % of a ternary telluride, etching in CP4 etchant alone was found to be satisfactory. For alloys of higher tellurium content the CP4 etchant produced a brown coloration which was removed by further etching with a solution of sodium dithionate in sodium hydroxide plus distilled water heated to 90°C. Room temperature values of conductivity and Hall coefficient were obtained by the same methods described previously for similar alloys of InSb (7, 8). For these highly degenerate materials, these electrical results are found to be independent of temperature, and hence the room temperature values were taken as characteristic of the materials. Optical transmission measurements were also made on the same ranges of alloy composition to determine the values of optical energy gap E_g at room temperature. Again the method was the same as that described previously (7, 8).

Results

InSb-In₂GeTe.—Specimens with compositions in the range 0-50 mole % In₂GeTe were investigated. Alloys quenched from the melt at 800°C

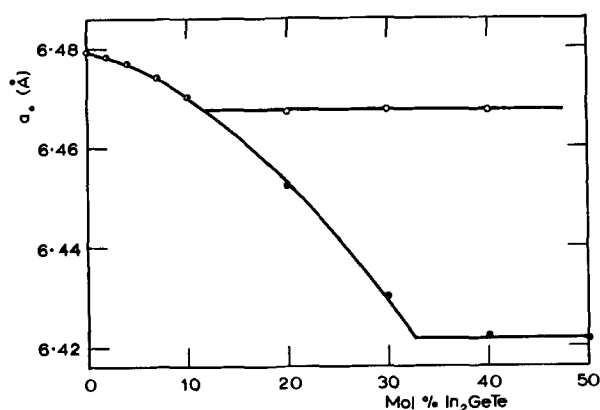


Fig. 1. Variation of zinc blende phase lattice parameter a_0 with composition for InSb-In₂GeTe alloys. ●, alloys quenched from melt at 800°C; ○, alloys annealed at 400°C.

showed reasonably sharp x-ray lines and lattice parameter values could be obtained for these. Powdered specimens were annealed at temperatures in the range 400°-450°C for 14 days, and Fig. 1 shows values of the lattice parameter of the zinc blende phase for both quenched specimens and those annealed at 400°C. The form of these results is typical of a pseudobinary section and hence the range of single phase solid solution is easily determined. Thus for the quenched materials, solid solubility extends out to about 33 mole % In₂GeTe, but this is reduced to 12 mole % for alloys annealed at 400°C. The x-ray photographs for alloys beyond these limits showed the presence of a second phase, but as only the zinc blende phase was of interest here, the lines of the second phase were not analyzed. For alloys annealed at 430° and 450°C, approximately the same range of solid solution was observed as in the case of the alloys annealed at 400°C. Alloys containing 30 and 40 mole % In₂GeTe showed signs of partial melting when annealed at 450°C, indicating the presence of a eutectic or peritectic horizontal in the vicinity of 450°C.

As a check on the x-ray work, photomicrographs were taken of various alloys. Of the alloys annealed at 400°C, the 2 and 10 mole % In₂GeTe alloys appeared single phase, but the 20 mole % In₂GeTe alloy was definitely two phase. The 20 mole % In₂GeTe alloy was also observed in the quenched state. The main part of the alloy appeared single phase but a small amount of second phase was observed at grain boundaries. A similar effect was observed with the other alloy systems described below.

For the electrical and optical measurements, alloys of less than 10 mole % In₂GeTe were observed. The values of the Hall coefficient R_H showed that all alloys were n type, and assuming that $R_H = 1/ne$ for these materials, values of n were obtained as shown in Fig. 2. It is seen that the value of n reaches a maximum of approximately $6 \times 10^{18}/\text{cm}^3$ at 0.5 mole % In₂GeTe and with increase in In₂GeTe content falls to $3 \times 10^{18}/\text{cm}^3$ at 10 mole % In₂GeTe. A corresponding result is obtained with the optical transmission measurements as shown in Fig. 2, the observed values of E_g rising (as would be expected due to the Burstein effect) to a maximum of

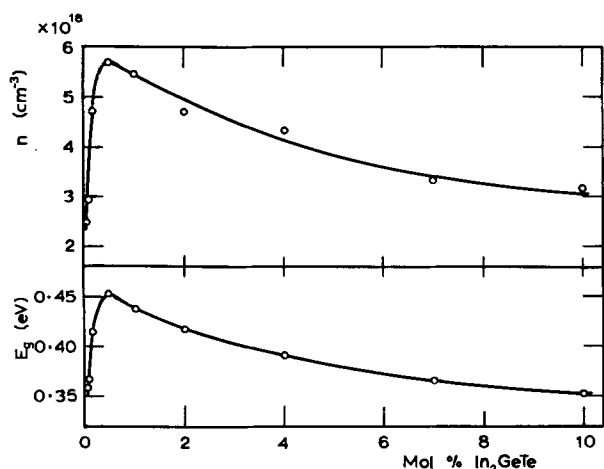


Fig. 2. Variation of room temperature values of electron density n and optical energy gap E_g with composition for InSb-In₂GeTe alloys.

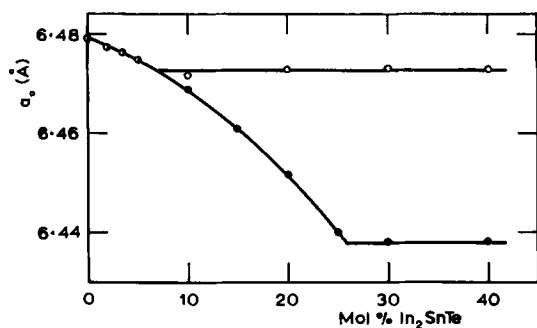


Fig. 3. Variation of zinc blende phase lattice parameter a_0 with composition for InSb-In₂SnTe alloys. ●, Alloys quenched from melt at 800°C; ○, alloys annealed at 400°C.

0.45 eV at 0.5 mole % In₂GeTe and then falling with increased In₂GeTe content.

InSb-In₂SnTe.—As in the previous case, alloys in the composition range 0 to 50 mole % In₂SnTe gave reasonable x-ray photographs when quenched from the melt at 800°C, so that lattice parameter values could be obtained for these quenched specimens and also for alloys annealed for 6 weeks at temperature in the range 400°–450°C. The variation of lattice parameter of the zinc blende structure with composition is shown in Fig. 3. Again pseudobinary behavior is observed. The range of solid solution for quenched alloys is 26 mole % In₂SnTe but this is reduced to 7 mole % for alloys annealed at 400°C, with a similar value for annealing temperatures up to 450°C. Beyond these composition limits, the x-ray photographs showed the presence of a second phase, but again no attempt was made to investigate this phase. Alloys containing 30 and 40 mole % In₂SnTe were found to melt at 500°C and showed signs of melting when annealed at 450°C.

Photomicrographs again showed that the apparently single phase quenched alloys of higher In₂SnTe content had signs of a small amount of second phase at the grain boundaries. It was confirmed however that the annealed alloys used for the electrical work were satisfactorily single phase.

Hall coefficient measurements again showed all the alloys to be n type and the variation of n (=

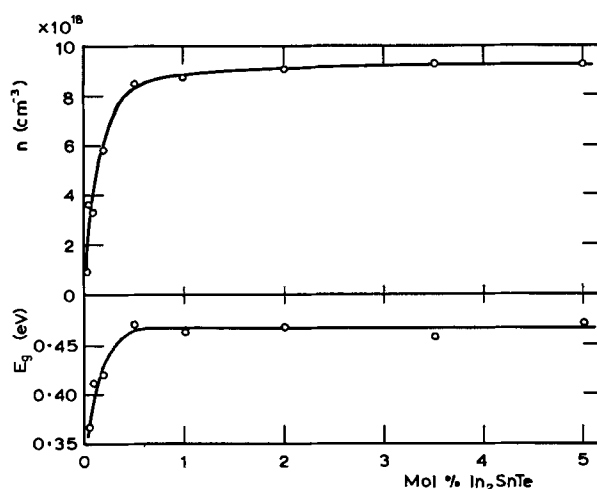


Fig. 4. Variation of room temperature values of electron density n and optical energy gap E_g with composition for InSb-In₂SnTe alloys.

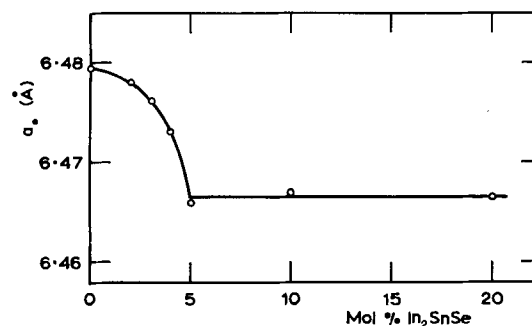


Fig. 5. Variation of zinc blende phase lattice parameter a_0 with composition for InSb-In₂SnSe alloys.

$1/eR_H$) with composition is shown in Fig. 4. In this case n rises to $9 \times 10^{18}/\text{cm}^3$ at about 1 mole % In₂SnTe and then remains practically constant at that value for larger In₂SnTe content. The optical energy gap E_g shows a corresponding behavior (Fig. 4) rising to a value of 0.47 eV and then remaining constant.

InSb-In₂SnSe.—Here alloys out to 20 mole % In₂SnSe were investigated. The x-ray photographs of alloys quenched from the melt at 800°C showed rather blurred lines in this case and so were not used to give lattice parameter values. The alloys were annealed in powder form at 400°C for 3 weeks and the resulting variation of zinc blende phase lattice parameter with composition is shown in Fig. 5. The results show an apparent pseudobinary behavior with the range of solid solution in InSb out to 5 mole % In₂SnSe, but for the alloys beyond 5 mole % it was difficult to observe the presence of a second phase. Photomicrograph work again confirmed the single phase condition of the alloys to be used for electrical and optical measurements.

Again all alloys showed n type behavior and the variations of carrier density n and optical energy gap E_g with composition are shown in Fig. 6. Here n reaches a maximum of $4.5 \times 10^{18}/\text{cm}^3$ at 1 mole % In₂SnSe and then falls with increased In₂SnSe content. E_g shows corresponding behavior.

InSb-CdSnSb₂.—Alloys in the composition range 0–50 mole % CdSnSb₂ were investigated. Here for

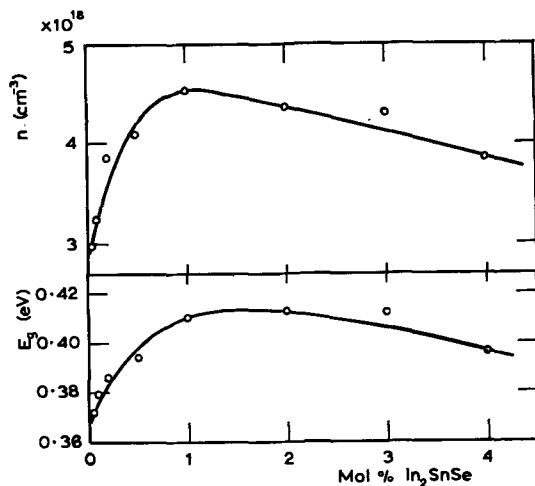


Fig. 6. Variation of room temperature values of electron density n and optical energy gap E_g with composition for InSb-In₂SnSe alloys.

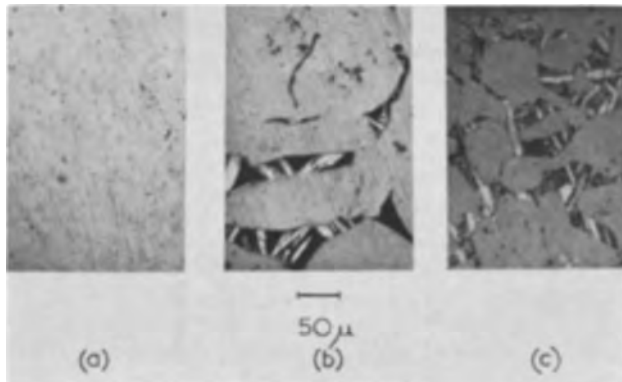


Fig. 7. Photomicrographs of annealed samples of InSb-CdSnSb₂ alloys. a, 2 mole % CdSnSb₂; b, 10 mole % CdSnSb₂; c, 30 mole % CdSnSb₂.

quenched specimens and for specimens annealed at 400°C for 12 weeks, no change in the lattice parameter of the zinc blende phase could be observed from the x-ray photographs. However lines corresponding to a second phase were visible for alloys containing 10 or more mole % CdSnSb₂ but not for the 5 mole % alloys, indicating a probable range of solid solution of between 5 and 10 mole %. This is a very different value from that of 50 mole % quoted by Goryunova and Prochukhan (6). However photomicrograph work supported this smaller value for the range of solubility. Photomicrographs of annealed samples containing 2, 10, and 30 mole % CdSnSb₂, respectively, are shown in Fig. 7. Here the 2 mole % alloy appears single phase, but the 10 and 30 mole % alloys do not. As the electrical and optical work was concerned with alloys containing 2 mole % or less of CdSnSb₂, more accurate estimates of the range of solid solution were not made.

Although the InSb used in the work was n type, the electrical measurements showed that all of the alloys measured (0.05 to 2 mole % CdSnSb₂) had a positive Hall coefficient and the variation of R_H with composition is shown in Fig. 8. This curve must return to a negative value of R_H for InSb itself and hence alloys containing smaller quantities of

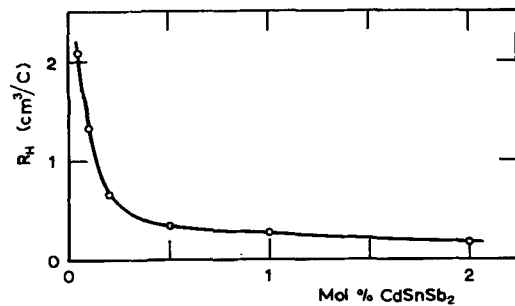


Fig. 8. Variation of room temperature values of Hall coefficient R_H with composition for InSb-CdSnSb₂ alloys.

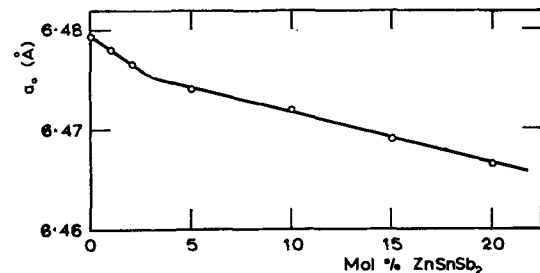


Fig. 9. Variation of zinc blende phase lattice parameter a_0 with composition for InSb-ZnSnSb₂ alloys.

CdSnSb₂ must be compensated, and so the simple single carrier interpretation of R_H cannot be used. Beyond 0.5 mole % CdSnSb₂ however, the hole density must be such as to allow the assumption $R_H = 1/pe$ and this gives a maximum observed value of p of $4 \times 10^{19}/\text{cm}^3$ at 2 mole % CdSnSb₂, the limit of the composition range investigated.

Because of the high carrier densities in these alloys, it was difficult to make optical transmission measurements, and so no values of E_g were obtained.

InSb-ZnSnSb₂.—Alloys in the composition range 0–40 mole % ZnSnSb₂ were investigated. Quenched alloys and alloys annealed at 400°C were x-rayed and the values of lattice parameter a_0 of the zinc blende phase showed that this system was not pseudobinary in character. Thus variation of a_0 with composition was observed for a range of composition where a second phase was clearly present. The results for the annealed alloys are shown in Fig. 9. The x-ray photographs of the 15 and 20 mole % ZnSnSb₂ alloys showed the presence of a second phase, although this was not observed at 10 mole %. However the form of the a_0 vs. composition curve would tend to indicate a limit of solid solubility at 3 mole % ZnSnSb₂. Again photomicrographs were used only to confirm the satisfactory condition of alloys used for electrical work. Thus photomicrographs showed the annealed 20 mole % sample to be definitely two phase, while the 2 mole % alloy (the limiting composition for electrical measurements) was single phase.

The variation of R_H with composition is shown in Fig. 10. It is seen that this is negative close to InSb but positive for alloys containing more than 0.15 mole % ZnSnSb₂. At 2 mole % ZnSnSb₂ it is possible to assume $R_H = 1/pe$ and the resulting value of p is $6 \times 10^{19}/\text{cm}^3$. As with the CdSnSb₂ alloys, no values of E_g were obtained.

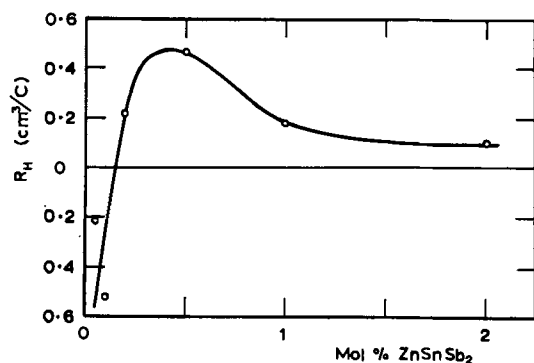


Fig. 10. Variation of room temperature value of Hall coefficient R_H with composition for InSb-ZnSnSb₂ alloys.

Discussion

As indicated in the beginning, effects of non-stoichiometry in the alloys cause the specimens to be degenerate semiconductors with large densities of electrons or holes depending on the type of derived ternary considered. A similar effect has already been observed in alloys of A^{III}B^V compounds with A₂^{III}B₃^{VI} compounds such as InSb-In₂Te₃, InSb-In₂Se₃, InAs-In₂Te₃, etc. (7-11). It is useful to discuss the data for these alloys first. In both the InSb-In₂Te₃ and InSb-In₂Se₃ systems the maximum observed electron concentrations were approximately $9 \times 10^{18}/\text{cm}^3$ in each case with a corresponding value of optical energy gap of approximately 0.45 eV, this maximum occurring for alloys containing less than 1 mole % A₂^{III}B₃^{VI} compound. In these cases the carriers are present because the number of lattice vacancies in the A sublattice is considerably less than the stoichiometric value, and hence uncompensated tellurium (or selenium) atoms on the B sublattice are acting as donors, in the same way as when tellurium (or selenium) is dissolved in InSb. It is assumed that the excess antimony is segregated to grain boundaries or lost as a vapor phase. An important question which arises is what factors determine the limiting value of $9 \times 10^{18}/\text{cm}^3$. One possibility is that this value represents the limit of solid solubility of tellurium (and selenium) in InSb, and that further addition of In₂Te₃ (or In₂Se₃) to InSb produces a correct number of compensating lattice vacancies. Parrott (12) has applied thermodynamic analysis to this problem and claims to account for the variation of n with composition in terms of these ideas.

However a second possibility is that the band structure of InSb is a determining factor. In this case it is suggested that many more tellurium (or selenium) atoms than those giving 9×10^{18} electrons per cubic centimeter act as donors in the alloys, but that further electrons enter other much broader conduction band minima, e.g., the <111> minima, and thus, having a much larger effective mass than electrons in the (000) minimum, are not observed by Hall effect measurements. Also because of the much higher density of states in the <111> minima a noticeable further increase in E_g due to Burstein effect does not occur. In such a case the maximum observed value of n should be

the density of electrons required to fill the (000) minimum up to the lowest level of the <111> minima and the observed maximum in E_g should give the height of the <111> minima above the valence band maximum. These values should then be independent of the source of electrons provided the band structure is not affected by the addition of the donor atoms. The similarity of the results for In₂Te₃ and In₂Se₃ alloys with InSb tends to support this view. Now a further check can be made with the various n type alloys described above.

For the three n type alloys considered, the observed maximum values of n and E_g are $9 \times 10^{18}/\text{cm}^3$ and 0.47 eV for In₂SnTe alloys, $6 \times 10^{18}/\text{cm}^3$ and 0.45 eV for In₂GeTe alloys, and $4.5 \times 10^{18}/\text{cm}^3$ and 0.42 eV for In₂SnSe alloys. However here one must now consider the possible variation in band shape due to alloying. Consider the InSb-In₂GeTe alloys. If the relative energy of the <111> minima is reduced by addition of one or two mole % In₂GeTe, then the observed maximum values of n and E_g would be smaller than expected. There is some evidence for such a change in the In₂GeTe results in that beyond 0.5 mole % In₂GeTe, the value of E_g falls with increased In₂GeTe content, the average rate of fall being 0.012 eV/mole %. To investigate whether this corresponds to a change in energy of the <111> minima, reflectivity measurements in the visible or u.v. may be used, as has already been indicated by Greenaway and Cardona for the InSb-In₂Te₃ alloys (13). For InSb the reflectivity peak E_1 at approximately 1.8 eV has been attributed to a direct transition of the L point in k space. Although recent work may now attribute this peak to a direct transition at a point near (1/6, 1/6, 1/6) in k space (14), the variation in energy of the reflection peak can still give an indication of the general movement of the Δ branch of the conduction band and hence give some indication of the movement of the <111> minima. The energy of this E_1 peak was therefore determined for InSb and alloys containing 2, 4, 7, and 10 mole % In₂GeTe, respectively. It was found that the energy of E_1 falls with increased In₂GeTe content, the mean rate of change being 0.014 eV/mole %. This is in reasonable agreement with the value from the E_g data and seems to confirm a movement of the <111> minima as In₂GeTe is added to InSb. By extrapolating the E_g vs. composition curve, the value corresponding to InSb itself is 0.47 eV.

For the In₂SnTe alloys, it is seen that the value of E_g of 0.47 eV remains constant in the range 0.5 to 5 mole %, indicating no change in relative energy of the <111> minima with addition of In₂SnTe. Reflectivity measurements confirm this, the energy of the reflectivity peak E_1 having the same value for the 5 mole % alloy as for InSb. Hence again an extrapolated value of 0.47 eV is obtained for InSb itself. For the In₂SnSe alloys, the values of E_g would indicate here also a change in energy of the <111> minima with composition, but the very limited range of solid solution makes this more difficult to investigate, and reflectivity measurements were not made. It can be said, however, that

the data is not inconsistent with the above considerations.

As indicated above, Greenaway and Cardona (13) have obtained similar reflectivity data for the InSb-In₂Te₃ alloys, and have correlated it with the observed variation of E_g (7). In this case also the extrapolated value of E_g at InSb is 0.47 ev.

On the basis of the above data, it would appear that in InSb at room temperature, the <111> minima of the conduction band are 0.47 ev above the valence band maximum, and that the (000) minimum of the conduction band will accept about 9×10^{18} electrons/cm³ before it is so filled that electrons mainly go into the <111> minima.

In the case of the p type alloys described above, the structure of the valence band of InSb is such that no similar effect can occur. Thus all holes produced by nonstoichiometry should be observed in the Hall measurements and the value of p thus obtained may be considerably greater than 9×10^{18} /cm³ and should differ from one alloy system to another, being determined by thermodynamical considerations similar to those given by Parrott (12). This is observed to be the case for the two p type systems investigated. Similarly if one considers n type alloys of such a compound as GaSb where the difference in effective mass between electrons in the (000) and <111> minima is relatively small, all conduction band electrons should have some effect on the Hall coefficient. This is confirmed in work reported elsewhere (15) on alloys of GaSb with Ga₂Se₃ and Ga₂Te₃, where carrier densities of the order 10^{20} - 10^{21} /cm³ are observed.

Finally, if the above analysis for InSb is correct, then a similar result should apply for InAs. Results for InAs-In₂Te₃ and InAs-In₂Se₃ (8, 9) indicate that for InAs the <111> minima be at about 0.85 ev above the valence band maximum.

Acknowledgments

The authors are indebted to Professor L. F. Bates for the facilities of his laboratory. They wish to thank Dr. K. W. Blazey for making the reflectivity measurements. The work described forms part of an investigation carried out for the Admiralty.

Manuscript received May 21, 1963.

Any discussion of this paper will appear in a Discussion Section to be published in the December 1964 JOURNAL.

REFERENCES

1. C. H. L. Goodman, *J. Phys. Chem. Solids*, **6**, 305 (1958).
2. J. H. Wernick and R. Wolfe, *Electronics*, **33**, (Feb. 12, 1960).
3. D. B. Gasson, P. J. Holmes, I. C. Jennings, B. R. Marathe, and J. E. Parrott, *J. Phys. Chem. Solids*, **23**, 1291 (1962).
4. A. J. Strauss and A. J. Rosenberg, *ibid.*, **17**, 278 (1961).
5. W. G. Spitzer, J. H. Wernick, and R. Wolfe, *Solid State Electronics*, **2**, 96 (1961).
6. N. A. Goryunova and V. D. Prochukhan, *Soviet Physics Solid State*, **2**, 161 (1960).
7. J. C. Woolley, C. M. Gillett, and J. A. Evans, *J. Phys. Chem. Solids*, **16**, 138 (1960).
8. J. C. Woolley and P. N. Keating, *Proc. Phys. Soc.*, **78**, 504 (1961).
9. J. C. Woolley, B. R. Pamplin, and J. A. Evans, *J. Phys. Chem. Solids*, **19**, 147 (1961).
10. D. B. Gasson, P. J. Holmes, I. C. Jennings, J. E. Parrott, and A. W. Penn, *Proc. Int. Conf. on Semiconductor Physics*, Czech Acad. Sciences, p. 1032, Prague (1961).
11. D. N. Nasledov and I. A. Fel'tin'sh, *Soviet Physics Solid State*, **2**, 755 (1960).
12. J. E. Parrott, *J. Phys. Chem. Solids*, **23**, 1437 (1962).
13. D. L. Greenaway and M. Cardona, *Proc. Int. Conf. on Physics of Semiconductors*, Exeter, p. 666 (1962).
14. J. C. Phillips, D. Brust, and F. Bassari, *ibid.*, p. 564 (1962).
15. J. C. Woolley and K. W. Blazey, To be published.

Electrolytic Reductive Coupling

I. Acrylonitrile

Manuel M. Baizer

Central Research Department, Monsanto Chemical Company, St. Louis, Missouri

ABSTRACT¹

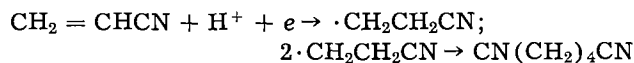
The electrolysis of concentrated solutions of acrylonitrile in aqueous tetraethylammonium p-toluenesulfonate at lead or mercury cathodes and at controlled pH yields adiponitrile in virtually quantitative yields and at current efficiencies close to 100%. If the catholyte has acrylonitrile concentrations much below 10% or contains alkali metal cations, increasing quantities of propionitrile appear as by-product. An explanation is offered for this shift in product distribution. Variations in laboratory cell design and supporting electrolyte composition are discussed.

The commercial desirability of reductively dimerizing acrylonitrile to adiponitrile, a key Nylon 66 intermediate, has been recognized for some time (1). The very poor yields obtained in effecting this conversion by means of sodium amalgam and water (2)

or magnesium in methanol (3) did not invite further work. However, new impetus was provided by the publications of Knunyants and his co-workers (4) in which they claimed that acrylonitrile and other derivatives of α , β -unsaturated acids, dissolved or suspended in strong mineral acid and treated with alkali metal amalgams which were generated elec-

¹ A preliminary announcement of the scope of this work appeared in *Tetrahedron Letters*, 1963, 973-977.

trochemically, gave good yields of "hydrodimer."² Under special conditions, acrylonitrile was said to yield adiponitrile in over 60% yield; a small quantity of propionitrile was produced as by-product but no amines or polymers were formed. Knunyants proposed that a free radical intermediate dimerized to yield the product



The inconsistency between the postulated intermediacy of free radicals and both the absence of polymer in the case of the above reaction and the absence of deuterated ethyl propionate when ethyl acrylate was hydrodimerized in the presence of deuterated ethanol was noted by Knunyants. The rationalization offered was that the properties of free radicals at a cathode must be different from the properties of free radicals in solution.

Our economic appraisal indicated that no reasonable modification of Knunyants' indirect electrochemical method would provide a commercially feasible competitive adiponitrile process. While other types of reductive coupling processes (6) have had limited success in certain areas,³ they did not appear applicable to the highly reactive and easily polymerizable acrylonitrile. A direct electrochemical conversion of acrylonitrile to adiponitrile in an aqueous system, on the other hand, would ideally consume only water and electrical energy and would offer prospects of meeting the stringent production cost requirements.

Electrolytic reductive coupling of α , β -unsaturated ketones, preferably in acid solution, to yield 1,6-diketones is well known (8). More germane to our problem was the successful coupling of cinnamic acid and derivatives in acidic medium (via a free radical path) to adipic acids (9). This type of procedure was recognized by the authors, however, as having limited applicability. It is inoperative when the monomer is easily polymerized by free radical initiation. Indeed, cathodic polymerization of acrylonitrile and related vinylic compounds in acid solution has been described (10). The bright outlook for an electrolytic adiponitrile process was therefore clouded by known serious hazards. Additional ones presented themselves (11) as this work progressed.

Experimental

Preliminary experiments.—A 7-hr run was made according to Knunyants' apparatus and procedure, except that the potassium amalgam, instead of being generated electrochemically, was formed by plunging small pieces of potassium into the external mercury pool (under a layer of toluene). The K-Hg diffused into the reaction area which contained acrylonitrile in 20% HCl. It was observed that the phenolphthalein indicator turned pink at the surface of the mercury in spite of the presence of an excess of free acid. Adiponitrile was isolated in about the yield reported for a 7-hr quasi-electrolytic run. The

² The term hydrodimerization was introduced by Knunyants *et al.* (5).

³ Dimerization of acrylonitrile to 1,2-dicyanocyclobutane followed by catalytic reduction has also been described as a route to adiponitrile (7).

coupling was apparently occurring under alkaline conditions at the surface of the mercury.

An attempt to electrolyze acrylonitrile in aqueous alcoholic potassium acetate at a mercury cathode gave no adiponitrile but, instead, a good yield of β -ethoxy-propionitrile. While this evidence of cyanoethylation of alcohol in an aqueous medium was surprising, it indicated that electrolysis of acrylonitrile in aqueous alkaline medium, though avoiding polymerization, would encounter other difficulties. An attempt to conduct the electrolysis in a phosphate buffer system was unsuccessful.

Initial choice of electrolytes.—Knunyants had proposed that a free radical intermediate was involved in the alkali metal amalgam hydrodimerization of acrylonitrile. At the time of our investigation Platonova (12), alone among those who had studied the polarographic reduction of acrylonitrile (13), solved the equation of the polarographic wave and concluded that a two-electron uptake was indicated.⁴ Regardless of the true reaction mechanism, since a coupled product (adiponitrile) was desired, it seemed advisable to use an electrolyte which would furnish a high concentration of acrylonitrile in the catholyte. For economic reasons a totally aqueous system was preferred. Further, the electrolyte would have to be stable to alkali and to discharge of its anion.

An initial answer to the electrolyte problem was found in McKee's "hydrotropic" solvents (14). Saturated aqueous solutions of alkali metal arylsulfonates dissolved large quantities of acrylonitrile (15): a saturated solution of equimolar quantities of sodium and potassium *p*-toluenesulfonates, *e.g.*, yielded a catholyte containing 20.9% by weight of acrylonitrile at room temperature. Such solutions were therefore chosen for further study.

Apparatus.—A convenient cell, constructed from a 500 ml resin flask and similar to one described in the literature (16) was used in the bulk of this work. The cathode, when mercury, was a 110 ml pool exposing a surface of 55 cm². The anode was an 18-gauge Pt wire sealed in glass. The membrane was an alundum cup⁵ cut to size and held in place by a rubber stopper. Stirring was by magnetic bar which rode on the surface of the mercury when that metal was used as cathode or rotated at the bottom of the flask when solid cathodes were used. The cell had Dry Ice condensers for anode and cathode compartments. It was placed in an open cooling bath containing acetone to which Dry Ice was added as required. Solid cathodes were cast from high purity metals⁶ in the shape of hollow cylinders 3 in. in outer diameter, ¼ in. thick, and 2 7/8 in. high. The alundum cup was suspended in the center of the cathode cylinder. The latter had numerous 3/8 in. perforations to allow for better circulation of the catholyte. Tabs of the same metal used as cathode extended well beyond the catholyte.

Electrolyses of Acrylonitrile in Mc Kee's Salts

Effect of changes in the cation.—The electrolysis

⁴ She concluded that propionitrile was the reduction product.

⁵ Norton Company, Worcester, Mass., mix RA84.

⁶ American Smelting and Refining Co., South Plainfield, N. J.

of saturated solutions of acrylonitrile⁷ in aqueous lithium, sodium and potassium p-toluenesulfonates individually was studied. While the concentrations of acrylonitrile (AN) in the three catholytes were very similar (12-13.7%), the yields of adiponitrile (ADN)⁸ relative to propionitrile (PN) decreased in the order Na > K > Li. This is the reverse of the order found by Knunyants in reducing with metal amalgams. The pH was prevented from becoming excessively high in the catholyte by occasional addition of acid. The products were isolated by fractional distillation through a Todd column. While a direct electrochemical formation of ADN was indicated, PN was the major product (ratio of grams PN/grams ADN 1.8-3.9).

Effect of change in AN concentration.—For reasons discussed above, it was desired to increase the AN concentration in the catholyte and to electrolyze to only partial conversion. In a series of runs the AN concentration was increased from 8 to 20.9% (saturation) in sodium-potassium p-toluenesulfonates. In general there was a favorable effect upon the ADN/PN ratio, although PN was still predominant. Increasing the AN concentration enormously by using dimethylformamide as a co-solvent finally yielded more ADN than PN but the latter was still a very important by-product. The catholyte pH was not controlled in these runs and substantial quantities of bis-(2-cyanoethyl)ether (BCE) were formed.

Effect of pH control.—To eliminate the cyanoethylation of water as a side reaction, a series of runs was made in which the alkalinity of the catholyte was adjusted. In one, acetic acid was added at ca. 10 min intervals to the catholyte to keep it just alkaline to phenolphthalein; the average alkalinity was 0.08N. In a second, acetic acid was added continuously to the catholyte so that it would never have required more than 2-3 additional drops to discharge the phenolphthalein color. In a third, a smaller concentration of AN was used and again continuous near-neutralization of the catholyte. In

⁷ Redistilled and stabilized by a trace of p-nitrosodimethyl-aniline (17).

⁸ Identity of ADN was always confirmed by comparison with authentic samples with respect to physical constants, infrared spectrum, and V.P.C. retention time.

both the second and third experiments mentioned no BCE was formed. Thereafter, except when pH control was imperfect, no BCE was encountered.

Effect of changes in current density.—The same factors which prompted the use of high AN concentrations in the catholyte suggested that high current densities would favor the hydrodimerization. The results obtained in progressing from 5.5 to 12.7 amp/dm² indicated that these expectations were borne out, but at best PN had by no means been reduced to the role of a minor by-product (ADN/PN = 1.35).

Source of PN by-product.—Since a combination of high current density and high AN concentrations was not sufficient to eliminate PN, it was necessary to inquire into the mechanism of its formation. Were the hydrodimerizations described above electrochemical processes or were they only *in situ* amalgam reductions? (The presence of alkali metal amalgam was noted at the end of each run.) If the former were true, improvement in the ADN yield might be profitably sought; if the latter were true, the prospects of improving substantially over the Russian workers' results were poor.

Two approaches were taken. First, solid high hydrogen-overvoltage cathodes were used in place of Hg (Table I). The same electrolyte system was retained. While Na-Pb alloys have been employed in some instances in place of sodium amalgam (18), it was unlikely that they would form under the conditions of these electrolyses. Formation of ADN at Pb, Cd, and Sn cathodes indicated that here at least a direct electrochemical process was involved. Second, use of an electrolyte containing a cation which, unlike the alkali metal cations, could not be discharged under the operating conditions again circumvented the intermediacy of an amalgam. Table II shows that the electrolysis of a 40% solution of AN in a concentrated aqueous solution of tetraethylammonium p-toluenesulfonate yielded ADN and no PN.

The elimination of PN in run 28 Table II was not due to the high AN concentration in the catholyte since a solution containing an even higher concentration of AN in alkali metal p-toluenesulfonates had yielded substantial PN. It will also be shown later that reducing the AN concentration to 20% in

Table I. Hydrodimerization of acrylonitrile at solid cathodes. McKee's salts as electrolytes; 25°; 3 amp/dm²

Run	Cathode		Area, dm ²	Anolyte	Catholyte		Amp hr	pH	Yield ratios*			
	Metal	Form			G salt soln.	G AN			PN	ADN	BCE	Other
19	Sn	a	2.40	b	283b	76.0	13.5	c	100	trace	106	269†
20	Pb	d	2.46	b	227b	60.0	13.2	e	100	49.2	None	—
21	Pb	d	2.46	b	227b	60.0	8.5	e	100	45.6	None	—
22	Pb	f	2.43	b	227b	60.0	12.1	e	100	46.2	None	—
23	Cd	d	2.43	b	227b	60.0	11.5	e	100	14.9	None	—
24	Sn	d	2.43	b	227b	60.0	12.0	e	100	96	None	>100†

* The catholyte was neutralized at the end of the run and exhaustively extracted with methylene chloride. The dried extracts were concentrated. The per cent yields of CH₂Cl₂, AN, PN, ADN, and BCE were determined by the V.P.C. methods described later in this paper. The yields of products based upon AN which had reacted were calculated. For comparison purposes, the yield of PN was assigned the number 100.

† Organo-tin compound, probably Sn(CH₃CH₂CN)₄. Cf. (19).

a. Four layers of foil rolled into a hollow cylinder to surround the porous cup.

b. A saturated solution of equimolar quantities of sodium and potassium p-toluenesulfonates.

c. Rising alkalinity not checked.

d. Surfaces polished by fine sandpaper before use. Only area facing anode used in calculating current densities.

e. Maintained just alkaline to phenolphthalein by adding acetic acid continuously to catholyte.

f. Surface prepared electrolytically by a standard procedure.

Table II. Electrolyses of acrylonitrile at a mercury cathode and at 25° in electrolytes CH₃—O—SO₃Z at current densities of 5.5 amp/dm²

Run	Anolyte Z=	Catholyte		% AN	Amp hr	pH	PN	Yield ratios*	
		G salt soln.	G AN					ADN	BCE
25	Li	308d	47.5	13.3	9.0	a	100	13.3	None
26	Na	308d	47.5	13.3	9.0	a	100	65.6	None
27	K	308d	47.5	13.3	9.0	a	100	62.5	None
28	Et ₄ N	141e	94.5	40.0c	10.1	b	None	f	None

* Absolute yields were not determined when ADN was only a minor product.

a. Acetic acid added continuously to maintain catholyte just alkaline to phenolphthalein.

b. Acetic acid used but very little required.

c. Catholyte volume only 260 ml in this experiment.

d. Saturated aqueous solutions.

e. A 56.5% solution.

f. An absolute yield of 75.2% based on AN not recovered was obtained.

tetraalkylammonium p-toluenesulfonate solutions still leads to only very minor quantities of PN. Therefore, the formation of PN must be associated with the presence of alkali metal cations in the electrolyte.

The polarographic reduction of acrylonitrile has been variously reported (13) to proceed in one wave at $-E_{1/2}$ of 1.94 to 2.05v (vs. S.C.E.). In a stirred system the alkali metal cations also discharge in this range. Due to this coincidence, electrolysis of AN in a catholyte containing alkali metal cations is a dual process. During electrolysis the requisite cathode voltage is reached and reductive coupling of AN to ADN can occur. In addition simultaneous discharge of the alkali metal cations makes possible a chemical reaction wherein the alkali metal can add 1,2- or 1,4- to the acrylonitrile molecule.⁹ The rate of this alternate reaction may equal or exceed the rate of electrochemical coupling; hydrolysis of the organometallic adducts leads to PN.¹⁰ In an electrolyte system containing cations not discharged in the -1.94 to $-2.05v$. range (vs. S.C.E.) the chemical route leading to PN can be eliminated and purely electrochemical hydrodimerization of AN occurs. The dual nature of amalgam reductions has been discussed in connection with the Clemmensen Reduction (21).

Batch Electrolyses of Acrylonitrile in Quarternary Ammonium Electrolytes

The formation from AN of ADN without PN or BCE (Table II, run 28) indicated that detailed investigation of this process was warranted. Yields, material balances, and current efficiencies (copper coulometer) were determined. For simplicity, tetraethylammonium p-toluenesulfonate was always used in a catholyte of 260 ml.

Preparation of tetraethylammonium p-toluenesulfonate.—Two hundred grams (1.00 mole) of purified ethyl p-toluenesulfonate was dissolved in 100 ml of absolute ethanol in a four-necked round-bottomed flask equipped with stirrer, thermometer, reflux condenser protected by a calcium chloride tube, and addition funnel. In the course of 15 min 101g (1.01 mole) of triethylamine was added with stirring. No exothermic reaction occurred. The mixture was heated slowly. At 60°–70° an exothermic re-

action started. The heating mantle was removed, and the reaction allowed to proceed spontaneously until alcohol stopped refluxing. The mixture was then heated under reflux for 6 hr. The alcohol and slight excess of amine were stripped off by aspirator. The residual white solid was washed by decantation three times with dry ether. Residual solvent was removed by aspirator. The crude hygroscopic product weighed 297g (99%). A saturated solution at room temperature contains ca. 80% of the salt. A sample after recrystallization from ethanol melted at 104°. Calculated for C₁₅H₂₇NO₃S: C, 59.76; H, 9.03; N, 4.65; found, C, 59.46; H, 9.01; N, 4.53

Procedure.—The anode and cathode chambers were charged, the cell assembled, stirring started, and the porous diaphragm allowed to soak for 30 min. The direct current was turned on and the cell voltage regulated to furnish 2.0–3.2 amp. As the electrolysis proceeded, glacial acetic acid was added dropwise to the catholyte to maintain the pH in the range required for a green color on Alkacid Test Paper. The water was replenished in the anolyte from time to time and the anolyte level was maintained ½ in. to 1 in. above that of the catholyte. No hydrogen was evolved. After an electrolysis the cell was cooled to ca. 20° and the cathode chamber contents transferred quantitatively to a separatory funnel using methylene chloride and water to aid in the transfer.¹¹ The catholyte was diluted with ca. 2 volumes of water and the mercury, when used, was drawn off. The aqueous layer was then extracted with 7 to 10 50-ml portions of CH₂Cl₂. The extracts were washed with water, dried over Drierite, filtered, and stripped of most of the solvent through a Todd fractionating column. An aliquot of the concentrated residue was analyzed by vapor phase chromatography (V.P.C.) and infrared spectroscopy. The remainder was fractionated; weight and purity of the ADN obtained were checked against the results obtained analytically.

Analytical method.—Initially the gas chromatographic analyses of CH₂Cl₂, AN, PN, ADN, and BCE were made in two stages using a Perkin-Elmer 154-C Vapor Fractometer. The low-boiling components were measured on a two-meter column containing 20% polypropylene glycol on C-22 Firebrick at 46°C. The "high boilers," ADN and BCE, were analyzed on a two-meter column packed with 20%

⁹ Addition of alkali metals to olefins is well known (20).

¹⁰ An alternate statement would be that the ion-pair (2M)⁺⁺(AN) is more easily disrupted by H₂O than by AN.

¹¹ Additional AN stabilizer was added.

Table III. Hydrodimerization of acrylonitrile

Run	Anolyte	G salt soln.	G AN	% AN	°C	Metal	Area, dm ²	Amp	Amp hr	Yields*		% AN accd	Current† efficiency
										ADN	PN		
29	a	141a	94.5	40	25	Hg	55	2-3	11.6	90.0	0	97.3	99
30	a	141a	94.5	40	25	Pb‡	243	2.6-4.8	10.9	88.4	0	96.9	"102"
31	a	204a	53.0	20.6	25	Hg	55	1.9-3.0	12.1	99.0	1.3	99.1	"106"
32	a	141a	94.5	40	25	Hg	55	2.0-3.2	22.3	100	1.1	100.7	100
33	b	141a	94.5	40	35	Hg	55	2.6-3.6	12.0	83.2	Trace	95.0	98
34		207b	149.0	40	30	Cu‡	89	3-5	10.0	Trace	—	—	—

* Based on AN not recovered.

† One F yields 0.5 mole (54 g) ADN.

‡ Surface prepared by a standard electrolytic procedure.

a. A 56% aqueous solution of tetraethylammonium p-toluenesulfonate.

b. A 55% aqueous solution of methyltriethylammonium p-toluenesulfonate.

D.C. Silicone Fluid 550 on C-22 Firebrick at 196°C. Later the analysis was adapted to an F and M Model 500 Programmed Temperature Gas Chromatograph using a two-meter column of 5% Tween 80 on Chromasorb P. The program rate was 13°/min from ambient temperature to 220°. Practically all components were resolved in approximately one-half hour. Blank determinations on single components and on synthetic mixtures yielded empirical factors which were used to correct volume per cent of components to weight per cent. These factors were: CH₂Cl₂ X 1.20; AN X 0.9; PN X 1.16; ADN X 1.17.

Yields and Current Efficiencies.—Table III summarizes the results of the most significant experiments on the hydrodimerization of AN. Lead and mercury were approximately equally effective; copper, as anticipated, was inoperative. Both yields and current efficiencies approached 100%.

Concentration of acrylonitrile in the catholyte.—Run 31 (Table III) demonstrated that reducing the initial AN concentration from 40% to 20% did not materially affect the ADN/PN ratio. In order to determine whether batch electrolyses had to be run to only partial conversion of AN or could be taken to virtually complete utilization of AN it was necessary to investigate the effect upon the ADN/PN ratio of operating at lower and lower AN concentrations. Table IV presents the data obtained in four separate experiments in which the initial AN concentration was successively reduced from 40% to 5%. It is clear that at AN concentrations down to ca. 10% insignificant quantities of PN are formed.

When the AN concentration in the catholyte fell below ca. 10%, other conditions being equal, the yield of PN rose sharply at the expense of ADN. This conclusion was verified in a single experiment (Table V) in which a solution containing initially

20.6% AN in the catholyte was electrolyzed at constant cathode potential until the AN concentration was below 3%. Aliquots were removed periodically and analyzed. Except for inconsistencies due to experimental difficulties, it was again found that at very low AN concentration PN becomes a major product. Platonova's conjecture (22) that PN is the product of the polarographic reduction of AN is probably justified.

Laboratory Process Variations

Exploratory continuous process.—While a number of schemes have been proposed for conducting a continuous electro-organic process (e.g., 28), a particularly attractive laboratory device which could accommodate all the requirements of the electrolytic ADN process was at hand in a liquid-liquid extractor in which the extraction chamber was made the electrolytic cell. Figure 1 illustrates schematically the apparatus used in this work.

Acrylonitrile was used in the boiler flask. It was distributed in the catholyte by means of a sintered glass disk and was discharged (desirably) in the vicinity of the cathode. The solubility of AN in aqueous tetraethylammonium p-toluenesulfonate varies with the concentration of the salt. The salt solution was chosen so that, at saturation, the AN concentration in the catholyte was within a safe range for avoiding propionitrile (PN) formation. Excess AN, constantly circulating, extracted ADN, formed an upper layer, overflowed through a water-washing device and thence to the boiler. The water wash removed most of the salt which had been simultaneously extracted by the AN; it was concentrated in vacuo and returned to the catholyte. The adjustment of pH in the catholyte took place by adding acetic acid through a tube which extended

Table IV. Hydrodimerization of acrylonitrile at a mercury cathode; 25°, 260 ml catholyte, 55 cm²

Run	% AN in catholyte*		Amp/dm ²	Cathode† voltage	Amp-hr	G ADN/ g PN
	Initial	Final				
31‡	40	21.5	5.45	—	22.3	92.5
32‡	20.6	10.3	5.45	—	12.1	99.
35	10.0	6.4	0.91	-1.90	ca. 3.6	7.1
36	5.0	0.385	1.82 to 0.73	-1.90	ca. 5.1	1.7

* A 56% aqueous solution of tetraethylammonium p-toluenesulfonate.

† Vs. SCE.

‡ Included from Table III for comparison.

Table V. Hydrodimerization of acrylonitrile with attrition. Incremental changes in formation of products

Electrolysis period	Amp hr	AN conc. at start of period*	G formed within periods		G ADN/ g PN
			PN	ADN	
I	11.5	20.6	0.342	23.3	68‡
II	6.0	11.3	1.33	8.9	6.7
III	5.1	6.5	0.91	10.0	11
IV	3.0	3.3	4.23	0.4	0.095

* The concentration at the end of a period is the starting concentration of the next period.

‡ The lower than usual ratio may be due to a KCl leak from the salt bridge leading to the reference calomel cell.

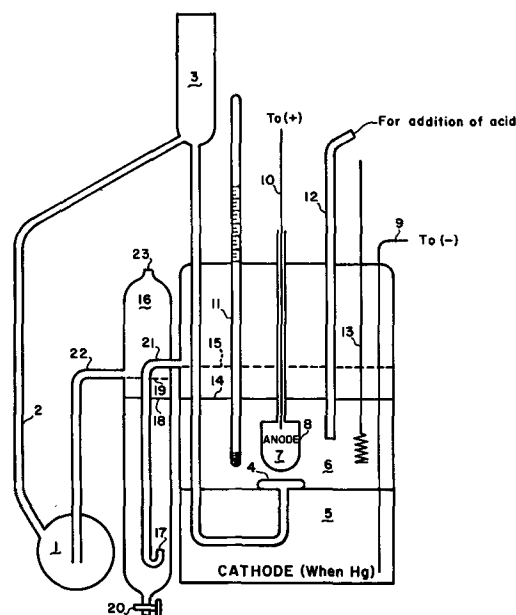


Fig. 1. Schematic drawing of continuous laboratory cell: 1, boiler; 2, riser; 3, condenser; 4, disperser; 5, cathode when Hg; 6, catholyte solution; 7, anode chamber; 8, diaphragm; 9, lead to cathode; 10, lead to anode; 11, thermometer; 12, inlet tube; 13, stirrer; 14, catholyte level; 15, level of supernatant AN; 16, washer; 17, disperser; 18, water level; 19, supernatant level; 20, stopcock; 21, overflow tube; 22, overflow tube; 23, water inlet.

well below the supernatant layer. The extraction chamber was jacketed and cooled by circulating ice water. In a typical run the catholyte contained a solution of 136 ml of AN in 249 g of 40% tetraethylammonium *p*-toluenesulfonate; an additional 136 ml of AN formed a supernatant layer just sufficient to overflow through the side arm. A mercury pool was used as cathode. The anode was a stout platinum wire hooked to a platinum screen. The anolyte was the above salt solution in sufficient quantity to form a head above the catholyte. An alundum cup was used as diaphragm. About 300 ml of AN was charged into the boiler and heated. When the extraction system was operating smoothly, a current of 3.5–5.0 amp was applied to the cell. In a run in which 55.4g ADN was produced in 5.5 hr, 40.7g had accumulated in the boiler, 13.7g was present in the supernatant AN layer in the extraction chamber and 0.96g remained in the aqueous layer.

Undivided cell.—The advantages with respect to choice of anode, pH control and decreased electrical resistance of employing a diaphragmless cell are obvious. While the highly reactive olefin AN might be expected to suffer oxidation at the anode, processes have been described (29) in which AN is formed under rather drastic conditions in the presence of oxygen. There was some prospect, then, of achieving simplicity in cell design at the cost of some AN loss. The cell described before was used except that the alundum cup and the rubber stopper holding it were removed. The anode was a rolled up platinum screen hooked to a platinum lead wire; the cathode was mercury. The electrolyte (*ca.* 190 ml) contained 69g AN dissolved in 103g of 56.5% aqueous tetraethylammonium *p*-toluenesulfonate. Electrolysis at 3 amp for a total of 14 amp-hr yielded 22.1g ADN,

39.6g recovered AN, and a small amount of tar. The yield of ADN based upon consumed AN was about 80%. Further work on the undivided cell was deferred.

Screening of electrolytes (with James D. Anderson).—In view of the unfavorable effect upon ADN yields of having alkali metal ions present in the catholyte and the favorable effect of maintaining a high AN concentration, specifications for a variety of suitable electrolytes (Z^+Y^-) could be drawn up:

1. The cation Z^+ must not discharge at the cathode voltage at which hydrodimerization occurs.

2. Y^- must not discharge at the anode. If a diaphragm is used, Y^- must not form an insoluble acid HY which would clog the pores of the diaphragm. (This requirement does not obtain in an undivided cell since the solution is maintained constantly slightly alkaline). Y^- must not form an acid HY which decomposes.

3. ZY must be very water soluble and must ideally provide a solution containing *ca.* 20% by weight of acrylonitrile preferably without the addition of a water-miscible organic solvent.

These requirements were met by a considerable number of salts, among them: benzyltrimethylammonium *p*-toluenesulfonate; *N*-trimethyl-*N'*-trimethyl ethylenediammonium di-*p*-toluenesulfonate; methyl tri-*n*-butyl-phosphonium *p*-toluenesulfonate; trimethylsulfonium *p*-toluenesulfonate; benzyltrimethylammonium acetate, benzoate and thiocyanate; methosulfates of tetramethylammonium, methyltriethylammonium, methyltripropylammonium, methyl tri-*n*-butylammonium, methyltriethylammonium, methyltrihexylammonium; benzyltrimethylammonium 2-naphthalenesulfonate; tetraethylammonium methanesulfonate. Others were suitable if a co-solvent such as acetonitrile or dimethylformamide were used to boost AN solubility: tetraethylammonium sulfate; di-tetraethylammonium benzenephosphonate; benzyltrimethylammonium phosphate; di-benzyl trimethylammonium *m*-benzenedisulfonate.

In all cases semiquantitative electrolyses were run in which it was verified by analysis and by isolation that ADN with little or no PN was formed. For this screening series purified salts were not used. Several types of preparation were involved:

1. Benzyltrimethylammonium salts were prepared by neutralizing the commercially available free base with the appropriate acid under cooling and removing the water in vacuo.

2. Methyl *p*-toluenesulfonate was added to the appropriate tert-amine or phosphine in an inert solvent. After reaction, the solvent was removed in vacuo and the residue thoroughly washed with dry ether to remove traces of starting materials.

3. Methosulfates were prepared by adding dimethyl sulfate to the tert-amine in a procedure similar to 2 above.

Several of the above salts merit special comment.¹² The methosulfates were found to be excellent "hydro-tropic" solvents for a variety of water-insoluble organic compounds. Tetraalkylammonium salts in

¹² Many of these salts may be excellent supporting electrolytes in polarography since they would avoid the use of an auxiliary solvent.

which several n-butyl groups were present were very "hydrotropic" and were also substantially soluble in methylene chloride. In the course of our usual workup procedure they were partially extracted with the products and were not completely removed by backwash with water. They could be removed by (a) retention on activated alumina, or (b) removing the methylene chloride and using ether to separate the products from the salt. Alternatively they could be allowed to remain as a residue after vacuum distillation of the products. The phosphonium salt was freely soluble in methylene chloride. The preparation and properties of two of the salts is given below.

Preparation of methyl tri-n-butylphosphonium p-toluenesulfonate.—In an atmosphere of nitrogen a solution of 50 ml (ca. 0.2 mole) of chilled tri-n-butylphosphine in absolute alcohol was mixed with 40g (0.20 mole) chilled methyl p-toluenesulfonate also in 50 ml of ethanol. The mixture warmed spontaneously to 31° and was heated under reflux for 3 hr. After standing overnight, the alcohol was removed on a water bath by aspirator. The residual liquid was shaken vigorously four times with dry ether; the ether washes were decanted through a separatory funnel. Traces of solvent were then removed in vacuo. The residual syrup (76.3g) slowly solidified, m.p. about 58°. It formed an 80% solution in water.

$C_{20}H_{37}O_3PS$: calculated, C, 61.82; H, 9.60; S, 8.25; found, C, 60.13; H, 9.27; S, 8.75.

Preparation of trimethylsulfonium p-toluenesulfonate.—To a solution of 31.0g (0.5 mole) of dimethyl sulfide in 50 ml of absolute alcohol was added a solution of 93g (0.5 mole) of methyl p-toluenesulfonate in a like volume of solvent. There was no exothermic reaction. The mixture was allowed to reflux overnight. After the first several hours 10 ml of dimethyl sulfide was added to compensate for any losses of this volatile material. The alcohol and excess sulfide were removed by aspirator. The residual solid after thorough washing with dry ether and drying weighed 116.5g. It was not hygroscopic. For analysis a sample was recrystallized from absolute ethanol, m.p. 177°.

$C_{10}H_{16}O_3S_2$: Calculated, C, 48.35; H, 6.49; S, 25.83. Found: C, 48.12; H, 6.43; S, 26.11.

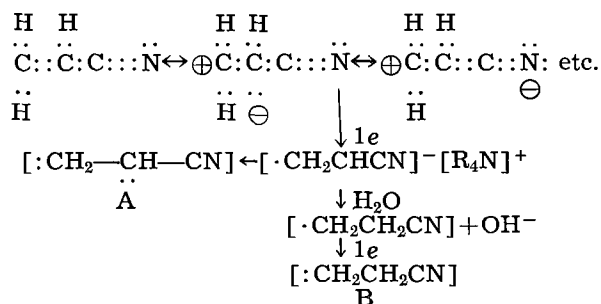
Discussion of Results

While the formation of PN along with ADN during the electrolysis of AN in electrolytes containing alkali metal cations can be rationalized by the postulated formation of organo-metallic intermediates and their hydrolysis, another explanation must be sought for its formation in quaternary ammonium electrolytes. In this system there is no evidence for the formation of free radical intermediates (which are well known to couple in concentrated solution): (a) the hydrodimerization of AN is not inhibited by hydroquinone or p-nitrosodimethylaniline; (b) there is no polymer formation¹³; (c) polarography

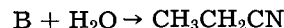
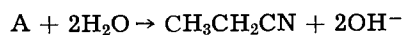
¹³ Knunyants and co-workers (5) cite the evidence against free radical formation in their M-Hg reductions but offer no alternative to the formation of $\cdot CH_2CH_2CN$ as an intermediate.

(22) does not indicate a one-electron uptake. It is proposed that:

1. At the cathode AN undergoes an over-all two-electron uptake. This probably occurs in two one-electron stages (23, 24) with the second electron being acquired at a more positive voltage than the first.¹⁴ Present data do not permit a firm decision to be made regarding the sequence of reactions in which the intermediate radical-anion is involved (26). Except when there is a great paucity of proton donor in the catholyte¹⁵ the radical-anion, whose negative charge is delocalized over a three-atom system, may react with water¹⁶ before the second electron is taken up at the β -position



2. The carbanions (A, B) may attack either water or, at the β -position, highly polarized molecules of AN which are attracted to the cathode:



Attack upon AN is favored by maintaining a high concentration of this substrate.

3. Interaction of the adiponitrile anion(s), in which again there is charge delocalization, with water, terminates the reaction^{17, 18} and yields ADN and OH^- .

Acknowledgments

It is a pleasure to acknowledge my indebtedness to: Dr. Carroll A. Hochwalt, Monsanto, for providing the impetus for the study of an adiponitrile ex acrylonitrile process; Drs. E. W. Gluesenkamp, F. C.

¹⁴ In this sense we agree with Knunyants *et al.* (5) that the behavior of a free radical at a cathode is different from its behavior in solution: in this system it acquires another electron at the cathode. Feoktistov and Zhdanov (25) report that the second stage of the two-electron reduction of $\text{ICH}_2\text{CH}_2\text{CN}$ —in which the equivalent of $\cdot\text{CH}_2\text{CH}_2\text{CN}$ must be involved—occurs at -1.5v , which is considerably more positive than the cathode voltage required for AN reduction.

¹⁵ The products of reduction of AN in catholytes containing little water are discussed in a subsequent paper.

¹⁶ Attack of the proton donor may be at the more basic N rather than at the α -carbanionic center.

¹⁷ Long after this work was completed, Feoktistov and Zhdanov (27) formulated a similar proposal via dianions to explain electrolytic hydrodimerization of AN.

¹⁸ Dr. M. J. S. Dewar, University of Chicago, in a private conversation suggested the following mechanism in order to avoid the need for postulating two adjacent carbanionic centers:



This does not appear to the author to be consistent with the ready reducibility of the anion-free radical nor with the influence of water on the ADN/PN ratio, nor with the fact that electrolysis of AN in the presence of an easily polymerized substance such as 2-phenylbutadiene—to be reported later—leads to no polymer.

Meyer and E. J. Prill, Monsanto, for encouragement and support; Drs. S. Swann, Jr., University of Illinois, and W. H. Urry, University of Chicago, for stimulating discussions; Dr. Stanley Wawzonek, State University of Iowa, for illuminating the role of polarographic data in an interpretation of reaction mechanism; Mr. G. D. Winget for technical assistance, Summer, 1960; Mr. D. Beasecker and his Instrumental Analytical group for vapor-phase chromatographic and infrared spectrophotometric measurements and interpretations; Mr. C. C. Richiusa for economic analyses which helped define our experimental goals; Mr. James D. Anderson for excellent technical assistance during the latter phases of this work.

Manuscript received Mar. 14, 1963; revised manuscript received Sept. 27, 1963. This paper was presented at the New York Meeting, Sept. 29-Oct. 3, 1963.

Any discussion of this paper will appear in a Discussion Section to be published in the December 1964 JOURNAL.

REFERENCES

- O. Bayer, *Angew. Chemie*, **61**, 229 (1949).
- Gg. Spiegelberger and O. Bayer, German Pat. Applic. 71937; P. B. Report 20545, Frames 3065-3066 (March 26, 1942).
- R. M. Leekley, U. S. Pat. 2,439,308, April 6, 1948.
- (a) I. L. Knunyants, *et al.*, U.S.S.R. Pat. 105,286, July 7, 1954; (b) *Izvest. Akad. Nauk SSSR, Otdel Khim. Nauk*, **1957**, No. 2, 238-240; (c) *Doklady Akad. Nauk, Otdel Khim. Nauk*, **113**, 112 (1957); (d) *Soveshchanie Po Elektrokhemii*, 4th Moscow 1956 (October 1-6), *Chem. Abs.*, **54**, 9811b(1960); (e) V. G. Khomyakov, *Khim Nauka i Prom.*, **3**, No. 4, 432 (1958).
- I. L. Knunyants and N. P. Gambaryan, *Uspekhi Khim.*, **23**, 781-820 (1954).
- Reference (5) and: (a) H. S. Taylor and D. G. Hill, *J. Am. Chem. Soc.*, **51**, 2922 (1929); (b) J. C. Jungers and H. S. Taylor, *J. Chem. Phys.*, **6**, 325 (1938); (c) L. Vanhaeren and J. C. Jungers, *Bull. Soc. Chim. Belg.*, **54**, 236 (1945); (d) E. P. Kohler and N. Drake, *J. Am. Chem. Soc.*, **45**, 1281 (1923); (e) Melville, *Proc. Roy. Soc. London*, **163**, 511 (1937).
- K. Senewald *et al.*, German Pat. 1,104,936, Appl. 7/11/59; *Chem. Abs.*, **56**, 332h (1962).
- R. Pasternak, *Helv. Chim. Acta*, **31**, 753 (1948).
- (a) C. L. Wilson and K. B. Wilson, *Trans. Electrochem. Soc.*, **84**, 153 (1943); (b) C. L. Wilson, *ibid.*, **92**, 369 (1947).
- (a) W. Kern and H. Quast, *Makromolekulare Chemie*, **10**, 202 (1953); (b) E. Dineen, *et al.*, *Trans. Electrochem. Soc.*, **96**, 226 (1949); (c) G. Parravano, *J. Am. Chem. Soc.*, **73**, 628 (1951).
- (a) J. W. Breitenbach and H. Gabler, *Monatsh.*, **91**, 202 (1960); (b) A. Zilkha, *et al.*, *J. Polymer Sci.*, **49**, 231 (1961).
- M. N. Platonova, *J. Anal. Chem. U.S.S.R.*, **11**, 317 (1956).
- (a) W. L. Bird *et al.*, *Anal. Chem.*, **24**, 586 (1952); (b) G. C. Claver and M. Murphy, *ibid.*, **31**, 1682 (1959); (c) M. Murphy *et al.*, *J. Polymer Sci.*, **54**, 107 (1961).
- (a) R. H. McKee, *Ind. Eng. Chem.*, **38**, 382 (1946); (b) H. S. Booth *et al.*, *ibid.*, **40**, 1491 (1948).
- (a) E. Klein *et al.*, *J. Chem. and Eng. Data*, **2**, 72 (1957); (b) N. M. Bikales *et al.*, *Ind. Eng. Chem.*, **50**, 87 (1958).
- M. J. Allen, "Organic Electrode Processes," Chapman and Hall Ltd., p. 36 (1958).
- Japanese Patents 1969-71(1959); *Chem. Abs.*, **54**, 9770b(1960).
- H. Stenzl and F. Fichter, *Helv. Chim. Acta*, **17**, 669 (1934).
- A. P. Tomilov and L. V. Kaabak, *Zhur. Priklad. Khim.*, **32**, 2600 (1959); *Chem. Abs.*, **54**, 7374i(1960).
- (a) K. Ziegler *et al.*, *Ann.*, **473**, 36 (1929); (b) C. K. Ingold, *J. Chem. Soc.*, **1935**, 717; (c) C. B. Wooster, *Chem. Revs.*, **11**, 1 (1932).
- (a) T. Nakabayashi, *J. Am. Chem. Soc.*, **82**, 3909 (1960); (b) D. Staschewski, *Angew. Chem.*, **71**, 726 (1959).
- M. N. Platonova, *J. Anal. Chem. U.S.S.R.*, **11**, 317 (1956).
- (a) R. Pasternak, *Helv. Chim. Acta*, **31**, 753 (1948); (b) P. J. Elving and B. Pullman, AECU Report 4317, U.S. Atomic Energy Commission, 1959.
- S. Wawzonek, E. W. Blaha, R. Berkey, and M. E. Runner, *This Journal* **102**, 235 (1955).
- L. G. Feoktistov and S. I. Zhdanov, *Izvest. Akad. Nauk, S.S.S.R., Otdel Khim. Nauk*, **1962**, 2127.
- (a) H. A. Laitinen and S. Wawzonek, *J. Am. Chem. Soc.*, **64**, 1765 (1942); (b) G. J. Hoijsink *et al.*, *Rec. Trav. Chim.*, **73**, 355 (1954); (c) G. J. Hoijsink, *Rec. Trav. Chim.*, **76**, 885 (1957).
- S. I. Zhdanov and L. G. Feoktistov, *Izvest. Akad. Nauk, S.S.S.R., Otdel Khim. Nauk*, **1963**, 53.
- M. J. Allen, 120th Meeting of The Electrochemical Society, Detroit, Mich., Oct., 1961, Abstract No. 163.
- Distillers Co. Ltd., Brit. Pat. 848,924, Sept. 21, 1960; *Chem. Abs.*, **55**, 5348i (1961).

June 1964 Discussion Section

A Discussion Section, covering papers published in the June-December 1963 JOURNALS, is scheduled for publication in the June 1964 issue. Any discussion which did not reach the Editor in time for the December 1963 Discussion Section will be included in the June 1964 issue.

Those who plan to contribute remarks for this Discussion Section should submit their comments or questions in triplicate to the Managing Editor of the JOURNAL, 30 East 42 St., Rm. 1806, New York, N. Y., 10017, *not later than March 2, 1964*. All discussion will be forwarded to the author(s) for reply before being printed in the JOURNAL.

Electrolytic Reductive Coupling

II. Derivatives of Mono-Olefinic α , β -Unsaturated Acids

Manuel M. Baizer and James D. Anderson

Central Research Department, Monsanto Chemical Company, St. Louis, Missouri

ABSTRACT

Electrolytic hydrodimerization of a variety of derivatives of α , β -unsaturated acids is reported, *e.g.*, methacrylonitrile, cinnamionitrile, ethyl acrylate, ethyl maleate, di-2-ethylhexyl fumarate, N, N-diethylacrylamide, acrylamide. The double bond may be endocyclic, as in 1-cyano-1-cyclopentene. The relationship of structure to hydrodimerizability is discussed. Evidences of stereo-preference in electrolytic hydrodimerization are presented.

Knunyants and co-workers reported the alkali metal-amalgam hydrodimerization of a number of derivatives of α , β -unsaturated acids as well as the formation of adiponitrile from acrylonitrile (1). In general, yields of hydrodimer decreased in the order Li-Hg > K-Hg > Na-Hg, "parallel to the decrease in the normal potential of these amalgams." The authors also proposed that the yields of hydrodimer, presumably formed via a free radical intermediate, decreased as the degree of interference with the conjugated system $>C=C-C=O$ increased. Thus, *e.g.*, ethyl acrylate (K-Hg) gave 52% diethyl adipate, N,N-diethylcinnamide (K-Hg) gave 22.7% hydrodimer and methacrylonitrile (K-Hg or Li-Hg) gave no hydrodimer. Also, shielding of the β -position, as in ethyl β , β -dimethylacrylate, reduced or eliminated hydrodimerization.

The results we obtained in the electrolytic hydrodimerization of acrylonitrile at a mercury cathode in electrolytes containing on the one hand alkali

metal arylsulfonates and on the other quaternary ammonium arylsulfonates suggested additional explanations for some of the shortcomings in the application of Knunyants' process:

1. In a stirred system, at a mercury cathode, the alkali metal cations discharge at *ca.* $-1.9v$ (*vs.* S.C.E.). If a given reduction requires a substantially more negative cathode potential (as determined polarographically), it cannot be effected by an alkali metal amalgam, not even Li-Hg.

2. In an alkali metal-amalgam reduction, there is a postulated competition between coupling of intermediates which lead to hydrodimers and formation of organo-metallics which can lead to dihydro-compounds. If the speed of the latter reaction is greater than that of the former, little or no hydrodimer can form.

3. If the activating group is $-\text{CONH}_2$ or a similar group which can react with alkali metals, little or

Table I. Comparison of reported amalgam process and new electrolytic process for hydrodimerization of derivatives of α , β -unsaturated acids in quaternary ammonium electrolytes

Expt. No.	Monomer	Monomer		Hydrodimer		Electrolytic process ^b	
		Amalgam process % Hydrodimer by	Li-Hg	K-Hg	Li-Hg	% Hydrodimer ^a	- Cathode v vs. S.C.E.
		$2RR'C=C(R'')X \rightarrow RCR'-CH(R'')X$					
		$\begin{array}{c} RCR'-CH(R'')X \\ \\ RCR'-CH(R'')X \end{array}$					
1	CH ₂ =CH-CN	62.2	—	—	75-100	1.81 to 1.91	
2	CH ₂ =C(CH ₃)CN	0	0	—	75.3 ^{c,*}	2.01 to 2.05	
3	(CH ₃) ₂ C=CHCN	0	37	—	87-93 ^d	2.08 to 2.11	
4	CH ₂ =CHCOOEt	52	—	—	74-87	1.85	
5	(CH ₃) ₂ C=CHCOOEt	0	31.4	—	66.2 ^e	2.10 to 2.18	
6	CHCOOEt	7.3	—	—	61.5 ^f	1.32 to 1.40	
	Cis						
	CHCOOEt						
7	C ₆ H ₅ CH=CHCOOEt	51.3	—	—	28 ^f	1.57 to 1.61	
8	CH ₃ CH=CHCONEt ₂	0	0	—	61.4 ^{g,*}	2.03 to 2.12	
9	CH ₂ =CHCONEt ₂	0	0	—	73.3 ^h	1.91 to 1.95	
10	CH ₂ =CHCONH ₂	0	0	—	39.6	1.82 to 2.00	

^a Based on current passed.

^b When the hydrodimerization occurs at a cathode voltage more positive than that required for discharge of alkali metal cations, solubility factors being equal, it may be expected that good results will be obtained even in the presence of alkali metal cations.

^c bp, 128°/0.75 mm; n_D²⁰ 1.4323. Anal. calcd. for C₈H₁₂N₂: C, 70.54; H, 8.88; N, 20.57. Found: C, 70.05; H, 8.81; N, 20.49.

^d mp, 133°. Anal. calcd. for C₁₀H₁₀N₂: C, 73.12; H, 9.82; N, 17.05. Found: C, 73.24; H, 10.23; N, 17.35.

^e bp, 128°/1.7 mm; n_D²⁰ 1.4480; Anal. calcd. for C₁₄H₂₀O₄: C, 65.08; H, 10.14; mol wt, 258.75. Found: C, 67.29%; H, 10.77; mol wt, 258.

^f Purified.

^g bp, 171°/0.4 mm, n_D²⁰ 1.4754. Anal. calcd. for C₁₈H₂₂N₂O₂: C, 67.56; H, 11.03; N, 9.85. Found: C, 67.46; H, 11.55; N, 9.92.

^h Crude.

* New compound.

no hydrodimerization can be expected in an alkali metal-amalgam process.

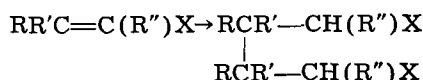
4. Monomers which, unlike acrylonitrile, have very low solubility in aqueous mineral acid would not be expected to give good yields of coupled product.

5. The ability to achieve more negative potentials with Li-Hg than with other alkali metal-amalgams should favor difficult hydrodimerizations, but this may be offset by the greater readiness to form organo-metallics and therefore dihydrocompounds.

Experimental Results and Discussion

Since the difficulties engendered by the presence of alkali metal cations can be eliminated by electrolysis in quaternary ammonium electrolytes (1), a comparison (Table I) was made between the best reported yields¹ in hydrodimerizing a selected group of monomers by alkali-metal amalgams and by the above electrolytic method. In most cases single electrolyses were run to partial conversion and the conditions were therefore not necessarily optimum. The apparatus, procedure and method of separating unchanged starting materials from products were similar to those described before (1). Isolation of product was by fractional distillation or crystallization as applicable. The cathode was always mercury. The anolyte was a diluted solution of the salt used in the catholyte.

In addition, a number of other derivatives of α , β -unsaturated acids (Table II), having a variety of structural features, were successfully hydrodimerized electrolytically. Again, usually single runs were made to establish the occurrence of the reaction. In all these and preceding cases, the products obtained are those to be expected from coupling at the β -position and acquisition of H at the α -positions



The relationship of half-wave potentials to constitution of electroreducible organic molecules has been discussed (2). In the presently reported hydrodimerizations, it will be noted that:

1. The double bond may be endocyclic; the cathode voltages are then more negative than those required for reduction of the open-chain analogs.

2. Two β -alkyl groups do not nullify the hydrodimerization process but, when an additional alkyl group is present in the α -position, coupling ceases.

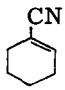

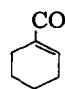
3. Phenyl groups extend the conjugation and expectedly shift the cathode voltage in a positive direction.

4. Ethyl, n-butyl, and 2-ethylhexyl maleates form hydrodimer about equally well; fumarates are reduced at a slightly more positive cathode voltage than are maleates.

5. Two activating groups (as in diethyl benzal-malonate and diethyl ethyldienemalonate) cause reduction at a more positive cathode potential than one activating group.

¹ Knunyants references cited in (1).

Table II. Electrolytic hydrodimerization of derivatives of α , β -unsaturated acids. Variation of cathode potential with structure of monomer

Expt. No.	Monomer	Hydrodimer	-Cathode v ^a vs. S.C.E.	% Hydrodimer ^b
	Monomer			
11	CH ₃ CH=CHCN		2.08-2.11	87 ^c
12	(CH ₃) ₂ C=C(CH ₃)CN		ca. 2.15	0
13	C ₆ H ₅ CH=CHCN		1.42-1.60	60.3 ^d
14			2.15-2.20	66.4
15			2.13	29 ^{e,*}
16	CH ₃ CH ₂ CH=CHCN		1.97-2.20	58 ^{f,*}
17	$\begin{array}{c} \text{CHCN} \\ \\ \text{NCC} \end{array}$		1.00-1.03	— ^g
18	C ₂ H ₅ OCH=CHCOOEt		2.22	57 ^h
19	Cis $\begin{array}{c} \text{Et} \\ \\ \text{CHCOOCH}_2\text{CH}(\text{CH}_2)_3\text{CH}_3 \\ \\ \text{CHCOOCH}_2\text{CH}(\text{CH}_2)_3\text{CH}_3 \\ \\ \text{Et} \end{array}$		1.41	66
20	$\begin{array}{c} \text{CHCOO}(\text{CH}_2)_3\text{CH}_3 \\ \\ \text{CHCOO}(\text{CH}_2)_3\text{CH}_3 \end{array}$		1.30	70
21	Trans $\begin{array}{c} \text{Et} \\ \\ \text{CHCOOCH}_2\text{CH}(\text{CH}_2)_3\text{CH}_3 \\ \\ \text{CHCOOCH}_2\text{CH}(\text{CH}_2)_3\text{CH}_3 \\ \\ \text{Et} \end{array}$		1.22	80
22	C ₆ H ₅ CH=C(COOEt) ₂		1.38-1.47	45 ⁱ
23	CH ₃ CH=C(COOEt) ₂		1.41-1.68	90
24			2.05-2.11	— ^k
25	C ₆ H ₅ CH=CHCONEt ₂		1.67-1.73	— ^m

^a All of these potentials were measured experimentally in the course of the electrolyses. The half-wave potential for most of these compounds are not reported in the literature. Electrolysis began at a potential somewhat more positive than the half-wave potential.

^b Based on current passed.

^c bp, 147°/4.2 mm; n_D²⁵ 1.4524. Anal. calcd. for C₆H₁₂N₂: C, 70.54; H, 8.89; N, 20.57. Found: C, 70.17; H, 8.86; N, 20.28. Properties of the hydrodimers are given only when new compounds (*) are involved or when the physical constants of old compounds differed from those reported in the literature. Where β to α coupling was conceivable, analysis of the infrared and n.m.r. spectra showed that this had not occurred.

^d Two isomers, mp, 151°-153° (known) and 98°, respectively. Anal. calcd. for C₁₈H₁₆N₂ (98° isomer): C, 82.44; H, 6.92; N, 10.68. Found: C, 82.42; H, 6.33; N, 10.47.

^e bp, 148°-150°/1.8 mm; n_D²⁵ 1.4939. Anal. calcd. for C₁₂H₁₀N₂: C, 76.60; H, 8.50; N, 14.90. Found: C, 76.10; H, 8.41; N, 13.87.

^f bp, 154°-157°/3.3 mm; n_D²⁵ 1.4565. Anal. calcd. for C₁₀H₁₀N₂: C, 73.12; H, 9.82; N, 17.06. Found: C, 72.54; H, 9.91; N, 16.02.

^g Two isomers, mp, 148°-152° and 122°-123°, respectively. Anal. calcd. for C₈H₈N₂: C, 60.75; H, 3.82; N, 35.43. Found: C, 60.45; H, 4.05; N, 35.32 and C, 60.60; H, 3.88; N, 35.35 respectively.

^h bp, 130°/5 mm; n_D²⁵ 1.4302. Anal. calcd. for C₁₄H₂₀O₆: C, 57.91; H, 9.03. Found: C, 58.43; H, 9.17.

ⁱ bp, 196°/0.9 mm. Anal. calcd. for C₂₈H₃₀O₈: C, 67.45; H, 6.87. Found: C, 68.31; H, 6.83.

^k Two isomers, mp, 216°-218° and 86°-87° respectively. Anal. calcd. for C₁₈H₂₀O₄: C, 69.64; H, 9.74. Found: C, 69.77; H, 9.53 and C, 69.85; H, 9.03 respectively.

^m mp, 47°-48°. Anal. calcd. for C₂₀H₂₀N₂O₂: C, 74.43; H, 8.88; N, 6.85. Found: C, 76.12; H, 8.95; N, 6.70.

* New compound.

Table III. Catholytes used in Tables I and II

Expt. No.	Monomer	Monomer, g	Catholyte composition Salt, g	Co-solvent, g
1	$\text{CH}_2=\text{CHCN}^a$	94.5	141 of 56% ^b	None
2	$\text{CH}_2=\text{C}(\text{CH}_3)\text{CN}^a$	93.0	93 of 73% ^b	37.2 DMF
3	$(\text{CH}_3)_2\text{C}=\text{CHCN}^c$	105.0	105 of 75% ^b	26.7 DMF
4	$\text{CH}_2=\text{CHCOOEt}^a$	76.0	75.8 of 76% ^d	88.6 DMF
5	$(\text{CH}_3)_2\text{C}=\text{CHCOOEt}^e$	75.0	82.0 of 86.5% ^f	88.6 CH_3CN
6	Cis— $\begin{array}{c} \text{CHCOOEt}^a \\ \\ \text{CHCOOEt} \end{array}$	105	106 of 75% ^b	47.6 DMF
7	$\text{C}_6\text{H}_5\text{CH}=\text{CHCOOEt}^a$	108	108 of 89% ^g	22.5 H_2O
8	$\text{CH}_3\text{CH}=\text{CHCONEt}_2^h$	104	104 of 75% ^b	52.0 H_2O
9	$\text{CH}_2=\text{CHCOONEt}_2^h$	104	104 of 75% ^b	52.0 H_2O
10	$\text{CH}_2=\text{CHCONH}_2^a$	85	85 of 85% ^b	42.5 H_2O
11	$\text{CH}_3\text{CH}=\text{CHCN}^a$	97.4	97.4 of 75% ^b	37.2 DMF
12	$(\text{CH}_3)_2\text{C}=\text{C}(\text{CH}_3)\text{CN}^j$	41.7	41.7 of 80% ^b	48.0 CH_3CN
13	$\text{C}_6\text{H}_5\text{CH}=\text{CHCN}^a$	95.6	98.0 of 80% ^b	45.0 DMF
14	$\begin{array}{c} \text{CN}^k \\ \\ \text{C}_6\text{H}_5 \end{array}$	88.4	88.4 of 76.5% ^d	81.5 DMF
15	$\begin{array}{c} \text{CN}^m \\ \\ \text{C}_6\text{H}_5 \end{array}$	82.0	81.0 of 80% ^b	70.4 DMF
16	$\text{CH}_3\text{CH}_2\text{CH}=\text{CHCN}^n$	52.9	69.0 of 80% ^b	43.0 CH_3CN
17	$\begin{array}{c} \text{CHCN}^a \\ \\ \text{NCCH} \end{array}$	75.3	83.5 of 75% ^b	91.0 CH_3CN
18	$\text{C}_2\text{H}_5\text{OCH}=\text{CHCOOEt}^p$	91.0	91.0 of 80% ^b	66.3 DMF
19	Cis— $\begin{array}{c} \text{Et} \\ \\ \text{CHCOOCH}_2\text{CH}(\text{CH}_2)_3\text{CH}_3^a \\ \\ \text{CHCOOCH}_2\text{CH}(\text{CH}_2)_3\text{CH}_3 \\ \\ \text{Et} \end{array}$	92.0	92.0 of 89% ^g	46.0 $\text{C}_2\text{H}_5\text{OH}$
20	$\begin{array}{c} \text{CHCOO}(\text{CH}_2)_3\text{CH}_3 \\ \\ \text{CHCOO}(\text{CH}_2)_3\text{CH}_3 \end{array}$	130.0	130.0 of 89% ^g	None
21	Trans— $\begin{array}{c} \text{Et} \\ \\ \text{CHCOOCH}_2\text{CH}(\text{CH}_2)_3\text{CH}_3^a \\ \\ \text{CHCOOCH}_2\text{CH}(\text{CH}_2)_3\text{CH}_3 \\ \\ \text{Et} \end{array}$	63.2	63.2 of 89% ^g	113.8 $\text{C}_2\text{H}_5\text{OH}$
22	$\text{C}_6\text{H}_5\text{CH}=\text{C}(\text{COOEt})_2^a$	86.6	86.6 of 80% ^b	80.0 DMF
23	$\text{CH}_3\text{CH}=\text{C}(\text{COOEt})_2^a$	95.5	95.5 of 80% ^b	61.7 DMF
24	$\begin{array}{c} \text{COOEt}^g \\ \\ \text{C}_6\text{H}_5 \end{array}$	80.0	80.0 of 89% ^g	8.0 CH_3CN
25	$\text{C}_6\text{H}_5\text{CH}=\text{CHCONEt}_2^r$	57.7	101.2 of 80% ^b	86.6 DMF

^a Purchased.^b Tetraethylammonium p-toluenesulfonate.^c Prepared according to ref (3).^d Methyltriethylammonium p-toluenesulfonate.^e Prepared according to ref (4).^f Tetraethylammonium benzenesulfonate.^g Methyltri-n-butylammonium p-toluenesulfonate.^h Prepared according to ref (5).^j Prepared according to ref (6).^k Prepared according to ref (7).^l Prepared by an adaptation of ref (7).^m Prepared by the pyrolysis of α -acetoxyvaleronitrile at 500° through a 3-ft column packed with glass beads. Satisfactory elemental analyses for the product were obtained.ⁿ Prepared according to ref (8).^o Prepared according to ref (9).^p Prepared according to ref (10).

6. A β -alkoxy-substituent shifts the cathode potential considerably toward the negative but still permits coupling.

7. Acrylamide yielded adipamide in spite of the presence of an unprotected $-\text{CONH}_2$ group.

Not all of the monomers used in this work dissolved completely in the hydrotropic quaternary salt solutions without the aid of a co-solvent. The catholytes used for the experiments summarized in Tables I and II are given in Table III.

Stereochemistry

Wilson and Wilson (11) had obtained slightly more meso- than dl-diphenyladipic acid by hydrodimerizing cinnamic acid in acidic medium (presumably via a free radical path). In our hydrodimerizations, which we believe occur via carbanion intermediates, there was scattered evidence, not further pursued at this time, that stereopreference was involved. While the 2,5-dimethyladiponitrile obtained from methacrylonitrile (expt. 2, Table II) was found to give two equal peaks in a vapor phase chromatogram, the hydrodimer from crotononitrile (expt. 11, Table II) showed no resolution into two components under a variety of conditions. Of 25.9g of crude hydrodimers obtained from cinnamonitrile (expt. 13, Table II), at least 17.9g (69%) was in the form of one isomer, mp 151° - 153° ; only 1.1g of the other isomer, mp 98° , could be recovered from mother liquors. The bulk of the hydrodimer obtained

from 1-cyclohexene-1-carbonitrile was the higher melting isomer, mp 216° - 218° ; only a small quantity of an isomer, mp 86° - 87° was present.

Acknowledgment

Mr. D. R. Beasecker and his Instrumental Analysis group performed all V.P.C., n.m.r., and infrared measurements.

Manuscript received Mar. 14, 1963; revised manuscript received Sept. 27, 1963. This paper was presented at the New York Meeting, Sept. 29-Oct. 3, 1963.

Any discussion of this paper will appear in a Discussion Section to be published in the December 1964 JOURNAL.

REFERENCES

1. M. M. Baizer, *This Journal*, **111**, 215 (1964).
2. I. M. Kolthoff and J. J. Ligane, "Polarography," 2nd ed., Vol. II, p. 631, Interscience Publishers (1952).
3. D. M. Trakhtenberg and M. M. Shemyakin, *J. Gen. Chem., U.S.S.R.*, **13**, 477 (1943).
4. W. H. Perkin, *J. Chem. Soc.*, **1896**, 1957.
5. H. R. Snyder and P. E. Putnam, *J. Am. Chem. Soc.*, **76**, 33 (1954).
6. L. Henry, *Bull. Acad. Roy. Belg.*, **36**, 241 (1898).
7. S. M. McElvain *et al.*, *J. Am. Chem. Soc.*, **77**, 4571 (1955).
8. W. J. Croxall and H. J. Schneider, *ibid.*, **71**, 1257 (1949).
9. J. A. Gardner and H. N. Rydon, *J. Chem. Soc.*, **1938**, 48.
10. D. Papa *et al.*, *J. Am. Chem. Soc.*, **72**, 3885 (1950).
11. (a) C. L. Wilson and K. B. Wilson, *Trans. Electrochem. Soc.*, **84**, 153 (1943); (b) C. L. Wilson, *ibid.*, **92**, 369 (1947).

Electrolytic Reductive Coupling

III. Some Derivatives of 1,3-Butadiene

Manuel M. Baizer and James D. Anderson

Central Research Department, Monsanto Chemical Company, St. Louis, Missouri

ABSTRACT

Ethyl sorbate has been hydrodimerized in aqueous tetraalkylammonium *p*-toluenesulfonate to give a good yield of a mixture of isomers. 1-Cyano-1,3-butadiene in a similar system underwent at least 65-70% coupling through the δ -position to furnish, after catalytic hydrogenation, sebaconitrile in quantitative yield. The major by-product identified was 3,4-diethyladiponitrile. A hydrotetramer was also formed, presumably from a dimer present in the starting material. This distribution of isomers is very different from that reported in the "radical dimerization" of butadiene by sodium.

In Paper II of this series (1), there was described the hydrodimerization in quaternary ammonium electrolytes of a variety of derivatives of monoolefinic α , β -unsaturated acids. The presence of aromatic substituents at the β -position extended the conjugation, shifted the required cathode potential to the positive, and probably contributed also to stereo-regulation in the mixture of isomeric hydrodimers obtained, but it could not, of course, alter the fact that coupling occurred through the β -position. Of greater interest was a study of the more complex case in which extended chain conjugation occurred, as in ethyl sorbate and 1-cyano-1,3-butadiene (CBD).

Wilson and Wilson (2) have reported an excellent study of the reductive dimerization of sorbic acid. In acid solution, the yield of hydrodimers ("pinacol") was virtually quantitative; the composition of the isomer mixture was not given.

Experimental Results and Discussion

Apparatus.—The electrolytic cell used has been described previously (3). The cathode was mercury.

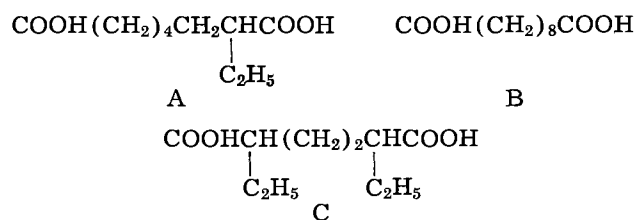
Hydrodimerization of ethyl sorbate.—In a brief study it was found that electrolysis of ethyl sorbate in methyltri-*n*-butyl *p*-toluenesulfonate plus dimethylformamide under mildly alkaline conditions gave 76.5% (based on current) of a redistilled mix-

ture of hydrodimers, bp 118°/0.55 mm to 132°/0.65 mm, n_D^{25} 1.4635. Carbon, hydrogen, and molecular weight determinations were satisfactory. Further examination of this mixture was deferred.

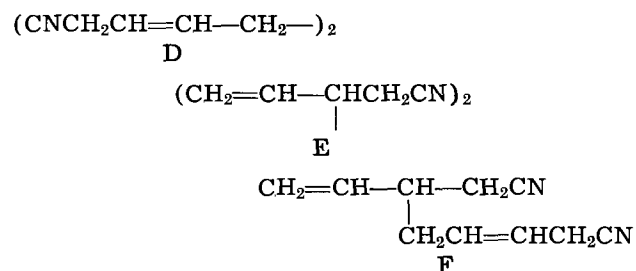
Hydrodimerization of CBD.—A more thorough investigation of the hydrodimerization of CBD was warranted because:

1. It could lead to a novel route to the commercially important products sebaconitrile, 1,10-diaminodecane and sebacic acid.

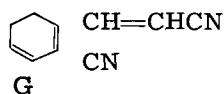
2. The distribution of isomers obtained electrolytically from a diene containing a polar end-group could be compared to the isomers obtained from butadiene itself in a "radical dimerization" process effected by sodium (4). In the U.S. Industrial Chemicals Company process, there is obtained, after carbonation and reduction, a mixture of 51% 2-ethyl-suberic acid (A), 38% sebacic acid (B), and 11% 2,5-diethyladipic acid (C):



Our supply¹ of CBD was furnished with the typical analysis: 89.8% cis-, 8.4% trans-, 0.9% cis-crotonitrile, and 0.9% unknown. It was anticipated that hydrodimerization via a carbanion intermediate would lead to a mixture of 1,8-dicyano-octa-2,6-diene (D), 3,4-divinyladiponitrile (E), and 1,6-dicyano-5-vinyl-2-hexene (F):



In addition, trans-CBD readily undergoes a Diels-Alder reaction with itself (5) to form the dimer G:



and it was possible that at the cathode voltage required for hydrodimerization of CBD dimer G could either hydrodimerize or undergo mixed reduction coupling² with available CBD.

After exploratory runs, crude hydrodimers were hydrogenated at the double bonds before gross fractionation and/or V.P.C. analysis in order to avoid imposing the complications of geometric upon position isomerism.

Catholyte.—CBD is very soluble in 70-80% aqueous tetraethylammonium p-toluenesulfonate and

catholytes containing 50% by weight of CBD were readily prepared. However, the catholytes were usually diluted with a little acetonitrile or dimethylformamide in order to conserve raw material.

Procedure.—The general electrolysis procedure and method of separation of the nitriles from the electrolyte were similar to what has been previously reported (3).

In one experiment, a solution of 100g of freshly redistilled CBD (to which a trace of p-nitrosodimethylaniline had been added) in 100g of 80% aqueous tetraethylammonium p-toluenesulfonate plus 20 ml acetonitrile was electrolyzed at 25° for 12.1 amp-hr (copper coulometer). The cathode voltage was -1.49 to -1.59 (*vs.* SCE). The theoretical yield of hydrodimer (based on current input) was 36.1g. After stripping unchanged starting materials on the water-bath at 10 mm, there remained a residue of 39.4g. Vacuum distillation yielded (i) 29.1g (80.5%) of crude hydrodimers boiling mainly at 130°/0.15 mm to 132°/0.34 mm, (ii) 1.9g bp 187°/0.30 mm to 248°/0.40 mm, and (iii) 8.4g of viscous residue. Fraction (i) mainly crystallized in the receiver. Crystallization from methanol gave in several crops, 15.8g (more than 50% of the weight of the crude hydrodimers) of 1,8-dicyano-octa-2,6-diene, mp 49°-50°, having the correct elemental and molecular weight analyses.³ A 6.64g portion of this diene from two different experiments was suspended in 100 ml of absolute ethanol and hydrogenated on the Parr shaker at 40 lb in the presence of 0.4g of 5% Pd/C. Hydrogenation was complete in 10 min. The product had n_D^{25} 1.4458 before and after distillation at 162°/4 mm -164°/5 mm. The infrared spectrum of the distilled product was superimposable upon that of an authentic sample of sebaconitrile.⁴

In another experiment, a solution of 95.5g of freshly redistilled and stabilized CBD in 107g of 75% tetraethylammonium p-toluenesulfonate was electrolyzed at 25°-55° for 12.4 amp-hr (\approx 37.0g hydrodimers). The cathode voltage was -1.55 to -1.62v (*vs.* SCE). The high-boiling residue weighed 35.4g.⁵ It was directly hydrogenated as above. Catalyst had to be filtered off and replaced by a fresh change several times. The crude hydrogenated nitriles weighed 32.8g.⁶ Of this, 78% boiled in the range expected for sebaconitrile and isomers.⁵ V.P.C. analysis of the distillate showed 86.7% sebaconitrile, 4.7% of an impurity having the same retention time as 3,4-diethyladiponitrile (1) and 2.8% and 2.6%, respectively, of two additional components. The material which had not distilled up to 143°/0.13 mm had n_D^{25} 1.4752; C, H, N and molecular weight determinations were in agreement with the values calculated for a hydrotetramer of CBD.

In a third experiment, conducted similarly to the first one above, the distilled hydrodimers weighed 32.5g (88% based on current). Hydrogenation and

³ Isomers (?) of this product have been reported to melt at 43° (6) and 44° (7).

⁴ Purchased from K and K Labs, Jamaica 33, N. Y. n_D^{25} 1.4452.

⁵ The possibility that some polymerization occurred during distillation cannot be excluded.

⁶ Mechanical losses.

¹ Monsanto Chemical Company, Hydrocarbons Division, Texas City, Texas.

² This type of reaction will be discussed in a subsequent paper.

distillation yielded 32.5g of saturated dinitriles, bp 126°-133°/0.25 mm, n_D^{25} 1.4521. V.P.C. analysis showed 76.7% sebaconitrile content.

Manuscript received Mar. 14, 1963; revised manuscript received Sept. 27, 1963.

Any discussion of this paper will appear in a Discussion Section to be published in the December 1964 JOURNAL.

REFERENCES

1. M. M. Baizer and J. D. Anderson, *This Journal*, **111**, 223 (1964).
2. C. L. Wilson and K. B. Wilson, *Trans. Electrochem. Soc.*, **80**, 139 (1941).
3. M. M. Baizer, *This Journal*, **111**, 215 (1964).
4. (a) C. E. Frank and W. E. Foster, U. S. Pat. 3,013,071, Dec. 12, 1961; (b) C. E. Frank and J. F. Nobis, U. S. Pat. 2,824,118, Feb. 18, 1958; (c) C. E. Frank and W. E. Foster, *J. Org. Chem.*, **26**, 303, 307 (1961).
5. H. R. Snyder and G. I. Poos, *J. Am. Chem. Soc.*, **71**, 1395 (1949).
6. G. Boffa and D. Costabello, U.S. Pat. 2,956,075, Oct. 11, 1960.
7. W. W. Pritchard and G. M. Whitman, U. S. Pat. 2,524,833, Oct. 10, 1950.

The Possible Mechanisms of Complex Reactions Involving Consecutive Steps

Paul C. Milner

Bell Telephone Laboratories, Incorporated, Murray Hill, New Jersey

ABSTRACT

A new systematic method for generating complete sets of reaction mechanisms is described, and several examples of its application are given to illustrate its utility in postulating mechanisms from which kinetic relations may be derived for comparison with experimental results. Starting with a choice of possible intermediate species, the procedure leads directly to the desired set of mechanisms, which are shown to be limited to those containing a number of steps no more than one greater than the number of intermediate species and which, therefore, can be obtained explicitly as unique solutions to a series of easily derived simultaneous equations.

One of the principal purposes of kinetic studies is the elucidation of reaction mechanisms. For many complex reactions, however, kinetic measurements cannot provide sufficient information for the direct and unambiguous specification of mechanism and therefore this process must depend on the comparison of experimental measurements with quantities derived from postulated mechanisms by means of appropriate kinetic laws. For such a procedure to be successful in identifying reaction mechanisms, all of the possible mechanisms must be considered. The following discussion provides a simple systematic method for generating the required complete sets of possible mechanisms and includes several examples of its use.

General considerations.—The course of reaction is often pictured as the motion of a point over a surface representing the energy of a group of the reacting species as a function of what are usually termed reaction coordinates (1). The path traced by this point, from one minimum across a saddle-point to an adjacent minimum and so on, is simply a pictorial description of the reaction mechanism, in which the minima correspond to groups of stable species produced from the original reactants by the elementary reactions or unit steps represented by the transitions across the saddle-points. These unit steps, in sum, make up the over-all reaction and are the smallest segments of it whose equilibrium and kinetic behavior can, at least in theory, be studied individually.

For a complex reaction, the energy surface may contain many minima so that many paths may be traced across it, each leading from a point corresponding to the reactants of the over-all reaction to a point corresponding to its products and each representing a possible mechanism. Considered in this way, it is clear that many mechanisms are represented by paths involving circles that return to a given minimum once or many times and are thus not microscopically reversible. These, and in fact all possible paths, including those in which two or more paths are simultaneously considered, are simply trivial combinations of a finite set of direct paths, each of which is unique in the sense that it cannot be considered to result from the superposition of any of the other members of the set.

These direct paths are not necessarily linearly independent of one another in the usual mathematical sense of the term. Such independence would require that it be possible to combine mechanisms in ways resulting in the cancellation of segments of the paths. Mathematically, this is feasible; but kinetically and with respect for physical reality, no two mechanisms containing a given unit step can be equivalent to a third in which it does not appear. Thus, these direct paths are kinetically distinct from one another; and, while they may not be linearly independent of one another, the unit steps of which each of them is composed are. This latter conclusion follows from the consideration that if one step were not independent, it would be equivalent to some

combination of other steps and the mechanism would involve some cyclic or alternate path.

Since the possible unit steps determine the possible mechanisms and are, in turn, determined by the species which may exist in the system under consideration, any systematic examination of possible reaction mechanisms must begin its detailed considerations at this point. The remainder of the development then leads in a straightforward and unambiguous fashion to the generation of the set of mechanisms corresponding to the set of direct paths.

Reactant, Product, and Intermediate Species and Possible Unit Steps

The list of species which may exist in a given system begins, of course, with the known reactants and products of the over-all reaction. In the most general case it will also include all the possible combinations of all the atomic species present, considered in all their possible states of oxidation and in all possible nonequivalent physical locations and orientations with respect to one another. At a more practical level, however, this latter group can be reduced to a small number of species which previous experience and common sense suggest as plausible participants in the reaction. Such participants may be species formed from the reactants and products of the over-all reaction, and they may include species classified as catalysts, third bodies, or solvent. In any case, they are quite generally characterized by the fact that they do not appear as reactants or products in the over-all reaction and so may be included in a general class and denoted as intermediates.

A typical selection of intermediates for the hydrogen-gas electrode reaction would, of course, include adsorbed hydrogen atoms, while a similar choice for the oxygen-gas electrode reaction might involve hydroxyl and hydroperoxyl radicals, oxygen atoms, and hydrogen peroxide or hydroperoxide ions, depending on the pH of the solution. Such selections of intermediates are admittedly arbitrary. They do, however, provide an easily modified starting point for the consideration of possible reaction mechanisms; and they occur at a point where reasonable assumptions can best be made.

From the list of possible species, the possible unit steps can readily be generated. They are simply all the reactions that can occur among the members of this set of species. Since it may be generally assumed that the order of a unit step is never greater than three and, at least in condensed phases, is unlikely to exceed two, it is usually necessary to consider only the possible reactions of the species individually, with themselves, and with each one of the other possible species in order to obtain a complete set of possible unit steps appropriate to the system being considered.

Stoichiometric Numbers and Reaction Mechanisms

Any over-all reaction, then, must consist of a series of steps selected from the complete set of possible unit steps; thus any reaction mechanism can be described completely by specifying the num-

ber of occurrences of each of the possible unit steps for each occurrence of the over-all reaction. In the terminology of Horiuti, these are the stoichiometric numbers associated with the specified reaction mechanism and represent his generalization (2) of the original concept of Horiuti and Ikusima (3), which dealt in a much more restricted fashion with the stoichiometry of the rate-determining step in the hydrogen electrode reaction at platinum. Outside of the work of Horiuti and his co-workers and that of Oldham (4), Mauser (5), and Riddiford (6), little use appears to have been made of stoichiometric numbers defined in this general way, although stoichiometric numbers have been associated with rate-determining steps in a number of treatments of electrode kinetics, most notably those of Parsons (7) and Makrides (8), and, in this restricted form, have been much used as diagnostic criteria in the determination of reaction mechanisms.

In these terms, the generation of possible reaction mechanisms reduces to the choice of appropriate sets of stoichiometric numbers, each set specifying the number of occurrences of each of the possible unit steps for one occurrence of the over-all reaction. These choices are, of course, subject to the restriction that they result in the over-all reaction. Thus, when the chemical equation for each unit step is multiplied by its stoichiometric number and these products summed, the coefficients of the intermediate species must vanish and the coefficients of the reactants and products must be those of the chemical equation for the over-all reaction.

This restriction yields two sets of relations among the stoichiometric numbers. If there are S unit steps involving I intermediates and R reactants and products, there will be S stoichiometric numbers, ν_s . With a_{is} as the coefficient of intermediate i and a_{rs} as the coefficient of reactant or product r in the chemical equation for step s , multiplication of each step by its stoichiometric number ν_s and summation of these products gives I relations of the form:

$$\sum_s a_{is} \nu_s = 0 \quad [1]$$

and R relations of the form

$$\sum_s a_{rs} \nu_s = b_r \quad [2]$$

where b_r is the coefficient of the reactant or product r in the over-all reaction.

Any set of ν_s 's satisfying relations [1] and [2] corresponds to a mechanism; and since there will usually be more stoichiometric numbers than there are independent equations relating them, there will usually be an infinite number of sets of solutions to [1] and [2] and, hence, an infinite number of mechanisms. This number includes the desired direct paths as well as all the possible combinations of them, so that an additional restriction is required to limit the choice to those sets of stoichiometric numbers which correspond to the former group.

The Complete Set of Direct Paths

The necessary restriction may be obtained from a consideration of the relations [1], which form

a system of I homogeneous linear equations in S variables. A fundamental theorem of algebra (9) states that if the matrix of the coefficients, (a_{is}) , has rank H , then all the solutions can be expressed as linear combinations of $S-H$ linearly independent solutions. For the purposes of this discussion it is necessary only to point out that the rank of a matrix is given by the dimension of the largest nonvanishing determinant which can be formed from it (10). In the present case, this requires that H be less than or equal to I , so that the number of linearly independent solutions to the set of relations [1] and, hence, the number of linearly independent reaction routes is greater than or equal to $S-I$.

The discussion of the preceding paragraphs parallels in many respects that given by Horiuti and Nakamura (11) though from a decidedly different viewpoint. Their considerations lead to the same conclusion regarding the number of independent reaction routes, and this number is interpreted as being the degrees of freedom of varying the reaction route in an analogy to the phase rule.

As Horiuti and Nakamura point out, however, a set of independent reaction routes consists of members which are not necessarily unique. They will, in fact, be selected from the desired set of direct paths, which may now be delineated as those reaction routes that are unique by virtue of the fact that the set of relations [1] has, for each path, no more than one solution. From the inequality derived above, it therefore follows that the number of variables, S , usable in describing a direct path is less than or equal to $I + 1$ or, in terms of stoichiometric numbers, that the number of nonzero stoichiometric numbers specifying a direct path can be no more than one greater than the number of intermediates. This useful and important result has not, to the author's knowledge, been previously derived.

The same conclusion may be based on the required linear independence of the unit steps appearing in any direct path. The details of the argument are given in the appendix.

With this restriction, the relations [1] must reduce to a set of I equations in $I + 1$ unknowns if the solution is to represent a direct path. Any one of the relations [2] is then sufficient to determine the precise values of the stoichiometric numbers. There will, in general, be $C(S, I+1) = S! / [(I+1)!(S-I-1)!]$ ways in which the relations [1] may be reduced; but since the solutions obtained for the reduced sets will not always be nonzero or different from one another, $C(S, I+1)$ represents an upper limit to the number of direct paths.

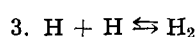
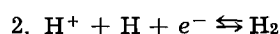
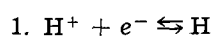
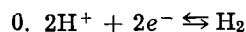
Examples

The following sections provide some illustrations of the principles developed in the preceding discussion. In each case, a choice of intermediates is made, the possible unit steps are generated, the necessary relations [1] and one of the set [2] are given, and, finally, the possible reaction mechanisms corresponding to direct paths are derived.

Table I. Possible mechanisms for the hydrogen-gas electrode reaction

	A	B	C
ν_1	1	2	
ν_2	1		2
ν_3		1	-1

I. *The hydrogen-gas electrode reaction.*—The overall reaction is $2\text{H}^+ + 2e^- \rightleftharpoons \text{H}_2$. A single intermediate, the adsorbed hydrogen atom, is assumed. The possible unit steps, limited to second order or less without consideration of the electrons, are



Step 0 is the over-all reaction itself and need not be considered further. Identifying the stoichiometric numbers by subscribing the number of the unit step, the single relation [1] is

$$\nu_1 - \nu_2 - 2\nu_3 = 0$$

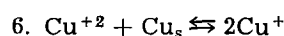
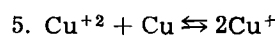
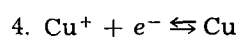
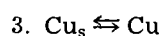
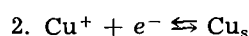
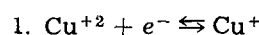
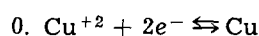
and, using the coefficient of H^+ for the one necessary relation [2],

$$\nu_1 + \nu_2 = 2$$

With one intermediate, no more than two stoichiometric numbers can be nonzero to give direct paths. The three possible solutions are readily found by setting each of the stoichiometric numbers in succession equal to zero and are given in Table I.

Mechanisms A and B are familiar. Mechanism C, in which Step 2 occurs twice in the forward direction and Step 3 occurs once in the reverse direction, is not; and it may be noted that should it be the only possible mechanism at some specific electrode material, it would be impossible to evolve hydrogen on a surface free of hydrogen atoms in the absence of hydrogen gas. Actually, Step 1 would presumably eventually provide sufficient hydrogen atoms; and the observed behavior would involve only an induction period.

II. *The copper-cupric ion electrode reaction.*—The over-all reaction is $\text{Cu}^{+2} + 2e^- \rightleftharpoons \text{Cu}$; and the intermediates Cu^+ and Cu_s , adsorbed copper atoms, are assumed. The possible unit steps, again limited to those of second order or less without regard for electrons, are



Step 3 shows the transfer of copper atoms between two nonequivalent physical locations, the surface

Table II. Possible mechanisms for the copper-cupric ion electrode reaction

	A	B	C	D	E	F	G	H	I	J
ν_1	1	2	1	2						
ν_2	1				2	2	1	2		
ν_3	1	1			2	1			-1	
ν_4			1				1		2	2
ν_5				-1	1			-1		1
ν_6		-1				1	1	2	1	

and the lattice; and step 0 is again the over-all reaction. The relations [1] among the stoichiometric numbers are

$$\nu_1 - \nu_2 - \nu_4 + 2\nu_5 + 2\nu_6 = 0$$

$$\nu_2 - \nu_3 - \nu_6 = 0$$

and the coefficient of Cu in the over-all reaction gives

$$\nu_3 + \nu_4 - \nu_5 = 1$$

With two intermediates, a direct path can have no more than three nonzero stoichiometric numbers. The ten mechanisms that result are given in Table II.

III. The oxygen-gas electrode reaction in alkaline solution.—The over-all reaction $4\text{OH}^- \rightleftharpoons \text{O}_2 + 2\text{H}_2\text{O} + 4e^-$ is assumed to have OH, O, O_2H , and O_2H^- as possible intermediates. The possible unit steps are

- $\text{OH}^- \rightleftharpoons \text{OH} + e^-$
- $\text{OH}^- + \text{OH} \rightleftharpoons \text{O} + \text{H}_2\text{O} + e^-$
- $\text{OH}^- + \text{O} \rightleftharpoons \text{O}_2\text{H} + e^-$
- $\text{OH}^- + \text{O}_2\text{H} \rightleftharpoons \text{O}_2 + \text{H}_2\text{O} + e^-$
- $2\text{OH}^- \rightleftharpoons \text{O} + \text{H}_2\text{O} + 2e^-$
- $\text{OH}^- + \text{O}_2 \rightleftharpoons \text{O} + \text{O}_2\text{H} + e^-$
- $\text{O}_2\text{H}^- \rightleftharpoons \text{O}_2\text{H} + e^-$
- $\text{O}_2\text{H}^- + \text{OH}^- \rightleftharpoons \text{O}_2 + \text{H}_2\text{O} + 2e^-$
- $\text{O}_2\text{H}^- + \text{OH} \rightleftharpoons \text{O}_2 + \text{H}_2\text{O} + e^-$
- $\text{O}_2\text{H}^- + \text{O} \rightleftharpoons \text{O}_2 + \text{OH} + e^-$
- $2\text{OH} \rightleftharpoons \text{O} + \text{H}_2\text{O}$
- $\text{OH} + \text{O} \rightleftharpoons \text{O}_2\text{H}$
- $\text{OH} + \text{O}_2\text{H} \rightleftharpoons \text{O}_2 + \text{H}_2\text{O}$
- $\text{O} + \text{O}_2\text{H} \rightleftharpoons \text{O}_2 + \text{OH}$
- $2\text{O} \rightleftharpoons \text{O}_2$
- $\text{O}_2\text{H}^- + \text{O} \rightleftharpoons \text{O}_2 + \text{OH}^-$
- $\text{O}_2\text{H}^- + \text{OH} \rightleftharpoons \text{O}_2\text{H} + \text{OH}^-$
- $\text{OH}^- + \text{O} \rightleftharpoons \text{O}_2\text{H}^-$

The relations [1] and the coefficient of OH^- give

$$\nu_1 - \nu_2 - \nu_9 + \nu_{10} - 2\nu_{11} - \nu_{12} - \nu_{13} + \nu_{14} - \nu_{17} = 0$$

$$\nu_2 - \nu_3 + \nu_5 + \nu_6 - \nu_{10} + \nu_{11} - \nu_{12} - \nu_{14} - 2\nu_{15} - \nu_{16} - \nu_{18} = 0$$

$$\nu_3 - \nu_4 + \nu_6 + \nu_7 + \nu_{12} - \nu_{13} - \nu_{14} + \nu_{17} = 0$$

Table III. Possible mechanisms for the oxygen-gas electrode reaction in alkaline solutions, assuming $\nu_{15} = 1$ and $\nu_4 = \nu_5 = \nu_6 = \nu_8 = \nu_9 = \nu_{10} = \nu_{13} = \nu_{14} = \nu_{16} = 0$

	A	B	C	D	E	F	G	H	I	J	K
ν_1	2	4									
ν_2	2		4	2	2	2	2				
ν_3				2		2		4		4	
ν_7					2		2		4		4
ν_{11}	2	-2						2	2	2	2
ν_{12}				-2			-2	-4			-4
ν_{17}					-2	-2			-4	-4	
ν_{18}						-2	2			-4	4

$$\nu_7 + \nu_8 + \nu_9 + \nu_{10} + \nu_{16} + \nu_{17} - \nu_{18} = 0$$

$$\nu_1 + \nu_2 + \nu_3 + \nu_4 + 2\nu_5 + \nu_6 + \nu_8 - \nu_{16} - \nu_{17} + \nu_{18} = 4$$

Of the 18 stoichiometric numbers, no more than five can be nonzero for a direct path, so that the complete set of mechanisms may be found. There are, however, $C(18,5) = 8568$ sets of simultaneous equations to be considered in this case; and the results of this tedious process are inappropriate to this discussion.

A very much more limited set of mechanisms may be obtained if it can be assumed for some particular electrode material that two electron transfers do not occur and that oxygen gas is produced or used only in step 15. With these limitations, $\nu_{15} = 1$ and the stoichiometric numbers of steps 4, 5, 6, 8, 9, 10, 13, 14, and 16 are zero. The resulting mechanisms are given in Table III.

Conclusion

The preceding sections provide and illustrate a systematic procedure for generating complete sets of reaction mechanisms, each of which corresponds to a kinetically distinct direct path made up of consecutive unit steps. The method requires only that a suitable set of possible intermediate species be assumed; beyond this point, the generation of possible unit steps and their combination into appropriate mechanisms are shown to follow quite mechanically when it is recognized that the number of unit steps in a direct path cannot be more than one greater than the number of intermediates. These direct paths may, of course, be combined in a multitude of ways to account for the behavior of systems in which simultaneous mechanisms are thought to be occurring.

With regard to the analysis of kinetic measurements in terms of possible mechanisms, it should be noted that for a complex reaction with several intermediates, the number of mechanisms will usually be extremely large. It is, therefore, important to narrow the range of possibilities by every available means, eliminating intermediates and unit steps from consideration wherever possible. It is equally important to recognize that this range of possibilities is an inherent characteristic of complex reactions and that their mechanisms cannot be regarded as unambiguously determined unless all of the possible paths are considered. As exemplified by the oxygen-gas electrode reaction, this clearly demands the type of systematic approach described here, in

which assumptions can be clearly identified and methodical procedures used to provide complete sets of reaction mechanisms.

Although the illustrations given above are drawn from the field of electrochemistry, the methods are of equal applicability in generating sets of mechanisms for any reaction. For the reaction $H_2 + Br_2 = 2HBr$ with H and Br as intermediates, eight possible mechanisms can be postulated in addition to the simple over-all reaction, three of the eight being the well-known chain reaction with different initiating steps.

Acknowledgment

The author is indebted to F. H. Stillinger and U. B. Thomas for their helpful comments and discussion during the course of this work.

Manuscript received May 16, 1963; revised manuscript received Aug. 19, 1963. This paper was presented at the Los Angeles Meeting, May 6-10, 1962.

Any discussion of this paper will appear in a Discussion Section to be published in the December 1964 JOURNAL.

REFERENCES

1. S. Glasstone, K. J. Laidler, and H. Eyring, "The Theory of Rate Processes," pp. 85-152, McGraw-Hill Publishing Co., New York (1941).
2. J. Horiuti, *J. Research Inst. Catalysis*, Hokkaido University, **1**, 8 (1948).
3. J. Horiuti and M. Ikusima, *Proc. Imperial Academy*, Tokyo, **15**, 39 (1939).
4. K. B. Oldham, *J. Am. Chem. Soc.*, **77**, 4697 (1955).
5. H. Mauser, *Z. Elektrochem.*, **62**, 419 (1958).
6. A. C. Riddiford, *J. Chem. Soc.*, 1175 (1960).
7. R. Parsons, *Trans. Faraday Soc.*, **47**, 1332 (1951).
8. A. C. Makrides, *This Journal*, **104**, 677 (1957).
9. See, for example, G. Birkoff and S. MacLane, "A Survey of Modern Algebra," p. 269, Macmillan, New York (1941).
10. *Ibid.*, p. 291.
11. J. Horiuti and T. Nakamura, *Z. Phys. Chem. N. F.*, **11**, 358 (1957).

APPENDIX

Considering a system composed of the species S_n , it is desired to determine the number of linearly independent reactions of the type

$$\sum_n \sigma_n S_n = 0$$

that can take place. There will exist a set of e chemical entities, E_e , such that each of the species S_n may be taken to be a combination of them; thus

$$S_n = \sum_e m_{en} E_e$$

Since the entities E_e must be conserved in any reaction

$$\sum_n m_{en} \sigma_n = 0 \quad \text{for all } e$$

These relations form a set of e homogeneous linear equations in n unknowns; and, as in the body of the text, the number of linearly independent solutions of such a set and hence the number of independent reactions is less than or equal to $n - e$.

If now r of the n species are identified as reactants and products of an over-all reaction so that there are $n - r = i$ intermediates, it may be noted that e must be greater than or equal to $r - 1$; otherwise there will be an insufficient number of entities E_e to describe the system. Thus, the number of linearly independent reactions is less than or equal to $n - e$, which must be less than or equal to $n - r + 1 = i + 1$. This is then the maximum number of unit steps that can occur in a direct path, since these unit steps must be linearly independent.

An Electrochemical Study of Thin Adsorbed Oxygen Films on Rhodium in Oxygen-Saturated Acid Solution

James P. Hoare

Research Laboratories, General Motors Corporation, Warren, Michigan

ABSTRACT

The rest potential of rhodium electrodes in oxygen-saturated acid solutions was determined as a function of time, pH, partial pressure of oxygen, and history of electrode preparation. Two electrode systems are distinguished. The Rh/Rh-O system consists of an adsorbed layer of oxygen atoms on the Rh surface, and the rest potential is a mixed potential, 930 ± 20 mv. The Rh/Rh₂O₃ system consists of an adsorbed layer of Rh₂O₃ on the Rh surface, and the rest potential is a mixed potential, 880 ± 10 mv. These oxygen films are good electronic conductors but poor catalysts for the decomposition of peroxides. Evidence is presented to show that the nature and the chemical and electrochemical properties of the two films are quite different which may be traced to two different types of bonding between the rhodium and oxygen atoms.

In previous work (1, 2), it was suggested that many of the differences in electrochemical properties of the Pt-O₂-acid and the Au-O₂-acid systems might be traced to differences in the nature of the thin adsorbed oxygen films present on the metal surface. One of the chief differences is expressed in the distinction between a thin film of adsorbed oxygen atoms and a thin film of adsorbed oxide.

With respect to its interaction with oxygen, rhodium seems to be quite similar to platinum (3),

and the oxygen layers formed on rhodium surfaces seem to be not much thicker than a monolayer (3-5). However, it appears that rhodium is not as good a catalyst for the O₂/H₂O reaction as Pt is. Therefore, it seemed to be a matter of interest to study the properties of these thin adsorbed oxygen films on Rh by investigating the rest potential of Rh electrodes in oxygen-saturated sulfuric acid solutions as a function of pH, partial pressure of oxygen, and history of electrode preparation.

Experimental

At the end of rhodium wires (99.9+% pure), small beads (0.1-0.13 cm in diam) were melted in an oxygen torch. The beads were cleaned by heating white hot in a H_2 flame followed by quenching in concentrated HNO_3 . This procedure was repeated about fifteen times. After this treatment, the beads were mirror-bright but had a bluish-black cast when compared to the appearance of a bright platinum bead. Three test beads, as checks, were mounted in the right side of a dual Teflon cell, and an α -Pd-H reference electrode (6) was mounted in the left side as described before (1, 2). All purification techniques and all cell and electrode preparations were carried out as before (1, 2). This investigation was done at a temperature of $25^\circ \pm 1^\circ C$, and the potentials were recorded with respect to the normal hydrogen electrode (NHE) unless otherwise stated. The purity of the system was checked by polarizing the Rh bead when the system was saturated with hydrogen with an electronic current interrupter and observing the resulting high pseudocapacitance (7). The potential was measured with a Model 1230-A General Radio Electrometer having a variable input impedance.

Results and Discussion

Rest potential as a function of time.—After the Rh bead had been polarized anodically in O_2 -saturated 2N sulfuric acid solution for about 15 min at about 1.8v, the circuit was broken, and the potential was followed as a function of time. The potential dropped rather quickly (within 15 min) to a minimum value between 710 and 770 mv. The system was then stirred with hydrogen gas (200 cm^3/min) to remove any peroxides produced during

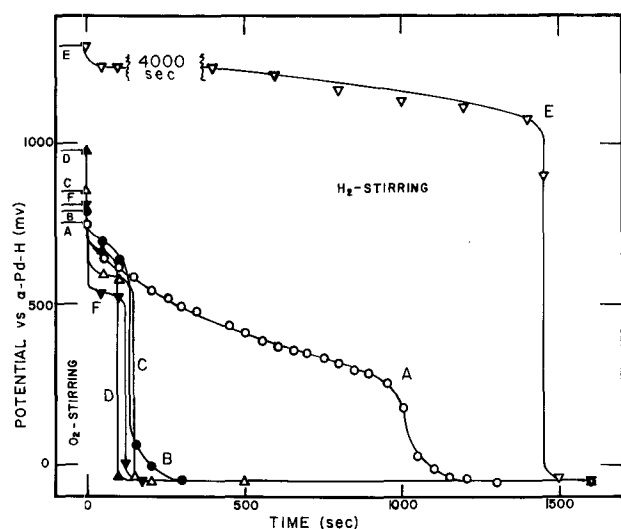


Fig. 1. Plot of the open-circuit potential vs. α -Pd-H as a function of time for the reduction of the adsorbed oxygen film on various electrodes with H_2 -stirring. The H_2 -stirring was between 200 and 250 cm^3/min in all cases. The curves begin with the electrodes at steady state with O_2 -stirring. At zero time the O_2 -stirring is replaced with H_2 -stirring. Curve A is the plot for a Rh/Rh $_2$ O $_3$ electrode; curve B, a Rh/Rh-O; curve C, an anodized Pt-O; curve D, a Pt-O; curve E, a Au/Au $_2$ O $_3$; curve F, a Au/Au-O. The hydrogen potential is -50 mv vs. α -Pd-H and is the point where it is assumed that all of the oxide is reduced. The points are direct readings from the meter, and the shapes of the curves were obtained from the recorder traces.

the period of anodic polarization. Although a platinum electrode in the same solution came to the hydrogen potential (-50 mv vs. α -Pd-H) within 5 min (curve C, Fig. 1), about 1300 sec, on the average, were required for the rhodium electrode to reach the same point. Over this 1300-sec period, the potential fell along a more or less smooth curve as shown by curve A in Fig. 1.

This behavior is different from that observed by a system in which the metal surface is covered by many layers of the metal oxide. The reduction curve obtained with H_2 -stirring in this case is shown by curve E in Fig. 1 for the reduction of the oxide layer on a Au/Au $_2$ O $_3$ electrode in H_2 -stirred acid solution (2). Such a curve exhibits a relatively long plateau (over 4000 sec) followed by a precipitous drop from the oxygen adsorption region to the hydrogen adsorption region. The reduction curve for the case where the adsorbed film is a monolayer of adsorbed atoms of oxygen also has a different form than curve A of Fig. 1 has. Here the film is completely reduced within 200 or 300 sec, and also the abrupt transition between the region of oxygen adsorption and hydrogen adsorption is observed. This behavior is demonstrated by the Pt/Pt-O electrode (1) in H_2 -stirred acid solution (curve D in Fig. 1) and by the Au/Au-O electrode (2) in H_2 -stirred acid solution (curve F in Fig. 1).

These observations indicate that the adsorbed oxygen film formed on a Rh surface during anodization must be very strongly held to the Rh surface, since the transition from the region of oxygen adsorption to that of hydrogen adsorption is relatively gradual. In fact, the transition is so gradual that these regions may overlap, which is understandable if this adsorbed oxygen film on Rh is not only tightly bound to the Rh surface but is also a good electronic conductor itself. These suggestions are supported by the polarization data obtained by Böld and Breiter on Rh (3) and on Pt (8) using the triangular waveform method of Will and Knorr (9). The oxygen reduction peak appears very close to the point where hydrogen begins to adsorb on Rh, Fig. 2a of ref. 3, whereas the peak in the Pt system, Fig. 5a of ref. 8, is some distance away. In fact, the current gets close to zero in the case of Pt after the oxygen reduction peak is passed but is far from zero in the case of Rh. Also, they observed that the adsorbed oxygen film on Rh does not increase in thickness much beyond a monolayer with continued anodic polarization, which indicates that the adsorbed layer is a good electronic conductor.

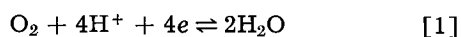
After the Rh bead had reached the hydrogen potential (after 1300 sec), the H_2 -stirring was replaced with O_2 stirring. The potential rose quickly to about 600 mv (within 100 sec) after which it steadily rose more slowly until a steady value of 930 ± 20 mv was reached in about 24 hr. When this electrode was treated with H_2 -stirring, the hydrogen potential was reached within 300 sec as shown by curve B in Fig. 1. In this case, the rhodium-oxygen system behaves in a manner very similar to the Pt/Pt-O and Au/Au-O cases. Therefore, a rhodium-oxygen electrode prepared by the

adsorption of oxygen from an O_2 -stirred solution after being maintained at the hydrogen potential with H_2 -stirring will be referred to as a Rh/Rh-O electrode. It is suggested that in this case the rhodium surface is covered by a monolayer of adsorbed oxygen atoms as in the Pt/Pt-O and Au/Au-O cases (1, 2).

Rest potential as a function of the partial pressure of oxygen.—The partial pressure of oxygen, P_{O_2} , was varied by diluting the oxygen with nitrogen as described before (1, 2) and was estimated from the rotameter readings. It was found that the rest potential, before treatment with H_2 -stirring, was dependent on the partial pressure of oxygen and sensitive to the stirring rate. The appearance of such a bead was the mirror-bright one with a bluish-black cast which was observed before the bead was anodized. After this bead had been treated with H_2 -stirring followed by O_2 -stirring to form the Rh/Rh-O electrode, it still retained the mirror-bright appearance with a bluish-black cast.

It was observed that the rest potential of the Rh/Rh-O electrode was dependent on the partial pressure of O_2 and independent of the stirring rate. The data for four different runs on four different beads are presented in Fig. 2. The points represent the experimental data and lines, having a slope of 15 mv, were drawn through these points to show that the data are not inconsistent with a four-electron process.

Then, these data may be explained through an over-all potential-determining reaction involving the O_2/H_2O reaction



If Eq. [1] were the only rate-determining process, a potential of 1.23v would be observed. Since this case is not observed and since a four-electron process is indicated, it is suggested that the observed rest potentials are mixed potentials (10) similar to those observed in the platinum-oxygen system

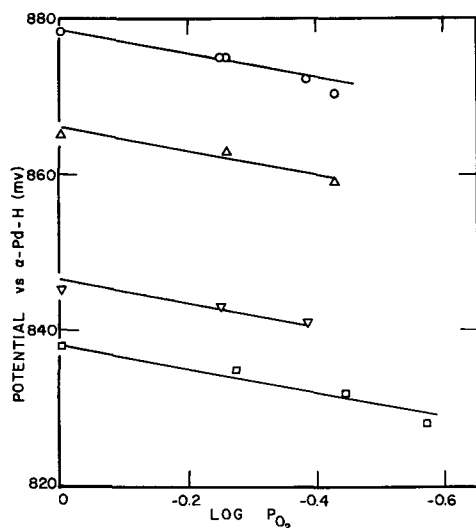
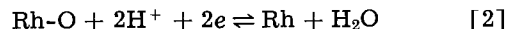


Fig. 2. Plot of the rest potential as a function of the partial pressure of oxygen. The points represent the experimental data. Lines with a slope of 15 mv per unit change in P_{O_2} were drawn through the points to indicate that the data are consistent with a four-electron process.

(1). This proposal requires that the potential-determining process occurring at a Rh/Rh-O electrode should consist of the O_2/H_2O reaction, Eq. [1], and a reaction involving Rh and Rh-O, such as

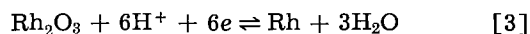


The steady state is reached at a potential of 930 ± 20 mv. When nitrogen was bubbled over this electrode for about 20 hr, the potential fell to a fairly steady value of 810 ± 15 mv. In this case, if it may be assumed that the O_2/H_2O reaction is suppressed and that, now, Eq. [2] is potential-determining, the standard potential for the Rh/Rh-O reaction is near 810 mv.

Rest potential as a function of pH.—The pH was varied by diluting the 2N H_2SO_4 with 2N Na_2SO_4 to keep the ionic strength constant, and its value was determined at the end of an experiment from the potential difference between a saturated calomel electrode (SCE) and a Pt/ H_2 electrode in the same solution. It was observed that all potentials vs. α -Pd-H were independent of pH. This indicates that all potential-determining reactions depend on the hydrogen ion activity in the same way as the α -Pd-H electrode reaction does (11). Therefore, for each electron transferred, a hydrogen ion is involved. This relationship is obeyed by both Eq. [1] and [2].

Rh/Rh₂O₃ electrode.—In order to study the behavior of the oxygen layer produced by anodization and yet free of the presence of peroxides, the following experiment was performed. Three Rh beads were prepared and mounted in a clean Teflon cell in the manner described before (1, 2). The cell was filled with 2N H_2SO_4 solution and pre-electrolyzed against a removable auxiliary Pt electrode for at least 24 hr. In a second clean dual Teflon cell (1), an α -Pd-H reference electrode was mounted in the left side. This cell was also filled with 2N H_2SO_4 solution and pre-electrolyzed for at least 24 hr. At the end of this time, H_2 was bubbled in the left side until 50 mv was observed on the Pd bead against a Pt/ H_2 electrode in the same solution for at least 2 hr. Next, hydrogen was bubbled through the right side for 20 min to remove peroxides, after which the H_2 -stirring was replaced with O_2 -stirring for 20 min to saturate the solution with oxygen. Finally, the Rh beads were removed from the first cell and placed in the right side of the second cell in O_2 -saturated, peroxide-free 2N H_2SO_4 solution. The cell was sealed up and potential measurements were taken.

In this case, the potential did not fall rapidly to much lower values as observed previously. Instead, the potential fell very slowly from about 1320 through 1050 mv in 8 hr to about 900 mv in 24 hr. Finally, the potential became steady at 880 ± 10 mv. This value is very close to the value (0.87v) quoted by Latimer (12) for the reaction

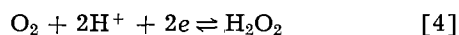


When such an electrode was treated with H_2 -stirring, it required about 1300 sec for the potential to fall to the hydrogen potential.

It was found that the observed potentials in this case were independent of P_{O_2} , and so it appears that a metal-metal oxide reaction similar to Eq. [3] is potential-determining. Sidgwick (13) states that the only stable oxide formed by rhodium is Rh_2O_3 and that this may be formed by heating Rh in air. A cleaned Rh wire was heated white hot in a H_2 flame and allowed to cool down in air. This wire was then plunged into an O_2 -saturated acid solution and the potential observed. It was found that the potential came to a steady value of about 875 mv in about 3 hr. Therefore, the system that is obtained by the anodic polarization of Rh and requires about 1300 sec to reduce the oxide film with H_2 -stirring will be referred to as the Rh/Rh $_2O_3$ system.

From the polarization data and coulometric studies of Butler and Drever (5) and Böld and Breiter (3), it appears that the oxide layers on Rh do not grow much beyond a monolayer. Therefore, in view of the experimental evidence, it is suggested that a layer of Rh_2O_3 , not much thicker than a monolayer, is formed on a rhodium surface with anodic polarization and that the rest potential is determined by the Rh/Rh $_2O_3$ reaction, Eq. [3], with a standard value of about 0.87v.

It is interesting to note that the potential never did reach the low value of about 740 mv in the absence of peroxide. It appears that the presence of peroxide has a greater effect on the rest potential in the Rh- O_2 system than in the Pt- O_2 system. Even though the oxygen layers on Rh are good electronic conductors, as they are on Pt, it may be possible that the Rh/Rh $_2O_3$ surface is such a poor peroxide-decomposing catalyst that relatively large amounts of peroxide accumulate in the vicinity of the electrode. In this case, the potential is pulled toward the potential of the O_2/H_2O_2 reaction



with a standard potential of 0.682v (12). It appears that Eq. [4] is established under these conditions since the potential is dependent on the partial pressure of oxygen. When peroxide is not present, the potential does not drop below 880 ± 10 mv, and it is independent of the partial pressure of oxygen.

Polarization data at low current densities.—The test electrodes were cathodically polarized in the same manner as described before (1, 2). In Fig. 3, the plot of the polarization (potential, E , minus the open-circuit potential, E_{oc}) against the logarithm of the apparent current density (estimated from the recorded potential, the geometric area of the bead, and the estimated value of the input impedance) is presented for both the Rh/Rh-O and the Rh/Rh $_2O_3$ systems. In curve A, the Rh/Rh-O electrode was cathodized with oxygen flowing at about 280 cm 3 /min. Although there is a hysteresis in coming back down the curve, the open-circuit value can be recovered within 1000 sec, after which the points on curve A can be reproduced within about 10 mv. When O_2 -stirring is replaced with N_2 -stirring, curve B is obtained. Here, the polarization is much larger and the hysteresis is very pronounced since it requires 5000 sec for the potential to return to the open-circuit value after being polarized.

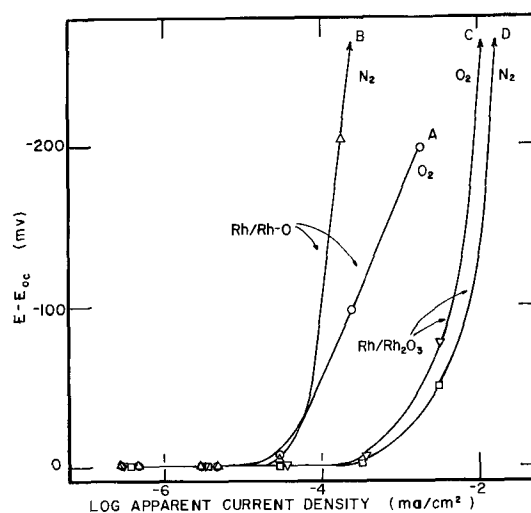


Fig. 3. Plot of the polarization, $E - E_{oc}$, as a function of the logarithm of the apparent current density for the Rh/Rh-O system with O_2 -stirring, curve A, and with N_2 -stirring, curve B; for the Rh/Rh $_2O_3$ system with O_2 -stirring, curve C, and with N_2 -stirring, curve D.

These data indicate that most of the current goes into the reduction of oxygen when the system is stirred with oxygen. In the N_2 -stirred case, the current has to go into the reduction of the adsorbed, Rh-O layer, and the system is polarized to high negative potentials quickly because there is not enough active material to support the demanded current density. If permitted, the potential would go to the point where hydrogen ion would be reduced. The hysteresis occurs because it takes time to repair the reduced film of Rh-O.

Curve C is obtained by cathodizing a Rh/Rh $_2O_3$ electrode with O_2 -stirring and curve D, with N_2 -stirring. However, the hysteresis is extremely pronounced since it required about 6 hr for the open-circuit potential to be reached after the system had been polarized in O_2 -stirring and about 9 hr in N_2 -stirring. It is interesting to note that the polarization is less for the N_2 curve than for the O_2 curve, although the curves are very close to one another. It appears that most of the current goes into the reduction of Rh $_2O_3$ in either case since the curves are so close to one another. Since the O_2 -stirred and N_2 -stirred curves are different, this indicates that rest potentials observed at Rh/Rh $_2O_3$ electrodes are mixed potentials and not true metal-metal oxide potentials such as those at Au/Au $_2O_3$ electrodes (2). Here, at the rest potential value, the local cell current is such that the O_2/H_2O reaction is polarized down to the Rh/Rh $_2O_3$ reaction (Eq. [3]). Then the rest potential is determined by Eq. [3] alone, and this explains why the observed open-circuit potentials in the Rh/Rh $_2O_3$ system are independent of P_{O_2} .

The hysteresis may be explained by two factors: (a) the difficulty in repairing the reduced Rh $_2O_3$ film and (b) the presence of peroxide produced by the reduction processes. Since, as in the case of curves A and B, the hysteresis is less with oxygen-stirring, it appears that the presence of oxygen promotes the repair of the adsorbed film. Therefore, curve C should have less pronounced hysteresis than curve D. As shown above, however, the Rh/Rh $_2O_3$

surface appears to be a poor peroxide-decomposing catalyst, and interfering concentrations of peroxide may accumulate in the vicinity of the electrode when oxygen is reduced (14). This may also be true when Rh_2O_3 is reduced and could explain why the polarization is greater in the case of O_2 -stirring than in the N_2 -stirred case. If reduction of O_2 produces more peroxide than reduction of Rh_2O_3 for a given current density, the potential should be less noble in the O_2 case than in the N_2 case, and curve C should fall to the left of curve D as it was observed to do.

It appears that rhodium is inferior to platinum as a catalyst for the reduction of oxygen because the adsorbed oxygen films on Rh, although they may be good electronic conductors, are much poorer peroxide-decomposing catalysts than those on Pt.

When a clean, oxygen-free Rh surface is permitted to adsorb oxygen from an acid solution by replacing H_2 -stirring with O_2 -stirring a film of adsorbed oxygen atoms about a monolayer thick is formed similar to that formed in the case of Pt. However, when the surface is anodically polarized the layer does not thicken much beyond a monolayer (3-5), but the oxygen becomes more tightly bound to the Rh to the extent that the layer may now be considered as one of an oxide, Rh_2O_3 . Evidence for the existence of the two types of adsorbed oxygen layers in the Rh- O_2 system is found in the data for the reduction of these films with H_2 -stirring, which certainly involves the bond between the adsorbed layer and the metal. The adsorbed film on the Rh/Rh-O electrode is reduced in about 300 sec while that on the Rh/ Rh_2O_3 electrode is reduced in about 1300 sec, over four times longer (curves A and B of Fig. 1). Also, the repair of these films is more difficult in the case of Rh_2O_3 , as shown by the greater hysteresis in the polarization data of Fig. 3 for the Rh/ Rh_2O_3 system. In Fig. 3, the plot of the polarization for the Rh/Rh-O electrode with O_2 -stirring (curve A) gives a Tafel-like region whereas the plot for the Rh/ Rh_2O_3 electrode (curve C) does not.

Apparently, the chemical and electrochemical properties of these layers are quite different in the two cases. It may be possible to trace these differences to the possibility that, in the Rh/Rh-O case, the adsorbed oxygen layer is composed of a mono-

layer of adsorbed oxygen atoms. In the Rh/ Rh_2O_3 case, however, the adsorbed oxygen layer may be described as an alloy of dissolved oxygen in the first surface layers of the Rh metal which may approximate an adsorbed monolayer of Rh_2O_3 . Two such different types of bonding of the oxygen with rhodium could produce the observed phenomena. This may be similar to the different types of bonds postulated in the literature in the case of adsorbed hydro- helpful comments and stimulating discussion.

Acknowledgment

The author wishes to express his gratitude to Dr. Paul Delahay, of Louisiana State University, and Dr. Raymond Thacker and Dr. John L. Griffin, of the General Motors Research Laboratories, for their helpful comments and stimulating discussion.

Manuscript received Mar. 8, 1963; revised manuscript received Aug. 19, 1963.

Any discussion of this paper will appear in a Discussion Section to be published in the December 1964 JOURNAL.

REFERENCES

1. J. P. Hoare, *This Journal*, **109**, 858 (1962).
2. J. P. Hoare, *ibid.*, **110**, 245 (1963).
3. W. Böld and M. Breiter, *Electrochim. Acta*, **5**, 169 (1961).
4. K. J. Vetter, "Elektrochemische Kinetik," p. 497, Springer Verlag, Berlin (1961).
5. J. A. V. Butler and G. Drever, *Trans. Faraday Soc.*, **32**, 427 (1936).
6. D. J. G. Ives and G. J. Janz, "Reference Electrodes," p. 112, Academic Press, New York (1961); J. P. Hoare, *G. M. Eng. J.*, **9**, No. 1, 14 (1962).
7. S. Schuldiner and J. P. Hoare, *J. Chem. Phys.*, **26**, 1771 (1957).
8. W. Böld and M. Breiter, *Electrochim. Acta*, **5**, 145 (1961).
9. F. Will and C. A. Knorr, *Z. Elektrochem.*, **64**, 258 (1960).
10. C. Wagner and W. Traud, *ibid.*, **44**, 391 (1938).
11. S. Schuldiner, G. W. Castellano, and J. P. Hoare, *J. Chem. Phys.*, **28**, 16 (1958).
12. W. H. Latimer, "Oxidation Potentials," Prentice-Hall, New York (1952).
13. N. V. Sidgwick, "Chemical Elements and Their Compounds," p. 1533, Oxford Press (1950).
14. A. V. Akopyan, *Zhur. Fiz. Khim.*, **33**, 82 (1959).
15. C. H. Presbrey and S. Schuldiner, *This Journal*, **108**, 985 (1961).
16. T. C. Franklin and S. L. Cooke, *ibid.*, **107**, 556 (1960).

Dynamic Analysis of Activation Overpotential

Leonard Karasyk,¹ Richard W. Law,² and Henry B. Linford

Department of Chemical Engineering, Columbia University, New York, New York

ABSTRACT

The differential equation describing the transient behavior of activation overpotential has been revised to take into consideration the fact that the sum $\alpha_c + \alpha_A$ does not equal one. Exact and approximate solutions to this equation are given. Using a digital computer program, estimates of the electrode kinetic parameters have been obtained from single charging curves. The values so calculated are in good agreement with those obtained by extrapolation and slope of Tafel lines drawn from several charging curves.

Activation overpotential has been characterized by the model of a resistance and a capacitance in parallel (1, 2). This representation has led to the derivation of a charging equation for a galvanostatic build up of overpotential (2)

$$\frac{d\eta_A}{dt} = -\frac{1}{C_A(t)} \left\{ i - i_o \left(\exp \left[-\frac{\alpha_c F \eta_A(t)}{RT} \right] - \exp \left[-\frac{(1 - \alpha_c) F \eta_A(t)}{RT} \right] \right) \right\} \quad [1]$$

where $\eta_A(t)$ is the activation overpotential (v), t time of charging (sec), $C_A(t)$ the capacitance in the model, often assumed to be the double layer capacity (f/cm²), i the total net current density (amp/cm²), i_o the exchange current density (amp/cm²), α_c the cathodic transfer coefficient, and F , R , T have their usual significance.

Derivation and Solution of Equations

Equation [1] is, however, not strictly valid for all cases, and a more accurate expression would be

$$\frac{d\eta_A}{dt} = -\frac{1}{C_A(t)} \left\{ i - i_o \left(\exp \left[-\frac{\alpha_c F \eta_A(t)}{RT} \right] - \exp \left[-\frac{\alpha_A F \eta_A(t)}{RT} \right] \right) \right\} \quad [2]$$

where α_A is the anodic transfer coefficient. The sum of $\alpha_A + \alpha_c$ has not been found to equal unity for many cases; for instance, for copper deposition and dissolution in a sulfate bath, the sum was experimentally found to be approximately 2 (3, 4).

For the sake of generality, assume

$$\alpha_A + \alpha_c = \theta = \text{constant} \quad [3]$$

where θ must always be $\leq Z$, the net valence change occurring in the deposition or dissolution.

Using Eq. [2] and [3], a general charging equation is obtained

$$\frac{d\eta_A}{dt} = -\frac{1}{C_A(t)} \left\{ i - i_o \left(\exp \left[-\frac{\alpha_c F \eta_A(t)}{RT} \right] - \exp \left[-\frac{(\theta - \alpha_c) F \eta_A(t)}{RT} \right] \right) \right\} \quad [4]$$

Equation [1], a special case of Eq. [4], is obtained by setting $\theta = 1$. For simplicity, the assumption is made that $C_A(t)$ is constant during the charging. While this assumption is not strictly true, it makes solution of Eq. [4] possible in special cases.³ In the absence of additional information, the substitution of an average value of $C_A(t)$, C_A , in Eq. [4] is reasonable.

$$\frac{d\eta_A}{dt} = -\frac{1}{C_A} \left\{ i - i_o \left(\exp \left[-\frac{\alpha_c F \eta_A(t)}{RT} \right] - \exp \left[-\frac{(\theta - \alpha_c) F \eta_A(t)}{RT} \right] \right) \right\} \quad [5]$$

Rojter, Juza, and Polujan (5) obtained a solution to Eq. [5] for the specific case of $\theta = 1$, $\alpha_c = 0.5$. Their solution, in addition to being very complicated, is valid only for the limited case mentioned.

Tabulated below, in Tables I and II, are exact and approximate solutions to Eq. [5]. The solutions cover a wider range of cases, and the approximate solutions are applicable to the completely general case where

$$0 < \alpha_c \leq \theta \leq Z$$

Derivations for these solutions are presented in the Appendix.

Application of Equations

A digital program has been written in Fortran (6, 7) language to obtain estimates of the kinetic parameters from the data of only one charging curve of activation overpotential vs. time. This program employs nonlinear least squares.

The computation assumes the overpotential to be given by the following expression

$$\eta_A(t) = \frac{1}{\alpha_c b} \ln \left[\rho + (1 - \rho) \exp \left[-\frac{\alpha_c b i t}{C_A} \right] \right] \quad [7]$$

³ The assumption that $C_A(t)$ remains constant during the growth of overpotential is perhaps an unrealistic condition which might make the solutions to Eq. [4] merely "idealized" calculations. Perhaps in the range of overpotentials for the system examined (0-200 mv for deposition of Cu from an acid CuSO₄ bath) $C_A(t)$ might well be approximated by an average capacity, C_A , for the fact remains that the solutions described in this paper have been successfully used to obtain good estimates of the kinetic parameters for this system! Of course additional tests with other systems would be helpful in further evaluation of the usefulness of these calculations. While the equations derived here might suffer from the approximation of an average double layer capacity, they are not limited by the often unrealistic restriction that η_A be less than several (0-5) mv, a condition which has been stipulated in previous solutions of equations of this sort, and therefore have the possibility of application to many more practical situations. Furthermore, the realization that $C_A(t)$ does change with potential makes the estimation of an integrated average double layer capacity from a single charging curve more meaningful than the estimation of $C_A(t)$ at zero overpotential from the initial slope of the charging curve.

¹ Present address: Socony Mobil Oil Company, Inc., New York, New York.

² Present address: Esso Research & Engineering Company, Madison, New Jersey.

Table I. Exact solutions to Eq. [5]

Eq. No.	$\eta_A(t)$	α_c	Restrictions	Other
[6]	$\eta_A(t) = -\frac{1}{\alpha_c b} \ln \left[\frac{r_1 K \exp[(r_1 - r_2)t] + r_2}{\alpha_c b B (K \exp[(r_1 - r_2)t] + 1)} \right]$ (See Notes 1, 2, 3, 4)	$\alpha_c = \frac{\theta}{2}$		None
[7]	$\eta_A(t) = \frac{1}{\alpha_c b} \ln \left[\rho + (1 - \rho) \exp \left[-\frac{\alpha_c b i t}{C_A} \right] \right]$ (See Notes 1, 5)	$\alpha_c = \frac{\theta}{2}$		$\rho \leq 0.15$
[8]	$\eta_A(t) = \frac{1}{b} \ln \left[\frac{\exp \left[-\frac{b i (1 + \rho) t}{C_A} \right] + \rho}{1 + \rho} \right]$ (See Notes 1, 5)	$\alpha_c = \theta$		None
[9]	$\eta_A(t) = -\frac{1}{\theta b} \ln \left[\frac{\exp \left[\theta b \left(\frac{1 - \rho}{C_A} \right) i t \right] - \rho}{1 - \rho} \right]$ (See Notes 1, 5)	$\alpha_c = 0$		None

$$1. b = \frac{F}{RT}$$

$$2. B = \frac{i_0}{C_A}$$

$$3. r_1 = \frac{\alpha_c \left(\frac{F}{RT} \right)}{2C_A} \left[i + \sqrt{i^2 + 4i_0^2} \right], r_2 = \frac{\alpha_c \left(\frac{F}{RT} \right)}{2C_A} \left[i - \sqrt{i^2 + 4i_0^2} \right]$$

$$4. K = - \left[\frac{i_0 - \frac{1}{2}(i - \sqrt{i^2 + 4i_0^2})}{i_0 - \frac{1}{2}(i + \sqrt{i^2 + 4i_0^2})} \right]$$

$$5. \rho = \frac{i_0}{i}$$

Table II. Approximate solutions to Eq. [5]

$$0 < \alpha_c \leq \theta \leq Z$$

Eq. No.	$\eta_A(t)$	Relationship of approximate solution to exact solution (unknown)
[7]	$\eta_A(t) \approx \frac{1}{\alpha_c b} \ln \left[\rho + (1 - \rho) \exp \left[-\frac{\alpha_c b i t}{C_A} \right] \right]$	$\approx \eta_A(t)$ exact*
[10]	$\eta_A(t) \approx \frac{1}{\alpha_c b} \ln \left[\frac{\rho + \exp \left[-\frac{\alpha_c (1 + \rho) b i t}{C_A} \right]}{1 + \rho} \right]$	$\approx \eta_A(t)$ exact

$$\text{Note: } b = \frac{F}{RT}, \rho = \frac{i_0}{i}$$

* $\eta_A(t)$ exact = that function $\eta_A(t)$ whose derivative with respect to time exactly fits Eq. [5] subject to no limitation on α_c except the one that $0 < \alpha_c \leq \theta \leq Z$.

The regression that was used was nonlinear since the parameters to be estimated in Eq. [7] appear in nonlinear form. The least squares approach [see ref. (8)] can be understood by considering the following equation

$$\beta = f(\epsilon_1, \dots, \gamma_k; \gamma_1 \dots \gamma_p) \quad [11]$$

Equation [11] connects a response β (in our case, activation overpotential) with levels of the variables $\epsilon_1, \dots, \epsilon_k$ (for instances, time, temperature, pressure, etc.); $\gamma_1, \dots, \gamma_p$, are unknown parameters. For this study, p is three and the unknown parameters are α_c, i_0 , and C_A .

Now, if $\beta = f(\epsilon, \gamma)$ is the solution of the differential equations for the observed response at some particular set of experimental conditions ϵ , and if y is the observed value of β at these conditions, then least squares estimates of the p constants γ would be obtained by minimizing the quantity

$$S(\gamma) = \sum [y - f(\epsilon, \gamma)]^2 \quad [12]$$

where the summation is over the n sets of experimental conditions (2). With the assumption that the experimental errors are normally distributed, the estimates γ so obtained are also maximum likelihood estimates.

Table III. Results of averaging parameter values with digital program

Cathode	Digital program	α_c	Tafel line	$i_0, \text{ ma/cm}^2$		$C_A, \mu\text{F/cm}^2$	
				Digital program	Tafel line	Digital program	Slope of charging curve
Atomizer	0.57 ¹			10.8 ¹		50 ¹	
Clean cathode	0.54 ¹	0.58 ³ ± 0.02		11.4 ¹	8.3 ³ ± 3.2	49 ¹	53 ⁴
	0.62 ¹			11.1 ¹		48 ¹	
	0.57 ²			10.6 ²		53 ²	
						16	
Soiled cathode ⁵	0.30	0.32 ⁶		22.8	18.0 ⁶		25

¹ These values all from same single charging curve using different data points with different grid spacings.

² Different current density on the same cathode.

³ Tafel line directed by 7 data points.

⁴ Initial slope of charging curve, footnote 1.

⁵ Soiled with the equivalent of one monolayer stearic acid, freshly applied (20 min); 107 coulombs/cm² prior deposition.

⁶ Tafel line directed by 6 data points.

The above least squares approach was used in the digital program. The procedure starts with a collection of data points from a charging curve consisting of the observed overpotential $\eta_{A,j}(t)$ ($j = 1, 2, \dots, N$) and the corresponding values of time, t_j . These data are then read into the computer. A guess is made for the parameters, α_c , i_0 , and C_A . For this combination of parameter values and a value of t_j , a predicted value $\hat{\eta}_{A,j}$ is computed using Eq. [7]. The quantity

$$\text{SUM} = \sum_{j=1}^N (\eta_{A,j}(t) - \hat{\eta}_{A,j}(t))^2 \quad [13]$$

is then calculated and stored by the digital computer. The value of C_A is then incremented by a specified amount while holding α_c and i_0 constant at their original value. For this new set of parameter values, the computer calculates and stores the quantity represented by Eq. [13]. This procedure of incrementing one parameter value at a time is continued until all possible combinations (as determined by the range and increment specified in the input data for each parameter) of parameter values have been used in calculation of Eq. [13].

Since experimental data are being considered, there is uncertainty in the value of overpotential used in calculating Eq. [13]. Therefore, the calculated set of three parameters yielding the minimum sum define a point which lies in the same region as the set of three parameters giving the true minimum and which differs from these true values by some error.

The average uncertainty in the activation overpotential as determined from the experimental charging curves⁴ was ±5 mv. Now, the standard deviation of residuals is given by (2)

$$S_e = \left[\frac{\sum (\eta_A(t) - \hat{\eta}_A(t))^2}{N - p} \right]^{1/2} \quad [14]$$

where p is the number of parameters estimated and N is the number of data points used. Thus, if one were trying to determine three parameters from 11 data points, and if the uncertainty in the overpotential is ±5 mv, then the sum of the squares of the residuals could come out as high as

⁴ The charging curves were photographs measuring 7 × 5½ cm.

$$\sum (\eta_A - \hat{\eta}_A)^2 = (5)^2 \cdot (11-3) = 200$$

and still be a possible solution.

Therefore, what is done in this digital program is to accept all sets of parameter values for which the following expression holds

$$\sum (\eta_A - \hat{\eta}_A)^2 \leq (5)^2 (N-p) \quad [15]$$

The parameter values that satisfy Eq. [15] are then averaged to obtain the least-squares estimates of the parameters.

These techniques were applied to galvanostatic charging curves, plots of activation overpotential vs. time, obtained for the deposition of copper from an acid sulfate bath (9). In that study both clean and reproducibly soiled (with stearic acid) copper cathodes were studied. Excellent agreement with the experimental results was obtained by using the above method of averages to estimate the kinetic parameters. Table III summarizes the results obtained using the digital program and compares these results with those obtained by the use of the Tafel Line.

There are two distinct advantages in using this digital program to get the estimates of the kinetic parameters:

1. With this program, an integrated C_A is obtained. This C_A is more representative of the true C_A of the charging process than the C_A obtained from the initial slope of the charging curve. An integrated C_A is more meaningful than a constant C_A since the double layer capacitance does change as the overpotential varies.

2. Only one charging curve is required to obtain the kinetic parameters with this digital program. The importance of using only one charging curve to get estimates of the parameters cannot be overemphasized. Previously, the parameters for the soiled electrodes were determined from at least two separate measurements, each on a different electrode. This procedure introduced an additional source of variation, namely, a different electrode with the same apparent aggregate soil density on the surface.

The computer program described here does not represent the only approach to the problem of obtaining kinetic parameters from one charging curve. The method of steepest descents (10) might be prof-

itably employed as an efficient means of approaching the minimum from well-spaced starting points situated in the permissible region.

While the averaging process used here is vital, it is important to point out the danger inherent in averaging minimum points which are not well-spaced in the acceptable region, *i.e.*, if the sets of calculated minimum points differ from the true minimum point by an error in the same direction, the calculated average would be biased.

Nevertheless, the averaging process when properly used (with provisions to minimize bias) should minimize an objection raised by Matsen (11) to using one charging curve to estimate kinetic parameters. On the basis of his analog computer solutions to the charging equation, Matsen argued that small errors in reading overpotentials from the charging curves would result in large errors in the kinetic parameters. However, it appears as shown by the values in Table III that these errors can be dramatically reduced by the averaging process.

Acknowledgment

The authors are indebted to the American Electroplaters' Society for the financial support and encouragement they provided for a portion of this research under A.E.S. Project No. 12.

Manuscript received Feb. 20, 1963; revised manuscript received Sept. 6, 1963. This paper was prepared for delivery before the Pittsburgh Meeting, April 15-18, 1963.

Any discussion of this paper will appear in a Discussion Section to be published in the December 1964 JOURNAL.

REFERENCES

1. J. N. Agar, *Ann. Rep. Prog. Chem.*, **44**, 5 (1947).
2. E. Mattson, *Trans. Roy. Inst. Technol., Stockholm*, **96**, 47 (1955).
3. E. Mattson and J. O'M. Bockris, *Trans. Faraday Soc.*, **55**, 1586 (9/1959).
4. D. R. Turner and G. R. Johnson, *This Journal*, **109**, 798 (1962).
5. W. A. Rojter, W. A. Juza, and E. S. Polujan, *Acta Physicochim. U.R.S.S.*, **10**, 389, 845 (1939).
6. IBM, *Reference Manual*, 1620 Data Processing System (1961).
7. IBM, *Data Processing Systems Bulletin*, IBM 1620 Fortran: Preliminary Specifications, Bulletin No. 26-4200-2, (May 1961).
8. G. E. P. Box and M. A. Coutie, *Proc. Inst. Elec. Engrs., London*, **103**, Pt. B (1), 100 (1956).
9. L. Karasyk and H. B. Linford, *This Journal*, **110**, 895 (1963).
10. O. L. Davies, "Design and Analysis of Industrial Experiments," pp. 495-501, Hafner Publishing Co., New York (1960).
11. J. M. Matsen, *This Journal*, **110**, 222 (1963).
12. N. W. McLachlan, "Ordinary Non Linear Differential Equations in Engineering and Physical Sciences," 2nd Ed. Clarendon Press, p. 12 (1952).
13. H. S. Mickley, T. K. Sherwood, and C. E. Reed, "Applied Mathematics in Chemical Engineering," 2nd Ed., pp. 148-152, McGraw-Hill Book Co., New York (1957).
14. *Ibid.*, p. 141.

APPENDIX

I. Exact Solutions to Eq. [5]

$$\frac{d\eta_A}{dt} = -\frac{1}{C_A} \left[i - i_0 \left(\exp \left[\frac{-\alpha_c F \eta_A(t)}{RT} \right] - \exp \left[\frac{(\theta - \alpha_c) F \eta_A(t)}{RT} \right] \right) \right] \quad [5]$$

Letting

$$b = \frac{F}{RT}, \quad A = \frac{i}{C_A}, \quad B = \frac{i_0}{C_A} \\ u = \exp [-\alpha_c b \eta_A(t)]$$

Eq. [5] becomes

$$\frac{du}{dt} = -\alpha_c b A u - \alpha_c b B u^2 + \alpha_c b B u^{2-\theta/\alpha_c} \quad [5a]$$

when $\alpha_c = \theta/2$, Eq. [5a] reduces to

$$\frac{du}{dt} = -\alpha_c b A u - \alpha_c b B u^2 + \alpha_c b B \quad [5b]$$

which is of the form of the Riccati equation (12). By defining a new variable

$$Z = \exp [\alpha_c b B \int u dt] \quad [5c]$$

Eq. [5b] is converted to

$$\frac{d^2 Z}{dt^2} - (\alpha_c b A) \frac{dZ}{dt} - (\alpha_c b B)^2 Z = 0 \quad [5d]$$

This equation is a standard second order linear differential equation whose solution is given by (13)

$$Z = K_1 \exp [r_1 t] + K_2 \exp [r_2 t] \quad [5e]$$

where K_1, K_2 are constants of integration and

$$r_1 = \frac{\alpha_c b}{2} [A + \sqrt{A^2 + 4B^2}] = \frac{\alpha_c b}{2C_A} [i + \sqrt{i^2 + 4i_0^2}] \\ r_2 = \frac{\alpha_c b}{2} [A - \sqrt{A^2 + 4B^2}] = \frac{\alpha_c b}{2C_A} [i - \sqrt{i^2 + 4i_0^2}]$$

Solving Eq. [5e] for $\eta_A(t)$ leads to

$$\eta_A(t) = -\frac{1}{\alpha_c b} \ln \left[\frac{r_1 K_1 \exp [r_1 t] + r_2 K_2 \exp [r_2 t]}{(\alpha_c b B) (K_1 \exp [r_1 t] + K_2 \exp [r_2 t])} \right] \quad [5f]$$

Dividing the expression in brackets by $K_2 \exp [r_2 t]$ results in

$$\eta_A(t) = -\frac{1}{\alpha_c b} \ln \left[\frac{r_1 K \exp [(r_1 - r_2)t] + r_2}{(\alpha_c b B) (K \exp [(r_1 - r_2)t] + 1)} \right] \quad [6]$$

where $K = K_1/K_2$.

Using the boundary condition that $\eta_A(t) = 0$ when $t = 0$, the constant of integration is found

$$K = -\frac{[i_0 - \frac{1}{2}(i - \sqrt{i^2 + 4i_0^2})]}{[i_0 - \frac{1}{2}(i + \sqrt{i^2 + 4i_0^2})]}$$

Some simplifications.—When $i_0/i \leq 0.15$, the assumption that $\sqrt{i^2 + 4i_0^2} = i$ is in error by less than 5%. Under these conditions

$$K \approx -\frac{i_0}{i_0 - i}$$

Letting $\rho = i_0/i$ and assuming that $\rho \leq 0.15$, Eq. [6] is simplified to

$$\eta_A(t) = \frac{1}{\alpha_c b} \ln \left[\rho + (1 - \rho) \exp \left[-\frac{\alpha_c b i t}{C_A} \right] \right] \quad [7]$$

When $\alpha_c = \theta$, Eq. [5] becomes

$$\frac{d\eta_A}{dt} = B \exp [-b\eta_A(t)] - (A + B) \quad [7a]$$

Letting $W_1 = \exp [-b\eta_A(t)]$ reduces Eq. [7a] to the form of Bernoulli's equation (14)

$$\frac{dW_1}{dt} = b(A + B)W_1 - bBW_1^2 \quad [7b]$$

which can be directly integrated if a new variable $V = 1/W_1$, is substituted into Eq. [7b]. Solving for $\eta_A(t)$ gives

$$\eta_A(t) = \frac{1}{b} \ln \left[\frac{K_3 \exp[-b(A+B)t] + bB}{b(A+B)} \right] \quad [7c]$$

At $t = 0$, $\eta_A(t) = 0$, so that $K_3 = bA$.

Substituting this value of K_3 , i/C_A for A , and i_0/C_A for B into Eq. [7c] leads to

$$\eta_A(t) = \frac{1}{b} \ln \left[\frac{\exp \left[-\frac{bi(1+\rho)t}{C_A} \right] + \rho}{1+\rho} \right] \quad [8]$$

When $\alpha_c = 0$, Eq. [5] becomes

$$\frac{d\eta_A}{dt} = (B-A) - B \exp[\theta b \eta_A(t)] \quad [8a]$$

Defining a new variable $W_2 = \exp[-\theta b \eta_A(t)]$ transforms Eq. [8a] to a form which can be directly integrated. Using the boundary condition, that $\eta_A(t) = 0$ at $t = 0$, and remembering the definitions for A and B leads to Eq. [9]

$$\eta_A(t) = -\frac{1}{\theta b} \ln \left[\frac{\exp \left[\frac{\theta b(1-\rho)it}{C_A} \right] - \rho}{1-\rho} \right] \quad [9]$$

II. Approximate Solutions

If the variable $W_1 = \exp[-b\eta_A(t)]$ is defined, Eq. [5] may be written as

$$\frac{dW_1}{dt} = W_1 \left[\left(\frac{1}{\rho} \right) - W_1^{\alpha_c} + W_1^{\alpha_c - \theta} \right] \quad [9a]$$

where

$$W_1^{\alpha_c - \theta} = \exp[(\theta - \alpha_c)b\eta_A(t)]$$

Since

$$\eta_A(t) \leq 0$$

$$0 \leq W_1^{\alpha_c - \theta} \leq 1$$

so that

$$W_1 \left[\left(\frac{1}{\rho} \right) - W_1^{\alpha_c} \right] \leq \frac{dW_1}{dt} \leq W_1 \left[\left(\frac{1}{\rho} \right) - W_1^{\alpha_c} + 1 \right] \quad [9b]$$

Integrating

$$W_1 \left[\left(\frac{1}{\rho} \right) - W_1^{\alpha_c} \right] = \frac{dW_1}{dt}$$

results in Eq. [7]

$$\eta_A(t) \cong \frac{1}{\alpha_c b} \ln \left[\rho + (1-\rho) \exp \left[-\frac{\alpha_c b i t}{C_A} \right] \right] \quad [7]$$

when the boundary condition that $\eta_A(t) = 0$ at $t = 0$ is employed.

Similarly integration of

$$\frac{dW_1}{dt} = W_1 \left[\left(\frac{1}{\rho} \right) - W_1^{\alpha_c} + 1 \right]$$

results in Eq. [10]

$$\eta_A(t) \leq \frac{1}{\alpha_c b} \ln \left[\frac{\rho + \exp \left[-\frac{\alpha_c(1+\rho)bit}{C_A} \right]}{1+\rho} \right] \quad [10]$$

when the same boundary condition is stipulated.

SYMBOLS

A	i/C_A
B	i_0/C_A
C_A	double layer capacity, assumed a constant independent of time
$C_{A(t)}$	the double layer capacitance as a function of time
F	Faraday constant
K, K_1, K_2, K_3	constants of integration
N	number of data points read from charging curve
R	gas constant
T	absolute temperature
W_1	$\exp[-b\eta_A(t)]$
W_2	$\exp[-\theta b\eta_A(t)]$
Z	$\exp[\alpha_c b B \int u dt]$
b	F/RT
i	the net current density
i_0	exchange current density
P	number of unknown parameters
r_1	$\alpha_c b / 2C_A (i + \sqrt{i^2 + 4i_0^2})$
r_2	$\alpha_c b / 2C_A (i - \sqrt{i^2 + 4i_0^2})$
S_e	the standard deviation of residuals defined by Eq. [12]
$S(\gamma)$	defined by Eq. [12]
t	time
t_j	the time associated with the j^{th} data point
u	$\exp[-\alpha_c b \eta_A(t)]$
v	$1/W_1$
y	the observed overpotential
z	the total valence change in a deposition
α_A	anodic transfer coefficient
α_c	cathodic transfer coefficient
β	any dependent variable; defined by Eq. [11]
$\gamma_1 \dots \gamma(P)$	unknown parameters
$\epsilon_1, \dots, \epsilon_K$	independent variables
$\eta_A(t)$	activation overpotential at time t
$\hat{\eta}_A(t)$	the value of the activation overpotential at time t calculated from Eq. [7]
$\eta_A(t)$ exact	that function $\eta_A(t)$ which represents an exact solution to Eq. [4]
ρ	i_0/i , the ratio of the exchange current density to the apparent current density
θ	a constant such that $0 < \theta \leq Z$

Ethyl Alcohol Oxidation at Platinum Electrodes

R. A. Rightmire, R. L. Rowland, D. L. Boos, and D. L. Beals

The Standard Oil Company (Ohio), Cleveland, Ohio

ABSTRACT

The oxidation of ethyl alcohol at platinum electrodes was studied by a-c differential capacitance measurements, current density measurements, rates of change of current density with time, constant current, voltage-time traces, and product analyses. Capacitance measurements can be interpreted as indicating that ethyl alcohol adsorbs on platinum electrodes in 1N H₂SO₄ as CH₃CHOH in the voltage range from +0.3 to 1.0v (NHE) and as CH₃CH₂O* in the voltage range from 0.9 to 1.4v. Above 1.2v platinum forms an irreversibly adsorbed oxide film which is not catalytically active and which weakly adsorbs ethyl alcohol. On reduction of this platinum oxide an "activation" occurs resulting in high catalytic activity. Current density peaks at 0.9 and 1.2v are consistent with postulated adsorption properties. Similar studies indicated that acetaldehyde reacts in an analogous manner. Thus, the suggestion of other investigators that the minimum in the alcohol curve arises because of poisoning by acetaldehyde appears to be refuted.

The oxidation of ethyl alcohol at both smooth and platinized platinum electrodes has been studied extensively recently (1, 2). In spite of this effort, there is at present very little agreement on the mechanism of the reaction.

The purpose of the present research was to gain some insight into the mechanism of the reaction of ethyl alcohol at Pt electrodes by investigating the relationship between surface properties of the electrode and polarization curves (*i vs. E*) obtained under controlled conditions. Polarization curves were obtained by slowly increasing or decreasing in a stepwise manner the potential of a platinized platinum test electrode relative to a reference electrode and measuring current at a preset time after the step voltage change. Analogous curves were obtained for acetaldehyde for comparison. These polarization curves were then compared to the results of the following four experiments: (a) differential capacitance values, measured at smooth platinum electrodes under nearly identical conditions; (b) product distributions, measured as a function of time at constant electrode potential; (c) variations of current densities with time, determined

during the transient period following a step change in electrode potential; and (d) constant current, voltage-time traces, measured after electrode "activation."

Experimental Techniques

Polarization curves.—The cell shown in Fig. 1 was used to carry out polarographic scans on large platinized platinum electrodes. The cell consisted of two chambers separated by a fritted glass disk. An extra electrode was provided for pre-electrolysis *vs.* the counter electrode. The solution was swept with N₂ prior to electrolysis test runs. Because of the greatly increased surface area of the platinized platinum electrodes, surface poisoning from minor impurities was much less likely than for the smooth platinum.

The potential of the test electrode was controlled by a potentiostat designed and built in this laboratory. The curves were obtained under quasi-steady-state conditions by allowing 15 sec for double-layer effects to decay off after every voltage change. Measurements were taken at 0.025v intervals corresponding to an average sweep rate of 0.1 v/min. In the 0.05-0.65v region, measured currents were equal within experimental error to those taken at sweep rates of 0.025 v/min with 1-min decay intervals and were very nearly zero. This indicated that double-layer effects were negligible. Slow current decays of a few per cent per minute were observed in each peak region, but the general shape of the curve remained unchanged. Voltages were swept from zero volts (NHE) up to 1.7v and back to zero. Additional sweeps gave results within experimental error of the initial sweep.

Product distribution analyses. Product distribution studies were carried out in the cell described in the previous section. The potential was held constant during electrolysis. Product analyses were carried out for nonvolatile components by direct injection of electrolyte plus products into a gas chromatograph.

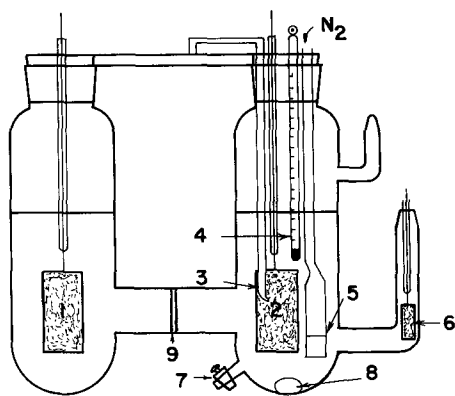


Fig. 1. Cell design: 1, counter electrode; 2, test electrode; 3, Luggin capillary; 4, thermometer; 5, fritted glass bubbler; 6, pre-electrolysis electrode; 7, Teflon stopcock; 8, Teflon stirrer; 9, fritted glass disk.

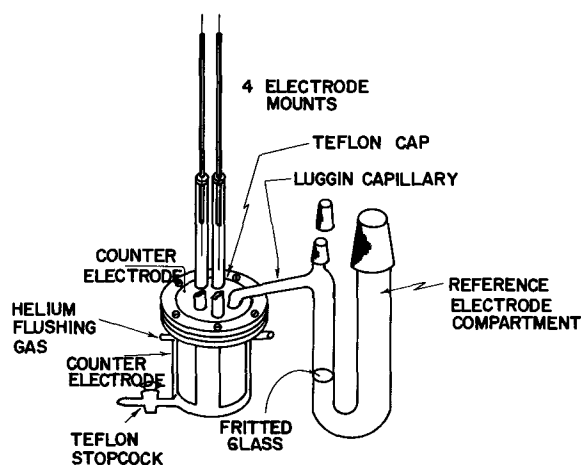


Fig. 2. Cell design for capacitance and transient current-time measurements.

Capacitance measurements.—Figure 2 is a diagram of the cell used for capacitance measurements. The cell consisted of an electrolytic beaker with the top ground flat and sealed with a Teflon cap clamped to the beaker. A large platinized platinum counter electrode was mounted around the inside surface of the beaker with contacts sealed into the Teflon cap. A Luggin capillary and four test electrodes were also mounted in the cap. The four test electrodes were maintained above the electrolyte in Pyrex tubes and slid freely through Teflon seals. The Luggin capillary supplied the bridge to the reference electrode compartment and was rotated in order to maintain the tip of the capillary adequately close to any one of the test electrodes.

A hydrogen reference electrode was used throughout these experiments so that any variation in reference voltage resulting from variations in hydrogen ion activity or from the presence of ethyl alcohol would be compensated by the same variation of the test electrode. The potential of the hydrogen reference electrode in electrolyte containing 5% (by weight) alcohol was tested against a silver-silver chloride reference electrode and a voltage of $0.223 \pm 0.002\text{v}$ was measured. This was in good agreement with the reported values of 0.255v in the absence of alcohol and 0.219 in the presence of 10% alcohol (3); hence, the voltage variation with variations in alcohol concentration cannot be greater than a few millivolts and therefore introduces no significant error into the measurements.

Excess sulfuric acid of the composition used in the experiment was contained in a large external vessel and pre-electrolyzed with two large platinized platinum electrodes for several weeks. This solution was then allowed to flow into the cleaned and sealed cell through the Luggin capillary tube. Purified ethyl alcohol was then added.

Cathodic pre-electrolysis was carried out for 30-60 hr on the first test electrode and withdrawn from the solution. Because of the high surface area of the counter electrode and because it had been undergoing anodic reactions, it was not withdrawn from the solution. The second test electrode was then immersed in the solution and the desired run conducted. After a given run, the second test elec-

trode was used for pre-electrolysis for 20 more hours. The procedure was then repeated for electrodes 3 and 4 with an additional 20 hr pre-electrolysis after electrode 3.

The platinum electrodes have been assayed at 99.998% purity and the initial sulfuric acid at 99.992% purity. The conductivity of the water used was measured at $4 \times 10^{-7} \text{ohm}^{-1} \text{cm}^{-1}$. Ethyl alcohol (99% purity) was doubly distilled through a fractionation column estimated to have about ten theoretical plates. Chromatographic analysis showed no volatile impurity peaks.

The platinum electrodes were prepared by sealing in soft glass and annealing for several minutes to insure that a water-tight seal was obtained. The electrodes were then etched slightly in aqua regia, rinsed thoroughly in conductivity water, heated in concentrated sulfuric acid, and rewashed in conductivity water.

Figure 3 is a block diagram of the electronic circuit used for the capacitance measurements. The d-c voltage was held constant by a high a-c impedance potentiostat. A sine wave was generated by an audiogenerator and sent to the output transformer. This signal was then fed to a decade resistance box which was in series with the cell. To obtain the capacitance of the cell, the voltage drop across the resistance box, across the cell, and then across the two in series were measured. These outputs were fed through a differential amplifier and a preamplifier to be monitored on an oscilloscope and measured by an a-c voltmeter. The capacitance was calculated from these values by an electronic computer using a series circuit analogue.

Capacitance measurements were made by advancing the voltage 0.05v every 2 min and allowing 90 sec for a quasi-steady-state condition to be attained. An a-c frequency of 100 cps and an amplitude of 5 mv (peak to peak) were used for all measurements. It was found possible to obtain good reproducibility by allowing all electrodes to equilibrate at 0.7v for at least 5 hr. The run started at 0.7v and scanned down to 0.05v up to about 1.80v and back to 0.05v . In most cases, reproducibility to about $\pm 7\%$ was obtained. In a few runs, large deviations occurred indicating either contaminated electrodes or imperfect sealing of the electrodes in the glass tubes. These runs were rejected.

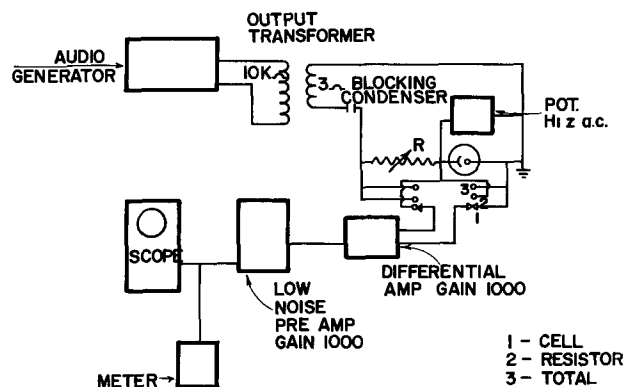


Fig. 3. Block design of electronic circuit used for a-c differential capacitance measurements.

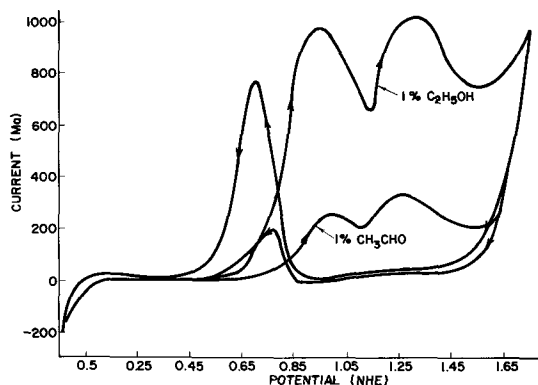


Fig. 4. Polarization curves at platinized platinum electrodes in 1N H_2SO_4 .

Transient current-time, voltage-time traces.—The cell shown in Fig. 2 was also used for the current-time and voltage-time traces. For current-time curves, the potentiostat was switched from one reference voltage to another by means of a mechanical switch, and current was followed as a function of time. Since the transient periods of interest were of the order of minutes, switching transients were negligible.

Constant current voltage-time curves were obtained by switching from a constant voltage state to constant current and recording voltage *vs.* time.

Experimental Results

Polarization curves.—Figure 4 shows polarization curves measured for both ethyl alcohol and acetaldehyde at platinized platinum electrodes in 1N H_2SO_4 . As is seen from Fig. 4, both ethyl alcohol and acetaldehyde show two maxima on the forward sweep but only one on the reverse. Furthermore, the maximum was shifted considerably more negative on the reverse sweep. At 0.65v, the current was about 10 times greater on the reverse scan than on the forward and indicated some type of "activation" of the electrode. The activation was not a stable condition as was indicated by the downward drifts in current over periods of a few minutes.

Capacitance measurements.—Figures 5 and 6 show the results of the capacity *vs.* voltage for 0, 1, and 5% (by weight) C_2H_5OH in 1N H_2SO_4 for scans from 0.05v (NHE) to about 1.9v and from 1.9 to 0.05v, respectively. Duplicate results are plotted for 0% alcohol and triplicate results for 1% alcohol.

Ethyl alcohol was found to reduce the capacitance over the entire range from below 0.2 to 1.8v. Platinum electrodes in 1N H_2SO_4 (0% C_2H_5OH) showed a characteristic increase in capacitance on the forward voltage scan (Fig. 5) from 0.9 to 1.2v. The capacitance went through a maximum at 1.25v and then decreased until reaching the voltage of oxygen evolution. The voltage region between 0.5 and 0.9v was very flat in the presence of 1-5% ethyl alcohol and appeared to be concentration independent.

On the reverse scan, from 1.8 to 0.8v the difference in capacitance between 0% alcohol and 1% alcohol was small. For 5% alcohol between 1.4 and 0.8v the difference was also slight. However, below 0.8v, large differences were observed. The peak at

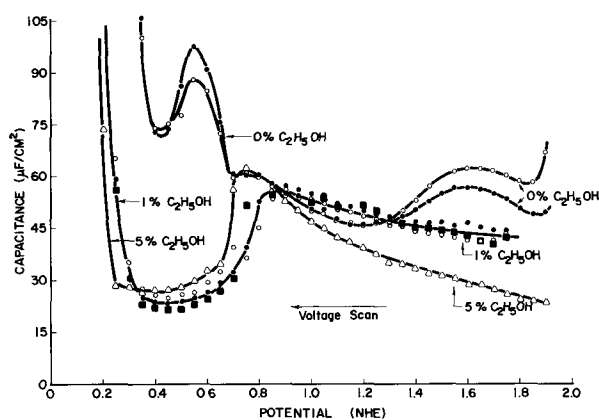


Fig. 5. Capacity vs. potential for forward voltage scan

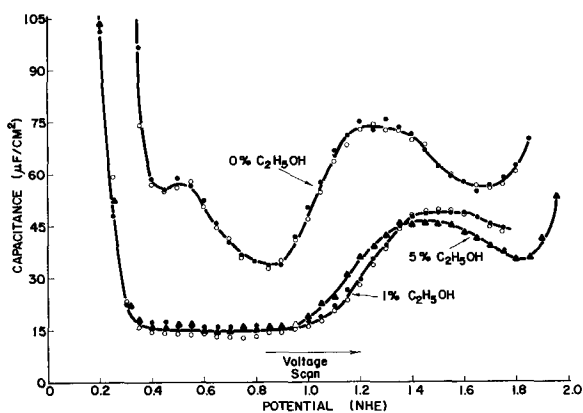


Fig. 6. Capacity vs. potential for reverse voltage scan

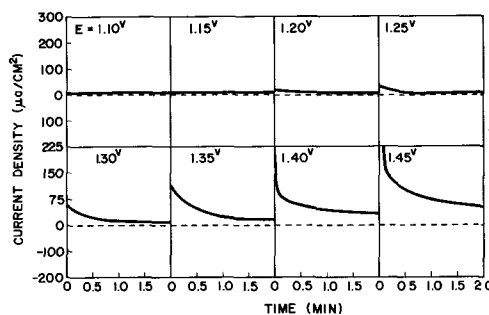


Fig. 7. Current transients at 0.70v (NHE) obtained after anodizing 2 min at voltage E . Electrolyte = 1% C_2H_5OH in 1N H_2SO_4 .

0.6v (0% alcohol) was not stable and decayed slowly with time.

Transient current-time curves.—Figure 7 shows anodic current transient obtained after anodizing for 2 min at a voltage E which varies from 1.1v to 1.45v and then switching to 0.70v. The latter voltage was near the maximum of the peak on the reverse scan. As is seen from Fig. 7, no activation of the electrode occurred until the electrode was anodized at voltages greater than 1.15v.

Figure 8 shows the effects of anodizing at 1.80v for 30 sec, then switching to the voltage E which varies from 0.750v to 0.475v. At voltages above about 0.700v, there was a momentary cathodic current followed by an increasing anodic current which rose through a maximum and then decayed to a very small current. Below 0.700v the initial rise was too fast to follow, and only the decay was observed. The largest current decay occurred in the first 2

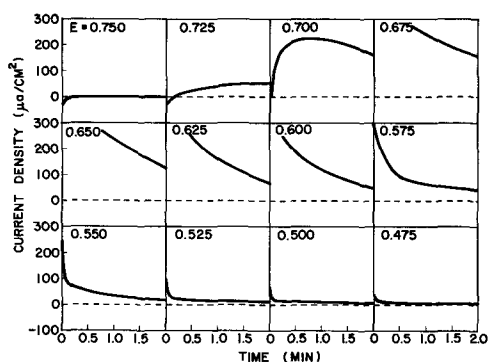


Fig. 8. Current transients at voltage E obtained after anodization for 2 min at 1.80v (NHE). Electrolyte = 1% C_2H_5OH in 1N H_2SO_4 .

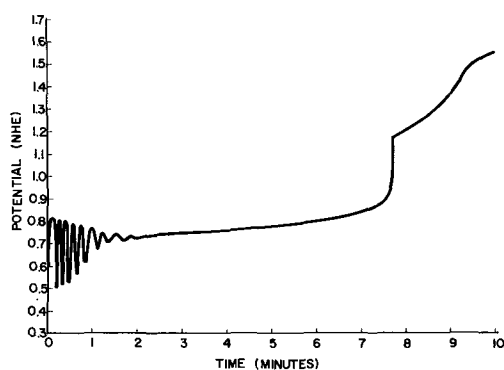


Fig. 9. Ethyl alcohol product distribution at 0.75v (NHE)

min and then gradually tailed out over a period of a few hours depending on the voltage.

Constant current voltage-time curve.—Figure 9 shows the voltage-time trace at constant current of a smooth platinum electrode which had first been activated by anodization at 1.8v for 2 min, followed by short cathodization at 0.3v. The electrode was then charged at constant current. The resulting oscillations in no way reflected an interaction with the instrumentation as the same effect could be obtained with a battery-resistance constant current source.

Product analyses.—The results of the product analysis studies are shown in Fig. 10. As is seen from Fig. 10, at 0.75v (over platinized platinum surface) the primary product is acetaldehyde with only small amounts of acetic acid building up. Acetic acid and acetaldehyde accounted for 100% of the products based on number of coulombs within the experimental error of the analyses. Analysis of Fig. 10 showed that the rate constants for the reactions of ethyl alcohol and acetaldehyde were in the ratio of approximately 3:1. Polarographic scans in acetic acid solutions showed no reaction which also indicates that this oxidation product does not react further.

Discussion

Figure 11 is a simultaneous plot of the polarization curve for 1% ethyl alcohol (Fig. 4) and the corresponding capacity curve under identical conditions (Fig. 5 and 6).

Hydrogen adsorption region.—On the forward scan in the presence of alcohol between 0 and 0.2v, the double-layer capacity was very large. It

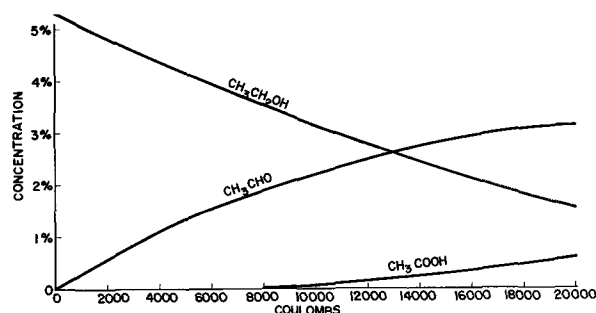


Fig. 10. Ethyl alcohol product distribution at 0.75v (NHE)

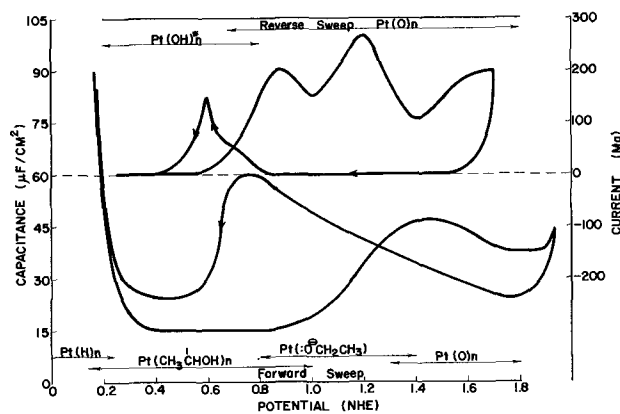


Fig. 11. Comparison of capacity and current curves for 1% C_2H_5OH in 1N H_2SO_4 .

has been fairly well established that in this range atomic hydrogen is adsorbed and desorbed (4-8). The amount of hydrogen adsorbed was severely depressed between 0.2 and 0.4v by the presence of the alcohol as is seen by comparing 0% alcohol with 1 and 5% in Fig. 5.

Double-layer region.—The flat, depressed region between 0.3 and 0.90v in the presence of alcohol is similar to that observed when surface active substances are adsorbed on mercury (9). In interpreting the significance of this region, a model of the double-layer originally suggested by Frumkin (10) of two capacitors in parallel is used. In this model the charge on the electrode is given by

$$q_{\theta} = \theta \cdot q_{(\theta=1)} + (1-\theta) q_{(\theta=0)}$$

The capacitance can be obtained through differentiation of this equation,

$$C_{\theta} = \theta \cdot C_{\theta=1} + (1-\theta) C_{\theta=0} + [q_{(\theta=1)} - q_{(\theta=0)}] \frac{d\theta}{dE}$$

where the C 's are the differential capacities of the electrodes with $\theta=0$ or $\theta=1$, respectively. The usefulness of this equation has been further demonstrated by the work of Delahay and co-workers (11). It is assumed that the flat region corresponds to a condition of $\theta_{alc} = 1$ and that $C_{\theta=1} \approx 15 \mu F/cm^2$. $C_{\theta=0}$ is evaluated from the curve for 0% alcohol and at 0.8v is equal to approximately $32 \mu F/cm^2$.

The flatness of the curve between 0.3 and 0.9 and the independence of capacitance on concentration, especially for a low molecular weight material such as ethyl alcohol, strongly suggests that the alcohol is chemisorbed rather than physically adsorbed in this region. Since below 0.9v, platinum is known not

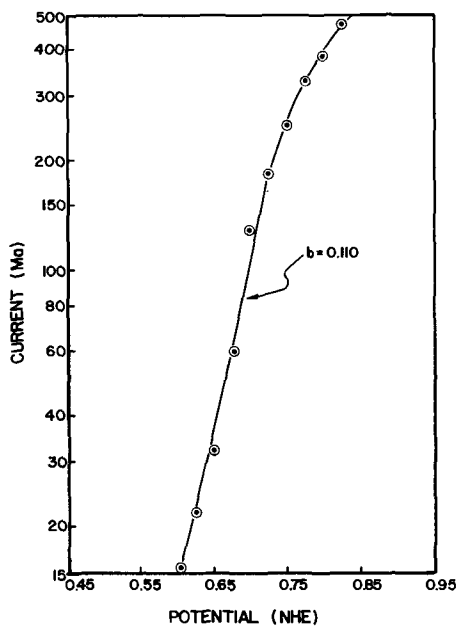
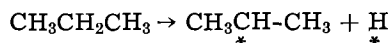


Fig. 12. Tafel plot of polarization curve from 0.45 to 0.95v (NHE) for 1% C_2H_5OH in 1N H_2SO_4 .

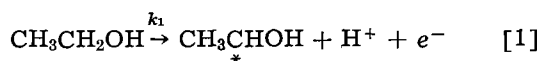
to undergo any surface oxidation or oxide film formation (5-7), it is not likely that a Pt-O linkage is involved in this chemisorption step. A more likely explanation involves the formation of a carbon-platinum surface bond analogous to that proposed for the chemisorption of saturated hydrocarbons on platinum catalysts. Bond and Addy (12) point out, for example, that in deuterium exchange reactions with propane over group VIII metals, the propane probably adsorbs as



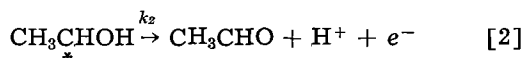
An analogous reaction for ethyl alcohol would involve chemisorption as $CH_3\overset{*}{C}HOH$, $CH_2\overset{*}{C}HOH$, or $CH_3\overset{*}{C}H_2$.

The current-voltage curve in the region of 0.55-0.75v (Fig. 4) gives a reasonable Tafel plot with a slope of 0.11v (Fig. 12), corresponding to a simple electrochemical rate-limiting step involving a single electron transfer. This would seem to eliminate $CH_3\overset{*}{C}H_2$ as a possible chemisorbed intermediate. As in the case of adsorbed propyl radicals, a dynamic equilibrium probably exists between $CH_3\overset{*}{C}HOH$ and $\overset{*}{C}H_2\overset{*}{C}HOH$.

A mechanism consistent with the above considerations involves a fast oxidation and chemisorption step,

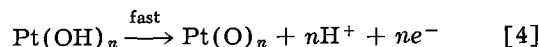
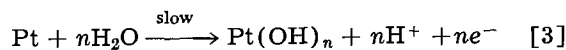


followed by a rate-limiting electrochemical step



Surface oxidation region.—The rise in capacity above 0.9v in the absence of ethyl alcohol has been

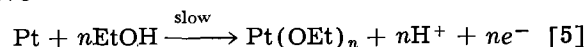
shown by Laitinen and Enke (7) to be directly related to the degree of surface oxidation of the platinum. It has been further postulated by Feldberg (5), as the result of detailed kinetic studies, that the formation of the oxide film proceeds by the following two-step mechanism



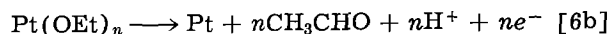
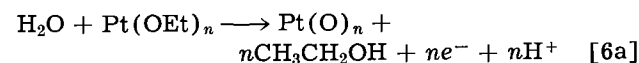
In the presence of ethyl alcohol, an analogous increase was observed in the same voltage region. However, the capacity was significantly reduced and nearly independent of concentration, indicating strong alcohol adsorption in this region also. This behavior suggested that a surface oxidation analogous to [3] and [4] was occurring, but was strongly influenced by the presence of an ethyl alcohol film adsorbed on the surface.

It is known that the presence of an oxide film poisons the ethyl alcohol reaction [2] yet the reaction during a slow voltage sweep showed a second current peak in this voltage region. Attempts to get a product analysis at 1.25v failed because this second current peak decayed off too rapidly to build up detectable quantities of product.

A reasonable explanation can be found by postulating a reaction of platinum with adsorbed alcohol through a Pt-O linkage analogous to [4] above



However, $Pt(OEt)_n$ can undergo two competing reactions



If reaction [6b] were significantly faster than [6a], poisoning of the electrode would not occur rapidly while reaction [6b] would account for the second current peak. Poisoning would gradually occur however through slow formation of PtO_n either through reaction [6a] or reactions [3] and [4]. Such a mechanism would explain the presence of a second peak and at the same time account for its decay. One should also expect that the first peak would be nearly concentration independent while the second peak because of increased poisoning rate at lower concentrations from the competing reactions [3] and [4] should show a concentration dependence. Experimentally, an attempt was made to measure these effects, but the scatter of data made it difficult to draw any conclusions. There did appear to be a correlation with concentration in the second peak while the scatter of data at any given concentration from the first peak was greater than variations observed with changes in concentration.

The first peak was relatively insensitive to sweep rate, while the second peak was more sensitive because of decay.

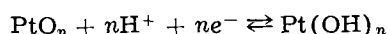
Reverse scan.—On the reverse scan (Fig. 6), ethyl alcohol apparently is weakly adsorbed down to

about 0.8v as is shown by the strong concentration dependence. It is generally agreed that the surface in this region is covered by a platinum oxide film; hence, the adsorption probably occurs on top of the oxide layer. As is seen from the polarization curves, this surface is completely inactive toward the oxidation of ethyl alcohol or acetaldehyde.

The reduction of platinum oxide occurs at about 0.8v (4-8) leaving an "activated" electrode as is seen from the great increase in reaction rate over that of the forward sweep. Below 0.8v, there was probably no experimentally significant difference between the 1% and 5% curves; but the strong deviation from the 0% curve indicates strong adsorption of alcohol.

There is considerable controversy as to the cause of this activation. Knorr (8) attributes this activation to a light platinization or roughening of the surface, while Feldberg, Enke, and Bricker (6) attribute the activation to the formation of an unstable platinum suboxide.

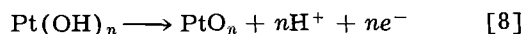
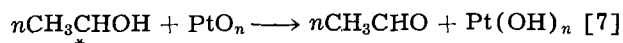
The large capacitance peak in the 0% alcohol curve between 0.8 and 0.5v has been studied extensively by Feldberg *et al.* They attribute this peak to the pseudocapacitance of the reversible reaction



The $\text{Pt}(\text{OH})_n$ is referred to as the semireduced state which only slowly decays to the clean platinum surface.

Figure 4 shows that the "activation" peak for alcohol oxidation occurs at exactly the same voltage as is observed for the proposed pseudocapacitance peak. To investigate the suggestion of Enke and Feldberg that this semireduced state might be responsible for the activation effect, current transient curves shown in Fig. 7 and 8 were measured. Figure 7 shows that anodization above 1.15v is necessary for the activation. Figure 8 shows that activation is greatest between 0.7 and 0.58v and the drop off in activity with voltage is quite rapid below 0.58v.

These curves seem to indicate that the electrode is catalytically active only when both oxide and semioxide are present and readily reversible. This is consistent with a reaction of the type



Above 0.8v reaction [7] will not proceed while below 0.5v reaction [8] does not proceed.

A further interesting test of this concept is shown in constant current, voltage-time trace shown in Fig. 9. At 0.3v the electrode was presumed to be completely reduced to the semireduced state and was not catalytically active. As the voltage increased, a range was reached where the catalyst became increasingly active, hence the voltage dropped even though anodic current was flowing into the electrode. The resultant decrease in voltage produced a decrease in activity, causing the voltage to rise, hence an oscillation was observed. These data appear to lend strong support to the catalytic effects of the semireduced state as causing the activation effect.

Acknowledgments

Helpful discussions with Professors R. W. Laity and C. G. Enke of Princeton University are gratefully acknowledged.

Manuscript received May 20, 1963; revised manuscript received Aug. 12, 1963. This paper was presented at the Los Angeles Meeting, May 6-10, 1962.

Any discussion of this paper will appear in a Discussion Section to be published in the December 1964 JOURNAL.

REFERENCES

1. C. Marie and G. Lejune, *J. Chim. Phys.*, **26**, 237 (1929).
2. G. A. Bogdanovskii and A. I. Shlygin, *Zhur Fiz. Khim.*, **37**, 57 (1960). For further references see work cited in this paper.
3. D. G. Ives and G. J. Janz, "Reference Electrodes, Theory and Practice," Academic Press, New York (1961).
4. M. W. Breiter, *This Journal*, **109**, 42 (1962).
5. S. W. Feldberg, Thesis, Princeton University, 1961.
6. S. W. Feldberg, C. G. Enke, and C. E. Bricker, Paper presented at the Society Meeting, Los Angeles, May 7-10, 1962.
7. H. A. Laitinen and C. G. Enke, *This Journal*, **107**, 779 (1960).
8. C. A. Knorr, WADC Technical Report 59-687, Wright Air Development Division (April, 1960).
9. A. Frumkin, "Second International Congress of Surface Activity," **3**, p. 58, J. H. Schulman, Editor, Academic Press, Inc., New York (1957).
10. A. Frumkin, *Z. Physik*, **35**, 792 (1926).
11. P. Delahay, "Transactions of the Symposium on Electrode Processes," p. 291, E. Yeager, Editor, John Wiley & Sons, Inc. N. Y. (1961).
12. G. C. Bond and J. Addy, "Chemisorption," p. 132, W. E. Garner, Editor, Academic Press, New York (1957).

An X-Ray Study of Oxidized Uranium Surfaces

L. Leibowitz, J. D. Bingle, and M. Homa
Argonne National Laboratory, Argonne, Illinois

As part of an investigation of the kinetics of oxidation of uranium (1), an examination was made of the oxidized metal surface using both x-ray and electron diffraction techniques. In that work, at 200° and 295°C only UO_2 was found until almost all the metal was consumed. The uranium-oxygen system is a fairly complex one, however, and there is a notable lack of agreement of interpretation among the various workers in this area (2-5). As an example, Aronson *et al.* (4) hold that oxidation of UO_2 proceeds via a UO_{2+x} solid solution, while Blackburn *et al.* (5) maintain that oxidation of UO_2 is controlled by diffusion of oxygen through a U_3O_7 layer. Recent crystallographic work by Belbeoch, Piekarski, and Perio (6) and by Hoekstra, Santoro, and Siegel (7) has done much to clarify the situation. The latter authors have discussed in some detail the complications of identification and the sources of conflict in the earlier work. Because of these recent findings it was decided to re-examine the oxidized surfaces of uranium using an x-ray diffractometer.

Experimental

Cubes of uranium were oxidized at 100° and 200°C in the constant pressure volumetric apparatus used previously (1). At 300°, 400°, 500°, and 600°C samples were oxidized in the heat-sink apparatus described by Baker and Bingle (8). At these higher temperatures self-heating of the metal would ordinarily preclude isothermal oxidation. In the heat sink apparatus, however, the uranium specimen is compressed between two massive stainless steel blocks which remove heat at a sufficient rate to maintain nearly isothermal conditions. All runs were carried out at an oxygen pressure of about 200 mm. For each case, when the desired amount of oxidation has occurred, the reactor was evacuated and samples allowed to cool in vacuum. It would have been useful to carry out the x-ray examination at the reaction temperatures; this could not be done with the equipment available. Thin adherent oxide films were formed after 400-1100 $\mu\text{g O}_2/\text{cm}^2$ were consumed, with no evidence of flaking. All x-ray diffraction patterns were measured using a G.E. XRD-5 diffractometer with Cu K_α radiation. Wide variations of the operating conditions were used to obtain maximum resolution. In no case was resolution of the K_{α_1} - K_{α_2} peaks found.

Results and Discussion

In Fig. 1 are shown sections of the diffraction tracings obtained from these samples. These are principally of oriented UO_2 patterns which, however, show some interesting details pertaining to the

kinetics of uranium oxidation. A marked change in the appearance of the tracings occurs at about 400°C. The diffraction maxima in the regions $2\theta = 55^\circ$ and 75° which are broad and diffuse up to 400°C are quite sharp at 500° and 600°C. The maximum in the region $2\theta = 33^\circ$ shows a similar change between 300° and 400°C.

It is interesting to note that a change in the kinetics of oxidation of uranium occurs at 450°C (8). Below that temperature an accelerating oxidation rate was found, proportional to $(\text{time})^{5/4}$ while above 450°C a decelerating rate proportional to $(\text{time})^{5/6}$ holds. It is reasonable to ascribe this change in reaction kinetics to the changed character of the oxide.

Although some of the line broadening observed at the lower temperatures may be attributed to small crystallite size, not all the changes in the

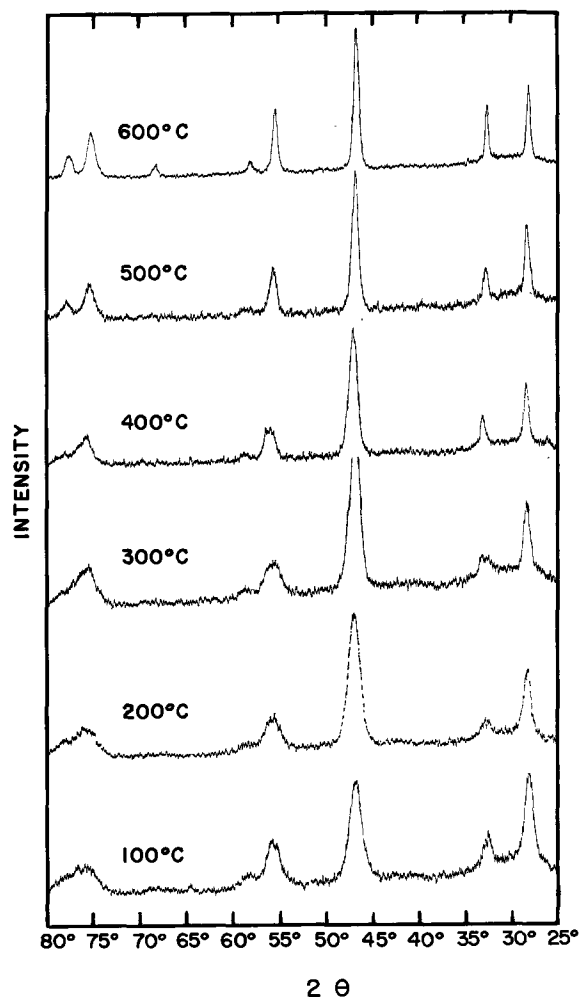


Fig. 1. X-ray diffractometer tracings of thin uranium oxide films formed at various temperatures.

nature of the diffraction patterns can be explained in this way. The splitting of the peaks at $2\theta = 33^\circ$ and 56° is most likely to be due to lattice distortion rather than small crystallite size. A semiquantitative assessment of these two effects may also be made. In general for a given x-ray wave length and fixed reflecting plane, line broadening due to lattice distortion is proportional to $\tan \theta$ while that due to small crystallite size is proportional to $1/\cos \theta$ (9-11) where 2θ is the diffraction angle. This, if β is the pure diffraction breadth, the constancy of the two parameters $\beta/\tan \theta$ and $\beta \cos \theta$ will be a measure of the contribution of the two effects. An examination of these values as a function of θ shows that at 100° , 200° , and 300°C distortion is the predominant effect. At the higher temperatures no clear distinction between the two possibilities can be made.

The work of Hoekstra, Santoro, and Siegel (7) leads us to believe that what is involved is the formation at the lower temperatures of another oxide phase. There are two cubic and three tetragonal phases that must be considered. The cubic phases are UO_2 and U_4O_9 . The tetragonal phases and their c/a ratios are: $\alpha\text{-U}_3\text{O}_7$ 0.989; $\beta\text{-U}_3\text{O}_7$ 1.031; $\text{UO}_{2.3}$ 1.016. Because these c/a values are so close to unity and because of the poor definition of the overlapping diffraction maxima, a clear distinction between these phases was not possible. Unfortunately in the back reflection region where such a distinction should theoretically have been possible, inadequate tracings were obtained.

The x-ray data are consistent with the uranium-oxygen phase diagram (7), if it is assumed that the molar ratio of oxygen to uranium in the oxide film is only slightly greater than 2. At 100°C we are then observing a two-phase $\text{UO}_2 + \alpha\text{-U}_3\text{O}_7$ region, at 200° , 300° , and 400°C a $\text{UO}_{2+x} + \text{U}_4\text{O}_9$ region exists, while at 500° and 600°C there is a single UO_{2+x} phase. These assignments are, of course, highly speculative, and the principle point we wish to make is that there is a change in the character of the oxide in the neighborhood of 400°C .

In none of this work involving thin oxide films did we see evidence for the presence of U_3O_8 . This is in contrast with the work of Loriers (9) who reports that above 240°C a crystalline structure appears, orthorhombic like U_3O_8 . Since Loriers states

that these layers scaled off readily it is evident that he was working with fairly heavily oxidized uranium. Under those conditions we also observe the formation of U_3O_8 (8).

Summary

There appears to be a change in the character of the oxide formed on uranium at about 400°C . Below 400°C the adherent oxide is distorted and seems to contain an oxide higher than UO_2 , possibilities being U_3O_7 , U_4O_9 , and $\text{UO}_{2.3}$. At 500° and 600°C the oxide seems to be a single UO_2 phase. When oxidation continues to such an extent that flaking of the oxide occurs, U_3O_8 forms but there is no evidence for the presence of U_3O_8 in thin adherent oxide films. This change in the oxide near 400°C coincides roughly with a change that has been found in the oxidation rate law. It seems reasonable that this change in the oxide is responsible for the change in oxidation kinetics.

Acknowledgment

The authors acknowledge with thanks the interest and advice of L. Baker, Jr. and J. G. Schnizlein. The review of the manuscript by R. Schablaske and S. Siegel is also gratefully acknowledged.

Manuscript received Jan. 10, 1963. Work performed under the auspices of the U. S. Atomic Energy Committee under Contract No. W-31-109-Eng-38.

Any discussion of this paper will appear in a Discussion Section to be published in the December 1964 JOURNAL.

REFERENCES

1. L. Leibowitz, J. G. Schnizlein, J. D. Bingle, and R. C. Vogel, *This Journal*, **108**, 1155 (1961).
2. K. B. Alberman and J. S. Anderson, *J. Chem. Soc.*, **303** (1949).
3. F. Gronvold, *J. Inorg. Nucl. Chem.*, **1**, 357 (1955).
4. S. Aronson, R. B. Roof, Jr., and J. Belle, *J. Chem. Phys.*, **27**, 137 (1957).
5. P. E. Blackburn, J. Weissbart, and E. A. Gulbransen, *J. Phys. Chem.*, **62**, 902 (1958).
6. B. Belbeoch, C. Piekarski, and P. Perio, *J. Nuclear Materials*, **3**, 60 (1961).
7. H. R. Hoekstra, A. Santoro, and S. Siegel, *J. Inorg. Nucl. Chem.*, **18**, 166 (1961).
8. L. Baker, Jr., and J. D. Bingle, To be reported.
9. A. Kochendorfer, *Z. Krist.*, **105**, 393 (1944).
10. J. Bouman, "Selected Topics in X-ray Crystallography" p. 59, 80, Interscience Publishers, New York (1951).
11. H. P. Klug and L. E. Alexander, "X-ray Diffraction Procedures," p. 530, John Wiley & Sons, Inc., New York (1954).

Effect of Vacuum Annealing of Oxide Films on the Oxidation of Copper-Nickel Alloy

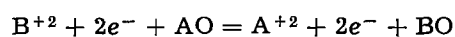
T. Yamashina and T. Nagamatsuya

Faculty of Engineering, Hokkaido University, Sapporo, Japan

It has been found that the oxidation kinetics are greatly influenced by the annealing of the oxide films during high-temperature oxidation of metals and alloys (1-3).

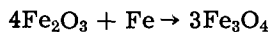
The change in oxidation kinetics with annealing could be due to a change in the physical properties of the oxide films and displacement reactions between different oxides in the film. Levin and Wagner (1) studied the oxidation of copper-zinc al-

loys and copper-nickel alloys to determine the occurrence of a displacement reaction of the type



as proposed by Wagner (4). They found that the oxidation rates were considerably changed by annealing in an inert gas, and it was concluded that decrease of oxidation rates after annealing was due to the formation of the more impermeable oxide

layer. A more detailed investigation of the annealing effect on the oxide film structure was made by Caule and Cohen (2); they found that the annealing reaction consumes hematite and produces magnetite in the oxidation of iron at 463°C. They considered that it is reasonable to write the reaction as



In the present study, the effect of vacuum annealing of the oxide film on the oxidation kinetics of copper, nickel, and copper-nickel alloy has been studied to clarify the possibility of displacement reactions. The change in the oxide structure of the copper-nickel alloy was compared with the kinetic data by means of x-ray diffraction.

Experimental Procedure

Samples used in the experiment were copper, nickel, and copper-nickel alloy containing 68 wt. % copper. Specimens of 5 cm² surface area were cut from sheets of cold-rolled metals and alloy 0.15 mm thick. After polishing through 600 grit silicon carbide and degreasing in benzene-methanol solution, the specimen was fixed on the hook of a Gulbransen-type microbalance. Oxygen and hydrogen were prepared by electrolysis of 0.5N NaOH solution and were purified by passing through silica gel, H₂SO₄, and P₂O₅ cells. After evacuating the microbalance system containing the specimen, hydrogen at 32 mm Hg was admitted at 800°C for 1 hr to remove surface contaminants. It was then evacuated for several minutes to get a pressure of 2×10^{-5} mm Hg, which was the minimum pressure used in the experiment. Oxygen was released into the system to bring the pressure to 55 mm Hg. In all the experiments, pretreatment in hydrogen, oxidation, vacuum annealing, and reoxidation were carried out at 800°C. After oxidation for 10 or 20 min, vacuum annealing was conducted at the same temperature as the oxidation, by rapidly pumping out the oxygen; then the specimen was reoxidized under the same condition as before annealing.

Results and Discussion

Figures 1, 2, and 3 show the oxidation curves of copper, nickel, and copper-nickel alloy involving the annealing effect. Annealing was carried out for 100 min in each case. In Fig. 1, little difference was found in the curves before and after annealing, and only a small change was found in the weight of the

¹ No visible change in the weight during vacuum annealing was detected in a blank test.

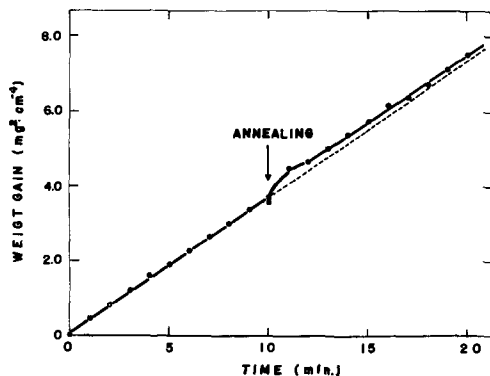


Fig. 1. Oxidation curve of copper at 55 mm Hg O₂ and 800°C, interrupted by a 100 min isothermal annealing *in vacuo*.

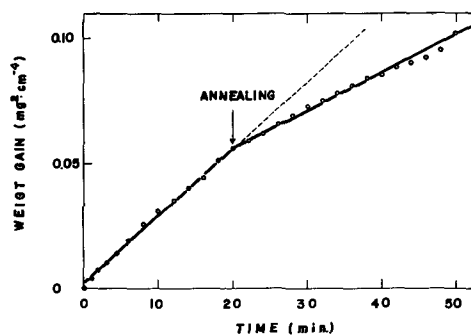


Fig. 2. Oxidation curve of nickel at 55 mm Hg O₂ and 800°C, interrupted by a 100 min isothermal annealing *in vacuo*.

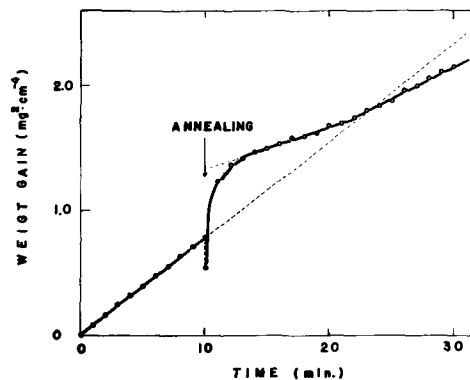


Fig. 3. Oxidation curve of copper-nickel alloy at 55 mm Hg O₂ and 800°C, interrupted by a 100 min isothermal annealing *in vacuo*.

specimen after annealing.¹ In the case of nickel oxidation (Fig. 2), the oxidation rate was decreased by annealing, being about half the rate before annealing. No visible break in kinetics was found during continuous oxidation for 1 hr (without annealing). On the other hand, in the oxidation of the alloy (Fig. 3), a considerable weight loss was seen after vacuum annealing, and the reoxidation curve showed a lower oxidation rate than before annealing. The weight loss during annealing was nearly constant, regardless of annealing times from 1 to 200 min. Weight losses during the 100-min annealing were 0.022 mg/cm² for copper and 0.143 mg/cm² for the copper-nickel alloy. The total weight gains after oxidation for 10 min (before annealing) were 1.916 mg/cm² for copper and 0.880 for the copper-nickel alloy; therefore, the ratios of weight losses to total weight gains become 1.15% (Cu) and 16.25% (Cu-Ni), respectively. To clarify the cause of the unusual change in the oxidation curve of the copper-nickel alloy, the oxide structure was examined by means of a Nolerco-type x-ray diffractometer. Samples for x-ray diffraction were prepared by quenching to room temperature after vacuum annealing at 800°C. Figure 4 shows the change of oxide structure with annealing time after 10 min oxidation. The oxides were compared by means of the diffraction pattern from (111) faces. In Fig. 4, the intensity from the oxide film formed in 10 min is shown at A (before annealing), and the intensity from the oxide film on reoxidizing for 1 min after 100 min annealing is shown at C. It is seen that the intensity of CuO in the oxide was greatly decreased; and that of Cu₂O was greatly increased by only 1 or 2 min annealing. After 100 min annealing (B), reoxidation for only 1 min (C) restored the original relation of CuO and Cu₂O. On the other

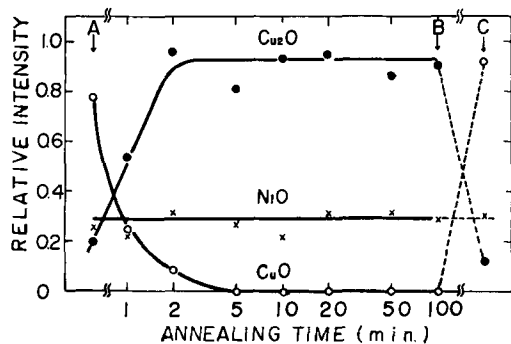
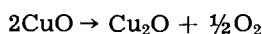


Fig. 4. X-ray diffraction intensities of the oxide film on copper-nickel alloy as a function of annealing time.

hand, the intensity of the pattern from NiO was found to be nearly constant regardless of annealing or reoxidation.

From the results presented above, the annealing reaction in copper-nickel alloy evidently consumes cupric oxide and produces cuprous oxide:



According to Sartell and co-workers (3), the oxide structure on 62 at. % copper-nickel alloy (nearly the same composition as the alloy sample in this experiment) was observed to be CuO in the outer layer and Cu₂O + NiO in the inner layer at atmospheric pressure of oxygen and 620°-927°C. In our experiment, the same oxide structure (the outer CuO and the inner Cu₂O + NiO) could be expected. Because of the large decomposition pressure of CuO at 800°C, it could be transformed easily to Cu₂O. Rapid reversal in the reoxidation can be explained if the oxide layer reduced to Cu₂O is porous enough so that oxygen can diffuse into and through it. In the oxidation of copper, no visible change in x-ray diffraction patterns was observed with annealing and reoxidation. The relative oxidation rates² with those before annealing as the unit, are presented as a function of annealing time in Fig. 5. The rate after annealing in copper did not change with increase of annealing time, but in nickel and the alloy they were decreased in nearly the same way, being rapidly decreased in the first 2 min of annealing.

² The oxidation rates of copper-nickel alloy after annealing were estimated from the linear part after 3 min reoxidation as seen in Fig. 3.

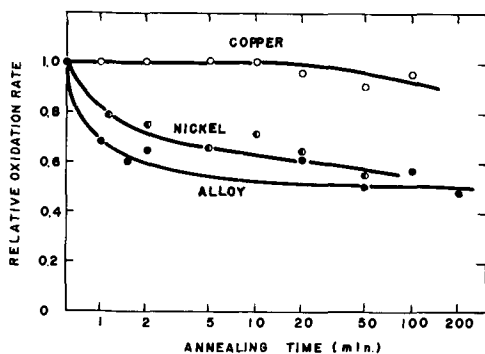
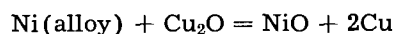


Fig. 5. Relative oxidation rates as a function of annealing time. Relative oxidation rate = K_2/K_1 , where K_1 is the rate before annealing and K_2 the rate after annealing.

From these results and Fig. 4 in which there was no change in the intensity of NiO with annealing, it is concluded that the cause of the decrease in the oxidation rate after vacuum annealing can not be due to the displacement reaction described as



by Levin and Wagner (1), but can be due to the change in physical properties of the NiO structure with vacuum annealing, such as formation of voids or decrease of the defect density in the oxide with annealing.

Acknowledgment

The authors wish to thank Dr. K. Funaki and Dr. Y. Shimizu, Tokyo Institute of Technology, for the X-ray diffraction data.

Manuscript received July 8, 1963.

Any discussion of this paper will appear in a Discussion Section to be published in the December 1964 JOURNAL.

APPENDIX

Determination of the parabolic rate constants.—The data in Fig. 1, 2 and 3 were plotted as $(\Delta m_1/A + \Delta m_2/A)^2 = (\Delta m_3/A)^2$, in which, Δm_1 is the weight gain before annealing, Δm_2 the weight gain after annealing, and Δm_3 the total weight gain. Levin and Wagner (1) plotted their data as $(\Delta m_1/A)^2$ before anneal + $(\Delta m_2/A)^2$ after anneal = $(\Delta m_3/A)^2$, in which the first term was a constant after the isothermal anneal. By

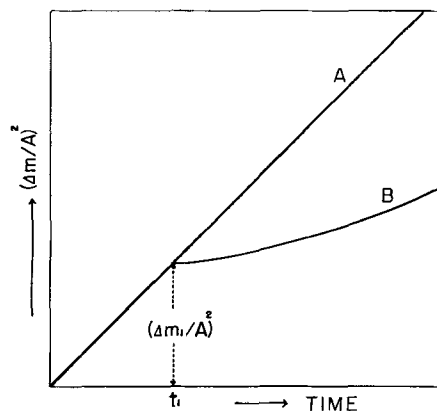


Fig. 6. Data which follow parabolic law (curve A) replotted after time t , as $(\Delta m_1/A)^2 + (\Delta m_2/A)^2 = (\Delta m_3/A)^2$.

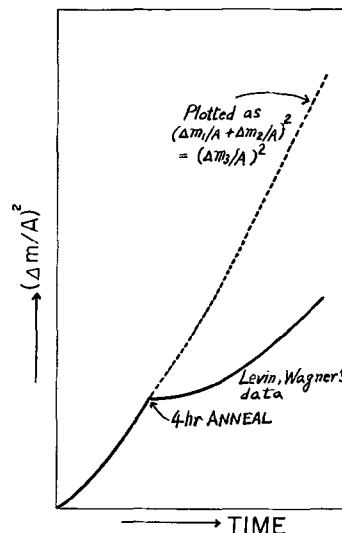


Fig. 7. Levin and Wagner's data replotted

using their expression the oxidation rate of Cu-Ni alloy after 4 hr annealing in argon gas appears to decrease by a factor of about 3 (Fig. 10, *This Journal*, **108**, 958 (1961).) This result is based on an error in their method of plotting the data parabolically. Let us assume data which exactly obey a parabolic rate law (curve A in Fig. 6). When these data are plotted according to Levin and Wagner's expression, the points after oxidation time t_1 fall on curve B. This gives the false impression of a major change in oxidation kinetics at time t_1 , whether the specimen has been annealed at this time or not. In Fig. 7, the oxidation curve

of Cu-Ni alloy by Levin and Wagner (1) is compared with the same curve, plotted as the expression $(\Delta m_1/A + \Delta m_2/A)^2 = (\Delta m_3/A)^2$.

REFERENCES

1. R. L. Levin and J. B. Wagner, Jr., *This Journal*, **108**, 954 (1961).
2. E. J. Caule and M. Cohen, *ibid.*, **108**, 834 (1961).
3. J. A. Sartell, S. Bendel, T. L. Johnston, and C. H. Li, *Trans. ASM*, **50**, 1047 (1958).
4. C. Wagner, *This Journal*, **99**, 369 (1952).

The Cathodoluminescence of Mn^{2+} - and Fe^{3+} -Activated Magnesium Aluminate Spinel

F. A. Hummel and J. F. Sarver¹

Department of Ceramic Technology, College of Mineral Industries,
The Pennsylvania State University, University Park, Pennsylvania

The spinel structure consists of a face-centered cubic lattice, the molecular formula of which can be represented as AB_2O_4 or $A_8B_{16}O_{32}$ on the basis of 32 cubic close-packed oxygens per unit cell. The unit cell contains 32 octahedral interstices, half of which are normally occupied, and 64 tetrahedral interstices of which only an eighth are normally occupied.³ The A and B sites may be occupied by cations having charges between one and six, the limitation being primarily ionic size and total positive charge over the A and B sites, e.g., $ZnAl_2O_4$, Mg_2TiO_4 , and $LiAl_5O_8$. In spinels such as $LiAl_5O_8$, in which Li^{1+} and Al^{3+} ions are distributed over both A and B sites, Datta (1) has shown that at low temperatures a cation ordering phenomenon may occur which leads to extra x-ray diffraction lines and the diffraction pattern is then indexed on the basis of a primitive cubic cell rather than a face-centered cell which is required for a true spinel structure by definition. Datta's work indicated that $MgAl_2O_4$ has a true spinel structure above 1240°C, although the proportion of Al^{3+} in tetrahedral sites at this temperature is not known. An increase in the proportion of Al^{3+} in the octahedral sites with increase in temperature above 1240° is indicated, i.e., $MgAl_2O_4$ tends to become a normal³ spinel at high temperatures. Below 1240°, some ordering is possible, similar to that discussed for $LiAl_5O_8$.

It was the purpose of this work to incorporate small concentrations of the isoelectronic ions Mn^{2+} and Fe^{3+} in $MgAl_2O_4$, to observe their effect on cathodoluminescent emission, and to relate the emission to activator environment, especially in view of the fact that the Fe^{3+} ion is known to exhibit a preference for tetrahedral sites in ferrite spinels. Compositions were prepared from c.p. basic

magnesium carbonate, reagent grade aluminum hydroxide, phosphor grade manganese carbonate, and ferric oxide. The batch materials were homogenized by mixing in acetone in an automatic agate mortar and pestle. In the case of the Mn^{2+} -activated phosphor, 1 mole % of the magnesium was replaced by manganese, and the composition was fired in a platinum crucible in a vertical tube furnace at 1350°C for 6 hr in a 5% H_2 , 95% N_2 atmosphere with a gas flow rate of 2 ft³/hr. The iron-activated phosphor was fired at 1400° for 6 hr in oxygen. The controlled atmosphere firings were intended to develop as much divalent manganese or trivalent iron as possible in each sample. Both samples were cooled slowly to room temperature in the furnace in the same atmosphere used at peak temperature. The samples were white, and x-ray diffraction patterns indicated well-crystallized magnesium aluminate spinel. No evidence of cation ordering during the cooling process was observed since this is a very slow process with $MgAl_2O_4$.

The visual cathodoluminescence of both the Mn^{2+} -activated and Fe^{3+} -activated phosphors was a deep green, considerably less bright than Mn^{2+} -activated

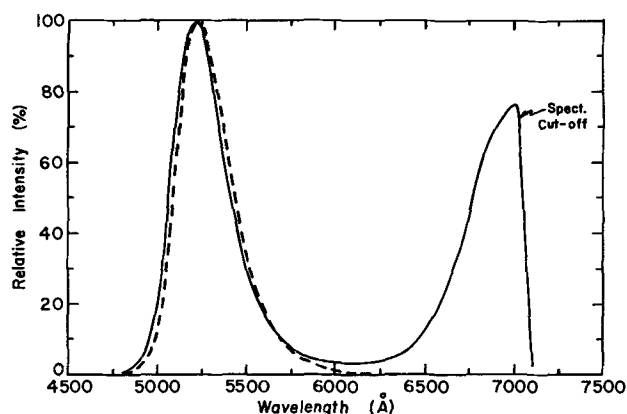


Fig. 1. Cathodoluminescence curves for $MgAl_2O_4$ activated with manganese and iron: solid line, 0.002 Fe^{3+} ; dashed line, 0.01 Mn^{2+} .

¹ Present address: Lighting Research and Development Operation, Lamp Division, General Electric Company, Nela Park, Cleveland, Ohio.

² Defect spinels such as gamma alumina are known in which vacant cation sites occur. However, the total positive charge distribution over the tetrahedral and octahedral sites in the unit cell is sixty-four.

³ In a normal spinel such as AB_2O_4 , B ions occupy only octahedral sites. In an inverse spinel, half the B ions are distributed over tetrahedral sites.

zinc orthosilicate. The emission spectra of the two phosphors were measured on a G.E. recording spectroradiometer and the normalized curves are shown in Fig. 1. The Mn^{2+} -activated phosphor was excited by 16 kv electrons with a current density of $1 \mu a/cm^2$ whereas the Fe^{3+} -activated phosphor was excited with a current density of $0.5 \mu a/cm^2$. The peak emission for the Mn^{2+} -activated phosphor occurred at 5240\AA whereas the Fe^{3+} -activated phosphor exhibited two emission peaks, one at 5210\AA and one around 7000\AA which was not completely recorded because of spectroradiometer cut-off. The peak emission of an NBS $Zn_2SiO_4:Mn$ standard occurred at 5250\AA . The green bands of the two phosphors have practically identical band widths at corresponding relative intensities, indicating that the Mn^{2+} and Fe^{3+} centers responsible for the green emission probably have very similar crystallographic environments and that there is little energy difference in the radiative transitions which occur in the two centers. The long wavelength band of the Fe^{3+} -activated sample probably can be attributed to the presence of some octahedrally coordinated Fe^{3+} . Magnesium ferrite contains Fe^{3+} in both tetrahedral and octahedral sites and can be represented approximately by the formula $(Mg_{0.1}Fe_{0.9})(Mg_{0.9}Fe_{1.1})O_4$. It is therefore likely that a solid solution of magnesium ferrite in $MgAl_2O_4$ would lead to two different types of Fe^{3+} fluorescent centers. The relative proportion of Fe^{3+} in the two different crystallographic environments would probably be very difficult to evaluate quantitatively with such small concentrations and is probably a function of firing temperature and rate of cooling.

With regard to the similarity of the green emission bands produced by the isoelectronic Mn^{2+} and Fe^{3+} activators, Kröger (2) discussed a related

phenomenon in the case of $Mg(Mg, Ti)O_4$ (inverse spinel) activated with manganese or chromium. It was found that the average valence of manganese in this phosphor, as determined by chemical analysis, was between three and four in air or oxygen firings. Excited by 3650\AA radiation, the Mn- and Cr-activated phosphors had visible red emissions which were very similar with respect to both band structure and position. This suggests that in the case of the Mn-activated compound, Mn^{4+} was responsible for the fluorescence since it is isoelectronic with Cr^{3+} . Since Cr^{3+} invariably prefers octahedral coordination to tetrahedral coordination, it is not unlikely that small concentrations of either Mn^{4+} or Cr^{3+} enter octahedral sites in this spinel, giving rise to the red emission.

Acknowledgment

Emission data were obtained through the cooperation of Majorie Brines of the Chemical Products Plant, General Electric Company. The investigation was made possible by the support of the Chemical Products Plant, General Electric Company, Cleveland, Ohio.

Contribution No. 62-6 from the College of Mineral Industries, The Pennsylvania State University, University Park, Pennsylvania.

Manuscript received Aug. 13, 1963.

Any discussion of this paper will appear in a Discussion Section to be published in the December 1964 JOURNAL.

REFERENCES

1. R. K. Datta, "Order-Disorder in Spinels," Ph.D. Thesis, Dept. of Geophysics and Geochemistry, The Pennsylvania State University, 157 pages, December, 1961.
2. F. A. Kröger, "Some Aspects of the Luminescence of Solids," Elsevier Publishing Co., Inc., New York (1948).

Diffusion of Sulfur, Selenium, and Tellurium in Gallium Arsenide

T. H. Yeh

Components Division, International Business Machines Corporation, Poughkeepsie, New York

A major problem in the diffusion of N-type impurities into P-type gallium-arsenide has been the compound formation on the surface of the GaAs (1, 2). By developing a diffusion technique that prevents such a compound formation and allows the N-type impurity to diffuse into P-type GaAs to form an N-P junction, one of the major difficulties in making a mesa or planar-type double-diffused PNP GaAs transistor would be removed.

The author has found (3) that silicon monoxide can be used as a masking material against the diffusion of Cd and Zn in GaAs. Further studies show that a thin layer of SiO evaporated onto the surface of P-type GaAs wafer prevents the formation of Ga_2S_3 , Ga_2Se_3 , Ga_2Te_3 ¹ on the wafer's surface during

the diffusion of sulfur, selenium, and tellurium into GaAs. This process allows each N-type impurity to diffuse into P-type GaAs and to form an N-P junction.

Experimental Procedure

Cadmium-doped P-type single crystals of GaAs with (111) orientation, with net impurity concentration of $3.0 \times 10^{17} \text{ cm}^{-3}$ and electron mobility of $160 \sim 190 \text{ cm}^2/v\text{-sec}$ were used in this study. Chemically polished wafers (4, 5), as well as optically polished ones, were used.

Experiments were conducted to investigate the prevention of compound formation upon GaAs wafer surfaces and the subsequent formation of an N-layer upon P-type GaAs during diffusion of S, Se, and Te. Silicon monoxide film thicknesses of approximately

¹ Determined by x-ray and spectrographic analysis.

1000Å, 2000Å, and 3000Å were evaporated onto half of the wafer's surface. Two experiments were carried out for each particular film thickness, and two wafers were used in each diffusion experiment.

In the study of Se and Te diffusions, elemental Se and Te were used as the diffusant. Wafers were placed onto a flat quartz plate which was then inserted into a quartz capsule. In the general case, a small quartz capillary containing either 0.3-1.4 mg of selenium² or 2.3 mg of tellurium and a small quartz cup containing the necessary amount of arsenic (6) to suppress the wafers' decomposition were placed beneath the quartz plate. The quartz capsule (about 20 ml) was attached to a high vacuum system, was pumped down to about 2.0×10^{-6} mm Hg, and then sealed off.

In the case of sulfur diffusion, sulfur-doped GaAs crystals with net impurity concentration of $3.8 \times 10^{18} \text{ cm}^{-3}$ (in the form of small chips) were used as the diffusant. The sulfur doped GaAs chips were weighed to give a chip-to-wafer weight ratio of approximately 100. The corresponding surface ratio was much higher than the weight ratio. These high weight and surface ratios ensure the sulfur vapor's pressure being maintained approximately constant during the diffusion period. The weighted sulfur-doped GaAs chips were put into a quartz boat. Wafers were placed onto the GaAs chips and the boat was then inserted into a quartz capsule (about 20 ml) which was evacuated and sealed off. The necessary amount of arsenic (6) to suppress the wafers' decomposition was also placed into the capsule.

All the diffusion experiments were carried out at 1040°C for 120 hr. After the heating period, the capsules were cooled with a cold zone at one end to avoid condensation of arsenic, sulfur, selenium, or tellurium upon the GaAs wafers. After the diffusion was completed, the SiO on the wafer's surface was removed with hot concentrated HF solution. The optically polished (or chemically polished) surface was preserved after the diffusion process only when the surface was protected by sufficient thickness of SiO film to prevent the compound formation. Hall measurements and N-P junction delineation (7) by diluted nitric acid were performed on each wafer. The necessary thickness of SiO film to prevent the compound formation and yet allow the diffusion to proceed can be determined by the surface condition, examined metallographically and electrically and by the presence or the absence of an N-P junction, examined by staining and Hall measurements on the GaAs wafer.

Results and Discussion

The experiments indicate that with approximately 2500Å of SiO film on the GaAs wafer surface, one can diffuse selenium or tellurium into a P-type GaAs wafer to form an N-P junction and prevent compound formation, such as Ga_2Se_3 or Ga_2Te_3 , on the wafer's surface. In the case of sulfur diffusion, an SiO thickness of only 2000Å prevents the formation of Ga_2S_3 on the wafer's surface. The surface conditions of GaAs wafers after sulfur, selenium, or tel-

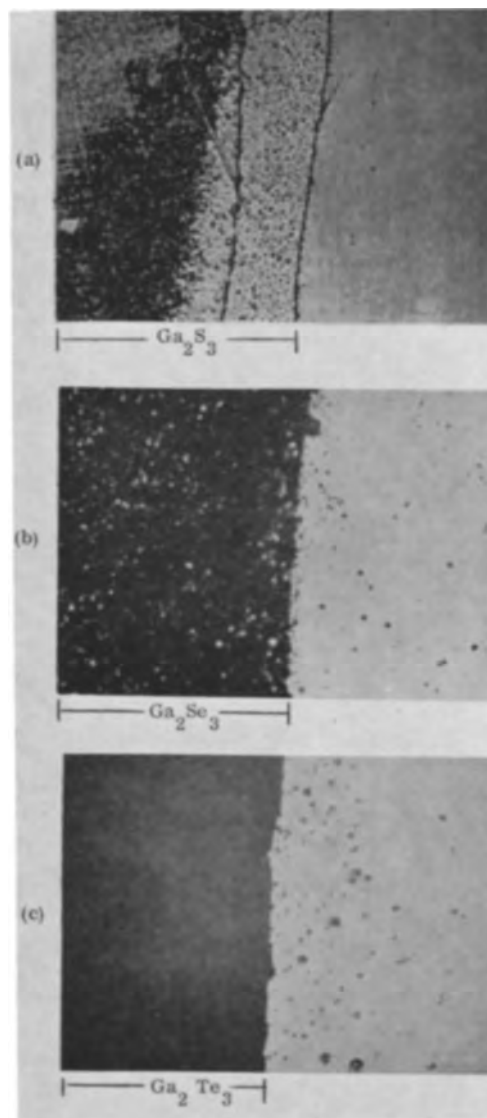


Fig. 1. Ga_2S_3 , Ga_2Se_3 , and Ga_2Te_3 formed on GaAs wafer surface at left; no compound formed on surface at right because of SiO protection. Magnification 150X (reduced to approximately 110X).

lurium diffusion, with or without the SiO protection, are shown in Fig. 1. Figure 2 shows N-P junctions formed separately by sulfur, selenium, or tellurium diffusion, respectively, with the protection of SiO on the P-type GaAs wafer surface. However, by using a dense vapor source, i.e., 30 mg of selenium, Ga_2Se_3 formed even on the surface having a SiO film thickness of 3000Å.

These experimental results indicate that there is a critical value of concentration of Group VI elements for GaAs, above which value chalcogenide formation always takes place. However, if the concentration of these elements is reduced below this critical value, either by using a very small amount of impurity source³ or by diffusing through a sufficient thickness of SiO film, the chalcogenide formation can thus be prevented, hence allowing Group VI elements to diffuse into GaAs and form N-type layers.

Attempts were made to determine whether the silicon monoxide can be used as a masking material against the diffusion of sulfur, selenium, or tel-

² In some experiments, 30 mg of selenium were used.

³ Not determined in this study.

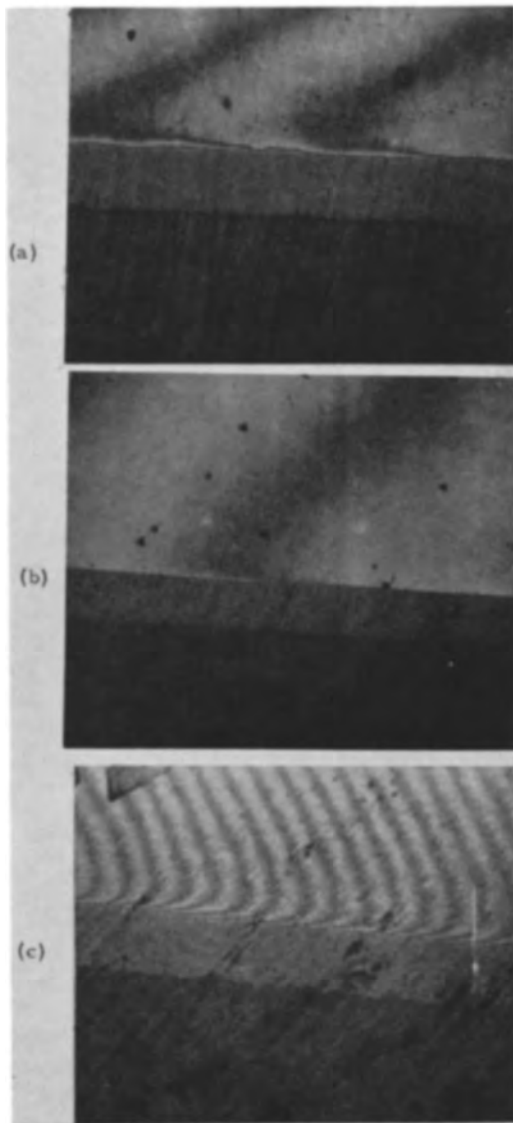


Fig. 2. N-P junction of GaAs formed by (a) sulfur diffusion, (b) selenium diffusion, (c) tellurium diffusion at 1040°C, 120 hr; junction delineated by diluted nitric acid; (measured by superimposed interference fingers). Magnification 150X (reduced to approximately 110X).

lurium in GaAs, as in the case of cadmium or zinc (6). Experimental results indicated that with an SiO film thickness of even 20,000Å on the P-type GaAs wafer surface, sulfur, selenium, or tellurium still could diffuse through and form an N-P junction. A typical example is shown in Fig. 3, for the case of selenium diffusion at 1050°C for 120 hr, where a shallow junction depth of 0.224 mil resulted on a wafer which had 20,000Å SiO, compared to a junc-



Fig. 3. Differentiated N-P junction of GaAs formed by selenium diffusion at 1050°C, 120 hr. (Wafer surface at left had 20,000Å SiO, wafer surface at right had only 2500Å SiO.) Magnification approximately 150X (reduced to approximately 110X).

tion depth of 0.307 mil in the case of 2500Å of SiO. Therefore, to achieve complete masking against selenium, sulfur, or tellurium diffusion, a much thicker SiO film would still be required on the GaAs wafer surface.

The work described above shows how to eliminate a major obstacle for making mesa-type PNP double-diffused GaAs transistors. However, due to the inability of reasonable thicknesses of SiO to mask against diffusions of N-type impurities, a planar-type P-N-P structure still remains a problem to be solved.

Acknowledgments

The author wishes to thank Dr. G. A. Silvey and Dr. A. E. Blakeslee for their valuable discussions, and R. M. DeFries, J. R. Garcia, and E. F. Gorey for their assistance in performing the experiments and the Hall measurements, respectively.

Manuscript received July 2, 1963; revised manuscript received Sept. 20, 1963.

Any discussion of this paper will appear in a Discussion Section to be published in the December 1964 JOURNAL.

REFERENCES

1. B. Goldstein, *Phys. Rev.*, **121**, 1305 (1961).
2. L. J. Vieland, *Phys. & Chem. of Solids*, **21**, No. 3/4, 318 (1961).
3. T. H. Yeh, *This Journal*, **110**, 341 (1963).
4. C. S. Fuller and H. W. Allison, *ibid.*, **109**, 880 (1962).
5. M. V. Sullivan and G. A. Kolb, *ibid.*, **109**, 204c (1962).
6. J. Van der Boomgaard and K. Schol, *Philips Research Repts.*, **12**, 125 (1957).
7. T. H. Yeh and A. E. Blakeslee, *This Journal*, **110**, 1018 (1963).

Evaluation of Concentration Distributions by Test Diffusion and Junction Delineation

K. M. Busen, J. J. Casey, and E. R. Skaw

Research Center, Sprague Electric Company, North Adams, Massachusetts

The solid-state diffusion of doping elements into semiconductor materials has been shown to result, under certain ideal conditions, in concentration distributions (or profiles) which can be represented by well-known conventional formulas. These ideal cases have been thoroughly discussed in the literature by a number of authors and an informative summary has been given by Smits (1).

Diffusion also occurs under conditions where the resulting profiles cannot be calculated at all, or not without considerable error, by use of conventional formulas. Such conditions are met, for example, when diffusion and growth during epitaxy proceed simultaneously, when the diffusion coefficient is not constant, or when bulk factors such as high densities of structural faults cause enhanced or retarded diffusion. Sils and Wang recently discussed a method for obtaining a "panoramic view" of impurity profiles arising during epitaxial growth (2). The technique involves junction delineation after diffusion into a low-angle bevelled n^+/n epitaxial structure, as illustrated in Fig. 1, which is reproduced from the above mentioned reference, but contains some added notations. From the figure it is possible to determine (i) the doping level of the substrate (point 1), (ii) the location (point 2) in the epitaxial layer where the impurity concentration becomes equal to the surface concentration of the test impurity, (iii) the place (point 3) where the resistivity in the epitaxial layer becomes constant, and (iv) a rather crude impurity profile utilizing these three points.

Because of the potential application of this method for the general study of impurity profiles, the present authors have further developed it by showing the degree of precision to which unknown profiles can be evaluated.

This has been accomplished by first studying the capabilities of the method analytically and then

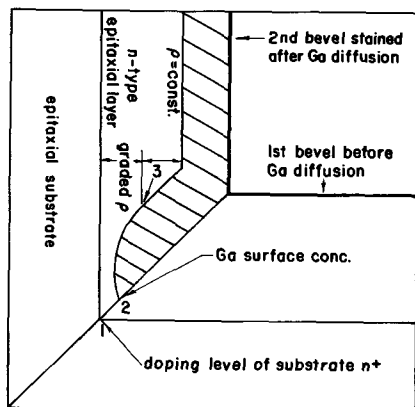


Fig. 1. Illustration of the test diffusion as carried out by Sils and Wang (2).

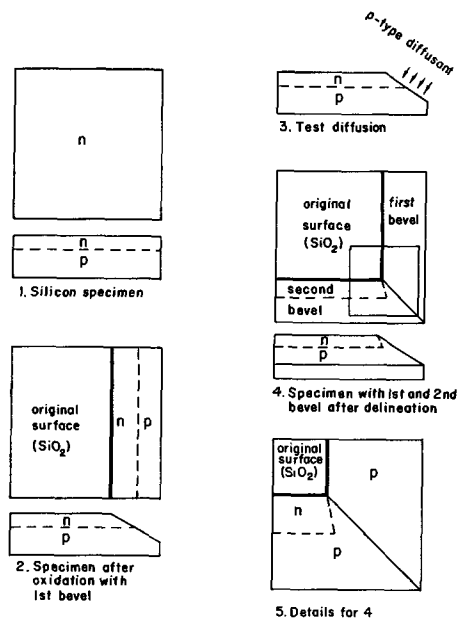


Fig. 2. Processing of a silicon sample for evaluation by test diffusion.

creating an "unknown" impurity profile (by indiffusion under well standardized conditions) followed by diffusion of a conductivity type opposite to that of the "unknown" profile (test diffusion) to find out how closely the profile can be determined.

Figure 2 illustrates the details of processing a silicon sample. It is for this process that the analysis is made and experimental verification presented. The oxidation step is useful in limiting the test diffusion to the area of the first bevel, but may be left out in cases where the part of the profile near the top of the 2nd bevel is of no special interest. It is assumed as a first approximation that the time and temperature of the test diffusion are not drastic enough to cause a significant change of the unknown profile.

The analysis is indicated in Fig. 3a for the case where the surface concentration of the profile from the p-type test diffusion is lower than the surface concentration of the "unknown" profile.

The method of analysis is to assign to each profile a series of depths corresponding to positions, x , of interference fringes on the first and the second bevel which would be obtained by laying a glass plate first parallel to the original surface and then to the first bevel as reference planes. To each fringe the corresponding calculated concentration is then assigned, and the intersections of fringes, corresponding to equal impurity concentrations, delineate a junction between the test profile and the "unknown" profile. Figure 3a shows the relations for a

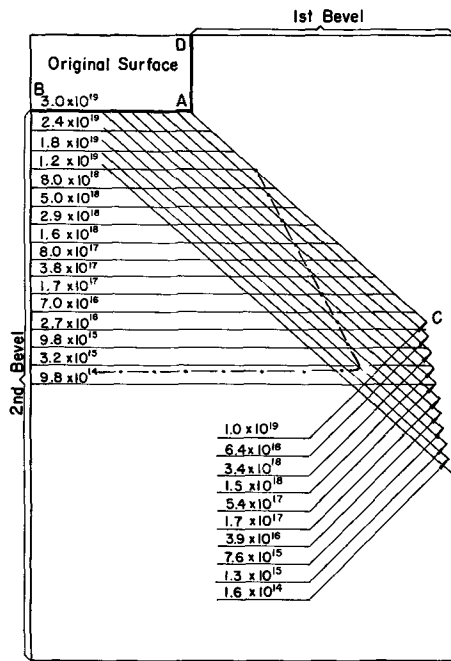


Fig. 3a. Test diffusion analysis. The surface concentration from the test diffusion is lower than the surface concentration of the "unknown" profile.

p-type silicon sample where the background concentration is $1.3 \times 10^{15} \text{ cm}^{-3}$ and where the "unknown" profile is represented by $C_0 \operatorname{erfc} x/\lambda$ with $C_0 = 3 \times 10^{19} \text{ cm}^{-3}$ and $\lambda = 2\sqrt{Dt} = 5.11$ fringes. D is the diffusion coefficient in $\text{cm}^2 \text{ sec}^{-1}$ and t is the time in seconds. (In the experimental work, one fringe corresponded to about $2.97 \times 10^{-5} \text{ cm}$.) The data for the test profile below the first bevel are assumed to be $C_0 = 10^{19} \text{ cm}^{-3}$ and $\lambda = 2.95$ fringes. The assigned impurity concentrations for consecutive fringes were calculated from these data. The dashed-dotted line in Fig. 3a indicates the position to be expected for the junction formed by the two profiles. When the process was carried out on a specimen with experimental conditions very close to those assumed for the analysis, the result shown in Fig. 3b was obtained, on actual delineation by copper plating (3).

Having shown that a junction can be constructed graphically from two known profiles, it remains to be shown how the unknown profile of a specimen

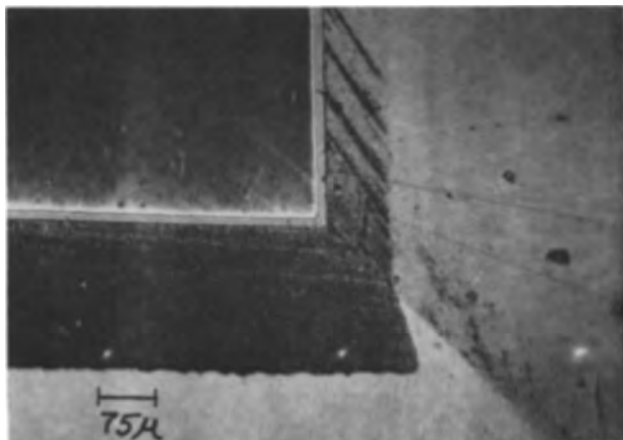


Fig. 3b. Sample after test diffusion and junction delineation

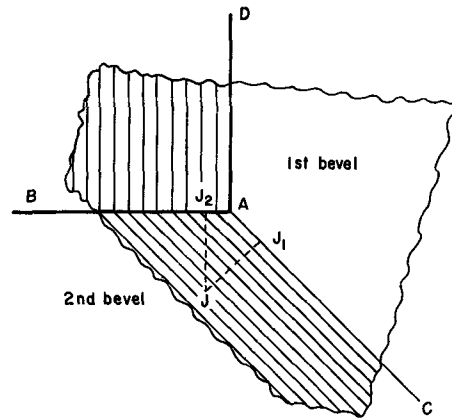


Fig. 4. Illustration for the evaluation of junction depths

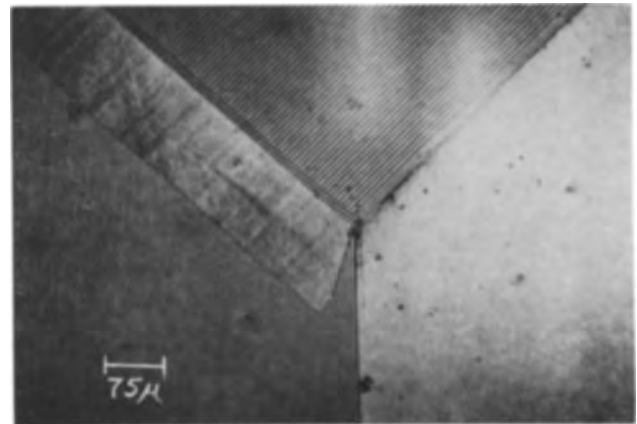


Fig. 5. Sample after test diffusion and junction delineation. This sample was used for the following numerical evaluations.

can be analyzed by means of the junction obtained by test diffusion and delineation.

An important simplification of the analysis can be achieved by showing that the depth in both directions of any particular point from the reference planes is obtainable from a single interference fringe system as depicted in Fig. 4. The number of fringes crossed in going from J to J_1 obviously is a measure of the depth of J with respect to the surface ADC, while simple geometrical considerations prove that the number of fringes traversed in going along the path J - J_2 , normal to AB , is a measure of the depth of J with respect to the plane ABD .

A set of points representing the intersections between interference fringes and a junction formed by a test diffusion is shown in Fig. 5. For each of these points the two depths were determined as indicated in Fig. 4. The data obtained from Fig. 5 were listed as shown in Table I and were used to plot the open circles as shown in Fig. 6. Curve I in this figure represents the p-type test profile $C = 10^{19} \operatorname{erfc} (x/2.95)$ and curve II is a plot of the "unknown" profile, which was already established from other methods of evaluation and was determined to follow the relation $C = 3 \times 10^{19} \operatorname{erfc} (x/5.11)$. It can

Table I.

Test	(JJ ₁)	1	2	3	4	5	6	7	8
Unknown	(JJ ₂)	2.5	4.5	7	9	11	13	14.5	16

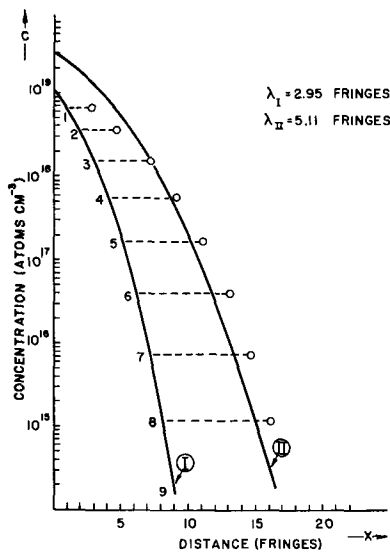


Fig. 6. Graphical evaluation for the sample of Fig. 5

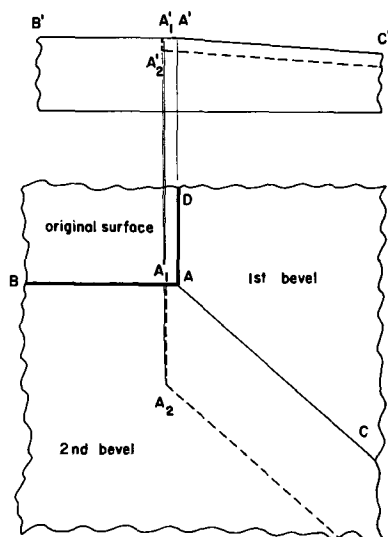


Fig. 7. Shape of a junction originating from test diffusion into a homogeneously doped sample.

be seen that the agreement between the open circles and the established profile is mostly within a factor of three, which is sufficient for many diffusion problems.

When a mask is used to protect the original surface against penetration by test diffusion, the front of the test profile advances underneath the mask in a direction parallel to $A'C'$ (see upper part of Fig. 7) and in a direction perpendicular to $A'C'$ whereby $A'_1A'_2 \approx A'_1A'_1$. Assuming that the specimen in Fig. 7 is homogeneously doped with an impurity of a conductivity type opposite to that of the diffusant, one obtains after angle lapping and junction delineation a structure as shown in the lower part of Fig. 7. It can be seen there that the second bevel magnifies the distance $A'_1A'_2$ but not the distance $A'_1A'_1$. For most of the diffusion experiments which are carried out in semiconductor technology, the resulting distance A_1A is very small and therefore does not show up in normal photomicrographs. Consequently, we let A_1 coincide with A in the following Fig. 8a. Because the front of the test profile in Fig.

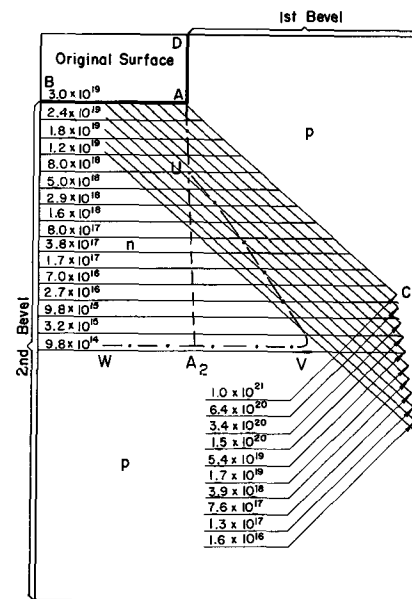


Fig. 8a. Test diffusion analysis. The surface concentration from the test diffusion is higher than the surface concentration of the "unknown" profile.

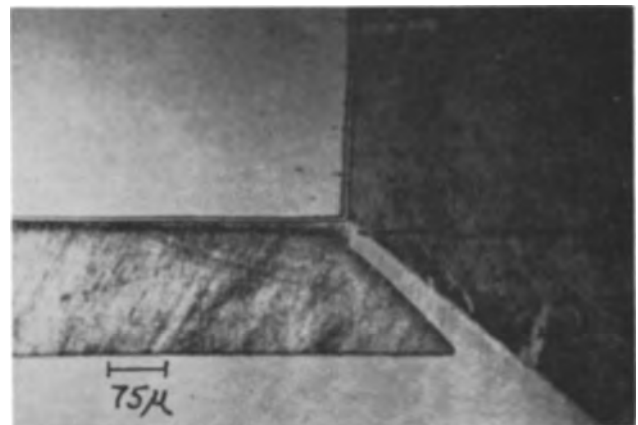


Fig. 8b. Sample after test diffusion and junction delineation

8a stops at A_2 , intersections between fringes of equal impurity concentrations are possible only below a certain concentration (below about $5 \times 10^{18} \text{ cm}^{-3}$) and a structure results as shown by the dashed dotted line $AUVW$. Obviously no identification of the "unknown" profile is possible above $5 \times 10^{18} \text{ cm}^{-3}$. The next Fig. 8b shows a photomicrograph of a sample which has been prepared under conditions which were similar to those in Fig. 8a. The statements above lead to the conclusion that the surface concentration of the test profile must be equal to or smaller than that of the "unknown" profile if structures as shown in Figs. 8a and 8b are to be avoided.

For quick reference, the function $C/C_0 = \text{erfc } x/\lambda$, which is suitable for a test profile, has been plotted vs. λ (Fig. 9). The parameter of the curves is the depth x in steps of fringes.

The method as outlined above is applicable when time and/or temperature for the test diffusion are kept low enough to leave the unknown profile practically unchanged. In many cases one already has more or less complete information on the diffusion

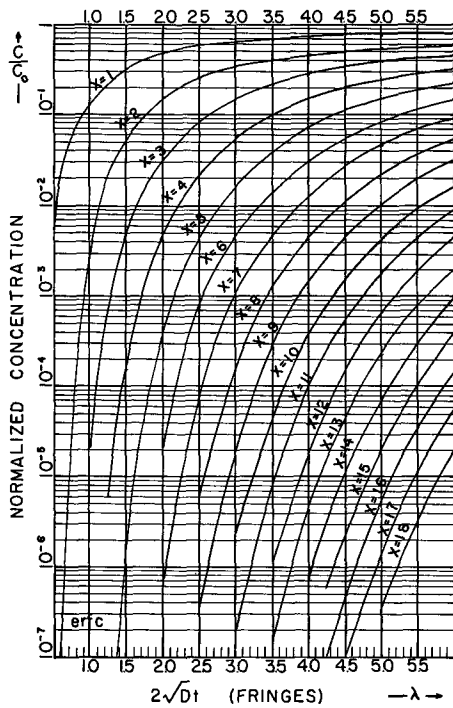


Fig. 9. (C/C_0) from $(\text{erfc } x/\lambda)$ vs. λ with x as parameter

parameters D and t of the unknown profile and if, therefore, the profile were to be checked by a test profile, the parameters D and t for the test diffusion could be adjusted suitably. If, however, the information on the unknown profile is very scant, as in the case of the application of a new diffusant with an unknown diffusion coefficient, one can proceed as outlined in the following suggested steps:

1. Divide the specimen to be analyzed into several pieces.
2. Apply a junction delineation to a piece and determine the junction depth.
3. Subject the piece of step 2 to a heat-treatment as it would be desired for a test diffusion.
4. Determine by another junction delineation whether the junction depth has been changed significantly. If there is no change, proceed with the test diffusion into another piece.
5. If there is a significant change, repeat steps 2 through 4 for one or more other pieces and try to find combinations of diffusion temperature and time, where the change becomes tolerable.
6. Select a suitable D and t for the test diffusion.

The first part of the "unknown" profile (open circles in Fig. 6) is lower than the actual curve II, and a curve through the circles would give an extrapolated C_0 of $\sim 10^{19} \text{ cm}^{-3}$. This may be explained qualitatively when for a depth of about 5 fringes we substitute the erfc, which describes curve II, by a Gaussian function and compute the change which the Gaussian function undergoes when the test diffusion is performed. In our example curve II is described by

$$C_{II} = 3 \times 10^{19} \text{erfc} \frac{x}{2\sqrt{10^{-13} \times 5.76 \times 10^4}}$$

where x is expressed in centimeters. The amount of material diffused during $t_{II} = 5.76 \times 10^4 \text{ sec}$ is (4)

$$M_t = \frac{C_{oII}}{\sqrt{\pi}} \lambda_{II} = 2.57 \times 10^{15} \text{ at. cm}^{-2}$$

If this amount M_t were predeposited at time 0 at the surface of the sample, then after time t the profile would be

$$C = \frac{M_t}{\sqrt{\pi D t}} \exp \left[-\frac{x^2}{4 D t} \right]$$

The expression in front of the e-function is the surface concentration for the Gaussian function and from

$$C)_{at \ x=0} = C_{oII} = 3 \times 10^{19} = \frac{2.57 \times 10^{15}}{\sqrt{\pi \times 5.33 \times 10^{-13} t}} \text{ at. cm}^{-3}$$

we obtain $t = 4.37 \times 10^3 \text{ sec}$ with the diffusion coefficient taken as shown above. After time $t_I = 3.6 \times 10^3 \text{ sec}$ (time for test diffusion) and for $D = D_I$

$$C_0 = \frac{M_t}{\sqrt{\pi D (t + t_I)}} = 2.3 \times 10^{19} \text{ at. cm}^{-3}$$

This indicates that the test diffusion lowered the surface concentration sensibly for the specimen.

When the specimen is being prepared for test diffusion care should be taken to avoid substantial surface damage originating from improper lapping of the first bevel. Another important point to be observed is the reliability of the junction delineation itself. Sometimes oxide layers, old plating solutions, contaminated surfaces, and other influences can obscure the junction. Therefore a certain amount of experience is required to determine whether a delineation is adequate for evaluation of the unknown profile or not.

For the evaluation of photomicrographs as shown in Fig. 5 it was found convenient to mark the intersections between interference fringes and the junction by punching them with a fine needle. The distance $J-J_2$ was measured by using a small transparent square. The square was oriented in such a way that the base matched an intersection and that the left vertical side was normal to AB (as in Fig. 4). Then the interference fringes along the left vertical side were counted. For samples with masking layers of SiO_2 , one has to correct for the silicon incorporated into the oxide.

Acknowledgment

The authors appreciate the work by A. Thibert, who took care of the angle lapping and the junction delineation.

Manuscript received July 31, 1963. This paper was presented at the Pittsburgh Meeting, April 15-18, 1963.

Any discussion of this paper will appear in a Discussion Section to be published in the December 1964 JOURNAL.

REFERENCES

1. F. M. Smits, *Proc. I.R.E.*, **46**, 1049 (1958).
2. V. Sils and P. Wang, Abstract No. 80, paper presented at the Electrochemical Society Meeting, Los Angeles, 1962.
3. D. R. Turner, *This Journal*, **106**, 701 (1959).
4. J. Crank, "The Mathematics of Diffusion," p. 31, Oxford University Press, London (1957).

A High Intensity Carbon-Arc-Image Furnace and Its Application to Single Crystal Growth of Refractory Oxides

G. J. Goldsmith, M. Hopkins, and M. Kestigian¹

RCA Laboratories, Radio Corporation of America, Princeton, New Jersey

Of the several techniques available for the attainment of temperatures in the range between 2500° and 3700°C, the arc-image system (1) appears to be especially adaptable to the growth of single crystals. Since, with this technique, heat is applied to the growing crystal by means of a focussed beam of radiant energy in the wavelength range where many common materials are transparent, the ambient atmosphere in which the crystal is grown, as well as the size and location of the hot zone, may be controlled easily. The system described herein was constructed specifically for the purpose of growing crystals by the powder fusion technique. It is designed to operate continuously over arbitrary periods of time and with an arbitrary choice of ambient atmosphere. It is adequately versatile so as to be adaptable to other crystal growth methods and to conventional high-temperature chemical investigations.

The principle of the arc-image furnace and its general applicability have been described by several investigators (1-7). The present furnace employs a double ellipsoidal optical system (1), one that permits ready manipulation of the radiant beam.

An outline of the furnace is shown in Fig. 1. The energy sources are a pair of high intensity blown carbon-arc motion picture projectors (Strong Electric Company, Toledo, Ohio) which contain both the carbon arc and the primary ellipsoidal reflector. Because of the ellipsoidal optics, it is possible to employ a small plane reflector to turn the beam 90°

¹ Present address: Sperry Rand Corporation, Sudbury, Massachusetts.

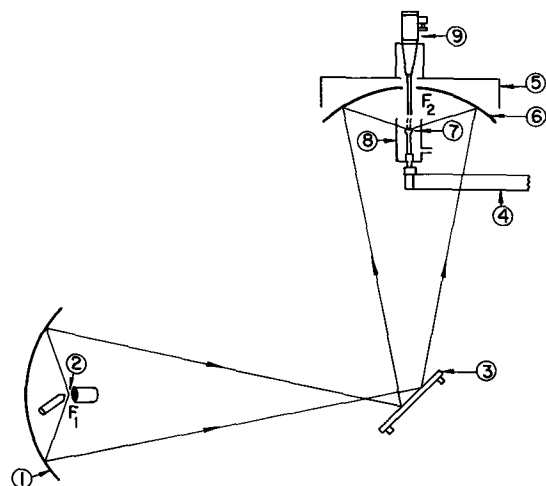


Fig. 1. Vertical arc image crystal growing furnace: 1, primary mirror; 2, carbon; 3, transfer mirror; 4, crystal support; 5, housing to hold reimagining mirror; 6, reimagining mirror; 7, crystal; 8, Pyrex cylinder around crystal; 9, feed hopper.

toward the reimagining mirror. This geometry yields an image of the burning arc which has its large dimension in a horizontal plane, a more desirable configuration for powder-fusion growth. The two sources are operated sequentially to permit continuous operation since anode life limits the uninterrupted operating time of each arc to only 15 min. Switching from one arc to the other is achieved by means of an inertial rotator on the plane reflector.

The feed hopper is located above the reimagining mirror with its delivery tube passing through a central hole to a point immediately above the focal plane. The hopper design and operation have been reported elsewhere (8).

The reimagining mirror, hopper, and crystal support are mounted on a separate assembly attached rigidly to the ceiling girders. This was done to isolate the growing crystal from any vibration caused by operation of the arcs and the transfer mirror. The hopper is mounted on a two-dimensional slide to provide accurate location of the feed flow relative to the reimagining mirror. The entire mirror-hopper assembly is mounted on a second two-dimensional slide for accurate positioning in the optical path. Further there is a three-point tilt mechanism for the reimagining mirror. The crystal support pedestal is mounted in a chuck which is attached to a rigid blade-shaped support. Positioning of the chuck in the horizontal plane is accomplished by means of a jewelers' lathe slide rest. Vertical motion is provided by a pair of lead screws on which are mounted a pair of preloaded ball bearing nuts. The lead screws are driven from a flexible coupling through a synchronizing bar. Two vertical speed ranges are available, one at 15 in./min for coarse positioning and one that is continuously variable from 0-4 in./hr for crystal growth. A pair of telescopes with eyepiece crosshairs are placed at 90° to one another in the image plane for sample positioning. Crystal growth is observed through the telescopes or by means of a projected image produced by a sequence of prisms and lenses.

The plane transfer mirror is a flat, 1/8 in. thick quartz disk, 6 in. in diameter, aluminized on its front surface. It is clamped to a water-cooled copper support which has provisions for adjustment of the tilt angle. The transfer mirror will rotate from one arc to the other in 90 ms. This is accomplished by an inertial rotation system. A small motor with a heavy flywheel is brought to a speed of 10,000 rpm, power is then removed from the motor, and a magnetic clutch is engaged causing the mirror to rotate. Accurate positioning of the mirror

limits is obtained through the use of ball-loaded detents and magnetic stops. The mirror rotation sequence is automatically programmed.

Exact matching of the images formed at the re-imaging mirror focal point with respect to position, size, and flux density is necessary for successful crystal growth. Preliminary mechanical alignment of the optic axes of the arcs is done with the aid of a cathetometer. Optical alignment is then carried out by placing plastic light pipes in the position of the positive carbon. The light pipes are illuminated by incandescent lamps to form a luminous object in the place where the arc would appear. These light pipes permit the entire optical system to be traced out and adjustments of reflector locations to be made without actually operating the arcs. Superposition of the images produced by each of the arcs is determined by a "target" placed at the focal point of the re-imaging mirror. Final adjustment of the arcs is conducted by operating the furnace and heating a flat zirconia plate located at the focal point of the re-imaging mirror. Satisfactory alignment is indicated when the size, shape, and location of the melted area in the zirconia plate are identical for both sources.

Because of the lack of reliable thermometry in this temperature region, no attempt was made to measure precisely the temperature attained. A rough temperature measure was obtained by melting pressed pellets (1 x 1 cm) of various refractory compounds with "known" melting points. The compounds, TiO_2 , Al_2O_3 , MgO , ZrO_2 , and ThO_2 , were melted and remelted in this way demonstrating that temperatures up to at least $3300^\circ C$ could be reached with materials of low emissivity.

A total irradiance calorimeter (A. D. Little, Inc.) was employed for the measurement of heat flux, heat flux profiles, and stability. This calorimeter is of the flow type in which water is circulated through a blackened copper receiver at a known rate, and the temperature difference between the incoming and outgoing water measured.

Various reflecting surfaces and mirror materials were investigated for life and efficiency including polished aluminum, glass with first-surface aluminum, glass with second-surface silver, and glass with first-surface multielectric coating. With the arc running under normal conditions, 160 amp at 72v, the heat flux with a glass first-surface aluminum reflector was found to be $230 \text{ cal/cm}^2 \text{ sec}$ with a variation of $\pm 2\%$ over the life of the anode carbon. With the more durable glass second-surface silver reflector, the flux density is reduced to $190 \text{ cal/cm}^2 \text{ sec}$. The polished aluminum reflector was found to overheat and to distort seriously. By far the best compromise is the glass first-surface multielectric reflector which is substantially more durable than the first-surface aluminum, and which yields about 20% higher flux, or about $275 \text{ cal/cm}^2 \text{ sec}$.

Heat flux profiles (Fig. 2, 3) of the image were measured by manipulating the calorimeter in three dimensions. It will be noted that the heat distribution is approximately Gaussian with a width at 0.9

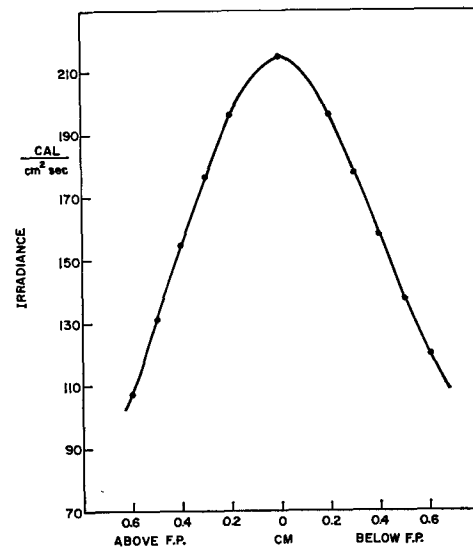


Fig. 2. Vertical profile of focal point

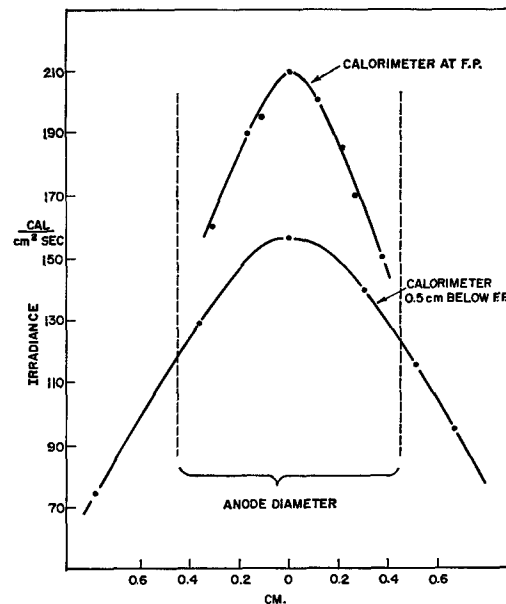


Fig. 3. Horizontal profile of focal point

of maximum of 3 mm in the horizontal plane, and of 4 mm in the vertical plane.

The internal stabilization systems built into the Strong Jet-arcs consist of an optical feed-back anode positioning control plus a current-controlled cathode feed rate. No additional control of output was found to be necessary as evidenced by the stability demonstrated in Fig. 4 which is taken over a 15 min period. The points at which the arcs were switched are obvious on the plot. Similar stable behavior was observed over many hours of continuous operation.

In a typical crystal growth experiment, the support rod, usually of stabilized zirconia, is positioned just below the image focal point and the carrier gas turned on. The feed material is slowly introduced by raising the voltage on the hopper solenoid and the support rod raised toward the focal point until the falling powder forms a sintered cone. The pedestal is further raised until the tip of the cone becomes molten. The crystal is then allowed to grow

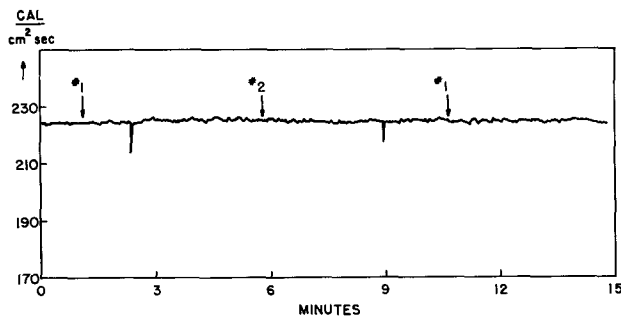


Fig. 4. Image furnace time stability



Fig. 5. HfO₂ crystal

closer to the focal point until the desired diameter is reached. The pedestal is then lowered at a rate equal to the growth rate. Upon completion of crystal growth, the boule is slowly lowered out of the focal point with the furnace running in order to minimize thermal shock. Generally the pedestal is mounted inside a 3 in. diameter Pyrex cylinder 8 in. long with ports near its base for escape of the carrier gas. This permits surrounding the growing crystal with a protective atmosphere.

Initial crystal growth studies were conducted on a familiar system, TiO₂, which melts at 1840°C. The melting temperature was reached and maintained at a point somewhat beneath the focal point. Colorless, nearly stoichiometric rutile crystals were grown at the rate of ¼ in./hr in an atmosphere of oxygen. This is in contrast with the crystals obtained by ordinary flame fusion which are invari-

ably black in color because of oxygen deficiency which must be removed by heat treatment in air or oxygen.

The most refractory crystals grown were those of ZrO₂ and HfO₂ containing CaO for the purpose of stabilizing a cubic phase. The initial concentrations of CaO ranged between 5 and 38 mole %. The best single crystals, cubic by x-ray analysis, were obtained in the region of 12 mole % CaO; a concentration which lies close to the phase boundary between cubic ZrO₂-CaO solid solution and the mixed phases, monoclinic ZrO₂ + cubic ZrO₂ solid solutions, according to Duwez, Odell, and Brown (9). Suitable feed material for the ZrO₂ crystals was prepared by calcining either zirconium lactate or zirconium sulfate nonahydrate with appropriate amounts of CaCO₃. The former compound was obtainable in unusually high purity and yielded the best crystals. HfO₂ feed was prepared directly from CP grade oxide by calcining with CaCO₃. Face-centered cubic crystals of HfO₂ and ZrO₂ were obtained with dimensions up to 5 mm x 4 cm long (Fig. 5). They are colorless and transparent. X-ray studies indicate that ZrO₂ normally grows 17° off the [111] crystallographic axis. These materials have also been grown successfully with rare earth and transition metal impurities. The furnace has also been employed in the study of diffusion of transition metal oxides in MgO and for the preparation of a number of refractory nitrides.

Acknowledgment

The authors wish to thank G. Neighbor who performed the x-ray studies.

Manuscript received July 22, 1963; revised manuscript received Sept. 23, 1963. This paper was presented at the Los Angeles Meeting, May 6-10, 1962.

Any discussion of this paper will appear in a Discussion Section to be published in the December 1964 JOURNAL.

REFERENCES

1. R. E. De La Rue and F. A. Halden, *Rev. Sci. Inst.*, **31**, 35 (1960).
2. P. E. Evans and G. Wildsmith, *Brit. J. Appl. Phys.*, **13**, 68 (1962).
3. H. W. Newkirk and B. B. Brenden, *J. Am. Ceram. Soc.*, **43**, 146 (1960).
4. M. R. Null and W. W. Lozier, *Rev. Sci. Inst.*, **29**, 163 (1958).
5. M. R. Null and W. W. Lozier, *J. Soc. Motion Picture Television Engrs.*, **68** [2], 80 (1959).
6. P. E. Glaser, *This Journal*, **107**, 226 (1960).
7. R. P. Poplawsky and J. E. Thomas, Jr., *Rev. Sci. Inst.*, **31**, 1303 (1960).
8. M. Kestigian, *ibid.*, **33**, 1293 (1962).
9. P. Duwez, F. Odell, and F. H. Brown, Jr., *J. Am. Ceram. Soc.*, **35**, 109 (1952).



Structure of Electroless Cobalt Films

R. D. Fisher and D. E. Koopman

The National Cash Register Company, Dayton, Ohio

The chemical (electroless) deposition of cobalt and nickel on catalytic surfaces (Fe, Ni, Al, Co, Pd) was reported by Brenner in 1947 (1). Electroless deposition is essentially a controlled autocatalytic reduction of cobalt and nickel ions on an active or catalytic surface by means of hypophosphite ions. The deposits inherently contain 1-12% phosphorus depending on the experimental conditions. Electroless nickel has been reported by Goldenstein *et al.* to be amorphous (2). However, Graham *et al.* have reported recently that electroless nickel is an extremely fine grained, supersaturated solid solution of phosphorus in crystalline nickel (3).

In this communication, the crystallinity and orientation of electroless cobalt films as a function of the hypophosphite ion concentration in the electroless solution is reported. The structure was studied by x-ray and electron diffraction and electron microscopy. Polycrystalline cobalt deposits are obtained, although in certain instances deposits appear to be amorphous.

The solution composition and deposition conditions for film preparation were: hypophosphite ion from 0.016 to 0.163M; 0.0315M cobalt ion; 0.23M ammonium chloride; and 0.094M citric acid monohydrate. The solution volume was 2 liters and the pH was adjusted to 8.2 with sodium hydroxide. Solution temperature was 80°C, controlled by means of a heating mantle. The cobalt deposits were prepared on Mylar at a constant thickness of approximately 6,000Å. The thickness was determined from the density of cobalt corrected for an average phosphorus content of approximately 4% by weight. The Mylar substrate was previously treated with an adhesive to enhance adhesion of the cobalt films and was activated or catalyzed by immersing in

stannous chloride, rinsing, and immersing in palladium chloride (4).

In general, the x-ray diffraction patterns showed a hexagonal close packed structure with a $10\bar{1}0$ preferred orientation parallel to the plane of the deposit (see Table I). Laue patterns of the films showed that the "c" axis was randomly oriented and parallel with respect to the plane of the deposit. Increasing the hypophosphite ion concentration from 0.016 to 0.132M results in a decreasing but still preferred $10\bar{1}0$ orientation and an increase of the $11\bar{2}0$ orientation. In general, the over-all intensity of the diffraction peaks decreases with increasing hypophosphite concentration, although the thickness of the deposits was constant. At a concentration of 0.163M hypophosphite ion, the deposits showed no x-ray diffraction pattern. Thus, as far as x-ray diffraction is concerned, these deposits could be considered amorphous, similar to electroless nickel deposits. No evidence of a cubic structure or the presence of any cobalt phosphide was obtained.

Table I. X-ray diffraction peak heights as a function of hypophosphite concentration*

Molar concentration,		Peak heights, counts/sec,				Thickness, Å
H ₂ PO ₂ ⁻	Co ⁺⁺	10 $\bar{1}1$	10 $\bar{1}0$	0002	11 $\bar{2}0$	
0.016	0.0315	208	880	32	48	6000
0.033	0.0315	128	1224	32	32	6000
0.066	0.0315	112	976	0	64	6000
0.082	0.0315	112	704	48	88	6000
0.099	0.0315	104	648	40	168	6000
0.132	0.0315	176	480	20	176	6000
0.163	0.0315	0	0	0	0	6000

* Molybdenum K α radiation with a zirconium filter.

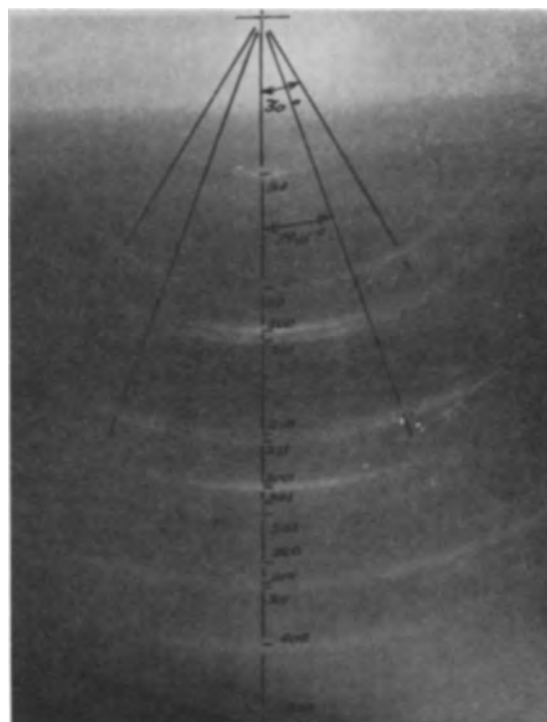


Fig. 1. Electron diffraction (reflection) pattern of as-deposited cobalt film prepared at 0.016M hypophosphite ion; acceleration voltage 50 kv.

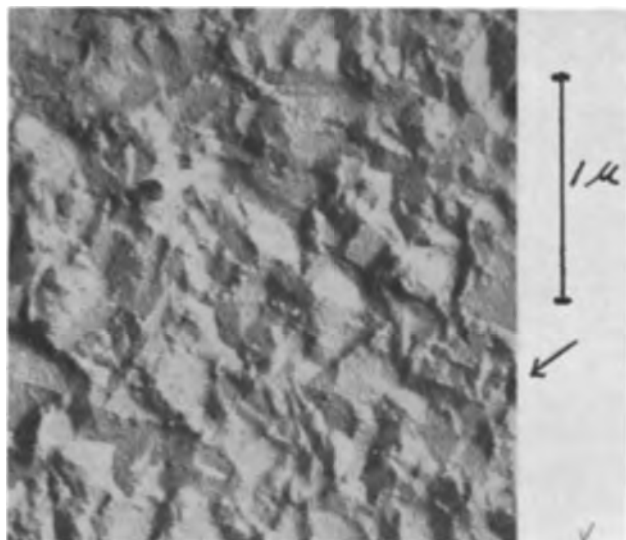


Fig. 2. Electron micrograph (30,000X); surface of electroless cobalt film prepared with 0.016M hypophosphite ion.

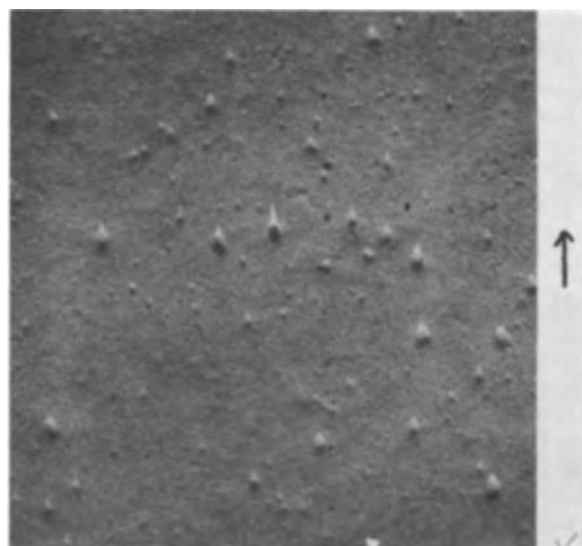


Fig. 3. Electron micrograph (30,000X); surface of electroless cobalt film prepared with 0.163M hypophosphite ion.

Electron diffraction (by reflection) of the same deposits (Fig. 1) confirmed a $10\bar{1}0$ preferred orientation, and with increasing hypophosphite ion concentration the diffraction rings became broader and more diffuse, i.e., a decrease in intensity and definition until at a maximum concentration of 0.163M, the films showed no diffraction pattern.

Thus, the surface layer structure of the deposits was similar to the structure of the bulk deposits.

Electron micrographs at 30,000 diameters of the same films were obtained by replication using a collodion-platinum shadowed carbon technique. Deposits prepared at the low hypophosphite ion concentrations (0.016-0.063M) have a relatively uniform surface texture displaying a crystallinity with observable crystalline faces having an average dimension in the range of 0.2-0.3 μ (Fig. 2). Deposits prepared with the higher hypophosphite ion concentration (0.163M) which appear amorphous from both x-ray and electron diffraction have a very fine surface texture with an estimated grain size of 0.01-0.02 μ (Fig. 3); considerable hydrogen pitting is also apparent. The fact that the deposits exhibit ferromagnetic properties which could be observed from their hysteresis loop characteristics is further evidence that the deposits have a crystalline structure and are not amorphous.

In conclusion, the structure of electroless cobalt on Mylar is hexagonal close packed and microcrystalline, with a $10\bar{1}0$ orientation; the degree of orientation and grain size is determined by the hypophosphite ion concentration, at least when the cobalt ion concentration is constant. The electroless cobalt deposits are similar to electroless nickel films which have been reported to be amorphous when prepared at high hypophosphite ion concentrations, and similar to electroless nickel films which have been reported to be crystalline when prepared at low hypophosphite ion concentrations. Thus, the influence of hypophosphite ion concentration on the degree of crystallinity may explain the apparent contradictions in crystallinity of electroless nickel films observed by different workers.

Acknowledgment

The authors would like to acknowledge the assistance of Dr. A. F. Prebus, of Ohio State University.

Manuscript received Sept. 10, 1963.

Any discussion of this paper will appear in a Discussion Section to be published in the December 1964 JOURNAL.

REFERENCES

1. A. Brenner and G. E. Riddell, *J. Research Natl. Bur. Standards*, **3**, 31 (1946).
2. A. W. Goldenstein, W. Rostoker, F. Schossberger, and G. Gutzeit, *This Journal*, **104**, 104 (1957).
3. A. H. Graham, R. W. Lindsay, and H. J. Read, *ibid.*, **109**, 1200 (1962).
4. R. D. Fisher and W. H. Chilton, *ibid.*, **104**, 485 (1962).

The Application of Radiography to the Study of the Structure and Operation of Porous Electrodes

M. Bonnemay, G. Bronoël, E. Levart, and G. Peslerbe

Laboratoire d'Electrolyse, Centre National de la Recherche Scientifique, Bellevue, S. & O., France

ABSTRACT

Homogeneity, porosity, and catalyst distribution in porous materials can be determined by x-ray techniques. In addition, the distribution of the gas and electrolyte phases and their variation as a function of parameters, such as pressure and polarization, can be evaluated. These possibilities render radiography a powerful and often irreplaceable tool for the study of the operation of triple-contact porous electrodes such as those used in fuel cells.

Certain electrochemical problems, in particular the interpretation of the operation of porous electrodes, necessitate at the present time hypotheses concerning the structure of the reaction volume in which depolarization processes take place. It is the object of the present work to show electrochemists the possibility of verifying certain of these hypotheses by the use of x-rays. It will be shown that this technique is a powerful tool for the determination of: (A) The structure of porous materials; in particular, (a) the global porosity of an electrode and its homogeneity, and (b) the distribution of a catalyst in a porous material. (B) The localization of the gas and electrolyte phases in triple-contact porous electrodes frequently used in fuel cells.

The systematic study of the phenomena taking place during the operation of porous electrodes necessitates the realization of known, reproducible and homogeneous porosities. The verification of this is normally carried out by the determination of apparent densities with a hydrostatic balance, and by the use of the mercury porometer.

Apparent density determinations lead to an average value of the pore density and thus cannot give information concerning the pore distribution in the sample. In addition this technique often necessitates an anti-wetting treatment which leads to surface poisoning and renders the electrode useless for further studies.

In a similar manner, the mercury porometer, while giving valuable information concerning pore distribution, also leads to surface pollution and, in certain cases, to catalyst poisoning. This technique is impossible to employ when the possibility of amalgam formation exists (silver electrodes for example).

The search for a technique free from the above mentioned difficulties led to a study of the possibilities of the use of x-ray techniques. It is well known that microcavity diameters (having values ranging lower than 0.1μ) in homogeneous porous materials may be determined by the analysis of centrally diffused x-rays (1). However, it does not appear that the analysis of the global absorption of x-rays has as yet been applied to the determination

of the apparent density of these materials. An application to porous electrodes having cavity diameters between 1 and 50μ will be given here. This nonpolluting method also allows the detection of heterogeneities and preferential canal orientation.

It is often of interest, in order to study diverse catalysts, to disperse them in a reproducible and homogeneous porous support. The catalyst distribution in such a support is thus an important parameter. Metallography is the classical method for this determination for a metallic element in a porous support. It consists in microscopic examination of a metallographic cut of the sample which must be exactly representative of the initial material. In the case of a carbon support, the tearing or crushing of a metallic deposit is difficult to avoid even using the most exacting manipulations. The use of a radiographic technique avoids these difficulties.

While different techniques may be used for the determination of the above mentioned parameters, the localization of the gas and electrolyte phases in the interior of a porous electrode may only be carried out with an x-ray technique. This technique has not as yet been used, to our knowledge, for this purpose, thus, data concerning the electrolyte position in the electrode are at best hypothetical.

It is, however, important to know the effective position of the different phases in the porous support. For example, in many cases the drop of electrode performance, as a function of time, is generally attributed to electrode flooding. The study of the gas and electrolyte distributions as a function of working conditions is thus important and is made possible by the use of radiography. In addition, recent work has shown that, for certain types of electrodes, possible variations of the concentration of the electrolyte in the pores may be determined (2).

Experimental and Results

In all of the studies of the structure and operation of electrodes a Philips PW 1009 x-ray generator was employed. This generator (G, Fig. 1) is characterized by: a maximum acceleration voltage of 50 kv; a possible filament current of as high as 50 ma;

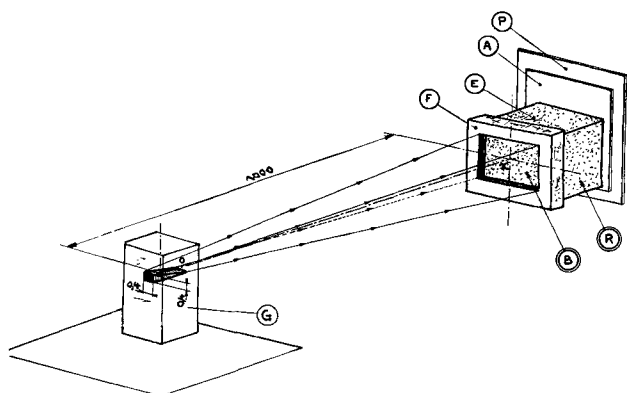


Fig. 1. Experimental set up for x-ray study. A, Aluminum screen; B, x-ray entry plane; E, porous sample; F, lead window; G, x-ray generator Philips PW 1009 (for clarity only one beam has been shown). Note: dimensions in millimeters.

and four independent windows allowing four experiments to be carried out simultaneously. Interchangeable tubes allow the use of various types of x-rays. In addition, certain tubes allow extremely fine beams to be employed (for example the apparent slit dimensions of a Cu anticathode are 0.4×0.4 mm). Classical x-ray generators, while perhaps more powerful, are seldom so versatile.

In view of the considerable importance of the operating procedure in this work it appears necessary to briefly review the fundamental rules governing x-ray techniques. Thus the sample (E, Fig. 1) must be placed far enough from the source, taking into account its surface area, so that it receives a uniform x-ray intensity. It should, however, not be placed at a distance such that there is too much energy loss from air absorption. The sample is placed between and in contact with a photosensitive plate (P) and a lead window (F) used to eliminate lateral diffusions. Further, for certain metals, such as nickel, an aluminum screen must be placed between the sample and the film in order to absorb the secondary fluorescent radiations of the metal under study.

The image obtained under these conditions will have better definition, the further the sample is from the source, the better the contact between sample and film, and the thinner the sample. In addition, the entry plane (B) of the x-rays must be perfectly normal to the beam axis (OX) and perpendicular to the lateral reference plane (R).

Porous Material Structural Study

This study involves the determination of the homogeneity and apparent density, as well as the catalyst localization, in a porous support. In these cases x-ray studies may be carried out either on complete electrodes (nondestructive experiments) or on samples cut from the original electrodes (destructive experiments).

In the first case studies were carried out on disk electrodes to determine the radial porosity or catalyst distributions. These studies are particularly adapted to the case of single porosity electrodes. They give useful information concerning the radial homogeneity of the electrode at different stages of

its fabrication, *i.e.*, after compression, sintering, etc.

In the second case, the experiments are carried out on parallelepiped specimens of the sample. This allows the study of porosity or catalyst distributions in directions other than radial. The studies are adapted for multilayer porous electrodes.

Experimental technique.—Porosity and homogeneity.—The x-rays used for this work must sufficiently penetrate the material, for example, in the case of carbon supports the $K\alpha$ rays of Cu are suitable for thicknesses up to 20 mm. On the other hand, the use of harder rays, such as that of Mo, is indispensable for the analysis of a Ni sample having a thickness as low as 3 mm.

Catalyst localization.—To localize a catalyst in a porous support, the x-ray should be strongly absorbed by the catalyst with relatively small support absorption. The case of a metallic element deposited in a carbon support is particularly favorable, since the absorption coefficient of carbon is considerably smaller than that of most of the metals studied. The film should be of sufficiently fine grain to enable clear enlargements to be obtained (use of maximum resolution Kodak plates: 1000 lines/mm).

Results.—Porosity measurement.—It is known that the absorption of an x-ray of initial intensity I_0 in a solid of uniform density ρ and of thickness x , is given by

$$A = I_0 - I = I_0 \left[1 - \exp \left(-\frac{\mu}{\rho} x \right) \right] \quad [1]$$

where μ is the linear absorption coefficient of the solid (3,4).

The intensity of the x-ray flux emerging from a sample may be determined by measurement of the optical density of a photosensitive film after its exposure.

The relation between the optical density (\mathcal{D}), of the film (in the linear portion of the characteristic curve) measured by photometry, and the intensity I of the emerging beam, is of the form

$$\mathcal{D} = \gamma \log I \quad [2]$$

γ is a characteristic emulsion coefficient. From this a linear relation is obtained between the optical density of the film and the metal thickness through which the x-ray beam has passed. Hence (with $\log I_0 = \text{constant}$).

$$\mathcal{D} = -ax + b \quad [3]$$

This function has been experimentally determined for different metallic electrodes. Figure 2 shows a representative curve for Ni. This curve is a calibration curve and was traced using pure solid Ni samples having thicknesses varying from 0.5 to 2 mm. For each sample the film is more exposed the thinner the sample using identical exposure times.

The linear absorption coefficients of metals have values considerably larger than those of gases, thus the absorption in a porous metal electrode filled with air will principally be a function of the length traversed by the x-rays through the metallic phase.

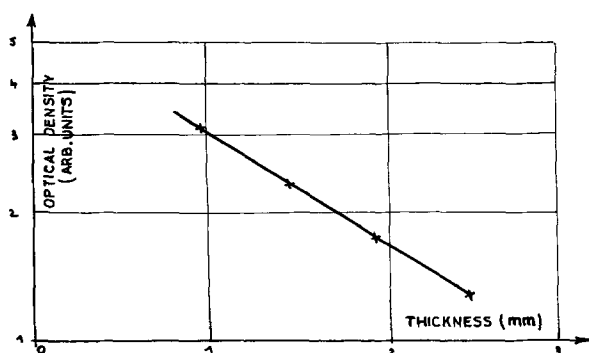


Fig. 2. Calibration curve

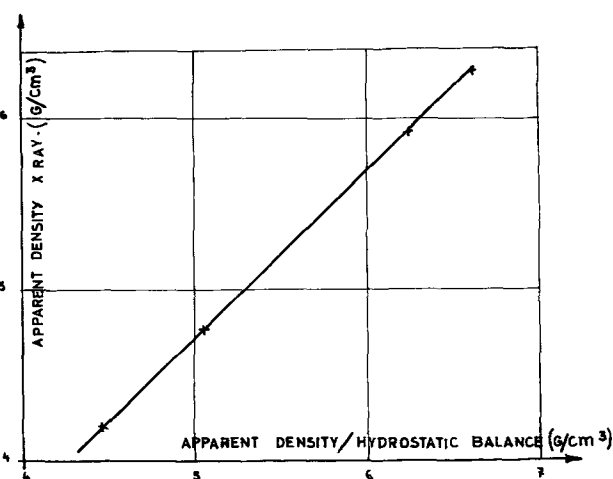


Fig. 3. Verification curve for a porous Ni sample

In the case of a homogeneously porous sample the ratio between its total thickness and the x-ray path length should be equal to the ratio of the density of the metal in the sample to the apparent density of the sample. The path length in the metallic portion of the sample is obtained from the calibration curve. The validity of this method has been verified using Ni samples of varying porosities, comparing the density values found with those obtained using a classical method (volume measurement using a hydrostatic balance), and the results are shown in Fig. 3.

In the case of preferential cavity orientation, this may be observed by the comparison of three photographs taken in different directions while conserving the same x-ray path length.

Catalyst localization in a porous support.—For these studies electrolytic Ag deposits using a classical cyanide solution were made on carbon electrodes of different porosities (22 and 60 μ) under rigorously identical electrolysis conditions.

The data were obtained by examination, under microscope, of the x-ray plates. Under these conditions it may be seen that the metal is deposited not only on the surface of the electrode, but also in the interior of the pores. Thus, radiography allows, in this case, the depth of penetration of the metal deposit to be determined. It has been observed that this depth varies greatly as a function of the support porosity.

Study of the Gas and Electrolyte Phase Distribution in a Porous Electrode

It has just been shown that radiography allows direct information concerning the texture of porous material, in particular those destined for use as electrodes in fuel cells, to be obtained.

Radiography may equally furnish information concerning the phenomena taking place in the interior of a porous electrode under operating conditions. Thus the gas and electrolyte phase distributions may easily be studied by this technique as a function of electrode texture and its operating conditions (pressure, temperature, polarization, etc.).

A first series of experiments were carried out on double-porosity electrodes. It is known that these electrodes were created (5) with the purpose of rendering the gas electrolyte interface relatively independent of external parameters (especially the differential pressure). It was thought that experimental verification of this would be of interest. A second study was undertaken concerning the influence of electrode polarization on the position of the gas-electrolyte interface. This work was carried out on single-porosity electrodes.

Experimental.—A special type of electrolytic cell was constructed specifically for this study (see Fig. 4). It consists of two compartments (A and B) between which the sample (C) is inserted. The latter is parallelepiped in shape and was cut from a porous electrode such that the original thickness was conserved (a, Fig. 4). The x-ray path length (represented by dimension b) was chosen according to the electrode material so as to obtain reasonable exposure times. For example, an exposure time of 15 sec was required for a carbon electrode 10 mm in thickness (x-ray: Cu, K α), whereas for a Ni elec-

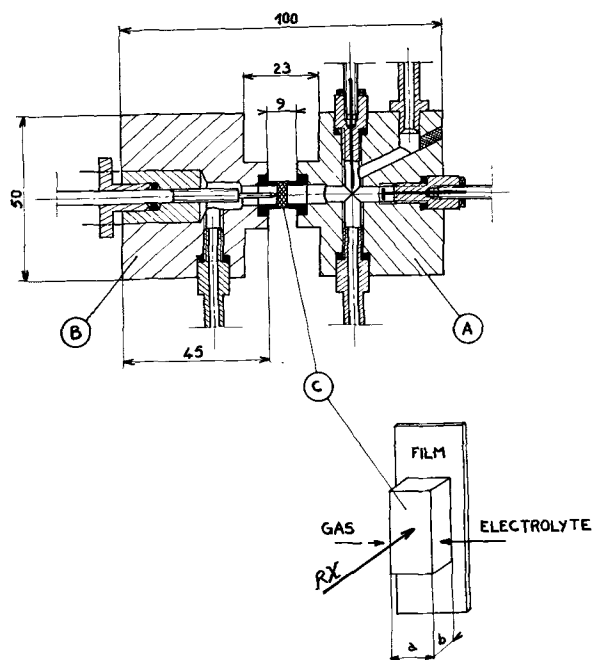


Fig. 4. Electrolytic cell for the study of phase distribution in a porous electrode. A, Electrolyte compartment; B, gas compartment; C, porous electrode. a, Original electrode thickness. b, X-ray path length. Note: dimensions in millimeters.

trode 3 mm in thickness an exposure time of 1 hr was required (x-ray: Mo, $K\alpha K\beta$).

Compartment A of the cell is an electrolyte compartment consisting of a counterelectrode, reference electrode, electrolyte input, and degassing device. Compartment B is connected to a gas circuit constructed such that the gas pressure is variable. The lateral electrode plane-compartment contacts were sealed using an appropriate polymer.

To obtain a well defined x-ray plate in this work the same radiographic conditions as those in the preceding study must be fulfilled. However, the absorbing power of 30 wt % KOH, normally used in fuel cells is, at times, insufficient to assure good contrast between the dry and wet portions of the electrode. In this case, the addition of an agent having strong absorption powers is quite necessary. Thus for the studies on Ni electrodes, using pressure as the variable, the addition of ammoniacal silver salts to the KOH permitted good image contrast to be obtained. However if electrochemical studies were to be carried out on these same electrodes, this addition would be out of the question. A possible solution to this problem would be to increase the KOH absorptive power by the addition of CsOH. For the studies carried out on activated carbon no additives were necessary for good image contrast.

The exploitation of x-ray plates must be made by examination on a suitable negatoscope. It is not possible to obtain exact information from the prints of these plates, since the paper normally cannot reproduce the contrasts present in the original negative. Thus the photographs reproduced in this article are unable to give an exact indication of the contrasts present in the original negative.

Results

Observation of the gas-electrolyte interface in a double porosity nickel electrode.—An initial photograph was taken of the dry electrode before introducing the electrolyte. On this photograph (Fig. 5, No. 1) two zones of different porosities may be distinguished: (i) a clear zone 0.8 mm thick corresponding to the small pores ($2\text{--}5\mu$ diameter); and (ii) a dark zone 2 mm thick corresponding to the large pores ($30\text{--}50\mu$ diameter).

The electrolyte was then introduced into the cell and a gas pressure of 300 g/cm^2 was applied. For this system this pressure is slightly below that at

which bubbling occurs. A second photograph was then taken (Fig. 5, No. 2) which differs from the first in that the small porosity zone is no longer visible. This indicates that this zone is completely filled with electrolyte. The large porosity zone exhibits no modification whatsoever.

Following this the differential pressure was varied between 300 and 50 g/cm^2 . Photographs taken under these conditions were essentially identical to photograph 2, thus indicating that the gas-electrolyte interface remained in a relatively constant position.

These experiments verify the generally accepted hypothesis that, in double porosity electrodes, the gas-electrolyte interface remains at the junction of the two zones in a large range of differential pressures.

Another hypothesis, more controversial than the precedent, concerns the possibilities of regeneration of an electrode after flooding occurs. Certain authors (6) admit that when an accidentally flooded electrode is submitted to a differential pressure superior to that at which bubbling occurs for a few moments the flooded large porosity zone is completely purged of liquid.

In order to verify this an electrode was deliberately flooded by elimination of the differential pressure. A photograph was taken under these conditions (Fig. 5, No. 3). A differential pressure superior to that at which bubbling occurs (350 g/cm^2) was then applied for a few moments. The pressure was then returned to 300 g/cm^2 and a photograph taken (Fig. 5, No. 4), which shows the existence of clear zones in the large porosity section of the electrode indicating that electrolyte pockets remain in this region of the electrode.

Thus it may be stated that the proposed procedure (6) to eliminate the liquid in the large porosity zone of a flooded electrode by increasing the differential pressure does not restore the electrode to its initial condition. This could explain, in certain cases, the observed drop in electrode performance after accidental flooding.

Radiographic observations of a polarized electrode.—In this study radiography is applied to the observation of electrochemical phenomena occurring in the interior of porous electrodes. Thus the effect of polarization on the position of the gas-electrolyte interface is examined. Carbon electrodes (oxygen cathodes) are particularly suited to such a study, since they possess high electrochemical activity (even at low temperatures) in addition to excellent x-ray absorption properties.

The electrode used in this work was made of a carbon support 4 mm in thickness covered with a 13 mm thick layer of activated carbon. The photographs are shown in Fig. 6: No. 1 is of the dry electrode; No. 2 was taken after introduction of the electrolyte and application of a gas pressure slightly lower than that at which bubbling occurs. It can be seen that the electrolyte wets the entire portion of the electrode.

Following this, the electrode was submitted to a cathodic current of 2 ma/cm^2 for approximately 10

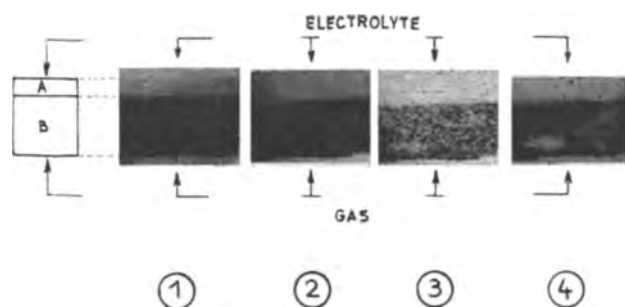


Fig. 5. X-ray plates of the gas-electrolyte interface position in a double porosity Ni electrode. a. Small porosity zone. b. Large porosity zone. 1, Dry electrode; 2, wet electrode; 3, flooded electrode; 4, regenerated electrode.

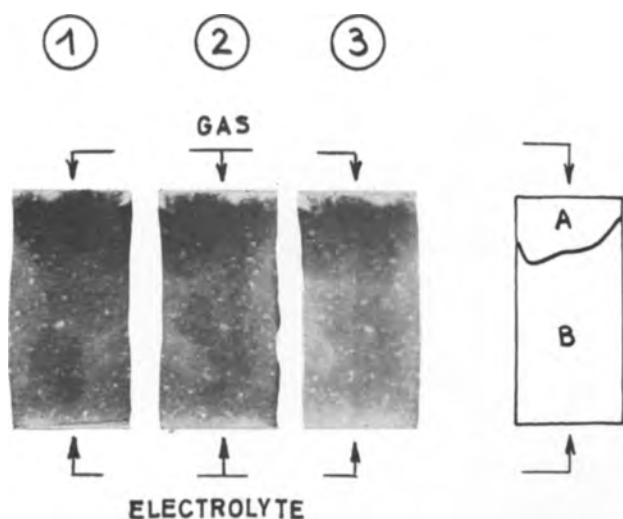


Fig. 6. X-ray plates obtained in a study of a working carbon electrode. 1, Dry electrode; 2, wet electrode; 3, polarized electrode.

min. Photograph 3 (Fig. 6) was taken under these conditions. It can be seen that the wet region of the electrode has absorbed the x-rays to a greater extent than initially. Experiments then performed for higher currents and longer electrolysis times resulted in essentially identical photographs. In addition an x-ray taken after current rupture resulted in a similarly identical photograph. The interpretation of the phenomena observed requires further study. However it seems probable that the variation in absorption is due to a progressive wetting of micropores initially filled with gas.

Conclusion

The purpose of this paper was to indicate to electrochemists the possibilities of a technique which, to the present time, has not been employed in this field. As has been seen, varied and important information may be obtained through radiographic studies, usually requiring relatively simple, rapid, and inexpensive experiments.

Further work will certainly give information concerning the operating mechanism of porous electrodes and allow a choice among the different hypotheses proposed to explain the electrochemical properties of these electrodes. X-ray techniques may be used, not only to verify the porosity and homogeneity of porous electrodes, but also for the verification of these properties for all other porous materials of more general interest. Electrochemical applications of radiographic techniques are not limited to the examination of the texture and operation of porous electrodes, for which fundamental studies are difficult. Thus, it is often necessary to use simple models, such as monotubular triple-contact electrodes. The position and morphology of the meniscus in such electrodes may be studied using x-ray techniques (2, 7). Here again radiography is a powerful and frequently irreplaceable tool for the electrochemist.

Acknowledgments

The authors wish to express their thanks for financial support of this work by the Delegation Generale à la Recherche Scientifique et Technique (Contract No. 61 FR 075).

Manuscript received Feb. 27, 1963; revised manuscript received Oct. 12, 1963. This paper was presented at the Boston Meeting, Sept. 16-20, 1962.

Any discussion of this paper will appear in a Discussion Section to be published in the December 1964 JOURNAL.

REFERENCES

1. A. Guinier, *Technique des Rayons X*, Dunod, Paris (1962).
2. M. Bonnemay, G. Bronoel, and E. Levart, *Electrochem. Acta*, To be published.
3. A. J. Rose, *Tables et Abagues*, Centre National de la Recherche Scientifique, Paris (1957).
4. W. J. Wiltshire, *Principes Physiques de la Radiographie*, Dunod (1948).
5. F. T. Bacon, French Pat. No. 667,298 (1950).
6. F. Justi and A. Winsel, French Pat. No. 1,170,574 (1957).
7. M. Bonnemay, G. Bronoel, E. Levart, Presented at the 13th Meeting C.I.T.C.E., Rome (Sept. 1962).

Electrochemical Behavior of Nickel Compounds

I. The Hydrogen Evolution Reaction on NiSi, NiAs, NiSb, NiS, NiTe₂, and Their Constituent Elements

A. K. M. Shamsul Huq and Arthur J. Rosenberg

Tyco Laboratories, Inc., Waltham, Massachusetts

ABSTRACT

The cathodic polarization behavior of NiSi, NiAs, NiSb, NiTe₂, and NiS at room temperature has been determined in 1M perchlorate solutions at pH 0.04 and pH 10.8 up to -1.0v vs. the reversible hydrogen electrode. Measurements were also made on Ni, Si, Sb, Te, and on Ni electrodes exposed to As₂O₃ and H₂S. Sb, Te, Si, and Ni + As₂O₃ exhibit kinetic peculiarities which are probably attributable to hydride formation, but these features are not generally shown by the corresponding nickel compounds. With the exception of Si in acid solution, all of the electrodes show an extended Tafel line indicating the hydrogen evolution reaction with the following characteristics. In alkaline solution, the Tafel slope is greater than 100 mv for all metals, while the exchange current is between 10^{-5} and 10^{-8} amp/cm². In acid solution, Ni, Sb, NiSi, NiSb, and Ni + As₂O₃ have slopes close to 120 mv, while Te, NiTe₂, Ni + H₂S, and NiS show slopes between 50 and 80 mv. The exchange currents in acid solution vary from about 10^{-5} for Ni to about 10^{-11} amp/cm² for Te. For NiAs, NiTe₂, and NiSi, there exist regions where the current densities at a given overpotential exceed those on either of the individual elements. Results are discussed with a view to distinguishing the role of atomic and crystal factors in the electrocatalytic activity of the electrode materials. The intrinsic chemical properties of the surface atoms appear to dominate the mechanism of the hydrogen reaction, while the crystalline properties strongly influence the rates.

Two general approximations are useful in interpreting the chemical activity of crystalline surfaces. The first, which may be designated the "atomic approach," cites the intrinsic reactivity of the individual surface atoms and treats the crystal environment as a perturbation. This approach has been effective, for instance, in treating the chemisorption of oxygen on metalloid surfaces (1), the dissolution reactions of compound semiconductors (2), and the excess reactivity of line dislocations (3). The alternative approach concentrates on the structural and electronic properties of the crystal as a whole and attaches but secondary significance to the specific atomic composition. Advocates of this "crystal approach" point, for example, to chemisorption and catalysis on transition metal alloys (4) and on semiconducting oxides (5).

In electrochemical surface reactions, evidence can be found to support both views. Thus, the rates of redox reactions such as the ferrous/ferric ion reaction at mercury and platinum surfaces (6) are determined by the electronic properties of the electrode as a whole. On the other hand, the passivation of titanium by trace additions of platinum (7) seems to imply that hydrogen discharge is an intrinsic property of the platinum atoms themselves. A particularly interesting case is the anodic dissolution of germanium. At low current densities, the course of reaction is strongly conditioned by the chemical properties of the surface atoms, while at high current densities, the rate is limited by what

is unambiguously a crystal property, *viz.*, the diffusion of electron holes to the reacting interface (8).

The distinction between the atomic and crystal factors is of heuristic value in studies of surface reactivity. Either approximation provides a point of departure for elaborating the details of mechanism and, at the same time, comprises an immediately useful guideline for optimizing the properties of new technical materials.

The objective of the present series of studies is to clarify the influence of crystal environment on the electrochemical, and particularly the electrocatalytic, properties of a transition metal atom. We have chosen to examine several compounds of nickel with elements from groups IVB, VB, and VIB of the Periodic Table. The use of such compounds was favored for two reasons: the clear chemical differences between the component elements, and the highly ordered atomic coordination.

Each of the compounds is a semimetal whose cohesive energy is concentrated in large part among directed covalent bonds between nickel and its companion element. Direct cation-cation valencies are also present, however, and are evidenced by the various crystal structures (9). For example, NiAs and NiSb both take on the B8₁ structure in which the nickel sublattice exhibits simple hexagonal symmetry, while the interpenetrating As or Sb sublattice exhibits close-packed hexagonal packing. If direct interactions between the nickel

atoms were absent, the *c/a* ratio of the crystals would equal 1.33 in consequence of the anion sublattice. Actually, *c/a* = 1.390 for NiAs and 1.308 for NiSb, the distortion being attributable to direct cation-cation interaction in the *c*-direction (10).

In the present paper, we describe the cathodic polarization characteristics of NiSi, NiAs, NiSb, NiS, and NiTe₂ electrodes and compare the results with those obtained on their constituent elements. The elements have been studied in the form of bulk crystals (Ni, Sb, Si, and Te) or as adsorbed films on nickel (As). Special emphasis is placed on electrocatalysis of the hydrogen evolution reaction (h.e.r.).

Experimental Procedures

The compounds were prepared from spectroscopically pure elements by direct fusion of stoichiometric mixtures in evacuated quartz capsules, directional freezing from the melt, and annealing just below the melting points. The melting points and relevant phase diagrams are given by Hansen (11). The ingots were all obtained as single phase material; the NiAs, NiSb, and the NiTe₂ consisted of several large crystal grains, while the NiS and NiSi were dense but microcrystalline. The elemental Ni, Sb, Si, and Te samples all consisted of single crystal sections. The silicon sample was semiconductor grade material doped with 1 ppm of phosphorus, which imparts an electrical conductivity of 1 (ohm-cm)⁻¹.

Cylindrical specimens were cut from each sample and mounted in a close-fitting Pyrex holder with Kel-F wax (12). Flat surfaces with a geometric area of ~ 0.75 cm² were exposed by grinding, followed by mechanical polishing, and, where possible, by chemical or electrolytic polishing. The samples were then washed ultrasonically, treated with chromic acid/sulfuric acid cleaning solution, thoroughly rinsed with triply distilled water, and transferred directly to the test cell.

An all-Pyrex three-compartment cell was employed in which the working electrode was separated from a platinum counter electrode by a glass frit. The solutions employed were 1M perchloric acid (pH 0.04) and 1M sodium perchlorate adjusted to pH 10.8. Potentials were measured against a reversible hydrogen electrode in the same solution. Potentiostatic and, occasionally, galvanostatic methods were used to obtain steady-state polarization data. The solutions were stirred by a stream of hydrogen or nitrogen which was purified by passage through a liquid nitrogen trap. The temperature was 25° ± 0.1°C.

The electrode under study was transferred to the test solution and was immediately polarized stepwise to potentials negative to the reference hydrogen electrode in the same solution. When the cathodic current exceeded 0.3 amp/cm² or the potential exceeded -1.0v, the path was retraced to the rest potential (in galvanostatic measurements), or until the direction of the current was reversed by the onset of anodic dissolution (in potentiostatic measurements).

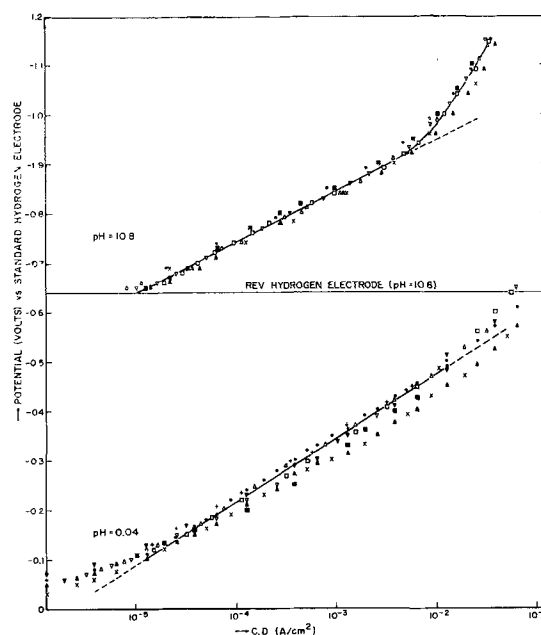


Fig. 1. H.e.r. on nickel in 1M HClO₄, pH 0.04 and in 1M NaClO₄ + 10⁻² NaOH, pH 10.8 at 25°C. Solution preelectrolyzed at 30 ma for 6 hr. Results of ten runs at pH 0.04 with mean *b* = 0.125v, *i*₀ = 2 × 10⁻⁶ amp/cm² and of six runs at pH 10.8 with *b* = 0.105v, *i*₀ = 1 × 10⁻⁵ amp/cm².

Results

The results are summarized in Fig. 1-6 as plots of potential vs. logarithm of the current density. All potentials are referred to the standard hydrogen electrode; the current densities (C.D.) are in amperes per unit geometric area of the electrode surface. In each figure, the results for elemental nickel are given for ready comparison. The dispersion in the nickel data, shown in detail in Fig. 1, covers the results for about ten independent experiments in which the effects of remounting the electrode, of mechanical vs. electrochemical polishing, of extended preelectrolysis, and of recycling were observed. The degree of reproducibility and the absolute values of the data on nickel compare favorably with other work (13). Included in the bands of data are slight hysteresis effects, *i.e.*, higher overpotentials in the direction of decreasing current than in the opposite direction.

Virtually all of the results show a positive deviation from the Tafel line at C.D.'s exceeding 10⁻² amp/cm². Since the deviation depends on current rather than potential, it is unlikely to result from a fundamental effect, such as increasing surface coverage by hydrogen atoms. It is more probably an artifact due to partial blocking of the surface by hydrogen bubbles generated by the h.e.r.

NiSi and Si.—Figure 2 summarizes the results for Ni, Si, and NiSi, in both acid and alkaline solutions. Elemental silicon shows a complex behavior, probably attributable to the effects of SiO₂ which is stable throughout the potential range under study. (SiO₂ + 4H⁺ + 4e = Si + 2H₂O; *E*₀ = -0.86v) (14).¹ In the direction of increasing overpotential the polarization curve shows a sharp upswing at currents exceeding ~ 0.5 ma/cm². In this region,

¹ IUPAC convention adopted in 1953 is followed.

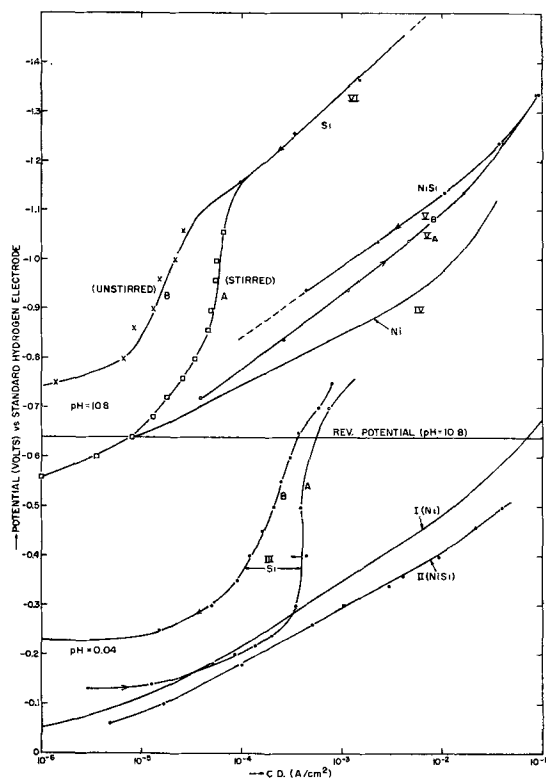


Fig. 2. Cathodic polarization curves (log C.D. vs. potentials) for NiSi and Si in 1M HClO_4 , pH 0.04, and in 1M $\text{NaClO}_4 + 10^{-2}\text{M}$ NaOH , pH 10.8 at 25°C. At pH 0.04, I, Ni (for comparison); II, NiSi; III_A, Si toward higher cathodic potentials (up); III_B, Si, toward lower cathodic potentials (down). At pH 10.8, IV, Ni (for comparison); V_A, NiSi (up); V_B, NiSi (down); VI, Si (A, stirred, B, unstirred).

the variation of current at constant potential showed a curious time dependence. The current decreased, e.g., from 1.2 ma/cm² to 0.4 ma/cm² at 0.5v, then jumped back to the original value from whence it repeated the decay with a frequency of about 1 cycle/2 min. The apparent decrease in the cathodic current may result from an increase in oxide thickness by the slow anodic oxidation which occurs even at negative potentials. Under the conditions of the experiment the surface appears unchanged; the absence of interference colors implies a total oxide thickness < 1000Å. The rapid jump to higher cathodic currents implies mechanical breakdown of the oxide when the thickness exceeds a critical value. The total anodic current must be smaller than that corresponding to the predominant cathodic reaction; which is doubtlessly hydrogen evolution. Further evidence for anodic film formation comes in the return to lower potentials after a prolonged period at -700 mv. During the return there is no longer evidence for the cyclic growth and breakdown, but as the potential is adjusted to values below -300 mv, a pronounced anodic transient is observed before the cathodic current takes over.

In the direction of decreasing overpotential the current decreases linearly with potential. The apparent ohmic resistance is 1200 ohm-cm²; assuming an average film thickness of 100Å in this potential region, one obtains a resistivity $\rho \sim 10^9$ ohm-cm, which is not unreasonable for SiO_2 . It is probable,

therefore, that the characteristics of the cathodic polarization curve on Si in acid solutions are determined primarily by the oxide film. A similar conclusion was reached by Turner (15).

The results on Si in alkaline solution bear a superficial resemblance to those in acid solution. One important distinction is the direct dependence of the current on stirring in the region of sharply rising overpotential. This implies that the rate is limited by a diffusion process in the region of the electrode-electrolyte interface. We tentatively suggest that the current in this region is not due to h.e.r., but to the direct reduction of Si to SiH_4 , ($\text{Si} + 4\text{H}_2\text{O} + 4e = \text{SiH}_4 + 4\text{OH}^-$; E_0 (pH 10.8) = 0.541v) (16). This reaction would be followed by the formation of silicate ion, ($2\text{OH}^- + \text{SiH}_4 + \text{H}_2\text{O} = 4\text{H}_2 + \text{SiO}_3^{2-}$) which is thermodynamically stable throughout the potential range. The unusual, but entirely reasonable, feature of the proposed reaction is that the reduction of Si to SiH_4 promotes the formation of SiO_3^{2-} . The diffusion of SiH_4 or SiO_3^{2-} from the electrode may then be responsible for the observed enhancement of the rate by stirring. At sufficiently high potentials Tafel behavior is observed with $i_0 = 10^{-7}$ amp/cm² and $b = 180$ mv.²

NiSi in both acid and alkaline solutions exhibits none of the peculiarities associated with elemental silicon. The polarization is characteristic of the h.e.r. The Tafel parameters in acid are $b = 113$ mv and $i_0 = 4 \times 10^{-6}$ amp/cm², which are similar to those on nickel itself. The data at pH 10.8 exhibit hysteresis, with the overpotential in the direction of decreasing current exceeding that in the reverse direction. The exchange current is $\sim 10^{-5}$ amp/cm², i.e., about the same as on Ni, but the Tafel slope is ~ 160 mv.

NiAs and As.—In acid solutions NiAs exhibits Tafel behavior in the range 2×10^{-5} - 2×10^{-3} amp/cm² with $b = 56$ mv, and $i_0 = 5 \times 10^{-8}$ amp/cm². The polarization curve thus crosses that of Ni (Fig. 3).

The high resistivity of elemental arsenic prohibits the direct measurement of hydrogen overpotential on the arsenic electrode. An estimate of the Tafel parameters for the h.e.r. on arsenic was obtained by the following procedure: 10^{-3} M/1 As_2O_3 was added to a solution with a nickel electrode biased at -300 mv. The current diminished slowly to a steady-state value of 3×10^{-6} amp/cm². Polarization measurements then revealed Tafel behavior in the range 10^{-6} to 3×10^{-5} amp/cm² with $b = 120$ mv and $i_0 = 10^{-8}$ amp/cm², the results being unaffected by stirring. Between 2×10^{-4} and 2×10^{-3} amp/cm² (galvanostatic measurements were specially employed) the potential became independent of current. However, the polarization curve in this current range exhibits an extraordinary dependence on stirring, viz., the overpotential increases with stirring. As the current is increased beyond 10^{-2} amp/

² Further evidence for the proposed scheme is the well-known corrosion of Si in alkaline solution. According to the present data the hydrogen overpotential on Si in alkaline solutions is such that corrosion currents exceeding 10^{-4} amp/cm² could not be supported by the h.e.r. It appears, therefore, that the cathodic component of the normal corrosion reaction may be the reduction of Si to SiH_4 .

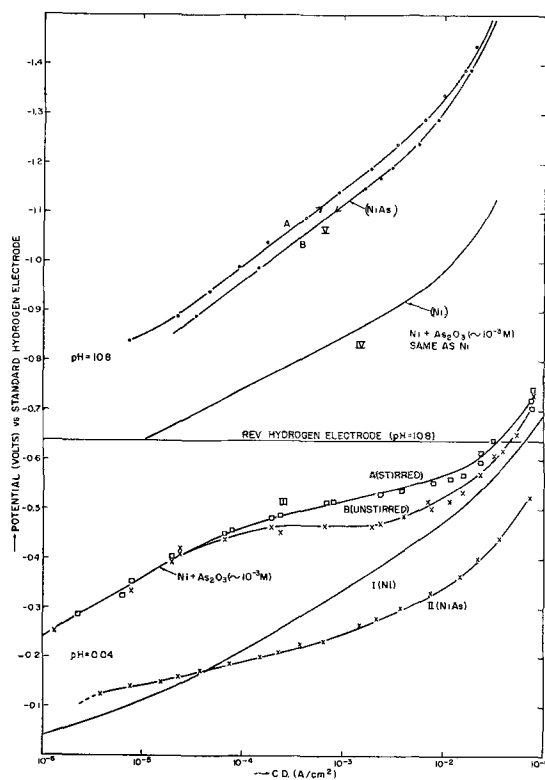


Fig. 3. Cathodic polarization curves (log C.D. vs. potentials) for NiAs and Ni + 10^{-3} M As_2O_3 in 1M HClO_4 , pH 0.04, and in 1M NaClO_4 + 10^{-2} M NaOH , pH 10.8 at 25°C. At pH 0.04, I, Ni; II, NiAs, mean of 5 runs; III, Ni with addition of $\sim 10^{-3}$ M As_2O_3 in solution; (A stirred, B, unstirred). At pH 10.8, IV, Ni, no effect of $\sim 10^{-3}$ M As_2O_3 added to solution. V, NiAs (A, "up"; B, "down").

cm^2 , the curves approach that of Ni, regardless of stirring.

We offer the following interpretation of these results. As_2O_3 is unstable with respect to As at all negative potentials: $\text{As}_2\text{O}_3(\text{aq}) + 6\text{H}^+ + 6e = 2\text{As} + 3\text{H}_2\text{O}$; $E_0 = 0.247\text{v}$ (16). We assume accordingly that As is deposited on the nickel surface, but that the reaction stops at monolayer coverage, because of a high overpotential for reduction of As_2O_3 on As. The residual current is then due to the h.e.r. on a chemisorbed arsenic monolayer. It is also possible that the steady-state current is due to the h.e.r. on a small residue of bare nickel, although this seems improbable. As the potential is increased, the reduction of As to AsH_3 becomes thermodynamically feasible, ($\text{As} + 3\text{H}^+ + 3e = \text{AsH}_3$; $E_0 = 0.60\text{v}$) (16). The formation of AsH_3 would compete with the h.e.r. exposing bare Ni. The C.D. would then increase toward the value characteristic of the h.e.r. on Ni. Counteracting this effect will be the diffusion of fresh As_2O_3 to the surface and the restoration of the As film. Stirring will assist diffusion and will thus oppose the tendency to increased h.e.r. currents. At sufficiently high C.D.'s, the formation of AsH_3 becomes more rapid than the diffusion rate so that the surface will remain effectively free of As, regardless of stirring. The polarization curve will then approach that of the h.e.r. on pure nickel. Our suggestion that the deposition of As is limited to a monolayer is based on the observation that pro-

longed electrolysis at -300 mv does not affect the results.

In alkaline solutions NiAs exhibits some hysteresis, but generally obeys the Tafel relation with $b = 155$ mv and $i_0 = 7 \times 10^{-7}$ amp/ cm^2 . In contrast to the results in acid solution, addition of 10^{-3} M/l As_2O_3 has no effect on the h.e.r. on nickel electrodes.

NiSb and Sb.—In acid solutions NiSb exhibits a Tafel behavior with $b = 108$ mv and $i_0 = 2 \times 10^{-8}$ amp/ cm^2 over the C.D. range 5×10^{-5} to 10^{-2} amp/ cm^2 (Fig. 4). At lower currents, the overpotential is less than that extrapolated from the Tafel line and is time dependent. In the case of Sb there is evidence for Tafel behavior only at currents exceeding 10^{-3} amp/ cm^2 (with $b \sim 180$ mv and $i_0 = 2 \times 10^{-6}$ amp/ cm^2). At lower currents, there is a sharp drop to lower overpotentials; the currents in this region ($|\eta| < 0.4\text{v}$) are steady and still substantial, thus ruling out cathodic depolarization by the reduction of traces of oxygen or by the reduction of a residual surface oxide. This general effect is even more pronounced in alkaline solution. Here the break occurs at a higher overpotential ($|\eta| \sim 0.5\text{v}$), and the approach to a steady-state current is very slow. Since the antimony oxides are all unstable at negative potentials (16), the results, which are similar to those observed by others (17), are explicable only in terms of hydride formation. However, the reported potentials for the formation of SbH_3 are too negative so that a lower hydride, e.g., Sb_2H_4 , may be involved.

Tafel behavior with values of $b \sim 250$ mv are observed in alkaline solution for both NiSb and Sb.

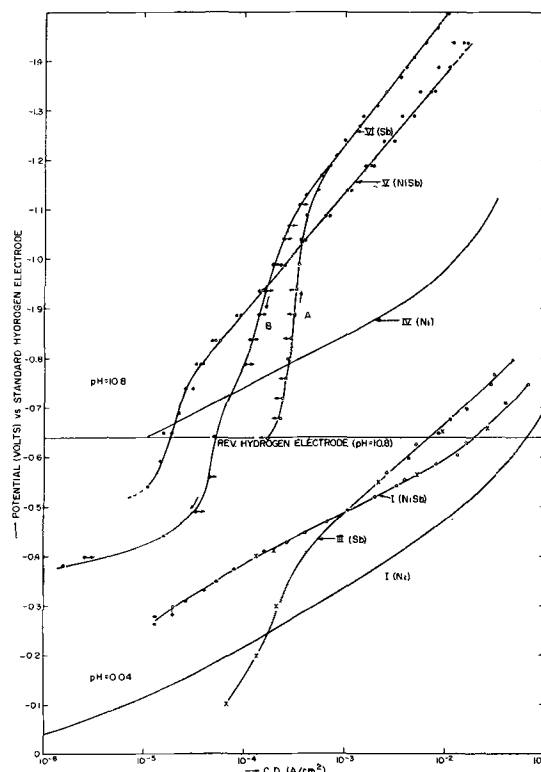


Fig. 4. Cathodic polarization curves (log C.D. vs. potentials) for NiSb and Sb in 1M HClO_4 , pH 0.04, and in 1M NaClO_4 + 10^{-2} M NaOH , pH 10.8 at 25°C. At pH = 0.04, I, Ni; II, NiSb; III, Sb. At pH = 10.8, IV, Ni; V, NiSb; VI, Sb. (A, "up"; and B, "down").

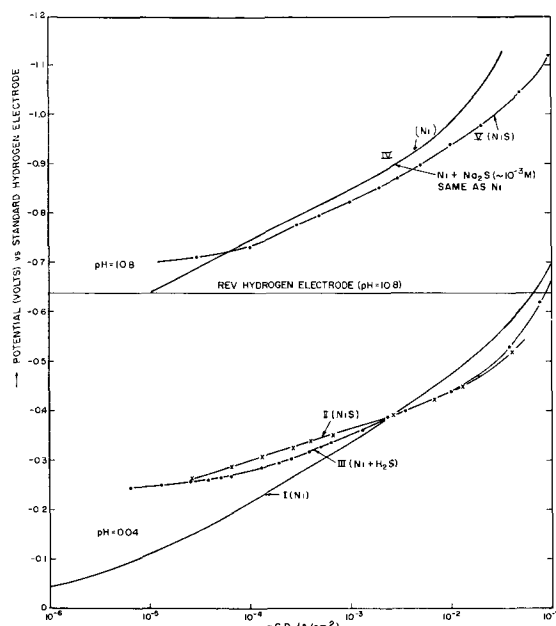


Fig. 5. Cathodic polarization curves (log C.D. vs. potentials) in 1M HClO_4 , pH 0.04 and in 1M $\text{NaClO}_4 + 10^{-2}\text{M NaOH}$, pH 10.8 at 25°C. At pH = 0.04, I, Ni; II, NiS (odor of H_2S in the effluent gas); III, Ni in presence of H_2S , added as Na_2S . At pH = 10.8, IV, Ni; V, NiS, no effect of addition of $\sim 10^{-3}\text{M Na}_2\text{S}$.

NiSb also shows an apparent depolarization at $|\eta| < 150$ mv, i.e., cathodic currents are observed at potentials positive to the reversible hydrogen electrode.

NiS and Ni+ H_2S .—The results for these systems are given in Fig. 5. NiS in acid solution follows the Tafel relationship between 3×10^{-5} and 10^{-2} amp/cm², with $b = 62$ mv and $i_0 = 7 \times 10^{-8}$. The polarization curve thus crosses that of Ni. The odor of H_2S was detected in the effluent gas stream during these runs. The addition of 10^{-3} M/1 Na_2S to the solution had no effect on the polarization curve.

The addition of 10^{-3} M/1 Na_2S to an acid solution has a strong and reproducible tendency to shift the polarization characteristics of a nickel electrode toward that of NiS.

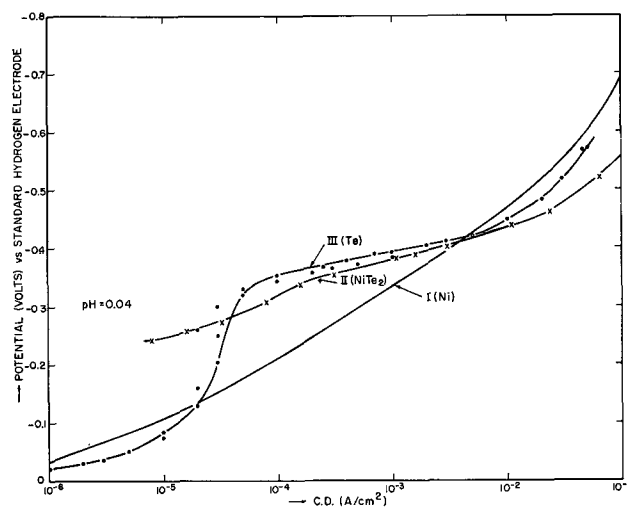


Fig. 6. Cathodic polarization curves (log C.D. vs. potentials) in 1M HClO_4 , pH 0.04, at 25°C. I, Ni; II, NiTe_2 ; III, Te.

In alkaline solution the behavior of NiS closely resembles that of Ni. The addition of Na_2S to alkaline solution has no apparent effect on Ni.

NiTe_2 and Te.—Experiments were limited to acid solutions and are summarized in Fig. 6. The results for Te, which are highly reproducible, show the same apparent depolarization as observed for Sb. Similar results have been observed by Awad (18) who tried to explain them by postulating the formation of an intermediate hydride, H_2Te_2 .

NiTe_2 shows some evidence of a break in the Tafel curve at the same potential where Te exhibits its transition. The Tafel parameters for Te are $b \sim 48$ mv, and $i_0 \sim 10^{-11}$ amp/cm², while those for NiTe_2 are $b \sim 55$ mv, and $i_0 \sim 10^{-8}$ amp/cm². The uncertainty in the value of i_0 for NiTe_2 is considerable, however, and its polarization curve can be virtually superposed on that of Te by a shift in the abscissa.

Discussion

Under the present experimental conditions, the cathodic reaction on nickel electrodes is confined to the hydrogen evolution reaction. In all other cases, excepting silicon, the h.e.r. is also dominant over extended potential regions, giving rise to Tafel behavior, i.e., $\eta = -b \log i/i_0$ where η is the overpotential relative to the reversible hydrogen electrode, b is the Tafel slope, and i_0 is the exchange current. The values of these parameters and their range of applicability are summarized in Table I.

The cathodic polarization curves on each of the elements, except nickel, exhibit features which suggest side reactions such as hydride formation or oxide reduction. In the case of Sb, these features are partially reflected in the behavior of NiSb. However, NiAs, NiTe_2 , and NiSi do not show significant side effects, illustrating that the surface chemical reactions of As, Te, and Si atoms are basically conditioned by their particular crystal environment. Since the kinetics of h.e.r. on the compounds differ from those on Ni itself, it is unlikely that the absence of side reactions on a nickel compound can be attributed simply to chemical depletion of the companion element in the surface region. We shall not dwell on the side reactions, however, but shall limit our discussion to a resolution of the atomic and crystal contributions to the h.e.r.

Atomic approach.—In the simplest atomic approximation it is assumed that each of the surface

Table I. Tafel parameters for the hydrogen evolution reaction

	pH 0.04		pH 10.8	
	b, mv	$-\log i_0$, amp/cm ²	b, mv	$-\log i_0$, amp/cm ²
Ni	125	5.3	105	5.0
Ni + As_2O_3	120	8.0	no effect on Ni	
NiAs	56	7.3	155	6.1
Si	no Tafel region		168	7.5
NiSi	113	5.4	145	5.4
Sb	170	5.7	260	5.3
NiSb	108	7.6	245	5.0
Te	48	11	—	—
NiTe_2	55	8	—	—
Ni + H_2S	80	9.4	no effect on Ni	
NiS	62	7.2	100	4.9

atoms reacts independently. The over-all reaction rate at a specified potential would then be given by a linear combination of the contributions of the component atoms. These contributions may be estimated from the behavior of the elemental electrodes, proper account being made of the relative surface concentrations on the elements and the compound.

In the cases of NiAs, NiTe₂, and NiSi in acid solution, there are potential regions where the C.D.'s on the compounds are greater than on either of the component elements. This immediately rules out the simple atomic description since the surface concentration of either component, regardless of crystallographic orientation, does not exceed that of its elemental form. The electrodes have interesting qualitative features, however. The general shape of the Tafel line on NiTe₂ resembles that of Te, while a similar correspondence exists for NiSi and Ni. This implies that the mechanism for these systems is determined by only one of the components, suggesting in turn that the surface consists predominantly of this component. The effect may originate from anisotropic corrosion leading to the exposure of a stable crystallographic plane in which only one component is present. This phenomenon is now well documented for III-V intermetallic compounds such as InSb and GaAs and leads to striking differences of chemical reactivity on opposite (111) crystallographic surfaces (2). However, both the stability of the Si-O bond and the hydride formation indicated for elemental tellurium would argue against the requisite configurations on NiSi and NiTe₂. In any event, it would still be necessary that the rate of the h.e.r. on Ni atoms in NiSi and Te atoms in NiTe₂, be faster than on the corresponding elemental crystals. In these cases, then, atomic properties may govern the mechanism of the reaction, but crystal properties apparently govern the magnitude of the reaction rate.

Similar considerations may also apply to NiS. However, the experimental results for the h.e.r. on "sulfur" were obtained by exposing a nickel electrode to H₂S. Since H₂S was also detected in the gas stream coming from the cell in which NiS was under study, it is not improbable that the latter may in fact be equivalent to the "Ni + H₂S" electrode. In alkaline solution, however, H₂S has no effect on the polarization behavior of Ni which indicates that H₂S is not adsorbed on the electrode. The NiS electrode behaves similarly to nickel, although the h.e.r. proceeds at a smaller rate; it is plausible that sulfur in the surface region of NiS is removed by electrochemical discharge of H₂S (NiS + 2H₂O = H₂S + 2 OH⁻ + Ni; E₀ = -0.77v).

For the remaining cases under study, it is evident that the over-all rate of the h.e.r. is not a specific atomic property, and that interactions between the surface atoms or between adsorbed hydrogen atoms at neighboring sites on the crystal surface play a prominent role. It is possible, however, that the atomic approach may still be valid for one or more of the reaction steps in the over-all mechanism. In order to elucidate this possibility we shall briefly

discuss the generally acknowledged mechanism of the h.e.r.

Mechanism of the hydrogen evolution reaction (19).—It is self-evident from its stoichiometry and its heterogeneous character that the hydrogen evolution reaction involves one or more reaction intermediates which are adsorbed at the electrode surface. By analogy to gas-phase dissociative chemisorption of hydrogen it has long been supposed that the predominant intermediate is an adsorbed hydrogen atom which is produced by the reduction of an adsorbed hydronium ion or water molecule, i.e.,

I. Discharge:



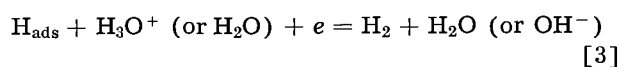
The discharge step may be followed by a bimolecular combination of H_{ads}, i.e.,

II. Combination desorption:



or an electrochemical desorption step,

III. Electrochemical desorption:



Other intermediates have been proposed. In particular, Horiuti has theorized that the adsorbed hydrogen-molecule ion, H₂⁺, may play an important role for many electrodes (20). This species may be regarded formally as a stable intermediate in III.

The reaction kinetics involve the quantity θ , which is the fractional coverage of the available surface by hydrogen atoms. The cathodic current is given by

$$V_{\text{I}} = k_{\text{I}}^0 (1 - \theta) e^{-\alpha n F / RT} \quad [4]$$

$$V_{\text{II}} = k_{\text{II}}^0 \theta^2 \quad [5]$$

$$V_{\text{III}} = k_{\text{III}}^0 \theta e^{-\alpha n F / RT} \quad [6]$$

where the k's are rate constants and include the activity of H₂O or H₃O⁺, and α is a transfer coefficient.

At equilibrium, i.e., $\eta = 0$, the rates of I, II, and III are given by

$$i_o^{\text{I}} = k_{\text{I}}^0 (1 - \theta_o) \quad [7]$$

$$i_o^{\text{II}} = k_{\text{II}}^0 \theta_o^2 \quad [8]$$

$$i_o^{\text{III}} = k_{\text{III}}^0 \theta_o \quad [9]$$

where θ_o , the equilibrium coverage, is determined by the free energy of adsorption of H₂ on the particular electrode in the particular solution. When i_o^{I} is much smaller than either i_o^{II} or i_o^{III} , the reaction kinetics are controlled by slow discharge and do not depend on the mechanism of desorption. Adsorbed hydrogen comes to equilibrium with the ambient gas by step II, and θ remains independent of η . Equation [4] or [6] reduces to the Tafel equation with $b = 2.3 RT / \alpha F = (59/\alpha) \text{mv}$ at 25°C. There is strong empirical evidence that α generally approximates $\frac{1}{2}$ (19) so that $b \sim 120 \text{mv}$.

When II is rate-controlling, the rate is given by Eq. [5]. With increasing overpotential θ increases as

$$\theta \simeq \theta_o e^{-\eta F / RT} \quad [10]$$

This result may be substituted in Eq. [5] and leads to a Tafel equation with $b = 2.303 RT / 2F = 29 \text{mv}$

at 25°C. Finally, when III is rate-limiting, substitution of Eq. [10] into Eq. [6] leads to a Tafel equation with $b = 2.3 RT/\gamma$ where γ is believed to change from 3/2 ($b \sim 40$ mv) at low θ to 1/2 ($b \sim 120$ mv) at high θ (19).

An explicit test of the various mechanisms requires an experimental determination of θ vs. η . This has been carried out by Devanathan and Selvaratnam (21) for Ni in 2N NaOH, and Makrides (22) has shown that the data, which exhibit a change in θ from 0.04 to 0.4 as η is increased from 40 to 200 mv, can be explained on the assumption $i_o^I \sim i_o^{II} \gg i_o^{III}$. Because of the relative values of b , the discharge step plays the prime role in molding the kinetics. The case of Ni in acid solution has not been clarified, but it is generally believed that slow discharge controls the kinetics (13).

It is apparent from the foregoing that the association of two different atoms in an intermetallic compound could lead to a basic modification in the kinetics of a surface reaction, even though the reactivity is inherently an atomic property. Thus, it is conceivable that discharge could be faster on atoms of one element, say A, while electrochemical desorption may be faster on the second element, B. In this case, if discharge on A were followed by transfer to a neighboring B atom, the over-all rate of the h.e.r. on the compound AB would be faster than on either element by itself. In the event that desorption proceeds through II, the effect could be even more pronounced since combination desorption requires the juxtaposition of two adsorbed hydrogen atoms, a process which will be strongly conditioned by the atomic configuration of the surface. In this way specific atomic properties may still underlie the kinetics, although the rates on the compound and on its elemental constituents may differ significantly. A clear distinction can still be made between the case of a compound and of a physical admixture of two elemental phases where, in the absence of significant grain boundary effects, the rate must be given by a linear combination of the rates on the elements.

Application to nickel compounds.—The Tafel slope b is useful in diagnosing the rate-limiting step of the h.e.r. Three groups are distinguishable according to the range of b ; the samples within each are listed below in order of decreasing i_o :

Class A:
 $b < 80$ mv pH 0.04:
 Ni+H₂S, NiS, NiAs, NiTe₂, Te

Class B:
 $105 < b < 125$ mv pH 0.04:
 NiSi, Ni, NiSb, Ni+As₂O₃
 pH 10.8:
 Ni, NiS, Ni+H₂S,* Ni+As₂O₃*

Class C:
 $b > 155$ mv pH 0.04: Sb
 pH 10.8: Sb, NiSi, NiAs, Si

(* No observable effect on adding H₂S or As₂O₃ to Ni at pH 10.8.)

The low value of b in class A probably means that desorption, by either II or III, is rate-limiting. On the other hand, I is presumed to control the rate on nickel, desorption being inherently faster. Since the Tafel lines of the class A materials approach or actually cross that of nickel, discharge on these materials is faster than on nickel, while the converse is evidently true for desorption.

Desorption on Ni is believed to proceed through II (22) which nominally requires the interaction of adsorbed hydrogen atoms on neighboring surface atoms. This interaction depends on the potential energy variation of H_{ads} as it moves normal and parallel to the surface. The former motion depends on the activation energy for adatom migration. The adsorption energy should parallel the M-H bond energy which is similar for all of the elements under study (23). The localization of the hydrogen atom depends as well on the directional character of the bond, i.e., the degree of covalence. The relative rate of II should thus decrease with increasing covalence, which is weakest for nickel and decreases generally with increasing electronegativity. There is supporting evidence for this view from studies of chemisorption of molecular hydrogen on the elements. For example, Ni chemisorbs H₂ dissociatively at room temperature while As does not react measurably under the same conditions (24). Since the bond energies of Ni-H and As-H are similar, the difference must be in the activation energy for dissociative chemisorption. This difference should apply as well to the activation energy for the reverse reaction which is identical to II. It is thus reasonable that II would be strongly inhibited by the presence of As, and that the desorptive mechanism might shift from II to III. This would apply whether the arsenic were present as chemisorbed atoms or as a fundamental crystal constituent, as in NiAs.

The case of NiAs is particularly interesting since it exhibits class A behavior, although the individual elements show class B behavior. While the h.e.r. on Ni is presumed to be limited by the discharge rate, the rate-limiting step on As is open to conjecture. According to the foregoing reasoning, III will likely control the rate. Supporting this contention is the fact that, if discharge were rate-limiting, $i_o^I(\text{As})/i_o^I(\text{Ni}) \sim 10^{-3}$; this ratio is exceptionally small in view of the fact that the energies of adsorption and the work functions (25), both of which should affect i_o^I , are apparently similar for Ni and As. Assuming rate control by III, the As film must be nearly saturated with hydrogen atoms, i.e., $\theta \rightarrow 1$, to account for a Tafel slope of 120 mv.

We suggest, therefore, that the h.e.r. on As proceeds by I + III. The same factors which underlie this, namely, localized adsorption, should persist in NiAs, particularly since the As-As distance on an arsenic monolayer on Ni and the Ni-As distance in NiAs are similar (9). One would expect then that the h.e.r. reaction on As atoms in NiAs proceeds independently of the reaction on nickel. The association of Ni and As has two important effects, however. First, it inhibits II on the Ni atoms by sharply reducing the number of near Ni-Ni neighbors and

shifts the desorption mechanism to III. Second, it increases the discharge rate on nickel itself by about an order of magnitude as shown by the experimental results.

While the decrease in the rate of an elementary electrochemical step such as I or III might be discussed as an artifact of adventitious inhibition, an enhancement of the rate obviously requires a change in the basic properties of the surface. This effect, which is common to many of the present results, may, in the simplest instance, be related to the work function ϕ_m of the electrode. The experimental results (19) for the h.e.r. on a series of transition metals follow the relation

$$-\log i_o^I = \text{const.} + C \phi_m$$

with $C \sim 2.5(\text{ev})^{-1}$. This equation shows that an increase of 0.5 ev in the electrode work function brings about an order of magnitude increase in i_o^I . This is not an implausible consequence of the chemical liaison between Ni and As, both of which individually show $\phi_m \sim 5.0$ ev.

Despite the similar crystal structure of NiAs and NiSb, the latter exhibits class B behavior in acid solutions. A self-consistent explanation would be that slow discharge on the Ni atoms is rate controlling on NiSb, but with an exchange current which is ten fold smaller than on elemental nickel. This result may also stem from a decrease in ϕ_m . It also seems likely that slow discharge controls the rate on NiSi in acid solution, requiring that $\phi_{\text{NiSi}} > \phi_{\text{Ni}}$.

In the case of NiTe₂ and NiSi in acid solution, the h.e.r. appears to be dominated by electrochemical desorption on the group VI atoms. Assuming that the rate of I on these materials is inherently faster, one would deduce that i_o^I increases in the order: NiSb, Ni, NiS \sim NiTe₂, NiSi, NiAs. There is, however, no simple correlation with chemical factors, such as electronegativity difference, or the energy of compound formation (27) which might be expected to influence ϕ_m .

The situation in alkaline solutions is even more complex. For all compounds, the Tafel slope is higher than in acid solutions, which may indicate a shift in mechanism. Alternatively, the magnitude of b may be taken to signal a change in the structure of the electrolytic double layer, for example, of specific adsorption of hydroxyl ions. In the case of NiAs, where the exchange current is smaller by two orders of magnitude than on nickel, the changes in work function and interatomic distances discussed above imply that the polarization curve in alkaline solution is determined by electrochemical desorption at high θ . This conjecture may be viewed in the light of the fact that Ni itself shows high θ in the potential range in question (21) despite the inherently less favorable condition (for achieving high θ) that desorption on Ni is by reaction II rather than by reaction III.

In conclusion, the electrocatalysis of the h.e.r. on nickel compounds cannot be explained in terms of the intrinsic chemical properties of the surface atoms. The most pointed demonstration is that the

over-all rate of reaction at a given potential is frequently greater than on either of the individual elements. Nevertheless, the atomic approach is a useful point of departure for interpreting the effects of composition and crystal structure on electrocatalytic activity. The use of this approach was illustrated for NiAs, NiTe₂, and NiSi. Further work along these lines, together with complementary studies of the electronic properties and gas phase chemisorption characteristics, promises to be useful from both a scientific and a technical standpoint.

Acknowledgments

The authors wish to acknowledge the expert technical assistance of Miss Mary Loud and Miss MaryJane MacLaren and the valuable technical comments of Dr. A. C. Makrides. This work was supported by the Office of Naval Research under Contract Nonr-3765(00).

Manuscript received June 20, 1963; revised manuscript received Sept. 19, 1963.

Any discussion of this paper will appear in a Discussion Section to be published in the December 1964 JOURNAL.

REFERENCES

1. A. J. Rosenberg, *J. Phys. Chem. Solids*, **14**, 175 (1960).
2. H. C. Gatos, *Science*, **137**, 311 (1962).
3. H. C. Gatos and M. C. Lavine, *This Journal*, **107**, 427 (1960).
4. D. A. Dowden, *J. Chem. Soc.*, **1950**, 242.
5. K. Haufler, "Advances in Catalysis," Vol. 7, p. 213 (1955).
6. J. E. B. Randles and K. W. Somerton, *Trans. Faraday Soc.*, **48**, 937, 951 (1952).
7. M. Stern and H. Wissenberg, *This Journal*, **106**, 759 (1959).
8. W. H. Brattain and G. G. B. Garrett, *Bell System Tech J.*, **34**, 129 (1955).
9. W. B. Pearson, "Handbook of Lattice Spacing and Structures of Metals and Alloys," Pergamon Press, New York (1958).
10. A. J. Cornish, *Acta Met.*, **6**, 371 (1958).
11. M. Hansen, "Constitution of Binary Alloys," 2nd ed., McGraw-Hill Publishing Co., New York (1958).
12. "KEL-F Brand Polymer Wax, Grade KF 200" obtained from Chemical Div., Minnesota Mining Manufacturing Co., St. Paul, Minn.
13. J. O'M. Bockris and E. C. Potter, *J. Chem. Phys.*, **20**, 614 (1952).
14. W. M. Latimer, "Oxidation Potentials," 2nd ed., Prentice Hall, Inc., New York (1959).
15. D. R. Turner, "Electrochemistry of Semiconductors," J. P. Holmes, Editor, Academic Press, New York (1961).
16. Ref. (14).
17. R. Piontelli, *et al.*, "Research on Hydrogen Overvoltage on Metallic Single Crystal," Tech. Documentary Report No. ASD TN 61-158, March 1962, Contract No. AF 61 (052)-144.
18. S. A. Awad, *J. Phys. Chem.*, **66**, 890 (1962).
19. J. O'M. Bockris, "Modern Aspects of Electrochemistry," Vol. 1, Butterworth, London (1954).
20. J. Horiuti, "Trans. Symposium on Electrode Processes," p. 17, E. Yeager, Editor, John Wiley & Sons, Inc., New York (1961).
21. M. A. V. Devanathan and M. Selvaratnam, *Trans. Faraday Soc.*, **56**, 1820 (1960).
22. A. C. Makrides, *This Journal*, **109**, 977 (1962).

23. L. Pauling, "The Nature of Chemical Bonds," 3rd ed., Cornell Univ. Press, New York (1960).
24. B. M. W. Trapnell, "Chemisorption," Butterworths, London (1955).
25. "Handbook of Chemistry and Physics," 41st ed., p. 2557, Chemical Rubber Publishing Co. (1960).
26. J. O'M. Bockris and R. Parsons, *Trans. Faraday Soc.*, **47**, 914 (1951).
27. G. F. Raynor, "The Physical Chemistry of Metallic Solutions and Intermetallic Compounds," Vol. 1, p. 312, Chemical Publishing Co., New York (1960).

Electrochemical Behavior of Nickel Compounds

II. Anodic Dissolution and Oxygen Reduction in Perchlorate Solutions

A. K. M. Shamsul Huq, A. J. Rosenberg, and A. C. Makrides

Tyco Laboratories, Inc., Waltham, Massachusetts

ABSTRACT

The anodic dissolution of Ni, Si, and Sb and of the compounds NiSi, NiSb, NiAs, and NiS was studied in molar perchlorate solutions at pH 0.04 and 10.8. In all cases, except with Si in acid solution, active dissolution at low anodic potentials is followed by a transition to a passive state where the anodic current density is nearly independent of potential. In acid solution, the critical potentials of NiSi, NiAs, and NiS are less positive than that of Ni and the critical currents are less by two to three orders of magnitude. The critical potential of NiSb is about the same as for Sb, but the critical current is substantially less. The anodic current in the passive region for the compounds is greater than for passive Ni. NiSi, NiAs, and NiS show a transpassive region in which Sb, As, and S are probably oxidized to ions of a high valence state. In alkaline solution, NiSi, NiSb, and NiS show an active-passive transition at the same potential as pure Ni. However, the rate of oxidation of these compounds in the passive state is again considerably greater than for passive Ni. It is suggested that in acid solution the passive film on nickel compounds is either a mixed oxide or an oxide having the basic structure of the second element; in alkaline solution, nickel oxide is formed first, but it probably has a different structure than the oxide formed on passive Ni. The difference between acid and alkaline solutions arises from the difference in the stability of nickel oxide in the two electrolytes. A stable, passive oxide on Ni is formed in acid solution only when the dissolution rate is sufficiently large to cause nickel hydroxide to precipitate at the electrode surface, a condition not fulfilled during the dissolution of any of the compounds. In general, the oxide of the companion element or a mixed oxide is more stable than nickel oxide in acid solution at low potentials. This situation is reversed in alkaline solution, and in this case the initial passive film is nickel oxide.

The electrocatalytic reduction of oxygen on nickel and nickel compounds occurs in the potential region where a passive film is stable. The order of catalytic activity for oxygen reduction is Ni > NiAs > NiSi in acid solution, and NiS > Ni > NiSi ~ NiSb > NiAs in alkaline solution.

In a preceding paper (1) the electrocatalysis of the hydrogen evolution reaction on various nickel compounds was compared with the behavior of the corresponding elements. The results suggested that the general form of the reaction mechanism was determined by the intrinsic chemical properties of the surface atoms, while the rates of the individual reaction steps were strongly affected by the structure and the electronic properties of the crystal as a whole. Under the experimental conditions, *i.e.*, potentials negative to the reversible hydrogen electrode, the surfaces of all of the electrode materials, except Si and NiSi, could be presumed free of oxide and chemically invariant with time.

In the present paper we discuss the behavior of NiAs, NiSb, NiSi, and NiS with respect to anodic dissolution and to the electrocatalytic reduction of oxygen. In both cases, the electrode surface under-

goes continuous change, although it does achieve a steady-state chemical configuration at each value of the electrode potential. In anodic dissolution, there is a loss of electrode material to the electrolyte. The solid-state diffusion coefficients in the nickel compounds are too small at room temperature to permit a rapid readjustment of the bulk composition in response to the preferential removal of one element. Thus a steady-state dissolution rate exceeding 10^{-5} amp/cm², *i.e.*, about one monolayer equivalent per minute, implies that both elements undergo the same net rate of reaction. Rate control may, however, be associated with the removal of the less active component.

Dynamic surface changes are also inescapable for the electrocatalytic reduction of oxygen, since the reaction proceeds at potentials where anodic dissolution is also taking place. Indeed, oxygen reduc-

tion, coupled with anodic dissolution, is the basis of normal corrosion in the absence of an applied potential.

Results and Discussion

The compounds were prepared from spectroscopically pure elements by direct fusion of stoichiometric mixtures in evacuated quartz capsules, directional freezing from the melt, and annealing just below the melting points. Melting points and relevant phase diagrams are given by Hansen (2). Ingots were obtained as single phase material. The NiAs and SiSb consisted of several large crystal grains, while the NiS and NiSi were dense but microcrystalline. The elemental Ni, Sb, and Si samples all consisted of single crystal sections. The silicon sample was semiconductor grade material doped with 1 ppm of phosphorus, which imparts an electrical conductivity of 1 (ohm-cm)^{-1} .

Cylindrical specimens were cut from each sample and mounted in a close-fitting Pyrex holder with Kel-F (3). Flat surfaces with a geometric area of $\sim 0.75 \text{ cm}^2$ were exposed by grinding, followed by mechanical polishing and, where possible, by chemical and electrolytic polishing. Samples were then washed ultrasonically, treated with chromic acid/sulfuric acid cleaning solution, thoroughly rinsed with distilled water, and transferred directly to the test cell.

An all-Pyrex three-compartment electrolytic cell was used in which the working electrode was separated from a platinum counter electrode by a glass frit. A platinized platinum reversible hydrogen electrode in the same solution was used as a reference and was connected through a Luggin tip positioned close to the working electrode. Measurements were carried out at $25^\circ \pm 0.2^\circ \text{C}$.

Results are shown in Fig. 1-7, where a complete polarization cycle is depicted for the case of N_2 -

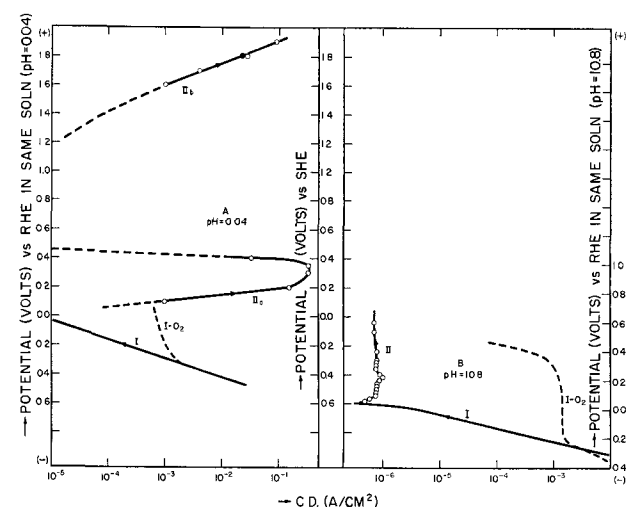


Fig. 1. Polarization curves for Ni. Fig. 1A, pH = 0.04 (1M HClO_4): curve I, cathodic h.e.r., curve IIa, anodic dissolution and passivation of Ni; curve IIb, transpassive region. Passivation current $< 10^{-5} \text{ amp/cm}^2$. Curve I- O_2 , O_2 reduction—Tafel region masked by anodic dissolution of Ni at $\sim 80 \text{ mv}$ (vs. RHE). Fig. 1B, pH 10.8 (1M NaClO_4): curve I—cathodic h.e.r.; curve II, initial anodic dissolution and passivation; curve I, O_2 , O_2 reduction—extends into passivation region.

saturated, molar perchlorate solutions at (A) pH 0.04 and (B) pH 10.8. The potentiostatic cycle was started at a potential sufficiently negative to a reversible hydrogen electrode in the same solution (RHE) to produce a hydrogen evolution current of $\sim 10^{-1} \text{ amp/cm}^2$. The potential was raised stepwise with a potentiostat to $+2.0 \text{ v}$ vs. RHE during which the cathodic current (I) decreased and was overtaken by an increasing anodic current (II). The potential was then lowered stepwise to the starting point; the anodic and cathodic current during this part of the cycle are designated III and IV, respectively.

Experiments were also carried out with oxygen-saturated solutions. Only the initial cathodic phases, (I- O_2) are shown in the figures.

Salient features of the polarization cycle will be discussed in order.

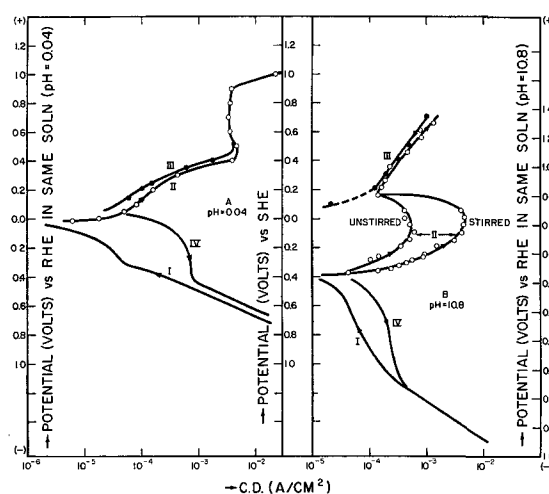


Fig. 2. Polarization curves for Sb. Fig. 2A, pH 0.04 (1M HClO_4): curve I, cathodic h.e.r.; curve II, anodic current for dissolution and passivation, toward increasing potentials; curve III, anodic currents, toward decreasing potentials; curve IV, cathodic currents, toward decreasing potentials, following curve III; O_2 reduction not observed. Fig. 2B, pH 10.8 (1M NaClO_4): curves I and IV, cathodic processes including h.e.r.; curve II, anodic dissolution and passivation, toward increasing potentials, stirring-dependent current in the active/passive transition region; curve III, reverse of curve II; no O_2 reduction observed.

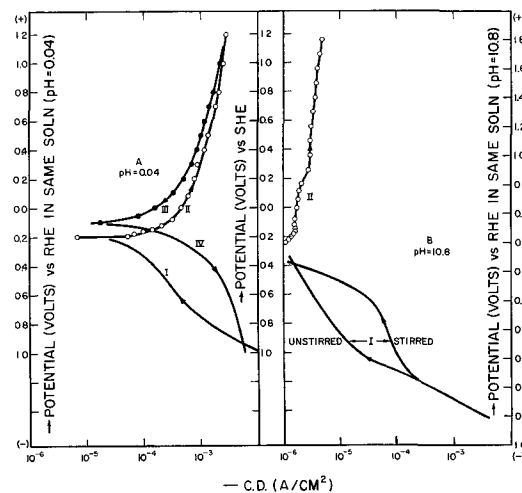


Fig. 3. Polarization curves for Si. Fig. 3A, pH 0.04 (1M HClO_4): Fig. 3B, at pH 10.8 (1M NaClO_4): passivation in alkaline solution; no O_2 reduction observed.

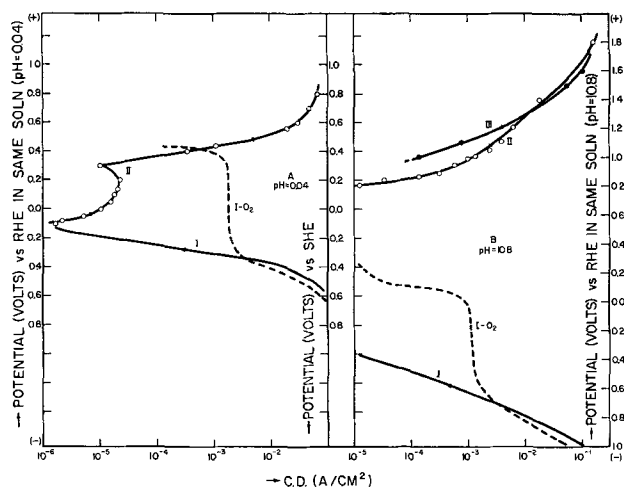


Fig. 4. Polarization curves for NiAs. Fig. 4A, pH, 0.04 (1M HClO_4): curve I, cathodic h.e.r.; curve II, anodic current for dissolution and passivation of NiAs; curve I-O₂, cathodic O₂ reduction, Tafel region masked by anodic dissolution of NiAs. Fig. 4B, pH 10.8 (1M NaClO_4): curve I, cathodic h.e.r.; curve II, anodic dissolution of NiAs, toward increasing potentials; curve III, same as II, toward decreasing potentials; curve I-O₂, O₂ reduction.

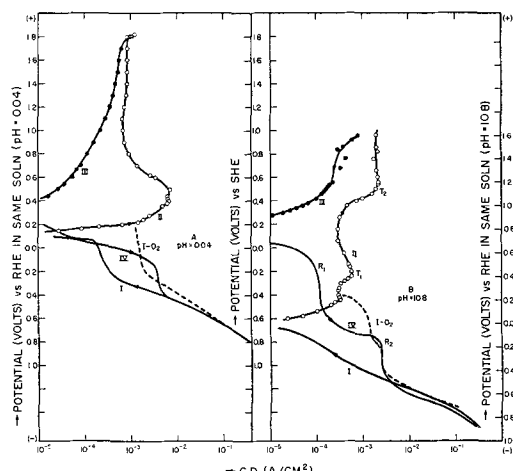


Fig. 5. Polarization curves for NiSb. Fig. 5A, pH 0.04 (1M HClO_4): curves I and IV, cathodic processes including h.e.r.; curve II, (toward increasing potentials) anodic dissolution and active/passive transition; curve III, (toward decreasing potentials) anodic current with no active/passive transition; curve I-O₂, O₂ reduction, Tafel region masked by anodic dissolution of electrode. Fig. 5B, pH 10.8 (1M NaClO_4): curve I, cathodic h.e.r.; curve IV, oxide reductions (R₁ and R₂) and h.e.r.; curve II, (toward increasing potentials) anodic currents, two transitions (T₁ and T₂) observed; curve III, reverse of curve II; curve I-O₂, O₂ reduction.

Hydrogen evolution reaction.—This phenomenon, observed in phases I and IV, has been discussed in detail in the preceding paper (4). Tafel behavior is observed in all cases except Si in acid solution. The differences in the Tafel regions of I and IV are evidently related to the presence of dissolved species released during II and III. This effect is pronounced for NiAs in acid solution where the deposition of As following anodic dissolution strongly inhibits the rate of hydrogen evolution.

Other cathodic processes.—Positive deviations from the cathodic Tafel line at low C.D.'s observed in several cases are evidently due to the onset of compensating anodic processes. The negative deviation

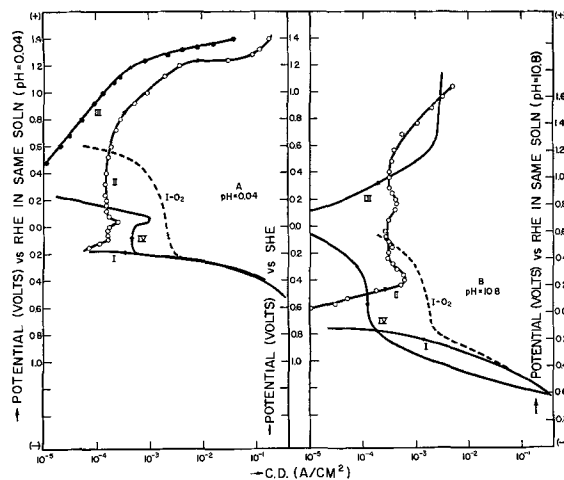


Fig. 6. Polarization curves for NiS. Fig. 6A, pH 0.04 (1M HClO_4): curve I, cathodic h.e.r.; curve IV, oxide reduction and h.e.r.; curve II, (toward increasing potentials) anodic dissolution and passivation current; curve III, (toward decreasing potentials); curve I-O₂, reduction currents for O₂-reduction. Fig. 6B, pH 10.8 (1M NaClO_4): curves I, II, III, and IV have same meanings as in Fig. 6A.

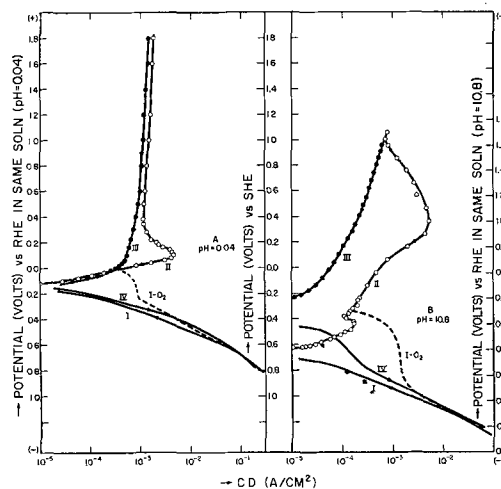


Fig. 7. Polarization curves for NiSi. Fig. 7A, pH 0.04 (1M HClO_4): curves I and IV, cathodic h.e.r.; curves II and III, anodic currents for dissolution and passivation of NiSi; curve II, (traced toward increasing potentials) shows active/passive transition; curve I-O₂, O₂ reduction, masked by anodic dissolution of electrode. Fig. 7B, pH 10.8 (1M NaClO_4): Curves I, II, III, and IV have same meanings as in Fig. 7A; curve II shows two transitions; curve I-O₂ shows pronounced O₂ reduction current.

tions in the cases of Sb and NiSb have been attributed to the formation of a hydride of antimony. The negative deviation observed with Si in alkaline solution is believed to involve the formation of SiH_4 followed by hydrolysis. In phase IV there is also a substantial cathodic current at positive potentials on NiS, NiSb, Sb, and, to a lesser extent, on NiSi in acid solutions, which suggests the reduction of an oxide or other anodically liberated species. The similarity in the phase IV behavior of NiSb to that of Sb is noteworthy.

Active anodic dissolution.—As the applied potential is raised beyond the rest potential, the anodic current rises rapidly. A generalized expression for the anodic reaction is

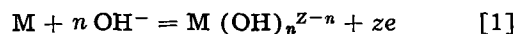


Table I. Values of E_{-5}^*

	M HClO ₄ at pH 0.04		M NaClO ₄ at pH 10.8	
	E_{-5} , v†	b, v	E_{-5} , v†	b, v
Ni	-0.10	0.05	-0.40	0.12
Sb	-0.03	0.12	-0.48	0.10
Si	-0.27	0.10	(+0.14)	0.32
NiAs	-0.02	0.09	(+0.16)	0.06
NiSb	+0.12	0.05	-0.64	0.10
NiS	-0.30	0.16	-0.61	0.10
NiSi	-0.12	0.08	-0.64	0.16

* All potentials vs. the standard hydrogen electrode (SHE).

† E_{-5} is the potential at an anodic current density $i_a = 10^{-5}$ amp/cm².

for which the current-voltage relationship at potentials sufficiently far from equilibrium should be

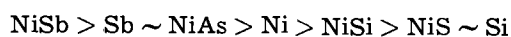
$$E = b(\log i - n \text{pH} - \log k) + E^{\circ}_{\text{H}} \quad [2]$$

where E°_{H} is a reference potential, i.e., the potential of the standard hydrogen electrode (SHE), and E is the applied potential vs. SHE. The Tafel slope, b , equals $59/\alpha z$ mv at 25°C, where α is a transfer coefficient, z is defined in Eq. [1], and k includes the specific rate constant for the reaction. It is convenient to define a parameter E_{-5} as the value of E for which $I = 10^{-5}$ amp/cm². Values of E_{-5} have been estimated by interpolating or extrapolating the apparent anodic Tafel lines in Fig. 1-7, and are listed in Table I. According to Eq. [2] and the definition of b , E_{-5} is a function of k , z , α , and n . The product αz can be obtained directly from the Tafel slope, but accurate values cannot be derived because of incipient passivation (see below).

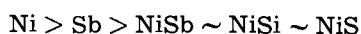
Despite a considerable variation, the values of b generally fall within the range of 100-160 mv. Since α is probably in the neighborhood of $\frac{1}{2}$, this implies that z lies between 0.8 and 1.3.

An estimate of n can be made from the pH dependence which is, approximately, $\Delta E/\Delta \text{pH} = bn = 59n/\alpha z$ mv. The results show a considerable variation, which implies significant difference in the value of α , z , and n for the rate-limiting step on the various electrodes. The apparent values of n are all substantially less than unity. This fact, together with the significant changes in the values of b , implies a change in mechanism with increasing pH.

Because of the apparent differences in the value of b , it is not possible to separate k from Eq. [2] for a quantitative comparison of rate constant against composition. There are, nevertheless, several qualitative features of the results which bear notice. The nobleness of the electrodes in acid solutions as measured by increasingly positive values of E_{-5} is in the order



while in alkaline solution, the sequence is



(Results for Si and NiAs in alkaline solution are indefinite.) Thus, NiSb is more noble in acid solution than either of the elements, while the converse holds for alkaline solution. NiSb, NiSi, and NiS be-

have very similarly in alkaline solution, but all are less noble than Ni.

These results should be considered in light of the fact that, while steady-state dissolution of a compound implies equal dissolution rates of the constituents, rate control is probably associated with the detachment of one or the other element. The identification of this element is an interesting problem. The transition state for dissolution is determined by the intersection of the potential energy curves for the atom in a lattice position at the surface and that for the ion in the solution. The latter is independent of the substrate, but the former is strongly conditioned by it. The problem then reduces to an evaluation of how the potential energy of a surface atom depends on its crystal environment.

Each of the compounds under study has, of course, a negative free energy of formation from the elements and apparently has a negative heat of formation as well. The effect of compound formation is to lower the energy of the more active element and to raise that of the less active element. Generally speaking, there will be a corresponding effect on the activation energy for detachment, e.g., the more active element will be rendered less active. In the simplest cases, then, the rate of dissolution of the compound would be somewhat faster than that of the less active element by itself. This observation coincides with the results for NiSi in acid solution.

These comments apply to dissolution only if the nature of the bonding in the compound is the same as in the elements. Where there is a substantial electronegativity difference between the two kinds of atoms there will be a shift in charge which tends to make the crystal more ionic. In the extreme case of an ionic crystal, solvation becomes paramount and dissolution will occur by nonelectrochemical processes. In less extreme cases, the electronegativity difference tends to raise the valence of the less electronegative element and lower that of its companion. An effective decrease in valence should tend to render the more electronegative element more stable to anodic oxidation. This observation coincides with the enhanced nobleness of NiSb in acid solutions.

However, these simple chemical considerations are obviously unable to account for all of the present results. In particular, the rates of dissolution of NiSi, NiSb, and NiS in alkaline solution are nearly identical which suggests that the detachment of Ni is rate-limiting. However, there are substantial differences in the heats of formation and in the electronegativity differences of the compounds (5). The apparent independence of the energy of activation for detachment of Ni cannot be explained in any simple way, e.g., compensation effects.

Active-passive transitions.—Nickel itself exhibits an active-passive transition in which the anodic current decreases rapidly with increasing anodic potential and reaches eventually a limiting current which is constant over a considerable range of potentials. An interpretation of this phenomenon in

Table II. Summary of results
Molar perchlorate solution of pH 0.04

	Passivation potential E_t , v	Critical C. D. i_t , amp/cm ²	C. D. in passive region i_p , amp/cm ²	Passive potential range ΔE_p , v	$\Delta E_t/\Delta pH$
Ni	+0.3	3×10^{-1}	$\sim 10^{-6}$	0.4 to 1.4	-0.074
Sb	+0.4	4.5×10^{-3}	3.5×10^{-3}	0.4 to 0.9	-0.041
Si	—	—	$\sim 10^{-3}$	—	—
NiAs	+0.2	2.3×10^{-5}	$\sim 10^{-5}$	—	—
NiSb	+0.45	7×10^{-3}	7×10^{-4}	0.8 to 1.8	-0.082
NiS	-0.10	1.5×10^{-4}	1.5×10^{-4}	-0.1 to 0.7	-0.026
NiSi	+0.10	4.5×10^{-3}	$\sim 10^{-3}$	0.4 to 1.8	-0.050

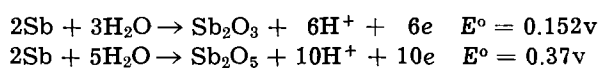
1M NaClO₄ at pH 10.8

	Passivation potential E_t , v	Critical C. D. i_t , amp/cm ²	C. D. in passive region i_p , amp/cm ²	Passive potential range ΔE_p , v
Ni	-0.5	10^{-6}	7×10^{-7}	—
Sb	-0.04	5×10^{-4} (unstirred) 5×10^{-3} (stirred)	$\sim 10^{-4}$	—
Si	-0.16	1.7×10^{-6}	1.6×10^{-6}	-0.16-2.0
NiAs	—	$< 10^{-6}$	$< 10^{-6}$	—
NiSb	-0.44 (0.56)	3×10^{-4} (2×10^{-3})	3×10^{-4} (2×10^{-3})	-0.44-0.37 (0.56-1.0)
NiS	-0.39	6×10^{-4}	3×10^{-6}	-0.39-0.56
NiSi	-0.44	1.7×10^{-4}	1.2×10^{-4}	—

terms of a higher valence oxide film has been proposed by Sato and Okamoto (6). According to this view, NiOH⁺ produced during dissolution accumulates near the electrode surface, until the solubility product of nickel hydroxide or nickel oxide is exceeded and the oxide precipitates at the electrode surface. With further increase of potential, a higher oxide, probably approaching Ni₃O₄ in composition, is formed as a compact film, and this probably constitutes the passive film. The current in the passive region is determined by the rate of solution of the oxide film. As the potential is raised further, the thickness of the oxide increases until the rate of film growth matches that of film dissolution so that the residual steady-state current remains independent of potential.

The anodic polarization curves of the nickel compounds also show evidence of active-passive transformations. The transitions are characterized by a transition potential (E_t); the current (i_t) at the transition potential; the current in the passive region (i_p); and, the range of potentials in which passivity occurs. Results are summarized in Table II. In the case of Ni, E_t decreases approximately 59 mv per pH unit, and the values of i_t and i_p decrease substantially with increasing pH.

In the case of Sb there are also distinctive transitions in both acid and alkaline solutions. In acid solution $i_t \sim i_p \sim 5 \times 10^{-3}$ amp/cm². In alkaline solution $i_p \sim 10^{-4}$ amp/cm², but increases with potential; i_t increases sharply with stirring, consistent with a mechanism based on passivation by a partially soluble oxide film. The formation of an oxide was further evidenced by a visible darkening of the original polished surface. In acid solutions, the relevant oxidation potentials for antimony are (7)



The last potential is in accord with E_t , which is strong inferential evidence that the passivating film consists of Sb₂O₅. The value of i_t in acid solution implies a dissolution rate of ~ 15 monolayer equivalents per second. There is virtually no hysteresis in retracing the polarization curve (III), suggesting that the actual passivating film is very thin, although there may be growth of a noncompact oxide above it. The latter could contribute to the large cathodic currents observed in phase IV.

In alkaline solutions, anodic dissolution begins at -0.40v and the transition to the passive state occurs at -0.04v.¹ Anodic dissolution probably occurs by oxidation to the soluble +3 oxide according to the reaction



with a potential $E = -0.42\text{v}$ at pH 10.8. The local decrease of pH caused by this reaction favors the formation of Sb₂O₅, and this oxide is probably responsible for passivity. The enhancement of the critical current by stirring is due either to increased diffusion of OH⁻ to the dissolving surface or to the removal of SbO₂⁻ from the interface.

In acid solutions, Si does not show an active-passive transition. Anodic dissolution begins at -0.20v, and the current gradually approaches an essentially constant value of 10^{-3} amp/cm². This limiting current is independent of stirring, and hence must be controlled by diffusion through a surface film, which is probably hydrated SiO₂. In alkaline solutions, there is an ill-defined transition at -0.16v.¹ The current in the passive region is $\sim 3 \times 10^{-6}$ amp/cm² and shows a slight increase at higher potentials. Anodic passivation of Si in KOH was also observed by Turner (8).

It is surprising that the anodic oxidation rate of Si in alkaline solution, where SiO₂ is soluble, is less

¹ Against a standard hydrogen electrode.

than in acid solution. This difference in rates implies that the surface oxide formed in acid solution is noncoherent.

Active-passive transitions of nickel compounds.— There is clear voltammetric evidence (Fig. 4-7) of active-passive transformations on the nickel compounds under study. Before discussing the data it will be useful to consider briefly the theory of such transitions.

Although the phenomenon of anodic passivation of intermetallic compounds is not unexpected, the interpretation is highly complex. Consider the following sequence of anodic reactions of an intermetallic compound AB in which the excess solubility of A or B is very small: As the potential is raised, anodic dissolution of both A and B increases until the proper conditions are achieved for the formation of a protective oxide film. Direct contact of the compound and the electrolyte is then prevented, and continued reaction requires the field-induced diffusion of cation defects (interstitials or vacancies) through the oxide film. As with elemental electrodes, the current drops to a low value, and the thickness of the oxide film at a given potential adjusts to a stationary value at which the field-induced transport of cations through the film exactly matches the rate of dissolution at the oxide/electrolyte interface. The transport rate may be limited either by the transfer of ions across the electrode/oxide interface or by their diffusion through the film. In the former case, the rate depends on the concentration, C_i , of the relevant species at the inner interface and its effective charge, Z_i , in the transition state; in the latter case it depends on the concentration, C_o , of the defects in the film and their diffusion coefficient.

Let us first consider the case where the passivating film consists essentially of pure oxide of A, here denoted by AO, and that interstitial cations are the predominant defects. In the passive region, where the steady-state current is independent of potential, the rate of chemical dissolution of AO is balanced by the transport of A ions through the film. However, ion transfer can only take place if B atoms are liberated as well. Since the excess B atoms cannot redistribute in AB (restricted solid solubility), they must accumulate at the metal/oxide interface. It is obvious that a steady state cannot be achieved in this case unless diffusion of B ions through AO also takes place. Therefore, although the intrinsic dissolution rate of AO still determines the over-all reaction rate, the thickness of the oxide is adjusted so as to permit a fast enough transport of the slower moving ion species through the film. In this model, the stationary current in the passive region is $\left(1 + \frac{Z_B}{Z_A}\right)$ times that observed on pure A electrodes, and the film thickness depends on the mobility of A through the AO oxide.

As a second possibility, it may be assumed that a mixed oxide of A and B is formed. In this case, the properties of the mixed oxide, including its chemical dissolution rate, determine the steady-state current

in the passive region. The passive current will differ, in general, from that observed on either pure A or pure B.

There are no simple precedents for deciding which model may be applicable to intermetallic compounds. The most relevant studies have been carried out with InSb. The rate of anodic oxidation of InSb in a KOH solution in which In_2O_3 is almost totally insoluble, and where, consequently, thick oxide films can be formed, depends on the rate of transfer of ions across the InSb/oxide interface (9). Because of the higher charge of Sb, the transfer of In is rate-limiting. The crystal structure of the oxide film was not determined, but it was found that the ratio of In to Sb in the film was unity from the InSb/oxide interface to within 100Å of the oxide/electrolyte interface where the ratio increased sharply, presumably because of the much larger solubility in KOH of Sb relative to In (9). A unit ratio of In to Sb in the oxide film is not expected on the basis of the proposed mechanism if transport through the film is by interstitials. This ratio may be explained if the mobile species are cation vacancies generated at the electrolyte/oxide interface. Although such a mechanism is contrary to the known high-temperature defect mechanism in In_2O_3 , it is consistent with the fact that anodically formed oxides rectify in a sense which indicates the presence of cation vacancies (10).

In the thermal oxidation of InSb at high temperatures, a protective film of In_2O_3 is formed, and further growth is limited by the chemical rather than the field-induced diffusion of interstitial In^{+3} ions through the oxide (11). In this case, Sb liberated by the oxidation of In is precipitated in an elemental phase at the InSb/ In_2O_3 boundary, as evidenced by electron diffraction. The Sb layer does not deter significantly the diffusion of In atoms at high temperatures and consequently has little effect on the kinetics. The experiments with InSb illustrate the general pattern of oxidation behavior which may be expected with an intermetallic compound if the rate is determined by one component. There are, however, a number of possible complications which may occur in other systems. For example, if the rate of diffusion of B through an AO oxide is small, the film cannot grow rapidly enough to balance the dissolution rate of AO, and the intermetallic compound will form an imperfectly protective oxide film. It is also possible that more than one oxide will form at the surface. A disparity between the rates of growth and dissolution of individual crystallites in such a mosaic would lead to mechanical instability of the film as a whole. Finally, a single oxide of either A or B may be formed, but it may differ in structure from that on the pure element.

The results on nickel compounds in the passive region may be summarized as follows (see Fig. 1-7 and Table II):

1. NiSi, NiAs, NiSb, and NiS all show passivation both in acid and alkaline solutions.
2. In acid solutions (pH 0.04), the critical potentials for passivation of NiSi, NiAs, and NiS are all

different from that for Ni, and the critical current on all these compounds is two orders of magnitude less than on Ni. The critical current and potential for NiSb are close to those found with elemental Sb.

3. In alkaline solutions (pH 10.8), the critical potentials for passivation of NiSi, NiSb, and NiS are about the same as for Ni, but the critical current density is three orders of magnitude larger than for Ni.

4. The current densities in the passive region lie between 10^{-4} and 10^{-3} amp/cm² for NiSi, NiSb, and NiS in both acid and alkaline solutions. The passive current on NiAs, like that on Ni, is orders of magnitude less.

5. An increase of current at potentials below the oxygen evolution (transpassive behavior) is observed with NiAs and NiS in both acid and alkaline solutions, and with NiSb in alkaline solution.

A noteworthy feature of the polarization curve of NiSb in acid solution is hysteresis between the curves obtained on increasing and decreasing the potential. This is indeed a general characteristic, although less pronounced, of the anodic behavior of all the compounds. It should be remembered that the present experiments are, in effect, an extension to very low rates (20 mv/30 sec) of the potentiostatic sweep method and that even at this rate a steady-state surface configuration may not be achieved. It is also possible that the composition of the oxide film varies with anodic potential. In this case, there may be relatively long time constants for re-establishing the appropriate concentration profile throughout the film.

The results with the intermetallic compounds point to the following general mechanism for passivation. In acid solution, the critical current depends on the kinetics of dissolution of the compound and varies in the way discussed above for dissolution in the active region. At potentials close to the transition potential, a stable surface oxide is formed, and this grows as the potential is further increased. Contrary to the case of Ni, the formation of the surface oxide is not preceded by the precipitation of a hydroxide of either element (the critical current is several orders of magnitude less than the diffusion-limited current) in the electrolytes. Since the critical potential is substantially less than that for Ni and since it is different for different compounds, it must be assumed that the passive film is a mixed oxide of both elements.

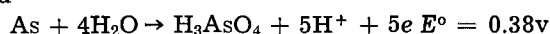
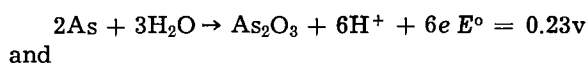
As the potential is increased beyond the critical value for passivation, both Ni and the second element migrate through the film. The higher rate of oxidation, compared to that of Ni, suggests that the films on the compounds are more soluble than the passive film on elemental nickel. The rate-limiting step is probably the oxidation of Ni rather than the oxidation of the second element. For example, in the case of NiSb the intrinsic rate of transfer of Sb across the metal/oxide interface is probably greater than for Ni since the charge of the Sb ion is greater; similarly, the field-induced rate of migration of Sb across the film is also expected to be greater, again because of the bigger charge and smaller size of the

Sb cation. Consequently, the rate at which NiSb oxidizes is probably controlled by the rate of removal of Ni, whether the rate-limiting step is the transfer of an ion across the metal/oxide interface or across the oxide itself.

The hysteresis observed with NiSb in acid solution suggests that the composition of the film changes on cycling. This may come about if the rate of dissolution of Sb from the oxide is greater than that for Ni (compare the anodic behavior of Ni and Sb). On increasing the potential during the anodic sweep, Sb is continuously introduced into the film, together with Ni, at a rate which is larger than the dissolution rate of the mixed oxide, causing the oxide film to grow. The composition of the film is probably maintained at some constant ratio of Ni to Sb, probably not far from unity. When the potential is decreased, the dissolution rate exceeds the rate of film formation, and the film therefore decreases in thickness. It appears that during this process Sb is removed preferentially from the oxide and the passive film approaches the characteristics of the film formed on elemental Ni, *i.e.*, its dissolution rate is now less by an order of magnitude.

NiS also shows a large hysteresis loop on anodic polarization. On increasing the potential, there is a small oxidation peak about 0.1v which corresponds to a reduction peak on the "down" run. The current is independent of potential up to about 0.6v; at higher potentials, a transpassive region sets in, and the current increases rapidly to very high values. Since the oxidation of S to a soluble SO_3^- species is thermodynamically possible above 0.5v, it is probable that the onset of the transpassive region corresponds to the oxidation of sulfur to the +4 state. The oxidation state of sulfur below 0.5v and the form in which it is incorporated in the film are uncertain. It is clear, however, that the passivating oxide on NiS is different from that on Ni since both the critical potential and the current in the passive region differ substantially from those found with Ni. It should be noted that the passive state on a pure Ni electrode breaks down when H_2S is added to the electrolyte. This observation shows that elemental S in NiS is not released as S^- to any large extent.

NiAs shows a distinctive active-passive transition at 0.2v, but passivity breaks down at slightly more positive potentials and the current increases rapidly. Apparently, a transpassive region (oxidation to a higher valency state) follows closely the passive region of NiAs. The potential range for both phenomena is probably determined by the oxidation reactions of As. The thermodynamic potentials for the couples



correspond closely to the potentials where the passive and transpassive regions for NiAs set in. Thus, it is probable that a protective oxide formed at lower potentials breaks down above 0.3-0.4v where oxidation of As to the +5 state becomes possible.

NiSi shows a regular active-passive transition at 0.1v and a passive region extending to very high potentials ($> 1.8v$). The current in the passive region is substantial (10^{-3} amp/cm²) and corresponds to a dissolution rate for the oxide of about 300 monolayers per minute. This rate is not much different from that of Si at comparable potentials and suggests that the passive oxide is similar to the oxide on elemental Si.

In alkaline solution, NiSi, NiSb, and NiS all show a transition at 0.2v (*vs.* H⁺/H₂ in the same solution) which corresponds closely to the transition observed with pure Ni. It is clear, therefore, that Ni oxide is formed first in all three cases. However, both the critical current and the passive current are largely by 2-3 orders of magnitude than on pure Ni. NiSi is particularly interesting in this respect since the dissolution rate of this compound in the passive region is greater by 2 orders of magnitude than the rate for either of the pure elements. Pronounced hysteresis is observed with all three compounds, the anodic current on decreasing the potential being in all cases less than on increasing the potential. These results suggest that the initial passivating film is nickel oxide but of a different structure than the passive oxide formed on pure Ni. It is not clear whether the second element is introduced in the film at more positive potentials. The increase of the current at potentials more passive than 0.2v in the case of NiSi and NiSb suggests that Si and Sb are in fact incorporated in the film. This conclusion is supported by the hysteresis observed on decreasing the potential which suggests a change in the composition of the film upon cycling as in the case of acid solutions.

In summary, the anodic behavior of nickel compounds in acid solution shows that the passive film is either a mixed oxide or an oxide having the basic structure of the second element. In alkaline solution, nickel oxide is formed first but probably has a different structure than the oxide formed on passive Ni. At higher potentials, substantial amounts of the second element are probably introduced in the film, particularly in the case of NiSi and NiSb. The difference between acid and alkaline solutions arises from the difference in stability of nickel oxide in the two electrolytes. A stable, passive oxide on Ni is formed in acid solution only when the dissolution rate is sufficiently high to cause nickel hydroxide to precipitate at the electrode surface, a condition which is not fulfilled during dissolution of any of the compounds. In general, the oxides of the companion elements are more stable in acid solution at low potentials than is nickel oxide. This situation is reversed in alkaline solution, and in this case the initial passive film is basically nickel oxide.

Oxygen reduction.—Oxygen reduction takes place on all the four compounds studied as well as on Ni, but there is no evidence of O₂ reduction on elemental Si and Sb. For the sake of comparison, two parameters were selected, *viz.*, i_{max} , the maximum reduction current, and E_{-4} , the potential for a reduction current of 10^{-4} amp/cm², and are shown in Table III. For all the materials (except Sb and Si), i_{max}

Table III. Oxygen reduction in molar perchlorate solutions

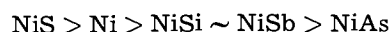
	pH	i_c (max), amp/cm ²	E_{-4} , v*
Ni	0.04	1.0×10^{-3}	—
	10.8	1.3×10^{-3}	-0.2
NiAs	0.04	1.4×10^{-3}	+0.43
	10.8	1.2×10^{-3}	-0.52
NiSb	0.04	1.3×10^{-3}	—
	10.8	1.4×10^{-3}	-0.38
NiS	0.04	2.0×10^{-3}	+0.58
	10.8	1.8×10^{-3}	-0.04
NiSi	0.04	0.8×10^{-3}	0.0
	10.8	1.5×10^{-3}	-0.34

* E_{-4} is the potential relative to the standard hydrogen electrode at a cathodic C. D. of 10^{-4} amp/cm².

is essentially the same (10^{-3} amp/cm²) and is consistent with a diffusion limited current for molecular O₂ in the solution. A higher activity of the electrode toward O₂ reduction is expressed by more positive values of E_{-4} . The order of decreasing activity in acid solution is



The value of E_{-4} for Ni and NiSb cannot be estimated since the oxygen reduction current is overwhelmed by the anodic dissolution current in the prepassive region. In alkaline solution, the values of E_{-4} decrease in the order



The order in the activity of the materials remains essentially independent of pH except that NiSi is more active than NiAs in alkali and that the reverse is true in acid. A significant observation is that O₂ reduction takes place in the potential region in which the materials are generally passive and are probably covered with surface oxides. The observed differences between these compounds indicate that the presence of the negative element (Si, S, Sb, As) modifies the nature of the surface oxide to produce changes in the electrocatalytic activity.

Acknowledgment

The authors wish to acknowledge the expert technical assistance of Miss Mary A. Loud and Miss MaryJane MacLaren. The authors are grateful to the Office of Naval Research for support under Contract Nonr-3765(00).

Manuscript received July 24, 1963; revised manuscript received Sept. 25, 1963.

Any discussion of this paper will appear in a Discussion Section to be published in the December 1964 JOURNAL.

REFERENCES

1. A. K. M. S. Huq and A. J. Rosenberg, *This Journal*, 111, 270 (1964).
2. M. Hansen, "Constitution of Binary Alloys," 2nd Ed., McGraw-Hill Book Co., New York (1958).
3. "KEL-F Brand Polymer Wax, Grade KF200" obtained from Chemical Division, Minnesota Mining and Manufacturing Co., St. Paul, Minn.
4. Ref. (1).
5. G. F. Raynor, "The Physical Chemistry of Metallic

- Solutions and Intermetallic Compounds," Vol. 1, p. 312, Chemical Publishing Co., New York (1960).
6. N. Sato and G. Okamoto, *Trans. Japan Inst. Metals*, **2**, 113 (1961).
 7. W. M. Latimer, "Oxidation Potentials," 2nd ed., Prentice Hall, Inc., New York (1959).
 8. D. R. Turner, *This Journal*, **105**, 469 (1958).
 9. J. F. Dewald, *ibid.*, **104**, 244 (1957).
 10. W. Ch. van Geel and J. W. A. Scholte, *Philips Res. Rept.*, **6**, 54 (1951); H. E. Haring, *This Journal*, **99**, 30 (1952); D. A. Vermilyea, *J. Appl. Phys.*, **27**, 963 (1956).
 11. A. J. Rosenberg and M. C. Lavine, *J. Phys. Chem.*, **64**, 1135 (1960); A. J. Rosenberg, *ibid.*, **64**, 1143 (1960).

Formation of Polynuclear Species during the Electroreduction of Chromic Acid

J. Levitan

Department of Inorganic and Analytical Chemistry, Hebrew University, Jerusalem, Israel

ABSTRACT

Chromic dimer and a second species, probably a chromic polymer, of still unknown structure, which were found during the electroreduction of chromic acid in the presence of sulfates, are oxidation products of the reaction between chromic acid and chromous ion, formed during the electrolysis. The formation of chromous ion is discussed. The same species are formed in the reaction between chromous perchlorate and chromic acid solutions. These species are not directly responsible for the metallic chromium deposition. The species decompose in the plating solution with the formation of $\text{Cr}(\text{H}_2\text{O})_6^{+3}$ ion. The fact that $\text{Cr}(\text{H}_2\text{O})_6^{+3}$ ion is not formed as a result of the direct reduction of hexavalent chromium is also discussed.

The mechanism of the electroreduction of chromic acid is of great interest, not only from the theoretical point of view, but also because of its application in the industry. Decorative and hard chromium plating are carried out using chromic acid solution as the electrolyte.

The products formed in the electrolyte during the electroreduction are the object of investigation, discussed in this paper.

Experimental

Cation exchange resin DOWEX-50, 100-200 mesh, cross-linking 2% in hydrogen form, was used. The resin was regenerated, after elution with $\text{La}(\text{ClO}_4)_3$, with citrate solution. Columns of 16 mm diameter and 200 mm height were employed.

Spectrophotometer OPTICA Milano Model CF-4 was used with 1 and 4 cm Pyrex cells.

Chromic acid solution was prepared by dissolving the reagent grade CrO_3 . The concentration of CrO_3 was determined iodometrically and spectrophotometrically.

$\text{La}(\text{ClO}_4)_3$ was prepared by dissolution of the reagent grade $\text{La}(\text{OH})_3$ in perchloric acid solution. The pH of $\text{La}(\text{ClO}_4)_3$ solution was kept at 2.

$\text{Cr}(\text{ClO}_4)_2$ was prepared by electrolytic reduction of chromic perchlorate under nitrogen. The cell consisted of two compartments, divided by sintered glass, a mercury cathode, and a cathodic solution of $\text{Cr}(\text{ClO}_4)_3$.

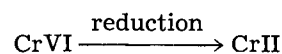
Chromium content was determined by oxidizing to bichromate by boiling with HClO_4 until fumes appeared. Then the solution was boiled for an additional 10 min, cooled, diluted, and boiled for 1/2 hr. The formed bichromate was determined iodometrically in an inert atmosphere.

A large number of investigations in this field have not led to a satisfactory explanation of the mechanism of the process or its specific properties.

Some investigators have interpreted the chromium deposition as a result of gradual reduction of the hexavalent chromium and discharge of the trivalent chromium on the cathode (1). In 1905 Caveth and Curry (2) expressed the view that the hexavalent chromium is directly discharged, and not the trivalent. This view was supported by the works of Muller (3), Kasper (4), and others. Ogburg and Brenner (5) prepared plating solutions with radioactive chromium in trivalent or hexavalent state. Their data supported the view that the metallic chromium deposition is a result of discharge of hexavalent chromium.

The following cathode processes were considered (6, 6a): (a) $\text{Cr}_2\text{O}_7^{-2} + 14\text{H}^+ + 6e \rightarrow 2\text{Cr}^{+3} + 7\text{H}_2\text{O}$, $E = 1.36$; (b) $\text{Cr}_2\text{O}_7^{-2} + 14\text{H}^+ + 8e \rightarrow 2\text{Cr}^{+2} + 7\text{H}_2\text{O}$, $E = 0.9$; (c) $\text{Cr}_2\text{O}_7^{-2} + 14\text{H}^+ + 12e \rightarrow 2\text{Cr}^0 + 7\text{H}_2\text{O}$, $E = 0.4$; (d) $2\text{H}^+ + 2e \rightarrow \text{H}_2$, $E = 0.0$; (e) $\text{Cr}^{+3} + e \rightarrow \text{Cr}^{+2}$, $E = -0.4$; (f) $\text{Cr}^{+2} + 2e \rightarrow \text{Cr}^0$, $E = -0.91$; (g) $\text{Cr}^{+3} + 3e \rightarrow \text{Cr}^0$, $E = -0.74$.

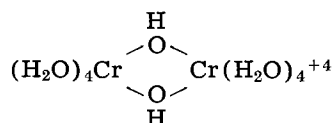
Conditions during electrolysis are favorable for processes (a) to (d). The strong hydrogen evolution is explained by the easy penetration of hydrogen ions through the cathodic film. Formation of chromous ions by process (b) is thermodynamically favorable and should be considered. The formation of chromous ions during the process is only vaguely mentioned by the former investigators who suggested paths such as the following



and $\text{CrII} + \text{CrVI} \longrightarrow \text{CrIII}$

No evidence, however, of the actual formation of the chromous ion was given.

Ardon and Stein (7) oxidized chromous perchlorate with oxygen and obtained the dimeric chromium ion. Its structure, spectrum, and other properties were investigated and published in later papers (9, 10, 12). The structure of the dimer was found to be



Ardon and Plane (10) obtained this dimeric ion by oxidizing chromous perchlorate solution with a number of oxidants. The dimer was also obtained by action of bichromate solution on chromous perchlorate solution (10).

If chromous ion is formed during the electroreduction of chromic acid solution, it will react with the bichromate ion in the solution with the formation of the dimeric and chromium hexaquo ions.

To determine if the dimer is indeed formed, a solution, containing 287.2 g/l CrO_3 and 2.5 g/l sulfates was electrolyzed at 30°C with a lead anode and chromium cathode. Cathode current density was 75 ma/cm^2 . After electrolysis the electrolyte was diluted to 1:10 to minimize the decomposition of the formed species, and passed through a cation exchange column. A green layer was obtained at the top of the column, the second (main) layer was blue-violet, and the bottom layer, being obtained in small amounts, was green, easily eluted with 0.5M perchloric acid. According to Knorr (8) this fraction is chromic sulfate complex. The second blue-violet layer was eluted with 1-1.5M perchloric acid and identified as the chromic hexaquo ion $\text{Cr}(\text{H}_2\text{O})_6^{+3}$. The first layer could not be eluted even with a 3M HClO_4 solution. When more concentrated HClO_4 was used, the layer spread over the column and a satisfactory elution was impossible. To elute this layer a $\text{La}(\text{ClO}_4)_3$ solution was employed. During the elution of the upper green layer with $\text{La}(\text{ClO}_4)_3$, it separated into 2 fractions: the first, colored blue-green, which was eluted with $\text{La}(\text{ClO}_4)_3$ 0.2M, and the second, colored yellow-green, which was eluted only with $\text{La}(\text{ClO}_4)_3$ 0.4-0.45M. Both solutions were studied spectrophotometrically. Results are given in Fig. 1.

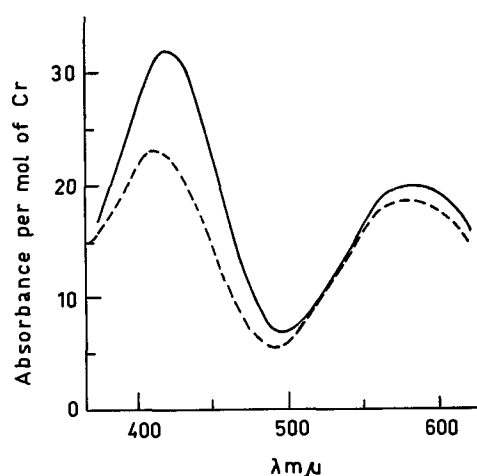


Fig. 1. Spectrum of solutions, eluted with $\text{La}(\text{ClO}_4)_3$. - - - - Blue-green solution (A); peaks; $415.5 \text{ m}\mu$, $\epsilon = 23.05$ and $580.5 \text{ m}\mu$, $\epsilon = 18.5$; ——— yellow-green solution (B); peaks; $422.5 \text{ m}\mu$, $\epsilon = 31.7$ and $581 \text{ m}\mu$, $\epsilon = 19.7$.

The spectrophotometric study and the manner of separation by ion exchange chromatography identify them as: solution A, the dimeric chromium ion (7, 9-12); Solution B, the species obtained by Laswick and Plane (9) in a boiling chromic nitrate solution and called "species B" in this paper.

The amounts of the reduction products obtained after the electrolysis are given in Table I.

For comparison, the reaction between chromous perchlorate solution and chromic acid was carried out. Chromous perchlorate solution was added to a vessel containing chromic acid solution. Nitrogen was passed through the CrO_3 solution for 15 min before the mixing and for 30 sec after it. The mixed solution was immediately diluted and analyzed as described above. Dimer, species B, and chromium hexaquo ions were obtained in ratios similar to that found after the electrolysis (Table II). The experiments showed the growing yield of polynuclear species in more dilute chromic acid solution.

In order to study the stability of the dimer and species B in the plating solution, the solution of CrO_3 with sulfates of usual concentration was electrolyzed under conditions similar to that described above. After the electrolysis the vessel with the solution was kept in a thermostat at a temperature of $30.1 \pm 0.1^\circ\text{C}$. Samples of the solution were taken

Table I. Composition of CrIII species formed during electrolysis of chromic acid solutions at 30°C and $D_c = 75 \text{ ma/cm}^2$

No.	Composition of the solution	Time of the electrolysis, min	Amounts of CrIII species in per cents of the total CrIII			
			Hexaquo with sulfato complex	Dimer	Species B	Species B + dimer
1	287.2 g/l CrO_3 2.5 g/l SO_4^{-2}	5	71	18.6	10.4	29
2	287.2 g/l CrO_3 2.5 g/l SO_4^{-2}	5	70.2	20.7	9.1	29.8
3	287.2 g/l CrO_3 2.5 g/l SO_4^{-2}	16	77	14.9	8.1	23
4	291.1 g/l CrO_3 2.7 g/l SO_4^{-2}	40	82	11.9	6.1	18
5	144.6 g/l CrO_3 1.3 g/l SO_4^{-2}	6.3	66.6	18.8	14.6	33.4

Table II. Composition of the CrIII species formed during the oxidation of chromous perchlorate by chromic acid

No.	Composition of the solution	Amounts of CrIII species in per cents of the total CrIII			
		Hexaquo ion	Dimer	Species B	Species B + dimer
1	287.5 g/l CrO ₃	72	18.8	9.2	28
2	287.5 g/l CrO ₃	66.4	23.2	10.4	33.6
3	287.5 g/l CrO ₃	71.25	20.45	8.3	28.75
4	100 g/l CrO ₃	63.4	29.2	7.4	36.6
5	60 g/l CrO ₃	58.4	32.2	9.4	41.6
6	30 g/l CrO ₃	53.2	32	14.8	46.8

after different time intervals and analyzed as described above. The dimer and species B were found to be unstable in the plating solution: they decompose with the formation of the chromic hexaquo ion. Kinetic measurements showed that the decomposition reactions of the polynuclear species are of the first order given under the conditions of the experiment

$$K_{\text{dec.dim}} = 2.62 \cdot 10^{-4}$$

$$K_{\text{dec.sp.B}} = 2.43 \cdot 10^{-4}$$

To determine whether the dimer and/or species B are the ions discharged on the cathode surface producing the metallic chromium deposit, 0.6M chromous perchlorate solution was added to a sulfate-free, pure chromic acid solution under an atmosphere of nitrogen. When this solution containing the chromium hexaquo, dimeric, and specie B ions in amounts similar to that in the plating solution, was electrolyzed with a copper cathode, no chromium deposit was obtained.

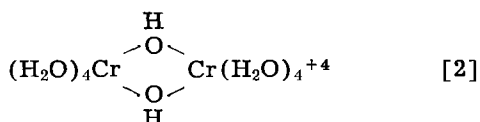
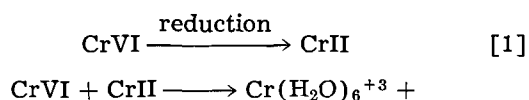
Discussion

The formation of chromic dimer and species B during the chromium plating process can be explained by the formation of chromous ion, as a product of electroreduction of the hexavalent chromium on the cathode surface, followed by its oxidation with chromic acid to yield the dimer, species B, and Cr(H₂O)₆⁺³ ions.

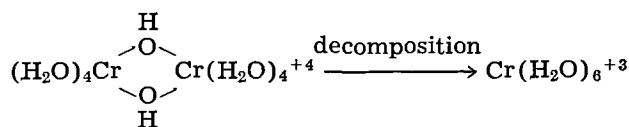
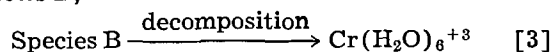
Although the possibility of the formation of these polynuclear species by direct electroreduction on the cathode surface of the hexavalent chromium, without passing through the bivalent state, cannot be ruled out, the similarity of the results obtained by the action of chromic acid on CrII perchlorate support the conclusion that CrII ion is formed during the electroreduction of chromic acid in presence of sulfates.

The oxidation products of chromous ion are dimer, specie B, and Cr(H₂O)₆⁺³ ions.

The following reactions take place



+ Species B;



As a result the chromic hexaquo ion being the most stable form is accumulated in the solution. The dimer and species B are not directly responsible for metallic chromium deposition, being only products of secondary reactions, especially products of oxidation of the chromous ion by the hexavalent chromium.

The structure of the dimeric ion has been studied (9-12). The structure of the yellow-green fraction, species B, is unknown. Its charge according to its behavior on the cation exchange resin should be more positive than that of the dimer, probably +5. Possibly the ion is formed from more than two chromium atoms. Its structure is being investigated.

The results of the electrolysis of chromic acid were compared with the results obtained by mixing Cr(ClO₄)₃ with CrO₃ solutions (Tables I and II). Experiments in Table I were compared with experiments in Table II. The electrolysis was run for about 5 min to obtain determinable amounts of reaction products and to minimize the time of decomposition of the polynuclear species.

The similar yields of the CrIII species in the electrolysis of the chromic acid solution and reduction of CrO₃ by chromous perchlorate solution suggest that the same mechanism operates in both cases. Direct formation of tervalent chromium cannot take place on the cathode surface because, if it is formed on the cathode with the Cr⁺² ion, the proportion of Cr(H₂O)₆⁺³ would be much greater than that obtained. The ion formed on the cathode surface as a reduction product is the chromous and not the chromic ion.

Conclusions

1. Polynuclear species are formed during the electroreduction of chromic acid in the presence of sulfates.

2. One of these species is the chromic dimer, the other, being of unknown structure, found by former investigators (9).

3. The nature of these species is in agreement with the assumption that they are formed by the (chemical) oxidation of Cr⁺² ion by hexavalent chromium.

4. Chromous ion is formed during the electroreduction process.

5. The dimeric and species B ions are not directly responsible for the metallic chromium deposition.

6. The chromic hexaquo ion is not formed as a result of direct reduction on the cathode surface. Its formation is a result of secondary chemical reactions.

Acknowledgment

The author wishes to thank Dr. M. Ardon for much helpful discussion.

Manuscript received July 8, 1963; revised manuscript received Oct. 22, 1963. This work is taken from the PhD thesis to be submitted by J. Levitan to the Senate of The Hebrew University, Jerusalem, Israel.

REFERENCES

1. E. Liebreich, *Z. Elektrochem.*, **30**, 186 (1924); **33**, 69 (1927); **39**, 628 (1933); **40**, 73 (1934).
2. H. Caveth and B. E. Curry, *J. Phys. Chem.*, **9**, 353 (1905).
3. E. Muller, *Z. Elektrochem.*, **30**, 208 (1924); **32**, 399 (1926); **33**, 72 (1927); **35**, 84 (1929); **46**, 82 (1940); **49**, 280 (1943); **50**, 172 (1944); *Arch. Metallkund.*, **2**, 11 (1933).
4. Ch. Kasper, *J. Research Natl. Bur. Standards*, **9**, 353 (1932); **11**, 515 (1933).
5. F. Ogburn and A. Brenner, *This Journal*, **96**, 347 (1949).
6. W. M. Latimer, "Oxidation States of the Elements and Their Potentials in Aqueous Solutions," 2nd ed., pp. 245-250, Prentice Hall, New York (1952).
- 6a. M. J. Udy, "Chromium," Vol. 1, p. 134. Reinhold Publishing Corp., New York (1956).
7. M. Ardon and G. Stein, *J. Chem. Soc.*, **1956**, 2095.
8. C. A. Knorr, G. Munster, and H. Feigl, *Z. Elektrochem.*, **63**, 59 (1959).
9. J. A. Laswick and R. A. Plane, *J. Am. Chem. Soc.*, **81**, 3564 (1959).
10. M. Ardon and R. A. Plane, *ibid.*, **81**, 3197 (1959).
11. M. Ardon and A. Linenberg, *J. Phys. Chem.*, **65**, 1443 (1961).
12. R. Plane, Private communications.

X-Ray Determination of Residual Stresses in Electrodeposited Coatings

Glenn W. Bush

Research and Development Laboratory, National Steel Corporation, Weirton, West Virginia

and Harold J. Read

The Pennsylvania State University, University Park, Pennsylvania

ABSTRACT

Experimental and mathematical procedures were developed and tested for x-ray determination of stress in deposits from data secured with an x-ray diffractometer. The effects of deposit thickness, variations in elastic modulus, and stresses owing to differential thermal expansion between deposit and basis metal have been evaluated. Work on nickel deposits showed stress can be evaluated to $\pm 6,000$ psi and that stress was uniformly distributed over the area irradiated by the x-ray beam.

Residual stresses in electrodeposits were reported as early as 1877 (1) and have received considerable attention since then. Interest in the subject has resulted from the effects of the stresses on the properties and serviceability of both protective coatings and electroforms.

The basis for the present methods of measuring residual stress is the deformation of a cathode owing to the bending effects of the stress. Deformation data can be used for calculation of the residual stress when the size and geometry of the cathode meet certain very restrictive requirements not found in most items of manufacture. Consequently, most measurements are restricted to instruments or cathodes made solely for the purpose of stress determinations. Such tests serve well as routine checks for certain protective and decorative coatings and for the evaluation of plating variables, but, unfortunately, do not determine the stresses in the actual electroformed or electroplated articles.

In addition to physical restrictions, the deformation technique is not free of other problems. The mathematical derivation of the basic equations and the practical application of these methods involve three assumptions: (i) there is no stress gradient normal to the surface of the deposit; (ii) stress is

uniformly distributed; and (iii) average values or "handbook" values may be used for the elastic modulus of the deposit. The most important result of these assumptions is that the measured stress is an average value for the entire deposit on the instrument. These assumptions may not cause serious error in the measured values, but they should be evaluated for a better understanding of the tests and of related phenomena.

Because x-ray stress determinations have been useful in some other fields, an investigation of its applicability to deposits was undertaken. The principal advantage to be gained is the development of a nondestructive test that can be used on a multitude of plated articles with little, if any, size or shape limitations. Furthermore, the x-ray technique would permit evaluation of the underlying assumptions in the deformation method of measuring stress. Also, knowledge of the correct stress distribution should be particularly valuable for studying related problems, such as stress corrosion and the mechanical properties of electrodeposited metals.

For illustrative purposes, the x-ray technique described herein was developed for electrodeposited coatings of nickel on steel because of the commercial importance of such coatings. However, the the-

ory developed in this investigation is applicable to all metallic coatings regardless of the method of deposition.

Theory

In x-ray stress determinations, as in any method of stress determination, strain is measured experimentally and converted to stress by the use of theoretical equations. An excellent derivation of the basic equations relating macrostress and the lattice strains measured by the x-ray techniques is given by Taylor (2).

These equations may be simplified (3, 4) and written as

$$\sigma_1 + \sigma_2 = K_1 (2\theta_{\perp} - 2\theta_0)$$

$$K_1 = \frac{E \cot \theta_0}{2\nu} \quad [1]$$

$$\sigma_{\phi} = K_2 (2\theta_{\perp} - 2\theta_{\psi})$$

$$K_2 = \frac{E \cot \theta_0}{2(1 + \nu) \sin^2 \psi} \quad [2]$$

where σ_1 and σ_2 are the principal stresses, σ_{ϕ} is a component of stress in the specimen surface, ψ is the angle of rotation of the specimen, E is Young's modulus, ν is Poisson's ratio, K_1 and K_2 are constants, θ_0 is the Bragg angle for the unstressed specimens, and $2\theta_{\perp}$ and $2\theta_{\psi}$ are the normal and inclined diffraction angles, respectively, for the stressed specimens.

If a state of plane stress is assumed, inclined measurements made at three azimuthal angles and one normal measurement permit calculation of the components of stress in three directions and, subsequently, calculation of the principal stresses in the irradiated volume of metal. Therefore, by making these measurements at several locations, it is possible to determine the distribution of stress over the surface of a specimen.

It is incorrect to use average mechanical property values in the above equations for the determination of stress directly from diffraction measurements because these properties may vary with plating conditions (5, 6). Also, nickel is one of the metals which can be electrodeposited with some degree of common crystallographic orientation and values of 16.1, 28.2, and 36.4×10^6 psi have been reported for the elastic modulus of single crystals of nickel (7). Thus, the elastic constants of deposits should be determined for the particular lattice planes being investigated for each set of plating conditions. Because of the extreme difficulty encountered in determining the appropriate elastic constants, recourse can be made to the use of calibration curves as indicated by Eq. [1] and [2]. In this case, the "ordinary" elastic modulus may be determined and used to apply known stresses to specimens for the purpose of calibration.

Choice of radiation.—In order to obtain precise spacing measurements from one set of planes as required for stress determinations, the radiation used must have a longer wavelength than the absorption edge of the specimen and must yield a high-

angle diffraction peak of sufficient intensity. Although either iron, chromium, or cobalt radiation would be satisfactory, iron radiation was chosen because it is of intermediate wavelength and gives strong, high-angle diffraction peaks at approximately $144^{\circ} 2\theta$ (222) and $132^{\circ} 2\theta$ (311). For a reason to be explained later, all of the measurements reported in this paper were of the (311) planes and were made with iron radiation at 40 kv and 8 ma with a manganese filter.

Selection of the radiation also determines the maximum angle of rotation for the inclined measurement, i.e., $\psi = \theta^{\circ}$, but the diffracted intensity decreases rapidly as ψ is increased. The maximum angle at which a strong peak can be easily obtained must be determined experimentally. In this case, the angle was found to be about 45° , and all inclined measurements were made at this angle.

Effect of specimen thickness.—A choice of radiation as described above tacitly assumes that the specimens are "infinitely thick" and, hence, that reflections from the basis metal would not interfere with reflections from the deposit. Because most protective and decorative nickel deposits are not infinitely thick, stress determinations on thin deposits may be complicated by such interference.

Infinite thickness represents the depth of penetration of the x-ray beam and depends on the sensitivity of the intensity measurements. The total diffracted intensity, I , from a specimen is given by (3)

$$I = \int_0^{\infty} \frac{I_0 ab}{\sin \theta} \exp[-2\mu x/\sin \theta] dx \quad [3]$$

where I_0 is the incident intensity, a and b are constants, μ is the linear absorption coefficient, and x is the depth of the infinitesimal layer. Practically, infinite thickness may be taken as the layer of metal such that the intensity of the diffracted beam from the back surface of the layer is 1/1000 of the intensity of the diffracted beam from the front surface (3). Thus, infinite thickness, t_{∞} , can be defined as

$$t_{\infty} = \frac{3.45 \sin \theta}{\mu} \quad [4]$$

For the normal measurements on nickel specimens, infinite thickness is 0.96, 1.49, and 1.85 mils, respectively, for chromium, iron, and cobalt radiations. A similar approach can be used to show that infinite thickness for the inclined measurements at 45° is smaller; in particular, it is 1.00 mil for iron radiation.

The total diffracted intensity from a thin specimen can now be expressed as a fraction, G_x or G_x' , of the total possible diffracted intensity by use of Eq. [3].

For normal measurements

$$G_x = 1 - \exp[-2\mu x/\sin \theta] \quad [5]$$

For inclined measurements

$$G_x' = 1 - \exp \left[\frac{-\mu x \{ \sin(\theta + \psi) + \sin(\theta - \psi) \}}{\sin(\theta + \psi) \sin(\theta - \psi)} \right] \quad [6]$$

Substitution of appropriate values into these expressions yields the results shown in Table I.

Table I. Fraction of total intensity diffracted by surface layers of nickel for iron K_{α} radiation

Measurement	Thickness of surface layers, in mils				
	0.15	0.25	0.50	1.00	1.50
$\psi = 0^{\circ}$	0.50	0.69	0.90	0.99	0.999
$\psi = 45^{\circ}$	0.71	0.87	0.98	0.999	0.999

Because appreciable diffraction intensity can be produced by the basis metal for thin deposits, spacing measurements must be restricted to such planes and radiation where no interference occurs. For iron radiation, it was found that the (220) peak from the basis metal, iron, could interfere with the (222) peak from the overlying nickel deposit. Therefore, spacing measurements were restricted to the (311) planes of nickel.

Equation [4] also defines the principle of a method for detecting the existence of extreme stress gradients normal to the specimen surface. Use of different radiations would yield the average stresses in surface layers of different thicknesses. Gross differences in the resulting values would indicate a stress gradient.

Equipment

A General Electric XRD-3 diffractometer equipped with a Berkley scaler was used for all measurements. Use of a diffractometer for stress measurements is advantageous because the diffracting planes for the normal measurement are parallel to the specimen surface as required by Eq. [1], and greater accuracy is obtained than in the back-reflection technique where the diffracting planes are slightly inclined to the specimen surface. Furthermore, previous experience (8-11) has indicated that interpretation of the back-reflection results is difficult because of the effect of the electrodeposited grain size on the x-ray pattern.

A precision specimen mount shown in Fig. 1 was designed to obtain the diffraction angles required for Eq. [1] and [2]. The mount was designed to fit the XRD-3 diffractometer, but can be adapted for use on other instruments. Each specimen can be

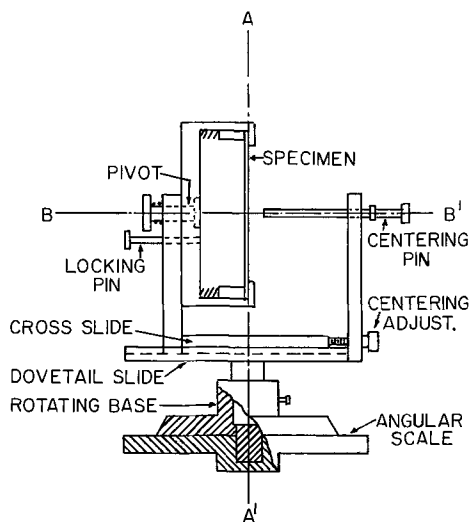


Fig. 1. Schematic sketch of specimen mount

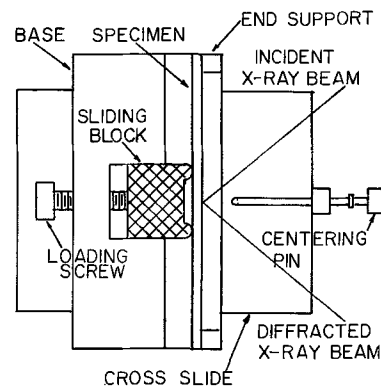


Fig. 2. Schematic sketch of bending fixture

centered easily in the axis of the goniometer with the aid of the centering pin. The mount also permits rotation of the specimen about the goniometer for the inclined measurements and about a horizontal axis for the measurements at azimuthal angles of 45° . Electroplated sheet specimens up to approximately 3 in. square can be accommodated in the mount. This size is the maximum which will permit both rotations of the specimen without major alteration of the diffractometer.

In order to determine calibration curves, a special bending fixture was designed to stress a specimen while simultaneously making spacing measurements. The fixture, shown in Fig. 2, attaches to the cross slide of the specimen mount in order to use the same aligning and centering facilities. Specimens in the form of rectangular beams, about 1 in. wide, 6 in. long, and 70 mils thick, are deformed by four-point loading in the fixture so that the component of applied stress in the irradiated volume of metal is constant.

Elastic modulus measurements were made on a Dillon testing machine with the aid of a low-carbon steel dynamometer ring and Tuckerman optical strain gauges. Stress-strain curves were determined on a Baldwin-Lima-Hamilton universal testing machine. Strains were measured with SR-4 gauges.

Specimens

All of the deposits used in this investigation were prepared from a Watts-type nickel bath having the composition: $\text{NiSO}_4 \cdot 6\text{H}_2\text{O}$, 300 g/l; $\text{NiCl}_2 \cdot 6\text{H}_2\text{O}$, 60 g/l; H_3BO_3 , 38 g/l. The solution was chemically and electrolytically purified (12, 13). Each bath was agitated during plating, and periodic additions were made to the bath to control pH and surface tension.

For the residual stress determinations by this technique, a one-mil deposit of nickel was plated on each of ten pieces of cold-rolled and annealed steel sheet having an ASTM grain size of nine. The steel cathodes were approximately 3 in. square and 40 mils thick and were cut so that the rolling direction could be identified. The specimens were prepared in two different plating runs, in each of which five specimens were plated consecutively from the bath at the following nominal conditions: current density, 40 asf; pH, 2.50; temperature, 59°C ; surface tension, 30-40 dynes/cm. Each cathode was degreased and cleaned immediately before plating. The thickness

Table II. Average thickness of test specimens

Sample	Thickness, mils
1	1.11
2	1.12
3	1.11
4	1.13
5	1.11
6	1.10
7	1.10
8	1.08
9	1.17
10	1.14

of each deposit was calculated from the gain in weight and is shown in Table II.

In order to avoid the problems encountered in the handling and mechanical testing of thin electrodeposits for purposes of calibration, nickel sheets were electroformed to provide material representative of electrodeposited metal but of sufficient thickness for easy testing. Four nickel sheets approximately 4 x 6 in. and 70 mils thick were plated on passivated stainless steel cathodes. These deposits were prepared under various plating conditions which were chosen to represent extreme cases. Strips 1 in. wide were taken from each sheet to use as rectangular beams in the bending fixture, and several strips from each sheet, about 3/4 in. wide, were machined into tensile specimens for mechanical testing.

Discussion of Results

Mechanical property values.—The determination of Young's modulus for each electroformed nickel sheet was the first step to be taken in developing the over-all procedure. At the start of each modulus test, a small initial load was applied to the specimen so that the shackles could be adjusted until equal strain readings were obtained from gauges on each face of the specimen. Simultaneous strain readings on each gauge were then taken as the load was increased. Young's modulus was taken as the slope of the line of best fit for the data points which lay on a straight line. The elastic limit for the specimen was not determined because the strain measured by the x-ray technique is only the elastic strain and therefore could not exceed it. Experimental results and various plating conditions are shown in Table III. These results substantiate previous results (5, 6) showing that the elastic modulus of electrodeposited metals depends on the plating conditions.

The definition of elastic modulus used above creates an arbitrarily defined proportional limit which may lie below the actual elastic limit of the

metal. Thus, calibrations based on the elastic modulus may be in error. The error thus introduced is represented by the difference in stress given in the extrapolated modulus line and the experimental stress-strain curve for a given strain. It was determined experimentally that a stress of 40,000 psi is about 1200 psi high and a stress of 50,000 psi is about 3400 psi high. The magnitude of this difference is smaller than the experimental error for low stresses and need only be applied as a correction factor to stresses about 50,000 psi or greater.

Calculation of peak positions.—Examination of preliminary specimens indicated that diffraction peaks obtained in stress determinations on electrodeposits are extremely broad, and it would be necessary to develop a special technique to determine their positions before proceeding with the calibration. The broadening results from the extremely fine grain size of the deposit and from any plastic strain that may have occurred during deposition. Also, for measurements at $\psi > 0^\circ$, an additional broadening of the peak and a shift in position resulted from the change in focusing conditions. With appropriate changes in the x-ray system, it was possible to obtain very symmetrical diffraction peaks. Hence, the position of each diffraction peak could be taken as its center of symmetry, which was represented by the axis of the parabola that could be fitted to the data in the vicinity of the diffraction maximum. A 3° collimator was used, and the receiving slit and Soller baffle were removed for all measurements. The angular shift in position resulting from these changes was determined experimentally and applied as a correction factor.

Consideration was given to two methods of fitting parabolas to the data; a simplified three-point method proposed by Koistinen and Marburger (14) and a least-squares method. Calculations and preliminary tests were conducted for comparative purposes. These results indicated that the least-squares method was the more reliable for an investigation of this nature. To simplify subsequent calculations, intensity measurements were made at five angular positions spaced at intervals of 0.2° and 0.3° for the normal and inclined measurements, respectively. At each position, the time, t_i , to receive three counts of 20,000 or more was measured and averaged. The peak position, 2θ , was calculated from these data according to the following equation

$$2\theta = \bar{2\theta}_i + \frac{X\sum(2\theta_i - \bar{2\theta}_i)t_i}{Y\sum t_i - Z\sum(2\theta_i - \bar{2\theta}_i)^2 t_i} \quad [7]$$

where $\bar{2\theta}_i$ is the mean angular position of the measurements, and X, Y, and Z are constants. A derivation of Eq. [7] is given in Appendix A. Figure 3 shows a typical fit of a curve to the data. It should be noted that the data are the reciprocals of intensity, and that the curve is fitted to these data without conversion.

Theoretical correction of peak asymmetry.—The breadth of the diffraction peaks encountered in stress determinations also gives rise to effects which may cause a shift in peak position. The principal factors which affect the diffracted intensity, thus

Table III. Young's moduli of electroformed sheets

Sheet	pH	Plating conditions		E x 10 ⁻⁶ , psi*
		Current density, asf	Temperature, °C	
A	2.15	30	52	29.2
B	2.15	40	64	28.3
C	5.00	20	39	27.5
D	3.40	55	74	26.5

* Average value for two or more specimens.

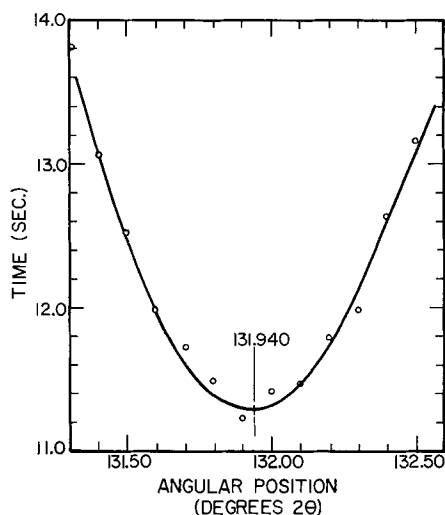


Fig. 3. Curve of best fit for an inclined measurement. (Intensity measurements were made at 131.3, 131.6, 131.9, 132.2, and 132.5°.)

causing an apparent shift in position of the peak, and which are applicable to this problem are the Lorentz-polarization factor and an absorption factor. Koistinen and Marburger (14) showed that a change in diffracted intensity, as a result of these factors, is sufficient to distort the shape of the peak, thereby causing an apparent shift in the peak position to lower values of 2θ . These investigators introduced the following factors that could be applied to the data to compensate for the changes in diffracted intensity

$$CF_{\psi=0^\circ} = \frac{LP_\theta}{LP_{\theta_1}} \quad [8]$$

$$CF_{\psi=\psi^\circ} = \frac{LP_\theta (1 - \tan \psi \cot \theta)}{LP_{\theta_1} (1 - \tan \psi \cot \theta_1)} \quad [9]$$

where $CF_{\psi=0^\circ}$ and $CF_{\psi=\psi^\circ}$ are the correction factors for the normal and inclined measurements, respectively, LP_{θ_1} is the Lorentz factor for the lowest angle, θ_1 , and LP_θ is the Lorentz factor for the angular position, θ , of the intensity measurement. Values of the Lorentz-polarization factors are constants and may be obtained from standard references (3).¹ These values are applicable to both the normal and inclined measurements for diffractometers. The absorption factor applies only to the inclined measurements and for specimens that are infinitely thick. For thinner specimens, the factor depends on the thickness and diffraction angle as shown by Eq. [6]. Hence, an additional variation in diffracted intensity could occur over the width of a broad diffraction peak. Calculations show that this effect will become significant only for deposits less than 0.25 mil in thickness or in cases where extremely broad peaks are encountered.

Application of the above correction factors indicated that the resulting shifts in peak positions were

¹ A reviewer has informed us that the function usually tabulated for the LP factor correction, $\frac{1 + \cos^2 2\theta}{\sin^2 \theta \cos \theta}$, is not the correct one to use in this application. He states that the correct function is $\frac{1 + \cos^2 \theta}{\sin^2 \theta}$ and that ref. (4) has been corrected accordingly. This change would result in a slight change in the magnitude of the measured stresses, but would not affect the results of this study significantly.

Table IV. Change in angular position resulting from intensity corrections

Specimen	Angular shift, degrees 2θ	
	Normal measurement	Inclined measurement
A	0.013	0.046
B	0.013	0.046
C	0.010	0.044
D	0.012	0.041
E	0.014	0.056
F	0.012	0.035

approximately constant for given sets of angular positions. Therefore, the magnitudes of these correction factors were determined for each different set of angular positions and were applied as constant factors to the experimental data. Table IV lists the magnitude of the angular shifts resulting from this correction.

Calibration of technique.—After determination of the elastic modulus of the nickel sheets, calibration curves were obtained by bending a beam cut from an electroformed sheet and simultaneously making spacing measurements. This type of experimental determination of values for the stress constants, K_1 and K_2 , in Eq. [1] and [2] depends only on the change in the applied stress and does not require a stress-free specimen. The width of the beam was such that an SR-4 strain gauge could be attached to the face of the beam adjacent to the irradiated area. Surface strains were converted to stress by use of the appropriate elastic modulus. The beam was deformed in several increments as the x-ray measurements were made. A line of best fit was drawn for the resulting data in order to obtain a calibration curve.

Data for the normal measurements on a specimen from sheet B are shown in Fig. 4 in accordance with Eq. [1]. The line of best fit was determined by the method of least squares and is given by the equation

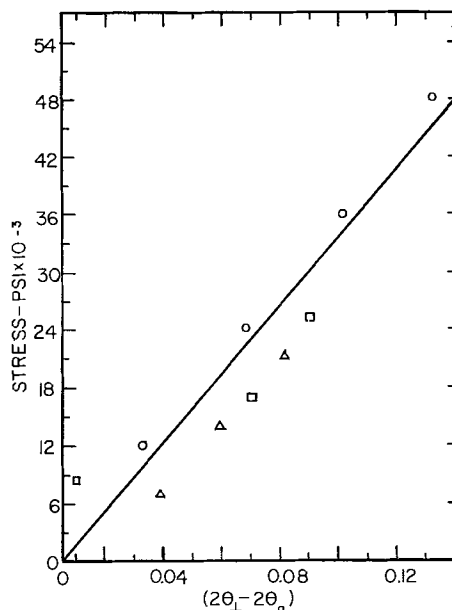


Fig. 4. Calibration curve for the sum of the principal stresses: □, 1st; △, 2nd; ○, 3rd.

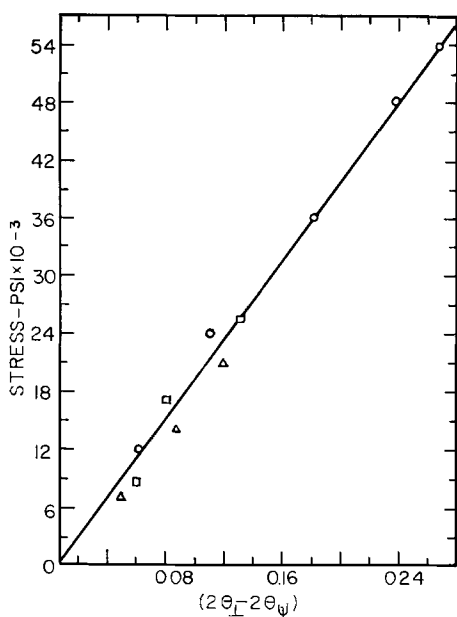


Fig. 5. Calibration curve for a component of stress: □, 1st; △, 2nd; ○, 3rd.

$$\sigma_1 + \sigma_2 = 354,700 (2\theta_{\perp} - 2\theta_{\psi}) - 2300 \quad [10]$$

The average error for these data is 3800 psi and the maximum error is 7400 psi. These values correspond to an error of $\pm 0.02^\circ$ in determining $(2\theta_{\perp} - 2\theta_{\psi})$.

The calibration curve shown in Fig. 4 is relative and therefore of restricted use because knowledge of the unstressed state of deposit is required. However, by use of Eq. [2] it is possible to circumvent this problem. That is, the stress in the deposit can be determined without knowledge of the unstressed state of the deposit. The data for the "two exposure" method are shown in Fig. 5 and are described by

$$\sigma_{\phi} = 206,900 (2\theta_{\perp} - 2\theta_{\psi}) - 1600 \quad [11]$$

The average error is 1300 psi, and the maximum error is 2600 psi. These values correspond to a precision of approximately $\pm 0.02^\circ$ in the quantity $(2\theta_{\perp} - 2\theta_{\psi})$.

Determination of error in calibration curves.—Spatial requirements limited the thickness of the beam used for calibration. As a result, a stress gradient normal to the specimen surface was produced. Therefore, the measured strains which were correlated with the surface stress are average strains over the depth of penetration. To determine the extent of this error, the resulting weighted average stress was calculated for comparison. Combining Eq. [5] with the well-known flexural formula results in the following expression for the weighted average stress, σ_w :

$$\sigma_w = \frac{2M\mu}{l \sin \theta} \int_0^x (c-x) \exp[-2\mu x/\sin \theta] dx \quad [12]$$

where M is the bending moment, l is the moment of inertia, c is the distance from the neutral axis to the surface of the beam, and x is the distance of the layer from the surface of the beam. Substitution of values into Eq. [9] for a 1-mil layer in a beam 70 mils thick gives a weighted stress of 49,300 psi for a

Table V. Components of stress in the plated specimens

Specimen	Stress, psi			σ_{average}
	$\sigma_{\phi 1}$	$\sigma_{\phi 2}$	$\sigma_{\phi 3}$	
1	52,000	62,000	54,000	56,000
2	42,000	48,000	50,000	47,000
3	48,000	50,000	50,000	49,000
4	54,000	48,000	50,000	51,000
5	60,000	58,000	54,000	57,000
6	36,000	34,000	34,000	35,000
7	42,000	40,000	38,000	40,000
8	42,000	40,000	40,000	41,000
9	48,000	48,000	46,000	47,000
10	32,000	36,000	34,000	34,000

surface stress of 50,000 psi. Thus, the calibration curves are only slightly more than 1% low.

Stress determination.—After development of the technique and determination of the calibration curves, the test specimens were evaluated. One normal and three azimuthal measurements were made at the center of each specimen to permit calculation of the components of stress.

The experimental data for the "as plated" condition of the test specimens are given in Table V. They indicate that the components of stress, $\sigma_{\phi 1}$, $\sigma_{\phi 2}$, $\sigma_{\phi 3}$, in three azimuthal directions, at intervals of 45° , in the surface of each specimen are probably within the limits of experimental error. It is concluded from these results that a uniform distribution of macro-stress exists in the irradiated volumes of the electrodeposits. Hence, future reference will be made to the averages of these values for each specimen.

There is poor agreement among the ten specimens plated under ostensibly the same conditions. The range of stress values is from 32,000 to 62,000 psi and is much larger than the error estimated from the calibration data. Specific stress values of 25,000, 25,600, and 13,000 psi have been reported for one-mil deposits of nickel from Watts' baths (15-17). It has also been reported (18) that values of 20,000 to 95,000 psi can be obtained in deposits from Watts' baths, depending on the purity of the solution. It is likely, then, that the high values for the present specimens result from contamination of the bath, either by soluble impurities from the anode or by the use of Duponal ME as a wetting agent.

Immediate comparison of the ten values as indicated above is not wholly warranted because of the possible change in composition and structure of the specimens that may occur as the result of being plated consecutively from a bath that is not being purified continuously. The results may be divided into two groups which reflect the order of plating of the specimens. The average values for the first five specimens, or group I, fall within the range $52,000 \pm 5,000$ psi whereas those of the second, group II, fall within the range $39,000 \pm 8,000$ psi. Within each group, the precision is about equal to that expected from the calibration data.

In order to resolve the accuracy and precision of the measurements, the ten specimens were stress relieved at several temperatures and re-examined. Because each specimen constitutes a bi-metal thermostat, it is possible to calculate the residual stress in the specimens after each heat treatment. Assum-

Table VI. Thermal stresses after stress-relief treatments

Specimen	Stress, psi		
	4 hr at 400°F	6 hr at 600°F	84 hr at 500°F
1	15,000	19,000	4,000
2	14,000	17,000	14,000
3	14,000	13,000	7,000
4	18,000	7,000	6,000
5	9,000	13,000	8,000
Group I average	15,700	13,000	7,700
6	6,000	11,000	6,000
7	10,000	7,000	10,000
8	5,000	9,000	7,000
9	10,000	3,000	3,000
10	7,000	3,000	12,000
Group II average	9,500	5,300	7,700
Theoretical	7,700	11,800	9,800

ing that the residual stress in the specimen is completely removed at the given temperature, the resulting thermal stress, σ , is given by

$$\sigma = K_3 \Delta T \quad [13]$$

where K_3 is a constant and ΔT is the change in temperature (see Appendix B). After an initial treatment at 400°F for 4 hr, the specimens were stress-relieved 6 hr at 600°F. Finally, to insure complete removal of stress from the basis metal as well as from the deposits, the specimens were stress-relieved at 500°F for 84 hr. The experimental and theoretical values resulting from these heat treatments are given in Table VI. Although there is much less variation from specimen to specimen after the 400° and 600° treatments, the values may still be divided into groups. The final heat treatment, however, eliminated the group-to-group variation and resulted in stresses that agree remarkably well with the theoretical values. On the basis of these results, the precision in the measurements appears to be approximately 6,000 psi. Hence, it must be concluded that the two sets of deposits originally had different residual stresses.

Summary

The x-ray technique of measuring lattice strains can be adapted for use on electrodeposited specimens of nickel without interference from the basis metal. By suitable modification of the x-ray system, it was possible to obtain diffraction peaks whose positions could be determined by a special parabola fitting technique.

The experimental x-ray data were corrected for the Lorentz-polarization and the absorption effects. A basis was given for other correction factors to compensate for the change in diffracted intensity which occurs in the case of extremely thin deposits.

Experimentally determined calibration curves were used to convert the appropriate differences in angular positions of the diffraction peaks to stress. The use of calibration curves was necessitated by the fact that mechanical tests on specimens of electroformed nickel indicated that the elastic modulus varied with plating conditions.

A precision of about 6000 psi was attained in determining the residual stresses in electrodeposited

nickel specimens. Within these limits of error, it was found that the stress in several electrodeposited specimens was uniformly distributed over the irradiated area of the specimens. With the plating procedures used in this investigation it was not possible to reproduce the same level of residual stress in two groups of electrodeposited specimens. After suitable stress relief of the specimens, it was found that the experimentally determined stress agreed with the stress theoretically calculated for the specimen.

Acknowledgment

The authors are indebted to the General Electric Company for sponsoring the fellowship under which this research was conducted.

Manuscript received June 25, 1963; revised manuscript received Sept. 25, 1963.

Any discussion of this paper will appear in a Discussion Section to be published in the December 1964 JOURNAL.

REFERENCES

1. E. J. Mills, *Proc. Roy. Soc. (London)*, **A26**, 504, (1877).
2. A. Taylor, "X-ray Metallography," J. Wiley & Sons, Inc., New York (1961).
3. B. D. Cullity, "Elements of X-ray Diffraction," Addison-Wesley, Reading, Mass. (1956).
4. Measurement of Stress by X-ray, SAE Handbook Supplement 182, 1960.
5. A. Brenner and C. W. Jennings, *Am. Electroplaters' Soc.*, **35**, 31 (1948).
6. H. J. Read and A. H. Graham, *This Journal*, **108**, 73 (1961).
7. M. Yamamoto, *Science Repts. Research Insts., Tohoku University*, **A3**, 308 (1952).
8. W. Hume-Rothery and M. R. J. Wyllie, *Proc. Roy. Soc.*, **A181**, 331 (1943).
9. W. A. Wood, *Phil. Mag.*, **15**, 553 (1933); **20**, 964 (1935); and **24**, 772 (1937).
10. E. M. Mahla, *This Journal*, **77**, 145 (1940).
11. M. R. J. Wyllie, *J. Chem. Phys.*, **16**, 52 (1948).
12. A. K. Graham, "Electroplating Engineering Handbook," Reinhold Publishing Co., New York (1955).
13. B. C. Case, *Proc. Am. Electroplaters' Soc.*, **34**, 228 (1947).
14. D. P. Koistinen and R. E. Marburger, *Trans. Am. Soc. Metals*, **51**, 537 (1959).
15. J. B. Kushner, *Plating*, **41**, 1146 (1954).
16. K. G. Soderberg and A. K. Graham, *Proc. Am. Electroplaters' Soc.*, **34**, 74 (1947).
17. A. Brenner and S. Senderoff, *ibid.*, **35**, 53 (1948).
18. R. Pinner, *Electroplating and Metal Finishing*, **10**, 7 (1957).
19. S. P. Timoshenko, "The Collected Papers of Timoshenko," McGraw Hill Book Co., New York (1953).

APPENDIX A

Use of the least squares method of fitting curves to data is laborious but desirable because it gives the most probable curve for the experimental data. Fortunately, mathematical treatment of this method for the present case can be simplified considerably by making an odd number of intensity measurements at equally spaced angular intervals. Then, by grouping the angular positions of the measurements, $2\theta_i$, about their mean value, $2\bar{\theta}_i$, the equation for the parabola which describes the data can be written as

$$t_i = X(2\theta_i - 2\bar{\theta}_i)^2 + Y(2\theta_i - 2\bar{\theta}_i) + Z \quad [A1]$$

where t_i is the time to receive a given number of counts and X, Y, and Z are constants. Complete solution of the resulting normal equations is not required to determine the position of the parabola. Only the quo-

Table AI. Constants for calculating peak positions from data at angular positions

Constant	Interval between angular positions, degrees 2θ				
	0.1	0.2	0.3	0.4	0.5
X	0.035	0.140	0.315	0.560	0.875
Y	0.100	0.400	0.900	1.600	2.500
Z	5.000	5.000	5.000	5.000	5.000

tient of X and Y must be determined. The resulting expression for the difference in position $(2\theta - \bar{2}\theta)$, between the axis of the parabola and the mean angular interval is

$$(2\theta - \bar{2}\theta) = \frac{-\Sigma(2\theta_i - \bar{2}\theta_i)t_i}{\Sigma(2\theta_i - \bar{2}\theta_i)} \left[\frac{\Sigma(2\theta_i - \bar{2}\theta_i)^2 \Sigma(2\theta_i - \bar{2}\theta_i)^2 - n \Sigma(2\theta_i - \bar{2}\theta_i)^4}{\Sigma(2\theta_i - \bar{2}\theta_i)^2 \Sigma t_i - n \Sigma(2\theta_i - \bar{2}\theta_i)^2 t_i} \right] \quad [A2]$$

Further simplification is attained by making the intensity measurements over constant angular intervals.

$$(2\theta - \bar{2}\theta) = \frac{X \Sigma(2\theta_i - \bar{2}\theta_i)t_i}{Y \Sigma t_i - Z \Sigma(2\theta_i - \bar{2}\theta_i)^2 t_i} \quad [A3]$$

The values of the constants X, Y, and Z for several sets of angular intervals are given in Table AI. The necessary summations can be obtained in a few minutes on a statistical calculating machine.

APPENDIX B

Derivation of Equation for Thermal Stresses

The particular thermal stress problem encountered here is identical to the commonly treated problem of bimetal thermostats. That is, it is desired to calculate the change in stress induced in a bi-metal couple as the temperature of the couple is changed. If it is assumed that the basis metal and the electrodeposited layer are stress-free at the stress-relief temperature, the stress resulting from the difference in the thermal contractions of the metals as the specimen is cooled can be calculated.

On cooling a bimetallic specimen from temperature, T °C, to a lower temperature, T_0 °C, uniformly distributed thermal stresses will be developed in the specimen if the coefficients of thermal expansion, α_b , of the basis metal and, α_c , of the coating are different.

For the purposes of this derivation, assume that $\alpha_c > \alpha_b$. Then, a tensile force, P_c , will be developed in the coating and an equal compressive force, P_b , will be developed in the basis metal. Of necessity, the strain in the coating will be equal to the strain in the basis metal at the interface. These strains are the sums of the strains due to the thermal contractions, the axial

forces, and the bending moments, and may be equated as follows [using the notation of Timoshenko (19)]

$$\alpha_b(T_0 - T) - \frac{P_b}{E_b a_b w} - \frac{a_b}{2\rho} = \alpha_c(T_0 - T) + \frac{P_c}{E_c a_c w} + \frac{a_c}{2\rho} \quad [B1]$$

where E_b and E_c are the elastic moduli of the basis metal and the coating, a_b and a_c are the thicknesses of the basis metal and coating, w is the width of the specimen, and ρ is the radius of curvature of the composite. It can be shown that

$$M_b + M_c = \frac{E_b l_b}{\rho} + \frac{E_c l_c}{\rho} = \frac{1}{2} P(a_b + a_c) \quad [B2]$$

where l_b and l_c are the moments of inertia for the basis metal and coating and $P = P_b = P_c$. Solving Eq. [B1] and [B2] for $1/\rho$ results in

$$\frac{1}{\rho} = \frac{(\alpha_b - \alpha_c)(T_0 - T)}{\left(\frac{2}{a_b + a_c}\right)\left(\frac{1}{w}\right)(E_c l_c + E_b l_b) \left(\frac{1}{E_c a_c} + \frac{1}{E_b a_b}\right) + \left(\frac{a_b + a_c}{2}\right)} \quad [B3]$$

The value of $1/\rho$ as calculated from the above equation may be substituted into Eq. [B2] to determine the magnitude of P .

$$P = \frac{2}{(a_b + a_c)} \left(\frac{w}{\rho}\right) \left(\frac{E_b a_b^3}{12} + \frac{E_c a_c^3}{12}\right) \quad [B4]$$

The stress in the electrodeposited coating is the sum of the tensile stress and the bending stress.

$$\sigma_{\max}^{\min} = \frac{P}{a_c w} \pm \frac{a_c E_c}{2} \quad [B5]$$

The maximum stress is developed at the interface, and the minimum stress is developed at the surface of the deposit. Substitution of the appropriate values into Eq. [B3], [B4], and [B5] gives

$$\sigma = (K_3 \pm K_4) \Delta T \quad [B6]$$

where K_3 and K_4 are constants and $\Delta T = T_0 - T$. For the particular conditions of the present investigation, K_3 is 37.7 psi/°C and K_4 is 0.1 psi/°C if $E_c = 28 \times 10^6$ and $E_b = 30 \times 10^6$; K_3 is 43.4 psi/°C and K_4 is 0.1 psi/°C if $E_b = E_c = 30 \times 10^6$. For either case, the stress gradient is only 100 psi at 315°C (600°F) and may be neglected for this investigation.

The contribution of the bending moment to the stress in the deposit is included in Eq. [B6] and can be shown to be negligible for this particular case. The thermal stress equation developed by Soderberg and Graham (16) does not include this factor.

The Effect of Thiocompounds on the Structure of Copper Electrodeposits

S. C. Barnes¹

Department of Industrial Metallurgy, University of Birmingham, Birmingham, England

ABSTRACT

Divalent sulfur compounds added to copper sulfate baths reduced the cathodic polarization and modified the crystal habit of copper deposited on the (100) surface of copper single crystals. These phenomena are attributed to surface adsorption effects.

The growth habit of epitaxial copper deposits is known to depend to a large extent on the orientation of the substrate (1, 2) and on the particular condi-

tions of formation (3, 4). Considerable evidence is available to show that such deposits, formed on copper single crystals near the cube orientation from acid sulfate solutions, develop under certain conditions plate-like growth features (1, 5-7) (Fig. 1).

¹ Present address: Chemistry Department, Joseph Lucas Group Research Centre, Birmingham, England.



Fig. 1. Layer growth structure on a copper single crystal with a surface near (100). Typical deposition conditions: 20 ma/cm², 30 min, from a N CuSO₄ + N H₂SO₄ solution at 35°C. X435.

Furthermore, it has been shown that habit modifications occur when the deposition conditions are altered (3, 4, 8, 9). These observations have been taken by some investigators to indicate that deposit habit is related in some simple way to cathodic polarization, and experimental evidence that the supposition is correct has been obtained for solutions free from surface active material (4).

Preliminary experiments designed to explore the possibilities of there being a more general relationship between deposit habit and cathodic polarization have shown, however, that under certain conditions the expected relationship is not observed [for example, ref. (8) and (9)].

Addition agents in electroplating solutions (added commercially to give enhanced properties to the deposit, e.g., brightness, lower internal stress, etc.) usually increase cathodic polarization (10). There are, however, certain compounds which, when added to acid copper sulfate plating solutions, cause a reduction in the overpotential. Shreir and Smith (10) quote the following as being typical of this group: hydrogen sulfide, carbon disulfide, sodium thiosul-

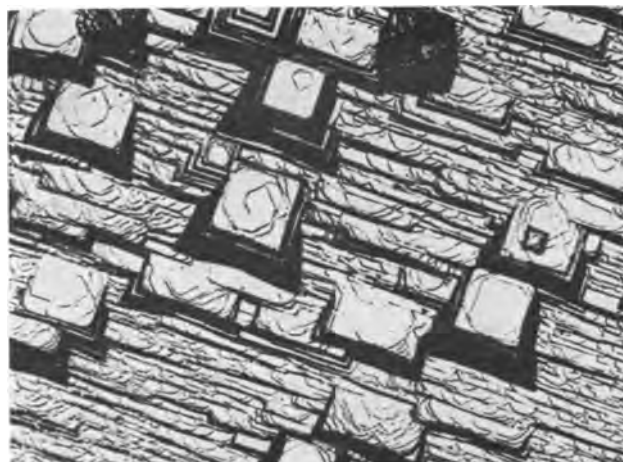


Fig. 2. Cubic growth structure of deposit on a copper single crystal with a surface near (100). Typical deposition conditions: 30 ma/cm², 20 min from a N CuSO₄ + N H₂SO₄ solution at 35°C. X435.

fate, and certain concentrations of thiourea. Sukava and Winkler (11) have reported that cysteine behaves similarly. It will be noted that all these are sulfur containing compounds.

Chemicals with this stimulatory action on the copper deposition process, which according to an earlier classification (10) cause deposition of material of a coarser grain size, have been observed in the present investigation not only to reduce the cathodic polarization to a great extent, but also to cause the deposit on single crystal substrates to grow in a new habit form.

Experimental Details

Full details of the procedure adopted in the growing, sectioning, and preparation of the single crystal electrodes are given in previous communications (1-4). The particular orientation selected for the work described here was a surface near the cube face, but inclined some $8^\circ \pm 2^\circ$ along a [110] zone from an exact (100).

This surface was selected since previous workers have shown that from purified solutions, the deposit habit is very well-defined (3) and is clearly related to the cathodic polarization (3, 4).

The methods used to examine the deposit, i.e., x-ray diffraction, optical and electron microscopy, and optical goniometry, and the techniques employed in the measurement of cathodic polarization are described elsewhere (1-4, 12).

The electrolyte, a previously carbon-purified N H₂SO₄ + N CuSO₄ solution (2, 3), unless otherwise stated, was maintained at 35°C, and any portion containing the addition agent was only used once unless the experiment was designed specifically to investigate the effect of continued use. Plating was carried out until 36 coulombs had passed per unit cathode area, i.e., assuming deposition to be 100% efficient, to a deposit thickness of 13.7 μ .

The following addition agents were studied: sodium thiosulfate, thioglycolic acid, thiosemicarbazide, rubeanic acid (thiooxamide), thioacetamide, and sodium sulfite.

Experimental Results

Standard electrolyte.—Experimental results are recorded in Fig. 1-4, which illustrate the structural characteristics of the deposits obtained, together with the polarization accompanying their deposition. It is at once apparent that, when the addition agents cause marked depolarization, the deposit transforms in habit.

Figure 3 is a typical example of the type described as "pyramidal." X-ray examination showed that deposits of this type were complete single crystal extensions of the base, and optical goniometry that the pyramids had flat, highly reflecting (111) faces.

Sodium sulfite additions were found to have no effect at concentrations of 10^{-6} , 10^{-4} , and 10^{-3} M/l, at 20 ma/cm². However, 10^{-2} M/l caused a slight reduction in the polarization, but failed to alter the deposit structure.

Nonstandard electrolytes.—Since the above experiments indicated that under certain conditions thiocompounds cause depolarization and changes

in crystal habit, the effect of one of them, thioacetamide, in two other N CuSO_4 baths was studied, one $5N$ in H_2SO_4 , the other neutral. Results are given in Table I.

Discussion

Several mechanisms have been suggested to explain the varying actions of addition agents in elec-

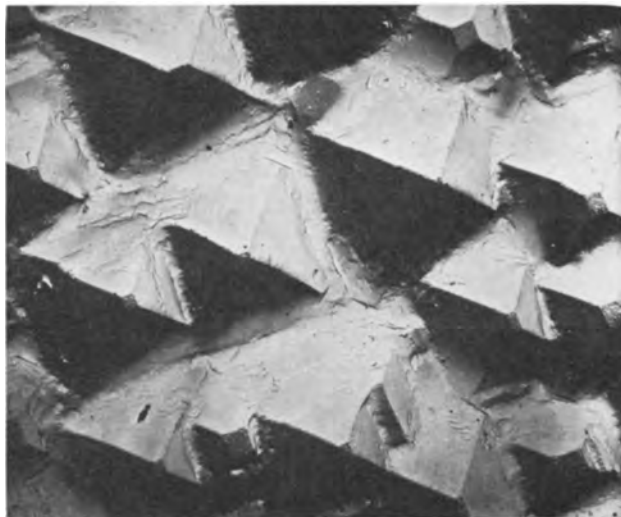


Fig. 3. Pyramidal growth structure of deposit formed on copper single crystal surface near (100) in the presence of thiocompounds. Typical deposition conditions: 50 ma/cm^2 , 12 min from a N $\text{CuSO}_4 + N$ H_2SO_4 solution containing 10^{-5} M/l $\text{Na}_2\text{S}_2\text{O}_3$ at 35°C . X5200.

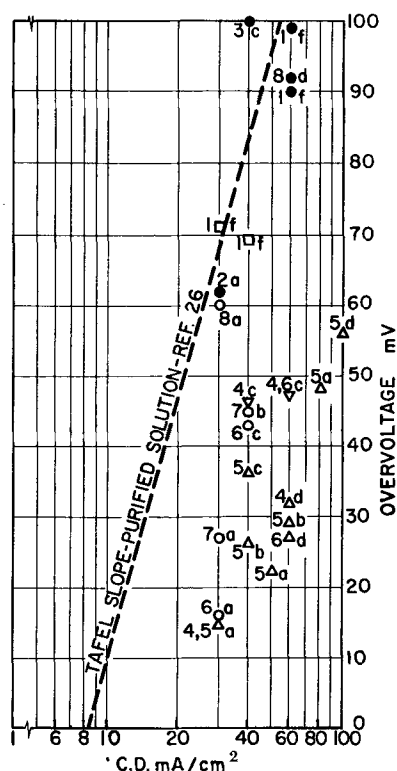


Fig. 4. Relationship between deposit structure, polarization and concentration of addition agent for N $\text{CuSO}_4 + N$ H_2SO_4 bath at 35°C . \circ , Layer growth, Fig. 1; \square , cubic growth, Fig. 2; Δ , pyramidal growth, Fig. 3; \bullet , polycrystalline; ∇ , matte, epitaxial. 1, Purified solution; 2, 10^{-2} M/l additions; 3, 10^{-3} M/l additions; 4, 10^{-4} M/l additions; 5, 10^{-5} M/l additions; 2×10^{-5} M/l in case of thioglycolic acid; 6, 10^{-6} M/l additions; 7, 10^{-7} M/l additions; 8, 10^{-8} M/l additions. a, $\text{Na}_2\text{S}_2\text{O}_3$; b, thioglycolic acid; c, thiosemicarbazide; d, rubenic acid; e, thioacetamide; f, no additions.

Table I. Effect of thioacetamide additions on the deposition of copper from electrolytes of varying H^+ concentration

Conc.	Added H_2SO_4	C. D., ma/cm^2	Polarization, mv	Structure
Nil	Nil	40	40	Polycrystalline
10^{-4}	Nil	40	150	Polycrystalline
Nil	$5N$	60	107	Polycrystalline
10^{-4}	$5N$	60	44	Pyramidal (Fig. 3)
10^{-4}	$5N$	100	36*	Polycrystalline
10^{-4}	$5N$	100	43	Pyramidal (Fig. 3)

* In this experiment the polarization was 700 mv for the first 20 sec of deposition, and only fell to 36 mv when the solution was gently agitated. During the early stages of deposition, visible gas evolution also occurred.

trodeposition processes. Of these, the surface adsorption theory seems the most pertinent in the present context. It was used by Ke *et al.* (13) to explain the action of thiourea on the copper electrodeposition process. Their work and later work by Llopis *et al.* (14, 15) and Barnes and Storey (16) show this to be the most probable explanation in cases where it acts as an inhibitor. It is well known however that under certain circumstances thiocompounds cause stimulation of electrochemical processes (17, 18), the electrodeposition of copper being but one example (10, 16).

Previously published results (4, 19) indicate that the addition of sulfuric acid to a neutral copper sulfate solution causes an increase in cathodic polarization. It is thus possible that the added hydrated hydrogen ions in some way inhibit the reaction, but it is doubtful whether this inhibition could arise purely as a result of physical blocking in view of the small size and high mobility of the hydrogen ions. On the other hand, it is possible that hydrogen ions, or discharged hydrogen atoms, could be chemisorbed on the metal surface. [The bond strength Cu-H has been estimated to be of the order 60 kcal/mole (20).]

It is postulated, from the observation that the catalytic activity of thiocompounds is only apparent in acidified electrolytes, that they owe this activity through preventing hydrogen ion (or atom) adsorption.

It has been observed that most of the compounds found to lower cathodic polarization contain divalent sulfur, *e.g.*, thioacetamide, rubenic acid, etc., and it is known that in acid solutions compounds of this type invariably contain the $-\text{SH}$ grouping (21). The thiosulfate anion has also been reported to act as though it contained this radicle (22).

It is possible, therefore, that divalent sulfur compounds prevent H^+ ion inhibition by themselves forming a barrier between the cathode surface and the electrolyte. This could be visualized as occurring via a displacement mechanism, whereby the $-\text{HS}^-$ anions become adsorbed on the metal surface in preference to other molecular or ionic species. On account of the high polarizability of the $-\text{HS}^-$ anion the electrochemical discharge reaction is stimulated, and additionally, since growth now occurs on a cathode surface covered with an adsorbed film of different characteristics, habit modifications

ensue. However, it would be premature to advance any definite mechanism without further knowledge of the structure of the metal/solution interface, of the effect of the adsorbed film on growth velocities and on the kinetics of the actual discharge process.

It would however be of interest to study the effect on polarization and crystal structure of related compounds such as thioketones, thiophen, etc., and also other sulfur containing compounds and anions, e.g., the thionates, sulfones, sulfoxides, sulfinic and sulfonic acids, thio and isothiocyanates, etc. The analogous stimulations observed during the corrosion of metals (17, 18), the cathodic evolution of hydrogen (23), and other electrochemical reactions (24, 25), are also worthy of further study.

It might be found that any compounds which stimulate one type of electrochemical reaction will stimulate others. For example, certain alkaloids lower the hydrogen overpotential (23). Is it possible they behave similarly when electrodeposition occurs from similar types of solution?

Acknowledgment

The author expresses his appreciation to the directors of Joseph Lucas Ltd. for their financial assistance, and to Professor E. C. Rollason for the provision of laboratory facilities.

Manuscript received April 3, 1962; revised manuscript received Oct. 2, 1963. This paper was delivered before the Detroit Meeting, Oct. 1-5, 1961.

Any discussion of this paper will appear in a Discussion Section to be published in the December 1964 JOURNAL.

REFERENCES

- H. J. Pick, G. G. Storey, and T. B. Vaughan, *Electrochim. Acta*, **2**, 165 (1960).
- G. G. Storey and S. C. Barnes, *Trans. Inst. Met. Finishing*, **37**, 11 (1960).
- S. C. Barnes, G. G. Storey, and H. J. Pick, *Electrochim. Acta*, **2**, 195 (1960).
- S. C. Barnes, *ibid.*, **5**, 79 (1961).
- V. R. Howes, *Proc. Phys. Soc.*, **74**, 616 (1959).
- G. Poli and L. P. Bicelli, *Metallurgia Ital.*, **51**, 548 (1959).
- I. Giron and F. Ogburn, *This Journal*, **108**, 842 (1961).
- R. Sroka and H. Fischer, *Z. Elektrochem.*, **60**, 109 (1956).
- H. Seiter and H. Fischer, *ibid.*, **63**, 249 (1959).
- L. L. Shreir and J. W. Smith, *Trans. Faraday Soc.*, **50**, 393 (1954).
- A. J. Sukava and C. A. Winkler, *Can. J. Chem.*, **33**, 961 (1955); **34**, 128 (1956).
- T. B. Vaughan and H. J. Pick, *Electrochim. Acta*, **2**, 179 (1960).
- B. Ke, J. J. Hoskstra, B. C. Sison, and D. Trivich, *This Journal*, **106**, 382 (1959).
- J. Llopis, J. M. Gamboa, and L. Arizmendi, "Proc. 9th Meeting C.I.T.C.E.," p. 448, Butterworths, London (1959).
- J. Llopis, J. M. Gamboa, and L. Arizmendi, *Electrochim. Acta*, **3**, 75 (1960).
- S. C. Barnes and G. G. Storey, *This Journal*, **106**, 1081 (1959).
- T. P. Hoar, "Modern Aspects of Electrochemistry," Butterworths, London (1959).
- W. Wesley, *Trans. Inst. Met. Finishing*, **33**, 452 (1956).
- L. L. Shreir and J. W. Smith, *This Journal*, **99**, 64 (1952).
- P. Ruetschi and P. Delahay, *J. Chem. Phys.*, **23**, 195 (1955).
- A. E. A. Werner, *Sci. Proc. Roy. Dublin Soc.*, **22**, 387 (1941).
- F. C. Page, Private communication.
- J. O. M. Bockris, B. E. Conway, and B. Lovrecek, "Proc. 6th Meeting C.I.T.C.E.," p. 207, Butterworths, London (1955).
- A. G. Stromberg, *J. Phys. Chem. U.S.S.R.*, **20**, 409 (1946).
- R. Brdicka, *Colln, Czech. Chem. Comm.*, **5**, 112, 148, (1933).
- E. Mattson and J. O'M. Bockris, *Trans. Faraday Soc.*, **55**, 1580 (1959).

Growth Habits of Electrodeposited Nickel and Cobalt

D. R. Cliffe and J. P. G. Farr

Department of Industrial Metallurgy, The University, Birmingham, England

ABSTRACT

A brief range of temperature and current density has been found over which the surface topography of growing nickel and cobalt cathodes reflects the atomic configuration of the original cathode surface, and their development is consistent with the theory of growth by a bunching mechanism.

Industrially one of the most important plating metals is nickel, and an understanding of growth processes for this metal should eventually lead to a knowledge of the factors governing the mechanical, physical, and chemical properties of the deposits.

In view of this, the present experiments aimed first to investigate the reasons for the absence in the literature of reports of sharp metallographic structures. Weil and Cook (1) have previously used the electron microscope to study the very fine struc-

tures obtained in nickel electrodeposition and were able to produce evidence of platelet growth.

Second, the investigation into copper and zinc systems, recently reviewed by Keen and Farr (2), showed that epitaxial growth occurred with coarse crystallographic facets developing on the surface of the electroplate. These structures could be related to the atomic configuration of the original substrate surface and to the conditions at the interface between the metal and the electrolyte. It was intended to compare and contrast the growth habit of nickel

with those of copper and zinc. As cobalt is in many ways similar to nickel, a parallel investigation was carried out.

The study was largely metallographic and crystallographic, under conditions comparable to the electrodeposition of copper and zinc, using single crystal substrates (9) and a chloride free electrolyte.

Investigations are still proceeding on the physical and chemical properties of the resulting electroplate.

Experiment

Growth of single crystal cathodes.—Electron beam floating zone melting is an ideal method for the production of single crystals of refractory metals in an extremely pure form (3), and this method has been used successfully in the present investigation. The zone was traversed at approximately 1 cm/min along specimens of spectrographically standardized metals 5 mm diameter x 15 cm long in a vacuum maintained between 10^{-5} and 5×10^{-4} millibars. It was found that in many cases a single pass was sufficient to produce a single crystal. The resulting crystals did not have very even surfaces, but with careful control a tolerable surface was obtained, over a length of about 6 cm.

Back reflection x-ray technique.—The complete orientation of the crystals, and of the cathodes before and after plating, was determined by the back reflection von Laue method (4). A "Unicam" x-ray goniometer was used, with a specimen to film distance of 3 cm, and a 0.5 mm diameter collimator. With white molybdenum radiation produced at 15 ma and 45 kv, the exposure time was approximately 30 min. The resulting diffraction patterns were interpreted by using a Greniger chart, a stereographic net, and a standard projection of the relevant system (4).

In the case of the cobalt, where the initial crystallographic system was in doubt due to the possibility of retained cubic metal from the sluggish allotropic transformation, a Debye-Scherrer photograph was taken. Cobalt white radiation was used at 10 ma, 35 kv with an exposure time of 1 hr. A comparison of the film with a standard obtained from the A.S.T.M. card index, showed that the main structural type present was close-packed hexagonal. This was in agreement with Uwents (5).

Specimen preparation.—For the work described in this paper it was necessary to cut 5 mm diameter single crystal rods to expose desired crystal plane. Mechanical cutting with a jeweller's saw was found to give very local distortion of the crystals. Vaughan (6) designed the apparatus which was used to hold the crystal in a suitable position.

Following the sectioning of single crystals to give the required faces, the specimens were mounted. This was carried out by holding the specimens in clips and covering each unit with powdered polythene which was then fused to give a stable film. Alternatively the specimens were wrapped in P.T.F.E. tape, which was then sintered at 350° – 400° C for from 15 to 60 min according to thickness.

The crystal specimens were polished under flowing water on silicon carbide papers, followed by

polishing on a rotating "Selvyt" cloth impregnated with 1μ diamond paste. They were degreased with trichlorethylene, rinsed in alcohol, and finally washed with distilled water. The flowed layer of metal produced in cutting and polishing was removed by electropolishing. This was confirmed and the orientation of the cathodes was finally established by x-ray diffraction.

Electropolishing.—During electropolishing (7) of both nickel and cobalt vigorous stirring was necessary, owing to the large amount of gas evolved.¹

In the case of nickel, the cathode employed was nickel, the electrolyte 390 ml H_2SO_4 and 290 ml of distilled water, and the time 4–6 min at 2v and room temperature. Specimens were removed from the polishing bath with the current still flowing. For cobalt, a stainless steel cathode was used, 500 ml hydrochloric acid and 500 ml ethyl alcohol electrolyte, and a time of 2–3 min at 2v and room temperature.

Immediately after electropolishing the nickel cathodes were washed with dilute nitrous acid to remove the anodic film. Cobalt cathodes were washed with boiling distilled water. This was essential otherwise interference with subsequent plating resulted.

Specimens were rinsed in distilled water, then in alcohol, and finally dried in a current of warm air.

Plating cell and plating technique.—The electroplating technique has been described by Keen and Farr (2). However, due to the high temperature required, a Pyrex beaker was used, heated by a Bunsen burner, and the whole enclosed by a draught shield. The electrolytes were made up from analytical grade reagents and double distilled water. Bath compositions were: 30 g/l boric acid, 240 g/l nickel sulfate, pH 3.0, for nickel; 45 g/l boric acid, 504 g/l cobaltous sulfate, pH 5.0, for cobalt. A simple sulfate bath was used in order that the results would compare with the work carried out on copper and zinc. Chloride is often present in commercial plating baths, and its principal function is to improve anode dissolution by reducing polarization. It was not added in the present investigation as even very small amounts of chloride grossly affect the topography of growing electrodeposits. Chloride is also known to influence strongly the mechanism of cathode reactions at some electrodes.

Experiments in a closed cell with solutions purified by continuous circulation through exhaustively cleaned charcoal (14) gave identical deposits. Similarly preelectrolysis of the plating solutions did not affect the structures produced.

Examination of deposits.—The bench microscope, Vickers projection microscope, and the electron microscope were used to examine surface details, and polycrystalline material was indicated by Debye-Scherrer rings at the Bragg angles corresponding to the wavelengths of the characteristic radiation present, and to the reflecting planes.

The Philips EM75B electron microscope had a resolution of 40Å. Carbon replicas were obtained from a

¹Electropolishing unit, Nash & Thompson Ltd., Surbiton, Surrey, England.

formvar film, with a bedacryl backing to prevent wrinkling (8).

Reproducibility.—To ensure that the plating conditions remained unaltered during each experiment, a test specimen of known orientation was plated under standard conditions at regular intervals. Whenever there were changes, the results from that solution were rejected, and the whole experiment repeated.

A satisfactory criterion for the quality of the electrolytes was based on the sensitivity of the topography of nickel and cobalt deposits grown on a near (111) nickel surface and a near (0001) cobalt surface, respectively, to solution impurity. The typical standard deposit structures are shown in Fig. 2.1 and 7.1. The surface structures of electro-deposits shown in the illustrations were reproducible, as were the transitions from one structure to another.

Experimental Results

Nickel.—The variables were base orientation, temperature, time, and current density, while the base material, base condition, and electrolyte composition were kept constant. In addition to the extremely fine nature of the deposits, hydrogen was evolved during plating, causing variable structures in the neighborhood of attached surface bubbles and some pitting.

The first phenomenon of note was a rapid coarsening of structure above a critical temperature. Figure 1 shows that at about 94°C a more defined structure begins to appear, surrounded by a fine irresolvable background. Between 94° and 98°C the amount sharply increases until the large structure predominates.

X-ray diffraction patterns, carried out before and after plating, showed whether each deposit was a complete continuation of the base. Where metallographic examination showed coarse nodular deposits (e.g., at 98°C, current densities above 10 ma/cm²) the patterns showed rings. Where coarse crystallographic deposits were obtained (98°C, 10 ma/cm²) sharp spots resulted, showing epitaxy. The fine irresolvable structures produced at temperatures below 90°C gave a series of diffuse spots. Cobalt deposits resembled nickel ones. In each case the deposit thickness was theoretically 12μ.

Although the structure change occurred over a relatively small temperature range, it is evident from Fig. 1 that it was not instantaneous. At about 90°C small "nuclei" appeared which had the same structure as the final deposit at 98°C. The small areas were uniformly distributed across the section and increased progressively in size as the temperature was increased. No further change was observed between 98°C and vigorous boiling.

Figures 2 and 3 show the influence of the base orientation on the deposit structure, at the temperature for maximum development of the structure. Flat facets appeared in some of the deposits, and ridge-type structures in the others. Considerable differences occurred in the appearance of the surface structures developed on bases of different orientations. As with copper deposits (9), it is

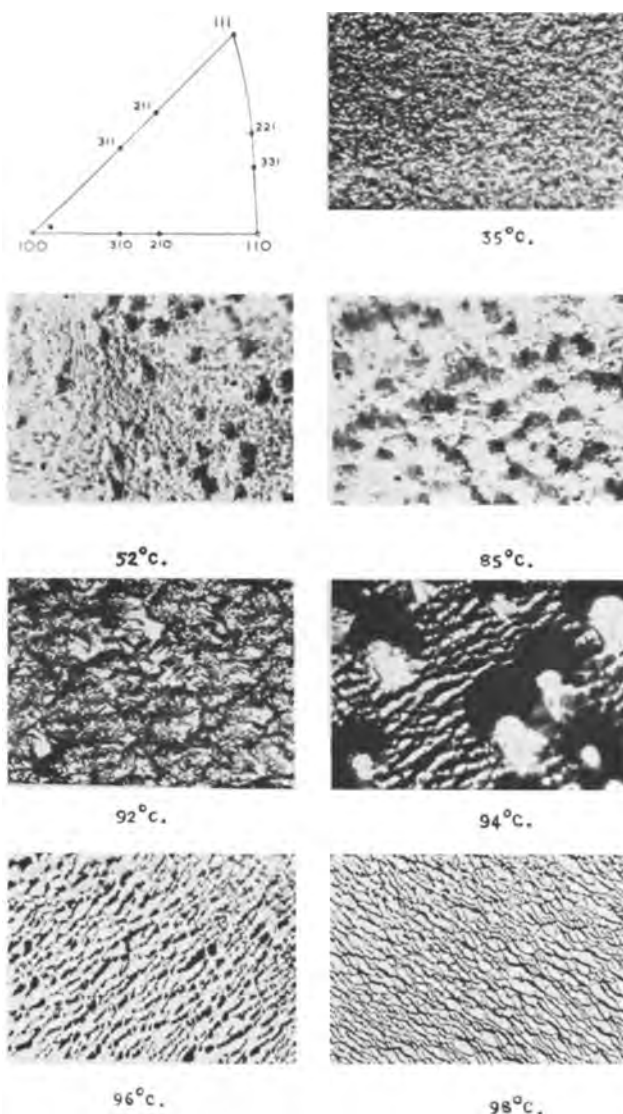


Fig. 1. Effect of increasing temperature, plated for 1 hr at 10 ma/cm². Orientation of the single crystal nickel base is shown in the stereographic projection. Magnification approximately 625X.

thought that the surfaces consisted of facets of low indices. Micrograph number 2 has an overlapping platelet structure, which has upper faces corresponding to (100) planes. As the angle between the cathode surface and the (100) plane increases, a limiting value is reached for which platelet structures are formed, e.g., numbers 6 and 11.

Surfaces closer to a (111) plane again developed flat-type facets, but the sides were pyramidal, with sharp edges, e.g., number 1.

Ridge forms appear near a (110) plane (numbers 3 and 10) with the ridges aligned parallel to a projection of the <110> direction on the surface.

The electron micrographs indicate that the facets were free from detail, although number 2 shows fine detail at the edges of some of the platelets.

The development of deposits with plating time is shown in Fig. 4. A number of specimens were plated, each for a different time, so that the deposit could be examined at any stage of growth. However, it is recognized that this method produces isolated stages in the process of growth, and the mechanism by

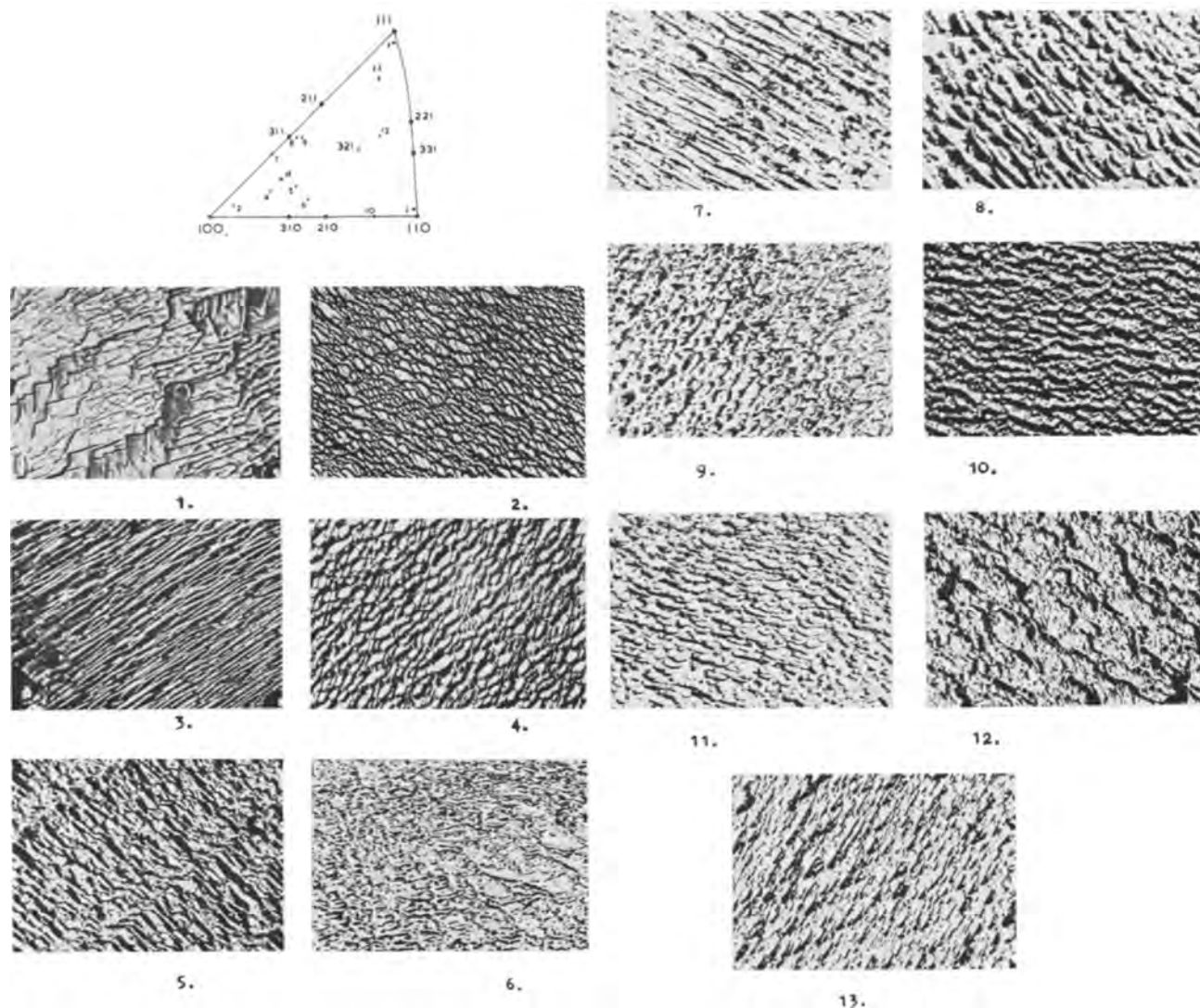


Fig. 2. Orientation series. Deposits formed at 10 ma/cm^2 for 1 hr and at 98°C on various single crystal nickel surfaces. Magnification approximately $650\times$.

which the structure at any instant transformed into that seen at a later stage could only be inferred.

Nuclei appeared at an early stage and fine growth features became more crystallographic, and finally covered the whole surface to produce a platelet-type structure. Similar observations have been made by other workers, *e.g.*, Vaughan on copper (15).

Figure 5 concerns the effect of current density, and the plating times were adjusted so that all the deposits were the same thickness (12μ). The structures reported and discussed in this paper were those observed at the centers of the specimens, as the current density at the peripheral areas was abnormal. This is in accordance with the findings of previous workers working on other metals.

The irresolvable structures at lower current densities are shown to be replaced by increasing proportions of the structures typical of the base orientation up to a maximum of 10 ma/cm^2 . Above this current density dark nodules appeared, increasing until the whole surface was covered.

Cobalt.—The deposits of cobalt appeared to be affected by temperatures in the same way as those of

nickel. Figure 6 shows the surface deposits with the temperature increasing in the same range as for the nickel. A coarser, more sharply defined structure formed at about 90°C , which increased in proportion across the surface, up to 100°C . However, the structure at this temperature did not appear to be fully resolved, and possibly higher temperatures would have produced a more defined structure.

The (0001) plane is equivalent to the (111) plane in the cubic nickel system and the corresponding micrograph shows similarity with (111) nickel, also to the (111) copper, and (0001) orientated zinc deposit (2). The lack of clearly defined facets makes positive comparison difficult.

Figures 7 and 8 show that both platelet and ridge structures result with varying base orientation. Fine detail is observed in all of the micrographs, which suggests that the growth structures are not fully developed. Electron micrograph number 1 shows facets which resemble quite closely the structure obtained on a (111) plane during nickel electrodeposition.

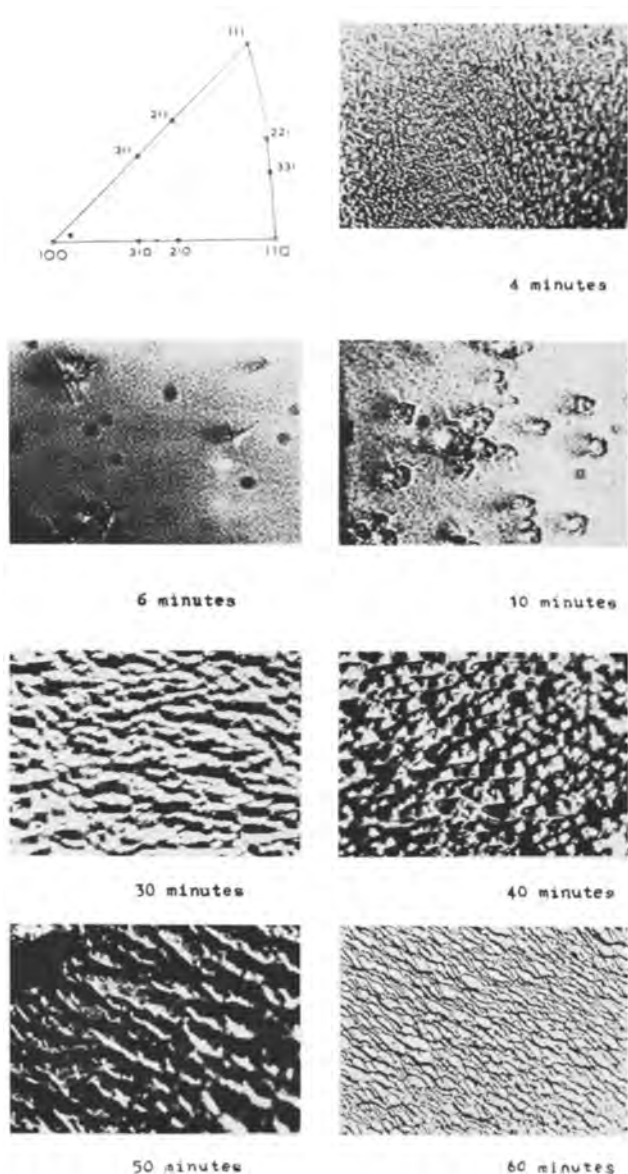


Fig. 4. Effect of plating time. Current density 10 ma/cm^2 , temperature 98°C . Magnification approximately 625X.

density in conditions where coarse nickel deposits formed did not produce resolvable structure changes corresponding to those for copper. Increase of current density could cause the overvoltage quickly to become large enough for break-away. The nodular polycrystalline structure resulted instead of the gradation in epitaxial structure types found on copper. Hoar (13) notes the incorporation of deposited nickel hydroxide, possibly colloiddally dispersed, due to hydrogen-ion discharge causing a rise in the pH.

The present investigation has shown that coarse growth structures in nickel electrodeposits begin to appear at temperatures above 92°C . Further work is in progress on this transition, in particular on the possibility that the codeposition of hydrogen in some form interferes with the crystal growth of nickel.

In its electrochemical behavior, cobalt occupies a position between nickel and iron. Kersten (16) has shown that cobalt deposited from sulfate solutions

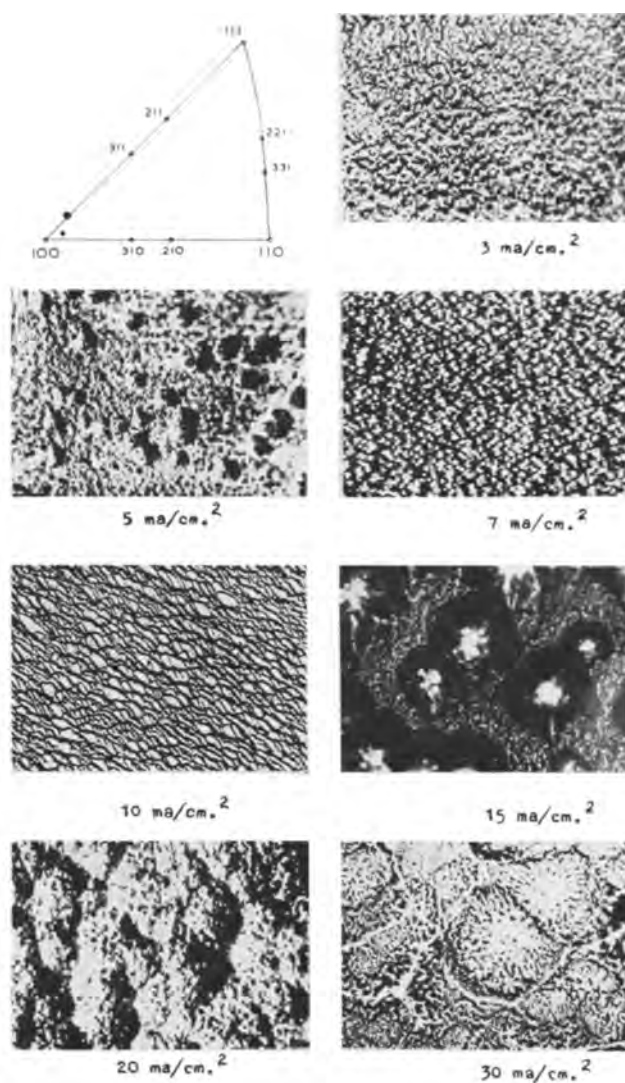


Fig. 5. Effect of current density. Deposits produced by 36 coulombs/cm^2 at 98°C . Magnification approximately 625X.

with a similar pH to those in the present investigation has a hexagonal structure, which changes into a mixture of hexagonal and cubic as the pH is decreased. Cobalt resembles nickel in the temperature effect. Within the critical temperature range the cobalt (0001) deposit resembles the nickel (111), although the structure is smaller and less sharply defined. This might be expected since a (0001) cobalt plane is equivalent to a (111) nickel plane.

A similarity exists between the electrodeposits of cobalt and zinc, both of close-packed hexagonal crystal structure, but the cobalt deposits contain considerable secondary detail. After 1 hr plating at 10 ma/cm^2 both copper and nickel were observed to produce similar structures, depending on the orientation of the substrate, but with the copper structures larger and more sharply defined. We therefore conclude that we have observed a similar growth process, i.e., within our narrow range of conditions, the growth of nickel and cobalt is consistent with a "bunching" mechanism. Further work is proceeding on the properties of this electroplate.

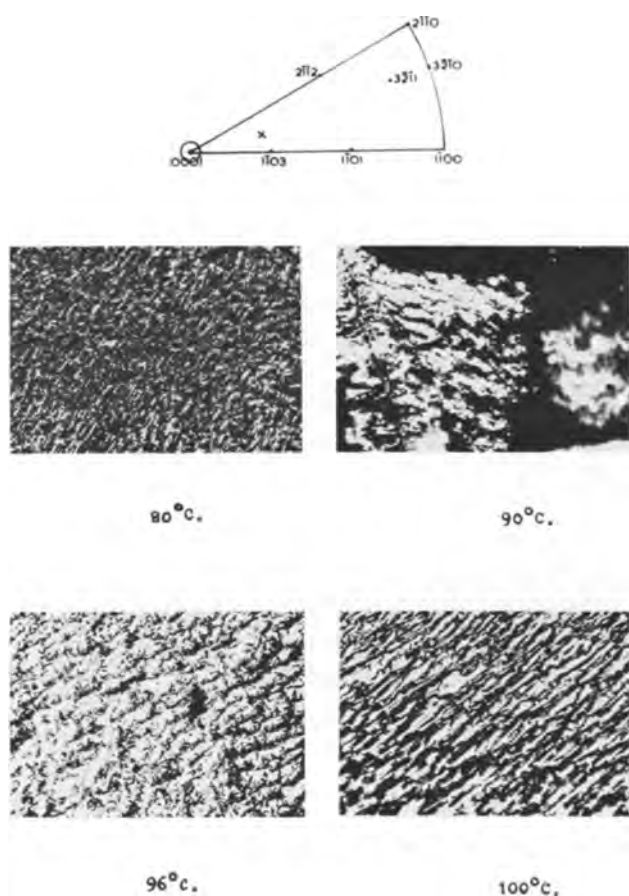


Fig. 6. Effect of increasing temperature on the structure of cobalt deposits, plated 1 hr at 10 ma/cm². Magnification approximately 600X.

There is no evidence to suggest that some impurity constituent is present in the nickel electrolyte, which produced the observed structures. Nickel electrodeposits formed under our conditions appear to be less sensitive to the presence of impurity than do copper electrodeposits grown from similar solutions. (We should emphasize that our conditions differ from those of commercial nickel deposition.) This may be due to (a) the higher temperature, of deposition and (b) the higher overvoltage, as compared with copper. Antropov (17) emphasizes that a high overvoltage leads to a high surface charge which can repel impurity ions. He suggests that the structures of cathodic deposits are connected with the magnitude of this charge. Also hydrogen co-deposited may, under certain circumstances, act as the positive pole of the M-H bonds, and their action on the discharge of metallic ions is considered to be like the action of adsorbed foreign cations. Antropov shows that the formation of finely crystalline deposits may result from both of these effects.

Conclusions

A brief range of temperature and current density has been found over which the surface topography of growing nickel and cobalt cathodes reflects the atomic configuration of the original cathode sur-

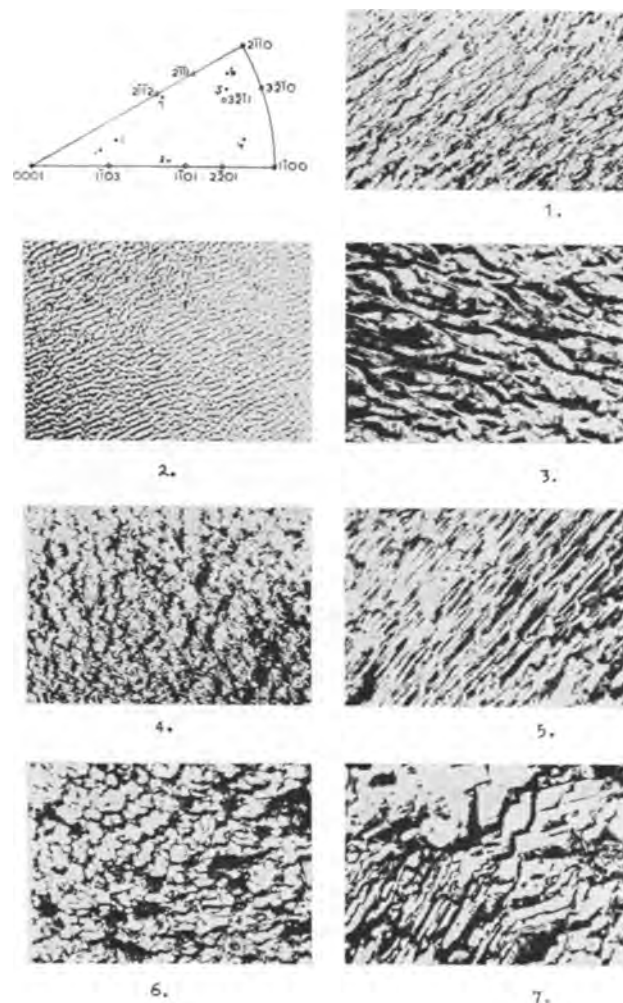


Fig. 7. Orientation series. Deposits formed at 10 ma/cm² for 1 hr at 100°C on various single crystal cobalt surfaces. Magnification approximately 600X.

face. The development of the deposit structures, from chloride-free electrolytes, is consistent with the theory of growth by a bunching mechanism.

Acknowledgments

The authors thank Professor E. C. Rollason for his interest and for the provision of laboratory facilities, and the Principal of the Wolverhampton and Staffordshire College of Technology for study leave for one of the authors (D.R.C.). They acknowledge the assistance of Mr. R. Brownsword in the production of cathode material by electron bombardment zone melting. Thanks are also due to Messrs. Joseph Lucas Ltd. for financial aid.

Manuscript received May 27, 1963. This paper was delivered at the New York Meeting, Sept. 29-Oct. 3, 1963.

Any discussion of this paper will appear in a Discussion Section to be published in the December 1964 JOURNAL.

REFERENCES

1. R. Weil and H. C. Cook, *This Journal*, **109**, 295 (1962).

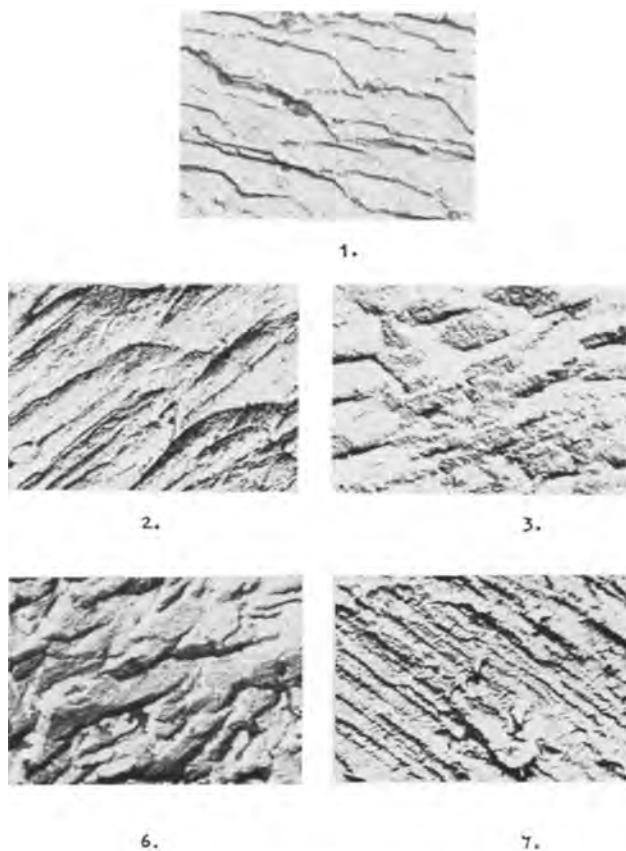


Fig. 8. Orientation series, electron micrographs. Deposits formed at 10 ma/cm^2 for 1 hr at 100°C on various single crystal cobalt surfaces. The orientations are shown in Fig. 7. Magnification approximately 6600X.

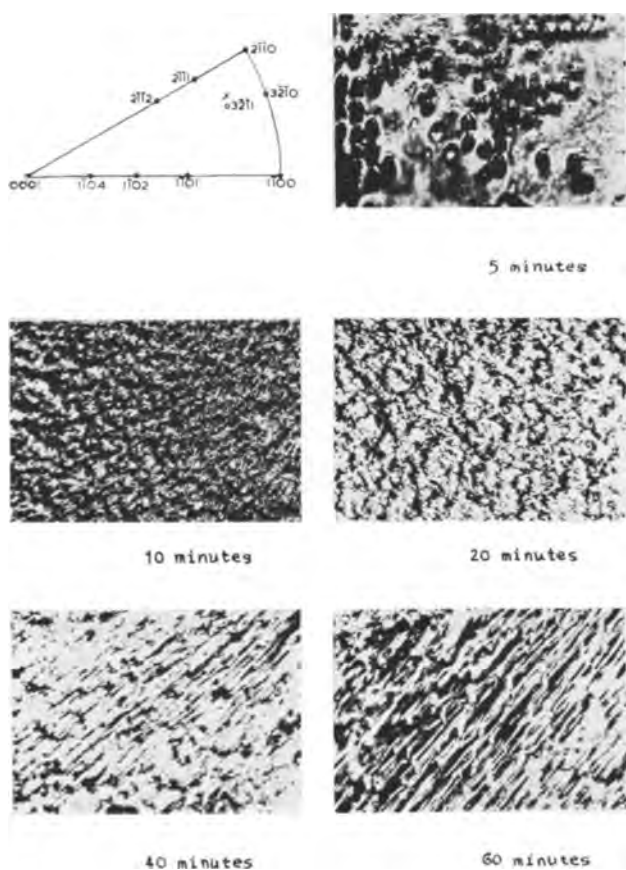


Fig. 9. Effect of plating time. Current density 10 ma/cm^2 , temperature 100°C . Magnification approximately 625X.

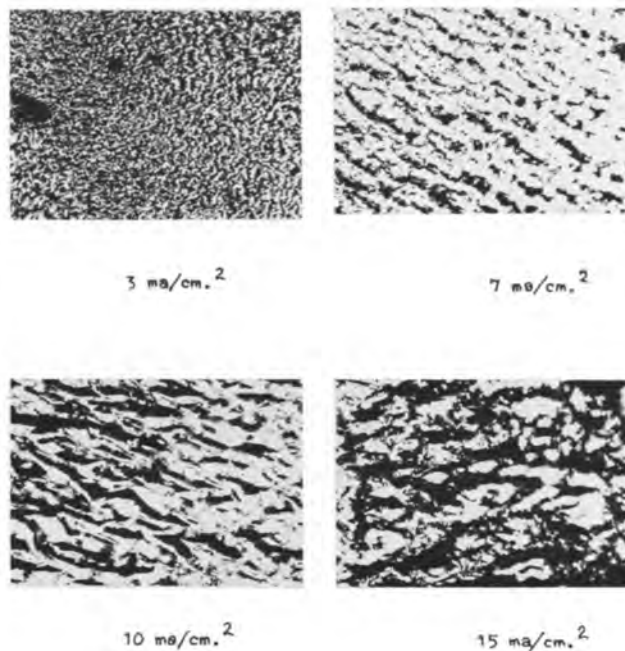
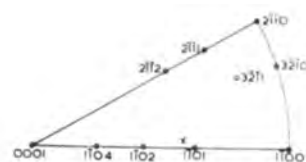


Fig. 10. Effect of current density on the surface structure. Deposits obtained at 36 coulombs/cm^2 on a single crystal base, electrolyte temperature 100°C . Magnification approximately 600X.

2. J. M. Keen and J. P. G. Farr, *ibid.*, 668.
3. F. E. Birbeck and A. Calverley, *J. Sci. Inst.*, **36**, 460 (1959).
4. C. S. Barrett, "Structure of Metals," McGraw Hill & Co. Ltd. (1952).
5. H. Uwents, S. E. R. L. Techn. Report No. M. 80, 36 (1959).
6. T. B. Vaughan, *J. Sci. Inst.*, **35**, 147 (1958).
7. W. J. McG. Tegart, "The Electrolytic and Chemical Polishing of Metals," Pergamon Press Ltd., London (1956).
8. D. Kay, "Techniques for Electron Microscopy," Blackwell Scientific Publications Ltd. (1961).
9. S. C. Barnes, G. G. Storey, and H. J. Pick, *Electrochem. Acta*, **2**, 165 (1960).
10. A. T. Vagramyan and L. A. Uvarov, *Trans. Inst. Metal Finishing*, **39**, 59 (1962).
11. A. Brenner *et al.*, *Plating*, **39**, 865 (1952).
12. D. R. Turner, *This Journal*, **100**, 15 (1953).
13. T. P. Hoar, *Trans. Inst. Metal Finishing*, **39**, 166 (1962).
14. G. C. Barker, in "Modern Electro-Analytical Methods," p. 122, G. Charlot, Editor, Elsevier Publishing Co., New York (1958).
15. T. B. Vaughan and H. J. Pick, *Electrochem. Acta*, **2**, 179 (1960).
16. H. Kersten, *Physics*, **2**, 274 (1932).
17. L. I. Antropov, "Kinetics of Electrode Processes and Null Points of Metals," C.S.I.R., New Delhi (1960).

Electroluminescence in Oxide Phosphors

Shannon Jones

Lamp Metals and Components Department, General Electric Company, Cleveland, Ohio

ABSTRACT

Certain oxide phosphors have been observed to exhibit substantial electroluminescence (EL) in high electric fields. This electroluminescence may be induced either by an alternating field, in which case insulating films may be interposed between the phosphor and the electrodes, or by a direct field, in which case an insulating film between the electrodes is not permissible. The voltage required is about 20 times that needed for equal brightness in commercial EL lamps using copper-activated zinc sulfide phosphors.

Unlike EL zinc sulfide phosphors, oxide phosphors by themselves do not exhibit EL when imbedded in substantial quantities of liquid or solid dielectrics. However, a small amount of organic material, such as shellac, may be used to hold oxide phosphor grains in place without seriously impairing the luminescence. Furthermore, Lehmann (1) has shown that oxide phosphors in oil and in contact with sharply pointed metal grains may exhibit EL at the contacts.

Among the oxide phosphors studied, some good lamp phosphors show good electroluminescent response; others do not. Similarly, some good oxide-type cathode-ray phosphors show good electroluminescent response while others do not. The phosphors examined were mostly variously activated binary oxides, such as borates, silicates, phosphates, or tungstates ("self-activated") of calcium, strontium, zinc, or cadmium. Most of the phosphors had been optimized for maximal brightness under cathode rays, 2537Å, or 3650Å radiation. They were not given any special washing, coating, refring, or other treatment before being tested in the EL cells.

The existence of electroluminescence in oxide phosphors is interesting in part because of the practical considerations of the wide range of colors obtainable, the large number of compounds and activators which provide phosphor systems, and the relative ease of manufacture of many of the oxide phosphors.

History.—Lossew observed light emission, not due to incandescence, from silicon carbide crystals through which an electric current was flowing (2). This effect is now believed to be the result of the recombination of positive and negative charge carriers at p-n junctions in a semiconductor. The effect is called injection electroluminescence and has been the subject of considerable research. However, it has not yet produced a practical light source.

Destriau observed light emission from copper-activated zinc sulfide phosphors when they were suspended in oil and subjected to high electric fields (3). This Destriau effect has been the subject of much research, many papers, and patents. It is the basis of the present commercial electroluminescent lamp. Many believe that in the Destriau effect electrons are emitted from inhomogeneities in the crystal under the influence of the field, then accelerated to velocities sufficient to produce light on

collision with a fluorescent region of the crystal. This process has been called acceleration-collision electroluminescence (4).

In contrast to the large amount published on injection electroluminescence in semiconductors and acceleration-collision electroluminescence in sulfide phosphors, little has been published on "electroluminescence" in oxide phosphors. Among reports and papers in the published literature, several of the most pertinent to this report are a note by Bowtell and Bate (5) on electroluminescence in oxide phosphors coated with an ionizable salt, a paper by Lehmann (1) on electroluminescence in oxide phosphors in contact with conducting particles, and papers by Kolomoitsev *et al.* (6) and by Palilla and Rinkevics (7) on electroluminescence in oxide phosphors (some of them uncoated and not mixed with conducting grains) in electric fields in air. Herwelly (8), Thorington (9), Morosin and Haak (10), and Lehmann (11) have proposed and discussed mechanisms of electroluminescence in certain aspects which may be related to the phenomena here described.

Construction of EL Lamps Using Oxide Phosphors; Some Observations

Different constructions are preferred or required, depending on whether the lamp or cell is to be used with a.c. or d.c., in air or in vacuum. Possible types of construction are as follows:

Type I. (for a.c., in air).—On a flat metal base plate, e.g., zinc-coated steel 5 cm², a thin, uniform, tacky coating of plasticized polyisobutyl methacrylate is deposited by evaporation from solution. The thickness of the tacky layer may be about 15 μ . The coated plate is then covered smoothly with an excess of a size-graded phosphor, such as manganese-activated zinc silicate through 100, on 200 mesh screen (per inch). The phosphor is pressed on the tacky layer under a pressure of about 3 kg/cm². The excess phosphor is tapped off the plate. A piece of 125 μ cellulose acetate film extending perhaps 5 mm beyond the base plate on all sides is placed on the phosphor layer. A piece of glass with a transparent conducting layer on one side only is placed on the plastic film with the conducting surface next to the film. The assemblage is clamped together, and electrical connections are made to the base plate and the conducting glass. The clamping pressure is not critical; ordinary spring clothespins

giving about a kilogram pressure at each corner are satisfactory.

With an alternating sinusoidal field of about 900v rms 60 cps applied to the above assemblage, luminescence is observable in a darkened room and without appreciable dark adaptation. With increasing voltage the brightness increases rapidly until dielectric breakdown occurs.

Type II. (for a.c., in air or vacuum).—This cell is similar to the Type I cell except for the presence of a layer of cadmium pyroantimonate grains next to the metal base plate and under the phosphor. Cadmium pyroantimonate is a semiconductor. Its presence in contact with the phosphor reduces the threshold field required for luminescence to about 500v. It also makes the cell capable of electroluminescence in vacuum, unlike the Type I cell, which glows poorly, if at all, in vacuum. It is probable that with this construction the luminescent mechanism is similar to that in the oil cells of Lehmann, who reported "contact electroluminescence" in phosphors in contact with semiconductors.

Type III. (for a.c. or d.c., in air or vacuum).—This is similar to Type II except that no dielectric film is interposed between the conducting glass and the phosphor. It has been difficult to obtain reproducible cells of this type. Often the glow will appear only at tiny spots. However, it has sometimes been possible to obtain uniform and steady glows over an area of about 1 cm². In this type of cell, it is probable that the resistance of the cadmium antimonate layer prevents arcing and catastrophic breakdown of the cell at some localized site.

While these cell constructions have been described specifically, many variations are permissible. Starting with the base plate and going up, these variations are next described in order.

As base metals, zinc-coated steel, cadmium-plated steel, plain cold-rolled steel, copper, molybdenum, aluminum, nickel, brass, and other alloys have been tried. Other things being equal, more light should be obtained from the metals of higher reflectivity. Apart from this effect, it is doubtful that the base metal has an appreciable effect on the efficiency.

The tacky or adhesive layer may be any one of a number of materials or may be eliminated entirely. It was used to provide a simple means of obtaining a monolayer of phosphor grains on the base plate. A Glyptal¹ varnish has been used successfully for the tacky layer. It is important, however, that the phosphor be not completely surrounded by a gross amount of the adhesive. Good cells have been made in which phosphors have been suspended in thin shellac solutions and sprayed on cellulose acetate sheets. These sheets were then placed between thin metal plates and conducting glasses. A good cell was made up using an aqueous solution of Polyox.¹ With either Polyox or shellac, the ratio of residual organic material to phosphor should be low, pre-

ferably of the order of 1% or less.

As a substitute for cadmium antimonate, silicon carbide of about the same grain size was tried. It did not act like cadmium antimonate to reduce the threshold voltage substantially. Neither did a layer of molybdenum powder, much finer than the cadmium antimonate, reduce the threshold voltage. Further evidence was obtained indicating that the reduction in threshold voltage with cadmium antimonate was not merely due to the increased roughness of the electrode surface. Roughening a cold-rolled steel base plate with coarse silicon carbide grain did not lower the threshold voltage when the plate was used alone, *i.e.*, without the cadmium antimonate layer.

There are substantial differences in electroluminescent response between different classes of oxide phosphors. In general, phosphors with calcium or strontium as cations are poor, those with zinc or cadmium are good.

A number of dielectric films other than the 125 μ cellulose acetate were tried. Among them were 6 μ Mylar,¹ 10 μ Saran,¹ 50 μ Tedlar,¹ 75 μ Lexan,¹ 34 μ cellophane, 22 μ cellulose acetate, 160 μ microscope cover glass. The 125 μ cellulose acetate and the Lexan gave the best and most consistent results. Some of the films were tried either as single or multiple layer insulators. The differences in threshold voltages for luminescence between cells using 125 μ cellulose acetate and cells using thinner dielectrics were surprisingly small. In Type I cells, electroluminescence could occur with dielectric films on both sides of the phosphor, *i.e.*, with dielectric next to both the metal and to the conducting glass.

Instead of conducting glass for the top electrode, a wire screen of about 100 mesh and having a light transmission of about 40% has been used successfully.

Discussion

Comparison of various phosphors.—Evidence of a relation between the metal cation of the phosphor and the electroluminescent efficiency is shown in the following lists. The better EL response of phosphors with zinc or cadmium cations, compared with calcium or strontium, was consistently observed. A few phosphors other than oxides are listed.

The phosphors with poor EL response, based on visual observation, were calcium halophosphate:Sb; calcium halophosphate:Sb, Mn; calcium cadmium halophosphate:Sb, Mn (1% Cd); calcium pyrophosphate:Sb, Na; calcium orthophosphate:Ce, Mn; calcium tetraborate:Pb, Mn; calcium potassium aluminum tetraborate:Pb, Mn; calcium silicate:Pb, Mn; strontium orthophosphate:Sn; strontium octaborate:Mn; barium titanium phosphate; magnesium arsenate:Mn; magnesium stannate:Ti; antimony tetroxide:Mn, B; salicylic acid; rhodamine B on silicic acid; sodium salicylate.

A fair EL response was obtained from calcium pyrophosphate:Dy; calcium lead tungstate (1% Pb); magnesium tungstate; magnesium germanate:Mn; magnesium aluminum silicate:Mn; zinc phosphate:Mn; anthracene.

¹ Glyptal, General Electric Company, based on glyceryl phthalate. Polyox, Union Carbide Corporation, polyethylene oxide. Mylar, E. I. du Pont de Nemours and Company, polyester. Saran, Dow Chemical Company, polyvinylidene chloride. Tedlar, E. I. du Pont de Nemours and Company, polyvinyl fluoride. Lexan, General Electric Company, polycarbonate.

Good EL response was obtained from magnesium aluminate:Mn (fired in reducing atmosphere); zinc silicate:Mn; zinc germanate:Mn; zinc borate:Mn; zinc tungstate; zinc aluminate:Mn; cadmium borate:Mn; cadmium silicate:Pb, Mn; cadmium chlorophosphate:Mn; cadmium tungstate; gadolinium oxide; zinc sulfide:Ag; zinc oxide:Zn.

Relative luminances of three phosphors in Type I cells at 3000v were measured and found to be:

Phosphor	Relative luminance	Approximate relative energy between 4000 and 7000Å
Zinc silicate: Mn	100	100
Calcium silicate: Pb, Mn	16	32
Calcium halophosphate: Sb, Mn	6	9

Effect of cadmium antimonate.—The effects of the cadmium antimonate layer on the threshold voltage for luminescence were examined. A-C cells were made using cadmium borate:Mn phosphor, with and without cadmium antimonate. They were operated in air and in vacuum. The results were as follows:

	A-C threshold voltage	
	In air	In vacuum, $4 \cdot 10^{-6}$ Torr
With cadmium antimonate	700	1600
Without cadmium antimonate	900	3100*

* At 3100v the pressure began to rise after a few seconds and the plastic broke down. The voltage required to induce luminescence in the absence of incipient plastic breakdown would probably have been much higher.

Similar effects of the cadmium antimonate in reducing threshold voltage were observed qualitatively with other phosphors, including zinc silicate:Mn and cadmium chlorophosphate:Mn.

Relation of voltage to appearance and brightness of oxide EL cells.—At threshold voltage and slightly above, only a few of the phosphor grains in the cell light up, and some of these flash off and on in an apparently random manner. As the voltage is increased slightly, the number of continuously lighted grains increases, although some will still appear to flash off and on or to move under the influence of the field. These actions often give a "crawling" effect to the oxide EL cell when it is operated at voltages perhaps 50% above the threshold voltage. At higher voltages, virtually all of the phosphor grains glow continuously, and the crawling effect disappears.

The relative luminances for various voltages were determined for a zinc silicate:Mn Type I cell, with the following results:

Volts, 60 cps	Galvanometer deflection, relative luminance
920	Visual threshold, not detected by cell and galvanometer
1700	Not detected by galvanometer
2040	12
2380	29
2720	53
3060	79
3400	99

Resistivity of oxide phosphors.—In an attempt to explain the differences in EL response between phosphors with calcium or strontium as cations and those with zinc or cadmium, it was postulated that the poorer calcium and strontium phosphors might charge up more under electrical bombardment than the better phosphors. Such charging would repel

further bombardment and this reduce or extinguish phosphor excitation. The tendency to become charged would be associated with high resistance. Using this argument, it was thought that the calcium phosphors should have higher resistance than the zinc or cadmium phosphors. The opposite was found to be true.

The various phosphors were placed between two steel electrodes arranged so that a high linear pressure could be applied to the phosphor. The dimensions of each electrode were 0.32 x 2.54 cm. The length of the phosphor pack was variable, but usually was about 0.03 cm. The pressure applied was over 70 kg/cm². Resistance varied little with pressure in this region.

The applied voltages varied with the resistance, but in no case was there evidence of nonlinearity in the voltage-current relation. A d-c source, variable from 10 to 500v, and a galvanometer were employed.

It appeared that what was being measured was probably surface conduction by ions, the ions made mobile by adsorption of water vapor from the atmosphere. The measured conduction depended on the history and treatment of the samples. However, the calcium phosphors generally had lower resistance than those of zinc or cadmium.

In one test, the electrical resistivity of cadmium silicate:Pb, Mn under an estimated linear pressure of more than 70 kg/cm² was more than 10¹³ ohm-cm under a field of about 5000 v/cm. Excitation of the top surface of the phosphor pack by 2537Å radiation did not produce a detectable increase in conductivity, but it must be noted that the volume of phosphor subjected to appreciable excitation was probably less than 1% of the total volume. The direction of the exciting radiation incident on the phosphor pack was normal to the common direction of pressure and electric field; thus the excited volume was in parallel electrically with the unexcited volume.

Further resistance measurements were obtained on other phosphors under linear pressures of about 70 kg/cm² at room temperature and 55% relative humidity. In column A below are measurements on the phosphors "off-the-shelf;" in column B are measurements on some of the phosphors shortly after baking them at 135°C for 3 hr; in column C the unbaked phosphors had been mixed with heavy white mineral oil of negligible conductivity to form a thick paste.

Phosphor	Resistivity, 10 ⁸ ohm-cm		
	A	B	C
Calcium halophosphate: Sb, Mn			
Sample 1	10		
Sample 2	7	100	600
Calcium silicate: Pb, Mn			
Sample 1	30	30	
Sample 2	70		
Cadmium chlorophosphate: Mn	40		
Cadmium silicate: Pb, Mn			
Sample 1	300	900	70,000
Sample 2	200		
Zinc silicate: Mn	100		
Zinc sulfide: Ag	100		

Dielectric constants and loss factors.—Dielectric constants and loss factors at 1000 cps were determined on a number of oxide phosphors, some of which were relatively good in electroluminescent response; others were poor. No consistent relation of dielectric constant or loss factor to electroluminescent response was evident.

Efficiency.—Electrical power input measurements were made calorimetrically on a zinc silicate:Mn cell and on a General Electric commercial flexible blue sulfide cell. The cells were operated at visible energy outputs estimated to be about equal. The energy inputs were determined by immersing the cells in kerosene in a Dewar vessel and observing the rate of temperature rise. It was necessary to enclose the zinc silicate cell in a cellophane bag. The silicate cell used about 20 times the power of the sulfide cell. Thus the efficiency of the silicate cell for conversion of electricity to visible energy was about 5% of the sulfide cell.

With equal currents passing through the two cells, the visible radiant energy output was about the same. However, the voltage on the sulfide cell was 120 while it was 2400 on the oxide cell. The current through each cell was 1 ma; the area of each was 17 cm². Thus the oxide cell required 20 times the volt-amperes of the sulfide cell for equal visible energy output. Since the oxide cell also required about 20 times the watts, the power factors of the two cells were about equal.

Effect of a-c frequency.—In one test on a Type II zinc silicate:Mn cell, the light output at 600v and 600 cps was lower than at 600v 60 cps. This is in qualitative agreement with a result of Kolomoitsev *et al.* (6), who found that, unlike the sulfide phosphors, zinc silicate:Mn lost brightness with increasing frequency in this range.

Maintenance.—Two zinc silicate:Mn cells, a Type I and a Type II in vacuum, were run about 16 hr. Qualitative visual observations did not indicate much brightness loss in this period.

In a Type I cell with magnesium tungstate and zinc tungstate phosphor side by side, the zinc tungstate started out at a lower threshold voltage and gave higher brightness than the magnesium tungstate. But after 15 min of operation at 1900v, the zinc tungstate was dimmer than the magnesium tungstate, which appeared fairly constant in brightness over this short period.

In a Type III cell on d.c. in air, using zinc silicate:Mn, polarization occurred after 10 hr so that the cell then glowed steadily only with the cadmium antimonate negative, giving only a short light pulse when the terminals were reversed. This polarized cell, when operated on a.c. of 60 cps, glowed steadily on 510v rms.

Mechanism.—In the case of Type I cells, it seems likely that the luminescence is the result of bombardment of the phosphor by electrons or gaseous ions, although the possibility of phosphor excitation by very short wavelength ultraviolet radiation (below 2000Å) has not been ruled out completely. As pointed out by Palilla and Rinkevics (7), energy may be transferred to the phosphor by the recom-

bination of ions at or near the phosphor surfaces, resulting in light emission.

In the case of electroluminescent oxide cells without the semiconductor, it appears that corona discharge starts at about the same voltage as the luminescence. It does not appear that excitation of the phosphor by ultraviolet radiation generated in the cell produces an appreciable part of the luminescence. In one experiment, nonfluorescent calcium pyrophosphate was placed between the base plate and a 50 μ film of Tedlar, which has good transmission for ultraviolet down to below 2000Å. A wire screen was used for the top electrode and another sheet of Tedlar was placed on the wire screen. With this arrangement, a considerable proportion of any 2000-4000Å ultraviolet generated should have been available to excite phosphors placed on the top sheet of Tedlar. With this cell under a high a-c field, no luminescence was observed in good oxide EL and photoluminescent phosphors placed on top.

Differences in ultraviolet excitation spectra of the various phosphors, at least down to 1000Å, do not seem to be sufficient to account for the differences in EL response. Sodium salicylate is reported to be excited fairly well and with virtually constant quantum efficiency down to below 1000Å, yet it was relatively poor in EL response.

In a demountable cathode-ray tube, operated at voltages varied from about 750 to 10,000, there was little visual difference between screens of cadmium silicate:Pb, Mn and calcium silicate:Pb, Mn, side by side. Yet in Type I cells, the cadmium silicate phosphor was much brighter than the calcium silicate. In order to account for this difference in EL response, while retaining the hypothesis that the luminescence arises from particulate bombardment, it seems necessary to assume that, in the EL cells, the type of phosphor is a factor in determining the amount of bombardment the phosphor receives.

It has been suggested that soft x-rays may be responsible for the luminescence (12). This possibility has not been explored.

In the case of the Type III cells operated on d.c., the polarization that occurs after several hours burning suggests that the cadmium antimonate then acts as an electron emitter, exciting the phosphor at the contact points between the phosphor and semiconductor.

Comparisons with other studies.—Bowtell and Bate (5) state that oxide phosphors must be given a coating of an ionizable salt in order to exhibit electroluminescence. This has not been found to be true in this study.

Lehmann (1) apparently worked mostly with oil-filled EL cells. He pointed out that in these oil cells, contact between phosphor and conducting grains was essential for electroluminescence with many phosphors, which he listed. However, one might reasonably infer from his paper that conducting grains are necessary for EL ". . . even with air as the embedding material." This, of course, is contrary to the results of the present work.

The results of Kolomoitsev *et al.* (6) are substantially in accord with this study. They reported calcium halophosphate phosphor as electroluminescent, along with other phosphors having zinc or cadmium as cations. They did not report on the relative brightness of the various phosphors. Apparently they did not use a solid dielectric film in their cells. They introduced the phosphor directly between a metal plate and conducting glass.

Palilla and Rinkevics (7) examined a number of phosphors activated by rare earths, as well as alumina activated by Cr or Mn. In general, their observations on what they called Type II emission were similar to those observed by the author in self-activated tungstates and in binary oxides activated by Mn or by Pb + Mn. The effects of frequency and of liquid embedment were similar in both investigations. However, they found it necessary to provide a special thermal treatment of their phosphors, while the author gave no special treatment to the phosphors he examined.

Conclusions

Many oxide phosphors exhibit electroluminescence, giving light outputs equal to sulfide phosphors at about the same current, but at about 20 times the voltage and 20 times the wattage.

Electroluminescence in oxide phosphors is believed to be due to bombardment of the phosphor by electrons or ions or to recombination of charged particles on or near the phosphor surface. Bombardment may occur at an air-phosphor interface or at a semiconductor-phosphor interface, depending on cell construction. Photoluminescence plays a negligible role in the cells described.

Oxide phosphors with zinc or cadmium as the metallic cation are in general more efficient than those with calcium or strontium.

The threshold voltage required for EL in oxide phosphors is reduced by providing contacts between the phosphors and cadmium pyroantimonate semiconductor grains. Such contacts also make oxide EL cells operable in high vacuum.

The existence of electroluminescent oxide phosphors as efficient as sulfides does not seem an impossibility. Crystal aggregates containing both electron-emitting and fluorescent phases would seem to have electroluminescent potentialities in oxide systems.

Acknowledgment

The assistance of Herman Ogrinc in this project is gratefully acknowledged.

Manuscript received Aug. 29, 1963.

Any discussion of this paper will appear in a Discussion Section to be published in the December 1964 JOURNAL.

REFERENCES

1. Willi Lehmann, *This Journal*, **104**, 45 (1957).
2. O. W. Lossew, *Telegrafia i Telefonija*, **18**, 61 (1923).
3. G. Destriau, *J. chim. phys.*, **33**, 620 (1936); **34**, 117 (1937).
4. H. F. Ivey, *This Journal*, **104**, 740 (1957).
5. J. N. Bowtell and H. C. Bate, *Proc. Inst. Radio Engrs.*, **44**, 697 (1956).
6. F. I. Kolomoitsev, V. P. Izotov, and E. V. Stauer, *Optics and Spectroscopy*, **12**, 64 (1962).
7. F. C. Palilla and M. Rinkevics, *This Journal*, **110**, 750 (1963).
8. A. Herwelly, *Acta Phys. Austriaca*, **5**, 30, (1951).
9. L. Thorington, Paper presented at Electrochemical Society Meeting, Philadelphia, 1952 (Abstract 52).
10. B. Morosin and F. A. Haak, *This Journal*, **108**, 477 (1961).
11. W. Lehmann, *ibid.*, **109**, 540 (1962).
12. A. Addamiano, Private discussion.

Spectral Properties of Rare Earth Oxide Phosphors

R. C. Ropp¹

Sylvania Electric Products Inc., Towanda, Pennsylvania

ABSTRACT

A study of rare earth oxide phosphors activated by rare earths revealed that fluorescence occurs only in those matrices where the cation possesses no unpaired electrons. The fluorescent intensities of the rare earth activators were divided into three categories, strong, medium, and weak, each having a characteristic excitation spectrum.

The study of spectral properties of rare earth activated phosphors is fundamental for an understanding of the luminescence process. In the rare earths, transitions among the f-electron energy levels result in line emission because the outer shielding electrons ($5s^25p^6$) minimize the perturbing influence of the crystal field. In the more usual case involving d-electrons, considerable perturbation occurs, resulting in broad emission bands.

The general field of oxide phosphors has been long neglected because of the low fluorescent intensities associated with such phosphors. Bonding involves a high degree of ionic character, and activators in which d-electron transitions take place do not produce high-intensity fluorescence. In such ionic solids, the excitation energy required for fluorescence at the d-electron activator site probably is dissipated in part by phonon processes via vibronic coupling or by spin-orbit exchange. However, with f-electrons, such a process should be minimized

¹ Present address: Westinghouse Electric Corporation, Bloomfield, New Jersey.

and thus permit the oxide-matrix combination with rare earth activation to produce phosphors of higher efficiency.

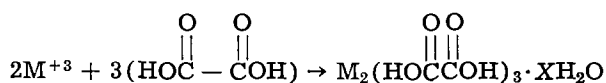
The rare earths form a series of homologous oxides having a cubic defect structure (1, 2). The state of present knowledge regarding the specific transitions involved in rare earth excitation and fluorescence is not extensive, nor is the nature of the transitions well defined. However, the energy levels of the trivalent ions are known quite well, the identification of the levels (SLJ) being complete in most cases up to 40,000 cm^{-1} (3). The correlation between the free ion levels and observed levels in a crystal is quite close, of the order of 100 cm^{-1} , in contrast with those of d-electron activators.

A study of rare earth activated, rare earth oxide phosphors was initiated to study activator matrix interactions and to elucidate the luminescent mechanisms of the rare earths as activators. Such a choice minimizes experimental difficulties to a certain degree.

Previously known phosphors include: $\text{Gd}_2\text{O}_3 \cdot \text{X}^{+3}$, where X^{+3} is Sm, Eu, or Tb (4); $\text{Y}_2\text{O}_3 \cdot \text{X}^{+3}$, where X^{+3} is Eu, Tb, Pr, Dy, or Er (5), and Sm (6); $\text{CeO}_2 \cdot \text{X}^{+3}$, where X^{+3} is Sm, Gd (6); and $\text{La}_2\text{O}_3 \cdot \text{Pr}$ (7).

Experimental Procedure

All materials were at least 99.99% pure. Impurities other than rare earths were not detected spectrographically. The nitrates (or the oxides dissolved in concentrated nitric acid) of the requisite rare earths were dissolved to form 0.40M solutions. Mixtures of the ions in solution were made so that the required volumes totaled one liter before precipitation. The activator ratio was 0.05 mole/mole of Gd^{+3} , Y^{+3} , La^{+3} , or other desired cation, so that in the total volume, the ratio of activator to cation remained constant. Oxalic acid as a 10% solution was used as the precipitant, assuming the reaction to be quantitative in the presence of 5M % excess acid (8)



where $X = 2$ to 6 when the precipitation is carried out at 80°C. The precipitate was dried at 110°C overnight and fired in air at 1000°C to form the phosphor, using open silica crucibles.

Measurements of spectral properties were made with a spectrofluorimeter described previously (9). Only visible fluorescence, and in one case ultraviolet emission, was measured. No attempt to measure luminescence below 14,400 cm^{-1} (6940Å) was made. It is probable that infrared emission occurs in many, if not all, of the phosphors. This aspect was not of interest in the present investigation.

Experimental Results

In general, calcination of the rare earth oxalate gave the rare earth sesquioxide. In the case of Ce and Pr, CeO_2 and Pr_6O_{11} were formed when the corresponding oxalates were fired in air. However, when fired in N_2 , they gave the expected sesquioxide (10). The experimental investigation was conducted in three steps: determination of effective matrices;

investigation of spectral properties; and correlation of excitation and emission properties.

Effective Matrices

To ascertain the effective rare earth activator-rare earth oxide combinations and yet not exceed the bounds of experimental feasibility, it was necessary to restrict the choice of possible activators. In a study of rare earth-activated Al_2O_3 , Adams and Mellickamp (11) found that only Sm^{+3} , Eu^{+3} , Gd^{+3} , Tb^{+3} , and Dy^{+3} were effective. It is also well known (12) that these same rare earth activators produce much higher intensities of fluorescence than any of the other rare earths. Therefore, limiting the choice to these five activators could be justified experimentally; it is unlikely that any other rare earth activator would produce significantly different results.

Fluorescence was evaluated by its presence or absence. The wave-number range, 14,400 cm^{-1} to 45,500 cm^{-1} , was scanned to determine if excitation was obtained. The data in Table I were obtained in this manner. The fluorescent intensities varied, by a factor of ten, from weak to strong.

The oxides were identified by x-ray powder diffraction patterns of the activated phosphors. Note that only Y_2O_3 , La_2O_3 , and Gd_2O_3 gave activated matrices. There is a correlation between activation, electron configuration, and body color (Table II). In the effective matrices, there are no unpaired spins, and the body color is white, i.e., no absorption

Table I. Visible fluorescence in the rare earth oxide matrices

Matrix	Structure	Activator*				
		Sm ⁺³	Eu ⁺³	Gd ⁺³	Tb ⁺³	Dy ⁺³
Y_2O_3	Cubic	w	s	w	m	m
La_2O_3	Hexagonal	w	s	m	s	m
$\text{Ce}_2\text{O}_3^{**}$	Hexagonal	—	—	—	—	—
$\text{Pr}_2\text{O}_3^\dagger$	Hexagonal	—	—	—	—	—
Nd_2O_3	Hexagonal	—	—	—	—	—
Sm_2O_3	Monoclinic	—	—	—	—	—
Gd_2O_3	Cubic	w	s	—	s	m
Dy_2O_3	Cubic	—	—	—	—	—
Ho_2O_3	Cubic	—	—	—	—	—
Er_2O_3	Cubic	—	—	—	—	—
Yb_2O_3	Cubic	—	—	—	—	—

* w = weak; m = medium; s = strong intensity.

** Fired in N_2 . Firing in air produces cubic CeO_2 which has the fluorite structure.

† Fired in N_2 . Firing in air produces the cubic Pr_6O_{11} .

Table II. Correlation of visible luminescence, electron configuration, and body color

Matrix	Activation obtained	Outer electron configuration	No. of unpaired spins	Body color	
Y_2O_3	X	4f ⁰	4s ² 4p ⁶	0	White
La_2O_3	X	4f ⁰	5s ² 5p ⁶	0	White
Ce_2O_3		4f ¹	5s ² 5p ⁶	1	White
Pr_2O_3		4f ²	5s ² 5p ⁶	2	Green
Nd_2O_3		4f ³	5s ² 5p ⁶	3	Blue
Sm_2O_3		4f ⁵	5s ² 5p ⁶	5	Cream
Gd_2O_3	X	4f ⁷	5s ² 5p ⁶	7	White
Dy_2O_3		4f ⁹	5s ² 5p ⁶	2	Cream
Ho_2O_3		4f ¹⁰	5s ² 5p ⁶	3	Pink
Er_2O_3		4f ¹¹	5s ² 5p ⁶	4	Pink
Yb_2O_3		4f ¹³	5s ² 5p ⁶	6	White

in the visible region, whereas in those matrices where unpaired electrons exist, no visible luminescence was observed. This is exactly what would be expected, since the presence of an unpaired electron implies the presence of low-lying energy levels. Cations with a closed-shell electron configuration require very high ionization energy, and no low-lying levels will be present. In the case of two or more electrons, it is unusual to find spin-pairing, except in the presence of a strong crystal field (13). Thus, in the rare earth oxides with unpaired 4f electrons, many low-lying levels are present and absorption occurs in the visible region. Excitation energy is easily dissipated or results in infrared emission. The special stability of a half-filled electron shell is well recognized and for Gd^{+3} results in only a few energy levels between 0 and 40,000 cm^{-1} (3). Activation was obtained only in the matrices where the cation has no unpaired electrons, i.e., no angular momentum and no low-lying energy levels, thus minimizing interaction of the activator site with the matrix.

Effective Activators

Using the three oxides, La_2O_3 , Y_2O_3 , and Gd_2O_3 , as matrices, fluorescent properties of the rare earth activators were investigated. In previous investigations, Dieke and his co-workers (14) have found that most of the rare earths produce luminescence in $LaCl_3$. In the present case, not all of the rare earths, when incorporated in oxide matrices, give rise to fluorescence. The results found are given in Table III. Ultraviolet excitation was obtained by scanning the wave-length range until maximum response was found.

The results obtained parallel those obtained by previous investigators (8, 12) concerning fluorescent intensities of rare earths. Thus, Sm^{+3} , Eu^{+3} , Gd^{+3} , Tb^{+3} , and Dy^{+3} gave the highest fluorescent response to ultraviolet excitation, which was varied between 14,400 cm^{-1} and 45,500 cm^{-1} in order to evaluate the luminescence properties. The intensities differed by a factor of ten between weak and strong intensities.

Excitation-Emission Properties

The spectral properties were measured using a commercial radiometer (9). In all cases, the excitation spectrum of the strongest emission line was

Table III. Activation in La_2O_3 , Y_2O_3 , and Gd_2O_3 matrices

Activator	Ground state	Matrix		
		La_2O_3	Gd_2O_3	Y_2O_3
Ce^{+3}	$^2F_{5/2}$	—	—	—
Pr^{+3}	3H_4	m	—	—
Nd^{+3}	$^4I_{9/2}$	—	—	—
Sm^{+3}	$^6H_{5/2}$	w	w	w
Eu^{+3}	7F_0	s	s	s
Gd^{+3}	$^8S_{7/2}$	m	—	w
Tb^{+3}	7F_6	s	s	m
Dy^{+3}	$^6H_{15/2}$	m	m	m
Ho^{+3}	5I_8	w	—	w
Er^{+3}	$^4I_{15/2}$	w	—	w
Tm^{+3}	3H_6	w	—	—
Yb^{+3}	$^2F_{7/2}$	—	—	—
Lu^{+3}	1S_0	—	—	—

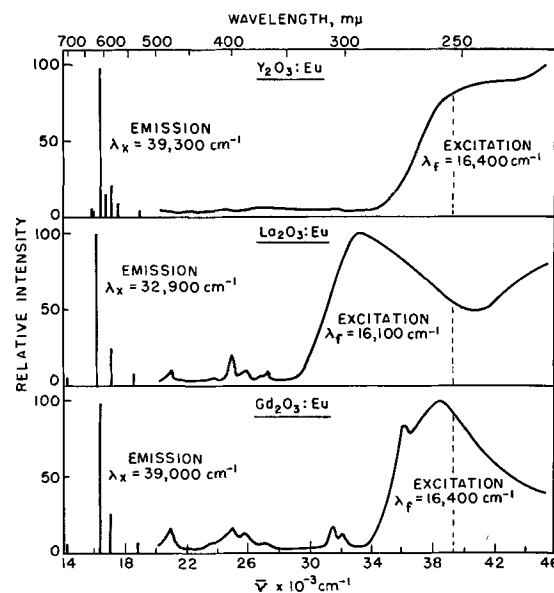


Fig. 1. Fluorescence of Eu^{+3} in rare earth oxide matrices

measured, and then the emission lines were re-measured to determine if change in excitation wavelength induced a change in emission lines. Only visible fluorescence was measured. Thus, the transition of Er^{+3} from its lowest fluorescent state, according to Dieke and Singh (15), would occur at 11,900 cm^{-1} (8440Å), a region which was not evaluated for fluorescence. The spectra are all normalized. The excitation beam was maintained at constant energy. The band pass of the instrument in the ultraviolet was about 2-10Å, depending on wavelength. Thus, spectral accuracy was believed to be within 100 cm^{-1} of the true values.

High-intensity emission.—High-intensity emission was observed with the activators Eu^{+3} and Tb^{+3} . The strongest line for Eu^{+3} is at 16,100 cm^{-1} in La_2O_3 , and at 16,400 cm^{-1} in Y_2O_3 and Gd_2O_3 , as shown in Fig. 1. The excitation spectra consist of broad bands with some lower intensity structure. The spectral properties are tabulated in Table IV for the main excitation bands and emission lines for each activator, exclusive of the levels attributable to transitions within the 4f configuration (ionic levels).

The emission lines were found to be nearly the same, but the excitation bands differed considerably. Because the 43,800 cm^{-1} band in La_2O_3 phosphors appears in all cases, regardless of activator (see below), it is probably a matrix excitation band. Ex-

Table IV. Spectral properties of Eu^{+3} and Tb^{+3} in rare earth oxide matrices

	Matrix					
	La_2O_3		Y_2O_3	Gd_2O_3		
	Emission, cm^{-1}	Excitation, cm^{-1}	Emission, cm^{-1}	Excitation, cm^{-1}	Emission, cm^{-1}	Excitation, cm^{-1}
Eu^{+3}	16,100	33,500	16,400	41,500	16,400	36,100
		44,000		>46,000		38,600
Tb^{+3}	18,400	36,500	18,400	32,700	18,300	33,200
		43,800		35,600		43,200

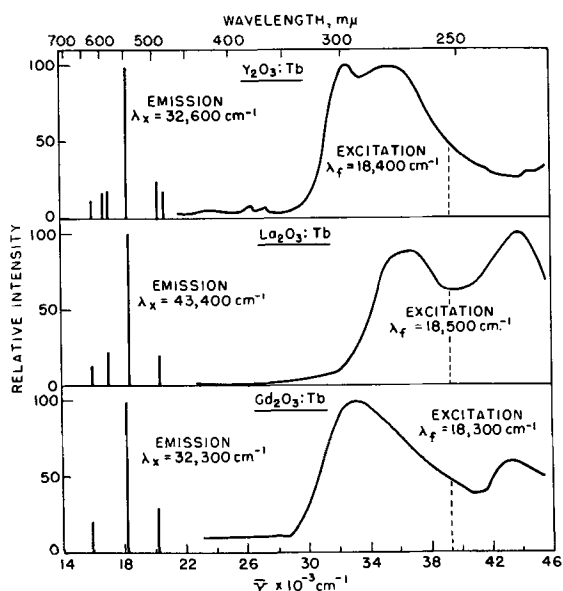


Fig. 2. Fluorescence of Tb^{+3} in rare earth oxide matrices

citation of the La_2O_3 matrix produced the same fluorescence as excitation in the lower intensity energy levels of the ionic activator. Excitation of the ionic levels of Eu^{+3} (transitions within the 4f configuration) was obtained in all cases, but excitation of Tb^{+3} ionic energy levels, for the most part, was absent, as shown in Fig. 2. The excitation spectrum of Y_2O_3 is suggestive of a band beyond the limits of measurement, and this hypothesis was confirmed by separate measurement (16). The second excitation band appears at $50,000\text{ cm}^{-1}$. The rather narrow peak at $36,200\text{ cm}^{-1}$ in $Gd_2O_3:Eu$ can be correlated to an excitation of the 6I_7 levels of the Gd^{+3} ion. This peak appears in most phosphors involving the Gd_2O_3 matrix.

Thus, for those phosphors having intense emission, fluorescence occurs by excitation which produces transitions within the 4f configuration, host lattice excitation (host sensitization) or excitation in an intense broad energy band which is probably related to a perturbed level of the activator. This band may be contrasted with the aforementioned rather narrow low-energy excitation bands which represent nonperturbed 4f transitions.

Medium intensity emission.—Medium intensity fluorescence was observed for the activators Sm^{+3} , Dy^{+3} , and Pr^{+3} , depending on the matrix. For Dy^{+3} , the spectra shown in Fig. 3 can be again divided into separate phenomena. The rather narrow excitation bands are associated with nonperturbed 4f transitions. The main emission lines and excitation peaks for $La_2O_3:Dy$, $Gd_2O_3:Dy$, and $Y_2O_3:Dy$, exclusive of ionic levels, are shown in Table V, as well as those for $La_2O_3:Sm$ (see Fig. 3).

In La_2O_3 , the matrix excitation band appears at $43,500\text{ cm}^{-1}$ in addition to the 4fⁿ excitation transitions. Both give rise to the main emission line of Dy^{+3} at $17,500\text{ cm}^{-1}$. Those phosphors based on the La_2O_3 matrix generally produced phosphors of medium intensity emission.

In Y_2O_3 , the matrix excitation band is not in a measured range, so that the main excitation peak indicated is a transition within the 4fⁿ configuration.

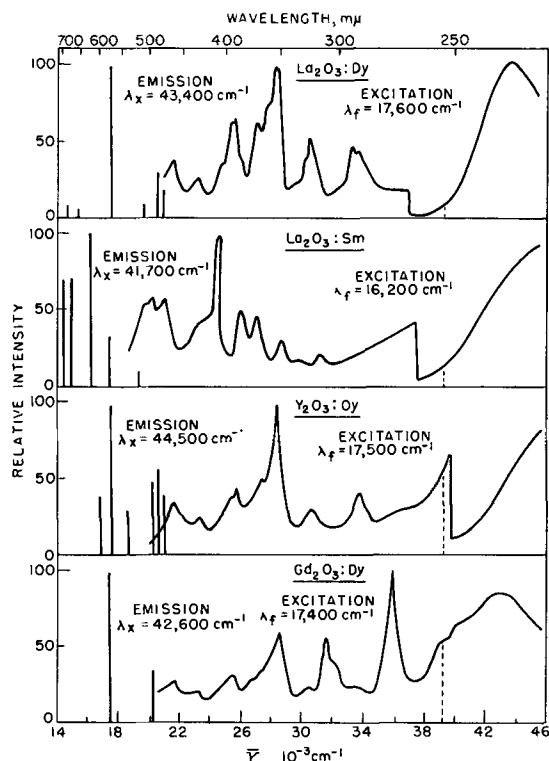


Fig. 3. Fluorescence of Dy^{+3} in rare earth oxide matrices

In Gd_2O_3 , there is a broad excitation band, apparently belonging to the matrix, but the strongest excitation band belongs to the 6I_7 levels of Gd^{+3} (3). There are Gd^{+3} ionic levels superimposed on the broad excitation band at $39,100\text{ cm}^{-1}$ and $40,200\text{ cm}^{-1}$. These are probably 6D_7 levels superimposed on the matrix excitation band. Thus, in this case, two types of excitation bands can be identified, non-perturbed 4fⁿ transitions and matrix excitation bands, but not the perturbed band involving one of the excited states of the activator found for the intense emitters.

Pr^{+3} .— Pr^{+3} in La_2O_3 leads to a medium intensity phosphor with the typical broad band perturbed level, probably associated with a Pr^{+3} excited state. In addition, the matrix excitation band is present at $43,600\text{ cm}^{-1}$ (see Fig. 7). The strongest fluorescence line is at $19,600\text{ cm}^{-1}$.

Weak intensity emission.—The systems which are relatively weak in emission intensity are those in which only 4fⁿ transitions are involved and little perturbation is evident.

Gd^{+3} .—In La_2O_3 , medium intensity is observed because host excitation occurs additionally (see

Table V. Spectral properties of Dy^{+3} in rare earth oxide matrices

	Matrix					
	La_2O_3		Y_2O_3		Gd_2O_3	
	Emission, cm^{-1}	Excitation, cm^{-1}	Emission, cm^{-1}	Excitation, cm^{-1}	Emission, cm^{-1}	Excitation, cm^{-1}
Dy^{+3}	17,500	43,500				
	19,400	35,700	17,500	44,500	17,400	43,000
Sm^{+3}	16,200	44,000	Too weak to measure			
Pr^{+3}	19,600	43,600	none			

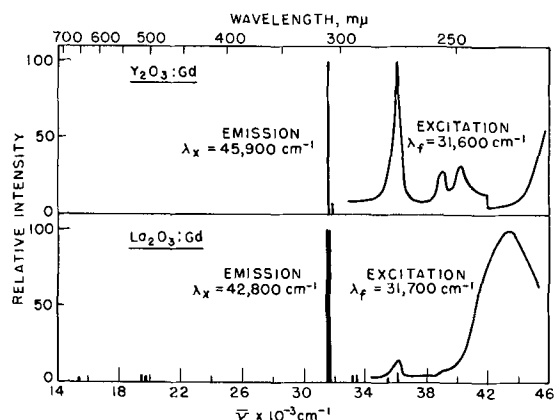
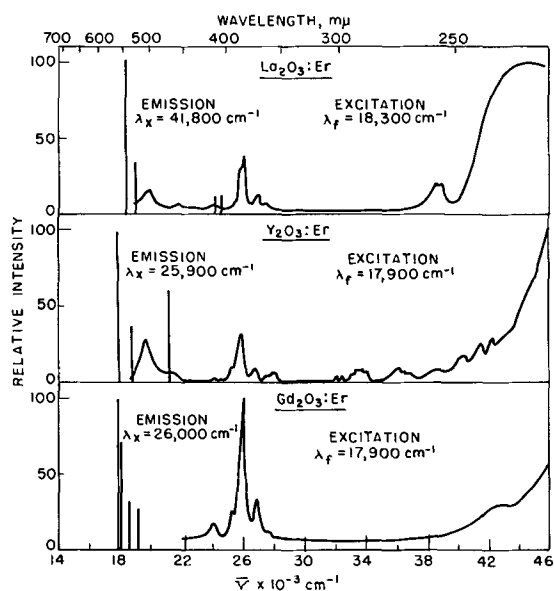
Fig. 4. Fluorescence of Gd^{+3} in rare earth oxide matricesFig. 5. Fluorescence of Er^{+3} in rare earth oxide matrices

Fig. 4). In $Y_2O_3:Gd$, the main excitation band is the Gd^{+3} triplet level, Table VI. This gives rise to the ultraviolet line emission. Thus, weak emission intensity is again associated with the absence of a perturbed excitation state of the activator.

Er^{+3} .—The emission intensity associated with Er^{+3} activator is always weak. The spectra are given in Fig. 5. In La_2O_3 , excitation in the matrix band does not produce intense emission. Apparently, the host sensitization process is not efficient, and the reso-

Table VI. Spectral properties of Gd^{+3} in rare earth oxide matrices

	Matrix			
	La_2O_3		Y_2O_3	
	Emission, cm^{-1}	Excitation, cm^{-1}	Emission, cm^{-1}	Excitation, cm^{-1}
Gd^{+3}	31,600) 31,700) 19,600	43,400	31,600	36,200
Intensity	medium		weak	

nance coupling is not strong between cation sites and activator. The transfer of energy would be expected to occur by resonant states of the matrix and activator (exciton states and excited dipole states). In Y_2O_3 , the emission lines of Er^{+3} are extremely weak and differ slightly from those found for Er^{+3} in La_2O_3 . The excitation spectrum shows considerable structure. The ionic excitation levels are very weak, and there is no matrix excitation in the range measured. In Gd_2O_3 , a similar situation prevails, except that the ionic levels are much more intense. The 6I state of Gd^{+3} is absent, indicating that host lattice resonance coupling, while stronger than Y_2O_3 , is not very efficient, and that the sensitization process is not strong. There is a band at $43,000\text{ cm}^{-1}$, indicative of host matrix excitation, but it is extremely weak. The main excitation and emission lines of Er^{+3} are summarized in Table VII, which includes the properties of Ho^{+3} in the same matrices (see Fig. 6).

The spectra of Er^{+3} in rare earth oxides consist of many interconfiguration transitions involved in excitation and emission.

For Ho^{+3} in the rare earth oxides, the emission intensity is also weak compared with other activators. In La_2O_3 , the usual matrix excitation band is present, and the coupling, *i.e.*, sensitization, seems to be somewhat stronger than for Er^{+3} in the same matrix. In Gd_2O_3 , an excitation state of Ho^{+3} is seen which is not present in the La_2O_3 phosphor. Further study of these phosphors is necessary to determine the effect of structure on relative intensity of the $4f^n$ excitation transitions.

Tm^{+3} .—In La_2O_3 , Tm^{+3} gives a single blue emission line at $21,700\text{ cm}^{-1}$ and a resonance line at $27,000\text{ cm}^{-1}$ (Fig. 7). The intensity is very low. Excitation in the matrix band yields these emission lines, but

Table VII. Spectral properties of Er^{+3} in rare earth oxide matrices

	Matrix					
	La_2O_3		Y_2O_3		Gd_2O_3	
	Emission, cm^{-1}	Excitation, cm^{-1}	Emission, cm^{-1}	Excitation, cm^{-1}	Emission, cm^{-1}	Excitation, cm^{-1}
Er^{+3}	17,900	21,700 26,000 14,000	17,900	19,700 25,900	17,900	24,100 26,100 27,000 43,000 (w)
Intensity	weak		weak		weak	
Ho^{+3}	18,000	19,800) 21,200) 43,400	18,200	21,100) 21,600) 21,900)	18,100	20,100) 20,700) 27,300) 43,000 (w)
Intensity	weak		weak		weak	

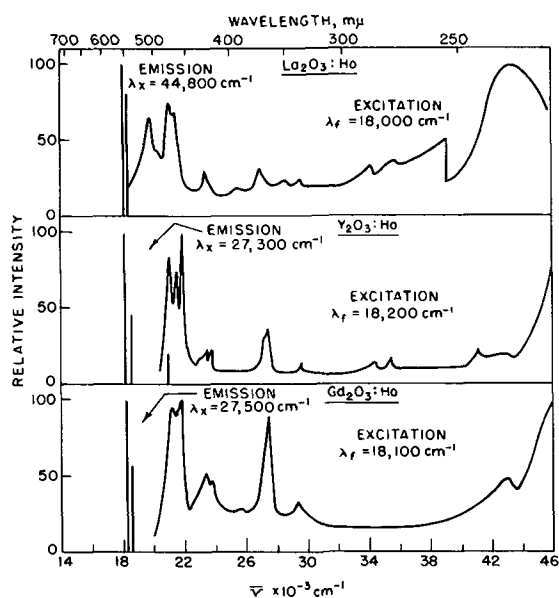


Fig. 6. Fluorescence of Ho^{+3} in rare earth oxide matrices

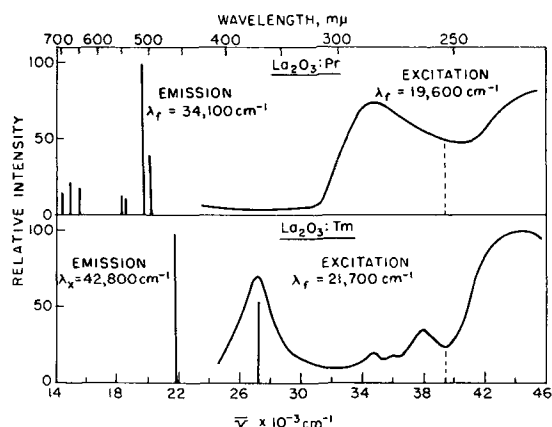


Fig. 7. Fluorescence of Pr^{+3} and Tm^{+3} in rare earth oxide matrices

the ionic levels are too weak to produce enough energy for measurement, except for the resonance line.

Conclusions

It has been shown that fluorescence is present in these systems where the cationic matrix component possesses the inert gas electron configuration (ns^2np^6). This corresponds to the case for d-electron activators. Since line spectra are observed, it is probable that perturbation of the emitting state is not large.

Correlation of the excitation spectra shows that the phosphors in each of the three emission intensity categories possess characteristic excitation spectra. For the weak emitters, only $4f^n$ configuration excitation transitions were noted. For the medium intensity phosphors, host sensitization seems to be the primary mechanism, but weak $4f^2$ excitation transitions were also present. For the intense emitters, the broad perturbed band, probably representing an excited state of the activator, predominates over all other features. Thus, intensity is associated with degree of perturbation.

The fundamental question of the origin of the broad excitation bands, other than those attributed to matrix excitation bands, is a difficult one, since excitation of Eu^{+3} or Tb^{+3} could involve either intraconfiguration transitions, as is more common in the d-electron activators, *i.e.*, changes in angular momentum, or transitions within the same configuration, the excited state of which is perturbed by the crystal field. The emitting state most certainly involves a $4f^n$ energy level, but it has become obvious (10) that the excitation and emission states are not one and the same. The excited states involve SLJ states which could belong either to the $4f^{n-1}5d$ or $4f^n$ configurations. If the former possibility prevailed, then one would expect line broadening in emission. This was not observed. The possibility that a transition between one of the excited states of the $4f^{n-1}5d$ configuration and a metastable state of the $4f^n$ configuration could occur prior to emission appears unlikely. Thus, the broad intense excitation band is probably associated with an excited state of the $4f^n$ configuration perturbed by the crystal field. Recently, Dieke and Crosswhite (3) have estimated the positions of the $4f^{n-1}5d$ states of the trivalent rare earths to be above $50,000\text{ cm}^{-1}$. If this estimate is correct, then there is little ambiguity as to the origin of the intense excitation bands found for Eu^{+3} and Tb^{+3} . The reasons for the unique behavior of these activators in a cation site of C_{3v} symmetry (*c*-type rare earth oxide) have not been explained. The logical choice to explain the nature of the high-intensity fluorescent transitions seems to be "induced electric dipole" transitions in which the selection rule becomes nonvalid when the nucleus of the activator is situated at a site whose symmetry lacks a center of inversion (17).

Acknowledgment

The author wishes to thank Dr. R. W. Mooney for his advice and encouragement, and H. D. Layman for preparation of the materials.

Manuscript received June 12, 1963; revised manuscript received Sept. 23, 1963.

Any discussion of this paper will appear in a Discussion Section to be published in the December 1964 JOURNAL.

REFERENCES

1. I. Warshaw and R. Roy, *J. Chem. Phys.*, **65**, 2048 (1961).
2. L. Pauling and M. D. Shappell, *Z. Krist.*, **75**, 128 (1930).
3. G. H. Dieke and H. M. Crosswhite, *Appl. Optics*, **2**, 675 (1963).
4. G. Urbain, *Ann. chim. phys.*, **18**, 293 (1909).
5. K. L. Wickersheim and R. A. La Fever, Unpublished data.
6. R. Tomaschek, *Z. Elektrochem.*, **36**, 737 (1930).
7. H. Gobrecht and R. Tomaschek, *Ann. Phys.*, **29**, 324 (1937).
8. K. G. Broadhead and H. H. Heady, *Anal. Chem.*, **32**, 1603 (1960).
9. W. Slavin, R. W. Mooney, and D. T. Palumbo, *J. Opt. Soc. Am.*, **51**, 93 (1961).
10. R. C. Ropp, Unpublished data.
11. I. Adams and J. W. Mellickamp, *J. Chem. Phys.*, **36**, 2456 (1962).

12. K. Hellwege, *Ann. Phys.*, **40**, 529 (1942).
 13. D. S. McClure, "Solid State Phys.," Vol. 9, F. Seitz and D. Turnbull, Editors, Academic Press, New York (1959).
 14. G. H. Dieke and R. Sarup, *J. Chem. Phys.*, **36**, 371 (1962); F. Varsanyi and G. H. Dieke, *ibid.*, **31**, 1066 (1959); F. Varsanyi and G. H. Dieke, *ibid.*, **36**, 835 (1962); H. M. Crosswhite and G. H. Dieke, *ibid.*, **35**, 1535 (1961).
 15. G. H. Dieke and S. Singh, *ibid.*, **35**, 555 (1961).
 16. J. E. Eby, Private communication.
 17. B. R. Judd, *Phys. Rev.*, **127**, 750 (1962).

The Dependence on Deposition Conditions of the Dopant Concentration of Epitaxial Silicon Layers

R. Nuttall

Ferranti Ltd., Wythenshawe, Manchester, England

ABSTRACT

Methods of doping epitaxial silicon layers produced by the hydrogen reduction of silicon tetrachloride are discussed, and a technique by which a constant concentration of dopant in the silicon tetrachloride vapor may be achieved is described. A function termed the conversion efficiency, η , is estimated for the various reactions taking place in the deposition cell, and the influence of various reaction conditions on η for several dopants are reported. The uniformity of dopant concentration in the epitaxial layers is discussed and methods for controlling the concentration gradient present at the substrate/epitaxial interface are indicated.

The epitaxial growth of silicon has been of particular interest in the silicon device field in view of the great potentialities of this technique. The most popular method by which epitaxial deposition is carried out is the hydrogen reduction of silicon tetrachloride, and the experiments described here were performed with a view to observing the influence of deposition conditions on the various reactions which take place during the deposition of doped silicon using this reaction.

Apparatus

The apparatus used in these experiments is similar to that described by Theuerer (1) and is shown in the flow diagram Fig. 1. The basic materials used in the construction are quartz and "Teflon." The hydrogen flow is controlled by tap T_1 which allows hydrogen to pass directly into the cell and tap T_2 which allows the hydrogen to pass through an evaporator filled with SiCl_4 and contained in a thermostatic bath. Tap T_4 allows the gas to run to waste for a period during which the flow is stabilized, while T_3 directs the flow into the deposi-

tion cell. By operating the thermostatic bath at various temperatures and varying the relative flow rates a large range of molar ratios SiCl_4/H_2 may be obtained. The deposition cell is constructed from quartz, and the pedestal is prepared from high purity graphite over which is placed a quartz cap. The graphite used was grade AGW obtained from British Acheson Electrodes Ltd., England.

The silicon slices used as substrates for the depositions were cut at 90° to the 111 axis and diamond polished, the final polishing being carried out using $\frac{1}{4}\mu$ particle size. The slices were cleaned by initially swabbing them with cotton wool soaked in methylene chloride followed by several rinses in clean methylene chloride. They were then dried using a clean dry nitrogen blast. Immediately before introducing each slice into the cell it was given a 2 min dip in hydrofluoric acid followed by several rinses in deionized water. It was then again dried with the nitrogen blast.

The mean resistivity of the epitaxial layers produced was calculated from four probe measurements and junction depth measurements, the latter being determined by the lapped bevel technique. In the system used the mean resistivity of the epitaxial layer deposited was found to be relatively independent of the substrate resistivity and type. However, in view of the possibility of gross contamination of the epitaxial layer by the substrate dopant reported by Basseches *et al.* (2), relatively high resistivity silicon of approximately 1-10 ohm-cm and of opposite conductivity type to the layer deposited was selected for the substrate. The conditions under which one may expect appreciable dopant transfer from the substrate are in fact suggested from the data obtained during these experiments. Each substrate was heated to 1250° in a

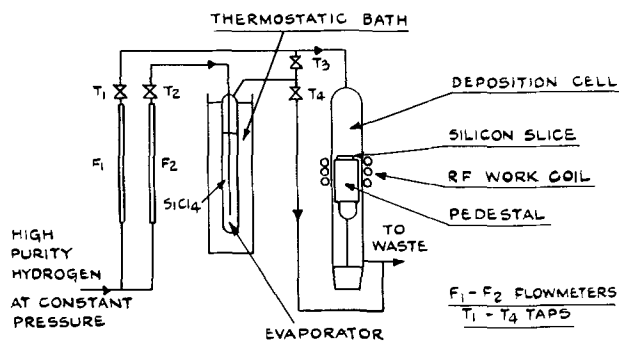


Fig. 1. Schematic flow diagram of equipment

stream of hydrogen for 20 min prior to deposition to remove oxide and anneal the mechanically polished surface. This type of surface yields a relatively large number of crystal faults in the deposited layer compared with a chemically etched surface but is more suitable for junction depth measurements. The thickness of the layers deposited was between 10-20 μ in each case.

The experiments were carried out in the following manner. The conditions, *i.e.*, flow rate, molar ratio, and temperature, were adjusted for each deposition, using a selected dopant, the conditions being selected randomly to eliminate the possibility of "hold-up" effects. For a given series of depositions using a specific dopant the final deposition was carried out under identical conditions to the first deposition and the results compared. These results in the majority of cases agreed within 20% of the bulk resistivity measurements. Where larger discrepancies were observed the experiments were repeated. The cell and pedestal were cleaned repeatedly during the experiments.

Doping of Epitaxial Layers

Production of doped silicon tetrachloride vapor mixtures.—The intrinsic silicon tetrachloride used in the experiments were prepared by distillation techniques. To evaluate this silicon tetrachloride, it was converted into a rod of silicon by reduction with hydrogen at molar ratio 0.07 (SiCl₄/H₂) and a flow rate of 3 liters/min and then float zone refined. After one pass in argon a resistivity profile of 400-100 ohm-cm N-type was found. Repeated vacuum refining gave a residual boron profile corresponding to 1000-800 ohm-cm P-type.

The two methods of introducing impurities into the vapor in these experiments were as follows:

(a) Direct addition of dopant to the silicon tetrachloride liquid in the evaporator, *i.e.*, liquid mixing. This is applicable where the "effective" vapor pressure of the dopant is similar to the vapor pressure of SiCl₄ (*e.g.*, PCl₃, BBr₃, and BCl₃).

(b) The pure dopant is incorporated in an evaporator in parallel with the intrinsic silicon tetrachloride evaporator with the relative hydrogen flows and evaporator temperatures controlling the concentration, *i.e.*, vapor mixing. This is more applicable to dopants of relatively low vapor pressures (*e.g.*, SbCl₃).

Liquid mixing.— This method was investigated in some detail as it is a relatively simple technique. The following factors are involved in such a system.

As with any two component system the rate of evaporation of the silicon tetrachloride and dopant will depend on their relative vapor pressures. It can be derived for such a system assuming ideal behavior and applying Raoult's law, that the change in concentration in the liquid phase is given by

$$\frac{y}{y_0} = \left[\frac{N}{N_0} \right]^{(\sigma-1)} \quad \text{providing } y \ll 1 \quad [A]$$

where N_0 is the initial total number of moles of dopant and SiCl₄ in the liquid phase, y_0 is the initial fraction dopant/SiCl₄ in the liquid phase, N is the

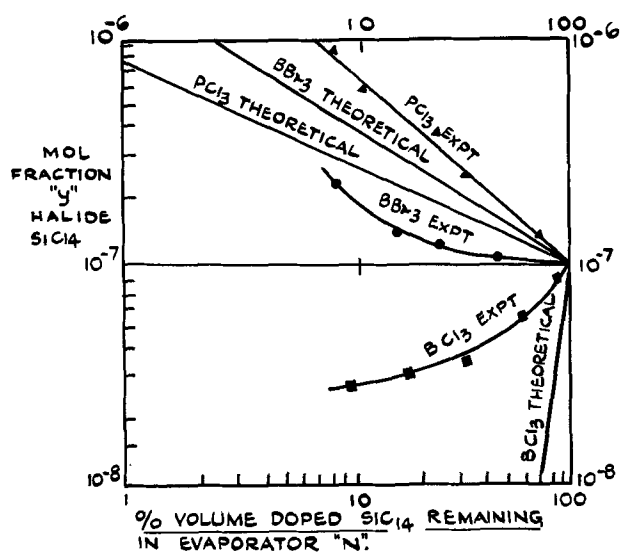
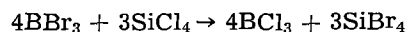


Fig. 2. Change in mole fraction on evaporation of doped SiCl₄

total number of moles of dopant and SiCl₄ remaining after evaporation of a given fraction of the original total volume, y is the mole fraction dopant/SiCl₄ after evaporation of the same fraction of the original volume, σ equals P_a/P_b , P_a is the vapor pressure of pure dopant, and P_b is the vapor pressure of pure SiCl₄.

This expression is basically the same as that described by Theuerer (1). Figure 2 shows the results obtained both by applying the equation and also those found by experiment. The temperature of the SiCl₄/dopant during evaporation was 20°C, the vapor pressures of the various components at this temperature being shown in Table I.

From Fig. 2 it can be seen that PCl₃ and BCl₃ exhibit vapor pressures which are less than expected, possibly due to intermolecular attraction. BBr₃ however, shows an increase in the expected vapor pressure suggesting some metathesis is taking place, *i.e.*,



This, together with the possible formation of mixed halogen compounds would result in higher vapor pressures being observed and possibly cause the nonlinearity of the BBr₃ curve. The nonlinearity of the BCl₃ is not clearly understood.

It can also be seen from Fig. 2 that there is a large change in the ratio of PCl₃/SiCl₄ vapor during evaporation, and this results in a corresponding large change in the concentration of phosphorus in the deposited silicon. This was also reported by Theuerer (1), who has since suggested a method of overcoming the effect (3). An alternative method, which unlike Theuerer's technique is independent of flow rate, has been derived and makes use of a "compensating evaporator." The compensating

Table I. Vapor pressure

Component	SiCl ₄	PCl ₃	BBr ₃	BCl ₃
Vapor pressure at 20°C mm Hg	190	93	52	1000

evaporator containing pure undoped SiCl_4 is placed before and in series with the doped evaporator, *i.e.*, between T_2 and the input side of the doped evaporator shown in Fig. 1. It is set at a predetermined temperature so as to compensate for the relative loss of SiCl_4 from the doped evaporator. For such a system a relationship similar to [A] can be derived, *i.e.*,

$$\frac{y}{y_0} = \left[\frac{N}{N_0} \right] \left(\frac{P_a - P_b + P_{b'}}{P_b - P_{b'}} \right) \quad [\text{B}]$$

The nomenclature is the same as for Eq. [A] with the addition of $P_{b'}$ which is the vapor pressure of the pure undoped SiCl_4 in the compensating evaporator.

It can be seen that the mole fraction y remains constant if

$$P_a = P_b - P_{b'}, \text{ i.e. } \sigma = 1 - \frac{P_{b'}}{P_b}$$

For practical purposes the value of σ is determined from the experimental data and is referred to as σ' . Using the value of σ' determined from Fig. 2, this requires for PCl_3 that

$$\frac{P_{b'}}{P_b} = 0.74$$

For example, if the temperature of the doped evaporator is 20°C (when P_b is 190 mm), then $P_{b'}$ should be 140 mm, *i.e.*, the temperature of the compensating evaporator will be 12.5°C for uniform concentration to be achieved.

The use of the compensating evaporator has proved successful in practice, particularly in the case of phosphorus trichloride doped SiCl_4 . Table II shows the mean resistivity of consecutive epitaxial layers produced using SiCl_4 doped with PCl_3 to a concentration to produce layers of mean resistivity of 2.5 ohm cm N-type. Column C shows typical results obtained using the compensating evaporator technique, while column D shows the change in resistivity found without the compensating evaporator. All the layers in each case were between 10-12 μ thickness.

Table II. Mean resistivity of consecutive epitaxial layers

C	D
2.7	2.5
2.9	
2.5	2.3
2.2	
2.0	
2.5	2.05
2.7	
2.5	
2.8	1.75
2.5	
2.7	
2.9	1.5
2.7	
2.9	
2.9	1.25
2.2	
2.9	
2.8	0.8

These results were obtained from evaporators containing initially the same volume of doped SiCl_4 . The 18 depositions carried out resulted in a 77% reduction of the original volume in the case of column D which produced the resistivity change indicated. Every third slice was evaluated. In the case of column C the volume reduction will be less due to the compensating evaporator continually adding SiCl_4 to the doped evaporator as a function of the compensating mechanism. The new "effective" volume V_E of a given doped SiCl_4 evaporator used in conjunction with a compensator will be given by

$$V_E = \left[\frac{P_b}{P_b - P_{b'}} \right] V$$

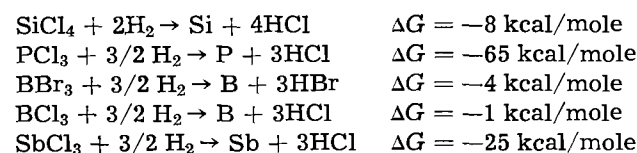
where V is the volume of doped SiCl_4 in evaporator and V_E is the volume of doped SiCl_4 + volume of pure SiCl_4 evaporated from the compensating evaporator. The technique can be applied to other dopants providing the ratio σ' is relatively constant throughout evaporation and is sufficiently high to warrant the use of a compensating evaporator.

For dopants having vapor pressures greater than that of SiCl_4 for the same temperature Eq. [B] and of course the technique will not apply. However, a more complex equation may be derived which is based on the replacement of the pure SiCl_4 in the compensating evaporator with SiCl_4 more heavily doped with the particular dopant selected, than the actual doped SiCl_4 evaporator. Using such a system it should be possible to compensate for the depletion of dopant occurring in the doped evaporator. This was not attempted during the experiments as the only applicable dopant used was BCl_3 which does not necessarily require compensation as the change in concentration with evaporation is relatively small over the latter part of the evaporation (see Fig. 2).

Gaseous mixing.—This method as previously indicated was used for dopants of low vapor pressure, which in the experiments carried out was confined to antimony trichloride. The equipment was modified for these experiments the dopant being contained in an evaporator placed in a thermostatic bath. Hydrogen was metered through this evaporator into the SiCl_4/H_2 stream and directed to waste or to cell with the SiCl_4/H_2 stream. Using this method for all the dopants investigated attempts were made to estimate the relative values of the conversion efficiencies of the dopant compared to the conversion efficiency for SiCl_4 under specific reaction conditions. The results obtained are discussed in the following section.

Estimation of the Relative Values of the Conversion Efficiency of Dopants Compared with Silicon

From the free energy/temperature data available in the literature (4, 5) the free energy changes accompanying the following reactions have been estimated at 1500°K .



There is some disagreement in the literature regarding the values of ΔG for the above reactions but there is sufficient difference between the group III elements and silicon for it to be argued that PCl_3 and SbCl_3 should be reduced much more readily than SiCl_4 under the reaction conditions indicated. They may be expected to be reduced before reaching the slice surface and if so the incorporation of P and Sb into the silicon lattice would be partly dependent on their vapor pressures and affinity for silicon (6). From the ΔG values for BCl_3 and BBr_3 it may be expected that they would not be so readily reduced as SiCl_4 , however because of the similarity of the basic chemistry of boron and silicon, side reactions may occur which will complicate the reduction.

The relative conversion efficiency η_1 was determined for the above dopants. η_1 is the ratio of the conversion efficiency for the dopant compared with the conversion efficiency for silicon, *i.e.*

$$\eta_1 = \frac{\eta_D}{\eta_{\text{Si}}}$$

where

$$\eta_D = \frac{S_D}{G_D} \quad \text{and} \quad \eta_{\text{Si}} = \frac{S_{\text{Si}}}{G_{\text{Si}}}$$

S_D is the number of atoms of dopant in the epitaxial layer, S_{Si} is the number of atoms of silicon deposited in the epitaxial layer, G_D is the number of molecules of dopant halide passing over the slice, and G_{Si} is the number of molecules of silicon tetrachloride passing over the slice.

η_1 was determined for PCl_3 , BBr_3 , and SbCl_3 using the following deposition conditions: gas flow rate 5 liters/min, molar ratio $\text{SiCl}_4/\text{H}_2 = 0.03$, and a reaction temperature of 1270°C .

For PCl_3 a value of 1 was obtained for concentrations corresponding to the range 10^{14} to 10^{19} atoms P/cc Si in the epitaxial layer produced. BBr_3 gave a value of 0.2 for concentrations of 10^{16} - 10^{19} atoms B/cc Si in the epitaxial layer. SbCl_3 produced a very low value compared with BBr_3 and PCl_3 , namely 0.03, which is much lower than can be expected from considerations of the free energy change of the reduction reaction, and is possibly due to the low affinity of Sb for Si (6). The figure of 0.03 was observed for the concentration range of 10^{15} - 10^{17} atoms Sb/cc Si in the resultant deposited layer. Although the figures quoted for η_1 are only approximate due to the large number of factors which have to be maintained constant during depositions, the figures indicate the marked differences in the readiness with which a particular dopant may be incorporated into the growing silicon layer. These values for η_1 are also dependent on the reaction conditions used for the deposition.

Effect of Deposition Conditions on the Conversion Efficiency of the Deposition and Doping Reactions

The conversion efficiency for silicon has been defined as

$$\eta_{\text{Si}} = \frac{S_{\text{Si}}}{G_{\text{Si}}}$$

as $S_{\text{Si}} \propto$ thickness of silicon deposited/min W , and

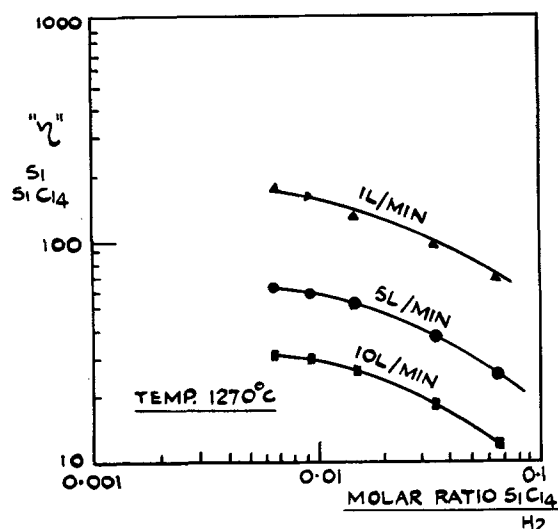
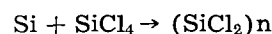


Fig. 3. Change in conversion efficiency Si/SiCl_4 with molar ratio and flow rate.

$G_{\text{Si}} \propto$ molar ratio $\text{SiCl}_4/\text{H}_2 \times$ gas flow/min *i.e.*, $M \times F$ then

$$\eta_{\text{Si}} \propto W/MF$$

In the experiments M and F were varied and W/MF plotted against M for different flow rates F . Figure 3 shows the results obtained. It should be noted that the values of " η_{Si} " are not absolute and that the graph only indicates the change in η_{Si} for a given change in conditions. The units used for the deposition rate are μ/min and flow rate liters/min. As space velocity appears to be a more valid measurement of flow it should be noted that from the deposition cell dimensions 1 liter/min = space velocity of 2.5 cm/sec. From Fig. 3 " η_{Si} " falls with both molar ratio and flow rate, possibly produced by the "etching reaction" (1.7), *i.e.*, the competing reaction



together with the limiting reaction rate at the surface of the substrate.

The variation of the conversion efficiency of the dopants with deposition conditions was determined as follows

$$\eta_D = \frac{S_D}{G_D}$$

For a constant concentration of dopant in the SiCl_4 vapor $G_D \propto$ molar ratio $\text{SiCl}_4/\text{H}_2 \times$ flow rate. The number of atoms dopant in the epitaxial layer $S_D =$ volume of epitaxial layer \times conc D atoms/cc Si.

For substrates of constant diameter the volume of the epitaxial layer \propto thickness.

\therefore Conversion efficiency

$$\eta_D \propto \frac{C \times W}{M \times F}$$

where C is the concentration dopant in layer in atoms/cc Si and is determined from the mean resistivity of the layer, W is the thickness of layer in μ deposited/min, M is the molar ratio of doped SiCl_4/H_2 , and F is the total gas flow rate measured in liter/min.

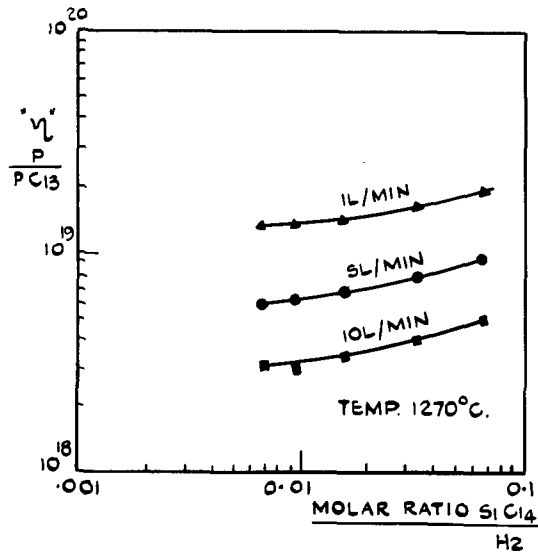


Fig. 4. Effect of molar ratio and flow rate on conversion efficiency of P/PCl₃.

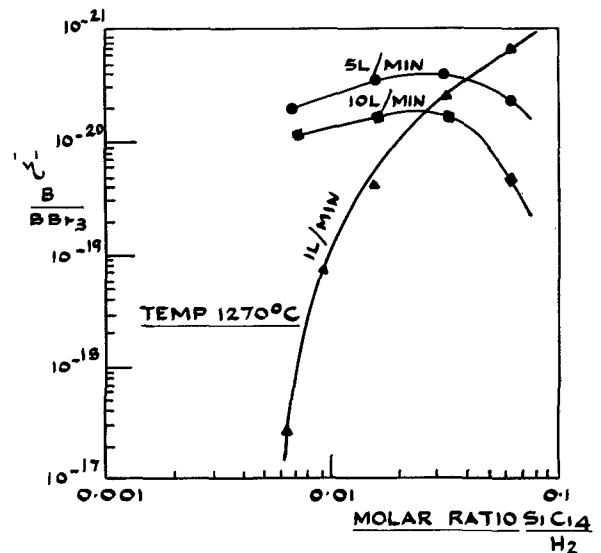


Fig. 6. Effect of molar ratio and flow rate on conversion efficiency of B/BBr₃.

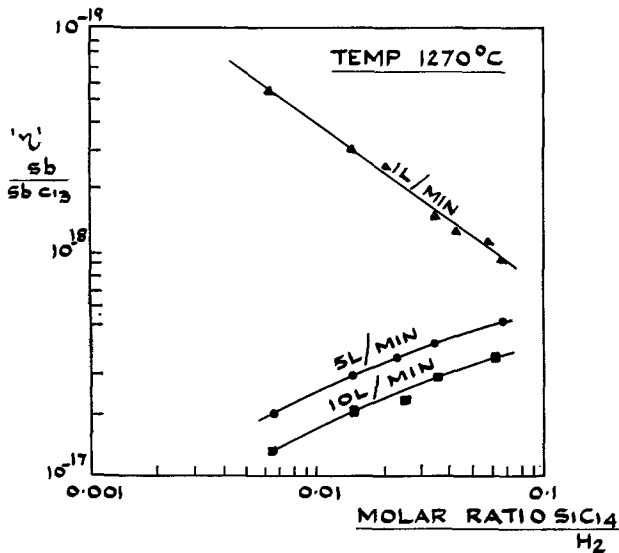


Fig. 5. Effect of molar ratio and flow rate on conversion efficiency of Sb/SbCl₃.

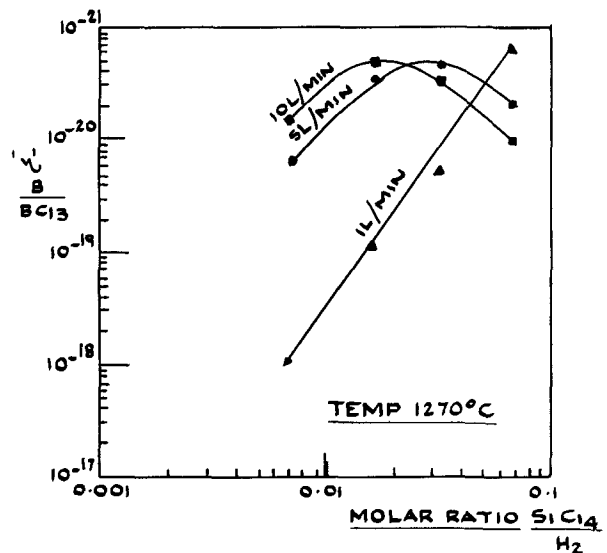


Fig. 7. Effect of molar ratio and flow rate on conversion efficiency of B/BCl₃.

This value for "η" is again not an absolute value but by varying the deposition conditions the changes in "η" can be noted.

Figure 4 shows the results obtained using PCl₃ as the dopant. By comparison with the efficiency curves for SiCl₄ an increase in molar ratio from 0.01 to 0.05 would increase the concentration of phosphorus in the layer by a factor of 4. The effect of flow rate is relatively small as this affects η_{Si} and η_P to a similar degree for a given molar ratio. These results are characteristic of those obtained for epitaxial layers produced with concentrations of phosphorus between 10¹⁴-10¹⁹ atoms/cc. The effect of molar ratio on the conversion efficiency of SbCl₃, Fig. 5, is similar to phosphorus at the higher flow rates although there is a tendency for the rate of change of "η_{Sb}" to fall with increasing molar ratio unlike phosphorus, whose rate increases. This phenomenon would appear significant in that at 1 liter/min "η_{Sb}" falls steadily with increasing molar ratio. This behavior has been noted in producing epitaxial layers of con-

centrations of 10¹⁵-6 x 10¹⁷ atoms Sb/cc Si. Figures 6 and 7 show the large changes of conversion efficiency for BCl₃ and BBr₃ with flow rate and molar ratio. At 1 liter/min the effect of a change in molar ratio of 0.008-0.05 increases "η_B" by a factor of 200 for BBr₃.

This effect could be partly explained by the BCl₃ and BBr₃ reduction reactions being inhibited by reaction products both from the reaction and the SiCl₄ reduction reaction. This is substantiated by the fact that epitaxial layers deposited under flow rate conditions of 1 liter/min and at low concentrations of BCl₃ and BBr₃ produced layers of which the first few microns were P-type while the remainder was N-type. The results shown on the graphs are characteristic when producing epitaxial layers of concentration 10¹⁶-10¹⁹ atoms B/cc Si.

Temperature also influences the conversion efficiency of the reactants as shown in Fig. 8. η₀ is a reduced form of η in that the efficiencies of each reaction at 1290°C has been equated to 1 to enable

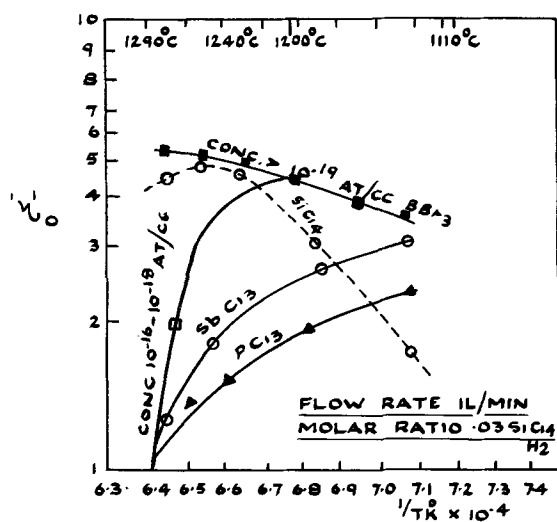
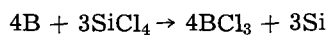


Fig. 8. Change of conversion efficiency with temperature

comparison of the relative changes in efficiencies. PCl_3 and $SbCl_3$ show a decrease in η with increasing temperature as might be expected. Boron behaves differently at high concentrations than low concentrations. At high concentrations there is a steady increase in η_B which would be expected assuming no side reactions. At low concentrations however, there is a sharp fall in η_B above 1240°C which may be associated with the reaction



It is also noted that the η_{S1} curve also shows this phenomenon but to a lesser degree. The above reaction has been suggested by Theuerer (1) as the reason for the large increase in deposition rate he observed when producing P-type layers using BBr_3 as the dopant. This increase was not observed during these experiments.

From over-all consideration of the graphs it is apparent that maximum control over resistivity of the layer is favored by the higher flow rates and lower temperatures.

The variation of resistivity and possibly conductivity type with reaction conditions may be used as a method of indicating the purity of silicon tetrachloride used in epitaxial depositions, particularly where compensation is suspected.

Epitaxial Layer Characteristic

It is apparent from the experimental results described that the conversion efficiency should indicate the most favorable conditions under which layers of uniform resistivity can be grown using a specific dopant. In the horizontal plane, i.e., across the slice, the only variable to be expected would be temperature. Therefore for a given temperature gradient across the slice during deposition, the lower the average temperature the more even would be the resulting resistivity of the subsequent layer. This will be limited however by the temperature dependence of the crystal perfection of the layer (1).

The variation in efficiency would also affect the concentration in the vertical plane, but other considerations are also of importance. Providing tight

control of flow rates and molar ratio is achieved during deposition the most marked variation in dopant concentration would be expected to occur during the initial deposition, i.e., at the substrate/epitaxial layer boundary. The factors which are responsible for the substrate/epitaxial concentration gradient are:

(a) The conversion efficiency which during the initial stages of deposition would vary until a steady state is achieved. This can be minimized by using deposition cells of small reaction volume together with high gas flow rates, which would tend to shorten the time taken to attain steady state conditions.

(b) The transfer of dopant from the substrate which may take place to a marked degree during the initial deposition and to a lesser degree during the latter stages of deposition. This has been referred to in recent papers as "autodoping" (8, 9).

(c) The diffusion of the dopants at the substrate/epitaxial layer interface. This has been discussed in some detail in a recent paper (10).

As already suggested the factor (a) can be minimized. The phenomenon indicated in (b) from consideration of the conversion efficiencies of the dopants would be expected to depend on the dopant involved and also the conditions of deposition. This follows if we assume that the incorporation of dopant from the substrate into the growing layer proceeds through a similar mechanism as the same dopant deliberately added in the gas phase. This means that it should be possible to select different dopants for the substrate and deposition gas mixture such that the conditions of deposition are unfavorable for the substrate dopant to be incorporated into the layer but favorable for the dopant in the deposition gas mixture. Conditions may be selected by comparison of the conversion efficiencies.

Suppression of Autodoping during Preparation of N/N + Structures

The structure consisting of a lightly doped N-type layer deposited on a heavily doped N-layer is familiar starting material for many device applications. Using arsenic or phosphorus doped substrate, the N/N + junction is considerably graded and may be an embarrassment when using such slices for certain device applications. Experiments carried out using arsenic as a dopant indicate that its conversion efficiency is similar to phosphorus. However, in all the experiments carried out with antimony trichloride as the dopant, antimony has shown a much lower relative conversion efficiency than phosphorus, i.e., approximately 0.03/1 for Sb/P. Therefore it follows that much less "autodoping" would be expected from antimony doped substrates than phosphorus or arsenic doped substrates. This has been substantiated by experiments. The average resistivities of N-type epitaxial layers deposited on 0.01 ohm-cm antimony doped substrates were always higher than those obtained using 0.01 ohm-cm arsenic doped substrates, for a given N-type dopant level in the gas phase, e.g., layers deposited on 0.01 ohm-cm arsenic doped substrates from prepared

PCl_3 doped SiCl_4 produced layers of resistivity of 3 ohm-cm N-type while corresponding layers deposited on 0.01 ohm-cm antimony doped gave a resistivity of 10 ohm-cm N-type. The resistivities were estimated by both reverse breakdown measurements and by using high resistivity P-type check slices deposited simultaneously.

Dope Transfer in Multi-Slice Systems

In systems where a horizontal flow system is used and in which several slices may be processed, transfer of dopant from one substrate to another may be observed in the direction of the gas flow during the initial deposition. This has been demonstrated by placing in such a system a low resistivity P-type, (boron doped) slice followed by in one case several 0.01 ohm-cm arsenic doped slices and in the other 0.01 ohm-cm antimony doped slices. The deposition was carried out using SiCl_4 doped with PCl_3 to give 5 ohm-cm N-type layers and under conditions which would give high boron efficiencies, i.e., high flow rates. On sectioning and copper staining the layers produced on antimony doped substrates, a P-type stripe was observed which proved to be the initial few microns of the epitaxial layer. This was deduced from fringe count measurements of the P and N layers, the total thickness agreeing with the total thickness normally expected for the deposition conditions used. Further verification was made by measuring the stacking faults (11). The thickness of the P-type stripe varied from 1-3 μ .

The layers deposited on arsenic doped substrate did not show a P-type stripe on sectioning. From these results it is apparent that sufficient arsenic is being transferred from the substrate to overdope the initial P-type contamination, whereas, although antimony would be released from the substrate, it is largely rejected by the growing surface.

The effects of the contamination P-type substrate are of course reduced as the layer is deposited as this in itself is "sealed" by the high resistivity layer which is being deposited. Experiments carried out using antimony doped substrates without the low resistivity P-type slice in the system produced N-type layers without a P-type stripe.

Other Dopants

So far P-type dopants other than boron have not been investigated but from consideration of free energy changes for halide reduction (4), volatility

and affinity (6), aluminum gallium, and indium may have certain advantages over boron as the substrate dopant. In all cases it is also necessary to consider whether the advantages gained by specific deposition conditions outweigh the disadvantages produced by possibly low deposition rates and high temperatures, i.e., excessive diffusion at the substrate/epitaxial layer interface, and the time for the system to achieve a steady state.

Conclusions

From the experimental data it is apparent that by selection of different dopants for the substrates and for epitaxial layers, and by the selection of the most suitable reaction conditions the degree of "autodoping" or dopant transfer can be minimized. This is particularly important when producing very thin epitaxial layers of high resistivity, and also in systems where multiple depositions are carried out.

Acknowledgment

Part of the work reported in this paper was carried out under contract from the Royal Naval Scientific Service. The author wishes to thank them for permission to publish this work.

Manuscript received April 29, 1963; revised manuscript received Oct. 10, 1963.

Any discussion of this paper will appear in a Discussion Section to be published in the December 1964 JOURNAL.

REFERENCES

1. H. C. Theuerer, *This Journal*, **108**, 649 (1961).
2. H. Basseches, R. C. Manz, C. O. Thomas, and S. K. Tung, A.I.M.E. Semiconductor Conference, Los Angeles, Aug. 1961. Published in *Metallurgy of Semiconductor Materials*, **15**, 69 (1962).
3. H. C. Theuerer, *This Journal*, **109**, 742 (1962).
4. Argonne National Laboratory ANL-5750, "Thermochemical Properties of the Oxides, Fluorides, and Chlorides to 2500°K, Alvin Glassner; "Metallurgical Thermochemistry," O. Kubashevski and E. L. L. Evans, *Bur. Mines Bull.* 476; and K. K. Kelley, *ibid.*, 477.
5. A. Mark, *This Journal*, **108**, 880 (1961).
6. S. E. Bradshaw and A. I. Mlavsky, *J. Electronics*, 134 (1956).
7. E. G. Bylander, *This Journal*, **109**, 1071 (1962).
8. C. O. Thomas, D. Kahng, and R. C. Manz, *ibid.*, **109**, 1055 (1962).
9. J. J. Grossman, Semiconductor Symposium, Electrochemical Society Meeting, Los Angeles, May 1962.
10. D. Kahng, C. O. Thomas, and R. C. Manz, *This Journal*, To be published.
11. W. Dash, *J. Appl. Phys.*, **2395** (July 1962).

Polarographic Studies in Acetonitrile and Dimethylformamide

IX. Behavior of α,β -Unsaturated Carbonyl Compounds

S. Wawzonek and A. Gundersen

Department of Chemistry, State University of Iowa, Iowa City, Iowa

ABSTRACT

Benzalacetophenone, benzalacetone, cinnamaldehyde, and crotonaldehyde were reduced stepwise at the dropping mercury electrode in anhydrous dimethylformamide. Large-scale electrolytic reductions were performed on the compounds in the presence and absence of carbon dioxide. Carbonation of the dianions of benzalacetophenone and benzalacetone gave α -phenyl- β -benzoyl propionic acid and α -phenyllevulinic acid, respectively. In the absence of carbon dioxide, the dianion of benzalacetophenone gave a polymer. The anion-free radical of benzalacetophenone in the presence of carbon dioxide gave a monomeric dicarboxylic acid and a dimeric monocarboxylic acid. In the absence of carbon dioxide a trimer was obtained. The reduction of cinnamaldehyde and crotonaldehyde gave tars.

Previous polarographic studies in acetonitrile and dimethylformamide have shown that this method is capable of furnishing evidence for the existence of stable anion-free radicals in the reduction of aromatic hydrocarbons (1, 2), aromatic ketones and aldehydes (3), and quinones (4).

In the present study the polarographic behavior and the electrolytic reduction of α,β -unsaturated ketones and aldehydes have been investigated to determine whether anion-free radicals and dianions are produced in dimethylformamide.

Experimental

The solutions were studied in a cylindrically shaped cell with a mercury pool anode and fitted with side arms for the anode connections and for admission of nitrogen. All measurements were made in a water thermostat at $25^\circ \pm 0.1^\circ$.

The current-voltage curves were obtained with a Sargent Model XII polarograph having a current scale calibration of $0.00497 \mu\text{a}/\text{mm}$ at a sensitivity of one.

The dropping mercury electrode was operated at 45 cm pressure and had a drop time of 3.60 sec in dimethylformamide (open circuit). The $m^{2/3}t^{1/6}$ value was $2.10 \text{ mg}^{2/3} \text{ sec}^{-1/2}$.

The dimethylformamide was purified in a manner similar to that reported previously (1). The compounds used were obtained from a stock and purified by crystallization or distillation.

Electrolytic Reductions

Electrolytic reductions of the various carbonyl compounds were carried out at a mercury cathode in a similar manner to that described earlier (1). The area of the cathode was 65 cm, and the line voltage was 85v. Typical procedures are illustrated below. The results are given in Table II.

Reduction of benzalacetophenone.—The electrolysis cell was filled with 300 ml of 0.155M potassium iodide in dimethylformamide. To the cathode compartment was added 20g of benzalacetophenone, and

nitrogen was bubbled through the cell for 1 hr. Direct current was passed through the cell for 6 hr.

The catholyte was poured into 1 liter of water which contained 20 ml of 10% acetic acid. The mixture was shaken with ether and allowed to stand overnight. The solid material which separated was collected on a filter and washed thoroughly with ether. Treatment of this white solid (6.2g) with acetone gave a trace of insoluble material melting at 271° - 274° . This material was not characterized further. The acetone filtrate was heated to boiling and water added to the cloud point. Upon cooling a white solid was obtained which, after two recrystallizations from benzene, gave a trimer (XV) which melted at 285° - 287° . A molecular weight determination of this compound using the freezing point method with 2-methyl-2-nitropropane as the solvent gave values of 616 and 629. The calculated value is 624.

Anal. Calc'd. for $\text{C}_{45}\text{H}_{36}\text{O}_3$: C, 86.53; H, 5.70. Found: C, 86.87; H, 5.74.

The ether layer from the extraction of the catholyte-water mixture was separated, dried over anhydrous sodium sulfate, and then the ether was removed by distillation. A red viscous oil remained which decomposed on distillation under diminished pressure. Analysis of this oil on the gas chromatograph at a column temperature of 325° showed that there was no benzalacetophenone or benzylacetophenone present.

A similar electrolysis of benzalacetophenone using 0.155M tetrabutylammonium iodide as the supporting electrolyte was carried out for 18 hr. The catholyte was poured into 600 ml of water which contained 20 ml of 10% acetic acid solution, and the resulting mixture was extracted with ether and filtered from the white solid formed; yield 6.1g. This compound was insoluble in all common solvents, but could be recrystallized from acetophenone; mp 426° with decomposition. An infrared spectrum of this compound in Nujol was almost

identical with the spectra of *meso*-1,3,4,6-tetra-phenyl-1,5-hexandione.

Anal. Calc'd. for $(C_{15}H_{13}O)_n$: C, 86.12; H, 6.22. Found: C, 85.81; H, 6.16.

Nitrogen analysis showed that no nitrogen was present in this molecule. The ether layer gave 9 ml of a dark brown tar.

Reduction of benzalacetophenone in the presence of carbon dioxide.—The electrolysis cell was filled with 300 ml of 0.155*M* potassium iodide in dimethylformamide. To the cathode compartment was added 10g of benzalacetophenone. Carbon dioxide was bubbled through the solution for 1 hr prior to the start of the reduction and during the reduction. Direct current was passed through the cell for 6 hr.

The solid material which precipitated from the cathode was filtered. This material was dissolved in water and filtered. The water was removed and the residue was washed with ether. The residue was a pink solid and weighed 1.85g. A potassium determination of this solid (I) gave a value of 21.73% (calc'd. 20.85). Upon acidification the compound lost carbon dioxide and gave 1.3g of α -phenyl- β -benzoylpropionic acid (III); mp 151°-152° (5).

The catholyte was poured into 1 liter of water and extracted with ether. The water solution was acidified and extracted with ether again. Removal of the ether left a yellow residue (5g). This material was washed with benzene and 3.2g of a white solid (IV); mp 225°-227° dec. was obtained.

Anal. Calc'd. for $C_{31}H_{26}O_4$: C, 80.50; H, 5.63. Found: C, 80.54; H, 6.03.

A neutralization equivalent of this compound was obtained by titration with sodium ethoxide in methanol and the value was found to be 464. The calculated value for a dimeric monocarboxylic acid (IV) is 462.

This acid from its infrared spectrum in Nujol and reaction with base proved to be 1,3,4-triphenyl-1-hydroxy-2-benzoyl-5-carboxycyclopentane (IV).

The acid (IV) (0.3g) when dissolved in water (150 ml) containing ethanol (3 ml) and 20% potassium hydroxide (2.5 ml) and heated at reflux for 5 min, gave *dl*-1,3,4,6-tetraphenyl-1,5-hexanedione; yield, 0.24g. The melting point after successive recrystallizations from benzene and ethanol was 192°-194°. A mixture with an authentic sample (6) melted at the same point. The infrared spectra in Nujol were identical.

In a similar electrolysis using 0.155*M* tetra-*n*-butylammonium iodide as the supporting electrolyte the resulting catholyte was poured over ice containing 10 ml of 10% acetic acid and extracted with 200 ml of methylene chloride. The insoluble white material formed was filtered and recrystallized from chloroform. This compound (0.9g) melted at 258°-261° and did not depress the melting point of *meso*-1,3,4,6-tetraphenyl-1,5-hexanedione (6).

The methylene chloride layer was shaken with three 50-ml portions of 10% sodium bicarbonate solution. Acidification followed by extraction with ether gave 3.9g of α -phenyl- β -benzoylpropionic acid; mp, 145°-147°. Recrystallization from a 1:2

mixture of benzene and petroleum ether (bp 100°-106°) gave a product with a melting point of 151°-152° (5). The neutralization equivalent obtained by titration with sodium methoxide in absolute methanol was 254.6.

Removal of the solvent from the methylene chloride extract gave a reddish tan-like material which could not be characterized.

Reduction of benzalacetone in the presence of carbon dioxide.—The electrolysis cell was filled with 300 ml of 0.155*M* tetra-*n*-butylammonium iodide in dimethylformamide. To the cathode compartment was added 10g of benzalacetone. Carbon dioxide was bubbled through the solution for 1 hr prior to the start of the reduction and during the reduction. Direct current was passed through the cell for 20 hr.

Twenty milliliters of 10% acetic acid was added to the catholyte, and the solvent was removed under diminished pressure. The residue was extracted with ether. The ether extract was shaken with three 50-ml portions of 10% sodium bicarbonate solution. Acidification of the combined sodium bicarbonate extracts and extraction with ether gave an oil which when recrystallized from water gave 2.1g of a white solid; mp 125°-127° [the literature value (7) for the melting point of α -phenyllevulinic acid is 126°]. A semicarbazone was prepared from this compound, and it melted at 217°-218°.

Anal. Calc'd. for $C_{12}H_{15}N_3O$: C, 57.81; H, 6.06. Found: C, 57.38; H, 6.16.

The nonacidic fraction from the reduction was a red oil (5.8 ml) which could not be crystallized. A distillation of this oil at reduced pressure (1 mm) gave decomposition.

Results

The polarographic data obtained for the various α,β -unsaturated carbonyl compounds in dimethylformamide are given in Table I.

To help formulate electrode reactions and identify the intermediate species large-scale electrolytic reductions were carried out with benzalacetophenone, benzalacetone, cinnamaldehyde, and crotonaldehyde. The results for the reductions in which identifiable materials were obtained are given in Table II. The products were characterized by neutralization equivalents, molecular weight determinations, preparation of derivatives, or comparison with authentic reference compounds. Infrared spectra furnished evidence for the structure of some of

Table I. Polarographic behavior of α,β -unsaturated ketones and aldehydes in dimethylformamide containing 0.155*M* tetra-*n*-butylammonium iodide

Compound	Concn. ^a	$E_{1/2}$ (v) vs. HG pool		I_d^b	
		1st Wave	2nd Wave	1st Wave	2nd Wave
Benzalacetophenone	0.952	-0.86	-1.48	1.03	0.84
Benzalacetone	1.01	-1.08	-2.06	1.06	0.76
Cinnamaldehyde	0.717	-0.97	-1.57	1.18	0.93
Crotonaldehyde	0.88	-1.39	—	1.11	—

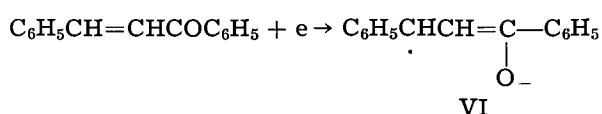
^a Millimoles per liter.

^b $I_d = i_d/Cm^{2/3}t^{1/6}$.

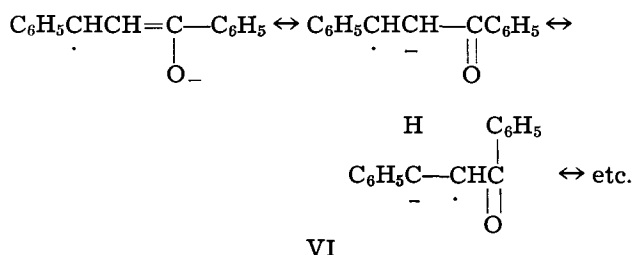
the second to the ketone group. The hydroxyl stretching of the carboxyl group appeared in the 2500-2700 cm^{-1} region and the alcohol group at 3490 cm^{-1} .

Decomposition of this acid (IV) occurred in alkaline solution by heating and gave *dl*-1,3,4,6-tetraphenyl-1,5-hexanedione (V). The infrared spectrum of this compound (V) in Nujol indicates that *dl*-1,3,4,6-tetraphenyl-1,5-hexanedione is present as a cyclic tautomer. Bands were obtained at 1660 cm^{-1} for the carbonyl group and at 3460 cm^{-1} for the hydrogen-bonded hydroxyl group.

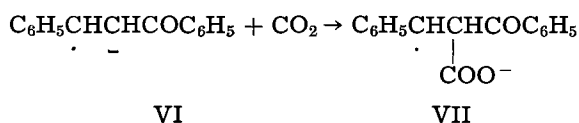
The products obtained in the electrolysis indicate that the reduction using potassium iodide as the supporting electrolyte must proceed by the addition of one electron to benzalacetophenone and gives an anion-free radical (VI)



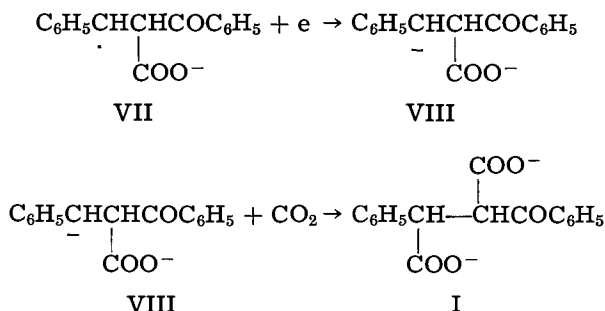
which is resonance stabilized



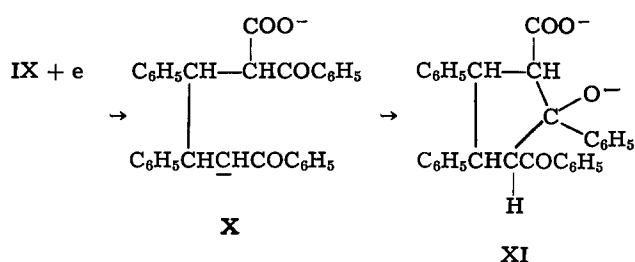
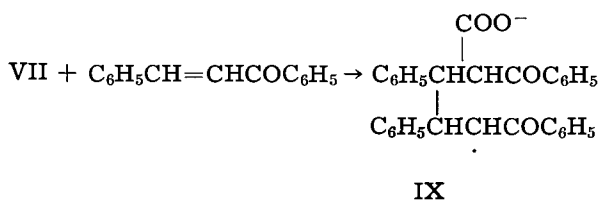
Carbonation of this intermediate is followed by further reduction and



carbonation to the dicarboxylate anion (I).

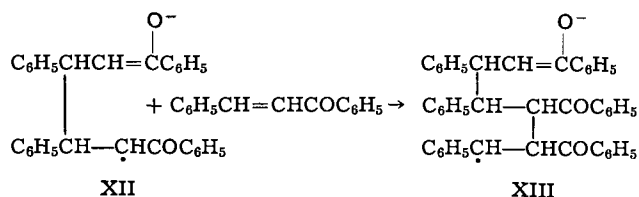


The anion-free radical (VII) may not be reduced to the dianion VIII immediately, but may add first to the double bond of another benzalacetophenone molecule and then would be reduced further.

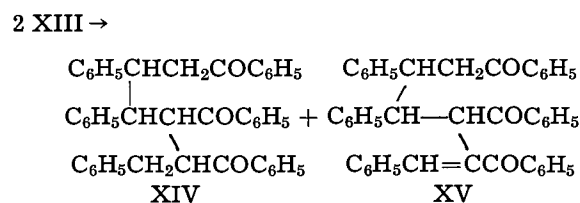


The resultant anion (X) would form the cyclopentane derivative (XI) which on protonation would give the compound (IV) isolated.

In the absence of carbon dioxide the one-electron reduction of benzalacetophenone gave a trimer. The actual structure of this compound is not known with certainty. The infrared spectrum of this compound in Nujol pointed to two different carbonyl groups. One occurred at 1685 cm^{-1} which is probably due to a benzoyl type ketone, and the other occurred at 1669 cm^{-1} which is in the range for a doubly unsaturated ketone group such as occurs in benzalacetophenone. A possible structure which would fulfill these requirements is represented by formula XV and would result from the addition of the anion-free radical (VI) to another molecule of benzalacetophenone. The resulting anion-free radical (XII) would add to another

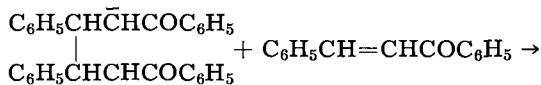
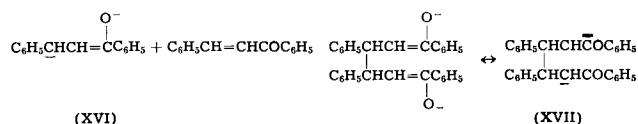


molecule of benzalacetophenone and this intermediate (XIII) could either disproportionate into the saturated (XIV) and unsaturated trimer (XV) or could lose a hydrogen atom to the other anion-free radicals (VI, XII) in the system

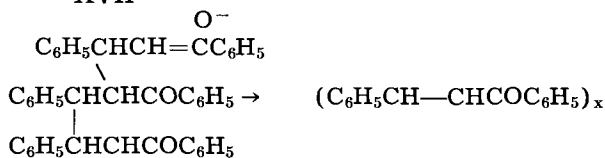


Neither the saturated ketone (XIV) or products from the anion free radicals (VI, XII) were isolated from the mixture of products obtained. The unsaturated trimer (XV) was obtained pure only after several crystallizations.

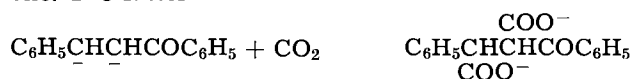
When tetra-*n*-butylammonium iodide was used as the supporting electrolyte, a two-electron reduction of benzalacetophenone occurred and gave a polymer which melted at 426° and was soluble only in boiling acetophenone. The infrared spectrum of this compound in Nujol was almost identical with the spectrum of *meso*-1,3,4,6-tetraphenyl-1,5-hexanedione. The compound must have resulted from a series of Michael-type additions of the dianion intermediate (XVI) to benzalacetophenone.



XVII



Reduction of benzalacetophenone under the same conditions but in the presence of carbon dioxide gave α -phenyl- β -benzoylpropionic acid and a small amount of *meso*-1,3,4,6-tetraphenyl-1,5-hexanedione. The latter



compound resulted from a Michael-type addition of the dianion to a benzalacetophenone molecule as shown in the scheme for the polymer formation.

Cinnamaldehyde and crotonaldehyde form much less stable reduction intermediates. In the presence and absence of carbon dioxide only oily products were obtained from the large-scale electrolytic reduction of these compounds. Benzalacetone behaved similarly in the absence of carbon dioxide, but could be carbonated to α -phenyllevulinic acid.

Results obtained in the absence of carbon dioxide are similar to those reported by Law (9) for the re-

duction of cinnamaldehyde, benzalacetone, and crotonaldehyde at a copper or lead cathode in aqueous medium. Unless the pH of the solution was controlled carefully only resinous material could be obtained.

The large-scale electrolysis indicated that α,β -unsaturated carbonyl compounds when suitably substituted as in benzalacetophenone will form stable anion-free radicals and dianions which may add to the parent compound. This addition may cause a lower diffusion current in polarographic analysis than what would be expected ordinarily. Such an addition reaction may make a quantitative determination of polymerizable monomers difficult in anhydrous media.

Manuscript received Aug. 2, 1963. This paper is based on the Ph.D. Thesis of A. Gundersen (June 1961) and was presented at the New York Meeting. The research was supported by the Office of Ordnance Research under Contract Da-11-022-ORD-1868.

Any discussion of this paper will appear in a Discussion Section to be published in the December 1964 JOURNAL.

REFERENCES

1. S. Wawzonek, E. W. Blaha, R. Berkey, and M. E. Runner, *This Journal*, **102**, 235 (1955).
2. S. Wawzonek and D. Wearing, *J. Am. Chem. Soc.*, **81**, 2067 (1959).
3. S. Wawzonek and A. Gundersen, *This Journal*, **107**, 537 (1960).
4. S. Wawzonek, R. Berkey, E. W. Blaha, and M. E. Runner, *ibid.*, **103**, 456 (1956).
5. R. Anschütz, P. Walter, and C. Hahn, *Ann.*, **354**, 148 (1907).
6. L. R. Finch and D. E. White, *J. Chem. Soc.*, **1950**, 3367.
7. Huan, *Bull. Soc. chim. (France)*, **5**, 1341 (1938).
8. R. Pasternak, *Helv. Chim. Acta*, **31**, 753 (1948).
9. H. D. Law, *J. Chem. Soc.*, **101**, 1030 (1912).

The Polarographic Reduction of Some Aryl Diketones

Robert H. Philp, Jr., Robert L. Flurry, and R. A. Day, Jr.

Department of Chemistry, Emory University, Atlanta, Georgia

ABSTRACT

The polarographic reduction of several diketones has been studied in aqueous and nonaqueous solvents. The Kalousek switching technique has been employed to detect oxidizable intermediates. Evidence was found for oxidizable enediols in the reduction of benzil and *p*-diacetylbenzene in aqueous media. Free radicals are produced by a number of diketones in dimethylformamide. The mechanism of reduction is discussed, including evidence for reversibility of electrode processes.

The polarographic reduction of various diketones has been reported by numerous investigators (1-17). The behavior of an individual compound depends, of course, on the structural relationship between the two carbonyl groups, as well as the presence of conjugation or aromatic groups in the molecule. It is difficult to generalize about the behavior of such compounds.

The present work reports results obtained on the polarography of a number of aryl diketones over a wide range of pH in aqueous-ethanol media. In addition to classical methods we have used such techniques as controlled potential coulometry and the

Kalousek switching method (18) in an attempt to gain information regarding the mechanism of reduction of selected diketones. Some studies were also carried out in dimethylformamide. The diketones, benzil, and *p*-diacetylbenzene, were studied in greatest detail. Preliminary results are also reported on the compounds 1,3-indanedione, 2-phenyl-1,3-indanedione, ninhydrin, *m*-dibenzoylbenzene, *o*-dibenzoylbenzene, and trans-dibenzoylethylene.

Experimental

Polarographic data were obtained with a L&N Electrochemograph Type E. Half-wave potentials

Table I. Half-wave potentials of diketones^a

Substance	pH	Wave 1		Wave 2	
		$-E_{1/2}$	<i>I</i>	$-E_{1/2}$	<i>I</i>
Benzil	3.1	0.45	2.5		
	4.6	0.55	2.2		
	7.6	0.72	2.0		
	8.7	0.79	1.9		
	9.4	0.79	2.1	1.53	0.5
	11.0	0.82	2.2	1.59	0.9
	12.0	0.81	2.2	1.61	1.3
p-Diacetylbenzene	2.0	0.78	2.4		
	3.7	0.85	2.5		
	5.0	0.94	2.5		
	5.8	0.99	2.2	1.45	0.7
	6.8	1.11	2.3	1.52	1.5
	7.9	1.22	2.1	1.60	2.1
	9.5	1.25	2.4	1.66	2.5
	11.0	1.26	2.5	1.70	2.3
	12.0	1.25	2.5	1.71	1.9
	Ninhydrin	2.8	0.89	1.6	1.19
4.2		0.96	1.6	1.26	1.9
6.0		1.09	1.9	1.40	1.9
7.3		1.14	1.9	1.43	1.9
8.6		1.20	1.8	1.48	1.5
10.8		1.21	1.5	1.63	1.7
12.1		1.26	1.5	1.62	1.2
1,3-Indanedione	2.8	0.92	2.0		
	4.2	1.00	2.0		
	6.0	1.14	2.1	1.52	0.9
	7.3	1.25	1.6	1.57	0.9
	8.6	1.32	0.4	1.65	2.9
	10.8			1.65	2.8
	12.0		1.70	2.5	
2-Phenyl-1,3-indanedione	2.8	0.91	1.8		
	4.2	0.98	1.8		
	6.0	1.18	1.7	1.50	1.8
	7.3	1.37	0.7	1.60	2.0
	8.9			1.61	3.0
	10.8			1.66	2.7
	12.0		1.72	2.5	
Benzoylacetone	2.9	1.19	1.6		
	4.3	1.27	1.5		
	5.3	1.33	1.6		
	6.9	1.42	1.6		
	8.5	1.48	1.2	1.66	0.6
	9.0	1.48	1.2	1.63	0.7
	9.8			1.60	1.5
	12.0			1.71	0.2
Dibenzoylmethane	1.6	0.93	0.9		
	2.6	1.07	0.9		
	4.1	1.15	0.8		
	4.9	1.21	0.9		
	7.4	1.35	0.7	1.53	0.7
	8.7	1.40	0.8	1.65	0.9
	10.5			1.65	0.9
	12.1			1.65	1.0
m-Dibenzoylbenzene	3.0	1.01	^b		
	3.9	1.03	^b	1.25	^b
	5.0	1.05	1.9	1.23	1.9
	5.7	1.10	1.9	1.23	1.8
	6.8	1.22	3.7		
	8.2	1.27	3.1		
	9.8	1.33	1.3	1.52	1.3
	11.7	1.33	1.2	1.51	1.2

^a All $E_{1/2}$ values vs. SCE; diffusion current constants $I = i_d / \text{cm}^{2/3} t^{1/6}$.

^b Waves were not well defined.

were corrected for IR drop and for lag caused by galvanometer damping. The electrolysis cell, experimental procedure and buffer solutions were the same as described previously (19). All pH values are of the cell solution, that is, the apparent pH of the aqueous-ethanol mixed solvent. The final cell solution was made by mixing equal volumes of aqueous buffer and a 0.002M solution of the diketone in 95% ethanol, except in one case. The concentration of p-diacetylbenzene was 5×10^{-4} M in a 20% ethanol solution in the runs reported in Table I. The dropping mercury electrode operated with a head of 40 cm giving values of $t = 5.0$ sec, $m = 1.48 \text{ mg sec}^{-1}$ in 0.01M sodium hydroxide in 25% ethanol with an open circuit.

All organic compounds of Eastman white label or equivalent grades were used without further purification. Compounds of uncertain purity were recrystallized. All inorganic compounds were reagent grade. The DMF was Matheson, Coleman, and Bell Spectroquality Reagent and was used without further treatment. All DMF solutions were 0.1M in tetra-n-butylammonium iodide, obtained as a polarographically pure grade from Southwestern Analytical Chemical Corporation. Polarograms in DMF were carried out in a Heyrovsky cell with an internal mercury pool anode.

Macroelectrolyses and coulometric measurements were carried out using a potentiostat of the Lingane-Jones type (20). The cell, electrodes, and experimental procedures were essentially those recommended by Lingane (21).

The circuit designed for use of the Kalousek technique is shown in Fig. 1a. The basic difference between this and circuits used by other workers is that the auxiliary potentiometric circuit contains a separate working cell. This eliminates the necessity of making any connections inside the commercial instrument.

The switching was effected by a specially constructed cam operating against a s.p.d.t. microswitch. The cam was driven by a Hurst synchronous motor (60 rpm) and was designed so that the switch was in each position three times each revolution. This gave a frequency of 3 cps compared to that of 5 cps originally employed by Kalousek (18).

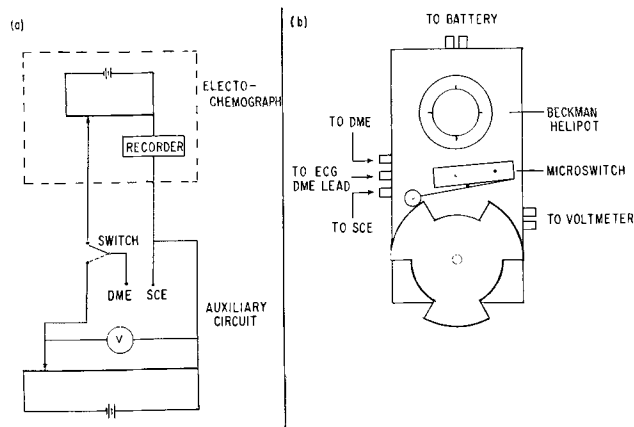


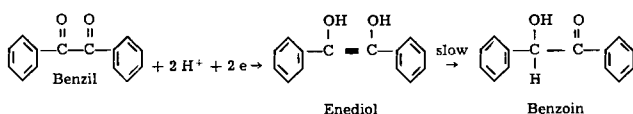
Fig. 1. Apparatus for application of Kalousek's technique. (a) Circuit. (b) Switching device.

The auxiliary potential was set by use of a Beckman helipot (500 ohms). The voltage was registered on a Simpson Model 127 Voltmeter (0-3v at 1000 ohms/v). It was realized that some loading might result from this circuit. The calculated value of the differential between the potential difference and the voltage read was of the order of 15 mv, and this was verified by measurements of the output using a potentiometer. Furthermore, as long as the auxiliary potential was at a value corresponding to the plateau of the reduction wave in question, the exact potential was not critical for the purpose of the experiments made. A diagram of the apparatus is shown in Fig. 1b.

The damping position 2 of the Electrochemograph was found to be most satisfactory. When less damping was employed, very large current oscillations caused by the drops, with smaller, superimposed oscillations caused by the switching were observed.

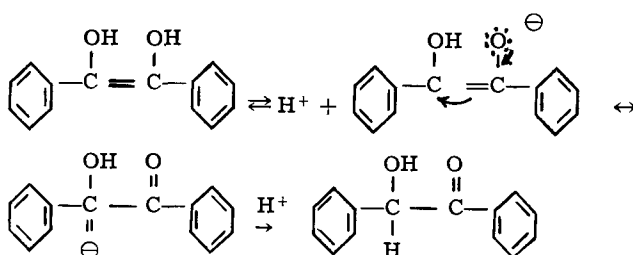
Discussion of Results

Benzil and related diketones.—The first diketone studied in some detail was benzil. Pasternak (6, 7) found one presumably two-electron wave over the pH range 1-11 and isolated benzoin as the product of macroelectrolysis. Since no wave was observed for the product, benzoin, which itself is reduced at somewhat higher potentials, it was assumed that the reduction proceeded through an enediol which was slow to rearrange to benzoin at the mercury drop. The reaction would be



Later Bobrova and Tikhominova (10) reported observing a second wave in the reduction of benzil. Day, Philp, and Flurry (22) confirmed this observation, noting that the wave was well formed at pH 10, and that it did occur at the potential at which benzoin was reduced. In solutions of low pH, however, the wave was not observed, even though benzoin itself normally produced a wave under these same conditions. Hence, it is evident that the rearrangement of the enediol to benzoin is facilitated in basic media.

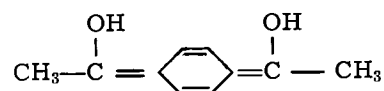
A mechanism to account for the effect of acidity on the rearrangement is as follows



The resonance hybrid of the enolate ion has a very basic center on a carbon atom and can be protonated directly. This mechanism would make reasonable the fact that no second wave is observed with

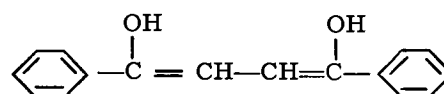
benzil at low pH, but is at high pH. It would require that the ease of rearrangement depend on the acid strength of the enediol; that is, the stronger the acid the lower the pH required to form appreciable concentrations of anion and consequently to observe the second wave.

The half-wave potentials obtained for several other diketones at different pH values are shown in Table I. Of these compounds p-diacetylbenzene is perhaps the most analogous to benzil in that the enediol shown below can be postulated



Rearrangement of this enediol to the keto structure restores aromatic character to the benzene ring. Hence, the anion structure should be favored and the second wave should be obtained at lower pH values, as is found to be the case.

Some studies were attempted with o-dibenzoylbenzene, since its structure allows the formation of an enediol intermediate. However, inconclusive results were obtained. At pH 2.7 one well-defined wave ($E_{1/2}$ of 0.81v, $I = 2.0$) was observed. At pH 4.7 the wave of 0.92v was followed by a somewhat drawn out wave around 1.25v. This behavior continues at higher pH values and for this reason no data are included in Table I. The compound ninhydrin also should be capable of forming the enediol structure and does form two waves even in fairly acidic solutions. We obtained no direct evidence for an oxidizable intermediate with this compound, but Holleck, Lehmann, and Mannl (23) recently reported the isolation of enediol salts in the reduction of ninhydrin in the pH range 4-11. The compound dibenzoyl ethylene, studied by Pasternak (7), should form an enediol intermediate



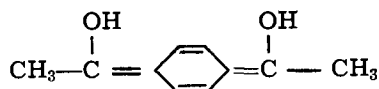
According to Pasternak's results, both cis- and trans-dibenzoyl ethylenes show the second wave about pH 7.2. We confirmed this behavior for the trans compound.

Other diketones.—Of the other diketones whose behavior is given in Table I, benzoylacetone and dibenzoylmethane cannot form the enediol intermediate. Current values correspond more nearly to one electron process for both waves. A second wave does appear in the pH range 7 to 8 but the first wave disappears at still higher pH. Enolization can occur in these molecules, of course, and the wave-splitting observed is similar to that found in the polarographic reduction of acids whose reducible groups are influenced by the presence of either the free acid or its anion form. The disappearance of the first wave is consistent with this concept. The behavior of 1,3-indanedione and 2-phenyl-1,3-indanedione is similar, and even though it is possible

for these compounds to form enediol structures the evidence does not support the formation of such intermediates.

The molecule *m*-dibenzoylbenzene is interesting since its structure is such that it cannot form the enediol structure, nor can it enolize. Apparently the carbonyl groups are reduced independently and the polarographic behavior is strikingly similar to that of a simple aromatic ketone, such as benzophenone (19). Two waves are observed in acid media, the first *pH* dependent, the second *pH* independent. The two waves merge about *pH* 6 and separate again at high *pH*. Coulometric data confirmed that complete reduction (4 electrons) occurred at high *pH*. The half-wave potentials observed are very close to the values obtained for benzophenone.

Studies using the Kalousek technique.—Since the intermediate proposed in the reduction of several diketones has the enediol structure and since enediols are oxidizable at the dropping mercury electrode, we investigated the possibility of detecting intermediates by an oxidation procedure. It was of further interest to see if any diketone-enediol system might be reversibly oxidized and reduced. In particular the intermediate obtained from *p*-diacetylbenzene shown below



is interesting since it represents a case analogous to the *p*-benzoquinone-hydroquinone system except that the quinone-like structure is the reduced rather than the oxidized form.

During the course of this work Berg (17) reported observing a stable, polarographically oxidizable intermediate in the photosensitized and catalytic reduction of benzil. Muller (16) also observed an oxidizable intermediate when benzil was reduced with hydrogen in a buffer solution of *pH* 2.4.

We chose the method introduced by Kalousek (18) to see if intermediates could be detected. This method, which has not been widely used, changes the polarizing voltage discontinuously. Recent papers in which the technique has been employed are those of Bauer (24), Bauer and Berg (25), and Holubek and Volke (26). As described under the experimental section, we used the circuit usually designated in the literature as K-11. With this circuit, if an oxidizable product is produced during reduction an anodic wave will be obtained along with the reduction wave providing the potential scan is initiated at a sufficiently positive value. The theoretical forms of current-potential curves under the conditions of Kalousek's experiments have been discussed by Kambara (27), Koutecky (28), and Matsuda (29). It can be shown that a system forming a reversible couple in the ordinary sense (reaction rate fast compared to diffusion) will exhibit a merged anodic-cathodic wave when K-11 conditions are applied.

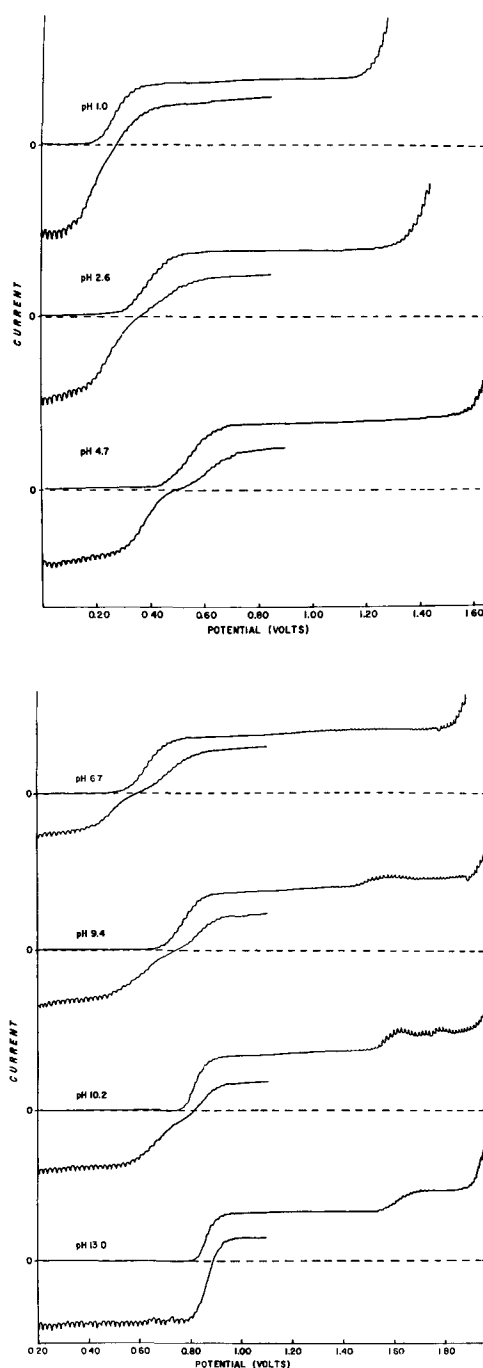


Fig. 2. Ordinary and K-11 polarograms of benzil at different *pH* values.

Figure 2 shows the ordinary and K-11 polarograms for benzil at different *pH* values. In all of the latter polarograms the auxiliary potential applied to produce the reduction product corresponded to the top of the first normal wave. In very acid solutions, the K-11 polarogram gives an almost merged wave, the half-wave potential of the combined wave being almost the same as that of the ordinary polarogram. However, the process is not strictly reversible. As the *pH* is increased, the waves split into anodic and cathodic components, and both waves show a shift to more negative potentials. In the *pH* range 9-10 there is a discernible trend toward merging, and at *pH* 13, only a merged, reversible wave is observed.

Some runs were made using the K-11 technique with the auxiliary potential corresponding to the top of the second wave (at pH values where the second wave was observed). An anodic wave of somewhat decreased height was obtained at the potential of the first wave. It had little if any cathodic component until the potential of the second reduction wave was reached. This behavior can be rationalized by assuming the four electron addition at potentials corresponding to the top of the second wave must be stepwise. The oxidizable intermediate must, in cases where the anodic wave is observed, have at this potential a life-time sufficient to allow detection by the K-11 technique.

Since the K-11 data at pH 13 indicated that the system was reversible, an undamped polarogram was run at this pH to determine n , the number of electrons in the potential determining step, from the slope of the polarogram. A slope of 27.5 mv was obtained, close to the theoretical value of 29.6 mv for a two-electron step. The K-11 data at pH 1 clearly indicated irreversibility, and the corresponding log plot deviated from linearity near the head of the wave. Since there was no clear evidence through the whole pH range which indicated a change in mechanism, we feel that the potential determining step in both acidic and basic media is a two-electron process. A mechanism is proposed later.

Figure 3 shows the ordinary and K-11 polarograms obtained with *p*-diacetylbenzene at different pH values. It can be seen that in the pH range 1-3 the K-11 data indicate reversibility. At pH 4.7 some separation of the anodic and cathodic waves is apparent. At pH 8.8 (and higher pH) the second cathodic wave is well defined, and the anodic current has fallen almost to zero. This latter behavior indicates that the enediol has rearranged to the keto form which is not reoxidized at the potential

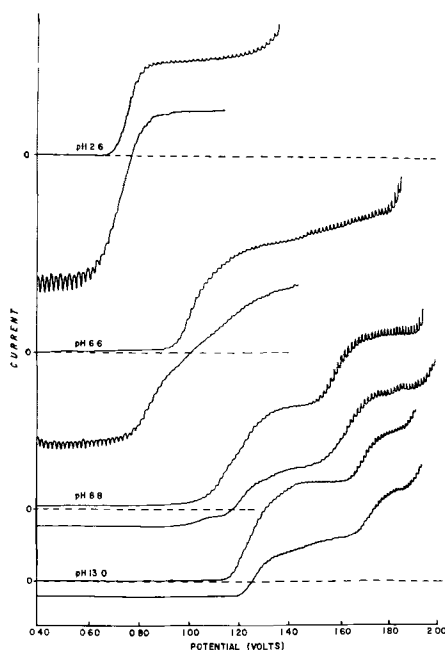


Fig. 3. Ordinary and K-11 polarograms of *p*-diacetylbenzene at different pH values.

being applied. The log plot of the data in acid solution gives a good straight line with a slope of 31.0 mv, indicating a two-electron potential controlling process. These observations will also be rationalized in the mechanism proposed later.

The normal polarographic behavior of *trans*-dibenzoylbenzene was found to be the same as previously reported by Pasternak (7). The K-11 polarograms showed merged anodic and cathodic components in the pH range 1-5 (same as for *p*-diacetylbenzene, Fig. 3). The results indicated a reversible two-electron step up to pH 5; at higher pH values the anodic and cathodic waves separated with the anodic current disappearing above pH 7. Above pH 10 no meaningful results could be obtained because the compound rapidly decomposed.

The only other ketones on which K-11 polarograms were run were *m*-dibenzoylbenzene, *o*-dibenzoylbenzene, and 1,3-indanedione. None of the three compounds gave anodic waves. This was not surprising in the case of *m*-dibenzoylbenzene, since the enediol intermediate cannot be formed. In the case of the *ortho* compound the enediol structure is possible, although the requirements of coplanarity in the structure might make the intermediate improbable. As previously mentioned it is also possible for 1,3-indanedione to form an enediol. However, the evidence here supports that obtained from ordinary polarograms indicating that such an intermediate is not formed. Although we did not try ninhydrin by this technique, Lehmann and Mannl (23), as previously mentioned, have reported isolation of enediol salts in the reduction of this compound.

Studies in dimethylformamide.—Dimethylformamide (DMF) is a highly aprotic solvent and allows electron addition to be observed without accompanying complications due to protonation. Since no previous work has been reported on diketones in DMF, it was thought desirable to determine their behavior in this solvent. Aromatic olefins, hydrocarbons, quinones, aldehydes, and ketones have been reduced in DMF (30-32) and intermediate free radicals have been detected by electron paramagnetic resonance measurements (33, 34).

The results obtained in DMF were generally reasonable, although attempts to gain information by adding phenol as a proton donor were generally unsuccessful. Polarographic data on several diketones are given in Table II. Benzil, *p*-diacetylbenzene, and *o*-dibenzoylbenzene gave two waves, *m*-dibenzoylbenzene gave one, and *trans*-dibenzoylbenzene gave three. In all cases the K-11 data indicated that the initial step was a reversible one involving the addition of one electron. Well-defined merged anodic-cathodic waves were obtained with the auxiliary potential corresponding to the top of the first wave.

Macroelectrolysis experiments with benzil definitely indicated the formation of a free radical. The potential was set at a value on top of the first wave and about 2 min after the start of the electrolysis, a deep blue color appeared, later changing to a deep green. The solution retained its color for long peri-

Table II. Half-wave potentials of diketones in dimethylformamide

Substance	$-E_{1/2}$ (vs. Hg pool)	I
Benzil	0.58	1.6
	1.28	1.5 ^a
trans-Dibenzoylethylene	0.32	1.5
	0.62	0.6
	1.48	0.7
p-Diacetylbenzene	0.91	1.8
	1.39	2.0
m-Dibenzoylbenzene	1.07	^b
o-Dibenzoylbenzene	1.05	1.5
	1.31	1.5

^a Benzoin gave a wave at $-1.22v$ with $I = 1.6$.

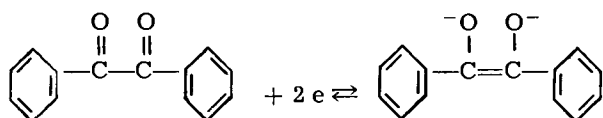
^b The first wave is followed by a large poorly defined current rise starting from $1.2v$. It appears to be two waves with a combined wave height (I) of about 3.0.

ods of time, but quickly reverted to a yellow color on exposure to air.

With the Kalousek technique, the auxiliary potential corresponding to that on top of the second wave, benzil behaved as it did in aqueous media, whereas p-diacetylbenzene produced an anodic wave not only at the potential of the first wave but also at that of the second wave (merged). This was the only case observed where there was evidence for two polarographically oxidizable intermediates. Results with trans-dibenzoylethylene were similar to those with benzil.

An investigation of the use of lithium chloride as a supporting electrolyte in DMF led to some interesting observations. With this salt as the electrolyte benzil gives only one wave of twice the height observed in tetrabutylammonium iodide (TBNI), indicating a single two-electron reduction step. The use of TBNI has been extensively studied (35) and lithium chloride has been reported to give anomalous results (36). For these reasons we investigated this result in more detail.

The single benzil wave in lithium chloride occurred at $E_{1/2} = 0.64$ and the value of I was 3.3. K-11 polarograms with the auxiliary potential on top of this wave gave a well-defined merged wave indicating a reversible couple. Addition of phenol resulted in the appearance of a second wave and in diminished K-11 anodic current. These results suggest that benzil is reversibly reduced in a two-electron step to a dianion which species may be more stabilized by the small lithium cation than by the bulky tetraalkyl

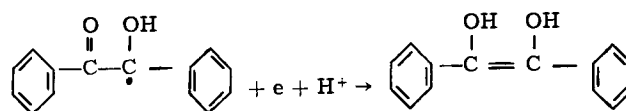
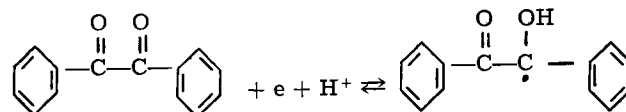


ammonium cation. Addition of the proton donor may facilitate rearrangement to benzoin which reduces to give the second wave.¹

¹ Evidence obtained by cyclic voltammetry and EPR supports these conclusions (37).

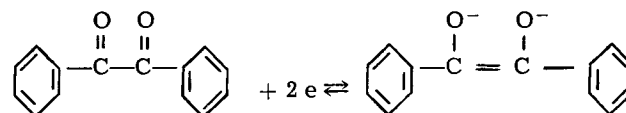
Conclusions Regarding Mechanism of Reduction

Benzil.—In ethanol-water solutions at low pH the experimental evidence does not clearly indicate the nature of the observed wave. From the wave height and the fact that benzoin is the product, we prefer to conclude that the enediol is formed and this species is that which produces the anodic current when the Kalousek technique is employed. One can assume a step-wise process



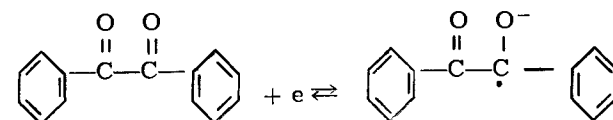
in which the second step is irreversible. This might be termed a "pseudoquinone" type system in that many quinones are not "well-behaved" in acid media with respect to log plots, etc.

In very basic media, the K-11 data and log plot indicate that the system is a reversible two-electron process

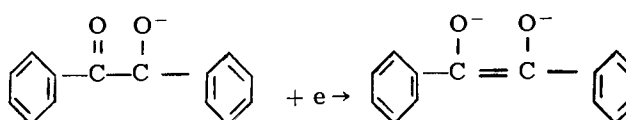


We found no conclusive evidence for the free radical postulated by Berg (38).²

In solutions of DMF both electrolysis and K-11 data support a one-electron reversible step for the first wave

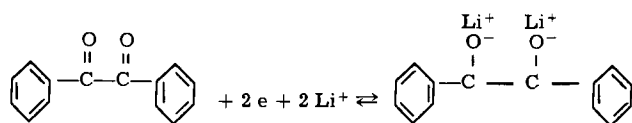


The second wave probably results from the further reduction of the radical to the enediol dianion

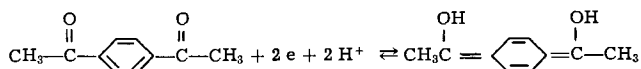


With lithium chloride as the supporting electrolyte, however, the process is apparently a reversible two-electron step

² Unpublished results of Ralph N. Adams and R. H. Philp, University of Kansas, using cyclic voltammetry with a hanging mercury drop in 50% ethanol, 0.1M sodium hydroxide shows a reversible couple which could be either the radical or enediolate. The EPR did not show any clear evidence for a free radical as would be expected for a semiquinone under these conditions.

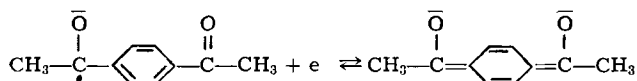
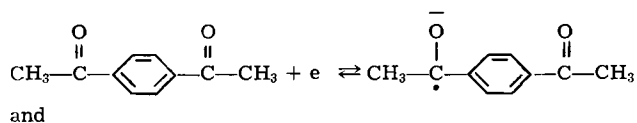


p-Diacetylbenzene.—In ethanol-water solutions under acidic conditions the data support a two-electron reversible step for the first wave



In basic media the enediol rearranges rapidly to *p*-(α -hydroxyethyl) acetophenone. This accounts for the disappearance of anodic current in the K-11 polarograms above pH 8.8. The second cathodic wave is, of course, due to the further reduction of the rearranged product.

In DMF solutions two polarographically oxidizable products were detected by the K-11 technique. These can be accounted for by the reactions



Other diketones.—In aqueous-ethanol media at low pH, trans-dibenzoyl ethylene showed similar behavior to *p*-diacetylbenzene, giving a reversible two-electron wave. In slightly basic medium the anodic current in the K-11 polarogram disappears and above pH 10 the compound apparently is unstable. The first two waves in DMF are apparently one-electron steps, as postulated for *p*-diacetylbenzene. The third wave is probably due to further reduction of the carbonyl group in the rearranged intermediate.

It has already been pointed out that the two carbonyl groups in *m*-dibenzoylbenzene are reduced independently. No enediol intermediate can be formed. The compounds benzoylacetone, dibenzoylmethane, 1,3-indanedione, and 2-phenyl-1,3-indanedione resemble each other in their polarographic behavior and no evidence was found for the enediol type of intermediate. Inconclusive results were obtained with *o*-dibenzoylbenzene. Further study of this compound and of ninhydrin is planned.

Manuscript received April 26, 1963; revised manuscript received Sept. 25, 1963.

Any discussion of this paper will appear in a Discussion Section to be published in the December 1964 JOURNAL.

REFERENCES

- I. Tachi, *J. Agr. Chem. Soc., Japan*, **13**, 692 (1937); *Mem. Coll. Agr. Kyoto Imp. Univ.*, **42**, 1 (1938).
- H. Adkins and F. W. Cox, *J. Am. Chem. Soc.*, **60**, 1151 (1938).
- A. Winkel and G. Proske, *Ber.*, **69**, 1917 (1936); **71**, 1785 (1938).
- G. Semerano and B. Polaczek, *Gazz. chim. ital.*, **70**, 448 (1940).
- R. Pasternak and H. von Halban, *Helv. Chim. Acta*, **29**, 190 (1946).
- R. Pasternak, *ibid.*, **30**, 1984 (1947).
- R. Pasternak, *ibid.*, **31**, 753 (1948).
- S. Harrison, *Coll. Czech. Chem. Commun.*, **15**, 818 (1950).
- E. Gagliardo, *Ricerca Sci.*, **20**, 1282 (1950); *C. A.*, **45**, 4176 (1951).
- M. I. Bobrova and N. S. Tikhominova, *Zhur. Obschei Khim.*, **22**, 2107 (1952); *C. A.*, **47**, 5818 (1954).
- K. Schwabe and H. Berg, *Z. Electrochem.*, **56**, 952 (1952).
- N. J. Leonard, H. A. Laitinen, and E. H. Mattus, *J. Am. Chem. Soc.*, **75**, 3300 (1953).
- A. Ryvolova, *Chem. Listy*, **50**, 1918 (1956).
- S. Wawzonek and J. H. Fossum, Proc. Int. Polarographic Congress, Prague, Part 1, 548 (1951), in K. Schwabe "Polarographic und Chemische Konstitution Organischer Verbindung," p. 73, Akademie, Verlag, Berlin (1957).
- A. Anhalt and H. Berg, *Z. Electrochem.*, **63**, 694 (1959).
- O. H. Muller, "Advances in Polarography," Vol. I, p. 277, I. S. Langmuir, Editor, Pergamon Press, New York (1959).
- H. Berg, *Naturwiss.*, **48**, 100 (1961).
- M. Kalousek, *Coll. Czech. Chem. Comm.*, **13**, 105 (1948).
- R. M. Powers and R. A. Day, Jr., *J. Am. Chem. Soc.*, **80**, 808 (1958).
- J. J. Lingane and S. L. Jones, *Anal. Chem.*, **22**, 1169 (1950).
- J. J. Lingane, "Electroanalytical Chemistry," 2nd Ed., p. 351, Interscience Publishers, Inc., New York (1958).
- R. A. Day, Jr., R. H. Philp, and R. L. Flurry, *This Journal*, **108**, 181C (1961).
- L. Holleck, O. Lehmann, and A. Mannl, *Naturwiss.*, **47**, 108 (1960).
- E. Bauer, *Z. Anal. Chem.*, **186**, 118 (1962).
- E. Bauer and H. Berg, *Roczniki Chem.*, **35**, 329 (1961).
- J. Holubek and J. Volke in "Advances in Polarography," Vol. III, p. 847, I. S. Langmuir, Editor, Pergamon Press, New York (1960).
- T. Kambara, *Bull. Chem. Soc., Japan*, **27**, 529 (1954).
- J. Koutecky, *Coll. Czech. Chem. Comm.*, **21**, 433 (1956).
- H. Matsuda, *Z. Electrochem.*, **62**, 977 (1958).
- S. Wawzonek, E. W. Blaha, R. Berkey, and M. E. Runner, *This Journal*, **102**, 235 (1955).
- S. Wawzonek, R. Berkey, E. W. Blaha, and M. E. Runner, *ibid.*, **103**, 456 (1956).
- S. Wawzonek and A. Gundersen, *ibid.*, **107**, 537 (1960).
- D. E. G. Austen, P. H. Given, D. J. E. Ingram, and M. E. Peover, *Nature*, London, **182**, 1784 (1958).
- P. H. Given and M. E. Peover, "Advances in Polarography," Vol. I, p. 948, I. S. Langmuir, Editor, Pergamon Press, New York (1959).
- P. H. Given and M. E. Peover, *J. Chem. Soc.*, **1959**, 1602.
- P. H. Given, M. E. Peover, and J. Schoen, *J. Chem. Soc.*, **1958**, 2674.
- R. N. Adams and R. H. Philp, Private communication (University of Kansas, To be published).
- H. Berg, *Z. Chemie*, **2**, 237 (1962). See also ref. (17).

Voltammetry and Controlled Potential Oxidation of 3,4-Dimethoxypropenylbenzene at a Rotating Platinum Electrode in Unbuffered Acetonitrile and in Acetonitrile-Pyridine Solution

James J. O'Connor¹ and Irwin A. Pearl

The Institute of Paper Chemistry, Appleton, Wisconsin

ABSTRACT

In unbuffered 0.5M sodium perchlorate-acetonitrile solution, 3,4-dimethoxypropenylbenzene (DMPB) gave three voltammetric waves of approximately equal height at a rotating platinum microelectrode. Waves II and III were usually defined poorly and often appeared to merge into a single wave. Wave I corresponded to a diffusion-controlled, one-electron oxidation which fulfilled substantially the various criteria for voltammetric reversibility. Attempts to carry out a large-scale, controlled potential oxidation were only partially successful since hydrogen ion liberated in a secondary reaction of the electrode product catalyzed the dimerization of DMPB to dimethyldiisoeugenol. The primary oxidation product appeared to be a dimeric perchlorate of DMPB with the structure of a cyclic lignan. An oxidation mechanism involving free radical dimerization at the β -carbon atoms of the side chains followed by ring closure and ejection of hydrogen ion has been suggested to account for the experimental results. Under similar conditions in the presence of pyridine, DMPB is oxidized in a two-electron, irreversible process. The course of the reaction has been established by means of voltammetric and coulometric studies as well as by the isolation of nearly quantitative yields of a dipyridinium diperchlorate of DMPB in a preparative-scale, controlled potential electrolysis.

Although lignin and lignin model compounds have been subjected to a great many oxidative degradations and ligninlike monomers have been subjected to many types of chemical and biochemical oxidative dehydrogenation in an attempt to learn more about lignin and lignification, comparatively little attention has been given to the electrochemical method of oxidation in these studies. The greater selectivity and means for control of electrochemical oxidation as compared with the usual methods of chemical oxidation suggest this method for the study of both oxidative degradation of the lignin polymer and the oxidative dehydrogenation of the lignin monomer. The voltammetric method of analysis used in conjunction with the technique of controlled-potential electrolysis should provide much useful information concerning the relative ease of oxidation of the methoxylated *p*-hydroxyphenylpropane moieties in the lignin polymer and the lignin model compounds, the reaction mechanisms of the oxidations, and the effect of substituents in altering the reaction paths. The present paper is concerned with the voltammetry and controlled-potential oxidation of the lignin model compound 3,4-dimethoxypropenylbenzene (DMPB) at a rotating platinum electrode. Sodium perchlorate-acetonitrile was chosen as the supporting electrolyte-solvent system because of the wide range of potential available compared with aqueous or mixed aqueous-organic solutions and because of the low solubility of DMPB in aqueous systems.

Experimental

Chemicals.—Acetonitrile (Matheson, Coleman & Bell, Practical grade) was purified by the method of Wawzonek and Runner (1). Water content of the purified acetonitrile was one to two millimolar as measured by the Karl-Fischer titration. The ultraviolet spectrum showed less absorption than commercially available spectral-grade acetonitrile.

Sodium perchlorate (G. F. Smith, Reagent grade anhydrous) was recrystallized from water and dried in a vacuum oven at 140° for 10 to 20 hr before use. The dried material was stored in a dark, covered bottle in a desiccator over phosphorus pentoxide.

3,4-Dimethoxypropenylbenzene (DMPB) (Brothers Chemical Co.) was vacuum distilled under nitrogen to a constant refractive index ($n_D^{20} = 1.5685$). The refractive indices for the *cis*- and *trans*-forms of DMPB are n_D^{20} 1.5616 and 1.5692, respectively (2). No apparent differences were observed between the voltammetric behavior of freshly distilled and aged DMPB.

1-Veratryl-2-methyl-3-ethyl-5,6-dimethoxyindan (dimethyldiisoeugenol) was prepared by boiling DMPB with sulfuric acid under reflux according to Müller and co-workers (3) and was obtained as fine white needles melting at 88°, even after repeated recrystallization from methanol. Müller (3) reported a melting point of 88° for the crude product, but after repeated recrystallization from methanol, he obtained the α -racemate of the indan melting at 106°. Dimethyldiisoeugenol was also prepared by treatment of DMPB with hydrochloric acid and zinc

¹ Present address: Kimberly-Clark Corporation, Neenah, Wisconsin.

chloride and was obtained as fine white needles melting at 93°-95° from methanol, presumably, a dimorphic form of the α -racemate of the indan (4). The infrared spectra of this compound and the 88° isomer were identical when run in carbon tetrachloride solution. However, spectra of the solid materials run in potassium bromide pellets were similar, but not identical.

Reagent-grade pyridine (Mallinckrodt, Baker) and spectral-grade pyridine (Matheson, Coleman, & Bell) gave deformed voltammetric waves in 0.5M sodium perchlorate-acetonitrile solution at approximately 1.5v vs. SCE. The several grades of pyridine were combined and distilled. The distilled pyridine was stored in a dark, all-glass container equipped with a glass siphon and stopcock for delivery. Voltammograms of the distilled product showed no waves.

Prepurified nitrogen (Matheson) passed through separate tubes of magnesium perchlorate and phosphorus pentoxide was employed in all distillations.

Apparatus.—The voltammetric cell used was patterned after a general description given by Kolthoff and Coetsee (5). As observed by these authors, a solid plug formed in the end of the agar bridge of the saturated calomel electrode after prolonged immersion in the acetonitrile solution. This was minimized by storing the agar bridge in a saturated (aqueous) solution of potassium chloride between runs. Contrary to the findings of Kolthoff and Coetsee, however, the presence of the plug seemed to have little effect on the measured cell resistance. The cell resistance of the voltammetric cell was usually between 1700 and 2000 ohms.

The voltammetric anode was constructed from 24-gauge platinum wire sealed into the tip of a soft-glass tube with the long axis of the wire parallel to that of the glass tube. The wire was heated in an oxygen flame to provide a rounded tip and a smooth, shiny surface before sealing into the glass tube. The electrode, having an exposed geometric area of 0.0075 cm², was rotated by means of a 600 rpm Sargent synchronous motor. Stroboscopic measurements gave a value of 618 rpm for the actual rate of rotation.

The cell used for controlled potential electrolyses consisted of a 600 ml capacity anode compartment which was immersed in a constant temperature bath. A 400 ml capacity cathode compartment was connected to the anode compartment by means of a 4 in. long tube into which was sealed a 1 in. diameter fine-grade frit. A ball and socket joint in the tube permitted easy dismantling and cleaning of the cell. A saturated calomel electrode (SCE) was used as the reference electrode and was connected with the anode compartment in the same manner described for the voltammetric cell. The anode used in the electrolysis cell was a platinum gauze cylindrical electrode obtained commercially (E. H. Sargent & Co., Chicago, Ill., Catalog No. 29625). A mercury pool served as an auxiliary electrode.

Potential-current curves were obtained with a Sargent-Heyrovsky polarograph, Model XII used in conjunction with a Sargent Chart Recorder with a

one second full-scale response. Controlled potential electrolyses were carried out using an Analytical Instruments Inc. Potentiostat. Potentials were checked before running the voltammograms and periodically during the course of controlled potential electrolyses by means of a L&N Student Potentiometer.

Resistance measurements were made with a General Radio Z-Y Bridge, Type 1603A using a Hewlett-Packard audio-oscillator, Model 200B to provide a 3700 cps a-c source. A Type 502 Tektronix, Inc. oscilloscope was employed as a null detector. Resistance measurements were made with an applied voltage of less than 0.05v.

Infrared curves were run on a Perkin-Elmer Model 21 spectrophotometer. Ultraviolet curves were obtained with a Beckman Model DK-2 spectrophotometer. Refractive indices were measured with a Bausch and Lomb Abbé refractometer.

All weighings were made on an analytical balance enclosed in a dry-box. Relative humidity within the dry-box was maintained between 5 and 10% by means of a silica gel column and blower together with traps of phosphorus pentoxide. However, in the humid summer months the relative humidity occasionally rose to 20% within the dry-box.

Voltammetric procedure.—Stock solutions of 0.5M sodium perchlorate in acetonitrile were prepared fresh each morning and used for the day's voltammetric runs. Ten milliliter stock solutions, usually 0.25M in DMPB and 0.5M in sodium perchlorate were prepared similarly each day even though stock solutions several weeks old showed no significant changes in voltammetric behavior.

Twenty-five milliliters of the supporting electrolyte-solvent stock solutions were pipetted into the cell and deaerated by passing dried nitrogen through the solution for approximately 10 min. The cleaned electrode was introduced into the cell, and a residual current curve recorded. The desired quantity of the electroactive species was introduced into the cell by means of a micropipet. After thorough mixing of the solution with a stream of nitrogen, the cleaned electrode was inserted, and the voltammogram recorded. During the recording of the voltammogram, a stream of nitrogen was directed over the surface of the anolyte solution.

The cell was controlled by thermostat and maintained at 25.0° ± 0.2° for all voltammetric measurements. Curves were recorded at a polarization rate of 2.95 mv/sec and were corrected for residual currents and iR drop through the cell.

The electrodes were cleaned in concentrated nitric acid or dichromate cleaning solution. The oxide film formed on the platinum surface by the cleaning procedure was removed by soaking the electrode in acidic ferrous ammonium sulfate solution for several minutes. The electrode was then rinsed thoroughly with distilled water followed by acetonitrile and transferred to the cell where it was allowed to equilibrate for several minutes before running the voltammogram.

Controlled potential electrolysis.—Six hundred milliliters of 0.5M sodium perchlorate-acetonitrile

solution were added to the anode compartment and 400 ml to the cathode compartment. After pre-electrolysis for 30 min at 1.5v vs. SCE, 10.08g of DMPB (0.0565 mole) was added to the anode compartment, and the control potential reset to 0.98v. Because of the slow drift in the potential of the SCE in acetonitrile with time, the final controlled potential of 0.98v should be considered a "long-time" measurement.

The electrolysis was characterized by a rapid decrease in current and the development of a cherry-red color which intensified to a deep purple as the electrolysis progressed. Periodically during the electrolysis 2-3 ml samples of the anolyte were removed, diluted with 50% acetonitrile-water solution, and titrated potentiometrically for hydrogen ion with 0.01M sodium hydroxide. The procedure was checked by titrating known amounts of perchloric acid in the same solvent system and was found to be accurate within $\pm 1.0\%$. The shape of the titration curves for the anolyte aliquots was identical with those obtained with the perchloric acid solutions.

The electrolysis was terminated after 17 hr, at which time the current had decreased to 5% of its original value. Integration of the current-time curve indicated that approximately 58% of the DMPB was oxidized assuming a one-electron oxidation.

The anolyte from the oxidation was placed in the refrigerator and allowed to stand overnight. No precipitate formed,² and the solution was concentrated under reduced pressure below 40° to near dryness. The concentrated solution was stirred into 1000 ml of ether, and the precipitate was filtered and extracted with chloroform to leave a residue of pure sodium perchlorate.

Ether and chloroform solutions, on concentration and cooling, both deposited a little ammonium perchlorate which was identified by its nitron reaction and its infrared absorption spectrum. Qualitative paper chromatography and thin layer chromatography of the ether and chloroform solutions indicated single major components in each with several fluorescent minor components in both. These materials were extracted from both solutions with water, and the water extracts were combined and concentrated under reduced pressure to yield several hundred milligrams of white crystals. Recrystallization from methanol gave colorless crystals melting at 184°-194° giving a positive perchlorate reaction. The infrared absorption spectrum indicated the presence of perchlorate and carbonyl and the absence of ester and carboxyl groups. Chromatographic and fluorescence behavior were very similar to those of the material formed by addition of perchloric acid to DMPB. Thus, this product appears to be a secondary product formed by the action of perchloric acid liberated during electrolysis.

The ether solution containing 8.73g of solids was

²In several preliminary oxidations carried out under identical conditions except that the concentration of DMPB was 50% or less of that in the present experiment, 5-10 mg of yellow needles were obtained in every case by allowing the solution to stand overnight. The material sublimed at 335°, and its infrared absorption spectrum was identical with that of authentic 2,3,6,7-tetramethoxyanthraquinone (6a).

evaporated to dryness, and the residue covered with cold methanol and allowed to stand in the refrigerator. The residual crystals were recrystallized from methanol to give long needles and clusters of fine needles. The two types of crystals were separated mechanically and dried over phosphorus pentoxide to give melting points of 88° and 105°, respectively. The infrared absorption spectrum (KBr pellet) of the 88° compound was identical with that of the 88° isomer of dimethyldiisoeugenol obtained by the action of sulfuric acid on DMPB (3). The infrared spectra (KBr pellets) of the 88° and 105° melting crystals and of the 95° melting isomer of the dimethyldiisoeugenol obtained by the action of zinc chloride and hydrochloric acid on DMPB (4) were very similar, but not identical. The compounds appear to be dimorphic forms of a single stereoisomer of dimethyldiisoeugenol, since the infrared spectra of all three in carbon tetrachloride are identical. Ultraviolet absorption spectra of the three compounds in ethanol are identical, and qualitative thin-layer and paper chromatography for the three are also identical.

The chloroform solution containing 2.91g of solids was concentrated under reduced pressure and stirred into excess carbon tetrachloride. The purple precipitate was filtered and washed. All attempts to crystallize the material failed, but precipitation with nitron acetate, explosion when heated on a platinum foil, solubility behavior in chloroform and carbon tetrachloride, and infrared absorption spectrum characterized this material as an organic perchlorate. Treatment of the purple material with sodium hydroxide yielded a pale yellow product containing no perchlorate groups and having an infrared absorption spectrum with bands at 2.90, 3.40, 6.20, 6.60, 6.81, 7.93, 8.77, 9.72, 11.9, 12.3, and 13.3 μ , and almost identical with that of 1,2-trans-2,3-cis-1-(3,4-dimethoxyphenyl)-1,2,3,4-tetrahydro-6,7-dimethoxy-2,3-naphthalenedimethanol (6b) except that the hydroxyl absorption bands were absent.

Electrolysis in the presence of pyridine.—Six hundred milliliters of 0.5M sodium perchlorate in acetonitrile 1.0M in pyridine was added to the anode compartment of the electrolysis cell and 400 ml to the cathode compartment. The solution was pre-electrolyzed at 1.2v vs. SCE for 1 hr during which time the anolyte developed a pale yellow color, and the current decreased to a low, constant value. After addition of 4.99g (0.028 mole) of DMPB to the anode compartment, the electrolysis was continued for 8 hr at a control potential of 1.2v vs. SCE. The pale yellow color of the anolyte intensified only slightly during the electrolysis.

During the oxidation, 0.023 mole of DMPB was consumed as estimated from the magnitudes of the initial and final currents. The theoretical current consumption for the two-electron oxidation is 4440 coulombs. Actual current consumption by integration of the current-time curve was 4285 coulombs. The calculated *n*-value is thus 1.93 electrons/molecule, in agreement with the voltammetric estimates.

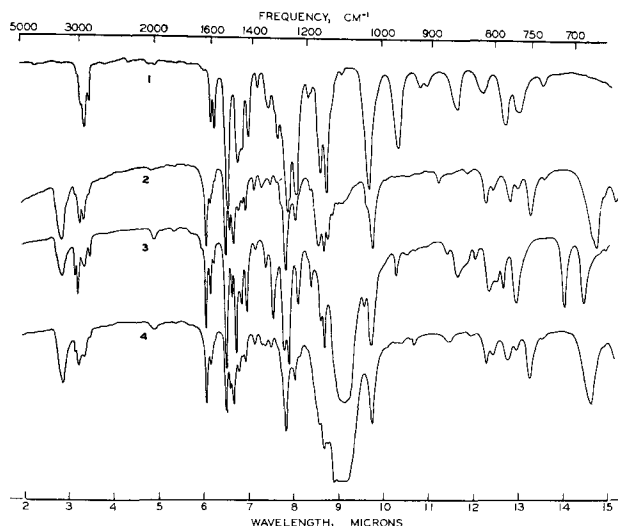


Fig. 1. Infrared spectra of 3,4-DMPB and certain derivatives: 1, 3,4-DMPB; 2, 3,4-DMPB-dipyridinium diiodide; 3, Yellow needles melting at 235°; 4, 3,4-DMPB-dipyridinium diperchlorate.

The anolyte was concentrated under reduced pressure and poured into 200 ml of ice-water. The crystalline precipitate was filtered, and the filtrate was concentrated and cooled to yield more crystals. The total yield of 12.5g of crystals was recrystallized twice from 90% ethanol to give colorless crystals melting at 110°. Its infrared spectrum (Fig. 1, curve 4) together with its reaction with sodium hydroxide to yield pyridine, explosion when heated, positive perchlorate reaction with nitron, and solubility tests indicated that the compound is the dipyridinium diperchlorate of DMPB.

Analysis for $C_{21}H_{24}O_{10}N_2Cl_2$: calculated, C, 47.11; H, 4.52; N, 5.23; Cl, 13.24; found³, C, 47.93, 47.96; H, 4.70, 4.61; N, 5.15; Cl, 12.94.

Treatment of this perchlorate in 90% ethanol with excess sodium iodide and cooling gave bright yellow needles which were filtered and recrystallized three times from ethanol to give yellow needles melting at 174° (decomposition), which proved to be the dipyridinium diiodide of DMPB containing a slight impurity of the diperchlorate which could not be removed by recrystallization. Its infrared absorption spectrum is shown in Fig. 1, curve 2.

Analysis for $C_{21}H_{24}O_2N_2I_2$: calculated, I, 42.8, found, I, 38.9, 38.9.

Treatment of the perchlorate with two equivalents of sodium hydroxide in aqueous solution yielded a strong odor of pyridine and pale yellow needles melting at 235°. Positive nitron test, explosion when heated and infrared absorption spectrum (Fig. 1, curve 3) indicated a perchlorate, but the compound was not characterized further.

Acid catalyzed dimerization of DMPB.—A $1.0 \times 10^{-3}M$ solution of DMPB in 0.5M sodium perchlorate-acetonitrile (25 ml) was added to the voltammetric cell and a voltammogram recorded. The electrode was removed, cleaned, and replaced in the

cell. One hundred microliters of 0.5M perchloric acid in glacial acetic acid was added to the cell, the solution was mixed with a vigorous stream of nitrogen, and a current reading was made at an anode potential of 1.05v vs. SCE. Similar current readings were taken at approximately 5-min intervals during the early stages of the reaction and approximately once every 30 min after the initial sharp drop-off in current had taken place. Between measurements the electrodes were disconnected from the voltammetric circuit. At the end of the run the electrode was again cleaned and a voltammogram recorded.

Similar experiments were carried out with 250, 500, and 5000 microliters of 0.5M perchloric acid added to the solution of DMPB in acetonitrile. Since the emf was applied across the cell only long enough to make a current reading, less than 0.5% of the observed current drop could be attributed to electrolysis of DMPB.

Results and Discussion

Voltammetry.—In unbuffered 0.5M sodium perchlorate-acetonitrile solution DMPB gave three voltammetric waves at a rotating platinum electrode. The waves had poorly defined diffusion plateaus which made it difficult to obtain accurate estimates of the diffusion current constants, $I_d = i_d/C$, where i_d is the diffusion current and C is the concentration of the electroactive species. A typical voltammogram is shown in Fig. 2, curve 1.

The half-wave potential ($E_{1/2}$) of wave I was $0.98 \pm 0.03v$ vs. SCE. The $E_{1/2}$'s of waves II and III were approximately 1.2 and 1.4v vs. SCE, respectively, at low concentrations of DMPB and increased with increasing concentration of the compound. Waves II and III were poorly defined, and in some cases appeared as a single, drawn-out wave. The diffusion current constants of waves II and III proved to be extremely erratic, but were usually between one and two times the height of wave I. In the present study the primary emphasis has been placed on the elucidation of the reaction corresponding with wave I.

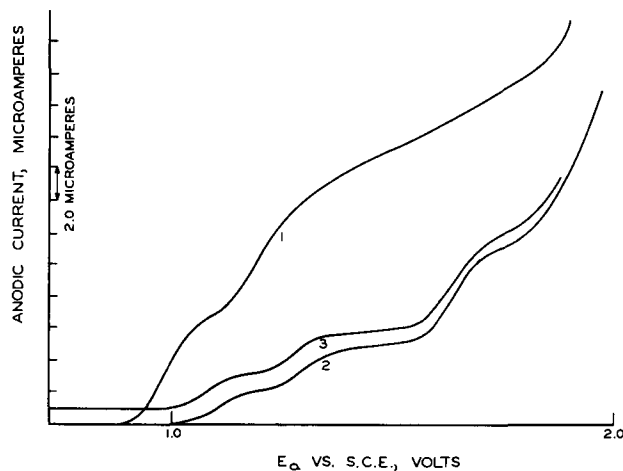


Fig. 2. Voltammograms in 0.5M sodium perchlorate-acetonitrile solution: 1, $1.092 \times 10^{-3}M$ DMPB; 2, $1.092 \times 10^{-3}M$ DMPB + $2.0 \times 10^{-3}M$ $HClO_4$; 3, $0.532 \times 10^{-3}M$ dimethyldiisoeugenol.

³ Analyses were performed by Geller Microanalytical Laboratory, Bardonia, N. Y.

Current-controlling process.—The temperature coefficient of the diffusion currents for both waves I and II was 3.0% per degree over the temperature interval from 25.7° to 37.1°. This value is of the order expected for the temperature coefficients of the diffusion currents of organic molecules at a rotating solid electrode. The indicated conclusion that diffusion is the current-controlling process is supported by the observation that the heights of the diffusion currents for both waves decreased with decreasing rate of rotation of the electrode.

Estimation of the electrode n -value.—The diffusion current constant, I_d , for DMPB was 6.34. On the same electrode with the same stirring conditions, anthracene in the presence of 0.1M pyridine gave an I_d of 13.0 and DMPB in the presence of 0.01M pyridine gave an I_d of 12.5. Under these conditions both anthracene (7) and DMPB are oxidized in two-electron steps with the formation of dipyridinium diperchlorates. In addition, anthracene and DMPB have identical molecular weights. Thus, a one-electron oxidation is indicated for DMPB in unbuffered acetonitrile solution. Hydroquinone, which presumably oxidizes in a two-electron step in unbuffered acetonitrile (8), gave an I_d of 11.5.

Reversibility of the electrode process.—Plots of $\log i/(i_d - i)$ vs. E for wave I always gave straight lines with slopes varying from 53 to 60 mv over a concentration range from 1.2×10^{-4} moles/liter to 60.0×10^{-4} moles/liter. These observations indicate strongly that the potential-determining electrode reaction corresponding to wave I is voltammetrically reversible. The temperature coefficient of $E_{1/2}$ for wave I was 2.3 mv/degree over the range 25.7°–37.1°. This value is somewhat higher than might be expected for a reversible electrode process (9). Similar log plots of wave II showed significant deviations from straight-line plots at negative values of $\log i/(i_d - i)$. The straight-line portions of the plots had slopes of 100–110 mv. This behavior is typical of an irreversible process.

Effect of hydrogen ion.—The concentration independence of $E_{1/2}$ for wave I in unbuffered acetonitrile noted earlier suggested that hydrogen ion was not involved in the electrode process. This was confirmed by examining the voltammetric behavior of wave I in the presence of 1.1M water, 0.2M acetic anhydride, 1.0M acetic acid, and 1.3mM perchloric acid. In no instance was either the diffusion current constant or the half-wave potential altered significantly when the voltammograms were run within a short time after addition of the various species noted. Perchloric acid, after prolonged standing in contact with DMPB, caused a decrease in I_d of all three waves. This has been attributed to the removal of DMPB by acid-catalyzed dimerization and is discussed in more detail later in this paper.

Although the present paper is concerned primarily with the reaction corresponding with wave I, it is of interest to note that both water and acetic anhydride caused a twofold increase in the height of wave II, while acetic acid caused a threefold increase. Perchloric acid, on the other hand, had no significant effect on wave II when the voltammo-

grams were run immediately after the addition of the acid.

Controlled potential oxidation.—The finding of ammonium perchlorate in this oxidation can be accounted for by the hydrolysis of the acetonitrile with perchloric acid formed during the electrolysis and small quantities of water present even in the dried acetonitrile. The equivalent quantity of acetic acid which would be formed by such a mechanism was actually detected by means of gas chromatographic analysis.

The primary oxidation product obtained was a purple-colored material which accounted for only about 30% of the original DMPB on a weight basis. Although attempts to purify this material were unsuccessful, it was possible to convert the compound to a pale-yellow solid by treatment with sodium hydroxide. The light-colored material contained no perchlorate groups, and its infrared absorption spectrum bore a striking resemblance to that of 1,2-trans-2,3-cis-1-(3,4-dimethoxyphenyl)-tetrahydro-6,7-dimethoxy-2,3-naphthalenedimethanol (6b). The only major difference in the spectra was the absence of hydroxyl absorption bands in the spectrum of the unknown, which contained absorption maxima at 3.40, 6.20, 6.60, 6.81, 7.93, 8.77, and 9.72 μ .

In the DMPB molecule the strong donor tendency of the *p*-methoxylated phenyl nucleus effects an electron shift in the direction of the β -carbon atom. Thus, of the representative contributing structures to the resonance hybrid shown in Fig. 3, B, C, and D are most important in describing the hybrid. Structures such as E and F contribute little to the description of the molecule.

The localization of the electrons at the β -carbon is shown in the acid-catalyzed dimerization of DMPB where proton addition to the β -carbon atom decreases the activation energy of the system sufficiently to permit chain initiation to occur (10). The importance of structure B is shown by the ready loss of the β hydrogen ion from the protonated form of structure B. A similar attack at the center of greatest electron density is expected in the electrolytic oxidation of DMPB. Thus, wave I of DMPB in unbuffered acetonitrile corresponds to the removal of a single electron from the vicinity of the β -carbon atom with the formation of a highly reactive carbonium ion radical. Although such a species may stabilize in a variety of ways (dimerization, fragmentation, addition of radicals and nucleophiles, ejection of hydrogen ions, or a combination of these processes), it appears that the DMPB carbonium ion radical stabilizes primarily by a single mechanism. This is shown by the presence of only one major oxidation product by chromato-

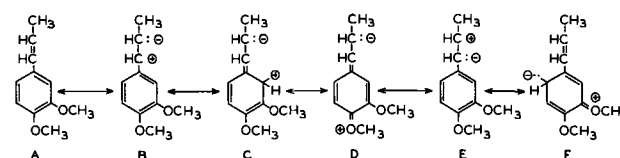


Fig. 3. Representative contributing structures to the resonance hybrid of DMPB.

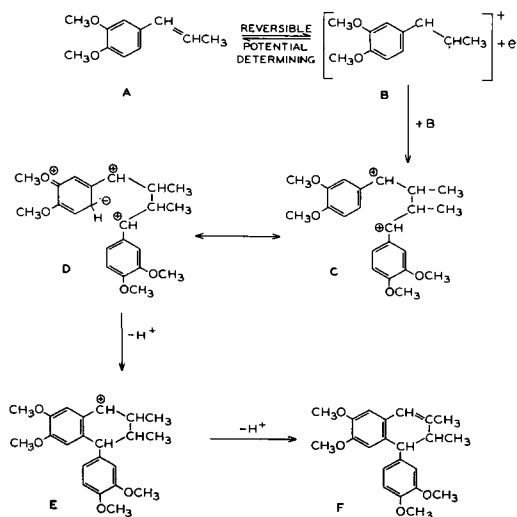


Fig. 4. Suggested reaction mechanism

graphic examination of the anolyte. Based on these considerations the reaction mechanism of Fig. 4 is suggested.

In the proposed reaction scheme the carbonium ion radical (B) formed in the electrode reaction undergoes a free radical dimerization with a second radical ion to give a divalent carbonium ion dimer (C) linked through the β -carbons of the side chain. Stabilization by ring closure and the ejection of hydrogen ion follows essentially the path described by Müller and co-workers (3) for the acid-catalyzed dimerization of propenylphenol ethers. The monovalent carbonium ion may stabilize by the addition of a nucleophilic reagent such as the perchlorate anion or by ejection of a second hydrogen ion. In the latter case, the loosely held hydrogen on carbon-2 of the tetralin nucleus would probably be lost with the formation of compound F. The purple-colored material is believed to be the perchlorate of E, and the product obtained by treatment of this material with base is believed to be the corresponding unsaturated compound F.

The postulated reaction mechanism requires the liberation of from 0.5 to 1.0 hydrogen ion per molecule of oxidized DMPB depending on the stabilization mechanism of the monovalent carbonium ion. Potentiometric titrations of aliquots of the anolyte taken after varying electrolysis times showed a gradual accumulation of hydrogen ion in the solution. The equivalents of hydrogen ion liberated as a function of electrolysis time is shown in Fig. 5. Also shown is a plot of equivalents of electrons transferred as a function of electrolysis time. The latter data were obtained by integration of the current-time curve. During the early stages of electrolysis, approximately one hydrogen ion was liberated per molecule of DMPB consumed, assuming a one-electron oxidation mechanism. This value gradually decreased to approximately 0.5 hydrogen ion per molecule as the electrolysis continued. It is to be expected that part of the decrease is due to migration of hydrogen ions into the cathode compartment of the electrolysis cell (11).

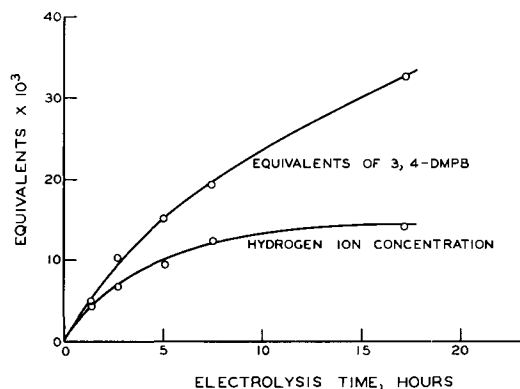
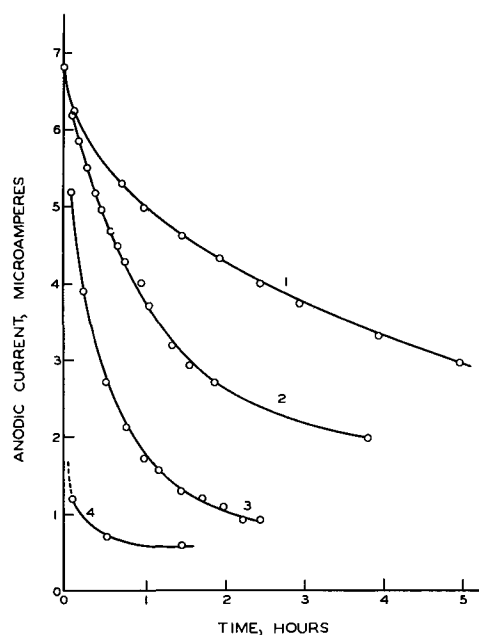


Fig. 5. Variation of equivalents of DMPB and equivalents of hydrogen ion liberated with electrolysis time.

It has been shown that the bulk of the DMPB originally present was converted during the electrolysis to dimethyldiisoeugenol. This material is normally synthesized by the acid-catalyzed dimerization of DMPB, and its presence in the anolyte is not surprising in view of the comparatively high concentration of hydrogen ion liberated in the oxidation reaction discussed earlier. Since no previous studies of the acid-catalyzed dimerization of DMPB in acetonitrile solution have been reported it was of interest to demonstrate that this mechanism was responsible for the formation of dimethyldiisoeugenol in the anolyte. Furthermore, some estimate of the rate of dimerization in this system would be helpful in explaining the experimental results because the rapid decrease in current during the electrolysis was obviously due to simultaneous oxidation of DMPB and its removal by acid-catalyzed dimerization.

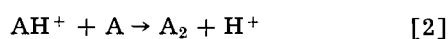
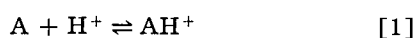
Acid dimerization of DMPB.—The current decrease as a function of time for DMPB in 0.5M sodium perchlorate-acetonitrile solutions contain-

Fig. 6. Variation of current due to the acid-catalyzed dimerization of 1.092 mM DMPB in 0.5M sodium perchlorate-acetonitrile with time: 1, 2.0×10^{-3} HClO₄; 2, 5.0×10^{-3} HClO₄; 3, 10.0×10^{-3} HClO₄; 4, 100.0×10^{-3} HClO₄.

ing varying concentrations of perchloric acid is shown in Fig. 6. The current was measured periodically at a potential of 1.05v vs. SCE. Less than 0.5% of the total current decrease is attributable to oxidation of DMPB since the potential was applied only long enough to measure the current at intervals.

Voltammograms of DMPB in 0.5M sodium perchlorate-acetonitrile solution after treatment with perchloric acid are well defined, although the heights of the waves are less than 50% of the heights of waves under conditions of no acid treatment. These results are in accord with the expected behavior for dimerization; that is, complete dimerization would effectively reduce the concentration of the electroactive species by 50%. A decrease in diffusion current somewhat greater than 50% would be expected because of the increased size, and, hence, decreased diffusivity, of the dimer. For comparison purposes a voltammogram of dimethyldiisoeugenol is also included. The concentration of the dimethyldiisoeugenol is approximately that of the dimer formed by the action of perchloric acid. The curves are identical with respect to the number of waves, the half-wave potentials, and the diffusion current constants.

With the nature of the product established, a more detailed description of the process was attempted. It has been shown that if styrene or anethole is dimerized by the action of deuterated hydrochloric acid, both the dimer and the unreacted monomer will contain deuterium (3). Furthermore, the rate of dimerization was found to be dependent on the acid concentration, and this suggested a reaction mechanism of the following type (3).



in which the second step is a slow, irreversible process. Thus, the rate of consumption of A will be given by

$$-\frac{dA}{dT} = k(AH^+)(A) = kK_{eq}(A)^2(H^+) \quad [3]$$

where

$$K_{eq} = \frac{(AH^+)}{(A)(H^+)} \quad [4]$$

and therefore, will be first order with respect to hydrogen ion and second order with respect to A. If the hydrogen ion is present in sufficiently large quantity to be treated as a constant, or if the concentration of AH^+ is negligibly small with respect to the hydrogen ion concentration, Eq. [3] may be integrated to give the familiar second-order rate equation

$$1/A_2 - 1/A_1 = kK_{eq}(H^+)(t_2 - t_1) \quad [5]$$

Assuming that the equilibrium position of reaction [1] is far to the left and that the only significant contribution to the current is given by DMPB mon-

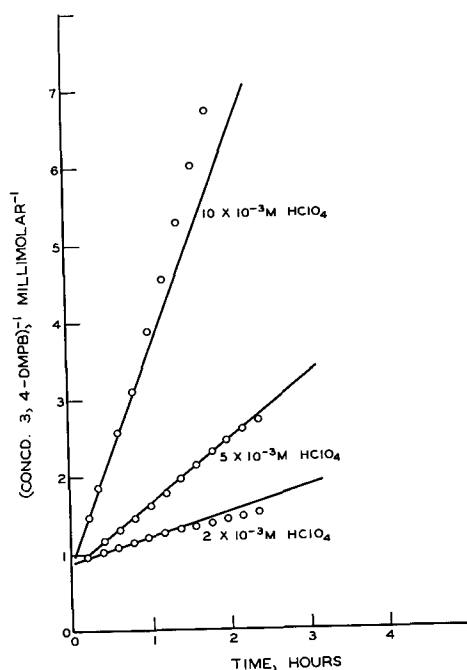


Fig. 7. Second-order plot for the acid-catalyzed dimerization of $1.092 \times 10^{-3}M$ DMPB in 0.5M sodium perchlorate-acetonitrile.

omer and dimethyldiisoeugenol, the following expressions may be written:

Letting a = concentration of DMPB at $t = 0$, and $(a - x)$ = concentration of DMPB at $t = t$, $x/2$ = concentration of dimethyldiisoeugenol, then

$$i = k(a - x) + (0.1)(x/2) \quad [6]$$

where i is taken as a positive quantity for purposes of convenience. The factor 0.1 is included in the second term, since the current height for dimethyldiisoeugenol is 0.1 times that of an equal concentration of DMPB at the potential used for the experiments.

Solving for $(a - x)$ in terms of a and i in Eq. [6] gives

$$(a - x) = [i - 0.05ka]/0.95k \quad [7]$$

Using Eq. [5] with $A = (a - x)$ and the data of Fig. 6, the plots of Fig. 7 were obtained. Although some deviation from a straight-line plot was obtained at longer times, the data were in surprisingly good agreement with Eq. [5] in view of the assumptions made in the derivation.

Since the slope is equal to $kK_{eq}(H^+)$ where the only variable is (H^+) , the predicted values for hydrogen ion concentrations of 2.0, 5.0, and 10.0 mM should have the ratio 1:2.5:5.0. The actual ratio obtained using the initial portions of the plots was 1:2.5:7.9. Thus, the rate of acid-catalyzed dimerization of DMPB is first order with respect to hydrogen ion concentration and second order with respect to the concentration of DMPB. A description of the current-time curve in the controlled potential oxidation itself would be somewhat more complicated, since hydrogen ion concentration

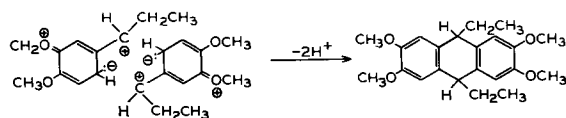


Fig. 8. Mechanism of dimerization of DMPB

gradually increases during the electrolysis, while DMPB is consumed both by oxidation and by acid-catalyzed dimerization.

It is also of interest to note that when perchloric acid is added to a solution of DMPB in acetonitrile, a bright cherry-color develops immediately. Thus, the red color observed in the electrolysis of DMPB is probably a result of the liberation of perchloric acid at the anode and the formation of a halo-chromic salt with unoxidized DMPB. The more intensely colored purple material appears to accumulate only slowly during the electrolysis.

One observation which has not been explained satisfactorily is the relatively low yield of oxidation product obtained in comparison with the coulombs of electricity consumed in the oxidation. One possible explanation is that comparatively small amounts of material are oxidized to a much greater degree by another mechanism. For example, it has been shown that the acid-catalyzed dimerization of DMPB yields small quantities of 2,3,6,7-tetramethoxy-9,10-diethyl-9,10-dihydroanthracene. A possible mechanism is the dimerization of two molecules of protonated DMPB as pictured in Fig. 8 (12). In the present study small quantities of 2,3,6,7-tetramethoxyanthraquinone and a fluorescent material resembling 2,3,6,7-tetramethoxy-9,10-ethylanthrone and its carbonium salts have been isolated. These materials most probably were formed in the electrolytic oxidation of 2,3,6,7-tetramethoxy-9,10-diethyl-9,10-dihydroanthracene formed by the acid-catalyzed dimerization of DMPB as shown in Fig. 8. The formation of these highly oxidized species would, of course, require considerably more than one electron per DMPB molecule.

Voltammetry in pyridine solutions.—In the presence of pyridine, DMPB shows only a single, deformed wave at a rotating platinum electrode in acetonitrile solution. At high anodic potentials the current decreases to low values. This effect is usually attributed to the formation of an insoluble film or tar on the electrode surface which acts as an effective barrier to the transfer of electrons. Similar film formation on a platinum electrode in the presence of pyridine was observed by Geske (13) in a study of the oxidation of iodide ion, Lund (14) in the oxidation of fluorenol, and Vermillion (15) in the oxidation of hindered phenols.

That the surface of the electrode was in some way altered was confirmed by attempts to retrace the voltammograms without cleaning the electrode between runs. In every case a significant reduction was obtained in the height of the voltammetric wave. Attempts to remove the "film" by cathodic reduction were only partially successful. Voltammograms comparable with those obtained initially

Table I. Voltammetric data for DMPB in 0.5M sodium perchlorate-acetonitrile solution 1.0M in pyridine

Concentration DMPB, mM	$E_{1/2}$, v vs. SCE	I_d , μ amp-1/mM
0.052	1.070	19.3
0.104	1.060	18.3
0.208	1.045	15.1
0.417	1.064	17.8
1.46	1.094	11.0
3.54	1.086	13.6

were obtained only after cleaning the electrode surface with nitric acid or dichromate cleaning solution.

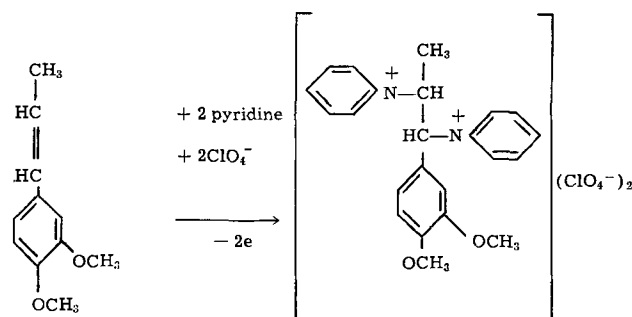
At high concentrations of DMPB a reduction in I_d was observed as shown in Table I. It is believed that this decrease is not attributable to a change in the nature of the electrode reaction, but rather is a reflection of the more rapid formation of the film on the electrode surface. On this basis, estimates of the n -value of the electrode reaction from the diffusion current constant should be most reliable at low concentrations of DMPB.

Anthracene, whose molecular weight and, presumably, diffusivity are the same as that of DMPB is oxidized in a two-electron process at a rotating platinum electrode in 0.5M sodium perchlorate-acetonitrile solution containing pyridine (7). Using the same electrode and stirring conditions as had been used for DMPB, an I_d of 23.5 was obtained. This value is approached by the I_d of DMPB at low concentrations indicating a two-electron oxidation for DMPB. This estimate was confirmed by a preparative-scale controlled potential oxidation of DMPB which is discussed in more detail below.

As shown in Table I, the half-wave potential of DMPB was constant and independent of the concentration of DMPB. Plots of $\log i/(i_d - i)$ vs. E , where i is the current at the potential E and i_d is the diffusion current, deviated significantly from straight lines at negative values of $\log i/(i_d - i)$. From the slopes of the linear portions of the curves α values of from 0.55 to 0.60 were calculated. These data indicate that the potential-determining electrode reaction is irreversible.

Oxidation of DMPB at a platinum electrode in 0.5M sodium perchlorate-acetonitrile solution 1.0M in pyridine yielded a water-soluble dipyridinium diperchlorate of DMPB. At a control potential of 1.2v vs. SCE the product was obtained in approximately 95% yield based on the starting DMPB at a current efficiency of nearly 100%. Thus, pyridine does not function merely as a proton acceptor as in the oxidation of anisyl alcohol, but participates in the electrode reaction decreasing the energy required to remove a second electron from the DMPB molecule. The oxidation may be pictured as a reaction involving a concerted push-pull attack by the unshared electron pair of the pyridine molecule and the positively charged electrode surface. The delocalization of the positive charge at the α -carbon atom due to coordination with pyridine may account for the decreased potential required to remove the second electron. The over-all reaction

without regard to mechanism may be summarized as follows:



It should be noted that the exact position of addition of the pyridine molecules has not been established conclusively. In chemical oxidations of DMPB which are not sufficiently drastic to effect side chain cleavage, the products are usually substituted at the α - and β -carbon atoms of the side chain.

Manuscript received Dec. 26, 1962; revised manuscript received Oct. 10, 1963. This paper is from the thesis of J. J. O'Connor prepared in partial fulfillment of the requirements of The Institute of Paper Chem-

istry for the Ph.D. degree from Lawrence College, Appleton, Wisconsin, June 1962.

Any discussion of this paper will appear in a Discussion Section to be published in the December 1964 JOURNAL.

REFERENCES

1. S. Wawzonek and E. Runner, *This Journal*, **99**, 457 (1952).
2. "Moderne Methoden der Pflanzenanalyse," p. 415, Band III, Julius Springer Pub., Berlin (1955).
3. A. Müller, M. Meszaros, K. Körmeny and A. Kucsman, *J. Org. Chem.*, **6**, 787 (1952).
4. A. Müller, M. Raltschewa and M. Papp, *Ber.*, **75**, 692 (1942).
5. I. M. Kolthoff and J. F. Coetzee, *J. Am. Chem. Soc.*, **79**, 870 (1957).
6. "Sadtler Standard Spectra-Midget Edition," Sadtler Research Laboratories, Philadelphia (1961), a, No. 6902; b, No. 6910.
7. H. Lund, *Acta Chem. Scand.*, **11**, 1323 (1957).
8. D. H. Geske, *J. Am. Chem. Soc.*, **81**, 4145 (1959).
9. L. Meites, "Polarographic Techniques," p. 108, Interscience Publishers, New York (1955).
10. A. Müller, *Acta Chim. Acad. Sci. Hung.*, **2**, No. 2-3, 231 (1952).
11. J. P. Billon, *J. Electroanal. Chem.*, **1**, 486 (1960).
12. A. Müller, *J. Org. Chem.*, **17**, 1077 (1952).
13. D. H. Geske, Doctor's Dissertation, Iowa City, State University of Iowa, 1957.
14. H. Lund, *Acta Chem. Scand.*, **11**, 491 (1957).
15. F. J. Vermillion, Jr., The Institute of Paper Chemistry, Private communication.

The Thermodynamic Properties of Cesium Chlorotitanates

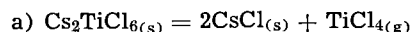
R. L. Lister and S. N. Flengas

Department of Metallurgical Engineering, University of Toronto, Toronto, Ontario, Canada

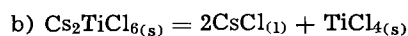
ABSTRACT

The equilibrium decomposition pressures of pure cesium hexachlorotitanate have been measured at various temperatures. Measurements were also made in the presence of cesium chloride. It was found that cesium hexachlorotitanate in excess of cesium chloride produced a new compound, cesium octachlorotitanate (Cs_4TiCl_8). The vapor pressure curves are given by the following equations:

For the reactions

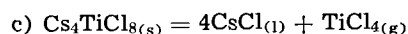


$$\log_{10} P_{(\text{mm Hg})} = \frac{-8358}{T} + 11.762 \quad (870^\circ - 918^\circ\text{K})$$



$$\log_{10} P_{(\text{mm Hg})} = \frac{-9223}{T} + 12.714 \quad (918^\circ - 950^\circ\text{K})$$

and



$$\log_{10} P_{(\text{mm Hg})} = \frac{-5171}{T} + 7.901 \quad (918^\circ - 1040^\circ\text{K})$$

Various properties of the alkali metal chlorotitanate compounds are also discussed.

Interest in fused salt electrolysis as a means of producing titanium metal has been aroused in the past decade. Titanium tetrachloride is too volatile to be used directly in a fused salt bath, and recent investigations have been directed toward production of stable compounds containing the titanium species. Investigations have shown that the solu-

bility of titanium tetrachloride in various salt baths could be explained in terms of compound formation and was found to be dependent on the temperature and surrounding atmosphere (1).

The first compound studied was potassium hexachlorotitanate, which has been shown to be insufficiently stable (2). In the present investigation,

the reactions between gaseous TiCl_4 and solid CsCl were studied.

The compound Cs_2TiCl_6 was synthesized, and the pressures of titanium tetrachloride in equilibrium with the solid compound at various temperatures were investigated. It was found that, in the presence of an excess of cesium chloride, the new compound Cs_4TiCl_8 was formed.

The thermodynamic properties of cesium hexachlorotitanate have also been measured by Morozov and Toptygin (3), and are compared to the values obtained herein.

Experimental

The cesium hexachlorotitanate was prepared by the direct reaction of the solid alkali metal chloride and titanium tetrachloride vapor, as described in a previous publication (5). The cesium chlorides were of reagent grade purified further by sublimation. The titanium tetrachloride was of the commercial grade purified by refluxing the liquid in the presence of finely divided copper filings, under a dry atmosphere, and by a double distillation of the refluxed liquid. A quantitative analysis of the hexachlorotitanates indicated a mole ratio of $\text{MCl}/\text{TiCl}_4 = 2.00 \pm 0.02$, and further identification was made by x-ray diffraction patterns.

Small amounts of spectrographically pure alkali chloride salts were obtained also and used to prepare the corresponding hexachlorotitanate compounds which were employed as comparison standards in the pressure measurements.

A static method was used for the vapor pressure measurements, the apparatus for which is shown in Fig. 1. It consists of the following major sections: the furnace heating the reaction cell; the vacuum system; the heated air bath; and the titanium tetrachloride trap.

To obtain a constant temperature zone, a heavily insulated tubular furnace, 25 in. long, with a 1-in. internal diameter, was used. The wiring consisted of one continuous coil over the whole length of the inner tube, and three equal resistance coils superimposed on this, each independently controlled by a variac. The power was supplied through a voltage stabilizer and with a fairly constant room temperature, a steady state heat flow gave an excellent tem-

perature control of $\pm 0.25^\circ\text{C}$ for long periods of time over the middle 6 in. of the furnace.

The reaction cell constructed of quartz was connected to the Pyrex spoon gauge by a graded seal; the external part of the gauge was connected to a manometer and a two-way stopcock. To allow for evacuation of the system, a by-pass of the spoon gauge was made with a helium-leak-tested, high-temperature, metal valve installed to close off this part when desired. The spoon gauge was made totally of Pyrex and acted as a null point detector, while keeping the corrosive titanium tetrachloride vapor separated from the mercury in the closed-end manometer. The sensitivity of the spoon gauge was such that pressure differences of better than one-half millimeter could be detected easily.

To prevent breakage of the gauge, the pointer was kept at about the null position at all times by adjusting the pressure on the outside jacket through a two-way stopcock. After the temperature had equilibrated and remained constant for about 5 hr for vapor pressure readings under 400 mm, and about 3 hr for vapor pressure readings above 400 mm, the spoon pointer was adjusted precisely to the zero point. This adjustment was made accurately by the use of a cathetometer. The cathetometer was also used for precise readings of the manometer differential.

To prevent condensation of titanium tetrachloride gas, the spoon gauge and cell connections were heated in an air furnace to a temperature above the dew point of titanium tetrachloride. The air furnace was heavily insulated and thermally controlled at $145^\circ \pm 5^\circ\text{C}$.

To investigate the stability of the hexachlorotitanate compound, vapor pressure measurements were made on mixtures of the hexachlorotitanate with the respective alkali metal chloride as well as on the pure compound. The mixtures were prepared by two methods: either by adding a known amount of alkali chloride salt to a known amount of the corresponding hexachlorotitanate, or by withdrawing from the reaction cell containing the hexachlorotitanate at a high temperature known amounts of titanium tetrachloride vapor.

For the latter, a cold trap immersed in liquid air was connected in series with the metal valve leading to the vacuum pump. When the metal valve was opened, titanium tetrachloride vapor from the cell was withdrawn and condensed in the trap. As the amount of alkali hexachlorotitanate initially placed in the cell was known, and the amount of titanium tetrachloride condensed in the trap was found by analysis, the ratio of MCl/TiCl_4 remaining in the cell could be readily calculated.

Between 5 and 10g of alkali hexachlorotitanate were transferred to the quartz cell in a dry box and the cell was immediately sealed into the system. The apparatus was evacuated at room temperature for a period of 3 hr. To remove the small amount of adsorbed titanium tetrachloride, which was always present with the hexachlorotitanate prepared by the direct method (5), the cell was heated to 150°C for a period of 12 hr. The valve was then

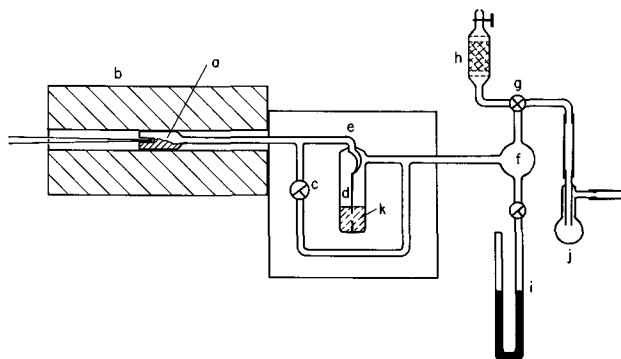


Fig. 1. Apparatus for the vapor pressure measurements. a, Reaction cell; b, furnace; c, metal valve; d, Pyrex spoon gauge; e, hot box; f, air reservoir; g, two-way stopcock; h, drying tube and air inlet; i, mercury manometer; j, cold trap connected to vacuum pump; k, silicone oil.

Table I. Compositions investigated

Run	Mole ratio CsCl/TiCl ₄	
1	2.02	Pure Cs ₂ TiCl ₆
2	2.00	
3	6.59	Mixtures prepared by mixing known amounts of CsCl + Cs ₂ TiCl ₆
4	6.66	
5	2.06	Mixtures prepared by withdrawing titanium tetrachloride from the Cs ₂ TiCl ₆ in the cell
6	2.41	
7	2.41	
8	2.69	
9	2.81	
10	2.97	
11	3.12	
12	3.85	

re-opened and the system was evacuated for only 5 min. The metal valve was then closed and pressure measurements were begun.

Results

Preliminary vapor pressure measurements with pure Cs₂TiCl₆, and in the presence of an excess of cesium chloride, exhibited two entirely different but well-defined pressure curves, indicating that with an increased content of cesium chloride, a new phase had appeared. It was, therefore, decided to

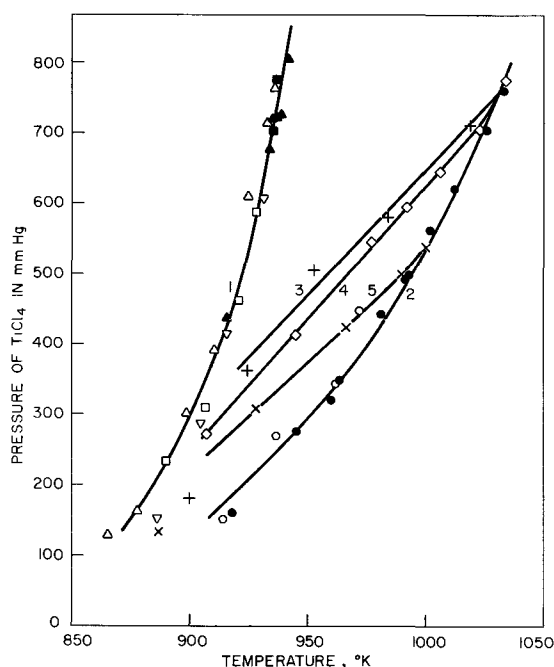


Fig. 2. Equilibrium decomposition pressures of the system Cs₂TiCl₆ + CsCl at various compositions and temperatures.

CsCl/TiCl ₄		
Curve 1	2.00	▲ Compound Cs ₂ TiCl ₆
	2.02	■
	2.06	△
	2.41	□
	2.41	▽
Curve 2	6.59	○ Compound Cs ₄ TiCl ₈
	6.66	●
Curve 3	2.97	+
Curve 4	3.12	◇
Curve 5	3.85	×

investigate the equilibrium pressures over a wide composition range by the methods described previously. The compositions investigated are given in Table I.

Figure 2 represents the two distinct vapor pressure curves for the decomposition of pure Cs₂TiCl₆, and in the presence of an excess of cesium chloride with mole ratios of CsCl/TiCl₄ ≥ 4. The two vapor pressure curves found, indicate the existence of two entirely different compounds.

Pressure readings of compositions ranging from the pure material to a mole ratio of CsCl/TiCl₄ of 2.4 are represented by curve 1 in Fig. 2. Compositions having a mole ratio greater than 4 are represented by curve 2. In the intermediate composition range, that is from mole ratios of approximately 2.4 to 3.85, the vapor pressure curves at low temperatures appeared to follow curve 1, while at higher temperatures they deviated and followed curve 2. Curves 3, 4, and 5 on Fig. 2 are typical of this anomalous behavior of the system. They represent mixtures of cesium chloride and cesium hexachlorotitanate, having the calculated mole ratios of 2.97, 3.12, and 3.85, respectively.

It should be noted that the pressures indicated by curve 1 in Fig. 2 were relatively irreversible with respect to temperature. Reproducible readings were obtained only during increasing temperatures. The system represented by curve 2 was completely reversible, and those of 3, 4, and 5 reversible to approximately the middle of the deviation range.

Figure 3 represents the log₁₀P_(mm) vs. 1/T curve plotted from the data of curves 1 and 2 in Fig. 2. On Fig. 3 the data obtained from the previous work

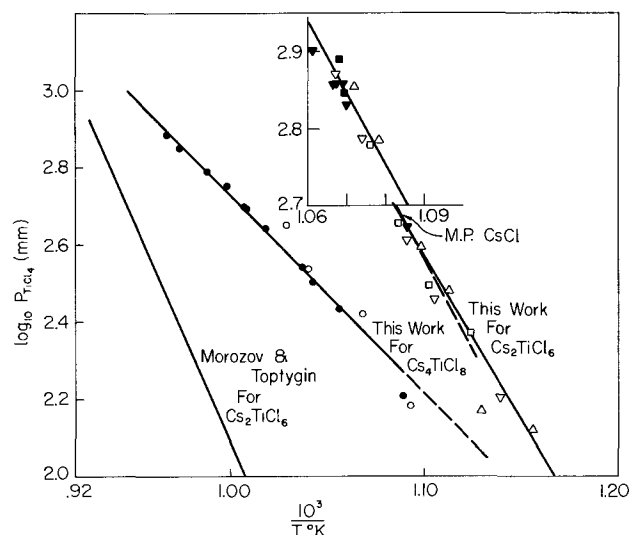


Fig. 3. Plot of log₁₀ P_(mmHg) vs. 1/T for the compounds Cs₂TiCl₆ and Cs₄TiCl₈

CsCl		
TiCl ₄		
Curve 1	2.00	▲ Compound Cs ₂ TiCl ₆
	2.02	■
	2.06	△
	2.41	□
	2.41	▽
Curve 2	6.59	○ Compound Cs ₄ TiCl ₈
	6.66	●

Table II. Summary of thermodynamic calculations

Reaction	$\log_{10}P_{(\text{mm})}$	$\Delta H^\circ T$, kcal/mole	$\Delta S^\circ T$, eu	Decomp. temp, °C	Temp range, °C
* $\text{K}_2\text{TiCl}_6(\text{s}) = 2\text{KCl}(\text{s}) + \text{TiCl}_4(\text{g})$	$\frac{-5930}{T} + 10.3636$	$+27.1 \pm 0.4$	-34.30 ± 0.5	520	350-550
* $\text{Rb}_2\text{TiCl}_6(\text{s}) = 2\text{RbCl}(\text{s}) + \text{TiCl}_4(\text{g})$	$\frac{-7524}{T} + 11.069$	$+34.43 \pm 1.0$	-37.51 ± 1.0	645	525-650
$\text{Cs}_2\text{TiCl}_6(\text{s}) = 2\text{CsCl}(\text{s}) + \text{TiCl}_4(\text{g})$	$\frac{-8358}{T} + 11.762$	$+38.24 \pm 2.0$	-40.98 ± 2.0	—	600-645
$\text{Cs}_2\text{TiCl}_6(\text{s}) = 2\text{CsCl}(\text{l}) + \text{TiCl}_4(\text{g})$	$\frac{-9223}{T} + 12.714$	$+42.21 \pm 1.0$	-45.21 ± 1.0	665	645-675
$\text{Cs}_4\text{TiCl}_8(\text{s}) = 4\text{CsCl}(\text{l}) + \text{TiCl}_4(\text{g})$	$\frac{-5171}{T} + 7.901$	$+23.66 \pm 1.0$	-22.97 ± 1.0	757	645-770

* Data for these reactions have been obtained in previous investigations (2, 10, 11) and have been included for comparison. The data for the decomposition of Rb_2TiCl_6 represent the results of a preliminary investigation not yet completed.

of Morozov and Topygin (3) are also included. Ehrlich and Framm (4) were not able to investigate this system satisfactorily due to what they called "a tremendous volatility at these temperatures."

Discussion

The experimental work done herein has indicated that the Cs_2TiCl_6 is not stable in the presence of an excess of cesium chloride. When the ratio of $\text{CsCl}/\text{TiCl}_4$ became equal to, or larger than, four, a totally new pressure curve was observed. Because of the composition range at which this new curve exists, it is postulated that the new compound formed is Cs_4TiCl_8 . This is supported further by the known existence of the two titanate acids H_2TiO_3 and H_4TiO_4 , which in this case are represented by the two families of compounds, respectively, having the general formulas M_2TiCl_6 and M_4TiCl_8 . It should be noted that neither potassium (2-10) nor rubidium (11) was found to exhibit the second type.

X-ray diffraction patterns were taken on reacted mixtures of $\text{Cs}_2\text{TiCl}_6 + \text{CsCl}$ in the intermediate composition range, specifically for compositions represented by the mole ratios of $\text{CsCl}/\text{TiCl}_4$ equal to 3 and 3.85, and the patterns indicated the main characteristic peaks for the Cs_2TiCl_6 compound, as well as peaks of a new compound postulated to be the Cs_4TiCl_8 . Furthermore, the observed peaks for Cs_2TiCl_6 in the mixture were slightly displaced, when compared with those of the pure compound, indicating solid solubility.

The equilibrium vapor pressures for the reaction

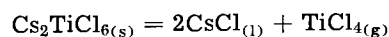


were calculated from the data by the method of least squares and are given by the equation

$$\log_{10}P_{(\text{mm})} = \frac{-8358}{T} + 11.762 \quad [1]$$

(between 870° — 918°K)

Similarly, the equilibrium vapor pressures for the reaction



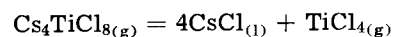
are given by equation

$$\log_{10}P_{(\text{mm})} = \frac{-9223}{T} + 12.714 \quad [2]$$

(between 918° — 950°K)

The heats of decomposition, as determined by the Van't Hoff equation are 38.24 ± 2.0 kcal/mole below 918°K, and 42.21 ± 1.0 kcal/mole above 918°K. The difference of 3.97 ± 3 kcal/mole is due to the latent heat of fusion for two moles of cesium chloride at its melting point. This value is lower than the approximate value of 7.2 kcal given in the literature (8). The decomposition temperature is 665°C. Morozov and Topygin have reported a decomposition temperature of 795°C and a heat of decomposition of 33.33 kcal/mole.

For the reaction



the equation for the equilibrium vapor pressure curve is

$$\log_{10}P_{(\text{mm})} = \frac{-5171}{T} + 7.901 \quad [3]$$

over the temperature range of 918°-1040°K, indicating a decomposition temperature of 757°C with a heat of decomposition of 23.66 ± 1.0 kcal/mole. The thermodynamic data for all the stable chlorotitanate compounds are summarized in Table II.

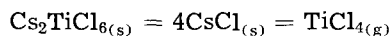
From the vapor pressure curves in Fig. 2, it is seen that at any given temperature over the range investigated, the compound Cs_4TiCl_8 has the lower equilibrium pressure and therefore is the more stable compound.

To explain the shift in the pressure curves with changing composition for the cesium compounds, the following should be taken into account:

(a) In a closed system at constant temperature, where the reactants cesium chloride and titanium tetrachloride are present in fixed amounts corresponding to a mole ratio of $\text{CsCl}/\text{TiCl}_4$ exactly equal

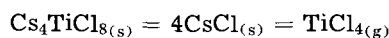
to two, the only compound which can be formed is Cs_2TiCl_6 .

The pressure of titanium tetrachloride in the system will then represent the equilibrium



(b) Considering the ratio of $\text{CsCl}/\text{TiCl}_4$ greater than two, and less than four, the reaction product in the cell should be a mixture of Cs_2TiCl_6 and Cs_4TiCl_8 . However, as long as Cs_2TiCl_6 is present, it will still control the equilibrium pressure in the system. The existence of these two competing reactions should also explain the relative irreversibility, with respect to temperature of the decomposition pressures of Cs_2TiCl_6 given by curve 1 on Fig. 1.

(c) When the mole ratio of $\text{CsCl}/\text{TiCl}_4$ becomes greater than four, Cs_2TiCl_6 cannot be formed any longer, and the pressure of titanium tetrachloride in the system should now represent the equilibrium due to the decomposition of the compound Cs_4TiCl_8 , following the reaction



In the actual experimental cell, the available titanium tetrachloride is present in two forms: as chemically bound in the compounds Cs_2TiCl_6 and Cs_4TiCl_8 , and as free titanium tetrachloride required to fill the volume of the apparatus at the corresponding pressure and temperature. The latter amount depends also on the volume of the apparatus and could be quite large when compared to the titanium tetrachloride available in the rather small quantity of Cs_2TiCl_6 initially placed in the cell.

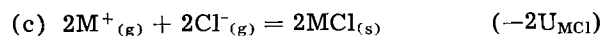
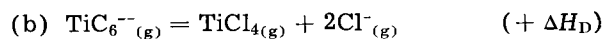
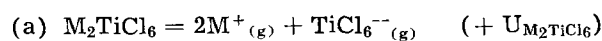
It is evident that the mole ratio of $\text{CsCl}/\text{TiCl}_4$ in the solid phase reaches the critical value of four, with an over-all composition corresponding to a much lower value, thus explaining the appearance of the curves for the compound Cs_4TiCl_8 at compositions below the theoretical.

It may also be calculated from the ideal gas law that the number of moles of titanium tetrachloride which is required to fill the free volume of the apparatus should be larger at the higher temperatures. Accordingly, it should be expected that, in the intermediate composition range, *i.e.*, $4 > \text{CsCl}/\text{TiCl}_4 > 2$ the pressure curves should follow at low temperatures the curve for Cs_2TiCl_6 , and at the higher temperatures the curve for Cs_4TiCl_8 .

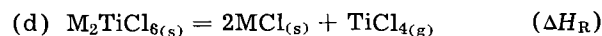
The behavior of the system in the intermediate composition range is further complicated by the evidence of solid solubility between the two components, Cs_2TiCl_6 and Cs_4TiCl_8 . The effect of solid solubility should be to change further the shape of the curves. Thus, the middle portions of curves 3, 4, and 5 in Fig. 2 could be interpreted as representing the partial pressures of Cs_2TiCl_6 in the solid solutions.

Ionic radius effect.—Potassium(1), rubidium(11), and cesium form stable hexachlorotitanates, the stability of which increases with the ionic radius of the corresponding cations. However, lithium and sodium do not form these compounds. The increasing stability of the hexachlorotitanates, with increasing

ionic radius of the alkali metal cation, may be accounted for by considering the following reactions



By adding Eq. (a), (b), and (c), we obtain the over-all reaction:



$$\text{and } \Delta H_R = \Delta H_D - (2U_{\text{MCl}} - U_{\text{M}_2\text{TiCl}_6}) \quad [4]$$

$U_{\text{M}_2\text{TiCl}_6}$ and U_{MCl} represent, respectively, heats which are equal to the lattice energies of M_2TiCl_6 and MCl . ΔH_D is the heat of dissociation of the complex anion TiCl_6^{--} and ΔH_R is experimentally measured heat of decomposition of the solid hexachlorotitanates.

The difference in the lattice energies, $2U_{\text{MCl}} - U_{\text{M}_2\text{TiCl}_6}$, is always positive because of the smaller size of the Cl^- anion, as compared to the size of the TiCl_6^{--} complex. This difference should increase going from a larger to a smaller metal cation.

As the heat of dissociation of the TiCl_6^{--} ion is the same in all three hexachlorotitanates, it follows that the heat of decomposition ΔH_R for the hexachlorotitanates should increase with increasing ionic radius. From the results in Table II, it may be seen that the heat of decomposition increases from 27 kcal/mole for K_2TiCl_6 to 42.2 kcal/mole for Cs_2TiCl_6 , which is in agreement with the theory.

Therefore, it may be predicted that the solubilities of gaseous titanium tetrachloride in molten mixtures containing alkali chlorides should be greater the larger the ionic radius of the alkali metal cations in the mixture.

From the previous investigations (5, 7), it has been found that the hexachlorotitanate structure consists of an alkali metal cation and a complex anion consisting of six chlorine atoms symmetrically coordinated about a titanium ion. X-ray diffraction by both Engel (6) and Bland and Flengas (7) have shown the crystal structures of K_2TiCl_6 , Rb_2TiCl_6 , and Cs_2TiCl_6 to be cubic and isomorphous to the hexachloroplatinate. The titanium ion in all three of these compounds is octahedrally co-ordinated by the six chlorine atoms at $2.35 \pm 0.03\text{\AA}$, and only the M-Cl distance changes.

For a complex compound of this type to crystallize in the cubic system in the octahedral manner, it can be readily calculated from geometric considerations (9) that the radius ratio of cation to anion must lie between 0.414 and 0.732. If it is assumed that the radius of the anion complex is equal to the co-ordinate distance of 2.35\AA , then the minimum and maximum permissible ionic radius of an alkali metal ion can be determined, as 0.97\AA and 1.72\AA , respectively. Values for the Pauling ion radii of Li^+ , Na^+ , K^+ , Rb^+ , and Cs^+ are -0.78 , 0.95 , 1.33 , 1.49 , and 1.65 , respectively, and accordingly, the lithium and sodium ions are too small to form stable hexachlorotitanates while the potassium, ru-

bidium, and cesium all lie within the prescribed range.

Silver and thallium also exhibit radii ratios within this required range, and considering the geometric factor, production of their respective hexachlorotitanates appears possible. Although silver compounds have not as yet been synthesized, thallium hexachlorotitanate has been produced and studied by Morozov and Toptygin (3).

With respect to their ionic behavior, it may be postulated that doubly ionized hexachlorotitanate compounds could also exist as indicated by the large difference in the M-Cl and Ti-Cl distances.

Acknowledgments

Acknowledgment is made to the National Research Council of Canada for a fellowship to one of the authors (R.L.L.) and for its financial assistance in support of this work.

Manuscript received March 25, 1963; revised manuscript received Oct. 23, 1963. This paper was presented at the Pittsburgh Meeting, April 15-18, 1963.

Any discussion of this paper will appear in a Discussion Section to be published in the December 1964 JOURNAL.

REFERENCES

1. S. N. Flengas, *Ann. N. Y. Acad. Sci.*, **79**, 11, 853 (1960).
2. J. H. Mui and S. N. Flengas, *Can. J. Chem.*, **40**, 997-1008 (1962).
3. I. S. Morozov and D. Ya. Toptygin, *Russ. J. Inorg. Chem.*, **5**, 1, 42 (1960).
4. P. von Ehrlich and E. Framm, *Z. Naturforsch.*, **98**, 324 (1954).
5. R. L. Lister and S. N. Flengas, *Can. J. Chem.*, **41**, 1548 (1963).
6. G. Engel, *Z. Krist.*, **90**, 341 (1935).
7. J. A. Bland and S. N. Flengas, *Can. J. Phys.*, **39**, 941 (1960).
8. O. Kubaschewski and E. LL. Evans, "Metallurgical Thermochemistry," Pergamon (1955).
9. F. A. Cotton and G. Wilkinson, "Advanced Inorganic Chemistry," Interscience (1962).
10. S. N. Flengas and T. R. Ingraham, *Can. J. Chem.*, **38**, 813 (1960).
11. R. L. Lister, The Formation and Thermodynamic Properties of Rubidium and Cesium Hexachlorotitanates, M.A.Sc. Thesis, Dept. of Metallurgical Engineering, Univ. of Toronto, 1962.

Mechanochemical Anodic Dissolution of Austenitic Stainless Steel in Hot Chloride Solution at Controlled Electrode Potential

T. P. Hoar and J. C. Scully¹

Department of Metallurgy, University of Cambridge, England

ABSTRACT

The influence of metal yielding on the anodic dissolution rate of 18Cr-8Ni stainless steel in 42 weight per cent (w/o) aqueous magnesium chloride solution at 154°C has been examined under conditions of controlled potential. At -0.14v (e_H) in solution flowing at 52 cm/sec to eliminate concentration polarization, yielding of the metal anode at ca. 100 %/min increases the anode current density by a factor of $>10^4$. A preliminary discussion of the mechanism of the mechanochemical effect is given; probably the intense disarranging of the deforming metal surface during the arrival of dislocation pile-ups produced by restricted slip results in a large transient increase in the density of anodically active surface sites.

Many investigators have studied the influence of prior cold-work on susceptibility to stress-corrosion cracking, but few have attempted to determine what influence a yielding surface has on the dissolution rate of metals and alloys. This is of critical importance in the mechanism of crack propagation in austenitic stainless steels stressed and exposed to chloride solutions, proposed by Hoar and Hines (1-3); the crack is supposed to propagate on account of the very rapid anodic dissolution of the yielding ductile metal at the advancing edge of the crack. Consequently, Hoar and West (4, 5) studied macroscopic yielding 18Cr-8Ni steel anodes galvanostatically and reported a drastic lowering of the overpotentials required to produce current densities up to 0.5 amp/cm² as compared with those required for static anodes. However, van Rooyen (6) using a similar technique was unable to obtain

so large an effect and criticized certain aspects of the overpotential measurements of Hoar and West.

The influence of several strain rates on the dissolution rates of 18Cr-8Ni steel in the concentrated chloride solution has now been examined potentiostatically. The anode current density increases found indicate that there is a large effect; the results are in harmony with those of Hoar and West.

Materials

The stainless steel wire 18-8(b) of Hoar and Hines (1) was used throughout this work in the as-received condition, fully softened after drawing and slightly work-hardened by subsequent coiling and uncoiling. The wire, 0.05 cm in diameter, had the composition Cr, 17.1; Ni, 9.2; Si, 1.0; C, 0.09; Mo, 0.18; N, 0.06; Nb + Ta, 0.05; Cu, 0.2; Ti, 0.05%; balance Fe.

The corrosive solution was 42 w/o aqueous magnesium chloride solution boiling at 154°C, prepared

¹ Present address: Olin Mathieson Chemical Corporation, New Haven, Connecticut.

Table I. Influence of metal strain rate and solution flow rate on anode current density at -0.14v (e_H)18Cr-8Ni steel; 42 w/o aqueous MgCl_2 ; 154°C

	Flow rate, cm/sec	0	20	40	52
	Strain rate, %/min	ma/cm ²	ma/cm ²	ma/cm ²	ma/cm ²
Stress-corrosion cracking, ca. 400 cracks/cm of wire	0	0.013*	0.013*	0.013*	0.013*
	4	0.24	—	—	—
	13	0.35	—	—	—
General dissolution	40	—	52	60	—
	107	3.0	—	119**	161†

* From polarization curve results of Hoar and West (5).

** Mean of 9 experiments—120, 120, 116, 114, 119, 111, 124, 131, and 123 ma/cm².† Mean of 5 experiments—160, 164, 153, 171, 151 ma/cm².

by adding small amounts of distilled water to the commercially pure hexahydrate.

Apparatus and Procedure

A modified Hounsfield tensometer was used for applying stress and achieving known macroscopic strain rates of the wire specimen, as described by Hoar and West (5). The electrode potential of the specimen was measured *vs.* a saturated calomel electrode with a high impedance electronic voltmeter monitoring a Honeywell Brown recorder, and converted to an approximate normal hydrogen scale by adding 254 mv, equivalent to the approximate procedure previously used (1-5). A Wenking-Bank extended range potentiostat was used to control the potential, and current from the instrument was recorded on a $\frac{1}{4}$ -sec Honeywell Brown electronic 10 mv fast recorder. By recording the p.d. across any one of several resistors, several current ranges could be used.

Two separate arrangements were used for experiments in stationary solution and in flowing solution. The vessel and the procedure used for the experiments in stationary solution were as described by Hoar and West (5). For experiments in flowing solution, the arrangement used by Hoar and

West was modified; a Luggin capillary probe passed through the cylindrical platinum cathode and came to within 0.05 cm of the wire. This apparatus and the main electrical circuitry are shown in Fig. 1.

In either arrangement, when the solution had regained its boiling point after setting up (about 5 min), the potentiostat was switched into circuit, the recorder chart set in motion, the current range selected, and the Tensometer motor started. For experiments in flowing solution, the glass top of the reservoir was closed and a stop watch started simultaneously when the Tensometer gauge indicated that the wire had begun to yield. Yielding occurred only in the hot, cracking or dissolving, length of wire, for which the strain rate was calculated from the extension rate of the whole length of the wire.

Results and Interpretation

Correction for local cathodic current.—Specimens held potentiostatically at -0.14v (e_H) showed a small over-all cathodic current density of 0.13 ma/cm^2 ,² caused by dissolved oxygen in the solution. The local anodic current density on static specimens in stagnant or flowing solution at this potential is ca. 0.013 ma/cm^2 , according to the polarization curve experiments of Hoar and West (5). Special experiments at -0.18v (e_H) showed that the somewhat higher cathode current density, 0.20 ma/cm^2 ,² found at that potential, where no anodic current flows, was scarcely influenced either by straining the wire specimen or by flowing the solution. Consequently, for all experiments at -0.14v , $0.13 + 0.013 = 0.14\text{ ma/cm}^2$ was added to the measured current density to obtain the total anode current density. The correction turns out to be of little importance, as will be seen.

Influence of strain rate and solution flow on anode current density.—Table I shows the influence of metal strain rate and solution flow rate on the anode current density at -0.14v (e_H). The salient features of the results are:

1. At the lower strain rates, stress corrosion cracking with a high crack density occurred, as found by Hoar and West in their galvanostatic experiments at the lower current densities. No doubt the actual strain rates at the advancing edges of the cracks, and the anode current densities there, were very considerably greater than those recorded, by a factor

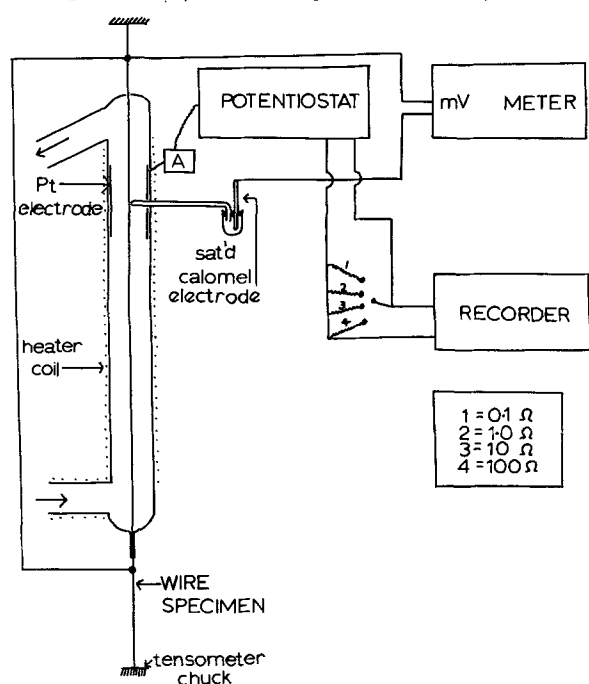


Fig. 1. Main electrical circuitry for apparatus used in flowing solution experiments.

² In agreement with the value observed by Hoar and Hines (3).

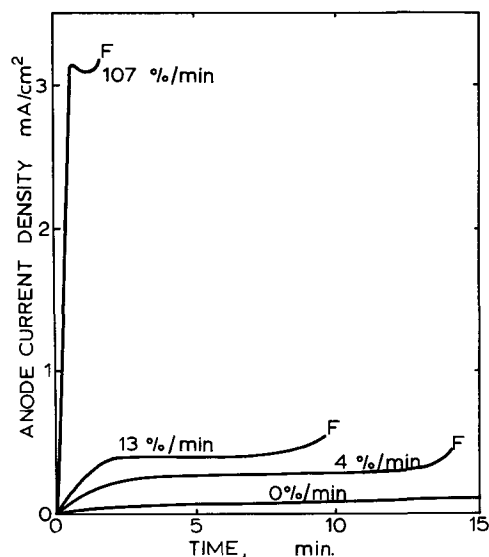


Fig. 2. Current density/time curves for 18Cr-8Ni wires strained at 4, 13, and 107 %/min while maintained at $-0.14v$ (e_H). F: fracture.

$$\frac{\text{Length of cracking wire}}{\text{Total width of advancing edges of cracks}}$$

which could well be 1000 or more.

2. At the higher strain rates, general dissolution occurred, and with flowing solutions high current densities were found. The two most interesting results, in the last line of Table I, were replicated many times with the excellent concordance recorded. The highest current density, 161 ma/cm², is about one-third of the 500 ma/cm² found by Hoar and West (5) to be sustained at potentials in the range -0.13 to $-0.17v$ with the *ca.* 3 times higher strain rate of *ca.* 300 %/min, and is evidently in complete harmony with the earlier result. It represents a mechanochemical increase of $> 10^4$ times in anode current density for a strain rate of about 100 %/min.

Rates of production and disappearance of mechanochemical effect.—In the experiments with stagnant solution, it was easily possible to record the rate of current density rise when straining began. Some typical results are shown in Fig. 2. The rise is not instantaneous, although at the highest strain rate it is fast; at the lower strain rates the rise in 2-3 min or so doubtless corresponds to crack initiation, and at the highest, to the noninstantaneous setting up of the most mechanochemically active surface.

In some experiments at low strain rates with stagnant solution, giving stress corrosion cracking, straining was interrupted, and the specimen either (a) left under the stress obtaining or (b) left without any applied stress; then after a short interval, straining was restarted in either case. Curves (a) and (b) of Fig. 3 show typical results of the above two programs. In (a), the cessation of macroscopic straining leads to a relatively slow fall of anode current density, because the stress left on maintains a slower yielding at the crack advancing edges; and the restarting of macroscopic straining produces a

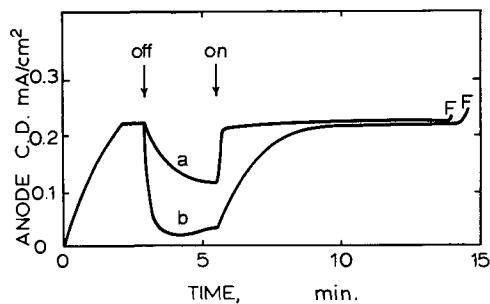


Fig. 3. Current density/time curves for 18Cr-8Ni wires strained at 4 %/min in stagnant solution while maintained at $-0.14v$ (e_H). Straining stopped for 2½ min during experiment; (a) load maintained (b) load removed. F: fracture.

very rapid return to the original current density, because the still-yielding advancing edges at once return to their previous strain rate. In (b), the cessation of macroscopic straining and the removal of stress gives a relatively rapid, but notably not instantaneous, fall of current density, because the now nonyielding crack edges quite quickly resume the anode properties of static material; and the restarting of straining produces a relatively slow return to the original current density, because the cracks have to be re-initiated.

It was not possible with the present apparatus to investigate similar transients on specimens undergoing general dissolution at high strain rates in flowing solutions, because of the very short duration of each experiment; such fast transients may well give important quantitative information about the mechanochemical process, and are now being examined (7).

Influence of prior cold work on the mechanochemical effect.—Specimens of the 18-8 wire were prestressed well into the plastic range, some to fracture. They were then tested in stagnant solution at $-0.14v$ (e_H) and a strain rate of 4 %/min, with the results shown in Table II; the corresponding result for as-received specimens is included for comparison. All the specimens except those prestressed to fracture showed qualitatively similar stress corrosion cracks.

The decrease of time to fracture with increase of prestress up to 90,000 psi reflects merely the smaller available extension of the cold-worked specimens during the test. The scarcely significant increase of total anode current density with increase of pre-

Table II. Influence of prior cold work on anode current density at $-0.14v$ (e_H)

18Cr-8Ni steel; 42 w/o aqueous MgCl₂; 154°C; stagnant solution; strain rate 4 %/min.

Apparent prestress, psi	Time to fracture, min	Crack density, cracks/cm	Anode C.D., ma/cm ²
0	14	380	0.24
50,000	11.5	490	0.24 ₅
70,000	8.5	500	0.24 ₆
90,000	4	610	0.25
111,700*	0.75	Nil	0.05

* Specimens prestressed to fracture.

stress, coupled with the moderate increase of crack density, probably means that each crack advancing edge is narrower, a reasonable supposition for the stiffer cold-worked material. The specimens prepared by stressing to fracture showed a net current density of -0.09 ma/cm^2 (indicating an anode current density of 0.05 ma/cm^2) before straining, no change of this during straining for the short period before they fractured in the test, and no stress-corrosion cracks; the fracture was almost brittle, in one case above the liquid level. This is striking evidence that a considerable degree of ductility of the metal is an essential condition for the development of both the anodic mechanochemical effect and stress corrosion cracking.

Discussion

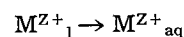
The present results obtained potentiostatically are in complete harmony with those obtained galvanostatically by Hoar and West (5) and confirm the reality of mechanochemical or yield-assisted anodic dissolution for 18Cr-8Ni austenitic steel in hot, concentrated chloride solution. Additionally, the transient results are further support for the mechanism of stress corrosion cracking of these steels put forward by Hoar and Hines (1). We report elsewhere (8) some similar results with a series of iron-nickel alloys; those that stress corrosion crack show a marked mechanochemical effect, whereas those that are not susceptible to cracking do not.

It is too early to propose too specific a mechanism for mechanochemical dissolution. However, evidence is accumulating that when stress corrosion cracking occurs in fcc lattices, those showing a high density of stacking faults and the correlated restricted slip (9) are the most susceptible (10-14). Stacking faults might play one or both of two roles: (i) their initial preferential dissolution [demonstrated for copper alloys under anodic polishing conditions by Swann and Nutting (10)] could provide very narrow stress-raising slots for initiating cracks; (ii) their interference with cross-slip leads to deformation by restricted slip and thus to very large pile-ups of dislocations at and near the surface of the deforming material; these pile-ups may initiate rupture in two ways (a) mechanical fracture, either ductile or brittle (15), because of the high local tensile stresses that they involve, or (b) preferential anodic dissolution leading to tunnels or slots, as demonstrated by the electron microscope studies of Nielsen (16). Further, the intense disarraying of the deforming surface during the arrival of pile-ups (17) may be expected to produce a transiently much greater increase in the density of anodically active surface sites than the increase produced by the arrival of single or small groups of unpiled-up dislocations coming from cross-slip. Consequently, the mechanochemical effect should be much more pronounced in lattices showing restricted slip than in those showing cross-slip, and crack propagation much assisted.

The possible correlation of the mechanochemical effect with the production of pile-ups in restricted

slip is now being studied (7), as are the transients in the mechanochemical effect at high and varying strain rates and high current densities, which should give information on the rate of creation and of annihilation of anodically active surface sites during this type of plastic deformation.

It is important to emphasize that the most rapid mechanochemical dissolution requires, as well as the rapid production of large numbers of active sites on the metal surface, a rapid arrival of suitable reacting entities in the solution at the metal/solution interface and a rapid removal of the reaction products. In the present case, chloride ions and water molecules are evidently the required "solution" reactants, and complex cations are the products, and they need to be respectively supplied and removed by forced convection as well as by natural diffusion. Chloride ion is probably a powerful catalyst for the over-all reaction



where M^{Z+}_1 is an iron, chromium, or nickel ion in the lattice and M^{Z+}_{aq} the same ion in aqueous solution, as well as being a complex-forming ligand; the recent demonstration of the very ready adsorption of chloride ion on austenitic stainless steel (18) may also have relevance.

Acknowledgments

The authors are grateful to Imperial Chemical Industries Ltd. for a maintenance grant to one of them (J. C. S.) during the course of which this work was carried out, and for other generous financial assistance. They are much indebted to Dr. J. G. Hines of the company for several valuable discussions.

Manuscript received July 8, 1963. This paper was presented at the New York Meeting, Sept. 29-Oct. 3, 1963.

Any discussion of this paper will appear in a Discussion Section to be published in the December 1964 JOURNAL.

REFERENCES

1. T. P. Hoar and J. G. Hines, *J. Iron Steel Inst.*, **182**, 124 (1956).
2. T. P. Hoar and J. G. Hines, "Stress Corrosion Cracking and Embrittlement," W. D. Robertson, Editor, John Wiley & Sons, Inc., New York (1956).
3. T. P. Hoar and J. G. Hines, Proc. 8th Meeting Int. Comm. Electrochem. Therm. Kin. (CITCE), Madrid 1956, p. 273, Butterworths, London (1958).
4. T. P. Hoar and J. M. West, *Nature*, **181**, 835 (1958).
5. T. P. Hoar and J. M. West, *Proc. Roy. Soc.*, **A268**, 304 (1962).
6. D. van Rooyen, First International Congress on Metallic Corrosion, p. 309, Butterworths, London (1962).
7. T. P. Hoar and G. P. Rothwell, work in progress.
8. J. C. Scully and T. P. Hoar, Second International Congress on Metallic Corrosion, To be published, New York (1963).
9. P. B. Hirsch, *J. Inst. Metals*, **87**, 406 (1958-9).
10. P. R. Swann, Thesis, Cambridge (1960).
11. P. R. Swann and J. Nutting, *J. Inst. Metals*, **90**, 133 (1961-2).

12. A. Howie and P. R. Swann, *Phil. Mag.*, **6**, 1215 (1961).
 13. S. Barnartt, R. Stickler, and D. van Rooyen, *Corrosion Sci.*, **3**, 9 (1963).
 14. P. R. Swann, Second International Congress on Metallic Corrosion, To be published, New York (1963).
 15. N. J. Petch, "Progress in Metal Physics," No. 5, B. Chalmers and R. King, Editors, p. 1, Pergamon, London (1954).
 16. N. A. Nielsen, Second International Congress on Metallic Corrosion, To be published, New York (1963).
 17. J. G. Hines, *Corrosion Sci.*, **1**, 21 (1961).
 18. D. N. Staicopoulos, *This Journal*, **108**, 900 (1961).

Thermodynamic Studies of Ternary Liquid Metallic Systems Containing Miscibility Gaps

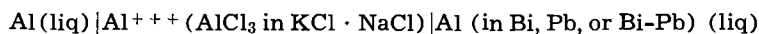
I. The Aluminum-Bismuth-Lead System

T. C. Wilder¹ and J. F. Elliott

Department of Metallurgy, Massachusetts Institute of Technology, Cambridge, Massachusetts

ABSTRACT

The partial and integral molar thermodynamic properties of the liquid Al-Bi-Pb system have been determined by emf measurements of the reversible concentration cell



in the range 700°-1000°C and distribution measurements of the two-phase alloys at 900°C. The measured properties of this system have been compared with estimates based on several theoretical treatments contained in the literature. The partial and integral molar properties of mixing, *i.e.*, F_1^M , S_1^M , H_1^M , F^M , H^M , and S^M , in this system have higher positive deviations from ideality than the theoretical treatments would indicate. The miscibility gaps at 900°C of the Al-Pb and Al-Bi systems are not as wide as those reported previously in the literature.

A reversible high-temperature concentration cell, similar to the one described previously by the authors (1), was used to determine the thermodynamic properties of the ternary liquid metallic system, Al-Bi-Pb, in the range of 700°-1000°C. The system is completely liquid at all temperatures of the study and exhibits a miscibility gap which is bounded by the two binary edges, Al-Bi and Al-Pb (Fig. 1). Distribution measurements at 900°C for the two-

¹ Present address: Ledgemont Laboratory, Kennecott Copper Corporation, Lexington, Massachusetts.

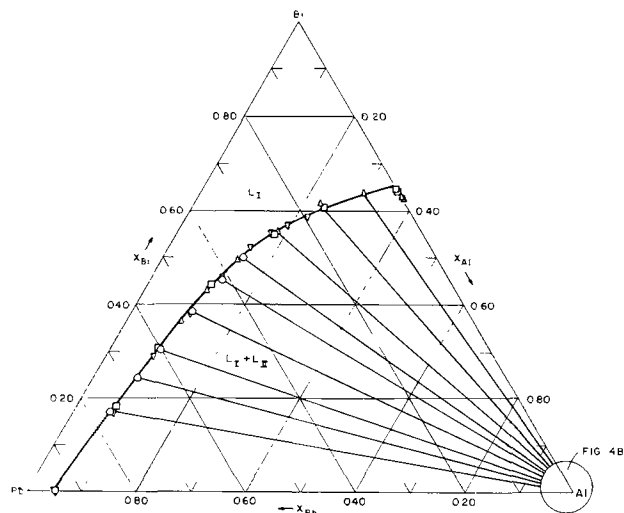
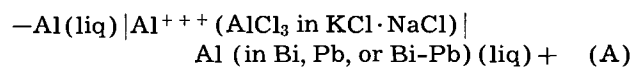


Fig. 1A. Al-Bi-Pb isotherm at 900°C. ▽, Run No. 82; ○, run No. 88; △, run No. 90; □, cell runs.

phase alloys located the conjugate compositions making up the boundary of the miscibility gap. The larger region of homogeneity, L_I , is adjacent to the Bi-Pb edge, which is miscible in all proportions. The very small L_{II} region is adjacent to the pure aluminum corner.

The cell under study was



for which, on completion of the circuit, the over-all reaction is

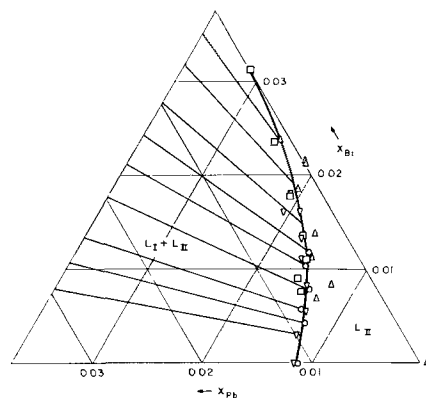
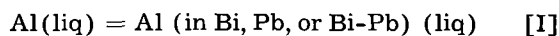


Fig. 1B. Enlargement of aluminum corner of Al-Bi-Pb isotherm at 900°C. ▽, Run No. 82; □, run No. 87; ○, run No. 88; △, run No. 90.

In this investigation the reference state for each metal is the pure liquid. From the measurements of the potential of the cell (A) as a function of temperature and composition, the following partial molar properties of aluminum, the most electro-positive metal in the system, are obtained

$$\bar{F}_{Al} - F_{Al}^{\circ} = F_{Al}^M = -3FE = RT \ln a_{Al} \quad [1]$$

$$\bar{S}_{Al} - S_{Al}^{\circ} = S_{Al}^M = -(\partial F_{Al}^M / \partial T)_{X_{Al}} = 3F(\partial E / \partial T)_{X_{Al}} \quad [2]$$

$$\bar{H}_{Al} - H_{Al}^{\circ} = H_{Al}^M = F_{Al}^M + TS_{Al}^M = -3F[E - T(\partial E / \partial T)_{X_{Al}}] \quad [3]$$

where F is the Faraday (23,063 cal/v equivalent), and E is the reversible electromotive force of the cell in volts. The valence, n , of the aluminum ion in the molten electrolyte is taken to be 3. Experimental justification of this is developed later.

Experimental

The plan of this investigation was to measure the emf of cells consisting of anodes of pure liquid aluminum and cathodes of the alloys of the larger region of homogeneity (L_1) of Al-Bi-Pb along the binary edges Al-Bi and Al-Pb and five "pseudo-binary" systems Al-(Bi/Pb = 0.25, 0.50, 1.0, 2.0, and 4.0) in the temperature interval 700°-1000°C. It was necessary to supplement the cell measurements with phase distribution measurements to obtain a complete picture of the system at 900°C.

Cell design.—A new cell design as shown in Fig. 2 was used. The various parts of the cells, *e.g.*, electrolyte, tantalum contact leads, chromel-alumel thermocouples, refractories, etc., were purified or prepared as described earlier (1). The closed-end Morganite (recrystallized 99.7% Al_2O_3) tube which was used to hold the pure aluminum standard, contained two ports: one for completion of the electrolyte bridge between electrodes, and the other for equalizing the levels of the electrolyte inside and outside the standard tube. Alloying additions were made at specified intervals through the addition tube. The alloy cathode was very large in comparison with the standard anode, because most of the alloy compositions were very dilute in aluminum. The large difference in electrode size also helped to minimize errors which may have occurred

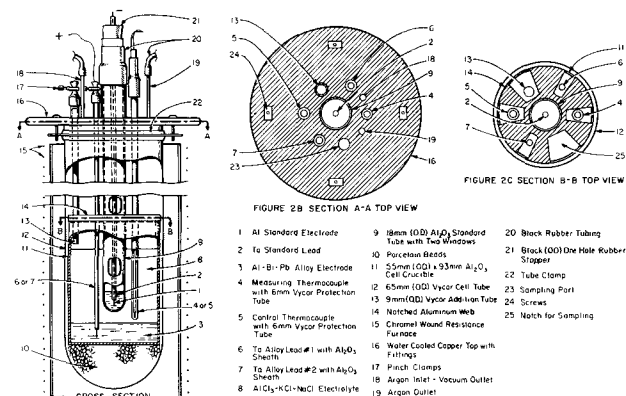


Fig. 2. Cell design (only one of the two thermocouples and one of the two contact leads are shown).

Table I. Assay of electrode metals
(All values in weight per cent)

	Lead*		Bismuth*		Aluminum**
Fe	0.0001	Mn	0.0001	Fe	0.002
Bi	0.00005	Pb	0.0001	Si	0.001
Cu	0.00005	Fe	0.0001	Cu	0.002
Pb	99.999+	Cu	0.0001	Al	99.995 (bal)
		Ag	0.0004		
		Bi	99.999+		

* Supplied by the American Smelting and Refining Company.
** Gift of the Aluminum Company of America.

from polarization of the cell. There were two shielded chromel-alumel thermocouples in the electrolyte. The first thermocouple was used to measure the temperature; the second was for temperature control. The notched aluminum disk on top of the cell crucible separated the various components of the cell and helped minimize vertical temperature gradients.

Cell operation.—Preparation of the cell was carried out as previously described (1), except that initially the alloy cathode was simply 300-400g of pure lead, bismuth, or a Bi-Pb alloy of premeasured atomic ratio of Pb/Bi. The anode chamber contained 6-7g of aluminum. Analyses of the pure metals are listed in Table I.

When the cell was brought to temperature (800° or 900°C) a small amount of aluminum, weighed to the nearest 0.1 mg, was added to the cathode through the addition tube. The aluminum dropped through the fused electrolyte, melted, and alloyed with the remainder of the cathode. The progress of solution of it was observed by measuring the cell emf as a function of time. After several hours, when the emf became constant with time, the alloy was homogeneous.

For each alloy investigated, potential measurements were made at three different temperatures: 700°, 800°, and 900°C in a staggered sequence. For alloys known to be two-phased at 700° or 800°C, readings were taken at three temperatures (one of which was 900°C) where the alloy was known to be single-phased. Steady and reproducible readings were obtained at 1000°C. Two samples (one at 900°C) for chemical analysis were withdrawn from the alloy cathode if it contained less than 0.5% Al by weight. At compositions over this value, only one sample was withdrawn at 900°C.

When the temperature in the cell was changed, at least 2 hr were allowed for equilibration of temperature and composition before potential readings were taken again. After the third temperature was studied for the first alloy, more aluminum was added through the addition tube. The resulting new alloy cathode was allowed to homogenize for at least 6 hr before readings were taken again. The above procedure was then repeated.

The cells were operated for 4 to 6 days, depending on how long the $AlCl_3$ would remain in the electrolyte. It was possible to study two alloy compositions a day; accordingly, as many as 12 alloys were studied in a single experiment. Occasionally the electrolyte was sampled and analyzed for aluminum.

The cell potentials became vague, or insensitive, if the AlCl_3 level in the electrolyte fell below 0.02% by weight. Alloys on or near the miscibility gap took so long to reach equilibrium that data obtained from most of them were discarded. For those two-phase alloys that were studied, the potentials were low (< 1 mv) and changed very little with temperature. With such alloys, measurements were taken only at 900°C , since for them $\partial E/\partial T$ is meaningless in terms of S_{Al}^M .

Distribution measurements.—The boundary of the two-phase region at 900°C was determined by equilibrating a series of two-phase alloys at $900^\circ \pm 1.5^\circ\text{C}$ for 24 hr under a protective cover of pre-purified KCl-NaCl azeotrope and argon gas. A portion of each of the two phases was removed for chemical analysis. The apparatus used for this was similar to that shown in Fig. 2, except that the crucible containing the alloy was a 6-in. long, closed-end Morganite alumina tube. The alundum thermal shield contained holes for the two thermocouples and a sampling port. The starting composition was located on either the Al-Bi or Al-Pb edge of the ternary system. After equilibration and sampling, a weighed amount of the third component was added, the system was equilibrated, and samples were withdrawn again. This was repeated several times. Additional compositions along the L_1 boundary of the miscibility gap were obtained from emf cells where the alloys were known to be two-phased.

Experimental Results

The potentials of each of the cells investigated were plotted against temperature. It was found that for a given cell having a homogeneous cathode, the potential varied linearly with temperature. Thus, for each cell the values of E and $\partial E/\partial T$ at 900°C on which all subsequent calculations are based were read from this plot. A reader interested in a tabulation of these data can obtain it by writing to the authors (J.F.E.).

The experimental data were transformed into the alpha and beta functions (2) of aluminum defined as follows

$$\alpha'_{\text{Al}} \equiv \frac{F_{\text{Al}} E}{(1-X_{\text{Al}})^2} = \frac{RT \ln a_{\text{Al}} - RT \ln X_{\text{Al}}}{(1-X_{\text{Al}})^2} = \frac{-3FE - RT \ln X_{\text{Al}}}{(1-X_{\text{Al}})^2} \quad [4]$$

$$\beta_{\text{Al}} \equiv \frac{H_{\text{Al}}^M}{(1-X_{\text{Al}})^2} = \frac{-3F[E - T(\partial E/\partial T)]}{(1-X_{\text{Al}})^2} \quad [5]$$

Table II. Alpha and beta functions for the liquid Al-Pb-Bi system

Binary or pseudobinary system	Composition range L_1 region	$\alpha'_{\text{Al}}, 900^\circ\text{C}, \text{kcal/gfw}$	$\beta_{\text{Al}}, \text{kcal/gfw}$
Al-Pb	$0 < X_{\text{Al}} < 0.0489$	$7.83 - 1.69X_{\text{Al}} (\pm 0.06)^*$	$10.28 - 31.9X_{\text{Al}} (\pm 0.16)^*$
Al-(Bi/Pb = 0.253)	$0 < X_{\text{Al}} < 0.0714$	$7.19 - 1.27X_{\text{Al}} (\pm 0.03)$	$8.99 - 12.67X_{\text{Al}} (\pm 0.08)$
Al-(Bi/Pb = 0.50)	$0 < X_{\text{Al}} < 0.0876$	$6.16 + 1.83X_{\text{Al}} (\pm 0.03)$	$8.36 - 6.38X_{\text{Al}} (\pm 0.06)$
Al-(Bi/Pb = 1.0)	$0 < X_{\text{Al}} < 0.118$	$5.96 + 3.33X_{\text{Al}} (\pm 0.02)$	$7.55 - 3.47X_{\text{Al}} (\pm 0.03)$
Al-(Bi/Pb = 2.0)	$0 < X_{\text{Al}} < 0.179$	$5.28 + 3.40X_{\text{Al}} (\pm 0.07)$	$6.94 - 2.74X_{\text{Al}} (\pm 0.11)$
Al-(Bi/Pb = 4.0)	$0 < X_{\text{Al}} < 0.245$	$4.75 + 3.73X_{\text{Al}} (\pm 0.03)$	$6.23 + 0.23X_{\text{Al}} (\pm 0.11)$
Al-Bi	$0 < X_{\text{Al}} < 0.20$	$4.02 + 3.72X_{\text{Al}} (\pm 0.035)$	$5.80 - 2.31X_{\text{Al}} + 15X_{\text{Al}}^2 (\pm 0.07)$
	$0.20 < X_{\text{Al}} < 0.35$	$4.01 + 2.52X_{\text{Al}} + 6.07X_{\text{Al}}^2 (\pm 0.035)$	$5.17 + 3.83X_{\text{Al}} (\pm 0.07)$

* Standard deviation in kcal/gfw.

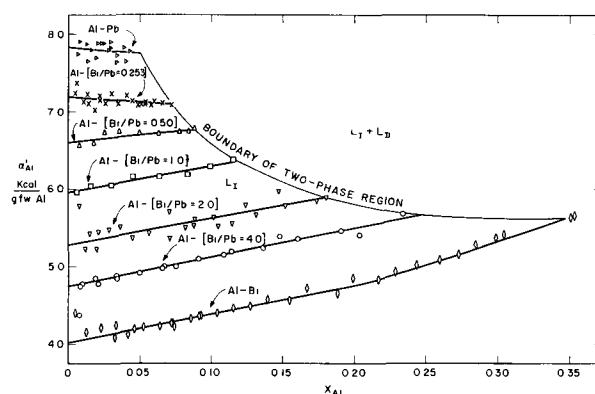


Fig. 3. Alpha function for binary and pseudobinary systems in liquid Al-Bi-Pb system at 900°C .

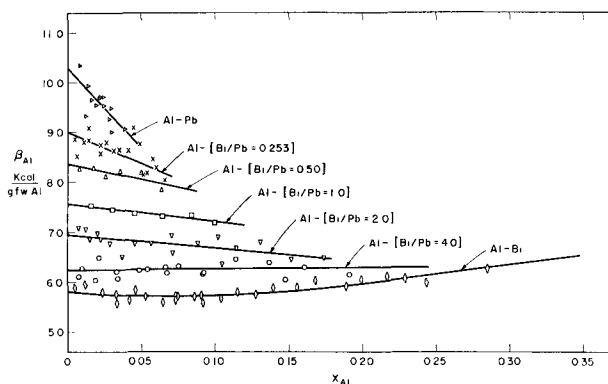


Fig. 4. Beta function for binary and pseudobinary systems in liquid Al-Bi-Pb system.

The alpha and beta functions, as plotted in Fig. 3 and 4, were used to determine the partial and integral molar thermodynamic properties of the system. The equations of these functions, determined by the method of least squares, are given in Table II. The alpha function is primed to differentiate it from the more usual form, $\alpha_i = \ln \gamma_i / (1-X_i)^2$.

There have been developed methods for applying the Gibbs-Duhem integration to ternary systems (3-5) when the thermodynamic property of interest for one of the components is known as a function of composition at the temperature of interest. Darken's (3) method requires that the compositional variable be the concentration (usually mole fraction) of the component whose partial molar property is known, i.e., Al. The integration is made along lines of constant ratio of the other two components, $X_{\text{Bi}}/X_{\text{Pb}}$. Thus the lines for integration are the binary and pseudobinary lines of this experimental work.

The excess partial molar property for aluminum, G_{Al}^E , may be expressed in terms of the compositional variable and the molar property in the usual manner

$$G_{Al}^E = G^E + (1-X_{Al}) (\partial G^E / \partial X_{Al})_{X_{Bi}/X_{Pb}} \quad [6]$$

Dividing by $(1-X_{Al})^2$ and rearranging

$$\left\{ \frac{\partial [G^E / (1-X_{Al})]}{\partial X_{Al}} \right\}_{X_{Bi}/X_{Pb}} = \frac{G_{Al}^E}{(1-X_{Al})^2} \quad [7]$$

In the case that G^E is replaced by F^E or H^M , the term on the right in Eq. [7] is α'_{Al} or β_{Al} , respectively. Integration of the equation between the limits $X_{Al}=0$ and X_{Al} gives

$$G^E = (1-X_{Al})$$

$$\left\{ \left[\int_{X_{Al}=0}^{X_{Al}} \frac{G_{Al}^E}{(1-X_{Al})^2} \cdot dX_{Al} \right] + G^E_{X_{Al}=0} \right\}_{X_{Bi}/X_{Pb}} \quad [8]$$

The integration constant, $G^E_{X_{Al}=0}$, is the integral excess property in the binary Bi-Pb system at the ratio of X_{Bi}/X_{Pb} being considered. With the help of Klepa's (6) calorimetric results² on the Bi-Pb system, Eq. [8] was used to calculate F^E , H^M , and S^E .

With G^E known (Eq. [8]) for the ternary field where liquid L_I is the single stable phase, it is possible to obtain G_{Pb}^E and G_{Bi}^E by Eq. [6] along lines of constant ratios of X_{Al}/X_{Bi} and X_{Al}/X_{Pb} , respectively. It is to be noted that Eq. [8] and [6] combine to become the familiar integrated form of the Gibbs-Duhem equation for simple binary systems (2). In such a case the term on the right in Eq. [8] is zero.

Wagner (4) derived a method for obtaining the partial molar properties of mixing of all components in a ternary system if (i) the partial molar properties of one component are known, and (ii) the partial molar properties in the binary system of the other two components are known. Introducing the independent compositional variable, y , where for this system

$$y = \frac{X_{Bi}}{X_{Bi} + X_{Pb}} \quad [9]$$

and then substituting y into the general Gibbs-Duhem equation for a ternary system followed by other mathematical transformations, Wagner (4) obtained expressions for excess partial molar free energies of mixing. They appear below as applied to present work along the pseudobinary systems, y .

$$F_{Pb}^E(y, X_{Al}) = F_{Pb}^E(y, X_{Al} = 0) +$$

$$\left\{ \int_{X_{Al}=0}^{X_{Al}} \left[\alpha'_{Al} - y \frac{\partial}{\partial y} \alpha'_{Al} \right] dX_{Al} - X_{Al}(1-X_{Al})\alpha'_{Al} \right\}_y \quad [10]$$

$$F_{Bi}^E(y, X_{Al}) = F_{Bi}^E(y, X_{Al} = 0) + \left\{ \int_{X_{Al}=0}^{X_{Al}} \left[\alpha'_{Al} + \right. \right.$$

² H^M is symmetrical with respect to composition for liquid Bi-Pb alloys, so the system is assumed to be regular, i.e., $S^E = 0$, and $H^M = F^E$.

$$\left. \left. (1-y) \frac{\partial}{\partial y} \alpha'_{Al} \right] dX_{Al} - X_{Al}(1-X_{Al})\alpha'_{Al} \right\}_y \quad [11]$$

These relations were used to determine F_{Pb}^E and F_{Bi}^E along the pseudobinary lines in the Al-Bi-Pb system at 900°C. Subsequently, a_{Pb} , a_{Bi} , γ_{Pb} , and γ_{Bi} , were calculated. The corresponding partial molar heats of mixing of Pb and Bi, respectively, were also obtained by Eq. [10] and [11] with β_{Al} substituted for α'_{Al} and H_i^M for F_i^E .

Equations [10] and [11] are well suited for the calculations in the L_I region and were used in these calculations rather than Eq. [6] and [8] because they can be treated analytically; i.e., the curves of α'_{Al} vs. y at constant values of X_{Al} can be fitted readily to an equation of two variables. The equation of each curve may then be differentiated with respect to y in order to determine its slope at particular values of y . The intercepts thus obtained when plotted vs. X_{Al} at constant y can be treated analytically. Each step involves the dependence of one variable on a second, and only when this dependence leads to a very peculiar relationship is it necessary to resort to a graphical integration.

The various thermodynamic properties of mixing, as determined from Eq. [4] through [11] and the data of Table II are shown in Fig. 5 through 12. In Fig. 5 to 8 the circles are points obtained directly from the experimental data.

The boundary of the miscibility gap (Fig. 1) on the L_I side of the Al-Bi-Pb system could not be determined precisely by distribution measurements. Instead, it was found that it could be determined more accurately from knowledge of the boundary of the L_{II} field, the direction of the tie lines crossing the two-phase field and the equations of α'_{Al} vs. composition (Table II). Since the field L_{II} is almost pure Al, it may be assumed that $a_{Al} = X_{Al}$ in the field and along the L_{II} boundary of the two-phase region. The superscript II indicates that the property is for the boundary composition in phase II. Cor-

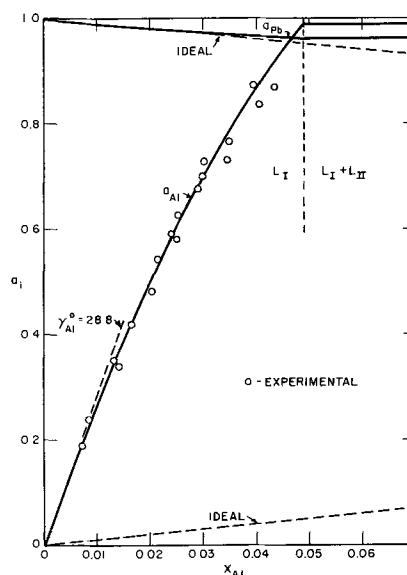


Fig. 5. Activities in the Al-Pb system at 900°C

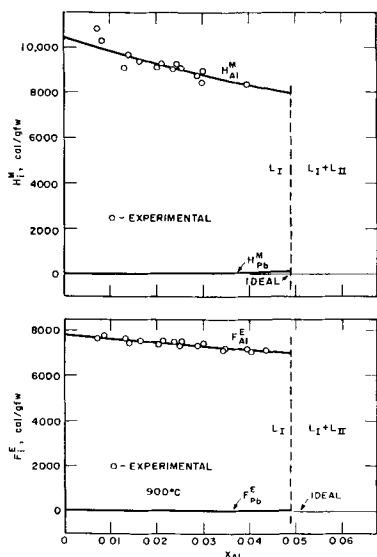


Fig. 6. H_1^M and F_1^E in the liquid Al-Pb system

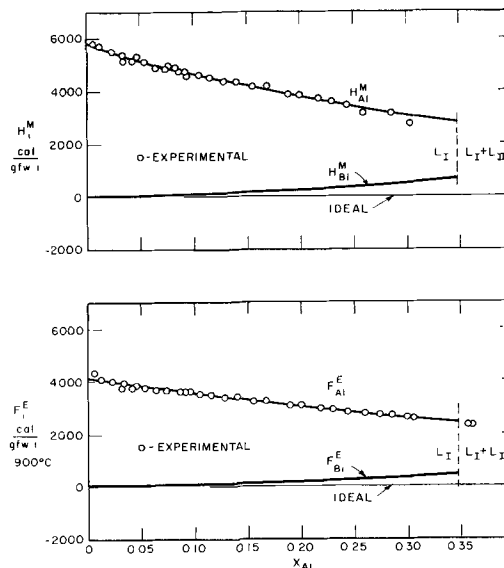


Fig. 8. H_1^M and F_1^E in liquid Al-Bi system

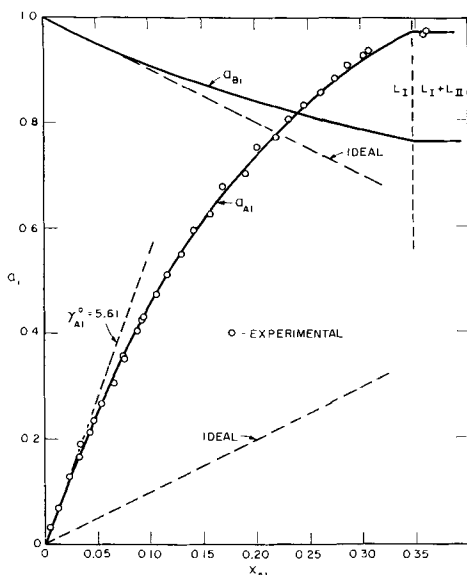


Fig. 7. Activities in the Al-Bi system at 900°C

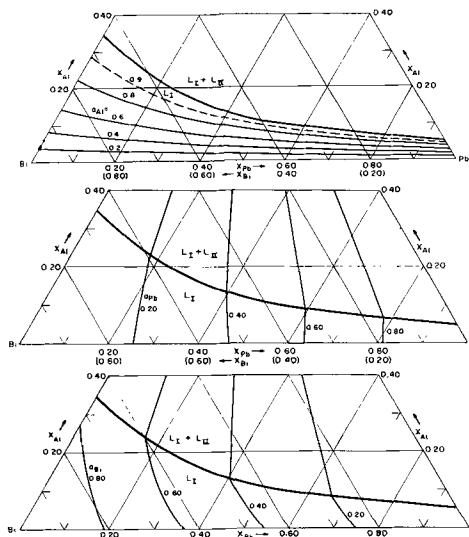


Fig. 9. Activities in the L_I region of the Al-Bi-Pb system at 900°C

respondingly, the superscript I designates that it is for the boundary for phase I. The activity of a component is constant along a tie line, hence

$$a_{Al}^{II} = X_{Al}^{II} = a_{Al}^I \quad [12]$$

and

$$\gamma_{Al}^I = a_{Al}^I / X_{Al}^I = X_{Al}^{II} / X_{Al}^I \quad [13]$$

Accordingly

$$(\alpha'_{Al})^I = \frac{RT \ln (X_{Al}^{II} / X_{Al}^I)}{(1 - X_{Al}^I)^2} = A + BX_{Al}^I + C(X_{Al}^I)^2 \quad [14]$$

where A, B, and C are the constants of the alpha function equations in Table II, C being zero for all the systems except Al-Bi. X_{Al}^I is then calculated by successive approximations for each of the binary and pseudobinary systems. The values of X_{Al}^I from the four distribution runs and the solution from thermodynamic data via Eq. [12], [13], and [14] are in excellent agreement as shown in Fig. 1. The disagreement is less than $\pm 0.002X_{Al}$ for Al-Pb and the ternary field, and $\pm 0.02X_{Al}$ in the Al-Bi system.

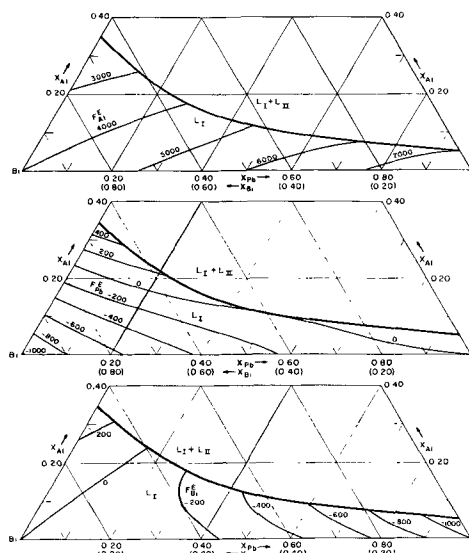


Fig. 10. Excess partial molar free energies of mixing in the L_I region of the Al-Bi-Pb system at 900°C. Values are in cal/gf.w.

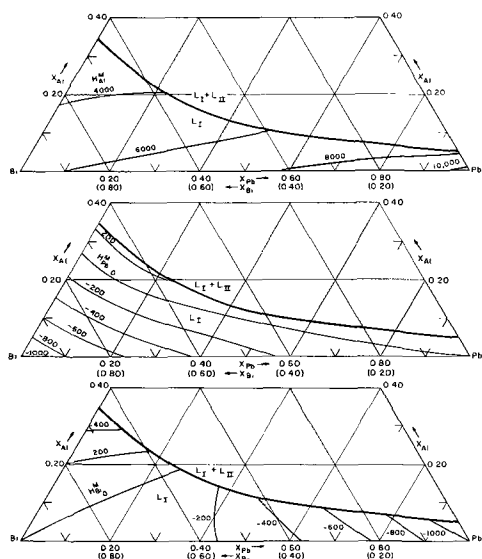


Fig. 11. Partial molar heats of mixing in the L_I region of the Al-Bi-Pb system. Values are in cal/gfw.

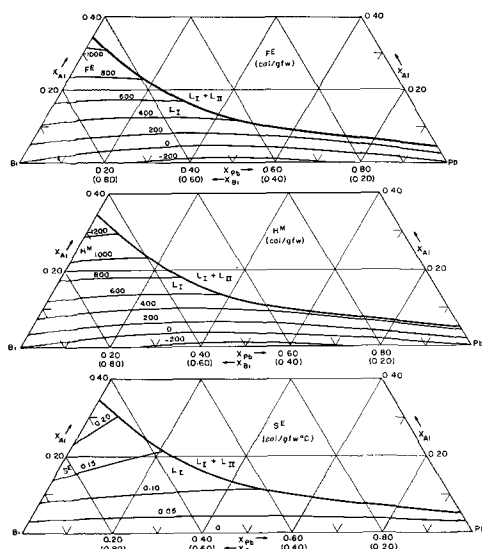
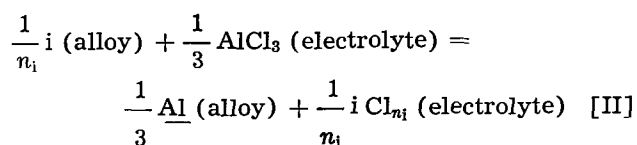


Fig. 12. Excess molar properties of mixing in the L_I region of the Al-Bi-Pb system at 900°C.

Sources and Analysis of Errors

It is essential, when studying the thermodynamic properties of alloys by a cell technique, that the cell be reversible, and that the reaction occurring is actually the one desired. The arguments concerning reversibility of the cell reaction of the previous paper (1) are also applicable in this case, except for the observations listed below.

Displacement reactions.—Using the treatment of Wagner (7) and the data of ref. (8), it was determined that errors in the activity of aluminum at 900°C, arising from exchange reactions of the type



where i is either bismuth or lead, and n_i is the valence of bismuth (3) or lead (2) in their respective chlorides, were in all cases less than 0.01%. Similarly, errors arising from exchange reactions of KCl

and NaCl of the supporting electrolyte with Al, Bi, or Pb in the alloys are negligible and need not be considered.

Solution of Ta in pure Al.—Tantalum was used for connecting leads because it was the only metal that resisted attack by liquid Al. There was no attack by alloys in the L_I region, or by pure Al below 850°C. Solution was slow in pure Al above 850°C. Accordingly, the standard electrode lead was replaced every 2-3 days. The effect of Ta on the activity of Al was measured in a cell having a massive anode containing 75g of Al and a cathode containing 15g of pure Al and 15g of $\frac{1}{4}$ in. lengths of Ta wire. The anode lead was touched to the electrode only for a short period when a measurement was made; the lead to the cathode remained in contact all during the experiment. The potential of this type of cell varied between 0.09 and 0.30 mv at 900°C. A sample taken from the cathode after 2 days at 900°C was found by chemical analysis to contain less than 0.3 wt % Ta ($<0.001 X_{\text{Ta}}$). This effect may contribute an appreciable error in emf for measurements with compositions very near the boundary of phase L_I . However, such measurements were not weighed heavily in establishing the equations of α' vs. X_{Al} (Table II) nor were they used in obtaining the boundary of phase L_I . Contamination of the Al standard by Ta probably causes an error in potentials above 10 mv which is equivalent to that arising from an uncertainty of 1°C in the cell potential at 900°C.

Loss of aluminum from the alloys.—In many of the cells containing homogeneous alloys which were very dilute in aluminum, the potentials were observed to drift very slowly to higher values with time. This indicated a slight continuing loss of Al from the cathode as the experiment proceeded. The composition of the cathode alloy could have been calculated from the aluminum charged with a small correction for the loss. Instead, it was decided that the results from chemical analyses of samples taken from the bath were more reliable. Accordingly, samples of the alloys for analysis were taken after all readings at 900°C and also at 800°C for the dilute alloys ($\text{Al} < 0.5\%$ by weight). All compositions reported in Fig. 3 and 4 are from analyses of the samples. The value for a dilute alloy was the average of the two analyses.

Since readings at 900°C were immediately followed by samples being taken from the alloy, activity and free energy values derived therefrom are not affected by the aluminum loss. However, the entropy and enthalpy calculations are not exact because the provision that X_{Al} remain constant in Eq. [2] and [3] is not fulfilled precisely. Most of the alloy cathodes contained over 0.5% Al by weight. In such cases the aluminum concentration seldom decreased more than 1% of its original percentage. Accordingly, the discrepancy in values of $\partial E/\partial T$ from this effect for these alloys is not greater than 2%.

In general, the great majority of the alloys investigated were in a range which was not so dilute as to cause significant errors from loss of aluminum yet not so near the boundary of the miscibility gap

that errors from the attack on the tantalum contacts by the standard become important.

Equivalence of aluminum.—The above observation, together with the results of a study by Russell, Martin, and Cochran (9) indicate the possibility of the reaction



occurring in the electrolyte. Such a reaction would remove aluminum from both the anode and cathode of cell (A), but even more important, it might affect the value of the equivalence of the aluminum ion in the electrolyte owing to the presence of a second valence state.

In order to determine the equivalence of the aluminum ion in the electrolyte, Faraday yield experiments were performed at 900°C. The experimental circuit consisted of a rectifier, variable resistor, copper coulometer, and the regular emf cell modified slightly to contain two electrodes of Al-Ag alloys. The Al-Ag alloys were used because the activity of aluminum is strongly depressed by silver (1). This improved the experiment because the attack on the Ta leads was avoided, and the activity of Al was reduced to the level where the spurious effect was most noticeable in the regular cells.

The results of two such experiments gave n as 2.997 and 2.942. The weight loss of Al from the anode was used in the calculation because the deposit at the cathode was somewhat dispersed and it was not possible to obtain a suitable quantitative result from the cathode material. From these experiments it appears that the amount of Al^+ in this electrolyte is very small and need not be considered in the calculations. On the other hand, it is possible that the electrolyte possesses some slight electronic conductivity, in which case the equivalence of the aluminum ion measured would be $n_{\text{Al}}/(1 - t_e)$ where t_e is the fractional contribution by electrons to the passage of current. Nevertheless, the effective value of n , with or without electronic conduction, is that measured by the experiments just described. It was taken to be 3 in all calculations.

Other sources of error.—All chromel-alumel thermocouples used in this study were taken from the same lots of wire. Three of the thermocouples, (one of which had been used for about 10 runs, another for one run, and the third freshly made) were standardized against the melting points of pure aluminum and pure silver. All three checked to within 1°C of the accepted melting points of Al (660°C) and Ag

(960.7°C). The thermocouples were checked and replaced by new ones frequently.

With the control thermocouple immersed in the electrolyte just above the alloy surface, the temperature control in the cells was $\pm 1/2^\circ\text{C}$. The vertical temperature gradient in the cells was about 1°C from the top of the electrolyte to the bottom of the alloy. It is assumed that the true temperature of a cell is within $\pm 1.5^\circ\text{C}$ of the temperature reported. In the distribution experiments, the uncertainty was slightly larger, being $\pm 2^\circ\text{C}$.

Aluminum was analyzed in the alloys as Al_2O_3 after removal of Pb and Bi by an ion exchange resin column and precipitation of $\text{Al}(\text{OH})_3$ by NH_4OH . The true aluminum concentrations are probably within $\pm 1\%$ of the value reported. Bismuth (as BiOCl) and lead (as PbCrO_4) were also determined gravimetrically. The values of X_{Bi} and X_{Pb} charged agreed with the results of chemical analysis to within $\pm 0.5\%$.

Analysis of Experimental Results

The Al-Bi-Pb isotherm, 900°C.—Comparison of the results of the distribution measurements with data of other investigations is limited to the binary Al-Pb and Al-Bi systems (see Table III). There is good agreement between the results of this study and those of Kempf and Van Horn (12), Paic (13), and Claus and Herrmann (14) for the solubility of lead and bismuth in aluminum at 900°C. No measurement of the limits of solubility of Al in Bi above the melting point of Bi is available. However, Hansen (15) estimated the solubility curve. The value of Dardell (10) for the solubility of Al in Pb at 900°C is considerably lower than that of this study or of previous work in this laboratory (11). In general, both the Al-Pb and Al-Bi systems at 900°C were found to have narrower miscibility gaps than has been reported earlier.

Thermodynamic properties of the Al-Bi-Pb system.—In order to estimate the errors in the values of the thermodynamic functions presented in the foregoing sections, the standard deviations of the alpha and beta function equations (Table II) were carried through the calculations. Table IV gives the results of the estimates. The errors for the partial molar free energy and activity of aluminum decrease in the vicinity of the miscibility gap because of the method used in correlating the emf measurements with the distribution data. No such method was available for H_{Al}^{M} ; thus, the errors in this property

Table III. Comparison of solubility limits in Al-Pb and Al-Bi systems at 900°C

System and boundary	Calc., Eq. [14]*	This study Experimental	Other investigations		
Al-Pb					
L _I , X _{Al}	0.0489	0.0510	0.037 (10)	0.050 (11)	
L _{II} , X _{Pb}	—	0.0115	0.011 (12)	0.011 (13)	0.008 (14)
Al-Bi					
L _I , X _{Al}	0.35	0.37	0.06 (15) **		
L _{II} , X _{Bi}	—	0.0308	0.03 (12)		

* And Table II.

** Estimated.

Table IV. Estimated average errors* in thermodynamic properties of mixing in Al-Bi-Pb system

Quantity	Errors	
	Vicinity of Bi-Pb binary	Vicinity of miscibility gap
F_{Bi}^E, F_{Pb}^E (900°C)	±20 cal/gfw	±25 cal/gfw
F_{Al}^E (900°C)	±50 cal/gfw	±10 cal/gfw
H_{Bi}^M, H_{Pb}^M	±20 cal/gfw	±30 cal/gfw
H_{Al}^M	±100 cal/gfw	±100 cal/gfw
F^E (900°C)	±20 cal/gfw	±20 cal/gfw
H^M	±20 cal/gfw	±35 cal/gfw
S^E (900°C)	±0.01 cal/gfw°C	±0.015 cal/gfw°C
a_{Bi}, a_{Pb} (900°C)	±0.004	±0.005
a_{Al} (900°C)	±0.004	±0.001

* Based on standard deviations of equations in Table II.

are slightly increased as X_{Al} is increased. As can be seen from Fig. 4, the scatter in β_{Al} is greater than for α'_{Al} . There are no thermodynamic data in the literature on the ternary alloys so a comparison with other results is not possible.

Interaction coefficients.—Of general interest in multicomponent systems is the so-called interaction coefficient, ϵ , which is defined

$$\epsilon_j^i = \left. \frac{\partial \ln \gamma_i}{\partial X_j} \right\} \begin{array}{l} X_i \rightarrow 0 \\ X_j \rightarrow 0 \end{array} \quad [15]$$

In the L_I region of the Al-Pb-Bi system at 900°C, the effect of Al on its own activity coefficient is obtained directly from the linear equations of the alpha functions (Table II)

$$\epsilon_{Al}^{Al} = \left. \frac{\partial \ln \gamma_{Al}}{\partial X_{Al}} \right\} X_{Al} \rightarrow 0 = \frac{-2A + B}{RT} \times 10^3 \quad [16]$$

with A and B being the constants in the equations. The effect of Bi additions on the activity coefficient of Al in Al-Pb alloys (ϵ_{Al}^{Bi} for Al-Pb) in the Pb corner of the ternary system was determined by plotting $\ln \gamma_{Al}$ vs. X_{Bi} along the Bi-Pb binary from $X_{Al} = 0, X_{Pb} = 1$. The slope of this plot at $X_{Bi} = 0$ is equal to ϵ_{Al}^{Bi} in Pb. The other interaction coefficients given in Table V were obtained in a similar manner.

Alpha function theories.—Worrell (16), Wriedt (17), and Wagner (18) have derived linear expressions for the alpha functions on either side of a miscibility gap for a binary system. Worrell (16) and Wriedt (17) used the "sub-regular" solution model [after Hardy (19)]; Wagner (18) used the Guggenheim (20) relation for the excess molar free energy. All these treatments require an accurate knowledge of the location of the miscibility gap, and all arrive essentially at the same equations for α'_i . Using Worrell's (16) treatment, if X_{Al}^I is the mole fraction of Al on the boundary of the gap near Bi or Pb, and X_{Al}^{II} the mole fraction of Al on the boundary of the gap near Al, then the two equations

Table V. Interaction coefficients in the L_I region of the Al-Bi-Pb system at 900°C

System	ϵ_{Al}^{Al}	Other
Al-Pb; ($X_{Pb} \rightarrow 1$)	-7.44	$\epsilon_{Al}^{Bi} = -1.29$
Al- $\frac{Bi}{Pb} = 0.253$	-6.72	—
Al- $\frac{Bi}{Pb} = 0.50$	-4.86	—
Al- $\frac{Bi}{Pb} = 1.0$	-3.68	—
Al- $\frac{Bi}{Pb} = 2.0$	-3.06	—
Al- $\frac{Bi}{Pb} = 4.0$	-2.46	—
Al-Bi; ($X_{Bi} \rightarrow 1$)	-1.85	$\epsilon_{Al}^{Pb} = 1.54$
Pb-Bi; ($X_{Pb} \rightarrow 1$)	—	$\epsilon_{Bi}^{Al} = -1.64$
($X_{Bi} \rightarrow 1$)	—	$\epsilon_{Pb}^{Al} = 1.62$

$$RT \ln \frac{X_{Al}^I}{X_{Al}^{II}} + (1-X_{Al}^I)^2 (A + BX_{Al}^I) - (1-X_{Al}^{II})^2 (A + BX_{Al}^{II}) = 0 \quad [17]$$

and

$$RT \ln \frac{(1-X_{Al}^I)}{(1-X_{Al}^{II})} + (X_{Al}^I)^2 \left(A - \frac{B}{2} + BX_{Al}^I \right) - (X_{Al}^{II})^2 \left(A - \frac{B}{2} + BX_{Al}^{II} \right) = 0 \quad [18]$$

may be solved simultaneously to determine the constants A and B. In this instance, the constant A has the value $RT \ln \gamma_{Al}^0$, or F_{Al}^E at infinite dilution, and B is the slope of the linear α'_{Al} vs. X_{Al} plot. Again the two constants have the same significance as in Eq. [16].

The same treatment may be used to estimate the alpha function of either component of a pseudobinary system which contains a miscibility gap if the conjugate compositions on both boundaries of the gap are in the same pseudobinary system. This is only approximately true for the pseudobinary systems of this study in the Al-Bi-Pb ternary; nevertheless, Eq. [17] and [18] may be used to estimate α'_{Al} in the system from the boundaries of the miscibility gap.

Figure 13 shows comparisons among the alpha functions predicted by Worrell (16), Wriedt (17), and Wagner (18) treatments, those obtained experimentally by this investigation, and those which would result from the assumptions of α_{Al} being linear in X_{Al} (Henrian behavior) for the two binary systems, Al-Pb and Al-Bi. It is evident that the theoretical alpha function equations become less accurate as the regions of miscibility become wider. In fact, for the Al-Bi and Al-(Bi/Pb = 2.0 and 4.0) systems, assumption of Henry's law for Al is a better approximation at infinite dilution.

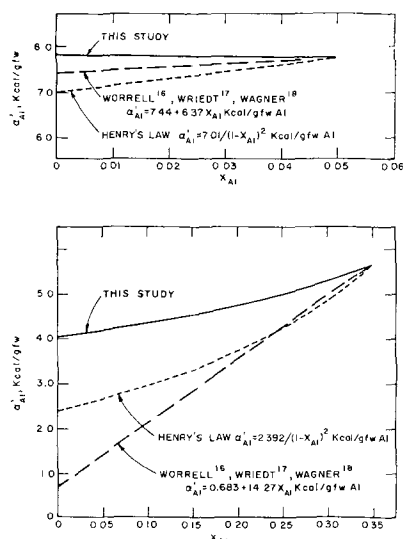


Fig. 13. Comparison of alpha functions for binary and pseudo-systems of Al in Al-Bi-Pb at 900°C: top, Al-Pb system; bottom, Al-Bi system.

The theories being discussed do, however, predict the linear alpha function, which is the actual case with the binary and pseudobinary systems of Al in the L_I region except for the Al-Bi edge, which has a linear alpha function only in the dilute range. The lack of agreement between the theoretical and experimental equations for the alpha function lies in the fact that the theories assume that each alpha function is linear over the entire composition range. Specifically, in the Al-Pb system, the theoretical equation for α'_{Al} in the L_I region would be the same as that for the L_{II} region. This assumption is not generally applicable because binary systems which have been found experimentally to possess linear alpha functions across their composition range are systems of metals or compounds which have similar chemical properties and hence they do not have ranges of immiscibility in the liquid state.

Binary system with an infinitely dilute third component.—Alcock and Richardson (21) have developed the following relationship for the activity coefficient of component 1 at infinite dilution along the 2-3 binary side of the 1-2-3 ternary system

$$RT \ln \gamma_1[X_1, X_2/X_3] = X_2 RT \ln \gamma_1[X_2 \rightarrow 1] + X_3 RT \ln \gamma_1[X_3 \rightarrow 1] - F^E[X_1 \rightarrow 0, X_2/X_3] \quad [19]$$

In terms of the present work, component 1 is Al, and 2 and 3 are Pb and Bi, respectively. If the third term on the right approaches zero, i.e., the 2-3 system is essentially ideal, the value of $\ln \gamma_1$ at infinite dilution in the 2-3 system is a linear function of composition. The experimental values of F_{Al}^E for each of the pseudobinary lines plotted vs. X_{Bi} fall on the straight line joining F_{Al}^E for the Al-Bi and Al-Pb systems. Elliott and Chipman's (22) results indicate that the curve of F^E for the Bi-Pb system at 500°C is small and slightly negative with a minimum of approximately -100 cal/gfw at $X_{Bi} = 0.5$, although the actual value is probably closer to -250 cal/gfw from Kleppa's (6) values of H^M ($X_{Pb} = 0.5$) and assuming that the Bi-Pb

system is regular. It is to be expected, then, that Eq. [19] will give essentially a straight line for $\log \gamma_{Al}^0$ in the Pb-Bi system.

The L_{II} region, estimated properties.—In order to complete the picture of the Al-Bi-Pb system, it is necessary to determine the thermodynamic properties of the alloys in the L_{II} region. As mentioned earlier, because of the high concentration of Al in this phase, satisfactory potentials could not be obtained from cells between Al and these alloys. However, the distribution measurements permit the calculation of α'_{Bi} and α'_{Pb} along the L_{II} boundary of the miscibility gap. From these calculations, reasonable estimates of F_{Pb}^E , F_{Bi}^E , a_{Pb} , and a_{Bi} in L_{II} can be made.

The values of α'_{Bi} and α'_{Pb} at experimental tie-line positions on the boundary of the L_{II} region were computed from the alloy composition and values of F_{Bi}^E and F_{Pb}^E for the equilibrium compositions of phase L_I (Fig. 10). Values of alpha for suitable binary and pseudobinary lines crossing phase L_{II} were obtained from Fig. 14. As $(1-X_{Bi})$ and $(1-X_{Pb})$ are essentially unity in this field, it may be assumed that the alpha functions are linear

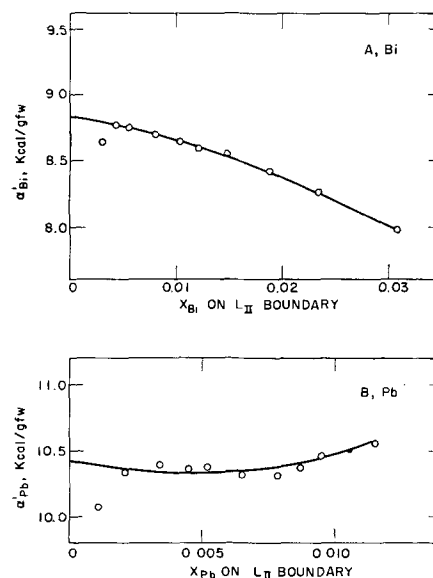


Fig. 14. Alpha function of Bi and Pb on the L_{II} phase boundary at 900°C.

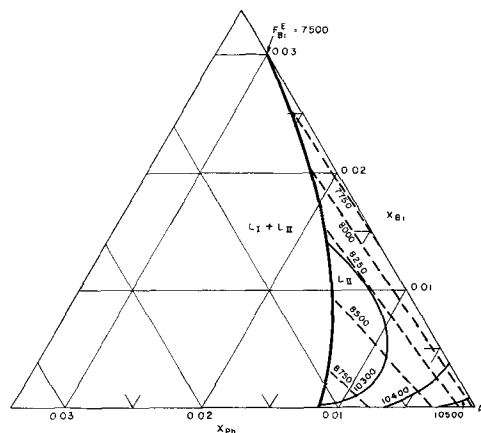


Fig. 15. Excess partial molar free energy of mixing for bismuth and lead in L_{II} region of the Al-Bi-Pb system at 900°C; - - -, F_{Bi}^E ; —, F_{Pb}^E (cal/gfw).

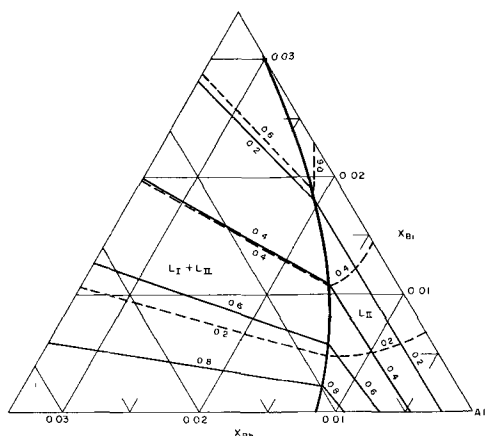
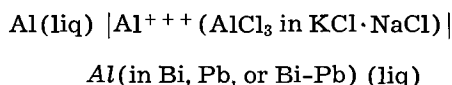


Fig. 16. Activities of bismuth and lead in the L_{II} region of the liquid Al-Bi-Pb system at 900°C . Note that $a_{\text{Al}} \sim X_{\text{Al}}$ in phase L_{II} . - - -, activity of bismuth; ———, activity of lead.

and horizontal for each of the binary lines. With this information F_1^E and a_i for Bi and Pb are calculated as shown in Fig. 15 and 16. The interaction coefficients and activity coefficients at infinite dilution for this region are contained in Table VI. The properties $\epsilon_{\text{Pb}}^{\text{Bi}}$ and $\epsilon_{\text{Bi}}^{\text{Pb}}$ in Al cannot be determined accurately because of the uncertainties in F_{Pb}^E and F_{Bi}^E .

Summary and Conclusions

The thermodynamic properties in the larger region of homogeneity, L_I , of the liquid Al-Bi-Pb system were determined at 900°C by potential measurements of the high-temperature reversible concentration cell



in the temperature range 700°C – 1000°C and by distribution measurements of the two-phase alloys at 900°C .

The properties α_i , γ_i , F_1^E , H_1^M , F^E , and H^M were determined for each of the binary edges, Al-Bi and Al-Pb and for the ternary alloys in the L_I region. These determinations may best be obtained by referring to Fig. 1 and 6 through 12. For alloys within the L_{II} region, a_{Bi} , a_{Pb} , F_{Bi}^E , and F_{Pb}^E at 900°C were estimated from the measured properties in the L_I region and the ternary isotherm. These estimates are presented in Fig. 15 and 16.

The conclusions of this investigation are summarized as follows:

1. The solubility of Al in Pb and Bi at 900°C is greater than previously reported.
2. The alloys of the L_I and L_{II} regions show very high positive deviations from ideality, the devia-

Table VI. Activity coefficients at infinite dilution and interaction coefficients for the Al-Bi and Al-Pb systems in phase L_{II} at 900°C

System	$\gamma^{\circ}\text{Pb}$	$\gamma^{\circ}\text{Bi}$	$\epsilon_{\text{Pb}}^{\text{Pb}}$	$\epsilon_{\text{Bi}}^{\text{Bi}}$
Al-Pb	93	—	—9	—
Al-Bi	—	30.5	—	—7

tions being higher the narrower the regions of miscibility.

3. The components do not follow Henry's law in the composition range studied. Deviation from Henry's law is greater the wider the ranges of miscibility.

4. Binary and pseudobinary systems of aluminum in the L_I region follow sub-regular solution behavior (linear α' function) except in the case of Al-Bi, where sub-regular solution behavior is exhibited only for homogeneous alloys in the range $0 < X_{\text{Al}} < 0.20$.

5. Linear alpha function equations for the dilute regions of homogeneity on either side of a miscibility gap in binary systems, derived from theoretical treatments of Worrell (16), Wriedt (17), and Wagner (18) yield thermodynamic properties which have less positive deviations from ideality than obtained experimentally. Experimental deviations from the derived alpha function become greater as the range of miscibility becomes wider.

Acknowledgment

The authors wish to express their sincere appreciation to the United States Atomic Energy Commission, for its financial support of this work under Contract No. AT (30-1)-1888. The authors are also indebted to Donald L. Guernsey and William T. Martin, Jr. for their chemical analyses of the many alloy and electrolyte samples.

Manuscript received March 22, 1963; revised manuscript received Sept. 30, 1963. This paper was presented at the Boston Meeting, Sept. 16-20, 1962, and is based on a thesis submitted by one of the authors (T. C. W.) in partial fulfillment of requirements for the Ph.D. degree at M.I.T.

Any discussion of this paper will appear in a Discussion Section to be published in the December 1964 JOURNAL.

REFERENCES

1. T. C. Wilder and J. F. Elliott, *This Journal*, **107**, 628 (1960).
2. L. S. Darken and R. W. Gurry, "Physical Chemistry of Metals," McGraw-Hill Book Company, Inc., New York (1953).
3. L. S. Darken, *J. Am. Chem. Soc.*, **72**, 2909 (1950).
4. C. Wagner, "Thermodynamics of Alloys," Addison-Wesley Press, Inc., Cambridge, Mass. (1952).
5. R. Schuhmann, Jr., *Acta Met.*, **3**, 219 (1955).
6. O. J. Kleppa, *J. Phys. Chem.*, **59**, [4], 354 (1955).
7. C. Wagner and A. Werner, *This Journal*, **110**, 326 (1963).
8. O. Kubaschewski and E. L. Evans, "Metallurgical Thermochemistry," 3rd ed., Pergamon Press, New York, London (1958).
9. A. S. Russell, D. E. Martin, and C. N. Cochran, *J. Am. Chem. Soc.*, **73**, 1466 (1951).
10. Y. Dardell, *Light Metals*, **9**, 220 (1946).
11. T. C. Wilder, Masters Thesis, Department of Metallurgy, M.I.T. (1959).
12. L. W. Kempf and K. R. Van Horn, *Trans. AIME*, **133**, 81 (1939).
13. M. Paic, *Rev. Met.*, **44**, 363 (1947).
14. W. Claus and I. Herrmann, *Metallwirtschaft*, **18**, 957 (1939).
15. M. Hansen and K. Anderko, "Constitution of Binary Alloys," 2nd ed., McGraw-Hill Book Company, Inc., New York (1958).
16. W. L. Worrell, U.S.A.E.C. Report NYO 4688 (1961).

17. H. A. Wriedt, *Trans. Met. Soc. AIME*, **221**, 377 (1961).
 18. C. Wagner, "Contribution to the Thermodynamic Evaluation of Ternary Phase Diagrams," Unpublished (1957).
 19. H. K. Hardy, *Acta Met.* **1**, 202 (1953).
 20. E. A. Guggenheim, *Trans. Faraday Soc.*, **33**, 151 (1937).
 21. C. B. Alcock and F. D. Richardson, *Acta Met.*, **6**, 385 (1958).
 22. J. F. Elliott and J. Chipman, *J. Am. Chem. Soc.*, **73**, 2682 (1951).

Some Characteristics of Arc Vaporized Submicron Particulates

J. D. Holmgren,¹ J. O. Gibson, and C. Sheer²

Vitro Laboratories, West Orange, New Jersey

ABSTRACT

The technique of producing ultrafine powders by vaporization in the high-intensity arc has been applied to a number of refractory materials, including oxides, carbides, and metals. Particle size ranges of the products obtained lie generally between 100 and 1000Å. Following a brief resume of the processing technique, a description of particulate characteristics is presented. Such properties as average size, shape, size distribution, sinterability, and chemical reactivity are examined, chiefly by electron microscopy, x-ray diffraction, sintering tests, and solution rates.

The purpose of this paper is to describe some features of various finely particulated materials produced by the vaporization of these materials in the high-intensity arc. The basic properties of the high-intensity arc and its utilization as a practical means of comminuting refractory materials were described in considerable detail in a previous paper (1). Therefore, only a brief review of the technique employed is presented here.

The High-Intensity Arc

The high-intensity arc, discovered by Beck in 1910, and for many years of interest only to search-light engineers as a brilliant source of light, is now attracting increasing attention in the field of electrochemical processing. Its basic distinction from the more commonly used form of arc is the fact that most of the arc input energy is transferred to the material of the anode. This is caused by the intense

concentration of energy which occurs in the anode sheath region when the high-intensity mode of arc operation is established. A comparison of the voltage distributions for the two types of arcs (with carbon electrodes) is shown in Fig. 1. From these curves it is clearly evident that in the case of the high-intensity mode the major fraction of the arc input energy is dissipated at the anode.

Particulation Technique

Practical utilization of the high-intensity arc effect requires that the feed material be incorporated into the body of the anode in order to take full advantage of the unique energy transfer capability inherent in this mode of arc operation. When this is done, the anode material is rapidly vaporized and heated to temperatures in the order of 7000°K. This material issues from the arc discharge in the form of the characteristic anode tail flame, which is essentially a plasma jet of anode vapor. A photograph of a typical high-intensity arc is shown in Fig. 2. Owing to the conditions under which it is formed, the tail flame issues as a well-defined, unidirectional, plasma jet. At 1 atm ambient pressure the velocity of this vapor jet is in excess of 150 ft/sec.

When the material to be comminuted is a non-conductive refractory, an anode fabrication step is required prior to arc vaporization. The fabrication technique consists of adding a minor percentage of a conducting constituent, *e.g.*, carbon, which is mixed with the material to be treated in the form of a coarse powder. After a suitable binder and extrusion aid are added to the mix, the latter is then extruded and baked, to provide a rod-shaped anode of good mechanical strength and sufficient electrical conductivity to carry the current required to maintain the arc.

If the material to be treated is intrinsically conductive, *e.g.*, a metal, then the arc may be struck to a crucible containing a molten pool of the metal. Figure 3 is a photograph of this type of operation

¹ Present address: Westinghouse Electric Corporation, Pittsburgh, Pennsylvania.

² Present address: Columbia University, New York, New York.

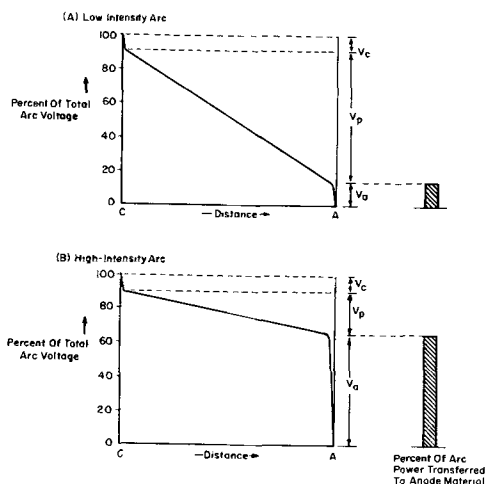


Fig. 1. Voltage distribution across the conduction path in low- and high-intensity arc discharges. V_c , Voltage drop across cathode sheath; V_p , voltage drop across arc plasma; V_a , voltage drop across anode sheath.

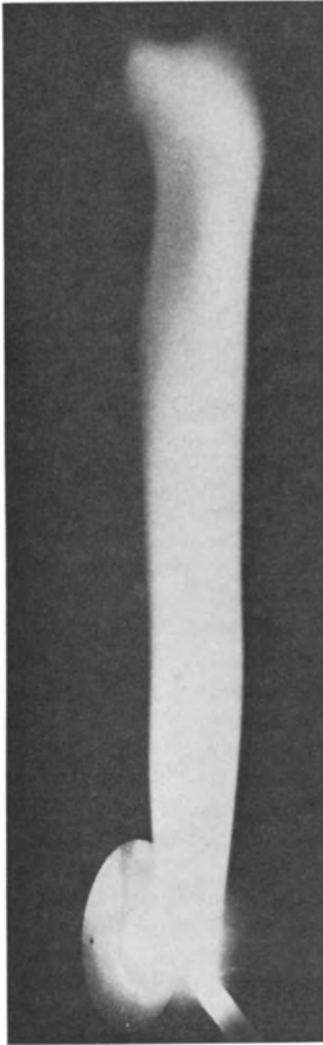


Fig. 2. High intensity arc tail flame in air: anode: $\frac{5}{8}$ in. diameter, 15% carbon + 85% complex silicate; cathode: $\frac{3}{8}$ in. diameter, graphite.



Fig. 3. High intensity arc tail flame in argon: anode: graphite crucible containing metallic aluminum; cathode, $\frac{3}{8}$ in. diameter, graphite.

utilizing a crucible containing molten aluminum. Regardless of which modification is employed, the action of the high-intensity arc in establishing a high-speed, ultrahigh temperature tail flame of anode vapor provides an excellent means for subdividing the material into extremely fine particle sizes. Because of the ultrahigh initial temperatures, the tail flame drops very rapidly in temperature after it leaves the arc, owing to the very high rate of radiation. As soon as the vapors have cooled below the dew point of a condensible constituent, rapid condensation occurs in the form of extremely

fine particles. The extremely fine state of subdivision, which was found to be characteristic of the tail flame condensate, is due largely to the high density of electric charges present in the tail flame. These electric charges, in the form of positive ions and free electrons, are always present in high concentration in an arc-generated plasma and form excellent centers of nucleation in the supercooled vapor. The nucleation of a condensed phase by charged particles in supercooled media is a well-known phenomenon and forms the basis for the familiar Wilson cloud chamber. In the case of the high-intensity arc tail flame, the large number of centers of nucleation result in a large number of individual particles. Because of the high boiling point of the anode material and the rapid temperature drop in the flame, the particles have little time to grow to any appreciable size. Thus the particles emerge from the tail flame in the size range of 100-1000Å.

The tail flame configuration also offers some opportunity for altering the particle size range. This can be done by increasing the cooling rate and/or diluting the plasma in the region of maximum condensation so that the growth of a condensed particle is inhibited. Conversely, particle size may be increased by decreasing the cooling rate and confining the vapor so as to promote particle growth. The effect of increasing the quenching rate on reducing particle size is illustrated in Fig. 4 and 5. Figure 4

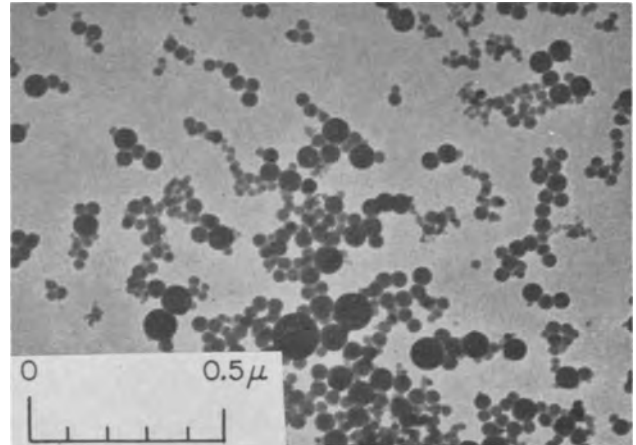


Fig. 4. Electron micrograph of arc vaporized silica. $\times 50,000$

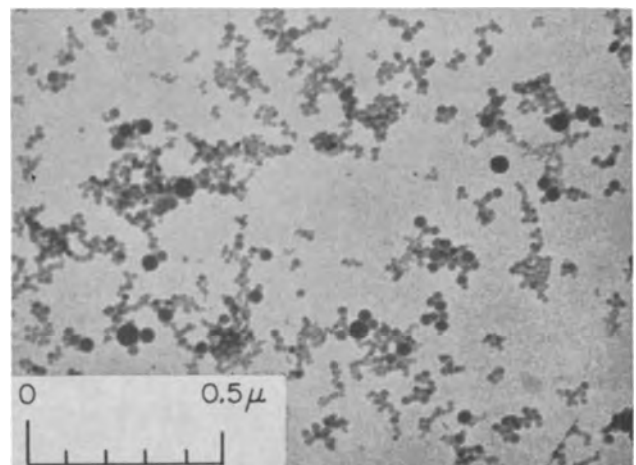


Fig. 5. Electron micrograph of arc vaporized silica, air quenched. $\times 50,000$.

Table I. Submicron materials produced using the high intensity arc process

Oxides	Metals	Carbides	Multicomponent systems	
SiO ₂	C	ThC	Ferrites	(Zn, Mn, Cu, Fe)O
Al ₂ O ₃	Al	TiC	Kaolin	Al ₂ O ₃ ·SiO ₂ ·Fe ₂ O ₃
Fe ₂ O ₃	Li	B ₄ C	Spodumene	LiAl(SiO ₃) ₂
ThO ₂	Ni	UC	Rhodonite	MnO·SiO ₂
MnO ₂	Fe	TaC	Ferrosilicon	Fe·Si
Cb ₂ O ₅	W	SiC	Chromite	FeO·Cr ₂ O ₃
NiO	Mo		Euxenite	Y ₂ Er ₂ Ce ₂ U ₂ (Ta,Cb) ₄ O ₁₅ ·xH ₂ O
Y ₂ O ₃			Boron carbide·silicon carbide	B ₄ C·SiC
UO ₂			Uranium carbide·columbium carbide	UC·CbC
MoO ₃			Uranium carbide·thorium carbide	UC·2·25ThC
ZrO ₂				
MgO				
WO ₃				

shows an electron micrograph of arc-vaporized silica, which condensed from an undisturbed flame. We note that the silica fume product is essentially spherical in shape. The average particle size of this material is approximately 440Å. Figure 5 is a photograph of the product obtained under identical processing conditions except that several cubic feet per minute of cold air was injected into the flame to increase the quenching rate. In this case an average particle size of 170Å was obtained.

Description of Typical Particulated Products

The application of this process in the field of particulation has been investigated in our laboratory for over four years. Table I is a list of submicron particulates made by this method. All of the materials were prepared by one or the other of the several modifications of consumable anode vaporization in a high-intensity arc. The materials which have been prepared include oxides, metals, carbides, and multicomponent systems of these three categories.

In the case of the oxides, the ambient atmosphere was ordinary air; whereas, for the carbides and metals, an inert atmosphere such as argon was used, often at reduced pressures. In addition to direct vaporization, some experiments have been carried out in which the material was particulated first as the oxide and subsequently reduced to the metal in a hydrogen atmosphere, *e.g.*, W, Ni, Fe, and Mo.

In addition to methods of preparation, some of the properties of the various fine particles have been investigated. While this investigation is far from complete, and is still under way, enough interesting characteristics for arc vaporized materials have been revealed to merit a description at this time.

Particle size.—The particle size range of the materials which have been prepared varies from less than 50Å up to approximately 2000Å, as determined by electron microscopy. The particle size distributions for specific materials have varied widely within this general range. Both the mean particle size and the dispersion about the mean vary primarily with the physical properties of the material and secondarily with the conditions of arc vaporization, *e.g.*, power level, ambient pressure, forced quenching, etc. Only meager quantitative data on size distribution are available at the present time. How-

ever, a rough guess would put the dispersion at approximately half the mean for most of the materials made without forced quenching. This subject is under study at the present time.

Mean particle sizes for the materials thus far investigated lie between 50 and 1000Å. Although the majority of these materials were particulated by the standard technique during which no effort was made to control particle size, neither the average size nor the dispersion for a given material are necessarily fixed. A reduction of 2½ to 1 in average particle size by air quenching has already been mentioned in the case of silica. In addition, it was determined from a study of the electron micrographs that the size distribution is sharply peaked at the mean particle size in the air-quenched sample, showing a reduction in size dispersion as well as average size. This and similar results with other materials indicate that closely controlled size distributions can be obtained.

For the same processing conditions, *i.e.*, mass flow rate of vapor, temperature gradient, ambient pressure, etc., particle size is determined largely by the physical properties of the material being treated. An important parameter is the vapor density, or concentration of molecules in the supercooled vapor. A low concentration would result in smaller particles and *vice-versa*. Naturally, individual growth rates will be influenced by such intrinsic factors as heat transfer coefficients, latent heats, etc. In general, however, for the same mass flow rate of vapor, high molecular weight materials tend to yield smaller particles than those of low molecular weight, other things being equal. Another relevant factor is the condensation temperature of the material. The data show a definite trend for the more refractory materials to condense into finer particles. Table II is a tabulation of three materials processed under ap-

Table II. Relation of physical properties to particle size

Material	MP, °C	BP, °C	Estimated relative vapor density	Equivalent sphere diam-avg. Å
MoO ₃	795	Sublimes	high	862
SiO ₂	1710	2800	high	331
TaC	3875	5500	low	56

proximately similar vapor flow conditions, showing a rough correlation between average particle size, condensation points, and density.

For a given material, control of particle size can of course be achieved only by control of effluent vapor density. The latter is a function of the ambient pressure, the arc power level, and amount of diluent present, if any. For the case of refractory oxides requiring carbon in the electrodes, a certain amount of CO is always present in the effluent vapor. This serves to dilute the vapor independently of any external quench gas. The partial pressure of CO in the flame is determined largely by the percentage of carbon in the electrodes. Hence, for such materials, particle size can be controlled to some extent by electrode composition.

Mean particle size of the samples was determined by surface area measurement from which the average diameter of equivalent spheres can be obtained. As expected the surface areas of the arc-produced particulates are high. They vary from 10 to 150 m^2/g depending on the density of the material and degree of particulation. In the case of the low density, finely divided silica, the surface area was approximately 150 m^2/g . In contrast, the more finely divided tantalum carbide with a correspondingly higher density had a surface area of 72 m^2/g . All of the values were determined using the Brunauer-Emmett-Teller nitrogen absorption technique (2). Surface area values for typical materials are illustrated in Table III.

Particle shape.—Particle shape is of course revealed by electron microscopy. On examination of the electron micrographs of the various samples thus far studied, one finds that the majority of the particles are spherical or at least spheroidal in shape. This finding is consistent with the method of preparation, which, in most cases, involves rapid successive phase transitions from vapor to liquid to solid. While in the liquid phase, the natural shape of the droplet is spherical. If, as is the case here, the time duration of the liquid phase is short, the droplet may congeal before it has had a chance to assume its natural crystal habit. This is apparently the case for most of the materials investigated.

Table III. Surface area values of typical submicron materials

Material	Surface area, m^2/g	Equivalent sphere diam-avg, \AA
SiO_2	70	331
SiO_2^*	152	152
Al_2O_3	28	580
Fe_2O_3	17.4	658
ZrO_2	23	470
MgO	67	250
MoO_3	20	700
Al	39	580
Ni**	24.3	277
Fe**	9.0	850
W**	29	110
TaC	72.4	56
ThO_2	18	400

* Air quenched.

** Vaporized as the oxide and subsequently reduced in hydrogen.

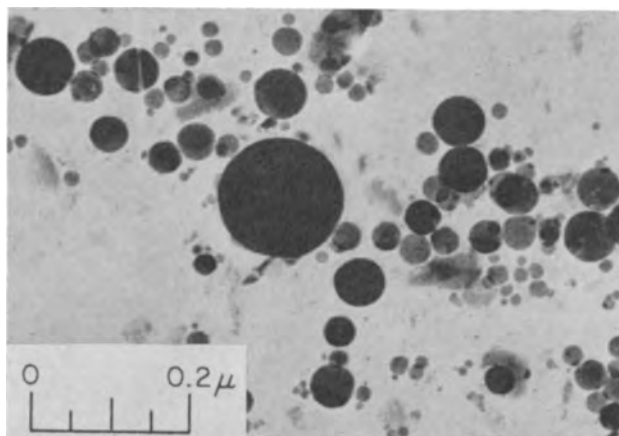


Fig. 6. Electron micrograph of arc vaporized alumina. $\times 100,000$

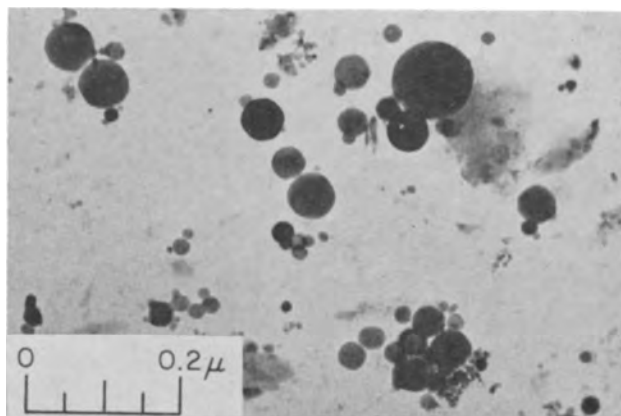


Fig. 7. Electron micrograph of arc vaporized zirconia. $\times 100,000$

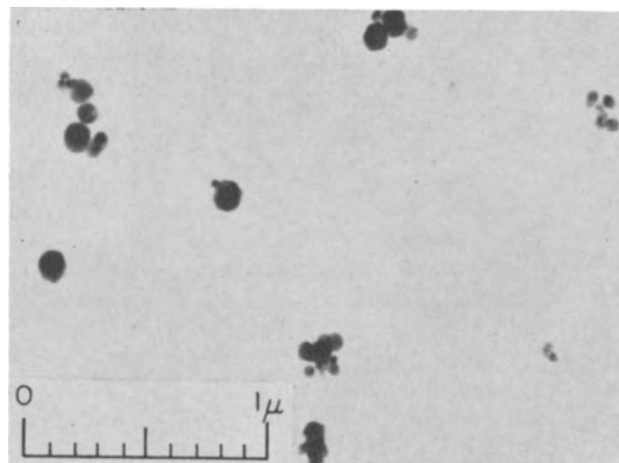


Fig. 8. Electron micrograph of arc vaporized iron oxide. $\times 31,500$

There are, however, specific materials such as iron oxide, molybdenum oxide, thorium oxide, tantalum carbide, and titanium carbide, which exhibit distinct crystalline shapes, including hexagonal, octahedral, cubic, and plate-type particles.

Examples of both spheroidal and crystalline particles are shown in Fig. 6-18. Figure 6 shows Al_2O_3 , which, like the SiO_2 particles previously shown, are clearly spherical in shape. A sample of ZrO_2 is shown in Fig. 7. Here the material is also spherical. The next few photographs present examples of materials which, while generally spheroidal in character, exhibit some tendency to assume a crys-

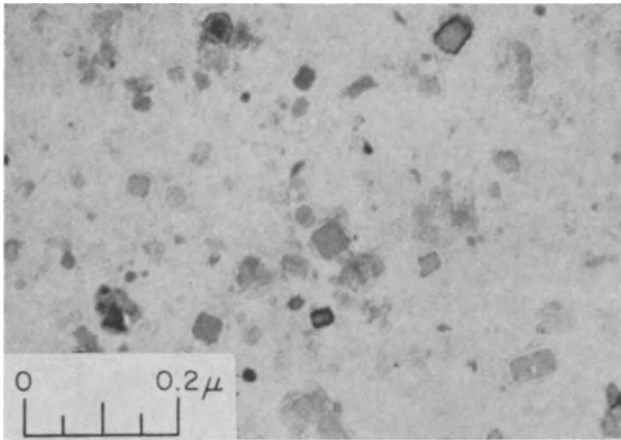


Fig. 9. Electron micrograph of arc vaporized magnesium oxide. $\times 100,000$.

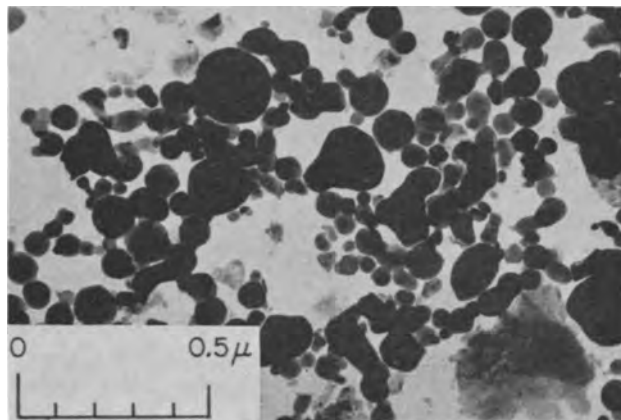


Fig. 10. Electron micrograph of submicron iron metal, produced by hydrogen reduction of arc-vaporized oxide. $\times 50,000$.

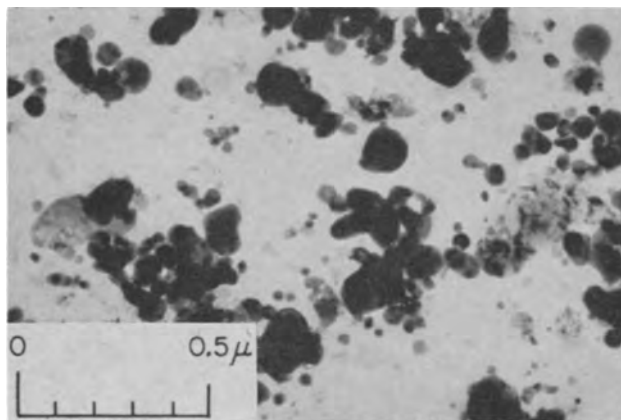


Fig. 11. Electron micrograph of submicron nickel metal, produced by hydrogen reduction of arc-vaporized oxide. $\times 50,000$.

talline shape. For example in Fig. 8, showing Fe_2O_3 , the shape is only roughly spheroidal, and a distinct trend toward a particle shape having a hexagonal outline can be observed. Similarly, Fig. 9, of MgO , shows a tendency for the particles to assume a cubic shape.

The next three materials, shown in Fig. 10, 11, and 12, are examples of submicron metal powders produced by arc-vaporization of the respective oxides followed by subsequent reduction in hydrogen. Conceivably, therefore, the crystalline form could have been influenced by the reduction process. Figures

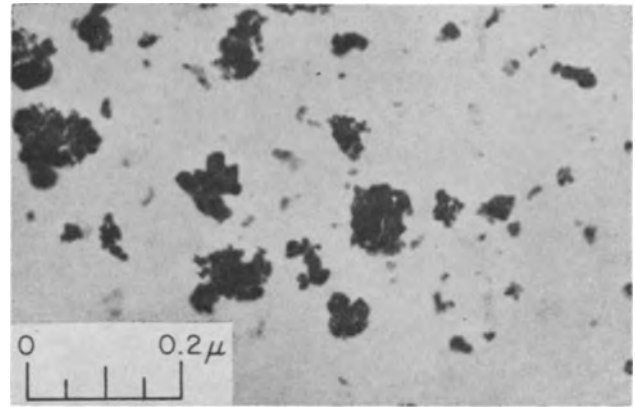


Fig. 12. Electron micrograph of submicron tungsten metal, produced by hydrogen reduction of arc-vaporized oxide. $\times 100,000$.

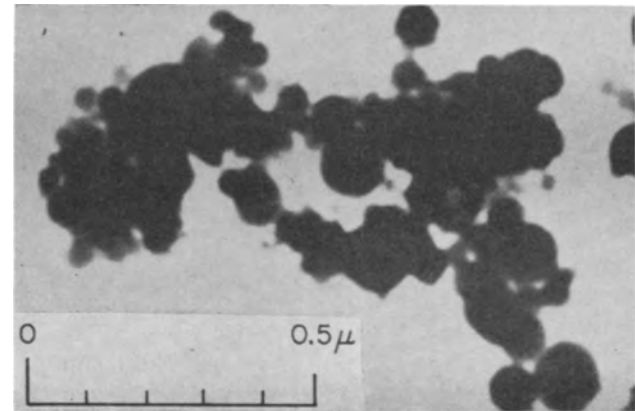


Fig. 13. Electron micrograph of arc vaporized aluminum. $\times 75,000$.

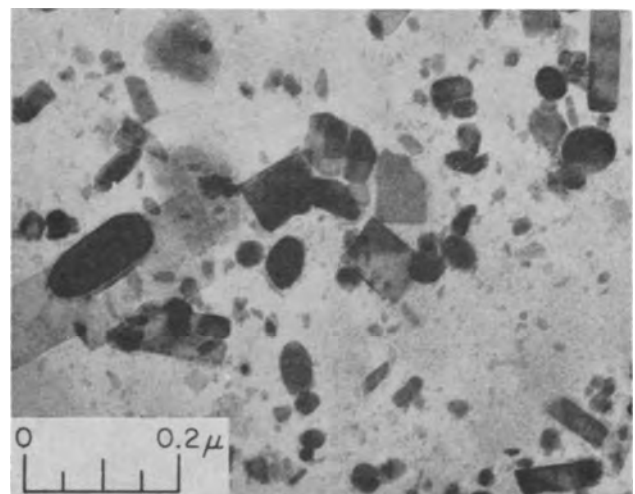


Fig. 14. Electron micrograph of arc vaporized molybdenum oxide. $\times 100,000$.

10 and 11, showing particulates of iron and nickel, respectively, exhibit a distinct crystalline trend. In particular, in the photograph of Ni (Fig. 11) it is observed that the larger particles are essentially spheroidal whereas the small particles appear to assume a more definite crystalline shape. In the case of W (Fig. 12), the shape is irregular and not clearly defined. It is definitely not spheroidal, however. A prismatic form could possibly present such an aspect, but further examination is necessary to define the shape.

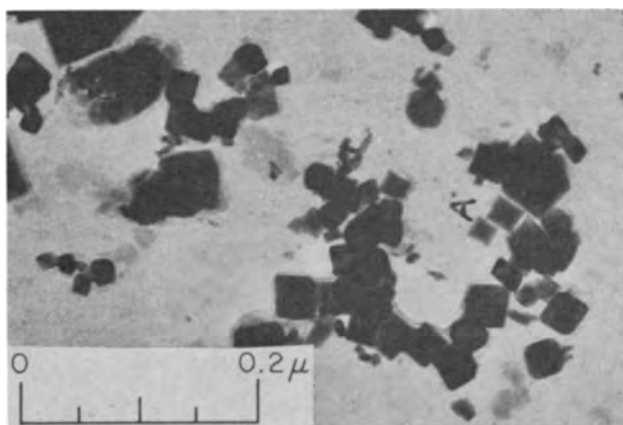


Fig. 15. Electron micrograph of arc vaporized thoria. $\times 150,000$

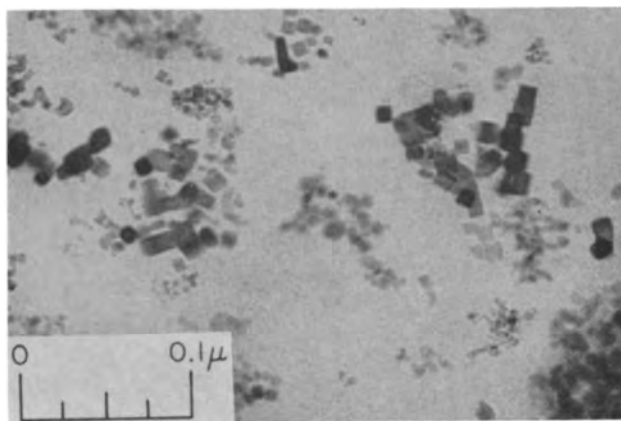


Fig. 16. Electron micrograph of arc vaporized tantalum carbide. $\times 225,000$.

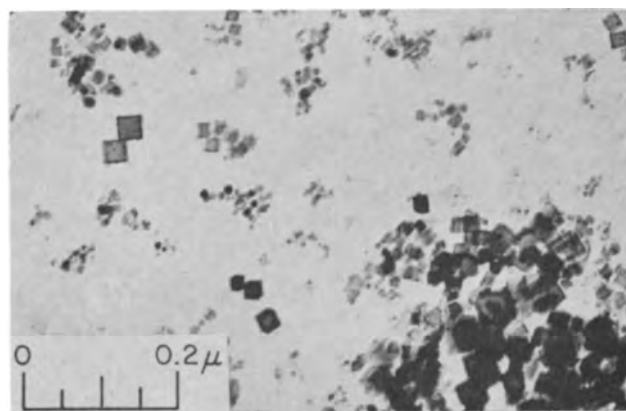


Fig. 17. Electron micrograph of arc vaporized titanium carbide. $\times 100,000$.

We next come to examples of materials for which the particle shape is distinctly crystalline. Figure 13 shows Al, produced by direct arc vaporization of the metal. Although the resolution on the particular picture is not as good as might be desired, the particle shape is definitely hexagonal with rounded corners. Figure 14, showing MoO_3 particles, clearly reveals a plate-like shape for the particles, and in Fig. 15, the thoria particles are well-defined octahedra. Figure 16 shows TaC particles at a magnification of 225,000. The cubic nature of these particles is quite clear. Similarly, Fig. 17 of TiC also exhibits a distinct cubic form.

In addition to the spherical and crystalline particle shapes, a filamentary or fibrous form was ob-

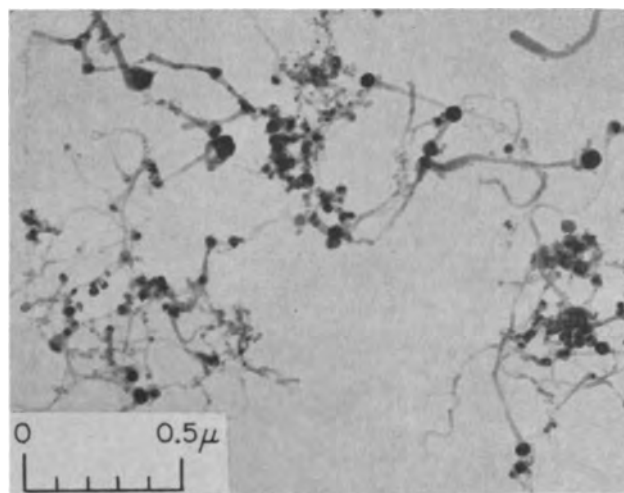


Fig. 18. Electron micrograph of submicron ferrosilicon, produced by arc-vaporization of a stoichiometric mixture of iron oxide, silica, and carbon. $\times 40,500$.

tained in the case of ferrosilicon. This material was produced by vaporizing a mixture of iron oxide, silica, and carbon in stoichiometric proportion to produce a sample which analyzes essentially to ferrosilicon. A photomicrograph of this sample is shown in Fig. 18. Both spherical particles and thin fibers, between 200 and 400 Å in width, are observed. It is interesting to note that in nearly every case a fiber appears to be attached to a sphere. The basis for the peculiar structure of this material is as yet unexplained.

Chemical properties.—Characterization of the chemical and solid-state properties of arc-produced particulates is still at an early stage of progress and is at present the subject of intensive effort. While results in this respect are still fragmentary, the tests conducted thus far reveal some unusual properties for this type of particulated material. The methods being used in this study include chemical analysis, x-ray diffraction analysis, chemical reactivity tests, and sinterability.

Chemical analysis has been used to evaluate product purity. In virtually every case the purity of the product was at least comparable to that of the starting material. In many cases product purity was improved by the arc-vaporization technique, especially when the impurities in the feed material were more volatile than the product and were distilled away as noncondensable vapors. This upgrading or beneficiation effect is particularly noted when the arc is operated at very low ambient pressures, and the partial pressure of the vaporized impurity constituent is below the equilibrium partial pressure for condensation.

X-ray diffraction analysis has revealed both ordered and partially disordered atomic arrangements among the spherically shaped particulates. Crystalline particulates have always shown an ordered array, as expected. However, the diffraction pattern from SiO_2 showed only a few diffuse bands, with many of the lines expected for a fully ordered array missing. Consequently, the silica fume is apparently produced in a semi-amorphous solid state.

On the other hand, the Al_2O_3 spheres yielded a pattern which indicated a much more ordered lattice arrangement despite the fact that the two materials look exactly the same under the electron microscope. It was interesting to note that in the case of Al_2O_3 , about 90% of the particulated material was in the delta phase. Another interesting item was revealed by x-ray diffraction analysis in the case of arc-vaporized carbon. When ordinary amorphous carbon was used as the starting material, the product was also found to be amorphous in structure, as expected. However, when graphite was vaporized, the major portion of the product was also found to be graphitic in nature. This "memory" effect of the material passing through the vapor state is strongly suggestive of the idea that, in the case of graphite, the material vaporized in polyatomic form. For example, if the vapor were predominantly triatomic, initial condensation into six-atom carbon rings, which is the basis structure of the graphite crystal, would be favored. This conjecture is consistent with both theoretical (3) and experimental (4) studies on the form of graphite vapor, which is shown to be polyatomic, in the vicinity of the sublimation temperature at least, with species containing an odd number of carbon atoms predominating.

The chemical reactivity of the arc-produced particulates was observed to be unusually high in nearly every case. Practically all of the metals, and metal carbides were highly pyrophoric and would burst into flame on exposure to the atmosphere, often with explosive violence. Such powders could be passivated by allowing a thin film of oxide to build up on the surface at a slow rate. For example, if the powder were transferred to a bottle and tightly stoppered while in an argon atmosphere, before removal from the arc chamber, and then allowed to remain for several hours, it could subsequently be opened to the atmosphere without igniting. This is attributed to the inleakage of traces of air through the stopper in amounts sufficient to form a film of oxide on the particles but insufficient to cause combustion. In the case of tantalum carbide, the bottle was observed to become very hot during the first few minutes after removal to the atmosphere indicating a partial oxidation of the product. The presence of Ta_2O_5 was subsequently verified by x-ray diffraction analysis. Aluminum powder handled in this fashion could safely be exposed to the atmosphere, but would still ignite at elevated temperatures. It could be ignited, for example, by a match flame. The oxide content of the aluminum powder was determined analytically to be about 25 wt %. Since this material has a particle size corresponding to 200Å equivalent sphere diameter, this oxide content is equivalent to a monomolecular layer of Al_2O_3 . The chemical reactivity of the oxide powders was investigated by solubility tests. In comparison to the behavior of macroscopic powders, the solubility of the arc-vaporized particulates in various reagents was anomalously high. For example, it was possible to dissolve silica and alumina completely in cold dilute acids, whereas

Table IV. Sintering properties of typical submicron materials

Material	MP, °C	Arc vaporized submicron	Sintering temperature of various size fractions, °C	
			Commercial 1μ	Commercial -325 mesh
SiO_2	1710	925	—	1125
Al_2O_3	2015	1150	—	1400
TaC (a)	3875	1800	>3000	—
TaC (b)	3875	1100*	—	—

* Presintered.

the starting materials were almost completely insoluble.

One of the most striking effects observed for the submicron particulates is the effect of the small particle size on sintering temperature. Proposed theories on sintering indicate that the sintering rate is inversely proportional to particle size. Apparently, the driving force in this process is the tendency of a polycrystalline material to minimize its surface energy by grain growth. This effect is illustrated by a lowering of the sintering temperature and/or a decrease in sintering time, when submicron particles are used. This was demonstrated in a test with arc-vaporized silica, in which the powder was deposited as a thin film on a sheet of platinum. After drying, the specimen was inserted into a furnace at 1100°C, held for 4 min, and then withdrawn. The resulting film was uniform, transparent, and dense, resembling fused quartz in appearance. A more striking example of enhanced sinterability is the case of tantalum carbide which normally requires a high sintering temperature. This is illustrated in Table IV, along with some results for silica and alumina. These tests show that the sintering temperatures for the arc-vaporized submicron materials are reduced to almost half that of coarser commercially available powders. The two samples of TaC were handled completely anaerobically. A benzene vehicle was used to prevent surface film oxidation, thus retaining the high surface energy of the particles. Sample a was raised to 1800°C in an argon atmosphere and the furnace immediately shut off. Although no heat soak was used the specimen was completely sintered. In the case of sample b the specimen was raised to 1100°C and held at this temperature for 2½ hr. Definite evidence of presintering was observed, and it is considered possible that a longer sintering time would result in complete sintering even at this comparatively low temperature.

Summary

In summary, the high-intensity arc process appears to be uniquely adaptable to the production of submicron particulates. The method is quite versatile with regard to the characteristics of the end product. While a considerable amount of work remains to be done in studying the properties of these products and in evaluating their usefulness in various applications, it is already clear that these prod-

ucts represent a new class of ultrafine powders having interesting and potentially useful characteristics.

The method of treatment seems amenable to relatively inexpensive production. From a cost standpoint it should be at least comparable to current chemical processing methods. Production factors relevant to the comminution of oxide-type materials have been studied (5) on a small pilot plant scale. During this study the particulated material was produced under practical, semicontinuous running conditions at rates of 10-20 lb/hr. The other types of fine particulates mentioned in this paper have thus far been produced only in pound quantities and under laboratory conditions. In general, however, the arc-vaporization method does not seem at this point to be faced with any unsolvable scale-up problems.

The investigation thus far has indicated that it is relatively easy to produce the fine particulates in the size ranges of greatest potential interest. The significant advantages ascribed to these materials are high surface energy, enhanced chemical reactivity, improved sintering characteristics, and flexibility with regard to particle size and distribution.

Acknowledgment

The authors wish to acknowledge the advice and consultation of Dr. S. Korman throughout this work, and the valuable service of Mr. R. Weidman in the fabrication of consumable electrodes for the arc-vaporization process.

The bulk of this work was carried out under the sponsorship of the Manufacturing Methods Division, AMC, Contract AP 33(600)-42916, Aeronautical Systems Center, Wright-Patterson Air Force Base.

Manuscript received Nov. 3, 1961; revised manuscript received Oct. 3, 1963. This paper was presented at the Indianapolis Meeting, April 30-May 3, 1961.

Any discussion of this paper will appear in a Discussion Section to be published in the December 1964 JOURNAL.

REFERENCES

1. C. Sheer and S. Korman, "The High-Intensity Arc in Process Chemistry," in "Arcs in Inert Atmospheres and Vacuum," W. E. Kuhn, Editor, pp. 169-183, John Wiley & Sons, Inc., New York (1956).
2. S. Brunauer, P. H. Emmett, and E. Teller, *J. Am. Chem. Soc.*, **60**, 309 (1938).
3. K. S. Pitzer and E. Clementi, *ibid.*, **81**, 4477 (1959).
4. R. E. Honig, *J. Chem. Phys.*, **22**, 126 (1954).
5. V. Harris, J. D. Holmgren, S. Korman, and C. Sheer, *This Journal*, **106**, 874 (1959).

The Pd/O₂ Electrode in Sulfuric Acid Solution

Sigmund Schuldiner and Robert M. Roe

U. S. Naval Research Laboratory, Washington, D. C.

ABSTRACT

Open-circuit potential behavior of palladium in helium-stirred sulfuric acid solutions which were virtually free of oxygen was determined. The experimental results indicated that traces of oxygen in the helium stream would eventually remove hydrogen dissolved in the palladium. Effects of oxygen partial pressure and pH showed that no simple equilibrium relations existed. At low pH, oxygen partial pressure, after a certain minimum, affected potential slightly. At pH values above 1.7, however, a slope of about 0.04v per decade of oxygen partial pressure change and 0.037v/pH unit was found. It is believed that these relations indicate mixed potentials due to several equilibria.

This investigation was carried out for the purpose of finding the open-circuit potential behavior of palladium in helium-stirred sulfuric acid solutions which were virtually free of oxygen. In addition, open-circuit relations between potential, oxygen partial pressure, and pH were determined.

Experimental

The experimental technique was essentially the same as that used in a recent study of the Pt/O₂

electrode (1). The cell was also the same except that a Pt electrode was present only when calibrating the glass reference electrode in hydrogen-saturated solution, before the run was started, and immediately at the conclusion of a run. The electrodes (99.97% Pd) used are shown in Table I.

The solutions used were 2.5, 1.95, 0.71, 0.23, 0.073, 0.024, 0.01, 0.0028, and 0.0012N H₂SO₄. The pH of these solutions was determined with a pH meter at the close of each series of runs. The temperature was 25° ± 1°C.

Low oxygen partial pressures were obtained by electrolytically generating oxygen and mixing with helium as described (1). High oxygen partial pressures (above 1 Torr) were obtained by mixing purified tank oxygen with nitrogen. The oxygen partial pressure was determined with a polarographic type Beckman Oxygen Analyzer and occasionally checked with a magnetic susceptibility type Beckman Oxygen Analyzer.

Table I. Palladium electrodes

Type	Dimensions	Area, cm ²	Volume, cm ³	Volume/area, cm
Bead	0.17 cm diam bead at end of 0.06 cm diam wire, 0.11 cm long	0.111	0.0029	0.026
Wire	0.0127 cm diam wire, 2 cm long	0.08	0.00025	0.0031
Spiral	0.0127 cm diam wire, 152 cm long	6.06	0.0192	0.0031
Foil	6.25 cm ² , 0.00127 cm thick	12.5	0.00794	0.000635

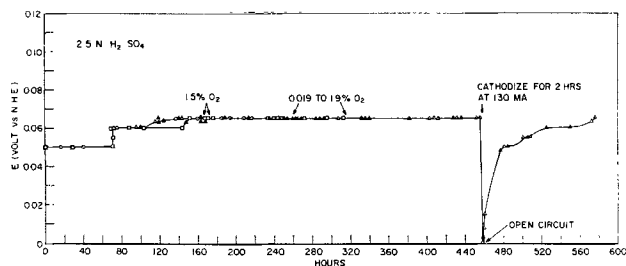


Fig. 1. Potential vs. time relation of palladium bead in helium-saturated solution. Arrows indicate time intervals at which indicated amounts of oxygen were added to the gas stream. Open circle with a dot, open box with a dot, open triangle with a dot refer to three separate runs.

Palladium Rest Potentials in Helium-Saturated Solutions

The potential-time relation for the Pd bead electrode in 2.5N H_2SO_4 solution is shown in Fig. 1. At zero hour the flow of hydrogen was replaced with helium. The potential remained constant at 0.05v for about 70 hr and then rose to a rest value of 0.065v. Small additions of oxygen during the time intervals indicated on the graph did not affect the rest potential. At the 455th hour the electrode was cathodized for 2 hr at 130 ma. The instantaneous potential on open-circuit was zero against the normal hydrogen electrode (NHE), but became more positive with time until it eventually returned to 0.065v, at which time the experiment was terminated. The 50 mv rest potential during the first 70 hr confirmed previous work at this laboratory (2) as well as the work of others (3). However, the rise to a very steady rest potential of 65 mv was observed for the first time.

Another experiment in helium-saturated 0.35N H_2SO_4 gave the results shown in Fig. 2. Here the rise to 65 mv was faster than in 2.5N acid for the bead electrode. The wire electrode reached the steady 65 mv potential even faster. In this experiment after the addition of small amounts of oxygen the potential on the bead electrode rose to only 75 mv, but the wire electrode showed a strong sensitivity to oxygen partial pressure.

The behavior of the spiral and foil electrodes in 1.95N H_2SO_4 is shown in Fig. 3. Here the rest potential was maintained at about 65 mv for 100 hr for the spiral, whereas, the foil rose above that value after about 50 hr. The addition of oxygen caused a large shift in potential for both electrodes. The removal of oxygen resulted in a slow decrease in positive potential with the Pd spiral coming down to a value of 0.3v. The decrease in positive potential for both electrodes was similar to the behavior of platinum under equivalent conditions (1).

The low rest potentials in pure helium-saturated solutions and the return of potential to the low positive values shown in Fig. 2 and 3 show that under these conditions palladium is not soluble in sulfuric acid solution. These experiments also show that the partial pressure of oxygen must be extremely low in the helium-saturated solutions. Also, after the addition of oxygen the adsorbed oxygen and/or oxygen-bearing species react or are spontaneously desorbed from the palladium surface.

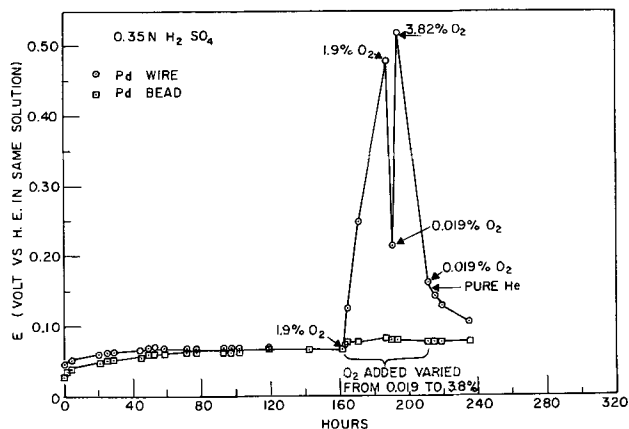


Fig. 2. Potential vs. time relation of palladium wire and bead. Arrows indicate changes from pure helium flow in the composition of gas bubbled through the sulfuric acid solution.

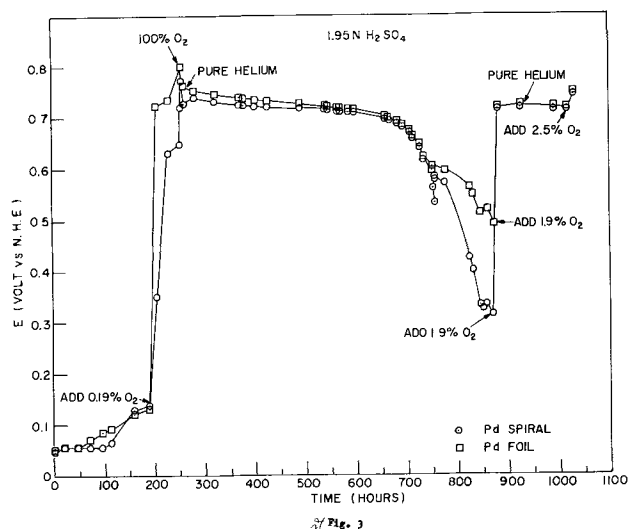


Fig. 3. Potential vs. time relation of palladium spiral and foil. Arrows indicate changes from pure helium flow in the composition of the gas bubbled through the sulfuric acid solution.

There is a possibility that on the addition of oxygen a palladium oxide is formed which can then dissolve in sulfuric acid solution. In any case, the results show that the amount of Pd ions in oxygen-bearing solutions must be very small.

Results shown in Fig. 1-3 indicate that there is a volume/area relation with rest potentials in both helium-saturated and oxygen-containing solutions and time. The rest potentials in helium-saturated solutions are undoubtedly dependent on the amount of hydrogen dissolved in the α -phase Pd-H alloy. Whether the rise in potential is a function of the rate of dissolved hydrogen being spontaneously transported from the metal phase to the solution, or the hydrogen is removed by reaction with traces of oxygen in the solution, is not entirely clear at this point. There is undoubtedly some trace amount of oxygen in solution so some of the hydrogen must be removed by reacting with it.

Using the data for the palladium foil and spiral shown in Fig. 3, it is apparent that after about 150 hr the potential is positive enough to indicate that a large part of the hydrogen originally in the α -phase alloy ($H/Pd = 0.03$) of these electrodes is

removed. A calculation of the amount of oxygen stoichiometrically required to remove all of the hydrogen from both electrodes shows that, if all of the oxygen that enters the cell reacts with hydrogen, the partial pressure of oxygen in the helium stream would be about 3×10^{-7} atm. The amount of oxygen in the helium stream was so low that mass spectroscopic analyses were indefinite because the limit of sensitivity of the instrument had been reached. This indicated that the oxygen partial pressure was less than 10^{-6} atm. Even though all of the oxygen flowing through the cell will not react with hydrogen on the palladium surfaces and all of the hydrogen is not removed, the indications are that the rise in potential on the palladium electrodes is due to hydrogen loss as a result of reaction with oxygen leaking into the cell. The amount of oxygen reacting will depend on the exposed area of the electrode. Thus, the Pd bead in Fig. 1 showed that the amount of hydrogen lost over a period of 460 hr was rather small even though, during part of the time, some oxygen was deliberately added. This was because little of the oxygen comes into contact with this very small electrode.

Whether hydrogen spontaneously leaves the α -phase and is swept out by the helium gas flow, or the hydrogen dissolved in the metal is in equilibrium with hydrogen ions (2) in solution, cannot be fully answered without further experimentation. The evidence appears to be that a hydrogen dissolution owing to zero hydrogen partial pressure, if it does occur, would be very slow. Experiments in closed systems with carefully controlled traces of oxygen could resolve this question. It is possible that the rate of potential change in low volume/area electrodes could be used as a method of determining very small amounts of oxygen.

Dependence of Potential on Oxygen Partial Pressure

The relation between rest potential and oxygen partial pressure in various pH solutions is shown in Fig. 4. The values shown in this figure are all for the palladium foil electrode. The spiral electrode was also used in these measurements, but it was found that the rate of attaining steady-state values was extremely long compared to the foil electrode. This is attributed to the much larger amount of hydrogen contained in the spiral electrode and the much longer diffusion path for its removal by reaction with oxygen. A run made in zero pH solution comparing the foil and spiral electrodes after several weeks exposure to oxygen-containing solution gave essentially the same results for each electrode. In subsequent work, however, the spiral electrode was not exposed long enough to give the steady values found for the foil electrode.

The pH dependence shown in Fig. 4 is interesting inasmuch as at zero pH the oxygen partial pressure affects potential slightly whereas, as the pH increases, the dependence on oxygen partial pressure increases and then more or less levels off at pH values above 1.3. The pH dependence at two oxygen partial pressures is shown in Fig. 5. The rise in potential with increasing pH up to pH = 1.7 cannot

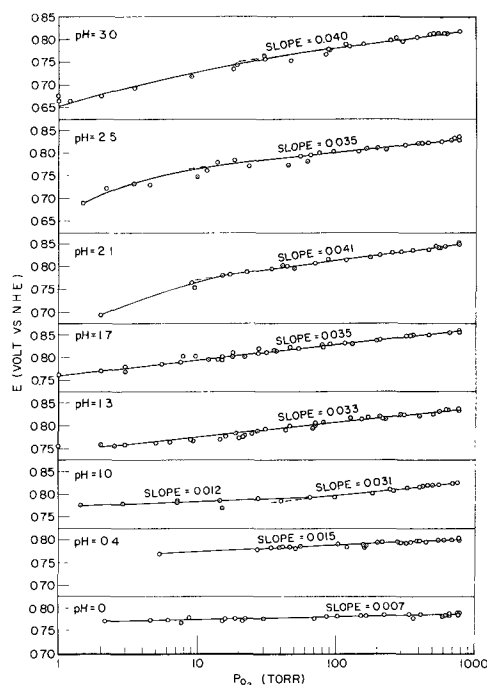


Fig. 4. Effect of oxygen partial pressure on open-circuit potential on palladium foil in sulfuric acid solutions of various pH.

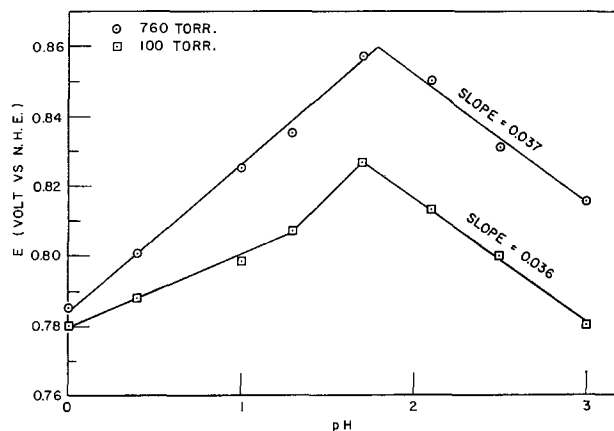
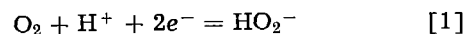


Fig. 5. Potential vs. pH relation at given oxygen partial pressures

be explained on the basis of any equilibrium potentials concerning oxygen and its species. A possible explanation is that the solubility¹ of palladium increases with both pH (up to 1.7) and oxygen partial pressure. This could be tied in with the formation of a palladium oxide or oxygen-bearing compound.

At pH values of 1.7 and above, a more normal relation between pH and potential is observed in Fig. 5. The slope of 0.037 cannot be readily related with any known equilibrium reaction, neither does the slope of about 0.04 for the relation between potential and oxygen partial pressure. It is possible that several equilibria may be occurring in parallel in this pH region and that they would together give such odd value slopes. Not many likely equilibria give a pH vs. potential slope less than 0.059. One possibility is



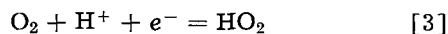
where, at 25° (5)

$$E = 0.34 - 0.029 \text{ pH} + 0.029 \log [P_{\text{O}_2}/a_{\text{HO}_2^-}] \quad [2]$$

¹ Vetter and Berndt (4) showed that in 1N H₂SO₄ palladium does undergo a corrosion maximum in the range from 0.9 to 1.1v.

The calculated $a_{\text{HO}_2^-}$ is about 10^{-19} M/l, which means that essentially no peroxide ion exists in solution. However, this species could exist in significant amount on the electrode surface. One would also have to assume that the activity of adsorbed peroxide ion is independent of oxygen partial pressure in the linear ranges shown in Fig. 4.

There are several parallel reactions in this pH range that could account for the slopes shown in Fig. 4 and 5. The equilibrium



where at 25° (5)

$$E = 0.13 - 0.059 \text{ pH} + 0.059 \log [P_{\text{O}_2}/a_{\text{HO}_2}] \quad [4]$$

occurring in parallel with Eq. [1] could account for these slopes. Indications were that this oxygen/perhydroxyl radical equilibrium could exist on platinum (1). Here also, the concentrations of perhydroxyl radical would be negligibly small in solution

but could be appreciable and constant on the electrode surface.

Acknowledgments

The mass spectroscopic analyses of helium for oxygen content were made by Dr. F. E. Saalfeld and R. Olfsky.

Manuscript received June 26, 1963. This paper was presented at the Pittsburgh Meeting, April 15-18, 1962.

Any discussion of this paper will appear in a Discussion Section to be published in the December 1964 JOURNAL.

REFERENCES

1. S. Schuldiner and R. M. Roe, *This Journal*, **110**, 1142 (1963).
2. S. Schuldiner, G. W. Castellan, and J. P. Hoare, *J. Chem. Phys.*, **28**, 16 (1956).
3. J. P. Hoare, *This Journal*, **106**, 640 (1959).
4. K. J. Vetter and D. Berndt, *Z. Elektrochem.*, **62**, 378 (1958).
5. M. Pourbaix, in "Le Mécanisme de l'Oxydation," Inst. International de Chimie Solvay. 8th Conseil de Chimie, 10-15th Sept. 1950, p. 485, R. Stoop, Brussels (1950).

Constant Current Transition Time Investigations of the Electrochemical Oxidation of Formate-Formic Acid at a Smooth Platinum Electrode

Ronald A. Munson

Research Laboratory, General Electric Company, Schenectady, New York

ABSTRACT

Transition times have been measured for various current densities on a smooth platinum electrode in aqueous formate solutions in the pH range 0-14 at 25°C. In strongly basic solutions there is no evidence for the supply of formate to the electrode during the current pulse. Results obtained in acidic and strongly buffered solutions to pH 10 indicate the presence of a slow preelectrochemical reaction. The electrochemical oxidation and the decomposition of formic acid share in part a common mechanistic path.

The nature of the interaction of formic acid with metal interfaces has long been an object of investigation. Deville and Debray (1) first reported the slow decomposition of formic acid to carbon dioxide and hydrogen on rhodium. Mueller and collaborators investigated the decomposition of formic acid on various dispersed metals in aqueous solutions (2) as well as its electrochemical oxidation (3) on a number of metal surfaces. For the low potential anodic oxidation Mueller (4) proposed a three-step mechanism consisting of a one-electron discharge of formate to HCOO^\cdot radical, decomposition of the adsorbed radical to carbon dioxide and adsorbed hydrogen, and electrooxidation of the adsorbed hydrogen. Evidence for this mechanism is insufficient, but it does explain the production of hydrogen during electrooxidation on certain metals which do not catalyze the electrooxidation of hydrogen. Schwab (5) has emphasized the importance of the electronic factor in decomposition on metals and alloys.

Schwabe (6) found that, following the inception of formic acid decomposition on finely divided metals, the potential went through a maximum while the rate of hydrogen production decreased to a small constant value. The mechanistic steps of Schwabe consist of adsorption of molecular formic acid, decomposition to carbon dioxide and adsorbed hydrogen, and hydrogen desorption. Schwabe postulated that formic acid rather than hydrogen is potential determining and that formic acid decomposition is hindered by slow desorption of hydrogen. A similar mechanism involving hydrogen desorption has been proposed by Gerischer and Held (7).

Formic acid adsorbs dissociatively onto metal surfaces from the vapor phase (8, 9) according to



There is disagreement concerning the degree of ionicity of the surface formate (10). These surface

formates have been shown to be intermediates in the decomposition to hydrogen and carbon dioxide at room temperature and above (11). Tamaru (12) found that the hydrogen formed from the decomposition of formic acid desorbed and formic acid continued to be adsorbed according to the process above until the surface was covered with surface formate. Only when the surface was covered with formate did a slow steady-state production of carbon dioxide begin.

Interpretation of constant current transition time measurements.—An anodic constant current (i) applied to an inert electrode in a solution containing a substance electrooxidizable at that electrode causes the depletion of the electrooxidizable material at or on the electrode surface. Removal of the electroactive species at the electrode surface leads to a gradual increase in the electrode overpotential until the electroactive species is no longer present at the surface. At this point the overpotential increases rapidly until a second electrode reaction supplies the constant current. The characteristic time representing initial complete depletion of the electroactive species at the electrode surface, which is easily identifiable by the sudden potential jump, is called the transition time (τ). When an electrooxidizable species is present on the electrode surface, but no additional electrooxidizable material reaches the electrode during the pulse, the $i\tau$ product will be constant. If there is no adsorption, and diffusion to the electrode alone limits the supply of electrooxidizable material at the surface, then the $i\sqrt{\tau}$ product will be constant (13). In general, the relationship between the applied current and the transition time is dependent on the nature of the preelectrochemical reactions present. The transition time-current density relationship for a homogeneous first order preelectrochemical step (14) and the effect of a heterogeneous first order preelectrochemical step (e.g., adsorption) (15) have been derived. Both treatments predict linear $i\sqrt{\tau}$ vs. i plots of negative slope at low current density if a rate-limiting preelectrochemical step is present. For the case of a rapid reversible heterogeneous step the $i\sqrt{\tau}$ vs. i plot will have a positive slope at low current densities.

Experimental

The experimental arrangement has been described (15). One molar sodium perchlorate was prepared by the neutralization of analytical reagent 70% perchloric acid with 50% sodium hydroxide (reagent) and dilution with triple-distilled water. Formic acid was purified by distillation at 62 mm Hg and was present in concentrations of 0.012N or less. The buffers were composed of reagent or CP grade chemicals, and the basic constituent of the buffer was, with one exception, at least 0.08N. Tank nitrogen and hydrogen (when used) was scrubbed by passage through concentrated sulfuric acid, chromous sulfate, 50% sodium hydroxide, and triple-distilled water.

The transition times were, in general, well defined and could be determined to within 2% by in-

spection. Under very high current densities and in basic solutions the transition times were determined to $\pm 5\%$ using the assumption of constant double-layer capacity.

The working platinum electrode was activated by single anodic pulses of 200 msec duration at an apparent current density of 14 ma/cm² until the transition times became reproducible. Following activation, the electrode was returned to 0.4v of the reversible hydrogen potential by cathodic polarization. Nitrogen was bubbled vigorously through the solution for 90 sec following activation. The electrode and solution then remained quiescent for 30 sec prior to the experimental pulse. Somewhat different activation current densities were employed to study competitive adsorption and to follow the potential change after activation. Better reproducibility was obtained when the activation procedure was repeated several times before each experimental pulse. The choice of activation procedure is more critical in formate-formic acid studies than it is in the case of the hydrogen on platinum electrode (15). Following activation, formate undergoes rapid initial decomposition on the freshly reduced platinum surface to hydrogen. This decomposition tends to deplete the formate species close to the electrode and at the same time produces hydrogen both on and in the immediate vicinity of the electrode surface. The rate of this decomposition decreases rapidly. Depending on the constituents of the solution partial deactivation of the electrode occurs in 10-30 min following activation. The activation procedure employed makes use of the time interval following the initial rapid decomposition but preceding deactivation. Stirring with nitrogen removes most of the hydrogen and reestablishes the bulk formate concentration in the vicinity of the electrode surface. The activation procedure chosen is arbitrary, but care in following it yields consistent meaningful results.

Results

At high current densities the transition times are more nearly the result of oxidation of species present on the electrode only, as the transition times are too short to permit significant diffusion to the surface. Figures 1, 2, and 3 show potential-time oscillograms for a 1N perchloric acid solution saturated with hydrogen, saturated with hydrogen in the presence of 0.005N formic acid, and with the formic

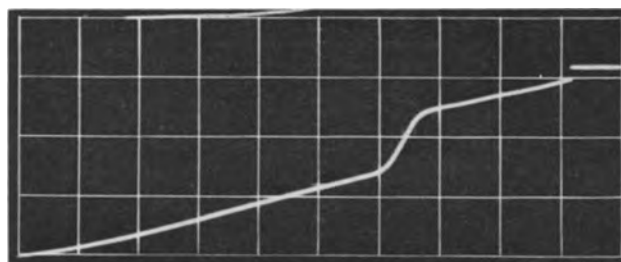


Fig. 1. Potential-time oscillogram for the oxidation of hydrogen from the surface of platinum in 1N perchloric acid. Current density 43 ma/cm². Potential increasing from top to bottom 0.50v per large division. Time increasing from right to left 5.0 msec per large division.

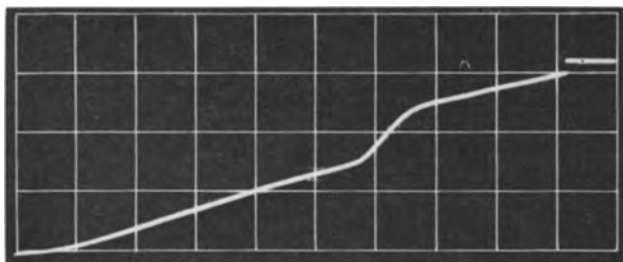


Fig. 2. Potential-time oscillogram for an anodic current density of 43 ma/cm^2 on platinum in $1N$ perchloric acid. Hydrogen saturated solution $0.005N$ in formic acid. Coordinates as in Fig. 1.

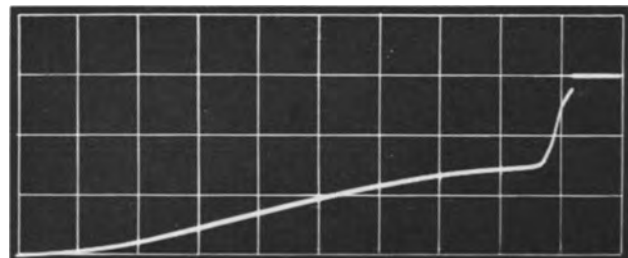


Fig. 3. Potential-time oscillogram as in Fig. 2 except solution is nitrogen saturated.

acid in a nitrogen saturated solution, respectively. The length of these transition times is little influenced by diffusion from the bulk of the solution due to the low solubility of hydrogen and preelectrochemical kinetic limitation on the formic acid oxidation. Therefore, the time to the potential transition is nearly proportional to the surface concentration of the species oxidizing at that potential. Formic acid and hydrogen electrooxidation do not overlap. Formic acid adsorbs hardly at all in the presence of hydrogen, and hydrogen surface coverage is decreased by not more than 5% by the presence of formic acid in solution. Formic acid in the absence of dissolved hydrogen in the bulk adsorbs to form essentially a monolayer, but some hydrogen is present on the surface from formic acid decomposition.

The open-circuit potential of a freshly activated platinum electrode in dilute formic acid describes a maximum as a function of time. The amount of hydrogen adsorbed on the surface, determined by high current density transition time pulses, also passes through a maximum. When the solution is stirred both maxima occur sooner.

One hundredth molar formate in tenth and one molar sodium hydroxide.—The transition time is poorly defined but the $i\tau$ product remains constant over four orders of magnitude in the transition time up to 10 sec. There is no evidence for the supply of formate to the electrode during the current pulse. *Borate and phosphate buffers in 1N NaClO₄ pH 1-10.*—An analysis of the relationship between the transition times and current densities employed allows interpretation of the preelectrochemical kinetics as discussed above. The results, an example of which is displayed in Fig. 4, indicate a rate-determining preelectrochemical step. When extended to short transition times these results also show the oxidation of a formate species adsorbed on the

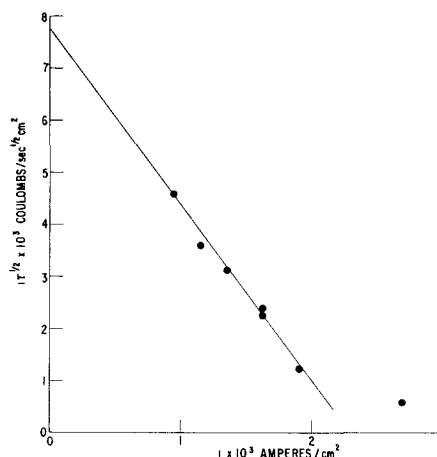


Fig. 4. Low current density experimental results in a phosphate buffer of pH 2.5, Σ formate = 0.012.

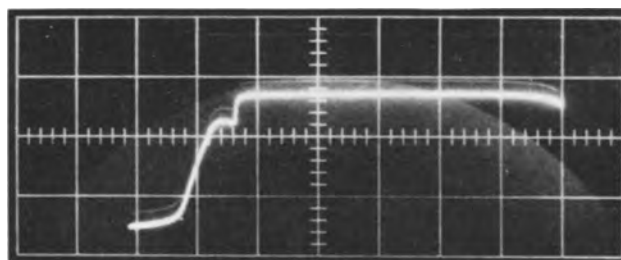


Fig. 5. Oscillogram illustrating two transition times at a current density of 1.97 ma/cm^2 at pH 3.0 Σ formate = $2.4 \times 10^{-2}N$. Abscissa: time increasing from right to left 1 sec per full division. Ordinate: potential increasing from top to bottom $0.50V$ per full division.

electrode surface. From pH 1.4 to 6.0 two transition times are observed (Fig. 5). The first, the $i\tau$ product of which becomes negligibly small at high current densities, corresponds to a direct electrooxidation of a formate species without significant prior adsorption. The second, which shows a constant $i\tau$ product at high current densities, corresponds to oxidation of both a formate species on the electrode surface and concurrent direct electrooxidation. Above pH 6.0 only one transition time is observed. Figure 6 illustrates the effect of pH on the rate of the preelectrochemical step. A minimum in the slope corresponds to a maximum in the rate. The actual pH at the electrode is, despite the strong buffering capacity, somewhat lower due to production of protons at the anode during current flow. *Perchloric acid and bisulfate buffers in 1N NaClO₄.*—The transition time-current density relationship shows the presence of a rate-determining preelectrochemical step. These results are in accord with those obtained potentiodynamically by Breiter (16) who found that the current maxima were not proportional to formic acid concentration as expected for a diffusion controlled process. Potential fluctuations often occurred.

Discussion

In strongly basic solutions there is no evidence for the supply of formate to the electrode during the current pulse. The formate ion adsorbs extremely slowly on platinum in a basic environment and does not oxidize without prior adsorption. This

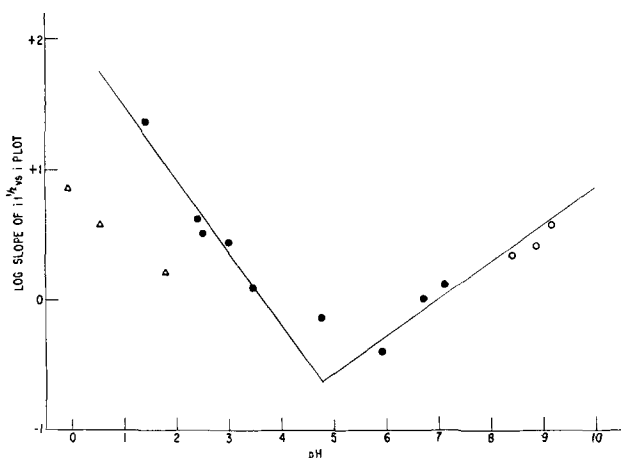


Fig. 6. Logarithm of the limiting slope of $i\tau^{1/2}$ vs. i plots against pH. ●, Phosphate buffers; ○, borate buffers; △, bisulfate buffers and perchloric acid.

confirms earlier work (17, 18) in which it is reported that the electrooxidation of methanol in strong base yields formate with essentially 100% efficiency. The formate produced from the oxidation of methanol must be desorbed and is not then susceptible to oxidation to carbonate.

Figure 3 exhibits a short transition time at low potential which is indicative of the presence of some hydrogen on the platinum surface. This hydrogen results from the dissociative adsorption of formic acid on the electrode (reaction *a*). The hydrogen surface concentration is kept low by its ready desorption and diffusion away from the electrode. Other experiments have shown that the surface equilibrium between adsorbed and dissolved hydrogen on newly activated platinum surfaces is rapid and reversible (15). In agreement with this, agitation is found to facilitate hydrogen transport from the electrode surface and to rapidly decrease the hydrogen surface concentration.

The sizable hydrogen exchange current density on platinum requires hydrogen to play an important role in electrode potential determination when it is present, *viz.*

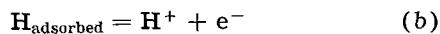
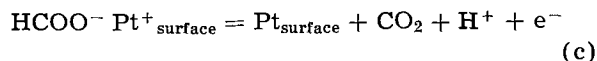


Figure 3 shows that adsorbed formate oxidizes at a potential higher than that of hydrogen, thus



The hypothesis that an adsorbed formic acid species is potential determining at open circuit on recently activated platinum is untenable. Rather a small amount of hydrogen from dissociative adsorption is primarily responsible for the open-circuit potential.

The rate of decomposition of formic acid on platinum to hydrogen and carbon dioxide has been found to be pH dependent (6). The rate has a maximum at pH 4.2. The preelectrochemical slow step observed in these experiments has an over-all maximum rate at approximately pH 5. The similarity in the pH dependence indicates that, at the very least, the electrochemical oxidation and the decomposition of formic acid share in part a common mechan-

istic path. The nature of the common precursors or steps is difficult to ascertain from the low and inexact value of the exponent of the hydrogen ion dependence (Fig. 6). Apparently specific anion influences are also present. The tendency of aqueous formic acid solutions to form hydrogen bonded oligomers (19-21) suggests the possibility of hydrogen bonded intermediates in homogeneous solution. A slow preelectrochemical conversion of the formic acid to an electroactive hydrogen bonded intermediate could explain the observed common pH dependence of the electrooxidation and decomposition reactions. Such an electroactive intermediate could involve the buffer itself, but the evidence is not conclusive.

It might be supposed that electrochemical oxidation of hydrogen follows the decomposition of formic acid to carbon dioxide and hydrogen on the platinum surface. However, the steady-state decomposition of formic acid to hydrogen and carbon dioxide is too slow (6) to support the observed current densities. In addition, formate oxidation is found to occur at potentials removed from those associated with hydrogen electrooxidation. Therefore, the complete decomposition of formic acid cannot precede the electrochemical oxidation. Rather the shared mechanism must precede the complete decomposition to carbon dioxide and hydrogen and may involve either or both dissociated adsorption or homogeneous reaction in solution. Therefore the mechanism envisaged for the electrooxidation of formic acid-formate includes a pH dependent rate-limiting step(s) either preceding or included in reaction (*a*) followed by steps (*b*) and (*c*) although, under certain conditions of pH, adsorption does not appear to be a necessary preliminary for electrooxidation. The decomposition to hydrogen and carbon dioxide would appear to involve a similar mechanism, excepting the electrochemical ones, followed by a quite slow steady-state decomposition of the surface formate.

Manuscript received March 14, 1963; revised manuscript received Sept. 7, 1963. This work was made possible by the support of the Advanced Research Projects Agency (Order No. 247-61) through the United States Army Engineer Research and Development Laboratories under Contract No. DA-44-009-ENG-4853.

Any discussion of this paper will appear in a Discussion Section to be published in the December 1964 JOURNAL.

REFERENCES

1. Deville and Debray, *Compt. rend.*, **78**, 1782 (1874).
2. E. Mueller, *Z. Elektrochem.*, **28**, 307 (1922); E. Mueller and J. Keil, *ibid.*, **29**, 395 (1923); E. Mueller and F. Mueller, *ibid.*, **30**, 493 (1924); E. Mueller and K. Schwabe, *ibid.*, **34**, 170 (1928).
3. E. Mueller, *ibid.*, **33**, 561 (1927); E. Mueller and S. Tanaka, *ibid.*, **34**, 256 (1928).
4. E. Mueller, *ibid.*, **29**, 264 (1923).
5. G.-M. Schwab, *Trans. Faraday Soc.*, **42**, 689 (1946).
6. K. Schwabe, *Z. Elektrochem.*, **61**, 744 (1957).
7. H. Gerischer and J. Held, *ibid.*, **64**, 1111 (1960).
8. G. Rienaecker and N. Hansen, *Z. anorg. u. allgem. Chem.*, **285**, 283 (1956).
9. K. Hirota, K. Fueki, Y. Nakai, K. Shindo, and K. Kuwata, *Bull. Chem. Soc. Japan*, **31**, 780, 861 (1958); K. Hirota, K. Kuwata, S. Asai, *Nippon Kagaku Zasshi*, **80**, 701 (1959); *C.A.*, **54**, 9432b.

10. R. E. Eischens and W. A. Pliskin, 2nd International Congress on Catalysis (1960).
11. J. Fahrenfort and H. F. Hazebroek, *Z. physik. Chem. (Frankfurt)*, **20**, 105 (1959); J. Fahrenfort, L. L. van Reizen, and W. M. H. Sachtler, *Z. Elektrochem.*, **64**, 216 (1960).
12. K. Tamaru, *Trans. Faraday Soc.*, **55**, 824 (1959).
13. H. J. S. Sand, *Phil. Mag.*, **1**, 45 (1901).
14. P. Delahay and T. Berzins, *J. Am. Chem. Soc.*, **75**, 2486 (1953).
15. R. A. Munson, *J. Phys. Chem.*, **66**, 727 (1962).
16. M. W. Breiter, Private communication.
17. T. O. Pavela, *Ann. Acad. Sci. Fennicae, A59, II. Chemica*, (1954).
18. R. P. Buck, L. R. Griffith, R. I. MacDonald, and M. J. Schlatter, Proceedings 15th Annual Power Sources Conference (1961).
19. D. L. Martin and F. J. C. Rossotti, *Proc. Chem. Soc.*, **1959**, 60.
20. P. Koteswaram, *Z. Phys.*, **112**, 395 (1939).
21. D. R. Cartwright and C. B. Monk, *J. Chem. Soc.*, **1955**, 2500.

Technical Note



A Practical Reference Electrode

J. Giner

Pratt & Whitney Aircraft, Division of United Aircraft Corporation, East Hartford, Connecticut

In this note a practical reference electrode of almost general application in aqueous solutions is described and its applicability to different conditions demonstrated.

The reference electrode consists of a platinized platinum electrode (electrode A in Fig. 1) which is cathodically polarized with the help of another similar auxiliary electrode (electrode B). On electrode A H_2 is evolved in aqueous solutions. Under these conditions, if an adequate constant current is used the potential of A differs only slightly from the reversible hydrogen electrode. This difference is a constant correction term of 40-20 mv at a current of 1 ma/cm². This term depends slightly on the composition of electrolyte, temperature, etc.

Two Pt-electrodes (Fig. 1) of approximately 2 cm² (1x1 cm) surface are welded to Pt-wire, sealed to glass tube, and introduced into a wider glass tube with a fine glass frit at the end to provide electrolytic contact with the main compartment of the cell. This tube is filled with the same solution as the main cell. Between electrode A and B a current of approximately 1 ma/cm² is forced, with help of a

small 45v Battery E with 45 kilohm resistor (R) in series. The cathode A should be kept approximately 1-2 cm lower than the O_2 anode B to avoid most of the O_2 diffusing from the auxiliary electrode which works as O_2 evolving anode.

The potential of the working electrode is measured against the potential of electrode A as indicated in Fig. 1.

For the evaluation of this electrode a cell as represented schematically in Fig. 1 was used, and the potential of the polarized reference electrode A was measured against a bubbling reversible H_2 electrode, which replaced the working electrode (WE).

Stabilization of the potential.—Immediately after introducing the reference system into the cell and closing the reference load circuit, the potential of the polarized reference electrode (H_2 -evolving electrode) stays 800-300 mv higher than the reversible bubbling H_2 electrode. This high potential is due to the fact that O_2 and surface oxides of Pt have to be reduced before the potential of the hydrogen evolution can be reached. It takes approximately 20 min at 1 ma/cm² until the potential drops to the steady potential of the H_2 evolution.

This time is comparable (or smaller) to the time required usually to deaerate the measuring solution, saturate with reactant gas, etc. Faster stabilization is reached if, before applying the 1 ma (current we have selected as convenient), 10 ma are applied for 2 min. This is practically done by using, instead of a 45 kilohm resistance, a 40 and a 5 kilohm in series and short-circuiting for 2 min the 40 kilohm resistance. After 2 min the reference electrode is practically stabilized (changes of less than 2 mv in 20 hr).

The time dependence of the reference potential was studied using a voltage recorder. The effect is not much higher than the time dependence of other usual electrodes when used without special precautions (it was always smaller than 5 mv in several days).

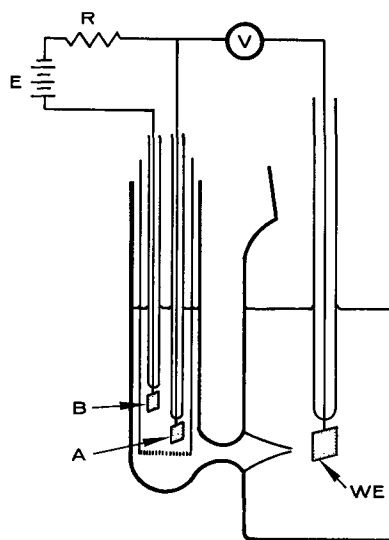


Fig. 1. Reference electrode

Table I. Correction term of potential referred to reversible H₂ electrode vs. electrolyte concentration and temperature millivolt, European sign convection

Electrolyte	Room temp	30°C	40°C	60°C	92°C
1M KOH	-21	-22.8		-18.5	
4M KOH	-32				
5M KOH	-38	-35	-33	-31	-33
			-40		
0.5M H ₂ SO ₄	-16	-18		-21.5	
1M H ₂ SO ₄	-17				-19
5M H ₂ SO ₄	-26				

The correction term.—In Table I the correction terms for different conditions of temperature and electrolyte have been summarized. These values should be taken only as an example. For accurate measurement each special configuration should be calibrated before use.

Possible causes of error.—When using the polarized reference electrode in not buffered solution in the middle pH range the possibility of a pH change on the polarized electrode caused by the slow H⁺ or OH⁻ diffusion has to be considered. In such case the correction term can amount to several hundred millivolts, if the current flowing through the polarized reference electrode is higher than the H⁺ or OH⁻ diffusion limiting current, but also here the correction term will be constant.

If the electrolyte contains substances which are reducible at potentials more positive than the potential of hydrogen evolution, the reference electrode can cease to work as a H₂ evolving electrode, and a special study should be made as to whether the process at the more positive potential could serve as reference. Another possibility, of course, would be to use a highly impermeable diaphragm similar to those of the calomel electrode to avoid the presence of the reducible compound at the reference electrode. When working with solutions saturated with O₂ and using a medium glass frit we did not find such difficulties, probably due to the low solubility of O₂.

Additions of reactants which are oxidable at a potential more positive than the H₂ potential do not affect the potential of the polarized reference electrode. For instance, the addition of some drops of CH₃OH to the chamber of the reference system did not show any effect; only during 3 min was the potential by 10 mv more positive, probably due to the dissolved oxygen contained in the added methanol solutions; neither did NH₃ additions to 5M KOH have appreciable effect.

Another precaution is to avoid shaking the reference electrode because this causes the potential to become suddenly more positive by 15 to 20 mv by the diffusion of O₂ to the electrode. The potential recovers, however, in approximately 1 min. This effect could be minimized by insulating the dynamic reference electrode (A) with a diaphragm from the auxiliary electrode (B). But since this effect appears only by intentional strong shaking, it seems that such a step is not necessary.

Examples of Applicability

The polarized reference electrode has been used satisfactorily by the author as reference electrode in fuel cell research, in both alkaline and base electrolyte with anodes using fuels such as methanol, ethylene, saturated hydrocarbons, ammonia, and with oxygen electrodes, both in stationary and transient measurements.

A very good example of demonstrated applicability is 75-95% H₃PO₄ in the range of 150°-200°C. Under these extreme conditions this polarized reference electrode gives consistent reference potentials. The advantages of the polarized reference electrode has been also confirmed by other workers (1-3).

Discussion

Comparing this dynamic electrode with such electrodes as calomel, mercuric oxide, mercuric sulfate, silver chloride, this electrode has the following advantages:

1. It does not introduce impurities such as Cl⁻ ions, or Hg²⁺ ions; the small amounts of hydrogen and oxygen which can diffuse into the main compartment are usually removed by sweeping gas.

2. It gives directly the potential against the reversible hydrogen electrode under the same conditions as the measured electrode, with a correction term which amounts only to few millivolt. (This type of reference potential against the reversible hydrogen electrodes under the same condition is particularly meaningful in studies of fuel cell electrodes.)

3. It does not have a temperature limitation as do most of the usual reference electrodes (calomel, silver chloride, mercury oxide, etc.).

4. It is applicable at any pH with a diaphragm of low resistance as long as no incompatible product is present in electrolyte.

5. Since the resistance of the diaphragm is low, this electrode appears to be more adequate than the commercial calomel electrode or glass electrodes for oscilloscopic measurements; also it should be adequate for fast transients where the resistance between reference electrode and working electrode has to be kept small.

Compared with the bubbling reversible H₂⁻ electrode, this electrode has the advantage that a gas supply is not necessary and that contamination by hydrogen in the solution is minimized. It should be emphasized that this electrode is not supposed to compete with the classical reference electrodes when extreme accuracy is required and the classical reference electrodes are adequate.

Manuscript received April 9, 1963; revised manuscript received Dec. 2, 1963.

Any discussion of this paper will appear in a Discussion Section to be published in the December 1964 JOURNAL.

REFERENCES

1. W. Vielstich, *Z. Instrumentenkunde*, **71**, 29 (1963).
2. H. Binder, A. Kohling, H. Krupp, K. Richter, and G. Sandstede, paper presented at the symposium on fuel cells of the A.C.S. Meeting in New York, Sept. 1963.
3. G. W. Fleischman, G. Johnson, and A. Kuhn, To be published.

The Application of an X-Ray Technique to the Examination of Electrodeposits

R. Brownsword and J. P. G. Farr

Department of Industrial Metallurgy, The University, Birmingham, England

In studies on electrolytic crystal growth, particularly of single crystals, it is important to confirm epitaxy between the deposit and the substrate. The normal Laue back-reflection x-ray technique is not ideal for determining this in cases where the deposit and substrate are of the same metal. Diffraction spots on a back-reflection x-ray photograph of a single crystal substrate may also appear on the corresponding photograph of the plated specimen. These may derive from an epitaxial deposit, but it is often possible for the substrate to make a sufficiently large contribution to the diffraction pattern to make the latter inconclusive.

It seemed that a Berg-Barrett technique [e.g., (1)] involving a glancing incidence of x-rays on the specimen surface would be more useful in establishing epitaxy. By adjustment of the angle of incidence, the penetration of the x-rays may be controlled according to the deposit thickness so as to reduce the possible contribution of the substrate to the diffracted pattern to an insignificant level.

The absorption of x-rays by a material is expressed by the relation $I/I_0 = e^{-\mu x}$ where I_0 and I are the radiation intensities before and after absorption respectively, μ is the absorption coefficient, and x is the thickness of absorbing material. Application of this formula yields a value of x for the length of x-ray path in the absorber to give for example I/I_0 less than 5%. This value is related to the angle of x-ray incidence θ as illustrated in Fig. 1. Under these conditions Berg-Barrett images

showing only the structure of the deposit are obtainable.

The technique has been applied to a study of the epitaxy of nickel deposits formed, as has been described previously (2), on a nickel single crystal substrate from a sulfate electrolyte. The single crystal was grown in an electron bombardment zone-melting furnace in such a way as to contain a "striation" substructure (3). Misorientation between neighboring elements was about $\frac{1}{2}^\circ$. This structure was readily recognizable in Berg-Barrett photographs, and the continuation into the deposit of this fine structure would provide clear proof of epitaxy.

In the present Berg-Barrett apparatus chromium radiation was used with a source-specimen distance of 80 cm. The incident beam was collimated with a 10 mm evacuated lead tube. Kodak B10 photo-

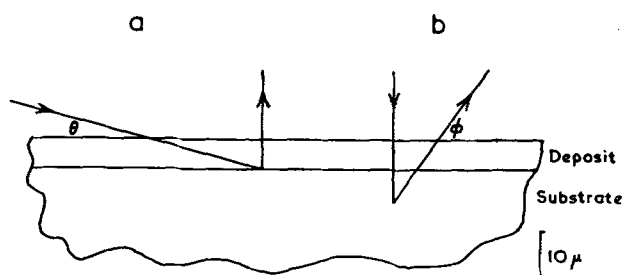


Fig. 1. A comparison of the penetration of x-rays into an electrodeposit in (a) Berg-Barrett technique and (b) Laue back-reflection technique, showing the deeper penetration in the latter. In each, the length of x-ray path in the metal is the same, giving in this case 98% absorption of the x-rays. Extreme cases are illustrated as the angle θ is usually less than shown giving less penetration and the angle ϕ greater than shown giving more penetration.

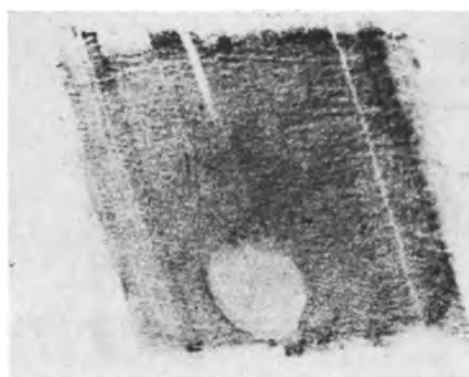


Fig. 2. A Berg-Barrett image of a nickel single crystal substrate containing a striation substructure. X15.



Fig. 3. A Berg-Barrett image of an electrodeposit formed at 15°C on the substrate shown in Fig. 2. X15.

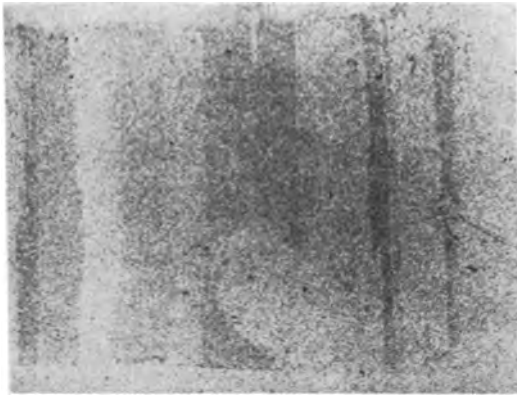


Fig. 4. A Berg-Barrett image of an electrodeposit formed at 99°C on the substrate shown in Fig. 2. X15. The images in Fig. 2 and 3 are formed by the same Laue diffraction spot; the image in Fig. 4 is formed by a different Laue spot.

graphic plates were placed within 1-3 mm of the specimen to record the image. Angles of incidence of 10°-15° were used, and these gave substrate contributions to the image of less than 2%. Exposure times of 30 min were used.

Cliffe and Farr (2) found marked differences in the topography of deposits formed above and below a critical electrolyte temperature range of 94°-98°C. In order to compare these deposit structures, plating was carried out at 10 ma/cm² for 30 min (giving a 6μ thick deposit) at 25° and at 99°C.

Figure 2 is a Berg-Barrett image of the substrate, and the linear striation substructure is seen as light and dark bands. The circular area corresponds to a porosity hole formed in freezing the metal. This feature proved useful as a location mark.

In the image from the deposit formed at 25°C (Fig. 3), the hole may be seen, but there is no evidence of the striation substructure. In contrast, the striation structure has clearly been reproduced in the deposit formed at 99°C (Fig. 4).

It appears therefore that deposits formed above 98°C are epitaxial with the substrate. While Laue spots were still obtainable from the deposit formed at 25°C, the deposit no longer conformed so closely to the structure of the substrate.

Acknowledgments

The authors thank Professor E. C. Rollason for his interest and for the provision of laboratory facilities. Thanks are also due to Messrs. Joseph Lucas Ltd. for generous financial assistance.

Manuscript received Oct. 21, 1963.

Any discussion of this paper will appear in a Discussion Section to be published in the December 1964 JOURNAL.

REFERENCES

1. J. B. Newkirk, *Trans. AIME*, **215**, 483 (1959).
2. D. R. Cliffe and J. P. G. Farr, *This Journal*, **111**, 299 (1964).
3. R. Brownsword and J. P. G. Farr, *Nature*, **195**, 373 (1962).

The Mechanism of Electrolytic Rectification

A. Middelhoek

N. V. Philips Gloeilampenfabrieken, Zwolle, The Netherlands

It has been known for a long time that the system metal/metal oxide/electrolyte, where the metal is Ta, Al, etc. (so-called valve metals), exhibits rectification. When the metal is anodically polarized, there is a "small" current, the leakage current; when the metal is cathodically polarized, a "high" current flows, the forward current.

Various theories, as mentioned in Schmidt's article (1), have been proposed to explain the phenomenon of electrolytic rectification, *viz.*, semiconductor theories; mechanical defect theories: pores, flaws, microfissures; electrochemical theories. A conclusive explanation has not yet been found.

A number of more or less well-known phenomena concerning the electrolytic rectification have been collected below, and on this basis a new theory is proposed (proton current mechanism).

A. On polarizing Ta anodically in an electrolyte an oxide film is formed; its thickness is proportional to the forming potential at constant current density. Subsequent cathodic polarization causes a "high" current flow; hydrogen is developed, and after some time the Ta metal becomes hard and brittle (2).

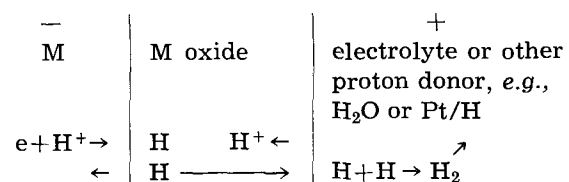
B. The system Al/Al₂O₃/metal or Ta/Ta₂O₅/metal probably exhibits no rectification in an absolutely dry state. The presence of moisture (H₂O) seems essential for rectification (3).

C. Anodic oxide films, obtained by forming, are not porous if well prepared. With the electron microscope one can detect very few or no pores; furthermore it is known that Al₂O₃ membranes are able to withstand gas pressure differences of 0.14 atm without leakage (1).

D. The system, Ta/Ta₂O₅/evaporated Pt, exhibits a higher conductance in a H₂ atmosphere. Au or Al counterelectrodes do not exhibit this effect (1).

E. It is possible to separate Al₂O₃ films from the underlying Al metal by an excessive H₂ development, *e.g.*, by switching d.c. or a.c. The developed H₂ hardly dissolves in Al at room temperature and acts as a wedge between the Al and the oxide film (4).

These phenomena can be interpreted in terms of the following mechanism:



When the valve metal is negatively polarized, protons from the electrolyte can diffuse through the

oxide film under the influence of the applied field (see above). The latter is considerably smaller than the forming field, and therefore the assumption is made that the mobility of the protons in the oxide is considerably larger than that of the Ta or Al ions. The protons arriving at the metal/metal oxide interface will be neutralized to H atoms.

These H atoms can either dissolve interstitially in the metal (point A) or collect at the interface. The H₂ gas so formed can either diffuse back to the electrolyte or crack the oxide film and disappear as H₂ gas (point E). Point B is also consistent with the suggested mechanism because moisture (H₂O) might act as a source of protons.

The mechanism suggested here differs considerably from the theory based on pores, etc., as proposed by Young (2), Vermilyea (12), and Kleefstra (14). Point C, however, indicates that at least in many cases, there are very few or no pores in the oxide layer (15). It is believed therefore that the mechanism suggested in this paper is better justified.

A further justification for the proposed mechanism can be found in the behavior of the glass electrode which is known to act as a membrane permeable for H⁺ ions. It is known that anodic oxide films, obtained by forming at moderate temperatures, are amorphous and glassy. The author is thinking of a parallel with the glass electrode. The diffusion of very small charged particles (protons) is much more probable than the diffusion of uncharged, bigger particles (H atoms) as Schmidt proposes. Moreover, the hypothesis of Schmidt necessitates an electronic current to flow through the oxide to promote the reaction $H^+ + e \rightarrow H$ or $(H_3O)^+ + e \rightarrow H + H_2O$ at the interface oxide/electrolyte. In this case it is also difficult to see why the H₂ should not choose the much easier way of escaping via the liquid electrolyte. It may be remarked that in principle the same theory may be valid under certain conditions for other "small" positive ions, e.g., Na⁺. In that case the dehydration energy of the cation must play an important role and acts as an extra barrier

in the double layer near the oxide/electrolyte interface.

A difficult point in the aforementioned mechanism was the fact that the "solid" Ta capacitor exhibits rectification even when encased in a "moisture-free" can. In recent literature, however, it is found that pyrolytic MnO₂ contains various amounts of hydrogen (16-19) so that the MnO₂ can act as the proton donor.

There are strong indications that the electrolytic rectification phenomena can be fully explained with the hypothesis of proton conduction through bulk oxide, although mechanical defects may play a certain minor role.

Manuscript received Nov. 22, 1963.

Any discussion of this paper will appear in a Discussion Section to be published in the December 1964 JOURNAL.

REFERENCES

1. P. F. Schmidt, *J. Phys. Chem. Solids*, **15**, 270 (1960).
2. L. Young, *Trans. Faraday Soc.*, **55**, 842 (1959).
3. J. Burnham, *I.R.E. Trans. on Comp. Parts*, **4**, 73 (1957).
4. A. Güntherschulze, "Elektrolytkondensatoren," 2nd ed., p. 63 (1952).
5. H. E. Haring, *This Journal*, **99**, 30 (1952).
6. B. M. Tareev, *Soviet. Phys. Solid State*, **2**, 2217 (1961).
7. Y. Sasaki, *J. Phys. Chem. Solids*, **13**, 177 (1960).
8. J. W. A. Scholte, *Philips Research Repts.*, **8**, 47 (1953).
9. A. J. Dekker, *ibid.*, **5**, 303 (1950).
10. A. W. Smith, *Can. J. Phys.*, **35**, 1151 (1957).
11. A. W. Smith, *ibid.*, **37**, 591 (1959).
12. D. A. Vermilyea, *J. Appl. Phys.*, **27**, 963 (1956).
13. R. W. Berry, *Proc. I.R.E.*, **47**, 1070 (1959).
14. M. Kleefstra, *Ann. Radioelectricité*, **57**, 223 (1962).
15. L. Masing, *Dielectrics*, **1**, 45 (1963).
16. V. Srb, *Coll. Czechoslov. Chem. Comm.*, **26**, 1231 (1961).
17. O. Glemser, *Nature*, **183**, 943 (1959).
18. J. P. Brenet, *Electrochimico Acta*, **8**, 273 (1963).
19. K. Appelt, *ibid.*, **8**, 559 (1963).
20. W. Ch. van Geel, *Philips Research Repts.*, **14**, 123 (1959).
21. P. Winkel, *ibid.*, **13**, 501 (1958).

Studies on the Oxygen Gradients in Oxidizing Metals

I. Zirconium

J. P. Pemsler

Ledgemont Laboratory, Kennecott Copper Corporation, Lexington, Massachusetts

ABSTRACT

The oxygen gradient beneath the oxide film on zirconium oxidized at 850°C for times ranging from 8 to 305 hr has been measured. The technique used involves the measurement of the rate of dissolution of interference colored oxide films. Experimentally determined gradients are in good agreement with a theoretical expression involving the diffusivity, time, and oxide film thickness. Metallography and microhardness measurements demonstrated the existence of a number of "phases" in the oxygen containing metal substrate. These are believed to be associated with order-disorder reactions. No evidence of zones of constant composition or steady-state gradients, as reported by previous investigators, were observed.

The oxidation of groups IVA and VA metals differ from that of other metals in that during oxidation significant quantities of oxygen dissolve in the metal substrate simultaneously with the growth of oxide, so that a metal zone rich in oxygen forms beneath the oxide layer. The role that oxygen solution plays in the mechanism of oxidation of these metals is not clearly understood.

Wallwork and Jenkins (1) studied the oxidation of titanium in the temperature range 800°-1000°C. They propose an initial parabolic rate associated with the formation of an oxygen diffusion gradient in the metal, followed by a linear rate associated with the establishment of a constant oxygen gradient in the metal. Steady-state gradients were also reported for zirconium and hafnium although no additional details were provided. Kofstad, Anderson, and Krudtaa (2) studied the oxidation of titanium in the temperature range 800°-1200°C. They report that the concentration of oxygen in the outer layers of the metal tends toward a limiting value corresponding to $\text{TiO}_{0.35}$, and that the oxygen gradient remains approximately constant after a period of time. Both of these observations are correlated with changes in the kinetics from parabolic to linear behavior.

Osthagen and Kofstad (3) found the rate of oxidation of zirconium-oxygen alloys increased with rising oxygen content up to 12 to 15 at. %, above which there was no further increase in rate with oxygen content. Microhardness studies on specimens oxidized for various lengths of time up to 11 hr at 800°C suggested that oxygen in an outer layer of the metal reached a "saturation" value corresponding to 12 to 15 at. %. The authors propose that accelerated oxidation commences due to cracking of this "saturated" layer. Akram and Smeltzer (4) studied the oxidation of zirconium at 800° and 850°C. On the basis of microhardness measurements they report that after 60 hr at 850°C the concentration of oxygen as a function of distance in the metal beneath the oxide film is defined by a steady-state configuration during linear oxidation. A model for the oxidation through a duplex scale consisting of a porous and compact oxide is given based on a steady-state oxy-

gen concentration in the metal during linear oxidation.

Three of the publications cited above (1-3) thus assign a causative role to the oxygen gradient in determining the kinetics of oxidation of group IVA metals. Both zones of constant composition and steady-state gradients are reported.

In a previous investigation the author (5) studied the oxygen gradient in zirconium alloys corroding in an approximately parabolic manner in steam at 650° and 750°C. The "mottling" of anodically deposited films was used to measure oxygen concentration. The data fit a theoretical expression involving a parabolic oxidation rate. No evidence was found for a zone of constant oxygen composition adjacent to the oxide.

The present study represents a further investigation into the nature of the oxygen gradient in oxidized metals and the effect of the gradient on the oxidation mechanism.

Theory

Calculation of the oxygen gradient beneath the film on oxidized metals necessitates the solution of a moving interface diffusion problem with the oxidation rate as a boundary condition. The solution to this problem for the case of zirconium oxidizing at a parabolic rate has been derived elsewhere (5).

The oxygen concentration C at a distance x' from the oxide/metal interface is given by the expression

$$C = C_s \frac{\operatorname{erfc} \left[(x'/2\sqrt{Dt}) + \left(\frac{V_{\text{Zr}}}{V_{\text{ZrO}_2}} \right) \left(\sqrt{\frac{k'}{D}} \right) \right]}{\operatorname{erfc} \left[\left(\frac{V_{\text{Zr}}}{V_{\text{ZrO}_2}} \right) \left(\sqrt{\frac{k'}{D}} \right) \right]} \quad [1]$$

where C_s is the oxygen concentration in zirconium coexisting with ZrO_2 , D is the diffusion coefficient of oxygen in zirconium at the experimental temperature, V_{Zr} is the atomic volume of zirconium, V_{ZrO_2} is the molar volume of zirconium oxide, and k' is the parabolic rate law constant.

The above equation may be rewritten in the form

$$C = C_s \frac{\operatorname{erfc}(x/2\sqrt{Dt})}{\operatorname{erfc}(s/2\sqrt{Dt})} \quad [2]$$

where s is the distance of the oxide-metal interface from the position of the initial surface and $x = x' + s$. Integration of Eq. [2] gives the total quantity of oxygen present in the metal beneath the oxide film

$$M = 2C_s\sqrt{Dt} \left[\frac{\exp(-s^2/4Dt)}{\sqrt{\pi} \operatorname{erfc}(s/2\sqrt{Dt})} - \frac{s}{2\sqrt{Dt}} \right] \quad [3]$$

where M is the quantity of oxygen dissolved in the metal per unit area of surface.

No solution to the general case where the metal oxidizes at a nonparabolic rate has been given. However, in the case of zirconium oxidizing in a protective manner where $s \ll 2\sqrt{Dt}$, substitution of numerical values in Eq. [2] indicates that the diffusion gradient is relatively independent of the value of the oxide thickness and depends primarily on values of the diffusion coefficient D and the time t . If it is then assumed that during oxidation the concentration of oxygen at the metal/oxide interface is equal to the saturation value of oxygen in zirconium and that oxidation occurs by diffusion through a protective film, then Eq. [2] ought to represent a good approximation to the oxygen gradient obtained during nonparabolic protective kinetics.

Anodically deposited interference colored oxide films have been used by the author to determine the diffusion coefficient of oxygen in zirconium (6) and in hafnium (7). Uniform interference colored films were deposited on samples anodically, and the samples were then heated in vacuum at an appropriate temperature for varying lengths of time. The observed decrease in film thickness ΔL , as noted by a corresponding change in interference color, is related to the displacement of the oxide/metal boundary x' by the following expression involving the respective molar volumes

$$x' = \frac{V_{\text{Zr saturated}}}{V_{\text{ZrO}_2}} \quad [4]$$

The displacement of oxide/metal boundary is in turn related to the diffusivity by the equation

$$x' = 2b\sqrt{Dt} \quad [5]$$

where b is found to satisfy the equation

$$b(1 + \operatorname{erfb}) = \frac{1}{\sqrt{\pi}} \frac{C_o}{m_o} e^{-b^2} \quad [6]$$

The quantity C_o is the difference between the saturated concentration C_s and the initial concentration of oxygen in the metal, and m_o represents the weight of oxygen removed from the ZrO_2 consumed in the generation of unit volume of saturated zirconium ($\text{ZrO}_{0.40}$). The diffusion coefficient of oxygen in alpha zirconium was found to obey the equation

$$D_{\text{cm}^2/\text{sec}} = 5.2 \exp [(-50,800 \pm 870)/RT] \quad [7]$$

in the range $400^\circ\text{--}1500^\circ\text{C}$.

In the above study, metal of negligible oxygen content was used. If, however, a sample of oxidized

metal is polished normal to the oxide film, there will be a gradient in the oxygen concentration in the metal near the oxide film. Anodization of the polished face will produce a nearly uniformly thick interference colored oxide film. When such a sample is annealed in vacuum to allow the interference film to dissolve into the metal, a film whose thickness is related to the initial oxygen content of the metal will result. Thus, sufficiently far into the metal substrate the film will decrease in thickness according to the rate of diffusion of oxygen in oxygen-free metal. In the oxygen-containing zone near the metal/oxide interface the rate of decrease in thickness of the interference colored film will be less than in the oxygen-free substrate. Immediately adjacent to the metal/oxide interface there can be no decrease in film thickness with time, since the metal is already saturated with oxygen.

Substitution of the proper numerical values into Eq. [5], [6], and [7] demonstrates that the rate of decrease in film thickness is nearly proportional to the fraction saturation of the metal. Thus, after diffusion, the oxygen-rich zone in the metal will reveal interference colors ranging from the initial anodized color at the metal/oxide interface to a maximum change in color at a point in the metal where the oxygen content becomes negligible. A quantitative measure of the gradient can therefore be obtained by anodic deposition and diffusion and subsequently measuring the thickness of interference color oxide as a function of distance from the metal/oxide interface.

Experimental

Since diffusion of oxygen in zirconium is highly anisotropic, it was desirable to make observations on single grains. Therefore, a coarse-grained rod was prepared by zone melting crystal bar zirconium. Disks 7 mm in diameter and 4 mm thick with grain sizes of the order of 3 mm in diameter were cut from near the center of the zone melted rod. Samples were polished with emery cloth to a 4/0 finish, etched for 30 sec in an aqueous solution of 50% nitric and 5% hydrofluoric acids, and exposed to oxygen at 850°C and 1 atm for different periods of time. After cooling, the samples were polished normal to one of the circular faces and cut in half normal to the direction of the polish. Extreme care was taken to prevent fracture of the oxide and the embrittled metal zone adjacent to the oxide. One of the two half-portions of each sample was anodized; the other was saved for comparison purposes. Anodization took place in a 1 wt % KOH solution with the samples as anode and a platinum wire as cathode. Specimens were anodized for 10 min at 20v to produce light-blue colored films 580\AA (6) thick. Small portions in the center of the samples remote from the diffusion zone were anodized at 35v to produce films 1015\AA thick. The anodized half-samples were then heated in vacuum for 145 min at 510°C at a pressure of less than 10^{-5} Torr. This treatment did not significantly alter the gradient in the metal substrate. About 550\AA of oxide diffused into the metal in the oxygen-free zone so that metal remote from the oxide/metal interface had no interference color re-

maining. The exact extent of oxide solution in oxygen-free metal was measured by comparison of the color of the portion of the specimen which had been anodized at 35v with appropriate standards. The two half-samples were then butted against each other separated by a mica insulating spacer and held tight in a plastic jig. Contact was made to the control half-specimen through a tantalum wire. The entire jig could thus be immersed during anodization with only the control half-specimen being anodized. The control specimen was then anodized successively in 2v increments. After each anodization the mounted samples were examined at 800 diameter magnification in a Leitz metallograph with a projection screen. Since there is a small difference in the interference color obtained on anodization of oxygen-rich metal compared with oxygen-free metal, the comparison of colors between the control and diffused specimen was facilitated by using a control specimen of identical oxygen gradient to that of the sample. The distance was measured from the metal/oxide interface in the diffused sample at which its color corresponded to that of the anodized control an equal distance from the metal/oxide interface. By this means the oxygen concentration could be determined as a function of distance from the metal/oxide interface.

In order to calculate the theoretical gradient according to Eq. [2], it is necessary to know the diffusion coefficient of oxygen in zirconium at 850°C. Since measurements were carried out on single grains and the diffusion of oxygen in zirconium is orientation-dependent, it was necessary to determine separately the diffusion coefficient of oxygen in each grain in the direction of diffusion, that is, normal to the originally polished face. Subsequent to the above gradient measurements, therefore, the samples were removed from the jig and the oxide film and oxygen-rich zone normal to the initially polished face were removed by abrasion. The diffusion coefficient of oxygen in the direction of oxidation was then determined by subsequent anodization and diffusion as previously described (6). Results are presented in Table I.

Results

The oxygen concentration gradient was determined by the color comparison method for each of five samples exposed to oxygen at 850°C and 1 atm pressure for times ranging from 8 to 305 hr. The data points are shown in Fig. 1. The solid lines indicate the theoretical gradient as calculated from Eq. [2]. The fit of the experimental points to the theoretical equation is good and indicates that, although Eq. [2] was derived rigorously only for the case of parabolic oxidation, the expression may be used to

Table I. Diffusion coefficient of oxygen in single grains at 850°C

Sample, oxidation time, hr	$D_{850^\circ\text{C}}, \text{cm}^2/\text{sec}$
8	6.22×10^{-10}
24	6.55×10^{-10}
68	8.16×10^{-10}
117.5	8.85×10^{-10}
305	6.24×10^{-10}

define oxygen gradients in samples oxidizing by non-parabolic protective kinetics.

In the above samples measurements were made at areas covered initially by black adherent oxide films, which showed no evidence of cracking when examined under polarized light. A single specimen from the "finish end" of the zone melted rod was exposed for 64 hr to oxygen at 850°C and 1 atm. This apparently contaminated sample was covered for the most part with flaky, white oxide. In other areas a duplex scale existed, consisting of a white cracked outer layer and a dark adherent inner layer. Anodization and diffusion experiments carried out using this sample indicated that the depths of oxygen penetrations were much less than the values calculated from Eq. [2].

During metallographic observation zones of optically active metal were observed beneath the oxide/metal interface. These zones were best observed in unetched samples which had been extensively polished. Figure 2 shows these optically active zones in a polycrystalline sample. Hardness traverses were obtained on two of the single grain samples using a

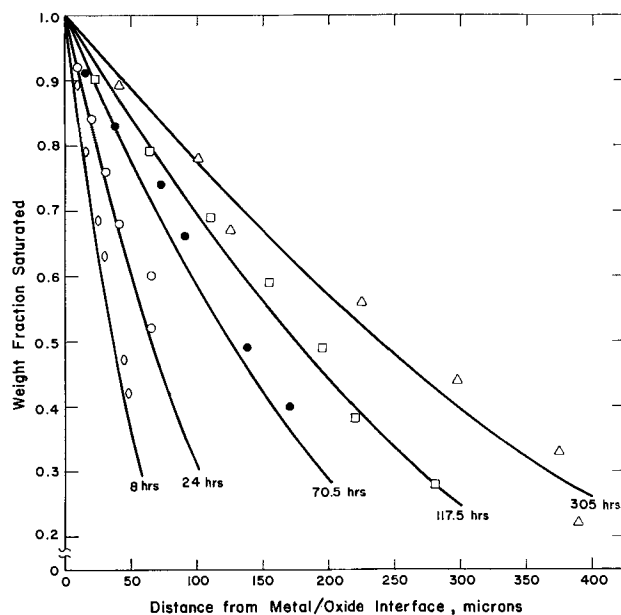


Fig. 1. Oxygen gradients in zirconium oxidized at 850°C

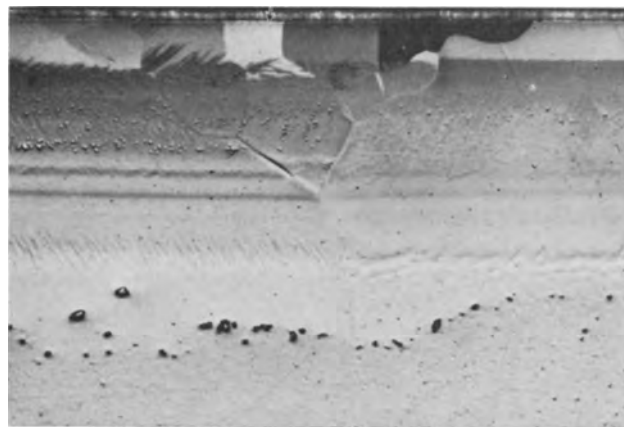


Fig. 2. Structure of zirconium-oxygen solid solution in oxidized polycrystalline zirconium. Oxide-metal interface is at top. (see arrow).

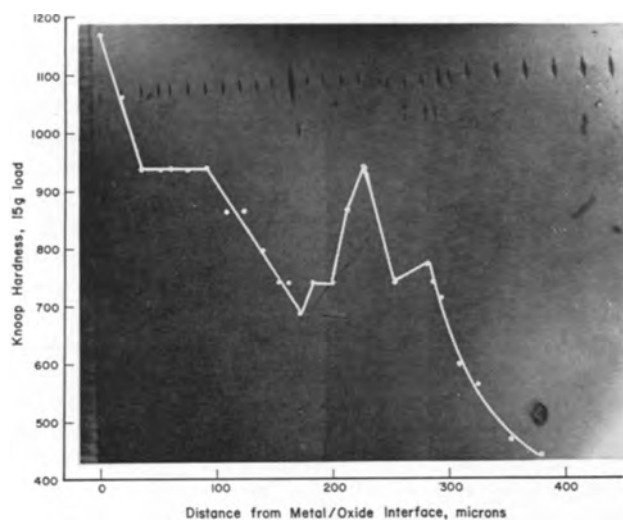


Fig. 3. Microhardness data for zirconium oxidized at 850°C for 305 hr.

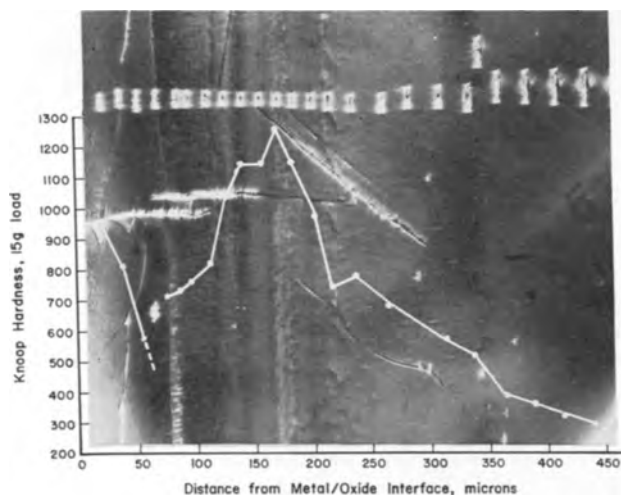


Fig. 4. Microhardness data for zirconium oxidized at 850°C for 117.5 hr.

Knoop indenter with a 15g load. The microhardness data superimposed on photomicrographs are shown in Fig. 3 and 4. Discontinuities in the microhardness curves correlate well with the position of zones in the photomicrographs. The oxygen concentrations at these phase boundaries as determined from Fig. 1 are given in Table II.

Table II. "Phase boundary" concentrations in zirconium substrate exposed to oxygen at 850°C and 1 atm

Exposure time, hr	"Phase boundary" concentrations			
	ZrO _{0.32}	ZrO _{0.26}	ZrO _{0.21}	ZrO _{0.16}
117.5				
305	ZrO _{0.31}	ZrO _{0.25}	ZrO _{0.22}	ZrO _{0.17}

"Phase boundaries" correspond approximately to concentrations equivalent to Zr₃O, Zr₄O, Zr₅O, and Zr₆O. The appearance of the photomicrographs suggest that order-disorder reactions take place in oxygen-containing zirconium at some temperature below that of the oxidation. The Zr₃O structure has been previously identified by x-ray studies and found to have a homogeneity range up to the solu-

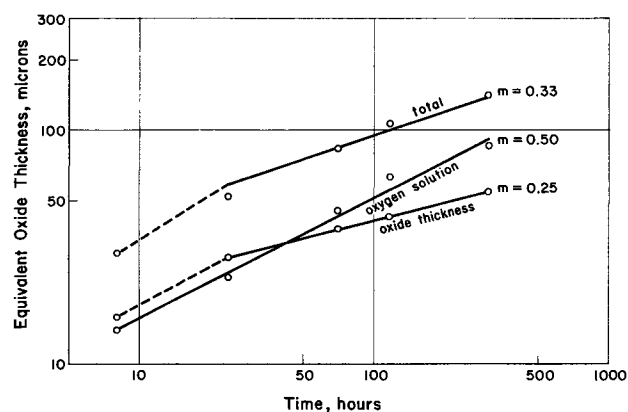


Fig. 5. Distribution of oxygen in zirconium oxidized at 850°C

bility limit (ZrO_{0.40}) (8). That the Zr₃O structure does not represent a zone of constant composition is readily seen by examination of a diffused sample which shows a continuous variation of color (and hence, oxygen concentration) through the Zr₃O phase boundary up to the solubility limit.

Kinetic data derived from experimental measurements of the oxide film thickness and diffusion gradients are shown in Fig. 5. The increase in oxygen contained in solid solution in the metal obeys a parabolic rate law, as would be expected from diffusion kinetics. Surprisingly, the increase in film thickness after the first 8 hr obeys an approximately "quartic rate law." No special significance is attached to the value of the rate exponent, except to indicate a rapidly decreasing rate. For those orientations examined the differences in orientation of the grains oxidized appears to play a less significant role in the rate of film thickness growth than in the diffusion of oxygen into the metal substrate since grains side by side had nearly equivalent film thicknesses but not necessarily equivalent oxygen diffusion gradients. The total weight gain obtained by summation of the contributions of the film thickness and oxygen in solution best fits a cubic rate law which has been found by other investigators to be obeyed over a wide range of temperatures for zirconium.

The conformity of zirconium oxidation to the cubic rate law at 850°C is very surprising, since in effect at this temperature it represents the summation of an approximately "quartic" film growth and parabolic oxygen solution. At lower temperatures the contribution of oxygen solution is negligible so that in fact that rate of film growth itself must be cubic. The reason for this is not understood.

Discussion

Examination of Fig. 1 indicates that no steady-state gradient is attained as had been reported by Akram and Smeltzer (4). This disagreement is probably due to several reasons. First, the previous investigators used a heavier load in their microhardness studies, producing a much larger indentation than used in the current investigation. Thus, the hardness reading was an average over a larger range of oxygen concentration. Second, the current investigation has shown that the hardness of zirconium-oxygen solutions is highly orientation de-

pendent and that extremely hard zones are present in the metal. In the previous work five hardness scans were taken and the arithmetic average for each determination used. This average may differ considerably from an indication of the true oxygen content. Furthermore, according to Eq. [2] and using the weight gain data of the previous investigators, the oxygen gradients obtained after 60 hr and after 100 hr do not vary greatly, and the difference between them was undoubtedly beyond the limit of detection of the method used.

The "saturation" value of the gradient reported by Osthagen and Kofstad (3) on the basis of microhardness studies undoubtedly represents a zone of constant hardness, such as that shown near the oxide/metal interface in Fig. 3. However, on the basis of anodization-diffusion measurements, it has been clearly demonstrated in this investigation that this zone does not represent a zone of constant composition.

In summary, the conformity of the oxygen gradient to a theoretical expression involving protective oxidation kinetics indicates that the oxygen gradient is the effect and not the cause of the observed oxidation kinetics. During protective oxidation the depth of oxygen penetration will continue to increase. When the oxide film starts to crack and a duplex oxide film forms with an outer cracked layer and inner adherent layer, oxidation will proceed at an accelerated rate and the oxygen gradient will be consumed at a rate more rapid than it can replenish itself. Under these circumstances the depth of oxygen penetration will decrease with time. When the entire oxide film consists of a cracked white oxide layer, the depth of penetration of oxygen beyond the oxide/metal interface can shrink to a very small value. That the cracking of the oxide

layer is not associated with a critical value of the gradient is apparent from the fact that white and dark areas are found to exist on the same sample and to persist during periods of continued oxidation. While cracking of the oxide film may be associated with an inner brittle layer of oxygen-containing metal, there is no conclusive evidence in the literature to support this hypothesis.

The oxygen gradients in oxidized hafnium are being studied in this laboratory and will be reported in a subsequent communication.

Acknowledgments

The author is indebted to Mr. J. Litchfield for technical assistance and suggestions throughout the course of this investigation. Thanks are also expressed to Mrs. M. Plumridge for metallographic preparation and Mr. R. Leite for the microhardness determinations. The zirconium rod was zone melted at Materials Research Corporation, Orangeburg, New York.

Manuscript received Sept. 10, 1963.

Any discussion of this paper will appear in a Discussion Section to be published in the December 1964 JOURNAL.

REFERENCES

1. G. R. Wallwork and A. E. Jenkins, *This Journal*, **106**, 10 (1959).
2. P. Kofstad, P. B. Anderson, and O. J. Krudtaa, *J. Less-Common Metals*, **3**, 89 (1961).
3. K. Osthagen and P. Kofstad, *This Journal*, **109**, 204 (1962).
4. K. H. Akram and W. W. Smeltzer, *Can. Metallurgical Quart.*, **1**, 41 (1962).
5. J. P. Pemsler, *J. Nuclear Materials*, **7**, 16 (1962).
6. J. P. Pemsler, *This Journal*, **105**, 315 (1958).
7. J. P. Pemsler, *ibid.*, **106**, 1067 (1959).
8. B. Holmberg and T. Dagerhamn, *Acta Chem. Scand.*, **15**, 919 (1961).

A Hypothesis for the Change in Potential of Iron on Uncoupling from Tin in Citric Acid Solution

W. Roger Buck, III, A. N. J. Heyn,¹ and Henry Leidheiser, Jr.

Virginia Institute for Scientific Research, Richmond, Virginia

ABSTRACT

When electrical contact is broken between electrodes of iron and tin immersed in boiling 0.2M citric acid containing Sn(II), the potential of the iron moves in the noble direction for a short time and then in the active direction for a much longer time until a steady-state value is reached within several hours. The largest shift in the noble direction and the slowest rate of return to a steady-state value were obtained with pure iron. Potential measurements, electron microscope studies, electron diffraction studies, studies using radioactive tin, and measurements using elliptically polarized light were made in order to explain the phenomenon. The following hypothesis was proposed to explain the potential changes observed. When iron and tin are in electrical contact under the experimental conditions used, an iron-tin alloy is formed on the iron surface. Simultaneously with the formation of the alloy, or as a secondary process, there is formed a small amount of excess tin. The shift to the noble value after uncoupling is a result of the dissolution of this excess tin. The slow drift to the steady-state value is a consequence of the dissolution of a minute amount of the iron-tin alloy with the resulting formation of a definite ratio of anodic/cathodic surface area.

One of the more intriguing facts about the electrochemical behavior of the iron-tin couple in acid solution is the so-called "uncoupling shift." When electrical contact is broken between electrodes of iron and tin in citric acid containing Sn(II), the potential of the iron moves in the noble direction for a short time and then in the active direction for a long time. This phenomenon was first observed by Koehler (1) at 60°.

The purpose of this paper is to summarize many new experimental observations related to the uncoupling shift and to offer a hypothesis for the behavior of the iron electrode.

Experimental

All the experiments carried out in this study were conducted at the boiling point under reflux in 0.2M citric acid. Potential measurements were made against a saturated calomel electrode (S.C.E.) maintained at room temperature in a small vessel bridged to the reaction vessel by means of a capillary tube. Potential-time curves were recorded with a Sargent Recording Potentiometer. Electrical contact with the metal specimens was made through the center of a Teflon assembly. The specimens made firm contact with the end of the Teflon so that only the metal specimens, and not the electrical connections, made contact with the solution.

Metals used.—Tin was obtained from the Vulcan Detinning Company and had a listed purity of 99.998%. Ferrovac-E iron was used in the majority of experiments and was obtained from Vacuum Metals Corporation as ½ in. rods. A typical analysis as given by the manufacturer showed: C 0.007%, Ni 0.005%, Co 0.005%, Cu 0.004%, Al 0.005%, Si

0.008%, Sn 0.001%, S 0.005%, P 0.003%, Mn 0.003%, N₂ 0.0003%, O₂ 0.015%, and Fe 99.92%. Armco iron was obtained from the Armco Steel Company. The analysis of this material as given by the supplier was: C 0.02%, Mn 0.03%, P 0.009%, and S 0.016%. Battelle high purity iron was obtained from Battelle Memorial Institute in the form of a slab, ½ in. in thickness. The iron was identified as Specimen F of Ingot B-1313. Actual analysis was: C 0.006%, O₂ 0.0022%, N₂ 0.00007%, H₂ 0.00002%, less than 50 ppm Sb, As, Si, and V; less than 5 ppm of Be, B, and P; less than 50 ppm of Cd and Ga; less than 1 ppm Pb and W; 4 ppm Al and Ni; 1 ppm Ca, Cu, Cr, Mn, and Sn; 10 ppm Co and Mo; and 2 ppm Mg. Type-L steel was obtained as a hot-rolled bar manufactured by the United States Steel Corporation. It had a mill ladle analysis of: C 0.04%, Mn 0.30%, P 0.012%, S 0.039%, Si 0.009%, Cu 0.02%, Ni 0.03%, Cr 0.01%, and As 0.007%. The bar had been hot-rolled from a mechanically capped ingot. JM spectrographic iron was obtained from Johnson Matthey Company, Ltd. The analysis furnished with the rods indicated: C 0.03%, O₂ 0.01%, and N₂ 0.01%. The following elements were present in amounts given in ppm: Si 7, Mn 4, Cu 3, Ni 2, Mg 1, and Ag, Na, and Li less than 1. Thirty-nine other elements including the transition elements were specifically sought and not detected. Puron iron was obtained about 10 years ago from Westinghouse Electric Corporation as 5 mm rods and had the following analysis: Al, B, Ca, Cr, Ga, Ir, Ag, W, and V less than 0.00005%, Ba 0.00003%, Pb 0.00003%, C 0.005%, O₂ 0.04%, Co 0.001%, Ni 0.0015%, Cu 0.0008%, Mg 0.0001%, Mn 0.00001%, S 0.003%, N₂ 0.004%, Zn 0.0008%, P less than 0.001%, Si less than 0.001%, Mo less than 0.0001%, Ti less than 0.00001%, and Sn less than 0.002%.

¹ Present address: Department of Physics, Auburn University, Auburn, Alabama.

Table I. Potential vs. S.C.E. in boiling 0.2M citric acid

	In absence of Sn (II), v	With 10 ⁻³ M Sn (II), v
Iron	-0.58	-0.52
Tin	-0.62	-0.56
Iron-tin couple	-0.60	-0.56
Iron, after uncoupling from tin (maximum value)	—	-0.42 to -0.45

In all the experiments with machined samples the irons were etched in 2M HCl in order to remove the work-hardened surface resulting from the machining operation and were then etched for a short time in the acid under test. In those experiments in which it was necessary to reduce surface roughness to a minimum, the samples were polished chemically in MirroFe.²

Immediately after polishing, the samples were immersed for short periods of time in NaOH and H₂SO₄ solutions prior to washing with distilled water.

Results

The great interest in the uncoupling shift phenomenon stems from the fact that the potential of an iron sample coupled to tin in boiling citric acid solution containing Sn(II) becomes significantly more noble after uncoupling than that of an uncoupled iron sample in the same medium. Another interesting feature of this system is that the potential of an iron sample is significantly more noble in boiling 0.2M citric acid containing Sn(II) than it is in the same medium in the absence of dissolved Sn(II). Table I gives representative figures for the potential of Ferrovac-E iron and tin electrodes exposed to boiling 0.2M citric acid solution.

Uncoupling shift phenomenon.—Many experiments have been carried out with iron of different purity and with several steels. Representative experiments for 6 different materials are summarized in Fig. 1. In these experiments the iron and tin were coupled externally for 30-120 min prior to uncoupling and the Sn(II) concentration was 10⁻⁴ to 10⁻³M. It will be noted that the commercial type-L steel used in the manufacture of tin plate gave

² Obtainable from McDermid Company, Waterbury, Connecticut.

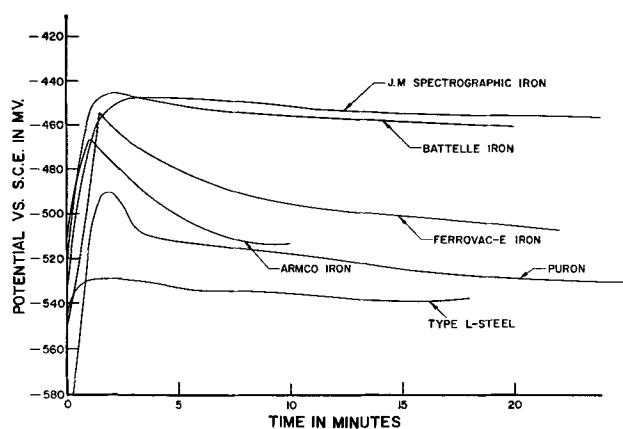


Fig. 1. Potential behavior of 6 samples of iron after uncoupling from tin in boiling 0.2M citric acid containing either 10⁻⁴ or 10⁻³M dissolved tin.

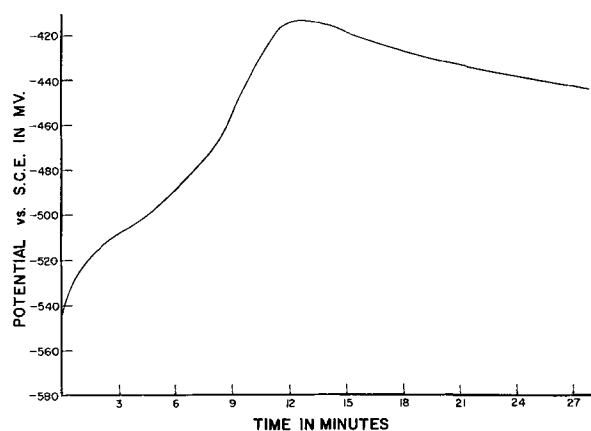


Fig. 2. Uncoupling shift curve showing an example of the tendency towards a plateau.

an insignificant uncoupling shift under the conditions used and within a short period of time assumed a potential characteristic of the steel in boiling citric acid containing dissolved tin. The Puron iron yielded a small uncoupling shift. Armco iron, a moderately pure commercial iron, gave a sharp uncoupling shift. The vacuum-cast, commercially pure iron, Ferrovac-E, gave a bigger shift in the noble direction and took a longer time to reach the value characteristic of that in citric acid containing Sn(II). The two pure laboratory irons, Johnson Matthey Spectrographic iron and the sample obtained from Battelle Memorial Institute, gave the maximum shift in the noble direction and a very slow drift back to the value characteristic of that in citric acid containing Sn(II).

The most noble potential ever observed at the maximum was -410 mv and was obtained with the spectrographic iron. As a general rule, however, the potential at the maximum was -420- -450 mv with Ferrovac-E iron, which was used in the great majority of the experiments.

In some cases an inflection was observed in the curve during the change to the most noble value. Figure 2 is an example of this inflection. Curves with a major inflection were most often obtained under the following conditions: exposures for several days to the boiling acid containing Sn(II) long coupling times of the order of 16-24 hr, and tin concentrations slightly in excess of 10⁻³M. It was also noted that when a curve with a major inflection was obtained, it could not be reproduced on the same specimen without another long period of coupling.

Pronounced uncoupling shifts of the same general type as those observed in citric acid were also obtained in hydrochloric, sulfuric, and sulfamic acids containing 10⁻³M dissolved Sn(II).

Pronounced uncoupling shifts were also obtained in the presence of As(III) in citric acid under the same conditions under which uncoupling shifts were obtained in the presence of Sn(II). No uncoupling shifts or insignificant shifts were obtained in the presence of In(III), Cd(II), Pb(II), or Bi(III) ions.

Uncoupling shifts could not be obtained using an applied potential and an inert anode in boiling

citric acid solutions in the absence of Sn(II). Uncoupling shifts were obtained, however, in citric acid solutions containing no dissolved tin provided that the iron was first made the cathode in a solution containing very low concentrations of tin.

Exposure to air for 1 sec or more of an iron electrode which had previously been coupled to tin, followed by reimmersion in the boiling acid, resulted in a potential approximately the same as that of the most noble value during the uncoupling shift, namely -420 – -450 mv.

Estimate of the number of coulombs required to yield the uncoupling shift.—The following experiments were carried out using current measurements as an aid to learning something about the character of the iron surface prior to uncoupling. In order to make these measurements it was necessary to establish an assumed standard surface on the iron. This was accomplished as follows: an iron sample surfaced in MirroFe was exposed to boiling 0.2M citric acid containing 10^{-3} M Sn(II) for three days. It was then coupled to a tin electrode of equal surface area overnight and successively uncoupled and recoupled for short periods of time until a rapid uncoupling shift was obtained. During this series of experiments the maximum value during the change in the noble direction was -420 mv.

After this standard state had been achieved, the iron sample was coupled to tin through a variable rheostat which was manually operated so as to give essentially potentiostatic conditions at the iron electrode. The potential of the couple was within 1 mv of that of tin in this medium. A recording potentiometer indicated that the potential remained constant to ± 2 mv. Coupling times were varied from 1 to 1000 sec and the potential was varied in 10 mv increments from -500 to -540 mv. The iron was recoupled to tin when the potential from a previous uncoupling reached -470 mv. This potential was not critical and was chosen for convenience only. The potential at the most noble value was determined as a function of polarizing potential and the current passing through the cell.

Plots of the maximum value reached after prior polarization to a known potential *vs.* the time of coupling were prepared and these plots were extrapolated to the time necessary to give the maximum value of -420 mv. The current flowing through the system was calculated from a knowledge of the potential difference between the electrodes and the external resistance. The extrapolated value was then used to calculate the amount of current required to establish the iron electrode in a condition whereby the most noble value (-420 mv) would have been obtained.

These results (Table II) indicate that the number of coulombs necessary to give the maximum uncoupling shift increases with a decrease in the polarizing potential. Extrapolation of these values on a semilogarithmic plot indicated that 0.0015 coulombs are required when the iron electrode is polarized to the tin potential by direct coupling of the two metals each exposing an equivalent surface area of 3.5 cm². This number of coulombs is

Table II.

Polarizing potential, mv	Time required to give maximum uncoupling shift (extrapolated), sec	Estimated coulombs required to give maximum uncoupling shift, coulombs
-540	85	0.0070
-530	170	0.014
-520	400	0.032
-510	1250	0.092
-500	2500	0.17

equivalent to 1.4×10^{15} atoms of tin per cm² assuming reduction from the divalent state. For reference purposes the number of atoms on the (100) face of iron is approximately 2×10^{15} per cm².

Polarization curves of iron in boiling 0.2M citric acid in the presence and absence of Sn(II).—Potential-current measurements were made on cylindrical iron electrodes which were each supported at the end of a Teflon electrode assembly. The current was measured with a microammeter and the potential was continuously recorded. Potential pickup was by means of a Luggin capillary.

The reproducibility of the polarization curves in separate experiments was poor but the relative position of the pairs of anodic and cathodic curves in the presence and absence of dissolved Sn(II) was always the same. In all cases, the estimated exchange currents differed by approximately two orders of magnitude, with the Sn(II)-containing solution always yielding the lower exchange current. These results are in accord with those of Kamm and Willey (2) who made polarization curve determinations in 0.1M citrate buffer at room temperature and found that the exchange current on steel was greatly decreased in the presence of 35 ppm dissolved tin. Extrapolation of their values leads to an estimate that the exchange current is decreased to 0.01 of its uninhibited value in the presence of tin. Koehler (3) also found that the exchange current of a steel electrode in citrate buffer containing 50 ppm dissolved tin at 37.8° was decreased to 0.01 of its former value after the steel had been in electrical contact with a tin electrode.

Corrosion potential of an iron-tin alloy.—Covert and Uhlig (4) prepared samples of FeSn₂ by immersing iron (99.95%), $\frac{3}{8} \times \frac{5}{8} \times \frac{1}{8}$ in., in molten tin at 488° for 7–9 days. The unalloyed iron and tin were removed by exposure to 50 volume per cent HNO₃. X-ray diffraction analysis indicated the presence of FeSn₂, Sn, and FeSn. It was estimated that the product contained 95% FeSn₂. The following corrosion potentials were determined in 0.1M citric acid saturated with hydrogen: FeSn₂ -0.516 v, Fe -0.539 v, Sn -0.606 v.

Luner and Murray (5) have prepared thin films of FeSn₂ by removal of both the tin and iron from tinplate using modified stripping techniques. The resulting thin film had a corrosion potential more noble than either iron or tin, namely -0.43 to -0.51 v. The most noble values were in the range of those obtained at the maximum of the uncoupling shift in 0.2M citric acid at the boiling point.

In the present study it was decided to determine the potential of an iron-tin alloy formed by diffus-

ing tin into iron at a temperature slightly above the melting point of tin. Iron samples were coated with very thin layers of tin by short cathodic treatment in citric acid solution containing very low concentrations of Sn(II). A tin-iron alloy of unknown composition was then formed by heat treatment in mineral oil at 250°-280°. In three separate experiments the potential of the tin-alloyed iron in boiling citric acid containing 10^{-3}M Sn(II) was -482, -462, and -477 mv. The potential remained approximately constant for a period and then slowly changed over a period of 16 hr to the steady-state value of -510 mv.

These results confirm those of Covert and Uhlig and of Luner and Murray in that they indicate that an iron-tin alloy has a potential in boiling citric acid containing dissolved tin appreciably more noble than that of either tin or iron in the same medium.

Reflection electron diffraction studies.—These studies were carried out with the assistance of Dr. Kenneth Lawless, Department of Chemistry, University of Virginia. The objective of these studies was to determine the composition of any film on the surface of iron after exposure to boiling citric acid containing Sn(II). Experiments were carried out on iron samples both with and without coupling to tin.

No diffraction patterns characteristic of elemental tin or of either FeSn or FeSn₂ were ever identified with certainty. The patterns generally consisted of elemental iron or of iron oxides. In a number of cases a pattern consisting of the following "d" spacings was observed: 3.12, 1.91, 1.63, 1.57, 1.35, 1.24, 1.10, and 1.04Å. A similar pattern has been observed by workers at the United States Steel Corporation laboratory (6) from a sample which had been prepared by stripping a matte tin coating with HCl at constant current in an inert atmosphere. They also were unable to identify the constituent giving rise to the pattern. The similarity of the pattern to that from silicon, aluminum phosphide, zinc sulfide, and cuprous chloride suggests that the unknown exists in the zinc blende or diamond structure with an a_0 spacing of approximately 5.41Å.

Electron microscope and electron diffraction studies of extraction replicas.—The surface of iron at various stages of the uncoupling shift was studied using a carbon extraction replica technique. Carbon was evaporated on the iron surface and extraction replicas were obtained by immersing the iron in 5-25% hydrochloric acid for short periods of time.

Figure 3 is a representative electron micrograph of an extraction replica removed from an iron sample which had been metallographically polished and exposed to boiling 0.2M citric acid containing 10^{-3}M Sn(II) for 30 min while coupled to a tin electrode of equal area. The dark areas (A) with apparent holes (B) represent the film which was extracted from the iron surface. The torn places, where the holes appear, are attributed to imperfect separation of the film from the iron surface. The presence of the carbon film in the (B) areas is indicated particularly at (C) where the polishing

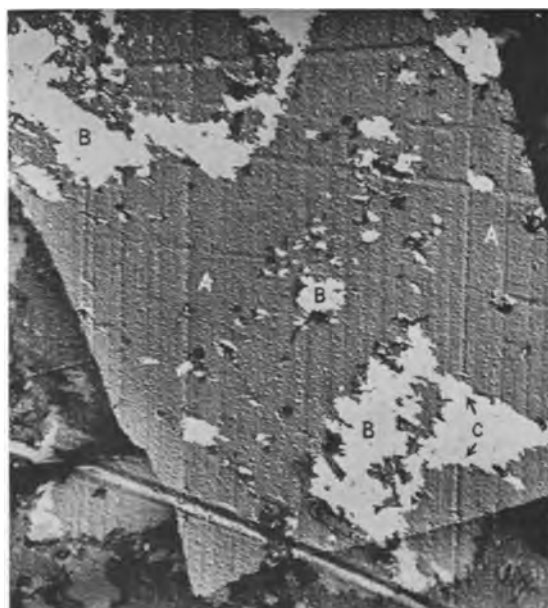


Fig. 3. Extraction replica of surface of an iron sample which had been coupled to tin for 30 min in boiling 0.2M citric acid containing 10^{-3}M Sn(II).

streak is visible in the apparent hole area. The small isolated islands of dark film adjacent to (C) are also indicative that the carbon film is present over the entire area of the photograph.

Extraction replicas of an iron surface which had been exposed to the boiling acid containing 10^{-3}M Sn(II) for 0-30 min after uncoupling indicated that a film was present on the iron surface during the entire period. Immediately prior to uncoupling, the film was relatively tough, solid, and of consistent structure. During the final stage it was very much thinner and the replica had a discontinuous, flimsy appearance. At intermediate stages the thickness of the film appeared to be between these two extremes.

Electron diffraction studies of the extraction replicas yielded an amorphous-like pattern, with a single scattering ring not observed with control samples. No crystalline diffraction pattern was observed.

Measurements using elliptically polarized light.—These experiments were carried out with the assistance of Dr. Jerome Kruger of the National Bureau of Standards. A commercial instrument manufactured by O. C. Rudolph and Sons was used. End points were determined by a photocell detector assembly. The 5461Å line of mercury and a 60° angle of incidence were used. In this instrument the incident radiation is elliptically polarized by passage through a polarizer and quarter-wave plate in such a manner that on reflection from the metal surface the light becomes plane polarized.

The iron samples used in these studies were mechanically polished through 4/0 emery paper and immediately before use were chemically polished. After polishing, the samples were freed of any major amount of surface film by dipping successively in 10% NaOH, 5% H₂SO₄, followed by thoroughly washing in distilled water. The samples were attached by means of a threaded rod to a Teflon holder which was rigidly mounted.

The following representative experiments indicate that any film which is formed at room temperature on iron in 0.2M citric acid containing dissolved Sn(II) is very thin:

(A) A sample was exposed to 0.2M citric acid containing 10^{-3} M Sn(II) for 24 hr. No precautions were taken in this experiment to remove dissolved air from the solution. The instrument readings indicated that no film thicker than 3Å formed on the surface during the time after the first reading was made, approximately 5 min after immersion.

A reference experiment was carried out using uninhibited 0.2M citric acid. The instrument readings indicated apparent film thicknesses of 10-100Å over a 20-hr period, but the sample was actively corroding as shown by the discoloration of the solution after 20 hr. The film thickness values do not have any significance here since the liquid film adjacent to the sample probably had a different refractive index than the bulk of the solution as a result of the corrosion process.

(B) Another experiment similar to (A) was carried out except that the solution was boiled to expel dissolved air and hydrogen, purified by passage through palladium, was bubbled through the solution during cooling and during the first 32 min during which ellipsometer measurements were made. The thickness of any film on the surface did not exceed 2Å during exposure to the solution for 18 hr.

In a second series of experiments, four samples of iron were exposed separately to boiling 0.2M citric acid containing 10^{-3} M (Sn)II for 7 days. The samples were removed from the solution and were then transported in a desiccator to Dr. Kruger's laboratory for the measurements. The measurements were made 5-7 hr after removal of the samples from the solution. Four additional samples were polished with MirroFe and were immediately placed on the stage of the ellipsometer for study. Thus, four samples representing the starting condition and four representing exposed samples were used. Table III gives an indication of the reproducibility of the results and the film thickness as represented by this experimental procedure.

The difference between the average polarizer readings of the two sets of samples, namely 1.4° , is equivalent to a film thickness of approximately 14Å.

In a third series of experiments, the samples which had been polished with MirroFe in the second series were immersed in boiling 0.2M citric acid containing 10^{-3} M Sn(II) for 6 days. The sam-

Table III.

Samples polished with MirroFe			Samples polished with MirroFe and then exposed to boiling inhibited citric acid for 7 days		
Sample No.	Avg polarizer reading	Avg analyzer reading	Sample No.	Avg polarizer reading	Avg analyzer reading
1	28.7°	143.2°	5	27.3°	143.2°
2	28.7°	142.5°	6	27.1°	142.6°
3	29.1°	143.4°	7	27.4°	142.5°
4	29.1°	142.4°	8	28.2°	142.6°
Average	28.9°	142.9°	Average	27.5°	142.6°

Table IV.

Sample No.	Samples polished with MirroFe		Samples polished with MirroFe and then exposed to boiling, inhibited citric acid for 6 days	
	Avg polarizer reading	Avg analyzer reading	Avg polarizer reading	Avg analyzer reading
1	28.7°	143.2°	27.4°	142.8°
2	28.7°	142.5°	27.6°	143.1°
3	29.1°	143.4°	27.4°	142.8°
4	29.1°	142.4°	27.4°	143.1°
Average	28.9°	142.9°	27.4°	143.0°

ples were removed from the solution and were then transported to Dr. Kruger's laboratory in Washington, D. C., for the measurements. As in the second series, the measurements were made 5-7 hr after removal of the samples from the solution. The results of these measurements are summarized in Table IV.

The difference between the average polarizer readings of the samples before and after immersion in the acid is 1.5° and is equivalent to a film thickness of approximately 15Å. Thus, the results of the second and third series of experiments were the same.

Radioactivity measurements with Sn¹¹³.—Measurements with Sn¹¹³ were made with the assistance of Mr. Emerson Newton and Dr. Robert Epple in the laboratories of Arthur D. Little, Inc.

Boiling citric acid solutions with an activity equivalent to 2.855 $\mu\text{C}/\text{ml}$ of Sn¹¹³ and a total Sn(II) concentration of 1.1×10^{-3} M added as the chloride, were used. The rate of pickup of tin by iron samples which had been metallographically polished was equivalent to 2×10^{-8} g/cm²-sec^{1/2}. This value should be compared with a value of 1×10^{-8} g/cm²-sec^{1/2} obtained by extrapolation of the data of Frankenthal and Loginow (7) to 100°. The rate of formation of tin on the surface of an iron sample coupled to tin in the boiling acid was approximately the same as the rate for an uncoupled sample, although there appeared to be a short induction period in the case of the coupled samples.

Some indication of the chemical state of the tin on the surface was obtained from electrolytic stripping studies using a standard method for stripping tin from iron. The stripping procedure removes elemental tin but not tin present as FeSn₂. An iron sample was coupled to tin for 60 min in the boiling acid containing dissolved Sn(II). The activity of the iron after this time was 17,000 counts/cm²/min equivalent to 3 monolayers of elemental tin. After electrolytic stripping in 5% NaOH for 5 min at a current density of 1 amp/dm², the count was reduced to 8800 counts/cm²/min, equivalent to approximately 2 monolayers of tin. An additional 5-min electrolytic treatment in the NaOH reduced the count further to 7500 counts/cm²/min. These results are taken to mean that approximately half the tin which had been picked up during the coupling existed in the form of an iron-tin alloy, not readily removed by electrolytic treatment.

Discussion

It has been amply demonstrated previously (8) that tin ions are very effective in inhibiting the corrosion of iron in boiling 0.2M citric acid. The electron microscope studies furnished confirming evidence for this conclusion reached previously on the basis of optical microscope and gravimetric measurements.

The electron microscope, electron diffraction, elliptically polarized light, and radioactivity measurements all indicated that any tin species on the surface is present in low amount. The radioactivity measurements, in fact, indicated that the rate of pickup of tin by uncoupled iron during the first few hours in boiling citric acid containing 10^{-3} M Sn(II) is approximately 2×10^{-8} g/cm²-sec^{1/2} which is equivalent to approximately 0.1 atom layer/cm² sec^{1/2}. If this value is assumed to be constant over a period of one week, it may be estimated that a film equivalent to 78 atom layers of tin would be formed. The measurements using elliptically polarized light, however, indicated that the thickness of the film after one week was only 14Å, equivalent to approximately 5 atom layers of tin. The order of magnitude difference between these values is considered good agreement in view of the extrapolation of the short-time radioactivity measurements to long times and of the fact that there may be an equilibrium film thickness at which point the rate of formation is equivalent to the rate of dissolution. One of the most important questions raised by this research is "what is the nature of the species on the surface which affords such excellent corrosion resistance to iron in boiling citric acid containing dissolved tin?" The corrosion inhibition is so great that the iron surface may be considered inert. No unequivocal answer can be given to this question, but the following available evidence supports the view that the protective film is FeSn₂.

1. The rate of pickup of tin by iron (2×10^{-8} g/cm²-sec^{1/2}) as determined by the radioactivity measurements is not greatly different from the extrapolated value of Frankenthal and Loginow (7) for the rate of formation of FeSn₂ when iron and tin are in contact (1×10^{-8} g/cm²-sec^{1/2}).

2. The potential of iron at the most noble value (−420 to −450 mv) in the uncoupling shift is approximately the same as the corrosion potential of FeSn₂ as determined by Luner and Murray (5) on a film of FeSn₂ stripped from an iron surface.

3. Intermetallic compounds have been found on the surface of gold (9), antimony, copper, silver, and palladium, when these metals were in electrical contact with tin in boiling 2M HCl solutions containing dissolved tin. The rate of formation of the intermetallic compounds varied greatly.

Hypothesis for the uncoupling shift.—When iron is exposed to boiling 0.2M citric acid containing a concentration of Sn(II) of 10^{-5} M or more, it is suggested that the compound FeSn₂ is formed on the iron surface by the reaction, $\text{Fe} + 2 \text{Sn}^{++} + 4e^- \rightarrow \text{FeSn}_2$. This compound has a very low activity in the boiling acid as shown by the fact that it cannot be stripped from a tin-plated surface by treat-

ment with citric or hydrochloric acids. When iron is brought into electrical contact with tin under the same experimental conditions, the potential of the iron approaches that of elemental tin. Under these conditions a small amount of elemental tin, of the order of a monolayer, is also formed. The current measurements concerned with the uncoupling shift indicated that a number of coulombs equivalent to less than a monolayer of tin was sufficient to give the maximum value of the uncoupling shift. A small proportion of this tin may react with the iron to form additional FeSn₂, but the majority of it is presumed to remain on the surface as elemental tin.

When electrical contact between the iron and tin is broken, the small amount of elemental tin on the surface goes into solution and the FeSn₂ layer is exposed. It is assumed that the anodic reaction during this phase of the uncoupling shift is $\text{Sn} - 2e^- \rightarrow \text{Sn}^{++}$ and the cathodic reaction is $2\text{H}^+ + 2e^- \rightarrow \text{H}_2$. As the surface area of tin exposed is decreased by dissolution, the anodic curve moves to the left with the consequence that its intersection with the cathodic curve is at more noble values and the potential moves in a noble direction until it reaches the most noble value, at which point essentially all of the elemental tin has been dissolved. It has been shown earlier (8) that the rate of corrosion of tin in boiling 0.2M citric acid is 0.018 mg/cm²/hr, which value is equivalent to slightly more than a monolayer of tin per minute. In the majority of the experiments, the uncoupling maximum was reached in 30-120 sec, very close to the time expected if the shift to the maximum value was a consequence of the dissolution of a monolayer of tin.

At the most noble value, a small amount of the FeSn₂ dissolves, thus exposing elemental iron and increasing the area on which the anodic reaction, $\text{Fe} - 2e^- \rightarrow \text{Fe}^{++}$, occurs. The anodic area increases until the potential reaches its steady-state value where the steady-state area of elemental iron is exposed. Several electrode reactions presumably take place under these conditions. It is suggested that the predominant reactions involve the dissolution of iron and tin and the predominant cathodic reactions involve the evolution of hydrogen and the formation of FeSn₂. The over-all electrode reactions take place at such a low rate that it would be difficult to determine the reactions experimentally.

The lack of an uncoupling shift with type-L steel and the failure of the potential to reach the most noble value in the case of the Armco and Puron samples are attributed to the presence in these samples of impurities. These impurities exert their influence immediately after uncoupling by increasing the rate of the hydrogen evolution reaction. Since the dissolution of tin is under cathodic control, the impurities have the net effect of reducing the time after uncoupling before the steady-state value is reached.

Acknowledgment

Appreciation is expressed to the United States Steel Corporation for their support of this research.

The assistance of Dr. Jerome Kruger, Mr. Emerson Newton, Dr. Robert Epple, and Dr. Kenneth Lawless in carrying out some of the experimental work is gratefully acknowledged.

Manuscript received Feb. 18, 1963; revised manuscript received Sept. 23, 1963. This paper was presented at the Houston Meeting, Oct. 9-13, 1960.

Any discussion of this paper will appear in a Discussion Section to be published in the December 1964 JOURNAL.

REFERENCES

1. E. L. Koehler, *This Journal*, **103**, 486 (1956).

2. G. G. Kamm and A. R. Willey, *Corrosion*, **17**, 77t (1961).
3. E. L. Koehler, *ibid.*, **17**, 93t (1961).
4. R. A. Covert and H. H. Uhlig, *This Journal*, **104**, 537 (1957).
5. C. Luner and M. V. Murray, *ibid.*, **110**, 176 (1963).
6. M. W. Lightner, Private communication, Feb. 1, 1960.
7. R. P. Frankenthal and A. N. Loginow, *This Journal*, **107**, 920 (1960).
8. W. R. Buck, III, and H. Leidheiser, Jr., *ibid.*, **108**, 203 (1961).
9. T. G. Carver and H. Leidheiser, Jr., *ibid.*, **109**, 68 (1962).

Kinetics of Redox Reactions on Passive Electrodes

A. C. Makrides

Tyco Laboratories, Inc., Waltham, Massachusetts

ABSTRACT

Overpotential measurements for the $\text{Fe}^{+++}/\text{Fe}^{++}$ couple on passive Ni, Fe, and Ti, were carried out in solutions of fixed ionic strength but of varying pH. Tafel lines were generally obtained with exchange currents between 10^{-7} and 10^{-5} amp/cm² and cathodic transfer coefficients of about 0.45. The anodic transfer coefficients were less, particularly with Ti and Fe electrodes. A limiting anodic current, which was unrelated to diffusion of Fe^{++} ion in solution, was observed under certain conditions on Fe and Ti. The contribution of ionic current to the total current through the film is negligible in most cases. In general, the passive film has rectifying properties, the easy direction of electron flow being from metal to solution. This rectification is additional to the usual Faradaic rectification observed with most electrochemical reactions. The apparent transfer coefficients, calculated from the anodic and cathodic polarization curves, yield sums significantly less than unity. The results demonstrate the existence of a potential drop across the passive film, the magnitude of which depends on the thickness and composition of the film.

The formation of a surface oxide is an important factor in the kinetics of oxygen evolution and oxygen reduction on practically all metallic electrodes (1). In general, a superficial oxide is expected to change the specific interaction of oxygen (or of reaction intermediates) with the electrode, to alter the potential distribution between metal and electrolyte, and to modify the dissolution kinetics of the metal. The change in the kinetics of dissolution has been studied in detail, since it is the characteristic phenomenon in passivity (2-6). However, relatively little work has been done on the effects of oxide films on electrochemical reactions other than corrosion reactions. The general features of electrode processes on superficially oxidized metals are examined in this paper using as a model a simple, one-electron redox reaction.

Aside from specific effects, *e.g.*, changes in the energy of adsorption of reactants or of intermediates, superficial oxides may influence the kinetics of an electrochemical reaction by providing a barrier to electron transfer between the metal and an ion or molecule at the oxide/electrolyte interface. With thick films, the oxide is the electrode, the underlying metal serving merely as a contact. The chemical character of the bulk oxide and its electrical properties, *e.g.*, its semiconducting properties, enter then into the description of its electrode characteristics. At the other extreme, very thin oxide films may be

considered as simply providing a barrier through which electrons must tunnel in order to participate in the reaction. The upper limit for tunneling is about 30Å; conduction through the oxide is necessary for electron transfer with thicker films. However, if the film is only 100-200Å, its electrical characteristics are influenced strongly by the underlying metal, and this interaction may be important in the description of the electrode behavior of superficially oxidized electrodes.

A simple way of examining the general electrochemical effects of surface oxides is to compare the kinetics of an elementary electron transfer reaction on oxide-covered and oxide-free electrodes. Specific effects, *e.g.*, adsorption, should be at a minimum for the redox couple chosen. The $\text{Fe}^{+++}/\text{Fe}^{++}$ couple was selected in this study because its kinetic behavior on oxide-free electrodes is straightforward (7, 8). Furthermore, since its reversible potential falls in about the middle of the potential region over which a number of common metals and alloys are passive, both the oxidation of ferrous ion and the reduction of ferric ion can be followed without gross interference from corrosion reactions.

Experimental

The electrochemical cell was described previously (9). Potentials were measured through a Luggin-Haber capillary probe 0.05 cm OD placed 0.10 cm

from the electrode surface. The iR drop between electrode and capillary probe was negligible at all currents. A high impedance circuit (residual current less than 10^{-12} amp) was used in measuring potentials. Constant current was drawn from high capacity batteries through variable resistances. The cell was thermostated to within $\pm 0.05^\circ\text{C}$.

The cell and its attachments were cleaned in concentrated chromic + sulfuric acid solution (cleaning solution). Ground-glass joints were of the cup type and were sealed with water. The solution around the electrode was stirred with argon which had been passed over copper at 500°C and through a cold trap (dry ice-acetone). Laboratory distilled water was distilled from dilute KMnO_4 into a two-stage, quartz still and from there into quartz storage flasks. Reagents were of C.P. grade. A series of experiments with twice-recrystallized ferrous and ferric salts showed no significant differences from experiments with C. P. reagents.

Electrodes were rods or spheres of about 1 cm^2 in projected area and were mounted on assemblies in which only glass and Teflon, besides the electrode, came in contact with solution (10). The electrodes were cleaned in cleaning solution followed by rinsing with boiling, triply distilled water. The passive film was formed in the solution after cathodic treatment of the electrode. Nickel and titanium passivated spontaneously in the ferric solutions. Electrolyte compositions are given in the tables and figures.

Exploratory studies showed that the current densities at which appreciable polarization is observed with all of the above electrodes (when passive) were substantially less than the expected diffusion-limited currents for both Fe^{+++} and Fe^{++} ions. An estimate of the diffusion-limited current density, i_d , can be made from

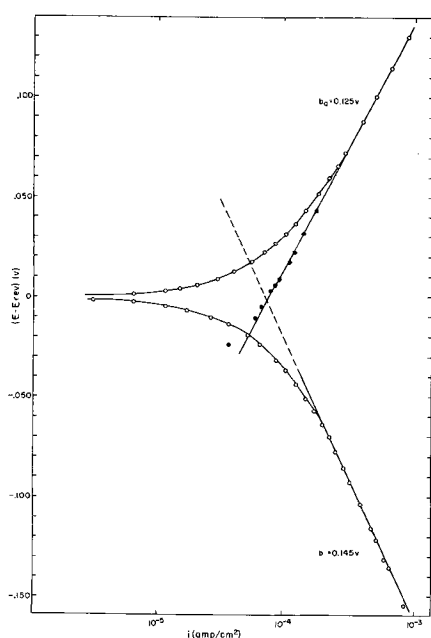


Fig. 1. Polarization curves for the $\text{Fe}^{+++}/\text{Fe}^{++}$ couple (0.05M) on Ni electrodes in M MgSO_4 at $\text{pH} = 2.3$ and at 30°C . Current densities corresponding to the full circles are calculated from $i_{\text{ox}} = i_{\text{appl}} + i_{\text{red}}$ where i_{red} is given by the extrapolated cathodic curve.

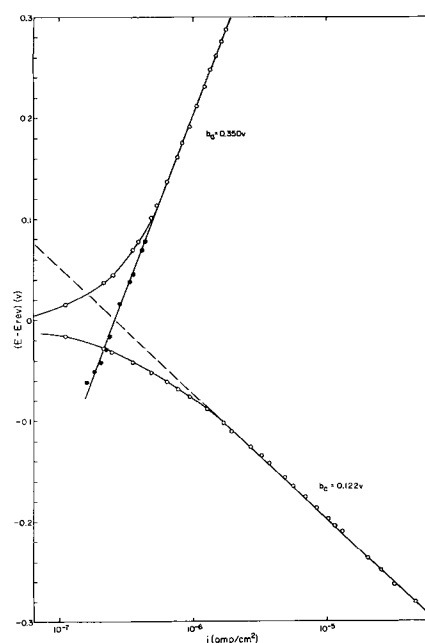


Fig. 2. Polarization curves for the $\text{Fe}^{+++}/\text{Fe}^{++}$ couple (0.05M) on Ti electrodes in M MgSO_4 at $\text{pH} = 2.3$ and at 20°C . Current densities corresponding to the full circles are calculated from $i_{\text{ox}} = i_{\text{appl}} + i_{\text{red}}$ where i_{red} is given by the extrapolated cathodic curve.

$$i_d = nFkc = nF \frac{D}{\delta} c \quad [1]$$

where the heterogeneous rate constant, k , is given by the ratio of the diffusion constant, D , to the effective thickness, δ , of the boundary layer for diffusion. Although neither D nor δ are known precisely, good estimates for both quantities are available. A conservative estimate of D is $5 \times 10^{-6} \text{ cm}^2/\text{sec}$ (11); δ is about $5 \times 10^{-3} \text{ cm}$ for stirring by gas (12). The diffusion rate constant is then $1 \times 10^{-3} \text{ cm}/\text{sec}$ and the diffusion-limited current at $c=0.05 \text{ M/liter}$ is $5.10^{-3} \text{ amp}/\text{cm}^2$. The maximum applied current density was substantially less than this, except in the case of nickel. With other than nickel electrodes, direct proof of the absence of concentration polarization was provided by the insensitivity of the measured potential to stirring. On nickel electrodes there was a difference of about 15 mv between the potential measured in stagnant and in stirred solutions at a current density of $10^{-3} \text{ amp}/\text{cm}^2$. We estimate the concentration overpotential in stirred solutions at $10^{-3} \text{ amp}/\text{cm}^2$ to be less than 5 mv.

Discussion

The overpotential parameters derived from the polarization curves of Fig. 1-3 are given in Table I.

Table I. Overpotential parameters for the $\text{Fe}^{+++}/\text{Fe}^{++}$ couple $C_{\text{Fe}^{+++}} = C_{\text{Fe}^{++}} = 0.05\text{M}$

Electrode	H_2SO_4	T, $^\circ\text{C}$	i_0 , amp/cm 2	α_c	α_a	$\alpha_c + \alpha_a$
Ni	M/100 ^a	30	7.5×10^{-5}	0.41	0.49	0.90
Fe	M/20 ^b	40	(1×10^{-5})	0.69	(0.23)	(0.92)
Ti	M/20 ^a	20	2.6×10^{-7}	0.47 ₅	0.16 ₅	0.64
Pt ^c	M	25	1.5×10^{-2}	0.42	0.58	1.00

^a Solution M in MgSO_4 .

^b Solution M/10 in Na_2SO_4 .

^c Results of Gerischer, ref. (7).

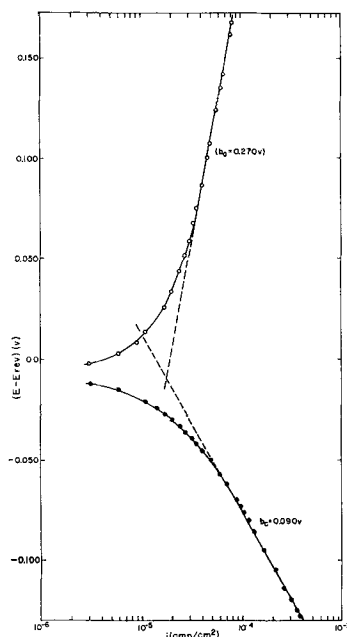


Fig. 3. Polarization curves for the $\text{Fe}^{+++}/\text{Fe}^{++}$ couple on Fe electrodes at 40°C . The solution was 0.30M in Fe^{+++} , 0.03M in Fe^{++} , and $\text{M}/20$ in H_2SO_4 and $\text{M}/10$ in Na_2SO_4 . The anodic curve was obtained after the electrode was kept for 30 min at 0.20v vs. E_{rev} for $\text{Fe}^{+++}/\text{Fe}^{++}$.

Noteworthy features are the low exchange currents, the unusual values of the transfer coefficients, and the pronounced asymmetry of the anodic and cathodic reactions on iron and titanium. These characteristics may be contrasted with results on Pt electrodes in $\text{M H}_2\text{SO}_4$ (7). The exchange current on Pt with $C_{\text{Fe}^{+++}} = C_{\text{Fe}^{++}} = 0.05 \text{ M/liter}$ is $1.5 \times 10^{-2} \text{ amp/cm}^2$; the anodic transfer coefficient is 0.58 ± 0.02 and the cathodic transfer coefficient 0.42 ± 0.02 (7). It should be noted that experiments in $\text{M H}_2\text{SO}_4$ without salt show that MgSO_4 , the inert electrolyte used for keeping the composition of the double layer essentially constant, does not participate in the reaction nor does it have any major effect on the kinetics.

Previous work with redox reactions on superficially oxidized electrodes has been concerned mainly with the kinetics of redox reactions on stainless steel (13-15) where redox couples can be used to inhibit dissolution. Redox reactions on passive stainless steel have been discussed in a conventional way (14), although they exhibit features similar to those noted here, *i.e.*, extremely small exchange currents and unusual values of transfer coefficients with sums generally less than unity (13).

Meyer (16) studied a number of cathodic reactions on anodically oxidized zirconium electrodes. He showed that the unusual transfer coefficients and reaction orders which he observed can arise from a dual energy barrier and suggested a model in which the reaction rate depends both on the potential drop across the oxide and across the electrolytic double layer. The present results also suggest that a significant potential drop exists across the surface oxide and that it is important in determining the over-all reaction rate. However, the dual barrier model as formulated originally (16) does not entirely fit the

present results. It is assumed in this model that two potential dependent processes occur, one corresponding to a film reaction and the other to a double layer reaction. Their rates are given by

$$i_c = i_{o,f} \exp(-\alpha_f V_f) \quad [2a]$$

and

$$i_c = i_{o,e} \exp(-\alpha_r V_r) \quad [2b]$$

where the potentials are in units of RT/F , and where

$$E = V_f + V_r \quad [3]$$

The apparent cathodic transfer coefficient is

$$\alpha_c = \left(\frac{\partial \ln i_c}{\partial E} \right)_T = - \frac{\alpha_f \alpha_r}{\alpha_f + \alpha_r} \quad [4]$$

Similarly, the apparent anodic transfer coefficient is

$$\alpha_a = \left(\frac{\partial \ln i_a}{\partial E} \right)_T = \frac{\beta_f \beta_r}{\beta_f + \beta_r} \quad [5]$$

where

$$\alpha_f + \beta_f = 1 \quad \text{and} \quad \alpha_r + \beta_r = 1 \quad [6]$$

From Eq. [4-6] and the experimentally determined anodic and cathodic apparent transfer coefficients we can calculate α_f and α_r (or β_f and β_r). The values so calculated are not reasonable. This can be demonstrated easily if we assume $\alpha_r = \beta_r \approx 0.5$. If then $\alpha_f \approx 0.5$, the apparent anodic and cathodic coefficients should be ~ 0.25 with a sum of 0.5. These values do not correspond with what is observed generally. If, on the other hand, we choose α_f so as to make the apparent cathodic coefficient reasonably close to what is observed, then the anodic coefficient calculated from Eq. [6] is unreasonable. For example, assuming again $\alpha_r = \beta_r \approx 0.5$ and taking $\alpha_f = 0.90$, the apparent cathodic coefficient, $\alpha_c = 0.32$, is not far from what is found on most electrodes. However, the calculated apparent anodic transfer coefficient is now only 0.08, which is substantially less than observed. In general, fractional values of α_f and β_f do not lead to the experimentally observed apparent transfer coefficients assuming for α_r and β_r either 0.5, or the values found on Pt.

The redox reaction.—In interpreting the results presented here, we note that all molecular processes for the $\text{Fe}^{+++}/\text{Fe}^{++}$ reaction occur on the aqueous side of the interface and that the electrode serves only as a reservoir of electrons at a fixed electrochemical potential. We expect in a first approximation that the exchange current and the transfer coefficients on oxide-free, inert electrodes, *e.g.*, Pt or Hg, are characteristic of the couple (17-19). If the surface layer on oxidized electrodes modifies electron transfer between electrode and solution in a major way, substantial changes in the redox kinetics may occur. It is assumed in the following discussion that the redox reaction proper occurs in a normal fashion and that differences of characteristic kinetic parameters between passive and metallic electrodes are due to the electron transfer process through the superficial film.

The fundamental concepts of electron exchange between a metal and a redox couple in solution developed by Gurney (17) were recently reformulated

and extended to semiconductors by Gerischer (19). The basic postulate of the theory is that a weak electronic interaction occurs between the ion and the electrode (18); consequently, electron exchange is adiabatic, *i.e.*, it occurs between the same energy levels in the two phases. Gerischer (19) introduced the concept of electron energy states in a redox electrolyte in analogy to the notion of energy levels in a solid. For example, the energy of unoccupied states is defined by the energy change accompanying the introduction of an electron from infinity to the lowest state of an oxidized ion without changing its solvation structure. It can be shown that the equilibrium distribution of available energy levels follows a Fermi distribution function where the "Fermi" level of the electrolyte is directly related to the mean free energy change accompanying the redox reaction.

The current flowing from electrode to electrolyte is given by (19)

$$i_c = e_0 \int_{-\infty}^{+\infty} P(\epsilon) \cdot D_{el}(\epsilon) \cdot f(\epsilon - \epsilon_{f,el}) \cdot D_{redox}(\epsilon) \cdot f(\epsilon_{f,redox} - \epsilon) d\epsilon \quad [7]$$

Here, e_0 is the electronic charge, D_{el} and D_{redox} the density of states functions for the electrode and electrolyte, respectively, and $f(\epsilon - \epsilon_{f,el})$ and $f(\epsilon_{f,redox} - \epsilon)$ the Fermi distribution functions for the two phases. $P(\epsilon)$ is a proportionality factor which contains the frequency with which electrons arrive at the electrode/electrolyte boundary and the tunneling probability through the potential barrier between the two phases.

The exchange current, i_c at $\eta = 0$, can be drastically smaller for semiconductors than for metal electrodes, since the actual density of states near the Fermi level (where most of the exchange takes place on metal electrodes) may be very small for a semiconductor. Thus, a main result of the theory is that the exchange current on semiconductor electrodes may be smaller than on metals by orders of magnitude.

The small exchange currents found for the Fe^{+++}/Fe^{++} reaction on passive electrodes can be viewed as a consequence of a decrease of $P(\epsilon)$. This may be due either to a substantial decrease in the tunneling probability or to the semiconducting character of the superficial film. It is shown below that

the current changes by only a small factor (<10) when the film thickness changes by a factor of about 2. This rules out a rate limiting process involving electron tunneling across the oxide. It is probable that the small exchange currents (Table I) are a consequence of the semiconductor characteristics of the passive film.

Rectification.—For most redox reactions, the i - E characteristics are not entirely symmetrical on anodic and cathodic polarization, the effect being described as Faradaic rectification. The rectification ratio is small generally; for example, the Fe^{+++}/Fe^{++} reaction on Pt exhibits anodic and cathodic transfer coefficients of 0.58 and 0.42 (Table II), so that the corresponding currents at $\eta = 100$ mv are in the ratio of 1/0.55. A considerably more pronounced rectification in the opposite direction is observed with passive electrodes (*e.g.*, Fe and Ti, Table II). In general, the transfer coefficient for Fe^{+++} reduction on passive electrodes is close to the value found on platinum; however, the anodic transfer coefficients are invariably smaller, frequently by a substantial amount.

Rectification by anodically formed surface oxides is well-known for valve metals (Ta, Zr, etc.) (20-23). The direction of easy electron flow is from metal to electrolyte and the magnitude of the current depends in a complicated way on the conditions of formation of the oxide and on surface preparation. In general, the current can be increased by cathodic "deformation" but is restored to its previous value by subsequent anodic polarization (23).

A number of possible mechanisms for rectification by anodic oxide films have been advanced (21-25). Vermilyea (25) demonstrated the existence of weak spots in oxide films on valve metals and showed that most of the cathode current flows through these imperfections. Although rectification was attributed to areas of defective oxide, no mechanism for the rectifying properties, as contrasted to its higher conductivity, was suggested for the defective oxide (25). The most likely explanation of rectification, which applies either to the film as a whole, or to weak or thin spots in the film, is that due to van Geel who postulates a p-n junction within the oxide (23, 24).

The rectification observed with passive films is similar in some respects to that observed with oxides on valve metals. However, the thinness of the passive

Table II. Nickel^a

pH	T, °C	E_{corr} , V	i_0 extrapolated from cathodic curve, amp/cm ²	i_0 from $\left(\frac{\partial i}{\partial E}\right)_{(E-E_{rev})=0}$ (i_0) _c	(i_0) _a	α_c	α_a	$\alpha_c + \alpha_a$
2.3	10	-0.0003	2.6×10^{-5}	2.5×10^{-5}	2.5×10^{-5}	0.415	0.484	0.90
	20	-0.0006	4.55×10^{-5}	4.4×10^{-5}	4.4×10^{-5}	0.40	0.495	0.90
	20	-0.0012	7.6×10^{-5}	7.45×10^{-5}	7.15×10^{-5}	0.41	0.49	0.90
0.35	30	-0.0006	8.6×10^{-5}	8.6×10^{-5}	7.5×10^{-5}	0.46	(0.60) (0.375)	—
0.00	0	-0.0003	5.0×10^{-5}	—	—	0.47	—	—
	10	-0.0008	8.0×10^{-5}	—	—	0.47	—	—
	20	-0.0005	$11. \times 10^{-5}$	10.2×10^{-5}	8.0×10^{-5}	0.47	—	—
	30	-0.001	$14. \times 10^{-5}$	12.8×10^{-5}	7.0×10^{-5}	0.47	(0.33)	—

^a All solutions $C_{Fe^{+++}} = C_{Fe^{++}} = 0.050M$ and M $MgSO_4$.

film makes it unlikely that the continuum description implied by the term "semiconductor" is applicable. It is preferable to adopt a chemical approach to the description of the electrical characteristics of the film, as was done by Vetter (26) and more recently by Nagyama and Cohen (27). The latter authors suggest that the passive film in the case of Fe consists of an inner layer approaching Fe_3O_4 and an outer layer of " $\gamma\text{-Fe}_2\text{O}_3$ " with a defect structure of the form $\text{Fe}_{x+6}\text{Fe}_{2-2x+3}\square_x\text{O}_3$. Although a film of this sort may be described as a "semiconductor," it could not possibly support a fully developed space-charge region similar to that which gives rise to the rectifying properties of semiconductor junctions.

Rectification by passive electrodes is probably caused by the distribution of the total potential drop from metal to solution between the film and the oxide/electrolyte interface. The potential drop across the passive film appears to be a constant fraction of the total applied potential. Therefore, the overpotential for oxidation of Fe^{++} is $(1-\gamma)\eta$, and the apparent transfer coefficient for the anodic reaction is $(1-\gamma)\beta_r$, where γ is the fraction of the total potential which is across the film. This argument is developed in more detail in a subsequent communication dealing with the kinetics of the $\text{Fe}^{+++}/\text{Fe}^{++}$ reaction on passive Fe-Cr alloys.

Ionic and electron currents.—Both an ionic current and an electronic current may flow through a passive electrode at any potential. The steady-state ionic current, which may be observed in the absence of the redox couple, is generally a small fraction of the total current plotted in Fig. 1-3. For example, the steady-state corrosion current (equivalent to the ionic current) for Ti is less than 10^{-7} amp/cm² and is independent of the potential in the passive region. The total current with a redox couple in solution depends, of course, on the potential and can be as much as 10^{-3} amp/cm². In the discussion above it was assumed that all the current which flows when a redox couple is added to the solution is electronic.

Although the ionic process does not contribute significantly to the observed current (however, see the case of Fe below), it may still have a substantial effect on the total i - E characteristics either because of changes in film thickness with potential or because of changes in film composition, particularly on anodic polarization. The commonly accepted account of the kinetics of growth and of dissolution of passive films is due to Vetter (26). Oxide growth is assumed to be by field-assisted migration of cations through the film. Contrary to the case of oxides on valve metals, the passive film dissolves in common electrolytes by a purely chemical reaction with a rate independent of potential. In the steady state, the rate of film growth equals its dissolution rate at some (stationary) oxide thickness. If the potential is changed to a more positive value, oxide formation is initially faster than dissolution but as the film grows, the field across it is reduced until the formation and dissolution rates again balance each other. This mechanism accounts for the most notable characteristic of passive electrodes, namely, a steady-state,

anodic oxidation current which is independent of potential.

Consider an electrode on which the film has grown to its steady-state thickness at the potential corresponding to the reversible $\text{Fe}^{+++}/\text{Fe}^{++}$ couple. If the electrode is polarized anodically, an ionic and an electronic current flow across the film. The ionic current is originally larger than its steady-state value since the potential gradient across the film is increased. The ionic current decreases as the film thickens and approaches eventually its former value which is of the order of 10^{-7} amp/cm² for Ti and 10^{-6} amp/cm² for Ni. The oxide thickness must, therefore, increase continuously with potential on anodic polarization. On the other hand, the oxide thickens and approaches eventually its former value at the reversible potential on cathodic polarization if the dissolution rate is 10^{-6} amp/cm² or less, and if substantial electrochemical reduction of the film does not occur in the potential range in question. This can easily be seen when the dissolution rate is translated into film equivalents. At 10^{-6} amp/cm², about 15 min would be required to remove about 10 Å of film ($\sim 10^{-3}$ coulomb/cm²), or approximately a unit cell of oxide. Thus, it is probable that the film thickness on passive Ni or Ti does not change in the course of a cathodic run. However, if the dissolution rate is substantially higher (10^{-5} amp/cm²), as it is in the case of iron, significant changes in film thickness must occur during cathodic polarization also.

Nickel electrodes.—The $\text{Fe}^{+++}/\text{Fe}^{++}$ reaction on nickel electrodes was examined at various pH and temperatures. Since films of varying stationary thickness are produced at different pH, it is possible to observe changes (if any) in the redox kinetics with oxide thickness. Results are given in Table II and Fig. 4-6.

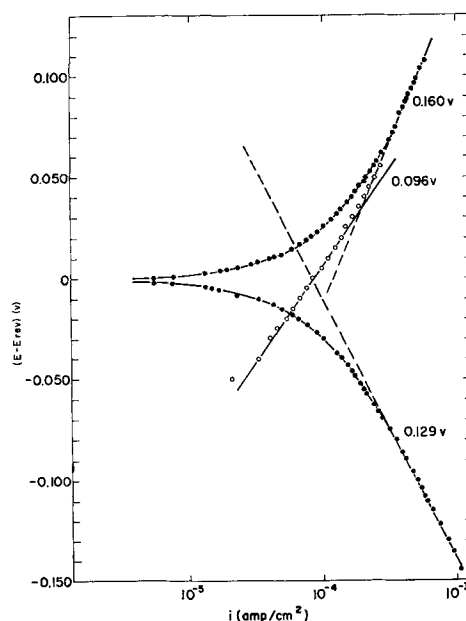


Fig. 4. Polarization curves for the $\text{Fe}^{+++}/\text{Fe}^{++}$ couple (0.05M) on Ni electrodes in M MgSO_4 at pH = 0.35 and at 30°C. Current densities corresponding to the open circles are calculated from $i_{\text{ox}} = i_{\text{appl}} + i_{\text{red}}$ where i_{red} is given by the extrapolated cathodic curve.

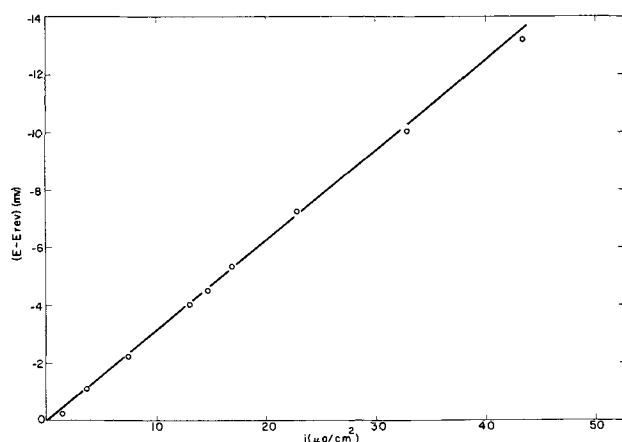


Fig. 5. Linear plots of $(E - E_{rev})$ vs. current density for the Fe^{+++}/Fe^{++} couple (0.05M) on Ni electrodes in M $MgSO_4$ at $pH = 0.35$ and at $30^\circ C$. The apparent stoichiometric number, determined from the cathodic polarization curve, is unity.

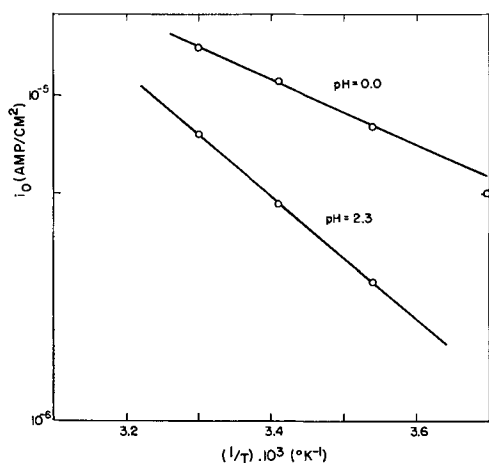


Fig. 6. Arrhenius plots for the Fe^{+++}/Fe^{++} couple (0.05M) on Ni electrodes in M $MgSO_4$. The exchange current, i_0 , is that extrapolated from the cathodic curve. The activation energies are 8.5 kcal at $pH = 2.3$ and 4.5 kcal at $pH = 0.0$.

The exchange current increases with decreasing pH and approximately doubles between pH of 2.3 and 0.0. The cathodic transfer coefficient increases from 0.41 to 0.47 over the same pH range. Therefore, the total cathodic current at any given overpotential increases by a factor of slightly greater than 2 in this acidity range.

Figure 4 shows that the anodic polarization curve changes in a substantial way when the pH decreases. The total anodic current at overpotentials between -0.050 and $+0.050$ v was calculated as before from the applied current and the extrapolated cathodic current (compare to Fig. 1). The anodic current can be approximated by two Tafel lines showing a transition from a low to a high Tafel slope at about $+0.05$ v. A similar change in the anodic kinetics is also observed at pH 0.00.

In interpreting the change in kinetics with pH , we note that the total potential drop between electrode and solution is given by

$$E = V + \psi_s + (\text{const}) \quad [8]$$

Here V is the potential drop across the oxide and ψ_s that across the oxide/electrolyte interface. In view of

the large excess of inert electrolyte we may assume in the first approximation that ψ_s does not change with pH . Therefore, for the same $C_{Fe^{+++}}$ and $C_{Fe^{++}}$ or, what is equivalent, at a fixed E_{rev} for the Fe^{+++}/Fe^{++} couple, we have the same V , independent of pH . Since the rate of dissolution increases with acidity, the stationary film thickness must be less in the more acid solutions.

The dissolution rate of passive Ni in 0.5M $SO_4^{=}$ is 10^{-7} amp/cm² at pH 3.1. Therefore, the direct contribution of ionic current to the total oxidation current is negligible even at low pH . That this is the case is shown by the fact that the rest potential of passive Ni in a Fe^{+++}/Fe^{++} solution is just the reversible Fe^{+++}/Fe^{++} potential.

The coincidence of the rest potential with the Fe^{+++}/Fe^{++} reversible potential makes it possible to obtain the stoichiometric number for the process from polarization measurements at small current densities. A plot of i vs. $(E - E_{rev})$ at small $(E - E_{rev})$ is shown in Fig. 5. The values of $(i_0)_c$ and $(i_0)_a$ given in Table II were obtained from the slope of such plots and the relation

$$\nu = \frac{F}{RT} i_0 \left/ \left(\frac{\partial i}{\partial E} \right)_{(E - E_{rev})=0} \right. \quad [9]$$

The stoichiometric number of a simple one-electron reaction, such as the Fe^{+++}/Fe^{++} reaction, must be unity. Therefore, Eq. [9] can be rewritten as

$$i_0 = \frac{RT}{F} \left(\frac{\partial i}{\partial E} \right)_{(E - E_{rev})=0} \quad [9a]$$

Consequently, the measurement of $\partial i/\partial E$ at small $(E - E_{rev})$ provides a check on the exchange currents found by extrapolation from large overpotentials. Specifically, comparison of i_0 determined in these two ways shows whether the potential-current relation is the same over the whole of the potential range examined or whether a change in film characteristics takes place as the potential is altered from its equilibrium value.

The results in Table II and Fig. 4 and 5 suggest that the reaction rate and apparent transfer coefficient depend on the thickness of the film and on the pH of the solution in which the film is formed. The increase of the exchange current at low pH is probably caused by changes in film composition which apparently affect its electrochemical characteristics. It has been suggested that protons migrate into surface oxides and are responsible for an increase in conductivity (29, 30). Since the concentration of protons in the film is probably decreased by the additional field imposed on anodic polarization, a more or less continuous increase in the anodic polarization characteristics at low pH is expected as the potential becomes more positive. This is borne out by the low $(i_0)_a$ values calculated from $\left(\frac{\partial i_a}{\partial E} \right)_{(E - E_{rev})=0}$ which indicate that the an-

odic current increases less rapidly at pH of 0.35 and 0.00 than is predicted from the usual expression for the net current at potentials close to equilibrium. The change in the energy of activation for reaction

(as calculated from the temperature coefficient of the exchange current, Fig. 6) from 8.5 kcal/mole at pH 2.3 to 4.5 kcal/mole at pH 0.00 also shows that the electrode characteristics are modified substantially by changes of pH.

Iron electrodes.—The passive film on iron is considerably less stable than on nickel. Consequently, high concentrations of ferric ion (0.3M) were necessary to maintain the electrode in the passive region. Even at this concentration, the rest potential was more active by 10-60 mv than the reversible $\text{Fe}^{+++}/\text{Fe}^{++}$ potential because of the relatively large corrosion current of passive iron.

The anodic polarization curve on iron electrodes shows hysteresis when overpotential measurements are made relatively rapidly. The time-dependence of the potential suggests that the contribution of the ionic current decreases with time at a fixed anodic current density. An anodic curve was obtained by first polarizing the electrode at $120 \mu\text{a}/\text{cm}^2$ until the potential became constant and then rapidly making measurements in decreasing order of current density. In this way, an approximately semilogarithmic polarization curve can be obtained. Measurements under these conditions are shown in Fig. 2.

The polarization curves on passive iron are strongly asymmetrical. The anodic process was examined in detail in M MgSO_4 at pH 1.45. The anodic current was held at each value until the potential became constant (~ 1 mv change in 5 min). This required from 10 to 100 min, depending on the current. Figure 7 shows that the anodic current reaches a limiting value which is proportional to the Fe^{++} concentration. This is not a diffusion-limited current. The estimated maximum diffusion currents at the various concentrations used are 10^{-3} to 10^{-2} amp/cm², i.e., at least two orders of magnitude greater than the observed limiting currents. Furthermore, comparison with Ni shows that appreciably larger anodic currents can be drawn in that case without any significant contribution from concentration polarization in solution (see Fig. 1).

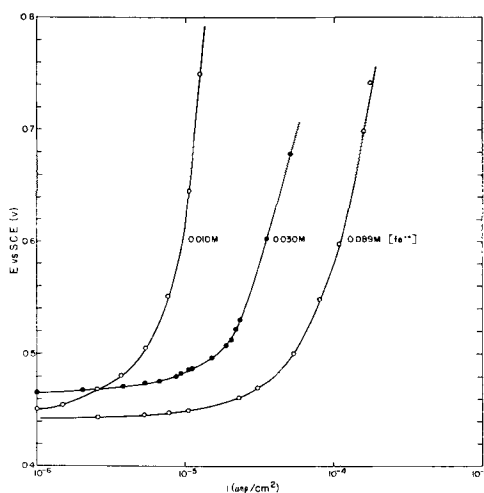


Fig. 7. Anodic polarization curves for the $\text{Fe}^{+++}/\text{Fe}^{++}$ couple on iron in M MgSO_4 at pH = 1.45. The Fe^{+++} concentration was 0.3M. The current was kept constant at each value shown until the potential changed by less than 1 mv in 5 min.

The i - E characteristics with passive Fe are analogous to those of a rectifying junction and may be described by an equation formally similar to that applicable to such a junction. Thus, assuming that the current from metal to solution is proportional to the (Fe^{+++}) concentration (as it is with other passive electrodes) we have for the net current in the anodic direction

$$i_a = k_1 C_{\text{Fe}^{++}} - k_2 C_{\text{Fe}^{+++}} \exp(-\alpha E)$$

or

$$i_a = k_1 C_{\text{Fe}^{++}} [1 - \exp(-\alpha E)] \quad [10]$$

where $k_1 C_{\text{Fe}^{++}} = k_2 C_{\text{Fe}^{+++}}$.

The results with passive Fe are not inconsistent with the general picture of passive films obtained from corrosion studies in the absence of a redox couple in solution (26, 27). For example, Vetter (26) has suggested a model for the passive film in which a potential drop of about 0.6v is assumed to exist within the oxide. A potential difference across the oxide with no current flowing presupposes a distribution of charge carriers similar to that suggested by the present results.

Titanium electrodes.—Titanium behaves similarly to Fe at temperatures of 30°C and above. Tafel lines are obtained at lower temperatures if the electrode is first anodized at the maximum current density used during a run. Curves similar to those of Fig. 3 are obtained at 0° and 10°C. Curves obtained at 30° and 40°C are shown in Fig. 8.

The time dependence of the potential (Fig. 9) suggests that the film thickens appreciably on anodic polarization at temperatures above 30°C. At lower temperatures, it is probably unchanged during a cathodic run; it may grow somewhat during an anodic run (see Fig. 9).

The temperature coefficient of the exchange current in the range in which the film thickness was approximately constant yields an energy of activa-

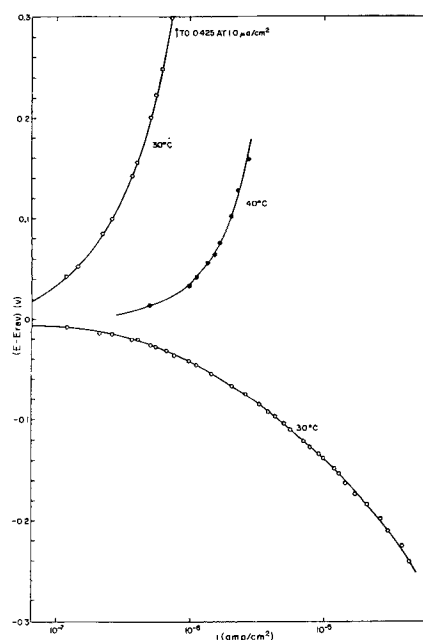


Fig. 8. Polarization curves for the $\text{Fe}^{+++}/\text{Fe}^{++}$ couple (0.05M) on Ti electrodes in M MgSO_4 at pH = 2.3.

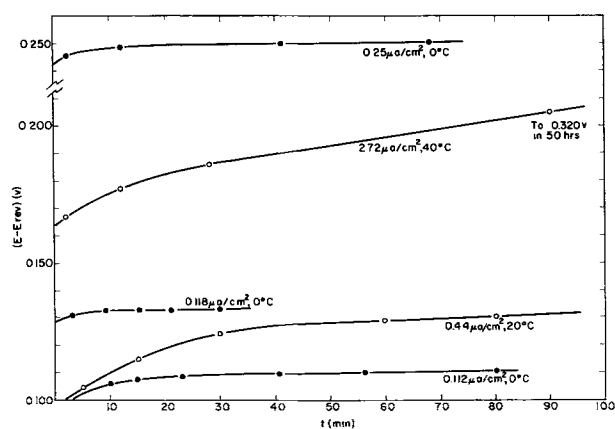


Fig. 9. Time dependence of the potential of Ti electrodes in a $\text{Fe}^{3+}/\text{Fe}^{2+}$ (0.05M) solution. M in MgSO_4 and of pH = 2.3. The applied anodic current densities are given in the figure together with the temperature for each measurement.

tion of about 15 kcal/mole. This is only an estimate, since the $\log i_0$ vs. $1/T$ plots are not straight lines even in this narrow temperature range.

Summary of polarization characteristics.—The polarization behavior of the $\text{Fe}^{3+}/\text{Fe}^{2+}$ couple on passive Ni, and Ti is given by an expression of the form (potentials in units of RT/F)

$$i = i_0 \{ \exp[-\alpha_r(E-E_{rev})] - \exp[\beta_r(E-E_{rev} - V)] \} \quad [11]$$

Here V is the potential drop within the oxide and is, in general, a function of the current density. The results suggest that V is proportional to E , i.e.

$$V = \gamma(E-E_{rev}) \quad [12]$$

In this case

$$i = i_0 \left\{ \exp[-\alpha_r(E-E_{rev})] - \frac{\exp[\beta_r(1-\gamma)(E-E_{rev})]}{\exp[\beta_r(1-\gamma)(E-E_{rev})]} \right\} \quad [13]$$

Consequently

$$\alpha_c + \alpha_a = (\alpha_r) + \beta_r(1-\gamma) = 1 - \gamma\beta_r \quad [14]$$

with an apparent stoichiometric number of

$$\nu = \pm i_0 \left/ \left(\frac{\partial i}{\partial E} \right)_{(E-E_{rev})=0} \right. = 1 - \gamma\beta_r \quad [15]$$

Equations [12-14] are followed by passive Ni at pH = 2.3 and by Ti at pH = 1.5 and for $T \leq 20^\circ\text{C}$. The coefficient γ is 0.15 for Ni and 0.60 for Ti. Fe, Ni at low pH, and Ti at higher temperatures show a more complicated behavior on anodic polarization.

Summary and Conclusions

1. Passive electrodes generally function as inert, indicator electrodes for the $\text{Fe}^{3+}/\text{Fe}^{2+}$ couple. The ionic current through the passive films of Ni and Ti is negligible compared to electron current. The ionic current is a significant fraction of the total current in the case of passive Fe. The rest potential of passive Fe is a mixed potential and is 10 to 60 mv more negative than the reversible $\text{Fe}^{3+}/\text{Fe}^{2+}$ potential at pH 1.45.

2. The electrode kinetics of the $\text{Fe}^{3+}/\text{Fe}^{2+}$ reaction on passive electrodes differ substantially from

those on oxide-free electrodes, e.g., Pt. The exchange current is substantially smaller on passive electrodes. The anodic transfer coefficient is about the same as on Pt. The sum of the apparent anodic and cathodic transfer coefficients on passive electrodes is significantly less than unity.

3. The i - E characteristics of the metal/passive film/redox electrolyte system are asymmetrical. The direction of easy electron flow is from metal to solution. A limiting anodic current, which is unrelated to diffusion of Fe^{2+} in solution, is observed on Fe and Ti in certain cases.

4. The polarization characteristics of the $\text{Fe}^{3+}/\text{Fe}^{2+}$ reaction on passive Ni, Fe, and Ti, specifically the unusual behavior summarized in 2 and 3, suggest that a potential drop exists within the oxide and that this potential is particularly important in anodic polarization. This conclusion is consistent with other studies of the growth and dissolution of passive films.

Acknowledgment

The author thanks Miss Mary Loud who assisted skillfully in the experimental part.

This work was supported by the Office of Naval Research under Contract Nonr-3765(00).

Manuscript received July 1, 1963; revised manuscript received Oct. 17, 1963.

Any discussion of this paper will appear in a Discussion Section to be published in the December 1964 JOURNAL.

REFERENCES

1. M. Breiter in "Advances in Electrochemistry and Electrochemical Engineering," vol. I, p. 123, John Wiley & Sons, New York (1961).
2. K. F. Bonhoeffer and K. J. Vetter, *Z. Phys. Chem.*, **196**, 127 (1951).
3. K. J. Vetter, *Z. Elektrochem.*, **58**, 230 (1954); **59**, 67 (1955).
4. U. F. Franck and K. G. Weil, *ibid.*, **56**, 814 (1952).
5. K. G. Weil, *ibid.*, **59**, 711 (1955).
6. Y. M. Kolotyrkin, *ibid.*, **62**, 664 (1958).
7. H. Gerischer, *ibid.*, **54**, 362 (1950).
8. J. E. B. Randles and K. W. Somerton, *Trans. Faraday Soc.*, **48**, 937 (1952).
9. A. C. Makrides, *This Journal*, **109**, 977 (1962).
10. M. Stern and A. C. Makrides, *ibid.*, **107**, 782 (1960).
11. C. V. King and L. Weidenhammer, *J. Am. Chem. Soc.*, **58**, 602 (1936); A. C. Makrides and N. Hackerman, *This Journal*, **105**, 156 (1958).
12. C. V. King, *This Journal*, **102**, 193 (1955).
13. M. Stern, *ibid.*, **104**, 559, 600 (1957).
14. F. A. Posey, *ibid.*, **106**, 582 (1959).
15. T. Ishikawa and G. Okamoto, First Inter. Congress Met. Corrosion 1961, p. 104, Butterworths, London.
16. R. E. Meyer, *This Journal*, **107**, 847 (1960).
17. R. W. Gurney, *Proc. Roy. Soc. (London)*, **A134**, 137 (1931).
18. R. A. Marcus, *J. Chem. Phys.*, **24**, 966 (1956); also in "Electrode Processes," p. 239, John Wiley & Sons, New York (1961).
19. H. Gerischer, *Z. Phys. Chem., N. F.*, **26**, 223, 325 (1960); **27**, 48 (1961).
20. A. Charlesby, *Acta Met.*, **1**, 348 (1953).
21. D. A. Vermilyea, *ibid.*, **2**, 346 (1954).
22. A. W. Smith, *Can. J. Phys.*, **35**, 1151 (1957).
23. W. Ch. van Geel and J. W. A. Scholte, *Philips Research Repts.*, **6**, 54 (1951); J. W. A. Scholte and W. Ch. van Geel, *ibid.*, **8**, 47 (1953).

24. H. E. Haring, *This Journal*, **99**, 30 (1952).
 25. D. A. Vermilyea, *J. Appl. Phys.*, **27**, 963 (1956).
 26. K. J. Vetter, *Z. Elektrochem.*, **62**, 642 (1958).
 27. M. Nagayama and M. Cohen, *This Journal*, **109**, 781 (1962).
 28. N. Sato and G. Okamoto, *Trans. Japan. Inst. Metals*, **2**, 113 (1961).
 29. P. F. Schmidt, *J. Appl. Phys.*, **28**, 278 (1957).
 30. P. D. Lukovtsev and G. J. Slaidin, *Acta Electrochim.*, **6**, 17 (1962).

Kinetics of the $\text{Fe}^{+++}/\text{Fe}^{++}$ Reaction on Fe-Cr Alloys

A. C. Makrides

Tyco Laboratories, Inc., Waltham, Massachusetts

ABSTRACT

The electrode kinetics of the $\text{Fe}^{+++}/\text{Fe}^{++}$ couple on passive Fe-Cr alloys were studied in acid solutions of constant ionic strength (M MgSO_4). Tafel behavior is generally observed with exchange currents of the order of 10^{-6} amp/cm² ($C_{\text{Fe}^{+++}} = C_{\text{Fe}^{++}} = 0.050\text{M}$), a cathodic transfer coefficient of 0.40, and an anodic transfer coefficient of 0.36. The electrochemical reaction order is unity both for oxidation of Fe^{++} and reduction of Fe^{+++} ; the heat of activation at the reversible potential is 10.8 kcal/mole. The results show that an appreciable fraction of the total potential drop on anodic polarization occurs within the passive film. This potential drop is probably associated with changes in the average oxidation state of cations between the inner and outer layers of the surface oxide. The electrochemical characteristics of the film depend on the pH of the solution, probably because of the migration of protons into the passive film. A change in the kinetics of Fe^{++} oxidation which occurs in the transpassive region of the Fe-Cr alloy is due to the production of Fe^{+3} or Cr^{+6} ions in the inner oxide layer.

The kinetics of the $\text{Fe}^{+++}/\text{Fe}^{++}$ couple on superficially oxidized electrodes present a number of interesting features (1-4). In general, the exchange currents are low ($\sim 10^{-6}$ amp/cm²), the transfer coefficients have unusual values and sums less than unity, and the anodic and cathodic curves are generally asymmetrical (1-4). These features appear to be basic to an electrode covered with a thin oxide (i.e., a passive electrode) and not to be related to the specific nature of the redox couple. They are probably connected with electronic processes within the surface oxide and are expected, therefore, to occur with any redox reaction taking place at such an electrode (4). In particular, they undoubtedly play a major role in oxygen evolution and reduction on electrodes which form surface oxides in the relevant potential region.

A study of the kinetics of the $\text{Fe}^{+++}/\text{Fe}^{++}$ reaction on passive Fe, Ni, and Ti electrodes was presented in a previous communication (4). This redox couple was chosen as a model reaction because its kinetics are straight-forward on oxide-free electrodes (5, 6) and because both oxidation of Fe^{++} and reduction of Fe^{+++} can be followed over a relatively wide potential range.

A detailed study of the redox kinetics of the $\text{Fe}^{+++}/\text{Fe}^{++}$ reaction on Fe-Cr alloys is presented here. These alloy electrodes, which show the same general features as other superficially oxidized electrodes, are convenient experimentally, since they have small dissolution rates in acid solutions. In addition to the usual experimental quantities required for a more or less complete characterization of a redox reaction (Tafel parameters, reaction order, pH dependence, and temperature coefficient), the dependence of the kinetics on the electrochemical

conditioning of the surface film (e.g., "deforming") was also determined.

Experimental

The electrolytic cell, measuring circuits, and experimental procedure were described previously (4, 7). Galvanostic measurements were generally employed. Under all experimental conditions, the diffusion-limited current for either Fe^{++} or Fe^{+++} was at least one order of magnitude greater than the applied current (4). Constant potential measurements were carried out with an electronic potentiostat similar to the one described by Gerischer and Staubach (8).

Fe-Cr alloys, prepared from electrolytic iron and electrolytic chromium, had as the main constituents 13.17% Cr, 0.008% C, 0.011% S, and the balance Fe. A limited amount of work was also done with a commercially available alloy (12.4 Cr, 0.44 Mn, 0.24 Ni, and 0.12% Cu).

The solution was M in MgSO_4 . The large excess of bivalent, inert electrolyte insured a constant composition of the electrolytic double layer even at the highest concentration of Fe^{+++} and Fe^{++} ions. Reagents were of C.P. grade.

In general, potentials were measured both against a platinized Pt electrode in the same solution with the working electrode and a SCE electrode. Fe-Cr electrodes are reversible to the $\text{Fe}^{+++}/\text{Fe}^{++}$ couple under most conditions as shown by their response to (Fe^{++}) or (Fe^{+++}) at fixed ionic strength (see, for example, Fig. 1). The reversible potential of the $\text{Fe}^{+++}/\text{Fe}^{++}$ couple is pH-dependent because of equilibria involving $\text{Fe}(\text{OH})^{++}$ and possibly $\text{Fe}(\text{OH})^+$ (9). The pH dependence of a platinized Pt electrode at a fixed (Fe^{+++})/(Fe^{++}) and fixed

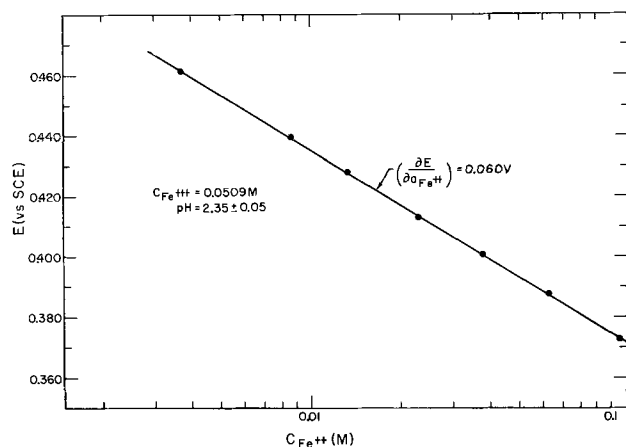


Fig. 1. Potential of passive Fe-Cr electrodes as a function of ferrous ion concentration at fixed ionic strength (M MgSO₄) and fixed ferric ion concentration and at 30°C.

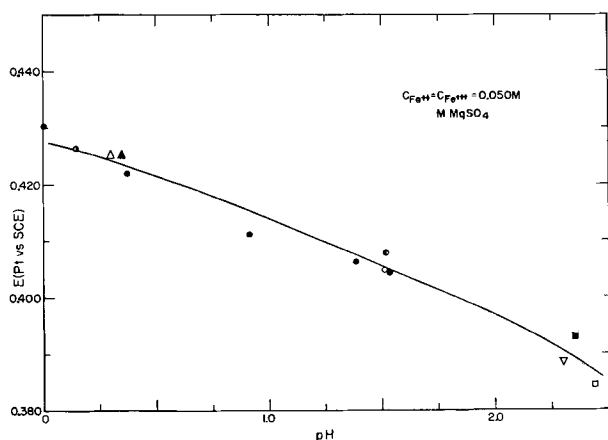


Fig. 2. Potential of platinized Pt at fixed $C_{Fe^{+++}}/C_{Fe^{++}}$ (0.05M) and fixed ionic strength (M MgSO₄) as a function of pH at 30°C.

ionic strength (M MgSO₄) is shown in Fig. 2. The potentials in Fig. 1 and 2 include an appreciable liquid junction potential, which is, however, constant and independent of the (Fe⁺⁺⁺) and (Fe⁺⁺) concentrations and of the pH.

The concentrations of (Fe⁺⁺) and (Fe⁺⁺⁺) were determined by titration with K₂Cr₂O₇ in the standard way using diphenylamine sodium sulfonate as the end-point indicator.

Results

Reproducibility.—Tafel curves were obtained for the Fe⁺⁺⁺/Fe⁺⁺ reaction on Fe-Cr electrodes as was the case with passive Fe, Ni, and Ti electrodes (4). Typical polarization curves for Fe-Cr are shown in Fig. 3. The anodic polarization curve was not semilogarithmic under certain conditions; its complicated behavior is described in detail below.

In general, the potential assumed a steady value within a short time after the current was set to a new value. Overshoot or undershoot, depending on whether the current was increasing or decreasing, was observed in certain potential ranges. These cases are discussed below.

The reproducibility of current-potential curves obtained with a given electrode over extended periods (~100 hr) is illustrated in Table I. The initial slow change, which comes to an end after about 24

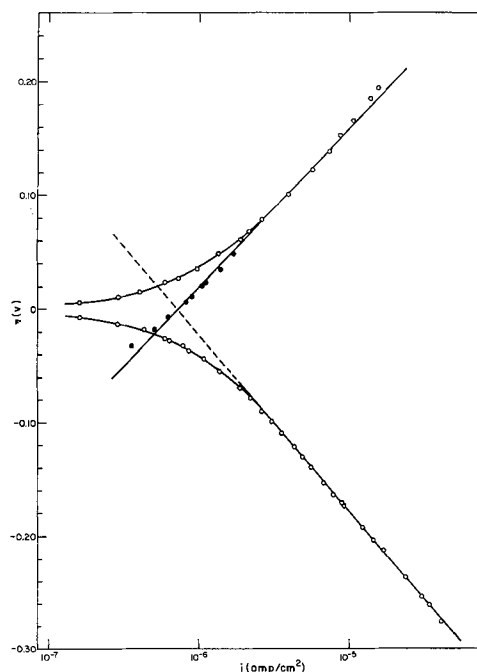


Fig. 3. Polarization curves of the Fe⁺⁺⁺/Fe⁺⁺ couple (0.050M) on passive Fe-Cr in M MgSO₄ at pH = 2.2. Solid circles are calculated from $i_a = i_c \pm i_{appl}$ where i_c is the extrapolated cathodic current and i_{appl} the externally applied current (30°C).

hr, is probably due to a change in the film. The rest-potential, which is originally about -20 mv vs. the reversible Fe⁺⁺⁺/Fe⁺⁺ potential, slowly changes toward zero indicating a continuously diminishing contribution from corrosion reactions. The rest potential is within 3-5 mv of the reversible potential after about 24 hr in almost all of the solutions used here. In general, the electrodes were extremely stable after the first 24 hr and showed little susceptibility to poisoning. This is probably due in part to the smaller tendency of oxide-covered surfaces, as compared to oxide-free surfaces, for adsorbing impurities and in part to the relatively high, positive electrode potential.

Reaction orders.—Current-potential curves in a solution of constant pH and M in MgSO₄ were determined for (Fe⁺⁺) and (Fe⁺⁺⁺) concentrations between 0.01 and 0.06M. The currents at a fixed anodic (0.60v vs. SCE) and fixed cathodic (0.20v vs. SCE) potentials are shown in Fig. 4. Both electrochemical reaction orders

$$\left(\frac{\partial \log i_a}{\partial \log (Fe^{+++})} \right)_{E_a} = 1 = \left(\frac{\partial \log i_c}{\partial \log (Fe^{+++})} \right)_{E_c} \quad [1]$$

are equal to unity in solutions containing a large excess of inert electrolyte (M MgSO₄).

Table I. Oxidation of Fe⁺⁺ *

t, hr	i_0 , amp/cm ²	b, v	Rest potential
2	5.0×10^{-7}	0.190	-0.022
24	3.8×10^{-7}	0.161	-0.006
80	3.8×10^{-7}	0.159	-0.001
120	4.0×10^{-7}	0.156	-0.0005

* $C_{Fe^{++}} = C_{Fe^{+++}} = 0.050M$; M MgSO₄; pH = 0.30.

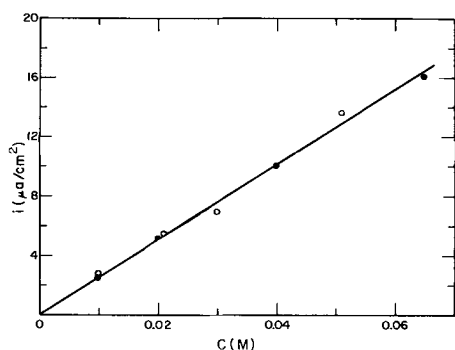


Fig. 4. Current at a fixed potential as a function of the concentration of ferrous or ferric ions —○— oxidation of Fe^{2+} at 0.600v vs. SCE; —●— reduction of Fe^{3+} at 0.200v vs. SCE (30°C).

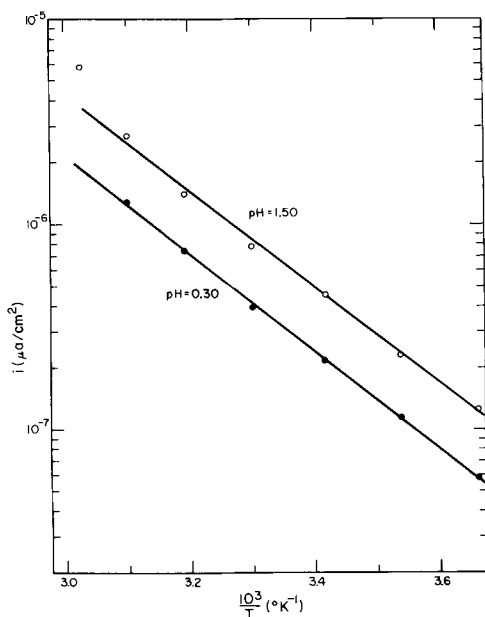


Fig. 5. Temperature coefficient of exchange current (extrapolated from the cathodic curve) for $\text{Fe}^{3+}/\text{Fe}^{2+}$ (0.50M) in M MgSO_4 .

Temperature coefficient.—The temperature dependence of i_0 , determined by extrapolation of the cathodic Tafel line, in solutions of $\text{pH} = 1.50$ and 0.30 is shown in Fig. 5. The energy of activation is essentially independent of pH and is $\Delta H^* = 10.8$ kcal/mole.

Corrosion reactions.—The rest potential is negative to the $\text{Fe}^{3+}/\text{Fe}^{2+}$ reversible potential in solutions of low pH and low in (Fe^{3+}) or (Fe^{2+}) indicating that the corrosion current is significant in comparison to i_0 . In these cases, the polarization curves were corrected for the steady-state corrosion current by assuming that the latter was independent of the potential as it is known to be from potentiostatic measurements in the absence of the redox couple. The corrosion current was obtained from the anodic current required to polarize the electrode from its rest potential to the $\text{Fe}^{3+}/\text{Fe}^{2+}$ reversible potential. The curves were then corrected by subtracting this quantity from the anodic applied current and adding it to the cathodic applied current as shown in Fig. 6 for the commercial Fe-Cr alloy. The assumption of constancy of i_{corr} was checked by comparing i_{corr} determined as described

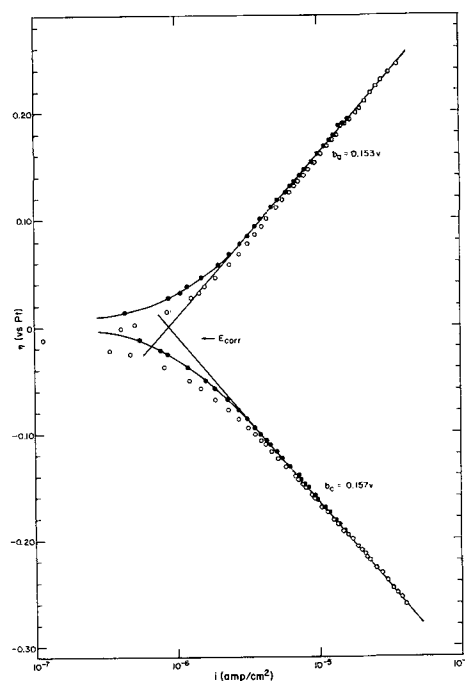


Fig. 6. Current-potential curves for the $\text{Fe}^{3+}/\text{Fe}^{2+}$ couple (0.05M) on commercial Fe-Cr alloys. Full circles are obtained after correction for corrosion current (30°C).

above with the value calculated from the difference between the corrected cathodic curve and the corrected anodic curve extrapolated to the rest potential. Table II shows that values of i_{corr} obtained in these two ways agree closely.

pH dependence.—The exchange current and the Tafel slopes decrease with decreasing pH as shown in Fig. 7. The exchange current at $\text{pH} = 1.35$ is less than that at $\text{pH} = 2.2$ by a factor of about 3. This decrease is probably connected with changes in the concentration of ionic species in solution (e.g., $\text{Fe}(\text{H}_2\text{O})^{3+}$, $\text{Fe}(\text{OH})^{2+}$, $\text{Fe}(\text{OH})^+$, etc.) which are also responsible for the change of the reversible potential with pH .

At pH of 1.5 or less, a qualitative change in the anodic polarization curve can be induced by a brief cathodic pulse or may appear spontaneously after the electrode has been in solution for some time. This is described in detail below.

"Forming" and "deforming" of the surface film.—It was observed that in solutions of low pH , the anodic and cathodic curves did not extrapolate to

Table II. Corrosion currents of commercial Fe-Cr alloy $N \text{ H}_2\text{SO}_4$ at 30°C

Fe^{2+} , M/liter	Fe^{3+} , M/liter	E_{corr} , v	i_{corr}^a , amp/cm ²	$(i_c - i_a)$ at E_{corr}^b , amp/cm ²
1.09×10^{-3}	1.38×10^{-2}	-0.026	4.0×10^{-7}	3.3×10^{-7}
1.09×10^{-3}	2.83×10^{-2}	-0.025	4.2×10^{-7}	3.6×10^{-7}
1.09×10^{-3}	4.92×10^{-2}	-0.020	4.0×10^{-7}	3.2×10^{-7}
1.09×10^{-3}	6.94×10^{-2}	-0.018	5.0×10^{-7}	4.6×10^{-7}
2.07×10^{-3}	6.94×10^{-2}	-0.014	4.5×10^{-7}	4.0×10^{-7}
4.05×10^{-3}	6.94×10^{-2}	-0.013	3.0×10^{-7}	3.5×10^{-7}
5.90×10^{-3}	6.94×10^{-2}	-0.010	4.3×10^{-7}	3.0×10^{-7}

^a Applied anodic current for $\eta = 0$.

^b From extrapolated polarization curves after corrections for i_{corr} .

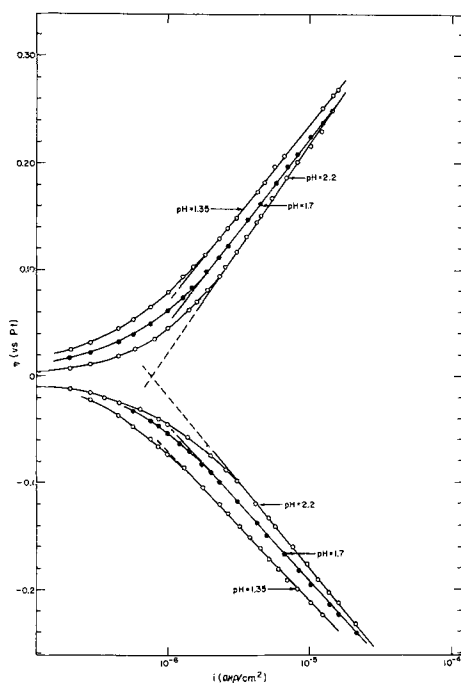


Fig. 7. Polarization curves of the Fe⁺⁺⁺/Fe⁺⁺ couple (0.10M) on passive Fe-Cr in M MgSO₄ at different pH (30°C).

a common i_0 , although the rest potential coincided with the reversible Fe⁺⁺⁺/Fe⁺⁺ potential. In particular, the anodic curve appeared to consist of two Tafel lines, the lower one extrapolating to about the same i_0 as the cathodic curve. This change from a single anodic Tafel line to the type of curve shown in Fig. 8 was delayed or was even absent if the film

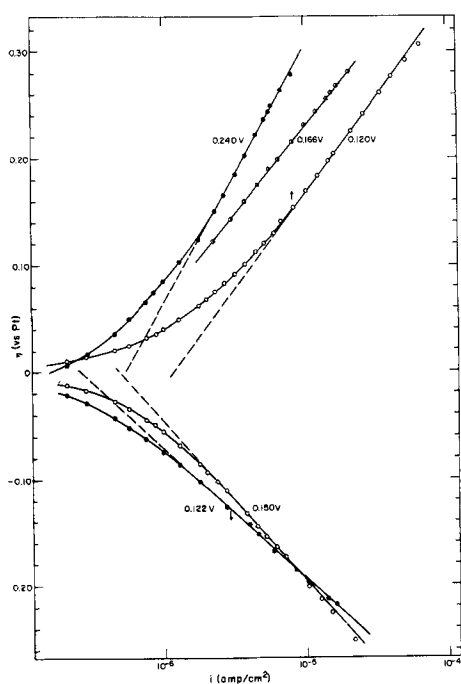


Fig. 8. Effect of anodic (dark circle) and cathodic (open circle) pulsing on polarization curve of the Fe⁺⁺⁺/Fe⁺⁺ couple (0.10M) on passive Fe-Cr in M MgSO₄ at pH = 1.35. Curve corresponding to (dash half dark circle dash) was obtained with electrodes which had not been pulsed (30°C). Arrows show points at which potential begins to drift in indicated direction. Measurements in these potential ranges were made rapidly and do not correspond to a steady state.

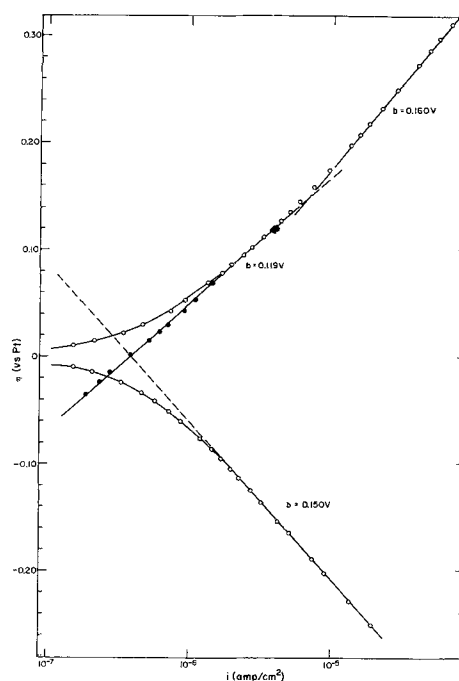


Fig. 9. Anodic polarization curve for Fe⁺⁺ oxidation on passive Fe-Cr alloy after cathodic pulsing. Measurements were made 24 hr after pulsing.

was formed in a solution of high pH, and the pH was later adjusted to a lower value. Also, it proved possible to induce this change by a brief cathodic pulse and to reverse it by an anodic pulse. These phenomena are obviously related to changes in the composition or structure of the surface film. The term "deforming" is used here to denote the change produced by a cathodic pulse, while "forming" refers to the change induced by an anodic pulse.

Polarization curves obtained with electrodes pulsed anodically or cathodically are shown in Fig. 8. The effect of a cathodic pulse on the cathodic polarization curve is slight. An anodic pulse displaces the cathodic curve in the direction of higher overpotentials, but the effect is relatively small. However, at overpotentials more negative than about -150 mv, the electrode potential at a fixed current density increases rapidly with time, a phenomenon not observed with electrodes which had not been pulsed.

The kinetics of oxidation of Fe⁺⁺ are changed substantially both by cathodic and by anodic pulses. The anodic curve after "deforming" is no longer semilogarithmic but is approximated by two Tafel lines with a fairly sharp transition (Fig. 9). The cathodic pulse does not increase the corrosion rate since the reversible potential and the rest potential after deforming are still the same. Furthermore, the effects of a cathodic pulse are not transitory. Anodic curves obtained shortly after a cathodic pulse are the same as those obtained 100 hr later. The curves shown in Fig. 8 and 9 were obtained 24 hr after the pulse was applied.

Anodic pulses displace the anodic curve toward higher overpotentials and increase the Tafel slope to relatively high values. The effects of anodic or cathodic pulses are essentially independent of the

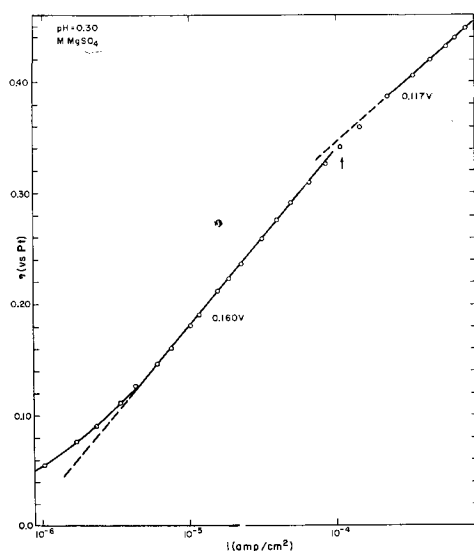


Fig. 10. Anodic polarization curve for Fe^{++} (0.050M) oxidation in M MgSO_4 at $\text{pH} = 0.30$. Note change in slope in transpassive region ($\eta > 0.35\text{v}$ or $E > 0.70\text{v}$ vs. SCE) (30°C). Arrow shows point where overshoot of potential is first observed.

previous history of the electrode, i.e., of the order in which the electrode was pulsed.

Transpassive region.—The potential was always kept within the passive region for the Fe-Cr alloy in the measurements described above. At high anodic potentials the alloy begins to dissolve again at a steady rate which depends on the potential. The onset of anodic dissolution in the transpassive region has a pronounced effect on the kinetics of oxidation of Fe^{++} . First, there is an overshoot of the potential on increasing the current and an undershoot when the current is decreased. Second, the Tafel slope for Fe^{++} oxidation decreases substantially in the transpassive region of the alloy (Fig. 10). It might appear at first that the increase in total current is due to the additional anodic current corresponding to metal oxidation. However, measurements of the anodic polarization curve in the absence of the redox couple show that the metal oxidation current is entirely negligible (Fig. 11). For example, at $E = 0.850$ vs. SCE ($\eta = 0.425\text{v}$) the total current is $400 \mu\text{a}/\text{cm}^2$, and the metal oxidation current is only $1.5 \mu\text{a}/\text{cm}^2$.

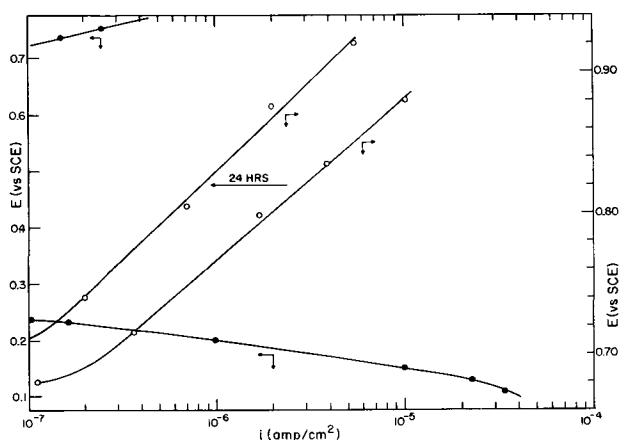


Fig. 11. Potentiostatic anodic polarization curve of Fe-Cr electrodes in M MgSO_4 at $\text{pH} = 0.30$ and at 30°C .

Table III. $\text{Fe}^{+++}/\text{Fe}^{++}$ on passive Fe-Cr
 $T = 30.0^\circ\text{C}$

Fe^{+++} , M/liter	Fe^{++} , M/liter	pH^a	α_c	α_a
5.0×10^{-3}	5.0×10^{-3}	0.30	0.40	0.37
5.0×10^{-2}	5.0×10^{-2}	0.30	0.38	0.37
1.0×10^{-1}	1.0×10^{-1}	1.35	0.43	0.36
5.0×10^{-2}	5.0×10^{-2}	1.5	0.40	0.35
1.0×10^{-1}	1.0×10^{-1}	1.7	0.41	0.35
1.0×10^{-1}	1.0×10^{-1}	2.1	0.38	0.30
1.4×10^{-2}	5.0×10^{-3}	0.60 ^b	0.42	0.38
4.1×10^{-2}	5.0×10^{-3}	0.60 ^b	0.40	0.38
5.0×10^{-2}	5.0×10^{-2}	0.30	0.40	} 0.58 ^c 0.37
5.0×10^{-2}	5.0×10^{-2}	1.35	0.42	
Avg $\alpha_c = 0.40 \pm 0.01$				
$\alpha_a = 0.36 \pm 0.02$				

^a All solutions M in MgSO_4 except where noted.

^b No MgSO_4 added.

^c Two Tafel slopes on anodic polarization; data not included in average α_c or α_a .

Discussion

The low exchange currents and the unusual values of the Tafel slopes (see Table III) are characteristic features of redox reactions on superficially oxidized electrodes. In general, the sum of the apparent transfer coefficients on passive electrodes is less than unity. For example, Table III shows that $\alpha_a + \alpha_c = 0.76 \pm 0.03$ on Fe-Cr alloys; similar results were reported for other passive electrodes (1, 4). The parameters are in contrast to those obtained on oxide-free electrodes. For example, the exchange current on Pt electrodes with $C_{\text{Fe}^{+++}} = C_{\text{Fe}^{++}} = 0.05\text{M}$ is 1.5×10^{-2} amp/cm² and the transfer coefficients are $\alpha_a = 0.58 \pm 0.02$ for the anodic and $\alpha_c = 0.42 \pm 0.02$ for the cathodic reaction (5, 6). The main difference in the kinetics (aside from difference of the exchange current) is in the apparent transfer coefficient for the anodic reaction. The cathodic transfer coefficients on passive Fe-Cr and on passive Ni and Ti (4) are all about the same as on Pt.¹ The results $\alpha_a + \alpha_c < 1.0$ on passive electrodes is due to the smaller value of α_a on these electrodes and indicates that the anodic reaction is not a simple electrochemical process as it is on Pt.

It should be pointed out that in other respects the electrode behavior of passive metals toward the $\text{Fe}^{+++}/\text{Fe}^{++}$ couple is similar to that of an inert electrode. Thus, the rest potential generally coincides with the reversible $\text{Fe}^{+++}/\text{Fe}^{++}$ potential, a result which implies that the surface oxide film has a reasonable electronic conductivity. Also, passive electrodes respond to changes in the concentration of either (Fe^{++}) or (Fe^{+++}) in the simple way expected for a first order, one-electron reaction without the complications usually associated with specific adsorption of either ion. Thus, the electrochemical reaction order is unity provided sufficient excess of inert electrolyte is present to suppress effects arising from the diffuse part of the double layer. In less concentrated salt solutions, the composition of the double layer is not independent of

¹ A cathodic transfer coefficient of 0.69 is observed for Fe^{+++} reduction on passive Fe(4). However, in this case the ionic current on cathodic polarization is probably a large fraction of the total current.

the (Fe⁺⁺⁺) or (Fe⁺⁺) concentration and the kinetics are more complicated.

Ionic and electronic currents.—The anodic reaction on passive electrodes involves probably both oxidation of the metal and oxidation of Fe⁺⁺. Therefore, the total applied current is the sum of an ionic current corresponding to the formation or reduction of the surface film, and of an electronic current equivalent to the rate at which the redox reaction is taking place. When no external current is applied, the anodic ionic current is equal to the net reduction current of Fe⁺⁺⁺ at the resting potential. If the ionic current is appreciable, the rest potential is negative to the reversible potential (a mixed potential). If, however, the ionic current is negligible in comparison to the exchange current for the Fe⁺⁺⁺/Fe⁺⁺ couple, the reversible and rest potentials coincide, and the alloy functions essentially as an inert, indicator electrode.

The kinetics of film growth may be involved in determining the polarization curves either directly through the contribution of the ionic current to the total current, or indirectly through the possible effect of changes of film thickness and composition on the distribution of the total potential drop between the film and the electrolytic double layer. Consider a passive Fe-Cr electrode in a solution 0.05M in Fe⁺⁺⁺ and Fe⁺⁺ ions, M in MgSO₄, and of pH = 1.5. The steady state dissolution rate of the alloy is less than 10⁻⁷ amp/cm², which is negligible in comparison to the exchange current. The distribution of potential from metal to electrolyte at the reversible Fe⁺⁺⁺/Fe⁺⁺ potential may be described by

$$E_{\text{rev}} = V + E_{\text{dl}} = \text{Constant} \quad [2]$$

where V is within the oxide, and E_{dl} is a potential drop across the oxide/electrolyte interface. If the electrode is polarized anodically, say to a potential E , an ionic and an electronic current flow across the film. The former corresponds to the rate of growth of the oxide and the latter to the rate of oxidation of Fe⁺⁺. As the film thickens, the ionic current eventually decreases to its previous value, i.e., 10⁻⁷-10⁻⁸ amp/cm². The electronic current depends on the kinetics of ferrous oxidation and is given by

$$i_a = i_o \exp(\beta_r \eta_{\text{dl}}) \quad [3]$$

where η_{dl} is in units of RT/F , and β_r is the transfer coefficient for Fe⁺⁺ oxidation.

The results show that in all cases studied [see also ref. (4)] an appreciable fraction of the applied potential on anodic polarization is across the film. This implies that the transfer of electrons from the oxide/solution interface to the metal, or of holes in the opposite direction, occurs over a potential barrier. If it is assumed that the potential drop across the film is a constant fraction, say γ , of the total applied potential, and since

$$\eta = E - E_{\text{rev}} = \Delta V + \eta_{\text{dl}} = \gamma \eta + \eta_{\text{dl}} \quad [4]$$

then the fraction of the overpotential across the double layer is

$$\eta_{\text{dl}} = (1 - \gamma) \eta \quad [5]$$

Substituting in Eq. [3] we have for the anodic current

$$i_a = i_o \exp[\beta_r(1 - \gamma)\eta] \quad [6]$$

On the other hand, the transfer of electrons from metal to the oxide/solution interface is apparently accompanied by a negligible change in the total potential drop across the film, and consequently

$$i_c = i_o \exp(-\alpha_r \eta_{\text{dl}}) = i_o \exp(-\alpha_r \eta) \quad [7]$$

where α_r is the transfer coefficient for Fe⁺⁺⁺ reduction ($\alpha_r + \beta_r = 1$).

The sum of the apparent transfer coefficients is

$$\alpha_a + \alpha_c = (1 - \gamma) \beta_r + \alpha_r = 1 - \gamma \beta_r \quad [8]$$

so that in the particular case of Fe-Cr alloys ($\alpha_a + \alpha_c = 0.76$) γ is 0.4.

An alternative interpretation of the unusual transfer coefficients may be considered. If it is assumed that the transfer of electrons across the film gives rise to a potential drop, V_f , according to the dual barrier model proposed for redox reactions on valve metals, e.g., Zr (11), then the anodic current across the film may be expressed by

$$i_a = i_{o,f} \exp(\alpha_f V_f) \quad [9]$$

where the subscript f refers to the film. The current across the double layer is, of course, the same and is given by Eq. [8], while the total potential drop from metal to solution is again $\eta = V_f + \eta_{\text{dl}}$. Although the polarization curve defined by Eq. [8] and [9] is not semilogarithmic, it may be approximated by a Tafel curve over a narrow range of current densities (11). It is difficult to decide on the basis of the polarization characteristics alone (the range of accessible current densities being relatively small) whether the dual-barrier model or the one advanced above is applicable. However, the electrochemical reaction orders can be used to differentiate between these two alternative interpretations. According to the dual-barrier model, the reaction order is

$$\left(\frac{\partial \ln i}{\partial \ln C} \right)_E = \frac{\alpha_f}{\alpha_f + \beta_r} \quad [10]$$

On the other hand, the account given above requires that

$$\left(\frac{\partial \ln i}{\partial \ln C} \right)_E = 1 \quad [11]$$

since V , and consequently E_{dl} , are constant at constant E . The experimental results agree with Eq. [11] and show that the transfer of electrons across the film is not described by Eq. [9].

It should be noted that the postulated potential drop within the oxide film does not appear in the expression for the electrode potential when the Fe⁺⁺⁺/Fe⁺⁺ is at equilibrium. The argument here parallels the analysis which shows that the thermodynamic potential of any redox couple is independent of the actual potential drop across the solid/electrolyte interface of an inert, indicator electrode.

Similarly, the experimental results on anodic polarization do not refer to the absolute magnitude of potential drop within the oxide, but rather to changes of this potential.

The electronic properties of the surface oxide which give rise to the observed behavior may be described in terms of the continuum properties of semiconducting oxides, *e.g.*, it may be supposed that the oxide next to the solution is of p-type while that next to the metal is of n-type. However, it is doubtful that these terms are relevant, since the thickness of the oxide is of the order of 100Å. Therefore, it is preferable to consider charge transfer within the oxide in terms of changes in chemical composition which may occur as the potential is changed to more or less positive values.

Consider, for example, a surface film of iron oxide in which the layers next to the solution are essentially Fe₂O₃, while the layers next to the metal may approach FeO. On cathodic polarization, an electron is transferred to a ferric ion in solution and a higher valency ion is left behind. The higher valency ion can accept an electron from a ferrous ion in the film which is in turn oxidized to the +3 state and eventually accepts an electron from the metal. On anodic polarization, an electron is transferred from a ferrous ion in solution to either a ferric ion in the film or to an ion of a higher valence, say Fe⁴⁺, which may be associated with a cation vacancy. Further charge transfer must occur by transfer of an electron to a ferrous ion in the inner layer or by transfer to a ferric ion which may be produced next to the metal. Since the first alternative is not likely, transfer will depend on the production of ferric ions in the inner layer. This is associated with an overpotential which apparently constitutes an appreciable fraction of the total applied potential difference. A similar analysis is applicable to other oxide films (*e.g.*, NiO) present on passive metals (4). The fraction of the overpotential which appears within the film is large in the case of Ti (0.60) and Fe-Cr (0.40), but is relatively small (0.15) in the case of Ni(4). In the case of Fe and Ti, and under circumstances previously discussed (4), practically all of the potential drop occurs in the oxide. In these cases, a substantial increase of the thickness of the oxide film apparently takes place on anodic polarization.

Changes of film characteristics.—The electrochemical characteristics of the surface oxide are changed either by an anodic or cathodic pulse. Furthermore, they are obviously also different in the transpassive region of the alloy. A change in the anodic polarization curve once a certain overpotential was exceeded was previously reported by Stern (1) who tentatively attributed it to the onset of oxygen evolution. The present study shows that oxygen evolution cannot be involved since the potential is in all cases less than the reversible oxygen potential.

The change of slope in the transpassive region is probably connected with the introduction into the film of large numbers of ions of higher valence (Fe³⁺, Cr⁶⁺). The potential drop within the oxide in the transpassive region apparently increases much more slowly with the total potential. As long as the

metal oxidation current is negligible in comparison to the oxidation of Fe⁺⁺, the total *i-E* characteristics should approach that for the anodic oxidation of Fe⁺⁺. In particular, the apparent transfer coefficient should approach 0.60. The observed change in the Tafel slope is in the expected direction.

The effects of anodic and cathodic pulses suggest that the potential drop across the oxide changes after a pulse. Stated differently, these results suggest that the electronic characteristics of the oxide are altered substantially by pulsing. A cathodic pulse apparently decreases the fraction of the potential drop which is across the oxide; an anodic pulse has the opposite effect. The apparent anodic transfer coefficient changes accordingly toward larger or smaller values. The origin of this effect is not clear at present. It may be connected with migration of protons into or out of the film since a change similar to that produced by a cathodic pulse also occurs when the pH is lowered (12). Apparently, proton migration is a slow process since the changes produced by pulsing persist for a least 100 hr after the pulse. This conclusion is supported by the observation that the characteristics of a film formed in a solution of high pH remain the same for some time after the pH is adjusted to a lower value.

Summary and Conclusions

1. Passive Fe-Cr alloy electrodes function as inert, indicator electrodes for the Fe⁺⁺⁺/Fe⁺⁺ couple. The steady-state, ionic current is generally negligible compared with the electron current.
2. Tafel curves are obtained on both anodic and cathodic polarization. The transfer coefficients are 0.36 for the anodic and 0.40 for the cathodic reaction. The exchange current is of the order of 10⁻⁶ amp/cm² for C_{Fe⁺⁺⁺} = C_{Fe⁺⁺} = 0.05M. The electrochemical reaction orders are unity for both Fe⁺⁺ and Fe⁺⁺⁺. The temperature coefficient of the exchange current yields ΔH* = 10.8 kcal/mol.
3. The polarization characteristics suggest that an appreciable fraction of the total potential drop between electrode and solution is across the passive film. The potential drop across the film increases linearly with the total applied potential. This dependence leads to an apparent transfer coefficient for the anodic reaction which is substantially less than what is expected for the oxidation of Fe⁺⁺.
4. The electrochemical characteristics of the passive film depend on the pH and can be modified by anodic or cathodic pulses. The film characteristics are also changed significantly when the potential is within the transpassive region for the alloy.

Acknowledgment

The author thanks Miss Mary Loud who assisted skillfully in the experimental part.

This work was supported by the Office of Naval Research under Contract Nonr-3765(00).

Manuscript received July 1, 1963; revised manuscript received Oct. 17, 1963.

Any discussion of this paper will appear in a Discussion Section to be published in the December 1964 JOURNAL.

REFERENCES

1. M. Stern, *This Journal*, **104**, 559, 600 (1957).
2. F. A. Posey, *ibid.*, **106**, 582 (1959).
3. A. C. Makrides and M. Stern, *ibid.*, **107**, 877 (1960).
4. A. C. Makrides, *ibid.*, **111**, 392 (1964).
5. H. Gerischer, *Z. Elektrochem.*, **54**, 362 (1950).
6. J. E. B. Randles and K. W. Somerton, *Trans. Faraday Soc.*, **48**, 937 (1952).
7. A. C. Makrides, *This Journal*, **109**, 977 (1962).
8. H. Gerischer and K. E. Staubach, *Z. Elektrochem.*, **61**, 789 (1957).
9. W. M. Latimer, "Oxidation Potentials," p. 224, Prentice-Hall, New York (1952).
10. K. J. Vetter, *Z. Elektrochem.*, **58**, 230 (1954); **59**, 67 (1955).
11. R. E. Meyer, *This Journal*, **107**, 847 (1960).
12. J. S. L. Leach, *J. Inst. Metals*, **27** (1959).

Factors Affecting the Morphology and Growth of FeSn₂

Charles Luner¹ and M. V. Murray

Applied Research Laboratory, United States Steel Corporation, Monroeville, Pennsylvania

ABSTRACT

So that an insight could be gained into the factors affecting alloy nucleation and growth, the morphology of the alloy formed during the melting of tin that had been previously deposited on iron substrates was examined by electron microscopy. Tin was electrodeposited from a phenolsulfonic acid electrolyte or vacuum deposited at 10⁻⁵ Torr on single crystals or polycrystalline substrates. Apparently the nucleation and growth of the alloy was greatly influenced by impurities from the electrolyte and substrate. The different crystal faces of iron (100), (110), and (111) gave rise to characteristic alloy morphologies. The morphologies of the alloy formed by melting vacuum-deposited tin on the (110) and (111) orientations were similar to those obtained when tin, deposited from a phenolsulfonic acid electrolyte on the same substrates, was melted. With vacuum-deposited tin very little alloy was formed on the (100) face of iron, presumably because an oxide formed on this more reactive surface during annealing or deposition.

As one of the processing steps in the manufacture of tinplate, the electrodeposited tin is melted either by induction or by resistance heating so as to give the surface a bright appearance. During the melting, an intermetallic compound, FeSn₂ (1, 2) is formed between the steel and the tin. For many years the alloy in the tinplate was considered an undesirable effect of melting, since it interfered with the soldering and manufacture of the tin can. A recent study (3) indicated that the structure of the alloy is important in the corrosion of tinplate, and preliminary observations (4) have been made on the growth of FeSn₂ on polycrystalline iron.

This paper describes the factors affecting the nucleation and growth of the alloy formed by heating an electrodeposited or vacuum-deposited tin film. These results are based primarily on electron-microscopic observations.

Materials and Experimental Work

Preparation and plating conditions.—The chemical compositions of the steels used in this investigation are given in Table I. The N250 material was obtained from a vacuum-melted heat prepared at U. S. Steel's Applied Research Laboratory, whereas the M1150 material was a commercial grade of low-carbon steel. Single crystals of different orientations were prepared from the N250 material by the strain-anneal method (5). After being thoroughly cleaned with toluene, the polycrystalline samples were vacuum-annealed for about 3 hr at 800°C at a pressure of about 5 x 10⁻⁵ Torr to degas the steel and to promote grain growth. Samples were mechanically

polished from 1/0 through 4/0 emery paper and then polished with diamond-polishing compound. Immediately before the samples were plated, they were cathodically cleaned in a 1% sodium carbonate solution, rinsed with distilled water, dipped in a 5% H₂SO₄, rinsed again, and then immersed for 30 sec in a chemical polishing solution maintained at 30°-35°C. It is estimated that about 1 x 10⁻⁶ cm of the iron surface was removed by this method. The samples were then quickly transferred to a 10% solution of NaOH for an immersion period of 2-5 sec. They were water-rinsed and agitated in a 5% by weight solution of H₂SO₄ until the brown iron hydroxide film formed during the caustic dip dissolved. After another water rinse, the samples, while still wet, were placed into the plating bath.

Table I. Analyses of samples

Sample No.	Composition, %	
	Laboratory vacuum-melted, N250	Low-carbon, L M1150
C	0.003	0.09
Mn	0.01	0.35
P	0.001	0.009
S	0.004	0.020
Si	0.018	0.003
Cu	0.002	0.52
Ni	0.023	0.01
Cr	0.006	0.02
Mo	N.D.*	0.003
	≤0.005	
Ti	N.D.*	—
	≤0.002	
Al	0.002	—

¹ Present address: Argonne National Laboratory, Argonne, Illinois.

* N.D., not detected.

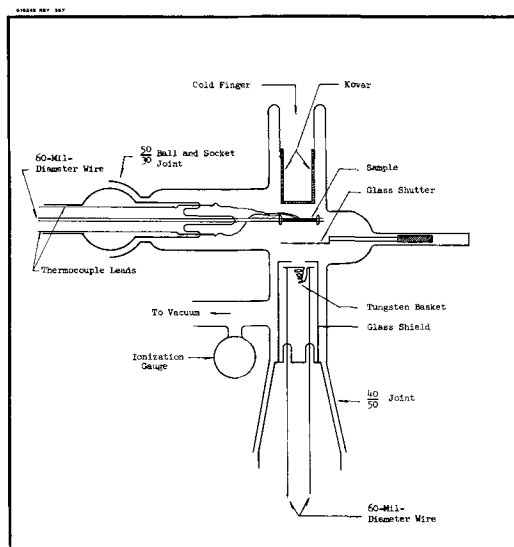


Fig. 1. Schematic view of a vacuum deposition cell

The chemical polishing solution was made by mixing one part of Mirrofe (a chemical polishing concentrate made by MacDermid, Inc., Waterbury, Connecticut), one part of water, and one part of 30% hydrogen peroxide.

Tin was electroplated from a phenolsulfonic acid electrolyte. The plating conditions and the composition of the bath are as follows:

Phenolsulfonic acid electrolyte

Sn ⁺⁺	35 grams per liter (g/l)
Free acid as H ₂ SO ₄	20 g/l
Total sulfate as H ₂ SO ₄	40 g/l
Dihydroxydiphenyl sulfone	6 g/l
Temperature	25°-30°C
Current density	25 amp/ft ²

Vacuum deposition of tin.—Figure 1 shows a sketch of the apparatus used in the vacuum evaporation of tin. Evaporated tin films were prepared by evaporating 99.99% pure Sn through a hole in a glass shield from an electrically heated 15-mil diameter tungsten wire in the shape of a conical basket. The evaporation rate was controlled by the current to the basket. The thickness of the deposited film was controlled by varying the time of evaporation. The cell was provided with a ground-glass joint through which passed two 60-mil diameter nickel lead-in wires for heating the tungsten basket. Similar wires, sealed through a ball-and-socket joint, were used to heat the substrate. The substrate, 1 x 3 cm, was placed between the wires and fastened by nichrome wire to maintain electrical contact. When single crystals were used as a substrate, it was more convenient to use infrared heating (6). This was accomplished by focusing two 150-watt Sylvania projection lamps, with an internal reflector, on the sample. The thermocouple wires also entered through the ball-and-socket joint. The ball-and-socket joint provided flexibility for the movement of the substrate so that, when necessary, it could be placed against the cold finger by a slight movement of the joint. The cell was also provided with a glass shutter that could be placed between the substrate and tung-

sten coil when either one was being degassed. This prevented contamination of the substrate and tin.

The following procedure was used to conduct an experiment. The substrate was first degassed for 3 to 4 hr at 800°C. The pressure at the end of the degassing period was about 1×10^{-6} Torr. The tin was then melted and degassed at a temperature at which condensation was visible on the walls of the vessel. During the degassing, the shutter was placed between the substrate and the tungsten coil. After the tin and substrate had been degassed, the current in the tungsten coil was rapidly increased to a predetermined value to give the desired evaporation rate. Removal of the shutter exposed the substrate to the tin vapor. Pressures of about 10^{-5} Torr were maintained during evaporation. The substrate was cooled by adding liquid nitrogen to the Kovar cold finger and bringing the sample into contact with the cold finger. The temperature of the substrate was measured by the thermocouple spot-welded to the sample. After the tin was deposited the sample was removed from the vacuum system and the alloy was formed by heating the sample at 242°C or at 225°C in a well-stirred oil bath. Replicas of the alloy layer were prepared by dissolving the tin coating anodically in a 5% solution of NaOH (7), evaporating a layer of chromium at a 45° angle, and then evaporating a layer of carbon onto the alloy specimen. The composite film was then separated from the specimen by immersing the sample in a solution of 5% bromine in ethanol, which dissolved the underlying alloy and thus freed the film.

Results and Discussion

Electrodeposition.—Figure 2 shows two typical electron micrographs of replicas obtained by melting tin (242°C) which had been deposited from a phenolsulfonic acid electrolyte. The substrate used was the vacuum-melted polycrystalline iron. These micrographs show that the morphology of the alloy and coverage of the substrate by the alloy varies with crystallographic orientation. On some grains of the iron substrate the alloy forms a relatively compact layer, whereas on other grains the alloy crystallites are in an approximately orthogonal array which leaves considerable areas of the substrate exposed. Indeed this alloy structure is characterized by the relatively large areas of substrate exposed on certain grains.

In unpublished work recently conducted at the Applied Research Laboratory, the morphology of the



Fig. 2. Typical electron micrographs of alloy, FeSn₂, formed on a polycrystalline substrate. Tin electrodeposited from a phenolsulfonic acid electrolyte. Magnification 17,000X before reduction for publication.

alloy layer formed on single-crystal substrates of iron having (111), (110), and (100) orientations was investigated. It was shown that on both the (111) and (110) crystal faces the alloy forms a compact layer. On the (100) face, however, the alloy does not form a compact layer, but instead the crystallites are arranged in an orthogonal network in which large portions of the base metal are exposed. It was concluded that a reasonable interpretation of the various alloy-layer structures on polycrystalline substrates can be made solely in terms of the alloy-layer structure observed on the (111), (110), and (100) crystal faces. On the basis of this single-crystal study it can be concluded that grain A in Fig. 2, which exhibits poor alloy coverage, was close to the (100) orientation.

To obtain a better insight into the initial stage of alloy growth, samples that had been electrodeposited from a phenolsulfonic acid electrolyte were heated at a lower temperature, 225°C . Replicas of some typical areas are shown in Fig. 3. The thickness of the alloy, uniform coverage being assumed, was estimated coulometrically to be about 500\AA . It appears that growth commences by a nucleation process which leads to the formation of small islands. These islands, which exhibit a high degree of orientation, gradually coalesce to form, in some instances, a relatively compact surface. The uniform size of the particles suggests that all the particles were nucleated simultaneously.

Vacuum deposition.—Since electrodeposition is but one of several methods of depositing crystals, it was of interest to grow a tin deposit by another method and to compare the alloy morphology obtained by melting the resulting deposit. Therefore, tin was evaporated from the liquid phase in a vacuum, and the vapor was condensed on the iron substrate maintained at room temperature or below. The use of this method of depositing tin meant that the complicating factors such as addition agents, aqueous media, and pH, which may influence the alloy structure, could be avoided.

Because the surface temperature of the substrate could rise considerably during the deposition of tin on a metal surface, it was possible to form alloy dur-

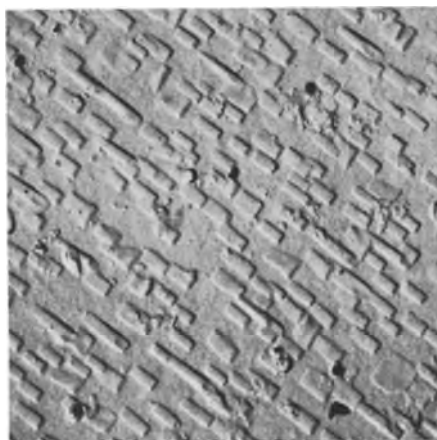


Fig. 3. Electron micrograph showing the initial stage of growth of FeSn_2 . Tin electrodeposited from a phenolsulfonic acid electrolyte. Magnification 17,000X before reduction for publication.

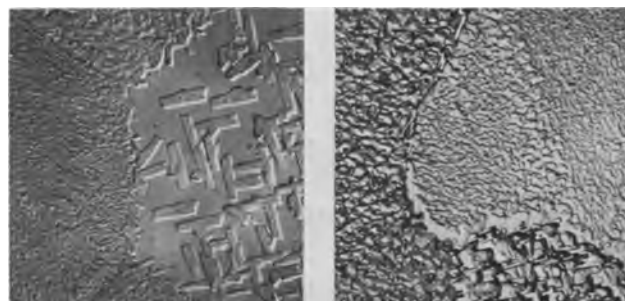


Fig. 4. Typical electron micrographs of the alloy, FeSn_2 , formed on different polycrystalline substrates. Tin deposited by vacuum evaporation. Left, vacuum-melted iron substrate (N250). Right, low-carbon-steel substrate. Magnification 7000X before reduction for publication.

ing the deposition process. This possibility was investigated by depositing tin on a polycrystalline iron substrate maintained at room temperature, at -70°C , and at -106°C . Immediately after tin deposition, the samples were maintained at liquid nitrogen temperatures until they were placed in the detinning solution, which was maintained at 4°C . After the samples were detinned they were washed and dried, and the surface was analyzed by reflection electron diffraction. In all samples, FeSn_2 was identified on the surface of the substrate. But when tin was electrodeposited from a phenolsulfonic acid bath, FeSn_2 could not be identified on the detinned surface. These experiments indicate that alloying occurred when the tin condensed from the vapor because of the temperature increase of the surface layers during deposition. Such alloying has been reported for other systems (8).

Although the formation of an alloy during deposition could be expected to affect the nucleation and the morphology of the alloy formed by reflowing the Sn, no marked difference was observed in the alloy structure as a function of substrate temperature. Replicas of the alloy obtained by melting tin (242°C) that had been vacuum-deposited on the carbon steel and on vacuum-melted (N250) iron are shown in Fig. 4. In both instances the morphology varied with substrate grain orientation. However, although the alloy covered the grains uniformly on the low-carbon steel, the coverage of certain grains on the vacuum-melted iron was incomplete. The replicas on the N250 material also show that on those grains which are not uniformly covered with alloy the alloy particles were larger and less numerous. It appears then that once the alloy is nucleated it continues to grow, with very few, if any, new nuclei being formed, as evidenced by the uniformity in size of the alloy particles.

To determine the relationship between the morphology of the alloy and the crystallographic orientation of the substrate, single crystals of the vacuum-melted iron of the (100), (110), and (111) orientation were used as substrates for tin deposition. The alloy was formed by heating the single crystals at 242°C .

Electron micrographs of the replicas of different crystal faces showed the (111) and (110) crystal faces to be uniformly covered with alloy, whereas

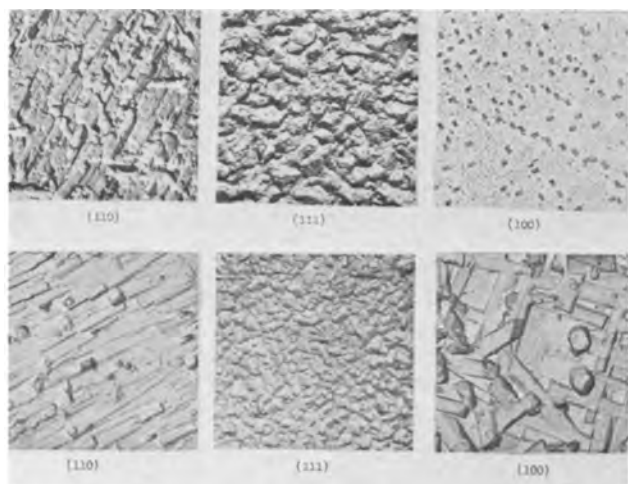


Fig. 5. Comparison of morphology of the alloy formed by melting electrodeposited tin (lower) with that obtained by melting vacuum-deposited tin (upper) on single-crystal substrates (N250). Electron micrographs magnification 17,000X before reduction for publication. Optical micrographs, upper right hand corner, 500X before reduction for publication.

the (100) face was only sparsely covered with relatively few large crystals of alloy, Fig. 5 (upper figures). It can be surmised that the sparsely covered ferrite grains on the polycrystalline material, N250 Fig. 4, were near the (100) orientation.

Since the (100) face of iron has been shown by Bardolle (9) to oxidize more readily than the (111) or (110) orientations at low pressures, it is suggested that the sparsity of alloy on the single crystal of the (100) orientation and on the (100) grains on the polycrystalline material can be attributed to the preferred oxidation of the (100) surface with the residual oxygen during annealing. The oxide(s) thus formed inhibit the interaction of tin and iron to form FeSn_2 . A contributing factor to the inhibition may be that silicon present at a relatively high level in this material (0.02%) may be oxidized to silica at low pressures of oxygen. This reaction appears to take place preferentially on the (100) face. There is independent evidence to indicate that the (100) face of Si-Fe alloys shows increased reactivity in the presence of traces of oxygen or water vapor (10). The uniform growth in the case of the low carbon steel can be attributed to the removal of oxide by the carbon in the steel during the annealing.

A comparison of the morphology of the alloy obtained by melting vacuum-deposited tin with that obtained by melting electrodeposited tin (phenol-sulfonic acid electrolyte) on the same substrate (N250) shows that the alloy morphology on the (110) and (111) orientations produced by either method is similar for a given orientation, Fig. 5 (lower figures). This would indicate that the growth process is the same regardless of either mode of deposition. A comparison of the (100) face cannot be made because of the complicating factors discussed above.

These experiments show that the growth characteristics of an intermetallic compound, as a result of interdiffusion of Sn and Fe, have many features in common with other forms of growth. For instance, Pashley and co-workers (11) have shown, particularly by electron diffraction and electron microscopy, that the initial stages of growth processes by vapor deposition, electrodeposition, and oxidation often involve the formation of isolated three-dimensional nuclei. The electron micrographs in this report also show that alloy growth is not uniform and is a result of growth by discrete particles.

It is now well established that the growth of a chemical compound on a crystal surface often occurs in such a way that the compound crystal shows a definite orientation relative to that of the metal (epitaxy). Although there have been many examples of oriented overgrowth on metals and salts (12), none have been reported for the growth of an intermetallic compound. The results obtained in this investigation clearly show that there is a large degree of epitaxy in the formation of the intermetallic compound FeSn_2 when tin is melted on an iron substrate. The degree of epitaxy, or orienting influence, is dependent on the mode of deposition of tin and on impurities.

Acknowledgment

The authors are indebted to H. Biber of U. S. Steel's Applied Research Laboratory for preparing single crystals of iron with different orientations and for permitting them to refer to his unpublished work on the morphology of the alloy layer found on these crystals.

Manuscript received Aug. 23, 1963; revised manuscript received Oct. 23, 1963. This paper was presented at the New York Meeting, Sept. 29-Oct. 3, 1963.

Any discussion of this paper will appear in a Discussion Section to be published in the December 1964 JOURNAL.

REFERENCES

1. W. E. Hoare and E. S. Hedges, "Tin and Its Uses," Edward Arnold and Company, London (1959).
2. P. A. Stoll, Special Technical Publication ASTM No. 262 (1959).
3. G. G. Kamm and A. R. Willey, "1st Int. Congress on Metallic Corrosion," Butterworth's Press, London, 495 (1961).
4. C. Luner and M. V. Murray, *This Journal*, **110**, 176 (1963).
5. P. E. Stein and J. K. Low, Jr., *Trans. AIME*, **221**, 744 (1961).
6. B. J. Bliss, "Vacuum Technology Transaction," p. 145, Pergamon Press (1960).
7. G. G. Kamm, A. R. Willey, R. E. Beese, and J. L. Krickl, *Corrosion*, **17**, 84t (1961).
8. Y. Fujiki, *J. Phys. Soc. Jap.*, **14**, 913 (1959).
9. T. Bardolle and C. R. Head, *Sci.*, **239**, 706 (1954).
10. J. L. Walter and C. G. Dunn, *Acta Met.*, **8**, 497 (1960).
11. C. A. Bassett, S. W. Menter, and D. W. Pashley, "The Structure and Properties of Thin Films," A. A. Neugebauer, J. B. Newkirk, and D. A. Vermilyea, Editors, J. Wiley & Sons, New York (1959).
12. D. W. Pashley, *Advances in Physics*, **5**, 173 (1956).

Kinetics of Electroluminescent Deterioration in Some ZnS Phosphors

L. A. Rogers¹

Corning Glass Works, Corning, New York

ABSTRACT

The deterioration of ZnS:Cu:halogen electroluminescent phosphors with time is shown to follow second order kinetics. The activation energy for deterioration was found to be about 11 kcal/mole for three chloride coactivated phosphors and 23 kcal/mole for one bromide coactivated phosphor.

The decrease in brightness of an electroluminescent phosphor was found by Roberts (1) to fit the "empirical" equation

$$\frac{B_0}{B} = 1 + \frac{t}{t_{1/2}} \quad [1]$$

where B is brightness at time t , B_0 is the initial brightness, and $t_{1/2}$ is a time constant equal to that when the brightness reaches one half the initial brightness. Differentiation of Eq. [1] gives for the decay rate

$$\frac{dB}{dt} = \frac{-B^2}{B_0 t_{1/2}} \quad [2]$$

Roberts postulated that the second order dependence results from the recombination of dissociated activator and coactivator pairs under the influence of an electric field, and Jaffe (2) suggests diffusion of the anion away from its equilibrium position near the acceptor (copper). Thornton (3) suggested that the decay is associated with trapping states "several tenths of an electron volt below the conduction band."

Taking a general form of the second order rate equation

$$\frac{dA}{dt} = \frac{dB}{dt} = k(A)(B) \quad [3]$$

and letting n_0 and m_0 be the initial concentrations of A and B and letting x be the decrease in concentration of A and B (for the reaction $A + B \rightarrow$ products) at time t , one obtains

$$\frac{dx}{dt} = k(n_0 - x)(m_0 - x) \quad [4]$$

and for the case where n and m are equal Eq. [4] integrates to

$$t = \frac{1}{k(n_0 - x)} - \frac{1}{kn_0} \quad [5]$$

Assuming electroluminescent emission to be directly related to the number of emission centers ($n = n_0 - x$) Eq. [5] can be written as

$$t = \frac{1}{kn} - \frac{1}{kn_0} \quad [6]$$

or $n_0/n = 1 + kn_0 t$.

A plot of time against reciprocal brightness should give a straight line with the slope equal to the

reciprocal of the rate constant. Further, Eq. [6] is identical to Eq. [1] if one assumes

$$kn_0 = 1/t_{1/2} \quad [7]$$

On this basis the "empirical" equation by Roberts is not so empirical after all, but a special case of the second order equation, and the half time constant is the reciprocal of the rate constant times the initial concentration of active centers.

The activation energy for decay can be found by plotting (i) $\ln(1/t_{1/2})$ against $(1/T)$, where T is the absolute temperature, to obtain the Arrhenius activation energy (E_a), or by plotting (ii) $\ln(1/t_{1/2}T)$ against $1/T$ to obtain the absolute reaction rate activation energy (ΔH^\ddagger).

Experimental

Experimentally, three different phosphors were tested in ceramic (glass) cells: U.S. Radium Corporation (USR 3633), Westinghouse (W 133-P), and a ZnS:Cu:Cl phosphor of our own manufacture (CGW).

The cells were operated in a light-tight oven equipped with a window (VYCOR Brand plate glass) to transmit the light to an uncorrected 1P21 phototube. Operation frequency was 400 cps and the applied voltage was adjusted to a field strength of 100 v/mil. Figure 1 is the data obtained for the CGW phosphor plotted according to Eq. [1] so the slope is equal to the reciprocal of the half time constant. Similar plots for data on the USR and W phosphor were also made. Straight lines also were found for these other phosphors with the only com-

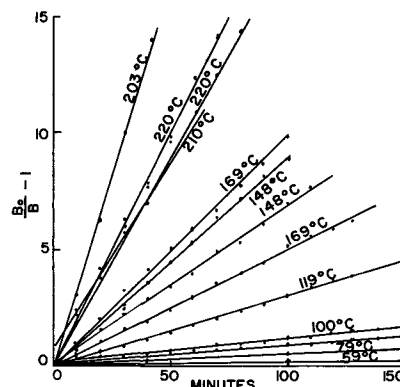


Fig. 1. Plots of brightness-time data in accordance with Eq. [1] for the CGW phosphor in ceramic cells.

¹ Present address: Lawrence Radiation Laboratory, Livermore, California.

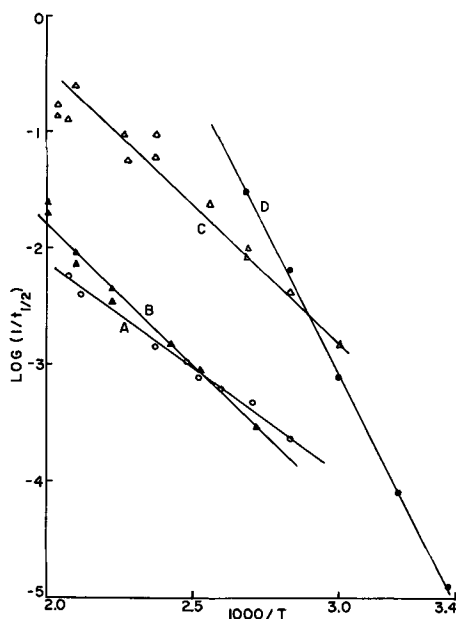


Fig. 2. Arrhenius plots for the deterioration data. A(O)-W; B(\blacktriangle)-USR; C(\triangle)-CGW; D(\bullet) Westinghouse proprietary ZnS:Cu:Br phosphor.

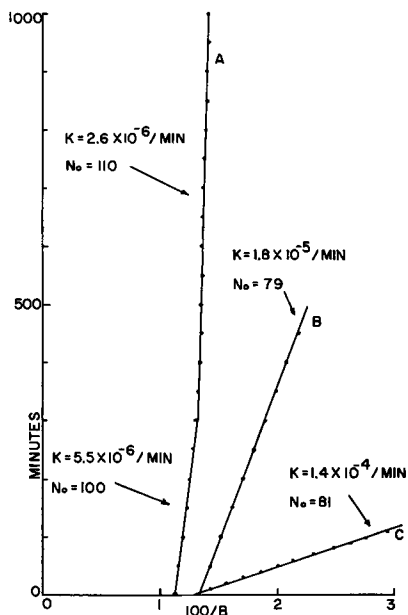


Fig. 3. Typical plots for the brightness-time data plotted in accordance with Eq. [6].

plications being that initial increases in brightness caused the straight line portion of the plots to miss the origin a small amount when they were extrapolated to zero time, and the W phosphor data had changes in slope around 300 min.

Arrhenius plots for the phosphors are given in Fig. 2. An Arrhenius plot for some data taken from a Westinghouse report (4) on some proprietary (ZnS:Cu:Br) phosphor is also included in Fig. 2. Plots of time against $1/B$ for three sets of decay data are given in Fig. 3 in accordance with Eq. [6] where the slope is equal to the reciprocal of the rate constant. The value of n_0 is then found by substituting the rate constant back into Eq. [6]. A thermoluminescence, or glow, curve and an emission as a function of temperature, or thermal quenching curve,

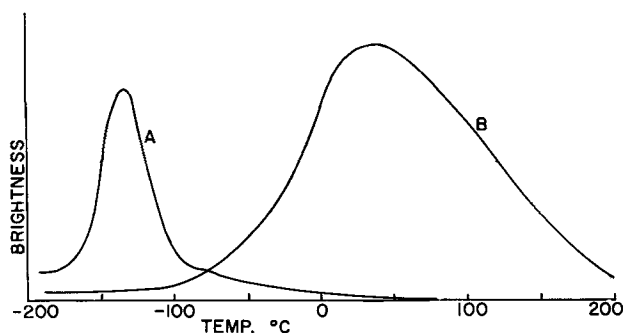


Fig. 4. Glow curve (A) and thermal quenching curve (B) for the CGW phosphor in ceramic cells.

Table I. Activation energies and half times from Arrhenius plots

	E_a , kcal/mole from Arrhenius plots	$t_{1/2}$ @ 25°C, hr.
Corning	11	80
US Radium 3663	11	2000
Westinghouse 133-P	8*	600
Westinghouse Proprietary	23	1200

* For times less than 300 min; for longer times the activation energy is higher, but its value was not evaluated for this study.

is given in Fig. 4. A tabulation of the activation energy and half time constants is given in Table I.

Discussion

The present results are consistent with the postulates of others (1-3) in that second order rate equations are obeyed and that the activation energies for deterioration are several tenths of an electron volt. For the CGW phosphor the thermal quenching of the electroluminescence occurred both above and below room temperature. Apparently some thermal energy combined with the electrical field is required for electroluminescence, and either too much or too little thermal energy quenches the emission.

The exact mechanism has not been determined from the limited data, but in view of the difference in activation energies between the Br coactivated Westinghouse proprietary phosphor and the Cl activated USR, W, and CGW phosphors one would suspect diffusion of the halide ion in the ZnS lattice, or along defects in the lattice, as suggested by Jaffe, to be the rate-controlling step. Another possible mechanism, which seems as likely as that proposed by others, is that diffusion occurs rapidly (possibly the relatively smaller copper ions) and the slow, or rate-controlling, step is the reaction of the copper and halide ions to annihilate a luminescent center. The limited results of the present study, however, are not sufficient to distinguish between the two possible mechanisms.

Manuscript received Oct. 15, 1963.

Any discussion of this paper will appear in a Discussion Section to be published in the December 1964 JOURNAL.

REFERENCES

1. S. Roberts, *J. Appl. Phys.*, **28**, 262 (1957).
2. P. M. Jaffe, *This Journal*, **108**, 711 (1961).
3. W. A. Thornton, *J. Appl. Phys.*, **28**, 313 (1957).
4. R. W. Wollentin, Westinghouse Electric Corp., Bloomfield, New Jersey, A.F. Contract 30(602)-2431, AD291606 ASTIA number.

Chemical Equilibria in the Germanium-Iodine and Germanium-Bromine Systems by Weight-Loss Measurements

F. Jona, R. F. Lever, and H. R. Wendt

Thomas J. Watson Research Center, International Business Machines, Yorktown Heights, New York

ABSTRACT

Simple heterogeneous equilibria can be elucidated by determining the total amount of solid that goes in the gas phase under the action of a known amount of gaseous solvent at a given temperature. This method was first tested satisfactorily with the germanium-iodine system, for which thermodynamic data are already available, and then applied to the germanium-bromine system. The data make it possible to calculate the ratio between total density of germanium atoms and total density of halogen atoms in the gas phase within a wide range of temperatures and pressures. These calculations enable one to predict the direction and the amount of diffusive vapor transport in closed or open vapor-growth systems.

The technique of growing crystals by means of chemical transport reactions (1) has received increasing attention in recent years for its application to the field of epitaxial growth of semiconductors at relatively low temperatures. Several theories have been developed (1-6) which enable one to calculate the diffusion-limited vapor transport of solid in sealed-tube systems, and in a few cases these theories have found satisfactory quantitative confirmation by experiment (1, 7, 8). The pertinent calculations require knowledge of the chemical equilibria involved. Unfortunately, in a number of interesting cases thermodynamic data are only known inaccurately or not at all. In the case of germanium, for example, the usefulness of the growth technique by the iodide process (9) has stimulated a detailed investigation of the germanium-iodine system by Lever (10), who extended the data of Jolly and Latimer (11) concerning the disproportionation of solid GeI_2 . However, data concerning the equally interesting germanium-bromine system are scarce. The heat of formation of germanium tetrabromide is known from Evans and Richards (12), and the entropy from Jolly and Latimer (11), but no reliable information is available concerning germanium dibromide. It is the purpose of the present investigation to collect data capable of clarifying the heterogeneous equilibrium in the germanium-bromine system, and to examine the possibilities and the limitations of this system for the diffusion-limited vapor-growth of germanium. The method of weight-loss measurements chosen for this study, and described below, was first tested, with satisfactory results, on the germanium-iodine system for which thermodynamic data are now available (10).

Method

We are concerned with the heterogeneous system involving solid germanium and a gaseous halogen X_2 , where for this discussion X is either I or Br. Following Lever (10), we assume a model in which the only species present in the gas phase are GeX_4 , GeX_2 , X_2 , and X, but the concentrations of the two

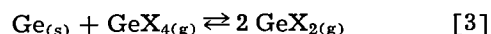
latter species, X_2 and X, are negligible. Suppose that the system is in equilibrium in some volume V at the temperature T and that we have some means to determine the total number of moles of Ge in the gas phase (n_{Ge}) as well as the total number of moles of the halogen X ($n_{\text{X}}^{\text{tot}}$). Calling n_{GeX_4} and n_{GeX_2} the amounts of GeX_4 and GeX_2 , respectively, in the gas phase it follows for the model assumed that

$$\text{and } \left. \begin{aligned} n_{\text{Ge}} &= n_{\text{GeX}_4} + n_{\text{GeX}_2} \\ n_{\text{X}}^{\text{tot}} &= 4 n_{\text{GeX}_4} + 2 n_{\text{GeX}_2} \end{aligned} \right\} \quad [1]$$

from which we can calculate

$$\left. \begin{aligned} n_{\text{GeX}_4} &= \frac{1}{2} n_{\text{X}}^{\text{tot}} - n_{\text{Ge}} \\ n_{\text{GeX}_2} &= 2 n_{\text{Ge}} - \frac{1}{2} n_{\text{X}}^{\text{tot}} \end{aligned} \right\} \quad [2]$$

With these quantities, we are in a position to calculate the equilibrium constant of the disproportionation reaction



[(s) = solid, (g) = gas], namely

$$K = p_{\text{GeX}_2}^2 / p_{\text{GeX}_4} = n_{\text{GeX}_2}^2 RT / n_{\text{GeX}_4} V \quad [4]$$

In principle, then, the experiment can be carried out as follows. A piece of Ge, properly cleaned and accurately weighed, is introduced into a suitable container of volume V which is evacuated and then backfilled with a predetermined amount of halogen ($n_{\text{X}}^{\text{tot}}$). The tube is then introduced into a furnace already at the temperature T (a flat temperature profile over the length of the tube is of course necessary to avoid vapor transport during the run) and kept at this temperature for a period of time judged sufficient to attain equilibrium. The tube is then extracted from the furnace, rapidly quenched to room temperature, and finally cut open. The Ge piece is weighed again and the difference between initial and final weight is the amount sought (n_{Ge}) provided that certain precautions are taken which are discussed below.

The experiment as described above yields directly the ratio between the density of germanium atoms

and that of halogen atoms in the gas phase, a quantity that has been previously denoted by η and has been shown to be convenient for discussing problems of vapor-solvent growth (5, 13). Knowledge of this quantity as a function of temperature allows one to make predictions about the direction of diffusive vapor transport in sealed systems, even if the gaseous species involved are not known and the related chemical equilibria are very complicated. In simple systems such as those considered in the present study weight-loss experiments can yield also thermodynamic data, as shown above.

The precautions needed for the experiments to be meaningful are discussed in the following.

(a) Quenching of the sample tube at the conclusion of each run is conveniently done by spraying cold water directly onto the tube-end opposite that in which the Ge piece is located. In this way, one avoids condensation of the germanium halides onto the germanium piece whose weight-loss is to be determined.

(b) Within the model assumed here, the behavior of η at a given temperature T is depicted schematically in Fig. 1 as a function of halogen density. The value of η cannot be lower than 0.25, which corresponds to a vapor phase consisting exclusively of GeX_4 (unless the density of free halogen becomes appreciable, as happens at high temperatures and low pressures in the germanium-iodine system and is indicated by the dotted curve in Fig. 1), and cannot be higher than 0.5, which corresponds to a vapor phase consisting exclusively of GeX_2 . It is obvious that one will want to work with halogen densities in the immediate vicinity of point A in Fig. 1, not only because this will minimize the errors involved in the determination of very small quantities but also because of the following point. Much to the right of point A, i.e., at high pressures (and, in particular, low temperatures) one runs the risk of exceeding the vapor pressure of GeX_2 . If this happens, the weight-loss of the Ge sample will obviously not be representative of the germanium content in the gas phase, and the conclusions drawn from such an experiment will be erroneous.

Experimental Procedure

The containers used for the runs were silica tubes with internal diameter of 22-23 mm and approximately 30 cm long. The volume was measured before each run using a simple water-filling procedure

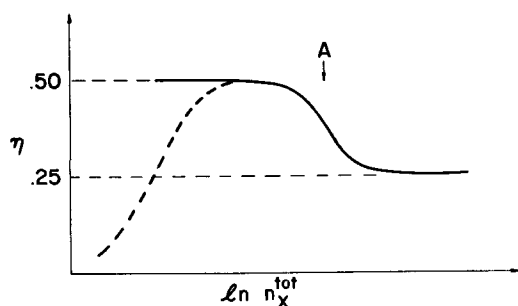


Fig. 1. Dependence of $\eta = N_{\text{Ge}}/N_{\text{X}}^{\text{tot}}$ on density of halogen X at a given temperature T (schematic). Dashed curve: typical low-pressure and high temperature behavior for X = iodine.

and was found to range between 100 and 110 cm^3 . The Ge samples were 1 cm long parallelepipeds (approximately 0.5g in weight) cut from zone-refined, polycrystalline, intrinsic germanium ingots (~ 40 ohm-cm). They were etched for 3 min in "white etch" ($5\text{HNO}_3:1\text{HF}$) and thoroughly rinsed with demineralized water just before they were weighed and introduced into the silica tubes.

These tubes were connected, through a constriction, to a quartz chamber containing either the iodine or the bromine capsule previously prepared (see below). The quartz chamber, in turn, was provided with a ground-glass joint that allowed connection of the whole assembly to the vacuum system. After flaming in vacuo of the order of 10^{-6} Torr the assembly was sealed off the system with a torch. The halogen capsule was broken with a magnet hammer and the halogen distilled into the sample tube by cooling the latter with liquid nitrogen. Finally, the sample tube was sealed off at the constriction.

Known amounts of iodine were introduced into the tube by preparing capsules with a procedure similar to that described by Silvestri and Lyons (14). It is estimated that, taking into account the corrections required by the procedure, the error in the amount of iodine was $\pm 1\%$, causing an error of $\pm 10\text{-}20\%$ in the value of the equilibrium constant K , the larger error being in the range of low values of K .

A different procedure was followed for the preparation of bromine capsules. A certain amount of bromine was distilled in vacuo into a precision-bore capillary tube that was previously provided with a break-off tip and finally sealed off. The bromine volume was then measured by determining the height of the bromine column with a cathetometer; a correction for the meniscus curvature was applied by assuming semispherical shape for the meniscus. The radius of the precision-bore capillary ($r = 7.63 \times 10^{-2}$ cm) was measured in advance by determining the height of a mercury column whose weight was measured with a microanalytical balance. The final amount of bromine was calculated by taking into account also the bromine vapor contained in the space above the liquid within the break-off tip capsule. It was estimated that the error in the final bromine amount was as high as $\pm 1\%$ in the range of small bromine contents, much smaller for the larger bromine contents.

The weights of the germanium slugs were measured on a microanalytical balance with an accuracy of ± 0.01 mg. Therefore, in the range of small germanium weight losses (of the order of 2 mg), the error involved may have been as high as $\pm 1\%$, which alone would cause an error in K of about $\pm 25\%$. In the range of large values of K the experimental error is expected to be markedly smaller.

Results

Figure 2 depicts the equilibrium constant K of the disproportionation reaction [3] as a function of reciprocal temperature. The dashed line represents the result obtained earlier by Lever (10) for the germanium-iodine system on the basis of total pres-

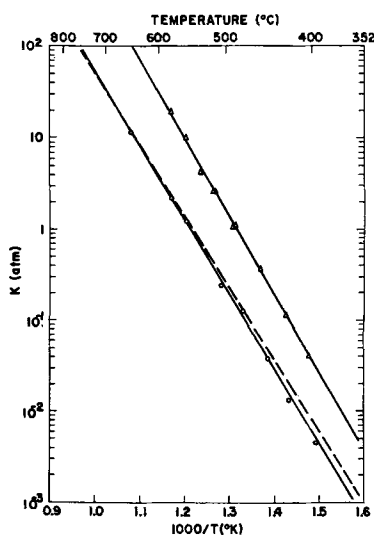


Fig. 2. Equilibrium constant vs. reciprocal temperature. Germanium-iodine system: the dashed line represents Lever's result (10), the circles (and the solid line through them) the result of the present weight-loss measurements. Germanium-bromine system: triangles represent results of weight-loss runs.

sure measurements by means of a Bourdon gauge. The solid line (and the circles) is the result of the present study of the same system. The agreement between the two results is to be considered very good within the range of the experimental errors of both methods. The solid line through the triangles represents the result of the present weight-loss measurements in the germanium-bromine system. The pertinent thermodynamic data are summarized in Table I.

Two more experiments were carried out that are not apparent in Fig. 2. The purpose of these experiments was only to check the model for the germanium-bromine system, *i.e.*, to confirm that even in the high-temperature and low-pressure range there are no considerable amounts present, in the vapor phase, of halides lower than GeBr_2 . This was done by checking that in that range the quantity η does not exceed the value 0.50 considerably (see Fig. 1), although the data obtained were not sufficiently accurate for the calculation of K values. The two experiments, carried out with a bromine density of the order of 10^{-2} moles/liter at 920° and 1000°K yielded η values of 0.49 and 0.48, respectively, thus confirming that the model assumed initially is substantially correct within the temperature range of interest.

Discussion

As mentioned earlier, it is convenient for vapor-growth purposes to know the behavior of the quan-

Table I. Enthalpy ΔH and entropy ΔS of the disproportionation reaction $\text{Ge}_{(s)} + \text{GeX}_{4(g)} \rightleftharpoons 2 \text{GeX}_{2(g)}$ in the temperature range $T \cong 900^\circ\text{K}$

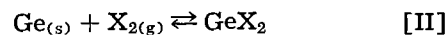
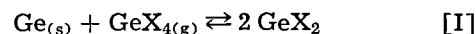
Method	ΔH , kcal/mole		ΔS , cal/mole deg	
	X = I	X = Br	X = I	X = Br
Total-pressure measurements (Bourdon gauge) (10)	36.3	—	44.3	—
Weight-loss measurements	37.7	39.4	45.8	51.9

tity η over a wide range of temperatures and pressures. It has been shown previously (5) that the diffusive transport of solid J_s in a vapor-solvent growth system can be calculated as

$$J_s = -ND(N_x^{\text{tot}}/N)(d\eta/dx)$$

where N is the total molar density of the vapor phase, D an average diffusion coefficient applying to every pair of vapor species, $N_x^{\text{tot}} = n_x^{\text{tot}}/V$ the total gram atomic density of all solvent atoms in the gas phase, and $(d\eta/dx)$ the gradient of the quantity η previously defined. If the dependences of ND and N_x^{tot} upon x are neglected, J_s is given essentially by $(d\eta/dx)$, or, in a closed tube system, by $(\Delta\eta/\Delta T)(\Delta T/\Delta x)$ where ΔT is the temperature difference between source and seed located a distance Δx apart from one another.

It was decided, therefore, to use the thermodynamic data presently available in both the germanium-iodine and the germanium-bromine systems to calculate η beyond the range of pressures and temperatures covered by the present experimental work. For this purpose, the assumption made initially, that the densities of molecular and atomic halogen in the vapor phase are negligible, was relieved. It was chosen to describe each system with the three following equilibria:



For both $X = \text{I}$ and $X = \text{Br}$, the equilibrium constants K_I of reaction [I] are known from Lever's (10) and the present work. The heats of formation of GeBr_4 and GeI_4 were taken from Evans and Richards (12), the entropies from Jolly and Latimer (11) and the remaining thermodynamic data necessary to calculate the equilibrium constants K_{II} and K_{III} of reactions [II] and [III], respectively, were taken from the compilation of Kubaschewski and Evans (15) for both $X = \text{I}$ and $X = \text{Br}$.

The calculation procedure was the following. Given a temperature T , the values of K_I , K_{II} , and K_{III} were calculated. Then, given a series of values for p_{GeX_2} , the corresponding values of p_{GeX_4} were calculated from K_I , of p_{X_2} from K_{II} and of p_{X} from K_{III} , where p_{GeX_2} , p_{GeX_4} , p_{X_2} , and p_{X} are the respective partial pressures of the species written as subscripts. It was then possible to calculate

$$p_{\text{Ge}} = N_{\text{Ge}}RT = p_{\text{GeX}_4} + p_{\text{GeX}_2}$$

$$p_{\text{X}}^{\text{tot}} = N_{\text{X}}^{\text{tot}}RT = 4p_{\text{GeX}_4} + 2p_{\text{GeX}_2} + 2p_{\text{X}_2} + p_{\text{X}}$$

and hence the ratio of the two latter quantities, $p_{\text{Ge}}/p_{\text{X}}^{\text{tot}} = \eta$, which could then be plotted as a function of $p_{\text{X}}^{\text{tot}}$ (see Fig. 1). For practical purposes, it was found convenient to plot the final results in the way depicted in Fig. 3 for the germanium-iodine and in Fig. 4 for the germanium-bromine system.

In these plots, lines of constant values of $(\eta \times 100)$ have been drawn as a function of halogen density and of temperature. For convenience, the ordinate has also been converted, on the right hand side, into

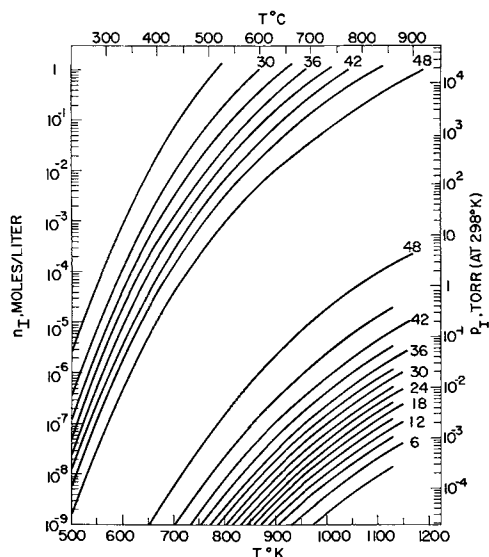


Fig. 3. Germanium-iodine system: curves of constant ($\eta \times 100$) as functions of iodine density N_I and of temperature. The quantity p_I is the pressure that the iodine would exert as a monoatomic gas in the given container at room temperature.

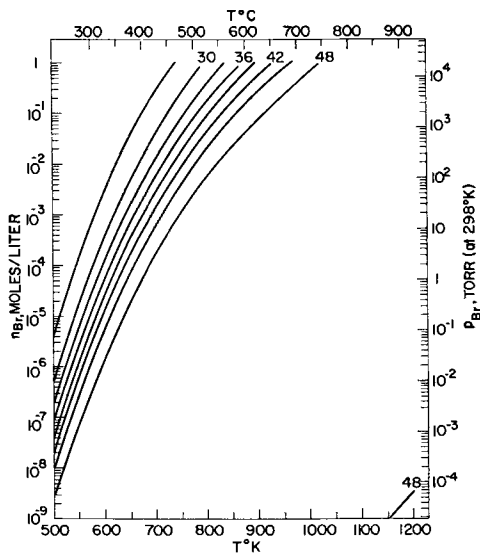


Fig. 4. Germanium-bromine system: curves of constant ($\eta \times 100$) as functions of bromine density N_{Br} and of temperature. The quantity p_{Br} is the pressure that the bromine would exert as a monoatomic gas in the given container at room temperature.

the pressure in Torr that the halogen would exert as a monoatomic gas at room temperature. We see that the two vapor-growth systems considered here differ from one another in at least one aspect. In both systems there are regions, at low temperatures and moderate to high pressures, where the diffusive transport of solid occurs from higher to lower temperatures ("hot to cold"). For example, in the germanium-iodine system (Fig. 3), if the source is located at 500°C and the seed at 450°C, in a closed tube filled with 100 Torr of I the value of η will decrease from 0.39 at the source to 0.33 at the seed, and transport will obviously occur in the direction of decreasing η , hence from hot to cold. However, at high temperatures and low pressures the situation is reversed in the germanium-iodine system, and transport has in fact been observed (16) to

occur from cold to hot. This is not the case in the germanium-bromine system (Fig. 4), at least in the range of conveniently attainable bromine pressures.

It may be of interest to point out that in a plot of $\ln p_X^{tot}$ vs. $1/T$ the curves of constant η would be straight lines in the present cases. This can be seen as follows. Since η is essentially given by

$$\eta(2p_{GeX_2} + 4p_{GeX_4}) = p_{GeX_2} + p_{GeX_4}$$

and hence

$$p_{GeX_2}/p_{GeX_4} = (4\eta - 1)/(1 - 2\eta)$$

we can express p_{GeX_2} in terms of the equilibrium constant K from the relationship

$$K = (p_{GeX_2})^2/p_{GeX_4} = p_{GeX_2}(4\eta - 1)/(1 - 2\eta)$$

Thus, since

$$p_X^{tot} = 2p_{GeX_2} + 4p_{GeX_4} = 2p_{GeX_2}/(4\eta - 1)$$

we obtain

$$p_X^{tot} = 2K(1 - 2\eta)/(4\eta - 1)^2$$

and hence

$$\ln p_X^{tot} = \ln K + f(\eta)$$

For a single-reaction system, the plot of $\ln p_X^{tot}$ vs. $1/T$ will then consist of a family of straight lines all parallel to the line giving $\ln K$ vs. $1/T$. In the germanium-iodine system, where two different reactions predominate in different regions, the same plot will consist of two families of straight lines with different slopes, given by the two different equilibrium constants.

While the η -plots depicted in Fig. 3 and 4 are useful for work with closed-tube vapor-growth systems, when doing experiments with "open-tube" or continuous-flow systems a change of ordinate becomes necessary. In such systems the appropriate variable is the ratio of the pressure of halogen to that of the carrier gas, e.g., p_X^{tot}/p_{He} if helium happens to be the carrier gas.¹ Thus, instead of plotting η as a function of p_X^{tot} and temperature, it is more convenient, for open-tube work, to plot it as a function of the aforementioned ratio and temperature. This ratio can be calculated with the same procedure outlined above, since

$$p_X^{tot}/p_{He} = p_X^{tot}/(1 - P)$$

where P is the total pressure in atmospheres exerted by all gaseous species except helium

$$P = p_{GeX_4} + p_{GeX_2} + p_{X_2} + p_X$$

In a practical open-tube experiment, where the over-all pressure is 1 atm, the temperature of the halogen bed (i.e., the vapor pressure of the halogen) is what establishes the actual value of said ratio. This is given by

$$p_X^{tot}/p_{He} = 2p^*/(1 - p^*)$$

where p^* is the vapor pressure of the halogen X_2 expressed in atmospheres.

¹ The total fluxes of halogen and carrier gas must be conserved since neither sources nor sinks exist for these substances within the system. Hence the ratio of these fluxes must be constant throughout the system. For viscous flow conditions, this implies a constant ratio of the corresponding densities from which follows the constancy of the ratio p_X^{tot}/p_{He} .

Acknowledgment

We like to express our appreciation for the partial support of this study by the Air Force Office of Scientific Research of the Office of Aerospace Research under Contract AF 49 (638) -1201.

Manuscript received July 11, 1963. This paper was presented at the New York Meeting, Sept. 29-Oct. 3, 1963.

Any discussion of this paper will appear in a Discussion Section to be published in the December 1964 JOURNAL.

REFERENCES

1. H. Schaefer, "Chemische Transportreaktionen," Verlag Chemie, Weinheim (1962).
2. G. Mandel, *J. Phys. Chem. Solids*, **23**, 587 (1962).
3. R. F. Lever and G. Mandel, *ibid.*, **23**, 599 (1962).
4. R. F. Lever, *J. Chem. Phys.*, **37**, 1174 (1962).
5. R. F. Lever, *ibid.*, **37**, 1078 (1962).
6. G. Mandel, *ibid.*, **37**, 1177 (1962).
7. F. Jona, *J. Phys. Chem. Solids*, **23**, 1719 (1962).
8. F. Jona and G. Mandel, *J. Chem. Phys.*, **38**, 346 (1963).
9. R. P. Ruth, J. C. Marinace, and W. C. Dunlap, *J. Appl. Phys.*, **31**, 995 (1960).
10. R. F. Lever, *This Journal*, **110**, 775 (1963).
11. W. L. Jolly and W. M. Latimer, *J. Am. Chem. Soc.*, **74**, 5754 (1952).
12. D. F. Evans and R. E. Richards, *J. Chem. Soc.*, **1952**, 1292.
13. R. F. Lever and F. Jona, *J. Appl. Phys.*, **34**, 3139 (1963).
14. V. J. Silvestri and V. J. Lyons, *This Journal*, **109**, 963 (1962).
15. O. Kubaschewski and E. LL. Evans, "Metallurgical Thermochemistry," Pergamon Press, New York (1958).
16. R. F. Lever, Unpublished work.

Effect of Solution Trace Impurities on I-V Characteristics of Electrodeposited Surface Barrier Diodes

G. M. Krembs and M. M. Schlacter

Philco Scientific Laboratory, Blue Bell, Pennsylvania

ABSTRACT

Radioisotopes were used to determine the surface concentrations of metallic impurities introduced on mechanically polished Ge surfaces during acid clean-up etching and jet electrodeposition. Reagent grade chemicals, to which were added radioactive metallic ions in the concentration range below 1 ppm, were used in the experiments. Surface coverage ranged from fractional monolayers in acid etching to several monolayers in jet electrolysis. In jet electrodeposition, autoradiograms revealed that noble metal impurities are chemically plated onto Ge electrodes, the distribution being a function of the hydrodynamic flow pattern, but independent of current density. The strong influence of these metallic impurities on the reverse I-V characteristics of surface barrier diodes is due to a p-type channel.

Trace metal impurities, present in reagent grade chemicals in the concentration range below 1 ppm, have been reported to influence the electrical characteristics of a germanium surface (1-4). In this paper, a similar investigation is reported on surface barrier metal contacts. Radiochemical methods were utilized in a study of acid clean-up etching and jet electrodeposition to measure quantitatively the amount of selected metallic impurities deposited on Ge surfaces, and to correlate these chemical data with the I-V characteristics of the metal-semiconductor contacts prepared by this method.

Metallic Impurities Deposited from Acid Etchants

In the initial experiment, the objective was to measure the surface concentration of metallic impurities introduced by the etchant used to remove the mechanically damaged surface layer prior to electrodeposition of the surface barrier contact. The etchant was prepared with electronic grade reagents in the concentration 15 parts by volume acetic (glacial), 8 parts HNO₃ (70%), and 5 parts HF (49%). Ag and Fe were chosen to represent the groups of metallic impurities which are more noble and more active, respectively, than hydrogen in the electromotive series. From a spectrographic analysis, it was deter-

mined that the 15:8:5 etch used in these experiments had 5 ppb of Ag and 50 ppb of Fe before the addition of the radiotracers. To this etchant were added standardized solutions obtained from Oak Ridge National Laboratories received with 99% radiochemical purity. Because of the dilution by the starting etchant, no further purification of the radiochemicals was necessary.

Ge disks with a total front and back surface area of 7.6 cm² were mechanically polished on the (111) face and then dipped into the etchant for a range of time intervals. From the measured count rates, it was found that a 5-sec etch was sufficient for a steady state to be established between the deposition of the impurity and its continued removal via the etching process. The wafers were then rinsed in deionized water and dried in an air jet.

No Fe-59 was detected on the Ge wafer at the highest concentration tested, which was 4 ppm. The minimum surface coverage of Fe detectible for these experimental conditions was 7.4 x 10¹⁰ at./cm² or about 10⁻⁴ monolayers. [Holmes (1) has reported that Fe was deposited from alkaline etchants, such as KOH or NaOH.]

Ag-110 was readily detected on the Ge wafer at an etchant concentration of 50 ppb and, based on pre-

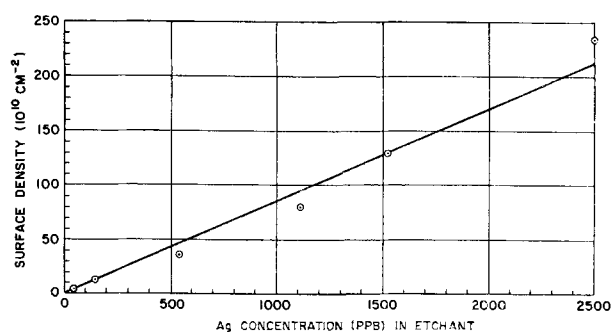


Fig. 1. Steady-state surface density of Ag on Ge as a function of etchant concentration.

vious instrument calibration, was calculated to be 5×10^{10} at./cm². Similar measurements, taken over the range of silver concentration up to a maximum of 2.5 ppm, indicated that this surface coverage increased directly with Ag concentration in the etchant, as shown in Fig. 1. The linear curve was considered the best fit to the experimental points.

To achieve reproducible data in these experiments, careful control of the rinsing technique was required. By reproducible data is meant the time average counting rate (after correction for background) was within the variance of the statistical Poisson distribution. The lowest net surface coverage for a specific solution concentration was obtained when the Ge disk was removed from the etchant and immediately washed in a water jet. Hence, this procedure was standardized for the collection of these data. Flushing the etchant from the beaker with a large stream of deionized water or transporting the wafer through a 4 sec room air exposure to an ultrasonic rinsing bath resulted in nonreproducible, higher counting rates.

Deposition of Ag Impurities during Jet Electrolysis of Cd

In the study of jet electrolysis, the objective was to measure the surface concentration and distribution of metallic impurities which are deposited simultaneously with the surface barrier metal contact on the Ge electrode, and to compare this surface concentration with that previously obtained for the acid-etched surface.

The Ge blanks [0.7 ohm-cm n-type polished on (110) surface] were soldered to a Ni tab for an ohmic contact and pre-etched in the jet stream in a 15:8:5 etchant for 3 sec with 0.15 ma etching current. The jet orifice had a diameter of 9 mils and the pressure was 10 psi. With the same pressure and current, the Cd dot was deposited in 10 sec from an electrolyte of the following composition: 15.15g Cd (BF₄)₂ solution, aqueous (assay 50.3%); HBF₄ to adjust pH between 2.1 to 2.4; 0.14 ml acid addition agent (Enthone, Inc., New Haven, Conn.); 990 ml deionized water; 0.222 ml AgNO₃ solution (assay 0.028%) for 40 ppb formulation. The experimental procedure is similar to that described by Tiley and Williams (5). After a subsequent rinse for 10 sec in a deionized water stream the Ge electrodes were dried in a gas jet of the same composition as the surrounding atmosphere and counted in a G-M gas flow counter.

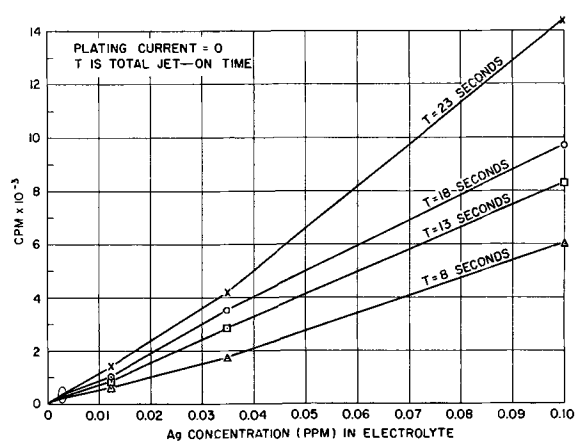


Fig. 2. Total radioactive Ag on Ge surface as a function of electrolyte concentration.

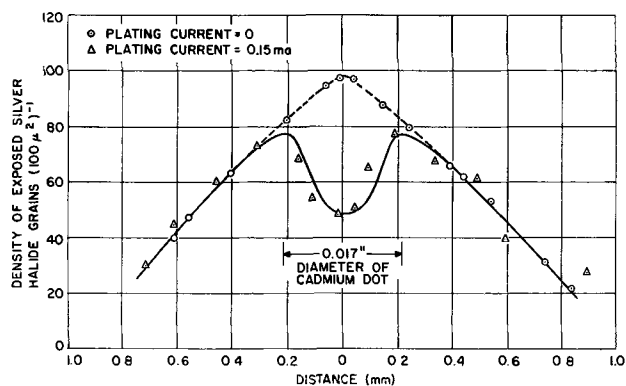


Fig. 3. Topological distribution of Ag co-deposited with Cd.

Without any applied external potential, radioactive Ag was deposited on the Ge blank, as shown in Fig. 2; the activity increased with electrolyte concentration and with the length of time the jet was in contact with the Ge surface. Units made from a recycled electrolyte had a slightly lower activity due to depletion of the Ag from the fresh solution.

In Fig. 3 is shown the result from grain counting of an autoradiogram prepared on the radioactive unit made at zero current density. In comparison to the noble metal surface concentration measured after acid etching, the average surface concentration following jet electrodeposition was 10^4 times higher. Ag-110 was detected over the entire Ge blank, but was more highly concentrated under the impinging jet. When an external potential was applied, the resulting Cd deposit fogged the nuclear film superimposed on it. Therefore, autoradiograms were prepared as shown in Fig. 4. Saran film was used to prevent a chemical reaction between the nuclear emulsion and the Cd deposit. The films were subsequently exposed for 4 hr while stored in a refrigerator at 3°C and developed; there was no influence on the emulsion when the Cd deposit was covered by the protective film of Saran.

Figure 5 is a photomicrograph taken at the edge of the Cd deposit, showing the individual grains of this autoradiogram. When this grain density was counted outside of the region of the Cd deposit, there was no increase in the Ag concentration over that measured for zero plating current. The distribution

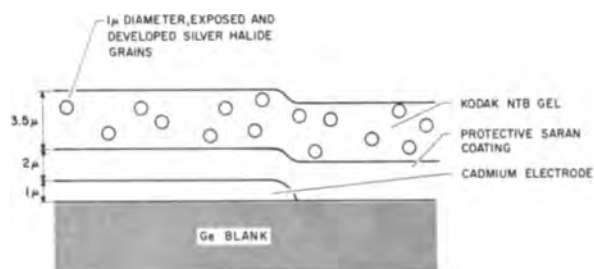


Fig. 4. Cross section of nuclear film formed on Ge electrode

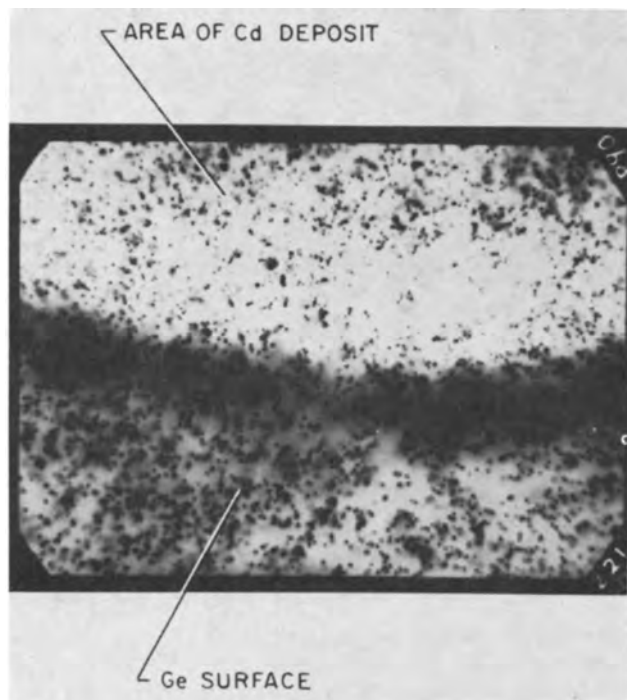


Fig. 5. Photomicrograph of autoradiogram developed and observed *in situ*. The lighter region is due to the greater reflectivity of the Cd metal deposit. (1200X).

of grain density in this case with plating current is shown in Fig. 3 for comparison. Since the resolution of autoradiography is limited to about 5μ , it is not possible to determine with this technique whether the Ag nucleated at localized sites on the Ge surface as reported by Frankl for Cu on Ge (6). If a homogeneous surface coverage is assumed, a grain density of 100 per 100 square microns is equivalent to 2.2 monolayers on the (110) plane, after corrections are made to account for beta backscattering and the counting efficiency of the gas-flow Geiger-Mueller counter. Although it has been shown by Holmes and Neuman (7) with electron diffraction that the adsorbed silver forms oriented crystallites on Ge surface, the average surface coverage can be stated in equivalent monolayer coverage.

The decrease in developed grain density near the Cd deposit is due to absorption of the beta particles. Gamma rays and energetic beta particles are not efficient in exposing NTB emulsion, compared to the less energetic (8) beta rays. Furthermore the weak beta ray in Ag-110m, which is the most probable particle emission (9), has a maximum range in Cd metal of 10μ (10). Since the thickness of Cd in the

center of the deposit is about 5μ , the observed decrease in grain density can be explained as due to absorption of these weak beta rays within the Cd deposit. To prove that the nuclear film was not stretched by the Cd deposit, an optical lens system with small depth-of-focus was used to check the film thickness by sweeping the field and observing the two extremes at which developed grains came into focus. The emulsion thickness was 3.5μ over the entire surface area.

Correlation with Electrical Characteristics

To determine the influence of this concentration range of Ag impurities on the reverse I-V characteristics of a surface barrier diode, a diode testing station was constructed inside a glove box, together with a jet etch-plate station, a water jet rinse, and a gas jet dryer. After plating the Cd deposit, a deionized water rinse was used to clean the surface of residual electrolyte. The atmosphere inside the glove box could be changed from room air of $50\pm 5\%$ relative humidity to argon containing less than 100 ppm of water vapor, as measured on a Meeco moisture analyzer. The gas used in the dryer was the same as the glove box atmosphere.

Figure 6 shows the I-V characteristics, as displayed on an X-Y oscilloscope, where only the trace associated with increasing voltage has been reproduced. The normal hysteresis loop observed during the return trace with decreasing voltage is not included to preserve graphic simplicity. Zero time is defined to be the start of the jet drying time.

The higher leakage currents and higher breakdown voltage of the diodes containing the surface coverage of silver are characteristic properties of an inversion layer and cannot be attributed to an oxide layer since all diode surfaces had an oxide layer formed during the various processing steps of etching, deposition, rinsing and drying. In other words, Ag forms a p-type channel on these oxidized Ge electrodes, similar to that reported for adsorbed Cu by Morrison (2). To confirm this conclusion, we measured the same diodes after 30-min exposure to

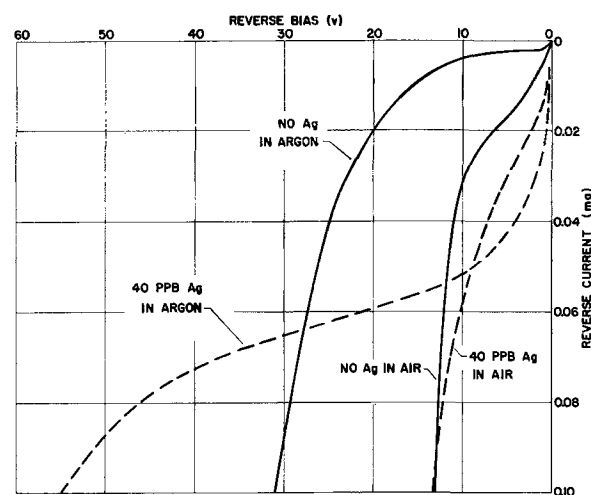


Fig. 6. Reverse I-V characteristics of surface barrier diodes prepared by jet electrodeposition after 3 min in a controlled atmosphere.

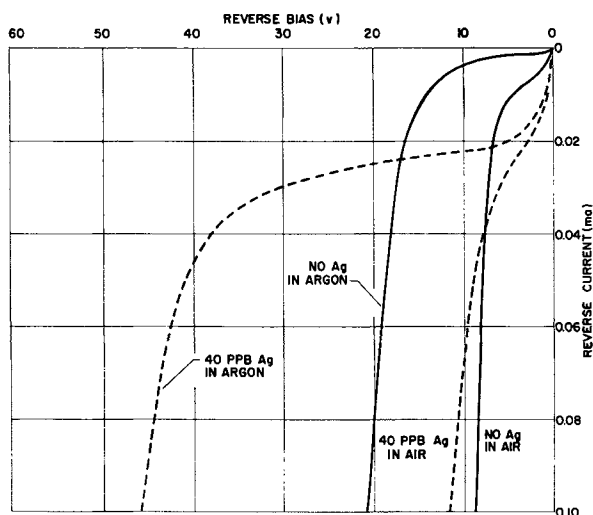


Fig. 7. Reverse I-V characteristics after 30 min in controlled atmosphere.

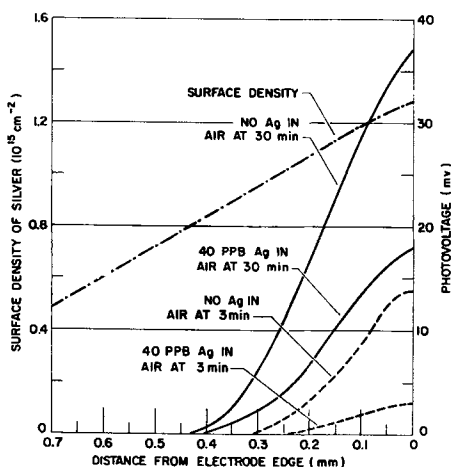


Fig. 8. Photoresponse of the surface barrier diode prepared by jet electrodeposition.

their respective atmospheres. Figure 7 shows the characteristic n-type shift due to the slow states generated by the water adsorbed on the surface and in equilibrium with moisture in the glove box atmosphere. The growth of this accumulation layer causes a lower leakage current and breakdown voltage compared to the data taken at 3 min in Fig. 6.

In addition to the change of surface potential, surface recombination velocity increases, as is apparent in the photoresponse data taken simultaneously with the previous I-V curves, and shown in Fig. 8. The photon source was a flying spot scanner imaged through a lens mounted in the glove box wall.

Deposition of Other Trace Impurities during Jet Electrolysis

Similar experiments were conducted with Cu-64 in both the acid etchant and jet electrolyte. For the same range of Cu-64 in the starting solutions, surface coverage was qualitatively comparable to Ag-110m in both cases. In reference to the electromotive series, Ag and Cu would be expected to behave similarly, and the extension of this study to other noble metal ions would also follow the laws of electrokinetics.

Conclusion

It has been shown experimentally that noble metal impurities are chemically plated onto Ge surfaces during both acid etching and jet electrodeposition, and that electropositive elements, such as Fe, if present at all, were deposited at a much lower concentration. The average surface coverage of Ag and Cu ranged from approximately 10^{-4} monolayers in acid etching to several monolayers after jet electrodeposition. Electrical measurements showed that Ag is an active recombination center on the oxidized Ge surface as well as a p-type dopant. At trace solution concentrations, such noble metal impurities had strong influence on the reverse diode electrical characteristics.

Acknowledgment

The authors are grateful to B. Cahan and Dr. G. Schnable for helpful discussions, and to F. Acampora for assistance in collection of the experimental data. Special thanks are due to C. V. Bocciarelli and R. A. Williams for their continued interest in this work.

Manuscript received Feb. 25, 1963. This paper was presented at the Los Angeles Meeting, May 6-10, 1962.

Any discussion of this paper will appear in a Discussion Section to be published in the December 1964 JOURNAL.

REFERENCES

1. P. J. Holmes, "The Electrochemistry of Semiconductors," P. J. Holmes, Editor, p. 333, Academic Press, New York (1962).
2. S. R. Morrison, *Phys. Chem. Solids*, **14**, 214 (1960).
3. D. R. Frankl, *This Journal*, **109**, 238 (1962).
4. P. J. Boddy and W. H. Brattain, *ibid.*, **109**, 812 (1962).
5. J. W. Tiley and R. A. Williams, *Proc. Inst. Radio Engrs.*, **41**, 1706 (1953).
6. D. R. Frankl, *Phys. Rev.*, **128**, 2609 (1962).
7. P. J. Holmes and R. C. Newman, *Proc. I.E.E.*, **B106**, (Suppl. 15), 287 (1959).
8. G. A. Boyd, "Autoradiography in Biology and Medicine," p. 46, Academic Press, New York (1955).
9. D. Strominger, J. M. Hollander, and G. T. Seaborg, *Rev. Mod. Phys.*, **30**, 683 (1958).
10. "Radiological Health Handbook," S. Kinsman, Editor, p. 85, R. A. Taft Sanitary Engineering Center, Cincinnati (1954).

Controlled Massively Defective Crystalline Solutions with the Fluorite Structure

Della M. Roy and Rustum Roy

*Materials Research Laboratory and Department of Geochemistry and Mineralogy,
The Pennsylvania State University, University Park, Pennsylvania*

ABSTRACT

Fluorite-structure compounds form a rare example of ionic species containing vacancies and interstitials in very high concentrations (up to 50 mole-%). With the formation of substitutional defects incorporating the "half-breed" derivatives of the type NaLnF_4 (Ln = lanthanon and yttrium) the possibility of controlling a whole series of properties of fluorite for applications such as lasers is apparent. Crystalline solubility is extensive in binary systems of the type $\text{CaF}_2\text{-NaLnF}_4$, $\text{CaF}_2\text{-LnF}_3$, and $\text{NaLnF}_4\text{-LnF}_3$, and in ternary systems $\text{CaF}_2\text{-NaLnF}_4\text{-LnF}_3$. Unit cell dimension, density, and refractive index measurements confirm the existence of interstitial F^- as the major defect in $\text{CaF}_2\text{-LnF}_3$ and $\text{NaYF}_4\text{-YF}_3$ type structures, while simple substitutional defect structures exist between CaF_2 and NaLnF_4 . Ternary compositions can show a controlled combination of the two types of defect. Certain of the crystalline solutions have been shown to exhibit photoluminescence and cathodoluminescence.

All crystalline solids are "defective" in some respect, chemically or physically, if described on a sufficiently small scale, and a knowledge of the type and concentration of defects under a prescribed set of conditions is important in understanding the physical and chemical properties of the material. Some defect types readily attain an equilibrium value under a given set of conditions, while others do not. The present investigation undertakes to describe certain equilibrium defects resulting from chemical substitutions on a gross scale in the fluorite structure. This structure, the chemical entity CaF_2 and the structural family which bears its name, is especially interesting in that it may contain a large concentration of defects, as well as a variety of defects. Furthermore, the CaF_2 structure is one of the most important host crystals for solid-state lasers, and the variety of possible substitutions creates interesting possibilities for control of properties. For example, the substitution of a range of rare earth fluorides in the fluorite structure may be expected to produce considerable variation in the properties of the resultant crystal. Furthermore, because of the high concentration of defects attainable, it is possible to relate the concentration to measurable gross physical properties such as density, refractive index and lattice parameter. It has already been shown (1) that changes in defect concentration in this phase have a marked effect on diffusion rates and, hence, on solid-state reactivity.

Strong evidence for the existence of interstitial fluorine defects was first obtained by Zintl and Udgard (2), who postulated this model to explain an "abnormally high" density of an impure $\text{CaF}_2\text{-YF}_3$ crystalline solution. Recently in this laboratory Short and Roy (1) by careful density measurements unequivocally confirmed this model for a wide range of high purity $\text{CaF}_2\text{-YF}_3$ crystalline solutions having values closely approaching theoretical density for a

fluorite structure with all the excess anions in interstitial sites. Similar interstitial F^- defects have been reported, largely on the basis of x-ray patterns, for the systems $\text{BaF}_2\text{-UF}_3$ (3) and $\text{SrF}_2\text{-LaF}_3$ (4). Contrariwise, anion vacancies up to perhaps 4% (1) have been suggested for CaF_2 . Anion-vacancy and interstitial-anion structural models were postulated by Ure (5) for NaF- and YF_3 -doped CaF_2 samples, respectively, on the basis of ionic conductivity measurements. Finally, simple substitutional and half-breed derivatives are known such as NaYF_4 (6), NaPuF_4 and NaCeF_4 (7), and, hence, many intriguing possibilities for controlled defect materials are suggested.

The present investigation was undertaken in order to provide a systematic crystal chemical study for fluorides based on the CaF_2 structure, to determine the extent of crystalline solubility with a variety of substituents, and to make diagnostic measurements which define the type of resulting structure. The types of defect formed in the present study are described in three general categories: simple substitutional defects, interstitial-anion, and anion-vacancy structures. With a thorough knowledge of the type of defect present under a given set of conditions one should then be able to control the environment of substituent "impurities" and as a result control the structure-dependent properties.

Experimental Techniques

The chemicals used were: Baker's Analyzed Reagent Grade CaF_2 and NaF obtained from Allied Chemical Corporation; 99.9% YF_3 obtained from Research Chemicals; and additional C. P. rare earth fluorides from A. D. Mackay, Incorporated. Some single crystals of Harshaw CaF_2 were used. NaF and rare earth fluorides were dried approximately 30 min at 700° in high-purity dry nitrogen; CaF_2 was dried at 900° . In any instance where oxidation was

Table I. "Half-breed" derivatives of CaF₂

Compound	Unit cell dimension	Refractive Index	Miscellaneous
NaLaF ₄ (9)	$\begin{cases} a = 6.167 \\ c = 3.819 \end{cases}$	$\begin{cases} \omega = 1.486 \\ \epsilon = 1.500 \end{cases}$	Hexagonal
NaPuF ₄ (7)	$\begin{cases} a = 6.129 \\ c = 3.753 \end{cases}$	$\begin{cases} \omega = 1.523 \\ \epsilon = 1.552 \end{cases}$	
NaCeF ₄ (7)	$\begin{cases} a = 6.152 \\ c = 3.778 \end{cases}$	$\begin{cases} \omega = 1.493 \\ \epsilon = 1.514 \end{cases}$	
NaPrF ₄	$\begin{cases} a = 6.133 \\ c = 3.749 \end{cases}$	$\begin{cases} \omega = 1.501 \\ \epsilon = 1.531 \end{cases}$	
NaSmF ₄	$\begin{cases} a = 6.077 \\ c = 3.651 \end{cases}$	$\begin{cases} \omega = 1.500 \\ \epsilon = 1.528 \end{cases}$	
NaGdF ₄	$\begin{cases} a = 6.053 \\ c = 3.601 \end{cases}$	$\begin{cases} \omega = 1.488 \\ \epsilon = 1.512 \end{cases}$	
NaHoF ₄	$\begin{cases} a = 5.991 \\ c = 3.536 \\ a_c = 5.485 \end{cases}$	$\begin{cases} \omega = 1.487 \\ \epsilon = 1.512 \end{cases}$	Hex ↑ 760° Cubic } Dimorphic
NaErF ₄	$\begin{cases} a = 5.983 \\ c = 3.504 \\ a_c = 5.465 \end{cases}$	$\begin{cases} \omega = 1.478 \\ \epsilon = 1.505 \\ n = 1.452 \end{cases}$	Hex ↑ 775° Cubic } Low temp—hex High temp—cubic
NaYF ₄	$\begin{cases} a = 6.000 \\ c = 3.583 \\ a_c = 5.47 \end{cases}$	$n = 1.438$	Hex ↑ 705° Cubic } $\rho = 4.14$ Cubic } $\rho = 3.80$
NaYbF ₄	$a_c = 5.415$	$n = 1.458$	

(9) and (7) Data from references; others measured in the present study.

* Symbols used: ω and ϵ are the refractive indices for the ordinary and extra-ordinary rays, respectively, in hexagonal crystals; ρ is density; cell dimensions are in Å.

evident, the compound was refluoridated in a nitrogen atmosphere by reacting with NH₄HF₂, first in the range 300°–400° and then at 700°.

After weighing, mixtures were ground together in an agate mortar under ethyl acetate, dried again by heating in a nitrogen atmosphere, and then usually sealed in Au or Pt tubes. Most runs were made in Kanthal- or platinum-wound quenching furnaces at atmospheric pressure, although some were made at elevated pressures in hydrothermal pressure vessels (8). Accurate lattice spacings were measured using slow scanning speeds on a Norelco wide-range x-ray diffractometer externally standardized with silicon.

Pycnometric densities were measured by immersion in thallium formate-thallium malonate liquids with densities up to 4.4. Samples were immersed in the liquid, centrifuged, and the density of the liquid adjusted gradually until the sample remained suspended. Densities can be measured with slightly greater precision on flawless single crystals than with the pressed powder pellets. Cleavage fragments of single crystals of Harshaw CaF₂ were measured to be 3.180 (cf. 3.1803 theoretical density), while the method using pressed powder yielded results which were not more than 1% lower than theoretical density. However, best reproducibility of results in the present study was obtained by using pellets pressed from finely powdered samples at 50 kilobars pressure, where inaccuracies caused by bubbles and problems of wettability are avoided.

Results

Half-breed derivatives of CaF₂.—A variety of rare earth ions were combined with Na to form

compounds (NaLnF₄)¹ which are derived from 2CaF₂ by substituting Na⁺ and Ln³⁺ for two Ca²⁺ ions. Table I and Fig. 1 give data on the compounds formed. Only Yb, Er, Ho, and Y yield cubic fluorite structures with the Na⁺ and Ln³⁺ ions in statistically disordered 8-coordinated positions. The larger

¹Ln is the symbol used for "lanthanon," to represent the rare earths and yttrium throughout the paper.

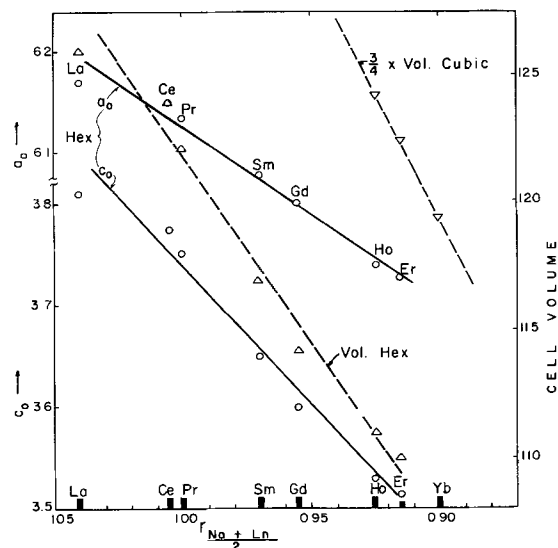


Fig. 1. Cell size of hexagonal and cubic NaLnF₄ compounds vs. average radius $\frac{Na^+ + Ln^{3+}}{2}$. Solid lines through circles give a_0 and c_0 for hexagonal cell; dashed lines through triangles give cell volume for hexagonal and cubic structures. $Z = 2$ for cubic cell and $Z = 3/2$ for hexagonal cell; equivalent cell volumes are plotted. Values for Y are omitted because it is not a rare earth.

cations, Gd to La form a hexagonal ordered structure (C 32), the so called $\beta_2\text{Na}_2\text{UF}_6$ of Zachariasen (9), with one Ln^{3+} in a 9-coordinated position and $\frac{1}{2}\text{Ln}^{3+}$ and $1\frac{1}{2}\text{Na}^+$ ions in 6-coordinated positions in each unit cell. Figure 1 gives the cell dimensions a and c of the various hexagonal structures (C 32) as a function of the average radius of the cation $(\text{Ln}^{3+} + \text{Na}^+)/2$. Departures from the curves for the hexagonal structures may be explained in part by a smaller effective ionic radius for Ln^{3+} ions in the 6-coordinated position. Also given is a plot of the cubic structures, which assume about 10% greater cell volume than the hexagonal structures. Whereas only representative rare earth ions were selected for study, it is expected that compounds of the complete rare earth series La . . . Lu will fit the curves of Fig. 1 with Nd, Pm, Eu, Tb, and Dy forming hexagonal structures and Tm and Lu forming cubic structures. The principal question remaining concerns the possibility of polymorphism of Tb and Dy. On the basis of the present results, cubic fluorite-type compounds might be expected to be formed also with the nonrare earths Tl^{3+} and In^{3+} which have ionic sizes in the proper range. Preliminary data obtained with NaInF_4 and NaTlF_4 , however, indicate that these structures are considerably more complex.

The compounds with the larger ions melt incongruently at temperatures in the vicinity of 750° – 850° , and apparently no high-temperature disordered structure can be formed before melting. Details of the melting behavior have not been worked out for the compounds with the smaller ions, although they are in general higher-melting.²

NaHoF_4 , NaErF_4 , and NaYF_4 are dimorphic, having the hexagonal structure at low temperatures and the fluorite structure at high temperatures. Table II gives an indexing of the x-ray pattern of hexagonal NaHoF_4 according to the NaLaF_4 cell. Zalkin and Templeton (11) suggested a different hexagonal cell for NaHoF_4 with $a = 3.86$ and $c = 5.041$, but the present data do not fit the latter cell. The approximate inversion temperatures (at atmospheric pressure) for the hexagonal to cubic polymorphs are given in Table I. Investigations made at pressures

² Confirming these observations are those of Thoma and co-workers (10) who also found an anomalous melting behavior for NaYF_4 ; it gradually disproportionates to a YF_3 -rich crystalline solution + liquid rather than having a sharp melting point.

Table II. X-ray data for hexagonal NaHoF_4 *

d, Å		hkl	Rel. Int., measured
Measured	Calculated		
5.22	5.19	100	10
3.00	3.00	110	8
2.926	2.92	101	5
2.614	2.59	200	2
2.292	2.28	111	1
2.094	2.093	201	6
1.966			0.5
1.771			0.5
1.731	1.728	300	4
1.716	1.715	211	4
1.675	1.673	102	0.5

* Data obtained on Norelco Wide-Range diffractometer using filtered Cu radiation.

up to 1000 atm showed that the transition temperature in NaHoF_4 increases with increasing pressure, which is to be expected on the basis of the volume relationships: approximately 12% increase in cell volume takes place on change from the hexagonal to cubic structure in NaHoF_4 (see Fig. 1).

The heat of transition (ΔH_{tr}) for the hexagonal-cubic transformation was calculated from the Clausius-Clapeyron relationship

$$\Delta H_{\text{tr}} = \frac{dP}{dT} \times T \Delta V$$

Values used were the experimentally determined dP/dT ³ (i.e., the slope of the P - T curve for the transition) and the volume change ΔV calculated from measured lattice parameters. Using $T = 1033^\circ\text{K}$, ΔV (1 mole NaHoF_4) = + 8.9 Å³, and $dP/dT = 47.6$ atm/ $^\circ\text{C}$ the ΔH_{tr} calculated = 6440 cal/mole. Considering the maximum experimental error, that for determination of the P - T curve, the calculated value for ΔH_{tr} is believed to be accurate to $\pm 10\%$. The slopes of the P - T curves for the transitions in the other compounds were not determined, but in view of similar changes in cell volume, heats of transition are expected to be of the same order of magnitude.

Crystalline solutions of NaLnF_4 compounds in CaF_2 .—Determination was made of the extent of crystalline solubility of various NaLnF_4 compounds in CaF_2 . Crystalline solutions were formed at optimum subsolidus temperatures for obtaining a maximum amount of solid solution, and yet having sufficiently high reaction rate to achieve equilibrium rapidly. The CaF_2 -rich compositions were crystallized at around 1200° , while the lower-melting NaLnF_4 -rich compositions were crystallized in the range 700° – 1000° . No attempt was made to determine detailed melting phase equilibria for the various systems.

Crystalline solubility is complete between CaF_2 and the cubic structures NaYF_4 and NaYbF_4 . Preliminary evidence indicates that solubility is extensive between CaF_2 and the Ho and Er compounds, although the data are incomplete. Solubility is limited with the hexagonal compounds, extending from CaF_2 up to about 66 mole % $\text{NaPrF}_4/2$, and about 75 mole % $\text{NaGdF}_4/2$.

Properties of some of the phases formed are shown in Fig. 2 and 3. The density change is linear with composition between CaF_2 and NaYF_4 indicating that these crystalline solutions are formed by a simple ion-for-ion replacement in normal lattice sites of 2 Ca by (Na + Y) throughout the series.⁴ The refractive indices show the same type of relationship. Within the limit of error of measurement this property also follows a linear pattern of change with composition for Y and Yb throughout the continu-

³ An increase of 10° in transition temperature for corresponding pressure increase from 8,000 to 15,000 psi was found by quenching experiments.

⁴ The measured density of NaYF_4 is 3.81, the same as calculated according to the fluorite cell using measured cell volume with 2 moles NaYF_4 per unit cell: 1 Na and 1 Y substitute for 2 Ca positions. The linearity in the measured densities between CaF_2 and NaYF_4 therefore indicates a simple ion-replacement substitution with no significant amount of either cation vacancy or interstitial anions present in intermediate compositions. The other NaLnF_4 solid solution structures are assumed to be the same by analogy.

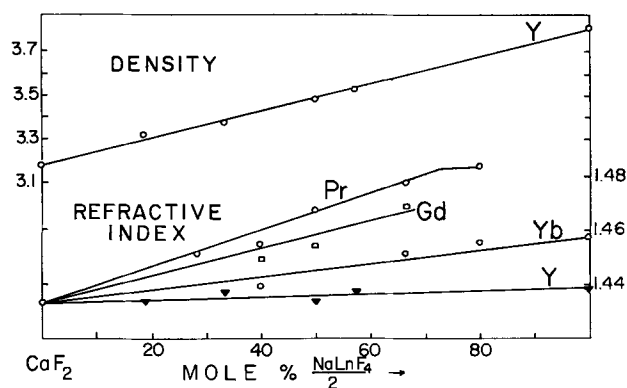


Fig. 2. Density and refractive index measurements of $\text{CaF}_2\text{-NaLnF}_4$ crystalline solutions.

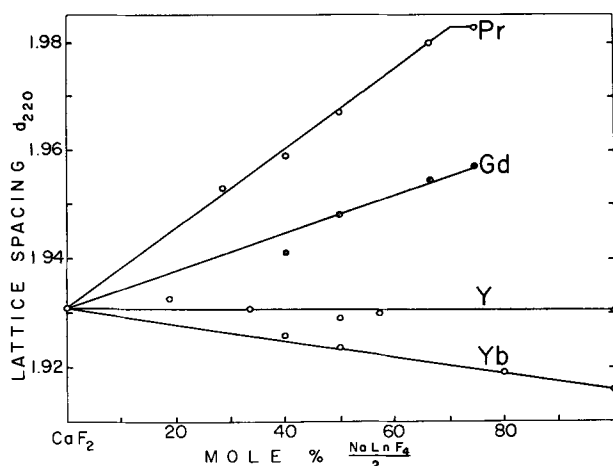


Fig. 3. Lattice spacing d_{220} of $\text{CaF}_2\text{-NaLnF}_4$ crystalline solutions

ous crystalline solution range. Refractive indices provide a particularly useful measurement for confirming the cation replacement substitution model for the NaYbF_4 crystalline solutions, where densities near NaYbF_4 were too high for measurement by the technique used. The crystalline solutions with NaPrF_4 and NaGdF_4 behave in a similar manner to those with the Y and Yb compounds up to the limit of crystalline solubility. The change in lattice parameter with composition is also linear throughout the complete series of crystalline solutions of CaF_2 with NaYF_4 and NaYbF_4 (Fig. 3) and, up to the solubility limit is linear with addition of NaGdF_4 and NaPrF_4 , suggesting that crystalline solutions are formed by a simple balanced substitution of $\text{Na} + \text{Ln}$ for two Ca ions.

The variation in properties of cubic crystalline solutions of NaLnF_4 in CaF_2 as a function of ionic radius (i.e., the average of $\text{Na}^+ + \text{Ln}^{3+}$) is given in Fig. 4. The variation in both lattice spacing and refractive index with average ionic radius is linear. Values for Y were omitted: because Y is not a rare earth, it would not be expected to fit in regularly with the rest of the series and, indeed, values for Y fall below the curve, behaving as though it were a smaller ion.

Interstitial fluorine structures.—The substitution of a variety of trivalent rare-earth fluorides in CaF_2 resulted in crystalline solutions in which as much as one out of five fluoride ions was in an interstitial

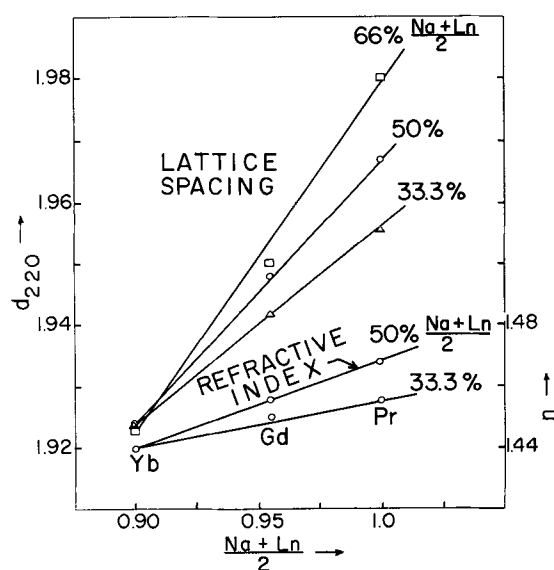


Fig. 4. Lattice spacing d_{220} and refractive index of $\text{CaF}_2\text{-NaLnF}_4$ crystalline solutions vs. average ionic radius $\frac{\text{Na}^+ + \text{Ln}^{3+}}{2}$.

position. Crystalline solutions of YF_3 and YbF_3 in CaF_2 were limited to slightly greater than 50 mole % of the trivalent fluoride, while those with larger ions such as Gd and Pr incorporated slightly less. The density measurements show conclusively that the additional fluorines added through the substitution of trivalent fluoride are very largely in interstitial sites. Figure 5 gives data for crystalline solutions formed by reaction at approximately 1200°C . The density curve for $\text{CaF}_2\text{-YF}_3$ is taken from previous work of Short and Roy (1) in this laboratory.

Because of the higher densities of the rare earths than yttrium, it was not possible, by means of the immersion method, to measure densities of crystalline solutions containing as large percentages of these ions as with yttrium. However, the values measured correspond to those expected on the basis of a theoretical interstitial fluorine model.⁵ Furthermore, the refractive index measurements increase in a linear fashion with increasing substitution, showing a trend parallel to that of the density measurements. Among the individual rare earths, however, the order is reversed from that of the density measurements: larger rare earth cations produce crystalline solutions with higher refractive indices.

⁵ Short and Roy (1) describe this model in more detail. The following comparison between x-ray densities calculated on the basis of two models with measured pycnometer values shows that the densities are close to those expected from an interstitial anion model, with nearer approximation reached the higher the LnF_3 concentration.

Compound ratio	V (Å ³)	M (vacancy)	M (interstitial)	ρ (vac)	ρ (int.)	ρ (meas.)
$3\text{CaF}_2 \cdot 1\text{GdF}_3$	169.2	398.4	448.1	3.92	4.40	4.24
$4\text{CaF}_2 \cdot 1\text{HoF}_3$	166.7	388.4	427.2	3.87	4.26	4.12
$4\text{CaF}_2 \cdot 1\text{YbF}_3$	164.8	394.2	433.6	3.97	4.37	4.294
$3\text{CaF}_2 \cdot 2\text{YF}_3$	170.7	350.8	421.2	3.42	4.10	4.12
$2\text{CaF}_2 \cdot 1\text{YF}_3$	168.7	345.2	402.5	3.40	3.96	3.95
$4\text{CaF}_2 \cdot 1\text{YF}_3$	166.2	333.2	367.0	3.33	3.67	3.63
$9\text{CaF}_2 \cdot 1\text{YF}_3$	163.8	323.2	339.3	3.27	3.44	3.37
$9\text{CaF}_2 \cdot 1\text{SmF}_3$	165.0	346.5	363.9	3.48	3.65	3.55

V, unit cell volume; M, molecular weight; ρ , density. Cation vacancy model $\text{Ca}_2\text{F}_4\text{Ca}_{0/5}\text{Ln}_{1/5}\text{F}_4$ (for $3\text{CaF}_2 \cdot 1\text{GdF}_3$) Interstitial anion model $\text{Ca}_2\text{F}_4\text{CaGdF}_5$

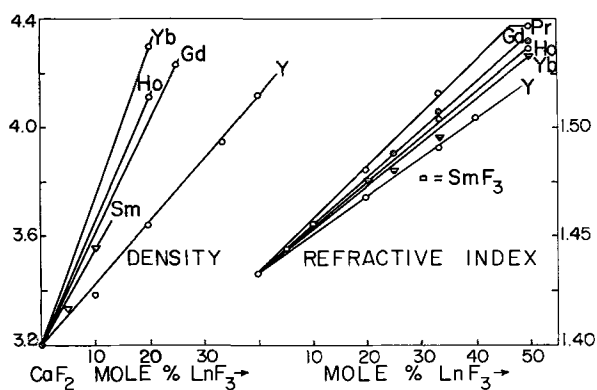


Fig. 5. Density and refractive index measurements of $\text{CaF}_2\text{-LnF}_3$ crystalline solutions.

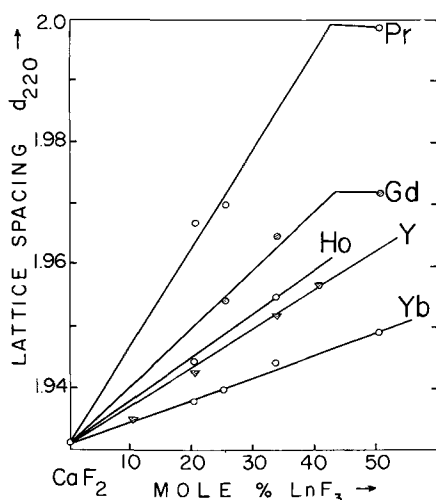


Fig. 6. Lattice spacing d_{220} of $\text{CaF}_2\text{-LnF}_3$ crystalline solutions

Lattice spacings of these same crystalline solutions are shown in Fig. 6. These increase in a linear fashion with increasing crystalline solution. The cell constants of the structures are of course much larger with the larger cations. One might expect that ideally an interstitial fluorine structure could be produced having the same cell size as pure CaF_2 , especially if the "interstitial" fluorine ion actually fits in a vacant cube center. It has, however, been demonstrated that even with structures containing cations smaller than Ca (Y and Yb) this is not the case. The repulsive forces resulting from the additional fluorine anions must be strong especially if the extra anions are not directly paired with a trivalent cation.⁶

It should be noted that in the above figure, as in Fig. 5, values for 50% Pr and Gd fall below the extrapolation of the line. These compositions contain a second phase in addition to the fluorite crystalline solution. The phase in equilibrium with this crystalline solution containing a maximum amount of LnF_3 is apparently the hexagonal polymorph⁷ (LaF_3 structure) in the PrF_3 and GdF_3 containing systems.

⁶Friedman and Low (12) in an attempt to reconcile different paramagnetic resonance spectral data obtained with CaF_2 structures containing Gd^{3+} impurities showed that in annealed crystals the Gd migrated to sites having axial symmetry, with the interstitial fluorine apparently closely associated with the Gd^{3+} , while crystals quenched from high temperatures showed more random distribution of the Gd^{3+} .

⁷Zalkin (13) and Zalkin and Templeton (11) discuss the polymorphism of the rare earth fluorides.

With Y and Yb the orthorhombic (stable) LnF_3 modification was expected. However, in the latter systems also a hexagonal phase, resembling the LaF_3 -type structure was formed. It is not clear whether this phase is a crystalline solution of CaF_2 in YF_3 and YbF_3 , stabilizing the more dense hexagonal structure, or a "compound" with about a 1:3 or 1:4 ratio of $\text{CaF}_2\text{:LnF}_3$ having a structure similar to LaF_3 .

An attempt was made to obtain further data on pure YF_3 in order to explain these new observations. The results obtained confirmed the results of previous investigations (14). The normal form of YF_3 is orthorhombic, and on heating it undergoes a reversible rapid inversion at about 1050° , accompanied by a substantial endothermic heat effect. The high-temperature modification is not quenchable. High-temperature x-ray patterns obtained in the present study, in attempt to obtain additional information on the structure, were inconclusive because partial oxidation took place even in a supposedly inert atmosphere.

The variations in refractive index and lattice spacing measurements of cubic $\text{CaF}_2\text{-LnF}_3$ crystalline solutions as a function of ionic size of Ln^{3+} are given in Fig. 7. The size of the cation has a profound effect on the lattice spacing, and the variation with size is linear. The refractive index in contrast is much more affected by the percentage of interstitial fluorine than the particular cation present.

$\text{NaYF}_4\text{-YF}_3$ interstitial fluorine structures.— Interstitial anion structures were also formed by incorporation of trivalent fluorides in cubic half-breed derivative structures. Hund (6b) suggested the existence of extensive solid solubility of YF_3 in NaYF_4 , and Thoma (10) in contemporaneous work presented a phase diagram of the NaF-YF_3 system showing this solubility up to about 75 mole % YF_3 . In the present study, these crystalline solutions were investigated more extensively and an interstitial anion defect model established.

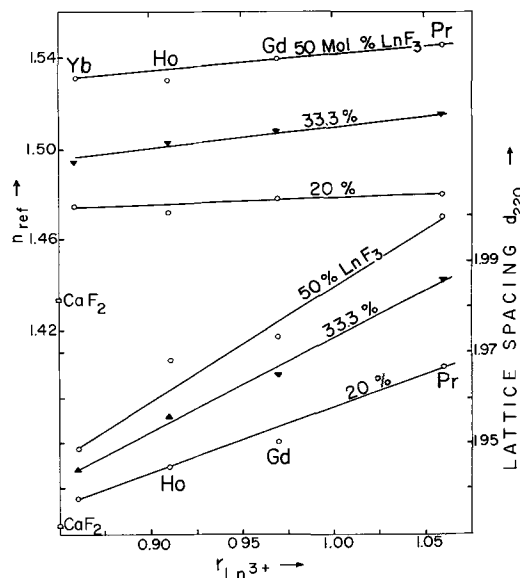


Fig. 7. Refractive index and lattice spacing of $\text{CaF}_2\text{-LnF}_3$ crystalline solutions vs. radius of Ln^{3+} .

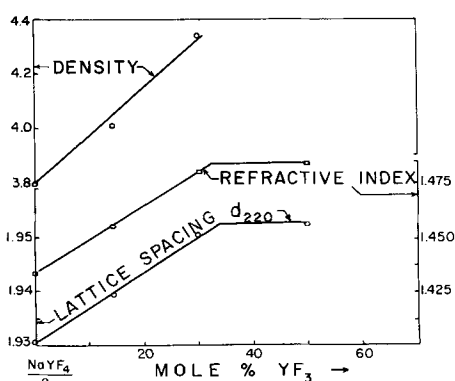


Fig. 8. Density, refractive index and lattice spacing of NaYF_4 - YF_3 interstitial anion structures.

Figure 8 gives measurements of density, refractive index, and lattice spacing of the crystalline solutions formed which confirm this model. The density of the 14.5 YF_3 (85.5 $\text{NaYF}_4/2$) composition is very close to theoretical density for the interstitial fluorine type structure, while the 30 YF_3 composition is slightly more dense than predicted. (This higher value may be the result of some undetected free YF_3 in the sample.)

Although NaYF_4 is dimorphic, having a low-temperature hexagonal form, there is little tendency of the "stuffed" cubic crystalline solution to exsolve once formed. Beyond the limit of crystalline solution the orthorhombic modification of YF_3 is formed as a second phase, in contrast to the hexagonal phase formed in equilibrium with CaF_2 - YF_3 crystalline solutions.

CaF_2 -NaF anion vacancy structures.—Substitution of NaF in the CaF_2 structure was attempted, and data obtained by different methods are summarized in Table III. High-temperature x-ray data have shown that about 4% NaF is taken into the CaF_2 structures just below the solidus (1). Diffusion of NaF into single crystals of CaF_2 held for a month just below the eutectic temperature resulted in a phase slightly less dense than pure CaF_2 , suggesting that the resulting phase does indeed contain some anion vacancies.

Furthermore, mixtures of powders reacted above the eutectic temperature resulted in products having lower densities than the original CaF_2 . However, since the measured densities of the CaF_2 phase were approximately the same with 1, 2, and 5 mole % NaF additions, it is assumed that saturation is reached by 1% NaF. At least, this would be the

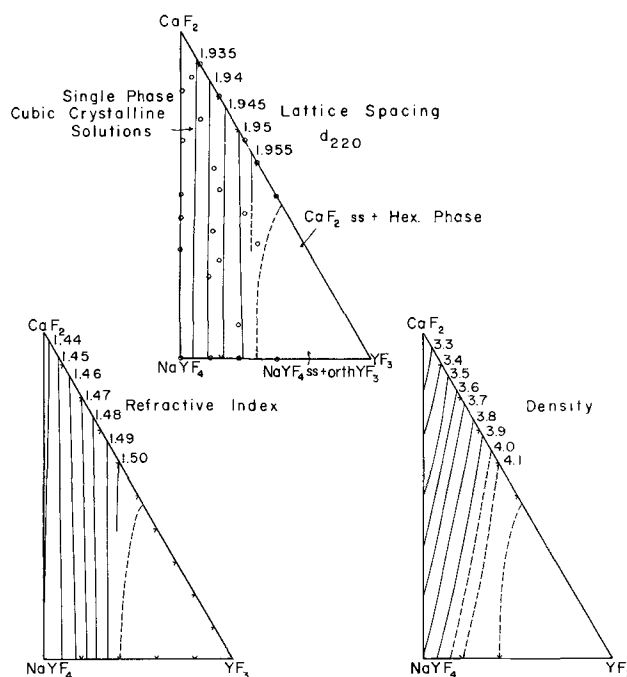


Fig. 9. Properties of CaF_2 - YF_3 - NaYF_4 ternary crystalline solutions. Dashed boundary curve shows limit of one-phase area. a, Lattice spacing d_{220} ; b, refractive index; c, density. Phases were crystallized below the solidus: approximately 1200°C in the CaF_2 -rich region, decreasing to the range 1000°C - 750°C in the lower part of the triangles.

maximum which can be retained in the structure quenched to room temperature. Furthermore, refractive indices of the three are the same, confirming the maximum of 1 per cent.

CaF_2 - LnF_3 - NaLnF_4 solutions.—The last model considered involves ternary crystalline solutions, which could incorporate two types of defect. The example investigated in most detail was the CaF_2 - YF_3 - NaYF_4 system, and Fig. 9 (a, b, and c) summarizes briefly some results obtained on this system.

Crystalline solution is complete between CaF_2 and NaYF_4 along the vertical join, extends just past 50 mole % YF_3 along one side, and along the bottom from NaYF_4 to approximately 70 mole % YF_3 30% NaF.⁸ The vertical join is a simple substitutional relationship whereas the bottom and side have interstitial anion structures. A single phase CaF_2 -crystalline solution area covers a very large part of the triangle, and the properties of the phase change in a gradual and systematic manner.

Lattice spacings (d_{220}) (Fig. 9a) nearly parallel the CaF_2 - NaYF_4 vertical. Isofracts (Fig. 9b) (lines

⁸ Thoma (10) suggests that this may extend to 75 mole % YF_3 .

Table III. Anion-vacancy CaF_2 structures

Starting material	Treatment	Properties or evidence of anion vacancy
Single crystal CaF_2 (Harshaw) $\rho = 3.1803$ $n = 1.4338$	NaF powder diffused in at 760° 1 month	$\rho = 3.170$
Pre-reacted powders CaF_2 -NaF	High temperature x-ray diffraction 750°C	2nd phase appears beyond 4% NaF
Mixed powders at } 880°C (eutectic) } 1% NaF 2% NaF 5% NaF	880°C in sealed Pt tube	$n = 1.431, \rho = 3.079$ $n = 1.431$ $n = 1.431, \rho = 3.099$ } 2nd phase present

ρ is the pycnometric density; n the refractive index.

Table IV. Luminescence of defect fluorites

Sample No.	Composition	Temp prepared, °C	Cathode ray excitation	UV 2537
329	90 CaF ₂	1100	Bright pink—peach	Strong pink-red
336	10 SmF ₂ 90 CaF ₂	1100	Weak pink—peach	Weak whitish pink
328	5 SmF ₂ 5 SmF ₃ 80 CaF ₂	1100	Much weaker than 336, same color	Neg.
72	20 SmF ₃ NaSmF ₄ *	700	Mod. bright greenish white	Neg.
339	CaF ₂ 99.9 MnF ₂ 0.1	1300	Intense blue	Neg.
334	CaF ₂ 75 YF ₃ 25 MnF ₂ 0.1	1100	Bright bluish white	Neg.
Mn Ca Nd	80 CaF ₂ 10 MnF ₂ 10 NdF ₃	1100	Bluish white < 334	Neg.
199	CaF ₂ 50** GdF ₃ 50	1100	Greenish white—some dark spots	Strong pink
341	CaF ₂ 99.9 GdF ₃ 0.1	1300	Blue < 339	Slight pink
293	CaF ₂ 2 ⁺ NaF 3 GdF ₃ 3	1000	Bright bluish white	Slight pink
82	NaGdF ₄ *	800	V. wk.	Slight pink
80	NaGdF ₄ ⁺	800		
335	CaF ₂ 75 YF ₃ 25 GdF ₃ 0.1	1100	V. dull—red-brown?	Strong pink Neg.
342	CaF ₂ 75 YF ₃ 25 GdF ₃ 0.1	1300	Blue < 341	
340	CaF ₂ 99.9 NdF ₃ 0.1	1300	Mod. intense whitish blue < 339	Mod. wk. white
Mn Nd Ca	80 CaF ₂ 10 MnF ₂ 10 NdF ₃	1100	Bluish white > 335 < 334	Neg.
203	3 CaF ₂ PrF ₃	800	Inhomogeneous: purple-white, dark greenish blue?	Neg.
228	2 CaF ₂ 1 PrF ₃	1200	V. faint (bluish green)?	Neg.
296	CaF ₂ ⁺ NaF PrF ₃	1000	Faint bluish-white	Neg.
140	NaPrF ₄ *	750° N ₂	Greenish white; some darker purple	Neg.
330	YF ₃	1100	v. v. intense white (sl. greenish-yellow)	White
144	2 CaF ₂ 1 YF ₃	800	Mod. strong greenish white	Neg.
287	35 NaF 65 YF ₃	1000	Bright greenish white > 292	Neg.
270	NaYF ₄	900	Bright greenish white sim. 287	Neg.
292	4 CaF ₂ 1 NaYF ₄	650	Faint bluish green-white	Neg.
334	CaF ₂ 75 YF ₃ 25 MnF ₂ 0.1	1100	Bright bluish-white	Neg.
339	CaF ₂ 0.1 MnF ₂	1300	Intense blue	Neg.
335	CaF ₂ 75 YF ₃ 25 GdF ₃ 0.1	1100	Dull v. wk. red-brown?	Neg.
342	CaF ₂ 75 YF ₃ 25 GdF ₃ 0.1	1300	Blue 341	
197	2 CaF ₂ 1 HoF ₃	1100	Mod. strong dark red	Neg.
195	NaHoF ₄ *	700	Red mod. strong sim. 197	Neg.
239	4 CaF ₂ 1 YbF ₃	1300-1200	V. weak	Neg.
139	NaYbF ₄ ***	750° N ₂	V. wk. or none—one area yellow-peach	Neg.
196	NaErF ₄ *	700	V. dull, faint greenish?	Neg.

Except where indicated by symbol, the samples were cubic CaF₂-based crystalline solutions.

* Hexagonal NaLnF₄ phase.

** Cubic phase and little excess hexagonal GdF₃.

+ Cubic phase and little excess hexagonal NaLnF₄ phase.

++ Differs from other NaGdF₄ samples in that it was melted and cooled.

*** Cubic NaLnF₄ phase.

of equal refractive index) very nearly parallel these lines. Density (Fig. 9c) increases with increasing Y, much more rapidly however, in the predominantly interstitial anion structures than where simple substitution predominates.

Detailed phase equilibria in the region rich in YF_3 were not determined, for they appear to be rather complex. A hexagonal phase is formed from YF_3 -rich compositions along the CaF_2 - YF_3 side, while orthorhombic YF_3 exists along the bottom: ternary compositions may contain various combinations of the two, or additional phases.

Similar investigations were made of the systems CaF_2 - PrF_3 - NaPrF_4 and CaF_2 - YbF_3 - NaYbF_4 . These were of a preliminary nature and therefore will not be described in detail here. The Yb-containing system bears a very strong resemblance to the yttrium system as would be expected from the similarities between the respective binary systems. The extent of crystalline solubility in the Pr-containing system was considerably smaller, a result of the larger cation size and the limited crystalline solubility between CaF_2 and NaPrF_4 .

Luminescence of Defect Fluorites

Little information is available on the effect of the host structure on the optical spectra of rare earth ions incorporated in the fluorite structure, except for a few dopants which exhibit fluorescence having potential application for optical masers (15). White (16) recently calculated the crystal field splitting of rare earth ions in a cubic field and, as more experimental spectral data are available, better comparison may be made with theory. The few qualitative observations made on the visible fluorescence characteristics of some of the defect crystalline solutions investigated in the present study have, therefore, been included as a preliminary indication of the variation within a single anion environment. These results are summarized in Table IV.

Attempts to obtain visible fluorescence spectra of representative samples on a Beckmann DK-2 spectrometer were not very successful, perhaps because the excitation energy of the 3000-4000Å Hg band was insufficient. A few samples fluoresced when excited by a Hg 2537 "mineral light," as indicated in the last column in Table IV. A large number of samples luminesced brightly under cathode ray excitation,⁹ including many which failed to fluoresce under either type of u.v. excitation. Furthermore, in some cases the wavelength of radiation emitted under cathode ray excitation is apparently shorter than that stimulated by u.v. excitation (e.g., some Gd^{3+} samples fluoresce red with u.v. excitation, while the cathodoluminescence is blue). Other tentative indications are that temperature of equilibration may have an effect on the first and second spheres of coordination of the Gd^{3+} and, hence, on the luminescence: CaF_2 - YF_3 (Gd 0.1) samples prepared at 1100° exhibit only a very weak luminescence while those prepared at 1300°C luminesce strongly: this may, of course, be due to

a number of causes. In the noncubic environment of hexagonal NaGdF_4 , the Gd-luminescence was observed to be weak; however, one sample which was melted and cooled has strong luminescence. The explanation for this latter observation is not clear. The fluorescence characteristics of Sm^{2+} and Sm^{3+} in the CaF_2 lattice are quite different: under the conditions of excitation used the divalent ion produces a strong luminescence, the trivalent ion a weak luminescence, which may prove useful in determining ratios of the two in a specific material. A further difference is seen in the wavelength of the radiation emitted from Sm^{3+} in the CaF_2 and NaSmF_4 structures: this may be a result of the differences in the symmetry of the crystal field,¹⁰ but detailed spectral data would be necessary to confirm this.

Conclusions and Summary

The results of this investigation illustrate the relative importance of two mechanisms of equilibrium defect formation in the CaF_2 structure: simple substitutional defects produced by balanced substitution of the type $\text{Na}^+ + \text{Ln}^{3+}$ for 2Ca^{++} ; and interstitial anion structures formed by the substitution of Ln^{3+} for Ca^{2+} , with the additional fluorine ion stuffed into the structure. It is apparent from the results of the present study that the anion vacancy is a much less important mechanism in these fluoride structures than in counterpart oxide systems. This is, of course, partly the result of availability of substituent cations for producing anion-vacancy type structures: with oxides such as ZrO_2 (18), a wide variety of trivalent ions are available, while with CaF_2 the substituent cations must be monovalent and proportionately more different from the host Ca^{++} ion. Other crystal-chemical considerations such as relative binding energies, must be important, however, for the oxides form anion-vacancy structures also with CaO and MgO substitution (19).

It has been possible to vary certain properties of crystalline solutions based on CaF_2 by small controlled changes in composition of the starting material. Density, unit cell size, and refractive index values may be varied via small increments, and it is expected that other related properties may be similarly controlled. Frequencies of vibration of a given ion pair resulting in absorption in the infrared region are known to be modified by the surrounding crystal field, and it may be expected that visible fluorescence spectra will also be influenced, if not resulting in actual change in wavelength, then at least in intensity of emission as a result of differences in binding in the second coordination sphere. Preliminary examination of fluorescence characteristics of certain of the structures has been made, but the interpretations given are only tentative.

Note Added After Review.—An unpublished paper by Thoma *et al.* called to our attention by the reviewers reports that the crystalline solubility extent of the fluorite phase in the system NaF - YF_3 at

⁹ A maximum accelerating voltage of 30,000v was applied, which of course is orders of magnitude greater than the energy required for optical transitions.

¹⁰ Such differences have been observed for the Eu ion by Tomaschek and Deutschbein (17).

800°C is from 50% to about 65% YF₃, in excellent agreement with our less detailed measurements. Similar good agreement with our data was obtained on the refractive indices [1.476 vs. 1.472 (Thoma) both probably ± 0.002 for the maximum YF₃ phase] and cell constant ($a_0 = 5.52$ vs. 5.53). Interesting and quite peculiar melting behavior and subsolidus reactions are also reported by these authors.

Acknowledgments

The authors would like to express their appreciation to Mrs. Alice Jordan, who assisted in much of the experimental part of this study. Mr. Seymour Merrin also assisted with part of the high pressure work. This research was part of a program on defect solids supported by the Bausch and Lomb Optical Company.

Manuscript received June 10, 1963. Contribution No. 62-95, College of Mineral Industries. Much of this material was presented at the New York Meeting of the American Ceramic Society, May 1, 1962.

Any discussion of this paper will appear in a Discussion Section to be published in the December 1964 JOURNAL.

REFERENCES

1. J. Short and R. Roy, *J. Phys. Chem.*, (1963); see also J. M. Short, Ph.D. Thesis, The Pennsylvania State University, University Park, Pa.

2. E. Zintl, and A. Udgard, *Z. anorg. u. allgem. Chem.*, **240**, 150 (1939).
3. R. W. D'Eye and F. S. Martin, *J. Chem. Soc.*, **61**, 1847 (1957).
4. J. A. A. Ketelaar and P. J. H. Willems, *Rec. Trav. Chim.*, **56**, 9 (1937).
5. R. W. Ure, *J. Chem. Phys.*, **26**, 1363 (1957).
6. F. Hund, (a) *Z. Anorg. Chem.*, **261**, 106 (1950); (b) **263**, 102.
7. C. J. Barton, J. D. Redman, and R. A. Strehlow, *J. Inorg. Nucl. Chem.*, **20**, 45 (1961).
8. R. Roy and O. F. Tuttle, "Physics and Chemistry of the Earth I," Chap. VI, 138-180, Pergamon Press, London (1956).
9. W. H. Zachariasen, *J. Am. Chem. Soc.*, **70**, 2147 (1948).
10. R. E. Thoma, Progress Report OrNL3262, 10-13, May 4, 1962.
11. A. Zalkin and D. H. Templeton, *J. Am. Chem. Soc.*, **75**, 2453 (1953).
12. F. Friedman and W. Low, *J. Chem. Phys.*, **33**, 1275 (1960).
13. A. Zalkin, Ph.D. Thesis, University of California, Berkeley, Calif. (1951).
14. R. E. Thoma, *J. Phys. Chem.*, **65**, 1096 (1961).
15. L. F. Johnson, *J. Appl. Phys.*, **34**, Pt. 1, 897 (1963).
16. J. A. White, *J. Phys. Chem. Solids*, **23**, 1787 (1963).
17. R. Tomaschek and O. Deutschbein, *Glastech. Ber.*, **35**, 148 (1939).
18. F. Hund, *Z. Elektrochem.*, **55**, 363 (1951).
19. F. Hund, *Z. physik. Chem.*, **199**, 142 (1952).

Electrolytic Titanium from TiCl₄

I. Operation of a Reliable Laboratory Cell

Myron J. Rand¹ and Lawrence J. Reimert

New Jersey Zinc Company, Palmerton, Pennsylvania

ABSTRACT

The design and operation of a laboratory electrolytic cell for the production of ductile Ti with continuous TiCl₄ feed is described. The cell is metal, with an alumina diaphragm; the electrolyte is LiCl-KCl-NaCl plus several per cent Ti ion, at 550°C. Reproducibility of results was good, and the cell was used chiefly to study the effects of varying operating conditions on metal quality. Observations are reported on the influences of Ti ion valence and concentration, current density, agitation, salt melt purity, air leakage, and gaseous and metallic impurities on the cathode deposit. A pronounced improvement in metal quality, with no sacrifice in yield, was achieved by delaying the immersion of the main deposition cathode for a considerable period after the start of electrolysis.

This report presents a summary of results from the operation of a laboratory-scale cell for the production of metallic titanium directly from the tetrachloride by fused-salt electrolysis. The work was done in a 7-in. diameter Hastelloy C cell with a central graphite anode, an Alundum diaphragm, and a metal cathode to which the deposit adheres. The electrolyte was the LiCl-KCl-NaCl eutectic (f.p. 340°C) maintained at 550°C, with TiCl₄ dripped onto the quiescent melt surface in an argon atmosphere. The cell usually operated at 4-5v, 20-30 amp, for 36-48 hr, producing about a pound of Ti. Runs comprised concentration buildup, prolonged steady-state operation, and stripping stages. For metal eval-

uation the cathode was generally raised out of the melt and the cell allowed to cool before opening.

The cell was under close material and electrical control, and the product has been so reproducible that metal quality is a reliable index of the effect of operating variables. Of the more than two hundred runs, each lasting 36-48 hr, carried out in this referee cell, all but three were completed successfully.

As far as practicable the conditions of operation were those considered desirable for a commercial process, for example, continuous TiCl₄ feed. Several per cent Ti ion was maintained in the melt most of the time, thereby minimizing the effects of concentration polarization. The relatively low 550°C electrolysis temperature simplifies materials and cor-

¹ Present address: Bell Telephone Laboratories, Inc., Allentown, Pennsylvania.

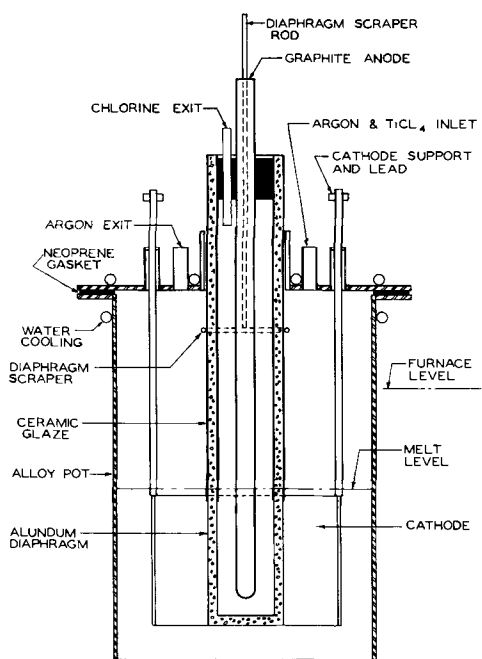


Fig. 1. Schematic cross-section of the electrolytic cell

rosion problems. The cell was metal. No mechanical agitation was necessary.

$TiCl_4$ is the preferred feed for a large-scale process because of its ease of preparation from ores and relative simplicity of purification and handling. Experiments on $TiCl_4$ for cell feed, and the many problems inherent in its efficient electroreduction, have been summarized by workers at the National Lead Co. (1-4). Apparently they found it necessary to operate in a cyclic rather than a continuous fashion, building up the Ti ion concentration in the melt and then nearly stripping it. Alternatively, with continuous operation with the basket cathode (4), the Ti ion concentration was kept under 1%. Recent reports by Russian investigators of pilot-plant work with semicontinuous and continuous $TiCl_4$ feed at high temperatures stress materials corrosion problems and deposit contamination (5). References to Ti electrowinning at temperatures below $800^\circ C$ are fragmentary, with little data on metal quality.

Cell Construction and Operation

The cell is shown in schematic cross section in Fig. 1. It is essentially a cylindrical can with a flange to which a cover may be bolted tightly. The $\frac{1}{2}$ -in. diam graphite anode in the center is surrounded by a 2-in. od diaphragm of high-purity sintered alumina, completely enclosing the anolyte and anode, and glazed above the melt level so that chlorine cannot diffuse through and back-react.

The diaphragm was Norton Company RA-186 or RA-139. Wall thickness of the former was $\frac{1}{4}$ -in.; porosity is about 30% and permeability about $0.005 \text{ cm}^3/\text{sec}/\text{cm}^2/\text{cm}/\text{cm Hg}$. Both $\frac{1}{8}$ -in. and $\frac{3}{16}$ -in. RA-139 diaphragms have been used; for the $\frac{1}{8}$ -in. wall, porosity is about 40% and permeability 0.04. The RA-139 grade is preferred to the RA-186 since it is as efficient, allows higher current, and gives less endosmosis. This phenomenon

is rarely troublesome, however, and on the few occasions when lowered anolyte level resulted in the appearance of anode effect a short period of operation at reduced current restored conditions to normal.

The cathode was usually a 5-in. diam cylindrical sheet 2 to 3- $\frac{1}{2}$ -in. high of 18-gauge Hastelloy C suspended by two $\frac{3}{16}$ -in. diam leads 180° apart. Many other cathode designs were tried: multilayer screens, perforated sheets, hemicylinders, blades, and rods. No differences in adherence or crystallinity were evident, barring those due to excessive current density on rod cathodes.

Not shown in Fig. 1 are ports in the cell top for a thermocouple well, for adding molten salt, for withdrawing melt samples for analysis, and for the ring scraper surrounding the diaphragm. Periodic operation of this scraper prevents the deposit from bridging to the diaphragm and hastening its failure.

The metal cell pot may serve as cathode during any portion of a run. During this time the deposition cathode may be suspended above the melt, out of the circuit, so that if desired the first metal made may be prevented from collecting on it. Later the deposition cathode may be immersed and activated, with the pot left electrically floating. This delayed-immersion or pre-electrolysis technique was almost always employed to some degree; it will be shown that this method of operation always resulted in a marked improvement in the crystallinity, purity, and adherence of the product.

Current densities, in amperes/square inch, were 0.3-1.6 on the deposition cathode, 0.8-1.7 on the outside wall of the diaphragm, and 4-10 on the anode. The cell was charged with 4.5 kg of molten salt, providing a bath 5 in. deep at the usual $550^\circ C$ operating temperature. The concentration-buildup stage was controlled at 1 mole of Ti added per 2 faradays passed, in theory enough current to reduce all the $TiCl_4$ to $TiCl_2$. Buildup was most often to 2- $\frac{1}{2}$ % Ti, although concentrations from a few tenths to 7% Ti have been investigated. In the next stage, the steady-state operation, $TiCl_4$ was fed to the cell continuously at 1 mole/4 faradays, and there was little change in concentration. The duration of steady-state is limited only by the ability of the cell to hold the metal made. During this stage typical operating characteristics were cell voltage, 4-5; current 25 amp; open-circuit emf 2.2-2.6.

It is of course not necessary to strip a melt of Ti values to produce Ti metal, but this step was usually carried out so that the mixture of metal and salts harvested from the cell would have no entrapped Ti ion able to react with air or moisture and contaminate the metal during separation. Stripping was accomplished by stopping the $TiCl_4$ feed and continuing electrolysis until the open-circuit emf rose sharply to 3.5v (at low current).

Materials

Salt melts were prepared and stored (under argon) in fused silica pots. While salts were being melted a stream of HCl gas was bubbled through the liquid. This minimized hydrolysis of LiCl to LiOCl or LiOH, which would have introduced ox-

xygen into the melt. Salts were of reagent grade, from three manufacturers, varying in foreign metals content from 0.02 to 0.28%, and with the LiCl containing up to 5% water. The molten salt mixture was dried by either of two equally effective methods: vacuum at 550°C for 12 hr, or gassing with argon at $650^\circ\text{--}675^\circ\text{C}$ for 48 hr. After drying moisture contents were 20–200 ppm.² The latter would add about 0.2% oxygen to the Ti produced if it all ended up in the deposit; since no such serious contamination was observed the water must have been largely scavenged out before the deposition cathode was immersed.

In general, metal quality was not sensitive to melt purity, within the limits of the treatment described above. There were no detectable effects of using different batches of salts, moisture contents, or storage times.

TiCl_4 is considered the most likely source of impurities detrimental to the Ti quality. The raw material for most of the work reported here was commercial-grade TiCl_4 made by the chlorination of either titaniferous slag or ilmenite. A considerable variety of vanadium-removal treatments was tried: H_2S , carbon, copper, soap, or oil. A batch distillation followed, with a fore-run cut to remove SiCl_4 . Finally, before use the TiCl_4 was distilled again, under argon, through a laboratory Vigreux column into a reservoir from which it was fed to the cell without further exposure. Such material was colorless and always analyzed $< 0.0005\%$ V, $< 0.001\%$ Fe and Al, and $< 0.003\%$ S. The vanadium-removal treatment used had no influence on metal quality. An extensive study of the effect of TiCl_4 impurity content on metal quality was carried out, and is reported as Part II of this paper (6).

The tank argon for the cell atmosphere (Linde Air Products Company) had a guaranteed purity of 99.99+%. In the early part of this work a furnace containing Ti sponge at $900^\circ\text{--}950^\circ\text{C}$ was inserted into the argon line, but it was eliminated after a series of runs had shown no advantage for this special purification.

Electrochemical Phenomena in the Melt

The cell construction permitted taking melt samples at will without exposure to the atmosphere or interruption of the electrolysis. These were analyzed for total Ti ion and average Ti ion valence. The Ti^{++} was determined by hydrogen evolution from a weakly acid solution, with the hydrogen swept out with CO_2 and collected over strong KOH in a gas buret. All the Ti ion was then reduced to Ti^{+3} with zinc and titrated with ferric ammonium sulfate using an ammonium thiocyanate indicator. Since there was no evidence of finely divided Ti metal when the frozen melt samples were dissolved, the Ti^{+3} content was assumed to be the difference between total Ti and divalent Ti^{+2} .³

²This determination was devised by Dr. N. F. Miller of this laboratory and is unpublished. The method consists in heating the salt sample with calcium carbide and absorbing the liberated acetylene in ammoniacal cuprous chloride. Cuprous acetylide, after oxidation to Cu^{++} , is determined iodimetrically in the usual way.

³The method described was devised by Dr. A. C. Elm of this laboratory; it is similar to one which has been reported (7) for NaCl-SrCl_2 melts.

With melt analyses available, a rather complete description of cell performance may be deduced. The TiCl_4 feed rate is monitored carefully, and any TiCl_4 expelled with the anode gases is caught in a trap. At any time, the difference between the net Ti fed and that found in the melt can only represent metal made to that point. Furthermore, since the cell is run at constant current, periodic and cumulative over-all current efficiencies may be calculated also.

Samples were taken from the cell during many runs, with reproducibility under similar operating conditions (and duration) within ± 0.05 valence unit. It was not expected that the ion valence would be exactly 2 even near the end of a prolonged electrolysis, since earlier investigation of the $2\text{Ti}^{+3} + \text{Ti} \rightleftharpoons 3\text{Ti}^{+2}$ equilibrium at 550°C , in the salt melt used, had shown an average equilibrium valence of 2.09 at 2½% Ti and 2.11 at 6% Ti.

Results of the melt sampling show that by the time enough Ti has been absorbed into the melt to allow a meaningful analysis, *i.e.*, about ½%, the valence was about 2.40. A level >2 during the 2 faraday per mole buildup stage reflects some deposition of metal rather than poor current efficiency. By the end of buildup to 2½% Ti the valence was down to 2.28. During steady-state operation this value fell slowly, approaching the equilibrium valence asymptotically. In the stripping stage, the valence was close to 2.10; by this time about three "turnovers" of the steady-state Ti ion content of the cell had occurred.

Equilibrium valence was approached more rapidly when the melt was agitated mechanically. Valence at the end of the buildup stage was then about 2.15, and reached 2.10 halfway through the run. If the agitation was stopped at this point, valence levels soon reverted to those normal for an unstirred melt.

Of course it is quite possible to prepare melts with Ti ion valences much higher than those cited. A melt with normal Ti^{++} content could be fed TiCl_4 very rapidly until the valence was nearly 3. When this melt was then electrolyzed at steady-state (4 faradays/mole TiCl_4 feed), nearly all the current went to reduce the valence and little metal was made until valence = 2.4; from this point equilibrium valence was approached more slowly.

However, if a cell had been operating long enough to accumulate considerable metal, it was difficult to raise the valence above 2.4 by increasing TiCl_4 feed. Metal dissolved rapidly with accelerated feed even when it was presumably protected by a 2–3v cathodic bias. Thus, metal once plated out does not necessarily remain so during the rest of the electrolysis, since reworking—solution and later re-deposition—may occur whenever it is not strongly cathodically biased. For example, metal deposited on a "scavenging" cathode, or on the cell wall, is no longer protected when the main deposition cathode is immersed; it will slowly dissolve even at valence = 2.20 and be redeposited on the main cathode.

Over-all current efficiencies (c.e.), calculated from metal made and current passed, are as follows: at

2½% Ti, with RA-186 diaphragm, 90 ± 4%; with the more permeable RA-139 diaphragm, 89 ± 4%. At 6% Ti, with RA-186, c.e. = 82 ± 5%. Periodic c.e.'s determined over short periods may be lower, e.g., after prolonged steady-state operation at 2½% Ti, 85%, and at 6% Ti about 70%. Minimum c.e. usually coincides with maximum expulsion rate of TiCl₄ from the anolyte. Current efficiency during the buildup stage is close to 100%, as it is near the end of stripping.

Metal recoveries average 92 ± 4% of the Ti values of the net TiCl₄ feed, independent of Ti ion concentration in the melt. Ti not recovered escapes as gas with the chlorine or with the catholyte argon flow; due to imperfect stripping some also remains in the melt, and the diaphragm.

Both the metal on the cathode and the metal in the cell pot were recovered in each run. Surprisingly, the fraction of the product harvested on the cathode is little affected by delay in cathode-immersion. With the deposition cathode immersed at the end of the buildup stage ("no delay"), metal adhering represents about 93% of total recovery. Considering deposition time as time exclusive of the buildup stage, immersion delay of 30% of deposition time still achieves a yield on the cathode of 91% of total recovery. The high yield with immersion delay is explained by reworking of metal on the cell walls.

Product Evaluation

There is considerable frozen salt occluded in the cold cathode deposit, but the form of the deposit is evident. Furthermore, with the coarser products it is possible to leach the deposit on the cathode and to dissolve the salt without dislodging any metal. The Ti appears as a finely divided dark powder in a layer near the cathode surface and then, in sharp contrast, as well-drained, well-formed, lustrous dendritic crystal agglomerates in the remainder of the deposit. The boundary is abrupt, although the operating cell shows no discontinuity in electrical characteristics. With the delayed-immersion technique the layer of fines is thinner or absent; the deposit is more coarsely crystalline, lower in salt content, and less voluminous. Coarse crystals are found throughout the deposit, and those adjacent to the cathode surface are anchored firmly to it. The proximal side of the cathode is covered with a continuous foil of ductile, low-oxygen Ti as much as 15 mils thick.

Deposits contain 5-10g of Ti crystals per cubic inch. Adherence is never a problem. High Ti ion

Table I. Properties of electrolytic Ti ingots

R _A	B.H.N.	% O ₂	% Cold reduction to cracking
30	81	0.04	>95
35	91	0.07	>90
40	106	0.10	90
45	123	0.13	85
50	145	0.18	70
55	171	0.26	55
60	200	0.38	40
65	238	0.57	15

concentration and high current density each encourage branching and raggedness in the crystal agglomerates, but the effect is not marked unless both occur together. Rotating a plate cathode continuously did not make the deposit more compact; neither did mechanical agitation of the melt.

An inverse correlation between deposit crystallinity and frozen salt content was observed. A deposit of poor crystallinity may hold five times its weight of salt, while deposits yielding satisfactorily ductile Ti had 30-35% metal, and very coarse deposits (such as are obtained using long cathode-immersion delays) were 50% metal or higher.

The frozen salt was separated from the metal by either of the two methods: (i) vacuum evaporation in an induction furnace at 1400°C, with the sample contained in a perforated graphite crucible; a sinter cake results. (ii) Leaching, usually in ½% HCl, followed by water elutriation to separate and discard the -44μ size fraction. This latter method was eventually adopted for most of the product recovery work since it sacrifices little in yield but is much simpler and gives better metal.

The standard method of metal evaluation was the measurement of Rockwell A (R_A) and 1500-kg Brinell (B.H.N.) hardnesses at several points on a 30-40g ingot. The compressed metal crystals were melted on a water-cooled copper hearth under argon by a d-c arc of 18-25v 200-600 amp, with the Ti the anode. Most of the ingots were also cold-rolled in many passes to determine the per cent cold reduction possible without cracking. Oxygen and hydrogen analyses by vacuum fusion were done routinely. Correlations among the metal properties are shown in Table I.

Typical values for metal hardness are given in Table II, where the striking effect of cathode-immersion delay is shown. As already noted, this improvement in metal quality is not necessarily accompanied by poorer yield; in fact, the superior crystallinity more than compensates for any differ-

Table II. Summary of product quality

Time when cathode immersed	Salt removal by vac. evap. and sinter		Salt removal by leaching		
	No. of runs	B.H.N.	No. of runs	% + 44μ	B.H.N.
At start	7	180 ± 7 ^a	—	—	—
End of buildup period	14	130 ± 10	11	82.0 ± 2.5	116 ± 10
After 30% of dep. time*	3	100 to 112	6	93.2 ± 2.3	86 ± 9
During stripping only	6	79 to 93	—	—	—

* "Deposition time" = time exclusive of buildup stage.
^a Average deviation from the mean.

Table III. Particle size and impurity content

%	-28 μ	44-53 μ	74-99 μ
O ₂	1.14	0.35	0.22
H ₂	0.076	0.022	0.010
N ₂	0.013	0.008	0.004
Cu	0.05	0.035	0.025
Al	0.04	0.025	0.02
Ni	0.03	0.01	0.0045
Cr	0.045	0.035	0.025
Fe	0.015	0.004	0.0025
Mo	0.02	0.0045	0.003
Sn	0.007	—	—
Pb	0.012	0.009	0.012
Mn	0.0008	0.0012	0.0012
Mg	0.002	0.0015	0.002
Total	1.45	0.51	0.33

ence in proportion of recovered metal adhering to the cathode. Defining "useful recovery" as the per cent of the net Ti feed which is recovered on the cathode as $> 44\mu$ crystals, this is 70% for immersion at the end of buildup and 77% for immersion after 30% of "deposition time."

Chemical analyses of the product vary with crystallinity, as expected. Oxygen content of the best products is 0.05%. Hydrogen may be up to 0.02% on leached crystals, but after arc-melting is 10-50 ppm. Nitrogen is $< 0.015\%$. Foreign metals contents, in ppm, range as follows: Si, < 100 ; Cu, 5-500; Al, 100-700; Ni, 30-300; Cr, 100-500; Fe, 20-200; Mo, 10-200; Sn, 10; Pb, 50-300; Mn, 5-40; Mg, 10-50. The chief sources of impurities are: Cu, from the hearth during arc-melting; Al, from the alumina diaphragm; and Ni, Cr, Mo, Fe, and Mn from the Hastelloy cell.

Correlations between crystal size and the concentration of impurities are shown in Table III, for three elutriated fractions of a leached cathode deposit. From several such sets of analyses the general conclusion is drawn that whenever the prospective impurity is present in the cell in relative abundance, *e.g.*, the gaseous contaminants, aluminum, and the major components of Hastelloy, the concentration in the metal will vary inversely as the particle size, whereas the adventitious impurity contents, Cu, Pb, Mg, and Mn, are independent of particle size. Of course the existence of a relationship between purity and particle size does not distinguish which is cause and which effect; but it is clear that the electrolytic process, unlike the Kroll process, has a built-in impurity-rejection mechanism.

Some Effects of Operating Conditions

The standard Ti ion concentration in the melt was $2\frac{1}{2}\%$, but many runs were done at 6-7% Ti. Little effect of the higher concentration on product quality was observed; in any case these effects are inseparable from those of current density. No effect of cathode c.d. was seen in the usual operating range of 0.3-1.3 amp/in.², nominal, but at $2\frac{1}{2}\%$ Ti only fines were obtained at more than 3 amp/in.², and at 7 amp/in.² the deposit did not adhere at all. At 6% Ti, c.d. can be carried to 8 amp/in.² before fines start to deposit. A deposit at excessive c.d. changes to coarse crystals when it has grown to such size

Table IV. Effect of air leakage

	B.H.N.	%O ₂ (ingot)	%N ₂ (ingot)
Result if all added air contaminates deposit	> 220	0.44	1.2
Actual result (3 runs)	145-170	0.15-0.22	0.05
Standard result for conditions of electrolysis	110 ± 10	0.09	0.01

that the effective c.d. is below the critical limit; the transition is abrupt and gives a sharply defined junction in the deposit.

Too low a Ti ion concentration is definitely harmful; a run at 0.4% Ti gave all fine material, with many fragile platelets. Furthermore, it is noticeable that a thin layer of fines appears on the outside of even the coarsest products. This evidently represents the last material deposited; it is not present when metal is harvested without stripping. Such fines probably result from extreme concentration polarization, probably attended by deposition of alkali metal.

Experiments with vigorous agitation of the melt by a propeller stirrer show poorer deposit adherence and crystallinity during the steady-state operation—this despite the advantages of faster $TiCl_4$ absorption, lower average Ti ion valence, and improved thermal and material homogeneity.

The effect of air leakage into the cell was tested in three runs in which 0.5 v/% of room air was deliberately bled in continuously to the argon over the catholyte. This would add 0.35% O₂ to the metal if it were all absorbed by the deposit. Results are shown in Table IV. The cathode deposit is obviously degraded but again some selective rejection of the contaminant has occurred. Analysis of elutriated size fractions showed normal oxygen content for the crystal size; air leakage simply causes a higher proportion of fines. There was voluminous cell-bottom sludge also, containing $\sim 5\%$ O₂ and 1.5% N₂.

Similarly, opening and discharging the cell hot (550°) showed no measurable oxygen contamination of the $+44\mu$ crystals where these constituted $> 90\%$ of the product. Where these were 80-90% of the product, however, an oxygen pickup of about 0.05% resulted. This indicates a different particle-size distribution in the latter deposit, with more material near the small end of the range.

One final source of oxygen contamination comes in reclaiming metal from frozen entrained salt when the melt has not been stripped. Absorption of atmospheric moisture by LiCl, followed by reaction with Ti lower chlorides, contaminates the deposit with oxygen-bearing hydrolysis products. These cannot be separated by the vacuum evaporation procedure: in three products with 1-2% Ti ion remaining in the melt the ingot was 40-240 B.H.N. above standard. However, with leaching in $\frac{1}{2}\%$ HCl at ice temperature the hydrolysis products apparently can be washed off the metal crystals by agitation or floated off during elutriation. With $2\frac{1}{2}\%$ Ti ion in the salt the $+44\mu$ crystals were as soft as those from comparable runs with the melt stripped. It is reassuring for the prospects for large-scale

electrolytic titanium that it is not necessary to strip the cell before harvest if the leaching is done with care.

Manuscript received Oct. 11, 1962.

Any discussion of this paper will appear in a Discussion Section to be published in the December 1964 JOURNAL.

REFERENCES

1. M. B. Alpert, F. J. Schultz, and W. F. Sullivan, *This Journal*, **104**, 555 (1957).
2. M. B. Alpert, J. A. Hamilton, F. J. Schultz, and W. F. Sullivan, *ibid.*, **106**, 142 (1959).
3. W. R. Opie and K. A. Svanstrom, *Trans. AIME Met. Soc.*, **215**, 253 (1959).
4. W. R. Opie and O. W. Moles, *ibid.*, **218**, 646, (1960).
5. A. V. Ivanov *et al.*, *Titan i ego Splavy*, *Akad. Nauk S.S.S.R. Inst. Met. im. A. A. Baikova*, **1961**, 124, 136, 153.
6. L. J. Reimert and M. J. Rand, *This Journal*, **111**, 434 (1964).
7. S. Mellgren and W. Opie, *Trans. AIME, J. Metals*, **9**, 266 (1957).

Electrolytic Titanium from $TiCl_4$

II. Influence of Impurities in $TiCl_4$

Lawrence J. Reimert and Myron J. Rand¹

New Jersey Zinc Company, Palmerton, Pennsylvania

ABSTRACT

Titanium tetrachloride for an electrolytic titanium process was prepared on a pilot-plant scale and the impurities identified. Data are given allowing a quantitative estimation of contaminants by infrared spectrophotometry on 10-cm liquid paths. Each impurity was tested for its effect on electrolytic cell performance and Ti metal quality using the laboratory cell described in a previous paper. The most common impurity, Si_2OCl_6 , is harmless. Deposit quality was most sensitive to sulfur-containing agents such as COS, CS_2 , and S_2Cl_2 , and to CO_2 . Results are also reported for HCl, $COCl_2$, $SiCl_4$, $VOCl_3$, $SnCl_4$, $AsCl_3$, $POCl_3$, and CCl_3COCl . Impurities are shown to concentrate strongly in the smaller crystals of the cathode deposit and in the cell sludge, often making it possible to obtain acceptable metal from contaminated $TiCl_4$ by screening the deposit. All detrimental impurity levels are such that economical large-scale preparation of good cell feed $TiCl_4$ should present no problem.

Several factors make $TiCl_4$ purity of extreme importance in processes for Ti metal. Ti absorbs many impurities quickly at elevated temperatures, and small amounts of those which dissolve interstitially destroy metal ductility. Furthermore, since $TiCl_4$ contains only 25% Ti, there may be a four-fold concentration of impurities in the metal. Finally, the method of manufacture and the inherent powerful dehydrating and solvent powers of $TiCl_4$ make it susceptible to contamination by a wide variety of substances during preparation, purification, storage, and handling.

In an electrolytic process, impurities inhibit crystal growth and are concentrated in the smaller particles of the cathode deposit. These fines may either drop off the deposit, forming cell sludge, or, if they adhere, be separated later by elutriation. In either case, a potential impurity-rejection mechanism operates. With continuous $TiCl_4$ feed, however, impurities are replenished constantly. The result could be a more serious degradation of average crystal size, with greater oxygen and hydrogen pickup during metal recovery.

In order to study the effects of $TiCl_4$ impurities on the quality and yield of electrolytic Ti, the following conditions must be met: (a) A highly reproducible electrolytic operation must be available; (b) A par result for product crystallinity and hardness

must be established for pure $TiCl_4$, or for $TiCl_4$ of known and readily-attainable purity; (c) As completely as possible, the impurities in this $TiCl_4$ of cell-feed grade must be identified and their concentrations determined; (d) Controlled changes in these concentrations must be made and the effect on deposit quality observed.

The first requirement has been met by the work described in Part I of this paper: a reliable laboratory-scale fused-salt cell producing ductile Ti at 550°C from continuous $TiCl_4$ feed dripped onto the melt surface (1). Continued operation of this reference cell has given further improvement in deposit quality and reproducibility. In the work described here, redistilled $TiCl_4$ samples with controlled amounts of various impurities were fed to the cell and a standard electrolysis carried out: a 2 faraday/mole concentration buildup stage to 2½% Ti ion in the melt, at the end of which the deposition cathode was immersed; a prolonged steady-state electrolysis, during which the current and $TiCl_4$ feed were kept in balance; and finally, a stripping stage. Runs lasted about 36 hr (850-900 amp-hr), and about 350g of Ti were made. The product was harvested cold, and after leaching in ice-cold ½% HCl was wet-screened on 200-mesh (74μ) with distilled water.

Preparation of $TiCl_4$

It is the purpose of this study to determine the quality of Ti which can be produced not from $TiCl_4$

¹ Present address: Bell Telephone Laboratories, Inc., Allentown, Pennsylvania.

of the highest attainable purity but from $TiCl_4$ which may be prepared with reasonable economy for large-scale operation, and to discover the levels at which the contaminants begin to degrade the electrodeposited metal. Thus some description of the production of the $TiCl_4$ used is necessary. This process was on the pilot-plant scale throughout and readily capable of being scaled up to full commercial size.

The starting material was either ilmenite ore or titaniferous slag. These were briquetted with coal, using either clay or sulfite liquor as binder, and reacted with chlorine autogenously at 900° - $1000^\circ C$ in a continuous-feed column (2). Under these conditions chlorides and oxychlorides of many substances contaminate the product: Fe, Si, Al, and V from the ore or slag; S, C, H, O from the coal or binder. Some of these are separated readily during product condensation, or later by distillation, whereas others persist to at least some extent to the final "pure" material.

Vanadium removal was generally accomplished by H_2S gassing. The amount used was arbitrary, based on the analysis of the crude $TiCl_4$ and what experience had shown was required to reduce the vanadium level below 5 ppm. The $TiCl_4$ next went to a continuous still with two 7 ft x 4 in. diam columns packed with $\frac{1}{2}$ -in. Berl saddles. In the first of these, $SiCl_4$ (b.p. 57°) was removed; in the sec-

ond, $TiCl_4$ was taken off overhead, leaving behind less volatile metal chlorides and, especially, the oxides and oxychlorides of indeterminate composition arising from air exposure, called "hydrolysis product." The still was operated with high reflux ratios, with a throughput of only 4 gal/hr. At this stage the $TiCl_4$ was clear and colorless. Finally, just before use the material was distilled into a reservoir from which it was fed to the cell without further exposure.

Impurities in $TiCl_4$

The identification and determination of contaminants in the purified $TiCl_4$ was carried out chiefly by the infrared absorption spectrum of deep liquid layers. $TiCl_4$ is quite transparent up to 9μ , and with a 10-cm absorption path impurities have detection limits in the range 1-200 ppm. Many of these are listed in Table I, with quantitative characterization of the absorption bands. Some of the assignments have been published earlier (3, 4) and some appear here for the first time. The absorptivity referred to is the constant a in the Beer law equation $\log I_0/I = abc$. Absorptivities differ from those of ref. (4) by a factor of three, emphasizing that for accurate work the absorption bands should be calibrated with the spectrophotometer to be used.

The following substances have been detected in the purified $TiCl_4$ fed to the cell: HCl , CO_2 , $SiCl_4$, Si_2OCl_6 , COS , CS_2 , $VOCl_3$, $COCl_2$, $SnCl_4$, $AsCl_3$, and

Table I. Infrared detection of impurities in $TiCl_4$

Impurity	Absorption maximum, μ		Absorptivity, wt % ⁻¹ cm ⁻¹		Detection limit, ppm	
	This work	Ref. 4	This work	Ref. 4	This work	Ref. 4
HCl	3.53	3.53		30		2
	3.41	3.41		19.3		3
Si_2OCl_6	8.98		38		1	
	5.43		0.56		40	
	6.49					
$TiOCl_2^*$	12.18	12.18		426		0.1
	8.46	8.45		4.3		8
	7.37	7.37		5.5		6
COS	4.89	4.89 ^a		450 ^a		0.2
CO ₂	4.28	4.28		164		0.8
CS ₂	6.57	6.58	260	780	0.04	0.07
COCl ₂	5.50	5.52		110		2
	6.05	6.05		9.2		15
VOCl ₃	9.66		62			
	4.84	4.84	0.29	1.15	50	40
CCl ₃ COCl	5.53	5.55	15	95	1	0.6
POCl ₃	7.95	7.91	57	139	2	1
	8.21	8.16		80		1.6
CH ₂ Cl ₂	7.93		8.9		5	
CHCl ₃	8.24		17		2	
CCl ₄	6.44		0.33		100	
SOCl ₂	8.09	8.06	64	150	0.5	1
	4.06					
SO ₂ Cl ₂	7.04		55		2	
C ₃ N ₃ Cl ₃	6.65		93		0.5	
	7.92					
SiCl ₄	8.18	8.18	0.37	0.81	115	200
C ₆ Cl ₆		7.69		20.3		5
$TiCl_4$ bands**	9.03	($\nu_4 + 2\nu_3$)				
	7.96	($2\nu_1 + \nu_3$)				
	7.37	($\nu_1 + 2\nu_3$)				
	6.79	($3\nu_3$)				

* "Hydrolysis product", composition uncertain.

** See also refs. (3, 6).

^a From ref. 5.

Table II. Summary of results

Run	Treatment	Cathode deposit			Deposit analysis, %		
		% + 200 Mesh	% Useful recovery	B.H.N. + 200 mesh	+ 200 Mesh	- 200 Mesh	Cell sludge
271	AlCl ₃ -Cl ₂	86.5	80.0	95			
178	None (standard run)	86.1	77.9	96	H	0.002	
242	None (standard run)	87.5	78.5	99	S	0.002	
263	None (standard run)	86.9	79.6	96	Si	0.005	
250	None, no redistillation	82.6	72.2	99			
253	None, no redistillation	80.2	70.9	99			
256	None, no redistillation	84.1	75.6	104			
248	0% Si ₂ OCl ₆	77.6	72.2	104	Si	0.01	0.01
266	0% Si ₂ OCl ₆	81.8	74.0	96			
263	0.084% Si ₂ OCl ₆	86.9	79.6	96			
249	0.19% Si ₂ OCl ₆	86.0	79.8	94	Si	0.01	0.21
251	0.24% Si ₂ OCl ₆	89.8	79.0	90	Si	0.01	0.22
257	0.42% Si ₂ OCl ₆	95.5	82.1	92			
261	0.48% Si ₂ OCl ₆	88.2	77.2	104			
255	0.92% Si ₂ OCl ₆	82.7	70.3	99	Si	0.01	1.04
226	470 ppm S as S ₂ Cl ₂	79.6 ^a	78.1	156	S	0.03	0.06
229	140 ppm S as S ₂ Cl ₂	79.8	71.2	139	S	0.02	0.07
245	100 x normal COS (0.1% est.)	84.7 ^a	72.4	151	S	0.004	0.033
273	40 ppm CS ₂	82.4 ^a	72.8	109	S	0.003	0.010
275	21 ppm CS ₂	94.0	80.6	101			
234	Sat. CO ₂ (100 x normal)	58.4	49.6	128			
236	Near sat. HCl (4 x normal)	81.0	71.5	106	H	0.002	
247	COCl ₂ 100 x normal	77.6	67.4	115			
238	330 ppm Si as SiCl ₄ *	77.9	68.0	103	Si	0.004	0.35
270	740 ppm Si as SiCl ₄ **	90.1	81.2	90			
240	150 ppm V as VOCl ₃	84.2	75.1	110	V	0.014	0.024
268	82 ppm V as VOCl ₃	85.5	77.4	99			
267	600 ppm Sn as SnCl ₄ (60 x normal)	86.7	75.9	98	Sn	0.089	0.20
269	210 ppm As as AsCl ₃ (10 x normal)	82.0	73.5	110	As	0.007	0.030
262	0.22% POCl ₃ (100 x normal)	74.7	66.0	131	P	0.015	0.028
233	520 ppm CCl ₃ COCl	87.5	79.2	99			

^a Proportion of + 100 mesh crystals noticeably substandard.

* Plus 0.014% Si as Si₂OCl₆.

** Plus 0.025% Si as Si₂OCl₆.

the TiCl₄ hydrolysis product. Si₂OCl₆ is the most common, probably because its boiling point (137°) is identical to that of TiCl₄. It was present to about 1500 ppm in TiCl₄ made from slag, but only to about 300 ppm in TiCl₄ from ilmenite. VOCl₃ (b.p. 127°), SnCl₄ (114°), AsCl₃ (130°), and S₂Cl₂ (136°) are also difficult to separate by distillation, but none of these is believed to exceed 25 ppm. Estimated levels of other impurities are: SiCl₄ and HCl, 200 ppm; CO₂ and COCl₂, 50 ppm; COS and CS₂, < 10 ppm. POCl₃ (b.p. 105°), and CCl₃COCl (118°) were not detected, but because they are common impurities in TiCl₄ they were included in this investigation.

Usually the cell feed for the experiments was prepared by adding the desired contaminant in known amount to the freshly redistilled material in the feed reservoir in such a way that there was negligible exposure to the atmosphere; for example, liquid contaminants were added by breaking a fragile ampoule under the surface of the TiCl₄ with a plunger. Alternatively, a hypodermic syringe with a long needle could be used. Thorough stirring with argon followed. Gaseous contaminants were added simply by bubbling the pure gas through the TiCl₄ in the reservoir. Often the exact concentration of the contaminant was known from the weight added; but the composition of the cell feed was always checked by analysis, either by infrared spectrophotometry or by standard wet chemical methods.

Results

Three criteria were selected for evaluating the result of an electrolysis: (a) the per cent of the cathode deposit retained on a 200-mesh screen; (b) the per cent of the net Ti fed to the cell which was recovered on the cathode as +200 mesh crystals, the so-called "per cent useful recovery;" (c) the Brinell hardness of an ingot made by arc-melting the +200 mesh crystals under argon. Standard runs, as defined earlier, were made at intervals among the impurity runs to establish reproducibilities and par values. From these and from earlier experience (1), it was decided that the effect of an impurity could be considered negligible if the metal evaluation gave: % +200 mesh > 80, % useful recovery > 70, Brinell hardness < 105.

Table II is a condensed summary of all pertinent data and results. In this table clearly substandard results are shown in italic numbers.

In run 271 the TiCl₄ was treated at boiling temperature with aluminum chloride hexahydrate and gassed with chlorine in an attempt to make super-pure material (3). This procedure destroys organic compounds, and also changes sulfur monochloride to dichloride (b.p. 59°) so that it is separated in the subsequent distillation. Si₂OCl₆ is not affected. By comparison with the standard runs, the next three entries in the table, it is seen that there is no advantage to this special treatment; the standard

TiCl_4 preparation yields a cell feed which it is unnecessary and uneconomical to improve upon.

Runs 250, 253, and 256 used the product of the pilot-plant still without the final redistillation; the material was simply poured through the air into the cell feed reservoir. The results are only slightly inferior to the optimum. The still product is evidently entirely suitable for an electrolytic process for Ti of ductility equal to that of the best current commercial metal.

In eight runs the influence of Si_2OCl_6 was studied. Runs 248 and 266 are the only ones in Table II with none of this oxygen-bearing impurity. For these the TiCl_4 was distilled through activated carbon at 400° , and then given still another distillation to reduce the high CO_2 and HCl concentrations caused by this treatment. Removal of Si_2OCl_6 is indicated by transparency at 8.98μ .

There is no evidence of any harmful effect of even 1% Si_2OCl_6 . In fact, there is some indication of a slight beneficial effect in the range 0.2-0.4%; runs 251 and 257 are outstanding. It may well be that Si_2OCl_6 never gets into solution in the 550° melt at all, but decomposes to SiCl_4 (which distills out of the cell) and insoluble silicon oxides.

On the other hand, the sulfur-containing compounds— S_2Cl_2 , COS , CS_2 —in concentrations of the order of 0.01% severely degrade the cathode deposit. The poor quality of the products was obvious to the most cursory inspection; in addition, metal from these runs, including the on-grade 275, suffered twice the normal weight loss during arc-melting. The electrolytic process is considered more sensitive to sulfur than to any other impurity investigated.

High CO_2 concentration is also harmful. However, the amount of contaminant used in run 234 is much greater than would be found in any TiCl_4 batch which had been stored and handled with reasonable care. Excessive CO_2 can be removed by simple distillation.

Other impurities which are considered detrimental only in quantities some ten times normal are COCl_2 , VOCl_3 , AsCl_3 , and POCl_3 . There seems little need for concern about the concentration of SiCl_4 , SnCl_4 , and trichloroacetyl chloride.

Analytical results for the deposit crystals and for metal recovered from the cell sludge, also presented in Table II, are quite instructive. With the single exception of tin, no appreciable amount of any impurity tried was introduced into the +200-mesh Ti crystals. The -200-mesh fraction was much more contaminated, and the cell-bottom metal worst of all. The impurity-segregating mechanism in the production of electrolytic Ti evidently operates as a result of the inhibition of growth of any crystals into which some critical amount of foreign material is incorporated.

Acknowledgment

The authors are indebted to John L. Rodda of these laboratories for his aid in obtaining infrared spectrograms.

Manuscript received Oct. 11, 1962.

Any discussion of this paper will appear in a Discussion Section to be published in the December 1964 JOURNAL.

REFERENCES

1. M. J. Rand and L. J. Reimert, *This Journal*, **111**, 429 (1964).
2. H. M. Cyr *et al.*, U. S. Pat. 2, 723, 903 (1955); L. D. Fetterolf and C. M. McFarland, *Chem. Eng. Prog.*, **56**, 68 (1960).
3. R. B. Johannesen *et al.*, *J. Res. Nat. Bur. Standards*, **53**, 197 (1954); W. S. Clabaugh *et al.*, *ibid.*, **55**, 261 (1955).
4. D. I. Tsekhovol'skaya *et al.*, *Zavodskaya Lab.*, **25**, 300 (1959); D. I. Tsekhovol'skaya and T. A. Zavaritskaya, *Zhur. Analiticheskoi Khim.*, **16**, 623 (1961); T. A. Zavaritskaya, *Titan i ego Splavy*, *Akad. Nauk SSSR, Inst. Met.*, **1961**, 195-200 [C. A. **58**, 269c].
5. T. A. Zavaritskaya and I. A. Zevakin, *Zhur. Priklad. Khim.*, **34**, 2783 (1961).
6. N. J. Hawkins and D. R. Carpenter, *J. Chem. Phys.*, **23**, 1700 (1955).

A Study of Surface Oxides on Platinum Electrodes

Jaspal S. Mayell and Stanley H. Langer¹

Central Research Division, American Cyanamid Company, Stamford, Connecticut

ABSTRACT

Surface oxides on smooth platinum, electrodeposited platinum black, and platinum black-polytetrafluoroethylene molded electrodes have been characterized by anodic oxidation and cathodic stripping. The oxidation sequence for smooth platinum and platinum black electrodes is $\text{Pt} \rightarrow \text{Pt}(\text{OH})_2 \rightarrow \text{Pt}(\text{O})_2$. At higher potentials smooth platinum forms $\text{Pt}(\text{O})_4$ and PtO while platinum black forms $\text{Pt}(\text{O})_{2.5(\text{approx.})}$. The initial oxidation of platinum to $\text{Pt}(\text{OH})_2$ and subsequent reduction has been used as a basis for the determination of platinum electroactive surface areas. The formation of a "tight" PtO structure on smooth platinum at higher potentials may account for some of the unusual properties of smooth platinum electrodes. The failure of platinum black to form tight PtO may be due to irregular platinum atom arrangement and related to its catalytic properties.

Platinum surfaces and surface platinum oxidation states are the subject of a great number of modern investigations and considerable controversy despite the fact that the unique properties of platinum and platinized platinum electrodes have been known for many years. Historical perspective and current views on some of the effects of the platinum oxidation states have been reviewed recently in several places (1-5). Our own interest in platinum catalysts and electrocatalysis led to an investigation of oxidation states on smooth platinum, electrodeposited platinum black, and molded polytetrafluoroethylene-platinum black electrodes.

Modern workers (6-17) recognize that platinum electrodes are not inert, as often had been assumed, and that oxidized and reduced surface states determine the properties of the electrode under consideration. However, much disagreement centers around the question: do platinum oxides form or is oxygen merely chemisorbed on the surface during initiation of platinum surface oxidation? Surface platinum-oxygen ratios have still not been established for many oxidizing conditions. It is this latter problem that we have addressed since, as will be shown, it can be approached from a stoichiometric viewpoint. Furthermore, the question of oxygen bonding may not be answerable in terms of contemporary bonding concepts and may be avoided for the present.

Another major objective of this work has been to investigate the use of platinum oxide formation as a basis for the determination of surface area from an electrochemical viewpoint.

A number of workers have noted distinct changes in electrode reactions when a platinum electrode is reduced or oxidized prior to reaction. In many instances, these changes have been studied only in terms of the effect on a particular reaction at the electrode rather than in terms of alterations of the platinum surface oxidation states. Lingane (3) reports that direct reduction of oxygen at a platinum cathode is diffusion controlled in the presence of a

small amount of platinum oxide, but kinetically controlled if a minimum amount of platinum oxide is not present. Hoare (4) also has discussed recently the important catalytic effect of platinum oxide on oxygen reduction. Earlier, Baker and MacNevin (18) reported the oxidation of arsenous and ferrous ions to be inhibited by the presence of platinum oxide while Kolthoff and Nightingale (19) contended that the Fe(II)—Fe(III) couple was more reversible in the presence of the oxide. Anson (20, 21) noted an increase in chronopotentiometric oxidation transition time for ferrous ion in the presence of surface PtO and has claimed (22) surface oxides make the iron couple less reversible. Giner (23) states that the oxidized electrode inhibits oxalic acid oxidation so that only oxygen is evolved from aqueous solution. Hickling and Wilson (24) and Bianchi, Mazza, and Mussini (25) have discussed the decomposition of hydrogen peroxide on platinum oxide surfaces to form oxygen and postulate that PtO may enter into the reaction as an intermediate.

Despite the recognized importance of surface pretreatment, the principal surface oxides at platinum electrodes have not been studied to give a coherent picture. Relatively little attention has been given to the development of reliable methods for measurement of electroactive areas at platinum surfaces. We implemented the present study of the behavior of platinum electrodes under galvanostatic and potentiostatic oxidation conditions, since the published literature left little doubt that platinum surface oxide state is important in electrocatalytic reactions involving hydrogen and oxygen.

Experimental

Apparatus.—The constant current source was model 151 B, Quan-Tech Laboratories (Boonton, New Jersey). The current passing through the cell was measured by means of a potentiometer, from the voltage drop across a standard resistor. The potentiostat was an Elektronischer Potentiostat nach Wenking obtained from Brinkmann Instruments, Inc. The potential-time behavior was observed on

¹ Present address: Chemical Engineering Department, University of Wisconsin, Madison, Wisconsin.

a Sargent SR recorder used in conjunction with a Sargent pH Recording Adapter. All experiments were performed at $25.00^\circ \pm 0.05^\circ\text{C}$ in a water bath. A conventional H-type electrolysis cell, Fig. 1, was used. The cathode and anode compartments were separated by a sintered glass disk of 3 cm diameter and a 3% solution of agar agar, applied toward the auxiliary compartment of the sintered disk. [Note: Since this work was completed much of it has been repeated without agar agar and with a standard hydrogen electrode. Results are substantially the same as those reported here.] The auxiliary electrode was a smooth platinum sheet of 4 cm^2 area. The reference electrode was mercury, mercurous sulfate, and saturated potassium sulfate ($+0.64\text{ v}$ vs. the normal hydrogen electrode). The platinum surface oxidation states were determined on a smooth shielded platinum electrode of 1.0 cm^2 area, a shielded platinum black-polytetrafluoroethylene molded electrode, and a shielded electrodeposited platinum black electrode.

In order to observe the electrode surface, a work inspection mirror C-2 of Ullman Products Corporation (Norwalk, Connecticut) was placed below the electrolysis cell but inside the water bath. The Burton Fresnel light source was focussed on the mirror to get a clear image of the electrode surface, Fig. 2. *Preparation of the electrodes.*—The shielded smooth platinum electrode was prepared exactly as recommended by Bard (26).

The electrodeposited platinum black electrode was prepared by depositing platinum electrolytically on a 1.0 cm^2 smooth shielded platinum electrode of "J" configuration. The J-shaped configuration was a result of bending the electrode holder (see Fig. 1) so that the shielded platinized platinum electrode faced the surface of the solution and was parallel to the solution surface. This preserved a reproduc-

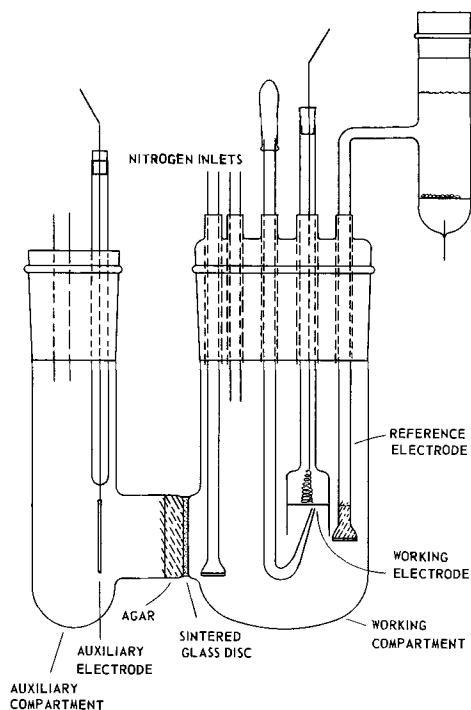


Fig. 1. Electrolysis cell

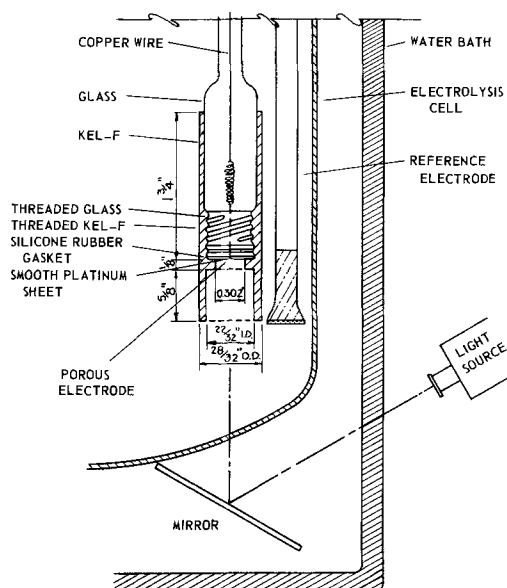


Fig. 2. Polychlorotrifluoroethylene electrode holder assembly for porous electrodes.

ible surface since any detached platinum stayed in contact with the surface. An aqueous solution of H_2PtCl_6 (5%) containing 0.03% lead acetate was used for electrodeposition. Deposition was performed at a constant current of 170 ma in three $\frac{1}{2}$ -min stages because of the interference of gas bubbles. The weight of the platinum deposited was 2.6 mg.

The platinum black-polytetrafluoroethylene molded electrode contained 30.8 mgm of platinum black plus 15% of polytetrafluoroethylene. It was cut from a larger sheet on which a platinum black-polytetrafluoroethylene paste had been spread on platinum screen and molded at 340°C . For the platinum black-polytetrafluoroethylene molded electrode, a shielded polychlorotrifluoroethylene electrode holder was fabricated. This shielded holder has the advantage of permitting interchange of electrodes so that the same area of the electrode was exposed to the solution. Moreover, it was not necessary to seal the electrode in glass tubing. The electrode holder assembly is shown in Fig. 2. Threaded glass (from a small glass vial) was screwed into the threaded polychlorotrifluoroethylene holder pushing silicone rubber sealing gaskets against the electrode so that the electrode was positioned in the shield. The porous electrode was backed with a piece of smooth platinum sheet to prevent leakage into the holder. The connection to the electrode was made by silver soldering a copper wire to the smooth platinum sheet used to back up the porous electrode. *Reagents.*—These were all of analytical grade. The platinum sheet was from Engelhard Industries.

Procedure.—The electrodes which were being studied were oxidized to various potentials at constant current or at constant potential. The oxidized electrode was kept at open-circuit voltage for 3 to 4 min and then reduced at constant current.

The working compartment contained 150 ml and the auxiliary compartment contained 50 ml of the supporting electrolyte. Both solutions were de-

aerated with nitrogen to remove dissolved oxygen before and after oxidation. A nitrogen atmosphere was maintained while performing both the oxidation and the reduction.

After oxidation, during open-circuit decay, any oxygen, if evolved, was removed by the dropper (see Fig. 1). Electrolyte from the vicinity of the electrode was removed also after every oxidation. The solution was routinely deaerated during the time of open-circuit voltage. During reduction, the potential of the oxidized electrode was recorded with respect to time as is done in chronopotentiometry. The transition time, τ , was taken at a potential of 0.34v. Transition times are the average for three reductions. All potentials reported here are referred to a normal hydrogen electrode although the work was performed with a Hg, Hg₂SO₄, saturated K₂SO₄ reference electrode ($E^\circ = +0.64v$ vs. the normal hydrogen electrode). In the present study the transition time, τ , does not depend on the mass transfer conditions and is thus proportional to concentration and may be interpreted in terms of coulombic equivalents.

Results

Smooth platinum electrode.—Curves from galvanostatic and chronopotentiometric studies of smooth platinum are shown in Fig. 3. Curve I for 34 μ a, curve II for 1.018 ma represent the change of potential with time during constant current oxidation of a smooth shielded platinum electrode. Curves III, IV, and V represent change of potential with time during reduction at a constant current of 34 μ a after the electrode was oxidized to 1.24, 1.64, and 1.93v, respectively. Oxidation of the electrode was initiated at an open-circuit voltage of about 0.86v. The dotted lines show the potential drop of the oxidized electrode 3-4 min after the circuit was broken. The potential dropped slowly when the electrode was oxidized up to 1.54v. At higher voltages (above 1.74v), the voltage dropped abruptly to approximately 1.50v when the circuit was broken, and then it decreased slowly with time. Subsequently as indicated by curve V, the potential dropped immediately to about 0.5v when the current for reduction was applied.

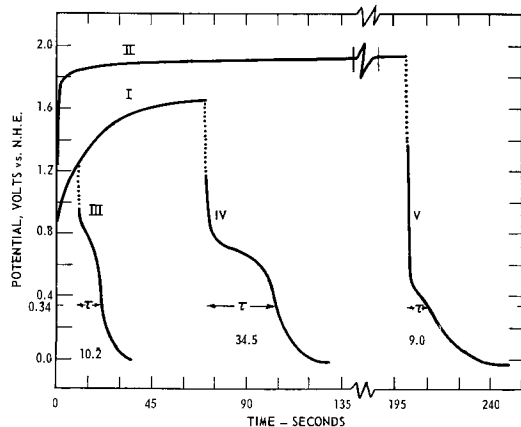


Fig. 3. Variation of potential with time when the smooth platinum electrode was oxidized (curves I, II) and reduced (curves III, IV, V) at constant current in 2N H₂SO₄.

The transition time τ to a potential of 0.34v vs. N.H.E. was measured from the potential-time plot for the reduction of the oxidized electrode. All reductions were performed at constant current. The log of μ coul ($i\tau$) required to reduce the oxidized electrode was plotted against the potential to which the electrode was oxidized. The rationale for plotting $\log i\tau$ vs. potential stems from an equation developed by Bockris and Huq (27) from kinetic considerations

$$\frac{\partial \eta}{\partial \log_{10} t} = 2.303 \frac{RT}{\alpha F} \quad [1]$$

where RT has usual significance, F is the Faraday, η is overpotential, t is time, α is the transfer coefficient, $\alpha = \frac{RT}{F} \frac{\partial \ln i_a}{\partial \eta}$, and i_a is anodic current. The devel-

opment of Eq. [1] is based on the assumption that the oxidation of a particular entity (OH⁻ or H₂O) takes place on a bare metal heterogeneous surface. Upon oxidation of H₂O or OH⁻ at previously active sites, these sites become inactive. The reduction process essentially measures (in terms of $i\tau$) that anodic current which is associated with the oxidation of the platinum surface; it appears (*vide infra*) that the chronopotentiometric oxidation potential is a function of the platinum surface state. In the Bockris and Huq development, surface coverage is proportional to t whereas in our work it is considered to be equal to $i\tau$ as i is constant and the oxidation potential E is employed in place of the over potential η .

Curve I, Fig. 4 shows a plot of log microcoulombs required to reduce the smooth platinum electrode vs. the potential to which the electrode was oxidized at constant current in 2N H₂SO₄. Data are presented in Table I. Essentially, the reduction process is used to measure the number of oxygen atoms attached to the platinum surface. It can be seen that the plot of curve I is linear over certain discrete ranges. It appears then that the platinum surface is altered in

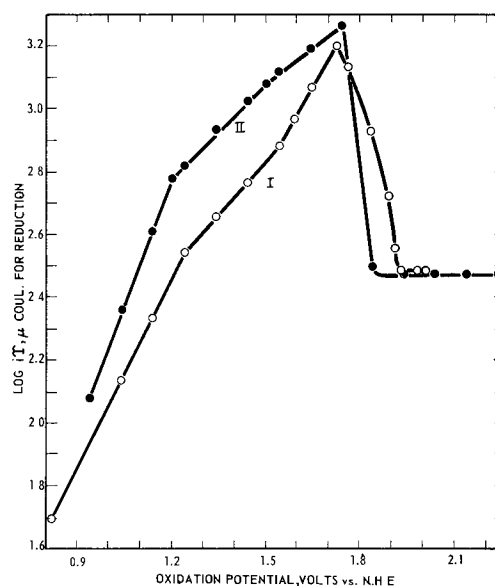


Fig. 4. Plot of log microcoulombs required to reduce the oxidized smooth platinum electrode surface vs. the potential to which the electrode was oxidized in 2N H₂SO₄, curve I (oxidation at constant current), curve II (oxidation at constant potential).

Table I. Galvanostatic oxidation of a smooth shielded platinum electrode* in 2N H₂SO₄

Potential to which the electrode was oxidized, v vs. N.H.E.	Current for oxidation, $\mu\text{a}/\text{cm}^2$	Time for oxidation, sec	τ For reduction,† sec	$i\tau$ For reduction, μcoul	Rest potential after 3½ min, v vs. N.H.E.
0.82	34.0	0.00	1.45	49.3	0.82
1.04	34.0	3.20	4.00	136.1	0.89
1.14	34.0	6.25	6.30	214.2	0.94
1.24	34.0	10.70	10.20	347.0	0.97
1.34	34.0	15.47	13.43	457.0	0.98
1.44	34.0	21.50	17.00	578.0	1.00
1.54	34.0	38.50	22.37	760.0	1.04
1.59	34.0	42.00	27.00	919.0	1.08
1.64	34.0	70.50	34.50	1172.0	1.14
1.72	34.0	394.00	46.00	1564.0	1.26
1.76	198.0	24.00	40.00	1360.0	1.22
1.83	198.0	150.00	25.00	850.0	1.34
1.89	1018.0	46.00	15.50	527.0	1.30
1.91	1018.0	80.00	10.60	360.5	1.35
1.93	1018.0	200.00	9.00	306.0	1.37
2.01	3029.5	70.00	9.00	306.0	1.37

* A smooth platinum electrode which was cleaned by nitric acid and washed with distilled water several times was prerduced many times until a consistent value of about 1.45 sec was obtained.
† Current i for reduction in all cases was 34 μa .

steps and that each stage begins, approximately, after the preceding state is terminated. From a kinetic viewpoint one should assume that during any particular oxidation stage, the proportion of oxygen discharges effective in altering the platinum surface is constant.

Data for potentiostatic oxidation and subsequent reduction in 2N H₂SO₄ and 1M HClO₄ are given in Table II. Similar work was also performed in 0.1M KOH. For comparison with chronopotentiometric oxidation, results from potentiostatic oxidation in 2N H₂SO₄ are shown as curve II, Fig. 4.

Constant current oxidation.—It can be seen from Table I that the time required to oxidize the electrode to 1.24v is almost the same as is required to reduce it, when the oxidation and reduction of the electrode are performed at a constant current of 34

Table II. Potentiostatic oxidation of a smooth shielded platinum electrode in two electrolytes

Potential to which the electrode was oxidized, v vs. N.H.E.	2N H ₂ SO ₄			1M HClO ₄		
	τ For reduction, sec	$i\tau$ For reduction, μcoul	Rest potential after 3½ min, v vs. N.H.E.	τ For reduction, sec	$i\tau$ For reduction, μcoul	Rest potential after 3½ min, v vs. N.H.E.
0.94	3.60	119.0	0.87	3.80	125.4	0.89
1.04	6.90	228.0	0.95	7.30	241.0	0.97
1.14	12.25	405.0	1.02	15.50	511.0	1.04
1.20	18.10	597.0	1.05	21.00	693.0	1.08
1.24	20.00	660.0	1.07	24.25	801.0	1.09
1.34	26.25	866.0	1.11	29.85	985.0	1.16
1.44	32.00	1058.0	1.17	37.25	1229.0	1.21
1.50	36.20	1195.0	1.22	39.30	1297.0	1.25
1.54	39.50	1303.0	1.25	42.00	1387.0	1.27
1.64	47.10	1552.0	1.29	47.60	1570.0	1.33
1.74	55.60	1837.0	1.35	51.10	1685.0	1.38
1.84	9.50	314.0	1.37	9.00	297.0	1.42
1.94	9.00	297.0	1.39	9.00	297.0	1.45
2.61	9.00	297.0	1.37	9.00	297.0	1.43

* Current i for reduction in all cases was 33.0 μa .

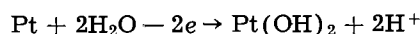
Table III. Calculated coulombs required to cover a smooth platinum surface

Major planes of face-centered cubic lattice	Packing densities of Pt at./cm ² of smooth Pt	Calculated μcoul required to cover a monolayer of smooth Pt (1 cm ²) when the electron change involved in the reaction is:	
		2 electrons	8 electrons
100	1.30×10^{15}	418	1672
110	0.93×10^{15}	298	1192
111	1.51×10^{15}	484	1936

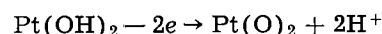
μa . This shows that the platinum surface oxide alone is being formed up to 1.24v, and no other reaction takes place. The number of coulombs used in oxidation from 1.24v upward is more than for reduction of the electrode surface indicating side reactions. Up to 1.54v, no oxygen bubbles were visible. It is possible that water from 1.24 to 1.54v is oxidized to intermediates which result in the formation of a higher surface oxide of platinum. Laitinen and Enke (2) have suggested that when water is oxidized, intermediates (OH) are produced which cause the formation of PtO. Above 1.60v, excess coulombs for oxidation can be attributed to oxygen evolution, readily seen on the platinum surface.

Based on the packing densities of the platinum atoms per square centimeter in different planes of a face-centered cubic lattice (2, 28), the calculated number of microcoulombs required to cover a monolayer of platinum atoms for a 2 and 8 electron change in the electrochemical reaction is shown in Table III. The experimental validity of this method has been argued by others (2, 11, 14, 29, 30). The experimental data of Table I (microcoulombs required to reduce the oxidized electrode) can be compared with Table III and curve I of Fig. 4 to interpret the results.

The number of microcoulombs required to reduce the electrode when oxidized to 1.24v is 347.0. This, when compared to data in Table III, most nearly corresponds to a two-electron change, showing the formation of a monolayer of Pt(OH)₂ according to the reaction



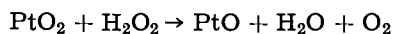
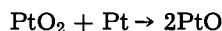
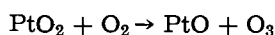
When the electrode is oxidized to 1.54v, the number of microcoulombs required for reduction is 760.0 which corresponds to a four-electron change. This is consistent with Pt(OH)₂ being converted to Pt(O)₂ as follows



Curve I in Fig. 4 shows two breaks at 1.24 and 1.54v, signifying the complete formation of a monolayer of Pt(OH)₂ and Pt(O)₂, respectively. The number of coulombs required to reduce the electrode continues to increase as the oxidation potential is increased to 1.72v. The number of microcoulombs (1564.0) used for reducing the electrode after oxidation to 1.72v corresponds to an eight-electron change. This represents the presence of four oxygen atoms per platinum atom. It seems possible that, up to the oxidation potential of 1.72v, one oxygen molecule per

platinum atom is chemisorbed on a PtO₂ surface. There is the additional possibility that PtO₂ changes to PtO₃ and then one oxygen atom per platinum atom (or O₂ molecule for 2 platinum atoms) is chemisorbed on the PtO₃ surface.

As the oxidation potential is raised above 1.72v, the platinum oxidation state begins to decrease, the reverse of what one might expect. Above an oxidation potential of 1.93v, the number of microcoulombs (306.0) for reduction remains constant. This corresponds to a two-electron change or a monolayer of PtO. This PtO seems to be different from the Pt(OH)₂ formed when the electrode was oxidized to 1.24v. We prefer to think of it as a "tight" PtO structure. The mechanism of formation of "tight" PtO is not yet clear. Some of the possible ways could be



Constant potential oxidation.—The electrode was oxidized utilizing the potentiostat. Initial experiments involving oxidation to 1.24v for different lengths of time and then reduction at a constant current of 33 μa showed that after 2 min the electrode was almost completely oxidized. In our experiments, the electrode was oxidized to different potentials for 5 min.

As initial experiments were in 2N H₂SO₄, it was thought that at higher potentials sulfate ion might be oxidized to persulfate and cause a change in the electrode surface. In order to study this point, the same experiments were repeated in 1.0M HClO₄ and 0.1M KOH. The data of Table II show that, in general, the oxidation behavior of platinum surfaces in perchloric acid is similar to that in sulfuric acid.

The potentiostatic data of Table II when compared with Table III indicate that in acid medium, Pt(O)₂ is formed at a potential of 1.24v. At 1.54v, the reduction data correspond to three oxygen atoms per platinum atom; at 1.74v, a maximum of four oxygen atoms per platinum atom is attained. At potentials greater than 1.84v, formation of the tight PtO surface is characteristic. Oxidation of the platinum electrode at 1.80v in acidic media followed by reduction did not give reproducible results. Coulombs used in reduction corresponded to an electron change between eight and two, consistent with a surface in a state of transition.

Platinum surface potentiostatic behavior in 0.1M KOH was similar to that in acidic media. A two-electron change corresponding to formation of Pt(OH)₂ at 0.24v and a four-electron change at 0.44v corresponding to formation of Pt(OH)₆⁴⁻ was found. The maximum number of $\mu\text{coul}_{(1105.0)}$ for reduction at 0.94v corresponded to a six-electron change which may indicate formation of PtO₄²⁻. The formation of similar chemical compounds in basic solution has been discussed by Latimer (31). At potentials beyond 1.0v, a two-electron change was observed showing the formation of the tight PtO structure. Addition of 0.77v (31) (the difference in

Table IV. Galvanostatic oxidation of electrodeposited platinum black electrode in 2N H₂SO₄

Potential to which the electrode was oxidized, v vs. N.H.E.	Current for oxidation, ma	Time for oxidation, sec	τ For reduction, sec	$i^*\tau$ For reduction, μcoul	Rest potential after 3½ min, v vs. N.H.E.
0.94	9.81	0.4	2.0	0.196×10^5	0.865
1.04	9.81	1.9	3.2	0.314×10^5	0.916
1.14	9.81	4.0	5.5	0.540×10^5	0.985
1.24	9.81	6.2	8.2	0.805×10^5	1.020
1.34	9.81	8.2	9.8	0.960×10^5	1.080
1.44	9.81	10.4	11.8	1.158×10^5	1.130
1.54	9.81	12.5	13.9	1.363×10^5	1.190
1.64	9.81	22.5	16.0	1.569×10^5	1.245
1.74	9.81	170.0	19.0	1.863×10^5	1.390
1.88	19.91	170.0	19.7	1.932×10^5	1.400
2.09	29.89	170.0	20.0	1.961×10^5	1.420
2.64	49.82	120.0	20.0	1.961×10^5	1.410

* Current i for reduction in all cases was 9.81 ma.

E° value for the evolution of oxygen between 1.0M acid and 0.1M basic solution) to the above potentials makes them more nearly correspond to values for surface oxides obtained in acid solution.

Electrodeposited platinum black.—Surface area.—The electrochemically active surface area of an electrodeposited platinum black electrode was measured by oxidizing it to 1.24v at constant current and comparing the number of coulombs required to reduce the oxidized surface (see Table IV) with that used to reduce the bright platinum electrode surface under similar conditions, 347 $\mu\text{coul}/\text{cm}^2$. The calculated surface area was 232 cm² or 8.92 m²/g. Calculated surface areas for measurements at 1.34 and 1.44v were 8.08 and 7.70 m²/g, respectively. Krypton adsorption measurements using the BET method gave 11.4 m²/g of platinum on a similar electrode.

This method of measuring surface areas gives a value relative to smooth platinum and assumes a roughness factor of one for the smooth platinum. A roughness factor of 1.1 might be preferable (2). Furthermore, this measured surface area is related to the electrochemical active surface area while the Krypton adsorption method measures surface area which may or may not be electrochemically active. Inherent in this method of surface area measurement is the assumption that the platinum black and bright platinum surface are in the same oxidation state at 1.24v, *vide infra*, and that the surface crystalline state or combination of surface crystal planes is the same for platinum black as for bright platinum.

Constant current oxidation.—As might be expected, it is more difficult to define integral surface oxidation states for platinum black than for bright platinum. A number of platinum black electrodes were studied by oxidation at constant current followed by reduction. The data of Table IV are typical. Oxidation of the platinum black apparently is more efficient, and all discharged oxygen (after correcting for an apparent partial preoxidized state) is attached to the platinum surface up to 1.54v. At about 1.60v, gaseous oxygen is evolved. A plot of log

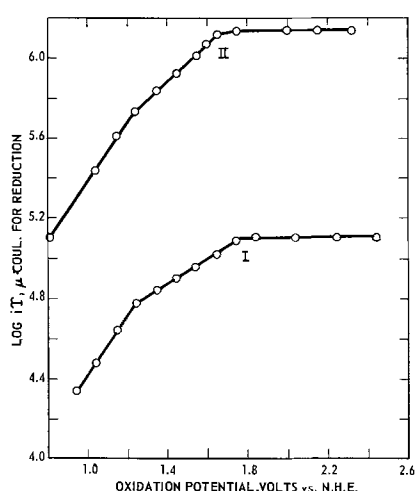


Fig. 5. Plot of log microcoulombs required to reduce the oxidized electrode surface vs. the potential to which the electrode was oxidized in $2N H_2SO_4$ at constant current, curve I (electrodeposited platinum black electrode), curve II (platinum black-polytetrafluoroethylene molded electrode).

microcoulombs vs. oxidation potential similar to curve 1 of Fig. 3 is shown as curve 1 of Fig. 5.

Multiplying the data of Table III by the surface area factor of 232, the number of microcoulombs used for 2, 4, and 5 electron reductions in various crystal planes can be calculated and compared with the reported $i\tau$ values of Table IV. These indicate that the platinum surface oxidizes to $Pt(OH)_2$ at 1.24v and $Pt(O)_2$ at about 1.64v. Above 1.85v the number of coulombs used in reduction becomes constant and corresponds to $Pt(O)_{2.5}$ (approximately). The break in curve 1 of Fig. 5 at about 1.24v is consistent with the formation of $Pt(OH)_2$ at this potential (*vide supra*). Otherwise (see Fig. 4), it does not appear that surface oxide states of platinum black and bright platinum are comparable at voltages vs. N.H.E. above 1.24v.

Constant potential oxidation.—Upon potentiostatic oxidation (for 5 min), platinum surface oxides similar to those for constant current oxidation were indicated. The states were defined in terms of microcoulombs necessary for reduction and rest potentials were consistent with those observed for constant current oxidation. $Pt(OH)_2$ (rest potential 1.02v) was formed at 1.04v and $Pt(O)_2$ was formed between 1.24 and 1.34v (rest potential 1.18–1.26v). At potentials above 1.74v, $Pt(O)_{2.5}$ (approximately) was observed (rest potential 1.45v).

Platinum black-polytetrafluoroethylene molded electrode.—**Surface area.**—The electrochemically active surface area of this electrode was determined in a manner similar to that used for the electrodeposited platinum black electrode. The calculated surface area when oxidized to 1.24v at constant current (see Table V) was 723 cm^2 or $5.08 \text{ m}^2/\text{g}$ of Pt (geometrical area of the electrode was 0.462 cm^2). Krypton adsorption measurements (BET method) gave an area of $4.96 \text{ m}^2/\text{g}$.

Krypton adsorption measurements on the platinum black powder used in the molded electrode gave a value of $22.9 \text{ m}^2/\text{g}$. The results reported above for the molded electrode indicate surface area are di-

Table V. Galvanostatic oxidation of a platinum black-polytetrafluoroethylene molded electrode in $2N H_2SO_4$

Potential to which the electrode was oxidized, v vs. N.H.E.	Current for oxidation, ma	Time for oxidation, sec	τ For reduction, sec	$i\tau$ For reduction of 0.462 cm^2 of geometric area, μcoul	Rest potential after $3\frac{1}{2}$ min, v vs. N.H.E.
0.81	0.00	0.0	6.00	0.584×10^5	0.81
1.04	9.74	9.5	13.00	1.268×10^5	0.88
1.14	9.74	19.0	19.50	1.900×10^5	0.92
1.24	9.74	24.0	25.75	2.505×10^5	0.96
1.34	9.74	31.0	33.00	3.215×10^5	0.99
1.44	9.74	40.5	40.00	3.895×10^5	1.02
1.54	9.74	53.0	49.50	4.820×10^5	1.07
1.59	9.74	78.0	56.00	5.450×10^5	1.13
1.64	9.74	141.0	63.00	6.135×10^5	1.22
1.74	9.74	216.0	66.00	6.420×10^5	1.27
2.31	14.83	225.0	66.00	6.420×10^5	1.30

* Reductions were performed at constant current of 9.74 ma.

minished considerably through the molding process if special precautions are not taken in molding.

Constant current oxidation.—Data for constant current oxidation are given in Table V. From the time of oxidation and τ for reduction it appears that all oxygen produced up to 1.50v is attached to the platinum surface, a consequence of the catalytic properties of the electrode. A plot of logarithm microcoulombs required for reduction vs. oxidation potential is shown as curve 2 of Fig. 5. Multiplying the data of Table III by the surface area factor of 723, the number of microcoulombs used for 2, 4, and 5 electron reduction in different crystal planes can be calculated and compared with the reported $i\tau$ values of Table V. These indicate that the platinum surface oxides are $Pt(OH)_2$ at 1.24v and $Pt(O)_2$ at about 1.54v. Above 1.74v, the number of coulombs used in reduction becomes constant and corresponds to $Pt(O)_{2.5(\text{approx.})}$. The break in curve 2 of Fig. 5 at about 1.24v is consistent with the formation of $Pt(OH)_2$ at this potential.

Constant potential oxidation.—A study of surface oxidation at 1.24v showed that the major portion of the oxidation was completed in the initial 60 sec. For our experiments, five minutes of oxidation was performed at each predetermined potential and complete oxidation seems to have occurred in this time. The stability of the platinum oxide layer formed at 1.24v was checked by allowing it to stand for $\frac{1}{2}$ hr at open circuit and reducing the oxide layer in the regular way. Only after 1 hr did the number of coulombs necessary for reduction begin to decrease.

Because of the electrode shield configuration and evolved oxygen, the circuit tended to be broken before 5 min of oxidation at potentials above 1.74v. The oxygen formed a gas pocket which pushed solution away from the solution.

Over-all behavior, in terms of surface oxidation states, as determined from the number of coulombs required to reduce the electrode when oxidized at various potentials agrees with that noted for constant current oxidation. $Pt(OH)_2$ was formed at about 1.04v (rest potential 0.98v) and $Pt(O)_2$ at about 1.24v (rest potential 1.08v). The situation is

Table VI. Representative data for potentiostatic oxidation of a molded platinum black-tetrafluoroethylene electrode in 2N H₂SO₄

Potential to which the electrode was oxidized, v vs. N.H.E.	τ For reduction, sec	$i^*\tau$ For reduction of 0.462 cm ² geometric area, μcoul	Rest potential after 3½ min, v vs. N.H.E.
1.04	22.00	2.140×10^5	0.980
1.14	34.20	3.322×10^5	1.030
1.24	44.00	4.280×10^5	1.100
1.44	61.00	5.940×10^5	1.250
1.54	69.00	6.700×10^5	1.290
1.64	84.50	8.210×10^5	1.345
1.74	86.00	8.352×10^5	1.360
1.94	81.60	7.960×10^5	1.350
2.60	78.20	7.650×10^5	1.340

* Reduction at constant current of 9.74 ma.

more ambiguous at higher potentials as can be seen by referring to some of the representative potentiostatic data of Table VI. Higher oxidation states may actually exist or appear to exist because of occluded oxygen in the porous electrode structure or because of seepage into compressed boundaries between adjacent particles.

Discussion

Platinum oxidation states.—The results presented herein (Table VII) show the following platinum surface oxides at the indicated potentials. We use parentheses to imply surface platinum/oxygen ratios rather than compounds *per se*.

In defining the surface platinum oxides, the galvanostatic results based on kinetic considerations and the treatment of Bockris and Huq (27) is probably the most precise. On the other hand, the results apply to a kinetic rather than to a final equilibrium situation. The potentiostatic results give clear cut trends, but are more ambiguous, especially since pure compounds in thermodynamic equilibrium probably are not present.

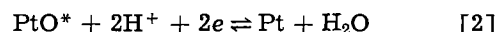
Galvanostatic oxidation to the initial state of Pt(OH)₂ where all surface oxide is measured by cathodic stripping is probably the best defined oxidation state and the one to which the Bockris and Huq (27) treatment, as discussed here, best applies. The value of 1.23v is not reached until the platinum surface is completely covered as PtO or Pt(OH)₂. However, if an electrode is oxidized po-

tentiostatically in the region of this potential, 1.24v, one obtained essentially surface Pt(O)₂ after 5 min; chronopotentiometrically, the potential rises readily above 1.23v, without complete formation of Pt(O)₂ until 1.54v.

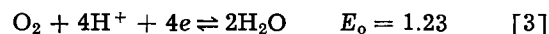
Our designation of one surface oxide of platinum as Pt(O)_{2.5}(approx.) actually results from many experiments in which the oxygen/platinum ratio varied from 2.3 to 2.7 but never clearly reached 3 (except in the questionable case of the molded platinum black electrode). However, in those instances where we have designated the surface oxide as Pt(O)_{2.5}(approx.) it may be correct to think of the surface as predominantly Pt(O)₃. This is especially interesting since preparations of PtO₃ (32, 33) often show oxygen deficiencies and PtO₃ does decompose in sulfuric acid with evolution of oxygen (7).

It cannot be presumed that the properties of the surface oxides encountered here correspond to those of the stoichiometrically similar pure platinum compounds which can be isolated (17). The commencement of the formation of the Pt/Pt(OH)₂ couple at the open-circuit potential of 0.82v on bright platinum was observed when about 50 μcoul were required for reduction (see Table I). El Wakkad (13) reports the starting potential of the Pt/PtO couple to be 0.82v in acid solution. Calculations based on the thermochemical data on pure compounds show E° values (31) of 0.98v and about 1.10v for Pt/Pt(OH)₂ and Pt(OH)₂/PtO₂ couples, respectively.

Hoare (4) found the rest potential of a platinum electrode in nitrogen stirred 2N H₂SO₄ to be 0.88v and ascribed it to the following equilibrium



where PtO* is a surface oxide. However, in an oxygen stirred solution, the electrode potential becomes 1.06v. The latter is postulated to be a mixed potential from reactions [2] and [3].



It is the latter reaction, PtO catalyzed (4), which corresponds to the reversible oxygen electrode and is a desired fuel cell reaction. However, the PtO surface is destroyed by reduction at potentials higher than 0.88, and reaction [3] takes place on a platinum oxide surface in equilibrium with platinum. *Double layer capacity.*—This has also been the sub-

Table VII. Galvanostatic oxidation

Electrode	Potential (v) vs. N.H.E.				
	1.24	1.54	1.64	1.74	1.92
Smooth platinum	Pt(OH) ₂	Pt(O) ₂	—	Pt(O) ₄	PtO
Electrodeposited platinum black	Pt(OH) ₂	← Pt(O) ₂ →	—	Pt(O) _{2.5} (approx.)	Pt(O) _{2.5} (approx.)
Platinum black-polytetrafluoroethylene molded electrode	Pt(OH) ₂	Pt(O) ₂	—	Pt(O) _{2.5} (approx.)	Pt(O) _{2.5} (approx.)
Potentiostatic oxidation					
Electrode	Potential (v) vs. N.H.E.				
	1.04-1.14	1.24-1.34	1.64-1.74	1.84	
Smooth platinum	Pt(OH) ₂	Pt(O) ₂	Pt(O) ₄	PtO	
Electrodeposited platinum black	Pt(OH) ₂	Pt(O) ₂	Pt(O) _{2.5} (approx.)	Pt(O) _{2.5} (approx.)	
Platinum black-polytetrafluoroethylene molded electrode	Pt(OH) ₂	Pt(O) ₂	—	—	

ject of considerable study and speculation (2, 5, 15, 17, 34, 35). Our concern, here, is only to the extent that it may effect our estimate of the composition of surface oxides. If one accepts an average value of $50 \mu\text{f}/\text{cm}^2$ (in agreement with most recent investigations) then over a discharge range of 0.67v, the correction for double layer capacity is of the order of 30 microcoulombs. A correction of this order of magnitude does not appreciably effect the arguments presented here. Where the double layer capacity correction assumes a greater value, other compensating influences diminish its effect on coulometric values and any attempt at correction does not significantly alter our conclusions.

"Tight" PtO structure.—The most striking difference between the smooth platinum electrode and the two others (electrodeposited platinum black and platinum black-polytetrafluoroethylene molded electrode) is the formation of PtO on the smooth electrode surface at higher potentials. The platinum black type electrodes tend to form $\text{Pt}(\text{O})_{2.5(\text{approx.})}$. We have called the higher potential platinum oxide the "tight" PtO structure. Curve 5, Fig. 3 is the characteristic curve observed during cathodic stripping for this form of PtO.

The tight structure PtO appears to adsorb no oxygen (from the coulometric data). Its rest potential is higher than the $\text{Pt}(\text{OH})_2$ observed at lower potentials. It might be explained by a platinum structure in which every surface Pt atom is linked to others by oxygen bridges. These bridges effectively seal off the electrode surface and sorbing secondary valence forces so that the surface tends to be stable and relatively inert.

It is probably the tight structure which is most resistant to solution in hydrochloric acid-sodium chloride solution. Anson and Ligane (1) in studies of platinum surface oxides noted that some platinum oxides were stripped from platinum electrodes in 20 min while others were stripped in 60 min. The latter surface platinum oxide was obtained after treatment with strong oxidizing agents or at high anodic potentials. Becker and Breiter (15) report a large decrease in double layer capacity to virtually zero on oxidation of smooth platinum at higher potentials. The formation of the tight PtO phase is equivalent to passivating the smooth platinum electrode. The tight platinum structure is probably also associated with the electrochemical generation of ozone (36). The electropolishing of the electrode may result in uniform aligned platinum atoms at the surface suitable for tight structure formation.

Smooth platinum electrodes are much better than platinum black electrodes for the Kolbe synthesis (in aqueous solution) which involves discharge of carboxylate ions at potentials of about 1.90v. This is well above the discharge potential of oxygen in water and is probably possible because of the "inert" PtO structure. Shukla and Walker (37) found the Kolbe synthesis commences at the critical potential of 2.14v. At this potential, tight PtO was observed in our experiments. Alternatively a similar passivated structure may be formed, involving a carboxylate radical (38).

Surface area.—The large surface area of platinum black as compared to smooth platinum has been hypothesized as one of the explanations for the high catalytic activity of platinum black. Our results show that such increased surface area effects do exist from an electrochemical viewpoint. Using data from galvanostatic oxidation at 1.24v, the surface areas which we measure (see results) compared favorably with those obtained by the BET method and indicate strongly that this approach to measurement of electroactive surface area is a valid and useful one.

The surface area of smooth platinum itself is a subject of controversy and a critical factor for electrochemical surface area measurements. The roughness factor, ratio of real to geometric area, has been estimated from 1.5 to 3.0 with a value of 2.0 (13, 17) being commonly used. Laitinen and Enke (2) have quoted data from N. Hackerman's laboratory, obtained by gas adsorption techniques, which indicate a roughness factor of 1.12 ± 0.10 . This would support an estimate of a roughness factor of 1 as being a reasonable choice at least for comparison purposes.

Our surface area measurement for electrodeposited platinum black is in agreement with Frumkin and Slygin (10) who found the specific area of electrodeposited platinum black to be of the order of 10^2 - 10^4 greater than smooth platinum. Wakkad and Emara (13) found a factor of 180 based on double layer capacity considerations and a roughness factor of 2.

Platinum catalytic activity.—The formation of $\text{Pt}(\text{O})_{2.5(\text{approx.})}$ by platinum black as contrasted to PtO for smooth platinum may be another clue to the catalytic activity of platinum black. Platinum black may be in such crystalline disarray that it cannot form the tight structure. This would imply many platinum atoms in corners and cracks with unshared d-electrons and available bonding orbitals. It may be these platinum atoms, capable of being involved in loose surface bonding, with other substances (hydrogen, olefin, etc.) which impart some of the characteristic catalytic properties of platinum black.

With respect to catalytic activity of platinum black, it is interesting to compare coulombs used for oxidation and reduction on smooth platinum and platinum black in the PtO - $\text{Pt}(\text{O})_2$ range. From Table I for smooth platinum, we see that only about 60% of the current used for oxygen evolution in the $\text{Pt}(\text{OH})_2$ - $\text{Pt}(\text{O})_2$ region results in further oxidation of the platinum surface. However, from Tables IV and V, we see that almost all of the oxygen evolved on platinum black is effective for surface oxidation. This could be ascribed to the catalytic properties of the black itself in bringing about its own oxidation.

Rest potential.—Most recently, Hoare (4) has reviewed and discussed the factors affecting surface rest potential. In the absence of solution impurities, especially oxygen, this may be determined by surface platinum oxide composition. In our work in acid medium, rest potentials increased up to an oxidation potential of 1.74v. Rest potentials were de-

Table VIII. Rest potentials

Electrode	$\text{Pt} + 2\text{H}_2\text{O} \rightleftharpoons \text{Pt}(\text{OH})_2 + 2\text{H}^+ + 2e$	$\text{Pt}(\text{OH})_2 \rightleftharpoons \text{PtO}_2 + 2\text{H}^+ + 2e$	Formation of tight PtO	Formation of $\text{PtO}_{2.5}$ (approx.)
Smooth platinum	0.97-0.99	1.04-1.07	1.37-1.43	—
Electrodeposited platinum black	1.02	1.16-1.17	—	1.39-1.45
Platinum black-polytetrafluoroethylene molded electrode	0.96-0.98	1.07-1.10	—	1.30-1.35
E° values (31)	0.98	Estimated 1.10	—	<2.0

terminated by surface oxidation state and were independent of method of oxidation. Results are summarized in Table VIII. These potentials may be compared to those obtained by Grube (7) for chemical compounds as well as potentials given by Latimer (31). The close agreement between our rest potentials for surface $\text{Pt}(\text{O})_{2.5}$ (approx.) and those (1.40-1.48v) found by Grube (7) for chemically prepared PtO_3 (which spontaneously decomposes) is especially noteworthy.

Overvoltage.—Formation of $\text{Pt}(\text{O})_2$ apparently precedes oxygen evolution. We find oxygen overvoltage values, potentiostatically, of 0.41v for smooth platinum and 0.21v for both platinum black electrodes in agreement with reported values (39, 40).

Acknowledgment

The authors thank Dr. R. A. Hermann of this laboratory for surface area determinations by the BET method. It is a pleasure to acknowledge constructive suggestions and helpful discussion from Professors B. E. Conway and A. J. Bard.

Manuscript received April 10, 1963; revised manuscript received Sept. 13, 1963. This paper was presented at the Pittsburgh Meeting, April 15-18, 1963.

Any discussion of this paper will appear in a Discussion Section to be published in the December 1964 JOURNAL.

REFERENCES

- F. C. Anson and J. J. Lingane, *J. Am. Chem. Soc.*, **79**, 4901 (1957).
- H. A. Laitinen and C. G. Enke, *This Journal*, **107**, 773 (1960).
- J. J. Lingane, *Electroanal. Chem.*, **2**, 296 (1961).
- J. P. Hoare, *This Journal*, **109**, 858 (1962).
- M. W. Breiter, *Electrochim. Acta*, **7**, 601 (1962).
- R. Lorenz and P. E. Spielmann, *Z. Elektrochem.*, **15**, 293 (1909).
- G. Grube, *ibid.*, **16**, 621 (1910).
- J. A. V. Butler and G. Armstrong, *Proc. Roy. Soc.*, **A137**, 604 (1932).
- G. Armstrong, F. R. Himsworth, and J. A. V. Butler, *ibid.*, **143A**, 89 (1933).
- A. N. Frumkin and A. Slygin, *Acta Physicochim. U.S.S.R.*, **3**, 791 (1935); **4**, 911 (1936); **5**, 819 (1936).
- A. Hickling, *Trans. Faraday Soc.*, **41**, 333 (1945).
- B. Ershler, *Discussions Faraday Soc.*, **1**, 269 (1947).
- S. E. S. El Wakkad and S. H. Emara, *J. Chem. Soc.*, **1952**, 461.
- M. Breiter, C. A. Knorr, and W. Volkl, *Z. Elektrochem.*, **59**, 681 (1955).
- M. Becker and M. Breiter, *ibid.*, **60**, 1080 (1956).
- E. Lange and G. Rädlein, *ibid.*, **61**, 724 (1957).
- J. Giner, *ibid.*, **63**, 386 (1959).
- B. Baker and W. MacNevin, *J. Am. Chem. Soc.*, **75**, 1476 (1953).
- I. M. Kolthoff and E. R. Nightingale, Jr., *Anal. Chim. Acta*, **17**, 329 (1957).
- F. C. Anson, *J. Am. Chem. Soc.*, **81**, 1554 (1959).
- F. C. Anson, *Anal. Chem.*, **33**, 934 (1961).
- F. C. Anson, *ibid.*, **33**, 939 (1961).
- J. Giner, *Electrochim. Acta*, **4**, 42 (1961).
- A. Hickling and W. Wilson, *This Journal*, **98**, 425 (1951).
- G. Bianchi, F. Mazza, and T. Mussini, *Electrochim. Acta.*, **7**, 457 (1962).
- A. J. Bard, *Anal. Chem.*, **33**, 11 (1961).
- J. O'M. Bockris and A. K. M. S. Huq, *Proc. Roy. Soc.*, **237**, 277 (1956).
- R. W. G. Wyckoff, "The Structure of Crystals," 1930-1934 Supplement to the Second Edition, Reinhold Publishing Co., New York (1935).
- K. J. Vetter, "Electrochemische Kinetik," p. 500, Springer-Verlag, Berlin (1961).
- J. A. V. Butler, "The Behavior of Oxygen and Hydrogen at Electrodes," in "Electrical Phenomena at Interfaces," J. A. V. Butler, Editor, p. 204, Macmillan, New York (1951).
- W. M. Latimer "Oxidation Potentials," pp. 204-209, 39, Prentice Hall, New York (1961).
- N. V. Sidgwick, "Chemical Elements and Their Composition," Vol. II, p. 1626, Oxford Press (1950).
- L. Wohler and F. Martin, *Ber.*, **42**, 3326 (1909).
- D. G. Peters and J. J. Lingane, *J. Electroanal. Chem.*, **4**, 193 (1962).
- M. W. Breiter, *This Journal*, **109**, 425 (1962).
- H. Boer, *Recueil*, **67**, 217 (1948); *ibid.*, **70**, 1020 (1951).
- Shukla and O. J. Walker, *Trans. Faraday Soc.*, **27**, 722 (1931).
- B. E. Conway and M. Dzieciuch, *Can. J. Chem.*, **41**, 21 (1963).
- S. Glasstone and A. Hickling, "Electrolytic Oxidation and Reduction," p. 63, Chapman and Hall Ltd. London (1935).
- J. J. Lingane, "Electroanalytical Chemistry," p. 208, Interscience, New York (1958).

Transport Numbers in Stabilized Zirconia

D. T. Bray and U. Merten

John Jay Hopkins Laboratory for Pure and Applied Science,
General Atomic Division of General Dynamics Corporation, San Diego, California

ABSTRACT

A simple theoretical treatment of conduction in solids shows that apparent electron transport numbers determined by different experimental techniques are not identical. The techniques considered for stabilized zirconia were oxygen-transfer measurements and emf measurements on galvanic cells having oxygen at two different activities at the electrodes. Transport numbers for stabilizing cations can be determined by measuring compositional changes that result from passage of an electric current through the electrolyte. The principal current carrier in stabilized zirconia is known to be the oxide ion. The apparent electron transport number in an yttria-stabilized zirconia at 900°-1100°C is found to be ≤ 0.005 in an oxidizing atmosphere and ≤ 0.011 in a reducing atmosphere. The apparent transport number for yttrium ions is found to $\leq 4 \times 10^{-9}$.

Transport numbers in solid oxides are of considerable importance in their use as electrolytes in galvanic cells for high-temperature thermodynamic measurements (1) and in their possible use in fuel cells (2). Wagner (3) and Schottky (4) are primarily responsible for the early development of the theory of transport numbers in solids. Recently, Pal'guev and Neuimin (5), Weissbart and Ruka (6), and Schmalzreid (7) have reported results of transport-number measurements in calcia-stabilized zirconia. Certain aspects of transport-number determination in such systems are discussed below, and some experimental results on yttria-stabilized zirconia are presented.

Significance of Transport Numbers

Transport numbers in solid electrolytes are readily discussed if the flow of each charged species is written as the sum of two terms, one representing the diffusion of the carriers in the crystal lattice and the other the motion of the lattice as a whole:¹

$$\vec{J}_i = -\alpha_i \text{grad } \mu'_i + c_i \vec{v} \quad [1]$$

where \vec{J}_i is the flux of the i^{th} component, μ'_i its electrochemical potential, c_i its concentration, α_i an appropriate coefficient related to the mobility of the i^{th} species, and \vec{v} the velocity of the lattice with respect to our reference frame. The electrochemical potential is given by

$$\mu'_i = \mu_i + q_i \phi$$

where μ_i is the local chemical potential, q_i is the charge of the i^{th} species, and ϕ is the local electrostatic potential. We assume an isotropic crystal and isothermal conditions. Cross terms other than those between charged particles inherent in the use of the electrostatic potential are neglected. If the chemical potentials of all charged species are constant in the crystal, we may rewrite Eq. [1] as

¹ An equation of this form is readily obtained as a simple case of more complete diffusion expressions given, for example, by de Groot (8), who discusses in some detail the use of $\text{grad } \mu'$ as a driving force for diffusion.

$$\vec{I}_i = q_i \vec{J}_i = -\sigma_i \text{grad } \phi + q_i \cdot c_i \vec{v} \quad [2]$$

where

$$\sigma_i = q_i^2 \alpha_i \quad [3]$$

The total current is

$$\vec{I} = \sum_i I_i = -\sum_i \sigma_i \text{grad } \phi + \vec{v} \sum_i q_i c_i = -\sigma \text{grad } \phi \quad [4]$$

where $\sigma = \sum_i \sigma_i$ and the second term must be zero if charge neutrality is to be maintained in the crystal. This last equation is just Ohm's law and we identify σ as the total conductivity. The σ_i 's can, then, be regarded as partial conductivities and we may define transport numbers as

$$t_i = \sigma_i / \sigma \quad [5]$$

The magnitude of \vec{I} in Eq. [4] does not depend on \vec{v} , and the determination of σ is therefore not sensitive to the relative velocities of the crystal lattice and the reference frame. The \vec{I}_i 's, on the other hand, depend on \vec{v} , and the determination of the σ_i 's depends on the knowledge of \vec{v} . This problem is quite analogous to that encountered in ordinary diffusion, where the importance of appropriate markers fixed in the lattice to the determination of the diffusivities of individual components of solutions is well recognized as the Kirkendall effect (9, 10).

If under the assumptions of Eq. [2], the \vec{I}_i 's are measured in a reference frame in which $\vec{I}_i = 0$ (i.e., the particles of species i are at rest), then

$$\vec{v} = (\sigma_i / q_i c_i) \text{grad } \phi \quad [6]$$

and

$$\vec{I}_i = [-\sigma_i + \sigma_i (q_i c_i / q_i c_i)] \text{grad } \phi = -\sigma_{ia} \text{grad } \phi \quad [7]$$

We may now define

$$t_{ia} = \sigma_{ia} / \sigma \quad [8]$$

as an apparent transport number in this particular reference frame, and it is this number which is most often determined experimentally.

The determination of true transport numbers is

possible in some cases through measurement of the tracer diffusion coefficient for one of the species in the system of interest, and calculation of its partial conductivity with the help of the Nernst-Einstein relation. Bardeen and Herring (10) and Wagner (3,11) have pointed out that the tracer diffusion coefficient will be numerically different from the ordinary diffusion coefficient needed in this calculation, but where the direct exchange of particles suggested by Wagner does not occur, only the small and calculable correction pointed out by Bardeen and Herring will apply. Once a single partial conductivity, σ_1 , is known, \vec{v} , and therefore the relation between true and apparent transport numbers, can be defined for any given experiment. Thus, if \vec{I}_1 , the current arriving at the surface of an electrode in contact with the sample, is measured for some value of $\text{grad } \phi$, then the use of Eq. [2] permits calculation of \vec{v} in a coordinate system fixed in the electrode-sample interface.

Apparent Transport Numbers in Stabilized Zirconia

In practical electrochemical problems, the determination of an apparent transport number in a particular frame of reference is usually all that is required. In the experiments on stabilized zirconia electrolytes reported here, the apparent transport numbers of interest were those for electrons and for the stabilizing cations.

Methods for determining electron transport numbers in solids have been discussed at some length by Wagner (12) and by Hebb (13). These authors have also reviewed much of the previous experimental work in this field. The importance of the choice of reference frame has not always been recognized. Imagine a simple cell consisting of two inert electrodes (electronic conductors) in contact with an oxide electrolyte and with separate sources of oxygen at two different activities. Each electrode may be in electrical contact with the electrolyte via an electronic process involving simply the transfer of an electron between the electrode and an appropriate electronic level in the electrolyte and via an ionic process involving the formation of oxide ions from uncharged oxygen molecules and electrons from the electrode and the decomposition of such ions.

Since our ultimate interest is in the fraction of the total current which crosses the electrode-electrolyte interfaces by each of these mechanisms, we choose a coordinate system fixed in one of these interfaces. We will concern ourselves first with a binary oxide electrolyte in which the average oxidation state of the cation does not change appreciably over the range of oxygen activities of interest, and the cation lattice may, then, be taken as fixed in our reference frame. (This assumption, incidentally, removes any concern about possible motion of the second interface with respect to our chosen coordinate system due to changes in volume of the electrolyte.)

From Eq. [1] and [4], the fluxes through the electrolyte may be written as

$$\left. \begin{aligned} \vec{J}_o &= -\alpha_o \text{grad } \mu_o + c_o \vec{v} \\ \vec{J}_x &= -\alpha_x \text{grad } \mu'_x + c_x \vec{v} \\ \vec{J}_e &= -\alpha_e \text{grad } \mu'_e + c_e \vec{v} \end{aligned} \right\} \quad [9]$$

$$\vec{I} = q_x \vec{J}_x + q_e \vec{J}_e = -\sigma_x \text{grad } (\mu'_x/q_x) - \sigma_e \text{grad } (\mu'_e/q_e) + (c_x q_x + c_e q_e) \vec{v} \quad [10]$$

where the subscripts o, x, and e refer to uncharged oxygen, oxygen ions, and electrons, respectively. For a nonporous ionic crystal, the mobility and concentration of uncharged oxygen will generally be essentially zero, so $\vec{J}_o = 0$. In this case all oxygen transfer must occur via the oxide ion current, \vec{J}_x , and the magnitude of \vec{J}_e may be evaluated by comparing the electric current passed to the amount of oxygen transferred between the two electrodes. If the two electrodes are essentially reversible and the electronic contact resistances small, and if the range of values of μ_x and μ_e is small enough so that σ_e and σ_x are essentially constant throughout the electrolyte, then t_{ea} , an apparent transport number for electrons, can be evaluated by substituting $(\vec{I} - q_x \vec{J}_x)$ for \vec{I}_e in Eq. [7].

An alternative approach has been suggested by Wagner (12). This requires the determination of the open-circuit potential of a galvanic cell having oxygen at two different activities in contact with the two electrodes. Since there is no external current flow, $\vec{I} = 0$ and Eq. [10] becomes

$$\sigma_x \text{grad } (\mu'_x/q_x) + \sigma_e \text{grad } (\mu'_e/q_e) - [(c_x q_x + c_e q_e)/c_1 q_1] \sigma_1 \text{grad } (\mu'_1/q_1) = 0 \quad [11]$$

where we have used the procedure of Eq. [6] to eliminate \vec{v} , and the subscript 1 here refers to the cations. For a stoichiometric electrolyte, the chemical potential of the electrolyte compound will be essentially constant through its thickness, so we may write

$$q_x \mu'_1 + q_1 \mu'_x = a \text{ constant} \quad [12]$$

$$\text{grad } \mu'_1 = -(q_1/q_x) \text{grad } \mu'_x \quad [13]$$

and Eq. [11] becomes

$$\{\sigma_x + [(c_x q_x + c_e q_e)/c_1 q_1] \sigma_1\} \text{grad } (\mu'_x/q_x) + \sigma_e \text{grad } (\mu'_e/q_e) = 0 \quad [14]$$

or setting

$$\{\sigma_x + [(c_x q_x + c_e q_e)/c_1 q_1] \sigma_1\} = \sigma_{xa'} \quad [14']$$

then

$$\sigma_{xa'} \text{grad } (\mu'_x/q_x) + \sigma_e \text{grad } (\mu'_e/q_e) = 0 \quad [15]$$

In this case apparent transport numbers

$$t_{xa'} = [\sigma_{xa'}/(\sigma_{xa'} + \sigma_e)] \text{ and } t_{ea'} = [\sigma_e/(\sigma_{xa'} + \sigma_e)] \quad [16]$$

can conveniently be defined, but they are not, in general, the true transport numbers, nor even the usual apparent transport numbers of Eq. [8].

Under conditions of local chemical equilibrium, the electrochemical potentials of the species of interest are related by the equation

$$\mu'_x = \mu_o + (q_x/q_e)\mu'_e \quad [17]$$

which, together with Eq. [15], yields

$$\begin{aligned} \text{grad}(\mu'_e/q_e) &= -[\sigma_{xa'}/(\sigma_e + \sigma_{xa'})] \text{grad}(\mu_o/q_x) \\ &= -t_{xa'} \text{grad}(\mu_o/q_x) \end{aligned} \quad [18]$$

Integrating from one electrode-electrolyte interface to the other, we obtain

$$E \equiv -\frac{1}{q_e} \int_{\mu'_e(1)}^{\mu'_e(2)} d\mu'_e = (1/q_x) \int_{\mu_o(1)}^{\mu_o(2)} t_{xa'} d\mu_o \quad [19]$$

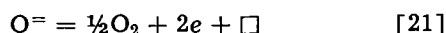
This is just the expression for the emf of the cell, E , derived by Wagner (3) and Schottky (4) except that in their cases the cations were assumed immobile so that $\vec{v} = 0$ and $t_{xa'} = t_x$.

For small $\Delta\mu_o$, $t_{xa'}$ may be assumed constant and Eq. [19] becomes

$$E = -\Delta\mu'_e/q_e = (t_{xa'}/q_x)\Delta\mu_o \quad [20]$$

Thus, if $\Delta\mu_o$ is known from the oxygen activities at the electrodes and E is measured, we may calculate $t_{xa'}$. The value of $t_{ea'}$ is, of course, $1 - t_{xa'}$.

Schmalzreid (7) has recently examined zirconia cells with large $\Delta\mu_o$, assuming a particular relationship between $t_{xa'}$ and μ_o , which makes the integration of Eq. [19] possible. He assumes that carrier electrons are formed by the reaction



where \square is an oxygen vacancy, and obtains

$$t_{xa'} = 1/[1 + (P^*_{\text{O}_2}/P_{\text{O}_2})^{1/4}] \quad [22]$$

for the oxide ion transport number at oxygen partial pressure P_{O_2} , where $P^*_{\text{O}_2}$ is a constant corresponding to the oxygen partial pressure at which $t_{xa'} = 0.5$.

On integrating Eq. [19], Schmalzreid then obtains an expression which we may write as

$$P^*_{\text{O}_2} = P_{\text{O}_2}(2) \left\{ \frac{1 - \exp\left[\frac{q_e(E - E_o)}{kT}\right]}{\exp\left(\frac{q_e E}{kT}\right) - 1} \right\}^4 \quad [23]$$

which may be used to calculate $P^*_{\text{O}_2}$ from the actual open-circuit voltage, E of a cell having a theoretical (i.e., assuming $t_{xa'} = 1$) open-circuit voltage, E_o , and an oxygen partial pressure, $P_{\text{O}_2}(2)$, on the oxygen-rich side of the cell. If the oxygen partial pressures on the two sides are sufficiently greater and less, respectively, than $P^*_{\text{O}_2}$, then

$\exp[q_e(E - E_o)/kT] \ll 1$ and $\exp(q_e E/kT) \gg 1$ so Eq. [23] reduces to

$$P^*_{\text{O}_2} = P_{\text{O}_2}(2) \exp(-4q_e E/kT) \quad [24]$$

In the simple cell which we have been discussing, the apparent cation transport number of a binary oxide electrolyte would be zero, regardless of the relative mobilities of anions and cations, since the

cations are not formed or discharged at the electrodes.

In stabilized zirconia, the situation is made more complicated by the fact that there are two different cations. Unmixing may therefore occur during direct-current passage if the mobilities of the two cations are unequal. Returning to Eq. [1] we may write \vec{J}_m and \vec{J}_s , the fluxes of the majority and stabilizing cations, respectively, as

$$\vec{J}_i = -\alpha_i \text{grad}(\mu_i + q_i\phi) + c_i\vec{v} \quad [25]$$

Assuming that Raoult's and Henry's laws apply to the majority and minority cations respectively, i.e.

$$\text{grad} \mu_i = (kT/c_i) \text{grad} c_i \quad [26]$$

we replace $\alpha_i kT/c_i$ by the ordinary diffusion coefficient, D_i , which we will assume to be independent of c_i . Thus,

$$\vec{J}_i = -D_i[\text{grad} c_i + (q_i c_i/kT) \text{grad} \phi] + c_i\vec{v} \quad [27]$$

Again, choosing a coordinate system in which the majority cations are at rest, i.e.

$$\vec{J}_m = 0 \quad [28]$$

$$\vec{v} = \frac{D_m}{c_m} [\text{grad} c_m + (q_m c_m/kT) \text{grad} \phi] \quad [29]$$

and substituting for \vec{v} in Eq. [27], the stabilizing ion flux becomes

$$\begin{aligned} \vec{J}_s &= -D_s[\text{grad} c_s + (q_s c_s/kT) \text{grad} \phi] \\ &+ (c_s D_m/c_m)[\text{grad} c_m + (q_m c_m/kT) \text{grad} \phi] \end{aligned} \quad [30]$$

which may be simplified by writing

$$\begin{aligned} c_m + c_s &\cong \text{a constant} \\ \text{grad} c_m &= -\text{grad} c_s \end{aligned} \quad [31]$$

therefore,

$$\begin{aligned} \vec{J}_s &= -D_s\{[1 + (D_m c_s/D_s c_m)] \text{grad} c_s \\ &+ [1 - (D_m q_m/D_s q_s)] c_s q_s/kT \text{grad} \phi\} \end{aligned} \quad [32]$$

It is apparent that under boundary conditions like those used earlier, which permit no discharge of cations at the electrodes (as will generally be the case for zirconia stabilized with such oxides as calcia and yttria), a steady state must be established after a long period of constant current flow in which

$$\vec{J}_s = 0 \quad [33]$$

and

$$\text{grad} \ln c_s = -\{[1 - (D_m q_m/D_s q_s)]/[1 + (D_m c_s/D_s c_m)]\} q_s/kT \text{grad} \phi \quad [34]$$

Prediction of the steady-state concentration distribution requires a knowledge of the relative mobility of the two cation species. Thus, if the majority cations are highly immobile, i.e., $D_m \ll D_s$, then at steady state

$$\text{grad} \ln c_s = -(q_s/kT) \text{grad} \phi \quad [35]$$

or, integrating

$$\ln(c_{s1}/c_{s2}) = -(q_s/kT)(\phi_1 - \phi_2) \quad [36]$$

where the subscript 1 refers to the cathodic surface of the electrolyte and the subscript 2 to its anodic surface.

Discussions of stabilized-zirconia fuel cells generally assume operation near 1000°C, with an electrostatic potential difference across the electrolyte (due to ohmic losses) of the order of 0.1v. Under these circumstances, $c_{s1}/c_{s2} = 15$ for a triply-charged stabilizing element. This result clearly indicates that electrolyte unmixing can be a problem of practical significance. In fact, in general the single-phase cubic range is sufficiently narrow so that unmixing of the magnitude indicated would result in precipitation of a new phase at one of the electrodes.

Since steady-state unmixing experiments do not lead to an experimental determination of D_s , but only to relative values for the two cations, it is of interest to examine the transient case.

Assuming a constant voltage gradient across an infinite slab of electrolyte of thickness L , and again assuming $D_m \ll D_s$, Eq. [32] becomes

$$J = -D[(dc/dx) - Hc] \quad [37]$$

where the subscript s has been dropped and

$$H = [q_s(\phi_1 - \phi_2)/kTL] \quad [38]$$

The rate of accumulation of stabilizing cations in a differential volume element is just

$$\partial c(x,t)/\partial t = -\partial J/\partial x = D[\partial^2 c(x,t)/\partial x^2] - HD[\partial c(x,t)/\partial x] \quad [39]$$

where t is time and will be measured from the beginning of a constant-current-density experiment.

Solution of Eq. [39], subject to the appropriate boundary conditions

$$c(x, 0) = \text{constant} \equiv c_0 \quad [40]$$

and

$$(1/L) \int_0^L c(x, t) dx = c_0 \quad [41]$$

is given in terms of three dimensionless parameters as follows

$$\begin{aligned} \bar{c}(\beta, \tau) = & \frac{\lambda}{2 \sinh \lambda/2} \exp \left[\lambda\beta - \left(\frac{\lambda}{2} \right) \right] \\ & + \frac{16\pi}{\lambda^2} \exp \left[\left(\frac{\lambda\beta}{2} \right) - \tau \right] \sum_{n=1}^{\infty} \frac{[1 + (-1)^{n+1} \exp(-\lambda/2)] n}{[(4\pi^2 n^2/\lambda^2) + 1]^2} \\ & \left(\sin n\pi\beta + \frac{2\pi n}{\lambda} \cos n\pi\beta \right) \exp \left[\left(-\frac{4\pi^2 n^2}{\lambda^2} \right) \tau \right] \quad [42] \end{aligned}$$

where the dimensionless parameters are

$$\begin{aligned} \beta &= x/L \\ \tau &= DH^2 t/4 \\ \lambda &= HL \end{aligned}$$

$$\bar{c}(\beta, \tau) = c(x, t)/c_0$$

This solution was programmed for the IBM-7090 and runs were made for values of τ from 10^{-5} to 100, λ from 0.5 to 10, and β from 0 to 1. Figures 1 and 2 present data at the two surfaces ($\beta = 0, \beta = 1$) as a function of λ and τ . The concentration distribution across the electrolyte is shown in Fig. 3 at various τ for the particular condition of $\lambda = 6$. It is note-

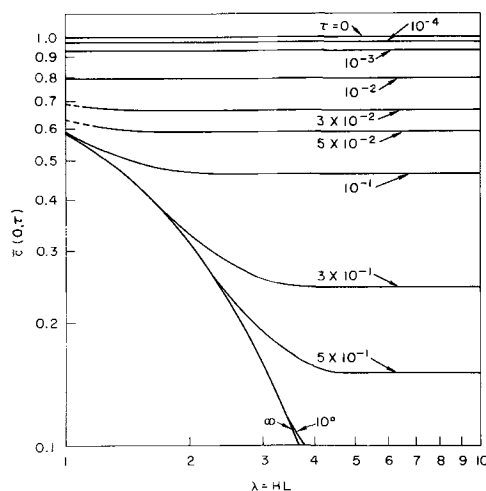


Fig. 1. Variation of surface concentration on anode side of electrolyte.

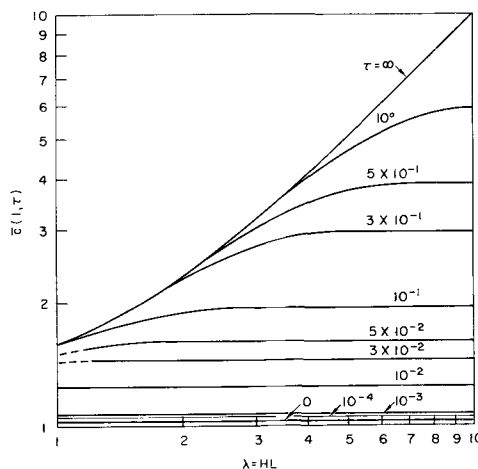


Fig. 2. Variation of surface concentration on cathode side of electrolyte.

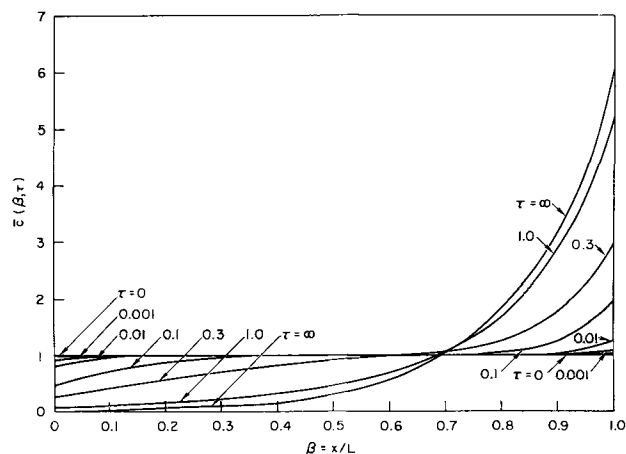


Fig. 3. Variation of concentration across electrolyte at various τ for $\lambda = 6.0$.

worthy, from an experimental point of view, that the square of the voltage gradient appears in τ . As a result, experiments to determine the extent of separation can be greatly accelerated by increasing the current density employed.

Experimental Results for Yttria-Stabilized Zirconia

Transport numbers for electrons.—Thin disks ~ 2.5 cm in diameter and ~ 0.1 cm thick of $ZrO_2 - 10$ mole

Table I. EMF of an air-oxygen cell

Temperature, °C ± 1°	Measured emf, mv ± 0.1	Theoretical emf, mv ± 0.1	Deviation from theoretical, %
916	40.1	40.0	+0.2
979	42.2	42.2	0
1065	45.0	45.1	-0.2
1109	46.5	46.5	0

% Y₂O₃ were prepared from reagent-grade materials and were supported in a tube furnace between the ends of two alumina tubes which allowed the two faces of the disk used in a particular experiment to be exposed to different gases and contacted with electrodes for voltage and current measurements. The total gas pressure on both sides of the disk was always atmospheric. The voltage developed between metallic electrodes in contact with the two surfaces was measured and compared with the theoretical emf of the cell in question, calculated on the assumption that oxide ions (O⁼) were the only current carriers.

For the data presented in Table I, the reactants were air and 99.8% pure oxygen, the electrodes were Nichrome V screens, and the temperature and voltage-measuring procedures used were good to ±1°C and ±0.1 mv, respectively.

In a second experiment, the reactants were 100.0% pure hydrogen and a hydrogen-nitrogen gas mixture, both saturated with water at room temperature. The dry hydrogen-nitrogen mixture was analyzed chromatographically and mass-spectrometrically and found to contain 29.0% ± 0.5% hydrogen by volume. The electrodes in this case were of palladium. The results of these cell measurements are given in Table II.

The results of these experiments indicate agreement with theory within experimental error. (The relatively large uncertainty in the theoretical emf's indicated in Table II is a direct result of the uncertainties in the analytical results for the hydrogen-nitrogen mixture used.)

These data indicate that in zirconia-10 mole % yttria the apparent electron transport number of Eq. [16] is ≤0.005 in the oxidizing atmosphere of the oxygen-air cell and ≤0.011 in the reducing atmosphere of the wet hydrogen cell, in the 800°-1100°C range. The consistency of the deviations and the fact that the activation energy for electronic conduction would be expected to be different from that for ionic conduction, give added reason to believe that t_{ea} is actually well below these limits over most of this temperature range. These results are in agreement with those of Weissbart and Ruka (6), who found $t_{ea} \leq 0.005$ for zirconia-15 mole % calcia

at 1000°C in oxygen by a Faraday's law experiment; they also found good agreement between the theoretical and the measured open-circuit voltages for wet hydrogen vs. oxygen cells.

In the wet-hydrogen experiment, the H₂/H₂O ratio was 9.1 on the 29%-H₂ side of the electrolyte. From the data obtained and Eq. [23], we can estimate that at 1100°C, $P^*_{O_2} \leq 9 \times 10^{-26}$ atm based on Schmalzreid's work (7). In an effort to pursue this question further, an alternate form of Schmalzreid's experiment was carried out.

Schmalzreid used a calcium-calcium oxide mixture on one side of his electrolyte, but since calcium is a substantially better reducing agent than zirconium, the surface of the electrolyte was almost certainly reduced. Thus, the effective oxygen activity was determined by the zirconium-zirconia couple, not the calcium-calcia couple. In the present experiments, surface reduction of the zirconia on one side of the cell was caused by filling the chamber behind one electrode with hydrogen and sealing it, then making the electrode in this chamber cathodic for 2 to 10 min by passing a current of 100 to 700 ma/cm² through the cell from an external source.

After the current was interrupted in each experiment, the voltage across the cell at 1000°C dropped promptly to 1.90v, then over a period of a few seconds or minutes to a value of 1.66v, which held constant for a period of many minutes in most runs before the reoxidation proceeded to such an extent that the decay continued. It is not obvious which of two voltages reported is the more significant because the derivation of Eq. [19] assumes that the electrodes are reversible, i.e., it is assumed that local equilibrium as expressed by Eq. [17] is attained. The initial value, 1.90v, may well be high because of some slowly decaying polarization component, while the plateau value, as well as the voltage measured by Schmalzreid, may well be low owing to the polarization effects connected with the internal steady-state currents. Substitution of the two voltages into Eq. [24] yields $P^*_{O_2} = 2 \times 10^{-31}$ atm ($E = 1.90v$) and $P^*_{O_2} = 1.3 \times 10^{-27}$ atm ($E = 1.66v$). Use of the approximate Eq. [24] is justified if the effective E_0 is assumed to be close to that for the oxidation of Zr to ZrO₂² which is 2.16v (14) at 1000°C.

Cation transport numbers.—A disk of ZrO₂-10 mole % Y₂O₃ like those used for electron-transport-number studies was placed between two porous pellets of manganese oxide, which served as electrodes, and supported in a tube furnace flooded with oxygen at 1000°C. A current of 0.600 amp/cm² was passed through the sample for 600 hr. At the conclusion of the experiment, both sides of the electrolyte disk were examined by x-ray diffraction techniques. Only the cubic zirconia phase was detected, with lattice parameters of 5.1402 ± 0.0005Å on the cathode side and 5.1397 ± 0.0005Å on the anode side. (The errors quoted are estimates of the reproducibility in the experimental arrangement used rather than the absolute accuracy of the determinations.) Thus, the difference in lattice parameter between the two sides

Table II. EMF of a hydrogen-nitrogen-29 vol-% hydrogen cell

Temperature, °C ± 1°	Measured emf, mv ± 0.01	Theoretical emf, mv ± 0.08	Deviation from theoretical, %
824	58.31	58.52	-0.36
930	64.02	64.20	-0.28
990	67.17	67.40	-0.34
1027	69.18	69.38	-0.29
1135	74.88	75.09	-0.28

² The value of E_0 will not be exactly 2.16v, because of the solubility of oxygen in zirconium metal and the presence of calcia in the zirconia phase.

was $\leq 0.0015\text{\AA}$. The data of Duwez *et al.* (15) indicate that this difference in lattice parameter corresponds to a difference in composition of ≤ 0.5 mole % Y_2O_3 ; *i.e.*, the concentration ratio between the two sides is ≤ 1.05 .

From Fig. 1 and 2, it is apparent that this limit on the concentration ratio requires $\tau \leq 1 \times 10^{-4}$. Using the definition of τ given in connection with Eq. [39] and taking the resistivity of the sample as 10 ohm-cm (16), we calculate that at 1000°C

$$D_{sa} \leq 7 \times 10^{-15} \text{ cm}^2/\text{sec}$$

and from the Nernst-Einstein relation, $\sigma_i = D_{ic}e^2/kT$, we estimate

$$\sigma_{sa} \leq 4 \times 10^{-10} \text{ ohm}^{-1} \text{ cm}^{-1}$$

and

$$t_{sa} = \frac{\sigma_{sa}}{\sigma} \leq 4 \times 10^{-9}$$

where the subscript a has been added to emphasize that these are apparent limits, based on the assumption of negligible zirconium-ion mobility.

Finally, some comments on the zirconium-ion mobility are possible. With the current density and sample thickness used in the above transport experiment, it takes an oxygen ion about 1.33 hr, on the average, to traverse the disk. Thus, the entire oxygen inventory was removed and replaced about 450 times during this run. Despite this fact, the texture and markings on the surface of the pellet after the test appeared to be the same as at the beginning, suggesting that any movement of the cations within their own sublattice was very small. This is confirmed in a closely related system by Rhodes and Carter's (17) observation that the tracer diffusion coefficients for the cations in two ZrO_2 -CaO solutions are 10^6 smaller than the corresponding anion diffusion coefficients. Kingery *et al.* (18) compared diffusion coefficients for oxygen in ZrO_2 -15 mole % CaO with the conductivity of the same material and concluded that vacancy migration in the anion sublattice could account for all the observed conductivity, and Hund (19) has established the existence of a high concentration of anion vacancies and an essentially complete cation lattice in both calcia- and yttria-stabilized zirconia. Thus, it seems probable that the zirconium ions move very little with

respect to one another, and that the apparent electron and stabilizing-ion transport numbers reported here are true transport numbers in the sense of Eq. [5].

Acknowledgment

The authors are indebted to B. W. Roos and R. W. Preisendorfer of this Laboratory for obtaining a solution to Eq. [39].

Manuscript received March 7, 1963; revised manuscript received Nov. 1, 1963.

Any discussion of this paper will appear in a Discussion Section to be published in the December 1964 JOURNAL.

REFERENCES

1. K. Kiukkola and C. Wagner, *This Journal*, **104**, 379 (1957).
2. E. Bauer and H. Preis, *Z. Elektrochem.*, **43**, 737 (1937).
3. C. Wagner, *Z. Phys. Chem.*, **21B**, 25 (1933).
4. W. Schottky, *Wiss. Veröff. Siemens-Werken*, **14**, 10 (1935).
5. S. F. Pal'guev and A. D. Neumin, *Trans. (Trudy) of Inst. of Electrochem.*, No. 1, p. 90 (translation from Russian by Consultants Bureau, New York, 1961).
6. J. Weissbart and R. J. Ruka, *This Journal*, **109**, 723 (1962).
7. H. Schmalzried, *Z. Elektrochem.*, **66**, 572 (1962).
8. S. R. de Groot, "Thermodynamics of Irreversible Processes," pp. 114 and 127-133, North Holland, Amsterdam (1959).
9. E. O. Kirkendall, *Trans. Am. Inst. Mining, Met. Petroleum Engrs.*, **147**, 104 (1942).
10. J. Bardeen and C. Herring, in "Atom Movements," pp. 87-111, American Society for Metals (1951).
11. C. Wagner, in "Atom Movements," pp. 153-173, American Society for Metals (1951).
12. C. Wagner, in "Proceedings 7th Meeting of International Committee on Electrochemical Thermodynamics and Kinetics," pp. 361, 377, Butterworths, London (1957).
13. M. H. Hebb, *J. Chem. Phys.*, **20**, 185 (1952).
14. J. P. Coughlin, *Bureau of Mines Bull.*, 542 (1954).
15. P. Duwez, F. H. Brown, Jr., and F. Odell, *This Journal*, **98**, 356 (1951).
16. J. M. Dixon, L. D. LaGrange, U. Merten, C. F. Miller, and J. T. Porter II, *ibid.*, **110**, 276 (1963).
17. W. H. Rhodes and R. C. Carter, *Bull. Am. Ceram. Soc.*, **41**, 283 (1962).
18. W. D. Kingery *et al.*, *J. Am. Ceram. Soc.*, **42**, 393 (1959).
19. F. Hund, *Z. Elektrochem.*, **55**, 363 (1951), and *Z. physik Chem.*, **199**, 142 (1952).

Pores in Tantalum Oxide Films and Their Influence on the Photoresponse

R. Dreiner and J. Schimmel

Research Center, Sprague Electric Company, North Adams, Massachusetts

ABSTRACT

Experimental evidence is presented which indicates that HF attacks preferentially along cracks, pores, or other singularities which exist in anodic tantalum oxide films. These defects when enlarged by the HF etch permit an electrochemical emf to arise. It is discussed how the electrochemical emf affects the photoresponse of tantalum oxide.

Many phenomena observed with electrolytic capacitors or anodized valve metals have been connected to pin holes or flaws in the oxide layer. It is known that, for a given field across the oxide film, the anodic leakage current density cannot be reproduced very well and that the leakage current density increases with increasing oxide thickness. This is in agreement with the concept of flaws or microfissures which penetrate the oxide and whose effect becomes more severe as the oxide thickness increases. Young (1) measured $\tan \delta$ as a function of frequency and found by varying the electrolyte conductivity that the increase of $\tan \delta$ at low frequencies is due to microfissures in the oxide. He suggested that the rectification properties of the anodized valve metals are also connected to the pores which are blocked by oxygen gas but remain more or less free during hydrogen evolution. A model based on the idea that the formation of oxide above surface irregularities will cause stresses in the oxide, and hence cracks, was also proposed by Young (2). The onset of recrystallization (3), which occurs at the metal-oxide interface in the presence of a strong electric field, also will lead to cracks. Further support of "weak" spots in the oxide film is reported by Vermilyea (4) who tested Ta_2O_5 films with small area contacts. It was found that the Ta_2O_5 layer is a good insulator except where it is formed over singularities at the tantalum surface. It is proposed that the oxide formed over these small imperfections is highly conductive.

In this work we are concerned with tantalum, and it is probably safe to assume that its oxide film has pores or "weak" spots. The density of these imperfections will depend on the purity of the tantalum metal, the pretreatment, and the anodization. These imperfections, if present, may be attacked differently than the bulk oxide by HF solutions. Vermilyea (5) found by comparison with an optical step gauge that the dissolution of Ta_2O_5 in HF is uniform. However, the method of optical comparison would not be sensitive enough to reveal minute preferential etching in HF. In a very recent paper Vermilyea (6) showed electron micrographs of flaws in anodic Ta_2O_5 films. Several possibilities leading to flaws were outlined and discussed. On comparing the measured capacity with that calculated from the optical thickness, Vermilyea concluded that the etching occurs preferentially along

the flaws as well as uniformly along the surface. This was confirmed by electron microscopy studies. A very sensitive indicator should also be the leakage resistance of the oxide film. Preferential etching along "weak" spots will change the leakage resistance and should, therefore, affect leakage currents during anodic charging, open circuit voltage decay, and the photovoltage or photocurrent.

Experimental

Tantalum foils of ~ 18 cm² area and with narrow tabs were punched from 10 mil tantalum sheet (Fansteel, impurities less than 0.1%). The samples were degreased, chemically polished for 15 sec in 5:2:2, conc H_2SO_4 :conc HNO_3 :48% HF, leached in boiling deionized water for 10 min and then vacuum annealed ($< 10^{-4}$ Torr) at 2100°C for 30 min. The foils were then anodized in 0.1% H_2SO_4 solution at about 34°C by applying a constant current of 2 ma/cm² until a pre-set potential was reached, and then continuing at constant voltage for 1 hr. The anodized foil was placed in a large polyethylene and Teflon cell containing bright platinum counterelectrodes with an area of 170 cm². The HF etching solution used in these experiments consisted of 9 parts deionized water to 1 part 48% HF. Large volumes of electrolyte solutions (~ 0.8 liter) were used and were well stirred to prevent the character of the solution from changing markedly during the experiments.

A Keithley 610A electrometer was used for the current and voltage measurements. It should be noted that the electrometer measures the voltage drop across various standard resistors. Thus the ordinates of the curves shown are labeled "potential" rather than directly as current. A Hanovia quartz lamp was used to provide the full spectrum of a high pressure mercury arc for the photoinvestigations. However, only one side of the samples was irradiated during the experiment.

The bright platinum electrode was compared to a standard saturated calomel electrode in order to establish some reference for the results of the tantalum to platinum potential measurements. A potential of 0.67v was measured between a platinum electrode (positive) and a saturated calomel electrode (negative) in a 0.1% H_2SO_4 electrolyte. However, when a tantalum electrode was introduced into the system and a charging current was passed

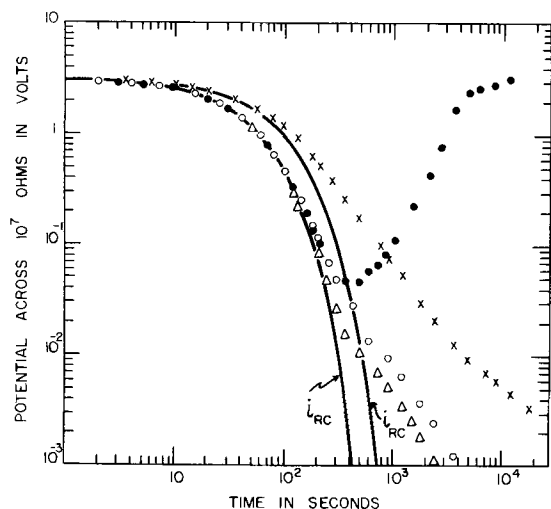


Fig. 1. Current vs. charging time with a 3v anodic bias. \circ , First charging curve, 0.1% H_2SO_4 ; Δ , second charging curve, 0.1% H_2SO_4 ; \bullet , third charging curve, diluted HF solution; \times , fourth charging curve, 0.1% H_2SO_4 .

between the tantalum (positive) and the platinum (negative), the above potential was reduced to 0.64v. When the current was discontinued and all electrodes put on open circuit, the platinum-SCE potential returned to the initial value of 0.67v within 10 min. The open-circuit potential between platinum and SCE electrodes in the 9:1 H_2O :HF electrolyte was 0.64v (platinum positive) and this was reduced to 0.62v with the passage of the charging current.

Results

Leakage current.—In Fig. 1 the results of current measurements during charging are plotted which were made with the anodized foil in (a) 0.1% H_2SO_4 electrolyte, and (b) in the diluted HF solution. The foil was anodized to 54v. Initially, the current corresponded to the RC-charging current but deviated after about 100 sec. The theoretical RC-curves (solid lines) in Fig. 1 were calculated with τ values obtained from semilog plots of the initial charging current vs. time. In the case where 0.1% H_2SO_4 electrolyte was used, a slowly decaying leakage current was observed after long charging times. The leakage currents were not reproducible. However, with the anodized foil in the diluted HF solution, the current passed through a minimum and increased to a value which was higher than the ratio of the externally applied potential to the series resistor. The additional power source must be within the cell and is thought to be the electrochemical emf of the system Ta/diluted HF solution/Pt in series with the externally applied potential. The emf, however, should only be observed when the diluted HF solution comes into contact with the metal. From capacitance measurements at 120 cps before ($C = 4.36 \mu\text{F}$) and after ($C = 4.80 \mu\text{F}$) etching, it appeared that only about 80 or 90A of oxide had been removed (assuming $\epsilon = 27.6$). No change in the interference color, which remained uniform, could be detected with certainty by comparison with an optical step gauge (5v steps). Therefore, the HF solution, besides removing a thin layer of oxide, must have penetrated into pores or

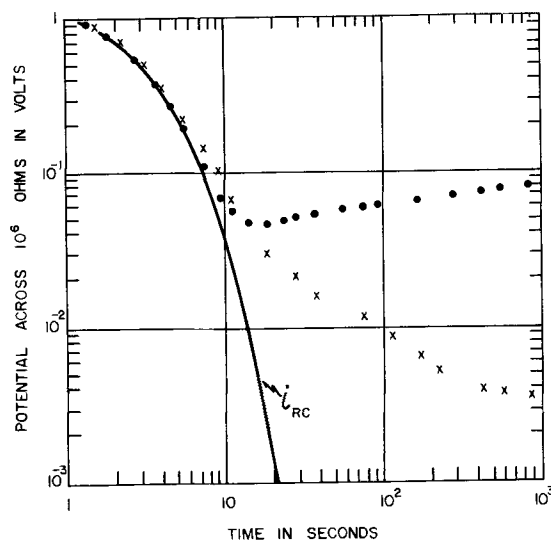


Fig. 2. Current vs. charging time with a 1.56v cathodic bias.

preferentially etched "weak" spots of the oxide to make contact with the metal. After etching, and with the foil back in 0.1% H_2SO_4 , the charging was repeated and, as seen, the leakage current remained at a higher level.

A second tantalum foil was anodized to 107v, but subjected to the same charging field. In general, the effects discussed above were confirmed. One might state, however, that the increase of the current due to the etching occurred sooner though at the same current level.

In Fig. 2 the results obtained with a tantalum foil anodized to 107v but charged cathodically (tantalum negative) to 1.56v are shown. Prior to the runs the foil was anodically charged to 45v for 20 min and shorted for 5 min. The results are qualitatively the same as those observed with an anodic bias, but it will be seen that the increase in leakage current due to preferential etching occurs in a much shorter time (about 12 sec as compared to 400 sec in Fig. 1). This indicates that the HF solution penetrates the pores almost immediately but that the effect will not be noticed until the current through the defects becomes comparable to (i) the RC charging current and/or (ii) the leakage current.

Voltage decay.—Two foils, anodized to 54v (Fig. 3) and 107v (Fig. 4), were immersed in 0.1% H_2SO_4 or HF solution and charged for 20 sec to 22.5v (Fig. 3) and 45v (Fig. 4) (when in the HF solution, 20 sec from time of immersion). After charging, the external circuit was interrupted and the open-circuit voltage decay recorded. The potential decreased slowly when the diluted sulfuric acid was the electrolyte. In the HF solution, the potential decayed more rapidly, changed polarity and leveled off at 1.38v with the tantalum negative. With an unanodized tantalum foil immersed in the HF solution, an open-circuit potential of 1.38v was measured (tantalum negative). Therefore the internal emf source is related to the electrochemical reaction of the Ta/HF solution/Pt system. For this to occur the HF solution must penetrate through flaws, since the capacitance measurements (before: $C = 4.8 \mu\text{F}$; and after: $C = 4.36 \mu\text{F}$) indicated that only

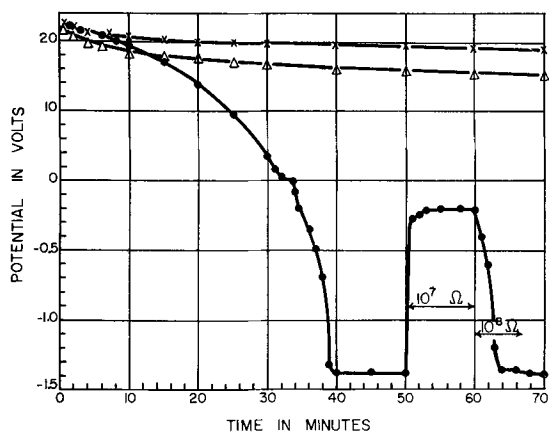


Fig. 3. Open circuit voltage decay. X, First run in 0.1% H_2SO_4 ; ●, second run in diluted HF solution; Δ , third run in 0.1% H_2SO_4 . External resistors 10^7 and 10^8 ohms indicate approximate internal impedance. Note scale change of ordinate.

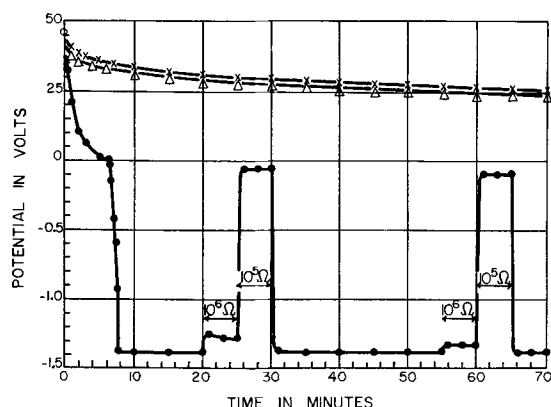


Fig. 4. Same as Fig. 3 except that oxide thickness and charging voltage are twice as large. Note scale change of ordinate.

about 40Å of oxide were etched off. No conclusive thickness change could be determined from the comparison with the optical step gauge. The internal resistance, Fig. 3, of the emf was about 5×10^7 ohms.

After the foil which had been treated as described above had soaked for 30 min in deionized water and was put back into the 0.1% H_2SO_4 electrolyte, the open-circuit potential was again such that the tantalum was positive and slowly increased to 0.12v within 60 min. It was expected that the emf of the system Ta/0.1% H_2SO_4 /Pt would appear, but apparently the residual potential from previous chargings still dominated. However, the etching caused changes in the oxide, which were not eliminated by a 20 sec charging to the same potential, as seen from the third open-circuit decay, Fig. 3.

Continuous etching was expected to increase the number and size of the pores. This should lower the internal resistance of the emf of the system Ta/HF solution/Pt. Eventually this internal resistance should approach about 10^2 ohms as observed with a bare Ta-foil. So the foil used for the runs plotted in Fig. 3 was etched for an additional 14 hr in the diluted HF solution and indeed the internal resistance decreased to about 3×10^4 ohms. The interference color had changed uniformly, and by comparison, the oxide thickness had changed from a thickness corresponding to the initial formation

potential of 56v to about 35v (before: $C = 4.36 \mu\text{F}$; after: $6.90 \mu\text{F}$).

After soaking for 30 min in deionized water, the foil described above was again immersed in 0.1% H_2SO_4 electrolyte. Now the open-circuit potential remained negative, tantalum low, and declined over a time period of 50 min from 1.11 to 1.06v. The run continued to a total of 250 min and the potential stayed constant. Recharging for 20 sec to 22.5v with 10^4 ohms in series did not heal the remaining oxide layer as was seen from a subsequent open-circuit decay.

That thicker oxide films have more flaws is clearly demonstrated by a comparison of Fig. 3 and Fig. 4. The foil used for the runs plotted in Fig. 4 was anodized to twice the potential of the foil in Fig. 3. However, the open-circuit decay (in the HF solution) to the electrochemical potential occurred more rapidly. After approximately the same etching time, the internal resistance of the emf was two orders of magnitude less, about 5×10^5 ohms.

Photoinvestigations.—It is well-known that Ta_2O_5 responds to light of wavelengths shorter than about 300 $\text{m}\mu$. During the discharge of a tantalum oxide electrolytic capacitor and the open-circuit voltage (residual voltage) build-up and decay, the photosensitivity of the oxide has been found to extend to much longer wavelengths (7). For the following experiments, no selected light frequencies were used, and therefore, the results will give only a qualitative explanation of how pores in a tantalum oxide film affect the photoresponse.

When a foil anodized to 55v was immersed in 0.1% H_2SO_4 and the oxide illuminated during the open-circuit voltage decay, the potential very rapidly dropped to a negative value (the Pt-counter-electrode positive) and the internal resistance of this potential source was about 10^5 ohms, Fig. 5. This value depends, of course, on experimental conditions such as light intensity, spectral distribution, etc.

We picture the photovoltage and the electrochemical voltage as two potential sources with characteristic internal resistances and further we assume that these two cells are in parallel. As soon as the electrochemical emf, E_e , is equal to the maximum open-circuit photovoltage, E_{ph} , no open-circuit photoresponse of the tantalum oxide should be ob-

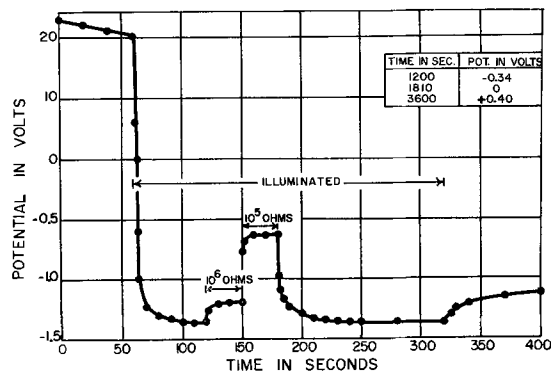


Fig. 5. Open-circuit voltage decay in 0.1% H_2SO_4 after 20 sec charging to 22.8v as influenced by illumination. Note scale change of ordinate.

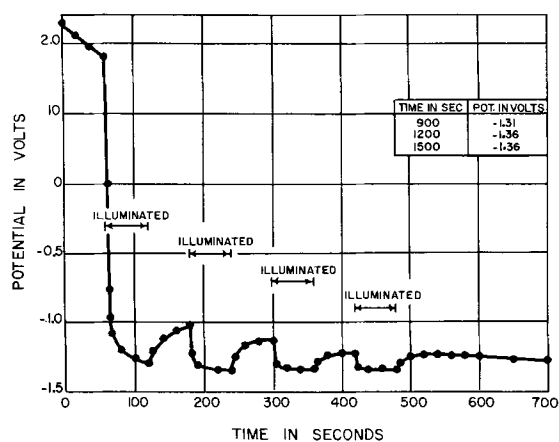


Fig. 6. Open-circuit voltage decay in diluted HF solution after 20 sec charging to 22.8v as influenced by repeated illuminations. Note scale change of ordinate.

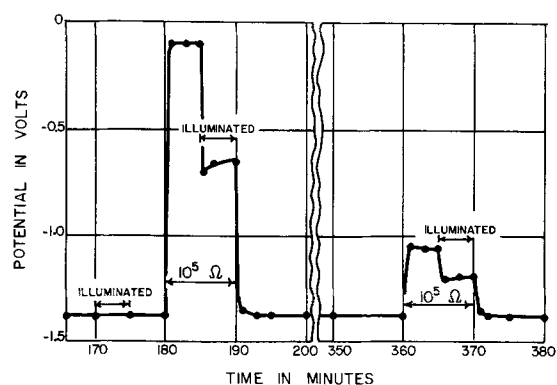


Fig. 7. Continuation of Fig. 6. Although the open-circuit photoresponse had ceased, a photocurrent could still be observed.

served. With the anodized foil in the diluted HF solution, the difference between the photopotential and the dark potential diminished (Fig. 6) as the etching proceeded. Fig. 7 is a continuation of the run in Fig. 6. We see from Fig. 7 that the open-circuit photoresponse finally could not be detected anymore. The ratio of the current supplied by the two cells in parallel depends on the ratio of the internal resistors for $E_e \approx E_{ph}$. It was mentioned above that the internal resistance of the "electrochemical battery" was a function of the time the foil had been in the HF solution. Therefore, a photocurrent should be detectable even after the open circuit voltage can no longer be affected by light, provided the internal resistance of the photosource is not much larger than the internal resistance of

the electrochemical voltage source. This indeed was observed, Fig. 7. Here a current of about $1 \mu\text{a}$ increased rapidly to approximately $7 \mu\text{a}$ and leveled off at $6.5 \mu\text{a}$ when the oxide was illuminated. As is further seen, the photocurrent (the difference between the dark and the total current) decreased as the etching proceeded. After the run, the interference color was still uniform on each side but the illuminated side had etched faster as indicated by the difference in interference colors.

An additional experimental observation can be explained by assuming that the oxide is penetrated by pores. An anodized foil which had been etched for some time so that the internal resistance of the electrochemical emf was about 10^8 ohms and the open-circuit photoresponse had disappeared was immersed in deionized water for two hr. When the foil was put back in the HF solution, the open circuit potential reacted to light but this response vanished with time as described above. It is suggested that the deionized water had filled the pores and the HF solution needed some time to make contact with the tantalum and restore the electrochemical potential, and thus conceal the open circuit photoresponse.

It has previously been proposed (8) that a surface barrier exists close to or at the oxide electrolyte interface since the photoeffect disappeared and the cathodic current increased after a thin layer of oxide was removed by etching in HF. Here, however, the conclusion is made that an anodic oxide layer on tantalum always responds to light of adequate frequency regardless of whether layers are etched off or not. The etching, however, increases the porosity of the oxide and thus causes the electrochemical potential to arise. As explained above, this eventually conceals the photoresponse of the tantalum oxide.

Manuscript received April 29, 1963; revised manuscript received Aug. 8, 1963.

Any discussion of this paper will appear in a Discussion Section to be published in the December 1964 JOURNAL.

REFERENCES

1. L. Young, *Trans. Faraday Soc.*, **55**, 842 (1959).
2. L. Young, *Acta Met.*, **5**, 711 (1957).
3. D. A. Vermilyea, *This Journal*, **102**, 207 (1955).
4. D. A. Vermilyea, *J. Appl. Phys.*, **27**, 963 (1956).
5. D. A. Vermilyea, *Acta Met.*, **2**, 482 (1954).
6. D. A. Vermilyea, *This Journal*, **110**, 250 (1963).
7. R. Dreiner, *This Journal*, **111**, 27 (1964).
8. P. F. Schmidt, F. Huber, and R. F. Schwarz, *J. Phys. Chem. Solids*, **15**, 270 (1960).

Short-Pulse Techniques

I. Kinetics of the Triiodide/Iodide Reaction on a Platinum Electrode in Neutral Solution

Sigmund Schuldiner and Clifton H. Presbrey, Jr.

U. S. Naval Research Laboratory, Washington, D. C.

ABSTRACT

The subject application permits observation of polarization changes on an electrode surface in times as short as 25 nanosec. The required miniaturization of the electrolytic cell is achieved by the use of a solion. Short pulses limit electrochemical processes so that only those reactants already present at the metal/solution interface are available for reaction. The perturbation time of iodide ions in the compact double layer was estimated to be 3×10^{-8} sec. Kinetic relations for polarization build-up and decay are derived and applied to this redox system for both anodic and cathodic polarization. The variability of the transfer coefficient, α , found by Newson and Riddiford, is confirmed over a wide range in both the anodic and cathodic directions. Kinetic parameters are determined, and the equations based on the Vetter electron transfer step, with some modifications, are verified. Surface coverage determinations indicate that the fraction of available platinum surface covered with adsorbed iodine atoms at zero overvoltage (θ_0) for adsorbed iodine atoms is 0.09. Parameters are also determined for the hydrogen formation reaction at potentials where all of the iodine is reduced. A model for the adsorption of iodine species on the electrode surface is given in order to explain the relationship between surface coverage of these species and the exchange current density.

The object of this investigation was twofold. The first aim was to devise a technique which would allow the determination of transient polarization effects as soon as possible after the imposition or discontinuation of a perturbation. The second aim was to apply such a technique to the study of a redox system.

A solion cell was selected for this work because such a cell physically meets the requirements for polarization measurements at times less than $1 \mu\text{sec}$ after changes are applied to the system. The careful construction of these cells and the purity of the reagents used are also conducive to studies of fundamental reaction kinetics.

Instrumentation

Circuitry.—The basic circuit used in this investigation is the same as that given in an earlier paper (1) with the omission of the horizontal oscilloscope input, since these measurements are all made from simple time base displays. One modified circuit, shown in Fig. 1, was used for very fast pulses having a rise time of 4 nanosec. These pulses were used to check for evidence of cell reactions at very

short time intervals following the incidence of a pulse. The use of a nominal value of 100 ohms for R_{std} was found to seriously increase the pulse rise time so this was reduced to 10 ohms, a value sufficient to provide usable current measurement voltages but not large enough to materially affect the rise time. Furthermore, essentially constant current conditions exist because of the high solution resistance of the cell. The capacitance existing between the reference and the working electrode caused very large overshoot and some ringing on the pulses observed at the reference electrode. The 200-ohm series resistor was used to greatly reduce the overshoot and eliminate the ringing. Higher values of resistance introduced undesirable stray capacitance effects. Since the pulse generator required a nominal 50-ohm load (45 ohms for optimum square wave pulse shape), it was necessary to shunt the cell circuit with a 68-ohm resistor to provide this load. Thus the internal resistance of the solion cell turns out to be approximately 125 ohms.

Since no evidence of cell reactions occurred in the first 25 nanosec following pulse incidence, a longer pulse generator with a pulse rise time of 25 nanosec was used with the circuit shown in Fig. 2 for subsequent measurements. The longer rise time eliminated the overshoot and ringing problem, so that the 200-ohm resistor shown in Fig. 1 could be omitted and the 10-ohm R_{std} could be increased to the nominal 100 ohms once more, permitting more accurate voltage readings under essentially constant current conditions. Since load matching is not so critical with this generator, the internal 93-ohm load gave a very good wave form with the cell circuit of Fig. 2. Since this generator had a relatively high cutoff current, particularly on

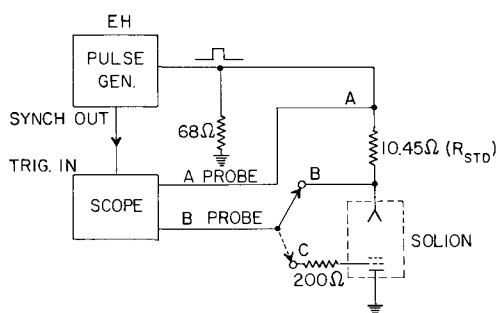


Fig. 1. Block diagram of very short-pulse circuit

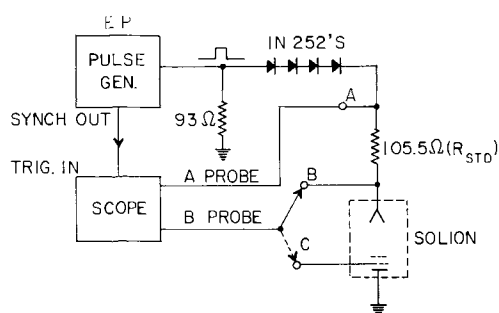


Fig. 2. Block diagram of pulse circuit using Electro Pulse pulse generator.

the positive output polarity, the four 1N252 diodes were inserted in the cell circuit to hold this down to an insignificant value, as in the former polarization studies (1).

While using the circuit of Fig. 1 with the short-pulse generator, the measurements and calculation method were checked by testing with a dummy cell circuit which utilized carefully measured, known values of components.

Equipment.—The short-pulse generator used in the circuit in Fig. 1 was the Model 121 manufactured by the E-H Research Laboratories, Inc. It will supply a $50\text{v} \pm$ pulse to a 50-ohm load. The pulse rise and fall times are 4 nanosec, and the pulse width is variable from 20 to 1000 nanosec. Repetition rate is from 10 cycles to 10 megacycles. In addition there is a single-pulse pushbutton.

The long-pulse generator used in the circuit in Fig. 2 was the Electro-Pulse Model 3450D manufactured by the Servo Corporation of America. It will produce a positive or negative 75v pulse into a 100-ohm load, with a rise and fall time of 25 nanosec. Pulse width ranges from 50 nanosec to 1 sec, using two modules. Repetition rate is from 0.05 cycles to 2 megacycles, using two modules. There is also a single-pulse pushbutton.

The oscilloscope used in taking these measurements was a Tektronix Type 585. This is the successor to the Type 535 used in the polarization studies covered by the paper referred to above (1). It is practically identical in its specifications but it has response up to 100 MCS, with a rise time of 3.5 nanosec. This response is necessary for use with the short-pulse generator. The dual-trace, switched-input, plug-in amplifier unit (Type 82) available with this scope was used for the simultaneous display of traces recorded with a Polaroid camera using fast film with 10,000 ASA rating.

The 1N252 diodes are a fast-switching type manufactured by Transistron. The maximum inverse operating voltage is 20v; the maximum average forward current is 40 ma; and the maximum recovery time is $0.15 \mu\text{sec}$.

The solion cell used in these studies is described in detail elsewhere in this report, and an enlarged diagram is given in Fig. 3.

Procedure.—Initial tests on the solion cell resulted in polarization curves such as those illustrated in Fig. 4. These show the superposition of the pulse at the reference electrode on the original pulse shape

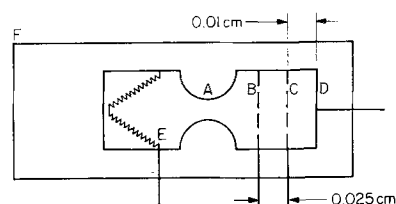


Fig. 3. Integrator solion. A. Cross-section at neck from 0.05 to 0.1cm; B. Pt shield electrode (diam = 0.4 cm with 7 holes of 0.005 cm diam); C. Pt reference electrode (diam = 0.4 cm with 7 holes of 0.005 cm diam); D. Pt working electrode (diam = 0.4 cm); E. counterelectrode (80 mesh Pt gauze, 0.254 cm x 0.953 cm); F. cylindrical plastic case (1 cm diam x 4 cm long) surrounding a glass envelope which contains electrodes and electrolyte.

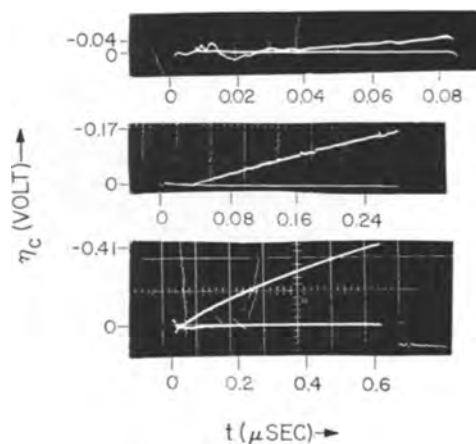


Fig. 4. Cathodic polarization oscilloscope traces at short times $i \approx 3 \text{ amp/cm}^2$.

at the very start of the pulse. This is done by means of the electronic switching circuitry contained in the scope preamplifier unit. Three different time bases are used, primarily showing progressive charging of the double layer capacitance up to approximately $1 \mu\text{sec}$. Two Type P6008 probes having a 10 megohm input resistance and 7 pfd input capacitance (designed specifically for use with the Type 82 plug-in unit) were found to give the best possible wave shape when carefully grounded through BNC connectors to the small shielding box containing the cell. All leads in the box were kept very short, to minimize stray inductance and capacitance, and the box was mounted right on the output connector of the pulse generator. The probes were connected to points A and C in Fig. 1, and pulse widths of approximately 0.08, 0.3, and $0.8 \mu\text{sec}$ were used, at repetition rates between 100~ and 500~. This pulse spacing was sufficient to permit return to equilibrium between pulses. Cell current was obtained by measuring pulse voltages at points A and B with the calibrated scope vertical amplifier. The current is equal to the difference in voltage at points A and B divided by 10.45 ohms.

Similar measurements were made with the long-pulse generator using the circuit of Fig. 2. With the use of 0.8, 8, 45, and $80 \mu\text{sec}$ pulse widths, a single-pulse technique was necessary in order to permit the cell to return to equilibrium between the longer pulses. It should be observed that the polarity of the 1N252 diodes must be reversed with a reversal of the input pulse polarity; otherwise their high

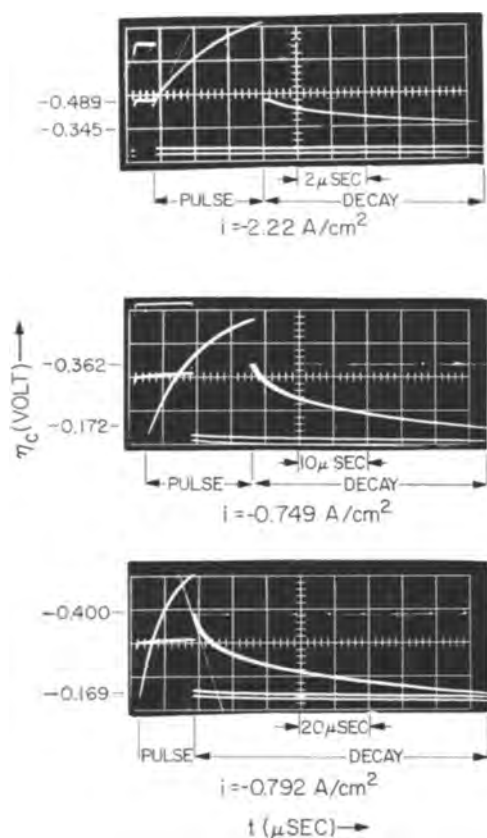


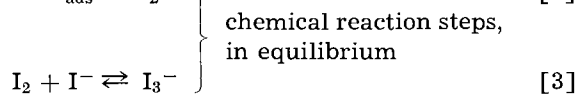
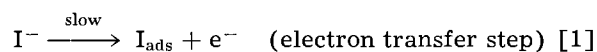
Fig. 5. Typical cathodic pulse and decay oscilloscope traces. Note: the two rectangular pulses in each picture of this and succeeding figures were used to determine current.

back resistance will prevent application of the pulse to the cell. The curves in Fig. 5 show typical pulse shapes at the reference electrode. The pulses appear inverted because the actual measurements were taken on the reference electrode (it was necessary to ground the working electrode in arriving at a practical circuit). The curves in Fig. 5 also show pulse decay characteristics. With this circuit, the current is equal to the difference in voltage at points A and B (see Fig. 2) divided by 105.5 ohms. This current may be considered constant insofar as its effect on the polarization curves is concerned because the polarization voltage changes are an insignificant proportion of the total applied pulse voltage.

A dummy cell circuit was assembled in an attempt to approximate the curves obtained from the cell and to calculate the known values of R and C by measurements taken from them. In making these measurements, the time base of the scope was carefully calibrated, along with the vertical amplifier voltage calibration. Measurements were taken from pulse photographs, using both pulse generators and pulse polarities. The calculated component values were in reasonable agreement with the measured ones, proving that such measurements are a reliable quantitative source of data when applied to the unknown values in an electrolytic cell.

Triiodide/Iodide Reaction

Vetter (2, 3) reviewed the kinetics of this reaction and concluded that the reaction mechanism would follow the path



here I_{ads} is a chemisorbed iodine atom. Newson and Riddiford (4) have recently confirmed this mechanism.

Experimental

A diagram of the "Tracor solion electrical readout integrator" is shown in Fig. 3. The solution was reported by the manufacture to consist of very carefully purified 1.0M KI plus about 0.0025M I_2 and less than 0.01% citric acid dissolved in pure water. The cell was constructed of lead-free soft glass in which all the electrodes were sealed. The glass housing was encapsulated in an epoxy potting resin. The oxygen concentration inside the cell was reduced to essentially zero by boiling the solution, out-pumping the gases, and then filling the cell under vacuum. The apparent area of the working electrode was 0.123 cm^2 , while that of the counterelectrode was about 50 times larger. The reference electrode was of the same dimensions as the working electrode, except that to provide an electrolytic path, six 0.005 cm holes were equally spaced in a circle midway on the disk, with another hole of the same size in the center of the electrode. The shield electrode shown in Fig. 3 was not used. The temperature was $25^\circ \pm 1^\circ\text{C}$.

It was found that when pulses were first applied, polarization was high compared to values obtained when the working electrode was first anodized with a succession of about ten 80 μsec pulses. This anodizing process undoubtedly cleaned the surface and gave lower polarization results for both anodic and cathodic polarizations. It is possible that this treatment also may have removed any adsorbed citric acid. Double layer capacitance *vs.* overvoltage measurements indicated that no such substance was adsorbed to an important extent on the working electrode surface. The solubility of citric acid in water would also tend to minimize both its rate of adsorption and the amount adsorbed. Measurements were then taken, usually in a period of less than 1 hr, and in that time the results were reproducible enough so that poisoning effects were not too severe. This was especially true for anodic polarization. Polarization in the cathodic direction, being more subject to poisoning effects, was not quite as reproducible.

The solion was subjected to single, constant-current (varying from 0.1 to 3 amp/cm^2) anodic and cathodic pulses of about 0.8, 8, 45, and 80 μsec duration. The current density was controlled by varying the pulse voltage, and its value was calculated for each pulse from measurements of the voltage drop across R_{std} , determined from two pulses usually recorded on the same film with the voltage-time trace for the working electrode. Decay curves were determined by applying single pulses ranging from about 3 to 25 μsec in duration and recording

both the pulse and the potential-time decay trace. Figure 5 shows typical cathodic short pulses followed by decay curves. The rectangular pulses shown on these curves were used to determine current density.

The fact that a pulsed working electrode returned to its original open-circuit potential before the application of a succeeding pulse was demonstrated in two ways: first, by photographing a succession of two pulses which coincide on superposition, and second, by extending the decay time to a point where the decay potential coincided with the potential at the initiation of the pulse. This return to the original open-circuit potential occurred in less than 1000 μ sec. Intervals between successive pulses were of much longer duration. Repeated pulses of a length greater than 80 μ sec caused accumulative effects and some coloration at the anode due to the formation of iodine. However, this condition was carefully avoided during the collection of data.

Open circuit potentials between each electrode were equal to zero. The calculated equilibrium potential, E_{eq} , for the triiodide/iodide redox couple is obtained from the equation

$$E_{eq} = E_o + \frac{RT}{2F} \ln \frac{I_3^-}{I^-} \quad [4]$$

with $E_o = 0.536$ v (5). For 1M KI and 0.0025M I_3^- , the mean activity coefficient of KI = 0.646 (6), and assuming a unit activity coefficient for I_3^- , $E_{eq} = 0.476$ v. The measured E_{eq} for this solution was reported to be essentially the calculated equilibrium value. The pH of the solution is close to seven. The I_3^-/I^- reaction is apparently at equilibrium at open circuit, so polarization can be represented as an overvoltage. That equilibrium is attained, follows also from the findings of Newson and Riddiford (4), who showed that the potential of the triiodide/iodide redox electrode under similar conditions was essentially at its reversible value.

Kinetic Relations

In this investigation constant-current pulses were kept to short durations so that only reactants initially adsorbed on the electrode surface or in the immediate vicinity of the electrode surface would be available for reaction. Transport of iodine or triiodide to and from the electrode, being a relatively slow process (2), does not occur significantly during the application of these pulses. Calculations show that the I_3^- concentration in solution at the interface will drop to zero within a few microseconds at the lowest current densities applied. Also the rate of diffusion of I_3^- from the interior of the solution to the electrode surface will be virtually insignificant during the pulse time used. Iodide ion, however, is present in such a relatively large amount that concentration changes of this ion at the electrode interface will be relatively insignificant at the current densities and pulse times used.

The high current-density pulses used in this work gave potential-time curves in which the overvoltages were high enough so that the back reaction could be considered to be negligible. The correct-

ness of Vetter's mechanism was assumed, giving the following equations for the rate-controlling anodic and cathodic electron transfer steps

$$i_a = i_o \exp(2.3\eta_a/b_a) \quad [5]$$

$$i_c = i_o (\theta/\theta_o) \exp(-2.3\eta_c/b_c) \quad [6]$$

where the subscripts a and c denote anodic and cathodic, carrying respective positive and negative signs, i is the current density, i_o is the exchange current density, η is the overvoltage, b is the Tafel slope ($=2.303 RT/\alpha F$), θ is the fraction of available platinum surface covered with adsorbed iodine atoms,¹ θ_o is the same fraction at zero overvoltage, α is the transfer coefficient, and R , T , and F have their usual meanings. Equation [5] does not contain concentration terms because the iodide ion concentration would be virtually constant for the experimental conditions applied. Changes in surface concentration of adsorbed iodine atoms would be significant in Eq. [6] because of low concentrations and slow diffusion of I_3^- to the surface.

Transient equations [7, 8] were derived for constant-current pulse application and also for decay of potential after the application of a pulse, assuming the simple model of an electrode interface as a double layer capacitance in parallel with a faradaic impedance (the latter being a function of the rate of electron transfer) with no back reaction. On polarization with a constant-current pulse, and with insignificant concentration changes, the following differential equation describes the rate of overvoltage change:

$$\frac{d|\eta|}{dt} = \frac{|i|}{C} - \frac{i_o}{C} \exp(2.3|\eta|/b) \quad [7]$$

where t is the time and C is the double layer capacitance. Integration of this equation gives

$$|\eta| = \frac{|i| t}{C} - b \log \frac{|i| - i_o + i_o \exp(2.3 |i| t/bC)}{|i|} \quad [8]$$

On cathodic polarization, where changes in the concentration of adsorbed iodine atoms are significant, Eq. (7) must be modified. Here

$$\frac{d\eta_c}{dt} = \frac{i_c}{C} + \frac{i_o}{C} \frac{\theta}{\theta_o} \exp(-2.3\eta_c/b_c) \quad [9]$$

Since

$$\theta = \theta_o + \frac{N_A \times 10^{-6} i_f t}{2 \times 10^{15} F} = \theta_o + 3.125 \times 10^{-3} i_f t \quad [10]$$

where N_A is Avogadro's number, i_f is the faradaic current density in amp/cm², t is in μ sec, and 2×10^{15} is the estimated number of adsorption sites (Pt atoms) per square centimeter on the Pt electrode. Since

$$i_c = i_c + i_f \quad [11]$$

Where i_c is the capacitive current density, with

$$i_c = C d\eta_c/dt = C \eta_c' \quad [12]$$

¹ Although the adsorbed species will be indicated in the text and figures as iodine atoms, an equivalent of iodine molecules, triiodide ions, or a combination of these may actually exist. More concerning these species will be discussed later.

Hence

$$\theta = \theta_0 + (i_c - C\eta_c') 3.125 \times 10^{-3} t \quad [13]$$

Substituting into Eq. [9]

$$\eta_c' = \frac{i_c}{C} + \frac{i_0 \theta_0}{C \theta_0 \exp(2.3\eta_c'/b_c) + 3.125 \times 10^{-3} C i_0 t} \quad [14]$$

Transient measurements made from potential decay traces after application of a constant-current pulse contain important simplifications. This is due to the fact that when the polarizing current pulse is switched off, the current flow through the electrode/solution interface has only a single path. In other words, the double layer capacitance is in series with the faradaic impedance instead of in parallel as in the case of the application of a pulse. This leads to a simplification of Eq. [7]

$$\frac{d|\eta|}{dt} = \frac{-i_0}{C} \exp(2.3 |\eta|/b) \quad [15]$$

Another inherent simplification in decay measurements is that the effects of changes of reactants adsorbed on the electrode surface are canceled out. This is because changes in the number of reactant particles at the time the pulse is switched off affect the exchange current density inversely as these same changes affect potential decay.

Integration of Eq. [15] gives the relation

$$|\eta_0| - |\eta_t| = b \log \left(1 + \frac{2.3 |i_i| t}{bC} \right) \quad [16]$$

where η_0 is the overvoltage at the time the pulse is switched off, η_t is the overvoltage at time t after the pulse is switched off, and i_i is the current density of the series arrangement of double layer capacitance and faradaic reaction at the instant after the pulse is switched off. Eq. [16] differs from the equation derived by Frumkin (9) inasmuch as in Frumkin's case a constant current was applied until a steady-state voltage was achieved at the electrode. This meant that at current interruption the double layer was fully charged and all of the current flowed through the faradaic impedance. Hence the current density in the series double layer and faradaic impedance at interruption time was equal to the applied current density. In the cases investigated in this paper, steady-state conditions are not reached and the double layer is not fully charged at pulse cut-off time. Hence the current density, i_i , will be less than the current density applied by the constant-current pulse. This is because just after the pulse switch-off time the net current flowing in the series double layer and faradaic impedance will depend on the state of charge of the double layer.

Experimental Results

Double layer capacitance at open circuit was determined by applying a 0.8 μsec pulse in both anodic and cathodic directions. The initial slope of the traces was used to determine double layer capacitance from the relation

$$C = i\Delta t/\Delta\eta \quad [17]$$

For anodic polarization, $C = 7 \pm 1 \mu\text{fd}/\text{cm}^2$ and for cathodic polarization $C = 6 \pm 1 \mu\text{fd}/\text{cm}^2$.

As first demonstrated by Frumkin (9), the relation in Eq. [16] can be used to determine the Tafel slope, b , from a plot of overvoltage vs. $\log t$. Tafel b values were thus found from all polarization decay traces. Typical overvoltage vs. $\log t$ decay curves after polarization are shown in Fig. 6. These curves show that b is dependent on the total number of coulombs applied in the polarizing pulse. The relation between these quantities is shown in the decay curves of Fig. 7 and 8. The dependence of b on the overvoltage at the time the pulses were switched off is shown in the decay curves of Fig. 9 and 10.

The decay curves in Fig. 7 and 8 show that during application of a pulse, b is not constant for the I_3^-/I^- reactions but can be expressed by the relation

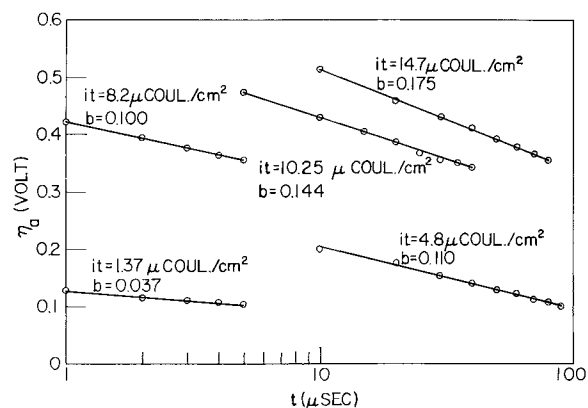


Fig. 6. Typical η_a vs. $\log t$ decay curves

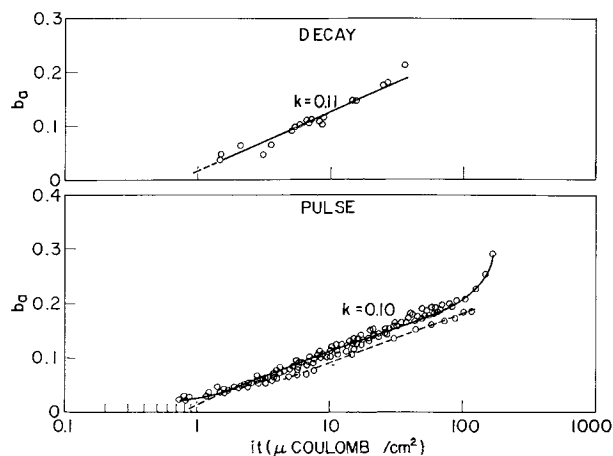


Fig. 7. Relation between anodic Tafel, b_a , and $\log it$ for pulse and decay measurements. Note: the dashed line under the pulse curve indicates that those points came from a single pulse.

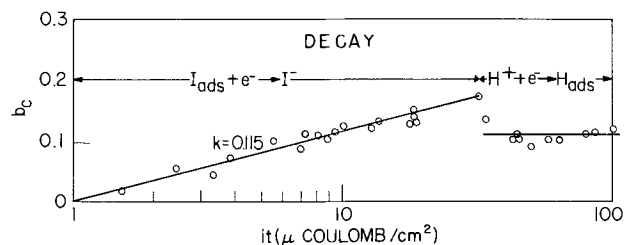


Fig. 8. Relation between cathodic Tafel, b_c , and $\log it$ for decay measurements. Note: the H^+ ions indicated in this and other graphs refer to water $\text{H}^+ - \text{O} = \text{H}^+$.

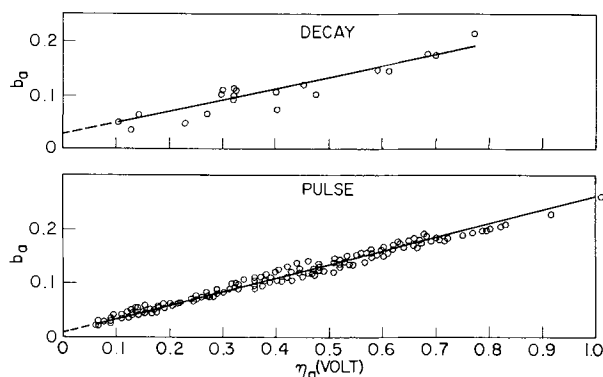


Fig. 9. Relation between anodic Tafel, b_a , and η_a for pulse and decay measurements.

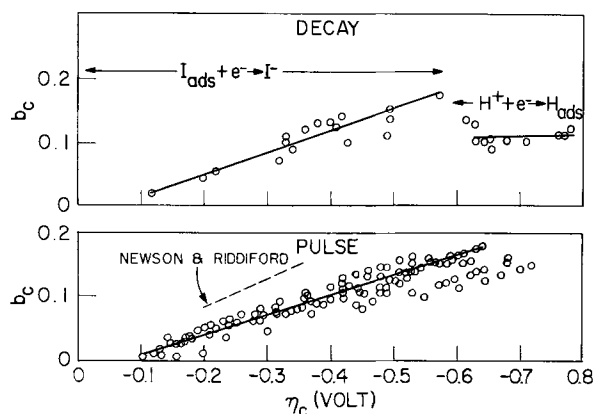


Fig. 10. Relation between cathodic Tafel, b_c , and η_c for pulse and decay measurements.

$$b = a + k \log it \quad [18]$$

where a is the value of b at $it = 1 \mu\text{coulomb/cm}^2$, k is the slope of the b vs. $\log it$ curve and it is the number of $\mu\text{coulombs/cm}^2$ applied in the polarizing pulse. This means that Eq. [7] must be modified to

$$\frac{d|\eta|}{dt} = \frac{|i|}{C} - \frac{i_0}{C} \exp(2.3|\eta|/(a + k \log it)) \quad [19]$$

or

$$k = \frac{|\eta|}{\log it \log [(i - C|\eta'|)/i_0]} - \frac{a}{\log it} \quad [20]$$

where $\eta' = d\eta/dt$.

The exchange current density i_0 was determined from the decay curves by using Eq. [16] to determine i_i and then applying the relation

$$i_0 = i_i \exp(-2.3|\eta_0|/b) \quad [21]$$

These relations are usable because b is determined by the number of coulombs used to polarize the electrode and, as shown in Fig. 6, b remains constant during decay. For anodic decay, a random scatter of the values of i_0 was obtained with an average value of $2 \times 10^{-4} \text{ amp/cm}^2$. Although the scatter was about one order of magnitude, most of the points lay in a reasonable range (0.9 to $2 \times 10^{-4} \text{ amp/cm}^2$). For cathodic decay, however, the i_0 values could not be considered to be constant and the relation found in Fig. 11 was observed.

Using the average i_0 value of $2 \times 10^{-4} \text{ amp/cm}^2$ found from the anodic decay curves, Eq. [20] was

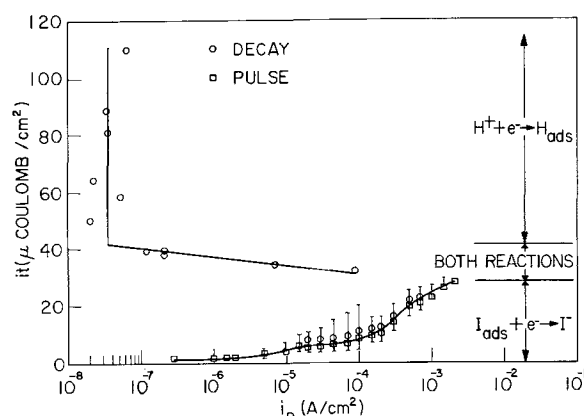


Fig. 11. Relation between exchange current density and amount of charge for cathodic pulse and decay measurements.

solved for k for discrete experimental values found in the pulse traces. From the k values thus determined, b_a was calculated using the decay curve parameters indicated in Fig. 7, which upon applying Eq. [18] gave $b_a = 0.015 + 0.11 \log it$. The b_a values so determined are shown on the pulse curve in Fig. 7. This latter curve gave the empirical relationship, $b_a = 0.015 + 0.10 \log it$. The concordance between the decay and pulse curves shown in Fig. 7 indicates that the kinetic relations used are valid.

Since i_0 values were not constant for the cathodic decay curve, it was not possible to run a similar check. Instead, the Eq. [18] relation $b_c = 0 + 0.115 \log it$ found from the decay curve of Fig. 8 was used to determine i_0 values for the pulse traces for cathodic overvoltage. This was done for the iodine reduction reaction which terminated at pulse charges above $30 \mu\text{coulomb/cm}^2$. Solving Eq. [14] for i_0 gives

$$i_0 = \frac{\exp(2.3\eta_c/b)}{\frac{1}{\eta_c' C - i_c} - \frac{3.125 \times 10^{-3} t}{\theta_0}} \quad [22]$$

The value of θ_0 was determined from Fig. 8 which clearly showed that when more than $30 \mu\text{coulomb/cm}^2$ of charge was applied, all of the adsorbed iodine atoms were ionized and hydrogen ions in water were reduced. This allowed a calculation of the number of iodine atoms adsorbed at open circuit. This was found to be $1.9 \times 10^{14} \text{ atoms/cm}^2$. Assuming that there are $2 \times 10^{15} \text{ Pt atoms/cm}^2$ of apparent area of the working electrode, then $\theta_0 = 0.09$. The i_0 values determined from the cathodic pulses are shown in Fig. 11 together with the values found from the cathodic decay curves.

Double layer capacitance relationships are shown in Fig. 12-14. Decay values of capacitance in Fig.

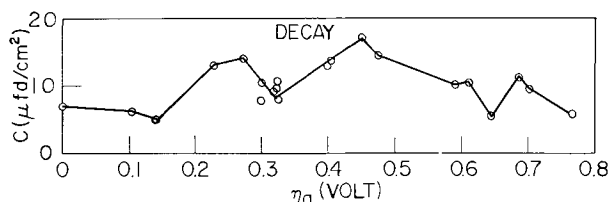


Fig. 12. Relation between double layer capacitance and overvoltage at time pulse was switched off. From anodic decay measurements.

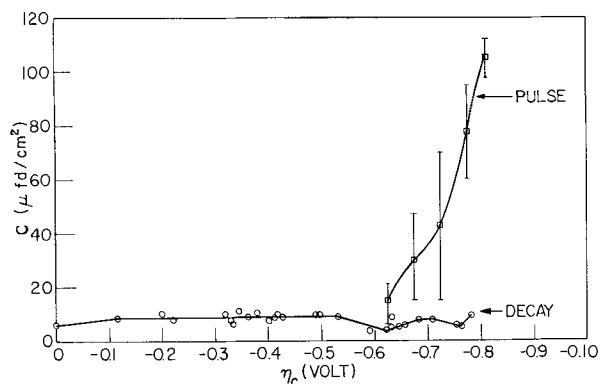


Fig. 13. Relation between double layer capacitance and cathodic overvoltage. η_c for decay measurements is the overvoltage at pulse switch-off time.

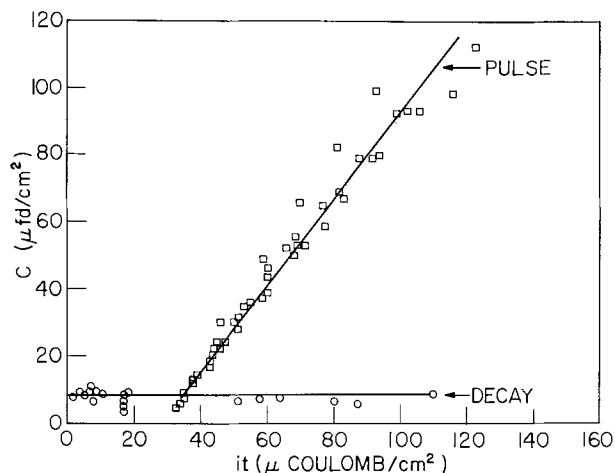


Fig. 14. Relation between double layer capacitance and amount of cathodic charging for pulse and decay measurements.

12 and 13 were determined by multiplying the calculated i_i values for each of the decay oscilloscope traces by the slope, $\Delta t/\Delta \eta$ at the beginning of each overvoltage decay. Within the experimental precision, the decay curves indicate that the double layer capacitance is essentially independent of overvoltage. For the cathodic polarization curves, after the application of $30 \mu\text{coulomb}/\text{cm}^2$ of charge, the predominant reaction is the reduction of water to hydrogen atoms. In this case $i_0 \approx 3.5 \times 10^{-8} \text{ amp}/\text{cm}^2$ (Fig. 11) and $b = 0.11$ (Fig. 8). These parameters show the normal expected behavior of this reaction. Using Eq. [8] and solving for C , the results shown in Fig. 13 and 14 (pulse curves) were obtained.

Relationships between b and overvoltage from the pulse traces are shown in Fig. 9 and 10. The relation between the number of iodide ions oxidized or the number of electrons consumed and the overvoltage for the anodic or cathodic pulses, respectively, are shown in Fig. 15 and 16. These measurements were corrected for the number of coulombs used to charge the double layer. The curve marked with X's in Fig. 16 represents the relation between overvoltage and the number of hydrogen atoms formed, corrected for the amount of charge used to reduce iodide ions.

The limits of experimental scatter shown in Fig.

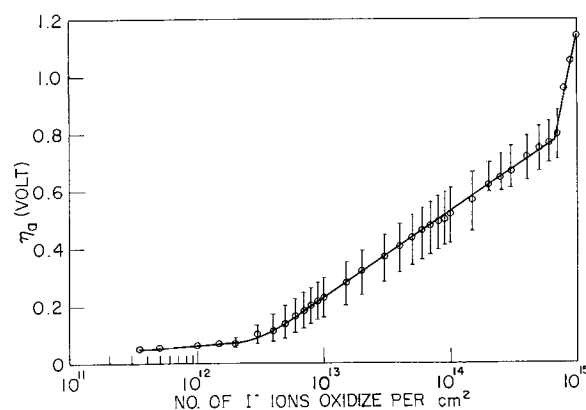


Fig. 15. Relation between anodic overvoltage and number of I^- ions oxidized per square centimeter.

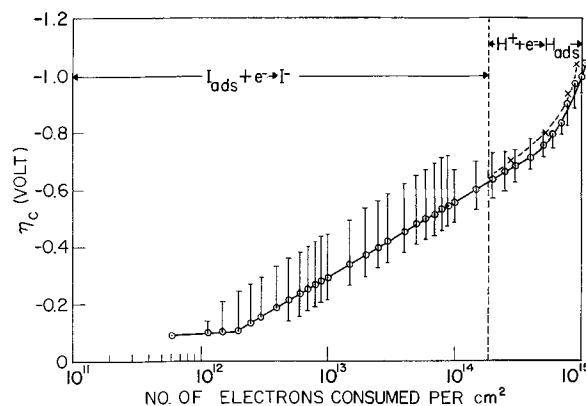


Fig. 16. Relation between cathodic overvoltage and number of electrons consumed per square centimeter. Broken line with X's represents number of hydrogen atoms formed.

11, 13, 15, and 16 by the vertical lines show the scatter of sets of curves rather than individual points. All points from each individual pulse trace essentially follow the same course as shown by the curve. The curves were drawn through the median of the region of maximum density of individual curves.

Discussion

The experimental results indicate that the triiodide/iodide reaction is a very complex one and that the simple mechanism shown in Eq. [1-3] is not completely adequate. An interesting possible application of the very short pulses, such as shown in Fig. 4, is to determine the perturbation (or relaxation) time of ions in the compact double layer. Extrapolating back to zero overvoltage on the $0.08 \mu\text{sec}$ curve indicates a perturbation time of $3 \times 10^{-8} \text{ sec}$ for iodide ions. Much more work, however, is required to really understand the physical significance of this measurement.

Newson and Riddiford (4) found that for cathodically polarized electrodes, the transfer coefficient α was dependent on the bulk concentration of triiodide ion, iodide ion, and the rate of stirring. Their data showing overvoltage dependence was calculated and plotted in Fig. 10. One of the interesting results of the present investigation is the indicated dependence of the Tafel b slope on the number of

coulombs used to charge the electrode (Fig. 7 and 8 or on the overvoltage Fig. 9 and 10). Thus the transfer coefficient is primarily dependent on the number of adsorbed iodine atoms. The maximum value of α occurs near open-circuit conditions. In this case it can go up to three, an astonishingly high value. On either anodic or cathodic polarization, α decreases with either an increase or decrease in the number of adsorbed iodine atoms. In the cathodic direction when all of the iodine atoms are ionized, the hydrogen formation reaction gives a constant Tafel slope of 0.11 ($\alpha = 0.54$), as shown in Fig. 8, which is essentially the value expected for this charge transfer reaction.

Newson and Riddiford (4, 10) explained the variation of α as due to non-uniformity of the electrode surface and they postulated that the anodic and cathodic sites differed. This work shows that essentially the same relation holds (see Fig. 7 and 8) for the change in the number of adsorbed iodine atoms and the Tafel b slope in either the anodic or cathodic direction. It is difficult to understand why the transfer coefficient should be so dependent on the concentration of reactant in the cathodic case and on the concentration of product in the anodic case. A relation to the number of active sites, however, seems to be apparent.

With the fast-pulse techniques used (especially at very short times), the mechanisms involved could be different from the steady-state condition represented by Vetter (Eq. [1-3]), since equilibrium of the chemical steps (Eq. [2 and 3]) may not have had enough time to be established. Thus α values greater than one, which were obtained at very short times, may represent a faradaic impedance controlled by the chemical combination/dissociation reaction (Eq. [2]) or the complexing of iodine to triiodide (Eq. [3]). At longer times, equilibrium could have been established for these steps and consequently the charge transfer step (Eq. [1]) would be rate-controlling.

Figure 16 shows that on open circuit there are about 2×10^{14} iodine atoms/cm² adsorbed on the electrode surface. From Fig. 15 it can be seen that when an additional 7×10^{14} atoms/cm² are formed to give a total of 9×10^{14} iodine atoms/cm², a limiting condition is reached, causing a sharp rise in potential. This would indicate that only about one-half the total number of Pt atoms available on the surface are active insofar as the oxidation of iodide ions is concerned. Thus it appears that each adsorbed iodine atom could share bonds with two Pt atoms. This saturation of the active sites with iodine atoms, molecules, and/or triiodide ions indicates also that diffusion away from the surface, into the solution is not a limiting factor.

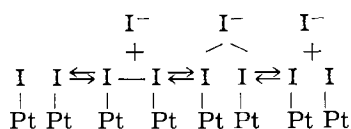
The curves shown in Fig. 13 and 14, respectively, relate double layer capacitance with cathodic overvoltage and with the number of coulombs per square centimeter used to charge the electrode. The decay curves in both figures show only minor variation, whereas the pulse curves show a sharp rise at the point where formation of adsorbed hydrogen atoms becomes the predominant reaction. The fact that

the rise in capacitance occurs only during pulsing can be due to the removal of iodine atoms which act as an electrode poison and tend to lower the capacitance. The low capacitance found for decay curves, even in the range where the predominant reaction before pulse cutoff was the formation of hydrogen, indicates that removal of the polarizing current was accompanied by readsorption of enough poison to lower the double layer capacitance even though part of the reaction during pulse decay may still be the formation of hydrogen atoms. The absence of capacitance peaks in all of the double layer capacitance curves, other than for the hydrogen formation reaction, indicates also that citric acid was not adsorbed on the working electrode.

The fact that the exchange current density on anodic polarization showed no dependence on the number of coulombs used to charge the electrode is expected since the concentration of I⁻ ions remains effectively constant. A very strong dependence is indicated for the cathodic case, as Fig. 11 shows. For small changes in the amount of charge, the exchange current density increases very rapidly with the amount of charge. A reduction in the rate of change of i_0 with charge is evident at about 10 μ coulomb/cm². At 30 μ coulomb/cm² the adsorbed iodine is virtually completely removed and the exchange current density drops off very rapidly as the hydrogen formation reaction takes over. Eventually the hydrogen reaction dominates, to give an essentially constant i_0 for this reaction at about 3.5×10^{-8} amp/cm². The increase in i_0 in the range of the iodine reaction is accompanied by a very rapid decrease in the number of iodine atoms available for reaction. This increase in i_0 is surprising since i_0 is a direct function of concentration and, therefore, the opposite effect would be expected. This can only mean that the activation energy for the reduction of adsorbed iodine atoms decreases as the number of iodine atoms decreases. Since the activation energy term in the kinetic equation is an exponential, the effect of lowered activation energy overwhelms the effect of lowered concentration of reactant.

The determination of i_0 for anodic and cathodic polarization does not necessarily indicate the i_0 which would be found near open circuit. It appears that i_0 at $\eta \rightarrow 0$ would be about 2×10^{-4} amp/cm², the value found for anodic polarization. At short times, very little current would flow in the faradaic arm with a resultant rapid rise in the potential primarily due to the charging of the double layer. The maximum i_0 value of 2×10^{-3} amp/cm² found for the cathodic iodine reduction reaction (see Fig. 11) would be the effective exchange current density for the electron transfer step under steady-state cathodic polarization where the rate of the reaction is controlled by the diffusion of triiodide ions to the electrode surface.

In this paper we have in a general way referred to the adsorbed reactant on cathodic polarization as iodine atoms, without specifying how these atoms were associated on the surface. The adsorption can be visualized as



where an equilibrium between iodine atoms, molecules and triiodide ions is assumed. The concentration of each of these species on the surface is not known, although it is quite likely that the triiodide ion dominates. The increase in i_0 as the concentration of these reactants decreases from the open-circuit value of $\theta_0 = 0.09$ may be due to a large increase in the heat of adsorption of the chemisorbed species. The evidence of Vetter (2) and Newson and Riddiford (4) indicates that the reduction of the adsorbed species is a one-electron step. However, the reduction may take place from any one or all of these species. As the electrode becomes more negative, the bonds between the iodine atoms and the iodide in the triiodide ion could be weakened due to repulsion of the iodide. This would tend to favor the formation of either adsorbed iodide atoms or molecules. This also could favor the direct reduction of triiodide ions.

On anodic polarization, the surface is undoubtedly largely covered with adsorbed iodide ions (11, 12). Thus the effective concentration of reactant remains relatively constant, as indicated by the independence of the exchange current density from the amount of charge passed. The additional coverage of the surface with iodine atoms, molecules, and triiodide ions at increasing polarization does not materially affect the activation energy for the oxidation of iodide ions. Effects of the back reaction are negligible at the overvoltages obtained.

This investigation has demonstrated the effectiveness of the short-pulse technique when used to obtain information concerning a very complex electrode process. Much more work is indicated in order

to clarify the many complex features of the triiodide/iodide system.

Acknowledgments

We are indebted to Dr. Ray M. Hurd, of Tracor, Inc., for furnishing the integrator solution used in this study and for the information he gave concerning the construction and properties of this cell. We gratefully acknowledge the assistance of Mrs. Janet P. Mason in making computations on the Naval Research Laboratory digital computer (NAREC) and the professional aid of Dr. H. A. Hauptman, members of the Applied Mathematics Staff of the Naval Research Laboratory.

Manuscript received May 20, 1963. This paper will be presented at the Toronto Meeting, May 3-7, 1964.

Any discussion of this paper will appear in a Discussion Section to be published in the December 1964 JOURNAL.

REFERENCES

1. C. H. Presbrey, Jr., and S. Schuldiner, *This Journal*, **108**, 985 (1961).
2. K. J. Vetter, *Z. physik. Chem.*, **199**, 22, 285 (1952).
3. K. J. Vetter, "Elektrochemische Kinetik," p. 374, Springer Verlag, Berlin (1961).
4. J. D. Newson and A. C. Riddiford, *This Journal*, **108**, 699 (1961).
5. W. M. Latimer, "The Oxidation States of the Elements and Their Potentials in Aqueous Solution," 2d Edition, p. 64, Prentice-Hall, Englewood Cliffs, N. J. (1952).
6. H. S. Harned and B. B. Owen, "The Physical Chemistry of Electrolytic Solutions," 3d Edition, p. 731, Reinhold Publishing Co., New York (1958).
7. V. A. Roiter, V. A. Yuza, and E. S. Poluyan, *Zhur. Fiz. Khim.*, **13**, 605, 805 (1939).
8. V. L. Kheifets and A. B. Sheinin, *Russ. J. Phys. Chem.*, **33**, 233 (1959).
9. A. N. Frumkin, *Acta Physicochim. U.S.S.R.*, **18**, 23 (1943).
10. W. A. Ledger and A. C. Riddiford, *Nature*, **194**, 1233 (1962).
11. A. N. Frumkin and E. Ajkazyan, *Doklady Akad. Nauk, U.S.S.R.*, **100**, 315 (1955).
12. L. T. Shanina, *ibid.*, **134**, 141 (1960).

Anodic Oxidation of Formic Acid at Platinum Electrodes

M. H. Gottlieb

Bell Telephone Laboratories, Incorporated, Murray Hill, New Jersey

ABSTRACT

From measurements on electrode potentials and rates of carbon dioxide formation on open circuit and on passing currents, it was concluded that the open-circuit potential of the HCOOH, H₂SO₄, Pt system is a mixed potential, determined by the direct anodic oxidation of formic acid and the cathodic reduction of hydrogen ion. The value for the exchange current for formic acid oxidation is smaller than 10⁻¹⁰ amp/cm², and the rates of the mixed reactions on open circuit are between 10⁻⁸ and 10⁻⁷ amp/cm². The slope of the potential-log current curve for the formic acid oxidation is approximately 100 mv per decade of current. It was also concluded that the only effect of platinizing the electrode in this system is to increase the surface area, and that specifically active catalytic sites are not introduced by the platinization process.

The anodic oxidation of organic compounds on platinum at potentials which are considerably more cathodic than those corresponding to the oxygen electrode has been known for at least some forty

years (1). In recent years, there has been renewed interest in these reactions because of their potentialities in the fuel cell field (2). To a very large extent, the mechanism whereby these low potential

oxidation processes occur is not understood. The theories which have been proposed include the adsorption and decomposition of the organic compound with adsorbed hydrogen as the electrochemically active species (1, 3), direct reaction of the organic compound or an intermediary product (4-6), and oxidation by hydroxyl radicals (7). It has also been suggested that the cathodic evolution of hydrogen may accompany the anodic oxidation reaction (8). More recently Buck and Griffith (9) and Gilman and Breiter (10) have presented extensive voltammetric data and have interpreted these data on the tacit assumption that electron transfer is directly from the organic compounds.

The present paper will attempt to decide among the various hypotheses with regard to the electrochemical oxidation of formic acid. This compound was studied in order to avoid complications due to stable oxidation products intermediary to carbon dioxide formation. Open-circuit and polarization behavior of electrodes of smooth platinum and of two degrees of platinization were studied. Although it is known that the effects of impurities are magnified with smooth or low surface area electrodes, electrode polarization with high surface area electrodes is often due to limitations of mass transfer, which are extraneous to the purpose of this paper. The use of electrodes of various degrees of platinization also permits clarification of the role of platinizing in these systems, *i.e.*, whether specific catalytic activity is introduced, or whether increase in activity is due solely to increased surface area.

Experimental and Results

General Procedures.—Unless otherwise noted all data refer to experiments in 1.0N H₂SO₄ and all potentials are with respect to the hydrogen electrode at 1 atm in 1.0N H₂SO₄. All experiments were done at 23° ± 1°C in a temperature controlled room.

All chemicals employed were the highest purity grades available and unless otherwise noted, were used without further purification. Redistillation of triply distilled water from alkaline permanganate and percolation of formic acid over silica gel did not affect the results. The platinum used was stated to have an impurity content of less than 0.001%.

Three different electrodes were used, one bright platinum, one moderately covered with platinum black, and one more heavily coated with platinum black. The first two electrodes were wires, 0.8 mm in diameter and 20 mm long; the third was a square, 1.0 cm on a side. All electrodes were sealed in the (Pyrex glass) extensions of male standard taper joints.

The square electrode and one of the wire electrodes were platinized in a solution of 2% H₂PtCl₆ in 1.0M HCl at a current density of 2.0 ma/cm² of electrode area for periods of 60 min and 5 min, respectively. The counterelectrode in this procedure was a perforated cylinder of platinum. The solution was stirred by a magnetic stirrer and the electrode being platinized was rotated several times during the course of the platinization.

The cell used was a 100 ml round bottom flask with four standard taper joint necks. The counterelectrode was a platinum wire, also sealed in glass, but with a capillary opening to permit venting of the gas formed at this electrode. A fritted glass disk separated the counterelectrode compartment from the bulk solution. A saturated calomel electrode with a fine capillary tip was connected to the cell through a bridge of solution of the same composition as that used in the experiment. This bridge, which contained a plug of glass wool, terminated in a fine capillary which extended to within a few millimeters of the working electrode.

Highest purity nitrogen was bubbled successively through alkaline pyrogallol, distilled water, and a solution of the same composition as used in the experiment proper, before being bubbled through the solution at a rapid rate. Bubbling of N₂ was continued for 1-2 hr before each experiment was started. Unless otherwise stated, all experiments were conducted with bubbling at a rate sufficiently rapid so that further increases in the bubbling rate did not affect the potential.

Currents were measured to ±1% with a multi-range ammeter which had been calibrated by accurately measuring the potential drop across a known resistance with various current flows. The current source was a 45v dry cell battery in series with a variable resistance.

Potentials were measured with a high impedance Keithley electrometer, since the small currents drawn by most potentiometers on or approaching balance would be significant as compared to the currents used with the smooth platinum electrode. A Varian potential recorder, with a maximum speed of 8 in./min, was placed across the recorder output terminals of the Keithley. In some cases a Leeds and Northrup K-2 potentiometer was used for more accurate measurement.

The potential of the saturated calomel electrode, in contact with a 1.0N solution of sulfuric acid, was found to be +0.267v with respect to a platinized platinum electrode immersed in the acid solution after hydrogen bubbling had been substituted for nitrogen. Potentials in solutions of other acid contents were put on this hydrogen scale with no correction made for the change in liquid junction potential with solution composition. The difference in junction potential between saturated KCl and concentrated acid and alkali solutions, respectively, is of the order of 0.020v.

Carbon dioxide was determined by sweeping nitrogen through the solution and bubbling the effluent gas through a fritted glass gas bubbler immersed in 20 ml of 0.0050N Ba(OH)₂ for 30 min. The change in concentration of the Ba(OH)₂ solution was determined conductometrically, by comparison with a calibration curve previously established. The "blank" measurement, with no electrode in the cell, was 0.002 meq of CO₂. Experiments in which known quantities of CO₂ were generated, by addition of known aliquots of K₂CO₃ solution to the sulfuric acid solution, agreed to within 5% of theoretical.

Electrode Characteristics

The "true" surface areas of the platinum electrodes were determined (in 1.0N H₂SO₄) by two methods, double layer capacitance and quantity of PtO formed on anodizing to a given voltage. In the former method, the electrode was made anodic at a current density sufficient to maintain a steady state potential of +1.25 to +1.50v, placed on open circuit for 5 min and made cathodic at a current sufficiently large so that reduction of PtO occurs within minutes, but sufficiently small so that the transition in potential in the region in which only double layer charging occurs took place over readily measurable time periods. The double layer capacitance was determined by dividing the cathodic current by the rate of voltage change in the region +0.65 to +0.45v. In this region the voltage-time course was always found to be linear. The results were not significantly dependent on the preanodization current or on the cathodic current. The method of determining relative surface areas from the quantity of PtO formed at a given potential of anodization is based on the observation of Laitinen and Enke (11) that the quantity of PtO formed at a given anodization potential is, except for very short periods of time, independent of the length of time for which the electrode is held at that potential. The anodic current necessary to maintain a steady state potential of +1.52v was determined empirically for each electrode. The electrode was held at that potential for various periods of time, and after a 5 min open circuit stand, made cathodic at the same current used for the anodic treatment. The time for reduction of the potential to +0.45v was recorded. The drop in potential below +0.60v is rapid so that little error is involved in estimating the end of the reduction. The number of coulombs of PtO formed was found to be independent of the time for which the electrode was held at the given anodization voltage. The true areas were determined on the basis of 24 $\mu\text{F}/\text{cm}^2$ for double layer capacity and 0.70 millicoulombs/cm² of PtO formed at 1.52v (11). A summary of the characteristics of the three platinum electrodes used is given in Table I. The results of the two methods are seen to agree within a factor of 2.

Polarization Behavior

On exposing electrodes No. 1 and No. 2 to formic acid solution, the potential rapidly dropped to some minimum value, remained constant there for up to a minute, and then slowly began to increase toward more anodic values becoming constant in an hour at potentials about 0.2v more positive than the minimum previously attained. With electrode 3 the minimum in the open circuit potential was maintained for at least 2 hr to $\pm 0.001\text{v}$; after a 16 hr period the

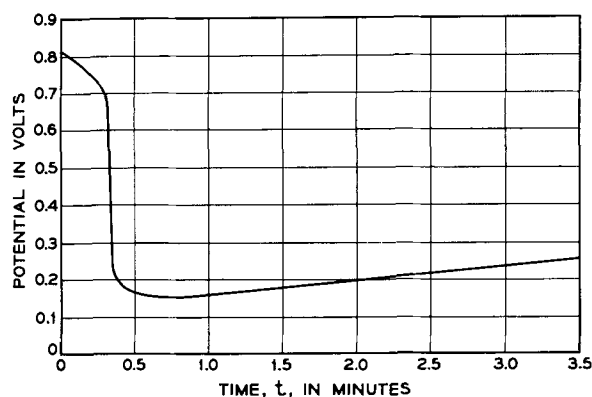


Fig. 1. Behavior of platinum electrode following exposure to formic acid solution. Electrode No. 1, 0.1M HCOOH, 1.0N H₂SO₄.

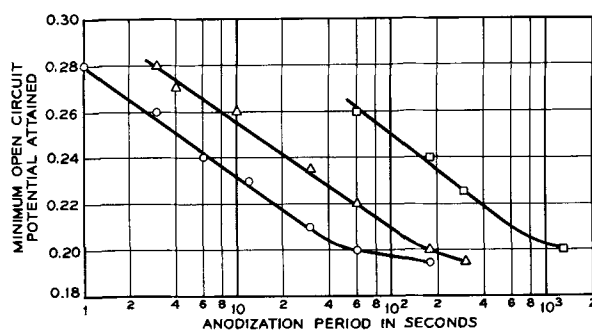


Fig. 2. Minimum open circuit potential attained in formic acid solution as a function of time of preanodization. Electrode No. 2, 0.010M HCOOH, 1.0N H₂SO₄. \circ , $i = 600 \times 10^{-6}$ amp/cm², $E = 0.74$ to 0.76v ; \triangle , $i = 300 \times 10^{-6}$, $E = 0.55$ to 0.65 ; \square , $i = 150 \times 10^{-6}$, $E = 0.55$.

potential increased by approximately 0.1v. Similar behavior was encountered when the electrodes were placed on open circuit following passage of an anodic current. Figure 1 shows the changes in potential with time for electrode No. 2 following immersion in 0.010M HCOOH in 1.0N H₂SO₄. Figure 2 indicates the minimum open circuit potentials obtained after ceasing anodic polarization, as a function of anodizing conditions. If the electrode was anodized at potentials greater than 1.35v, the resultant minimum potential was independent of both time and current of anodization. The minimum open circuit potentials obtained under these conditions were, for solutions of the same composition, the same for electrodes No. 1 and No. 2, and further, equal to the originally constant potential attained with electrode No. 3. Qualitatively similar behavior was obtained in 1.0M HClO₄ solution and in methanol-sulfuric acid solution. The following procedure was adopted in obtaining each polarization point with electrodes No. 1 and No. 2. The electrodes (immersed in the formic acid, sulfuric acid solution) were first sub-

Table I. Characteristics of Electrodes

Number	Form	Apparent area, cm ²	Double layer capacity, μF	PtO formed at 1.52v, mcoul	True area from D.L. capacity, cm ²	True area from PtO formation, cm ²
1	Wire	0.32	18	0.40	0.75	0.57
2	Wire	0.32	1,300	22	54	31
3	Square	2.0	240,000	3200	10,000	4600

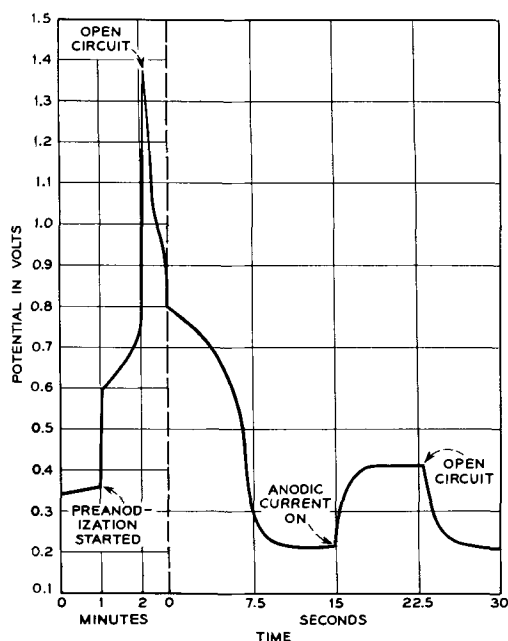


Fig. 3. Electrode potential during preanodization and anodic polarization measurements. Electrode No. 2, 0.01M HCOOH, 1.0N H₂SO₄, $i = 400 \times 10^{-6}$ amp.

ject to preanodization at currents of 200 μ a, and 4 ma, respectively, until the potential reached +1.35v. The system was then placed on open circuit and the potential allowed to decay through the platinum oxide and double layer regions until it was observed to remain constant at its minimum for about 5 sec. The anodic current of the desired magnitude was then initiated and continued for another 5 sec. The system was then open circuited, whereupon the potential returned to the neighborhood of the original open circuit value. This procedure is analogous to that used by Breiter (8) in the study of the adsorption of methyl alcohol. For about 90% of the runs, the second open circuit potential was within 0.010v of the first; measurements in which the discrepancy was greater were not accepted. A plot of this potential time sequence is shown in Fig. 3. Usually a series of measurements with increasing anodic currents were first made, followed by a series with decreasing anodic currents and concluded by a series with increasing anodic currents. The open circuit potentials and polarizations obtained in this way were reproducible to ± 0.01 v.

Figure 4 indicates a comparison of polarization

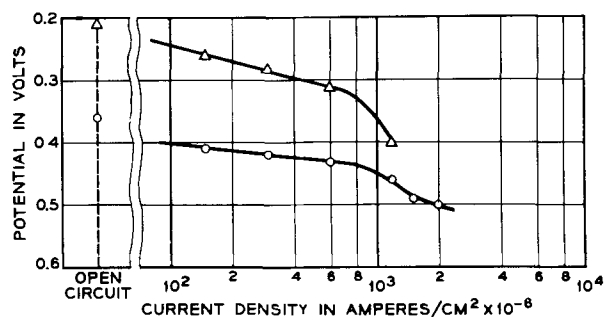


Fig. 4. Comparison of anodic polarization data with and without preanodization. Electrode No. 2, 0.010M HCOOH. Δ with preanodization, \circ without preanodization.

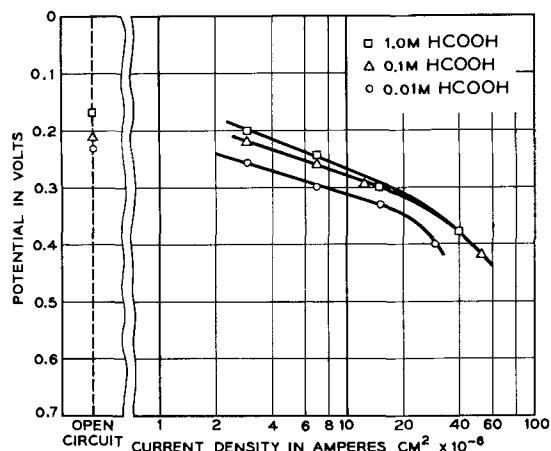


Fig. 5. Electrode potential as a function of current density (apparent area). Electrode 1, 1.0N H₂SO₄.

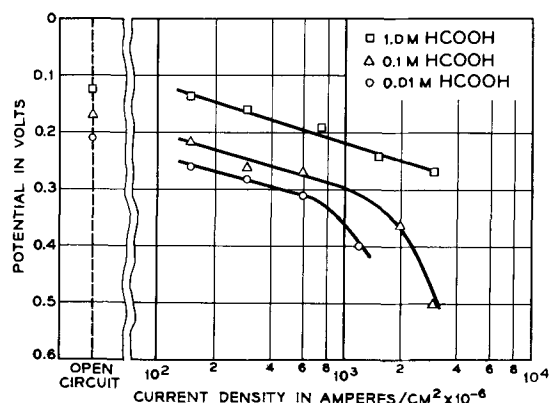


Fig. 6. Electrode potential as a function of current density (apparent area). Electrode 2.

data for electrode No. 2 as obtained using the preanodization technique and as obtained with no preanodization. In the latter case the electrode was on open circuit for 5 min between the measurements at the various currents. No effect of preanodization on polarization was noted in the case of electrode No. 3. In Fig. 5, 6, and 7 the potentials as a function of current density on a superficial area basis are shown for electrodes 1, 2, and 3 in 0.01, 0.10, and 1.0M HCOOH in 1.0N H₂SO₄ solution. In Fig. 8, the open circuit potentials are shown as a function of solution pH for electrode 3 in 1.0M HCOOH.

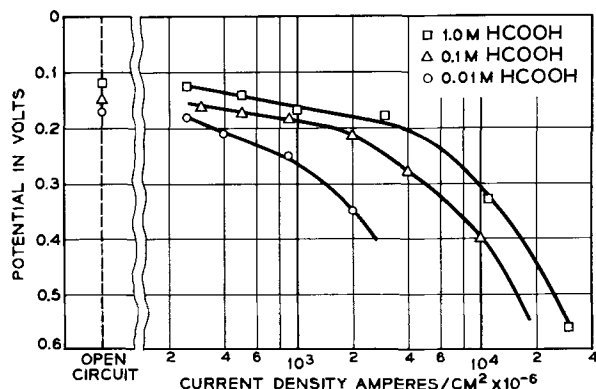


Fig. 7. Electrode potential as a function of current density (apparent area). Electrode 3.

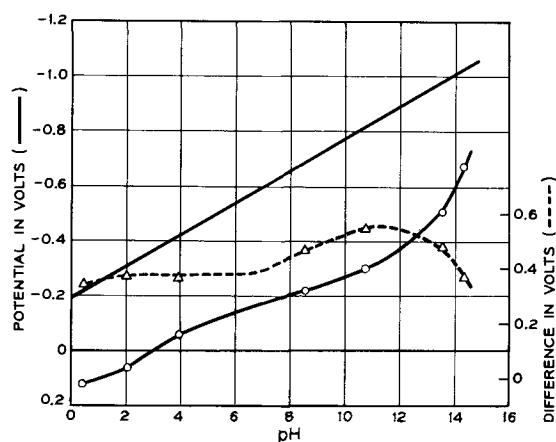


Fig. 8. Open circuit potential as a function of pH, O, Electrode 3, 1.0M HCOOH. Theoretical curve for HCOOH electrode, and difference, Δ , between observed and theoretical potentials also included.

When electrodes 1 and 2 were anodically polarized at low current densities, with no preliminary anodization treatment, the potential rapidly attained a value at which it stayed constant for a few minutes and then slowly decreased by about 20–50 mv, arriving at a new constant value. Buck and Griffith (9) reported that a similar maximum in the polarization occurred when a platinized platinum electrode was in contact with the solution for 10 min prior to passage of an anodic current, and that it did not occur when the anodic current was initiated within a minute of contact of the electrode with the solution.¹

When the current was permitted to flow for more than a few minutes at the higher current densities, wide periodic oscillations in potential were obtained with electrodes 1 and 2, and more moderate variations were obtained with electrode 3. These effects are illustrated in Fig. 9a and b for electrodes No. 1 and No. 3 in 0.10M HCOOH. The wide oscillations observed with electrodes 1 and 2 invariably terminated with the potential rising above 1.25v and remaining there until the current was stopped. The moderate fluctuations in potential obtained with electrode 3 could apparently be maintained indefinitely. These phenomena were not studied in detail, but some data on the currents and times of current

¹ Enke *et al.* (13) have recently attributed "activation" by pre-anodization to the presence of a residual partially reduced oxide of platinum which is left on the electrode after cathode reduction of the oxide formed at higher voltage ($>1.25v$). In view of the data of Fig. 2, in which "activation" is attained following anodization at voltages as low as 0.55v, this explanation is not believed to apply to the "activation" process encountered here.

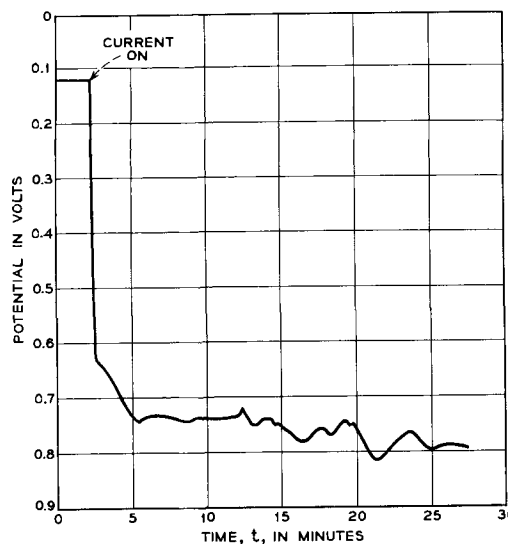
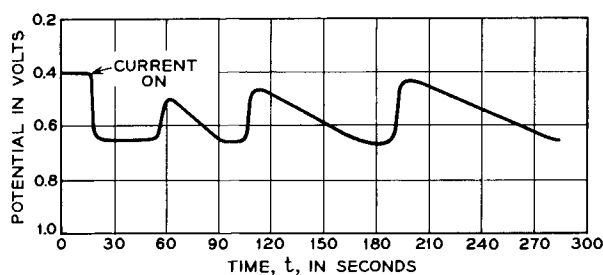


Fig. 9. Periodic potential behavior, 0.10M HCOOH, 1.0N H₂SO₄. a. Electrode No. 1, $i = 60 \mu\text{a}/\text{cm}^2$. b. Electrode No. 3, $i = 24 \text{ma}/\text{cm}^2$.

flow at which periodic behavior was observed are shown in Table II. Periodic behavior was also observed with HClO₄ as electrolyte, and with methanol.

Reaction Products

Within the limits of the analytical procedure used, the only product of the anodic oxidation is CO₂. In Table III, the yields of carbon dioxide obtained are shown as a function of current. Particular attention was paid to the verification of CO₂ formation on open circuit.

No formaldehyde could be detected in 100 ml of 1.0N H₂SO₄, 1.0M formic acid solution in which electrode 3 was immersed for 16 hr, using a procedure which could detect formaldehyde at concentrations as low as 10⁻⁷ moles/liter (14). Thus formaldehyde as formed by catalytic disproportionation of formic acid at platinum, is ruled out as the reactive electrochemical species.

Table II. Oscillatory behavior

Electrode No.	Solution concentration, moles/liter	Anodizing current, amp/cm ²	Preoscillatory steady-state potential, v	Period for which steady-state potential was maintained, min	Maximum potential observed during oscillations, v	Minimum potential observed during oscillations, v
1	0.10	15 × 10 ⁻⁶	+0.45	>30	None observed	
		30 × 10 ⁻⁶	+0.50	5	+0.74	+0.41
		60 × 10 ⁻⁶	+0.65	0.5	+0.74	+0.40
2	0.01	0.6 × 10 ⁻³	+0.43	>30	None observed	
		1.2 × 10 ⁻³	+0.46	1	+0.75	+0.35
		1.6 × 10 ⁻³	+0.49	0.5	+0.85	+0.43
		2.0 × 10 ⁻³	+0.50	0.25	+0.86	+0.42
		4.0 × 10 ⁻³	+0.56	>30	None observed	
3	1.0	8.0 × 10 ⁻³	+0.60	2	+0.75	+0.46
		11 × 10 ⁻³	+0.34	>30	None observed	
		24 × 10 ⁻³	+0.61	1	+0.82	+0.74

Table III. Rates of carbon dioxide formation, electrode 3, 1.0N H₂SO₄, 1.0M HCOOH

<i>i</i> , amp/cm ²	CO ₂ formation rate, meq/hr cm ²	Current equivalent of CO ₂ formation rate, ma/cm ²
Anodic		
0.00	1.85 ± 0.08 × 10 ⁻³ (four runs)	0.050 ± 0.002
0.050 × 10 ⁻³	3.5 ± 0.2 × 10 ⁻³ (four runs)	0.095 ± 0.007
0.25 × 10 ⁻³	10.5 × 10 ⁻³	0.28
0.50 × 10 ⁻³	20 × 10 ⁻³	0.54
1.0 × 10 ⁻³	38 × 10 ⁻³	1.02
Cathodic		
0.15 × 10 ⁻³ (<i>E</i> = +0.020v)	0.25 ± 0.05 × 10 ⁻³	0.007 ± 0.002

Effect of Formic Acid on Hydrogen Potentials

Formic acid was not found to have any effect on the response of the electrodes to hydrogen. The same open circuit potential (±0.001v) was obtained by electrode 3 on introducing H₂ gas into the system both in the presence and absence of formic acid. The cathodic hydrogen evolution characteristics are not affected by the presence of formic acid. In Fig. 10, the hydrogen overvoltage is shown as a function of current for electrode No. 1 and various formic acid concentrations.

Effect of Carbon Dioxide on Formic Acid Open Circuit Potentials

Switching from nitrogen bubbling to carbon dioxide bubbling did not affect the open circuit potential of electrode 3 in 1.0N H₂SO₄, 0.10M HCOOH (Δ*E* < 0.001v). Bubbling of CO₂ was continued for 1-2 hr, so that it may be assumed that the solution was saturated with CO₂ under these conditions. Also, in alkaline solution, addition of potassium carbonate sufficient to increase the carbonate concentration of 1.0N KOH, 0.10M HCOOK solution to 0.10M, did not affect the open circuit potential (22).

Discussion

In Fig. 11 the polarization curves of the three electrodes are plotted on a "true" area basis, with "true" area here being defined by the double layer capacity. A similar series of curves would have been obtained if the areas determined from PtO formation were used for true areas, since the ratio of the areas obtained by the two methods are essentially constant. Except for points for which the current

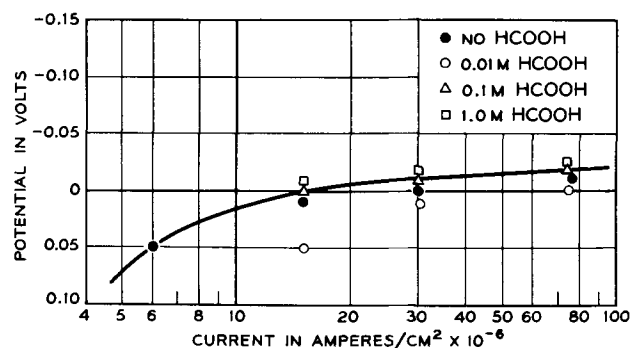


Fig. 10. Cathodic hydrogen overvoltage in 1.0N H₂SO₄ for electrode 2 in 1.0N H₂SO₄ solutions of various HCOOH contents.

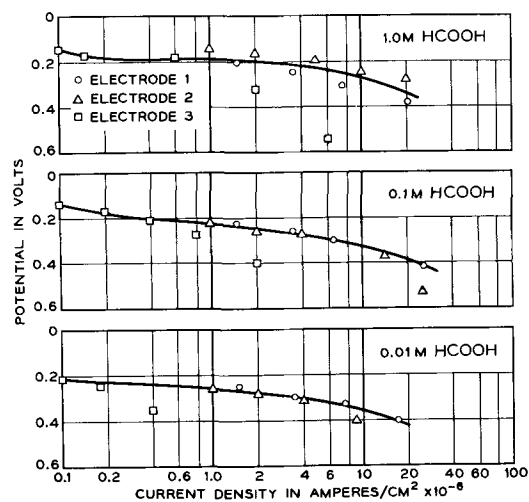


Fig. 11. Electrode potential as a function of current density (true area basis).

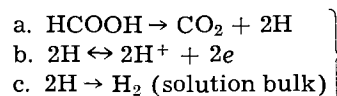
densities on an apparent area basis are greater than 2 × 10⁻³ amp/cm² in 0.010M and 0.10M solutions, and 10⁻² amp/cm² in 1.0M solutions, and at which therefore concentration polarization is likely to be significant, the data for the three electrodes are quite similar. This indicates that the only effect of platinization is to increase the true area of the electrode and that there is no introduction of catalytic sites specific for the oxidation reaction. It also indicates that the polarization data for the three electrodes, considered on a true area basis, may be treated as a unit using the curves of Fig. 11.

The open circuit potential which is calculated for the reversible reaction



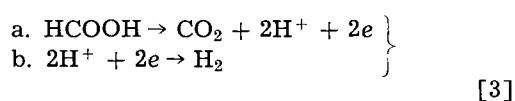
is -0.196v at unit activity of reactants and products (16). Since the activity of carbon dioxide in the solution was kept well below that in equilibrium with 1 atm of the gas, the open circuit potential should be significantly more negative than this value. Thus the values of +0.12 to +0.17v which were obtained indicate that there must be some irreversible step in the oxidation of formic acid to carbon dioxide. Of the various mechanisms which have been proposed, the most important distinction to be made is between those which indicate a direct reaction of the formic acid at the electrode and those in which a preliminary decomposition of formic acid occurs, followed by electrochemical oxidation of the resulting hydrogen. The suggestion that hydroxyl radicals, formed by the discharge of water molecules, are responsible for the reaction need no longer be considered, since it is now fairly well established that discharge of water does not begin at potential less than almost half a volt more anodic than the observed open circuit potentials (14).

Preliminary decomposition of formic acid and subsequent oxidation of hydrogen may be indicated by the following over-all scheme



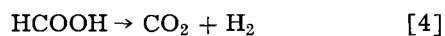
The first step here is meant to include all mechanisms of nonelectrochemical formation of oxidizable hydrogen at a rate which is independent of electrode potential. The third step here indicates that some of the hydrogen formed diffuses away from the electrode. It is this step which would be responsible for the irreversible behavior, since in its absence on open circuit hydrogen would accumulate on the electrode until reaction [2a] attained equilibrium. This equilibrium quantity of hydrogen would then give rise, via reaction [2b], to the open circuit potential calculated for the over-all reaction occurring reversibly.

Alternately, the simplest scheme for an irreversible process involving the direct extraction of electrons from formic acid is that of a mixed potential process, in which hydrogen is evolved cathodically at the same rate as formic acid reacts anodically on open circuit, *i.e.*,



Reactions [3a] and [3b] are meant to signify over-all electrochemical reactions; it is not meant to imply that the mechanisms of these reactions are necessarily as simple as the equations indicate.²

On open circuit the sum of reactions [2, a, b, c] are equal to those of [3 a, b], stoichiometrically, *i.e.*,



However the mechanisms can be distinguished by the rates at which CO₂ formation on open circuit would have to occur in order to be consistent with the open circuit and polarization potential data observed. Thus the decomposition reaction, [2a], would have to occur at a rate at least equal to the current which can be continuously drawn without causing large degrees of polarization. Otherwise, at currents greater than the rate of reaction [2a], the quantity of hydrogen at the electrode would soon be depleted and the potential would increase to that characteristic of the next process possible, here oxidation of platinum. According to Fig. 7, a current of 3 x 10⁻³ amp/cm² can be passed through electrode 3 with only 0.060v of polarization in 1.0M HCOOH and up to 11 x 10⁻³ amp/cm² could be passed for long time periods at constant polarization. However, according to Table II, the rate of reaction [4], which is the rate of CO₂ formation on open circuit, is only 55 x 10⁻⁶ amp/cm². Even if the rate of production of oxidizable hydrogen atoms were equal to the rate of formic acid decomposition, this reaction rate is clearly too small to account for the low polarization observed. Further, the data of Table III indicate that the rate of CO₂ formation at low anodic currents is the sum of that produced by the current and that produced on open circuit. This indicates that even if hydrogen were formed by decomposition of formic acid, it would be necessary to conclude that it dif-

fused away from the electrode before it could be anodically oxidized. Hydrogen formed by a nonelectrochemical decomposition process is apparently not a significant factor in the electrochemical behavior of the system.

On the basis of the mixed potential model, the rate of reaction [4] corresponds to the currents necessary to polarize reactions [3a and b] anodically and cathodically, respectively, to the same potential. At currents corresponding to potentials 50-100 mv more positive than the observed open circuit potentials the rate of reaction [3b] would be small compared to that of [3a] and the slope of the curves of Fig. 11 in this region may be taken as corresponding to reaction [3a]. Thus as indicated by Fig. 11 this reaction is polarized to the extent of approximately 0.10v per decade of current, and since the potential at, *e.g.*, 1 x 10⁻⁶ amp/cm² of true area, corresponds to ~0.38v of polarization from the calculated reversible potential (-0.20 -0.18v), the exchange current density for reaction [3a] is at least 4 decades less than this measured current density, or 10⁻¹⁰ amp/cm² of true area. This is an upper limit for this quantity, since the true open circuit potential, corresponding to the presence of far less than unit activity of carbon dioxide, is less than -0.20v. The rates of reactions [3a and b] on open circuit can be estimated in several ways. The order of magnitude of the maximum currents which can be drawn without significantly increasing the potential above the measured open circuit potential is from Fig. 11, about 0.1 x 10⁻⁶ amp/cm² of true area. Since lower currents are therefore insignificant compared to the open circuit currents, this must also be the order of magnitude of the rates of reaction on open circuit. From the data of Fig. 10, which indicate that the hydrogen evolution characteristics are not significantly modified by the presence of formic acid, a cathodic current of 3 x 10⁻⁶ amp/cm² of superficial area, or 0.06 x 10⁻⁶ amp/cm² of true area is required to polarize electrode 2 to the open circuit potential observed with formic acid. The rate of CO₂ production on open circuit obtained with electrode 3 corresponds to 0.01 x 10⁻⁶ amp/cm² of true area. This degree of agreement among the three methods is considered to be good.

The mixed potential hypothesis is also consistent with the dependence of the open circuit potential on formic acid concentration, 0.032 ± 0.008v per decade of concentration and the lack of dependence on carbonate or carbon dioxide concentration. At potentials about 100 mv removed from the open circuit potential, the rate of the reverse reaction is completely negligible and changes in the concentrations of reactants for the reverse reaction have no effect on the potential. The rate of the forward reaction is, of course, significant and dependent on the concentration of reactants at all potentials. Similarly, the mixed potential hypothesis is consistent with the observation that the rate of CO₂ formation at low currents is equal to that produced on open circuit plus that calculated from the current. The cathodic reduction of hydrogen ions will occur as long as the potential is not far removed from the observed open

² A reaction sequence involving the rapid decomposition of formic acid to CO, followed by electrochemical oxidation of the CO to CO₂, cannot be distinguished on this basis from the direct reaction of formic acid, since the standard potentials of the two reactions are similar.

circuit value, irrespective of whether or not there is a net anodic current.

Finally, the marked decrease in the rate of CO_2 evolution on making the electrode potential more negative than the open circuit value by passing a cathodic current (Table III), is a most convincing indication that the formation of CO_2 on open circuit is the result of an electrochemical process, and that the open circuit potential is a mixed potential.

Since the open circuit potentials are resultants of two irreversible processes, it is not surprising that the dependence on solution pH is not simple. The rates of the cathodic and anodic reactions depend on the concentrations of reactive species at the electrode solution interface, which in turn are functions of the charge on these species, the charge on the electrode, and the total salt concentration. The dissociation constant of formic acid is 1.8×10^{-4} . Thus at pH values less than 4, the species being anodically oxidized is HCOOH , while at pH greater than 4, the dominant species is HCOO^- . The increase in deviation from the theoretical potential at pH 4 in Fig. 8 is probably due to the change from HCOOH to HCOO^- as the reactive species. The effect of pH on the cathodic hydrogen evolution on platinum is not large. The maximum change with pH, of polarizations at constant currents of even greater than the magnitudes of interest here, $\leq 100 \times 10^{-6}$ amp/cm², is about 10 mv over the range pH 1-12 (17).

Oscillatory behavior of the potential, at constant currents, has been previously observed at platinum electrodes in sulfuric acid solutions during oxidation of methanol (18) and hydrogen (19). In the former case, the increase in potential was ascribed to the depletion of methanol from the neighborhood of the electrode due to its reaction. The subsequent fall of potential was ascribed to the reaccumulation of the methanol as current went into the higher potential process, oxidation of platinum. It was necessary to assume that the electrochemical oxidation of methanol did not occur on the oxidized platinum surface and that the latter was reduced by a nonelectrochemical process at a rate which was less than the rate of diffusion of methanol to the electrode. Although these latter assumptions have been found to be valid (20), it is not believed that this explanation holds for the data presented in Table II. The current densities in Table II are not high enough (except for electrode No. 3) for concentration polarization to be significant. Indeed, in the case of electrode No. 1, the lowest current density at which periodic behavior was observed would require a period of some 10^6 sec for depletion of formic acid molecules at the surface of the electrode even if all stirring were absent and formic acid molecules arrived at the electrode solely by diffusion [as indicated by the standard constant current potentiometry equation (21)]. Second, it is now known that oxidation of platinum does not occur until potentials of $\sim 0.8\text{v}$ are attained (15). The potentials attained at the maxima in the oscillations did not exceed this value in the present work in several instances, or 0.75v in reference (18). The explanation given for the oscillatory behavior in the case of hydrogen (19)

was that the latter is depleted at the electrode surface and that hydrogen dissolved in the electrode becomes the electrochemically active species, being oxidized in the region 0.4 to 1.0v. Activation of the electrode at the higher potentials was cited as a contributory factor in the recovery of the electrode to lower potentials. It is believed that a similar explanation holds for the data presented in this paper. Formic acid which has been adsorbed onto the electrode is depleted as a result of the anodic current and the potential increases. At the same time the electrode is activated so that the rate of adsorption of formic acid increases, until it becomes greater than the anodic current, the potential thereupon decreasing. There is direct evidence for the adsorption of methyl alcohol on platinum in the potential region of interest here (8, 18). The necessity for an adsorption step, prior to the electron transfer step of reaction [3a], is also indicated by the fact that other metals, mercury and bright gold, do not respond to formic acid addition (22). The same activation process may well be responsible for the periodic behavior, the minimum in the open circuit potential following anodic polarization, and the decrease in potential after a few minutes of current flow. One possibility is the removal of impurities from the electrode by oxidation at the higher potentials.

Manuscript received April 8, 1963; revised manuscript received Nov. 18, 1963.

Any discussion of this paper will appear in a Discussion Section to be published in the December 1964 JOURNAL.

REFERENCES

1. E. Muller, *Z. Electrochem.*, **29**, 264 (1923).
2. See, for example, Abstracts of Papers presented at Electrochemical Society Meeting, Chicago, May 1962.
3. G. V. Elmore and H. A. Tanner, *This Journal*, **108**, 669 (1961).
4. R. P. Buck *et al.* Proceeding 15th Annual Power Sources Conference, USASRDL (1961).
5. T. O. Pavela, *Ann. Acad. Sci. Fennicae* (1954).
6. A. K. Korolev and A. J. Shlygin, *Zhur. Fizi. Khim. U.S.S.R.* **XXXVI**, 314 (1962).
7. A. Hickling and F. Rodwell, *J. Chem. Soc.*, 90 (1943).
8. M. V. Breiter and S. Gilman, *This Journal*, **109**, 622 (1962).
9. R. P. Buck and L. R. Griffith, *ibid.*, **109**, 1005 (1962).
10. S. Gilman and M. W. Breiter, *ibid.*, **109**, 1099 (1962).
11. H. A. Laitinen and C. Enke, *ibid.*, **107**, 773 (1959).
12. M. W. Breiter, *ibid.*, **109**, 425 (1962).
13. S. W. Feldberg, C. G. Enke, and C. E. Bricker, *ibid.*, **110**, 826 (1963).
14. F. Feigl, "Spot Tests," 2nd English Edition, p. 328, Nordeman Publishing Co., New York (1939).
15. W. Bold and M. Breiter, *Electrochim. Acta*, **5**, 145 (1961).
16. W. M. Latimer, "Oxidation Potentials," 2nd Edition, p. 130, Prentice Hall, New York (1952).
17. S. Schuldiner, *This Journal*, **101**, 426 (1954).
18. T. O. Pavela, *Suomen Kemistelehti*, **B30**, 138 (1957).
19. G. Armstrong and J. A. V. Butler, *Disc. Faraday Soc.*, 122 (1947).
20. M. H. Gottlieb, In preparation.
21. P. Delahay, "New Instrumental Methods in Electrochemistry," p. 182, Interscience Publishers, New York (1954).
22. Unpublished observations.

Cation-Exchange between Molten Salts and a Special Porcelain of High Sodium Content

R. J. Labrie

Metallurgy Division, National Bureau of Standards, Washington, D. C.

ABSTRACT

In an earlier paper a special porcelain of high sodium content, 7.16% by weight, was shown to serve as a membrane conductive to sodium ions, and it was therefore useful for molten salt experiments. Because of its importance to further experimental application, the ability of this material to rapidly undergo cation-exchange when immersed in certain molten salts is studied now. In melts of potassium, rubidium, or silver salts, exchange was complete and reversible; in melts of lithium, cuprous copper, and cesium salts, partial exchange or reaction took place. It was found possible to obtain mechanically sound pieces of porcelain which could serve as ion-conductive membranes after exchange by potassium, lithium, and silver. The porcelain did not have a strong enough retention for potassium, rubidium, or silver ions to separate them effectively from sodium ions in the molten mixtures which were studied.

A special porcelain of high sodium content, 7.16% by weight, has potential usefulness in experiments involving molten salts when a membrane having a fairly high sodium ion conductivity is required at high temperatures, as has been shown in experimental measurements of the transference numbers of the ions in molten sodium nitrate (1). In the course of these experiments it was noted that the porcelain was able to exchange cations rapidly with a variety of molten salts. Since such exchange must be understood and considered when using the porcelain in such applications, and because similarly useful porcelains conductive to other cations might be prepared by ion-exchange, a study of the exchange properties of this porcelain in molten salts seemed warranted.

That the sodium in glass can exchange with other cations from molten salts has long been known (2, 3). Some studies also have been made concerning ion-exchange between molten salts and minerals of a chemical composition somewhat similar to this porcelain (4, 5).

Over-all chemical composition of the porcelain used in this study, based on analysis of the clays as given by Meyer and Klinefelter (6), may be expressed as 53.1% SiO_2 , 35.4% Al_2O_3 , and 9.65% Na_2O by weight. Analysis of the fired porcelain showed a content of potassium equivalent to 0.2% K_2O . The body is white, smooth, and translucent, and completely nonporous. Despite its high sodium content, the material withstands temperatures as high as 1100°C before softening and loses only a small fraction of a milligram per square centimeter of surface area after an hour in boiling water. Its electrical conductivity is relatively high, about 100 times that of Pyrex glass at any given temperature (7). Conduction is by electromigration of sodium ions rather than electronic (7). Powder-diffraction x-ray analysis showed it to be mainly noncrystalline and to contain only a small amount of a crystalline component identified as mullite.

Experimental

Preparation of the porcelain.—In a one-gallon jar mill, 128g of anhydrous sodium silicate, Na_2SiO_3 , 107g of dried and finely ground alumina, 117g of powdered flint, 54g of Kentucky ball clay No. 4, and 71g of Georgia kaolin were milled dry with flint pebbles for 10 hr. The mixture was removed, packed into fire-clay crucibles, and fired for 4 hr at 1100°C to form a glass. This glass was crushed, ground to 200 mesh, and then milled dry for 10–15 hr. Then, to the total amount of the glass were added 142g of Kentucky ball clay, 111g of Georgia kaolin, and 400 to 500 ml of water. If a deflocculant seemed necessary, $\frac{1}{4}$ g of sodium silicate or carbonate was added, and the slip was milled for 10 to 12 hr. Slip casting was done in plaster of Paris forms (made of 40 parts of plaster to 36 parts of water). The green body was fired by heating at 150°C/hr to a temperature between 1205°–1260°C, equivalent to cones 5 through 8. Drying and firing shrinkage totaled about 16%.

Exchange procedure.—Specimens of porcelain used for ion-exchange experiments were tubes from 1 to 2 cm long, about 1 cm in diameter, and about 1 mm in wall thickness. Exchange took place more slowly with specimens in this form than with a powder, but weighing was facilitated, and physical changes such as erosion or cracking could be observed. Tubes were immersed in the melts to effect exchange. They were periodically removed, cooled, and cleaned of adhering melt by suitable chemical means in order to make weighings and observe physical changes. In general, the degree of exchange was judged from the weight change of the pieces especially when no chemical attack was evident. Pieces were weighed to the nearest tenth milligram on an analytical balance. At intervals fresh melt was used. Melt temperatures were maintained constant to about $\pm 10^\circ\text{C}$. In general they were as low as the salt or mixture allowed in order to minimize melt decomposition or evaporation.

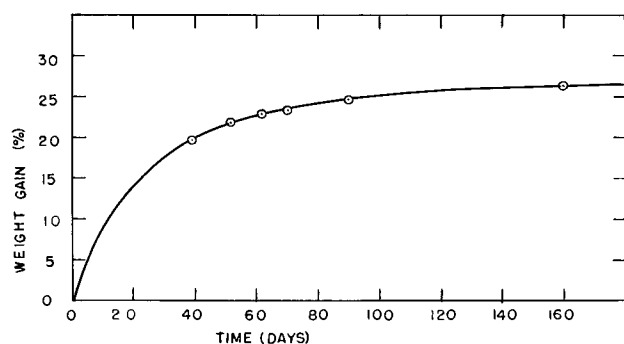


Fig. 1. Weight gain of the porcelain when immersed in molten silver nitrate at 220°-230°C.

Results

Silver.—Complete exchange of silver for sodium resulted from immersing a piece of the porcelain in molten silver nitrate at a temperature of 220°-230°C as indicated by weight increases shown in Fig. 1 and Table I. That the change of weight was due to exchange of silver for sodium was confirmed by analysis of another exchanged specimen, which contained 25.6% silver and approximately 0.25% sodium. The pieces did not crack nor appear to be reduced in strength by exchange, but acquired a pale cream color. An increase in temperature of 50°C approximately tripled the rate of exchange, but also caused slight etching of the porcelain.

A melt composed of one mole of silver nitrate and two moles of sodium nitrate exchanged at equilibrium 54% of the sodium which the porcelain initially contained. This result can be compared to that obtained by Guenterschulze and Mohr (8) who found that traces of silver were totally extracted by glass from a sodium nitrate melt but not from a sodium bromide melt.

The piece of porcelain containing 25.6% silver and 0.25% sodium by weight was immersed in molten sodium nitrate. It lost weight at a rate decreasing with time so that after 14 days the loss amounted to 20.1%, and no further weight loss took place. The final loss in weight was the amount to be expected by complete re-exchange of sodium ions for silver ions which shows the exchange to be reversible.

Potassium.—After immersion in molten KNO_3 for three days at 400°C, less than half of the sodium ions

were exchanged. The exchange by potassium ions caused considerable stress as evidenced by the disintegration of the porcelain to a coarse powder, and the continued disintegration of bits of this powder even after washing and drying.

Complete and stoichiometric exchange by potassium was obtained by immersing the porcelain in molten potassium chloride for 6-10 hr at 800°C as shown in Table I. However, this exchange invariably produced a few cracks, probably from stresses caused by uneven exchange throughout the entire piece of porcelain. Uncracked pieces could be obtained if the piece was exchanged stepwise, first using an equimolar melt of sodium and potassium chlorides, then pure potassium chloride. The composition shown in Table I of the porcelain exchanged in the equimolar melt is an equilibrium value. This was shown by the fact that the porcelain reached approximately the same composition starting with either unexchanged sodium porcelain, or with a porcelain completely exchanged by potassium. Pieces completely exchanged by potassium could be re-exchanged by sodium without cracking by immersing them in molten sodium nitrate.

Rubidium.—Immersion of the porcelain in molten rubidium chloride resulted in complete exchange of rubidium ions for sodium ions (Table I). The exchange always produced a few cracks even when gradual exchange was effected with a series of sodium chloride-rubidium chloride melts. A piece of porcelain exchanged by potassium gained the stoichiometric weight for complete exchange by rubidium ions when immersed in rubidium chloride, but also cracked in the process.

Hydrogen.—A piece of porcelain immersed in molten sodium bisulfate, which likely was somewhat decomposed at the temperature used, in the neighborhood of 300°C, lost 4.1% in weight after 20 days as shown in Fig. 2 and Table I. Theoretical weight loss corresponding to complete replacement is 7.0%. By analysis the sodium content of the piece was shown to be 3.0%, the amount to be expected if the 4.1% weight loss represents exchange of sodium by hydrogen ions. Ehrmann, deBilly, and Zarzycki have also shown that hydrogen from a molten acid sulfate, in this case ammonium bisulfate, can exchange for sodium in glass (9).

Lithium.—Ion-exchange that occurred when the porcelain was immersed in lithium nitrate at a

Table I. Melts which produce stoichiometric exchange

Melt composition, moles	Time, days	Weight change, %		
		Observed	For complete exchange*	Na exchanged
AgNO_3	159	26.3	26.8	98
KCl	0.5	5.1	5.0	100
1 KCl + NaCl	0.5	3.5-3.7		69-73
RbCl	4	20.0	19.7	100
0.14 RbCl + 0.86 NaCl	4**	3.7		19
0.33 RbCl + 0.67 NaCl	5**	7.8		40
0.59 RbCl + 0.41 NaCl	7**	10.8		54
NaHSO_4	20***	-4.1	-7.0	58

* Assuming exchange of 7.16% sodium and 0.17% potassium.

** The same piece of porcelain was immersed in each of this series of melts until no further weight change took place.

*** The experiment was halted at this point because the porcelain had broken into a number of small pieces even though equilibrium did not appear to have been reached. See Fig. 2.

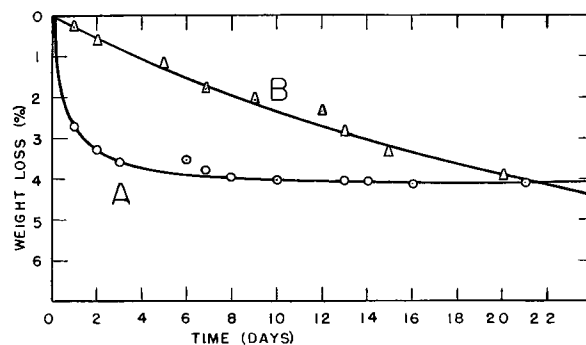


Fig. 2. Weight loss of the porcelain when immersed in: A. molten lithium nitrate, LiNO_3 , at 260°-270°C; B. molten sodium bisulfate, NaHSO_4 , in the neighborhood of 300°C.

temperature close to its melting point caused maximum weight loss within about 6 days, as shown in Fig. 2. The resulting porcelain was strong and uncracked, but was microscopically crazed. However, it was not porous as evidenced by the fact that the exchanged porcelain in the form of a closed tube would contain molten lithium nitrate to a depth of 3 cm for at least 8 hr without any leakage. It was hygroscopic, but immersing it in boiling water for a few minutes caused a small weight loss which appeared to be removal of the hygroscopic material. Higher melt temperature favored attack of the porcelain probably by decomposition products of the melt. A number of pieces showed an over-all weight loss of 4.0-4.2%. Analysis of one of these pieces after being boiled in water showed a loss of sodium equal to 87% of the sodium initially contained, and a gain of lithium sufficient to replace 100% of the sodium, which indicates that a side reaction took place.

Electrical conduction of the porcelain exchanged by lithium was due almost solely to migration of lithium ions as was shown by the following experiment. A test-tube-shaped piece of lithium-substituted porcelain, 3 cm long, containing molten lithium nitrate, was dipped into more lithium nitrate in a larger container so that the wall of the tube separated the two melts. A platinum anode was used in the tube at which the reaction, $2\text{NO}_3^- \rightarrow 2\text{NO}_2 + \text{O}_2 + 2e^-$ was assumed to take place stoichiometrically. The changes in weight of the tube and of the contents were measured, corresponding to passage of a known charge between the internal and external electrodes. Loss of lithium nitrate amounted to 1.2757g when 1785 coulombs was passed. Theoretical weight loss would be 1.2759g. Passage of 1966 coulombs caused the porcelain to lose 0.1% in weight, and another 1800 coulombs caused a further weight loss of only 0.04%, although the total charge was sufficient to replace all of the lithium and sodium in the porcelain tube about 10 times.

Copper, cesium, and thallium.—The weight gains shown in Table II, corresponding to immersion of porcelain tubes in cuprous chloride and cesium bromide, are the maxima which occurred even with continued immersion. In molten thallium chloride pieces of porcelain continued to gain weight slowly. No chemical analyses of the porcelain pieces were made after immersion in any of these melts, and consequently it cannot be stated with certainty that the weight gains were due to ion-exchange for sodium. Immersion in cuprous chloride caused

Table II. Melts which produced exchange of uncertain stoichiometry

Melt	Time, days	Weight change, %		Appearance after immersion
		Observed	For complete exchange	
LiNO_3	10	-4.0 to -4.2	-5.2	Surface crazed but strong and non-porous
CuCl	34	6.3	12.8	Surface crazed but strong. Olive-green
CsBr	9	6.7	34.7	Surface roughened
TlCl	20	3.9	57.3	No change

Table III. Melts which did not produce ion-exchange

Melt composition, moles	Time, days	Weight change, %	
		Observed	For complete exchange
1 NH_4NO_3 + 0.14 NaNO_3 + 0.08 NaCl	13	0.0	-1.7
1 NH_4NO_3 + 0.2 NH_4Cl	1	-0.05	-1.7
1 MgCl_2 + 1.3 NaCl	5	0.2	-3.5
1 $\text{Ca}(\text{NO}_3)_2$ + 2 $\text{Na}(\text{NO}_3)$	10	0.1	-1.0
BaCl_2	2	0.7	14.4
ZnCl_2	18	-0.5	3.0
PbCl_2	12	0.0	25.4
1 CdCl_2 + 1 NaCl	7	0.0	10.4

the porcelain tube to acquire an olive-green color through its entire thickness. Its surface was slightly crazed, but the tube remained quite strong. After standing in air, a whitish, powdery coating developed. Immersion of sodium-porcelain in cesium bromide caused only a slight etching of the surface; and in thallium chloride no observable change in appearance or strength resulted.

Ions not exchanging.—A molten mixture of ammonium nitrate and ammonium chloride at 140°C was used to test for exchange by ammonium ion. None occurred.

No significant weight change occurred in melts containing divalent ions as shown in Table III. The small weight changes which did occur were likely due to chemical attack of the surface of the porcelain by the melt.

Crystallinity and electrical conductivity of exchanged porcelain.—If immersion of the porcelain in molten salt produces a chemical reaction, instead of ion-exchange, then probably the products of the reaction would be sufficiently crystalline to yield significant x-ray patterns, so powder diffraction patterns of the porcelain after exchange for silver, copper, lithium, potassium, and rubidium were taken. They showed the same lack of crystallinity, except for the presence of a small amount of mullite, as did the pattern for the unexchanged sodium porcelain.

Approximate measurements of the electrical conductivity of the porcelain exchanged by silver or lithium showed that for each material it is the same order as that of the sodium porcelain. It is likely that electrical conduction in porcelain exchanged by other ions would occur by migration of the exchanged ion, as was the case for porcelain exchanged by lithium, but experiments were not performed to demonstrate this.

Discussion

The ease with which this porcelain undergoes ion-exchange is consistent with its high ionic conductivity, inasmuch as the process in both cases involves the migration of ions. This high conductivity, which is about one hundred times that of Pyrex glass, can be accounted for if the porcelain is pictured as being composed of two phases, one mullite, $3\text{Al}_2\text{O}_3 \cdot 2\text{SiO}_2$, a poor electrical conductor, and the other a glass which has good conductivity. If some of the alumina content of the porcelain is present in the mullite phase, then the composition of the

glass phase would be such that its electrical conductivity approximates that of the porcelain. Bryson (10) has measured the electrical conductivity of a series of glasses which, starting with the approximate composition, $\text{Na}_2\text{O} \cdot 4\text{SiO}_2$, were formed by replacement of varying amounts of silica by alumina. His data show that a composition which contains about 5 mole per cent alumina would be about as conductive as this porcelain and so could be similar in composition to the glassy phase. Moreover, a two phase structure, one phase mullite and the other a glass, is consistent with the x-ray information. It must be realized, however, that the porcelain probably has some of the properties of a colloidal system, and so its properties will differ from those expected of a simple mixture of mullite and glass. For instance, a glass which has the composition of the glass phase might soften considerably at 500°C and might lack other desirable properties that this porcelain has, such as low coefficient of thermal expansion and good mechanical strength.

The fragmentation of the porcelain when exchanged by potassium ions from potassium nitrate but not from potassium chloride is of interest. A potassium ion occupies about twice the volume of a sodium ion and it is probably necessary to break and reform silicon-oxygen bonds to accommodate the larger ion. Apparently, at the temperature at which potassium nitrate was used, about 400°C , silicon-oxygen bonds do not reform well. Consequently, the porcelain fragments. But at 800°C , the temperature at which potassium chloride was used, bond-reforming takes place. Re-exchanging potassium ions with sodium ions, which are smaller, can occur without bond-breaking so that temperature is unimportant. The few cracks which form at 800°C when rubidium ions exchange for potassium or sodium ions are not to be taken as an indication that bonds are not reformed at this temperature. Silver ions, although slightly larger than sodium ions, can be polarized so as to accommodate to the cation site. Thallium ions are probably too large to enter the glass network at an appreciable rate, at least at the 500°C temperature used. The slight crazing which occurs when lithium ions exchange for sodium ions has been observed by others and is accounted for by a reduction in volume of the porcelain which first takes place at the surface,

causing it to shrink. The surface then crazes in order to accommodate its reduced area to the underlying porcelain which is still unexchanged. Probably the increase in total cation content after exchange by lithium ions is due to inclusion of lithium or sodium compounds in these microcracks. This is consistent with the observed hygroscopicity and the minor weight loss in boiling water. At a sufficiently high temperature, using lithium chloride, instead of lithium nitrate, annealing might allow exchange by lithium ions to take place without crazing.

Probably divalent ions do not enter the glass network for the same reason that they do not undergo electromigration in glass. Presumably, this is because there is an extremely small probability that there will occur two cation sites sufficiently close to each other to accept a single divalent cation and which are also simultaneously vacant.

Acknowledgment

This research was carried out under sponsorship of the U.S. Atomic Energy Commission under Contract No. NBS 0806-11-08474.

Manuscript received May 13, 1963; revised manuscript received Nov. 4, 1963.

Any discussion of this paper will appear in a Discussion Section to be published in the December 1964 JOURNAL.

REFERENCES

1. R. J. Labrie and V. A. Lamb, *This Journal*, **110**, 810 (1963).
2. G. Schulze, *Ann. Physik.*, **40**, 335 (1913).
3. A. Heydweiller and F. Kopfermann, *ibid.*, **32**, 739 (1910).
4. W. C. Orr *et al.*, Eighth Ann. Report on Distribution Studies between Melts and Solid Phases, Univ. of Connecticut, June 30, 1960, AEC Contract No. AT(30-1)-1154.
5. V. E. Plyushchev, *Izvest. Vysshikh Ucheb. Zavedenii Khim. i Khim. Tekhnol.*, **4**, 463 (1961); *C. A.*, **56**, 8065.
6. W. W. Meyer and T. A. Klinefelter, *J. Research Nat. Bur. Standards*, **19**, 65 (1937).
7. R. J. Labrie and V. A. Lamb, *This Journal*, **106**, 895 (1959).
8. A. Guenther-schulze and O. Mohr, *Z. tech. Physik*, **13**, 356 (1932); *Ceram. Abstracts*, **11**, 611 (1932).
9. P. Ehrmann, M. deBilly, and J. Zarzycki, *Verres et refractaires*, **15**, 63, 131 (1961).
10. F. F. S. Bryson, *J. Soc. Glass Technol.*, **11**, 331 (1927).

A Simple Gas Electrode Structure for the Evaluation of Catalysts (Electrocatalysts) in Working Fuel Cells

W. T. Grubb and Carol J. Michalske

Research Laboratory, General Electric Company, Schenectady, New York

The problem of catalytically promoting electrode reactions in fuel cells is apparently more complex than that of promoting gas-solid surface reactions if only for the reason that, in the important case of gaseous fuels, three rather than two phases of matter are involved. To distinguish the more complex process occurring at a fuel cell gas electrode from conventional heterogeneous catalysis, Liebhafsky (1) has used the term electrocatalysis. Little is known in detail about electrocatalysis in fuel cells. Parallels with ordinary heterogeneous catalysis with regard to the efficacy of various catalyst substances are rather poor (2). It is therefore necessary to evaluate electrocatalysts for fuel cells by direct tests in a porous gas electrode geometry.

Typical electrodes for fuel cells (3-5) have the difficulty that interchanging of catalyst materials is not easy or that the type of catalyst is restricted to a certain class of materials, *e.g.*, carbon based catalysts. These restrictions result from the fact that porosity is usually attained in the electrode structures by sintering of metal powders or by employing a porous (*e.g.*, carbon) matrix.

This note reports a new fuel cell gas electrode structure which offers moderately high performance capability and is easily prepared from any high area powder (with some electronic conductivity). With pyrophoric materials, it can be prepared in a glove box under an inert atmosphere and assembled into a cell without exposure to air.

Experimental

Preparation of the electrode is simple. For example an aqueous slurry of platinum black is applied by spatula to a metal screen, then touched to an absorbent surface, such as a filter paper, leaving a smooth, porous platinum-black surface with the black embedded in the meshes of the screen. The electrode is dried out thoroughly by exposure to a dry gas atmosphere over night or for 2 hr in a rough vacuum. It is then treated with solution of a hydrocarbon wax in an organic solvent to make it hydrophobic. When assembled into a hydrogen-oxygen fuel cell with an immobilized aqueous electrolyte, such an electrode is surprisingly good.

In detail the following procedure produced satisfactory platinum black electrodes. A weight of 0.5g of Englehard 100% platinum black (BET surface area by Shell Sorptometer measurement 20 ± 5 m²/g) was mixed with a spatula thoroughly on a

glass plate with 0.5 ml of distilled water. The slurry was then spread smoothly on a 3.8 cm (1.5 in.) diameter platinum screen [45 x 45 mesh 0.0198 cm (0.0078 in.) wire diameter] which was provided with a platinum tab for electrical connection in the assembled fuel cell. After being dried superficially by touching the back (unspread side) with a filter paper, further drying was accomplished by pumping off in a bell jar for two hours. Wetproofing was achieved by three times saturating the electrode with 0.2 ml of a solution containing 2% by weight of ceresin wax (white ceresin wax, Code 2410, from General Chemical Division, Allied Chemical Corporation) dissolved in *n*-hexane (99 mole % minimum, Phillips Petroleum Company). Solvent hexane was removed between applications and after the last one by 15-min drying periods in dry air or by pumping off in a rough-vacuum bell jar. The weight of ceresin in the finished electrode was approximately 0.008g.

The resultant electrode, pictured in the photograph of Fig. 1, has good electrical and gas-diffusion properties and is useful in both acidic and basic electrolytes. Its mechanical strength is sufficient for use with immobilized electrolytes.

With two electrodes assembled in a small cell housing of design previously described (6) polarization curves were taken in conventional manner. A satisfactory immobilized electrolyte was Permaplex C-20¹ ion-exchange membrane saturated with

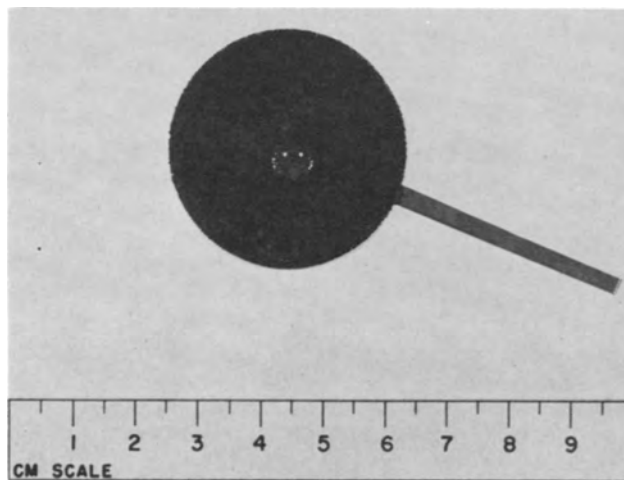


Fig. 1. Platinum black fuel cell electrode of pasted screen structure showing hydrophobicity.

6N aqueous sulfuric acid (acid electrolyte) or Permaplex A-20¹ saturated with 5.5N aqueous potassium hydroxide (alkaline electrolyte). Asbestos was also used as an immobilizer, but the gas impermeability of ion-exchange membranes was better. The cells were operated with H₂ and O₂ pressures of about 15 cm H₂O above atmospheric.

Results

In Fig. 2 and 3 are plotted the current density vs. voltage curves for hydrogen-oxygen cells at room temperature with representative catalysts, including platinum black, a high area nickel,² unsupported silver, and a silver-activated carbon prepared by the method of Yeager (7). It is evident that the structure is quite active with these types of electrocatalysts.

Mechanical mixtures of electrocatalysts may also be used in the present structure. It was found that an anode containing a mechanical mixture of equal weights of platinum black and a low area silver powder gave the same performance with an alkaline electrolyte as a platinum black anode.

The structure described has been used for comparing various catalytic materials up to 65°C in fuel cells. A rather extensive empirical survey of

¹ United Water Softeners, Ltd., Gunnersbury Ave., London W.1, England.

² Ultrafine Nickel, National Research Corp., Cambridge 42, Mass.

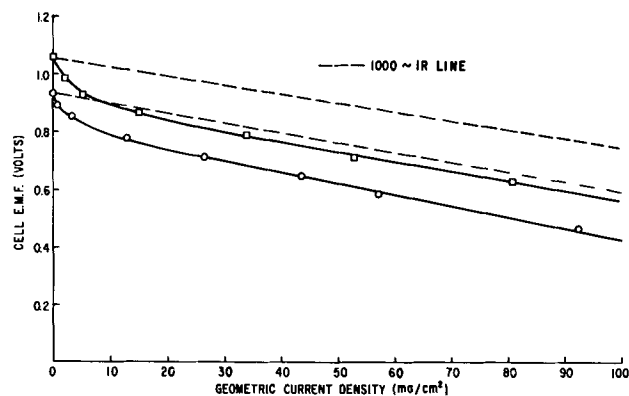


Fig. 2. Current density vs. voltage curve for H₂-O₂ cells with platinum black electrodes with acid electrolyte \circ and with alkaline electrolyte \square . The 1000 \sim resistance was measured using a General Radio Model 650A impedance bridge.

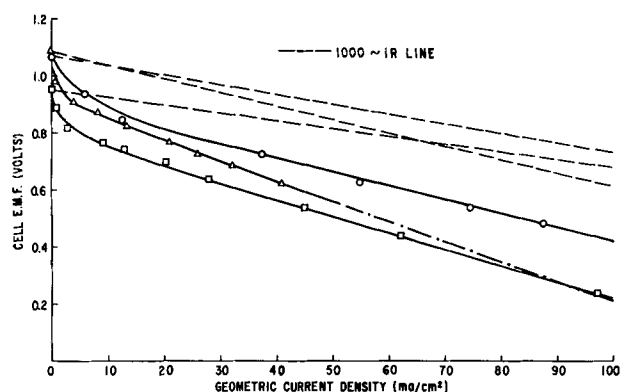


Fig. 3. Current density vs. voltage curve for H₂-O₂ cells with alkaline electrolyte, platinum black cathodes, and various anodes: N.R.C. ultrafine nickel (see text) Δ ; silver \circ ; and silver on Nuchar C-190N (Yeager method, see text) \square .

elements for catalytic activity at fuel cell anodes with several fuels has been described elsewhere (2).

Manuscript received June 4, 1963; revised manuscript received Oct. 25, 1963. This work was made possible by the support of the U.S. Army Engineer Research and Development Laboratories under Contract No. DA-44-009-ENG-4909.

Any discussion of this paper will appear in a Discussion Section to be published in the December 1964 JOURNAL.

REFERENCES

1. H. A. Liebhafsky and E. J. Cairns, Proceedings of the Pacific Energy Conversion Conference, August 1962, San Francisco, California, p. 11-1.
2. W. T. Grubb, Proceedings 16th Annual Power Sources Conference, May 1962, pp. 31-34.
3. E. Justi *et al.*, "High Drain Hydrogen Diffusion Electrodes Operating at Ambient Temperature and Low Pressure," Academy of Sciences and Literature (Mainz) Komm.-Verlag, F. Steiner, Wiesbaden (1959).
4. F. T. Bacon, "High Pressure Hydrogen-Oxygen Fuel Cell," in "Fuel Cells," G. J. Young, Editor, pp. 51-77, Reinhold Publishing Corp., New York (1960).
5. K. Kordesch, "The Hydrogen-Oxygen (Air) Fuel Cell With Carbon Electrodes," in "Fuel Cells," G. J. Young, Editor, pp. 11-22, Reinhold Publishing Corp., New York (1960).
6. L. W. Niedrach, *This Journal*, **109**, 1092 (1962).
7. E. Yeager, Progress Report No. 12, Contract NONR 2391(00) Project NR359-277, Astia Document No. AD 240883, p. 24.

The Electrical Characteristics of Germanium Oxidic Films

Robert D. Wales

Materials Sciences Laboratory, Lockheed Missiles and Space Company, Palo Alto, California

The electrical characteristics of oxidic films of different metals have been of increasing interest. The accumulation of such knowledge is of value, particularly as pertains to the microminiaturization of electrical components. The methods of preparation and characterization of such films have been discussed (1-3).

The electrochemical parameters and properties of anodically formed germanium dioxide films have

been presented (5, 6). The differential field strength in the oxide has been given as 2.1×10^6 v/cm (5) and the resistivity has been given as 2.3×10^{10} ohm-cm (2, 6).

Germanium oxidic films have been formed using previously described electrochemical techniques (5) and some of the electrical characteristics of the dry film determined. These results are discussed below.

Experimental

Oxidic films.—The germanium oxidic films were formed on polycrystalline intrinsic germanium using apparatus and techniques previously described (4, 5). These techniques consisted of the anodic oxidation of germanium at constant current in an electrolyte solution of 0.6 mM LiNO₃, 0.105M HAc, 0.278M H₂O, and 0.011 mM GeO₂ in acetic anhydride. The currents used were between 25 and 250 μ amp/cm², and the film thickness was calculated using the current efficiency previously determined (5).

Electrical measurements.—The capacitance and dissipation factor of the films were measured with a General Radio Type 1650A Impedance Bridge using an oscilloscope as an external null indicator and a Hewlett Packard Audio Signal Generator, Model 205AG, as the external frequency generator. The resistance measurements were made with a Variable Voltage Megohmmeter, M.S.E. No. 11.¹

Electrical contacts.—Mercury was found to give the best electrical contact with the dry oxidic film. The apparent area of the mercury contact was 0.036 cm². A large-area contact of air dried conductive silver, DuPont No. 4922, was found to be satisfactory as a contact to the polycrystalline germanium.

Results and Discussion

Capacitance of wet and dry films.—The series capacitance of the film during formation and of the dry film are compared in Fig. 1. The capacitance was determined at a frequency of 1 kc. The capacitance was measured at various times during formation, and the film thickness, after each time interval, was calculated from efficiency data (5). The solid line in Fig. 1 represents the average of six series of such data and has an average deviation of about 7%. The points in this figure represent the series capacitance of dry films of various thicknesses.

If the usual assumption is made concerning pores and cracks in the film (1), then the greater conductivity of the electrolyte would result in a lower capacitance for the wet films than that obtained for

¹ This instrument was designed and built by H. R. Kaiser, of the Electronic Sciences Laboratory of Lockheed Missiles & Space Co., for determination of leakage resistance of capacitors as a function of applied voltage.

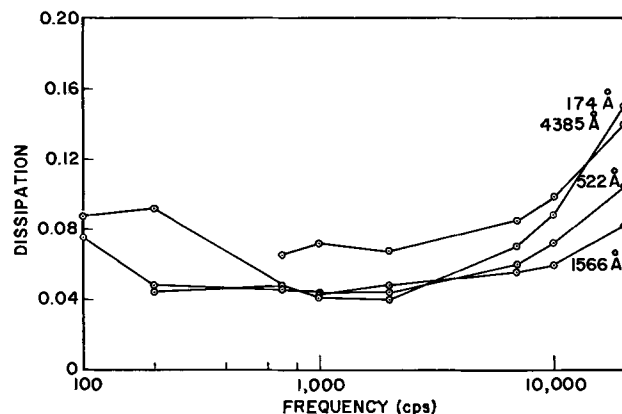


Fig. 1. Variation of dissipation factor with frequency for dry anodically formed germanium dioxide films.

the dry films, if the film is porous. The data in Fig. 1 thus indicate that there is considerable porosity in the thin films which decreases as the film thickness increases up to about 500Å. There is essentially no difference in the data for films of greater than 500Å in thickness. Thus, for the thicker films, there is apparently very little porosity or the pores are either much smaller or not as deep. The dielectric constant of the germanium dioxide film, using data for the thicker films, was calculated to be 6.4 at 1 kc.

The variation of the capacitance with thickness for the dry films may be represented empirically by

$$C_s/A = a + c/d$$

$$a = 7.0 \times 10^{-9} \text{ farads/cm}^2$$

$$c = 3.80 \times 10^{-5} \text{ farads } \text{Å}/\text{cm}^2$$

where C_s = capacitance in farads, A = area in cm², and d = thickness in Angstroms.

Capacitance of dry films.—The variation of the capacitance with frequency for dry films is indicated in Fig. 2. There was a linear variation of the reciprocal capacitance with the logarithm of the frequency for most of the films, the capacitance decreasing by about 6% for a 100 fold increase in frequency.

Dissipation in dry films.—The variation of the dissipation factor with frequency for dry films is indicated in Fig. 3. The dissipation factor is apparently

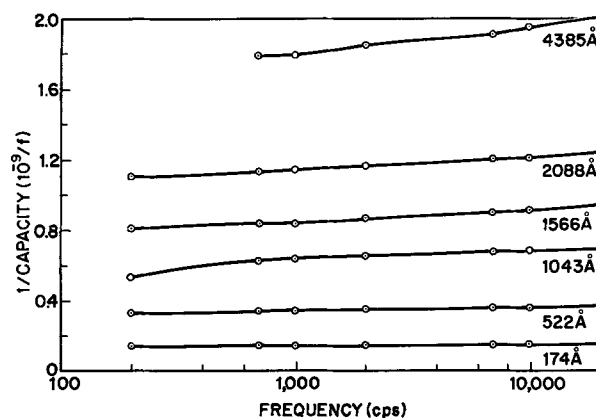


Fig. 2. Variation of capacitance with frequency for dry anodically formed germanium dioxide films.

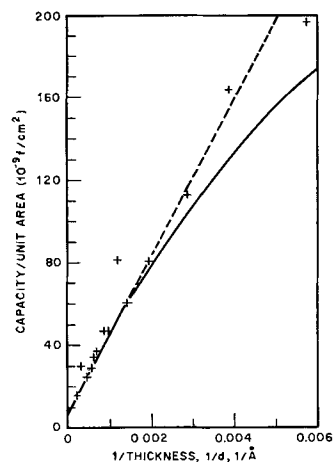


Fig. 3. Variation of capacitance at 1 kc with thickness for wet (solid line) and dry (+) anodically formed germanium dioxide films.

Table I. Resistivity of anodically formed germanium oxidic films

Film thickness, d , Å	Resistance at 1.60v, ohms	Resistivity,* 10^{12} ohm cm
872	9.0×10^8	3.7
1461	1.6×10^9	4.0
1566	9.0×10^8	2.1
4385	9.0×10^{10}	74

* Contact area = 0.036 cm².

independent of film thickness and a nonlinear function of the logarithm of the frequency between 100 and 20,000 cps.

The data indicate a minimum dissipation factor of approximately 0.04 at about 2000 cps. There is approximately a linear relationship with frequency for frequencies greater than 2000 cps, and a linear relationship with 1/frequency for frequencies less than 2000 cps.

Resistivity of the films.—The d-c resistivity (at 1.60v) of several of the dry films is tabulated in Table I. The average value of the resistivity for the thinner films is 3.3×10^{12} ohm-cm. The resistivity of anodically formed germanium oxidic films has been quoted to be approximately 2.3×10^{10} ohm-cm (2, 6) for wet films up to about 1200Å in thickness.

Conclusions

Films of less than 500Å in thickness are fairly porous while thicker films are indicated to have little porosity. The dielectric constant of the germanium dioxide films was estimated to be 6.4 at 1 kc. The capacity of the films (at 1 kc) may be represented by the empirical equation

$$C_s/A = 7.0 \times 10^{-9} + 3.80 \times 10^{-5}/d$$

where the capacitance, C_s , is in farads, the area, A , is in cm², and the film thickness, d , is in Angstroms.

The dissipation factor probably can be represented by an equation of the type

$$D = a\omega + b/\omega$$

where D is the dissipation factor, ω is $2\pi f$ (f = frequency), and a and b are constants. The reciprocal of the capacity increases linearly with the logarithm of the frequency, increasing about 6% for a 100 fold increase in frequency. Apparently no simple model exists which will explain the data obtained.

The d-c resistivity of several of the films was found to be about 3.3×10^{12} ohm-cm.

Acknowledgment

This work was done under the Lockheed Independent Research Program.

Manuscript received May 16, 1963; revised manuscript received Oct. 3, 1963.

Any discussion of this paper will appear in a Discussion Section to be published in the December 1964 JOURNAL.

REFERENCES

1. L. Young, "Anodic Oxide Films," Academic Press, New York (1961).
2. P. J. Holmes, "The Electrochemistry of Semiconductors," Academic Press, New York (1962).
3. D. A. McLean, N. Schwartz, J. K. Werner, and M. Gresh, Bell Telephone Laboratory Report No. 25309-E (Jan. 15, 1960), Army Contract No. DA 36-039SC74996.
4. R. D. Wales, *This Journal*, **110**, 946 (1963).
5. R. D. Wales, *ibid.*, **110**, 914 (1963).
6. S. Zwerdling and S. Sheff, *ibid.*, **107**, 338 (1960).

Some Observations on the Electroplating and Deplating of Silver

J. J. Becker

Research Laboratory, General Electric Company, Schenectady, New York

The electrodeposition of one metal upon another quite generally proceeds by the nucleation of the deposited metal at isolated sites on the substrate, followed by the growth of these nuclei until they coalesce into a more or less continuous deposit. The isolated sites are particularly striking in the deposition of silver from aqueous silver nitrate solutions. Figure 1 shows the appearance under the microscope of a typical deposit from a solution of 1N silver nitrate. The cathode was a 2-mil sheet of platinum with a total cross-sectional area of 1 cm². The "current density" corresponding to the total cathode area is obviously an average of a very much higher value at the particles and zero over most of the cathode surface. Very similar deposits were observed on cathodes of gold, graphite, tin-oxide-coated glass, and sputtered films of gold and platinum.

Effect of Cathode Pretreatment on Deposit Morphology

The appearance of the deposit was similar for almost any pretreatment of the platinum cathode, such

as cleaning in nitric acid, in sulfuric-chromate cleaning solution, or heating in a flame. It was also the same if the platinum was previously made anodic in a solution of nitric acid, so that oxygen was

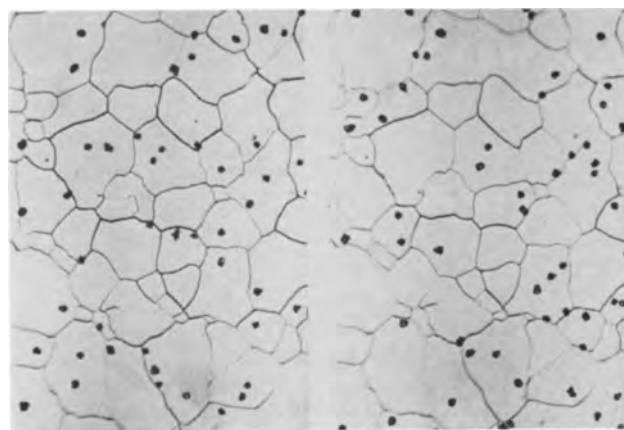


Fig. 1. Successive deposits of silver on a platinum substrate after anodic pretreatment. Platinum grain boundaries are thermally etched. 1N AgNO₃, 6.7 ma, 5 sec. Magnification 125X.

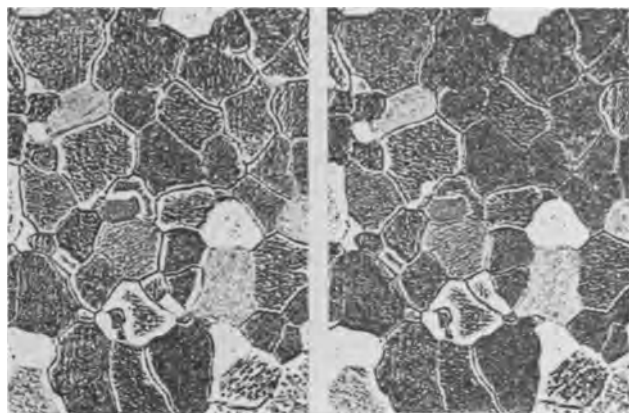


Fig. 2. Successive deposits of silver on same platinum substrate areas in Fig. 1 after successive cathodic pretreatments. 0.1N $\text{AgNO}_3 + 1\text{N HNO}_3$, 6.7 ma, 30 sec. Magnification 125X.

evolved for several seconds, then rinsed and placed in the plating bath. All of these treatments probably leave a film of adsorbed oxygen on the surface. Figure 1 shows two successive deposits on the same cathode area after two successive cleanings and anodic pretreatments. The locations of the deposit sites appear to be quite random, with no suggestion of preference for grain boundaries or other sites, and no spots of any sort that seem to be favored twice in a row.

If, however, the cleaned platinum cathode is made cathodic in nitric acid solution, so that hydrogen is evolved for several seconds, then rinsed and made cathodic in the silver nitrate solution, the appearance of the deposit, as shown in Fig. 2, is totally different. Figures 1 and 2 contrast the appearance of the silver deposits on the same cathode area after cathodic and anodic pretreatments. In one case the plating solution contained some HNO_3 , which tends to enhance the development of crystal faces, but it is not necessary. The removal of the adsorbed oxygen layer by the cathodic pretreatment has evidently greatly reduced the work of nucleation, which is now dependent on the crystallographic nature of the surface. The extreme increase in the number of deposition sites is obvious. It is also evident that the orientation of the silver is determined by that of the platinum grain on which it is growing. The practically complete avoidance of some grains shows the influence of surface orientation on the nucleation work. The avoidance of some areas near grain boundaries, where thermal grooving changes the orientation of the surface, shows the same effect. Figure 2 shows two successive deposits on the same area after two successive cleanings and cathodic pretreatments. The great detail in which the deposit morphology is reproduced is in striking contrast to the random deposits after successive anodic pretreatments shown in Fig. 1.

In a general way one might expect coarse-grained deposits from solutions in which metals are deposited at positive potentials, at which oxygen films on the cathode material would tend to be stable. This would be the case for the more noble metals deposited from simple salts. Silver deposited from the cyanide complex is much finer grained than that from silver

nitrate. It is interesting to note that the equilibrium electrode potential from normal nitrate solution is +0.8v relative to the normal hydrogen electrode, while from a cyanide solution it is -0.3v, a much more reducing potential (1). An adsorbed oxygen film would be much more likely to be stable at the more positive potential.

Incomplete Deplating

If a cell contains aqueous silver nitrate solution, a silver electrode, and a platinum electrode, and if the silver is made anodic with respect to the platinum by an applied potential across the cell, silver will dissolve anodically and deposit on the platinum. If the solution is fairly concentrated and the electrodes of any reasonable size, most of the applied voltage appears as IR drop in the electrolyte, as was verified with a silver-silver nitrate reference electrode (2) and a Luggin probe, and the current is linear with voltage, at least up to a volt or more. If, however, the clean platinum is made anodic, no current flows until the applied voltage across the cell exceeds 0.7v, that is, when the platinum is more than 0.7v positive with respect to the Ag-Ag^+ electrode. Under these conditions, silver is deposited on the silver electrode, while the anode reaction at the platinum is the formation of an oxy-nitrate of divalent silver (3). This substance can be seen to form as dark, lustrous needles or pyramids.

If, to begin with, the clean platinum is made cathodic, and any small voltage of less than 0.7v is applied across the two electrodes of the cell for a given length of time, silver is deposited on the platinum. The total amount of deposit should correspond to the total number of coulombs. If now the same small voltage is applied with the opposite polarity, one might expect that current would flow as long as there was deposited silver to go back into solution and that the current would drop to zero when all the deposited silver had been redissolved, the same number of coulombs having flowed in the opposite direction. When this simple experiment was tried, however, it was found that the reverse current stopped after only about 80% of the original coulombs had gone through the cell on the deplating cycle. Figure 3 shows a typical pair of current-time traces. There are a number of possible causes for this behavior, but microscopic examination of the

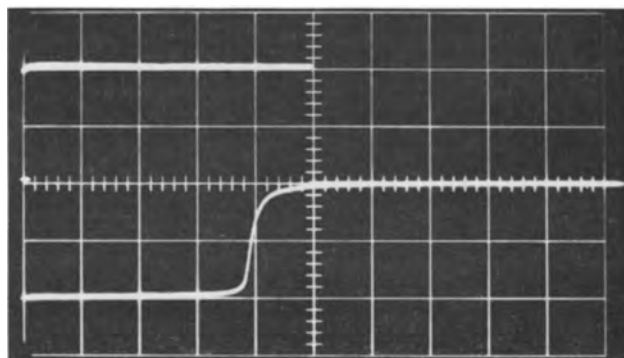


Fig. 3. Current (vertical) vs. time (horizontal, left to right) for plating and deplating process. 1 large division = 1 sec by 0.67 ma. Upper trace shows 5-sec plating cycle. Lower trace shows current flow resulting from reversing same voltage after plating.

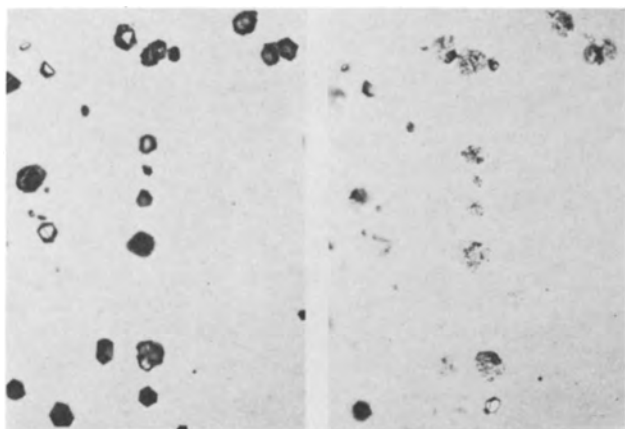


Fig. 4. (a, left) Platinum electrode with silver deposit produced by 0.47 ma for 15 sec, 1N AgNO₃; (b, right) same field after deplating. Magnification 145X.

platinum readily reveals that what is happening is that not all of the deposited silver comes off. Starting with an initial deposit on the usual relatively small number of sites, as in Fig. 4a, one finds, after the deplating current has stopped, a residue from the original deposit, Fig. 4b. This residue is at least largely silver, as shown by electron diffraction and by its chemical behavior.

It is possible, by gradually raising the applied voltage from zero, to grow a single crystal deposit (4). If this is observed under the microscope, it can be seen to grow by steps sweeping across the crystal faces. When the current is reversed, the observed solution process is not at all the reverse of growth. Solution begins much more generally along the edges and over the faces of the crystal, which soon becomes wrinkled and shrunken, and then quite suddenly stops dissolving. No other obvious change occurs. At this point, the voltage can be raised until the anodic oxy-nitrate forms all over the platinum, but still the silver residue does not go into solution.

In many instances it appears that the reason the silver stops deplating may be that it loses electrical contact with the substrate. This certainly appears to be the case when solution stops early and leaves a large piece of the original crystal, an example of which can be seen near the bottom of Fig. 4b. Sometimes during the solution process small pieces of a deposited crystal can be seen to come loose and fall to the surface, by the sort of undercutting process Vermilyea associates with anode slime (5). When the platinum electrode is vertical, one can sometimes see that portions of the original deposit have moved down the platinum during deplating. Upon replating, if the silver residue were in electrical

contact with the platinum, one would certainly expect the deposition to start on the residue again, but usually only a small fraction of the residual sites are active sites for redeposition. For fine grained deposits on a previously cathodically treated substrate, the incomplete deplating is still present but less pronounced.

It was discovered that a variety of addition agents greatly increase the incompleteness of the deplating. SO₄²⁻ ions at a concentration of 10⁻⁴M increase the irreversibility, as do similar concentrations of HPO₄²⁻, I⁻, and MnO₄⁻. Other ions, such as PO₄³⁻, acetate, ClO₃⁻, F⁻, and ClO₄⁻, have no effect. In both cases some of the ions mentioned produce precipitates, of course, but this does not seem to be relevant. 10⁻²g/l of gelatin has a very pronounced effect, as does 10⁻³g/l of thiourea. In all cases, the effect was the same if the plating was done in a solution without the additive and the deplating in a solution containing the additive. Presumably these substances, particularly the strongly adsorbed organic molecules, are inhibitors for anodic solution and would tend to distribute the anodic solution process more evenly over the surface of the crystal and thus enhance the tendency to geometrical undercutting.

A coulometric method for the quantitative analysis of small amounts of silver has been described (6). The silver is first deposited on a platinum electrode, and then the coulombs necessary to deplate it are measured. In these experiments, it was found that after plating with a fixed current for a fixed time, only about 80% of the plating coulombs were returned on deplating. The authors attributed this to deplating current efficiencies greater than 100% because of mechanical stripping, but it seems equally likely that the phenomena described above were responsible for the discrepancy.

Manuscript received Oct. 7, 1963; revised manuscript received Dec. 13, 1963.

Any discussion of this paper will appear in a Discussion Section to be published in the December 1964 JOURNAL.

REFERENCES

1. W. K. Latimer, "Oxidation Potentials," Prentice-Hall, Inc., Englewood Cliffs, N. J. (1952).
2. G. N. Lewis and M. Randall, "Thermodynamics," p. 414, McGraw Hill, Inc., New York (1923).
3. J. W. Ritter, *Gehlen's neue J.*, **3**, 561 (1804); J. A. McMillan, *Chem. Rev.*, **62**, 65 (1962).
4. V. Kohlschutter and A. Torricelli, *Z. Elektrochem.*, **38**, 213 (1932).
5. D. A. Vermilyea, *This Journal*, **105**, 547 (1958).
6. S. S. Lord, Jr., R. C. O'Neill, and L. B. Rogers, *Anal. Chem.*, **24**, 209 (1952).

The Kinetics of Epitaxial Growth of Silicon from the Trichlorosilane-Hydrogen Reaction

Andrew M. Stein

Space and Information Systems Division, North American Aviation, Inc., Downey, California

Epitaxy refers to orientated intergrowth between two solid phases. The surface of one crystal provides, through its structure, preferred orientation for the deposition of the second crystal. The concept of epitaxial growth as a means of preparing single crystal semiconductor materials has been the subject of extensive investigation recently (1-4). This technique appears to offer certain advantages over solidification from the molten state. Crystals can be grown and selectively doped with impurities at temperatures low enough that undesirable diffusions are minimized. The ability to deposit alternate layers of n and p type material is also a distinctive advantage of the epitaxial growth process. It is also possible, in principle, to build single crystal layers of ultra high purity, since the impurity content of the vapors above the growing crystal can be arbitrarily chosen and/or controlled. Crystal growth, in general, is a kinetic process. The study of kinetics provides knowledge about the rates and mechanisms of chemical and physical change (5-8). In generating single crystals by vapor deposition from vapor phase chemical reactions there are two types of kinetics involved; gas phase reaction kinetics and crystallization kinetics. For the work reported herein it is assumed that a heterogeneous surface reaction is involved. The following mechanism is proposed: 1, reactants diffuse to the wafer surface; 2, reactants form activated complex with surface; 3, activated complex decomposes to products; 4, silicon becomes preferentially orientated on substrate surface; 5, gaseous products diffuse away.

It was decided to employ the reaction between trichlorosilane and hydrogen because the kinetics involved are probably comparatively simple. The objective was to study the epitaxial growth rate as a function of the partial pressure of trichlorosilane, and the absolute temperature. The subject of material preparation, i.e., single crystal growth and surface treatment of semiconductors has been discussed in the literature (9-16) and will not be repeated. The substrate material employed for the work reported herein was 10 ohm-cm p-type and was of high perfection. The hydrogen flow rate employed in this study was 7.9 cc/sec. Electrolytic grade hydrogen was employed, and further purification to remove water and other condensable gases was accomplished by methods similar to that of reference (2). Finally, the resulting hydrogen was bubbled through trichlorosilane to ensure saturation. The partial pressure of trichlorosilane in hydrogen was obtained by saturating hydrogen for several thermostat temperatures and could be reproduced with reasonably good accuracy.

The kinetics of epitaxial growth was investigated as a function of the partial pressure of trichlorosilane

for the partial pressure range 1.45-45 mm for several temperatures. In another series of experiments, the epitaxial growth kinetics was determined as a function of the absolute temperature for several partial pressures of trichlorosilane. The wafer temperature was determined by means of an optical pyrometer, and the temperatures referred to in this paper are corrected by the method of Allen (17). The rate of epitaxial growth was determined by placing single crystal silicon wafers of {111} surface orientation on a quartz pedestal heated by means of a radio frequency field, as shown (Fig. 1), and passing the trichlorosilane hydrogen mixture into the reactor at the experimental temperature for a given time. The growth rate was determined by weight gain of wafers with suitable corrections being made for weight loss due to surface evaporation of silicon. No correction was made for surface etching which could result from hydrogen chloride attacking the silicon wafer. The mole fraction of hydrogen chloride was relatively low, and it was assumed that the amount of silicon removed by etching was small compared to the amount deposited.

Discussion

It was difficult to obtain epitaxial growth at the lowest temperature investigated. This observation was applicable to all experiments conducted at partial pressures of trichlorosilane greater than 1.45 mm.

The deposition rate of silicon from the reduction of trichlorosilane with hydrogen on the silicon substrate is depicted in Fig. 2. In Fig. 3 the deposition rate is plotted vs. the square root of the dimensionless partial pressure of trichlorosilane for the several temperatures investigated. It is seen that curves approximating straight lines were obtained when the curves were drawn through the average distribution of experimental points. Finally, a plot of the logarithm of the deposition rate vs. the reciprocal of the absolute temperature is depicted in Fig. 4. It is seen that the curves approximate straight lines for the two partial pressures shown.

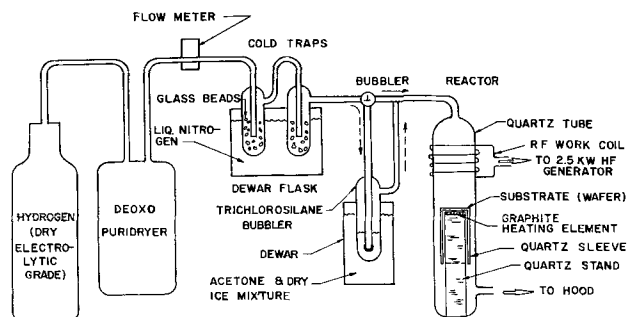


Fig. 1. Schematic of hydrogen purification system and reactor for vapor deposition.

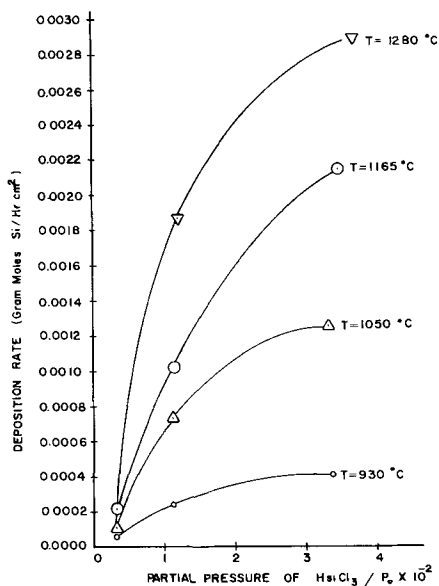


Fig. 2. Deposition rate of silicon vs. partial pressure of trichlorosilane. $P_0 = \text{total pressure} = 1 \text{ atm}$. $\text{H}_2 \text{ flow} = 7.9 \text{ cm}^3/\text{sec}$.

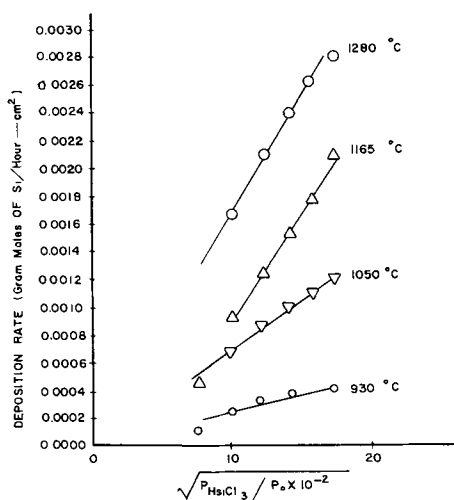


Fig. 3. Deposition rate vs. dimensionless partial pressure of trichlorosilane.

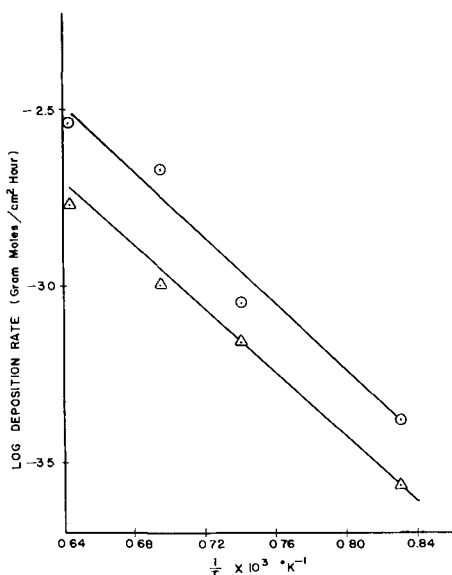


Fig. 4. Deposition of silicon vs. temperature. \odot , Partial pressure $P_{\text{HSiCl}_3} = 3.38 \times 10^{-2} P_0$. \triangle , Partial pressure $P_{\text{HSiCl}_3} = 1.12 \times 10^{-2} P_0$. Apparent energy of activation per mole = 22,500 cal. Hydrogen flow rate = 7.9 cm^3/sec .

Conclusions

From the above, several conclusions may be drawn:

1. The apparent order of the deposition kinetics is one-half, since approximately straight lines were obtained when deposition rates were plotted vs. square root of concentration of trichlorosilane. This finding would apparently support the conclusion that the deposition reaction may be a surface reaction. Homogeneous gas phase kinetic processes have been observed to obey zero order, first order, second order, and, in rare instances, third order kinetics.

2. The apparent energy of activation of the deposition process is independent of the partial pressure of trichlorosilane, for a range of partial pressures. It is observed that the slopes of the curves depicted in Fig. 4 are essentially the same.

3. The relatively low value of the activation energy, 22,500 cal/mole of silicon deposit, is also an indication of the surface reaction.

4. Good epitaxial growth can be achieved at 1050°C and higher temperature, at reasonable rates. Deposition rates must be very low if epitaxial growth is to be carried out at 1000°C or lower temperature.

Acknowledgments

The author takes this opportunity to acknowledge the assistance of several colleagues at Pacific Semiconductors, Inc., where this research was performed. Acknowledgment is also due North American Aviation, Inc., for clerical assistance provided in the final preparation of the manuscript. The research was supported by the United States Air Force under Contract No. AF33(600)-43029, ASD Project 7-850.

Manuscript received Feb. 5, 1963.

Any discussion of this paper will appear in a Discussion Section to be published in the December 1964 JOURNAL.

REFERENCES

A partial account of this work was reported previously before the American Physical Society, Bulletin APS, Series II, Vol. 7, August 1962.

1. IBM Journal of Research and Development, 4, No. 3, July 1960.
2. J. M. Craig and B. A. Joyce, *This Journal*, **109**, 957 (1962).
3. R. Glang and E. S. Wajda, AIMME, Semi-conductor Conference, Los Angeles, August 1961.
4. H. C. Theuerer, *This Journal*, **108**, 649 (1961).
5. C. N. Hinshelwood, "Kinetics of Chemical Change," Oxford University Press (1926).
6. S. Glasstone, "Textbook of Physical Chemistry," D. Van Nostrand Co., Inc., New York (1946).
7. S. Glasstone, K. J. Laidler, and H. Eyring, "The Theory of Rate Processes," McGraw-Hill Book Co., New York (1941).
8. Mollwyn-Hughes, "Principles of Physical Chemistry," 2nd Edition, Pergamon Press (1961).
9. W. C. Dash, *J. Appl. Phys.*, **29**, 736 (1958).
10. W. C. Dash, *ibid.*, **30**, 459 (1959).
11. W. C. Dash, *ibid.*, **31**, 736 (1960).
12. Gottfried Greger, *Z. Angew. Phys.*, **13**, 49 (1961).
13. Joseph R. Ligenza, U. S. Pat. 2,930,722, March 29, 1960, to Bell Telephone Laboratories, Inc.
14. Harry Robbins and Bertram Schwartz, *This Journal*, **106**, 505 (1959).
15. Ben H. Alexander, U. S. Pat. 2,809,103, Oct. 8, 1957, to Sylvania Electric Products, Inc.
16. Douglass L. Cox, U.S. Pat. 2,827,367, March 18, 1958, to Texas Instruments, Inc.
17. F. G. Allen, *J. Appl. Phys.*, **28**, 1510 (1957).

Transmission Electron Microscope Investigation of Removal of Mechanical Polishing Damage on Si and Ge by Chemical Polishing

R. Stickler

Westinghouse Electric Corporation, Research and Development Center, Pittsburgh, Pennsylvania

and G. R. Booker

Cavendish Laboratory, University of Cambridge, Cambridge, England

A procedure often used during the preparation of Ge and Si surfaces for solid-state devices, *e.g.*, transistors, molecular blocks etc., is mechanical polishing of the specimens to a mirror finish and then removal of the resulting surface damage by subsequent chemical polishing. However, the latter usually causes a marked deterioration in the smoothness and flatness of the surface, and it is often difficult to decide when to terminate the chemical polishing treatment.

The kind of deterioration which occurs is illustrated in Fig. 1 for a single crystal Ge specimen mechanically polished along random directions with 0.25μ diamond, and subsequently chemically polished with a modified CP4 (1).² During this chemical polishing treatment, a series of "scratch-marks" is rapidly revealed, which gradually broaden and eventually cannot be detected. At the same time, the surface becomes progressively wavy on a coarse scale. In practice, a chemical treatment of approximately 10-15 sec is commonly used, and hence it can be seen that the resulting surface still exhibits numerous scratch-marks. A similar behavior occurs when Si is mechanically polished with 0.25μ diamond, and is then chemically polished with CP4.³

The scratch-mark structure arises from the 0.25μ diamond surface damage, while the waviness is characteristic of the CP4 chemical polishing process (1).

¹ 200 ml NHO_3 : 120 ml HF : 120 ml CH_3COOH : 1.6g Ge: 1.2 ml liquid Br_2 .

² 200 ml NHO_3 : 120 ml HF : 120 ml CH_3COOH .

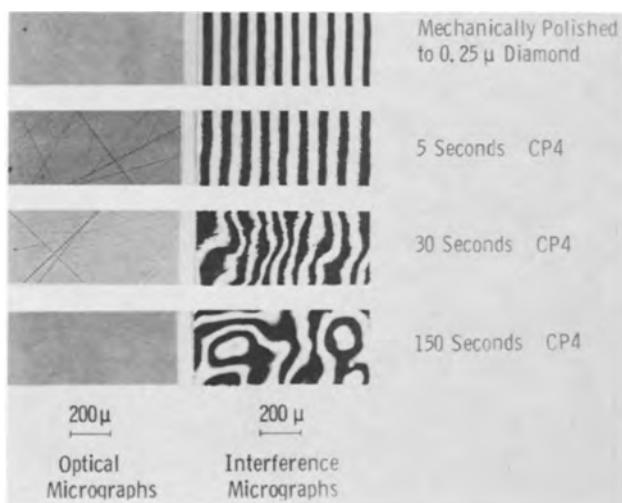


Fig. 1. Optical and interference micrographs showing progressive stages of chemical polishing of Ge with CP4. The initial mechanical polishing was performed using 0.25μ diamond at random directions.

However, the reason why the scratch marks are not eliminated until after chemically polishing for 150 sec, corresponding to the removal of a layer approximately 60μ thick, is not immediately clear. This is because the damage for the 0.25μ diamond polishing is usually considered to extend only the order of 1μ beneath the surface.

In order to explain this apparent anomaly, Faust (2) suggested that the damage is completely removed after chemically polishing for only approximately 5 sec. However, the attack occurs preferentially along lines of damage and so gives rise to series of grooves having the appearance of scratch marks. Considerable additional chemical polishing is then required before these grooves are smoothed out.

Similar observations concerning the occurrence of scratch marks when mechanically polished Ge and Si specimens are subsequently chemically polished have also been reported by Ida *et al.* (3). These workers used optical interference techniques together with electron microscope studies of surface replicas in order to investigate the scratch marks. Although the geometry of the scratch marks was thereby determined, it was not possible to observe the actual damage or see how the damage was removed. No detailed explanation for the occurrence of the grooves was given.

In order to understand how such damage is removed during chemical polishing, it is first necessary to establish the precise nature of the damage. This has been done by the authors (4) using the transmission electron microscope method of examination, a method possessing the advantage that the resolution is high and the structure within the damaged layer can be directly observed. It was found that for Si specimens polished with 0.25μ diamond particles on a rotating cloth pad, the damage was orientation dependent. In particular, for (111) specimens, polishing along $\langle 110 \rangle$ directions gave dislocations only, while polishing along $\langle 211 \rangle$ directions gave dislocations together with surface chipping and cracking. This damage was estimated to extend only approximately 0.2μ below the surface.

The authors have now used the transmission electron microscope method to determine how 0.25μ diamond surface damage is removed during chemical polishing. The chemical polishing was performed with CP4 in order that the findings would be applicable to the previous observations (1). It was found that there was little, if any, difference in the behavior of Ge and Si specimens. Conse-

quently, although all of the transmission electron micrographs used below to illustrate the results are for Si, they may also be considered as being representative of Ge.

Experimental

High-purity (approximately 50 ohm-cm) single crystal Ge and Si slices were cut parallel to the (111) plane, lapped on both sides to 20 mils thick, and chemically polished with CP4 until all of the lapping damage was removed. The slices were then mechanically polished with 0.25 μ diamond slurry on a cloth pad using kerosene as a lubricant for a few minutes, applying a light hand pressure. Individual slices were then chemically polished with CP4 for either 1, 3, 5, 30, or 150 sec, immediately rinsed first with water and then with alcohol, and then dried.

For the electron microscope examination, the slices were chemically thinned from the side not polished with 0.25 μ diamond, using a jet of 9:1 HNO₃/HF solution (5). In order to ensure that no etching of the reactive mechanically polished surface by acid fumes, etc., could occur, the surface was covered with a thin protective layer of wax. As soon as the jet chemical thinning caused a small hole to appear, the specimen was rinsed and dried, the wax dissolved, and the thin portions surrounding the hole examined in transmission in the electron microscope.

Results

A transmission electron micrograph of a Si specimen unidirectionally abraded along a $\langle 110 \rangle$ direction with 0.25 μ diamond is shown in Fig. 2a. For this abrasion, the cloth pad contained well-used 0.25 μ diamond slurry, conditions similar to those previously used by the authors (4). The damage consists of lines of dislocations running along the $\langle 110 \rangle$ abrasion direction.

A Si specimen unidirectionally abraded along a $\langle 110 \rangle$ direction but using a cloth pad freshly charged with 0.25 μ diamond slurry, is shown in Fig. 2b. The damage is similar to that of Fig. 2a, but is

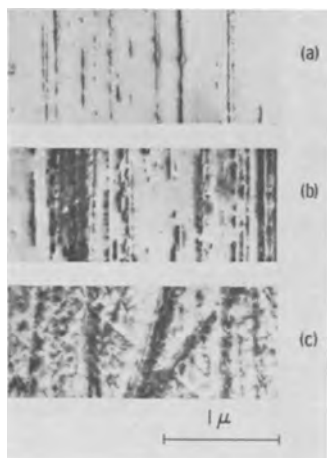


Fig. 2. Transmission electron micrographs showing the surface damage of Si specimens mechanically polished with 0.25 μ diamond: a, unidirectionally abraded in a $\langle 110 \rangle$ direction on a cloth pad with used diamond slurry; b, unidirectionally abraded in a $\langle 110 \rangle$ direction on a cloth pad freshly charged with diamond slurry; c, randomly abraded on a cloth pad freshly charged with diamond slurry.

more severe. In addition to the lines of dislocations, some chipping and cracking appear to have occurred.

A Si specimen abraded in random directions using a cloth pad freshly charged with 0.25 μ diamond slurry is shown in Fig. 2c. The severity of the damage is again greater. Broad lines of damage up to 1000 Å across, numerous narrow lines of damage, and a mottled background structure are present. Chipping and cracking are more pronounced.

For the remainder of the present investigation, all of the specimens were randomly abraded using freshly charged pads, *i.e.*, the damage introduced corresponded to that shown in Fig. 2c. In this way, it was considered that greater uniformity in the polishing conditions, and hence better reproducibility of the surface damage, would result. Moreover, the effect being investigated, namely, the influence of the damage on subsequent chemical polishing, was likely to be more pronounced.

A different area of the specimen of Fig. 2c is shown in Fig. 3. Abrupt changes in contrast can be seen, the changes usually occurring at lines of damage. The changes indicate a small rotation of the crystal lattice, while the bounding lines of damage suggest that the rotation results from severe strains associated with these lines. It is presumed that the strains arise when the specimen is mechanically polished, and that the strains are partly relieved when the specimen is jet chemically thinned from the undamaged side to a final thickness of the order of 1 μ by a slight rotation of the crystal lattice.

A 0.25 μ diamond Si specimen chemically polished with CP4 for approximately 1 sec is shown in Fig. 4a. The lines of damage are preferentially attacked. The damage is partly removed, and grooves occur along the lines. The grooves are slightly wider than the original damage lines and are up to approximately 2000 Å across. The mottled background structure is almost completely absent. The general degree of attack varied slightly from area to area of the specimen on a coarse scale indicating small differences in wetting etc. For example, the attack has proceeded further in Fig. 4b than in Fig. 4a.

A similar specimen chemically polished with CP4 for 3 sec is shown in Fig. 5a. It should be noted that the magnification for Fig. 5 is half that of Fig.

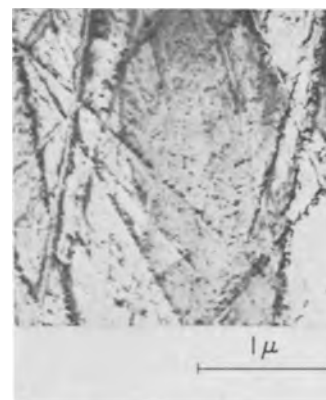


Fig. 3. Transmission electron micrograph of a different area of the specimen shown in Fig. 2c. Abrupt changes of contrast occurring along the lines of damage indicate a small rotation of crystal lattice.

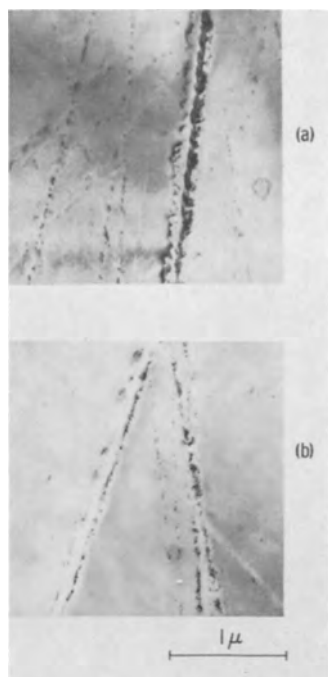


Fig. 4. Transmission electron micrographs of a Si specimen showing the effect of 1 sec CP4 chemical polish after abrading similarly to the specimen of Fig. 2c. Figure 4a and 4b are different areas of the same specimen; note the varying degree of attack.

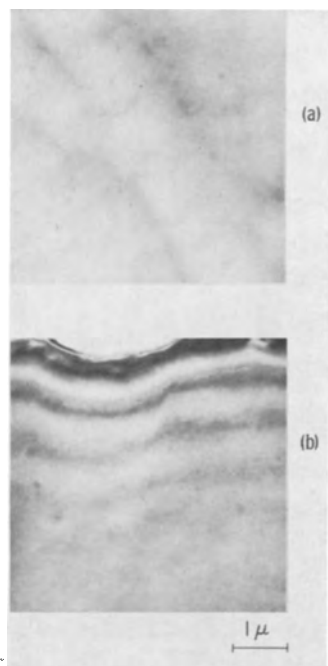


Fig. 5. Transmission electron micrographs of a Si specimen showing the effect of 3 sec CP4 chemical polish after abrading similarly to the specimen of Fig. 2c. Visible damage is completely removed. Shallow grooves remain, the profile of which can be deduced from the thickness fringes shown in Fig. 5b.

2 to 4. Damage is no longer observed, only surface grooves. The grooves are up to approximately $20,000\text{\AA}$ across, *i.e.*, are much wider than those shown in Fig. 4a and b. By following the more pronounced grooves to the edge of the thinned specimen and suitably tilting the specimen in the electron microscope, thickness fringes were obtained as shown in Fig. 5b. Because the side from which the specimen was thinned is considered to be smooth,

the profile of the groove can be obtained from the fringes. Although these fringes arise in a different manner from optical interference fringes, they are nevertheless contours of equal thickness, and so can be similarly interpreted. The fringes appear at specimen thickness intervals of 750\AA (this interval corresponds to the extinction distance for a $\langle 220 \rangle$ reflection (6), the reflection used for this micrograph). A displacement of a fringe for a fraction (ds) of the lateral fringe spacing (s) corresponds to a change in the specimen thickness for a fraction of the extinction distance ds/s 750\AA . Thus, for the groove of Fig. 5b, the maximum depth is estimated to be approximately $0.6 \times 750\text{\AA}$, *i.e.*, 450\AA .

Similar specimens chemically polished with CP4 for times longer than 3 sec all showed no damage. Moreover, it was difficult, if possible, to detect the surface grooves. The insensitive nature of the transmission electron microscope method of examination for detecting such grooves, compared with the optical microscope method, is due to the different mechanisms by which the image contrast arises in the two cases.

Discussion

The transmission electron micrographs of the (111) Si specimens polished with 0.25μ diamond show that the damage consists in general of chips, cracks, and dislocations. Moreover, the nature and amount of the damage varies markedly with the manner in which the polishing is performed. Its dependence on the polishing direction was reported previously (4). The present results show that it also depends on whether the 0.25μ diamond abrasive is fresh or well-used. This is in agreement with an observation recently made by the authors (7) concerning abrasion with either diamond or SiC particles. Thus, starting with fresh abrasive, the abrasion rate, *i.e.*, amount of material removed per unit time, was high for the first few minutes, and then dropped to a low value. The initial rate was often as much as five times the subsequent rate. The probable explanation is that the particles responsible for most of the initial abrading, namely, the larger and sharper particles, are rapidly either broken into smaller particles or worn down.

Hence, the observations show that when polishing (111) Si specimens with 0.25μ diamond on a rotating cloth pad, least damage occurs when the pad contains well-used abrasive and the abrasion is performed unidirectionally along a $\langle 110 \rangle$ direction. On the other hand, most damage occurs when the pad contains fresh abrasive and the abrasion is randomly performed.

When specimens abraded with 0.25μ diamond to give most damage were jet chemically thinned from the opposite side, small lattice rotations occurred as indicated by contrast changes in the transmission electron micrographs. These localized rotations are undoubtedly due to strains associated with the lines of damage. Other evidence for such strains was previously reported by the authors (4) as a result of transmission electron microscope studies on annealed 0.25μ diamond Si specimens. Thus, new dis-

locations had propagated from several lines of damage into the surrounding regions during annealing, and the driving force for these dislocations was considered to be the associated stresses.

However, although strains are present beneath the "visible" damage, *i.e.*, the chips, cracks, and dislocations, little appears to be known about their nature or extent. The strains are elastic and arise from the stresses imposed by the "visible" damage, and also perhaps from the presence of point defects, *e.g.*, vacancies. Such point defects could be present without being detected by the transmission electron microscope method.

When such specimens are chemically polished with CP4, the transmission electron micrographs show that the attack commences preferentially at the lines of damage. After 1 sec, the damage is partly removed and grooves begin to form along the lines of damage. After 3 sec, no damage can be detected and the grooves are appreciably wider. Thereafter, the grooves continue to increase in width, but not apparently to change much in depth. The latter may also be deduced from the interference micrographs of Fig. 1. The sequence is illustrated diagrammatically in Fig. 6. The reason for the preferential attack is undoubtedly due to the strains associated with the lines of damage.

The question still remains as to why the scratch-

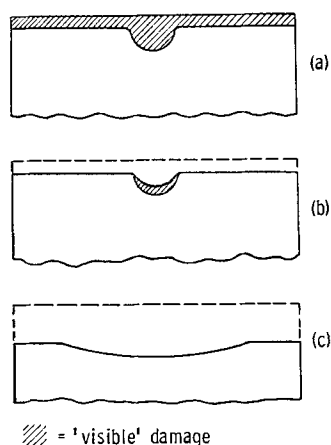


Fig. 6. A diagrammatic representation of the formation and elimination of grooves by chemical polishing (cross sections): a, as abraded; b, after approx. 1 sec chemical polishing; c, after approx. 5 sec chemical polishing (compare with Fig. 1).

mark structure persists for such a long time during the CP4 chemical polishing process. There appear to be two main possibilities. First, when the visible damage is removed, the associated stresses are removed, and hence the elastic strains caused by these stresses are removed. However, because the specimen is at room temperature, point defects beneath the lines of damage remain and cause local increases in the dissolution rate. The effect of these rate increases is to delay the smoothing over of the initial grooves.

The second possibility is simply that once grooves have formed, they are extremely difficult to smooth over by chemical polishing with CP4 (2). The dissolution rate at the middle of a groove is the same as that at the surface away from the groove, while the dissolution rate at the edges of the groove is slightly faster. Consequently, the groove remains approximately the same in depth, but becomes progressively wider.

In view of the lack of information concerning the occurrence of point defects beneath the visible damage and their likely effect on the dissolution rate, it is not possible to decide unambiguously between the two possibilities. However, it is considered that if the point defect mechanism does occur, then it is most unlikely that it would still be operative at depths of more than a few microns. Hence it is thought that the predominant mechanism is simply the difficulty of smoothing over the grooves once they are formed.

Manuscript received Nov. 27, 1963.

Any discussion of this paper will appear in a Discussion Section to be published in the December 1964 JOURNAL.

REFERENCES

1. G. R. Booker and R. Stickler, *This Journal*, **109**, 1167 (1962).
2. J. W. Faust, Jr., reported in ref. (1).
3. I. Ida, Y. Arai and M. Suzuki, Review of the Electrical Communication Lab., Nippon Telegraph and Telephone Public Corp., Tokyo, Japan, **10**, 547 (1962).
4. R. Stickler and G. R. Booker, *Phil. Mag.*, **8**, 859 (1963).
5. G. R. Booker and R. Stickler, *Brit. J. Appl. Phys.*, **13**, 446 (1962).
6. A. Howie and M. J. Whelan, Private communication.
7. R. Stickler and G. R. Booker, To be published.

Effect of Aging on Surface Roughness of Thin Films

R. J. Prosen, J. Kivel,¹ B. E. Gran, and J. S. Sallo

Honeywell Research Center, Hopkins, Minnesota

The aging of thin films has been studied previously with respect to adhesion and resistivity (1). Recently, techniques have become available (2-4) which permit the study of surface roughness. One such method has been applied to the study of variations of surface roughness of thin films with time. This paper presents the results of this study.

Experimental

Sample preparation.—The evaporated thin films were prepared in a bell jar evacuated to 10^{-5} Torr. Thin films of nickel, iron, Permalloy (83% Ni-17% Fe), copper, and gold were prepared. All films were circular with $\frac{3}{4}$ -in. diameters. The metals were heated in an alumina crucible (Morganite) by resistance heating and evaporated onto Corning code No. 2915 microscope cover glasses to a thickness of

¹ Present address: Atlantic Research Corporation, Alexandria, Virginia.

1000Å. The substrate temperature was 250°C. The thickness was determined by multiple beam interferometry. A more detailed experimental procedure has been reported elsewhere (5).

Permalloy films (83% Ni-17% Fe) were also deposited by cathodic sputtering. These films were deposited in a three electrode system. The cathode current and voltage were 2 amp and 40v, respectively. The target voltage and current density were 1.5 kv and 2 ma/cm². The substrate was placed approximately 2 mm from the target, and deposition rate was from 200-250 Å/min. This work was done in a continuous flow argon atmosphere at a pressure of 3×10^{-4} Torr.

Adsorption phenomena.—The radiochemical technique by which the adsorption properties of hexadecyltrimethyl ammonium bromide (HMAB) have been utilized to determine relative values of surface area has been reported (2) for glass and for iron-nickel thin films. A "monolayer plateau" was shown to occur in the $3-8 \times 10^{-4}$ M HMAB concentration range. Adsorption isotherms were determined for iron, nickel, copper, and gold. All these metals yielded identical adsorption isotherms to those previously studied, indicating that a similar adsorption mechanism occurs, and hence, areas could be compared for these dissimilar metals.

The surface area and roughness of each thin film were determined. Samples were immersed in a 5.72×10^{-4} M C¹⁴-labeled HMAB aqueous solution until equilibrium was reached (15 min) and then vertically withdrawn at a rate of 2 mm/min by means of a small motor. Samples were counted using a thin window gas flow counter and compared with standards previously calibrated against a 0.19 ± 0.019 microcurie carbon-14 source. Although this results in a $\pm 10\%$ absolute error, this error does not apply to the relative values reported. Conversion of the counting data to atoms of HMAB adsorbed and attributing 20.5Å² to each molecule adsorbed (2) enabled surface areas to be determined. A minimum of two samples was used for each determination throughout this study, and each sample was used only once. All samples for a given run were prepared in the same evaporation or sputtering runs.

Aging experiments.—The thin films were removed from the bell jar, exposed to atmospheric conditions, and immediately placed in the desired environment at 20°C. Samples were placed in dry and 100% RH air, dry and 100% RH helium, and vacuum (10^{-5} Torr) environments. Dry air and dry helium aging were carried out in chambers containing magnesium perchlorate as the desiccant. The desiccant was replaced by a beaker of water in the 100% RH humidity experiments. After being stored for the desired time interval, the samples were removed from the chamber and immediately placed in the HMAB solution. The roughness of these samples was determined by the procedure discussed above.

Experiments were also carried out at 150°C with Permalloy and iron in dry air and dry helium by procedures similar to those previously mentioned.

There exists the possibility that the HMAB solution alters the surface roughness of the film. In order to determine whether this is a source of error, a series of bulk nickel samples were studied. Some of these were anodized to form an oxide layer. After the 15-min time required to reach adsorption equilibrium with the HMAB (2), there was no further change in the determined surface area, for either the fresh or oxidized nickel surfaces. A plot of HMAB adsorption vs. time for Permalloy thin films has been published (2).

Results

The roughness, or roughness factor, of a sample is defined in this investigation as the ratio of the surface area obtained from the HMAB adsorption data to the geometric area. No attempt has been made to determine the nature of the roughness, i.e., no distinction can be made between a sample having a few large defects and another having a great number of smaller defects. The roughness of the cover glasses has been determined to be 2.5 (2).² Figure 1 shows plots of roughness of the metal film divided by the roughness of the glass substrate (relative roughness). The change in relative roughness with time in dry air at 20°C is shown in this figure. All the metals studied, except gold, undergo an increase in surface area as a result of aging in dry air. Figure 2 shows electron micrographs prepared by surface replication, comparing the surface of a freshly prepared copper film with a copper film that has been exposed to dry air for 107 days at 20°C. The micrographs confirm the roughening of the film with time.

An increase in roughness, similar to that in dry air, was observed for Permalloy films in vacuum and dry helium. However, 100% relative humidity appears to inhibit the roughening mechanism. Figure 3 shows the change in roughness obtained for Permalloy films in different environments. The data have

² This value, and all other roughness values obtained in this investigation, is based on calculations using 20.5Å² as the area of surface covered by one HMAB molecule. This figure has not been verified experimentally and, therefore, all roughnesses reported in this investigation should be considered as relative.

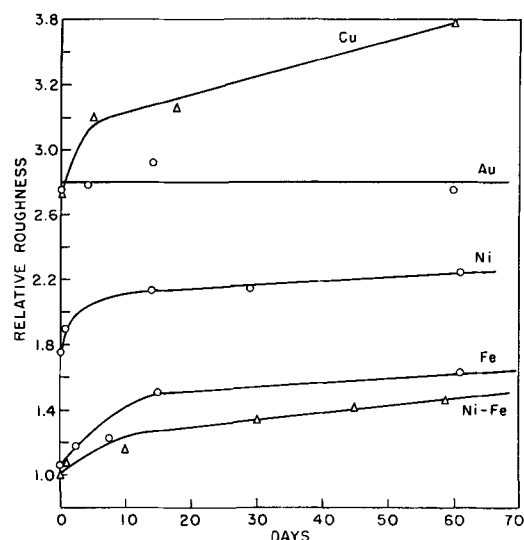


Fig. 1. Change in relative roughness (roughness of film/roughness of glass) with time in dry air.

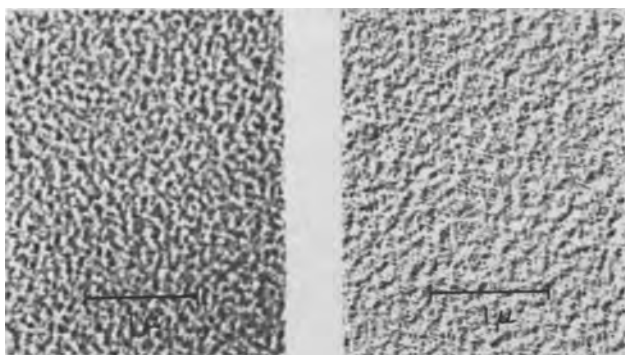


Fig. 2. Electron micrograph of freshly evaporated copper film (left) and copper film after 107 days in dry air environment at 20°C.

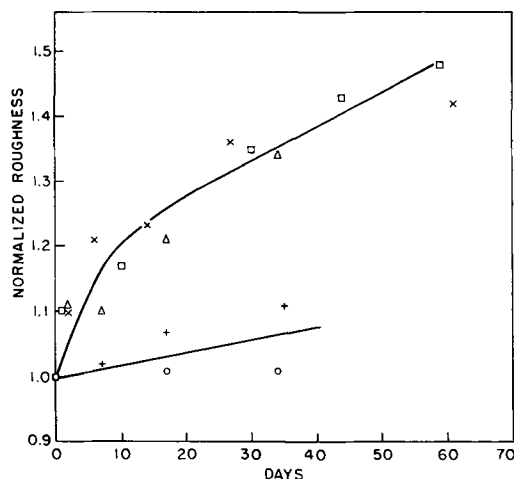


Fig. 3. Change in relative roughness for Permalloy in various environments. All roughnesses normalized to an initial roughness of 1. □, dry air; X, vacuum; Δ, dry helium; ○, 100% RH helium; +, 100% RH air.

been normalized to an initial roughness of 1.0 to facilitate comparison with other systems. Sputtered Permalloy films gave results identical to those obtained for evaporated Permalloy.

Although Permalloy films exhibited an increase in surface area in dry helium and vacuum similar to that in dry air, this was not observed for any other metal. Figure 4 shows the results obtained by aging iron films in various environments. Nickel and copper gave similar results. It can be seen that the aging effect on these metals is suppressed in all environments other than dry air. Again, the data have been normalized to an initial roughness of 1.0.

Similar observations were noted at 150°C (Fig. 5). It is seen that the roughening of Permalloy films was identical in dry air and in dry helium. The iron films, although exhibiting a considerable increase in roughness in dry air, did not roughen in a dry helium environment.

Discussion

As seen in Fig. 1, the films studied show differing roughness in their initial state. These initial roughnesses are in the inverse order of the recrystallization temperature or melting points of the metal. In fact, a plot of initial roughness *vs.* melting point of the metal is nearly linear. Since all of the

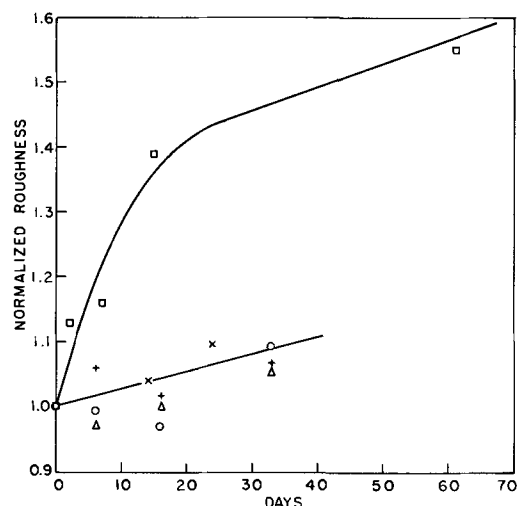


Fig. 4. Change in relative roughness for iron in various environments. □, dry air; X, vacuum; Δ, dry helium; ○, 100% RH helium; +, 100% RH air.

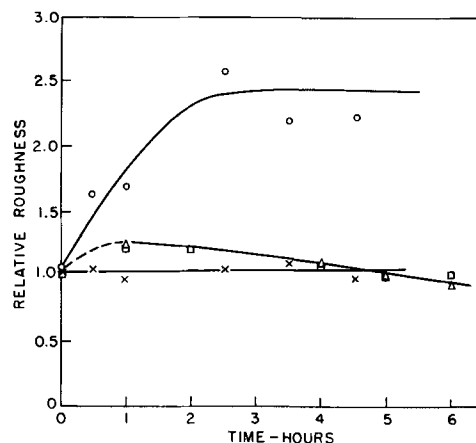


Fig. 5. Roughening of Permalloy and iron films at 150°C. □, Permalloy in dry air; Δ, Permalloy in dry helium; ○, iron in dry air; X, iron in dry helium.

evaporations were carried out at a constant substrate temperature, the metals with lower recrystallization temperatures will exhibit more crystal growth. This process should lead to an increase in surface roughness, explaining the initial points in Fig. 1. As an alternative possibility, the lower melting point metals may have more mobility on the substrate and more clumping of the film may occur.

The roughening of thin metallic films at room temperature may be due to an oxidation process or to an atomic rearrangement. The fact that gold films do not age under any of the conditions studied suggests a mechanism involving oxidation. The failure of Cu, Ni, and Fe to roughen under nonoxidizing conditions lends support to this mechanism in these cases. The inhibiting effect of moisture may be due to the adsorption of a layer of water on the surface of the film, inhibiting the oxidation process. Such inhibition of oxidation by water, although certainly unusual for iron, is not unknown for other materials (6, 7).

Results for Permalloy are of the greatest interest, particularly since oxides are thought to play

a role in the origin of anisotropy in magnetic films (8). In this case, results are different from those obtained for the unalloyed metals. As for Ni or Fe films, moisture is seen to inhibit the aging process. However, Permalloy is seen to age in nonoxidizing atmospheres provided they are dry. This may imply that aging in Permalloy is due to diffusion of oxygen or oxides to the surface from the interior of the film. Such a model has previously been suggested to explain the origin of the magnetic anisotropy (9). Whatever the driving force for this migration, it is inhibited by a water layer at the surface. Clearly, such an interpretation cannot be rigorously drawn from the available data, and a truly satisfactory explanation of this data cannot be made at this time.

Experiments at 150°C further support the conclusions drawn from room temperature studies. In the case of Permalloy an additional mechanism, leading to subsequent smoothening of the films, seems to be in operation at this temperature.

It has been shown that thin metallic films become rougher on aging at room temperature due to an oxidative process. The process is inhibited by moisture. Permalloy films also become rougher in nonoxidizing environments, provided moisture is absent. This process is not understood at the present time.

Acknowledgment

Many helpful discussions with Dr. J. A. Sartell, who suggested the correlation of recrystallization temperature with initial roughness, are gratefully acknowledged. The authors also wish to acknowledge the assistance of Mr. L. L. Egan and Mr. C. C. Isakson.

Manuscript received July 12, 1963; revised manuscript received Nov. 28, 1963. This paper was presented at the Pittsburgh Meeting, April 15-18, 1963.

Any discussion of this paper will appear in a Discussion Section to be published in the December 1964 JOURNAL.

REFERENCES

1. C. Weaver and R. M. Hill, *Advances in Physics*, **8**, 375 (1959).
2. J. Kivel, F. C. Albers, D. A. Olsen, and R. E. Johnson, *J. Phys. Chem.*, **67**, 1235 (1963).
3. J. E. Lewis and R. C. Plumb, *Intern. J. Appl. Rad. Isotopes*, **1**, 33, (1956).
4. M. C. Kordecki and M. B. Gandy, *ibid.*, **12**, 27, (1962).
5. R. J. Prosen, J. O. Holmen, B. E. Gran, and T. J. Cebulla, *J. Appl. Phys.*, **33**, 1150 (1962).
6. C. G. Sidwell, H. Salwin, and R. B. Koch, *J. Food Sci.*, **27**, 255 (1962).
7. K. V. Ingold, "Symposium on Foods; Lipids and Their Oxidation, p. 102, Air Publishing Co. (1962)
8. R. D. Heidenreich, E. A. Nesbitt, and R. D. Burbank, *J. Appl. Phys.*, **30**, 995 (1959).
9. R. J. Prosen, J. O. Holmen, B. E. Gran, and T. J. Cebulla, *J. Phys. Soc., Japan*, **17**, B-1, 580 (1962).

Brief Communication



Incorporation of Boron into Epitaxially Grown Silicon

Y. Matukura, K. Suzuki, and Y. Miura

Semiconductor Division, Nippon Electric Company, Limited, Kawasaki, Japan

Theuerer (1) and Corrigan (2) have reported the incorporation of boron into silicon during epitaxial growth. The transfer ratio (the ratio of boron-to-silicon ratio in solid to boron-to-silicon ratio in gas) of boron from BBr_3 contained in SiCl_4 into the epitaxially grown silicon is smaller than unity and depends on the fraction of BBr_3 in the SiCl_4 solution. These properties cannot be understood by considering alone the simple reactions such as the reduction of BBr_3 by hydrogen. Here, we report on the epitaxial growth of p-type silicon by using SiCl_4 solution containing a larger amount of BBr_3 than that normally contained as a doping source, and by using a preheating chamber and/or a water-cooled reduction chamber.

BBr_3 is mixed with SiCl_4 in an argon atmosphere so that the fraction of BBr_3 is 11.4, 1.17, or 0.11 mole %. Hydrogen gas samples saturated with the above and with nondoped SiCl_4 solution are introduced together into the deposition chamber as shown in Fig. 1. When the preheating chamber is operated above room temperature, the cooling water of the

deposition chamber is removed. The epitaxial growth is carried out at 1220°C with the flow rate of 1 liter/min H_2 gas containing approximately 3 mole % of the mixture of SiCl_4 and BBr_3 . Resistivity and Hall coefficient measurements on the grown p-type layers show that impurities with deep levels are not incorporated into the grown layer. The boron concentration of the p-type growth layer is determined from the resistivity measurements. Epitaxial layers with reproducible resistivities are obtained by this method.

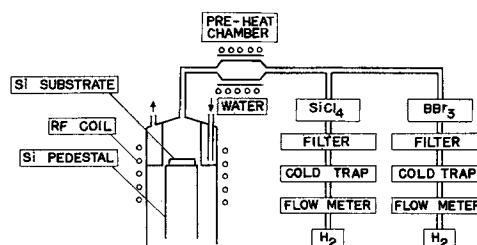


Fig. 1. Apparatus for silicon film growth by the hydrogen reduction of SiCl_4 .

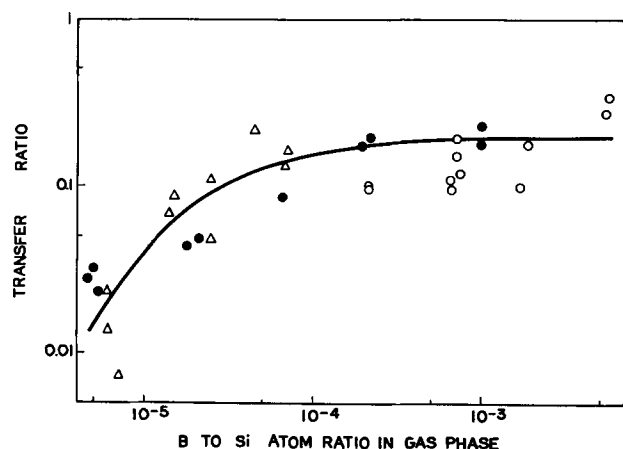


Fig. 2. Variation of transfer ratio with boron-to-silicon atom ratio in the gaseous phase: \circ , 11.4 mole % BBr_3 ; \bullet , 1.17 mole % BBr_3 ; \triangle , 0.11 mole % BBr_3 .

The transfer ratio is obtained without using the preheating and water cooling, and the results are shown in Fig. 2, in which the transfer ratio is given as a function of the boron-to-silicon atom ratio in the gaseous phase. It is seen that the transfer ratio increases with increasing boron-to-silicon atom ratio in the reactant gases in the range below 10^{-4} , while in the range above 10^{-4} the transfer ratio is shown to be approximately 0.2. These tendencies are in agreement with Theuerer's and Corrigan's results. The deposition temperature is varied over the range 1150° – 1250°C , but the results obtained show that the transfer ratio does not depend on the deposition temperature in the above range.

The remarkable influence of the preheating condition on the transfer ratio is shown in Table I. In the case of a preheating condition of 820°C , slight decomposition of SiCl_4 can be seen on the quartz tube of the preheater, while at 750°C no deposition of silicon can be observed. The silicon layers deposited using the water-cooled deposition chamber have scattered values of resistivity ranging from 1 to 12 ohm-cm.

As shown in Fig. 2, the transfer ratio does not depend on the mole per cent of BBr_3 in the SiCl_4

Table I. Transfer ratio obtained for various preheating conditions

Preheating condition, $^{\circ}\text{C}$	Resistivity of grown layer, ohm-cm	Transfer ratio
820	0.05	0.6
750	1	0.03
25	1	0.03
Water-cooled*	~ 5	~ 0.006

* Data obtained have scattered values of resistivity.

solution used as a gas doping source. This fact indicates that reaction of BBr_3 and SiCl_4 in the liquid phase does not affect the transfer ratio of boron. Corrigan (2) has reported that the use of BCl_3 as a doping material gives the same results as that obtained with BBr_3 . As shown in Table I, the preheating processes at 750° and 25°C give the same value of transfer ratio. In the gaseous phase, therefore, the reaction of BBr_3 and SiCl_4 does not affect the incorporation of boron.

The preheating process at temperatures such that the decomposition of SiCl_4 occurs results in a large increase of transfer ratio. In this case, the decomposition of SiCl_4 in the preheating chamber gives a change in boron-to-silicon ratio in the gaseous phase and the growth rate of the silicon layer decreases from 1 to $0.8 \mu/\text{min}$. However, this cannot be responsible for such a large increase in transfer ratio. On the other hand, epitaxial growth using the water-cooled chamber gives small and irregular values of the transfer ratio in comparison with that obtained by using the preheating and/or the room temperature chamber, in spite of the fact that BBr_3 is decomposed more easily by hydrogen than by SiCl_4 .

The above-mentioned properties indicate that boron does not incorporate directly from the form of BBr_3 into silicon during the epitaxial growth using SiCl_4 , but incorporates through other intermediate products of boron. If it is assumed that these intermediate products are formed simultaneously when SiCl_4 is reduced by hydrogen, the results shown in Table I will be reasonable. These products may be a complex composed of silicon, boron, chlorine, and/or bromine. Furthermore, if it is assumed that these products have two or more boron atoms, the decrease of transfer ratio with decreasing boron-to-silicon atom ratio can be understood, that is, it seems that the incorporation of boron into silicon during the decomposition of SiCl_4 is not caused by a reaction of the first order but of higher orders, of boron in gaseous phase.

Acknowledgment

The authors wish to thank Dr. H. Osafune for his usual encouragement.

Manuscript received Dec. 3, 1963.

Any discussion of this paper will appear in a Discussion Section to be published in the December 1964 JOURNAL.

REFERENCES

1. H. C. Theuerer, *This Journal*, **108**, 649 (1961).
2. W. J. Corrigan, "Metallurgy of Semiconductor Materials," J. B. Schroeder, Editor, p. 103, Interscience Div. of John Wiley & Sons, Inc., New York (1962).

The Reaction at the Iron Alkaline Electrode

Alvin J. Salkind and C. J. Venuto

The Carl F. Norberg Research Center, The Electric Storage Battery Company, Yardley, Pennsylvania

and S. Uno Falk

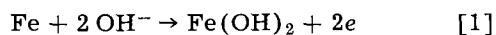
Svenska Ackumulator AB Jungner, Oskarshamn, Sweden

ABSTRACT

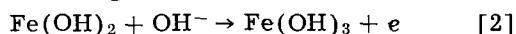
The discharged state of the iron (Edison) electrode in alkaline solution has been reported historically as a number of materials, usually as either FeO or Fe(OH)₂. Recent x-ray crystallography data, obtained independently in the two laboratories represented by the authors, indicates the material to be Fe(OH)₂ or Fe₃O₄, depending on the conditions of discharge. X-ray patterns were obtained by in situ techniques with electrodes cycled in sealed polyethylene bags, as well as with washed and dried active materials.

The alkaline iron electrode was investigated by both Thomas A. Edison and Waldemar Jungner for use as a negative electrode, with different types of nickel hydroxide positive electrodes, and was brought to a commercial product by Edison approximately 60 years ago. The charged active material has been consistently reported as Fe from the earliest mentions of the system in the literature, except for one patent of Jungner's (1) which indicates the charged material to be Fe(OH)₂. However, the discharged active material has been reported at various times at FeO (2), Fe(OH)₃ (1), Fe(OH)₂ (3), and Fe₃O₄ (4). Since the actual identification of the material had in general been done by analytical chemical rather than crystallographic techniques, a reinvestigation of the discharged iron active material was initiated.

The most thorough and extensive of the early researches into the electrochemistry of the alkali-iron powder electrode were those of Foerster, Herold and their associates (3, 5) in the period 1905-1910. Foerster found two potential stages on discharging iron electrodes and stated that the first stage was connected with the reaction



and the second stage



Chemical analysis carried out on three samples of active iron after stage I indicated 64-69% metallic iron, 19-22% valence two iron, and 11-14% valence three iron. But, Foerster attributed the 3-valent iron to a disturbance connected with air oxidation. Krassa (4), however, found a mixture of Fe(OH)₂ and Fe₃O₄ at a similar point of discharge. After stage II, Foerster found 39-43% metallic iron, 16.2-16.9% valence two iron, and 40-45% valence three iron.

Recent electrochemical studies have been carried out by Winkler (6) and Frumkin (6) and his associates.

Experimental

The iron active material investigated by the American co-authors was obtained from the Nickel Alkaline Battery Division of the Electric Storage

Battery Company (successors to the Edison Storage Battery Company). The material investigated by the Swedish co-author was prepared by the Svenska Ackumulator AB Jungner. In addition to these materials, prepared by the conventional Edison type processes described in the literature (7), iron active material made by electrolytic deposition was also checked. These preparations result in slightly different materials. NABD and electrolytical preparations result in a material which is solely a mixture of iron and its oxidized form. The former contained a slight amount of added sulfur, the latter contained none. On the other hand, the material prepared from the Jungner process contained a small amount of coprecipitated cadmium. The powder materials before forming into electrodes were identified by x-ray diffraction as a mixture of α Fe and Fe₃O₄ for the American materials and α Fe, Fe₃O₄, and CdO for the Swedish material. The active material powders were compressed between woven nickel screens into pellets of the type used in nickel-cadmium button cells and cycled between a pair of standard sintered-nickel positive electrodes (4.2 cm x 5 cm x 0.6 mm) in 20% KOH. In the first approach to preparing the materials for x-ray examination the pellets were removed from the electrolyte, washed in running water for 16 hr, and then rinsed in acetone three or four times to remove residual water and air-dried. These tests were carried out with materials in various stages of charge or discharge, and on extensively cycled as well as fresh active material. The x-ray reflections obtained always corresponded to the ASTM patterns for α Fe and Fe₃O₄. In retrospect, it appears that oxygen in the water, and air oxygen as well, were reacting with Fe(OH)₂ to form Fe₃O₄.

Another series of experiments was conducted with button pellet electrodes which were washed in a reducing solution of distilled water and invert sugar for 1 hr, rinsed in acetone, and air dried. The invert sugar reduction solution was obtained by inverting a 10% sucrose solution with 30 cc/liter of 87 weight per cent H₂SO₄. This was diluted further to different concentrations. It was observed that when the washing was conducted with solutions of concentration

greater than 0.05%, the reducing sugars interacted with the discharged material of the iron electrodes, so that only x-ray patterns of alpha iron were obtained. When rinsed in reducing sugar solutions of 0.05% the iron electrodes were stable and did not heat on exposure to air; the latter phenomenon was observed when the electrodes were washed in pure distilled water. A third series of experiments was conducted in which a pellet of active iron material was cycled against a nickel hydroxide electrode sealed in a polyethylene bag. This technique has previously been reported by Falk (8) and eliminates the possibility of a change in chemical composition due to air oxidation, washing, or drying, and is a modification of the technique reported by Salkind and Bruins (9). X-rays were taken through the bag for three or more cycles of charge and discharge. In the in situ x-ray experiments carried out in Sweden, current was maintained on the electrodes continuously in order to stabilize the active material and to prevent open circuit reactions.

Results

The charged active material, in all cases, yielded x-ray patterns listed in the ASTM file (10) as belonging to αFe .

The crystallographic data obtained with the last two methods of stabilizing electrodes discussed in the experimental section, were similar. The material found in the early part of the discharge curve of iron electrodes fits exactly the ASTM pattern for $\text{Fe}(\text{OH})_2$. A typical discharge curve for the potential of an iron electrode discharged at the 5-hr rate measured against a Hg-HgO-20% KOH reference is shown in Fig. 1. A first voltage plateau existed until the discharge voltage of -0.85v against the reference was obtained. During this plateau only patterns of $\text{Fe}(\text{OH})_2$ and αFe were observed when in situ techniques were used with the Swedish iron as is shown in Fig. 2. When the reducing solution technique was used with the American iron the pattern contained the reflections of Fe_3O_4 as well as $\text{Fe}(\text{OH})_2$ and αFe as given in Table I. These differences may be attributable to reaction with oxygen contained

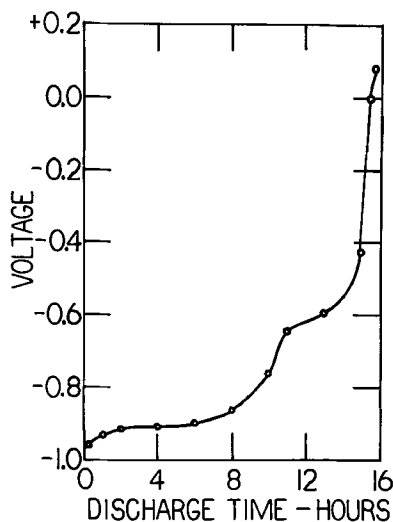


Fig. 1. Discharge curve for an iron electrode measured against a Hg-HgO reference in 20% KOH.

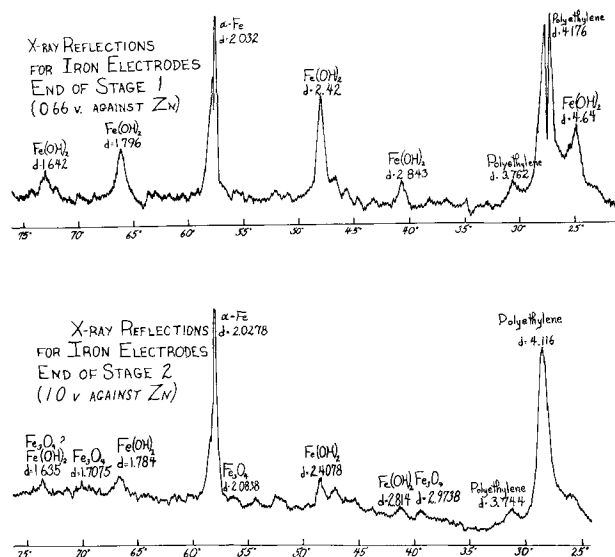


Fig. 2. X-ray patterns from iron electrodes obtained by in situ bag cycling technique.

in the wash solution. However, it is also possible that the Cd-content of the Swedish iron tends to stabilize that material at the $\text{Fe}(\text{OH})_2$ stage against chemical reaction with oxygen. On continuation of discharge a second voltage range was obtained, which, although not a true plateau, was in the range of -0.5 to -0.65v . The x-ray reflections obtained for material in this region fit the ASTM pattern for Fe_3O_4 . In both voltage regions reflections of undischarged αFe were obtained.

The ASTM standard lines for αFe , Fe_3O_4 , FeO , and $\text{Fe}(\text{OH})_2$ are included in Table I for comparison. No unidentifiable refraction lines were encountered with the American iron materials except a minor peak at 2.22\AA , which appeared whenever strong patterns of αFe were obtained.

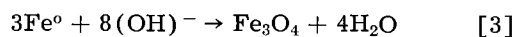
Discussion and Conclusions

The crystallographic data indicate that the half-cell reaction at the iron alkaline electrode is initially

$$\text{Fe} + 2\text{OH}^- \rightarrow \text{Fe}(\text{OH})_2 + 2e \quad [1]$$

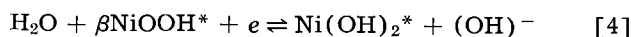
confirming the earlier experiments of Foerster and co-workers.

On complete discharge the reaction



takes place. The authors recalculated the chemical analysis reported by Foerster for material after stage II, deducting the amount of Fe^{3+} attributed by Foerster (after stage I) to a disturbance connected with air oxidation, and found that the recalculated data approximately fit the stoichiometry of Fe_3O_4 .

If these equations are combined with the nickel electrode half-cell reaction proposed by Wynne-Jones *et al.* (11), Salkind and Bruins (9), Falk (8), Conway and Bourgault (12), Kornfeil (13) and others

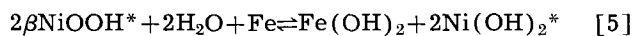


where the * indicates unknown amounts of hydration and adsorbed alkali, then the cell reactions in the nickel iron cell are

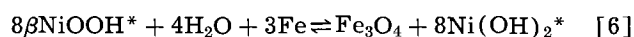
Table I. X-ray reflections from iron electrodes using reducing sugar wash technique comparing experimental data with ASTM standards

α -Fe		ASTM Standards						Experimental data		
		Fe ₃ O ₄		FeO		Fe(OH) ₂		Discharge to -0.85v*	0.00*	+0.60*
d, A	I/I ₁	4.85	40			4.61	80	4.59		
		2.97	70			2.82	50			
		2.53	100					2.52	2.53	2.51
				2.49	80					
		2.42	10			2.42	100	2.41		
		2.10	70	2.15	100					
2.03	100							2.03	2.03	2.03
		1.71	60			1.79	28			
		1.61	85			1.64	36			
				1.52	60	1.54	20			
1.43	19	1.48	85					1.43	1.43	1.43

* Voltages vs. Hg-HgO reference.



and



Equation [5] agrees with the reaction reported by Glemser and Einerhand (14) who used it in their study of the nickel electrode. The authors rechecked the records of the Nickel Alkaline Battery Division of The Electric Storage Battery Company to ascertain how the original identification of the material as FeO was made. The discharged material had been found to have approximately equal stoichiometric quantities of oxygen and iron, and it was on this basis that the material was identified as FeO in the early records. A recent recheck of the present active material indicates the same chemistry. The authors feel that the over-all stoichiometry of almost equal amounts of oxygen and iron can be accounted for by a mixture of the two materials. The possibility of lumps of Fe₃O₄ having Fe cores must also be considered. Metallographic examinations at 500 magnification, indicate that the active material grains are composed of an irregular mixture of two phases, but the identification has not yet been established with certainty.

The theoretical capacity of iron electrodes based on Eq. [5] would be 0.96 A.H./gram of iron and on Eq. [6] 1.28 A.H./gram of iron. However, practical nickel-iron cells are designed with a large excess of iron, so the second voltage range of the iron electrode is rarely met in practice.

Acknowledgment

The authors would like to acknowledge the assistance of Mr. M. J. Mackenzie in carrying out electrode preparation and cycling and Mr. R. Hedell for his assistance in the in situ x-ray experiments.

Manuscript received Oct. 23, 1963. Revised manuscript received Dec. 9, 1963.

Any discussion of this paper will appear in a Discussion Section to be published in the December 1964 JOURNAL.

REFERENCES

- W. Jungner, Swedish Patent No. 15567, Jan. 22, 1901.
- E. F. Roeber, *Trans. Am. Electrochem. Soc.*, **2**, 195, (1902); Kirk-Othmer, "Encyclopedia of Chemical Technology," Vol. 3, p. 309 Interscience, New York (1949); F. C. Anderson, *This Journal*, **99**, 244C (1952).
- F. Foerster, *Z. Electrochem.*, **14**, 285 (1908); M. Kammerhoff, "Der Edison akkumulator," p. 13, Julius Springer, Berlin (1910).
- P. Krassa, *Z. Electrochem.*, **15**, 490 (1909).
- Foerster and Herold, *ibid.*, **16**, 461 (1910).
- H. Winkler, *Deut. Elektrotechnik*, **6**, 355 (1952); B. Kabanov, R. Burnstein, and A. Frumkin, *Disc. Faraday Soc.*, **1**, 759 (1947).
- G. W. Vinal, "Storage Batteries," 4th ed., p. 89, John Wiley & Sons, New York (1955); (Discusses in part ref. 3 and 13.)
- S. U. Falk, *This Journal*, **107**, 666 (1960).
- A. J. Salkind and P. F. Bruins, *ibid.*, **109**, 356 (1962); A. J. Salkind, *Dissertation Abstracts*, **19**, 497 (1958); A. J. Salkind, "Nickel-Cadmium Cell," MIC-58-2880, University Microfilms, Ann Arbor, Mich.
- A.S.T.M. "X-ray Powder Data File" Special Technical Publication 48-L, A.S.T.M. Philadelphia (1962).
- E. Jones and W. F. K. Wynne-Jones, *Trans. Faraday Soc.*, **52**, 1260 (1956); W. D. Briggs and W.F.K. Wynne-Jones, *ibid.*, **52**, 1272 (1956).
- B. E. Conway and D. L. Bourgault, *Can. J. Chem.*, **37**, 292 (1959).
- F. Kornfeil, "The Charge-Discharge Process of the Nickel-Oxide Electrode," Proc. 12th Ann. Battery Res. Dev. Conf. 18-22, Fort Monmouth (1958).
- O. Glemser and J. Einerhand, *Z. Electrochem.*, **54**, 302 (1950).
- S. A. Rozentsveig and Z. V. Shcherbakova, *Russian J. of Phys. Chem.*, **35**, 1259 (1961).

Investigation of Manganese Dioxides

II. Surface Area and Water Content

Robert F. Amlie and Aladar Tvarusko¹

The Carl F. Norberg Research Center, The Electric Storage Battery Company, Yardley, Pennsylvania

ABSTRACT

The surface areas of natural ores, electrolytic, chemical, and synthetic hydrous MnO₂ samples were determined by both low-temperature nitrogen gas adsorption and water vapor adsorption at 25°C, using the B.E.T. adsorption isotherm relationship. These various types of manganese dioxides have distinctly different surface areas as determined by the two methods. The water content retained at 110°C and corrected total water content were found to be surface area dependent. The synthetic hydrous MnO₂ samples occupy a unique position due to their high water content.

The ease of electrochemical reduction of a manganese dioxide electrode is affected by the number and distribution as well as the state of the sites available for the reaction of protons with the oxide depolarizer. It is recognized in the Leclanché dry cell industry that the activity of an oxide is intimately involved with its water content and that oxides with higher water content often exhibit more satisfactory performance. The surface area of an MnO₂ material is also known to be an important physical parameter in determining cathodic performance. It was therefore of interest to study the correlation of the water content of oxides with their surface areas. In the present work, surface areas were determined by both low-temperature nitrogen and room temperature water-vapor adsorption techniques and related to the quantity of water retained at 110°C and the total water content.

The B.E.T. surface area (1) of various MnO₂ samples has been measured by numerous authors and was found to depend on: (a) the type of MnO₂ (2-13), (b) the preparation (4, 7), (c) temperature of degassing (10, 14), and (d) particle size distribution (10). Several investigators have reported that as the MnO₂ samples were heated the surface area remained almost constant initially and then decreased with increasing temperature (5-7, 14). Hirai *et al.* (15) tried to measure the surface area by liquid-phase adsorption method, but no correlation was found with B.E.T. surface area. Scott's effective surface area (16) was only about 12% of the B.E.T. surface area.

Attempts were made to correlate the B.E.T. surface area with: (a) the depolarizing activity (3) (not successful), (b) depolarizing capacity (8) (valid only within the same structure type), and (c) ion exchange properties (7), Zn⁺⁺ adsorption, and amount H⁺ released (14) (linear dependence). The loss of water content is assumed to be responsible for the small increase of surface area when the degassing temperature is low (10, 14). According to Gattow *et al.* (7), γ -MnO₂ samples of higher surface areas contain more OH⁻ than products of lower surface areas.

Adsorption isotherms of MnO₂ for water vapor were determined by Foote *et al.* (17). They found that the surface adsorption of water is markedly reduced only when the temperature is raised above the decomposition temperature. However, Sasaki *et al.* (18) and one of us (19) showed that the amount of water adsorbed decreases gradually with the increasing temperature. On the basis of B.E.T. surface area and water vapor adsorption isotherms of heated electrolytic MnO₂, Sasaki *et al.* (18) found that the experimental value of the water vapor adsorption is close to the value corresponding to monolayer adsorption by B.E.T. theory. Ninagi *et al.* (20) measured the adsorption isotherms of water vapor on various manganese dioxides and calculated the apparent surface area. They found that the apparent surface area depends on the crystal type of MnO₂ and decreases with the increasing temperature of the heat treatment.

The surface areas of natural ores, electrolytic, chemical, and synthetic hydrous MnO₂ samples, described earlier (19), were determined in this study by both low-temperature nitrogen gas adsorption and room-temperature water vapor adsorption, using the B.E.T. adsorption isotherm relationship (1). Furthermore, these surface areas were correlated with their water contents determined previously (19).

Experimental

Surface area determination by low-temperature N₂ adsorption.—In order to realize a more rapid analysis time and to avoid difficulties normally encountered with the conventional high-vacuum B.E.T. apparatus, the surface areas were determined by low-temperature nitrogen gas adsorption, described by Loebenstein *et al.* (21). This simplified technique is based on the selective adsorption of nitrogen gas from nitrogen-helium gas mixtures at pressures in the order of barometric pressures. The isotherm measurement and calculations were normally carried out in less than 3 hr, since the adsorption equilibria could be attained rapidly by the repeated cycling of the gas mixture through the sample. Furthermore, time was saved by not having to wait to remove the helium (the presence of helium does not interfere with the adsorption of N₂)

¹ Present address: Department of Industrial and Engineering Chemistry, Swiss Federal Institute of Technology, Zurich, Switzerland.

and to recool the adsorption tube prior to admitting nitrogen gas (21).

Liquid nitrogen is normally employed with the high vacuum B.E.T. apparatus as the sample refrigerant. In this study, however, the nitrogen adsorption was measured at the temperature of liquid oxygen to obtain an expanded range of the partial pressures. Under a pressure of 735 mm Hg, liquid nitrogen boils at approximately 77°K, whereas pure liquid oxygen boils at 90°K. It can be readily calculated that at 90°K, liquid nitrogen is in equilibrium with its vapor at a pressure of 2700 mm Hg. Since the free-surface B.E.T. equation is usually valid only with the adsorbate in the relative pressure (p/p_0) range of 0.05-0.3, it is evident that a nitrogen pressure range of about 680 mm Hg is realized at 90°K. In comparison, this working pressure range at 77°K is reduced to approximately 180 mm Hg. At the higher temperature, the expanded pressure range provided better resolution and consequently a more accurate isotherm determination. The pressures in the apparatus were maintained in the range of about 100-900 mm Hg. Since the total gas mixture could not be allowed to greatly exceed barometric pressure, it is evident that a nitrogen relative pressure of 0.3 was the upper limit at 90°K. Liquid nitrogen was the refrigerant when it was desired to go higher than 0.3 p/p_0 .

A greatly improved reproducibility was obtained for the lower surface area samples by using a dead-space calibration procedure different from that of Loebenstein *et al.* (21). Prior to the determination of the nitrogen adsorption isotherm, the quantity of the helium (in moles) in the dead space of the apparatus was measured as a function of the helium equilibrium pressure. For each calibration plot, a straight line should be obtained which has to pass through the origin since helium behaves essentially as an ideal gas, even at the temperature of liquid oxygen. The slope of this line can be very accurately determined and failure of the line to pass through the origin indicates the calibration to be in error.

In the determination of the nitrogen adsorption isotherm, the quantity of the nitrogen in the dead space is calculated by multiplying the corrected nitrogen gas pressure at equilibrium by the value of the calibration slope. The surface area values are calculated by a method similar to that used for conventional B.E.T. adsorption isotherm calculations.

The MnO_2 samples were oven-dried at 110°C for 24 hr with the exception of synthetic hydrous MnO_2 samples which were dried for 48 hr. Each sample was then placed in the sample holder between layers of glass wool and degassed at 110°C in a slow stream of helium gas for 4-8 hr.

Surface area determination by water vapor adsorption at 25°C.—It is known that surface areas of various materials can be calculated from the amount of the water vapor adsorbed determined either gravimetrically or volumetrically. Ninagi *et al.* (20) determined gravimetrically the water vapor adsorption of MnO_2 samples in various humidities and calculated the apparent surface areas from the adsorption isotherms. In the present study,

the gravimetric method was selected over the volumetric method because of its inherent simplicity and reproducibility. The surface areas of the various MnO_2 samples were calculated from the water vapor adsorption isotherms.

Initially, a "static atmosphere" method of water vapor adsorption on predried MnO_2 samples was carried out in partially evacuated vacuum desiccators over various saturated salt solutions (their p/p_0 was between 0.1 and 0.3) for at least three days. However, this method was abandoned in favor of the Nesbitt bulb "dynamic method." The Nesbitt absorption bulb was chosen for the determination of the water vapor adsorption at various relative pressures (of water vapor) because the weight increase due to the adsorbed water can be determined without exposing the sample to the ambient atmosphere and without the accidental loss of MnO_2 sample. Furthermore, equilibrium in a given water vapor atmosphere can be attained in a shorter time than in a "static atmosphere" by forcing the water vapor of certain relative pressure through the sample.

A weighed amount of the MnO_2 sample was placed in a Nesbitt absorption bulb interspersing the sample between layers of glass wool to prevent packing and consequent channeling of the water vapor stream. The Nesbitt bulb so prepared was weighed and the MnO_2 sample was degassed at 100°C in vacuum for a period of about 15 hr and then reweighed. A water-vapor trap cooled by an acetone-dry-ice mixture was placed between the Nesbitt bulb and the vacuum pump. After reweighing, the Nesbitt bulb was connected to the apparatus and evacuated. Water vapor of certain relative pressure was slowly and intermittently pumped from the constant-humidity chamber (*i.e.*, sulfuric acid reservoir) through the MnO_2 sample for a certain time (3-5 hr, depending on the type of MnO_2). The Nesbitt bulb was removed and immediately reweighed. The weight increase over the weight of the bulb after degassing gave the amount of water vapor adsorbed. Equilibrium was considered attained when the weight of the bulb remained constant.

The relative pressure of the aqueous vapor in the constant humidity chamber depends on the concentration, *i.e.*, specific gravity, of the aqueous sulfuric acid solutions. During the equilibration of the MnO_2 , water is removed from the aqueous sulfuric acid solution. If a large enough amount of sulfuric acid solution is present, the decrease of the relative pressure of aqueous vapor due to the concentration change of the sulfuric acid solution is small. To obtain the correct relative pressure of aqueous vapor at equilibrium, the specific gravity of the aqueous sulfuric acid solution was measured with a Westphal density balance immediately after the removal of the Nesbitt bulb. The corresponding relative pressure value was read from a diagram of p/p_0 vs. density. The apparatus for the determination of surface areas by water vapor adsorption was kept in a constant temperature cabinet and all results refer to 25.0° ± 0.2°C.

The water vapor adsorption of each MnO_2 sample was determined at four or more different rela-

Table I. Surface areas of MnO₂ samples determined by low-temperature nitrogen and water vapor adsorption at 25°C

Name	Surface area, m ² /g		H ₂ O vapor adsorption 25°C	Water content	
	N ₂ adsorption Conventional	90°K		110°C, %	Corrected total, %
Natural ores					
African, Ghana	10.3	9.5	9.2	0.88	3.3
Montana	17.5	16.6	28.2	2.40	5.2
California	12.4	11.6	18.4	1.54	3.0
Moroccan	7.4	7.1	6.3	0.53	1.2
Mexican	—	16.6	19.4	2.25	4.3
Grecian A	—	14.1	25.9	2.74	5.5
Grecian B	—	11.2	22.3	2.28	—
Caucasian	—	12.7	10.4	1.19	3.2
Electrolytic MnO₂					
Sample A	45.0	44.7	35.2	3.82	5.9
Sample B	46.2	42.4	35.6	3.56	5.8
Sample C	29.8	28.0	16.2	3.35	6.2
Sample D	43.5	44.3	30.6	3.44	6.5
Sample E	—	41.8	30.5	3.33	6.0
Sample O	—	45.0	30.5	3.18	—
Sample P	—	36.5	24.1	3.05	—
Chemical MnO₂					
Sample F	95.5	88.2	48.5	5.56	7.1
Sample G	90.4	78.1	53.7	5.37	6.8
Sample H	—	81.1	36.5	5.88	7.4
Sample Q	—	57.5	32.0	5.73	—
Synthetic hydrous MnO₂					
Sample J	17.1	17.0	211	15.13	20.2
Sample K	—	14.6	150	14.07	20.7
Sample L	11.5	5.6	50	10.01	14.2
Sample M	—	25.8	105	15.89	19.6
Sample N	—	90.9	147	17.19	22.0
Sample R	—	2.7	152	11.81	—
Sample S	—	29.1	155	15.62	—

tive pressures of water vapor which were selected to fall in the B.E.T. range, namely $p/p_0 = 0.1$ to 0.3 .

Results and Discussion

The surface areas of the manganese dioxide samples classified by their origin, namely, natural ores, electrolytic, chemical, and synthetic hydrous MnO₂ samples, described earlier (19), were determined by nitrogen adsorption at 90°K. Surface areas of some of the MnO₂ samples were also determined by the conventional B.E.T. apparatus at 70°K. Both results are given in Table I. In general, the surface area values determined at 90°K are slightly lower than those determined by the conventional B.E.T. apparatus. The surface area values for the natural ores and electrolytic MnO₂ samples are comparable and the agreement is good. For the chemical MnO₂ samples and some of the synthetic hydrous MnO₂ samples, the deviation in the two surface areas is large and can be explained only by changes taking place in the higher vacuum employed in the conventional B.E.T. apparatus.

The results clearly indicate that the surface area depends on the type of MnO₂, a conclusion drawn by various authors (2-13). The various groups of MnO₂ samples, with the exception of synthetic hydrous MnO₂, have distinctly different surface area values and the deviation in the surface areas within the group is small.

Table II. Surface area as a function of equilibrium time. Water vapor adsorption at 25°C

Determined by	Surface area, m ² /g	
	African ore	Montana ore
"Static method"	12.6	31.5
"Dynamic method"		
2 Hr equilibration	7.39	25.0
3 Hr equilibration	8.10	26.7

In the surface area determinations by water vapor adsorption at 25°C, the attainment of the equilibrium with the water vapor is very important. Table II shows the surface areas of two natural ores calculated from data obtained after various periods of equilibration. It can be clearly seen that increasing the length of the equilibration time increases the calculated surface area of the sample. This is to be expected since the re-adsorption depends on time and the equilibrium is approached asymptotically. The surface areas obtained by the "static method" are slightly higher than those obtained by the "dynamic method." The reproducibility of the "static method," however, was inferior to that of the "dynamic method."

The surface areas of the various MnO₂ samples obtained by water vapor adsorption are also shown in Table I. It is quite evident that these surface area values in most cases differ significantly from the surface areas determined by the low-temperature nitrogen adsorption. The deviation between the two surface area values seems to increase with the decreasing degree of crystallinity, i.e., with the increasing water content (19). Ninagi *et al.* (20) observed that the apparent surface area determined by water vapor adsorption depends on the crystal type of the MnO₂.

The water originally present in the MnO₂ is first eliminated and then it is allowed to re-adsorb at different relative pressures of water vapor. On the basis of the amount of the re-adsorbed water, the surface areas are calculated. Ninagi *et al.* (20) found that the apparent surface areas decreased with the increasing temperature of the heat treatment. This is due, as was found by Sasaki *et al.* (18) and one of us (19), to the decreased re-adsorption of the water vapor by the heated MnO₂ sample. In most cases, however, all the water removed at 110°C is resorbed by the MnO₂ sample. Accordingly, a linear relationship should exist between the surface area values of various MnO₂ samples determined by water vapor adsorption, and the water content at 110°C (19); this is shown in Fig. 1. The correlation is reasonably good for all types of MnO₂ with the exception of the synthetic hydrous MnO₂ samples for which it is only fair.

Figure 2 shows the corrected total water content, see ref. (19), of the various MnO₂ samples as a function of their surface area, determined by water vapor adsorption (S.A. — H₂O). As expected, on the basis of Fig. 1, the corrected total water content increases with the surface area regardless of the type of the MnO₂ sample. The different nature of the synthetic hydrous MnO₂, however, clearly shows

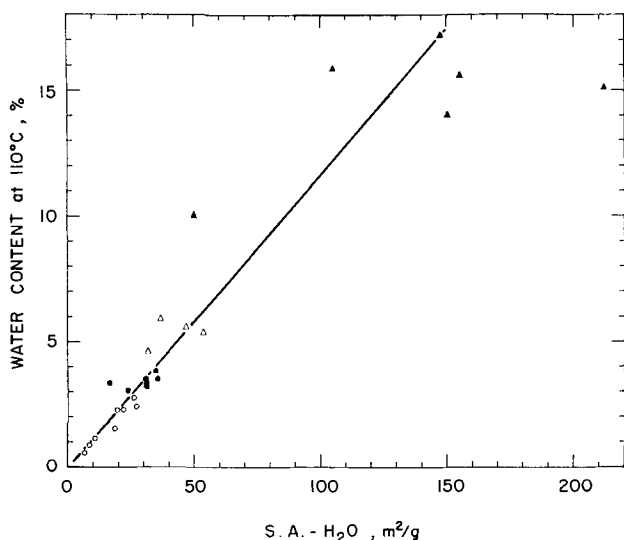


Fig. 1. Water content at 110°C as a function of surface area determined by water vapor adsorption at 25°C. ○ Natural ores, △ chemical MnO₂, ● electrolytic MnO₂, ▲ synthetic hydrous MnO₂.

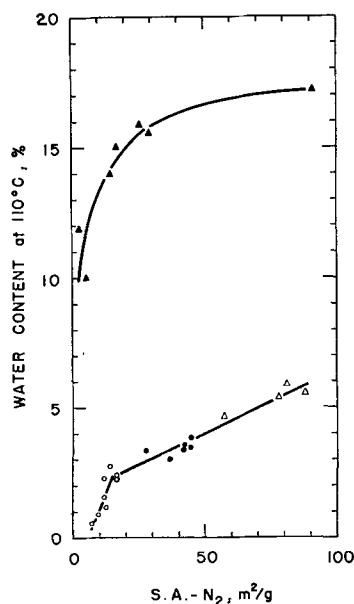


Fig. 3. Water content at 110°C as a function of surface area determined by nitrogen gas adsorption at 90°K. Legend the same as in Fig. 1.

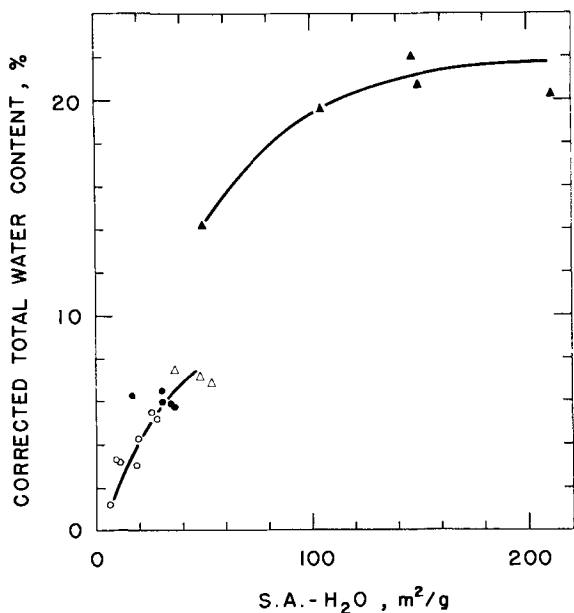


Fig. 2. Corrected total water content as a function of surface area determined by water vapor adsorption at 25°C. Legend the same as in Fig. 1.

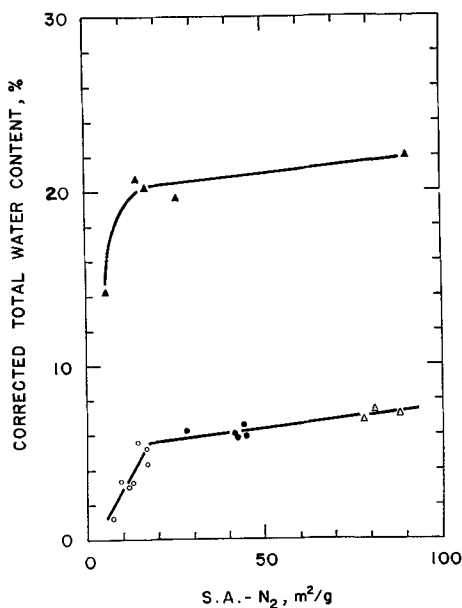


Fig. 4. Corrected total water content as a function of surface area determined by nitrogen gas adsorption at 90°K. Legend the same as in Fig. 1.

up. Furthermore, it is evident that the water content of the MnO₂ samples seems to approach a constant value with the increasing surface areas. If the surface areas of the other three types of MnO₂ could be increased to the values of the synthetic hydrous MnO₂ samples, the water content curves would still be below the curve representing the synthetic hydrous MnO₂ samples. The numerical difference between the two water content curves is about 7%; this could be assumed to be the water that reacted with the amorphous MnO₂.

Because of the possibility of a reaction between the water vapor and the MnO₂, it was of interest to establish the relationship between the different water contents and the surface areas as determined

by low-temperature nitrogen adsorption. Figure 3 shows the water content at 110°C as a function of surface area obtained by nitrogen adsorption (S.A. — N₂). The linear relationship of Fig. 1 is not found here. The MnO₂ samples of various types form distinct groups; within all these groups, the water content at 110°C increases with the increasing surface area. With the exception of the synthetic hydrous MnO₂ samples, this relationship is approximately linear for all groups. By extrapolating the curve for the synthetic hydrous MnO₂ samples to the ordinate, representing the water content, the curve seems to intercept at about 7 to 8%. This is in good agreement with the value obtained from Fig. 2.

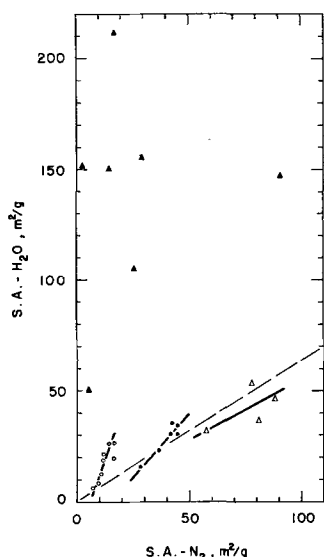


Fig. 5. Relationship between surface area determined by water vapor adsorption at 25°C and surface area determined by nitrogen gas adsorption at 90°K. Legend the same as in Fig. 1.

Figure 4 shows the corrected total water content as a function of the surface area, determined by nitrogen adsorption. This figure resembles Fig. 3. Because of the similarity of the upper and lower curve of Fig. 4, it can be expected that the difference in the corrected total water content has some significance; this difference is about 13-15%. On the basis of the results of Fig. 2 and 3, it can be assumed that about 7% water is combined to various degrees with the synthetic hydrous MnO₂. By adding to this the corrected constitutional water content (19), 12 to 14% is obtained for the water reacted, to various degrees, with the MnO₂; this is about equal to the numerical difference in the water content between the two curves of Fig. 4. These high water contents of the synthetic hydrous MnO₂ materials are responsible for the beneficial effect realized when combined with natural ores in the Leclanché cells (22).

Correlation of the two water contents with surface areas measured by water vapor and nitrogen adsorption techniques showed that the various types of MnO₂ fall into two distinct groups. It was also of interest to see what relationships exist between the two surface area measurements and these data are plotted in Fig. 5. The broken line in Fig. 5 shows the linear relationship which would result with monolayer coverage assuming that the N₂ molecule occupies an area of 17.0Å² at 90°K (23) and the water molecule covers 10.8Å² of surface at 25°C (24). The various MnO₂ types are seen to form distinct groups and approximate linear relationships exist for the natural ores, electrolytic, and chemical MnO₂ samples; the synthetic hydrous MnO₂ samples are scattered and form no distinct group. This is, however, to be expected since they are not as uniform physically and chemically as the other three groups.

Conclusions

The reproducibility of the low surface area values, determined by the low-temperature nitrogen ad-

sorption, was improved by using a dead-space calibration procedure different from that of Loebenstein *et al.* (21). The surface area determination by water vapor adsorption can be used for the natural ores, electrolytic and chemical MnO₂ samples, but it is not suitable for the synthetic hydrous MnO₂ samples due to a reaction between the MnO₂ and the water and the presence of certain alkalies. On the other hand, this determination allows one to obtain information not evident from the surface area measurement by nitrogen adsorption. The deviation between the two surface area values seems to increase with the decreasing degree of crystallinity, *i.e.*, with the increasing water content (19).

The water content at 110°C and the corrected total water content increase with the increasing surface area of the sample, whether nitrogen gas or water vapor was used for its determination. The natural ores, electrolytic, and chemical MnO₂ samples form one loosely coherent group, whereas the synthetic hydrous MnO₂ samples behave quite differently. This is due to their high content of water, the larger portion of which is combined in different extents with the MnO₂.

Since the water content and the surface area of the various MnO₂ samples are interdependent, it can be assumed that the discharge capacity and the rate of discharge will increase with the increasing surface area and hence the water content; the different slopes of the various groups of manganese dioxides indicate that the latter relationship is valid only within a given group. This is in agreement with Srb's observation (8) that the B.E.T. surface area and depolarizing capacity correlation is valid only within the same structure type.

Acknowledgment

The authors are indebted to Mr. Michael S. Kisiel, Jr. for carrying out the adsorption isotherm measurements.

Manuscript received Sept. 9, 1963; revised manuscript received Nov. 29, 1963.

Any discussion of this paper will appear in a Discussion Section to be published in the December 1964 JOURNAL.

REFERENCES

1. S. Brunauer, P. H. Emmett, and E. Teller, *J. Am. Chem. Soc.*, **60**, 309 (1938).
2. A. Kozawa, *This Journal*, **106**, 79 (1959).
3. M. Fukuda, *J. Electrochem. Soc. Japan*, **28**, 67 (1960).
4. W. C. Vosburgh, *This Journal*, **106**, 839 (1959).
5. O. Glemser, G. Gattow, and H. Meisiek, *Z. anorg. u. allgem. Chem.*, **309**, 1 (1961).
6. G. Gattow and O. Glemser, *ibid.*, **309**, 121 (1961).
7. G. Gattow and O. Glemser, *ibid.*, **309**, 20 (1961).
8. V. Srb, *Collection Czechoslov. Chem. Commun.*, **26**, 1231 (1961).
9. W. Buser and P. Graf, *Helv. Chim. Acta*, **38**, 830 (1955).
10. M. Fukuda, T. Hirai, and H. Manabe, *Natl. Tech. Rept.*, **5**, 127 (1959).
11. N. C. Cahoon and M. P. Korver, *This Journal*, **109**, 1 (1962).
12. J. Euler, *Electrochim. Acta*, **4**, 27 (1961).
13. J. F. Laurent and B. Morignat, Paper presented at the Third International Battery Symposium, Bournemouth, England, October 1962.

14. A. Kozawa, *This Journal*, **106**, 552 (1959).
15. T. Hirai, H. Manabe, and M. Fukuda, *Natl. Tech. Rept.*, **7**, 16 (1961).
16. A. B. Scott, *This Journal*, **107**, 941 (1960).
17. H. W. Foote and J. K. Dixon, *J. Am. Chem. Soc.*, **52**, 2170 (1930).
18. K. Sasaki and A. Kozawa, *J. Electrochem. Soc. Japan*, **25**, 115 (1957).
19. A. Tvarusko, *This Journal*, **111**, 125 (1964).
20. S. Ninagi and Y. Miyake, *J. Electrochem. Soc. Japan*, **30**, 727 (1962).
21. W. V. Loebenstein and V. R. Deitz, *J. Research Natl. Bur. Standards*, **46**, 51 (1951).
22. A. Tvarusko, *This Journal*, **109**, 557 (1961).
23. P. H. Emmett, *Advances in Colloid Sci.*, **1**, 1 (1942).
24. H. K. Livingston, *J. Colloid. Sci.*, **4**, 447 (1949).

The Oxidation of Iron Single Crystals around 200°C

P. B. Sewell and M. Cohen

Division of Applied Chemistry, National Research Council, Ottawa, Ontario, Canada

ABSTRACT

The oxidation of electropolished iron in the temperature region of 200°C is highly dependent on the surface orientation in respect to both the total thickness and phase composition of the oxide. In general, surface orientations close to the (001), (011), and (111) planes oxidize to give films with a large proportion of Fe₃O₄. The thick oxide formed on the (001) surface has a thin outer layer containing a high percentage of γ -Fe₂O₃. Specimens with orientations remote from the above low index planes oxidize to form films containing a smaller percentage of Fe₃O₄. On the (112) surface, α -Fe₂O₃ develops in the outer layer of the oxide at an earlier stage than on the (001). No discrete phase boundaries exist between the oxide phases. These trends are also shown at higher temperatures. Thin films of Fe₃O₄ (up to about 100Å) on the (001) and (112) surfaces behave differently with regard to cathodic reduction, with mainly formation of Fe⁺⁺ from magnetite on the (001) surface, and a mixed reaction with a large amount of reduction to metallic iron on the (112) surface. A change in surface preparation can change the distribution of phases in the oxide.

The oxidation of polycrystalline iron around 200°C has been investigated in some detail by Davies, Evans, and Agar (1) and Vernon *et al.* (2) and a brief summary of the findings was given by Evans (3). In general it was concluded that the oxide formed at low temperatures was cubic (Fe₃O₄ and γ -Fe₂O₃) while the oxide formed above 175°C is more complex, consisting of α -Fe₂O₃ at the oxide/gas interface and a cubic spinel-type oxide (either γ -Fe₂O₃ or Fe₃O₄) at the oxide/metal interface (3). The total thickness and the amounts of α -Fe₂O₃, γ -Fe₂O₃, and Fe₃O₄ at temperatures up to 350°C appeared to vary considerably with the purity of the iron specimen, surface pretreatment, and conditions of oxidation.

The above conclusions were drawn from extensive studies on polycrystalline iron specimens (1-5) on which the surfaces were prepared by abrasion, chemical etching, and hydrogen reduction. While there is no doubt that many valid conclusions have been made from the above mentioned investigations, a more detailed study of the fundamental mechanisms of the oxidation of iron can be made using carefully prepared, smooth surfaces of known crystallographic orientation on iron crystals of high purity. The importance of this approach to the study of thin film oxidation phenomena has been demonstrated by Gwathmey and his co-workers in their work on the low-temperature oxidation of copper (6-8).

Some dependence of the oxidation behavior of iron on crystallographic orientation has already

been demonstrated (9, 10). In the latest work Wagner, Lawless, and Gwathmey (10) measured the kinetics of the oxidation of several carefully prepared surfaces parallel to low index planes on an iron single crystal using interference colors. However, due to the formation of at least two oxide phases on iron, this optical technique may not be satisfactory for the estimation of total oxide film thickness (11). Furthermore it is desirable to determine the relative amounts of the various phases present in the oxide film, as well as the total thickness.

The determination of α -Fe₂O₃ and Fe₃O₄ in oxide films on polycrystalline iron specimens has been carried out with considerable success using gravimetric and electrometric methods for the film thickness range from 100 to 20,000Å (1, 12). However, general conclusions drawn from these experiments on polycrystalline iron must be taken with some reservations in view of the anisotropy of oxidation of iron in this region and the variation of oxidation behavior with surface preparation, etc. Recently a study was made of thin oxide films in the 10-25Å range using a combination of electrometric and electron optical methods. However, to date, no careful investigation of structures of oxide films of intermediate thickness on single crystal iron surfaces of known orientation has been reported.

A detailed study of the kinetics of oxidation of iron single crystals of reproducible surface condition is clearly a formidable task. In this paper an

attempt is made to demonstrate how some aspects of the problem may be approached. Electron diffraction, electrochemical and gravimetric methods have been applied to the investigation of oxide films grown on electropolished surfaces of iron single crystals at temperatures up to 360°C. The limitations of the experimental techniques are discussed in relation to the estimation of the various oxide phases. Although absolute quantitative determination of these phases has not been possible, electron diffraction and cathodic reduction studies have helped to reveal the composition of the oxide films in considerable detail. A marked anisotropy in (a) the total film thickness and (b) the film composition has been established for the oxidation of the (001) and (112) iron surfaces.

Experimental

Material.—Both polycrystalline Ferrovac E iron sheet and large strain annealed single crystals were used. Details regarding the origin and purity of these specimens have already been reported (13).

Surface preparation.—The iron surfaces were prepared initially using electropolishing conditions which produce "atomically smooth" surfaces covered by a thin film of oxide some 15-25Å thick (14). From the previous study (13) it is known that the composition of this oxide varies with the time of exposure in air or vacuum at a rate dependent on the temperature. However this change is slow at room temperature and fairly reproducible conditions could be obtained by carrying out oxidation within 30 min of electropolishing. In some cases this pretreatment was varied to observe the effect on subsequent oxidation.

No attempt was made to study the oxidation of hydrogen reduced surfaces of the type used in other studies (5, 12). A preliminary examination of the surface microstructure and contamination that may result following hydrogen reduction has indicated that marked structural changes occur during such treatment (15). Thus, for the present the investigation has been restricted to the oxidation behavior of electropolished surfaces.

Oxidation.—Oxidation experiments were carried out in a conventional quartz vacuum furnace arrangement similar to that used by Caule, Buob, and Cohen (12). The heating zone of the furnace was uniform over the region where the specimen was mounted to about $\pm 1.5^\circ\text{C}$, and this temperature was constant to within the same limits. Samples were brought to the oxidation temperature in a vacuum of about 5×10^{-6} Torr and oxygen then admitted. All oxidation experiments were carried out in 20 Torr of dry oxygen for a period of 120 min. Following the oxidation, the assembly was cooled rapidly to room temperature in the oxygen atmosphere to prevent the reduction of any Fe_2O_3 in the surface layers to magnetite by diffusion of iron from the substrate (16).

Electron diffraction.—Reflection electron diffraction observations were made using a 50 kv beam in a General Electric diffraction apparatus. The results of the electron diffraction investigations car-

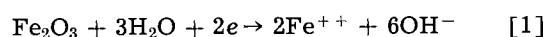
ried out in connection with this study are reported and interpreted in more detail in a separate paper (17).

Estimation of film thickness.—Two methods of estimating film thickness were used, (a) gravimetric and (b) electrometric (1, 18). As mentioned above, interference colors give uncertain results. The vacuum microbalance technique was not used because an absolute weight curve, rather than weight-gain time curves, was required.

Gravimetric.—For thin films about 100Å in mean thickness, formed during short periods of oxidation around 200°C, the gravimetric technique used has limited accuracy. Because of the areas required and the thickness of the single crystal specimens a Mettler Microbalance with a sensitivity of about $\pm 1 \mu\text{g}$ was used. With specimen areas of 5-9 cm^2 and an oxygen uptake in the range of 1-2 $\mu\text{g}/\text{cm}^2$ the weighing errors were about $\pm 8\%$ for most specimens and as high as $\pm 30\%$ for small specimens.

Cathodic reduction and interpretation.—The cathodic reduction of iron films in the oxygen-free, HCl borate buffer of pH 7.6 has been described in detail in previous publications (18, 19). As pointed out in these publications, during cathodic reductions, observations can be made on the immersion potential (before current is applied), the potential of any arrests, and the current efficiency (based on Fe^{++} found in solution) during the various parts of the process.

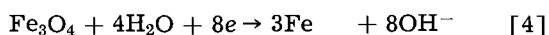
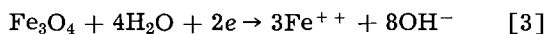
In the previous work it was found that for oxides formed at room temperature and at high temperatures distinct arrests and waves could be observed for $\gamma\text{-Fe}_2\text{O}_3$ (-0.3 to -0.4v) and $\alpha\text{-Fe}_2\text{O}_3$ (-0.6v), respectively. Both of these oxides reduced with high current efficiencies based on the Fe^{++} in the solution and the reaction



The arrest potentials for the two oxides are sufficiently different to determine the phase which is present. In both cases the Fe_3O_4 arrest potential came at the same place (-0.7v) and current efficiencies for the production of Fe^{++} were very low. In the high temperature case weight gains were sufficiently high that Fe_3O_4 could be determined by weight differences. In the low temperature case a combination of reduction to Fe^{++} in solution and reduction to metallic iron was used to calculate the thickness of Fe_3O_4 .

In the temperature range discussed in this paper compositions either mixed or intermediate between $\gamma\text{-Fe}_2\text{O}_3$ or $\alpha\text{-Fe}_2\text{O}_3$ are formed. This has led to cathodic reduction curves in which there are often no sharp arrests for either $\gamma\text{-Fe}_2\text{O}_3$ or $\alpha\text{-Fe}_2\text{O}_3$. However high current efficiencies are still maintained until the Fe_3O_4 potential is reached. The decision on the structure of the oxide has been made with the aid of electron diffraction. In that the iron analysis is quite accurate the thickness of total Fe_2O_3 (as α and γ) can be estimated with good accuracy.

In contrast to the Fe_2O_3 , the accurate estimation of the thickness of Fe_3O_4 is very difficult. At -0.7v three reactions are possible



Reaction [2] accounts for the low current efficiency. In some cases reaction [3] has been found to take place with a current efficiency as high as 10%. In other cases (20), all the oxide reduction current is used for direct formation of iron as in reaction [4] with a current efficiency of about 40%. In some cases both reactions take place. The particular course of the reduction appears to depend on the thickness of the magnetite and on the orientation of the substrate iron surface. Two methods were therefore used in estimating the thickness of the oxide.

Method A.—Assume that all the oxide is reduced to Fe^{++} in solution following reaction [3]. The thickness of the magnetite is then simply calculated from the amount of Fe^{++} in solution.

Method B.—Assume that the oxide is reduced by both reactions [3] and [4]. The thickness of the magnetite is then twice that corresponding to the Fe^{++} in solution.

The decision as to which of these two methods was used was aided by balancing the calculated total oxide obtained by cathodic reduction against the total weight gain. A second criterion was electron diffraction from the iron surface after cathodic reduction. If reaction [4] had taken place, rings corresponding to cubic oxide formed by room temperature oxidation of the redeposited iron were observed.

In practice the procedure used was as follows. The cathodic reduction could be stopped at various points on the cathodic reduction curve and the solution drained (with nitrogen flowing) for chemical analysis. If the specimen was removed for electron diffraction analysis it was washed quickly with conductivity water and then redistilled anhydrous methanol. During this handling of the specimen any exposed magnetite would be oxidized to $\gamma\text{-Fe}_2\text{O}_3$ to a thickness of some 10Å (19). If the air-exposed specimen was further cathodically reduced a correction was made for the Fe^{++} which came from this $\gamma\text{-Fe}_2\text{O}_3$ with almost 100% current efficiency. The ferrous ion was analyzed by the orthophenanthroline method.

Results and Discussion

Polycrystalline Samples

The initial gravimetric and electrometric investigations of low temperature oxidation were carried out using coarse grained (grains larger than 2-3 mm across) Ferrovac E iron sheet. Following electropolishing and oxidation at 200°C the measured weight gains for these samples corresponded to the development of oxide films whose total mean thickness ranged from $75 \pm 15\text{Å}$ to $125 \pm 15\text{Å}$. This variation was later correlated with the distribution of crystal orientations in the surfaces of the specimens. For example, the specimen showing the smallest weight gain contained no visible grains having

surface orientations within 5° of the low index planes (001), (011), and (111). However the specimen exhibiting the largest weight gain, corresponding to a total oxide of $125 \pm 15\text{Å}$, was found to have about 25% of its surface within 5° of the above low index planes.

Cathodic reduction of the oxide was carried out until all the readily reducible oxide was removed and the reduction potential reached that was characteristic of Fe_3O_4 . On removing the samples from the cell, certain grains were observed to be almost metallic in appearance, others were covered with a pale straw film, while some grains were covered with a much darker, brown film.

Back reflection x-ray diffraction was used to establish the orientation of selected grains covered with residual oxide films of varying thicknesses. The results are illustrated by plotting surface normals to the grains in the stereotriangle Fig. 1. The darkest films of residual oxide were found in surfaces within about 5° of the low index faces (001), (011), and (111). Much lighter films (presumably thinner) were observed when the surface normals were slightly greater than 5° from the above major planes. On grains with surfaces more remote from these low index planes there was no visible oxide film.

Reflection electron diffraction patterns obtained from a dark film on an (001) iron surface at the edge of one of the specimens, were similar to the pattern B of Fig. 5 and indicated that the residual film was highly oriented cubic oxide, either $\gamma\text{-Fe}_2\text{O}_3$ or Fe_3O_4 . However, the potential during cathodic reduction suggested that the residual oxide film was predominantly Fe_3O_4 .

Previous studies of the oxidation of iron have established that the total oxide film thickness is dependent on the crystallographic orientation of the iron substrate (9, 10). The above observations suggest that the relative amounts of the $\alpha\text{-Fe}_2\text{O}_3$ and Fe_3O_4 (and possibly $\gamma\text{-Fe}_2\text{O}_3$) also vary with substrate orientation.

To investigate this problem more carefully, studies were made on oxides formed on the surface of iron single crystals. In particular it was desirable to investigate surface orientations showing

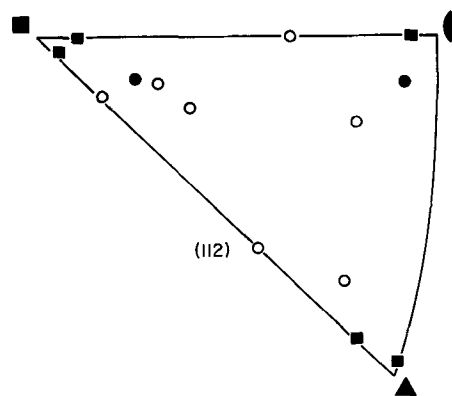


Fig. 1. Stereo-triangle showing orientation of iron crystals in relationship to thickness of residual magnetite films following cathodic reduction of oxide formed at 200°C. ■ Darkest Fe_3O_4 films, ● visible Fe_3O_4 films, ○ invisible Fe_3O_4 films.

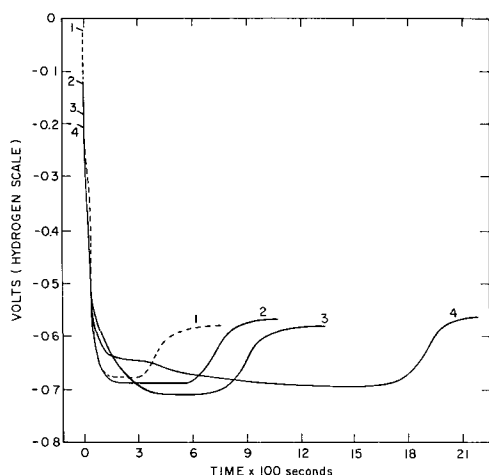


Fig. 2. Cathodic reduction curves from oxides formed at various temperatures on the (112) iron surface. 1. 25°C, 19 day exposure; 2. 175°C for 120 min; 3. 200°C for 120 min; 4. 260°C for 120 min.

markedly different oxidation behavior, as evidenced by Fig. 1. For this purpose, available crystals having near (001) and (112) surface orientations were used.

(112) Crystal

The use of the cathodic reduction method for the analysis of oxide film grown on the (112) iron surface is illustrated in Fig. 2. Reduction curve 1 was obtained from an electropolished specimen that had been exposed to dry air for 19 days. It shows a high immersion potential (at zero time) and a definite arrest around $-0.3v$, both of which are characteristic of $\gamma\text{-Fe}_2\text{O}_3$. Following the reduction of about 16\AA of this surface oxide the potential drops rapidly to the region of $-0.68v$ where Fe_3O_4 is reduced. Finally, when the reduction of Fe_3O_4 is complete, the potential rises to a value of $-0.58v$, characteristic of the discharge of hydrogen on the (112) iron surface (19).

The reduction curves 2, 3, and 4 show the same general trend, but the reduction period for the complete removal of Fe_3O_4 is longer and the reduction behavior of the initial surface oxide is somewhat different.

The reduction curves 2 and 3, obtained from oxide films grown at 175° and 200°C , respectively, show no evidence of a $\gamma\text{-Fe}_2\text{O}_3$ arrest. Here, during the initial reduction the potential changes quite rapidly to the region of $-0.68v$, during which time Fe^{++} appears in solution with high current efficiency. The composition of the surface oxide on these specimens has been discussed elsewhere (17), in the light of electron diffraction evidence. It is thought that at these temperatures the first stages of the nucleation and growth of $\alpha\text{-Fe}_2\text{O}_3$ can be observed, but the surface layer is not entirely crystalline $\alpha\text{-Fe}_2\text{O}_3$.

Following oxidation at 260°C , the cathodic reduction curve 4, shows a definite arrest at about $-0.65v$, indicating that $\alpha\text{-Fe}_2\text{O}_3$ is being reduced. This curve will be discussed in more detail in connection with a combined electron diffraction and cathodic reduction analysis of the oxide.

Estimates of the thickness of the "reducible" oxide and the Fe_3O_4 , are given in Table I. The two methods

Table I. Estimation of oxide thickness on (112) crystal

Cathodic reduction curve No.	Oxidation temp, °C	"Reducible" oxides	Oxide mean thickness, Å		
			Fe_3O_4	Total oxide	Total oxide gravimetric
Method A					
1	25	15	10	25	
2	175	23	20	43	
3	200	43	32	75	100 ± 30
4	260	115	44	159	175 ± 20
Method B					
1	25	15	10	25	
2	175	23	30	53	
3	200	43	54	97	100 ± 30
4	260	115	75	189	175 ± 20

A and B, described previously, are used for estimating Fe_3O_4 . The total thickness, estimated from cathodic reduction analysis is given, and where possible, compared with the film thickness determined gravimetrically.

The use of both electron diffraction and cathodic reduction analysis for the examination of the oxide film formed at 260°C on the (112) surface is illustrated in Fig. 3. The diffraction pattern A, taken directly after oxidation, shows strong reflections from $\alpha\text{-Fe}_2\text{O}_3$, the crystallites being oriented with respect to an underlying cubic oxide, either $\gamma\text{-Fe}_2\text{O}_3$ or Fe_3O_4 . The interpretation of this pattern is given elsewhere (17). At point B' on the reduction curve, the Fe^{++} in solution was sufficient to account for $115 \pm 5\text{\AA}$ of "reducible" oxide, some of which was clearly $\alpha\text{-Fe}_2\text{O}_3$. On removing the specimen from the cell electron diffraction pattern B was obtained. This shows predominantly reflections from the spinel-type oxide, presumably Fe_3O_4 with some 10\AA of its surface oxidized to $\gamma\text{-Fe}_2\text{O}_3$ by air exposure. After further reduction at the Fe_3O_4 potential of -0.68 to $-0.69v$, the potential finally changed to that at C', characteristic of hydrogen discharge on the (112) iron surface. The electron diffraction pattern C, obtained at this stage shows two main features: (i) strong, elongated reflections from the iron substrate crystal [the (112) surface from the $[11\bar{1}]$ azimuth]; and (ii) a series of arced semi-rings, identified as either Fe_3O_4 or $\gamma\text{-Fe}_2\text{O}_3$.

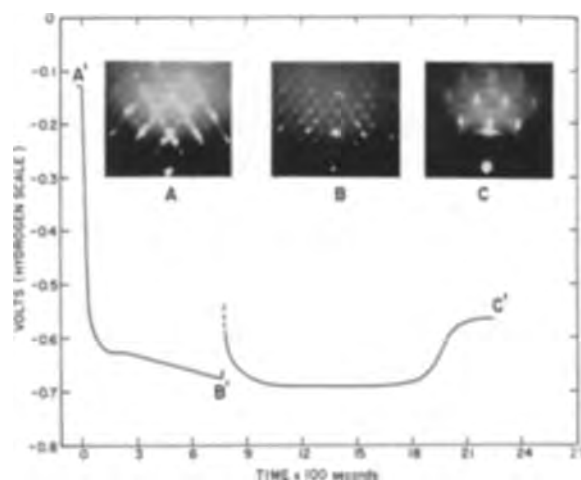


Fig. 3. Electron diffraction and cathodic reduction analysis of oxide formed at 260°C for 120 min on (112) iron surface.

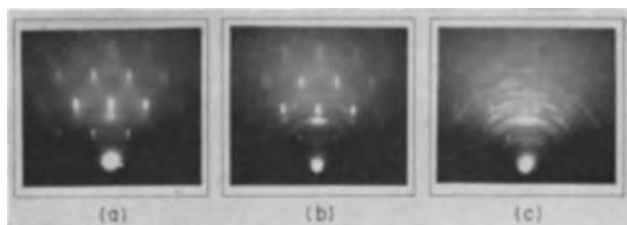


Fig. 4. Electron diffraction patterns from (112) iron surface [111] azimuth, following cathodic reduction of various amounts of Fe_3O_4 listed in Table II.

There is good evidence, that this arced semi-ring pattern results from the air oxidation of iron crystallites produced during the cathodic reduction of Fe_3O_4 .

Reduction of Fe_3O_4 to Fe

It is convenient to discuss the possible reduction of Fe_3O_4 to metallic iron at this juncture, as the most striking evidence of this process was obtained during the reduction of oxide films on the (112) iron surface.

In our discussion of experimental procedure, it was emphasized that there is considerable uncertainty about the precise mechanisms operating during the cathodic polarization of Fe_3O_4 in the HCl-borate buffer. If we assume that all the Fe_3O_4 is reduced to Fe^{++} in solution in accordance with reaction [3], then, when the specimen is examined by electron diffraction at the end of the reduction run (such as point C' of Fig. 3), it should show in addition to the iron substrate pattern, only reflections from a highly oriented, air formed oxide film some 10-20Å thick. On single crystal iron specimens, oxide films of this type are readily detected if the surface is smooth (14, 13).

On (112) surfaces, diffraction patterns of the above type were obtained when the Fe^{++} ion resulting from reduction at the Fe_3O_4 potential was less than $1 \mu\text{g cm}^{-2}$. However when the Fe^{++} from the Fe_3O_4 plateau was greater than this amount, extra features were visible in the diffraction patterns shown, for example, in Fig. 4. The amounts of Fe^{++} in solution obtained from the reduction of Fe_3O_4 in these cases are listed in Table II, together with estimates of Fe_3O_4 film thicknesses determined by methods A and B described previously.

In Fig. 4a, two diffuse rings, corresponding to the (113) and (440) spinel reflections are visible, in addition to the features described above. These weak semi-rings suggest that iron crystallites, resulting from the reduction of Fe_3O_4 , have oxidized on air exposure to produce a small amount of randomly oriented cubic oxide. In Fig. 4b and 4c the intensity of this extra pattern is quite strong, suggesting that

Table II. Estimation of Fe_3O_4 on (112) crystal

Fig. No.	Oxidation temp, °C	Fe^{++} $\mu\text{g cm}^2$	Mean thickness of film in A		
			Fe_3O_4 Method A	Fe_3O_4 Method B	Fe_3O_4 Reduced to iron
4 a	175	1.2	33	54	22
4 b	200	1.6	44	74	32
4 c	260	1.85	50	88	39

larger amounts of this "reduced" iron have been oxidized on air exposure. In no cases have semi-rings from iron been observed. This is consistent with the view that this finely divided iron is completely oxidized on air exposure as for the case of iron powder (1) at 40°C.

The detection of these oxidized crystallites by electron diffraction will depend on: (a) the mean thickness of the iron film resulting from the reduction of Fe_3O_4 , and (b) the orientation of the crystallites (and the subsequent oxide) with respect to the substrate crystal.

The absence of detectable features in patterns, following the reduction of thin Fe_3O_4 films, may therefore be accounted for by either the small quantities of iron liberated by reaction [2] or alternatively by the possibility that this iron is highly oriented with respect to the substrate crystal. In the latter case, the resulting air formed oxide may not be distinguishable from the air formed film on the substrate crystal.

Unfortunately, neither the quantity nor the detailed manner of deposition of iron can be estimated from electron diffraction examination of the resulting oxide. However, the electron diffraction evidence presented above, and the appearance of Fe^{++} ion in solution, both support the proposals that thin Fe_3O_4 films on iron may be reduced in the HCl-borate buffer, most likely according to the mechanisms of Eq. [3] and [4].

The (001) Crystal

Electron diffraction observations of the surface oxide on (001) iron single crystals have shown that the $\alpha\text{-Fe}_2\text{O}_3$ phase does not develop on this surface as early as on the (112) surface (17). In addition both gravimetric and electrometric measurements reported here indicate that the total oxide film thickness on the (001) surface is greater than on the (112).

Cathodic reduction and electron diffraction analyses applied to an oxide film grown at 200°C in the (001) surface are given in Fig. 5. Directly after oxidation, the electron diffraction pattern A indicates that the surface oxide is predominantly cubic. This

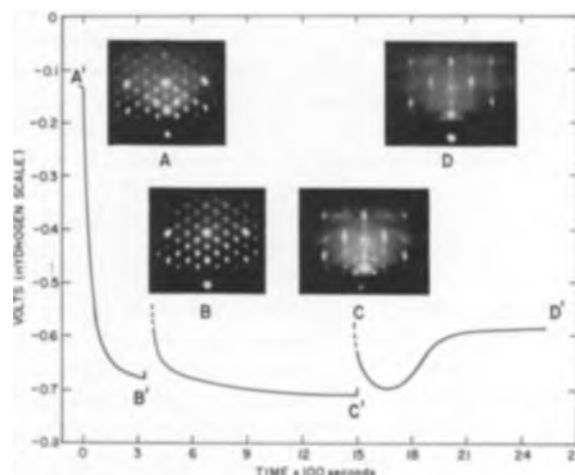


Fig. 5. Electron diffraction and cathodic reduction analysis of oxide film formed at 200°C on (001) iron surface.

pattern exhibits some spiking in the $\langle 111 \rangle$ directions around the strong spots, which we believe to be due to the initial stages of development of $\alpha\text{-Fe}_2\text{O}_3$ (17). Cathodic reduction between the points A' or B' results in the appearance of Fe^{++} ion in solution equivalent to a mean thickness of about 41Å of "reducible" oxide. The lack of an arrest in this curve suggests the presence of a mixed $\alpha\text{-Fe}_2\text{O}_3/\gamma\text{-Fe}_2\text{O}_3$ structure in the surface film.

The electron diffraction pattern B was obtained from the surface after removal from the reduction cell at point B'. The spikes of pattern A are now absent and diffuse reflections from the highly oriented microcrystalline Fe_3O_4 film are observed. Following further reduction to point C' at a potential characteristic of the reduction of Fe_3O_4 , $2.7 \mu\text{g Fe}^{++} \text{ cm}^{-2}$ was found in solution. At this point the diffraction pattern C was obtained from the surface of the specimen. Three distinct features are visible: (i) strong, elongated spots from the iron substrate; the (001) surface from the [011] azimuth; (ii) an array of weak, diffuse reflections characteristic of the oriented cubic oxide (as for pattern B). This is believed to be due to traces of the original Fe_3O_4 film which has not yet been cathodically reduced; (iii) a series of arced semi-rings from an almost randomly oriented spinel type oxide. This contribution to the pattern is believed to be due to the oxidation of a small amount of metallic iron formed by direct reduction of some of the Fe_3O_4 to metallic iron, as for the case of the (112) crystal.

After the final cathodic treatment to D' diffraction pattern D was recorded. The oriented oxide [contribution (ii) above] of pattern C appears to have been removed. The pattern again shows strong iron reflections and suggests that areas of the iron surface where the oxide was completely reduced at point C' are now covered with a thin oriented oxide film due to air exposure. The semi-rings are again believed to arise from the air oxidation of metallic iron crystallites produced during the reduction of Fe_3O_4 .

The oxidation of the (001) surface at 260°C results in the development of a surface oxide which is still predominantly the cubic oxide. Some weak spots due to $\alpha\text{-Fe}_2\text{O}_3$ are visible but the predominant feature in the pattern is the spiking along the $\langle 111 \rangle$ directions of the cubic type pattern (17). During cathodic reduction of this oxide, there was a slight arrest at the $\alpha\text{-Fe}_2\text{O}_3$ potential and about 65Å of "reducible" oxide appeared in solution before the Fe_3O_4 reduction potential was reached. The measured oxygen uptake of such a specimen corresponded to a total oxide film thickness of about $300 \pm 15\text{Å}$ so that the estimated amount of Fe_3O_4 on this surface was about $225 \pm 20\text{Å}$.

Cathodic reduction of such thick Fe_3O_4 films was not practicable, as the films separated from the metal substrate during reduction. However these film fragments could be collected and examined by transmission electron diffraction. They proved to be composed predominantly of highly oriented Fe_3O_4 .

Examples of film thickness observations on the (001) crystal are given in Table III. The good agree-

Table III. Estimation of total oxide on (001) crystal

Oxidation temperature, °C	"Reducible" oxide	Mean thickness, Å		
		Fe_3O_4	Total oxide electro-metric	Total oxide gravi-metric
200	45	89 (Method A)	134	120 ± 30
200	45	158 (Method B)	203	120 ± 30
260	65 ± 5 (Electro-metric)	225 ± 20 (Gravimetric)		300 ± 15

ment between the total oxide thickness determined gravimetrically and that determined by our method A from cathodic reduction results, suggests that most of the Fe_3O_4 is reduced directly to Fe^{++} for this particular crystal orientation. The electron diffraction pattern C of Fig. 5 also supports this view to some extent. For example, during the reduction period B'C' a total of $2.7 \mu\text{g Fe}^{++} \text{ cm}^{-2}$ appears in solution. Using our method B for calculation of the total Fe_3O_4 thickness, we would obtain 134Å Fe_3O_4 . Of this, about 10Å would have been converted to $\gamma\text{-Fe}_2\text{O}_3$ and hence reduced entirely to Fe^{++} . Another 62Å, as Fe_3O_4 , would have been reduced to Fe^{++} and another 62Å of Fe_3O_4 reduced directly to metallic Fe. On air exposure of this microcrystalline iron it should all convert to the cubic oxide and give an intense pattern of semi-rings (assuming random orientation). However the semi-ring pattern from the oxide in C of Fig. 5 is relatively weak compared with that of pattern C of Fig. 4 which is believed to result from the reduction of only 39Å of Fe_3O_4 to metallic iron on the (112) surface. Furthermore if the iron surface at point C' was covered with the above mentioned 62Å of oxide together with some nonreduced oxide from the original film, then the total Fe_3O_4 reduced during period C'D', estimated from the Fe^{++} in solution at D' should have been greater than 62Å. However only $0.65 \mu\text{g Fe}^{++}$

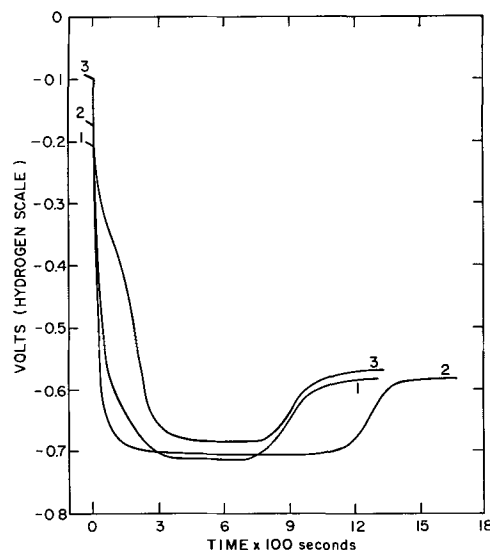


Fig. 6. Cathodic reduction curves from oxide films formed on the (112) surface at 200°C following various surface pretreatments. 1. Normal electropolished. 2. Annealed. 3. Electropolished and air exposed for 12 days.

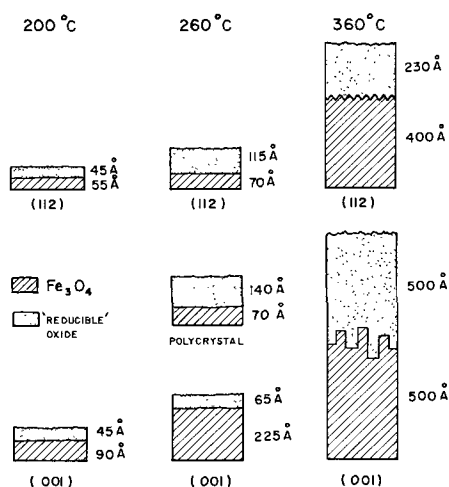


Fig. 7. Schematic representation of distribution of oxide on the (112) and (001) crystals at various temperatures.

cm^{-2} was found at D' correspond to either (A) 17Å or (B) 24Å of Fe_3O_4 . All evidence pertaining to the reduction of Fe_3O_4 on the (001) iron surface, leads to the conclusion that it is converted essentially to Fe^{++} in solution with only a small percentage being reduced to metallic iron.

Effects of Surface Preparation

The effect of the oxide film present on the surface of the specimen on the subsequent oxidation at higher temperatures is illustrated by the reduction curves of Fig. 6. These curves were obtained from oxide films grown on the (112) iron surface at 200°C following initial surface preparation as follows:

1. Specimen electropolished, loaded into furnace tube and brought to 200°C in vacuum of 5×10^{-6} Torr over period of about 10 min. Oxidation commenced within 30 min of electropolishing.

2. Specimen electropolished and loaded as for case 1, but given an anneal for 30 min at 200°C in 5×10^{-6} Torr prior to oxidation at 20 Torr.

3. Specimen electropolished and exposed to dry air for period of 12 days. Brought to oxidation temperature as for case 1.

Estimates of the oxides present, determined from Fe^{++} in solution, are given in Table IV. Bearing in mind the magnitude of the errors in these estimations and the fact that calculations of the type B are believed to apply most favorably for the (112) crystal, the following observation can be made:

(a) There is little difference in the total oxide following pretreatments 1 and 2. The longer vacuum anneal of 2 gives rise to a somewhat thicker Fe_3O_4 layer in the final oxide film, possibly resulting from a larger Fe_3O_4 component in the original oxide.

Table IV. Effect of pretreatment on oxide composition on (112) crystal

Cathodic reduction curve	Mean thickness, Å		
	"Reducible" oxide	Fe_3O_4 Method B	Total oxide
1	43	54	97
2	33	84	117
3	62	50	112

(b) While there is no marked difference in the total thickness following pretreatment 3, the oxide film at the oxide/gas interface for this case is entirely different to that of 1 and 2. A definite $\gamma\text{-Fe}_2\text{O}_3$ potential arrest is observed and about 60Å of $\gamma\text{-Fe}_2\text{O}_3$ is reduced. The electron diffraction pattern from this surface indicated that the oxide had random orientation, rather than the highly preferred orientation of cases 1 and 2.

The relatively small difference in the composition of the films in cases 1 and 2 suggests that slight variations in the time required to bring samples to the oxidation temperature should not markedly affect its oxidation behavior.

Growth Mechanism

A representation of the distribution of the oxides is shown in Fig. 7. Results at 360°C have been added to show consistency at higher temperatures and results from oxidation of polycrystalline iron at 260°C are also given. The lower oxide is magnetite, with reducible oxide above. Further details of the range of composition in the reducible oxide is reported elsewhere (17). In that at the lower temperatures at least part of the reducible oxide is $\gamma\text{-Fe}_2\text{O}_3$, and there is an intermediate structure between $\gamma\text{-Fe}_2\text{O}_3$ and $\alpha\text{-Fe}_2\text{O}_3$, no sharp boundary exists between the oxide phases. It can be seen that the difference in the amounts of the oxides on the (112) and (001) persists even up to 360°C.

The marked anisotropy of growth of the cubic oxide on a cubic metal is difficult to explain (21). Lawless and Gwathmey (7) suggested that the different rates of oxidation on low index faces on a copper single crystal might be explained in terms of the number of equivalent orientations of the oxide with respect to the metal. The maximum oxidation rate for copper is found on the (001) surface (6) on which there are four equivalent orientations of the oxide. Much lower oxidation rates are observed on the (110) and (113) surfaces on which the oxide grows with one single orientation.

For both the (001) and (112) iron surfaces investigated here, the Fe_3O_4 grows with a single orientation. However our results have shown a marked difference in their oxidation behavior. While "multiple" positioning of the oxide may not be the principal controlling factor for oxidation anisotropy, it is quite likely that "grain" boundaries between individual oxide crystallites do play an important role in the growth process. Electron diffraction and electron microscope observations on stripped iron oxide films have shown that for oxides formed at temperatures up to about 360°C, the oxide particle size is generally in the range of 20-50Å (15). These oxide films, up to some 1000Å thick, may be described as compact arrays of microcrystals in which the size and orientation of the microcrystals is governed in part by the orientation of the substrate metal and in part by the conditions of oxidation. In such thin oxide films it is likely that the principal diffusion paths are through defect regions between the small crystallites. In this connection Roberts (22) has found from kinetic studies of the growth of thin

oxides on evaporated iron films that the activation energy for the steady growth process (most probably cation diffusion) is much lower than that for the diffusion of Fe^{++} through bulk magnetite. The significance of this observation in relation to the diffusion mechanism in iron oxide films has been discussed by Adams and Roberts (23).

While it is difficult to obtain measurements of the activation energy for diffusion of Fe^{++} in microcrystalline Fe_3O_4 and its variation with particle size, it appears that a more detailed investigation of this aspect of the oxidation process may help clarify some of the problems of oxidation anisotropy.

Manuscript received June 24, 1963.

Any discussion of this paper will appear in a Discussion Section to be published in the December 1964 JOURNAL.

REFERENCES

1. D. E. Davies, U. R. Evans, and J. N. Agar, *Proc. Roy. Soc.*, **A225**, 443 (1954).
2. W. H. J. Vernon, E. R. Calnan, C. J. B. Clews, and T. J. Nurse, *ibid.*, **A216**, 375 (1953).
3. U. R. Evans, "The Corrosion and Oxidation of Metals," Edward Arnold Limited (1960).
4. H. R. Nelson, *J. Chem. Phys.*, **6**, 606 (1938).
5. E. A. Gulbransen, *Trans Electrochem. Soc.*, **81**, 327 (1942).
6. F. W. Young, J. V. Cathcart, and A. T. Gwathmey, *Acta Met.*, **4**, 145 (1956).
7. K. R. Lawless and A. T. Gwathmey, *ibid.*, **4**, 153, (1956).
8. W. W. Harris, F. L. Ball, and A. T. Gwathmey, *ibid.*, **5**, 574 (1957).
9. R. F. Mehl and E. L. McCandless, *Trans. Am. Inst. Mining Met. Engrs.*, **125**, 531 (1937).
10. J. B. Wagner, K. R. Lawless, and A. T. Gwathmey, *Trans Met. Soc. AIME*, **221**, 257 (1961).
11. E. J. Caule, *Corrosion Science*, **2**, 147 (1962).
12. E. J. Caule, K. H. Buob, and M. Cohen, *This Journal*, **108**, 829 (1961).
13. P. B. Sewell, C. D. Stockbridge, and M. Cohen, *ibid.*, **108**, 933 (1961).
14. P. B. Sewell, C. D. Stockbridge, and M. Cohen, *Can. J. Chem.*, **37**, 1813 (1959).
15. P. B. Sewell, E. G. Brewer, R. Ramasubramanian, and M. Cohen, "5th Int. Congress for Electron Microscopy," Vol. 1, Abstract GG-8, Academic Press, New York (1962).
16. E. J. Caule and M. Cohen, *This Journal*, **108**, 834 (1961).
17. P. B. Sewell and M. Cohen, *ibid.*, **111**, 508 (1964).
18. K. H. Buob, A. F. Beck, and M. Cohen, *ibid.*, **105**, 74 (1958).
19. C. D. Stockbridge, P. B. Sewell, and M. Cohen, *ibid.*, **108**, 928 (1961).
20. M. Nagayama and M. Cohen, *ibid.*, **109**, 781 (1962).
21. O. Kubaschewski and B. E. Hopkins, "Oxidation of Metals and Alloys," 2nd edition, pp. 53-64, Butterworth & Co. Ltd. (1962).
22. M. Wyn Roberts, *Trans. Faraday Soc.*, **57**, 99 (1961).
23. M. Wyn Roberts, "First International Congress on Metallic Corrosion," p. 84, Butterworth (1961) Discussion by A. M. J. Adams.

An Electron Diffraction Study of Thin Oxide Films on Iron Single Crystals

P. B. Sewell and M. Cohen

Division of Applied Chemistry, National Research Council, Ottawa, Ontario, Canada

ABSTRACT

Electron diffraction patterns from thin films of Fe_3O_4 (or $\gamma\text{-Fe}_2\text{O}_3$), formed at low temperatures on the (112) and (001) iron surfaces, exhibit diffuse spiking parallel to the $\langle 111 \rangle$ directions in reciprocal space. At higher temperatures, intensity maxima on these spikes are replaced by the strongest reflections from highly oriented $\alpha\text{-Fe}_2\text{O}_3$, which grows with its oxygen planes parallel to those of the cubic oxide; (00.1) α // (111) spinel. The spikes about the strongest reflections of the spinel pattern are interpreted as evidence of stacking faults in the closest packed oxygen planes. The appearance of stacking faults is regarded as the first indication of the nucleation of $\alpha\text{-Fe}_2\text{O}_3$ in the films. On the (112) iron surface, $\alpha\text{-Fe}_2\text{O}_3$ develops in the outer layer of the oxide at an earlier stage than on the (001).

The identification of the oxide phases present during the early stages of low-temperature oxidation of iron has been carried out with considerable success in the past by electron diffraction (1-4) and electrochemical techniques (5, 6): the former gives certain crystallographic information about the surface layers of the oxide, while the latter, combined with gravimetric measurements, may permit the quantitative estimation of the relative amounts of Fe_3O_4 and $\alpha\text{-Fe}_2\text{O}_3$, when these are the principle oxides present (5-7). However, it is clear from the numerous publications on the early stages of oxidation of iron that the composition and mean thickness of the resulting oxide film is dependent on the pur-

ity of the specimen and the initial surface preparation as well as the conditions of oxidation.

In this paper the results of a detailed examination of electron diffraction observations on thin oxide films formed on single crystals of iron by low-temperature oxidation are reported. In particular, the early stage of formation of the $\alpha\text{-Fe}_2\text{O}_3$ phase near the oxide-gas interface is discussed. The weight-gain and cathodic reduction behavior in this temperature region has been discussed previously (8).

Experimental

The specimen material, electropolishing technique, and oxidation procedure are the same as those used

in previous work (8-10). All specimens were oxidized for 120 min in 20 Torr oxygen and cooled rapidly in the oxygen atmosphere. Thermocouple measurements on test specimens showed that a specimen cooled from a temperature of 350° to 50°C in 3 min, if still in the oxidizing atmosphere. This rapid cooling in oxygen is desirable in order to prevent any reduction of the α -Fe₂O₃ phase to Fe₃O₄ by iron diffusion through the cubic oxide (5, 11).

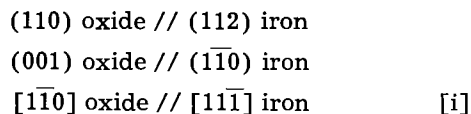
Specimens were examined by electron diffraction at grazing incidence using a 50 kv electron beam, in a General Electric diffraction apparatus.

In order to interpret the electron diffraction patterns from the highly oriented α -Fe₂O₃ films, it was found convenient to construct a model of hexagonal reciprocal space in which the allowed reflections for α -Fe₂O₃ were indexed from x-ray diffraction information. For this reason the indices of reflections and zones for the α -Fe₂O₃ patterns referred to in this article are given in the short hexagonal form rather than the more common rhombohedral notation.

Results

Thin oxide films on iron single crystal surfaces parallel to the {001} and {112} planes have been studied. These surface orientations are of particular interest since the first formed cubic oxide has only one discrete orientation with respect to the substrate metal. On the {011} iron surface, the first formed cubic oxide has two equivalent orientations (10, 12, 13). Since up to four principal orientations of α -Fe₂O₃ have been found on a single orientation of the cubic oxide on the {001} surface, some eight orientations of α -Fe₂O₃ might be expected in overgrowths on the {011} surface. Due to the complexity of electron diffraction patterns from specimens of this type, studies on the {011} and {111} iron surfaces were not pursued.

The {112} iron surface.—The orientation of the first formed cubic oxide on this surface has been reported previously (10, 12, 14) as follows



This simple or single positioning of the cubic oxide was observed in the present oxidation experiments for all temperatures between 25° and 360°C. The presence of this orientation alone between the metal/oxide interface and the cubic/hematite interface was confirmed by examining stripped oxide films by transmission electron diffraction.

If the cubic oxide with orientation [i] is examined with the electron beam parallel to the $[\bar{1}\bar{1}0]$ oxide zone, then a pattern of diffuse reflections, corresponding to the section of the spinel reciprocal lattice, Fig. 1, is observed. Such a pattern of weak spots was recorded when a (112) iron surface was examined following either (a) electropolishing and air exposure, or (b) cathodic reduction and air exposure. In these cases, reflections from the iron substrate were also visible since the oxide film was only some 15Å thick (10).

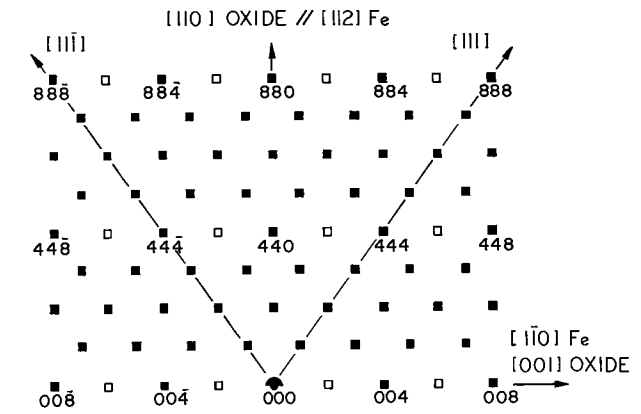


Fig. 1. Section of reciprocal lattice of cubic oxide, Fe₃O₄, grown on (112) iron surface. Electron beam parallel to $[\bar{1}\bar{1}0]$ oxide zone. □ Spots due to double diffraction.

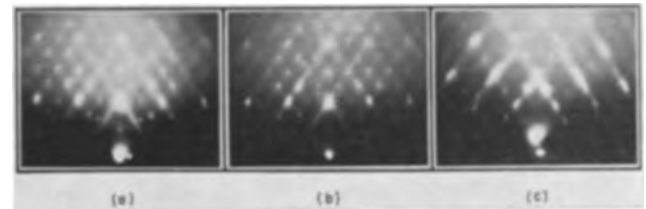


Fig. 2. Diffraction patterns from oxide film on (112) iron surface; electron beam parallel to $[\bar{1}\bar{1}0]$ cubic oxide zone. (a) 50Å oxide formed at 175°C; (b) 100Å oxide formed at 200°C; (c) 175Å oxide formed at 260°C, showing strong reflections from α -Fe₂O₃ layer less than 75Å thick.

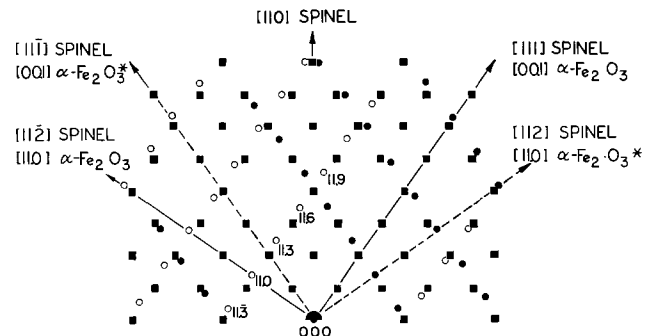


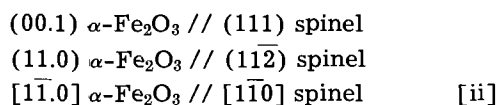
Fig. 3. Interpretation of diffraction pattern Fig. 2c. ■ Reflections from underlying spinel; ●, ○ reflections from two equivalent orientations of α -Fe₂O₃. Electron beam parallel to $[\bar{1}\bar{1}0]$ zone in both oxides.

Oxidation at 175°C produced an oxide film about 50Å thick which gave rise to the diffraction pattern Fig. 2a. Here, diffuse streaks parallel to the $\langle 111 \rangle$ directions of reciprocal space appear around the strong spinel reflections, particularly the (440).

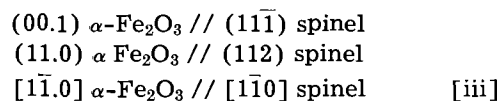
After oxidation at 200°C, the oxide film was about 100Å thick and streaking through the stronger oxide reflections was more clearly defined, as shown in Fig. 2b. Extra, weak diffraction maxima, not belonging to the spinel pattern, are present on spikes through the (440) spinel reflection, these being clearly visible on the original plates.

Oxidation at 260°C resulted in an oxide film some 175Å thick, which exhibited reflections from both the spinel type oxide and the hexagonal α -Fe₂O₃, as seen in Fig. 2c. The principal diffraction maxima present in this pattern are shown in the reciprocal lattice section, Fig. 3. The original spinel orientation

[i] is still present, and in addition strong reflections from α -Fe₂O₃ arise from two equivalent orientations as follows

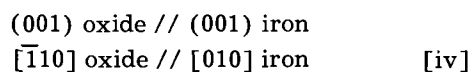


and



Orientations [ii] and [iii] result from the parallel growth of the closest packed oxygen planes of the hexagonal α -Fe₂O₃ with the {111} oxygen planes of the cubic oxide. The two equivalent orientations are observed since there are two equivalent {111} planes of the cubic oxide parallel to the electron beam when the specimen is examined from the $[\bar{1}\bar{1}0]$ spinel azimuth. The weak maxima present of the spikes around the (440) reflection of Fig. 2b have developed into the strong (11.3), (11.6), and (11.9) reflections from α -Fe₂O₃, shown in Fig. 3.

The {001} iron surface.—The orientation of the air-formed film of cubic oxide on this surface has been reported previously as (10, 13)



The x-ray studies of Wagner, Lawless, and Gwathmey (12), together with our own examination of

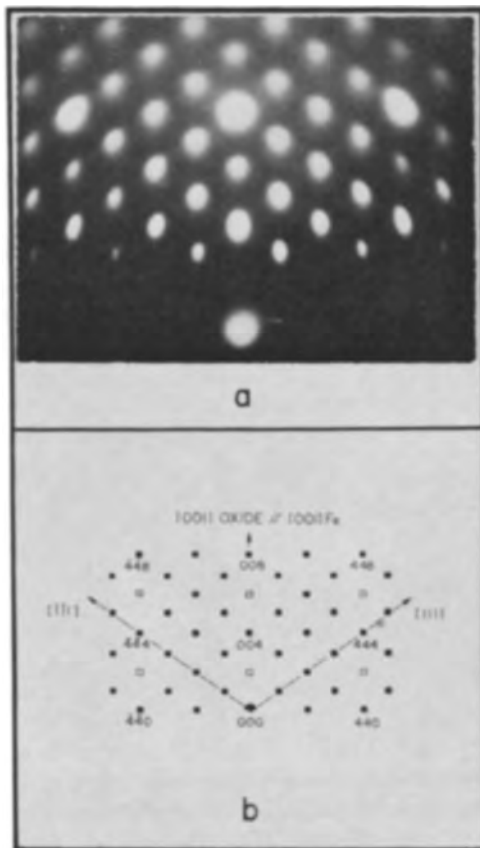


Fig. 4a. Diffraction pattern from oriented microcrystalline film of Fe₃O₄ on (001) iron surface. b. Section of reciprocal lattice corresponding to Fig. 4a. Electron beam along $[\bar{1}\bar{1}0]$ oxide zone. □ Spots due to double diffraction.

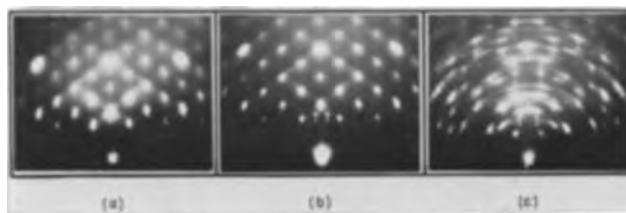


Fig. 5. Diffraction patterns from oxide films on (001) iron surface; beam along $[\bar{1}\bar{1}0]$ spinel zone as for Fig. 4. a. 120Å oxide formed at 200°C; b. 300Å oxide formed at 260°C; c. 1000Å (500Å Fe₃O₄, 500Å α -Fe₂O₃) formed at 360°C. Pattern from α -Fe₂O₃ only, beam parallel to underlying $[\bar{1}\bar{1}0]$ spinel. Arrows in 5b and 5c show (11.3) α -Fe₂O₃ reflections.

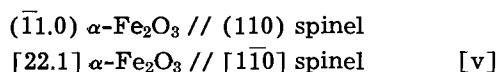
stripped oxide films have shown that this single orientation exists for the cubic oxide in films up to some 500Å mean thickness, formed at temperatures as high as 350°C.

A film of Fe₃O₄ with the above orientation [iv], gave rise to the diffraction pattern Fig. 4a, when observed with the beam parallel to the $[\bar{1}\bar{1}0]$ oxide zone. Major reflections in this pattern are indexed in Fig. 4b. For this particular specimen, outer layers of α -Fe₂O₃ and reducible oxide were removed by cathodic reduction, and the resulting Fe₃O₄ film was about 100Å thick. The reflections are diffuse but exhibit no spiking. The oxide film is composed of an array of highly oriented microcrystals some 30-50Å across.

During the oxidation of the {001} iron surface, the first evidence for any change in the spinel pattern was observed after 120 min at 200°C. Spikes parallel to the $\langle 111 \rangle$ spinel directions appeared around the strong spinel reflections, particularly the (004), as shown in Fig. 5a.

After oxidation at 260°C, the oxide was some 300Å thick and the predominant pattern was still from the cubic oxide, as seen in Fig. 5b. Strong, well defined spikes parallel to the $\langle 111 \rangle$ spinel directions are visible again, together with some very weak reflections from α -Fe₂O₃ with orientation [v] below.

Strong reflections from α -Fe₂O₃ appeared in diffraction patterns following oxidation at higher temperatures. For example, after oxidation at 350°C the total oxide thickness was 1000Å, determined gravimetrically. Of this total some 500Å was α -Fe₂O₃, determined electrometrically. When this outer α -Fe₂O₃ layer was examined with the electron beam parallel to a $\langle 110 \rangle$ zone of the underlying cubic oxide, the pattern Fig. 5c was recorded. Detailed interpretation of patterns from oxides formed at 350°C will be discussed elsewhere (15). Four equivalent orientations of the type [ii] above were observed on the four equivalent {111} spinel planes. It follows from this multiplicity of orientations that when the electron beam is parallel to the $[\bar{1}\bar{1}.0]$ α -Fe₂O₃ zones of orientation [ii], it is also nearly parallel to a $[22.1]$ zone of α -Fe₂O₃ on the (111) and ($\bar{1}\bar{1}1$) spinel planes. As a result of this, primary and secondary reflections appear in patterns of the type Fig. 5c, corresponding to the section of reciprocal space where



The strong $\alpha\text{-Fe}_2\text{O}_3$ reflections of orientation [ii] in Fig. 5c have replaced the spikes which developed around the strong spinel reflections of Fig. 5a and 5b. For example, the (11.3) $\alpha\text{-Fe}_2\text{O}_3$ reflections of Fig. 5c occur in the positions occupied by the regions of maximum intensity (indicated by arrows) on the spikes around the (004) spinel reflection of Fig. 5b.

Discussion

The orientational relationship between $\alpha\text{-Fe}_2\text{O}_3$ and the cubic oxide which is common to the oxidation of both {112} and {001} iron surfaces, is that of type [ii] above, where the closest packed oxygen planes of the two structures are parallel. This same relationship has been observed in overgrowths of hematite on magnetite in mineral samples (16) and during the early stages of oxidation of magnetite single crystals (17) at 600°C. Parallel orientation of the oxygen planes in the transformation of $\gamma\text{-Fe}_2\text{O}_3$ to $\alpha\text{-Fe}_2\text{O}_3$ has been reported by Mackay (18) and Kachi, Momiyama, and Shimizu (19) during electron microscope studies of small single crystals.

The closest packed oxygen planes in Fe_3O_4 (or $\gamma\text{-Fe}_2\text{O}_3$) occur with the cubic close packing sequence ABCABCABC . . . , while in $\alpha\text{-Fe}_2\text{O}_3$ the oxygen planes have the hexagonal close packing sequence ABABAB . . . (20). Since it has been shown that the oxygen planes occur with parallel orientation for the earliest stages of formation of $\alpha\text{-Fe}_2\text{O}_3$ on the underlying cubic oxide, it is likely that a region of oxygen close packing with a high density of stacking faults occurs between the two more regular sequences of these oxides.

The spikes or diffuse streaks parallel to the $\langle 111 \rangle$ directions in patterns for the cubic oxide are attributed to the presence of stacking faults in the {111} planes of the oxide. Similar effects have been observed due to the presence of stacking faults in the close packed planes of the spinel $\gamma\text{-Al}_2\text{O}_3$ (21).

When oxidation conditions begin to favor a structure approaching $\alpha\text{-Fe}_2\text{O}_3$, the oxygen stacking sequence (and the distribution of cations within this sequence) should show some evidence of hexagonal close packing. At this point weak maxima corresponding to certain $\alpha\text{-Fe}_2\text{O}_3$ reflections should appear on the streaks in diffraction patterns. This stage of the oxidation was observed at 200°C of the {112} surface. Finally, when the hexagonal close packing is sufficiently extensive and the distribution of cations has established the $\alpha\text{-Fe}_2\text{O}_3$ phase, diffraction maxima from the hematite lattice should be prominent, as seen in Fig. 3c and Fig. 5c.

If the diffuse streaks appearing in the diffraction patterns from the cubic oxide are regarded as the first evidence for the nucleation of the $\alpha\text{-Fe}_2\text{O}_3$ phase, then there is clear evidence for such nucleation in 50Å oxide films produced at 175°C on the {112} surface. For the {001} surface, hematite nucleation only was observed in oxide films some 175Å thick produced at 200°C, and also in 300Å films pro-

duced at 260°C. However, in 175Å films produced on the {112} surface at 260°C, the hexagonal $\alpha\text{-Fe}_2\text{O}_3$ structure was well developed.

Quantitative measurements on the composition of these oxide films (8) have shown that on the {001} surface both (a) the total oxide thickness, and (b) the thickness of Fe_3O_4 are greater than observed on the {112} plane. There is evidence (22, 23) that the growth of magnetite occurs primarily by cation diffusion, and the late appearance of $\alpha\text{-Fe}_2\text{O}_3$ on the {001} surface might be explained by the particularly high rate of cation diffusion through orientation [ii] of the spinel. The nucleation of $\alpha\text{-Fe}_2\text{O}_3$ may not occur until the thickness of the cubic oxide is sufficient to reduce the total cation flux to a level which favors the formation of the hexagonal structure, since it is known that $\alpha\text{-Fe}_2\text{O}_3$ may be reduced to Fe_3O_4 by cation diffusion at low temperatures (5, 11).

In the present article, the oxide film between the metal substrate and the $\alpha\text{-Fe}_2\text{O}_3$ has been referred to in general terms as a cubic oxide of the spinel type. There is good electrochemical evidence that much of this oxide, particularly that adjacent to the metal, is Fe_3O_4 . However, the outer region of this cubic oxide has not been positively identified as either Fe_3O_4 or $\gamma\text{-Fe}_2\text{O}_3$. This oxide gives rise to electron diffraction patterns similar to those from Fe_3O_4 , which frequently exhibit extra reflections which could be attributed to $\gamma\text{-Fe}_2\text{O}_3$. Unfortunately, to date, lattice parameter measurements have not established an accurate unit cell dimension. However this oxide is cathodically reduced with a relatively high current efficiency and in this way resembles $\gamma\text{-Fe}_2\text{O}_3$.

From present electron diffraction and electrochemical evidence, it seems reasonable to consider that an intermediate oxide some 50Å thick separates the Fe_3O_4 from the $\alpha\text{-Fe}_2\text{O}_3$. This oxide is composed of an array of oxygen planes with cubic close packing and has a distribution of cations resembling that of $\gamma\text{-Fe}_2\text{O}_3$. From a consideration of this structure, together with the stacking fault mode of nucleation of $\alpha\text{-Fe}_2\text{O}_3$, our present concept of the thin oxide films formed on iron single crystals is illustrated in Fig. 6. The thickness of each of the layers AB, BC,

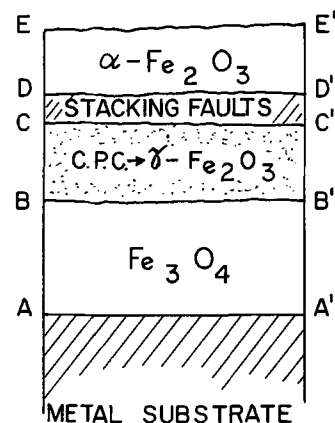


Fig. 6. Schematic of proposed cross-section of thin oxide films formed on iron single crystal surfaces.

CD, and DE is dependent on both the orientation of the substrate and the conditions of oxidation and is probably influenced by the metal purity and the initial surface treatment. To complicate the interpretation of both electron diffraction and electrochemical measurements on these thin oxide films, there is electron microscope evidence that the interfaces BB', CC', and EE' are quite irregular even for oxides grown on smooth single crystal surfaces.

Manuscript received June 24, 1963.

Any discussion of this paper will appear in a Discussion Section to be published in the December 1964 JOURNAL.

REFERENCES

1. H. R. Nelson, *J. Chem. Phys.*, **6**, 606 (1938).
2. P. D. Dankov and N. A. Shishakov, *Zhur. Fizi. Khim.*, **23**, 1031 (1949).
3. W. H. J. Vernon, E. A. Calnan, C. J. B. Clews, and T. J. Nurse, *Proc. Roy. Soc.*, **A216**, 375 (1953).
4. J. Moreau and J. Bardolle, *Compt. rend.*, **240**, 524 (1955).
5. D. E. Davies, U. R. Evans, and J. N. Agar, *Proc. Roy. Soc.*, **A225**, 443 (1954).
6. K. H. Buob, A. F. Beck, and M. Cohen, *This Journal*, **105**, 74 (1958).
7. E. J. Caule, K. H. Buob, and M. Cohen, *ibid.*, **108**, 829 (1961).
8. P. B. Sewell and M. Cohen, *ibid.*, **111**, 501 (1964).
9. P. B. Sewell, C. D. Stockbridge, and M. Cohen, *Can. J. Chem.*, **37**, 1813 (1959).
10. P. B. Sewell, C. D. Stockbridge, and M. Cohen, *This Journal*, **108**, 933 (1961).
11. E. J. Caule and M. Cohen, *ibid.*, **108**, 834 (1961).
12. J. B. Wagner, K. R. Lawless, and A. T. Gwathmey, *Trans. Met. Soc. AIME*, **221**, 257 (1961).
13. O. Haase, *Z. Naturforsch.*, **119**, 46 (1956).
14. E. A. Gulbransen and R. Ruka, *This Journal*, **99**, 360 (1952).
15. P. B. Sewell *et al.*, To be published.
16. C. Palanche, H. Berman, and C. Frondell, Editors, "Dana's System of Mineralogy," 7th edition, p. 527, John Wiley & Sons, New York (1952).
17. V. I. Arkharov and B. S. Borisov, *Doklady Akad. Nauk S.S.S.R.*, **114**, 293 (1957).
18. A. L. Mackay, "Reactivity of Solids," Proc. 4th International Symp. Reactivity of Solids. Amsterdam 1960, p. 571.
19. S. Kachi, K. Momiyama, and S. Shimizu, *J. Phys. Soc. Japan*, **18**, 106 (1963).
20. G. D. Nicholls, *Adv. in Phys.*, **4**, 122 (1955).
21. J. M. Cowley, *Acta Cryst.*, **6**, 53 (1953).
22. D. Fuller, *Acta Met.*, **8**, 743 (1960).
23. M. Wyn. Roberts, *Trans. Faraday Soc.*, **57**, 99 (1961).

The Kinetics of Anodic Oxidation of Iron in Neutral Solution

I. Steady Growth Region

Norio Sato¹ and Morris Cohen

Division of Applied Chemistry, National Research Council, Ottawa, Ontario, Canada

ABSTRACT

Iron was anodically oxidized under both potentiostatic and galvanostatic conditions. It was found that the rate of film growth could be expressed by the over-all equation $i = k' \exp(\beta E - Q_T/B)$ where Q_T is the film thickness, E the potential, and k' , β , and B are constants. A model is proposed based on a "place-exchange" mechanism in which all the M-O exchanges in a given row take place simultaneously. β is then related to the transfer of oxygen from the OH⁻ in the solution to the oxide and B is related to the activation energy for an equivalent ion-pair exchange. The activation energy for a single place exchange was calculated to be 3.5 kcal. This mechanism would lead to an increase of activation energy with thickness and a probable change of mechanism at some finite thickness.

A large amount of work has been reported on the passivity of iron where very thin oxide films of the order of 20-30Å in thickness are formed, but only a few experimental studies of the detailed kinetics of the thickening of passive films are to be found in the literature. Vetter (1) and Weil (2) measured the rate of growth of anodic films on iron in sulfuric acid solution, and by assuming that the rate of dissolution of the oxide film was independent of potential during both increasing and constant film thickness, described the growth process by the equation $i = A' \exp(B'E/d)$ (where i is the rate, E the electrode potential, d the film thickness, and A' and B' are constants). This equation is similar to that obtainable from the Mott-Cabrera (3) theory. In a recent pub-

lication, however, Nagayama and Cohen (4) showed that the kinetics of anodic oxidation of iron in a neutral solution followed a logarithmic law rather than the inverse logarithmic type referred to above. The same type of logarithmic film growth was reported by Brasher and Kingsbury (5) for film formation on iron in a chromate solution.

In the present work the rate of anodic passive oxide film growth on iron in a neutral borate-boric acid buffer solution was measured as a function of the electrode potential and film thickness, in the potential range where no measurable dissolution of the oxide occurred, using both potentiostatic and galvanostatic methods. The results which were obtained could best be fitted to a logarithmic equation. This equation was then derived theoretically on the

¹ N.R.C. Post-doctorate Research Fellow. Present address: Faculty of Engineering, Hokkaido University, Sapporo, Japan.

basis of a place exchange mechanism and the activation energy for film growth calculated.

Experimental

The methods and materials used were essentially the same as those reported previously (4). Ferrovac E was used as specimen material. The iron was annealed at 700°C in hydrogen and electropolished. Solutions were made from 0.15N boric acid and 0.15N sodium borate. An equivolume mixture of these solutions gives a pH of 8.43. The solution was de-aerated by prolonged bubbling with purified nitrogen. The electrolytic cell was a cylindrical glass vessel of 80 ml capacity. The volume of solution used was 30 ml. The cell had an outer jacket through which constant temperature water could be circulated. Two Pt auxiliary electrodes of large surface area were used as counter electrodes. The potential of the electrode was measured against a saturated calomel electrode via a bridge filled with the electrolyte. All potential data reported here are referred to the saturated calomel electrode.

Two different electrical circuits, a potentiostatic circuit of the Gerischer-Stauback type, and a galvanostatic circuit were used for polarizing the specimens. When the potentiostat was used an additional resistance of 11 kohms was inserted in series with the cell to reduce the initial current to a value which could be followed easily by the chart recorder. When the rate of current change had slowed down sufficiently the resistance was removed from the circuit. This sequence was necessary to obtain an accurate measure of the total coulombs passed. The circuit could be changed from the potentiostat to the galvanostat and the direction of the polarization could be changed rapidly by means of a multiple switch.

Solutions for analysis were drained from the cell under nitrogen while polarization was still being applied. Iron was analyzed by the orthophenanthroline method with an accuracy of about $\pm 1\%$.

Most of the experiments were carried out at $25^\circ \pm 1^\circ\text{C}$. Other temperatures were obtained with the use of a water-jacketed cell and were maintained to $\pm 0.1^\circ\text{C}$.

In order to obtain good reproducibility in these studies the specimens were first given preliminary anodic oxidation at constant potential for 1 hr. The potential was then changed to a higher potential and the kinetics of further oxidation measured.

Results

Formation of initial oxide.—Before anodic polarization the specimens were cathodically treated at a current density of $10 \mu\text{A}/\text{cm}^2$ until the air-formed or passive oxide film was completely reduced (4). The solution was then changed at least three times in order to remove the ferrous ion formed by the cathodic reduction. The specimen was then anodically oxidized at various constant potentials more noble than 0.05v for 1 hr. This potential region was chosen because the amount of iron formed in solution is less than $0.005 \mu\text{g}/\text{cm}^2$ (equivalent to less than $0.016 \text{mC}/\text{cm}^2$). An example of the change of current density with time is shown in Fig. 1. The

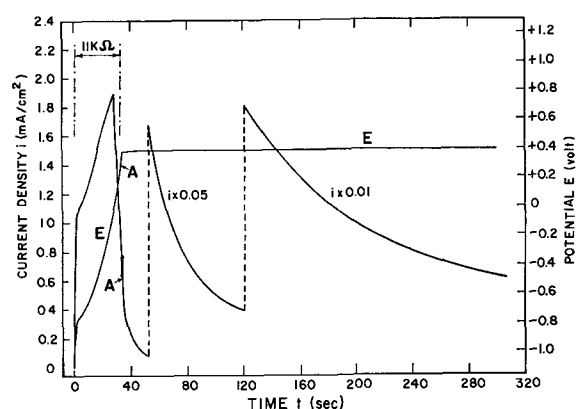


Fig. 1. An example of the change in anodic current density and potential with time during preliminary oxidation; an additional resistance of 11 kohm inserted in potentiostat circuit was removed at the point marked with A.

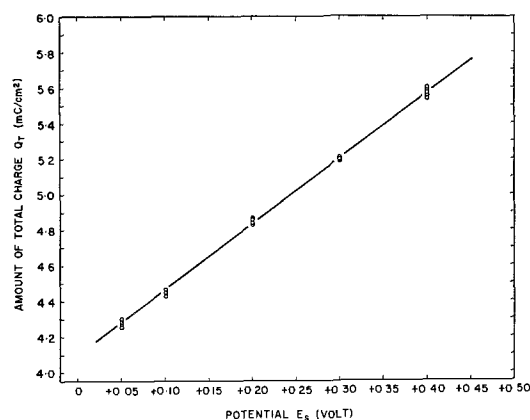


Fig. 2. Effect of potential on the amount of total charge passed during 1 hr preliminary oxidation.

E_s, v	+0.050	+0.100	+0.200	+0.300	+0.400
	4.284	4.459	4.855	5.203	5.568
	4.289	4.442	4.825	5.189	5.594
$Q_T,$	4.298	4.464	4.841	5.182	5.555
mC/cm^2	4.277	4.430	4.862	5.194	5.540
	4.260	4.461	4.826	5.196	5.604
Mean	4.282	4.451	4.840	5.193	5.572

resistance of 11 kohms was removed about 35 sec after the start of the oxidation, the time being marked as A in Fig. 1. The quantity of electric charge passed can be obtained by graphic integration of the curves. The calculated amount of charge passed during 1 hr of this preliminary oxidation, sQ_T , at five different potentials ranging from 0.05v to 0.40v is shown in Fig. 2. The experimental error appears to be less than 1%. In that there is no iron found in solution and these potentials are well below the potential at which oxygen is evolved, this charge is all accumulated in the formation of the surface oxide film and is an exact measure of the amount of film formed.

Potentiostatic oxidation.—Immediately after the preliminary oxidation treatment the potential was changed to a more noble potential and the change in anodic current with time was followed until the anodic current was $< 0.1 \mu\text{A}/\text{cm}^2$. Where necessary, the external resistance was inserted into the circuit for about 20 sec. The charge accumulated during this potentiostatic oxidation was again determined

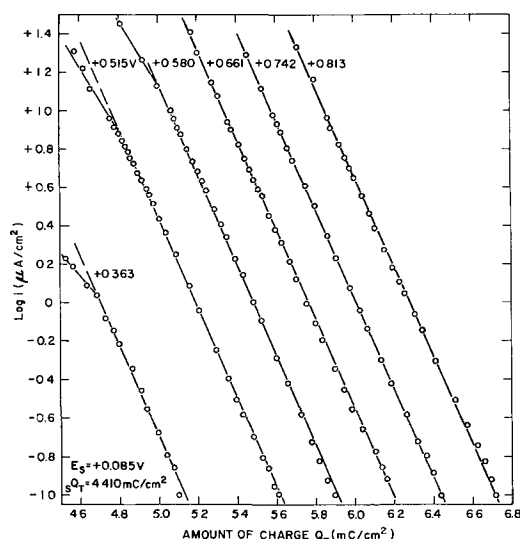


Fig. 3. Change of anodic current with thickness of the anodic oxide film during potentiostatic oxidation carried out at six different potentials after 1 hr preliminary oxidation at E_S (+0.085v); $Q_T = sQ_T + \int_0^t i dt$, Q_T is the amount of total charge accumu-

lated in the oxide film, sQ_T the amount of charge passed during preliminary oxidation.

$$i = A \exp \left(-\frac{Q_T}{B} \right)$$

E, v	$2.3026B,$ mC/cm^2
+0.363	0.426
+0.515	0.430
+0.580	0.426
+0.661	0.430
+0.742	0.434
+0.813	0.432

by graphic integration. The quantity of total charge Q_T in the passive film was then calculated as the sum of the initial charge sQ_T and the charge passed during the potentiostatic oxidation.

Figure 3 shows results of a set of experiments performed at six different constant potentials on specimens with the same starting condition of 1 hr preoxidation at 0.085v. All the points shown on this figure were obtained after the additional outside resistance had been removed. In all cases there is a large initial current which then decreases rapidly. In general a plot of the logarithm of the current density vs. the amount of total charge in the film gives a straight line, except for an initial short period of time. The final slope at all the potentials is the same but the amount of total charge is greater the more noble the potential. This leads to the empirical rate equation for the growth of the anodic oxide film.

$$i = A \exp \left(-\frac{Q_T}{B} \right) \quad [1]$$

where A and B are constants related to the position and slope of the $\log i - Q_T$ curve, respectively. Constant A increases with increasing potential, whereas the value of B is independent of the potential and is equal to

$$B = 0.430/2.3026 \text{ mC/cm}^2, 25^\circ\text{C} \quad [2]$$

The results do not fit the equation, $i = A' \exp(B'E/d)$, found by Vetter (1) and Weil (2) for the film growth on iron in acid solutions.

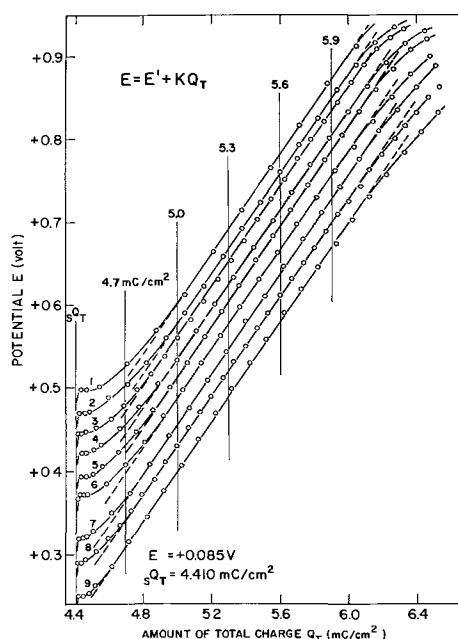


Fig. 4. Change of potential with thickness of the anodic oxide film during galvanostatic oxidation carried out at various anodic current densities after 1 hr preliminary oxidation at E_S (+0.085v); $Q_T = sQ_T + it$, Q_T is the amount of total charge accumulated in the oxide film, sQ_T the amount of charge passed during preliminary oxidation.

No.	$i,$ $\mu\text{A/cm}^2$	$K,$ $v/mC/cm^2$
1	16.67	0.308
2	11.11	0.310
3	7.78	0.308
4	5.56	0.302
5	3.33	0.303
6	2.22	0.303
7	1.11	0.302
8	0.667	0.296
9	0.333	0.299

Galvanostatic oxidation.—Constant anodic currents ranging from 0.3 to 23 $\mu\text{A/cm}^2$ were applied to the specimens immediately after 1 hr of preliminary oxidation treatment by switching the polarizing circuit from the potentiostat to the galvanostat, and the resulting change of the anodic potential with time was followed at each current density. The results for a set of experiments using a starting potential of 0.085v are plotted in Fig. 4. The amount of total charge accumulated in the film was calculated as

$$Q_T = sQ_T + it$$

where i is the anodic current density and t the time of galvanostatic oxidation. It can be seen that a rapid rise of potential is immediately followed by a potential arrest after which the potential rises gradually then passes through a steady growth region and finally reaches the oxygen evolution potential region. In the steady growth region which holds for the major part of the curves, the potential is seen to be a linear function of the total amount of charge Q_T . The slope is independent of applied current density as is seen in the tabular column in the caption of Fig. 4, although the polarization potential is lower with lower current densities. The slope of the $E - Q_T$ curve thus obtained galvano-

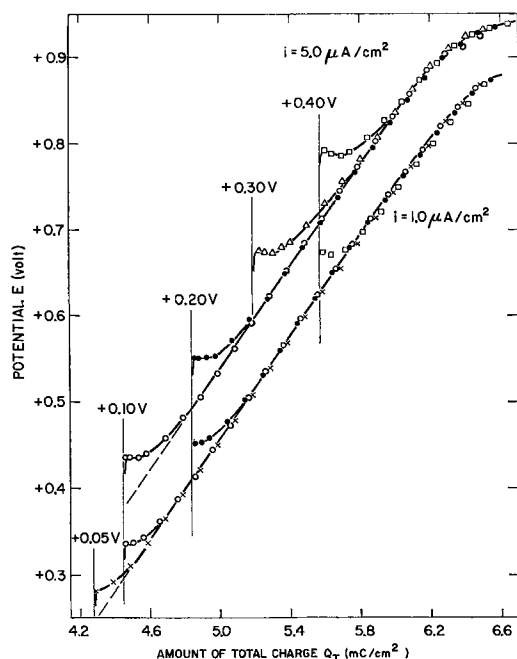


Fig. 5. Effect of the starting potential E_S on the galvanostatic oxidation curve (Q_T vs. E); preliminary oxidation was done at E_S for 1 hr. E_S : X, +0.05v; O, +0.10v; ●, +0.20v; Δ, +0.30v; □, +0.40v.

statically is the same as that obtained from the potentiostatic oxidation curves (data from Fig. 2).

Figure 5 presents the results of a set of experiments carried out at two different current densities from five different starting potentials (and hence five different initial film thicknesses). It is seen that the initial parts of the $E - Q_T$ curves are markedly dependent on the starting potentials but that the points of the succeeding main part of the curves at different starting potentials lie on a single straight line for each current density. It would thus appear that the polarization potential in the steady growth region is a direct function of the film thickness and current density, independent of the initial film thickness and the starting potential. It should therefore be reasonable to derive polarization curves at various constant film thicknesses from the steady-state

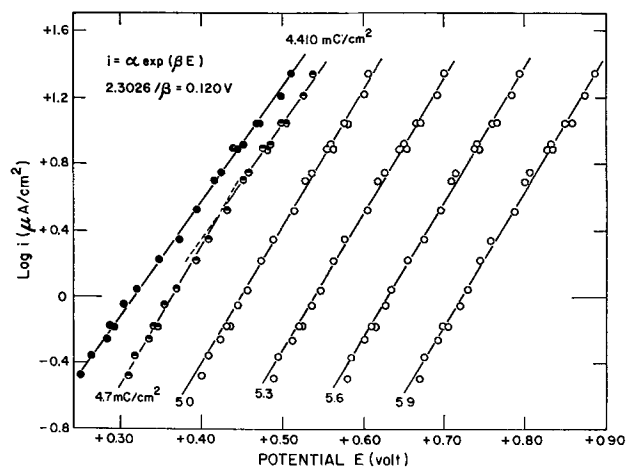


Fig. 6. Polarization curves of the thickening of anodic oxide at different thicknesses, which were obtained from the curves in Fig. 4; —●—, initial arrest potential (E_i vs. $\log i$); —○— (half solid circle), transition region; —○—, steady growth region.

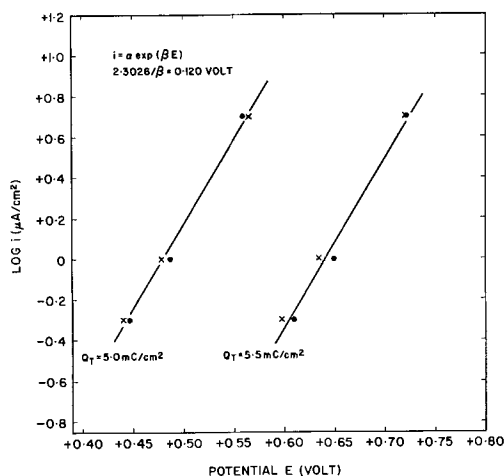


Fig. 7. Effect of pH on the polarization curve of the thickening of anodic oxide at two different thicknesses in steady growth region. ●, pH 8.38; X, pH 9.24.

region of the $E - Q_T$ curves obtained galvanostatically.

The potentials estimated at five different film thicknesses in the $E - Q_T$ curves in Fig. 4 are plotted as a function of the logarithm of the current density in Fig. 6. The polarization curves thus obtained for the steady growth regions are straight lines of constant slope obeying the Tafel relationship

$$i = \alpha \exp(\beta E) \quad [3]$$

where α and β are constants. The constant β is independent of film thickness and is estimated to be

$$2.3026/\beta = 0.120v \quad [4]$$

whereas the value of α decreases with increasing film thickness. Transition of the polarization curve from the initial region to the steady growth region can be seen in Fig. 6 where the dark circles pertain to points before the steady growth has been reached.

The polarization curves obtained at two different pH's are shown in Fig. 7. The pH was adjusted by changing the ratio of boric acid to sodium borate. No appreciable effect of pH on the polarization curve was observed.

Effect of temperature.—Potentiostatic experiments were carried out at four different temperatures ranging from 0° to 36°C at +0.700v after 1 hr of preliminary oxidation at 0.100v. The results are shown in Fig. 8. Kinetic Eq. [1] is followed at all temperatures, although the deviation in the initial period increases with decreasing temperature. It can also be seen that the slope of these $\log i - Q_T$ curves, i.e., the value of the constant B in Eq. [1] is definitely dependent on the temperature.

Discussion

The film growth in both the potentiostatic and galvanostatic experiments can be divided into two parts; an initial region immediately after changing the potential or the anodic current density, and a steady growth region. This discussion will deal with the steady growth region. The initial region will be dealt with in a subsequent publication.

In the steady growth region the rate of film growth depends on both the film thickness and the

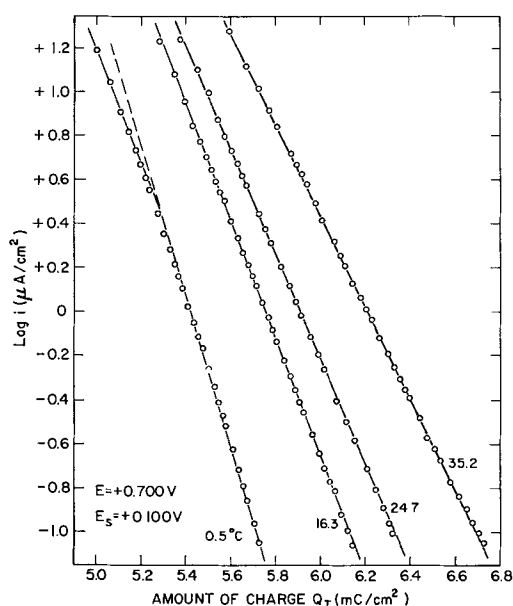


Fig. 8. Effect of temperature on the potentiostatic oxidation curve (Q_T vs. $\log i$); oxidation was done at +0.700v after 1 hr preliminary oxidation at +0.100v.

$$i = A \exp \left(-\frac{Q_T}{B} \right)$$

Temp. °C	$\frac{2.3026B}{mC/cm^2}$
0.5	0.303
16.3	0.377
24.7	0.422
35.2	0.481

potential and can be expressed by the two equations

$$i = A \exp \left(\frac{-Q_T}{B} \right) \text{ at constant } E \quad [5]$$

and

$$i = \alpha \exp (\beta E) \text{ at constant } Q_T \quad [6]$$

These may be combined to give the equation

$$i = k' \exp (\beta E - Q_T/B) \quad [7]$$

Any theory which accounts for the kinetics of the anodic growth of oxide film on iron in neutral solutions should result in an equation of this form.

Results conforming to Eq. [5] have been found in both chemisorption and oxidation studies and have been interpreted in many ways. Hauffe and Ilschner (6) used a modification of the Mott theory (7) which is based on the assumption that the rate controlling step is the flow of electrons from the metal through the oxide by tunnelling. They derived an equation similar to [5], with, however, a constant B which must be independent of temperature. Grimley and Trapnell (8) proposed that the field across the p-type oxide was created by adsorbed ions on the surface of the oxide and that the field strength was independent of film thickness. This led to a constant B which is proportional to the absolute temperature. Uhlig (9), on the other hand, proposed that the rate is determined by the transfer of electrons across the metal-metal oxide interface and derived a constant B which was also proportional to the temperature. None of these theories can account for all the results obtained in this study, nor do

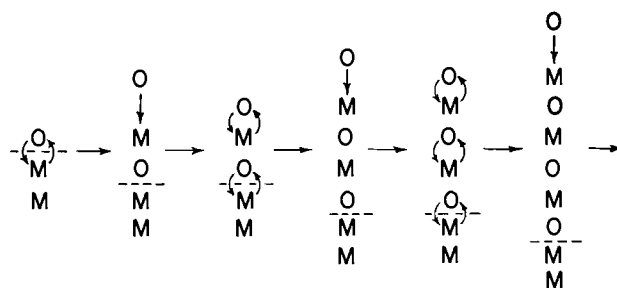


Fig. 9. Schematic representation of the "place exchange" process; M, metal ion; O, oxygen ion.

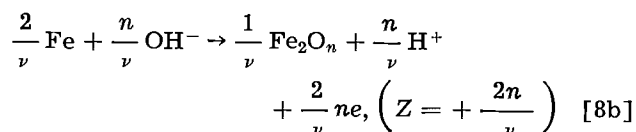
other theories based on specialized flow paths due to various types of "imperfect" structures (10-13).

An anodic growth rate of the type given by Eq. [5] can result from a process in which the activation energy increases linearly with thickness. Such a process can be derived from a mechanism which involves simultaneous place exchange, *i.e.*, rotation of M-O systems such as is shown in Fig. 9. This mechanism for ion movement was first proposed by Lanyon and Trapnell (14) and subsequently by Green (15) and Law (16) to account for the initial oxidation of metals. An oxygen atom is adsorbed and exchanges places (possibly by rotation) with an underlying metal atom. A second oxygen atom is then adsorbed and the two M-O pairs rotate simultaneously. This process repeats, with the number of pairs which exchange increasing with thickness. If all exchanges must be simultaneous then the activation energy should increase linearly with thickness. In the following discussion this place exchange mechanism is used to derive equations which conform with the results described above. From previous work (4) it is assumed that the oxide is an ordered spinel (Fe_3O_4 - Fe_2O_3) and that the rate can be calculated on the basis of concentrations, activation energies and potential gradients.²

Although the anodic oxide formed on iron in a neutral solution has been shown to be duplex in character, as a first approximation the film can be treated as a face centered cubic lattice of oxygen ions into which ions are fitted to give a composition varying between Fe_3O_4 and γ - Fe_2O_3 , with an oxygen lattice parameter between 4.20 and 4.16. The overall reaction for the anodic formation will then be



where n is the ionic valency of the iron ion in the oxide and Z the number of electrons involved in the reaction. If the rate determining step occurs ν times when the over-all reaction occurs once, then it is reasonable to write the reaction as



where ν is the stoichiometric number of the reaction.

A schematic arrangement of the system is shown in Fig. 10. The potential of this system is equal to

²The general treatment is a combination of that given by Young (17) and Darken and Gurry (18).

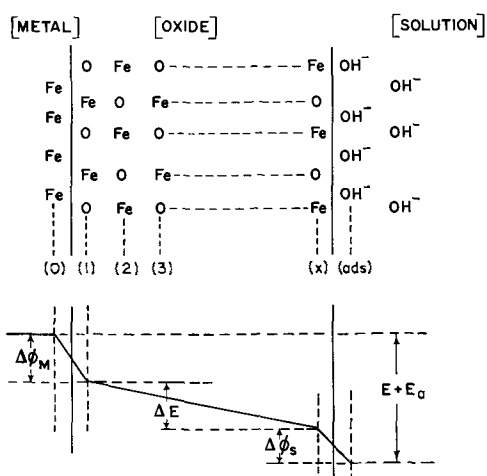


Fig. 10. Phase scheme of the electrode and the inner potential level.

the sum of all the potential differences which exist between the metal and the solution, so that

$$E = (\Delta\phi_M + \Delta E + \Delta\phi_S) - E_0 \quad [9]$$

where

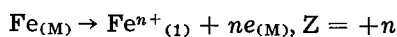
$$E_0 = (\chi_S - \chi_M) - \Delta E_S - C$$

where $\Delta\phi_M$ is the potential difference at the metal-metal oxide interface, ΔE the potential difference across the oxide, $\Delta\phi_S$ the potential difference at the metal oxide-solution interface, ΔE_S the potential difference in solution, C a constant dependent on the reference electrode, and χ_S and χ_M the surface potential differences of the solution and the metal. Since χ_S and χ_M are properties of the given solution and metal, E_0 can be considered constant when the ionic strength of the solution is large enough to diminish ΔE_S to zero.

In the steady growth region equivalent numbers of iron ions and oxygen ions are transferred from the metal phase and solution phase into the oxide. The over-all chemical reaction for the flow of iron is



where $Fe_{(M)}$ is an iron atom at the metal lattice just inside the metal surface, $Fe^{n+}_{(x)}$ the iron ion at the outermost oxide lattice layer. The first step of this reaction is the transfer of the iron ion from the metal to the first lattice layer of the oxide



The activation energy for this reaction can be split into a chemical part and an electrostatic part such that

$$A_n = W_M - \alpha\Delta\phi_M nF$$

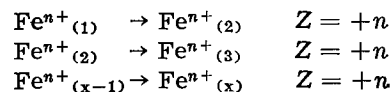
where W_M is the difference between the chemical potential of the iron ion in the activated state and the metallic state, α the transfer coefficient, and F the Faraday. In general the transfer coefficient α may have any value between zero and one. For an elemental step of the type given in Eq. [10] it is reasonable to assume that $\alpha = 0.5$.³

³ Put in another way this assumes that the activated state is in the center of the potential gradient between the two iron ions in the lattice.

The probability that an iron will transfer from the metal to the activated state is equal to the equilibrium constant for the activation reaction and is given by

$$P_1 = \exp [-(W_M - 0.5 \Delta\phi_M nF)/RT] \quad [11]$$

At the same time a group of other reactions involving exchange between the lattice layers in the oxide take place as follows:



where $Fe^{n+}_{(m)}$ represents an iron ion at the m th lattice layer of oxide (Fig. 10). The activation energy for each of these reactions, assuming a transfer coefficient equal to 0.5 will be

$$A_o = W_o - 0.5 \epsilon_m a n F$$

where W_o is the difference in chemical potential between an iron ion in the activated state and the normal state in any lattice layer, ϵ_m is the gradient of the potential difference at the m -th layer of the oxide film and a the distance between two adjacent layers in the oxygen lattice (and hence $\epsilon_m a$ is the potential difference between the $(m-1)$ -th and m -th lattice layers). The probabilities for occurrence of the activated state for these reactions are given by

$$\begin{aligned} P_2 &= \exp [-(W_o - 0.5 \epsilon_2 a n F)/RT] \\ P_3 &= \exp [-(W_o - 0.5 \epsilon_3 a n F)/RT] \\ P_x &= \exp [-(W_o - 0.5 \epsilon_x a n F)/RT] \end{aligned}$$

If one assumes that the ion movement takes place by the place exchange mechanism and hence all steps are simultaneous then for reaction all the ions in a given row must be in the activated state. The probability for this is

$$\begin{aligned} P &= P_1 \times P_2 \times P_3 \times \dots \times P_x \\ &= \exp \frac{[-\{W_n - W_o + xW_o - 0.5\Delta\phi_M nF - 0.5(\epsilon_2 a + \epsilon_3 a - \dots - \epsilon_x a)nF\}]}{RT} \\ &= \exp [-(W_n - W_o + xW_o - 0.5(\Delta\phi_M + \Delta E)nF)/RT] \end{aligned}$$

The number of rows with completely filled activated ions is equal to $({}_oN_{Fe})P$ where ${}_oN_{Fe}$ is the number of iron ions per unit area of oxide at the metal surface. The rate of incorporation of iron into the lattice, assuming there is no back reaction in the applied potential field of anodic oxidation, is equal to

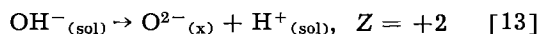
$$\frac{kT}{h} ({}_oN_{Fe} P)$$

Since reaction [10] must occur $2/\nu$ times when the rate determining step of reaction [8b] occurs once, the rate of anodic oxidation can be expressed as

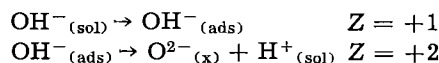
$$\begin{aligned} R_{Fe} &= \frac{kT}{h} ({}_oN_{Fe})^{2/\nu} (P)^{2/\nu} = \frac{kT}{h} ({}_oN_{Fe})^{2/\nu} \\ &\exp \frac{[-2(W_M - W_o + xW_o) + nF(\Delta\phi_M + \Delta E)]}{\nu RT} \quad [12] \end{aligned}$$

where R_{Fe} is the rate of influx of Fe to form $1/\nu Fe_2O_n$, k the Boltzmann constant, and h the Planck constant.

The transfer of oxygen from the solution to the outermost lattice layer of the oxide



can be considered to take place in two steps



If the adsorption step controls the rate of the oxygen ion uptake the rate of reaction [13] should be dependent on the activity of OH^- ion in the solution (19). However, if incorporation into the lattice is the rate controlling step then the rate of reaction [13] should be proportional to the total number of surface sites available for OH^- adsorption (19). The results shown in Fig. 7 indicate that there is no appreciable dependence of the rate of growth on the pH and hence the growth rate should be dependent on the number of surface sites only.

The activation energy for the incorporation process can be given in the same way as for iron in Eq. [11].

$$A_S = W_S - 0.5\Delta\phi_S \cdot 2 \cdot F$$

Since the oxygen uptake reaction [13] occurs n/ν times when the rate determining step of [8b] occurs once, the rate of the anodic oxidation can be given by

$$R_{ox} = \frac{kT}{h} (N_S)^{n/\nu} \exp[-(W_S - \Delta\phi_S nF)/RT] \quad [14]$$

where N_S is the total number of surface sites on the oxide for OH^- adsorption.

Under the conditions of steady state thickening of the anodic oxide, R_{Fe} should be equal to R_{ox} so that

$$R = R_{Fe} = R_{ox} \quad [15]$$

where R is the rate of the anodic oxidation.

By combining Eq. [12], [14], [15], and [9] the rate of oxide film growth is

$$\begin{aligned} i &= 2FR = 2F \sqrt{R_{Fe} \cdot R_{ox}} \\ &= K' \exp \left[\frac{n(\Delta\phi_M + \Delta E + \Delta\phi_S)F}{2\nu RT} - \frac{xW_O}{\nu RT} \right] \\ &= K \exp \left[\frac{nEF}{2\nu RT} - \frac{xW_O}{\nu RT} \right] \quad [16] \end{aligned}$$

where

$$K = \frac{2FkT}{h} \sqrt{N_S^{n/\nu} (oN_{Fe})^{2/\nu}} \exp \left[\frac{nE_0F}{2\nu RT} - \frac{W_M - W_O + 0.5nW_S}{\nu RT} \right]$$

The total activation energy A_T for the over-all process of film thickening will vary with the thickness

$$A_T = \frac{W_O}{\nu} x + \left\{ \frac{1}{\nu} (W_M - W_O + 0.5nW_S) - \frac{n}{2} F(E + E_0) \right\} \quad [17]$$

since x is proportional to the film thickness.

The rate equation is of the same form as the kinetic equation obtained experimentally

$$i = k' \exp \left(\beta E - \frac{Q_T}{B} \right) \quad [7]$$

Hence the constant β would appear to be

$$\beta = \frac{nF}{2\nu RT}$$

Using the value of β obtained experimentally $\left(\frac{2.3026}{\beta} = 0.120v \right)$ it can be seen that $\nu = n$. For

all practical purposes $n = 3$. This stoichiometric number of 3 corresponds to the rate determining step being the transfer of oxygen from the adsorbed OH^- to the oxide lattice (Eq. [8a] and [8b]).

The number of lattice layers x , in the oxide film can be calculated from the total charge, Q_T passed in forming the films.

$$\begin{aligned} x &= \frac{Q_T}{(\text{No. of oxygen atoms/cm}^2/\text{lattice layer}) \times 2e} \\ &= \frac{l^2}{4e} Q_T \end{aligned}$$

where e is the charge of the electron, l is the lattice distance of oxygen in the elemental face centered cubic cell of oxygen in the lattice and each oxygen atom has two electrons associated with it. Substituting for x and taking $\nu = n$ the rate of the over-all reaction can be expressed as

$$i = K \exp \left(\frac{0.5F}{RT} E - \frac{l^2 W_O}{4neRT} Q_T \right) \quad [18]$$

The physical meaning of the constants in Eq. [7] are therefore

$$k' = K \quad [19]$$

$$\beta = \frac{0.5F}{RT} \quad [20]$$

and

$$1/B = \frac{l^2 W_O}{4neRT} = \frac{l^2}{4neR} \left(\frac{\Delta H_O^*}{T} - \Delta S_O^* \right) \quad [21]$$

where W_O has been split into an enthalpy term ΔH_O^* and an entropy term $T\Delta S_O^*$.

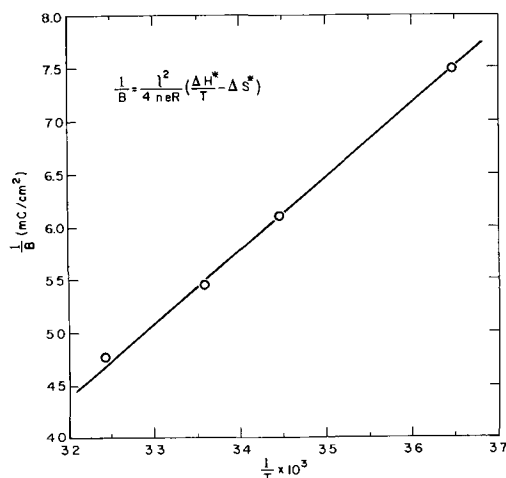


Fig. 11. Effect of temperature on the constant B

It can be seen from Fig. 11 that the relationship between B and T derived in Eq. [21] is obeyed experimentally. It should be emphasized that this formulation is independent of the relative magnitudes of the individual potential differences $\Delta\phi_M$, ΔE , and $\Delta\phi_s$.

From the data given in Fig. 11 one can calculate the values of ΔH_O^* and ΔS_O^* using the known values of the constants, i.e., $l = 4.18$, $n = 3$, $R = 1.9865$ cal/mole, $e = 1.602 \times 10^{-16}$ mC and the experimental values of B .

$$\Delta H_O^* = 15.5 \text{ kcal/ion pair}$$

$$\Delta S_O^* = 40 \text{ cal/degree}$$

so that the activation energy for each iron ion exchange at 25°C is

$$W_O = \Delta H_O^* - T\Delta S_O^* = 3.5 \text{ kcal}$$

From this it can be seen that the activation energy will change with temperature. This is a fairly small value and may indicate the presence of some cooperative phenomenon between layers or rows.

As pointed out above the total activation energy at any thickness is directly dependent on the number of lattice layers. When this becomes sufficiently large the activation energy for the "place-exchange" process will exceed that for either lattice diffusion by a vacancy mechanism or a pore or "loose structure" mechanism and one of the latter processes will take over.

Manuscript received May 7, 1963.

Any discussion of this paper will appear in a Discussion Section to be published in the December 1964 JOURNAL.

REFERENCES

1. K. J. Vetter, *Z. Elektrochem.*, **58**, 230 (1954).
2. K. G. Weil, *ibid.*, **59**, 711 (1955).
3. N. Cabrera and N. F. Mott, *Rept. Progress in Physics*, **12**, 163 (1949).
4. M. Nagayama and M. Cohen, *This Journal*, **109**, 781 (1962).
5. D. M. Brasher and A. H. Kingsbury, *Trans. Faraday Soc.*, **54**, 1214 (1958); O. Kubaschewski and D. M. Brasher, *ibid.*, **55**, 1200 (1959).
6. K. Hauffe and B. Ilschner, *Z. Elektrochem.*, **58**, 382 (1954).
7. N. F. Mott, *J. Inst. Metals*, **65**, 333 (1939).
8. T. B. Grimley and B. M. W. Trapnell, *Proc. Roy. Soc. London*, **234A**, 405 (1956).
9. H. H. Uhlig, *Acta Met.*, **4**, 451 (1956).
10. D. Davies, U. R. Evans, and J. Agar, *Proc. Roy. Soc.*, **225A**, 443 (1954).
11. U. R. Evans, *Trans. Electrochem. Soc.*, **83**, 335 (1943).
12. U. R. Evans, *Nature*, **157**, 732 (1946).
13. H. Miley, *Trans. Electrochem. Soc.*, **81**, 413 (1942).
14. A. H. Lanyon and B. M. W. Trapnell, *Proc. Roy. Soc.*, **227A**, 387 (1955).
15. M. Green, *Progress in Semiconductors*, **4**, 37 (1960); M. Green, J. A. Kafalas and P. H. Robinson, "Semiconductor Surface Physics," p. 349. University of Pennsylvania Press (1957).
16. J. T. Law, *J. Phys. Chem. Solids*, **4**, 91 (1958).
17. L. Young, "Anodic Oxide Films," p. 14, Academic Press, London (1961).
18. L. S. Darken and R. W. Gurry, "Physical Chemistry of Metals," p. 467, McGraw-Hill Book Co., Inc., New York (1953).

The Kinetics of Anodic Oxidation of Iron in Neutral Solution

II. Initial Stages

Norio Sato¹ and Morris Cohen

Division of Applied Chemistry, National Research Council, Ottawa, Ontario, Canada

ABSTRACT

When passive iron is oxidized galvanostatically a potential arrest is observed in the initial region. Polarization curves obtained using the arrest potentials at different current densities lead to an equation of the form

$$i = \alpha' \exp(\beta' E_i)$$

The value of β' decreases with increasing film thickness and is smaller than that observed in the steady state region. Cathodic reduction experiments showed that the ratio of iron in the outer layer of the film to charge passed is considerably smaller in the initial region than in the following steady growth region. It was concluded that in the initial region the charge passed was used in the formation of iron-ion vacancy-electron pairs and the transfer of oxygen from the solution to the outer layer of the oxide. The extent of this reaction depends on the film thickness in that the latter determines the distribution of the potential drops between the metal and the solution.

In a previous paper (1) it was shown that during both the potentiostatic and galvanostatic oxidation of iron in a neutral buffer solution some time of polarization was required before a steady state

¹ N.R.C. Post-Doctorate Research Fellow. Present address: Faculty of Engineering, Hokkaido University, Sapporo, Japan.

was reached. An understanding of the kinetics of the reaction during this initial period should be helpful in any attempt to elucidate the whole mechanism of anodic film formation. In this paper some results obtained in this early period are presented.

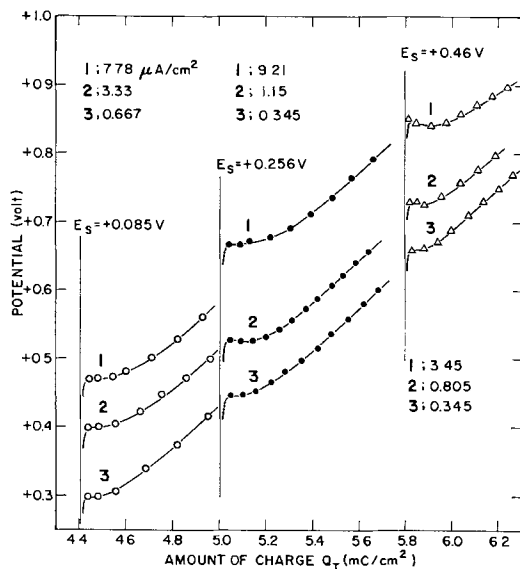


Fig. 1. Change of potential with thickening of the anodic oxide film during galvanostatic oxidation at various anodic current densities after 1 hr preliminary oxidation at three different starting potentials (E_s).

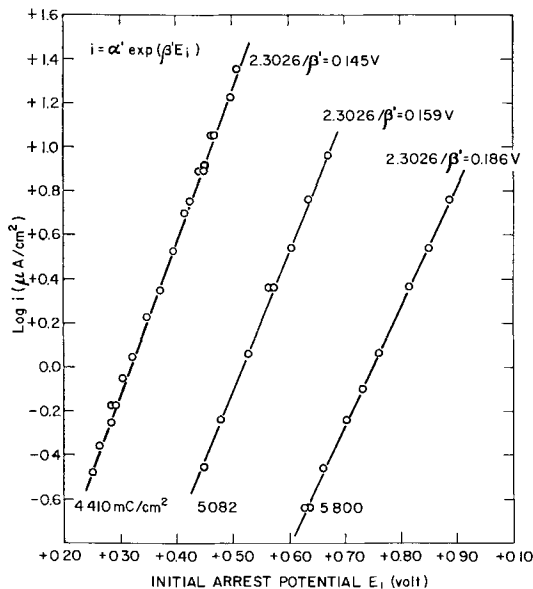


Fig. 2. Initial polarization curve of oxide-thickening at three different thicknesses.

Experimental

The materials and methods are the same as those presented in the preceding paper (1).

Results

Specimens which had been pre-polarized for 1 hr at various constant potentials were oxidized galvanostatically over a range of current densities. A typical set of results is shown in Fig. 1. It can be seen that on applying the constant current after the pre-polarization there is a sharp rise in potential followed by a potential arrest which is then followed by a gradual merging into a region where the potential varies linearly with total charge.

A polarization curve can be constructed for the oxide film growth in the initial region by plotting the value of the potential arrest, E_1 , vs. the current density. Figure 2 shows three polarization curves

obtained in this way by galvanostatic oxidation from three different starting potentials (and hence three different initial oxide thicknesses). As shown for the steady state region in the previous paper the polarization curves appear to obey the Tafel equation

$$i = \alpha' \exp(\beta' E_1) \quad [1]$$

It can be seen that the value of β' decreases with increasing film thickness and that it is smaller than that obtained in the steady growth region (1).

The composition of the film during galvanostatic oxidation was determined by stopping the anodic current at various times and immediately switching to a cathodic reduction circuit. The cathodic current density was $10 \mu\text{A}/\text{cm}^2$. As in previous work (2) measurements were made of both the number of coulombs used in the first wave of the cathodic reduction and of the amount of iron formed in the solution. The previous study (2) had shown that only the outer layer of the oxide film is electrolytically dissolved to form ferrous ion in solution during the first part of the cathodic process. The results are shown in Fig. 3 and 4. It can be seen that the amount of iron in the film increases only very slowly in the initial region of the galvanostatic oxidation and only later on becomes a function of the total charge. This relationship is the same as that observed between the potential and total charge. In contrast to this the charge accumulated in the outer layer shows no arrest but increases linearly from the beginning of the galvanostatic oxidation.

Discussion

The results indicate that the initial arrest in the potential during galvanostatic oxidation is associated with the formation of iron-ion vacancies (or excess oxygen ion) in the outer layer of the oxide.

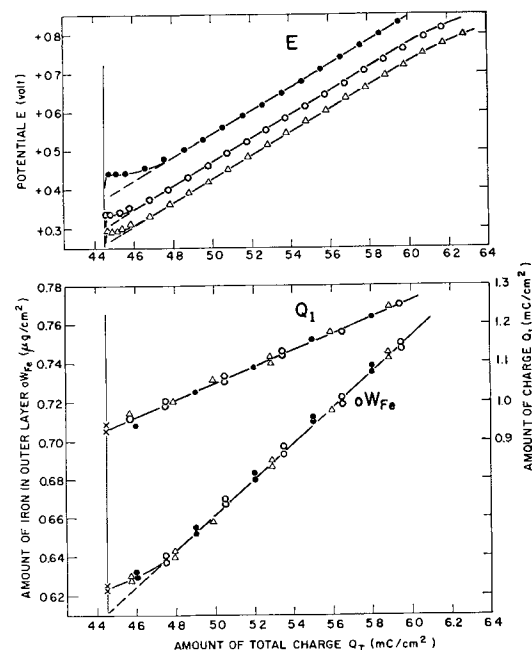


Fig. 3. Change of the amount of iron in the outer layer of oxide film during galvanostatic oxidation; Q_1 is the amount of charge associated with the first wave of cathodic reduction curve. i ($\mu\text{A}/\text{cm}^2$): Δ , 0.5; \circ , 1.0; \bullet , 5.0; $E_s = +0.100$ v.

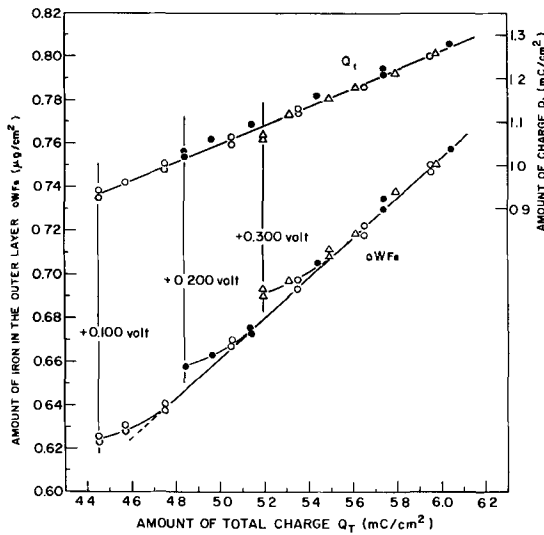
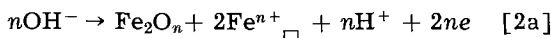
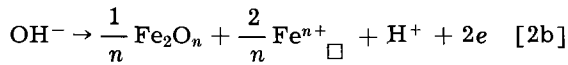


Fig. 4. Effect of the starting potential E_s on the change in ΔW_{Fe} and Q_1 during galvanostatic oxidation. E_s volt: \circ , +0.100; \bullet , +0.200; \triangle , +0.300; $i = 1.0 \mu a/cm^2$.

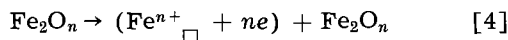
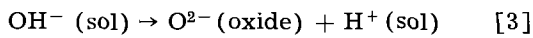
It is, therefore, reasonable for the initial region to write the reaction as



or

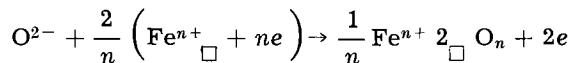


where $Fe^{n+} \square$ is the iron-ion vacancy with the positive charge of n . Reaction [2b] can be split into two reactions involving the transfer of oxygen ion from the OH^- from the solution into the oxide and the formation of iron-ion vacancies in the outermost part of the oxide



where $(Fe^{n+} \square + ne)$ is the vacancy-electron pair.

These reactions are followed by the combination of the oxygen-ion and iron-ion vacancy in the oxide



The rate equation for the transfer of oxygen ion from the solution into the oxide was derived theoretically in the previous paper (1) and is found to be

$$R_{ox} = \frac{kT}{h} N_s \exp \left(-\frac{(W_s - \Delta\phi_s F)}{RT} \right) \quad [5]$$

where N_s is the total number of surface sites on the oxide for OH^- adsorption, W_s the chemical term of the activation energy, $\Delta\phi_s$ the inner-potential difference at the metal oxide-solution interface, k the Boltzmann constant, h the Planck constant, and F the Faraday. In that the electrode potential is the sum of the potential differences which exist between the metal and the solution, $\Delta\phi_s$ is related to the electrode potential E by the equation

$$E = (\Delta\phi_M + \Delta E + \Delta\phi_s) - E_o \quad [6]$$

where $\Delta\phi_M$ is the inner potential difference, ΔE the potential difference across the oxide, and E_o the arbitrary constant.

The vacancy-electron pair, $(Fe^{n+} \square + ne)$ is electroneutral in itself and consequently it is reasonable for the formation of the vacancy-electron pair to assume an activation energy which is independent of the electrostatic field applied. The number of the vacancy-electron pairs formed in the oxide must be related to the number of oxygen-ions transferred from the solution into the oxide in such a way that the transfer of one oxygen-ion corresponds to the formation of two n -th of one vacancy-electron pair. The rate of the oxide growth due to the formation of vacancy-electron pairs, therefore, can be given by

$$R_v = (xN_{Fe})^{2/n} \frac{kT}{h} \exp(-2W_v/nRT) \quad [7]$$

where xN_{Fe} is the number of iron-ion sites in the outer most part of the oxide, and W_v is the activation energy for the formation of the vacancy-electron pair. The rate R_v should be equal to the rate R_{ox} ; then the rate of oxide growth can be expressed by

$$R = R_{ox} = R_v \quad [8]$$

Combination of Eq. [5], [6], [7], and [8] leads to the rate equation of the oxide growth for the initial region as

$$\begin{aligned} i &= 2F \sqrt{R_{ox} R_v} = K' \exp \left(\frac{0.5F}{RT} \Delta\phi_s \right) \\ &= K'' \exp \left(\frac{0.5F}{RT} \kappa E \right) \end{aligned} \quad [9]$$

where

$$\begin{aligned} K'' &= 2F \left(\frac{kT}{h} \right) \sqrt{N_s (xN_{Fe})^{2/n}} \\ &\quad \exp \left(\frac{0.5F}{RT} \kappa E_o - \frac{W_v + 0.5W_s}{nRT} \right) \end{aligned}$$

$$\kappa = \Delta\phi_s / (\Delta\phi_M + \Delta E + \Delta\phi_s) = \Delta\phi_s / (E + E_o)$$

Since $1 > \kappa > 0$, the potential dependence of the rate in this equation is smaller than that for the rate in the steady growth region which is equal to $0.5 F/RT$ (1). This is in agreement with the observed smaller slope of the initial polarization curve than the slope for the subsequent steady growth (1).

The numerical value of factor κ can be calculated from the slope of the initial polarization curves (Fig. 2), and the results of the calculation are shown in Table I. The value of κ is seen to decrease with the film thickness. This is what one would expect if the potential difference E in the oxide film increases with the film thickness. All the values of

Table I. Relation between κ and oxide film thickness

Starting potential E_s (v)	Oxide thickness s_{Q_T} (mC/cm ²)	$\kappa = \Delta\phi_s / (\Delta\phi_M + \Delta E + \Delta\phi_s)$
+0.085	4.410	0.821
+0.256	5.082	0.748
+0.460	5.800	0.640

κ are also seen to be larger than 0.5. This suggests that at the initial moment of the anodic oxidation immediately after increasing the anodic current the major part of the potential difference between the metal and the solution is located at the metal oxide-solution interface

$$\Delta\phi_s > \Delta\phi_M + \Delta E$$

This equation, however, cannot apply to the steady growth region, since the relative magnitude of the three individual potential differences may change with the lapse of time of anodic oxidation.

As the vacancy concentration increases in the outermost part of the oxide, the rate of the formation of iron-ion vacancies will slow down and the flow of iron-ion from the metal will take over. This would be the cause of the transition from the initial region to the steady growth region.

On the basis of the above and the preceding paper (1) the kinetics of the oxidation process can be

described in the following manner. On first applying the current, either potentiostatically or galvanostatically, a charge is set up at the oxide solution interface which leads to the formation of iron-ion vacancy-electron pairs and oxygen ion entrance into the lattice. After a certain period of time this process is superseded by the place-exchange of oxygen-iron ion pairs until such a time as the thickness of the layer is too large (*i.e.*, the activation energy increases to a large value) and a new mechanism involving either cation diffusion via vacancies or some other process takes over.

Manuscript received May 7, 1963.

Any discussion of this paper will appear in a Discussion Section to be published in the December 1964 JOURNAL.

REFERENCES

1. N. Sato and M. Cohen, *This Journal*, **111**, 512 (May 1964).
2. M. Nagayama and M. Cohen, *ibid.*, **109**, 781 (1962).

Effect of Cold-Work on Corrosion of Iron and Steel in Hydrochloric Acid

Z. A. Foroulis and H. H. Uhlig

Corrosion Laboratory, Massachusetts Institute of Technology, Cambridge, Massachusetts

ABSTRACT

Zone-refined iron corrodes at the same rate whether cold-worked or annealed. Cold-working of iron containing 0.007-0.15% carbon increases the corrosion rate in 0.12N HCl ($\text{pH} = 1.01$), the rate increasing still more after heat treating the iron at 77°-100°C for 2 hr. Cold-working of iron containing 0.01-0.02% nitrogen increases the corrosion rate only after heat treatment at 77°-200°C. Two maxima in the rate appear for heat treated N alloys but only one for C alloys, corresponding to precipitation of two different nitrides but only one iron carbide. Heat treatment above 200°C reduces the corrosion rate for both alloys, but pure iron is not affected by any heat treatment schedule. Polarization measurements show that corrosion in all instances is controlled cathodically.

These results are explained by lower H_2 overvoltage of imperfection sites introduced by cold-work, and associated with C or N atoms (Cottrell atmospheres). In absence of C and N, imperfection sites have the same apparent H_2 overvoltage as iron, and their tendency to dissolve anodically is not pronounced. The C and N atoms segregated at imperfections come from interstitial sources as well as through dissociation of carbides and nitrides, the compounds being less stable than the corresponding Cottrell atmospheres. Increase in corrosion caused by cold-work, especially when followed by heat treatment at 77°-200°C, is in part explained by annealing out some imperfections, such as lattice vacancies, causing re-formation of carbides or nitrides in finely divided form. Increased peripheral area of the precipitate increases galvanic action. Carbides dissociate more rapidly at low temperatures than do nitrides, accounting for the observed difference in behavior of Fe-N and Fe-C alloys. Effect of cold-work on corrosion of metals in general is greatest when a second phase precipitates to form active galvanic cells, whereas the increase in internal energy of a disarrayed metal lattice has little if any effect. Preferred grain orientation of surface metal sometimes resulting from cold-work may either increase or decrease corrosion.

Cold-working or plastic deformation of metals is usually assumed to increase corrosion tendency. Tammann and Neubert (1) came to this conclusion from results they obtained with electrolytic iron cold-rolled up to 85% reduction in thickness, annealed at various temperatures, and subsequently

corroded in 3N H_2SO_4 . Corrosion rates for cold-rolled iron were 20 times rates for annealed iron. They also found cold-rolling to increase corrosion of Mg, Al, cerium, and Zn. Evans (2) stated that disarray in the atomic structure brought about by cold-work is likely to facilitate detachment of the

atom from the metallic phase and its passage into the liquid. He pointed out that preferred orientation, also mentioned by Tammann, or change in surface composition induced by cold-work may also be factors in altering the corrosion rate. Furthermore, for some metals particularly in environments other than acids, damage to oxide films may account for an increase of attack. Hoar (3) stated that cold-working produces more active sites of low activation energy for anodic dissolution than does annealed material.

Harwood (4) stated that the published evidence relating to the influence of stress on general corrosion is somewhat confused, some authors finding stress to increase corrosion, others finding no effect and still others reporting a decrease. He concluded that there is no consistent change in corrosion rate with stress but rather that the effects are quite specific both to the metal and to its environment. Zaretsky (5) concluded that cold-work increases corrosion, the effect of strain being one of rupturing oxide films on the metal surface or decreasing ohmic resistance of microcells such as by breaking up the grain structure. He also indicated that in some instances microfissures are formed or that there may be precipitation from super-saturated solid solutions.

Straumanis and Wang (6) found that 99.99% Al, cold-rolled to 90% reduction in thickness, corroded in 1N HF at the same rate as annealed material. Similarly, cold-rolling had no effect on the dissolution rate in 0.5N barium hydroxide. Only severe hammering on an iron anvil produced an increase of attack by Ba(OH)₂ by as much as 30%, which the authors ascribe to slip bands plus microscopic or submicroscopic shear cracks. However, it is also possible that the increase in corrosion they found was caused by iron contamination picked up during the severe hammering operation. With respect to nickel and some nickel-base alloys, Copson (7) presented data showing that on the average there is no significant effect of cold-work on the corrosion rate in acids and in alkalis.

For iron in aqueous media, it is known that the effect of cold-work is negligible when corrosion is controlled by oxygen depolarization, but in non-oxidizing acids previously reported data indicate that the corrosion rate invariably increases (1, 5, 8, 9). This paper is concerned with the effects of cold-work on corrosion of pure iron, specifically in an acid medium, as a function of nitrogen and carbon content of the iron. The mechanism of attack is studied by appropriate polarization measurements.

Experimental Procedure

For some experiments, zone-refined iron of high purity was used as prepared and analyzed at Battelle Memorial Institute. It contained <0.001% C and 0.0003% N. For alloys of iron with carbon or with nitrogen, decarburized remelted electrolytic iron was the starting material. This was melted in a vacuum induction furnace employing pure alumina crucibles to which additions of spectrographic carbon were made; alternatively for nitrogen alloys, the melt was held in a pure N₂ atmosphere. For the carbon alloys, purified helium blanketed the furnace after melting, and the alloys were suction-cast by drawing them into 7 mm Vycor tubes and quenching in water. Nitrogen alloys were cast similarly in a nitrogen atmosphere. Castings were homogenized by sealing them in individual evacuated quartz tubes and heating at 1050°C for 48 hr. The castings were then cold-rolled at 0.015 in. per pass in the direction of the long axis, usually to a final 50% reduction in thickness. Analyses are given in Table I.

Heat treatment of cold-rolled specimens followed differing procedures depending on temperature. For treatment at 77°C, specimens were immersed in boiling ethyl acetate. At 100°C, specimens enclosed in glass tubes were immersed in boiling water. At 150°-250°C, they were immersed in a low melting Bi-Sn-Zn alloy bath thermostatically controlled. For temperatures above 250°C, temperature-controlled furnaces were employed with specimens contained in individually evacuated and sealed quartz tubes.

Specimens were kept at room temperature for one week following cold-rolling in order to insure that they had all undergone the same amount of room-temperature aging and recovery. Measurements of corrosion rates were started immediately after any particular heat treatment schedule.

Specimens for corrosion rate measurements were rectangular in shape and about 4 to 6 cm² total area. A small hole was drilled at one end from which the specimen was suspended by a glass hook. They were abraded through 4-0 emery paper, pickled in dilute HCl to remove effects of abrading or machining, washed in H₂O, and dried by successive immersion in acetone and benzene. After being weighed, specimens were suspended from the side of a tubular glass chimney contained in a glass-stoppered flask (Fig. 1). The corrodent was 0.12N HCl (pH 1.01) which was deaerated beforehand by bubbling purified H₂ (passed over Pd catalyst at

Table I. Analysis of iron and steels

	Treatment	% C	% N	% O	% S
Zone-refined iron	—	<0.001	0.0003	0.0015	
Remelted electrolytic iron	—	0.007	0.0005	0.004	0.003
Remelted electrolytic iron	Decarburized	0.002	0.0005		
Remelted electrolytic iron	Added carbon	0.023	0.005		
Remelted electrolytic iron	Added carbon	0.076	0.003		
Remelted electrolytic iron	Added carbon	0.15	0.005		
Remelted electrolytic iron	Added nitrogen	0.002	0.01		
Remelted electrolytic iron	Added nitrogen	0.002	0.023		

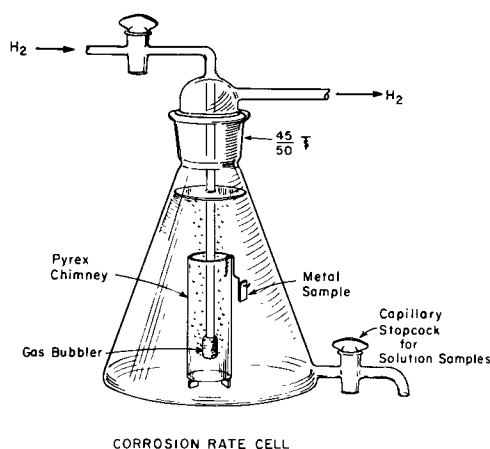


Fig. 1. Cell for measuring corrosion rates by weight loss and by solution analyses.

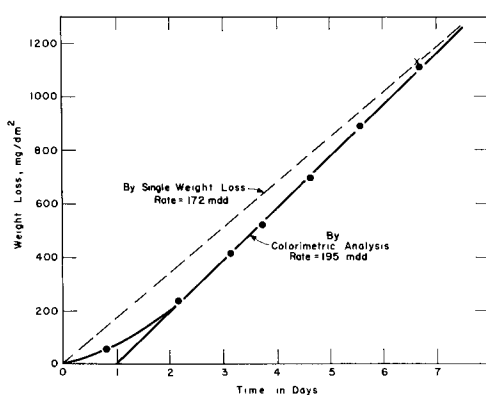


Fig. 2. Weight loss-time behavior of cold-rolled 0.002% C steel in deaerated 0.12N HCl, 25°C.

room temperature and Ru catalyst at 300°C) through the acid for 12 hr. Hydrogen was also passed at a slow rate through the solution during the test, the actual rate of which was found to have no effect on corrosion.

Corrosion rates were determined by periodic analyses of the acid for Fe^{++} using the colorimetric orthophenanthroline method (10). Results were checked by comparison with weight loss measurements at the end of each run. The comparison was close but not exact because of a slow initial rate sometimes lasting one or more hours preceding a higher steady-state rate (Fig. 2). Only steady-state rates are reported herewith for exposure periods averaging 4 to 6 days, and for minimum exposure time of two days.

Polarization measurements were carried out in H_2 -deaerated 0.12N HCl using a three compartment cell. The design of the cell and of the iron electrode using Teflon gaskets was the same as that described previously (11).

Results

Pure iron and carbon steels.—Steady state corrosion rates obtained for cold-rolled iron containing <0.001–0.15% C are plotted as a function of heat treatment in Fig. 3 and 4. Cold-rolling increases the corrosion rate to a greater extent the higher the carbon content. Attack was uniform in all cases.

For 0.15% C steel, the cold-rolled material corrodes at a rate 10 times higher than the annealed

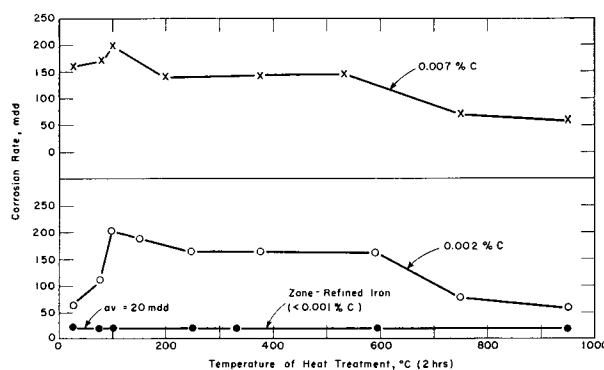


Fig. 3. Corrosion rates in deaerated 0.12N HCl of carbon steels cold-rolled 50% and subsequently heat treated at various temperatures for 2 hr.

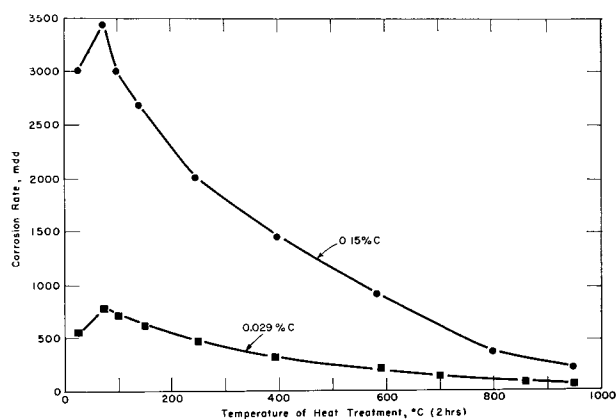


Fig. 4. Corrosion rates in deaerated 0.12N HCl of carbon steels cold-rolled 50% and subsequently heat treated at various temperatures for 2 hr.

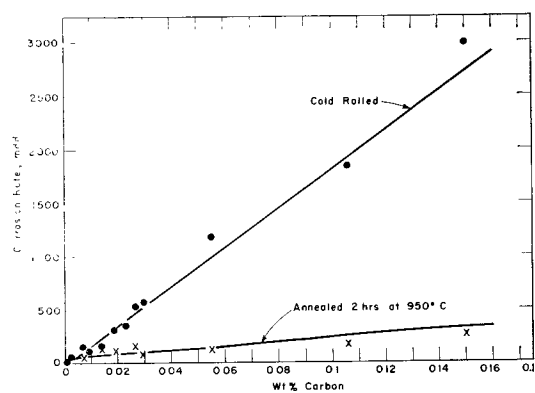


Fig. 5. Effect of carbon in steels cold-rolled 50%, or subsequently annealed, on corrosion in deaerated 0.12N HCl, 25°C.

material. But for the 0.029% C steel, the ratio is only 5 times, for the 0.007% C steel it is still less (3 times), and for iron containing 0.002% C or <0.001% C, the annealed and cold-rolled materials corrode at the same rate. The corrosion rate plotted vs carbon content of various steels either annealed or cold-reduced 50%, is shown in Fig. 5. The rate increases linearly with carbon content for cold-rolled and annealed steels, the slope, however, for annealed steel being appreciably lower. Rates extrapolated to zero carbon content show no differences for cold-rolled or annealed material, which confirms the results obtained using zone-refined iron (Fig 3).

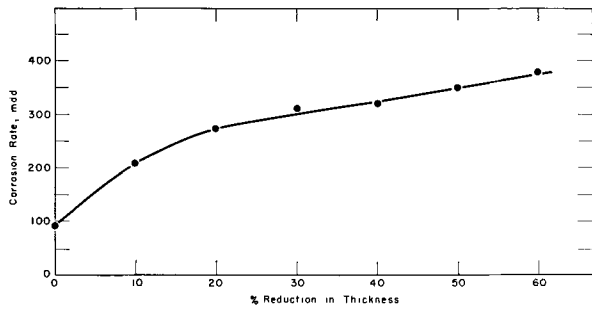


Fig. 6. Effect of degree of cold-work on corrosion of 0.023% C steel in deaerated 0.12N HCl, 25°C.

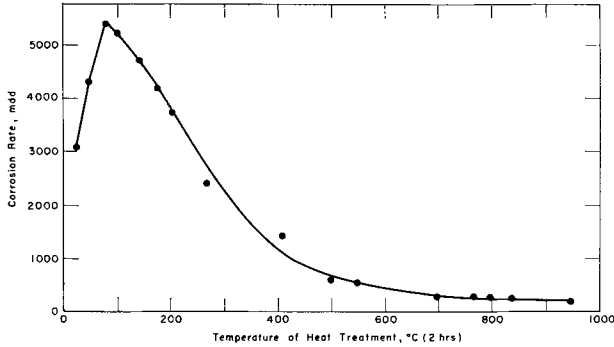


Fig. 7. Corrosion rates in deaerated 0.12N HCl of 0.076% C steel cold-rolled 85% and subsequently heat treated at various temperatures for 2 hr.

For cold-rolled carbon steels, the rate increases on low temperature heat treatment at 77°-100°C for 2 hr. At higher temperatures the rate decreases, tending toward a minimum above the critical temperature for austenite-ferrite transformation. For zone-refined iron, heat treatment at 77°-100°C has no effect. The corrosion rate remains at 20 mdd after cold-rolling as well as for any subsequent condition of heat treatment.

Trend of the corrosion rate with extent of cold-rolling for 0.023% C steel is shown in Fig. 6. The rate continues to climb at 60% reduction in thickness, which was the maximum extent to which this particular steel was cold-rolled. In Fig. 7, data are plotted for 0.076% C steel cold-reduced 85%. The rates are appreciably higher than for 50% reduction in thickness as can be seen from interpolated data of Fig. 5.

Nitrogen Steels.—Corrosion rates for two cold-rolled nitrogen steels are shown in Fig. 8. For either steel, the rates for cold-rolled and annealed material are about the same. Low-temperature heat treatment, however, accounts for an appreciable increase

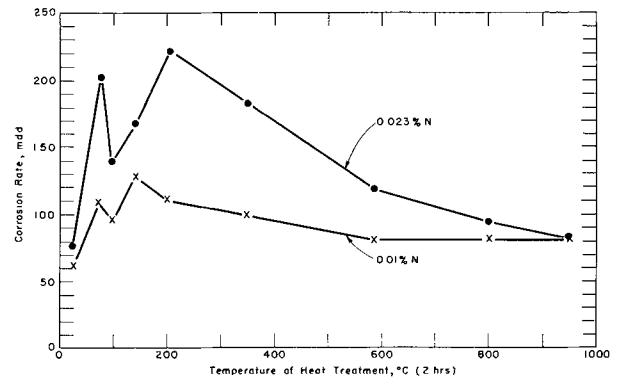


Fig. 8. Corrosion rates in deaerated 0.12N HCl of nitrogen steels cold-rolled 50% and subsequently heat treated at various temperatures for 2 hr.

in rate, the proportionate effect of which is much larger than for carbon steels. Unlike carbon steels, two maxima appear instead of one, each of which lies at or below 200°C. Beyond 200°C, the rate decreases, as is the case for carbon steels, reaching a minimum at or above the critical temperature. Analyses show that the 0.023% N alloy heated for 2 hr at as high a temperature as 950°C did not lose nitrogen. Hence, the decrease in rate on heat treatment is not explained by change in composition.

Polarization measurements.—Cathodic polarization measurements over at least two orders of magnitude of current density i were used to establish values of the slope for potential *vs.* $\log i$ and of the exchange current density i_0 . Data shown in Table II were readily reproducible. Anodic polarization measurements, on the other hand, exhibited typical hysteresis depending on whether measurements were recorded for increasing or decreasing current, as pointed out previously by Stern (12). It was not possible, therefore, to report values of anodic constants for the Tafel equation.

Referring to Table II, values of exchange current density for cold-rolled 0.15% C steel are definitely higher (lower H₂ overvoltage) than for the same steel annealed. For zone-refined iron, on the other hand, the values are about the same for either cold-rolled or annealed material, and they lie appreciably below the values for 0.15% C steel. This behavior is in accord with a lower corrosion rate of zone-refined iron, and also with a corrosion rate not sensitive to cold-work. For pure iron, values of the Tafel slope β and exchange current density i_0 are in reasonable agreement with values reported by

Table II. H₂ overvoltage constants for pure iron and steels in H₂-saturated 0.12N HCl (pH 1.01), 25°C

Electrode	Treatment	Corrosion potential, H ₂ scale	Tafel slope, β (v)	Exchange current density, i_0 , ma/cm ²
Zone-refined iron	Cold-rolled	-0.305	0.10	3.3×10^{-5}
Zone-refined iron	Annealed 950°C, 2 hr, quenched	-0.303	0.10	3.7×10^{-5}
0.002% C steel	Cold-rolled	-0.275	0.10	1.6×10^{-4}
0.15% C steel	Cold-rolled	-0.26	0.12	2.5×10^{-2}
0.15% C steel	Annealed 950°C, 2 hr, quenched	-0.26	0.12	2.0×10^{-3}
0.01% N steel	Cold-rolled	-0.33	0.10	5.4×10^{-5}

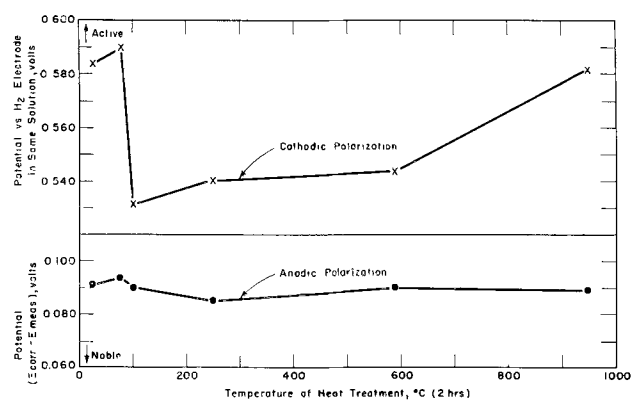


Fig. 9. Anodic and cathodic polarization potentials in deaerated 0.12N HCl at 10 ma/cm² of 0.002% C steel cold-rolled 50% and subsequently heat treated at various temperatures for 2 hr.

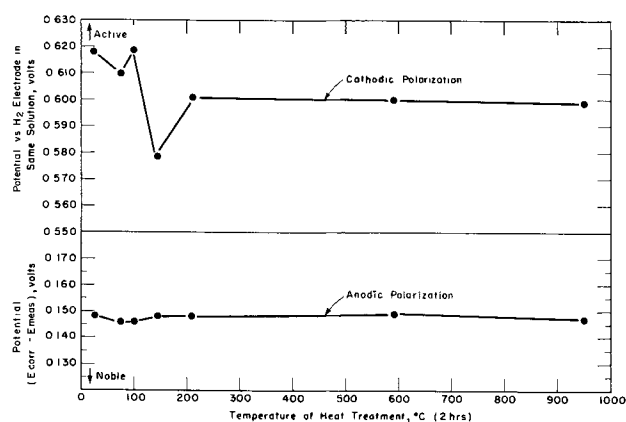


Fig. 10. Anodic and cathodic polarization potentials in deaerated 0.12N HCl at 10 ma/cm² of 0.01% N steel cold-rolled 50% and subsequently heat treated at various temperatures for 2 hr.

Stern for iron in HCl + 4% NaCl solutions at pH 1 and 2 (13). Anodic and cathodic polarization values at 10 ma/cm² for 0.002% C and 0.01% N steels cold-rolled 50% and heat treated at various temperatures are shown in Fig. 9 and 10. Marked change with heat treatment is found only for the cathodic values, the changes of anodic polarization being small or within experimental error. Two minima are found in the cathodic polarization curves for the nitrogen steels corresponding to two maxima in the corrosion rates.

Discussion

The corrosion potential of cold-rolled 0.002% C steel is -0.275 v (Table II) and the polarized potential as cathode (Fig. 9) in 0.12N HCl of pH 1.01 is $-0.584 - 0.059 \times 1.01 = -0.644$ v. The electrode, therefore, is polarized as cathode $-0.644 - (-0.275) = -0.369$ v. As anode, on the other hand, it is polarized only 0.091v (Fig. 9). In general, for either cold-worked or annealed 0.002% C steel, and also for nitrogen steels, cathodic polarization predominates over anodic polarization for a given current density.

Polarization data of Fig. 9 and 10 clearly demonstrate, therefore, that in HCl, corrosion of iron whether cold-worked or annealed is cathodically controlled. This fact, with regard to annealed iron at least, has been recognized in the literature for a long time and is not new. Since the increased corrosion rate of cold-worked carbon steels is depend-

ent on carbon content, as data of Fig. 5 show, the function of carbon is to reduce hydrogen overvoltage at cathodic sites of the metal surface. Such sites may consist of dislocations and other imperfections, and also of precipitated cementite, Fe₃C. Severe cold-working is known to increase number of dislocations, the density of which changes from perhaps 10⁸ for annealed iron to 10¹²/cm² (14) for cold-worked iron. Dislocations, consequently, may serve as one source of reduced hydrogen overvoltage provided, however, they are associated with carbon atoms (Cottrell atmospheres). Without carbon, dislocations have no effect on the corrosion rate in HCl as data for zone-refined iron show (Fig. 3 and 5). Suits and Low (15) found analogously that etch pits in cold-worked silicon steel marking the presence of dislocations were observed only if sufficient carbon were present.

The sources of carbon atoms in iron are interstitial carbon, present in small amount, and also Fe₃C present as a second phase. As explained later, Fe₃C probably dissociates in presence of dislocations and other imperfection sites into interstitial C and Fe. Cementite itself has a low hydrogen overvoltage, and accelerates corrosion corresponding to the amount present and its particle size (extent of peripheral area in galvanic contact with ferrite).

The first effect, therefore, following formation of more imperfection sites, is the migration of C atoms to such sites. But some imperfection sites such as lattice vacancies slowly anneal out during and after the cold-rolling process, hence carbon atoms associated with such imperfections react to form cementite¹ again, but now in finely divided form. One effect of cold-working, therefore, quite apart from mechanical break up of inclusions, is to produce small particle size cementite which accelerates corrosion over and above the rate typical of steel containing the same amount of cementite in more massive form, e.g., as in pearlite. The appreciable effect of cementite particle size on corrosion is observed in earlier data on effect of heat treating carbon steel as reported by Heyn and Bauer (16) combined with electron photomicrographs obtained subsequently by Lement, Averbach, and Cohen (17, 18). Heyn and Bauer found that tempering of martensite at 300°-400°C, at which temperature cementite in smallest particle size is formed, accounted for the highest corrosion rate in sulfuric acid compared to tempering treatments at lower temperatures (less cementite precipitated) or higher temperatures (agglomeration of cementite to larger particle size). Along the same lines, the effect of low temperature heat treatment (77°-100°C) of cold-worked steel to increase the corrosion rate (Fig. 3, 4 and 7) can be explained by increased diffusion of carbon atoms to imperfection sites, followed in some instances by precipitation of finely divided Fe₃C.

In view of the fact that the source of carbon atoms includes Fe₃C, this situation implies that carbon atoms associated with imperfections in iron forming Cottrell atmospheres are thermodynamically more

¹ Perhaps also finely divided agglomerated carbon is formed. Some carbon is found as a residue when carbon steels are dissolved in acid.

stable than Fe_3C . Internal friction data obtained by Dykstra (19), interpreted in terms of the interstitial solubility of nitrogen in ferrite, confirm that this is the case. For example, solubility of nitrogen in cold-worked iron was found to be 0.0025% at 300°C, and 0.006% at 400°C, but for unworked iron in presence of Fe_4N particles at the same temperatures, the solubility increased to 0.012% and 0.025%, respectively. Increased solubility corresponds to increased activity of nitrogen atoms in presence of iron nitride, compared to lower solubility and activity of nitrogen atoms associated with imperfections (greater stability). Kunz (20) also concluded from internal friction measurements that strain of carbon-iron alloy crystals followed by aging at 25°C apparently dissociates iron carbides, the carbon atoms segregating at dislocations.

Heat treatment at 100°C reduces hydrogen overvoltage (by 0.05v, Fig. 9) because of Cottrell atmospheres and precipitated Fe_3C . It has little or no influence on anodic polarization.

Heat treatment above 100°C serves to agglomerate carbides into larger particles, but without appreciable effect on H_2 overvoltage because the total exposed area of Fe_3C remains constant. The total peripheral area of Fe_3C , however, diminishes with time and temperature. As mentioned earlier, this reduces the galvanic action between ferrite and carbides which is focused largely at the interface between the two phases. Corrosion control continues to depend on the cathodic and not the anodic reaction. The hydrogen overvoltage of cold-rolled 0.002% C steel increases again upon heat treatment at 950°C, caused perhaps by crystal reorientation.

The effect on corrosion of iron containing nitrogen is analogous but not identical to that of iron containing carbon. First of all, cold-rolled 0.01 or 0.023% N steel corrodes in 0.12% N HCl at a rate only about 1/3 to 1/5 the rate of cold-rolled 0.01 or 0.02% C steel. Furthermore, nitrogen steels corrode at about the same rate whether cold-rolled or annealed, unlike carbon steels which corrode at a higher rate when cold-rolled. This suggests that the hydrogen overvoltage of dislocations in iron is decreased to a lesser extent through association with nitrogen than with carbon atoms, but an alternative explanation is also available as discussed later. Nevertheless, low temperature heat treatment of cold-rolled nitrogen steels increases the corrosion rate proportionately more than of cold-rolled carbon steels.² For example, for 0.01% and 0.023% N steels the increase of corrosion after 2 hr heat treatment is a maximum of 100 and 190%, respectively, whereas for 0.007% and 0.029% C steels, the increase is a maximum of 25 and 35%, respectively. Another distinguishing difference is that there are two peaks in the corrosion rate plotted with increasing temperature of heat treatment, whereas for carbon steels only one appears. The two peaks correspond to a two-stage precipitation of iron nitrides, the final nitride Fe_4N being preceded by an unstable nitride (19, 21). Both nitrides have lower hydrogen over-

voltage than does ferrite in accord with a higher corrosion rate of iron in their presence. Cathodic polarization curves correspondingly show two minima for nitrogen steels, but only one minimum for carbon steels (Fig. 9 and 10).

The lesser change of hydrogen overvoltage for cold-worked nitrogen steels compared to cold-worked carbon steels may relate in part to a higher activation energy for dissociation of iron nitrides compared to cementite. Hence, interstitial N atoms may be unable to form in sufficient concentration at cold-work temperatures in order to associate with imperfection sites. At slightly higher temperatures, however, dissociation proceeds more rapidly, and the increase in corrosion rate then becomes appreciable. Measurements on stress corrosion cracking of carbon and nitrogen steels (22) in nitrate solutions have led to an estimate for the activation energy for dissolution of iron nitrides in ferrite equal to 48 kcal/mole, compared to an average of 37 kcal/mole for cementite. This corresponds to a dissociation rate at room temperature smaller for nitrides than for carbides by a factor of about 10^8 and could, therefore, exert an appreciable effect. Hence, low temperature heat treatment of cold-worked nitrogen steels accelerates the dissociation of iron nitrides and produces a larger proportional change in the corrosion rate than for carbon steels for which the formation of Cottrell atmospheres and their decomposition into finely divided carbides proceeds during cold-working as well as at some subsequent higher temperature.

It is obvious that the present data do not support the point of view that a disarranged lattice or increased active sites for dissolution of Fe are the cause of increased corrosion following cold-work of iron or steel. Anodic polarization data for either cold-worked or annealed iron or steel show no significant differences. Instead, the effect of cold-work is to accelerate the cathodic reaction, which is generally the reaction that controls corrosion of iron in nonoxidizing acids.

It should be noted that cold-working of iron increases its internal energy, but this increase is not a significant contribution to the reaction tendency. Lack of an effect on corrosion is expected, and can be predicted from the small value of residual energy measured calorimetrically for severely cold-worked iron. The maximum value is about 7 cal/gram (23). Whether the stresses in cold-worked iron are localized or uniformly distributed is not an important consideration. The uniform corrosion of cold-worked iron, the lack of any large potential differences for cold-worked *vs.* annealed iron in any medium, and the similar polarization behavior as anode (Fig. 9 and 10) suggest that the localized fraction of iron atoms in an energy state higher than the average is not large.

From the thermodynamic relations: $\Delta G = \Delta H - T\Delta S$ and $\Delta G = -EnF$, where ΔG is the change in free energy, ΔH refers to enthalpy change, ΔS to entropy change, E to change in electromotive force, n equals 2, and F is the Faraday, it follows that the maximum expected change in electromotive force

² The behavior of the 0.002% C steel (Fig. 3) is anomalous in this respect.

corresponding to $\Delta H = 7$ cal/gram for severely cold-worked iron is 0.008v. This is too small a value to have an appreciable effect on the current produced by a corrosion cell.

The above calculation neglects change in entropy, which for a cold-worked metal is positive, and which according to Titchener and Bever (23) does not contribute greatly to ΔG . The value of E corrected for entropy, in any event, is expected to be less than the value just cited rather than greater. A similar calculation also holds for metals other than iron, and explains why pure metals in general show no large effect of cold-work on the corrosion rate or on the potential. Such effects as are found are caused mostly by changes in grain orientation, and hence cold-working of pure metals can either increase or decrease the corrosion rate depending on the crystal face which is developed by cold-work parallel to the metal surface. This explains some of the present seeming inconsistencies for the effect of cold-work reported in the literature. But when a second phase is precipitated through cold-working as, for example, carbides and nitrides in iron, or when impurities segregate at imperfections (Cottrell atmospheres), galvanic cells are established which usually lead to an increase in the corrosion rate. In other words, cold-work exerts a maximum effect when composition gradients within the metal are established by plastic deformation, a smaller effect usually results from change in crystal face of surface metal, and the increase in energy of the distorted metal is least important of all.

Acknowledgment

The authors are pleased to acknowledge support of this research by a fellowship grant from the National Steel Corporation. Appreciation is also expressed to the American Iron and Steel Institute for supplying a sample of zone-refined iron.

Manuscript received Sept. 11, 1963. This paper was presented at the New York Meeting, Sept. 29-Oct. 3, 1963.

Any discussion of this paper will appear in a Discussion Section to be published in the December 1964 JOURNAL.

REFERENCES

1. G. Tamman and F. Neubert, *Z. anorg. Chem.*, **207**, 87 (1932).
2. U. R. Evans, "Corrosion and Oxidation of Metals," p. 386, Edward Arnold Ltd., London (1960).
3. T. P. Hoar in "Modern Aspects of Electrochemistry," vol. 2, J. Bockris, Editor, p. 334, Butterworth's, London (1959).
4. J. Harwood, *Corrosion*, **6**, 256 (1950).
5. E. Zaretsky, *J. App. Chem. U.S.S.R.*, **24**, 521 (1951).
6. M. Straumanis and Y. Wang, *Corrosion*, **12**, 177t (1956).
7. H. Copson in "Corrosion Handbook," H. H. Uhlig, Editor, p. 576, John Wiley & Sons, Inc., New York (1948).
8. O. Bauer, O. Kröhnke, and G. Masing in "Die Korrosion Metallischer Werkstoffe," I, p. 314, S. Hirzel, Leipzig (1936). Also "Corrosion Handbook," H. H. Uhlig, Editor, p. 138, John Wiley & Sons, Inc., New York (1948).
9. J. Friend, *Carnegie Schol. Mem.*, **11**, 103 (1922); *J. Iron and Steel Inst.*, **117**, 639 (1928).
10. E. B. Sandell, "Colorimetric Determination of Traces of Metals," p. 271, Interscience Publishers, New York (1944).
11. R. Covert and H. Uhlig, *This Journal*, **104**, 537 (1957).
12. M. Stern, *ibid.*, **102**, 609 (1955).
13. M. Stern, *ibid.*, **102**, 663 (1955).
14. L. Darken in "The Physical Chemistry of Metallic Solutions and Intermetallic Compounds," Vol. II, 4G, Nat. Phys. Lab. Symp. No. 9 (London) (1959).
15. J. Suits and J. Low, *Acta Met.*, **5**, 285 (1957).
16. E. Heyn and O. Bauer, *J. Iron and Steel Institute*, **79**, 109 (1909).
17. B. Lement, B. Averbach, and M. Cohen, *Trans. Am. Soc. Metals*, **46**, 851 (1954).
18. H. H. Uhlig in "Relation of Properties to Microstructure," pp. 189-207, Am. Soc. Metals, Cleveland (1954).
19. L. Dykstra, *J. Metals*, **1**, 252 (1949); A. Cottrell, "Dislocations and Plastic Flow in Metals," p. 134, Oxford Press (1954).
20. F. Kunz, *Acta Met.*, **3**, 126 (1955).
21. G. Lagerberg and B. Lement, *Trans. Am. Soc. Metals*, **50**, 141 (1958).
22. J. Sava and H. Uhlig, *Trans. Quarterly Am. Soc. Metals*, **56**, 361 (Sept. 1963).
23. A. Titchener and M. Bever, *Prog. in Metal Phys.*, **7**, 247 (1958).

Conduction Properties of $\text{Cd}_2\text{Nb}_2\text{O}_7$ and $\text{Pb}_{1.5}\text{Nb}_2\text{O}_{6.5}$

R. Mazelsky and W. E. Kramer

Research Laboratories, Westinghouse Electric Corporation, Pittsburgh, Pennsylvania

ABSTRACT

Materials having the pyrochlore structure, $\text{Cd}_2\text{Nb}_2\text{O}_7$, $\text{Pb}_{1.5}\text{Nb}_2\text{O}_{6.5}$, and their solid solutions were prepared and their conduction properties examined. The cadmium pyrochlore has a large ionic contribution to the conductivity while the lead pyrochlore is almost exclusively electronic. By means of resistivity measurements as a function of temperature and oxygen pressure, mass action equations are derived describing the generation of electronic carriers. Equilibrium constants and the energies involved in the conduction process are calculated.

Pyrochlore is a mineral of the approximate composition $\text{NaCaNb}_2\text{O}_6\text{F}$. Materials of this structural type became of interest when ferroelectric properties were observed in $\text{Cd}_2\text{Nb}_2\text{O}_7$ (1,2). Cook and

Jaffe further reported a defect pyrochlore of the composition $\text{Pb}_{1.5}\text{Nb}_2\text{O}_{6.5}$. Jona, Shirane, and Pepinsky (3) clarified the structure of $\text{Cd}_2\text{Nb}_2\text{O}_7$. They reported a network of NbO_6 corners sharing octa-

hedra with the seventh set of oxygens and the cadmium ions occupying open spaces in the lattice. These relatively "unattached" ions lead to the possibility of ionic conductivity. The same situation exists for $\text{Pb}_{1.5}\text{Nb}_2\text{O}_{6.5}$ except that some of the lead and oxygen sites are vacant. On the other hand electronic conduction is possible as a result of the variable valency exhibited by both lead and cadmium ions (CdO via Cd interstitials and PbO with its positive two or four valence). The purpose of this paper is to elucidate the conduction type in these materials.

Preparation

The materials were made from Nb_2O_5 (99.7% minimum purity) CdO and PbO (Fisher Certified). For the purpose of comparison cadmium and lead oxides were prepared from 99.999+ % metal by means of solution of the metal, precipitation, and careful oxidation to the monoxide.

The oxides were weighed to yield a product of the appropriate composition. The reactants were mixed thoroughly, compacted into a cylinder, and pre-fired at 800° for 24 hr. Weight losses of less than 1 part per thousand were observed. The pellet was placed in a platinum cylinder and put into a quartz tube which was previously sealed at one end. For the sample $\text{Cd}_2\text{Nb}_2\text{O}_7$ a small excess of CdO , equivalent to the weight loss observed, was added. The quartz tube was evacuated and back filled with oxygen to about $\frac{1}{4}$ atm and then sealed. The tube was heated near the melting point of $\text{Cd}_2\text{Nb}_2\text{O}_7$, approximately 1400° , for 3 hr. A similar procedure was used for the preparation of $\text{Pb}_{1.5}\text{Nb}_2\text{O}_{6.5}$. A final firing temperature of approximately 1290° was used.

The resulting products were rounded on the edges, indicative of incipient melting. They were quite crystalline and yellow-orange in color. Small pieces were chipped off for x-ray identification photographs and symmetrical cylinders were cut out for measurements. All samples used for measurement had a density $95 \pm 2\%$ of the theoretical density, ignoring the effects of vacancies.

Experimental

Using the procedure described above, a series of solid solutions of the type $(1-x)\text{Cd}_2\text{Nb}_2\text{O}_7-x\text{Pb}_{1.5}\text{Nb}_2\text{O}_{6.5}$ was prepared. Chemical analyses were made on samples where $x = 0.15$ and $x = 0.85$ and the compositions as reported agree with the analysis within experimental error. The results are shown on Table I. A complete range of solutions appears to exist, the lattice parameter varying nonlinearly with composition as shown in Fig. 1. The powder diffraction photographs were taken with a Phillips camera having 114.6 mm diameter.

Table I. Results

	$0.85\text{Cd}_2\text{Nb}_2\text{O}_7-0.15\text{Pb}_{1.5}\text{Nb}_2\text{O}_{6.5}$		$0.15\text{Cd}_2\text{Nb}_2\text{O}_7-\text{Pb}_{1.5}\text{Nb}_2\text{O}_{6.5}$	
	Theoretical, %	Experimental, %	Theoretical, %	Experimental, %
Pb	8.72	8.39	44.86	43.41
Cd	35.76	35.6	5.73	6.36
Nb	34.78	35.5	31.55	32.0

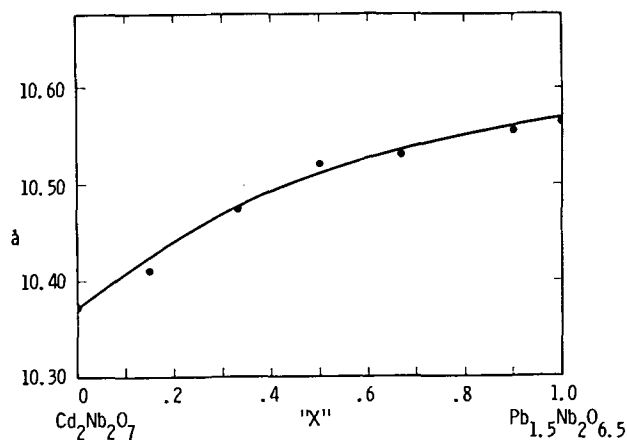


Fig. 1. Lattice parameter vs. "x" (mole fraction $\text{Pb}_{1.5}\text{Nb}_2\text{O}_{6.5}$)

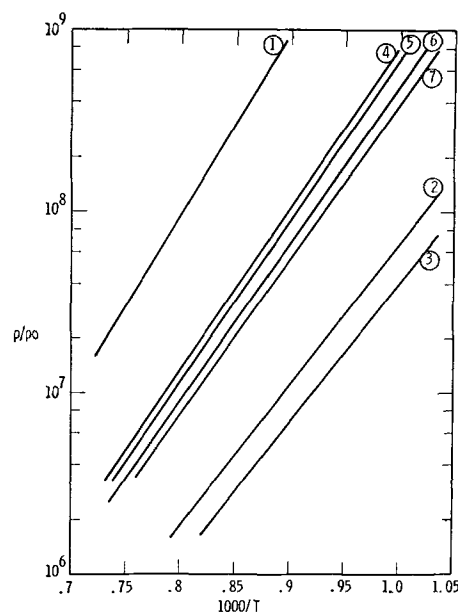


Fig. 2. ρ/ρ_0 vs. $1000/T$

Identification No.	ρ_0	"x" (mole fraction $\text{Pb}_{1.5}\text{Nb}_2\text{O}_{6.5}$)
1	4.4×10^{-6}	0.00
2	1.2×10^{-4}	0.05
3	1.8×10^{-4}	0.15
4	3.9×10^{-5}	0.50
5	5.5×10^{-5}	0.70
6	3.1×10^{-5}	0.85
7	3.4×10^{-5}	1.00

Resistance measurements as a function of temperature were made using an impedance bridge. The pellets used were cylindrical specimens the ends of which were painted with platinum paste and fired to decrease contact resistance. Spring loaded platinum electrodes were used. The sample and holder were heated in a resistance furnace in air. The results are shown in Fig. 2. The activation energies calculated from the $\ln \rho$ vs. $1000/T$ are shown on Fig. 3. A minimum in the activation energy is observed at about $x = 0.15$. If one plots isothermal resistivity (ρ) vs. composition, at all the temperatures between 800° and 1150°C , a resistance minimum is observed at $x = 0.10$ with a broad maximum over the center range of composition ($x = 0.3-0.8$) the resistivity dropping back to approximately that of $\text{Pb}_{1.5}\text{Nb}_2\text{O}_{6.5}$ at $x = 0.9$.

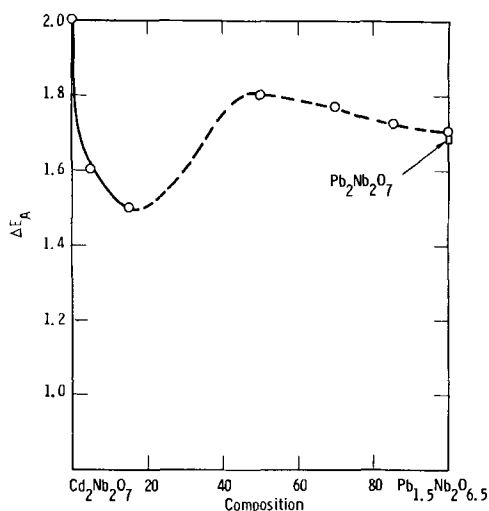


Fig. 3. Activation energy vs. "x" (mole fraction $\text{Pb}_{1.5}\text{Nb}_2\text{O}_{6.5}$)

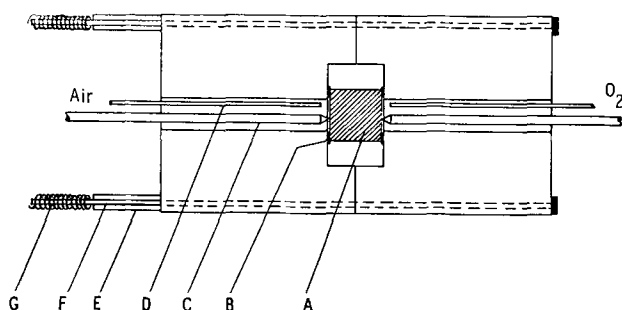


Fig. 4. Emf measurement holder. A, Sample; B, gold O rings; C, Pt-Pt 10% Rh thermocouple; D, quartz delivery tube; E, ceramic rod; F, stainless steel rod; G, spring.

A cell using the samples described above as an electrolyte was set up. Cylindrical pellets were used to measure emf with a pressure ratio $P_2/P_1 = 5$ where P_2 and P_1 were pressures of oxygen on opposite sides of the pellet. Figure 4 is a schematic of the holder used. The thermocouples are used for temperature measurements on both sides of the specimen. The platinum legs on both sides are further used as lead wires to measure emf. The holder proper is made of lavite, the steel rods being of a length such as to keep the springs outside the furnace. The specimen faces are platinum coated to insure contact between the thermocouple and the

Table II. Results

Material	% Ionic conduct		Porosity (%)
	850°C	900°C	
$\text{Ca}_{0.15}\text{Zr}_{1.70}\text{O}_{1.85}$	94		7
$\text{Cd}_2\text{Nb}_2\text{O}_7$	57	12	6
$0.95\text{Cd}_2\text{Nb}_2\text{O}_7-0.05\text{Pb}_{1.5}\text{Nb}_2\text{O}_{6.5}$	14	7	8
$0.9\text{Cd}_2\text{Nb}_2\text{O}_7-0.1\text{Pb}_{1.5}\text{Nb}_2\text{O}_{6.5}$	10	5	5
$0.5\text{Cd}_2\text{Nb}_2\text{O}_7-0.5\text{Pb}_{1.5}\text{Nb}_2\text{O}_{6.5}$	0	0	5
$\text{Pb}_{1.5}\text{Nb}_2\text{O}_{6.5}$	0	0	10

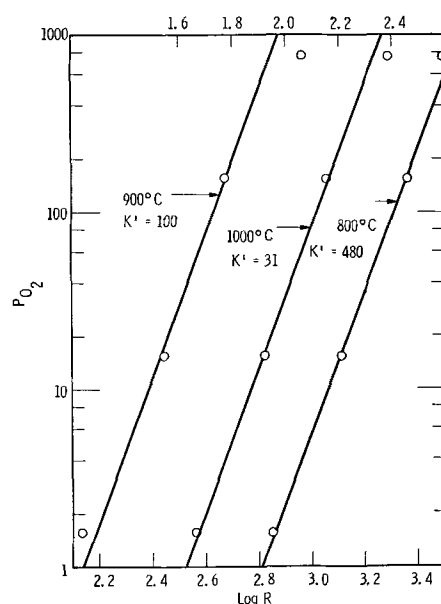


Fig. 5. Log resistance vs. ($A/l = 0.735$) vs. log of oxygen pressure at 800°, 900°, 1000°C of $\text{Pb}_{1.5}\text{Nb}_2\text{O}_{6.5}$ (overhead scale for 1000°C points).

sample. The reaction that occurs at the electrode is assumed to be $\text{O}_2 + 4e^- \rightleftharpoons 2\text{O}^-$ and the per cent oxygen ion conductivity was based on the calculated value derived from the Nernst relation. This procedure has been discussed previously (4). Due to the high resistance of the sample, the sensitivity of the emf measurements was low at temperatures less than 850°C. Measurements were taken at 850° and 900°. The results are summarized on Table II. The value obtained for the stabilized cubic zirconia is shown for comparison.

Resistivity measurements as a function of oxygen pressure were made on $\text{Cd}_2\text{Nb}_2\text{O}_7$ and $\text{Pb}_{1.5}\text{Nb}_2\text{O}_{6.5}$. Oxygen pressures of 1.5-760 mm Hg were used and the log pressure was plotted vs. log resistivity. $\text{Cd}_2\text{Nb}_2\text{O}_7$ showed little if any dependence on oxygen pressure below 900°C. At 1050°C a variation in resistance with pressure to $1/12$ power was observed, but the results were not conclusive. This is due to the fact that at low oxygen pressures cadmium metal is formed which has a tendency to volatilize. (Distillation from a sample of $\text{Cd}_2\text{Nb}_2\text{O}_7$ was collected and identified as cadmium by an x-ray photograph.) Measurements of $\text{Pb}_{1.5}\text{Nb}_2\text{O}_{6.5}$ at 800°C, 900°C, and 1000°C are shown on Fig. 5. The resistivity is observed to vary with the pressure of oxygen to the $1/4$ power. The data for the end members and solid solutions are shown on Table III.

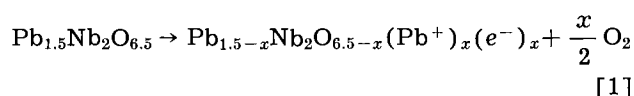
Seebeck coefficient measurements vs. platinum were made in air. Due to the high resistivity of the samples at the measuring temperatures (900°-1000°C), the results were unreliable. However, the sign of the Seebeck coefficient is negative.

Table III.

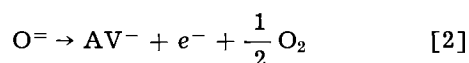
	$\text{Cd}_2\text{Nb}_2\text{O}_7$	$x = 0.05$	$x = 0.15$	$x = 0.5$	$x = 0.7$	$\text{Pb}_{1.5}\text{Nb}_2\text{O}_{6.5}$
800°C	Indep of P_{O_2}	Indep of P_{O_2}	$P_{\text{O}_2}^{1/9}$	$P_{\text{O}_2}^{1/4.4}$	$P_{\text{O}_2}^{1/4.4}$	$P_{\text{O}_2}^{1/4}$
900°C	Indep of P_{O_2}	Indep of P_{O_2}	$P_{\text{O}_2}^{1/4.6}$	$P_{\text{O}_2}^{1/4.4}$	$P_{\text{O}_2}^{1/4.4}$	$P_{\text{O}_2}^{1/4}$
1000°C	Slight O_2 dep.	$P_{\text{O}_2}^{1/6}$	$P_{\text{O}_2}^{1/4.4}$	$P_{\text{O}_2}^{1/4.4}$	$P_{\text{O}_2}^{1/4.4}$	$P_{\text{O}_2}^{1/4}$
1050°C	$P_{\text{O}_2}^{1/12}$	$P_{\text{O}_2}^{1/6}$	$P_{\text{O}_2}^{1/5}$			$P_{\text{O}_2}^{1/3.8}$

Discussion

The data are consistent in that at certain temperatures $\text{Cd}_2\text{Nb}_2\text{O}_7$ has an appreciable ionic contribution to the conductivity which rapidly diminishes as $\text{Pb}_{1.5}\text{Nb}_2\text{O}_{6.5}$ is added. This is shown by the emf measurements and verified by the fact that the resistivity shows little dependence on the pressure of oxygen at 800°C . $\text{Pb}_{1.5}\text{Nb}_2\text{O}_{6.5}$ on the other hand within the accuracy of the measurement shows no indication of ionic conductivity at the working temperature, and, in fact, shows a marked dependence of the resistivity on the oxygen pressure as is seen in Fig. 5. This behavior can be described by the chemical mass action equations. If one considers the reaction



it can be seen that loss of oxygen results in excess lead present in the lattice with the consequent generation of electrons. Alternatively



For the purpose of calculation the second equation will be used. Using mass action equations

$$K = P_{\text{O}_2}^{1/2} (\text{AV}^-) (e^-) \quad [3]$$

This assumes the anion vacancy to have one electron in it, the other being contributed to the lattice for conduction. Therefore, assuming $\text{AV}^- = n^-$ or e^- , the number of electrons

$$(n) = K^{1/2} P_{\text{O}_2}^{-1/4} \quad [4]$$

If the loss of an oxygen results in lead being reduced to the zero state, a dependence of $P_{\text{O}_2}^{-1/6}$ is derived. Since the charge carriers (e^-) are related to resistivity by the equation

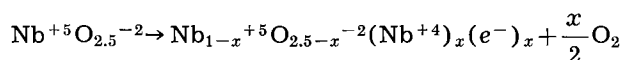
$$\rho = \frac{1}{ne\mu} \quad [5]$$

One obtains by combining Eq. [4] and [5]

$$\rho = K' P_{\text{O}_2}^{1/4} \text{ where } K' = \frac{1}{K^{1/2} e\mu} \quad [6]$$

This is in agreement with the observed data on Fig. 5.

It should be noted that the same equilibrium relation as that described above for lead can be derived assuming the niobium is the source of the electronic carriers.



Therefore, $n = K^{1/2} P_{\text{O}_2}^{-1/4}$, identical to the case derived above. Furthermore, it is not possible to distinguish between the two mechanisms. This indicates that the electrical conduction in the temperature range under discussion is done by electrons. The fact that negative Seebeck voltages were observed confirms the electron mechanism for conduction.

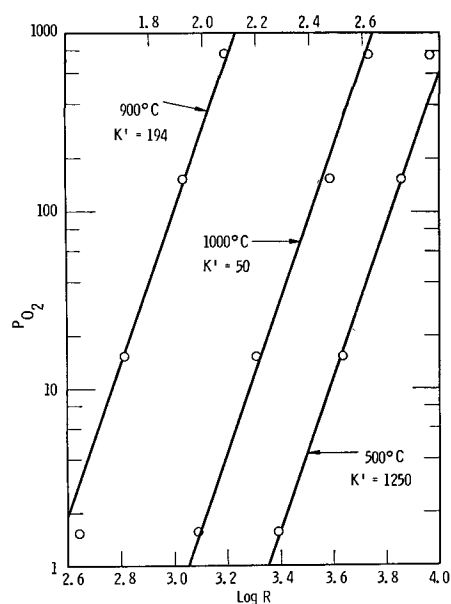


Fig. 6. Log resistance ($A/I = 0.554$) vs. oxygen pressure at 800° , 900° , and 1000°C for $0.7\text{Pb}_{1.5}\text{Nb}_2\text{O}_{6.5}-0.3\text{Cd}_2\text{Nb}_2\text{O}_7$ (overhead scale for 1000°C points).

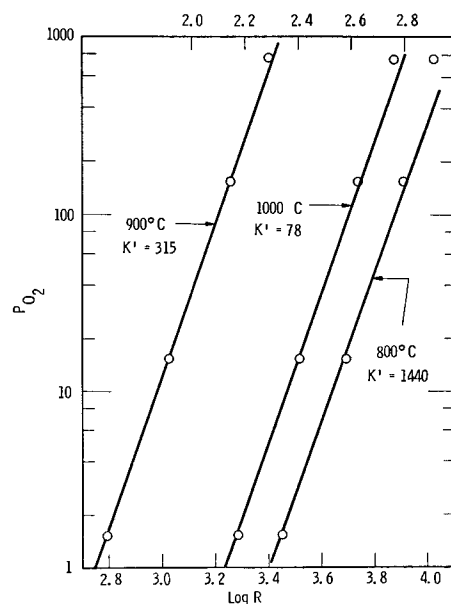


Fig. 7. Log resistance ($A/I = 0.566$) vs. log oxygen pressure at 800° , 900° , and 1000°C for $0.5\text{Pb}_{1.5}\text{Nb}_2\text{O}_{6.5}-0.5\text{Cd}_2\text{Nb}_2\text{O}_7$ (overhead scale for 1000°C points).

Other composition ranges were also examined. The results are not so simple. On Fig. 6 and 7 are seen the $\log P$ vs. resistance curves for $0.7\text{Pb}_{1.5}\text{Nb}_2\text{O}_{6.5}-0.3\text{Cd}_2\text{Nb}_2\text{O}_7$ and $0.5\text{Pb}_{1.5}\text{Nb}_2\text{O}_{6.5}-0.5\text{Cd}_2\text{Nb}_2\text{O}_7$. The data are fit best by a line of slope = 4.4. On Fig. 8 the dependence of resistivity on oxygen pressure at 1050°C is shown for pure $\text{Cd}_2\text{Nb}_2\text{O}_7$ and for $\text{Cd}_2\text{Nb}_2\text{O}_7$ with 5% and 15% $\text{Pb}_{1.5}\text{Nb}_2\text{O}_{6.5}$. The larger the concentration of $\text{Pb}_{1.5}\text{Nb}_2\text{O}_{6.5}$ the greater the amount of electron conductivity. However, the high vapor pressure of cadmium oxide and cadmium metal at these temperatures can lead to errors in the measurements. However, it is interesting to note that $\text{Cd}_2\text{Nb}_2\text{O}_7$ alone and with small amounts of lead pyrochlore seem to have a pressure dependence of the resistivity to the $1/6$ power, indicating a

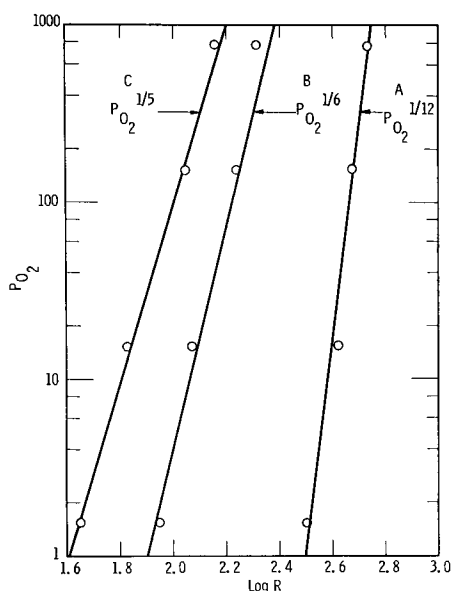


Fig. 8. Log resistance vs. log oxygen pressure for (A) $\text{Cd}_2\text{Nb}_2\text{O}_7$; (B) $0.95\text{Cd}_2\text{Nb}_2\text{O}_7-0.05\text{Pb}_{1.5}\text{Nb}_2\text{O}_{6.5}$; (C) $0.85\text{Cd}_2\text{Nb}_2\text{O}_7-0.15\text{Pb}_{1.5}\text{Nb}_2\text{O}_{6.5}$.

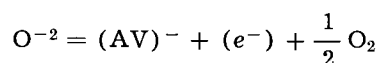
two electron/mole process. This would indicate that the cadmium, at least in part, is involved in producing the carriers. (Even the transitory existence of Nb^{+3} is unlikely.) It would seem that the pressure dependence of 4.4 is due to one of the mass action equations above plus some cadmium contribution.

If one uses Eq. [6] the equilibrium constant can now be calculated for these systems by the equation

$$\log P_{\text{O}_2} = C \log \rho + C \log K'$$

where $C = 4$ for $\text{Pb}_{1.5}\text{Nb}_2\text{O}_{6.5}$ and $C = 4.4$ for the solid solutions described above. For the compositions other than $\text{Pb}_{1.5}\text{Nb}_2\text{O}_{6.5}$, the fact that "C" is not an integral number indicates that the equilibrium equations are more complicated than those written above. This would possibly be due to some contribution of cadmium toward the conductivity.

It has been shown previously that the data as presented are not true equilibrium constants, the true values differing by a factor of the charge carriers and mobility. However, it will be assumed that this is a small effect for the purposes of calculating the heat content of the reaction. Using this assumption the values of K' calculated from Fig. 5 to 7 are related to the equilibrium constant by $K = 1/K'^2$. We can then plot $d \log K$ vs. $1/T$ to get the enthalpy. This is shown in Fig. 9. Furthermore assuming the relation $K = 1/K'$ is approximately true free energies can be calculated by $\Delta G = -RT \ln K$. Then from the relation $\Delta F = \Delta H - T\Delta S$ entropies can be calculated. These equations describe the reaction



modified by the fact that $e^{-} \neq 1/\rho$.

The validity of the above assumption can be checked. The resistivity change was taken as a function of temperature at a constant oxygen pres-

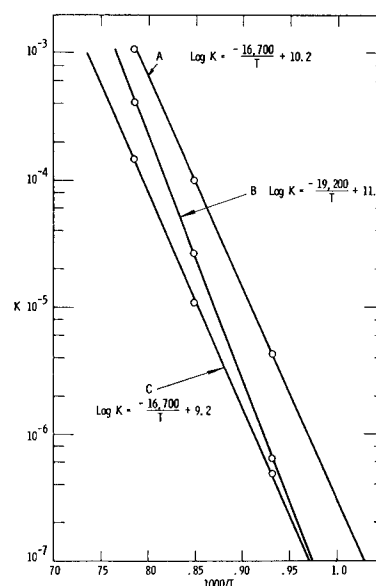


Fig. 9. $\log K$ vs. $1000/T$ for (A) $\text{Pb}_{1.5}\text{Nb}_2\text{O}_{6.5}$ $\Delta H = 76.3$ kcal; (B) $0.7\text{Pb}_{1.5}\text{Nb}_2\text{O}_{6.5}-0.3\text{Cd}_2\text{Nb}_2\text{O}_7$ $\Delta H = 87.7$ kcal; (C) $0.5\text{Pb}_{1.5}\text{Nb}_2\text{O}_{6.5}-0.5\text{Cd}_2\text{Nb}_2\text{O}_7$ $\Delta H = 76.3$ kcal.

sure, approximately 150 mm Hg. The equations fit the form

$$\rho = \rho_0 e^{Q/RT} \quad [7]$$

It has also been shown that

$$\rho = K' P_{\text{O}_2}^{1/A} \quad [8]$$

where $A = 4$ for $\text{Pb}_{1.5}\text{Nb}_2\text{O}_{6.5}$ and $A = 4.4$ over most of the solid solution range. Also $K' = 1/K^{1/2} e\mu$ and K' and K are a function of temperature. Taking logarithms and differentiating at constant pressure

$$\left[\frac{\partial \ln \rho}{\partial (1/T)\Delta} \right]_P = \frac{Q}{R} \quad [9]$$

$$\left(\frac{\partial \ln \rho}{\partial (1/T)} \right)_P = \frac{\partial \ln K'}{\partial (1/T)} = -\frac{\Delta H}{R} \quad (\text{by definition}) \quad [10]$$

Therefore,

$$Q = -\Delta H \quad [11]$$

If the $\log K'$ is plotted vs. $1000/T$ the slope (or enthalpy) should be equal to the activation energies shown in Fig. 3. This is shown in Fig. 10. The two values are within 10% of one another, quite good agreement. It has been stated that

$$K' = \frac{1}{K^{1/2} e\mu} \quad [12]$$

Therefore

$$\ln K' = -\frac{1}{2} \ln K - \ln e - \ln \mu \quad [13]$$

and

$$\left(\frac{\partial \ln K'}{\partial (1/T)} \right)_P = -\frac{1}{2} \left(\frac{\partial \ln K}{\partial (1/T)} \right)_P - \left(\frac{\partial \ln \mu}{\partial (1/T)} \right)_P \quad [14]$$

$$\Delta H' = -\frac{1}{2} \Delta H_{\text{React}} - \Delta H_{\mu}$$

The heat of reaction calculated from resistivity data is the true value provided the energy required for the jump mechanism is small. Comparison of

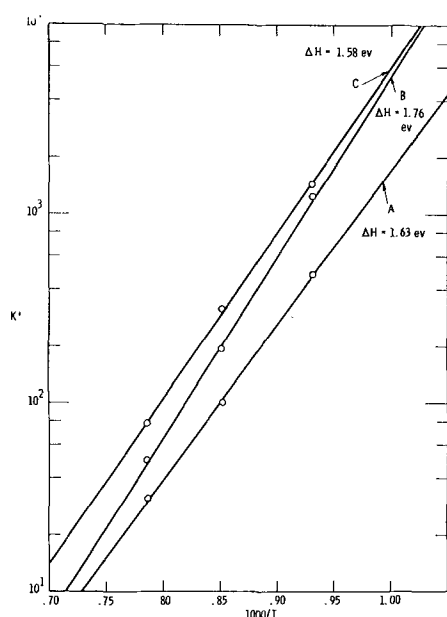


Fig. 10. $\log K'$ vs. $1000/T$ for (A) $\text{Pb}_{1.5}\text{Nb}_2\text{O}_{6.5}$; (B) $0.7\text{Pb}_{1.5}\text{Nb}_2\text{O}_{6.5}-0.3\text{Cd}_2\text{Nb}_2\text{O}_7$; (C) $0.5\text{Pb}_{1.5}\text{Nb}_2\text{O}_{6.5}-0.5\text{Cd}_2\text{Nb}_2\text{O}_7$.

$\Delta H'$ with $\frac{1}{2} \Delta H$ shows them to be of approximately the same magnitude, indicating the ΔH_μ term is perhaps 10% of the total energy. The calculated values for K are, therefore, the correct order of magnitude. It remains to consider how the charge carriers, ionic and electronic, can migrate through the lattice. It seems likely that oxygen ions can move via the loosely bound oxygen ion associated with the lead or cadmium site, the oxygen ions being displaced from site to site acting as the charge carriers. Since the distance between these sites is over half a lattice distance and these positions are separated by an NbO_6 octahedron, the high resistances observed are not surprising. Although the ionic conductivity in $\text{Pb}_{1.5}\text{Nb}_2\text{O}_{6.5}$ was not measured due to the abundance of electronic carriers present, the same process must also occur in this material.

The conduction mechanism in $\text{Pb}_{1.5}\text{Nb}_2\text{O}_{6.5}$ and most of its solution range with $\text{Cd}_2\text{Nb}_2\text{O}_7$ is predominantly electronic. The origination of these carriers comes from the reduction of one or more of the metal ions as described by the mass action equations derived above and verified by resistivity-vapor pressure and Seebeck coefficient measurements. However, the observed resistivity of these semiconductors is quite high, of the same order of magnitude as the predominantly ionic $\text{Cd}_2\text{Nb}_2\text{O}_7$. This leads one to suspect that the electrons are trapped quite strongly in the lattice and have an exceedingly low mobility.

It is now of interest to consider the meaning of the activation energy calculated from the resistivity-temperature curves. It is apparent that the electrons are localized and the broad band picture is not applicable. If one considers $\text{Pb}_{1.5}\text{Nb}_2\text{O}_{6.5}$, it can be seen

that more than one process is involved in the transport of carriers. There is first the energy required to displace the carrier from its parent ion. This is essentially an ionization energy modified by the crystal environment. Second there is the energy required to move the carrier from its initial site, through a potential barrier to the neighboring site. These have been described previously. When that section of the solid solution range is reached where ionic conductivity is also present, a third energy of activation is required for the transport of ionic carriers.

Furthermore, even these energies vary within the series. The presence of a large number of vacancies can act as traps for the electron carriers. (At 25% $\text{Pb}_{1.5}\text{Nb}_2\text{O}_{6.5}$ there is one anion and one cation vacancy per unit cell. This is perhaps a reason for the anomalous increase in activation energy near this point.) The distance between available sites has an effect on activation energy, the greater the distance to be traveled, the greater the energy. The distortion of the lattice can affect the energy required for the transport of carriers. This may account for the higher than expected activation energy for $\text{Pb}_2\text{Nb}_2\text{O}_7$ (see Fig. 3). Since the relative order of magnitude of these energies is not known, only qualitative use can be made of these numbers to describe the transport of carriers throughout the solid solution.

Conclusion

The system $\text{Pb}_{1.5}\text{Nb}_2\text{O}_{6.5}-\text{Cd}_2\text{Nb}_2\text{O}_7$ has been shown to form a complete range of solid solution. Over a small part of the range ionic conductivity is shown to be present although electronic conductivity predominates. Although the microscopic mechanism by which conductivity occurs is not clear, the method by which carriers are produced is shown. Thermodynamic values for the $2\text{O}^{-2} \leftrightarrow \text{O}_2 + 4e^-$ reaction cannot be exactly calculated since the number of carriers is not known directly but only through the resistivity. Therefore, the only energies that can be calculated are the combined energies for the formation of carriers and the energy to release the carriers from their sites. These energies can be separated roughly and show that the hopping energy is a small portion of the total energy for conductivity.

Acknowledgment

The authors wish to acknowledge helpful discussions with Drs. L. Dykstra, R. Ruka, and A. Panson. Chemical analysis was done by Mrs. M. L. Theodore. This work was supported by the Advanced Research Projects Agency through the Office of Naval Research.

REFERENCES

1. W. R. Cook, Jr., and H. Jaffe, *Phys. Rev.*, **88**, 1426 (1952).
2. W. R. Cook, Jr., and H. Jaffe, *ibid.*, **89**, 1297 (1953).
3. F. Jona, G. Shirane, and R. Pepinsky *ibid.*, **98**, 903 (1955).
4. J. Weissbart and R. Ruka, *Rev. Sci. Instr.*, **32**, 593 (1961).

Self-Activated Luminescence of M^{2+} Niobates and Tantalates

A. Wachtel

Westinghouse Electric Corporation, Bloomfield, New Jersey

ABSTRACT

Among 22 compounds examined for photoluminescence, only $Mg_4Nb_2O_9$, $CaTa_2O_6$ and the metaniobates of Mg, Ca, Zn, and Cd show appreciable room temperature emission. With the exception of $Mg_4Nb_2O_9$, all of these have the columbite structure; moreover, the only essentially nonluminescent columbite-type compound noted was $ZnTa_2O_6$. The absorption edges of the luminescent niobates lie at shorter wavelengths than those of otherwise similar compositions. This indicates a relationship between luminescence and the separation of energy states within the Nb-O bond, as influenced by structure.

Relatively few self-activated inorganic phosphor systems are known. In these, luminescence is generally assumed to originate from one of the constituent ions, e.g., UO_2^{2+} or WO_4^{2-} , while perturbations due to differences in ionic environment, lattice dimensions, and structure influence the optical characteristics to a varying extent. Recent investigations in this laboratory have shown that certain niobates and tantalates of divalent cations exhibit photoluminescence whose general characteristics appear to be of the self-activated type. Moreover, crystallographic differences seem to be accompanied by large differences in luminescence properties.

Experimental

Compounds were prepared from Nb_2O_5 (Kawecki Chemical Company) or Ta_2O_5 (Fansteel) purified in this laboratory,¹ and the respective luminescence grade carbonates or oxides, using at least two firings in air (2 hr each) with intermediate grinding so as to ensure the formation of homogeneous products. The ratio of the component oxides was usually chosen to be stoichiometric. In some cases, a slight excess of the divalent oxide was used to avoid the presence of unreacted Nb_2O_5 . Difficulties were encountered only in the case of MgO, whose reaction with Nb_2O_5 appeared to be sluggish even at 1500°C and always resulted in some $Mg_4Nb_2O_9$. Pure $MgNb_2O_6$ was therefore prepared from $MgSO_4 + Nb_2O_5$, while the purest $Mg_4Nb_2O_9$ was obtained by reaction of $MgO + Nb_2O_5$ in fused anhydrous $MgCl_2$. Due to the poor luminescence of the tantalates, the possibility of similar complications with respect to $MgTa_2O_6$ were not investigated. Conditions necessary to form $Mg_3Ta_2O_8$ (1) or the analogous niobate were not attainable on our present equipment.

X-ray powder diffraction analyses were performed on a Philips x-ray diffractometer operated at

35 kv and 15 ma, using a Cu target and Ni filter, and were employed to identify compounds wherever comparison with published values of d could be made. Several compounds were, in addition, indexed here, the detailed results to be reported elsewhere (2). Temperature dependence was measured with a Spectra Brightness Spot Meter² (eye-sensitivity corrected) focussed on samples mounted on a copper block within a quartz dewar. Excitation and absorption spectra (the latter defined here as 100% diffuse reflectance) were taken on a B & L 500 mm grating monochromator, using a H_2 arc lamp as source. Correction for equal excitation energy was made by means of a sodium salicylate standard. Emission spectra were obtained on the same apparatus under 2537Å (Mineralight) excitation.

Results

Table I summarizes crystallographic data and visual observations of luminescence. The notation "same as published" means that our x-ray powder diffraction pattern essentially agreed with published values, and no further analysis was undertaken. It can be seen that, with the exception of hexagonal $Mg_4Nb_2O_9$, the only compounds with discernible room temperature luminescence are $CaTa_2O_6$ as well as the metaniobates of Mg, Ca, Zn, and Cd. These have orthorhombic symmetry with lattice dimensions approximately in the ratios of 5:15:5.7. The Cd (3,4), Mg (5), and Zn (5) compounds are reported to have the columbite structure. The tetragonal symmetry of $ZnNb_2O_6$ reported by Harrison and Delgrosso (6) is based on data which are very similar to ours except for several weak lines in our pattern which made the analysis more satisfactory on the basis of orthorhombic symmetry. It should be mentioned that Larach (7) investigated this compound but found it to be non-luminescent. The structure of $CaNb_2O_6$

¹ By fusion with K_2CO_3 and treating the 3:1 K-salts in aqueous solution with H_2S and organic reagents, followed by precipitation with NH_4Cl . Spectrographic analyses semi-quantitative) were as follows:

	Al	B	Bi	Cu	Fe	Mg	Mn	Ni	Pb	Si
Nb_2O_5 as received	FT-	n.d.	n.d.	VF+	FT	FT	FT	FT-	FT-	FT-
Nb_2O_5 purified	FT-	n.d.	n.d.	VF-	n.d.	VF	n.d.	n.d.	n.d.	FT
Ta_2O_5 as received	FT-	n.d.	T	VF	FT-	FT+	VF	n.d.	n.d.	FT-
Ta_2O_5 purified	FT-	FT-	FT-	n.d.	n.d.	n.d.	n.d.	n.d.	FT-	FT-

where T = 100-1000 ppm, FT = 10-100 ppm, VF = 1-10 ppm, and n.d. = not detected. Plus or minus signs indicate concentrations within the higher or lower end of the range indicated. The limit of detection for K is high (1%), and it may therefore have been present in appreciable amounts.

² Photo Research Corporation, Hollywood, California.

Table I. Niobate and tantalate compounds investigated

Compound	Firing temp., °C	Present crystallographic data (2)	Symmetry or structure	Published crystallographic data			Ref.	Lumin. exc. by 2537Å	
				a_0	b_0	c_0		Room temp.	-196°C
MgNb ₂ O ₆	1200	Orthorhombic $a_0 = 5.02$, $b_0 = 14.16$, $c_0 = 5.69$	Columbite	5.017	—	5.665	(5)	w. blue	s. blue
Mg ₄ Nb ₂ O ₉	1200	Hexagonal $a_0 = 5.155$, $c_0 = 13.98$	—	—	—	—	—	m. bl.-violet	s. white-purple
MgTa ₂ O ₆	1250	—	Tetragonal (Trirutile)	4.713	—	9.187	(1, 18)	—	w. blue
Mg ₄ Ta ₂ O ₉	1250	MgTa ₂ O ₆ + Mg ₄ Ta ₂ O ₉ + MgO	Orthorh., pseudotetrag.	10.238	11.456	10.065	(1, 19)	—	v. w. green
Mg ₄ Ta ₂ O ₉	1250	MgTa ₂ O ₆ + Mg ₄ Ta ₂ O ₉ + MgO	Hexagonal (Ilmenite)	5.162	—	14.038	(19, 20)	—	v. w. green
CaNb ₂ O ₆	1250	Same as published	Orthorhombic	5.22	14.94	5.73	(21)	v. s. blue	v. s. blue
CaTa ₂ O ₆	1350	Complex	Columbite	—	—	—	(4)	v. w. blue	m. blue
Ca ₂ Nb ₂ O ₇	1250	Same as published	Monoclinic	13.36	5.50	7.70	(21)	—	m. blue
Ca ₃ Nb ₂ O ₈	1400	Same as published*	Cubic, face cent.	7.978	—	—	(21, 22)	—	—
SrNb ₂ O ₆	1200	Complex	Perovskite**	—	—	—	(23)	—	v. w. blue
SrTa ₂ O ₆	1250	—	Tetragonal	—	—	—	(24)	—	—
BaNb ₂ O ₆	1200	Same as published	Hexagonal	12.07	—	3.95	(25)	—	—
BaNb ₂ O ₆	1400	Same as published	Orthorhombic	12.194	10.268	7.065	(25)	—	v. v. w. gr.-yel.
BaTa ₂ O ₆	1250	—	Tetragonal	—	—	—	(24)	—	—
Ba ₅ Nb ₄ O ₁₅ ***	1350	—	Hexagonal	5.795	—	11.784	(25)	—	v. w. green
ZnNb ₂ O ₆	1050	Orthorhombic $a_0 = 5.04$, $b_0 = 14.2$, $c_0 = 5.71$	Columbite	5.036	14.18	5.715	(5)	m. blue	v. s. blue
ZnTa ₂ O ₆	1200	—	Columbite	5.058	14.08	5.682	(5)	—	w. white-green
CdNb ₂ O ₆	1050	Same as published	Orthorh. (Columbite)	5.13	14.75	5.842	(3, 4, 26, 27)	v. s. blue	v. s. deep blue
CdT ₂ O ₆	1300	Complex	—	—	—	—	—	—	—
Cd ₂ Nb ₂ O ₇	1100	Same as published	Cubic (Pyrochlore)	10.35	—	—	(26, 28)	—	v. v. w. yellow
Cd ₂ Ta ₂ O ₇	1200	Complex	Cubic (Pyrochlore)	10.36	—	—	(28)	—	—
PbNb ₂ O ₆ ***	1100	Same as published	Rhombohedral	7.184	[$\alpha R = 93^\circ, 55'$]	—	(15, 29, 30)	—	—
PbNb ₂ O ₆	1275	Same as published	Orthorh., pseudotetr.	17.65	17.91	7.736	(15, 29, 30)	—	v. w. gr.-yellow
PbTa ₂ O ₆	1100	Rhomb. + unknown	Rhombohedral	7.147	[$\alpha R = 94^\circ, 47'$]	—	(15)	—	—
PbTa ₂ O ₆	1350	—	Orthorhombic	17.68	17.72	7.754	(15)	—	—

* The orthorhombic modification $a_0 = 11.51$, $b_0 = 5.754$, $c_0 = 7.990$ Å (22) could not be obtained.** Sr_{0.2}Ba_{0.2}Nb₂O₆ reported orthorhombic (pseudotetragonal) $a_0 = 12.41$, $c_0 = 3.92$ Å (31).

*** Ba-niobates with different stoichiometry (25) were found nonluminescent; Pb-niobates with different stoichiometry were not prepared.

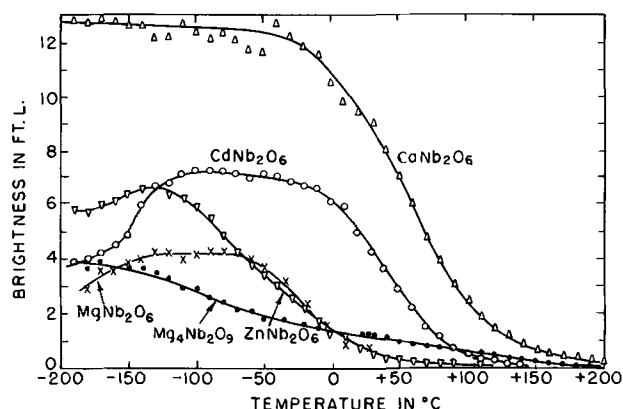


Fig. 1. Brightness of niobates under 2537Å excitation as a function of temperature.

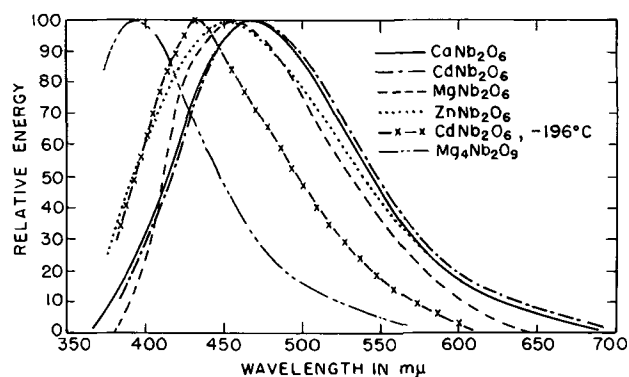


Fig. 2. Spectral distribution of emission of niobates under 2537Å excitation at room temperature, and of CdNb₂O₆ at -196°C.

does not seem to have been reported; however, in view of the similarity in symmetry and lattice dimensions as compared with those of the Cd, Mg, and Zn compounds, it is almost certainly also columbite.

The brightness of luminescent niobates as a function of temperature is shown in Fig. 1. A more valid comparison of phosphor performance (e.g., total energy) may be made by taking the ratio of brightness at various temperatures to the room temperature luminosity (η), values of which are shown in Table II along with data on MgWO₄ excited under the same conditions. The reproducibility of brightness in CdNb₂O₆ proved to be somewhat poorer than that of the other compounds, and values up to 6.5 ft.-L at 25°C (on the same scale) have been obtained on phosphors prepared from CdCO₃ precipitated in this laboratory. The decrease in brightness of CdNb₂O₆ toward lower temperatures is accompanied by a color change to deep blue ($\eta = 0.180$ as indicated by the emission spectra shown in Fig. 2, and

Table II. Emission characteristics of niobates at 25°C

Compound	Brightness in ft.-L. from Fig. 1	Luminosity factor, η	ft.-L./ η
MgWO ₄ (standard)	15.7	0.395	39.7
MgNb ₂ O ₆	0.69	0.251	2.75
Mg ₄ Nb ₂ O ₉	1.23	0.0525	23.4
CaNb ₂ O ₆	9.38	0.324	28.9
CdNb ₂ O ₆	4.75	0.339	14.0
ZnNb ₂ O ₆	0.69	0.282	2.45

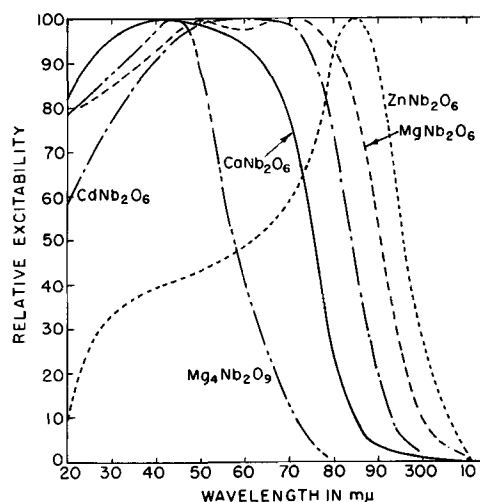


Fig. 3. Room-temperature excitation spectra of niobates

the ratios of brightness/luminosity at -100° and -196°C are the same (21.2). Conversely, the originally violet-blue emitting Mg₄Nb₂O₉ becomes more luminous (purple-white) below about -80°C, but no emission spectrum of this was taken at low temperatures, and therefore the luminosity under these conditions is not known. The other compounds exhibited only a slight shift to shorter wavelengths at the lowest temperatures. All tantalates were much more weakly luminescent than the niobates of similar composition. The reason for this need not necessarily be sought in structure (which is often different), since energy levels in electronic transitions involving the respective ions are likely to differ in spite of similarity in ionic size and coordination. In this connection, it should be noted that among the tantalates now investigated, only CaTa₂O₆ (4) and ZnTa₂O₆ (5) are reported to have the columbite structure, and only the former proved to be luminescent at room temperature.

The excitation spectra of the luminescent niobates are shown in Fig. 3. Their appearance suggests at least two peaks which are indicated quite clearly in the case of MgNb₂O₆ and ZnNb₂O₆. There is therefore a qualitative resemblance to the excitation spectra of the alkali metavanadates reported by Gobrecht and Heinsohn (8), although the peaks of the niobate spectra are located at shorter wavelengths. Compounds reported as non-luminescent (Table I) also failed to show visible emission under excitation by a source of continuous u.v. (H₂ arc). However, the possibility of emission in the u.v. or the necessity for excitation by wavelengths less than about 2200Å (limit of H₂ arc with Corning No. 9863 filter) was not investigated.

Absorption spectra are shown in Fig. 4 and grouped so as to facilitate comparisons between selected compounds. Assuming that alkaline earths do not introduce absorption bands in the region investigated, the absorption observed should be due entirely to niobate or tantalate ions, respectively, but influenced by the particular environment. Figure 4a shows that the absorption edges of the niobates lie at longer wavelengths than those of the

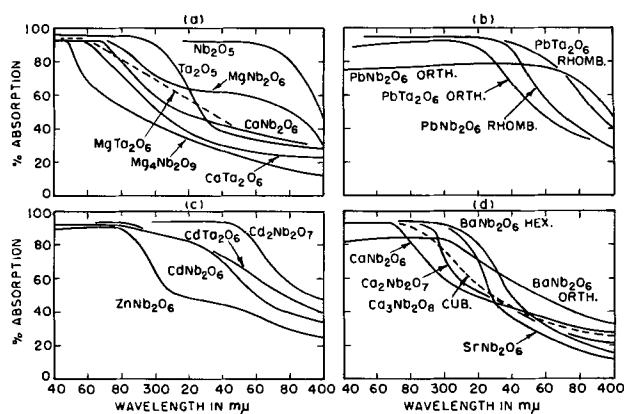


Fig. 4. Room-temperature absorption spectra (as 100-% diffuse reflectance) of some niobates and tantalates.

tantalates, in accordance with the positions of the absorption bands of Nb_2O_5 and Ta_2O_5 themselves. The additional absorption of $MgNb_2O_6$ at longer wavelength coincides with that of Nb_2O_5 and disappears in the case of $Mg_4Nb_2O_9$, and other products of firing Nb_2O_5 with an excess of MgO over the 1:1 ratio. This absorption may therefore be caused by traces of Nb_2O_5 undetected by x-ray diffraction. On the other hand, the long wavelength absorption of the Pb compounds (Fig. 4b) indicates the possibility that this is caused by Pb itself. At least in the rhombohedral compounds, the relative locations of the absorption edges of the niobate and tantalate are reversed from those of Fig. 4a. Contrary to $PbWO_4$, the present Pb compounds show only weak luminescence at low temperatures, and it was also observed that small additions of Pb to $CaNb_2O_6$ progressively decreased the brightness which is also contrary to the behavior of Pb in $CaWO_4$ (9). Figure 4c again shows absorption bands at longer wavelengths which might be caused by processes involving the divalent elements (Zn or Cd); in this case, however, the metaniobates are luminescent, and the additional absorption bands are weak enough to allow the main absorption edges to be resolved. These are located in the same vicinity as those of the isostructural Mg and Ca metaniobates. Going from $CdNb_2O_6$ to cubic and nonluminescent $Cd_2Nb_2O_7$ we also see a shift to longer wavelengths and disappearance of the original absorption edge. Figure 4d again includes only alkaline earth cations and compares the location of the absorption edges of luminescent $CaNb_2O_6$ with that of the nonluminescent compounds, *i.e.*, $SrNb_2O_6$, $BaNb_2O_6$, $Ca_2Nb_2O_7$, and $Ca_3Nb_2O_8$. Returning to Fig. 4a, it is also noted that the absorption edge of the luminescent $Mg_4Nb_2O_9$, like those of the other luminescent compounds, lies at short wavelengths, *e.g.*, below $280\ m\mu$. Finally, it should be observed that the positions of the absorption edges of the luminescent niobates are in fair agreement with those of the long wavelength peaks, or edges, of the excitation spectra.

No reflectance measurements were taken in the visible region, but as may be extrapolated from the data shown, most of the compounds appeared lightly tinted when directly compared with MgO . Appreciable coloration was noted only on orthorh. $PbNb_2O_6$

(yellow-white), orthorh. $BaNb_2O_6$ (light gray), $Ca_3Nb_2O_8$ (green-white), and $Cd_2Nb_2O_7$ (light yellow, turning gray-purple on exposure to ambient light). The absorption spectrum of $Cd_2Nb_2O_7$ shown was taken on a sample freshly bleached by heating to $300^\circ C$.

Only a few qualitative observations were made on the effect of substitution of V for Nb in $CaNb_2O_6$. Increasing concentrations (5, 10, 20 mole %) resulted in increasingly yellow body color and a shift in emission to longer wavelengths (green) as well as drastic reduction in brightness. The effect increased with increasing firing temperature. It was interesting to note that V-containing samples sometimes also displayed a red luminescence under 3650\AA excitation, particularly at liquid N_2 temperature, as for instance $Ca(0.8Nb, 0.2V)_2O_6$ or $Ca(0.95Nb, 0.05V)_2O_6$, fired at 1000° and $1100^\circ C$, respectively. Since the emission color of $Ca_2V_2O_7$ is reported to be blue, and in view of the appreciable efficiency observed on pyrovanadates (10), as well as the fact that $Ca_2Nb_2O_7$ is non- or only poorly luminescent, it is seen that any analogy between niobate and vanadate phosphors must be limited. No x-ray investigations were made on these V-substituted compounds or on known vanadate phosphor compositions.

Discussion

It has been shown that the spectral regions where both excitation and absorption occur, are those where absorption is most likely to be caused by the niobate groups, rather than by electronic transitions involving the divalent cation. Accordingly, the luminescence process would involve mainly excitation and relaxation of the Nb (or Ta)-O bond. This is also supported by the similarity in emission spectra and the observation that at low temperature most of the compounds displayed at least a weak luminescence. The mechanism is therefore analogous to that proposed for other self-activated phosphor systems, *e.g.*, molybdates (11), tungstates (12), vanadates (8), and the more complex Ti or Zr containing compounds (13, 14). Since in all of the present compounds, niobium or tantalum is octahedrally linked to six oxygen atoms, structural differences are often minor [such as orthorhombic distortion of tetragonal symmetry in $PbNb_2O_6$, $PbTa_2O_6$ (15)] and are mainly the result of differences in the arrangement of the octahedral groups within the unit cell, *e.g.*, as between the brookite and rutile (16) and the brookite and columbite (17) structures.

The principal question concerns the conspicuous influence of structure on luminescence as observed on the present compounds. As already noted, strong luminescence of niobates occurs only in the columbite structure, with the one exception of $Mg_4Nb_2O_9$. There is also a slight indication that stronger luminescence ($CaNb_2O_6$) is associated with an absorption edge shifted to shorter wavelength, although more precise measurements on single crystals would be required to establish such a relationship with certainty. All other niobates (with different structure) absorb at longer wavelengths. From this, one may conclude that in the meta compounds, the con-

figuration of the ground and excited states of the Nb-O bond is favorable to luminescence in compounds with the columbite structure, while in other structures, crossing-over of the ground and excited states may occur at lower energies, leading to quenching at lower temperatures.

Acknowledgment

The writer wishes to thank Miss I. Walinski and Mr. D. W. Morgan for their help in sample preparation and optical measurements, Dr. C. K. Lui Wei for the numerous x-ray powder diffraction analyses, and Dr. E. C. Subbarao, Dr. W. A. McAllister, and Professor E. Banks for helpful discussions.

Note Added in Proof

A recent paper by Ballman, Porto, and Yariv (32) describes the preparation and properties of single crystals of CaNb_2O_6 doped with rare earths for laser application. The pulled crystals were stated to be essentially the same as the mineral fersmite (33) (CaNb_2O_6) whose space group, P_{bcn} , is the same as that of columbite. The authors did not, however, mention any host-crystal luminescence of the compound.

Manuscript received Aug. 22, 1963. This paper was presented at the Toronto Meeting, May 3-7, 1964.

Any discussion of this paper will appear in a Discussion Section to be published in the December 1964 JOURNAL.

REFERENCES

1. Y. Baskin and D. C. Schell, *J. Am. Ceram. Soc.*, **46**, 176 (1963).
2. C. K. Lui Wei, To be published.
3. B. Lewis and E. A. D. White, *J. Electronics*, **1**, 646 (1956).
4. E. Aleshin and R. Roy, *J. Am. Ceram. Soc.*, **45**, 18 (1962).
5. K. Brandt, *Arkiv kemi, mineral., geol.*, **17A** [15], (1943).
6. R. W. Harrison and E. J. Delgrosso, *This Journal*, **110**, 205 (1963).
7. S. Larach, *J. Chem. Phys.*, **19**, 1318 (1951).
8. H. Gobrecht and G. Heinsohn, *Z. Physik*, **147**, 350 (1957).
9. F. A. Kröger, "Some Aspects of the Luminescence of Solids," p. 124, Elsevier Publishing Co. (1948).
10. J. Kotera and T. Sekine, *Bull. Chem. Soc. Japan*, **27**, 13 (1954).
11. F. A. Kröger, "Some Aspects of the Luminescence of Solids," p. 108, Elsevier Publishing Co. (1948).
12. H. W. Leverenz, "An Introduction to Luminescence of Solids," p. 100, John Wiley & Sons, New York (1950).
13. S. T. Henderson and P. W. Ranby, *This Journal*, **98**, 479 (1951).
14. D. E. Harrison, N. T. Melamed, and E. C. Subbarao, *ibid.*, **110**, 23 (1963).
15. E. C. Subbarao, G. Shirane, and F. Jona, *Acta Cryst.*, **13**, 226 (1960).
16. L. Pauling and J. H. Sturdivant, *Z. Krist.*, **68**, 239 (1928).
17. J. H. Sturdivant, *ibid.*, **75**, 88 (1930).
18. A. Byström, B. Hök, and B. Mason, *Arkiv. kemi mineral. geol.*, **15B**, [4] (1941).
19. Battelle Memorial Institute, A.S.T.M. Index No. 8-252.
20. *Ibid.*, Index No. 8-265.
21. J. F. Rawland, N. F. H. Bright, and A. Jongejan, *Proc. 7th Ann. Conf. Ind. Appl. X-ray Analysis*, Denver (1958).
22. M. Ibrailim and N. F. H. Bright, *J. Am. Ceram. Soc.*, **45**, 325 (1962).
23. H. J. Goldschmidt, *Metallurgia*, p. 211-50, Nov. and Dec. 1960.
24. J. F. Ismailzade, *Soviet Physics-Crystallography*, **4**, 618 (1959).
25. R. S. Roth and J. L. Waring, *J. Research Natl. Bur. Standards*, **65A**, 337 (1961).
26. A. de Bretteville, Jr., F. A. Halden, T. Vasilos, and L. Reed, *J. Am. Ceram. Soc.*, **40**, 86 (1957).
27. R. S. Roth, *ibid.*, **44**, 49 (1961).
28. A. Byström, *Arkiv. kemi mineral. geol.*, **18A** [21], (1944).
29. M. H. Francombe, *Acta Cryst.*, **10**, 696 (1958).
30. R. S. Roth, *J. Research Natl. Bur. Standards*, **62**, 27 (1959).
31. M. H. Francombe, *Acta Cryst.*, **13**, 131 (1960).
32. A. A. Ballman, S. P. S. Porto, and A. Yariv, *J. Appl. Phys.*, **34**, 3155 (1963).
33. H. S. Hess and H. J. Trumpour, *Am. Mineralogist*, **44**, 1 (1959).

Copper-Activated Alkaline-Earth Phosphate Phosphors

R. C. Ropp¹

Sylvania Electric Products, Inc., Towanda, Pennsylvania

ABSTRACT

Spectral properties of the alkaline earth pyrophosphates and a condensed strontium phosphate, all activated by copper, are described. Of the pyrophosphates, only $\alpha\text{-Ca}_2\text{P}_2\text{O}_7$, $\beta\text{-Ca}_2\text{P}_2\text{O}_7$, and $\delta\text{-Ba}_2\text{P}_2\text{O}_7$ produce moderately intense emission when activated by copper. In the condensed phosphate systems, only $\text{Sr}_5(\text{P}_3\text{O}_{10})_2\text{:Cu}$ produces intense luminescence. An explanation in terms of d-electron interaction or coupling is proposed.

Copper, in its early use as an activator, was restricted to sulfide and silicate phosphors. Later work showed that carbonates, oxides, halides, and phosphates could also be activated by copper (1). Such materials as ThSiO_4 (2), aluminosilicates (3), and phosphates such as calcium apatite (4) or calcium metaphosphate (5), activated by copper, have been

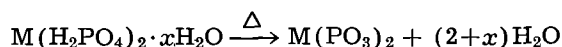
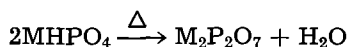
reported. More recently, it has been shown that cuprous copper would activate both orthophosphates (6) and certain apatites (7) of the alkaline earths. The quantum efficiencies of such phosphors have been high (8), and the luminescent state was obtained only when the matrix containing the copper was subjected to a neutral or reducing atmosphere during firing.

¹ Present address: Westinghouse Electric Corporation, Bloomfield, New Jersey.

This contribution describes some observations on the alkaline-earth phosphates activated by copper, including the pyrophosphates and certain members of the condensed phosphates. The work was part of a survey of various activators in the alkaline-earth pyrophosphates.

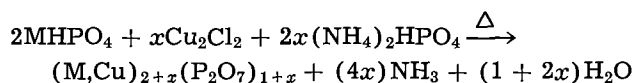
Method of Preparation

High-purity raw materials were prepared by methods given previously (9). The pyrophosphates or condensed phosphates were prepared by ignition of the corresponding dibasic or monobasic phosphate, according to the reactions



where M is an alkaline earth, and x may be 0 to 2 moles.

The method of addition of the activator was not critical and any copper salt gave activation, although Cu_2Cl_2 was preferred. Activator concentrations ranged between 0.0005 mole to 0.15 mole per mole of phosphor. Activation was obtained only when the fired materials were subsequently refired in a reducing atmosphere containing 95% N_2 -5% H_2 . In the case of the condensed phosphates of strontium, reduction was not required to obtain activation when cuprous chloride was employed, but it was possible to obtain inert materials by overfiring. In the pyrophosphates, additional phosphate was added to give a stoichiometric material, according to the reaction



where M is any alkaline earth.

Methods of measurement followed those described in a previous work (10).

Calcium Phosphate Phosphors

Copper was found to activate the α - and β -forms of the calcium pyrophosphates but not the γ - or δ -forms. This difference is probably due to the low degree of crystallinity obtained which is related to the low transition temperatures involved. Only in β - $\text{Ca}_2\text{P}_2\text{O}_7$ was the position of the emission peak observed to be dependent on copper content. An increase in activator concentration caused a shift in the emission band to longer wavelengths, but the most characteristic feature of materials with higher Cu contents was the appearance of a prominent new excitation band at 3240Å in the β -form, the effect being observed beginning with 0.005 mole Cu^+ per mole of pyrophosphate (Fig. 1). The shift in emission spectrum of β - $\text{Ca}_2\text{P}_2\text{O}_7$ phosphors was pronounced, activation by 0.001 mole Cu producing an emission band peaking at 4840Å, when excited by 2537Å, while activation by 0.1 mole Cu gave an emission band at 5430Å, when excited by 3240Å.

In the high-temperature form, α - $\text{Ca}_2\text{P}_2\text{O}_7$:Cu, increasing the copper concentration did not change

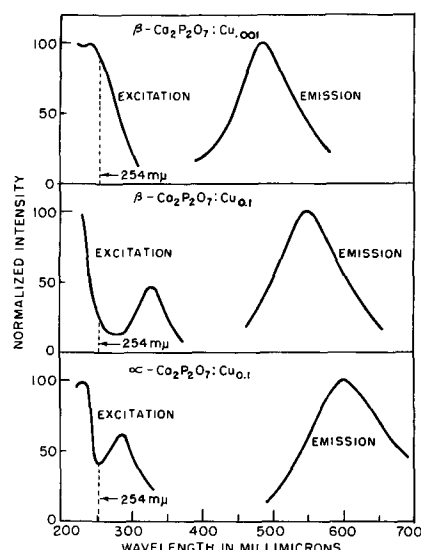


Fig. 1. Copper-activated calcium pyrophosphates

the position of the excitation and emission bands, although higher concentrations of copper seemed to promote the phase transformation from β - $\text{Ca}_2\text{P}_2\text{O}_7$ to α - $\text{Ca}_2\text{P}_2\text{O}_7$, as deduced from x-ray powder diffraction data. A change to lower firing temperatures served to counteract any such phase transition, and the β forms containing high copper contents were obtained in this manner.

The effect of copper concentration on plaque brightness of β - $\text{Ca}_2\text{P}_2\text{O}_7$:Cu is shown in Table I. The data show that these phosphors, compared with a commercial phosphor, $\text{Ba}_2\text{TiP}_2\text{O}_9$, are of intermediate brightness.

Attempts to produce a condensed phosphate of calcium activated by copper were futile, and none of the known forms gave a phosphor.

Strontium Phosphate Phosphors

The pyrophosphates of strontium are not activated by copper, at least not at excitation energies between 2180Å and 7050Å. No reason can be given for this, in terms of structure, since both α - $\text{Sr}_2\text{P}_2\text{O}_7$ and β - $\text{Sr}_2\text{P}_2\text{O}_7$ closely resemble the corresponding salts of calcium (11). A very low level of luminescence was seen in α - $\text{Sr}_2\text{P}_2\text{O}_7$:Cu, but measurement of the optical properties gave results close enough to the strontium tripolyphosphate (see below) so that it is probable that the pyrophosphate decomposed to form the more stable structure in the presence of copper.

In contrast to the other alkaline-earth condensed

Table I. Effect of Cu content in β - $\text{Ca}_2\text{P}_2\text{O}_7$:Cu

Cu content (moles/mole phosphor)	% Plaque brightness (vs. $\text{Ba}_2\text{TiP}_2\text{O}_9$) (2537Å excitation)	
0.001	Blue 37	Green 29
0.005	46	36
0.01	35	29
0.05	19	14
0.10	23	21

Table II. Dependency of composition on copper concentration

Moles Cu per mole of metaphosphate	Firing temperature (°C)	Phases present in per cent*		% Relative red brightness (3550Å excitation)
		β -Sr(PO ₃) ₂	α -Sr(PO ₃) ₂	
0.001	900	—	100	80
0.005	900	10	90	100
0.01	900	30-50	70-50	95
0.05	900	100	—	50
0.10	900	100	—	50
0.005	815	—	100	60
0.005	870	—	100	90

* Estimated by x-ray methods.

phosphates, copper activation in the strontium system gave two phosphors, as shown in Table II.

X-ray powder diffraction data showed the presence of the two forms, β -Sr(PO₃)₂ and α -Sr(PO₃)₂, as found by Thilo and Grunze (12) and others (13). Both forms were activated by copper.

Chemical analysis showed the average formula Sr_{1.0}(PO₃)_{2.1}. Infrared analysis of these forms showed that the absorption bands of β -Sr(PO₃)₂ correspond to those expected for the trimetaphosphate structure, Sr₃(P₃O₉)₂.² The infrared absorption bands of α -Sr(PO₃)₂ appeared to be those of the tripolyphosphate structure, Sr₅(P₃O₁₀)₂.² The former is a cyclic structure, whereas the latter consists of linear chains of indeterminate length. Of the two forms, the tripolyphosphate, when activated by copper, possesses twice the brightness of the trimetaphosphate (see Table II). The phosphor structure and brightness were found to be functions of copper content and firing temperature. The higher copper concentrations promoted the formation of the low-temperature β -Sr(PO₃)₂ form, as shown in Table II.

To obtain the brightest phosphor, the preparation conditions were those which promoted the formation of the phosphor Sr₅(P₃O₁₀)₂:Cu. If the material were fired at too high a temperature, the tripolyphosphate was not formed and the material was inert. Copper activation of Sr₅(P₃O₁₀)₂ gave a strongly emitting phosphor when activated by 3100Å radiation, as shown in Fig. 2. The emission peak is broad, and a considerable part of the emission lies beyond the peak emission wavelength of 6550Å into the near infrared region of the spectrum. This phosphor

² It should be noted that these formulas are structural formulas, indicating the structural units, not chemical compositions. The chemical formula remained one metal atom per two atoms of phosphorus. This behavior is common in condensed systems.

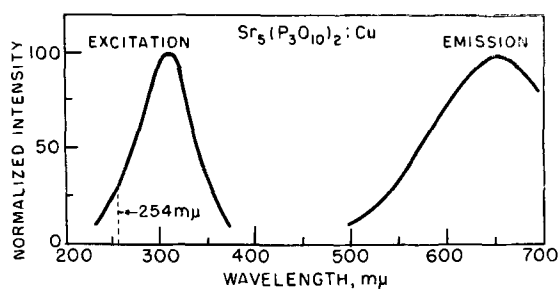


Fig. 2. Copper-activated strontium tripolyphosphate

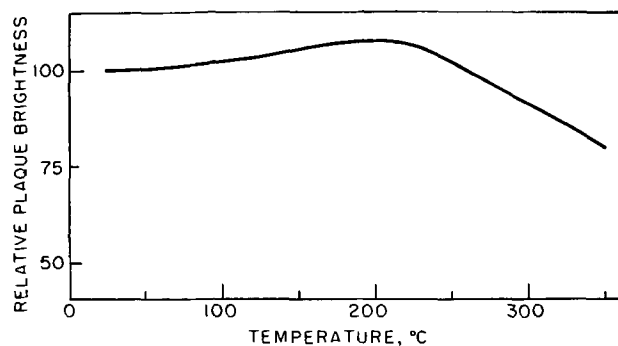


Fig. 3. Temperature dependence of luminescence of Sr₅(P₃O₁₀)₂:Cu

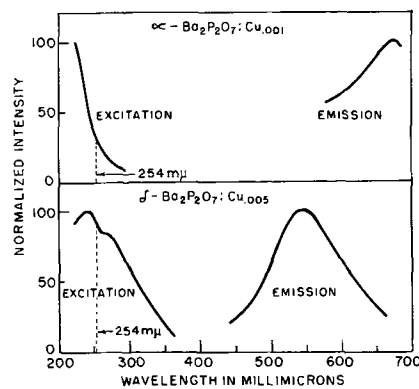


Fig. 4. Copper-activated barium pyrophosphates

was easily prepared by calcining Sr(H₂PO₄)₂ to form the condensed phosphate, although it was possible to use SrCO₃ + 2(NH₄)H₂PO₄. Much superior phosphors resulted from the former method.

The intensity of fluorescence of this phosphor in ambient air was maximum at 205°C, as shown in Fig. 3. Excitation was accomplished by radiation from a F4BL lamp peaking at 3550Å, and the heating rate was approximately 8°C per min. The results show that the phosphor might be suitable as a high-temperature mercury-vapor (HPMV) lamp phosphor. No attempt was made to evaluate the stability of the phosphor in the lamp-making process or during lamp operation.

Barium Phosphates

Copper activation in the barium pyrophosphates produces either a dull red (emission peak of 6750Å) or a green-yellow phosphor (emission peak of 5460Å) when excited by 2537Å, depending on which of the two crystal structures is formed. The low-temperature form, α -Ba₂P₂O₇:Cu, is much less efficient than the high-temperature form, δ -Ba₂P₂O₇:Cu. The former was a dull red phosphor, too inefficient to permit precise measurement of its spectral properties. Therefore, the data in Fig. 4 are accurate only for δ -Ba₂P₂O₇:Cu, but the measured properties of α -Ba₂P₂O₇:Cu are given for the sake of completeness. A change in copper concentration did not cause a change in the excitation or emission bands. The optimum concentration was about 0.005 mole Cu per mole of phosphor. The emission of the high-temperature form, δ -Ba₂P₂O₇:Cu, was of medium intensity, as shown by the comparison of plaque brightness data in Table III. Of the materials

Table III.

Phosphor	Emission color	Excitation maximum (Å)	% Plaque brightness (vs. Ba ₂ TiP ₂ O ₆) (2537Å excitation)		
			B	G	R
β -Ca ₂ P ₂ O ₇ :Cu _{0.001}	Blue-green	2410	46	36	—
β -Ca ₂ P ₂ O ₇ :Cu _{0.1}	Blue-green	3380	23	21	—
α -Ca ₂ P ₂ O ₇ :Cu _{0.005}	Yellow-green	2960	16	28	—
δ -Ba ₂ P ₂ O ₇ :Cu _{0.005}	Green-yellow	(2440) (2720)	29	42	33

investigated, the phosphors listed in Table III gave the greatest response to 2537Å irradiation.

Discussion

Several experimental differences were noted in the separate systems. In the calcium pyrophosphate system, the emission peak varied according to both the structure formed and the amount of copper activator present. At low concentrations, the excitation band was fairly broad, but the edge shifted to higher energy as the copper content was increased in β -Ca₂P₂O₇:Cu. The new excitation band at high concentrations is attributed to excitation of copper-activator centers, while the excitation band at lower concentrations may be due to absorption in a localized copper-oxygen complex or to the matrix itself. In contrast, the α -Ca₂P₂O₇:Cu phosphor shows only the band attributed to absorption in the copper centers, plus the high-energy excitation band. The similarity of x-ray diffraction patterns of α -Ca₂P₂O₇, α -Sr₂P₂O₇, and α -Ba₂P₂O₇ is well known (14), yet only the calcium compound is activated at room temperature by copper. Likewise, β -Ca₂P₂O₇ and β -Sr₂P₂O₇ are isomorphic [tetragonal, P₄¹ (11)], but only β -Ca₂P₂O₇:Cu shows luminescence. It must, therefore, be concluded that there is an appreciable effect on luminescent intensity due to the nature of the cation in the matrix. The experimental firing data imply that the copper activator is probably in the cuprous state. Cuprous activator has the outer electronic structure 3s²3p⁶3d¹⁰, and ground state ¹S₀. The first excited state is a ³D₃ state, but the transition is not allowed by dipole rules. The transition to the next state, a ³P₃ state, is allowed. The position of the activator in the lattice cannot be ascertained in the present study. It is not inconceivable that the copper activator could be associated with a trapped electron to give a Cu⁺ net charge. Such a center would also have an allowed transition.

In the tripoly phosphate Sr₅(P₃O₁₀)₂:Cu, the narrow excitation band indicates the presence of a single activator level. The extremely broad emission band is indicative of a considerable amount of crystal field perturbation of the activator center in the crystal during the luminescence process. The

temperature dependence found for Sr₅(P₃O₁₀)₂:Cu shows that the matrix-activator center vibronic coupling is not large, since any such process would lead to nonradiative energy transfer.

In the pyrophosphates, the differences observed in luminescent properties due to the presence of various cations in the same structure are more easily explained as the interaction of matrix cations having d-electrons with the activator center by an electronic coupling process, or possibly spin-exchange. In Ca₂P₂O₇, where no d-electrons are present, luminescence of copper is observed at room temperature, in contrast with the same structure where spin interaction, involving d¹⁰-electrons between cation sites in Sr₂P₂O₇ and the activator center, leads to nonradiative energy transfer and phonon dissipation of energy.

Acknowledgment

The author is indebted to H. D. Layman for the preparations, C. W. W. Hoffman for the x-ray and infrared data, and to M. A. Aia and R. W. Mooney for many stimulating discussions.

Manuscript received July 8, 1963; revised manuscript received Dec. 2, 1963.

Any discussion of this paper will appear in a Discussion Section to be published in the December 1964 JOURNAL.

REFERENCES

1. F. A. Kröger, "Some Aspects of The Luminescence of Solids," Elsevier Publishing Co., New York (1948).
2. H. W. Leverenz, "An Introduction to The Luminescence of Solids," p. 266, John Wiley and Sons, Inc., New York (1950).
3. E. W. Claffy and J. H. Schulman, *This Journal*, **98**, 408 (1951).
4. E. Inmore, *Sci. Papers Inst. Phys. Chem. Research (Tokyo)*, **27**, 1 (1935).
5. D. G. Engle, *J. Optical Soc. Am.*, **11**, 599 (1925).
6. Y. Uehara, Y. Kobuke, and I. Masuda, *This Journal*, **106**, 1027 (1959); W. L. Wanmaker and C. Bakker, *ibid.*, **106**, 1027 (1959); W. L. Wanmaker and A. Spier, *ibid.*, **109**, 109 (1962); P. W. Ranby and D. Hobbs, *ibid.*, **110**, 280 (1963); H. W. Rimbach, U. S. Pat. 3,025,425 (1962).
7. B. E. Hunt and A. H. McKeag, *This Journal*, **106**, 1032 (1959).
8. Y. Uehara, Y. Kobuke, and I. Masuda, *ibid.*, **107**, 1 (1960).
9. R. C. Ropp, M. A. Aia, C. W. W. Hoffman, T. J. Veleker, and R. W. Mooney, *Anal. Chem.*, **31**, 1163 (1959).
10. R. C. Ropp and R. W. Mooney, *This Journal*, **107**, 15 (1960).
11. R. W. Mooney and M. A. Aia, *Chem. Rev.*, **61**, 433 (1961).
12. E. Thilo and I. Grunze, *Z. anorg. u. allgem. Chem.*, **290**, 223 (1957).
13. E. Stegar, *ibid.*, **298**, 305 (1958); W. Wieker and E. Thilo, *ibid.*, **306**, 40 (1960); E. Thilo, *Acta Chim. Acad. Sci. Hung.*, **12**, 221 (1957).
14. P. W. Ranby, D. H. Mash, and S. T. Henderson, *Brit. J. Appl. Phys., Suppl. No. 4*, S18 (1955).

The Role of Calcium Manganese Orthophosphate in Halophosphate Phosphors

J. G. Rabatin and G. R. Gillooly

Luminescent Materials Laboratory, Lamp Metals and Components Department,
General Electric Company, Cleveland, Ohio

ABSTRACT

The pink coloration often found in calcium halophosphate phosphors has been found to be associated with the presence of an impurity phase of $\beta(\text{Ca, Mn})_3(\text{PO}_4)_2$ which forms on partial degradation of the phosphor. The identification, preparation, properties, and mode of formation of this impurity are described. The pink coloration is due to trace amounts of Mn^{+3} . Because Mn^{+3} absorbs strongly in both the visible and ultraviolet regions, it has a deleterious effect on phosphor brightness.

The present understanding of the nature and amounts of deleterious impurities associated with halophosphate phosphors is incomplete. Butler (1) and more recently Aia and Mooney (2) describe the properties of calcium antimonates usually found in the finished phosphors. Studies regarding reactions which may be involved in the formation of the apatite structure have been reported (3-5), but these do not elucidate the factors influencing the stability of the phosphor at high temperatures. There remains the perplexing problem of why manganese-containing halophosphate phosphors may tend to develop a light pink discoloration during firing (under ambient atmosphere conditions). Bergin *et al.* (6) have described certain procedures to remove this discoloration. Butler (7) has shown that inert atmosphere preparation of halophosphates will reduce this pink body color. However these procedures have not further identified the nature of this deleterious impurity.

In the course of our studies on halophosphate phosphors, this pink coloration has been identified

as being associated with the solid solution of manganese in $\beta \text{Ca}_3(\text{PO}_4)_2$. Some of the manganese is in a higher oxidation state than Mn^{+2} . The identification, preparation, properties, and mode of formation of this impurity are reported here.

Identification of $\beta \text{Ca}_3(\text{PO}_4)_2$ in Halophosphates

The first evidence for the presence of $\beta \text{Ca}_3(\text{PO}_4)_2$ was found in cool white halophosphate phosphors by x-ray diffraction analysis of a phosphor sample which was refired in an open container at 1150°C for 3 hr. The phosphor body color had the typical light pink coloration sometimes seen during the manufacture of halophosphate phosphors. Figure 1 shows x-ray diffractometer traces between 27° and $35^\circ 2\theta$ for a cool white halophosphate compared with the same halophosphate refired in an open container. The x-ray diffractometer traces were recorded using the log scale setting in order to emphasize the presence of the minor constituents. The three extraneous x-ray diffraction lines in the refired sample approximated the principal lines of pure $\beta \text{Ca}_3(\text{PO}_4)_2$, namely, the 31.05° , 34.32° , and $27.76^\circ 2\theta$ lines (as listed in the ASTM Index for $\text{Cu K}\alpha$ radiation). These extraneous lines are indicated by arrows in Fig. 1. Note that otherwise the two patterns are identical in intensity and d-spacings. Examination of the traces between 20° and $80^\circ 2\theta$ shows that the normal apatite structure is still present accompanied by the appearance of this new phase of $\beta \text{Ca}_3(\text{PO}_4)_2$. It was further found that the d-spacings of the $\beta \text{Ca}_3(\text{PO}_4)_2$ lines were shifted to smaller values possibly indicating some solid solution of manganese in the $\beta \text{Ca}_3(\text{PO}_4)_2$.

Preparation

On the basis of this evidence a study was made of the extent of solid solution of manganese in $\beta \text{Ca}_3(\text{PO}_4)_2$. For this purpose samples were prepared by combining the following ingredients in the proportions shown. In all cases electronic grade reagents were used.

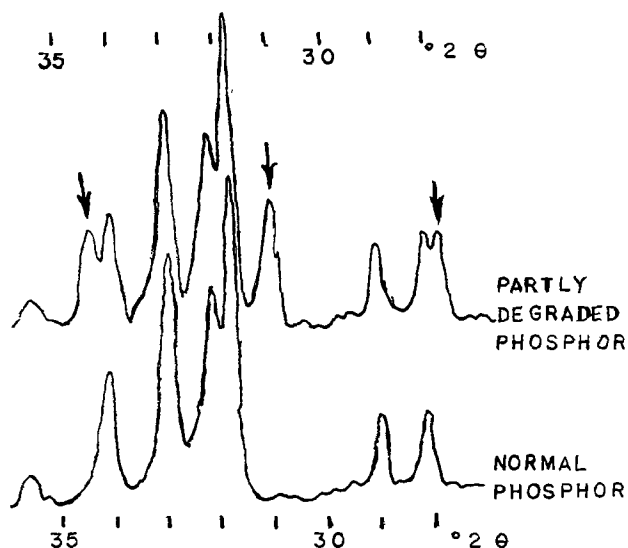
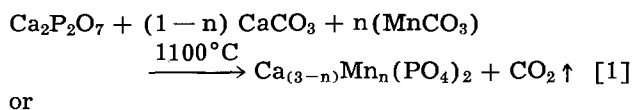
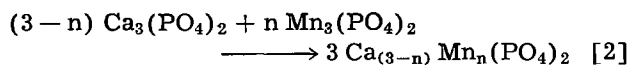


Fig. 1. Diffractometer traces of normal and partly degraded halophosphate phosphors between 28° and $35^\circ 2\theta$ using $\text{Cu K}\alpha$ radiation. Arrows point to the principal lines of $\beta(\text{Ca, Mn})_3(\text{PO}_4)_2$ found in degraded phosphor.



The mixtures were thoroughly blended, fired in open crucibles at 1100°C for 4 to 18 hr, reblended, and refired for 4 hr at 1100°C. The samples prepared in this manner possessed a light pink body color, indicating that a small amount of the manganese had been oxidized.

The fired preparations were examined by standard methods involving the use of a GE XRD-5 x-ray diffraction unit, a continuous recording spectroradiometer, petrographic microscope, a Beckman D U spectrophotometer, and a plaque brightness meter.

Magnetic susceptibility measurements were made by the Gouy method. An electrodynamic microbalance was used to determine the change of weight of the sample tube in the magnetic field. Weighings were made at a number of magnetic field strengths ranging from 1800 to 13,500 gauss.

Results and Discussion

Change in *d*-spacings.—Positive evidence for the solid solution of manganese in $\beta \text{Ca}_3(\text{PO}_4)_2$ was established by the presence of a progressive decrease in the *d*-values as the manganese concentration is increased. This decrease is compatible with that expected when a smaller manganese ion substitutes in the $\beta \text{Ca}_3(\text{PO}_4)_2$ structure leading to a contraction of the lattice. The results for the change in the 31.05° 2θ line (*d* = 2.88) are illustrated in Fig. 2. The limiting value for manganese solid solution appears to be about 12 mole % $\text{Mn}_3(\text{PO}_4)_2$ since no further changes in *d*-values were noted.

Change in refractive index.—Examination of the various preparations under the petrographic microscope show the presence of birefringent crystals with only traces of foreign material. The refractive indices of the various solid solutions were determined; the results are presented in Fig. 3. Since no further change in the index of refraction occurs beyond about 12 mole % $\text{Mn}_3(\text{PO}_4)_2$, it is suggested that this is the limiting solid solution.

Absorption spectra.—Since most of the preparations were light pink in color after air firing, reflectances

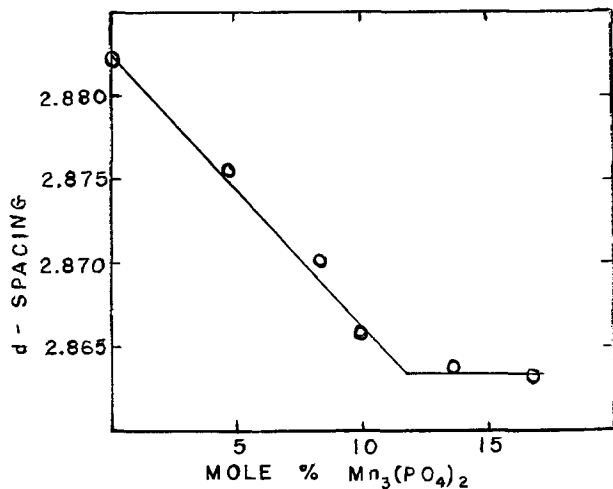


Fig. 2. Effect of manganese solid solution on the *d*-spacings of the principal line of $\beta \text{Ca}_3(\text{PO}_4)_2$.

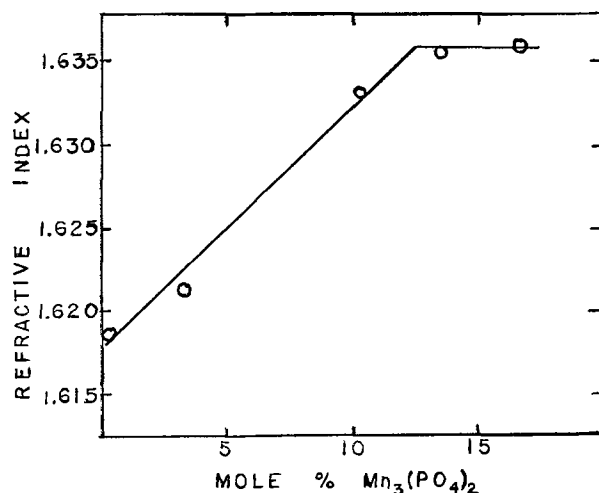


Fig. 3. Effect of manganese solid solution on the refractive indices of $\beta \text{Ca}_3(\text{PO}_4)_2$.

were measured on a Beckman D U spectrophotometer between 2500 and 8000Å. The results presented in Fig. 4 are for two preparations with different manganese contents. Broad absorption peaks occur at 2900 and 5300Å. The latter absorption in the blue-green region is similar to that described by Kumar and Sen (8) for Mn^{+3} in glass and accounts for the pink body color found in all of these preparations. Even 0.6 mole % $\text{Mn}_3(\text{PO}_4)_2$ solid solution in $\beta \text{Ca}_3(\text{PO}_4)_2$ will exhibit this body color. The absorption spectrum of $\beta \text{Ca}_3(\text{PO}_4)_2$ which contains no Mn shows no structure between 2500 and 7000Å, typical of highly reflective materials such as MgO.

Reflectance measurements were also made at 2537Å. The absorption results, calculated from one minus reflectance (1-R), are presented in Fig. 5. It will be noted that the absorption increases rapidly initially up to about 2.5 mole % $\text{Mn}_3(\text{PO}_4)_2$ solid solution, but then is relatively insensitive to further increase in solid solution of manganese in $\beta \text{Ca}_3(\text{PO}_4)_2$. This point is further elucidated in the next section on magnetic susceptibility measurements.

Magnetic susceptibility measurements.—Since the pink coloration might be attributed to manganese

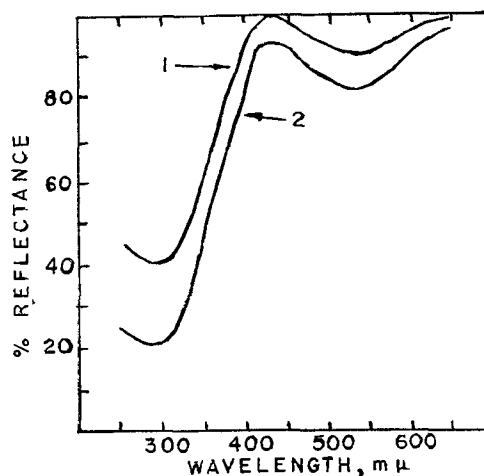


Fig. 4. Reflectance curves for two $\beta (\text{Ca}, \text{Mn})_3(\text{PO}_4)_2$: curve 1, $\text{Ca}_{2.946} \text{Mn}_{0.054} (\text{PO}_4)_2$; curve 2, $\text{Ca}_{2.8} \text{Mn}_{0.2} (\text{PO}_4)_2$.

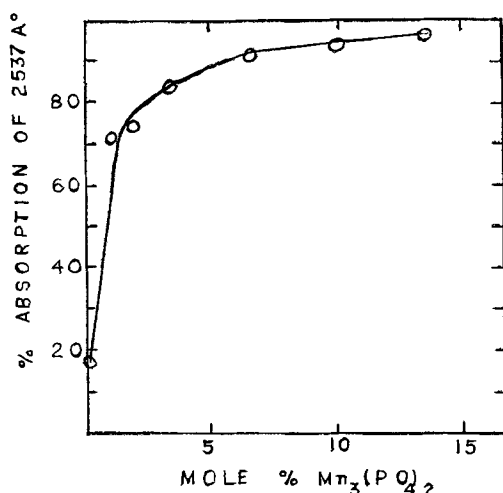


Fig. 5. Effect of manganese solid solution in β $\text{Ca}_3(\text{PO}_4)_2$ on the absorption of 2537 Å Hg line.

as Mn^{+3} , it was of interest to determine to what extent the higher oxidation state of manganese may occur in β $\text{Ca}_3(\text{PO}_4)_2$ which contains manganese in solid solution. Magnetic susceptibility measurements can best be made on samples with manganese content considerably less than that found in the cool white halophosphate. The magnetic susceptibility of $\text{Ca}_{2.98}\text{Mn}_{0.02}(\text{PO}_4)_2$ [0.67 mole % $\text{Mn}_3(\text{PO}_4)_2$ in solid solution] was determined to a precision of about 2%. Calculations indicate that at these concentrations of manganese only about 13% is present as Mn^{+3} . In other words only about 0.0026 mole of Mn^{+3} is present in the β $\text{Ca}_{2.98}\text{Mn}_{0.02}(\text{PO}_4)_2$. The remaining manganese of 0.0174 mole is in the Mn^{+2} state. Temperature dependence of the susceptibility shows that the Weiss constant is zero and that, therefore, Mn^{+3} is uniformly distributed in the orthophosphate structure with no clustering. These results preclude the possibility that the Mn^{+3} is present in the form of a manganese compound since otherwise the Weiss constant would not be zero.

Several pink samples of β $\text{Ca}_3(\text{PO}_4)_2$ with manganese in solid solution were refired in forming gas (95% N_2 -5% H_2) at 1100°C. The body color, on cooling, was now white. Susceptibility measurements now showed that the manganese was divalent in orthophosphate. No concurrent shift in 2θ values was noted for these samples, suggesting that there was no further increase in manganese solid solution as the Mn^{+3} was reduced to the Mn^{+2} state. These results confirm that the "pinkness" is due to a small amount of Mn^{+3} ions intimately associated with the β $\text{Ca}_3(\text{PO}_4)_2$ structure. The charge compensation required by the higher oxidation state of manganese could be a defect structure, presumably calcium vacancies, which may limit the extent of Mn^{+3} permissible. Interestingly, the samples which on refiring in forming gas became white, once again exhibited pink body color when fired a third time in air.

Effect of $\beta(\text{Ca}, \text{Mn})_3(\text{PO}_4)_2$ on luminescence of cool white halophosphates.—Spectroradiometer traces are shown in Fig. 6 for a cool white phosphor and the same phosphor partly degraded by refiring

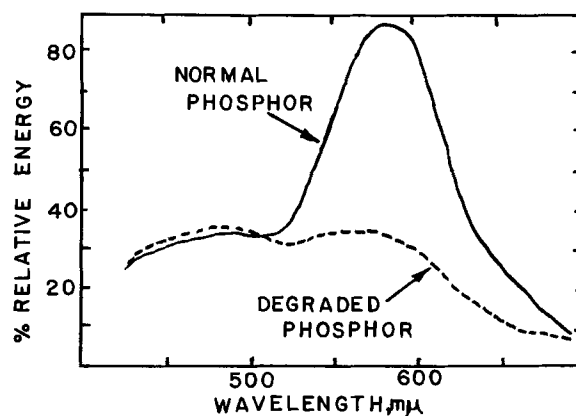


Fig. 6. Spectroradiometer traces of a normal cool white halophosphate and a partly degraded cool white halophosphate.

to produce a light pink body color. X-ray diffraction analyses reveal that the major constituent is still the normal fluor-chlor apatite. The minor constituent of β $\text{Ca}_3(\text{PO}_4)_2$ is present to the extent of only about 7 weight per cent (w/o). The 31.0° 2θ line of $\text{Ca}_3(\text{PO}_4)_2$ has shifted to about 31.2° which indicates manganese in solid solution to the extent of about 12 mole % (see Fig. 2). This would correspond to a formula of about $\text{Ca}_{2.6}\text{Mn}_{0.4}(\text{PO}_4)_2$. It might be expected if only 7% of the phosphor were degraded to yield simply β $\text{Ca}_3(\text{PO}_4)_2$ then most of the manganese would still be present in the luminescent apatite and the phosphor might still luminesce with a nearly normal cool white color. However, the luminescence of the partly degraded phosphor (Fig. 6) reveals that the manganese emission band peaking at 5900 Å is greatly depressed. Examination of the spectral curves based on observations described by Butler (9) and Nagy *et al.* (10) clearly indicates a major reduction in the amount of manganese activator now present in the phosphor. Analysis of the spectral distributions (11) shows that 60% of the manganese was removed from the phosphor during degradation. This loss agrees closely with the amount of manganese which was found in solid solution in the β $\text{Ca}_3(\text{PO}_4)_2$. The broad antimony emission peaking at about 4900 Å is increased as would be expected when manganese content is decreased (9, 10). These results clearly indicate that a large per cent of manganese ions have left the phosphor to become incorporated in the β $\text{Ca}_3(\text{PO}_4)_2$ which formed during the high-temperature partial degradation.

The next step was to prepare mixtures of 1, 2, and 5 w/o β $\text{Ca}_3(\text{PO}_4)_2$ with cool white halophosphate and fire the mixtures in covered crucibles for 1 hr at 1150°C. (On cooling the phosphors produced luminescent colors showing a decrease of manganese emission.) The spectroradiometer traces were similar to that shown in Fig. 6 for the degraded phosphor. X-ray diffraction patterns for the unfired and fired mixtures were identical, respectively, except that the β $\text{Ca}_3(\text{PO}_4)_2$ lines were shifted indicating maximum solid solution of manganese. Measurements similar to those described previously for the degraded phosphor were performed on these samples. Results are presented in Table I. These results show that the per cent of manganese which formed

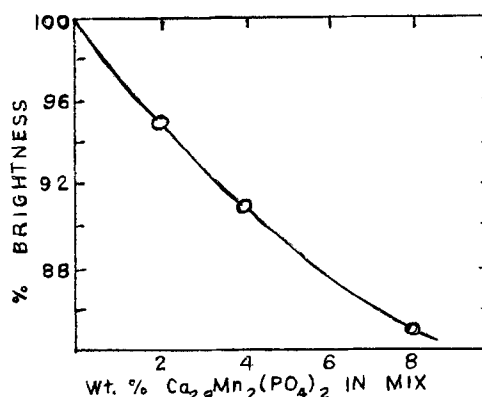
Table I. Distribution of manganese content in fired mixtures of halophosphate phosphor containing β $\text{Ca}_3(\text{PO}_4)_2$

Wt. % β $\text{Ca}_3(\text{PO}_4)_2$ in mixture	% of Mn found in β $(\text{Ca,Mn})_3(\text{PO}_4)_2$ based on max. solid soln.	Emission analysis, % Mn lost from phosphor
1	7.2	8.5
2	14.3	15.4
5	36.7	31.5

solid solution in β $\text{Ca}_3(\text{PO}_4)_2$ was in close agreement with the amount of manganese which was lost from the phosphor as calculated from the spectral curves. From these results it can be concluded that on firing manganese will migrate from the apatite to the β $\text{Ca}_3(\text{PO}_4)_2$.

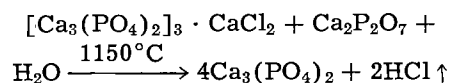
Spectroradiometer traces of several mechanical mixtures of a cool white halophosphate with a pink colored $\text{Ca}_{2.8}\text{Mn}_{0.2}(\text{PO}_4)_2$ preparation show normal cool white emissions, but with lower relative energies due to the strong but nonuseful absorption of 2537Å mercury radiation by trace amounts of Mn^{+3} found in β $\text{Ca}_{2.8}\text{Mn}_{0.2}(\text{PO}_4)_2$. The relative brightness of a cool white phosphor is decreased by the presence of β $\text{Ca}_{2.8}\text{Mn}_{0.2}(\text{PO}_4)_2$ as shown in Fig. 7. This decrease in brightness is not due solely to physical dilution of the phosphor with a nonluminescent phase. For example when 8 w/o β $\text{Ca}_3(\text{PO}_4)_2$ was blended in with a cool white phosphor, the brightness decrease was only 5% compared to a 15% decrease in brightness when 8 w/o β $\text{Ca}_{2.8}\text{Mn}_{0.2}(\text{PO}_4)_2$ was blended with the phosphor. These results also confirm that the color change in the degraded halophosphate is not due to the presence of a given amount of β $(\text{Ca, Mn})_3(\text{PO}_4)_2$, but is a result of manganese migration from the phosphor to the β $\text{Ca}_3(\text{PO}_4)_2$ impurity.

Mode of formation of β $\text{Ca}_3(\text{PO}_4)_2$ in halophosphates.—Since β $\text{Ca}_3(\text{PO}_4)_2$ appears as a consequence of a partial decomposition of the apatite structure, it was of interest to investigate some factors which may be related to this degradation process. Chemical analyses of the degraded phosphors reveal some chloride losses. For example, the degraded product represented in Fig. 1 and 6 had a chloride content of 0.40% compared to an original chloride content of 0.62%. Based on these observations, investigations were made of the following compositions: (a) chlorapatite; (b) chlorapatite + $\text{Ca}_2\text{P}_2\text{O}_7$ (equimolar); (c) fluorapatite + $\text{Ca}_2\text{P}_2\text{O}_7$ (equimolar) by firing each in open crucibles at 1150°C for up to 16 hr. Weight losses, chloride

Fig. 7. Effect on brightness of various amounts of β $\text{Ca}_{2.8}\text{Mn}_{0.2}(\text{PO}_4)_2$ mixed with a cool white halophosphate phosphor.

contents, and x-ray diffraction analyses were performed on each. Results presented in Table II show that fluorapatite is stable even in the presence of a large amount of calcium pyrophosphate.

Chlorapatite is only slightly unstable when heated alone at 1150°C. But in the presence of $\text{Ca}_2\text{P}_2\text{O}_7$ (atmospheric water probably needed), it rapidly decomposes to β $\text{Ca}_3(\text{PO}_4)_2$. This decomposition may be written as



Similarly a fluorochlorapatite of a cool white halophosphate composition (0.62% chloride) can also decompose to some extent if $\text{Ca}_2\text{P}_2\text{O}_7$ is present. In the case where 0.40 w/o chloride is present after degradation, the amount of $\text{Ca}_2\text{P}_2\text{O}_7$ necessary to cause this decomposition is only about 0.8 w/o $\text{Ca}_2\text{P}_2\text{O}_7$.

Summary

Beta calcium manganese orthophosphate has been identified as the principal factor related to the "pinkness" of manganese containing calcium halophosphate phosphors which are prepared in ambient air. Manganese will form a solid solution in β $\text{Ca}_3(\text{PO}_4)_2$ to about 0.4 moles (or about 12 w/o) manganese per mole of orthophosphate. Associated with this solid solution may be a pink coloration due to the oxidation of a small portion [less than 0.01 moles per mole of β $(\text{Ca, Mn})_3(\text{PO}_4)_2$] of the manganese to Mn^{+3} .

The deleterious effect of this substance on phosphor brightness is due to two factors. First, it ab-

Table II. Chloride loss and x-ray diffraction analysis of mixtures heated at 1150°C

Composition	Chloride, % lost				X-ray examination after 4 hr
	½ hr	1 hr	2 hr	4 hr	
1) Chlorapatite	1.3	2.5	4.3	5.0	Chlorapatite (major) + trace β $\text{Ca}_3(\text{PO}_4)_2$
2) Chlorapatite + $\text{Ca}_2\text{P}_2\text{O}_7$	26	39	65	85	β $\text{Ca}_3(\text{PO}_4)_2$ (major) + some chlorapatite
3) Fluorapatite + $\text{Ca}_2\text{P}_2\text{O}_7$	—	—	—	0	Fluorapatite + $\text{Ca}_2\text{P}_2\text{O}_7$
4) Fluorochlorapatite* + 0.03 mole $\text{Ca}_2\text{P}_2\text{O}_7$	—	—	—	36	Fluorochlorapatite** + β $\text{Ca}_3(\text{PO}_4)_2$

* Initial chloride content 0.62 w/o.

** Chloride loss limited due to the low amount of $\text{Ca}_2\text{P}_2\text{O}_7$ initially present.

sorbs strongly in both the visible and ultraviolet regions thus resulting in less radiant energy being available for the luminescent process. Also when $\text{Ca}_3(\text{PO}_4)_2$ is formed by a degradation process at high temperatures, some of the manganese is removed from the phosphor to form $(\text{Ca, Mn})_3(\text{PO}_4)_2$. This results in a decrease in the manganese emission, and thus the luminescent color shifts toward the blue antimony emission with a corresponding decrease in luminous efficiency.

Acknowledgments

The authors gratefully acknowledge the contributions of Dr. John Parodi in the measurement and interpretation of the magnetic susceptibility data, and Dr. R. L. Brown for the reflectance measurements. Their thanks are also extended to Drs. E. F. Apple and H. C. Froelich for their helpful criticisms and discussions.

Manuscript received Sept. 9, 1963. This paper was prepared for delivery at the Toronto Meeting, May 3-7, 1964.

Any discussion of this paper will appear in a Discussion Section to be published in the December 1964 JOURNAL.

REFERENCES

1. K. H. Butler, M. J. Bergin, and V. M. B. Hannaford, *This Journal*, **97**, 117 (1950).
2. M. A. Aia, R. W. Mooney, and C. W. W. Hoffman, *ibid.*, **110**, 1048 (1963).
3. W. L. Wanmaker, A. H. Hoekstra, and M. G. A. Tak, *Philips Research Repts.*, **10**, 11 (1955).
4. W. L. Wanmaker and M. L. Verheyke, *ibid.*, **11**, 1 (1956).
5. D. Robbins, Paper presented at ECS Los Angeles Meeting in 1962, Abstract 37.
6. M. J. Bergin, K. H. Butler, and H. H. Homer, Paper presented at ECS Cincinnati Meeting in 1955, Abstract 46.
7. K. H. Butler, U. S. Pat. 2,755,254 (1956).
8. S. Kumar and P. Sen, *Phys. and Chem. Glasses*, **1**, 175 (1960).
9. K. H. Butler and C. W. Jerome, *This Journal*, **97**, 265 (1950).
10. Rudolph Nagy, R. W. Wollentin, and C. K. Lui, *J. (and Trans.) Electrochem Soc.*, **95**, 187 (1949).
11. G. R. Gillooly, Paper presented at ECS Los Angeles Meeting in 1962, Abstract 39A.

Semiconducting Properties of AgIn_3Te_5

Daniel F. O'Kane and Donald R. Mason

The Department of Chemical and Metallurgical Engineering, The University of Michigan, Ann Arbor, Michigan

ABSTRACT

The congruently melting ($699^\circ \pm 3^\circ\text{C}$) compound, AgIn_3Te_5 , which can be described as 25 mole % Ag_2Te -75 mole % In_2Te_3 , was found as a result of a study of the Ag_2Te - In_2Te_3 pseudobinary phase diagram. Zone refining was used to prepare polycrystalline samples of the compound for electrical measurements. Electrical conductivity, Hall effect, Seebeck coefficient, and thermal conductivity data above room temperature are reported.

Previous work on the Ag_2Te - In_2Te_3 system consists of crystal structure determinations on various compositions by Hahn (1). No attempt was made to interpret the pseudobinary phase diagram or suggest the existence of a congruently melting compound at 25 mole % Ag_2Te -75 mole % In_2Te_3 (AgIn_3Te_5). Electrical measurements have been reported on the composition 50 mole % Ag_2Te_3 -50 mole % In_2Te_3 (AgInTe_2) by Austin *et al.* (2) and Zhuze *et al.* (3).

In the present work, differential thermal analysis measurements were made on seven compositions within the Ag_2Te - In_2Te_3 pseudobinary phase diagram. These results led to zone refining experiments which separated a congruently melting compound from the composition 30 mole % Ag_2Te -70 mole % In_2Te_3 . Chemical analysis showed the separated compound to be 25 mole % Ag_2Te -75 mole % In_2Te_3 , AgIn_3Te_5 , which has a melting point of $699^\circ \pm 3^\circ\text{C}$. Microscopic examination of zone refined and cast samples of AgIn_3Te_5 showed this composition to be single phase. Denning (4) reported the crystal structure of AgIn_3Te_5 to be either diamond ($\text{Fd}3\text{m}$) or sphalerite ($\text{F}43\text{m}$) with a lattice parameter of $a_0 = 6.2476 (\pm 0.001) \text{ \AA}$.

A density calculation, using Mooser-Pearson rules and assuming that the tellurium forms a close-packed lattice, shows that the material contains 27 ± 1 mole % Ag_2Te and 73 ± 1 mole % In_2Te_3 .

Experimental Procedures

The compound was prepared by fusing stoichiometric quantities of the elements (99.999% purity indium and tellurium, and 99.99% purity silver) in sealed quartz tubes (5) which were evacuated to a pressure of 5×10^{-5} mm Hg. After fusion, the compound was zone refined for one to six passes at $\frac{3}{4}$ in./hr. All samples were examined microscopically at 400X magnification to verify that they were homogeneous. The thermal conductivity sample was prepared by slowly freezing a sample of zone refined material.

The apparatus used for the electrical conductivity, σ , and Hall coefficient, R_H , measurements with direct current and a magnetic field of 2100 gauss, is described by LaBotz *et al.* (6). Ohmic electrical contacts were made to the sample by fusing hot platinum wires to the surface. The Seebeck coefficient was measured in the same apparatus prior to taking each σ and R_H reading in a hydrogen atmosphere.

to be estimated from the slope. The values are substantially identical with those obtained from the conductivity measurements and are listed in Table I.

The Seebeck data provide an indication of the temperature at which the intrinsic region begins and the relative purity of the samples. Seebeck coefficient data in Fig. 2 for sample number 735, the only sample not zone refined, show a change from p-type to n-type near 150°C. The decrease in Seebeck coefficient in the intrinsic range followed by a gradual rise near 425°C is similar to that observed on the two zone refined samples.

The Seebeck data are plotted against reciprocal absolute temperature in Fig. 4. The slopes of the data for 217 (1), 238 (1C), and 238 (4A) are linear in the approximate ranges of 250°-440°C and 500°-640°C. The slope in the high temperature range is about four times higher. These data were fitted to the relationship (8) $\alpha = (m/T) + c$, which permits the calculation of the electron-to-hole mobility ratio, b , from

$$m = -\frac{k}{q} \left(\frac{b-1}{b+1} \right) (E_{go}/2k) \quad [1]$$

where k is the Boltzmann constant and q is the electronic charge. This assumes that the spherical energy band approximation is valid and that lattice scattering predominates. Since the fit of the Seebeck data to the equation appears to be good, this model may apply in the low temperature range for AgIn_3Te_5 . The model is only valid for a two-band semiconductor in the intrinsic region.

Using the energy gap of 1.1 eV obtained from electrical measurements, the mobility ratios are 6.1 and 7.2 for samples 217 (1) and 238 (4A), respectively, in the temperature range below 440°C. These results are shown in Table I. The temperature dependence of the energy gap, a , was calculated from the equation (8)

$$c = -\frac{k}{q} \left[\left(\frac{b-1}{b+1} \right) \left(\frac{a}{2k} + 2 \right) + \frac{3}{4} \ln(m_n^*/m_p^*) \right] \quad [2]$$

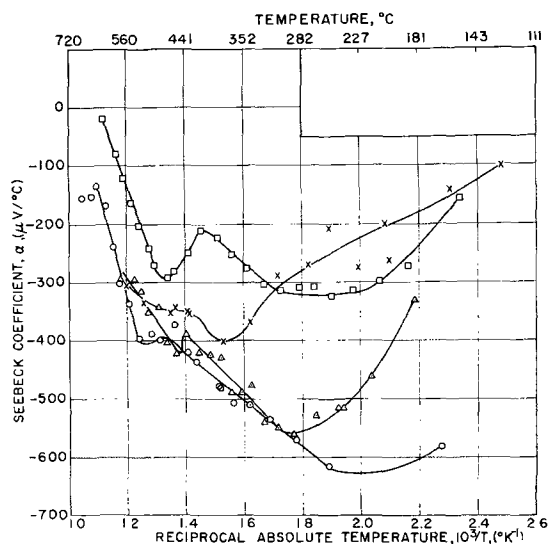


Fig. 4. Seebeck coefficient vs. reciprocal absolute temperature for AgIn_3Te_5 . AgIn_3Te_5 : Circle with dot, No. 217 (1); X, No. 217 (2) first heating cycle; triangle with dot, No. 238 (1C); box with dot, No. 238 (4A).

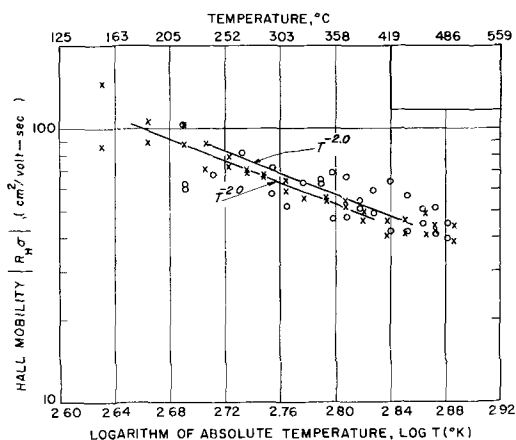


Fig. 5. Logarithm of Hall mobility $|R_H\sigma|$ vs. logarithm of absolute temperature for AgIn_3Te_5 . AgIn_3Te_5 : O, No. 238 (1C); X, No. 238 (4A).

where m_n^* and m_p^* are the effective masses of the electrons and holes, respectively.

Using the α vs. $10^3/T$ data below 440°C, values of $a = -6 \times 10^{-4}$ eV/°K and $a = -1.3 \times 10^{-3}$ eV/°K were obtained for 217 (1) and 238 (4A), respectively. This assumes the mobility ratio is proportional to $(m_p^*/m_n^*)^{5/2}$. The slope of α vs. $10^3/T$ in the high temperature region above 500°C gives a negative mobility ratio which implies that the theory does not hold.

In the temperature region where the material shows intrinsic behavior the following relationship is valid.

$$R_{H,i}\sigma_i = \beta(\mu_n - \mu_p) \quad [3]$$

where β is the ratio of the Hall mobility to the drift mobility. These data are plotted in Fig. 5 and show a temperature dependence of $T^{-2.0}$ for the two samples. The temperature ranges used were 244°-440°C for 238 (1C) and 189°-389°C for 238 (4A). Extrapolation of the mobility data back to 300°K results in a value of 250 $\text{cm}^2/\text{v-sec}$ for the $R_{H,i}\sigma_i$ product. When a value of $3\pi/8$ for β is used with the average mobility ratio of 6.6 obtained above, it follows directly that the electron mobility at room temperature is 250 $\text{cm}^2/\text{v-sec}$ and the corresponding hole mobility is 38 $\text{cm}^2/\text{v-sec}$.

Thermoelectric Properties

The thermal conductivity of AgIn_3Te_5 is shown in Fig. 6 for ingot number 206. Between 0° and 70°C,

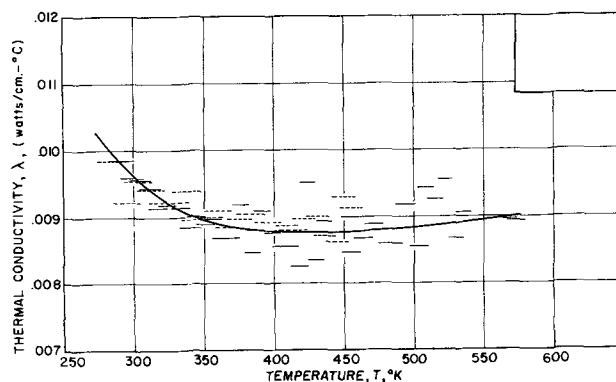


Fig. 6. Thermal conductivity vs. absolute temperature for AgIn_3Te_5 . AgIn_3Te_5 : No. 206, - - - run No. 1; — run No. 2.

the thermal conductivity decreases from 0.010 to 0.009 w/cm°C and then remains constant up to 300°C. The electrical conductivity and Hall coefficient data in Fig. 1 and 3 suggest that the intrinsic conduction region begins above 300°C in this ingot. The maximum contribution from the electronic component of thermal conductivity will occur at 300°C where the electrical conductivity is a maximum over the temperature range in which thermal conductivity measurements were made.

The carrier component of the thermal conductivity is the sum of the Wiedemann-Franz contribution, $2(k/q)^2 \sigma T$, and the ambipolar contribution (9), $4(k/q)T[(\sigma_+ \sigma_-)/(\sigma_+ + \sigma_-)] [(E_g/2kT) + 2]^2$, where σ_+ is the hole component of the electrical conductivity and σ_- is the electron component of the electrical conductivity. At 300°C, the Wiedemann-Franz contribution is equal to 5×10^{-7} w/cm°C, and the ambipolar contribution is equal to 1×10^{-5} w/cm°C. These are considerably less than the total thermal conductivity of 9×10^{-3} w/cm°C.

The thermoelectric figure of merit, Z , can be estimated from the thermal conductivity of sample number 206 and the σ and α data on sample number 217. The latter sample has the highest Seebeck coefficient and should provide a rough estimate of Z . Any difference in thermal conductivity between numbers 206 and 217 would be expected to result from the electronic contribution which is small compared to the total at 300°C.

Using σ equal to 0.01 mho/cm, α equal to $-600 \mu\text{V}/^\circ\text{C}$, and λ equal to 0.009 w/cm°C, the thermoelectric figure of merit, $Z = \alpha^2 \sigma / \lambda$, of AgIn_3Te_5 is $4.0 \times 10^{-7}/^\circ\text{K}$ and ZT is equal to 1.8×10^{-4} at 450°K. It is not possible to calculate an optimum figure of merit, Z_{max} , from Simon's paper (10) because the dimensionless parameters obtained from the data on AgIn_3Te_5 result in a value which is beyond the limits of the graphs provided. There is little doubt that the figure of merit for AgIn_3Te_5 is low, especially since the mobility is low.

Discussion

The variation in energy gap found between the cast sample and the zone refined samples of AgIn_3Te_5 may be attributable to the characteristics of the pseudobinary phase diagram of $\text{Ag}_2\text{Te}-\text{In}_2\text{Te}_3$ in the vicinity of 25 mole % Ag_2Te -75 mole % In_2Te_3 . The extent of the solubility region for the compound AgIn_3Te_5 is unknown.

AgIn_3Te_5 can be considered as In_2Te_3 with 1/10 of the indium atoms replaced by silver atoms; three silver atoms replace each indium atom. The diamond or sphalerite structure (4) reported for AgIn_3Te_5 with 1/5 of the metal sites vacant is only slightly different from the zinc blende or antiferite structures claimed for In_2Te_3 (11), with 1/3 of the metal sites vacant.

The effect of introducing silver into the vacant sites of the In_2Te_3 lattice and the replacement of some indium atoms can be seen by comparing the electrical properties of AgIn_3Te_5 with ordered In_2Te_3 . With an energy gap of 1.1 eV for AgIn_3Te_5 , there is no significant difference from the value of

1.12 eV reported by Zhuze *et al.* (12) for ordered In_2Te_3 and 1.02 given by Gasson *et al.* (13). The mobility of AgIn_3Te_5 , which was measured as 120 $\text{cm}^2/\text{v-sec}$ at 155°C and extrapolated to a value of 250 $\text{cm}^2/\text{v-sec}$ at 300°K, is higher than the 5 $\text{cm}^2/\text{v-sec}$ to 70 $\text{cm}^2/\text{v-sec}$ for In_2Te_3 (12) at room temperature. Also, the mobility of AgIn_3Te_5 has a temperature dependence of $T^{-2.0}$, whereas Zhuze (12) reports that the mobility of In_2Te_3 is independent of temperature between about 50° and 350°C.

The thermal conductivity of AgIn_3Te_5 , 0.009 w/cm°C, is essentially the same as that of ordered In_2Te_3 , 0.011 w/cm°C, reported by Zaslavskii (14). However, Gasson *et al.* (13) have reported the thermal conductivity of In_2Te_3 as 0.008 w/cm°C whereas Wooley and Pamplin (15) have reported a value of 0.014 w/cm°C. These values are indicative that more definitive work remains to be done on In_2Te_3 as discussed by O'Kane and Mason (16).

Acknowledgments

The authors wish to express their appreciation for assistance given by Messrs. P. W. Chiang, E. K. Parrott, and P. H. Smith. Contribution No. 15 from the Semiconductor Materials Research Laboratory, The College of Engineering, The University of Michigan, Ann Arbor, Mich. This work has been supported by Texas Instruments, Inc., Dallas, Texas.

Manuscript received May 14, 1963; revised manuscript received Nov. 15, 1963. This paper was presented at the Pittsburgh Meeting, April 15-18, 1963.

Any discussion of this paper will appear in a Discussion Section to be published in the December 1964 JOURNAL.

REFERENCES

- H. Hahn, G. Frank, W. Klingler, A. D. Meyer, and G. Storger, *Z. anorg. u. allgem. Chem.*, **271**, 153 (1953).
- I. Austin, C. Goodman, and A. Pengelly, *This Journal*, **103**, 609 (1956).
- V. P. Zhuze, V. M. Sergeeva, and E. L. Shtrum, *Soviet Physics-Technical Physics*, **3**, 1925 (1958).
- R. M. Denning, Private communication to D. R. Mason.
- N. L. Hozak, J. S. Cook, and D. R. Mason, *This Journal*, **103**, 105 (1961).
- R. J. LaBotz, D. R. Mason, and D. F. O'Kane, *ibid.*, **110**, 127 (1963).
- R. J. LaBotz and D. R. Mason, *ibid.*, **110**, 121 (1963).
- V. A. Johnson and K. Lark-Horovitz, *Phys Rev.*, **92**, 226-232 (1953).
- A. F. Ioffe, "Physics of Semiconductors," p. 284, Academic Press (1960).
- R. Simon, Symposium on Thermoelectric Power Conversion, Dallas, Texas (January 1961). Preprint obtained from Battelle Memorial Institute, Columbus, Ohio.
- J. C. Woolley, B. R. Pamplin, and P. J. Holmes, *J. Less Common Metals*, **1**, 362 (1959).
- V. P. Zhuze, V. M. Sergeeva, and A. I. Shelykh, *Soviet Physics—Solid State*, **2**, 2545 (1961).
- D. B. Gasson, P. J. Holmes, I. C. Jennings, J. E. Parrot, and A. W. Penn, *Proc. of the International Conference on Semiconductor Physics, Prague, 1960*, p. 1032, Czechoslovak Academy of Sciences, Prague (1961).
- A. I. Zaslavskii, V. M. Sergeeva, and I. A. Smirnov, *Soviet Physics—Solid State*, **2**, 2565 (1961).
- J. C. Woolley and B. R. Pamplin, *This Journal*, **108**, 874 (1961).
- D. F. O'Kane and D. R. Mason, *ibid.*, **110**, 1132 (1963).

Epitaxial Deposition of Silicon Layers by Pyrolysis of Silane

S. E. Mayer and D. E. Shea

Trancoa Chemical Corporation, Reading, Massachusetts

ABSTRACT

The pyrolysis of silane diluted by a carrier gas in a horizontal-type system is described. Films of closely controlled thickness have been obtained. Control of the electrical resistivity of the films by admixture of suitable dopants is shown. The effect of various process parameters on growth rate is discussed. Experimental data on migration of dopant from the substrate to the grown layer are presented, and the mechanism involved is discussed. Some characteristics of devices using such layers are shown.

The pyrolysis of silane has been one of the methods used for the preparation of high-purity silicon from the very beginning (1). When epitaxial growth became of interest, it was naturally one of the methods that suggested itself. In considering the differences between such a pyrolysis and the hydrogen reduction of a halide, first of all it is obviously of interest to consider the basic thermodynamics of the reaction.

The first point to be noted in this connection is that silane is always prepared by some indirect reaction; most simply, as in our case, by reaction of hydride ion either in ether or salt solution with the halide or, alternatively, by action of acid on certain silicides or by direct reaction of silicon and hydrogen with aluminum. In each of these cases, large heats of reaction are involved which completely overshadow the heat of formation of silane. No reliable information on its magnitude can, therefore, be obtained in this way, nor for that matter, even on its sign as the reactions are complex with evidently very different rates for the various component reactions. Hence, no conclusions can be drawn on the stability of any of the substances involved.

The study of the decomposition is also ambiguous as the heat of decomposition is very small compared with many possible side reactions with oxidizing

substances so that even a small amount of side reaction will appreciably affect the results. The most reliable value of $\Delta H = 7.3$ kcal (2) leads to a ΔH curve as shown in Fig. 1 and a ΔF curve as shown in Fig. 2. It means that the material is unstable even at low temperatures and that the well-known fact that silane can be stored indefinitely at room temperature and for long periods of time at temperatures as high as 450°C is due to low reaction rates; even though the equilibrium is very strongly towards complete decomposition.

We can, therefore, conclude that at the temperatures of interest here, the decomposition rates and growth rates will be determined by kinetic considerations only. In this connection it has been shown that the decomposition of many related hydrides are strongly surface catalyzed (3). We find the same to be true for the silane-silicon system at the higher temperatures of interest here, although at lower temperatures the reaction has been reported as homogeneous (4). This fact is primarily responsible for the ability to confine decomposition to a silicon surface and so to avoid gas phase pyrolysis and unwanted deposition on parts of the equipment.

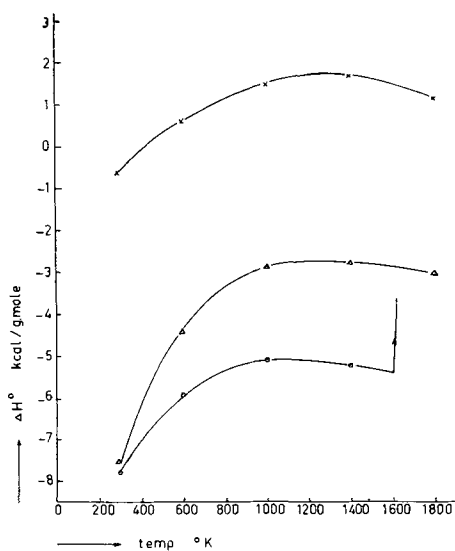


Fig. 1. Standard heat of decomposition vs. temperature. X, Phosphine (PH_3); O, silane (SiH_4); Δ , diborane (B_2H_6).

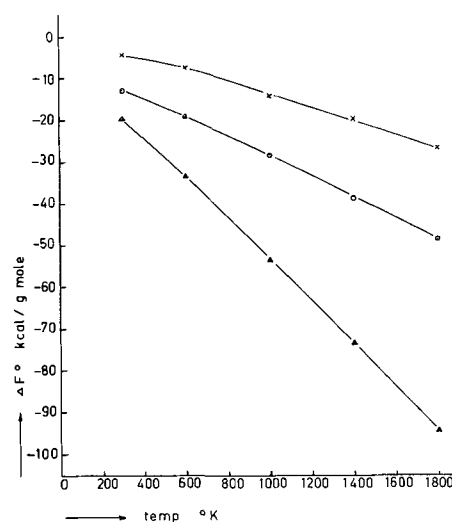
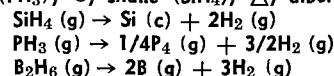


Fig. 2. Standard free energy of decomposition vs. temperature. X, Phosphine (PH_3); O, silane (SiH_4); Δ , diborane (B_2H_6).



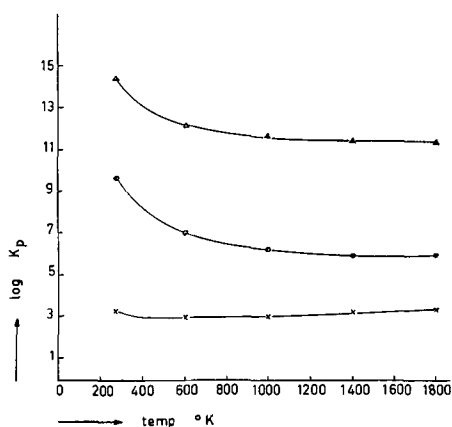


Fig. 3. Equilibrium constant of decomposition vs. temperature. X, Phosphine (PH_3); O, silane (SiH_4); Δ , diborane (B_2H_6).

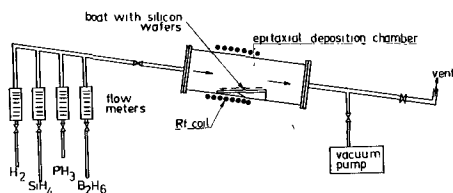


Fig. 4. Epitaxial deposition system. Reaction: $\text{SiH}_4 \rightarrow \text{Si} + 2\text{H}_2$

Another rather important consideration is to find substances for gas doping of which the thermodynamics are similar to those of the basic material. Among the rather obvious choices are phosphine and diborane. Plots of the thermodynamic data of these substances compared to silane as a function of temperature are shown in Fig. 1, 2, and 3. These data are based on room temperature requirement and the following calculated expressions for C_p as a function of temperature

$$\text{SiH}_4 \quad C_p = 1105 + 8.78 \times 10^{-3}T - 3.05 \times 10^5 T^{-2} \quad [1]$$

$$\text{PH}_3 \quad C_p = 9.11 + 5.72 \times 10^{-3}T - 1.71 \times 10^5 T^{-2} \quad [2]$$

$$\text{B}_2\text{H}_6 \quad C_p = 13.68 + 18.60 \times 10^{-3}T - 5.37 \times 10^5 T^{-2} \quad [3]$$

It will be seen that the requirement of similar thermodynamic properties is fulfilled reasonably well. It still remains to be seen, of course, whether the kinetics are sufficiently similar to make these particular materials usable for reliable doping.

Experimental Technique for Deposition

The growth of films was carried out in the equipment shown in Fig. 4. Pure silane was stored at 200 psi and used as such. Electrolytic hydrogen was further purified by passage through a deoxo palladium catalyst followed by a molecular sieve trap cooled with liquid nitrogen and then passed through a cellulose filter to remove dust from the molecular sieve. Dopants were made up with prepurified hydrogen and used without further treatment. The whole of the gas supply system was constructed of stainless steel heliarc welded. Small-bore tubing was used in a spiral immediately in front of the furnace and experience has shown that adequate mixing of the feed gases was obtained at all times. The deposition tubes were air-cooled on the outside—experiments with water cooling having shown that

the growth conditions are not changed thereby to any significant extent.

As a slice carrier, slabs of fine-grained deposited silicon were used; these were generally about 6 in. long by $2\frac{1}{2}$ in. wide by $\frac{1}{2}$ in. thick. The slabs were of high resistivity and could not be R.F. heated at the frequency used (450 kc) from cold. A small low-resistivity antimony-doped slug was therefore used at the exit end. Once the system was heated, the starting slug was at a lower temperature than the top surface of the carrier so that evaporation was very small and system contamination was minor. On high resistivity substrates, layers of over 25 ohm-cm could be obtained with ease. Carriers were initially used in the etched condition and re-etched periodically.

The wafers used in this work were electropolished and cleaned by conventional methods, the last operation being a hydrofluoric acid dip followed by water and solvent washing.

Prior to deposition, wafers were preheated in hydrogen (after the system was thoroughly flushed), silane and dopants required were then admitted for the necessary time. Cooling again took place in hydrogen. As far as the obtaining of structurally perfect films was concerned, a very short preheating time of only some minutes was required to remove residual oxide films. However, the preheating cycle was varied from time to time as it has a marked effect on system doping as will be seen.

Control of Deposition Rate

The basic parameters involved here are time, temperature, gas composition, gas flow rate, and system geometry. We will discuss their various effects in this order.

Time.—The deposition rate is found to be quite constant with time as shown in Fig. 5. No induction period has ever been observed.

Temperature.—Figure 6 shows the deposition rate as a function of temperature for two gas-flow conditions. Wafer temperatures are measured optically

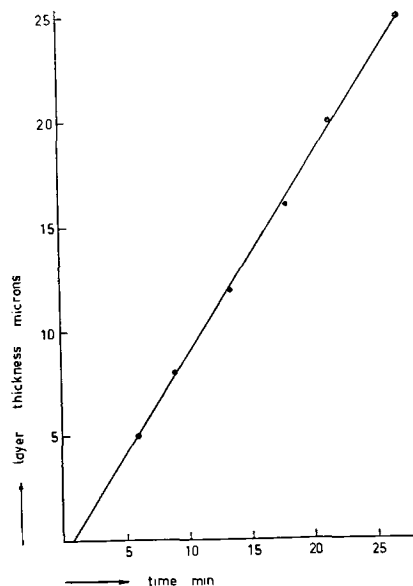


Fig. 5. Layer thickness vs. time. Hydrogen flow 15 liter/min, silane flow 33 cc/min, temperature 1220°C .

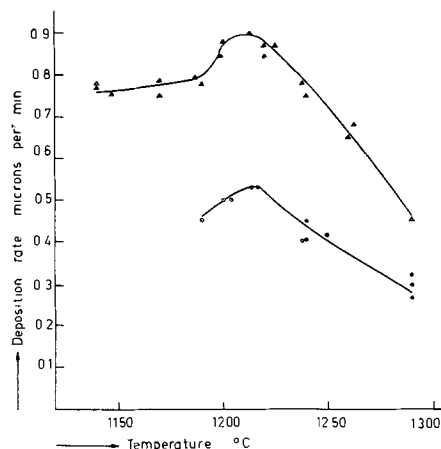


Fig. 6. Deposition rate vs. temperature. Δ , SiH_4 33 cc/min, H_2 13 liters/min; \circ , SiH_4 19 cc/min, H_2 17 liters/min.

and then corrected for emissivity. Of particular note, of course, is the temperature peak shown at 1210°C . It is interesting to note that Li (8) and also Joyce (9) found a peak in deposition rate at essentially the same temperature in using the hydrogen reduction of trichlorosilane.

In view of what we have concluded before about the essentially surface catalytically controlled nature of the silane cracking process, we conclude that the rather rapid departure from the Arrhenius plot has something to do with a rapid change in the nature of the surface, very possibly a reduction of the number of available surface sites, due to the presence of silicon vapor near the surface. In this connection, it has been observed that the perfection of the layers as determined by conformity of electrical characteristics of diodes to theory deteriorates very rapidly once deposition temperatures of 1210° to 1220°C are exceeded.

Gas composition.—Figure 7 shows growth rate vs. hydrogen-silane ratio at a temperature of 1220°C . Plots at other temperatures are similar. It can be seen that over a wide range of conditions, a gradual change of rate occurs.

Gas flow rate.—Deposition rates depend on flow rates as shown in Fig. 8. For a given hydrogen-silane ratio, the rates level off above a certain figure, in general the rate being higher for greater dilution.

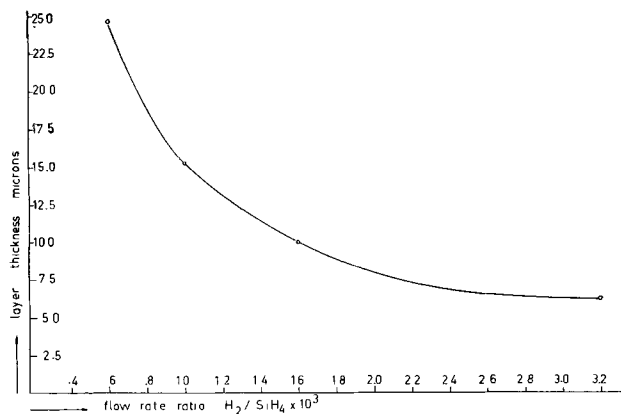


Fig. 7. Hydrogen-silane ratio vs. layer thickness. Conditions: hydrogen flow 15 liters/min, time 45 min, temperature 1220°C .

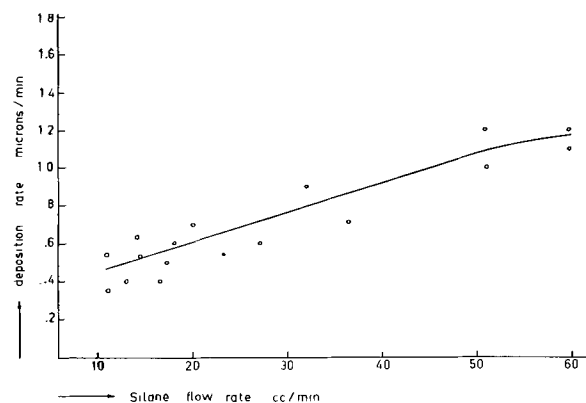


Fig. 8. Deposition rate vs. SiH_4 flow rate. Hydrogen/silane ratio 500:1, temperature 1220°C .

Gas flow rates practically do not affect the distribution of deposition rates at all in small systems, as long as some circulation is present. As soon as systems become larger, it is found that with low flow rates, the deposition decreases along a boat. Gradual increases of flow rate will even out these conditions. However, an excessive increase in flow rate is undesirable as it is found to increase dendrite formation. It has been established that the reason for this is the settling of minute amounts of dust from gas phase decomposition on the wafers. Under conditions of moderate flow, much dust settles on the cold parts of the equipment and, in any case, appears to be formed to a much lesser extent. Gas flow rates are, therefore, increased to only a moderate extent, the maximum gas speed being about 100 cm/sec. Further evening out of deposition rates is achieved by suitable modification of the system geometry.

There is an advantage in high deposition rates in that it cuts down substrate doping as will be seen. It is, therefore, desirable to aim for a geometry that will allow relatively high gas speeds without dendritic growth appearing.

System geometry.—We have confined ourselves essentially to horizontal systems, the reasoning being that in such a system it is easier to arrange comparable conditions for a large number of wafers than in a vertical system. For the gas flow rates used in this work, less than 50 liters/min through a 65 mm tube, the Reynolds number is so small (of the order of 50) that stream line flow is to be expected. On the other hand, due to the temperature differences in the gas stream, considerable convection at right angles to the direction of flow will take place. This circulation at right angles to the flow direction is very desirable to insure comparable conditions as far as gas in direct contact with the wafers is concerned along the length of a long carrier. Such circulation is assisted by departing somewhat from the horizontal position. Figure 9 shows the thickness for wafers in a typical run for the two conditions. It can be seen that the tilted arrangement has flattened out gradients very considerably. The slight dip in growth rate in the center of the carrier does not appear to be due to an area effect in the sense that it still persists if large areas in this vicinity are masked by oxidation, but is probably due to thermal effects in the gas layer.

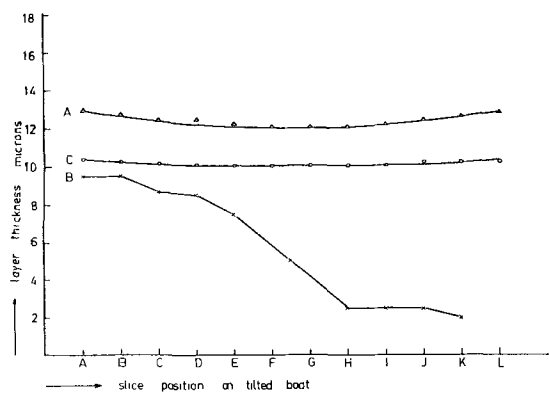


Fig. 9. Layer thickness vs. slice position on tilted (A and C) and horizontal (B) boat. Conditions: temperature 1220°C, H₂ 18 liters/min; SiH₄ 38 cc/min; thickness measurements by infrared.

Temperatures on the carrier are uniform within better than ±5°C. It has also been found that changes in the size of the carrier, either in length or cross section, do affect deposition rates somewhat. However, the effects are minor; changes in rate being of the order of 10-15%. Study of dust-flow patterns in the tubes has shown that, once again, this is largely a flow-pattern effect.

Changes in tube size have similar effects, but in this case, not only the flow pattern but also the temperature gradients across the gas stream are affected and changes are correspondingly larger.

The number of slices present on a boat has no effect on deposition rate as long as the temperature is kept constant.

As might be expected from the layer thickness distribution of wafers within a given run, the distribution of thickness within a wafer is very close indeed as shown in Fig. 10. These measurements were taken by angle sectioning and staining, and the only thing that can be concluded is that the control is well within the accuracy of the measurement.

Resistivity Control

High-resistivity substrates.—The most straightforward situation as far as doping layers is concerned occurs where substrates of sufficiently high resistivity are used such that no contribution of dopant from the substrate is to be expected. In this case, measurement by conventional four-point probe techniques is possible. This is done most easily when the substrate is of the opposite type to that of the deposited layer in which case no correction is neces-

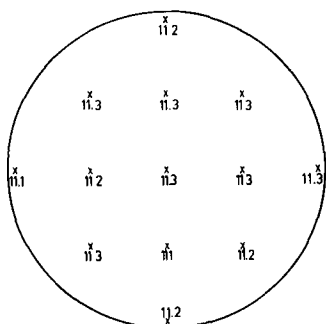


Fig. 10. Layer thickness (microns) vs. position on slice. Growth rate 0.8 μ/min.

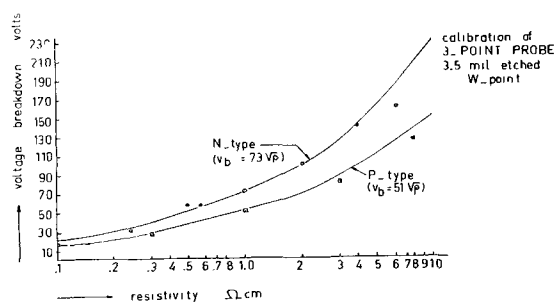


Fig. 11. Resistivity vs. atoms per million PH₃ in SiH₄, furnace No. 1, batch No. 28. Substrate 200 ohm-cm p-type, gas flow rate, 15 liters/min, H₂-SiH₄ ratio 500:1, temperature, 1220°C.

sary; less easily, but still quite reliably, when the layers are of the same type and a correction has to be made.

Figure 11 shows such a plot for N-type layers on high-resistivity (200 ohm-cm) P-type for a typical set of growing conditions. It has been found that the extent of these doping effects is temperature-dependent in the sense that at higher temperatures, less dopant is introduced into the film, particularly in the case of phosphorus. In any case, the amounts of dopant introduced are far less than the ratio present in the gas phase (by a factor of the order of 10³). It is believed that this is related to evaporation from the surface. A further indication in this direction is obtained from the fact that the deposits on cold parts of the apparatus, particularly towards the exit end, contain much larger amounts of doping elements than the epitaxial layers.

Low-resistivity substrates.—*Method of resistivity measurement.*—For the measurement of resistivity of layers on low-resistivity substrates of the same type, the measurement of breakdown of surface point contact diodes due to Brownson (10) has been chosen. Calibration plots for N and P layers using a chemically etched 3.5 mil whisker are shown in Fig. 12.

In order to obtain surfaces similar to those to be measured, N layers on P substrates previously measured by four-point probe measurement were used for calibration. The slices were treated with hydrofluoric acid just before measurement and carefully

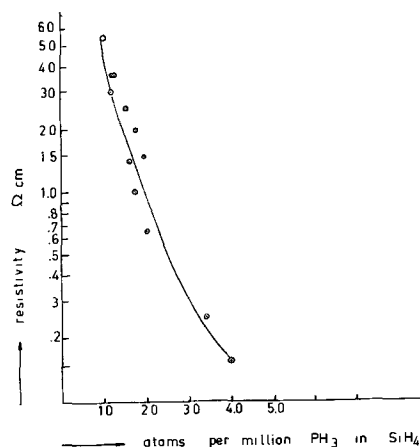


Fig. 12. Resistivity vs. voltage break down. O, Actual measurements on N-type, $v_b = 73 \sqrt{\rho}$; □, actual measurements on P-type, $v_b = 51 \sqrt{\rho}$.

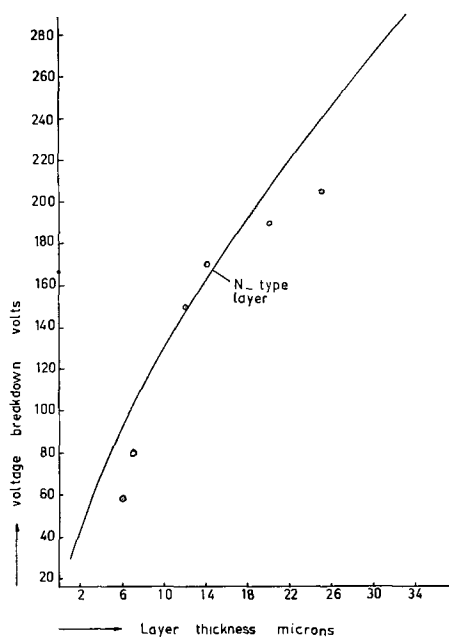


Fig. 13. Silicon epitaxial layer thickness vs. theoretical maximum voltage breakdown. O, Measured points on N-type. $W_B = [2E\rho\mu v_B]^{1/2}$.

dried after washing with water and solvents. It was found that normal slices could not be used for calibration, evidently because the polishing procedure was not readily usable on high-resistivity slices and the surfaces were, therefore, not perfect enough for this type of measurement. If the layer thickness is greater than the depletion layer width, the breakdown measured on a deposited layer will be a direct measurement of resistivity. Figure 13 shows plots for maximum surface breakdown voltages obtainable as a function of layer thickness for typical approximate formulas for N-type diodes. The maximum voltages actually obtained for various thicknesses for such diodes is also indicated and it can be seen that agreement with theory is quite good.

If the layers contain gradients in the sense that resistivities near the substrate are lower than on the surface, this implies that the measured resistivity is lower than the true surface reading and also that the depletion layer will not penetrate to the interface.

Gradients in layers have been determined by using the same technique on angle sections.

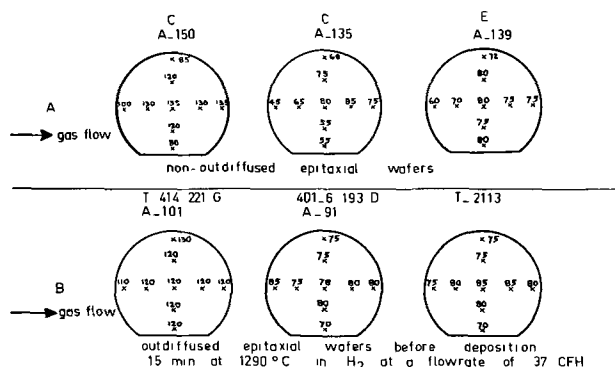


Fig. 14. Surface breakdown voltage of point contact diodes on wafers with different pretreatment (by 3-point probe).

Experiments on resistivity control.—Figure 14 shows a typical plot obtained by surface measurement of wafers deposited on with only a brief hydrogen prefire. It can be seen that the breakdown voltages are lowest around the edges of the slices and also that there is a marked gradient in the direction of gas flow. This effect could be a geometric one or it could be a flow effect. In order to answer this question, a similar run was carried out after outdiffusing the wafers for a time at a temperature considerably higher than the deposition temperature. In this case, the edge effect has virtually been eliminated and the flow effect is no longer observable. It is observed that these effects are minimized by high deposition rates. As has been pointed out before, however, deposition rates are limited by considerations relating to layer perfection. Even before dendrites appear, the perfection of the layers, as judged by electrical measurements on diodes, is adversely affected.

In order to gain some further insight into the mechanism involved in dopant transfer, sections were taken through a number of typical slices.

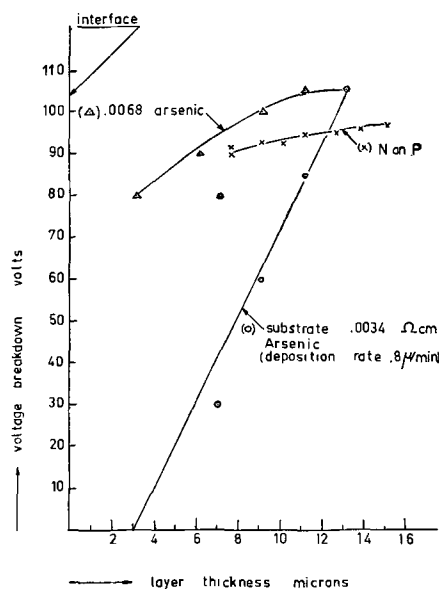


Fig. 15. Voltage breakdown vs. epitaxial layer thickness

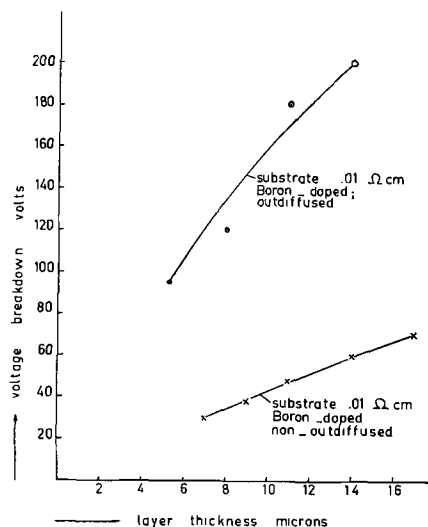


Fig. 16. Voltage breakdown vs. layer thickness, P-type

Figure 15 shows such sections for layers of nominally the same resistivity deposited on different substrates, in each case without outdiffusion. It is evident that the substrate-doping effect depends on layer thickness in an almost linear manner, the slope of the curve depending on the doping level in the substrates. The doping effects in layers deposited on boron-doped substrates are very similar as shown in Fig. 16. Other findings are:

1. The effect is somewhat less marked in antimony doped substrates than arsenic-doped ones of the same resistivity.

2. Masking of the back surface by formation of an oxide film does not inhibit the effect to any marked extent.

3. Masking by pre-depositing high resistivity silicon on the back of the wafer very considerably cuts down the doping effect on the front.

Discussion of Mechanism Involved

As has been shown in this system, the decomposition reactions both for silicon and dopant are irreversible. The only possible mechanisms of dopant transfer are, therefore, evaporation with outdiffusion, surface diffusion coupled with outdiffusion, and bulk diffusion. Bulk diffusion has been studied by various workers (11) and, while it accounts for the doping profile near the interface (which we have not studied here in detail), it cannot account for the profiles in the main part of the layer.

A decision between the two other possible mechanisms cannot be arrived at easily. From the experiments cited above, it is clear that the back surface of the wafers plays an important part, particularly in view of the observed edge effects. The fact that masking by oxidation does not eliminate these effects but silicon masking does, is not conclusive as oxide at the relatively high temperatures involved here is known not to be an effective barrier to the interchange between silicon and the gas phase.

We have no quantitative data on the surface-diffusion coefficients on silicon at this time. Sufficiently large diffusion coefficients to account for the observed effects, however, might be expected from the bulk diffusion coefficients having regard to the usual ratio of bulk to surface diffusion coefficients.

Whichever of the two mechanisms is responsible has, however, to account for the falling off of the doping levels with time and layer thickness. We would suggest, tentatively, that this may be due to the gradual silicon masking taking place around the edges where small amounts of silicon are deposited. If this is correct, it would indicate that surface diffusion is at least partly responsible. Such edge masking, while it could be expected to cut down surface diffusion, did not similarly cut down evaporation from the back surface.

Diode Characteristics

The making of diffused diodes on epitaxial layers has gradually become the final criterion for judging the perfection of epitaxial layers. The measurement of some of the properties of such diodes, such as peak inverse voltage, only confirms information on

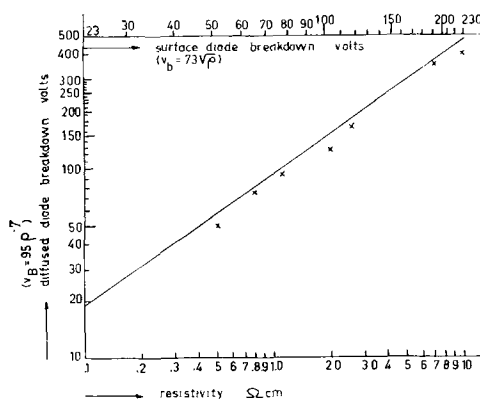


Fig. 17. Voltage vs. resistivity for shallow diffused diodes on epitaxial wafers. X, Actual measured points.

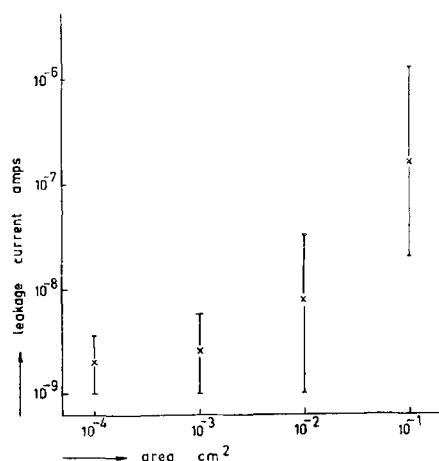


Fig. 18. Leakage current of diffused diodes. C_0 , 2×10^{19} boron; ρ_N , 6 ohm-cm; depth 6μ ; leakage measured at 100v.

resistivity and resistivity gradients which usually already has been obtained by nondestructive methods. The leakage currents of diodes of various sizes, on the other hand, give a good indication of the number and distribution of any defects that may be present. In addition, measurement of forward characteristics and pulse recovery may be used as an indication of life-time.

First of all, to consider reverse characteristics, Fig. 17 shows a plot of peak inverse voltage vs. resistivity for N-type films. The drawn curve is that due to McKay (12) for step junctions which can be expressed as $V_B = 95\rho^{0.7}$ for the resistivity range of interest. The measured points indicate actual results obtained on various layers and it can be seen that the agreement is quite reasonable. It is also clear that if either the diffusions are sufficiently shallow to approach step junctions or, alternatively, allowance is made for gradient (13), a more precise measurement of resistivity is obtained than by the three-point probe method as the voltage breakdown depends to a greater extent on resistivity in the range considered here. Also, premature breakdown due to surface effects is much less likely than with the three-point probe.

Figure 18 shows the mean leakage current and spread thereof for diodes of various sizes made from a typical slice. It can be seen that there is a very definite size effect, no doubt due to the presence of defects in the layers.

We have no quantitative data on lifetime at this time. However, indications are that greater perfection, as measured by reverse characteristics, goes together with higher lifetime.

Further progress in this field will mainly have to be directed toward the elimination of defects so as to make epitaxial deposition (now that adequate thickness and resistivity control have been obtained) usable for the manufacture of large-area devices.

REFERENCES

1. J. M. Wilson, *Research*, **10**, 166 (1957).
2. S. R. Gunn, *J. Phys. Chem.*, **65**, 779 (1961).

3. H. Taylor, *Can. J. Chem.*, **33**, 838 (1955).
4. T. R. Hogness, T. L. Wilson, and W. C. Johnson, *J. Am. Chem. Soc.*, **58**, 108 (1956).
4. Altschuller, *J. Phys. Chem.*, **23**, 761 (1955).
6. Altschuller, *J. Am. Chem. Soc.*, **77**, 4220 (1955).
7. Webb, Men, and Pitzer, *J. Phys. Chem.*, **17**, 1007 (1949).
8. C. H. Li, *This Journal*, **109**, 952 (1962).
9. J. M. Charig and B. A. Joyce, *ibid.*, **109**, 957 (1962).
10. J. Brownson, Electrochem. Soc. Meeting, Los Angeles, May 1962.
11. D. Kahag, C. O. Thomas, and R. C. Manz, *This Journal*, **109**, 1106 (1962).
12. K. G. McKay, *Phys. Rev.*, **94**, 877-884 (1954).
13. C. D. Root, D. P. Lieb, and B. Jackson, *IRE Trans. Electron Devices*, **7**, 257-262 (1960).

1/f Noise in Thin Films of Semiconductors

K. M. Kiser

Research Laboratory, General Electric Company, Schenectady, New York

ABSTRACT

Measurements have been made of the 1/f noise produced by thin films of indium oxide on a gelatin substrate and of thin films of copper iodide on a polycarbonate substrate. Only the audiofrequency range was examined. For relatively small d-c currents the noise power for the indium oxide films is strictly $\propto f^{-1}$. This proportionality is preserved at the higher current levels but anomalies appear in these spectra. The noise power decreases slightly with temperature and increases somewhat when oxygen is removed. Moisture has little effect on the 1/f noise. In the case of the copper iodide films, the noise apparently has two components, a f^{-1} component detectable at low frequencies and high currents, and a single time constant component $\propto [1 + \omega^2\tau^2]^{-1}$ detectable at high frequencies and low currents.

Semiconductors, vacuum tubes, point contacts, and certain thin metal films, when biased by a d-c voltage, all exhibit a noise whose power spectrum, $E(f)$, varies inversely with the frequency, f , of the fluctuations. This noise, variously called "1/f noise," "excess noise," "flicker noise," or "current noise" depending on where it is observed, is commonly interpreted as a fluctuation in the conductivity of the material. The physical origin of 1/f noise, in spite of the large effort which has been devoted to its study, is still a matter of some dispute. There does not appear to be even general agreement as to whether it is a surface phenomenon (1, 2) or a bulk effect (3) except perhaps in the case of single-crystal semiconductors where the mechanism is thought to be one of surface trapping of current carriers (2, 4). Whatever the origin of 1/f noise, so far as has been determined experimentally, it extends over the whole range of frequencies; it has been observed from frequencies as low as 2.5×10^{-4} cps (5) up to the highest of frequencies where it becomes lost in the thermal noise.

Besides following an inverse frequency relationship, it has also been observed that the noise power, $E(f_1)$, where f_1 is any given frequency, increases with some power, usually the square, of the applied d-c current.

Working with platinum and tungsten, Bernamont (6) observed 1/f noise in thin vapor-deposited films. Though he realized that these films could not simply

be thin sheets of the parent metal, he was unable to account for the 1/f form of the noise power spectrum. More recently, Borel (7) made extensive measurements on thin films of silver and indium (resistance about 10^8 ohms/square) which, from electron microscopic examination he knew to have a discontinuous structure. He observed both the inverse frequency dependence and (at least for low currents) also the square law dependency of $E(f_1)$ on the mean current. Borel suggested that the particulate structure was the source of the 1/f noise.

It is the purpose of this paper to present some of the noise characteristics of thin indium oxide (In_2O_3) and copper iodide (CuI) films prepared on polymeric substrates by vapor deposition methods. Both materials are semiconductors and so may be expected to exhibit 1/f noise on this basis alone. The two films differ physically from each other, however. Whereas the CuI films are relatively thick and, so far as can be ascertained, continuous, the In_2O_3 films are apparently neither of these. Electron microscopic and electron diffraction examination suggest that the latter films consist of individual "islands" of conductor. If so, the observed noise may then be associated with an interparticle tunneling of conduction electrons just as is the case for the discontinuous metal films.

On the other hand, the resistance of these films is low, of the order of a few thousand ohms/square. This suggests that the In_2O_3 particles are really in-

terconnected in such a way as to form a two-dimensional network of conduction paths. Simple (bulk) semiconductor noise is obtainable from this structure, but it is possible that the spectrum will be more complex because of another noise generating process. Osman (8) has recently presented a case for 1/f noise from semiparticulate structures based on the idea of small volume contacts between particles with a conductor trapping process occurring at the constrictions. Thus $E(f)$ for the In_2O_3 films can have contributions from the bulk semiconductor, from the point contacts, and even from the discontinuities, just as in the discontinuous metal films. It seems probable that a two-dimensional structure is at least responsible for the high conductivity of these films even if it is not the main source of the 1/f noise.

Experimental Technique

Films of In_2O_3 were prepared by first vapor depositing indium metal on gelatin substrates and in the presence of small quantities of oxygen (oxygen pressures of $\approx 25\mu$). Subsequently these films were heated for 4 hr in air at 100°C . This, it has been observed, increases both the conductivity and the transparency of In_2O_3 films (9, 10). X-ray diffraction measurements of the final films showed them to be almost entirely In_2O_3 with only small quantities of indium metal remaining. They further showed that the In_2O_3 was present primarily in the form of many single crystals randomly oriented on the substrate. Some electron micrographs of the deposits substantiated this and also showed the films to have a particulate structure with the individual "islands" of material consisting essentially of at most a few crystals of In_2O_3 . One of these films is shown in Fig. 1. These films were all of the order of 100\AA to 150\AA thick.

The copper iodide film was obtained by iodiding metallic copper films which had been vapor deposited on Lexan¹ in the presence of oxygen (oxygen

¹ A General Electric trademark.

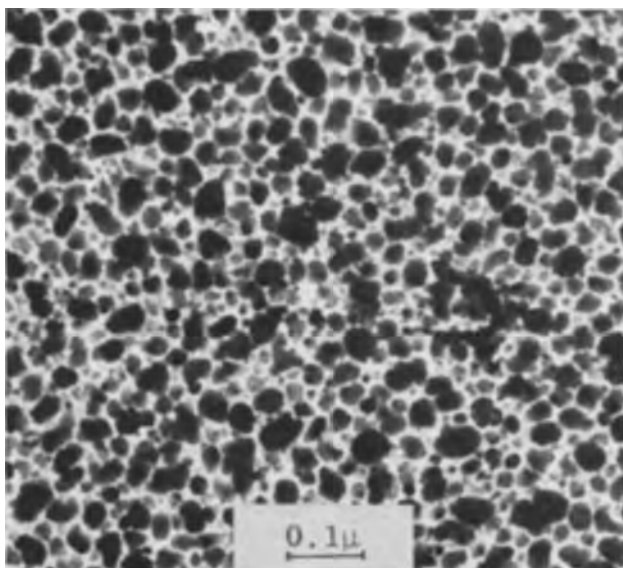


Fig. 1. Indium oxide on gelatin: 100-150Å. Magnification 100,000X.

pressure $\approx 30\mu$). Some of the properties of these films are discussed elsewhere (11). The structure of this film is not known nearly as well as that of the In_2O_3 films. Indirect measurements (light interference colors) place its thickness around 1000\AA , so it is reasonable to assume that it was a continuous film of polycrystalline material. Electron micrographs made of carbon replicates of this film would appear to support this assumption.

All noise measurements were made using the two-terminal method. While this arrangement is generally considered to be inferior to the four-terminal method, it was found to be more than adequate for present purposes. Each specimen tested was 1 cm long between terminals and 0.5 cm wide. The ends of the specimens were painted with silver to assure the best possible contact. In a few cases the silver point was omitted for comparison. Except for a more erratic behavior, however, no important difference in the noise power spectra was noted. Beyond this, the influence of the contacts on the observed noise was not determined.

A d-c bias voltage was applied to the film in series with a load resistance that could be varied so as to change the current passing through the film. The voltage drop across the film was amplified by a linear, low-noise, a-c amplifier, the output of which was fed to a 4-cps band pass wave analyzer. Only the audiofrequency range (20 to 16 kcps) was examined. The conductor and electrodes were enclosed in glass and the enclosure shock was mounted.

The background noise of the circuit was determined for each film by shorting the film, using a piece of metal, and also by substituting for the film a wire-wound resistor. $E(f) = 2.2 \times 10^{-14} \text{ v}^2\text{-sec}$ was observed for both cases. This background noise had a flat frequency spectrum and, except at the highest frequencies, was well below the 1/f noise level of the films. Corrections were made only at the higher frequencies.

Most of the measurements presented here pertain to the In_2O_3 films in room air (27°C and 25% relative humidity). For these, the noise measurements were made at several current levels at 27°C and for one current level, at temperatures ranging from 27° to -196°C . Measurements also were made on these films when they were placed in atmospheres of different gases.

In the case of the copper iodide film, only the first of the above-mentioned measurements were made.

Experimental Observations

The spectral density of the noise power, $E(f) \equiv \overline{e_r^2}/\Delta f$ is shown in Fig. 2 for one of the In_2O_3 films of thickness (nominal) 150\AA and in Fig. 3 for a copper iodide film about 1000\AA thick. $\overline{e_r^2}$ is the mean square value of the voltage fluctuation measured at the noise frequency, f , and contained in the interval Δf , where Δf is the pass band width of the wave analyzer.

The simple 1/f form for the spectra was obtained for all the In_2O_3 films examined so long as the d-c current was kept low. When currents in excess of about $10^3 \mu\text{amp}$ were used, the measured spectra

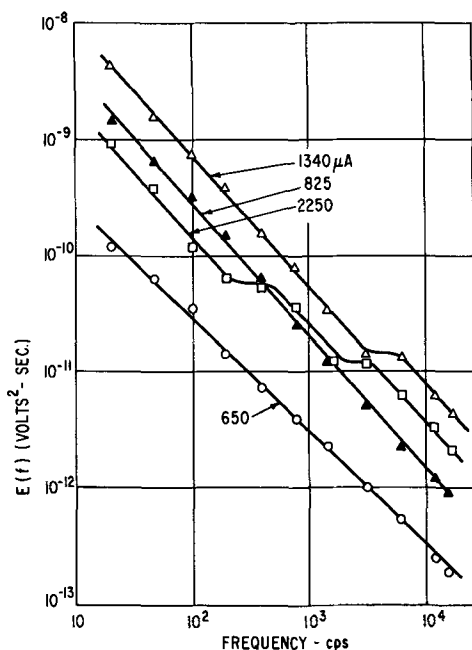


Fig. 2. Noise spectra for an indium oxide film

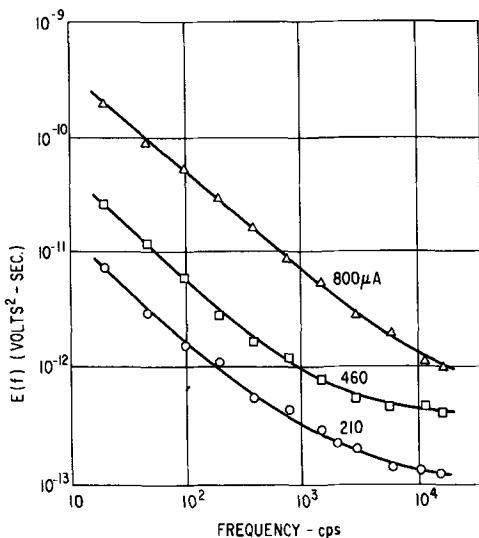


Fig. 3. Noise spectra for a copper iodide film

still exhibited a $1/f$ form, but here some anomalies appeared. These are manifested in the spectra as "bumps" or "jogs" in the otherwise smoothly decreasing curves. As indicated in Fig. 2, the number of these anomalies tended to increase with increasing current.

Almost simultaneous with the appearance of these anomalies, the noise power was observed to decrease with additional increases in current, and a large increase in current beyond the peak noise current invariably resulted in the failure of the conductor. The particular In_2O_3 film from which the data of Fig. 2 were taken failed at $2400 \mu\text{amp}$, for example.

For one of the CuI films, as the measurements of Fig. 3 show, a $1/f$ form for the noise was obtained but only for frequencies below 10^3 cps. Above 10^3 cps the noise is more nearly characteristic of a single time constant process as is indicated by the general flattening of the spectra. The same flattening was observed in other samples of this conductor. Unfor-

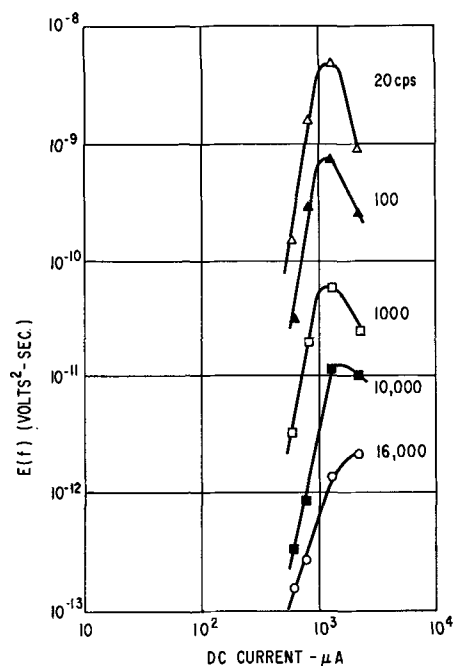


Fig. 4. Noise-current characteristics for an indium oxide film

tunately, the measurements were limited to the audio range of frequencies and therefore it was not possible to confirm this as a generation-recombination (GR) process. In order to preserve these films for subsequent measurements, the currents were kept small so as not to alter their properties by resistive heating. No anomalies like those observed in the In_2O_3 films were observed here, but then, the currents were not so high for these films.

Figure 4 shows, for the In_2O_3 film of Fig. 2, a power law relationship between the noise power, $E(f_1)$, and the mean current, I_{DC}

$$E(f_1) \propto I_{DC}^n \quad [1]$$

when the currents are small ($< 10^3 \mu\text{amp}$). f_1 is the noise frequency at which the measurements were made. The exponent, n , is clearly not constant but varies from about 6 at a noise frequency of 20 cps to about 3 at 10^4 cps for this film. Very similar results were obtained with other films of indium oxide. It was observed, however, that n depends not only on the frequency, f_1 , but also the particular film, most probably its structure. None of the films examined in this work obeyed the I_{DC}^2 law usually obtained for $1/f$ noise although they tended to approach this at the highest frequencies measured.

In the case of the CuI films (Fig. 5) the I_{DC}^2 law seems to have been obtained, at least for the lowest currents. This is so even at the high frequencies where the spectrum deviates sharply from the $1/f$ form. Since $E(f_1)$ for GR noise should vary as I_{DC}^2 also, the agreement with [1] for the highest frequencies is taken to be evidence that the single time constant process is a GR process.

Several In_2O_3 films were exposed sequentially to atmospheres of different gases where the sequence was from humid air (45% relative humidity) where it had been stored prior to measurement, to dry air for 6 hr, to dry N_2 for 16 hr and finally back to

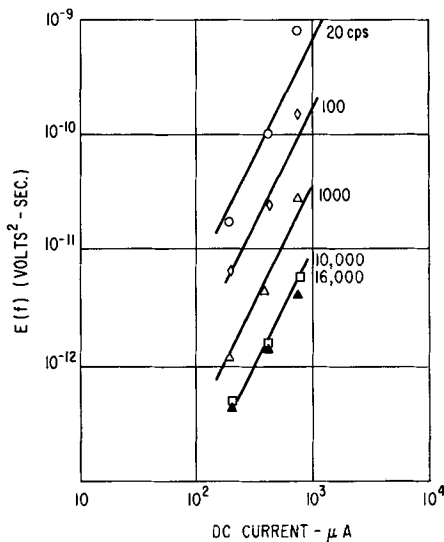


Fig. 5. Noise-current characteristics for a copper iodide film

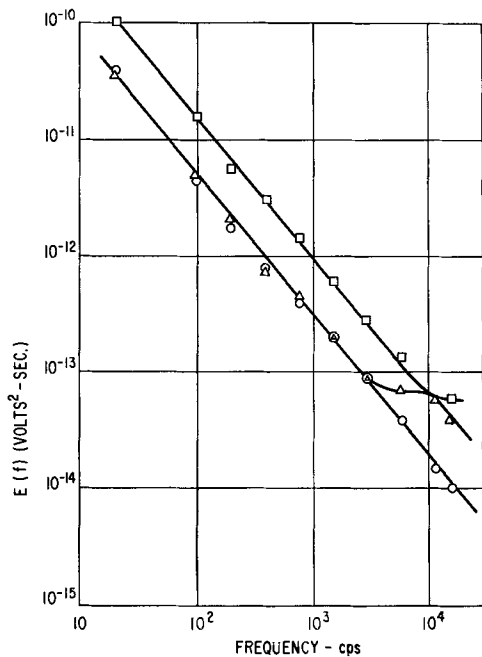


Fig. 6. Noise spectra for an indium oxide film under different environmental conditions. \circ , Air, 45% RH; Δ , air, dry; \square , nitrogen dry.

humid air again. The results of this operation are presented in Fig. 6. As may be seen from the measurements, removal of water vapor had little effect on the 1/f noise. It did, however, introduce an anomaly at a frequency of about 6 kcps. Removal of oxygen, on the other hand, resulted in a general increase in $E(f)$, but introduced no additional anomalies.

Finally, there is presented in Fig. 7 the effect of temperature upon the noise power. A small but steady decrease with decreasing temperature is noted here. Not all of the change in $E(f)$ can be attributed to a simple temperature effect because these data were not obtained with the same current. The current through the films decreased with decreasing temperatures at least partially because their temperature coefficient of resistance is negative. Rather than return the current to its initial value every

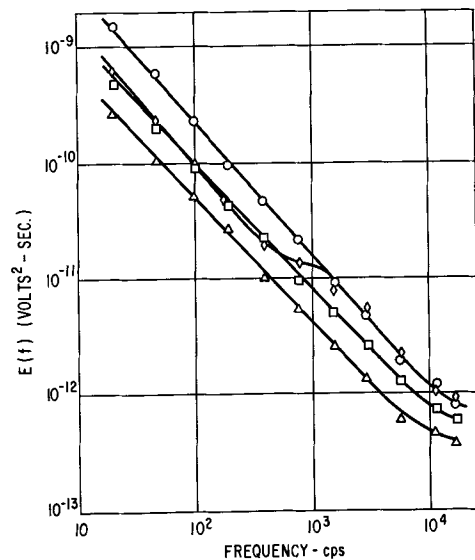


Fig. 7. Noise-temperature characteristics for an indium oxide film. \circ , 27°C; \diamond , 0°C; \square , -78°C; Δ , -196°C.

time the temperature was lowered, and risk an irreversible change in the properties of the film, the new current levels were accepted. However, since the changes in the current were relatively small, 625 μ amp at 27°C to 582 μ amp at -196°C, the corrections are probably small.

Discussion

Discussion of the results for the CuI films will be reserved until later, and the In_2O_3 films taken up first.

The measurements are most easily explained if the In_2O_3 films have a 2-D network structure, i.e, a quasi-continuous structure formed by the aggregates of the deposit all making point contacts with one another as suggested by Osman (8). The low resistances, the decrease in the noise power with a decrease in temperature, and even the photomicrographs showing the "apparent" discontinuous structure of these films are regarded as evidence for this structure.

From the measurements, some of which are presented in Fig. 2, it is observed that $E(f)$ follows very closely the power law relationship

$$E(f) = Af^{-m} \quad [2]$$

with $m = 1.07 \pm 0.04$ for reasonably low d-c currents. This value for m is in good agreement with values reported in the literature (3, 7, 12) and so there is little doubt that what is observed can be classed as 1/f noise. At the higher currents, certain anomalies appear in the spectra which are difficult to explain. But even at these high currents, the spectra seem basically to consist of 1/f noise.

If the anomalies observed in the spectra were due to a GR-type phenomena then it would be expected that the measurements could be fitted by an equation of the form

$$E(f) = A I_{DC}^2 f^{-1} + \sum_i B_i I_{DC}^2 (1 + \omega^2 \tau_i^2)^{-1} \quad [3]$$

where $\omega \equiv 2\pi f$ and $\tau_i \equiv (2\pi f_i)^{-1}$; f_i being the characteristic frequency of the GR-phenomenon, I_{DC} the

d-c current through the film, and B_1 a characteristic constant. Since this cannot be done it seems unlikely that the anomalies are associated with any phenomenon of this nature. The fact that the anomalies are observed most frequently at the highest current levels, levels near which the film is known to fail by resistive heating, suggests that they are more likely associated with localized failures in the film. For small currents, the noise measurements are always reproducible. But once the anomalies appear in the spectra, the original current characteristics can no longer be reestablished. Very similar "bumps" in the spectra were observed by van Vliet (13) and his co-workers for the noise in several types of thermistors.

As was pointed out earlier, contributions to the measured $1/f$ spectra can be expected from no less than three sources in these films: the bulk material, small volume contacts, and interparticle tunneling processes. From theory and from experiment (with very few reliable exceptions) all three noise sources show $E(f_1) \propto I_{DC}^n$ with $n \approx 2$. The large deviations from $n = 2$ for the In_2O_3 films are not explained. Most probably this is related to the semicontinuous structure, for in the course of making the measurements, it was observed that when the films were bent slightly concave or even vibrated (hence the need for shock mounting) the total noise was enhanced.

From other measurements (not here reported) the resistance of these films is known to be appreciably higher when measured in moist air or nitrogen than when measured under dry conditions but only slightly higher in dry air and oxygen than in dry nitrogen. Quite the reverse appears to be the case for the noise properties as may be seen in Fig. 6; moisture has little or no effect while the effect of removing oxygen is to increase the noise. The increased resistivity of the films in the presence of moisture is explained by the swelling of the gelatin which causes the network structure of the film to open. Gelatin has been reported as absorbing as much as 20 to 30% by weight water at normal room temperatures and relative humidities of 30 to 70% (14). It is surprising, however, that such a change in the dimensions of the film does not also affect the noise.

Oxygen sorbed on the films, either on the islands of In_2O_3 or on the exposed substrate between the islands seems to play an important role in the $1/f$ noise generating processes. Whether this be by carrier injection (or suppression) or by chemical modification of the film is not known. Measurements by Rupprecht (10) show that the conductivity of thin In_2O_3 films decrease sharply with decreasing oxygen pressure at temperatures of the order of 500°C and higher but is little affected for temperatures below about 100°C. Thus chemical modifications would seem not to be important here. However, since $1/f$ noise is sensitive to small variations in the number of charge carriers, it may always be argued that there is significant dissociation even at room temperatures. Whatever the mechanism, it is a reversible one for on readmission of air after be-

ing in nitrogen (or under vacuum) the original noise and resistance characteristics are recovered.

It would seem that the above is evidence for the noise being associated with bulk semiconductor properties and not point contacts as previously suggested. However, this apparent conflict is resolved if it is true that the noise in semicontinuous films is governed largely by surface trapping of current carriers at the small volume constrictions of the contacts.

The CuI films will now be discussed briefly since only a very limited amount of information was obtained.

These films are considerably thicker than the In_2O_3 films and almost certainly possess a continuous structure. It is to be expected therefore that they will behave like other semiconductor films, for example, like the PbS films examined by Barber (15) and by Lummis and Petritz (16). And indeed they do. Following their procedure, the data of Fig. 3 and 5 for the CuI films can be fitted by the semiempirical equation of Herzog and van der Ziel (17)

$$E(f) = AI^2f^{-1} + BI^2[1 + (f/f_0)^2]^{-1} \quad [4]$$

indicating that the noise spectra consists of a contribution from $1/f$ noise and a contribution from a single time constant phenomenon, possibly G-R noise. f_0 is the characteristic frequency of this process. The latter contributes to the measured spectra only in the region of the highest frequencies measured. Unfortunately, the measurements could not be extended beyond the audio range to permit an accurate determination of the characteristic relaxation time $\tau_0 = (2\pi f_0)^{-1}$. τ_0 appears to be of the order of several hundred to 1000 μsec , however.

Acknowledgment

The author thanks C. S. Herrick for the samples of CuI film used in this work.

REFERENCES

1. H. C. Montgomery, *Bell System Tech. J.*, **31**, 950 (1952).
2. A. V. MacRae, *J. Appl. Phys.*, **33**, 2570 (1962).
3. D. A. Bell, "Electrical Noise," p. 219, D. Van Nostrand Co., New York (1960).
4. A. L. McWhorter, Res. Lab. Elect., MIT, Tech. Rept. No. 295 (1955).
5. B. V. Rollin and I. M. Templeton, *Proc. Phys. Soc.* **B66**, 259 (1953).
6. J. Bernamont, *ibid.*, **49**, 138 (1937).
7. J. P. Borel, *J. phys. radium*, **17**, 224 (1956).
8. M. S. Osman, Rept. ESL-R-149, MIT, Cambridge, Mass. (1962).
9. L. H. Mauk, Battelle Mem. Inst., WADC Tech. Rept. 54-325, Part 3, ASTIA Doc. No. AD 118184 (1957).
10. G. Rupprecht, *Z. Physik*, **139**, 504 (1954).
11. C. S. Herrick and A. D. Tevebaugh, *This Journal*, **110**, 120 (1963).
12. E. J. Harris, *Electronic Eng.*, **20**, 145 (1948).
13. K. M. van Vliet, C. J. van Leeuwen, J. Block, and C. Ris, *Physica*, **20**, 481 (1954).
14. C. E. Mees, "The Theory of Photographic Processes," Macmillan Co., Rochester, N. Y. (1954).
15. D. Barber, *Proc. Phys. Soc.*, **B68**, 898 (1955).
16. F. L. Lummis and R. L. Petritz, *Phys. Rev.*, **105**, 502 (1957).
17. G. B. Herzog and A. van der Ziel, *ibid.*, **84**, 1249 (1951).

The Hall Effect in Semiconducting Glasses

W. F. Peck, Jr. and J. F. Dewald*

Bell Telephone Laboratories, Incorporated, Murray Hill, New Jersey

ABSTRACT

Hall effect measurements on semiconducting glasses from the systems, arsenic-tellurium-iodine and arsenic-tellurium-bromine, are reported. The Hall field is linear in the drift field up to 4.6 v/cm and in the magnetic field up to 70 kilogauss. The sign of the Hall effect in these systems indicates n-type semiconductors which is in apparent contradiction with the sign of the thermoelectric effect which indicates p-type conductivity. The carrier mobilities are of the order of 0.05 cm²/volt-sec, with only small temperature dependence.

This paper reports the conductivity, Hall effect, and measuring techniques on a group of semiconducting glasses from two new systems found by Pearson and Northover (1). The new systems are As-Te-I and As-Te-Br.

Studies of the basic properties of glassy semiconductors have been quite limited; most of the published work having come from Kolomiets and co-workers (2). Conduction in common glasses is usually considered ionic. In the past few years, however, inorganic glasses have been found showing electronic conduction (1,3). A triangular phase diagram of one of these systems, arsenic-tellurium-iodine, is illustrated in Fig. 1. The glass-forming region is within the island shown, while outside this region the system is at least partially crystalline. Rough constant conductivity curves have been plotted on this island, and these show that the electronic conduction in this system varies roughly exponentially with iodine content from approximately 10⁻³ (ohm-cm)⁻¹ at low iodine to approximately 10⁻⁸ (ohm-cm)⁻¹ at the highest iodine concentration. The data points shown represent compositions of the samples studied.

Previous work on glassy semiconductors has shown simple exponential dependence of conductivity on reciprocal temperature (2,4). This dependence was confirmed in the intrinsic region above room temperature in the systems studied. An example of four glasses showing this exponential de-

pendence is shown in Fig. 2. These glasses were composed of 53 atomic per cent (a/o) As, 43 a/o Te, and 4 a/o of Element X, the X representing either I or Br in the halogen systems, or Se or S in the previously reported systems.

In intrinsic germanium, a consistent picture of the variation of conductivity with temperature in the intrinsic region is obtained if the variation is ascribed to carrier density changes. Although the glassy semiconductors do not possess the extended long-range ordering found in crystals, current theories on the structure of glass postulate the existence of short-range ordering among the atoms. Therefore, it is not unreasonable to use Hall effect and conductivity measurements as in crystalline semiconductors to examine the source of the variation of conductivity with temperature. It should be noted, however, that in the glassy semiconductors it is not, at present, known if the Hall mobility equals the drift mobility.

Uphoff and Healy (4) suggest that well over half this variation of conductivity in the glassy semiconductors is kinetic in origin, that is, a variation of mobility with temperature. They stated this only tentatively, however, since their Hall measurements were restricted to a single temperature.

Experimental

Samples were prepared as follows: Cylinders of the glasses in evacuated quartz vials were air

* Deceased.

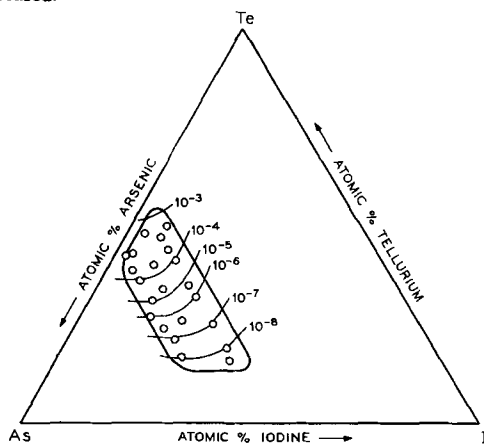


Fig. 1. Rough constant-conductivity contours in the system As-Te-I.

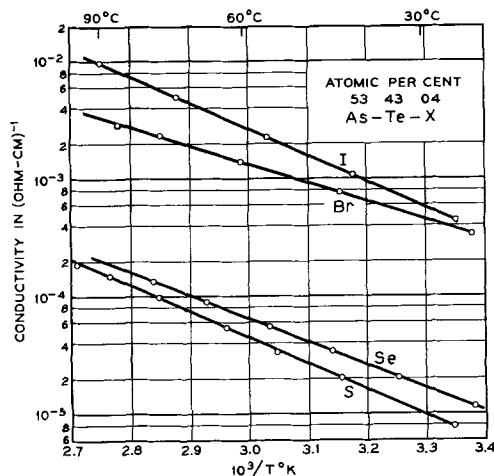


Fig. 2. Conductivity vs. 1/temperature plot of four glass systems

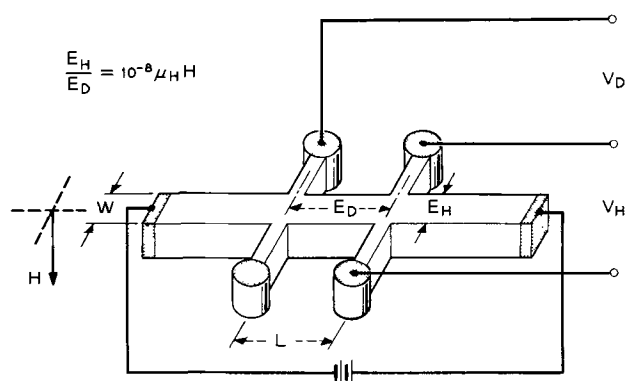


Fig. 3. Sample "bridge" arrangement for Hall effect and conductivity measurements.

quenched from 700°C. Wafers were cut from these cylinders using either an abrasive wheel or chemical etch saw and were lapped to the required thickness using a fine abrasive. Bridges were then cut from these wafers using a vibrating die. A picture of a sample bridge is shown in Fig. 3. Connection points on the bridges were covered with evaporated gold to a thickness of approximately 5000Å; fine copper wires were soldered to these points using gold-saturated solder. The bridges were lightly sandblasted to assure uniform surface condition. For the Hall effect measurements, the bridges were assembled to thermally regulated fixtures. The bridge to be measured was supported in a cryostat evacuated to approximately 10^{-3} mm Hg for thermal isolation from the outside. The sample within the cryostat was centered in an Arthur D. Little Inc. "Bitter Type" solenoid magnet, model number BS-3. This magnet developed up to 105,000 gauss in a $2\frac{1}{8}$ in. diameter throat with a field uniformity of 1.2% within a cylindrical section $\frac{1}{2}$ in. in radius and $\frac{1}{2}$ in. each side of center.

The equation below relates Hall mobility to the Hall, drift, and magnetic fields.

$$\frac{E_H}{E_D} = \frac{V_H/W}{V_D/L} = 10^{-8} \mu_H H \quad [1]$$

Noting Fig. 3 again, E_H is the Hall field (v/cm), V_H is the Hall voltage (v), W is the distance between the Hall arms (cm), E_D is the drift field (v/cm), V_D is the drift voltage (v), L is the distance between the drift arms (cm), H is the magnetic field (gauss) perpendicular to the current in the sample, and μ_H is the Hall mobility ($\text{cm}^2/\text{volt-sec}$). In the sample "bridges" constructed, $W = 0.15$ cm and $L = 0.28$ cm. The drift voltage was measured using a L&N K-3 potentiometer. The Hall voltage was measured using a L&N stabilized d-c microvolt amplifier, model number 9835-A, and a Varian recorder, model number G-10. Because the bridges were not perfectly symmetrical, an asymmetry voltage developed across the Hall arms and had to be cancelled. This was accomplished by recording the voltage between the Hall arms while the magnetic field was reversed in polarity. The Hall voltage developed was, therefore, half the difference between the two steady-state values.

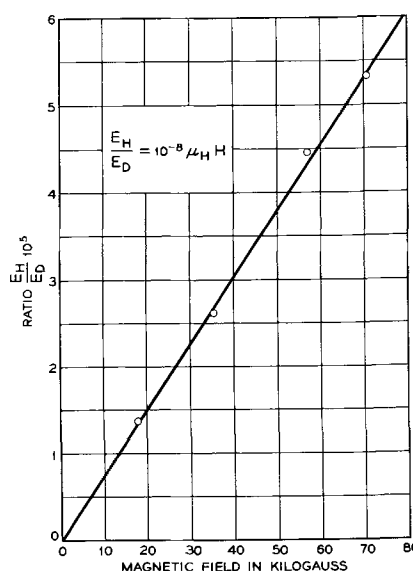


Fig. 4. Variation of Hall to drift field ratio with magnetic field in the system As-Te-I 53 43 04.

Results

In using these very large magnetic fields, it was questioned whether the Hall effect measurements in the glass systems were dependent on the magnetic field, since germanium starts showing such a dependence around 5 kilogauss. Figure 4 shows a plot of the Hall to drift field ratio *vs.* magnetic field on one of the As-Te-I glasses, composed of 53 a/o arsenic, 43 a/o tellurium, and 4 a/o iodine. Hall effect measurements were taken at magnetic fields up to 70 kilogauss. The experimental points lie on a straight line passing through the origin, indicating that the Hall mobility, μ_H , is constant and not magnetic field dependent up to 70 kilogauss. Experiments also showed that μ_H is independent of drift field polarity and magnitude up to 4.6 v/cm.

In order to determine the temperature dependence of the Hall mobilities in these glasses, Hall measurements were made at various temperatures from room temperature to 90°C. Figure 5 shows a comparison of the Hall mobility and the electrical conductivity *vs.* reciprocal temperature on the same

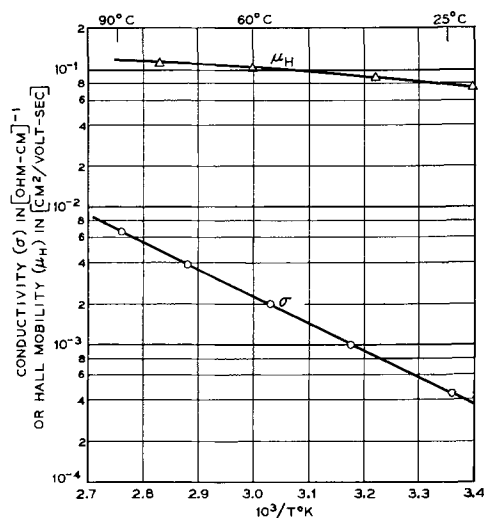


Fig. 5. Variation of conductivity (σ) and Hall mobility (μ_H) with $1/\text{temperature}$ in the system As-Te-I 53 43 04.

As-Te-I composition as above. In this composition the Hall mobility only changes from approximately 0.08 at room temperature to 0.12 cm²/volt-sec at 90°C. In other compositions of the systems, As-Te-I and As-Te-Br, Hall mobilities varied with the same small temperature dependence, from approximately 0.01 to 0.1 cm²/volt-sec. The composition plotted and also the other compositions studied showed the temperature dependence of their Hall mobilities to be only about 15% that of their conductivities, indicating that the variation of conductivity with temperature is due mainly to carrier density change and only slightly to mobility change.

Discussion

The indication as to the source of the variation of conductivity with temperature in the glass systems is complicated by the fact that the sign of the Hall effect indicates the glasses studied are n-type semiconductors while the sign of the thermoelectric effect, measured at room temperature with a thermal gradient of a few degrees, indicates they are p-type. Possible causes of this anomaly, taken from a discussion by Pearson (5), are briefly:

1. If the system involves two carriers, the Hall and thermoelectric effects can undergo sign reversals as the temperature varies, but, in general, the two effects would not change sign at the same temperature so that there might be a region where the two effects have opposite signs.

2. The usual semiconductor concepts may not apply since the semiconducting glasses lack the periodicity of normal crystal lattices.

3. The conduction process may depend on a "hopping" mechanism between atoms; and in this case it has not, at present, been rigorously established that the Hall and thermoelectric effects should have the same sign.

4. The existence of a second phase might also account for this sign inconsistency. The likelihood of

this particular possibility has been discussed by Pearson (6).

The investigation is still underway to resolve this situation, and until this apparent contradiction is explained, the deduction that the variation of conductivity with temperature in the glass systems studied is due mainly to carrier density changes can only be made tentatively.

Acknowledgment

The authors are indebted to A. David Pearson for supplying the semiconducting glasses and for his helpful comments and assistance during the course of this work.

Manuscript received Oct. 4, 1963. This paper was presented at the Boston Meeting, Sept. 16-20, 1962.

Any discussion of this paper will appear in a Discussion Section to be published in the December 1964 JOURNAL.

REFERENCES

1. A. D. Pearson, W. R. Northover, J. F. Dewald, and W. F. Peck, Jr., "Advances in Glass Technology," Plenum Press, New York (1962).
2. B. T. Kolomiets and N. A. Goryunova, *J. Tech. Phys. (USSR)*, **25**, 984 (1955); T. N. Vengel and B. T. Kolomiets, *Soviet Phys.—Tech. Phys.*, **2**, 2314 (1957); N. A. Goryunova, B. T. Kolomiets, and V. P. Shilo, *Soviet Phys.—Solid State*, **2**, 258 (1960); B. T. Kolomiets and T. F. Nazarova, *ibid.*, **2**, 369 (1960); B. T. Kolomiets *et al.*, "Structure of Glass," Vol. 2, (Translated from Russian), Consultants Bureau, N. Y. (1960).
3. E. P. Denton, H. Rawson, and J. E. Stanworth, *Nature*, **173**, 1030 (1954).
4. H. L. Uphoff and J. H. Healy, "Semiconducting Properties of Inorganic Amorphous Materials, Part II," U. S. Government Printing Office, Cat. no. AD 260780 (1961).
5. A. D. Pearson, "Sulfide, Selenide and Telluride Glasses," "Modern Aspects of the Vitreous State," Vol. 3, J. D. Mackenzie, Editor, Butterworths, Washington, D. C. In press.
6. A. D. Pearson, Recent News Paper presented at ECS Meeting, New York 1963.

Correction

In the paper by S. Schuldiner and C. H. Presbrey "Short-Pulse Techniques, I. Kinetics of the Triiodide/Iodide Reaction on a Platinum Electrode in

Neutral Solution," Vol. 111, No. 4, pp. 457-465, 1964, page 460, right-hand column, second paragraph, should read "Transient Equations (7, 8)..."

The Oxidation Kinetics of Zirconium in the Temperature Range 400°-600°C

R. J. Hussey and W. W. Smeltzer

Department of Metallurgy and Metallurgical Engineering, McMaster University, Hamilton, Ontario, Canada

ABSTRACT

The oxidation kinetics of zirconium were determined in the temperature range 400°-600°C at subatmospheric pressures for exposure times of 650 hr at 400°C to 160 hr at 600°C by a microbalance technique. From scale thickness measurements, it was shown that at temperatures between 500°-600°C the amount of oxygen in the metal varies from 14 to 23% of the total oxygen consumption respectively. Further both the oxidation kinetics and the oxygen distribution between the metal and the oxide were found to be independent of changes of oxygen pressure from 0.25 to 50 cm Hg. The kinetics were fitted to a parabolic rate relation after an initial deviation. In the parabolic range, oxidation behavior approximated to a model in which the oxidation rate was determined by oxygen diffusion in both the oxide and metal.

Zirconium is one of those few metals which is capable of dissolving relatively large quantities of oxygen. When it is heated in this gas at elevated temperatures, an oxide layer is built up concurrently with the establishment of an oxygen concentration gradient in the metal. In any study of the reaction of zirconium with oxygen, therefore, both the mechanism of oxide scale growth and diffusion of oxygen into the metal must be considered.

The kinetics of the oxidation, giving the over-all consumption of oxygen with time, have been studied extensively over a large range of temperatures (1-9). Both parabolic and cubic equations have been used to express the kinetic data for short term oxidation experiments. However, there is little reported work on the long term oxidation behavior of zirconium at intermediate temperatures (3, 5), and it was considered that extended time studies might prove more fruitful in the elucidation of the kinetics.

Accordingly, the present paper is devoted to an investigation of the oxidation kinetics of zirconium in pure oxygen at temperatures in the range 400°-600°C for periods up to several hundred hours.

Experimental

The iodide-refined zirconium used in this study was 99.92% pure and the analysis of the metal is given in Table I. Specimens were cut from 0.030 in.

Table I. Analysis of zirconium impurity content

Element	p.p.m.	Element	p.p.m.
Al	45	Mo	25
B	<0.2	N	21
C	50	Ni	<10
Cd	<0.3	O	140
Co	<5	Pb	<5
Cr	44	Si	<40
Cu	<25	Sn	<10
Fe	218	Ti	<20
H	3.7	V	<5
Hf	68	W	<25
Mg	<10	Zn	<50
Mn	<10		

sheet to sizes of 2 x 1 and 1.5 x 1 cm. The oxygen gas (supplied by Matheson Co. Ltd.) was listed as 99.6 volume per cent (v/o) pure. It was further purified by passage through heated cupric oxide, ascarite, Linde 5A molecular sieves, and a trap immersed in solid carbon dioxide to remove traces of hydrogen, water vapor, carbon monoxide, and carbon dioxide.

The kinetic experiments were carried out using a vacuum microbalance apparatus (10). Two separate microbalances of sensitivities 1.55 and 5.00 $\mu\text{g}/\text{division}$ were found necessary to ensure that the kinetics could be followed for long times over the temperature range under consideration. Furnace temperatures were controlled to $\pm\frac{1}{2}^\circ\text{C}$ using a temperature controller with a platinum resistance thermometer as the sensing element. Prior to admitting the oxygen, a specimen was subjected to a vacuum of 10^{-6} mm Hg for a period of 16 hr at room temperature. The specimen was subsequently heated to 650°C, annealed at this temperature for 1 hr in a vacuum of 10^{-6} mm Hg, and then cooled to reaction temperature, whereupon oxygen was admitted. The first readings were taken 5 min after the admission of oxygen.

In order that the metal surface presented to the oxidizing gas was representative of the bulk metal, it was necessary to ensure that the deformation inevitably introduced into the surface of the metal during specimen preparation was removed as far as was possible. Two approaches were examined to this end, namely, a mechanical and a chemical polish.

In the former, the specimen was abraded on SiC papers from 240 through 600 mesh grit under water and then polished for several hours on a napped cloth, impregnated with 8μ diamond paste and lubricated with kerosene. During the abrasion deformation is produced in the surface layers of the metal to a considerable depth. For example, finishing with a 600 grit paper this amounts to 15μ for 70:30 brass (11) and 2.2μ for stainless steel (12). As yet no measurements of this type have

been made for zirconium and so it was necessary to remove at least as much deformation as has been detected on other metals and alloys. Subsequent diamond polishing has been shown to remove this deformation in the case of the brass and the stainless steel, the polishing rate decreasing as the melting point of the material increases. Since the melting point of zirconium is much higher than that of either of the two alloys the polishing rate would be expected to be very low (13).

The chemical polish, which consisted of a 2 min swabbing at room temperature with an HF/HNO₃/distilled H₂O mixture (10:45:45) was preceded by abrasion to 2/0 emery under petroleum ether. During this polish a thickness of metal estimated to be about 16-20 μ was dissolved which means that the gross deformation from the abrasion processes was removed.

To examine the variations in oxidation behavior shown by specimens prepared by the two methods, four specimens were polished, two by each method and then oxidized at 400°C in oxygen at a pressure of 10 cm Hg for about 150 hr. Prior to oxidation one of each pair was heated at 650°C for 1 hr; hereafter this treatment is referred to as an anneal. All experiments on the effects of temperature and pressure on oxidation kinetics were carried out with the chemically polished annealed specimens.

It is possible to obtain an estimate of the amount of oxygen in the metal knowing the total weight gain of a specimen and the thickness of the oxide film. Metallographic examinations were made of the oxide formed on the metal during oxidation by sectioning a few selected specimens mounted in bakelite. The metallographic preparation consisted of an abrasion through 240 to 600 mesh SiC wet papers, a polish on an 8 and a 1 μ diamond lap successively, and a final polish on a Syntron vibratory polisher using a water slurry of 0.3 μ γ -Al₂O₃ on a Selvyt cloth.

Results

Surface preparation.—The kinetic curves, which were obtained for the chemically polished and abraded specimens, are shown in Fig. 1. It is immediately evident that the chemically polished spec-

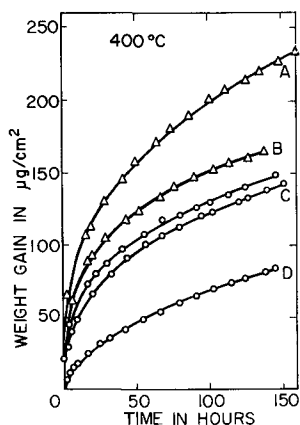


Fig. 1. Oxidation of zirconium at 400°C in oxygen at 10 cm Hg pressure. Curve A, abraded with anneal; Curve B, abraded without anneal; curve C, chemically polished with anneal; curve D, chemically polished without anneal.

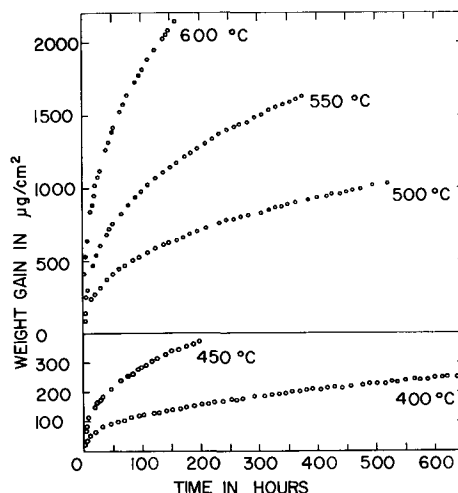


Fig. 2. Oxidation of zirconium at 400°-600°C in oxygen at 10 cm Hg pressure.

imens oxidize to a lesser extent than the abraded ones. Further, there is a marked difference between the annealed and unannealed specimens prepared by the same method.

In both methods of specimen preparation the deformation may be removed satisfactorily, but since the chemical polish method was very much more rapid than the abrasive method, it was chosen as the standard method. The reproducibility obtained in the kinetic curves using chemically polished/annealed specimens as shown in Fig. 1 is within $\pm 5\%$. Thus, if kinetic reproducibility be a criterion for a representative surface, all other experimental conditions being the same, then the method adopted is satisfactory.

Effect of temperature.—A series of zirconium specimens was oxidized in oxygen at a pressure of 10 cm Hg of oxygen at temperature intervals of 50° over the range 400°-600°C. The oxidation period varied from 650 hr at 400°C to 160 hr at 600°C. A family of curves, plotted as weight gain in $\mu\text{g}/\text{cm}^2$ vs. time in hours, is shown in Fig. 2. The reproducibility of the data for 400°, 500°, and 600°C was about $\pm 5\%$ in each case. At all temperatures the kinetic curves show an initial rapid rate of oxidation which decreases continuously with time.

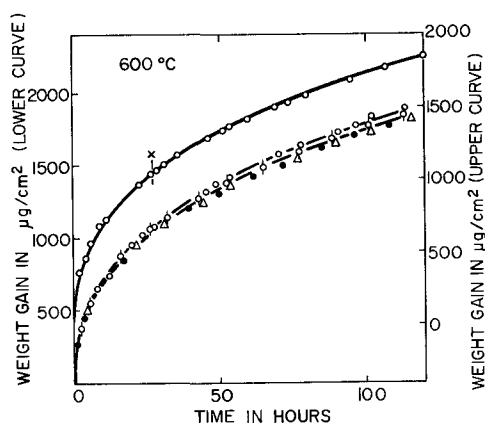


Fig. 3. Lower curve, oxidation of zirconium at 600°C in oxygen at pressure of 0.25, 1, 10, and 50 cm Hg; upper curve, oxidation of zirconium at 600°C in oxygen, at x the pressure was reduced from 10 to 1 cm Hg. •, 50 cm; ○, 10 cm; △, 1 cm; ◊, 0.25 cm.

Effect of pressure.—To investigate the effect of pressure change on the oxidation kinetics, specimens were oxidized at 600°C at pressures of 0.25, 1, 10, and 50 cm for 150 hr. The kinetic curves obtained are shown in Fig. 3. It is evident that within the experimental error, the over-all oxygen consumption is unaffected by pressure change over the range covered by this investigation. To confirm this, a specimen was oxidized at 600°C at a pressure of 10 cm Hg for 27 hr and then the pressure was reduced to 1 cm Hg and the oxidation kinetics were followed for a further 139 hr. As is shown in Fig. 3, the curve continues without a break.

Metallographic examination.—The scale formed on the specimens oxidized at all temperatures from 400°-600°C showed the characteristic dark gray color (2) and was strongly adherent to the metal core, even on cooling. Metallographic examination of the sectioned specimens in bright field showed the oxide on the surface to be dark gray in color and dense (Fig. 4). Under polarized light the oxide was observed to be columnar in structure. Occasionally a thickening of the scale was seen, usually in the area of a crack or blister.

The edges of the specimens oxidized at the higher temperatures showed a white piping of oxide. The piping consists of thicker areas of scale which have cracked and exfoliated from the metal/oxide interface (Fig. 5); here this interface has become quite rounded, as was found by Wallwork and Jenkins (4). Under polarized light the exfoliated oxide was

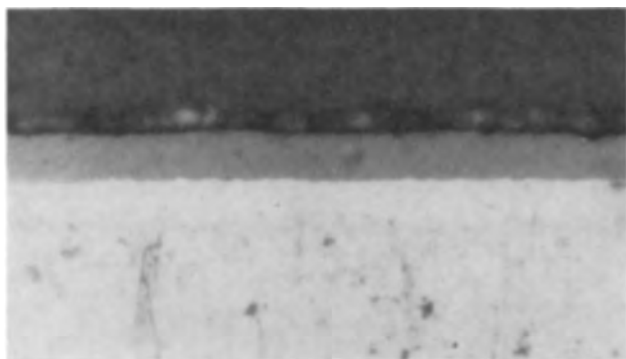


Fig. 4. Section showing oxide on specimen surface. Magnification X500.

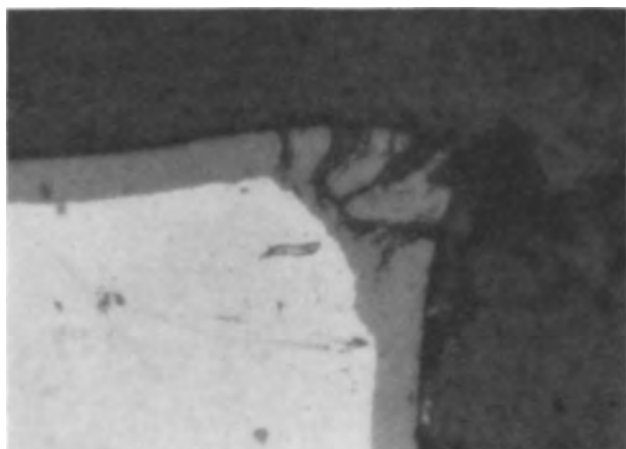


Fig. 5. Section showing oxide at specimen edge. Magnification X500.

Table II. Influence of pressure on the amount of oxygen in zirconium oxidized at 600°C

Time, hr	Pressure, cm Hg	Film thickness, μ	% Oxygen in metal ^a
123	0.25	10.3	18 \pm 8
115	1.0	10.1	16 \pm 9
156	10.0	11.1	23 \pm 7
108	50.0	9.7	17 \pm 5

^a Determined from film thickness.

characteristically of a two-fold nature; the outer part consisted of a translucent columnar layer, the thickness of which was of the same order as the oxide scale on flat surfaces, while the inner oxide was dense and apparently structureless.

Examination of the specimens after oxidation showed that while the specimens oxidized at pressures of 1, 10, and 50 cm Hg were the characteristic dark gray color, the sample oxidized at the lowest pressure of 0.25 cm Hg showed interference colors.

The oxidation kinetics have been shown to be insensitive to large pressure changes. In order to show whether the oxygen distribution between the oxide and metal was influenced by pressure change, metallographic examinations were made of the specimens oxidized in the pressure range 0.25-50 cm. These results are shown in Table II. Within the experimental precision, the distribution was unaffected by pressure.

These measurements establish that approximately 20% of the total oxygen consumption is present in the metal at 600°C. That oxygen diffuses into the metal to an appreciable extent even at the lower temperatures is illustrated in Table III. At the temperature of 500° and 550°C, it is shown that the amounts of oxygen in the metal core are of the order of 15%. The difficulties in using the metallographic technique for measuring scale thicknesses on specimens oxidized at 400°C lead to a large error in the determination of the amount of oxygen in the metal (Table III), but the measurements suggest that oxygen is dissolved in the metal phase.

Discussion

The present studies were carried out to extend the existing data to longer times in the temperature range 400°-600°C in order to elucidate more fully the oxidation mechanism. In common with other investigators (1) who have studied the oxidation behavior of zirconium in the thin scale region, it has been found difficult to decide the type of oxidation rate relationship being followed. Generally the

Table III. Influence of temperature on the amount of oxygen in zirconium oxidized at a pressure of 10 cm Hg

Time, hr	Temperature, °C	Film thickness, μ	% Oxygen in metal ^a
644	400	1.2	29 \pm 24
519	500	5.9	14 \pm 13
377	550	9.1	16 \pm 8
156	600	11.1	23 \pm 7

^a Determined from film thickness.

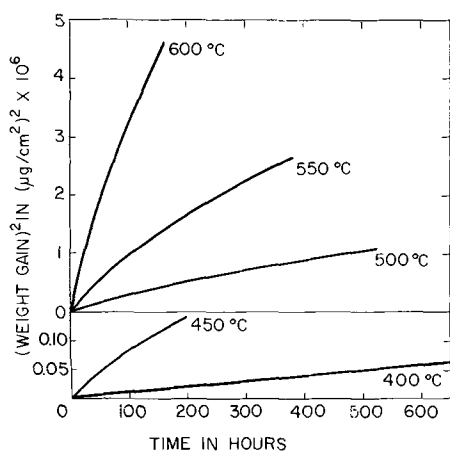


Fig. 6. Oxidation of zirconium at 400°-600°C in oxygen at 10 cm Hg pressure (in parabolic form).

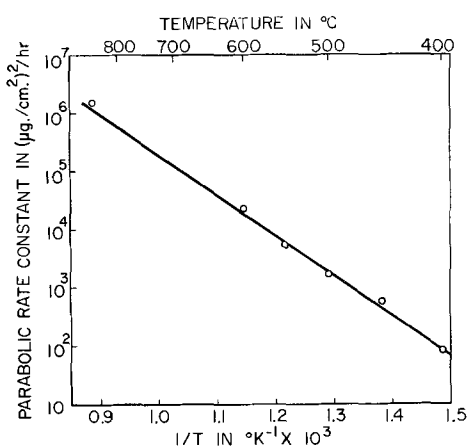


Fig. 7. Variation of the parabolic rate constant with temperature

indecision has arisen in connection with those experiments carried out over relatively short intervals.

At each temperature after an initial deviation it was found that the data obeyed the parabolic rate equation. The kinetic data for the temperature range 400°-600°C were plotted in this form as the square of the weight gain vs. time (Fig. 6). It is evident that the period of deviation from parabolic behavior decreases markedly with increasing temperature; at 400°C the deviation lasts 400 hr, whereas at 600°C it is only 100 hr in duration.

From this data the parabolic constant, K_p , for each temperature was determined from the slope of the line (using least mean squares) passing through the last ten points on the graph. The values of K_p given in Table IV plotted in Arrhenius form as $\log K_p$ vs. $1/T$ are shown in Fig. 7. The straight line through the points shows the activation energy, E , to be 31.9 kcal/mole which is in good agreement with previous values of 28.6 and 32.0 kcal/mole

Table IV. Experimental values of the parabolic rate constants

Temperature, °C	K_p ($\mu\text{g}/\text{cm}^2$) ² /hr
400	8.37×10
450	5.83×10^2
500	1.65×10^3
550	5.48×10^3
600	2.33×10^4

(2, 14). The value of the parabolic rate constant, given by Wallwork *et al.* (9) for the oxidation of diamond polished zirconium at 850°C for 200 hr also lies on the same straight line.

The over-all oxygen consumption was unaffected by pressure change at 600°C. Furthermore, the final rates of oxidation, as defined by drawing the best line through the last five points on the kinetic curves plotted in the parabolic form for each of the pressures, were within $\pm 10\%$ of each other and showed no trend with change in pressure. This behavior is consistent with the established oxide model for parabolic kinetics where oxidation proceeds lattice diffusion of oxygen in the n-type oxide by anion vacancies (15). Accordingly, the concentration gradient of oxygen across the oxide film is not markedly affected by oxygen pressure, and it is therefore reasonable to assume that the degree of oxygen solution into the metal would be unaffected over the investigated pressure range. This conclusion is borne out by the results given in Table II where the percentage of oxygen in the metal was approximately 20% at all oxygen pressures.

The dark gray oxide formed during the parabolic stage of oxidation was columnar and adherent to the metal suggesting that it acts as a diffusion barrier. Although there was evidence for oxide break-away at the edges of specimens (Fig. 5), its overall contribution to the kinetics by an increase in reaction area and a localized decrease in the effective oxide diffusion thickness was found to be within the experimental error. The oxidation curves showed no evidence of discontinuities.

The deviations from parabolic oxidation may be largely due to a large number of short circuit diffusion paths in the initially formed oxide such as dislocation pipes or grain boundaries. Smeltzer *et al.* (17) have advanced a simple model for this type of oxidation where the density of oxygen sites in the short circuit paths decreases by a first order rate mechanism; the effective diffusion constant for oxygen is time dependent, its value finally being equal to that for lattice diffusion only. This being so, the initial rate would be greater than parabolic as was found in the present experiments. Although the data may be fitted to the derived equation, which approximates to a parabolic equation for long times, the model does not account for oxygen solution in the metal. It is therefore not feasible to analyze the data for temperatures in the range 500°-600°C because 15-20% of the oxygen consumed is present in the metal. Also this equation was not adopted to analyze the kinetics at 400°C where the magnitudes of the rates were markedly dependent on surface preparation (Fig. 1). At this temperature it was not possible to distinguish between the relative amounts of oxygen present in the oxide or metal (Table III).

The linear Arrhenius plot of the parabolic constants, the negligible effect of oxygen pressure change on the oxidation kinetics, the degree of oxygen solution in the metal, the occurrence of compact oxide and the absence of discontinuities in the oxidation curves all suggest that the mechanism

of parabolic oxidation remains the same over the investigated temperature range.

In the present study there was an initial deviation from parabolic behavior and so this type of oxidation only approximates to the model advanced by Wagner (16) for the growth of a superficial reaction product layer and concurrent solution of the diffusion reactant in the substrate, because this model requires the oxidation kinetics to obey a parabolic equation from zero time. At 850°C, however, the Wagner model was found to be applicable by Wallwork *et al.* (9) for exposures to 200 hr. Moreover, the value of the parabolic constant determined by these investigators was found to lie on the Arrhenius plot of this investigation (Fig. 7), which suggests that the mechanism of parabolic oxidation remains the same over the temperature range 400°-850°C. Unfortunately, there are insufficient data available at the lower temperatures to evaluate parabolic constants from a consideration of a model such as that considered by Wallwork *et al.* (9).

Several investigators have interpreted the kinetic data over a similar temperature range for shorter times in terms of a cubic equation (1, 5, 7). When the present data for the chemically polished specimens are plotted to this equation as the cube of the weight gain *vs.* time, the curves are convex to the time axis. The kinetic data at 400°C for the abraded specimens show good agreement to the cubic equation. This behavior has also been reported by Charles *et al.* (3) for the oxidation kinetics of abraded zirconium at 350° and 450°C. At present there is no adequate model to account for cubic oxidation of zirconium, although it has been suggested that such kinetics may be partially due to oxygen solution in the metal (7, 18). Consequently, it appears more appropriate, at least for long exposures, to represent the extensive data for the chemically polished specimens from this investigation in terms of a parabolic equation accounting for lattice diffusion of oxygen in the oxide and oxygen solution in the metal.

Conclusions

The oxidation kinetics for zirconium over the temperature range 400°-600°C may be described by the parabolic rate equation apart from the initial deviation. It is suggested that this behavior is associated with both diffusion of oxygen in the oxide and oxygen solution into the metal. The initial period of oxidation, where the rate was greater than parabolic, may be due to the time dependence of

the effective diffusion constant of oxygen in the oxide.

The oxidation kinetics at 600°C were not affected by change of oxygen pressure from 0.25 to 50 cm Hg, and the distribution of oxygen between the oxide and the metal did not vary over this pressure range. The amount of oxygen present in the metal over the range 500°-600°C varied from 14-23% of the total oxygen consumption respectively. At 400°C the distribution of oxygen between the oxide and the metal could not be reliably determined.

Acknowledgments

The authors were indebted to Dr. G. R. Wallwork, University of New South Wales, for helpful discussions. This work forms part of a research project sponsored by the U.S. Air Force Office of Scientific Research, Office of Aerospace Research and the Defence Research Board, Ottawa, Canada.

Manuscript received Nov. 5, 1963. This paper was presented at the New York Meeting, Sept. 29-Oct. 3, 1963.

Any discussion of this paper will appear in a Discussion Section to be published in the December 1964 JOURNAL.

REFERENCES

1. J. Belle and M. W. Mallett, *This Journal*, **101**, 339 (1954).
2. E. A. Gulbransen and K. F. Andrew, *J. Metals*, **9**, 394 (1957).
3. R. G. Charles, S. Barnartt, and E. A. Gulbransen, *Trans. AIME*, **212**, 101 (1958).
4. G. R. Wallwork and A. E. Jenkins, *This Journal*, **106**, 10 (1959).
5. H. A. Porte, J. G. Schnizlein, R. C. Vogel, and D. F. Fischer, *ibid.*, **107**, 506 (1960).
6. K. Osthagen and P. Kofstad, *ibid.*, **109**, 204 (1962).
7. K. A. Sense, *ibid.*, **109**, 377 (1962).
8. K. H. Akram and W. W. Smeltzer, *Can. Met. Quart.*, **1**, 41 (1962).
9. G. R. Wallwork, W. W. Smeltzer, and C. J. Rosa, *Acta Met.*, **12**, 409 (1964).
10. E. A. Gulbransen, *Rev. Sci. Instruments*, **15**, 201 (1944).
11. L. E. Samuels, *J. Inst. Metals*, **85**, 51 (1956-57).
12. L. E. Samuels and G. R. Wallwork, *J. Iron Steel Inst.*, **186**, 211 (1957).
13. L. E. Samuels, *J. Inst. Metals*, **81**, 471 (1952-53).
14. D. Cubicciotti, *J. Am. Chem. Soc.*, **72**, 4138 (1950).
15. M. W. Mallett and W. M. Albrecht, *This Journal*, **102**, 407 (1955).
16. C. Wagner, "Diffusion in Solids, Liquids and Gases," W. Jost, Editor, p. 71, Academic Press, New York (1952).
17. W. W. Smeltzer, R. R. Haering, and J. S. Kirkaldy, *Acta Met.*, **9**, 880 (1961).
18. P. Kofstad and K. Hauffe, *Werkstoffe u. Korrosion*, **7**, 642 (1956).

The Electrical Conductivity, and the Thermodynamic and Structural Properties of Molten AgCl-Ag₂S Mixtures

I. Thermodynamic and Structural Properties

M. C. Bell and S. N. Flengas

Department of Metallurgical Engineering, University of Toronto, Toronto, Ontario, Canada

ABSTRACT

The phase diagram and the densities for the entire AgCl-Ag₂S system have been determined. The emf's for the concentration cell



have been measured up to 20 mole % silver sulfide, and in the temperature range between 450° and 700°C. The results of the emf measurements indicate that silver chloride is completely dissociated and forms ideal solutions in dilute solutions of silver sulfide. Slight positive deviations from ideality occur in more concentrated solutions. Calculations from the phase diagram substantiate the results of the emf measurements and indicate further that silver sulfide, on the silver sulfide side of the phase diagrams, behaves like an associated liquid. The phase diagram shows a eutectic at 377°C and 35.6 mole % silver sulfide, and an incongruently melting compound at about 50 mole %. Molar volumes were also calculated from the density measurements and indicate negative deviations from additivity. These results are interpreted in terms of a gradual breakdown of the structure of associated silver sulfide by the addition of the ionic silver chloride.

In spite of the importance of the sulfide ores, there have been very few systematic investigations of the thermodynamic and electrical properties of molten metal sulfides and their mixtures with other salts.

Sulfides for which the electrical conductivities have been measured are generally those of the transition metals and are predominantly electronic conductors in the molten state. On mixing with the corresponding metal chlorides, the conductance changes from electronic to ionic, and it could be inferred that the recovery of metals by fused salt electrolysis of sulfide ores may become possible.

Thus, previous investigations (1-3) have shown that dilute solutions of lead sulfide in molten lead chloride are ionic conductors and that direct electrolysis of such mixtures may be carried out at high current efficiencies. Derge and Pound (4) have measured the electrical conductivities and current efficiencies of cuprous sulfide-cuprous chloride melts at high temperatures. They found the electrical conductivity decreases rapidly on the addition of cuprous chloride and the melts become predominantly ionic conductors at about 50 mole % cuprous chloride.

The present work was undertaken to investigate in detail the factors affecting the type of electrical conductance in molten mixtures of sulfides and chlorides, and the mechanism of the process. The silver chloride-silver sulfide system was chosen because of its relative thermal stability, its inertness with respect to silica glass containers, and the stoichiometric composition of the sulfide.

Preliminary experiments have indicated that the type of electrical conductivity is closely related to the structure of the melts. It was therefore decided to investigate first properties giving some indication of the structure of the liquid mixtures.

This paper establishes the phase diagram of the system and presents results on the density determination of the molten mixtures of silver chloride-silver sulfide over the entire composition range. The thermodynamic properties for dilute solutions of silver sulfide have also been determined from emf measurements. Electrical conductivities for the system over the entire composition range have also been measured and are reported in a separate publication.

Experimental

Preparation of materials.—Silver sulfide was prepared by precipitation from a boiling aqueous solution of reagent grade silver nitrate by sodium sulfide. The precipitate was thoroughly washed with distilled water and dried at 120°C. The product was further purified by treatment in a dry mixture of hydrogen sulfide and hydrogen, at $P_{\text{H}_2\text{S}}/P_{\text{H}_2} \approx 11$, at about 700°C. Small amounts of excess sulfur were then removed from this product by heating to about 150°C under vacuum.

Analysis of this product by titration for silver with thiocyanate, and by weight loss on thermal decomposition in air, gave the analytical formula of Ag_{1.99}S, or Ag₂S, within the error of the analysis. These results are in agreement with Wagner's (5) observation that stoichiometric silver sulfide may be prepared at temperatures below the α to β transfor-

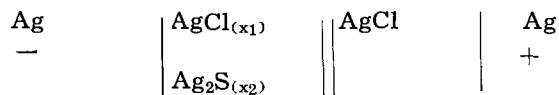
mation temperature which occurs at 178°C.

Anhydrous silver chloride was of analytical grade and was further dried under vacuum at 300°C.

Apparatus.—Cryoscopic measurements.—The liquidus for the AgCl-Ag₂S system was determined by cooling curves carried out in a quartz tube under a flow of dried purified argon. In the absence of air, silica glass was found to be an excellent material for containing the melts. The thermocouple well was made from thin walled quartz tubing, and the tubing was collapsed around the thermocouple head to insure good thermal contact with the melt. All thermocouples were calibrated with respect to the melting points of pure tin, zinc, and silver. The temperature was read at 20-sec intervals on a potentiometer. Cooling rates were approximately linear and on the silver chloride side of the diagram showed a well-defined plateau. Supercooling was generally less than 1°C, at a cooling rate of 1°C per min.

The composition of the melt in the tube could be changed by adding pellets of silver chloride or silver sulfide from a side arm feeding tube magnetically operated from outside the cell.

EMF measurements.—The thermodynamic properties of silver chloride in dilute solutions of silver sulfide up to 20 mole % were determined by measuring the reversible potential of the concentration cell



The cell was constructed from silica glass, the two electrode compartments being separated by an asbestos fiber sealed in silica tubing. The composition of the melt in the indicator half-cell compartment could be readily changed by the addition of silver sulfide pellets from a side arm feeding tube. All measurements were made under an atmosphere of purified argon.

The operation and the details of construction of similar cells have been described in previous publications (6, 7).

Density measurements.—The densities of the molten mixture of AgCl-Ag₂S over the entire range of compositions and at temperatures between 450°-900°C, were determined by the apparent loss in weight method of a density sinker immersed in the melt. The apparatus used is shown in Fig. 1.

The density sinker was made by sealing a ¼ in. diameter by ½ in. long tungsten rod under vacuum in silica glass tubing. A fine quartz fiber of 0.15-0.20 mm diameter was drawn from one end of the sinker so that surface tension effects and the volume of the stem were negligible. The sinker was then suspended from a quartz spring balance, as shown on Fig. 1. The extension of the spring could be read to the nearest milligram with a cathetometer. The sinker was calibrated at room temperature in a constant temperature bath containing distilled water. By the use of the glass pulley, shown on the upper part of the apparatus in Fig. 1, the level of the sinker in the melt could be adjusted and the

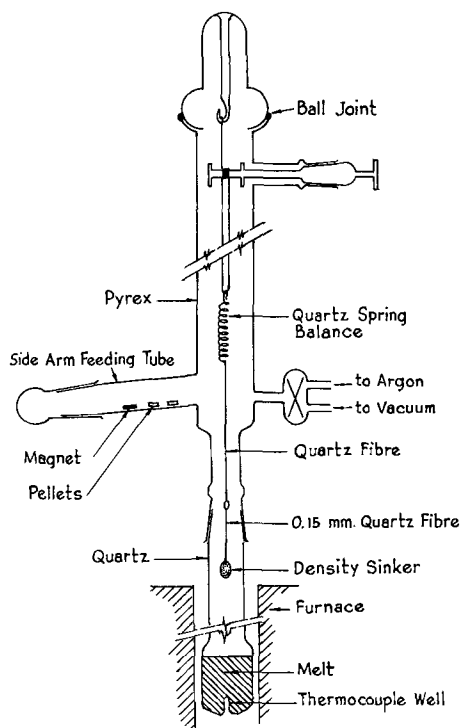


Fig. 1. Density measurement apparatus

entire sinker and spring balance system could be raised out of the hot zone of the furnace without opening the cell. The cell was vacuum tight, and all measurements were made in an atmosphere of dried purified argon. In order to obtain reproducible readings, it was found necessary to remove gas bubbles, which were invariably trapped inside the viscous sulphide melts, by evacuating the cell with the sinker in place.

Results and Discussion

Cryoscopic Measurements

The experimentally determined liquidus is shown in Fig. 2. The accuracy of the points on the silver chloride side of the phase diagram is better than

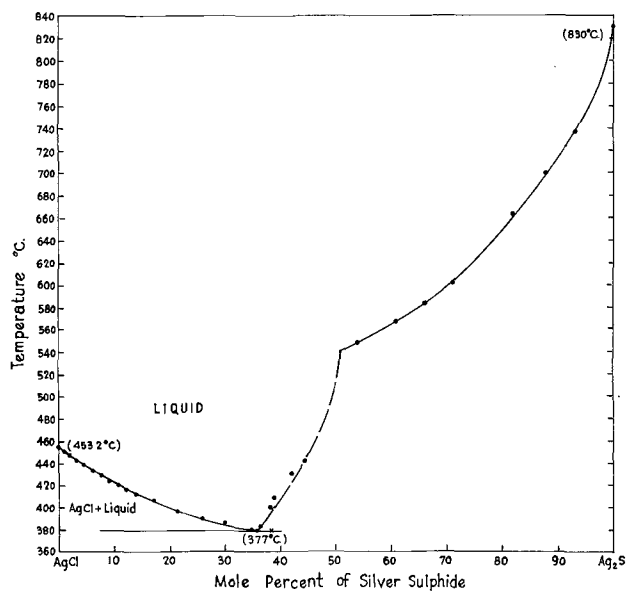


Fig. 2. Phase diagram of the AgCl-Ag₂S system

$\pm 0.5^\circ\text{C}$. Thus, the observed melting point of silver chloride is 453.2°C as compared with 454.8°C , quoted by Brewer (8).

On the silver sulfide side, the cooling curves were not as well defined due to the steepness of the liquidus and the glassy nature of the liquid mixtures. The melting point of pure silver sulfide could not be obtained accurately because of excessive supercooling. From electrical conductivity measurements (9), however, the melting point was determined as $825^\circ \pm 5^\circ\text{C}$. This value should be compared with $838^\circ \pm 2^\circ\text{C}$ reported by Kracek (10), 842°C by Kubaschewski and Evans (11), and 810° to 832°C , reported recently from electrical conductivity measurements by Velikanov (12).

The system has one eutectic that occurs at 377°C and 35.8 mole % silver sulfide. At about 50 mole % there is apparently a weak incongruently melting compound of unknown composition. X-ray patterns of material cooled from the eutectic showed no significant shift in the silver chloride peaks, indicating that solid solubility on the silver chloride side of the diagram is slight if it occurs.

It should be observed that the curvature of the liquidus on both sides of the diagram is opposite to that observed in a normal system.

Phase diagram calculations.—On the silver chloride side of the diagram, the freezing point depression may be calculated by the classical van't Hoff equation given below, assuming that the solutions are ideal and there is no solid solubility.

$$\ln a_{\text{AgCl}} = -\frac{\Delta H_f}{R} \left[\frac{1}{T_L} - \frac{1}{T_F} \right] \quad [1]$$

a_{AgCl} is the activity of liquid silver chloride at the liquidus temperature T_L (with respect to pure silver chloride at T_L as the standard state). T_F is the melting point temperature of pure silver chloride.

The temperature dependence of the heat of fusion (ΔH_f) has also been neglected in this equation, as any correction for the ΔC_p term should be small compared to the uncertainty in the published value of the heat of fusion of silver chloride, i.e., ± 100 cal.

The calculation of thermodynamic activities in ideal ionic molten salt solutions was derived by Temkin as the product of the individual ionic fractions and are given simply as the fraction of ions of similar sign. This statistical model implies the random distribution of cations on cation sites, and of anions on anion sites, regardless of the charge of the ions.

Flood, Forland, and Grotheim (13) modified Temkin's model to account for a vacancy introduced by a divalent ion in the molten salt structure. The thermodynamic activity is then calculated as the product of the equivalent ionic fractions for anions and cations.

Thus, in a mixture containing n_1 moles AgCl, and n_2 moles Ag₂S, the activity of silver chloride following these two models is given by either of the relationships

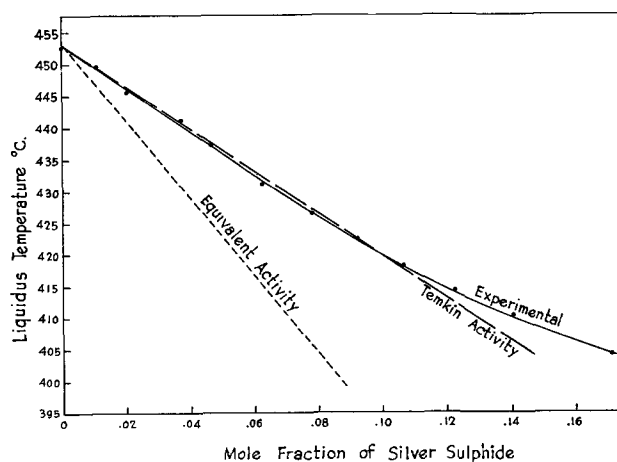


Fig. 3. Comparison between the experimental and the calculated liquidus on the silver chloride side of the phase diagram.

(a) in terms of the ionic fractions

$$a_{\text{AgCl}} = N_{\text{Ag}^+} \cdot N_{\text{Cl}^-} = \frac{n_1}{n_1 + n_2} = x_{\text{AgCl}} \quad [2]$$

(b) in terms of the equivalent ionic fractions

$$a_{\text{AgCl}} = N'_{\text{Ag}^+} \cdot N'_{\text{Cl}^-} = \frac{n_1}{n_1 + 2n_2} \quad [3]$$

It should be noted that because of the existence of a common cation, Temkin's activity is numerically equally to the conventional mole fraction (x_{AgCl}).

Figure 3 shows the comparison between the experimental and the calculated liquidus. The solid line is the best curve drawn through the experimental points. A straight line has been drawn from 0 to 8 mole % silver sulfide and the liquidus then curves off as shown. The dashed line is the theoretical liquidus calculated using Temkin's model, and the dotted line that calculated using the equivalent fraction model. It is evident that Temkin's model gives a good agreement with the experimental data, the deviation at 8 mole % being less than 100 cal, compared to the uncertainty of ± 100 cal for the published value of the heat of fusion of silver chloride. The conclusion that the simple Temkin model, rather than the equivalent ionic model, predicts the correct activity for a system containing mono- and divalent anions, is the same as that reached previously by numerous investigators (14-16) for systems containing mono- and divalent cations. The results indicate that silver sulfide is completely dissociated and forms essentially ideal mixtures up to 8 mole %. Divalent and monovalent anions are randomly distributed in all anion positions and divalent anions are not associated with additional vacancies in the melt.

Above 8 mole % silver sulfide, the experimental liquidus curve lies higher than that predicted from theory, indicating that positive deviations from ideality are occurring.

On the silver sulfide side of the phase diagram, the freezing point depression of Ag₂S on addition of AgCl may be calculated again from the van't Hoff

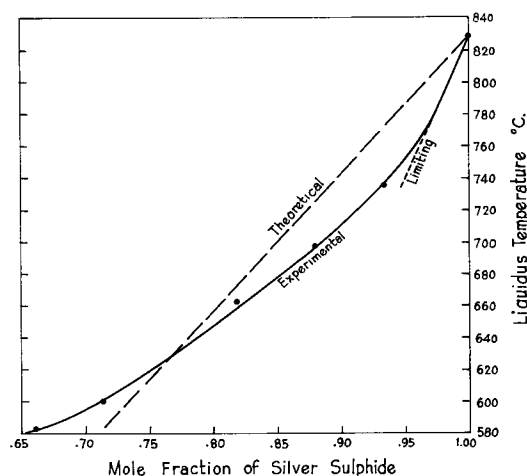


Fig. 4. Comparison between the experimental and the calculated liquidus on the silver sulfide side of the phase diagram.

equation, the published value of the heat of fusion of Ag_2S [2.7 kcal/mole (11)], and the observed melting point of pure silver sulfide. Assuming that silver sulfide is fully ionized in the liquid mixtures, Temkin's activity may be used to calculate the theoretical liquidus.

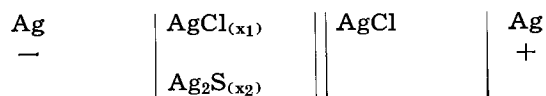
Figure 4 shows the result of this calculation. It is evident that the calculated liquidus is about 40°C , above the experimental curve, at 95 mole % silver sulfide. The discrepancy cannot be ascribed to solid solubility, as solid solubility would raise further the temperature of the calculate line. Furthermore, a higher value for the heat of fusion (17) or even a higher melting point of silver sulfide should also increase this difference.

Solid silver sulfide may be described in terms of a rather rigid chain network of sulfur atoms covalently bonded with the highly mobile silver atoms in interstitial positions (18). The low value of the entropy of fusion, i.e. only 3.1 e.u., indicates that the solid structure does not break down completely on melting, so that liquid silver sulfide should also be described as an associated liquid. If such were the case, then the number of structural units of silver sulfide would be less than that expected. Further breakdown could also be expected on addition of silver chloride. An estimate of the average chain length for $(\text{Ag}_2\text{S})_n$ required to give the observed limiting freezing point depression, 740°C and 95 mole % Ag_2S , gave the average value for n as approximately 2.4. This value appears consistent with the view that silver sulfide behaves as an associated liquid.

As more silver chloride is added, further breakdown should take place, the average chain length should decrease, and as a result, the heat of fusion of silver sulfide should increase. The experimental liquidus would then approach the ideal line calculated using Temkin's activities, as shown by the converging curves on Fig. 4 at about 25 mole % silver chloride. At even higher concentrations of silver chloride, the presence of the incongruently melting compound causes the experimental liquidus to deviate further from the ideal line, but in the opposite direction.

EMF Measurements

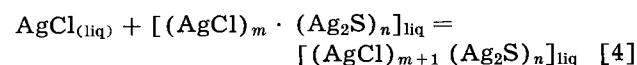
The reversible potentials for the concentration cell



were measured as a function of temperature and concentration. Measurement during an increasing and decreasing temperature cycle were in excellent agreement, and there was no sign of contamination of the silver chloride electrode with silver sulfide even after operating the cell continuously for a period of three weeks.

Potentials at concentrations higher than 30 mole % and particularly at the higher temperatures, could not be measured accurately because of what was subsequently (9) found to be excessive electronic conductivity in the melts. Thus, the dashed line in Fig. 5 and 6 represents the onset of electronic conduction as determined by the conductivity measurements. The interpretation of the data beyond this limit is questionable.

On the passage of one equivalent of electricity, the spontaneous cell reaction may be readily derived as



where m and n represent very large numbers. The free energy change for this reaction is by definition the partial molar free energy of mixing of silver chloride, the standard state being also defined as pure liquid silver chloride at the temperature of the experiments.

The equation for the cell potential is, therefore

$$E = - \frac{2303 RT}{F} \log x\gamma \quad [5]$$

where x and γ are, respectively, the mole fractions and the activity coefficient of silver chloride.

The liquid junction potential has not been included in Eq. [5] as previous measurements indicated that the junction potential between two melts having a common ion should be negligibly small at close compositions. Thus it was found (7) that across a fused asbestos fiber separating the equimolar mixture of potassium and sodium chlorides and a solution of silver chloride in the same solvent melt, the junction potential vanishes at all concentrations below 20 mole % of silver chloride in solution. Murgulescu and Sternberg (19) measured the junction potentials between pure liquid silver halides and the corresponding mixtures with alkali chlorides, and found that in all cases the corrections for the liquid junction potentials were less than 1 mv. The same conclusion was also reached recently by Laity (20) for the junction potential between molten silver nitrate and mixtures of silver nitrate and potassium nitrate.

It appears, therefore, that the use of the simple form of Eq. [5] for calculating the activities is justified on the basis of indirect experimental evidence.

The results of the potential measurements are given in Fig. 5. That relatively large entropy effects

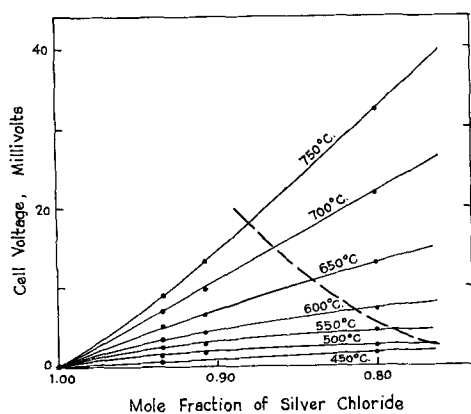
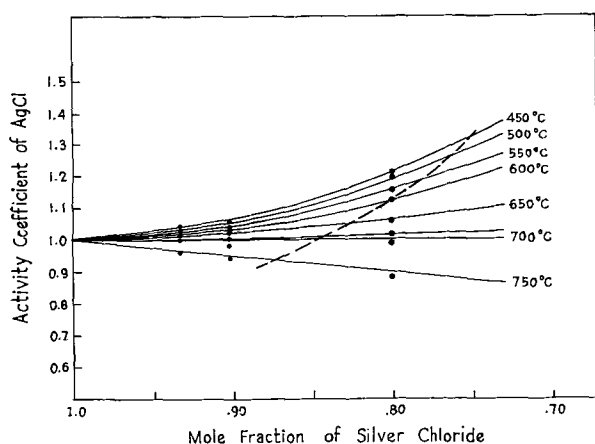
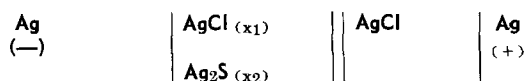


Fig. 5. EMF measurements of the cell:

Fig. 6. Activity coefficients of silver chloride in AgCl-Ag₂S mixtures.

occur in these mixtures is indicated by the large temperature dependence of the emf values.

The activity coefficients of silver chloride have also been calculated and are given in Fig. 6. It is evident that silver chloride in the presence of silver sulfide shows slight positive deviations from ideality, up to 10 mole % silver sulfide the solutions are very nearly ideal, in complete agreement with the calculation from the phase diagram. Kleppa (22) and Toguri *et al.* (21) have also observed positive deviations from ideality in mixtures containing a common cation. The activity coefficients increase with increasing silver sulfide content and decrease with increasing temperature; the solution approaching ideality at the higher temperatures. The slightly positive deviations from ideality at the lower temperature may be explained in terms of a change in configurational entropy because of a preferential distribution of the ions present.

At high temperatures, random distribution prevails, and the solutions become ideal. In any case, such small positive deviations from ideality should not be ascribed to the formation of complex species in the melt over the range of concentration investigated.

Density Measurements

The densities of the molten mixtures of Ag₂S-AgCl were measured as functions of temperature at

Table I. Observed densities of molten AgCl-Ag₂S mixtures

Mole fraction silver sulfide	Density = $a - b(t^\circ\text{C} - 500)$		Standard deviation	Temperature range, °C
	a	$b \times 10^3$		
0	4.832	0.87	0.0017	486-800
5.70	4.984	0.85	0.0025	480-800
20.37	5.396	0.87	0.002	480-800
30.01	5.475	0.75	0.0017	500-800
32.30	5.540	0.74	0.0027	500-800
39.14	5.654	0.73	0.0013	500-800
53.44	6.012	0.67	0.0028	650-950
65.59	6.159	0.45	0.002	700-960
78.31	6.407	0.55	0.003	700-960
85.50	6.535	0.52	0.005	700-960
97.98	7.439	2.6	0.016	860-960

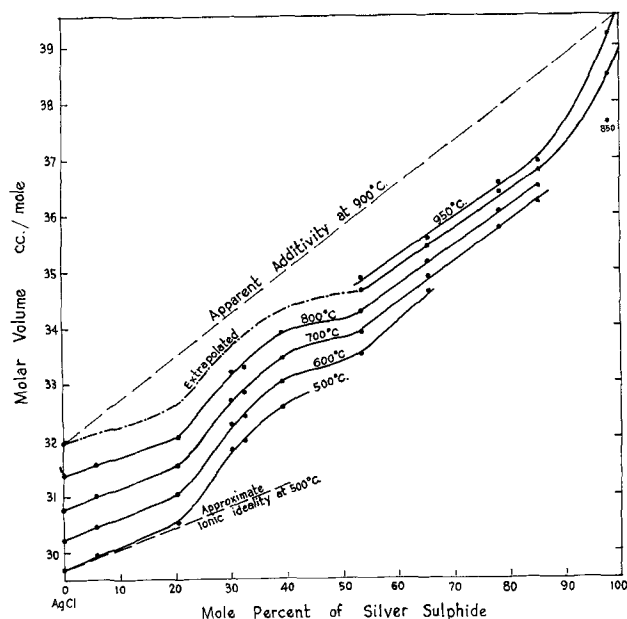
a number of compositions. The observed densities were linear functions of temperature for all compositions studied. Linear regression of the observed densities as a function of temperature yielded the constants a and b to fit the equation

$$d = a - b(t - 500) \quad [6]$$

where the temperature is in degrees centigrade.

The constants and the calculated standard deviations are shown in Table I. The measured densities of pure silver chloride are in excellent agreement, within 0.05%, to those reported recently by Spooner and Wetmore (23). The standard deviation shows the scatter of the measured data about a straight line and does not include absolute errors such as calibration errors and the effect of surface tension on the fine quartz fibers. That such errors are small is apparent from the excellent agreement with Wetmore's data, and the self-consistency of the data on independent determinations (see Fig. 7 at 30 and 32 mole % silver sulfide).

From the measured densities, the molar volumes of the melts were calculated by dividing the average molecular weight of the mixtures by the density. The molar volume isotherms plotted as a function of composition are shown in Fig. 7.

Fig. 7. Molar volumes of the AgCl-Ag₂S system

For compositions close to silver chloride, the increase in density on increasing the silver sulfide concentrations is that which might be expected for an ideal ionic mixture. The ionic radius of the sulfur ion, 1.82Å, is almost the same as that of the chloride ion, 1.80Å, so that the addition of completely ionized silver sulfide to silver chloride should increase the total molar volume by only the volume of one gram ion of silver ions per mole of silver sulfide added. If there are no changes in packing effects in the melts on the addition of silver sulfide, the approximate increase in molar volume on the addition of silver sulfide, using a hard sphere model for the calculation, would be that shown by the dashed line in Fig. 7 for the 500°C isotherms. It is evident that in dilute solutions of silver sulfide, the increase in molar volume with increasing silver sulfide concentration is that expected for completely ionized silver sulfide. The density measurements are then in good agreement with the calculations from the phase diagram in indicating that in dilute solutions silver sulfide is completely ionized, and that an additional vacancy is not introduced with the divalent sulfide ion.

The increase in molar volumes of the melts above the line for approximate ionic ideality, in the composition range 20-50%, indicates a tendency toward compound formation in the melts (24). This tendency is coincident with the incongruent melting compound shown in the phase diagram.

Pure silver sulfide has a large molar volume which decreases rapidly on the addition of silver chloride. Calculations from the phase diagram on the silver sulfide side of the system have already indicated that molten silver sulfide behaves like an associated liquid, with a network of covalently bonded sulfur atoms persisting from the solid. This structure would be expected to contain a relatively large amount of free volume, and hence to have a large molar volume. The partial molar volume of silver chloride, which may be determined graphically by the intercept of a tangent drawn to any of the isotherms shown in Fig. 7, would then be expected to be abnormally small. Thus at 900°C, the indicated partial molar volume of AgCl is about 23 cc/mole as compared with 32 cc/mole for pure AgCl at this temperature.

The rapid decrease in the molar volume of the melts on the addition of silver chloride indicates, in agreement with the phase diagram calculations, that the large structural units in silver sulfide are rapidly broken up on the addition of silver chloride. Between 55 and 85 mole % silver sulfide, the molar volumes appear to be essentially linear functions of composition, indicating that the partial molar volumes for both silver chloride and silver sulfide remain constant and are additive. Furthermore, the partial molar volumes of silver chloride in this area are approximately those of pure silver chloride. This suggests that the sulfide is no longer associated, so that its partial molar volume should represent the volume of the monomolecular liquid silver sulfide. It should be noted that the partial molar volume of silver sulfide in this area is greater than on the sil-

ver chloride side of the system because of a possible lower coordination number and the resulting larger amount of free volume in the melt.

Conclusions

The combined results of the phase diagram calculations, the emf measurements, and of the molar volumes of the mixtures, indicate the following:

Dilute solutions of silver sulfide in silver chloride are completely ionized and form ideal solutions. Additional vacancies are not introduced with the added divalent sulfur anions.

In more concentrated solutions, slight positive deviations from ideality occur at low temperatures. The deviations can be accounted for only by entropy effects due to a preferential distribution of the ions present. As the temperature is increased, the solutions tend toward ideality.

An incongruently melting compound appears at about 50 mole % silver sulfide. Pure liquid silver sulfide contains large structural units of covalently bonded sulfur atoms, persisting from the solid. These groups are rapidly broken up on the addition of silver chloride.

Acknowledgments

This work was carried out with financial assistance from the School of Engineering Research (S.E.R.) of the University of Toronto, and from the National Research Council of Canada. The authors wish to thank N.R.C. and Cominco for a maintenance grant to one of us (M.C.B.).

Manuscript received Aug. 22, 1963. This paper was presented at the Pittsburgh Meeting, April 15-19, 1963.

Any discussion of this paper will appear in a Discussion Section to be published in the December 1964 JOURNAL.

REFERENCES

1. H. Sawamoto and T. Saito, *J. Mining Inst. Japan*, **68**, 555 (1952).
2. H. Winterhager, *Forschungber. Wirtsch. u. Verkehr. Nordrhein-Westfalen*, No. 134, 1955.
3. H. Winterhager and R. Kammel, *Z. Erzbergbau. u. Metallhuttenu.*, **9**, 97 (1956).
4. L. Yang, G. M. Pound, and G. Derge, *Trans. AIME*, **206**, 783 (1956).
5. C. Wagner, *J. Chem. Phys.*, **21**, 1819 (1953).
6. S. N. Flengas, *Ann. N. Y. Acad. Sci.*, **79**, art. 11, 853 (1960).
7. S. N. Flengas and T. R. Ingraham, *This Journal*, **106**, 714 (1959).
8. L. Brewer *et al.*, "Chemistry and Metallurgy of Miscellaneous Materials: Thermodynamics," McGraw-Hill Book Co., New York (1950).
9. M. C. Bell and S. N. Flengas, *This Journal*, **111**, 575 (1964).
10. F. C. Kracek, *Trans. Am. Geophysics Union*, **27**, 364 (1947).
11. O. Kubaschewski and E. Evans, "Metallurgical Thermodynamics," Pergamon Press (1955).
12. A. A. Velikanov, *Ukrain. Khim. Zhur.*, **26**, 319 (1960).
13. H. Flood, T. Forland, and C. Grjotheim, *Inst. Min. Met. Symp. Molten Slags*, **46**, 1953.
14. T. Forland, *Discussion Faraday Soc.*, No. 32, 122 (1961).
15. K. J. Macleod and F. E. W. Wetmore, *Ann. N. Y. Acad. Sci.*, **79**, art. 11, 873 (1960).
16. H. Bloom and B. J. Welch, *Discussion Faraday Soc.*, No. 32, 115 (1961).

17. K. K. Kelley, *U.S.B.M. Bull.* 406, 1937.
18. A. F. Wells, "Structural Inorganic Chemistry," 136, Oxford (1960).
19. I. G. Murgulescu and S. Sternberg, *Discussion Faraday Soc.*, No. 32, 107 (1961).
20. R. Laity, *J. Am. Chem. Soc.*, **79**, 1849 (1957).
21. J. Toguri, H. Flood, and T. Forland, Unpublished results quoted *Discussion Faraday Soc.*, No. 32, 168 (1961).
22. O. J. Kleppa and S. V. Meschel, *J. Phys. Chem.*, **67**, 668 (1963).
23. R. C. Spooner and F. E. W. Wetmore, *Can. J. Chem.*, **29**, 777 (1951).
24. M. Bloom and J. Bockris, "Modern Aspects of Electrochemistry," No. 21, Butterworth (1960).

The Electrical Conductivity, and the Thermodynamic and Structural Properties of Molten AgCl-Ag₂S Mixtures

II. Electrical Conductivities

M. C. Bell and S. N. Flengas

Department of Metallurgical Engineering, University of Toronto, Toronto, Ontario, Canada

ABSTRACT

The specific conductivities of molten silver chloride-silver sulfide mixtures have been determined over the entire composition range. Pure molten silver sulfide is a good electronic conductor having a specific conductivity of 202 ohms⁻¹·cm⁻¹, with an almost negligible temperature dependence. The measured specific conductivity of pure molten silver chloride is in very close agreement with previous determinations. Silver chloride has a very low apparent activation energy for conduction. By comparison with the alkali halides, it is shown that the apparent activation energy for conduction of univalent salts is inversely proportional to their lattice energies. Dilute solutions of silver sulfide in silver chloride are ionic conductors. The specific conductivity in this region decreases and the apparent activation energy for conduction increases as the concentration of silver sulfide is increased. Above 20 mole % silver sulfide, the conductivity of the melts increases rapidly with increasing silver sulfide content and increasing temperature, as electronic conduction starts to occur. The activation energy for electronic conduction in this region is shown to be essentially composition and temperature independent. One per cent electronic conduction starts to occur at about 14 mole % silver sulfide at 750°C and at 24.5 mole % silver sulfide at 460°C. Above 50 mole % silver sulfide the conductivity increases very rapidly, and the temperature dependence of the conductivity becomes negative. Structural changes in these melts appear to influence the electronic conduction markedly.

The electrical conductivity of solid silver sulfide has been widely investigated (2, 3). It has been shown that the character of the conductivity changes from predominantly semiconductive to metallic at temperatures above 178°C. It is perhaps of historical interest that silver sulfide was the first semiconductive material discovered by Faraday in 1833.

Pure liquid silver sulfide is also a good electronic conductor having a specific conductivity of 202 mhos cm⁻¹ at 850°C, about half that of molten FeS (4), and about three times that of molten Cu₂S (5). On the other hand, molten silver chloride is an ionic conductor having a specific conductance of only 3.995 mhos cm⁻¹ at 500°C. It should therefore be expected that molten mixtures of these two compounds would exhibit both types of conductivity.

It was the purpose of this investigation to study the factors affecting the type of conductance prevailing in these mixtures.

In a previous publication (1), properties giving an insight into the structure of the silver chloride-silver sulfide mixtures, phase diagram, molar vol-

umes, and activity measurements, were investigated. In this paper, the electrical conductivities were measured over the permissible temperature range for a number of compositions across the phase diagram. The results are discussed in relation to the previously measured structural properties of the system.

Experimental

The preparation and purification of the materials used in this investigation have been described in a previous publication. Briefly, the materials were anhydrous and of reagent grade, and the silver sulfide was stoichiometric within the error of analysis.

The a-c conductivity bridge used in the investigation incorporated both the basic Jones and Joseph (6) and the Luder (7) bridge designs. The bridge was designed for accurate measurements over a wide range of resistances and frequencies. Leeds and Northrup, 697-C frequency independent, paired ratio arms, alike to 0.02%, of 10, 100, 1000, and 10,000 ohms, could be plugged into the bridge. A Leeds and Northrup a-c decade resistor (4755) having 1000, 100, 10, 1, and 0.1 ohm decades was used as

the standard resistor. A 0.01 ohm decade was made from Kanthal resistance wire and a decade switch. The power supply for the bridge was an Eico signal generator having a frequency response up to 100 kilocycles. A three-stage transistor amplifier having an amplification of about 2000 to 1 at low input signals was incorporated in the bridge design. The amplifier proved to be quite noise free in operation. A broad band oscilloscope tuned to the input frequency, or a harmonic of both 60 cycle and the input frequency, was used as the null point detector. The sensitivity of the bridge was 0.1 ohm in 10,000 ohms or 0.01 ohm in 100 ohms. No difference could be detected between using the Luder, or the Jones and Joseph systems of balancing the bridge, and the Jones and Joseph system was used as it required less precise balancing of the Wagner ground.

The conductivity cell used in the investigation is illustrated in Fig. 1. The cell was a simple U-tube silica glass capillary. Silica was found to be an excellent container for these melts, provided oxygen was rigorously excluded from the cell, and the cells showed no sign of attack even after several weeks of operation. It was found that the viscous melts would not readily come to the same hydrostatic level on either side of the U-tube when the capillary used was smaller than 1.5 mm ID. Therefore, the capillary used in the present investigation was 2.5 and 2.0 mm ID and cell constants of about 400 and 800 cm^{-1} were obtained. Bright platinum disk elec-

trodes were used on the silver chloride side of the system. Since platinum dissolves in molten sulfides, tungsten rod electrodes were used and found to be quite stable on the silver sulfide side of the system. The electrodes were fused to heavy silver wires which were taken out of the cell through vacuum-tight sliding seals. The resistance of the electrodes and of the leads were measured at several temperatures, and appropriate corrections were applied. The entire cell was immersed in a molten tin bath covered with carbon and maintained under an argon atmosphere. With the tin bath, the temperature gradient over the length of the cell, approximately 6 in., could easily be adjusted to less than $\frac{1}{4}^{\circ}\text{C}$, and could readily be maintained at a constant temperature during the time required for a reading.

It was found in preliminary experiments that the melts did not wet the quartz, and bubbles formed between the melt and the cell. It was therefore found necessary to evacuate the cells lightly to obtain reproducible resistances. The entire cell as constructed was vacuum tight, and was always maintained under a slight positive pressure of dried, purified argon, while the actual readings were being taken. Different pressures of argon could be applied to either side of the cell and the melt moved completely through the capillary to insure that no bubbles were present. This operation was repeated for each measurement to insure that the correct readings were obtained. The cell had a sidearm feeding tube magnetically operated from outside, so that the composition of the melt could be changed without opening the cell by adding pellets of either silver sulfide, or silver chloride.

The conductivity cells were calibrated at room temperature using 1 demal KCl solution for which the conductivity is accurately known (8). The temperature of the large distilled water bath used as a thermostat could be maintained constant to 0.001°C during the time required for calibration. The cells were calibrated for different amounts of solutions in the cells, and different amounts of electrode immersion at each level of solution. The level of the solutions in the cell was readily measured with a cathetometer by lowering the electrode assembly until electrical contact was established across the cell. The cell constant was then known regardless of the amount of melt in the cell, or the amount of electrode immersion. The capillary accounted for essentially all of the cell resistance, so that the total variation for the amount of electrode immersion and level of solutions in the cell was less than 0.3% of the cell constant. During calibration, the resistances were measured at frequencies from 2 to 12 kilocycles and extrapolated to infinite frequency. The extrapolation to infinite frequency was generally less than 1% of the total resistance when using the platinum disk electrodes, and slightly more when using the tungsten rod electrodes.

Results and Discussion

The resistance of the silver chloride-silver sulfide melts was measured at a number of concentrations over the entire composition range, as a

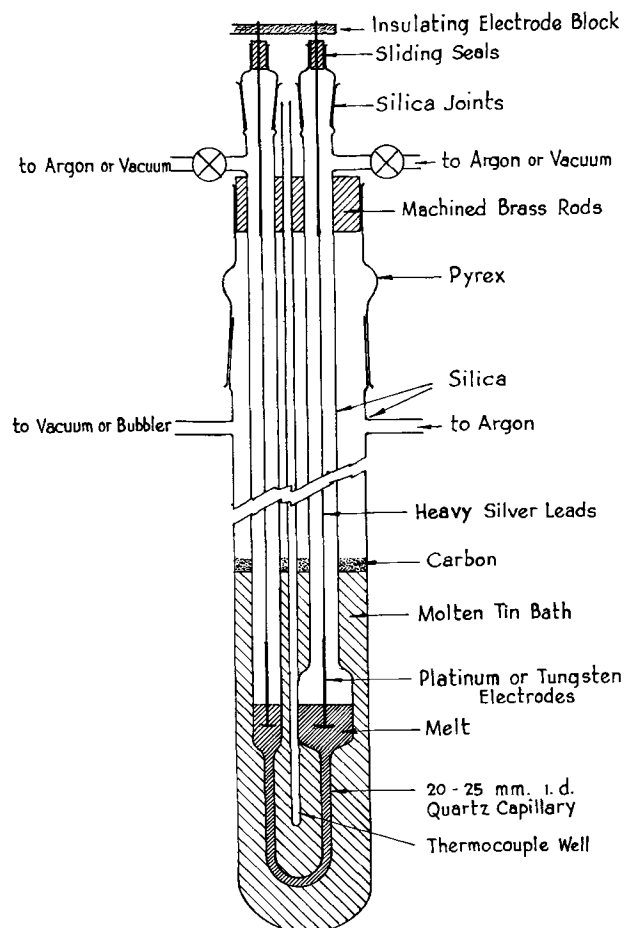


Fig. 1. Conductivity cell

function of temperature. The resistances were reproducible to within 0.2% over periods of several days on increasing and decreasing the temperature cycle. A large number of readings, about 30, were taken at each composition so that accurate curves could be drawn through the results. There was no measurable change in the observed resistances on changing the bridge frequency from 1 to 9 kilocycles. All measurements were therefore made at 3 kilocycles.

Ionic conduction.—The measured specific conductivities of the melts on the silver chloride side of the system up to the eutectic composition are shown in Fig. 2. Higher concentrations have conductivities well above the range of this graph.

The measured conductivities for pure silver chloride are 2.0–2.5% higher than those reported by Harrap and Heyman (9) and 0.7% higher than those reported more recently by Doucet and Bizouard (10). Our values are, however, in excellent agreement with those reported by Wetmore (11), being only 0.15% higher.

It is evident from Fig. 2 that the conductivities of the mixtures, up to 20 mole % silver sulfide, are lowered by the addition of silver sulfide, particularly at the lower temperatures. It was shown in a previous publication (1) that silver sulfide is completely ionized in this concentration range. Duke has shown that silver ions in molten silver chloride carry most of the current (12), so that the observed decrease in conductivity should be attributed to a lowering of the mobility of the silver ions due to the higher charge density of the divalent sulfur ions.

Above 20 mole% silver sulfide, as seen in Fig. 2, there is a very rapid increase in conductivity with temperature, and conductivities much higher than that for pure silver chloride are observed. This increase in conductivity is due to electronic conduction, as none of the ions in solution could have mobilities high enough to give the observed conductivities.

The specific conductivity for those compositions having ionic conductivities—up to 9.95 mole % silver sulfide at all temperatures, and the lower temperature region of the 19.83 mole % curve—could be exactly fit to an equation of the form

$$K_{\text{ionic}} = a + b(t - 400) - c(t - 400)^2 \quad [1]$$

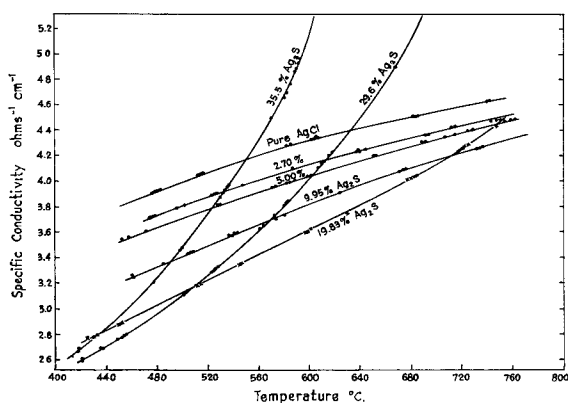


Fig. 2. Specific conductivities of molten AgCl-Ag₂S mixtures, on the silver chloride side of the composition range.

Table I. Ionic conduction in AgCl-Ag₂S melts. $K_{\text{ionic}} = a + b(t - 400) - c(t - 400)^2$ where t is the temperature in degrees centigrade

Mole fraction silver sulfide	a	$b \times 10^2$	$c \times 10^6$
0	3.580	0.4625	0.451
2.70	3.390	0.4463	0.375
5.00	3.309	0.4143	0.243
9.95	2.975	0.450	0.205
19.83	2.605	0.472	0.0
29.67	2.39*	0.49*	0*
35.5	2.36*	0.49*	0*

* Extrapolated values.

The determined values of the constants a , b , and c , are given in Table I. The coefficients for Eq. [1] were then extrapolated to give the coefficients, and therefore the expected ionic conductivities for the 29.7 and 35.5% compositions. The extrapolated values are quite close to the actual values observed at low temperatures and are also included in Table I. The electronic conductivity occurring at these compositions is the difference between the calculated and observed values and will be discussed subsequently.

From the measured specific conductivities and the densities reported previously (1), the equivalent conductivities in the area of ionic conduction were calculated, and plots of the logarithm of the equivalent conductivity vs. $1/T^\circ\text{K}$, were made. As was found in other accurate determinations (11, 15), none of the Arrhenius type plots were straight lines, and the "apparent activation energies" for conduction were determined at specified temperatures. The apparent activation energy for silver chloride is very low, and changes from 1.35 at 500°C to 1.14 kcal per equivalent, at 700°C.

At the present time, there is no comprehensive theory for ionic conduction in molten salts, and most of the empirical relationships have been derived by a comparison of the conductivities of the alkali halides. It is therefore instructive to compare the properties of silver chloride to those of the alkali halides. A comparison of some of the properties which might be expected to influence the conductivities are shown in Table II.

As it is difficult to compare the equivalent conductivities at the same temperature because of the wide range of melting points, Table II shows the equivalent conductivities at the arbitrary "equivalent temperature" of 1.1 times the melting point in degrees Kelvin used by Van Artsdalen (15). The conductivity and density data for the alkali halides are taken from the very accurate work of Yaffe and Van Artsdalen (15). For more accurate values, the original paper should be referred to. It is evident from Table II that the equivalent conductivity of silver chloride at the "equivalent temperature" is about the same as that of potassium chloride which has a larger cation radius, indicating that the equivalent conductivities are not in order of their ionic radii. Caution should be exercised in such a conclusion however, because of the arbitrary nature of the equivalent temperature, the wide differences

Table II. Comparison of the electrical conductivities and associated properties of silver halides, and the alkali halides

Salt	ΔA at $\theta = \frac{T \cdot K}{T_{M.P.}}$ = 1.1 ohms ⁻¹ cm ² equiv. ⁻¹	Apparent activation energy for conduction at $\theta = 1.1$ kcal/equiv.	Average temperature dependence of $\Delta H^\ddagger \times 10^2$ kcal equiv. ⁻¹ °C ⁻¹	Cation radius (solid state) (13) cm $\times 10^8$	Lattice energy (solid state) (13) kcal/mole	Volume change on melting (14) $\Delta V/V_s$ %	Expansivity $\times 10^3$ g cc ⁻¹ °C ⁻¹	Coeff. C in the attractive energy term $-C \cdot r^{-9}$ (12) (solid state) erg/cm ⁶ $\times 10^{60}$
AgCl	121.9	1.29	-0.10	0.97	203	8.9	0.87	767
LiCl	179.5	2.0	+0.03	0.70	195	26.2	0.433	113
NaCl	152	2.92	+0.14	1.00	180	25.0	0.543	180
KCl	122.7	3.4	-0.25	1.33	164	17.3	0.583	452
RbCl	100	4.4	-0.23	1.52	158	14.3	0.883	691
CsCl	87	5.25	-0.47	1.70	145	10.5	1.065	1530
AgBr (9)	100.5	1.20	—	0.97	197	8.2	1.04	967
LiBr	179.5	2.03	+0.15	0.70	185	24.3	0.6520	183
NaBr	144.2	3.2	+0.14	1.00	172	22.4	0.8169	271
KBr	107.8	3.7	-0.92	1.33	157	16.6	0.8253	605
RbBr	85.5	4.2	-0.72	1.52	152	13.5	1.0718	1330
CaBr	72.5	5.6	-0.69	1.70	—	—	1.2234	2070

in melting points, and the uncertainty of the ionic radii in molten salts.

The apparent activation energy for conduction is a relatively temperature insensitive property, and therefore offers a good basis for comparison of the alkali halides with silver chloride. It is evident from Table II that the apparent activation energies for conduction are not related by the ionic radii, but appear to be inversely proportional to the lattice energy of the salts. That such is the case for the alkali chlorides and silver chloride; and for the alkali bromides and silver bromide, is shown in Fig. 3. Such a correlation is quite reasonable, as one would expect the temperature dependence of the equivalent conductivities to be inversely proportional to attractive force field between the ions in the melt. Some of the deviations from the straight lines in Fig. 3, and the difference between the chlorides and bromides may be the result of different changes of lattice energies on melting.

It should be noted in Table II that the volume change on melting of the alkali halides and silver halides decreases as the polarization forces in those salts increase. This would indicate, as expected, that the salts with more deformable ions can melt with the introduction of less free volume into the melt structure. Furthermore, salts with small volume

changes on melting have a larger expansivity in the molten state regardless of their radii.

It would also appear from this Table that the average temperature coefficient of the heat of activation is positive for salts with low polarizability and negative for salts having higher polarizabilities.

A much more detailed knowledge of the forces acting in molten salts is required for a better understanding of the conductivity in ionic melts.

The apparent activation energy for equivalent conduction in mixtures of silver sulfide in silver chloride are shown in Fig. 4. It is evident that as divalent sulfide ion is added to the monovalent silver chloride melt, the apparent activation energy for conduction increases rapidly. This increase in activation energy parallels the decrease in the equivalent conductivity at low temperatures. This increase in activation energy, and the positive temperature coefficient for activation energy in these mixtures, are consistent with the view that the mobility of the silver ions becomes restricted by the presence of the divalent sulfur ions.

Electronic conduction.—It was shown in Fig. 2 that electronic conduction started to occur in the melts at concentrations above 20 mole % silver sulfide. The coefficients for Eq. [1] were fit for the ionic range of conductivities, and extrapolated to

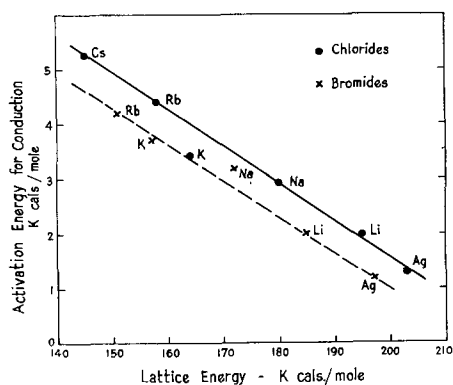


Fig. 3. Apparent activation energy of pure molten monovalent metal chlorides and bromides as a function of their lattice energies.

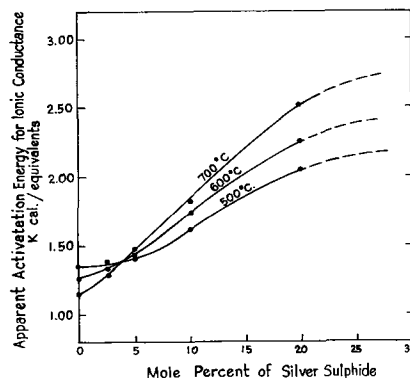


Fig. 4. Apparent activation energy for ionic conduction in molten AgCl-Ag₂S mixtures.

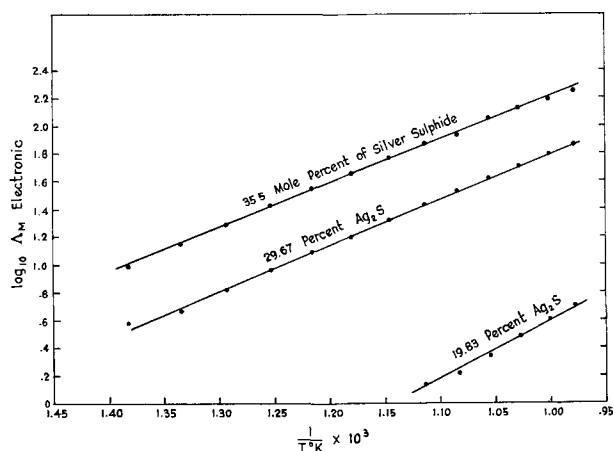


Fig. 5. Plot of the molar electronic conductance vs. $1/T$

give the expected contribution due to ionic conductivities for the 29.6 and 35.5 mole % silver sulfide compositions. The extrapolated values for the coefficients are shown in Table I, and give values quite close to the observed conductivities at low temperatures (400°C). The difference between the measured conductivities and the expected ionic conductivities calculated from the values in Table I, thus gives the amount of electronic conduction occurring at these compositions. At high temperatures there is a large difference between the measured conductivities and the expected ionic conductivities, so that small errors in extrapolation have little effect on the calculated amount of electronic conductivity. The specific electronic conductivity thus obtained was then multiplied by the molar volume to give the molar electronic conductivity, and express the conductivity per unit number of sulfur atoms in the melt. A plot of the logarithm of the molar electronic conductivity, thus calculated, is shown vs. $1/T^{\circ}\text{K}$ in Fig. 5.

It is evident that the electronic conductivity at these compositions obeys an equation of the form

$$\Delta_m (\text{electronic}) = D \cdot e^{-F/RT} \quad [2]$$

where T is given in degrees Kelvin, and that the "apparent activation energy" for electronic conduction is a unique value over a temperature range of 300°C . The curves moreover are almost parallel for compositions between 20 and 36 mole % Ag_2S , indicating that the apparent activation energy for electronic conduction is essentially composition independent in this region. Values of the constants to fit Eq. [2] are given in Table III. Different extrapolations for the expected ionic conductivities shown in Table I still give straight line plots with essentially parallel slopes, and values for D and F only slightly different from those shown in Table

Table III. Electronic conduction in AgCl-Ag₂S mixtures
 $\Delta_m (\text{electronic}) = D \cdot e^{-F/RT}$

Mole fraction silver sulfide	$\log_{10} D$	F
19.83	4.711	18,800
29.67	5.099	15,000
35.5	5.342	14,300

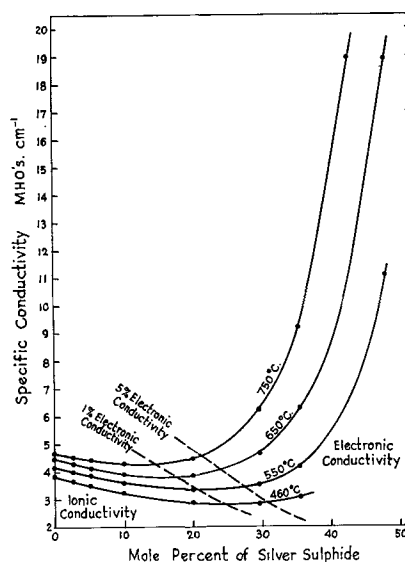


Fig. 6. Specific conductivity isotherms of molten AgCl-Ag₂S mixtures on the silver chloride side of the composition range.

III. The values for the 19.83% composition are less accurate than the other compositions because of the small amount of electronic conduction. The onset of electronic conductivity in these melts can best be seen in a plot of the conductivity vs. composition at various temperature isotherms, as shown in Fig. 6.

The conductivity isotherms decrease as the divalent sulfur ion lowers the ionic mobility of the silver ions and then there is a very dramatic increase as electronic conduction starts to occur. The very rapid increase in conductivity with temperature at the higher compositions is evident. The approximate lines for 1 and 5% electronic conduction were interpolated from the data given in Table III, and are shown by the dashed lines. It is evident that electronic conductivity starts to occur at steadily lower sulfide concentrations at higher temperatures. Presumably electrolysis of such mixtures could be carried out at high current efficiencies in the ionic regions.

The specific conductivity at a number of compositions on the silver sulfide side of the system was also measured as a function of temperature. The results of these measurements are given in Fig. 7.

It is readily seen that the specific conductivity of pure molten silver sulfide is practically temperature independent, changing from 202.5 at 840°C , to 201.5 mhos cm^{-1} at 960°C .

A small amount of sulfur condensed in the upper part of the conductivity cell during the measurements on pure silver sulfide. However, this did not have any measurable effect on the specific conductance of the liquid, as the measured value remained constant over a 24-hr period at the lower temperature. On the addition of silver chloride to silver sulfide the decomposition pressure of sulfur apparently decreased, and there was no sign of condensed sulfur in any of the subsequent runs with the mixtures. At temperatures below 830°C , the conductivity increased rapidly as the material changed its state from liquid to solid. At temperatures below 815°C , the conductivity of solid silver sulfide reached a value of approximately 700

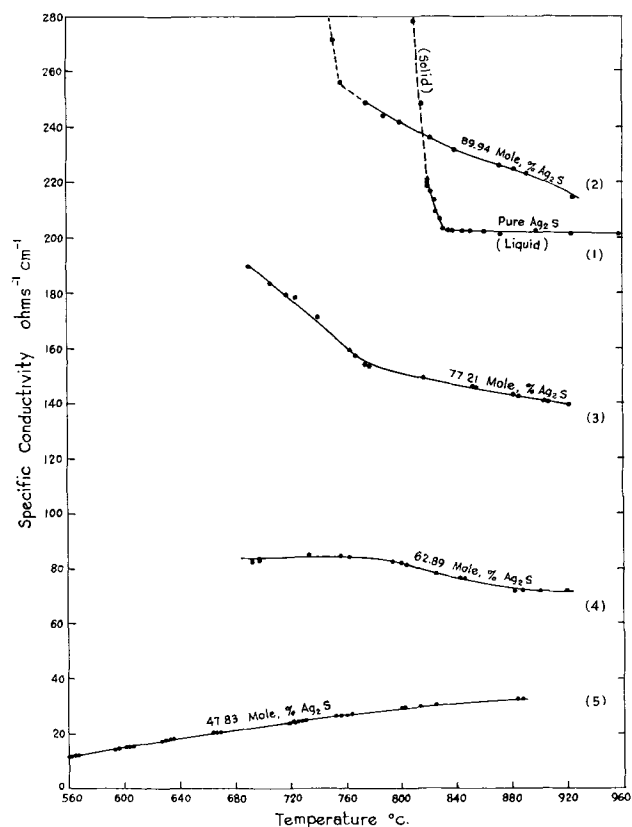


Fig. 7. Specific conductivities of AgCl-Ag₂S molten mixtures on the silver sulfide side of the composition range.

mhos cm⁻¹, which appeared to depend on the cooling rate. These figures, however, can be considered to be only approximate, as the apparatus was not designed to take into account shrinkage effects which occur in the solid state. These values are in agreement with the conductivities of solid silver sulfide reported recently by Velikanov (16), although the conductivities for pure liquid silver sulfide reported herein are about 50% greater than those measured by Velikanov in a capillary cell equipped with graphite electrodes.

The molar conductivities of the melts are shown in Fig. 8 for the entire composition range. The liquidus is also superimposed in this diagram for comparison.

The molar conductivity scale here ranges from 0 to 10,000 mhos per mole cm². The conductivities that have previously been described lie on the flat portion of curves below 50% silver sulfide, and are practically insignificant compared to the dramatic increase which occurs on the silver sulfide side of the system. As silver chloride is added to the molten silver sulfide, the conductivity increases and the temperature dependence of the conductivity inverts. As more silver chloride is added, the conductivity decreases rapidly until between 50 and 60%, approximately at the position of the break in the phase diagram, the temperature dependence again reverts to that observed on the silver chloride side of the diagram.

Proposed mechanism of electronic conduction.—Because of the absence of long range order in the liquid state, it seems necessary to abandon the band

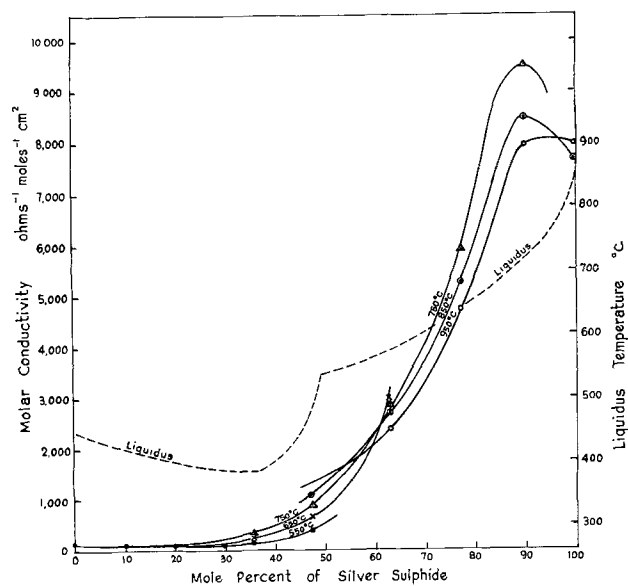


Fig. 8. Molar conductivity isotherms of AgCl-Ag₂S molten mixtures.

theory for electronic conduction as such and to consider instead a modified form of the random walk process proposed by Rice (17) for the case of metal-metal salt solutions. For such a mechanism we consider the sulfur atoms from silver sulfide to act as the electron donors, the electrons being produced by thermal excitation as in any other intrinsic semiconductor. The electronic migration will be a random discontinuous charge transfer between the sulfur species in the melt. The observed conduction would then depend on both the mobility and availability of electrons for conduction.

The mobility of the electrons on the silver sulfide side of the system should be primarily dependent on the continuity of the sulfur network in the melt, and the extent of covalency of the sulfur atoms. The availability of the conduction electrons will depend on the temperature, since they are thermally activated electrons, on the change in the sulfur electron levels with chloride ion substitution in the melt, and on the concentration of sulfur species in the melt.

The specific conductivity of pure silver sulfide in the solid just below the melting point is about three times that observed for liquid silver sulfide just above the melting point. This abrupt change reflects the breakdown of the continuous sulfur network of the solid state.

It is well known that silver sulfide in the solid state is an intrinsic semiconductor having predominantly n type conduction above 180°C, with the sulfur acting as the electron donors. High temperature x-ray data show that solid Ag₂S is a network of covalently bonded sulfur with highly mobile silver ions randomly distributed in the available positions (18).

As silver chloride is first added to the melt, the sulfur network is broken up so that the mobility of the conducting electrons will be lowered. The observed increase in conductivity in this region (95 mole % Ag₂S) implies that the availability of conduction electrons must have increased with in-

creasing silver chloride content, possibly because of a breaking down of the covalently bonded sulfur chains, and of the resulting increase in the energy levels of the electrons involved.

Phase diagram calculations and density measurements (1) have already indicated that molten silver sulfide is an associated liquid having an average chain length of about 2.4. As silver chloride is added to the sulfide, this structure in the liquid is further broken up and the sulfide appears to be essentially monomolecular between 55 and 80 mole % silver sulfide. The mobility of electrons in this region decreases as the sulfur network in the liquid breaks up, as the amount of sulfide in the melt decreases, and as the melt becomes more ionic. The availability of conduction electrons also decreases as the melt becomes more ionic, and as the sulfide content decreases, so that the conductivity decreases rapidly. The fact that the conductivity increases with decreasing temperature in this region is attributed to an increase in the electron mobility as the melts become more covalently bonded at the lower temperatures. This view is supported by the fact that the temperature dependence of the conductivity becomes less as the concentration of silver chloride is increased and the temperature dependence inverts when the melts become predominately ionic on the silver chloride side of the system.

Below 50 mole % silver sulfide, the melts become essentially ionic. The electronic component of the conductivity here increases with increasing temperature because of the increased thermal activation of the electrons on the sulfur ions. The fact that the observed "apparent activation energy" for electronic conduction is essentially composition and temperature independent implies that the electronic conduction is controlled by a single rate determining process. Whether this process is the energy required to remove an electron from a sulfur ion or the energy required to make an electron jump between two adjacent sulfur ions, cannot be determined from these data alone.

The structure of the molten mixtures is thus seen to play an important role in determining the type and amount of conductivity in the system.

Summary

The specific conductivities of molten silver chloride-silver sulfide mixtures have been accurately determined.

Molten silver chloride has a high apparent activation energy for conduction. By comparison with the alkali halides, the apparent activation energies for conduction in monovalent pure salts have been shown to be inversely proportional to the lattice energy of the salts.

In dilute solutions of silver sulfide in silver chloride, the melts are ionic conductors. The ionic con-

ductivity decreases and the apparent activation energy for conduction increases as silver sulfide is added because of the higher charge density on the divalent sulfur ion. As the concentration of silver sulfide is increased above about 20 mole % silver sulfide, small amounts of electronic conductivity start to occur in the melt. The amount of electronic conductivity increases with temperature and increasing concentration of silver sulfide. The activation energy for electronic conductivity is temperature and composition independent in this region.

Above 50 mole % silver sulfide, electronic conduction increases very rapidly, and increases with increasing temperature. Both an increase in electron mobility and availability are responsible for the high electronic conductivities. Structural changes in the melt appear to influence the electron mobility markedly in this region.

Acknowledgments

This work was carried out with the financial assistance of the School of Engineering Research (S.E.R.) of the University of Toronto, and of the National Research Council of Canada. The authors wish to thank N.R.C. for a scholarship for one of us (M.C.B.).

Manuscript received Aug. 22, 1963. This paper was presented at the Pittsburgh Meeting, April 15-19, 1963.

Any discussion of this paper will appear in a Discussion Section to be published in the December 1964 JOURNAL.

REFERENCES

1. M. C. Bell and S. N. Flengas, *This Journal*, **111**, 569 (1964).
2. P. Junad and Busch, *Helv. Phys. Acta*, **31**, 567 (1958).
3. M. H. Hobb, *J. Chem. Phys.*, **20**, 185 (1952).
4. D. Argyriades, G. Derge, and G. Pound, *Trans. Am. Inst. Mining Met. Engrs.* **215**, 909 (1959).
5. M. Bourgon, G. Derge, and G. Pound, *ibid.*, **209**, 1454 (1957).
6. Jones and Joseph: *J. Am. Chem. Soc.*, **50**, 1047 (1928).
7. Luder, *ibid.*, **62**, 89 (1940).
8. Jones and Bradshaw, *ibid.*, **55**, 1780 (1933).
9. B. S. Harrap and E. Heymann, *Trans. Faraday Soc.*, **51**, 259 (1955).
10. Y. Doucet and M. Bizouard, *Acad. Sci. Comp. Rend.*, **250**, 73 (1960).
11. R. C. Spooner and F. E. W. Wetmore, *Can. J. Chem.*, **29**, 777 (1951).
12. F. R. Duke, A. L. Bowman, E. Wolf, and H. Garfinkel, *Am. N. Y. Acad. Sci.*, vol. 79, art. 11, 1023.
13. E. A. Moelwyn-Hughes, "Physical Chemistry," Cambridge Press (1951).
14. V. H. Schinke and F. Sauerwald, *Z. anorg. Chem.*, **281**, 313 (1956).
15. I. S. Yaffe and E. R. Van Artsdalen, *J. Phys. Chem.*, **60**, 1125 (1956).
16. A. Velikanov, *Ukrain. Khim. Zhur.*, **26**, 319 (1960).
17. S. A. Rice, *Disc. Faraday Soc.*, N32, 181 (1961).
18. A. F. Wells, "Structural Inorganic Chemistry," 3rd ed., Oxford at the Clarendon Press (1962).

The 1010° and 800°C Isothermal Sections in the System $\text{Na}_3\text{AlF}_6\text{-Al}_2\text{O}_3\text{-SiO}_2$

D. F. Weill¹ and W. S. Fyfe

University of California, Berkeley, California

ABSTRACT

Isothermal sections at 1010° and 800°C have been determined in the system $\text{Na}_3\text{AlF}_6\text{-Al}_2\text{O}_3\text{-SiO}_2$ by the quenching technique. A determined solubility of 13-15 weight % for corundum in the $\text{Na}_3\text{AlF}_6\text{-Al}_2\text{O}_3$ system at 1010°C is in good agreement with recent revisions of that binary melting diagram. The steep nature of the corundum liquidus curve in the $\text{Na}_3\text{AlF}_6\text{-Al}_2\text{O}_3$ system is found to continue into the ternary system. Silica solubility which is less than 5% in molten Na_3AlF_6 at 1010°C increases rapidly with addition of Al_2O_3 to the system and reaches a maximum value of 69% at the invariant point. The refractive indices of quenched glasses plot smoothly against composition and vary from a maximum of 1.442 (at 17% Na_3AlF_6) to a minimum of 1.422 (at 50% Na_3AlF_6). Glasses richer than 50% in Na_3AlF_6 were difficult to quench. No evidence was found for liquid immiscibility or solid solution in the temperature range studied.

The widespread use of molten cryolite as a solvent for alumina in the electrolytic process for aluminum has prompted much interest in the liquidus portion of the $\text{Na}_3\text{AlF}_6\text{-Al}_2\text{O}_3$ phase diagram. Although some disagreement exists in the published details of the binary liquidus curves, the relatively large solubility of corundum is well established and indicates the possibility that molten cryolite may be a useful solvent of some equally "insoluble" refractories and silicates. As a foundation for the investigation of the solubilities of some aluminum silicates, the phase relations cryolite-corundum-silica-liquid in the ternary system $\text{Na}_3\text{AlF}_6\text{-Al}_2\text{O}_3\text{-SiO}_2$ were studied by the quenching method at 1010° and 800°C.

Experimental

Natural cryolite from Ivigtut, Greenland, was freed from minor inclusions of quartz by density separations. Synthetic corundum crystals from Union Carbide Corporation, Linde Division, and clear quartz crystals from Hot Springs, Arkansas, were also used as parent material. Homogeneous powdered mixtures of appropriate compositions were prepared from the 140-300 mesh size fraction. Approximately 100 mg of mixture were sealed in platinum tubes and heated in a platinum resistor furnace. A dozen closely spaced holes drilled in a cylindrical steel block were used to hold the samples in an effort to minimize temperature gradients. These holes also served as wells for a Pt-Pt₈₇Rh₁₃ thermocouple. The reproducibility of temperature readings between thermocouple positions and the occasional calibration of the thermocouple at the melting point of reagent grade NaCl indicated an uncertainty of ±2°C in the temperature. The majority of runs lasted 200-300 hr. The duration on occasional runs was varied from 12 to 1000 hr in order to determine any possible time effect on the results. The charges were frequently turned end over end during a run and quenched to room temperature in

2-3 sec at the end of the run. The contents were examined with a polarizing microscope and by x-ray diffraction. Refractive indices were measured in immersion media at 0.002 intervals using the Becke line method and are believed to be accurate to within ±0.001. A slight swelling of the sealed tubes was noticeable at the end of each run. The maximum amount of trapped gas, possibly including some volatile fluorides such as SiF_4 and NaAlF_4 which might be developing over the melt, was estimated in the following way. A length of platinum tubing, sealed and collapsed at one end, and connected to an oxygen pressure tank at the other end, was introduced into the furnace at 1010°C. The swelling could be reproduced rapidly at ca. 1 atm gauge pressure. The average available volume within the tubes during the runs was 0.2 cc. Applying the ideal gas law we conclude that the amount of trapped gas is too small ($<4 \times 10^{-6}$ moles) to be relevant in the interpretation of these results. There is no doubt also that trapped air accounts for a significant portion of the gas present.

Results

The results of 86 runs are shown in Fig. 1 as ternary phase diagrams at 1010° and 800°C. It should be pointed out that equilibrium between liquid and the various crystalline phases indicated (*i.e.*, the solubility of the latter) has not been positively demonstrated. In this connection two points are to be kept in mind. First, the equilibrium has been approached from only one direction (solids → liquid) so that the possibility exists that the solubilities shown are slightly low. The situation may be compared to phase diagrams determined by the cooling curve method where the approach to equilibrium is from liquid → solid and where the measured solubilities may be high due to the supersaturation necessary to nucleate the crystalline phases. Second, existing thermodynamic data [Richardson *et al.* (1)], and geologic evidence indicate that corundum plus silica are metastable with re-

¹ Present address: University of California, La Jolla, California.

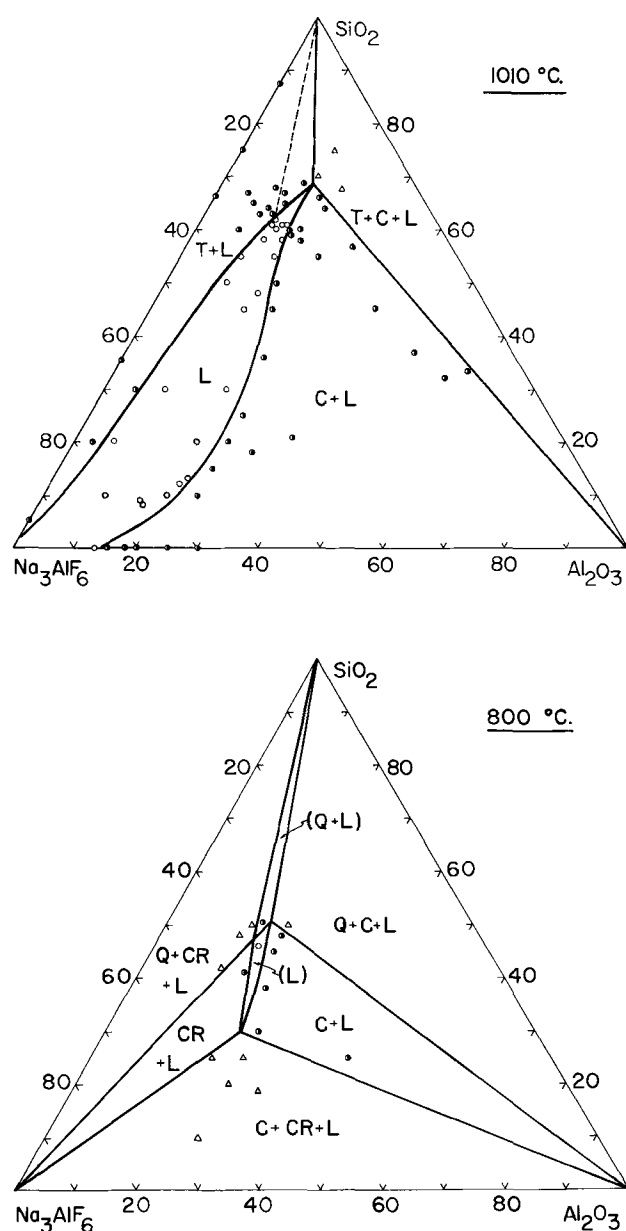


Fig. 1. $\text{Na}_3\text{AlF}_6\text{-Al}_2\text{O}_3\text{-SiO}_2$ system at 1010°C and 800°C. Compositions in weight per cent. See text for explanation of dashed line in 1010°C section. C is corundum, CR cryolite, L liquid, Q quartz, T tridymite.

spect to the Al_2SiO_5 polymorph sillimanite as well as mullite ($3\text{Al}_2\text{O}_3 \cdot 2\text{SiO}_2$) in the temperature range studied. It is best to reserve the label "equilibrium diagram" for those systems in which reversibility has been demonstrated. There are indications, however, that the solubilities of corundum and silica have been closely approached (*i.e.*, the diagrams in all probability nearly represent metastable solid-liquid equilibrium). In all regions of the ternary system formation of the fluid phase is very rapid. The bulk of the liquid is formed in a matter of minutes and no detectable change occurs after a few hours. This was verified at representative compositions near the solubility curves by varying the duration of runs nearly two orders of magnitude from 12 to 1000 hr. The results are independent of time within the experimental error. No spontaneous nucleation of the more stable aluminum silicate phases occurs

from the ternary liquids. This observation is consistent with the current view, Flood and Knapp (2) that free energy differences between the crystalline phases in the $\text{Al}_2\text{O}_3\text{-SiO}_2$ system are much smaller than suggested by published thermodynamic data.

Quartz was used as the silica source for all runs, but as expected tridymite was identified in all the runs quenched from 1010°C. The conversion to tridymite was complete in 300 hr or less except in the six runs whose bulk compositions lie to the right of the dashed line through the tridymite + liquid field in Fig. 1. Three of the six runs are in the tridymite + corundum + liquid field. The six runs are mainly distinguished from others in the tridymite stability field by a reduced concentration of Na_3AlF_6 in the co-existing liquid. One of the runs in the three-phase field was repeated for a duration of 600 hr at the end of which some quartz was still present. It seems clear that in this system the phase transformation quartz \rightarrow tridymite is greatly facilitated by the presence of a solvent and that the rate of growth of tridymite from the solvent is quite sensitive to its composition (quite apart from SiO_2 content which of course is at the tridymite saturation level). This may be due to the greater viscosity of the liquids resulting from the increase in SiO_2 and Al_2O_3 components or may be connected with the tolerance of the tridymite lattice for Na and Al "impurities" as emphasized by Buerger (3). The entire silica field at 1010°C is labeled tridymite in Fig. 1, since the difference in solubility between quartz and tridymite is beyond the accuracy of the diagram. This is to be expected since the free energy difference between the two is very slight at this temperature.

Above 560°C cryolite occurs in a cubic, high-temperature modification known as β -cryolite. It was found impossible to quench this modification, and the cryolite identified in all the quenched charges is the monoclinic α -cryolite. None of the crystalline phases examined showed any indication of ternary or binary solid solution detectable as variations in lattice parameters or refractive indices. Foster (4) and Rolin (5) found no evidence for solid solution in the binary system $\text{Na}_3\text{AlF}_6\text{-Al}_2\text{O}_3$, and solid solution of SiO_2 in corundum and Al_2O_3 in quartz are known to be negligible. The possible impurities entering the tridymite structure discussed above would represent a very restricted solid solution effectively outside the ternary system studied here.

The examination of the quenched charges is largely a matter of detecting small amounts of crystalline phases in a glassy matrix. The polarizing microscope is much more sensitive for this task than the x-ray diffraction technique. For instance, as much as 2-3% corundum may escape detection by the x-ray diffractometer, whereas a fraction of a per cent can easily be detected microscopically. Foster (6) has drawn attention to the dangers of relying exclusively on x-ray detection of small amounts of corundum in determining the liquidus curve for the $\text{Na}_3\text{AlF}_6\text{-Al}_2\text{O}_3$ system. There is some disagreement in the literature about the exact posi-

tion of the liquidus in this system. Curves determined by various authors are assembled for comparison in Phillips *et al.* (7). The differences are due in part to the small latent heat of crystallization of corundum which is difficult to identify on cooling curves. Also, the effect of supercooling may present difficulties. None of these problems is associated with the present method, since all phases except the liquid are initially present. In the usual application of the quenching method several preliminary fusions of the starting mixtures are usually carried out to insure a homogeneous composition in the charge. This was not done in the present study for two reasons. First, cryolite is unstable at the temperatures required to melt compositions relatively rich in alumina and silica. Second, in a system where there is a possibility that the crystalline phases may nucleate with difficulty, the use of glass charges may partially cancel whatever advantages the quenching method has over the cooling curve method. The supersaturation necessary to nucleate a crystalline phase in a reasonable time during a run in the quenching method is a source of uncertainty analogous to the supercooling problem in the cooling curve method. The uncertainty in the present measurements are connected with the approach to equilibrium from the undersaturated side, and the accuracy of the solubility curves depends on the closeness of the approach to the solubility limit in relatively long periods. Since it is much harder to maintain a superheated crystal than a supercooled liquid, it is not unreasonable to assume that the indicated solubilities are not far from the limiting values. The position of the Na_3AlF_6 - Al_2O_3 liquidus determined here (13-15% Al_2O_3 at 1010°C) is in good agreement with Phillips *et al.* (7) who arrived at a figure of 14% Al_2O_3 using a method of visual examination and Foster (4), 13% Al_2O_3 , by a quenching method. Investigations using the cooling curve method all give appreciably higher values. An examination of the corundum saturation curves at 800° and 1010°C in Fig. 1 reveals the steep nature of the corundum liquidus surface in that temperature interval. Such a small temperature dependence in corundum solubility indicates small latent heats of crystallization of corundum from the ternary liquids. It seems likely therefore that the cooling curve method would prove inadequate for determining the corundum liquidus surface in this ternary system for much the same reason it has been found insensitive in determining the corundum liquidus curve in the binary Na_3AlF_6 - Al_2O_3 system.

Liquids containing less than 50% Na_3AlF_6 were easily quenched to a clear, colorless glass. Figure 2 is a plot of the refractive indices of the quenched glasses. The indices of glasses quenched from 1010° and 800°C plot consistently indicating that the structure is effectively frozen in the glass below 800°C or that the effects on the refractive indices caused by the different thermal histories is too small for detection. The Na_3AlF_6 rich glasses are not plotted since it was impossible to prevent some cryolite from forming during the quenching of these liquids. This did not interfere with the determination

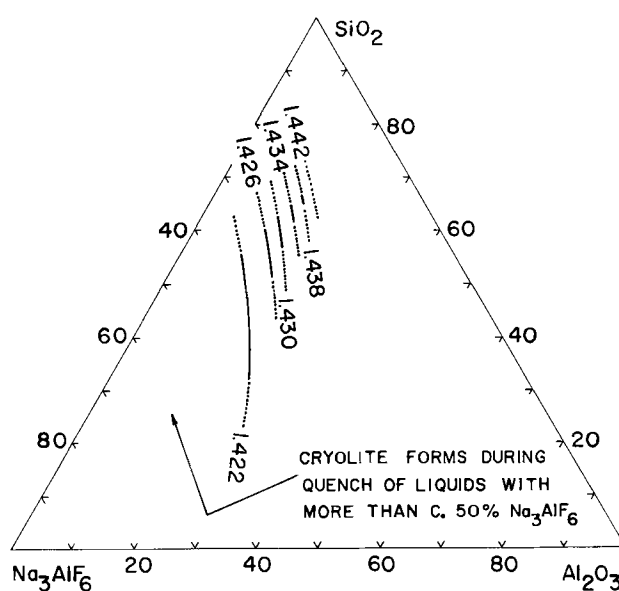


Fig. 2. Refractive indices (n_D) of glasses in the Na_3AlF_6 - Al_2O_3 - SiO_2 system. Compositions in weight per cent.

of the cryolite field at 800°C since the coarser cryolite of the initial mixture was easily distinguishable under the microscope from the microcrystalline variety which precipitated during the quenching period.

Conclusions

The relatively low solubility of silica (<5%) in the binary system SiO_2 - Na_3AlF_6 is strikingly increased by the addition of Al_2O_3 to the liquid. Rolin (8) has analyzed the melting point lowering of cryolite by various oxides using the extension of the regular solution equation for fused salts due to Temkin (9). While the simple dissociation scheme to the cation and O^- best fits the phase diagrams for most of the oxides studied (*e.g.*, Na_2O , MgO , CaO , ThO_2 , La_2O_3) the results for Al_2O_3 were inconclusive. A solution of alumina in cryolite may contain aluminate as well as oxyfluoride ions. Any proposed scheme for the structure of liquids in the Na_3AlF_6 - Al_2O_3 - SiO_2 system will have to account for the sharp increase in SiO_2 concentration along the SiO_2 isoactivity line represented by the silica saturation curve.

The large solubility of silica and corundum at the invariant points (69% SiO_2 -14% Al_2O_3 at 1010°C , and 50% SiO_2 -17% Al_2O_3 at 800°C) imply substantial solubilities for the aluminum silicates in this system. The restricted field of liquid at 800°C indicates that the liquidus surface does not extend much below this temperature. There are no indications of liquid immiscibility in the temperature range studied.

Acknowledgments

This work was supported in part by the Office of Naval Research and the National Science Foundation.

Manuscript received April 4, 1963.

Any discussion of this paper will appear in a Discussion Section to be published in the December 1964 JOURNAL.

REFERENCES

1. F. D. Richardson, J. H. Jeffes, and G. Withers, *J. Iron Steel Inst.*, **166**, 213 (1950).
2. H. Flood and W. Knapp, *J. Am. Ceram. Soc.*, **40**, 206 (1957).
3. M. J. Buerger, *Fortschr. Miner.*, **39**, 9 (1961).
4. P. A. Foster, Jr., *J. Am. Ceram. Soc.*, **43**, 66 (1960).
5. M. Rolin, *Bull. Soc. Chim. France*, 1201 (1960).
6. P. A. Foster, Jr., *This Journal*, **106**, 971 (1959).
7. N. W. F. Phillips, R. H. Singleton, and E. A. Hollingshead, *ibid.*, **102**, 648 (1955).
8. M. Rolin, *Bull. Soc. Chim. France*, 939 (1962).
9. M. Temkin, *Acta Physiochim. U.R.S.S.*, **20**, 411 (1945).

The Transport of Gallium Arsenide in the Vapor Phase by Chemical Reaction

R. R. Fergusson¹ and T. Gabor²

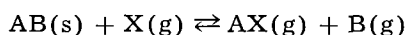
Research Laboratories, Westinghouse Electric Corporation, Pittsburgh, Pennsylvania

ABSTRACT

The heat contents and entropies have been derived as a function of temperature for gallium arsenide and the gaseous species which exist in equilibrium with it, in the temperature range 800°-1200°K when iodine or hydrogen chloride and hydrogen are also present. The important gaseous species are shown to be GaCl₃, GaI₃, GaCl, GaI, HI, I₂, I, HCl, As₄, and H₂. Under certain conditions the species As₂, AsCl₃, and Ga (liq.) may also be present. The free energy changes for reactions among the above species are derived. They are shown to be consistent with those isothermal equilibria that have been directly measured. The free energy changes are used, together with the conservation equations for nondepositing components (I, Cl, H, and As in excess of the stoichiometric Ga:As=1:1 ratio) to give the partial pressures of all the important species at any temperature in a temperature gradient in a constant pressure system. The results are applicable to the calculation of the flux of gallium arsenide in open flow or closed tube (diffusive transport) systems, and they are in good agreement with experimentally measured rates of transport in the system GaAs-H₂-Cl₂ in an open flow apparatus.

Deposition from chemically reacting species from the vapor phase offers particular advantages in the preparation of crystalline stoichiometric semiconducting compounds which cannot readily be obtained by freezing a melt because of peritectic decomposition, incongruent melting, or the need to work at excessively high temperatures or pressures. Since the extensive work on chemical transport reactions by Schäfer (1) and the observation by Antell and Effer (2) of the transport of gallium arsenide contained in a sealed tube, down a temperature gradient by reaction with iodine, the adoption of such methods has been widespread both for the preparation of gallium arsenide in quantity and for its deposition in the form of thin films. The aims of this paper are to analyze the physical chemistry of the reactions in the gallium-arsenic-halogen-hydrogen systems for the transport of this compound by iodine or chlorine and to determine the rate of transport in specific processes.

Consider the idealized gas-solid reaction



occurring simultaneously at two interconnected temperature regions T_1 and T_2 . The free energy gradient between the two temperatures is a measure of the driving force for the mass transfer of solid AB between the two regions. Provided none

of the chemical reactions is rate-limiting, the resistance against which this force is exerted will depend only on the particular flow mechanism by which transport occurs (diffusion, laminar or turbulent flow). The partial pressure differences between T_1 and T_2 of the gaseous species involved, calculable through the equilibrium constants from the free energy changes of the reactions at T_1 and T_2 , may therefore be used in the equations which define the flow process to determine the rate of mass transfer of AB between T_1 and T_2 .

Chemical Equilibria Involved in the Transport of Gallium Arsenide

In the system gallium arsenide, hydrogen, iodine within the temperature range 800°-1200°K possible stable species are: GaAs(s), Ga(l), GaI₃(g), GaI(g), HI(g), I₂(g), I(g), H₂(g), As₄(g), and As₂(g). The species GaI₂(g) and AsI₃(g) are unstable in this temperature range. Ga(l) and As₂(g) are only important at very low total (free and combined) iodine pressures. Calculations show that they may be neglected in determining the transport equilibria in the temperature range here considered.

In the case of gallium arsenide, hydrogen, chlorine system, in the same temperature range, 800°-1200°K, possible stable species are: GaAs(s), Ga(l), GaCl₃(g), GaCl₂(g), GaCl(g), HCl(g), Cl₂(g), H₂(g), As₄(g), and As₂(g). The species AsCl₃(g) is unstable and again Ga(l) and As₂(g) are only important at low total halogen pressures. Cl(g) also

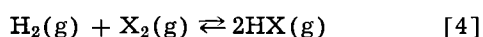
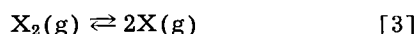
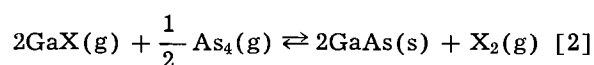
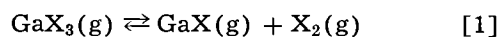
¹ Present address: Ministry of Aviation, ERDE, Waltham Abbey, Essex, England.

² Present address: Battelle Memorial Institute, Columbus, Ohio.

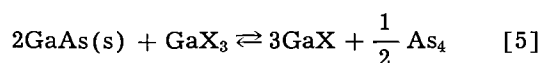
is unimportant and may be neglected in the temperature range 800°-1200°K.

Brewer (3) has estimated that the equilibrium $\text{GaCl}(g) + \text{GaCl}_3(g) \rightleftharpoons 2\text{GaCl}(g)$ is shifted to the right with increasing temperature. We have re-examined the vapor density data of Laubengayer and Schirmer (4) and of Nilson and Pettersson (5) and concluded (6) that the concentration of $\text{GaCl}_2(g)$ will be relatively unimportant below 1200°K. This species is neglected in the present paper.

The following reactions, in which X denotes Cl or I, are sufficient to describe the equilibria between the species involved in the transport of gallium arsenide by iodine or chlorine in the presence of hydrogen, between 800° and 1300°K



If no hydrogen is present, reaction [4] is not involved, and because the pressure of free halogen is small, reaction [3] may be omitted and reactions [1] and [2] replaced by the single reaction



Thermodynamic Data

In Table I are listed the values of the enthalpies and entropies of the species involved as a function of temperature. All standard heats of formation are based on experimental data in the literature. In those cases where values for $H^\circ_T - H^\circ_{298}$ and $S^\circ_T - S^\circ_{298}$

were not available, estimates were based on the values of related compounds in Kelley's compilation (7). Estimates of the values for S°_{298} for the gallium halides were based on the use of the empirical curves of Kubaschewski and Evans (8) or on Latimer's tables (9). The most uncertain values are the standard heats of formation at 298°K of GaI and GaAs, for which conflicting values exist. Gutbier's (10) value for H°_{298} (GaAs) is 5.2 kcal more negative than that of Drowart and Goldfinger (11). The former has been used in these calculations because it is consistent with the data of Silvestri and Lyons (12) on the GaAs-I₂ equilibrium, and because it is also consistent with results on other III-V compounds. The heat of dissociation of GaI(g) is -91 kcal from flame photometry work of Bulewicz, Phillips, and Sugden (13). Barrow (14) has reviewed the available spectroscopic data and suggested -81 kcal. We have chosen the intermediate value of -84 kcal. This is consistent within ± 2 kcal with both the Ga(1)-I₂ and GaAs-I₂ data of Silvestri and Lyons.

The standard free energy changes as a function of temperature for reactions [1-4] are obtained directly from the values of Table I and are listed in Table II. They are compared with the available experimental data in Table III.

The data of Tables I and II show that for reactions [1] and [2] the equilibria are well over to the left so that the partial pressures of free halogen will be small (less than 10^{-12} atm). Considering the

reaction $2\text{AsCl}_3(g) \rightleftharpoons 3\text{Cl}_2(g) + \frac{1}{2} \text{As}_4(g)$, for

which from the data of Table I, $\Delta F^\circ_{1000} = +122.8$ kcal, it may be seen that $\text{AsCl}_3(g)$ will be negligible.

Table I.

Species	$H^\circ_{298}(g)$ kcal	$S^\circ_{298}(g)$ e.u.	$H^\circ_T(g)$ cal	$S^\circ_T(g)$ e.u.	Comments and references
GaAs	(s) = -18.5	(s) = 15.6	(s) = 12.0T - 21,600	(s) = 11.96lnT - 53.0 + 1.6 × 10 ⁻³ T	From mass spectrometry. Ref. (10), (11).
GaI ₃	(s) = -51.0	(s) = 48.7	20.0T - 34,100	19.50lnT - 22.6	$H^\circ_{298}(s)$ from calorimetry. Ref. (8). $S^\circ_{298}(s)$ from Latimer's tables. Ref. (9).
GaCl ₃	(s) = -125	79.7	19.2T - 107,700	19.17lnT - 29.3	$H^\circ_{298}(s)$ from calorimetry. Ref. (8). $S^\circ_{298}(g)$ from Kubaschewski and Evans empirical plot. Ref. (8).
GaI	+10.5	61.0	8.9T + 7,800	8.94lnT + 10.0	Corresponds to -84 kcal for dissociation energy of GaI. Heat of vaporization of Ga from ref. (10).
GaCl	-16.2	56.4	8.9T - 19,000	8.93lnT + 5.2	$H^\circ_{298}(g)$ from spectra. Ref. (14), (20), (21).
I ₂	(s) = 0	62.2	8.9T + 12,200	8.94lnT + 11.4	Ref. (21) and (22).
Cl ₂	0	53.3	8.9T - 2,700	8.85lnT + 2.6	Ref. (21) and (22).
HI	+6.2	49.4	6.4T + 5,000	6.39lnT + 14.1	Ref. (21) and (22).
HCl	-22.0	44.6	6.3T - 23,300	6.27lnT + 9.9	Ref. (21) and (22).
I	+25.5	43.2	4.8T + 24,200	4.80lnT + 15.9	Ref. (21) and (22).
H ₂	0	31.2	6.5T - 1,600	6.52lnT - 5.3	Ref. (21) and (22).
As ₄	+34.5	75.0	19.8T + 28,300	19.84lnT - 38.6	Ref. (21) and (22).
AsCl ₃	-71.5	78.2	19.7T - 77,700	19.72lnT - 34.2	Ref. (21) and (22).

All standard heats of formation from experimental values in the literature.

Table II.

Reaction	ΔF°_T (Iodine) cal	ΔF°_T (Chlorine) cal
[1] $\Delta F^\circ_1 = -46.2T + 1.62T \ln T + 54,100$		$\Delta F^\circ_1 = -38.5T + 1.39T \ln T + 86,000$
[2] $\Delta F^\circ_2 = +100.5T - 5.06T \ln T - 60,750 - 3.2 \times 10^{-3}T^2$		$\Delta F^\circ_2 = +99.7T - 4.99T \ln T - 22,050 - 3.2 \times 10^{-3}T^2$
[3] $\Delta F^\circ_3 = -19.7T - 0.66T \ln T + 36,200$		$\Delta F^\circ_3 = -10.7T - 2.2T \ln T + 51,780$
[4] $\Delta F^\circ_4 = -24.7T + 2.68T \ln T - 600$		$\Delta F^\circ_4 = -25.5T + 2.83T \ln T - 42,300$

Table III.

Chemical reaction	From Table I (kcal)	Experimental values (kcal)
a. $\text{GaI}_3(\text{g}) + 2\text{Ga}(\text{l}) \rightleftharpoons 3\text{GaI}(\text{g})$	$\Delta F_{1000} = -6.6$ $\Delta H_{1000} = +52.2$	$\Delta F_{1000} = -6.4$ Ref. (12) $\Delta H_{1000} = +50.4$ Ref. (12)
b. $\text{GaI}_3(\text{g}) + 2\text{GaAs}(\text{s}) \rightleftharpoons 3\text{GaI}(\text{g}) + \frac{1}{2}\text{As}_4(\text{g})$	$\Delta F_{1000} = +17.5$ $\Delta H_{1000} = +107.5$	$\Delta F_{1000} = 19.4$ Ref. (12) $\Delta H_{1000} = +108.2$ Ref. (12)
c. $\text{GaAs}(\text{s}) \rightleftharpoons \text{Ga}(\text{l}) + \frac{1}{4}\text{As}_4(\text{g})$	$\Delta H_{1000} = +27.6$	$\Delta H_{1000} = +28.9$ Ref. (12) $\Delta H_{1000} = +27.0$ Ref. (10) $\Delta H_{1000} = +21.8$ Ref. (11)

Application to Vapor Transport Processes

Transport of gallium arsenide in the GaAs-X₂-H₂ systems may be carried out in several ways. In an open flow system AsCl₃(g) or As₄(g) may be reacted with GaX(g), GaX₃(g), or Ga(l) with or without H₂ being present; alternatively H₂ plus X₂ or HX [or in the case X = Cl, AsCl₃(g)] may be flowed over GaAs(s) so that gallium and arsenic vapor species are taken up into the gas phase and redeposited downstream at a different (lower) temperature. In a closed tube system in a temperature gradient, gallium arsenide at the hotter end may be transported to the cooler end if X₂, X₂ + H₂, or HX are also put into the tube. All of these cases may be analyzed within the framework of the theories developed in this section.

Open tube flow systems.—The changes in composition of the gas flowing along an open tube in a temperature gradient will depend, in the absence of turbulent flow, on the flow velocity, the diffusion coefficients of the species involved, and on the reaction rate constants. If chemical equilibrium exists at the solid-gas interfaces, and provided that none of the gaseous reactions is rate limiting, the system corresponds to a flow process with simultaneous diffusion. At sufficiently high flow rates the influence of diffusion on the transport process may be ignored. All the constituents in the vapor phase may be assumed to move at a uniform rate equal to the over-all space velocity. The effect on the rate of varying the space velocities will reveal any inadequacies in this assumption.

There is insufficient data on the kinetics of the reactions involved in the process to determine whether they will limit the transport of gallium arsenide. The equations are solved on the assumption that reaction rates are not limiting, and this is tested by comparison between theory and experiment.

The equations governing the transport process in conformity with the above restrictions and assumptions are:

The equilibrium equations

$$K_1(T) = \frac{p_{\text{GaX}} p_{\text{X}_2}}{p_{\text{GaX}_3}} \quad [6]$$

$$K_2(T) = \frac{p_{\text{X}_2}}{p_{\text{GaX}}^2 p_{\text{As}_4}^{1/2}} \quad [7]$$

$$K_3(T) = \frac{p_{\text{X}}^2}{p_{\text{X}_2}} \quad [8]$$

$$K_4(T) = \frac{p_{\text{HX}}^2}{p_{\text{H}_2} p_{\text{X}_2}} \quad [9]$$

the equation defining the total pressure, independent of temperature and constant throughout the tube³

$$P = p_{\text{GaX}_3} + p_{\text{GaX}} + p_{\text{X}_2} + p_{\text{X}} + p_{\text{HX}} + p_{\text{H}_2} + p_{\text{As}_4} \quad [10]$$

and the conservation equations

$$\frac{J_{\text{X}_2} RT}{S} = \frac{3}{2} p_{\text{GaX}_3} + \frac{1}{2} p_{\text{GaX}} + p_{\text{X}_2} + \frac{1}{2} p_{\text{X}} + \frac{1}{2} p_{\text{HX}} \quad [11]$$

$$\frac{J_{\text{H}_2} RT}{S} = p_{\text{H}_2} + \frac{1}{2} p_{\text{HX}} \quad [12]$$

$$\frac{J_{\text{As}} RT}{S} = 4p_{\text{As}_4} - (p_{\text{GaX}_3} + p_{\text{GaX}}) \quad [13]$$

In these equations the constants $K_1(T)$ etc., are determined through the equation $F^\circ_T = RT \ln K(T)$ by the data of Table II; p_{GaX_3} etc., denote the partial pressures (atm), S the linear space velocity (cm/sec), and the J 's denote the constant fluxes (moles/sec cm²) of total halogen, hydrogen, and arsenic in excess of the stoichiometric ratio Ga:As=1:1. These fluxes are conserved because the components which they represent do not exist, free or combined, as

³ For a tube of diameter of the order of one centimeter no measurable total pressure gradient would be sustained except at very low or very high pressures. The total pressure difference between the ends of the tube will be negligible as compared with the total pressure except for narrow tubes.

condensed phases in the temperature range 800°-1200°K.⁴

Equations [6]-[13], in which it might be noted that the space velocity S can be eliminated, since the flux ratios of the conserved components are constant, cannot be written explicitly as a function of a single variable. A minimization procedure was used based on a Fibonacci search (15), in which a minimum was sought in the difference of the partial pressures of arsenic as given by Eq. [7] and [13], respectively. The results are described in the next section.

The flux of gallium arsenide at a point in the flow system corresponding to a temperature T is given by the equation

$$J_{\text{GaAs}} = \frac{S}{RT} (p_{\text{GaX}_3} + p_{\text{GaX}})$$

or, eliminating S/RT by the use of Eq. [11]

$$\frac{J_{\text{GaAs}}}{J_{\text{X}_2}} = \frac{p_{\text{GaX}_3} + p_{\text{GaX}}}{\frac{3}{2} p_{\text{GaX}_3} + \frac{1}{2} p_{\text{GaX}} + p_{\text{X}_2} + \frac{1}{2} p_{\text{X}} + \frac{1}{2} p_{\text{HX}}} \quad [14]$$

The difference in the flux J_{GaAs} , between two temperatures T_1 and T_2 , is a measure of the gallium arsenide transported between these temperatures. Thus if halogen, hydrogen, and excess arsenic if present are flowed over solid GaAs at a source temperature T_1 , then the rate that GaAs will be transported in an open tube flow system from the source to the substrate at a temperature T_2 will be given by $J_{\text{GaAs}}(T_1) - J_{\text{GaAs}}(T_2)$ in which the values of $J_{\text{GaAs}}(T_1)$ and $J_{\text{GaAs}}(T_2)$, defined by Eq. [14], are found from the solutions to Eq. [6]-[13] appropriate to the values of the temperatures, the total pressure, and the conserved fluxes used.

Values for the ratio $J_{\text{GaAs}}/J_{\text{X}_2}$ are plotted against temperature for the system GaAs-I₂ in Fig. 1, for the system GaAs-I₂-H₂ in Fig. 2, and for the system GaAs-Cl₂-H₂ in Fig. 3.⁵ Flux ratios for the sys-

⁴ If the flux of halogen is so low that less gallium is transferred to the vapor phase from GaAs than is equivalent to the establishment of the equilibrium arsenic vapor pressure over GaAs, gallium in excess of the stoichiometric ratio Ga:As = 1:1 will be present as a condensed phase. The calculations only apply to stoichiometric GaAs as the sole condensed phase.

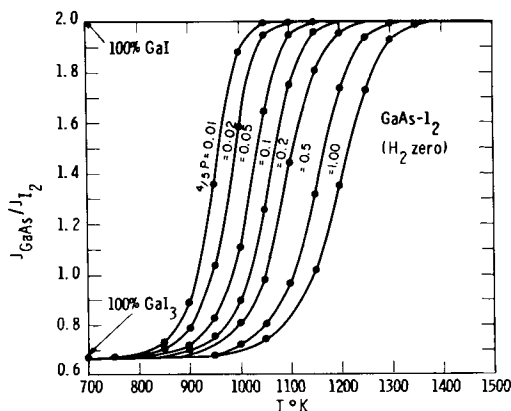


Fig. 1. Temperature dependence of gallium arsenide-iodine flux ratios for different fixed total pressures. These curves are also applicable to the gallium arsenide-chloride system.

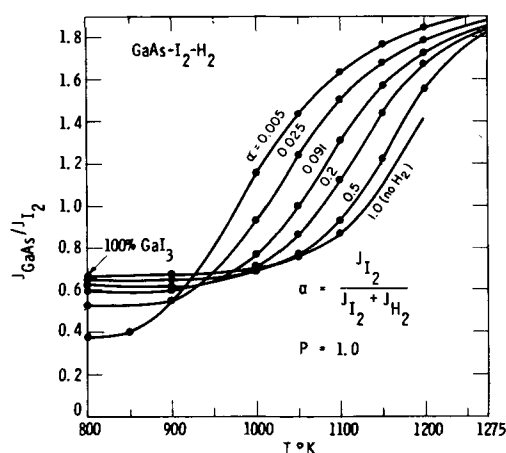


Fig. 2. Temperature dependence of gallium arsenide-iodine flux ratios for different iodine-hydrogen flux ratios. All the curves are for a total pressure of 1 atm.

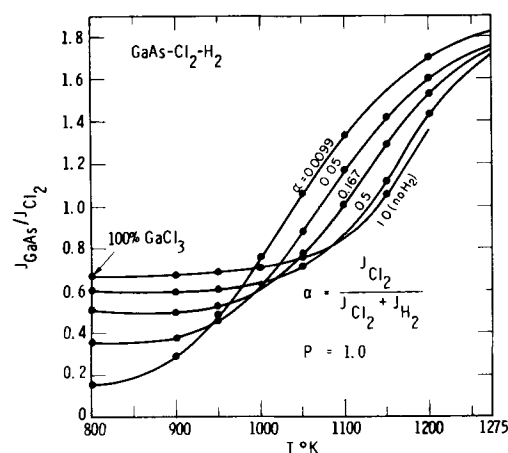


Fig. 3. Temperature dependence of gallium arsenide-chlorine flux ratios for different chlorine-hydrogen flux ratios. All the curves are for a total pressure of 1 atm.

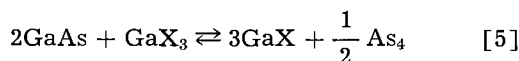
tems GaAs-I₂ and GaAs-Cl₂ are so similar that the curves for the latter system are not given.

Closed tube systems.—Schäfer and co-workers (16) have provided two models for the transport mechanism. (a) Diffusive transport applicable at pressures less than about 1-10 atm total pressure, in which the fluxes of the gaseous species are set equal to a diffusion coefficient multiplied by the gradient in the concentrations of these species. This treatment has been developed by Mandel and Lever (17-19) who considered transport occurring by both diffusion and convection in systems which would not sustain a total pressure gradient. Convection occurs in all pressure regions if the transport reaction involves a change in the number of gaseous molecules. (b) Transport predominantly by Poiseuille flow applicable at pressures greater than about 1-10 atm, where the differences in over-all vapor densities between the two ends of the tube, at which chemical equilibrium is assumed to exist, create a net pressure gradient down which transport occurs.

Only case (a) is considered for systems where only gallium arsenide and halogen are present and

⁵ The data of Fig. 1-3 and 4-6 have been calculated for stoichiometric Ga:As systems. A nonstoichiometric Ga:As system is treated in Fig. 8 and is discussed later.

the total pressure can be assumed uniform throughout the tube. Since below 1200°K, the concentration of free halogen may be neglected, the equilibrium is determined by the single chemical reaction



for which the equilibrium constant is given by the ratio $K_1(T)/K_2(T)$.

The total pressure is uniform throughout the tube, and the amount of gallium arsenide transported from the end at the higher temperature, denoted by T_1 , to the cooler end at T_2 is given (see Appendix) by the equation

$$Q_{\text{GaAs}} = \bar{D}c_{\text{X}_2} \frac{a}{l} \left[\left(\frac{p_{\text{GaX}_3} + p_{\text{GaX}}}{\frac{3}{2}p_{\text{GaX}_3} + \frac{1}{2}p_{\text{GaX}}} \right)_{T_1} - \left(\frac{p_{\text{GaX}_3} + p_{\text{GaX}}}{\frac{3}{2}p_{\text{GaX}_3} + \frac{1}{2}p_{\text{GaX}}} \right)_{T_2} \right] \quad [15]$$

where $\bar{T} = (T_1 + T_2)/2$ is the mean temperature. \bar{D} is an average diffusion coefficient at the mean temperature \bar{T} of the different gaseous species present for a total pressure equal to that present in the tube,⁶ c_{X_2} is the total halogen concentration (moles/cm³), a the cross-sectional area (cm²), and l the tube length (cm).

The data for the case of an open tube, plotted in Fig. 1, are applicable to Eq. [15] as may be seen by comparing Eq. [14] and [15], remembering that p_{X_2} and p_{X} are negligible, and p_{HX} is zero in the present case. The values for $(p_{\text{GaX}_3} + p_{\text{GaX}})/\left(\frac{3}{2}p_{\text{GaX}_3} + \frac{1}{2}p_{\text{GaX}}\right)$ to be used in Eq. [14] are the

values of $J_{\text{GaAs}}/J_{\text{X}_2}$ of Fig. 1 lying on that isobar for which, at $\bar{T} = (T_1 + T_2)/2$, the total pressure is appropriate to the concentration of halogen present in the tube. Thus suppose that the tube contains 1.35×10^{-6} moles/cc of iodine, and that T_1 is 1100° and T_2 900°K, hence, $\bar{T} = 1000^\circ\text{K}$, and the equivalent pressure that the iodine concentration would exert at this temperature is given by

$$\frac{3}{2}p_{\text{GaI}_3} + \frac{1}{2}p_{\text{GaI}} = c_{\text{I}_2}RT = 1.35 \times 10^{-6} \times 82 \times 10^3 = \frac{0.1}{0.9}$$

Inspection of Fig. 1 shows that the isobar for $\frac{4}{5}P =$

$$(p_{\text{GaI}_3} + p_{\text{GaI}}) = 0.1 \text{ corresponds to this value of } \frac{3}{2}$$

$p_{\text{GaI}_3} + \frac{1}{2}p_{\text{GaI}}$ at 1000°K. Hence the values of $(p_{\text{GaX}_3} + p_{\text{GaX}})/\left(\frac{3}{2}p_{\text{GaX}_3} + \frac{1}{2}p_{\text{GaX}}\right)$ to be used in Eq.

⁶ Gaseous diffusion coefficients are inversely proportional to the total pressure, their dependence on concentration is slight and is here neglected; they depend on temperature according to the equation

$$D = D_0(T/T_0)^{1.5} \text{ [ref. (1)]}$$

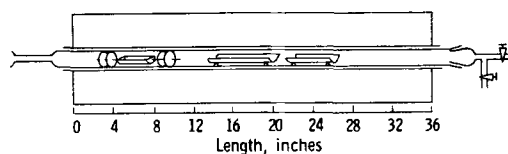


Fig. 4. Schematic drawing of furnace and transport tube

[14] are given by the values of $J_{\text{GaAs}}/J_{\text{I}_2}$ at 900° and 1100°K on this isobar. In general of course the value of the halogen concentration will not correspond exactly to a particular isobar so that it will be necessary to interpolate between the different curves.

Experimental

Gallium arsenide was transported in an open flow system at atmospheric pressure from a source region and deposited on a variety of substrates in the apparatus shown schematically in Fig. 4. It consisted of a 27 mm ID quartz reaction tube in a 36 in. long five zone furnace within which the source gallium arsenide was contained in a quartz boat, located between quartz baffles to promote temperature uniformity and to minimize counterdiffusion. Deposition occurred on substrates held on quartz racks further down the tube. Thermocouple activated temperature controllers allowed a constant temperature to be established along the source region.

The ingoing flux over the gallium arsenide source consisted of hydrogen purified by means of a palladium alloy diffusion tube (I. Bishop & Company) and vapor species (HCl and As₄) resulting from the decomposition of arsenic trichloride. The latter was introduced into the hydrogen stream from a temperature controlled saturator containing liquid arsenic trichloride. The chlorine/hydrogen flux ratios in the input stream were determined by chemical analysis. The uptake of gallium arsenide from the source was determined from weight loss measurements.

Flow rates employed ranged mostly from 60 to 150 cm³/min (at STP). These rates correspond to space velocities over the source of approximately 0.5 to 1.0 cm/sec. The space velocities over the baffles were about an order of magnitude higher. The temperature at the outgoing baffle was held close to the source temperature to minimize counterdiffusion. The results are given in Table IV.

Discussion

We restrict the discussion to the case of open flow systems. Figure 1 shows that by increasing the total pressure, one extends the range over which transport takes place to higher temperatures. The effect of the addition of hydrogen is shown in Fig. 2. The curves are not as steep as in the absence of hydrogen, i.e., the interconversion of GaI₃ and GaI extends over a much wider temperature range. Figure 2 also shows that the formation of gallium arsenide may be brought about without a temperature gradient. For example by flowing GaI₃ and arsenic in a tube at 800°K and adding a stream of hydrogen to decrease the total iodine concentration to 1/200 of its original value, nearly half of the combined gal-

Table IV.

T°K	J_{Cl_2}/J_{H_2}	J_{GaAs}/J_{Cl_2}	Mean value J_{GaAs}/J_{Cl_2}	
1190	0.016	0.87	1.71	
1190	0.023	1.14		
1190	0.025	1.78		
1190	0.036	1.82		
1190	0.036	1.95		
1190	0.036	2.37		
1190	0.036	2.51		
1190	0.036	2.48		
1190	0.042	0.88		
1190	0.042	1.27		
1160	0.036	1.58		1.58
1110	0.036	1.15		1.30
1110	0.036	1.53		
1110	0.036	1.24		
1110	0.036	1.29		
1100	0.036	1.33	1.26	
1100	0.036	1.04		
1100	0.036	0.91		
1100	0.036	1.04		
1100	0.036	1.06		
1100	0.036	1.06		
1100	0.036	1.64		
1100	0.036	1.86		
1100	0.036	1.44		
1100	0.049	1.21		
1090	0.036	1.24	1.24	
1060	0.036	0.96	0.89	
1060	0.036	0.83		
1040	0.003	0.96	1.30	
1040	0.003	1.42		
1040	0.003	1.54		
1030	0.003	1.41	0.95	
1030	0.003	0.58		
1030	0.004	1.39		
1030	0.004	0.93		
1030	0.004	0.93		
1030	0.036	0.47		
960	0.003	0.47	0.56	
960	0.004	0.58		
960	0.004	0.94		
960	0.009	0.53		
960	0.036	0.30		
920	0.044	0.35	0.35	

lium in the gas phase will be deposited as gallium arsenide. Figure 3 shows that for the case of GaAs-Cl₂-H₂ system the curves are even less steep than those of Fig. 2.

If Δ is defined as

$$(J_{GaAs}/J_{X_2})_{T_1} - (J_{GaAs}/J_{X_2})_{T_2} = \Delta \quad [16]$$

where $(J_{GaAs}/J_{X_2})_{T_1}$ and $(J_{GaAs}/J_{X_2})_{T_2}$, given by Eq. [14] represent the solutions to Eq. [6]-[13] for the source and deposition regions T_1 and T_2 , then the rate of transport between these regions is

$$(J_{GaAs})_{T_1} - (J_{GaAs})_{T_2} = J_{X_2}\Delta \quad [17]$$

The values of Δ as functions of pressure are plotted for the GaAs-I₂ system in Fig. 5 for three pairs of temperatures. These values were obtained by taking the difference in the ordinates for the de-

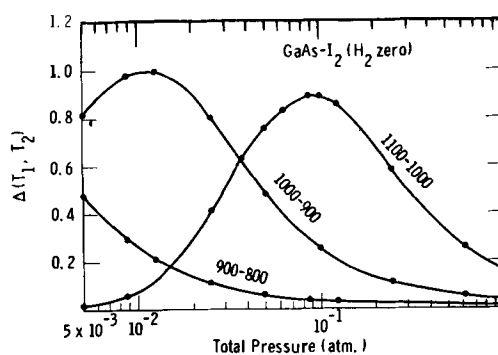


Fig. 5. Ratio of the rate of transport of gallium arsenide and iodine between two temperatures as a function of total pressure in the absence of hydrogen. These curves are also applicable to transport by chlorine.

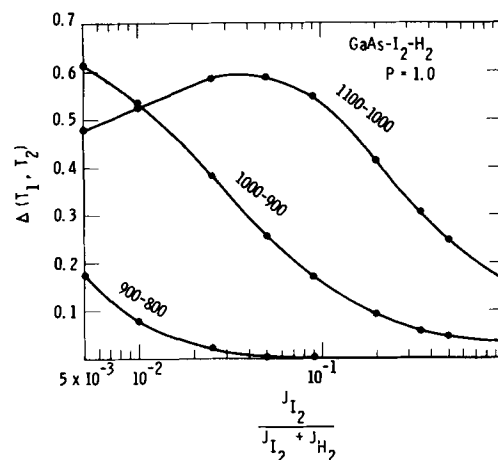


Fig. 6. Ratio of the rate of transport of gallium arsenide and iodine between two temperatures at a total pressure of 1 atm as a function of the fraction of iodine in the total iodine-hydrogen flux.

sired pairs of temperatures along the individual curves of Fig. 1. The maxima in the curves of Δ correspond to pressure regions where the best utilization of the transporting agent takes place. These maxima lie in relatively narrow pressure regions. At lower temperatures it is advantageous to work at relatively low pressures.

A comparison between Fig. 5 and 6 shows that when the hydrogen is present the flux ratio of gallium arsenide to iodine may be greater or smaller than in the absence of hydrogen. The fact that dilution by hydrogen may increase the efficiency of the halogen in the transport of gallium arsenide may be seen by comparing the values of Δ for transport between 1000° and 900°K at 1 atm total pressure in the presence and absence of hydrogen. Thus Δ is 0.03 in the absence of hydrogen under these conditions (Fig. 5), whereas it is 0.53 (an increase of almost 20 fold) when the iodine is diluted 100 fold with hydrogen (Fig. 6). Curves analogous to those shown in Fig. 6 for the GaAs-I₂-H₂ system are drawn in Fig. 7 for the GaAs-Cl₂-H₂ system.

Figure 8 shows the effect of excess arsenic. Even though a relatively large excess arsenic pressure is considered in this curve, its influence is seen to be not very pronounced. At high ratios of halogen to hydrogen fluxes, the effect of excess arsenic on the

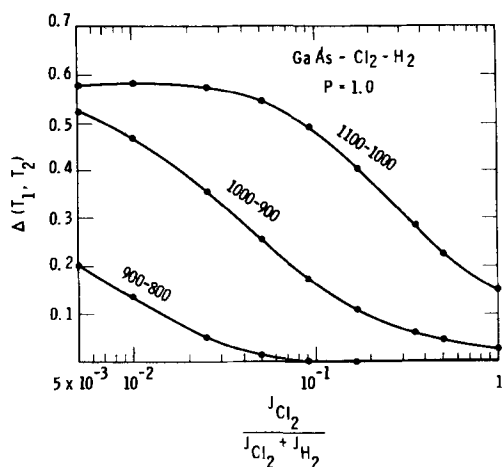


Fig. 7. Ratio of the rate of transport of gallium arsenide and chlorine between two temperatures at a total pressure of 1 atm as a function of the fraction of chlorine in the total chlorine-hydrogen flux.

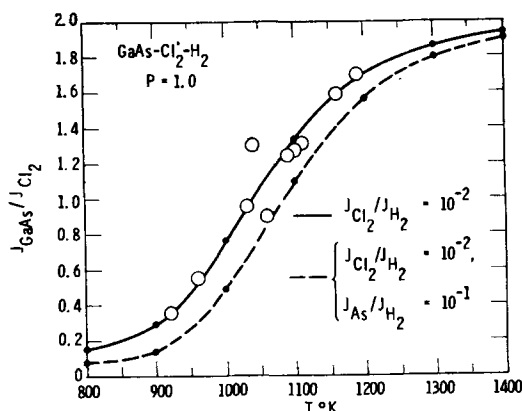


Fig. 8. Temperature dependence of gallium arsenide-chlorine flux ratios showing the influence of added excess arsenic. The circles represent experimental values.

gallium arsenide/halogen flux ratio has been found to be negligible.

The circles in Fig. 8 denote the mean values of all the measured gallium arsenide/total halogen flux ratios at the same source temperature (see section on Experimental, Table IV). The dotted curve in this figure was calculated for a rather higher J_{As}/J_{H_2} ratio than was used experimentally. The experimental results should fall in between the two curves of Fig. 8. There is no evidence from Fig. 8 and from the data of Table IV for departures from the idealized transport process in which counterdiffusion and undersaturation are assumed to be negligible. As the primary aim of the experimental work was to study the epitaxy of the deposited films, the flow rates were not varied over a sufficiently wide range to allow the analysis of the influence of flow rates on the transport process.

Acknowledgments

We thank H. Kleine and R. Fardo for writing the search program, T. A. Jeeves for allowing us the use of the computer, and K. Liang for his contribution to the experimental work.

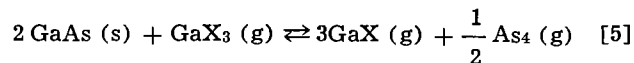
Manuscript received July 17, 1963. This paper was presented at the Pittsburgh Meeting, April 15-18, 1963.

Any discussion of this paper will appear in a Discussion Section to be published in the December 1964 JOURNAL.

APPENDIX

Derivation of the Equation for the Diffusive Transport of Gallium Arsenide in a Closed Tube

Consider the reaction



occurring at a constant temperature \bar{T} in a closed tube. For a stoichiometric Ga:As=1:1 ratio we have

$$4p_{As_4} = p_{GaX_3} + p_{GaX} \quad [18]$$

and a total pressure P given by

$$P = p_{As_4} + p_{GaX_3} + p_{GaX} \quad [19]$$

The system is bivariant, and the total pressure depends on both the temperature and the amount of halogen present. If one end of the tube is slowly heated to T_1 and the other end cooled to T_2 such that $(T_1 + T_2)/2 = \bar{T}$, the total pressure will remain invariant throughout the tube. Gallium arsenide if present at the hot end will react and be deposited from the vapor species at the cooler end at a steady rate until all the solid at the hot end had disappeared.

Transport of the gaseous species between T_1 and T_2 will occur by a combination of diffusion and flow. A net flow in one direction occurs because the reaction involves a change in the number of molecules in the gas phase. If the binary diffusion coefficients among the species GaI_3 , GaI , and As_4 are assumed to be equal, the general equations of transport in a multicomponent system (18) may be reduced to

$$J_{GaX_3} = \frac{Jp_{GaX_3}}{P} - \frac{\bar{D}}{RT} \frac{dp_{GaX_3}}{dx} \quad (\text{moles/sec/cm}^2) \quad [20]$$

and

$$J_{GaX} = \frac{Jp_{GaX}}{P} - \frac{\bar{D}}{RT} \frac{dp_{GaX}}{dx} \quad [21]$$

for the unidimensional fluxes of GaX_3 and GaX molecules through unit cross-sectional area at a point along the tube where $T = \bar{T}$. The algebraic sum of the fluxes of all the molecular species equals the net flux of all the molecules in one direction so that

$$J = J_{As_4} + J_{GaX_3} + J_{GaX}$$

The fluxes J_{GaX_3} and J_{GaX} depend on the coordinate x because the species they represent are interconvertible and the conversion is temperature dependent. Let j_{X_2} and j_{Ga} denote the equivalent fluxes of total halogen and gallium expressed as X_2 and Ga in moles/sec/cm², then

$$j_{X_2} = \frac{3}{2} J_{GaX_3} + \frac{1}{2} J_{GaX} \quad [22]$$

$$j_{Ga} = J_{GaX_3} + J_{GaX} \quad [23]$$

Combining Eq. [20]-[23] we can write

$$j_{X_2} = \frac{\frac{3}{2} p_{GaX_3} + \frac{1}{2} p_{GaX}}{P} J - \frac{\bar{D}}{RT} \frac{d\left(\frac{3}{2} p_{GaX_3} + \frac{1}{2} p_{GaX}\right)}{dx} \quad [24]$$

and

$$j_{Ga} = \frac{p_{GaX_3} + p_{GaX}}{P} J - \frac{\bar{D}}{RT} \frac{d(p_{GaX_3} + p_{GaX})}{dx} \quad [25]$$

Since the total halogen is conserved in the gas phase, j_{X_2} is zero. Therefore

$$J = \frac{\bar{D}P}{RT} \frac{d \ln \left(\frac{3}{2} p_{GaX_3} + \frac{1}{2} p_{GaX} \right)}{dx} \quad [26]$$

The elimination of J between [25] and [26] leads to an expression for the flux of gallium arsenide that can be integrated

$$j_{\text{GaAs}} = j_{\text{Ga}} = -\frac{\bar{D}}{RT} \left(\frac{3}{2} p_{\text{GaX}_3} + \frac{1}{2} p_{\text{GaX}} \right) \frac{d}{dx} \frac{(p_{\text{GaX}_3} + p_{\text{GaX}})}{\left(\frac{3}{2} p_{\text{GaX}_3} + \frac{1}{2} p_{\text{GaX}} \right)}$$

The equivalent flux of gallium equals the flux of gallium arsenide because of the requirements of stoichiometry. In the steady state the equivalent flux of gallium entering the gas phase at the hot end equals the flux leaving the gas phase at the cooler end. Gallium neither enters nor leaves the gas phase at points in between so the j_{Ga} is independent of x .

Integrating between T_1 where $x=0$ and T_2 where $x=l$ gives

$$Q_{\text{GaAs}} = a j_{\text{Ga}} = +\bar{D}c_{\text{X}_2} \frac{a}{l} \left[\left(\frac{p_{\text{GaX}_3} + p_{\text{GaX}}}{\frac{3}{2} p_{\text{GaX}_3} + \frac{1}{2} p_{\text{GaX}}} \right)_{T_1} - \left(\frac{p_{\text{GaX}_3} + p_{\text{GaX}}}{\frac{3}{2} p_{\text{GaX}_3} + \frac{1}{2} p_{\text{GaX}}} \right)_{T_2} \right] \quad [15]$$

where a is the cross-sectional area, and $c_{\text{X}_2} = (3/2 p_{\text{GaX}_3} + 1/2 p_{\text{GaX}})/RT$ is the total concentration of halogen in the tube.

REFERENCES

1. H. Schäfer, "Chemische Transportreaktionen," Verlag Chemie (1962).

2. G. R. Antell and D. Effer, *This Journal*, **106**, 509 (1959).
3. L. Brewer, Private communication.
4. A. W. Laubengayer and F. B. Schirmer, *J. Am. Chem. Soc.*, **62**, 1578 (1940).
5. L. F. Nilson and O. Pettersson, *Z. physik. Chem.*, **1**, 36, 461 (1888); *ibid.*, **2**, 661 (1888).
6. R. R. Fergusson and T. Gabor, To be published.
7. K. K. Kelley, *U. S. Bur. Mines, Bull.* 584 (1960).
8. O. Kubaschewski and E. L. Evans, "Metallurgical Thermochemistry," Pergamon Press, New York (1958).
9. W. M. Latimer, *J. Am. Chem. Soc.*, **73**, 1480 (1951).
10. H. Gutbier, *Z. Naturforsch.*, **16a**, 268 (1961).
11. J. Drowart and P. Goldfinger, *J. chim. phys.*, **55**, 721 (1958).
12. V. J. Silvestri and V. J. Lyons, *This Journal*, **109**, 963 (1962).
13. E. M. Bulewicz, L. F. Phillips, and T. M. Sugden, *Trans. Faraday Soc.*, **57**, 921 (1961).
14. R. F. Barrow, *ibid.*, **56**, 952 (1960).
15. S. M. Johnson, U. S. Air Force Project Rand Res. Memo, RM-1590, Nov. 18, 1955.
16. H. Schäfer, H. Jacob, and K. Etzel, *Z. anorg. Chem.*, **286**, 27 (1956).
17. G. Mandel, *J. Phys. Chem. Solids*, **23**, 587 (1962).
18. R. F. Lever, *J. Chem. Phys.*, **37**, 1078 (1962).
19. G. Mandel and R. F. Lever, *J. Phys. Chem. Solids*, **23**, 599 (1962).
20. C. N. Cochran and L. M. Foster, *This Journal*, **109**, 144 (1962).
21. Circular 500 National Bureau of Standards (1952).
22. Stull and Sinke, "Thermodynamic Properties of the Elements," Am. Chem. Soc. Advances in Chem. Series (1956).

Electrolytic Stibine Formation

L. Tomlinson

Chemistry Division, Atomic Energy Research Establishment, Harwell, Berkshire, England

ABSTRACT

The formation of stibine during the electrolytic reduction of aqueous antimony solutions has been investigated. Using a lead cathode, the rate of stibine formation is independent of temperature, current density, and stirring rate, but increases as a direct function of total current and pH. Stibine is formed 1.8 times more rapidly from SbIII than from SbV solutions (in 1N HCl). Cathode materials are without effect except mercury and porous graphite which gave higher rates of stibine formation. The process probably takes place in two main stages: the deposition of antimony metal; the reduction of this metal to stibine. When the antimony concentration is $>10^{-4}\text{M}$ the cathode is well covered with antimony, and the second stage is probably rate controlling. When the antimony concentration is $<10^{-4}\text{M}$ the first stage is probably the slowest step.

Stibine (SbH_3) is evolved at the cathode during the electrolysis of aqueous antimony solutions at high current density and when electrolytes containing no antimony ions are electrolyzed with an antimony metal cathode. A study of this latter method of stibine formation has been reported by Salzberg and Andreatch (1). These authors have shown that the rate of stibine formation increases with increasing current density, at least up to 0.5 amp/cm^2 and conclude that stibine is formed from reduced water molecules rather than from discharged hydroxonium ions.

Very little information has been published concerning the formation of stibine during the electro-

lysis of aqueous antimony solutions at inert electrodes. Grant (2) has described a suitable cell in which to prepare the hydride from antimony solutions and states that lead cathodes are to be preferred if high rates of stibine formation are to be achieved. However no experimental evidence is furnished to reinforce this statement. Reisman *et al.* (3) have shown briefly that stibine is also formed when platinum/iridium cathodes together with very high current densities ($10\text{-}100 \text{ amp/cm}^2$) are employed.

In the present paper a wide survey of the influences of many parameters on the electrolytic formation of stibine from aqueous antimony solutions is

reported for the first time. The aim has been to elucidate the broad features of the process rather than study in detail a small experimental region. In this preliminary study, the electrolysis current has been maintained constant, no attempt being made to measure or control the cathode potential.

Experimental

Apparatus and procedure.—A diaphragm cell was used similar to that devised by Grant (2) but somewhat smaller. The porous porcelain diaphragm of 40 ml capacity contained 20 ml of aqueous antimony solution. Either hydrogen or helium was passed through the cell at 130 ml/min. Substitution of helium for hydrogen had no effect on the rate of stibine formation. The gases passed from the cell *via* a splash head and calcium chloride drying tube to a silica decomposition tube heated to 800°C. The hydride was completely decomposed; 90% of the antimony forming a mirror on the tube wall and 10% passing on in particulate form to be caught by a sintered glass filter.

After several preliminary experiments, it was realized that the standard electrode potentials of Sb (+0.212v) and Pb (−0.126v) (4) are such that electrochemical displacement of Sb III by Pb could occur, before and after electrolysis, while the cathode is in contact with the solution. The rate of this electrochemical reaction was measured in our cell under normal conditions at 23°C. After a 10-min experiment in which no current was passed, the electrode was removed and found to be coated with a loosely adherent black deposit of antimony, amounting to 9% of that originally present solution (see Fig. 2). Following this result the contact time between solution and electrode was kept to a minimum. Before electrolysis this was 1 min and after electrolysis 2 min.

In a normal electrolysis run, air was swept from the system for several minutes before adding the antimony solution to the cathode compartment *via* a funnel. After electrolysis, the cathode was quickly removed and washed. The amounts of antimony remaining in solution and deposited on the electrode, silica tube, and sinter were measured so that a mass balance could be carried out. An average of 5% of the antimony was lost in each experiment, primarily by diffusion into the porcelain diaphragm.

Electrodes.—A conical lead cathode was made by sealing spectroscopically pure lead rod (6.5 mm diameter) into a glass tube with Araldite resin. The exposed area of the electrode was 1.0 cm². A second conical lead cathode of surface area 2.4 cm² was made in a similar way using rod of 11 mm diameter. Other electrodes (Pb, Pt, Pd, Au, Ag, Bi, Cu, graphite) were cut out from sheet to give a total surface area of 1 cm² (7 × 7 mm) and sealed into glass tubes with Araldite. The copper amalgam electrode was prepared, immediately prior to use, by cleaning a sheet copper electrode with dilute nitric acid, washing with distilled water, and then placing in clean mercury. The mercury was found to wet only part of the electrode surface. However on replacing the partially coated electrode in the dilute nitric acid,

the mercury spread out and gave a thick, uniform coating. The electrode was finally washed with distilled water. A small beaker placed on the bottom of the porous pot and containing mercury (surface area 1 cm²) served as a mercury cathode. Electrical connection was provided by a wire sealed into a glass tube. Both the conical and sheet lead electrodes were cleaned by scraping with a razor blade to expose a bright metal surface. Other sheet metal electrodes, except silver, were cleaned with CCl₄, acetone, dilute HCl, and distilled water. The silver electrode was cleaned with CCl₄, acetone, and distilled water. The graphite (Pile grade A) electrode was rubbed with fine emery cloth and soaked in water before use.

Analysis.—The rate of stibine formation was measured by a radioactive tracer method. Tracer solutions were prepared as follows. Spectroscopically pure antimony metal was irradiated in a nuclear reactor to produce ¹²⁴Sb (60 day). The metal was dissolved in 0.3 ml hot concentrated H₂SO₄, diluted and reduced to Sb III with SO₂. Excess SO₂ was boiled off. Dilute HCl and inactive Sb III solution (prepared from solid analytical grade SbCl₃) were added to the largest portion of this solution. Another portion was oxidized to Sb V with Cl₂, excess Cl₂ being boiled off. A third portion was diluted with 1N H₂SO₄ to give a sulfuric acid tracer solution. These solutions were used for the major part of the experimental work. A small number of experiments concerned with the pH effect were, however, carried out with tracer solution prepared from radioactive SbCl₃ dissolved in 5N HCl supplied by the Radiochemical Centre, Amersham, England. This had been made by dissolving irradiated, analytical grade Sb₂O₃ in concentrated HCl. Traces of Sb V in the solution were reduced to Sb III with SO₂ and the excess SO₂ boiled off. Sb III tracer solutions were then prepared as described previously.

In each experiment the following quantities were measured: concentration of antimony ions before and after electrolysis; amounts of antimony metal deposited on the cathode, silica tube, and sinter. The total of that found on the silica tube and sinter is equal to the amount of SbH₃ produced. The beta activity of the solutions was determined with a 10 ml liquid Geiger counter (20th Century Electronics, Ltd., type M6 or CV2145). The latter is a tubular counter with an outer annulus to contain the liquid. Before counting the solutions were adjusted to a constant acidity (1N). The antimony metal deposits were dissolved at room temperature in 4N HCl containing a small quantity of hydrogen peroxide. The acidity of these solutions was also adjusted to 1N before counting.

Results

Lead electrode.—This electrode, stated by Grant (2) to be the most efficient, was used to study the effects of a large number of parameters on the rate of stibine formation. Experiments were carried out with a conical lead electrode (surface area 1 cm²), using tracer solution prepared from radioactive Sb metal. Preliminary experiments showed that, using the same tracer solution, the method was quite re-

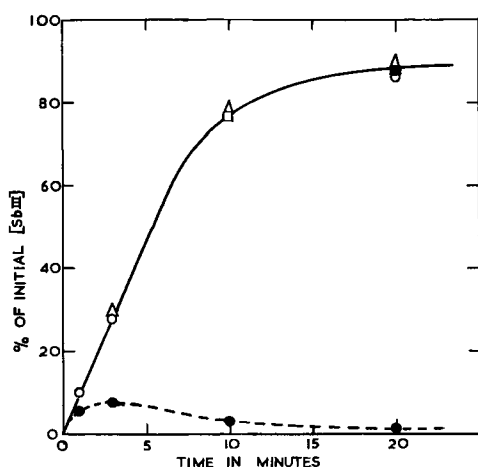


Fig. 1. Effect of initial temperature (4A, [Sb III] $4.1 \times 10^{-4}M$, 1N HCl). Open circle, 0°C; dark box, 10°C; open triangle, 23°C; open box, 35°C; dark circle, Sb on the cathode; — % Sb III converted to SbH_3 ; - - - - % Sb III deposited on the cathode.

producible; three runs with 20-min electrolysis times resulted in 85, 84, and 88% conversion of the antimony in solution to stibine. However, using the tracer solution prepared from radioactive $SbCl_3$ lower rates of stibine formation were observed (Fig. 3), but these were reproducible in themselves.

The percentage conversion of the antimony ions in solution to SbH_3 and the percentage deposited on the cathode are plotted or tabulated, in Fig. 1 to 4 and Tables I to III. Figure 1 shows the effect of initial cell temperature. Because of the cell resistance of 3 ohms, the temperature rises by a considerable amount during electrolysis. Thus, when 4 amp are passed for 20 min, the temperature rises from 23° to 60°C. Although the stated temperatures did not remain constant during a run, experiments which start at 0°C will operate during a fixed time period, over a different temperature range than those starting at 35°C. It is found however that the initial temperature has no effect on the yield of stibine after a given electrolysis time (Fig. 1), indicating that the process has either a zero or very small temperature coefficient.

The quantity of antimony found deposited on the electrode at the conclusion of an experiment is also independent of temperature, but varies with time (Fig. 1). This quantity is the sum of that deposited by electrolysis and by electrochemical displacement of lead, minus that converted into stibine. The displacement reaction does not occur during electrolysis because of the applied potential. In the absence of electrolysis, 9% of the antimony in solution is deposited on the electrode by displacement in 10 min

Table I. Effect of current density on the rate of stibine formation at conical lead cathodes [Sb III] $4.1 \times 10^{-4}M$, 1N HCl, 23°C, 3 min 4A

Surface area of electrode, cm^2	% Sb III initially in solution	
	Converted to SbH_3	Deposited on electrode
1.0	30	6.4
2.4	28	7.7

Table II. Effects of Sb V and H_2SO_4 on the rate of stibine formation at a conical lead cathode, $1 cm^2$ 23°C, 3 min, 5A, [Sb] $4.1 \times 10^{-4}M$

Conditions	% Sb initially in solution	
	Converted to SbH_3	Deposited on electrode
Sb III, 1N HCl	33	3.3
Sb V, 1N HCl	18	1.4
Sb III, 1N H_2SO_4	33	2.8

Table III. Effect of electrode material on the rate of stibine formation at sheet electrodes, $1 cm^2$ 23°C, 3 min, 5A, [Sb III] $4.1 \times 10^{-4}M$

Electrode material	% Sb initially in solution	
	Conv. to SbH_3	Dep. on electrode
Pt	28	0.2
Pb	29	2.9
Bi	27	0.5
Pd	26	0.2
Au	26	0.3
Ag	28	0.1
Cu	29	3.2
Cu/Hg	37	2.9
Hg	53	0.4
Graphite	37	0.2
Graphite	31	1.6
Graphite	42	0.5

(see "Apparatus and Procedure" and Fig. 2). The rate of the displacement reaction will depend on the antimony concentration, temperature, and thickness of the antimony layer on the electrode. It is therefore impossible to estimate accurately what amount of antimony is deposited on the electrode during the 2 min after the end of an electrolysis experiment and prior to removal of the electrode from the solution. However it is unlikely that this will exceed 2% of the antimony initially present in solution so that the general shape of the curve for antimony present on the electrode (Fig. 1) is probably correct. During the first few minutes of electrolysis the rate of deposition of antimony is therefore greater than its rate of removal but thereafter the amount on the electrode decreases steadily (Fig. 1).

A large increase in the rate of stibine formation occurs as the current is increased (Fig. 2), confirm-

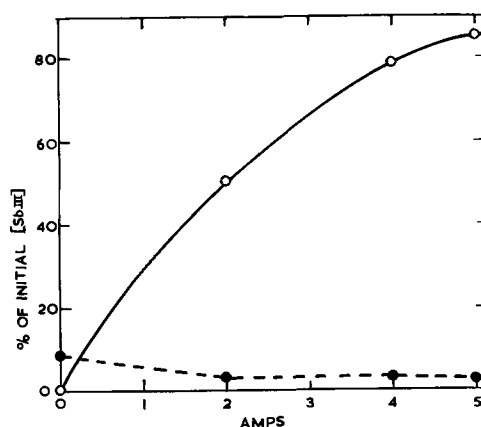


Fig. 2. Effect of current (23°C, 10 min, [Sb III] $4.1 \times 10^{-4}M$, 1N HCl); —○—, % Sb III converted to SbH_3 ; - - -●- - -, % Sb III deposited on the cathode.

ing the statement of Grant (2). The points at zero current represent the displacement of antimony by lead. Keeping the current constant and reducing the current density by using a conical electrode of higher surface area had no effect on the rate of stibine formation (Table I). Thus the rate of stibine formation is independent of current density but strongly dependent on the total current flow through the cell.

The effect of pH is shown in Fig. 3. Although the results with the two tracer preparations are quantitatively different, the trends, both as regards the rate of stibine formation and the amount of antimony deposited on the electrode, are the same. The difference between the tracer preparations is possibly due to impurities which affect both the rate of antimony deposition and stibine formation. The latter is probably controlled by the hydrogen overpotential, a quantity well known for its susceptibility to trace impurities.

By changing the gas flow through the cell the rate of stirring of the electrolyte could be altered. Increasing the stirring rate was found (Fig. 4) to have little effect on the yield of stibine, but increased the thickness of the deposited antimony. The effects of Sb V and a sulfuric acid electrolyte were also investigated and the results are shown in Table II.

A definite decrease in the rate of stibine generation occurs when the higher oxidation state of antimony is used. The quantity of antimony deposited on the electrode is also less. Substitution of sulfuric

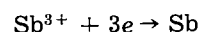
for hydrochloric acid is found to be without effect on the process.

Effect of electrode material.—In view of the electrochemical displacement which occurs when a lead electrode is placed in antimony solutions, other materials whose standard electrode potentials are such that a displacement reaction cannot occur have been investigated. Sheet electrodes were used in all cases (except for mercury) and the results are summarized in Table III. All the electrodes apart from mercury, copper amalgam, and graphite give the same yield of hydride in spite of the large differences in hydrogen overpotential at the various metal surfaces. After electrolysis, all the electrodes are coated with antimony metal.

Discussion

Although this work is a preliminary investigation of the formation of stibine during the electrolysis of aqueous antimony solutions, certain features of the process can be discerned. It would appear that two main steps are involved (the deposition of antimony by displacement of lead is neglected here):

1. Deposition of antimony on the electrode



2. Formation of stibine from deposited antimony

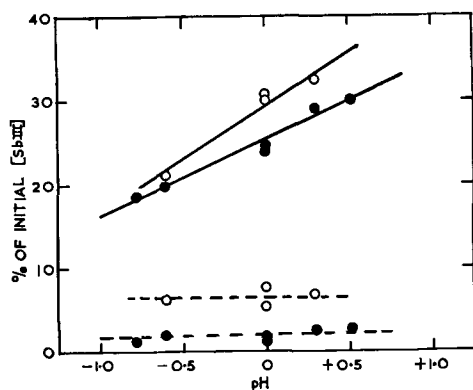
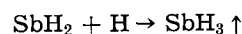
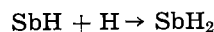
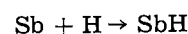


Fig. 3. Effect of pH (23°C, 4Å, 3 min, [Sb III] $4.1 \times 10^{-4}\text{M}$); ○, solution prepared from radioactive Sb metal; ●, solution prepared from radioactive SbCl₃ solution; ——— % Sb III converted to SbH₃; - - - - - % Sb III deposited on the cathode.

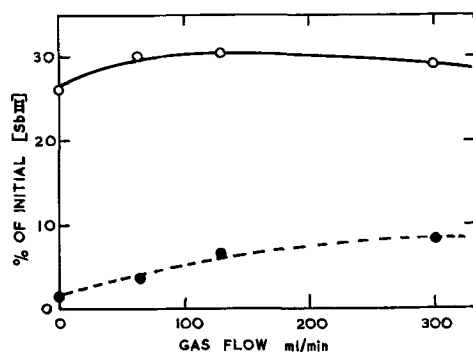


Fig. 4. Effect of stirring (23°C, 4Å, 3 min, [Sb III] $4.1 \times 10^{-4}\text{M}$, 1N HCl); ——— ○, % Sb III converted to SbH₃; - - - - - ●, % Sb III deposited on the electrode.

where H represents a hydrogen atom from an unspecified source (discharged H_3O^+ , reduced H_2O , or an adsorbed H atom) and SbH and SbH₂ are surface groups. Step 1 should follow the normal exponential rate law for the electrolytic deposition of metals (5). Step 2, on the other hand, may be expected to follow a linear rate law, as found by Salzberg and Andreatch (1) for the formation of stibine at an antimony cathode, as long as the electrode is completely covered with antimony.

In the region from 0 to 70% conversion of the antimony ions in solution to stibine (Fig. 1), the rate law is approximately linear. In this region, the electrode is well covered with antimony (Fig. 1) even when any antimony deposited by displacement after electrolysis is taken into account. (To form a monolayer of Sb, 2×10^{-8} moles are needed. In practice, however, many times more than this will be required to form an effective coating as the deposited antimony is powdery and loosely coherent.) The virtual absence of any effect of cathode material in this region (Table III), although the materials used have widely differing hydrogen over potentials, again indicates that the coating of antimony is of sufficient thickness to preclude any influence of the underlying metal. Furthermore the effects of temperature (Fig. 1), current (Fig. 2), and pH (Fig. 3) are very similar to results obtained with an antimony metal cathode by Salzberg and Andreatch (1). It is therefore concluded that in this region the electrode behaves as an antimony metal cathode and that step 2 is the slow step in the process. Salzberg

and Andreatch (1) explain the effects of temperature, current, and pH by assuming that the hydrogen overpotential is the factor which controls the rate of stibine formation. A similar explanation probably holds in the present system.

The high rate of stibine formation at a mercury cathode (Table III) could therefore be due to the high hydrogen overpotential at a mercury surface. This surface will actually consist of an antimony amalgam and have an overpotential somewhere between the 0.9v for Sb and the 1.4v for Hg (6). The higher rate of stibine formation also demands that the rate of deposition of antimony be higher than on other cathodes. This one would expect, since metals such as antimony which form amalgams have lower deposition potentials on mercury than on any other electrode material (7). (The high and unreproducible yields found with a graphite electrode are probably associated with the porous nature and high surface area of this material.)

When more than 70% of the antimony ions in solution have been converted into stibine (Fig. 1), the rate of stibine formation decreases. This is probably due to the electrode no longer being completely covered with antimony so that the process is now controlled by step 1, the rate of antimony deposition. The rate of this step will decrease exponentially with time, as the Sb III concentration falls (5).

The lower rate of stibine formation from Sb V ions compared to Sb III ions (Table II) is probably due to the slower rate of Sb deposition in the former case. This is indicated by the smaller amount of antimony found on the cathode when an Sb V solution is electrolyzed. The condition of antimony ions in

aqueous solutions has been described by Pitman *et al.* (8). It appears that, in the pH region used in the present work, Sb III will be present in solution almost entirely as SbO^+ while Sb V will be present as approximately equal numbers of SbO_2^+ and $\text{Sb}(\text{OH})_6^-$ ions. The rate of deposition from Sb III solutions would therefore be expected to be higher than from Sb V solutions since in the latter case the concentration of positive antimony ions is only half of the total antimony concentration.

Acknowledgments

The writer is indebted to Mr. G. N. Walton for valuable discussions. He also thanks Dr. G. C. Barker for advice on the theoretical aspects of the work and Mr. M. J. Bull for assistance with the experiments.

Manuscript received Sept. 23, 1963.

Any discussion of this paper will appear in a Discussion Section to be published in the December 1964 JOURNAL.

REFERENCES

1. H. W. Salzberg and A. J. Andreatch, *This Journal*, **101**, 528 (1954).
2. J. Grant, *Analyst*, **53**, 626 (1928).
3. A. Reisman, M. Berkenbilt, E. C. Haas, and A. Gaines, Jr., *This Journal*, **101**, 387 (1954).
4. W. M. Latimer, "Oxidation Potentials," 2nd ed., pp. 125, 157, Prentice-Hall Inc., Englewood Cliffs, N. J. (1952).
5. J. J. Lingane, "Electroanalytical Chemistry," p. 195, Interscience, New York (1953).
6. R. Parsons, "Handbook of Electrochemical Constants," pp. 95-97, Butterworths, London (1959).
7. Ref. (5), p. 199.
8. A. L. Pitman, M. Pourbaix, and N. Zoubov, *This Journal*, **104**, 595 (1957).

The Kinetic Order of Irreversible Reactions Following Electrolysis

Richard C. Pinkerton

Department of Chemistry, North Carolina State of the University of North Carolina, Raleigh, North Carolina

ABSTRACT

In the electrolysis of certain compounds, alternating currents result in some net production of material. This may occur because of the irreversible decomposition of an electrolytically formed intermediate. New mathematical derivations of the efficiency are outlined for first and second order mechanisms and for various wave shapes. It is concluded that the kinetic order may be determined using periodic current of any wave shape. The efficiency for a first order reaction is independent of current density; the characteristic of second order reactions is that the efficiency will be unchanged if the ratio (current density)/(frequency)² is held constant. These generalizations are valid even when a complete mathematical solution is unavailable. The relationship between the results of efficiency measurements and studies of the Faradaic impedance is examined.

In recent years, much progress has been made in the study of electrochemical mechanisms. This is borne out by Delahay's comprehensive review (1). The central problem is the determination of the rate of the electron transfer reaction. This is often accomplished under conditions greatly complicated by diffusion and adsorption. In so far as the species immediately involved in electron transfer are

concerned, the mechanism will usually be first order. The concept of reaction order, so paramount in the study of homogeneous kinetics, becomes submerged. In this paper, the possibility of second order reactions is considered.

Successful techniques have been developed for investigating chemical reactions which accompany the primary electrochemical step. A few representa-

tive cases will be cited because of their close relation to the present treatment. As one example, a metal ion produced by anodic oxidation may go on to complex with a certain number of ligands. The reaction order in terms of these ligands may then be found. The kinetic behavior in such cases has been considered by Kern (2), and in a series of papers by Gerischer (3). The reverse of the above process, that is, electrodeposition of a complexed metal ion, has also been considered. The mathematical analysis has been extended by Matsuda, Delahay, and Kleinerman to include complexing reactions which are irreversible (4). This sometimes permits the determination of rates for very fast chemical reactions occurring in the diffusion layer. A number of these have been investigated by Koryta and co-workers (5). Their treatment is based on a mathematical formulation of the problem due to Koutecky. Koryta has considered the limitations of such methods for determining the rates of associated chemical reactions (6). One important conclusion is that, ideally, the species involved should be uncharged.

Square wave techniques have played an important role in the experimental work. This subject has also been reviewed by Koryta (7). Smit and Wijnen have been particularly successful in applying square wave currents and voltages (8). For example, they were able to determine the transfer coefficient of the electron transfer reaction by a method in which diffusion does not interfere. The dimensionless transfer coefficient is obtained from a plot of two experimentally obtained voltages. Dimensionality plays an important part in these methods. The particular wave shape used may not be of concern; mathematical analyses are sometimes obtained in a form applicable to any time function of the current (9). Other advances in analytical methods continue to be reported (10, 11).

In the foregoing cases, the kinetics are first order in the initial product of electrolysis. There are important exceptions. Let us assume that an unstable organic radical is formed. Subsequent decay will often be irreversible. Then the problem of interest is to determine whether decay is first or second order. The Kolbe synthesis falls in this category. This century old reaction has never been adequately described. Yet it is involved in some recent problems of practical interest. The electrolytic oxidation of methanol, with its intermediate of formic acid, is related to the Kolbe synthesis. Within the past year, informative papers have been published by Conway and Dzieciuch (12), by Breiter (13), and by Juliard and Shalit (14). Conway and Dzieciuch explicitly consider the problem of kinetic order. For the prototype Kolbe reaction, the oxidation of formic acid, they reject a second order path *a priori*. Their reasoning is based on the fact that no peroxides are observed. This they consider the necessary result when two $\text{HCOO}\cdot$ radicals combine. However, the reaction $\text{HCOO}\cdot + \text{HCOO}\cdot \rightarrow \text{HCOOH} + \text{CO}_2$ should not be overlooked. Experimental evidence which they cite later in support of a first order

mechanism is complicated by competitive adsorption processes which also occur.

In this paper, a different approach to the problem of determining kinetic order will be examined. Wilson and Lippincott applied this method in a study of the Kolbe synthesis published in 1956 (15). They electrolyzed acetic and propionic acids using an alternating square wave current. Under these conditions, some net amount of the products is obtained, due to the irreversible nature of the reactions. The amounts fall off as higher frequencies are employed. Wilson and Lippincott attempted to establish the kinetic order by studying the effect of frequency on the current efficiency. Their conclusions are questionable, however, due partly to the form in which the efficiency equations were derived.

Since this is a potentially useful experimental approach, a more general mathematical model will be developed. Complicating factors such as diffusion, adsorption, and double layer capacitance will purposely be ignored. The models used in other work are admittedly more sophisticated. However, there is an advantage to be gained by focusing attention on the kinetic order. Certain basic requirements of dimensionality will become evident, and these must still apply when more complicated models are used.

Electrolyses with Square Wave Currents

The paper of Wilson and Lippincott (15) should be consulted for experimental details in what follows.

The initial electrochemical reaction may be written very generally as $\text{R}^- \rightarrow \text{R}\cdot + \text{e}$. R^- is the anion of a carboxylic acid and $\text{R}\cdot$ is a carboxy- or a hydrocarbon radical. In the latter case, CO_2 would be one of the implied products. There would then follow a reaction involving either one or two of these radicals. In the square wave electrolysis, only a fraction of the radicals initially produced are recovered on reversal of the current. Those which react chemically will form hydrocarbons. In this case they are gaseous. The volumes are measured and used to calculate a current efficiency.

First Order Case

Following the terminology of ref. (15), two differential equations are set down which describe the kinetics during the first half of a cycle of square wave current

$$d[\text{R}]/dt = I - k_1[\text{R}] \quad [1]$$

and

$$d[\text{P}]/dt = k_1[\text{R}] \quad [2]$$

$[\text{R}]$ is the concentration of radicals at the surface, $[\text{P}]$ the concentration of products, and k_1 the first order rate constant. The current density, I , is expressed in consistent units, containing within it the Faraday constant. For mathematical conciseness a change will be made to two new variables: $X = [\text{R}]/I$ and $Y = [\text{P}]/I$. Later on, this will also help in defining the critical parameters governing the efficiency. In the new form, the equations are

$$dX/dt = 1 - dY/dt \quad [1A]$$

and

$$dY/dt = k_1X \quad [2A]$$

For square wave current, the cycle time will be given by $1/f$, where f is the frequency in cycles per second. In the second half of the cycle, no new radicals will be produced. Any remaining will be destroyed.

In the treatment of ref. (15) the latter half-cycle is completely ignored. Limits of integration on the time are therefore set at $t = 0$ and $t = 1/2f$. This gives for X , which is a measure of that fraction of the current appearing as radicals on the surface

$$X = (1/k_1)[1 - \exp(-k_1t)] \quad [3]$$

At the end of the half-cycle

$$X = (1/k_1)[1 - \exp(-k_1/2f)] \quad [4]$$

The value of Y , which is a measure of the product obtained per unit of current during one cycle, is then obtained by integrating [1A]

$$Y = (1/2f) - (1/k_1) [1 - \exp(-k_1/2f)] \quad [5]$$

The efficiency may then be obtained by dividing Y by the maximum value which it can reach. This occurs when either k_1 is very large or the frequency is very low. Under these conditions, $Y = 1/2f$. The efficiency then is, on the basis of the assumptions of (15)¹

$$E(1) = 1 - (2f/k_1) [1 - \exp(-k_1/2f)], \text{ or} \\ 1 - (1/a) [1 - \exp(-a)], \text{ where } a = k_1/2f \quad [6]$$

The index (1) assigned to the efficiency identifies the first order case.

Before going further, it will be necessary to examine more closely the foregoing assumptions. It is seen that, by the end of the first half-cycle, there remain unreacted radicals. Since we must assume that the initial reaction is a reversible one, reversal of the current will commence to remove radicals. However, they will not be destroyed instantaneously. Unless some new mechanism is brought into play, they will disappear only as fast as the reverse current permits, and beyond that, only by further formation of product. This is illustrated in Fig. 1. The dashed line shows what the surface concentration of radicals would be if there were no product formation. The concentration will eventually become zero, but at some time which is greater than the time of a half-cycle. This new time should be used as the upper limit of integration.

Under these new conditions, a more general expression for the efficiency may be found. In the second half-cycle, the equation for X corresponding to [1A] is

$$dX/dt = -1 - dY/dt \quad [7]$$

Then, combining [1A] and [7]

$$Y = Y(\text{I}) + Y(\text{II}) = \int_0^{(1/2f)} dt - \int_{1/2f}^{\tau} dt - \int_0^{X(1/2f)} dX - \int_{X(1/2f)}^{X(\tau)} dX$$

or

$$Y = (1/f) - \tau \quad [8]$$

¹ There are several alternate ways of arriving at the efficiency, all of which give the same result. The expression given by ref. (15), which is their equation [7], lacks the factor 2 associated with f . This has no bearing on their arguments regarding kinetic order, and would make a difference only had a value been assigned to k_1 .

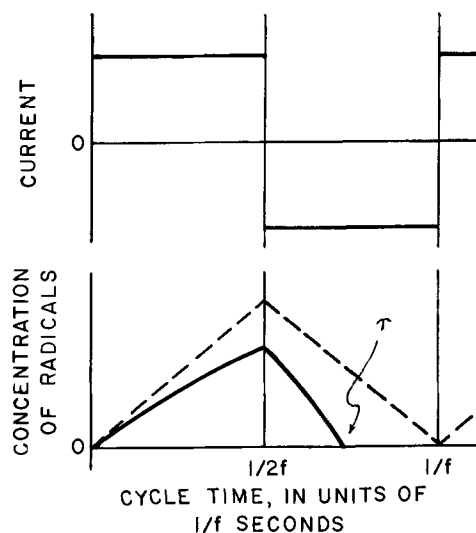


Fig. 1. Concentration of radicals at an electrode surface as a function of time, shown in relation to a cycle of square wave current.

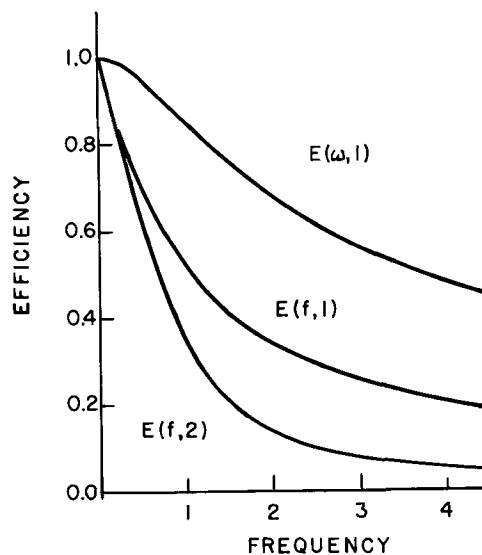


Fig. 2. Efficiencies for first and second order kinetics and for various wave shapes, as a function of frequency in dimensionless units. The units are, for $E(f,1)$, $2f/k_1$; $E(f,2)$, $2f/\sqrt{k_2f}$; $E(\omega, 1)$, ω/k_1 .

since $X(t = \tau) = 0$. The efficiency is again obtained by multiplying by $2f$

$$E(f) = 2(1 - f\tau) = 1 - 2f(\tau - 1/2f) \quad [9]$$

Here the index f appended to E refers to the square wave case. The expression applies for any reaction order, it being the time τ which is affected by the mechanism. In the first order case, τ is easily found by integrating Eq. [7], the second expression for X , along with [2A]. This gives

$$\tau - 1/2f = (1/k_1) \ln [2 - \exp(-k_1/2f)] \quad [10]$$

Substituting in [9], the revised efficiency becomes

$$E(f,1) = 1 - (1/a) \ln [2 - \exp(-a)] \quad [11]$$

in which $a = k_1/2f$ as before.

A plot of this function is shown as the lower curve in Fig. 2. The general shape of the curve resembles very much that of Eq. [6]. However, the associated value of k_1 is quite different.

In order to evaluate k_1 from experimental data, it is first necessary to ascertain whether first order kinetics really apply. As shown later, this had best not be done by curve fitting. The most reliable indication is that the efficiency is independent of current density. Then k_1 may be found by determining the frequency f' for which $E(f,1)$ has a prescribed value. For example, when $a = 1$, $E = 0.510$, so that

$$k_1 = 2f' \quad [12]$$

It may be that, because of experimental interferences, the middle portion of the curve is not reliable enough to be used in evaluating k_1 . An alternate method would be to use the slope. As can be seen from the graph, $dE(f,1)/df$ is reasonably straight in the initial, low frequency range. Taking the derivative of the general Eq. [9]

$$dE(f,1)/df = -2(\tau + f d\tau/df) \quad [13]$$

For the first order case

$$d\tau/df = -1/f^2 [2 - \exp(-a)] \quad [14]$$

Then in the limiting case

$$k = -2(\ln 2)/dE(f,1)/df(0) \quad [15]$$

Second Order Case

For the second order case, the differential equation replacing [2A] is

$$dY/dt = k_2 I X^2 \quad [16]$$

This equation, together with [1A], may be solved for the first half-cycle only, to give an efficiency corresponding to that obtained by Wilson and Lippincott (15). The result is

$$E(2) = 1 - (2f/\sqrt{k_2 I}) \tanh(\sqrt{k_2 I}/2f)$$

or

$$1 - (1/b) \tanh b, \text{ where } b = \sqrt{k_2 I}/2f \quad [17]$$

The expression given in ref. (15) was in series form, which caused difficulties in the interpretation of the results. In any case, the integration here will again be carried out until the time τ when all radicals disappear. The equation for the second half cycle is

$$dX/dt = -1 - k_2 I X^2 \quad [18]$$

Upon integration this gives

$$\tau = (1/2f) [1 + (1/b) \tan^{-1} \tanh b] \quad [19]$$

so that

$$E(f,2) = 1 - (1/b) \tan^{-1} \tanh b \quad [20]$$

This results immediately from the general Eq. [9]. Evaluation of the rate constant k_2 might be carried out by any of the methods suggested before. Using the derivative the relationship required is

$$dE(f,2)/df(0) = -\pi/\sqrt{k_2 I} \quad [21]$$

The efficiency curve for the second order case is shown in Fig. 2, along with the curve for the first order. Both are plotted in comparable, dimensionless frequency units, (b) and (a) respectively. The shapes of the curves alone do not distinguish the first from the second order. The logical procedure appears to be to vary the current density over a reasonably wide range. In the second order case,

an increase in I should improve the efficiency. Doubling the frequency should have the same effect as reducing I by a factor of one-fourth. As will be shown, this criterion is independent of the particular wave shape used.

An expression has also been obtained for the mixed first and second order case. Only the results are given. The value of τ to be used in [9] is $\tau = (1/2f) +$

$$(1/c) \ln \frac{k_1 + d \operatorname{ctnh}(d/4f) + 4k_2 I / (k_1 - c)}{k_1 + d \operatorname{ctnh}(d/4f) + 4k_2 I / (k_1 + c)} \quad [22]$$

where $c = \sqrt{k_1^2 - 4k_2 I}$ and $d = \sqrt{k_1^2 + 4k_2 I}$.

An alternate form may be obtained, which gives a more concise expression for E

$$E(f;1,2) = 1 - (4f/c) \operatorname{ctnh}^{-1}[(2k_1 + d) \operatorname{ctnh}(d/4f)/c] \quad [23]$$

The value of the slope of the efficiency curve is

$$dE(f;1,2)/df(0) = -(4/c) \operatorname{ctnh}^{-1}[(2k_1 + d)/c] \quad [24]$$

The efficiency referred to here is the total efficiency of electron utilization. If the two reaction paths in question lead to different products, the efficiency derived is actually the total of two separate quantities. The mathematical task of separating these two is a formidable one. Unfortunately, it may be that only one product is isolated in the experiment. It is quite possible that, in the work of Wilson and Lippincott (15), more than one mechanism is operative.

Electrolyses with Sign Wave Currents

For a number of reasons, one would like to have solutions for the sine wave cases. There are certain impedance measurements, closely related to the model being discussed, which would ordinarily be carried out with sine wave current.

The general differential equation to be solved is

$$dX/dt = \sin \omega t - dY/dt \quad [25]$$

In this case, X is defined as $X = [R]/I'$, where I' is the amplitude, and also, $Y = [P]/I'$. Equation [25] may be integrated immediately to give

$$0 = (1/\omega) (1 - \cos \omega \tau) - Y \quad [26]$$

the limits of integration for X being zero at both extremes. Y is again a measure of that fraction of the current going to form product, in a single cycle. If all of the current during the first, positive half of the cycle went into product, the value of Y would be $2/\omega$. Therefore, the efficiency will be

$$E(\omega) = (1/2) (1 - \cos \omega \tau)$$

or

$$1 - (1/2) (1 + \cos \omega \tau) \quad [27]$$

This equation applies for any order. The symbol ω , which is the frequency in radians per second, is also used to label E for the sine wave case.

First Order Case

The first order case is the only one for which a complete solution has been obtained, and this solu-

Table I. Numerical solutions

$\omega\tau$	$E(\omega, 1)$	ω/k_1
3.59	0.950	0.484
3.93, ($5\pi/4$)	0.854	0.975
4.19, ($4\pi/3$)	0.750	1.50
4.37	0.667	2.07
4.71, ($3\pi/2$)	0.500	3.64
5.05	0.333	7.13
5.23, ($5\pi/3$)	0.250	9.83
5.50, ($7\pi/4$)	0.147	18.64

tion is an implicit one. In order to find an expression for τ , Eq. [25] is solved for X after inserting k_1X for dY/dt . This gives

$$X = (1/\omega^2 + k_1^2) [k_1 \sin \omega t - \omega \cos \omega t + \exp(-k_1 t)] \quad [28]$$

When X reaches its second zero value, $t = \tau$. By defining again a characteristic parameter $a' = k_1/\omega$, an implicit solution for τ is obtained

$$a' \sin \omega\tau - \cos \omega\tau + \exp(-a'\omega\tau) = 0 \quad [29]$$

It will be noticed that, just as in Eq. [10], the magnitude of the current density does not enter into the solution for τ . Therefore, the efficiency is also independent of I' .

Numerical solutions for $E(\omega, 1)$ are given in Table I. They are listed in terms $1/a'$, or ω/k_1 , which may be regarded as a dimensionless frequency parameter. The first part of the curve of $E(\omega, 1)$ vs. ω/k_1 has been plotted in Fig. 2, along with the values for $E(f, 1)$. It will be noted that the change in wave shape of the applied current has had a marked influence on the shape of the efficiency curve. If the experimental wave shape is distorted the rate constants evaluated may be in error. For the sine wave case, E at the 0.5 level is attained when $k_1 = \omega/3.64$; if the frequency is read in cycles per second instead of radians, $k_1 = 1.73f$. In the square wave case, under similar circumstances, $k_1 = 2.08f$. In other words, the same efficiency may be achieved at a somewhat higher frequency if sine wave current is used.

The difference in the efficiency curve is even more pronounced at low frequencies. For the sine wave case, it is no longer possible to evaluate the rate constant k_1 from the derivative, as in [15]. By implicit differentiation of [29], it may be shown that $dE(\omega, 1)/d\omega(0) = 0$. However, there is a useful alternate expression. As ω becomes small, or as $k_1\tau$ takes on large values, the exponential term in Eq. [29] vanishes faster than the sine term. Over a certain region, $k_1 \sim \omega \tau n \omega\tau$. Then, from [27]

$$k_1 \sim \omega(E-0.5)/\sqrt{E(1-E)} \quad [30]$$

This expression may be used with an accuracy better than 2.5% in the range of E values greater than 0.85.

General Solutions Giving the Order with Any Wave Shape

In the second order, sine wave case, not even an implicit solution for τ is available. However, there is a powerful generalization which allows one to establish the kinetic order. Then, while absolute

values for the rate constant may not be obtained, a number proportional to it may be measured.

In the general second order case, one may always write

$$d[R]/dt = IF(\omega t) - k_2[R]^2 \quad [31]$$

where F is some function defining the wave shape. As long as it is a periodic function, ωt will appear as the independent variable. Let $\omega t = s$, and let $[R]$ be replaced by $[R] = (I/\omega)Z$. Then

$$dZ/ds = F(s) - (k_2 I/\omega^2)Z^2 \quad [32]$$

The relation between the constant $k_2 I/\omega^2$, which will be called b' , and the quantity b defined in Eq. [17], is immediately apparent. It is now appropriate to call b' the characteristic parameter for the case of second order kinetics. Now, since Eq. [32] will ordinarily satisfy the conditions for existence of a solution, a value for $s = \omega\tau$ may be obtained, in theory. This will be done by integrating with limits of zero on Z at both extremes. In so doing, the variable Z will be eliminated. A solution for s will be obtained in terms of b' alone. This term embodies all the experimental variables, which will appear only through b' . In the meantime, direct integration of the equation in a form similar to [25] leads to the efficiency. This equation will be characteristic of the wave shape used, but will be a function only of the particular value of s at $Z = 0$. Then it is possible to state that

$$E(2) = G(s) = G'(b') \quad [33]$$

This means that, beyond the specific case of Eq. [20], all second order kinetics will depend on the current density I . Further, the efficiency will not be affected if both I and ω are varied in such a manner that I/ω^2 remains constant.

In a similar way, it is possible to arrive at the characteristic first order parameter, $a' = k_1/\omega$. It is therefore possible to distinguish between first and second order kinetics using a periodic current of arbitrary wave shape, whether or not the equations can be integrated.

It will also be possible to find a relative value of the rate constant, which will be related to the absolute value by a constant. Some particular value of the efficiency is chosen, say $E = 0.5$. If the kinetics are second order, it is then possible to state that

$$k'_2 = Ck_2 = \omega'^2/I \quad [34]$$

where ω' is the value of ω at $E = 0.5$. The value of C will be fixed for any particular wave shape, although it may be undetermined. Such a relative value of the rate constant is perfectly adequate for determining the temperature dependence and from this the activation energy for the rate-determining step.

The simple model considered here will probably require some modification before it can be applied experimentally. The effects of diffusion and adsorption cannot be completely ignored. For example, in order to insure an ample supply of ions at the surface, one must restrict the current density to low values, or else use a high frequency. Otherwise, the

chronopotentiometric transition time will be exceeded. But under these conditions, the current lost in charging and discharging the double layer capacitance may have to be taken into account. There is hope that these difficulties can be overcome.

Relationship to Faradaic Impedance Measurements

A mechanism analogous to the one discussed here has been analyzed in terms of the Faradaic impedance (16). Grahame applied this to the hydrogen evolution reaction, in which there may be a second order recombination of hydrogen atoms (17). Much present day work is based on Grahame's approach, and it will be of interest to compare the results obtained.

The experimental conditions imposed when one studies the Faradaic impedance differ considerably from those used when measuring the efficiency. The part of the impedance which is affected by the electrochemical process is first separated from such other influences as the double layer capacitance. This Faradaic impedance may be represented as a series resistance and capacitance (or its parallel circuit equivalent). There is then a theoretical relation between these components of the impedance and the controlling rate constant.

Grahame considers the second order case in Section III of his paper. He sets down

$$dv_o/dt = i_o g + ag \sin \omega t - kv_o^2 \quad [\text{G50}]$$

In this equation, v_o is the concentration of hydrogen radicals at the surface. i_o represents a polarizing current and has some relation to the current density I' of the present paper.² The significance of g need not concern us here. Equation [G50] may then be compared to Eq. [25] in combination with [16]. However, the magnitude of the sine wave current $ag \sin \omega t$ is restricted to very small values. Electrolysis is to be carried out over a linear portion of the current-voltage curve. The sine wave current therefore contributes nothing to the net electrolysis. This allows certain second order terms to be ignored, and a complete solution of the differential equation is possible. The series resistance R_s and the capacitance C_s are then found. Grahame ultimately arrives at the important dimensionless relation

$$R_s C_s \omega = 2\sqrt{i_o k_2}/\omega \quad [\text{G61}]$$

in which k_2 is inserted for k_1 , and a factor g has been omitted. This is the same as $2\sqrt{b'}$, b' being the

² While it is true that there is no resultant d-c current in the situation considered previously, there may be at each individual electrode a rectification current whose magnitude depends on the efficiency. It will also depend on the magnitude of I' . Of course, in a real case, some other Faradaic process will intervene after τ is reached.

characteristic second order parameter of the present paper.

Grahame did not bother to show the solution for cases of different order, but this is easily done. For first order kinetics, one obtains

$$R_s C_s \omega = k_1/\omega = a' \quad [\text{35}]$$

It is apparent that these generalizations regarding kinetic order apply to widely differing formulations of the kinetic problem. In simple cases, a straightforward dimensional analysis may be sufficient. The particular wave shape used is of secondary importance. The exploration of radical reactions at the electrode surface remains a challenging area for experimental investigation. There are often formidable mathematical barriers to interpretation. It is hoped that some of these problems will soon be solved.

Acknowledgment

The author wishes to thank Professor Dan Trivich and others, for calling his attention to certain references, and the reviewers, for many pertinent comments.

Manuscript received July 31, 1963. Revised manuscript received Nov. 26, 1963. This paper was presented at the New York Meeting, Sept. 29-Oct. 3, 1963.

Any discussion of this paper will appear in a Discussion Section to be published in the December 1964 JOURNAL.

REFERENCES

1. P. Delahay in "Recent Advances in Electrochemistry and Electrochemical Engineering," P. Delahay and C. W. Tobias, Editors, pp. 233-318, Interscience Publishers, New York (1961).
2. D. M. Kern, *J. Am. Chem. Soc.*, **76**, 4234 (1954).
3. H. Gerischer, *Anal. Chem.*, **31**, 33 (1959).
4. H. Matsuda, P. Delahay, and M. Kleinerman, *J. Am. Chem. Soc.*, **81**, 6379 (1959).
5. J. Koryta and Z. Zabransky, *Collection Czech. Chem. Commun.*, **25**, 3153 (1960).
6. J. Koryta, *Z. Elektrochem.*, **64**, 23 (1960).
7. J. Koryta, *Electrochim. Acta*, **8**, 471 (1963).
8. W. M. Smit and M. D. Wijnen, *Rec. Trav. Chim.*, **79**, 5, 22, 203, 289 (1960).
9. H. Hoffmann and W. Jaenicke, *Z. Elektrochem.*, **66**, 7 (1962).
10. K. E. Reinert, *ibid.*, **66**, 379 (1962).
11. A. G. Stromberg, Abstract No. 4.43, C.I.T.C.E., 14th Meeting, Moscow, August 19-25, 1963. *Electrochim. Acta*, **8**, 1viii.
12. B. E. Conway and M. Dzieciuch, *Can. J. Chem.*, **41**, 21, 38, 55 (1963).
13. M. W. Breiter, *Electrochim. Acta*, **8**, 447 (1963).
14. A. L. Juliard and H. Shalit, *This Journal*, **110**, 1002 (1963).
15. C. L. Wilson and W. T. Lippincott, *J. Am. Chem. Soc.*, **78**, 4290 (1956).
16. P. Delahay, "New Instrumental Methods in Electrochemistry," p. 165, Interscience Publishers, New York (1951).
17. D. C. Grahame, *This Journal*, **99**, 380C (1952).

The Electrochemical Oxidation of Formic Acid on Platinum

C. W. Fleischmann, G. K. Johnson, and A. T. Kuhn

Leesona Moos Laboratories, Great Neck, New York

ABSTRACT

The anodic oxidation of formic acid has been investigated on platinum black electrodes in 5*N* sulfuric acid. The data presented pertain to the activation controlled process under approximately steady state conditions at four temperatures between 25° and 90°C. Tafel plots appear to have significant slopes, and the correlation of these slopes with experimentally measured electrode coverages supports the hypothesis of two distinct electrochemical oxidation mechanisms, advanced by other workers.

The electrochemical oxidation of formic acid has been studied by many workers (1-6), the most recent paper being one by Breiter (7) who studied electrode coverage and current-voltage relationships at ambient temperature with bright platinum electrodes. In the present work, coverage measurements and current-voltage data were obtained at four temperatures, 25°, 45°, 70°, and 90°C, using platinized platinum electrodes in a 5*N* H₂SO₄-1*M* HCOOH solution.

Although perchloric acid has frequently been used as an electrolyte for such work, it becomes an oxidizing agent at higher temperatures. With sulfuric acid, this effect is smaller.

The choice of concentration of formic acid was based on the observation that the current in all potential regions ceased to be dependent on concentration somewhere between 0.5 and 1.0 molar on the type of electrodes investigated and at the highest temperatures employed. This fact was taken to indicate the establishment of activation, rather than diffusion-controlled rates of reaction. This region of concentration is also that reported by Breiter (8) and Pavela (2) to be necessary to achieve saturated coverage of platinum electrodes in solutions of methanol. It may be noted in passing that the maximum current densities obtainable in these systems at moderate concentrations are considerably in excess of the limiting currents predicted by steady state diffusion calculations because of the convective stirring due to the evolution of carbon dioxide.

In view of Breiter's statement (for methanol) that extremely small amounts of hydrogen were observed on bright platinum electrodes at open circuit, while significant amounts of hydrogen have been measured in this work, the difference in the type of electrode is an important one. Schwabe (9) and others have measured the rate of heterogeneous decomposition of formic acid, using platinum black catalysts.

Experimental

Materials and electrodes.—Reagent grade formic acid (98 + %, Eastman) and sulfuric acid (Baker) were used throughout the work.

Platinized platinum electrodes were prepared from 0.003 in. platinum sheet. The plating solution was 1.7*N* HCl containing 2.4 weight per cent Pt (as H₂PtCl₆, Bishop) and a trace of lead ace-

tate. Deposition of the black was carried out simultaneously on all electrodes at 10 ma/cm² for 3 min followed by 50 ma/cm² for 2 min. The resulting surfaces were smooth and uniformly black. The geometric area of the electrodes was 2 cm² for the work at room temperature but was decreased for the work at higher temperatures in order to provide currents within the limitations of the instruments.

Instruments and methods.—The cells were of a modified H-type and constructed entirely of glass. A fine glass frit separated the anodic and cathodic compartments, and the former was fitted with a Luggin capillary leading to a separate reference compartment. Temperatures were maintained by immersing the cells in a constant temperature bath controlled within ± 0.1°C. Potentials were set with a Wenking potentiostat and voltages were measured with a Fluke differential voltmeter. All potentials quoted have been corrected for ohmic drop between the terminal of the potentiostat and the working electrode surface; these corrections were determined oscillographically by the galvanostatic pulse technique.

Current measurements for the Tafel plots were generally made by connecting the differential voltmeter across a 1 ohm standard resistor, which in turn was connected to the external measuring terminals of the potentiostat. During the coverage work, measurements of current from a regulated current power supply were made on a Sensitive Research milliammeter.

Estimates of surface coverage were made by a galvanostatic method previously described by Breiter (3). The electrode coverage with hydrogen is measured in the electrolyte alone by observing the hydrogen transition time on a cathodic charging curve taken from about + 600 mv. The quantity sQ_H , in millicoulombs/cm², obtained in this way is taken as an arbitrary standard of full coverage. In the presence of the organic species, the electrode is held potentiostatically at a selected potential for a determined period of time, after which the potentiostat is disconnected by means of a Western Electric 275A relay and a cathodic galvanostatic pulse is simultaneously applied. The transition time for the deposition of hydrogen is observed, and a quantity Q_H is determined. Q_H represents the extent of the sur-

face unoccupied. A total fractional coverage is then defined by $(sQ_H - Q_H)/sQ_H$.

Results obtained by this method do not agree with those obtained by the method of fast anodic sweeps, as Breiter (7) shows. As a measure of uncovered surface area, rather than area on which formic acid may be adsorbed, the method appears to be valid.

Reference electrodes and potential convention.—It has been found impossible to use calomel electrodes in this system because of the adsorption of chloride ions on the anode even when the reference and anode compartments are well isolated from each other. In some of the present work, a bubbling hydrogen electrode was used directly as the reference; in other cases a "dynamic hydrogen electrode" (10) (which has been calibrated against a hydrogen electrode) was employed. The latter is a slightly cathodically polarized platinum-black electrode and has been found to be a stable reference for this work at all temperatures. Diffusion of hydrogen from the reference to the anode during current-voltage measurements was prevented by the Luggin capillary and an asbestos fiber capillary on the electrode assembly itself. In addition, the anolyte was continuously purged with helium or nitrogen at a slow rate during all experiments, except when measurements were actually taken.

The potentials in this paper are designated on the scale of the bubbling hydrogen electrode at 1 atm total pressure in the same electrolyte (5N H_2SO_4). This scale is referred to as E^* , and potentials anodic to this reference are designated as positive.

Results

Coverage measurements.—The results of measurements of electrode coverage at four temperatures are given in Fig. 3 and 4. All of the data was obtained by holding the indicated potential for 2 min and then applying the cathodic pulse. Hydrogen was evolved for 30 sec at the end of the pulse; then the next potential was set, and the process repeated. The galvanostatic pulse currents were adjusted to give transition times for hydrogen deposition of a few milliseconds. It is believed that the surface concentration of chemisorbed species is not disturbed during such times. The electrode used to obtain the data in Fig. 3 and 4 had a maximum hydrogen coverage (sQ_H) in sulfuric acid alone of about 15 mCoulomb/cm². The percentage of coverage expressed on the vertical axes is based upon the value of sQ_H determined prior to each experiment.

An additional curve is shown in Fig. 3 which corresponds to the measured coverage minus that portion which was identifiable as adsorbed hydrogen by means of anodic charging taken from +100, 200, and 300 mv. This amount of hydrogen is seen to correspond to a large fraction of the measured coverage at 25°C; this fraction decreases with increasing temperature, however, and at 90°C adsorbed hydrogen accounted for a maximum (at 0 mv) of only 5% of the total coverage. The accuracy of the coverage values is estimated as ± 0.1 .

Current-voltage data and Tafel plots.—No logarithmic plots of current at 25°C are presented, since

even a close approximation to the steady-state at a large number of potentials is not experimentally feasible. Such plots were sometimes constructed from data obtained by slow sweep methods and were reasonably linear over the first 1 to 2 decades of current in the low potential region. They consistently exhibited slopes of approximately $2RT/F$, which corresponds to a one electron transfer mechanism.

The data illustrated in Fig. 1 at the three elevated temperatures were obtained by holding each potential for 2 min in the anodic direction. Data was also obtained in the cathodic direction, and it was noted that the current hysteresis decreased progressively as the temperature was increased.

At 45°C an average slope through the data is about 110 mv/decade, although a slight increase in slope appears at around 350 mv. This change is also exhibited by the data at 70°C. The simplest picture is presented at 90° where both anodic and cathodic slopes are quite linear over more than three decades of current. The slope in the anodic direction corresponds exactly to RT/F at 90°C (72 mv/decade). Tafel slopes were accurate to ± 5 mv.

In Fig. 1 it is also shown that a limiting current is reached in all three curves at about 500 mv. This is believed to represent a limitation imposed by the rate of a pre-electrochemical step. The current

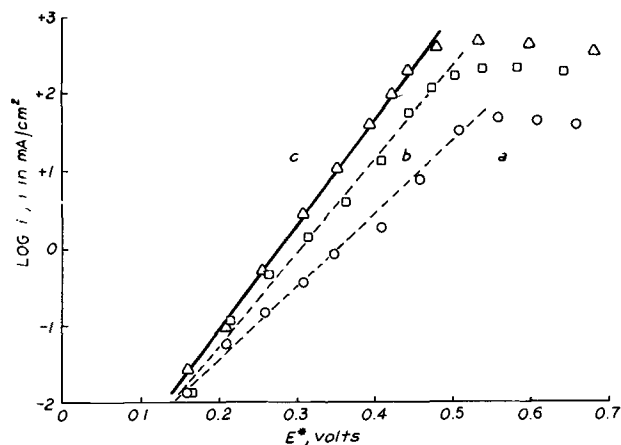


Fig. 1. Tafel plots of current due to the oxidation of HCOOH (2-min points) on platinum-black electrode of Fig. 3 and 4. Curves (a), (b), and (c) were taken in the anodic direction at 45°, 70°, and 90°C, respectively.

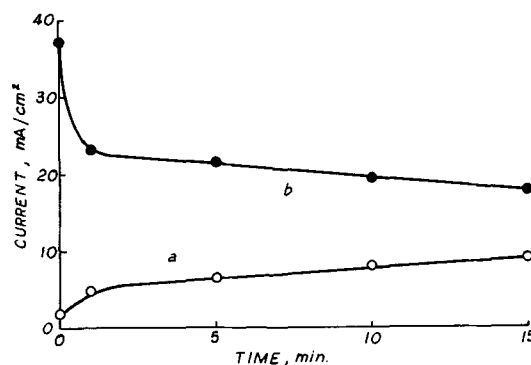


Fig. 2. Behavior of current in Fig. 1 at 600 mv E^* with time when the potential is approached from (a) less anodic potentials, and (b) more anodic potentials.

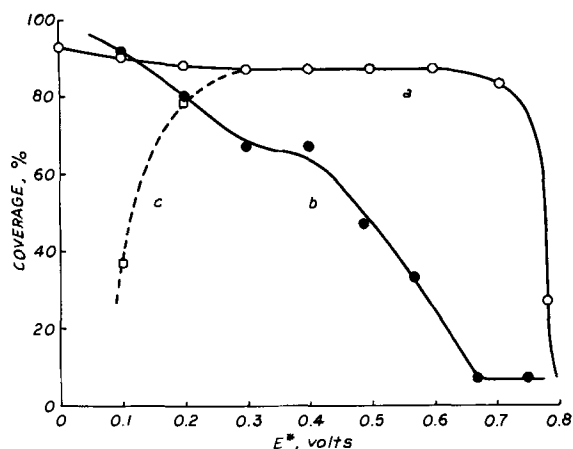


Fig. 3. Coverage of platinum-black electrode in 1M HCOOH at 25°C (2-min points) showing hysteresis in (a) anodic and (b) cathodic directions. Curve (c) is the anodic curve corrected for that part of the coverage identified as adsorbed hydrogen by anodic charging curves.

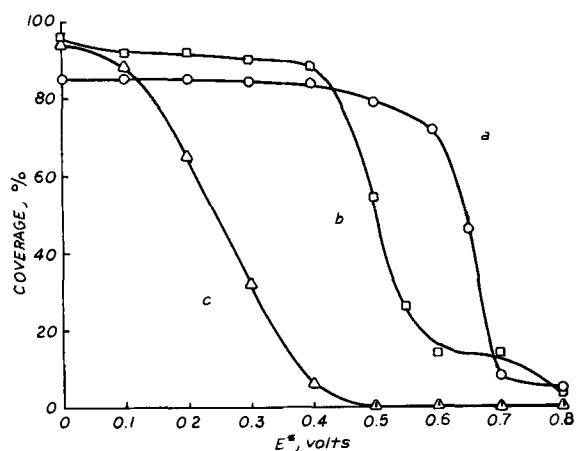


Fig. 4. Total coverage of electrode (2-min points, anodic direction) at: (a) 45°C, (b) 70°C, and (c) 90°C.

plateau did not appear to be shifted by stirring or by increasing concentration beyond 1M HCOOH. A similar limitation was observed polarographically at +500 mv by Vasil'ev and Bagotskii (11), and was ascribed to the formation of oxides. This explanation, however, is contrary to much evidence that no oxides are formed at such potentials on platinum in acidic electrolytes.

The apparent activation energy for such a pre-electrochemical step, as calculated from the current data of Fig. 1 at +500 mv, is about 12 kcal.

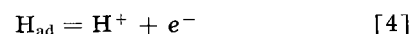
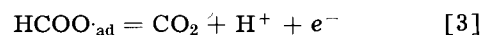
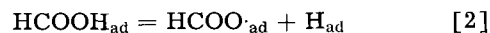
Approach to the steady-state.—This is shown in Fig. 2. It is seen that under certain conditions, the current at a given potential would increase with time. Not only does this show that the phenomenon involved is not conventional electrode "poisoning," it also provides strong evidence for the existence of two reactions, competing for a given number of platinum sites. Theories of this kind have already been advanced by Gilman (12) for the electro-oxidation of CO. A further relevance of this theory will be seen in the discussion section. The approach to the steady-state was faster at higher temperatures; its reproducibility is implicit in the reproducibility of the Tafel slopes. Similar observations

and deductions have been made for the electrochemical oxidation of acetylene (13).

Discussion

The data presented in this paper and the work of Breiter (7) and Gilman (13) all point to the existence of two distinct mechanisms by which simple organic molecules may be electrochemically oxidized.

Breiter (7) has suggested two alternative mechanisms for the oxidation of formic acid. His first mechanism is



That this mechanism is the predominant one in the low temperature region, is supported by the following facts that emerge from the present work. The coverage is large, and thus potential independent in the region under consideration. This coverage is known to be mainly a species other than hydrogen. The Tafel slope is $RT/2F$ as theory would predict. All these observations support Breiter's contention that the hindered discharge step is [3]. Breiter advances reasons for discounting the other steps as rate determining.

Recent work by Giner (14) on the electrochemical oxidation of "reduced" CO_2 provides further support. It is possible that Giner's reduced species and the adsorbed radical in [3] are identical. Gilman has a similar approach.

The high temperature electro-oxidation constitutes a more difficult problem. Breiter postulates a mechanism whereby the formic acid molecule strikes free electrode surface, and is immediately oxidized. Gilman has an analogous model for one of his two CO oxidation mechanisms. Neither author considers this mechanism in any greater detail. A simultaneous two electron transfer is felt to be unlikely, although it would give rise to the Tafel slope of RT/F observed in this work. If this is rejected, one must return to some concept of adsorbed intermediate. Though the assumption of a Temkin isotherm and activated adsorption would lead to slopes of RT/F at low coverages, this would still leave unexplained the behavior of the electrode in approaching its steady state. The authors feel that the possible explanation may lie in the varying orientations in which the formic acid molecule may be adsorbed on the electrode.

Acknowledgment

The authors would like to acknowledge the helpful comments of both referees.

Manuscript received Aug. 8, 1963.

Any discussion of this paper will appear in a Discussion Section to be published in the December 1964 JOURNAL.

REFERENCES

1. R. P. Buck and L. R. Griffith, *This Journal*, **109**, 1005 (1962).
2. T. O. Pavela, *Ann. Acad. Sci. Fennicae, Ser. A, II. Chem., Helsinki*, pp. 1-47 (1954).

3. M. W. Breiter and S. Gilman, *This Journal*, **109**, 622 (1962).
4. S. Gilman and M. W. Breiter, *ibid.*, **109**, 1099 (1962).
5. M. W. Breiter, *ibid.*, **110**, 449 (1963).
6. E. Müller, *Z. Elektrochem.*, **33**, 561 (1927).
7. M. W. Breiter, *Electrochim. Acta*, **8**, 457 (1963).
8. M. W. Breiter, *ibid.*, **7**, 533 (1962).
9. K. Schwabe, *Z. Electrochim.*, **61**, 743 (1957).
10. J. Giner, *This Journal*, **111**, 376 (1964).
11. Yu. B. Vasil'ev and V. S. Bagotskii, *Dokl. Acad. Nauk SSSR*, **148**, No. 1, 132-135 (1963).
12. S. Gilman, *J. Phys. Chem.*, **66**, 2657 (1962).
13. J. W. Johnson, H. Wroblowa, and J. O'M. Bockris. In press.
14. J. Giner, *Electrochim. Acta*, **8**, 857 (1963).
15. M. W. Breiter, *ibid.*, **7**, 601 (1962).
16. H. A. Laitinen and C. G. Enke, *This Journal*, **107**, 773 (1960).
17. M. W. Breiter, *ibid.*, **109**, 425 (1962).
18. G. C. Bond, "Catalysis by Metals," pp. 412-432, Academic Press, New York (1962).

Polarization Characteristics of the Hydrogen Gas Diffusion Electrode

Raymond P. Iczkowski

Research Division, Allis-Chalmers Manufacturing Company, Milwaukee, Wisconsin

ABSTRACT

The polarization characteristics of an electrode are obtained by combining the previously derived behavior of a single pore, with data on the pore size distribution and internal surface area of the electrode. Application is made to a cell in which the electrodes are sandwiched against a central porous electrolyte vehicle. The hydrogen electrode is made of nickel and NaOH is the electrolyte. The electrode pores are approximated by an idealized system of parallel cylinders. The total electrode current is considered to be a sum of contributions from each of the pores at the same polarization. Theoretically calculated curves are in moderately good agreement with experimentally determined curves except that they predict too much polarization at low currents and too little polarization at high currents. The dependence of the polarization curves on temperature and surface area is in general agreement with experiment.

It is customary to represent a porous hydrogen gas diffusion electrode by an idealized model in which the pores are considered to be parallel cylinders of various radii (1). The polarization characteristics of a single pore were obtained earlier (2). The aim of the present treatment is to obtain the polarization characteristics of an entire electrode by combining the results for a single pore with data on the pore size distribution and internal surface area of the electrode. This method is very similar to a method used in studies of the flow of fluids through porous media. In those studies, theoretical values of the permeability of a porous material are calculated by combining Poiseuille's law for the flow of a liquid through a cylinder with the pore size distribution of the material (3).

Type of Cell

The type of electrochemical cell considered here is one in which a porous nickel hydrogen anode and a platinum oxygen cathode are sandwiched against a central spacer of sheet asbestos. NaOH electrolyte is added to this system. This type of cell is diagrammed in Fig. 1 and has been described previously (4). Eighty per cent of the void volume of the intact asbestos fiber bundles corresponds to pores having radii less than 0.006μ (5). Less than 3% of the pore volume of the electrode is in the range below 0.01μ . It has been found that when electrolyte is added to such a cell it tends to concentrate in the

asbestos and will resist being driven out by pressure differentials up to 12 atm, and gravity forces greater than 10 G's (4). Experimental polarization curves for the hydrogen electrode were obtained by measuring the potential between the hydrogen electrode and a Luggin capillary (6) placed at the interface between the electrode and the asbestos.

Nature of the Pores and the Electrolyte Distribution inside the Electrode

The pore structure in an electrode may be most accurately pictured as the space between many sintered grains of nickel. As the saturation of the electrode by the electrolyte is increased, the electrolyte preferentially occupies the sharp pointed regions at the points of contact between granules (7), rather than flat or convex regions, and fills small vacancies between (or within) the grains before it fills larger ones. The electrolyte configuration is roughly sketched as the dark annular regions in

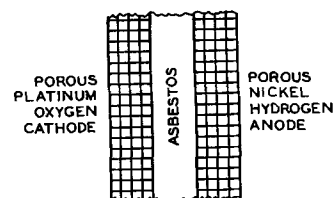


Fig. 1. Electrochemical cell with a porous electrolyte vehicle

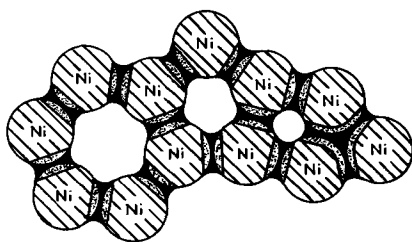


Fig. 2. Electrolyte configuration in a porous medium

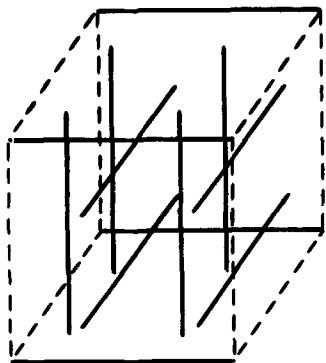


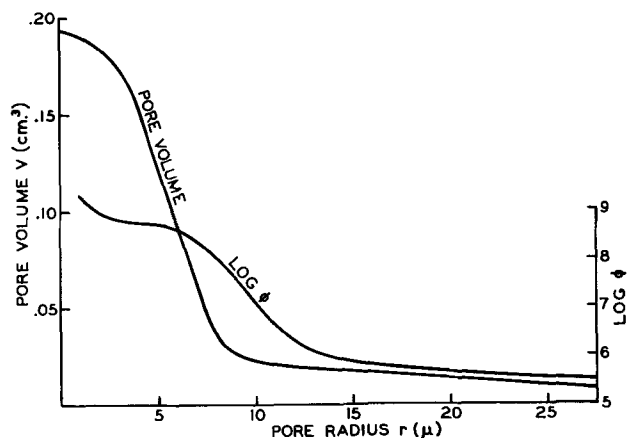
Fig. 3. "Parallel type" model of a porous medium

Fig. 2. The asbestos spacer can be completely saturated with electrolyte while the electrodes are only partially saturated, because a wetting electrolyte preferentially enters the smaller pores. Further addition of electrolyte over and above that necessary to completely saturate the asbestos, fills successively larger capillaries in the electrodes. Mercury (a nonwetting liquid) shows the opposite behavior, which is utilized in the mercury porosimeter method of determining the pore size distribution of porous electrodes (8).

The actual porous system and the configuration of the electrolyte menisci within it are too complicated to take into account exactly. For the purpose of making calculations, a simpler, idealized model of the porous system is used. The "parallel type" model (9) of a porous system is sketched in Fig. 3 for an electrode having the shape of a rectangular parallelepiped. According to this model, the pores are assumed to be right circular cylinders of various radii, the axial directions of the pores are assumed to be equally distributed in each of the three spacial directions, they pass completely through the electrode, and they intersect the external surfaces of the electrode at right angles. For this model, the quantity, ϕdr is defined as the number of pores having radii between r and $r + dr$, per square centimeter of the surface of the electrode, which the pores intersect. The pore size distribution function, ϕ , can be calculated from the volume distribution function, $V(r)$, (the volume of all pores having a radius greater than a given value, r), as obtained from mercury porosimeter measurements (8)

$$\phi(r) = \frac{-(dV/dr)}{3\pi r^2 V_s} \quad [1]$$

where V_s is the total external volume of the electrode. Typical distribution functions for an electrode made from sintered nickel powder are shown

Fig. 4. Distribution functions for a typical nickel electrode of thickness 0.0711 cm and area 3.59 cm².

in Fig. 4. In order to obtain a better graphical representation of this steeply inclined function, $\log \phi$ was plotted instead of ϕ .

When electrolyte is added to the porous system, the smaller pores will be filled up to some maximum radius, r_m . As an additional feature of the model, pores of radius less than r_m are taken to be micropores representing irregularities in the cylindrical surface of the macropores, and which only act to increase the surface roughness of those pores. Pores of radii larger than r_m will be wetted by a film of electrolyte. The actual shape of the wetting film is more nearly represented by the annular regions between the grains of nickel as shown in Fig. 2. However, for the purpose of having a workable idealized model, the film will be assumed to be of uniform thickness, t , in all parts of the electrode. Both r_m and t are proportional to the degree of saturation of the electrode by electrolyte, and they can be varied by adding more or less electrolyte to the electrode. For completeness, the polarization should be evaluated as a function of both parameters r_m and t . The film thickness, t , can take on values between zero and r_m . For simplicity in the present study, calculations will be presented only for t equal to its maximum value, r_m .

The polarization characteristics of a single pore having a uniform thin film of electrolyte were analyzed in a previous study (2). According to this "electrolyte film" mechanism, the reaction proceeds by means of the steps illustrated in Fig. 5. (i) Hydrogen from the gas phase dissolves in the outermost layer of the film. (ii) Hydrogen diffuses radially through the film and sodium hydroxide moves along the film to various points along the wall. (iii) The hydrogen is adsorbed as atoms on the surface of the nickel metal. (iv) Reaction of hydrogen and hy-

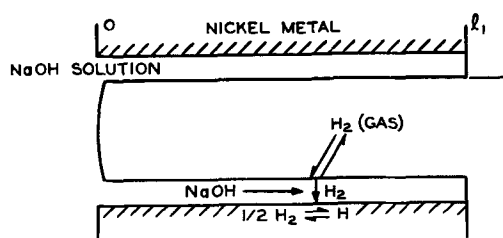


Fig. 5. "Electrolyte film" mechanism for reaction in a single pore

droxide ion occurs at points along the wall forming water and an electron, which goes into the metal. A numerical method was set up for solving the equations, which describe this mechanism, on an IBM 704 computer. In this way, the current produced by a single pore, J , can be expressed as a function of the polarization, η . The pore current is also a function of the radius of the pore, r , the length of the pore, l_1 , the temperature, T , the concentration of NaOH in the bulk solution, C_{OH^-} , the pressure of hydrogen, P , the surface roughness of the walls of the pore, s , and the thickness of the electrolyte film adhering to the wall of the pore, t .

The surface roughness ratio, s , is evaluated for a given sample of material as the ratio of the experimentally measured surface area, S , [obtained from the low temperature nitrogen adsorption method (10)] to the area of the operating pores as calculated from the pore size distribution function

$$s = S/A \quad [2]$$

where

$$A = 2\pi l_1 \int_{r_m}^{\infty} \phi(r) r dr$$

Calculation of the Current Density and Comparison with Experiment

The current density of an electrode, $I(\eta)$, at a polarization, η , is the sum of currents, $J(\eta, r)$ which would be produced at this value of the polarization by each of the individual pores of radius, r , in 1 cm^2 of electrode material

$$I(\eta) = \int_{r_m}^{\infty} J(\eta, r) \phi(r) dr \quad [3]$$

Pores of radius less than r_m (or t) are filled with electrolyte and are considered inoperative as far as the "electrolyte film" mechanism is concerned. However, they do act to increase the effective surface area, S , of the larger pores and act to increase the pore current, J , and therefore also the total electrode current, I .

In order to compare the experimentally observed polarization curves with those which would be expected theoretically from the same electrode, the comparison must be made for the same values of the parameters, l_1 , T , C_{OH^-} , P , s , and ϕ . Four different electrodes were cut from a sheet of porous nickel which had the volume distribution function shown in Fig. 4 and were operated in an electrochemical cell under the conditions listed in Table I. The calculations were performed on an IBM 704 computer. To facilitate making the calculations, the volume distribution function from mercury porosimeter data were curve fitted as a ratio of a sixth order polynomial in r in the numerator, and a third order

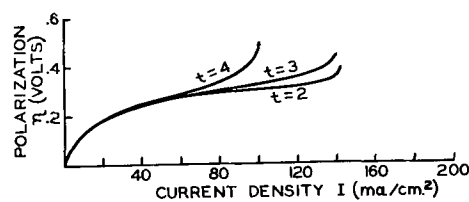


Fig. 6. Polarization curves as a function of film thickness

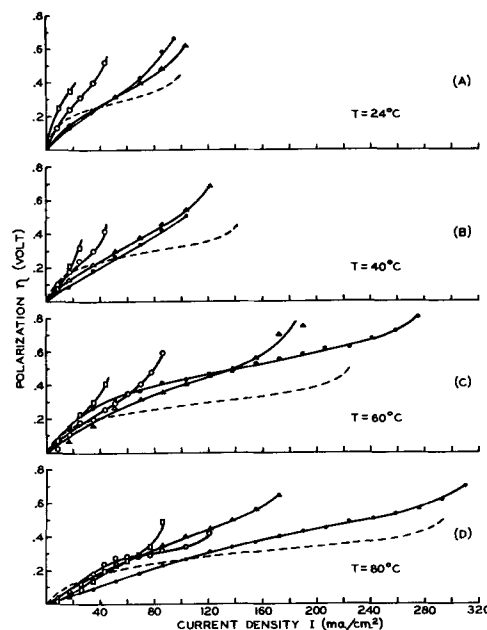


Fig. 7. Polarization curves as a function of temperature

polynomial in r in the denominator. The pore size distribution, ϕ , was evaluated from Eq. [1], by differentiation of the curve fitted volume distribution function. The product ϕr was integrated numerically to obtain the surface roughness ratio from Eq. [2]. At a polarization of 0.05v, the pore current, J , was calculated for several values of the pore radius, r , on an IBM 704 computer using the method described in ref. (2). These currents were curve fitted by a fourth order polynomial in r . The product, $J\phi$, was integrated numerically in Eq. [3] to yield the electrode current density at a polarization of 0.05v. The procedure was repeated for polarizations of 0.1, 0.15, 0.20, etc., to yield a complete polarization curve for the electrode. Calculations were performed for three values of the film thickness: 2, 3, and 4μ . The resulting curves are shown in Fig. 6. The curve for $t = 3\mu$ (shown as a dashed curve) is compared with the four experimental curves (shown by the four full curves and experimental points) in Fig. 7B.

To determine how well the calculated curves account for the temperature variation of the polarization, the experiments on the four electrodes and the

Table I. Properties of low surface area electrodes

Electrode thickness (length of pores)	l_1	0.0711	cm
Temperature	T	313.16	$^{\circ}\text{K}$
Concentration of NaOH	C_{OH^-}	0.006	moles/cm ³
Pressure of hydrogen	P	1.544	atm
Surface area of 1 cm^2 of the electrode	S	140	cm ² /cm ²
Film thickness		$t = 2$	$t = 3$
$2\pi l_1 \int_t^{\infty} \phi(r) r dr$		60.3	52.7
Surface roughness ratio	s	2.25	2.68
			$t = 4$
			43.3
			μ
			cm ² /cm ²

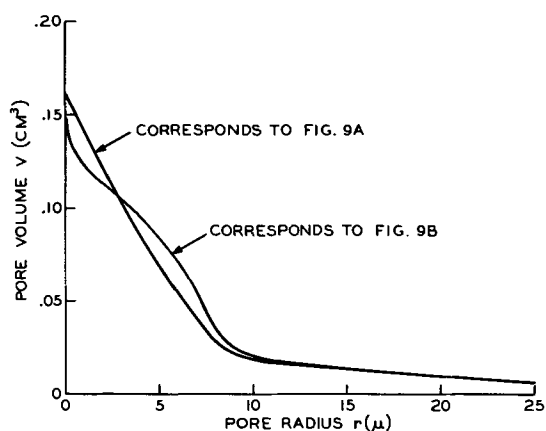


Fig. 8. Volume distribution functions for high surface area nickel electrodes of thickness 0.0711 cm.

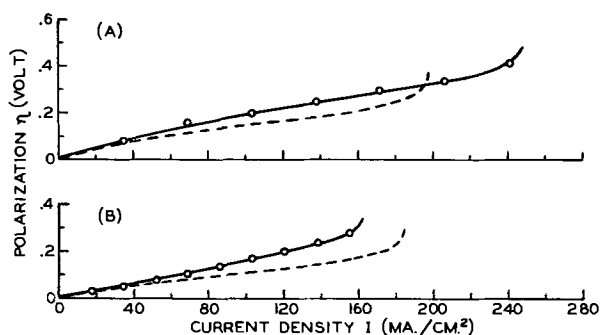


Fig. 9. Polarization curves for high surface area electrodes

calculations for $t = 3\mu$ were repeated at temperatures of 24° , 60° , and 80°C . The results are shown in Fig. 7A, 7C, and 7D. To determine how well the calculations take into account the variation of the polarization with a change in surface roughness, experiments were carried out on two samples of porous nickel having very high internal surface areas. The two samples had the volume distribution functions shown in Fig. 8 and had the other properties shown in Table II. Calculated and observed curves are shown in Fig. 9A and 9B.

Discussion

The calculated polarization curves at low currents are insensitive to variation of the film thickness. Increasing the film thickness decreases the maximum current which the electrode can deliver. The effective film thickness is related to the saturation of the electrode by electrolyte. The saturation could not be determined accurately due to the necessity of bolting the parts of the cell tightly together; the resulting compression of the asbestos spacer in-

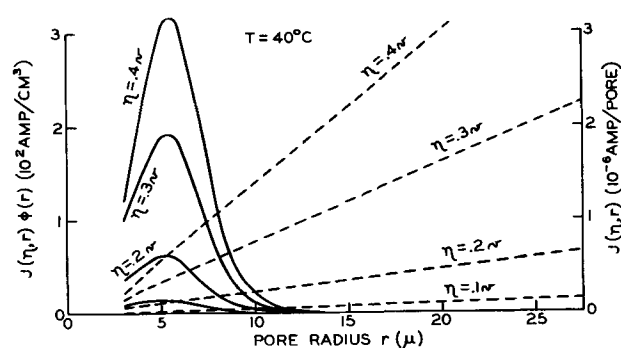


Fig. 10. Contribution of different sized pores to the total current for a film thickness of 3μ (full curves) and pore current as a function of radius (dashed curves).

creased the saturation of the electrode by an undetermined amount. By comparing the weight of the electrode after the experiment with the dry weight, it was found that the saturation was always greater than one-third.

The calculated curves change with temperature in approximately the same way as the experimental curves. Previously, a formula was derived for the limiting pore current, J_{\max} , when the diffusion of hydrogen through the film is the rate determining process (2), and differentiating Eq. [3] under the assumption that t (and r_m) are unaffected by the change in temperature, it can be shown that the maximum current for the electrode changes with temperatures in the same way that the pore current does

$$\frac{d \ln I_{\max}}{dT} = \frac{d \ln J_{\max}}{dT}$$

Figure 10 shows J (dashed curves) and the integrand of Eq. [3], $J\phi$ (full curves) as a function of η and r for a temperature of 40°C , and a film thickness of $t = 3\mu$. As the polarization is raised, the maximum in $J\phi$ changes by only a small amount, from 5.2 to 5.5μ . Ninety per cent of the total electrode current is produced by pores having a radius less than 8.5μ . Figure 11 shows the product, $J\phi$, at polarizations of 0.2 and 0.3v , for film thicknesses of 2 and 4μ . The current maximum occurs at from 5.0 to 5.5μ for the curves and is not very sensitive to changes in the film thickness or polarization. To a very good approximation, the pore current is a linear function of r .

$$J(\eta) = -a(\eta) + b(\eta)r$$

where a and b are positive constants which depend on η . Therefore the electrode current, from Eq. [3], is approximately of the form

Table II. Properties of high surface area electrodes

Sample shown in		Fig. 9A	Fig. 9B	
Electrode thickness (length of pores)	l_1	0.0711	0.0711	cm
Temperature	T	358.16	350.91	$^\circ\text{K}$
Concentration of NaOH	COH^-	0.006	0.006	moles/cm ³
Pressure of hydrogen	P	1.544	1.544	atm
Surface area of 1 cm ² of the electrode	S	820	2138	cm ² /cm ²
Film thickness assumed	t	3	3	μ
$2\pi l_1 \int_t^{\infty} \phi(r) r dr$		36.8	33.08	cm ² /cm ²
Surface roughness ratio	s	22.3	64.7	

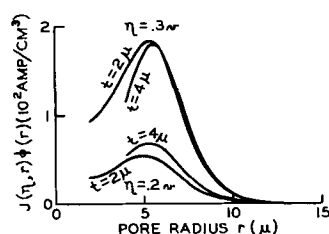


Fig. 11. Contribution of different sized pores to the total current for film thicknesses of 2 and 4 μ .

$$I(\eta) = -a(\eta)N + \frac{b(\eta)}{2\pi l_1} A$$

where $N = \int_{r_m}^{\infty} \phi dr$, is the number of pores of radius greater than r_m .

Analysis of the "parallel type" model of a hydrogen gas diffusion electrode yields polarization curves which are in moderately good agreement with the experimentally determined curves. However, the fact that the model usually predicts too much polarization at low currents and too little polarization near the maximum current is probably due to the idealized nature of the model. The actual electrolyte film is probably more like a sequence of annular pools, such as those shown in Fig. 2, rather than a circularly cylindrical shell of uniform thickness. These regions have a range of thicknesses and are connected to each other by narrow films or fissures of electrolyte. Because of these narrow regions, and also because of the longer tortuous length of the film, the electrical resistance of the film is much larger than that given by the uniform thickness approximation. As a result the present treatment probably underestimates the rate at which the polarization decreases from the electrolyte side to the gas side of the electrode. Similarly, the concentration polarization of NaOH is probably greater than that given by the model. The area encircling such annular pools is much greater than the area around a single meniscus in a cylindrical tube such as that considered in ref. (1). Therefore, the "surface diffusion" mechanism may account for a greater proportion of the current than was previously estimated for a single meniscus (2).

In the model, a decrease in the maximum current is associated with an increase in saturation of the electrode. Actual experimental curves show variations in the maximum current, even though they are made with electrodes which have the same volume distribution function and surface area. Although only rough measurements could be made on the saturation, it seemed unlikely that the variation in saturation could have been as great as that which would be required by the model in order to account for the observed variation in maximum currents. The variation in maximum current suggests that the particular configuration of electrolyte menisci within the pores is also important in determining the polarization behavior. It has been shown that at a given capillary pressure, the saturation is not a simple single valued quantity (11), but may have a range of values depending on the manner in which

the particular degree of saturation was formed. Therefore many different meniscus configurations are of equal (or nearly equal) stability (free energy). Two electrodes may have the same total saturation but may differ in the local saturation at a given point in the electrode. A more refined model of the porous electrode would probably require an analysis of the effect of detailed electrolyte configurations.

Manuscript received Aug. 19, 1963; revised manuscript received Nov. 21, 1963.

Any discussion of this paper will appear in a Discussion Section to be published in the December 1964 JOURNAL.

REFERENCES

1. E. Justi and A. Winsel, "Kalte Verbrennung," Chap. 3, Franz Steiner Verlag, Wiesbaden (1962).
2. R. P. Iczkowski, Previously submitted to *This Journal*. See also F. G. Will, *This Journal*, **110** 145, 152 (1963).
3. W. R. Purcell, *Trans. AIME*, **186**, 39 (1949); A. E. Scheidegger, *Producers Monthly*, **17**, 17 (1953).
4. R. A. Wynveen and T. G. Kirkland, in *Proc. 16th Annual Power Sources Conference*, p. 24, P.S.C. Publications Committee, Red Bank, N. J. (1962).
5. F. L. Pundsack, *J. Phys. Chem.*, **65**, 30 (1961).
6. G. Kortum and J. O'M. Bockris, "Textbook of Electrochemistry," p. 399, Elsevier Publishing Co., New York (1951).
7. W. Rose, *J. Appl. Phys.*, **29**, 687 (1958); W. von Englehardt, *Proc. World Petrol. Congr.*, Section I/C, 399, (1955); W. O. Smith, P. D. Foote, and P. F. Busang, *Phys. Rev.*, **36**, 524 (1930).
8. H. L. Ritter and L. C. Drake, *Ind. Eng. Chem., Anal. Ed.*, **17**, 787 (1945); L. G. Joyner, E. P. Barret, and R. E. Skold, *J. Amer. Chem. Soc.*, **73**, 3155 (1951).
9. A. E. Scheidegger, "The Physics of Flow through Porous Media," p. 117, MacMillan Co., New York (1960).
10. F. M. Nelsen and F. T. Eggertsen, *Anal. Chem.*, **30**, 1387 (1950).
11. R. E. Collins, "Flow of Fluids through Porous Materials," p. 29, Reinhold Publishing Corp., New York (1961).

LIST OF SYMBOLS

r	Pore radius.
l_1	Length of pore.
T	Temperature.
$C_{\text{OH}}^{\text{OH}}$	Concentration of NaOH in the bulk solution.
P	Pressure of hydrogen.
s	Surface roughness of the walls of the pore.
t	Thickness of the electrolyte film covering the walls of the pore.
J	Current produced by a pore at a given polarization.
J_{max}	Maximum current which can be produced by a pore.
$\phi(r)$	The number of pores having radii between r and $r + dr$, per cm^2 of surface area is equal to ϕdr .
$V(r)$	Volume of all pores which have a radius greater than a given value, r .
V_s	Total external volume of the electrode.
r_m	Pore radius below which all pores are filled with electrolyte.
I	Current density produced by an electrode at a given polarization.
I_{max}	Maximum current which can be produced by an electrode.
S	Total internal surface area in an electrode.
N	Number of pores having a radius greater than r_m : $N = \int_{r_m}^{\infty} \phi dr$
A	Internal surface area of all pores of radius greater than r_m , assuming a surface roughness factor of one: $A = 2\pi l_1 \int_{r_m}^{\infty} \phi r dr$.

The Effect of Metal Dissolution on the Rest Potential in the Palladium-Oxygen-Acid System

James P. Hoare

Research Laboratories, General Motors Corporation, Warren, Michigan

ABSTRACT

The rest potential of palladium electrodes in oxygen-saturated sulfuric acid solutions was studied as a function of pH and the partial pressure of oxygen. In the absence of anodic polarization, a rest potential of 870 ± 10 mv is obtained which is a mixed potential, and this system is referred to as a Pd/PdO electrode. After anodic polarization but in the absence of peroxide, a rest potential of 1470 ± 10 mv is obtained which is an equilibrium metal-metal oxide potential, and this system is referred to as a Pd/PdO₂ electrode. With time, a Pd/PdO₂ electrode is transformed to a Pd/PdO electrode because PdO₂ is unstable in acid solutions. In a certain potential region, Pd dissolves in acid solutions to form Pd⁺⁺ ions which greatly influence the rest potential. Evidence is presented which indicates that, of all the noble metals, possibly Pd is the only one for which the evolution of oxygen under anodic polarization proceeds through an oxide mechanism.

From thermodynamic considerations, an inert electrode serves only as a source or sink for electrons and as the catalytic surface on which the electrode processes may proceed. Recent work (1) indicated that although platinum is stable in acid solutions (2), it is not inert to oxygen. For this reason, the observed rest potentials in the Pt-O₂-acid system are mixed potentials, and the reversible oxygen potential cannot be observed. It was shown (3) that a platinum surface may be passivated in nitric acid. Such treatment renders the surface inert to oxygen, and a rest potential of 1.225 ± 10 mv on the normal hydrogen scale was observed in oxygen-saturated sulfuric acid solution. Possibly because the oxygen layers on gold (4) are poor electronic conductors, the reversible oxygen potential was not observed (3).

During these studies, it seemed to be of interest to consider the situation where the noble metal, under certain circumstances, would be slightly soluble in the electrolyte. Vetter and Berndt (2) have shown that in certain potential regions palladium is slightly soluble in sulfuric acid solutions.

The present investigation was undertaken to observe the effects of the presence of dissolved palladium on the rest potential in the palladium-oxygen-acid system.

Experimental

Small beads (0.1 to 0.15 cm in diam) were melted at the end of pure palladium wire (99.97% pure) in an oxygen torch and cleaned by heating white hot in a hydrogen flame followed by quenching in concentrated nitric acid as described before (1). Three Pd beads were mounted in the right side and an α -Pd-H reference electrode (5) in the left side of a clean dual Teflon cell in a manner previously described (1). The temperature at which these experiments were recorded was $25^\circ \pm 1^\circ\text{C}$. As before (1), all purification techniques and all cell and electrode preparations were carried out. The potential was measured with a General Radio electrometer, Model 1230-A, which has a variable input imped-

ance, and is reported with respect to the normal hydrogen electrode (NHE) unless otherwise stated. The purity of the system was checked by polarizing the Pd bead with an electronic current interrupter when the system was saturated with hydrogen and by observing the resulting high pseudocapacitance (6).

Results and Discussion

Potential-time behavior.—After a palladium bead had been anodized at about 2v in O₂-saturated 2N H₂SO₄ solution, the open-circuit potential came to a value of about 1470 ± 10 mv within a few minutes. The surface of such a bead appeared mirror-bright. Then, this potential began to decay to lower values after about 2 hr. A positive test for the presence of peroxide is obtained with TiSO₄ reagent (7). It was found (1) that the presence of peroxide interferes with the metal-oxygen system under study and may be removed by treating the system with hydrogen. When a palladium bead at a potential of 1470 mv was treated with hydrogen stirring, the potential fell along the curve similar to that shown in Fig. 1.

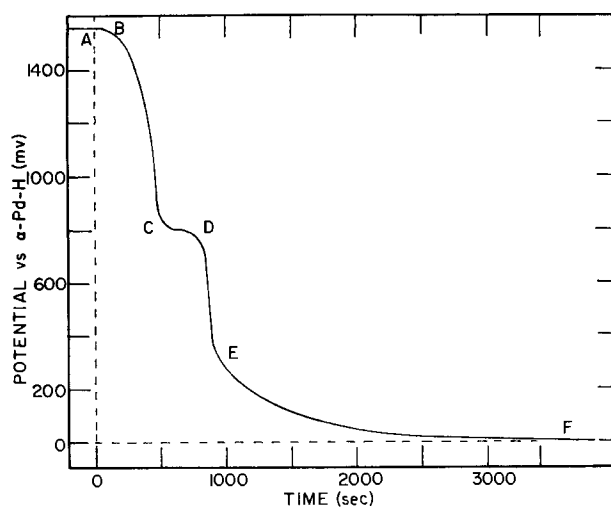


Fig. 1. Plot of open-circuit potential of a previously anodized Pd bead as a function of time with H₂-stirring. See text for details.

Zero time began at A when O₂-stirring was replaced with H₂-stirring (200 cc/min). A plateau in the potential, AB, was observed at about 1400 mv vs. α -Pd-H (1450 mv vs. NHE) followed by another, CD, at about 800 mv. Afterwards, the potential decayed rapidly to a point, E, at about 200 mv and finally came slowly to zero potential at F in about an hour. The two plateaus correspond, most likely, to the reduction of a higher and a lower oxide. Similar plateaus were observed by Vetter and Berndt (2) in their studies of the charging curves obtained on Pd electrodes. At the point E, all oxides were removed, and hydrogen began to be adsorbed. The hydrogen then dissolved in the bulk metal to form a palladium-hydrogen alloy (8). As the hydrogen content increased, the activity of the dissolved hydrogen increased, and the potential fell toward the potential (9) of α -Pd (50 mv vs. Pt/H₂ in the same solution; zero volt vs. α -Pd-H in Fig. 1).

After the potential of the Pd bead had fallen below the point E, H₂-stirring was replaced with O₂-stirring. The potential did not rise until all the dissolved hydrogen had been oxidized. Then, the potential rose rapidly to about 600 mv and more slowly thereafter, until a steady value of 870 \pm 10 mv was reached in about 10 hr. Such an electrode will be referred to as a Pd/PdO electrode. The upper plateau value could not be obtained without anodizing the bead again. Such a bead was mirror-bright.

Dependence of potential on partial pressure of O₂.—The partial pressure of oxygen, P_{O₂}, was varied by diluting the oxygen flow with nitrogen and was determined from the rotameter readings in the manner described before (1). A plot of the potential as a function of the logarithm of the P_{O₂} is presented in Fig. 2 for three different beads. Parallel lines with a slope of 33 mv may be passed through these points. This indicates that a 2-electron process is potential-determining.

Dependence of potential on pH.—The pH of the solutions was varied by diluting the 2N sulfuric

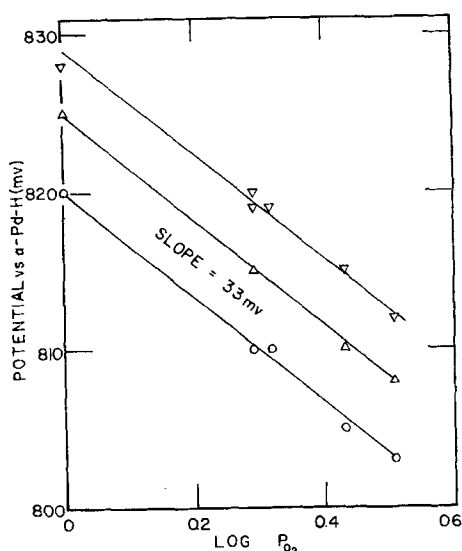


Fig. 2. Plot of rest potential of three different Pd/PdO electrodes as a function of the logarithm of the partial pressure of oxygen in atmospheres.

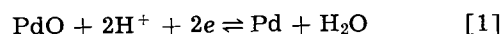
Table I. pH dependence of the potential of the Pd/PdO electrode

Solution composition	Potential of Pt/H ₂ vs. SCE (mv)	pH	Potential vs. α -Pd-H (mv)	$\Delta E/\Delta pH$	Potential vs. NHE (mv)
2N H ₂ SO ₄	-245	0	822	—	869
0.1N H ₂ SO ₄ + 2N Na ₂ SO ₄	-335	1.5	905	56	862
0.01N H ₂ SO ₄ + 2N Na ₂ SO ₄	-402	2.6	982	61	872

acid with 2N sodium sulfate solution. At the end of a run, the potential of a saturated calomel electrode (SCE) vs. a Pt/H₂ electrode in the same solution was determined. From these determinations, the pH may be found, and the recorded potentials may be converted from the α -Pd-H scale to the NHE scale. The data for a typical set of runs are presented in Table I. The potential values recorded in column four are the steady values obtained in the O₂-stirred solutions after 24-48 hr had passed.

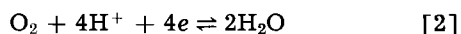
It is interesting to note that, as the pH increases or the hydrogen ion concentration decreases, the potential with respect to α -Pd-H increases. In the fifth column, the change in potential per unit change in pH is given. It is seen that this value is close to 59 mv which indicates that a one-electron reaction is involved. These two observations require the conditions that the potential-determining reaction be independent of the pH and that the $\Delta E/\Delta pH$ values reflect the dependence of the reference electrode on pH (9) (one electron transferred for each H⁺ ion involved). The last column shows that the potential vs. NHE is independent of pH and has a value of about 870 mv.

Potential-determining reactions.—Using constant current charging curves, several investigators (2, 10, 11) found that a monolayer of PdO was formed before oxygen was evolved. This layer began to form at about 800 mv which corresponds to the potential value observed at the first plateau in the charging curves. Hickling and Vrjosek (12) quote a value of 0.85v for the equilibrium potential of the Pd/PdO couple in N H₂SO₄ solution. The PdO, in this case, was chemically prepared. These values agree quite well with the value of 870 \pm 10 mv found for the rest potential in O₂-saturated 2N H₂SO₄. It is stated by Sidgwick (13) that PdO may be made by heating Pd in air. A palladium wire was cleaned in a H₂ flame and quenched in HNO₃. After a final heating, the wire was allowed to cool in air. Finally, the mirror-bright wire was plunged into O₂-saturated 2N H₂SO₄ solution and the potential recorded. Initially, the potential had a value of about 800 mv which came to a steady value of 860 mv in 7000 sec. These observations seem to indicate that the potential-determining reaction involves the Pd/PdO couple



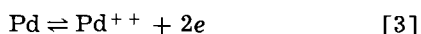
where PdO and H⁺ represent the hydrated species. The symbol for the oxygen film, PdO, was used instead of Pd-O because there seems to be some evidence that the film is a monolayer of true oxide

rather than an adsorbed layer of oxygen atoms. Also Blackburn and Lingane (14) have arrived at similar conclusions. Since this does not explain the fact that the rest potential depends on the partial pressure of oxygen, a mechanism involving a mixed potential (15) may be considered. If an attempt is made to explain the P_{O_2} dependence by considering the rest potential to be a mixed potential composed of Eq. [1] and of the O_2/H_2O reaction

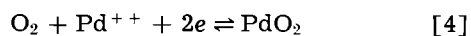


it is not possible to explain the fact that the rest potential is independent of pH. Therefore, neither of these reactions can be potential-determining, although they may be the path through which the Pd initially becomes covered with a monolayer of PdO.

Vetter and Berndt (2) have measured the rate of dissolution of Pd metal in sulfuric acid solutions as a function of potential. They find that below a potential of 800 mv Pd is passive, becomes transpassive between 800 and 1150 mv with a maximum rate of dissolution of $0.8 \mu a/cm^2$ at 900 mv, is passive again between 1150 and 1750 mv, and becomes transpassive above 1800 mv. The corrosion reaction is



It is suggested that the following sequence of events may offer an explanation consistent with the observed experimental data. When a sample of Pd is plunged into O_2 -saturated sulfuric acid, it is initially passive, and a monolayer of hydrated PdO is formed on the surface, most likely through Eq. [1] and [2]. Here the rest potential could be determined by Eq. [1]. The oxide layer causes the potential to rise to the point where Pd becomes active and, at certain active centers, Pd goes into solution according to Eq. [3]. Then it may be possible for the Pd^{++} ions in the immediate vicinity of the electrode to react with dissolved O_2 molecules in solution or adsorbed O_2 molecules on the electrode surface to form adsorbed molecules of PdO_2 on the electrode surface according to the equation



From the estimated values (16) for the ΔF of formation of the species in Eq. [4], this reaction is quite possible energetically.

The interaction of Eq. [3] and Eq. [4] adds PdO_2 molecules to the surface layers of PdO, and a point may be reached when the concentration of PdO_2 in the surface layers becomes so much greater than that of PdO that PdO_2 becomes the potential-determining entity on the surface. At this point, a mixed potential could be set up through Eq. [3] and [4]. The relative local cell current densities for the two partial reactions could be such that the potential of Eq. [3] would be polarized to that of Eq. [4] in a manner similar to that shown by the diagram in Fig. 2a of ref. 1. In this way, the rest potential would no longer be determined by Eq. [1], but by Eq. [4].

With Eq. [4] potential-determining, the experimental observations, (a) that the potential depends on the P_{O_2} , (b) that it is independent of pH, and

(c) that a 2-electron reaction is indicated, may be adequately explained.

Supporting evidence for these suggestions may be found in the following observations. When a Pd wire which had been heated in air was plunged into 2N H_2SO_4 , the potential was initially 760 mv vs. α -Pd-H and came to a steady value of 815 mv vs. α -Pd-H within 24 hr. However, when such a wire was plunged into 0.01N H_2SO_4 solution, the potential was initially 770 mv vs. α -Pd-H but then came to a steady value of 938 mv vs. α -Pd-H. Because the initial potentials vs. α -Pd-H were virtually independent of pH, the Pd/PdO couple, Eq. [1], may be potential-determining in this region, since the pH dependence is the same as that of the reference electrode (9). Then, as the potential rose and the corrosion process, Eq. [3], became important, the potential vs. α -Pd-H became dependent on the pH which indicated that, now, the PdO_2/Pd^{++} couple, Eq. [4], was potential-determining.

Another bit of evidence in support of this picture is the experimental fact that, if a Pd/PdO electrode which had been treated with O_2 -stirring for about an hour was treated with H_2 -stirring (200 cc/min), it required about 50 sec to reduce the oxide. Yet, when a Pd/PdO electrode, which had been treated with O_2 -stirring for over 24 hr, was treated with H_2 -stirring (200 cc/min), it required about 300 sec to reduce the oxide. This indicates that the nature of the adsorbed oxygen layer changes with time. It is suggested that this change reflects the addition of PdO_2 to the monolayer of PdO caused by the corrosion of the Pd.

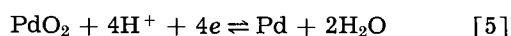
Since a steady, time-invariant (over 48 hr) potential was obtained, a steady state must have been set up such that the products of the local cell action were removed as fast as they were formed. From the polarization data obtained by Butler and Drever (11) and Hickling and Vrjosek (12), it was shown that, in the presence of acid, PdO_2 is unstable and decomposes spontaneously to PdO. Soon after the potential-determining concentration of PdO_2 is set up in the surface, PdO_2 spontaneously decomposes to PdO as fast as it is formed. The PdO layer does not build up because the back reaction of Eq. [1] becomes important, and a steady state is set up. In all cases these electrodes were mirror-bright. As indicated before (17), these layers probably do not build up much beyond a monolayer thick on open circuit.

Potential behavior with N_2 -stirring.—When O_2 -stirring was replaced with N_2 -stirring, the potential of a Pd/PdO electrode fell with time. After about 8 hr the potential became rather steady. The potential values vs. α -Pd-H are as follows: 742 mv in 2N H_2SO_4 , 750 mv in 0.1N H_2SO_4 , and 739 mv in 0.01N H_2SO_4 . These potentials are independent of pH and are near the initial potential values observed when a Pd wire that had been heated in air was plunged into oxygen-saturated acid solutions. Since the oxygen half reaction of any mixed potential would be suppressed by this procedure, these observations favor a value of 790 ± 10 mv for the standard potential of the Pd/PdO couple, Eq. [1]. Such a value

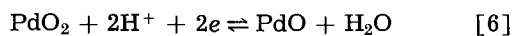
would be in better agreement with Hickling and Vrjosek's (12) experimental results (0.79v) than the value (0.85v) they obtained from the chemically prepared Pd/PdO electrode. After all, the chemically prepared species may not be the same as the electrochemically prepared species. Quite possibly the corrosion reaction, Eq. [3], affected the chemically prepared Pd/PdO system, and the potential was really determined by the PdO₂/Pd⁺⁺ couple, Eq. [4], rather than the Pd/PdO couple. The 0.85-v value is very close to the steady-state rest potential value presented in the last column of Table I which is considered to be determined by Eq. [4].

Pd/PdO₂ electrode.—It was observed by Butler and Drever (11) that, with continued anodization, a layer of PdO₂ several molecules thick may be formed. In order to study this system in the absence of interfering concentrations of peroxide produced in the anodization process, the Pd beads were anodized in a clean Teflon cell, and the solution was prepared in a second Teflon cell as described for the case of the Au/Au₂O₃ electrode (4). In this way, the anodized Pd beads were placed in O₂-saturated, peroxide-free, 2N H₂SO₄ solution. The potential came to a steady value of 1470 ± 10 mv within 2 or 3 min and remained steady for a period of 5 to 6 hr before drifting very slowly to less noble values. Such an electrode will be referred to as a Pd/PdO₂ electrode.

It was observed that the 1470-mv potential was independent of stirring and of the partial pressure of oxygen. Also, the potential *vs.* α-Pd-H was independent of pH which indicated that for each H⁺ ion involved an electron was transferred (9). Such observations could be explained if a reaction similar to the following were potential-determining



El Wakkad and El Din (10) suggested that the couple responsible for the 1470-mv potential was the PdO₂/PdO couple



Since both of these oxides, although hydrated, are in the solid phase, one would expect the potential to remain constant as long as the two solid phases are present. The potential should change rather sharply if one of these phases should disappear. It was shown (11, 12) that PdO₂ is unstable in acid solutions, and this fact is confirmed by the data presented in Fig. 3. Here, the rest potential of three different Pd/PdO₂ electrodes is plotted as a function of time. For all three electrodes, the potential remained steady at 1470 ± 10 mv for 5 or 6 hr before decaying to less noble values. The differences in the rate of decay for the three curves most likely represent different amounts of PdO₂ initially produced by varying conditions of time and current density during the forming-anodic prepolarization. It is to be noted that the rate of decay of potential falls along a smooth curve which may be explained better by the concept of a mixed potential. This may be true because a mixed potential could show a smooth transition from one potential-determining reaction

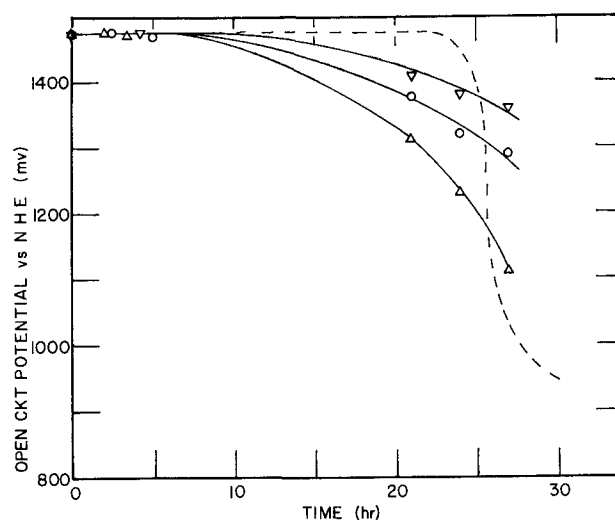


Fig. 3. Decay of open-circuit potential of three different Pd/PdO₂ electrodes with time. For explanation of dashed curve, see text.

to another, whereas the PdO₂/PdO-determining concept should show a rather sharp knee in the potential-decay curve similar to the dashed curve in Fig. 3.

It is proposed that, as soon as the anodic polarizing current which produces the film of PdO₂ is broken, concentration of PdO builds up in the surface film at the expense of the spontaneously decomposing PdO₂. Since the potential is constant over a period of 5 to 6 hr, this decomposition process is most likely a chemical reaction. A point is reached when the PdO concentration becomes high enough that the Pd/PdO reaction becomes important. Here a mixed potential is set up. As the relative concentrations of PdO₂ and PdO change, the relative local cell current densities change, and therefore, the polarization of the component reactions changes. As a result, the potential proceeds smoothly from that of the Pd/PdO₂ electrode to that of the Pd/PdO electrode. Of course, once the local cell is set up the local cell current accelerates the decomposition of PdO₂ and the rate of transition from the PdO₂ electrode to the PdO electrode increases as shown by the curves in Fig. 3. The over-all local cell reaction is equivalent to Eq. [6]; however, here the mechanism is a local cell instead of the equilibrium metal oxide-metal oxide system suggested by El Wakkad and El Din. Therefore, it is preferred that the 1470-mv potential be associated with the Pd/PdO₂ couple, Eq. [5], rather than the PdO₂/PdO couple, Eq. [6].

Polarization at low current densities.—The Pd beads were cathodically polarized at very low current densities by varying the input impedance of the electrometer as described before (1, 4). The cathodic polarization (the open-circuit potential, E_{oc} , minus the potential at the given apparent current density, E) is plotted as a function of the logarithm of the apparent current density in Fig. 4.

Curve A is a plot of the data for a Pd/PdO₂ electrode with O₂-stirring or with N₂-stirring. In either case, the points could be reproduced within ± 5 mv going up or down the curve. This indicates that nearly all of the current goes into the formation or reduction of PdO₂ at these very low current densities.

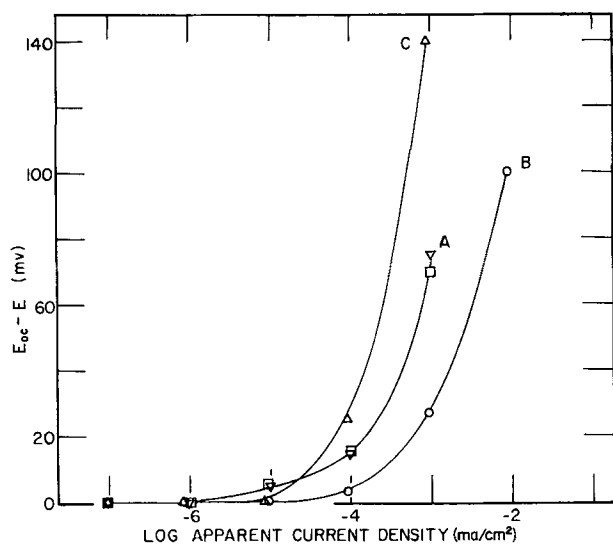


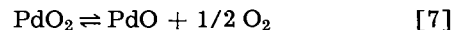
Fig. 4. Cathodic polarization, $E_{oc}-E$, of various Pd electrodes at low current densities in 2N H_2SO_4 solution: ∇ for Pd/PdO₂ electrode with O₂-stirring; \square for Pd/PdO₂ electrode with N₂-stirring; \circ for Pd/PdO electrode with O₂-stirring; \triangle for PdO electrode with N₂-stirring.

Apparently an oxygen reaction is not involved, and so the 1470 ± 10 -mv potential is an equilibrium metal-metal oxide potential. The potential-determining reaction is Eq. [5] with a standard potential of about 1470 mv.

This value of 1470 mv is somewhat higher than that (1.29v) found by Hickling and Vrjosek (12) for the chemically prepared Pd/PdO₂ electrode. They dried their PdO₂ over sulfuric acid, and Sidgwick (13) states that PdO₂ is stable only when hydrated. Again, this chemically prepared oxide is most likely not the same as the electrochemically prepared oxides. The low value of 1.29v could be the mixed potential resulting from the presence of both PdO and PdO₂. This suggestion is strengthened by the fact that they found a mixture of the chemically prepared PdO and PdO₂ gave nearly the same value as the chemically prepared PdO₂ alone. El Wakkad and El Din, Vetter and Berndt, and Blackburn and Lingane show well defined plateaus in the region of 1470 mv in their charging curves, but Hickling and Vrjosek show a very ill defined inflection. This may be true because they charged their electrodes too fast. The effect of the rate of charging is demonstrated by Vetter and Berndt (2). At a high charging rate (high current density), oxygen evolution is reached quickly, and the intervening plateaus are missed.

It is interesting to note that the point at which oxygen begins to evolve on a constant current charging curve coincides with the point where the potential is 1470 mv (2, 10, 14). The H₂-reduction data presented in Fig. 1 and the open-circuit data in Fig. 3 show that a definite, stable potential exists at 1470 ± 10 mv which may be associated with the Pd/PdO₂ equilibrium (the 1470-mv potential is obtained after anodic polarization, Fig. 3, and after cathodic polarization, Fig. 4). The fact that the potential, at which O₂ evolution begins, and the equilibrium Pd/PdO₂ potential coincide, suggests that

oxygen evolution proceeds through an oxide mechanism (18). Under steady-state, anodic polarization PdO₂ is formed from the layer of PdO as quickly as it is decomposed chemically to form PdO and O₂ according to



This may be why a layer of PdO₂ does not build up beyond a few molecules thick (11). In support of this the following is to be noted. As shown in the charging curves obtained by Vetter and Berndt (2) at higher current densities, an overvoltage is obtained. The oxygen evolution plateau becomes more noble with increasing current density instead of a second plateau corresponding to the oxidation of H₂O to O₂ appearing as in the case for Au (2).

Curve B is the polarization of a Pd/PdO electrode with O₂-stirring. The points could be reproduced within ± 5 mv either going up or down the curve. When a Pd/PdO electrode was polarized in N₂-stirred acid solution, curve C was obtained. In this case the polarization for a given current density is much higher, and the points could not be reproduced because of the presence of a large hysteresis. For Pd/PdO electrodes, most of the current goes into the reduction of oxygen either by Eq. [2] or Eq. [4]. When O₂-stirring is replaced with N₂-stirring at a given current density, enough active material is not present to support such a rate, and the potential moves quickly toward the value for the reduction of hydrogen ion.

The fact that the PdO layer is easily converted to a layer of PdO₂ with anodic polarization (11) indicates that the PdO layer is not as good an electronic conductor as the oxygen layer on platinum. As compared to similar polarization curves on Pt (1), however, it seems that palladium is just as good a catalyst as platinum is for the reduction of oxygen. It may be possible that the oxides of palladium are very good peroxide-decomposing catalysts. Some evidence for this is found in the fact that a Pd/PdO₂ electrode can maintain a potential of 1470 mv for over an hour in the presence of peroxide as noted at the beginning of this discussion.

Manuscript received June 3, 1963.

Any discussion of this paper will appear in a Discussion Section to be published in the December 1964 JOURNAL.

REFERENCES

1. J. P. Hoare, *This Journal*, **109**, 858 (1962).
2. K. J. Vetter and D. Berndt, *Z. Elektrochem.*, **62**, 378 (1958).
3. J. P. Hoare, *This Journal*, **110**, 1019 (1963).
4. J. P. Hoare, *This Journal*, **110**, 245 (1963).
5. D. J. G. Ives and G. J. Janz, "Reference Electrodes," p. 112, Academic Press, Inc., New York (1961); J. P. Hoare, *G. M. Eng. J.*, **9**, No. 1, 14 (1962).
6. S. Schuldiner and J. P. Hoare, *J. Chem. Phys.*, **26**, 1771 (1957).
7. F. D. Snell and C. T. Snell, "Colorimetric Methods of Analysis," Vol. II, 3rd ed. (1949).
8. J. P. Hoare and S. Schuldiner, *This Journal*, **102**, 485 (1955).
9. S. Schuldiner, G. W. Castellan, and J. P. Hoare, *J. Chem. Phys.*, **28**, 16 (1958).
10. S. E. S. El Wakkad and A. M. S. El Din, *J. Chem. Soc.*, **1954**, 3094.

11. J. A. V. Butler and G. Drever, *Trans. Faraday Soc.*, **32**, 427 (1936).
12. A. Hickling and G. G. Vrjosek, *ibid.*, **57**, 123 (1961).
13. N. V Sidgwick, "Chemical Elements and Their Compounds," p. 1558, Oxford Press (1950).
14. T. R. Blackburn and J. J. Lingane, *J. Electroanal. Chem.*, **5**, 216 (1963).
15. C. Wagner and W. Traud, *Z. Elektrochem.*, **44**, 391 (1938).
16. W. H. Latimer, "Oxidation Potentials," Prentice-Hall, New York (1952).
17. K. J. Vetter, "Elektrochemische Kinetik," p. 502, Springer Verlag, Berlin (1961).
18. W. G. Berl, *Trans. Faraday Soc.*, **83**, 253 (1943).

Reversible Oxygen Electrodes

N. Watanabe and M. A. V. Devanathan¹

The Electrochemistry Laboratory, The University of Pennsylvania, Philadelphia, Pennsylvania

ABSTRACT

The reversible oxygen electrode has been set up on anodized platinum in ultrapure sulfuric acid solutions. The essential conditions for establishing the reversible oxygen electrode are described. It is found that the variation of the electrode potential with partial pressure follows the theoretical expression. At other stable potentials exhibited by the platinum oxygen system the partial pressure effects give variations not consistent with any theoretical formula. Decay curves on open circuit have been measured and a dependence on the oxygen partial pressure has been observed. In ultrapure solutions the potential decays after several hours to a limiting value of 1.1v corresponding to the Pt-PtO₂-Pt(OH)₂ potential. When the solutions are impure the limit is lowered to about 0.84v which is the equilibrium potential of the PtOH-OH⁻ hydrogen peroxide system. The gold-oxygen system also exhibits a number of different oxide potentials, one of these is at 1.23v in normal acid solution. The apparent establishment of the reversible oxygen electrode potential on gold must be viewed with caution as the overpotential for the mixed reduction of gold oxide and oxygen can give rise to spurious Tafel lines. The oxygen partial pressure effect on gold electrodes does not follow the Nernst equation. It therefore appears that the reversible oxygen electrode is not set up on gold.

Although the reversible potential of the oxygen electrode can be calculated theoretically (1), it has been found extremely difficult to set up a reversible oxygen electrode. One reason is the small exchange current of the reaction estimated at about 10⁻¹⁰ amp cm⁻², which makes the system susceptible to poisoning by impurities. The other difficulty is the reproduction of a suitably catalytically active oxide surface on which the reaction can be made to proceed without interference from spurious oxide potentials. Bockris and Huq (2) reported the attainment of the reversible oxygen electrode potential, on oxidized platinum electrodes, in highly purified sulfuric acid solutions. In other attempts (3) to set up the oxygen electrode reported in the literature, the reversible potential has not been attained either due to insufficient solution purification or due to the lack of a suitably active surface. We report here the technique of establishing the reversible oxygen electrode on platinum and the effects of the variation of partial pressure of oxygen on platinum and gold electrodes.

Experimental

Cell.—A standard six electrode all Pyrex glass cell with greaseless seals as shown in Fig. 1 was used.

Preparation of materials.—**Sulfuric acid.**—Acid redistilled in vacuum was found to contain relatively large amounts of dissolved sulfur dioxide. Hence analytical reagent grade concentrated acid was used without any distillation.

Water.—Conductance water (1 x 10⁻⁷ mho cm⁻¹) was refluxed in all Pyrex glass still for about 2 hr in a current of purified oxygen. It was then distilled directly into the cell. The initial portions were used to wash and rinse the cell and the final portions used for solution preparation. The conductivity of the solution was measured with a conductance bridge and sulfuric acid added until the desired conductivity was attained.

Oxygen.—Tank oxygen was purified by passage through the following train: Silica gel, platinized asbestos at about 250°C, copper turnings at about 250°C, silica gel, soda lime, silica gel, three traps

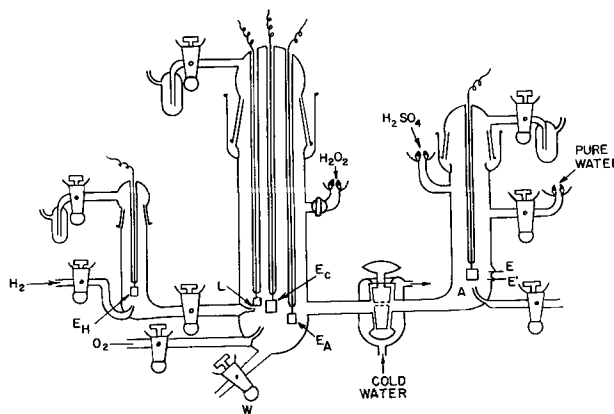


Fig. 1. Electrolytic cell. E_H, reference electrode; E_C, test electrode; E_A, pre-electrolysis electrode; E_E, conductance measurement electrode; L, Luggin capillary; W, waste tube; A, anodic compartment.

¹ Present address: Central Electrochemical Research Institute, Karaikudi, India.

containing charcoal at liquid oxygen temperature, and an empty trap also cooled to liquid oxygen temperature.

Helium.—The same train was used to purify the helium for experiments on partial pressure effects.

Hydrogen.—The hydrogen was required only for the reference electrode and was purified by passage through a standard hydrogen purification train.

Electrical instrumentation.—Polarization currents varying from 10^{-3} to 10^{-12} amp were obtained from 90v dry battery by dropping the potential through two 10K helipot and a variable 1M resistance in series. Currents were measured with a Keithley 410C micromicroammeter. Potentials were measured with a Doran valve potentiometer sensitive to ± 1 mv. For the partial pressure experiments a Leeds & Northrup K3 potentiometer with an electrometer amplifier sensitive to $100 \mu\text{v}$ as null detector, was used.

Preparation of electrodes.—The electrodes consisted of platinum or gold sheets (0.5 cm x 1.5 m) spot welded to a piece of platinum or gold wire which was pinch sealed to the electrode stem. The electrodes were degreased and allowed to soak in chromic sulfuric acid overnight. These were washed thoroughly in conductance water and anodically oxidized in the purification solution at a current density of 10^{-4} – 10^{-2} amp cm^{-2} for about 0.5–3.0 hr. They were then raised above the level of the solution, into the oxygen gas atmosphere in the cell, and remained there during further solution purification by anodic pre-electrolysis.

Procedure.—The cell was cleaned in chromic sulfuric acid followed by nitric sulfuric mixture. It was then washed several times in distilled water, rinsed with conductivity water, and set up in position. The all glass bridges from the gas supply points and water distillation unit, etc., were then assembled. The cell was rinsed by distilling water into it several times thus washing also the electrodes. After final distillation the required amount of sulfuric acid was added in order to attain the required strength as shown by the conductivity.

The electrodes were now anodized, raised above the solution, and anodic pre-electrolysis was commenced on an auxiliary electrode with 40 ma corresponding to a current density of 10^{-2} amp cm^2 . A conventional power supply was used for this purpose and the pre-electrolysis lasted 48 hr with steady oxygen bubbling.

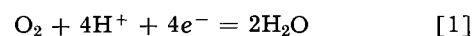
Partial pressure variation.—The required partial pressure of oxygen was attained by mixing with helium and controlling the composition with the aid of calibrated flow meters. The procedure used was to obtain first the equilibrium potential at a low partial pressure, e.g., 0.1 or 0.01 atm. When a steady potential was attained, pure oxygen was admitted and the potential changes measured at frequent intervals. The difference of the steady state values was taken as the effect due to a partial pressure change from 0.01 or 0.1 to 1 atm. This method avoids hysteresis effects in respect to the partial pressure effect on the oxygen concentration in the solution. Thus if to an oxygen saturated solution a helium

oxygen gas mixture at an oxygen partial pressure of 0.1 is bubbled, it takes several hours for the excess oxygen to be brought down to the equilibrium value. This was also confirmed by attempting to decrease the partial pressure and following the potential changes. It was found that it took over 20 hr for the potential to come down to the calculated value.

Results and Discussion

Reversible oxygen electrode.—The use of the technique described above made it possible to attain the reversible oxygen potential on platinum electrodes, readily and with satisfactory reproducibility. The steady potential was established in about half an hour after which it was constant for over an hour. Thereafter the potential showed a tendency to decrease. Typical time variations of the potential are shown in Fig. 2. The limits of reproducibility of the reversible oxygen potential on platinum in normal sulfuric acid solutions saturated with pure oxygen were found to be $1.23 \pm 0.02\text{v}$. This result is in agreement with the thermodynamic value of 1.229v. The limits of reproducibility must be considered satisfactory in view of the small exchange current of the system.

Effect of oxygen partial pressure.—The best proof of the establishment of the reversible oxygen electrode is to show that the system responds in the manner predicted by the Nernst equation as applied to this system. Writing the reaction as



the Nernst expression for the potential as a function of partial pressure is

$$E = E_0 + (RT/4F) \ln p_{\text{O}_2} \quad [2]$$

Hence a 15 mv change in potential is expected for every 10 fold change of partial pressure. In our experiments the partial pressures used were 1.0, 0.1, and 0.01 atm, so that 15 and 30 mv changes in potential are expected for a change over from unity to 0.1 and 0.01, respectively. In order to establish that the pressure response was the same whatever the direction, experiments were carried out with increasing and also with decreasing partial pressures. Typical potential variations are shown in Fig. 3,

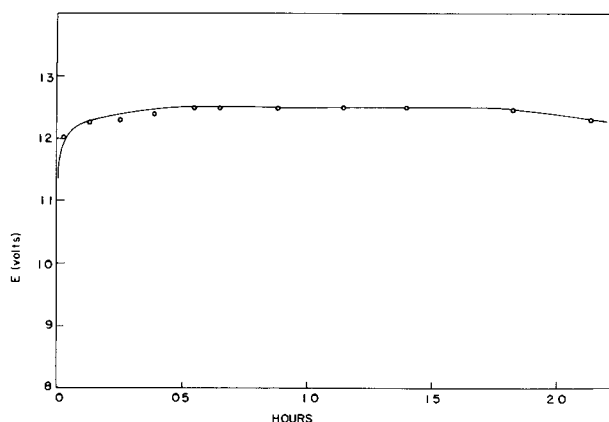


Fig. 2. Time variation of rest potential of oxygen electrode on anodized platinum. Electrode pre-oxidation, 10^{-3} amp/ cm^2 1 hr; solution preelectrolysis, 10^{-2} amp/ cm^2 , 48 hr; $P_{\text{O}_2} = 1$ atm.

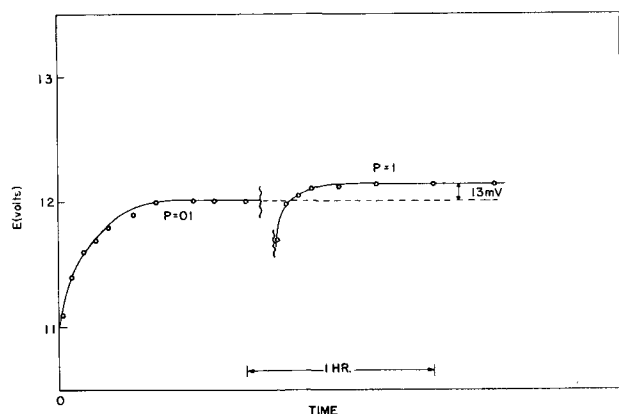


Fig. 3. Effect of variation of partial pressure of oxygen on the rest potential of oxygen electrodes.

and the results presented in Table I. These figures are in reasonable agreement with those expected from the Nernst equation, considering the difficulty of maintaining steady equilibrium potentials with reactions of small i_0 on solid substrates.

Potential decay curves.—When platinum electrodes polarized anodically for some time at 10^{-2} amp cm^{-2} are put on open circuit, the potential drops rapidly from about 1.9 to about 1.5v. The subsequent potential change is slow and decreases gradually to about 1.1v in purified acid solutions. The significant feature of such decay curves is the partial pressure dependence around the reversible oxygen potential. Figure 4 shows such decay curves at oxygen partial pressures of 1.0, 0.1, and 0.01 atm, respectively. The potential separations are 16 mv and 13 mv compared to the theoretical values of 15m and 30 mv, assuming the Nernst equation to be applicable here.

Partial pressure effect at other potentials.—The platinum-platinum oxide system exhibits many potentials corresponding to different electrode reactions. Of these the 1.1v potential observed in pure solutions corresponds to the reaction (4)

Table I. Oxygen partial pressure effects

Pressure range	Potential change	No. of runs
1 atm \leftrightarrow 0.1 atm	14 ± 3 (mv)	10
1 atm \leftrightarrow 0.01 atm	25 ± 4 (mv)	6

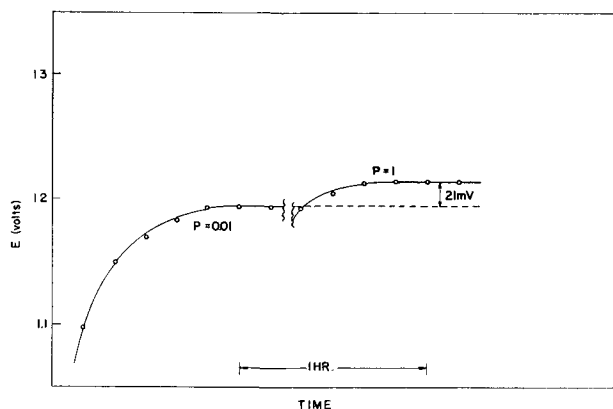
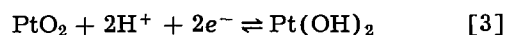
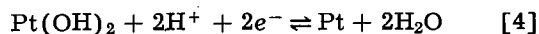


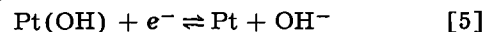
Fig. 4. Decay of potential on open circuit of oxygen electrodes at various oxygen partial pressures.



and the 0.98v potential corresponds to the reaction (5)



The 0.84 potential is due to the potential determining reaction



This latter potential is obtained readily by the addition of hydrogen peroxide, and as shown by Bockris and Oldfield (6) is oxygen partial pressure independent, but pH dependent. In impure solutions it was found that the potential did not stabilize at 1.1v but dropped to 0.84v. This is due to the oxidation of impurities accompanied by the reduction of oxygen in a corrosion like reaction (7). The product of oxygen reduction is hydrogen peroxide (8, 9) which then sets up the 0.84v potential. In an attempt to ascertain if any partial pressure effect was exhibited by the 1.1 and 0.98v potentials, similar experiments were carried out and no systematic partial pressure dependence was observed. The erratic and large variations are due to the adsorption of oxygen to various extents by these electrodes. Should these be even mixed potentials some partial pressure dependence would be noticed. We therefore conclude that the platinum oxide potentials corresponding to 1.1 and 0.98v do not involve molecular oxygen.

Conditions for establishing the reversible oxygen electrode.—From the above, it is evident that a reversible oxygen electrode can be set up on a platinum oxide surface. As is to be expected with catalytic surfaces, it is important to obtain the kind of surface on which the oxygen electrode reaction can proceed readily. The exchange current for this reaction is about 10^{-10} amp cm^{-2} . Hence the exchange currents for all other oxide reactions should be suppressed to below this value, only then will the reaction alone be potential controlling. It appears necessary to have anodically formed oxide films. It was also found essential to let the oxide surface be exposed to oxygen gas for some time. This happened to be the time during which the solution was pre-electrolyzed. The necessity for exposure to oxygen was shown by preparing two electrodes under identical conditions in the same cell and solution. One was submerged in the solution during pre-electrolysis, the other was exposed to the oxygen gas. The potentials registered by these two electrodes are shown in Fig. 5. That which was submerged gives a steady value of 1.1v, while the oxygen exposed electrode registers the reversible potential shortly after immersion in the same electrolyte. It seems likely that the anodic oxide film on platinum is sufficiently porous or presents sites suitable for the adsorption of oxygen from the gas phase. In confirmation of this view it may be noted that the adsorption of oxygen by platinum oxide to form oxides of composition PtO_2 and Pt_2O_4 in varying ratios have been reported (10). Lingane (11) has demonstrated that only on anodized platinum of composition $\text{PtO} + \text{PtO}_2$ in the ratio 6:1 the reduction of molecular oxygen proceeds readily. The compositions referred to may be regarded simply as

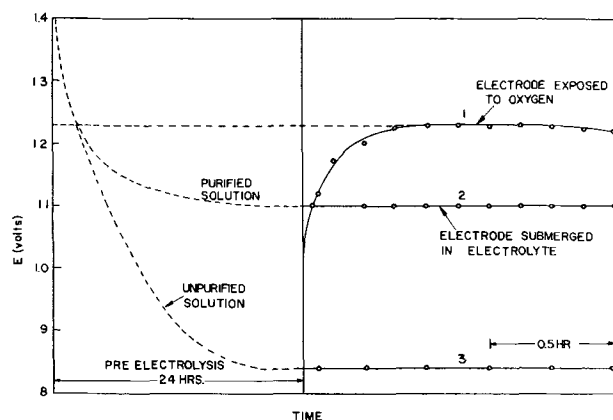


Fig. 5. Effect of exposure to oxygen gas of anodized platinum electrodes.

stoichiometric equivalents of adsorbed oxygen on a platinum oxide substrate. The corresponding adsorption of oxygen from the solution onto the submerged electrode will be diffusion controlled and is probably not comparable to the rate of desorption of the oxygen. The decrease of potential after about 90 min may also be due to this loss of oxygen activity by desorption. Experiments on the adsorption of oxygen by oxide are in progress in these laboratories and will be reported later.

Cathodic polarization curves.—Attempts were made to obtain the cathodic Tafel line by polarization, but starting from the reversible oxygen potential. It was found that the potentials were not steady and did not fall on a smooth line, until a current density of about 10^{-6} amp cm^{-2} was reached (12-17). Thereafter, a Tafel line with gradient about 0.1 was obtained until the oxygen reduction limiting current was reached. On retracing the polarization curve from high current density to low current density, potential plateaus as shown in Fig. 6, were obtained. With successive cycles the potential plateau was lowered until it reached a limit of 0.84v, after several cycles. This limit is also reached by the addition of a few drops of hydrogen peroxide. It therefore appears likely that hydrogen peroxide produced as an intermediate in oxygen reduction or

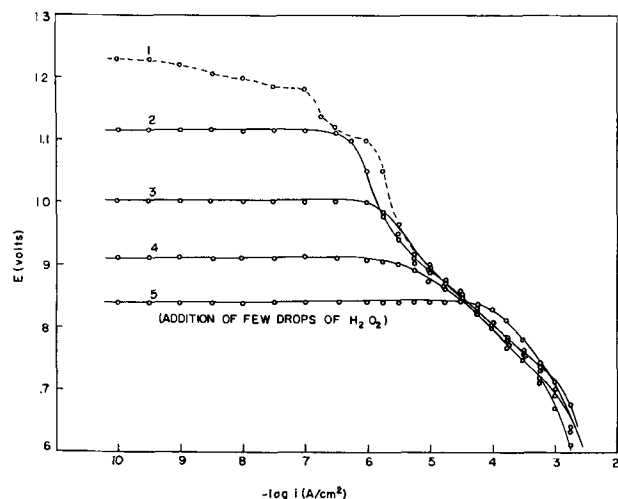


Fig. 6. Cathodic polarization curves of reversible oxygen electrodes.

in a side reaction is exerting potential control in very small quantities (less than 10^{-6} moles/liter). When the H_2O_2 concentration exceeds 10^{-6} moles/liter the potential is controlled by reaction [5] and is 0.84v as shown by Bockris and Oldfield.

Experiments with gold electrodes.—Anodized gold electrodes were also examined as possible substrates for the oxygen electrode reaction. It was found that a variety of potentials in the range 1.34 to 1.24v were obtained depending on the current density and duration of anodization. Cathodic polarization of such electrodes resulted in plots such as shown in Fig. 7. The proximity of the reversible oxygen potential to the gold oxide potential of 1.236v can be misleading and the cathodic polarization curves are more likely to be due to the reduction of gold oxide rather than of oxygen since the rapid technique was used. It appears that exposure of pure gold electrodes to oxygen gas at 1

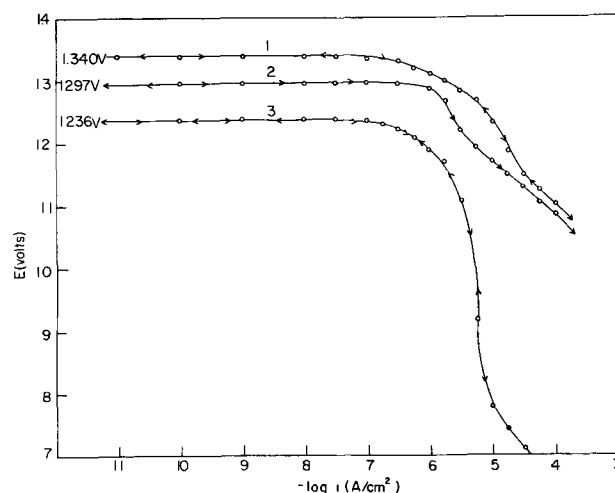


Fig. 7. Cathodic polarization curves of anodized gold electrodes

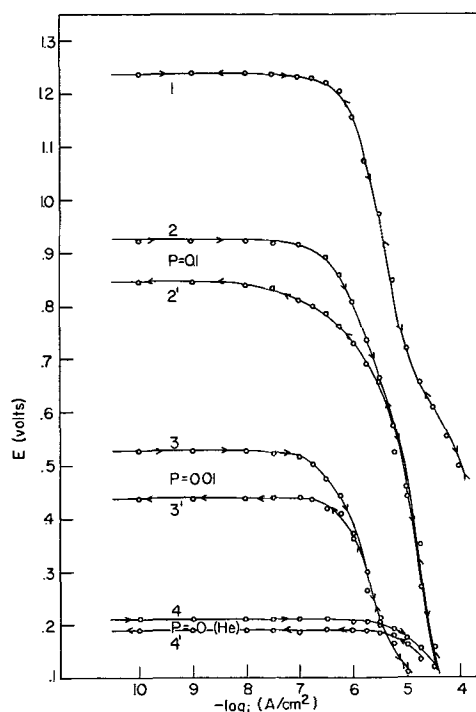


Fig. 8. Effects of oxygen partial pressure and cathodic polarization behavior of gold electrodes.

atm pressure results in the formation of a gold oxide with a stable potential of 1.236v. That this is not the reversible oxygen potential is shown by Fig. 8 which shows the effect of partial pressure changes. The potential changes do not follow the Nernst equation. It therefore appears unlikely that a reversible oxygen electrode can be established on gold or gold oxide substrates.

Acknowledgments

We thank Professor J. O'M. Bockris and Miss W. Visscher for discussions. One of us (N.W.) wishes to thank the Council of Kyoto University for leave of absence. This project was supported by the U.S. Army Signal Corps under contract No. DA 36-039-SC-889 21.

Manuscript received November 1, 1962. Revised manuscript received Nov. 12, 1963.

Any discussion of this paper will appear in a Discussion Section to be published in the December 1964 JOURNAL.

REFERENCES

1. W. M. Latimer, "The Oxidation States of the Elements and Their Potentials in Aqueous Solution,"

- p. 39, Prentice-Hall, New Jersey (1952).
2. J. O'M. Bockris and A. K. M. S. Huq, *Proc. Roy. Soc.*, **A237**, 277 (1956).
 3. J. P. Hoare, *This Journal*, **109**, 858 (1962).
 4. Ref. 1, p. 207.
 5. *Ibid.*, p. 205.
 6. J. O'M. Bockris and L. F. Oldfield, *Trans. Faraday Soc.*, **51**, 249 (1955).
 7. W. Visscher and M. A. V. Devanathan, To be published.
 8. R. R. Witherspoon, H. B. Urbach, E. Yeager, and F. Hovorka, Tech. Report 4, Western Reserve University, ONR Cont. Nonr. 581(00) 1954.
 9. W. G. Berl, *Trans. Electrochem. Soc.*, **83**, 253 (1943).
 10. S. M. Aviya, M. P. Morozova, G. S. Markevick, and A. A. Reikhardt, *Shornk Slatei Obshshei Khim., Akad. Nauk. S.S.S.R.*, **1**, 76-82 (1953).
 11. J. J. Lingane, *J. Electroanal. Chem.*, **2**, 296 (1961).
 12. T. P. Hoar, *Proc. Roy. Soc.*, **A142**, 628 (1933).
 13. V. I. Veselovski, "Soviet Electrochemistry," Vol. II, p. 163 (1961).
 14. A. N. Frumkin, *ibid.*, p. 199 (1961).
 15. A. Hicking and S. Hill, *Disc. Faraday Soc.*, **1**, 236 (1947).
 16. G. Armstrong and J. A. V. Butler, *ibid.*, **1**, 122 (1947).
 17. K. J. Vetter and D. Berndt, *Z. Electrochem.*, **62**, 378 (1958).

The Mechanism of Hydrogen Evolution on Iron in Acid Solutions by Determination of Permeation Rates

M. A. V. Devanathan¹ and Z. Stachurski

Electrochemistry Laboratory, University of Pennsylvania, Philadelphia, Pennsylvania

ABSTRACT

The permeation of electrolytic hydrogen in Armco iron membranes has been investigated by the electrochemical technique described elsewhere. In purified solutions it has been found that the permeation rate follows the equations previously derived. This rate is inversely proportional to the thickness and to the surface coverage with atomic hydrogen θ . The intercept of the plot of reciprocal of the permeation rate against the thickness varies inversely as the coverage as also predicted by the equation. Anomalies in the thickness dependence often reported in the literature have been traced to the adsorption of impurities and to redeposited iron, which then limit the over-all permeation rate. The variation of permeation with cathodic overpotential has been determined. It is found that at moderate overpotentials $d \ln \theta/d\eta = F/4RT$ indicating a slow discharge rate-determining step followed by Tafel recombination. At higher overpotentials $d \ln \theta/d\eta = 0$, indicating a constant coverage brought about by a transition to electrochemical desorption. In confirmation of this mechanism attempts have been made to determine the pseudocapacitance of the electrode system by galvanostatic cathodic transients. The results show the complete absence of pseudocapacity in acid solutions, thus proving that discharge of hydrogen ions is the rate-determining step.

The determination of the hydrogen evolution mechanism on iron electrodes is of more than academic interest in view of the practical importance of this reaction in respect to the corrosion behavior of iron. Bockris and Koch (1) concluded from studies of the comparative rates of hydrogen and deuterium evolution on iron cathodes that the rate-determining step was slow discharge. As has been shown elsewhere determination of the degree of coverage enables the identification of the subsequent steps (2, 3). From the point of view of mech-

anism diagnosis only, it is not necessary to know the absolute value of the coverage, but only its variation with potential. Such information can be readily obtained from studies of the rate of permeation.

Experimental

Permeation measurements.—Details of the cell and auxiliary apparatus used in these experiments have been described elsewhere (4) in connection with permeation studies on palladium membranes; only the cell diagram (Fig. 1) and electrical circuit (Fig. 2) are given here. For these investigations

¹ Present address: Central Electrochemical Research Institute, Karaikudi-3, India.

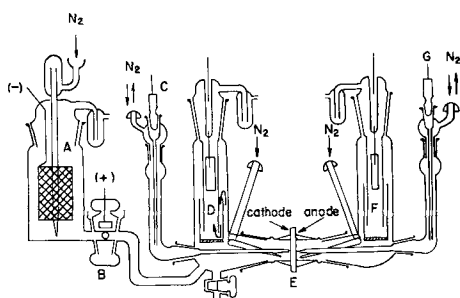


Fig. 1. Cell and pre-electrolysis vessel: A—Cathodic compartment of the pre-electrolysis cell. B—Anodic compartment of the pre-electrolysis cell. C, G—Saturated calomel electrodes. D, F—Auxiliary electrodes. E—Test electrode.

FIG 2

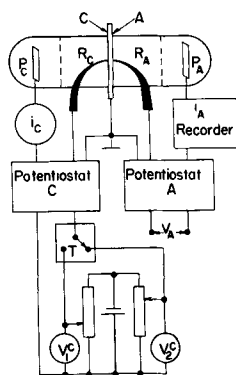


Fig. 2. Electrical circuit: C—Cathodically polarized side of the test membrane. A—Anodically polarized side of the test membrane. P_C , P_A —Auxiliary electrodes. R_C , R_A —Reference electrodes. T—Electrical timer & coupled relay.

Armco iron sheets prepared in the following way were used. Sheets of various thickness were degreased in benzene and heated to 700°C in an atmosphere of pure hydrogen and allowed to anneal. The membranes were then mounted in the cell as described elsewhere (4). The anodic compartment contained 1N NaOH and, to reduce the possibility of passivation, this side was coated with a thin electrodeposit of palladium. This thin coating did not materially affect the rate of permeation of atomic hydrogen which was rate controlled only in the iron membrane (5).

Attention was paid to purification of the solution, and pre-electrolysis was carried out in an external cell before admitting the solution in to the cell. In the permeation studies, the transients were recorded as described earlier for various cathodic potentials and various thicknesses of the membrane.

Capacity determinations.—The capacity of the iron electrode at various potentials was measured by using single sweep galvanostatic cathodic pulses. The electrode was polarized at a low cathodic current density of about 10^{-5} amp/cm² with a simple galvanostatic circuit consisting of two decade power resistors in series and a 120v dry battery. Across one decade box a fast rise time mercury relay was connected so that, on closing the contacts, the decade resistance box was shorted. Thus, it was possible to obtain a rapid change of current density from a low

value to the required high value. The attendant change in potential measured with respect to calomel reference electrode was registered by a Tektronix 535A oscilloscope with a type D preamplifier. The trace was recorded on Polaroid 46-C film with a Tektronix C12 camera. Calculations were made from tracings on graph paper at a magnification of 4 per cm of oscilloscope screen. The electrolyte solutions used were sulfuric acid, sodium hydroxide, and acetate buffer solutions. All measurements were carried out at room temperature which was $25^\circ \pm 2^\circ$ C.

Results and Discussion

Anomalies in the permeation.—A typical permeation transient is shown in Fig. 3. As shown elsewhere the diffusion constant can be calculated from this curve in as many as five different ways (5, 6). Since the identity of the diffusion constant D evaluated by the various methods has already been established, we have calculated D by measuring the time taken for the permeation to reach 0.6299 of its

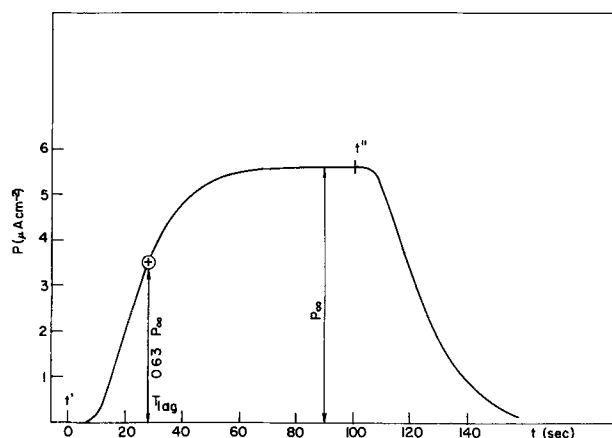


Fig. 3. Typical permeation transient

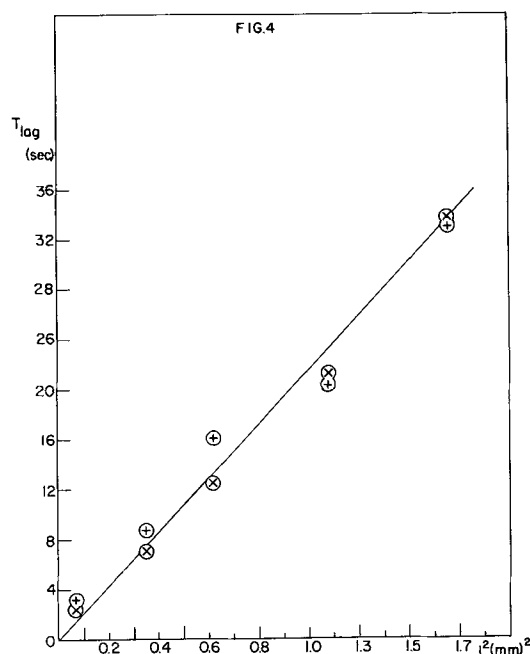


Fig. 4. Plot of time lag versus L^2 for $E = 1000$ mV vs. S.C.E. —plus with circle—plus with circle—. $E = 1400$ mV vs. S.C.E. —X with circle—X with circle.

limiting value. This time is the same as the classical time lag related to the diffusion constant by

$$T_p = 0.63 P_\infty = T_{\text{lag}} = L^2/6D \quad [1]$$

where $T_p = 0.63 P_\infty$ is the time required for the permeation rate to attain 63% of the steady-state value and L is the thickness of the membrane.

Hence a plot of $T_p = 0.6299 P_\infty$ vs. L^2 should be a straight line whatever the cathodic polarization conditions. Such a plot is shown in Fig. 4, and this linearity is the first proof of the constancy of the diffusion constant. A summary of these determinations for various thicknesses is presented in Table I. In the first place we may note that the diffusion constant is independent of thickness. Several investigators have reported a variation of the diffusion constant with thickness when calculated according to the classical time lag method. Thus Palczewska and Ratajczyk (7) find that for diffusion from the gas phase the diffusion constant increases from about $3.8 \times 10^{-7} \text{ cm}^2/\text{sec}^{-1}$ for Armco iron membranes of thickness 0.02 cm to about $3.1 \times 10^{-6} \text{ cm}^2/\text{sec}^{-1}$ for a thickness of 0.12 cm. They concluded that above a thickness of about 0.078 cm the diffusion constant is almost independent of thickness. It appears likely that this effect is due to the surface exerting a controlling influence on the diffusion. In our experiments in acid solutions we observed a black film of finely divided iron depositing on the cathode if the solution was not adequately pre-electrolyzed and if the corrosive solutions were allowed to be in contact with the electrode without a cathodic protection current. Whenever such a film was formed the permeation current dropped to about $3 \mu\text{A}$. Redeposited iron appears to be much less permeable to hydrogen as shown by Devanathan and Stachurski (8). Thus only membranes of sufficient thickness which have an overall permeation rate much less than $3 \mu\text{A}$ will be unaffected by this film. All thinner membranes will show a constant permeation of $3 \mu\text{A}$ whatever the thickness because this film controls the over-all rate of permeation. With careful purification and pre-electrolysis, complications due to surface control by this film can be avoided, and reliable permeation transients can be recorded. As shown elsewhere, the plot of the reciprocal of the permeation rate against the thickness should be a straight line (5, 6). In

Table I. Diffusion coefficients measured for various thicknesses

L, cm	t_0 , sec		$10^5 D$, cm^2/sec
	-1000 mv	-1400 mv	
0.129	33.0	—	8.4
0.129	—	33.7	8.2
0.104	20.1	—	8.9
0.104	—	21.0	8.6
0.079	16.0	—	6.5
0.079	—	12.4	8.4
0.059	8.7	—	6.6
0.059	—	7.0	8.3
0.026	3.2	—	3.5
0.026	—	2.6	4.3

D calculated from slope (Fig. 4)

8.3

Figure 5 we show such a plot for film-free iron. The above results and those obtained with palladium (4) show that attention must be paid to removing films which can control permeation when present at the surface (8).

It has been shown elsewhere that the rate of permeation of hydrogen under these experimental conditions should follow the equation (5, 6)

$$1/P = L k_{bs}/D \theta k_{sb} + 2/\theta k_{sb} \quad [2]$$

where P is the permeation rate through a membrane of thickness L and diffusion constant D , and k_{sb} and k_{bs} are the rate constants for the transfer of atomic hydrogen from the metal surface to the metal bulk and *vice versa*. Under potentiostatic control the coverage of the cathode with hydrogen atoms θ will be constant. Hence at constant η , Eq. [2] predicts a linear plot for $1/P$ vs. L . The slope and intercept are both dependent on the reciprocal of θ . Since in general θ is larger the higher the η value, for high overpotentials, both the gradient and the intercept should be smaller.

Such plots for iron in an acetate buffer of pH 3.6 and in 0.1N H_2SO_4 are given in Fig. 5 and 6, respectively. It is evident that the predictions of Eq. [2] are borne out, and this is the first proof of the validity of the assumptions used in its derivation (5, 6). One of these is that the rate constants k_{sb} and k_{bs} be large compared to the diffusion constant. From these plots it is possible to evaluate k_{bs} since θk_{sb} is known from the intercept and D is also known independently. The order of magnitude of k_{bs} has been found to be $10^{-2} \text{ cm}^2/\text{sec}^{-1}$, which is larger than the value of D . It will not be possible to evaluate k_{sb} until the absolute value of θ is obtained by independent methods.

Mechanism of the hydrogen evolution reaction on iron.—The following stages are possible for the hydrogen evolution reaction on iron.

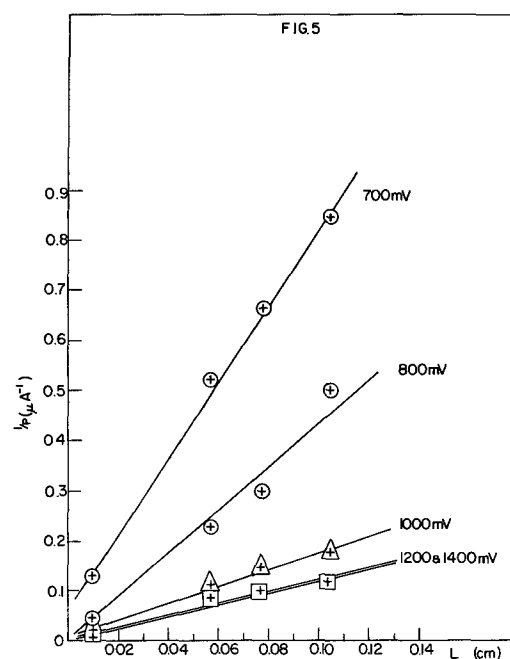


Fig. 5. Plot of reciprocal of permeation rate against thickness for various potentials in acetate buffer of pH 3.6.

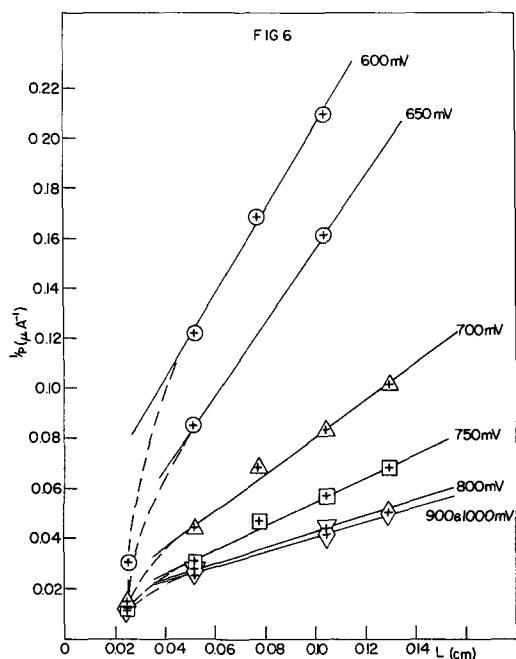
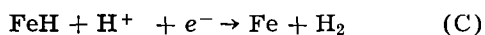
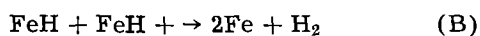
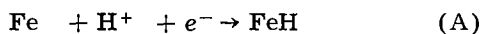


Fig. 6. Plot of reciprocal of permeation rate against thickness in 0.1N sulfuric acid.



In order to obtain information regarding mechanisms, the results of the permeation plots shown in Fig. 5 and 6 were analyzed as follows. The slope of the $1/P$ vs. L plot at constant η is according to [2] given by

$$g = k_{bs}/D k_{sb}\theta \quad [3]$$

Hence

$$d \ln \theta / d\eta = - d \ln g / d\eta \quad [4]$$

and the slope in a plot of $\ln g$ vs. η or $E_{(\text{S.C.E.})}$ yields the negative of $d \ln \theta / d\eta$. This derivative has characteristic values for certain mechanism sequences.

Thus if the reaction sequence involves the rate-determining slow discharge (A), followed by rapid Tafel recombination (B), then in the steady state we have

$$i_c = k_D (1 - \theta) \exp(-\alpha F\eta/RT) = k_T \theta^2 \quad [5]$$

When discharge is rate determining, θ is usually small, and in the limit of small θ , we may write the approximate form

$$\theta = (k_D/k_T)^{1/2} \exp(-\alpha F\eta/2RT) \quad [6]$$

Noting that α is 0.5, since the Tafel plot has a slope 1 of $2.303(2RT/F)$, logarithmic differentiation of [6] yields

$$d \ln \theta / d\eta = - F/4RT \quad [7]$$

If the reaction sequence is the rate-determining discharge (A) followed by fast electrochemical desorption (C) then for the steady state we have

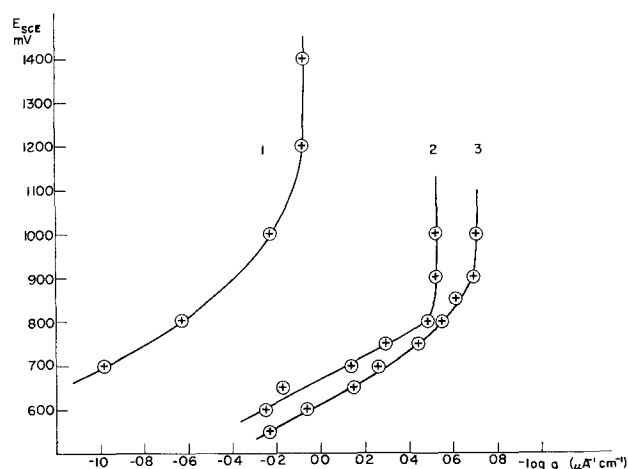


Fig. 7. Plot of $\log g$ vs. $E_{(\text{S.C.E.})}$ for: 1. Acetate buffer pH³; 2. 0.1N Sulfuric acid; 3. 0.5N Sulfuric acid.

$$i_c = k_D (1 - \theta) \exp(-\alpha F\eta/RT) = k_E \theta \exp(-\alpha F\eta/RT) \quad [8]$$

Hence

$$\theta/(1 - \theta) = k_E/k_D = \text{constant} \quad [9]$$

That is θ is potential independent, i.e.,

$$d \ln \theta / d\eta = 0 \quad [10]$$

We show in Fig. 7 plots of $\log g$ vs. $E_{(\text{S.C.E.})}$ for the various solutions. The curves consist of two linear sections. The first has a slope of about 0.36v^{-1} compared to $[(2.303)4RT/F]^{-1}$ which is 0.42v^{-1} , the second has zero slope. Hence in the above solutions the mechanism of the hydrogen evolution reaction must be slow discharge always; followed by Tafel recombination at low overpotentials and electrochemical desorption at high overpotentials.

Pseudocapacity.—With iron in acid solutions, the view that electrochemical desorption might be rate determining has also been suggested. Should this be the case then the preceding step (A) must be in equilibrium unless (A) is irreversible. In this case as shown by Bockris and Kita (9) a pseudocapacity should be observed. A typical transient used in evaluating the double layer capacity is shown in Fig. 8. The capacity in regions where the faradaic current is negligible is found to be about $40 \mu\text{F}$ (see

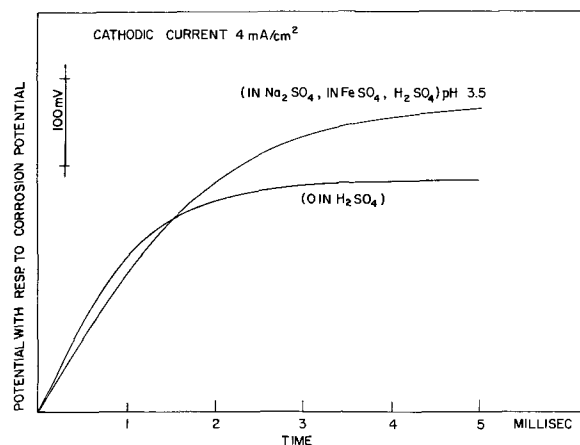


Fig. 8. Cathodic charging transient for iron at the corrosion potential in acid solution and in ferrous solution.

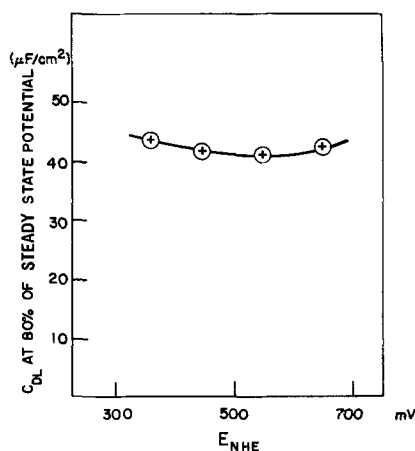


Fig. 9. Plot of differential capacity at 80% of steady state potential vs. $E_{(N.H.E.)}$ for iron in acid solutions. (Capacities were calculated from galvanostatic transients for various current densities.)

Fig. 9). These values are much too close to the double layer values, and it is reasonable to conclude the absence of pseudocapacity. This result also confirms the mechanisms suggested all of which involve discharge as the rate-determining step.

The high capacity reported for iron in ferrous sulfate sulfuric acid solutions appears to be dependent on the cathodic current density used. Thus as shown in Table II (part A) at low current densities the capacity is approximately the same whether ferrous ions are present or not. However, at high current densities, in ferrous ion containing solutions only, an increase in capacity to about 200 μF is observed (Table II, part B). Whenever such high capacities were encountered the iron cathode was found to have a coating of an iron electrodeposit. At the same cathodic current density in ferrous ion free solution the capacity was still about 30 μF . Therefore, it appears probable that the large values of pseudocapacity reported are due to a high faradaic contribution whenever the current density is sufficient for ferrous ion discharge.

Conclusions

From the above it is clear that the mechanism of the hydrogen evolution reaction is rate-determining discharge followed by Tafel recombination at low overpotential, and electrochemical desorption at high

Table II. Double layer capacity ($\mu\text{F}/\text{cm}^2$) from the initial slopes of the galvanostatic transients

i , ma/cm ²	0.1N H ₂ SO ₄	(1N FeSO ₄ , 1N Na ₂ SO ₄) adjusted with H ₂ SO ₄ to pH 3.5
A		
0.81	28	35
1.6	27	30
4.1	24	30
B		
8.1	25	69
12.2	—	104
16.3	25	184
32.5	27	158

overpotential (> 600 mv). These conclusions are also in harmony with the findings of Frumkin (10), who used a qualitative method of establishing the mechanism. (By observing the increase or decrease of overpotential at constant current of one side of an iron membrane, when additional hydrogen permeates on cathodically polarizing the opposite side.)

Acknowledgments

The authors wish to thank Professor J. O'M. Bockris and Dr. W. Beck for discussions and the Office of Naval Research for support of this work.

Manuscript received Nov. 2, 1962.

Any discussion of this paper will appear in a Discussion Section to be published in the December 1964 JOURNAL.

REFERENCES

1. J. O'M. Bockris and D. F. A. Koch, *J. Phys. Chem.*, **64**, 1941 (1961).
2. M. A. V. Devanathan, J. O'M. Bockris, and W. Mehl, *J. Electroanal. Chem.*, **1**, 143 (1959-60).
3. M. A. V. Devanathan and M. Selvaratnam, *Trans. Faraday Soc.*, **56**, 1820 (1960).
4. M. A. V. Devanathan and L. Stachurski, *Proc. Roy. Soc. (London)*, **A270**, 90 (1962).
5. M. A. V. Devanathan, ONR Technical Report No. 4 (1961).
6. M. A. V. Devanathan, *Trans. Faraday Soc.*, (in press). (1963).
7. W. Palczewska and I. Ratajczyk, *Bull. Acad. Polon. Sci.*, **9**, 267 (1961).
8. M. A. V. Devanathan and Z. Stachurski, In press.
9. J. O'M. Bockris and Hideaki Kita, *This Journal*, **108**, 676 (1961).
10. A. N. Frumkin, *Z. Physik. Chem.*, **207**, 321 (1957).



Kinetics of the Aging of Anodic Oxide Film on Iron

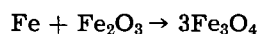
Norio Sato¹ and Morris Cohen

Division of Applied Chemistry, National Research Council, Ottawa, Ontario, Canada

In a previous study (1) of the kinetics of anodic oxide film growth on iron in a neutral solution, it was found that the rate of thickening of the oxide at constant potential varies with the film thickness in accordance with the equation

$$i = A \exp\left(-\frac{Q_T}{B}\right) \quad [1]$$

where Q_T is the amount of charge accumulated in the film and A and B are constants. In the process of anodic oxidation there is movement of both the iron and oxygen ions. If, after an oxide film has been formed, the supply of oxygen ion is cut off by removing the solution from the electrolytic cell, the iron ion may continue to flow to a new reaction zone to change the composition of the oxide. A possible reaction is



There is already some evidence for this process for both anodic oxide films (2) and with films formed by dry oxidation (3). The purpose of the present study was to compare the kinetics of the aging process with those of the anodic oxidation process.

Experimental Procedure

The methods and materials used have been described (1); the specimen was electropolished Ferrrovac iron sheet and the solution was an equal-volume mixture of 0.15*N* boric acid and 0.15*N* sodium borate (pH = 8.43). In a recent study (4) the cathodic reduction of the anodic oxide film on iron in the same solution as above has been studied and the reduction efficiency of the inner "Fe₃O₄" layer of the oxide film at the second wave of the cathodic reduction curve has been estimated; the efficiency was in the range 41.1-43.1% with an average of 42.0% for the oxide film formed in the potential range +0.1-+0.8v referred to the saturated calomel electrode (SCE). This was applied here as a convenient method to measure the thickness of the inner "Fe₃O₄" layer.

Before the measurement the air-formed or passive oxide film on the specimen was removed by cathodic reduction at 10 μa/cm², which was followed by the renewal of the solution. The specimen then was anodically oxidized at a constant potential of + 0.700v (SCE scale) at 25° ± 0.1°C for a period of 1 hr to establish an oxide film of definite

thickness. After the oxidation was stopped by rapidly pulling the solution out, the oxidized specimen was kept in the cell at the same temperature in a constant flow of purified nitrogen gas for different specified times of aging before being immersed again in the solution. Subsequent measurement of the cathodic reduction curve shows the change in the thickness of the inner "Fe₃O₄" layer caused by the aging.

Results

Figure 1 shows the change in the amount of charge Q_2 associated with the second wave of cathodic reduction curve with time of aging. From the data the mean film thickness and mean rate of thickening of the inner "Fe₃O₄" layer during specified time intervals can be calculated respectively as follows

$$i = \eta(\Delta\bar{Q}_2/\Delta t)$$

$$\bar{Q}_1 = \eta\bar{Q}_2$$

where i is the rate of thickening, \bar{Q}_1 the mean thickness of "Fe₃O₄" layer expressed in terms of the amount of charge \bar{Q}_2 required to reduce it to metallic iron, and η the current efficiency in cathodic reduction. The results of the calculation are plotted in a semilogarithmic fashion in Fig. 2. A straight line can be drawn to fit the calculated data with the equation

$$i = A \exp\left(-\frac{\bar{Q}_1}{B}\right) \quad [2]$$

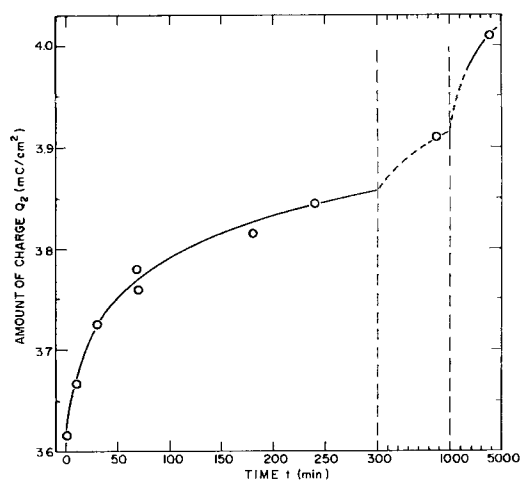


Fig. 1. Change in the amount of charge associated with the second wave of cathodic reduction curve during aging.

¹ Present address: Faculty of Engineering, Hokkaido University, Sapporo, Japan.

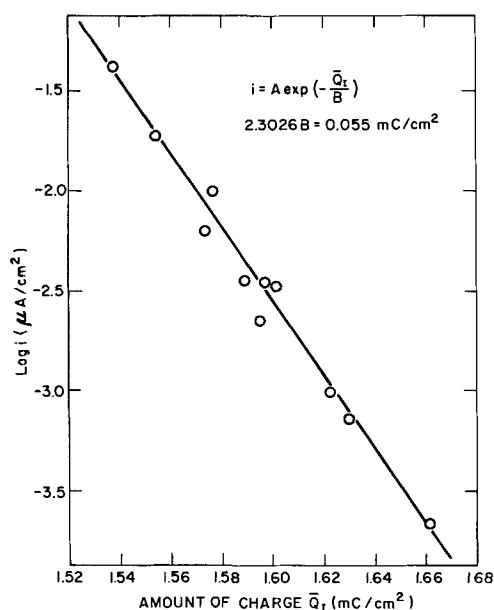


Fig. 2. Change in the rate of growth of the inner magnetite layer with its thickness.

where A and B are constants.

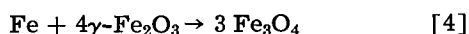
The rate equation thus obtained from the result is of the same form as Eq. [1], and consequently one can compare the kinetics of both aging and anodic oxidation by comparing the value of constant B of the rate equations. From the slope of the straight line in Fig. 2 the value of B for the aging reaction is calculated to be

$$B = 0.055 \text{ mC/cm}^2 \quad [3]$$

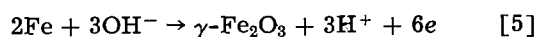
and it is compared with the value of B ($B = 0.430 \text{ mC/cm}^2$, 25°C) obtained for the anodic oxidation (1). It is seen that the value of B for the aging reaction is about one-eighth of that for the anodic oxidation; in other words the decrease in the rate of magnetite layer thickening during the aging is about eight times faster than the decrease in the rate of anodic oxide film thickening during the potentiostatic oxidation.

Discussion

During aging the inner magnetite layer thickens by a reaction between the underlying iron and the $\gamma\text{-Fe}_2\text{O}_3$ which composes the outer layer of the oxide film. Consequently, the over-all reaction of aging is written as



This reaction will be compared with the reaction of anodic oxidation which can be written as



In the strict sense, because of the duplex structure of the film, the reaction of anodic oxidation should be written as



but the value of n calculated from the composition of anodic oxide film is so close to 3 that for the present purpose one can write the anodic reaction as Eq. [5]; during the anodic oxidation the ratio of the magnetite layer to the total oxide film was estimated as 10~20% which corresponds to 2.91~2.95 for the value of n (4).

Since the reagents involved in reaction [4] are all solid state, the driving force of the reaction should be constant in the course of aging. In the anodic oxidation the driving force is also maintained constant at constant electrode potential. Accordingly, it is reasonable to compare the rate equation of the reaction of aging with that of potentiostatic oxidation. The results show that the rate of magnetite layer thickening during the aging obeys a kinetic equation of the same form as that of the potentiostatic growth of anodic oxide but the constant B in the equation differs considerably in the aging and anodic oxidation.

In both anodic oxidation and aging there is a flow of iron through the oxide to the site of reaction. Equation [4] shows that during the aging the flow of 1 g-atom of iron causes the transfer of 12 g-atom of oxygen from the γ -ferric oxide layer to the magnetite layer. On the other hand, the flow of 1 g-atom of iron during the anodic oxidation gives rise to the introduction of 1.5 g-atom of oxygen from the solution (probably from adsorbed OH^- ion) into the oxide film. In the previous paper (1) B was related to the re-arrangement of iron and oxygen in the film. The number of oxygen ions required to rearrange themselves per gram atom of iron is eight times as large in the case of the aging experiment as in the case of the anodic oxidation, and hence the rate of the reaction should be one-eighth as fast. This is what is observed experimentally.

Manuscript received May 7, 1963.

Any discussion of this paper will appear in a Discussion Section to be published in the December 1964 JOURNAL.

REFERENCES

1. N. Sato and M. Cohen, Submitted to *This Journal*.
2. M. Nagayama and M. Cohen, *ibid.*, **110**, 670 (1963).
3. E. J. Caule and M. Cohen, *ibid.*, **108**, 834 (1961).
4. M. Nagayama and M. Cohen, *ibid.*, **109**, 781 (1962).



Oxidation of Pyrolytic Carbon 1000° to 1500°C and Oxygen Pressures of 2 to 38 Torr

E. A. Gulbransen, K. F. Andrew, and F. A. Brassart

Physical Chemistry Department, Westinghouse Electric Corporation, Pittsburgh, Pennsylvania

In a recent paper (1) we presented a study of the oxidation characteristics of spectroscopic grade graphite having a density of 1.6. Below 800°C a chemical controlled reaction mechanism was found. Above 800°C the reaction was limited by either a chemical controlled process or gas diffusion controlled process. The transition between the two mechanisms depends on the pressure, sample size, and the nature of the reaction system.

Pyrolytic carbon (2), having a density of about 2.1, is a more dense form of carbon than the spectroscopic grade graphites and is highly anisotropic. Pyrolytic carbon is nearly impermeable to gases, and its oxidation rate is said to be less than that of spectroscopic grade graphites by a factor of 1/3 to 1/10 (2). Theoretically the oxidation rates should depend on the porosity and permeability if the internal surfaces of the graphite participate in the reaction. This difference in oxidation rates should not exist in the gas diffusion controlled region of oxidation.

This paper shows that pyrolytic and a spectroscopic grade of graphite oxidize with nearly identical rates in the gas diffusion region of the oxidation process.

The pyrolytic graphite has the following analyses in parts per million: Na<10, K<10, Li<10, Ba<1, Sr<1, Cr<10, Ca 2, Cu 2, Ag<1, Co<10, Ti<10, Zn<10, Sr<10, Cd<10, Mo<10, V<10, Al<10, Bi<10, Nb<10, W<100, Si 2, Mg<1, Mn<10, Fe<10, Zr<10, B<1, As<100. Flat plates of pyrolytic carbon were cut and machined into cylinders having a weight of 0.93g and surface areas of about 3.4 cm².

The experimental method was described in an earlier paper (1).

Results and discussion.—Weight loss-time curves were made at 5 pressures for temperatures between 1000° and 1500°C. Since the surface area changed during reaction, the rate of reaction dw/dt decreased with time. To compare the rates of oxidation, dw/dt was evaluated at time $t = 0$ using the differential form of Lagrange's interpolation formula (3).

Table I summarizes the rate data for pyrolytic carbon. The rates of oxidation are given in units of grams of C or atoms of C reacting per cm²-sec. The data show the reaction to be insensitive to temperature between 1000° to 1500°C. The effect of

pressure on the rate of oxidation is also small. For the temperature range of 1000°-1500°C, the data can be fitted to the equation

$$\frac{dw}{dt} = KP^{0.32 \pm 0.1} \quad [1]$$

Here dw/dt is the rate, P is the pressure in Torr, and K is a constant.

In our earlier paper (1) on the oxidation of spectroscopic grade of graphite, we devised an empirical equation to explain the rates of oxidation as a function of temperature for the temperature region 800°-1500°C. An equation of the same type can be used to explain the results for pyrolytic carbon with the exception that the constant 1.86×10^{-6} must be multiplied by the factor relating the specimen surface area 6.3/3.3. The rates of oxidation in the gas diffusion region of oxidation were inversely proportional to the surface area (1).

The following empirical equation explains the rates of oxidation

$$\frac{dw}{dt} = 3.5 \times 10^{-6} P^{0.32 \pm 0.1} e^{-\frac{3600}{RT}} \quad [2]$$

Here dw/dt is in g/cm²-sec, P is the pressure in

Table I. Summary of data, oxidation pyrolytic carbon
Sample areas, 3.18-3.46 cm², sample weight 0.92-0.94g

Reaction conditions		Rates of reaction		
Temp, °C	Pressure, Torr	dw/dt g/cm ² -sec	dn'/dt atom C/cm ² -sec	log dn'/dt
1200	2	1.47×10^{-6}	7.38×10^{16}	16.87
1400	2	1.58×10^{-6}	7.93×10^{16}	16.90
1500	2	1.49×10^{-6}	7.48×10^{16}	16.87
1200	5	2.56×10^{-6}	1.29×10^{17}	17.11
1400	5	2.47×10^{-6}	1.24×10^{17}	17.09
1500	5	2.44×10^{-6}	1.22×10^{17}	17.09
1200	9.5	3.03×10^{-6}	1.52×10^{17}	17.18
1400	9.5	2.78×10^{-6}	1.40×10^{17}	17.15
1500	9.5	3.03×10^{-6}	1.52×10^{17}	17.18
1200	19	2.69×10^{-6}	1.35×10^{17}	17.13
1400	19	3.69×10^{-6}	1.85×10^{17}	17.27
1500	19	3.17×10^{-6}	1.59×10^{17}	17.20
1000	38	3.17×10^{-6}	1.59×10^{17}	17.20
1200	38	3.50×10^{-6}	1.76×10^{17}	17.25
1400	38	3.47×10^{-6}	1.74×10^{17}	17.24
1500	38	4.50×10^{-6}	2.26×10^{17}	17.35

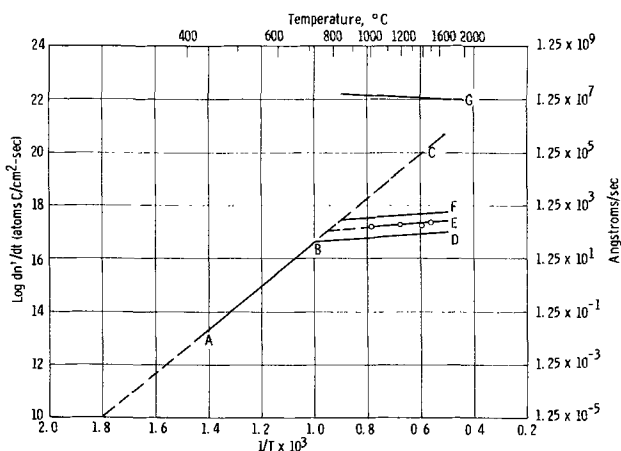


Fig. 1. $\log dn'/dt$ vs. $1/T$, ablation pyrolytic carbon, 38 Torr O_2 , 1000°-1500°C; A-B, chem control graphite; B-C, extrapolated; area ACD diffusion controlled; G, kinetic theory; E, experimental data 3.2 cm^2 samples; D, comparison data, graphite, 6.2 cm^2 ; F, same but for 1.2 cm^2 samples.

Torr, R is the gas constant, and T is the absolute temperature.

Figure 1 shows a $\log dn'/dt$ vs. $1/T$ graph of the data obtained at 38 Torr oxygen pressure together with our data obtained on spectroscopic grade of graphite. Line AB and its extension BC represents data obtained on spectroscopic grade of graphite for the chemical controlled region of oxidation. Line ABD was obtained using 6.0-6.3 cm^2 samples of spectroscopic grade of graphite. Line ABF was obtained using 1.2 cm^2 samples of spectroscopic grade of graphite. Line ABE is the projected line for the same material using 3.2 cm^2 samples. The circled points represent the experimental data for pyrolytic carbon using 3.3 cm^2 samples. The pyrolytic carbon data are in excellent agreement with the results previously found for spectroscopic grade of graphite.

A $\log dn'/dt$ vs. $1/T$ plot was also made for 2 Torr pressure. A similar agreement was found for the two sets of oxidation data.

Line G of Fig. 1 shows the calculated values of dn'/dt from kinetic theory assuming CO as the reaction product.

We interpret Fig. 1 as follows: two different types of oxidation processes exist (a) chemical controlled oxidation and (b) gas diffusion controlled oxidation. For spectroscopic grade of carbon, the chemical controlled region is line ABC and the gas diffusion controlled region lies to the right of line ABC. For pyrolytic carbon, the chemical controlled region of oxidation has not been determined. The experiments discussed in this paper in Table I, Eq. [1], and Fig. 1 are all in the gas diffusion controlled region of oxidation. The gas diffusion controlled regions are characterized by the following: (i) a small temperature and pressure dependence and (ii) the rates of oxidation dn'/dt are dependent on surface area A by the equation

$$dn'/dt \cdot A = k \quad [3]$$

We conclude that pyrolytic carbon and spectroscopic grade of graphite oxidize with nearly identical rates of oxidation at temperatures above 1000°C for pressures of 2-38 Torr in static gas atmospheres. Due to higher density (less porosity), it is expected that pyrolytic graphite should oxidize at a lower rate under conditions of chemical control. These are found at temperatures below 800°C and in high flow reaction conditions (4).

Manuscript received Dec. 11, 1963.

Any discussion of this paper will appear in a Discussion Section to be published in the December 1964 JOURNAL.

REFERENCES

1. E. A. Gulbransen, K. F. Andrew, and F. A. Brassart, *This Journal*, **110**, 476 (1963).
2. R. E. Nightingale, "Nuclear Graphite," p. 435, Academic Press, New York (1962).
3. T. R. Running, "Empirical Formulas," John Wiley & Sons, Inc., New York (1917).
4. E. A. Gulbransen, K. F. Andrew, and F. A. Brassart, "Ablation of Graphite in Oxygen and Air at 1000° to 1400°C Under Flow Conditions," Westinghouse Research Laboratories Scientific Paper, To be published.

Yellow and Red Emitting ZnS:Cu Phosphors

M. J. Presland, R. Marshall, and J. Franks

Research Laboratory, Associated Electrical Industries Limited,

Harlow, Essex, England

During an investigation of the effects of quenching on the structural, photo and electroluminescent properties of zinc sulfide, copper activated phosphors, a new method for preparing intense yellow and red emitting phosphors has been found.

If a slurry prepared in the normal manner is fired in an argon of H₂S atmosphere and quenched directly from the firing temperature in a bath of deionized water, then on subsequent drying at room temperature the phosphors display bright red

and yellow photoluminescence, at copper concentrations in the range $5 \cdot 10^{-4}$ to $10^{-3} \text{ g} \cdot \text{g}^{-1}$ ZnS. The effect of coactivators is only of secondary importance since yellow and red emissions occur equally well in ZnS:Cu, ZnS:Cu, Cl, and ZnS:Cu, Al phosphors. This method differs in many respects from those described previously [for example by Froelich (1) and Aven and Potter (2)] which require the total exclusion of oxygenous and halogeneous impurities, and the presence of a sulfur-rich atmosphere during firing. In addition other authors (3, 4) have suggested that the presence of hydrogen is essential for the production of the red center.

We have also observed that low temperature annealing causes first a conversion of the yellow emission to red and then subsequently, complete destruction of the red emission.

Further annealing causes a reversion to the more usual blue and green emissions. These effects are shown in Fig. 1.

Manuscript received April 29, 1963.

Any discussion of this paper will appear in a Discussion Section to be published in the December 1964 JOURNAL.

REFERENCES

1. H. C. Froelich, *This Journal*, **100**, 280 (1953).
2. M. H. Aven and R. M. Potter, *ibid.*, **105**, 134 (1958).
3. W. Van Gool and A. P. D. M. Clieren, *ibid.*, **106**, 672 (1959).
4. S. Shionoya, T. Koda, K. Era, and H. Fujiwara, "Luminescence of Organic and Inorganic Materials," H. P. Kallman and C. M. Spruch, Editors, John Wiley & Sons, London (1962).

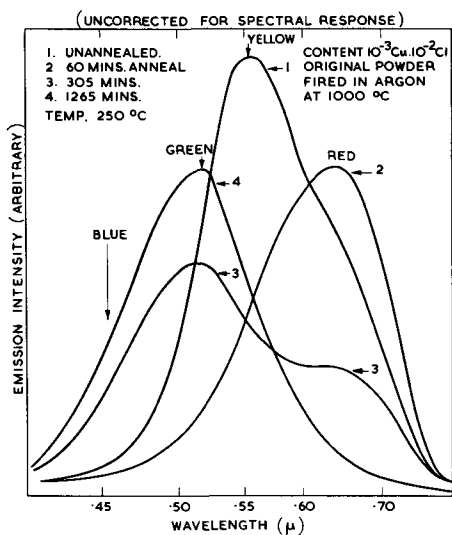


Fig. 1. Quenched ZnS:Cu:Cl phosphors. Four types of emission: 1, unannealed; 2, 60 min anneal; 3, 305 min; 4, 1265 min. Temperature 250°C. Content $10^{-3} \text{ Cu} \cdot 10^{-2} \text{ Cl}$. Original powder fired in argon at 1000°C. Uncorrected for spectral response.

Factors Affecting the Transport of Silver in Silver-Alkaline Batteries

T. P. Dirkse and L. A. Vander Lugt

Calvin College, Grand Rapids, Michigan

ABSTRACT

A study has been made of the factors which control the amount of silver which is introduced into the electrolyte during the operation of a silver-alkaline battery. Part of this work was done with the use of radioactive silver as a tracer. Silver is introduced into the electrolyte during all phases of the operation of a silver-alkaline battery. However, it can be increased by charging at lower current densities or by operation at the Ag/Ag₂O voltage level. A possible mechanism for the electrolytic formation of the oxides is also given.

One of the drawbacks to the more widespread use of silver-alkaline batteries is the fact that the silver oxides are soluble in the KOH electrolyte. Because of this, silver can be transferred to the negative plates of the battery and eventually cause internal shorting. This transport of silver can be, and is, lessened by the use of separators. However, after batteries have been cycled for some time there are extensive silver deposits on or in the separators. These too may eventually lead to internal shorting. In many instances the separators, in effect, delay the building up of internal shorts due to silver sufficiently so that cell failure is then due to other causes.

A large variety of products has been tested and tried as separators in silver-alkaline batteries. Combinations have also been tried, but no completely satisfactory material has been found. A completely satisfactory separator would be one which, in addition to other characteristics, would neither accumulate silver on or within it nor allow silver to diffuse through it. It is not known, of course, whether such a material can be produced.

However, in the search for such a product it may be helpful to learn more about the means by which silver is transported within a silver-alkaline battery. The purpose of this work was to carry out such a study.

In seeking to determine the mechanism or conditions for this silver transport, an attempt was made to answer two questions: (a) what effect does the passage of current or the presence of a voltage gradient have on this transport?; and (b) do some parts of a charge-discharge cycle contribute more heavily to this transport than other parts?

Migration of silver.—The first of these questions is related to the migration of the dissolved silver ions. In a strongly alkaline solution of the kind used as battery electrolyte one would expect the dissolved silver species to be an hydroxylated, negatively charged ion, e.g., Ag(OH)₂⁻. Such an ion would move towards the positive electrode and away from the negative electrode in the presence of a voltage gradient.

Several difficulties were encountered in seeking to determine the extent of silver migration. One of

these has to do with the electrodes. Silver electrodes would introduce silver into the electrolyte and this would complicate the interpretation of the analytical data. If other electrodes were used they could react with the dissolved silver oxides and also complicate the interpretation of the results. Electrodes at which gas is evolved are to be avoided because they, in effect, stir the electrolyte.

Experimental

The experimental arrangement finally used is shown schematically in Fig. 1. The cell case consisted of three compartments each made of Plexiglas and separators could be clamped between the compartments to prevent the free flow of electrolyte from one compartment to the other. Electrodes, 40 x 50 x 2 mm, could be inserted in spaces D and E. There was a small hole in the top of each compartment through which samples of electrolyte could be withdrawn for analysis.

The cell was assembled with two layers of microporous polyethylene between compartments C and A and between C and B. These were squares selected diagonally from each other in a larger square of the material. This was done to minimize the effect of nonuniformity of the polyethylene with respect to silver diffusion. The anode was sintered silver and the cathode was a fully charged sintered silver electrode. Each of these was wrapped in a layer of cellophane. Cellophane rapidly picks up practically all the silver dissolved in the electrolyte. Therefore, it would pick up any silver introduced into the electrolyte by the silver electrodes and it would prevent

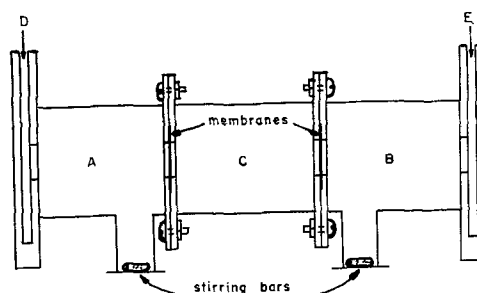


Fig. 1. Cell case used in silver migration study

such silver from getting into compartments A and B.

In addition, a layer of polyethylene was wrapped around the layer of cellophane. This was to minimize the amount of silver picked up by the cellophane from compartments A and B.

The cell was assembled in a dark room and kept there throughout the run to eliminate any possible photo effects. A dark room safe light was turned on briefly only when samples of electrolyte were removed for analysis. 50 ml of 30% KOH was saturated with Ag_2O , allowed to stand 48 hr in the dark, and then filtered through a fine Pyrex frit. A small amount of Ag^{110} was then added as a radioactive tracer. This solution was placed in compartment C. 90 ml of 30% KOH was placed in each of compartments A and B. At intervals 0.5 ml samples were removed from each compartment and counted for gamma emission in a well-type scintillation counter. The solutions in A and B were stirred for 1 min by means of the magnetic stirring bars just before samples were removed. The cell was kept on open circuit for 24 hr to establish the extent of diffusion and then a current of 30 ma was passed for 31 hr. At the end of the run each membrane and electrode was counted.

Results

The results are given on Fig. 2 and in Table I. The cellophane layer around the electrodes was black and appeared to have been effective in picking up the silver introduced into the electrolyte from the electrodes. The polyethylene covering the cellophane was only slightly colored and did pick up some silver. The polyethylene layers between the compartments were dark, the membranes in direct contact with the electrolyte in compartment C having more silver on them than the other layer. There was little difference in silver content of these polyethylene layers on the anode and the cathode side of the middle compartment. The use of the double layer, however, did not completely eliminate the effect of the nonuniformity of the material. The diffusion into the cathode compartment was greater, even on open circuit.

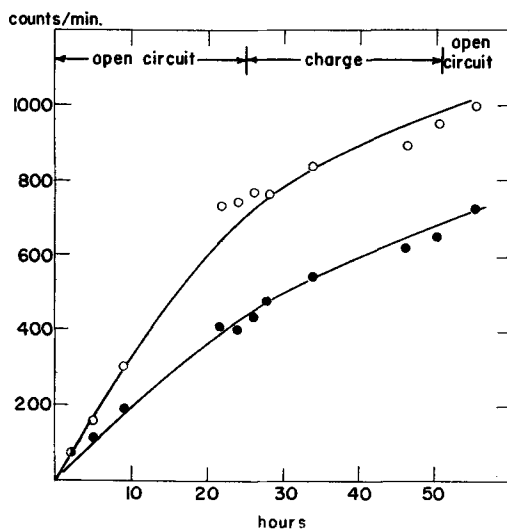


Fig. 2. Effect of current on transport of silver. Current is 30 ma; ○, cathode compartment; ●, anode compartment.

Table I. Radioactivity of cell components

Component	Counts per minute	
	Anode side	Cathode side
Electrode	40	930
Cellophane	16,800	30,500
Polyethylene around cellophane	12,700	33,900
Polyethylene layer 1	38,100	41,000
Polyethylene layer 2 (in direct contact with compartment C)	86,800	95,200

The results on Fig. 2 indicate that the passage of current through the cell did not alter the rate of diffusion of the silver from the center compartment. This diffusion, due to concentration gradients, began as soon as the cell was assembled. The curves through the experimental points are smooth and show no breaks. Slight irregularities appear in both anode and cathode electrolyte at the same time and to the same extent, indicating that these are experimental irregularities. The electrolyte, membranes, and electrode on the cathode side all have higher counts than the corresponding components on the anode side. This is due to differences in the permeability of the polyethylene layers between the compartments.

Under the conditions of the experiment, the passage of current did not alter the transport of silver into either anode or cathode compartment and this suggests that such transport is due primarily to diffusion. Any transport due to migration is relatively insignificant. This seems reasonable when one considers polarography as an analogy. In a silver-alkaline battery the KOH serves as the supporting electrolyte which suppresses current due to migration.

Effect of cycling on silver transport.—Two experimental methods were used to study the effect of cycling on the silver transport in a silver-alkaline battery.

The first method used radioactive silver as a tracer. The Plexiglas cell used in this work is shown on Fig. 3 and the experimental set up is shown on Fig. 4. The electrodes were 10 x 20 mm. The negative electrode was a sintered Cd/CdO and was wrapped in a double layer of polyethylene. The silver electrode was prepared by plating silver on a fine mesh expanded nickel grid from a silver cyanide bath to which had been added some Ag^{110} . Several

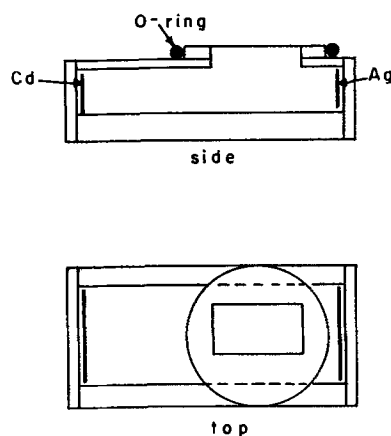


Fig. 3. Cell case used in cycling studies with $\text{Ag}^{110\text{m}}$

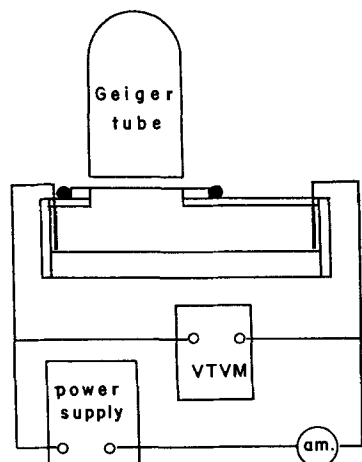


Fig. 4. Experimental arrangement for cycling studies with $\text{Ag}^{110\text{m}}$

preliminary experiments were first carried out to determine a satisfactory ratio of radioactive to non-radioactive silver for this run. After the electrodes had been sealed in the cell, about 20 ml of 30% KOH were added and the rectangular opening was covered with a tightly stretched piece of polyethylene held in place by an O-ring. The cell was then mounted in the Geiger tube housing with the rectangular opening directly below and less than 3 mm from the Geiger tube window. The cell was charged at 0.4 ma for 1.5 hr and then discharged at the same rate. During this cycle the voltage was always that of the $\text{Ag}_2\text{O}/\text{Ag}/\text{OH}^-$ system. The results are shown on Fig. 5. The vertical axis measures the change in counts/minute from that which was obtained at the start of the experiment. The electrolyte was not stirred or agitated in any way other than by convection and this accounts for the irregularities observed in the counting rates. Because of this, only a limited amount of work was done with this technique. The results, however, show that silver is introduced into the electrolyte as soon as the charging process begins.

The other approach to this problem involved the use of a cell of the type shown in Fig. 6. The two halves are clamped together by means of four screws, washers, and nuts, with a membrane covering the hole in the one wall of each half cell. Compartments A and B, 55 x 45 x 6 mm, contain the electrolyte and electrodes. In these runs a sintered silver electrode, a sintered Cd/CdO electrode, and

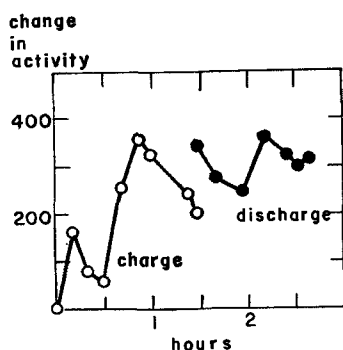


Fig. 5. Change in activity of the electrolyte during cycling on the $\text{Ag}_2\text{O}/\text{Ag}$ level.

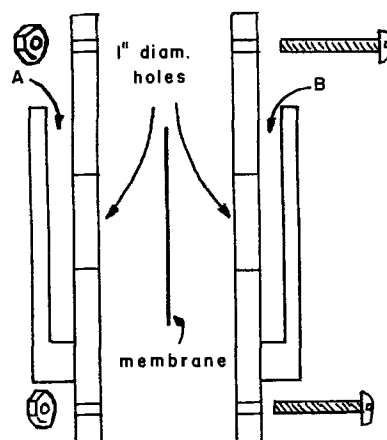


Fig. 6. Cell case used to determine the amount of silver introduced into the electrolyte during cycling.

30% KOH were used. The membrane in all cases was cellophane. This served to pick up practically all the silver that was introduced into the electrolyte. The cell was then charged and discharged under various conditions, after which the cellophane was removed, rinsed in distilled water, and treated with HNO_3 to remove the silver. The amount of silver was determined by potentiometric titration with KI (1).

In the first set of runs the same silver electrode was used throughout and the sequence of events was: (i) charged for 666 min at 20 ma only at the $\text{Ag}_2\text{O}/\text{Ag}$ voltage level; (ii) stand on open circuit for 24 hr; (iii) charged for 1099 min at 35 ma only at the $\text{AgO}/\text{Ag}_2\text{O}$ voltage level; (iv) stand on open circuit for 30 hr; and (v) discharged at 50 ma for 902 min. In each of these fresh electrolyte and a fresh cellophane membrane were used. Later a charged silver electrode was given a trickle charge at constant voltage for 24 hr. The current was about 6 ma throughout this charge.

The results of all these runs are given in Table II. From these it appears that silver is introduced into the electrolyte most readily during the early stages of charge. Charging at the $\text{AgO}/\text{Ag}_2\text{O}$ voltage level or discharging introduces silver into the electrolyte at a lower rate (see values in the right hand column of Table II). Applicable amounts of silver get into the electrolyte during open circuit in the charged state. However, more is introduced from an AgO electrode than from an Ag_2O electrode.

A second series of runs was then carried out. The purpose was to investigate further the effect of the

Table II. Distribution of silver during various parts of charge-discharge cycle

Cell case	Treatment	Quantity	Ag content $\times 10^{+4}$ g	Ag content per unit quantity, $\times 10^{+5}$ g
1	Charge	13.3 amp-min	5.44	4.1/amp-min
2	Stand	24 hr	4.20	1.7/hr
3	Charge	38.5 amp-min	6.43	1.7/amp-min
4	Stand	30 hr	8.97	3/hr
5	Discharge	45.1 amp-min	10	2.2/amp-min
6	Charge	8.64 amp-min	1.15	1.3/amp-min

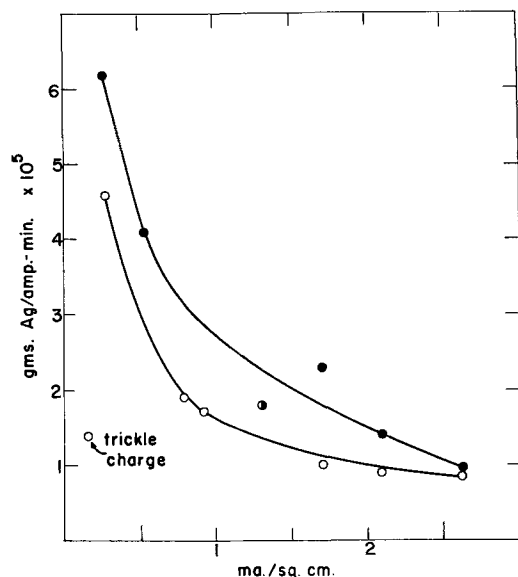


Fig. 7. Amount of silver introduced into the electrolyte during charging; ●, Ag/Ag₂O level; ○, Ag₂O/AgO level.

charging voltage level and also the effect of current density on the amount of silver introduced into the electrolyte. Silver-cadmium cells with a cellophane separator were assembled and charged at different current rates at the Ag/Ag₂O and Ag₂O/AgO voltage levels. The results are shown on Fig. 7. These results show that there is a current density effect. The current density values are calculated from the external dimensions of the silver electrodes and the area of both sides of the plate was included. As the current density is lowered the amount of silver introduced per ampere-minute of charge increases markedly. One exception is the one point on Fig. 7 which is designated "trickle charge." However, in this case the electrode was fully charged before the run began whereas with the other points on the AgO level curve, the electrode was charged on the AgO voltage level at the current density indicated.

The results on Fig. 7 also point out that more silver is introduced into the electrolyte by charging at the lower, or Ag₂O, voltage level than by charging at the higher voltage level. These results suggest that to minimize the amount of silver introduced into the electrolyte it would be better to charge at higher current densities. There appears to be no relationship between the amount of silver introduced into the electrolyte and the time allowed for charging, unless comparisons are made at a fixed current density. When different current densities were used, the amount of silver per unit time figure varied randomly.

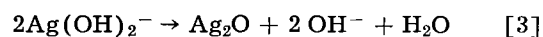
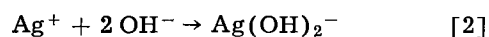
The fact that less silver is introduced into the electrolyte while the electrode is charging to AgO can be explained in terms of the insolubility of AgO in the alkaline solution (2). This accounts also for the small amount of silver introduced into the electrolyte during trickle charging. However, it should be noted that a fully charged silver electrode (AgO)

does introduce silver into the electrolyte at a greater rate on open circuit than does an Ag₂O electrode.

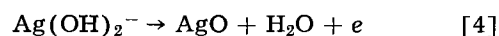
An alternative explanation would allow for an appreciable solubility of AgO in the KOH electrolyte. If one assumes that the silver in AgO is in the divalent state then the charge density on the silver (ion) in AgO is greater than in Ag₂O. This would give AgO greater acid properties than Ag₂O, *e.g.*, ref. (3). If this is so then AgO would dissolve or react more readily with the KOH solution than would Ag₂O. The result of this would be the formation of a hydroxylated ion perhaps Ag(OH)₂⁻ or something similar since the AgO readily decomposes in the KOH (2).

During charging on the AgO voltage level the potential of the silver electrode is greater than it is when charging at the Ag₂O voltage level. Consequently, the Ag(OH)₂⁻ ions are less likely to diffuse away from the silver electrode during charging at the higher potential of the AgO voltage level. This could also account for the small amount of silver introduced into the electrolyte during trickle charging. This argument is also consistent with the slope of the lines in Fig. 7. It may appear to be at variance with the earlier conclusion that transport of silver is by diffusion. However, the potential of the silver electrode in this case is at least 250 mv higher than that in the earlier runs and this may have modified the transport of silver somewhat.

If this explanation is correct then it may also be possible that the formation of silver oxides takes place in the solution phase with the oxide then being "plated" on the electrode. The following could represent such a series of reactions



or



The higher the potential on the silver electrode the more readily reactions [3] and [4] would occur and the less silver would be present as an ion dissolved in the electrolyte.

Acknowledgment

This work was carried out under contract AF 33(657)-8689 with the A.F. Aero Propulsion Laboratory at Wright-Patterson Air Force Base, Ohio.

Manuscript received Nov. 6, 1963; revised manuscript received Dec. 28, 1963.

Any discussion of this paper will appear in a Discussion Section to be published in the December 1964 JOURNAL.

REFERENCES

- H. L. Johnston, F. Cuta, and A. B. Garrett, *J. Am. Chem. Soc.*, **55**, 2311 (1933).
- P. Rüetschi and R. F. Amlie, *This Journal*, **108**, 813 (1961).
- E. S. Gould, "Inorganic Reactions and Structure," Revised edition, p. 74, Holt, Rinehart, Winston, New York (1962).

The Fluorination of Copper

Patricia M. O'Donnell and A. E. Spakowski

Lewis Research Center, National Aeronautics and Space Administration, Cleveland, Ohio

ABSTRACT

The reaction between fluorine gas and copper metal has been studied at 450°C and pressures from 10 to 130 mm Hg. The reaction was pressure dependent and followed the logarithmic law, $y = K \log (at + c) + C$. The logarithmic rate constant K varied with pressure according to the equation $\log K = m \log P - 6.11439$ where m is equal to 0.781. Analysis of the corrosion film yielded a F/Cu ratio of 1.11. A reaction mechanism is postulated, and from evidence presented fluorine is considered the migrating species in the reaction.

In the study of gas-solid reactions the variables to consider from a kinetic point of view are the effects that time, temperature, and pressure have on the rate of reaction. These variables have been studied in detail for the reactions of metals with oxygen, and many mechanisms have been postulated to account for the data; however, very little kinetic work has been attempted with the more reactive fluorine. The reaction of copper foil and fluorine gas has been studied at a pressure of 200 mm Hg and over the temperature range of 427°-649°C. The simple power law $y^n = kt$ was applicable at 427° and 482°C where n was 1.15 and 1.62 and k was 1.7×10^{-3} and 1.6×10^{-2} , respectively (1). A further increase in the temperature resulted not only in an increase in the rate of reaction but also in a change of rate law. In the temperature range 538°-649°C the logarithmic law $y = k' \log (\sqrt{t} + k'')$ was obeyed where k' varied from 1.2 to 1.5, and k'' was equal to 5.

Other studies of metal-gas reactions have reported both pressure dependent and pressure independent relationships. Hale *et al.* (2) found that the nickel-fluorine reaction was pressure dependent at high temperatures (594°-815°C) and pressures from 76 to 760 mm Hg. Brown, Crabtree, and Duncan (3) working at lower temperatures (100°-250°C) and pressures (6-60 mm Hg) found no pressure effect for the reaction between copper powder and fluorine. Jarry (4) using radiotracer techniques to study the mechanism of nickel fluorination has reported that fluorine is the migrating species in the nickel-fluorine reaction.

The object of this investigation was to study the effect of pressure on the reaction of copper and fluorine at 450°C and subatmospheric pressures and to set up a preliminary model of the mechanism.

Apparatus

Figure 1 is a schematic diagram of the apparatus used for the experiments. The entire system was Pyrex glass except for the pressure pickup and the connection between the system and the bottle of high-purity fluorine (99.8%) which consisted of copper tubing and a Teflon-packed Swagelok fitting. The cold trap, containing methyl cyclohexane slush (-116°C), was used to remove any hydrogen fluoride contaminant in the fluorine gas. The fluorine

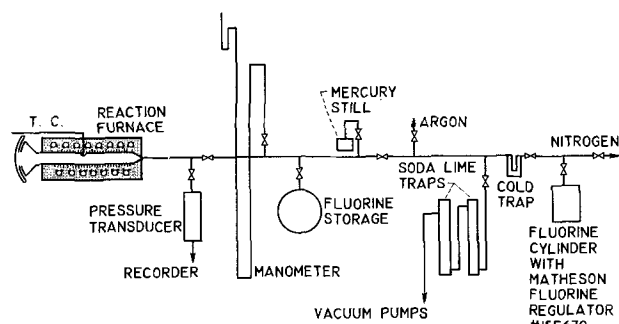


Fig. 1. Apparatus used for study of copper-fluorine reactions

was assayed by the mercury-reflux method (5). The mercury manometer used to measure the pressure in the storage bulb had a protective layer of fluorocarbon oil floated on top of the mercury to prevent the reaction of mercury and fluorine. All stopcocks and ground-glass joints were lubricated with fluorocarbon grease.

The quartz reaction tube was heated by a nichrome wound furnace, and its temperature was controlled to $\pm 1^\circ\text{C}$. The pressure in the reaction zone was measured to ± 0.05 mm Hg by a stainless steel transducer connected to the system by a Monel-to-glass ground joint. Ultradry argon of 99.995% purity as purchased was used as the purging gas.

Procedure

Before the system was put into use, it was passivated by repeated pressurization with fluorine, followed by prolonged evacuation. As a result of these steps, the concentration of impurities adsorbed on the walls was reduced to a negligible value. For blank runs the pressure changed only 0.23 mm Hg in 7.5 hr, which for this study was insignificant.

High-purity copper (oxygen content less than 0.002% as determined by vacuum fusion) was used for the metal specimens. The specimens in the form of $1.3 \times 15.3 \times 0.005$ cm plates were cleaned by using (a) trichloroethane, (b) 20% nitric acid, and (c) distilled water, acetone, and alcohol rinses. All samples were given a standard preheat treatment consisting of heating 0.5 hr at 538°C in vacuum. After pretreatment, the furnace was adjusted to the appropriate temperature and fluorine was introduced to the desired pressure. The drop in pressure in the system of known volume was a measure of the fluo-

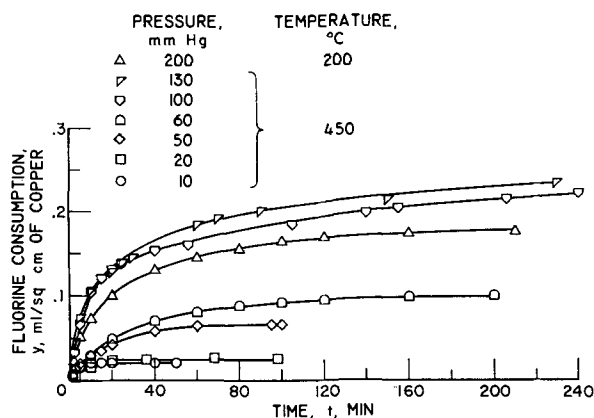
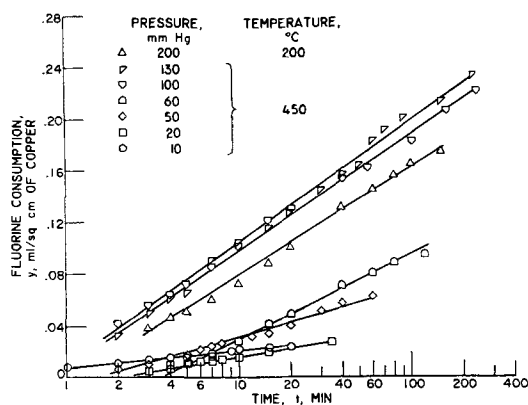
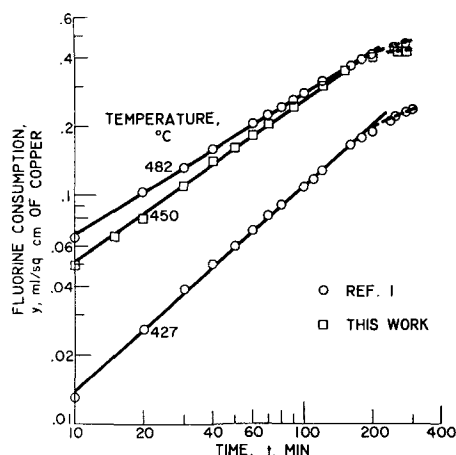


Fig. 2. Fluorination of copper

rine consumed. As fluorine was consumed, more fluorine was added to the reaction section to maintain the pressure within ± 2 mm Hg of the initial value for the 50–130 mm runs and within ± 1 mm Hg for the 10 and 20 mm runs. The run was continued until the consumption of fluorine had decreased to a negligible value. From the incremental pressure drops and the calibrated volume of the system, the amount of fluorine consumed was calculated. At the end of each run the furnace was cooled to 38°C before the fluorine was pumped out of the system through the soda lime traps. The system was then brought up to atmospheric pressure with argon and the copper plate was removed to a sample holder under flowing argon and sealed for later examination.

Results

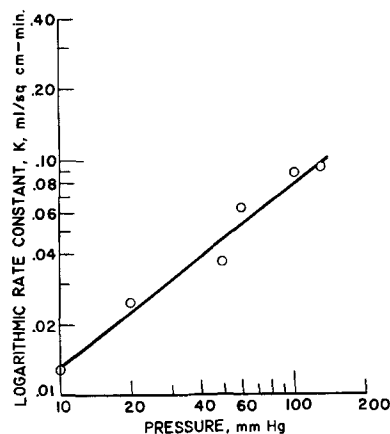
The data obtained over a pressure range of 10–130 mm Hg at 450°C are shown in Fig. 2 where y , the fluorine consumed in milliliters per square centimeter of copper surface, is plotted as a function of t , the time in minutes. The two or more runs made at each pressure showed an average reproductibility in values of y of 6%. In Fig. 3(a) the data are plotted according to the logarithmic equation $y = K \log(at + c) + C$ where K is the logarithmic reaction rate constant, a is taken as unity with the dimension of reciprocal time, and c is taken as zero. These data are represented by this expression; however, at higher pressures the data no longer fit, and therefore the mechanism must be different. Data

Fig. 3(a). Fluorination of copper, according to logarithmic law $y = K \log(at + c) + C$.Fig. 3(b). Fluorination of copper, according to power law $y^n = kt$ at pressure of 200 mm Hg.

taken at 200°C and 200 mm Hg appear to obey the same logarithmic law as the low pressure data at 450°C . The corrosion rate of the copper and fluorine as described by the aforementioned log law is therefore influenced by both temperature and pressure. In Fig. 3(b) data at 450°C and 200 mm Hg are plotted with similar data from ref. (1) according to the power law $y^n = kt$, and the consistency is quite good.

The variation of the rate constant, K , with pressure at 450°C is shown in the log plot of Fig. 4 where the rate constant is plotted as a function of the fluorine pressure according to the equation $\log K = m \log P - 6.11439$. The slope, m , is the order of the reaction with respect to the fluorine pressure and has the value of 0.781.

An interesting event was observed in that the corroded metal specimens lost their passivity when subjected to heat and vacuum. In Fig. 5, at point B, the fluorine gas was pumped out of the reaction section to 0.1μ pressure and the pumping continued for 15 min. The reaction section was then pressurized with fresh fluorine to 10 mm Hg. As seen in Fig. 5, the reaction starts anew. The same logarithmic law also describes this second reaction; however, the logarithmic rate constant, K , is slightly lower for the second reaction. This same effect was observed by Brown *et al.* (3) if the pumping was continued for 4 days at 100°C ; however, if the time of pumping

Fig. 4. Effect of pressure on logarithmic rate constant K

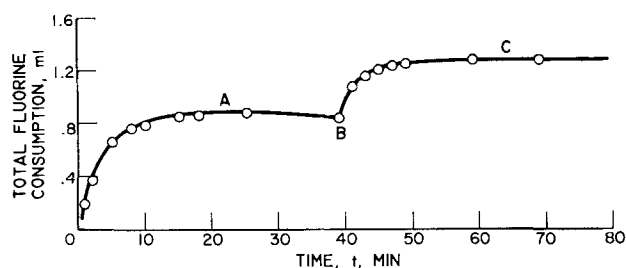


Fig. 5. Interrupted fluorination of copper; A and C 450°C and 10 mm Hg pressure, B evacuated 15 min at 450°C.

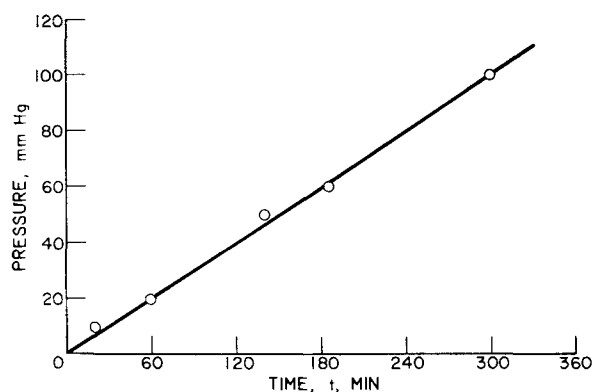


Fig. 6. Effect of pressure on passivation period of copper at 450°C

were shortened to 16 hr at the same temperature, they observed no effect. In our studies therefore, increasing the temperature by a factor of four decreased the pumping time by a factor of about 400.

The time it takes for the rate of reaction at 450°C to decrease to a negligible value ($<10^{-4}$ ml/cm²-min) is of interest. This time, which could be called the passivation period, is a linear function of pressure (shown in Fig. 6) where t , the time for the rate to decrease to the negligible value is plotted as a function of pressure. It must be pointed out that when the reaction reaches the negligible rate the logarithmic equation no longer holds.

Microscopic examination of the corrosion film showed the presence of both clear and red crystals. The red crystals are probably CuF and the colorless ones CuF₂. The total corrosion film was analyzed for copper and fluorine and the results indicate a F/Cu ratio of 1.11. Unfortunately because of the unstable nature of the corrosion products, they could not be positively identified. Most of the films formed at 450°C exfoliated on cooling, and examination of the metal surface underneath revealed many pits.

Discussion

In setting up a theoretical model to understand better the mechanism of the reaction between gaseous fluorine and a copper surface, it can be assumed that when the gas is introduced the reaction starts. The first thin film of reaction product forms a barrier between the two reacting phases, copper and fluorine. In order for the reaction to continue, therefore, it becomes necessary for either one or the other of the phases to migrate across this barrier. Based on evidence presented later, it can be postulated that the reaction includes at least the following three steps: (i) fluorine is absorbed on the outer surface;

(ii) fluorine migrates through the barrier layer; (iii) fluorine reacts with the copper. Initially, step (i) is predominant, but as soon as a film forms, step (ii) becomes rate controlling. The reaction in step (iii) is assumed to be very fast in comparison with the reactions in the other steps, and thus would not contribute significantly to the over-all reaction rate. If the migration through the barrier layer were strictly a diffusion controlled process, the data could be described by a parabolic rate law. As shown in Fig. 3(a), however, the data were best described by a logarithmic rate law, and therefore the reaction is not entirely diffusion controlled. Several theories based on various hypothetical rate-determining mechanisms have been put forward to explain the fact that under certain conditions the corrosion of metals obeys a logarithmic rate law (6). We have used the logarithmic rate equation as derived for the mechanism proposed by Vernon (7) who assumed that the reaction rate was dependent on the fraction of atoms penetrating the barrier layer. In addition we have assumed that this fraction is pressure dependent and therefore one would expect the rate constant K to vary with the pressure. This model is consistent with the data where K was found to vary with pressure according to the equation $\log K = m \log P - 6.11439$.

The logarithmic equation is

$$W = K \log (at + c) + C$$

where W is the weight of corrosion products formed and t is the time. c would be unity and C zero if the equation held from the onset where $t = 0$ and $W = 0$; however, in these experiments at $t = 0$, W has some finite value since a finite time is required for the reaction chamber to attain test pressure. Thus the equation does not hold at $t = 0$. C was calculated from the data in Fig. 3(a) assuming a and c to be equal to 1 and 0, respectively. The values of C and K are shown in Table I.

It is interesting to speculate on the location of the specific reaction. Two possibilities can be considered: (A) the copper can migrate through the barrier layer and react at the fluoride/fluorine interface or (B) the fluorine can migrate through the barrier layer and react at the fluoride/metal interface. Consider the following. The way in which the reaction rate constant varies with pressure infers at which interface the reaction is taking place. For example, reactions at the gas-corrosion layer interface usually are controlled by dissociation of the attacking diatomic gas and manifest themselves in a reaction rate constant that is a function of the square root of

Table I. Values of C and K

Temp, °C	Pressure, mm	K , ml/cm ² -min	C , ml/cm ²
450	10	0.013	0.008
450	20	0.025	-0.008
450	50	0.037	-0.005
450	60	0.063	-0.032
450	100	0.089	0.008
450	130	0.093	0.012
200	200	0.083	-0.004

the pressure (8). The experimental data show that this is not the relation between K and P under these test conditions. Second, it has been found in our earlier work (1) that pretreatment of the metal had a large effect on the rate. If the reaction were at the fluoride/fluorine interface, such a drastic effect on the rate would not be expected from the condition of the metal surface alone. Last, microscopic examination of the metal surface showed pits visible on the metal after the corrosion film was removed. Since pitting is not the result of an initial attack of a gas on a metal, but rather a localized attack for a period of time, pit formation could be favored by the gas having direct access to the metal. These points therefore tend to indicate that the reaction was carried out on the surface of the metal. From these data and from the work of Jarry (4) stating the probability of fluorine diffusion, fluorine is considered the migrating species in the copper fluorine reaction, and the reaction is considered to take place at the fluoride/metal interface.

Three possible ways for the fluorine to get to the metal would be (a) anion vacancy migration, (b) interstitial migration, and (c) grain boundary migration. Attack by migration along grain boundaries is common on metals at high temperature and has

been shown to be the way fluorine reacts with nickel (2). This, of course, is possible also with copper; however, the mechanism by which fluorine migrates through the corrosion barrier is still in question.

Manuscript received July 11, 1963; revised manuscript received Dec. 30, 1963.

Any discussion of this paper will appear in a Discussion Section to be published in the December 1964 JOURNAL.

REFERENCES

1. P. M. O'Donnell and Adolph Spakowski, NASA TN D-768, 1961.
2. C. F. Hale, E. J. Barber, H. A. Bernhardt, and K. E. Rapp, AECD 4292, 1959.
3. P. E. Brown, J. M. Crabtree, and J. F. Duncan, *J. Inorganic and Nuclear Chem.*, **1**, 202 (1955).
4. R. L. Jarry and J. Fisher, Metal Fluorine Reactions. Paper Presented at American Chemical Society Meeting, Chem. Eng. Div., Argonne National Lab., Sept. 1960.
5. R. E. Seaver, NASA TN D-1412, 1962.
6. U. R. Evans, "The Corrosion and Oxidation of Metals," St. Martins Press, Inc., 1960.
7. W. H. J. Vernon, E. I. Akeroyd, and E. G. Stroud, *J. Inst. Metals*, **65**, 320 (1939).
8. O. Kubaschewski and B. E. Hopkins, "Oxidation of Metals and Alloys," 2nd ed., Academic Press, New York (1962).

The Effect of Crystallographic Orientation on the Oxidation of Tin

W. E. Boggs, R. H. Kachik, and G. E. Pellissier

Applied Research Laboratory, United States Steel Corporation, Monroeville, Pennsylvania

ABSTRACT

The formation of oxide on five low-index faces of β -tin has been investigated in an attempt to determine the influence of the crystallographic orientation of the tin on the nucleation, growth, and orientation of the oxide. Orientation relationships between the metal and the oxide were determined using x-ray and electron diffraction. The number and size of the oxide particles formed in a given length of time under standard conditions of temperature and oxygen pressure were measured using an electron microscope. Crystallographic relationships were found to exist between the oxide and the metal; however, no simple over-all mechanism could be deduced that would explain the differences observed in the number or size of the oxide particles formed on the various tin crystal faces. Furthermore, there appeared to be little correlation between the number of oxide platelets and the number of different oxide orientations formed on each tin face. It is suggested that favorably oriented screw dislocations tend to increase the number of oxide platelets formed on certain tin faces. The experimental observations also indicate that crystal lattice matching between the metal and the oxide, in certain orientations, has an influence on the rate of oxidation.

For convenience, oxide films are often considered to be uniform, isotropic layers that cover the surface of a metal and thicken with time. This simplified concept is useful in the derivation of mathematical models to explain various empirical rate laws but often is not valid for the early stages of oxidation. Optical and electron microscopic studies have shown that the crystalline oxide is not continuous in the early stages of oxidation (1, 2). Benard has suggested that oxidation takes place

in the following sequence (3): at the beginning of oxidation the metal is covered by an invisible film, the thickness of which increases to a critical value of several tens of angstroms; the film continues to form and tends to accumulate at certain crystallization centers; then these nuclei grow laterally until they cover the entire metal surface. The number and morphology of these oxide platelets are strongly influenced by the crystallographic orientation of the metal substrate (4, 5).

Furthermore, recent low-energy electron diffraction studies by Germer (6) have indicated that even the earliest stages of the reaction of oxygen with metals are influenced by the crystallographic orientation of the substrate. Germer (7-9) and MacRae (10) have found that the adsorption of oxygen on the (100) and (110) faces of nickel progresses through the formation of several two-dimensional nickel-oxygen structures corresponding to one-tenth to one monolayer of adsorbed oxygen. The nickel atoms in the surface layers of the "open" (110) nickel face rearranged when exposed to oxygen. At elevated temperatures patches of crystalline NiO were found. The orientation of the oxide grown on the close-packed (100)Ni face was the same as that of the substrate but the orientation of the oxide grown on the (110)Ni face appeared to depend on the two-dimensional transition lattice formed by the oxygen-induced rearrangement of nickel atoms at the oxide-metal interface.

The effect of the crystallographic orientation of the substrate on the number and distribution of oxide nuclei have led to the suggestion that the formation of nuclei in the early stages of oxidation is assisted by defects such as dislocations (11) and stacking faults (12) in the metal substrate. However, the number of nuclei has been observed to change with oxygen pressure, even though there is no reason to expect that the number of crystallographic defects should change similarly with pressure. Young introduced predictable numbers of dislocations into pure copper crystals and found no correlation between the number of dislocations and the number of oxide nuclei (13). However, Hondros and Oudar (14) have reported that, under certain conditions of temperature and low oxygen pressure, oxide nuclei form more readily at the sites of emerging dislocations than at random sites on the surface of pure copper.

The present authors found, in a recent study of the oxidation of pure tin (15, 16), that crystalline tin oxide platelets grow laterally over the surface of the metal from tin grain boundaries and wheel-shaped structures termed "growth centers." The number of growth centers and the rate of lateral growth of the platelets varied from tin grain to tin grain. The rate of oxide growth normal to the tin surface also appeared to vary from tin grain to tin grain. Thus, the crystallographic orientation of the individual tin grains appeared to influence all visible phases of the oxidation of polycrystalline tin foils.

The number of growth centers and tin oxide platelets was essentially independent of oxygen pressure from 0.001 Torr to 100 Torr (16). Furthermore, the number of platelets was of the same order of magnitude as the number of crystallographically shaped pits that could be produced in the metal surface by etching. Thus, it was suspected that orientation-dependent defects such as dislocations emerging in the surface of the tin, might be effective as nucleation sites for tin oxide.

In view of the apparent influence of the crystallographic orientation of the tin substrate on the various stages of the oxidation of tin, a more detailed

study of the formation of oxide on several low-index faces of tin single crystals was undertaken. The experimental program consisted of determining the orientation relationships between the oxide and the metal, and determining the number and size of the oxide platelets formed on each of these crystallographic faces under controlled conditions of time, temperature, and oxygen pressure. In addition, electron-transparent tin films, prepared from previously oxidized foils, were examined by transmission electron microscopy, in an effort to find lattice defects, such as dislocations, that might have been clearly associated with tin oxide platelets.

Experimental Procedure

Preparation of tin single crystals.—The tin single crystals used in this study were grown in horizontal graphite boats according to the method described by Chalmers (17). The crystallographic orientations were controlled by seeding melts of 99.9999% tin with small tin single crystals having the required orientations. The Laue x-ray back-reflection technique (18) was used to check the orientation of the tin single crystals before the oxidation experiments.

The single crystals of tin obtained by the Chalmers technique were 8-10 in. long, 3/4 in. wide, and 1/16-1/4 in. thick. Since the vacuum microbalances normally used in the study of oxidation kinetics cannot support samples weighing more than about 0.5g, an attempt was made to reduce the single-crystal bars to single-crystal foils 0.003-0.006 in. thick. The bars were first planed using a spark-cutting machine developed by Metals Research Ltd. and then electropolished by a method described in an earlier paper (15). Strains were accidentally, but unavoidably, introduced in the tin during the preparation and handling of the single-crystal foils. As a result, the kinetic data were erratic and nonreproducible. Because of these difficulties, the microbalance investigation of single-crystal foils was abandoned, and the emphasis was placed on the study of the effect of the crystallographic orientation of the tin on the orientation, nucleation, and growth of oxide on bulk-tin single crystals that were thick enough to resist accidental structural damage.

Preparation and examination of tin oxide films.—The single-crystal bars of tin obtained by the Chalmers technique were electropolished, washed, dried, and suspended vertically in a vacuum system. After the system was evacuated to a pressure of 10^{-7} Torr, the bars were annealed at 200°C for 1 hr. The temperature was then reduced and equilibrated at 190°C, and oxygen was introduced at a pressure of 10 Torr. The free surface of each specimen (the surface that had not been in contact with the walls or bottom of the boat during tin-crystal growth) was examined by light microscopy and then the oxide films were stripped, using the technique described in earlier papers (15, 16). The oxide films were mounted on specimen support grids having rotational orientation reference markers so that the original orientation of the oxide on the metal could be preserved when the stripped oxide films were placed in an RCA-EMD electron diffraction unit. Since there are no lenses below the specimen in

this instrument, the diffraction patterns of the oxide are not rotated or inverted, and their orientation can be related directly to the previously determined orientation of the tin substrate. It is estimated that the combined error in the alignment of the specimen support grids was not more than $\pm 5^\circ$.

Several extraction replicas were obtained from each tin crystal face. The oxide platelets on each grid were counted on the viewing screen of an electron microscope, and typical platelets from each tin face were photographed.

Electrothinning.—Lattice dislocations and other imperfections in metal crystals have been studied extensively using transmission electron microscopy (12, 19). Thin electron-transparent tin foils (20) were prepared from pre-oxidized specimens of tin in an effort to find direct evidence of oxide nucleation on emerging dislocations and other crystal defects. The tin foils were thinned to provide electron-transparent areas using an electrolyte of 80.7% glacial acetic acid and 19.3% perchloric acid in an electropolishing microscope.¹

Background for the interpretation of crystallographic orientation relationships.—The mutual orientation relationships between oxide and metal crystals are generally considered to have important influences on nucleation and oxidation rates. Visual aids in the form of scale models of the respective β -Sn and α -SnO crystal lattices were employed in the present study to assist in the interpretation of the experimentally determined orientation relationships between the oxide and the metal.

Models of metallic tin and stannous oxide crystals were built to scale by gluing together plastic balls with diameters proportional to the atomic and ionic diameters given by Pauling (22) and the Tin Research Institute (23). The large white balls shown in the figures, represent the tin atoms in the β -Sn crystal, the gray balls represent oxygen ($O^{=}$) ions, and the small white balls represent tin (Sn^{++}) ions in the α -SnO crystal. The respective unit cell dimensions were obtained from the ASTM x-ray powder data file. Since most of the single crystal surfaces studied in this work consist of more than one layer of partially exposed tin atoms, these surfaces are termed "crystal faces" rather than planes and are

¹ The Zeiss (Jena) "Elypovist" (21).

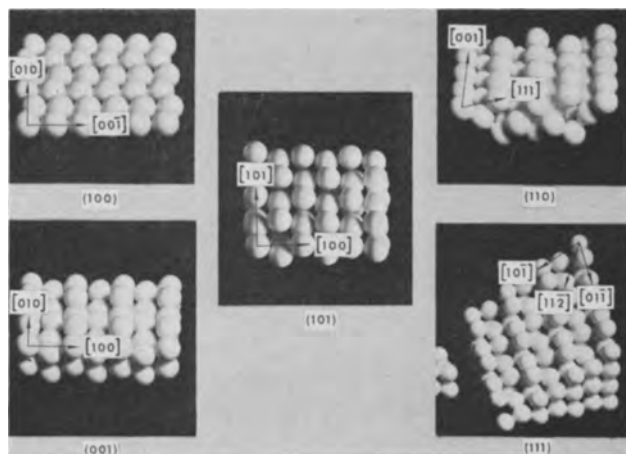


Fig. 1. Plastic models of the (100), (110), (101), (001), and (111) faces of β -Sn.

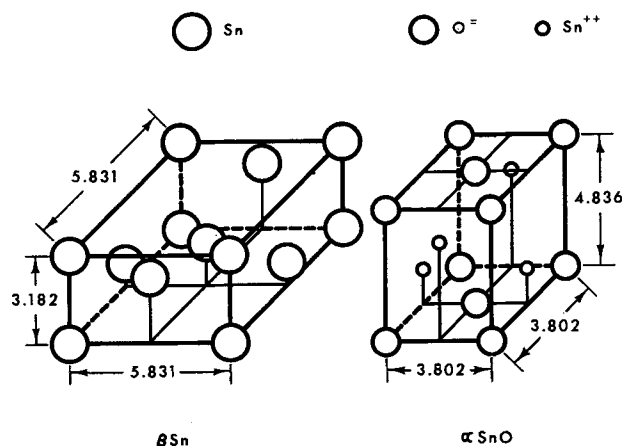


Fig. 2. Diagram of the unit cells of β -Sn and α -SnO

identified with the Miller indices of the respective parallel crystallographic planes. Models of the tin faces studied in this work are shown in Fig. 1.

Diagrams of the unit cells of β -Sn and α -SnO are shown in Fig. 2. Tin has a tetragonal structure with tin atoms in the corners, body center, and in the (010) and (100) planes at positions $(\frac{1}{2}, 0, \frac{3}{4})$ and $(0, \frac{1}{2}, \frac{1}{4})$, respectively. These {100} planes are the most closely packed planes in the tin crystal. Alpha stannous oxide also has a tetragonal structure. The oxygen ions are in the corners of the unit cell and in the center of the (001) planes. The tin atoms are located in the (010) and (100) planes at positions $(\frac{1}{2}, 0, \frac{3}{4})$ and $(0, \frac{1}{2}, \frac{1}{4})$, respectively.

Results and Discussion

Orientation Relationships Between the Oxide and the Metal After Short Periods of Oxidation

The major orientations of the oxide observed on the (100), (110), (101), (001), and (111) faces of

Table I. Major orientation relationships between tin and stannous oxide

Crystal face β -Sn substrate	Parallel plane α -SnO	Fraction of oxide in this orientation	Major directional relationships
(100)	(001)	0.57	$[100]SnO \pm 13^\circ [010]Sn$ $[110]SnO \pm 13^\circ [010]Sn$
	(111)	0.21	$[110]SnO 33^\circ [010]Sn$ $[110]SnO 76^\circ [010]Sn$
(110)	(001)	0.71	$[010]SnO // [001]Sn$
	(111)	0.12	$[110]SnO 10^\circ [001]Sn$
(101)	(001)	0.33	$[\bar{1}10]SnO // [0\bar{1}0]Sn$ $[\bar{1}10]SnO 28^\circ [0\bar{1}0]Sn$
	(111)	0.33	$[\bar{1}10]SnO -10^\circ [0\bar{1}0]Sn$ $[110]SnO +8^\circ [0\bar{1}0]Sn$
	(311)	0.17	$[0\bar{1}1]SnO -13^\circ [0\bar{1}0]Sn$
(001)	(111)	0.33	$[110]SnO 26^\circ [010]Sn$
	(110)	0.33	$[110]SnO 19^\circ [100]Sn$
	(113)	0.33	$[110]SnO // [2\bar{1}0]Sn$ $[110]SnO 42^\circ [2\bar{1}0]Sn$
(111)	(111)	0.31	$[011]SnO // [101]Sn$
	(311)	0.23	$[\bar{1}12]SnO // [110]Sn$ $[\bar{1}12]SnO // [101]Sn$
(102)		0.23	$[010]SnO // [101]Sn$
(113)		0.12	$[\bar{1}10]SnO // [\bar{1}\bar{1}0]Sn$

Table II. Atom spacings of β -tin and α -stannous oxide crystals

Direction	Atom distance center to center, A	Crystallographic planes parallel to listed directions
	Sn to Sn	
[001]Sn	3.182	(100) Sn, (110) Sn
[100]Sn	5.831	(100) Sn, (101) Sn, (001) Sn
[102]Sn	3.02, 9.066	(100) Sn
[302]Sn	3.768, 11.304	(100) Sn
[111]Sn	4.420	(110) Sn, (101) Sn
[110]Sn	8.246	(110) Sn, (001) Sn
[101]Sn	6.643	(101) Sn, (111) Sn
[112]Sn	10.416	(111) Sn
	O ⁼ to O ⁼	
[100]SnO	3.802	(001) SnO, (102) SnO
[110]SnO	2.688	(001) SnO, (110) SnO, (113) SnO
[001]SnO	4.836	(110) SnO, (100) SnO
[201]SnO	9.012	(102) SnO, (100) SnO
[101]SnO	6.152	(111) SnO
[112]SnO	5.533	(111) SnO, (311) SnO
[301]SnO	12.389	(113) SnO
[332]SnO	9.403	(113) SnO
[011]SnO	6.151	(100) SnO, (311) SnO
[130]SnO	6.012	(001) SnO, (311) SnO
	O ⁼ to Sn ⁺⁺ to O ⁼	
[021]SnO	2.253, 6.759	(100) SnO, (102) SnO
[023]SnO	4.095, 20.475	(100) SnO
	Sn ⁺⁺ to Sn ⁺⁺	
[112]SnO	3.616	(111) SnO
[010]SnO	3.802	(100) SnO

β -tin in 300 min at 190°C and an oxygen pressure of 10 Torr are given in Table I. A complete description of the orientation of the oxide with respect to the metal can be given by a statement of the crystallographic plane in the oxide found parallel to the particular tin face together with the relationship between a crystallographic direction in the oxide and one in the metal. Wherever possible in this discussion, the crystallographic directions chosen are the intersections (zone axes) between the crystallographic planes that are parallel to the oxide metal interface and easily identified low-index planes in the oxide or the metal. In this way, visualization of the orientations of scale models of the oxide on scale models of the five tin faces is facilitated. The atom spacings in various directions of the tin and the oxide crystal lattices are given in Table II.

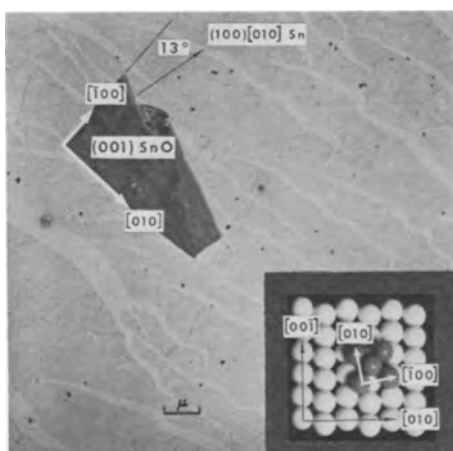


Fig. 3. Oxide platelet formed on (100)Sn face with (001)SnO // (100)Sn and [100]SnO 13° from [010]Sn orientation. Inset shows oxide model on tin model in the same orientation. Magnification approximately 5000X.

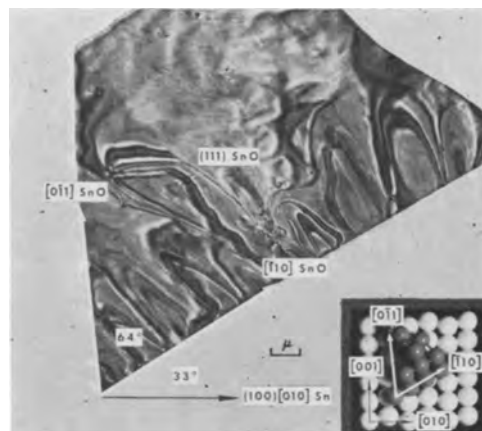


Fig. 4. Oxide platelet formed on (100)Sn face with (111)SnO // (100)Sn and [110]SnO 33° from [010]Sn orientation. Inset shows oxide and tin models in same relationship. Magnification approximately 8000X.

Oxide formed on the (100)Sn face.—The oxide platelets formed with (001) orientations were roughly rectangular, square or triangular in shape with at least one 90° corner, Fig. 3. The crystal edges intersecting at 90° were either parallel to [100]SnO or [110]SnO directions.

The platelets in the (111) orientations were usually triangular or trapezoidal with edges intersecting at angles of 64° or 52° to each other, Fig. 4. The edges intersecting at 64° were parallel to the [110]SnO and [101]SnO directions, while those intersecting at 52° were parallel to [101]SnO directions.

The (001) and (111) oriented lattice models of tin oxide could be fitted to the models of the (100) tin face, with a minimum amount of distortion in both lattices, in orientations approximating those experimentally determined. Perhaps the observed orientations of oxide on this tin face can be accounted for on the basis of the best fit of the oxide lattice to the metal lattice.

Oxide formed on the (110)Sn face.—The (001) oriented oxide crystals formed on the (110) tin face all had the same shape, that is, "arrowheads" formed by two triangles joined along their longest sides. These arrowheads always pointed in the [001]Sn direction, Fig. 5. This restricted crystal habit makes possible a detailed analysis of the growth of oxide on the (110)Sn face. The dominant feature of this face is a series of parallel troughs in the <001> directions, Fig. 1. It is evident from the shape of the oxide platelets that the oxide growth rate was highest in the direction parallel to these troughs, that is, the [010]SnO and [001]Sn directions. A second interesting feature of the (110) tin face is that the atoms in the parallel <001> ridges are also lined up parallel to the <111>Sn directions. Thus, there is a second series of shallow troughs or saddles between atoms in the four <111>Sn directions. The angle between the [001]Sn direction and the [111]Sn direction is 74°. The angle between the common side, that is, the [010]SnO // [001]Sn direction and the short side (~[310]SnO direction), of either oxide triangle in the arrowhead platelet, is also 74°.

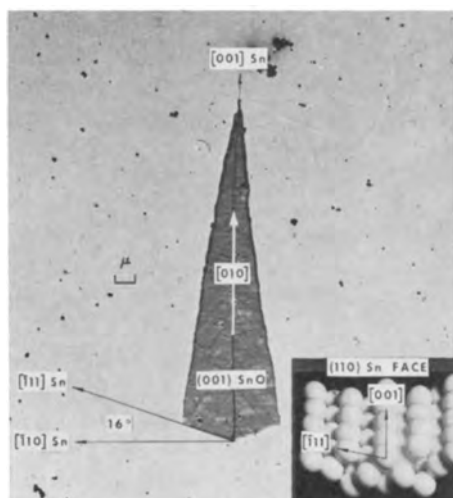


Fig. 5. Typical arrowhead-shaped oxide platelet formed on the (110) tin face in the (001) $[010]\text{SnO} // (110) [001]\text{Sn}$ orientational relationship. Magnification approximately 4500X.

The (110) face of tin is very similar in structure to the (110) face of nickel. Using low-energy electron diffraction, Germer (12) has been able to show that the migration of atoms on the (110) nickel face occurs mainly in the direction of the troughs between parallel rows of nickel atoms. Thus, it is suggested that the shape of the oxide platelets formed on the (110) face of tin is caused by rapid surface migration of atoms along the troughs in the $[001]\text{Sn}$ direction and slower migration over the saddles in the $[111]$ and $[\bar{1}\bar{1}1]\text{Sn}$ directions. The oxide platelets are about six times as long in the $[001]\text{Sn}$ direction as in the $[111]$ and $[\bar{1}\bar{1}1]\text{Sn}$ directions. The oxide platelets may have nucleated at the extreme rear of the arrowhead, where a $\langle 111 \rangle \text{Sn}$ vector intersected the $[001]\text{Sn}$ vector, and then grown fastest along the $[001]$ troughs toward the apex. As the apex advanced, the sheets of oxide spread laterally at a slower rate over the saddles in the $[111]$ and $[\bar{1}\bar{1}1]\text{Sn}$ directions, to give these oxide platelets their distinctive arrowhead shape.

If the surface of the (110)Sn crystals were perfectly oriented, it is to be expected that the oxide would grow equally rapidly in the $[001]\text{Sn}$ and $[00\bar{1}]\text{Sn}$ direction. The lack of appreciable oxide growth in the $[00\bar{1}]\text{Sn}$ direction is probably caused by a slight misorientation of the (110) face of the tin single crystal used in these experiments. This (110) tin face was tilted about 1° in the $[00\bar{1}]\text{Sn}$ direction. Because of this tilt, a new (110) plane was exposed and a step, one tin atom high, was formed every 182Å, or after every 57 tin atoms in the $[00\bar{1}]\text{Sn}$ direction. Thus, in cross section, the surface would have a stair step appearance, with the tread of each step 57 times as long as the height of the riser to the next step, and with the steps facing in the $[001]$ direction. This series of walls imparts an anisotropy to the surface, hindering atom migration in the $[00\bar{1}]\text{Sn}$ direction. Very few, if any, of these atomic steps running parallel to the $[110]\text{Sn}$ directions in the (110)Sn face serve as nucleation sites.

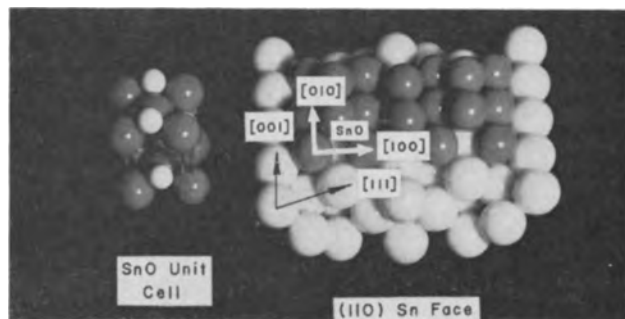


Fig. 6. Model of the oxide and the tin in the (001) $[010]\text{Sn} // (110) [001]\text{Sn}$ orientational relationship demonstrating the severe strain involved in a direct fit of the oxide to the metal.

There would be about 890 steps under the single oxide platelet shown in Fig. 5.

Scale models of the $\alpha\text{-SnO}$ crystal in the (001) orientation will not fit directly to the model of the (110)Sn face in the observed orientations without strain and distortion of the respective lattices. The fit of the oxygen ions is reasonable when the distance between the troughs is considered, but there is mismatching along the troughs, and the $(\frac{1}{2}, \frac{1}{2}, 0)$ oxygen ions would be displaced vertically from their normal positions in the (001)SnO plane, Fig. 6. Germer (12) has found that the adsorption of oxygen, even at room temperature, on a clean (110) nickel face produced a rearrangement of the surface nickel atoms. He deduced that the formation of this new surface arrangement involved a migration of nickel atoms along the troughs in the $\langle 110 \rangle$ directions. The nickel oxide formed on the (110) face fitted this rearranged nickel-oxygen transition lattice rather than the underlying (110) nickel lattice.

In view of the similarity in structure between the lattice of the (110) nickel face and that of the (110) tin face, it seems probable that a similar oxygen-induced rearrangement of the surface atoms occurs on the (110) face of tin. Thus, it is suggested that the oxide in the observed orientation, (001)SnO// (110)Sn and $[010]\text{SnO} // [001]\text{Sn}$, fits an intermediate, two-dimensional, oxygen-tin lattice rather than the tin lattice directly as exposed in the (110)Sn face. Unfortunately, a study of the adsorption of oxygen on tin single crystals by low-energy electron diffraction would be very difficult. In the first place, the low melting point of tin (231.9°C) precludes the apparatus bakeout necessary to achieve the ultra-high vacuum required by the technique. Furthermore, the removal of residual oxide from the surface of the tin, without introducing structural alteration of the crystal, would be nearly impossible.

Oxide formed on the (101) face of tin.—The atom arrangement in the (101)Sn face is more complex than that of either the (100)Sn face or the (110)Sn face. This face consists of two layers of tin atoms, one of which is 0.8Å higher than the other, Fig. 1. Alternate tin atoms in the $\langle 010 \rangle \text{Sn}$ directions and at 90° in the $\langle 101 \rangle$ directions, lie at alternate levels in the two layers, but all atoms in the $\langle 111 \rangle$ directions lies in a single layer. The oxide crystals formed on the (101)Sn face were mostly irregular in shape, so that it was difficult to discern a characteristic shape for each type of oxide orientation.

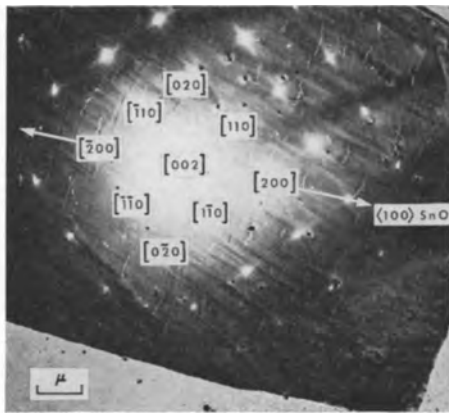


Fig. 7. Oxide platelet formed on the (101) face of tin. Superimposed electron diffraction pattern shows that one of the edges of the oxide crystal is parallel to the $[100]$ SnO direction. Magnification approximately 5000X.

Oxide crystals having edges intersecting at 90° were of the (001)SnO orientations. One of these edges was usually parallel to a $[100]$ SnO direction, Fig. 7.

Scale models of the oxide lattice could be made to fit, with some distortion, lattice models of the (101) face of the β -tin crystal for the experimentally determined orientations. However, it is more likely that rearrangement of the surface tin atoms takes place on exposure to oxygen, and that the orientation of the oxide is determined by the structure of this intermediate layer.

Oxide formed on the (001) face of tin.—Oxide with the (001)SnO plane oriented parallel to the (001)Sn plane was never found. If a simple best fit model is assumed, then the close-packed atoms parallel to the $\langle 110 \rangle$ directions in the (111) and (110) planes of oxide should fit in the troughs in the (001)Sn face parallel to the $\langle 100 \rangle$ Sn directions. The parallel sheets of oxygen atoms in the (001) planes of the oxide would have about the right spacing to fit in these troughs, if either the (111)SnO or (110)SnO planes were parallel to the (001) face of tin. As is shown in Table II, the $\langle 110 \rangle$ directions in the (111)SnO crystals diverged from the $\langle 100 \rangle$ Sn directions by 21° to 30° , and the $\langle 110 \rangle$ directions in the (110)SnO crystals diverged from the $\langle 100 \rangle$ Sn directions by 14° to 24° . This divergence is believed to be evidence of the rearrangement of the surface tin atoms in the (001)Sn face. The (111) and (110) planes of SnO probably fit on top of the two-dimensional tin-oxygen structure that results from this rearrangement.

The lattice of the (001)Sn face is even more complex than that of the (101)Sn face, Fig. 1, since the tin atoms lie in four levels— 0.8\AA , 1.6\AA , and 2.4\AA above the lowest level. Deep troughs lie parallel to one of the $\langle 100 \rangle$ directions. The removal of the top layer of atoms in the (001) face would change the direction of the troughs 90° . This surface is more complicated than any so far investigated by Germer. However, if adsorption-induced rearrangement of tin atoms occurs on the (110) face, it probably occurs more easily on the (001) face of tin, since a fourth of the tin atoms exposed in this face have three missing nearest neighbors.

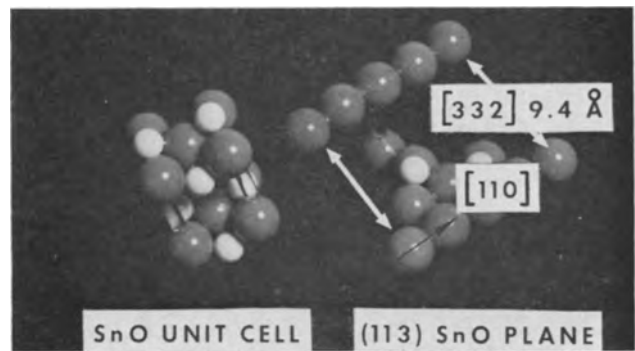


Fig. 8. Model of the (113) plane of α -SnO

About a third of the oxide crystals found were formed with the (113)SnO plane parallel to the (001)Sn face. The oxygen atoms in the (113) SnO plane lie in close-packed rows in the $[110]$ direction. These rows are about 9.4\AA apart, Fig. 8. In view of the great distance between atoms in the $[332]$ direction, it seems unlikely that the (113) plane of oxide would be compatible with the (001)SnO face. However, the angle between the (113)SnO plane and the (001)SnO plane is 31° , and the angle between the (001)Sn face and the (101)Sn face is 29° . The crystallographic direction in two of the (113)SnO diffraction patterns obtained from oxide stripped from the (001)Sn face corresponded exactly with observed orientations of (001) oxide formed on the (101)Sn face. The third (113)SnO pattern was rotated 45° and failed to line up with an observed orientation of (001) oxide on (101) tin by only 10° . A combined error of 10° in orienting the specimen support screens on the oxidized tin single crystals, and then in placing these grids in the electron diffraction unit, is not unlikely. These observations suggest that the (113) oriented oxide may have formed on facets parallel to the (101) planes of tin, rather than directly on the (001)Sn face; the oxide-metal interface probably consists of parallel steps rising at an angle of about 29° to the (001)Sn face, such as are shown in Fig. 9. Such facets were not found in replicas of unoxidized tin surfaces or on the areas between the platelets on partially oxidized tin surfaces.

Oxide formed on the (111) face of tin.—The tin atoms in the (111)Sn face lie at four levels in a

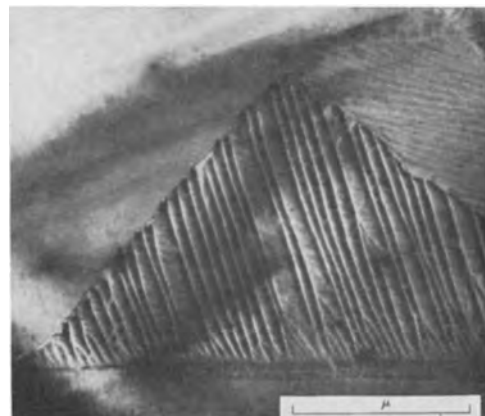


Fig. 9. Oxide platelet *in situ* on β -Sn showing parallel steps at oxide-metal interface. Conditions: 220°C , 10 Torr, 5 min. Magnification approximately 25,000X.

Table III. Missing nearest neighbors in the low index faces of β -tin

β -Sn crystal face	Number of missing nearest neighbors per surface atom				Number of missing nearest neighbors per cm^2
	Top layer	Second layer	Third layer	Fourth layer	
(100)	1				1.08×10^{15}
(110)	2				1.52×10^{15}
(101)	2	$1\frac{1}{2}$			1.72×10^{15}
(001)	3	1	1	1	1.76×10^{15}
(111)	3	2	2	1	1.87×10^{15}

manner similar to the atom layers in the (001) face, except that the structure is more open and the levels are farther apart, Fig. 1. The greatest number of different oxide orientations was found on the (111)Sn face, as would be expected in view of the complex nature of the atom arrangement in the metal surface. The (311) and (102) orientations of oxide appear to be unique to the (111)Sn face, whereas the (111) and (113) orientations of oxide appear to be the result of faceting of the tin parallel to the (101)Sn and (100)Sn planes, respectively. Scale models of both the (311) and the (102) planes of oxide fit a scale model of the (111) face of tin fairly well for the observed orientations. In view of the complex nature of the (111) tin face, it is believed that here again an intermediate, two-dimensional, rearranged tin-oxygen lattice occurs between the tin and the oxide. An intimate fit of the oxide lattice directly to the metal surface would require excessive strain and distortion of both crystal lattices.

Stability of the Tin Faces

The relative structural complexity of crystal surfaces is related to the number of nearest neighbors that are missing from the exposed surface atoms, Table III. Furthermore, according to Germer (24), the number of missing nearest neighbors per unit area is a measure of the relative stability of a surface; the greater this number, the more unstable is the surface. Thus, the (100) face of tin is the most

stable and the (111) face is the least stable of the five orientations studied in this work. Faceting to expose more stable surfaces, and/or rearrangement of the exposed atoms, are more likely to occur as the number of missing nearest neighbors increases. The number of different oxide orientations observed on the tin crystal faces tended to increase as the stability of these faces decreased. Micrographs of the oxide formed on the (100), (110), (101), (001), and (111) tin faces are shown in Fig. 10. The fine structure in the oxide formed on the (001) and (111) tin faces is believed to be evidence of faceting.

Orientation Relationships After Extended Periods of Oxidation

The orientation relationships between the tin substrate and the oxide are still evident after the surface of the metal is completely covered with crystalline oxide. Electron diffraction patterns of the oxide formed at 190° and 10 Torr for 7000-8500 min on the (100), (110), (101), and (001) faces of tin consisted of strong, single-crystal, oxide diffraction spots superimposed on the diffraction rings of randomly oriented oxide crystals. The single crystal spots, in the main, were more intense and slightly elongated segments of the random diffraction rings, indicating that the majority of the oxide crystals within the diffracting area were in essentially the same orientation.

The preferred orientation of oxide on the (100), (110), and (101) tin faces consisted of the (001) plane of oxide parallel to the tin surface. The tendency of the (001) oxide formed on the (110) tin face to have one specific orientation, $[010]\text{SnO}$ parallel to $[001]\text{Sn}$, was still evident. However, the oxide formed on the (100) tin face was considerably more randomly oriented than it had been after only 300 min of oxidation. Oxide films with (113)SnO, (111)SnO, or (311)SnO planes parallel to the tin surface were found to be the major oxide orientations on the (001) tin face.

The morphology of the oxide also varied with the tin surface orientation in these thick films. Figure 11

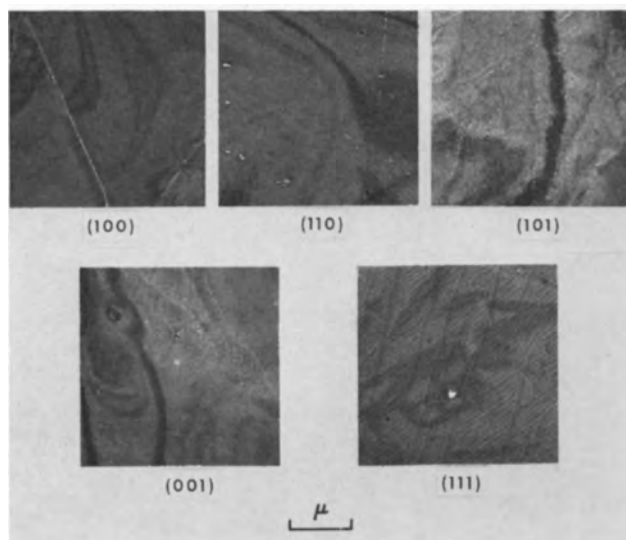


Fig. 10. Oxide removed from the (110), (101), (100), (111), and (001) planes of tin after oxidation for 180 min at 190°C and 10 Torr.

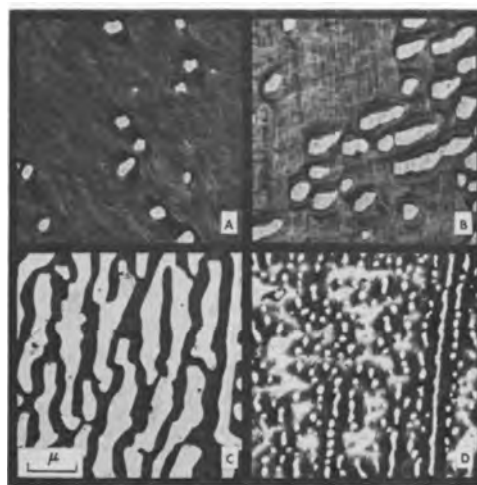


Fig. 11. Composite electron micrograph of oxide films stripped from the (100), (101), (001), and (110) faces of tin after 7000 to 8500 min at 190°C and 10 Torr. X15,000. A, (100)Sn face oxide thickness 179Å; B, (101)Sn face, oxide thickness 258Å; C, (001)Sn face, oxide thickness 319Å; D, (110)Sn face, oxide thickness 356Å.

Table IV. Oxide formed on tin single crystals in 300 min at 190°C and 10 Torr

Exposed face tin single crystal (hkl)	Number etch pits per cm ²	Number oxide platelets per cm ²	Average area per platelet, cm ²	Tin surface area covered by oxide platelets, cm ² SnO/cm ² Sn	Major oxide orientations, % (hkl)
(001)	1.1×10^7	19.8×10^3	63.3×10^{-8}	125.3×10^{-4}	33% (113), 33% (110), 33% (111)
(101)	3.3×10^6	18.3×10^3	24.5×10^{-8}	44.8×10^{-4}	33% (001), 33% (111)
(110)	1.6×10^7	7.9×10^3	72.7×10^{-8}	57.4×10^{-4}	71% (001), 12% (111)
(100)	1.2×10^7	3.3×10^3	43.7×10^{-8}	14.4×10^{-4}	57% (001), 21% (111)
(111)	Uniformly etched	2.3×10^3	29.5×10^{-8}	6.8×10^{-4}	31% (111), 23% (311), 23% (102), 12% (113)
Bulk polycrystal		1.2×10^5	20.6×10^{-8}	24.7×10^{-3}	
Polycrystalline foil 6-mil-thick		5.2×10^5	98.0×10^{-8}	51×10^{-2}	

is a composite of electron micrographs of representative oxide films stripped from the (100), (101), (001), and (110) faces of tin after 7000–8500 min of oxidation at 190°C and 10 Torr. The cavities (white areas), that previously had been observed in oxide films on polycrystalline tin (16), also appeared in the oxide formed on single-crystal faces. The size and area of the cavities appear to depend to some extent on the orientation of the tin substrate. The thickest oxide was formed on the (001) and (110) tin faces. As is seen in Fig. 11, there is a marked difference in the average size of the cavities in the oxide formed on these two tin faces. The geometric orientation (and shape) of the cavities does not appear to depend on the tin substrate, since it varies from oxide crystal to oxide crystal, on tin substrate of a single orientation.

The growth of cavities in the oxide at the metal-oxide interface appears to involve surface diffusion on the oxide, since the cavities, once nucleated, will grow in vacuum. It is possible that the formation of the cavities is, in part, a means of compensating for the periodic loss of registry between the oxide lattice and the underlying metal lattice.

Effect of Substrate Orientation on the Nucleation of Tin Oxide

The numbers of oxide platelets found on the five low-index faces of β -Sn after oxidation at 190°C and 10 Torr oxygen for 300 min are given in Table IV. The oxide platelets thus formed were large enough to be counted easily in the electron microscope but had not yet grown together to form a complete crystalline film. Assuming a one-to-one correspondence between oxide nuclei and the oxide platelets grown from oxide nuclei, these numbers represent nucleation rates at 300 min, under the experimental conditions.

A correlation between the different rates of oxidation of some crystal faces of copper and the number of equivalent orientations of oxide formed on these faces has been observed (25). These different oxidation rates are believed to be related to the numbers of oxide grains formed on the various copper crystal faces. A similar correlation between the number of tin oxide crystals and the number of equivalent orientations of tin oxide on the low-index tin faces was not observed. The (001) plane of oxide was formed parallel to the (100), (110), and (101) faces of tin. Four orientations of (001) oxide were observed on the (100) tin face, two on the (101)

face, and one on the (110) face. As is shown in Table IV, the number of tin oxide platelets was greatest on the (101) tin face, intermediate on the (110) face, and least on the (100) face.

The (001) plane is the most closely packed plane in the α -SnO crystal. Oxide with the (001) plane oriented parallel to the tin surface was most frequently observed for both single crystals and polycrystalline foils. Thus, it appears that the preferred orientation of α -SnO on β -Sn consists of the (001)SnO plane parallel to the oxide-metal interface. The frequency of occurrence of the (001) oxide orientation may serve as an index of the crystallographic factors that influence the formation of oxide nuclei on tin single crystals. On this basis, a greater number of oxide platelets would be expected to form on the (110)Sn face. This order, in fact, is observed for the (100) and (110) faces, but it cannot be extended to include the (001), (101), and (111)Sn faces.

Several experimental observations have led to the suggestion that some of the dislocations that intersect the tin surface may serve as nucleation sites for oxide: (i) An increase in oxygen pressure with its attendant increase in the number of oxygen atoms striking the metal surface did not produce a corresponding increase in the number of oxide particles, as would be expected if oxide nucleation occurred at random on the metal surface, under the influence of a surface diffusion equilibrium (16). (ii) The number of oxide particles that formed on the polycrystalline tin (exclusive of tin grain boundaries) was higher than the number formed on single crystals, Table IV. Dislocations are known to be easier to anneal out of single crystals than out of polycrystalline material. (iii) Fewer oxide crystals were found on tin single crystals that were relatively free of structural damage than were found on like faces of accidentally strained single crystals. A comparison of the number of oxide particles found on strained and unstrained tin single crystals is given in Table V.

In the absence of impurities, the type of dislocation most likely to act as an oxide nucleation site might be a perfect screw emerging perpendicular to a surface, since such a dislocation would provide a step of maximum height on the surface. Because perfect screw dislocations are, by definition, perfectly straight and have Burgers vectors parallel to their line length, the best oxide nucleation sites among emerging screw dislocations should be on

Table V. Comparison of oxide formed on good and damaged tin single crystals

Exposed face (hkl)	Number oxide platelets per cm ²	Average area per oxide platelet, cm ²	Tin surface area covered by oxide, cm ²	Major oxide orientations
(100) Unstrained	3.3×10^3	43.7×10^{-8}	14.4×10^{-4}	57% (001), 21% (111)
(100) Strained	12.7×10^3	47.0×10^{-8}	59.7×10^{-4}	80% (001), 20% (111)
(111) Unstrained	2.3×10^3	29.5×10^{-8}	6.8×10^{-4}	31% (111), 23% (311), 23% (102), 12% (113)
(111) Strained	7.9×10^3	45.3×10^{-8}	35.8×10^{-4}	60% (111), 20% (311), 20% (113)

Note: The x-ray Laue patterns of the damaged crystals consisted of two sets of reflections separated by about 1°.

those crystallographic faces that are perpendicular to the Burgers vector (*b*). Since the strain energy of a dislocation is proportional to b^2 , a whole dislocation will have a minimum strain energy when the value of *b* corresponds to the smallest lattice vector, that is, the close-packed direction. Therefore, the most favorable sites for oxide nucleation on emerging screw dislocations should occur on those tin faces that are perpendicular to the close-packed directions.

The most closely packed direction, and also the most common slip direction, in the tetragonal β -Sn lattice is the <001> direction. The atom-center-to-atom-center distance in this direction is 3.8Å. The <001> direction intersects the (001) plane at an angle of 90°, the (101) plane at 61°, and the (111)Sn plane at 52°. The <001> direction is parallel to the (110) and (100)Sn planes. Thus, pure screw dislocations will show the highest growth steps on the (001) face of tin, smaller steps on the (101) and (111) faces, and no steps on the (110) and (100) faces.

As is shown in Table IV, the greatest numbers of oxide platelets were found on the (001) and (101) planes of tin, and the least numbers were found on the (110), (100), and (111) planes. Thus, a qualitative correlation appears to exist between the expected angle of emergence of perfect screw dislocations in the (001), (101), (110), and (100) faces of tin and the number of individual oxide platelets formed on these faces. However, the number of oxide platelets found on the (111) face of tin was much lower than would be expected from the above arguments.

If the frequency of occurrence of oxide in (001) orientations and the angle of emergence of perfect screw dislocations in each tin face are added together, an interesting correlation is obtained be-

tween these sums and the numbers of oxide platelets actually found on each tin face, Table VI. Thus, it is suggested that in the absence of twin and grain boundaries, tin oxide nucleation rates are dependent on interactions between the crystal lattice of the tin and the parallel crystal lattice of the oxide, but that these tin oxide nucleation rates may be modified by the presence of screw dislocations emerging in the tin surface.

The number of dislocations to be expected in a well annealed tin single crystal apparently has not been reported in the literature, but a number in the order of 10^6 - 10^8 dislocations per square centimeter is usually quoted for most well annealed metals. The number of crystallographic etch pits formed on most of the tin faces is of the order of 10^6 - 10^7 per cm², Table IV. The number of oxide platelets found on tin single crystals is two to three orders of magnitude less than 10^6 . Thus, it appears that only a small fraction of the dislocations present in the tin could have been active as nucleation sites for oxide.

An effort was made to find direct evidence of tin oxide nucleated on emerging screw dislocations. Specimens of oxidized tin were electrothinned and examined by transmission electron microscopy, but no tin crystal dislocations that were clearly associated with oxide nuclei could be brought into contrast. Since the images of screw dislocations favorably oriented for oxide nucleation would be small and easily obscured by the relatively thick oxide platelets, the failure to observe dislocations associated with oxide nuclei does not prove that oxide nucleation cannot take place on some emerging screw dislocations.

The apparent correlation between the number of oxide nuclei on some tin crystal faces and the angle of emergence of screw dislocations is interesting but inconclusive. It might be postulated that the concentration of surface impurity atoms is orientation dependent, and that impurities, rather than dislocations, act as nucleation sites. On the other hand, it can be argued that the impurities in the tin render ineffective as oxide nucleation sites a majority of the dislocations emerging in the surface of the tin single crystals.

Significance of Growth Centers

The function of the characteristic "growth centers" in the formation of larger tin oxide platelets was discussed in earlier papers (16). About three-fourths of the oxide plates that were not nucleated on the grain boundaries of polycrystalline tin foils were associated with growth centers. Two types of

Table VI. Prediction of the number of oxide nuclei on tin single crystal faces

Exposed face tin single crystal (hkl)	Angle between <001> and (hkl)	Screw-dislocation-emergence angle in fractions of 90°	Fraction of oxide in (001) orientation	Sum of dislocation emergence-angle fraction and fraction of oxide in (001) orientation	Observed number oxide platelets per cm ²
(001)	90°	1.00	0.00	1.00	19.8×10^3
(101)	61°	0.68	0.33	1.01	18.3×10^3
(110)	0°	0.00	0.71	0.71	7.9×10^3
(100)	0°	0.00	0.57	0.57	3.3×10^3
(111)	52°	0.58	0.00	0.58	2.3×10^3

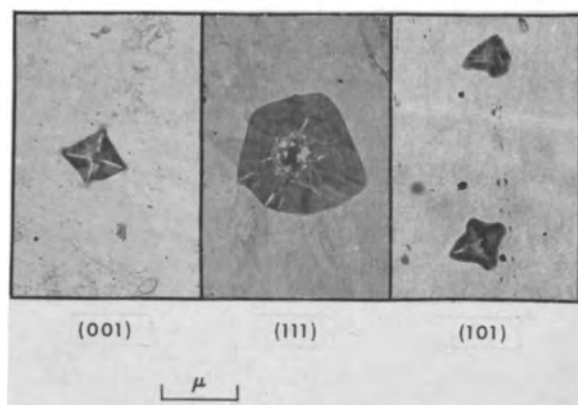


Fig. 12. Wheel-shaped and pyramidal growth centers formed on (001), (101), and (111) tin faces.

growth centers were observed: (i) wheel or spiral-shaped centers, and (ii) pyramidal or diamond-shaped centers, Fig. 12.

In contrast to the oxide formed on polycrystalline foils, most of the oxide platelets formed on tin single crystals were idiomorphic. Less than half of the oxide platelets were associated with growth centers. No growth centers formed on the (110) and (100) faces of bulk tin single crystals. The shapes of the growth centers that formed on the other faces appeared to depend on the exposed crystal structure of the tin. Pyramidal-shaped growth centers formed on the (101), (111), and (001) tin faces, but wheel-shaped growth centers formed only on the (111) and (001) faces of bulk tin single crystals.

The number of growth centers appeared to depend on the amount of accidental strain present in the tin crystals. For example, growth centers were formed on the (110) and (100) faces of thin foils prepared from bulk tin single crystals, although none were found on these same faces of the bulk single crystals themselves. Furthermore, greater numbers of growth centers were formed on the (101), (001), and (111) faces of single crystal foils than were formed on the same faces of bulk single crystals. Since the foils were unavoidably strained during preparation, it is suspected that the level of accidental strain was much higher in the thin foils than in the bulk single crystals. It is argued, therefore, that the tin oxide growth centers are related to dislocations emerging from the surface of the tin. Since the growth centers appear only on tin faces into which perfect screw dislocations would emerge at angles of 52-90°, it is suggested that the growth centers are most likely associated with screw dislocations.

Summary

The effects of the crystallographic orientation of the substrate on the orientation, nucleation and early growth of tin oxide have been investigated using electron and x-ray diffraction, and electron microscopy. Tin single crystals were prepared from 99.9999% pure tin in five orientations: (100), (110), (101), (001), or (111) plane parallel to the surface.

Estimates of the nucleation and early growth rates of oxide on the low-index tin faces were obtained by counting the number and measuring the

area of the oxide crystal platelets stripped from these tin faces, after oxidation for 300 min at 190°C and an oxygen pressure of 10 Torr. This treatment produced from 10^3 to 10^4 crystalline oxide platelets per square centimeter of tin surface with average areas per platelet of from 2×10^{-8} to 7×10^{-8} cm² depending on the orientation of the tin.

The (001) plane of SnO was parallel to the oxide-metal interface in over half of the oxide platelets formed on the (100) and (110)Sn faces. In the remainder of the oxide platelets, the (111)SnO plane was parallel to the interface. Oxide in the (001) and (111) orientations was also formed on the (101)Sn face. The (001) oxide plane was never found parallel to the (001) and (111) faces of the tin single crystals. In general, the number of different oxide orientations increased as the crystallographic complexity of the lattice plane in the surface of the tin increased. Some of the oxide platelets formed on the tin faces under investigation had distinctive shapes that could be associated with the orientation of the oxide and the exposed structure of the substrate.

Many of the observed oxide orientations could be explained by matching models of the oxide crystal lattice to models of the tin lattice. However, it was apparent that increasing strain and distortion would occur in both the oxide and the metal lattice as the complexity of the parallel tin and oxide lattice planes increased. In view of the findings of Germer (9) concerning the oxygen-induced metal-atom rearrangement in the (110) face of nickel, it is suspected that transition lattices usually form between the oxide and the tin. Some of the orientations of oxide found on the more complex tin faces could best be explained if microscopic facets formed in the metal surface, at certain angles to these faces, exposing some of the less complex tin-lattice planes.

The major oxide orientations persisted over extended periods of oxidation, although the electron diffraction patterns indicated an increased randomness in the orientations of the oxide. The surface of tin single crystals becomes covered with oxide much more slowly than do polycrystalline foils. This is believed to be due largely to the smaller number of oxide nuclei that form on the tin single crystals.

As the oxide crystals grow thicker on the surface of the single crystals, thin areas or cavities develop in the oxide. The shape and orientations of the cavities formed in the oxide grown on tin single crystals appear to be related to the crystal structure of the oxide rather than to the structure of the exposed tin face. It is suggested that the growth of the cavities is related in part to the periodic loss of registry between the metal and oxide crystal lattices.

The number of oxide platelets formed on some of the tin faces appeared to be influenced by direct or indirect oxide-to-metal lattice matching. There was also a suggestion that favorably oriented screw dislocations emerging in the tin surface might serve as nucleation sites and that this would increase the number of oxide platelets formed on some tin crystal faces. It appears that tin oxide nucleation rates

are dependent on the geometry of the substrate but are modified by the presence of favorably oriented emerging screw dislocations. A comparison of the number of oxide platelets with the expected number of dislocations, however, indicates that at most only one or two dislocations per thousand could have served as oxide nucleation sites. Direct electron-microscopic evidence of the involvement of dislocations was not obtained.

Acknowledgments

The authors wish to thank Dr. Fred Weinberg, of the Canadian Department of Mines and Technical Surveys (Mines Branch), Ottawa, Ontario, for kindly providing the tin single crystal seeds used in this work, and Dr. Alan J. Baker, of the U. S. Steel Applied Research Laboratory, for helpful discussions concerning the possible role of dislocations in nucleating tin oxide.

Manuscript received Sept. 11, 1963. This paper was presented at the New York Meeting, Sept. 29-Oct. 3, 1963.

Any discussion of this paper will appear in a Discussion Section to be published in the December 1964 JOURNAL.

REFERENCES

1. J. Bardolle and J. Benard, *Rev. met.*, **42**, 613 (1952).
2. E. A. Gulbransen, W. R. McMillan, and K. F. Andrew, *Trans. Am. Inst. Mining Met. Engrs.*, **200**, 1027 (1954).
3. J. Benard, *Acta Met.*, **8**, 272 (1960).
4. J. Bardolle, *Rev. met.*, **51**, 833 (1954).
5. F. W. Young, J. V. Cathcart, and A. T. Gwathmey, *Acta Met.*, **4**, 145 (1956).
6. E. J. Scheibner, L. H. Germer, and C. D. Hartman, *Rev. Sci. Instruments*, **31**, 112 (1960).
7. L. H. Germer, E. J. Scheibner, and C. D. Hartman, *Phil. Mag.*, **5**, 222 (1960).
8. L. H. Germer and C. D. Hartman, *J. App. Phys.*, **31**, 2085 (1960).
9. L. H. Germer and A. U. MacRae, *ibid.*, **33**, 2923 (1962).
10. A. U. MacRae, *Science*, **139**, 379 (1963).
11. E. A. Gulbransen and K. F. Andrew, *This Journal*, **106**, 511 (1959).
12. V. A. Phillips, *J. App. Phys.*, **33**, 712 (1962).
13. F. W. Young, *Acta Met.*, **8**, 117 (1960).
14. E. Hondros and J. Oudar, *Compt. rend. acad. sci. U.R.S.S.*, **256**, 2386 (1963).
15. W. E. Boggs, R. H. Kachik, and G. E. Pellissier, *This Journal*, **108**, 6 (1961).
16. W. E. Boggs, P. S. Trozzo, and G. E. Pellissier, *ibid.*, **108**, 13 (1961).
17. B. Chalmers, *Can. J. Phys.*, **31**, 136 (1953).
18. B. D. Cullity, "Elements of X-Ray Diffraction," p. 215, Addison-Wesley, Reading, Mass. (1956).
19. G. A. Bassett, J. W. Menter, and P. W. Pashley, "Structure and Properties of Thin Films," pp. 11-40, John Wiley and Sons, New York (1959).
20. J. T. Fourie, F. Weinberg, and F. W. C. Boswell, *J. App. Phys.*, **31**, 1136 (1960).
21. Jena Review, No. 1/1963, p. 58.
22. L. Pauling, "The Nature of the Chemical Bond," p. 346, Cornell University Press, Ithaca, New York (1948).
23. "The Properties of Tin," Tin Research Institute, Middlesex, England (1954).
24. L. H. Germer, Private communication.
25. K. R. Lawless and A. T. Gwathmey, *Acta Met.*, **4**, 153 (1956).

An Ellipsometer Investigation of Vapor Adsorption on Etched Silicon

B. H. Claussen

Standard Telecommunication Laboratories, Harlow, Essex, England

ABSTRACT

Ellipsometer measurements have been made of vapor adsorption on single crystal silicon etched in HF/HNO₃ mixtures. Approximate equations, derived originally by Drude from the exact theory of reflection, have been used to evaluate film thicknesses. Adsorption isotherms have been plotted for water, some lower monohydric alcohols, acetone, benzene, and hexane. The results confirm the feasibility of using an ellipsometer for this type of measurement. In the absence of further surface treatment the amount of adsorption is small, even at saturation. However, when the etched surface is either treated with caustic soda solution or boiled successively in nitric acid and deionized water, adsorption is enhanced and smooth type II isotherms result. This behavior is attributed to the removal of chemically bonded fluoride ions from the surface of the adsorbent. Monolayer thicknesses calculated from the experimental results agree reasonably well with those to be expected from the dimensions of the adsorbed molecules assuming the latter to have a particular orientation on the surface. Anomalous results obtained on some samples are thought to be due mainly to the existence of localized areas of the surface on which adsorption is inhibited.

A variety of experimental techniques are available for the study of adsorption on solid surfaces. In most cases, sensitivity considerations necessitate the use of powdered samples in order to obtain a sufficiently large surface area. However, it is possible to

determine the thickness of adsorbed layers on single crystal surfaces from an analysis of the state of polarization of light reflected from the surface of the adsorbent. This procedure has the added advantage that high vacua are not essential.

If the incident light beam is plane polarized with its plane of polarization inclined at 45° to the plane of incidence, the beam will in general be elliptically polarized. The ellipticity can be characterized by the phase difference Δ and the amplitude ratio $\tan \psi$ of two plane wave components vibrating parallel to and perpendicular to the plane of incidence. The parameters Δ and ψ are functions of the angle of in-

reported. The procedure used is essentially that described by Archer (14) in his study of the rate of oxide growth on silicon and germanium under normal atmospheric conditions. In evaluating α and β , Archer retained terms missing in the original Drude equations which significantly alter the values of the coefficients for semiconductors. α and β are then given by the expressions¹

$$\alpha = \frac{720 \cos \phi \sin^2 \phi (n_1^2 - 1) \left\{ \left(\frac{1}{n_1^2} - a \right) [\cos^2 \phi - a + \sin^2 \phi (a^2 - a_1^2)] + a_1^2 \right\}}{\lambda ([\cos^2 \phi - a + \sin^2 \phi (a^2 - a_1^2)]^2 + a_1^2)}$$

$$\beta = \frac{360 \sin 2\bar{\psi} \cos \phi \sin^2 \phi (n_1^2 - 1) a_1 \left\{ \left(\frac{1}{n_1^2} - a \right) (1 - 2a \sin^2 \phi) - [\cos^2 \phi - a + \sin^2 \phi (a^2 - a_1^2)] \right\}}{\lambda ([\cos^2 \phi - a + \sin^2 \phi (a^2 - a_1^2)]^2 + a_1^2)}$$

cidence, the wavelength of the light, the optical constants of the substrate, and the thickness and optical constants of any surface film. To determine the thickness of an adsorbed layer from a measurement of Δ and ψ approximate equations derived from the exact theory of reflection have to be employed. Drude (1) shows that if the exact equation is expanded and terms higher than the first order in thickness are neglected, linear relations can be derived between both Δ and ψ and film thickness.

$$\Delta = \bar{\Delta} - \alpha L$$

$$\psi = \bar{\psi} + \beta L$$

where $\bar{\Delta}$ and $\bar{\psi}$ are the values of Δ and ψ for a film free surface, L is the film thickness, and the coefficients α and β are dependent on the optical constants of film and substrate. A similar approach has been used by Tronstad (2) which enabled him to obtain an explicit expression for the refractive index of thin transparent film. Other more rigorous methods of determining the thickness and optical constants of thin films have been developed by Lucy (3), Vasicek (4), Partovi (5), and Bartell and Churchill (6). These have the advantage over the Drude-Tronstad approximations in that a wider range of film thickness can be studied, but for films of 100Å or less, little increase in accuracy can be gained to compensate for the somewhat laborious computations.

A number of investigations of adsorption on solid surfaces have been carried out using the reflection technique, notably by Frazer (7) (water and methyl alcohol on glass), Silverman (8) (methyl alcohol on rock salt), and Herschkowitsch (9) (gas sorption on metals). More recently, Bartell and Churchill (6) determined both the thickness and the adsorption spectra of molecular films adsorbed on to chromium, while Archer (10) has reported some vapor adsorption measurements on silicon. In addition, Rothen and Hanson (11), Faucher, McManus, and Trurnit (12), and Mertens, Theroux, and Plumb (13) have all shown agreement between thicknesses calculated from the Drude approximations and known thicknesses of adsorbed barium stearate films.

In this paper, the results of an investigation of vapor adsorption on etched single crystal silicon are

where ϕ is the angle of incidence, λ the wavelength of the light, n_1 the refractive index of the film, $a = (n^2 - k^2)/(n^2 + k^2)^2$ and $a_1 = 2nk/(n^2 + k^2)^2$. n and k are the real and imaginary parts of the complex refractive index $\hat{n} = n - ik$ of the reflecting substance, k being related to the absorption coefficient by the equation $\alpha = 4k/\lambda$.

Most metals and semiconductors are normally covered with a thin oxide layer so that it is difficult in practice to obtain a film free surface. However, Mertens *et al.* (13) have recently demonstrated that in a thickness measurement, the presence of an extraneous layer between the film under consideration and the metal (or semiconductor) surface is satisfactorily accounted for by its effect on the apparent optical constants of the substrate. Thus, if the silicon plus oxide is considered as the substrate for the adsorbed film, the thickness of the latter may be calculated using the apparent optical constants of the composite substrate to evaluate α and β . In the case of silicon, the presence of a thin oxide layer, though altering the apparent values of $\bar{\Delta}$ and $\bar{\psi}$, makes little difference to the magnitudes of α and β . This approach is not valid when changes in the oxide layer thickness occur during the experiment.

Experimental Technique

The optical measurements were carried out on an ellipsometer constructed in these laboratories. The instrument itself and the method of measurement have been described in detail in a previous paper (15) and will not be discussed further. However, since for silicon α is $\gg \beta$ and Δ can be determined with greater accuracy than ψ , film thicknesses were evaluated from a measurement of the polarizer setting, P , at extinction. With the fast axis of the quarter wave plate in $\pi/4$ azimuth, P is related to Δ by the equation

$$\tan \Delta = \sin \delta \cot 2P$$

where δ is the actual retardation of the plate (for the mercury green line used in these experiments δ was found to be 83°). The polarizer setting at extinction can be determined with an accuracy of $\pm 0.01^\circ$.

¹ The author is indebted to Dr. R. J. Archer for pointing out the mistakes in the expressions for α and β given in ref. (14).

The adsorption experiments were carried out on (III) slices P type silicon in the resistivity range 1-100 ohm-cm. The slices were mechanically polished using 0.25μ alumina as the final abrasive degreased in redistilled acetone and then etched for 2 min in a 1:5 mixture of 40% hydrofluoric acid and concentrated nitric acid. The majority of specimens were, in addition, either boiled successively in nitric acid and deionized water or etched for a further 10 min in a 40% caustic soda solution. A few measurements were also carried out on slices that had been annealed for 30 min at 1200°C in hydrogen purified by passage through a palladium tube.

After a final rinse with deionized water and blotting dry with tissue, the slice being studied was mounted in the ellipsometer and the sample holder adjusted until the light beam was centered on the slice. A gas tight covering having strain free windows normal to the incident and reflected beams was then placed over the sample holder and a stream of dry purified argon passed through the chamber at a rate of approximately 1 liter/min. The gas flow was continued for some 20 min after the polarizer reading had stabilized. As the dry argon contained less than 1 ppm of water it could then be presumed that the silicon surface was free from physisorbed water.

Vapor was introduced into the gas by passing the argon through a thermostated bubbler of the liquid under investigation. Prior to admission to the chamber, the saturated argon was mixed with pure argon, the final vapor concentration being determined by the relative flow rates of the two gas streams. The relative saturation was then calculated from these flow rates as measured by rotameter flow meters. To prevent fluctuations in relative saturation, the sample chamber was enclosed in an air thermostat maintained at the same temperature (27°C) as that of the bubbler. With this arrangement relative saturations calculated from the flowmeter readings were found to agree to within 1-2% with those determined from the weight increase of a suitable absorbent.

The liquids studied included water, some lower monohydric alcohols, acetone, hexane, and benzene. At each vapor concentration, optical measurement were started 1 min after the gas started flowing and were continued, initially every 2 min, and then every 5 min until equilibrium was established.

Results

Table I gives the refractive indices of the various liquids studied together with the appropriate values

Table I. Refractive indices of liquids

Liquid	Refractive index	α degrees/A
Water	1.33	0.109
Methanol	1.33	0.109
Ethanol	1.36	0.114
Iso-propanol	1.38	0.117
n Butanol	1.40	0.120
Acetone	1.36	0.114
Hexane	1.37 (5)	0.116
Benzene	1.50	0.134

for the coefficient α . The angle of incidence was chosen to be 61.26° for reasons of experimental convenience. Though this is somewhat far from the principal angle, reasonable sensitivity can still be obtained. In estimating α the complex refractive index of silicon was taken to be $4.05 - 0.03i$ (15, 16) and the refractive index of the adsorbed film was assumed to be the same as that of the bulk liquid.

The apparent thickness of the surface oxide layer usually lies in the range 10-25Å, though on some occasions much larger values are obtained for the nitric acid treated surface.

Water adsorption data for the various types of silicon surface studied are plotted in Fig. 1. Type III adsorption isotherms are obtained on the acid etched surface and on the surface reduced in hydrogen after etching. In both cases the amount of adsorption is small, even at saturation. After boiling in nitric acid and deionized water (and after etching in caustic soda) the amount of adsorption increases markedly and s shaped type II isotherms result. A similar, though less pronounced enhancement is observed with the organic vapors. Typical data for the nitric acid treated surface are plotted in Fig. 2, 3, and 4. Again, smooth type II isotherms are obtained although n butanol is an exception in that the adsorption appears to monomolecular, i.e., the data

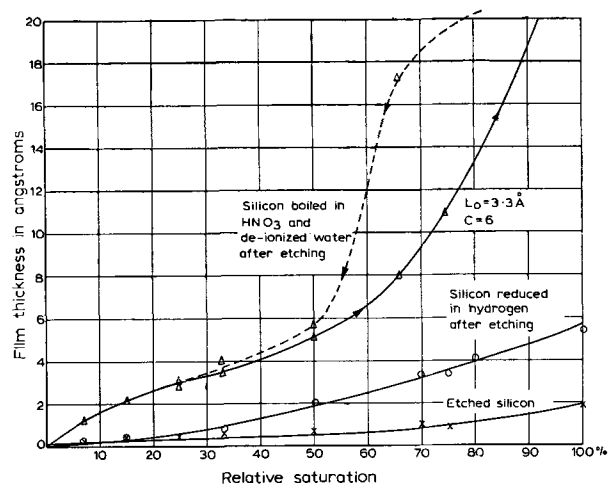


Fig. 1. Effect of surface treatment on the adsorption of water

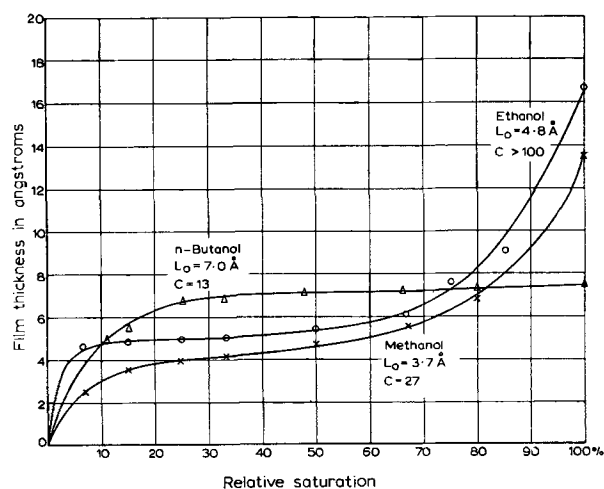


Fig. 2. Adsorption of methanol, ethanol, and n-butanol

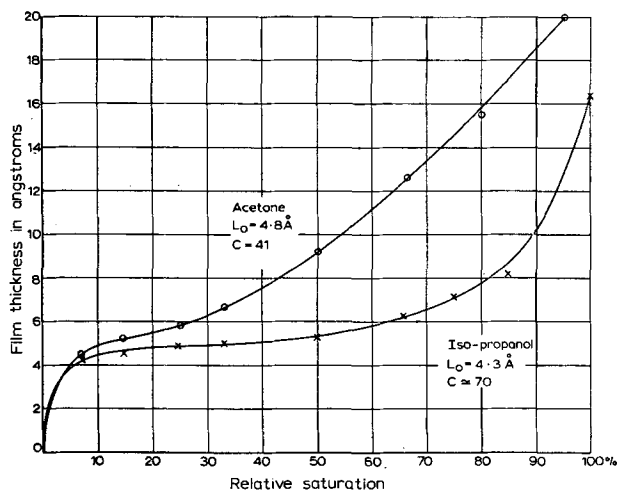


Fig. 3. Adsorption of iso-propanol and acetone

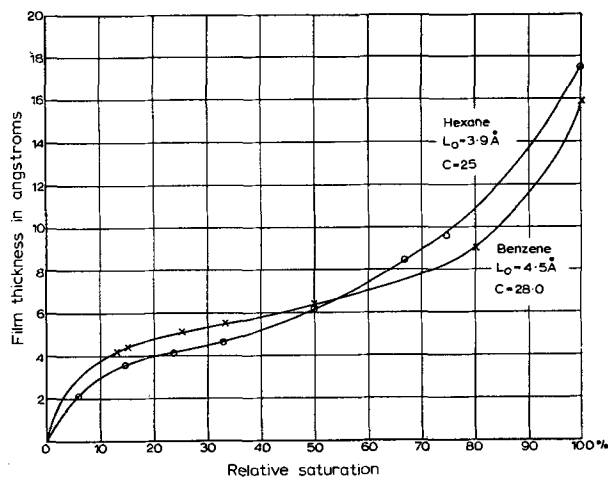


Fig. 5. B.E.T. plots

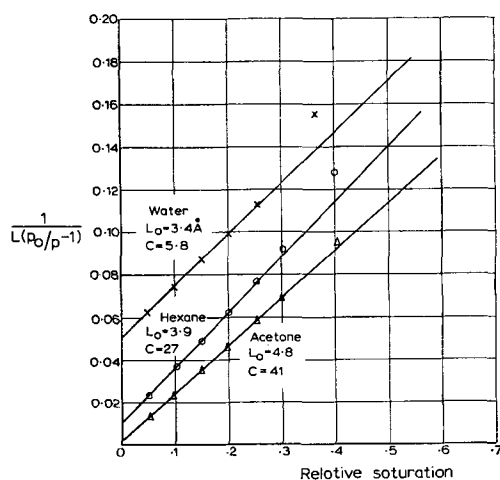


Fig. 4. Adsorption of benzene and hexane

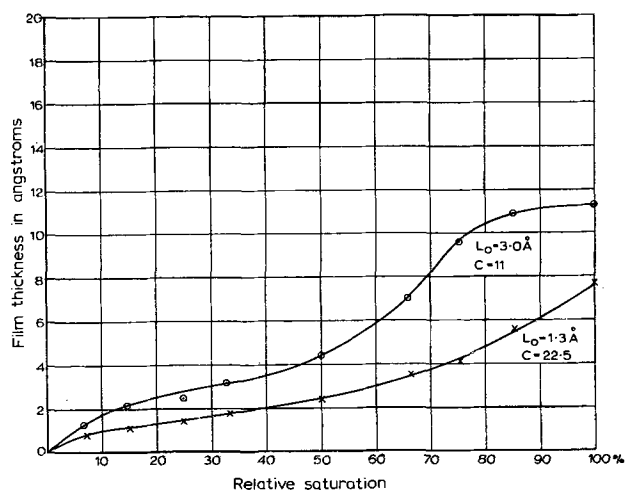


Fig. 6. Anomalous adsorption of water

approximate to a type I isotherm. There does, however, appear to be a tendency for the amount of adsorption at saturation to decrease as the hydrocarbons chain length of the primary alcohol increases. The isotherms, particularly in the case of water vapor, are not always reversible, as a hysteresis loop (Fig. 1) can be formed between the adsorption and desorption curves.

The type II isotherm can be described reasonably well by the B.E.T. equation (17), at least over the P/P_0 range 0.05-0.35. The latter may be written in the form

$$\frac{1}{L(P_0/P-1)} = \frac{1}{L_0 C} + \frac{(C-1)}{L_0 C} P/P_0$$

where L is the film thickness at a relative saturation P/P_0 , L_0 is the thickness of the complete monolayer, and $C = \exp(E_1 - E_L)/kT$. E_1 is the heat of adsorption of the first layer and E_L is the latent heat of condensation of the adsorbate. A plot of $\frac{1}{L(P_0/P-1)}$ against P/P_0 should then give a straight line from which it is possible to calculate both L_0 and C . Typical B.E.T. plots are shown in Fig. 5, the data marked on the other figures being obtained from an analysis of the straight line portion of curves of this type.

A number of measurements have been carried out with each adsorbate, the majority of which give monolayer thicknesses that agree fairly well with those to be expected from the known dimensions of the adsorbate molecules. However, some of the monolayer values obtained for the nitric acid treated surface (usually between 10 and 35% of the total) are much less than the estimated thickness. This behavior is illustrated by the type II water vapor isotherm plotted in Fig. 6. Surfaces etched in caustic soda, either before or after treatment with nitric acid, give far fewer of these anomalous results. Possible reasons for this behavior are discussed in the next section. The type IV isotherm also plotted in Fig. 6 occurs only rarely and cannot be satisfactorily explained.

Discussion

The marked difference in the amount of water adsorbed after the various surface treatments can be attributed to differences in both the structure and composition of the adsorbent surface. After etching in HF/HNO₃ mixtures, a silicon surface is normally covered with a thin oxide layer, usually less than 20Å thick, which would be expected to contain chemically bonded fluoride and hydroxyl groups. This view is supported by the work of Baird (18) on the water retention of silicon surfaces treated with

boiling water, hydrofluoric acid, and nitric acid. To explain his results, he proposed that the water treated surface is characterized by hydroxyl groups and oxygen bridges with some water entrapped within the oxide. Rinsing in hydrofluoric acid brings about the conversion of many of the hydroxyl groups to fluoride and extensive chemisorption of the acid. The resulting surface can be presumed to be very similar to the HF/HNO₃ etched surface though the latter is likely to contain less chemisorbed HF. The lack of water adsorption is attributed to the extensive hydrogen bonding between the surface fluoride and hydroxyl groups. Baird suggests that on heating the HF treated surface in nitric acid an extensively cross linked oxide layer is produced. This is considered to be free from fluoride and to contain little or no entrapped water. The proportion of hydroxyl groups on the surface depends on the exact details of the nitric acid treatment and is enhanced by boiling in deionized water. Such a surface is hydrophylic unlike the acid etched surface, adsorption taking place on the oxygen bridges and on the hydroxyl groups. A surface etched in caustic soda would also be expected to be free from fluoride and to terminate in hydroxyl groups, so that again adsorption should occur readily. On the other hand, annealing in hydrogen, through reducing the oxide thickness, will not completely remove the fluoride, so that the surface remains hydrophobic.

The smoothness of the type II isotherms and the way in which they can be fitted by the B.E.T. equation show that ellipsometer studies of vapor adsorption can yield meaningful results. In Table II monolayer thickness calculated from the B.E.T. equation are compared with those estimated from x-ray data assuming a particular orientation for the adsorbate molecules. Thus, the primary alcohols and methyl ketones are considered to be anchored to the surface via their active group with their hydrocarbon chains vertical (19). The alcohol thicknesses given in the table are calculated from the molecular volumes taking the cross sectional area of the molecules in the liquid state to be 21.5Å². The latter figure was obtained from x-ray measurements on methanol which suggested that each methyl group is surrounded by six others separated by roughly 5Å (20). Adsorption measurements on the acetone/silica system indicate a similar area for the acetone molecule (21). In contrast the molecules of both benzene and the long chain hydrocarbon hexane are thought to lie flat on the surface, the quoted figures being the effective thicknesses of the molecules in the solid state (22, 23).

Table II. Monolayer thicknesses

Adsorbate	Experimental, Å	Estimated, Å
Water	3.0	3.1
Methanol	3.6	3.2
Ethanol	4.8	4.6
Iso-propanol	4.5	
n Butanol	6.9	7.1
Acetone	5.0	(6.0)
Hexane	3.7	3.8
Benzene	4.5	4.6

The figures in the first column of the table are mean values obtained from a number of measurements with each adsorbate. In calculating these figures, monolayer thicknesses that are less than half the maximum recorded value, *i.e.*, those which are much less than the estimated thickness, have been excluded. The remainder normally lie within $\pm 0.5\text{Å}$ of the mean figure.

Inspection of the table shows that the measured and estimated thicknesses are in reasonable agreement thus confirming the proposed orientations of the various molecules. In the case of acetone, however, the measured thickness is much less than the estimated value, being closer to the values found for ethyl and isopropyl alcohols. This is not unexpected if these molecules are indeed anchored to the surface via their active groups. The most likely explanation for this discrepancy is that the area of an acetone molecule in the bulk liquid is higher than that in the adsorbed state.

For each adsorbate, there is considerable variation in the values obtained for the constant *C* and hence the heat of adsorption *E*. This must be attributed to differences in the surface properties of the silicon resulting from minor variations in the etching procedure. However, some sort of pattern can be discerned in that the heat of adsorption tends to be lower for the less polar molecules, *i.e.*, benzene and hexane. This is not unexpected since *E*₁ is a measure of the degree of attraction between adsorbent and adsorbate. Moreover hydrogen bonding will almost certainly occur between the hydroxyl groups of the surface oxide layer and the active groups of molecules such as water, acetone, and the alcohol.

As mentioned in the previous section, on quite a number of occasions the monolayer thickness is found to be much smaller than the value estimated from the dimensions of the adsorbed molecule. Moreover, Archer's (10) results on etched surfaces repeatedly gave monolayer thicknesses at least two times smaller than the appropriate molecular dimension unless the silicon surface was specially prepared. There are a number of possible explanations for this behavior:

Failure of the optical theory for monomolecular films.—A number of investigators claim to have shown that the Drude equations give valid results for dielectric films that are less than 100Å thick. However, there is usually a large discrepancy between the calculated refractive index of a thin film and the bulk refractive index of the same material. To explain this anomaly Mertens *et al.* (13) have recently suggested that an adsorbing region exists at the interface between a metal and dielectric for which explicit allowance should be made in calculating the thickness of very thin films. It is thought that the absorption results from the establishment of a space charge region within the film. In the case of silicon the refractive index of a thin surface film cannot be evaluated directly, since the changes in ψ are usually too small to be measured. Nevertheless, a complex refractive index could explain the lack of agreement between the thickness of the oxide layer as measured in this laboratory by ellipsometry and

that indicated by electron diffraction (24). Whether such an absorbing region would exist at the interface between the hydrated oxide and an adsorbed film is open to question. It is doubtful whether a hydrated oxide could be regarded as a perfect dielectric and consequently the space charge region would be unlikely to extend as far as the surface of the oxide layer. Moreover, when the adsorbed film is anchored to the surface by van der Waals forces, *e.g.*, hexane, no electrical double layer can be formed. However, there does appear to be a slight correlation between the monolayer thickness of an adsorbed water film and the apparent thickness of the oxide layer.

Inapplicability of the B.E.T. equation.—Though the B.E.T. equation is open to many criticisms, there is much evidence in the literature to show that it reproduces the experimental data with reasonable accuracy over the P/P_0 range 0.05-0.35 and gives satisfactory values for the monolayer capacity. In the present experiments linear B.E.T. plots have nearly always been obtained over this pressure range. Moreover, the inadequacies of the B.E.T. theory cannot account for the variable results obtained with each adsorbate.

Lack of surface smoothness.—In calculating the thickness of the adsorbed film it is usually assumed that the effect of surface irregularities, small compared to the area of the light beam, can be averaged out (3). However, Archer (10) has worked out a quantitative model which explains the anomalous results in terms of irregularities comparable in size to the adsorbed molecules. He has shown that on such a surface, the ellipticity change for films of the order of the monolayer thickness will be smaller than on a flat surface. Consequently the measured thickness will be less than the true thickness. This is due to the change in refractive index of the surface layer of the adsorbent caused by the gradual filling of the depressions in the surface by the film material. Since little is known about surface roughness on an atomic scale this explanation must remain a possibility in the absence of evidence to the contrary.

Nonuniform adsorption over the surface.—The film thickness determined in an ellipsometer experiment is an average value over the area of the surface covered by the light beam. If adsorption is inhibited on certain parts of this area, the effective refractive index of the adsorbed film will be less than that of the bulk material as a result of the presence of the air gaps. Consequently, the calculated thickness will be smaller than the true value. Such behavior could be due either to incomplete removal of chemically bonded fluoride or to surface contamination. That the cleanliness of the surface is of paramount importance is suggested by the following facts: (i) treatment with caustic soda of a surface boiled in nitric acid can result in a marked enhancement of the monolayer thickness with virtually no change in the thickness of the oxide layer, (ii) a hydrophobic silicon surface is gradually converted to a hydrophobic surface on exposure to the atmosphere (25), and (iii) repeated adsorption cycling, particularly with impure vapors, can bring a progressive decrease in the calculated monolayer thickness.

Since it is difficult to account for the above results on the basis of absorption within the adsorbed layer, or in terms of surface roughness, it would seem that the last explanation is most likely to be correct.

Conclusions

An ellipsometer investigation has been made of vapor adsorption on single crystal silicon etched in HF/HNO₃ mixtures. The liquids studied include water, some lower monohydric alcohols, acetone, benzene, and hexane. Approximate equations derived originally by Drude (1) and modified by Archer (14) to apply to semiconductors have been used to evaluate film thicknesses. These have then been plotted against relative saturation.

In the absence of further treatment the amount of absorption is small, the resultant curves approximating to type III isotherms. After boiling in nitric acid and deionized water and after treating in caustic soda solution the amount of adsorption increased markedly and smooth type II isotherms generally result. This behavior is attributed to the removal of chemically bonded fluoride from the surface oxide layer.

The type II isotherms can be fitted reasonably well by the B.E.T. equation, at least over the P/P_0 range 0.05-0.35. Monolayer thicknesses calculated by means of the B.E.T. equation are in quite good agreement with those estimated from x-ray data assuming a particular orientation for the adsorbed molecules. Thus the primary alcohols must be anchored to the surface with their hydrocarbon chains vertical, whereas both benzene and hexane appear to lie flat on the surface. These results show that useful information can be obtained from an ellipsometer investigation of this type.

On a number of occasions monolayer thicknesses much less than those to be expected from the size of the adsorbed molecules have been obtained. These are thought to be due mainly to the existence of localized areas of the surface on which virtually no adsorption takes place. However, the possibility of adsorption within the adsorbed film and the effects of surface roughness on an atomic scale cannot be discounted.

Acknowledgments

The author is grateful to Standard Telecommunication Laboratories for permission to publish this paper. Thanks are also due to Mrs. P. R. Gander for carrying out much of the experimental work.

Manuscript received Nov. 26, 1963.

Any discussion of this paper will appear in a Discussion Section to be published in the December 1964 JOURNAL.

REFERENCES

1. P. Drude, *Ann. physik*, **36**, 532 (1889).
2. L. Tronstad, *Trans. Faraday Soc.*, **31**, 1151 (1935).
3. F. A. Lucy, *J. Chem. Phys.*, **16**, 167 (1948).
4. A. Vasicek, *J. Optical Soc. Am.*, **37**, 145 (1947).
5. F. Partovi, *ibid.*, **52**, 918 (1962).
6. L. S. Bartell and D. Churchill, *J. Phys. Chem.*, **65**, 2242 (1961).
7. J. H. Frazer, *Phys. Rev.*, **33**, 97 (1929).
8. S. Silverman, *ibid.*, **36**, 311 (1930).
9. Herschkowitsch, *Ann. Physik*, **10**, 993 (1931).

10. R. J. Archer, Ellipsometer Symposium, 1963. National Bureau of Standards, Washington, D. C. Full report to be published in the Symposium Proceedings.
11. A. Rothen and M. Hanson, *Rev. Sci. Instruments*, **20**, 66 (1949).
12. J. A. Faucher, G. M. McManus, and H. J. Trurnit, *J. Optical Soc. Am.*, **48**, 51 (1958).
13. F. P. Mertens, P. Theraux, and R. C. Plumb, *ibid.*, **53**, 788 (1963).
14. R. J. Archer, *This Journal*, **104**, 619 (1957).
15. B. H. Claussen and M. Flower, *ibid.*, **110**, 983 (1963).
16. R. J. Archer, *J. Optical Soc. Am.*, **52**, 970 (1962).
17. S. Brunauer, "The Adsorption of Gases and Vapours," Vol. 1, p. 153, Princeton University Press, Princeton (1945).
18. S. S. Baird, Autumn Meeting of the Electrochemical Society, 1960, Electronics Division.
19. W. D. Harkins, "The Physical Chemistry of Surface Films," Reinhold Publishing Corp., New York (1952).
20. S. Glasstone, "Test Book of Physical Chemistry," p. 510, McMillan and Co., London (1946).
21. S. J. Gregg, "The Surface Chemistry of Solids," p. 102, Chapman and Hall Ltd., London (1951).
22. A. Muller, *Proc. Roy. Soc.*, **A127**, 417 (1930).
23. S. Glasstone, "Test Book of Physical Chemistry," p. 508, McMillan and Co., London (1946).
24. H. Wilman and J. N. King, Imperial College, London University, Private communication.
25. M. M. Atalla, E. Tannenbaum, and E. J. Scheibner, *Bell System Tech. J.*, **38**, 749 (1959).

The Very Rapid Oxidation of Aluminum at Room Temperature When in Contact with Mercuric Iodide

David A. Jackson, Jr.¹ and Henry Leidheiser, Jr.

Virginia Institute for Scientific Research, Richmond, Virginia

ABSTRACT

The rate of oxidation of aluminum, contaminated with solid HgI_2 , in moist air occurred linearly with time in the early stages of reaction. The rate of oxidation at 30°C increased with relative humidity and was a maximum at 80-100% relative humidity. The majority of the reaction was with oxygen, but a constant amount of reaction, $0.066 \text{ mg/cm}^2/\text{min}$, occurred with water vapor over the relative humidity range 36-100%. The total reaction of aluminum at 100% relative humidity was equivalent to $0.9 \text{ mg/cm}^2/\text{min}$. The reaction product exhibited no crystalline diffraction pattern when examined with electron or x-ray beams. The product lost a negligible amount of water when heated at 115°C but lost an average of 34% by weight when heated at 600°C . Aging of the product without dehydration resulted in the crystallization of the beta-trihydrate. An explanation of the strong dependence of the rate on the relative humidity was given, based on the supposition that the electrical properties of any oxide present on the surface are a function of the relative humidity.

It is well known that mercury has an extremely deleterious effect on aluminum in many environments. For example, the corrosion of aluminum in boiling 2M HCl containing 10^{-4} to 10^{-3}M HgCl_2 is increased 100-fold over that in the absence of mercury (1). Also, the rate of oxidation of aluminum is greatly increased in the presence of mercury as can be readily shown by applying a drop of mercury on an aluminum surface and scratching the surface in order to aid in penetration of the oxide film.

The purpose of the work reported herein was to make a quantitative study of the oxidation of aluminum in the presence of mercury and thereby to determine the more important variables. Preliminary experiments indicated that it was very difficult to obtain reproducible results with metallic mercury, presumably because of the inability to prepare a reproducible surface whose oxide coating was uniformly penetrated by mercury. Preliminary experiments with many mercury salts spread on the surface indicated that HgI_2 was a satisfactory reactant and that uniform attack was obtained over the entire surface when it was spread in a thin layer.

Quantitative experiments were then confined to HgI_2 .

Experimental Procedure

It was determined very early in the research that aluminum in contact with HgI_2 reacted with both oxygen and water vapor when both were present in the atmosphere. The major amount of reaction leading to a pressure change at all humidities took place with oxygen as indicated by the fact that there was a pressure decrease in a closed system containing air when the water vapor concentration was maintained constant. These observations led us to adopt pressure change in a closed system as the measured parameter for following the reaction as a function of time. Since the reaction with oxygen consumes $3/4$ mole of oxygen gas for every gram atom of aluminum and the replacement reaction with water evolves $3/2$ mole of hydrogen gas for every gram atom of aluminum, a small fraction of the total reaction involving water leads to a significant error in assessing the total amount of reaction from pressure decrease only. Gravimetric measurements were thus carried out in separate experiments in order to determine the relationship between pres-

¹ Present address, Research and Development Laboratory, Fort Belvoir, Virginia.

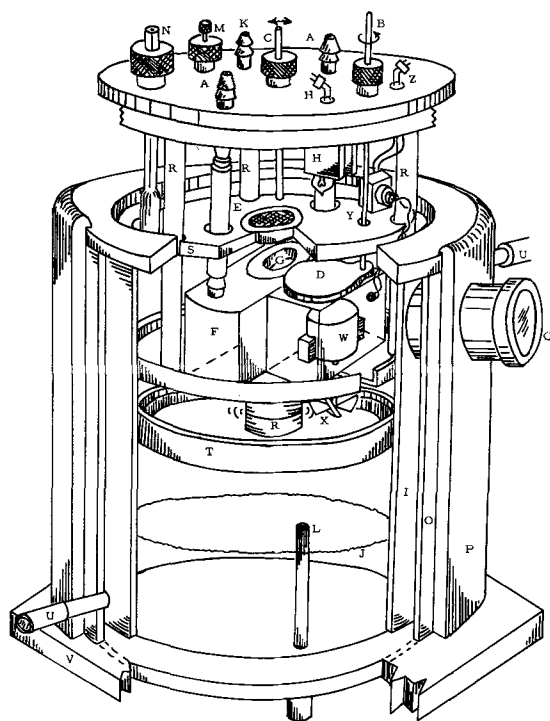


Fig. 1. Apparatus used in quantitative studies of oxidation of aluminum in contact with HgI_2 .

sure change and the total amount of reaction. All studies were carried out with air.

The reaction apparatus (Fig. 1) consisted of an insulated, double-walled copper chamber whose interior metal surface was heavily coated with a flat black paint. The sealed chamber was connected to a mercury capillary manometer at L and to a bellows-type pressure gauge at K. The chamber was maintained at constant temperature by passing water from a constant temperature bath between the double walls of the chamber. Temperature measurements were made by means of a thermometer passing into the chamber at N through an "O" ring seal.

The cylindrical sample was inserted in the plastic holder G which was cemented to the hollow support F through which water at constant temperature continuously circulated. The sample fits very tightly in the holder G so that only the upper circular surface was exposed to HgI_2 . The base of the plastic holder G was machined to a thickness of approximately 0.5 mm so as to interfere as little as possible with the transfer of heat from the specimen to the constant-temperature water circulating through F.

The desired relative humidity was obtained by placing a saturated salt solution in the plastic tray T and allowing the enclosed system to reach equilibrium during a 30-min period. Both thermal and humidity equilibrium were facilitated by the use of a small fan X which continually stirred the internal atmosphere. It was assumed that relative humidity equilibrium was achieved in these experiments because of the location of the fan blades immediately above the surface of the salt solution. At relative humidities less than 100%, Octoil-S was used as a spacer to control the internal volume of the chamber to 1000 cc. At 100% relative humidity, water was used as the spacer.

The HgI_2 was uniformly distributed over the sample surface by passing it through a Nylon sieve E by motion of the stainless steel rod C. A movable shield D prevented specks of the salt from coming into contact with the sample prior to the desired time.

The aluminum samples were prepared from 99.999% pure ingot obtained from Dr. Lee Craig of the Reynolds Metals Company. They were machined in the shape of cylinders, 1.3 cm in diameter. They were degreased in ether and were heavily etched in 2M HCl immediately prior to insertion into the reaction chamber. The appearance of the sample during the reaction was observed through the observation port Q and illumination was provided by the battery-operated lamp H.

Experimental Results

Rate measurements.—The rate curves, as determined by pressure change uncorrected for water replacement reaction, were all characterized by a linear segment in the early stages as shown by the representative curves in Fig. 2 and 3. At 100% relative humidity and 30°C there was an induction period which was as long as 40 min in some instances. This induction period decreased with decrease in relative humidity at 30°C and was much less at 40°C and 100% relative humidity than at 30°C. At low relative humidities the linear rates were not maintained for a long period and the reaction essentially ceased after 100–200 min. At high relative humidities the reaction rate decreased as the oxygen in the system approached a low value. A compilation of all the rate measurements is given in Fig. 4 in which the average value of the linear rate is plotted as a function of the relative humidity. The range of all the measurements at any one relative humidity is denoted by the bar.

At high relative humidities (90–100%) the oxide often grew as a continuous, thick, blue-white column. This column grew perpendicularly and had sufficient strength to lift the Nylon sieve from its

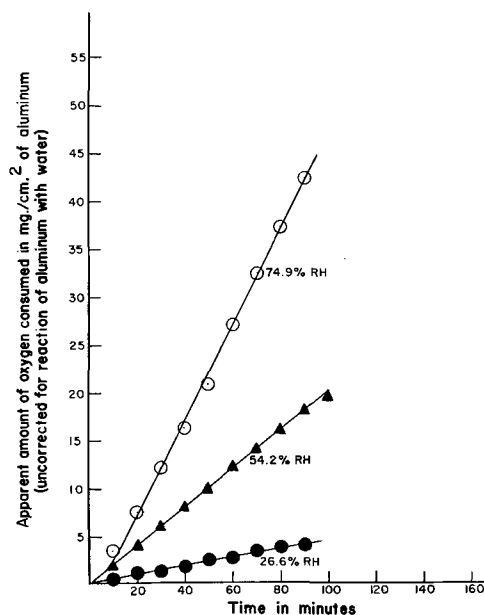


Fig. 2. Oxidation of aluminum in air in the presence of HgI_2 at 30° and different relative humidities.

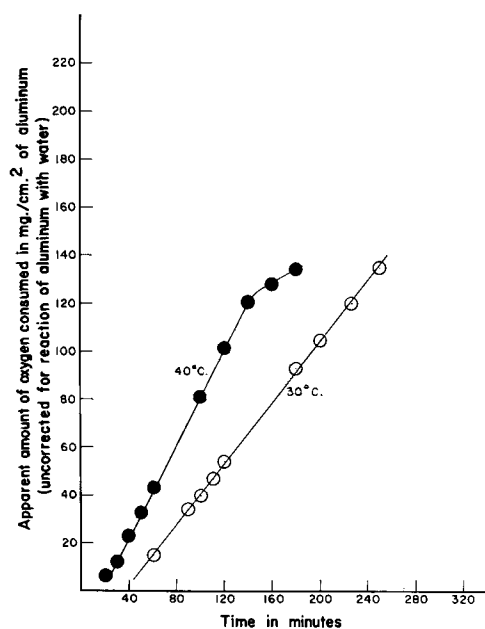


Fig. 3. Oxidation of aluminum in air at 100% relative humidity in the presence of HgI_2 .

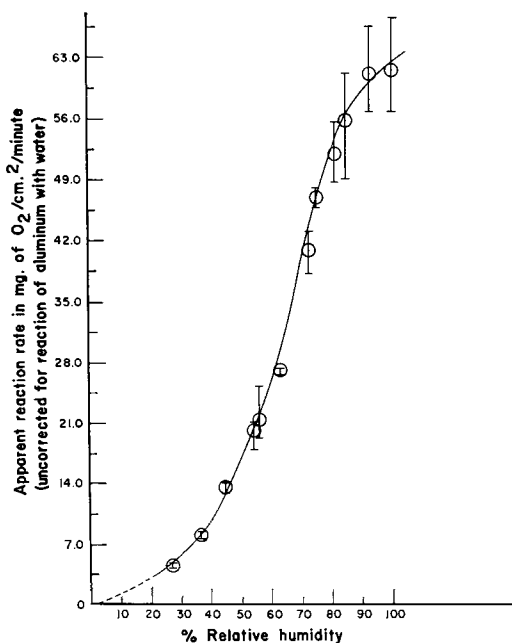


Fig. 4. Apparent reaction rate of aluminum with moist air at various relative humidities. Data are not corrected for the reaction of aluminum with water vapor. See Fig. 5 for corrected data.

support. At low relative humidities (20-50%), the oxide consisted of short fibers, somewhat powdery and pure white in color. At intermediate humidities and at high humidities long ribbons of oxide formed. Microscopic examination of the point of contact between the aluminum sample and a small crystal of HgI_2 indicated that metallic mercury was formed and that it rapidly spread over a large area from its point of origin. Oxide formed uniformly over the surface in the area covered by the spreading mercury.

As stated previously, it was known that a portion of the total over-all reaction involved a replacement reaction of water with aluminum. The method used to determine the fraction of reaction with oxygen

and with water vapor was as follows. Three to eight experiments, separate from those summarized in Fig. 4, were carried out at each of the following humidities: 36, 58, 73, 81, 85, 93, and 100%. The cylindrical samples of aluminum were rubbed in HgI_2 and were immediately placed in a closed system maintained at the desired humidity. The pressure change during the experiment was measured and the amount of aluminum consumed was determined gravimetrically. Errors in the gravimetric measurements resulting from the inability to remove the mercury completely from the surface at the end of the experiment were minimized by allowing the experiment to run for a sufficient length of time that the residual mercury represented only a small fraction of the total weight loss of the aluminum. The pressure measurements summarized in Fig. 4 were then used to calculate the amount of reaction with oxygen and the amount of the replacement reaction with water. The results of these experiments are summarized in Fig. 5.

Next, it appeared of interest to determine the rate of corrosion of aluminum in water under essentially the same conditions of amalgamation. Samples of aluminum were coated with HgI_2 , the iodide was washed off in a stream of water, and the samples were immersed for 1-24 hr in a 0.001M solution of HgCl_2 maintained at 30°. The rate of the reaction in seven experiments ranged from a low of 0.013 to a high of 0.035 $\text{mg/cm}^2/\text{min}$, with an average rate of 0.020 $\text{mg/cm}^2/\text{min}$. Thus the rate of reaction of aluminum with water vapor (0.066 $\text{mg/cm}^2/\text{min}$) was not greatly different from the rate of reaction with liquid water.

Oxidation product.—X-ray diffraction analysis of the product immediately after preparation indicated, by the absence of a diffraction pattern, that it was amorphous. This confirmed the observation made

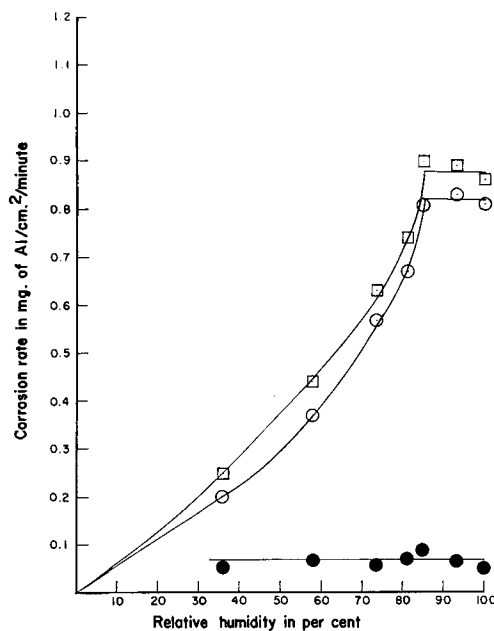


Fig. 5. Summary of the data showing the rate of reaction of aluminum with moist air as a function of relative humidity. \square , Total corrosion rate; \circ , that portion of corrosion rate due to reaction with oxygen; \bullet , that portion of corrosion rate due to replacement reaction with water.

previously by Straughan (2) on the product formed when mercury contacted a single crystal of aluminum. Subsequently, Heyn (3) noted that no crystalline pattern was obtained, using electron diffraction techniques, on the product formed on aluminum in the presence of mercury under room conditions. Lawless (4) confirmed that the product formed in the presence of HgI₂ at 100% relative humidity yields no crystalline electron diffraction pattern.

Exposure of the oxide to 100% relative humidity at room temperature for 10-21 days resulted in the crystallization of beta-Al₂O₃·3H₂O. The rate of crystallization of the trihydrate appeared to be greater for the product formed at 40°C and 100% relative humidity than at 30°C. Simultaneously with the crystallization, the sample decreased greatly in volume and it changed from its bluish-white translucent appearance to an opaque white color.

Dehydration of the product at 600°C for 3 hr resulted in a product which yielded no diffraction pattern. Rehydration of this dehydrated product by exposure to 100% relative humidity for 5-10 days resulted in the crystallization of the beta-trihydrate. Dehydration of the crystalline hydrate formed by hydration of the dehydrated, initially formed, amorphous oxide yielded anhydrous eta-Al₂O₃. The pattern obtained in this case was diffuse.

Negligible weight losses were obtained when the oxidation product was heated at 115°C for 1-10 hr. An estimate of the amount of water in the product was obtained by determining the weight loss when the sample was heated at 600°C for 3 hr. Analyses were performed on products formed at 81 and 100% relative humidity at 30°C and at 100% relative humidity at 40°C. The weight loss in eight samples ranged from a low of 31.0% to a high of 38.9% with an average loss of 33.7%. The difficulty in making accurate measurements of this type is a result of the fact that droplets of mercury and HgI₂ are occasionally trapped in the oxide during growth. This weight loss suggests that the approximate empirical composition of the product is Al₂O₃·3H₂O [or Al(OH)₃], in which the theoretical water content is 34.6% by weight.

Discussion

These experiments furnish additional convincing evidence for the highly reactive nature of aluminum when its oxide film no longer offers protection. The rate of oxidation in air at high relative humidity and 30°C, for example, was equivalent to the consumption of 0.9 mg of aluminum/cm²/min. The nonprotective nature of the reaction product was emphasized by the fact that the rate of reaction was linear with time as shown by experiments of the type reported in Fig. 2. Linear rates are often obtained with systems in which the reaction product develops faults such as cracks or pores.

Attempts to furnish a quantitative explanation for the oxidation behavior are severely limited by the inability to make measurements on or observation of the aluminum surface during reaction. The changing nature of the surface during reaction and the presence of the voluminous reaction product

precluded simultaneous rate measurements and meaningful electrical measurements, for example. It has been necessary, therefore, to attempt an explanation on the basis of measurements on samples of other types and on the basis of the electron microscope observations of Heyn (3).

The optical microscope studies indicated that the HgI₂ rapidly reacts with aluminum and the resulting free mercury spreads over the surface from its point of origin.

It is conjectured that the oxide film which forms on the mercury-contaminated aluminum surface is similar to that which is formed during anodic treatment (5) in which pores penetrate the oxide normal to the metal surface. These pores have been determined to be 100-300Å in diameter by electron microscope observations (6). It is further conjectured that the major fraction of the total oxidation of aluminum under the conditions used in these experiments is electrochemical in nature with metallic aluminum losing electrons as the anodic reaction and oxygen gaining electrons as the cathodic reaction. The rate under a certain range of experimental conditions might then be determined by the electrical properties of the oxide. Jason and Wood (5) and more recently Stover (7), have found that the impedance of anodically formed oxide films is a function of the relative humidity of the atmosphere surrounding the sample. Stover found, for example, that the impedance at 60 cycles/sec of an aluminum sample anodized with an alternating current in 50% sulfuric acid at 90°F and 12 amp/sq ft for 25 min was approximately 10⁸ ohms at 0% relative humidity, 10⁵ ohms at 40% relative humidity, 10⁴ ohms at 60% relative humidity, and approximately 2 × 10³ ohms at 100% relative humidity.

Jason and Wood found that the equivalent parallel resistance decreased from the order of 10⁷ ohms at 0% relative humidity to approximately 3 × 10³ ohms at 100% relative humidity for films formed by anodization in chromic acid, oxalic acid, and sulfuric acid. The equivalent parallel capacitance increased from 5 × 10² to 2 × 10³ microfarads at 0% relative humidity to 5 × 10⁵ microfarads at 100% relative humidity for samples anodized in the same three electrolytes.

If the properties of the films present on the surface in this study and the films studied by Jason and Wood are similar, then it may be said that the electrical properties are strongly a function of the relative humidity. Further, if the reaction is indeed electrochemical in nature, it is to be expected that the rate would be intimately related to the electrical properties of the film.

It is proposed that the passage of aluminum ions through the film occurs largely at pores whose diameter is of the order of 100Å. The electron micrograph of Heyn (3) clearly shows that the oxidation product is needle like in nature. Transport of aluminum ions through the pores apparently occurs readily and reaction with oxygen and water molecules apparently occurs within the pore or at the top surface. Transport of aluminum ions through the film necessitates the transport also of electrons. Their ready transport perhaps occurs at places

where mercury penetrates through the film, but they may also move through the film at other locations.

The positions of the pores in the film probably continually change as the aluminum at the base of the pore is consumed. Transport of aluminum atoms at the base of the pore may be facilitated by the presence of mercury and by the highly exothermic nature of the oxidation process.

The role of water in the reaction is a very complex one. It is apparent that the influence of water on the over-all rate of the oxidation of aluminum is more than simply an effect on the electrical properties of the film since water is an intimate component of the reaction product. Very little of the incorporated water was lost on heating at 115°C and the composition of the product as determined by dehydration at 600°C was equivalent to $\text{Al}_2\text{O}_3 \cdot 3\text{H}_2\text{O}(\text{Al}(\text{OH})_3)$. Storage at 100% relative humidity led to crystallization of the trihydrate. Water also was involved in a direct chemical reaction over the entire range of relative humidity in an amount equivalent to 0.066 mg of aluminum/cm²/min.

Acknowledgment

The assistance of W. Roger Buck, III, Frank V. Moore, and C. Jennings Connelly, Jr., in carrying out the experimental work is gratefully acknowledged. Support for this research was furnished by the Department of Defense.

Manuscript received July 15, 1963. This paper was presented at the Boston Meeting, Sept. 16-20, 1963.

Any discussion of this paper will appear in a Discussion Section to be published in the December 1964 JOURNAL.

REFERENCES

1. W. Roger Buck, III, and H. Leidheiser, Jr., *Corrosion*, **14**, 308t (1958).
2. V. E. Straughan, *Virginia J. Sci.*, **3**, 311 (1952).
3. A. N. J. Heyn, *This Journal*, **108**, 482 (1962).
4. K. Lawless, Private communication.
5. A. C. Jason and J. L. Wood, *Proc. Phys. Soc.*, **68B**, 1105 (1955).
6. F. Keller, M. S. Hunter, and D. L. Robinson, *This Journal*, **100**, 411 (1953).
7. C. M. Stover, "New Aluminum Oxide Humidity Element," Sandia Corp., Technical Memorandum, March 1962. Available from the Office of Technical Information Service, Washington, D. C.

The Electrical Resistivity of Pyrolytic Beta MnO_2

J. S. Wiley¹ and H. T. Knight

Rectifier-Capacitor Division, Fansteel Metallurgical Corporation, North Chicago, Illinois

ABSTRACT

In an investigation of the role of MnO_2 in the "solid electrolytic" tantalum capacitor, a technique was developed to produce samples of pyrolytic β - MnO_2 which could be used for electrical resistivity measurements without the necessity of grinding and pressing into pellets. The samples were prepared by repeatedly filling a test tube with $\text{Mn}(\text{NO}_3)_2$ solution and pyrolyzing it. The residue of MnO_2 in the tube was then used for resistivity measurements. The resistivity of such samples was approximately 0.1 ohm-cm which is two to three orders of magnitude below previously reported values from MnO_2 compacts. The effect of the addition of certain doping agents to the samples and the variation of resistivity with temperature was also studied. The only dopant of those studied which produced a lower resistivity was a vanadium-containing compound, ammonium vanadate. Two activation energies for conduction were found over the temperature range of -55° - 185°C . The more recently published values for resistivity and activation energies are summarized and compared with the present work.

The resistivity of β - MnO_2 has been investigated by several experimenters. All reported values have been on polycrystalline material. The usual technique has been to grind the sample to powder and to compact the powder to a pellet. The resistivity of such pellets has been reported to be from 10 to over 1000 ohm-cm (1-4).

In an investigation of the role of MnO_2 in the "solid electrolytic" tantalum capacitor where the oxide is used as a contacting agent between the surface of the Ta_2O_5 dielectric and the cathode, it was found that such resistivity measurements were of questionable value since the values obtained were strongly dependent on grinding and compaction. Measurements made directly on the MnO_2 produced from $\text{Mn}(\text{NO}_3)_2$ decomposition without grinding and compacting were found to

be somewhat more reproducible, and more important, it was felt that the results were more meaningful from a practical standpoint since the MnO_2 in a capacitor is usually deposited in this manner.

Experimental

Sample preparation.—Samples of β - MnO_2 were prepared by pyrolyzing A.C.S. reagent grade manganous nitrate solution (50%) in a Pyrex test tube. The residue in the bottom of the tube was moistened with the $\text{Mn}(\text{NO}_3)_2$ solution and again heated for a few minutes. This process was repeated a few times and then the sample was heated for a longer period to insure completion of the pyrolysis reaction. The tube was broken and parallelepiped samples approximately 1 x 1 x 0.5 cm were cut from the mass.

¹ Present address: Texas Instruments, Inc., Dallas, Texas.

The main body of the reaction product was confirmed to be $\beta\text{-MnO}_2$ by x-ray diffraction analysis. Samples had densities in the range of 3.6 to 4.0 g/cm^3 which represents 72-80% of the theoretical density. The material was surprisingly hard (Knoop hardness of 835 to 1180) which made it relatively simple to cut samples of desired dimensions.

X-ray and chemical analyses.—X-ray diffraction patterns of samples from the residue in the bottom of the tube showed them to be $\beta\text{-MnO}_2$. There was always a portion at the top of the sample which was porous and more fragile than the mass at the bottom. X-ray patterns showed it to be a manganese oxide with apparently smaller particle size than the bulk. Occasionally $\alpha\text{-Mn}_2\text{O}_3$ was detected in this upper portion. Material with small particle size is also observed on the exterior of anodes in the manufacture of solid tantalum capacitors.

Chemical analyses for available oxygen and total manganese were performed. Available oxygen was determined by the ferrous sulfate method as given by Katz *et al.* and total manganese by an indirect method of Schwartzenback and Biedermann (5, 6).

The portion of the sample remaining in the bottom of the tube was found to be nearly stoichiometric $\text{MnO}_{2.0}$. There was some residual material in these samples, which if it is assumed to be H_2O , amounted to about 0.04-0.09 mole/mole of MnO_2 . There was a general reduction of stoichiometry in samples along the sides of the tube above the main volume of MnO_2 . For example, one sample varied from 84.3% MnO_2 to 97.0% MnO_2 from the top of the tube to a point just above the main volume of MnO_2 .

Technique and results of resistivity measurements.—Samples for electrical resistivity measurements were cut from the bulk material which was most nearly stoichiometric. The resistivity of the samples was measured in a variety of ways including 4-probe, single probe, and voltmeter-ammeter methods.

Most of the samples were measured in a single probe device in which the parallelepiped samples were placed in a jig and two opposite ends were pressure contacted by indium coated, copper plates. Current was passed through the sample and a probe connected to a voltmeter measured the voltage profile across the MnO_2 sample. Current was supplied with a battery supply and voltage measured with a Keithley Electrometer, Model 610A.

This method eliminates the problems of contact resistance and rectifying contacts. A four probe apparatus as described by Valdes was also used to measure certain samples (7). A third method was a simple voltmeter-ammeter method. The ends of the samples were coated with silver paint and copper wire leads were imbedded in the paint. The paint was baked dry, thereby bonding the leads to the sample. A voltmeter-ammeter circuit was used to determine the resistance of the sample. This method was useful only on samples of relatively high resistance, since the contact resistance between the silver and the MnO_2 was about 0.1 ohm. The methods all gave values in good agreement.

Table I. Resistivity and density values of *in situ* MnO_2 samples

No. of fillings of test tube with $\text{Mn}(\text{NO}_3)_2$	Resistivity (ohm-cm)		Apparent density (g/cc)	
	Average	Standard deviation	Average	Standard deviation
1	1.56	0.37	2.50	—
2	0.18	0.09	3.59	0.16
3	0.14	0.03	3.92	0.18

$$\rho = KR \frac{A}{L}; K = \frac{\text{Apparent density}}{5.03}$$

With the single probe and voltmeter-ammeter measurements, resistivity was computed from

$$\rho = \frac{KRA}{L} \quad [1]$$

where ρ is resistivity in ohm-cm; R sample resistance; A cross sectional area of sample, cm^2 ; L sample length, cm; and K correction factor which is actually density/theoretical density.

The K in [1] is used in an attempt to correct for the porosity of the samples. It did not greatly affect the results, however, since its value was 0.72-0.80 in all cases. Table I shows the resistivity values obtained on various samples and the number of fillings of the test tube used.

The biggest drop in resistivity occurs after a second filling of the test tube. Other experiments showed that further fillings beyond three had no significant effect on resistivity values, so most subsequent measurements were made on samples with three fillings. The nonreproducibility between samples from a given number of fillings is probably due to the porous nature of the samples.

Certain experiments were done in order to validate the techniques of measurement and to insure that the resistivity being measured was really a property of the manganese oxide rather than an effect of surface treatment. The external surface area/volume ratio was changed on individual samples by a factor of two with no corresponding change in resistivity. This indicated that there was no significant effect due to the external surface.

Effect of pyrolysis conditions on MnO_2 .—Two parameters were varied in a study of the effect of the conditions of pyrolysis on the resulting manganese dioxide; these were (i) length of time, and (ii) temperature of pyrolysis.

The object of (i) above was to determine the length of time at various temperatures necessary to reach a constant value of resistivity. To do this, two platinum electrodes were introduced into the $\text{Mn}(\text{NO}_3)_2$ solution and the resistance of the solution during pyrolysis was monitored on a resistance bridge. As the $\text{Mn}(\text{NO}_3)_2$ decomposed, the resistance changed as shown in Fig. 1. The postulate is that section A-B of the curve represents the resistance of the liquid $\text{Mn}(\text{NO}_3)_2$ solution. After point B, enough MnO_2 is present so that the conduction is controlled by the electronic current in the MnO_2 rather than the ionic current of the solution. This results in a sharp decrease in the resistance as seen in section B-C. After point C, the resistance slowly increases and approaches a con-

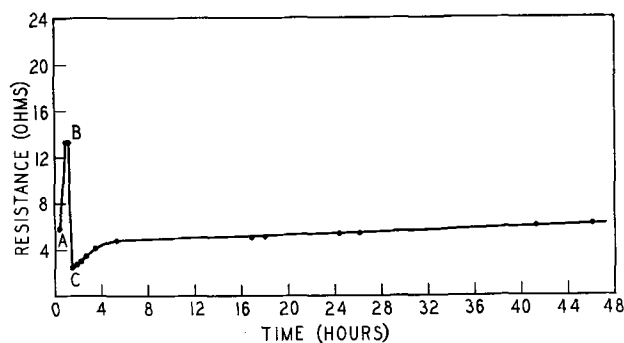


Fig. 1. Variation of resistance of $\text{Mn}(\text{NO}_3)_2\text{-MnO}_2$ at 250°C

stant value as the $\text{Mn}(\text{NO}_3)_2$ decomposition proceeds to completion.

Most samples were heated at 250°C for at least 20 hr which produced samples having nearly constant resistivity. It was found that samples pyrolyzed at 150° and 400°C required approximately 50 and 8 hr, respectively, to reach a resistance plateau. Thus, subsequent samples prepared at these temperatures were heated for at least these lengths of time.

Another area of interest is the effect of pyrolysis temperature on the resistivity of manganese dioxide. A series of 10 samples was prepared at 150° , 250° , and 370°C for a sufficient time to come to constant value of resistivity, and the room temperature resistivity was measured. One of the samples was then heated successively at 450° , 500° , 525° , 600° , and 650°C in order to extend the range of temperature. Table II summarizes these results.

There is relatively little change in the resistivity until the temperature range of $370^\circ\text{-}450^\circ\text{C}$ is reached. A later discussion will compare this behavior to thermal decomposition experiments by Brenet and correlate the composition and resistivity changes.

Effect of added impurities.—In an effort to change the resistivity of the MnO_2 samples, certain compounds were added to the $\text{Mn}(\text{NO}_3)_2$ solution and reacted with it during the pyrolysis. Table III shows the compounds with the cations being introduced and the resistivities of the resulting samples.

Generally if as much as 1 atomic per cent (a/o) was added to the MnO_2 , the resulting samples were soft and fragile and the $\beta\text{-MnO}_2$ crystal structure was disturbed. In the case of the aluminum dopant, however, the samples containing 1 a/o were still reasonably hard.

Only the 0.1 a/o vanadium dopant produced samples having resistivities out of the range of un-

Table II. Resistivity of MnO_2 formed at various pyrolysis temperatures

Temperature, $^\circ\text{C}$	Average resistivity (ohm-cm)	Standard deviation (ohm-cm)
150	0.15 (10 samples)	0.03
250	0.14 (10 samples)	0.03
370	0.17 (10 samples)	0.04
450	0.39	
500	1.20	
525	1.30×10^4	
600	3.60×10^5	
650	3.60×10^5	

Table III. Doping of MnO_2 samples

Compound introduced	Concentration (% metallic cations per Mn atom)	Resistivity (ohm-cm) Average values (2-6 samples for each concentration)
$\text{Al}(\text{NO}_3)_3 \cdot 9\text{H}_2\text{O}$	1.0	1.07
	0.1	0.20
As_2O_5	1.0	0.15
	0.1	0.15
$(\text{NH}_4)_6\text{Mo}_7\text{O}_{24} \cdot 4\text{H}_2\text{O}$	1.0	0.10
$\text{NH}_4 \cdot \text{VO}_3$	0.2	0.16
	0.1	0.02
$\text{Cr}(\text{NO}_3)_3 \cdot 9\text{H}_2\text{O}$	0.2	0.14
	0.1	0.17

Table IV. Reported values for activation energy of conduction in MnO_2

Author	Temperature range, $^\circ\text{C}$	E (ev)
Brenet	20-80	0.25-0.32
Das	10-143	0.13-0.19*
Bhide and Damle	0-140	0.10-0.30 (Observe anomaly at 50°C)
Present work		
Sample A (one tube filling)	-55-140	0.019
Sample B (three tube fillings)	140-190	0.096
	-55-115-130	0.022
	130-200	0.074

* Natural ores.

doped samples without significant crystalline disturbance.

Activation energy experiments.—A series of experiments was done whereby the variation of resistivity with temperature was measured. In all cases, the data could be fitted to an expression of the form $\rho = C \exp E/KT$, where C is a constant, E an activation energy, K Boltzmann's constant, and T the absolute temperature in degrees Kelvin. The samples were measured by painting on contacts as previously described and using a voltmeter-ammeter technique. The results are contained in Table IV for two typical samples.

Sample A was a singly pyrolyzed sample having a density of approximately 2.5 g/cc and sample B was a triply pyrolyzed sample having a density of approximately 4.0 g/cc. The undoped samples exhibit a change of slope in the region of $115^\circ\text{-}140^\circ\text{C}$. Although the samples A and B differ by about an order of magnitude in their apparent resistivity, the activation energies for the two samples are comparable and both samples show a change of slope at about the same temperature.

Discussion

Huston points out that there are a great many difficulties encountered in obtaining meaningful data on polycrystalline samples (8). Unfortunately, many materials, $\beta\text{-MnO}_2$ included, can be readily obtained only in such a condition and one is thus limited to measurements on such samples.

In the case of the present study, the uncertainty about the influence of the polycrystalline structure of the MnO_2 was somewhat negated, since the in-

Table V. Reported resistivity values of β - MnO_2

Author	Resistivity (ohm-cm) measured at room temperature	Form of samples
Sasaki and Kojima (1954)	350	Pressed pellets
Glicksman and Moorehouse (1956)	33-77	Pressed pellets*
Brenet (1959)	115	Pressed pellets
Bhide and Damle (1960)	10-1000	Pressed pellets**
Present work (1961)	20-70	Pressed pellets
	≈ 1.0	<i>In situ</i> samples, single pyrolysis
	≈ 0.14	<i>In situ</i> samples, triple pyrolysis

* Sample measured in press.

** Natural ores and artificial β - MnO_2 .

terest was in its relation to solid electrolytic capacitors where it is found in polycrystalline form anyway. Thus, although the properties reported may not represent exactly the behavior of a stoichiometric single crystal of MnO_2 , it is felt that these samples are similar to the MnO_2 in solid electrolytic capacitors. Furthermore, due to the technique of preparation, it is felt that these *in situ* samples represent the MnO_2 in such capacitors to a far greater extent than do pressed pellets.

Resistivity values.—Table V shows some of the more recent values of resistivity which have been reported. The date and form of the sample are also given.

There are rather large variations in these reported values of pressed samples. None of these, however, approach the low value of the *in situ* samples. The most obvious explanation of the difference is that the interparticle bonding is much stronger in the *in situ* samples as witnessed by the hardness and cohesion of these samples. The pressed samples, on the other hand, are quite fragile.

Pyrolysis conditions.—Figure 2 shows the resistivity *vs.* pyrolysis temperature behavior which was given in Table II. Adjacent to this curve is

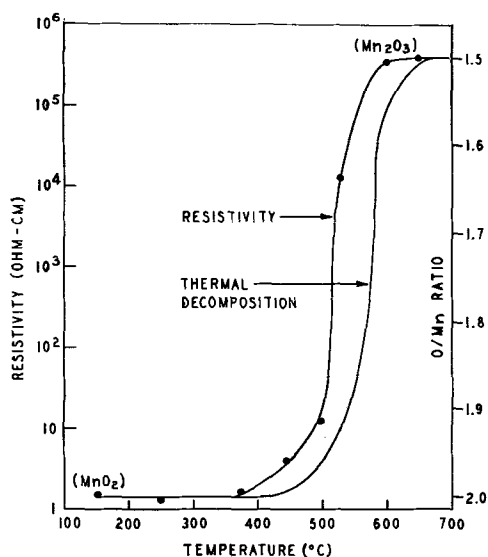


Fig. 2. Resistivity and thermal decomposition curves

a thermal decomposition curve by Brenet which shows the composition changes over the same range (9). The O/Mn ratio is plotted on the right ordinate of the figure.

The comparison of the two curves is interesting since they show similar behavior, namely constant values from 150° to 370°-450°C then a rapid rise. At a range of 600°-650°C the curves again approach a constant value. The resistivity curve changes at a somewhat lower temperature than the thermal decomposition curve, but this is probably explainable on the basis of the difference in equilibrium attained in the two processes. The resistivity samples were heated for approximately 100 hr or until the resistivity remained constant. Further, the resistivity values may be somewhat more sensitive to composition changes than the weight changes reported by Brenet.

Chemical analyses by the methods previously described showed that the Mn/O ratio was constant from pyrolysis temperatures of 150°-400°C. A change in the amount of residual material, assumed to be water, of from 0.09 to 0.04 mole/mole of MnO_2 was found with these samples. X-ray diffraction analysis showed only β - MnO_2 from samples pyrolyzed up to 400°C. At 450°C and above, α - Mn_2O_3 shows up, and at 600°C nothing but α - Mn_2O_3 is present.

Brenet indicates that water or OH^- may be lost from the samples above 350°C. Our own analyses tend to support this, thus some of the earliest changes in resistivity above 370°C may be due to loss of water. Above 450° the resistivity change becomes more rapid and the presence of α - Mn_2O_3 is detected. The great change in resistivity between 450° and 600°C can be attributed to the formation of Mn_2O_3 , a poor conductor. The resistivity again becomes constant at a value of 3.6×10^5 ohm-cm as the constant composition of Mn_2O_3 is attained.

Activation energy.—Values of activation energy for conduction reported by various authors or computed from their resistivity data are shown in Table V.

Again, the probable difference between pressed pellets and *in situ* samples is the difference in particle bonding. Although samples A and B have different resistivities, their activation energies are nearly the same. This indicates that the particle bonding and conduction mechanism are identical and the difference in apparent resistivity is due to the failure of the correction factor, K , in Eq. [1] to adequately allow for the sample porosity in sample A. In other words, the less dense a sample is, the greater is the error in Eq. [1] due to lack of knowledge of the equivalent sample cross section or length.

The change of slope at 115°-130°C is not fully understood. It is tempting to refer to it as an extrinsic-intrinsic conductivity transformation. There are, however, other possibilities which must be considered. One of these is that the point of the shift represents the ferroelectric Curie point. Bhide has reported such behavior, except at a lower temperature of about 50°C (4).

Another possibility is that a surface layer of a lower oxide of manganese such as Mn_2O_3 is formed which results in an increase in the activation energy. It is known that on heat treatment, various types of manganese dioxide form a surface film of lower oxide (11). A third possible cause is loss of water from the samples which has been reported by Sasaki and Kojima (1). Since the activation energy curves are reversible up and down the temperature range, this seems a likely cause. The $Mn_2O_3 \rightarrow MnO_2$ transformation has been reported by Otto to be quite slow, thus it seems less likely to be the cause (12).

Lack of information about the conduction mechanism in MnO_2 makes it difficult to interpret activation energy data. Das has shown that in naturally occurring ores, the carrier concentration is $\approx 4.3 \times 10^{19}$ per cc (10). Thermoelectric and Hall constant measurements show that the conduction is n-type with low mobility carriers. It seems obvious that further basic studies including studies of the effect of metal and oxygen defects are necessary before a complete model of the conduction process can be postulated. The information available, however, indicates that MnO_2 is a nearly degenerate semiconductor.

Acknowledgments

The authors wish to thank Messrs. A. Shtasel and R. Hoeckelman for many helpful discussions. The

aid of M. Cunningham and S. Kaski in the performance of the experiments is also gratefully acknowledged.

Manuscript received Aug. 8, 1963. This paper was presented at the Pittsburgh Meeting, April 15-18, 1963.

Any discussion of this paper will appear in a Discussion Section to be published in the December 1964 JOURNAL.

REFERENCES

1. K. Sasaki and K. Kojima, *J. Electrochem. Soc. Japan*, **22**, 564 (1954).
2. R. Glicksman and C. K. Moorehouse, *This Journal*, **103**, 149 (1956).
3. J. Brenet, *Schweizer Archiv., Angew. Wiss. U. Tech.*, **26**, (1), 10 (1960), *Compt. rend.*, **248**, 776 (1959).
4. V. G. Bhide and R. V. Damle, *Physica*, **26**, 33 (1960).
5. M. J. Katz, R. C. Clarke, and W. F. Nye, *Anal. Chem.*, **28**, 507 (1956).
6. G. Schwarzenback and W. Biedermann, *Helv. Chim. Acta*, **31**, 459 (1948).
7. L. B. Valdes, *Proc. Inst. Radio Engrs.*, **42**, 420 (1954).
8. A. R. Huston, in "Semiconductors," N. B. Hannay, Editor, Chapt. 13, p. 541, Reinhold Publishing Co., New York (1959).
9. J. Brenet and A. Grund, *Compt. rend.*, **240**, 1210 (1955).
10. J. N. Das, *Z. Physik*, **151**, 345 (1958).
11. A. Kozawa, *This Journal*, **106**, 79 (1959).
12. E. M. Otto, "Thermal Dissociation of Manganese Dioxides," paper presented at September 1960 Meeting of The Electrochemical Society.

Phase Equilibria and Manganese-Activated Luminescence in Portions of the System $Zn(PO_3)_2$ - $Cd(PO_3)_2$ - $Mg(PO_3)_2$

Jesse J. Brown and F. A. Hummel

Department of Ceramic Technology, The Pennsylvania State University, University Park, Pennsylvania

ABSTRACT

The equilibrium relationships in the system $Zn(PO_3)_2$ - $Cd(PO_3)_2$ were established by quenching and solid state experiments. At 810°C α - $Cd(PO_3)_2$ inverted to β - $Cd(PO_3)_2$, which melted congruently at 896°C. Small regions of solid solution exist at the extremities of the system, involving the low and high temperature forms of $Zn(PO_3)_2$ and $Cd(PO_3)_2$. The most noteworthy feature of the system is the large region of intermediate solid solution which ranges from 35 to 90 mole % $Cd(PO_3)_2$ and has a distorted $Mg(PO_3)_2$ structure.

Manganese-activated phosphors were prepared throughout the system $Zn(PO_3)_2$ - $Cd(PO_3)_2$ - $Mg(PO_3)_2$ and the cathodoluminescence emission peak and brightness values were obtained. The ternary system is dominated by a solid solution which has the $Mg(PO_3)_2$ structure. The phosphors are characterized by two emission peaks in the ranges 5950-5590Å and 6200-6420Å. Cadmium metaphosphate increases the intensity of the higher wavelength emission while $Zn(PO_3)_2$ and $Mg(PO_3)_2$ -rich compositions favor the lower wavelength emission.

This is the second of a series of papers intended to establish the phase equilibria relationships and to investigate and identify the host lattices which are responsible for luminescence in a portion of the system ZnO - CdO - P_2O_5 . Although this paper is primarily concerned with phase relationships and cathodoluminescence in the binary system $Zn(PO_3)_2$ - $Cd(PO_3)_2$, it also contains cathodoluminescence

data for preparations throughout the ternary system $Zn(PO_3)_2$ - $Cd(PO_3)_2$ - $Mg(PO_3)_2$.

The phase relationships and cathodoluminescence of phases in the system $Zn(PO_3)_2$ - $Mg(PO_3)_2$ have recently been investigated by Sarver and Hummel (1). Two previous papers by Katnack and Hummel (2) and Hummel and Katnack (3) have dealt with the phase relationships in the system ZnO - P_2O_5 and

the emission characteristics of the manganese-activated zinc phosphate compounds under cathode ray excitation.

Experimental Procedure

Compositions used for determining phase relationships.—The equilibrium relationships in the system $\text{Zn}(\text{PO}_3)_2\text{-Cd}(\text{PO}_3)_2$ were established using the fourteen compositions listed in Table II. The raw materials used were phosphor grade ZnO , MgCO_3 , MnCO_3 , and CdCO_3 , and C.P. grade ammonium dihydrogen phosphate, $\text{NH}_4\text{H}_2\text{PO}_4$. The batch materials for quench and DTA experiments were reacted in the solid state at 750°C for 24 hr, re-mixed, and reacted again at 750°C for 24 hr. Based on previous experience with metaphosphate compounds (1, 2), loss of P_2O_5 by vaporization has been found to be small under these conditions of preparation.

Portions of each composition were melted in platinum crucibles for 15 min between 1000° and 1200°C and the melts were air quenched. The glasses were crushed in a steel mortar and the -100 to $+120$ mesh size fraction was used for index of refraction measurements.

Heat treatments and physical measurements.—The melting, quenching, solid state reactions, phase identification, differential thermal analysis, and measurement of emission spectra were carried out as described previously (4).

X-ray diffraction data were obtained using $\text{CuK}\alpha$ ($\lambda = 1.5418\text{\AA}$) radiation from a Norelco diffractometer operating at 40 kv and 15 ma. Precise lattice spacings were obtained using silicon powder ($a_0 = 5.4305\text{\AA}$) as an internal standard and a diffractometer scanning rate of $\frac{1}{4}^\circ\text{-}2\theta$ min. Petrographic microscope determinations of refractive indices of glasses were accurate to ± 0.003 using immersion oils which had been calibrated with an Abbé refractometer. Cathodoluminescence spectral distributions were determined on a demountable television tube using an electron beam with a current density of $1.0 \mu\text{amp}/\text{cm}^2$ and an accelerating potential of 15 kv.

Results and Discussion

Cadmium metaphosphate.—It was determined by quench experiments that $\text{Cd}(\text{PO}_3)_2$ undergoes a sluggish reversible inversion at $810^\circ \pm 5^\circ\text{C}$ and melts

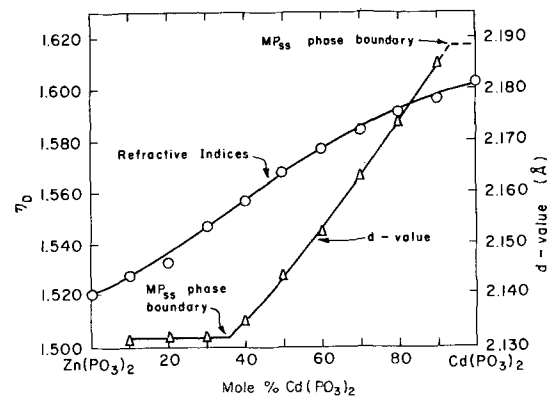


Fig. 1. Index of refraction of metaphosphate glasses and d -values of MP_{SS} (750°C) for reflection at $42^\circ\text{-}2\theta$.

congruently at $896^\circ \pm 5^\circ\text{C}$. Upon recrystallization an apparently metastable polymorphic phase initially crystallizes which rapidly reverts to the stable polymorph with increasing time of heat treatment. The powder x-ray diffraction data for the two stable cadmium metaphosphate polymorphs are shown in Table III.

Phase equilibrium relationships in the system $\text{Zn}(\text{PO}_3)_2\text{-Cd}(\text{PO}_3)_2$.—The indices of refraction and d -values for the reflection¹ at $42^\circ\text{-}2\theta$ for compositions in the $\text{Zn}(\text{PO}_3)_2\text{-Cd}(\text{PO}_3)_2$ system are tabulated in Table I and plotted as functions of composition in Fig. 1. These data were used extensively to determine phase boundaries from many of the quenches made in this system. The quench data shown in Table II were used to construct the phase equilibria relationships shown in Fig. 2.

The phase diagram is characterized by a large intermediate solid solution series (MP_{SS}) extending from 35 to 90 mole % $\text{Cd}(\text{PO}_3)_2$, a small region of $\beta\text{-Zn}(\text{PO}_3)_2$ solid solution which will accept a maximum of 10 mole % $\text{Cd}(\text{PO}_3)_2$ at 786°C , a small region of $\beta\text{-Cd}(\text{PO}_3)_2$ solid solution which will accept a maximum of 5 mole % $\text{Zn}(\text{PO}_3)_2$ at 840°C , and vanishingly small regions of $\alpha\text{-Zn}(\text{PO}_3)_2$ and $\alpha\text{-Cd}(\text{PO}_3)_2$ solid solutions. Since the α to $\beta\text{-Zn}(\text{PO}_3)_2$ inversion is irreversible, it was impossible to accurately determine the degree to which this transformation temperature was decreased by

¹ The MP_{SS} phase (Fig. 1) appears to have a structure of low symmetry (monoclinic or triclinic), consequently the reflection at $42^\circ\text{-}2\theta$ was the highest angle reflection suitable for d -value measurements.

Table I. Refractive indices of glasses and d -values for the $42^\circ\text{-}2\theta$ reflection from the MP_{SS} phase in the system $\text{Zn}(\text{PO}_3)_2\text{-Cd}(\text{PO}_3)_2$

Composition (mole %)		n_D of glasses	d (Å)
$\text{Zn}(\text{PO}_3)_2$	$\text{Cd}(\text{PO}_3)_2$		
100	0	1.521	—
90	10	1.528	2.131
80	20	1.533	2.132
70	30	1.547	2.132
60	40	1.557	2.135
50	50	1.568	2.144
40	60	1.577	2.152
30	70	1.584	2.163
20	80	1.591	2.174
10	90	1.596	2.185
0	100	1.603	—

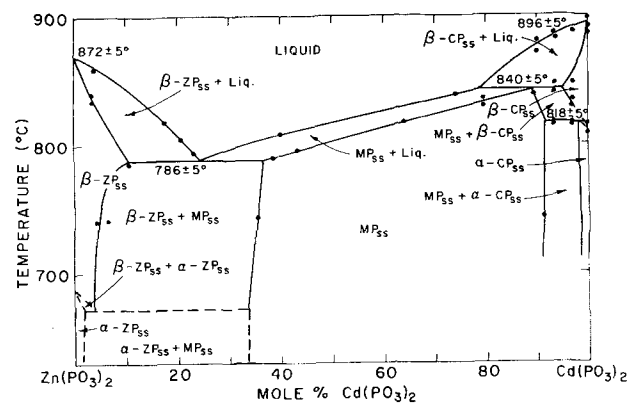


Fig. 2. Equilibrium relationships in the system $\text{Zn}(\text{PO}_3)_2\text{-Cd}(\text{PO}_3)_2$

Table II. Quench data for the system $Zn(PO_3)_2$ - $Cd(PO_3)_2$

No.	Composition (mole %)		Temp (°C)	Time	Phases*	Remarks
	Zn $(PO_3)_2$	Cd $(PO_3)_2$				
1	97	3	755	24 hr	β -ZP _{ss}	
			857	60 min	β -ZP _{ss}	
			862	90 min	β -ZP _{ss} + G	
			866	60 min	β -ZP _{ss} + G	Trace β -ZP _{ss}
2	93	7	755	24 hr	β -ZP _{ss} + MP _{ss}	
			3	90	10	755
783	35 min	β -ZP _{ss} + MP _{ss}				
4	80	20	804	30 min	β -ZP _{ss} + G	Trace G
			821	30 min	β -ZP _{ss} + G (18.5)	
			832	30 min	β -ZP _{ss} + G (12.0)	
			622	72 hr	β -ZP _{ss} + MP _{ss} + α -ZP _{ss}	Nonequilibrium
			665	1 wk	β -ZP _{ss} + MP _{ss} + α -ZP _{ss}	Nonequilibrium
			787	30 min	β -ZP _{ss} + G	Trace G
5	70	30	793	30 min	β -ZP _{ss} + G (24.0)	
			805	30 min	β -ZP _{ss} + G (20.0)	
			811	30 min	β -ZP _{ss} + G	Trace β -ZP _{ss}
			756	17 hr	β -ZP _{ss} + MP _{ss} (36.0)	
6	60	40	750	24 hr	MP _{ss}	
			794	45 min	MP _{ss}	
			799	45 min	MP _{ss} (45.0) + G	Trace G
			805	45 min	MP _{ss} + G	
			811	45 min	MP _{ss} + G (40.0)	
7	50	50	750	24 hr	MP _{ss}	
			810	3½ hr	MP _{ss} + G	Trace G
8	40	60	750	24 hr	MP _{ss}	
			816	35 min	MP _{ss} (66.5) + G	
			825	35 min	G	
9	30	70	750	24 hr	MP _{ss}	
10	20	80	750	24 hr	MP _{ss}	
			832	30 min	MP _{ss}	
			835	30 min	MP _{ss} + G	
			842	35 min	MP _{ss} + G (76.0)	
11	10	90	795	14 hr	MP _{ss}	
			805	14 hr	MP _{ss}	
			825	20 hr	MP _{ss}	
			846	30 min	β -CP _{ss} + G	
			854	60 min	β -CP _{ss} + G	
			862	60 min	β -CP _{ss} + G	
12	7	93	881	60 min	G	
			795	14 hr	MP _{ss} + α -CP _{ss}	
			805	14 hr	MP _{ss} + α -CP _{ss}	
			816	25 hr	MP _{ss} + α -CP _{ss}	
			821	20 hr	MP _{ss} + β -CP _{ss}	
			825	20 hr	MP _{ss} + β -CP _{ss}	
			837	15 hr	MP _{ss} + β -CP _{ss}	
			842	30 min	MP _{ss} + β -CP _{ss}	
			858	30 min	β -CP _{ss} + G	
			861	30 min	β -CP _{ss} + G	
			870	45 min	β -CP _{ss} + G	
			880	45 min	β -CP _{ss} + G	Trace β -CP _{ss}
13	3	97	888	60 min	G	
			902	60 min	G	
			800	14 hr	MP _{ss} + α -CP _{ss}	
			805	9 hr	MP _{ss} + α -CP _{ss}	
			807	24 hr	MP _{ss} + α -CP _{ss}	
			833	30 min	β -CP _{ss}	
			840	7½ hr	β -CP _{ss}	
			847	30 min	β -CP _{ss}	
			855	30 min	β -CP _{ss}	
			871	60 min	β -CP _{ss} + G	Trace G
14	0	100	890	60 min	β -CP _{ss} + G	Trace β -CP _{ss}
			805	12 hr	α -CP	
			810	5 hr	α -CP + β -CP	Nonequilibrium
			817	2 hr	α -CP + β -CP	Nonequilibrium
			830	1 hr	α -CP + β -CP	Nonequilibrium
			831	16 hr	β -CP	
			852	12 hr	β -CP	
			886	1 hr	β -CP	
			894	1 hr	β -CP	
			899	1 hr	G	

* G, glass; α -ZP_{ss}, α -Zn(PO₃)₂ solid solution; β -ZP_{ss}, β -Zn(PO₃)₂ solid solution; MP_{ss}, intermediate solid solution series with Mg(PO₃)₂ structure; α -CP_{ss}, α -Cd(PO₃)₂ solid solution; β -CP_{ss}, β -Cd(PO₃)₂ solid solution.

Table III. X-ray data for the system $Zn(PO_3)_2$ - $Cd(PO_3)_2$

$Mg(PO_3)_2$ ⁽¹⁾ d I/I ₀	$(Zn_{0.60}, Cd_{0.40})$ d $(PO_3)_2$ I/I ₀	$(Zn_{0.40}, Cd_{0.60})$ d $(PO_3)_2$ I/I ₀	$(Zn_{0.20}, Cd_{0.80})$ d $(PO_3)_2$ I/I ₀	$(Zn_{0.10}, Cd_{0.90})$ d $(PO_3)_2$ I/I ₀	α - $Cd(PO_3)_2$ d I/I ₀	β - $Cd(PO_3)_2$ d I/I ₀							
6.1	10	6.7	20	6.7	20	6.7	20	6.5	15	6.8	100	5.6	50
		6.3	55	6.3	65	6.4	65	6.9	55	4.8	10	4.4	5
		5.3	5	5.3	10	5.3	5	5.4	5	3.92	100	3.69	60
4.6	45	4.6	15	4.5	15	4.7	20	4.7	20	3.80	10	3.40	15
4.2	25	4.3	70	4.3	80	4.4	65	4.4	50	3.55	80	3.36	10
		3.83	10	3.87	10	3.88	10	3.90	5	3.41	25	3.29	100
		3.60	20	3.63	15	3.66	20	3.78	20	3.30	15	3.07	30
3.51	15	3.47	15	3.45	50	3.49	40	3.52	35	3.20	25	2.80	15
3.36	25	3.43	45							3.12	15	2.66	25
3.21	45	3.24	40	3.27	50	3.29	40	3.30	35	3.07	10	2.61	25
3.16	35												
2.99	100	3.05	100	3.07	100	3.10	100	3.11	100	2.92	5	2.49	50
2.86	20	2.89	25	2.91	25	2.96	25	2.94	25	2.84	20	2.37	10
2.72	5	2.75	—	2.76	5	2.77	5	2.78	5	2.77	70	2.25	10
		2.68	5	2.70	10	2.71	10	2.73	10	2.46	70	2.16	10
2.56	20	2.63	25	2.65	25	2.68	25	2.67	25	2.37	5	2.14	5
		2.53	10	2.50	10	2.56	15	2.56	10	2.33	10	2.12	5
2.37	15	2.44	25	2.45	30	2.48	30	2.49	25	2.32	10	2.05	15
		2.36	—	2.34	5	2.36	5	2.36	10	2.25	10	1.977	10
2.27	5	2.30	5	2.33	10	2.34	10	2.30	10	2.21	10	1.925	15
2.24	5	2.23	10	2.25	10	2.27	10	2.27	10	2.18	5	1.848	20
		2.21	5	2.23	5	2.23	10	2.24	10	2.17	5	1.834	10
2.18	10	2.19	10	2.20	10	2.19	5	2.21	10	2.10	10	1.794	10
2.09	20	2.14	30	2.15	30	2.17	20	2.18	20	2.06	10	1.787	5
1.940	5	1.989	10	2.00	10	2.02	10	2.03	10	2.05	10	1.752	5
Other reflections	Other reflections	Other reflections	Other reflections	Other reflections	Other reflections	Other reflections	Other reflections	Other reflections	Other reflections	Other reflections	Other reflections	Other reflections	Other reflections

the addition of $Cd(PO_3)_2$, therefore this region of the phase diagram is shown by dashed lines.

In Table III the x-ray diffraction powder data for various compositions in the MP_{ss} stability region are compared with that of the compound $Mg(PO_3)_2$.

It can be seen that these structures are very similar. Some additional weak reflections are present in the MP_{ss} patterns which may indicate structural distortion as a result of replacing Mg^{2+} by the larger Cd^{2+} ions.

Table IV. Composition and cathodoluminescence emission data for phosphors in the system $Zn(PO_3)_2$ - $Cd(PO_3)_2$ - $Mg(PO_3)_2$

No.	$Zn(PO_3)_2$	Composition (mole %)		$Mn(PO_3)_2$	Temp/Time (°C)/(hr)	Phase	Brightness (ft-L)	Peak wavelength	
		$Cd(PO_3)_2$	$Mg(PO_3)_2$					Primary	Secondary
1	—	—	99.0	1.0	750/24	MP	7.8	6080	—
2	—	9.9	89.1	1.0	750/24	MP _{ss}	7.9	5950	6180
3	—	19.8	79.2	1.0	750/24	MP _{ss}	10.3	5870	6160
4	—	29.7	69.3	1.0	750/24	MP _{ss}	23.3	5840	6190
5	—	39.6	59.4	1.0	750/24	MP _{ss}	22.8	5800	6210
6	—	49.5	49.5	1.0	750/24	MP _{ss}	22.9	6330	5790
7	—	59.4	39.6	1.0	750/24	MP _{ss}	14.3	6350	5770
8	—	69.3	29.7	1.0	750/24	MP _{ss}	9.1	6390	5700
9	—	79.2	19.8	1.0	750/24	MP _{ss}	9.4	6380	5680
10	—	89.1	9.9	1.0	750/24	MP _{ss}	8.3	6410	5670
11	—	99.0	—	1.0	800/24	α -CP	46.1	5580	—
12	—	99.0	—	1.0	835/10	β -CP	16.1	5850	—
13	99.0	—	—	1.0	600/96	α -ZP	12.9	6240	—
14	99.0	—	—	1.0	750/24	β -ZP	19.1	5880	6300
15	69.3	29.7	—	1.0	750/24	β -ZP _{ss} + MP _{ss}	23.1	5820	6290
16	59.4	39.6	—	1.0	750/24	MP _{ss}	27.6	5800	6320
17	49.5	49.5	—	1.0	750/24	MP _{ss}	21.3	5780	6360
18	39.6	59.4	—	1.0	750/24	MP _{ss}	19.2	6360	5760
19	29.7	69.3	—	1.0	750/24	MP _{ss}	16.9	6400	5710
20	19.8	79.2	—	1.0	750/24	MP _{ss}	12.1	6410	5660
21	9.9	89.1	—	1.0	750/24	MP _{ss}	9.2	6420	5590
22	9.9	9.9	79.2	1.0	750/24	MP _{ss}	10.2	5930	6190
23	19.8	19.8	59.4	1.0	750/24	MP _{ss}	20.4	5870	6250
24	9.9	29.7	59.4	1.0	750/24	MP _{ss}	25.9	5850	6220
25	29.7	9.9	59.4	1.0	750/24	MP _{ss}	16.1	5930	6320
26	29.7	29.7	39.6	1.0	750/24	MP _{ss}	30.8	5850	6230
27	14.85	44.55	39.6	1.0	750/24	MP _{ss}	26.0	5790	6290
28	44.55	14.85	39.6	1.0	750/24	MP _{ss}	27.9	5920	—
29	39.6	39.6	19.8	1.0	750/24	MP _{ss}	27.1	5750	6260
30	19.8	59.4	19.8	1.0	750/24	MP _{ss}	23.7	6330	5690
31	59.4	19.8	19.8	1.0	750/24	MP _{ss}	32.3	5650	—

It is interesting to note the analogy between the $\text{Zn}(\text{PO}_3)_2\text{-Cd}(\text{PO}_3)_2$ system which contains a large region of an intermediate solid solution phase with the $\text{Mg}(\text{PO}_3)_2$ structure and the $\text{Zn}_3(\text{PO}_4)_2\text{-Cd}_3(\text{PO}_4)_2$ system which contains a small region of an intermediate solid solution phase with the $\text{Mg}_3(\text{PO}_4)_2$ structure (4).

Luminescence

Table IV contains the compositions and cathodoluminescence emission data for the thirty-one phosphors prepared in the system $\text{Zn}(\text{PO}_3)_2\text{-Cd}(\text{PO}_3)_2\text{-Mg}(\text{PO}_3)_2$. All phosphors were activated with 1.0 mole % Mn^{2+} substituted for Zn^{2+} , Cd^{2+} , and/or Mg^{2+} and heat treated within the temper-

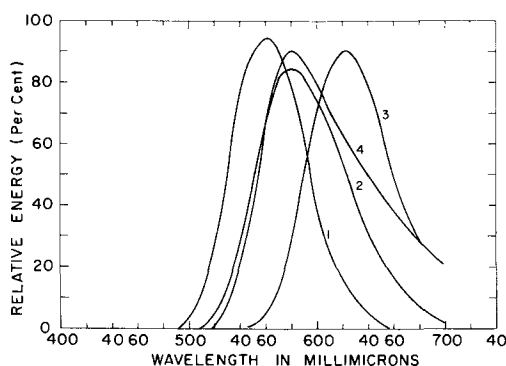


Fig. 3a. Cathodoluminescence emission curves of $\text{Zn}(\text{PO}_3)_2$ and $\text{Cd}(\text{PO}_3)_2$ polymorphs: 1, $\alpha\text{-Cd}(\text{PO}_3)_2$; 2, $\beta\text{-Cd}(\text{PO}_3)_2$; 3, $\alpha\text{-Zn}(\text{PO}_3)_2$; 4, $\beta\text{-Zn}(\text{PO}_3)_2$.

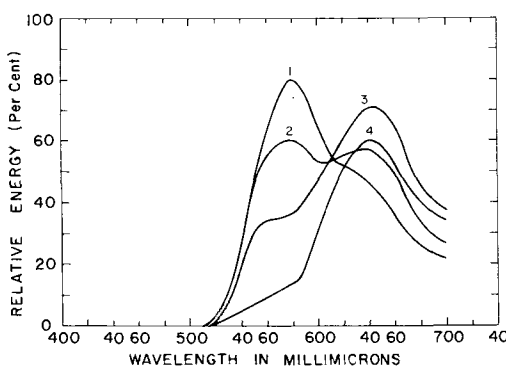


Fig. 3b. Cathodoluminescence emission curves of zinc-cadmium metaphosphate phosphors with $\text{Mg}(\text{PO}_3)_2$ structure: 1, $(\text{Zn}_{0.70}, \text{Cd}_{0.30})(\text{PO}_3)_2$; 2, $(\text{Zn}_{0.50}, \text{Cd}_{0.50})(\text{PO}_3)_2$; 3, $(\text{Zn}_{0.30}, \text{Cd}_{0.70})(\text{PO}_3)_2$; 4, $(\text{Zn}_{0.10}, \text{Cd}_{0.90})(\text{PO}_3)_2$.

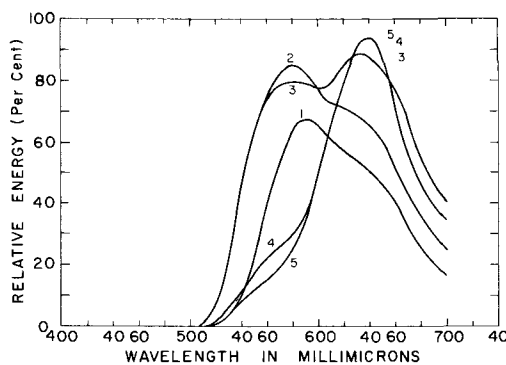


Fig. 3c. Cathodoluminescence emission curves of magnesium-cadmium metaphosphate phosphors with $\text{Mg}(\text{PO}_3)_2$ structure: 1, $(\text{Mg}_{0.90}, \text{Cd}_{0.10})(\text{PO}_3)_2$; 2, $(\text{Mg}_{0.70}, \text{Cd}_{0.30})(\text{PO}_3)_2$; 3, $(\text{Mg}_{0.50}, \text{Cd}_{0.50})(\text{PO}_3)_2$; 4, $(\text{Mg}_{0.30}, \text{Cd}_{0.70})(\text{PO}_3)_2$; 5, $(\text{Mg}_{0.10}, \text{Cd}_{0.90})(\text{PO}_3)_2$.

ature stability range for the phase under consideration.

The system $\text{Zn}(\text{PO}_3)_2\text{-Cd}(\text{PO}_3)_2$.—The spectral energy distribution (S.E.D.) curves for the high (β) and low (α) temperature $\text{Zn}(\text{PO}_3)_2$ and $\text{Cd}(\text{PO}_3)_2$ polymorphs are shown in Fig. 3a. $\alpha\text{-Zn}(\text{PO}_3)_2$ has a peak emission at 6240Å and a brightness of 12.9 ft-L; $\beta\text{-Zn}(\text{PO}_3)_2$ has a peak emission at 5880Å and possibly a secondary emission around 6300Å with a total brightness of 19.1 ft-L. $\alpha\text{-Cd}(\text{PO}_3)_2$ is a very bright phosphor (46.1 ft-L) emitting at 5580Å while $\beta\text{-Cd}(\text{PO}_3)_2$ emits at 5850Å with a much lower brightness of 16.1 ft-L.

The S.E.D. curves for four phosphors in the MP_{ss} stability region are shown in Fig. 3b. These phosphors are characterized by two emission peaks in the ranges 6290-6420Å and 5820-5590Å whose relative intensities can be related qualitatively to the $\text{Zn}^{2+}/\text{Cd}^{2+}$ ratio. When the $\text{Zn}^{2+}/\text{Cd}^{2+}$ ratio is larger than unity, the luminescence center that gives rise to the shorter wavelength emission is favored, when the ratio is less than unity the less energetic center (longer wavelength) predominates, and when there are an equal number of Zn^{2+} and Cd^{2+} ions present, both centers are equally active. In Fig. 4a the peak emission wavelengths for the MP_{ss} phosphors are shown as a function of composition. The solid lines indicate the primary emission peak and the dashed lines indicate the secondary emission. It can be seen that the two emission peaks tend to converge as the smaller Zn^{2+} ion concentration increases over the Cd^{2+} concentration.

The system $\text{Cd}(\text{PO}_3)_2\text{-Mg}(\text{PO}_3)_2$.—On the basis of x-ray identifications of the phosphors prepared in this system it appears that $\text{Mg}(\text{PO}_3)_2$ will accept at least 90 mole % $\text{Cd}(\text{PO}_3)_2$ in solid solution. The phase equilibria configuration for this system appears to be similar to that for the system $\text{Zn}(\text{PO}_3)_2\text{-Mg}(\text{PO}_3)_2$ (1).

The S.E.D. curves for five phosphors in this system which have the $\text{Mg}(\text{PO}_3)_2$ structure are shown

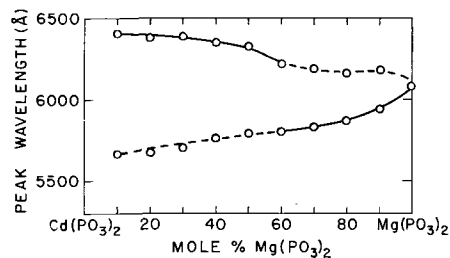
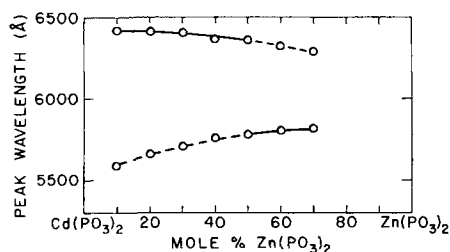


Fig. 4a (top). Peak emission as function of composition for zinc-cadmium metaphosphate phosphors with $\text{Mg}(\text{PO}_3)_2$ structure.

Fig. 4b (bottom). Peak emission as function of composition for magnesium-cadmium metaphosphate phosphors with $\text{Mg}(\text{PO}_3)_2$ structure.

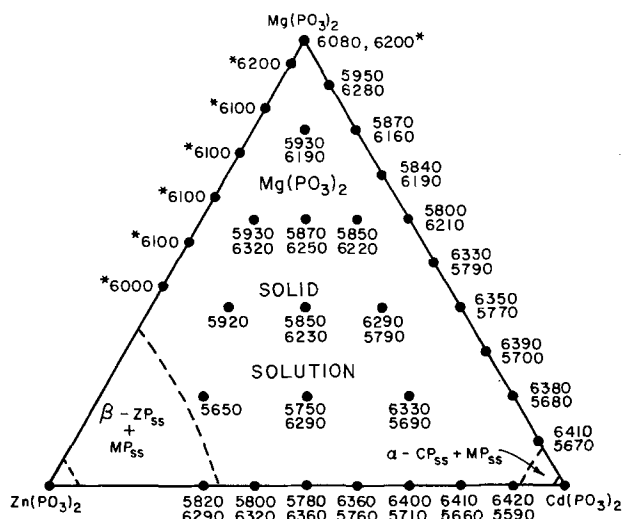


Fig. 5. Peak emission wavelengths of $\text{Zn}(\text{PO}_3)_2\text{-Cd}(\text{PO}_3)_2\text{-Mg}(\text{PO}_3)_2$ phosphors. Phase relationships indicated are for 750°C isothermal plane.

(*These compositions, previously reported by Sarver and Hummel (1), were heat treated at 850°C .)

in Fig. 3c, and the peak wavelengths are plotted as a function of composition in Fig. 4b. From these two figures it can be seen that two luminescence centers are again active, their intensities are related to the cation sizes, and they tend to converge to a single center at $\text{Mg}(\text{PO}_3)_2$.

The system $\text{Zn}(\text{PO}_3)_2\text{-Cd}(\text{PO}_3)_2\text{-Mg}(\text{PO}_3)_2$.—The peak emissions of the phosphors prepared in this system are shown in Fig. 5. For each composition the upper value is for the primary emission peak and the lower value represents the secondary emission peak. Also shown in this figure are the approximate phase boundaries on the 750°C isothermal plane as determined by x-ray identifications of the various phosphor preparations.

These results show that $(\text{Zn,Mg})(\text{PO}_3)_2$ phosphors emit in a single emission band ranging from 6000 to 6200\AA (1) and that adding moderate amounts of $\text{Cd}(\text{PO}_3)_2$ in solid solution tends to decrease the wavelength of this emission peak and introduces a weak secondary emission band. As the $\text{Cd}(\text{PO}_3)_2$ content reaches about 50 mole %, the two emission bands are equally intense and above 50 mole % $\text{Cd}(\text{PO}_3)_2$ the higher wavelength emission predominates. The brightnesses of these phosphors are highest when the two emission bands are equally intense. High concentrations of $\text{Cd}(\text{PO}_3)_2$ generally produce a decrease in brightness.

In the present work, appreciable differences in both brightness and peak emission wavelength have been observed for $\text{Mg}(\text{PO}_3)_2$ and its solid solutions with $\text{Zn}(\text{PO}_3)_2$, when compared with the previous results of Sarver and Hummel (1). These differences are most probably accounted for by the 100°C difference in firing temperature, since the meta-

phosphates are known to be especially sensitive to time and temperature of heat treatment.

Summary

1. Cadmium metaphosphate has a reversible inversion at 810°C and melts congruently at 896°C . The low temperature modification is a bright (46.1 ft-L) manganese-activated cathodoluminescent phosphor emitting at 5580\AA and the high temperature polymorph emits at 5850\AA with a much lower intensity (16.1 ft-L).

2. The $\text{Zn}(\text{PO}_3)_2\text{-Cd}(\text{PO}_3)_2$ phase relationships are characterized by small regions of $\alpha\text{-Zn}(\text{PO}_3)_2$, $\beta\text{-Zn}(\text{PO}_3)_2$, $\alpha\text{-Cd}(\text{PO}_3)_2$, and $\beta\text{-Cd}(\text{PO}_3)_2$ solid solutions and a large intermediate solid solution series extending from 35 to 90 mole % $\text{Cd}(\text{PO}_3)_2$ which has a distorted $\text{Mg}(\text{PO}_3)_2$ structure. Manganese-activated cathodoluminescence phosphors in this MP_{ss} region have two emission peaks in the ranges $5820\text{-}5590\text{\AA}$ and $6290\text{-}5590\text{\AA}$. The lower wavelength emission is favored by high Zn^{2+} concentrations and the higher wavelength emission is favored by high Cd^{2+} concentrations.

3. $\text{Mg}(\text{PO}_3)_2$ will accept at least 90 mole % $\text{Cd}(\text{PO}_3)_2$ in solid solution. These phosphors emit in two overlapping bands with $\text{Cd}(\text{PO}_3)_2$ favoring the higher wavelength emission and $\text{Mg}(\text{PO}_3)_2$ favoring the lower.

4. The ternary system $\text{Zn}(\text{PO}_3)_2\text{-Cd}(\text{PO}_3)_2\text{-Mg}(\text{PO}_3)_2$ is composed predominately of a single $\text{Mg}(\text{PO}_3)_2$ solid solution region that disappears only in the neighborhood of the compounds $\text{Zn}(\text{PO}_3)_2$ and $\text{Cd}(\text{PO}_3)_2$. Manganese-activated cathodoluminescent phosphors composed of $\text{Zn}(\text{PO}_3)_2$ and $\text{Mg}(\text{PO}_3)_2$, and lying in the region of $\text{Mg}(\text{PO}_3)_2$ solid solution, have single emission peaks. As $\text{Cd}(\text{PO}_3)_2$ is added, the secondary emission increases in intensity and above 50 mole % $\text{Cd}(\text{PO}_3)_2$ it dominates the emission spectrum.

Acknowledgment

Emission data were obtained through cooperation of Marjorie Brines of the Chemical Products Plant, General Electric Co., Cleveland, Ohio. This investigation was made possible through the financial assistance of the International Lead Zinc Research Organization. Contribution No. 63-16 from the College of Mineral Industries, The Pennsylvania State University, University Park, Pa.

Manuscript received Aug. 21, 1963.

Any discussion of this paper will appear in a Discussion Section to be published in the December 1964 JOURNAL.

REFERENCES

1. J. F. Sarver and F. A. Hummel, *This Journal*, **106**, 500 (1959).
2. F. L. Katnack and F. A. Hummel, *ibid.*, **105**, 125 (1958).
3. F. A. Hummel and F. L. Katnack, *ibid.*, **105**, 528 (1958).
4. J. J. Brown and F. A. Hummel, *ibid.*, **110**, 1218 (1963).

Purification of CdS by Partial Sublimation in a Gas Flow

A. Vecht, B. W. Ely, and A. Apling

Harlow Laboratories, Associated Electrical Industries Limited, Templefields, Harlow, Essex, England

ABSTRACT

A method of purifying cadmium sulfide by partial sublimation in a gas flow is described. Results of spectrographic and wet analysis are given.

Cadmium sulfide can be prepared by the vapor phase reaction of hydrogen sulfide or sulfur with cadmium metal, or by precipitation from aqueous solution. The vapor reaction leads to a product which may be contaminated with silicon and heavy metals (1) chiefly from the interaction with the reaction vessels, but which is usually free from anion impurities. Cadmium sulfide which is prepared by this method tends to be less stoichiometric than that formed by precipitation. Deviations from stoichiometry in the vapor-reacted material can often be detected by chemical analysis, but this is not generally sufficiently sensitive to detect any deviation in precipitated cadmium sulfide.

Precipitated cadmium sulfide is the more easily produced and is usually prepared by the reaction of an aqueous cadmium salt solution with hydrogen sulfide, ammonium sulfide, or organo-sulfur compounds. In all three cases two main types of contaminants are found. These are:

1. Heavy metals, usually those which form insoluble sulfides, especially Fe, Ni, Co, Ag, and Cu.

2. Nonmetal ions which formed the original salt solution of the cadmium metal as well as hydroxides, sulfates, sulfites, etc., which may be formed during precipitation or, more usually, on oxidation during the drying of the precipitate. A third type of impurity may arise from the absorption of soluble sulfides during precipitation. This is very typical when ammonium sulfide is used as the precipitant.

It thus becomes evident that precipitated cadmium sulfide requires further purification. Usually, a simple firing in argon removes a large proportion of the nonmetallic impurities. As zone refining would prove exceedingly difficult with this type of compound, sublimation or crystallization affords the only simple method of purification.

Flow methods for the production of cadmium sulfide are well known and were first developed by Frerichs in 1947 (2), and later improved by various authors [e.g., Fochs (3)]. Although it is evident that one of the advantages of the method is that purification does take place during a crystal growing run, the extent of the purification has not previously been assessed. The purpose of the present work was to determine the extent of the purification, and it was found that using two sublimation runs very pure material could be produced.

Experimental

Commercial luminescent grade cadmium sulfide precipitate (ex. Derby Luminescents Ltd.) was used as raw material. The heavy metal content of this

material is low, but it contains a considerable amount of nonmetal impurities. The halide and sulfate contents vary from about 0.1%-0.5%. The bulk of these ions is removed by one simple firing in argon at 800°C which reduces the sulfate and chloride content to between 60 and 200 ppm. The argon fired material is then used as starting material for the sublimation runs.

The apparatus used for partial sublimation is shown in Fig. 1 and is based on the apparatus used by Fochs (3). The temperature distribution is also shown.

To achieve the highest purity the following additional steps are taken:

1. A substrate of cadmium sulfide is first built up on the silica tube. This is done to prevent any contamination due to diffusion of impurities out of the silica tube into the cadmium sulfide crystals, since it is known that considerable impurities still exist in even the best type of commercially available silica. Diffusion of silicon into the cadmium sulfide is thereby also prevented.

2. Only about half of the cadmium sulfide in the charge is volatilized so that the charge retains the less volatile impurities.

3. Recrystallization runs are done as rapidly as possible to prevent contamination with less volatile constituents and to encourage flushing of more volatile components.

4. Only loosely attached crystals are removed from the substrate.

With a charge of 20g the average yield is between 5 and 8g. In the preparation of about 150g only two tubes were used. These tubes were thoroughly cleaned only when the substrate began to flake off. Cleaning after every run was deliberately avoided

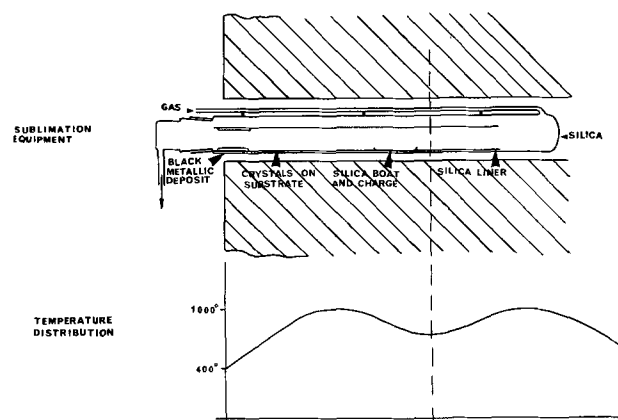


Fig. 1. Apparatus used for partial sublimation

Table I. Details of results

	Impurities					
	Chloride, ppm	Sulfate, ppm	Zinc, ppm	Copper, ppm	Silver, ppm	
Argon fired raw material	150	200	200	7	<0.5	Traces of Fe, Al, Pb, and Si
Crystals from a first run with a clean tube	65	40	100	0.7	<0.5	
Crystals from a final run before cleaning tube	20	20	50	<0.5	<0.5	
Residue left in boat after a run	40	20	320	0.9	<0.5	
Substrate taken after a final run	80	20	180	<0.5	<0.5	
Samples of a 150g stock of crystals	75	40	100	<0.5	<0.5	
	76	20	100	<0.5	<0.5	
	77	20	52	<0.5	<0.5	
	78	20	180	<0.5	<0.5	

to prevent the migration of impurities from the silica.

Details of results obtained are given in Table I. This table shows the difference in composition of an initial run and a final run (after 15 sublimations) and also gives a comparison between the composition of residue and substrate. Numbers 75, 76, 77, and 78 represent four samples taken out of a bottle containing some 150g of cadmium sulfide prepared as described. Since the crystals obtained were not crushed, some lack of homogeneity was to be expected, but this did not appreciably affect results.

To study the separation of impurities during a partial sublimation run the apparatus shown in Fig. 2 was set up. For this run the cadmium sulfide was deliberately doped with 5×10^{-3} g/g of a range of impurities. The cadmium sulfide in each section was analyzed, and some typical analytical figures

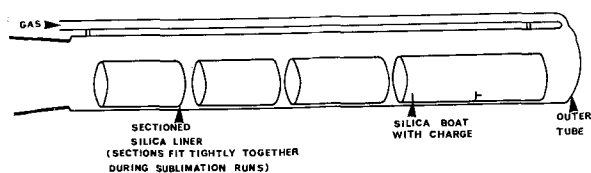


Fig. 2. Apparatus for separating definite fractions of crystals and substrate.

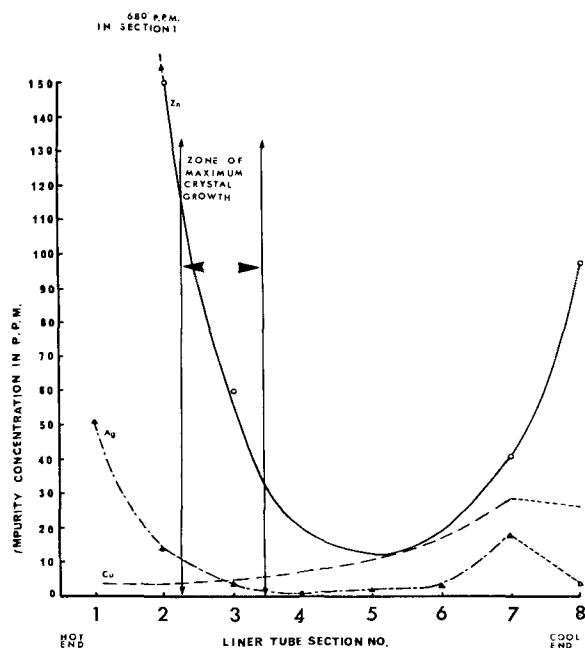


Fig. 3. Approximate impurity distribution curves for Zn, Ag, and Cu, using a deliberately doped charge.

are shown in Fig. 3. It is interesting to note that the main heavy metal impurities tend to a minimum in the crystal growing region providing that constant gas flow conditions operate. With a variation in gas flow the position of crystal growth and impurity profile will vary.

When nitrogen was used as the carrier gas a different range of impurities was obtained than with argon even with a similar gas flow (see Table II). The effect of changing the gas appears analogous to changing the gas flow rate; thus the crystal growing region is displaced with respect to the substrate. A change of carrier gas from argon to nitrogen gave a relative decrease in the zinc content and an increase in the copper content. This would be expected if crystallization takes place further down the tube.

Since sublimation gave such promising results it was decided to resublime the material produced after one crystallization. The resublimed material only contained traces of zinc and chloride (below the quantitative detection limit). No other impurities were detected.

Discussion and Conclusions

Analytical results show that partial sublimation or crystallization in an inert gas flow is a very effective method of purifying cadmium sulfide. This material gives consistent results in the preparation of photoconducting powder and is also used as starting material for the preparation of CdS crystals and thin films. It is interesting to note that the resublimed material shows phonon structure typical of pure CdS, as reported by Marshall and Fochs (4).

It should be emphasized that two aspects of the purity are still in doubt: first, the oxygen content, which could not readily be assessed by any known method once no sulfate could be detected; second, the degree of nonstoichiometry which can only be detected chemically if very large. In many publications, however, not only are these two aspects overlooked but no attempt is made at an analysis of the anion present. This must throw very great doubt on the validity of the conclusions drawn as to the

Table II. Range of impurities

Sample	Heavy metal impurities	
CdS crystals sublimed using argon gas	Zn 100 ppm	Cu <0.5 ppm
CdS crystals sublimed using nitrogen gas	Zn 25 ppm	Cu 1.3 ppm

effect of cations on the electrical and optical properties of the material.

Acknowledgments

The authors wish to acknowledge their thanks to Dr. J. Franks, Dr. P. D. Fochs, and Mr. B. Lunn for valuable discussion, and Dr. M. E. Haine for permission to publish.

Manuscript received Aug. 21, 1963.

Any discussion of this paper will appear in a Discussion Section to be published in the December 1964 JOURNAL.

REFERENCES

1. U. S. Government Report AD 276416 (1962).
2. R. Frerichs, *Phys. Rev.*, **72**, 594 (1947).
3. P. D. Fochs, *J. Appl. Phys.*, **31**, 1733 (1961).
4. R. Marshall and P. D. Fochs, To be published.

Copper-Activated Thorium Phosphate Phosphors

William F. Schmid and Richard W. Mooney

Chemical and Metallurgical Division, Sylvania Electric Products Inc., Towanda, Pennsylvania

ABSTRACT

Eight different copper-activated thorium phosphate phosphors were prepared, identified, and their fluorescence properties measured. The brightest phosphors, with their fluorescence maxima, are: $\text{Th}_3(\text{PO}_4)_4:0.045 \text{ Cu}$, 440 nm and 540 nm; $\text{Th}_3(\text{PO}_4)_4:0.48 \text{ Cu}$, 590 nm; $\text{Th}_2\text{Cu}(\text{PO}_4)_3$, 590 nm; $\text{Th}_2\text{Li}(\text{PO}_4)_3:0.04 \text{ Cu}$, 455 nm; and $\text{Th}_2\text{Ag}(\text{PO}_4)_3:\text{Cu}$, 565 nm. The copper concentration has a pronounced effect on the fluorescence color and phosphor composition. All the phosphors except $\text{Th}_2\text{Ag}(\text{PO}_4)_3:\text{Cu}$ have good temperature dependence. If the proper coating technique is used, these phosphors are highly efficient in high pressure mercury vapor lamps.

Copper-activated thorium phosphates were first prepared and studied by Ranby and Hobbs (1). The present work was undertaken to expand upon their original study, to identify the specific chemical compounds responsible for fluorescence, and to measure the luminescent properties of the phosphors.

The investigation of the thorium phosphate phosphors was facilitated by a previous systematic study of the $\text{ThO}_2\text{-P}_2\text{O}_5$ system by Burdese and Borlera (2). They identified three previously reported compounds; the metaphosphate, $\text{Th}(\text{PO}_3)_4$, pyrophosphate, ThP_2O_7 , and orthophosphate, $\text{Th}_3(\text{PO}_4)_4$, as well as two new phosphates; thoryl pyrophosphate, $(\text{ThO})_2\text{P}_2\text{O}_7$, and thoryl orthophosphate, $(\text{ThO})_3(\text{PO}_4)_2$.

Experimental Procedure

The preparation of the copper-activated thorium phosphate phosphors followed the general procedure prescribed by Ranby and Hobbs (1). However, in order to avoid any possible confusion, the specific preparative techniques are described.

The copper-activated phosphors were prepared by dry ball milling the stoichiometric quantities of ThO_2 , $(\text{NH}_4)_2\text{HPO}_4$, and $\text{Cu}(\text{C}_2\text{H}_3\text{O}_2)_2 \cdot \text{H}_2\text{O}$. Lindsay Chemical Company ThO_2 (Code 112) was employed with an average particle size of 0.5-2 μ . A copper oxide could be substituted for the acetate. After milling, the raw mix was pre-fired at 800°C resulting in some fusion and the evolution of ammonia and steam. After mortaring, the mix was re-fired between 1000°-1250°C, depending on the phosphor being prepared. This second firing formed the matrix and produced a dull phosphor having a greenish body color indicating the presence of some cupric ion. The phosphor was again mortared, and then re-fired (1000°-1150°C), and cooled in an atmosphere of nitrogen mixed with a 40 psi flow of

steam. A bright phosphor was produced with almost no cupric ion body color.

The final steam firing is the crucial step in preparing a bright phosphor. The phosphor does not gain or lose weight when fired in steam. It is a reversible reaction so that if the phosphor is deadened by heating in air, it can again be regenerated to a bright phosphor by steam firing. Steam and nitrogen at 1000°-1150°C appear to act as a reducing atmosphere; however, if a stronger reducing atmosphere of hydrogen with nitrogen is used, the copper is reduced to elemental copper and a poor phosphor results.

The methods used to measure fluorescence spectra (3) and temperature dependence curves (4) have been described previously. The x-ray diffraction data were obtained from diffractometer traces taken on a Philips Norelco unit using $\text{CuK}\alpha$ radiation. The scanning rate was one degree $2\theta/\text{min}$, and the chart speed 2 in./min.

Aside from characterizing the phosphors by their x-ray diffraction traces, their composition was verified quantitatively. The percentage of thorium and phosphorus was determined by x-ray fluorescence with the phosphor diluted in sodium borate glass pellets containing sodium fluoride flux. The copper was determined colorimetrically as the bromide complex.

Results

Thorium metaphosphate, $\text{Th}(\text{PO}_3)_4$.—Thorium metaphosphate has the lowest reaction temperature and is the first phosphate to form when ThO_2 and $(\text{NH}_4)_2\text{HPO}_4$ are fired. In order to prepare pure metaphosphate, four moles and a slight excess of $(\text{NH}_4)_2\text{HPO}_4$ were added and fired in four separate steps to prevent formation of a fused polyphosphate. The x-ray diffraction pattern of the resulting

thorium metaphosphate was in good agreement with the published data of Burdese and Borlera (2). However, repeated attempts in this laboratory to prepare a copper-activated thorium metaphosphate phosphor were unsuccessful.

Thorium pyrophosphates, ThP_2O_7 .—The copper-activated $\beta\text{-ThP}_2\text{O}_7$ phosphor was prepared by adding two moles of $(\text{NH}_4)_2\text{HPO}_4$ in two firing steps. The amount of ThO_2 was always less than one mole and calculated so that copper would substitute for the less than stoichiometric amount of thorium. The raw mix containing one mole of $(\text{NH}_4)_2\text{HPO}_4$ was first fired at 800°C for 30 min in air. After milling and adding the second mole of phosphate, it was fired at 1200°C in air for another 30 min. After mortaring, the phosphor was fired at 1150°C for 2 hr in a nitrogen-steam atmosphere. The x-ray diffraction data of $\beta\text{-ThP}_2\text{O}_7$ was in fair agreement with published results (2).

At very low activator concentrations (0.01 atom Cu/atom Th) $\beta\text{-ThP}_2\text{O}_7$ is inert. An efficient phosphor is found over a rather narrow range of Cu content (0.025–0.10 atom Cu/atom Th) with the brightest phosphor obtained at the upper end of this range, but still only 50% as bright as the best thorium orthophosphate phosphor. If one attempts to incorporate more than 0.1 mole of copper, the phosphor becomes brown, while the orthophosphate is still an efficient white-bodied phosphor with twice this amount of copper.

The excitation and emission spectra of the beta pyrophosphate are found in Fig. 1(C). As is the case for most copper-activated thorium phosphates, the excitation bands are very broad so that at best

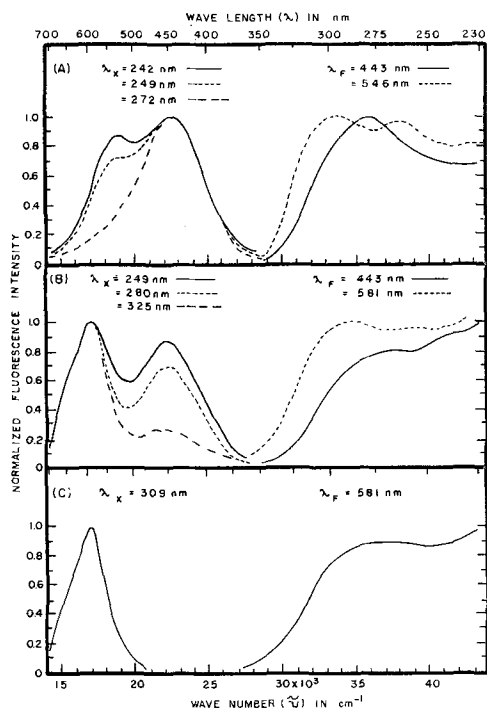


Fig. 1. Excitation and emission spectra of copper-activated thorium phosphate phosphors: (A) $\text{Th}_3(\text{PO}_4)_4:0.03 \text{ Cu}$; (B) $\text{Th}_3(\text{PO}_4)_4:0.3 \text{ Cu}$; and (C) $\text{Th}_2\text{Cu}(\text{PO}_4)_3$, $\beta\text{-ThP}_2\text{O}_7:0.1 \text{ Cu}$, $(\text{ThO})_3(\text{PO}_4)_2:0.15 \text{ Cu}$. λ_x and λ_f are the wavelengths in nanometers of excitation and fluorescence which apply respectively to the emission and excitation spectra.

one can state that the maximum excitation occurs in the region of 270 nanometers (nm). The fluorescence band extends from 490 to 730 nm with a maximum emission at 590 nm (yellow-orange).

Attempts to prepare the Cu-activated $\alpha\text{-ThP}_2\text{O}_7$ by rapid quenching were invariably unsuccessful, the product always ending up as $\beta\text{-ThP}_2\text{O}_7:\text{Cu}$. Apparently the presence of Cu stabilizes the $\beta\text{-ThP}_2\text{O}_7$ structure.

Thorium orthophosphates.—The procedure for preparing the orthophosphate phosphor, $\text{Th}_3(\text{PO}_4)_4:\text{Cu}$, was the same as for the beta-pyrophosphate phosphor except for the changes in stoichiometry with the addition of all the $(\text{NH}_4)_2\text{HPO}_4$ at the start. The final steam-nitrogen firing was at 1200°C . The x-ray diffraction data on our preparation agreed very well with the data reported by Ranby and Hobbs (1) and less well with that reported by Burdese and Borlera (2).

The concentration of copper had a pronounced effect on the emission of the orthophosphate [Fig. 1(A), 1(B), 2, and 3]. A blue phosphor resulted when the copper concentration was as low as 0.002 atom Cu/atom Th. The maximum blue emission occurred at 0.02 atom Cu/atom Th (Fig. 2). Above the ratio of 0.02 atom Cu/atom Th, a yellow-orange fluorescence band appeared and the blue band rapidly diminished in intensity.

In Fig. 3, the yellow-orange fluorescent intensity of two series (solid and dotted lines) of phosphor

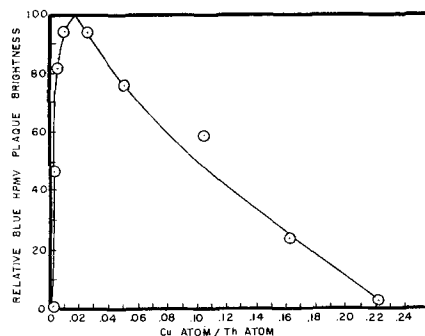


Fig. 2. Effect of copper activator concentration on the blue fluorescence intensity of thorium orthophosphate [$\text{Th}_3(\text{PO}_4)_4$] excited by high-pressure mercury-vapor light.

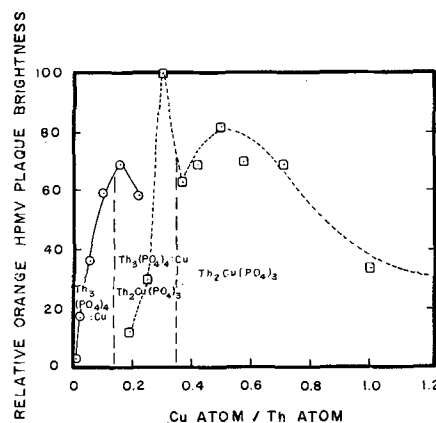


Fig. 3. Effect of copper activator concentration on the orange fluorescence intensity and composition of thorium orthophosphate excited by high-pressure mercury-vapor light. $\circ\text{---}\circ$, $>80\%$ $\text{Th}_3(\text{PO}_4)_4:\text{Cu}$; $\square\text{---}\square$, $>60\%$ $\text{Th}_2\text{Cu}(\text{PO}_4)_3$.

preparations are graphed. At lower copper concentrations (0.02–0.2 Cu atom/Th atom) the product is mainly orthophosphate activated by copper substituted for thorium. In this paper, wherever a phosphor formula appears followed by high activator concentration, the cuprous ions are assumed to substitute for the major cation. The maximum brightness for this phosphor is reached at 0.16 atom Cu/atom Th. However, at this concentration a new compound, $\text{Th}_2\text{Cu}(\text{PO}_4)_3$, starts to form as determined from the x-ray diffraction data. The region 0.16–0.35 Cu atom/Th atom contains a mixture of $\text{Th}_3(\text{PO}_4)_4$:Cu and $\text{Th}_2\text{Cu}(\text{PO}_4)_3$ as indicated by the dashed vertical lines. The two copper series (solid and dotted lines) do not join because the composition of the mixed phosphors were not the same. $\text{Th}_3(\text{PO}_4)_4$:Cu is formed in preference to $\text{Th}_2\text{Cu}(\text{PO}_4)_3$ if the final firing temperature is 1200°C; whereas $\text{Th}_2\text{Cu}(\text{PO}_4)_3$ is preferentially formed at 1100°C. A discontinuity in the fluorescence brightness curve of $\text{Th}_2\text{Cu}(\text{PO}_4)_3$ is observed at 0.3 Cu atom/Th atom. The brightest phosphor produced at this Cu/Th ratio had a composition of 80% $\text{Th}_2\text{Cu}(\text{PO}_4)_3$ and 20% $\text{Th}_3(\text{PO}_4)_4$:Cu as estimated from the x-ray diffraction pattern. The new compound $\text{Th}_2\text{Cu}(\text{PO}_4)_3$ was obtained in pure form without any $\text{Th}_3(\text{PO}_4)_4$ when a stoichiometric composition was reached, and as seen from Fig. 3, this also gave the brightest emission for pure $\text{Th}_2\text{Cu}(\text{PO}_4)_3$. X-ray fluorescence analysis of thorium and phosphorus as well as wet

chemical analysis of copper confirmed the stoichiometry of the compound $\text{Th}_2\text{Cu}(\text{PO}_4)_3$. Infrared absorption spectra indicated the presence of an orthophosphate (PO_4^{-3}) group (5). X-ray data on $\text{Th}_2\text{Cu}(\text{PO}_4)_3$ are given in Table I.

It is apparent from Fig. 2 that the blue-green emission of $\text{Th}_3(\text{PO}_4)_4$:Cu was very rapidly concentration quenched. The characteristic yellow-orange emission band (Fig. 3) increased rapidly, but also appeared to show marked concentration quenching above 0.16 atom Cu/atom Th. The phosphor $\text{Th}_2\text{Cu}(\text{PO}_4)_3$ was, however, efficient over a wide activator concentration range as would be typical of a structurally self-activated phosphor.

The blue emission of the orthophosphate was resolved into two broad bands; a more intense blue band with a maximum at 440 nm, and a weaker green band with a maximum at 540 nm [Fig. 1(A)]. There was some indication that, as the copper concentration increased, the green band intensity decreased faster than the blue band. However, this was difficult to determine since, as the copper concentration increased, a yellow-orange band at 590 nm began to appear and overlapped the green band [Fig. 1(B)]. Within the accuracy of the spectrometer, the yellow-orange band of the orthophosphate was identical with the emission of several other thorium phosphates [Fig. 1(C)], and the excitation giving rise to this fluorescence was also the same. The excitation spectrum giving rise to the blue emission band was well defined with a maximum at 278 nm. There appeared to be more than one excitation band giving rise to the green emission; one at about 300 nm and one at shorter wavelengths which excited the green band more effectively than the blue. The excitation and emission spectra of the $\text{Th}_2\text{Cu}(\text{PO}_4)_3$ phosphor were the same as for $\beta\text{-ThP}_2\text{O}_7$:Cu and $(\text{ThO})_3(\text{PO}_4)_2$:Cu phosphors [Fig. 1(C)].

$\text{Th}_2\text{M}^{\text{I}}(\text{PO}_4)_3$:Cu phosphors.—In the preceding section, it was shown that the most efficient of the Cu-activated thorium phosphate phosphors was predominantly $\text{Th}_2\text{Cu}(\text{PO}_4)_3$. Ranby and Hobbs (1) described a thorium phosphate phosphor activated by Cu in the presence of Li and one activated by Cu in the presence of Ag. It is proposed herein that both of these phosphors and a third one as yet undescribed have the composition $\text{Th}_2\text{M}^{\text{I}}(\text{PO}_4)_3$:Cu where M^{I} is a monovalent cation of Group I, specifically Li, Ag, or Na. The x-ray diffraction data of these phosphors are compared to $\text{Th}_2\text{Cu}(\text{PO}_4)_3$ in Table I. The data on $\text{Th}_2\text{Li}(\text{PO}_4)_3$ correspond almost exactly to those given by Ranby and Hobbs. In addition, a marked correspondence between $\text{Th}_2\text{Li}(\text{PO}_4)_3$ and $\text{Th}_2\text{Na}(\text{PO}_4)_3$ may be noted. The compound $\text{Th}_2\text{Ag}(\text{PO}_4)_3$ has essentially the same d spacings as the alkali-metal modified phosphates, but the intensities differ. The compound $\text{Th}_2\text{Cu}(\text{PO}_4)_3$ differs in both d values and intensities from the others, although there are still similarities in the patterns. The structures probably bear common characteristic groupings, but it is very unlikely that they are all isomorphous.

These phosphors were prepared in the same manner as the previously described orthophosphate

Table I. X-ray diffraction data of $\text{Th}_2\text{M}(\text{PO}_4)_3$ compounds

$\text{Th}_2\text{Cu}(\text{PO}_4)_3$ d / I		$\text{Th}_2\text{Ag}(\text{PO}_4)_3$ d / I		$\text{Th}_2\text{Na}(\text{PO}_4)_3$ d / I		$\text{Th}_2\text{Li}(\text{PO}_4)_3$ d / I	
10.4	<5						
		8.57	10	8.57	50	8.55	40
6.4	30	6.34	40	6.35	100	6.30	100
5.24	45	5.15	30	5.15	50	5.13	50
4.83	40	4.81	45	4.81	40	4.78	30
4.40	100	4.38	85	4.37	50	4.36	45
		4.28	25	4.27	45	4.27	35
				4.08	10	4.09	10
		4.00	30	4.00	30	3.99	20
3.55	10						
3.52	60						
3.47	30	3.49	30	3.49	25	3.49	25
		3.41	20				
		3.39	30	3.39	30	3.38	35
3.32	10	3.28	5				
		3.24	60	3.24	70	3.24	50
		3.19	35	3.19	50	3.19	50
		3.13	<5				
3.01	60	3.02	100	3.02	90	3.01	70
2.91	25	2.88	5	2.88	15	2.86	10
2.84	15						
2.83	35	2.85	45	2.85	35	2.85	30
2.78	10	2.76	55	2.76	50	2.75	50
2.73	5	2.71	10	2.71	20	2.70	20
2.61	10			2.62	10	2.62	10
2.49	10						
2.46	30	2.44	15	2.44	20	2.43	20
		2.40	10	2.40	10	2.39	10
		2.35	5	2.35	5	2.34	5
2.30	10	2.30	10	2.30	20	2.29	15
2.23	15	2.25	<5	2.25	5	2.24	5
2.20	5	2.19	<5				
2.16	15	2.17	25	2.18	20	2.17	20
2.14	10	2.15	30	2.14	30	2.14	20
2.09	15			2.11	20	2.10	20

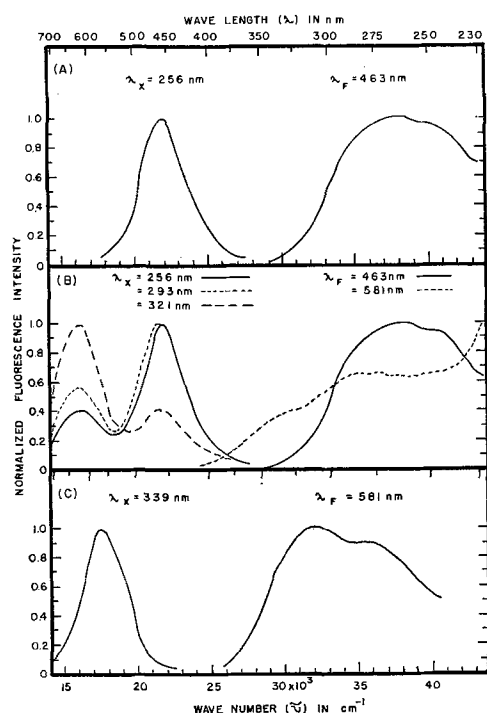


Fig. 4. Excitation and emission spectra of copper-activated complex thorium phosphate phosphors: (A) $\text{Th}_2\text{Li}(\text{PO}_4)_3:0.02 \text{ Cu}$; (B) $\text{Th}_2\text{Li}(\text{PO}_4)_3:0.2 \text{ Cu}$; and (C) $\text{Th}_2\text{Ag}(\text{PO}_4)_3:0.05 \text{ Cu} \cdot 3.4 \text{ ThO}_2$. λ_X and λ_F are wavelengths in nanometers of excitation and fluorescence which apply respectively to the emission and excitation spectra.

phosphors with the second firing at 1100°C for 1 hr and a 1-hr steam-nitrogen firing at 1100°C . The purest and most crystalline compound was formed when stoichiometric quantities were employed. However, an efficient, white-bodied $\text{Th}_2\text{Ag}(\text{PO}_4)_3:\text{Cu}$ phosphor was only prepared when a large excess of ThO_2 (3.4 mole excess $\text{ThO}_2/\text{mole Th}_2\text{Ag}(\text{PO}_4)_3:\text{Cu}$) was used corresponding closely to the Ranby and Hobbs (1) formulation. When the stoichiometric two moles of thoria were used, a dull phosphor was formed due to the presence of grayish material.

$\text{Th}_2\text{Li}(\text{PO}_4)_3:\text{Cu}$.—Changing the copper concentration of $\text{Th}_2\text{Li}(\text{PO}_4)_3$ had the same effect as with $\text{Th}_3(\text{PO}_4)_4$. However, unlike $\text{Th}_3(\text{PO}_4)_4:\text{Cu}$, $\text{Th}_2\text{Li}(\text{PO}_4)_3:\text{Cu}$ at low copper concentrations has one emission band only [Fig. 4(A)]. This blue band (455 nm) is at a longer wavelength than the blue emission of the orthophosphate. At higher copper concentrations (0.1 atom Cu/atom Th), the yellow-orange emission appears [Fig. 4(B)] and compared to the orthophosphate is also shifted to a longer wavelength (610 nm). The excitation giving rise to the blue emission starts at about 345 nm, reaches a maximum at 263 nm and drops off in the far ultraviolet. The excitation of the yellow-orange emission starts at 410 nm and is continuous into the far ultraviolet with several poorly defined bands.

$\text{Th}_2\text{Na}(\text{PO}_4)_3:\text{Cu}$.— $\text{Th}_2\text{Na}(\text{PO}_4)_3:\text{Cu}$ is a much less efficient phosphor than $\text{Th}_2\text{Li}(\text{PO}_4)_3:\text{Cu}$. It is almost nonluminescent and discolored when the copper concentration is as high as 0.1 atom Cu/atom Th. It has two broad emission bands, one in the deep blue (430 nm) and a much weaker one in the red (650 nm). The red emission is excited by longer wavelength ultraviolet than the blue emission.

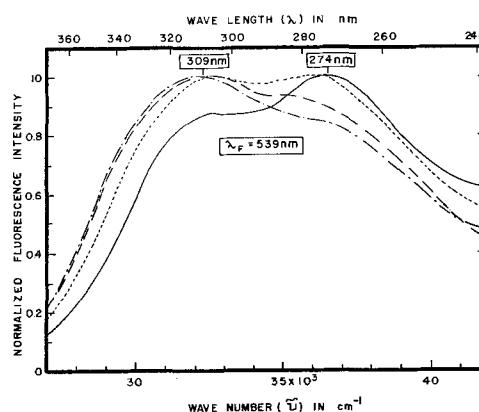


Fig. 5. Excitation spectra of copper-activated thorium silver orthophosphate, $\text{Th}_2\text{Ag}(\text{PO}_4)_3:\text{Cu} \cdot 3.4 \text{ ThO}_2$. Cu mole/Ag mole: —, 0.005; - - -, 0.016; ····, 0.064; - · - ·, 0.159.

$\text{Th}_2\text{Ag}(\text{PO}_4)_3:\text{Cu}$.— $\text{Th}_2\text{Ag}(\text{PO}_4)_3:\text{Cu}$ is the brightest of all the thorium phosphate phosphors. Without the copper it is comparatively nonluminescent, but only very small concentrations of copper (0.01 atom Cu/atom Th) are required to produce a bright yellow phosphor. The brightest phosphor was obtained when the starting materials were in the proportion 5.36 mole ThO_2 , 3.0 mole $(\text{NH}_4)_2\text{HPO}_4$, 0.89 mole AgNO_3 , and 0.06–0.08 mole of cupric acetate. Varying the copper concentration had no effect on the emission wavelength. As in the case of $\text{Th}_2\text{Li}(\text{PO}_4)_3$ and $\text{Th}_2\text{Na}(\text{PO}_4)_3$, silver shifts the copper emission. This time the blue emission is shifted to the yellow (565 nm). The excitation spectrum of this phosphor, unlike most of the thorium phosphates, has well-defined maxima at 309 nm and 274 nm. The excitation spectra of a series of $\text{Th}_2\text{Ag}(\text{PO}_4)_3 \cdot 3.4 \text{ ThO}_2$ phosphors with varying copper concentration are graphed in Fig. 5.

Thoryl phosphates.—The copper-activated thoryl orthophosphate, $(\text{ThO})_3(\text{PO}_4)_2:\text{Cu}$, phosphor was prepared by firing one mole of $\text{Th}_3(\text{PO}_4)_4$, and somewhat less than three moles of ThO_2 , depending on the amount of copper which would substitute for thorium, and copper acetate at 1250°C for 4 hr. The product was then mortared and nitrogen-steam fired for 1 hr at 1200°C . X-ray diffraction data on the product agreed very well with those reported by Burdese and Borlera (2). Unlike the orthophosphate and like the pyrophosphate, the thoryl orthophosphate is nonluminescent at low copper concentrations (0.01 atom Cu/atom Th). As was the case for thorium orthophosphate, when more than 0.1 atom Cu/atom Th was added, $\text{Th}_2\text{Cu}(\text{PO}_4)_3$ started to form in appreciable amounts. Thoryl orthophosphate has the same excitation and emission spectra as $\text{Th}_3(\text{PO}_4)_4:\text{Cu}$ and $\text{Th}_2\text{Cu}(\text{PO}_4)_3$ [Fig. 1(C)].

Relative brightness of thorium phosphate phosphors.—The relative efficiencies of the phosphors previously described are listed in Table II with data on $\text{Ca}_{2.65}\text{Zn}_{0.20}(\text{PO}_4)_2:\text{Sn}$ included for comparison purposes. The blue and orange fluorescence intensities are not inter-comparable because of the non-linearity of photomultiplier response and differences in the transmission of filters.

Temperature dependence.—As seen from Fig. 6, all the copper-activated thorium phosphate phosphors,

Table II. Relative efficiencies of phosphors

Phosphor	Cu concentration giving brightest phosphor (mole Cu/mole Th)	Relative HPMV** plaque brightness*		Fluorescence wavelength (nm)
		Orange	Blue	
Ca _{2.65} Zn _{0.20} (PO ₄) ₂ :Sn	—	57	39	—
β-ThP ₂ O ₇ :Cu	0.10	52	—	590
Th ₃ (PO ₄) ₄ :Cu	0.005	—	135	440 540
Th ₃ (PO ₄) ₄ :Cu	0.16	68	27	590
(ThO) ₃ (PO ₄) ₂ :Cu	—	46	—	590
Th ₂ Cu(PO ₄) ₃	0.50	81	—	590
Th ₂ Li(PO ₄) ₃ :Cu	~0.02	—	84	455
Th ₂ Li(PO ₄) ₃ :Cu	~0.1	—	—	455 610
Th ₂ Ag(PO ₄) ₃ :Cu	0.04	137	—	565
80% Th ₂ Cu(PO ₄) ₃ 20% Th ₃ (PO ₄) ₄	0.30	100	—	590

* Orange plaque brightness was obtained through Corning No. 3385 filter, blue through a Corning No. 5543 and No. 3389 filter. Photometer sensitivity was constant.

** HPMV = High pressure mercury vapor.

except Th₂Ag(PO₄)₃:Cu, have very good temperature dependence. In the case of Th₂Ag(PO₄)₃:Cu, even very small amounts of silver produce a phosphor which has poor temperature dependence. Like most phosphor temperature-dependence curves in the literature, the ones in Fig. 6 indicate that the phosphors become more efficient as the temperature increases above room temperature. The increase in brightness observed in Fig. 6 is due to (i) a broadening of the emission band as the temperature is raised, and (ii) a shift towards shorter wavelengths in the direction of greater photomultiplier sensitivity. Since the plaque tester (4), which was used to take the data shown in Fig. 6, measures the integrated fluorescence, the brightness increases are due to the above effects. Spectra taken at various temperatures on the spectrometer (3) show that the maximum fluorescence intensity actually decreases

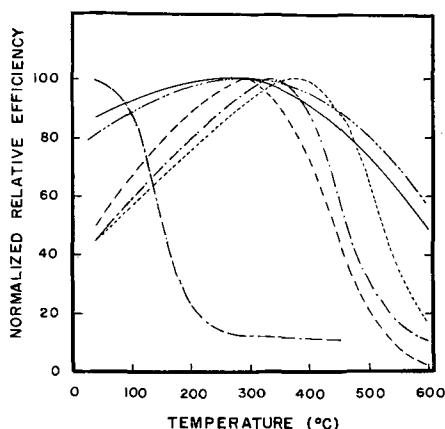


Fig. 6. Effect of temperature on the fluorescence intensity of copper-activated thorium phosphate phosphors excited by high-pressure mercury-vapor light. —, Ca_{2.65}Zn_{0.20}(PO₄)₂:Sn; - - -, β-ThP₂O₇:Cu; — · — ·, Th₃(PO₄)₄:Cu; — · — ·, Th₂Cu(PO₄)₃; - - - - - , Th₂Li(PO₄)₃:Cu; — · — ·, Th₂Ag(PO₄)₃:Cu.

with an increase in temperature. This may well be true for phosphors in general.

EPR spectra.—Electron spin resonance spectra were obtained for the various phosphors at 77°K using a Varian EPR Spectrometer, in the hope that they might give some insight into the nature of the luminescent centers. Each phosphor had considerable resonance absorption, but only in a few cases were the resonance peaks clearly resolved. Because the actual crystal structures of these phosphors are unknown, no detailed analyses of the spectra were possible.

However, certain general comments can be made. In the case of thorium orthophosphate, the resonance peaks of Cu²⁺ were well defined when there was a visible amount of cupric ion present. The two sets of four equally spaced peaks, one set centered around 2780 gauss and the other about 3100 gauss, each set having different spacing, were similar to those reported by Sands (6) for Cu²⁺ in glass. When this phosphor is reduced further, the same general spectral shape is retained, but the resonance peaks are no longer resolved.

Unactivated thorium phosphates showed no resonance absorption. The resonance absorption of the phosphors must then be attributed to copper or a reduced state of thorium. Divalent and elemental copper are paramagnetic and produce resonance, while monovalent copper has zero electron spin and is not detected by EPR. Since fluorescence from copper is normally attributed to the cuprous state, the electron spin resonance must then result from small amounts of Cu²⁺, Cu⁰, or less likely, Th⁺³.

Lamp data.—When copper-activated thorium phosphates were first tested in high-pressure mercury-vapor lamps, the phosphor was discolored in the lamp coating process resulting in reduced brightness and poor maintenance. However, when the coating procedure was changed to include the addition of (NH₄)₂HPO₄ as suggested by Ranby and Hobbs (7), the phosphor was no longer discolored and the maintenance of the lamps was excellent as seen from Table III.

Discussion

The luminescence of copper-activated thorium phosphates has been attributed to copper in a thorium orthophosphate [Th₃(PO₄)₄] matrix or a modified orthophosphate lattice under special conditions (1). This work has shown that copper activates many different thorium phosphate compounds: β-ThP₂O₇, Th₃(PO₄)₄, (ThO)₃(PO₄)₂,

Table III. Lamp performance data

Phosphor	(NH ₄) ₂ HPO ₄ added	LPW from 400w HPMV lamps		
		0 Hr	100 Hr	500 Hr
Ca _{2.65} Zn _{0.20} (PO ₄) ₂ :Sn	No	64	58	55
β-ThP ₂ O ₇ :Cu	No	57	53	—
β-ThP ₂ O ₇ :Cu	Yes	43	44	—
Th ₃ (PO ₄) ₄ :Cu	No	61	53	48*
Th ₃ (PO ₄) ₄ :Cu	Yes	64	59	—
Th ₂ Cu(PO ₄) ₃	No	56	50	45*
Th ₂ Cu(PO ₄) ₃	Yes	63	66	62

* 300 hr.

$\text{Th}_2\text{Cu}(\text{PO}_4)_3$, $\text{Th}_2\text{Ag}(\text{PO}_4)_3$, $\text{Th}_2\text{Li}(\text{PO}_4)_3$, and $\text{Th}_2\text{Na}(\text{PO}_4)_3$. The last four are a new class of compounds with the general formula $\text{Th}_2\text{M}(\text{PO}_4)_3$. As seen from their x-ray diffraction data (Table I) they may well have similar crystal structure characteristics. Wallroth (8) has reported the preparation of the double phosphates $\text{Th}_2\text{Na}(\text{PO}_4)_3$ and $\text{Th}_2\text{K}(\text{PO}_4)_3$. Ranby and Hobbs (1) attribute the blue emission of copper to a structural modification of the thorium orthophosphate lattice caused by adding lithium or by increasing the firing temperature to 1250°C. They considered the possibility that their blue phosphor might be a thorium lithium orthophosphate, but since the same x-ray pattern was obtained when the phosphor was fired at 1250°C in the absence of lithium, they discarded this hypothesis. We were unable to prepare a compound with the x-ray diffraction spectrum of $\text{Th}_2\text{Li}(\text{PO}_4)_3$ (Table I) in the absence of lithium. Only when a stoichiometric amount of lithium was used was a pure compound prepared. Therefore, the change from blue to yellow-orange emission is a property of the copper activator concentration and does not necessarily result from a change in structure. The blue emission of thorium phosphate phosphors is characteristic of low copper concentration (0.01 Cu atom/Th atom). The exception is $\text{Th}_2\text{Ag}(\text{PO}_4)_3$:Cu whose yellow emission is independent of copper concentration.

The yellow-orange emission of copper within the thorium phosphate structures, β - ThP_2O_7 , $\text{Th}_3(\text{PO}_4)_4$, $(\text{ThO})_3(\text{PO}_4)_2$, and $\text{Th}_2\text{Cu}(\text{PO}_4)_3$ is not shifted by the over-all crystal structure. All of these copper-activated phosphors have the same yellow-orange emission band thus indicating that copper is unperturbed by its oxygen-thorium environment in these matrices. In the case of the $\text{Th}_2\text{M}(\text{PO}_4)_3$ compounds where Cu⁺ substitutes for Li⁺, Na⁺, and Ag⁺ interactions occur between Th⁴⁺ and M⁺. Thus, the blue and, at higher copper concentrations, the yellow-orange emission are shifted somewhat depending on the monovalent cation which makes up the complex thorium phosphate salt.

Spectral reflectance measurements on copper-activated and unactivated thorium phosphates show that about 30% of the 80-98% ultraviolet light (254-309 nm) absorbed is absorbed by the host depending on the concentration of copper present. Therefore, most of the remaining (50-68%) exciting radiation is absorbed by copper. The unactivated compounds $\text{Th}_2\text{Ag}(\text{PO}_4)_3$ and $\text{Th}_2\text{Li}(\text{PO}_4)_3$ absorb about the same amount of u.v. light as $\text{Th}_3(\text{PO}_4)_4$ from 254-365 nm, showing that silver and lithium are not sensitizers.

In considering the possible relationship between half-height band width and temperature dependence, Ranby (1) and Wanmaker (9) report their results in wavelength units (Å). In order to com-

pare the band width of a blue band with a red band, it would be more meaningful to use frequency units (cm^{-1}) which are directly related to the energy. If this is done, then according to our results $\text{Th}_2\text{Cu}(\text{PO}_4)_3$ has a band width of 3000 cm^{-1} , $\text{Th}_2\text{Li}(\text{PO}_4)_3$:Cu 3100 cm^{-1} , and $\text{Th}_2\text{Ag}(\text{PO}_4)_3$:Cu 3500 cm^{-1} . The latter phosphor with a somewhat larger band width has the poorest temperature dependence (Fig. 6). Thus, within a particular phosphor and structural system comparing band-width and temperature dependence may be significant as suggested by Wanmaker (9). Phosphors of different systems cannot be meaningfully compared. For example, magnesium lithium antimonates (10) activated by U, or Mn, have narrow bands (1600 cm^{-1}), but poor temperature dependence.

Ranby and Hobbs (1) have pointed out the close comparison between the two copper emission bands of thorium orthophosphate with the weaker emission bands of hexagonal zinc sulfide. As seen from Fig. 1, all three copper bands were observed in this investigation: blue ($22,400 \text{ cm}^{-1}$), green ($19,000 \text{ cm}^{-1}$), and yellow-orange ($16,900 \text{ cm}^{-1}$). These compare very closely to the hexagonal zinc sulfide peaks at $22,400 \text{ cm}^{-1}$, $19,250 \text{ cm}^{-1}$, and $17,000 \text{ cm}^{-1}$ (11). The main green ZnS:Cu band is much weaker in the case of the thorium orthophosphate.

Acknowledgment

The authors are indebted to Dr. C. W. W. Hoffman for the x-ray diffraction measurements, and to Mr. Roman J. Wisniewski for the epr measurements. We would also like to thank Mr. Allan J. Comstock and Mr. James E. Mathers for the analytical determinations. The phosphor samples were prepared by Mr. Olney B. Bullock.

Manuscript received Dec. 10, 1963; revised manuscript received Jan. 20, 1964.

Any discussion of this paper will appear in a Discussion Section to be published in the December 1964 JOURNAL.

REFERENCES

1. P. W. Ranby and Doreen Y. Hobbs, *This Journal*, **110**, 230 (1963).
2. A. Burdese and M. L. Borlera, *Atti reale accad. Sci. Torino*, Part 1, *Classe sci. fis., mat. nat.*, **94**, 89 (1960).
3. W. Slavin, R. W. Mooney, and D. T. Palumbo, *J. Opt. Soc. Am.*, **51**, 93 (1961).
4. R. W. Mooney, *This Journal*, **107**, 101 (1960).
5. D. E. C. Corbridge and E. J. Lowe, *J. Chem. Soc.*, **1954**, 493.
6. R. H. Sands, *Phys. Rev.*, **99**, 1225 (1955).
7. P. W. Ranby and D. Y. Hobbs, British Pat. 834,024. May 4, 1960.
8. K. A. Wallroth, *Bull. soc. chim.*, (2) **39**, 316 (1883).
9. W. L. Wanmaker and C. B. Bakker, *This Journal*, **106**, 1027 (1959).
10. R. W. Mooney, *ibid.*, **108**, 1112 (1961).
11. S. T. Henderson, P. W. Ranby, and M. B. Halstead, *ibid.*, **106**, 27 (1959).

Preparation and Properties of GaAs-GaP, GaAs-Ge, and GaP-Ge Heterojunctions

Martin Weinstein, R. O. Bell, and A. A. Menna

Tyco Laboratories, Inc., Waltham, Massachusetts

ABSTRACT

Epitaxial films of GaAs and GaP have been deposited on GaAs, GaP, and Ge substrates by a vapor phase chemical reaction technique. The growth variables, such as source temperature, seed temperature, crystal orientation, surface preparation, and gas flow rate, have been investigated. The optimum conditions for the growth of epitaxial films and the electrical characteristics of these films are reported. GaAs-GaP junctions grown by a solution growth technique (TSM) are abrupt, whereas junctions grown by the vapor phase technique are graded. Detailed measurements of the I-V characteristics and capacitance of GaAs-Ge, GaAs-GaP, and GaP-Ge abrupt heterojunctions are interpreted in terms of Anderson's model. Kinks in the I-V characteristic are explained by discontinuities in the valence and conduction bands.

Considerable progress has been made recently in the growth of epitaxial films of III-V compounds from the vapor phase. All the techniques reported to date involve the chemical reaction of a Group III halide with a volatile Group V species, either in a closed tube or in an open tube with continuous flow. In the closed tube technique, the source III-V compound, or its constituents, is placed with the appropriate transfer reactant in the reaction zone of the furnace chamber, and the seed crystal upon which epitaxial growth occurs is placed in a lower temperature region of the furnace. Various transfer agents have been used for the epitaxial growth of GaAs and GaP. Moest and Shupp (1) used exclusively HCl as the transfer agent; Holonyak *et al.* (2) have grown films of these compounds with a halogen or metal halide as the transfer agent; Lyons and Silvestri (3) and Hagenlocher (4) have reported the growth of GaAs films with iodine as the transfer agent. Because of the ease of setup and the fast growth rates, the open tube continuous flow method has been extensively investigated. Williams and Ruehrwein (5) and Newman and Goldsmith (6) have used this method with an HCl transfer agent and a synthesized III-V compound. Ing and Minden (7) recently described the use of elemental gallium, arsenic, and phosphorus as source materials, together with HCl transfer gas. Frosch and Foy (8) reported the evaporation of GaAs and GaP at elevated temperatures in a flow of hydrogen gas and the subsequent redeposition of the compound in the cooler zone of the system.

Because of these advances it is now possible to prepare heterojunctions, *i.e.*, junctions between two different semiconducting compounds. Holonyak *et al.* (2) have reported the preparation and some of the electrical properties of GaAs-Ge, GaAs_xP_{1-x}-

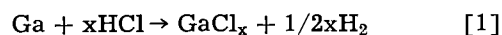
GaAs_yP_{1-y}, and GaP-GaAs heterojunctions. Moest and Shupp (1) and Ing and Minden (7) have described the preparation of GaAs-GaP and GaAs-Ge heterojunctions. Van Ruyven and Dekker (9) recently described the preparation of Ge-GaP junctions. Detailed analyses of the electrical properties of GaAs-Ge heterojunctions have been made by Anderson (10) and Nathan and Marinace (11). The former author proposes a model in which the conduction and valence band edges at the interface are discontinuous. Aven and Garwacki (12) have recently proposed a band model for ZnTe-CdS junctions. From their experimental evidence they concluded that these junctions possessed a PSN structure (S is a heavily compensated region) with levels near, or slightly above, the middle of the band gap of cadmium sulfide.

This paper describes the growth of epitaxial GaAs and GaP films and the heterojunctions which have been formed between GaAs and GaP, GaAs and Ge, and GaP and Ge.

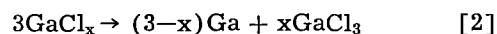
Epitaxial GaP and GaAs Films

Epitaxial, single crystal films of GaAs and GaP have been deposited on various substrates by HCl vapor transport in the open tube arrangement shown in Fig. 1.

The reaction between the source material and the HCl is given by



The reaction in the deposition region is



This deposition reaction is postulated (5) because large quantities of GaCl₃ and free As are found

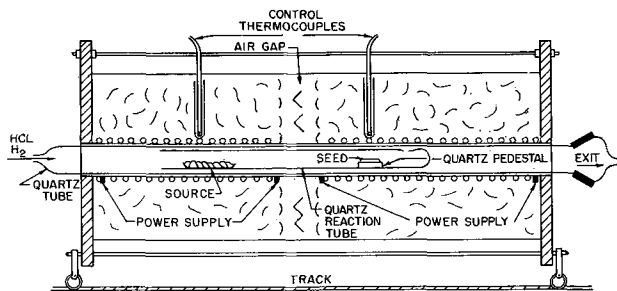


Fig. 1. Two-zone epitaxial furnace

at the exit sections of the reaction tube. The transfer mechanisms are obviously different for the two elements involved. The metal Ga forms lower halides which undergo a disproportionation reaction on the substrate surface, whereas the arsenic or phosphorus evaporates and is transported by the carrier gas to the seed crystal.

The HCl was introduced into the system through stainless steel or monel valves and was purified by passing it through a dry ice-acetone cold trap. The hydrogen was purified by passing it through a Deoxo¹ unit (platinized asbestos) to remove oxygen, and then into a drying tower to remove water vapor. Quartz was the only material, other than the seed and source materials, which was used in the hot zone of the reaction chamber. A large multiple tap furnace was used in the initial investigation of process variables (temperature, temperature gradient, crystal orientation, surface preparation, and gas flow rate) so that the source and seed temperatures could be varied with ease. For later investigations, as discussed below, the two-zone furnace shown in Fig. 1 was used to obtain large area, perfect (low defect density) epitaxial films.

The following experimental procedure was used. The source and seed materials were etched and the orientation of the seed noted. The seed crystals were carefully polished to a mirror-like finish (as described below), and the source and seed were placed in the quartz reaction chamber. After the system was purged with helium, hydrogen was passed through it for ½ hr. While the hydrogen was flowing, the furnace was moved on its track until the source and seed crystals were at the proper temperatures. At this time, the appropriate mixture of HCl and H₂ was passed into the reaction chamber. After the reaction period, the furnace was quickly moved away and the HCl flow stopped. Small amounts of powdered material, which could be removed by ultrasonic washing, were present on the surface of the epitaxial films at the end of each run. The results of over 100 experiments in which the optimum variables for epitaxial growth of perfect GaAs and GaP films were determined are discussed below.

Growth of GaAs epitaxial films.—The source temperature, substrate temperature, and temperature difference between the seed and substrate were found to be critical to the epitaxial growth process. When

¹ Manufactured by the Engelhard Industries, Inc., Newark, New Jersey.

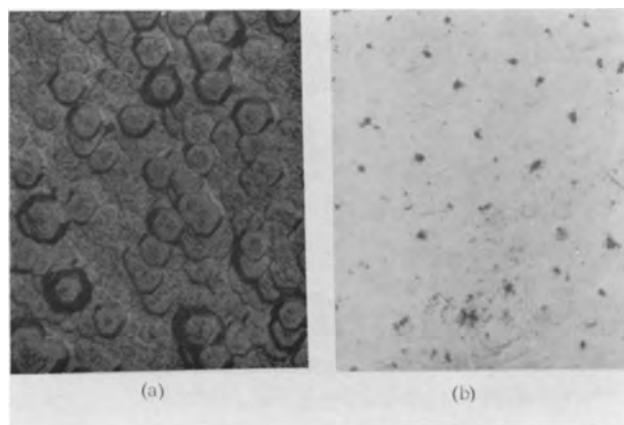


Fig. 2a. (left) Large etch figures on upstream portion of GaAs epitaxial layer. Fig. 2b. (right) Micro-orange peel pattern on downstream portion of GaAs epitaxial layer; unetched. Magnification approximately 200X.

the source temperature was higher than 870°C, the rate of material transfer was extremely fast, and very accurate control of the gas flow rate was necessary. In general, the source temperature was maintained at or below 870°C. The influence of the seed temperature on the perfection of the epitaxial deposit can be seen in Fig. 2a and 2b, which are, respectively, photomicrographs of the upstream and downstream portions of the same epitaxial GaAs film. The upstream portion, which was at approximately 800°C, contains large etch figures similar to the growth facets apparent on the surface of a (111) oriented GaAs crystal grown from solution. The downstream portion of the crystal, which was at 750°C, has a fairly smooth epitaxial deposit, which may be described as "micro-orange peel." Glang and Wajda (13) have determined for silicon epitaxy that this type of texture defines a perfect crystal film. When the temperature difference between the seed and source exceeded 150°C, polycrystalline deposition occurred; etching of the seed crystal occurred when the gradient was less than 75°C. These experiments indicate that the optimum temperatures for epitaxial growth are a source temperature of 870°C and seed crystal temperature of 735°C. These temperatures were easily obtainable in the two-zone furnace shown in Fig. 1.

The effect of gas flow rate on crystal growth in this system was also studied. Flow rates of 3 cc/min for HCl and 35 cc/min for H₂, and the optimum temperature difference of 135°C, yielded the epitaxial film with a chevron surface pattern shown in Fig. 3. With the lower flow rates of 2 cc/min for HCl and 30 cc/min for H₂, the epitaxial film shown in Fig. 4 was formed. Faceted growth probably results from the slower deposition rate. Satisfactory results were obtained with an HCl flow rate of 3 cc/min and an H₂ flow rate of 35 cc/min when the seed crystal was prepared as described below.

The deposition of smooth, highly perfect epitaxial films requires a polished substrate surface. Initially, the preparation of highly polished GaAs surfaces was difficult. Mirror-like finishes could be obtained by mechanical polishing, but strained surface layers normally prevented the deposition of smooth

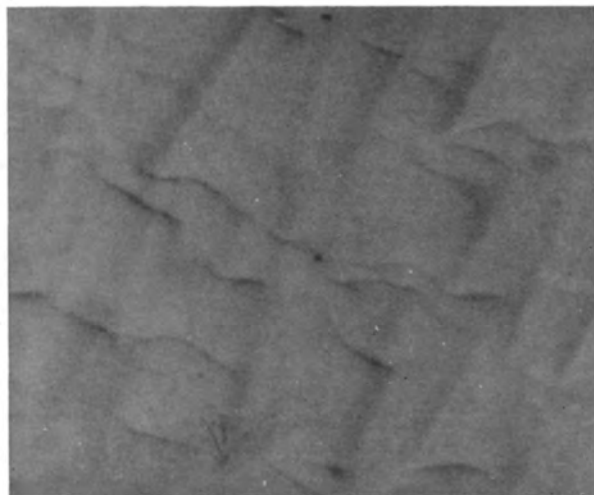


Fig. 3. Chevron type of epitaxial deposit, unetched. Magnification 300X.

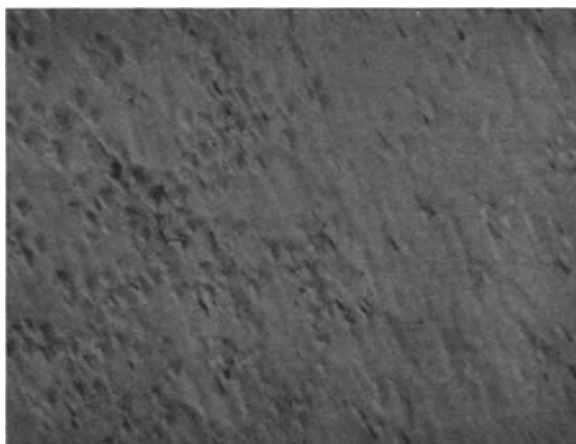


Fig. 4. Faceted growth caused by extremely slow deposition rate, unetched. Magnification approximately 200X.

epitaxial layers. Of all the common etches studied, aqua regia produced the best surfaces. Preferential etching, however, occurred in this case. An intensive study of surface preparation indicated that the etch described by Fuller and Allison (14), i.e., an organic liquid saturated with chlorine or bromine, yields smooth surfaces. For GaAs the best results were obtained with an etch prepared by bubbling chlorine gas slowly through methyl alcohol, with the specimen completely immersed. A reproducible etching rate of approximately 0.5 mils/min at 25°C was obtained with solutions completely saturated with gas.

With this surface preparation technique, and the optimum crystal growth parameters (source temperature 870°C, seed temperature 735°C, HCl flow rate 3 cc/min, and H₂ flow rate 25-35 cc/min) smooth, perfect epitaxial layers of GaAs were deposited on GaAs substrates in the two-zone furnace. Epitaxial films 1 cm² in area have been grown with only one or two of the wrinkled defects shown in Fig. 5. The rate of etching of the source material and the rate of crystal growth were highly reproducible. The average rate of crystal growth under the optimum conditions was 10 μ/hr. Because the rate of growth was constant with time, epitaxial layers with desired thicknesses of 1-100μ



Fig. 5. Smooth GaAs epitaxial film; films 1 cm² have been grown with only one or two of the wrinkled defects shown; unetched. Magnification approximately 200X.

could be prepared with accuracies of ±10%. The rate of film growth and the perfection of the film were independent of (111) crystal face polarity, as observed by Williams and Ruehrwein (5). However, the defects formed on the surface were characteristic of the specific crystal face. Thickness variations of less than 10% were observed over most of the substrate area.

Electrical evaluation of GaAs epitaxial deposits.—The electrical properties of the deposited GaAs layers were evaluated by measurements of point contact varactor diodes prepared from these layers. In all cases, n-type GaAs was deposited on high conductivity (0.0003 ohm-cm) n-type GaAs. An alloyed ohmic contact was made to the n⁺ side with an 80Au-20Sn alloy. The junction was prepared by pressing a 0.5 mil diameter phosphor-bronze point onto the epitaxial layer, and a standard ceramic package was used to encapsulate the diode. Capacitance measurements made at 1 Mc are given in Table I; the values include both the capacitance of the package (0.4 pf) and the junction. The high-frequency measurements were made at X-band. The built-in potential (ϕ) of all the point contact diodes tested was between 1 and 1.25v. The value of n in the relation

$$I = I_0 \left[\exp \left(\frac{eV}{nkT} \right) - 1 \right] \quad [3]$$

varied from approximately 1 to 2.05.

The effect of the source material resistivity on the epitaxial deposit resistivity was determined from measurements of voltage breakdown in these devices. GaAs epitaxial layers prepared from 0.01 ohm-cm source material exhibited breakdown voltages of 1-3v. These voltages correspond to a layer resistivity of 0.0006-0.001 ohm-cm, approximately the resistivity of the initial substrate material. When the source material had a specific resistivity of 0.1 ohm-cm, the epitaxial layers ex-

Table I. Electrical properties of GaAs varactor diodes

Exp	V _b , v @ 10 μa	V _f , v @ 3 ma	C _o , Pf	VSWR, db @ -0.4v	f _c , kMc @ -2v	φ, v	n
16	7.2	1.0	0.675	14.7	180	1.07	1.36
19	5.2	1.08	0.818	10.2	120	1.02	1.5
20	6.0	1.0	0.526	13.4	163	1.03	2.05

hibited voltage breakdowns of 6-10v. These values correspond to a resistivity of approximately 0.003-0.01 ohm-cm. With 1 ohm-cm source material, breakdowns of 20-25v, corresponding to a layer resistivity of approximately 0.1 ohm-cm, were obtained.

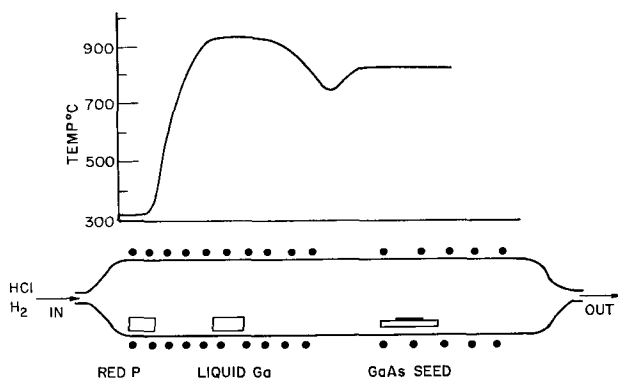
Although the pick-up of impurities, *e.g.*, silicon from the reaction tube and dopant from the high conductivity substrate, may be a factor in the increase in conductivity of the deposit, the contribution of these transfer processes should be small (carriers transferred must be $< 6 \times 10^{16}/\text{cm}^3$ as given by the carrier concentration of the highest resistivity layer) and of constant magnitude, irrespective of the impurity concentration of the source material. The experimental results therefore indicate that during the transport-deposition process the source crystal impurity tends to segregate in the epitaxial film rather than becoming randomly distributed throughout the deposition zone.

GaAs platelets were also deposited on gold-plated Kovar pins by the epitaxial deposition process. This device fabrication process does not require an alloy contact to the GaAs because Au and GaAs form an ohmic contact at the high deposition temperatures. Also, because there is no GaAs substrate, the series resistance of the device is low. Although the contact between the GaAs and Au in this case was slightly resistive, excellent varactor diodes ($f_c = 100$ kMc at -2v) were obtained by this technique.

Epitaxial growth of GaP films.—Epitaxial GaP films were grown in a system similar to that described by Ing and Minden (7). The transport process was the same as that for GaAs growth. However, the synthesis of GaP was accomplished directly in the reaction chamber by the passage of HCl gas in an H_2 stream over heated phosphorus and over gallium at a higher temperature. The epitaxial deposit was obtained on a substrate crystal which was at a lower temperature than the gallium. Because high-quality GaP seed crystals were not available, GaAs (111) oriented seed crystals were used in most GaP runs. A schematic diagram of the experimental arrangement is shown in Fig. 6. The source phosphorus was always at a temper-

ature of approximately $250^\circ\text{-}300^\circ\text{C}$. When the seed and source crystal temperatures determined in the GaAs epitaxial film study (Ga temperature 870°C and seed GaAs temperature $735^\circ\text{-}765^\circ\text{C}$) were used, fuzzy yellow deposits of GaP, which could be easily removed by an ultrasonic wash in acetone, were found on the seed crystal. At higher seed crystal temperatures, etching occurred. When the source Ga was kept at 970°C , in an effort to increase the rate of GaP formation, yellow GaP deposits again were observed on the substrate crystal; however, now red crystals of GaP were observed in the hotter sections of the furnace at approximately $800^\circ\text{-}850^\circ\text{C}$. When the seed crystal was placed in this zone with the source material at 950°C , massive deposits of red GaP were found on the substrate crystal. In some cases, GaP layers were observed on the surface of the GaAs substrate under polarized light, even though the crystal had shown a decrease in weight. This indicates that both etching and deposition occurred simultaneously. Epitaxial deposits from 2 to 150μ thick have been grown on GaAs substrates. The thicknesses were determined by metallographic angle lapping techniques. X-ray analysis indicated that the deposits were single crystal and had the same orientation as the substrate. In all cases, the GaP deposits appeared gray under ordinary light; under polarized light, the red color of GaP could be seen. Figure 7 is a photomicrograph of GaP as it appeared under polarized light. The deposit is approximately 150μ thick, and is extremely faceted.

The substrate temperature was much more critical for the formation of epitaxial GaP layers than for epitaxial GaAs growth. The critical temperature for GaP single crystal epitaxial deposition is $800^\circ \pm 5^\circ\text{C}$ under the existing furnace conditions. Reproducible rates of GaP epitaxial growth have been obtained with this substrate temperature, using either previously synthesized GaP or elemental Ga and P as source materials. GaP epitaxial films are generally much more faceted than GaAs epitaxial films. For the experimental conditions studied, the rate of GaP crystal growth was approximately $15\mu/\text{hr}$.



GaP EPITAXIAL DEPOSITION SET-UP

Fig. 6. GaP epitaxial deposition set-up

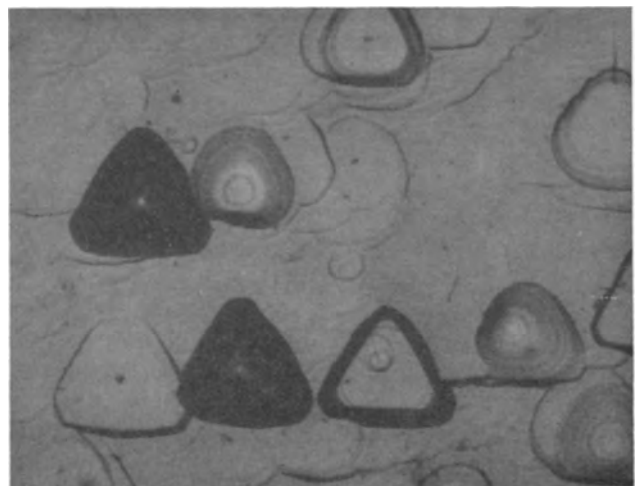


Fig. 7. Faceted surface of GaP deposit on GaAs, unetched, under polarized light. Magnification approximately 225X.

Table II. Electrical properties of GaP (on GaAs) varactor diodes

Sample description	$V_b, v @ 10 \mu a$	$V_f, v @ 3 ma$	C_o, Pf	$f_c, kMc @ -2v$	ϕ, v	n
Run No. 40						
Gap layer 1-6						
40-1	3.0	1.04	0.734	187	1.53	1.7
40-2	2.8	0.93	0.518	132	1.58	3.3
40-3	3.5	1.14	0.712	50		
Monsanto GaAs substrate						
M-1	2.6	1.13	0.610	90	1.0	
M-2	1.6	1.07	0.450	48	1.0	2.54
M-3	1.5	0.95	0.492	0	1.0	
Run No. 41	7.5	2.75	0.522	0	1.65	3.4
GaP layer 20-50						
Run No. 42	3.75	2.3	0.714	0	1.85	3.3
GaP layer 40-100						

Electrical evaluation of GaP epitaxial films.—Varactor diodes similar to those used in the evaluation of the GaAs epitaxial material were prepared from several GaP epitaxial deposits on GaAs substrates. Data from typical diodes are given in Table II.

Experimental results indicate that high Q varactor diodes can be made with epitaxial GaP material. This is in direct contradiction to the predictions of varactor theory in which it is assumed that mobility is the limiting factor in the efficiency of varactor diodes (15). The mobility of the GaP films in this case was probably 50-150 cm²/volt-sec. As the thickness of the GaP epitaxial layer increases, ϕ increases from 1.5 to 1.85. If ϕ is assumed to be an approximate measure of the energy gap, there is good correspondence between the values for GaP and GaAs. ($\phi_{GaAs} = 1.0-1.3$, $E_{g(GaAs)} = 1.39$; $\phi_{GaP} = 1.9$, $E_{g(GaP)} = 2.24$). Therefore, the space charge region of point contact diodes prepared from thin epitaxial GaP layers include both GaAs and GaP. The formation of a graded region between GaP and GaAs has already been reported by Holonyak *et al.* (2).

Diodes prepared from the material of runs 41 and 42 (Table II) behaved as microwave loads, *i.e.*, low VSWR, probably because of the high series resistance, R_s , of the thick GaP layer. The validity of the results obtained from the material prepared in run 40 was checked by measurements made on diodes constructed from the basic GaAs substrate material (0.0007 ohm-cm), as supplied by the Monsanto Chemical Corporation. These results confirm the contribution of the high resistance GaP layer to the microwave properties of the device. Because all the devices prepared with GaP were square law devices, ϕ could be accurately determined.

Heterojunctions

Junctions between oppositely doped regions of a given semiconductor have been studied extensively and are well understood. However, junctions between two different materials have not been studied to the same degree because it has been difficult to prepare well-behaved junctions. Junctions between dissimilar materials (heterojunctions) can now be

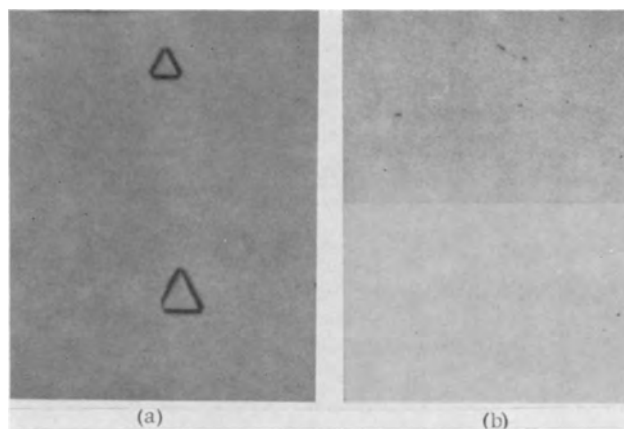


Fig. 8a. (left) Open triangular defect on GaAs film deposited on Ge. Fig. 8b. (right) Junction between GaAs and Ge (angle lap 20°) etched in HNO₃:H₂O. Magnification approximately 170X.

readily prepared by epitaxial growth from the vapor and from solution. The preparation and properties of GaAs-Ge, GaP-Ge, and GaAs-GaP heterojunctions are discussed below.

GaAs(n)-Ge(p⁺) heterojunctions.—Single crystal epitaxial films of GaAs were grown on Ge substrates using the same experimental arrangement and the same deposition parameters employed for growing GaAs on GaAs. The Ge surface was prepared by a chemical polishing technique, using an H₂O₂:NaOH solution in conjunction with a cotton pad soaked with 1 μ alumina. GaAs films prepared on germanium substrates were extremely perfect. The defect structures seen in Fig. 8a were different from those observed when GaAs substrates were used. The open triangle defect is normally found in epitaxial Ge or Si, and corresponds to stacking faults in these materials. Thus, not only the growth habit, but also the nature of the epitaxial GaAs

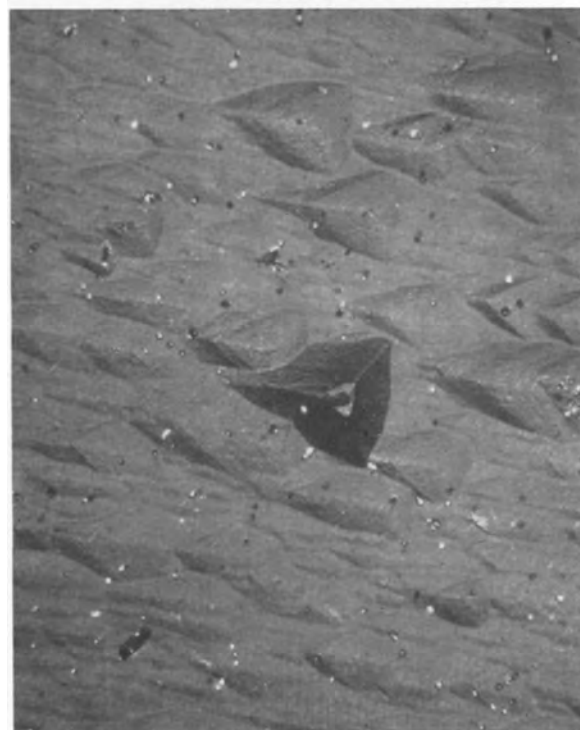


Fig. 9. Faceted nature of GaP film deposited on Ge, unetched. Magnification approximately 65X.

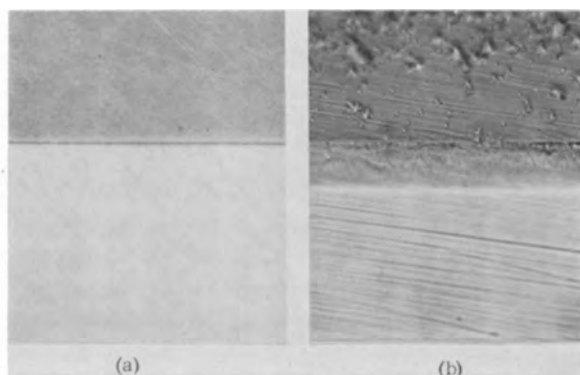


Fig. 10a. (left) Polished cross section of GaP-Ge junction. Fig. 10b. (right) Etched cross section of GaP-Ge junction showing transition region (20° angle lap). Magnification approximately 665X.

film is influenced by the Ge substrate. A cross section of the GaAs-Ge heterojunction, shown in Fig. 8b, demonstrates the highly perfect metallurgical nature of the junction.

GaP(n) on Ge(p⁺).—Single crystal oriented GaP films have been deposited on germanium by the HCl vapor transport technique previously described. In this case, the substrate temperature was again critical. Deviations of $\pm 5^\circ\text{C}$ from the desired temperature, 800°C , produced microcrystalline yellow deposits of GaP. The surface of the GaP film deposited on Ge is shown in Fig. 9. As shown in the photomicrograph, elongated pyramidal facets cover the entire surface. Figure 10a, a polished cross section of the GaP-Ge structure, shows no evidence of imperfections or diffusion at the junction. When the structure was etched, however, a transition region (possibly Ge in GaP) could be observed, as shown in Fig. 10b. The erratic electrical characteristics of these junctions, which are discussed below, are probably caused by this 2μ thick transition region.

GaAs(p)-GaP(n).—Heterojunctions of GaP-GaAs have been produced by epitaxial growth from the vapor phase of GaP on GaAs and by a solution growth technique (16). The surface of the vapor grown epitaxial GaP deposit on GaAs is shown in Fig. 7. These deposits were extremely faceted, the facet structure being mainly of the pyramidal type. Because the resistivity of the GaP layer was extremely high (approximately 10^4 to 10^6 ohm-cm), devices could not be prepared easily from this material.

GaP-GaAs heterojunctions which are discussed in this paper were prepared by the TSM solution growth technique (15). The preparation of these junctions may be easily described with the aid of Fig. 11. In this case, liquid gallium was used as the solvent zone, GaP as the seed crystal, and GaAs as the source crystal which is dissolved. Because of the variation in solubility of GaAs at the upper and lower liquid-solid interfaces, the GaAs tends to dissolve at the upper interface and redeposit at the lower interface. In this way, epitaxial growth of GaAs onto the GaP seed was obtained. No transition region was observed because the rate of solution of GaP in Ga at the experimental temperature is extremely small relative to the rate of solution

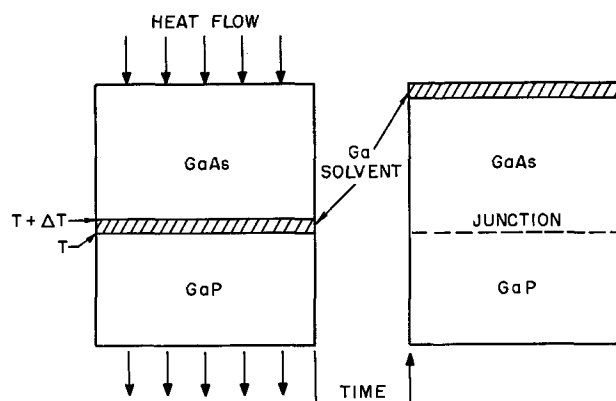


Fig. 11. Schematic representation of TSM for growth of GaP-GaAs heterojunction.

of GaAs at the upper interface. Specifically, a temperature gradient of 170°C was placed across the entire composite, the lower GaP (solid)-Ga liquid interface being at 650°C . The regrown GaAs was single crystal and had the orientation of the GaP seed crystal. A Ge-doped Ga liquid zone yielded regrown GaAs that was conductivity p-type.

Electrical Measurements

The capacity and current-voltage characteristics of the heterojunctions have been measured. Except for the junctions made by the deposition of GaP(n) on GaAs(p) by vapor transport, the heterojunctions had a square law dependence of capacitance on the reverse bias, indicating the abrupt character of the junctions. The GaP-GaAs vapor deposited junctions had a cube law dependence of capacitance on the bias voltage, indicating that these junctions were linearly graded. In general, the value of the built-in potential, ϕ , was between that of the two constituent semiconductors, as shown in Table III. Results obtained for the various heterojunctions are discussed below.

GaAs(n) on Ge(p).—In this heterojunction, 0.001 ohm-cm n-type GaAs was deposited on 0.002 ohm-cm Ge. Ohmic contacts were made to the GaAs with an 80:20 Au:Sn alloy and to the Ge with an In:Ag alloy. This device was encapsulated in a ceramic package. The I-V characteristic of this heterojunction was studied as a function of temperature. In Fig. 12 the oscilloscope traces of the forward characteristics at 23° , 80° , and 150°C are given. The forward currents for a diode of this area (0.2 cm^2) are higher than those which would be expected for GaAs. The reverse characteristics indicate that the leakage current is determined by the Ge region of the junction (Fig. 13). At 100°C

Table III. Value of ϕ for various junctions

$$C(V) = \frac{C_0}{(1 - V/\phi)^{1/2}}$$

Junction	ϕ
Ge(p ⁺) on Ge(n)	0.60
GaAs(p ⁺) on Ge(n)	0.78
GaAs(p ⁺) on GaAs(n)	1.0-1.3
GaAs(p ⁺) on GaP(n)	1.5
GaP(p ⁺) on GaP(n)	1.9-2.0

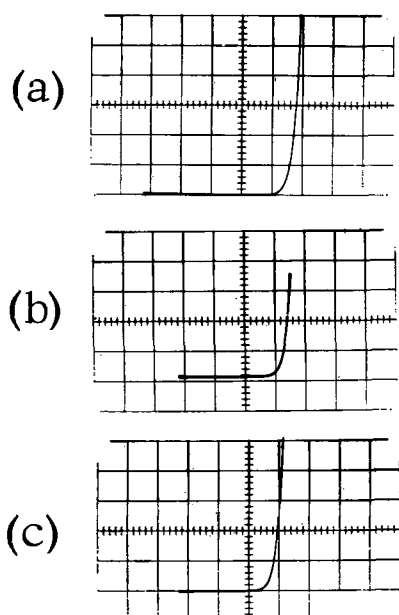


Fig. 12. Forward characteristics of GaAs-Ge diode as a function of temperature. Vertical scale is 1 ma/division and horizontal scale, 1/2 volt/division. a, 23°C; b, 80°C; c, 160°C.

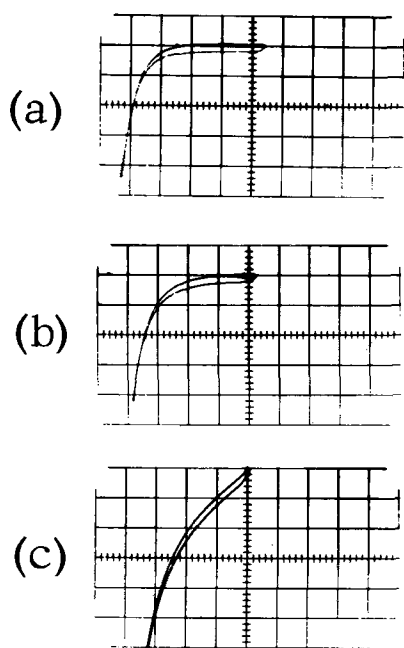


Fig. 13. Reverse characteristics of GaAs-Ge diode as a function of temperature. Vertical scale is 10 μ a/division and horizontal scale is 1/2 volt/division. a, 23°C; b, 80°C; c, 160°C.

the leakage becomes excessive, and above 120°C, where the Ge becomes conductive, the reverse characteristic is completely lost. This can be explained by the thermal generation of electron-hole pairs in Ge, as illustrated on the energy band diagram of this junction in Fig. 14.

Figure 15 is a semilog plot of current vs. voltage for a GaAs(n)-Ge(p) heterojunction. Initially, the current increases exponentially according to Eq. [3] with a value of $n = 2.6$. At 0.32v bias, the slope changes to a value of $n = 1.4$. Above 0.48v, the ohmic resistance of the sample becomes important.

If it is assumed that the transition to ohmic behavior at a bias of 0.48 occurs at the flat band posi-

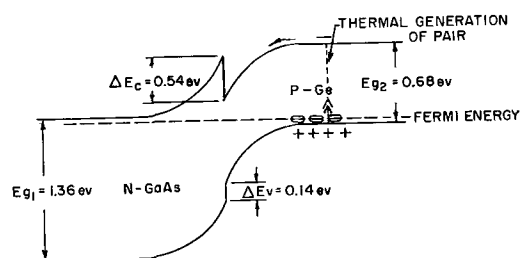


Fig. 14. Energy band diagram of GaAs-Ge heterojunction

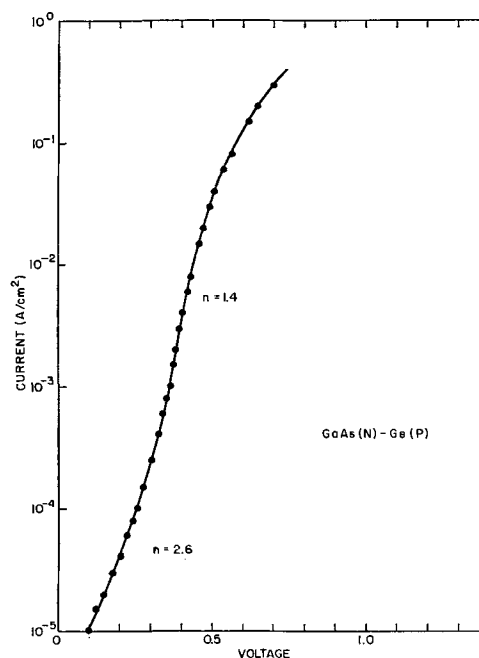


Fig. 15. Semilog plot of I-V characteristic for a GaAs(n)-Ge(p) heterojunction.

tion, the value of discontinuity of the valence band, ΔE_v , and conduction band, ΔE_c , can be calculated. The calculated values $\Delta E_v = 0.54$ eV and $\Delta E_c = 0.14$ eV are in good agreement with the results of Anderson (10). However, the capacity data yield $\phi = 1.02$ v, so that $\Delta E_v = 0.14$ eV and $\Delta E_c = 0.54$ eV. A discrepancy between values calculated from the capacity and current-voltage data occurred in a number of cases. Possible reasons for this are:

1. Interdiffusion which results in a gradual, rather than abrupt, transition of the conduction band from one material to the other;

2. Charge or surface states, which may cause energy band bending in the immediate vicinity of the junction.

3. Dislocations or strains, which may complicate the energy band structure. For example, dislocations that pass through the junction can reduce the potential barrier for current flow.

GaAs(n) on Ge(n).—Because the conduction and valence bands in GaAs and Ge are at different levels, it is possible to make a junction between these two semiconductors even though they are both n-type. One such diode which was tested had a reverse current of 10 μ a at -4 v and a forward current of 1 ma at 0.85v. Diodes of the GaAs(p) on Ge(p) and GaAs(p) on Ge(n) configurations exhibited nonreproducible characteristics.

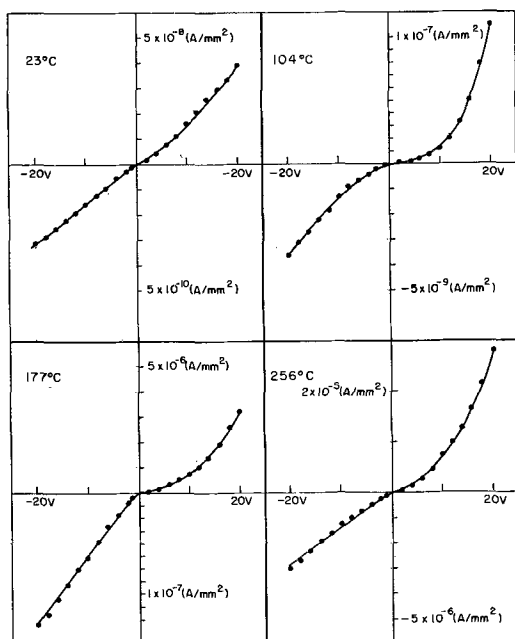


Fig. 16. Typical I-V characteristic for GaP(n) on Ge(p) heterojunction.

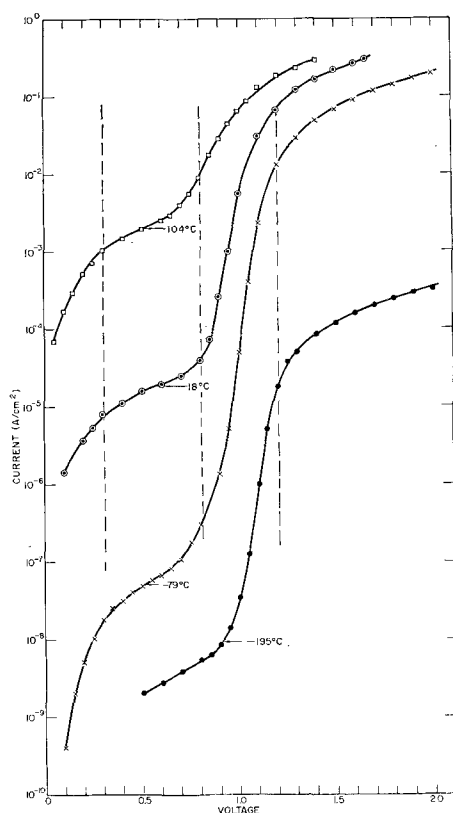


Fig. 17. Semilogarithmic plot of current vs. voltage for a solution grown GaP-GaAs heterojunction.

GaP(n) on Ge(p).—Initially, diodes constructed of GaP on Ge had junctions with very high resistances. A typical current-voltage characteristic for a GaP(n) on Ge(p) heterojunction is shown in Fig. 17. The characteristic can be explained by the assumption of a very high resistivity transition region between the two semiconductors. When the high resistivity of the transition region was reduced by the introduction of antimony into the vapor

transport system, the resulting heavily doped junctions had a forward current higher by a factor of 10^3 than the original value. Because the diode had a high reverse current, no reliable capacity measurements could be made. From the current-voltage characteristic, the flat band position was found at a forward bias of 1.2v, and the slope in Eq. [3] for small bias corresponded to $n = 2.1$.

GaP(n) on GaAs(p).—Heterojunctions of GaP on GaAs made by vapor transport and by the travelling solvent method of crystal growth (15) were evaluated. In the junctions made by vapor transport, the junction capacitance had a cube law dependence on voltage, characteristic of a linearly graded junction. A junction of this type is expected because GaAs and GaP are mutually soluble, and diffusion occurs readily at the preparation temperatures. The square law dependence of capacity on bias voltage observed in TSM-grown junctions indicated that these junctions were abrupt. For both junctions, the same general current-voltage characteristics were observed, although the kinks were more pronounced in the TSM diode. The diodes conduct about $10 \mu\text{a}$ at 7v reverse bias. A semilogarithmic plot of current vs. voltage for a TSM diode is given in Fig. 17, where several distinct kinks can be observed. This curve may be divided into four regions, in each of which the current may be roughly approximated by the diode equation with various values of n characterizing the slope (see Table IV). In region (I) the current is carried by electrons flowing across the junction. As the voltage is increased, because of the discontinuity of the conduction band, the current does not increase as rapidly (region II). With further increase in voltage injected current becomes important (region III). Finally, the ohmic resistance of the material limits the current.

Measurements were made at several temperatures between 104° and -195°C . In all cases the same general form for the current-voltage curve was observed. Similar behavior has been reported by Anderson (10) for a GaAs-Ge heterojunction, but without as clearly a defined plateau region.

If it is assumed that the capacity occurs mainly in the GaP side of the junction region, the number of carriers, N , can be estimated from the expression

$$C = \left[\frac{Ne\epsilon}{2(V + \phi)} \right]^{1/2} \quad [4]$$

where e is the electron charge, ϵ is the dielectric constant, V is the applied bias, and ϕ is the built-in potential. Equation [4] yields a value for N of $3 \times 10^{16} \text{ cm}^{-3}$ at room temperature. The position of the Fermi energy, E_F , with respect to the conduction

Table IV. Values of n in the diode equation for different ranges of voltage in GaAs-GaP heterojunctions

Temp, °C	n 0-0.3v	$I = I_0 \exp\left(\frac{eV}{nkT}\right) - 1$ 0.3-0.8v	0.8-1.2v
104	1.7	15	1.9
18	1.9	15	1.3
-79	1.8	18	1.4
-195	—	44	3.8

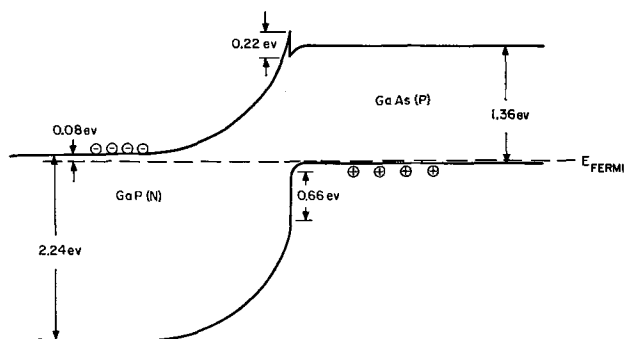


Fig. 18. Derived energy band diagram for the GaAs-GaP junction at zero bias.

band, E_c , can then be calculated by the expression

$$N \approx N_c \exp [(E_F - E_c)/kT] \quad [5]$$

where N_c is the density of states in the conduction band. Equation [5] yields a value for $(E_F - E_c)$ of 0.08 eV. This is in good agreement with conductivity measurements which give 0.07 eV for the activation energy in the GaP. Because the value of ϕ (1.50 eV) determined from the capacity data or current data gives the flat band position, ΔE_c and ΔE_v are estimated to be 0.22 and 0.66 eV, respectively. The derived energy band diagram for the GaAs-GaP junction at zero bias is shown in Fig. 18.

Acknowledgments

The authors wish to thank Dr. A. I. Mlavsky for extremely stimulating discussions and suggestions and Dr. G. Rupprecht for assistance in the interpretation of the electrical characteristics. The help of H. E. LaBelle in the preparation of diodes is appreciated. They also gratefully acknowledge the fi-

ancial support of the Bureau of Ships, Department of the Navy, under Contract No. Nobsr-87340.

Manuscript received Oct. 28, 1963; revised manuscript received Dec. 24, 1963.

Any discussion of this paper will appear in a Discussion Section to be published in the December 1964 JOURNAL.

REFERENCES

1. R. R. Moest and B. R. Shupp, *This Journal*, **109**, 1061 (1962).
2. N. Holonyak, Jr., D. C. Jillson, and F. S. Bevacqua, "Metallurgy of Semiconductor Materials," J. B. Schroeder, Editor, Metallurgical Society Conference, Vol. 15, Interscience Publishers, New York (1961).
3. V. J. Lyons and V. J. Silvestri, *This Journal*, **108**, 177C (1961).
4. A. Hagenlocher, *ibid.*, **108**, 213C (1961).
5. F. V. Williams and R. Z. Ruehrwein, *ibid.*, **108**, 177C (1961).
6. R. L. Newman and N. Goldsmith, *ibid.*, **108**, 127 (1961).
7. S. W. Ing, Jr., and H. T. Minden, *ibid.*, **109**, 995 (1962).
8. C. J. Frosch and P. W. Foy, *ibid.*, **108**, 127 (1961).
9. L. J. Van Ruyven and N. Dekker, *Physica*, **28**, 307 (1962).
10. R. L. Anderson, *J. Solid State Electronics*, **5**, 341 (1962).
11. M. I. Nathan and S. C. Marinace, *Phys. Rev.*, **128**, 2149 (1962).
12. M. Aven and W. Garwacki, *This Journal*, **110**, 401 (1963).
13. R. Glang and E. S. Wajda, "Metallurgy of Semiconductor Materials," J. B. Schroeder, Editor, Metallurgical Society Conference, Vol. 15, p. 27, Interscience, New York-London (1961).
14. L. S. Fuller and H. W. Allison, *This Journal*, **109**, 880 (1962).
15. J. Lowen and R. H. Rediker, *ibid.*, **107**, 26 (1960).
16. A. I. Mlavsky and M. Weinstein, *J. Appl. Phys.*, in press, Sept. 1963.

Anodic Oxide Films for Device Fabrication in Silicon

I. The Controlled Incorporation of Phosphorus into Anodic Oxide Films on Silicon

P. F. Schmidt and A. E. Owen¹

Research Laboratories, Westinghouse Electric Corporation, Pittsburgh, Pennsylvania

ABSTRACT

The preparation of phosphorus doped anodic oxide films on silicon is described. These oxide films can be used as phosphorus diffusion sources during heat treatment. The concentration and distribution of the phosphorus in the oxide film has been investigated by tracer techniques, the quality of the oxide film by electron microscopy. Oxide growth in the solutions and at the current densities investigated occurs preponderantly by cation migration. A novel method is described for measuring the amount of silicon converted into oxide per volt forming voltage. The density of the oxide can also be calculated by this method.

The anodization of silicon differs in certain respects from that of metals. Both the flux of ions from the silicon towards the electrolyte, and the electronic current from the electrolyte towards the silicon, due to the discharge of anions, can be blocked by the wide energy gap semiconductor (1).

¹ Present address: Department of Glass Technology, University of Sheffield, England.

The semiconducting substrate suggests various device applications: silicon dioxide films as masks against diffusion from the gas phase; doped oxide films as diffusion sources; device passivation by means of suitable oxide films, etc. All these applications are being studied at these Laboratories. Techniques for obtaining geometry control over anodic oxide film growth on n-type silicon, the use

of doped oxide film patterns as localized diffusion sources, the use of pure SiO_2 films for varactor purposes (2), and the incorporation of p-type dopants will be the subject of further communications.

In this paper (Part I) the incorporation of phosphorus into anodic oxide films on silicon is described and discussed. Of the later publications, Part II deals with the diffusion of the phosphorus into the silicon for device purposes, and Part III will be devoted to a study and analysis of the diffusion profile of phosphorus in silicon. The same or similar concepts as developed here for anodic oxide films on silicon apply to anodic oxide films on a number of other semiconductors.

General Considerations

Incorporation of impurities into anodic oxide films, a process analogous to alloy plating, has received scant attention in the past due to the lack of practical applications. In the preparation of electrolytic capacitors, for example, the tendency has been to make the oxide film as pure as possible. Nor has the subject attracted much academic investigation: potential measurements are almost worthless in detecting the presence of a second electrode reaction due to the continuously rising potential during oxide growth.

Incorporation of sulphate ions into anodic oxide films grown on aluminum in dilute sulphuric acid has been known for over 60 years (3), but the purpose of the sulphuric acid bath has been the production of thick, porous oxide films rather than the incorporation of sulphur. In 1958, Lewis and Plumb (4) made a tracer study of thin, nonporous oxide films grown on aluminum in an aqueous solution of $\text{KH}_2\text{PO}_4\text{-K}_2\text{HPO}_4$ and showed that the phosphorus was incorporated into the oxide in a uniform manner independent of thickness. Incorporation of small quantities of boron into oxide films grown on aluminum in borate solution has recently been noted by Bernard and Randall (5).²

The present work received its impetus from the consideration that a dopant content of several per cent in an anodic SiO_2 film should be sufficient to use the film as a diffusion source. Such thin oxide film sources would have several potential advantages over other diffusion sources presently in use in the industry:

1. No problems of uniformity of vapor flow can occur, source and substrate being contiguous. This fact in itself should result in better control over the diffusion process.

2. Dopant source and substrate are always at the same temperature, eliminating another possible cause of error.

3. The strength of the dopant source is dependent on the concentration of the dopant in the oxide film, and on the film thickness. The thickness of anodic oxide films can be regulated by the applied forming voltage to within a few Angstrom units. An unusual degree of control should result since the dopant content in the oxide can be kept constant or can be varied in a controlled fashion.

4. The oxide film contains such a minute total amount of dopant that doped oxide patterns can be used as localized diffusion sources without masking of the rest of the silicon surface by means of a thermally grown thick oxide film. Thus another process step could be eliminated in the manufacture of devices.

5. The silicon is coated with an oxide film at room temperature; impurities originally present on the surface would be either dissolved away or incorporated into the oxide film. Fast diffusing impurities like iron, copper, or gold thus should have no opportunity to diffuse into the silicon at the beginning of the heat treatment. These impurities are usually undesirable because they lead to soft breakdown characteristics of p-n junctions due to internal field emission (6) and because they can change the minority carrier lifetime in uncontrolled fashion.

In order to be incorporated into an anodic oxide film, the particular impurity must occur in the anodizing solution as an anion. If other anions, e.g., hydroxyl ions, are present as well, the reaction potential of the impurity ion must be low enough that its rate of incorporation is not too small compared to that of oxygen from other sources. It is thus to be expected that all factors which affect the electrochemical activity of the impurity anion will also affect its rate of incorporation. In addition, specific effects due to the affinity of the host oxide lattice for the particular impurity may be important.

Striking evidence for the importance of the host lattice, or for the importance of the potential distribution across the oxide/electrolyte interface, was provided by the fact that anodization in the same acidic phosphate solution which incorporates large amounts of phosphorus in the anodic films on Ta, Zr, and Si, did not lead to the incorporation of any phosphorus into the anodic oxide film on germanium, even though anodization proceeded readily and to high voltages.

Elements of Group V of the periodic system are used as n-type dopants in silicon, and the anions of these elements are therefore of special interest. Of the three elements commonly used as dopants, P, Sb, and As, the latter is readily incorporated into anodic SiO_2 but is largely lost to the surroundings during heat treatment at atmospheric pressure due to the volatility of the oxide. All the work reported here was done with phosphorus.

Anodization Process Anodizing Solution

In order to study the incorporation of phosphorus into the oxide film, and its subsequent diffusion into the silicon during heat treatment, the radioactive isotope P^{32} has been used. P^{32} has a half life of 14.3 days, and is a pure beta-emitter, maximum energy 1.7 Mev. Non-tracer solutions were employed where the information desired could be obtained from the electrical measurements on the silicon subsequent to diffusion treatment.

It was found that heavy incorporation of phosphorus occurs from phosphoric acid, the amount incorporated depending on the $\text{P}_2\text{O}_5\text{:H}_2\text{O}$ ratio of the solution. No incorporation occurs from aqueous so-

² Recently, L. L. Gruss and W. McNeill (*Electrochem. Tech.*, 1, 283 (1963)) studied the incorporation of various anions into (porous) oxide films on a variety of metals.

lutions of trisodiumphosphate; oxide growth in this medium apparently proceeds by reaction with hydroxyl ions. Even in alkaline solutions there occurs strong adsorption of phosphate ions on the surface of the oxide, and these ions cannot be removed by washing only, but the radioactivity disappears completely by isotopic exchange upon anodization to a slightly higher voltage in a non-tracer phosphate solution.

Anodization for device purposes should be carried out in a medium in which SiO_2 is completely insoluble in order to avoid pore formation in the oxide. Strongly acidic aqueous solutions and solutions of phosphate in certain organic solvents meet this requirement. The actual choice of the anodizing solution, however, depends also on the fact that process control is much easier with oxide films in the visible interference range. Both the increment of thickness per volt forming voltage (about $5\text{\AA}/\text{v}$, depending on the solution), and the refractive index of the oxide [1.5 in the visible for P_2O_5 doped SiO_2 (7)] are very low on silicon, and the maximum voltage obtainable in concentrated solutions without deterioration of oxide quality is not sufficient to produce even the first order blue. For this reason the work described here has been carried out in solutions of 15 volume per cent (v/o) of pyrophosphoric acid in tetrahydrofurfuryl alcohol, even though the invisible films grown in the undiluted acid contain enough phosphorus to be used as diffusion sources.

As the work progressed it became clear that even small traces of water, such as might be absorbed during anodization in a vessel open to the atmosphere, have a profound effect on the amount of phosphorus incorporated. It is therefore necessary to provide for a dry atmosphere during anodization if the same solution is to be used for a prolonged period of time. The dependence of phosphorus incorporated upon the water content in the solution can be utilized to produce different doping levels, but in general it is more convenient to achieve the same end by the addition of other oxygen-containing species, such as nitrate ions, to the solution. One of the limitations on the use of water is the deterioration of oxide quality with increasing water content of the solution.

Experimental Conditions

The P^{32} tracer used in these experiments was obtained from Nuclear of Chicago either in the form of P_2O_5 or of aqueous phosphoric acid. The P_2O_5 was reacted with an accurately measured quantity of water, and the acid was dehydrated by heating, until the desired $\text{P}_2\text{O}_5:\text{H}_2\text{O}$ ratio was reached. The activity was either 1 or 3 millicuries per millimole. Standards were prepared in the usual way and compared to a P^{32} simulated source obtained from Tracerlabs, Inc. The anodizing solution was stored in a closed vessel at all times and remained usable for weeks.

Anodizations were in general carried out in non-stirred solutions at room temperature or slightly above room temperature. At 65°C the thickness of

the oxide film per volt forming voltage increases noticeably, indicating the beginning of porosity; temperatures higher than 45°C were therefore avoided. A large area platinum foil served as the current carrying counter electrode, and the approximate potential of the anode was read by a platinum wire dipping into the solution and connected to a high input impedance vacuum tube voltmeter. The potential at constant current, or the current at constant voltage, were recorded as a function of time by means of a Moseley X-Y recorder, model 38 Autograph, and were found to be very reproducible from sample to sample. Anodizations were usually carried out at a constant current density in the range between 3 and $5\text{ ma}/\text{cm}^2$ (constant current power supply model C-633-A-M by Electronic Measurements Company, Inc.). When the desired forming voltage was reached, the operation was continued at constant voltage for 30 min, this being sufficient time for the leakage current to decay to a small value and to become practically independent of further anodization at constant voltage. A series of tests showed that the amount of phosphorus incorporated into the oxide in a given forming solution was independent of current density in the range between 3 and $5\text{ ma}/\text{cm}^2$. Current densities below $2.5\text{ ma}/\text{cm}^2$ lead to poor oxide quality, and

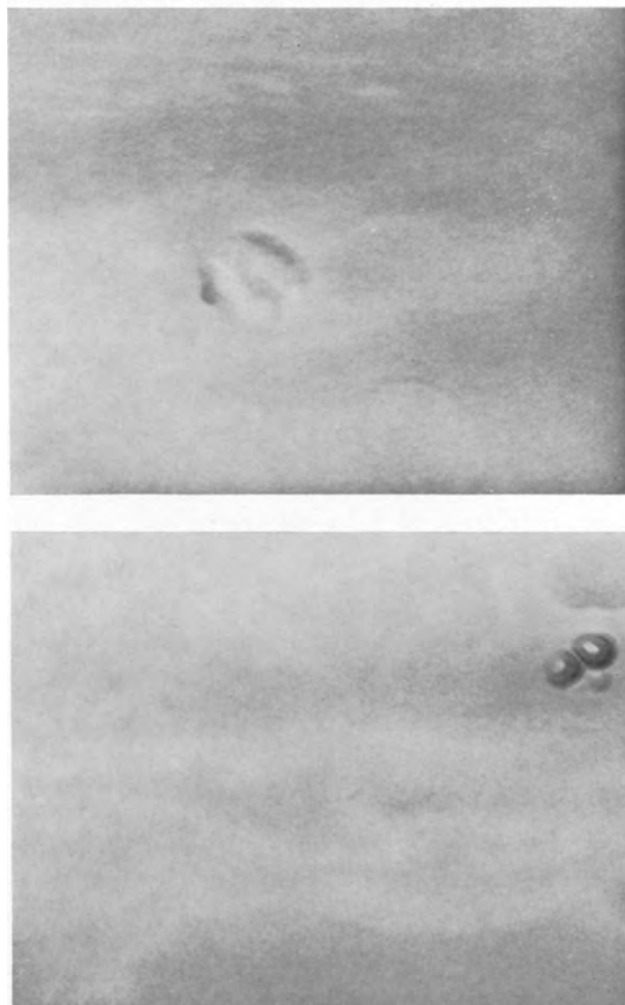


Fig. 1a (top) and 1b (bottom). Nonporous, phosphorus-doped anodic SiO_2 film. Magnification 62,000X.

current densities above 5 ma/cm² were not used in order to avoid Joule heating of the solution.

Structure and Uniformity of the Oxide

It is desirable that the oxide film should be nonporous, regardless of its further use as a diffusion mask, diffusion source, or electric insulator. Possible porosity of the oxide film has been checked by electron micrographs in transmission, after stripping of the oxide in dry chlorine at 800°C. Three types of films were noted: completely structureless films, nonporous even at a magnification of 62,000X (Fig. 1); films showing round spots of increased film thickness, surrounded by a ring of less-than-average thickness (Fig. 2); and films showing round holes of the same size as the thickenings (Fig. 3). On some specimens (c.f. Fig. 3) holes and thickenings can be seen side by side. The final leakage current during anodization, however, is not drastically different for the three types of films described (by a factor of 2-3). This observation probably rules out the presence of a large number of actual holes during anodization in the films shown in Fig. 3.

The random distribution of the structures suggested that they might be caused by bubbles ad-

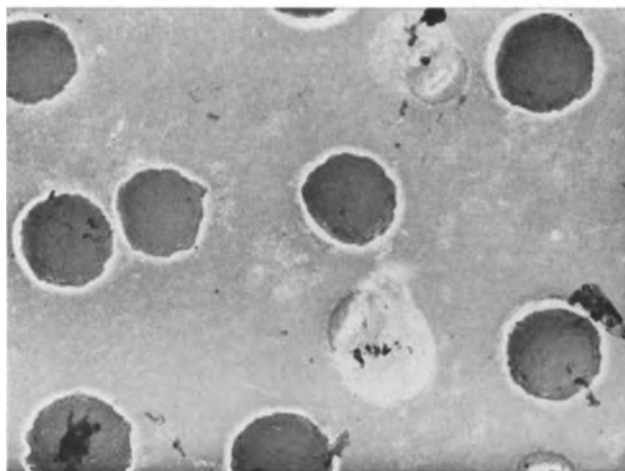


Fig. 2. Thickenings in anodic SiO₂ film, probably as a consequence of the adhesion of gas bubbles during anodization. Magnification 7800X.

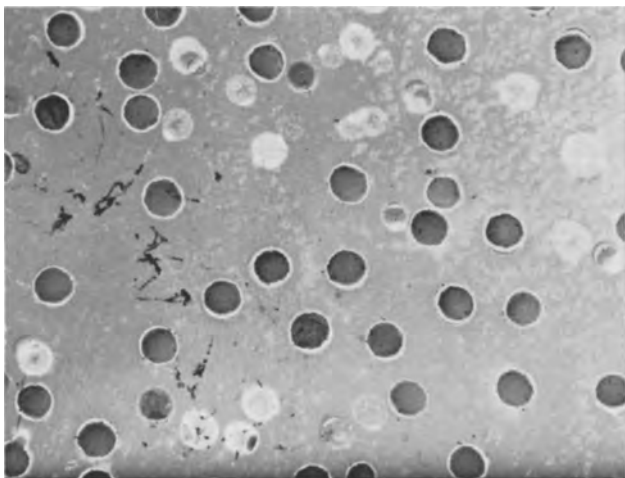


Fig. 3. Same as Fig. 2, but showing thickenings and holes side by side. Magnification 2800X.

hering to the surface during anodization. Observation of the postulated bubbles (diameter a few microns) proved possible using a high power microscope, 480X, the plane of the silicon surface being oriented at 45° both with respect to the axis of the microscope and the direction of the incident light. The bubbles were observed in solutions with a somewhat higher water content, but were absent in very "dry" solutions.

The following explanation is therefore suggested: the current efficiency during oxide formation on silicon is always very low (1), about 4%, in the solution employed here. Nevertheless, no macroscopic oxygen bubbles are visible at the Si anode under normal conditions. It must therefore be assumed that most of the charge passed serves to oxidize the alcohol; molecular diffusion of oxygen in the high viscosity electrolyte is unlikely to explain the absence of bubbles at the quoted current densities. Both in the presence of water, and in the presence of dust particles, etc., on the silicon surface, the evolution of oxygen is increased, resulting in bubble formation. For reasons not investigated further the oxide then grows thicker underneath the bubble but thinner around the bubble. This results in only a small increase of the leakage current. During subsequent etching in chlorine at high temperature the mechanically strained oxide at the periphery of the thickenings cracks; evolution of SiCl₄ gas then causes the whole structure to drop out, leading to the holes shown in Fig. 3.

Thus for device fabrication, especially for shallow diffusions or for insulation purposes, it is obviously necessary to observe a high degree of cleanliness during anodization, in keeping with the practices established in the electrolytic capacitor and semiconductor industries.

Procedure for measuring the P³² concentration in the oxide.—The activity can be measured both *in situ*, by placing the wafer underneath the window of a Geiger tube (Tracerlab Inc. TGC-2 Geiger tube, Nuclear of Chicago Model 186 Decade Scaler), or by dissolving the oxide in HF, evaporating to dryness in a suitable tray, and counting. Both measurements are relative because of the geometry factor and must be related to the P³² simulated source by measuring under conditions identical to those of the source. The experiments were carried out on bar-shaped samples because these are more conveniently anodized in strongly radioactive solutions. This shape of the samples requires tight-fitting special holders in order to position the samples always in exactly the same way under the window of the Geiger tube. Initially, dissolution of the oxide film in HF, followed by evaporation to dryness in a Teflon tray was used as the standard procedure. Later it was found that the data from the trays scatter considerably more than the data from carefully positioned wafers, and measurements on the wafers *in situ* were therefore added to the routine procedure. Measuring the activity *in situ* is a very convenient way of checking the constancy of phosphorus concentration in the oxide on different wafers prior to diffusion.

P_2O_5 distribution in the oxide film.—Uniformity of the phosphorus distribution in the direction parallel to the surface has been checked by three independent methods: uniformity of blackening of a nuclear track emulsion (Eastman-Kodak NTB-2 film) brought into direct contact with the radioactive sample (exposure time 70 hr); activity from different areas of a large anodized wafer; and planarity of p-n junctions produced in p-type silicon by diffusion from the oxide. All of these methods indicated complete uniformity.

The possible existence of a phosphorus gradient perpendicular to the surface was investigated by stepwise dissolution of the oxide in 0.04N HF kept at 0°C and magnetically stirred. The interference colors changed uniformly over the whole surface of the sample, indicating uniform dissolution. Both the activity transferred to the solution, and the activity remaining on the sample, were measured. Only films above 100 and below 250v (constant voltage) were tested. For this range an optical step gauge had been prepared by anodizing a long silicon bar in 25v steps. In addition, the total activity incorporated into the film (including film thicknesses less than 100v) was measured. It was found that the phosphorus concentration between 100 and 250v forming voltage is constant, except for a very thin region at the outer surface of the oxide, where it is somewhat reduced. The straight portion of the total activity vs. oxide thickness curve extrapolates almost (but not quite) to the origin, indicating that the phosphorus concentration is probably also constant for film thicknesses less than 100v. From the intercept on the abscissa (oxide thickness), the thickness of a pre-existing oxide film can be estimated to be approximately 50Å (Fig. 4). The drop in phosphorus concentration at the outer surface of the anodized film can probably be ascribed to the solubility of P_2O_5 in water (or most organic solvents as well) since, after anodization in tracer solution, the samples had to be rinsed with hot water in order to remove the adhering radioactive solution completely. Some wafers were also anodized to a somewhat higher voltage in non-tracer phosphate solution without a preceding water rinse; the results were the same in both cases. It

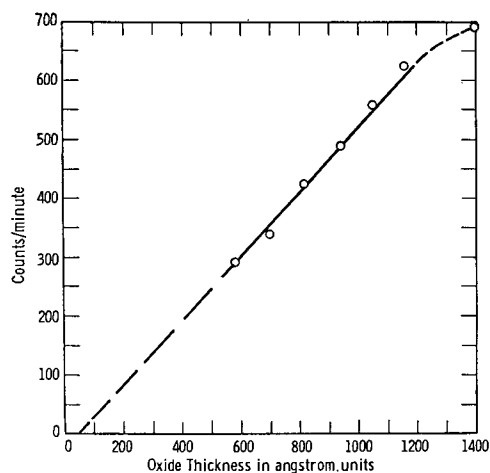


Fig. 4. Total P^{32} activity vs. oxide thickness. Film kept at 240v for 30 min.

seems that a soluble component of a mixed oxide film can be leached out of a very thin surface layer by a solvent, or can be replaced in this thin layer by an isotope of the same species during subsequent anodization. Analogous results have been reported for the anodization of InSb in dilute potassium hydroxide solution (8), resulting in a depletion of Sb at the surface of the oxide.

The highest phosphorus content observed so far in anodic SiO_2 films has been approximately 23 w/o. However, the whole range between 0 and 23% is accessible by a judicious choice of the electrolyte.

Thickness/Voltage Increment and Density of the Oxide

The thickness/voltage increment for either constant voltage or constant current operation was established by anodizing an optically flat p-type silicon wafer at or to 250v, dissolving away part of the oxide, evaporating silver over the step thus formed, and measuring the step height by double beam as well as by multiple beam interferometry. The thickness/voltage increment at constant voltage is a constant for a given solution and temperature, whereas the increment under constant current operation depends also on the geometry of the anodization vessel, the resistivity of the solution, and on the current density employed; it is therefore a constant only if the experimental conditions are kept constant. The average of several measurements was $5.81 \text{ \AA/v} \pm 5\%$ for constant voltage operation, and $4.66 \text{ \AA/v} \pm 5\%$, for constant current operation (3 ma/cm^2).

The amount of silicon converted to oxide per volt forming voltage (at constant voltage) was determined by masking the surface of an optically flat silicon wafer with a thick, thermally grown oxide film, etching a pattern of very fine lines (line width less than 2 mils) by means of photoresist techniques, removing the resist, and subjecting the sample to anodization at 250v for $\frac{1}{2}$ hr. All of the oxide was then stripped in HF, and the depression in the silicon produced by the anodization was measured by multiple beam interferometry. This depth was found to be $510 \pm 25 \text{ \AA}$.² It was not possible to determine in a similar fashion the amount of silicon converted to oxide at constant current operation, because the current density in the fine line pattern etched into the thermal oxide film would be a completely uncontrolled quantity. It is however reasonable to assume that the densities of oxides formed under constant voltage and under constant current conditions do not differ by more than a few per cent; no difference in percentage of phosphorus incorporated was, for instance, noted for constant voltage or for constant current operation. Making the assumption that the density of the oxide is indeed identical under the two sets of conditions, one can calculate a depth "etched" into the silicon per volt forming voltage at constant current from the ratio of oxide thicknesses quoted above. This increment turns out to be $1.64 \text{ \AA/v} \pm 5\%$.

² i.e., 2.04 \AA/v .

Table I. Silicon etching during anodization at constant current. Obtained from measurements of junction depth.

Specimen No.	No. of anodizations at 250v constant current only	μSi removed	$\mu\text{Si}/250\text{v}$
1	39	1.87	0.0480
	90	3.50	0.0389
	129	5.37	0.0416
2	70	2.82	0.0403
	90	4.08	0.0454
	160	6.90	0.0431
4	70	2.96	0.0423
	30	1.05	0.0350
	100	4.00	0.0400
6	70	2.74	0.0392
	10	0.51	0.0510
	80	3.25	0.0406

Average $\text{Si}/250\text{v} = 0.0420\mu$. Standard deviation = $\pm 10\%$.

The same parameter can be determined by periodic angle-lapping and junction delineation during the process of multiple anodization for diffusion profile determination in the silicon. This will be discussed in Parts II and III of this series.

This multiple anodization process was also carried out at a constant current density of $3 \text{ ma}/\text{cm}^2$ mainly to avoid the time consuming wait for the decay of the current in the constant voltage operation. These measurements, which are summarized in Table I, show that the "etching" depth per 250v at constant current is $420\text{\AA} \pm 10\%$ of silicon, *i.e.*, the increment is $1.68 \text{ \AA}/\text{v}$ of silicon removed. This result is in good agreement with the value obtained from the optical measurements quoted above, and in conjunction with the diffusion profile confirms that the physical location of the p-n junction occurs at the position of delineation (HF staining was used in these determinations of junction depth).

Knowing the thickness of the oxide film per volt forming voltage from the interferometric data, one can calculate the density of the oxide by converting the amount of silicon removed into silicon dioxide produced. This calculation involves the assumption that the oxide is fully stoichiometric and corresponds to the maximum valency of the cation. On metals like Si or Al this assumption is probably correct. Dividing the weight of the oxide thus calculated by the volume occupied yields the density of the film. This procedure is permissible, however, only if no component of the electrolyte other than oxygen is incorporated into the oxide film. In the present case, heavy incorporation of phosphorus is known to occur. This phosphorus may safely be assumed to exist in its highest valence state, *i.e.*, as P_2O_5 . Assuming that the density of P_2O_5 as incorporated into the anodic SiO_2 film is not drastically different from the density of bulk P_2O_5 , an approximate density of the phosphorus doped film can be calculated if the per cent phosphorus incorporated is known from the tracer data. Calculation of the oxide density from the above data without taking the incorporation of P_2O_5 into account would lead to the very low value of only $1.75 \text{ g}/\text{cm}^3$. The solution employed was known, from tracer data, to incorporate approximately 14 w/o P_2O_5 , which must be added to

the weight of the SiO_2 . This leads to an estimated density of about $2 \text{ g}/\text{cm}^3$ for the oxide film doped with 14 w/o P_2O_5 . A density of about $2 \text{ g}/\text{cc}$ seems reasonable in view of the determination by Archer (7) of the density of anodic oxide films formed on silicon in aqueous borate solution. Archer obtained a value of 1.82. It is, however, known that oxide films formed on silicon in aqueous solution are less dense than films formed in nonaqueous solvents.

Growth mechanism.—Anodic oxide films on silicon appear to grow preponderantly by cation migration. P^{32} doped films (grown in the pyrophosphoric acid-alcohol solution to 150v), were encapsulated in essentially pure SiO_2 films by subsequent anodization to twice the original forming voltage in a solution of KNO_3 in N, N-dimethylpropionamide. The oxide was then progressively dissolved in 0.1N cold HF, magnetically stirred, the interference colors changing in a uniform manner. Only a very small amount of activity was found in the solution until the original thickness of the P^{32} doped film had been almost reached (remaining film thickness equivalent to about 170v). The same experiment, performed with non-tracer phosphoric acid solution instead of the N, N-dimethylpropionamide gave essentially the same result. It is not possible to decide from the data whether the small amount of activity detected in the HF solutions of the outer portions of the oxide stems from localized deeper etching in very small pores, or is due to some fraction of the current in the oxide being carried by oxygen ions during anodization in the electrolytes and at the current densities investigated. In our opinion, it is necessary to restrict statements about the mechanism of oxide growth (by cation or anion migration) to the actual system investigated; whereas the supply of cations at the metal-oxide interface is probably more or less constant for any anodization of the given metal (except in the case of gross variations in the chemical composition of the oxide formed), it appears quite likely that the supply of oxygen ions may depend drastically on the particular electrolyte, especially if it contains ionic species preferentially adsorbed onto the oxide surface during anodization. The discrepant results in the literature on the mechanism of oxide growth on, for example, aluminum or tantalum (9) are quite likely due to different experimental conditions.

The fact that oxide growth on silicon occurs preponderantly by cation growth (under the given conditions) makes it possible to encapsulate doped anodic oxide films in anodic oxide films consisting essentially of pure SiO_2 , and to suppress out-diffusion during heat treatment, at least to some extent.

Conclusions

Phosphorus-doped anodic oxide films of good quality have been grown on silicon in pyrophosphoric acid or solutions of this acid in tetrahydrofurfuryl alcohol. As will be discussed in Part II, these doped anodic oxide films can be used as diffusion sources and appear to have certain advantages over conventional diffusion sources.

The phosphorus appears to be uniformly distributed throughout the oxide, both perpendicular to the

surface, and laterally. The thickness/voltage increment per volt forming voltage has been established for the electrolyte used, and an optical method has been used to estimate the oxide density in conjunction with tracer data. Oxide growth on silicon occurred by cation migration in the electrolytes and at the current densities investigated.

Acknowledgments

Thanks are due to Dr. R. Stickler for the electron micrographs, to Dr. D. R. Hamilton for the interferometric measurements, and to Dr. I. M. Mackintosh for discussions. Messrs. N. J. Roney and G. D. Rose helped with the other experiments. This work was sponsored jointly by the Electronic Technology Laboratory, Aeronautical Systems Division, Wright-Patterson Air Force Base, Ohio under Contract AF 33(657)-9897 and by Westinghouse Research Laboratories.

Manuscript received Nov. 15, 1963. This paper was presented at the Pittsburgh Meeting, April 15-18, 1963.

Any discussion of this paper will appear in a Discussion Section to be published in the December 1964 JOURNAL.

REFERENCES

1. P. F. Schmidt and W. Michel, *This Journal*, **104**, 230 (1957).
2. R. Lindner, *Bell Syst. Tech. J.* **XLI**, 803 (1962).
3. K. Norden, *Z. Elektrochem.*, **6**, 159, 188 (1899).
4. J. E. Lewis and R. C. Plumb, *This Journal*, **105**, 496 (1958).
5. W. F. Bernard and J. J. Randall, *ibid.*, **108**, 822 (1961).
6. A. Goetzberger and W. Shockley, *J. Appl. Phys.*, **31**, 1821 (1960).
7. R. J. Archer, *J. Optical Soc. Am.*, **52**, 970 (1962).
8. J. F. Dewald, *This Journal*, **104**, 244 (1957).
9. D. A. Vermilyea, *Acta Met.*, **2**, 482 (1954); W. J. Bernard, *This Journal*, **109**, 1082 (1962), and further references there; J. A. Davies *et al.*, *ibid.*, **109**, 999 (1962); G. Amsel and D. Samuel, *J. Phys. Chem. Solids*, **23**, 1707 (1962); J. A. Davies *et al.*, extended abstracts 167 and 168, Electrochemical Society Spring Meeting, Pittsburgh, 1963, Theoretical Division; J. A. Davies and B. Domeij, *This Journal*, **110**, 849 (1963).

Rates of Formation of Thermal Oxides of Silicon

H. C. Evitts, H. W. Cooper, and S. S. Flaschen

Semiconductor Products Division, Motorola Inc., Phoenix, Arizona

ABSTRACT

Oxidation growth rates of SiO_2 have been studied using as variables Si conductivity types, crystal growing methods, and bulk resistivity. Rates were determined in closed systems of both dry O_2 and steam over a temperature range of 800°-1300°C. The conclusion is drawn that the only factors controlling oxide growth rate were time, temperature, and ambient. Results reported include a study of the optical properties of the oxide films.

Because of the increased importance that oxide films have in the diffusion masking and surface passivation of planar silicon devices, it is highly desirable to know with precision the oxidation kinetics for silicon under various conditions of conduction type, resistivity, and ambient atmospheres.

This work was a two-fold one; first, to find better ways to measure these oxide films, and second, to obtain more information about the growth rate as a function of various parameters.

Experimental

The method of measuring the grown silicon dioxide films began with the usual technique of removing a section of the oxide with HF, metallizing the entire surface to obtain a sharper, clearer image, and placing the resulting "step" into a monochromatic interferometer. Since most interferometers do not have a sufficiently fine reticle scale, and the reading is often one more of guesswork than of accuracy, the image was photographed and then further magnified, employing a suitable measuring scale such as a wide-field filar micrometer eye-piece on a low-powered microscope. This procedure allows one to obtain accurate readings of the film thickness to within 50Å, and thereby reduced the variance in the data due to measuring errors.

The interferometer used throughout the experiment was a Zeiss, employing a monochromatic thal-

lium source with a half wavelength of 2675Å. Some of the readings, especially those falling near some multiple of this figure, were further checked on a multiple beam interferometer utilizing both thallium and sodium sources (1, 2).

The oxidation system used was a closed system, as shown in Fig. 1, consisting of a high temperature diffusion-type furnace, with all of the accompanying glassware constructed of high-purity quartz. On the left-hand side of the schematic is the ambient introduction area. For our "dry" system, line O_2 was passed through standard drying chambers, and then through a submicron filter to remove any contaminating particles picked up in the gas line or in the

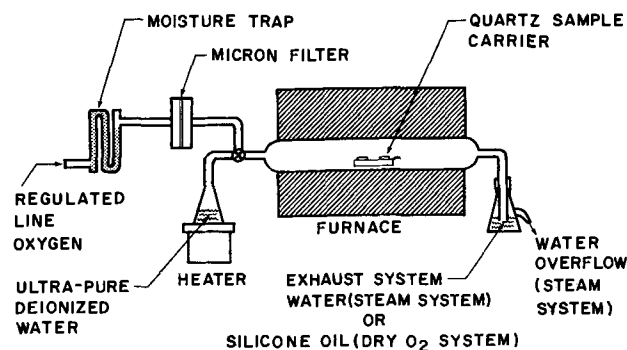


Fig. 1. Closed oxidation system

drying columns, and hence, into the furnace itself. At the exhaust end of the system the gas passes into a trap of silicone oil, which was chosen because of its very low vapor pressure.

The alternate system was for steam. In this case, oxygen was not used, but instead, the generator was filled with ultrapure water, and the steam was passed through the furnace tube to a water-filled trap. Since the amount of water vapor formed by this trap is insignificant when compared to the greater amount of steam introduced by the generator, the backflow can again be disregarded. An overflow syphon is used here to remove the condensed steam, and to keep the liquid level constant. As can be seen for both of these methods, the entire system is sealed from the outside atmosphere, insuring a high degree of purity. The pressure inside the furnace is kept as near to 1 atm as possible by maintaining as small a liquid head as practical in the tubes leading into the exhaust traps.

The variables studied were: Two bulk-conduction types (N or P), crystal fabrication method (either Czochralski or float-zoned material), and bulk resistivities ranging from a low value of 0.01 cm for each of the four above combinations, 1 cm of each, and a high value of 100 cm of each, giving a total of twelve wafers in each run. All of the wafers were cut on the <111> crystal plane, with final mechanical polishing with 0.25 μ Linde compound to a mirror-like, scratch-free surface. As stated, the ambient gases used were clean, dry oxygen, or steam at a pressure of 760 mm Hg, over a temperature range of 800°-1300°C, maintained at $\pm 1^\circ\text{C}$ throughout the experiments. The polished wafers were placed on a quartz boat, either flat or on edge (experimentally the positioning was immaterial to the growth rate, as long as the furnace was sufficiently stable and the temperature well controlled.)

Results

After a number of runs at various times and temperatures had been completed, the data was subjected to extensive statistical analysis to study the effects of the various variables, as well as their interactions with each other. The conclusion was that, within the limits of our measurements, (i) there was no difference statistically between N and P type materials; (ii) there was no difference between the material grown by either the Czochralski or the float-zoned methods, and (iii) over range used, there was no difference due to resistivity either (this is probably due to the fact that the concentration of phosphorous or boron impurities at these resistivities is much less than 0.01% and the lattice is still largely dominated by Si rather than phosphorous or boron atoms). Therefore, it was decided that it was not necessary to use all twelve wafers for each data point, although at least four wafers from each of the runs were read as a check on accuracy and reproducibility.

The resulting data points after some seventy-five runs are plotted in Fig. 2 and 3. Figure 2 is for the dry oxygen system. The scale is log-log, with time in seconds *vs.* the measured thicknesses for the various temperatures from 900° to 1300°C. The

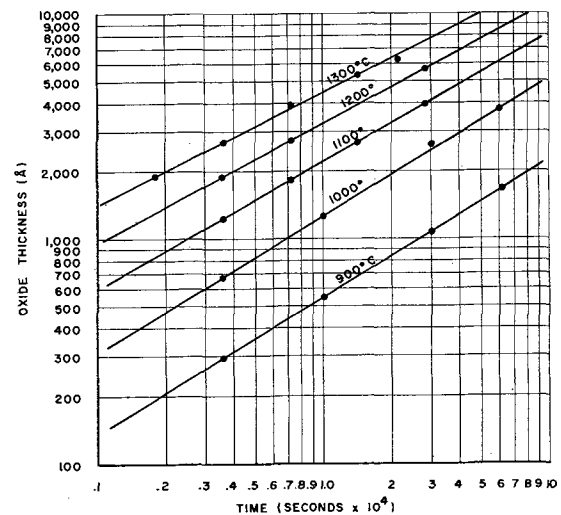


Fig. 2. Thermal oxide thickness for <111> silicon in dry oxygen at 1 atm pressure.

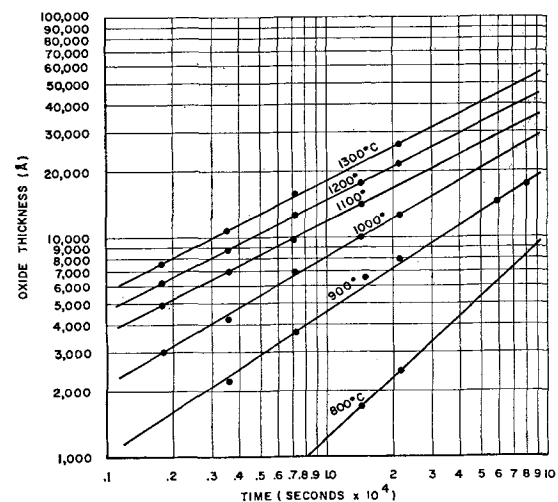


Fig. 3. Thermal oxide thickness for <111> silicon in steam at 1 atm pressure.

slope is very close to 0.5 above 1100°C. Each of the data points plotted represents more than 30 interferometric readings, with a majority of the readings within $\pm 70\text{\AA}$ of the average value.

Figure 3 is a similar one for the steam system. The slope of the higher temperature curves again has the value of 0.5, while the slope has increased to 0.8 for an 800°C steam atmosphere.

From the experimental data the following thermal oxidation growth rate equations for closed systems were calculated for $T \cong 1100^\circ\text{C}$, <111> silicon surface orientation, and 1 atm of pressure.

$$\text{Steam: } X^2 = 1.21 \times 10^9 t \exp(-0.8 q/kT)$$

$$\text{Dry O}_2: X^2 = 3.53 \times 10^9 t \exp(-1.33 q/kT)$$

where X is the oxide film thickness in Angstrom units, t time in seconds, q electron charge, k Boltzmann constant, and T temperature in degrees Kelvin.

These activation energies, 0.8 electron volt (ev) for the steam system and 1.33 ev for the dry oxygen, are somewhat lower than those previously published by Atalla (3) but agree closely with Deal's (4, 5) values of 0.87 ev and 1.26 ev, respectively.

Table I. Silicon dioxide interference color-thickness relationships

Color	Thickness, Å			
Gray	100			
Tan	300			
Brown	500			
Blue	800			
Violet	1000	2750	4650	6500
Blue	1500	3000	4900	6850
Green	1850	3300	5200	7200
Yellow	2100	3700	5600	7500
Orange	2250	4000	6000	
Red	2500	4350	6250	

As further convenience for the production workers who need to repeat a certain oxide growth run after run, where the accuracy need not always be within 50Å, a color *vs.* thickness chart was constructed, Table I.

Colors can be observed for oxide thicknesses of well over $1\frac{1}{2}$ to 2μ ; however, the colors begin to fade at around $\frac{3}{4}\mu$, or at 7500Å thickness, and a color chart becomes of questionable value past this limit. Since the colors are sufficiently intense up to 7500Å, one can use this chart for noncritical estimates with accuracy to 100Å.

Conclusions

1. Of the factors studied in this work, the rate of oxide growth on silicon is controlled only by time, temperature, pressure, and type of gas present in the oxidation system.

2. The properties of crystal fabrication, bulk resistivity, and type, and any interactions thereof, have no significant bearing on the oxide growth rates.

3. The activation energies for steam and dry oxygen systems are 0.8 eV and 1.33 eV, respectively, at temperature above 1100°C.

Acknowledgments

Our thanks are extended to our colleagues at Motorola Semiconductor Products Division for their suggestions and help, and especially to Mr. Gene Ladamoto for the use of special equipment. This work was supported in part by the Electronic Research Directorate, Air Force Cambridge Research Center, Air Research and Development Command.

Manuscript received April 24, 1963; revised manuscript received Feb. 13, 1964. This paper was presented at the Boston Meeting, Sept. 16-20, 1962.

Any discussion of this paper will appear in a Discussion Section to be published in the December 1964 JOURNAL.

REFERENCES

1. S. Tolansky, "Multiple Beam Interferometry of Surfaces and Films," Oxford Union Press, London (1948).
2. G. R. Booker and C. E. Benjamin, *This Journal*, **109**, 1206 (1962).
3. M. M. Atalla, E. Tannenbaum, and E. J. Scheibner, *Bell System Tech. J.*, **38**, (May 1959).
4. B. E. Deal, *This Journal*, **110**, 527, (1963).
5. *Ibid.*, **110**, 1292 (1963).

A Study of the Calcium Molybdate-Rare Earth Niobate Systems

L. H. Brixner

Pigments Department, Experimental Station,

E. I. du Pont de Nemours & Co., Inc., Wilmington, Delaware

ABSTRACT

The rare earth niobate-calcium molybdate systems are one class of a number of pseudobinary systems which can be described by the general formula $(\text{LnM}^I)_x(\text{CaM}^{II})_{1-x}\text{O}_4$, where Ln = trivalent rare earth, Sc^{+3} and Y^{+3} , $\text{M}^I = \text{Nb}^{+5}$, Ta^{+5} , and $\text{M}^{II} = \text{Mo}^{+6}$, W^{+6} . Calcium, furthermore, may be replaced by Sr^{+2} and Ba^{+2} . For some of these compositions, lattice parameters and intensity of fluorescent emission have been determined as a function of x . Single crystals were grown by the Czochralski technique, and the distribution coefficients were determined for a number of niobates in calcium molybdate. Stimulated emission was obtained from a 3 in. long NdNbO_4 doped CaMoO_4 crystal.

The advent of the solid state optical maser, realized by ruby, calcium tungstate, and calcium fluoride doped with rare earths, has stimulated considerable interest and activity in compositions of the "scheelite" or related structures. Nassau (1) recently published a detailed study on calcium tungstate, its Czochralski crystal growth characteristics, crystal perfection and possibilities for substitution both in the A^{+2} and B^{+6} sites of CaWO_4 . Although rare earth ions can be introduced into the scheelite lattice without a secondary compensating ion (creating a defect lattice), valence compensation by a second ion is generally preferred, since it simplifies the fluorescent emission spectrum and lowers the

threshold for laser action. The most commonly used scheme as outlined by Nassau (1) is the compensation by the pair $\text{Ln}^{+3}/\text{Na}^{+1}$ for every two Ca^{+2} ions replaced. Although the structural match for these ions is nearly perfect, there are problems with sodium because of its volatility at the high melt temperatures and its relatively low distribution coefficient. The thermodynamically very stable ABO_4 -type rare earth niobates and tantalates should be good doping agents for molybdates and tungstates. In a very recent paper, Nassau (2) also described this type of compensation for the $\text{CaWO}_4/\text{Nd}^{+3}$, Nb^{+5} system. The valence compensation here is such that for each Ca^{+2} being replaced by Ln^{+3} valence

balancing occurs in the W⁺⁶ or Mo⁺⁶ site by introducing the same amount of Nb⁺⁵ or Ta⁺⁵. Considering Ahrens (3) radii for Nb⁺⁵ (0.69Å), Ta⁺⁵ (0.68Å), W⁺⁶ (0.62Å), Mo⁺⁶ (0.62Å), Ca⁺² (0.99), and Gd⁺³ (0.93) as the middle representative of the lanthanons, isomorphous substitutions should be possible over considerable ranges. The rare earth niobates and tantalates of the type LnNbO₄ and LnTaO₄ have been recently characterized structurally by Keller (4), but their fluorescent properties were not described. Since they formed end-members in the solid solutions of the type (LnNbO₄)_x(CaWO₄)_{1-x}, all these compounds were prepared and their luminescent properties are reported. Although optically interesting species with the possibility of laser action could only be expected in the region of *x* from about 0.005 to 0.20, at least in some cases compositions with a considerable range of *x* were prepared in order to observe the transition from the scheelite to the fergusonite structure.

The close structural relationship between these two types became apparent during a study of compounds of the type LnTi_{0.5}W_{0.5}O₄, which can best be considered IV/VI substituted rare earth niobates or tantalates. Depending on the ionic radius of the Ln⁺³ ion, these compositions crystallize either in the scheelite or in the fergusonite lattice. Roth (5) already pointed out that the monoclinic GdNbO₄ transforms into a tetragonal structure at 840°C and Gingerich (6) identified this structure as the scheelite type, which again points to the close structural relationship of these two lattices. Since the A-site in CaWO₄ is 8 coordinated, but 6 coordinated in the fergusonite type, the effect of coordination number on the position of the fluorescence spectra could also be observed.

Experimental

All constituent oxides used in this investigation were of the best commercially available purity, usually 99.9+ % pure, and were not given any further purification treatment prior to the reactions. The

rare earth oxides were obtained from the Lindsay Chemical Division, WO₃ from Sylvania Electric Products Inc., MoO₃ from Merck, CaCO₃ was "Baker analyzed," and Nb₂O₅ and Ta₂O₅ were Kawecki "high-purity" quality. Only Sc₂O₃ was prepared from re-sublimed ScCl₃, which in turn was obtained by chlorinating thortveitite from Norsk Feldspat. With the exception of Ce, Pr, and Tb, all rare earths were in the trivalent state. The true sesquioxides of Ce, Pr, and Tb were obtained by hydrogen reduction at 1200°C, and all subsequent reactions with these oxides were carried out under purified argon. Tb readily goes to the trivalent state at high temperature, even in air, and so the argon treatment was limited to Ce and Pr compounds only.

The oxide components were weighed to the nearest 0.1 mg according to the desired stoichiometry and mixing was effected by ball milling in a mechanical agate ball mill under acetone. During a first firing step, the dried mixtures were heated to 1050°C in the case of the tungstates, and to 690°C in the case of the molybdates. The reaction products were then again wet ball milled and pressed into 1 in. diam. pellets under 20,000-40,000 psi. These pellets were then refired at 1200°-1350°C. After this procedure, homogeneous reaction products were obtained which did not give any x-ray patterns of the constituent components. Chemical analysis was only carried out in cases where the procedure could possibly have caused a concentration shift of components, as for instance, during Czochralski crystal pulling. This technique will be described in a separate paragraph. Most optical and electrical examinations were carried out with polycrystalline powders. The weight loss experienced during the different firing operations was always less than 0.1-0.2% for 1-5g charges, allowing for the loss of CO₂.

X-ray Study

Lattice parameters were determined on the basis of powder diffraction patterns obtained with a 114.6 mm Philips camera. All samples were ground to -325 mesh, sealed in 3 mm Lindemann glass capil-

Table I. Lattice parameters of the Ln_{0.5}Nb_{0.5}W_{0.5}O₄ series

Composition	a _t , Å	c _t , Å	Unit cell volume, Å ³	c/a	Space group	ρ, X-ray, g·ml ⁻¹	ρ, Pycn., g·ml ⁻¹
Sc _{0.5} Nb _{0.5} W _{0.5} Ca _{0.5} O ₄	Not formed: mixture of ScNbO ₄ and CaWO ₄						
Y _{0.5} Nb _{0.5} W _{0.5} Ca _{0.5} O ₄	5.202	11.180	302.540	2.149	I4 ₁ /a	5.858	5.80
La _{0.5} Nb _{0.5} W _{0.5} Ca _{0.5} O ₄	5.320	11.455	324.204	2.153	I4 ₁ /a	5.979	5.91
Ce _{0.5} Nb _{0.5} W _{0.5} Ca _{0.5} O ₄	5.292	11.402	319.316	2.154	I4 ₁ /a	6.083	5.98
Pr _{0.5} Nb _{0.5} W _{0.5} Ca _{0.5} O ₄	5.278	11.361	316.487	2.152	I4 ₁ /a	6.146	6.13
Nd _{0.5} Nb _{0.5} W _{0.5} Ca _{0.5} O ₄	5.263	11.347	314.302	2.155	I4 ₁ /a	6.224	6.17
Sm _{0.5} Nb _{0.5} W _{0.5} Ca _{0.5} O ₄	5.244	11.272	309.975	2.149	I4 ₁ /a	6.376	6.31
Eu _{0.5} Nb _{0.5} W _{0.5} Ca _{0.5} O ₄	5.234	11.245	308.054	2.148	I4 ₁ /a	6.434	6.29
Gd _{0.5} Nb _{0.5} W _{0.5} Ca _{0.5} O ₄	5.225	11.224	306.422	2.148	I4 ₁ /a	6.525	6.51
Tb _{0.5} Nb _{0.5} W _{0.5} Ca _{0.5} O ₄	5.216	11.200	304.714	2.147	I4 ₁ /a	6.579	6.44
Dy _{0.5} Nb _{0.5} W _{0.5} Ca _{0.5} O ₄	5.208	11.186	303.400	2.148	I4 ₁ /a	6.647	6.56
Ho _{0.5} Nb _{0.5} W _{0.5} Ca _{0.5} O ₄	5.196	11.173	301.653	2.150	I4 ₁ /a	6.713	6.68
Er _{0.5} Nb _{0.5} W _{0.5} Ca _{0.5} O ₄	5.191	11.161	300.749	2.150	I4 ₁ /a	6.758	6.63
Tm _{0.5} Nb _{0.5} W _{0.5} Ca _{0.5} O ₄	5.24*	11.30	—	—	I4 ₁ /a + I2/a	—	—
Yb _{0.5} Nb _{0.5} W _{0.5} Ca _{0.5} O ₄	5.24*	11.29	—	—	I4 ₁ /a + I2/a	—	—
Lu _{0.5} Nb _{0.5} W _{0.5} Ca _{0.5} O ₄	5.25*	11.26	—	—	I4 ₁ /a + I2/a	—	—

* These last three samples of Table I were in the 2-phase region and also contained the following monoclinic fractions:

Tm: a = 5.24Å, b = 10.87Å, c = 5.125Å, β = 93.90°
 Yb: a = 5.23Å, b = 11.05Å, c = 5.08Å, β = 93.42°
 Lu: a = 5.20Å, b = 10.90Å, c = 5.05Å, β = 93.32°

laries and then exposed to copper K_{α} radiation ($\lambda = 1.5418\text{\AA}$) at 25°C for 3-6 hr. The readings were taken visually at constant temperature with a Hilger and Watts film measuring rule with 0.05 mm vernier divisions. All films were corrected for film shrinkage.

Orientation patterns of Czochralski grown single crystals were obtained by the Laue back-reflection technique. The densities were determined on powdered specimens of -200 mesh, by weighing 1-2g samples into a 5 ml pycnometer and distilling pure CCl_4 onto the compound under vacuum. While the CCl_4 was frozen out with liquid nitrogen, it was possible to pump the system to 10^{-5} mm Hg or better.

Table I summarizes the structural parameters together with the x-ray and pycnometrically determined densities for the $(\text{CaWO}_4)_x(\text{LnNbO}_4)_{1-x}$ system with $x = 0.5$.

Lattice parameters were also determined for the corresponding molybdate systems as well as for both tungstates and molybdates in solid solution with the rare earth tantalates. The situation is almost identical with that represented in Table I, except that the a_t parameters for the molybdates are generally slightly smaller, c_t is slightly larger, and the unit cell volume is slightly smaller. It is also interesting to note that the transition to the fergusonite type for the molybdate solid solutions occurs between terbium and dysprosium, rather than between erbium and thulium as it does for the tungstates. In general, the transition line runs from approximately $x = 0.6$ for the lanthanum compounds to about $x = 0.4$ for the lutetium compounds, with the 2-phase region being about twice as wide for the Lu composition as it is for the La compounds. A more detailed study of the parameters as a function of x is given in Fig. 1 for the $\text{EuNbO}_4/\text{CaWO}_4$ system. Figure 2 summarizes the same situation for the $\text{YNbO}_4/\text{CaWO}_4$ system. In either case, the lattice parameters of the pure monoclinic end members agree quite well with those determined by Keller (4).

Fluorescent Properties

The fluorescent emission as a function of x for the different systems was determined next. Since generally a high site symmetry, that is a great number

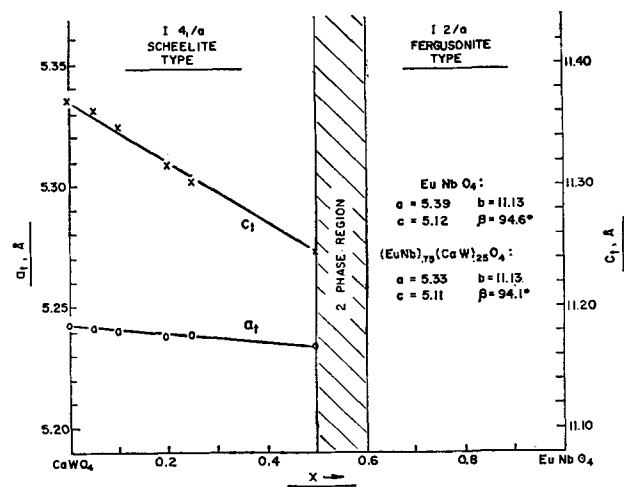


Fig. 1. Structure types as a function of X for the $(\text{EuNbO}_4)_x(\text{CaW})_{1-x}\text{O}_4$ system.

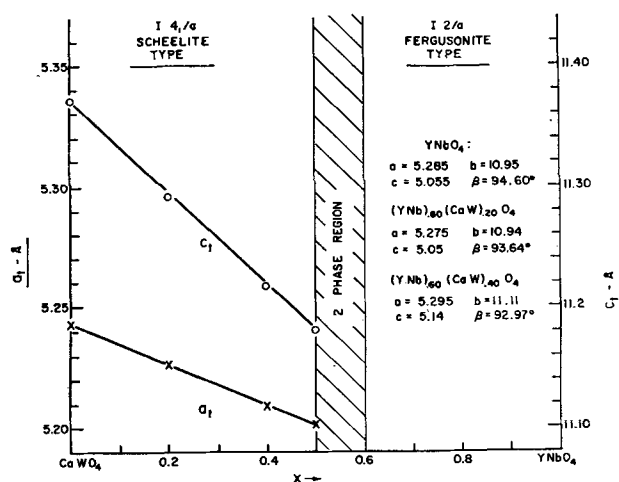


Fig. 2. Structure types as a function of X for the $(\text{YNbO}_4)_x(\text{CaW})_{1-x}\text{O}_4$ system.

of nearest neighbors, is a desirable situation for efficient fluorescence, it was to be expected that the rare earth in the 6 coordinated A site of the fergusonite would not be as readily excited as in the 8 coordinated A site of scheelite. However, since no fluorescent properties of the rare earth niobates and tantalates had been reported, these properties were studied both under 3650Å and 2537Å excitation, at

Table II. Intensity and color of fluorescent emission of ABO_4 type rare earth niobates and tantalates

Compound	Fluorescence color under 3650Å excitation at 25°C	Fluorescence color under 2537Å excitation at 25°C	Fluorescence color under 3650Å excitation at -196°C	Fluorescence color under 2537Å excitation at -196°C
YNbO_4	—	S Blue white	S Yellow	S Blue white
LaNbO_4	—	S White	M Peach	S Blue white
EuNbO_4	W Purple	W Purple	W Red purple	W Red purple
GdNbO_4	—	S Peach	S Yellow	S Peach
ErNbO_4	—	—	M Yellow	M White
TmNbO_4	—	S Blue white	S Yellow	S Blue white
ScTaO_4	—	—	W White	M White
YTaO_4	—	S Blue white	—	S Blue white
LaTaO_4	—	S Peach	—	S White
SmTaO_4	—	—	—	S Blue white
EuTaO_4	W Red purple	W Purple	M Red	S Red purple
GdTaO_4	—	S Peach	M Peach	S White
DyTaO_4	—	—	—	S Blue white
TmTaO_4	—	W Blue	—	W Blue white
LuTaO_4	—	W Blue white	—	M Blue white

room temperature and at liquid nitrogen temperature. These results are summarized in Table II. The compounds not listed did not exhibit any fluorescence under the conditions stated. The prefixes W, M, and S denote visually observed weak, medium, and strong fluorescence. It is interesting to note that compositions such as the Y, La, Gd, and Lu compounds were found to fluoresce, although on the basis of the reflectance spectra of the corresponding rare earth oxides, no absorption is noticed in the region of excitation. This indicates that probably the NbO₄³⁻ or TaO₄³⁻ anionic groups absorb and transfer the energy to the rare earths, which in turn emit.

The qualitatively observed fluorescence for the LnNbO₄/CaWO₄ system at $x = 0.5$ is summarized in Table III. Here again the compounds which did not luminesce are not listed. It is interesting to note that, for instance, the samarium compounds did not fluoresce at this concentration, while at lower concentrations it is one of the most intense emitters, fluorescing in the orange. Obviously, this is a case of concentration quenching. For further studies, the following rare earths were selected as candidates: Sm, Eu, Tb, and Dy. All of these fluoresce intensely in the visible and are relatively sharp line emitters. The intensity of fluorescent emission was first determined as a function of the activator concentration. The coarse fluorescent scans were obtained in a Beckmann DK 2 recording spectrometer with a fluorescent ultraviolet lamp F 4 T5/BL (GE designation). The detector used was a 1 P28 RCA photomultiplier tube. The more refined spectra were taken from samples excited by a filtered AH-3 mercury discharge lamp (primarily 3650Å radiation) on a Leeds and Northrup 0.5 meter Ebert mount grating spectrometer using again a 1 P28 photomultiplier detector. Figure 3 gives the intensity of fluorescent emission as a function of activator concentration for the DyNbO₄/CaMoO₄ system and Fig. 4 represents the same situation for the TbNbO₄/CaWO₄ system. The fact that the optimum doping concentration was observed to be lower for the molybdates than for the tungstates was generally true also for all other systems. Typical fluorescence spectra of compositions in the vicinity of the doping optimum are given in Fig. 5 and 6 for a europium and terbium doped tungstate at room temperature and in Fig. 7 and 8 for dysprosium and samarium both at

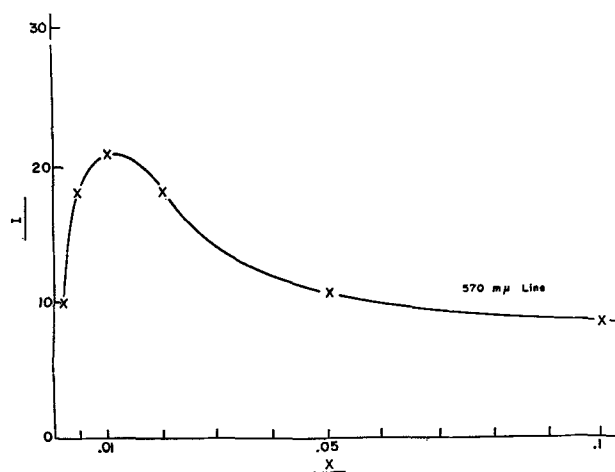


Fig. 3. Intensity of fluorescent emission as a function of X for the $(\text{DyNbO}_4)_x(\text{CaMoO}_4)_{1-x}$ system. 3650Å excitation.

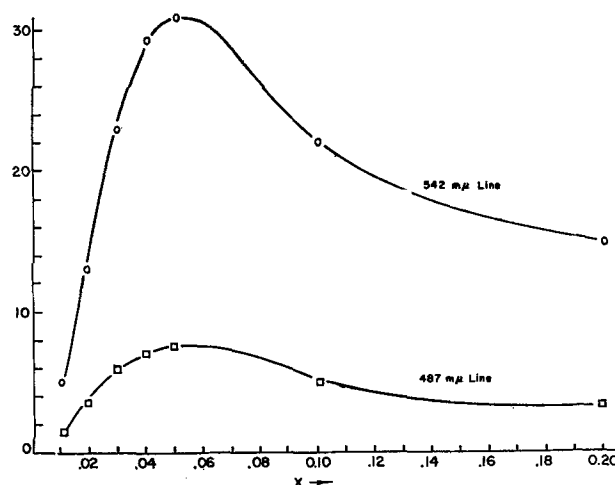


Fig. 4. Intensity of fluorescent emission as a function of X for the $(\text{TbNbO}_4)_x(\text{CaWO}_4)_{1-x}$ system. 3650Å excitation.

room temperature and liquid nitrogen temperature. The first two spectra show half widths of certain lines between 10 and 20Å at room temperature. For the latter two spectra, a significant sharpening of lines can be observed at liquid nitrogen temperature with half widths of 2-3Å.

As far as comparison of relative intensities is concerned, the terbium-doped compounds were outstanding. Table IV lists the intensities in arbitrary units for comparable conditions in various hosts and

Table III. Color of fluorescent emission of the Ln_{0.5}Nb_{0.5}W_{0.5}Ca_{0.5}O₄ series

Ln	Fluorescence color under 3650Å excitation at 25°C	Fluorescence color under 2537Å excitation at 25°C	Fluorescence color under 3650Å excitation at -196°C	Fluorescence color under 2537Å excitation at -196°C
Sc	—	S White	—	S Yellow white
Y	—	M Yellow white	—	S Green white
La	—	M Yellow white	W Blue	S Green white
Pr	—	S Green white	—	S Green white
Eu	—	S Red	S Red	S Red
Gd	—	S Yellow white	W Orange	S Green white
Tb	—	M Green	W Yellow green	S Green white
Er	—	—	M Yellow	M Yellow white
Tm	W Rose	S Yellow white	M Orange	S Green White
Yb	—	W Blue	—	M Blue white
Lu	—	W Blue	—	W Blue white

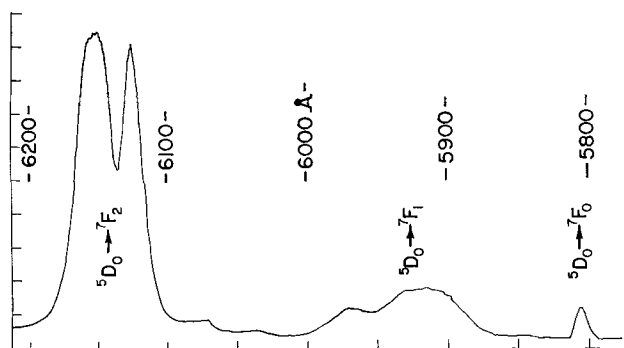


Fig. 5. Fluorescent emission spectrum of $(\text{EuNb})_{0.2}(\text{CaW})_{0.8}\text{O}_4$ at 300°K . 3650\AA excitation.

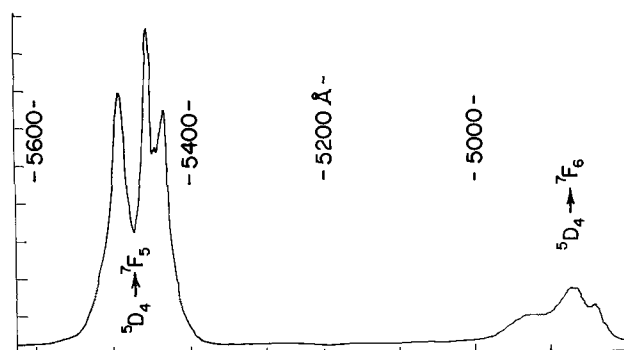


Fig. 6. Fluorescent emission spectrum of $(\text{TbNb})_{0.04}(\text{CaW})_{0.96}\text{O}_4$ at 300°K . 3650\AA excitation.

with both Nb^{+5} and Ta^{+5} as compensating ions. The wavelength of the most intense line for which the comparison is made is given in the last column. With the exception of the $\text{EuNbO}_4/\text{CaWO}_4$ case, we can see that the Nb/Mo combination is generally the best, indicating that intensity appears to be a function of the average atomic weight. This was further supported by experiments using SrMoO_4 , SrWO_4 , BaMoO_4 , and BaWO_4 as hosts for the various rare earth niobates and tantalates. In each case, a further reduction in intensity of fluorescent emission was obtained as the atomic weight of the host increased.

Crystal Growing Experiments

The apparatus used for the Czochralski growth of crystals is shown in Fig. 9. It is very similar to the setup described by Nassau (1); the principal difference is the rotation of the melt rather than the seed. As a power source, a 25 kw Westinghouse radio frequency generator, 450 kc/sec was used. An automatic radio frequency voltage controller, regulating

Table IV. Comparison of maximum observed emission for Tb, Dy, Sm, Eu, and Er in different host lattices under identical test conditions

Rare earth	Host and compensating ion				Wave length, $m\mu$
	Mo/Nb	Mo/Ta	W/Nb	W/Ta	
Tb	560	260	190	190	542
Dy	360	240	150	40	565
Sm	160	33	10	5	580
Eu	64	40	110	27	610
Er	85	65	37	31	548

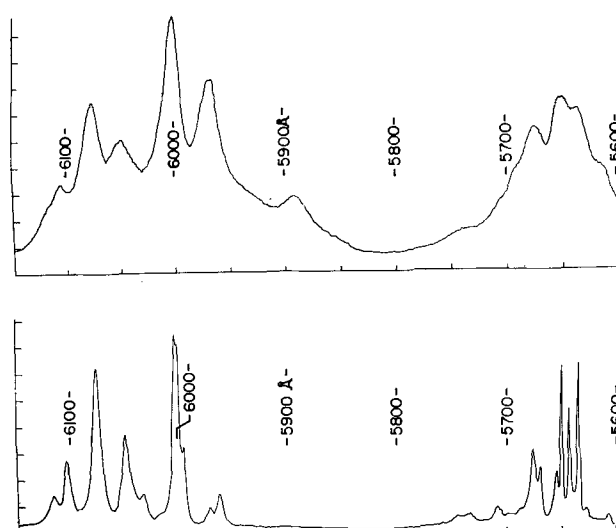


Fig. 7. Fluorescent emission spectrum of $(\text{SmNb})_{0.006}(\text{CaMo})_{0.994}\text{O}_4$ at 300°K (top) and 77°K (bottom). 3650\AA excitation.

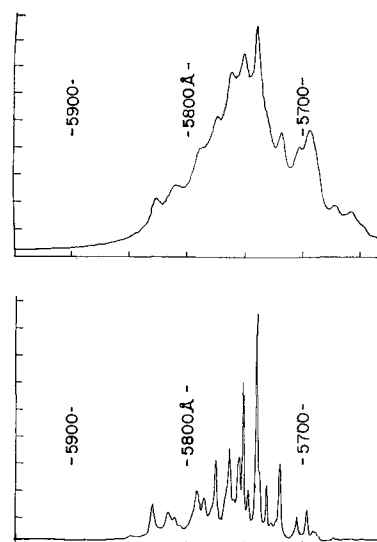


Fig. 8. Fluorescent emission spectrum of $(\text{DyNb})_{0.008}(\text{CaMo})_{0.992}\text{O}_4$ at 300°K (top) and 77°K (bottom). 3650\AA excitation.

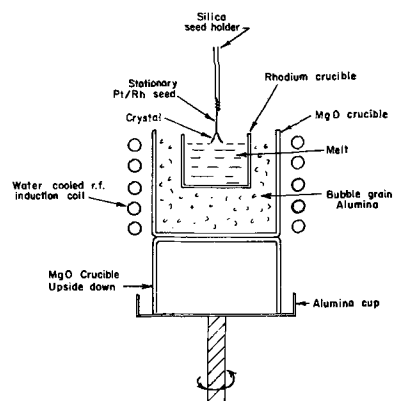


Fig. 9. Apparatus used for Czochralski growth of crystals

to $\pm 2\frac{1}{2}\%$ was found extremely helpful in obtaining better uniformity in cross-section of the single crystals. The rotation rate of the melt container was 6-10 rpm, pulling rate, generally $\frac{1}{2}$ -1 in./hr. Melt temperatures were observed visually with an optical pyrometer. An occasional check with a Pt/Pt 13%

Rh thermocouple indicated that due to the emissivity correction the optical measurements were about 40°C too low. Initial melt temperature for molybdates was about 1480°C; the tungstates melted about 100°C higher.

First seeds were obtained from monocrystalline fractions of boules grown on a Rh wire, and subsequent growths were exclusively made on seeds. Twofold symmetry of the Laue back reflection photographs of the spontaneously seeded crystals indicated that crystals grew in the a-axis and most subsequent crystals were oriented in the same direction, although it was possible by cutting an appropriate seed to grow crystals in the c-axis. The cross-section of these crystals was almost round as compared to the elliptical cross-section of a-axis crystals.

Although some doped tungstates were grown, most work was done on molybdates since the niobate doping gave a specific advantage. It is known (7) that if CaMoO₄ is grown by itself it tends to lose oxygen and turn blue. Although such a colored crystal can be reoxidized under pure oxygen at about 1300°C this is a rather undesirable feature, one which is not apparent with CaWO₄. If as little as 1/2 mole % of a rare earth niobate (with the exception of EuNbO₄) is added to the CaMoO₄ melt, it is stabilized to the point where no oxygen loss and hence no coloration occurs. The most striking examples are those with inherently uncolored rare earths such as Gd, Tb, Tm, and Yb which give colorless, waterclear crystals in CaMoO₄ as a host even without annealing in oxygen.

In pulling undoped CaMoO₄ from melts of commercially available material, considerable difficulties were experienced with cracking. Even double-pulled crystals, although to a much lesser degree, tended to crack. The precipitation of CaMoO₄ from a purified ammonium molybdate solution with a purified calcium nitrate solution gave an excellent starting material. The quality of this CaMoO₄ was such that even on first pulling, crack-free, sound crystals of high optical perfection were obtained. Ten calcium molybdate crystals doped with different

rare earths, of an average length of at least 2 in., were grown without cracks, clouds or inclusions of any kind. Figures 10 and 11 give some typical examples of crystals. Figure 11 represents the rather interesting case of EuNbO₄/CaMoO₄. This is the only example where very intense deep red coloring of the crystal after growing was observed. The color here, however, is not associated with a reduction of Mo⁺⁶, but rather with oxygen loss from Eu⁺³. Brauer (8) has recently described a novel europium oxide, Eu₃O₄, which is of deep red color. It is undoubtedly this combination of Eu⁺² and Eu⁺³ which gives the same red color in the crystal. The effect of annealing at 1300°C under pure oxygen is seen in the lower picture. All Eu⁺² is oxidized to Eu⁺³ and the red color disappears.

Top and bottom of each crystal were cut off with a diamond saw and were used for analytical evaluation and determination of the distribution coefficients. The analytical procedure was an x-ray fluorescence technique which provided results as seen for a small number of typical crystals in Table V. Also listed are the calculated distribution coefficients of the corresponding rare earth niobates in the host. The distribution coefficient is given by the ratio C_S/C_L, where C_S represents the concentration of the dopant in the solid, C_L that in the liquid. It was calculated according to Pfann (9) under the assumption that the stoichiometric ratio of Ln:Nb does not change appreciably, which is nearly correct as seen from some ratio calculations of CaO:MoO₃ and CaO:Nb₂O₅ on top and bottom of several crystals.

A few typical examples of the anion to cation ratios calculated from analytical data are given in Table VI. In no case of the eleven examples examined did the CaO:MoO₃ ratio deviate by more than 0.01 and no general trend for the shift of the Ln₂O₃:Nb₂O₅ ratio could be detected. In seven cases the ratio went up, down in four, but it always ex-

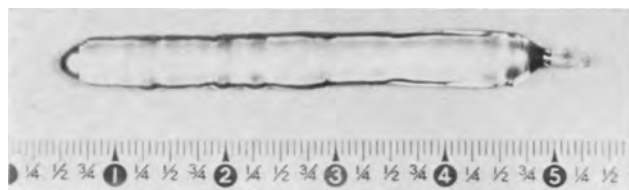


Fig. 10. Single crystal of CaMoO₄

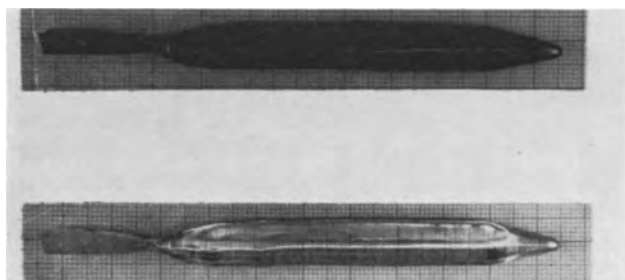


Fig. 11. Single crystal of (EuNb)_{0.01}(CaMo)_{0.99}O₄ after growing (top) and after oxidizing (bottom).

Table V. Analysis and distribution coefficients of some typical single crystals of the (LnNbO₄)_x(CaMoO₄)_{1-x} series

Ln	K=C _S /C _L	% MoO ₃	% CaO	% Ln ₂ O ₃	% Nb ₂ O ₅	Σ %
Pr	1.3	70.74	27.39	0.86	0.74	99.73
Nd	1.2	71.30	27.12	0.86	0.73	100.01
Sm	1.2	71.35	27.76	0.61	0.53	100.25
Eu	1.4	70.99	27.32	0.92	0.77	100.00
Gd	1.4	70.50	27.22	1.30	1.01	100.03
Tb	1.4	70.88	27.93	0.80	0.66	100.27
Dy	1.3	70.92	27.88	0.88	0.76	100.44
Ho	1.4	70.48	27.75	1.05	0.81	100.09
Er	1.3	70.70	27.72	1.09	0.88	100.39
Tm	1.2	70.92	27.28	0.92	0.89	100.01
Yb	1.2	70.07	27.75	1.04	0.87	99.73

Table VI. Cation to anion ratios for several dopants in CaMoO₄ host

Dopant	Cation/anion ratio		CaO:MoO ₃ ratio	
	Top	Bottom	Top	Bottom
NdNbO ₄	1:1.05	1:1.16	1:1.00	1:0.99
GdNbO ₄	1:1.05	1:1.09	1:0.99	1:0.99
TbNbO ₄	1:1.09	1:1.13	1:0.99	1:0.99
HoNbO ₄	1:1.09	1:1.07	1:0.99	1:0.99

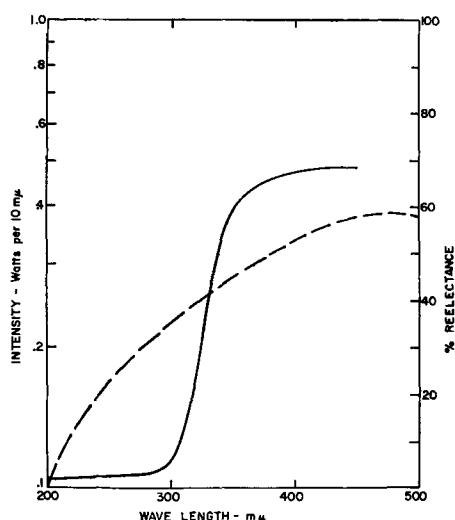


Fig. 12. Spectral characteristics of a xenon arc (---) compared with the reflectance spectrum of $(\text{EuNb})_{0.01}(\text{CaMo})_{0.99}\text{O}_4$ (solid line).

ceeded the nominal 1:1.00 ratio, indicating that in order to obtain true stoichiometry one should start with a $\text{Ln}_2\text{O}_3:\text{Nb}_2\text{O}_5$ ratio slightly rich in rare earths.

Nassau (2), however, found in a more refined study that Nb^{+5} and, for example, Nd^{+3} do segregate individually but tend to approach the desirable 1:1 ratio.

Evaluation of Crystals

Crystals of over 2 in. length were ground to laser specifications by A. Meller Co. Fluornoy (10) readily achieved stimulated emission from a rod doped with about 1 mole % NdNbO_4 and observed a threshold <10 joules at 135°K and a fluorescent lifetime of 159 μsec ; halfwidth of the laser line was <5Å.

Although the xenon flash lamp available did not appear to be the best source of excitation (as can be seen from a comparison of the absorption spectrum of $\text{Eu}_{0.01}\text{Nb}_{0.01}\text{Ca}_{0.99}\text{Mo}_{0.99}\text{O}_4$ in comparison with the spectral characteristics of a xenon arc in Fig. 12) we attempted to observe laser emission in the visible from rods doped with Sm^{+3} , Tb^{+3} , and Dy^{+3} , but even at pumping energies up to 6400 joules no laser action was observed.

Studies with all other compositions expected to have laser action in the infrared are still in progress.

Miscellaneous Other Data and Discussion

The structural characterization of the $\text{LnNbO}_4/\text{CaMoO}_4$ systems and the practical evaluation in single crystals indicated that these systems are ideal for doping materials of the scheelite type. The high thermal stability of the rare earth niobates and tantalates (melting in excess of 1700°C), combined with a very favorable distribution coefficient are desirable factors. The fact that distribution coefficients are above 1 indicates that the melt temperature of the host material, CaMoO_4 , is actually raised somewhat and the concentration C_s of the dopant in the solid is at all times slightly higher than the concentration C_L in the liquid. This leaves a very

slight concentration gradient decreasing from the top to the bottom of a single crystal. Although this gradient is apparently not detrimental to laser action (as the stimulated emission showed of $\text{Nd}_{0.01}\text{Nb}_{0.01}\text{Ca}_{0.99}\text{Mo}_{0.99}\text{O}_4$) it would be desirable to eliminate it. There are three possibilities: (i) to zone level the crystal after pulling, (ii) to add precalculated amounts of Nb_2O_5 and Nd_2O_3 during pulling, and (iii) to pull a relatively small crystal from a large melt reservoir. It would appear that solution (iii) is by far the simplest and most practical, if indeed a realistic need for complete homogeneity of the dopant in the crystal exists.

Since the same valence compensation principle would apply for rare earth vanadates and phosphates (tetragonal zircon structure) as it did for niobates and tantalates, it was of interest to see how calcium molybdate could be doped with these compounds. Sufficient solid solubility was first established by x-ray study. Although rare earth vanadates and phosphates per se are also quite temperature stable (GdVO_4 melts at $\sim 1750^\circ\text{C}$) if added to CaMoO_4 , the oxygen loss of that compound was worse than if pulled by itself, as judged from the deep blue-black color. Distribution coefficients for both the vanadates and phosphates were also below 1. This was a rather surprising result but it indicates that rare earth vanadates and phosphates show no advantage over niobate doping, particularly since the growing characteristics of these crystals were also much worse than for niobate doped ones. This constitutes just one other feature in favor of the Nb/Mo system.

Electrical properties were mostly measured on hot pressed or sintered pellets and indicated that the resistivities generally ranged from 10^{12} - 10^{13} ohm-cm with dielectric constants between 7 and 12. An interesting feature is the fact that luminescence did not quench up to 300°C, which may suggest some high temperature applications for these materials as phosphors. The Eu doped molybdate was also found to cathodoluminesce in the red.

Although it is recognized that the ultimate criterion for laser performance is the threshold energy and lowest thresholds have been reported for tungstates, it also appears that very little work has actually been done with CaMoO_4 . The results reported here may help to stimulate some new interest in this material as a host.

Acknowledgment

The author gratefully acknowledges the assistance of Mr. Fred Walls, who grew all crystals. Thanks are also due to Dr. G. Teufer, Engineering Technology and Materials Laboratories, for his cooperation in interpreting the x-ray diagrams, to Dr. E. Abramson, Central Research Department, and Mr. L. S. Brooks for determining numerous spectra and to Mr. Hoidal for the analytical evaluations. As mentioned in the text, Dr. P. A. Fluornoy, Engineering Physics Laboratory, demonstrated laser action in one of our crystals and will publish his detailed results separately.

Manuscript received Nov. 26, 1963. This paper was presented at the New York Meeting, Sept. 29-Oct. 3, 1963.

Any discussion of this paper will appear in a Discussion Section to be published in the December 1964 JOURNAL.

REFERENCES

1. K. Nassau, *J. Appl. Phys.*, **33**, 3064 (1962).
2. K. Nassau, *Phys. and Chem. of Solids*, In print.
3. L. H. Ahrens, *Geochimica Cosmochimica Acta*, **2**, 115 (1954).
4. C. Keller, *Z. anorg. allgem. Chem.*, **318**, 89 (1962).
5. R. S. Roth, "Rare Earth Research," p. 93, McMillan Co., New York (1961).
6. K. A. Gingerich, Annual Conference Application of X-Ray Analysis, Denver (1963).
7. L. F. Johnson, *J. Appl. Phys.*, **34**, 897 (1963).
8. G. Brauer, *Acta Crystall.*, **15**, 1059 (1962).
9. W. G. Pfann, "Zone Melting," p. 11, John Wiley & Sons Inc., New York (1958).
10. P. A. Flournoy, Unpublished. Dr. Flournoy kindly permitted us to quote his results.

Activity of Gallium in NiGa and Associated Gallium-Gallium Oxide Equilibria

A. U. Seybolt

*Metallurgy and Ceramics Research Department, Research Laboratory,
General Electric Company, Schenectady, New York*

ABSTRACT

The relative partial molal free energy of gallium and the activity of gallium in the compound NiGa have been obtained across the homogeneity range of this phase at 835° and 900°C. A solid state anion conductor (CaO-stabilized ZrO₂) was used as the electrolyte in a high temperature galvanic cell. It was found that the thermodynamic properties of NiGa change rapidly near 50 atom per cent gallium. A brief review is made of the metal/oxide equilibria and the free energies of the two gallium oxides Ga₂O₃ and Ga₂O.

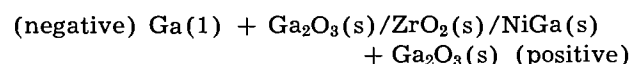
During the course of investigating (1) an oxygen-induced hardening in the CsCl structure compound NiGa, it became desirable to learn something about the variation of gallium activity with gallium concentration across the homogeneity range of NiGa. According to the phase diagram given by Hansen (2), the intermetallic compound NiGa has a homogeneity range of about 37-60 atom per cent (a/o) Ga at 900°C, rapidly decreasing to about 48-54 a/o Ga at 600°C and below.

Experimental Procedure

Five alloys were used, containing 41, 49.6, 51.6, 53.7, and 57 a/o Ga. The first and last alloys were not analyzed, but the composition of the other three alloys are the results of chemical analysis. Experience has shown that the intended composition was ordinarily achieved to within about 0.1% Ga. Gallium of four nines purity and carbonyl nickel were melted in a purified argon atmosphere in an induction furnace and 100g castings were poured into graphite molds to yield bars about 3/8 in. x 3/4 in. x 5 in. Metallographic examination showed single phase alloys except for the two extreme compositions, which showed two phases in the as-cast condition as predicted by the phase diagram (2). However, at the two temperatures selected for making activity measurements, 835°C and 950°C, these alloys are quite close to the phase boundaries. For the present purpose, the precise position of the extreme alloys with respect to the phase boundaries is not particularly important, as long as these compositions may be considered to approximate the compositional range of NiGa.

At the suggestion of Professor Wagner (3), it was decided to use the solid state galvanic cell technique

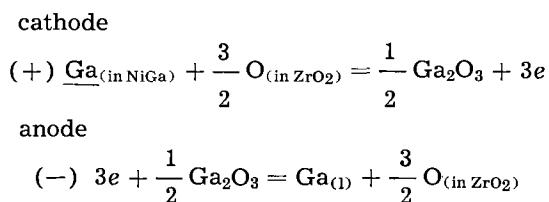
in which CaO-stabilized ZrO₂ is used as a solid electrolyte. This cell may be represented as follows:



This is a solid state cell where one electrode is a mixture of pure liquid gallium + solid Ga₂O₃, and the other electrode is a mixture of NiGa alloy of some desired composition also mixed with Ga₂O₃. Liquid gallium metal was mixed with an equal volume of Ga₂O₃ powder in a mortar and pestle, to make a stiff, dry paste. Similar quantities of -200 mesh NiGa alloy powder and Ga₂O₃ were mixed by the same technique. A B₄C mortar and pestle were used to avoid contamination. Both types of electrode material were pressed into thin (~50 mil) disks, 1/2 in. in diameter, with a steel die, using enough pressure to obtain pieces which could be handled without excessive breakage. A Ga/Ga₂O₃ disk and a NiGa/Ga₂O₃ disk laid on either side of the ZrO₂ electrolyte disk, of similar size, comprised the galvanic cell. The ZrO₂ (CaO-stabilized by about 14 mole/% CaO) acts as the electrolyte since ZrO₂ is an oxide with anion vacancies and conducts only oxygen anions. It is almost a pure ionic conductor. Since the activity of the Ga in NiGa is lower than in the liquid metal, there is a tendency for that in the Ga(1) + Ga₂O₃ electrode (which is negative) to ionize and for trivalent Ga (or Ga⁺⁺⁺) in the NiGa + Ga₂O₃ electrode to discharge into the alloy in an effort to equalize the activity in the two phases. There is therefore a tendency for Ga cations to pass from left to right as the cell is written above. However, this cannot occur since ZrO₂ passes only anions. Accordingly, oxygen anions tend to pass from right to left. In actual practice, there is only a very small

movement of anions, since the cell is not allowed to deliver power, but is measured in a reversible manner by a d-c potentiometer, which balances the cell's emf.

The electrode reactions can be written



Since the activity of Ga_2O_3 is unity, and is the same at both electrodes, and the activity of the migrating oxygen ion is the same also, on adding we get

$$\text{Ga}_{(\text{in NiGa})} = \text{Ga}_{(l)}$$

This is an expression of equilibrium, which is maintained by bucking out the difference in gallium activity by means of the emf of the potentiometer. Hence $\bar{F}_{\text{Ga}} = F^\circ_{\text{Ga}} - 3FE$ since 3 electrons are required in the electrode reactions above, where F = Faraday constant = 23,070 cal/v equivalent, E = measured emf in volts. By definition, $\bar{F}_{\text{Ga}} - F^\circ_{\text{Ga}} = \Delta\bar{F}_{\text{Ga}}$, where $\Delta\bar{F}_{\text{Ga}}$ is the relative partial molal free energy of gallium.

It will be noted that for this cell to produce meaningful results, the two oxygen pressures fixed by the two electrode equilibria noted above must not be altered by some other competing process. There was at first some concern about the possible presence of the gallium sub-oxide Ga_2O , and hence perhaps some ambiguity about establishing correct oxygen pressures demanded by the equilibria expected in the cell. As it turned out, there was no difficulty from this source; this topic will be expanded in a subsequent section.

Physically, the cell as it finally evolved was as sketched in Fig. 1. An argon atmosphere purified by zirconium chips at 850°C was slowly passed through the cell to keep out any atmospheric oxygen.

Experimental Results

In most cases the measured cell voltage was quite stable for several hours, often not varying more than

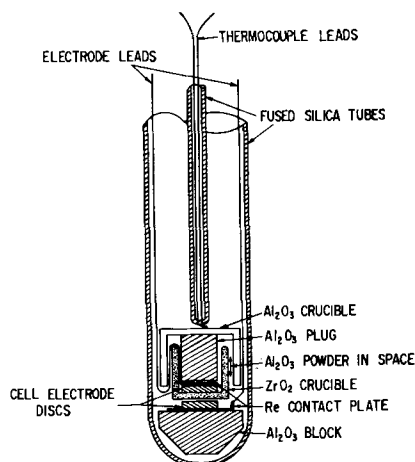
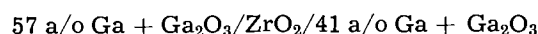


Fig. 1. Solid electrolyte galvanic cell

about 1 mv over a 3-hr interval. Constancy to about 2 mv over a 3-hr interval was considered to be evidence that equilibrium was probably reached, but a value was not accepted unless a temperature excursion of $835^\circ\text{--}950^\circ\text{C}$ and return reproduced the same result at 835°C . A run usually lasted 2 to 3 days, and the reading in the morning was usually fairly close to that of the preceding evening, within about 5 mv. Experiments were made using several alloys against pure gallium, and by using one alloy against another. This allowed a check on internal consistency, and a comparison of the relative molal free energy of gallium derived from two different routes.

Table I summarizes the data obtained from the cells: the emf values which were measured directly, and the free energy change derived from their values. Cell 3 means the following cell



The third column gives the free energy change for the cell as written. Hence, cell 3 gives the free energy obtained in reversibly transferring one mole of gallium from an alloy of 57 a/o Ga to that of 41 a/o Ga where the quantities of each alloy are sufficiently large so that no detectable concentration difference results in either alloy. Cells 1 and 2 give directly the partial molal free energy of gallium in the 41 a/o Ga alloy and in the 57 a/o Ga alloy, respectively, referred to pure liquid gallium. By subtracting from the emf at 835° and 950°C of cell 1 the corresponding emf values of cells 3, 4, 5, and 6, relative partial molal free energies of each alloy, referred to liquid gallium, may be obtained. These

Table I. Electromotive force (emf) of the cells, and free energy of cell reactions

Cell	emf (mv)	ΔF cell (cal/mole Ga)
(1) 41 a/o Ga vs. Ga		
835°C	157	-10,880
950°C	168	-11,650
(2) 57 a/o Ga vs. Ga		Calculation of ΔF_2 from cells 1 and 3
835°C	37	-2,570 -2,360 $\Delta(\Delta F) = 210$
950°C	36	-2,500 -2,170 $\Delta(\Delta F) = 330$
(3) 41 a/o Ga vs. 57 a/o Ga		
835°C	123	-8,530
950°C	137	-9,500
(4) 41 a/o Ga vs. 49.6 a/o Ga		
835°C	5	-347
950°C	23	-1,600
(5) 41 a/o Ga vs. 51.6 a/o Ga		
835°C	55	-3,810
950°C	63	-4,480
(6) 41 a/o Ga vs. 53.7 a/o Ga		
835°C	62	-4,320
950°C	76	-5,260
(7) 53.7 a/o Ga vs. Ga		Calculation of ΔF_7 from cells 1 and 6
835°C	80	-5,550 -6,470 $\Delta(\Delta F) = 1,020$
950°C	73	-5,070 -6,420 $\Delta(\Delta F) = 1,350$

Table II. Partial molal free energy of gallium relative to pure liquid gallium, and gallium activity, at several compositions

A/o Ga	$\overline{\Delta F}_{\text{Ga}}$ (835°C)	$\overline{\Delta F}_{\text{Ga}}$ (950°C)	a_{Ga} (835°C)	a_{Ga} (950°C)	How obtained
41	-10,880	-11,650	0.00723	0.0083	41 vs. Ga
49.6	-10,540	-10,100	0.00830	0.0158	41 vs. 49.6
51.6	-7,060	-7,200	0.0406	0.0520	41 vs. 51.6
{ 53.7	-6,570	-6,420	0.0506	0.0715	41 vs. 53.7
{ 53.7	-5,550	-5,070	0.0860	0.124	53.7 vs. Ga
{ 57	-2,570	-2,500	0.312	0.358	57 vs. Ga
{ 57	-2,360	-2,180	0.342	0.408	41 vs. 57

figures are listed in Table II in columns 2 and 3, along with the activities of gallium calculated from the $\overline{\Delta F}_{\text{Ga}}$ values according to the relationship

$$\overline{\Delta F}_{\text{Ga}} = RT \ln a_{\text{Ga}}$$

The activities are plotted in Fig. 2 against mole fraction Ga x 100 (a/o Ga). The filled circles and squares refer to measurements made on alloys which were measured with pure liquid gallium as the other electrode. Hence, these values are more directly obtained and preferred values, as opposed to the open points obtained in a less direct manner. This applies also to Fig. 3, where the relative partial molal free energies are plotted. The preferred values are underlined in Table II. It will be noted at once that the activity and partial molal free energy changes comparatively little from about 41 to 50 a/o Ga, but that above this concentration these quantities increase sharply.

The kind of relationship between a/o Ga and gallium activity shown in Fig. 2 was previously observed by Kachi (4) and by Trzebiatowski and Terpilowski (5) in the case of magnesium in AgMg, another intermetallic compound of CsCl structure.

It will be noted in Table II that while the free energy discrepancy for the 57 a/o Ga alloy ob-

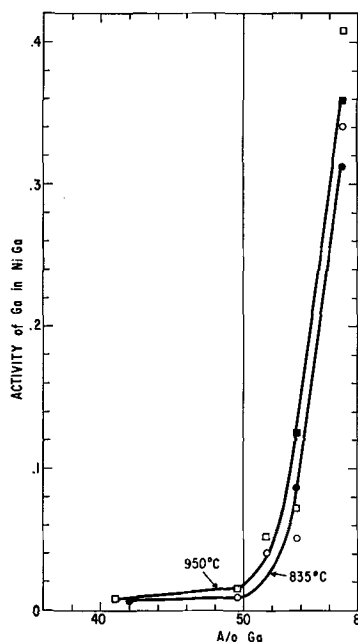


Fig. 2. Activity of gallium in NiGa as a function of composition

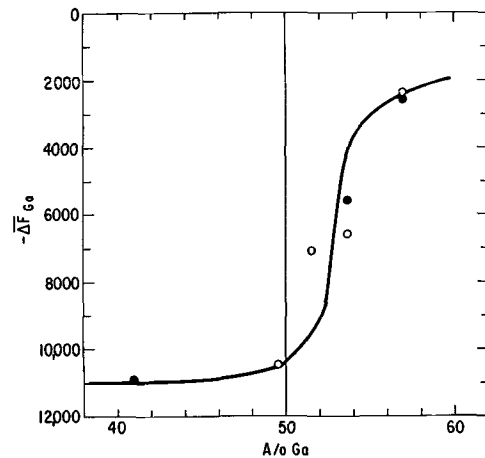


Fig. 3. Partial molal free energy of gallium in NiGa at 835°C as a function of composition.

served directly and indirectly is fairly small, there is a larger difference at 53.7 a/o Ga. The reason for the larger variation for the last alloy is not clear. It is possible that these observed variations are due to slight inhomogeneities of compositional differences in the alloy powder used to make the electrodes.

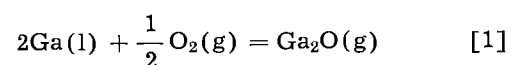
In summary, it has been observed that there are sharp changes in the relative partial molal free energy of gallium, and hence in gallium activity, with increasing gallium commencing at 50 a/o Ga.

Thermodynamics of the Gallium Oxides

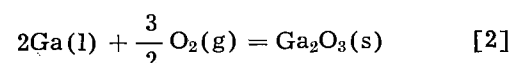
As noted above, it was necessary to establish that only one oxide of gallium (Ga_2O_3) was involved in the cell equilibria. The following is a brief summary of the metal-oxide equilibria of the two known gallium oxides which are compared here for the first time to this author's knowledge.

While the thermodynamic properties of Ga_2O_3 have apparently been fairly well established for some time, there has been some confusion regarding Ga_2O , the sub-oxide. For example, Coughlin's (6) tables list Ga_2O as a solid only, while more recent data indicate that at temperatures above 700°K, at least, its normal state is a gas. Glassner's (7) data shows it as a solid up to about 1000°K or somewhat lower, then as a gas whose free energy of formation is constant from 1000° to 2500°K, at the -55 kcal level.

Recently Cochran and Foster (8) studied reactions in systems involving gallium metal vapor, Ga_2O and other stable oxides such as SiO_2 , MgO , Al_2O_3 , and the like. In their paper they listed free energy functions for $\text{Ga}_2\text{O}_3(\text{s})$ and $\text{Ga}_2\text{O}(\text{g})$. Combining these functions with similar ones published by Stull and Sinke for $\text{Ga}(\text{l})$ and $\text{O}_2(\text{g})$ one can calculate the free energy of the following two reactions as a function of temperature



and



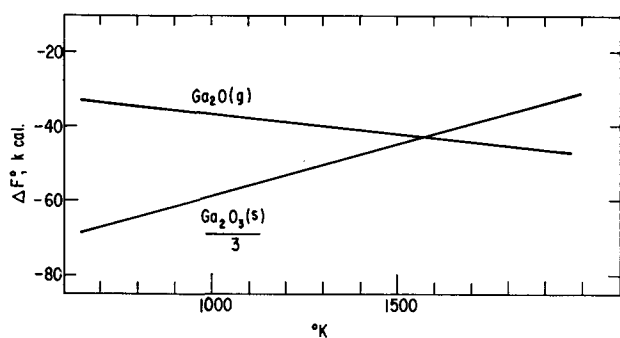
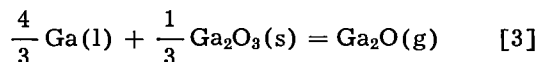


Fig. 4. Free energy of formation of Ga_2O and Ga_2O_3 per gram atom of oxygen as a function of temperature.

The results are plotted in Fig. 4 for $\Delta F^\circ_{\text{Ga}_2\text{O}}$ and $(\Delta F^\circ_{\text{Ga}_2\text{O}_3})/3$ so that each compound is put on a basis of equal oxygen content. The results for Ga_2O_3 agree quite closely with the older (1954) tables of Coughlin (6). However, the data for $\text{Ga}_2\text{O}(\text{g})$ are apparently new and at least have the appearance of credibility. For example, the negative slope of ΔF° vs. T for $\text{Ga}_2\text{O}(\text{g})$ seems correct since a gaseous product of higher entropy is being formed. It is particularly of interest to note that the free energy of formation per atom of oxygen of Ga_2O_3 is considerably more negative than Ga_2O in the temperature region of interest in this work; 1000°C and below.

Frasch and Thurmond (10) in a recent paper examined the reaction



and measured the vapor pressure of $\text{Ga}_2\text{O}(\text{g})$ over the temperature range 1073°–1273°K, the temperature range of interest in this work. Over this temperature range the pressure of Ga_2O varied from 1.56×10^{-4} atm to 9.90×10^{-3} atm, respectively. If one calculates the standard free energy of this reaction from this data one obtains +1490 cal/mole at 1200°K, while by combination of the two equations given previously one obtains +1400 cal/mole, very satisfactory agreement.

Since Ga_2O is a condensable gas, in a nonisothermal enclosure it will condense in cold parts of the system and disproportionate back to Ga and Ga_2O_3 . Hence its formation tends to remove Ga_2O_3 from the hot zone as Ga_2O . The important consideration for operation of the galvanic cell is that reaction [1] above can not compete with reaction [2] because Ga_2O_3 is more stable. Ga_2O can be formed, however, by reaction [3] but in this reaction oxygen gas is not involved, and therefore the presence of Ga_2O causes no ambiguity in establishing the desired electrode reactions and hence oxygen pressures. During

cell operation there was very little evidence of reaction [3], since the quartz cell enclosure showed only traces of a whitish deposit.

Application of the phase rule shows that on fixing temperature there are zero degrees of freedom, hence all phases are of fixed composition or pressure, including oxygen.

Summary

The activity of gallium referred to pure liquid gallium has been determined as a function of composition, across the phase field of the compound NiGa, at 835° and 950°C. It has been found that the activity increases slowly with composition as the gallium content reaches 50 a/o, but as the gallium content is increased, the activity increases very rapidly, (almost discontinuously), to the end of the homogeneity range.

A brief outline of the thermodynamic relationships between the two gallium oxides is included primarily in justification of the method used in the galvanic cell which employed the oxygen, gallium, Ga_2O_3 equilibrium.

Acknowledgments

The author is grateful to Professor Carl Wagner for suggesting the use of the ZrO_2 electrolyte galvanic cell. Helpful discussions were had with Professor John Elliott and Dr. Jack Westbrook. Drs. Stephen Spacil and John Cahn reviewed the manuscript. This work was sponsored by the Aeronautical Systems Division, U. S. Air Force.

Manuscript received July 18, 1963; revised manuscript received Dec. 18, 1963.

Any discussion of this paper will appear in a Discussion Section to be published in the December 1964 JOURNAL.

REFERENCES

1. A. U. Seybolt and J. H. Westbrook, To be published.
2. M. Hansen, "Constitution of Binary Alloys," 2nd ed., McGraw-Hill Book Co., New York.
3. Carl Wagner, Private communication.
4. S. Kachi, *Sci. Repts. Research Inst., Tohoku*, **A7**, 351 (1955).
5. W. Trzebiatowski and J. Terpilowski, *Bull. acad. polonaise des sciences*, **3**, 391 (1955).
6. James P. Coughlin, "Contributions to the Data of Theoretical Metallurgy," XII; "Heats and Free Energies of Formation of Inorganic Oxides," *Bull.* 542, U. S. Bur. Mines.
7. Alvin Glassner, "The Thermochemical Properties of the Oxides, Fluorides and Chlorides to 2500°K," ANL-5750 (Supt. Public Doc.).
8. C. N. Cochran and L. M. Foster, *This Journal*, **109**, 144 (1962).
9. D. R. Stull and G. C. Sinke, "Thermodynamic Properties of the Elements," ACS, Washington, D. C. (1956).
10. C. J. Frasch and C. D. Thurmond, *J. Phys. Chem.*, **66**, 877 (1962).

Electrolysis in Anhydrous Hydrogen Fluoride

I. The Drying of Hydrogen Fluoride by Electrolysis

H. H. Rogers, S. Evans, and J. H. Johnson

Research Department, Rocketdyne Division, North American Aviation, Inc., Canoga Park, California

ABSTRACT

Periodically reversing the direction of current in an electrolytic cell has been shown to lead to effective drying of hydrogen fluoride because it causes extensive depolarization. Its obvious advantage is that, by allowing a higher average current to pass, the time required for drying is greatly shortened and, thereby, the attack on the nickel electrode is reduced markedly. The portion of the current used for nickel dissolution was never greater with current reversal than in the conventional procedure where the current was not periodically reversed.

The use of hydrogen fluoride as an electrolyte often requires the removal of water to avoid the formation of unwanted oxygen-containing compounds during electrolysis. In addition, the electrochemical reactivity and properties of nonaqueous solvents are frequently quite different in the presence of even small amounts of water. Methods for producing pure dry hydrogen fluoride which are discussed by Runner, Balog, and Kilpatrick (1), all involve either potassium hydrogen fluoride or sodium hydrogen fluoride as an intermediate. These methods can produce very dry products which are characterized by very low conductivities approaching $10^{-6} \text{ ohm}^{-1} \text{ cm}^{-1}$; the values first measured invariably increase to about $10^{-4} \text{ ohm}^{-1} \text{ cm}^{-1}$ when the product is permitted to stand for a period of time. The extremely pure product is not generally needed for electrosynthetic work and, in addition, requires considerable time and equipment to prepare. These methods are, therefore, not usually employed for producing dry hydrogen fluoride prior to carrying out electrosynthetic experiments.

Simons (2) states that commercial hydrogen fluoride was dried by passing a current through it until fluorine was evolved. Water was removed as oxygen, oxygen difluoride, and hydrogen. This method was employed by Kongpricha and Clifford (3) who passed current until the conductivity was low and the cell gave a constant back potential for several hours after electrolysis was stopped. Although this electrolytic drying process has been used by other workers (4), no further details of either procedure or of the drying efficiency of the process have been found in the literature.

Experience with the electrolytic drying process (2) has indicated that hydrogen fluoride cannot be dried satisfactorily in a reasonable length of time, overnight for example, because of severe anodic polarization. On the other hand, if the electrode arrangement provided a very large electrode area [such as in the Simons' Cell (5)] in comparison to the amount of hydrogen fluoride to be dried, then it was apparently possible to pass sufficient amounts of current at a low average current density to dry the hydrogen fluoride in one or two days. It should

be pointed out that this process is accompanied by severe anode corrosion.

The results of experiments which contrast the effectiveness of conventional electrolytic drying of hydrogen fluoride (2) with a new procedure, drying by periodic current reversal, will be discussed.

Experimental

The electrolytic cell (Fig. 1) constructed almost entirely of welded stainless steel sheet, was designed for maximum cooling efficiency. Refrigerated methanol was circulated through a jacket that completely surrounded the cell except for the top. The temperature of the electrolyte was monitored with the aid of a copper-constantan thermocouple inserted into a stainless steel well which was located between the electrodes (Fig. 2). Suitable fittings

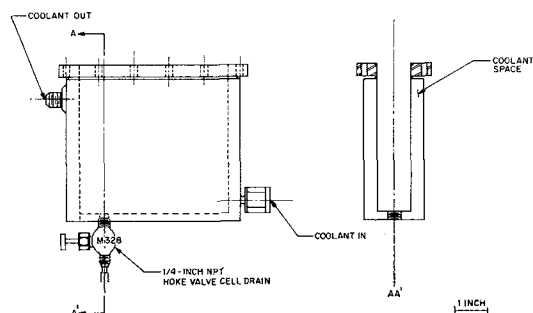


Fig. 1. Electrolytic cell (stainless steel welded)

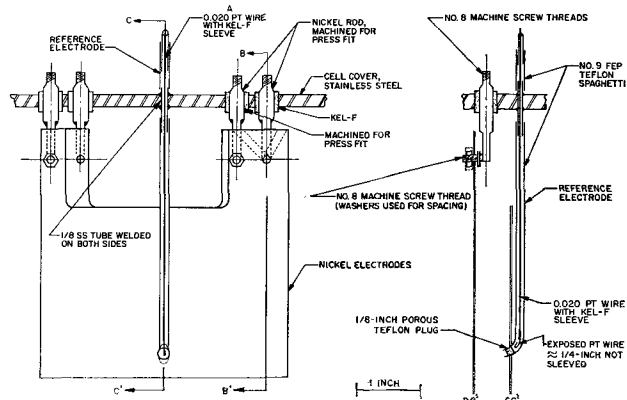


Fig. 2. Electrode assembly

were provided for the addition of liquid hydrogen fluoride (Matheson) directly from the cylinder. A reflux condenser, maintained at about -18° by circulating methanol, returned vaporized hydrogen fluoride to the cell.

The sheet nickel electrodes had an area (one side) of approximately 60 cm^2 exposed to the electrolyte when the cell was filled with 250 ml of liquid hydrogen fluoride; the useful capacity of the cell was from 40 to 360 ml. The electrodes were mounted on nickel rods, as shown. These rods were forced into short lengths of Kel-F rods which were, in turn, forced into the cover of the cell. In each instance, the holes were drilled very slightly smaller than the diameter of the rod, providing a vacuum-tight seal.

Electrical power was obtained from a Knight Battery Eliminator (6) connected in series with a current regulator (7). The circuit was modified to permit electrolyses to be conducted at constant current over a range from 0.001 to 15 amp. Current, input voltage, and electrode potential readings were recorded by Rustrak Model A Recorders connected with the appropriate shunts and multiplier resistors. A transistorized automatic reversing switch provided a means for reversing current periodically to the cell during reverse-current drying. An additional set of contacts also reversed connections to the voltage recorder. Although the transistorized switch was continuously adjustable to obtain either equal or unequal time intervals from 1 to 40 sec, a simple mechanical switch set to reverse connections about every 30 sec would have been satisfactory.

Current was brought into the electrodes through the nickel support rods. Cell voltage was measured across the other two nickel support rods, thereby virtually eliminating any errors due to a high-resistance connection to one of the electrodes. Electrode potentials were measured between the electrode under study and a platinum wire electrode with a General Radio 1230-A D.C. Amplifier and Electrometer or with a transistorized electrometer voltmeter (8). The platinum electrode in the measuring circuit, where there was negligible current drain, functioned satisfactorily as a poised reference rather than as a nonpolarizable reference electrode.

Additional experimental and procedural details are given below. Details of the operating conditions, typical of those used for electrolysis, are presented in Tables I and II.

Inert gas was used to dilute the gaseous products, thereby reducing the severity of explosions which sometimes occurred during electrolysis. A flow of about 50 cc/min of helium was found to be adequate.

The liquid level in the cell was found by using a probe made from a piece of Monel rod covered, except for the ends, with a thin Kel-F sleeve (electrical spaghetti). The probe, inserted into the cell through a Teflon "O" ring, was lowered slowly until it made electrical contact with the electrolyte as indicated by an ohmmeter. Since the depth to which the rod had been lowered was proportional to electrolyte level, not only could the quantity of electrolyte added be determined, but the loss of electrolyte during electrolysis as well.

Table I. Details of electrolysis experiments, electrical data

Internal cell temperature -8° to -16° .

Run	Reactants	Potentials, v	Current, amp	Length of run, hr	Reversal periods, sec
1	HF-200 ml	8.0 \rightarrow 15.4	5.2 \rightarrow 0.96	1.7	None
2	HF-228 ml	8.0 \rightarrow 15.0	5.6 \rightarrow 2.8	6.0	40
3	HF-280 ml	9.6 \rightarrow 26.8	3.2 \rightarrow 0.28	20.5	30
4a	HF-216 ml	10 \rightarrow 23**	6.0 \rightarrow 0.60**	17.5	40
4b	HF:NH ₃ *	5.3 \rightarrow 4.8	0.75	2.0	None

* Mole ratio 15:1.
** At end of 6.0 hr.

Table II. Details of results of electrolysis experiments

Nickel electrodes cleaned with abrasive paper before each run.

Run	Weight loss, g		Current equiv. of wt loss, amp	Products		Current reversal
	Anode*	Cathode*		Principal	Trace	
1	0.574	0.016	0.32	OF ₂	CF ₄	No
2	1.023	0.958	0.36	OF ₂	CF ₄ , NO ₃ F	Yes
3	1.045	0.870	0.086	Not determined		Yes
4a	1.735**	1.371**	0.16	Not determined		Yes
4b				NF ₃	CF ₄	

* Or electrode normally acting as anode or cathode.
** Total weight loss for parts a and b.

Results and Discussion

According to Burdon and Tatlow (9), the drying of hydrogen fluoride by electrolysis causes a reduction in current until the conductivity is almost zero when complete drying has occurred. If it is assumed that the current measured is proportional only to the quantity of water in the system, this amperometric measurement is valid.

Typical current and potential behavior monitored during the conventional electrolytic drying process (without current reversal) is shown in Fig. 3. In this graph it can be seen that the current did fall off as a function of drying time. However, the resumption of electrolysis after breaking the circuit resulted in an increased current. This indicated that electrode effects, rather than solution conductance,

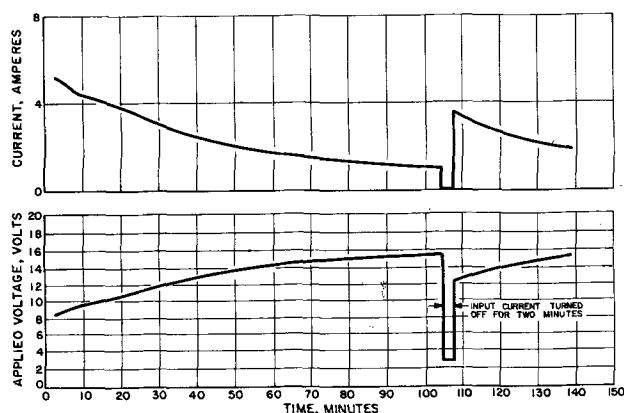


Fig. 3. Typical run, electrolytic drying of HF without current reversal.

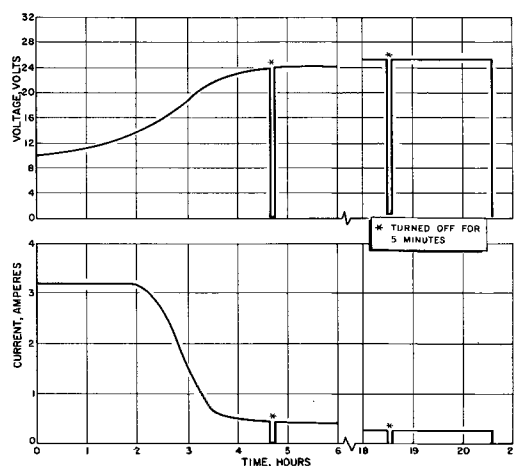


Fig. 4a (top). Typical run, electrolytic drying of HF with current reversal.

Fig. 4b (bottom). Typical run, electrolytic drying of HF with current reversal.

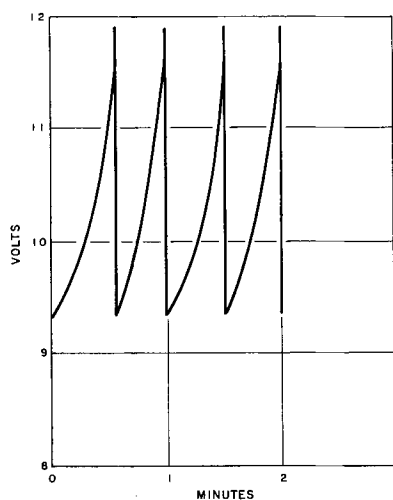


Fig. 4c. Typical run, electrolytic drying of HF with current reversal. Details of voltage curve at 0.6 hr.

were the limiting factor in determining the cell current. Therefore, any strict interpretation which relates current to solution conductance, *i.e.*, quantity of dissolved water, is not valid under these conditions. In six separate experiments hydrogen fluoride was dried in this manner for 2 to 3 hr prior to the addition of ammonia. Subsequent electrolysis of this system consistently yielded oxygen difluoride as a product, indicating that water removal was incomplete. Oxygen difluoride was still produced during electrolysis when the ammonia was predried over sodium.

In contrast, when the hydrogen fluoride was dried using periodically reversed current, the current and potentials were unchanged when electrolysis was resumed after a short time interval (Fig. 4). Thus, changes in current and potential observed previously must have been a function of solution resistance.

Further confirmation of the cause of this resistance change was obtained from analysis of diagnostic tests (Table III). Electrode potentials were measured at the end of a run between the platinum

Table III. Electrode potentials at end of typical runs

	Cell configuration*		E Anode	E Cathode
Conventional drying	C	RA	15	-0.9
Reverse drying	C	RA	12	-17
Reverse drying	A	RC	27	-2.3

* A is the anode, C the cathode, R the platinum reference electrode. Potentials (in volts) listed were measured with respect to reference electrode. Measured at 0.63 amp.

reference electrode and each of the nickel electrodes, observing the electrode configurations illustrated in Table III. The difference in anode as well as cathode potentials, as measured with both configurations, was caused by the IR drop in the solution. Based on previous results, it was reasonable to assume a real cathode potential of 1v (with insignificant IR contribution) and a total solution resistance of about 27 ohms was then calculated. Without any such assumption, however, the solution resistance calculated between the reference electrode and the nickel electrode, which is not in close proximity to it, was 25 ohms. On examination of the values obtained on conventional drying (Table III), it can be seen that there is a negligible contribution of solution resistance to the electrode potential value as measured between the reference electrode and the nickel electrode which is not in proximity to it.

While it is not justifiable to derive any value of specific conductivity from such resistance measurements, it is possible to correlate the observed high-solution resistance values with effectiveness of drying. Thus, when ammonia was added to hydrogen fluoride which was dried with the current reversal method, subsequent electrolysis did not yield oxygen difluoride or any oxygen-containing product (Run 4b, Tables I and II), indicating that water removal was essentially complete.

The drying of hydrogen fluoride with current reversal is effective because during electrolysis it is possible to pass higher average currents than during conventional drying processes. The variation of applied potential during current reversal is illustrated in Fig. 4. If it can be assumed that the polarization which occurred during conventional drying was a result of the onset of passivity, then it is possible that, by reversing the current, the passive film was removed cathodically, thereby causing gross depolarization. Clearly this is not the process which occurred. The buildup of passivity is associated with metal dissolution (to form a passive film some metal must dissolve) so that the periodic destruction and formation of a passive film must be accompanied by an additional weight loss. The average portion of the current which assists in the dissolution process, calculated from weight loss data, is never significantly larger for the current reversal process than for the conventional process (Table II). The depolarization observed with the current reversal process is not related to the loss of a passive film, but probably resulted from the obviation of other

forms of polarization, such as concentration polarization or gas-film polarization.

The additional current which passes with the current reversal process is related directly to the quantity of water removed and not to any further metal dissolution. The current reversal technique used in cells designed specifically for electrosynthesis permits more effective drying in shorter time periods than the conventional electrolytic procedure, and therefore, results in considerably less metal consumption.

Acknowledgments

The authors wish to express their appreciation to the Office of Naval Research for their support of this work under Contract Nonr 1818(00). Thanks are also due to Dr. Donald Pilipovich of these laboratories for several helpful discussions.

Electrolysis in Anhydrous Hydrogen Fluoride

II. The Hydrogen Fluoride-Nitrous Oxide System

H. H. Rogers, S. Evans, and J. H. Johnson

ABSTRACT

The electrolysis of nitrous oxide solutions in anhydrous hydrogen fluoride has been shown to yield nitrogen trifluoride consistently, while oxygen difluoride and nitroxy fluoride were also produced frequently. Since nitrosyl fluoride may have been an intermediate, the electrolysis of the hydrogen fluoride-nitrosyl fluoride system was also investigated. The results are consistent with a mechanism requiring the formation of fluorine at the anode and nitric oxide at the cathode.

The mechanism for the formation of products during electrolysis of nitrous oxide in anhydrous hydrogen fluoride is not completely understood. The products can arise from the electrolysis of some electroactive species which forms on the addition of nitrous oxide to hydrogen fluoride or from the interaction of electrolytically generated fluorine with some species present in the system. The purpose of this paper is to elucidate the electrochemical mechanism in the hydrogen fluoride-nitrous oxide system through a study of polarization characteristics.

An electrochemical study was conducted in the systems: hydrogen fluoride-sodium fluoride, hydrogen fluoride-sodium fluoride-nitrous oxide, and hydrogen fluoride-nitrosyl fluoride. Since nitrosyl fluoride was formed (2) on fluorination of nitrous oxide with elementary fluorine at 100°-900°, it was deemed worthwhile to determine if nitrosyl fluoride was an intermediate in the electrochemical process. Nitrosyl fluoride reacts with the hydrogen fluoride electrolyte to form very stable complexes (3).

Polarization curves were determined in each of the above systems with the objective of seeking an inter-relationship between polarization phenomena and the products formed on electrolysis.

Manuscript received Nov. 12, 1963.

Any discussion of this paper will appear in a Discussion Section to be published in the December 1964 JOURNAL.

REFERENCES

1. M. E. Runner, G. Balog, and M. Kilpatrick, *J. Am. Chem. Soc.*, **78**, 5183 (1956).
2. J. H. Simons, *This Journal*, **95**, 47 (1949).
3. S. Kongpricha and A. F. Clifford, *J. Inorg. Nucl. Chem.*, **18**, 270 (1961).
4. R. D. Dresdner and J. A. Young, *J. Am. Chem. Soc.*, **81**, 574 (1959).
5. J. H. Simons, U. S. Pat. 2,519,983, Aug. 22, 1950.
6. Cat. No. 83YX505J, Allied Radio Corporation.
7. H. H. Rogers, *Rev. Sci. Instruments*, **34**, 1440 (1963).
8. H. H. Rogers, *Rev. Sci. Instruments*, **34**, 250 (1963).
9. J. Burdon and J. C. Tatlow, in "Advances in Fluorine Chemistry," M. Stacey, J. C. Tatlow, and A. G. Sharpe, Editors, Vol. 1, p. 134, Academic Press, Inc., New York (1960).

Experimental

Apparatus.—The electrolytic cell and associated electrical equipment are fully described in the first paper (1) in this series. In addition, a stainless steel and Teflon vacuum line was used to collect and separate the products (Fig. 1). The system was also provided with storage cylinders and additional traps.

Procedure.—Referring to Fig. 1, hydrogen fluoride

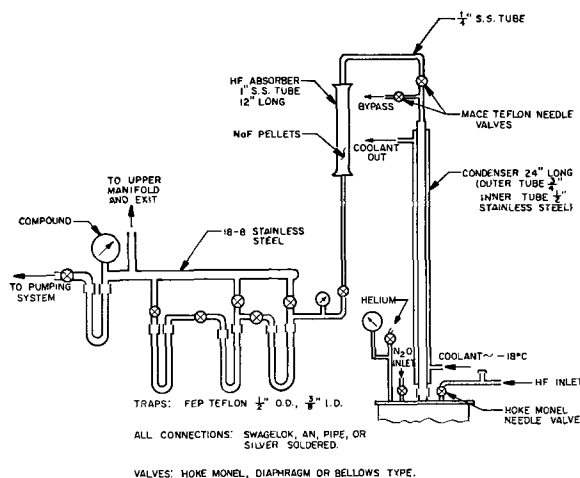


Fig. 1. Product handling equipment

(Matheson Company, minimum purity 99.9%) was added to the refrigerated cell as a liquid directly from the cylinder. Sodium fluoride (J. T. Baker Company, Reagent Grade), when used as a conductivity additive, was first dissolved in a small amount of hydrogen fluoride in a polyethylene bottle and then added to the electrolytic cell by means of a "T" in the inlet line. When anhydrous hydrogen fluoride was desired, the electrolyte was dried overnight by electrolysis using periodic current reversal (1). The products were identified by infrared analysis.

Hydrogen fluoride-nitrous oxide system.—The nitrous oxide (Matheson Company, 98.0% minimum purity) was added through an inlet valve in the cell cover; the gas was passed through the cell and condenser, and out the bypass valve to flush out all the helium, which had been used to prevent the entrance of moisture. After the bypass valve was closed, the cell pressure was permitted to rise to a maximum of 85 psig of nitrous oxide. This pressure was maintained for about one-half hour to ensure a saturated solution and then was reduced to atmospheric pressure by bleeding off the excess nitrous oxide. Any nitrous oxide remaining in the cell gas space was then purged with helium. The absorber (Fig. 1) removed any hydrogen fluoride which passed through the reflux condenser during electrolysis. A flow of about 30 cc/min of helium served to carry the products to the FEP Teflon traps which were cooled by liquid nitrogen. The products were separated from nitrous oxide by normal vacuum line techniques and were identified by their infrared spectra.

In this electrolysis, current was maintained constant at specific points over a range of 0.5–8.0 amp by a current regulator. The cell voltage was found to be between 5–8v depending on the current settings, temperature, etc. Cell temperatures (internal) varied between -8° to -22° . The length of runs varied from 1 to 3 hr. A porous Teflon divider (1/16-in. thickness, Porous Plastic Filter Company) was used in about half the runs to separate the anode and cathode compartments in the liquid phase only.

Hydrogen fluoride-nitrosyl fluoride system.—Electrolyses in the hydrogen fluoride-nitrosyl fluoride system were carried out in substantially the same manner described above. Since the hydrogen fluoride-nitrosyl fluoride system is a good electrical conductor, a conductivity additive was neither needed nor used. The nitrosyl fluoride prepared by the method of Seel (3), was added as a solution in hydrogen fluoride. Additional details which differ significantly from those described under the hydrogen fluoride-nitrous oxide system are: cell voltage, 5–11v; cell temperature, -4° to -16° ; mole ratios, hydrogen fluoride to nitrosyl fluoride, 16:1 to 35:1. The porous Teflon divider was used in all experiments in this system.

Results

The system, hydrogen fluoride-nitrous oxide.—The solubility of nitrous oxide (gas) in hydrogen fluoride (liquid) was determined as a part of this

study. Pressure measurements in this system showed that the solubility was adequate for synthetic purposes, although it was apparent that the products of the electrolysis would be contaminated with nitrous oxide. Henry's law constants (mole fraction/mm Hg) calculated from the experimental data, are 7×10^{-6} at -23° and 5×10^{-5} at -78° . The isotherms appeared to follow Henry's law throughout the range considered, indicating a lack of reaction between solute and solvent. This point was partially confirmed by rough electrical conductivity measurements which showed that an insignificant increase in conductivity occurs with the addition of nitrous oxide to hydrogen fluoride. Therefore, a conductivity additive (sodium or potassium fluoride) was used for all electrolyses in the hydrogen fluoride-nitrous oxide system.

Electrochemistry of the Hydrogen Fluoride-Nitrous Oxide System

Electrolysis of the hydrogen fluoride-nitrous oxide system yielded nitrogen trifluoride consistently. In addition, either oxygen difluoride or nitroxy fluoride (NO_3F) or both were generally formed. It appeared that the rate of formation of these latter products was greatest during the initial portion of the experiment. Varying the current during electrolysis did not appear to be significant in determining the nature of the products. Yields, based on current, of a typical experiment were: nitrogen trifluoride, 2%; oxygen difluoride, 2%; and nitroxy fluoride, 1%. The anodic weight losses during the electrolyses generally accounted for 50–80% of the current. Since the hydrogen fluoride had been thoroughly dried in two of the experiments in which oxygen-containing products appeared, it is apparent that they originated with the nitrous oxide.

Anodic and cathodic polarization curves were determined with respect to a platinum reference electrode (1) in the hydrogen fluoride-potassium fluoride and hydrogen fluoride-sodium fluoride systems before and after the addition of nitrous oxide, as well as after the electrolysis was concluded. These curves were reproducible in general form but varied from run to run with respect to potential regimes. Since the applied potential for a given current density was highly reproducible in all experiments, it was concluded that the platinum electrode did not function effectively as a poised-type reference electrode in the hydrogen fluoride-sodium fluoride system. It did, however, clearly define at which electrode the phenomena occurred.

The applied polarization curves were generally reproducible, and it was reasonable to concentrate on the lower portion of the curve to highlight the basic processes which occurred in this system. Linear plots of current density vs. applied potential in the low current density regions (i.e., up to 2 ma/cm² which corresponds to a current of 0.16 amp) yielded a consistent value for the decomposition voltage of dry hydrogen fluoride at nickel electrodes, namely, 3.9v (Fig. 2). A minimum current of 0.05 ma/cm² was chosen arbitrarily as that corresponding to decomposition. The results were de-

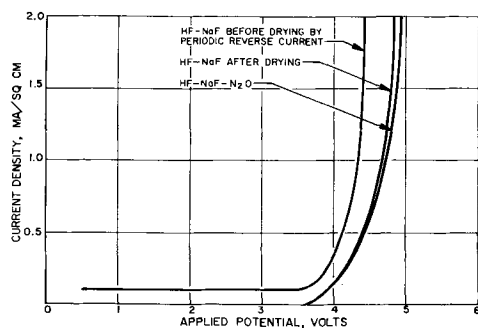


Fig. 2. Typical behavior of potential in low-current region

rived from several experiments in both the hydrogen fluoride-sodium fluoride and hydrogen fluoride-potassium fluoride systems. The shape and potential characteristics of the applied polarization curves obtained after the nitrous oxide was added and, after the electrolysis experiment was concluded, were virtually indistinguishable from those obtained in the absence of nitrous oxide.

Electrolysis in the hydrogen fluoride-nitrosyl fluoride system.—Electrolysis in the hydrogen fluoride-nitrosyl fluoride system yielded only reduction products of the NO^+ ion with one exception; oxygen difluoride and nitroxy fluoride were products of one experiment where the hydrogen fluoride had been only partially dried. Not even traces of these compounds were found in those experiments where the hydrogen fluoride had been dried using periodic current reversal (1).

According to Seel (3), the electrolysis of hydrogen fluoride-nitrosyl fluoride solutions in a cell containing a diaphragm, which was capable of separating the gaseous products, should result in nitric oxide and fluorine as products.

In our cell, where no separation of the gaseous products was attained, the spontaneous reaction of nitric oxide and fluorine to give nitrosyl fluoride would be expected; the latter would, no doubt, dissolve in the electrolyte. The nitric oxide which was found as a product was probably a result of insufficient fluorine available from the anodic reaction since a substantial part of the current was used for the dissolution of the nickel anode.

The synthesis of nitrous oxide at the cathode is readily explained. It would be expected that the NO^+ ion would reduce directly to nitric oxide, although, with a sufficiently high cathode potential, reduction to nitrous oxide could also occur. The polarization curves (Fig. 3) which were taken before the start of the run show clearly that a second reaction took place at the cathode at currents over 1 amp.

Discussion

Both the thermal fluorination (2) of nitrous oxide and the electrolysis of the hydrogen fluoride-nitrous oxide system resulted in the formation of nitrogen trifluoride. However, while nitrosyl fluoride was a product of the thermal reaction, oxygen difluoride and nitroxy fluoride were generally formed as a result of the electrolysis. The electrolysis of a hydrogen fluoride-nitrosyl fluoride solution produced neither oxygen difluoride nor nitroxy

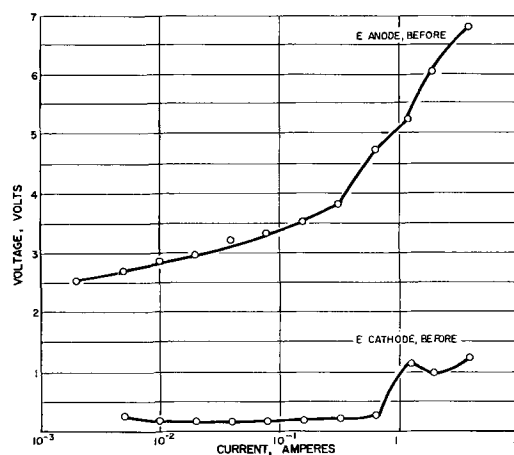
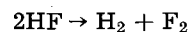


Fig. 3. Polarization curve HF-FNO

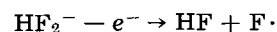
fluoride (with dry hydrogen fluoride). It is, therefore probable that the formation of oxygen difluoride and nitroxy fluoride in the electrolysis of the hydrogen fluoride-nitrous oxide system was not the result of further electrolysis of any nitrosyl fluoride originally formed as an electrolysis product.

Representative polarization curves for the hydrogen fluoride-sodium fluoride system with and without added nitrous oxide are shown in Fig. 2. The residual current present before the solution was electrolytically dried was due to water and other impurities in the hydrogen fluoride which were removed by electrolytic drying. Such behavior is typical of systems with trace impurities. After drying, there was no residual current noted and the decomposition potential was found to be reproducible.

Since the addition of nitrous oxide does not affect the polarization characteristics of the cell, it is reasonable to conclude that there is a basic electrochemical reaction which is common to both systems, namely, the decomposition of hydrogen fluoride



The anodic electrochemical reaction common to both systems appears to be



It is proposed that additional reactions were a result of the combination of the electrolytically generated "active" fluorine with nitrous oxide. Since the concentration of products which resulted from such a postulated reaction was found to be low, most of the active fluorine either formed fluorine or directly attacked the nickel anode. The current equivalent of the weight loss during electrolysis of hydrogen fluoride-nitrous oxide system is not significantly different from that derived from electrolysis of hydrogen fluoride-sodium fluoride. The bulk of the current utilized in the electrolysis in the hydrogen fluoride-sodium fluoride system can be related directly to the weight loss at the anode. While the anodic dissolution process might not have been a direct electrochemical reaction, it can be related to the amount of fluorine generated, assum-

ing that the nickel was directly attacked by the active fluorine.

Acknowledgment

The authors are indebted to the Office of Naval Research for their generous support of this research under Contract Nonr 1818(00).

Manuscript received Nov. 12, 1963.

Any discussion of this paper will appear in a Discussion Section to be published in the December 1964 JOURNAL.

REFERENCES

1. H. H. Rogers, S. Evans and J. H. Johnson, *This Journal*, **111**, 701 (1964).
2. F. D. Marsh, U. S. Pat. 3,032,400 May 1, 1962.
3. F. W. Seel, W. Birnkraut, and D. Werner, *Ber.* **95**, 1264 (1962).

Hydrogen Evolution and Surface Oxidation of Nickel Electrodes in Alkaline Solution

J. L. Weininger and M. W. Breiter

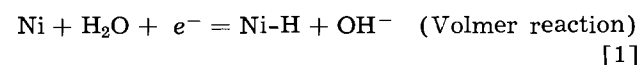
Research Laboratory, General Electric Company, Schenectady, New York

ABSTRACT

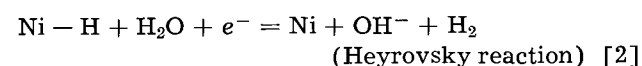
The electrochemical processes which occur on nickel electrodes in 4N KOH during a slow-speed anodic potential sweep between -300 and $+1500$ mv were studied. Tafel plots for hydrogen evolution were determined under different conditions, and the impedance was measured at 100 cps as a function of potential. The results are interpreted in terms of the adsorbed species. It is confirmed that hydrogen evolution between -300 and -100 mv is controlled by the discharge step of water molecules (Volmer reaction) and that the coverage with electrochemically active hydrogen atoms is small in this region. Prior to the formation of $\text{Ni}(\text{OH})_2$ an adsorbed layer of OH-radicals appears to be formed.

Recently we studied the anodic formation of $\text{Ni}(\text{OH})_2$ and NiOOH on different crystal planes of nickel and polycrystalline nickel in alkaline solution (1). It was shown that the formation of a surface film of hydroxide depended to some extent on the crystal structure of nickel. The region of special interest extended to anodic potentials of about 800 mv (with respect to a hydrogen electrode in the same solution). In this region a few molecular layers of hydroxide were formed and removed without drastically affecting the underlying structure, which on further oxidation was strongly disordered. A more detailed study of the nickel electrode, extending from -300 mv to about 1500 mv, appeared desirable in order to obtain information about the adsorbed species and reactions which occur in this potential range. Experimental results are here presented and interpreted in terms of cathodic hydrogen evolution, hydrogen adsorption, hydroxide adsorption, and nickel hydroxide formation.

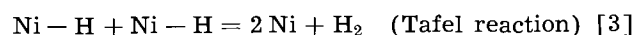
Hydrogen evolution and adsorption have been exhaustively studied and discussed (2), primarily for mercury and platinum metals but also, among other metals, for nickel in alkaline solution. Lukovtsev, Levina, and Frumkin (3) attributed the overvoltage to a hindered discharge step



except possibly in the most dilute alkaline solution. They suggested that reaction [1] is followed by the less hindered electrochemical desorption



The anodic current-potential curves showed a large increase of potential with current, as in the case of a diffusion-limited current. These curves were interpreted as resulting from the simultaneous oxidation of molecular hydrogen (reaction [2]) and of the nickel electrode. Later Frumkin (4) suggested that reaction [1] is rate-determining on the greater part of the surface, but that on a small part of the surface hydrogen evolution is limited by recombination



Even on those sites where reaction [1] is rate-determining the rate of removal of hydrogen atoms from the surface is not infinitely great. Bockris and Potter (5) confirmed a rate-determining discharge step. Devanathan and Selvaratnam (6) determined the hydrogen coverage, θ , experimentally as a function of cathodic current density. They arrived at a rate-determining Volmer reaction, followed by the less hindered reaction [3] without distinguishing different sites on the surface. Makrides (7) recently placed more emphasis on surface states existing on nickel electrodes (at least in 0.1N NaOH solution) which result from the pretreatment and history of the electrode. He concluded that the discharge step is rate-determining only on surfaces in an "initial" state with high affinity for hydrogen adsorption. Anodic-cathodic cycling produced a steady state for which the exchange rates of the discharge and combination steps were about equal, so that there was no single rate-determining step.

Oxygen evolution on nickel electrodes in alkaline solution may be accompanied by adsorption proc-

esses (of intermediate OH^- and O_2H^- , and of atomic and molecular oxygen) and by the formation of surface oxides. This has been discussed with respect to the surface coverage on inert electrodes by Ruetschi and co-workers (8). The presence of other adsorbed species during hydrogen evolution has been considered possible but otherwise has been largely ignored. On an active electrode of Ni in alkaline solution, because of the closeness of the electrode potential of $\text{Ni}(\text{OH})_2$ formation ($E^\circ = 0.106\text{v}$) to that of H_2 evolution, it is feasible that some overlap may exist of H and OH adsorption. This is taken into consideration in the evaluation of the present experimental results.

Similar impedance measurements on sintered nickel electrodes have also been reported by Kandler, Roemer, and Häusler (9).

Experimental

As in the previous work (1) current-potential curves were determined by impressing potentiostatically a linearly increasing potential. The potential sweep extended from -300 to 1500 mv (potentials were measured and are given against a hydrogen electrode in the same solution as the test electrode). The previous d-c procedures were followed with the following exceptions:

A lower rate of potential increase, 5 mv/sec, was used.

The nickel electrodes were maintained at -300 mv for 8 min before applying the initial as well as subsequent sweeps in order to remove any previously formed oxide.

Experiments were performed in solutions which were saturated with hydrogen or argon, respectively, and were stirred by continuous flow of these gases.

In addition to the circuit used in d-c measurements, Fig. 1 shows schematically the a-c instrumentation. The added units G, S, and A are shown in the dashed box of the figure. An a-c signal of 3 mv, generated by the oscillator G, is added to the signal from the function generator, F.G. Both sig-

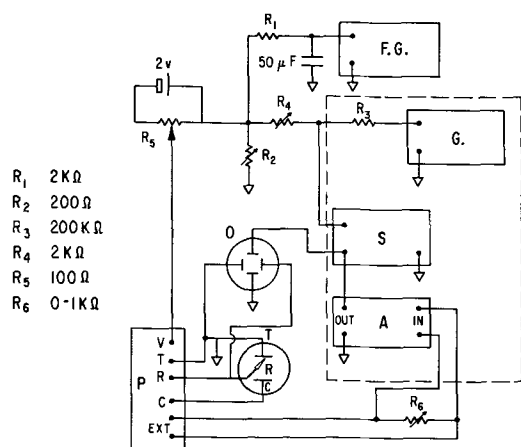


Fig. 1. Schematic circuit diagram: A, Tektronix type D plug-in unit in power supply used as pre-amplifier; G, Hewlett-Packard oscillator, type 200CD; S, Solartron-Resolved component indicator, Model VP 250; O, Tektronix 502 double beam oscilloscope; FG, Exact Electronics Function Generator, type 250; P, Wenking potentiostat with connections for V, applied voltage; T, test electrode; R, reference electrode; C, counter electrode; EXT, output.

nals across R_2 are applied to the test electrode by a Wenking potentiostat, P. It was found that the potentiostat applied a-c signals up to 3000 cps without introducing a noticeable phase shift. Therefore, the a-c signal across $(R_2 + R_4)$, instead of that between test and reference electrodes, was used as a reference signal of the a-c voltage for the Resolved Component Indicator, S, Model No. VP 250 manufactured by Solartron Laboratory Instruments Ltd. The latter allows a direct reading of the in-phase (ohmic) and out-of phase (here capacitive) components of the a-c current through R_6 . The amplifier, A, which was used with a gain of 50 and does not introduce a phase shift, amplifies the a-c voltage across R_6 . The circuit requires a ground-free input for this amplifier. The indicator is selective with respect to the frequency of the reference voltage. The oscilloscope, O, registers the amplitude of the a-c current flowing through the cell as a function of electrode potential.

As before, current-potential curves were recorded oscillographically. Two oscilloscopes were used in parallel. The input resistance of the combination was 5 megohms, using attenuator probes. On one scope, the current-voltage characteristics were recorded on an expanded voltage scale in the region -300 - 150mv . These data were used to construct Tafel plots because it was found that in this potential range Tafel plots did not depend on sweep rates at rates less than 10 mv/sec. The other oscilloscope covered the entire d-c range from -300 to 1500 mv. Its traces established the qualitative nature of the anodic reactions and, quantitatively, the thickness of hydroxide films (1).

The electrolyte was a solution of $4N$ KOH. In a few experiments, intended to test the effect of pH on the current-potential curves, the alkali concentration was varied from $0.001N$ to $1.0N$ NaOH with NaClO_4 added as supporting electrolyte.

Results

D-c measurements.—As in the previous study (1) a drastic change of the current-potential curves was observed between the first potential sweep, on a freshly polished surface, and subsequent sweeps. The change in the electrodes, presumably a

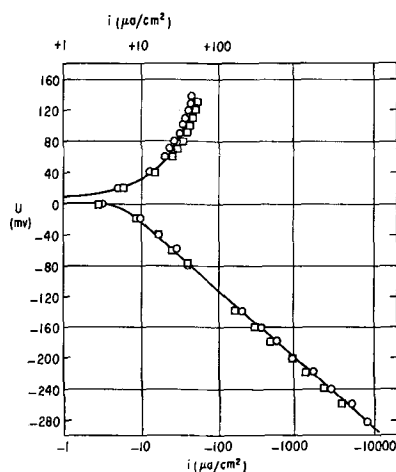


Fig. 2. Tafel plots for Ni electrodes with (100) plane in $4N$ KOH solution on second sweeps. Solution saturated with argon, $\square\square$, hydrogen, $\circ\circ$.

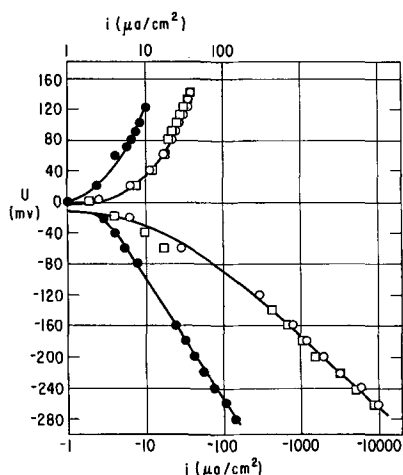


Fig. 3. Tafel plots for polycrystalline Ni electrodes in 4N KOH solutions saturated with argon: first sweep, ●●●; second sweep, ○○○; hydrogen: second sweep, □□□.

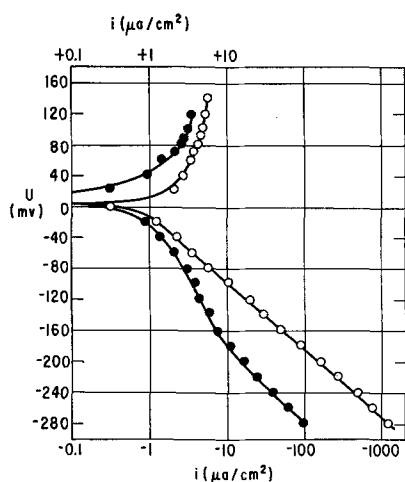


Fig. 4. Tafel plots for polycrystalline Ni electrode in 4N KOH after pretreatment with chromic acid: first sweep, ●●●; second sweep, ○○○.

disordering of the surface structure, took place between the first and second sweep.

Figures 2, 3, and 4 are semilogarithmic current-potential plots which were obtained for different nickel electrodes in 4N KOH solutions. Cathodic currents and potentials are plotted negatively. These curves were obtained by enlarging the oscillograms photographically by about 3X and then transcribing the curves point-by-point from the linear to the semilog plot. The experimental error of these measurements was $\pm 5\%$.

Within the limits of experimental error the nickel crystal planes (100), (110), and (111) showed the same electrode characteristics on "second" sweeps. Figure 2 is the Tafel plot for the (100) crystal on second sweeps in argon and hydrogen-saturated solutions. No appreciable difference was found between these experiments.

Figure 3 shows data obtained on first and second sweeps for polycrystalline nickel electrodes. In all cases the overvoltages and the Tafel constant b , e.g., 152 mv, were always larger on the first sweep than the corresponding reproducible values of b and of overvoltages on later sweeps. For later sweeps, b

was 89 to 93 mv for all electrodes; the exchange current density was about $10 \mu\text{A}/\text{cm}^2$.

In the experimental procedure, the electrodes were chemically polished, washed, and cathodically polarized. Since in some instances other workers used a chromic acid treatment instead of the chemical polish, experiments with such a procedure were also performed. Thus, Fig. 4 shows the Tafel plots for a polycrystalline nickel electrode in a first and second sweep, for which chemical polishing was replaced by chromic acid treatment. The plot for the first sweep shows a nonlinearity, resulting possibly from another cathodic reaction introduced by chromate ions. The second sweep gives the usual Tafel slope but the current densities are reduced by nearly an order of magnitude, compared to chemically polished electrodes during the second sweep, indicating the passivating effect of the chromic acid treatment.

The two curves of Fig. 2 show the same behavior during the second sweep in solutions saturated with either Ar or H₂. Likewise, there is no difference due to the different saturated solutions in the anodic behavior of the nickel electrodes, for which Fig. 5 is an example. This figure shows traces of the I-U curves during the first and second sweeps on a (110)

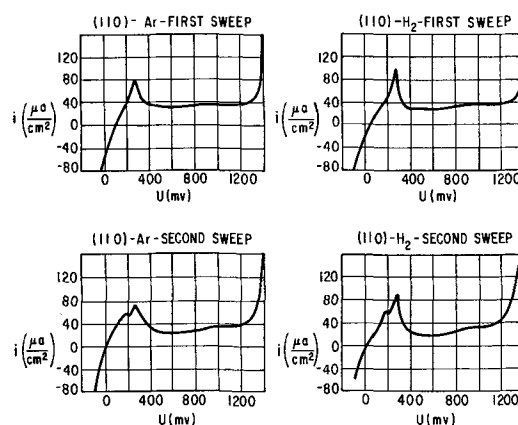


Fig. 5. Current-potential curves for single potential sweeps at 5 mv/sec on (110) crystal in 4N KOH saturated with Ar or H₂ as indicated.

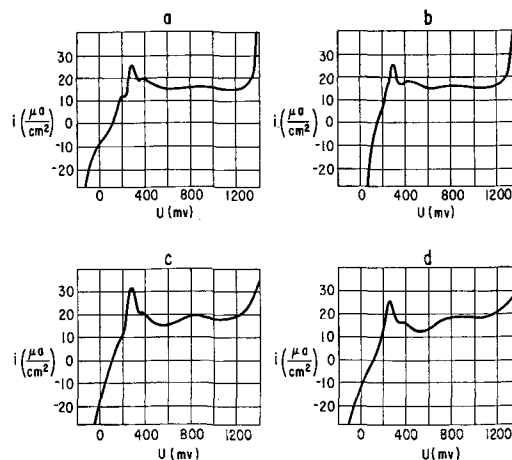


Fig. 6. Current-potential curves for the first sweep on polycrystalline Ni electrode in different solutions: a, 1.0N NaOH, 5N NaClO₄; b, 0.1N NaOH, 5N NaClO₄; c, 0.01N NaOH, 5N NaClO₄; d, 0.001N NaOH, 5N NaClO₄.

crystal plane in which the changes between successive sweeps can be noticed. The location of the peak, attributable to the formation of $\text{Ni}(\text{OH})_2$, differs from that given in ref. (1). This is due to the slower sweep rate (5 mv/sec vs. 110 mv/sec) and to the higher concentration of the electrolyte (4N vs. 0.2N KOH) in the present experiments.

The effect of changing pH is given in Fig. 6, which shows initial ("first" sweep) oscillographic current-potential traces on a polycrystalline nickel electrode in 5M NaClO_4 , with different additions of NaOH. The hydroxide concentration was varied by a factor of 1000 without affecting the location of the peak of nickel hydroxide formation. Since in each case the potentials were measured against a hydrogen electrode in the same solution as the nickel electrode, there was, therefore, an effective change in potential of about 59 mv on the potential scale, as expected for the $\text{Ni}(\text{OH})_2$ formation.

A-c measurements.—Most of the a-c measurements were made with polycrystalline electrodes because the behavior of the different planes is very similar for second sweeps. The values of C_p and $(1/R_p)$, calculated from direct readings, at 50 mv intervals of the d-c sweep, on the resolved component indicator are shown in Fig. 7 and 8 for argon stirring. These measurements, resulting from the superposition of a 3 mv peak-to-peak a-c voltage on the d-c voltage have an experimental accuracy of $\pm 5\%$. Since the difference in the a-c characteristics between the first and later sweeps is less drastic than in d-c measurements the more gradual changes are illustrated by showing the first, second, and third sweeps. Within the experimental limits, the same results were obtained with hydrogen stirring. They are, therefore, not shown separately.

The point by point plots of Fig. 7 and 8 show calculated values which may obscure some of the

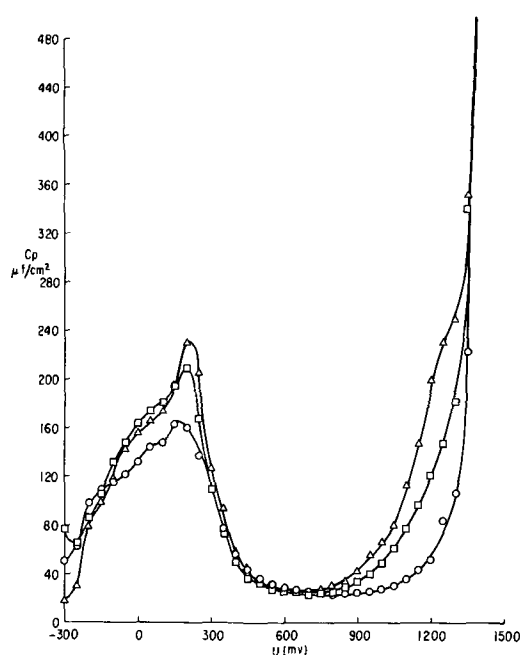


Fig. 7. Capacity, C_p , as a function of potential for polycrystalline Ni electrode in 4N KOH saturated with Ar, measured at 100 cps; \circ , first sweep; \square , second sweep; \triangle , third sweep.

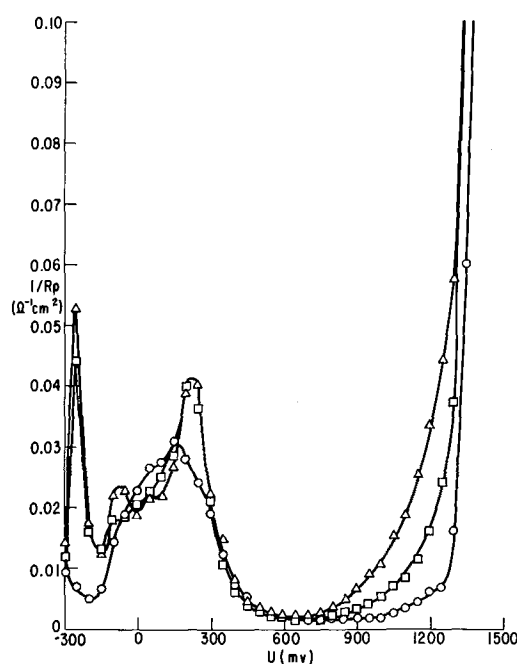


Fig. 8. Parallel conductance ($1/R_p$) as a function of potential for polycrystalline Ni electrode in 4N KOH solution saturated with Ar, measured at 100 cps; \circ , first sweep; \square , second sweep; \triangle , third sweep.

finer structure in the cathodic region. That this is not a serious problem is shown in Fig. 9, which is the continuous recording of the amplitude of the a-c current, $i_{a.c.}$, corresponding to the third sweep of Fig. 7. Qualitatively, these curves give the same information as Fig. 7 and 8. The continuous oscilloscope trace of $i_{a.c.}$ is very useful in locating peaks of the C_p and $(1/R_p)$ curves.

Discussion

It was the purpose of this study to elucidate the intermediate steps in the anodic formation of $\text{Ni}(\text{OH})_2$ on nickel and to gain some understanding of the surface changes that take place on cathodic reduction of a freshly prepared and oxidized nickel electrode. This electrode is very sensitive to its treatment prior to oxidation (7). Consequently, the electrode had to be studied by starting the potential sweeps at cathodic potential of -300 mv, where we expected that the oxide or hydroxide would be removed cathodically.

D-c measurements.—The current-potential curves obtained from d-c measurements, Fig. 3 through 5, point out the marked difference between the first

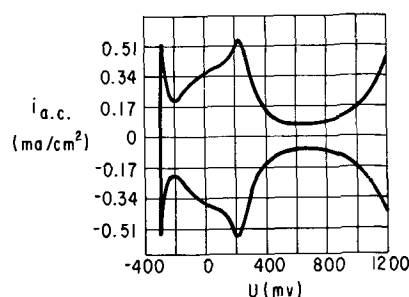
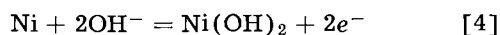


Fig. 9. Alternating current, $i_{a.c.}$, as a function of potential for polycrystalline Ni electrode in 4N KOH solution, at 100 cps. This is the third sweep, corresponding to impedance data of Fig. 7 and 8.

and subsequent potential sweeps on nickel electrodes. This behavior was previously found for anodic oxidation (1) and is now also shown for cathodic hydrogen evolution.

Practically the same current-potential curves were obtained for solutions stirred with hydrogen or with argon. This means that the steep rise of potential with current at potentials between 0 and +120 mv cannot be attributed to an anodic limiting current density of the Tafel reaction (3). This was concluded earlier (3) on the basis of similar experiments. An estimate based on the experimental precision of our measurements in the vicinity of zero overpotential leads to a contribution of less than 1 $\mu\text{a}/\text{cm}^2$ of the anodization of molecular hydrogen to the net anodic current density. The present value of the Tafel constant, $b=90$ mv, for hydrogen evolution, corresponds to those reported by other workers (3, 4, 10). The present exchange current density $i_0=10$ $\mu\text{a}/\text{cm}^2$, extrapolated from the cathodic Tafel plot, is smaller than that found by Devanathan and Selvaratnam (6), it is about the same as that of Makrides (7), and it is larger than the values given by Bockris and Potter (5), and by Lukovtsev *et al.* (3). Our d-c measurements, *i.e.*, the magnitudes of the Tafel slope and exchange current, and the relatively small values of the capacity C_p between -300 and -100 mv in Fig. 6 suggest that reaction [1] is the rate-determining step in this potential range, in agreement with the above-mentioned conclusions of others.

The pH dependence of the peak potential, shown to be about 59 mv/decade of hydroxide concentration, is in agreement with the reaction



It is likely that this reaction includes the anodic formation of an adsorbed layer of hydroxyl radicals as a first step. Evidence for this reaction will also be adduced from a-c measurements.

The abnormally high Tafel slope of the first sweep corresponds to a similar observation of the increase of hydrogen overvoltage on iron electrodes in alkaline solutions, which Frumkin (4) attributed to the presence of oxide on the iron electrode. By analogy, our results during first sweeps might be interpreted as being due to the influence of some oxide remaining from the chemical polishing of the electrodes. Such traces of oxide may not be removed by electrochemical reduction (12).

In a comparison with our previous d-c measurements (1), it should be noted that in the present experiments a very slow rate of potential sweep (5 mv/sec) was chosen in order to be able to make direct-reading a-c measurements. This procedure results in accurate a-c data, but the slow sweep rate introduces complications in d-c measurements due to possible side reactions, which were absent at the faster sweep rate of 110 mv/sec used previously.

A-c measurements.—With regard to the a-c measurements, inspection of the C_p - U curve of Fig. 7 shows a minimum of 22 $\mu\text{F}/\text{cm}^2$ in the region of +600 to +800 mv. This C_p value can be identified as the double layer capacity. Since it does not in-

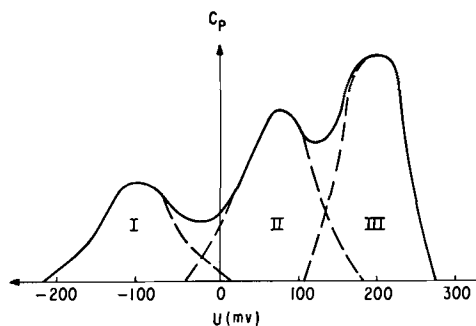


Fig. 10. Schematic capacitance-potential diagram in the low potential region for idealized Ni electrode in KOH.

crease on successive sweeps, it is concluded that the experimental procedure did not increase the surface area. The higher C_p values at more anodic and cathodic potentials are faradaic pseudocapacitances due to electrode reactions. The anodic part rises steeply to values of 500 to 550 $\mu\text{F}/\text{cm}^2$ at 1450 mv corresponding to the formation of the higher oxide, NiOOH. The region of lower potential is of greater interest because different adsorption processes and the formation of Ni(OH)₂ take place there. There are three distinct events which occur between -300 mv and +300 mv and which cause an increase in C_p with maxima at approximately -100, +100, and +200 mv. The exact locations of these peaks in the C_p vs. U curves depend on the experimental conditions, especially the rate at which the potentiostatically controlled voltage is varied. Since the reactions leading to the capacity peaks overlap each other to some extent, this obscures the representation of C_p as a function of U . The region of low potential in Fig. 7 can be schematically drawn as in Fig. 10 where the solid line, representing C_p , is the sum of three processes. These are drawn arbitrarily except for process III, which will be identified as the formation of Ni(OH)₂, and is therefore assumed to start closely to the thermodynamic standard potential of 106 mv. Processes I and II are attributed by us to electrochemical formation and removal of adsorbed layers of hydrogen atoms and hydroxyl radicals.

Frumkin (4) has interpreted measurements of hydrogen overvoltages on nickel in alkaline solutions (3) as indicating the existence of sites with different free energy of activation for the reactions [1] to [3]. Past and Jofa (11) in work on the same system have concluded from capacity data that the electrochemically active, *i.e.*, relatively weakly bonded, hydrogen atoms covered only a small fraction of the total surface. Whether or not the remaining surface was covered with strongly bonded hydrogen could not be determined. More recently, Devanathan and Selvaratnam (6) have quantitatively determined the fractional coverage of the Ni electrode by hydrogen atoms. They assumed that only one hydrogen species was present and that this was the electrochemically active one.

Process II can either be caused by a Volmer-type reaction involving strongly bound H atoms, or more likely, by a reaction between OH⁻ and adsorbed OH. The experimental data in Fig. 6 offer some evidence in favor of OH adsorption. The small hump which

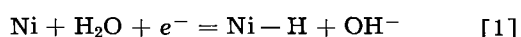
appears before the large peak of Ni(OH)₂ formation disappears gradually with decreasing concentration of OH⁻. The latter possibility is not taken into account by Devanathan and Selvaratnam, and makes their calculated fractional surface coverage (0.045 to 0.386 with overvoltages from -10 to -186 mv) doubtful.

Reaction III and its corresponding peak in the C_p-U curve is clearly due to the formation of Ni(OH)₂. This process can be estimated to lead to a thickness of two molecular layers on the basis of the d-c current-voltage measurements of Fig. 5.

Comparison of the (1/R_p) vs. U curve of Fig. 8 with the C_p vs. U curves of Fig. 7 shows it qualitatively to be the same, except at -300 mv where there is an additional peak in the (1/R_p) curve. This is due to a contribution to the impedance term by the increase of the ohmic component of process I at large overvoltages. Otherwise, the correspondence of the behavior of pseudocapacitance and pseudoconductance (1/R_p) confirms that at the frequency of 100 cps, chosen for these experiments, no extraneous electrode processes occur which would obscure processes discussed above.

In conclusion, the electrode processes discussed above can be interpreted as successive steps of cathodic hydrogen evolution, anodic formation of adsorbed hydroxide (or anodic oxidation of adsorbed hydrogen), and Ni(OH)₂ in the following approximate potential ranges:

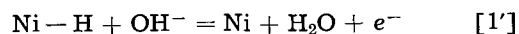
-300 to -100 mv: hydrogen evolution involving weakly bonded H atoms with the rate-determining step:



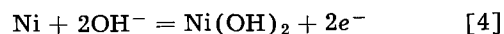
-100 mv up: Electrochemical adsorption of hydroxide:



This may be accompanied or even may be replaced by oxidation of firmly adsorbed H atoms:



+100 mv up: Formation of Ni(OH)₂:



where reaction [1'] is the reverse of reaction [1].

Manuscript received Aug. 4, 1963; revised manuscript received Nov. 30, 1963. This paper was presented at the New York Meeting, Sept. 30-Oct. 3, 1963.

Any discussion of this paper will appear in a Discussion Section to be published in the December 1964 JOURNAL.

REFERENCES

1. J. L. Weininger and M. W. Breiter, *This Journal*, **110**, 484 (1963).
2. See e.g., K. J. Vetter, "Elektrochemische Kinetik," Ch. IV, Springer Verlag, Berlin (1961).
3. P. Lukovtsev, S. Levina, and A. Frumkin, *Acta Physicochim. U.S.S.R.*, **11**, 21 (1939).
4. A. Frumkin, *Disc. Faraday Soc.*, **1**, 57 (1947).
5. J. O'M. Bockris and E. C. Potter, *J. Chem. Phys.*, **20**, 614 (1952).
6. M. A. V. Devanathan and M. Selvaratnam, *Trans. Faraday Soc.*, **56**, 1820 (1960).
7. A. C. Makrides, *This Journal*, **109**, 977 (1962).
8. P. Ruetschi, J. Bockermann, and R. Amlie, *ibid.*, **107**, 325 (1960).
9. L. Kandler, D. Roemer, and E. Häusler, *Electrochim. Acta*, **8**, 233 (1963).
10. F. P. Bowden and E. K. Rideal, *Proc. Royal Soc.*, **A120**, 80 (1928).
11. W. E. Past and S. A. Jofa, *Zhur. Fizi. Khim.*, **33**, 1230 (1959).
12. K. E. Heusler, Private communication.

Direct Current Measurement of Fused Salt Conductivity: Molten Nitrates

Lowell A. King¹ and F. R. Duke²

Institute for Atomic Research and Department of Chemistry, Iowa State University, Ames, Iowa

ABSTRACT

The practicability of a direct current technique for determination of fused salt specific conductivity has been demonstrated. Simple conductivity cell design and electrical circuits minimized many of the problems associated with alternating current techniques. Experimentally determined cell constants were very nearly those calculable from cell geometry. The direct current conductivities of LiNO₃, NaNO₃, KNO₃, and their binary mixtures were determined. The results were in agreement with published alternating current values, where available.

The high specific conductivity of most fused salt systems complicates the usual alternating current (a-c) measurement techniques. In order to achieve sufficiently high total resistance in the conductivity cell, it is necessary to resort either to a very long current path or to a small diameter cell. Since temperature control is difficult for a large cell, glass

capillaries, filled with fused salt, typically are used. Glass itself becomes relatively conductive at high temperatures and may introduce significant error in conductivity measurements. This is especially true for dipping cells. Furthermore, any attack of the cell wall by a melt will introduce a greater error if a small diameter cell is used than if a larger cell is employed.

Direct current (d-c) conductivity measurement techniques permit one to avoid the use of capillary

¹ Present address: Department of Chemistry, U.S. Air Force Academy, Colorado

² Present address: Department of Chemistry, Agricultural and Mechanical College of Texas, College Station, Texas.

tubes and allow the use of quite simple electrical circuits. On the other hand, two potentially serious problems exist. Conveniently prepared and used reversible electrodes must be available to measure voltage drop in the conductivity cell. Such electrodes are not necessarily easily devised for use in fused salt systems. Furthermore, the cell design must be such that no significant potential gradient appears across the surface of the probe electrodes, or an apparent cell current dependence of conductivity will be observed.

A few studies of aqueous solution d-c conductivities have been performed. Gunning and Gordon (1) reviewed the earlier literature and gave a general discussion of the problems associated with probe electrode design. It appears quite clear that at least for solutions of highly dissociated, nonhydrolyzed salts, d-c conductivities are not sensibly different from a-c conductivities.

Very little work has been performed on fused salt d-c conductivities. Grantham and Yosim (2) have compared a-c and d-c conductivities of various Bi-BiI₃ melts and found agreement to within 0.1%. They used a capillary cell with bare tungsten electrodes. The most recent work other than that of Grantham and Yosim, was done by Poincaré (3) in 1890. His results showed considerable scatter and were often in serious disagreement with a-c values which have been published since.

The systems chosen in this research to demonstrate the utility of the d-c technique in fused salts were LiNO₃, NaNO₃, KNO₃, and binary mixtures of these salts. Alternating current conductivities of most of these systems are well known and will be compared below with the findings of the present work.

Experimental

Materials and equipment.—"Baker analyzed" reagent AgNO₃ and Fisher certified reagent KCl were used without further purification. "Baker analyzed" reagent LiNO₃, NaNO₃, and KNO₃ were treated in the following manner: The dried salts were weighed, mixed if appropriate, then melted, and allowed to stand molten for 12 to 24 hr. To insure good mixing, the binary nitrate melts were thoroughly stirred for at least 1 hr while molten. Each melt was filtered through a medium or fine porosity sealing tube and allowed to cool in small porcelain crucibles. The resulting salt pellets were stored in a Mg(ClO₄)₂-charged desiccator before use.

Conductivity water for the KCl standardizing solution was prepared by passing tap distilled water through a Barnstead "Bantam" demineralizer column.

A 12-in. Marshall tube furnace, mounted vertically, was used to heat the conductivity cells. The furnace was provided with eight taps on the heater winding, across which shunts could be placed to maintain any desired temperature gradient along the axis of the furnace cavity. Near 280°C, the gradient across the voltage drop region of the conductivity cell was 0.2°. This gradient increased to 1.6° at a furnace temperature near 415°. Furnace temperature was maintained by a Bristol controller.

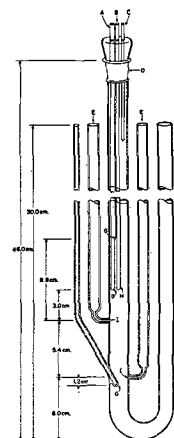


Fig. 1. Typical conductivity cell. A, 5 mm ID dual thermocouple well; B, 3 mm ID thermocouple well; C, 5 mm ID electrode access port; D, 29/42 standard taper on 17 mm ID central tube; E, 8 mm ID side-arms; F, 13 mm ID tube; G, H, thermocouple locations; I, 1 mm diam holes leading to side-arms.

Any given cell temperature was held constant to within less than a degree.

A typical Pyrex conductivity cell is shown in Fig. 1. Direct current was passed through the main channel of the U-tube and the voltage drop between points I was measured by reference electrodes in the side arms. The current-supplying electrodes were platinum wire helices. Provision was made for the immersion of four thermocouples in the melt. One thermocouple (at point H) led to the controller and the other three (at points G) were used to determine salt temperature in the voltage drop region.

Cell constants were determined at $25.00 \pm 0.02^\circ$ from the d-c conductivity of 1-demal KCl, prepared according to the specifications of Jones and Bradshaw (4). Beckman Model 39270 calomel electrodes were used in the side-arms to measure the voltage drop. Cell constants were corrected for the thermal expansion of Pyrex.

Silver-silver nitrate electrodes were used in the side arms to register the potentials developed across the voltage drop region in all experiments on fused salts. These electrodes consisted of small Pyrex tubes, open at the top and terminating in thin-walled bubbles through which electrical contact to the melt was attained. The electrodes were partially filled with a solution 10% by weight AgNO₃ in equimolar NaNO₃-KNO₃. Silver wires dipped into the silver nitrate solutions and extended out the tops of the tubes. Similar electrodes have been described by Inman (5).

The principal features of the electrical circuits employed are shown in Fig. 2. Direct current was drawn from a 12v storage battery bank or from a constant current source. Current control devices are not shown in the figure. Current was supplied to the conductivity cells through a Gray Instrument Company calibrated 10.003 ohm precision resistor. The 500 and 25 ohm variable resistors (Beckman Helipots) constituted a potentiometer circuit for measuring voltage drop across the 10.003 ohm resistor. In practice, current was adjusted such that for a given Helipot setting, depression of the tap

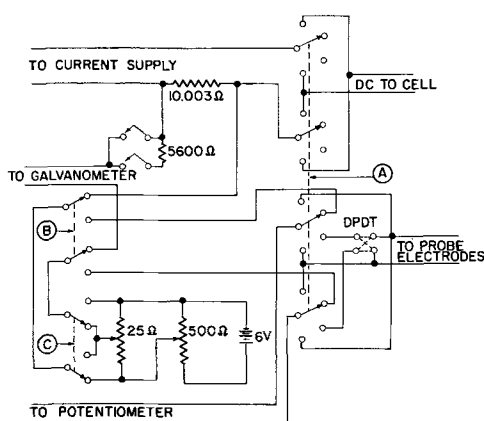


Fig. 2. Electrical circuits. A, Polarity switch; B, calibrate/operate switch; C, current range switch.

switches caused no deflection in a Leeds and Northrup Type 2420-A galvanometer.

A given Helipot setting provided for two current values, selected by the "current range switch." The Helipot could be set for any desired cell current by calibration with a Leeds and Northrup K-3 potentiometer. Such calibration was accomplished by appropriately positioning the "polarity switch" and the "operate/calibrate switch." When a Leeds and Northrup Type 2430-A galvanometer (attached to the K-3 potentiometer) showed no deflection, the number of millivolts with which the K-3 potentiometer was set divided by 10.003 was numerically equal to the number of milliamperes of cell current for which that given Helipot setting was adjusted.

The two lower gangs of the "polarity switch" connected the side-arm electrodes to the K-3 potentiometer. Electrode polarity was automatically changed as cell current polarity was changed. Provision was also made for measuring the potential difference between the side-arm electrodes when no current was flowing through the cell. Such a provision made possible a convenient check on polarization and on the eventual deterioration of the side-arm electrodes.

Procedure.—Fused salt and 1-demal KCl conductivities were measured in very nearly the same manner. The conductivity cell was charged with the liquid under study and the probe and working electrodes inserted. Once thermal equilibrium was reached conductivity measurements were commenced. Current was passed through the cell in one direction and the potential difference between the side-arm electrodes was recorded. Then the cell current was reversed and the new potential difference was noted. The probe electrode potential difference at zero current was measured before and after each of these two operations. The cycle was repeated at some new cell current value. Because two galvanometers and potentiometric circuits were available (see Fig. 2), it was possible to determine current and cell voltage drop simultaneously.

At any given cell current value, the measured potential differences were averaged for forward and reverse current. If this average did not agree with the average of the potential differences as cor-

rected for zero-current voltage, the data were discarded.

In the case of fused salt measurements, the entire sequence of voltage measuring steps was repeated at each new furnace temperature setting. Normally, the first conductivity measurements were made just above the melting point of the salt being investigated, and furnace temperature was increased in steps until either the electrodes failed or the salt began to decompose. In some cases, however, furnace temperature was changed in random order, or was reset to some previously used temperature. Observed conductivities did not appear to depend on the order of temperature settings.

The cell current potentiometer circuit was calibrated at sufficiently frequent intervals to insure continually accurate cell current determination.

All of the operations required for determining each fused salt conductivity value were carried out as rapidly as possible to minimize the effects of any thermal cycling in the furnace. The minimum time necessary was about 4 min.

Results and Discussion

Conductivity cell performance.—As Gunning and Gordon have pointed out (1), it is essential to consider two important problems when planning a d-c conductivity experiment. It is necessary first of all that the probe electrodes be reversible, or at least not significantly polarized by the act of measuring the voltage between them. The calomel (for 1-demal KCl) and silver-silver nitrate (for fused salts) electrodes employed in this work behaved very satisfactorily and gave no reason to suspect error to be introduced through polarization or lack of reversibility.

The most serious shortcomings of the silver electrodes were their limited useful temperature range and their sensitivity to melt composition. At temperatures below 300° the Pyrex bubbles became sufficiently nonconductive to render the galvanometric null-point difficult to determine accurately. As might be expected, this sluggish response was most pronounced at high mole fractions of KNO_3 . At temperatures in excess of 400°, the silver electrodes did not work well in LiNO_3 -rich melts.

The second problem pointed out by Gunning and Gordon is concerned with electrode geometry. To eliminate any apparent current dependency of specific conductivity, the reference electrodes ideally should be vanishingly small in the dimension parallel to the flow of cell current. The U-tube holes which led to the side-arms were made as small as was practicable (1 mm diameter). It is reasonable to assume that the potential difference between the hole sites would be equal to that seen in the side-arms at the actual electrode locations. In any event, any voltage developed within the side-arms would cancel as cell current was reversed.

As evidence of the successful elimination of cell current effects, specific conductivities did not change within experimental error as the current was changed 40-fold in the fused salt experiments and 16-fold in the KCl experiments. It does not appear

that the cell design of Ives and Swaroopa (6), who circumvented the problem of reference electrode geometry in another way, would be amenable to high temperature fused salt work.

The cell constants were within about 5% of the values which were calculable from cell geometry.

Table I. Experimental values of specific conductivity of LiNO_3 , NaNO_3 , KNO_3 , and their binary mixtures

Melt composition, mole %	Temperature, °C	κ , $\text{ohm}^{-1}\text{cm}^{-1}$	Melt composition, mole %	Temperature, °C	κ , $\text{ohm}^{-1}\text{cm}^{-1}$
100 LiNO_3	284.2	0.9676	25.0 ₅ LiNO_3	278.5	0.8651
	284.2	0.9696	74.9 ₅ NaNO_3	278.5	0.8660
	321.8	1.1756		300.8	0.9763
	321.8	1.1786		300.8	0.9777
	359.0	1.3880		327.2	1.096
	359.0	1.3884		327.2	1.099
				348.8	1.199
100 NaNO_3	330.5	1.089		349.2	1.203
	330.5	1.090		375.2	1.319
	349.0	1.168		375.3	1.320
	349.0	1.175		398.6	1.422
	398.6	1.382		398.8	1.422
	398.6	1.383		421.8	1.516
	444.5	1.558		421.8	1.516
	444.5	1.562			
			50.0 ₄ LiNO_3	283.8	0.9097
100 KNO_3	354.0	0.6785	49.9 ₆ NaNO_3	283.8	0.9175
	354.0	0.6789		303.6	1.0171
	374.8	0.7442		303.6	1.0185
	374.8	0.7470		331.5	1.1472
	398.2	0.8181		331.5	1.1560
	398.6	0.8190		355.1	1.2642
	422.2	0.8882		355.1	1.2645
	422.2	0.8894		394.2	1.4443
				394.2	1.4465
74.6 ₀ LiNO_3	285.8	0.9563	24.85 NaNO_3	280.0	0.5125
25.3 ₀ NaNO_3	286.2	0.9576	75.15 KNO_3	280.0	0.5128
	319.5	1.130		302.6	0.5929
	319.5	1.133		302.6	0.5930
	358.5	1.330		326.0	0.6741
	359.0	1.329		326.2	0.6749
	397.8	1.53		352.0	0.7624
				352.2	0.7620
				376.8	0.8429
23.3 ₁ LiNO_3	278.5	0.5139		377.0	0.8435
76.6 ₉ KNO_3	279.6	0.5236		399.0	0.9159
	302.6	0.5974		399.0	0.9165
	302.6	0.5977		420.8	0.9836
	325.8	0.6761		421.0	0.9841
	326.0	0.6772			
	350.2	0.7616			
	350.6	0.7626	50.31 NaNO_3	280.8	0.5989
	374.2	0.8398	49.69 KNO_3	282.2	0.6014
	374.2	0.8419		325.5	0.7730
	396.8	0.9172		326.2	0.7746
	397.2	0.9180		375.8	0.9555
	421.0	0.9951		375.8	0.9556
	421.2	0.9949		398.8	1.038
				399.0	1.039
50.1 ₂ LiNO_3	285.5	0.6445		422.2	1.117
49.8 ₈ KNO_3	286.9	0.6489		423.2	1.118
	312.0	0.7419			
	312.7	0.7440	75.09 NaNO_3	301.8	0.7923
	345.0	0.8685	24.91 KNO_3	302.1	0.7957
	345.1	0.8688		302.1	0.7971
	381.5	1.0048		302.8	0.7957
	381.5	1.0048		348.8	0.9909
	427.2	1.18		348.8	0.9977
				398.8	1.187
				398.8	1.190
74.8 ₀ LiNO_3	290.2	0.8025			
25.2 ₀ KNO_3	290.2	0.8034			
	330.2	0.9838			
	330.2	0.9866			
	370.2	1.155			
	370.8	1.154			

Table II. Specific conductivity equations for LiNO_3 , NaNO_3 , KNO_3 , and their binary melts

Melt composition, mole %	$\kappa = a + bt + ct^2 \text{ ohm}^{-1}\text{cm}^{-1}$			Root mean square deviation $\text{ohm}^{-1}\text{cm}^{-1}$	Temp range, °C
	a	b × 10 ⁸	c × 10 ⁶		
100 LiNO_3	-0.4424	4.4524	+1.8027	0.001	285-360
100 NaNO_3	-0.8007	6.9089	-3.5949	0.002	330-445
100 KNO_3	-0.8241	5.2218	-2.7583	0.0008	355-425
25.0 ₅ LiNO_3	-0.7763	6.7915	-3.2169	0.001	280-420
74.9 ₅ NaNO_3					
50.0 ₄ LiNO_3	-0.6253	5.9456	-1.7573	0.004	280-395
49.9 ₆ NaNO_3					
74.6 ₀ LiNO_3	-0.7441	6.5804	-2.2173	0.001	285-400
25.3 ₀ NaNO_3					
23.3 ₁ LiNO_3	-0.5769	4.2578	-1.2446	0.002	280-420
76.6 ₉ KNO_3					
50.1 ₂ LiNO_3	-0.4578	3.9418	-0.2828	0.001	285-430
49.8 ₈ KNO_3					
74.0 ₀ LiNO_3	-0.8902	6.9590	-3.8750	0.002	290-370
25.2 ₀ KNO_3					
24.85 NaNO_3	-0.6391	4.6240	-1.8254	0.0006	280-420
75.15 KNO_3					
50.31 NaNO_3	-0.7358	5.4550	-2.5391	0.002	280-425
49.69 KNO_3					
75.09 NaNO_3	-0.9017	6.8016	-3.9159	0.002	300-400
24.91 KNO_3					

Considering the difficulty of precise measurement of the inside diameter of the U-tubes, such close agreement is powerful evidence that the method of d-c conductivity determination is valid.

Fused salt conductivities.—The results obtained for d-c specific conductivities of alkali metal nitrates are given in Table I and are summarized in the form of empirical equations in Table II. These equations

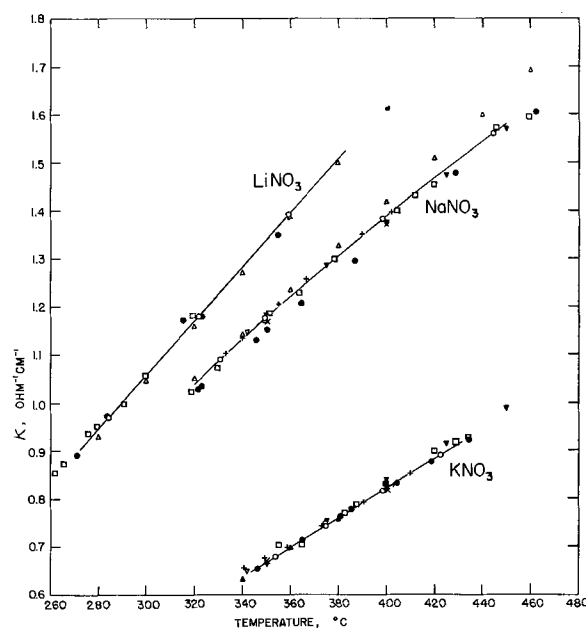


Fig. 3. Specific conductivities of LiNO_3 , NaNO_3 , and KNO_3 . ○, This work; ●, Jaeger and Kapma (7); △, Doucet and Bizouard, calculated from their equation (8); ▽, Doucet and Bizouard (9); ▲, Protsenko and Popovskaya (10); ▼, Murgulescu and Zuca (11); □, Goodwin and Mailey (12); ■, Polyakov (13); +, Kröger and Weisgerber (14); ×, Sandonnini (15).

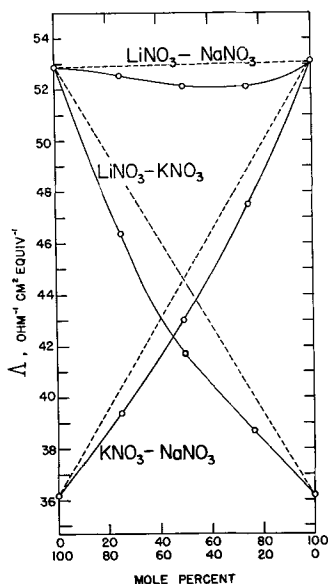


Fig. 4. Equivalent conductivities of binary melts at 350°C

represent the observed points within experimental error, as indicated in the root mean square deviation column. The temperature ranges indicated are those within which the data were obtained.

The present results are compared to values of specific conductivity obtained by other workers (all of whom used a-c techniques) in Fig. 3. Only the curves for the pure salts are shown. It is evident that there is considerable disagreement among various laboratories, especially concerning the conductivity of NaNO_3 . The present results agree quite closely with the more recently measured a-c values. The d-c data show less scatter than other workers have been able to attain with a-c techniques. Similar agreement was noted for those binary melts for which literature values were available.

It is worthwhile to show some typical equivalent conductivity isotherms for the three binary systems, inasmuch as they have not been published elsewhere in a single paper. Figure 4 shows 350° isotherms.

Density data of Murgulescu and Zuca (11) and Murgulescu and Volanschi (16) were used to calculate equivalent conductivities. Of particular interest are the strong deviations of equivalent conductivity from additivity (dashed lines in Fig. 4). The deviation is most pronounced for the LiNO_3 - KNO_3 isotherm, where the cationic radius difference is greatest. In the case of LiNO_3 - NaNO_3 melts, all mixtures actually are less conductive than either pure salt.

Manuscript received June 25, 1963. This work was performed in the Ames Laboratory of the U. S. Atomic Energy Commission, Contribution No. 1321.

Any discussion of this paper will appear in a Discussion Section to be published in the December 1964 JOURNAL.

REFERENCES

1. H. E. Gunning and A. R. Gordon, *J. Am. Chem. Soc.*, **81**, 3207 (1959).
2. L. F. Grantham and S. J. Josim, *J. Chem. Phys.*, **38**, 1671 (1963).
3. M. L. Poincaré, *Ann. Chim. (Paris)*, Ser. 6, **21**, 289 (1890).
4. G. Jones and B. C. Bradshaw, *J. Am. Chem. Soc.*, **55**, 1780 (1933).
5. D. Inman, *J. Sci. Instruments*, **39**, 391 (1962).
6. D. J. G. Ives and S. Swaroopa, *Trans. Faraday Soc.*, **49**, 788 (1953).
7. F. M. Jaeger and B. Kapma, *Z. anorg. allgem. chem.*, **113**, 27 (1920).
8. Y. Doucet and M. Bizouard, *Bull. Soc. Chim. France*, **1959**, 1570.
9. Y. Doucet and M. Bizouard, *Compt. rend.*, **248**, 1328 (1959).
10. P. I. Protsenko and N. P. Popovskaya, *J. Gen. Chem. USSR (English Transl.)*, **24**, 2089 (1954).
11. I. G. Murgulescu and S. Zuca, *Acad. Rep. Populare Romini, Studii Cercetari Chim.*, **7**, 325 (1959).
12. H. M. Goodwin and R. D. Mailey, *Phys. Rev.*, **26**, 28 (1908).
13. V. D. Polyakov, *Izv. Sektora Fiz. Khim. Analiza, Inst. Obshch. Neorgan. Khim., Akad. Nauk. SSSR*, **26**, 147 (1955).
14. C. Kröger and P. Weisgerber, *Z. Physik Chem. (Frankfurt)*, **5**, 192, (1955).
15. C. Sandonnini, *Gazz. Chim. Ital.*, **50**, Part 1, 289 (1920).
16. I. G. Murgulescu and C. Volanschi, *Rev. Chim. Acad. Rep. Populaire Roumaine*, **6**, 45 (1961).

December 1964 Discussion Section

A Discussion Section, covering papers published in the January-June, 1964 JOURNALS, is scheduled for publication in the December 1964 issue. Any discussion which did not reach the Editor in time for the June 1964 Discussion Section will be included in the December 1964 issue.

Those who plan to contribute remarks for this Discussion Section should submit their comments or questions in triplicate to the Managing Editor of the JOURNAL, 30 East 42 St., Rm. 1806, New York, N. Y., 10017, not later than September 1, 1964. All discussions will be forwarded to the author(s) for reply before being printed in the JOURNAL.

Direct Current Measurement of Fused Salt Conductivity

II. KCl-LiCl

F. R. Duke¹ and Lynn Bissell¹

Institute for Atomic Research and Department of Chemistry, Iowa State University, Ames, Iowa

ABSTRACT

Direct-current measurements were used to determine the electrical conductivity of the fused potassium chloride-lithium chloride system. Specific conductivity was determined for the pure salts and five of their mixtures as a function of temperature. In all cases, the specific conductivity increased with temperature. Agreement with other workers on the specific conductivity of KCl was excellent. The addition of water to dry lithium chloride was found to lower the specific conductivity at a given temperature. The equivalent conductivity and apparent activation energy of ionic migration were computed using the density data of other workers.

The determination of the electrical conductivity of LiCl presents many problems which can be shown by the large variation of values obtained by several workers (1-5). The high specific conductivity and great affinity for water make a-c measurements somewhat unreliable since capillary tubes must be used to obtain the high resistance needed in the conductivity cell.

The purpose of this work was to determine whether more reliable values of electrical conductivity could be obtained for LiCl and some of its mixtures and to demonstrate the utility of the d-c method described by King and Duke (6) at higher temperatures.

The system (KCl-LiCl) was chosen for this work. Previous work has been done on this system by Van Artsdalen and Yaffe (1) and Karpachev, Stromberg, and Podchainova (6), but it was thought worthy of reinvestigation. The specific conductivity of KCl seems to be well enough known (1-3, 7-9) to compare the a-c and d-c methods.

Experimental

The furnace setup, electrical circuits, and method of operation used in this work are described in a previous paper by King and Duke (5). Conductivity cells made of fused silica (Fig. 1) were also of a design similar to theirs. The voltage drop across the IR-region F (see Fig. 1) was measured using two Ag/AgCl reference electrodes located in tubes A. These electrodes consisted of a silver wire immersed in a mixture of alkali metal chlorides with a small amount of silver chloride added. This melt was enclosed in a Vycor tube in which a small thin bubble had been blown in one end. The electrode melts consisted of two mixtures. The first, used for the lower-melting salt mixtures, was made up of 35 mole % LiCl, 52 mole % KCl, 10 mole % NaCl, and 3 mole % AgCl. The second, used for the higher melting salt mixtures, consisted of 48 mole % NaCl, 49 mole % KCl, and 3 mole % AgCl.

The cell constants were calculated using 1-demal KCl according to Jones and Bradshaw (10). Rede-

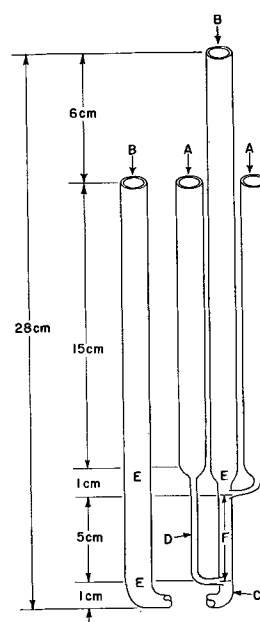


Fig. 1. Typical conductivity cell: A, 10 mm sidearms; B, 13 mm current arms; C, 6 mm tubing; D, 2 mm capillaries; E, thermocouple locations; F, IR region.

termination of the cell constant after 8 hr in contact with pure LiCl showed a change of only 0.04%.

Baker analyzed LiCl and KCl were used in this work. The pure salts were dried at 450°C for 36 hr in a vacuum apparatus connected to a dry ice bath. Samples treated in the same manner for 24 hr, weighed, then reheated in the vacuum apparatus for an additional 12 hr showed a loss in weight of only 0.008%.

Results

The specific conductivity of the pure salts and five of their mixtures was determined at several temperatures. These data are given in Table I. Equations of these curves of κ vs. t were computed by the method of least squares and are given in Table II. The agreement between this work and other publications done since 1945 for KCl (Fig. 2) indicates that the d-c method of determining electrical conductivity is feasible at higher temperatures also.

¹ Present address: Agricultural and Mechanical College of Texas, College Station, Texas.

Table I. Experimental values of specific conductivity of KCl, LiCl, and their binary mixtures

Composition, mole % KCl	Specific conductivity, mho/cm		Composition, mole % KCl	Specific conductivity, mho/cm		
	Temp, °C			Temp, °C		
100	787.2	2.193 ₂	29.6 ₄	603.2	2.420 ₈	
	803.2	2.240 ₆		650.0	2.635 ₈	
	803.5	2.241 ₄		686.0	2.784 ₇	
	812.5	2.262 ₉		686.2	2.788 ₂	
	818.8	2.280 ₈		463.0	2.032 ₀	
	819.0	2.282 ₅		463.5	2.042 ₁	
	822.8	2.287 ₁		474.5	2.170 ₄	
	837.0	2.326 ₉		485.8	2.261 ₂	
	851.5	2.358 ₆		486.0	2.264 ₁	
	860.8	2.378 ₃		493.0	2.307 ₁	
	864.8	2.396 ₆		506.5	2.394 ₇	
	883.6	2.414 ₁		507.0	2.397 ₀	
	80.0 ₄	731.5		2.163 ₈	507.8	2.389 ₄
		732.0		2.164 ₂	509.2	2.391 ₇
		747.4		2.213 ₆	528.2	2.509 ₉
		750.5		2.216 ₄	529.0	2.511 ₉
		769.2		2.276 ₀	529.8	2.512 ₁
		769.5		2.278 ₃	555.0	2.650 ₃
		790.2		2.345 ₀	555.2	2.656 ₀
790.8		2.344 ₀	573.8	2.762 ₀		
791.2		2.346 ₆	593.0	2.867 ₃		
792.5		2.340 ₂	593.2	2.868 ₂		
59.5 ₅	818.8	2.415 ₃	615.5	2.976 ₇		
	819.5	2.420 ₂	616.0	2.980 ₉		
	820.0	2.423 ₁	640.8	3.100 ₄		
	59.5 ₅	605.6	1.926 ₄	641.4	3.104 ₃	
		605.6	1.926 ₉	528.2	3.200 ₁	
		616.6	1.980 ₈	528.6	3.209 ₉	
		616.6	1.978 ₆	549.6	3.344 ₃	
		629.2	2.033 ₈	550.2	3.356 ₉	
		629.5	2.034 ₇	570.2	3.469 ₇	
		640.0	2.082 ₂	571.0	3.478 ₇	
656.0		2.150 ₀	593.2	3.595 ₄		
656.2		2.150 ₂	614.8	3.714 ₆		
676.2		2.230 ₀	615.0	3.717 ₃		
59.5 ₅	676.5	2.231 ₇	637.6	3.839 ₃		
	703.2	2.334 ₇	637.8	3.840 ₇		
	704.2	2.336 ₀	655.8	3.943 ₁		
	724.5	2.410 ₀	675.0	4.030 ₉		
	41.2 ₀	724.8	2.412 ₂	627.0	5.951 ₆	
		749.2	2.495 ₁	628.8	5.949 ₂	
		749.2	2.495 ₁	644.5	6.042 ₄	
		789.5	2.623 ₆	644.8	6.047 ₉	
		789.8	2.628 ₀	653.8	6.101 ₅	
		429.8	1.425 ₀	659.2	6.135 ₅	
450.0		1.571 ₉	663.5	6.157 ₈		
470.5		1.690 ₃	671.5	6.189 ₂		
470.7		1.692 ₅	671.5	6.178 ₁		
491.2		1.818 ₀	692.2	6.303 ₁		
510.2	1.927 ₉	692.8	6.293 ₅			
510.5	1.927 ₁	706.8	6.347 ₅			
529.5	2.035 ₂	709.4	6.391 ₇			
530.0	2.038 ₆	713.0	6.387 ₅			
547.8	2.136 ₄	713.2	6.390 ₃			
548.0	2.144 ₀	728.8	6.465 ₉			
578.5	2.298 ₃	728.8	6.448 ₈			
578.5	2.301 ₀	746.0	6.523 ₄			

The dependence of specific conductivity on temperature for LiCl (Fig. 3) differs by as much as 3.0% from other publications; however, except for the work of Blitz and Klemm (4), the relative shape of the curves are approximately the same. Both Van Artsdalen and Yaffe (1) and Edwards *et al.* (2) mention that considerable attack occurred on their cells while the measurements were being made. While Van Artsdalen and Yaffe were able to obtain

Table II. Specific conductivity equations as a function of temperature for (K-Li) Cl mixtures

Composition, mole % KCl	$\kappa = a + bt + ct^2$, mho/cm			Standard deviation, mho/cm	Temp. range, °C
	a	b	c		
100.00	-3.3855	1.1358	-0.5419	0.004	790-880
80.04	-1.7849	0.7590	-0.3000	0.003	730-820
59.55	-2.4172	0.9780	-0.4300	0.001	600-790
41.20	-2.3427	1.0969	-0.5091	0.003	430-690
29.64	-1.7588	1.0407	-0.4406	0.006	460-640
18.23	-2.0370	1.3324	-0.6433	0.004	530-680
0.00	1.0262	1.0356	-3.9786	0.009	630-750

values over a considerable temperature range, Edwards *et al.* obtained points at three different temperatures only with the cell resistance changing rapidly. Blitz and Klemm (4) and Bloom *et al.* (3) make no mention of any attack on their cells, and none was observed in this work.

Over a period of 2 hr, the addition of 5×10^{-2} moles of water to 30g of LiCl changed the cell constant by 2.7%, and the specific conductivity was

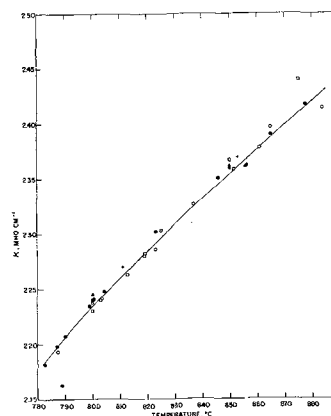


Fig. 2. Specific conductivity vs. temperature for pure KCl: —○—, this work; ●, data from Van Artsdalen and Yaffe (1); △, data from Doucet and Bizouard (7); ■, data from Lee and Pearson (8); +, data from Huber *et al.* (9); △, data from Edwards *et al.* (2); □, equations from Bloom *et al.* (3).

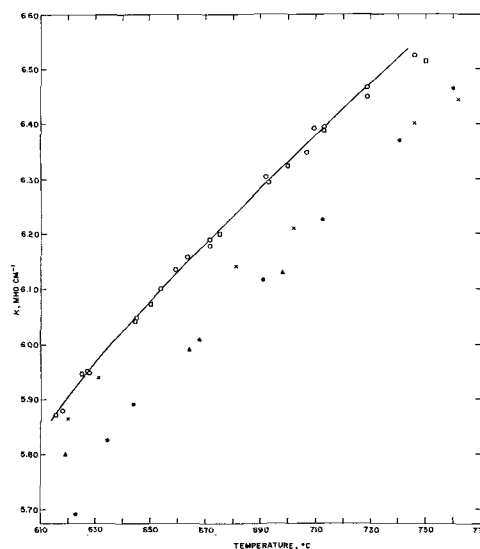


Fig. 3. Specific conductivity vs. temperature for pure LiCl; —○—, this work; ●, data from Van Artsdalen and Yaffe (1); ▲, data from Edwards *et al.* (2); □, equation from Bloom *et al.* (3); ×, data from Blitz and Klemm (4).

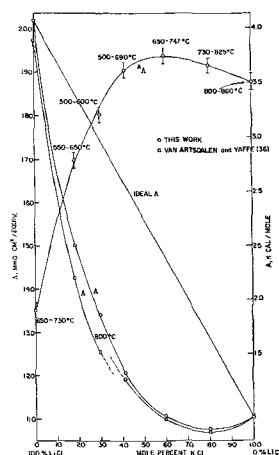


Fig. 4. Equivalent conductivity at 800°C and activation energy vs. composition for the KCl-LiCl system.

lowered by about 3.3%, which is a greater difference than that observed by the various workers. A very small amount of water will cause both attack on the cell and lower specific conductivity.

The specific conductivity vs. composition at 800°C is compared with those values obtained by Van Artsdalen and Yaffe (1) in Fig. 4. The percent difference in the two curves increases steadily from 0.2 to 6.4% through the composition range 100% KCl to the 29.64 mole % KCl mixture, respectively, then decreases to a 2.2% difference for 100% LiCl. A smooth curve can be drawn through the values determined in this work; however, there appears to be a break in their curve between the 29.64 and 41.20 mole % KCl mixtures.

The density equations² of Van Artsdalen and Yaffe were used to compute the equivalent conductivity by means of the equation

$$\Lambda = \frac{\kappa \bar{e}}{\rho}$$

where κ is the specific conductivity in mho/cm, \bar{e} is the mean equivalent weight, and ρ is the density of the melt in g/cm.

The average or apparent activation energy of ionic migration was calculated for each mixture over the temperature range covered in this work. The equation (12)

$$\Lambda = F e^{-A/RT}$$

² The value 1.9597 was substituted for the constant a for the 80.04 mole % mixture [see ref. (11)].

was used, where A is the activation energy of ionic migration, F is a constant known as the frequency factor, and Λ is the equivalent conductivity. The standard deviation of the $\log \Lambda$ vs. $1/T$ plot was about 0.0005 from linear for all melts if the values near the melting points were omitted. This small deviation still produced a probable error of ± 70 cal in the apparent activation energy.

The equivalent conductivity vs. composition plot at 800°C (Fig. 4) shows a minimum similar to that observed by Van Artsdalen and Yaffe at the 80 mole % KCl mixture. The activation energy of ionic migration (Fig. 4) shows a maximum near the equimolar mixture although there is some overlap in possible values due to probable error. The maximum deviation from the ideal Λ curve, which would be obtained if the equivalent conductivities were additive, is near the 45 mole % KCl mixture.

Acknowledgment

The authors are indebted to Dr. Lowell A. King for the use of his electrical apparatus and his helpful suggestions.

Manuscript received Sept. 9, 1963. This paper is Contribution No. 1386; work was performed in the Ames Laboratory of the United States Atomic Energy Commission.

Any discussion of this paper will appear in a Discussion Section to be published in the December 1964 JOURNAL.

REFERENCES

1. E. R. Van Artsdalen and I. S. Yaffe, *J. Phys. Chem.*, **59**, 119 (1955).
2. J. O. Edwards, C. S. Taylor, A. S. Russell, and L. F. Maranville, *This Journal*, **99**, 527 (1952).
3. H. Bloom, I. W. Knaggs, J. J. Molloy, and D. Welch, *Trans. Faraday Soc.*, **49**, 1458 (1953).
4. W. Blitz and W. Klemm, *Z. anorg. u. allgem. Chem.*, **152**, 267 (1926).
5. S. V. Karpachev, A. G. Stromberg, and N. Podchainova, *Zhur. Obshchei Khim.*, **5**, 1517 (1935).
6. L. A. King and F. R. Duke, *This Journal*, **111**, 712 (1964).
7. Y. Doucet and M. Bizouard, *Compt. rend.*, **250**, 73 (1960).
8. E. K. Lee and E. P. Pearson, *Trans. Electrochem. Soc.*, **88**, 171 (1945).
9. P. W. Huber, E. V. Potter, and H. W. St. Clair, U.S.A.E.C. Report BM-RI-4858 (Bureau of Mines), 1 (1952).
10. G. Jones and B. C. Bradshaw, *J. Am. Chem. Soc.*, **55**, 1780 (1933).
11. G. P. Smith and G. F. Petersen, *J. Chem. Eng. Data*, **6**, 493 (1961).
12. H. Bloom and E. Heymann, *Proc. Roy. Soc. (London)*, **188A**, 392 (1947).

The Journal of the Electrochemical Society regrets the delay in publishing the Brief Communication by M. J. Presland, R. Marshall, and J. Franks "The Effects

of Quenching on the Structural, Photo and Electroluminescent Properties of ZnS:Cu Phosphors," *This Journal*, **111**, 628 (1964).

Electric Conductivity of Fused $\text{LiNO}_3\text{-NaNO}_3\text{-KNO}_3$ Eutectic

Lowell A. King,¹ C. Lynn Bissell,² and F. R. Duke²

Institute for Atomic Research and Department of Chemistry, Iowa State University, Ames, Iowa

ABSTRACT

Simple, sensitive reference electrodes are described for use in direct current measurement of fused salt conductivity. They consist of silver wires dipping into a very dilute solution of Ag^+ in the salt under investigation. The ternary eutectic of LiNO_3 , NaNO_3 , and KNO_3 was chosen to demonstrate the technique. Specific conductivity of the system was measured from 134° to 384°C.

The practicability of a direct current technique for the measurement of fused salt electric conductivity has been demonstrated previously (1, 2). In those studies, glass bubble-enclosed, reversible $\text{Ag}^\circ\text{-Ag}^+$ electrodes were used to measure the voltage-drop across a known region of the conductivity cell. With proper selection of solvent and type of glass, such electrodes apparently can be used up to the melting temperature of silver. However, reasonably sturdy Pyrex bubbles become sufficiently non-conductive below about 300° to make accurate null-point determination difficult even with a sensitive galvanometer (1). Kust (3) successfully used $\text{Ag}^\circ\text{-Ag}^+$ glass electrodes in $\text{NaNO}_3\text{-KNO}_3$ eutectic at 235°; he employed an electrometer for null-point detection. His experience, and ours at 200°, indicates that glass-encased electrodes can be used with an electrometer providing the system is well shielded from stray electric fields.

At best, glass electrodes are extremely inconvenient for low temperature work. This paper describes a technique in which the glass membrane is eliminated by simply immersing silver wires into a very dilute solution of AgNO_3 in the salt whose conductivity is to be measured. The fused salt system chosen for study is the $\text{LiNO}_3\text{-NaNO}_3\text{-KNO}_3$ ternary eutectic (mole fractions: 0.3753, 0.1628, 0.4619, respectively), melting below 120° (4). The electric conductivity of the system has not been reported previously; therefore measurements were made from near the melting point to 385° and are reported below.

Experimental

Treatment of chemicals, design and calibration of the conductivity cells, design of the direct current electrical circuits, and the method of operation have been described previously (1, 2).

Each side-arm electrode was an 8-cm length of 1/16-in. diameter silver wire (Handy and Harmon, 99.99+ % Ag). The electrodes were immersed in the melt to a depth of about 1 cm. The other end of each wire was attached to a platinum lead extending out of the side-arm.

Results and Discussion

Conductivity measurements were made on ternary eutectic solution to which no AgNO_3 was added, and

¹ Present address: Department of Chemistry, U.S. Air Force Academy, Colorado.

² Present address: Department of Chemistry, Texas A & M University, College Station, Texas.

on solutions which were 0.12, 0.0056, and 0.00014 molal in AgNO_3 . In all four instances, the silver wire electrodes were extremely sensitive to the voltage drop across the cell.

As expected, a high and variable zero-cell current voltage existed between the electrodes immersed in the melt to which no AgNO_3 was added. Upon standing (1 to 2 days) the zero-current voltage stabilized considerably. Even then the electrodes were not useful, for they were easily polarized when searching for the galvanometric null-point. A small and extremely stable zero-cell current voltage was established immediately in 0.12M AgNO_3 , and the electrodes showed no evidence of polarization. Electrodes immersed in 0.0056M AgNO_3 stabilized in a few minutes and in 0.00014M AgNO_3 , in a few hours. The electrodes showed some tendency to become polarized in the latter case.

The conductivity data recorded in Table I were taken on a solution 0.0056M in AgNO_3 . This concentration was high enough to give stable, nonpolarized electrodes, yet low enough to introduce no significant error in conductivity by virtue of the contribution of AgNO_3 itself. The specific conductivities of AgNO_3 in LiNO_3 (5) and in KNO_3 (5, 6) solutions are nearly additive. One may assume additivity also to occur in $\text{AgNO}_3\text{-LiNO}_3\text{-NaNO}_3\text{-KNO}_3$ melts; 0.0056M AgNO_3 will lead to a conductivity value which is too high by $0.00015\text{-}1\text{ cm}^{-1}$ at 250°C. This assumption was checked by measuring the specific conductivity of 0.0056M AgNO_3 in an equimolar

Table I. Specific conductivity of $\text{LiNO}_3\text{-NaNO}_3\text{-KNO}_3$ eutectic

Temp, °C	ohm ⁻¹ cm ⁻¹	Temp, °C	ohm ⁻¹ cm ⁻¹	Temp, °C	ohm ⁻¹ cm ⁻¹
133.9	0.10733	230.8	0.43086	357.1	0.91948
133.9	0.10736	230.9	0.43148	357.1	0.92000
134.0	0.10773	230.9	0.43162	357.2	0.92037
134.1	0.10811	231.0	0.43188	383.9	1.01708
159.9	0.17896	260.5	0.54696	384.0	1.01728
160.0	0.17897	260.6	0.54748	384.1	1.01793
160.0	0.17901	260.6	0.54742		
160.0	0.17902	286.4	0.64657		
185.2	0.26237	286.6	0.64759		
185.3	0.26291	286.7	0.64763		
185.5	0.26346	309.8	0.73977		
195.5	0.29854	309.9	0.73966		
195.6	0.29908	310.0	0.74008		
213.8	0.36685	333.9	0.83170		
213.8	0.36697	333.9	0.83182		
214.0	0.36799	333.9	0.83189		
214.0	0.36825				

Table II. Empirical equations for specific conductivity of ternary eutectic

$\kappa = a + bt + ct^2 + dt^3$, $\text{ohm}^{-1}\text{cm}^{-1}$					Temp range, °C
a	$b \times 10^8$	$c \times 10^6$	$d \times 10^8$	Root mean square deviation, $\text{ohm}^{-1}\text{cm}^{-1}$	
-0.23879	+2.0767	+3.5295	—	0.0038	134-310
-0.67884	+5.2450	-2.1545	—	0.0003	285-385
-0.06512	-0.49491	15.670	-1.8356	0.0016	134-385

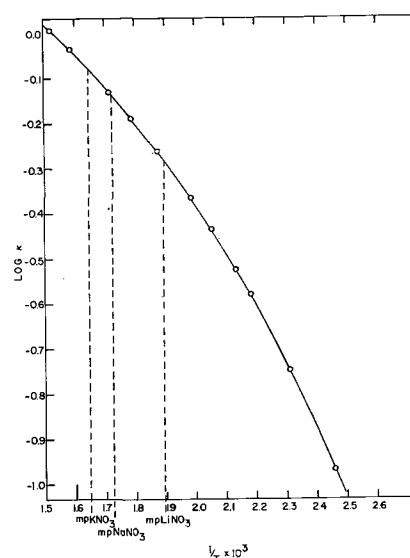
$\text{KNO}_3\text{-NaNO}_3$ mixture and found to be correct within experimental error. Results were corrected for the thermal expansion of Pyrex.

A plot of specific conductivity vs. temperature gives an S-shaped curve, concave upward at low temperatures and slightly concave downward at high temperatures. The data were divided into two overlapping temperature regions and are represented by empirical equations, given in Table II. The equations were obtained by the method of least squares. An IBM-7074 computer was used to obtain the cubic equation.

Figure 1 is a plot of $\log \kappa$ vs. reciprocal temperature.

Manuscript received Sept. 9, 1963. Contribution No. 1371. Work was performed in the Ames Laboratory of the U. S. Atomic Energy Commission.

Any discussion of this paper will appear in a Discussion Section to be published in the December 1964 JOURNAL.

Fig. 1. Plot of $\log \kappa$ vs. reciprocal temperature

REFERENCES

1. L. A. King and F. R. Duke, *This Journal*, **111**, 712 (1964).
2. C. L. Bissell and F. R. Duke, *ibid.*, **111**, 717 (1964).
3. R. N. Kust, Private communication.
4. "International Critical Tables," Vol. 4, p. 83, McGraw-Hill Book Co., New York (1928).
5. H. C. Cowen and H. J. Axon, *Trans. Faraday Soc.*, **52**, 242 (1956).
6. F. R. Duke and R. A. Fleming, *This Journal*, **105**, 412 (1958).

The Electrochemical Oxidation of Ethylene: An Experimental Study

Mino Green,¹ Jan Weber,² and Vera Drazic³

Electrochemistry Laboratory, University of Pennsylvania, Philadelphia, Pennsylvania

ABSTRACT

Both steady state and time dependent current-voltage curves of the anodic oxidation of ethylene were studied at the electrode Pt(Pt)|1M NaOH, C_2H_4 (diss.), conditions for obtaining the Tafel slope, found to be approximately $2RT/F$, were established. Ethylene partial pressure had no measurable effect on the steady state current-voltage curve in the Tafel region. The Pt electrode was found to become "passivated" at about 0v (NHE). Time dependent studies showed that the electrode became continuously less active. Experiments were carried out in a closed cell arrangement, where ethylene consumed at the anode and coulombs passed could be measured simultaneously. Within experimental error, one mole of ethylene was found to involve the passage of twelve Faradays, showing that ethylene is totally oxidized. An analysis of the experimental data in terms of single electron transfer steps, limiting surface coverage and Tafel transfer coefficients of $\sim 1/2$ leads to the conclusion that the OH^- discharge most likely plays the dominant role in the rate determining step.

The investigation reported in this paper was undertaken because of the present strong interest in fuel cells. There is a real need for the development

¹ Present address: Zenith Radio Research Corporation (U.K.) Ltd., Stanmore, Middlesex, England.

² Present address: Polarographic Institute CSAV, Opletalova, Ceskoslovenska.

³ Present address: Tehnoloski Fakultet, Univerzitet U Geogradu, Karneeljeva, Beograd.

of experimental techniques for investigating electrochemical reactions of possible fuel cell use and for understanding the mechanism of the reaction. Previous studies (1-3) of the electrochemical oxidation of ethylene have not been primarily directed toward determining those parameters of the reaction which are useful in diagnosing mechanism.

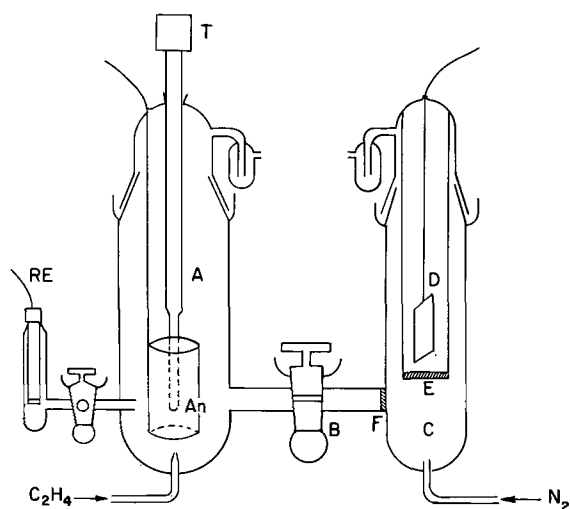


Fig. 1. Schematic arrangement of the electrolysis cell (without pre-electrolysis attachment).

Experimental

The electrode investigated was Pt(Pt)|1M NaOH, C₂H₄ (dissolved). The current-voltage characteristics of the electrode were determined as a function of temperature and ethylene pressure. The over-all stoichiometry of the electrode reaction was also determined.

Polarization Parameters

Electrolysis cell.—The current voltage characteristics for the anodic oxidation of ethylene were determined in the kind of cell shown on Fig. 1. The cell was constructed of Pyrex glass and consisted of three basic units. In the anode compartment, A, provision was made for introducing ethylene gas and also for thermostating the compartment by connecting a mercury-in-glass contact thermometer, T, with a power source supplying the heating mantle wrapped around the compartment. The anode compartment was separated from the cathode compartment, C, by means of a ground glass stop-cock, B, and a coarse glass fritted disk, F. B and F were introduced into the system in order to prevent transport of hydrogen to the anode. The cathode D, was contained in a glass tube terminated by a coarse fritted disk, E. Nitrogen was bubbled through C, to further reduce the steady state concentration of hydrogen in C. The saturated calomel reference electrode RE, was connected to A, via a stop-cock and a Luggin capillary.

Pre-electrolysis attachment.—The influence of impurities (over and above that occurring by glass dissolution) on the anodic reaction was studied by measuring the voltage-current characteristics of the electrode as a function of successively greater "purification" of the electrolyte. The cell shown in Fig. 1 was provided with a pre-electrolysis attachment such as shown in Fig. 2.

The contact thermometer, T, (Fig. 1) was discarded when the attachment was used: steady temperature being maintained by outside thermostating. The attachment shown in Fig. 2 consisted of three Pt gauze electrodes: electrode An, was the working anode, electrode X was the pre-electrolysis anode

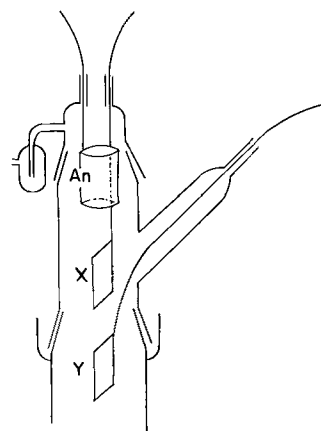


Fig. 2. Pre-electrolysis attachment for anode compartment of electrolysis cell.

and electrode Y was used as the pre-electrolysis cathode. Each electrode was attached to a ground-glass sliding joint so that it could be immersed in solution or withdrawn into the gas space above the liquid. The procedure used was first to carry out pre-electrolysis with X anodic and electrode D (of Fig. 1) cathodic. X was then withdrawn from solution and Y was immersed and made cathodic (with respect to D). During the pre-electrolysis, pure N₂ was continuously bubbled through the solution in order to keep the solution concentration of oxygen or hydrogen as low as possible. X was then withdrawn, N₂ was then replaced by C₂H₄ and finally the working electrode, An, was immersed in solution.

During the course of this work H. Wroblowa (in our laboratories) carried out a series of experiments in a Teflon cell, and obtained the same Tafel slopes for ethylene oxidation and the same potential-time dependences.

Electrode preparation.—The anode (and cathode) was a platinum gauze, 0.1 mm wire thickness, 52 mesh size, coated with platinum black. The platinizing procedure was as follows: The gauze was cleaned in hot aqua-regia for several minutes and then washed in distilled water. The platinum electrode was then platinized at a current density of 0.05 amp-cm⁻² (apparent area) for a period of 3 min. The counter electrode in this platinizing procedure was also platinum. The composition of the plating solution was 3% (w/w) platinic chloride and 0.02% (w/w) lead acetate dissolved in 0.1M HCl. During electrolysis the temperature of the solution, which was rapidly stirred, rose to ~50°C. The weight of the platinum deposit was ~2 mg cm⁻². The electrode was finally washed in distilled water. Electrodes, both planar and cylindrical, of various sizes were used, ranging from 20 to 120 cm². The platinized electrode (when employed as an anode) was activated just prior to use by an electrochemical pulsing technique. The electrode was cycled from anodic to

cathodic, going from oxygen evolution to hydrogen evolution, the cycle was carried out about three times and always terminated on the cathodic part of the cycle. The electrolyte was 1M H_2SO_4 and the electrolysis was carried out at a current density of 0.1 amp-cm^{-2} (apparent area).

This activation process was carried out at the start of each run. It was found to give highly reproducible results, obviating the necessity for a freshly platinized electrode before each run.

Gases.—The ethylene used in these experiments was C. P. grade supplied by the Matheson Corporation. The gas analysis was: 99.4% C_2H_4 , 0.5% C_2H_6 , and 0.1% CH_4 . Any traces of O_2 and H_2 were removed by passing the gas through 1m long columns of active copper powder and active copper oxide powder at 210°C . It was found that this purification procedure was not necessary and for later runs was discarded.

Nitrogen gas was 99.996% pure and further purification (cf. above) was found to be unnecessary.

Ethylene partial pressure.—In most of the runs carried out in the work reported here the pressure of ethylene above the electrolyte was 1 atm. However, it was sometimes desired to find the effect of lower solution concentrations of ethylene on the electrode process. Lower solution concentrations of ethylene were affected by mixing ethylene with nitrogen and passing the gas mixture through the electrolyte at a total pressure of 1 atm. The ethylene and nitrogen were metered by means of suitably calibrated flowmeters and in this way the ethylene partial pressure could be controlled from 10^{-2} to 1 atm.

Electrolyte.—The water used in preparing the sodium hydroxide solutions was conductivity water prepared by distillation and having a specific resistivity in excess of $2 \times 10^8 \text{ ohm-cm}$. The sodium hydroxide used was C.P. grade material (Baker, analyzed).

Electrical accessories.—Current-voltage curves for the anodic oxidation of ethylene were studied using potentiostatic and galvanostatic methods. A "Wenking" electronic potentiostat was used. The potentiostat had a maximum current output of 200 ma, its internal resistance was 0.01 ohm and the response time of the potentiostat was $2 \times 10^{-6} \text{ sec}$. The galvanostatic circuit consisted of the usual high voltage, stabilized d-c power supply connected in series to a large variable resistance. The anode potential was measured using a d-c vacuum tube voltmeter (about 10^7 ohm input impedance). The current time and voltage-time variations were recorded on mechanical recorders of about 1 sec response time.

Coulometric Apparatus

The apparatus shown in Fig. 3, was made in order to determine the amount of ethylene consumed during electrolysis by a known amount of electricity.

The cell, constructed from Pyrex glass, consisted basically of three chambers; an anode chamber, A, with gas burette, B; a cathode chamber, C; and, reservoir R. Liquid was circulated in the anode chamber by means of a magnetically operated cen-

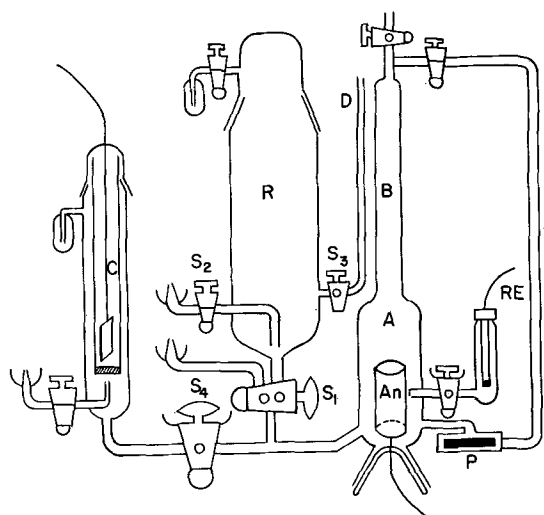


Fig. 3. Apparatus for the coulometric examination of the electrochemical oxidation of ethylene.

trifugal pump, P. The electrolyte was initially all contained in the reservoir R. While in R the electrolyte was saturated, via stopcock, S_2 , with ethylene gas at room temperature and at about 1 atm pressure. At the same time the rest of the apparatus was swept clear of air and filled with ethylene gas. The stopcock S_1 was then opened, and the ethylene saturated sodium hydroxide solution allowed to fill compartments A and C. Compartment A was filled to about one third of the way up the burette B, leaving about 25 ml of ethylene in the gas space. The pressure of ethylene in B was the prevailing atmospheric pressure plus the hydrostatic pressure of the solution corresponding to the difference in liquid levels between compartments B and R. The liquid level difference between B and side arm D was measured after opening stopcock S_3 . At this point the volume of ethylene gas in B was noted. With the liquid and the gas in A and B isolated from the rest of the system, the anode compartment was brought to 70°C and the pump P turned on. Electrolysis was started, there being adequate electrical conductivity across the closed but wetted stopcock S_4 . The anode An, in A, was a platinum gauze cylinder prepared as indicated above. The electrolysis was carried out galvanostatically and the potential of An was mechanically recorded. About every 15 min during the electrolysis, the stopcock S_1 was opened for a short time to admit ethylene saturated electrolyte to A in order to compensate for the decrease in the volume of gaseous ethylene in B. At the end of several hours of electrolysis, noting the number of coulombs passed, the anode compartment was allowed to cool to room temperature. The stopcock S_1 was then opened and the amount of ethylene in B determined as indicated at the beginning of this description.

Results

Steady-state current-voltage curves.—The results of extensive pre-electrolysis on the current-voltage behavior were largely negative. As already mentioned studies carried out by Wroblowa (4) in an all-Teflon cell failed to show any significant effect on the kinetic characteristics of the electrode due to the dissolution of glass. The only influence of puri-

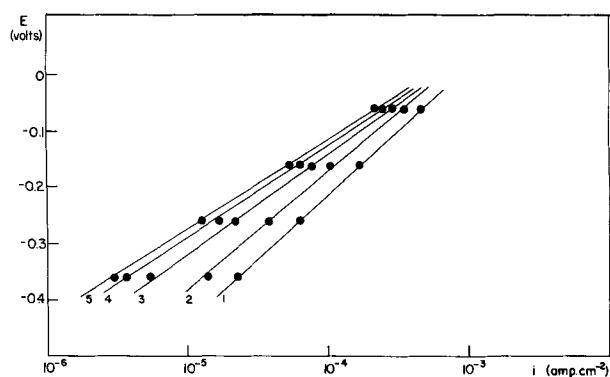


Fig. 4. Dependence of the "Tafel" slope on the degree of approach to steady state. Time passed from the beginning of the electrolysis: (1): 5 min; (2): 10 min; (3): 30 min; (4): 60 min; (5): 120 min. Potentiostatic circuit used. Electrode area 40 cm^2 (geom.). Temperature, 70°C . Ethylene pressure, 1 atm. Potentials given in NHE scale, current densities in $\text{amp}\cdot\text{cm}^2$ (geom. area).

fication noted was that the Tafel range of the current-voltage curve was extended to somewhat lower currents. Measurements of the electrode overpotential were found to be time dependent, approaching, after some time, a steady state. Steady state is arbitrarily defined as that value of potential (when using a galvanostatic arrangement) which changes less than 10 mV/hr , or that value of current (when using a potentiostatic arrangement) which changes less than $10\%/hr$.

The overpotential of the anode, $\text{Pt(Pt)}|1\text{M NaOH}$, 1 atm C_2H_4 (70°C), obeys the Tafel relation over the range of potential -400 mV to 0 mV [normal hydrogen electrode scale (NHE)]. Figure 4 shows the steady state current-voltage curve as well as current-voltage curves taken at intervals (time measured from start of electrolysis) before steady state (see Fig. 10). Curve 1 was obtained, using a potentiostatic arrangement, by plotting the 5 min points from a series of current-time curves. Curves 2, 3, and 4 correspond to the 10, 30, and 60 min points, respectively, and curve 5 corresponds to steady state obtained after 2 hr. Identical (*i.e.*, $\pm 10 \text{ mV}$) results (Fig. 4, curve 5) for the linear part of the Tafel curve were obtained from steady state galvanostatic measurements. It can be seen that the Tafel slope goes from 300 mV (per decade) to 155 mV . It is to be noted that once the current-time curve ($i-t$) or voltage-time curve ($E-t$) has reached the condition referred to as steady state, that the Tafel slope does not change so long as the set of i (or E) points are values taken for the same corresponding value of t . Thus on Fig. 4, curves 4 ($t = 60 \text{ min}$) and 5 ($t = 120 \text{ min}$) give essentially the same Tafel slope, although the extrapolated exchange current would be different. In electrochemical processes 300 mV is not a rational slope, whereas 155 mV , which corresponds to about $(2.303) 2 RT/F$ (in the limit of $\pm 20\%$), is a common, easily explained value in electrode kinetics. The argument just advanced is taken as justification for our selection of the steady state as a condition with meaning for mechanistic analysis.

Rest potential and lower limit of Tafel curve.—At 70°C in the absence of ethylene and with a freshly activated electrode, the rest potential of the electrode

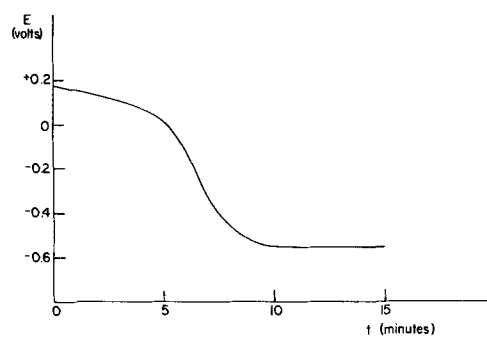


Fig. 5. Decay of the open circuit potential after passivation of the electrode. Electrode kept potentiostatically at $+0.2 \text{ v}$ (NHE) for 5 min, at time $t = 0$ the potentiostatic circuit was interrupted. Electrode area, 25 cm^2 (geom.). Temperature, 70°C . Ethylene pressure, 1 atm.

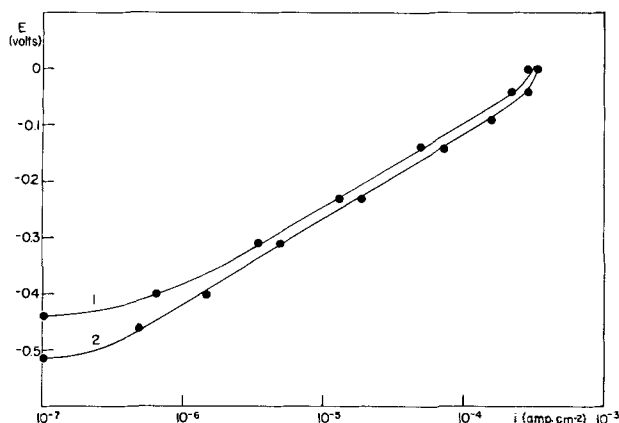


Fig. 6. Effect of pre-electrolysis on the slope of the Tafel curve. Curve 1, without pre-electrolysis; curve 2, after pre-electrolysis. Galvanostatic circuit, steady state conditions. Pre-electrolysis: 8 hr cathodically, 8 hr anodically, at current density $3 \text{ ma}\cdot\text{cm}^2$ (geom. area). Other conditions as for Fig. 4.

was $+50 \text{ mV}$ (NHE), on introducing ethylene the electrode rapidly ($<1 \text{ min}$) achieved a rest potential of -560 mV (NHE). If the electrode was not freshly activated, the time required to respond to the introduction of ethylene was longer, $\sim 5 \text{ min}$. If the electrode is kept potentiostatically at a potential corresponding to electrode passivation, *i.e.*, at $+240 \text{ mV}$ (NHE), and subsequently allowed to decay to the open-circuit potential, it is found that the process is slow as shown in Fig. 5. If the same is repeated, but with nitrogen, rather than ethylene, then there is no significant drop in potential when the circuit is opened.

Pre-electrolysis did not affect the value of the rest potential, but it did affect the shape of the current-voltage curve in the vicinity of the rest potential. This is shown on Fig. 6.

The temperature of the solution is important in determining the rate at which the rest potential is established when ethylene is freshly introduced into the anode compartment, the time necessary to establish the potential increasing with decreasing temperature. At room temperature ethylene had no influence on the potential of the electrode.

Upper limit of the Tafel curve.—Depending on experimental conditions, there is one of two reasons for an upper limit to the Tafel slope. The most important cause for the limit is that at about 0 mV

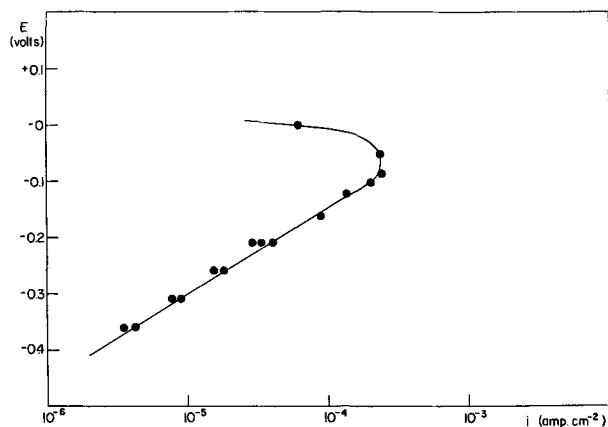


Fig. 7a. Upper limit of the Tafel curve-passivation of the electrode. Potentiostatic circuit, steady state conditions. Electrode area, 25 cm² (geom.). Other conditions as for Fig. 4.

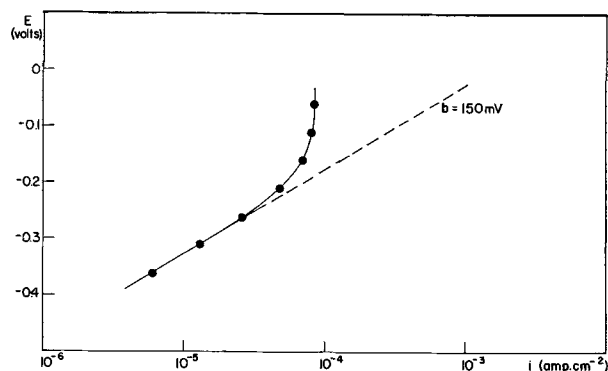


Fig. 7b. Upper limit of the Tafel slope-diffusion control. Ethylene pressure 0.05 atm, other conditions as for Fig. 7a.

(NHE) the platinum electrode passivates: this is shown on the potentiostatic voltage-current curves, Fig. 7a. The other cause for an upper limit is a limiting current associated with transport of ethylene to the electrode. In the latter case the limiting current is dependent on stirring and partial pressure of ethylene (see Fig. 7b).

Ethylene pressure.— There is no significant influence of ethylene partial pressure on the value of the Tafel slope or on the extrapolated exchange current: this is shown on Fig. 7b and Fig. 8. Figure 8 shows the effect of cycling the ethylene partial pressure between 1/10 and 1 atm. It can be seen that the transient effect of changing pressure from 1/10 to 1 atm decreases with time; furthermore there is no transient effect on going from the higher to the lower pressure.

Temperature effect.— The temperature dependence of the current was studied under potentiostatic conditions at $E = -160$ mv (NHE). Figure 9 shows the dependence of steady state current (after 2 hr) on temperature.

Time effects.— A typical $i-t$ curve (taken under potentiostatic conditions) is shown in Fig. 10. The curve was obtained when the electrode, which had been exposed to ethylene, and was at the rest potential, was suddenly polarized to a more positive potential. The initial current, up to ~ 1 min, is due to capacitive charging, and the remainder of the curve is associated with the Faradaic part of the

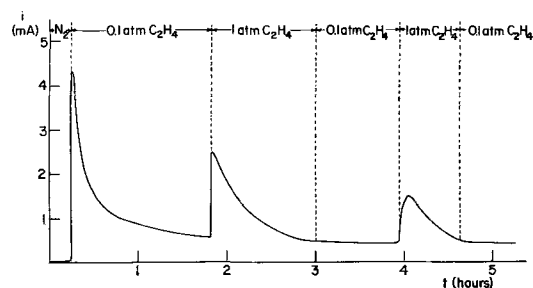


Fig. 8. Pressure dependence of the current. Potentiostatic circuit, $E = -260$ mv (NHE). Electrode, 40 cm² (geom. area). Temperature, 70°C. Pressure of ethylene cycled between 0.1 and 1 atm. Total current given in ma.

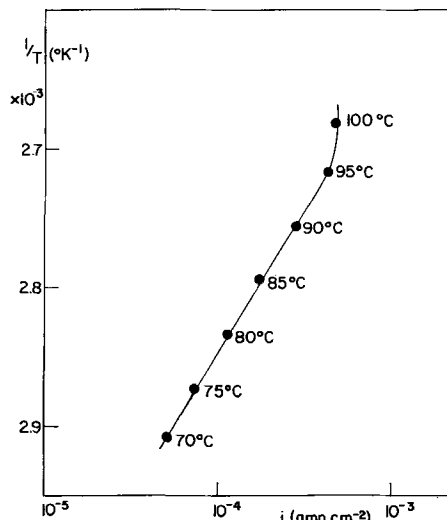


Fig. 9. Temperature dependence of the current. Potentiostatic circuit, $E = -160$ mv (NHE). Steady state conditions. Temperature in range, 70°-100°C. Other conditions as for Fig. 7a.

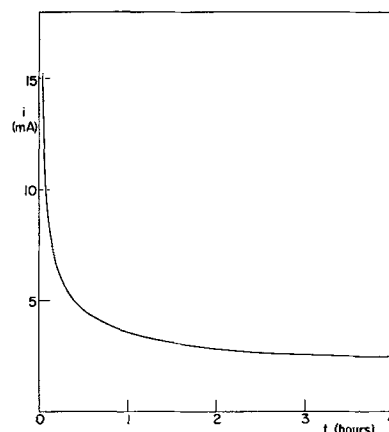


Fig. 10. Current-time curve. Potentiostatic circuit, $E = -160$ mv (NHE). Other conditions as for Fig. 4. Total current given in ma.

electrochemical reaction. There is no simple mathematical function which accurately describes the current decay, however a moderate range of the curve (approximately 10-200 min) can be described as a parabola.

The decay curves depend on the previous history of the electrode in the following way. If the electrode, with ethylene in solution, is first polarized at a high potential (more positive), i.e., just below the passivating potential and maintained until steady

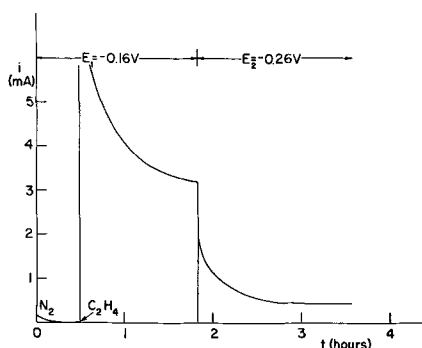


Fig. 11. Transient from higher to lower over-voltage. Potentiostatic circuit, potentials $E_1 = -160$ mv and $E_2 = -260$ mv (NHE). Other conditions as for Fig. 10.

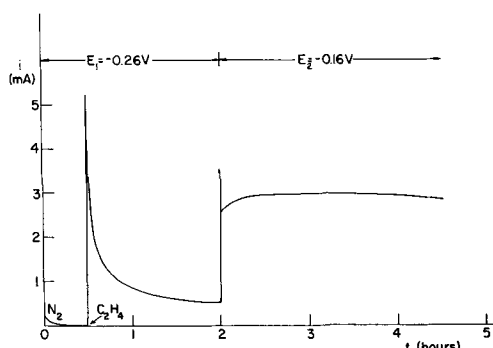


Fig. 12. Transient from lower to higher over-voltage. Potentiostatic circuit, potentials $E_1 = -260$ mv and $E_2 = -160$ mv (NHE). Other conditions as for Fig. 10.

state is reached, then as the potential is reduced step-wise at long intervals, a series of $i-t$ curves will be obtained as shown in Fig. 11. However if the electrode is first polarized at a low potential and the potential raised in a series of steps then a curve as shown on Fig. 12 results.

When the electrode is brought first to the passivation potential and then potentiostatically returned to a more negative potential, the electrode is completely reactivated, *i.e.*, the initial current, in an $i-t$ plot, is high and is identical in behavior with the curve shown on Fig. 10.

It was stated above that only the initial part of an $i-t$ curve is to be associated with capacitive charging. This was demonstrated in the following way. The electrode was maintained at -160 mv (NHE) in a nitrogen atmosphere thereby charging the double layer. When the current was steady, *i.e.*, charging was complete, ethylene was bubbled into the system, and the $i-t$ decay curve recorded. If account is taken of the time required to saturate the solution (~ 5 min) then it is found that the $i-t$ curve is here the same as the $i-t$ curve obtained starting with ethylene. This bears out the point that the long time part of the decay process is Faradaic.

Coulometric measurements.—The results of four coulometric measurements are given in Table I. It can be seen that the results are, within the experimental error of $\pm 5\%$, equivalent to the rational value of 12 electrons per ethylene molecule. This points to complete oxidation of ethylene. A rough confirmation of this result was obtained by titrating the carbonate formed as a result of the oxidation of

Table I. Stoichiometry of the anodic oxidation of ethylene. Ethylene consumed vs. coulombs passed

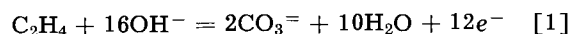
Experiment run number	1	2	3	4
Potential [mv (NHE)]	-160	-110	-80	-60
Amount of C_2H_4 consumed [millimoles]	0.63	1.08	1.24	1.20
Coulombs passed	816	1260	1464	1360
Number of Faradays per mole C_2H_4	13.5	12.1	12.2	11.8

the ethylene. Three independent runs gave the ratio of moles of carbonate in solution to moles of ethylene consumed as 2.2, 2.4, and 2.3. The expected value is 2, however it is difficult to keep a concentrated sodium hydroxide solution free of carbonate.

Discussion

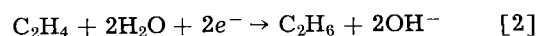
Experimental Results

One of the objects of this investigation was to determine those steady state parameters of the electrochemical oxidation of ethylene important to mechanistic analysis. In this connection there are three results of importance. (a) The over-all stoichiometry of the anodic reaction can be represented by the equation



(b) The Tafel slope is essentially $2RT/F$. (c) The effect of ethylene pressure is zero, *i.e.*, $(\partial \ln i / \partial \ln P_{C_2H_4})_E = 0$.

It is clear from the experimental results that the ethylene electrode is always far more positive than the hypothetical reversible ethylene electrode [calculated (5) to be -0.85 v]. The rest potential of -0.56 v found in this investigation can be understood in terms of two competing electrochemical reactions. The two reactions are the anodic process given in Eq. [1] and the cathodic process.



The standard thermodynamic reversible potential for reaction [2] is -0.31 v. There is ample experimental evidence for the occurrence of this reaction (6).

If the Tafel slope for the anodic reaction is extrapolated to -0.85 v the resulting apparent exchange current (using the geometrical area) of the electrode is 5×10^{-9} amp-cm $^{-2}$. In order to obtain the real exchange current it is necessary to know the roughness factor, B , of the platinized electrode. Various values of B have been determined. Thus comparing the rates of ethylene oxidation on platinized platinum and bright platinum gave ~ 100 . Capacitive charging gave $B \sim 200$, and adsorption of C^{14} labelled thiourea gave $B \sim 250$. B is then roughly between 100 and 300 giving a true i_0 of about 5×10^{-11} amp-cm $^{-2}$ to 10^{-12} amp-cm $^{-2}$.

Reaction Kinetics

The detailed mechanism of the electrochemical oxidation of ethylene is obviously most complex, and it is not the object of this discussion to postulate specific complete sets of reaction sequences. Here we are concerned with the examination of simplified steady state reaction sequences with a view to the

interpretation of the experimental data of the anodic ethylene reaction in terms of the concept of the rate determining step.

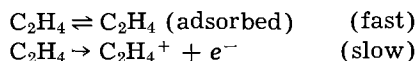
Assumptions.—When considering electrode processes the following simplifying assumptions are made (7, 8).

No multi-electron transfer processes are admitted as possible in a single step. The fractional coverage of the electrode (or that part of the electrode active in electrolysis) with reacting species is either taken to be limiting low, less than 1/10 coverage, or else the coverage tends to 1 in one species only, all other species having negligible low coverages. All steps are taken to be activation controlled, *i.e.*, there is no limitation due to diffusion. The electrochemical transfer coefficient, α , is taken to be $\frac{1}{2}$.

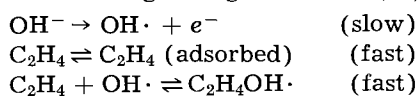
In the kinetics of simplified open reaction sequences each step in the reaction is taken to be simple and first order with respect to the intermediate species. All steps prior to the rate determining step (r.d.s.) are treated in equilibrium. Steps after the r.d.s. need not be in equilibrium but the forward path of these subsequent steps must be fast compared with the r.d.s.

The ethylene reaction.—The Tafel slope.—The Tafel slope for the anodic oxidation of ethylene was found to be essentially $2RT/F$. From an analysis of open chain reaction sequences (8) the following possibilities for a slope of $2RT/F$ exist.

(a) For low surface coverage, the first electron transfer step could be the r.d.s., *e.g.*



(b) For both low and high coverage, rate determining OH^- discharge can give $b = 2RT/F$, *e.g.*



(c) For high coverage of the intermediate in the forward step of an electron transfer r.d.s., which may be any stage in the sequence, we obtain $b = 2RT/F$.

Since the reaction velocity was found to be independent of ethylene pressure, it is clear that reaction scheme (a), above, cannot apply to our system. Reaction schemes (b) and (c) will show no dependence on ethylene pressure in the steady state and are therefore both admissible. Further analysis of the reaction mechanism requires that we appeal to other features of the experimental study of the anodic oxidation of ethylene.

Passivation of the electrode.—The passivation of the electrode at positive potentials has been noted in previous papers (9-11). This phenomenon is attributed to the formation of an oxide layer on which the rate of ethylene oxidation is insignificantly low. The onset of the formation of an oxide film on platinum at 0v (NHE) in alkaline solution is supported by various studies (12-15).

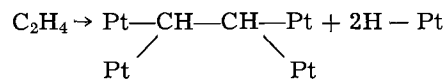
The formation of an oxide film in alkaline solution is taken as strong evidence for occurrence OH^- discharge. Thus, it is postulated that when the surface concentration of hydroxyl radicals achieves a

sufficiently high surface concentration so that the reaction



can occur, only then does oxide formation commence. Since there is evidence for extensive OH^- discharge near 0v (NHE) it seems reasonable to assume that OH^- discharge also occurs at more negative potentials.

Time effects.—The deactivation and reactivation of platinum electrodes reported above can only be understood in terms of high surface coverage of organic intermediate species. Furthermore recent experiments (16) carried out on the electrochemical oxidation of C^{14} -ethylene at platinum electrodes in alkaline solution at 70°C have shown that decreasing activity of the electrode is associated with increasing electrode coverage with C^{14} -containing material and that activation of the electrode is associated with removal of C^{14} -containing species. The high initial activity of the electrode may perhaps be associated with the dissociative chemisorption of ethylene according to the scheme (17-19)



whereupon the hydrogen formed will be rapidly oxidized. However, the $\begin{array}{c} \diagdown \quad \diagup \\ \text{CH}-\text{CH} \\ \diagup \quad \diagdown \end{array}$ fragment would be less susceptible to oxidation and since its surface concentration would build up in time, it may lead to decreasing surface activity, and a change in mechanism.

In Fig. 12 it was shown that on going from more negative to more positive potentials, that the current increased to a steady state value, rather than decreased. When we couple this observation with the observation that the corresponding increase in potential is associated with a decrease in surface coverage in carbon containing species (C^{14} -work) (16), we conclude that scheme (c) above is unlikely. This is so since scheme (c) requires that the reaction velocity be a linear function of the surface coverage of the organic species which appears in the r.d.s.

It should be noted here that $\theta \rightarrow 1$ need not correspond to the use of every platinum surface atom. Thus if a two-point attachment process is involved in the chemisorption of an organic molecule the maximum surface coverage will be about 92% (20). For four-point attachment the number of holes in a completed monolayer will be even greater than 8%. If surface strain is involved in the configuration of the adsorbed species there may only be certain geometrically favored sites which will accommodate two-point surface attachment (21, 22). This could lead to saturation surface coverages, *i.e.*, $\theta \rightarrow 1$, which corresponds to actual surface coverages which are much below a monolayer, based on a count of platinum surface atoms. This is in fact another way of stating the concept of active centers.

We have pointed out that "high" electrode coverage with organic species is likely, but that direct electron transfer from such species in the rate de-

termining step seems to be excluded. We are left with scheme (b). Thus, as previously pointed out, rate determining hydroxyl discharge should lead to a Tafel slope of $2RT/F$, and no ethylene pressure dependence, at the extreme conditions of intermediate species coverage. Furthermore the connection of the transient behavior with coverage of C^{14} -carbon species, mentioned above, can be understood when it is realized that this phenomena (shown in Fig. 12) occurs only at about -150 mv (i.e., about -150 mv from passivation potential). Here OH^- discharge becomes comparable in rate to the rate of build of oxidizably organic species, whence the reaction of OH radicals with the organic material on the electrode results in a decrease in organic species surface concentration, and a corresponding increase in area available for OH^- discharge. The result of more extensive OH^- discharge leads finally to surface oxide formation and passivation, as discussed above.

It should be noted that while the above conclusions are consistent with the data, much more elaborate experimental work is required to prove the complete truth of our conclusions.

Acknowledgments

We wish to thank Dr. H. Wroblowa of this Laboratory for making some unpublished work available to us and also for participating in discussions on the time effect. We wish to thank Mr. A. P. Saunders, the Chemistry Department Glass Blower, for his design of the centrifugal pump shown on Fig. 3. It is also a pleasure to acknowledge the generous support of this work by the Pratt & Whitney Aircraft Division of the United Aircraft Corporation.

Manuscript received April 9, 1963; revised manuscript received Feb. 4, 1964.

Any discussion of this paper will appear in a Discussion Section to be published in the December 1964 JOURNAL.

REFERENCES

1. J. M. Schlatter, American Chemical Society Meeting, Chicago, September 1961.
2. G. J. Young and R. B. Rozelle, "Fuel Cells," G. J. Young, Editor, p. 28, Reinhold Publishing Corp., New York (1960).
3. W. T. Grubb, Proceeding of 16th Annual Power Source Conference 1962.
4. H. Wroblowa, Private communication.
5. W. M. Latimer, "Oxidation Potentials," p. 135, Prentice Hall, New York (1952).
6. J. Giner, Private communication.
7. J. O'M. Bockris, *J. Chem. Phys.*, **24**, 817 (1956).
8. M. Green and P. H. Robinson, *This Journal*, **106**, 253 (1959).
9. K. Franke, C. A. Knorr, and M. Breiter, *Z. Electrochem.*, **63**, 226 (1959).
10. W. Bold and M. Breiter, *Electrochem. Acta*, **5**, 145 (1961).
11. M. Breiter, *ibid.*, **7**, 601 (1962).
12. A. I. Shlygin and A. N. Frumkin, *Acta Physicochim.*, **3**, 791 (1935).
13. K. J. Vetter and D. Berndt, *Z. Elektrochem.*, **62**, 378 (1958).
14. J. Giner, *ibid.*, **63**, 386 (1959).
15. W. Visscher and M. A. V. Devanathan, To be published.
16. H. Dahms, M. Green, and J. Weber, *Nature*, **196**, 1310 (1962).
17. O. Beeck, A. E. Smith, and A. Wheeler, *Proc. Roy. Soc. (London)*, **A177**, 61 (1940).
18. O. Beeck, *Rev. Mod. Physics*, **17**, 61 (1945).
19. G. C. Bond, "Catalysis by Metals," p. 233, Academic Press, New York (1962).
20. A. R. Miller, "The Adsorption of Gases on Solids," C.U.P., 1949.
21. G. H. Twigg and E. K. Rideal, *Trans. Faraday Soc.*, **36**, 533 (1940).
22. M. Green and A. Liberman, *J. Phys. & Chem. Solids*, **23**, 1407 (1962).

The Relative Electrocatalytic Activity of Noble Metals in the Oxidation of Ethylene

Harald Dahms¹ and John O'M. Bockris

The Electrochemistry Laboratory, University of Pennsylvania, Philadelphia, Pennsylvania

ABSTRACT

A comparative study of the anodic oxidation of ethylene on five noble metal electrodes (Au, Ir, Pd, Pt, Rh) in 1M sulfuric acid at 80°C is reported. Complete oxidation of ethylene to CO_2 was observed on Pt, Ir, and Rh. On Au and Pd practically no CO_2 could be detected and the main products of the reaction were aldehydes and acetone. The Tafel slopes as well as pH and pressure effects are also found to be different for the two groups of metals. The order of chemical reactivity in the two groups of metal catalysts is $Pt > Rh > Ir$ and $Pd > Au$.

There has been a recent surge of studies on the electro-oxidation of hydrocarbons because of their possible use in electrochemical energy conversion (1). Since most of these investigations concerned more or less technological aspects, the results are usually too complex to allow electrode kinetic analysis. The more fundamental aspects of a few organic

systems have been studied (2-8), but almost exclusively on platinum. Only a few attempts have been made to study the role of the metal in organic electro-oxidation (2). Hitherto, insufficient data have existed to form the basis of some first concepts of catalytic activity and its dependence on the metal for electro-oxidation. A parallelism of the relevant considerations to catalysis at the metal-gas inter-

¹ Present address: Thomas J. Watson Research Center, International Business Machines Corporation, Yorktown Heights, New York.

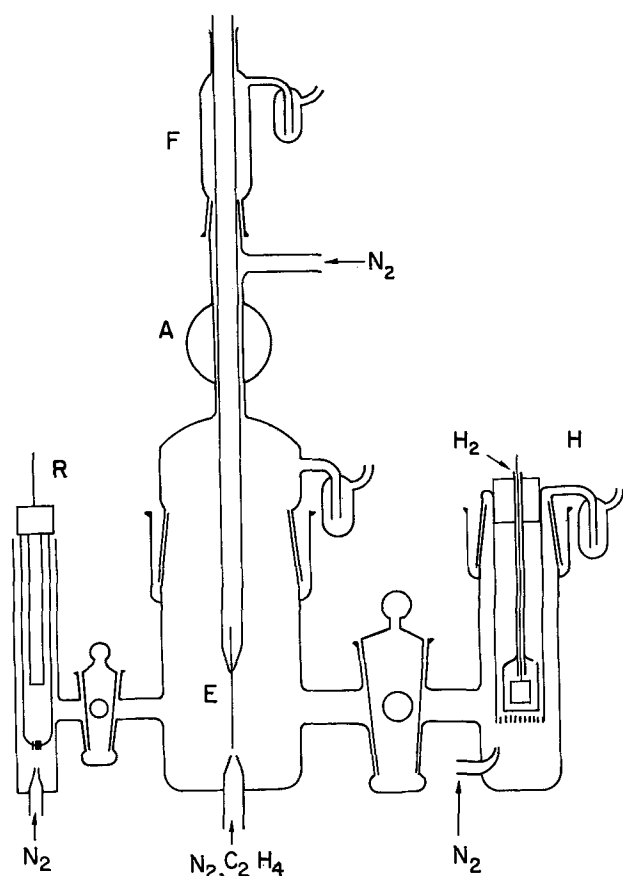


Fig. 1. Cell for pre-treatment of metals and electrode kinetic studies. F, electric furnace; A, stopcock; R, reference electrode; E, working electrode; H, hydrogen electrode used as counter electrode.

face (9) cannot be expected to be close. The electric field across the reaction zone and the structure of the double layer are factors in electrocatalysis which do not have analogues at the metal-gas interface. Furthermore, reaction products from the solvent (e.g., metal oxides in aqueous solutions) can take part in the reaction sequence.

Here, a study of the electro-oxidation of ethylene on bright noble metal electrodes (Au, Ir, Pd, Pt, Rh) in aqueous sulfuric acid solutions is reported.

Experimental

Cell.—The cell is shown in Fig. 1. Cells of this type have been used extensively in electrode kinetic studies of inorganic systems (10), but rarely in electro-oxidation. The electrode E can be treated in the furnace F in an inert atmosphere and can then be introduced into the cell through stopcock A without contacting air. The compartment containing the counter electrode (platinized platinum gauze/ H_2) is separated by a stopcock. In order to avoid any diffusion of hydrogen into other parts of the cell, the electrode is separated by a fritted glass over which nitrogen is passed continuously. The temperature in the compartment of the working electrode is controlled by a contact thermometer at $80^\circ \pm 1^\circ C$ in connection with an electric heating tape wound around the cell. The potential of the working electrode is measured against a saturated calomel electrode in another compartment separated by a stop-

cock. The reference electrode was kept at room temperature.²

Circuit.—The potential was applied from a lead acid battery over a potentiometer between the working electrode E and the hydrogen counter electrode H. The relative resistances of the potential divider and the circuit containing the cell allowed this arrangement to apply a constant potential between cathode and anode. The large relative area of cathode to anode made the arrangement that of a potentiostat for the anode. The circuit contained an electronic microammeter (voltage drop across the instrument <1 mv). A recorder was attached to the microammeter. A high impedance vacuum-tube millivoltmeter was used to measure the potential between the working anode and the calomel reference electrode.

The circuitry for recording galvanostatic transients on an oscilloscope (determination of the oxide coverage) has been described (14, 15).

Electrodes.—These were wires of 0.5 mm diameter sealed into glass (slip joints) exposing a geometric area of 1 cm². The purity was better than 99.9% for all metals.

The electrodes were pre-treated in two ways:

(A) The electrodes were introduced into the furnace and heated in a pre-purified nitrogen atmosphere for 1 hr to a temperature corresponding to one half of their melting points (in degrees Kelvin, e.g., Au $400^\circ C$, Pt $750^\circ C$, etc.). The electrodes were cooled down in the furnace to room temperature within 20-30 min. They were then lowered through the stopcock and immersed into the solution under a given potential.

(B) The electrodes were dipped into a cleaning solution of concentrated H_2SO_4 and nitric acid (1:1) for about 30 sec. They were then brought into contact with conductivity water for several minutes. The electrodes were then introduced into the cell and polarized up to hydrogen evolution for 5 min to reduce the oxides (except for Pd which was kept at a potential of $+150$ mv against the hydrogen electrode). The electrodes were then brought to $+0.4$ v (hydrogen scale). The hydrogen was swept out with N_2 before starting measurements.

Solution preparation.—Solutions were prepared from conductivity water and A.R. concentrated sulfuric acid. Pre-purified nitrogen was passed through the solution to sweep out other dissolved gases. Ethylene gas was then passed through the solution and bubbled throughout the experiment. The ethylene had a minimum purity of 99.5% (analysis of the impurities indicated ethane, propane, propylene, butane, butylene, no hydrogen).³ Lower concentrations of ethylene were obtained by mixing it with

² All potential values below are given against the standard hydrogen electrode at $80^\circ C$, i.e., the temperature of the working electrode. Therefore, the potential E' measured between the working electrode (80°) and the saturated calomel electrode ($+0.245$ at $25^\circ C$) had to be corrected by the temperature coefficient of the standard hydrogen electrode given by de Bethune *et al.* (11) as $dV/dt = +0.87$ mv/degree. Measurements of Fales and Mudge (12) show that this gradient is approximately constant with temperature. Hence, the potential, E , against the standard hydrogen electrode at $80^\circ C$, is given by

$$E = E' + 0.245 - 0.049$$

Liquid junction and Peltier potentials are insignificant (13).

³ Purification of the solution by pre-electrolysis had no effect on i_0 and the Tafel slope (7).

pre-purified nitrogen in controlled proportions and using calibrated flowmeters.

Procedure.—Measurements of the reaction rate as a function of potential, pH, and ethylene concentration.—The electrode (pre-treatment, see above) was immersed in sulfuric acid with pre-purified nitrogen passing through the system. The residual currents due to impurities and corrosion on Pd (17) were recorded. Then, ethylene was passed through the solution while the electrode was kept at a potential just less than that at which appreciable oxide formation commenced (see below. These potentials were: for Pt, + 850 mV_{NHE}, Au, + 950 mV_{NHE}, Pd + 700 mV_{NHE}, Ir and Rh, + 600 mV_{NHE}). After allowing time for the ethylene concentration to reach the equilibrium value (ca. 30 min) the measurements were started. The potential was changed stepwise and the current was recorded at each steady potential. After some 15 sec, the variation of current with time in the next 20 min was <10%. The criterion for steady state was that the same currents were obtained $\pm 10\%$ when the potential-current relation was recorded with decreasing and increasing electrode potential (see Fig. 2).

Determination of the over-all reaction.—Electrodes of larger areas were needed in order to detect and to determine the reaction products quantitatively. For Au, Pt, and Pd bright metal sheets and gauzes could be used (areas 40-500 cm²). For Ir and Rh, sufficient currents (5-40 ma) could be obtained only if the electrode surfaces consisted of black electro-deposits (high surface roughness).

A constant current was passed through the cell with the potential of the electrode having a value that was always on the linear part of the corresponding Tafel plot (see below). Ethylene was constantly bubbled through the cell. The outgoing gases were passed at first through a trap filled with saturated barium hydroxide solution. The carbon dioxide which was produced in a certain time at constant current was determined by titration with 0.05M HCl. Appropriate precautions to exclude extraneous CO₂ were taken. For another period of time the reaction products were collected in a trap cooled at -80°C and then analyzed by a gas chromatograph. After the run a sample of the electrolytic solution was also gas chromatographically analyzed.

Results

The over-all reaction.—The analytical results are given in Table I.

Table I. Reaction products of the electro-oxidation of ethylene (1M H₂SO₄, 80°C)

	Conversion to CO ₂	Reaction products in gas phase other than CO ₂	Reaction products in electrolyte solution
Pt	Complete*	—	—
Ir	Complete†	—	—
Rh	Complete†	—	—
Au	<5%	Acetaldehyde, acetone, propionaldehyde	Propionaldehyde, acetone, acetaldehyde
Pd	<5%	Acetaldehyde, propionaldehyde	Propionaldehyde, acetone, acetaldehyde

* Given in ref. (7) for platinized platinum (accuracy $\pm 1\%$); the result was confirmed on bright platinum.

† Accuracy $\pm 20\%$.

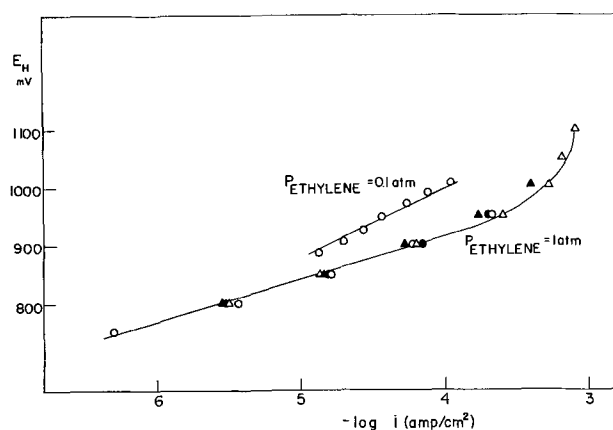


Fig. 2. Current-potential dependence of the electrode Au/1M H₂SO₄, ethylene (80°C). ●, Decreasing the potential, value measured after 15 sec; ▲, increasing the potential, value measured after 15 sec; ○, decreasing the potential, value measured after 3 min; △, decreasing the potential, value measured after 3 min.

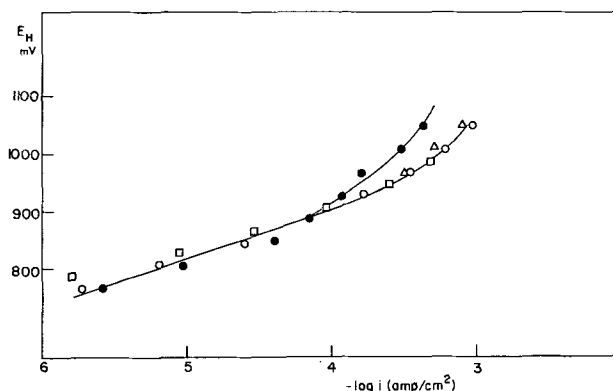
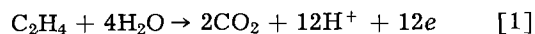


Fig. 3. Current-potential dependence of the electrode Au/1N Na₂SO₄, x, M H₂SO₄, ethylene (80°C); □, x = 2M; ○, x = 1M; x = 0.6M, ●, x = 0.1M.

Even though the accuracy of the CO₂ determination for Ir and Rh was only $\pm 20\%$, the conversion can be considered to be quantitative since no other reaction product could be detected. Hence, the over-all reaction for iridium and rhodium is identical to that given for platinum (7) as



The main reaction products on Au and Pd are aldehydes and ketones. Thus, the average number of transferred electrons per ethylene molecule is about $n = 2$.

The reaction rate as a function of potential, pH, and ethylene concentration.—Gold.—The current-

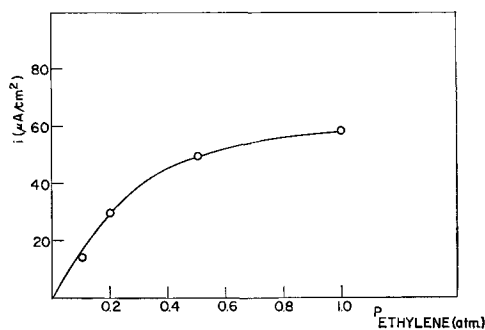


Fig. 4. Current-partial pressure of ethylene on Au/1M H_2SO_4 , ethylene (80°C) at constant potential $E_H = +0.900\text{v}$.

potential relation is given in form of a Tafel plot (Fig. 2). Note that the measurements at $p_{\text{ethylene}} = 0.1$ atm were recorded in the limiting current region. The two points at the lowest current densities are outside this region.

The current shows no appreciable change with the hydrogen ion concentration in the Tafel region (Fig. 3). The current is given as a function of the partial pressure of ethylene in the solution at constant potential in Fig. 4.

Palladium.—Tafel plots at different hydrogen ion concentrations are given in Fig. 5. The hydrogen ion concentration has no influence in the Tafel region. The current as a function of the ethylene partial pressure is plotted in Fig. 6.

Platinum.—Tafel plots in acid concentrations from 0.01M to 1.0M are given in Fig. 7.

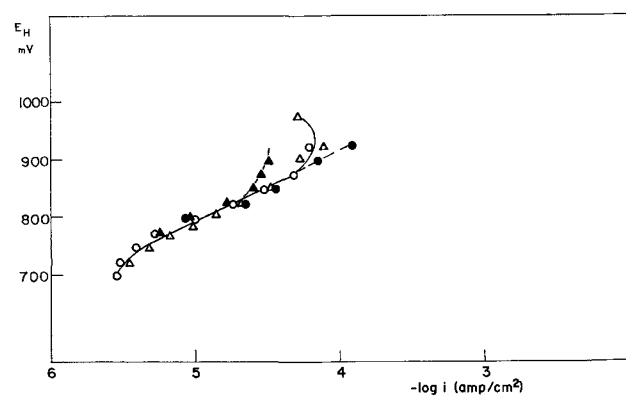


Fig. 5. Current-potential dependence of the electrode Pd/1N Na_2SO_4 , x , M H_2SO_4 , ethylene (80°C). \circ , $x = 1\text{M}$, decreasing the potential; Δ , $x = 1\text{M}$, increasing the potential; \bullet , $x = 2\text{M}$; \blacktriangle , $x = 0.1\text{M}$.

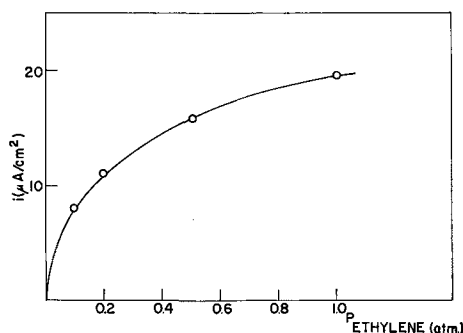


Fig. 6. Current-partial pressure of ethylene on Pd/1M H_2SO_4 , ethylene (80°C) at constant potential $E_H = +0.830\text{v}$.

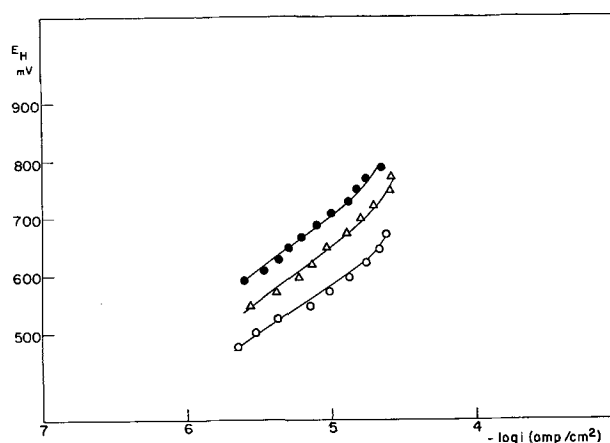


Fig. 7. Current-potential dependence of the electrode Pt/1N Na_2SO_4 , x , M H_2SO_4 , ethylene (80°C); \circ , $x = 0.01\text{M}$; Δ , $x = 0.1\text{M}$; \bullet , $x = 1.0\text{M}$.

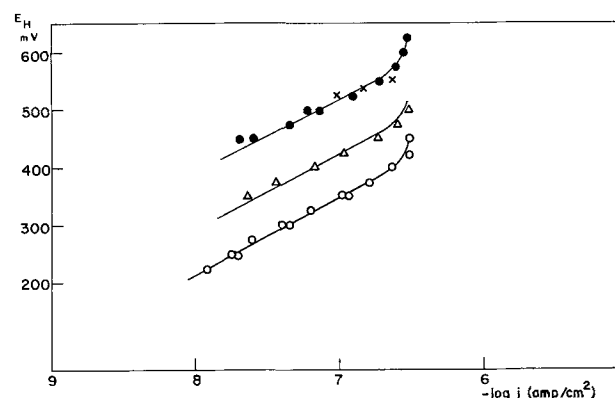


Fig. 8. Current-potential dependence of the electrode Ir/1N Na_2SO_4 , x , M H_2SO_4 , ethylene (80°C), \circ , $x = 0.01\text{M}$; Δ , $x = 0.1\text{M}$; \bullet , $x = 1.0\text{M}$; \times , $x = 1.0\text{M}$ (smooth electrode).

Iridium.—Because of the low current densities, measurements on smooth electrodes could be carried out only at high anodic potentials. The measurements were then extended to lower potentials using black iridium surfaces. By comparing the currents obtained on smooth and black electrodes at the same (high) anodic potential, the effective surface area of the black electrode could be obtained. The current densities given in Fig. 8 correspond to those at smooth electrodes.

Rhodium.—The technique used here was the same as that applied to iridium (Fig. 9).

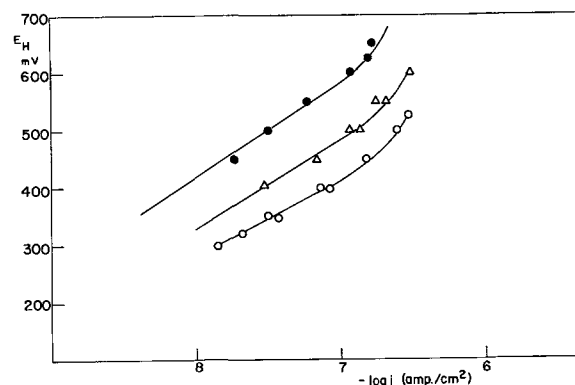


Fig. 9. Current-potential dependence of the electrode Rh/1N Na_2SO_4 , x , M H_2SO_4 , ethylene (80°C); \circ , $x = 0.01\text{M}$; Δ , $x = 0.1\text{M}$; \bullet , $x = 1.0\text{M}$.

Table II. Effect of surface pre-treatment on reaction rate

	A-electrodes		B-electrodes	
	i ($\mu\text{a}/\text{cm}^2$)	Tafel slope (mv)	i ($\mu\text{a}/\text{cm}^2$)	Tafel slope (mv)
Au*	270	80	540	70
Pd†	84	130	99	125
Pt‡	18.6	170	26.5	170

* Au at $E_H = 1000$ mv, 1M H_2SO_4 (80°C), 1 atm ethylene.
 † Pd at $E_H = 850$ mv, 1M H_2SO_4 (80°C), 1 atm ethylene.
 ‡ Pt at $E_H = 700$ mv, 0.1M H_2SO_4 , 1N Na_2SO_4 (80°C), 1 atm ethylene.

Table III. Calculated maximal oxygen coverages

	Molar volume, cm^3	Surface atoms per cm^2	Charge for monolayer per cm^2 $\mu\text{coulomb}$	R, Roughness factor*	Charge for monolayer per apparent cm^2 $\mu\text{coulomb}$
Pt	9.12	$1.63 \cdot 10^{15}$	523	1.2	630
Pd	8.77	$1.67 \cdot 10^{15}$	534	2.0	1060
Rh	8.27	$1.74 \cdot 10^{15}$	557	1.5	840
Ir	8.57	$1.70 \cdot 10^{15}$	544	1.5	810
Au	10.20	$1.53 \cdot 10^{15}$	490	1.2	590

* Obtained from galvanostatic charging curves taking the electrode capacity $C = 16 \mu\text{Fd}/\text{cm}^2$ for $R = 1$.

Reaction rates as a function of the pre-treatment of the electrode.—The influence of the pre-treatment (A and B see above) was studied on the metals that showed a sufficiently high current density to work on smooth electrodes of 1 cm^2 . The results are shown in Table II.

The oxygen coverage.—The amount of charge required to reduce the oxide (Fig. 10) was converted into coverage by using the maximal coverages obtained in Table III. The number of metal atoms lying at the surface is calculated from the molar volume. Assuming one atom of oxygen per surface atom of metal we obtain the charge for forming or reducing a monolayer. This value has to be multiplied by the roughness factor (determined from charging curves).

The coverages given in Fig. 11 are obtained by referring the experimentally determined values to the maximal charges calculated in Table III. The calculation of the coverages involves two assumptions: (A) The reduction of oxygen is complete. It has been shown, however, on a number of metals that the charge q_a required to form an oxygen layer differs from the charge required to reduce this layer q_c ($q_a > q_c$) (16, 17). (B) The ratio oxygen:surface atom = 1:1. In certain cases, however, this ratio was found to be different. These considerations do not affect essentially the relation between oxygen coverage and the rate of the ethylene reaction which is considered below.

Discussion

General Considerations

Thermodynamics of the reaction.—The equilibrium potential can be easily calculated from the thermodynamic data of the reaction products (18). For reaction [1] this value is found to be $E_o = 0.08$ at 80°C (hydrogen scale).

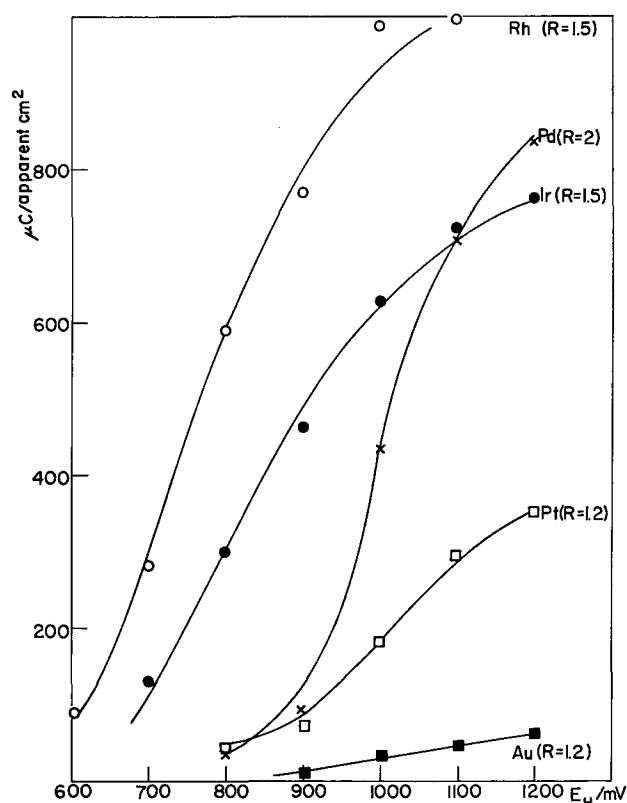


Fig. 10. Charge required for cathodic reduction of oxide on Au, Pt, Ir, Pd, Rh in dependence of potential. Solution: 1M H_2SO_4 , N_2 atmosphere ($R =$ roughness factor).

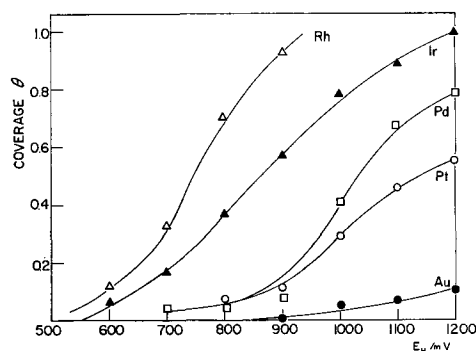


Fig. 11. Oxygen coverage in terms of θ calculated from Fig. 10

The rest potential of the system Me/ethylene appears to be a mixed potential (6, 8).

The "chemical" rate constant.—The rate of an activation-controlled reaction at an electrode is given by (19)

$$i = nFkc \exp \left[\frac{\alpha F (\Delta\zeta + \phi_M - a)}{RT} \right] \quad [2]$$

if there is no potential drop in the diffuse double layer and the rate of the back reaction is negligible; (n is the number of electrons, F Faraday, k rate constant, α transfer coefficient, $\Delta\zeta$ potential of electrode against standard hydrogen electrode, ϕ_M electronic work function in ev, a constant).

In order to bring out the "chemical" catalytic activity of the different metals we have to eliminate the influence of the applied electrical field. The electrical field across the interface can be written as (20)

$$\Delta\zeta = \Delta\psi + \Delta\chi \quad [3]$$

where $\Delta\zeta$ is potential difference against standard electrode (e.g., hydrogen electrode), $\Delta\psi$ potential difference due to excess charges of metal, $\Delta\chi$ potential difference due to orientation of dipoles.

It appears useful to define the "chemical" rate as the reaction rate at $\Delta\psi = 0$, i.e., at the potential of zero charge $\Delta\zeta = \Delta\zeta_{p.z.c.}$. As can be seen from Eq. [3], the potential of zero charge contains a dipole term. This term can be due to (a) the orientation of water dipoles at the interface, and (b) the adsorption of the reactant and of intermediate reaction products on the electrode. The orientation of the water dipoles appears not to differ at the potential of zero charge greatly from metal to metal, since Frumkin (21) found the approximate relation

$$\phi_{M_1} - \phi_{M_2} = \Delta\zeta_{M_1}^0 - \Delta\zeta_{M_2}^0 \quad [4]$$

where ϕ_M is electronic work function, $\Delta\zeta_M^0$ potential of zero charge.

The change of the $\Delta\chi$ potential with adsorption of the reactant and of the intermediates can be estimated from the change of the potential of zero charge on mercury with the adsorption of neutral (22) and charged (23) organic species: Typical values of this shift for full coverage of the electrode with neutral species are 0.1-0.2v. Charged species could cause higher shifts, if present at sufficient concentrations (e.g., $\theta > 0.1$), which is improbable in the present system. Hence, the dipole term in Eq. [4] could cause an error of 0.1-0.2v, which would lead to a maximal change of one power of ten in the "chemical" rate constant of Eq. [3] (α assumed = 0.5).

The definition of the "chemical" rate at $\Delta\psi = 0$ may be considered as indicative (within these limits) of the reaction rate on the various surfaces free from double layer effects.

The factors determining the "chemical" rate constant at the interface metal/gas (24, 25) are well known, e.g., they concern: (a) geometric factors which affect the activation energy of reactants (26, 27); (b) the electronic work function, which affects the heat of adsorption (28); (c) the d-band structure influences the heat of adsorption (e.g., in the adsorption of hydrogen and ethylene) (29).

For catalysis at the metal-electrolyte interface, one has to take into account these factors, remembering that they can act both on the solute reactant

and also on the solvent reactant; for example, oxides will be formed and may participate either directly, or as inhibitors, in determining the rate of the reaction.

The effect of the applied field.—A change of the field across the double layer will have mainly two effects: It will (a) change the rate of any reaction step involving charge transfer, and (b) change the adsorption energy of the reactants, i.e., vary their concentration in the reaction zone.

The surface concentration of the organic reactant depends on the applied electric field. Analogous to the adsorption on mercury (22), it has been found that there is a potential range of 0.2-0.4v on both sides of the potential of zero charge, where there is significant adsorption at the interface (30, 31). Roughly, the adsorption-potential relation is parabolic. Generally, there is a relation between the potential of zero charge and the potential of maximal adsorption [cf. adsorption on gold electrodes (30) and other metals (31)], but exceptions occur on certain metals (31).

In summary, the catalytic activity on an electrode is a resultant of the effects of the chemical rate constants and the double layer field effects, the degree of the effect of which is a function of the transfer coefficient, α . Hence, a low chemical rate constant on one metal can be compensated by a higher α on another.

Application to Present Reaction

Phenomenological.—(i) The over-all reaction. The products of the over-all reaction are given in Table IV.

(ii) The "chemical" rate constants. These are given in Table IV. The potentials of zero charge on which the calculations are based were determined experimentally only for Pt (32, 33), Au (34, 35), and Pd (33). The corresponding values for Ir and Rh were calculated from the empirical relation (21) between electronic work functions and potential of zero charge.

(iii) The effect of the applied field. The influence of the applied field on the reaction rate is given in Table IV.

(iv) The effect of pre-treatment. The two methods of pre-treatment of the electrode do not cause essential differences in the reaction rates (Table II).

Table IV. Ethylene oxidation and characteristic properties of the metals

Reaction product	"Chemical" reaction rate at p.z.c.,* amp/cm ²	pH dependence $\left(\frac{dE}{dpH}\right)_i$	Tafel slope $\left(\frac{dE}{2.3d\log i_{pH}}\right)$, mv	Lattice parameter Q[A], from ref. (36)	Potential of zero charge $\Delta\zeta_{p.z.c.}$, hydrogen scale	Vacant d orbitals per atom, from ref. (37)	Heat of sublimation L_s , kcal mole ⁻¹ , from ref. (25)
Platinum	CO ₂	1×10^{-7}	70	160	+0.30 (32, 33)	0.55	135
Iridium	CO ₂	1×10^{-11}	75	132	+0.05 \pm 0.1†	1.5	165
Rhodium	CO ₂	5×10^{-11}	70	155	0.05 \pm 0.1†	1.5	138
Gold	No CO ₂ , aldehydes	1×10^{-11}	0	72	+0.30 (34, 35)	0	84
Palladium	No CO ₂ , aldehydes	7×10^{-10}	0	80-110	+0.25 (33)	0.55	91

* Potential of zero charge (formerly: e.c.m.).

† Calculated Eq. [4] using electronic work functions (36).

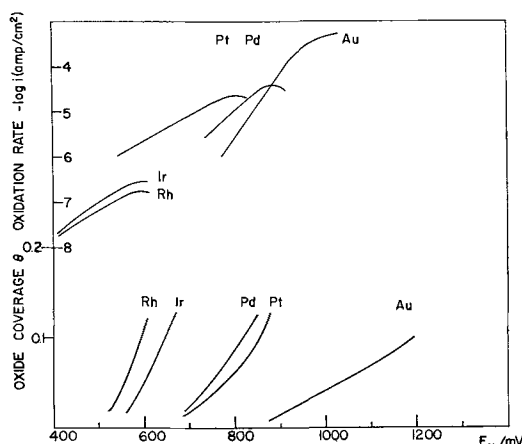


Fig. 12. Comparison of oxide coverage and Tafel lines of anodic ethylene oxidation in 1.0M H_2SO_4 on Rh, Ir, Pd, Pt, Au.

The slight (up to two fold) change in rate constants (but not in mechanism) is probably due to roughness factor effects.

(v) Effect of oxide coverage on the reaction rate.

The oxide coverage affects the reaction rate for all metals in the same way: The electrode potential at which the oxide coverage exceeds a value of about 0.1-0.2 (Fig. 11) corresponds to the potential (Fig. 12) at which the Tafel line goes into a limiting region. The fact that an oxide coverage of 0.1-0.2 causes a current decrease by a factor of 2 (compared to the extrapolated Tafel line) can be related to: (a) Geometric factors in the competitive adsorption of oxide and the organic species. Since C_2H_4 needs a four point attachment to the surface the blocking effect of small oxide coverages will be great (24). (b) The χ potential set up by the oxide. The dipole potential due to the oxide coverage will decrease the charge on the metal and, hence, lower the reaction rate.

Mechanistic considerations.—Since the complete oxidation of ethylene involves the transfer of 12 electrons considerable further work is needed to establish the mechanism with certainty. In view of this situation, it should be noted that our discussion of the factors determining the reaction rates applies to the same general type of reaction sequence represented by the mechanism given below.

Comparison of metals.—The metals (Table IV) fall into two groups of electrocatalytic activity: Group I (Pt, Ir, Rh) oxidizes the reactant quantitatively to CO_2 , shows approximately an identical Tafel slope (135-160 mv), and has the same pH dependence (~ 70 mv/pH). Group II (Au, Pd) reveals incomplete oxidation, has lower Tafel slopes, and no pH dependence. Furthermore, the "chemical" rate constants of the Group I (Pt, Ir, Rh) metals tend to be higher.

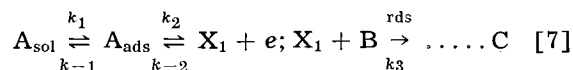
The heats of sublimation show a clear difference for the metals Pt, Ir, Rh; and Au, Pd, respectively. According to Pauling's equation, the bond strength for a partially covalent bond of the metal with an organic species is

$$D(\text{org-M}) = \frac{1}{2} \{D(\text{M-M}) + D(\text{org-org})\} + 23.06 (X_{\text{org}} - X_{\text{M}})^2 \quad [6]$$

where D is bond energies between the respective species in kcal/mole, X the electronegativities of the bond in Pauling units. Thus, for a given organic species the bond strength with metals of Group I (Pt, Rh, Ir) is higher by about 20 kcal than the bond strength with metals of Group II (Au, Pd).

The electronegativities of the metals (39) (Pd 2.0, Rh 2.1, Ir 2.1, Pt 2.1, Au 2.3) vary by 0.3 units. Taking the electronegativity of the organic species as 2.5 [value for C (38)] the electronegativity term changes by less than 5 kcal/mole for the metals examined. Thus the bond strength between metals of Group I and metals of Group II differs by about 20 ± 5 kcal/mole. Consequently, the bond metal-organic intermediate can be broken more easily with the Au, Pd metals: an incomplete oxidation would therefore be feasible, because intermediate oxidation products have a higher rate of desorption.

Gold and palladium.—Considering the effect of ethylene partial pressure on the reaction rate (Fig. 4, 6) and the current potential dependence in the Tafel line region (Fig. 2, 5) the reaction scheme can be given by

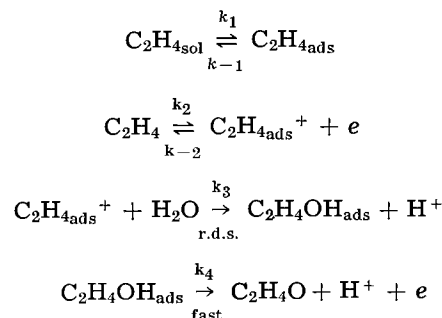


where A_{sol} , A_{ads} , B represent stable chemical species in the solution (excluding ions from water) and on the electrode, X_1 represents an intermediate. The current can be written as⁴

$$i = nFk_3 \frac{K_1 p_E}{1 + K_1 p_E} \cdot K_2 e^{VF/RT} \quad [8]$$

where n is the number of transferred electrons, $K_1 = k_1/k_{-1}$, $K_2 = k_2/k_{-2}$, p_E is pressure of ethylene, V electrode potential.

This scheme gives rise to a b-value in the Tafel equation of RT/F , its zero pH effect and (qualitatively, depending on the isotherm applied) the pressure dependence experimentally observed (Fig. 4, 6; Table IV). To suggest a specific scheme is made difficult by the fact that the reaction goes to at least three products, the dominant of which are aldehydes. It is difficult to find a reaction sequence which is consistent with the facts of Table IV. The following type of mechanism obeys this criterion, though it involves the assumption of a $C_2H_4^+$ intermediate. Evidence that reactions with this radical could be slow arises from its stabilization by solvation.



⁴This expression implicitly assumes a Langmuir isotherm with one-point attachment, whereas C_2H_4 is probably adsorbed with four-point attachment. However, no qualitative differences result in the interpretation of the pressure effect.

Then, the relatively greater chemical rate constant on Pd rather than Au may be roughly interpreted so: In the rate-determining reaction, the heats of activation will be determined primarily by the heats of adsorption of $C_2H_4^+$ and C_2H_4OH , as also by the thermionic work function of the metal. Other factors which determine the heat of activation at the potential of zero charge are, for example, the heat of hydration of the proton and other factors which are independent of the catalyst. Very roughly, one can now suppose that the heat of adsorption of $C_2H_4^+$ and that of CH_3CHO do not differ greatly; for they will be made up mostly of the energies of two M-C bonds. Thus, the major difference resides in the work function: the faster reaction will occur in the metal which has the higher work function, and the expected ratio of chemical rate constants will be

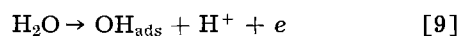
$$\frac{i_{Pd}}{i_{Au}} = e^{(\phi_{Pd} - \phi_{Au})\alpha F/RT}$$

The work function data for Pd and Au are scattered (36). The most probable are: Pd 4.9; Au 4.7. If these values are accepted, the difference in rates agrees fairly with that observed (expt.: $i_{Pd}/i_{Au} = 70$; theoret: $i_{Pd}/i_{Au} = 10^3$).

Similar remarks would apply to any mechanism of the oxidation of ethylene in which a stable chemical species is in equilibrium with an unstable one through a charge transfer reaction; and thereafter the unstable species goes to a stable one by a chemical (no net charge transfer) reaction.

Platinum, iridium, rhodium.—For platinum a substantial study of the mechanism of ethylene oxidation has been made by Weber and Green (6) (alkaline solution) and Wroblowa, Piersma, and Bockris (7) (alkaline and acid solutions). Since Tafel slope, pH dependence, and reaction products on Ir and Rh are identical to those on Pt (Table IV), these considerations apply to these metals as well.

Rate-determining water discharge is deduced for the whole pH range (7). All following reactions are in equilibrium and do not affect the over-all reaction rate. Hence, the relative catalytic power depends on factors which determine the rate of



Of these, the work function and the heat of adsorption of reactant and product depend on the catalyst.

It is difficult to make an estimate concerning the difference in the heat of adsorption of H_2O and OH on these metals. OH is chemisorbed (40). If water is chemisorbed (41, 42), then the bonding is likely to be between the metal and the two orbitals of oxygen, i.e., there is likely to be considerable compensation of any difference as both M-OH (in the final state) and M-OH₂ (in the initial state) would change in the same direction. Hence, the relative catalytic power is largely in terms of work function, i.e.

$$\frac{k_{chem, Pt}}{k_{chem, Rh}} = e^{(\phi_{Pt} - \phi_{Rh})\alpha F/RT} \quad [10]$$

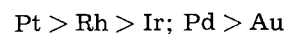
An analogous relation will hold for Ir. The work function data are fairly spread out. Taking the most probable value for Pt (5.3 eV) and Rh (4.9–5.1 eV) and Ir (4.9–5.0 eV) one obtains from Eq. [10] $k_{chem, Pt} \approx 10^3 k_{chem, Rh} \approx 10^3 k_{chem, Ir}$. The experimental values give a factor of $k_{chem, Pt} = 2 \cdot 10^3 k_{chem, Rh} = 10^4 k_{chem, Ir}$.

Conclusions.—In summary, the model arising from here is that on noble metal electrocatalysts there is a potential range in which C_2H_4 is adsorbed and its rate in the subsequent reaction depends primarily on the relation of the potential for the adsorption range to the thermodynamic reversible potential for a given reaction. If two possibilities are near, e.g., $C_2H_4 \rightarrow CO_2$ and $C_2H_4 \rightarrow CH_3CHO$, then, which occurs depends on the relative binding of the intermediate radicals: the smaller this is, the less likely the reaction is to go to completion. The final product, and path of reaction having been established by the factors mentioned, the "chemical" (or zero field standardized) rate constant is affected by one or two relatively simple properties such as work function or heat of adsorption of reactant and product. For the electrocatalysts studied here, these approaches are consistent with the facts.

Summary

The electrode kinetics of the oxidation of ethylene has been examined with special reference to its dependence on the electrocatalyst used. Aspects experimentally determined were the dependence of the current on potential, pH and ethylene partial pressure for the catalysts Au, Ir, Pd, Pt, and Rh in sulfuric acid solutions.

The experimental results showed the catalysts Pt, Rh, Ir to cause one path to occur (final product: CO_2) while on Pd and Au another takes place (final product: aldehydes). When, within these groups, the relative rates are expressed so that the effect of the interfacial electric field is eliminated, the sequence is



An important factor which determines electrocatalysis is the coincidence of the potential range (generally 0.2–0.4V) in which adsorption occurs and the thermodynamically calculated potential for a given over-all reaction. Differences between catalysis at the metal/gas interface and the metal/electrolyte solution interface concern the potential dependence of the concentration of reactants on the electrode, the fact that a solvent is always present which often participates in the reaction, and the accelerating effect of the interfacial electric field. Specific interpretations evolved from the present data indicate that the relative rate constants among the two groups (Pt, Rh, Ir; Pd, Au) depend largely on the relative work function. The velocity at which the oxidation reaction can occur is limited primarily by a competing oxide forming reaction, which becomes appreciable at higher anodic potentials in the order Rh, Ir < Pt; Pd < Au.

Manuscript received June 27, 1963; revised manuscript received Dec. 9, 1963.

Any discussion of this paper will appear in a Discussion Section to be published in the December 1964 JOURNAL.

REFERENCES

1. E. W. Justi and A. W. Winsel, "Cold Combustion, Fuel Cells," Franz Steiner Verlag Wiesbaden (1962); G. J. Young, "Fuel Cells," vol. I and II, Reinhold Publishing Corp., New York (1960 and 1963).
2. E. Müller, *Z. Elektrochem.*, **29**, 264 (1923); **33**, 561 (1927).
3. J. Giner, *Electrochim. Acta*, **4**, 42 (1961).
4. M. Breiter and S. Gilman, *This Journal*, **109**, 622, 1099 (1962).
5. R. P. Buck and L. R. Griffith, *ibid.*, **109**, 1007 (1962).
6. M. Green, J. Weber, and V. Drazic, *ibid.*, **111**, 721 (1964).
7. H. Wroblowa, B. J. Piersma, and J. O'M. Bockris, In course of publication.
8. J. Weber and M. Green, In course of publication.
9. G. J. Hooijink, in "The Mechanism of Heterogeneous Catalysis," J. H. de Boer, Editor, Elsevier (1960).
10. J. O'M. Bockris, D. Drazic, and A. R. Despic, *Electrochim. Acta*, **4**, 325 (1961).
11. A. J. de Bethune, T. S. Licht, and N. Swendeman, *This Journal*, **106**, 616 (1959).
12. H. A. Fales and W. A. Mudge, *J. Am. Chem. Soc.*, **42**, 2434 (1920).
13. G. M. Milazzo and G. Bombara, *J. Electroanal. Chem.*, **1**, 265 (1960).
14. W. Mehl, M. A. V. Devanathan, and J. O'M. Bockris, *Rev. Sci. Instruments*, **33**, 400 (1956).
15. M. A. V. Devanathan, J. O'M. Bockris, and W. Mehl, *J. Electroanal. Chem.*, **1**, 143 (1959-1960).
16. A. Hickling, *Trans. Faraday Soc.*, **41**, 333 (1945).
17. E.g., K. J. Vetter and D. Berndt, *Z. Elektrochem.*, **62**, 378 (1958).
18. W. M. Latimer, "The Oxidation States of the Elements and Their Potentials in Aqueous Solutions, Prentice Hall, Inc. (1961).
19. J. O'M. Bockris and E. Potter, *This Journal*, **99**, 169 (1952).
20. E. Lange and B. Miscenko, *Z. physik. Chem.*, **149**, 1, (1930).
21. A. Frumkin, *Z. Elektrochem.*, **59**, 807 (1955).
22. E. Blomgren, J. O'M. Bockris, and C. Jesch, *J. phys. Chem.*, **65**, 2000 (1961).
23. E. Blomgren and J. O'M. Bockris, *ibid.*, **63**, 1475 (1959).
24. B. M. W. Trapnell, "Chemisorption," Butterworths, London (1955).
25. G. C. Bond, "Catalysis by Metals," Academic Press, London, New York (1962).
26. A. A. Balandin, *Z. physik. Chem.*, **B2**, 289 (1929).
27. A. Sherman and H. Eyring, *J. Am. Chem. Soc.*, **54**, 2661 (1932).
28. O. H. Wansbrough-Jones and E. K. Rideal, *Proc. Roy. Soc.*, **A123**, 202 (1929).
29. O. Beeck, *Disc. Faraday Soc.*, **8**, 118 (1950).
30. H. Dahms and M. Green, *This Journal*, **110**, 1075 (1963).
31. J. O'M. Bockris and D. A. J. Swinkels, *ibid.*, **111**, 736 (1964).
32. F. P. Bowden and L. Young, *Research*, **3**, 235 (1950).
33. V. L. Kheifets and B. S. Krasikow, *Zhur. Fiz. Khim.*, **31**, 1992 (1957).
34. M. Green and H. Dahms, *This Journal*, **110**, 466 (1963).
35. G. M. Schmid and N. Hackerman, *ibid.*, **110**, 440 (1963).
36. Handbook of Chemistry and Physics, Chemical Rubber Publishing Co. (1963).
37. W. Hume-Rothery, "Atomic Theory for Students of Metallurgy," The Institute of Metals (1955).
38. L. Pauling, "The Nature of the Chemical Bond," Cornell University Press, Ithaca (1960).
39. W. Gordy and W. J. O. Thomas, *J. Chem. Phys.*, **24**, 439 (1956).
40. M. L. B. Rao, M. A. V. Devanathan, and J. O'M. Bockris, In course of publication.
41. F. Barry and E. P. Barrett, *J. Am. Chem. Soc.*, **55**, 3088 (1953).
42. C. Kemball, *Proc. Roy. Soc.*, **A190**, 117 (1947).

Adsorption of n-Decylamine on Solid Metal Electrodes

J. O'M. Bockris and D. A. J. Swinkels¹

The Electrochemistry Laboratory, The University of Pennsylvania, Philadelphia, Pennsylvania

ABSTRACT

The adsorption from solution of n-decylamine on five metals has been measured using a new method, which consists of adsorbing radioactively labeled organic compounds on a metal tape electrode and measuring the resulting radioactivity from the tape. After calibration of the counters and determination of the roughness factor of the tapes by the B.E.T. method using krypton, the amount adsorbed per actual square centimeter is calculated. The coverage has been determined as a function of potential and bulk concentration, and the free energy of adsorption has been calculated for each system. A consideration of thermodynamic cycles for water and for the organic adsorbate leads to a relationship between the free energy of adsorption and the solubility and vapor pressure of the organic compound. The adsorption arises largely from metal-adsorbate dispersion interaction differences between water and the organic. These vary little with the metal. The potential dependence arises primarily from the field dependence of the metal-water interaction.

A knowledge of the adsorption of organic compounds at the electrode-solution interface is needed for the understanding of organic electrode reactions and of the inhibitive action of organic compounds

on corrosion. However, the methods of measuring adsorption, which have been developed for mercury, cannot be applied to solid metals. Determination of adsorption from surface tension measurements is not possible for solid metals, while capacity measure-

¹Present address: Allison Division of General Motors Corporation, Dept. 8897, Indianapolis 6, Indiana.

ments (1, 2) are limited to a small potential range. Because of the small amounts of material involved in adsorption ($\approx 10^{-10}$ moles/cm²) measurements of the decrease in concentration in the solution (3) are inaccurate, except for the most dilute solutions.

The small quantities of adsorbate involved suggest the use of radioactively labeled compounds. The adsorption of several organic compounds on gold has been measured as a function of potential and concentration by using C-14 and S-35 labeled organic compounds and measuring the β -radiation through the thin ($\approx 2\mu$) gold foil electrode (4, 5). Most common metals cannot be obtained in the form of such thin foils, and since the penetrating power of the β -rays is not sufficient to pass through thicker metal foils, another method has been developed.

Experimental

The present method consists of adsorbing a radioactively labeled organic compound on a metal tape electrode. When equilibrium has been reached, the tape is withdrawn from the solution through a narrow slit in such a way that very little solution adheres to the tape ($\approx 1\mu$). The total radioactivity from the tape is then measured by placing proportional counters on both sides of the tape, which, after correction for the adhering solution, gives the amount adsorbed per geometrical square centimeter. The apparatus used and calibration procedures are described in detail elsewhere (6, 7).

The metals investigated are Ni, Fe, Cu, Pb, and Pt. The tapes used were 0.5 in. wide and 0.002 in. thick. These dimensions were determined by considerations of strength and flexibility. A lead tape of these dimensions does not have sufficient tensile strength, while a platinum tape is costly. In these cases, the metals are clad onto a nickel base to give a compound tape of the same dimensions.

C-14 labeled n-decylamine-HCl, as received from the supplier, was dissolved in distilled water. All solutions were made up from this stock solution by dilution with NaClO₄ electrolyte and adjustment of the pH.

One modification was made to the method in that foil was rolled onto both sides of the metal tape immediately after it came out of the adsorption bath. This was found necessary to prevent evaporation of volatile organic compounds, which would otherwise contaminate the counters over a period of several hours. Mylar foil, 1.5 in. wide, from supply rolls on either side of the tape, was pressed onto the tape by spring loaded glass rollers. The presence of the foil reduced the counter efficiency about 25% by adsorption of radiation in the foil. It also prevented the measurement of the thickness of the liquid film. But, since its thickness was found to be constant at $1 \pm 0.5\mu$, and since the correction for the radiation from this film was found to be small at the concentrations used, its accurate measurement was not required (6).

Accuracy.—The observed scatter of the data for a given potential and bulk concentration varies from 10 to 25% with the highest scatter occurring on iron. A detailed consideration of the sources of error shows (6) that the variation in roughness along a

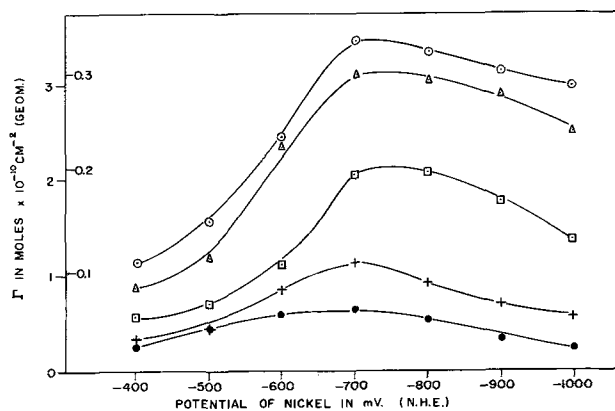


Fig. 1. Adsorption of n-decylamine on nickel from 0.9N NaClO₄, pH 12. Open circle with dot, 7.5×10^{-5} M n-decylamine; open triangle with dot, 5.0×10^{-5} M n-decylamine; open square with dot, 2.5×10^{-5} M n-decylamine; +, 1.0×10^{-5} M n-decylamine; dark circle, 0.5×10^{-5} M n-decylamine.

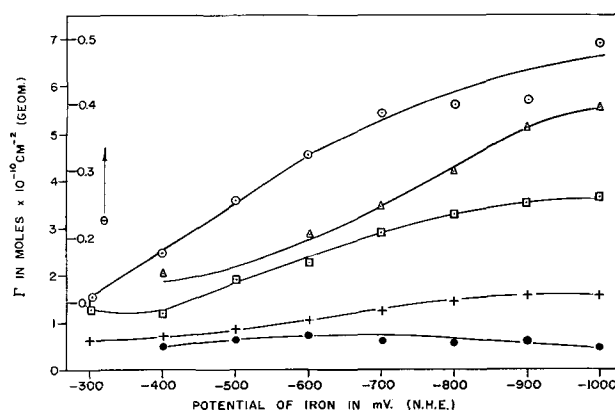


Fig. 2. Adsorption of n-decylamine of iron from 0.9N NaClO₄, pH 12. Open circle with dot, 1.0×10^{-4} M n-decylamine; open triangle with dot, 1.5×10^{-5} M n-decylamine; open square with dot, 5.0×10^{-5} M n-decylamine; +, 2.5×10^{-5} M n-decylamine; dark circle, 1.0×10^{-5} M n-decylamine.

tape is the largest contribution. Other sources of random errors are: counting errors, variations in thickness of the liquid layer on the tapes, and IR drop in the slits causing loss of potential control.

The absolute accuracy of the data is considerably less [$\pm 65\%$ ref. (1)] the main sources of error being the activity of the radiotracer ($\pm 15\%$) and the true surface area ($\pm 20\%$).

Results

The adsorption of n-decylamine on Ni, Fe, Cu, Pb, and Pt from 0.9N NaClO₄, 0.1N NaOH solution containing various amounts of n-decylamine are shown in Fig. 1-5. The value of the amount adsorbed (Γ) is the average of 4 to 6 separate measurements. The coverage θ was calculated in each case using the roughness factors determined by the B.E.T. method (Table I) and $\Gamma_m = 7.9 \times 10^{-10}$ moles/cm². The

Table I. Quantities relevant to the adsorption of n-decylamine on solid metals from 0.9N NaClO₄, 0.1N NaOH solution

	Roughness factor	$E_m(\theta \rightarrow 0)$, v	ΔG°_R at $E_m(\theta \rightarrow 0)$, kcal/mole
Ni	1.32	-0.7	-6.8
Fe	1.77	-0.7	-6.6
Cu	1.38	-0.9	-7.3
Pb	1.95	-1.0	-6.2
Pt	1.22	-0.4	-7.4

value of Γ_m used is that found for long hydrocarbon chains by surface balance measurements at the liquid-air interface (8). The potential range, in which adsorption measurements could be carried out, varied with the metal. It is limited on the cathodic side by hydrogen bubble formation, which interferes

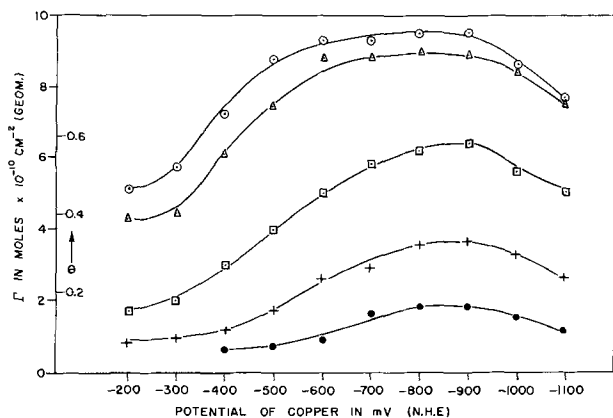


Fig. 3. Adsorption of *n*-decylamine on copper from 0.9*N* NaClO₄, pH 12. Open circle with dot, 7.0×10^{-5} M *n*-decylamine; open triangle with dot, 5.0×10^{-5} M *n*-decylamine; open square with dot, 2.5×10^{-5} M *n*-decylamine; +, 1.0×10^{-5} M *n*-decylamine; dark circle, 0.5×10^{-5} M *n*-decylamine.

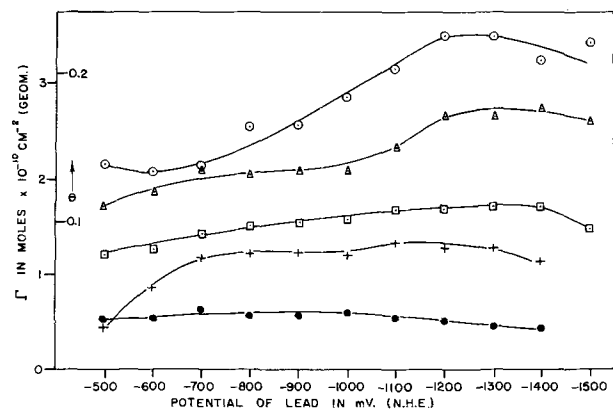


Fig. 4. Adsorption of *n*-decylamine on lead from 1*N* NaClO₄, pH 12. Open circle with dot, 9×10^{-5} M *n*-decylamine; open triangle with dot, 6×10^{-5} M *n*-decylamine; open square with dot, 4×10^{-5} M *n*-decylamine; +, 2×10^{-5} M *n*-decylamine; open circle with dot, 1×10^{-5} M *n*-decylamine.

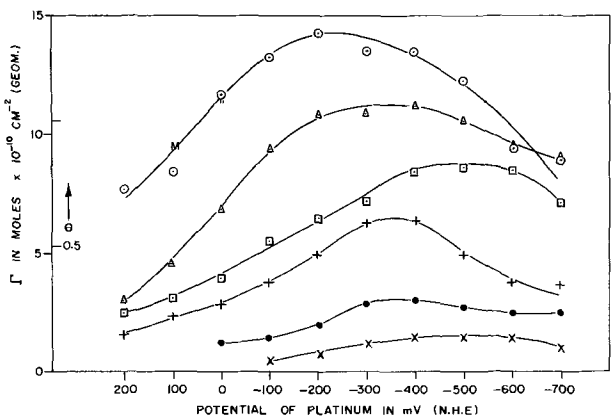


Fig. 5. Adsorption of *n*-decylamine on platinum from 0.9*N* NaClO₄, pH 12. Open circle with dot, 1.0×10^{-4} M *n*-decylamine; open triangle with dot, 8.0×10^{-5} M *n*-decylamine; open square with dot, 6.0×10^{-5} M *n*-decylamine; +, 4.0×10^{-5} M *n*-decylamine; dark circle, 2.0×10^{-5} M *n*-decylamine; X, 1.0×10^{-5} M *n*-decylamine.

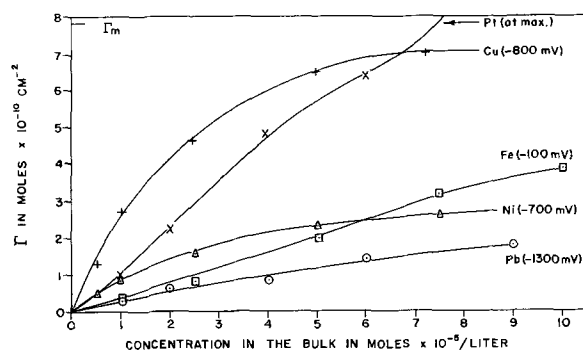


Fig. 6. Adsorption isotherms for *n*-decylamine

with the diffusion of adsorbate to the interface, while on the anodic side it is limited by metal dissolution or oxide formation.

Adsorption from acid solutions containing 10^{-4} moles/liter of *n*-decylamine was also measured for each metal, but the coverage was always less than 10%. Since the *n*-decylammonium ion is much more soluble than the amine molecule, its adsorbability is much less.

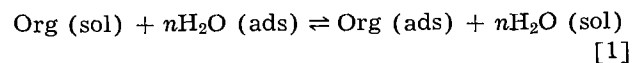
The potential of maximum adsorption (E_m) in Fig. 1-5, extrapolated to zero coverage to eliminate any $\Delta\chi$ -potential due to the adsorbate, is determined by the metal-water interactions, and will be treated in detail elsewhere (9).

Isotherms at the potential of maximum adsorption are shown in Fig. 6. A limiting coverage less than a monolayer is approached in each case except on platinum, where multilayer formation occurs.

The shift in the adsorption maximum to more negative potentials as $\theta \rightarrow 1$ indicates that a monolayer of *n*-decylamine molecules with the amine group towards the metal is first formed. A second layer then adsorbs more easily on the hydrophobic surface formed by all the hydrocarbon chains extending into solution.

Discussion

Free energy of adsorption.—The adsorption of an organic substance at the metal-solution interface may be written



where n is assumed to be independent of coverage or charge on the electrode. The standard free energy for the above process referred to unit mole fraction of organic or water in solution and on the surface is

$$\Delta G_a^\circ = -RT \ln \frac{(X_{\text{org,ads}})(X_{\text{w,sol}}^n)}{(X_{\text{w,ads}}^n)(X_{\text{org,sol}})} \quad [2]$$

For dilute solutions $X_{\text{w,sol}} = 1$ and $X_{\text{org,sol}} = C_{\text{org}}/55.4$. On the surface

$$X_{\text{org,ads}} = \frac{\Gamma_{\text{org}}}{\Gamma_{\text{org}} - \Gamma_{\text{w}}} \quad [3]$$

where Γ_{org} and Γ_{w} are the number of moles of organic material and water, respectively, per unit area. Using $\Gamma_{\text{org}} = \theta\Gamma_{\text{max,org}}$ and $\Gamma_{\text{w}} = n\Gamma_{\text{max,org}}$ we have

$$X_{\text{org,ads}} = \frac{\theta\Gamma_{\text{max,org}}}{\theta\Gamma_{\text{max,org}} + (1-\theta)n\Gamma_{\text{max,org}}} = \frac{\theta}{\theta + n(1-\theta)} \quad [4]$$

Similarly

$$X_{w,ads} = \frac{n(1-\theta)}{\theta + n(1-\theta)} \quad [5]$$

Introducing Eq. [4] and [5] into Eq. [2] we obtain

$$\Delta G_a^\circ = -2.3 RT \log \left[\frac{55.4}{C_{org}} \cdot \frac{\theta}{(1-\theta)n} \cdot \frac{\theta + n(1-\theta)^{n-1}}{n^n} \right] \quad [6]$$

The corresponding isotherm is

$$\frac{\theta}{(1-\theta)^n} \frac{\{\theta + n(1-\theta)\}^{n-1}}{n^n} = \frac{C_{org}}{55.4} \exp\left(\frac{-\Delta G_a^\circ}{RT}\right) \quad [7]$$

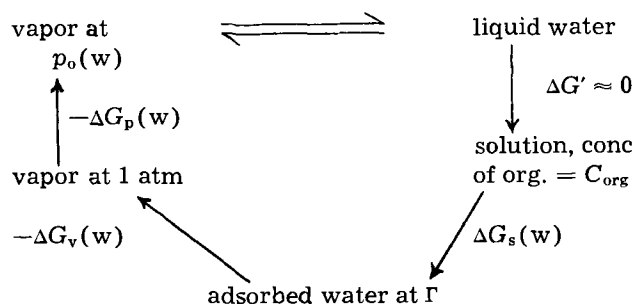
When $n = 1$, Eq. [7] reduces to the familiar Langmuir equation.

The standard free energy of adsorption at the adsorption maximum extrapolated to zero coverage for each system is given in Table I.

In the case of copper the coverage becomes sufficiently high so that lateral interactions become significant. The apparent standard free energy of adsorption calculated using Eq. [6] then varies with coverage as shown in Fig. 7.

Components of the standard free energy of adsorption.—Adsorption from solution is influenced by several interactions between the metal, the organic compound and the water both on the surface and in the bulk. To discuss these thermodynamically we will consider two cycles, one for the organic compound and one for the water.

Thermodynamic cycle for water



For water

$$\Delta G_s^\circ(w) = \Delta G_p^\circ(w) + \Delta G_v^\circ(w) \quad [8]$$

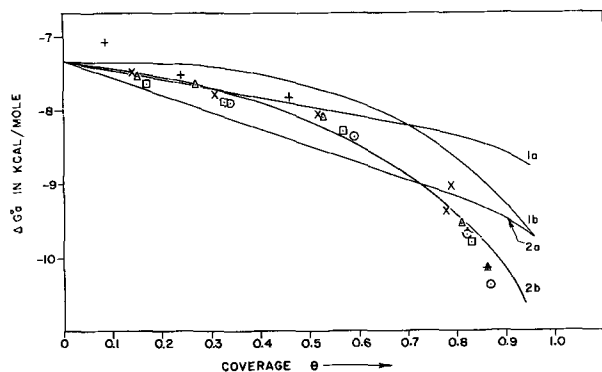
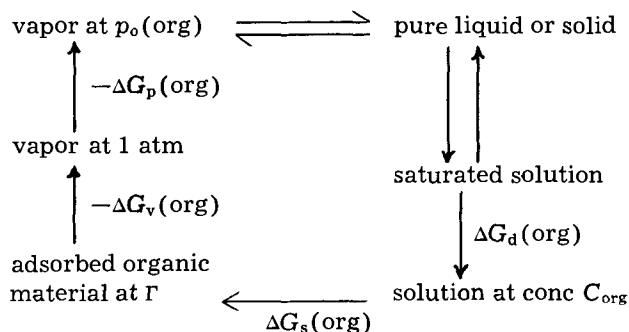


Fig. 7. ΔG_a° for n-decylamine on copper as a function of coverage. X, -1000 mv; open circle with dot, -900 mv; open square with dot, -800 mv; open triangle with dot, -700 mv; +, -600 mv.

where $\Delta G_s(w)$ = free energy of adsorption of water from solution; $\Delta G_v(w)$ = free energy of adsorption of water from the vapor phase at 1 atm; $\Delta G_p(w) = -RT \ln p_o(w)$; where $p_o(w)$ = vapor pressure of water at the temperature T .

Thermodynamic cycle for the organic material at the temperature T



For the organic compound

$$\Delta G_s^\circ(org) = -\Delta G_d^\circ(org) + \Delta G_p^\circ(org) + \Delta G_v^\circ(org) \quad [9]$$

where $\Delta G_s^\circ(org)$ = free energy of adsorption of the organic compound from solution at the concentration C_{org} and coverage Γ ; $\Delta G_d^\circ(org)$ = free energy of dilution = $RT \ln C_{org}/C_s$; C_s = saturation concentration of organic; $\Delta G_p^\circ(org) = -RT \ln p_o(org)$; $p_o(org)$ = vapor pressure of the pure organic material at temperature T ; $\Delta G_v^\circ(org)$ = free energy of adsorption of the organic compound from the vapor phase at 1 atm.

The standard free energy of adsorption from solution (ΔG_a°) defined earlier, which is really the free energy of replacement of water at the interface, is then

$$\Delta G_a^\circ = \Delta G_s^\circ(org) - n\Delta G_s^\circ(w) \quad [10]$$

Using the standard state of unit mole fraction of organic material or water at the interface and in solution, we have

$$\Delta G_a^\circ = -\Delta G_d^\circ(org) + \Delta G_p^\circ(org) - n\Delta G_p^\circ(w) + \Delta G_v^\circ(org) - n\Delta G_v^\circ(w) \quad [11]$$

$$= -RT \ln \frac{C_s}{55.4} - RT \ln \frac{p_o(org)}{p_o^n(w)} + \Delta G_v^\circ(org) - n\Delta G_v^\circ(w) \quad [12]$$

The first two terms of Eq. [12] do not change with the metal and hence make the same contribution to ΔG_a° for all metals. Equation [12] also shows that at a given concentration the amount of adsorption increases as the solubility (C_s) of the adsorbate decreases (10).

For the adsorption of n-decylamine at 25°C , $C_s = 5 \times 10^{-4}$ moles/liter (11) and $p_o(org) = 0.18$ mm (12) and $p_o(w) = 23.8$ mm.

Hence

$$\Delta G_a^\circ = -6.80 + 2.74 + \Delta G_v^\circ(org) - n\Delta G_v^\circ(w) \quad [13]$$

Thus, about half of the free energy of adsorption (cf. Table I) from solution is due to the escaping tendency from solution in the present case and the

remainder arises from interactions with the metal (ΔG°_v).

Dispersion interaction between water and metals.—The magnitude of ΔG°_a and its relatively constant value for different metals suggest that only physical forces are involved in the adsorption process. The dispersion interaction between an adsorbed molecule and a large plane metal surface is (13)

$$U_{\text{Disp}} = \frac{\pi \bar{N} C}{6R^3} \quad [14]$$

where \bar{N} is the number of metal atoms per cm^3 ; R the distance between the center of the molecule and the surface of the metal; C a constant for the system. Various expressions for C have been given (14) of which the following seems the most useful

$$C = 6 mc^2 \frac{\alpha_1 \alpha_2}{\left(\frac{\alpha_1}{\chi_1}\right) - \left(\frac{\alpha_2}{\chi_2}\right)} \quad [15]$$

where m is the mass of the electron = $9.11 \times 10^{-28} \text{g}$; c is the velocity of light = $3 \times 10^{10} \text{cm/sec}$; α_1, α_2 are the polarizability of water and metal, respectively; χ_1, χ_2 are the diamagnetic susceptibility of water and metal. Experimental determinations of α and χ are not available for most metals. Pierotti and Halsey (14) have calculated α for copper and iron from the refractive indices of these metals. However, since they used refractive indices determined at different wavelengths for the two metals, and since the refractive index of a metal varies greatly with wavelength, the polarizabilities so obtained cannot be compared.

Since the molar refraction of conductors is approximately equal to the molar volume we have

$$\alpha = \frac{3R_0}{4\pi N} \approx \frac{3V_m}{4\pi N} \quad [16]$$

where R_0 is the molar refractivity; V_m the molar volume. Values of α calculated in this way are listed in Table II. Mercury is included, since its polarizability has been measured (15) and was found to be $5.05 \times 10^{-24} \text{cc}$. This is 14% less than the value calculated from Eq. [16]. All calculated values of α are therefore reduced by 14%, to give the corrected values in column 2, which are used in the dispersion calculation. The atomic diamagnetic susceptibility of the metals was calculated from

$$\chi = \frac{-e^2 a_0^{1/2}}{4 mc^2} \sqrt{n\alpha} \quad [17]$$

where e and m are the electronic charge and mass, respectively, a_0 is Bohr radius, and n the number of electrons in the atom.

Agreement between $\chi(\text{calc})$ and measured values (16) is fair for mercury and lead. Iron, nickel, and platinum are paramagnetic, and the measured value for copper is low because of the presence of some paramagnetism (14). Using $\alpha(\text{corr})$ and $\chi(\text{calc})$ for each metal and the measured values of α and χ for water the constant C was calculated for each system. Using Eq. [14] with $R = 1.5 \text{\AA}$ the dispersion interaction between water and the various metals was calculated. The values found vary little among the metals. This agrees well with the rather constant value of ΔG°_a found for the different metals. The magnitude of U_{Disp} is very dependent on the value of R and hence may be as much as 50% in error, but this would not affect the relative magnitude among the metals unless R varies with the metal.

Dispersion interactions between adsorbed organic molecules and the metal substrate can also be calculated. The values for different metals will vary in the same proportions as for water, but will be somewhat larger, since the polarizability of the organic molecule is greater than that of water. Hence a net heat of adsorption, which varies with the polarizability of the metal results. However, since *n*-decylamine molecules are not spherical, the dispersion calculation becomes more complex (cf. next section).

Lateral attraction.—When there is lateral attraction between adsorbed organic molecules the free energy of adsorption becomes more negative with increased coverage. This is clearly the case on copper (Fig. 7).

The way in which the lateral interaction varies with coverage depends not only on the type of interaction (ion-dipole, dipole-dipole, or dispersion) but also on the type of adsorption (localized or non-localized). In the case of localized adsorption the distance between the sites on the substrate is fixed and invariant with coverage, while the occupancy of the sites varies linearly as the coverage. Hence (17), for localized adsorption the lateral interaction varies linearly with coverage.

For nonlocalized adsorption the distance between adsorbed molecules can vary continuously and specifically varies inversely as the square root of the coverage. If the interaction potential is of the form $U = B/r^m$ then U varies as $\theta^{m/2}$ and hence, the variation in lateral interaction with coverage depends on the type of interaction. In general, for an interac-

Table II. Quantities relevant to the dispersion interaction between water and various metals

	α (calc) in cm^3	α (corr) in cm^3	χ (calc) in c.g.s.	χ (meas.) in c.g.s.	C (Eq. [15])	U_{Disp} in kcal/mole
Ni	2.62×10^{-24}	2.25×10^{-24}	-1.68×10^{-29}	—	7.97×10^{-59}	16.2
Fe	2.82×10^{-24}	2.42×10^{-24}	-1.68×10^{-29}	—	8.16×10^{-59}	15.4
Cu	2.83×10^{-24}	2.43×10^{-24}	-1.78×10^{-29}	-0.87×10^{-29}	8.51×10^{-59}	16.0
Pb	7.24×10^{-24}	6.23×10^{-24}	-4.80×10^{-29}	-4.17×10^{-29}	22.53×10^{-59}	16.6
Pt	3.61×10^{-24}	3.10×10^{-24}	-3.30×10^{-29}	—	13.77×10^{-59}	20.3
Hg	5.87×10^{-24}	5.05×10^{-24}	-4.27×10^{-29}	-5.61×10^{-29}	19.48×10^{-59}	17.7
H ₂ O	—	1.45×10^{-24}	—	-2.16×10^{-29}	—	—

Table III. $\Sigma 1/r_i^n$ for various systems

	$n = 6$	$n = 3$ ($\uparrow\uparrow$)	$n = 3$ ($\uparrow\downarrow$)
Square array ^a	$\frac{4.64}{R^6}$	$\frac{7.8}{R^3}$	$\frac{2.68}{R^3}$
Hexagonal array	$\frac{6.42}{R^6}$	$\frac{9.24}{R^3}$	$\frac{4.5}{R^3}$

^a R is the distance between nearest neighbors at full coverage.

tion energy of the form B/r^n we have (6) for localized adsorption

$$\mu = B\theta \sum_{i=1}^{\infty} \frac{1}{r_i^n} \quad [18]$$

and for nonlocalized adsorption

$$\mu = B \left(\frac{n+2}{4} \right) \theta^{n/2} \sum_{i=1}^{\infty} \frac{1}{r_i^n} \quad [19]$$

where μ is the chemical potential due to lateral interaction; r_i the distance between a given molecule and the i 'th neighbor at full coverage. The summation is over all other molecules in the plane but converges rapidly when $n > 2$. The summations were evaluated for $n = 6$ (dispersion) and $n = 3$ (dipole-dipole) for square and hexagonal arrays until the terms became less than 1% of the first term. In the case of $n = 3$ both parallel and anti-parallel arrays were considered. The results are shown in Table III.

The lateral interactions in the system n-decylamine on copper can now be calculated on the basis of four models:

1a. Localized adsorption, n-decylamine molecules rigid.

The n-decylamine molecules are treated as rigid rods, perpendicular to the surface with the amine

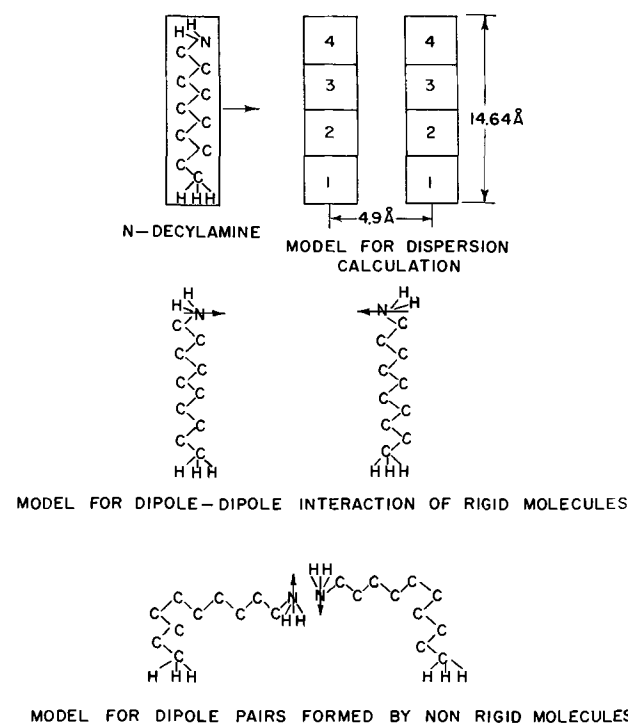


Fig. 8. Models for lateral interaction calculations between n-decylamine molecules.

group towards the solution and the dipole parallel to the surface (Fig. 8).²

To calculate the lateral interaction due to dispersion forces, we must calculate the difference in the dispersion interaction between two n-decylamine molecules and between a n-decylamine molecule and a volume of water equal to the second n-decylamine molecule. Since it is the hydrocarbon chain that is mainly concerned in the dispersive interaction, the polarizability (α) and molar volume (V_m) used for n-decylamine are taken as those of n-decane (18). The polarizability is calculated from the refractive index of n-decane ($n = 1.41$).

$$\alpha(\text{org}) = \frac{3V_m}{4\pi N} \frac{(n^2 - 1)}{(n^2 + 2)} = 19.2 \times 10^{-24} \text{ cc} \quad [20]$$

The dispersion interaction between two spherical molecules in a medium of dielectric constant ϵ is given by

$$U_{\text{Disp}} = \frac{-3h\nu\alpha_1\alpha_2}{4\epsilon r^6} \quad [21]$$

Since the n-decylamine molecule is a long cylinder, we will divide it into four approximately spherical units and sum the interactions between each unit in one molecule and the four units of the other molecule (cf. Fig. 8). The polarizability of each unit of the organic molecule is then $\alpha'(\text{org}) = \alpha(\text{org})/4 = 4.8 \times 10^{-24}$ cc. For a volume of water equal to one of these units we have

$$\alpha'(\text{w}) = \frac{V_m(\text{n-decane})}{4V_m(\text{water})} \times \alpha(\text{w}) = 3.94 \times 10^{-24} \text{ cc} \quad [22]$$

Thus

$$U_{\text{Disp}} = \frac{-3h\nu}{4\epsilon} i \alpha'(\text{org}) \{ \alpha'(\text{org}) - \alpha'(\text{w}) \} \sum_{i=1}^4 \sum_{j=1}^4 \frac{1}{r_{ij}^6} \quad [23]$$

where r_{ij} is the distance between the i 'th unit of one molecule and the j 'th unit of the other (Fig. 8); ν_i the characteristic frequency for the electrons, which both for saturated hydrocarbons and for water is about $3 \times 10^{15} \text{ sec}^{-1}$; h Planck's constant; and $\epsilon \approx n^2 \approx 1.9$.

Assuming a hexagonal array of adsorbed molecules the distance between nearest neighbors at full coverage is 4.9 \AA .

Hence

$$r_{ij} = \sqrt{(4.9)^2 + (|i-j| \times 3.66)^2} \quad [24]$$

Using these values we find $U_{\text{Disp}} = -0.19 \text{ kcal/mole}$ and

$$\mu_{\text{Disp}} = 6.42 \theta U_{\text{Disp}} = -1.22 \theta \text{ kcal/mole} \quad [25]$$

To calculate U_{Dipole} we have

$$U_{\text{Dip}} = \frac{-\mu^2}{\epsilon r^3} \quad [26]$$

where the dielectric constant ϵ varies with coverage. At low coverage the dipoles are separated by water molecules about 15 \AA from the electrode surface,

² This model is chosen because of the lack of variation of the potential of the maximum of adsorption with coverage, i.e., zero $\Delta\chi$ due to the organic molecule.

where the dielectric constant is that of bulk water ($\epsilon \approx 80$), while at full coverage the dipoles are separated by organic molecules ($\epsilon = 2$). Assuming a linear combination of these at intermediate coverages, we have

$$\epsilon = 80 - 78\theta \quad [27]$$

Hence

$$\mu_{\text{Dip}} = 4\theta U_{\text{Dip}} = \frac{-1.08\theta}{80 - 78\theta} \text{ kcal/mole} \quad [28]$$

The total change in free energy of adsorption with coverage is equal to $\mu_{\text{Disp}} + \mu_{\text{Dip}}$ (curve 1a on Fig. 7).

1b. Nonlocalized adsorption, n-decylamine molecules rigid.

In this case:

$$\mu_{\text{Disp}} = 6.42 \left(\frac{n+2}{4} \right) \theta^3 U_{\text{Disp}} = -2.44\theta^3 \text{ kcal/mole} \quad [29]$$

$$\mu_{\text{Dip}} = 4.5 \left(\frac{n+2}{4} \right) \theta^{3/2} U_{\text{Dip}} = \frac{-1.35\theta^{3/2}}{80 - 78\theta} \text{ kcal/mole} \quad [30]$$

The curve marked (1b) in Fig. 7 corresponds to this model.

2. Nonrigid molecules.

A long hydrocarbon chain can generally bend and twist in all directions. The fully stretched n-decylamine molecule is about 16Å long. Hence, if the average hydrocarbon chain bends through 90° in the middle of the chain, then the dipoles of two molecules can pair up even at 10% coverage (average distance between adsorbed molecules 14.5Å). At higher coverages, the hydrocarbon chain needs to bend less and less, until at full coverage the situation is almost the same as for rigid molecules. At low coverages the molecules can take up many orientations in which no dipole pair is formed, but since antiparallel dipoles attract pairing is favored. It is difficult to calculate exactly the probability of pair formation at a given coverage. We will assume that the fraction of adsorbed molecules forming pairs is proportional to θ and that at full coverage all molecules are paired up. The attractive force between two anti-parallel dipoles 3Å apart is $-\mu^2/r^3$, i.e., $U = 1.05$ kcal/mole. Hence $\mu_{\text{Dip pairs}} = \theta U = 1.05\theta$ kcal/mole.

To a first approximation the forming of pairs does not change the interaction between a given dipole and the remainder of the dipoles or the dispersion interaction. The contribution due to pairing is therefore added to the change in free energy calculated for models 1a and 1b to give the curves 2a and 2b in Fig. 7.

The agreement with experiment is best for model 2b, i.e., nonlocalized adsorption and nonrigid molecules.

Summary

The adsorption of n-decylamine from alkaline solution on a number of solid metals has been measured as a function of concentration in solution and electrode potential. The amount adsorbed was considerably less than a monolayer on Fe, Ni, and Pb. No significant change in ΔG_a° with coverage at a given potential was observed on these metals indicating no lateral interactions at these low coverages.

Essentially a monolayer of n-decylamine was adsorbed on copper at the higher concentrations. ΔG_a° in this case became more negative with increased coverage especially at $\theta > 0.5$ indicating lateral attraction between adsorbed molecules. This was calculated on the basis of four models. Best agreement with experiment was obtained assuming nonlocalized adsorption and nonrigid molecules allowing the formation of dipole pairs.

The absence of any shift of the potential of maximum adsorption with coverage on Cu, Ni, and Pb indicates that the net dipole moment of the organic layer is zero and hence n-decylamine is thought to adsorb with the polar amine group towards the solution. However, on platinum, where multilayer formation occurs, the first layer adsorbs with the amine group towards the metal and the second layer with the amine group towards the solution (cf. Fig. 5).

On iron the amine also adsorbs with the NH_2 -group to the metal as indicated by the large shift of the adsorption maximum to more negative potentials, but no multilayer formation occurs, since at the maximum concentration used, the first layer is less than half formed. The reason for the strong preference of the amine group for iron is not clear. The free energy of adsorption on iron is the same as for the other metals, so that strong chemibonding is unlikely. By considering a thermodynamic cycle for water and the organic adsorbate a relationship between the free energy of adsorption and the solubility and vapor pressure of the organic adsorbate is derived, showing that the lower the solubility the higher the adsorbability of an organic compound. The remaining part of the free energy of adsorption arises from interactions of organic and water with the metal.

The magnitude of ΔG_a° and its relatively constant value for the different metals is consistent with the model, that the energy of adsorption arises from the difference in dispersion forces of the organic and the water molecule, which varies little with the metal (Table II). The dependence of the adsorption on potential arises largely from the metal-water interactions (9).

Acknowledgments

The authors are grateful to the United States Steel Corporation for support of this work. One of us (D.A.J.S.) wishes to thank Union Carbide Chemicals Company for a research fellowship during part of the work. This paper is taken in part from the thesis presented to the University of Pennsylvania by one of us (D.A.J.S.) in partial fulfillment of the requirements for the Ph.D. degree.

Manuscript received Sept. 19, 1963.

Any discussion of this paper will appear in a Discussion Section to be published in the December 1964 JOURNAL.

REFERENCES

1. R. S. Hansen, R. E. Minturn, and D. A. Hickson, *J. Phys. Chem.*, **60**, 1185 (1956); **61**, 953 (1957).
2. M. W. Breiter, *This Journal*, **109**, 42 (1962); *Electrochim. Acta*, **7**, 533 (1962).
3. B. E. Conway, R. G. Barradas, and T. Zawidzki, *J. Phys. Chem.*, **62**, 676 (1956).

4. E. A. Blomgren and J. O'M. Bockris, *Nature*, **186**, 305 (1960).
5. H. Wroblowa and M. Green, *Electrochim. Acta*, **8**, 679 (1963).
6. D. A. J. Swinkels, Ph.D. Dissertation, University of Pennsylvania, 1963.
7. M. Green, D. A. J. Swinkels, J. O'M. Bockris, *Rev. Sci. Instruments*, **33**, 18 (1962)
8. I. Langmuir, *J. Am. Chem. Soc.*, **39**, 1848 (1917).
9. J. O'M. Bockris, M. Green, and D. A. J. Swinkels, *This Journal*, **111**, 743 (1964).
10. E. A. Blomgren, J. O'M. Bockris, and C. Jesch, *J. Phys. Chem.*, **65**, 2000 (1961).
11. D. J. Brown, *J. Colloid Sci.*, **13**, 286 (1958).
12. R. R. Dreisbach, "P.V.T. Relationships of Organic Compounds," Handbook Publishers Inc. (1952).
13. M. Polanyi, *Trans. Faraday Soc.*, **28**, 316 (1932).
14. R. A. Pierotti and G. D. Halsey, *J. Phys. Chem.*, **63**, 680 (1959).
15. H. Wolfsohn, *Z. Physik*, **83**, 234 (1933).
16. P. W. Selwood, "Magnetochemistry," Interscience Publishers, New York (1956).
17. A. R. Miller, *Proc. Cambridge Phil. Soc.*, **36**, 69 (1940).
18. A. F. Shepard, A. L. Henne, and T. Midgeley, Jr., *J. Am. Chem. Soc.*, **53**, 1948 (1931).

Adsorption of Naphthalene on Solid Metal Electrodes

J. O'M. Bockris, M. Green, and D. A. J. Swinkels¹

The Electrochemistry Laboratory, The University of Pennsylvania, Philadelphia, Pennsylvania

ABSTRACT

The adsorption of naphthalene on Fe, Ni, Cu, Pt from aqueous solution has been measured using a recently developed radio-tracer technique. The surface area of the metals was determined by the B.E.T. method using krypton. The amount adsorbed was found as a function of potential and concentration in solution. The results are discussed in terms of a "competition with water" model of the electrode-solution interface, in which water molecules are treated as simple dipoles perpendicular to the metal. The same treatment applies to the adsorption of decylamine on the metals stated. The free energy of adsorption is calculated for each system and is related to the free energy of solution and the metal-adsorbate dispersion interactions. Evidence for π -bonding, particularly between naphthalene and platinum is given.

A new radio-tracer method for measuring the adsorption of organic compounds at solid metal electrodes has recently been developed (1, 2) and the adsorption of n-decylamine on several metals has been investigated (3). Blomgren *et al.* (4) have found, that on mercury, aromatic compounds are adsorbed more readily than the corresponding aliphatic compounds.

In the present work the adsorption of naphthalene on Ni, Fe, Cu, and Pt from acid and alkaline solutions has been measured.

Experimental

The present method consists of adsorbing a C-14 labeled organic compound on a metal tape electrode, which, after equilibrium is reached, is withdrawn from the solution in such a way that very little solution adheres to the tape. The method is described in detail elsewhere (2).

C-14 labeled naphthalene was dissolved as received from the supplier in distilled water to give a 2×10^{-4} molar stock solution from which all other solutions were made up by addition of electrolyte and dilution.

The metal tapes were vapor degreased with trichlorethylene before insertion into the apparatus. Immediately before going into the adsorption cell each section of the tape was given anodic and cathodic treatment to produce a clean, oxide free surface for adsorption.

Results

The adsorption of naphthalene on Ni, Fe, Cu, and Pt from 1N NaClO₄ solution containing various

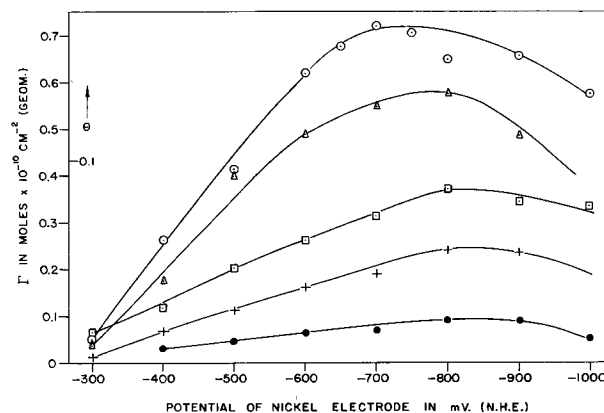


Fig. 1. Adsorption of naphthalene on nickel from 1N NaClO₄, pH 12. \circ , 7.5×10^{-5} M Naphthalene; Δ , 5.6×10^{-5} M naphthalene; \square , 3.8×10^{-5} M naphthalene; $+$, 1.9×10^{-5} M naphthalene; \bullet , 0.8×10^{-5} M naphthalene.

amounts of naphthalene are shown in Fig. 1 to 5. The value of the amount adsorbed (Γ) is the average of two to eight separate measurements. The coverage θ was calculated in each case using the roughness factors determined by the B.E.T. method (Table I) and $\Gamma_m = 3.26 \times 10^{-10}$ moles/cm² for naph-

Table I. Quantities relevant to the adsorption of naphthalene on solid metals from 1N NaClO₄ solution

Metal	Roughness factor	z.ch.p., v	References	E_{max} ($\beta \rightarrow 0$), v
Ni	1.32	-0.47 ± 0.05	(5-9)	-0.8
Fe	1.77	-0.5 ± 0.1	(5-7, 10-12, 19)	-0.7
Cu	1.38	-0.2 ± 0.2	(6, 8, 13-15)	-0.9
		-0.1		
Pt (Acid)	1.22	$+0.3 \pm 0.1$	(6, 13, 16-20)	+0.1
Pt (Alk)	1.22	-0.4 ± 0.1	(6)	-0.4

¹ Present address: Allison Division of General Motors Corp., Dept. 8897, Indianapolis 6, Indiana.

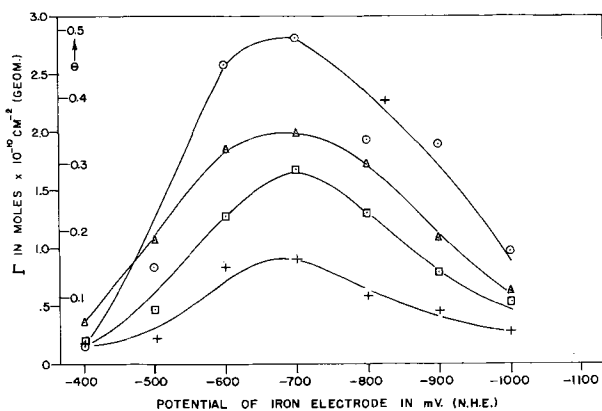


Fig. 2. Adsorption of naphthalene on iron from 0.9N NaClO_4 , 0.1N NaOH . \circ , 10^{-4}M Naphthalene; \triangle , $7.5 \times 10^{-5}\text{M}$ naphthalene; \square , $5 \times 10^{-5}\text{M}$ naphthalene; $+$, $2.5 \times 10^{-5}\text{M}$ naphthalene.

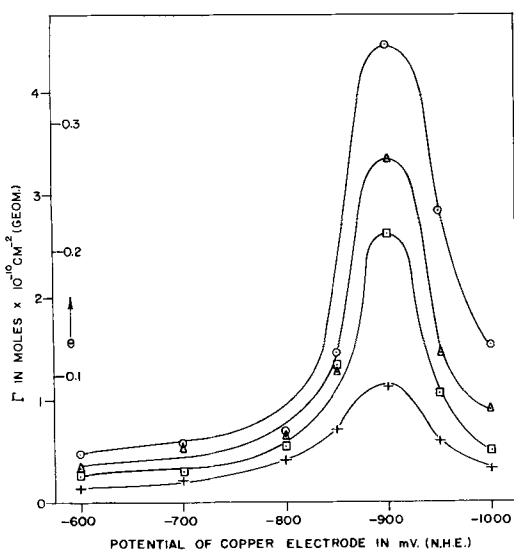


Fig. 3. Adsorption of naphthalene on copper from 1N NaClO_4 . \circ , 10^{-4}M Naphthalene; \triangle , $7.5 \times 10^{-5}\text{M}$ naphthalene; \square , $5.0 \times 10^{-5}\text{M}$ naphthalene; $+$, $2.5 \times 10^{-5}\text{M}$ naphthalene.

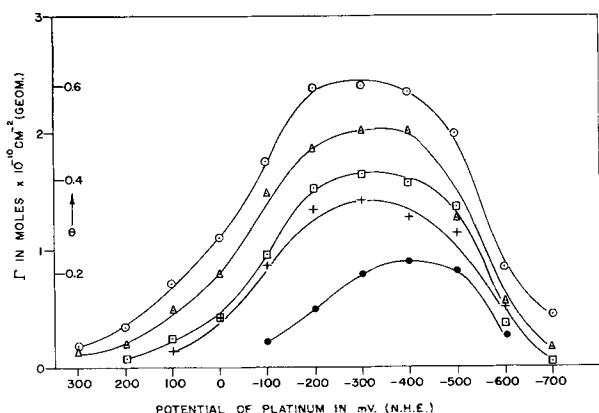


Fig. 4. Adsorption of naphthalene on platinum from 0.9N NaClO_4 , 0.1N NaOH . \circ , 10^{-4}M Naphthalene; \triangle , $5 \times 10^{-5}\text{M}$ naphthalene; \square , $1 \times 10^{-5}\text{M}$ naphthalene; $+$, $5 \times 10^{-6}\text{M}$ naphthalene; \bullet , $2.5 \times 10^{-6}\text{M}$ naphthalene.

thalene lying flat and $\Gamma_m = 8.9 \times 10^{-10}$ moles/cm² for naphthalene standing up at the interface.

The potential range in which adsorption measurements could be carried out varied for the metals. It is limited on the cathodic side by hydrogen bubble formation, which interferes with the diffusion of ad-

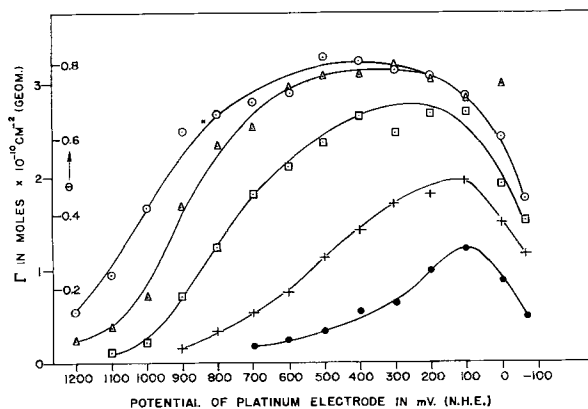


Fig. 5. Adsorption of naphthalene on platinum from 0.9N NaClO_4 , 0.1N HClO_4 . \circ , 10^{-4}M Naphthalene; \triangle , $5 \times 10^{-5}\text{M}$ naphthalene; \square , $1.25 \times 10^{-5}\text{M}$ naphthalene; $+$, $5 \times 10^{-6}\text{M}$ naphthalene; \bullet , $2.5 \times 10^{-6}\text{M}$ naphthalene.

sorbate to the interface, while on the anodic side it is limited by metal dissolution or oxide formation. Because of hydrogen evolution, adsorption from acid solution ($\text{pH} = 1$) on Fe, Ni, and Cu could only be measured to about -400 mV. The coverage in these systems was less than 10% in the potential range available at the highest concentration of naphthalene used (10^{-4}M).

A clear maximum is observed in the adsorption curves in Fig. 1-5. On platinum this potential of maximum adsorption (E_{max}) varies with coverage, indicating a $\Delta\chi$ -potential due to the adsorbed layer (see discussion). Values of E_{max} extrapolated to zero coverage are listed in Table I together with the zero charge potentials (z.ch.p.) of the systems. It should be stressed that the values of $E_{\text{max}}(\theta \rightarrow 0)$ are approximately the same as those found in the case of *n*-decylamine adsorption on these metals (3). Adsorption isotherms at the potential of maximum adsorption are shown in Fig. 6.

Discussion

Zero charge potentials.—Antropov and Banerjee (5) have suggested that, when two metals are at the same potential with respect to their z.ch.p., their charges and conditions of physical adsorption are the same. We will retain the first assumption, but must discard the second on the basis of the data in Table I at least for uncharged organic molecules.

The z.ch.p. were obtained by averaging the most reliable values found in the literature and correcting them for specific adsorption of the perchlorate

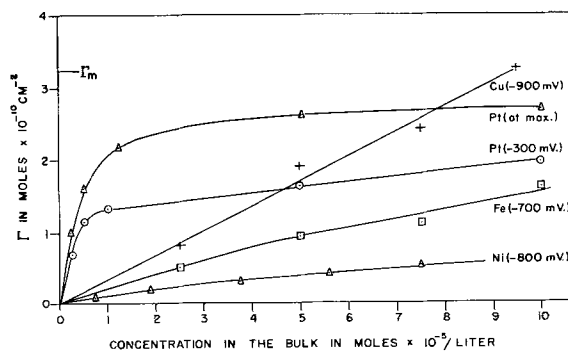


Fig. 6. Adsorption isotherms for naphthalene

ions, assuming this to be the same as on mercury (21).² The error limits of the z.ch.p. in Table I are estimated on the basis of detailed consideration of the data (1). In the case of platinum the z.ch.p. changes with the pH of the solution (6). The two values given in Table I correspond to pH \approx 1 and 13. The adsorption maximum is found to change with pH by about the same amount, suggesting a relationship between the z.ch.p. and $E_{\max}(\theta \rightarrow 0)$, which however, is not a constant for all metals as suggested by Antropov (5).

Model of the interface.—Bockris *et al.* (23) have reviewed models for the adsorption of organic compounds at the mercury-solution interface and suggested a "competition with water" model, in which water molecules are treated as simple dipoles perpendicular to the metal, the fraction of dipoles in each orientation depending on the charge on the metal and the noncharge-dependent binding forces in both orientations. We will extend this model to solid metals.

Consider a metal-solution interface with $N\uparrow$ water molecules in the "up" orientation (oxygen towards solution) each having an energy $E\uparrow$ and $N\downarrow$ in the "down" orientation (oxygen towards metal) each having an energy $E\downarrow$. The total number of water molecules (N_T) at the interface may change with their average energy at the surface (\bar{E}) but will be a maximum when \bar{E} is a minimum. We then have

$$E\uparrow = E^{\uparrow c} + \mu X - REc \quad [1]$$

$$E\downarrow = E^{\downarrow c} - \mu X + REc \quad [2]$$

where μ is the dipole moment of water, X the field at the interface, R equals $(N\downarrow - N\uparrow)/N_T$, E is the lateral interaction between two water molecules, c the coordination number, and E^c the noncharge dependent part of the binding energy.

The average energy \bar{E} of water at the interface is

$$\bar{E} = \frac{N\uparrow E\uparrow + N\downarrow E\downarrow}{N_T} \quad [3]$$

At the potential of minimum binding energy of the water

$$\frac{\partial \bar{E}}{\partial X} = 0 \quad \text{and} \quad \frac{\partial N_T}{\partial X} = 0 \quad [4]$$

Differentiating \bar{E} with respect to the field X and using $\partial N_T/\partial X = 0$ we find

$$\frac{\partial \bar{E}}{\partial X} = 0 = \frac{1}{N_T} \left(N\uparrow \frac{\partial E\uparrow}{\partial X} + E\uparrow \frac{\partial N\uparrow}{\partial X} + N\downarrow \frac{\partial E\downarrow}{\partial X} + E\downarrow \frac{\partial N\downarrow}{\partial X} \right) \quad [5]$$

From Eq. [1] and [2] we have

$$\frac{\partial E\uparrow}{\partial X} = - \frac{\partial E\downarrow}{\partial X} \quad [6]$$

and from [4]

²Detailed discussion of the various measurements of z.ch.p. is given in ref. (1). The assumption of similar specific adsorption on all metals is justified if specific adsorption is due to non-covalent forces (22). The correction for specific adsorption of perchlorate ions consisted of a shift of -0.08 v, since the E.C.M. of mercury is shifted by this amount (21).

$$\frac{\partial N\uparrow}{\partial X} = - \frac{\partial N\downarrow}{\partial X} \quad [7]$$

Hence

$$\frac{\partial \bar{E}}{\partial X} = 0 = \frac{1}{N_T} \left[(N\uparrow - N\downarrow) \frac{\partial E\uparrow}{\partial X} + (E\uparrow - E\downarrow) \frac{\partial N\uparrow}{\partial X} \right] \quad [8]$$

Mathematically speaking Eq. [8] has an infinite number of solutions. However, a consideration of the physical meaning of the terms on the right hand side of Eq. [8] shows that both terms must have the same sign. To add up to zero, each term must therefore be equal to zero. Since $E\uparrow$ and $N\uparrow$ change monotonically with the field X , $\partial E\uparrow/\partial X \neq 0$ and $\partial N\uparrow/\partial X \neq 0$ and hence the only physically possible solution is $(E\uparrow - E\downarrow) = (N\uparrow - N\downarrow) = 0$ or $E\uparrow = E\downarrow$ and $N\uparrow = N\downarrow$. Since no assumptions regarding the nature of E^c , E or the total number of water molecules at the interface were made, the deduction, that at the potential of minimum binding of water [*i.e.*, at $E_{\max}(\theta \rightarrow 0)$], $N\uparrow = N\downarrow$, and hence $R = 0$, is general for all metals.

Combining Eq. [1] and [2] we have at any potential

$$E\uparrow - E\downarrow = \Delta E^c + 2\mu X - 2REc \quad [9]$$

where $\Delta E^c = E^{\uparrow c} - E^{\downarrow c}$. At the adsorption maximum: $E\uparrow - E\downarrow = 0$ and $R = 0$.

$$\therefore \Delta E^c = -2\mu X_m \quad [10]$$

On mercury, X_m can be found from the charge on the electrode (q_m) since $X_m = 4\pi q_m/E$, where E is the potential with respect to the z.ch.p. but on solid metals, we can only estimate X_m (and hence ΔE^c) from the difference between E_{\max} and the z.ch.p. for each metal by assuming that the charge on the metals is the same for all metals at the same potential with respect to their own z.ch.p. (1). The values of q_m and ΔE^c so calculated are shown in Table II.

The values of q_m and ΔE^c for mercury have been included for comparison. The value for platinum is the average for acid and alkaline solutions.

Origin of ΔE^c .—Bockris *et al.* (23) suggested that on mercury ΔE^c may be due to a difference in the image interaction in the two orientations, favoring the case in which the oxygen atom is towards the metal, since the dipole is then 0.05–0.1 Å closer to the metal. This would, however, not vary much with the metal and could never amount to 4.2 kcal since the required asymmetry would be too great. For a dipole perpendicular to the surface

Table II. Quantities relevant to the adsorption of water and naphthalene on various metals*

	$E_m - E_{z.ch.p.}$, v	q_m , μ coulomb/cm ²	ΔE^c , kcal/mole	ΔG_a^0 (See Eq. (16)), kcal/mole
Ni	-0.33	-6	2	-6.0
Fe	-0.2	-3.6	1.2	-7.0
Cu	-0.7	-12.7	4.2	-7.0
Pt	-0.1	-1.8	0.6	-8.4
Hg	—	-2.0	0.7	—

* Columns 1-3 also apply to the adsorption of n-decylamine on these metals (3).

$$U_{\text{image}} = -\frac{\mu^2}{8r^3} \quad [11]$$

where μ is the dipole moment, and r the distance from the center of the dipole to the conductor. The difference for the two orientations is then

$$\Delta U_{\text{image}} = -\frac{\mu^2}{8} \left(\frac{1}{(r+d)^3} - \frac{1}{(r-d)^3} \right) \approx \frac{3\mu^2 d}{4r^4} \quad [12]$$

where d is the asymmetry of the dipole. For $d = 0.05\text{\AA}$, $r = 1.4\text{\AA}$, $\mu = 1.87$ Debye, this gives: $\Delta U_{\text{image}} = 0.5$ kcal/mole.³ Thus, to obtain a difference of 4.2 kcal from this source would require an asymmetry of almost 0.5\AA , which is unlikely in the water molecule.

Another factor which may contribute to ΔE^c is the dispersion interaction between the water molecule and the metal adsorbent (3). Since the lone pair electrons of the oxygen atoms can get closer to the metal than the bond electrons in the OH-bond, the dispersion forces will be greater for the case of oxygen towards the surface. Since the dispersion interaction between an adsorbed molecule and a plane surface is given by (3)

$$U_{\text{disp}} = \frac{\pi NC}{6r^3} \quad [13]$$

where N is the number of atoms per cubic centimeter of adsorbent, C a constant for each system, which depends mainly on the polarizability of water and the metal [see ref. (3)], and r the distance from the center of the adsorbed molecules to the surface. The difference for the two orientations is then

$$\Delta U_{\text{disp}} = \frac{\pi NC}{6} \left[\frac{1}{(r-d)^3} - \frac{1}{(r+d)^3} \right] \\ \approx \frac{-\pi NCd}{r^4} = \frac{-6d U_{\text{Disp}}}{r} \quad [14]$$

where d is the asymmetry parameter, *i.e.*, the electrons on the average, are a distance $2d$ further from the metal, when the H-atoms are towards the metal, than when the oxygen atom is towards the metal. Using $2d = 0.05\text{\AA}$ and U_{Disp} between water and the metals calculated elsewhere (1, 3) we find $\Delta U_{\text{disp}} = 1.62$ kcal/mole (Ni); 1.54 kcal/mole (Fe); 1.60 kcal/mole (Cu); 2.03 kcal/mole (Pt); and 1.77 kcal/mole (Hg).

Thus ΔU_{Disp} is of the right order of magnitude to explain ΔE^c but does not vary sufficiently with the metals (see the variation of the ΔE^c term with the metal, Table I).

If the amount of asymmetry in the water molecule varies with the metal, then both ΔU_{image} and ΔU_{Disp} will change correspondingly. This may occur as a result of the surface dipole of the metal. Since the positive and negative charge centers at the surface of a metal do not in general coincide, their exists at the surface a region of strong electric field,

which is the surface dipole (24). This may increase or decrease the asymmetry in the water molecule depending on the direction and magnitude of the field. If the asymmetry of the charge distribution of water in the absence of a field is assumed to be 0.05\AA , then the value of ΔE^c for iron and nickel indicates a negligible surface dipole for these metals. It is then necessary to assume a surface dipole with the positive end towards the metal for copper (25), since this would increase the asymmetry and hence ΔE^c , while a surface field with the negative end towards the metal for platinum and mercury would reduce the asymmetry and ΔE^c . Sinanoglu and Pitzer have suggested that the surface field may be obtained from a virial treatment of the adsorption of inert gases (26), but no calculations were made. The above consideration cannot be made more quantitative at this stage because of the lack of data on the surface dipoles of metals (24, 25).

Naphthalene at the interface.—Figure 6 shows the amount of naphthalene adsorbed at the potential of maximum adsorption as a function of the concentration in solution. Except for the case of copper, the coverage always remains below Γ_m for naphthalene adsorbed parallel to the surface and approaches a limiting coverage on platinum. Hence, naphthalene probably adsorbs parallel to the metal surface on Fe, Ni, and Pt.

On copper the isotherm is linear up to the maximum concentration investigated and at the highest concentration exceeds Γ_m for flat adsorption. This indicates either flat adsorption with multilayer formation or perpendicular adsorption, *i.e.*, the plane of the naphthalene molecule at right angles to the surface. The former is unlikely since the maximum concentration used was well below the saturation concentration of naphthalene and no multilayer formation was observed on the other metals at the same concentration.

The area occupied by a naphthalene molecule perpendicular to the surface depends somewhat on whether one or both rings are in contact with the surface. Assuming that both perpendicular orientations occur, the area per molecule is about 17\AA^2 and hence Γ_m in this case is 9.8×10^{-10} moles/cm². The coverage θ at the highest concentration (10^{-4}M) is then 0.37 and a linear isotherm up to this coverage is reasonable.

The adsorption peak for naphthalene on copper also differs from other metals in that it covers a much smaller potential range. Bockris *et al.* (23) showed that sharp peaks can be expected when the lateral interaction between the adsorbed water molecules is small. This may be the case here due to the fact that naphthalene molecules adsorb standing up. Thus the H-bonding of the adsorbed water with water in the second layers out from the electrode is disrupted and the energy of adsorption of water decreased increasingly as the maximum of adsorption is approached. This decrease adds to that being caused by the electrode field and, hence, the adsorption peak sharpens.

Shift in the adsorption maximum.—A considerable change in the potential of maximum adsorption

³ Bockris *et al.* (23) obtained 0.9 kcal/mole⁻¹ for the same displacement owing to the use of $\mu^2/4r^3$ in place of Eq. [11].

with coverage of naphthalene is observed only in the case of platinum. A very small change in the same direction is observed on nickel. Since the maximum coverage on nickel was less than 0.2, only the shift on platinum is treated quantitatively.

Since the adsorption maximum on platinum occurs close to the zero charge potential, the field in the double layer is small and hence the shift cannot be due to an induced dipole in the naphthalene. Hence, some degree of electron exchange between the π -orbitals of naphthalene and the platinum is suggested. To explain the observed shift in the adsorption maximum, the bond must have a dipole moment with its negative end towards the solution, *i.e.*, the metal becomes more positive with respect to the solution as the coverage increases. The dipole moment per molecule can be calculated from the observed shift which is 0.5 and 0.2v in going from $\theta = 0$ to $\theta = 1$ in acid and alkaline solution respectively. The dipole moment is found using $\Delta\chi = (4\pi n\mu)/\epsilon$, where n is the number of dipoles cm^{-2} which, assuming 5 bonds per naphthalene molecule is $5 \times 3.26 \times 10^{-10} \times 6.023 \times 10^{23}$; $\epsilon = n^2$, for naphthalene = 2.3. The dipole moment of each bond is then 0.31 and 0.12 Debye in acid and alkaline solutions respectively. A smaller amount of π -bonding may occur on nickel but not on copper. Suhrmann *et al.* (27) observed that the resistance of thin evaporated films of Ni, Fe, and Pt increased when benzene was allowed to adsorb on them indicating a removal of electrons from the metal (*cf.* Direction of dipole observed in this work) while no such effect was observed on gold and copper.

Free energy of adsorption.—The adsorption of an organic substance from an aqueous solution may be written as the following process

$\text{Org(sol.)} + n\text{H}_2\text{O(ads)} \rightleftharpoons \text{Org(ads)} + n\text{H}_2\text{O(sol)}$
where n is a size factor equal to the number of water molecules displaced by one organic molecule. The equilibrium constant for the above process referred to unit mole fraction of organic or water in solution and on the surface is

$$K = \frac{(X_{o,\text{ads}})(X_{w,\text{sol}}^n)}{(X_{w,\text{ads}}^n)(X_{o,\text{sol}})} \quad [15]$$

Hence, one obtains for the standard free energy of adsorption

$$\Delta G_a^\circ = -2.3RT \log \left[\frac{55.4\theta}{C_o(1-\theta)^n} \cdot \frac{\{\theta + n(1-\theta)\}^{n-1}}{n^n} \right] \quad [16]$$

where the mole fractions have been expressed in terms of concentration and coverage θ (1, 3).

Using Eq. [16] with $n = 6$ for naphthalene adsorbed flat on the surface and $n = 2$ in the perpendicular case, the standard free energies of adsorption were calculated for all systems. The value at the potential of maximum adsorption is given in Table II, where the value for platinum is the average of the values in acid and alkaline solutions (8.6 and 8.2 kcal/mole respectively).

On Fe, Ni, and Cu, ΔG_a° as calculated from Eq. [16] is independent of coverage indicating that lateral interactions are negligible in these cases.

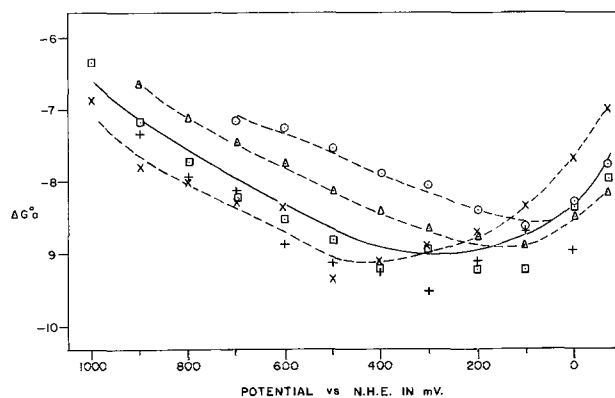


Fig. 7. Free energy of adsorption (ΔG_a°) of naphthalene on platinum from 0.9N NaClO_4 , 0.1N HClO_4 solution in kcal/mole. \circ , $2.5 \times 10^{-6}\text{M}$ Naphthalene; \triangle , $5.0 \times 10^{-6}\text{M}$ naphthalene; \square , $1.25 \times 10^{-5}\text{M}$ naphthalene; $+$, $5.0 \times 10^{-5}\text{M}$ naphthalene; \times , $1.0 \times 10^{-4}\text{M}$ naphthalene.

An apparent dependence of ΔG_a° on coverage or bulk concentration is observed on platinum, particularly from acid solution (Fig. 7). However, the free energy should be calculated at constant charge on the electrode, since the average energy of the water dipoles at the interface depends on charge. When the adsorption process does not change the potential significantly (no shift in adsorption maximum) then the charge varies linearly with potential (21) and hence ΔG_a° , when plotted on a potential scale, should still be independent of coverage in the absence of lateral interactions.

On platinum a significant shift in the adsorption maximum with coverage is observed and hence a similar shift occurs in the free energy curves plotted on a potential scale (Fig. 7). The curves can be put on an approximate charge scale by shifting them along the potential scale until the minima coincide, which reduces the apparent concentration dependence at a given potential to less than 1 kcal, which is the experimental scatter observed in all cases.

Summary

The adsorption of naphthalene on Fe, Ni, Cu, and Pt electrodes from acid and alkaline solutions has been determined as a function of potential and concentration using a radio-tracer technique.

A potential of maximum adsorption was observed, which was always more negative than the zero charge potential of the system.

The dependence of the adsorption on potential arises from the field dependent metal-water dipole interaction. The difference between the potential of maximum adsorption extrapolated to zero coverage and the z.c.p. was interpreted on the basis of this model as the difference in the binding energy of a water molecule in two orientations, favoring the orientation with the oxygen atom towards the metal. The dispersion interaction of water with the metal is greater in this orientation, since the electrons of water are then closer to the metal. Values of ΔU_{Disp} calculated on this basis are of the right order of magnitude. This asymmetry of water may vary with the metal, since qualitatively the surface field of the metal may increase or decrease the water distortion.

Shifts in the potential of maximum adsorption with coverage, particularly on platinum, indicate some π -bonding of naphthalene with that metal. Naphthalene adsorbs parallel to the surface on Pt (close to maximum coverage for that orientation) and probably on Ni and Fe but must adsorb perpendicular to the surface on Cu, since coverages of more than a monolayer must otherwise be assumed.

The free energy of adsorption of naphthalene was calculated for each system. It was found to be roughly constant for all metals but with a slightly higher value for platinum. This suggests that the amount of adsorption is determined mainly by the difference between the dispersive interaction with the metal of organic and water (3), with some π -bonding on platinum.

No significant lateral interactions between adsorbed molecules were observed.

Acknowledgments

The authors are grateful for financial support of this work by the National Science Foundation and the Esso Company. This paper is taken in part from a thesis by one of the authors (D.A.J.S.) presented to the University of Pennsylvania in partial fulfillment of requirements for the Ph.D. degree.

Manuscript received

Any discussion of this paper will appear in a Discussion Section to be published in the December 1964 JOURNAL.

REFERENCES

1. D. A. J. Swinkels, Ph.D. Dissertation, University of Pennsylvania, 1963.
2. M. Green, D. A. J. Swinkels, and J. O'M. Bockris, *Rev. Sci. Instruments*, **33**, 18 (1962).
3. J. O'M. Bockris and D. A. J. Swinkels, *This Journal*, **111**, 736 (1964).
4. E. A. Blomgren, J. O'M. Bockris, and C. Jesch, *J. Phys. Chem.*, **65**, 2000 (1961).
5. L. I. Antropov and S. N. Banerjee, *J. Indian Chem. Soc.*, **35**, 309, 531 (1958).
6. V. L. Kheifets and B. S. Krasikov, *Zhur. Fizi. Khim.*, **31**, 1992 (1957).
7. B. S. Krasikov and V. V. Sysoeva, *Bokl. Akad. Nauk. S.S.S.R.*, **114**, 363 (1957).
8. B. Jakuszewski and F. Kozlowski, *Roczniki Chem.*, **36**, 1873 (1962).
9. P. Lukovtsev, S. Levina, and A. N. Frumkin, *Acta Physicochim. U.R.S.S.*, **11**, 21 (1939); *Zhur. Fizi. Khim.*, **13**, 916 (1939).
10. J. Billiter, *Z. Elektrochem.*, **14**, 624 (1908).
11. D. M. Brasher, *Nature*, **181**, 1060 (1958).
12. E. O. Ayazyan, *Doklady Akad. Nauk. S.S.S.R.*, **100**, 473 (1955).
13. E. K. Wenström, V. I. Lichtman, and P. A. Rehbinder, *ibid.*, **107**, 105 (1956).
14. R. M. Vasenin, *Zhur. Fizi. Khim.*, **27**, 878 (1953).
15. J. J. McMullen and N. Hackerman, *This Journal*, **106**, 341 (1959).
16. N. Balashowa and A. N. Frumkin, *Doklady Akad. Nauk. S.S.S.R.*, **20**, 449 (1938).
17. L. Young, Ph.D. Dissertation, Cambridge, 1949.
18. A. N. Frumkin, A. W. Gorodetskaya, B. Kabanov, and N. Nekrassov, *Physik. Z. Sowjetunion*, **1**, 225 (1932).
19. T. N. Voropaeva, B. V. Deryagin, and B. N. Kabanov, *Izvest. Akad. Nauk. S.S.S.R.*, p. 257 (1963).
20. N. A. Balashowa, *Compt. rend. acad. sci. U.R.S.S.*, **103**, 639 (1955).
21. D. C. Grahame, E. M. Coffin, J. I. Cummings, and M. A. Poth, *J. Am. Chem. Soc.*, **74**, 1207 (1952).
22. T. N. Anderson and J. O'M. Bockris, *Electrochim. Acta*, **9**, 347 (1964).
23. J. O'M. Bockris, M. A. V. Devanathan, and K. Müller, *Proc. Roy. Soc.*, **A274**, 55 (1963).
24. C. Herring, "Metal Interfaces," American Society for Metals, 1951.
25. C. Herring and M. H. Nichols, *Rev. Mod. Physics*, **21**, 185 (1949).
26. O. Sinanoglu and K. S. Pitzer, *J. Chem. Phys.*, **32**, 1279 (1960).
27. R. Suhrmann, B. Hahn, and G. Wedler, *Naturwissenschaften*, **44**, 60 (1957).

Technical Notes



Solid Solubility and Amphoteric Behavior of Tin in Solution Grown Gallium Phosphide

F. A. Trumbore, M. Kowalchik, H. G. White, R. A. Logan, and C. L. Luke
Bell Telephone Laboratories, Incorporated, Murray Hill, New Jersey

The amphoteric behavior of group IV impurities in III-V compounds has been studied by a number of authors, particularly for the impurities germanium and silicon in gallium arsenide (1-5). In the present paper we consider the case of tin in gallium phosphide where the tin may substitute on either a gallium site or a phosphorus site, thus acting as a donor or an acceptor, respectively. Specifically, a thermal gradient technique has been used to grow gallium phosphide crystals from melts of compositions lying along the pseudobinary Sn-GaP liquidus

curve in the range from about 784° to 1085°C. Chemical analyses and surface barrier capacitance data indicate solid solubilities of $1-2 \times 10^{19}$ atoms/cc and (N_D/N_A) ratios of between 2 and 3 for tin in gallium phosphide under the present growth conditions. The distribution coefficient of tin in gallium phosphide increases with temperature in a manner similar to that observed for tin in silicon.

Experimental

The method and procedure used for the growth of the crystals involved the sealed tube thermal gra-

dient technique used previously (6) for the growth of tin-doped germanium and silicon. The gallium phosphide source material was boat grown or floating zone material obtained either from Merck or from L. Derick of these Laboratories. In the four experimental runs the thermal gradients were typically on the order of 2°-10°C/cm and growth times ranged from 4 to 7 weeks. Large grained samples, of the order of a cubic centimeter in volume, were obtained.

Surface barrier capacitance measurements were carried out on these samples using a technique described previously (7). By comparison with Hall effect measurements as a function of temperature, this method has been shown (7) to be an accurate and relatively simple way to determine the net impurity concentration ($N_D - N_A$) over the range of values encountered here. In order to check the possibility that either precipitation of tin or redistribution of tin on the gallium and phosphorus sites was present, one sample was heated to about 1000°C and quenched in the manner described previously (8) for germanium. No change in ($N_D - N_A$) was observed.

The samples were analyzed chemically for the total tin concentration. Prior to analysis the samples were crushed and digested in hot conc HCl to remove any occluded tin. [Previous work (9) on aluminum and gallium in germanium, where a direct check between electrical and chemical data was possible, indicates that with appropriate care the effect of occluded impurity can be eliminated in crystals grown by the thermal gradient method.] The analytical procedure involved solution of the powdered gallium phosphide in a H₂O-HNO₃-H₂SO₄ (2:1:1) mixture, removal of the HNO₃ by evaporation to white fumes and precipitation of the tin as the sulfide with added copper as co-precipitant. The amount of tin was then determined by the photometric phenylfluorone method (10). In these analyses particular care was taken to carry out the sulfide precipitation from a strong acid solution and to develop the colored phenylfluorone complex at a sufficiently low pH to prevent interference by traces of gallium or copper.

Results and Discussion

In the interpretation of the chemical and capacitance data, it is assumed that electrically active impurities or imperfections other than tin are present in negligible amounts¹ and, following Whelan *et al.* (2), that the tin atoms are randomly distributed on the gallium and phosphorus sites. Thus, ($N_D - N_A$) is assumed to be the excess of tin atoms on gallium sites over those on phosphorus sites and ($N_D + N_A$) is assumed to be equal to the total tin concentration. The results of the photometric ($N_D + N_A$) and the capacitance ($N_D - N_A$) measurements (all samples were n-type) are summarized in Table I along with the growth temperatures and calculated values of N_D/N_A . The accuracy of the chemical analyses is believed to be better than ±10% of the total tin

¹ Qualitative spectroscopic analyses indicated silicon to be the major contaminant in these crystals, as expected from the fact that the crystals were grown in silica tubes. Quantitative photometric analyses indicated a silicon concentration of less than $\sim 1 \times 10^{18}$ atoms/cc, the limit of sensitivity of the method.

Table I. Summary of capacitance and chemical data*

Temp. °C	($N_D - N_A$) (capacitance)	($N_D + N_A$) (chemical)	N_D/N_A
784 ± 10	$(6.3 \pm 3.1) \times 10^{18}$	1.22×10^{19}	3.1
950 ± 10	6.2×10^{18}	1.34×10^{19}	2.7
1070 ± 15	$(6.3 \pm 0.25) \times 10^{18}$	1.59×10^{19}	2.3
1085 ± 20	$(8.6 \pm 1.6) \times 10^{18}$	1.63×10^{19}	3.2

* All concentrations are atoms/cc.

concentration. The uncertainties quoted in Table I for ($N_D - N_A$) are the mean deviations of a number of measurements on that sample (except for the crystal growth at 950°C, on which only one measurement was made). The relatively large scatter in some of the capacitance data is probably due to local inhomogeneities in the samples such as occlusions or cracks rather than actual concentration fluctuations.²

By combining the results of the chemical analyses with Rubenstein's data (11) for the pseudobinary Sn-GaP liquidus curve, we may calculate the variation of the distribution coefficient, k , for tin in gallium phosphide as a function of temperature along this liquidus curve. (Here k is defined as $k = x^S/x^L$ where x^S and x^L are the atom fractions of tin in the solidus and liquidus alloys, respectively). The usual $\log k$ vs. $1/T$ plot is shown in Fig. 1. It is seen that k rises with temperature in a nonlinear fashion similar to the behavior observed for tin in silicon (6), which has nearly the same lattice constant as gallium phosphide and also melts between 1400° and 1500°C. In fact, in the temperature range studied, the solid solubility of tin in gallium phosphide is only about a factor of three lower than the solubility in silicon.

The question naturally arises as to whether or not the distribution coefficients obtained here correspond to equilibrium values. The presence of large

² It is of interest that the sample grown at 1070°C was part of a run containing four other crystals grown from gallium-rich solutions. Duplicate capacitance measurements on each of these crystals agreed to within better than ±5-10% and the optical quality of this group of crystals appeared significantly better than for the other crystals listed in Table I. Thus, the value of ($N_D - N_A$) for the 1070°C crystal in Table I is considered to be particularly reliable.

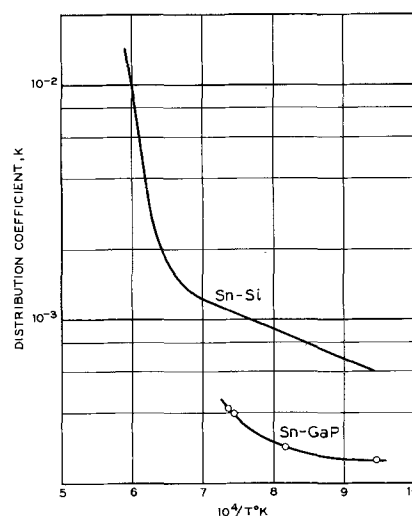


Fig. 1. Comparison of $\log k$ vs. $1/T$ plots for the Sn-GaP and Sn-Si systems. The experimental points are calculated from the data in Table I and Rubenstein's liquidus data from ref. (11). The Sn-Si plot is from ref. (6).

facet effects (12) in III-V compounds is well known. However, as discussed by Banus and Gatos (13) for indium antimonide, there is a decrease in the magnitude of the facet effect with increasing impurity concentration. A similar effect in germanium is implied by the failure to observe a facet effect in crystals grown from melts doped very heavily with antimony (14). The assumption of equilibrium growth conditions is, therefore, thought to be reasonable in the absence of data to the contrary.

The calculated values of (N_D/N_A) of between 2 and 3 indicate a strong preference of the tin for the gallium site. This is consistent with the better match between the gallium and tin tetrahedral radii as compared to the phosphorus and tin radii (15). The scatter in the capacitance data is sufficient to obscure any trend in (N_D/N_A) with temperature or melt composition. Further experiments are in progress to obtain such data for tin as well as for other group IV impurities in gallium phosphide.

Manuscript received May 16, 1963; revised manuscript received Jan. 13, 1964.

Any discussion of this paper will appear in a Discussion Section to be published in the December 1964 JOURNAL.

REFERENCES

1. C. Kolm, S. A. Kulin, and B. L. Averbach, *Phys. Rev.*, **108**, 965 (1957).
2. J. M. Whelan, J. D. Struthers, and J. A. Ditzemberger, *Proceedings of the International Conference on Semiconductor Physics, Prague, 1960*, p. 943; also "Properties of Elemental and Compound Semiconductors," H. C. Gatos, Editor, p. 146, Interscience Publishers, Inc., New York (1960).
3. J. O. McCaldin and R. Harada, *J. Appl. Phys.*, **31**, 2065 (1960).
4. R. Solomon, R. Newman, and N. R. Kyle, *This Journal*, **108**, 716 (1961).
5. L. J. Vieland and T. Seidel, *J. Appl. Phys.*, **33**, 2414 (1962).
6. F. A. Trumbore, C. R. Isenberg, and E. M. Porbansky, *J. Phys. Chem. Solids*, **9**, 60 (1959).
7. H. G. White and R. A. Logan, *J. Appl. Phys.*, **34**, 1990 (1963).
8. R. A. Logan, *Phys. Rev.*, **101**, 1455 (1956).
9. F. A. Trumbore, E. M. Porbansky, and A. A. Tagaglia, *J. Phys. Chem. Solids*, **11**, 239 (1959).
10. C. L. Luke, *Anal. Chem.*, **28**, 1276 (1956); *ibid.*, **31**, 1803 (1959).
11. M. Rubenstein, Electronics Division Abstracts of the Electrochemical Society, Vol. 11, No. 1, p. 129 (1962).
12. K. F. Hulme and J. B. Mullin, *Phil. Mag.*, **4**, 1286 (1959).
13. M. D. Banus and H. C. Gatos, *This Journal*, **109**, 829 (1962).
14. W. G. Spitzer, F. A. Trumbore, and R. A. Logan, *J. Appl. Phys.*, **32**, 1822 (1961).
15. L. Pauling, "The Nature of the Chemical Bond," p. 179, Cornell University Press, Ithaca, N. Y. (1945).

Growth of $(\text{Ga}_x\text{In}_{1-x})\text{As}$ Single Crystals by Vapor Phase Reaction

Richard Serrine

Lincoln Laboratory,¹ Massachusetts Institute of Technology, Lexington, Massachusetts

The epitaxial growth of single crystal III-V compounds by the halogen disproportionation mechanism in both open and closed systems has been reported by a number of people (1-4). The nonseeded growth of polycrystals has been discussed by Holonyak and co-workers (5). This note deals with the nonseeded growth of single mixed crystals $(\text{Ga}_x\text{In}_{1-x})\text{As}$ grown by the halogen vapor transport mechanism in a closed system.

There is considerable advantage to growing mixed single crystals in the closed tube process. The material can be homogenized by transporting several times before the final crystal is grown. The crystal grows with large, atomically flat faces, which are suitable for injection laser fabrication without polishing.

Crystals grown by this method without special precautions nucleate at a number of places on the quartz wall and grow inward, eventually forming a solid polycrystalline ingot. In order to grow single crystals without a seed the initial nucleation must be controlled and the environment must be such that the crystal grows out toward the quartz wall. The steps necessary to have this happen are:

1. In order to keep the area of initial nucleation small, the reaction vessel is drawn down to a point

which is connected to a heat sink. In drawing the quartz tube to a point, the wall is thinned down to reduce the thermal conduction along the wall.

2. In order to keep the reaction as close to equilibrium as possible but still maintain transport, the reaction vessel is placed in a temperature gradient such that the tip is only 10°-15°C below the source temperature. With such a small temperature difference, it is very necessary that the furnace have a uniform temperature in a plane perpendicular to the axis of the reaction vessel. This is accomplished in the furnace by centering a small diameter Mullite tube on the axis of the furnace and selecting the quartz tubing such that a snug fit exists between the reaction vessel and the inner wall of the Mullite tube.

3. In order to keep the partial pressure of the normal halide much larger than the partial pressure of the subhalide, the source temperature is chosen such that the normal halide is the dominant member, and a relatively large amount of chlorine is used.

The general procedure is as follows: the desired amounts of GaAs and InAs, undoped polycrystalline material, are placed in a reaction vessel such as shown in Fig. 1a along with a few milligrams of As and a dopant, usually Se. The vessel is connected to

¹ Operated with support from the U.S. Air Force.

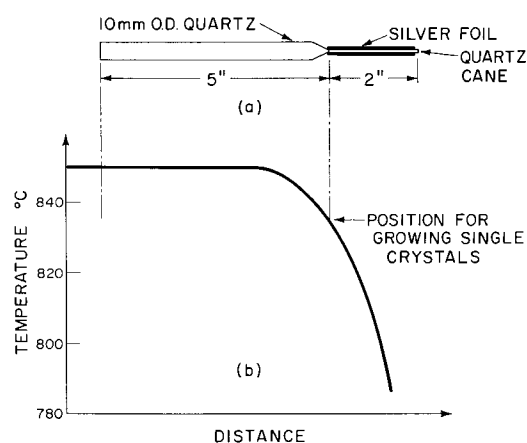


Fig. 1. (a) Reaction vessel and (b) temperature profile of furnace. The reaction vessel is positioned for growing single crystals.



Fig. 2. Photograph of $(\text{Ga}_{0.95}\text{In}_{0.05})\text{As}$ single crystal inside reaction vessel.

a vacuum system and pumped down to approximately 10^{-6} Torr, back filled with Cl_2 , and sealed off. As shown in the figure foil (silver or platinum) is wrapped around the quartz cane. The vessel is placed in a furnace with a profile as shown in Fig. 1b.

Figure 2 shows a crystal $(\text{Ga}_{0.95}\text{In}_{0.05})\text{As}$, grown according to the above discussion. The crystal, which was loosely bonded to the quartz, has been moved back from the tip by gentle tapping. The crystal was photographed while still in the quartz vessel and the spots seen on the top face are actually on the quartz. This crystal required 115 hr

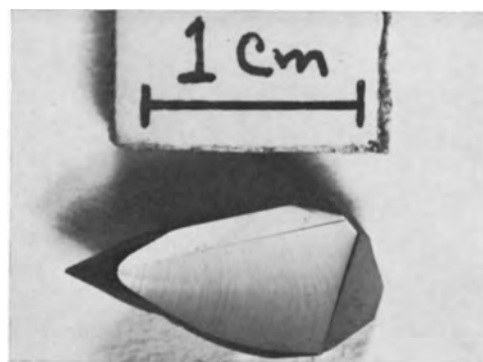


Fig. 3. Photograph of an "as grown" $(\text{Ga}_{0.97}\text{In}_{0.03})\text{As}$ crystal

for growth. Figure 3 shows another crystal $(\text{Ga}_{0.97}\text{In}_{0.03})\text{As}$ grown in a different furnace in a 72-hr period. The photograph is an "as grown" picture of the crystal and demonstrates how the crystal grows out toward the quartz wall. The top face, one just like it on the other side of the crystal, and the end face are all (111) faces. The fast growing direction is in the (111) plane, and the slow growing direction is the $\langle 111 \rangle$ direction. The crystal grows "up" the temperature profile until the thermal conduction is inadequate to maintain a sufficient temperature difference for deposition on the high-temperature side but continues to grow in thickness until the source material is exhausted. The line on the top face also appears on the other side and indicates that the crystal is twinned.

These compositions were chosen in the search for injection lasers at 8800\AA , a wavelength desired to pump a Nd^{+3} CaF laser. A single crystal of $(\text{Ga}_{0.20}\text{In}_{0.80})\text{As}$ has been grown which produced coherent light at 2.4μ .

Manuscript received Dec. 12, 1963.

Any discussion of this paper will appear in a Discussion Section to be published in the December 1964 JOURNAL.

REFERENCES

1. V. J. Silvestri and V. J. Lyons, *This Journal*, **109**, 963 (1962).
2. R. R. Moest and B. R. Shupp, *ibid.*, **109**, 1061 (1962).
3. San-Mei Ku, *ibid.*, **110**, 991 (1963).
4. F. A. Pizzarello, *ibid.*, **110**, 1059 (1963).
5. N. Holonyak, Jr., D. C. Jillson, and S. F. Bevacqua, "Metallurgy of Semiconductor Materials," J. B. Schroeder, Editor, Interscience Publishers, New York (1961).

Photorectifiers with Agar Gel Contacts

Karen E. Plain and Richard H. Bube

Department of Materials Science, Stanford University, Stanford, California

Several different types of photorectifiers have been described in recent years. Reynolds, Greene, and Antes (1) describe a photodiode consisting of a high-conductivity CdS crystal with one ohmic indium electrode and one rectifying diffused copper electrode. Photoexcitation of the rectifying junction decreases the reverse resistance of the cell, and rectification ratios of the order of 20 or more are obtained for low voltages; the operating range

of such a cell is for applied voltages less than about 2v. A radically different type of photorectifier is described by van Santen and Diemer (2) using a CdS photoconducting powder dispersed in a dielectric (3). This type of photorectifier is effective only for alternating and not for direct currents, and has an operating range in the hundreds of volts. This note describes another type of photorectifier employing photosensitive single crystals of CdS or

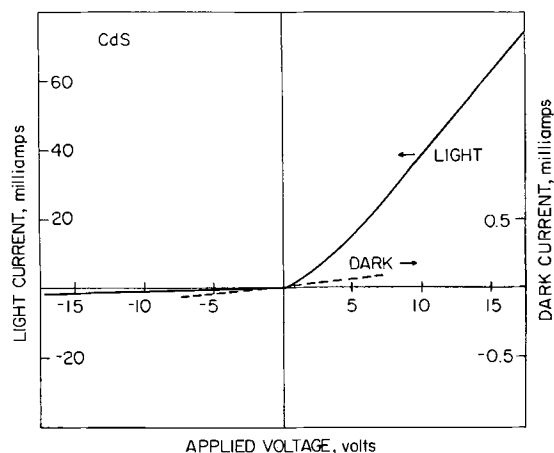


Fig. 1. Current vs. voltage characteristics of CdS single crystal with ohmic indium electrode and blocking agar gel electrode, in the dark and for illumination by microscope lamp. Voltage positive means indium electrode negative.

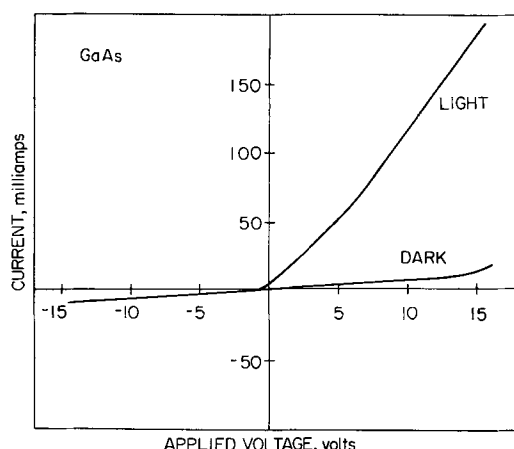


Fig. 2. Current vs. voltage characteristics of GaAs single crystal with ohmic indium electrode and blocking agar gel electrode, in the dark and for illumination by microscope lamp. Voltage positive means indium electrode negative.

GaAs, and an electrolytic agar gel blocking contact. Such a system is capable of giving rectification ratios of 20 to 50 or higher, with photocurrents in the forward direction of tens or even hundreds of milliamps, over an operating range of at least 20v.

Williams (4) has made extensive use of an electrolytic KCl aqueous solution as a blocking contact and has also discussed the photochemical processes in the Becquerel effect involving such contacts (5). The photorectifiers described in this note were constructed with one melted indium ohmic contact, and with a blocking contact consisting of a stiff agar gel, 4% agar in 0.1M KCl, which has electrical properties similar to those of a KCl solution.

Table I. Photorectifier cell characteristics

	Forward resistance, ohms		Reverse resistance, ohms	
	Dark	Light	Dark	Light
CdS	10^8	200	10^8	10^4
GaAs	2000	70	2000	2000

Typical curves for an n-type CdS single crystal are given in Fig. 1 and for an n-type GaAs single crystal in Fig. 2, for operation at room temperature in the dark and under a microscope lamp. Forward and reverse resistances of these two cells, meaningful quantities for applied voltages greater than about 2v, are summarized in Table I.

The CdS crystal shows a dark-to-light resistance ratio in the forward direction of almost 10^6 and a rectification ratio of about 50. Unfortunately a photochemical reaction in the forward direction (5) causes decomposition of the CdS crystal. The GaAs crystal was somewhat more conducting in the dark, but still shows a rectification ratio of about 30. No photochemical reaction in the forward direction (5) occurs for the GaAs, and its operation is unaffected by the passage of time. These values represent typical easily obtained magnitudes and should not be construed to be the result of any extensive attempt to optimize parameters.

The polarity of the applied voltage for the forward direction in these cells is for the ohmic indium electrode negative, consistent with the model of a photoconductor with high gain depending on the ability of the cathode to replenish electrons drawn out at the anode. In the reverse direction and near zero applied voltage, the photovoltaic effects described by Williams are significant (5).

Acknowledgment

Crystals used in this study were available through the courtesy of the RCA Laboratories.

Manuscript received Jan. 1, 1964. Work sponsored partially by the National Science Foundation for one author (K.E.P.) and by the Advanced Projects Research Agency of the Defense Department through the Center for Materials Research at Stanford University.

Any discussion of this paper will appear in a Discussion Section to be published in the December 1964 JOURNAL.

REFERENCES

1. D. C. Reynolds, L. C. Greene, and L. L. Antes, *J. Chem. Phys.*, **25**, 1177 (1956).
2. J. G. van Santen and G. Diemer, *Solid State Electronics*, **2**, 149 (1961).
3. R. H. Bube, *J. Appl. Phys.*, **31**, 2239 (1960).
4. R. Williams, *Phys. Rev.*, **117**, 1487 (1960); **123**, 1645 (1961); *J. Phys. Chem. Solids*, **22**, 129 (1961).
5. R. Williams, *J. Chem. Phys.*, **32**, 1505 (1960).



The Hall Effect-Seebeck Effect Sign Anomaly in Semiconducting Glasses

A. David Pearson

Bell Telephone Laboratories, Incorporated, Murray Hill, New Jersey

Peck and Dewald (1) have reported Hall effect and conductivity data on semiconducting glasses from the system arsenic-tellurium-iodine. Among the results that they noted was that all the samples tested, regardless of chemical composition, showed n-type semiconductivity. However, subsequent Seebeck effect measurements on samples of the same compositions indicated that they were p-type semiconductors. Similar anomalies between the sign of the Hall effect and Seebeck effect in semiconducting glasses have been noted by Kolomiets and Nazarova (2) on materials from the system arsenic-tellurium-selenium-thallium, and by Uphoff and Healy (3) on glasses from the system arsenic-tellurium-selenium. The work reported here was undertaken in an attempt to discover the source of this anomaly, a necessary procedure before any interpretations could be made based on Hall effect or Seebeck effect data in these glasses.

There are several possible sources for an anomaly such as described above. One would be a two carrier semiconductor, since the band theory only demands that the signs of the Hall and Seebeck effects be the same for a one carrier system. Another possibility is that, since the carrier mobilities are so low in these materials [Peck and Dewald (1) report a few parts $\times 10^{-2}$ cm²/volt-sec], the conduction process may be carried out by means of a hopping mechanism in which the mean free path of the charge carriers is comparable to the interatomic distance in the material. This sort of process is not yet well enough understood to be able to say with certainty whether or not the signs of the Hall effect and Seebeck effect should be the same. A third possibility is that the band theory does not apply to the semiconducting glasses at all. They lack the ordered crystalline lattice on which the band theory is based. There is a fourth possibility, which it was felt should be investigated before serious consideration of the previously mentioned ones. This is the effect of second phases. Wolfe, Wernick, and Haszko (4) have found an anomalous Hall effect and Seebeck effect in silver antimony telluride, which turned out to be due to the presence of a second phase consisting of silver telluride.

Seebeck effect investigation.—A series of arsenic-tellurium-iodine semiconducting glasses in sealed fused silica ampoules was quenched from 600°C

to room temperature. The Seebeck coefficients of the samples thus obtained were measured at room temperature and ranged from +940 to +1200 $\mu\text{V}/^\circ\text{C}$ depending on composition. The ease of devitrification of these glasses had already been noted and reported on samples which had been held a little above their softening temperatures (5). So the possibility existed that samples held at somewhat higher temperatures might contain crystals even though not readily visible. A second series of glasses having the same compositions as the first were therefore equilibrated at 400°C and quenched to room temperature. Two of these samples appeared crystalline even to the naked eye while the rest appeared glassy. Seebeck coefficients of the glassy samples had decreased somewhat from their original values, while the coefficients of the two grossly crystalline samples had dropped to less than 10 $\mu\text{V}/^\circ\text{C}$ although they were still positive. The electrical resistivities of these two samples had also dropped by several orders of magnitude. These data are consistent with an n-type crystalline phase precipitating from a p-type semiconducting glassy matrix.

Previous x-ray diffraction investigations of devitrified glasses from this system have shown the presence of arsenic and arsenic telluride in the crystalline phase (5). Presumably these crystals would not be pure, but would contain excess arsenic, tellurium, or iodine. Arsenic telluride doped with iodine or tellurium has already been reported to be n-type (6). These two compositions, along with the other three possible second phases, that is arsenic doped with tellurium or iodine, (in 1% excesses), and arsenic telluride doped with 1% excess arsenic were therefore prepared separately and examined with hot and cold probes. N-type conductivity regions were detected in the arsenic telluride doped with excess arsenic or tellurium. Arsenic telluride doped with excess arsenic, tellurium, or iodine would therefore appear to be a reasonable possibility for the second phase, if such is the cause of the Hall effect-Seebeck effect anomaly.

Previous examination of polished and etched surfaces of semiconducting glasses from the system arsenic-tellurium-iodine by means of ordinary laboratory microscopes had not revealed any inhomogeneities in the samples. It was therefore decided to

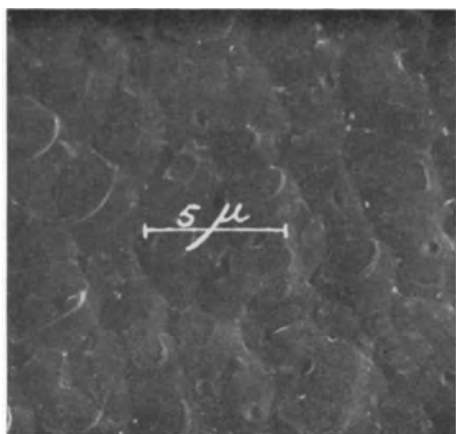


Fig. 1. Electron micrograph of As-Te-I glass (4 a/o I), polished and etched surface, two-step replica technique.

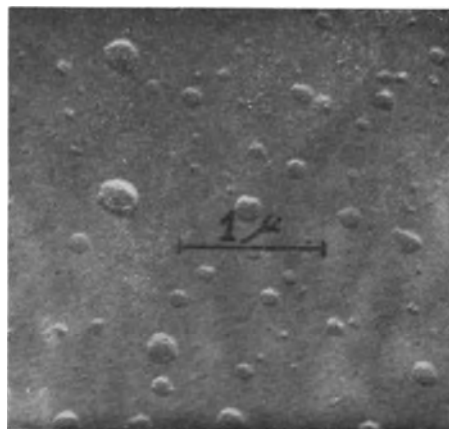


Fig. 3. Electron micrograph of $Tl_2SeAs_2Te_3$ glass, fresh fracture surface, direct replica technique.



Fig. 2. Electron micrograph of As-Te-I glass (20 a/o I), polished and etched surface, two-step replica technique.

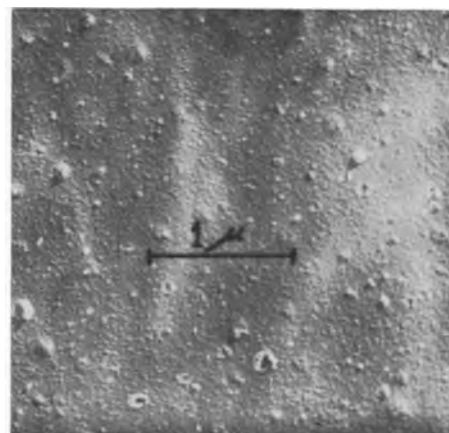


Fig. 4. Electron micrograph of $As_{10}SeTe_{12}$ glass, fresh fracture surface, two-step replica technique.

carry out an electron microscope investigation of these materials. Figure 1 shows an electron micrograph of a polished and etched sample of a glass consisting of 43 atomic per cent (a/o) arsenic, 4 a/o iodine, the remainder being tellurium. The material was originally quenched from $600^\circ C$ to room temperature. That the glass is not uniform is immediately apparent. The large structure is thought to be an etch pattern and not to represent inhomogeneity. The small irregularities are thought to be crystallites. Figure 2 shows an electron micrograph of a similar semiconducting glass containing a higher concentration of iodine (20 a/o). Here the irregularity of the material is even more apparent. The white particles are believed to be crystallites which have been ripped out of the surface of the sample by the collodion used to make the replica. Since the anomaly reported by Kolomiets and Nazarova (2) and Uphoff and Healy (3) was so strikingly similar to the one being discussed here, it was essential to check on their compositions to see whether the proposed explanation could apply to their results. Figure 3 shows an electron micrograph of a fresh fracture surface of the glass of composition $Tl_2SeAs_2Te_3$ reported on by Kolomiets and Nazarova (2), made by a direct replica technique. A second phase within the glassy matrix can be seen clearly. Similarly, Fig. 4 shows an electron micrograph of a fracture surface of the $As_{10}SeTe_{12}$ glass studied by Uphoff

and Healy (3) made by a two-step replica technique. Again the second phase is clearly evident.

Discussion.—The results described here are consistent with the picture of a p-type glassy matrix from which a small amount of a n-type crystalline phase has precipitated. In a Seebeck effect measurement, the low thermal conductivity of the glass causes it to support the temperature gradient and thus give a positive result. In a Hall effect measurement the relatively high carrier mobility of the crystalline phase causes it to dominate over the glassy matrix thus giving an n-type result. It must be pointed out that the results are only consistent with this picture and do not conclusively prove it. Conclusive proof will have to await the positive identification of the second phase, and calculations based on a knowledge of its carrier mobilities and Seebeck coefficients fitting in with the observed results on the two-phase materials. In the meantime, the fact that two phases have been seen in all the semiconducting glasses investigated in this study should give pause to workers attempting to interpret the results of electrical and Hall effect measurements on these materials.

Acknowledgments.—The author acknowledges the cooperation of Mr. R. Wolfe who made the Seebeck effect measurements, Miss Eloise Koonce who made the electron micrographs, and Mr. W. R.

Northover who assisted with the sample preparations.

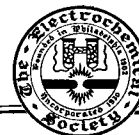
Manuscript received Jan. 13, 1964. This paper was presented at the New York Meeting, Sept. 30-Oct. 3, 1963.

Any discussion of this paper will appear in a Discussion Section to be published in the December 1964 JOURNAL.

REFERENCES

1. W. F. Peck, Jr. and J. F. Dewald, *This Journal*, In press.
2. B. T. Kolomiets and T. F. Nazarova, *Sov. Phys. Solid State*, **2**, 369 (1960).
3. H. L. Uphoff and J. H. Healy, A.S.T.I.A. Report No. AD 260780 (1961).
4. R. Wolfe, J. H. Wernick, and S. E. Haszko, *J. Appl. Phys.*, **31**, 1959 (1960).
5. A. D. Pearson, W. R. Northover, J. F. Dewald, and W. F. Peck, Jr., Paper presented at VI International Congress on Glass, Washington, D. C., July (1962).
6. T. C. Harman, B. Paris, S. E. Miller, and H. L. Goering, *J. Phys. Chem. Solids*, **2**, 181 (1957).

Discussion Section



This Discussion Section includes discussion of papers appearing in the JOURNAL of The Electrochemical Society, Vol. 110, No. 4, 7, 8, 9, and 12 (April-December 1963). Discussion not available for this issue will appear in the Discussion Section of the December 1964 JOURNAL.

Stresses in Anodic Films

D. A. Vermilyea (pp. 345-346, Vol. 110, No. 4)

E. M. Field and D. R. Holmes:¹ The discussion by Bradhurst and Leach² and by Evans³ of Vermilyea's paper reminds us of some calculations we made and some correspondence we had with Dr. Pringle on the subject of his paper "A Radiotracer Study of Anodic Oxidation" by Davies, Pringle, Graham, and Brown.⁴ These calculations were probably an oversimplification in view of the many uncertainties about the composition and structure of the corrosion products formed during the anodic oxidation of aluminum under varying conditions. We showed that if the ionic counter currents responsible for the growth of nonporous γ - Al_2O_3 are such as to give an inner stress-free film grown with zero volume change (as in the case of the magnetite films on mild steel studied by Potter and Mann⁵ and Adams *et al.*⁶) then 28% of the aluminum consumed must pass outwards through the film to regions beyond the original metal surface, either going into solution or reacting to lay down Al_2O_3 outside the original surface. If the film formed is porous then the percentage of aluminum passing outwards must be greater (for example for a film of density 3.1 instead of the theoretical 3.66, 40% of the aluminum would have to pass outwards). These calculated values lie within the range of values observed by Pringle *et al.*,^{4,7} for oxidation at various current densities, the lower values being associated with

¹ Central Electricity Research Labs., Leatherhead, England.

² D. H. Bradhurst and J. S. L. Leach, *This Journal*, **110**, Discussion Section, 1289 (1963).

³ U. R. Evans, *This Journal*, **110**, Discussion Section, 1290 (1963).

⁴ J. A. Davies, J. P. S. Pringle, R. L. Graham, and F. Brown, *This Journal*, **109**, 999 (1962).

⁵ E. C. Potter and G. M. W. Mann, p. 417, 1st International Congress Met. Corrosion 1961, Butterworth's (1962); also paper presented at the 2nd International Congress 1963.

⁶ A. M. Adams, E. M. Field, D. R. Holmes, and R. C. Stanley, paper presented at the 2nd International Congress Met. Corrosion, (1963).

⁷ J. P. S. Pringle and J. A. Davies, Contribution to The Electrochemical Society Meeting, Pittsburgh, April (1963).

⁸ D. H. Bradhurst and J. S. L. Leach, British Ceramic Soc. Conference on the Properties of Nonmetallic Crystals and Polycrystals, Hastings 1962.

⁹ D. H. Bradhurst, *Chem. and Ind.* (London) **472** (1962).

lower current densities. Bradhurst and Leach,^{8,9} have supplemented this information by showing that the stresses in anodically formed aluminum oxide films may change from compressive to tensile as the current density is increased. It would be interesting if the experiments in the two laboratories could be combined, to determine the value of outward counter-current at which the stresses in the oxide film change from compressive to tensile, so that the value predicted by the simple formula given below for growth at zero volume change could be checked.

For stress-free growth of oxide at porosity p (defined as the volume fraction of voids) we suggest the percentage of metal passing outwards will be given by:

$$100 \left[1 - \frac{nZ_o V_m (1-p)}{Z_m V_o} \right]$$

or

$$100 \left[1 - \frac{n\rho_o M_m (1-p)}{\rho_m M_o} \right]$$

where V_m is the unit cell volume of the metal

Z_m is the number of formula units per unit cell of metal

ρ_m is the theoretical metal density

M_m is the mass of a metal atom

V_o , Z_o , ρ_o are corresponding quantities for the oxide, M_o is the mass of an oxide formula unit, n is the number of metal atoms in an oxide formula unit.

It is interesting to note that the concept of ionic counter-currents giving rise to stress-free growth was also proposed by Czerski and Frank¹⁰ in their paper on the oxidation of nickel, before the more widely known independent suggestion by Potter and Mann.⁵

Conductivity and Thermoelectric Potential Measurements on Perylene: Metal Halide Complexes

M. S. Frant and R. Eiss (pp. 769-772, Vol. 110, No. 7)

L. I. Boguslavsky and A. V. Vannikov:¹¹ In Frant and Eiss's paper¹² it was found in the investigation of complexes of perylene with various metal halides that the value of σ_o calculated from the formula

¹⁰ L. Czerski and F. Frank, *Arch. Gornictwa i Hutnictwa*, **III**, 43 (1955).

¹¹ Institute of Electrochemistry, Academy of Sciences, U.S.S.R.

¹² M. S. Frant and R. Eiss, *This Journal*, **110**, 769 (1963).

Table I

Sample	σ_{20} , ohm ⁻¹ cm ⁻¹	ΔE ,* e.v.	σ_0 , ohm ⁻¹ cm ⁻¹	σ_v , ohm ⁻¹ cm ⁻¹	ΔE_v , e.v.
I 620°C	1.10 ⁻⁸	0.55	5.10 ⁻⁴	4.10 ⁻⁴	—
I 420°C	1.10 ⁻⁹	0.64	3.10 ⁻⁴	5.10 ⁻⁴	0.09
I** 420°C I	4.10 ⁻⁴	0.02	6.10 ⁻⁴	4.10 ⁻⁴	—
I** 420°C II	3.10 ⁻⁷	0.38	5.10 ⁻⁴	4.10 ⁻⁴	—
II 500°C	9.10 ⁻²	0.03	0.6	0.7	0.01
III 350°C	4.10 ⁻⁶	0.2	9.10 ⁻⁴	2.10 ⁻⁴	0.06

Table II

Samples	$\Delta\psi$, v.	σ_{20} , ohm ⁻¹ cm ⁻¹	ΔE ,* e.v.
I 360°C	0.51	1.10 ⁻¹¹	0.8
I 510°C	0.19	1.10 ⁻⁹	0.65
I 650°C	0.13	7.10 ⁻⁸	0.50
I 720°C	0	5.10 ⁻⁵	0.30

* Calculated from the formula.

** Samples differ in their iodine content.

$\sigma = \sigma_0 e^{-\Delta E/2KT}$ hardly depends on the nature of the complex, although the conductivity and the activation energy change widely. In this connection, it would be of interest to compare these results with the data obtained in the investigation over a wide frequency range of conductivity and activation energy of polyethylene modified by irradiation and heat treatment (I)^{14, 15} and of polymeric complexes formed by tetracyanethylene with some metals¹³.

Plotted in the logarithmic scale, the conductivity-frequency dependence is in the shape of a descending curve having a section independent of frequency. Generally, such a plateau on the curve is observed at a frequency of some tens of megacycles and depends on the previous treatment of the material. On the basis of a model of heterogenous structure, proposed in ref. 13, the parameters of regions of continuous conjugation should be those of the plateau. In that case, the values of σ_0 calculated from the direct current measurements and those of σ_v measured at high frequency within the plateau should coincide. In Table I are listed the results of these measurements for polytetracyanethylene (II), for the polymeric complex formed by tetracyanethylene with silver (III) and for (I) obtained at different temperatures in the presence of iodine additions and in their absence. The table shows that, just as in the case of complexes with perylene, various treatments hardly affect the regions of continuous polyconjugation, but they mainly change the probability of transfer of carriers from one region to another. This probability also depends on the presence of some additives, such as iodine. As it should be expected, σ_0 and σ_v do not depend on the iodine content in the sample, whereas σ_{20} and ΔE change greatly. In the case of substances studied there exists a marked activation energy of the carrier transfer from one region to another since the conduc-

tivity activation energies measured at a high frequency in the region of the plateau are much smaller than those obtained with direct current. The same conclusion may be drawn from the comparison of the differences in the work function of the samples (I), with other electric characteristics presented in Table II, the change in the work function being referred to the sample obtained at 720°C, which has a minimum work function. Similar dependences have been obtained for the films of a polymeric complex formed by tetracyanethylene with some metals¹⁶. On the basis of these results, we may draw the conclusion that the conductivity mechanism of the substances in question is determined apparently by the carrier transfer from one region of polyconjugation to another and by the conductivity within these regions characterized by an activation energy close to zero.

M. S. Frant¹⁷ and R. Eiss: We are pleased to have confirmation of our finding by Boguslavsky and Vannikov of a lack of variability of σ_0 within a series of related complexes. We now suspect that this phenomena may be much more generally applicable than has been previously realized.

The Influence of the Environment on the Corrosion of Zirconium and Its Alloys in High-Temperature Steam

J. N. Wanklyn, C. F. Britton, D. R. Silvester, and N. J. M. Wilkins
(pp. 856-866, Vol. 110, No. 8)

H. Spindler¹⁸: In respect to the authors, observations on the pressure dependence of steam corrosion of some zirconium alloys (see Table I of their paper) we must note that the stated behavior seems to be no general rule. As shown by own experiments published previously¹⁹, zirconium-niobium alloys with low niobium content in the range from 0.5 to 2.0 weight per cent (w/o) corrodes much faster in steam of 400°C at 1 atm than they do at 120 atm (i.e., \approx 1650 psi). The ratio between weight gain at 1 atm to weight gain at 120 atm is near 1.8; independent from niobium content in the range studied and from thermal and working history of the alloy. In line with the authors' conceptions we must therefore suggest a pronounced effect of niobium on the film properties, particularly its porosity, of the corrosion product layer on the alloys studied.

J. N. Wanklyn, C. F. Britton, D. R. Silvester, and N. J. M. Wilkins: We certainly agree that an increase of oxidation rate with steam pressure (e.g., our Table I) is not universal. Indeed, our capacity measurements for Zircaloy 2 (Fig. 5) indicate that less porous films are formed at high pressure than at low pressure. The influence of this "compensation effect" on weight gains is either to produce similar values at the two pressures (Fig. 3) or even, as with

¹⁶ L. I. Boguslavsky, *Zhur. Fiz. Khim.*, In press.

¹⁷ Present address: Prototech Incorporated, Cambridge, Massachusetts.

¹⁸ Zentralinstitut für Kernphysik Rossendorf der Deutschen Akademie der Wissenschaften zu Berlin, Bereich Werkstoffe und Festkörper.

¹⁹ R. Rauschenbach and H. Spindler, *Kernenergie*, 7, 19 (1964). (In German.)

¹³ L. I. Boguslavsky and L. S. Stilbans, *Doklady Akad. Nauk S.S.S.R.*, 147, 1114 (1962).

¹⁴ N. A. Bach et al., *Doklady Akad. Nauk S.S.S.R.*, 144, 135 (1962).

¹⁵ A. V. Vannikov, *Doklady Akad. Nauk S.S.S.R.*, 152, 905 (1963).

Dr. Spindler's Zr-Nb alloys, higher weight gains at the lower pressure (Fig. 4). These effects might possibly be rationalized by distinguishing alloys containing almost insoluble additions, e.g., Cu and Fe, from those containing Sn or Nb which are appreciably soluble in the matrix. Alternatively, a distinction might be based on the valence of the foreign ions present in the ZrO₂ film (Cu, Fe valence < 4, Sn, Nb valence \geq 4).

Finally, it is of interest to note that some recent experiments with unalloyed hafnium in steam at 500°C have shown markedly higher weight gains at 1 atm than at 1000 psi (e.g., 685 and 50 mg/dm² respectively at 21 days), with appropriate differences in capacity values.

A Technique for the Evaluation of Hydrogen Embrittlement Characteristics of Electroplating Baths

M. A. V. Devanathan, Z. Stachurski, and W. Beck (pp. 886-890, Vol. 110, No. 8)

G. Dubpernell²⁰: The authors have presented an interesting new technique for recording hydrogen permeation through thin metal membranes. However, the method is not described in very great detail. It would appear that what is actually recorded is the result of the change in potential of the anode side of the membrane. The higher values of permeation of 10 to 16 ma/cm² are higher than the cathode current density of 8.1 ma/cm² which was used. Since cadmium plating from cyanide baths is normally over 90% efficient this only leaves less than 1 ma/cm² for hydrogen evolution. What then is the meaning of permeations over 10 ma/cm²?

The diffusion of atomic hydrogen through the membrane is accepted as an actual fact rather than a theory. If the presence of atomic hydrogen has been demonstrated by anyone it might be well to give the reference.

The pretreatment of the membranes is not described in much detail, nor the need therefore. It is not clear how the annealing of Armco iron in hydrogen at 600°C for 2 hr can be replaced by cathodic treatment in 0.1N H₂SO₄ at 10 ma/cm² for 6 hr with high strength steel. Likewise it is not clear how these treatments can be compared and what is the nature of the need for them. It would be of interest to know the loss in weight and decrease in thickness of the high strength steel membrane after acid treatment.

Several minor or typographical errors were noted. The meaning of the expression "SCS" on page 887 is not given. On Fig. 6, "seconds x 10³" would be better expressed as "10³ seconds". Curve 1 in Fig. 3 does not seem to show an initial sigmoid shaped rise. Reference to the cadmium barrier in curves 2 and 3 in Fig. 3 would seem to be in error. The reference to the iron layer in curve 5, Fig. 6 should obviously be to curve 6 in Fig. 5.

²⁰ M&T Chemicals Incorporated, Detroit Research Lab., 1700 East Nine Mile Road, Detroit 20, Michigan.

M. A. V. Devanathan²¹, **Z. Stachurski**, and **W. Beck**²²: Details of the method have been described^{23,24}.

The idea of using a potentiostat is to study the rate of reaction at a constant potential. Hence there is no question of a change in the potential at the anodic side of the membrane.

Reference to figures will show that all permeation currents have been expressed in $\mu\text{a}/\text{cm}^2$. Hence the question of high ma permeation currents does not arise.

Regarding the other comments, reference to the previous two papers will make clear the need for annealing treatment, electrolytic charging, etc.

Oxidation of Molybdenum, 550°C to 1700°C

E. A. Gulbransen, K. F. Andrew, and F. A. Brassart (pp. 952-959, Vol. 110, No. 9)

D. R. Schryer²⁵: The conclusions drawn by the authors as the result of tests made in a static environment are essentially in agreement with those presented by Modisette and Schryer²⁶ based upon their work with flowing gases, that is, that the rate of oxidation of molybdenum can be either chemically controlled or diffusion controlled depending upon a number of environmental parameters. However, Gulbransen *et al.*, do not make it clear why this should be. I should like to present a picture of the oxidation of materials that form volatile oxides which, although very simple, is, I believe, both accurate and illuminating.

At temperatures at which the volatilization of its oxide is complete, such a material is vulnerable to direct attack by gaseous oxygen. In such a case oxidation may proceed so rapidly as to impose a serious drain on the oxygen supply adjacent to the reacting surface. Thus the rate of diffusion of fresh quantities of oxygen to the surface becomes important. If the rate of diffusion of oxygen is very rapid compared with the chemical reaction rate, the concentration of oxygen adjacent to the surface will not be significantly decreased and the reaction will be chemically controlled. Over whatever temperature range the chemical control holds the observed reaction rate will increase exponentially with increasing temperature.

However, if the rate of diffusion of oxygen to the surface is very slow compared with the chemical reaction rate, the concentration of oxygen at the surface will be severely depleted and the reaction will be diffusion controlled. The observed reaction rate will be relatively insensitive to temperature at temperatures where diffusion control applies.

²¹ Present address: Central Electrochemical Research Institute, Karaikudi-3, Madras, India.

²² Present address: Department of the Navy, Office of Naval Research, Branch Office, London, Navy 100, Box 39, F.P.O., New York, New York.

²³ M. A. V. Devanathan and Z. Stachurski, *This Journal*, 111, 619 (1964).

²⁴ *Proc. of the Royal Soc., A.*, 270, 90 (1962).

²⁵ National Aeronautics and Space Administration, Langley Research Center, Langley Station, Hampton, Virginia.

²⁶ J. L. Modisette and D. R. Schryer, "An Investigation of the Role of Gaseous Diffusion in the Oxidation of a Metal Forming a Volatile Oxide," NASA TN D-222, March 1960.

Depending upon the kinetics of the reaction and the existing environmental conditions, the transition between chemical and diffusion control may be gradual or fairly abrupt. Wherever a significant transition region exists, the observed oxidation rate will increase in some fashion with increasing temperature.

In much of the foregoing the word "transport" may be substituted for the word "diffusion," since in the most general case transport processes other than molecular diffusion may be involved (*e.g.*, convection or turbulence). It is this fact, perhaps, that is the reason for the statement made by Gulbransen *et al.*, that "simple diffusion of oxygen through a stagnant layer as proposed by Modisette and Schryer is not adequate."

It should be noted, however, that in many cases, both static and dynamic, molecular diffusion across some concentration gradient is the predominant transport process. One such case is the oxidation of specimens in a flowing gas stream under conditions such that laminar aerodynamic and concentration boundary layers are established. This is the specific case treated by Modisette and Schryer²⁶. The excellent agreement between the experimental and theoretical results presented in their paper is evidence of the applicability of the concept of diffusion control to the oxidation of molybdenum in flowing gas streams.

One further comment on the paper presented by Gulbransen *et al.*, is in order. The equation for the rate of oxidation when mobile absorption is the rate controlling process

$$v = C_g \frac{kT}{h} \frac{h}{(2\pi mkT)^{1/2}} e^{-\epsilon/kT}$$

can be reduced quite easily to

$$v = \frac{C_g \bar{V}}{4} e^{-\epsilon/kT}$$

since \bar{V} , the average velocity of the oxygen molecules, is given in kinetic theory²⁷ by $\bar{V} = \left(\frac{8kT}{\pi m}\right)^{1/2}$.

The term $\frac{C_g \bar{V}}{4}$ has a very simple interpretation; it is the rate of collision of the oxygen molecules with the metal surface²⁷. Since $e^{-\epsilon/kT}$ is the fraction of the oxygen molecules at temperature T , which have kinetic energies equal to or greater than ϵ , the rate equation for mobile absorption can be seen to be identical to that derived from simple collision theory. This equation, incidentally, is included in the theoretical treatment presented by Modisette and Schryer²⁶. It is important to realize that if the term C_g is taken as the concentration of oxygen just adjacent to the surface this equation applies to all circumstances, including transport control. However, if C_g is taken as the free stream or reservoir concentration of oxygen the equation applies only to the limiting case of chemical control.

E. A. Gulbransen, K. F. Andrew, and F. A. Brassart: We have attempted in our paper to study the oxidation behavior of molybdenum over the temperature range of 550°C to 1700°C. In the temperature range of 700°C to nearly 1400°C, we have demonstrated that the reaction was under chemical control with one activation energy. We have also delineated the exact conditions for our experimental system where diffusion or transport of oxygen to the reaction interface becomes rate controlling. We have also demonstrated the major influence of specimen size and system geometry on the observed rates of reaction. To our knowledge this has not previously been done by anyone, including the discussor.

Above 1400°C at 76 Torr pressure, we have found the reaction to be limited by diffusion or transport of gas to the surface for specimens of 0.12 cm² area. For reaction rates of 10¹⁹ atoms per cm²-sec of molybdenum reacting in our system, we postulate the model of oxygen diffusion through a stagnant layer of reaction products to be far too simple. Due to the large heat of reaction and volume changes associated with the formation of (MoO₃)₃, the reaction zone is not stagnant but very turbulent. The existence of the relation of surface area of sample \times rate of reaction per cm² equals a constant, only dependent upon the pressure and reaction system, eliminates the model proposed by the discussor.

We have treated the kinetics of surface reactions where volatile reaction products are formed since 1952²⁸ using the activated complex theory of surface reactions. We feel for most surface reactions this approach is a more general one than that proposed in the discussor's paper since the several processes required for chemical reaction are treated separately and the specific barriers for reaction identified.

We have not yet been bold enough nor do we have a very good insight into the treatment of the diffusion controlled region of chemical reaction. We do state emphatically that present treatments are inadequate.

D. Schryer: I have no criticism of either the technique or the results presented by Gulbransen *et al.*, and I did not mean to imply anything to the contrary in my original discussion. I do feel, however, that certain pertinent comments in amplification of their presentation were, and are, in order.

In addition, I feel that their statement that "simple diffusion of oxygen through a stagnant layer as proposed by Modisette and Schryer is not adequate" should be clarified. In my original discussion I suggested that perhaps the authors merely meant that the theoretical treatment presented by Modisette and Schryer²⁶ was not general enough to be applicable to many experimental situations—including the authors'—with which contention I readily agree. If this is the case I think the authors should state so unambiguously. In view of their reply to my first letter, however, in particular the last sentence in their reply, I am now forced to wonder whether the authors are challenging the applicability of the theoretical treatment in question even to the par-

²⁷ Earl H. Kennard, "Kinetic Theory of Gases," McGraw-Hill Book Co., New York, 1938.

²⁸ E. A. Gulbransen and K. F. Andrew, *Ind. Eng. Chem.*, **44**, 1034 (1952).

ticular experimental technique and conditions utilized by Modisette and Schryer²⁶. If this is the case the reasons for such a contention should be presented in sufficient detail to allow interested readers to evaluate the conflicting positions for themselves, and any experimental data referred to in such a case should certainly be taken under controlled flow conditions of a type to which the theory should apply.

Although the specific theoretical treatment presented by Modisette and Schryer²⁶ was intended to be strictly applicable only to rather restricted experimental conditions, the simple picture presented in my first discussion has a much broader applicability. In their reply Gulbransen *et al.*, state that "the existence of the relation of surface area times rate of reaction per cm^2 equals a constant, only dependent upon the pressure and reaction system, eliminates the model proposed by the discussor." On the contrary I feel that this relation is entirely compatible with the general picture I presented. In the paper under discussion Gulbransen *et al.*, state that "the relation of area A and dn/dt breaks down as dn/dt approaches $(dn/dt)_c$." In other words the product of the area and the oxidation rate per unit area—the total oxidation rate—is a constant only when the observed oxidation rate, dn/dt , is noticeably less than the intrinsic chemical reaction rate, $(dn/dt)_c$. According to the model in question, in this case the oxidation rate is transport controlled, that is the total oxidation rate is limited to the rate at which fresh quantities of oxygen can be transported to the reaction surface. Thus the total oxidation rate is fixed and the rate per unit area should vary inversely with the area, as observed. Also since the reaction is transport controlled the observed oxidation rate should be relatively independent of temperature but dependent upon pressure and the reaction system.

Finally, I would like to make clear that I have no quarrel with the authors' use of absolute reaction rate theory in their studies. This theory is admittedly a much more general approach to chemical kinetics than is simple collision theory. Nevertheless, the fact remains that in the case of the high-temperature oxidation of molybdenum both approaches yield the same equation, a fact which might not be obvious from the form of the equation used by the authors. As pointed out in my original discussion this equation is included in the theoretical treatment presented by Modisette and Schryer²⁶.

E. A. Gulbransen, K. F. Andrew, and F. A. Brassart:

The mechanism of gas diffusion of oxygen through a stagnant layer of reaction products we feel was conceived without adequate information as to the order of magnitude of rates of reaction, gas movement, volume changes, and heat evolved during reaction. The range of rates of reaction under discussion are of the order of 10^{18} to 10^{19} atoms of $\text{Mo}/\text{cm}^2\text{-sec}$. 10^{18} atoms of $\text{Mo}/\text{cm}^2\text{-sec}$ corresponds to an ablation rate of about 10^{-3} cm/min , while 10^{19} atoms of $\text{Mo}/\text{cm}^2\text{-sec}$ corresponds to 10^{-2} cm/min . The corresponding heat rates are of the order of 1/5

to 2 calories per $\text{cm}^2\text{-sec}$. Large volume changes also occur in the formation of the trimer $(\text{MoO}_3)_3$ from molybdenum and oxygen. These conditions are not those we would associate with a stagnant layer.

The simple picture proposed by Modisette and Schryer²⁶ implies that the rate of reaction should be independent of surface area, all other factors remaining constant. We have not found this to be true for our measurements in the range of 10^{18} to 10^{19} atoms of $\text{Mo}/\text{cm}^2\text{-sec}$. We cannot state that this surface area rate relationship also holds for the conditions used by Modisette and Schryer²⁶. Everything appears to be similar except for the pressure, flow, the reaction system and the presence of inert gases. The absolute values of the rates of reaction, the heat effects and the volume changes associated with the reaction are in the same range.

To decide the range of application of the simple picture it is essential to study the effect of temperature, pressure, flow, and surface area. We propose to make such experiments since the aerodynamicist's picture of fast chemical reactions in the gas diffusion region as we see it needs clarification.

D. E. Rosner and H. D. Allendorf²⁹: While it is evident that many earlier studies of the high temperature oxidation kinetics of molybdenum were carried out under conditions in which gaseous diffusion processes accounted in part for the observed rates, true kinetic data are now available from several sources³⁰⁻³². Taken together with work in progress at this laboratory^{33,44} as well as the paper under discussion, an interesting and rather complex picture of the oxidation kinetics begins to emerge. In the light of this recent evidence we would like to both comment, and solicit further comment, upon the mechanism of this reaction and some of its implications.

A common assumption in metal oxidation work is that in the "chemically controlled" regime the linear rate of oxidation at a given surface temperature depends only on the oxygen partial pressure in the immediate vicinity of the gas/solid interface. We are convinced this is not the case for high temperature molybdenum in O_2 -containing mixtures, the total pressure itself being important. Thus, the oxygen pressure can be varied in two distinct ways, and the apparent kinetic order should not be influenced by the choice made. Gulbransen *et al.*, vary the total

²⁹ AeroChem Research Laboratories, Incorporated, (a subsidiary of Pfaunder Permutit Inc.) Princeton, New Jersey.

³⁰ Materials Research Staff "High Temperature Oxidation of Molybdenum Under High-Altitude Conditions," North American Aviation Incorporated, Missile Development Division; Report AL-2617, Sept. 1, 1957; ASTIA AD 147 839.

³¹ J. Berkowitz, "Kinetics of Oxidation in the Mo-Si System," Aeronautical Systems Division (Wright-Patterson Air Force Base) Report ASD TDR 62-203, Part 1, May 1962; ASTIA AD 278-826.

³² J. B. Berkowitz-Mattuck, A. Buchler, J. L. Engelke, and S. N. Goldstein, *J. Chem. Phys.*, **39**, 2722 (1963).

³³ D. E. Rosner, and H. D. Allendorf, "Kinetic and Aerodynamic Aspects of the Oxidation of Metals by Partially Dissociated Oxygen," Propulsion Division, Air Force Office of Scientific Research, Contract AF 49(638)-1195.

ticular experimental technique and conditions utilized by Modisette and Schryer²⁶. If this is the case the reasons for such a contention should be presented in sufficient detail to allow interested readers to evaluate the conflicting positions for themselves, and any experimental data referred to in such a case should certainly be taken under controlled flow conditions of a type to which the theory should apply.

Although the specific theoretical treatment presented by Modisette and Schryer²⁶ was intended to be strictly applicable only to rather restricted experimental conditions, the simple picture presented in my first discussion has a much broader applicability. In their reply Gulbransen *et al.*, state that "the existence of the relation of surface area times rate of reaction per cm² equals a constant, only dependent upon the pressure and reaction system, eliminates the model proposed by the discussor." On the contrary I feel that this relation is entirely compatible with the general picture I presented. In the paper under discussion Gulbransen *et al.*, state that "the relation of area A and dn/dt breaks down as dn/dt approaches $(dn/dt)_c$." In other words the product of the area and the oxidation rate per unit area—the total oxidation rate—is a constant only when the observed oxidation rate, dn/dt , is noticeably less than the intrinsic chemical reaction rate, $(dn/dt)_c$. According to the model in question, in this case the oxidation rate is transport controlled, that is the total oxidation rate is limited to the rate at which fresh quantities of oxygen can be transported to the reaction surface. Thus the total oxidation rate is fixed and the rate per unit area should vary inversely with the area, as observed. Also since the reaction is transport controlled the observed oxidation rate should be relatively independent of temperature but dependent upon pressure and the reaction system.

Finally, I would like to make clear that I have no quarrel with the authors' use of absolute reaction rate theory in their studies. This theory is admittedly a much more general approach to chemical kinetics than is simple collision theory. Nevertheless, the fact remains that in the case of the high-temperature oxidation of molybdenum both approaches yield the same equation, a fact which might not be obvious from the form of the equation used by the authors. As pointed out in my original discussion this equation is included in the theoretical treatment presented by Modisette and Schryer²⁶.

E. A. Gulbransen, K. F. Andrew, and F. A. Brassart:

The mechanism of gas diffusion of oxygen through a stagnant layer of reaction products we feel was conceived without adequate information as to the order of magnitude of rates of reaction, gas movement, volume changes, and heat evolved during reaction. The range of rates of reaction under discussion are of the order of 10^{18} to 10^{19} atoms of Mo/cm²-sec. 10^{18} atoms of Mo/cm²-sec corresponds to an ablation rate of about 10^{-3} cm/min. while 10^{19} atoms of Mo/cm²-sec corresponds to 10^{-2} cm/min. The corresponding heat rates are of the order of 1/5

to 2 calories per cm²-sec. Large volume changes also occur in the formation of the trimer (MoO₃)₃ from molybdenum and oxygen. These conditions are not those we would associate with a stagnant layer.

The simple picture proposed by Modisette and Schryer²⁶ implies that the rate of reaction should be independent of surface area, all other factors remaining constant. We have not found this to be true for our measurements in the range of 10^{18} to 10^{19} atoms of Mo/cm²-sec. We cannot state that this surface area rate relationship also holds for the conditions used by Modisette and Schryer²⁶. Everything appears to be similar except for the pressure, flow, the reaction system and the presence of inert gases. The absolute values of the rates of reaction, the heat effects and the volume changes associated with the reaction are in the same range.

To decide the range of application of the simple picture it is essential to study the effect of temperature, pressure, flow, and surface area. We propose to make such experiments since the aerodynamicist's picture of fast chemical reactions in the gas diffusion region as we see it needs clarification.

D. E. Rosner and H. D. Allendorf²⁹: While it is evident that many earlier studies of the high temperature oxidation kinetics of molybdenum were carried out under conditions in which gaseous diffusion processes accounted in part for the observed rates, true kinetic data are now available from several sources³⁰⁻³². Taken together with work in progress at this laboratory^{33,44} as well as the paper under discussion, an interesting and rather complex picture of the oxidation kinetics begins to emerge. In the light of this recent evidence we would like to both comment, and solicit further comment, upon the mechanism of this reaction and some of its implications.

A common assumption in metal oxidation work is that in the "chemically controlled" regime the linear rate of oxidation at a given surface temperature depends only on the oxygen partial pressure in the immediate vicinity of the gas/solid interface. We are convinced this is not the case for high temperature molybdenum in O₂-containing mixtures, the total pressure itself being important. Thus, the oxygen pressure can be varied in two distinct ways, and the apparent kinetic order should not be influenced by the choice made. Gulbransen *et al.*, vary the total

²⁹ AeroChem Research Laboratories, Incorporated, (a subsidiary of Pfaunder Permutit Inc.) Princeton, New Jersey.

³⁰ Materials Research Staff "High Temperature Oxidation of Molybdenum Under High-Altitude Conditions," North American Aviation Incorporated, Missile Development Division; Report AL-2617, Sept. 1, 1957; ASTIA AD 147 839.

³¹ J. Berkowitz, "Kinetics of Oxidation in the Mo-Si System," Aeronautical Systems Division (Wright-Patterson Air Force Base) Report ASD TDR 62-203, Part 1, May 1962; ASTIA AD 278-826.

³² J. B. Berkowitz-Mattuck, A. Buchler, J. L. Engelke, and S. N. Goldstein, *J. Chem. Phys.*, **39**, 2722 (1963).

³³ D. E. Rosner, and H. D. Allendorf, "Kinetic and Aerodynamic Aspects of the Oxidation of Metals by Partially Dissociated Oxygen," Propulsion Division, Air Force Office of Scientific Research, Contract AF 49(638)-1195.

pressure of pure O_2 and report an order of 1.5 at a surface temperature of $1073^\circ K$ (the order at $1473^\circ K$ was not reported but from the apparent order obtained at $1873^\circ K$, the true order, *i.e.*, in the absence of a diffusional effect, must be very small, perhaps near zero). In ftnt. 30, the pressure level of air was varied from 2×10^{-2} to 760 Torr and the kinetic order was reported to be 0.62 at a surface temperature of $1413^\circ K$. On the other hand, the oxygen pressure can be varied by varying the composition of O_2 -containing mixtures at constant total pressure. In this way, Berkowitz³¹ obtains a kinetic order of 0.87 at a surface temperature of $1297^\circ K$, for partial pressures between 2.1 and 9.65 Torr. Helium/oxygen mixtures were used, presumably at a total pressure of 760 Torr. While the apparently discrepant data of ftnt. 30 and 31, which overlap in oxygen partial pressure, are suggestive of the effect we wish to emphasize here, differences in technique and surface temperature preclude a firm conclusion (the work of ftnt. 30 at $1413^\circ K$ is based on the reduction in electrically heated filament diameter at unspecified air flow rates, whereas, in the work of ftnt. 31 at $1297^\circ K$, the reaction rate is followed by monitoring the consumption of O_2). Owing to these differences we have studied the order of the reaction using the technique of ftnt. 30 and, at constant surface temperature, obtained the order of reaction in the 1 Torr region, first varying p_{O_2} by varying the total pressure of helium/oxygen mixtures of fixed composition and then varying the composition of both N_2/O_2 and He/O_2 mixtures of fixed total pressure. At a filament temperature of $1400^\circ K$, the kinetic order was found to be 0.62 with respect to total pressure in the first case, and 0.9 with respect to oxygen mole fraction in the second case (regardless of the identity of the carrier gas). These data, which on the basis of the absence of flow rate and carrier gas effects, are free of diffusional limitations, demonstrate an intrinsic role of total pressure level in the kinetics, quite apart from its influence on the O_2 partial pressure. The writers would therefore be interested in learning whether a similar effect has been observed in the research program leading to the paper under discussion. For example, would the reaction order at $1073^\circ K$ be 1.5 if all of the experiments were carried out at 76 Torr but in the presence of varying amounts of a diluent? That the true kinetic order is not independent of surface temperature seems surprising in view of the activation energy results discussed below. A temperature dependent order is also implicit in the mass spectrometer data of ftnt. 32 but at much higher surface temperatures ($1500^\circ - 2100^\circ K$).

With regard to the temperature dependence of the oxidation rate, it is of interest to compare the results of Gulbransen *et al.*, with other recent work in the diffusion-free regime. Perhaps the most meaningful comparisons can be made on the basis of an oxidation probability ϵ , defined here as the ratio of the flux $Z_{(Mo)}$ of molybdenum atoms (regardless of their chemical state of aggregation) away from the surface, to the collision flux Z_{O_2} of oxygen molecules

with the surface³⁴. This has been done in Fig. 1, which includes some unpublished results obtained at this laboratory, in addition to results computed from data of ftnt. 31, 32, 35, and 36. Three noteworthy features here are: (i) in the temperature range below about $1450^\circ K$, and with the exception of the data of ftnt. 36, there is comparatively good agreement on activation energy, with most values falling between 20 and 23 kcal/mole; (ii) at any given surface temperature, the magnitude of ϵ depends noticeably on both partial and total pressure as anticipated by the discussion of the previous paragraph³⁷; and, (iii) departures from simple Arrhenius behavior take place, particularly at temperatures above about $1450^\circ K$. This latter effect has also been observed in our experiments. Indeed, the data of ftnt. 32 reveals the existence of maxima in the oxidation probability at surface temperatures of the order of $1900^\circ K$ and above.

For a number of reasons we have been interested in the effect of oxygen atoms on the rate of molybdenum oxidation³⁸ and have been carrying out experiments in which helium/oxygen or argon/oxygen mixtures are subjected to a microwave discharge before passing over electrically heated filaments. Apart from their intrinsic interest, the results would appear to be of relevance here since any postulated mechanism of molybdenum oxidation in O_2 , if correct, should predict the effect of substituting O-atoms for O_2 molecules in the gas phase. In the diffusion-free regime, at 1 Torr total pressure, and for comparable collision fluxes of O and O_2 , we have found that the oxidation probability with O-atoms is two orders of magnitude higher than with O_2 at a surface temperature of about $1200^\circ K$. This enhancement ratio decreases with increased surface temperature since the O-atom oxidation reaction has an activation energy of only about 5 kcal/mole in this temperature range. It appears likely from the data obtained thus far that the two probabilities become comparable at some temperature well below the melting point of molybdenum. In the light of these observations it is by no means clear how the mechanism proposed by Gulbransen *et al.*, (*viz.*, mobile adsorption of O_2 on a monolayer of oxygen adatoms) can properly account for: (i) the significant departures from simple first-order kinetics discussed above³⁸; and, (ii) the large effect of dis-

³⁴ Computed using simple kinetic theory (Hertz-Knudsen equation) and based on the oxygen partial pressure in the feed gas. Since the actual oxygen partial pressure at the gas/solid interface may be slightly lower than this, apart from the effects of surface roughness the resulting probability always represents a lower bound to the true probability. The O_2 consumption data of ftnt. 31 were converted to oxidation probabilities by assuming the dominant reaction product to be $(MoO_3)_x$.

³⁵ J. L. Modisette and D. R. Schryer, *Planetary and Space Science*, 3, 31 (1961).

³⁶ J. W. Semmel, Jr., "High Temperature Oxidation of Molybdenum," "High Temperature Materials," R. F. Hehemann and G. M. Ault, Editors, p. 510, John Wiley & Sons, Inc., New York, (1959).

³⁷ In view of the implication of Gulbransen *et al.*, that the reaction order is strongly temperature dependent in the range $1073^\circ - 1873^\circ K$ it seems remarkable that curves a, e, g, which pertain to widely different partial and total pressures (*cf.* Fig. 1), should display similar slopes on the Arrhenius diagram. This aspect would appear to bear further investigation.

³⁸ Interestingly enough, our O-atom attack data reveal simple first-order kinetics at $1400^\circ K$ over the range of pressures investigated thus far ($1 \leq p \leq 5$ Torr; $2 \times 10^{-3} \leq p \leq 5 \times 10^{-2}$ Torr).

sociation on the rate of oxidation of molybdenum at intermediate temperatures. It should be added that a similar situation apparently exists in the case of the oxidation of platinum, *viz.*, the postulated mechanism³⁹ for oxidation in O₂ seems to us to be inconsistent with the observed effect of gas phase dissociation on the reaction probability⁴⁰ over the temperature range in which the oxide is volatile. Clarification of these mechanistic difficulties would be most welcome, and most useful.⁴⁴

Finally, additional words of caution may be in order concerning the transition regime investigated in part of Gulbransen *et al.*, (Class 3 to Class 4 transition) and previous workers^{35, 36}. In view of the complexity of the true kinetics of molybdenum oxidation in O₂-containing mixtures, any attempt to extract the kinetics from measurements made in the presence of a diffusional limitation, as typified by the work of ftnt. 35, is fraught with danger. For example, the data reduction procedure adopted in ftnt. 35 evidently fails to adequately account for the effects of: (i) nonunity reaction order; (ii) low Reynolds number and high interfacial mass velocity with their consequent influence on the oxygen mass transfer coefficient; (iii) molybdenum oxides and their polymers [*e.g.*, (MoO₃)₃] as they influence the effective Fick diffusion coefficient for O₂ through the gas mixture surrounding the specimen. For these reasons, if none other, the results shown in Fig. 1,

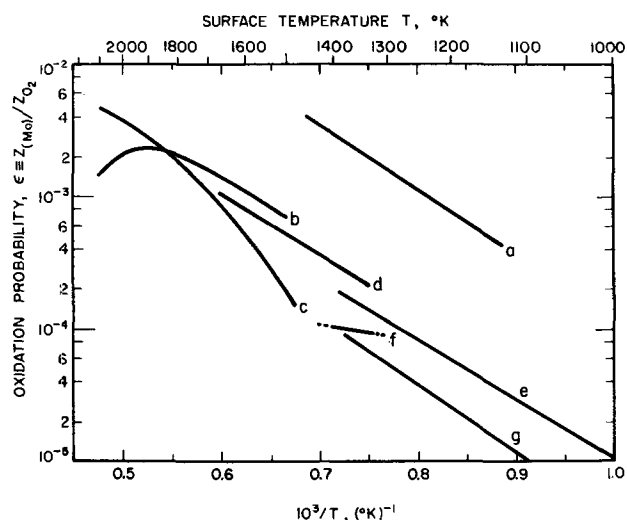


Fig. 1. Arrhenius plot on molybdenum oxidation possibilities

Curve	Source	p _{O₂} (Torr)	p (Torr)	Medium
a	Present work	3.0 × 10 ⁻²	1.0 × 10 ⁰	He/O ₂
b	ftnt. 32	0.61 × 10 ⁻³	0.61 × 10 ⁻³	O ₂
c	ftnt. 32	1.82 × 10 ⁻³	1.82 × 10 ⁻³	O ₂
d	ftnt. 35	1.59 × 10 ²	0.76 × 10 ³	air
e	Gulbransen <i>et al.</i>	0.76 × 10 ²	0.76 × 10 ²	O ₂
f	ftnt. 36	1.59 × 10 ²	0.76 × 10 ³	air
g	ftnt. 31	1.6 × 10 ⁰	0.76 × 10 ³	He/O ₂

³⁹ G. C. Fryburg and H. M. Petrus, *This Journal*, 108, 496 (1961).

⁴⁰ G. C. Fryburg, *J. Chem. Phys.*, 24, 175 (1956).

curve *d* would appear to be subject to large systematic errors. The theory of simple surface reactions in the transition regime with convective flow has recently been treated^{41, 42} and reviewed⁴³ by one of us. It is already clear that a considerable amount of work will have to be done before all of the important subtleties of a reaction such as molybdenum oxidation can be appropriately incorporated into the theory. This is especially true if accurate kinetics are to be inferred from data obtained in the presence of a non-negligible diffusion limitation.

E. A. Gulbransen, K. F. Andrew, and F. A. Brassart: Rosner and Allendorf have pointed out that the partial pressure of oxygen is not the only factor in determining the rate of oxidation at a given temperature. We would like to amplify this statement. The effect of oxygen partial pressure and inert gas pressure on the kinetics of oxidation depends upon the nature of the rate of controlling mechanism, *i.e.*, chemical control or gas diffusion control. No one rate equation can explain these two types of oxidation mechanisms. Providing sufficient gas flow is available to remove the volatile products of oxidation, the oxygen partial pressure is the important variable at a given temperature. With insufficient gas flow the reaction kinetics are a complex function of oxygen partial pressure, diluents, specimen size, reaction system, and temperature gradients. Our Table III illustrates this point nicely. The data at 800°C is for the chemical controlled region. Here the rate of oxidation followed the 1.5 power of pressure. At 1600°C the data are for the gas diffusion controlled region. Here the rate of oxidation followed the 0.14 power of the pressure.

The role of gas diluents was not studied in our paper. Again, the effect would depend upon the particular region of oxidation. We have not analyzed this problem in detail. More work is needed to determine the order of the kinetics of molybdenum oxidation. Both pressure and flow must be considered in interpretation of the experiments.

Rosner and Allendorf have proposed the use of the oxidation probability to relate the various experimental results. This is a useful unit. We prefer to express rates of oxidation in atoms of molybdenum per cm²-sec. Heats of activation can be calculated directly from log rate versus 1/T plots of the data. We also agree that comparison of rates of oxidation with collision theory is very useful and enlightening.

These discussers have questioned our suggested mechanism of mobile adsorption of oxygen on two grounds (i) the departure from first order kinetics and (ii) the large effect of dissociation. In defense, we would point out that the pressure de-

⁴¹ D. E. Rosner, *A.I.Ch.E. J.*, 9, 321 (1963)

⁴² D. E. Rosner, *Chem. Eng. Sci.*, 19, 1 (1964).

⁴³ D. E. Rosner, *AIAA J.*, 2, 593 (1964).

⁴⁴ A mechanism consistent with the observed rates of oxidation in partially dissociated oxygen is suggested in: D. E. Rosner and H. D. Allendorf, *AeroChem TP-84*, February 1964; *J. Chem. Phys.*, 40, (June 1964).

pendence has not been adequately studied under established conditions of pressure and flow. The 800°C data of Table III are the only data which can be used in our studies. Here a $P^{1.5}$ law was found. More work must be done to tie this point down. Dissociation of oxygen molecules to atoms should have a major influence on the adsorption of oxygen on the metal surface. We do not see how this phenomenon rules out the suggested mechanism.

The authors agree with Rosner and Allendorf concerning oxidation studies in the gas diffusion region of oxidation and the transition zone between gas diffusion and chemical controlled oxidation. In fact, we would go further and say that studies in the gas diffusion region are only useful for the particular system under consideration. Few generalizations can be made from such studies.

Ion Exchange Membrane Properties—Their Effect on the Development of the Dual Membrane Fuel Cells

R. M. Lurie, C. Berger, and H. Viklund (pp. 1173-1176, Vol. 110, No. 12)

P. V. Papat⁴⁵: In the three years since Lurie *et al.*, originally wrote their paper, rather significant advances have been made in ion-exchange membrane fuel cell technology. As a result of progress made in the areas of ion-exchange membrane synthesis, electrode technology and engineering design of the fuel cell battery, the technology of fuel cells with single ion-exchange membranes has reached the stage where all of the disadvantages listed by Lurie *et al.*, have been substantially eliminated, while the advantages of the solid electrolyte fuel cell over the dual membrane and liquid electrolyte types have been retained. These advantages include capability of operation in zero G, no electrolyte leakage, low specific weight and volume, no ionic concentration polarization, ease of heat and mass transfer control with a minimum of auxiliary equipment and proven safety, reliability and long life of the fuel cell.

One could also argue the greater merits of the present day membrane and electrode structures as opposed to those mentioned in the paper. In the final analysis, however, the reliability, safety, operational characteristics and life of a multi-cell battery are determined by deliberately incorporated safety provisions and by an engineering design which provides an efficient means for temperature stability and uniformity and for removal of product water.

Werner Glass⁴⁶: In the three years since Lurie *et al.*, originally wrote their paper, significant engineering advances have been made in dual-membrane fuel cell technology. The performance "predicted" in the paper has been far surpassed: resistances below 2 ohm-cm² per cell are obtained in present batteries as

compared to the then actual 5.5 ohm-cm² and predicted 4.7 ohm-cm². The safety and long life inherently associated with the DMFC design has been maintained. The high degree of reproducibility attainable with dual membrane fuel cells has been recognized by others, *e.g.*, General Electric's Space Sciences Laboratory⁴⁷, who have chosen the DMFC for their fuel cell work.

Heat Treatment of Anodic Oxide Films on Tantalum, The Effect on Dielectric Properties

D. M. Smyth, G. A. Shirn, and T. B. Tripp (pp. 1264-1276, Vol. 110, No. 12)

G. J. Korinek⁴⁸: We were also interested in the effect of heating on the dielectric properties of anodic oxide films on tantalum. Our experimental results agree in general with those of Smyth *et al.* Our experiments were performed on cleaned and vacuum annealed Ta wire. We found that the reproducibility with the wires was better than with the foil, but qualitatively the results on the wires and on the foil were the same.

It is our contention that by interpreting their results Smyth *et al.*, should have considered the possibility of creating mechanical defects such as cracks, microfissures and the like, in the anodic films during the heat treatment. These mechanical flaws would of course be "healed out" during subsequent reanodization and they could also explain the strong frequency and bias dependence of both the capacitance and ESR values.

Furthermore the large scatter of experimental results as referred to by Smyth would point in this direction.

If Smyth's picture is correct in its present form one would expect that a percentage increase in capacitance observed on specimens anodized at lower voltage should be higher than those anodized to higher voltage because the amount by which the thickness of the effective dielectric layer decreases should be mainly a function of time and temperature (being a diffusion process) and fairly insensitive to the total thickness of the oxide layer. From the results in Fig. 1 one can see that this is not the case; the change in capacitance on heating is essentially the same for all anodizing voltages shown and varies between 5-10% depending on frequency.

Fig. 2 shows an effect on capacitance of artificially introduced mechanical damage to the film (barely visible scratches ~ 0.2 mm long). The similarity between its capacitance frequency dependence to those of heated specimens is striking.

Where the mechanically damaged film differs from the heat treated ones is in its ability to reanodize. As can be seen by reanodization to its original voltage the capacitance value returns to its original value; in the case of the heat treated specimen that is not the case. A part of capacitance change is not removed on reanodization. This is in agreement

⁴⁵ Fuel Cell Laboratory, Direct Energy Conversion Operation, General Electric Company, West Lynn, Massachusetts.

⁴⁰ Ionics, Incorporated, Cambridge, Massachusetts.

⁴⁷ J. J. Konikoff, *et al.*, *Aerospace Medicine*, 34, 1129 (1963).

⁴⁸ Department of Rare Metals, CIBA Limited, Basle, Switzerland.

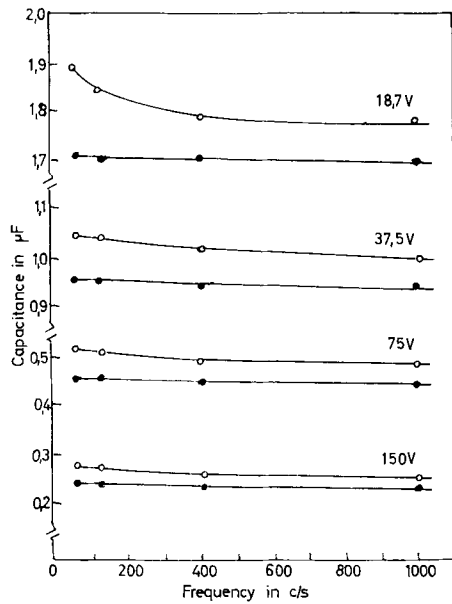


Fig. 1. Change in capacitance due to heating of Ta wires anodized to different voltages: \bullet , before heating; \circ , after heating (30 min at 400°C in air).

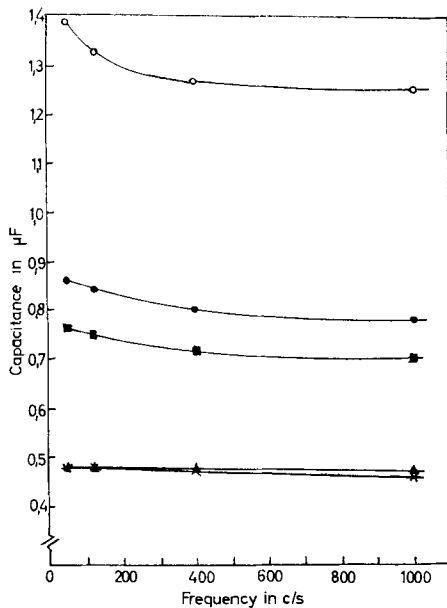


Fig. 2. Influence of mechanical damage on the capacitance of anodized Ta wires. Anodization voltage 75v: \blacktriangle , before mechanical damage; \blacksquare , one scratch ~ 0.2 mm long, hardly visible; \bullet , two scratches ~ 0.2 mm long, hardly visible; \circ , several scratches ~ 0.2 mm long, hardly visible; \times , reanodized at 75v for 1 hr.

with the results of Smyth *et al.* It is suggested that it is this irreversible part of capacitance increase which is the result of a possible oxygen diffusion from the oxide layer into the metal.

This suggestion is in agreement with results in Fig. 3, which shows the capacitance values as a function of the frequency on subsequent heating and reanodization. We can observe that the increase of the capacitance depends on the rate of heating. The wires which were slowly heated have slightly milder dependence on frequency and the irreversi-

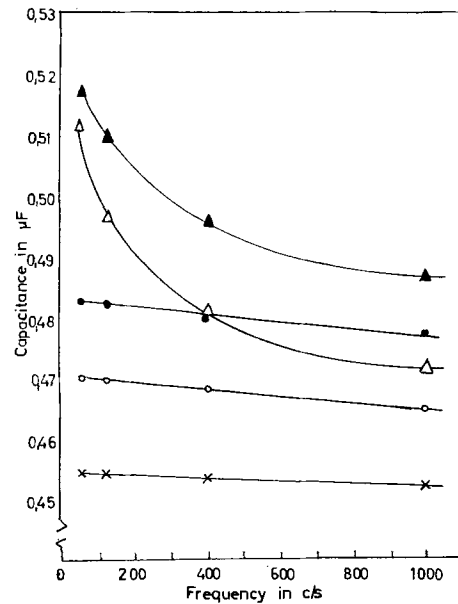


Fig. 3. Influence of the rate of heating on the capacitance of anodized Ta wires: \times before heating; \triangle after heating, (a) 30 min at 400°C in air; \blacktriangle after heating, (b) 30 min at 400°C in air plus 30 min heating-up and 30 min cooling-off time; \circ reanodized for 1 hr after heating, (a); \bullet reanodized for 1 hr after heating, (b).

ble change in capacitance is greater than by the fast heated ones.

We also found that by increasing the heating time from 10 min to 1 hr the irreversible change in the capacitance increased by a factor of about 2.

This agrees with results of Smyth *et al.*, shown in Fig. 5 where the $\% \Delta C$ (percentage increase of capacitance, relative to the reanodized capacitance) due to heat treatment in air decreases with the heating time.

This phenomenon would be expected when the contribution to the capacitance change from the mechanical defects stayed approximately constant or was even higher for short heating times due to the shock effect and the contribution from the diffusion of oxygen into the metal increased with the heating time.

It is also known that in the so-called solid electrolyte capacitor, based on Ta-Ta₂O₅-MnO₂ system, the scintillation voltage decreases and leakage current increases after one or more pyrolysis more strongly than one would expect from a small decrease in the thickness of the effective dielectric layer as indicated by the change in capacitance.

The results presented are part of work which will be published in detail, but they indicate that some of the conclusions in Smyth's paper should be re-examined.

We thank Dr. W. Scheller for helpful discussion and Mr. A. Henz for his assistance with the experiments.

D. M. Smyth, G. A. Shirn, and T. B. Tripp: We did not exclude the possibility that mechanical defects could contribute to the dielectric properties of heat-treated, anodized tantalum. On the basis of the experimental evidence, however, we did conclude

that such contributions are negligible. We retain that opinion.

Korinek has pointed out that deliberate damage to an anodic oxide film causes an increase in capacitance, and produces a frequency dependence of capacitance which is qualitatively similar to that of the Ta-Ta₂O₅ system after heat-treatment in air. This is certainly true; however, there are major differences in the behavior of heat-treated samples as compared with scratched samples. Perhaps the most serious discrepancy is the effect of a small DC bias (Ta positive) on the series capacitance and series resistance. The effect on heat-treated samples is reversible and reproducible for biases up to a third of the formation voltage. On the other hand, the application of even a one volt bias for a few minutes to a scratched 75v film causes permanent loss of a large fraction of the capacitance increase which resulted from the damage. The brief application of a 20v bias completely, and permanently, removes the capacitance increase.

Korinek has misinterpreted the consequences of our picture of the heat-treatment process on the increase of capacitance. It appears that during heat-treatment the compositions of the oxide at the Ta-Ta₂O₅ and Ta₂O₅-air interfaces rapidly reach equilibrium, and an appropriate composition gradient then extends across the film. Further heating, or reheating under the same conditions, will not change this gradient significantly. Moreover, since the compositions at the boundaries are thus fixed, the gradient will decrease with increasing oxide thickness (anodization voltage) such that the percentage increase of capacitance due to heat-treatment will be independent of oxide thickness. This is in agreement with the experimental results except for anodization voltages of less than 50v; below this the percentage increase becomes gradually smaller as the films become thinner.

The following points of behavior of heat-treated, anodized tantalum are presented as being consistent with our hypothesis, but inconsistent with a model based on mechanical damage:

1. The effect of DC bias on the dielectric behavior, as described above.

2. For samples of various types; *e.g.* wire, foil, and sintered, porous pellets; heat-treatment in air at 400° causes a capacitance increase of about 18%. It seems unlikely that the amount of mechanical damage would be so reproducible.

3. The capacitance is independent of the conductivity of the measuring electrolyte. The capacitance of damaged films shows a pronounced dependence⁴⁹.

4. Measurements of heat-treated samples made with small area metallic counterelectrodes (evapo-

rated gold or electroless nickel with area about 0.02 cm²) gave results which were in good agreement with our standard 18 cm² samples measured in 40% H₂SO₄. This would require a very uniform distribution of mechanical damage.

5. The characteristic temperature dependence of capacitance is not easily explained by mechanical damage.

6. The temperature dependence of capacitance has the same features when the measurement is made in an atmosphere of dry nitrogen with a counterelectrode of colloidal graphite covered with silver paint rather than in the usual counterelectrode of H₂SO₄.

7. The specific effect of partial reanodization on the temperature dependence of capacitance, as discussed in detail in the second paper of this series, is not consistent with the healing of mechanical damage.

8. The complete reanodization of heat-treated samples takes several hours at the original anodization voltage, whereas scratched samples are restored to their original condition within a few minutes at much lower voltage.

9. The effect of a small DC bias on the temperature dependence of capacitance is not readily explained by mechanical damage.

The following points are also pertinent:

10. When the heat-treatment is done in vacuum or hydrogen⁵⁰, the oxide no longer functions as a dielectric, *i.e.*, it becomes conducting throughout. The heating atmosphere should not have much effect on mechanical damage.

11. The effect of dielectric properties is reversibly dependent on the ambient oxygen pressure during heat-treatment.

12. Even stronger effects are observed with the Nb-Nb₂O₅ system, whereas no analogous behavior is exhibited by anodized aluminum. Niobium is a good solvent for oxygen, and Nb₂O₅ is known to be more readily reduced than Ta₂O₅⁵¹. Oxygen is not significantly soluble in aluminum and Al₂O₃ is extremely difficult to reduce.

13. The capacitance of a freshly scratched sample drifts downward for hours until as much as half of the original capacitance increase has disappeared. The capacitance of a heat-treated sample is stable within minutes after removal from the oven.

14. For a given increase in capacitance, the increase in series resistance of a heat-treated sample is several times larger than that of a scratched sample.

Further supporting evidence will be presented in future publications.

⁴⁹ D. A. Vermilyea, *Acta Met.*, 5, 113 (1957).

⁵¹ P. Kofstad, *This Journal*, 109, 776, (1962).

⁴⁹ L. Young, *Trans. Faraday Soc.*, 55, 842 (1959).

Morphology of PbO_2 in the Positive Plates of Lead Acid Cells

Jeanne Burbank

U. S. Naval Research Laboratory, Washington, D. C.

ABSTRACT

Several preparations of PbO_2 including positive active material from lead antimony and lead calcium cells were examined by electron microscopy. The morphology of the particles is believed to have a bearing on positive paste retention and plate performance in the lead acid cell. The anodic coating of PbO_2 formed on pure lead sheet in H_2SO_4 was found to be prismatic when first formed, but lost its prismatic character on prolonged anodization and on cycling.

The primary component of the positive plate in the fully charged lead acid cell is PbO_2 . This material exists in two polymorphic forms, the low-temperature α form is orthorhombic, and the high-temperature β form is tetragonal (1-3). Both phases have been observed in the positive plate active material of the battery and in anodic corrosion products on lead (4-7). The corrosion products, the surfaces of battery plates, and electrodeposits of PbO_2 have been examined by electron microscopy (7-11).

Mineral deposits of PbO_2 , plattnerite, do not commonly exhibit well-developed crystals, but occur in nodular masses (12). Synthetic β PbO_2 crystallized by hydrothermal treatment exhibits a morphology characteristic of its rutile structure type (13); however, most synthetic PbO_2 preparations do not give crystals large enough to be described by optical methods.

The lead calcium storage battery was developed for float service in the telephone system (14, 15) and has proved satisfactory in such installations. In recent years the lead calcium cell has been used on submarines in float service, but many failures were experienced in the early installations. As part of an investigation of this problem, the positive plates were examined by electron microscopy. The major difference between failing and successful cells was found to be a startling contrast in morphology of the particles of PbO_2 in the positives (16). It is generally agreed that the strength of particulate conglomerates is imparted by the morphology of the several species present. For example, Sliepcevich, Gildart, and Katz (17) discussing Portland Cement concrete state that ". . . the strength of the concrete is attributable to an abundance of crystals in the form of splines, needles and films matted together and bonded together by the amorphous mass." In agreement with this picturization, positive battery plates that contain mostly non-descript pebble-like nodular PbO_2 particles were found to soften and fail. On the other hand, plates made up of PbO_2 particles that were prismatic needles with many branches, possibly twinned, maintained capacity and retained a firm texture.

Astakhov, Kiseleva, and Kabanov (11) examined electrolytic deposits of the two polymorphs of PbO_2 by electron microscopy and indicated that there was a relation between mechanical strength and mor-

phology of the crystals in the electrode; they further suggested that the same considerations would apply to the stability of battery plates.

For this investigation commercial battery plates from several manufacturers in both lead antimony and lead calcium cells were examined by electron microscopy. Considerable variation was found in the particle morphology.

Experimental

Carbon replicas (18) were prepared of the specimens of PbO_2 , and, after removal of the PbO_2 by solution in dilute HNO_3 containing H_2O_2 , the replicas were examined in an RCA EMU-2B electron microscope.

Particulate specimens of PbO_2 were dispersed by floating on water in a crystallizing dish and picked up on parlodion films supported on specimen screens of the electron microscope. The carbon replicas were deposited by vacuum evaporation. After replication, the parlodion supporting film was dissolved in acetone by flooding the sample resting on a folded piece of filter paper from which the screens were then gently lifted with fine tweezers. The carbon replica would tend to be cemented to the screen mesh by any residual softened parlodion. The specimen was then touched to clean blotting paper and dropped onto the surface of the acid H_2O_2 solution. Following solution of the PbO_2 , a matter of a minute or two, the specimen was transferred to a surface of distilled water. After rinsing, it was transferred to blotting paper or onto a peg for air drying.

The active material from the battery plates and a cycled specimen of lead sheet were extracted with saturated ammonium acetate solution in order to obtain dispersion of the PbO_2 into discrete particles. Acid extraction of Pb_3O_4 also gave a residue of PbO_2 that was examined. The extracted material was dispersed by placing a drop of the run on slurry on the surface of distilled water in a crystallizing dish where the particles would float out across the surface, and these were then mounted for replication as described above.

Anodized lead sheet was replicated directly after blotting dry. The surface was scored into small squares, and the sample was gently lowered into dilute acetic acid containing H_2O_2 . Carbon films floated free on the surface and were transferred to

distilled water for rinsing. The films were then picked up on specimen screens of the electron microscope and air dried.

Results and Discussion

Anodic corrosion product on pure lead.—Earlier studies by electron diffraction (19) showed that the initial deposition of PbO_2 on pure lead by anodization in H_2SO_4 was preferentially oriented, and that on further anodization the deposit had random orientation. The initial deposit, Fig. 1, appears to be entirely prismatic, and clusters of crystallites of similar orientation are clearly discernible. This is the kind of deposit that is too thin to give x-ray diffraction patterns, but strong electron diffraction patterns are registered. The areas of similarly oriented crystallites confirm the electron diffraction observations of preferred orientation reported in the earlier studies. When the deposit was thickened by prolonged anodization, the coating began to spall from the surface. The electron micrograph, Fig. 2, of the anodic sample at this stage suggests that there is a total loss in prismatic character, and also shows the flaky nature of the coating. A coating of this type gives a polycrystalline diffraction pattern. As the specimen was cycled, the coating continued to shed, and it has been shown by Feitknecht and Gaumann (7-8) that the surface becomes covered with nodular concretions of PbO_2 . The individual particles are

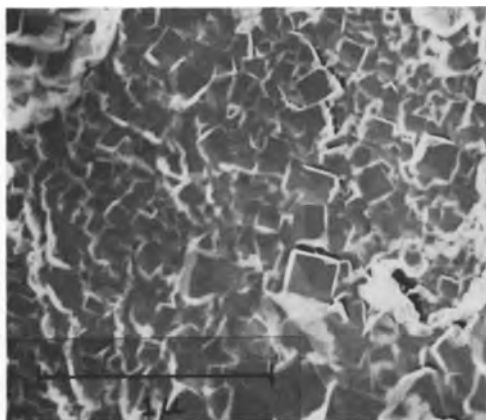


Fig. 1. Pure lead sheet anodized in H_2SO_4 for 68 hr. This thin coating of PbO_2 is prismatic and appears to exhibit definite areas of preferred orientation of the crystallites.

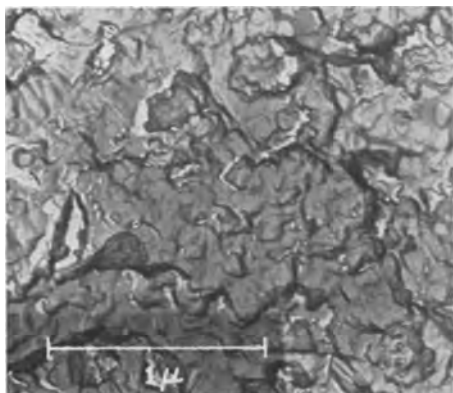


Fig. 2. Pure lead sheet anodized in H_2SO_4 for 1464 hr. The individual crystallites of thinner films (Fig. 1) have disappeared, and the coating is flaking away from the surface.

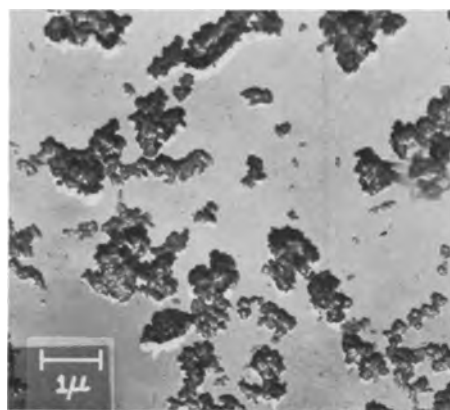


Fig. 3. Particles of PbO_2 isolated from a sheet of pure lead cycled 8 times in H_2SO_4 . The individual particles are difficult to disperse and tend to clump together; however, they appear to be approximately 0.1μ in diameter, and to be spheroidal. These particles are believed to be obtained by conversion from PbSO_4 and, unless bound by mechanical or chemical forces, readily detach themselves from the electrode surface.

submicron size and appear to be spheroidal. Figure 3 shows a carbon replica of such particles isolated from the surface of the cycled specimen. These particles are rather uniform in size and appear to be approximately 0.1μ in diameter. This is in the same range observed by Feitknecht and Gaumann and Burbank (8, 20); however, on the basis of x-ray line broadening, Feitknecht (7) estimated the particles to be about 100\AA . It is difficult to obtain good dispersion of such fine material by the techniques used in this work; however, these certainly lie within the colloidal range. It is these particles that form a reddish cloud in the electrolyte near the electrode surface if gas evolution is vigorous enough, and in turn give rise to lead trees as they circulate in the cell and come into contact with the negative electrode. As the anodic coating builds up, it tends to lose electrical contact with the lead surface and continuity between individual particles. In Planté plate formation it is necessary to retain the PbO_2 particles in a mass on the surface in order to get adequate capacity from the plates. Feitknecht's electron micrographs taken during self-discharge show that prismatic sulfate crystals grow during open-circuit stand. In a study of lead calcium cells (16) it was shown that even in pasted plates when the active material is composed of nondescript nodular PbO_2 particles, the plates would not give satisfactory capacity until sufficient prismatic PbSO_4 had been formed to bind the mass together. Planté in 1887 (21) described similar behavior thus: "A singular phenomenon frequently observed with secondary lead cells: it is found that immediately after charging, the battery will not pass enough current to heat a platinum wire, but after standing on open-circuit for about 24 hours it will heat the same wire to incandescence." He attributed this to a film of gas, but it appears from the electron microscopic investigations that during the 24 hr stand sufficient sulfate crystallized to cement the particles into a conducting mass.

Battery plates.—The positive active material from commercial battery plates shows a wide vari-

ety of particle morphology varying from complex prismatic crystals to nodular forms. Some commercial plates appear to be entirely prismatic in nature while others are entirely nondescript nodular formations. Still others contain clusters of well-developed prismatic crystals in a matrix of nondescript material. These formations are illustrated in the electron micrographs shown in Fig. 4-8. It

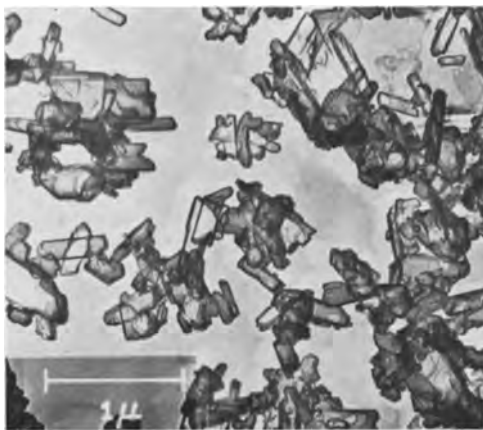


Fig. 4. Positive active material from lead calcium cells showing almost entirely prismatic crystallization. Plates composed of these particles remained firm and retained capacity in shallow cycling tests.

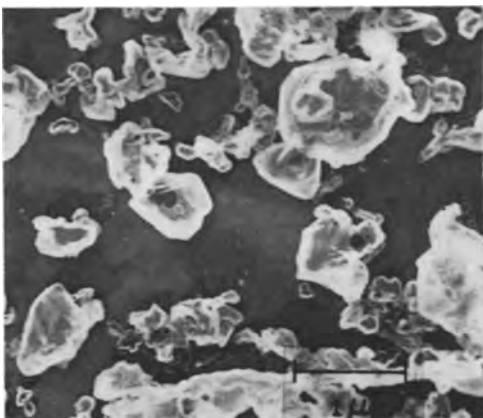


Fig. 5. Positive active material from lead calcium cells showing predominantly nodular crystallization. Plates composed of these particles softened and failed after a few weeks of shallow cycle testing.

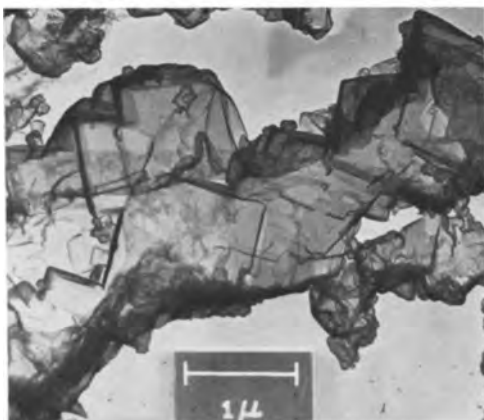


Fig. 6. Positive active material from a lead antimony cell. Massive prismatic conglomerates were characteristic of the active material in this sample.

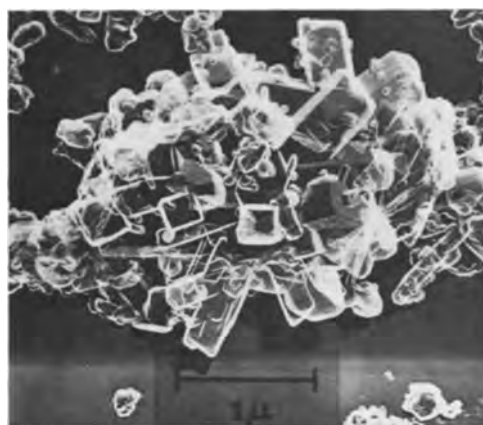


Fig. 7. A large cluster of prismatic crystals showing many side arms illustrating the interlocking believed to be associated with morphology of this type which is believed to impart mechanical strength to the positive paste.

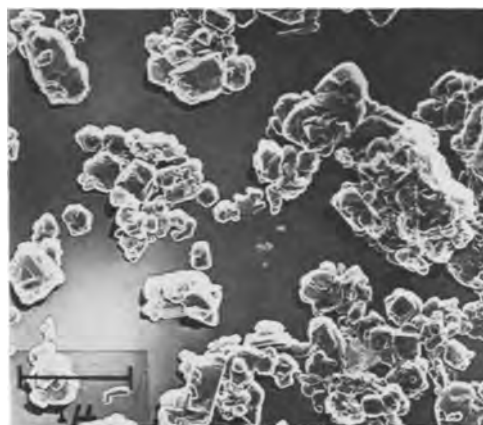


Fig. 8. Particles of positive active material showing an intermediate development of prismatic character. These particles retain some prismatic form, but are not characterized by intricate branching and would not be expected to impart mechanical strength to the active mass.

has been shown in an earlier study (16) that plates containing large amounts of prismatic material maintained capacity whereas plates comprised mainly of nondescript particles suffered drastic capacity loss and failed because of softening of the active mass. If the plates containing nondescript particles were operated in such a way as to retain prismatic sulfate crystals in the active material, satisfactory performance could be obtained from them. It is apparent that morphology of the particles plays a significant role in the retention of the positive active material in the lead acid cell.

Miscellaneous preparations.—Reagent grade PbO_2 was also examined as a matter of curiosity, and the sample available at this Laboratory showed a mixture of prismatic and nondescript particles Fig. 9. The growth habit of the prismatic crystals was different from that exhibited by the prismatic battery samples.

If Pb_3O_4 is extracted with acids that react with the divalent lead, PbO_2 is deposited. The lattice of Pb_3O_4 contains both di- and tetravalent lead, and the residue of PbO_2 is formed by deposition from solution. This material is not contained as such in

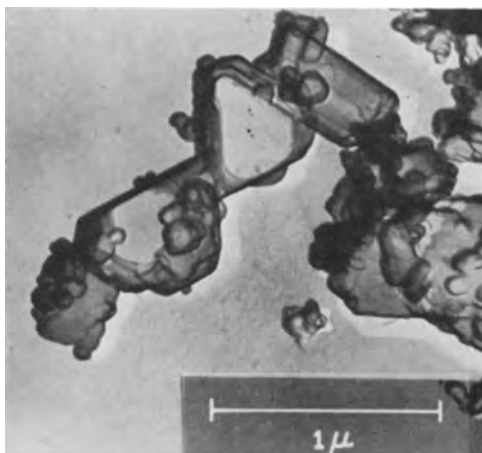


Fig. 9a. Particles of reagent grade PbO_2 . Prismatic crystals showing a growth habit different from those contained in the active material of the cells illustrated in Fig. 4, 6, and 7.

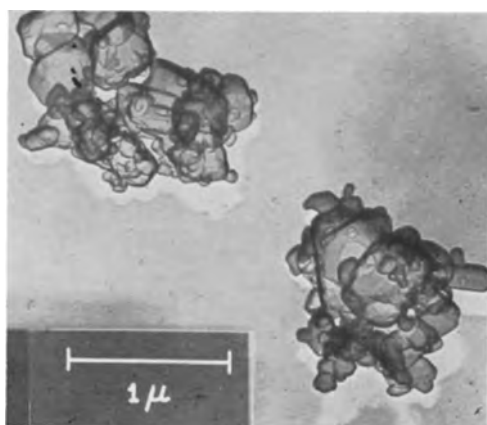


Fig. 9b. Particles of reagent grade PbO_2 . Mixture of nodular and prismatic forms. This type of material formed the bulk of the sample.

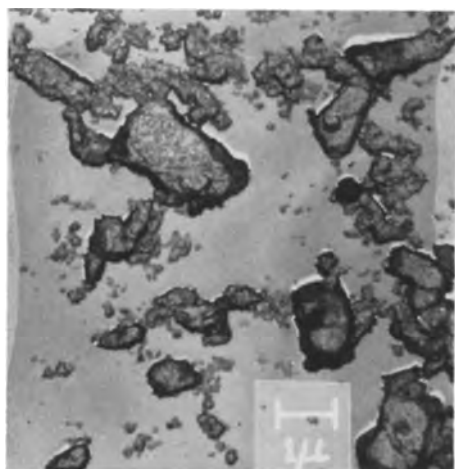


Fig. 10. PbO_2 obtained by extraction of Pb_3O_4 . The smallest individuals appear to be spheroidal, and the large particles may be conglomerates of these small units. There appears to be no tendency toward prismatic development.

the Pb_3O_4 lattice. Figure 10 is an electron micrograph of the PbO_2 residue obtained from extracting Pb_3O_4 and shows a lack of well developed crystals.

The individual particles are very small, and no prismatic forms were observed.

It is concluded that the morphology of battery active materials may be correlated with the performance of the plates at least under certain conditions. Optical microscopic examination of the active materials (22) has also shown variations in structure of a different order of magnitude. These studies suggest that improvements in battery performance may be expected to result from such examinations of structures and physical mechanisms of operation. It is hoped that this study will serve to stimulate further investigations of paste morphology and its relation to electrochemical and mechanical properties of battery active materials.

Manuscript received Jan. 28, 1964.

Any discussion of this paper will appear in a Discussion Section to be published in the June 1965 JOURNAL.

REFERENCES

1. A. I. Zaslavskii, Yu. D. Kondrashov, and S. S. Tol-kachev, *Doklady Akad. Nauk. S.S.S.R.*, **75**, 559 (1950).
2. A. I. Zaslavskii and S. S. Talkachev, *J. Phys. Chem. USSR*, **26**, 743 (1952).
3. W. B. White, F. Dacheille, and R. Roy, *Am. Ceram. Soc. J.*, **44**, 170 (1961).
4. H. Bode and E. Voss, *Z. Elektrochem.*, **60**, 1053 (1956).
5. P. Ruetschi and B. D. Cahan, *This Journal*, **104**, 406 (1957).
6. J. Burbank, *ibid.*, **106**, 369 (1959).
7. W. Feitknecht, *Z. Elektrochem.*, **62**, 795 (1958).
8. W. Feitknecht and A. Gaumann, *J. Chim. Phys.*, **49**, 135 (1952).
9. J. E. Buskirk, P. D. Boyd, and V. V. Smith, Paper presented at the Electrochemical Society Meeting, Houston, Texas, October 1960 (Extended Abstract 19).
10. D. Spahrbiel, Thesis: Zum elektrochemischen Verhalten der Bleidioxydelektroden Technischen Hochschule, Stuttgart, 1960.
11. I. I. Astakhov, I. G. Kiseleva, and B. N. Kabanov, *Doklady Akad. Nauk. S.S.S.R.*, **126**, 1041 (1959).
12. C. Palache, H. Berman, and C. Frondel, "Dana's System of Mineralogy," Vol. 1, p. 581, John Wiley & Sons, Inc., New York (1944).
13. H. R. Davidson, *Am. Min.*, **26**, 18 (1941).
14. H. E. Haring and U. B. Thomas, *Trans. Electrochem. Soc.*, **68**, 293 (1935).
15. U. B. Thomas, F. T. Forster, and H. E. Haring, *ibid.*, **92**, 313 (1947).
16. J. Burbank, Batteries, Proceedings of the 3rd International Symposium, Bournemouth, England, October 1962, p. 43.
17. C. M. Sliepevich, L. Gildart, and D. L. Katz, *Ind. Eng. Chem., Ind. Ed.*, **35**, 1178 (1943).
18. D. E. Bradley, *Brit. J. Appl. Phys.*, **5**, 65, 96 (1954).
19. J. Burbank, *This Journal*, **103**, 87 (1956).
20. J. Burbank, *ibid.*, **104**, 693 (1957).
21. G. Planté, Recherches sur L'Electricité, Librairie de A. Fourneau, Paris 1879, p. 72 ff.
22. A. C. Simon and E. L. Jones, *This Journal*, **109**, 760 (1962).

Thermogalvanic Cells with Silver Iodide as a Solid Electrolyte

J. L. Weininger

Research Laboratory, General Electric Company, Schenectady, New York

ABSTRACT

Experiments with the thermocells $\text{Ag}/\alpha\text{-AgI}/\text{Ag}$ and $\text{I}_2/\alpha\text{-AgI}/\text{I}_2$ are described and compared with theory. The combination of the solid electrolyte, $\alpha\text{-AgI}$, with iodine gas diffusion electrodes gives the iodine cell a figure of merit of $1 \times 10^{-3} \text{ deg}^{-1}$ and a theoretical efficiency of 5.1%. In operation of this cell, iodine gas is evolved at the cold electrode and consumed at the hot electrode. These electrode reactions are reversible. In the silver cell, complications are introduced by the formation of silver dendrites at the cathode.

Thermogalvanic cells, "thermocells" for short, are nonisothermal cells usually with identical electrodes in contact with an electrolyte. A difference in temperature of the two electrodes produces an emf (thermopotential) which causes a galvanic current to flow. The temperature coefficient of the thermopotential is the "thermoelectric power" of the electrolytic cell analogous to the thermoelectric power of electronic thermal converters.

Thermocells with solid electrolytes were first studied by Reinhold (1, 2) who was primarily interested in their thermodynamic aspects. Wagner (3) elaborated on the theory and studied the interrelation of the thermogalvanic effect with other heat effects. More recent investigations are due to Holtan (4, 5). A very recent and comprehensive review is due to Agar (6).

Among solid electrolytes silver halides have the largest ionic conductivities. Over the past years they have been studied in this Laboratory as electrolytes for galvanic cells (7, 8) as well as for thermocells. Alpha-silver iodide, a stable form of AgI in the temperature range $146^\circ\text{-}552^\circ$, is particularly suitable for use in thermocells. This report, therefore, deals with thermocells containing $\alpha\text{-AgI}$ as the electrolyte. Two types of thermocells are considered. In the "silver cell" the electrodes are silver ($\text{Ag}/\alpha\text{-AgI}/\text{Ag}$); in the "iodine cell" iodine gas diffusion electrodes are used ($\text{I}_2/\alpha\text{-AgI}/\text{I}_2$). Both cells are discussed, but more emphasis is placed on the

iodine cell which is thought to have more promise of practical application.

Mechanism.—The mechanisms of the present thermocells are shown in Table I. For the silver cell, the mechanism was proved by Reinhold; the present work experimentally verifies the mechanism of the iodine cell. The latter is also the subject of a recent patent (9). The thermoelectric power of the iodine cell and the dependence of this important parameter on the iodine vapor pressure were first reported by Wagener (10).

Silver Thermocell— $\text{Ag}/\alpha\text{-AgI}/\text{Ag}$

Cell construction.—Three cell types shown in Fig. 1 were used.

Cell I consists of two silver electrodes, 2 mm thick, which sandwich the AgI electrolyte. The lower electrode (anode) is heated. The electrolyte is a disk 4 mm thick and 5.07 cm^2 in area, contained in a Pyrex spacer to prevent deformation.

In Cell II the cathode (colder electrode) is a silver cup which is maintained above the transformation temperature of $\alpha\text{-AgI}$ (146°). AgI is melted and solidified in the cathode under an inert atmosphere to establish the electrolyte. The anode (hotter electrode) is a block of silver at the end of the tip of a soldering iron.

Cell III has the same electrodes and heating arrangement but the electrolyte is a porous ceramic disk (alumina) impregnated with AgI. The porous

Table I. Mechanism of thermocells

	Silver thermocell	Iodine thermocell
	$\oplus \text{Ag}/\alpha\text{-AgI}/\text{Ag} \ominus$ cold hot at T at $T + \Delta T$	$\oplus \text{I}_2(\text{Me})\alpha\text{-AgI}/\text{I}_2(\text{Me}) \ominus$ hot cold at $T + \Delta T$ at T where Me = inert electrode
Anode:	Temperature: $T + \Delta T$ Reaction: $\text{Ag} \rightarrow \text{Ag}^+ + e^-$	$\text{I}^- \rightarrow \frac{1}{2}\text{I}_2 + e^-$ (or, $\text{AgI} \rightarrow \frac{1}{2}\text{I}_2 + \text{Ag}^+ + e^-$) P_{I_2} increases
Electrolyte:	Ag^+ moves from hot to cold electrode.	Ag^+ moves from cold to hot electrode.
Cathode:	Temperature: T Reaction: $\text{Ag}^+ + e^- \rightarrow \text{Ag}$	$T + \Delta T$ $\frac{1}{2}\text{I}_2 + e^- \rightarrow \text{I}^-$ (or, $\text{Ag}^+ + \frac{1}{2}\text{I}_2 + e^- \rightarrow \text{AgI}$). P_{I_2} decreases
Net change per		
Faraday electricity:	transport of 1 mole of silver from hot to cold electrode.	transport of $\frac{1}{2}$ mole of iodine from cold to hot electrode.

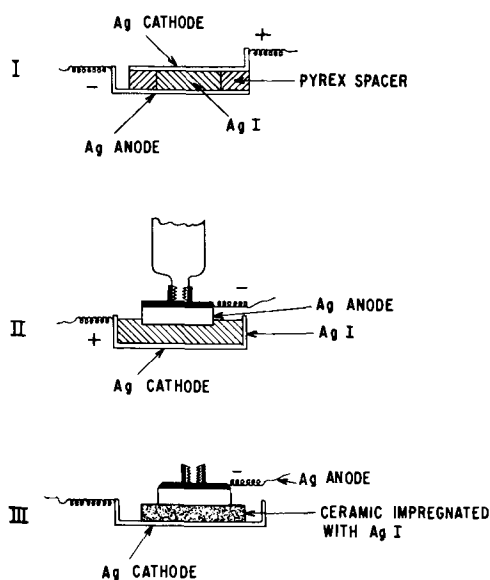


Fig. 1. Silver thermocells

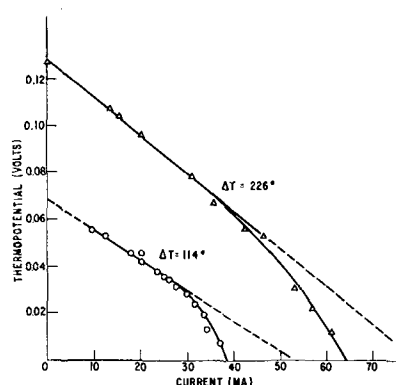


Fig. 2. Thermopotential-current curves for silver thermocell I

matrix was used in an attempt to overcome dendrite formation.

Results.—The experiments confirmed the known mechanism, *i.e.*, that transport of silver takes place from the hot to the cold electrode, with the former as the negative pole.

The thermopotential-current curves obtained with Cell I are shown in Fig. 2. The pertinent data of the two plots are:

$$\begin{aligned} \Delta T &= 114^{\circ}\text{C}, T_{\text{hot}} = 397^{\circ}, T_{\text{cold}} = 283^{\circ}, \Delta E/\Delta T \\ &= 0.60 \text{ mv/deg, slope} = 1.33 \text{ ohms} \\ \Delta T &= 226^{\circ}\text{C}, T_{\text{h}} = 382^{\circ}, T_{\text{c}} = 156^{\circ}, \Delta E/\Delta T \\ &= 0.56 \text{ mv/deg, slope} = 1.57 \text{ ohms.} \end{aligned}$$

With the given geometry the internal resistance should have been 0.056 ohm. Thus, the measured values indicated only about 4% effective contact. In another experiment at $\Delta T = 85^{\circ}$, an open cell voltage of 46 mv was measured. On passing a total of 290 coulombs in the external circuit, the anode had lost an amount of Ag equivalent to 373 coulombs, which was not deposited on the cathode. Thus, a 22% loss of Ag from the anode and almost constant cathode weight were evidence of an irreversible change. This was explained by the appearance of cell I at the end of the experiment, which is illustrated schematically in Fig. 3. The anode was

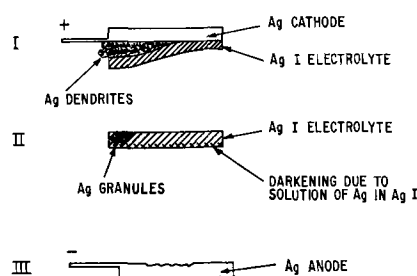


Fig. 3. Dendrite formation in operation of silver thermocell

etched in spots (III), indicating irregular dissolution of silver ions. These formed dendrites at the cathode (I) instead of depositing on the electrode. Silver grains extended also from the cathode into the electrolyte (II).

Better short-term performance was obtained with cell II because of its tighter construction and closer electrode spacing, but dendrite formation became an even more serious problem. At $\Delta T = 414^{\circ} - 150 = 264^{\circ}\text{C}$, by shorting the cell through the 0.011 ohm range of an ammeter a current of 500 ma was obtained. Dendrites were first seen 8 min after the start of the experiment and after 53 min the cell became internally shorted. As the current slowly decreased, a total passage of about 1000 coulombs was estimated.

With the construction of cell III, dendrite formation was slowed down, but some polarization occurred so that the lifetime of the cell was increased by a factor of 20 whereas the resistance of the cell increased by a factor of 5.

These experiments indicate that dendrite formation and the lack of deposition of silver at the cathode are formidable obstacles to the proper functioning of the silver thermocell. To obtain larger current production, commensurate with the large conductivity of the electrolyte, would require homogeneous deposition and migration of the carrier-ion (Ag^+). In the iodine thermocell, a different set of experimental difficulties are encountered.

Iodine Thermocell— $\text{I}_2/\alpha\text{-AgI}/\text{I}_2$

Both the iodine and silver thermocells have the same electrolyte with its highly desirable ionic conductivity ($\rho = 0.38 \text{ ohm-cm}$ at 500° , 0.47 ohm-cm at 350°) (11, 12). They differ, however, in that the carrier-ion (Ag^+) moves in opposite directions with respect to the temperature gradient. Hence, the net transport of material, iodine and silver, respectively, is in opposite directions. This is illustrated in Table I, which also shows that in the iodine cell the iodine pressure is increased at the cold electrode (anode) and decreased at the hot electrode (cathode).

Cell construction.—Two main problems in the design of the iodine cell are the use of gas diffusion electrodes, and the contraction of the room temperature form of AgI on heating and at the transition point $\beta\text{-AgI} \rightarrow \alpha\text{-AgI}$.

Most metals react with iodine at elevated temperatures. However, for preliminary experiments platinum and tantalum were chosen as electrodes because they had proved to be satisfactory for the

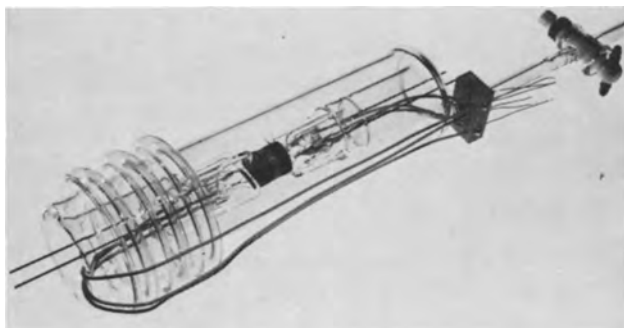


Fig. 4. Iodine thermocell

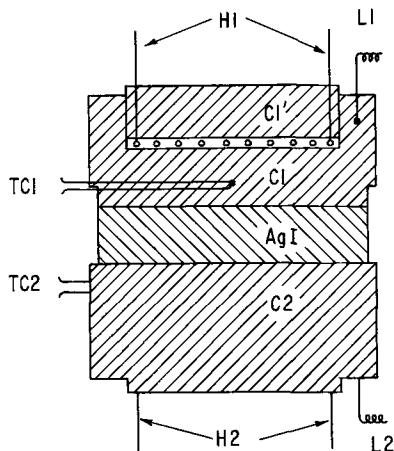


Fig. 5. Detail of iodine thermocell

iodine electrode in the galvanic cell $I_2/\alpha\text{-AgI}/\text{Ag}$ (8). Later on, porous carbon was found to be a preferable electrode material. Hence the electrodes were prepared from "Ultra-purity" graphite rods, supplied by the United Carbon Products Company. These electrodes had a porosity of 27% and a resistivity of 8×10^{-4} ohm-cm.

Below the temperature of transformation of $\beta\text{-AgI}$ to $\alpha\text{-AgI}$ at 145.80°C (12) and during this transformation the electrolyte contracts on heating. Thus, the cell must accommodate contraction and expansion of the electrolyte, on heating and cooling, without either losing contact between electrode and electrolyte, or putting undue strain on the electrodes and their supports. This presents a problem of cell design that was solved by mounting the cell on glass supports within the Pyrex housing which contained glass bellows. The cell is shown in the photograph of Fig. 4. Details of the cell are sketched in Fig. 5. The electrolyte is a disk of AgI, 14 mm in diameter and 3 mm thick. The electrodes, with the same diameter and a thickness of 6 mm, contain small doubly wound spiral heaters (H_1 and H_2) made of 0.010 in. platinum wires, which were insulated with a thin layer of Al_2O_3 . These heaters were covered with graphite plugs (e.g., Cl'). The thermocouple leads (TC1 and TC2) were also insulated and the electric leads (L_1 and L_2) were pressure-fitted into the graphite blocks. The two electrodes were identical except that on one there was a shoulder to provide a temporary wall (not shown) for melting the AgI under an inert atmosphere. For operation, iodine crystals were placed in the housing and the cell was evacuated and

Table II. Performance of the iodine cell

Experiment No.	T_h , °C	T_c , °C	ΔT , °C	ΔE , mv	$\Delta E/\Delta T$, mv/deg	Internal resistance, ohms
1	342	262	80	95	1.19	79
2	340	184	156	208	1.33	67*
3	498	218	280	347	1.24	91**
4	335	165	170	232	1.36	61

* At current < 0.6 ma.
** At current > 1 ma.

closed. At room temperature an iodine vapor pressure of approximately 0.3 mm Hg was then established.

Results.—Table II summarizes the thermopotential-current curves shown in Fig. 6. Within the experimental error the temperature coefficient of the thermopotential, the "thermoelectric power" of the cell, is in agreement with values calculated from thermodynamics. This is discussed below. The internal resistance of the cell, 70 ± 10 ohms, depends on the effective contact area of the interfaces between the inert electrode, the electrolyte, and the gas.

An important characteristic of the iodine thermocell is the advance of the solid electrolyte into the pores of the hot electrode. The coulombic (current-delivering) capacity of the cell, therefore, will be limited by the geometry of the electrodes, but reversing the temperature gradient will renew the capacity of the cell. A test of this capacity is shown in Fig. 7. The cell was discharged through an ex-

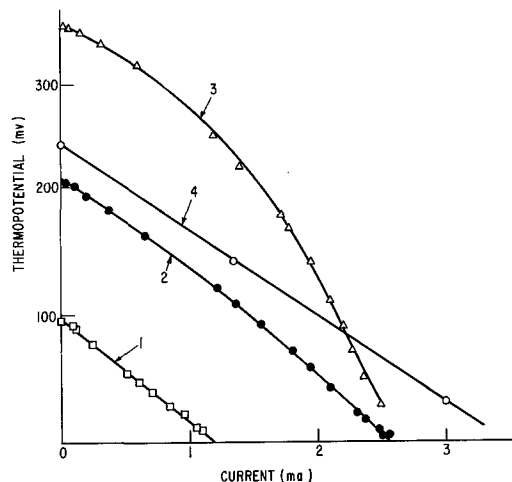


Fig. 6. Thermopotential-current curves for iodine cell

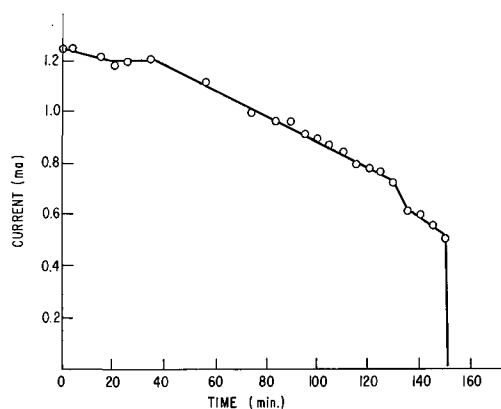


Fig. 7. Coulombic capacity of iodine cell; cell on 100 ohm load; capacity 8.5 coulombs.

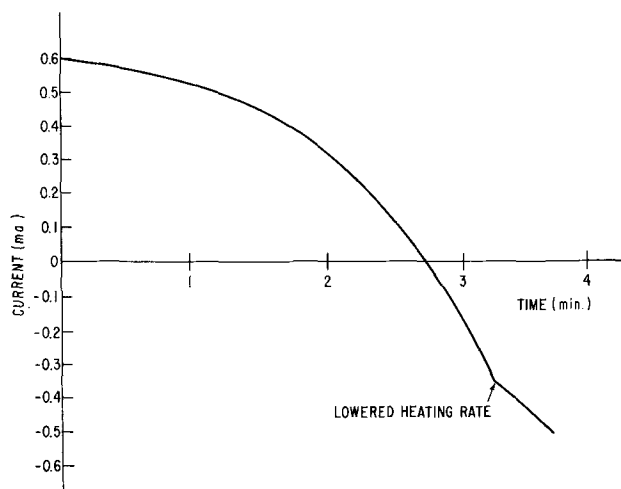


Fig. 8. Current output of iodine thermocell on reversal of temperature gradient.

ternal resistance of 100 ohms ($\Delta T = 150^\circ$, $T_h = 361^\circ$, $T_c = 211^\circ$, open cell potential = 204 mv, $\Delta E/\Delta T = 1.36$ mv/deg). The test was terminated when the current dropped to 0.5 ma, slightly more than one-half its original value. A total of 8.5 coulombs was obtained.

Response to a change in the temperature gradient seemed to be instantaneous. An illustration of this is the reversal of current on reversing the temperature gradient of the cell at the end of the above life test. This is shown in Fig. 8. At time zero the heating of the hot electrode was discontinued and the temperature of the other electrode was increased. The change from positive to negative current proceeded smoothly, and the indicated change of the slope of the curve was due to lowering the heating current of the newly "hot" electrode. This change in cell output was instantaneous.

The motion of the electrolyte was observed as a regularly advancing front of AgI at the outside of the hot carbon electrode. Likewise, it receded on reversing the thermal gradient. In fact, the data of Fig. 6 were obtained on current reversal after exhausting the cell in the reverse direction. The few steps in the current-time curve of Fig. 7 are believed to be real and due to blockage of some of the electrode's pores.

Increasing the iodine pressure by raising the temperature of the whole assembly did not improve the cell performance. This improvement would be expected if the diffusion of iodine in the electrodes were enhanced by reducing the pressure at the anode where iodine is formed, and by increasing the pressure at the cathode, where iodine is consumed. In the present cell, however, the anode and cathode were in one gaseous environment in which the iodine pressure was equalized by convection.

When the cell in one of its discharge cycles was nearly exhausted, an interesting current oscillation was observed. The current showed irregular but periodic fluctuations. This phenomenon is not yet understood, but it might be traced to the breakdown of the electrode/electrolyte/vapor interface. For example, the complete coverage of the inert electrode by the electrolyte, or the inability of the dif-

fusing gas to reach the site of the electrode reaction could account for these oscillations.

Summarizing the experimental results:

1. The thermoelectric power of 1.2 to 1.4 mv/deg has been experimentally established for the iodine cell.
2. The electrode reactions are very fast.
3. Reversal of the sign of the potential (hence current) on reversing the temperature gradient is instantaneous.
4. The internal resistance of the present cell, approximately 70 ohms, is large. A perfect three-phase interface with the present design would give a cell resistance of 0.11 ohm. Such a 700-fold improvement in cell performance may not be realized due to the specific nature of a gas diffusion electrode. However, this experimental fact points up the area in which further work should be pursued.

Discussion

Recently, Euler (13) has discussed the present iodine thermocell and has considered it as one of several promising unconventional thermal converters. In comparing it with other converters, the advantages of the thermocell are its basically simple construction and its reasonably large power output. These advantages are due to the combination of the solid electrolyte with iodine gas as the electrokinetically active species. As with other thermal converters the disadvantage of the thermocell is its inherently low efficiency of converting thermal into electrical energy. In the following discussion, before dealing with the thermal efficiency of the cell, the experimentally obtained thermoelectric power of the iodine cell is compared with that calculated from thermodynamic considerations. The efficiency of the thermocell and its applications are then considered (including the heat input into the thermocell in relation to solar energy conversion).

*Evaluation of the thermoelectric power of the iodine cell.*¹—The thermodynamic evaluation of the thermoelectric potential is complicated by the irreversibility of the nonisothermal system. In terms of entropy changes homogeneous transport processes and heterogeneous effects at the phase boundaries (electrodes) must be considered. From a modern viewpoint of ionic conductance, the homogeneous potential difference, which is due to the temperature gradient, is given in terms of heats of transport for interstitial ions (14). The heterogeneous effects include contact potential differences at the electrodes as well as the heterogeneous cell reactions. Fortunately, in the cell containing α -AgI as the electrolyte, the cell reaction overshadows all the other contributions to the over-all entropy of the process so that for a first approximation the Gibbs-Helmholtz equation may be applied. Presumably this is due to small magnitude of the transport entropies in the already disordered cationic lattice and due to the small magnitude of the contact potentials.

¹ An excellent comprehensive review of thermogalvanic cells, particularly of their theoretical aspects, has been published recently (6). The author states that the figure of merit for solid electrolytes is less than 0.5×10^{-3} deg⁻¹. However, for AgI the figure of merit is about 1×10^{-3} .

Table III. Variation of thermoelectric power of iodine cell with temperature

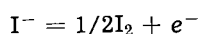
Temperature °C	Temperature °K	C_p	$S_T - S_{298^\circ}$ cal/deg mole	$\frac{1}{2}S_{I_2}$	dE/dT , mv/deg
550	823	9.06	9.15	35.5	+1.54*
500	773	9.05	8.60	34.7	1.50
400	673	9.03	7.32	34.6	1.49
300	573	9.01	5.85	33.8	1.46
200	473	9.00	4.14	33.0	1.43
150	423	8.99	3.15	32.5	1.41

* By convention a plus sign of the thermoelectric power corresponds to a positive current, at the cold interface, flowing in a direction from the electrode to the electrolyte.

Table IV. Comparison of experimental and calculated thermoelectric power

Experiment No.	Mean temperature, °K	Thermoelectric power	
		Experimental	Calculated
4	523	1.36	1.45
2	535	1.33	1.45
1	574	1.19	1.46
3	631	1.24	1.48

Following Holtan (4) for the cell reaction



we can calculate the thermopotential

$$\Delta E/\Delta T = -\Delta S/nF = -(1/2F) S_{I_2}$$

For small temperature gradients this has been shown to give good agreement for the cells $Cl_2/PbCl_2/Cl_2$, $Cl_2/AgCl/Cl_2$, and $Br_2/AgBr/Br_2$ (5). For the iodine cell $I_2/AgI/I_2$ the range of applicability of the equation should be even larger because of the greater ease of transport in the solid electrolyte.

The entropy of iodine gas at 25°C is given by Eastman, (15) $S_{I_2}(298^\circ K) = 61.8$ e.u., and the heat capacity is given by Kelley (16)

$$C_p = 8.94 + 0.14 \times 10^{-3}T - 0.17 \times 10^{-5}T^{-2}$$

from which we obtain the thermoelectric power for the iodine cell as shown in Table III.

In Table IV the experimental and calculated values of the thermoelectric power are compared at the mean temperatures at which the cell was operated. Although there is considerable experimental error in determining the thermoelectric power it is seen that the deviation of the experimental from the theoretical value becomes larger at higher temperatures. This may reflect the extent to which the above simplifying assumption in the calculation of $\Delta E/\Delta T$ were valid.

Efficiency of iodine thermocell.—Analogous to electronic thermoelectric converters the efficiency of electrolytic thermocells depends on the thermoelectric power of the cell, α , in volts/degree (above denoted by $\Delta E/\Delta T$), the electrical resistivity, ρ , in ohm-cm, and the thermal conductivity, k , in watts/centimeter-degree. These quantities are accurately known for the iodine cell except for the thermal conductivity of α -AgI, which is estimated to be $k = 0.004$ w/cm deg. At 500° and 350°C, $\rho = 0.38$

and 0.47 ohm-cm, respectively. With $\alpha = 1.3$ mv/deg a figure of merit, $Z = \alpha^2/\rho k$ of 1.1×10^{-3} at 500° and 0.9×10^{-3} at 350° is obtained.² This compares favorably with the best semiconducting elements. A change of the cell geometry would affect absolute values of power output and heat losses, but would not change the efficiency. This is illustrated by a relation due to Telkes (17)

$$\text{Efficiency} = \frac{1}{\frac{2T_h}{T_h - T_c} + \frac{4k\rho}{10^{-6}\alpha^2(T_h - T_c)}} \times 100 (\%)$$

where k , ρ , and α have the same meaning as before, but α is expressed in millivolt/degree, and T_h and T_c are the temperatures of the hot and cold side of the cell, respectively, in degrees K. The efficiency defined by this equation is the percentage of the maximum power output relative to the heat input at the hot electrode or junction. The first term in the denominator is a Carnot heat term; the second term resembles the above figure of merit. For the iodine cell, at a mean temperature of 350°C, and a temperature gradient of 300° this efficiency is 5.1%.

Applications of thermocells.—The efficiency of 5.1 represents the theoretical limit of the heat which can be converted into electrical energy by the iodine cell at a reasonable mean temperature and temperature gradient. It assumes that heat is conducted only from the hot to the cold electrode through the solid electrolyte without any heat losses except those due to the cell reaction. In practice the operating temperatures of the cells containing the AgI electrolyte are sufficiently low so that radiation effects can be neglected. Losses by conduction in the mechanical supports of the electrodes, and by convection of the iodine gas, must be minimized. At best an actual efficiency of a few per cent will be achieved. Thus, the application of thermocells is limited to the conversion of waste heat, and possibly to solar energy conversion.

In connection with solar energy conversion, the solar intensity must be increased by a factor of 10 in order to increase the heat input into the thermocell. For maximum cell output this can be shown to be necessary by matching the value of solar intensity with the geometrical requirements and thermal properties of the AgI electrolyte. It follows that for conversion of solar energy, in addition to the solution of design problems of the thermocell, provision must be made for a focusing device. Furthermore, for continuous operation of the iodine cell, means of reversing the temperature gradient must also be found.

Acknowledgments

The design of the iodine cell is largely due to W. R. Grams and W. L. Mowrey. Their assistance is greatly appreciated. The author is also indebted to R. E. Hoffman and T. O. Rouse for critical comments on the manuscript.

Manuscript received Aug. 27, 1963; revised manuscript received Feb. 15, 1964.

² An experimental determination of the thermal conductivity of α -AgI is now being made. The estimates of the figure of merit may have to be changed accordingly.

Any discussion of this paper will appear in a Discussion Section to be published in the June 1965 JOURNAL.

REFERENCES

1. H. Reinhold, *Z. anorg. u. allgem. Chem.*, **171**, 181 (1928).
2. H. Reinhold and A. Blachny, *Z. Elektrochem.*, **39**, 290 (1933).
3. C. Wagner, *Ann. Phys.*, **3** [5], 629 (1929).
4. H. Holtan, *J. Chem. Phys.*, **19**, 519 (1951); **20**, 539 (1952).
5. H. Holtan, *Koninkl. Nederland Akad. Wetenschap. Proc.*, **B56**, 498 (1953).
6. J. N. Agar, "Advances in Electrochemistry and Electrochemical Engineering," P. Delahay, Editor, Vol. 3, II, Interscience Publishers, New York (1963).
7. J. L. Weininger, *This Journal*, **105**, 439 (1958).
8. J. L. Weininger, *ibid.*, **106**, 475 (1959).
9. J. L. Weininger, (to General Electric Company) U. S. Pat. 2,890,259, June 1959.
10. K. Wagener, *Z. physik. Chem. (n.F.)* **21**, 74 (1959).
11. K. H. Lieser, *ibid.*, **9**, 302 (1956).
12. C. Tubandt and W. Lorenz, *Z. physik. Chem.*, **87**, 513 (1914).
13. J. Euler, *Chemie-Ing.-Techn.*, **34**, 567 (1962).
14. R. E. Howard and A. B. Lidiard, *Phil. Mag.*, (8) **2**, 1462 (1957).
15. E. D. Eastman, *J. Amer. Chem. Soc.*, **45**, 81 (1923).
16. K. K. Kelley, U. S. Bur. Mines Bull. 584 (1960).
17. M. Telkes, *J. Appl. Phys.*, **25**, 765 (1954).

The Effect of Abrasion on the Specific Surface Area of Metals and Glass

R. J. Adams, H. L. Weisbecker, and W. J. McDonald

Minnesota Mining & Manufacturing Company, St. Paul, Minnesota

ABSTRACT

The surface areas of polished and abraded surfaces have been investigated using adsorption from solution of carbon-14 tagged acetic acid, stearic acid, and N-ethyl-N-perfluorooctanesulfonylglycine. Adsorption rates, isotherms, heats of adsorption, and desorption characteristics are given for the unique acetic acid system. The effects of abrasion conditions on the surface area of steel have been investigated in detail. Specific surface areas ranging from two up to ten were obtained for various abrasive speeds, loads, and mineral types, and comparable surface areas were obtained for abraded surfaces of glass. Measured areas decreased with increased adsorbate chain length and with increased abrasion temperature. Accordingly, a possible mechanism for abrasion of steel is suggested which involves formation of microcracks. At the higher localized temperatures, more of these surface fissures may become sealed due to surface flow or reaction with oxygen.

Detailed studies of the processes of abrasion and polishing of metals are important for several reasons. Aside from surface finish and lubrication considerations, the new surfaces generated may have unique chemical properties and may influence bulk tensile and fatigue characteristics. Information has been contributed by many investigators [a partial listing is given (1-6)]; however, many questions remain unanswered. Samuels (7) has outlined the most pertinent of these.

Prominent among these problems is the question of the detailed microstructure of the so-called "deformed layer" formed by the abrasive action (1) and the effect of various abrasion parameters on this structure. One purpose of this work was to investigate the nature of abraded metal surfaces with respect to their specific surface area¹ and study the effect of abrasion conditions on this area. It was hoped that this study would afford an in-

sight into the mechanism of abrasion and structure of the deformed layer.

Work has appeared concerning the effect of surface area on the chemical reactivity of metal surfaces as regards the phenomena of oxidation, corrosion, and adhesion. Some of these studies have concerned abraded surfaces (8,9). However, difficulty in measuring and interpreting measurements of surface area has been a factor in the common neglect of this quantity in studies concerning surface reactivity. Another purpose of this study was to provide detailed reference data concerning surfaces generated by abrasion.

Adsorption from solution of carbon-14 tagged organic acids was used to estimate the surface area. This method was chosen because of its experimental simplicity, excellent sensitivity, and because adsorption phenomena at liquid-abraded metal interfaces are of interest *per se*. Several investigators have evaluated the merits of solution adsorption of tagged acids and other adsorbates for the measurement of surface area (9-12). In general, results for powders and planar metal surfaces using solution adsorption techniques have shown good agreement

¹ "Specific surface area" for planar solids is defined as the ratio of the true surface area (as approximated by the adsorption measurement) to the gross geometric area (planar area of the sample). Some authors have referred to this quantity as the "roughness factor" to avoid confusion with the specific surface area of powders (reported in square meters per gram); however we regard this term as misleading. In this work, the symbol R_s has been adopted to represent the specific surface area.

with values found by gas adsorption and other independent methods (13-16).

Three adsorbates were used in this work; acetic acid, N-ethyl-N-perfluoroöctanesulfonylglycine² and stearic acid, each tagged with carbon-14 in the carboxyl group. This permits an evaluation of the effect of adsorbate chain length on the measured surface area, since the chain lengths are in the ratio 1:6:9. The adsorption of stearic acid on powders and planar metal surfaces has been well characterized (12, 14). Results for acetic acid adsorbed on planar metal surfaces are of interest since, to our knowledge, this system has not been previously investigated. Acetic acid might be expected to give a better fit to micro-irregularities than the long chain acids which are commonly used. The glycine derivative was also chosen to permit comparison of these results with those of Ryan *et al.* (11) and to evaluate the effect of molecular cross-sectional area. Cyclohexane was chosen as the solvent based on low oxygen solubility and the results of Smith *et al.* (10) who found uniform monolayer coverage using this solvent.

It should be pointed out that surface areas measured by adsorption from solution should be considered as relative values due to resolution and the assumptions involving adsorbate molecular area and surface coverage which are needed to calculate the surface area. For an excellent discussion of the problems involved in surface area measurements, the reader is referred to a book by Adamson (17).

This study of surface area includes a detailed description of the effect of such variables as speed, load, and abrasive particle size. These quantities have usually been neglected in earlier work.

Experimental

Materials.—Acetic acid and stearic acid tagged with carbon-14 in the carboxyl position were obtained from New England Nuclear Corporation. Carbon-14 tagged N-ethyl-N-perfluoroöctanesulfonylglycine was obtained from Ryan *et al.* (11) who have described its preparation in a previous paper. Eastman Kodak white-label grade stearic acid and fractionally distilled Merck reagent grade glacial acetic acid (b.p. $116.5^\circ \pm 0.2^\circ\text{C}$) were used to dilute the tagged acetic and stearic acids. The specific activity of the adsorbates was determined by counting infinitely thin samples in a windowless Q-gas counter coupled with a Nuclear Chicago Model 186 scaler.

Stock solutions of the acids were prepared using cyclohexane exclusively as the solvent. These solutions (0.2*N* acetic acid, 0.02*N* stearic acid, and saturated glycine derivative) were diluted to obtain the working solutions used in this study.

Matheson technical grade cyclohexane was distilled, run through a column of activated alumina and silica gel, and finally redistilled in a fractionating column. The product did not spread when placed on clean acidic, basic, and neutral water surfaces.

²This compound is the fluorocarbon acid, $\text{C}_8\text{F}_{17}\text{SO}_2\text{N}(\text{C}_2\text{H}_5)\text{CH}_2\text{C}^*\text{OOH}$. In all subsequent references, the compound is referred to as the "glycine derivative."

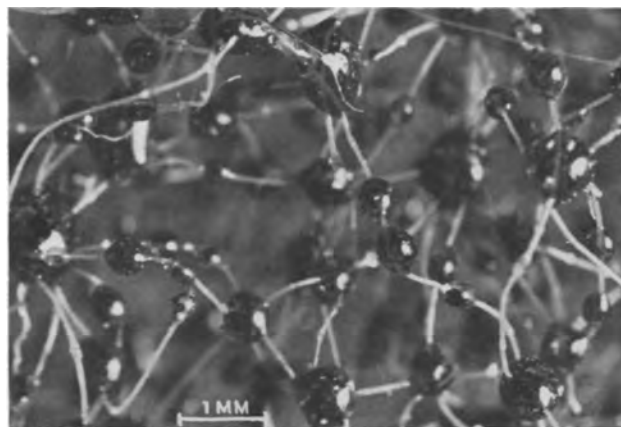


Fig. 1. Photomicrograph of "Scotch-Brite" brand abrasive material showing mineral particles embedded in binder globules which are dispersed throughout a nonwoven nylon web.

The solvent was stored in air-tight bottles containing sodium chunks until used in adsorption runs.

Disks of mechanically polished platinum and fire polished Corning No. 7740 Pyrex glass were used in this study. The steel samples used were cut from low carbon cold-rolled 1020 steel rod obtained from Bethlehem Steel Company. Circular samples, 1 in. in diameter by $\frac{1}{8}$ in. thick, were carefully machined from these bars so as to obtain relatively smooth surfaces. The samples were degreased in benzene and rinsed with acetone prior to the abrasive treatments. Analysis by emission spectroscopy yielded the following minor constituent concentrations in the steel: Mn, 1.0%; Cr, 0.1%; Ni, 0.3%; Si, 0.2%; C, 0.25%; P, 0.01%; and S, 0.02%.

Two distinctly different abrasive materials were used; resinbond coated abrasive disks and a low density abrasive product consisting of a nonwoven web of nylon fibers bonded with a relatively hard rigid binder containing mineral particles. A photomicrograph of this material is shown in Fig. 1. This latter material is sold under the name, "Scotch-Brite" Low Density Abrasive product.³ In the remainder of the paper this product will be referred to as "low density abrasive."

Procedure.—Three surface treatments were used; heat pretreatment at 500°C in a He atmosphere, abrasion in air, and abrasion under solvent. The first method, the heat pretreatment procedure, was the same as that used by Ryan *et al.* (11) of this laboratory. The second method involved holding the sample against the abrading tool in air for 2 min, followed by immersion in adsorbate solution. A delay of less than 1 sec occurred during the transfer from the abrading tool to the adsorbate solution. The third method consisted of abrading up to four samples under solvent for 2 min with constant load conditions followed by rapid transfer to the adsorbate solution so that the surfaces did not dry. Several experiments were carried out with tagged adsorbate in the abrading solution. No detectable differences in measured surface area were observed between these experiments and the ones involving transfer to adsorbate solution.

³Registered trade mark of the Minnesota Mining & Manufacturing Company, St. Paul, Minnesota. (See U.S. Patent 2,958,593 assigned to Minnesota Mining & Manufacturing Company, which describes in detail this type of low-density abrasive product.)

A typical experiment involved pretreatment of the sample by one of these techniques and immersion in the adsorbate solution for a predetermined time. The solutions were kept at $29.0^\circ \pm 0.1^\circ\text{C}$ and were stirred from time to time during the adsorption. Adsorbate concentrations were checked by radiochemical assay and fresh solutions were prepared when these concentrations deviated more than 3% from the desired value. The samples were removed and quickly blotted dry with absorbent tissues leaving only adsorbed acid on the surface. The reliability of this procedure was checked for several samples by immersion in the adsorbate solution, blotting, and counting followed by reimmersion, blotting, and counting. The two count rates agreed to within 0.5% for all samples. Smith and McGill (10) also observed this excellent reproducibility and both their results and this work agree with Ryan *et al.* (11) who used oleophobic surfaces.

The samples were mounted in brass holders which masked all but a 2.45 cm^2 circular area of the surface and were counted in a windowless Q-gas counter long enough to obtain less than 1% standard deviation in the count rate.

Specific surface areas were calculated from the isotherm plateau count rate using the adsorbate cross-sectional area, specific activity of adsorbate, counter efficiency, and the gross sample area (2.45 cm^2). The adsorbate molecular areas have been determined by others from film balance data on liquid substrates. The values used were 20.5 \AA^2 (18, 19) for acetic and stearic acids and 63 \AA^2 for the glycine derivative (11). The accuracy of these values was verified by area measurements on known smooth surfaces. All three adsorbates gave specific surface areas of near unity on polished glass surfaces when these molecular areas were used. The counter geometry factor was 50% as determined by using a standard carbon-14 source. The backscatter factors were checked with a standard source and agreed with values in the literature (20). Autoradiographs for all three adsorbates at various adsorption times were prepared by mounting samples containing activity on Eastman Kodak "No Screen" autoradiograph plates. These were stored in boxes containing drying agent to minimize loss of adsorbed acetic acid due to exchange with atmospheric moisture.

Results

Adsorption rates.—The rates of adsorption as a function of adsorbate concentration for acetic acid on steel abraded with CA-A-180⁴ are shown in Fig. 2. Similar rates were observed for 0.001N stearic acid and $3.0 \times 10^{-6}\text{N}$ glycine derivative. Adsorption rates for Pyrex glass were slightly higher than those for steel and nearly twice this rate was observed for heat pretreated platinum.

⁴ This notation designates the type of abrasive tool used. The first two letters indicate the type of tool; CA means coated abrasive disks, SB means "Scotch-Brite" Brand Low Density abrasive (described in experimental section). The second letter designates the type of abrasive mineral; A means Al_2O_3 and S means SiC. The last symbol refers to the abrasive mineral particle size; VF, Med., and C referring to Very Fine (avg. size 40μ), Medium (avg. size 134μ) and Coarse (avg. size 240μ) grades, respectively; this notation is used for "Scotch-Brite" Brand abrasives only. In the case of coated abrasives, the number refers to the particle size; grade 80 is 244μ , grade 180 is 94μ and grade 320 is 33μ .

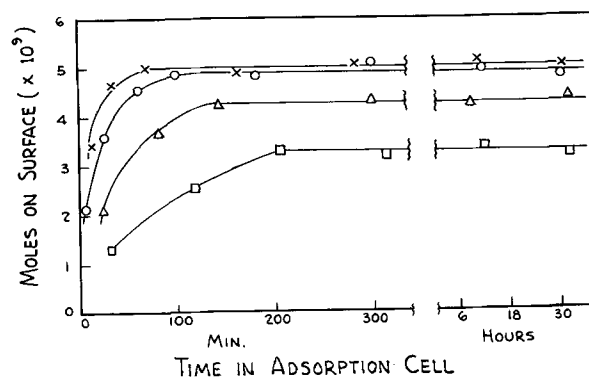


Fig. 2. Adsorption-time curves for acetic acid on abraded cold rolled steel. Samples abraded in air at 59 fps with CA-A-180 tool. Cyclohexane was the solvent, geometric sample area was 2.45 cm^2 and the temperature was 29.0°C . X, 0.004N; O, 0.002N; Δ , 0.001N; \square , 0.00025N.

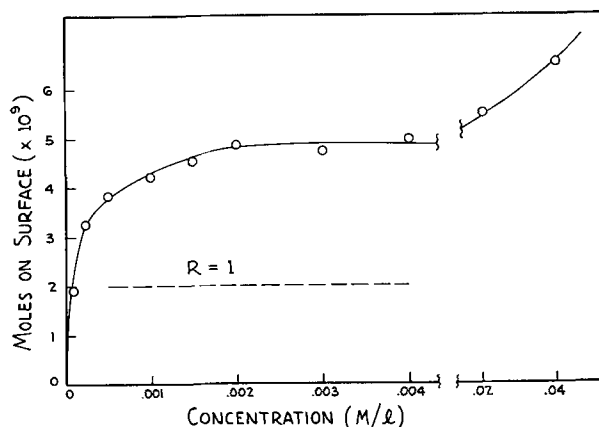


Fig. 3. Adsorption isotherm for acetic acid on abraded cold-rolled steel. Data in Fig. 2, together with additional data, were used to construct this isotherm; temperature 29.0°C .

Isotherm type.—Isotherms were constructed from the rate data by plotting the equilibrium value of adsorption as a function of adsorbate concentration. The isotherms obtained, one of which appears in Fig. 3, are of the variety classified as "Type I" by Brunauer (21) and can be interpreted as indicating formation of a monolayer with no further adsorption until higher adsorbate concentrations are reached. Isotherms of this type were obtained for all three adsorbates on cold rolled steel, platinum, and glass. The increase in adsorption at higher concentrations is probably due to multilayer formation and occurs at lower concentrations (relative to a saturated solution) for acetic acid than for stearic acid or the glycine derivative. This may reflect the fact that acetic acid forms a much thinner monolayer film compared with the long chain stearic acid and glycine derivative molecules, so that long range surface forces (*i.e.*, electrostatic dipole forces, etc.) induce formation of multilayers more easily than would be expected for the long chain adsorbates. The concentration ranges in which plateau adsorption occurred for stearic acid and the glycine derivative were 10^{-4} – 10^{-2}M and 2 – $4 \times 10^{-6}\text{M}$, respectively.

The isotherms were found to fit the Langmuir adsorption equation (22) rather nicely. A typical result appears in Fig. 4. In general, good agreement

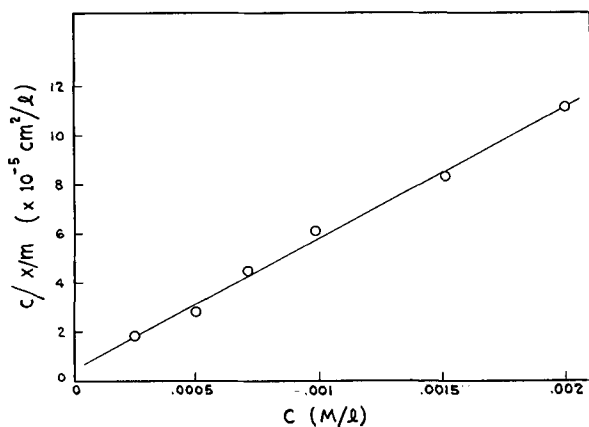


Fig. 4. A typical fit of the isotherm data of Fig. 3 to the Langmuir equation $C/(x/m) = 1/ab + C/a$, where C is adsorbate concentration, x/m is the number of moles of adsorbed acid per unit geometric surface area, a and b are constants. $R_{\text{slope}} = 2.3$; R_{plateau} of isotherm = 2.4.

in true surface area calculated from the slope of the Langmuir plot and from the isotherm plateau value was obtained.

Heat of adsorption.—Heats of adsorption were calculated from the temperature dependence of the parameter “ b ” in the Langmuir equation (23). The results (Table I) reveal excellent agreement between acetic and stearic acids independent of the measured surface roughness. This strongly suggests similar adsorption mechanisms independent of the abrasive treatment for these two acids. The glycine derivative yielded higher values for the heat of adsorption (4 kcal/mole higher). This quite probably reflects the fact that there are two possible adsorption sites for this molecule, the carboxyl group and the tertiary nitrogen atom. All of the values are definitely in the vicinity of that expected for chemisorption.

Reversibility of adsorption.—Data were taken on desorption of acetic acid, stearic acid, and the glycine derivative from steel by pure cyclohexane. Adsorption reversibility was exhibited by all three adsorbates; 60% of the adsorbed acetic acid was removed at infinitely long desorption time, 52% for stearic acid, and 29% for the glycine derivative. Since the heats of adsorption indicated chemisorption for these adsorbates, apparently the chemisorption products have sufficient solubility in cyclohexane to explain the desorption. Bordeaux and Hackerman (12) found partially reversible and partially irreversible adsorption for stearic acid on iron. Further work including solution analysis for metal content is needed to clarify the adsorption

Table I. Heats of adsorption for abraded steel

Adsorbate	SB-A-Med. in air 59 fps, kcal/mole	SB-S-VF under solvent 2.2 fps, kcal/mole
Acetic acid	14.0 (4.1) ^a	14.3 (7.5)
Glycine derivative	17.6 (2.5)	18.0 (4.4)
Stearic acid	14.1 (2.0)	

^a Measured specific surface areas are given in parentheses. Duplicate runs indicated an error of ± 1 kcal/mole.

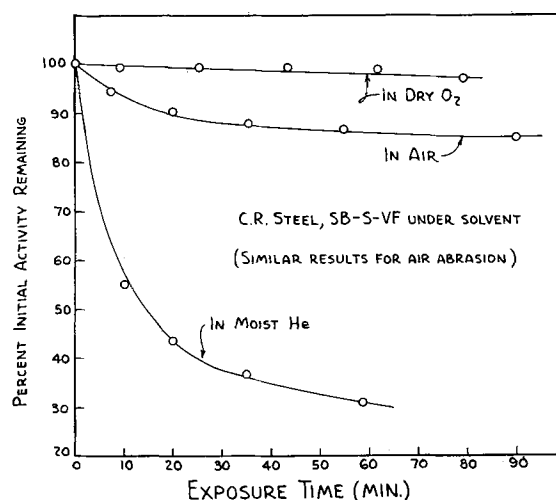


Fig. 5. Graph illustrating the “decay effect” for acetic acid adsorbed on cold-rolled steel. Abraded samples containing adsorbed radioactive acetic acid were counted at various intervals during exposure to three different atmospheres; dry O_2 , ambient air, and moist He.

mechanism. We were unsuccessful in attempts to obtain I. R. spectra of the adsorbed film by using the “Attenuated Total Reflectance” technique (24), due to the minute quantity of adsorbate on the samples.

Decay effect for acetic acid.—The amount of adsorbed acetic acid (presumably as a metal acetate) on a surface was found to decrease on exposure to the atmosphere (Fig. 5), no such loss being observed for stearic acid or the glycine derivative. This decay effect was not observed when the samples were kept in dry helium or in dry O_2 but storage in moist helium accentuated the effect. One likely explanation is that atmospheric moisture hydrolyzes the chemisorption product to yield free acetic acid. The rate of loss in air was slow enough to easily permit sample handling with negligible loss.

Surface area measurements.—Experimental results on surface areas are tabulated in terms of specific surface area (R_s) in Tables II-V. All single values represent the average of two or more runs and reproducibility of $\pm 10\%$ or better. Surface areas of polished platinum and glass surfaces, previously shown to be smooth (11), were measured with acetic acid. Specific surface areas close to unity (0.8-1.1) resulted, supporting the validity of the monolayer assumption and the value used for the acetic acid molecular area.

Table II presents the data on glass. Note that polished glass gives values of R_s near unity for all three adsorbates but that abraded samples give larger values, the increase being accentuated by the use of shorter chain length adsorbates.

Table III presents data on the effect of abrasion in air on the surface area of cold rolled steel. The effect of speed, mineral, abrasive type, and adsorbate are investigated. The following generalizations may be drawn from the data:

1. Decreases in abrasive speed always result in increases in specific surface area (R_s).

Table II. Specific surface areas for polished and abraded Pyrex glass

Pretreatment	Adsorbate		
	Acetic acid	Glycine der.	Stearic acid
Polished, heated in purified He	0.7-1.1 ^b	0.8-1.1	0.9
Abraded ^a under cyclohexane	8.1	4.8	2.3
Abraded ^a in air	7.5	4.6	2.2

^a Abraded samples treated with CA-A-180 2.2 fps for 10 min @ 2 psi load.

^b The range reported represents the results of twelve samples. Single values are averages of two or more runs with a $\pm 10\%$ reproducibility.

Table III. Specific surface area (R_s) on abrasion in air

Tool	Adsorbate		
	Acetic acid	Glycine derivative	Stearic acid
Tool speed: 59 fps			
CA-A-80	2.2	2.0	1.7
CA-A-180	2.4	2.6	2.0
CA-A-320	2.3	2.0	1.5
SB-A-VF	3.8	3.1	1.9
SB-S-VF	5.9	4.5	2.0
Tool speed: 2.2 fps			
CA-A-180	3.5	2.9	2.2
CA-S-180	3.7	3.0	2.0
SB-A-VF	4.7	3.3	1.9
SB-S-VF	6.5	4.9	2.0

Cold rolled steel samples, 1 psi load. Values shown are averages of at least two runs with a $\pm 10\%$ reproducibility.

2. SiC mineral produces larger values of R_s than Al_2O_3 .

3. Low density abrasives produce larger values of R_s than coated abrasives under identical conditions.

4. Increases in measured surface area are accentuated by the use of short chain length adsorbates.

Table IV considers the effect of abrasion in solvent. Generalizations 2-4, noted above, are seen to hold without exception, and another may be added:

5. Abrasion in solvent yields larger values of R_s than abrasion in air.

Table V considers a more detailed investigation of the effect of speed utilizing acetic acid. Generalizations 1-3, noted above, are seen to hold, again without exception.

Experiments on the effect of load showed the results to be insensitive to the effect of load over the range 0.25-4.0 psi. Grit size exerted negligible influence on R_s with coated abrasives, but coarser grits gave larger values with low density abrasives.

Discussion

Topographical model of abraded surfaces.—Profilometer contour traces and optical microscopic examination (resolution near wavelength of visible light) were carried out for all abrasion treatments studied. Specific surface areas estimated from these observations did not exceed 1.7, even for rather

Table IV. Specific surface area (R_s) on abrasion in solvent

Tool	Adsorbate		
	Acetic acid	Glycine derivative	Stearic acid
CA-A-80	4.7	3.4	2.2
CA-S-80	6.2	4.4	2.8
CA-A-180	5.2	3.2	1.8
CA-S-180	5.9	4.6	2.6
CA-A-320	5.2	3.3	1.9
CA-S-320	5.8	4.4	2.7
SB-A-VF	5.4	3.3	2.2
SB-S-VF	7.5	4.4	3.3

Speed: 2.2 fps, load: 1 psi, cold rolled steel samples. Observed error was $\pm 10\%$ or better for two or more runs.

Table V. Effect of speed on specific surface area (R_s)

Tool	Speed			
	0.39 fps	0.88 fps	2.2 fps	59 fps
Abrasion in air				
CA-A-180	4.1	3.8	3.5	2.4
CA-S-180	4.3	3.9	3.7	2.7
SB-A-VF	6.0	5.3	4.7	3.8
Abrasion under cyclohexane				
CA-A-180	5.5	5.4	5.2	
CA-S-180	6.8	6.3	5.9	
SB-S-VF	10.1	9.4	7.5	
SB-A-VF	7.7	6.5	5.4	

Adsorbate, acetic acid; load, 1 psi; cold rolled steel samples. Observed error was $\pm 10\%$ or better for two or more runs.

coarse grained abrasives. Other investigators have also found low values for abraded and sandblasted metal surfaces (25, 26). In view of the data found in this study ($R_s=2-10$) and other work (9, 12) the surfaces must contain numerous micro-irregularities which are unresolved by optical microscopy. It is difficult to observe micro-irregularity relief on the surface of abraded metals by standard electron microscopy techniques, however work is presently underway toward that end.

Plumb (27) has pointed out that large surface areas can be achieved conceptually by superimposing small asperities on large ones ad-infinitum. The authors noticed, however, that the present data suggests an interesting alternate possibility, namely that a significant portion of the surface area of abraded steel is contributed by the presence of microcracks which may be generated during abrasion.

This conclusion is corroborated by the following observations. First, abraded glass, which is known to contain Griffith microcracks (28), yielded high roughness factors (~ 8 for acetic acid) and successively lower values as the adsorbate chain length increased (Table II). The chain length effect can obviously be rationalized in terms of steric hindrance and/or increased tendency for "bridging" small surface fissures with increasing chain length. Griffith cracks on glass have been shown, by indirect means, to be as deep as the deepest grinding pits, yet very narrow at the surface (less than 50Å) and could well yield true areas several times larger

than the geometric area. They are far too small for observation by optical microscopy and, as yet, have defied observation by electron microscopy. When steel was abraded under certain conditions, the measured surface areas and chain length effect were strikingly similar to abraded glass (Table III and IV).

Second, the effect of abrasion conditions on the surface area of steel (and the chain length effect) are nicely explained by the microcrack hypothesis.

These effects may be stated as follows: The specific surface area is increased by lowering the speed of abrasion, by abrading in cyclohexane rather than air, by using low density abrasives rather than coated abrasives or by using SiC rather than Al_2O_3 .

Each of these conditions have the effect of lowering the abrasion temperature. Reduction in abrasive speed at constant load results in lower power consumption and reduced temperature. The presence of a solvent atmosphere will certainly result in reduced temperature. Stock removal and heat generated by coated abrasives is several times greater than for the unique, flexible low density abrasive. The latter product exhibits an abrasive action not unlike sandblasting since the flexible web construction allows freedom of motion of the abrasive grains, resulting in lower stock removal and a more shallow cut.

Retention of a microcrack type of surface topography would be especially sensitive to the surface temperature. These fissures would propagate under the influence of tensile stresses at the immediate side and rear areas of the abrasive grain as it traverses the surface. However, at higher abrasion temperatures, the cracks would be expected to reseal [localized abrasion temperatures may well equal the melting point of steel (29)] either by plastic flow or by augmented oxidation. Thus, there would be more retention of microcracks under conditions of low abrasion temperature, resulting in higher surface area and a more dramatic adsorbate chain length effect.

Abrasion in solvent has the effect of excluding air as well as lowering the temperature and both effects would tend to increase the surface area. An experiment designed to separate these effects is depicted in Fig. 6. Samples were prepared by abrasion in both air and solvent, and subsequently exposed to laboratory air prior to immersion in the adsorbate solution. A rapid decrease in the amount adsorbed was observed during the first 2 min of exposure to air, reaching a constant value which remained stable for at least 24 hr. However, this value is still significantly higher for samples abraded in solvent than for those abraded in air, indicating a permanent increase in surface area for abrasion in solvent. The initial drop is probably due to oxidation since the initial rate is very rapid; this conclusion is confirmed by solvent abrasion and exposure to helium.

The surprising but unmistakable difference between SiC and Al_2O_3 may also be explicable in terms of temperature. Silicon carbide is a much better thermal conductor than aluminum oxide and this

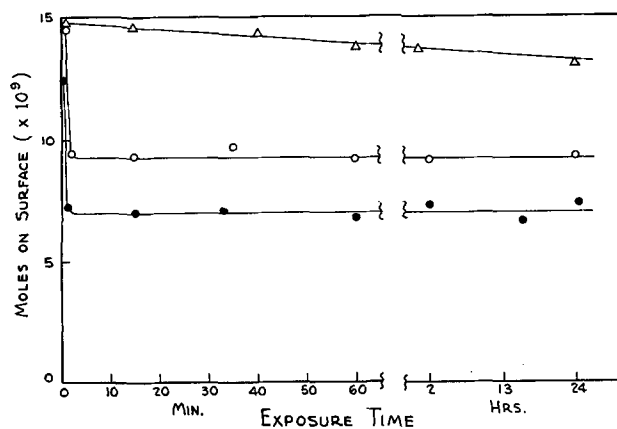


Fig. 6. Effect of exposure of abraded steel surfaces to various atmospheres. Samples abraded with SB-S-VF at 2.2 fps and 1 psi load were exposed to the media labeled on the curves. After various times they were placed in 0.004N tagged acetic acid solutions. When adsorption equilibrium had been attained, they were withdrawn, quickly dried, and counted. Δ , Solvent abraded—exposed in cyclohexane; \circ , solvent abraded—exposed in air; \bullet , air abraded—exposed in air.

would result in higher interface temperatures with Al_2O_3 . The rate of wear of SiC on ferrous metals has been reported to be higher than that obtained with Al_2O_3 (30). This may indicate that a stronger metal-abrasive interaction occurs for SiC than for Al_2O_3 , thus producing more severe tears.

One might not expect formation of such fissures on the surface of materials as ductile as metals. However, the structure and exact physical nature of the "deformed layer" (1) immediately underlying the oxide film on abraded surfaces are not well known. Interestingly enough, Atkinson (2) recently observed tears caused by polishing steel surfaces. The over-all dimensions of these tears are not far from the estimated dimensions of the proposed microcracks.

In order to rationalize the data at varying adsorbate chain length and the specific surface areas obtained, these cracks would have to be of the order of 50-150Å wide and approximately one to several microns in length and/or depth depending on the number of cracks per unit apparent area. If the fissures were, say, 5μ deep and 5μ long, there would have to be about 10^7 cracks/cm² to obtain R_s values in the vicinity of 5. This estimation assumes that the walls of the cracks are smooth and that the surface area contributed by the cracks is superimposed on a surface of specific surface area equal to two. Ernsberger (28) observed approximately 10^5 microcracks/cm² on the surface of unabraded glazing quality plate glass.

Adsorption method.—It should be noted that the surface area measurement used in this work is predicated on the monolayer assumption. For this reason, the authors would like to close by re-examining the evidence which supports this assumption and contradicts other assumptions which might be advanced.

Alternate possibilities might include: (a) multi-molecular layer formation; (b) retention of adsorbate solution in micro-irregularities on the surface; (c) amount of adsorption influenced more by

chemical reactivity of abraded surface (e.g., continuous reaction between adsorbate and metal oxide) than by true surface area.

As mentioned previously, the observed isotherms fit the Langmuir equation and exhibit discrete plateaus with the typical rise at higher concentrations. This would seem to rule out multilayer formation, particularly in view of the measured specific surface areas of unity on surfaces expected to be smooth. The excellent reproducibility of the blotting procedure has been mentioned, and one can also consider how unlikely it would be that such consistent abrasion effects could be measured if retention of liquid on the surface was a factor, the chain length effect would be particularly inexplicable from such a point of view.

Table I shows that the heat of adsorption is similar for all three adsorbates independent of the measured surface area. This discourages arguments based on assumed difference in chemistry of the surface as described in (c) above.

It appears at present that the most consistent argument is that saturated monolayers are formed and that the equilibrium amount adsorbed at "plateau" concentrations is an approximation of the true surface area. Furthermore, the results indeed show that higher resolution is achieved with acetic acid than with commonly used long chain adsorbates.

Autoradiographs prepared for steel samples abraded in air (for which lower R_s values were found) showed uniform adsorbate coverage, independent of adsorption time, within the relatively gross limits of resolution of this method. Samples for which higher surface areas were obtained, revealed concentration of adsorbate along the abrasive scratch pattern. This is consistent with the microcrack postulation since these fissures would be concentrated near the gross abrasive scratches.

The tentative hypothesis of the production of microcracks in grinding metals is sufficient to explain our results to date. This investigation is being extended to attempt direct observation of the postulated microcracks by electron microscopy. Double layer capacity measurements are also planned in an attempt to obtain independent correlation with the present surface area data.

Acknowledgments

The authors are grateful to Dr. John P. Ryan, of the Nuclear Research Group, for helpful discussions and for the use of some of his equipment in this work. They are also indebted to the staff of the Coated Abrasives and Low Density Abrasives Laboratories for their support and many helpful discussions.

Manuscript received Oct. 3, 1963.

Any discussion of this paper will appear in a Discussion Section to be published in the June 1965 JOURNAL.

REFERENCES

1. L. E. Samuels, "The Nature of Mechanically Polished Surfaces," pp. 122-127, American Electroplaters Society, 1959 Technical Proceedings.
2. R. H. Atkinson, *Plating*, **49**, 485 (1962).
3. T. M. Buck and F. S. McKim, *This Journal*, **103**, 593 (1956).
4. J. G. Poor, H. Chessin, and C. L. Alderuccio, *Plating*, **47**, 811 (1960).
5. J. Goddard, H. J. Marker, and H. Wilman, *Proc. Phys. Soc.*, **80**, 771 (1962).
6. R. P. Argawala and H. Wilman, *J. Iron Steel Inst.*, **179**, 124 (1955).
7. L. E. Samuels, *Plating*, **48**, 46 (1961).
8. P. M. Aziz and H. P. Godard, *This Journal*, **104**, 738 (1957).
9. R. C. Plumb and J. E. Lewis, *Int. J. Appl. Rad. and Isot.*, **1**, 33 (1956).
10. H. A. Smith and R. M. McGill, *J. Phys. Chem.*, **61**, 1025 (1957).
11. J. P. Ryan, R. J. Kunz, and J. W. Shepard, *ibid.*, **64**, 525 (1960).
12. J. J. Bordeaux and N. Hackerman, *ibid.*, **61**, 1323 (1957).
13. T. L. O'Connor and H. H. Uhlig, *ibid.*, **61**, 402 (1956).
14. M. C. Kordecki and M. B. Gandy, *Int. J. Appl. Rad. and Isot.*, **12**, 27 (1961).
15. S. H. Maron, E. G. Bobalek, and S. M. Fok, *J. Colloid Sci.*, **11**, 21 (1956).
16. J. W. Swaine, Jr., and R. C. Plumb, *J. Appl. Phys.*, **33**, 2378 (1962).
17. A. W. Adamson, "Physical Chemistry of Surfaces," pp. 425-454, 573-597, Interscience Publishers, Inc., New York (1960).
18. N. K. Adam, "The Physics and Chemistry of Surfaces," p. 24, Oxford University Press, Oxford (1938).
19. M. J. Vold, *J. Colloid Sci.*, **7**, 196 (1952).
20. H. Sobotka and S. Rosenberg, "Monomolecular Layers," pp. 175, 192, American Association for Advancement of Science (1951).
21. S. Brunauer, "The Adsorption of Gases and Vapors," vol. I, p. 166, Princeton University Press, Princeton, N. J. (1945).
22. I. Langmuir, *J. Am. Chem. Soc.*, **40**, 1361 (1918).
23. A. W. Adamson, "Physical Chemistry of Surfaces," p. 574, Interscience Publishers, Inc., New York (1960).
24. J. Fahrenfort, *Spectrochim. Acta*, **17**, 698 (1961).
25. A. G. Eubanks, W. A. Pennington, and D. G. Moore, *This Journal*, **109**, 382 (1962).
26. "The Finishing of Aluminum," G. H. Kissin, Editor, p. 195, Reinhold Publishing Corp., New York (1963).
27. R. C. Plumb, *This Journal*, **105**, 367 (1958).
28. F. M. Ernsberger "Advances in Glass Technology," pp. 511-523, Plenum Press, New York (1962).
29. E. P. Bowden and D. Tabor, "The Friction and Lubrication of Solids," p. 38, Clarendon Press, Oxford (1950).
30. E. J. Duwell and W. J. McDonald, *Wear*, **4**, 372 (1961).

The Corrosion of Uranium, Zirconium, and Some Alloys in Alkaline Solutions

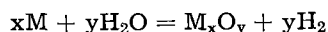
J. S. Llewellyn Leach and A. Y. Nehru

Department of Metallurgy, Imperial College of Science and Technology, London, England

ABSTRACT

The corrosion of uranium, zirconium, and an uranium-zirconium alloy was studied as a function of potential in some alkaline solutions. The behavior of zirconium was found to be in qualitative agreement with results previously obtained in more acid solutions. The interpretation of the data for uranium and the alloy involved assumptions concerning changes in the nature of the protective oxide layer associated with changes in the formation potential. Such differences are not shown on the pH-potential diagram generally accepted for the uranium-water system and a new diagram has been derived. Electron diffraction measurements were employed in an attempt to verify the present interpretation.

The high-temperature aqueous corrosion of uranium and zirconium has been the object of several detailed studies (1-5). The early work ascribed increases in the corrosion rate as well as the physical damage to the accumulation in the metal of the corrosion-product hydrogen formed during the reaction which, in the absence of oxygen, has the general form



Although it appears to be clearly established that hydrogen is active in the corrosion attack, there is some disagreement as to the precise nature of its role.

It was shown recently (1) that the corrosion rate of uranium, uranium-5 weight per cent (w/o) zirconium, and zirconium, cathodically polarized in a slightly acidic solution at temperatures below 100°C, was simply related to the hydrogen activity at the oxide-electrolyte interface over a wide range of potential. The corrosion rate was found to increase with increasing cathodic polarization indicating that the effect of the potential on the kinetics was greater than its effect in decreasing the thermodynamic driving force. This behavior was interpreted as resulting from the dissolution of hydrogen in the oxide leading to changes, within the film, of an electrical nature (causing increased ionic diffusion rates) rather than mechanical failure.

The present paper describes the results of corrosion rate measurements on uranium, uranium-10 w/o zirconium, and zirconium in alkaline solutions, with particular reference to the effect of cathodic polarization. It is shown that, although the behavior at high values of pH may be explained in the same general terms as the corrosion in acidic solution, the relationships with potential (*i.e.*, hydrogen activity) are much more complex for uranium and the alloy.

Experimental

The experimental method which has been described previously (1, 6, 7) permits measurement without removal of the specimen from the test en-

vironment. The technique involves the continuous measurement of the intensity of light reflected from the surface of the corroding specimen. Monochromatic light can be used giving interference effects superimposed on an absorption curve while white light gives absorption effects only.

To derive absolute values of oxide thickness requires a knowledge of either the refractive index or the absorption coefficient of the oxide depending on the method used. Over the range of thickness where both methods can be applied, the ratio of the refractive index to the absorption coefficient appears to be constant (1). As these two parameters depend on different physical properties it seems likely that they are independently constant. However, the exact magnitude of either is open to doubt, and in consequence the amount of oxidation is given in terms of relative oxide thickness rather than in absolute units.

In the present instance the white light method has been used which permits measurements of thicker oxide films due to the greater intensity available.

The test solutions were prepared by dissolving ANALAR reagents in distilled water and were constituted as follows:

pH 9.7 solution	0.2N Na ₂ CO ₃ + 0.2N NaHCO ₃
pH 11.6 solution	0.1N Na ₂ CO ₃
pH 13 solution	0.1N NaOH or 0.1N KOH

Oxygen-free nitrogen was continuously bubbled through the solutions before and during use to remove dissolved oxygen.

The marked corrosion resistance of zirconium necessitated making the measurements at higher temperatures (90°C). Additional features were incorporated in the test cell to provide a temperature control accurate to within $\pm 1^\circ\text{C}$.

Of the materials examined, the high purity zirconium was supplied by A.E.R.E.¹ (impurity analysis: O, 125 ppm; C, 50 ppm; N, 170 ppm; H, 24 ppm). No heat treatment was given before examin-

¹ Atomic Energy Research Establishment, Harwell, England.

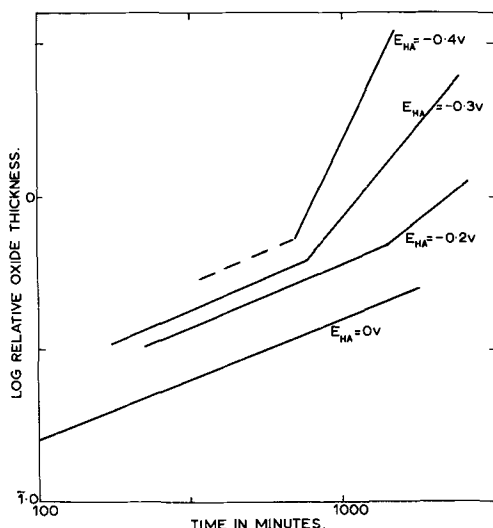


Fig. 1. Corrosion of zirconium, O_2 -reduced 0.1N KOH solution, $90^\circ C$.

ation. The uranium was supplied by A.E.R.E. and certified as 99.95% pure (impurity analysis: O, 40 ppm; N, 10 ppm; C, 30 ppm; Si, 8 ppm; Fe, variable 10-90 ppm; Al, 3 ppm). It was not subjected to a preliminary heat treatment. The alloy, prepared

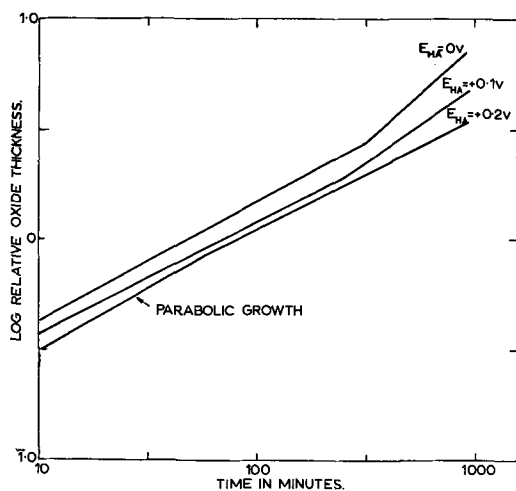


Fig. 2a. Corrosion of uranium, O_2 -reduced 0.2N Na_2CO_3 + 0.2N $NaHCO_3$ solution, room temperature.

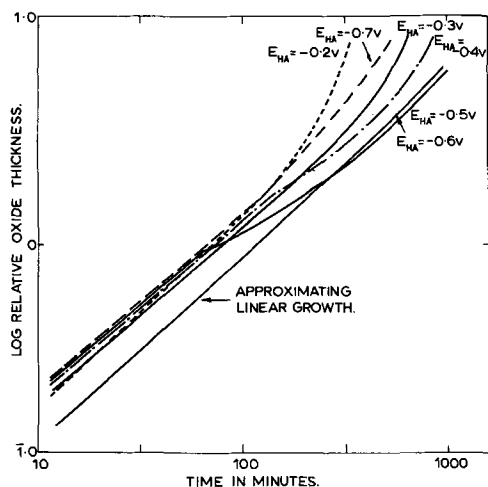


Fig. 2b. Corrosion of uranium, O_2 -reduced 0.2N Na_2CO_3 + 0.2N $NaHCO_3$ solution, room temperature.

from 99.95% pure uranium and low hafnium 99.9% pure zirconium (Van Arkel), was supplied in the arc-cast condition. Before testing, it was homogenized (by annealing in vacuo) at $1000^\circ C$ for seven days and then water-quenched. The methods used for mounting the specimen and preparation of the surface have been described previously (1, 6).

Results

Figure 1 illustrates the corrosion of zirconium in pH 9.7 solution at $90^\circ C$. The method of plotting enables calculation of the kinetics of film growth from the slope of the curves. The chief points of interest are given below:

(I). The corrosion rate increases with increasing cathodic polarization.

(II). A transition from less rapid to more rapid kinetics is easily distinguishable for two values of potential ($E_{HA} = -0.2v, -0.3v$),² and appears to take place at an approximately constant film thickness.

(III). The growth law governing the early stages of corrosion may be expressed by $y^{2.5} = kt$ where, y is the oxide thickness, k is a constant, and t is time.

Figures 2a and 2b show the corrosion behavior of pure uranium in pH 9.7 solution. The following observations are of interest:

(I). At and above $E_{HA} = 0v$ (Fig. 2a), the corrosion rate is either parabolic or parabolic changing to an approximately linear law. The corrosion rate increases with increasing cathodic polarization.

(II). Between $-0.2v$ and $-0.5v$ E_{HA} (Fig. 2b), the corrosion rate initially approximates to a linear law and changes in time to a complex law (accelerating rate). In this potential range, the rate decreases with increasing cathodic polarization.

(III). Below $-0.5v$ E_{HA} (Fig. 2b), there is a tendency for the initial corrosion to approximate more closely to the linear law. The rate increases with increasing cathodic polarization.

The corrosion of uranium-10 w/o zirconium in pH 9.7 solution is illustrated in Fig. 3a and 3b. It can be seen that the results indicate a continuation of the trends established for the pure metal with, however, two significant differences:

(I). The over-all corrosion rate of the alloy is lower.

(II). The changes in the corrosion process of the alloy occur at more negative potentials, i.e., first, between $-0.2v$ and $-0.3v$ E_{HA} (instead of between $0v$ and $-0.2v$ E_{HA}) and, second (apparently) below $-0.7v$ E_{HA} (instead of between $-0.5v$ and $-0.6v$ E_{HA}).

The corrosion behavior of pure uranium in pH 11.6 solution bears a marked resemblance to the behavior in pH 9.7 solution. Figures 4a and 4b show that the changes in corrosion process occur at approximately the same hydrogen activity potentials (E_{HA}), although the over-all corrosion rate is higher in the more alkaline solution.

The corrosion of uranium and the alloy in pH 13 solution has not been investigated in detail. How-

² $E_{HA} = E_H + 0.0591 \text{ pH}$ where E_H is the potential with respect to the normal hydrogen scale.

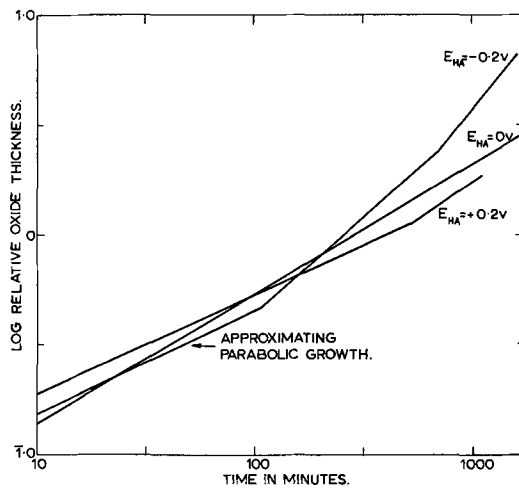


Fig. 3a. Corrosion of uranium-10 w/o zirconium, O₂-reduced 0.2N Na₂CO₃ + 0.2N NaHCO₃ solution, room temperature.

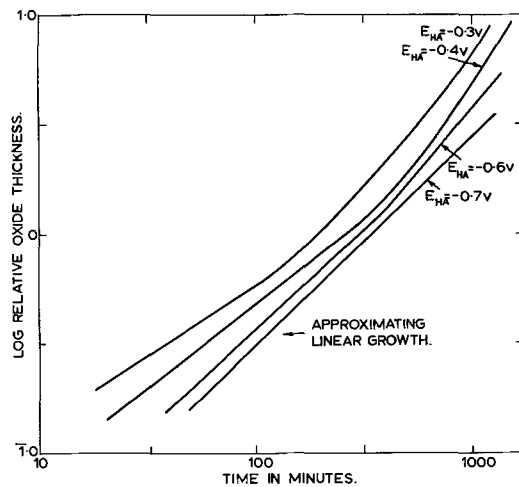


Fig. 3b. Corrosion of uranium-10 w/o zirconium, O₂-reduced 0.2N Na₂CO₃ + 0.2N NaHCO₃ solution, room temperature.

ever, the measurements which were made (Fig. 5) show the same type of complex behavior observed in other alkaline solutions. Again, it is clear that the over-all corrosion rate at any given potential is increased by greater alkalinity and decreased by alloying.

Discussion

A comparison of the present results with our earlier observations in pH 5.4 solutions shows that while the characteristics of the corrosion of zirconium remain virtually unaffected by the change in environment those of uranium and its alloys are significantly altered. The results obtained for the two metal systems will be discussed separately for the sake of simplicity.

Zirconium.—The low corrosion rate of zirconium in the temperature range to which this experimental technique is restricted makes it difficult to cause a change from protective to nonprotective kinetics within a reasonable length of time. Nevertheless, by cathodically polarizing the specimens it has been possible to show at 90°C (at least, in two instances) a kinetic sequence which is normally associated with very much higher temperatures. The increase in corrosion rates which accompanies cathodic polari-

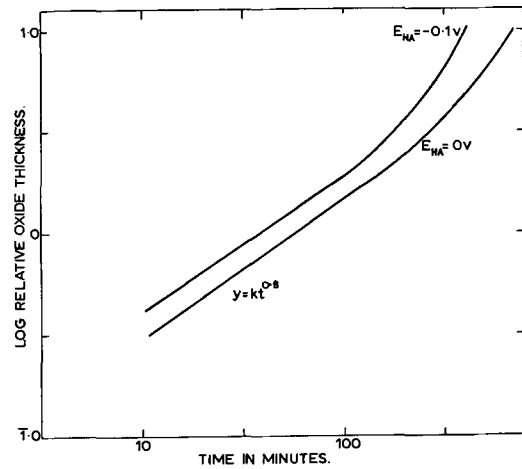


Fig. 4a. Corrosion of uranium, O₂-reduced 0.1N Na₂CO₃ solution, room temperature.

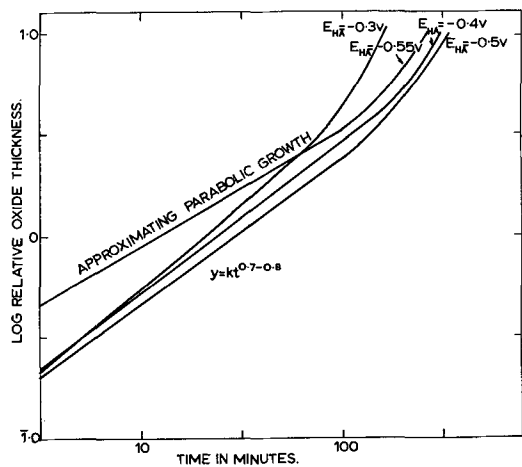


Fig. 4b. Corrosion of uranium, O₂-reduced 0.1N Na₂CO₃ solution, room temperature.

zation may be related to an increase in electronic conductivity of the corrosion-product oxide after the model previously proposed (1) to account for similar results obtained with uranium. If, as is thought to be the case (8), the oxide formed on zirconium is an anion-deficient n-type semiconductor, then the addition of a positively charged ion such as H⁺ is likely to cause the type of effect we have observed.

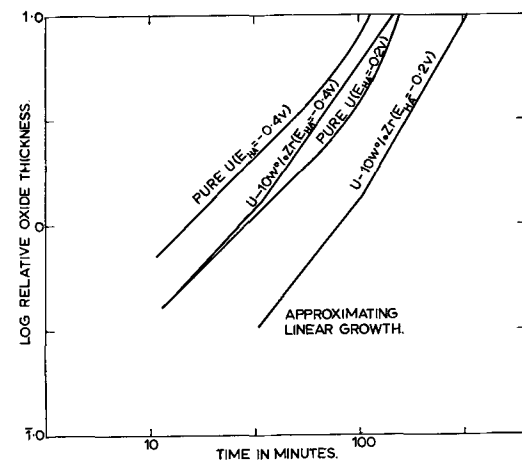


Fig. 5. Corrosion of uranium and uranium-10 w/o zirconium, O₂-reduced 0.1N NaOH solution, room temperature.

It should be pointed out, however, that in the initial stages of corrosion (up to 200 or 300 min), when the oxide film is still very thin, the sensitivity of the equipment was not always sufficient to allow accurate measurement, and in some cases the experimental scatter was considerable. In the series of measurements illustrated in Fig. 1, this scatter was particularly marked for the test carried out at $E_{HA} = -0.4v$, and it was difficult to obtain a reasonable straight-line fit for the period of protective growth. It is interesting, however, that in the cases where two well-defined growth laws can be seen, the transition from one to the other appears to take place at approximately the same film thickness. This observation may be compared with similar observations made by us on uranium in acidic solution from which it was concluded that cathodically induced hydrogen appears to change the corrosion rate without altering the protective thickness of the oxide (1, 9).

The kinetics of oxide growth bear a marked resemblance both in alkaline and acid solutions, although tests in the latter were not carried out for long enough to obtain a transition. The power of 2.5 for the protective growth law in pH 13 solution agrees reasonably with the exponent 2.66 found by us in acid solution, and both values compare favorably with the observations of other workers at higher temperatures (8, 10). The somewhat higher over-all rates in alkaline solution are difficult to explain from the present results. Coriou and co-authors (11) have pointed out from work on Zircaloy that such increases may be only in part due to the effect of pH, and that the oxides formed in alkaline solutions require further study.

Uranium and uranium-10 w/o zirconium.—The difference between the corrosion behavior of uranium in alkaline solutions and in pH 5.4 solution has been clearly established. Briefly, the present results show (i) that oxide growth in alkaline solutions is, in many cases, governed by complex laws, and (ii) that the direct relationship between corrosion rate and applied potential found in acidic environments is no longer apparent. In addition, visual observations of specimens tested in alkaline solutions have shown that the corrosion films are generally duller and less compact than their counterparts in acidic (pH 5.4) solution.

While it seems likely that such differences in behavior and appearance should correspond to a difference, either in structure or in composition, between the corrosion films formed in the two environments, the existence of two distinct species is not indicated by the data presented by Pourbaix and co-workers (2). Figure 6 shows the pH-potential diagram derived by these investigators, from thermodynamic data, for the uranium-water system. This figure has been recalculated from the original on the basis of hydrogen activity potentials to conform to the method adopted in this paper for the plotting of results. Here, the sole species considered stable in the pH-potential range of interest (pH 5.4 to pH 13 and $+0.2v$ to $-0.7v E_{HA}$) is given as UO_2 . Nevertheless, since the diagram has been

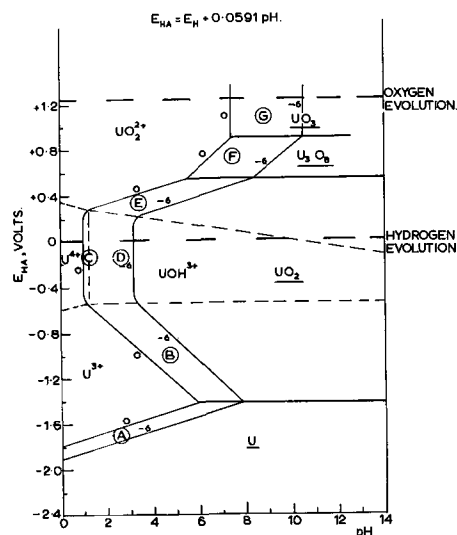


Fig. 6. pH-potential diagram for U-H₂O system (after Pourbaix)

derived for equilibrium conditions, it is possible that during processes of high irreversibility such as are encountered during the corrosion of uranium, the configuration may be significantly altered. As one example of this type of effect, it is worth noting that, although FeO is thermodynamically unstable with respect to Fe and Fe₃O₄, below 570°C, a layer of FeO has been found during the oxidation of iron at temperatures as low as 400°C (12). Of more specific interest to the present work is an observation made in the early stages of this investigation that rapid film growth occurs on uranium in very acid solutions (0.1N HCl, pH 1) where according to the thermodynamic data no solid phase should be stable.

There is, moreover, some evidence which suggests that the data from which the Pourbaix diagram for uranium-water is derived are incomplete and might not permit a comprehensive representation of the system. First, both Waber (13) and Katz and Rabinowitch (14) have observed and commented on the possible formation of the hydroxide $U(OH)_4$ instead of UO_2 in aqueous corrosion films on uranium. Pourbaix, himself, is not emphatic in denying the occurrence of this phase but prefers the alternative choice for his diagram. Second, some values for the free energy of formation used in calculating the Pourbaix diagram are 3-4% lower than values reported by Latimer (15). This is a noticeable disagreement in view of the fact that a relatively small difference in free energy can have considerable effect on the potential at which a given species is stable. Finally, Willardson, Moody, and Goering (16) have shown that the oxidation of UO_2 to higher oxides is accompanied by changes in type of semiconductivity caused by deviations from stoichiometry, and have identified two stable oxide phases U_4O_9 and U_3O_7 of O/U ratio intermediate to UO_2 and U_3O_8 . Capacity measurements on uranium electrodes in aqueous solutions have also been interpreted (17, 18) as showing the formation of higher oxides during corrosion, although it was difficult from the results to ascertain changes in semiconductivity. From the present point of view, the omission

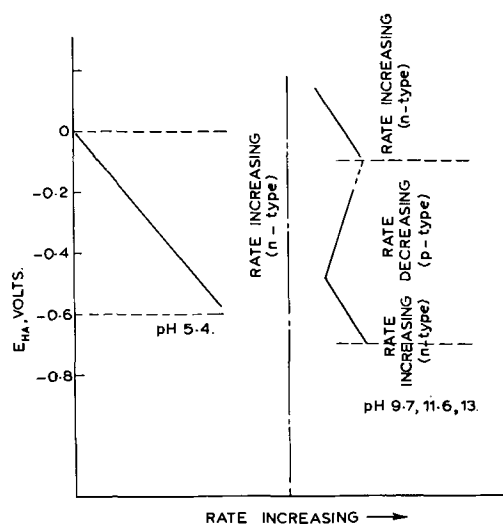


Fig. 7. Over-all corrosion rate of uranium as a function of pH and potential.

of the intermediate oxides from the diagram is serious since measurements in this investigation have been conducted within the potential range in which these species are most likely to be stable.

In view of these shortcomings and others which may arise when the conventional pH-potential diagram is applied to nonequilibrium conditions, it is not unreasonable to reconstruct relevant portions to fit the present results. It should be stressed, however, that the resulting diagram may be more in the nature of a metastable equilibrium diagram rather than a substitute for that proposed by Pourbaix (2) and his colleagues.

Figure 7 illustrates the differences between the corrosion trends of uranium in pH 5.4 solution and in alkaline solutions. A hypothetical demarcation has been shown at pH 7. The rate in pH 5.4 solution increases continuously with decreasing potential, whereas two transitions are found in alkaline solutions.

As pointed out earlier in the discussion, an increase in corrosion rate with increasing cathodic polarization suggests that the oxide forming is an n-type semiconductor. Conversely, a decrease in rate under similar circumstances would indicate the formation of a p-type oxide. Hence, the corrosion behavior of uranium in alkaline solutions may be ascribed to changes in the semiconductivity of the corrosion-product from n- to p- to n-type as the potential is decreased. It should be stressed, however, that the absence of parabolic growth at certain potentials in high pH solutions does not necessarily imply the absence of a diffusion process. Instead, as the over-all corrosion rate in these solutions is considerably higher than in pH 5.4 solution, it is believed that the period during which the diffusion-controlling film is growing is too short to allow detection by the measuring instrument. The over-all corrosion rate is defined as the amount of corrosion occurring in a given length of time and the use of this parameter becomes necessary in instances where it is difficult to define the corrosion rate in terms of the constants of the growth laws.

Changes in conductivity mechanism of the type described above could arise from the formation of nonstoichiometric phases during corrosion in alkaline solutions. Within the domain of stability of a given species, the oxygen-rich region (positive, in terms of potential) will tend to be p-type while oxygen deficiency will result in n-type semiconductivity (e.g., $UO_{2+x} \sim$ p-type, $U_4O_{9-x} \sim$ n-type, $U_3O_{8+x} \sim$ p-type). Note, that since the exact potentials at which the changes in mechanism occur are not known from the results, a division has been made in Fig. 7 at the arbitrarily chosen values $-0.1v E_{HA}$ and $-0.7v E_{HA}$. These two potentials, hence, bound the domain of stability of one species while immediately below lies the oxygen-rich region of a stable compound of lesser O/U ratio and immediately above is the oxygen-deficient region of the next phase. The fact that the transitions in the corrosion process of uranium-10 w/o zirconium occur at more negative potentials can be ascribed to the difference between the free energies of formation of pure oxides and those of the mixed oxides which result from the corrosion of the alloy.

Figure 8 shows the pH potential diagram constructed to fit the present results. The major differences between this figure and the diagram due to Pourbaix and co-workers are listed below:

1. The intermediate oxide phases U_4O_9 and U_3O_7 have been shown as occurring within the potential boundaries $-0.1v E_{HA}$ and $-0.7v E_{HA}$ and $+0.45v E_{HA}$ and $-0.1v E_{HA}$, respectively, and the hydroxide $U(OH)_4$ has been chosen in preference to UO_2 as the lowest oxidized phase of uranium. The complete sequence of solid phases is, therefore, U- $U(OH)_4$ - U_4O_9 - U_3O_7 - U_3O_8 - UO_3 . A consideration of the free energies of formation showed that the values determined theoretically from this particular sequence gave the best approximations to the available data, and differed by only 3-4% from those quoted by Pourbaix and co-workers. Values used by Pourbaix are compared with the recalculated values in Table I.

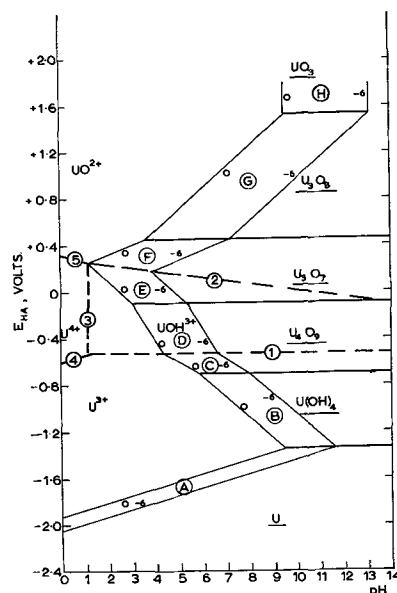


Fig. 8. pH-potential diagram for U-H₂O system (modified version)

Table I. Free energy of formation of solid species

	Pourbaix values, kcal/g mole	Calculated values, kcal/g mole
U(OH) ₄	-351.6	-351.6
U ₄ O ₉		-1041.9
U ₃ O ₇		-796.7
U ₃ O ₈	-804	-833
UO ₃	-273	-273

Table II. Free energy of formation of ionic species

	Pourbaix values, kcal/g mole	Calculated values, kcal/g mole
U ³⁺	-124.4	-131.1
U ⁴⁺	-138.4	-145.1
UOH ³⁺	-193.5	-200.2
UO ²⁺	-236.4	-243.1

2. The ionic activity lines of the Pourbaix diagram (marked A to G in Fig. 6) have been shifted 2 pH units to the right. This permits the differences between the corrosion behavior of uranium in acid and alkaline solutions to be ascribed to the existence of different species in the two environments. The free energies of formation for the ionic species recalculated after the shift are again found to differ only slightly from the values given by Pourbaix. Table II shows the values adopted by Pourbaix compared with the new ones used in Fig. 8.

Electron diffraction.—An attempt was made to verify the theoretical pH-potential diagram by electron diffraction measurements. Specimens of uranium were corroded at several values of potential between +0.8v E_{HA} and -1v E_{HA} in both pH 5.4 solution and in alkaline solutions, washed in ether and benzene, and transferred to a Hitachi HU 11 electron microscope which incorporated a special attachment for glancing angle diffraction. The diffraction chamber was provided with a vacuum seal which isolated it from the rest of the microscope and enabled the specimens to be under high vacuum within about 5 min of removal from the corrosion cell. This prevented serious atmospheric oxidation of the specimen before it could be photographed. Best results were obtained with a 50 kv electron beam.

The diffraction patterns were calibrated against a graphite d_{110} ring obtained by transmission using identical microscope settings. The results are summarized in Fig. 9 (the reference numbers indicate the sources where the lattice parameters of the relevant oxides were found).

The patterns obtained from specimens corroded in pH 5.4 solution were simple to identify, and showed that the corrosion product formed at all values of potential was UO₂. Corrosion in alkaline solutions gave some diffuse patterns with wide rings and these were, consequently, difficult to measure and interpret. The pattern for U₃O₇, however, was clearly identifiable as were several U₃O₈ lines in the oxide formed at +0.5v E_{HA} and +0.8v E_{HA} . The pattern obtained from the test at

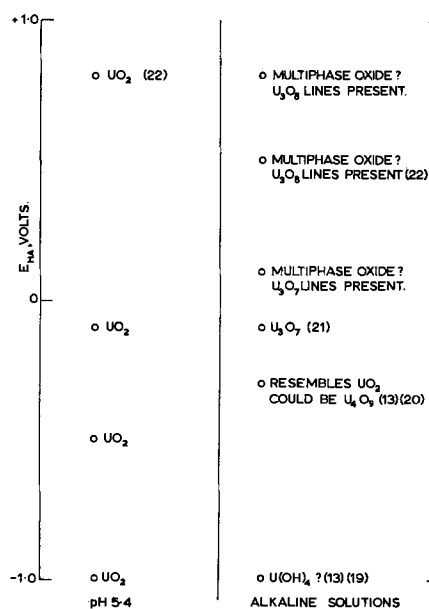


Fig. 9. Identification of uranium oxides by electron diffraction

-1v E_{HA} closely resembled that of UO₂, but the rings were very diffuse. On the basis of x-ray work, this is believed by some workers (13, 19) to indicate the presence of the hydroxide U(OH)₄.

Conclusions

It is established from the results that the corrosion of uranium and the uranium-zirconium alloy in alkaline solutions differs significantly from the corrosion in pH 5.4 solution, and this difference in behavior is ascribed to the formation of oxides other than UO₂ in solutions of high pH. The corrosion rate of zirconium in alkaline solutions is somewhat higher than in pH 5.4 but the mechanism appears to remain virtually unaltered. Zirconium ions are known to display a unique valency and oxides higher than ZrO₂ do not normally exist.

Electron diffraction measurements while failing to establish accurately the stability ranges of the various oxide phases shown in the newly constructed pH-potential diagram for uranium gave supporting evidence for their existence. The electron diffraction results agreed with the corrosion rate results to the extent of indicating clearly the marked difference between the corrosion products in the two types of environment.

Although the reversals in the corrosion rate of uranium and the alloy associated with cathodic polarization in alkaline solutions require a different and more complex explanation than does the simple behavior found in acidic solutions, the proposed mechanism of oxide growth remains the same. These results lend further support to the suggestion that a relationship exists between the electronic conductivity of the oxide, its hydrogen content, and the corrosion rate.

Acknowledgments

The authors wish to acknowledge the financial support of the United Kingdom Atomic Energy Authority during the investigation, and their indebted-

edness to Professor J. G. Ball for encouragement and for the provision of laboratory accommodation.

Manuscript received Dec. 3, 1963.

Any discussion of this paper will appear in a Discussion Section to be published in the June 1965 JOURNAL.

REFERENCES

1. J. S. Llewelyn Leach and A. Y. Nehru, "Corrosion of Reactor Materials," Vol. I, p. 58, I.A.E.A., Vienna (1962).
2. E. Deltombe, N. de Zoubov, and M. Pourbaix, Cebelcor Rapport Technique No. 31 (1956).
3. M. W. Burkart, U.S.A.E.C. Rept., Westinghouse Electric Corp., WAPD-127, Part III (1956).
4. J. E. Draley and W. E. Ruther, *This Journal*, **104**, 329 (1957).
5. D. E. Thomas and S. Kass, *ibid.*, **104**, 261 (1957).
6. A. Y. Nehru, Ph.D. Thesis, London University, 1963.
7. A. E. Stebbens and L. L. Shrier, *This Journal*, **108**, 30 (1961).
8. H. A. Porte, J. G. Schnizlein, R. C. Vogel, and D. F. Fischer, U.S.A.E.C. Rept. Argonne National Laboratory, ANL-6046 (1959).
9. J. S. Llewelyn Leach, "Properties of Reactor Materials and the Effects of Radiation Damage," p. 383, Butterworths, London (1962).
10. B. Lustman and F. Kerze, "Metallurgy of Zirconium," McGraw-Hill Book Co., New York (1955).
11. H. Coriou, L. Grall, J. Meunier, M. Perlas, and H. Willermoz, "Corrosion of Reactor Materials," Vol. II, p. 193, I.A.E.A., Vienna (1962).
12. E. A. Gulbransen and R. Ruka, *J. Metals*, Am. Inst. Mining & Met. Engr., **188**, 1500 (1950).
13. J. T. Waber, "Aqueous Corrosion of Uranium and its Alloys," Conf. on Aqueous Corrosion of Reactor Materials, Brussels (1959).
14. J. J. Katz and E. Rabinowitch, "The Chemistry of Uranium," Nat. Nucl. Eng. Series, Div. VIII-5, McGraw-Hill Book Co., New York (1951).
15. W. M. Latimer, "Oxidation Potentials," Prentice-Hall Inc., New York (1952).
16. R. K. Willardson, J. W. Moody, and H. L. Goering, U.S.A.E.C. Rept., Battelle Memorial Institute, BMI-1135 (1956).
17. J. S. Llewelyn Leach, *J. Inst. Met.*, **88**, 24 (1959).
18. H. S. Isaacs and J. S. Llewelyn Leach, *This Journal*, **110**, 680 (1963).
19. J. B. Schroeder, D. A. Vaughan, and C. M. Schwartz, *ibid.*, **106**, 486 (1959).
20. A. F. Wells, "Structural Inorganic Chemistry," Third ed., p. 966, Clarendon Press, Oxford (1962).
21. H. R. Hoekstra, A. Santoro, and S. Siegel, *J. Inorganic and Nuclear Chem.*, **18**, 166 (1961).
22. R. K. Hart, *Trans. Faraday Soc.*, **49**, 299 (1953).

The Effect of Heat-Treatment on the Corrosion and Hydrogen Pickup Behavior of a Zr-Sn-Nb Alloy in High Temperature Water and Steam

D. L. Douglass

Vallecitos Atomic Laboratory, General Electric Company, Pleasanton, California

and H. A. Fisch

Lamp Metals and Components Department, General Electric Company, Cleveland, Ohio

ABSTRACT

Heat-treatment was shown to increase the rate of corrosion of Zr-2Sn-2Nb over that of the annealed condition, but the rate of hydrogen pickup as a function of total corrosion was found to be relatively insensitive to heat treatment. The effects of heat treatment have been analyzed in terms of changes in: (i) alloy constitution, (ii) composition of microconstituents, and (iii) the metal texture and oxide orientation. Stereoscopic examination of oxide-film surfaces by electron microscopy revealed cracking both at grain boundaries and at interfaces between phases. Extensive and abrupt changes in film topography, which also were sites of film cracking, were observed.

A 2 atomic per cent (a/o) tin-2 a/o niobium alloy of zirconium in the annealed condition has been shown (1) to have mechanical properties superior to those of Zircaloy-2 and a corrosion resistance only slightly inferior to that of Zircaloy-2. Additional corrosion studies were warranted by this excellent combination of properties. The alloy is susceptible to heat-treatment with further improvement of its mechanical properties. This paper presents the results of a program to evaluate the corrosion behavior and hydrogen absorption of the annealed alloy and to determine the effects of heat-treatment on corrosion resistance.

Experimental Procedure

Sample preparation.—Two, 10-lb ingots were prepared by consumable arc melting in vacuum in a copper-cooled crucible. Ingots were remelted three times to obtain homogeneity. Ingot A (see Table I) was used to provide specimens for the investigation of the annealed alloy. Ingot B provided specimens for the heat-treatment studies.

Ingot A was jacketed with copper and Ingot B with mild steel before being extruded at 800°C. The extrusion reduced the ingots from the original 3-in. diameter to ¾-in. rod. These extruded rods were cold-rolled into 65-mil strips (3 passes with inter-

Table I. Chemical analysis of Zr-2Sn-2Nb ingots

	Ingot A		Ingot B	
	Weight per cent (w/o)	a/o	w/o	a/o
Tin	2.58	1.97	2.53	1.94
Niobium	1.97	1.93	1.94	1.90
Hydrogen	0.0022	0.20	0.0040	0.36
Nitrogen	0.0049	0.032	0.0110	0.072
Oxygen	0.1560	0.89	0.1000	0.57
Carbon	—	—	0.030	0.23
Zirconium	Balance		Balance	

mediate anneals) and cut into blanks which were vacuum-annealed at 775°C for ½ hr and fast-cooled (80°C/min). Corrosion coupons approximately 1x½-in. were machined from these blanks so that each specimen had four machined edges and two as-rolled surfaces.

Corrosion testing.—The coupons were degreased, pickled in HNO₃-HF-H₂O, and corrosion tested in water at 316° and 360°C and in steam at 400°, 440°, and 482°C, in static autoclaves of 347 stainless operated at 1500 psi. Deionized deoxygenated water was used in all tests. Twenty coupons were placed in an autoclave for each temperature condition. At the end of each incremental exposure, one coupon was removed and cut into six pieces. Hydrogen analysis by vacuum fusion and metallographic and x-ray examinations for hydride precipitation were performed on separate pieces of the coupon. The remaining coupons were left in the autoclave for longer exposures.

Heat treatment.—The blanks from Ingot B were heat-treated by sealing them, along with zirconium turnings, in quartz capsules under 1/3 atm of argon. Gettering of the atmosphere was performed before heat treatment by heating the turnings at one end of the capsule for several minutes. Quenching was performed by breaking the capsule under water after the desired time at temperature. Coupons were machined from these blanks and corrosion tested in 360°C water and 400°C steam.

X-ray diffraction.—The oxide films on the coupons from Ingot B were examined in a high-angle diffractometer with filtered copper radiation. A sample spinner was employed to rotate the sample about an axis perpendicular to the rolled surface of the strip.

Electron microscopy.—Oxide film surfaces were examined by electron microscopy using two-stage

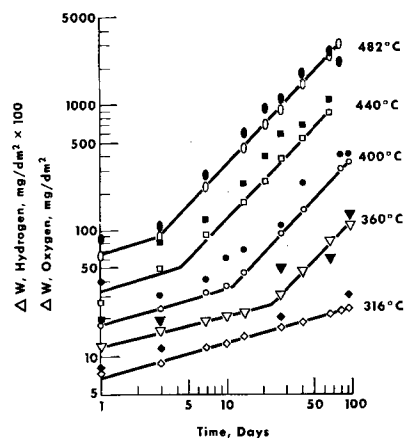


Fig. 1. Corrosion and hydrogen pickup kinetics of annealed samples. Open symbols, oxygen; closed symbols, hydrogen.

replication. Replicas were prepared by pressing replicating tape firmly against the surface, stripping off the tape, shadowing the tape with chromium at an oblique angle and finally shadowing with carbon normal to the surface of the tape. The carbon surface was coated with molten wax to prevent breakup of the replica, and the replicating tape was dissolved in acetone. The wax was dissolved subsequently, and the replicas were washed thoroughly. Stereo pairs were taken of all micrographs and subsequently studied with the aid of a stereoscope to determine the exact topographical nature of the oxide surfaces.

Results

Corrosion and Hydrogen Absorption of Annealed Samples

The effect of temperature on corrosion weight gain and associated hydrogen absorption for annealed samples is shown in Table II and in Fig. 1. As is characteristic for many zirconium-base alloys, the corrosion weight gain behavior follows a quasi-cubic rate law in the initial pretransition region, and a roughly linear rate in the post-transition region. On a log-log graph the transition point is arbitrarily taken to be the intersection of the lines representing the two rate law periods. The actual transition is gradual rather than abrupt. The slopes of the pretransition curves varied between 0.26 and 0.30 with no apparent relationship to exposure temperature. Posttransition slopes ranged between 1.01 and 1.08 and increased with increasing exposure temperature. These slopes are the exponents, n , in

Table II. Effect of temperature on corrosion and hydrogen pickup behavior on annealed alloy (70-Day exposure data)

Temp, °C	Medium	Oxygen weight gain, mg/dm ²	ppm, H ₂	Hydrogen pickup Per cent of theoretical	Weight gain, mg/dm ²	H:O weight gain ratio
316	Water	21.5	0	0	0	0
360	Water	81.0	16	6.3	0.6	0.0074
400*	Steam	(302)*	(94)*	(10.3)*	(4.0)*	(0.013)*
440	Steam	879	260	9.7	11	0.011
482	Steam	2585	601	27	8.4	0.010

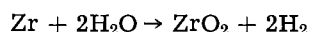
* 84-Day data.

Table III. Summary of rate law exponents

Sample history	Exposure temp, °C	Exponent from: $\Delta W = kt^n$	
		Pretransition	Posttransition
Annealed 775°C ¼ hr	316	0.26	—
Annealed 775°C ¼ hr	360	0.28	1.01
Annealed 775°C ¼ hr	400	0.30	1.02
Annealed 775°C ¼ hr	442	0.29	1.08
Annealed 775°C ¼ hr	482	0.29	1.08
Annealed 800°C 24 hr	360	0.25	1.00
Annealed 800°C 24 hr	400	—	1.06
Annealed 950°C 24 hr, furnace-cooled	360	—	0.73
Annealed 950°C 24 hr, furnace-cooled	400	—	0.74
Annealed 950°C 24 hr, water-quenched	360	—	0.78
Annealed 950°C 24 hr, water-quenched	400	—	0.83
Annealed 950°C 24 hr, water-quenched, tempered 24 hr at 600°C	360	—	0.84
Annealed 950°C 24 hr, water-quenched, tempered 24 hr at 600°C	400	—	1.09
Hot-rolled then cold-rolled 30%	360	0.26	0.94
Hot-rolled then cold-rolled 30%	400	—	0.89

the equation $\Delta W = kt^n$, in which ΔW is the weight gain in mg/dm² and t is the exposure time in days. Individual values for these slopes are given in Table III.

During the corrosion reaction, hydrogen is liberated according to the following reaction



A portion of this hydrogen is taken up by the metal, the remainder is released to the environment. The hydrogen pickup of the annealed alloy is shown in Table II and Fig. 1, 2, and 3. Figure 1 shows that hydrogen absorption kinetics closely follow the

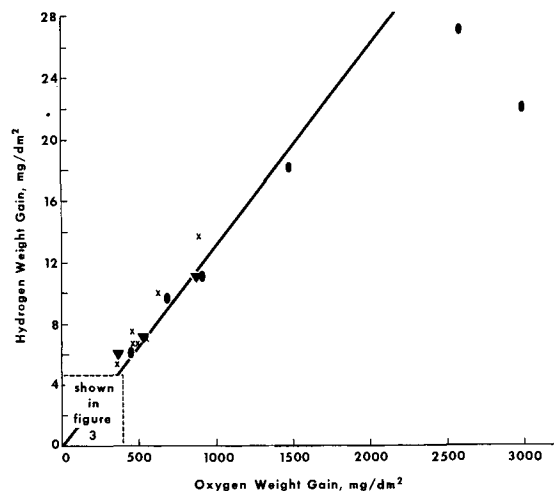


Fig. 2. Relationship between absorbed hydrogen and oxygen weight gains.

	Test temperature, °C				
	316	360	400	440	482
Annealed alloys posttransition	●	▲	■	▼	open oblong
Heat-treated alloys		+	×		solid oblong

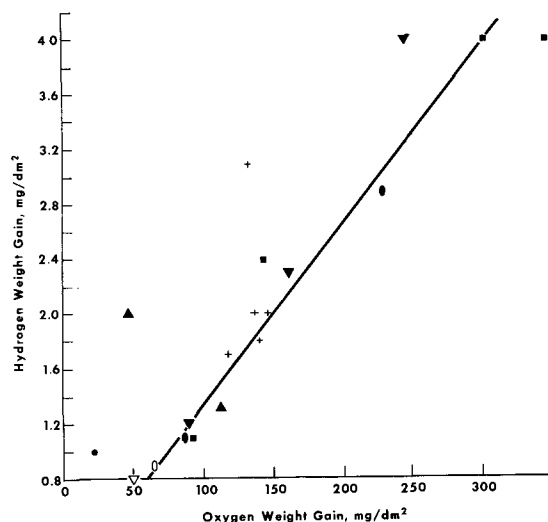


Fig. 3 Relationship between absorbed hydrogen and oxygen weight gains.

	Test temperature, °C				
	316	360	400	440	482
Annealed alloys					
Pretransition				▽	open oblong
Posttransition	●	▲	■	▼	solid oblong
Heat-treated alloys		+			

weight change kinetics. The absorbed hydrogen values in parts per million given in Table II are the differences between initial and final values. Since the hydrogen analyses were only accurate to ± 5 ppm, specimens with hydrogen absorption values below 5 ppm may be considered as having absorbed no hydrogen.

Figures 2 and 3 show that the ratio of hydrogen weight gain to oxygen weight gain of 0.013 is nearly constant over the temperature range investigated and that there is no difference between pickup in the pretransition and posttransition regions of the weight gain curve. This is in contrast to the observations of Cox (2) who found, for Zircaloy-2 and other zirconium alloys, that the curve for hydrogen absorption could be divided into three regions each having different ratios.

Effect of Heat-Treatment on Corrosion Resistance and Hydrogen Absorption

Total weight gain curves for heat-treated coupons exposed in 360°C water and 400°C steam are given in Fig. 4 and 5. All heat-treated coupons, with one exception, produced comparable corrosion weight gains after 100 days in 360°C water. A specimen which had been water-quenched from 950°C exhibited weight gains two or three times greater than the others. Tempering of the quenched structure for 100 hr at 500°, 600°, or 700°C resulted in weight gains comparable to those of both the fully annealed and cold-worked samples. The same general behavior was observed in 400°C steam. The as-quenched sample again showed greater weight gains than the others.

The increase in weight gain with time of the quenched samples did not follow the quasi-cubic to linear transition behavior observed with the an-

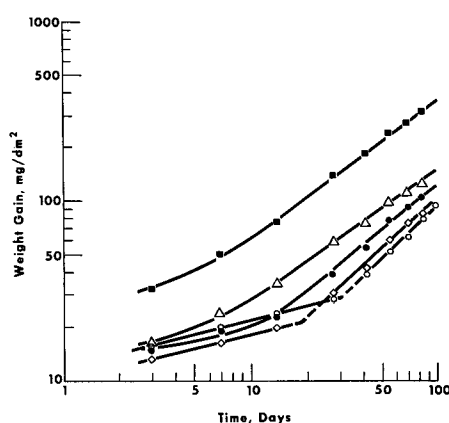


Fig. 4. Effect of heat treatment on 360°C water corrosion. ■, 950°C 24 hr, water quenched; △, 950°C 24 hr, furnace-cooled; ◇, hot rolled and cold rolled (~30%); ●, 950°C 24 hr, water-quenched, tempered at 600°C 100 hr; ○, annealed at 800°C 24 hr, furnace cooled.

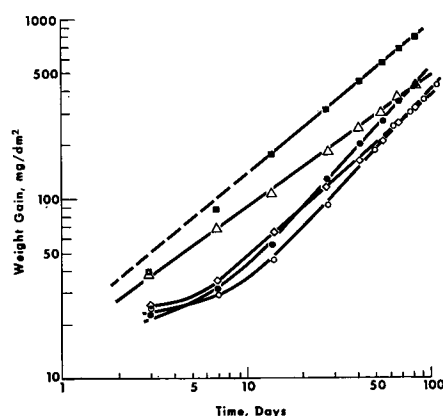


Fig. 5. Effect of heat treatment on 400°C steam corrosion. ■, 950°C 24 hr, water-quenched; △, 950°C 24 hr, furnace-cooled; ◇, hot rolled and cold rolled (~30%); ●, 950°C 24 hr, water-quenched, tempered at 600°C 100 hr; ○, annealed at 800°C 24 hr, furnace-cooled.

nealed specimens. In 360°C water, the specimen quenched from 950°C showed a continuously increasing slope which reached a limiting value of 0.78. This value, while not corresponding to any of the exponents for known rate laws, may be taken as the equivalent of the posttransition linear rate observed for the annealed specimens. Both the cold-

rolled and 800°C-annealed samples showed an initial quartic, rather than cubic, time relationship followed by a transition to a linear time relationship.

The same general behavior was observed in 400°C steam, but the initial slopes could not be determined. For the cold-rolled and 800°C-annealed specimens the slopes reached limiting values of 0.89 and 1.06, respectively. The samples which were furnace-cooled from 950°C showed a corrosion rate slope of 0.74 and the samples water-quenched from 950°C showed a corrosion rate slope of 0.83. These data are summarized in Table III.

The coupons were analyzed for hydrogen pickup after corrosion tests were completed. These results are given in Table IV. The per cent of theoretically available hydrogen which was absorbed by the heat-treated samples and the ratio of absorbed hydrogen to oxygen were generally higher than those for the fully annealed alloy. The median ratio for the heat-treated alloys, 0.015, was higher by a statistically significant amount than the value 0.013 observed for the annealed alloys.

Oxide Film Orientation

Monoclinic ZrO₂ films were observed on all samples investigated in this work. Although the film structures were identical on all alloys, differences in relative intensities of various ZrO₂ reflections are evidence of different film textures. Diffraction patterns of several samples are given in Table V, for both films and substrates.

According to Chirigos and Thomas (3) the monoclinic oxide on Zircaloy-2 is oriented with the (111) planes parallel with the (0001) planes of the metal; because of the similarity of Zircaloy-2 and Zr-2Sn-2Nb, a similar relationship of oxide-to-metal is to be expected for the latter alloy. The (111) oxide reflections on the annealed and cold-rolled samples were the strongest as shown in Table V. The strongest reflection from the substrate was for the (0002) planes (second order basal plane reflection). Evidently the oxide and metal both have the orientations observed by Chirigos and Thomas. However, the water-quenched samples showed weak basal

Table IV. Effect of heat treatment on corrosion and hydrogen pickup behavior
(98 Day exposure data)

Heat-treatment	Corrosion results			Hydrogen pickup		
	Corrosion conditions	Oxygen weight gain, mg/dm ²	ppm H ₂	Weight gain, mg/dm ²	Per cent of theoretical	H:O Ratio
Annealed 800°C, F.C. ^(a)	360°C water	112	33	1.3	9.6	0.012
Annealed 800°C F.C.	400°C steam	346	103	4.0	9.8	0.011
Betatized 950°C, F.C.	360°C water	139	40	1.8	10.2	0.013
Betatized 950°C, F.C.	400°C steam	495	150	6.7	10.9	0.014
Betatized 950°C, A.C. ^(b)	360°C water	136	45	2.0	11.8	0.015
Betatized 950°C, A.C.	400°C steam	471	150	6.7	11.5	0.014
Betatized 950°C, W.Q. ^(c)	400°C steam	900	310	13.6	12.2	0.015
Betatized 950°C, W.Q. + 100 hr 500°C	360°C water	132	71	3.1	18.9	0.023
Betatized 950°C, W.Q. + 100 hr 500°C	400°C steam	634	232	10.0	12.7	0.016
Betatized 950°C, W.Q. + 100 hr 700°C	360°C water	146	46	2.0	11.1	0.014
Betatized 950°C, W.Q. + 100 hr 700°C	400°C steam	551	155	7.0	10.1	0.013
Hot-rolled + 30% cold-work	360°C water	117	40	1.7	11.9	0.015
Hot-rolled + 30% cold-work	400°C steam	357	122	5.4	12.2	0.015

^(a) F.C., furnace-cooled; ^(b) A.C., air-cooled; ^(c) W.Q., water-quenched.

Table V. Relative intensities of x-ray patterns of uncorroded metal and of corrosion films

Phase	(hkl)	Corrosion tests									
		Base metal		360°C Water				400°C Steam			
		Annealed 800°C	Water- quenched from 950°C	Annealed 800°C	Annealed and cold-rolled	Water- quenched from 950°C	Water- quenched & 600°C tempering	Annealed 800°C	Annealed and cold-rolled	Water- quenched from 950°C	Water- quenched & 600°C tempering
ZrO ₂	(111)	—	—	100	100	8	14	100	100	12	36
α Zr	(100)	0	30	0	0	0	0	0	0	0	0
ZrO ₂	(002)	—	—	75	100	100	100	86	100	100	100
α Zr	(002)	100	10	0	0	0	0	0	0	0	0
ZrO ₂	(200)	—	—	50	60	0	0	0	0	0	0
ZrO ₂	(102)	—	—	40	65	55	38	55	50	55	50
α Zr	(101)	15	15	0	0	0	0	0	0	0	0
ZrO ₂	(211)	—	—	20	18	0	0	18	20	2	10
ZrO ₂	(21 $\bar{1}$)	—	—	20	20	25	20	32	20	23	15
α Zr	(102)	45	15	0	0	0	5	0	0	0	0
ZrO ₂	(220)	—	—	10	0	8	0	13	5	6	0
ZrO ₂	(013)	—	—	55	50	20	20	75	70	23	36
α Zr	(110)	8	100	0	0	0	50	0	0	0	0
ZrO ₂	(13 $\bar{1}$)	—	—	10	18	8	10	23	20	10	18
ZrO ₂	(11 $\bar{3}$)	—	—	25	25	2	5	32	30	4	12
α Zr	(103)	100	60	45	25	0	15	0	0	0	0
α Zr	(200)	0	5	0	0	0	0	0	0	0	0
α Zr	(112)	15	5	0	0	0	5	0	0	0	0
α Zr	(201)	0	0	0	0	0	0	0	0	0	0
ZrO ₂	$2\theta_{Cu} = 71.2$	—	—	25	40	50	28	45	50	40	43
α Zr	(004)	30	0	15	0	0	0	0	0	0	0
α Zr	(202)	0	0	0	0	0	0	0	0	0	0
α Zr	(104)	30	5	15	0	0	0	0	0	0	0
α Zr	(203)	0	0	0	0	0	0	0	0	0	0
ZrO ₂	$2\theta_{Cu} = 92.6$	—	—	12	0	0	0	0	0	0	0
α Zr	(210)	0	10	0	0	0	0	0	0	0	0
α Zr	(211)	0	10	0	0	0	0	0	0	0	0
α Zr	(114)	30	50	0	10	0	15	0	10	0	12
α Zr	(212)	0	0	0	0	0	0	0	0	0	0
ZrO ₂	$2\theta_{Cu} = 106$	0	0	25	10	0	0	0	0	0	0

plane reflections, the strongest x-ray peak being the (11 $\bar{2}$) reflection. The oxide on the quenched sample was oriented with the (001) planes parallel to the (11 $\bar{2}$) planes of the quenched metal. The (200), (211), (013), and (11 $\bar{3}$) oxide reflections on the annealed samples were strong but were non-existent or weak on quenched samples.

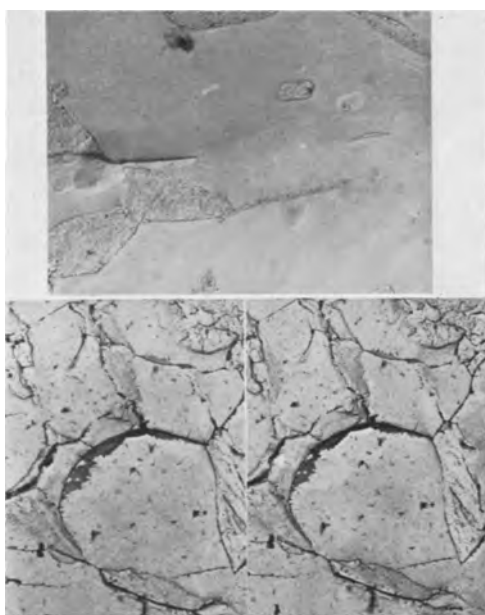


Fig. 6. Structure of annealed alloy, 24 hr at 800°C and furnace-cooled. Corroded 112 days in 360°C water. a (upper), Alloy substrate; b (lower), Stereo pair of oxide film surface (negative replica). Magnification approximately 3000X.

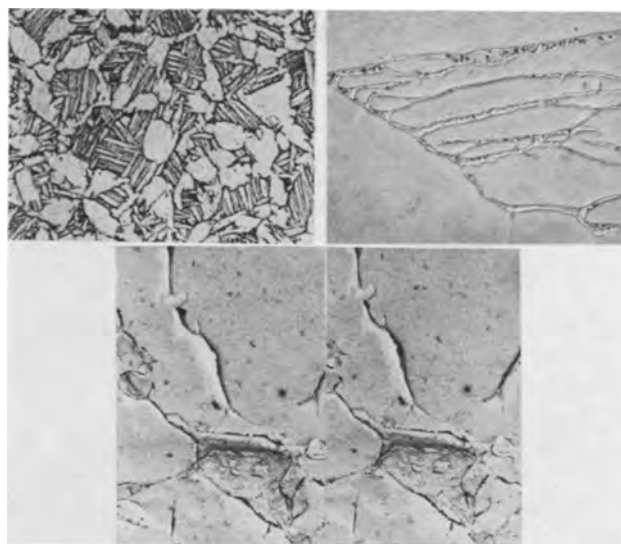


Fig. 7. Structure of 950°C annealed, furnace-cooled alloy. Corroded 100 days in 360°C water. a (upper), Alloy substrate; left, magnification approximately 250X; right, approximately 3000X. b (lower), stereo pair of oxide film surface (negative replicas); Magnification approximately 3000X.

Topography and Morphology of Oxide Films

The topographical features of the oxide films and the relationship of the film structure to the metal substrate structure were easily discernible in stereo pairs of electron micrographs. Four stereo pairs which were particularly informative are shown in Fig. 6, 7, 8, and 9, and may be viewed by the reader with a stereoscope.

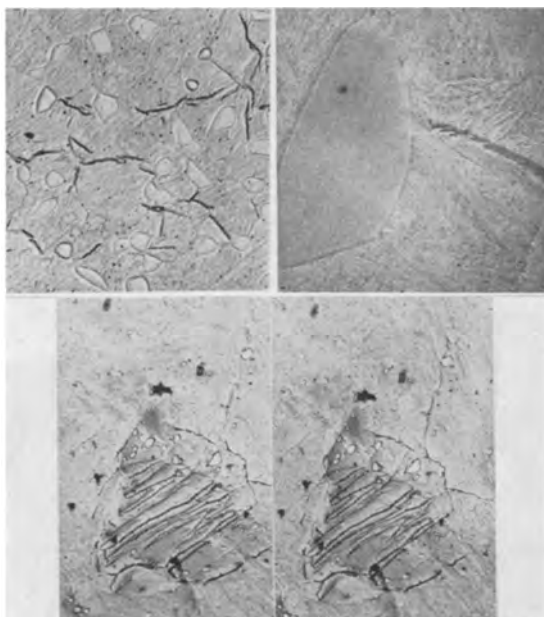


Fig. 8. Structure of quenched and tempered alloys. a (upper), Alloy substrate, quenched from 950°C and tempered 100 hr at 500°C, corroded 100 days in 360°C water; magnification, left, 250X; right, 3000X. b (lower), Stereo pair of oxide film surface (negative replicas). History same as a. 3000X.

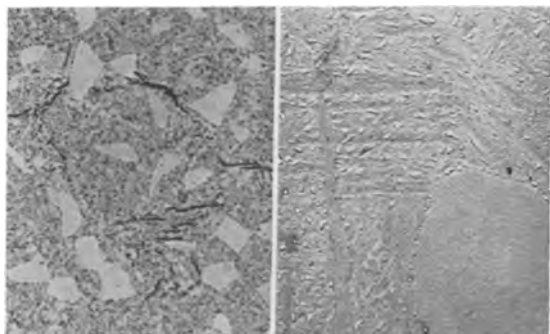


Fig. 8c. Alloy substrate, quenched from 950°C and tempered 100 hr at 600°C, corroded 100 days in 360°C water. Notice larger precipitate size and more advanced stages of martensite break down compared to a; left, 375X; right, 3000X.



Fig. 9. Structure of hot-rolled plus cold-rolled alloy, corroded 100 days in 360°C water. a (upper), Alloy substrate, 6000X. b (lower), stereo pair of oxide film surface (negative replicas). Magnification approximately 3000X.

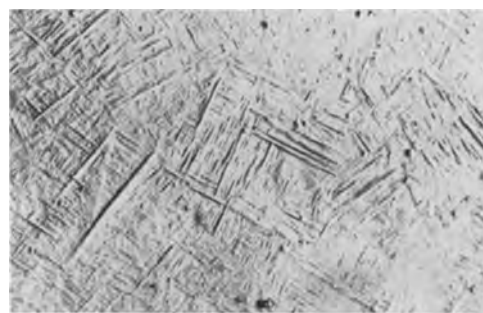


Fig. 10. Martensitic substrate structure, water-quenched from 1000°C. No primary alpha present, solution temperature was above $\beta/\beta + \alpha$ transus. Magnification approximately 250X.

Although macroscopic examination of the films indicated that they were crack-free and protective, the electron micrographs definitely established that many cracks were present. The cracks generally appeared at interfaces such as grain boundaries or the interfaces between two phases. An example of a grain boundary crack may be seen in Fig. 6, and an example of cracks between two phases may be seen in Fig. 7. Figure 7 also shows a crack which formed entirely within a primary alpha grain. Numerous interfacial cracks formed in the cold-rolled sample, Fig. 9. The quenched alloys were martensitic, consisting of a surface-roughened, acicular structure shown in Fig. 10. Much of the martensitic structure did not appear in the oxide films (such as in Fig. 8) indicating the oxide film masks out the structure of the substrate readily.

It should be emphasized that there are differences in the topography of the films which cannot be seen readily without a stereoscope. For example, the cracked patch in Fig. 8 is a raised mound in the replica (surface depression on the oxide surface) which probably resulted from a higher corrosion rate in this region. Another example of surface depressions in the oxide may be found in the negative stereo pair in Fig. 7 (the mottled region just below the center of the micrograph). This mottled region on the oxide is surrounded by a protruding ridge, at the bottom of which exists a crack (the black, fan-like structure). In most instances, the oxide films were cracked where the topography changed abruptly.

All stereo pairs revealed a significant amount of surface porosity as evidenced by small protruding whiskers in the replicas. The depth of these pores could be estimated from the height of the whiskers. It is not known whether the plastic replicating tape completely filled the pores or whether all of the tape was extracted from the pores during removal of the tape. The importance and nature of these features warrants further work.

Discussion

Rate Laws

Various heat-treatments effected appreciable differences in the corrosion behavior of the alloys, but it is difficult to analyze these differences in terms of the usual rate laws. It appears that many of the samples initially corroded in accordance with some frac-

tional-power-exponent rate law, which is indicative of some type of diffusion-controlled process. Eventually all of the samples exhibited a transition to corrosion in accordance with a more rapid rate law having higher values of the exponent. The higher values of the exponent are characteristic of a linear rate law in cases where $n \sim 1$, but the intermediate values, between 0.5 for a parabolic rate law and unity for a linear rate law, are puzzling. It is possible that a combination of rate laws is applicable because only a portion of the film area is protective (in which region a diffusion-controlled process takes place), while the remaining area of the sample is corroding according to a linear rate law. The fact that cracks in the film were observed rather extensively gives support to this idea. Further, the presence of porosity over certain areas, see Fig. 9, may allow those areas to corrode linearly, although it is not known if the porosity is deep enough to allow the reactants direct access to each other.

It is still doubtful that values of the exponent, n , obtained from log-log plots of weight gain *vs.* time are meaningful in view of Wanklyn's work (4) on individual grains of zirconium. Wanklyn has studied the formation of interference films by noticing color changes on numerous individual zirconium grains and has found a wide variety of rate laws for the grains. In addition to differences in over-all thickness, Wanklyn observed the formation of large "pustules" on grains which had the thinnest oxide films. Grains which oxidized rapidly appeared to form uniform thick films, whereas the more resistant grains eventually exhibited the highly localized attack in the form of pustules. Rate laws cannot be assigned with certainty to the oxidation of polycrystalline metals when the single grains exhibit such a wide variation in behavior.

Alloy Constitution

The difference in corrosion behavior as affected by heat-treatment can be analyzed in terms of the relative corrosion rates of the different phases. Let us consider how the constitution of the alloys can be changed by heat treatment.

The constitution of the alloy at the quenching temperature, 950°C, was $\alpha + \beta$ even though the isothermal sections of high-purity alloys indicate that the alloy should be entirely within the beta region (5). The primary alpha was stabilized by the presence of 1000 ppm oxygen, thus resulting in partitioning of the niobium to the beta phase and of the tin and oxygen to the alpha phase. Quenching resulted in supersaturation of the primary alpha and the transformation of the beta martensitically to a distorted alpha having a solute content in excess of that shown in the equilibrium diagram (5). The structure, therefore, consisted of two alpha-phases of different composition: primary alpha with ~ 1 a/o Nb and ~ 7 a/o Sn, and alpha prime with $\sim 1-2$ a/o Nb and $\sim 1-2$ a/o Sn.¹ The corrosion rate of the primary alpha would be higher than that of the

alpha prime due to the higher tin content of the former.

Tempering of the quenched structure improved the corrosion resistance considerably. This effect is related to the rejection of a precipitate from the martensitic alpha (see Fig. 8a and c). Tempering at 500°C produced a very fine precipitate; tempering at 600°C produced a much coarser precipitate. The primary alpha phase was void of precipitate whether tempering was performed at 500° or 600°C. This is rather surprising in view of the high tin content of the primary alpha which was considerably higher than the solubility limits at either tempering temperature. It was expected that rejection of Zr₄Sn would occur in the primary alpha, but electron microscopy failed to reveal any precipitation. Optical micrographs of the corroded samples, Fig. 8a and c, show the hydrides observed in the martensitic matrix of quenched alloys as well as tempered alloys. The hydrides did not form in the primary alpha phase, and when growing in the martensitic phase apparently were stopped on reaching the primary alpha particles.

Annealing at 800°C also was performed within the $\alpha + \beta$ region, but the composition of the two phases was markedly different from that of the alloy quenched from 950°C. The tin content of the primary alpha was lower, and the niobium content of the beta-phase was higher than the sample quenched from 950°C. If the niobium content of the beta-phase is high, transformation may be expected during cooling (6). According to the only isothermal sections available for high purity alloys (5), beta should decompose into three phases, $\alpha + \beta_f + \text{Zr}_4\text{Sn}$; the final beta, β_f , having a composition presently unknown but different from the original beta. The decomposition products of the high-temperature beta are seen in Fig. 6a as small polyphase regions. The fact that the samples annealed at 800°C were polyphase and also showed the most resistance to corrosion gives strong support to the supposition that the corrosion resistance of all the phases is nearly identical.

The good corrosion resistance of the cold-worked sample may be attributed to its similarity in structure to that of the sample annealed at 800°C. The cold-worked structure is elongated slightly by the rolling, but otherwise is very similar with respect to microconstituents.

Heat-treatment has been observed to have a strong influence on corrosion resistance in Zr-Nb binary alloys (7, 8), primarily due to gross changes in the composition of microconstituents. Klepfer (7) and Richter and Tverberg (8) showed that heat treatment in the $\alpha + \beta$ region for binary Zr-Nb alloys resulted in corrosion rates much higher than the corrosion rates for material annealed in the region below the monotectoid temperature. In the latter material an alpha-zirconium phase containing about 1% Nb is in equilibrium with a body-centered cubic phase of about 90% Nb-10% Zr; both phases have excellent corrosion resistance. Heating in the $\alpha + \beta$ region produces an alpha phase which is very similar to that formed below the monotec-

¹ These compositions were estimated from available ternary isotherms and unpublished research on the effect of oxygen on the constitution of Zr-Sn-Nb alloys.

toid temperature, but the body-centered cubic phase in equilibrium with the alpha contains between zero and ~20% Nb, depending on the temperature. Klepfer showed that as the annealing temperature within the $\alpha + \beta$ region increased, the niobium content of the beta-phase decreased. Richter and Tverberg showed a similar behavior for ternary Zr-Nb-Sn alloys for tin contents of up to 1%. It has been shown (1, 5, 7, 8) that the corrosion resistance of β -zirconium decreases with increasing niobium, and thus the over-all corrosion resistance of the two-phase alloy decreases as the amount of the beta-phase increases and/or as its niobium content increases.

Changes in Oxide and Metal Orientations

Another factor which may be partly responsible for the different corrosion behaviors after heat treatment could be the changes noted in orientations of both oxide and metal. The anisotropy of corrosion (9) would manifest itself in different corrosion kinetics as the texture of the substrate changed. Likewise, a change in oxide orientation might be expected to alter both the rate of oxygen diffusion through the oxide and the rate of growth of the oxide. Although no evidence exists for anisotropy of oxygen diffusion in zirconia (10), it is reasonable to expect diffusion anisotropy in low-symmetry structures as exemplified by self-diffusion in bismuth (11).

In this study, the strong (11 $\bar{2}$ 0) texture of the quenched samples and the strong (0001) texture of the annealed samples are the principal texture differences. Bibb and Fascia (9) have shown that metal orientation significantly affects the corrosion rate of single crystals of zirconium, some of their data are summarized in Table VI. Although Bibb and Fascia found that the weight gains in a given time of (0001) and (11 $\bar{2}$ 0) faces were similar, a shift in orientation from the (11 $\bar{2}$ 0) face of less than 16° gives an orientation of (21 $\bar{3}$ 1), the crystal face which they found to have the poorest corrosion resistance.

Pole figures were not run on the Zr-Sn-Nb samples, but the fact that medium intensities of the (10 $\bar{1}$ 3) and (11 $\bar{2}$ 4) reflections were observed in the quenched sample indicates that this sample did not have a perfect (11 $\bar{2}$ 0) texture and probably was close to the (21 $\bar{3}$ 1) texture. The (21 $\bar{3}$ 1) reflection for the quenched samples had a relative intensity

of 10, but this reflection was not detected in the annealed samples. Additional evidence supporting a (21 $\bar{3}$ 1) texture of the quenched samples may be obtained by considering the relative intensities of the low-multiplicity planes of zirconium powder, e.g., (21 $\bar{3}$ 1)—6 for powder *vs.* 10 for the quenched sample; (11 $\bar{2}$ 4)—3 for powder *vs.* 50 for the quenched sample.

The quenched samples showed a weight gain at a rate about two times that of the annealed samples, which is quantitatively similar to the ratio observed by Bibb and Fascia for the (21 $\bar{3}$ 1) and (0001) crystal face textures.

Hydrogen Pickup

The relative insensitivity of hydrogen pickup rate with respect to heat treatment and composition has been noted in binary Zr-Nb alloys by Klepfer (7). Richter and Tverberg (8) also studied binary Zr-Nb alloys and observed slight differences in hydrogen pickup rates, but no clear correlation between pickup and heat treatment or between pickup and composition could be established. Richter and Tverberg investigated several ternary Zr-Nb-Sn alloys and found that various alloys subjected to different heat treatments picked up hydrogen at about the same rate as that which Klepfer observed in the binary Zr-Nb alloys and as that observed in this study on Zr-2Sn-2Nb.

The location of hydrides (see Fig. 8) is somewhat puzzling. There appears to be no hydride in the primary alpha phase. The beta phase² is an equilibrium phase at 360°C, the corrosion test temperature, and if beta were present, one would expect that the hydrogen would locate preferentially in this phase due to a higher solubility than in alpha. However, the high temperature beta transformed to martensite during the quench, and no evidence of beta was found by x-ray diffraction after exposure at 360°C for 100 days. It would thus appear that tin restricts the solubility of hydrogen in alpha zirconium, whereas niobium increases the solubility. If it is assumed that the hydrogen was soluble at the test temperature, then precipitation should occur during cooling to room temperature.

No clear explanation of hydrogen pickup in zirconium alloys containing niobium has thus far been given. Fortunately, the rate of pickup is low in these alloys, and thus, if good corrosion resistance can be achieved, the amount of hydrogen absorbed will be low and integrity of mechanical properties can be maintained.

Manuscript received Aug. 30, 1963. This paper was presented at the New York Meeting, Sept. 29-Oct. 3, 1963.

Any discussion of this paper will appear in a Discussion Section to be published in the June 1965 JOURNAL.

REFERENCES

1. D. L. Douglass, "Nuclear Metallurgy," AIME, VII, 31 (1960).

² There are two beta phases present in the Zr-Nb system which exhibits a monotectoid reaction. The low temperature beta has the composition 10Zr-90Nb, whereas the high temperature form for the Zr-2Sn-2Nb alloy has a composition of less than 20% Nb, depending on the temperature. The high temperature form may transform to α' and/or ω upon quenching.

Table VI. Anisotropy of zirconium single crystal corrosion in 360°C water (9)

Crystal face	Weight gain, mg/dm ² after 100 days	Time to transition, days
(0001)	22	170
(10 $\bar{1}$ 4)	23	115
(10 $\bar{1}$ 1)	26	130
(21 $\bar{3}$ 1)	41	130
(21 $\bar{3}$ 0)	16.5	300
(11 $\bar{2}$ 0)	25	155

2. B. Cox, *This Journal*, **109**, 1 (1962).
3. J. N. Chirigos and D. E. Thomas, *Proc. A.E.C. Metallurgy Conf.*, March 1952. Report TID-5084.
4. J. N. Wanklyn, C. F. Britton, D. R. Silvester, and N. J. M. Wilkins, "The Corrosion of Zirconium and Its Alloys in High Temperature Steam. Part III. The Influence of the Environment on Oxidation," AERE-R 4130 (1962).
5. O. S. Ivanov and V. K. Grigorovich, "Structure and Properties of Zirconium Alloys," Peaceful Uses of Atomic Energy, Second Geneva Conference, Properties of Reactor Materials, **5**, 34 (1958).
6. R. F. Hehemann, *U.S.A.E.C. Symposium on Zirconium Alloy Development*, GEAP-4089, **1**, Paper 10 (1962).
7. H. H. Klepfer, *J. Nuc. Mat.*, In press.
8. H. Richter and J. C. Tverberg, *U.S.A.E.C. Symposium on Zirconium Alloy Development*, GEAP-4089, **I**, Paper 4 (1962).
9. A. E. Bibb and J. R. Fascia, Abstract in *J. of Metals*, **15**, 82 (1963), and personal communication.
10. D. L. Douglass, *Proc. International Conference on the Corrosion of Nuclear Materials*, IAEA, Salzburg, Austria, **2**, 223 (1962).
11. W. Seith and A. Keil, *Z. Elektrochem.*, **39**, 540 (1933).

The Trivalency of Gallium Ions Formed during the Dissolution of the Metal in Acids

M. E. Straumanis and K. A. Poush

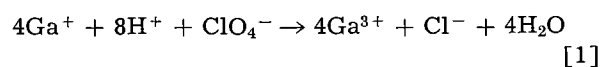
*Department of Metallurgical Engineering,
University of Missouri School of Mines and Metallurgy, Rolla, Missouri*

ABSTRACT

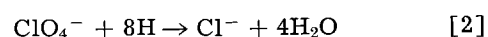
Gallium dissolves very slowly in dilute acids such as HCl, H₂SO₄, and HClO₄. The rate can be substantially accelerated if the metal is connected with a Pt electrode in the same solution. From the volume of the hydrogen developed the valency of 3 is calculated for the Ga ions going into solution. The same ionic charge is obtained from coulometric measurements using a Ga amalgam as an anode. This is in contradiction with the valency of one recently reported in the literature. However, microscopic observations revealed that the valency of one is only apparent, because Ga⁰ disintegrates partially while going into solution anodically. The diameter of the smallest observable Ga particles is less than 7 × 10⁻⁵ mm. If the solution is not cooled the formation of large metallic spheres is observed. Disintegration explains the deviation from Faraday's law, and the presence of the small particles—the reducing ability of the electrolyte. The postulation of Ga ions of lower valency is therefore, not necessary.

One of the basic problems in corrosion and anodic dissolution of metals is the valency or charge of ions with which the latter go into solution. There are investigations which seem to prove that, for instance, Be, Mg, and Zn, under certain conditions, may go into solution in the form of monovalent ions and then immediately react with the electrolyte or an oxidizer if present. Thus, the existence of lower valency ions cannot be proved directly, but the deviation from Faraday's law in the sense that more metal went into solution than calculated, points indirectly toward the anodic formation of lower valency ions.

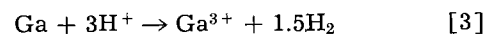
Such observations were also made on gallium anodes (1): more Ga went into solution than required by Faraday's law and the anolyte showed some reducing ability. It was concluded that in the initial stage of dissolution monovalent gallium ions were ejected by the anode. The existence of such ions was derived (2) from experiments in which Ga was dissolved in concentrated HClO₄, whereby this was assumed to be (partially) reduced to Cl⁻



A second possibility that the active hydrogen, developed during the dissolution reaction, might act as a reducing agent was not considered



The aim of the present contribution is to prove that Ga⁰ does go into solution in the form of Ga³⁺, and that the deviation from Faraday's law and the reducing ability of the anolyte are due to partial disintegration of the Ga anode into very fine particles which may act as a reducing agent. The experimental procedure is as follows: (i) collecting and measuring the volume of hydrogen evolved from the metal dissolving in acids provides confirmation of



(ii) determining the valency of Ga-ions going into solution from a Ga-amalgam electrode by measuring the number of coulombs, and (iii) examining the solvent for very fine metallic particles which may be expelled from the Ga anode while the current is flowing.

The Trivalency from the H₂-Volume Developed

Unfortunately, pure Ga metal dissolves so slowly in acids such as HCl, H₂SO₄, and HClO₄, even when they are hot and concentrated, that it was impossible to collect sufficient amounts of hydrogen to establish the stoichiometry of reaction [3]. The dissolution rates of Ga amalgams were even lower. Therefore, it was necessary to accelerate the veloc-

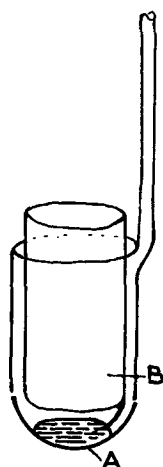


Fig. 1. Device for dissolving the Ga of the amalgam A by immersion into HCl, H₂SO₄, or HClO₄. B, Pt cylinder and connection with A.

ity of the reaction. This was achieved by connecting the Ga amalgam with a cylindrical platinized platinum electrode as a cathode (Fig. 1). Since this cathode has a low hydrogen overpotential, the gas can readily develop on it, while Ga is going into solution anodically.

About 0.13g of gallium (99.9% pure) were weighed precisely and dropped into some Hg; Ga amalgam was formed (3). Then this amalgam was connected with the hollow platinum cylinder and the couple was immersed in the acid, held in a flask. The contents were preheated to a temperature of 37°-38°C in a constant temperature water bath and saturated with hydrogen (4). Reaction [3] started at once. The gas was collected above water in a burette, using a leveling bulb.

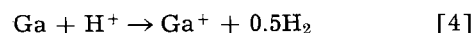
Volume-time curves were drawn to determine the end of the dissolution reaction, which required 3-6 hr. The valency of Ga ions was calculated from the weight of Ga dissolved and the volume of hydrogen developed. The results are summarized in Table I.

Table I. Valency of Ga ions going into solution anodically (from a Ga-amalgam anode)

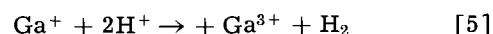
Acid	Normality	Valency	Average
H ₂ SO ₄	4.2	3.02	2.976
	4.0	2.98	
	7.2	2.98	
	7.2	2.93	
	8.6	2.97	
HCl	6.1	3.01	2.950
	6.1	2.88	
	6.1	2.96	
	6.1	2.94	
	6.1	3.01	
HClO ₄	9.2	2.79	2.884
	9.2	2.77	
	4.6	2.90	
	8.3	2.96	
	8.3	2.98	
	8.3	2.91	

Considering that there is still some hydrogen loss during the 3-6 hr of collection of the gas, it becomes clear from the valency numbers of Table I that Ga goes into solution as a trivalent ion, Ga³⁺. Besides, no Cl⁻ could be detected in the solutions of HClO₄ after the dissolution of Ga was completed, which indicates again that Ga⁺ was not formed during the experiments and that there were no reduction reactions according to [2].

Nevertheless, the objection can be raised that reaction [3] may proceed in two steps, according to Davidson and Jirik (1)



and



As the sum of reactions [4] and [5] is equal to reaction [3], Table I is no proof for the initial monovalency of Ga ions; it shows only that the stable valency of Ga-ions is 3.

However, there are the following objections against Eq. [4] and, as a consequence, against [5]: (i) The presence of Ga⁺ could not be proved in the solution, and therefore, it was previously assumed that Ga⁺ ions have only a very short lifetime (1); (ii) in the experiments as shown by Fig. 1, there was no reduction of ClO₄⁻, (hence there were no Ga⁺ ions (2), although a reaction similar to [5] could also proceed), and (iii) it was shown by James and Stoner (5) that in the case of Zn-amalgam only Zn²⁺ ions were formed during anodic dissolution. This might be also true with gallium (no expulsion of lower valency Ga ions).

The Trivalency of Ga Ions from Coulometric Measurements

As Ga electrodes are difficult to handle and may easily melt (melting point 29.8°C), another arrangement than described previously (5) was used for the coulometric proof of trivalency of Ga ions expelled by gallium amalgam. Figure 2 explains the method. A precisely weighed piece of Ga (about 0.015-0.028g) was dropped into mercury held in the beaker and covered with an acidic solution as

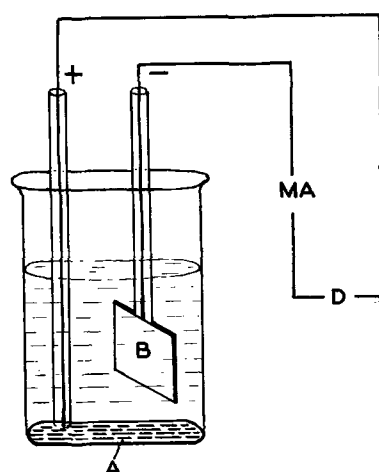


Fig. 2. Number of coulombs delivered by a certain amount of Ga: A, Ga-amalgam; B, platinized Pt electrode; MA, precise milliammeter; D, variable resistance.

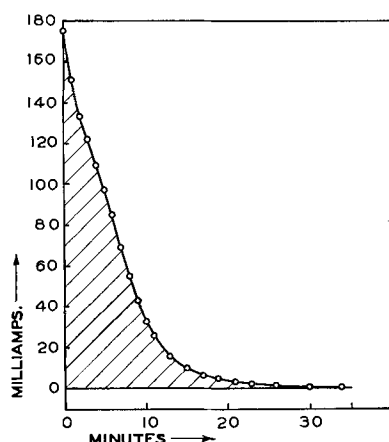


Fig. 3. Current delivered by the cell, Fig. 2, vs. time. Acid 0.5N HClO₄; shaded area: 69.5 amp sec (coulombs) = 0.0167g Ga.

shown in Fig. 2. Then a connection was made with the platinum electrode through a milliammeter. Immediately Ga went into solution and hydrogen was developed on the Pt cathode. The amount of current was plotted against the time as shown in Fig. 3. The experiment was continued until the current dropped to zero on the milliammeter. The milliampere minutes were determined from the shaded area of Fig. 3 by three methods: by weighing the paper of the shaded area, by direct counting of the square millimeters of that area, and by a planimeter. All three methods gave results in good agreement with each other. Then the milliampere-minutes were converted into coulombs and the amount of Ga present in the mercury was calculated assuming trivalency of Ga-ions (Eq. [3]). The results are summarized in Table II. This table shows clearly that Ga is going into solution solely as a trivalent ion. If the output values are slightly lower than the amount of Ga weighed in, then the difference is easily explained: slight formation of H₂-bubbles

Table II. Check of trivalency of Ga ions going anodically into solution from Ga amalgam

Acid	Input of Ga, g	Coulombs drawn	Output of Ga, g	Diff. Δ in %
1.8N H ₂ SO ₄	0.0082	33.8	0.0081	-1.2
1.8N H ₂ SO ₄	0.0170	69.4	0.0167	-1.7
1.8N H ₂ SO ₄	0.0296	119.0	0.0287	-3.4
1.8N H ₂ SO ₄	0.0156	63.7	0.0153	-1.9
1.8N H ₂ SO ₄	0.0194	80.8	0.0194	0
				Δ = -1.6
0.9N H ₂ SO ₄	0.0169	70.5	0.0169	0
0.9N H ₂ SO ₄	0.0284	115.0	0.0278	-2.1
0.9N H ₂ SO ₄	0.0093	37.6	0.0091	-2.1
				Δ = -1.4
0.45N H ₂ SO ₄	0.0154	62.1	0.0149	-3.2
0.45N H ₂ SO ₄	0.0176	70.4	0.0169	-4.0
0.45N H ₂ SO ₄	0.0131	53.0	0.0128	-2.3
				Δ = -3.2
0.5N HClO ₄	0.0137	57.6	0.0138	+0.7
0.5N HClO ₄	0.0091	36.0	0.0087	-2.2
0.5N HClO ₄	0.0207	86.5	0.0208	+0.5
0.5N HClO ₄	0.0166	69.5	0.0167	+0.6
0.5N HClO ₄	0.0206	84.0	0.0203	-1.4
				Δ = -0.3

was observed on the surface of the amalgam, except in perchloric acid, and some oxidation might also have occurred, as the work was done in presence of air. Thus, very slight amounts of Ga went into solution outside the circuit shown in Fig. 2. Besides, the differences obtained are nearly always within the limits of error.

Finally there is no reason to assume that Ga from a compact piece would go differently into solution, e.g., with a lower than 3 valency, as compared with the amalgam.

In order to check the correctness of the quantitative determination of active metals dissolved in mercury by the coulometric method (Fig. 2 and Table II), experiments with zinc were made: the differences between the input and output values were even smaller, they rarely exceeded 0.5%.

Disintegration of Gallium

If gallium goes into solution in acids solely as a trivalent ion, then why, using compact Ga as an anode, is more Ga dissolved than calculated from Faraday's law (1, 2)? The answer is a simple one: partial disintegration of the anode into very fine particles (6-10). Weight loss is caused not only because of faradaic current, but also because of the dropout of single Ga particles (11). If all the weight loss is attributed to the faradaic current, a lower calculated valency than 3 for the Ga ions going into solution follows automatically.

The partial disintegration of Ga anodes while the current was flowing was proved as follows: a Ga anode was made by pressing metallic Ga into a hole drilled in Plexiglass and having a Pt lead (Fig. 4). The anode was cooled down and immersed in cooled H₂SO₄. As soon as the circuit was closed a stream of grayish particles (sometimes interrupted by grayish flakes) started to drop from the anode to the bottom of the beaker. The particles were decanted with distilled water, dried, and observed under the microscope. Under high magnification (oil immersion) aggregates of very small particles could be seen. They were metallic because of their metallic luster (see Fig. 5). The particles were not held together by a surface oxide film as in the

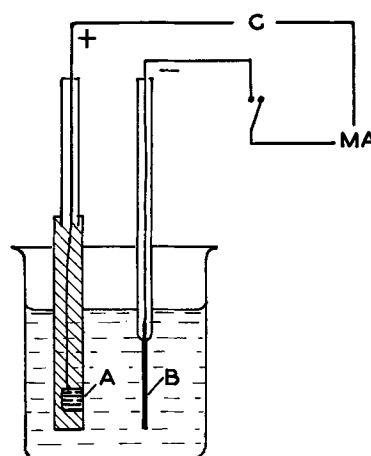


Fig. 4. Arrangement for observation of disintegration of a Ga anode A; B, cathode of Pt; electrolyte-0.5N H₂SO₄; current density 850 ma cm⁻²; C, battery; MA, milliammeter.

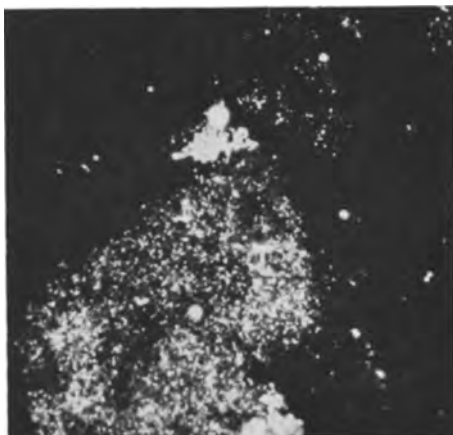


Fig. 5. Metallic Ga particles formed because of the partial disintegration of the Ga anode. Conditions: see Fig. 4. Magnification 1430X.

case of Mg (9, 10); they appeared separately, but easily stuck together to form particle aggregates. The diameter of the smallest visible particles was below 7×10^{-5} mm in diameter. If the anodic dissolution was performed without cooling, Ga spheres could frequently be observed. They were recognized by their larger size, spherical shape, and high metallic luster. X-ray pictures of the particles were not taken, because there was no doubt as to their metallic nature.

Discussion and Conclusions

Tables I and II show that 3-valent Ga-ions are produced in acidic solutions and that Ga-ions from Ga-amalgam go into solution as trivalent ions. Furthermore, there is no reason to assume that Ga-ions from a compact piece of the metal will be expelled with a charge lower than 3. While the metal is dissolving, it undergoes a partial disintegration into fine and very fine particles. This, of course, causes a deviation from Faraday's law, if the metal is dissolved anodically. The metallic particles, having a large specific surface, and an active potential (12) may act in the presence of oxidizers as reducers directly or through the active hydrogen developed on their surface. Thus, the ClO_4^- ion may be partially reduced to Cl^- (Eq. [2]). In the experiments of Fig. 1 (also Table I) no Cl^- ions could be found after the completion of the dissolution process, because the hydrogen was developed on the platinized Pt electrode which has a low hydrogen overpotential, inefficient in reduction processes, as molecular hydrogen is produced.

Disintegration of Ga anodes was observed at high current densities. There still may be a question as to whether disintegration also occurs at low current densities. This should happen because of the following reasons: an anode is rarely attacked evenly throughout, especially at low current densities; it will go into solution, as frequently observed, at preferential places (formation of etch pits) and, therefore, at high local current densities. Thus, if disintegration occurs, it will occur at these places. So it may be assumed that disintegration is to a certain degree proportional to the current density.

There is still a possibility that the 3 electrons of each Ga atom going into solution might not be released simultaneously but successively on the surface of the metal or of the amalgam. However, at present we have no experimental means to investigate this possibility. The question as to whether a Ga^+ is formed first and then immediately the Ga^{3+} by further release of two electrons, is therefore, useless.

Acknowledgment

We are grateful to the Office of Naval Research for financial support, to Dr. W. J. James, Professor of Physical Chemistry at the School of Mines and Metallurgy, for discussion, and to Mr. R. L. Martin for making the coulometric measurements.

Manuscript received Oct. 24, 1963. Revised manuscript received Dec. 16, 1963. This paper was presented at the New York Meeting, Sept. 29-Oct. 3, 1963.

Any discussion of this paper will appear in a Discussion Section to be published in the June 1965 JOURNAL.

REFERENCES

1. A. W. Davidson and F. Jirik, *J. Am. Chem. Soc.*, **72**, 1700 (1950).
2. K. Schug and A. Sadowski, *ibid.*, **83**, 3538 (1961).
3. E. S. Gilfillan, Jr. and H. E. Bent, *ibid.*, **56**, 1663 (1934). See also J. H. Hildebrand, "Regular Solutions," Prentice Hall, New York (1962).
4. G. Geffcken, *Z. physik. Chem.*, **49**, 257 (1904).
5. W. J. James and G. E. Stoner, *J. Am. Chem. Soc.*, **85**, 1354 (1963).
6. B. Roald and M. A. Streicher, *This Journal*, **97**, 283, 287, 288 (1950).
7. M. E. Straumanis and D. L. Mathis, *J. Less-Comm. Met.*, **4**, 213 (1962).
8. M. E. Straumanis and D. L. Mathis, *This Journal*, **109**, 434 (1962).
9. M. E. Straumanis and B. K. Bhatia, *Metall.*, **16**, 535 (1962).
10. M. E. Straumanis and B. K. Bhatia, *This Journal*, **110**, 357 (1963).
11. G. A. Marsh and E. Schaschl, *ibid.*, **107**, 960 (1960).
12. O. Stelling, *Z. Elektrochem.*, **41**, 712 (1935).

Distributed Network Analysis of Porous Electrode Capacitors

Jean Vergnolle

Centre de Recherches Techniques de la C.S.F., Paris, France

ABSTRACT

Assuming parameters distributed in a homogeneous anode of planar or cylindrical type, equations are given from which, with the aid of an analog computer, expressions are derived for equivalent series capacitance C , resistance (ESR) R , and for loss factor. Results are presented as families of curves, with the loss angle of the dielectric as a parameter, showing the decrease of C and R with frequency. The cathode has also a determinant influence on the characteristics.

In most capacitors with localized constants and relatively simple geometry, the equivalent impedance is easily determined. Electrolytic capacitors are a class apart, especially those in which the anode is a porous sintered mass with a useful area of a few tenths square meter per cubic centimeter. Such capacitors have a capacitance distributed inside the porous mass; the useful area has been coated with a very thin skin of dielectric, and the over-all capacitance results from the integration of the extremely small capacitances of the elementary areas facing the conducting material which impregnates the anode. A characteristic common to all capacitors of this type is the decrease of the apparent capacitance with frequency as well as the increase of the loss angle that may reach and even exceed $\pi/4$. Before attempting any calculation, it will be realized that the current, which passes between the porous metal and the conducting material filling its pores, by capacity effect, generates an energy in the dielectric skin by dielectric losses, as well as in the conducting material by the Joule effect; these phenomena determine the loss factor. At the higher frequencies, the resistance in the pores is shunted by the surrounding capacitance of the elementary capacitors; the effect of this low-pass filter is to prevent the current from entering the anode, resulting in a drop of the over-all capaci-

tance, which tends to become localized near the external surface of the anode (cf. Fig. 1 and 2).

Calculations will be made of the apparent capacitance and ESR, as well as the loss factor of the capacitors, taking into consideration characteristic parameters whose nature and number have been suggested by experimental data and by reasoning.

After examination of the complex anode impedance, the cathode (1) will be considered briefly, permitting an evaluation of the over-all impedance of a porous electrode capacitor.

Setting up the Anode Equations (2, 3)

We shall consider a porous anode as a homogeneous medium at the scale of the apparent dimensions with distributed capacitance, which will henceforth be referred to as nominal or specific capacitance, expressed in farads per cubic centimeter. The anode core is the porous metal mass relatively infinitely conducting: the cathode system is the impregnant, characterized by its finite conductivity χ that appears in the pores, multiplied by a factor p related to the state of division of the medium. The nominal capacitance per unit volume will be designated by K . Assuming an apparent intrinsic loss factor δ of the dielectric due, as will be seen later, partially to its nature and partially to an ESR distributed between the impregnant and the insulating skin itself, K will be a complex quantity given by

$$K = K_0(1-j\delta)(1+\delta^2)^{-1} \approx K_0(1-j\delta) \quad [1]$$

if δ is small enough; K_0 decreases slowly with angular frequency following an approximate law

$$K_0 = K_1 \omega^{-2\delta/\pi} \quad [2]$$

that is not the author's subject, and thus will not be discussed (4, 5).

Let us consider (cf. Fig. 3) a certain "current tube" whose shape is related to the macroscopic anode geometry, and in this tube an elementary volume dV between two equipotential surfaces, marked off by their abscissae x and $x+dx$ taken along a current line. The nominal capacitance of dV is

$$dC_1 = (\partial C_1/\partial x)dx = KdV = K(\partial V/\partial x)dx \quad [3]$$

and the resistance between the two surfaces (in the impregnant)

$$dR_1 = (\partial R_1/\partial x)dx = (dx/p\chi)(\partial V/\partial x)^{-1} \quad [4]$$

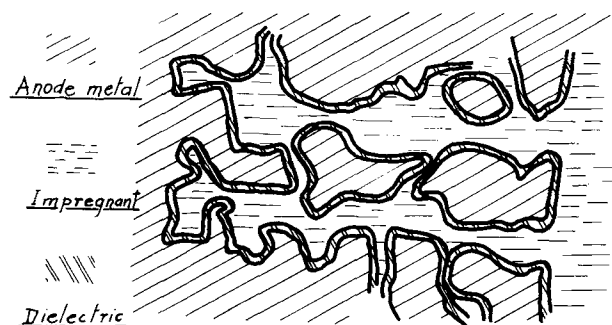


Fig. 1. Artist's conception of a cross section through a porous anode (current lines contained in the figure plane).



Fig. 2. Equivalent electrical network

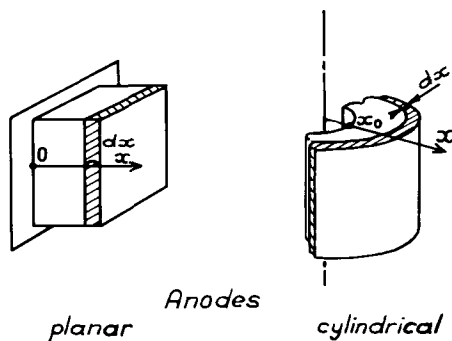


Fig. 3. Principal anodes structures investigated by using the corresponding dependence of $\partial V/\partial x$ on x .

Let $Z(x) = R(x) - j/\omega C(x)$ be the impedance between the anode and the plane $x > x_0$ in the case that no current would flow beyond this plane in the anode core, i.e., considering x as the outer surface of the porous anode. When increasing the thickness by dx , the impedance of the new structure becomes $Z + dZ$, where

$$(Z + dZ)^{-1} = (Z + dR_1)^{-1} + j\omega dC_1$$

from which

$$dZ = dR_1 - jZ^2\omega dC_1 \quad [5]$$

$$\left. \begin{array}{l} dR = dR_1 - 2(R/C)dC_1 \end{array} \right\} \quad [6]$$

$$\left. \begin{array}{l} d(1/C\omega) = \omega(R^2 - 1/C^2\omega^2)dC_1 \end{array} \right\} \quad [7]$$

This is where the macroscopic geometry of the anode comes in; it decides the shape of the current tubes and the expression for $\partial V/\partial x$. Two main structures are met with in practice: the so-called "planar" one in which the current lines are normal to a reference equipotential plane, and the so-called "cylindrical" one in which these lines are normal to a reference equipotential cylinder; the latter is by far the most common type. For planar anodes and a tube of unit section; $\partial V/\partial x = 1$; for cylindrical anodes and a "tube" contained between two cross-sectional planes one unit apart, $\partial V/\partial x = 2\pi x$. Taking into consideration the basic equations [3] and [4], the system [6] and [7] becomes, for planar types

$$\left. \begin{array}{l} dR/dx = 1/p\chi - 2KR/C \end{array} \right\} \quad [8]$$

$$\left. \begin{array}{l} dC/dx = (1 - R^2C^2\omega^2)K \end{array} \right\} \quad [9]$$

$$x_0 = 0$$

and for cylindrical types

$$\left. \begin{array}{l} dR/dx = (2\pi p\chi x)^{-1} - 4\pi KxR/C \end{array} \right\} \quad [10]$$

$$\left. \begin{array}{l} dC/dx = (1 - R^2C^2\omega^2)2\pi Kx \end{array} \right\} \quad [11]$$

$$x_0 \geq 0$$

When $x \rightarrow x_0$, i.e., when the porous material layer tends to be infinitely thin, ESR tends to zero, like capacitance, the over-all loss factor of the anode remaining. The variable will be normed using

$$\chi = K\omega x^2/2p\chi \quad [12]$$

Combined with an appropriate norm for R and C , a set of differential equations is obtained from [8]

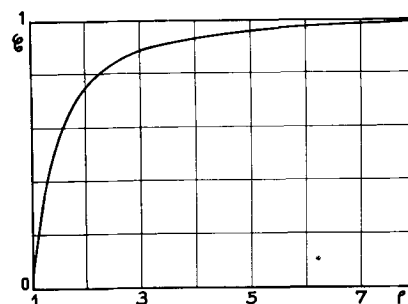


Fig. 4. Auxiliary function $G(\rho)$

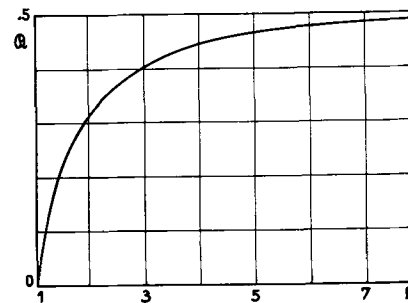


Fig. 5. Auxiliary function $R(\rho)$

and [9] (or [10] and [11]) which contains only one independent variable χ including both size dependence, x , and frequency dependence, ω . An appropriate norm for R and C is obtained when dividing by the limiting values for $\chi \rightarrow 0$, i.e., by the "initial values" C_i and R_i . One has, for planar types

$$C_i = Kx, \quad R_i = x/3p\chi \quad [13] [14]$$

for cylindrical types

$$C_i = \pi Kx^2G, \quad R_i = R/4\pi p\chi \quad [15] [16]$$

with the auxiliary functions of the ratio ρ (cf. Fig. 4 and 5)

$$G = 1 - 1/\rho^2 \quad [17]$$

$$R = 1/2 - (\rho^2 - 1)^{-1} + 2 \text{Ln } \rho(\rho^2 - 1)^{-2} \quad [18]$$

The normed values of C and R are

$$Y_C = C/Kx, \quad Y_R = 3p\chi R/x \quad [19] [20]$$

for planar types and

$$Y_C = C/\pi Kx^2G, \quad Y_R = 4\pi p\chi R/R \quad [21] [22]$$

for cylindrical types. It is remarkable that ESR of the cylindrical anodes remains constant, whatever be χ (low), either the radius x or the frequency ω be low; on the other hand, x remaining constant, when $\rho \rightarrow 1$, capacitance and ESR of the thin layer are given by the simplified formulas

$$C_i = 2\pi Kx^2(\rho - 1) \quad [23]$$

$$R_i = (\rho - 1)/6\pi p\chi \quad [24]$$

and when $\rho = \infty$ (no solid central core)

$$C_i = \pi Kx^2 \quad [25]$$

$$R_i = 1/8\pi p\chi \quad [26]$$

Invariant Curves for Anodes

Although mathematical solutions may be derived for the above differential systems, the author pre-

ferred using an ANALAC analog computer which gave invariant curves (\mathcal{Y}, \mathcal{X}) and whose interest becomes evident in the case of cylindrical anodes for which mathematics yield very complicated functions of Bessel's functions. Logarithmic coordinates are extensively and advantageously employed for these kinds of problems, and we shall now examine asymptotic solutions for $\mathcal{X} \rightarrow 0$ and $\mathcal{X} \rightarrow \infty$.

For planar types, like $Z = R - j/C\omega$

$$F = 6p\chi Z/x = 2\mathcal{Y}_R - 3j/\mathcal{X}\mathcal{Y}_C \quad [27]$$

with

$$\begin{aligned} \mathcal{X} &= K_c\omega x^2(1 - j\delta)/2p\chi(1 + \delta^2) \\ &= \mathcal{X}'(1 - j\delta)/(1 + \delta^2) \end{aligned} \quad [28]$$

For small values of \mathcal{X} ("initial range"), $\mathcal{Y}_C = \mathcal{Y}_R = 1$.

$$F = 2 - 3j/\mathcal{X} = 2\mathcal{Y}_R' - 3j/\mathcal{X}\mathcal{Y}_C' = 2 + 3\delta/\mathcal{X}' - 3j/\mathcal{X}'$$

ESR is represented by

$$\mathcal{Y}_R' = 1 + 3\delta/2\mathcal{X}' \quad [29]$$

and capacitance by

$$\mathcal{Y}_C' = 1 \quad [30]$$

$$\tan \Delta = RC\omega = (2/3)\mathcal{X}'\mathcal{Y}_R'\mathcal{Y}_C' = 2\mathcal{X}'/3 + \delta \quad [31]$$

In this range, capacitance is constant, ESR decreases like \mathcal{X}'^{-1} , while loss factor increases linearly with \mathcal{X}' from its initial value δ .

For high values of \mathcal{X}' ("extreme range")

$$\mathcal{Y}_R = 3/2\sqrt{\mathcal{X}'}, \quad \mathcal{Y}_C = 1/\sqrt{\mathcal{X}'} \quad [32] [33]$$

$$F = 3(1 - j)[(1 + \delta^2)(1 - j\delta)\mathcal{X}']^{-1/2} \quad [34]$$

Putting

$$T_\delta = [(1 + \delta^2)^{1/2} + \delta]^{1/2} \quad [35]$$

then

$$F = 3(T_\delta - j/T_\delta)/\sqrt{\mathcal{X}'} \quad [36]$$

Whence

$$\mathcal{Y}_R' = 3T_\delta/2\sqrt{\mathcal{X}'}, \quad \mathcal{Y}_C' = T_\delta/\sqrt{\mathcal{X}'} \quad [37] [38]$$

$$\tan \Delta = T_\delta^2 \quad [39]$$

Those formulas become, when δ is very small

$$T_\delta \simeq 1 + \delta/2 \quad [40]$$

$$\begin{aligned} \mathcal{Y}_R' &= 3(1 + \delta/2)/2\sqrt{\mathcal{X}'}, & \mathcal{Y}_C' &= (1 + \delta/2)/\sqrt{\mathcal{X}'} \\ & & & [41] [42] \end{aligned}$$

$$\tan \Delta = 1 + \delta \quad [43]$$

The "capacitance critical point" is important in practice, and defined, equating \mathcal{Y}_C' values derived from Eq. [30] and [38]

$$\mathcal{X}_C' = T_\delta^2 \quad [44]$$

Similarly, "ESR critical point" might be defined equating \mathcal{Y}_R' values derived from Eq. [29] and [37]. It is significant only when δ is negligible, then

$$\mathcal{X}_R' = 9T_\delta^2/4 \simeq 9(1 + \delta)/4 \quad [45]$$

For cylindrical types, like $Z = R - j/C\omega$

$$\begin{aligned} F &= 4\pi p\chi Z = \mathcal{R}\mathcal{Y}_R - 2j/G\mathcal{X}\mathcal{Y}_C \\ &= \mathcal{R}\mathcal{Y}_R' - 2j/G\mathcal{X}'\mathcal{Y}_C' \end{aligned} \quad [46]$$

For low values of \mathcal{X} , following the same computation process,

$$\mathcal{Y}_R' = 1 + 2\delta/G\mathcal{R}\mathcal{X}', \quad \mathcal{Y}_C' = 1 \quad [47] [48]$$

$$\tan \Delta = (1/2)(\mathcal{R}G\mathcal{X}'\mathcal{Y}_R'\mathcal{Y}_C') = \mathcal{R}G\mathcal{X}'/2 + \delta \quad [49]$$

For high values of \mathcal{X} , where

$$\mathcal{Y}_R = 1/\mathcal{R}\sqrt{\mathcal{X}'}, \quad \mathcal{Y}_C = 2/G\sqrt{\mathcal{X}'} \quad [50] [51]$$

$$\mathcal{Y}_R' = T_\delta/\mathcal{R}\sqrt{\mathcal{X}'}, \quad \mathcal{Y}_C' = 2T_\delta/G\sqrt{\mathcal{X}'} \quad [52] [53]$$

$$\tan \Delta = T_\delta^2 \quad [54]$$

The capacitance critical point is defined by

$$\mathcal{X}' = 4T_\delta^2/G^2 \quad [55]$$

Figures 6, 7, and 8 show the three invariant families of curves, depending on the parameter δ . for planar anodes. Figures 9, 10, and 11 are drawn as regards cylindrical types with $\rho = 8$ (as an example).

These curves represent variation of R, C , and $\tan \Delta$ with frequency ω , this variable being directly proportional to \mathcal{X}' , following Eq. [28]. The critical point is characterized by the "critical frequency" ω_c , which is an upper practical limit for utilization of the anode; above a frequency approximately $5 \omega_c$, capacitance and ESR decrease like $\omega^{-1/2}$. For planar types, \mathcal{X}' is simply the ratio $\omega/(\omega_c)_0$, and for cylin-

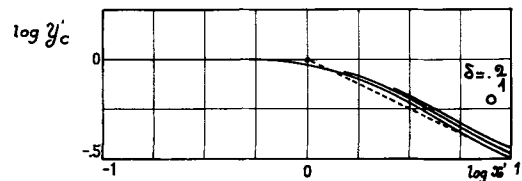


Fig. 6. Invariant family of curves ($\log \mathcal{Y}_C', \log \mathcal{X}'$) for planar anodes (δ as the parameter) (extreme asymptote in dotted line).

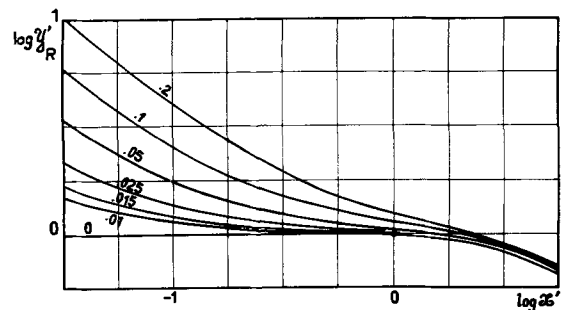


Fig. 7. Invariant family of curves ($\log \mathcal{Y}_R', \log \mathcal{X}'$) for planar anodes (δ as the parameter).

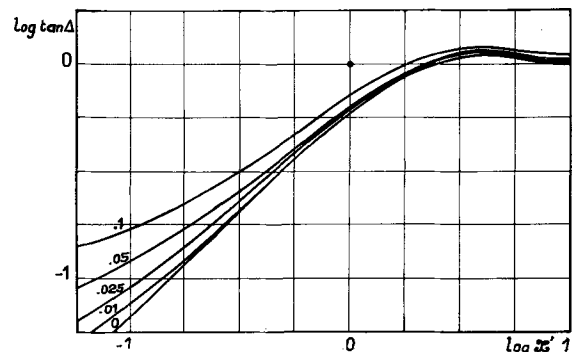


Fig. 8. Invariant family of curves ($\log \tan \Delta, \log \mathcal{X}'$) for planar anodes (δ as the parameter).

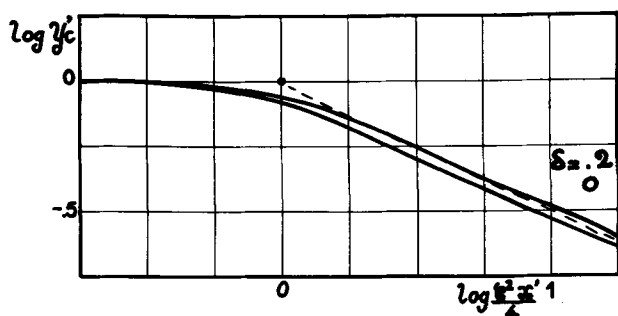


Fig. 9. Invariant family of curves ($\log Y'_c$, $\log X'$) for cylindrical anodes (δ as the parameter) ($\rho = 8$) (extreme asymptote in dotted line).

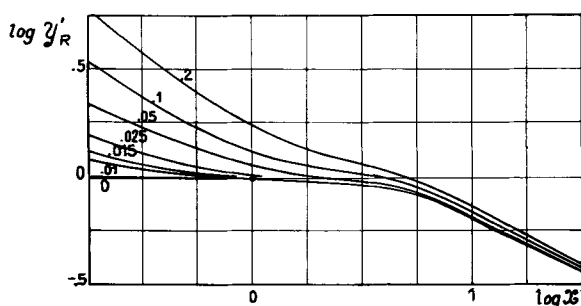


Fig. 10. Invariant family of curves ($\log Y'_R$, $\log X'$) for cylindrical anodes (δ as the parameter) ($\rho = 8$).

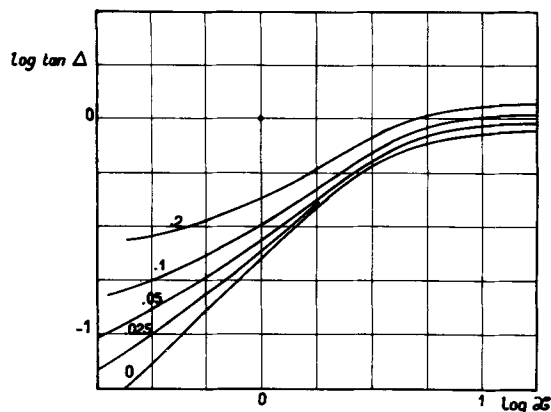


Fig. 11. Invariant family of curves ($\log \tan \Delta$, $\log X'$) for cylindrical anodes (δ as the parameter) ($\rho = 8$).

dical ones, it is similarly $(4/G^2)[\omega/(\omega_c)_0]$, $(\omega_c)_0$ being the critical frequency for a nil δ . Experimentally one may observe a slope of the curve ($\text{Ln}C$, $\text{Ln}\omega$) different from zero in the initial range, and higher than 0.5 in the extreme one, depending on Eq. [2], or possibly, another physical law.

Theoretical Comparison of Planar and Cylindrical Anodes

Before making any further assumptions it seems worthwhile comparing planar and cylindrical anodes with results already obtained; this comparison will make sense when made in respect to two anodes with the same useful volume and the same limit capacitance. Having first used anodes of unit cross section or unit length, it will now be necessary to take into consideration the area of cross section a or length l of the cylinder; the initial capacitances are then respectively Kax_p and πKx_c^2lG , the indices p

and c being applied to the values of x to distinguish the thickness x_p from the external radius x_c , i.e.

$$\pi x_c^2 l G = ax_p \quad [56]$$

Further on these indices will designate the magnitudes relative to the anodes of each of the two types. A new assumption will be added, i.e., the equality of the loss factors δ .

Under these conditions, the series resistances in the initial range, essentially laid down by δ , are necessarily the same. If δ is small, there is an intermediate range where $R \approx (R_i)_0$, and where

$$R_p/R_c \approx (G/3R)(2\pi x_c l/a)^2 = 4x_p^2/3GRx_c^2 \quad [57]$$

(throughout this range, the capacitances are still equal and constant). The ratio

$$\begin{aligned} (\omega_{cp})_0/(\omega_{cc})_0 &= (Gx_c/2x_p)^2 \\ &= Ga/4\pi x_p l = (a/2\pi x_c l)^2 \quad [58] \end{aligned}$$

compares practical upper utilization limits.

In the "extreme range," where only the apparent external areas come are considered, the following equation is valid for all values of δ .

$$R_p/R_c = C_c/C_p = 2\pi x_c l/a = 2x_p/Gx_c = 2(\pi l x_p/Ga)^{1/2} \quad [59]$$

Applications with Supplementary Hypothesis

The expressions derived for the equivalent series resistance and capacitance contain the parameter δ , which may be a function of frequency; it consists of an inherent, quasi frequency independent value δ_1 of the dielectric (and of the interface dielectric-impregnant) and of a frequency dependent loss arising from the series resistance of the impregnant in pores extending essentially perpendicular to the direction x ; thus

$$\delta = \delta_1 + \omega K_0/\alpha\chi = \delta_1 + 2pX'/\alpha^2 = \delta_1 + 2pX'/q \quad [60]$$

q (or α) is a new auxiliary parameter; q is dimensionless like p . A more thorough analysis of the effects would take into account the fact that, strictly, the new series resistance is depth dependent and thus frequency dependent; but we shall assume the critical frequencies of the narrowest pores are pushed back beyond the usual frequencies.

We shall now show how to utilize the computations and families of curves given in the previous section, taking due account of the introduction of new parameters. Instead of being constant, δ is linearly increasing with X' , according to Eq. [60]. And so, the invariant plots already made are still usable as charts for obtaining the new invariant curves (Y'_c , X'), (Y'_R , X'), and ($\tan \Delta$, X') arising from our additional assumptions. We shall suppose the new parameter q is always high enough to assure $\delta \ll 1$, whatever X' in a usual range, since values of δ_1 are lower than 1% for Ta_2O_5 .

Simple calculations lead to the following results. *Plane anodes—Initial range*

$$Y'_c = 1, Y'_R = 1 + 3p/q + 3\delta_1/2X' \quad [61] \quad [62]$$

$$\tan \Delta = \delta_1 + 2(1/3 + p/q)X' \quad [63]$$

Extreme range

$$Y'_c = (1 + \delta_1/2)/\sqrt{X'} + p\sqrt{X'}/q,$$

$$\mathcal{Y}_R' = 3/2[(1 + \delta_1/2)/\sqrt{X'} + p\sqrt{X'}/q] \quad [64] [65]$$

$$\tan \Delta = 1 + \delta_1 + 2pX'/q \quad [66]$$

Cylindrical anodes—Initial range

$$\mathcal{Y}_C' = 1, \quad \mathcal{Y}_R' = 1 + 4p/GRq + 2\delta_1/GRX' \quad [67] [68]$$

$$\tan \Delta = \delta_1 + (RG/2 + 2p/q)X' \quad [69]$$

Extreme range

$$\mathcal{Y}_C' = (1/G)[(2 + \delta_1)/\sqrt{X'} + 2p\sqrt{X'}/q,$$

$$\mathcal{Y}_R' = (1/R)[(1 + \delta_1/2)/\sqrt{X'} + p\sqrt{X'}/q] \quad [70] [71]$$

$$\tan \Delta = 1 + \delta_1 + 2pX'/q \quad [72]$$

As a general rule, in the initial range, capacitance is not affected by δ variations, but $\tan \Delta$ increases just a little more rapidly; in the extreme range, decreasing of capacitance is counter-balanced by an increasing term ($\sqrt{X'}$), whereas $\tan \Delta$ follows a linear growth. Loss factor depends mainly on the dielectric quality δ_1 at low frequencies, and on the anode porosity (p/q) at high frequencies (6).

Role of the Cathode

All the computations made so far have only introduced the impedance between an origin equipotential at the apparent external surface of the anode, but a conducting mass is necessarily inserted between the anode and the cathode: it is a layer of graphite, as in tantalum or niobium capacitors of the so-called "solid type," or a layer of electrolyte, as in those of the so-called "liquid" type. This layer, mainly in the latter case, introduces an additional resistance, τ , which can be taken as fixed at all frequencies. The cathode is an electrode which is relatively comparable to the anode, with its own capacitance, resistance, and loss factor; these parameters vary in a highly complex manner with frequency if, in a liquid electrolyte, the cathode is porous, in order to increase its surface area and to lower its impedance. In all cases a porous cathode can be considered as a thin layer of a material with electrical parameters distributed throughout its mass and deposited on a support which constitutes the last equipotential surface to be considered. Physically, capacitance is shunted by a very low resistance, what is equivalent to a very high capacitance with an ESR, both varying with frequency. The equivalent electrical diagram of a complete capacitor is therefore as follows (Fig. 12).

We might try to extend to the electrolytic cathode the conclusions of our previous calculations. Roughly, the capacitance per unit smooth area Γ increases with the electrolyte concentration, and, at the high concentrations used in porous electrodes capacitors, it goes through a maximum when the voltage between the electrode and the solution is zero; it decreases with frequency at a negative power with an absolute value decreasing with higher concentration (about -0.1 to -0.3). For a-c voltages, the only ones we are concerned with, a polarization series resistance Π appears, as inversely proportional to frequency. Unfortunately, a comparative examination of the curves (Π, ω) and (Γ, ω)

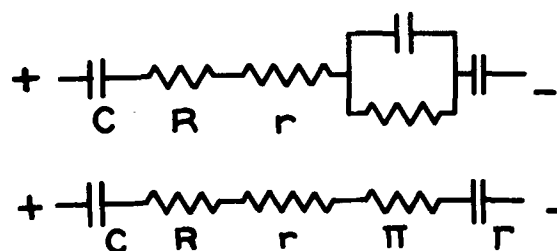


Fig. 12. Equivalent electrical diagrams of a complete capacitor

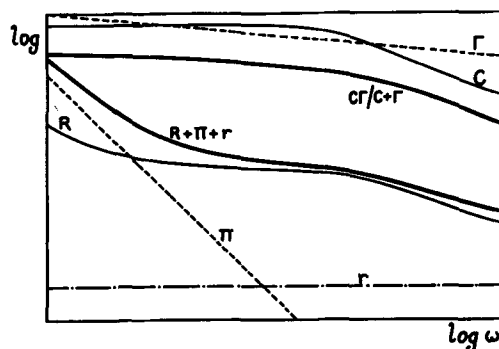


Fig. 13. Typical variations with ω of the different elements of the impedance of a liquid electrolyte capacitor with a smooth cathode.

relative to smooth cathodes with localized constants and to porous cathodes with distributed constants has so far failed to yield an explanation in terms of the criteria already adopted. In fact, for porous electrodes, Π and Γ decrease approximately like $\omega^{-1/3}$; coating a smooth silver cathode with a porous silver layer dipped in 40° Be sulfuric acid may divide Π by a factor of about 100 and multiply Γ by the same factor.

It is then easy to see the deteriorating effect of a smooth cathode with a capacitance of the same order of magnitude as C in the initial range: the resultant capacitance of the capacitor is halved. The cathode capacitance decreases whereas the anode capacitance hardly varies, so that the net capacitance decreases. These effects are illustrated in Fig. 13, drawn somewhat arbitrarily: in the extreme range it shows the over-all capacitance decreases more slowly than C ; the over-all ESR is considerable regarding R in the initial range; the two resistances then tend to come together, but at very high frequencies the resistance r causes the curves to diverge. With the same assumptions, substituting a porous cathode for a smooth one brings about a gain of Γ such that the resultant capacitance is practically equal to C . The over-all ESR, shown in Fig. 14, is hardly higher than R in the initial range, but in the extreme range both curves are necessarily again divergent; whatever be the upper validity range of our hypothesis, at the higher frequencies, r then dominates and the over-all ESR is not dependent on the nature of the cathode.

Conclusion

Returning to an idea that arose during the first physical and technological investigations on porous anode tantalum capacitors, we have attempted, with the collaboration of the ANALAC Analog Computing Center, to explain the dynamic behavior of electro-

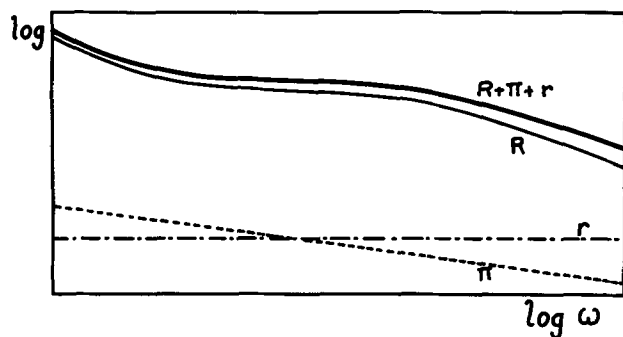


Fig. 14. Typical variations with ω of the different real elements of the impedance of a liquid electrolyte capacitor with a porous layer cathode.

lytic capacitors with liquid or solid semiconductor impregnant. We have tried to find the cause of observed variations of capacitance and loss factor with frequency and various characteristic parameters, more with regard to the "geometric" phenomena due to the low-pass filter action of porous anodes, than the deeper physical phenomena which affect the parameters themselves. We have shown how relatively simple families of curves allow the treatment of planar and cylindrical capacitors. These computations should assist in the interpretations of the experimental results. Using this tool and under light so projected, the author contemplates soon publishing as a whole experimental results as well on liquid electrolyte capacitors as on semiconductor ones; he preferred not to make heavy the present paper and to set aside the reported publication so as to show how study of an electric wave propagation through a porous anode permits to find again the theoretical preceding results.

Acknowledgment

For this work, done under contract MWDP F 61 MWP A 59, concerning general investigations on capacitors prepared by anodic oxidation and preferentially with a solid impregnant, we have enjoyed the aid of Dr. Kleefstra, who made experimental studies of the properties of electrolytic capacitors in the very low frequency range, and of Dr. Apter, who adapted the problem to the machine after the preliminary work of the late Dr. Ricou. Our sincere thanks are due to these engineers for the fundamental role they have played.

Manuscript received Dec. 4, 1962; revised manuscript received Nov. 1, 1963.

Any discussion of this paper will appear in a Discussion Section to be published in the June 1965 JOURNAL.

REFERENCES

1. N. Thien-chi and J. Vergnolle, *Onde Electrique*, **35**, 318 (1955).
2. P. Bourgault, A. C. Capacitance measurements of a porous electrode, Report for the Canadian Government.
3. J. S. Newman and C. W. Tobias, *This Journal*, **109**, 1183 (1962).
4. L. Young, "Anodic Oxide Films," Academic Press, London (1961).
5. J. Vergnolle and M. Kleefstra, C. R. (forthcoming paper).
6. D. A. McLean, *This Journal*, **108**, 48 (1961).

SYMBOLS

a	Cross-sectional area of a planar anode
l	Length of a cylindrical anode
x	Space coordinate (radial coordinate for cylindrical anode); also denoting space coordinate of outer position of porous anode
x_0	Space coordinate for solid anode core
ρ	x/x_0
G, R	Form factors for cylindrical anodes defined by Eq. [17] and [18] and represented in Fig. 4 and 5
$V(x)$	Volume within the surface, $x = \text{const.}$
$\partial C_1/\partial x$	Series equivalent capacitance per unit length of the porous anode
K	Complex equivalent series capacitance of the anode per unit volume
K_0	Real part of K
χ	Specific conductivity in the pores (impregnant conductivity)
$\partial R_1/\partial x$	Effective resistance per unit length of the pores
$p = \left(\frac{\partial R_1}{\partial x} \chi \frac{\partial V}{\partial x} \right)^{-1}$	A form factor characterizing porosity
δ	Effective loss factor of the dielectric
q	Another form factor characterizing porosity
T_δ	Function defined by Eq. [33]
δ_1	An intrinsic loss factor of the dielectric for the pore free case
$Z = R - j/C\omega$	Impedance between anode core x_0 and external surface x
ω	Angular frequency
$\tan \Delta = RC\omega$	Apparent loss factor of an anode or of a whole capacitor
χ	A dimensionless coordinate combining position, frequency, specific capacitance, and conductivity defined by Eq. [12]
χ'	Real part of χ . ¹
R_i, C_i	Asymptotic values for R, C , for $\chi' \rightarrow 0$ ("initial range")
R_∞, C_∞	Asymptotic values for R, C , for $\chi' \rightarrow \infty$ ("extreme range")
$(R_i)_0$	Asymptotic value for R in the initial range for $\delta = 0$
$\gamma_R = R/R_i$	A dimensionless coordinate, essentially representing R , and being a function of χ
$\gamma_{R'}$	The same one, function of χ' , (real) ¹
$\gamma_c = C/C_i$	A dimensionless coordinate, essentially representing C , and being a function of χ
$\gamma_{c'}$	The same one, function of χ' , (real) ¹
F	A dimensionless coordinate, essentially representing Z
$\chi_{R'}, \chi_{c'}$	Dimensionless abscissae at which $R_\infty = R_i$ and $C_\infty = C_i$, respectively (critical points)
ω_R, ω_c	Corresponding values of angular frequency (critical frequency)
r	Resistance of the structure outside of x (cathode-anode interval)
Γ	Cathode polarization equivalent series capacitance
Π	Cathode polarization equivalent series resistance

¹ Note: When considering capacitance as complex, or imperfect, we use χ and γ coordinates; when considering it as perfect and incorporating its imaginary part in ESR, we use χ' and γ' coordinates.

Growth of α -SiC Single Crystals from Chromium Solution

L. B. Griffiths and A. I. Mlavsky

Tyco Laboratories, Inc., Waltham, Massachusetts

ABSTRACT

The travelling solvent method of crystal growth has been successfully adapted to the growth of α -SiC single crystals, using pure chromium as the solvent. Since molten chromium does not wet chemically cleaned SiC in a uniform and reproducible manner, a prewetting procedure was developed which involves a heat treatment of the SiC at 1200°-1300°C *in vacua* at 10^{-9} - 10^{-10} Torr, followed immediately by the evaporation of a thin (10^4Å) film of pure chromium onto the clean surfaces. The chromium solvent zones were passed under the influence of a temperature gradient in a simple r. f. furnace; the average specimen temperature was 1750°C. Subsequent metallographic and x-ray examination revealed that good crystal growth had occurred. Growth rates of the order of 0.75 mm hr^{-1} were obtained under the above conditions. p-n junctions prepared by deposition, from chromium solution, of one conductivity type onto the opposite type were assembled into diode structures. Junction capacitance varies with bias in accordance with a $V \propto 1/C^2$ law, indicating an abrupt (step) junction. The forward I-V characteristics are unique for SiC devices in that the forward voltage drop is 1.2-1.5v compared to 2-5v reported for previous diodes at comparable current densities. The slope of the forward biased characteristics was found to be $e/2.4kT$. Considerable leakage is observed (under reverse bias); the peak inverse voltage, which ranges from 6-15v, is much lower than expected from the resistivity of the bulk material. This low voltage breakdown is tentatively discussed in terms of a peculiar dislocation structure in the region of the p-n junction. The over-all rectifying properties of the devices prepared by TSM persist up to at least 540°C.

Silicon carbide, a highly refractory semiconductor, occurs in two major crystallographic modifications. The so-called high-temperature, α -modification has a hexagonal structure which is most conveniently described as a distorted wurtzite structure. Depending on the polytype, of which a great number exist, the energy gap (1-3) is 2.7-3.2 ev. The β (cubic) modification, which is usually formed below 2000°C, has an energy gap of 2.3 ev (3).

The combination of high energy gap and refractoriness [decomposition (4) occurs at *ca.* 2800°C] makes α -SiC potentially very useful for high-temperature semiconductor devices. However, device development has been hampered by the difficulties encountered in the preparation of high-quality single crystals and p-n junctions.

α -SiC p-n junctions have been prepared by growth from the vapor phase (5-7), by the standard semiconductor techniques of alloying and diffusion (8, 9), and during growth from solution (10). This paper describes an improved version of the latter technique, the travelling solvent method of crystal growth (TSM) (11, 12).

TSM is based both on the temperature gradient zone melting technique of Pfann (13) and also a variant thereof (14) in which an aluminum-rich zone is passed through silicon under the influence of a temperature gradient to yield a large area p-n junction. Hergenrother (10) applied a similar technique to the growth of α -SiC p-n junctions, using a chromium-rich solvent. Modifications and improvements of these techniques have been made in this laboratory for the crystal growth of compound semiconductors. In the particular case of SiC, strin-

gent surface preparation of α -SiC insures uniform and ready wetting by the solvent and effects a considerable improvement in the basic technique.

Experimental

Principle of the method.—In the application of TSM, a temperature gradient is impressed across a thin solvent zone sandwiched between two pieces of the solid to be grown. Initially dissolution occurs at both solvent-solid interfaces. However, since the equilibrium solubility is greater at the hotter interface, a concentration gradient is established and solute diffuses across the liquid zone and precipitates onto the cooler seed crystal. The process may therefore be divided into several stages, *i.e.*, wetting of the solid by the solvent; dissolution at both interfaces; establishment of the concentration gradient; and finally precipitation of the solute on the seed crystal. Irrespective of which stage is rate determining, there is theoretically no dependence of the growth rate on the zone thickness. The driving force for passage of the solvent zone is provided solely by the concentration gradient which is a function of both the temperature gradient and also the slope of the liquidus at the particular temperature (average zone temperature) of growth.

Selection of a suitable solvent is based on the criteria that it should readily wet the solid in question, and exhibit increasing equilibrium solute content with increasing temperature, *i.e.*, the slope of the liquidus in the particular system should be positive. The solvent should preferably have a lower melting point than that of the solute, exhibit low vapor pressure at the temperature of growth, and

possess negligible solid solubility. The final feature is desirable from the viewpoint of the physical properties of the final crystal and is particularly significant for semiconductors.

Practical considerations.—TSM depends on a difference in solubility at the hot and cool solid-liquid interfaces. In principle, therefore, any alloy system exhibiting a liquidus of positive slope should favor zone movement. The liquidus slope ds/dT is given by:

$$\frac{ds}{dT} = \frac{F}{D \cdot \frac{dT}{dx}}$$

where F is the flux through the solvent zone, D the diffusion coefficient, and dT/dx the temperature gradient. If we consider an acceptable growth rate of 0.125 mm/hr, a liquid metal diffusion coefficient of 10^{-4} cm²/sec, and a temperature gradient across the solvent zone of 10°C/mm, which is a reasonable estimate, then:

$$\frac{ds}{dT} = \frac{1.25 \times 3.2 \times 10^{-2}}{10^{-4} \times 3.6 \times 10^3 \times 10^2} = 10^{-3}$$

i.e., expressing S as a percentage solubility, it is required that $ds/dT > 0.1$ at growth temperature.

The solvent zone must be sufficiently thick to provide stable interfaces with the solid over the entire contacting surfaces, while its maximum thickness is chosen to enable some solid material to be present always. The particular experimental arrangement used in the present work precluded the use of solvent zones thicker than 0.35 mm since both convection currents and r.f. stirring tended to destroy the temperature gradient in thicker zones.

The crystal growth experiments discussed in this paper were performed with chromium as the solvent. We have established a tentative constitutional diagram of the Cr-SiC alloy system in the region of interest (Fig. 1). The eutectic which occurs at about 1600°C is advantageous since it permits crystal growth well below the melting point of chromium. At the melting point, the vapor pressure of chromium is high and would cause serious experimental difficulties.

Silicon and platinum were initially used as solvents, but were discarded since the liquidus slopes

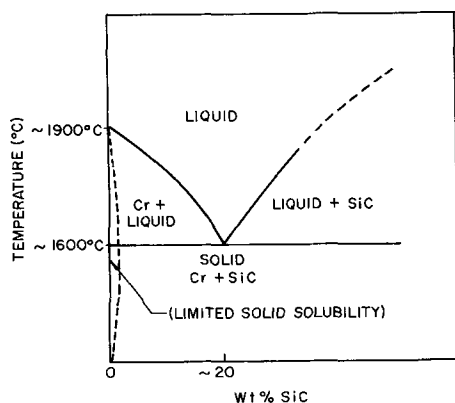


Fig. 1. Tentative constitutional diagram of chromium-rich end of Cr-SiC system.

in both systems are apparently too steep to provide growth rates of practical significance.

Specimen preparation.—Initial efforts of crystal growth were hindered by difficulties encountered in the wetting of SiC surfaces with chromium. This resulted in erratic zone movement. Good wetting was achieved when the silicon carbide surfaces were cleaned by the following procedure. After the specimens were machined to a suitable size and shape, they were heated by electron bombardment to about 1300°C in a vacuum of 10^{-9} to 10^{-10} mm Hg. The immediate visual result of the vacuum heat treatment was a greatly enhanced reflectivity. A thin film of chromium was then evaporated from a heated tungsten filament onto the specimens in the same apparatus. All experiments were performed utilizing (0001) crystallographic surfaces. Good adhesion between the evaporated films and the silicon carbide surfaces was obtained, as indicated by the lack of blistering or peeling of the films when they were heated to 1300°C. The apparatus used in this phase of the work is shown in Fig. 2.

Crystal growth and p-n junction fabrication.—Pairs of chromium-coated specimens were assembled in "sandwiches," with chromium slices of 0.1-0.3 mm thick between the coated surfaces. This assembly was heated in an argon atmosphere, inside the apparatus shown in Fig. 3. The upper surface of the sandwich was cooled by natural radiation; the maximum specimen temperature observed with an optical pyrometer was about 1750°C. SiC specimens

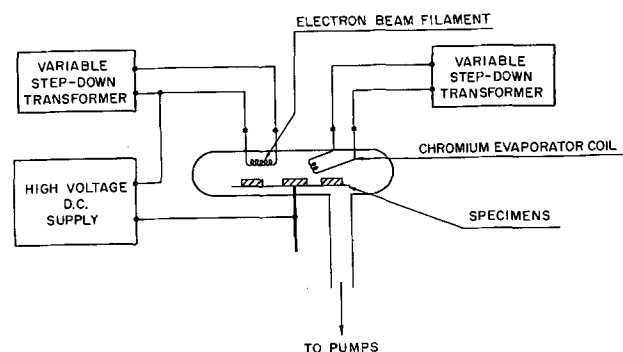


Fig. 2. Schematic of vacuum system with electron beam heating and chromium evaporation facilities.

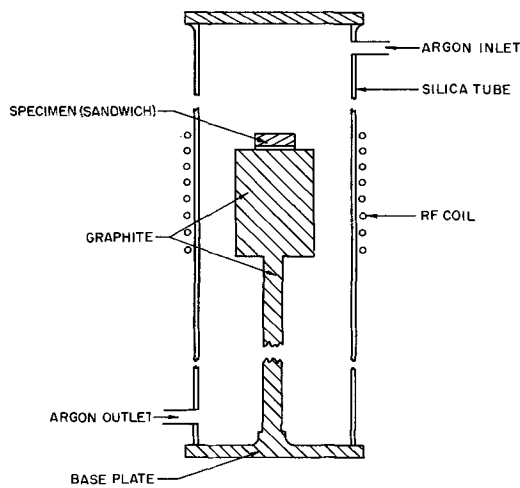


Fig. 3. Assembly for TSM crystal growth of SiC

Table I. Physical properties

Conductivity type	Hall coefficient, cm ² /coul	Resistivity, ohm-cm	Mobility, cm ² /volt-sec
p	57	9.0	6.3
n	2-35	0.4-4.0	83-107

of different thicknesses were used, and the time required for complete traverse of the chromium zone was recorded. The direction of growth was always in the "c" direction.

p-n junctions may be fabricated readily by TSM. The introduction of dopants into the solvent during crystal growth makes possible the deposition of either conductivity type. As a test of feasibility we took advantage of the fact that nitrogen is a strong n-type dopant in SiC and added a small quantity of N₂ to the argon atmosphere during growth of a p-type SiC crystal. The resultant crystal was subsequently examined metallographically.

Table I lists some physical properties of both p- and n-type SiC crystals obtained from Norton Company. The n-type material is green and transparent, while p-type is dark blue and also transparent. Using the procedures outlined above, p-type SiC has been deposited onto n-type seeds and *vice versa*. p-n junctions were thus fabricated using this partially characterized material without additional doping during crystal growth.

Contacting procedures.—Contacts of pure platinum were evaluated for use as ohmic contacts to p-n junctions. While exhibiting an excellent linear current-voltage relationship, they possessed very high resistances. Accordingly the use of platinum was discontinued.

An alloy of 99:1 Au-Ta doped with either aluminum or antimony was subsequently evaluated for contacting to p- and n-type material, respectively. Gold-tantalum alloys have been used both by Westinghouse Company (15) and also by Philips Research Laboratories (16). Tantalum additions aid in the wetting of gold to SiC. Quite excellent ohmic contacts were obtained when the alloy was heated in contact with the SiC in an r.f. furnace to 1150°C for a few minutes.

Results and Discussion

Figure 4a is a photomicrograph of a ground and polished crosssection through a typical SiC specimen after zone passing. The arrows indicate the initial position of the chromium layer; excellent regrowth is observed. Figures 4b and 4c, which show x-ray back reflection photographs of the seed and regrown material, respectively, demonstrate that true crystalline propagation of the seed has occurred. These results clearly demonstrate that the surface cleaning procedure is adequate to allow wetting of the SiC by the chromium. (There was no difficulty in wetting at Cr-Cr interfaces.) The high vacuum heat treatment was initially undertaken on the basis that a film of SiO₂ existed on the SiC and prevented wetting. Under high vacuum heating such a film would be removed by dissociation to SiO, which is volatile. Since the α -SiC struc-

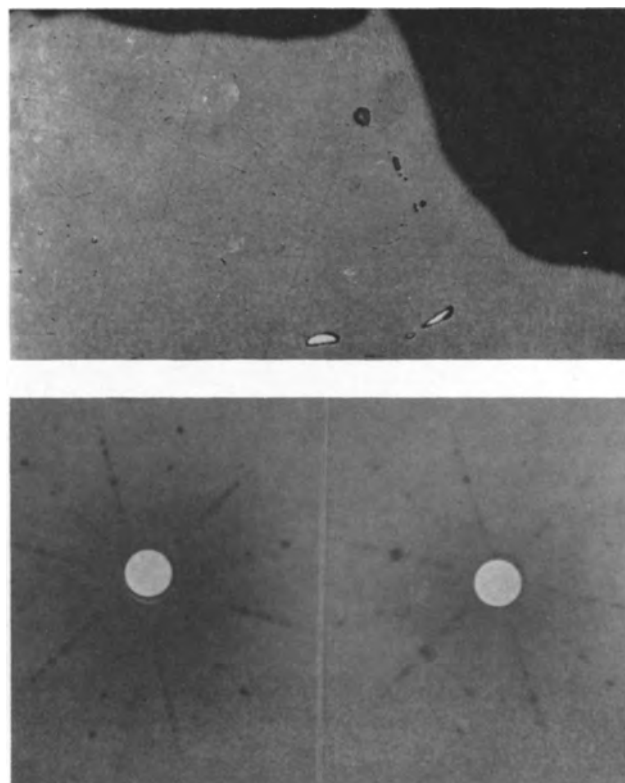


Fig. 4. Photomicrograph of cross section with corresponding x-ray patterns of TSM grown SiC crystal.

ture consists of alternate layers of silicon and carbon atoms tetrahedrally bound to their neighbors, only one surface of a SiC crystal is likely to be coated with a continuous SiO₂ film; the opposite surface terminates in a layer of carbon atoms. This surface "polarity" may be observed readily by etching SiC platelets; distinct differences in surface structure become clearly apparent.

A second possibility is that adsorbed gas on the SiC prevents wetting. However, unless the particular species is strongly chemisorbed, it appears unlikely that it would prevent wetting by chromium. The exact nature of the interface between chromium and "untreated" SiC is therefore still unresolved.

Of considerable interest is the fact that α -SiC (hexagonal) may be grown from chromium-rich solution at temperatures well below the β/α "transition" temperature of about 2000°C. This so-called transition in SiC is not a true allotropic, solid-state transition. In general, experimental evidence has demonstrated that preparation of SiC at temperatures below about 2000°C produces the cubic modification while the hexagonal form results, usually from vapor phase growth, above 2000°C. The transition is not sharp, and a wide range of hexagonal polytypes may be produced. Thermal cycling through 2000°C does not cause a crystallographic-type change. It appears that in the presence of an α -SiC seed and the particular experimental conditions of TSM the hexagonal modification may be grown below 2000°C. From the measurements of the time taken for passage of chromium-rich solvent through various thicknesses of SiC a growth rate of ~ 0.75 mm/hr was deduced. Figure 5 summarizes the data

which refer to a specimen temperature of 1750°C.

Figure 6 shows a photomicrograph of a cross section through the crystal doped with nitrogen during growth. It is clear that the quite flat, uniform junctions may be prepared by TSM, although at present we must resort to over-compensation to influence conductivity type. The junction shown in Fig. 6 was delineated by electrolytic etching in hydrofluoric acid at room temperature for 30 sec.

Using material of the type referred to in Table I, several crystals of 10 mm diameter, 2-3 mm thick, and containing a single p-n junction have been prepared. A die cut from one such crystal is shown in Fig. 7. This specimen measures 3 x 3 x 2 mm. The darker colored p-type material remained transparent after the chromium solvent zone had passed through it.

Several dice were cut from the junction-bearing crystal and provided with Au-Ta ohmic contacts in the manner previously described. The junction areas of the finished experimental diode structures were about 5 mm². A typical oscilloscope trace of the room temperature voltage-current character-

istics of silicon carbide diodes is shown in Fig. 8. Of particular interest is the forward characteristic in which turnover occurs at about 1.3v. This value is considerably lower than that previously observed in silicon carbide (17), but of the order expected for this material. Figure 9 illustrates the results obtained from point-by-point measurements in the forward direction. The forward characteristics may be represented by the empirical relationship

$$I = A \exp \frac{eV}{nkT} \quad (1)$$



Fig. 7. View of die cut from typical TSM crystal. Magnification 8X.

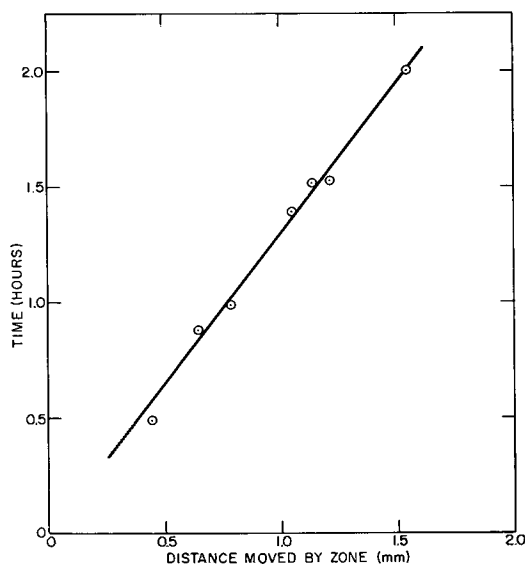


Fig. 5. Time-distance relationship for SiC crystal growth for chromium solution; temperature about 1750°C.



Fig. 6. Photomicrograph of cross section through SiC crystal showing junction produced by nitrogen doping during growth; electrolytically etched in HF solution. Magnification 250X.

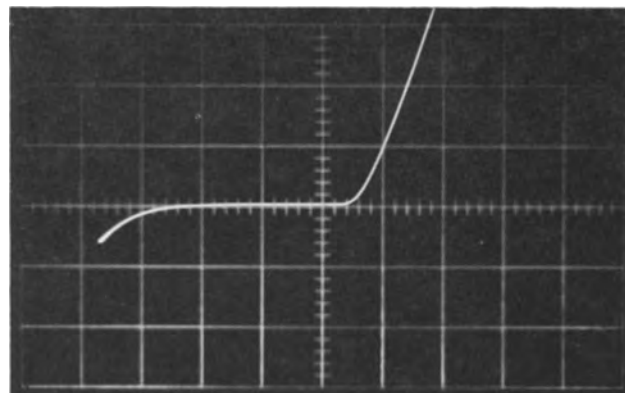


Fig. 8. Oscilloscope trace of room temperature characteristic of SiC p-n junction diode; vertical axis 5 ma/cm; horizontal axis 2 v/cm.

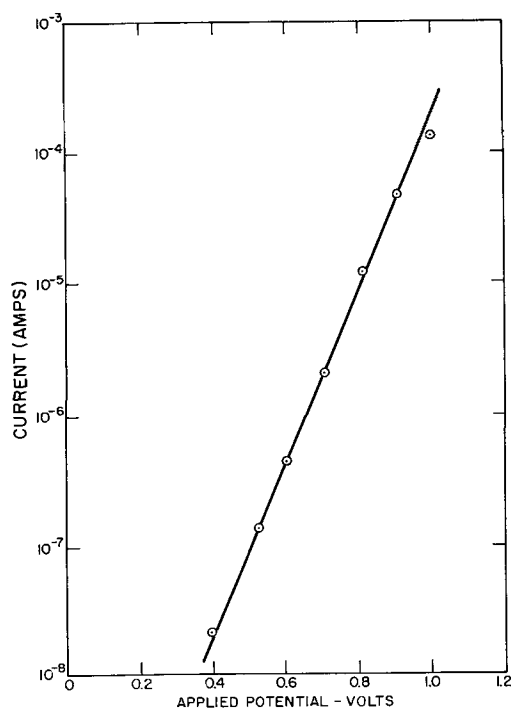


Fig. 9. Forward characteristic of SiC p-n junction diode

where V is the applied voltage, and A is the diffusion current. The quantity n is determined from the slope of the curve in Fig. 9 to be 2.4. Values of n of this order have been observed in silicon carbide diodes made from vapor grown junctions (2). Such high values may result from the relatively high impurity content of presently available material. To some extent, however, a high value of n reflects the nature of the junction, which in the case of SiC, frequently contains a thin semi-insulating region between the p and n sides. The physical extent of such a layer will be strongly influenced by the temperature of growth. In addition to affecting the value of n , the presence of a semi-insulating region will be reflected in the forward voltage drop. In fact, a contributory factor to the relatively low F.V.D. observed on many of our diodes (c.f., 1.3v) would appear to result from the temperature of crystal growth being several hundred degrees lower than that for vapor grown junctions.

Considerable information regarding the nature of p-n junctions is obtainable from the variation of junction capacitance with applied voltage. The theoretical dependence is given by the relation

$$C_v = \frac{C_o}{\left(1 - \frac{V}{\phi}\right)^x} \quad [2]$$

where C_v is the junction capacitance at a bias voltage V . C_o is the junction capacitance at zero bias, ϕ is the "built-in" junction potential, and x is 1/2 for an abrupt junction and 1/3 for a diffuse junction. Very careful measurements on TSM-grown silicon carbide junctions, Fig. 10, have yielded the relationship:

$$V \propto \frac{1}{C^2} \quad [3]$$

Extrapolation to infinite capacitance yields the value of ϕ which, in an ideal p-n junction, can be identified as that voltage which produces a flat band condition across the junction. The value of 2.1v shown in Fig. 10 is reasonable for α -SiC. For a simple p-n junction, ϕ cannot exceed the fundamental energy gap of the particular semiconductor, but, with the presence of a semi-insulating region be-

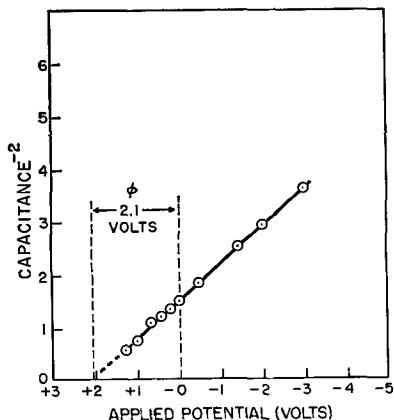


Fig. 10. Variation of SiC diode junction capacitance with applied voltage.

tween the p and n sides, Eq. [2] is inapplicable and ϕ has no real significance; extrapolation of $1/C^2$ vs. V plots yields voltages, corresponding to infinite capacitance which are very large and certainly greater than the band gap. This is understandable, since, in a true p-n junction structure, the capacitance is provided by the space charge region which varies with bias, whereas the capacitance of the semi-insulating region will be essentially independent of bias. Several diodes have exhibited large apparent values of ϕ . A detailed discussion of junction structure and properties in relation to growth parameters will be published elsewhere.

The temperature dependence of the diode characteristics is illustrated in Fig. 11, 12, and 13, which show oscilloscope traces for a typical junction at 30°, 320°, and 540°C, respectively. The forward

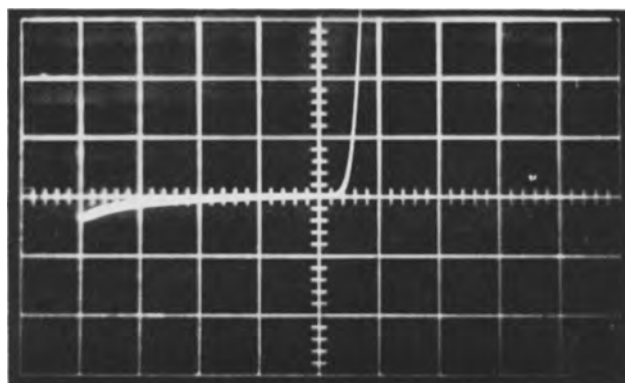


Fig. 11. Variation of SiC rectifier characteristics with temperature; vertical axis 5 ma/cm; horizontal axis 2 v/cm.

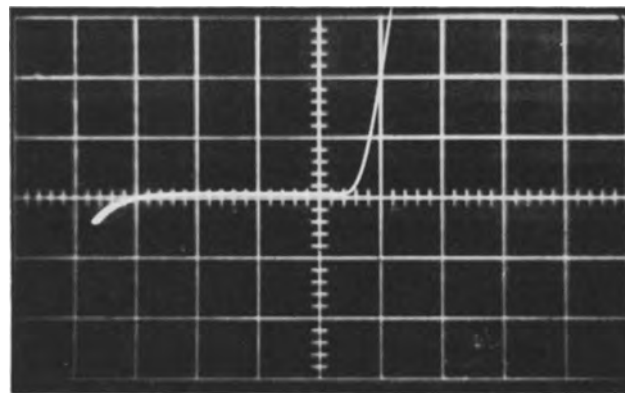


Fig. 12. (same as above)

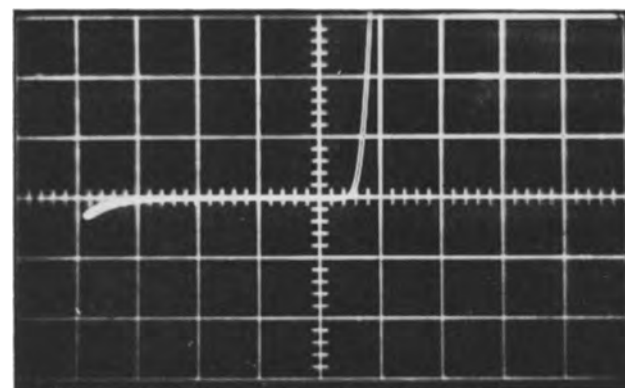


Fig. 13. (same as above)

characteristic improves continuously as the temperature increases. The reverse characteristic begins to "soften" only at temperatures above 500°C. Even at room temperature, the reverse characteristic of these devices is smaller than expected; typical values of peak inverse voltage range from 6v to about 15v. The low peak inverse voltages of TSM-prepared diodes may be the result of inadequate surface treatment of the assembled structure, *i.e.*, high surface leakage. However, repeated etching and washing treatments produced little or no improvement.

Metallographic examination of diode structures indicated that if, during alloying of contacts, the gold alloy flowed down the sides of a specimen and thus came into contact with the edges of the junction region, deep penetration of the junction by a thin film of gold occurred in times of the order of minutes only. It is recalled that in these structures the junction region coincides with the initial plane of crystallization. This plane is believed to contain a network of screw dislocations which allows the remarkably rapid penetration of gold. TSM grown crystals of other solids have revealed interesting and unique dislocation configurations (18) in the same general region. The presence of such a dislocation network in the vicinity of the junction could explain the rather high reverse leakage observed.

Summary

It has been shown that TSM is a simple technique for growing relatively large crystals of silicon carbide and of forming p-n junctions during crystal growth. Successful application of the method requires that SiC surfaces be rigorously clean. Uniform wetting by chromium is a prerequisite for successful zone passage and occurs only on ultra-clean SiC. The regrown material is α -SiC, even though the growth process is performed well below the β/α "transition" temperature of about 2000°C.

Acknowledgments

The authors wish to thank Mr. T. Fuller for valuable experimental assistance and Dr. A. J. Rosenberg for many helpful discussions during this work, which was performed under U.S. Air Force Contract No. AF 19(604) 8803.

Manuscript received July 26, 1963; revised manuscript received Oct. 17, 1963. This paper was presented at the Pittsburgh Meeting, April 15-18, 1963.

Any discussion of this paper will appear in a Discussion Section to be published in the June 1965 JOURNAL.

REFERENCES

1. L. Patrick, *J. Appl. Phys.*, **28**, 765 (1957).
2. W. J. Choyke and L. Patrick, "Silicon Carbide," p. 306, J. R. O'Connor and J. Smiltens, Editors, Pergamon Press Inc., New York (1960).
3. A. Addamiano, R. M. Potter, and V. Ozarow, *This Journal*, **110**, 517 (1963).
4. R. I. Scace and G. A. Slack, "Silicon Carbide," p. 24, Pergamon Press Inc., New York (1960).
5. A. H. Smith, "Silicon Carbide," p. 53, Pergamon Press Inc., New York (1960).
6. J. A. Lely, *Ber. deut. keram. Ges.*, **32**, 229 (1959).
7. D. R. Hamilton, *This Journal*, **105**, 735 (1958).
8. Hung-Chi Chang *et al.*, "Silicon Carbide," p. 496, Pergamon Press Inc., New York (1960).
9. R. N. Hall, *J. Appl. Phys.*, **29**, 914 (1958).
10. K. Hergenrother, U. S. Pat. 2,996,456 (1961).
11. A. I. Mlavsky and M. Weinstein, *J. Appl. Phys.*, **34**, 2885 (1963).
12. L. B. Griffiths and A. I. Mlavsky, Paper presented at the Pittsburgh Meeting, Electrochemical Society, April 1963.
13. W. G. Pfann, *Trans. AIME*, **203**, 961 (1955).
14. W. G. Pfann, "Zone Melting," p. 201, John Wiley & Sons, Inc. (1958).
15. Westinghouse Research Laboratories, Scientific Reports under Air Force Contract AF 19(604)-8499.
16. H. J. van Daal *et al.*, *Physics and Chemistry Solids*, **24**, 1 (1963).
17. H. J. van Daal *et al.*, *J. Appl. Phys.*, Suppl. to **32**, 2225 (1961).
18. M. Weinstein, H. LaBelle, Jr., and A. I. Mlavsky, Paper presented at Electrochemical Society Meeting, New York, 1963.

Measurement of the Resistivity of Epitaxial Vapor Grown Films of Silicon by an Infrared Technique

T. G. R. Rawlins

Northern Electric Research and Development Laboratories, Ottawa, Ontario, Canada

ABSTRACT

An infrared reflectivity technique is outlined whereby the reflectivity may be correlated with d-c resistivity of thin vapor deposited epitaxial silicon layers. The theory underlying the method is outlined and calculated curves for different planes of polarization are given. Experimental results are described for a range of resistivities between 0.03-60 ohm-cm. Limitations of the equipment used are discussed and the validity of the method examined.

It is well known that diffused transistors fabricated from epitaxial silicon (silicon having a thin lightly doped layer grown on top of a heavily doped single crystal substrate) have vastly improved characteristics over transistors fabricated from conventional material (1). In order to produce transis-

tors of controlled properties, it is necessary to measure the thickness and the resistivity of the layers. A nondestructive infrared interference method for the measurement of thickness has been proposed by Spitzer and Tannenbaum (2) and enlarged upon by Albert and Combs (3).

A variety of methods have been tried for measurement of resistivity, most of these have been electrical methods either direct or indirect. One method, that has been used extensively, has been to fabricate shallow junction diodes on the surface and calculate resistivity from the capacitance-voltage characteristics [see for example (4)]. This method is, however, destructive and comparatively time-consuming. Other methods in the case of silicon, which are nondestructive, rely on the properties of various types of contacts (5). These contacts do not usually have reproducible properties. In many instances these methods are not very practical and are limited in resistivity range.

It was with these many short-comings in mind that an infrared method was sought. The infrared method is also convenient in that thickness and resistivity may be measured on the same instrument.

In principle, high frequency resistivity (assumed proportional to d-c resistivity) may be found from the optical constants n and k . Thus any method of measurement which leads to values for n and k may be used, since the complex refractive index is given by

$$N = n - ik$$

and from Maxwell's equations

$$N^2 = \epsilon\mu - i4\pi\mu\sigma/\omega$$

where ϵ is the permittivity, μ permeability, σ conductivity (high frequency), and $\omega = 2\pi \times$ frequency.

Conventionally, reflectivity may be used to find n and k (6, 7). However, the case of epitaxial silicon reflectivity is different in that interference fringes are obtained, which somewhat complicate the situation, and a different expression for the reflectivity from a layer is obtained (8). In any case it becomes impracticable to measure resistivity in this way for, apart from the above factors, it is found that for the range of resistivities, which are usually of interest for epitaxial layers (0.1 ohm-cm - 100 ohm-cm), n is essentially constant and k is extremely small (9). In the case of conventional reflectivity measurements for reasonably accurate results, it is necessary that $k \geq 0.2$, i.e., significant absorption (6, 7). It therefore becomes necessary to "magnify" the very small values of k ($10^{-4} - 10^{-1}$) in order to be able to use reflection spectra for differentiating between layers of different resistivities. In addition, such a method must only allow penetration of the incident radiation into the topmost region of the deposited layer. In fact these requirements are met in the method of attenuated total reflection due to Fahrenfort (10) and Fahrenfort and Visser (11). The essentials of this method are such that radiation is allowed to travel in a dense medium towards a boundary between this medium and one which is less dense. The latter medium is the sample of immediate interest, having a finite (but usually small) value of k . The angle of incidence of the radiation on the boundary is arranged such that it is slightly greater than the critical angle. The reflectivity is then no longer 100% but depends quite markedly on the value of k for the sample [see (10, 11)]. This implies a transfer of energy into the second medium.

Some of this energy is absorbed, according to the value of k and the particular wavelength.

Theory

An outline of the theory, which is appropriate to the use of the method for resistivity measurement, will be given below.

The Fresnel coefficients may be obtained by applying the boundary conditions for radiation incident on an interface between dense and less dense media [c.f. (12)].

These expressions give the ratios of the amplitudes of the reflected or transmitted electric vectors for both planes of polarization of the incident electric vector. Analogous expressions may be obtained for the magnetic vectors.

Also

$$\begin{aligned} N_o \sin \phi_o &= N_1 \sin \phi_1 \quad (\text{Snell's law}) \quad [1] \\ N_o &= n_o \\ N_1 &= n_1 - ik_1 \end{aligned}$$

(Since N_1 is complex, it is apparent from [1] that ϕ_1 must be complex.)

Using the Fresnel equations, Snell's law and the definition of the Poynting vector, we may obtain equations for the reflectivity for the two planes of polarization, i.e., for polarization perpendicular to the plane of incidence

$$R_s = [(n_o \cos \phi_o - x)^2 + y^2] / [(n_o \cos \phi_o + x)^2 + y^2]$$

where x and y are parameters given by

$$x - iy = [(n - ik)^2 - n_o^2 \sin^2 \phi_o]^{1/2}$$

A similar expression may be obtained for the other plane of polarization. When various appropriate values of n_o , n_1 , k_1 , and ϕ_o are substituted in the reflectivity equations, results such as those shown in Fig. 1 and 2 are obtained. From these graphs it may be seen that, when the second medium has a finite non-zero value of extinction coefficient for angles of incidence greater than the critical angle, defined

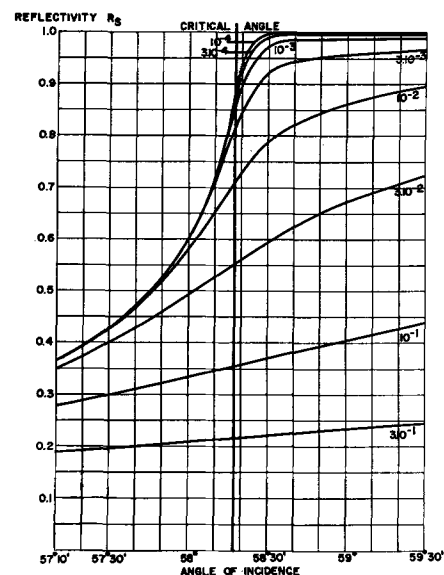


Fig. 1. Calculated reflectivity vs. angle of incidence curves for polarization perpendicular to the plane of incidence and various values of k : $n_o = 4.02$ (germanium), $n_1 = 3.42$ (silicon).

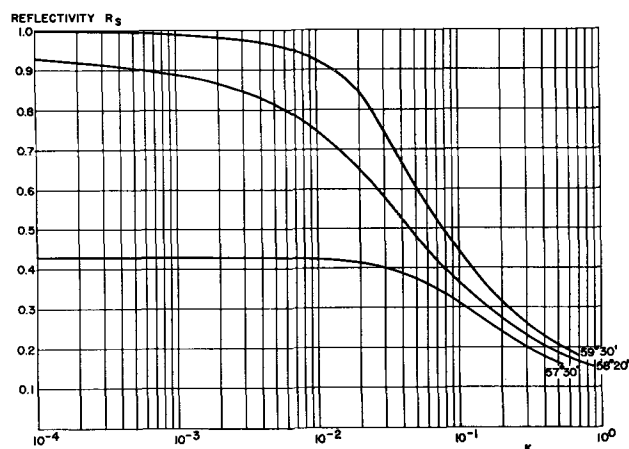


Fig. 2. Re-plotted version of Fig. 1, showing reflectivity vs. k for different angles of incidence.

as $\sin^{-1}(n_1/n_0)$, the reflectivity varies according to the value of k . This is also true for angles of incidence less than the critical angle. However, in this case, the difference in reflectivity for a given change in k very rapidly becomes much less (see Fig. 2). It is evident from the graphs that the difference is greatest at, or slightly above the critical angle.

Now according to electromagnetic theory

$$(n - ik)^2 = \epsilon\mu - i4\pi\sigma/\omega$$

or

$$n^2 - k^2 = \epsilon\mu = \epsilon \quad (\text{assume } \mu = 1)$$

$$nk = 2\pi\sigma/\omega = \sigma/v$$

Hence n and k are dependent on σ . Also experimentally (9) it is found that at a given wavelength the absorption coefficient increases with increasing carrier concentration, *i.e.*, since absorption coefficient $\alpha = 4\pi k/\lambda$, reflectivity must vary with carrier concentration. [For a more complete theoretical treatment, see ref. 13.]

Experimental

As the refractive index of silicon is (nominally) $3.42 - ik$ (14) it is necessary to pick another semiconductor, namely germanium, $n = 4.02$, as the optically denser medium (14). Since both incident beam and reflected beam should be attenuated as little as possible, it is preferable that the germanium should have small absorption, *i.e.*, intrinsic germanium so that little or no impurity absorption occurs and only that due to lattice vibrations is significant.

Further, it is apparent from the analysis (13) that the two media must be in intimate contact in order to give the best results, *i.e.*, there should be no intermediate air space. In practice this is difficult to achieve. However, various microwave experiments (15) show that the effect will still occur even when there is substantial separation. However, it is evident that the relative difference may be expected to be considerably reduced. Due to this fact, and to the fact that the surface of vapor-grown material is not perfectly flat, it is more convenient to be able to investigate a relatively small portion of the total area, since the variation in flatness may be expected to be less over the more restricted area.

Hence, better contact should be achieved. This requirement, therefore, suggests that a condensing system be used. A further factor, suggesting the necessity for a condensing system, is that it is convenient to have the same amount of energy incident on every sample. This means that the beam should be condensed sufficiently so that the whole of the beam will fall on the smallest and most irregular samples, without any portion of it being lost, *i.e.*, sampling area is maintained constant.

In order to ensure that the angular accuracy and reproducibility are maintained, a parallel beam should fall on the sample.

Most of these requirements are satisfied by a commercially available micro-attenuated total reflectance unit.¹

A schematic of the optical system of this unit is shown in Fig. 3 and 4. A condensing system is used to bring the beam to a focus just before the germanium hemicylinder. The cylindrical surface refracts the radiation such that a parallel beam falls on the sample [c.f., Fahrenfort (10)]. The size of the sample is approximately 1×6 mm, *i.e.*, the beam is condensed to this approximate size. The main drawback is that the angular accuracy is not as adequate as desirable [see (11)]. It is also necessary for the germanium hemicylinder to be very accurate and free from surface defects on the polished surfaces in order to prevent aberrations and scattering.

Results and Conclusions

Some typical reflectance curves, using random polarization, for a variety of epitaxial vapor-de-

¹ Connecticut Instrument Corp., Wilton, Conn.

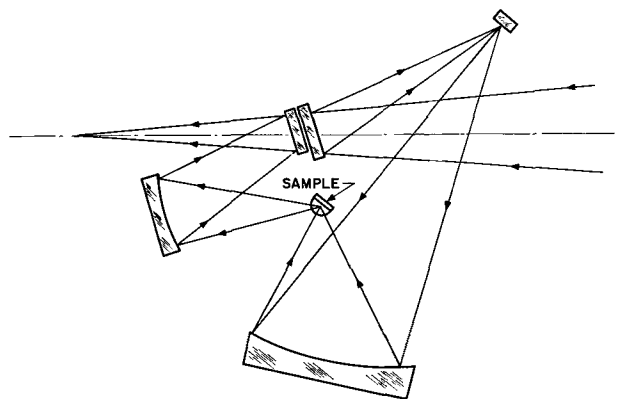


Fig. 3. Optical system of the micro-attenuated total reflectance unit.

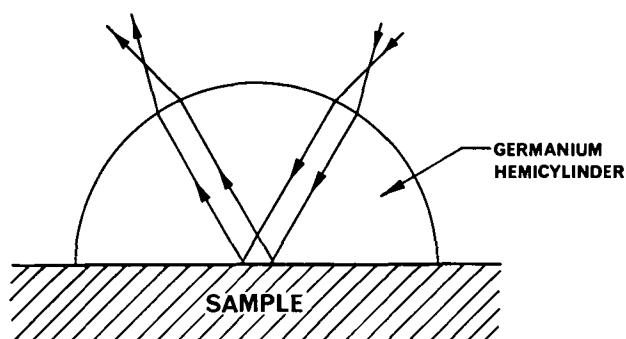


Fig. 4. Enlarged portion of Fig. 3 showing the sample and germanium hemicylinder.

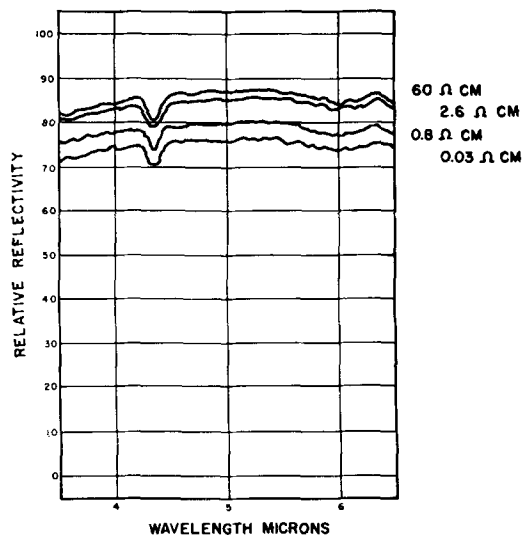


Fig. 5. Relative reflectivity vs. wavelength for epitaxial silicon slices of different resistivity.

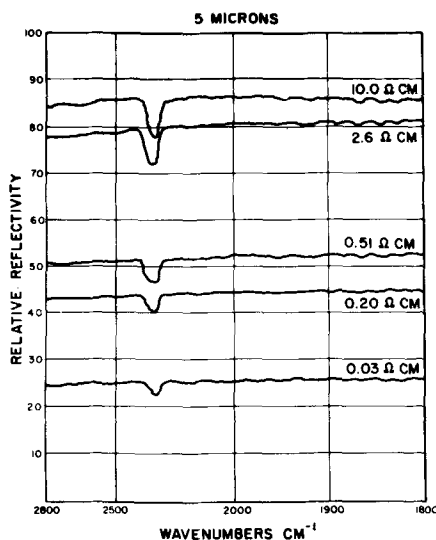


Fig. 6. Relative reflectivity vs. wavelength for further epitaxial silicon slices.

posited slices are shown in Fig. 5 and 6. In Fig. 5, which is a tracing of a number of curves, the reflection unit was placed in the sample beam of a Beckman I.R. 5A Rock Salt Spectrophotometer. A beam attenuator was used in the reference beam in order to increase the relative transmission. Usually the actual transmission in the sample beam was approximately 15-30%, which compares reasonably well with the 50-55% observed with an aluminized mirror substituted for hemicylinder prism and sample, *i.e.*, the sample etc. must cause some scattering, absorption, and reflection losses. Also evident in the spectra are atmospheric absorption bands, due to the longer sample beam path length. The layer resistivities were measured by means of the diode capacitance technique [c.f. (4)].

Figure 6 shows further tracings, in this case the curves were run on a Perkin-Elmer Model 21 Spectrophotometer under exactly the same conditions, except that scale expansion as well as beam

attenuation was used. As before the sample resistivities were measured by means of the diode capacitance-voltage technique. Figures 5 and 6 are unfortunately not directly comparable due to the scale expansion and beam attenuation used; it should be emphasized that the ordinate is relative reflectivity.

It is, therefore, apparent that the method is sound, although the difference in reflectivity is not as great as that which might be predicted from absorption measurements and the above calculated curves.

Further experimental work is required, both to improve and refine the technique, and to give a better idea of reproducibility and accuracy. First, as noted above, the reflectivity observed does not agree with that predicted from the theory. It is felt that the explanation for this lies first in the lack of angular accuracy inherent in the unit. Indeed, from this respect as well as others, such as convenience of loading the sample, it may be best to design an instrument for the specific purpose, probably with a fixed angle, as it has been found quite difficult to maintain the angle constant when samples are changed. Second it is felt that the germanium hemicylinder may not be sufficiently adequate for the purpose of the measurement. It is quite likely that the germanium is insufficiently pure (the resistivity was only close to intrinsic resistivity) and is, therefore, absorbing. Any absorption will cause a loss in reflected energy. It is also likely that the geometrical shape is inaccurate. Any variation in curvature will change the refracting power of the surface, so that the beam will not be parallel when it is incident on the sample. This in turn will cause further loss in energy. After the blank has been machined, it is necessary to polish it. This may introduce further sources of energy loss due to scattering, as well as change in dimensions or flatness. In addition, if the sample itself is not flat, or has a poor surface, or is not in contact with the germanium, additional energy will be lost.

Thus, it seems likely that the above-noted mechanisms account for any discrepancies. It should be noted that, in any case, limits should be set on the range of resistivities which may be measured; the limitation being the actual value of k . From the theoretical curves it may be expected that $k = 10^{-4}$ is the lowest practical value under most circumstances. This corresponds to approximately 10 ohm-cm at 10μ for n-type material (9). The high limit of k may be set by the ability to distinguish materials of different values of k . In practice the lower limit enables one to cover the whole conventional range of resistivities, from approximately 0.001 ohm-cm upwards, consistent only with being able to resolve sufficiently small changes in relative reflectivity.

It is difficult at this stage to give any exact idea of precision due to difficulties already noted, however it may be stated that, provided great care is taken to maintain a constant angle, a sample may be removed and replaced to give relative reflectivities constant to within a few per cent. As discussed above the accuracy is primarily limited by the unit

itself, although the roughness of the sample also contributes as does the sample area.

A further point should be made clear with reference to the practicality of the method for measuring resistivities in thin layers. It is obvious that for the epitaxial silicon to affect the reflectivity, there must be penetration into it. As epitaxial layers are usually only about 10μ thick, it is valid to question whether the substrate will have any effect on the measurement. It will become clear from the theory (13) that the penetration is less than a wavelength. Thus, a suitable wavelength may be chosen between the energy gap absorption region and the region of high lattice absorption (in germanium) such that penetration is no problem. In practice no difficulty is encountered, for interference fringes would be observed on scanning the whole spectrum if the penetration were substantial.

Finally it should be emphasized that the method gives only the resistivity of the surface layer.

Acknowledgments

I would like to thank R. R. Senechal and W. D. Westwood for useful discussions and M. Naqi for programming the reflectivity equations. This work was sponsored in part by the Defence Research Board of Canada.

Manuscript received Nov. 26, 1963. This paper was presented at the New York Meeting, Sept. 29-Oct. 3, 1963.

Any discussion of this paper will appear in a Discussion Section to be published in the June 1965 JOURNAL.

REFERENCES

1. H. C. Theuerer, J. J. Kleimack, H. H. Loar, and H. Christensen, *Proc. I.R.E.*, **48**, 1642 (1960).
2. W. G. Spitzer and M. Tannenbaum, *J. App. Phys.*, **32**, 744 (1961).
3. M. P. Albert and J. F. Combs, *This Journal*, **109**, 709 (1962).
4. C. O. Thomas, D. Kahng, and R. C. Manz, *ibid.*, **109**, 1055 (1962).
5. E. E. Gardner, J. F. Hallenback, Jr., and P. A. Schumann, Jr., *Solid State Electronics*, **6**, 311 (1963).
6. I. Simon, *J. Optical Soc. Am.*, **41**, 336 (1951).
7. D. G. Avery, *Proc. Phys. Soc. (London)*, **65B**, 425 (1952).
8. T. G. R. Rawlins, 9th Ottawa Symposium on Applied Spectroscopy, 1962.
9. W. G. Spitzer and H. Y. Fan, *Phys. Rev.*, **108**, 268 (1957).
10. J. Fahrenfort, *Spectrochimica. Acta.*, **17**, 698 (1961).
11. J. Fahrenfort and W. M. Visser, *ibid.*, **18**, 1103 (1962).
12. M. Born and E. Wolf, "Principles of Optics," p. 38, Pergamon Press (1959).
13. T. G. R. Rawlins, To be published.
14. C. A. Salzberg and J. J. Villa, *J. Opt. Soc. Am.*, **47**, 244 (1957).
15. W. Culshaw and D. S. Jones, *Proc. Phys. Soc.*, **66B**, 859 (1954).

Preparation of $\text{GaAs}_x\text{P}_{1-x}$ by Vapor Phase Reaction

W. F. Finch¹ and E. W. Mehal

Texas Instruments Incorporated, Dallas, Texas

ABSTRACT

A method for producing epitaxial $\text{GaAs}_x\text{P}_{1-x}$ utilizing an open tube flowing atmosphere system is presented. The various alloy compositions are synthesized and deposited by using AsCl_3 , PCl_3 , H_2 , and Ga as the initial reactants. The complete range of $\text{GaAs}_x\text{P}_{1-x}$ compositions has been prepared by varying the mole ratio PCl_3 and AsCl_3 introduced into the reactor gas stream. Experimental conditions required for achieving good epitaxial growth of these materials on $\langle 111 \rangle$ oriented GaAs substrates are discussed.

Preparation of III-V semiconductors by vapor phase reaction was first reported by Antell and Effer (1). Later Lyons and Silvestri (2) demonstrated epitaxial GaAs growth from a vapor. Others have continued this work in open and closed systems using volatile halides and oxides as transport media.

Gershenson and Mikulyak (3) prepared GaP by reaction of gallium suboxide with phosphorus in the vapor phase. A variety of oxygen compounds were also formed, and the GaP was thought to be doped with oxygen. Oxygen was later shown to cause a deep donor level (4) (0.4 eV) in GaP.

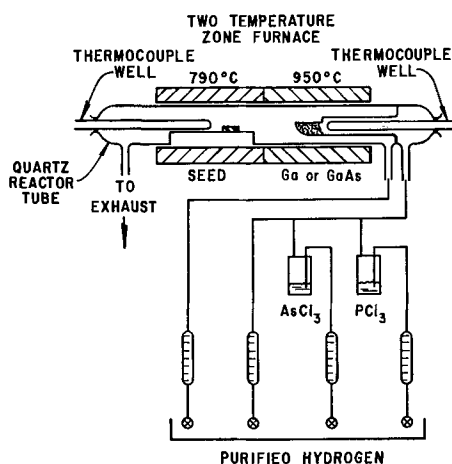
Pizzarello (5) prepared solid solutions of GaP in GaAs by transporting a mixture of GaAs and GaP with iodine in a closed system. The deposits were not epitaxial, but the entire composition range was synthesized and identified from x-ray powder diffraction patterns. Variation in band gap as a func-

tion of composition was measured. Also, lattice parameter variation was found to obey Vegard's law.

Halogen doping experiments by Antell (6) have shown that chlorine and iodine do not behave as donors or acceptors in InAs, GaP, and presumably other III-V semiconductors. For this reason halogen vapor transport systems seem better than oxygen systems for III-V semiconductor vapor growth. A variety of halide sources has been used in closed system experiments (7), but open tube experiments have used primarily HCl. Open systems offer considerable flexibility compared to closed systems, but HCl is difficult to obtain in high purity and is easily contaminated through reaction with metal valves and flow meters.

This paper describes the vapor phase reaction of Ga and GaAs with AsCl_3 and PCl_3 in an open system to form epitaxial $\text{GaAs}_x\text{P}_{1-x}$ deposits on GaAs substrates. This technique has several advantages over earlier open tube systems. High-purity AsCl_3

¹ IBM. Components Division, Poughkeepsie, New York.

Fig. 1. $\text{GaAs}_x\text{P}_{1-x}$ epitaxial deposition system

and PCl_3 can be prepared by laboratory distillation and can serve as a pure arsenic and phosphorus source as well as a halogen source. The vapor pressures of AsCl_3 and PCl_3 are high enough so that they can be transported as gases by displacement from a bubbler, thus avoiding contact with the usual metal parts necessary in HCl systems. Also, the ratio of arsenic to phosphorus introduced into the system can be varied during growth allowing graded composition structures to be grown in a single operation.

Experimental

Figure 1 shows the experimental apparatus. Hydrogen, purified by Pd diffusion, is metered into the system through four flow meters. Two are connected to AsCl_3 and PCl_3 bubblers while a third controls further dilution of the displaced AsCl_3 and PCl_3 vapors. The diluted vapors then pass over Ga or GaAs feed material² at an elevated temperature, and the reaction products are further diluted with hydrogen from the fourth flow meter. These gaseous products are swept through a decreasing temperature gradient to the cooler end of the reaction tube where they combine to deposit $\text{GaAs}_x\text{P}_{1-x}$ on a GaAs seed. Both mechanically and chemically polished (111) oriented seeds have been used with equal success.

Typical operating conditions are: feed material temperature, $900^\circ\text{--}950^\circ\text{C}$; seed temperature, $775^\circ\text{--}820^\circ\text{C}$; AsCl_3 bubbler flow rate, $10\text{--}100\text{ cm}^3/\text{min}$; PCl_3 bubbler flow rate, $1\text{--}10\text{ cm}^3/\text{min}$; dilution hydrogen flow rates, $20\text{--}200\text{ cm}^3/\text{min}$.

The chemical compositions of the $\text{GaAs}_x\text{P}_{1-x}$ deposits were identified primarily by x-ray diffraction. Since no composition difference was seen in $\text{GaAs}_x\text{P}_{1-x}$ deposited on a seed and on adjacent walls of the reaction tube, most of the x-ray measurements were done from powder patterns of material adjacent to the seed. A few wet chemical measurements were made and were found to be within 4% of the x-ray values.

Junction electroluminescence was used as an indirect measurement of composition. Zinc was diffused into several n-type deposits of different compositions to form p-n junctions. The light emitted on

²The Ga was six nines grade purity and the GaAs was prepared initially from five nines grade purity Ga and As. The AsCl_3 and PCl_3 were distilled reagent grade materials.

forward bias had a wavelength which corresponded to an energy transition approximately equal to the energy gap of the composition involved.

Transport properties were measured for two compositions of $\text{GaAs}_x\text{P}_{1-x}$. A 100μ thick deposit of $\text{GaAs}_{0.9}\text{P}_{0.1}$ was grown using $n \sim 10^{15}\text{ cm}^{-3}$ GaAs as feed material. The seed was lapped away and the deposit was cut into a $1.0 \times 0.2\text{ cm}$ rectangular bar. Direct current Hall effect and resistivity measurements showed $n = 1.4 \times 10^{17}\text{ cm}^{-3}$ and $\mu_H = 1.2 \times 10^3\text{ cm}^2/\text{volt-sec}$ at room temperature. This mobility is below what might be expected for this composition and doping level. It was later discovered that the PCl_3 used in this preparation was contaminated with POCl_3 .

A deposit of $\text{GaAs}_{0.6}\text{P}_{0.4}$ was grown on a high resistivity ($\rho \geq 10^6\text{ ohm-cm}$) seed using $n \sim 10^{16}\text{ cm}^{-3}$ GaAs as feed material. Hall effect and resistivity measurements showed $n = 3.0 \times 10^{16}\text{ cm}^{-3}$ and $\mu_H = 1.8 \times 10^3\text{ cm}^2/\text{volt-sec}$. These values seem reasonable for this composition.

Crystalline characteristics of the $\text{GaAs}_x\text{P}_{1-x}$ have been examined by staining techniques and microscopic observation. X-ray techniques were used to measure the orientation of the deposit. Deposit thickness was optically measured on a cleaved or angle lapped edge. No staining was necessary here because the deposit is a different color from the seed. Compositions having phosphorus greater than $\text{GaAs}_{0.35}\text{P}_{0.65}$ are transparent varying from dark red to greenish-yellow.

Results and Discussion

The complete composition range of $\text{GaAs}_x\text{P}_{1-x}$ has been grown epitaxially on GaAs. The two important variables that control the product composition are the composition of the feed material and the ratio of AsCl_3 to PCl_3 introduced into the system. The composition of the deposit was not dependent on the temperature of the feed material for the temperature range investigated ($900^\circ\text{--}950^\circ\text{C}$). Figure 2 shows the effect of the mole ratio of AsCl_3 to PCl_3 introduced into the system on the deposit composition for both Ga and GaAs feed material.

³The carrier concentration of the feed materials is presented as an order of magnitude number estimated from resistivity and emission spectrographic data.

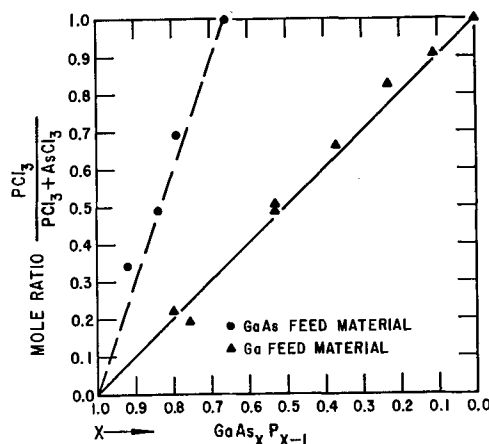
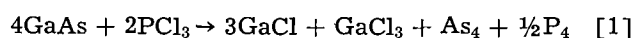
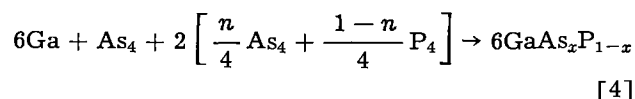
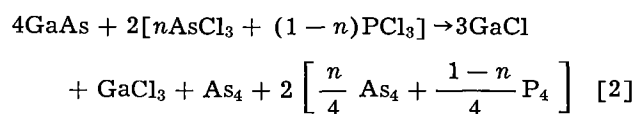


Fig. 2. $\text{GaAs}_x\text{P}_{1-x}$ deposit composition as a function of AsCl_3 and PCl_3 gas phase compositions.

The complete composition range has been synthesized using Ga feed material; however, $\text{GaAs}_{0.67}\text{P}_{0.33}$ was the highest phosphorus composition produced using GaAs as a feed material. This information can be used to give some insight into the nature of the chemistry involved. The literature generally agrees that a reaction between Ga and a halide source will form mono-, di-, and tri-halides. The di-halide is thought to be a loosely associated $\text{Ga}(\text{GaCl}_4)$ complex and does not exist in the gaseous state. The gallium feed data in Fig. 2 have shown that the composition of $\text{GaAs}_x\text{P}_{1-x}$ formed is roughly proportional to the mole ratio of arsenic to phosphorus present in the system. The GaAs feed data in Fig. 2 have shown that the reaction between PCl_3 and GaAs produces $\text{GaAs}_{0.67}\text{P}_{0.33}$. This indicates that the ratio of arsenic to phosphorus present in the deposition zone must be 2 to 1. Equation [1]



gives such a ratio. Knowing that under these temperature conditions 3 moles of GaCl are formed for every mole of GaCl_3 we can propose the following over-all series of reactions.



where $x = (2+n)/3$. First the GaAs reacts with the AsCl_3 and PCl_3 (Eq. [2]). In the decreasing temperature gradient the GaCl disproportionates (Eq. [3]) forming gallium which is then able to react (Eq. [4]) with the arsenic and phosphorus which are available in the gas phase.

The reaction shown in Eq. [2] is complicated by the fact that AsCl_3 and PCl_3 are reduced by hydrogen at elevated temperatures. This means that while the over-all reaction proposed in Eq. [2] is correct the mechanism may involve HCl as an intermediate.

The reactions with gallium feed material are similar to the gallium arsenide feed material reac-

tions except that, in the former, AsCl_3 is the only arsenic source.

The deposit growth rate has not been extensively investigated as such, but the following trends have been established. The two primary growth rate variables are the AsCl_3 and PCl_3 flow rates and the position of the seed in the temperature gradient.

The normal ranges of flow rates of H_2 saturated with AsCl_3 and PCl_3 vapor from the bubblers are 10-100 cm^3/min and 1-10 cm^3/min , respectively. (Vapor pressure of PCl_3 is approximately ten times higher than that of AsCl_3 .) In general, increased flow rates give increased growth rate. Very high flow rates, however, tend to etch the seed, and no deposition occurs. This is because the H_2 saturated with AsCl_3 and PCl_3 flow past the feed material too rapidly to react completely and are subsequently reduced to produce HCl as a by-product. The HCl then etches the GaAs seed at a rate higher than the growth can occur.

Figure 3 shows the deposition rates during a 4.5 hr growth with PCl_3 and AsCl_3 vapor flow rates of 4 and 20 cm^3/min , respectively. The gallium feed material temperature was 950°C . Six GaAs seeds were placed at 1-in. intervals in the cooler end of the reactor and the temperature gradient was adjusted to $10^\circ\text{C}/\text{in}$. No deposit grew on the hottest seed. On the second seed the deposition rate was 3.3 μ/hr , and no deposit occurred on the adjacent supporting quartz shelf. This indicates that the growth process is surface catalyzed at this point in the reactor. On the next seed a growth rate of 50 μ/hr was obtained, and a very thick deposit was formed on the surrounding quartz. The process here is probably a combination of surface catalysis and condensation of a supersaturated vapor species. On the next three seeds the deposition rate varied from 17 to 11 μ/hr with a moderate deposit on the quartz. This is a combination of surface catalysis and normal condensation from the vapor.

Values presented in Fig. 3 show a typical deposition rate gradient. The curve can be shifted to the left by raising the feed material temperature, but this tends to eliminate the region in which growth is by surface catalysis only.

Epitaxial growth is easily achieved in the surface catalyzed region, but the rate is too slow for practical use. Epitaxial growth in the region of rapid deposition is possible but unpredictable. The most reproducible, practical growth is achieved in the

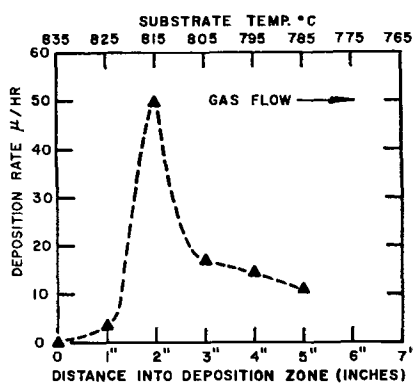


Fig. 3. Deposition rate as a function of position of substrate in deposition zone and temperature.

Table I. Physical characteristics of deposits produced at various substrate temperatures

Run No.	Seed temperature, °C	Result
7	650	"Powdery" deposit
8	675	Very fine grain polycrystalline
9	725	Large grain polycrystalline
11	775	Single-epitaxial, rough surface
29	790	Single-epitaxial, smooth surface
38	830	Single-epitaxial, slow growth rate
37	850	Seed etched, no deposit
63	790 → 600	Single-epitaxial, slightly rough surface

region immediately beyond the rapid deposition zone. Initially, only about 30% of the deposits grown in this region were epitaxial. Later, by beginning the growth at 840°C and slowly lowering the seed temperature to 790°C, about 80% of the deposits were epitaxial.

The series of runs shown in Table I was made to establish the temperature conditions for epitaxially depositing GaAs_{0.67}P_{0.33} on a GaAs substrate. In each run GaAs was used as a feed material at 915°C, and the substrates were placed in the deposition zone about 1.5 in. past the region of rapid deposition. Epitaxial growth was achieved when the substrate temperature was between 775° and 830°C. With the gas concentration and flow conditions used, vapor etching was noticed at the higher temperature, and nonepitaxial deposits were observed for lower temperatures.

The evidence that our epitaxial yield was increased from 30 to 80% by starting growth at 840°C and slowly lowering the seed temperature to 790°C suggested that initial nucleation was a critical phase of growth. Several runs, similar to run 63 in Table I, were made in which the temperature was substantially lowered in several steps after an initial period of 790°C growth. It was established that the deposit can remain epitaxial and single crystalline as low as 600°C. Below this temperature arsenic begins to

condense in the deposition zone making further growth difficult.

Acknowledgments

The authors wish to thank Dr. D. Miller for x-ray analyses, Dr. R. Biard for the information about the performance of the electroluminescent diodes he made from our samples, and Mr. T. Robertson for his assistance in the experimental work.

This work was supported by the Electronic Technology Division, Air Force Systems Command at Wright-Patterson Air Force Base, under Air Force Contract No. AF 33(657)-9196.

Manuscript received Sept. 5, 1963.

Any discussion of this paper will appear in a Discussion Section to be published in the June 1965 JOURNAL.

REFERENCES

1. G. R. Antell and D. Effer, *This Journal*, **106**, 509 (1958).
2. V. J. Lyons and V. J. Silvestri, *ibid.*, **108**, 177C (1961).
3. M. Gershenzon and R. M. Mikulyak, *ibid.*, **108**, 548 (1961).
4. M. Gershenzon and R. M. Mikulyak, *Solid State Electronics*, **5**, 313 (1962).
5. F. A. Pizzarello, *This Journal*, **109**, 226 (1962).
6. G. R. Antell, *J. Appl. Phys.*, **31**, 1686 (1960).
7. N. Holonyak, D. C. Jillson, and S. F. Bevacqua in "Metallurgy of Semiconductor Materials," **15**, pp. 49-59, Interscience Publishers, New York (1962).

Epitaxial Growth of Gallium Arsenide on Germanium Substrates

1. The Relationship between Fault Formation in

Gallium Arsenide Films and the Surface of Their Germanium Substrate

T. Gabor*

Research Laboratories, Westinghouse Electric Corporation, Pittsburgh, Pennsylvania

ABSTRACT

Morphological and etching studies on films of gallium arsenide deposited on germanium substrates have revealed twin planes, grains, and stacking faults. The evidence suggests that these defects are related to the faceting of the substrate and to the presence of oxide films.

The deposition of gallium arsenide films on low index planes of germanium substrates has been described (1-4), and recently films altogether free of stacking faults have been grown (5). We have found it much more difficult to avoid the formation of faults in films grown on {111} surfaces of germanium than in films grown on gallium arsenide substrates. The aim of the work described in this communication was to examine the causes of fault formation when germanium was used as substrate.

Experimental

Flow system.—A stream of hydrogen containing arsenic trichloride was passed over gallium arsenide in an open tube. The resulting gas mixture then flowed over germanium substrates in a lower temperature region. The substrates were lying horizontally on semicylindrical holders so that some growth

took place even on the sides that were facing downwards. The experimental conditions, the chemical equilibria, and transport taking place in this system have previously been described (6).

Substrates and outgassing.—{111} wafers cut from Czochralski-grown crystals and germanium webs were used as substrates. The latter are grown by pulling two dendrites from the melt, the material connecting the dendrites being pulled up by surface tension (7, 8). Various procedures were used for the cleaning of the crystals. The Czochralski-crystals were etched in CP4 while the webs were sometimes etched in CP4 at other times in aqueous HF. In most cases after etching the crystals were rinsed in water then in redistilled methanol. The second distillation of the methanol was performed in a quartz apparatus. The solvent was blown off the crystals with a stream of ultrapure hydrogen. A similar technique

* Present address: Battelle Memorial Institute, Columbus, Ohio

was also used with double-distilled water. On a few occasions, especially when no CP4 etching was performed, the substrates were washed with a non-ionic surface active agent, "SteroxAJ"¹ (2.5 cc/liter), in an ultrasonic bath followed by three washes with distilled water. In still other cases trichloroethylene was used for cleaning.

Before deposition, the substrates were heated at high temperatures ($\leq 650^\circ\text{C}$) for periods up to 20 min in a stream of hydrogen. In some experiments the furnace was heated to the deposition temperature, and the arsenic trichloride was added to the stream of hydrogen before the substrates were brought into the deposition region.

Contamination of substrates with antimony.—A stream of hydrogen was passed over antimony (55 mg) at 400°C and then over the substrates at 250°C for 10 min. The direction of the flow of gas was then reversed, and the deposition zone was heated in a stream of hydrogen to 610°C and kept there for 5 min before starting the growth experiment. This treatment was shown (9) to deposit $10^{14} - 10^{15}$ at. Sb/cm² Ge.

Results

Etching of cross sections of gallium arsenide films.

—On etching $\{211\}$ cross sections of gallium arsenide films with a solution of $\text{K}_3\text{Fe}(\text{CN})_6$ (2) : H_2O (25) : KOH (3), two different types of areas were delineated. One etched rapidly and gave a rough dark brown looking surface after only 30 sec. The other etched more slowly and took longer (2-3 min) before it appeared dark at magnifications up to 200X and showed etch pits at 500X.

The etching studies revealed the following defects:

1. Twin planes in the germanium substrate extended into the gallium arsenide film with unchanged spacing. Figure 1 shows a typical differentially etched $\{211\}$ section of the growth on the edge of a germanium crystal. The latter contained twin planes lying in $\{111\}$ planes perpendicular to the plane of the picture. (The picture was taken with the gallium arsenide deposit in focus; the germanium substrate has etched more slowly and was slightly out of focus so that only two of its three

¹ The author thanks Monsanto Chemical Company for the supply of the surface active agent.

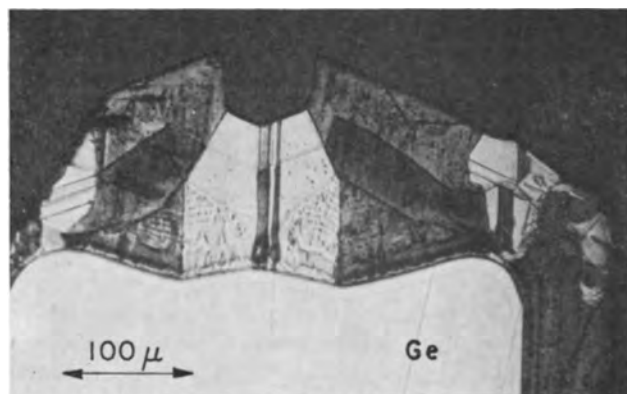


Fig. 1. $\{211\}$ section of GaAs grown on Ge. Twins contained in the latter propagate through the epitaxial film. Changes in polarity across the twins are shown by the differential etch.

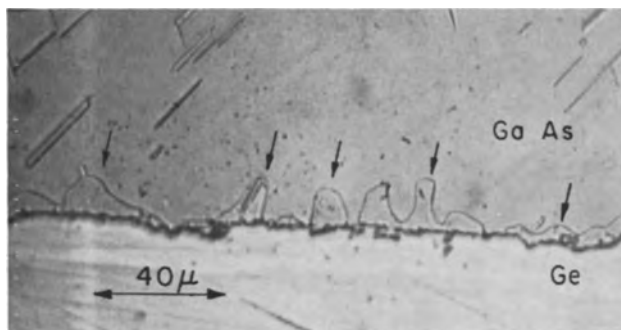


Fig. 2. Etched cross section of GaAs film grown on $\{111\}$ Ge substrate. Arrows indicate misoriented areas.

twin planes can be seen.) The $\langle 110 \rangle$ traces of the twins in the gallium arsenide deposit separate dark and light etched areas. Similar lines separating dark from light areas also originate at edges where macroscopic faces of the germanium substrate meet. Other etched $\{211\}$ cross sections showed the same phenomenon.

2. Etched cross sections of the growth on the $\{111\}$ planes showed grains. Figure 2 shows a cross section after a 10-sec etch (with long etching the roughness of the interface could not be seen because of the rapid dissolution of the gallium arsenide deposit and the attack of the etchant on the side of the exposed germanium). On longer etching and for cross sections cut in a $\{110\}$ plane, the grains remained the same color as the surrounding growth, whereas in $\{211\}$ cross sections they were of the opposite type to the growth surrounding them: they etched rapidly and became dark whereas the surrounding growth etched slowly and vice versa. In growth occurring at the edge of $\{111\}$ germanium wafers (Fig. 1) and also in growth on $\{111\}$ planes when the system was badly contaminated² grains were found not only at the interface but also throughout the deposit.

3. Lines propagating in the inclined $\{111\}$ planes away from the substrate were seen. These were never found to delineate dark and light areas.

Morphological studies.—Information about the early stages of growth was derived from the examination of growth islands that were found in some cases where growth was slow. Most of these islands were trigonal. In very few cases, probably due to

² For example when a large amount of zinc chloride was used as the transporting agent in a sealed tube.

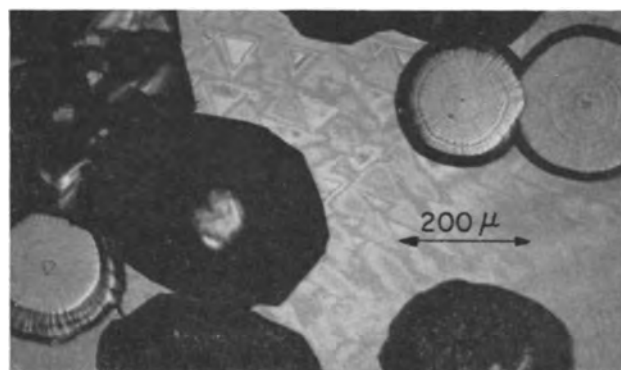


Fig. 3. Circular and triangular growth islands of GaAs observed on the downward facing plane of a $\{111\}$ Ge crystal.

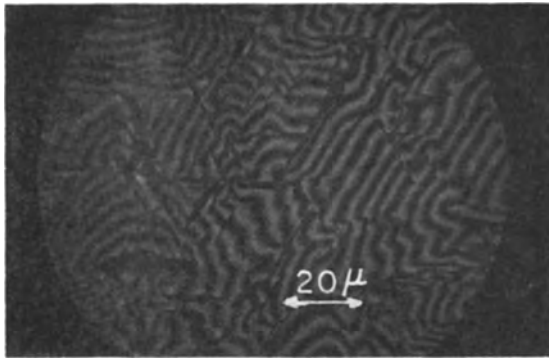


Fig. 4. Interference micrograph showing growth steps on the $\{111\}$ plane where faults propagating in the three inclined $\{111\}$ planes reach the surface.

some impurity preventing epitaxial growth, they were circular. Figure 3 shows a rare case where both were present. The triangles showed interference colors suggesting growth of only a few thousand angstroms thickness. The apices of some of these triangles point in the $[2\bar{1}\bar{1}]$ whereas others in the $[211]$ direction.

Stacking faults were formed on both the Czochralski crystals and on the webs, and none of the cleaning procedures (see Experimental section) resulted in their elimination. The intersection of the faults with the $\{111\}$ surface of the films was visible without etching because growth is faster along one side of the fault than along the other. Figure 4 shows an interference micrograph of the surface of a thick film in which the faults have interacted with each other as has been described for the case of stacking faults in silicon films by Booker and Stickler (10).

Films grown on substrates that had not been outgassed also showed faults. Growth islands obtained on such substrates had a feathered structure (Fig. 5), and films grown on them did not show the well-defined lines of the stacking faults that were obtained on outgassed samples but instead showed a diffuse structure (Fig. 6).

Deliberately contaminated substrates yielded unusual growth structures. For example, when the substrate was contaminated with antimony, a large number of whiskers and round hills like the one in Fig. 7 were found on the substrate that was nearest to the source region (highest temperature). This

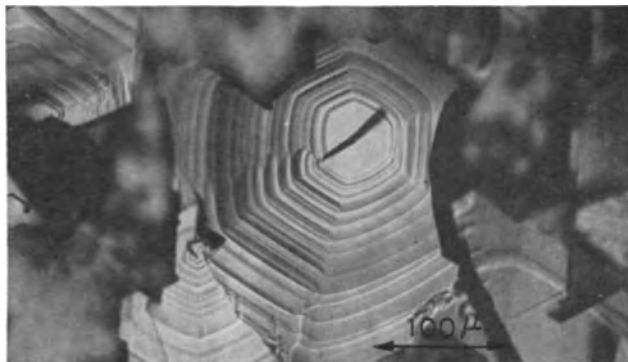


Fig. 5. Growth islands of GaAs showing feathered structure obtained on the downwards facing plane of an oxide-contaminated $\{111\}$ Ge crystal.

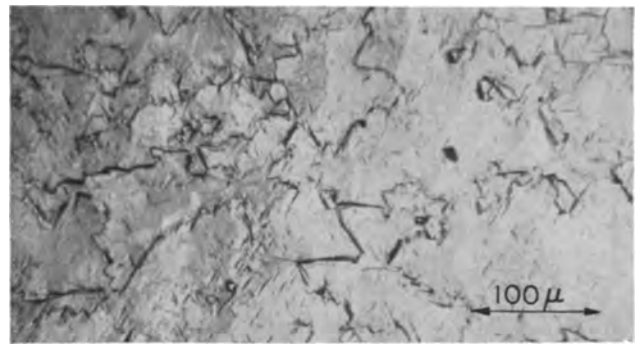


Fig. 6. Faults on surface of GaAs film grown on oxide-contaminated $\{111\}$ Ge substrate.

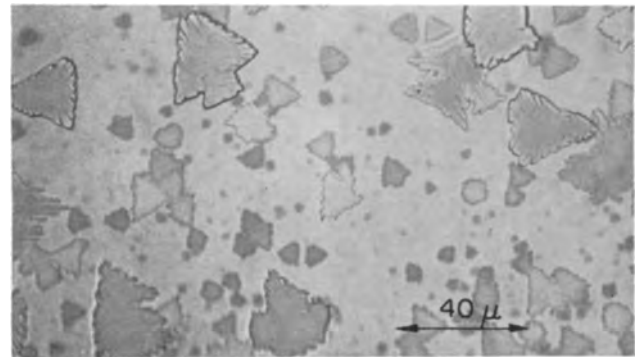


Fig. 7. GaAs growth structure obtained on Sb-contaminated $\{111\}$ surface of Ge crystal.

hill showed the interaction of growth steps from a dominant dislocation with those from small imperfect dislocations. In the same experiment, individual trigonal growth islands reached a height of 18μ on the crystal furthest away from the source region, whereas in the absence of antimony they did not grow higher than $3-4\mu$.

Discussion

In gallium arsenide, on one side of a twin plane it is the gallium atoms, on the other side the arsenic atoms that in a $\{211\}$ cross section have two broken bonds, the other type of atom having only one. The observation that the twin planes in the substrate propagate through the growing film and are revealed after etching as lines separating dark from light areas (Fig. 1) suggests that the etch distinguishes between the two possible types of polarity.

The two vertical lines in Fig. 1 that separate dark from light areas and originate where macroscopic faces on the edge of the crystal meet must similarly be intersections of twin planes with the $\{211\}$ cross section. A possible explanation for their formation may be the deposition of the same type of atom on both faces. For example, if the first layer that deposits on a macroscopic $\{111\}$ plane of germanium consists of arsenic atoms, then, on a $\{111\}$ facet that forms an angle of 70° with it, the first layer must consist of gallium atoms, or vice versa, otherwise mismatch will occur at the edge.³ Due to the difference in reactivity between the gallium and arsenic atoms (11), the first layer on all facets will consist of entirely gallium or arsenic atoms. Thus, depend-

³ This was first pointed out by A. I. Bennett.

ing on the orientations of adjacent facets, there is a probability that, if nucleation starts independently on both facets, the film will not be able to grow together without the formation of a fault. If the two grains join along a {111} plane, the boundary between them will be a twin plane.

Facets of atomic dimensions must be present on any substrate. However, these facets may not be large enough to allow independent nucleations to take place. Faceting on a macroscopic scale may however occur during the outgassing of the substrates (12).⁴

An additional cause of faceting may be the deposition of gallium and the absence of sufficient amounts of arsenic to form gallium arsenide at the beginning of the experiment. When outgassing is performed at high temperatures for prolonged periods, the source gallium arsenide must lose considerable amounts of arsenic, resulting in a gallium rich mixture when the carrier gas is introduced. The formation of a thin film, or of microscopic islands of gallium, on the surface of the substrates at 600°-700°C will result in melts containing 25-35% Ge (13). The dissolution of germanium should cause the formation of faceted pits (14).

The degree of misorientation in the growing film appeared to be related to the roughness of the substrate, and it decreased with the distance from the interface. This means that growth with one type of polarity was favored. On etching the surface of a film (> 100 μ thick) as described by Gatos and Lavine (11), well-developed triangular pits, all having an apex pointing in the $[\bar{2}11]$ direction, were obtained. This suggests that under the experimental conditions that were used in this work, the outermost layer consisted of gallium atoms.

The faults propagating in the three {111} planes inclined to the interface were similar to the stacking faults that have been described in films of germanium (15, 16) and silicon (17, 18). A possible explanation for the varying growth rates on the two sides of each fault may be the following: The growth may take place by the propagation of two-dimensional nuclei parallel to the surface. When such a layer reaches the intersection of a fault with the surface, its propagation may be prevented due to the stacking order being different on the two sides of the fault. The number of layers reaching the fault may be different on the two sides because it must depend on the probability of nucleations

occurring on different sides. These nucleation probabilities will themselves depend on the distribution of other faults.

The growth on a {111} substrate of triangles with an apex pointing in the $[\bar{2}11]$ direction (Fig. 3) must have involved the formation of a fault. We do not know whether this was caused by mismatched growth on facets or by impurities. In the case of Fig. 5, it was evidently the oxide contamination that caused the growth islands to have the feathered structure and some of them to be misoriented. Growth islands pointing in opposite directions cannot grow into an unfaulted layer and must result either in the formation of stacking faults or of grains that are misoriented relative to each other (Fig. 2).

Acknowledgments

The author thanks H. D. Larson for the cross sectioning and polishing work, K. Liang for his assistance in growing the films, and H. C. Chang and D. R. Hamilton for helpful discussions.

Manuscript received Dec. 6, 1963; revised manuscript received Feb. 10, 1964.

Any discussion of this paper will appear in a Discussion Section to be published in the June 1965 JOURNAL.

REFERENCES

1. N. Holonyak, Jr., D. C. Jillson, and S. F. Bevacqua, *Met. Soc. Conf.*, **15**, 49, (1961).
2. R. R. Moest and B. R. Shupp, *This Journal*, **109**, 1061 (1962).
3. T. Okada, T. Kano, and Y. Sasaki, *J. Phys. Soc. Japan*, **16**, 2591 (1961).
4. A. E. Blakeslee, Paper presented at Electrochemical Society Pittsburgh Meeting, May 1963.
5. A. E. Blakeslee, Private communication.
6. R. R. Fergusson and T. Gabor, *This Journal*, **111**, 585 (1964).
7. S. O'Hara and A. I. Bennett, *J. Appl. Phys.*, **35**, 686 (1964).
8. S. Dermatis and J. W. Faust, Jr., *Communication and Electronics (IEEE)*, **1**, (March 1963).
9. J. E. McNamara, *This Journal*, **108**, 199 (1961).
10. G. R. Booker and R. Stickler, *J. Appl. Phys.*, **33**, 3281 (1962).
11. H. C. Gatos and M. C. Lavine, *This Journal*, **107**, 427 (1960).
12. T. Gabor, *ibid.*, **111**, 821 (1964).
13. E. M. Savitskii, V. V. Baron, and M. A. Tytkina, *Zhur. Neorg. Khim.*, **3**, 763 (1958).
14. J. W. Faust, Jr., A. Sagar, and H. F. John, *This Journal*, **109**, 824 (1962).
15. T. B. Light, Metallurgy of Semicond. Materials, Proc. AIME Conf., Los Angeles (1961).
16. O. Haase, *ibid.*
17. H. J. Queisser, R. H. Finch, and J. Washburn, *J. Appl. Phys.*, **33**, 1536 (1962).
18. G. H. Schwuttke, *ibid.*, **33**, 1538 (1962).

⁴ Note added in proof: a method of preparing smooth, etched germanium substrates has recently been described [J. A. Amick, *RCA Rev.*, **24**, 555 (1963)].

Epitaxial Growth of Gallium Arsenide on Germanium Substrates

II. Deterioration of the {111} Surface of Germanium at 570°-850°C

T. Gabort†

Research Laboratories, Westinghouse Electric Corporation, Pittsburgh, Pennsylvania

ABSTRACT

It has been shown that on heating germanium crystals in hydrogen or in vacuum at temperatures 570°-850°C, deterioration of the 111 planes takes place. Temperature gradients and adsorbed impurities are the probable causes of the deterioration. Impurities cause the formation of etch- and growth-structures which in their absence would be unstable.

When preparing devices from germanium, one often has to heat the crystals to high temperatures. For example, in the epitaxial deposition of germanium or gallium arsenide on germanium substrates, the latter are exposed to high temperatures during outgassing, when impurities, especially oxides, are removed from the surface. This work was undertaken to examine whether the smoothness of the germanium surface can be preserved under such conditions. The effect of any deterioration on the crystallographic quality of gallium arsenide films is described in Part I (1) of this series.

Experimental

The crystals and the purification procedures have been described in Part I. Details of the heat treatments are given below. Numbers within the same bracket mean that these figures represent different areas of the same sample. The crystals were heated:

- A. With continuous pumping, Fig. [4, 7, 9].
 - B. In sealed quartz tubes
 - a. In vacuum, Fig. [1, 2, 3], [10], [11].
 - b. In hydrogen, Fig. [8].
 - C. In open flow systems in hydrogen, Fig. [5, 6].
- Specific details are given in Table I.

The quartz used for the sealed tube experiments was cleaned in aqua regia. The tubes had an approximate volume of 20 cc. The weight changes in nearly all of the experiments were within the experimental error of ± 0.2 mg. The two {111} faces of the wafers had a total area of about 1 cm², compared

† Present address: Battelle Memorial Institute, Columbus, Ohio.

Table I. Details

Fig.	Evacuation of tube			Heat treatment		
	Temp, °C	Hr	Pressure, mm Hg	Temp, °C	Hr	Pressure, mm Hg
4, 7, 9				820	15	2×10^{-7}
1, 2, 3,* a	500	2	3×10^{-6}	570	8	
10	500	3	1×10^{-6}	720	20	
11	500	3.5	2×10^{-6}	680	16	
8,* b	500	2	3×10^{-6}	570	8	150 (H ₂)
5, 6,* c				680	17	760 (H ₂)

* Heated in a temperature gradient: a, the sample at the highest temperature was at 780°C; b, the sample at the highest temperature was at 780°C, and that sample lost 1.0 mg weight; c, the sample at the highest temperature was at 700°C ("upstream").

to which figure the area of the edges may be neglected.

Observations

Some faceting was observed on nearly all samples that were heat-treated. The smoothness of the surface was best preserved when the last wash before heat-treatment was performed with double distilled water, and the latter was blown off the surface by a stream of hydrogen. The degree of deterioration increased with increasing temperature and with increasing temperature gradient. In case of experiments that were performed in an atmosphere of hydrogen, the roughening of the surface was the least prevalent when the hydrogen was purified by diffusion through a palladium alloy tube.

On nearly all samples, either some tetrahedral pits or growth triangles were observed. In addition to these many unexpected structures were found. Some of these are described below:

1. Simultaneous formation of pits and hillocks.— Figure 1 shows hillocks on a germanium crystal. The black dots are whiskers. They most likely consist of either germanium or of silicon dioxide, the latter originating from the quartz tube, although the composition of the whiskers could not be established from an electron diffraction pattern. Figure 2 shows a replica of the crystal, shadowed at an angle of 30° to the specimen plane. A cross section of the structure shown at the top of Fig. 2 is drawn in Fig. 3. The

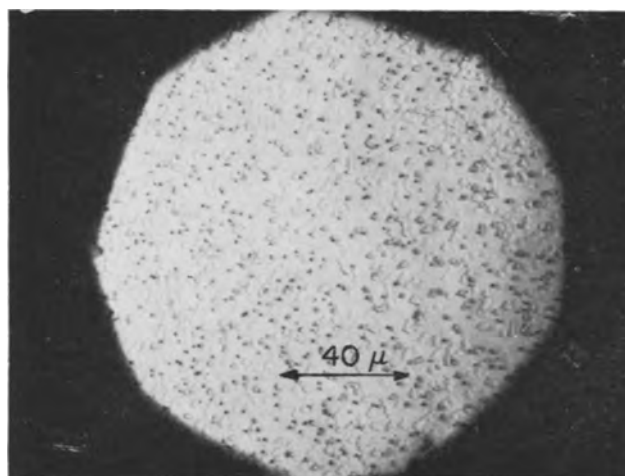


Fig. 1. Growth triangle and whiskers

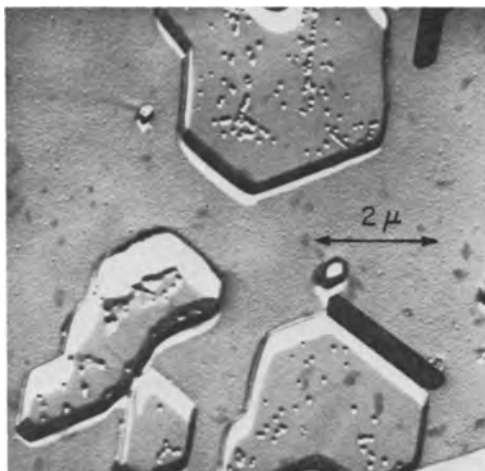


Fig. 2. Shadowed replica of part of Fig. 1

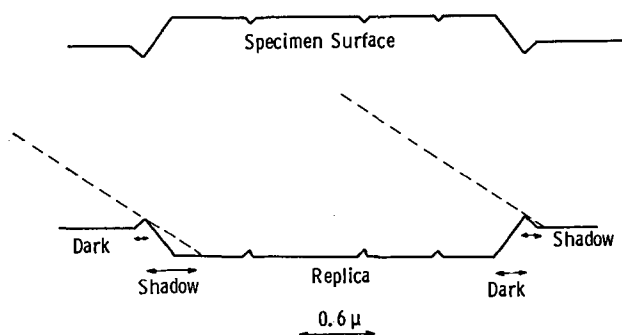


Fig. 3. Cross section of growth structure shown on top of Fig. 2

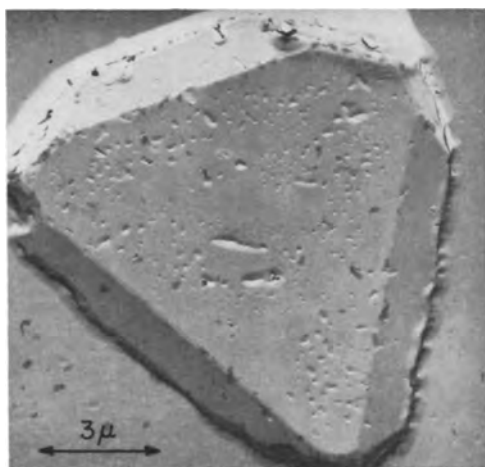


Fig. 4. Etch pit

vertical dimensions given in this figure are approximate. They were estimated from the width of the dark and light lines at the edge of the structure. The light lines represent areas that were in the shadow of protrusions on the replica. Figure 2 shows that the hillocks are surrounded by channels and that there are small pits on top of the hillocks.

On another crystal, the electron micrograph of the shadowed replica showed that small hillocks were formed at the bottom of the pits. This is illustrated in Fig. 4. A further example of simultaneous pit and hillock formation is shown in Fig. 5. The large

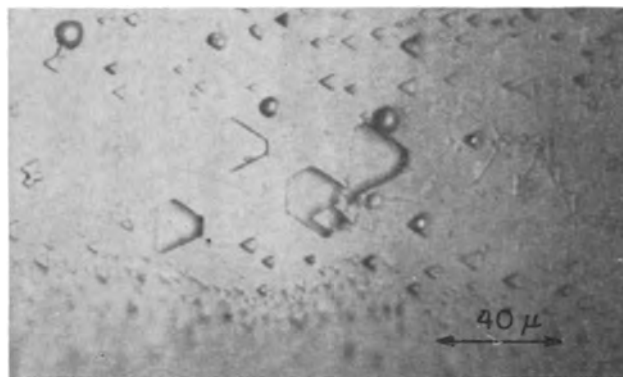


Fig. 5. Simultaneous formation of pits and hillocks

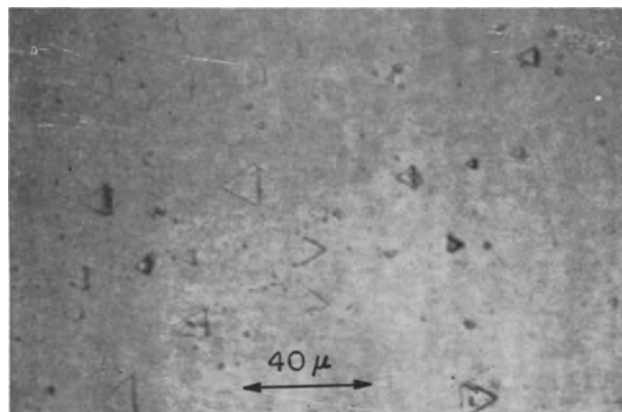


Fig. 6. Growth triangles pointing in opposite directions

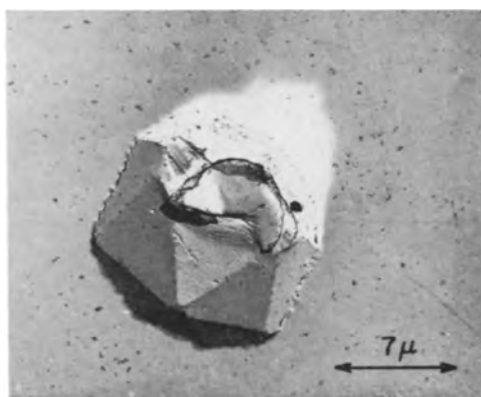


Fig. 7. Etch pit

truncated triangles are growth areas. Five or six circular growth structures can also be seen.

2. Growth triangles pointing in different directions.—Figure 6 shows another area of the same crystal used in Fig. 5. This picture was again taken using side illumination in order to show that all the triangles are growth structures.

3. Facets with orientations other than $\{111\}$.—In these experiments, facets other than $\{111\}$ were found both in pits and in hillocks. Figure 7 shows the replica of an etch pit, and Fig. 8 shows $\{100\}$ faces on some of the growth pyramids.

4. Other structures.—Examples of other unexpected structures are given here. Figure 9 shows the

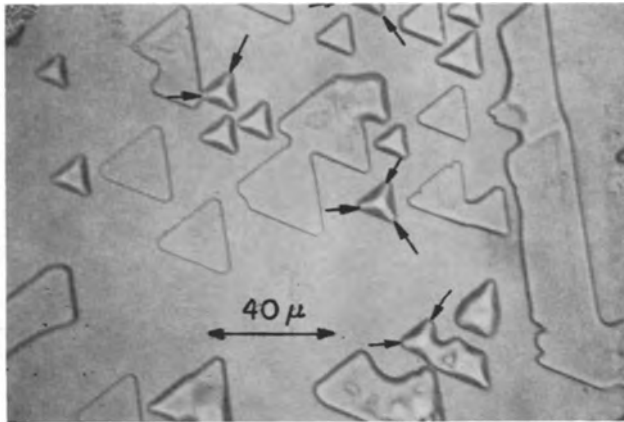


Fig. 8. Growth structures; some of the $\{100\}$ faces are shown by arrows.

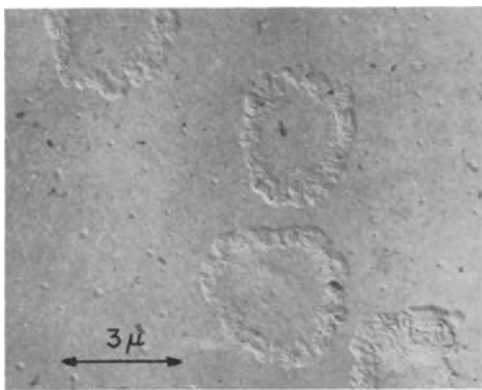


Fig. 9. Circular pattern

replica of a circular pattern, while Fig. 10 shows the replica of a rough structure that was obtained even though the temperature during the heat treatment was nearly uniform. Figure 11 shows a structure that was often encountered. This consists of lines running in $\langle 110 \rangle$ directions. Due to the small difference in height of the lines it could not be proved unequivocally, but it is thought that they are depressions. They have an appearance similar to the "Y-etch figures" found in evaporated epitaxial films of germanium by Courvoisier *et al.* (2).

Heat treatment at temperatures close to 850°C often resulted in the formation of wormlike structures (3).

Discussion

While this work was in progress, Gatos and Lavine (3) described the deterioration of germanium surfaces on heat treatment. They examined one crystal at a time, thereby eliminating the complicating phenomenon of transport of material from one crystal to the other. Our work was directed towards the examination of deterioration encountered during device fabrication in general, with special emphasis on deterioration taking place in epitaxial growth experiments. Therefore, (a) in most cases several samples were used, and these were spread out along the tube; (b) the effect of temperature gradients was also examined; (c) when working under vacuum, the pressures in most cases were above 10^{-6} mm Hg.

In order to make the deterioration of the surfaces easier to observe, the period of heat treatment given

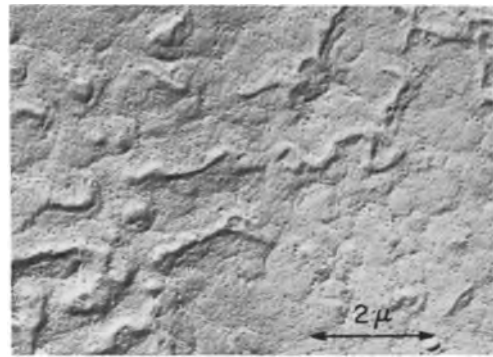


Fig. 10. Rough surface

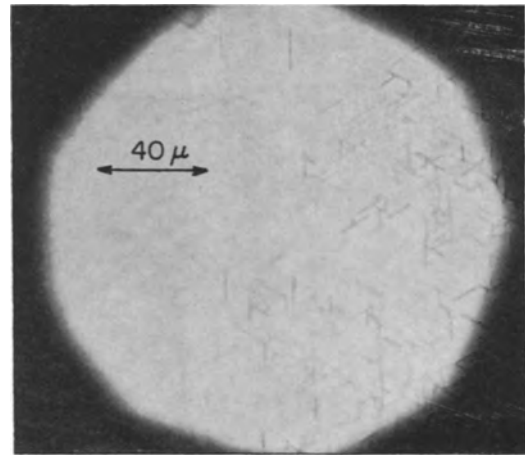


Fig. 11. Lines in $\langle 110 \rangle$ directions

to samples in this work was longer than that to which they would have been exposed during device preparation. However, deterioration to a lesser degree must occur over shorter periods. Similarly, the temperature gradients were larger than those usually encountered (see next paragraph).

When several crystals are used in the same experiment, it is difficult to assure that no temperature gradient occurs either during the heating up of the furnace or during the actual device preparation. Also, in experiments designed to examine the effect of deposition temperature on epitaxial growth, one may be tempted to place a series of substrates along a temperature gradient. Even when a gradient is not established on purpose, the gases, mostly flowing from the direction of a hotter source region, will establish a gradient along the cooler deposition region. Under such conditions, material may be transported from one sample to another through the vapor phase and also along the individual samples, both by surface diffusion and by transport in the gas phase.¹ In addition to the removal and deposition of complete epitaxial layers, the formation of tetrahedral pits with faces consisting of inclined $\{111\}$ planes and having an apex pointing in the $[\bar{2}11]$ direction, and the deposition of growth triangles with an apex pointing in the $[2\bar{1}\bar{1}]$ direction is to be expected (4).

The formation of misoriented growth islands like the triangles having an apex pointing in the $[\bar{2}11]$ di-

¹ The observation that, when hydrogen was used, the deterioration of the surface was a function of the purity of the gas suggested that traces of oxygen may play a major role in the transport of germanium.

rection (Fig. 6) was probably caused by the presence of adsorbed impurities (4). Similarly, it is probably impurities that caused the formation of the other unexpected structures. Even though a crystal plane may break up into a hill and valley structure if the total surface free energy of the resultant structure is lower than that of the original plane (5, 6), in case of clean germanium surfaces, the {111} plane is the closest packed and should therefore have the lowest specific surface free energy, γ_s .

A certain amount of impurities must be present on any semiconductor surface that was in contact with solvents. Reversible and irreversible electrochemical deposition is to be expected (7). In addition, the complete removal of the solvent is unlikely, even when the solvent is blown off the surface of the crystal; during drying, the nonvolatile impurities² dissolved in the solvent will deposit on the surface. The effect of impurities on γ_s has been shown for some other systems (9-11). Even though the concentration of impurities may be less than what can be detected by studies of adsorption of oxygen on germanium (12), they may sufficiently change γ_s to cause deterioration of the surface. In the present work the effect of impurities is most evident in the appearance of planes other than {111} and also in the circular structures³ shown in Fig. 9. The latter were probably caused by impurities deposited by the solvent.

Due to the relatively small weight changes, in most cases it was not possible to differentiate between the effect of flow to or from the vapor phase and that of surface diffusion. Thus three different explanations may be given for the formation of the structures shown in Fig. 1-3. The grooves around the hillocks may have been caused by deposition of an epitaxial film, this film not being able to grow around and link up with the faster growing areas. Or, if germanium was lost to the gas phase, the top of the hillocks may correspond to the original surface, perhaps the loss of germanium there being retarded by the presence of adsorbed impurities [a similar phenomenon was described by Rhead and Mykura (14)]; they found that when a silver crystal

² In case of organic solvents, such as methanol, oxidation and polymerization reactions can lead to the formation of nonvolatile residues (8).

³ A similar phenomenon was found by Hale (13) on thermal etching of silicon.

was heated, pyramids with shallow grooves around them were formed due to the loss of metal). Finally, the structures may have been formed by surface diffusion. The latter explanation may also hold in case of Fig. 4. Alternatively, in this case the growth at the bottom of the pits may have taken place by deposition during the cooling of the furnace.

Gatos and Lavine did not find any deterioration below 690°C. In this work, deterioration occurred even at 570°C. This discrepancy was probably caused by transport due to a thermal gradient, and also by the presence of impurities that were liberated from the quartz during sealing off when the experiments were performed in closed tubes.

Acknowledgments

The author thanks R. J. Engle for the electron micrographs, K. Liang for help with the experiments, and H. C. Chang, H. F. John, R. Stickler, and W. A. Tiller for helpful criticism of the manuscript.

Manuscript received Oct. 21, 1963. This paper was presented at the New York Meeting, Sept. 29-Oct. 3, 1964.

Any discussion of this paper will appear in a Discussion Section to be published in the June 1965 JOURNAL.

REFERENCES

1. T. Gabor, *This Journal*, **111**, 817 (1964).
2. J. C. Courvoisier, L. Jansen, and W. Haidinger, *Transactions 9th Nat. Vacuum Symp.*, Amer. Vacuum Soc., **14** (1962).
3. H. C. Gatos and M. C. Lavine, *Ann. N. Y. Acad. Sci.*, **101**, 983 (1963).
4. G. R. Booker and R. Stickler, *J. Appl. Phys.*, **33**, 3281 (1962).
5. C. Herring, *Phys. Rev.*, **82**, 87 (1951).
6. W. W. Mullins, *Phil. Mag.*, **6**, 1313 (1961).
7. G. B. Larrabee, *This Journal*, **108**, 1130 (1961).
8. H. F. John, *Symp. Cleaning Electronic Device Components and Materials*, Tech. Pub. No. 246, Amer. Soc. Test. Materials (1958).
9. J. L. Walter and C. G. Dunn, *Acta Met.*, **8**, 497 (1960).
10. G. R. Hennig, *Proc. 1st and 2nd Conf. Carbon*, **103** (1956).
11. J. M. Blakely and H. Mykura, *Acta Met.*, **9**, 595 (1960).
12. M. Green and A. Liberman, *Phys. Chem. Solids*, **23**, 1407 (1962).
13. A. P. Hale, *Vacuum*, **13**, 93 (1963).
14. G. E. Rhead and H. Mykura, *Acta Met.*, **10**, 843 (1962).

Epitaxial Growth of Gallium Arsenide on Germanium Substrates

III. Deposition on High Index Planes and on Curved Surfaces

T. Gabor¹

Research Laboratories, Westinghouse Electric Corporation, Pittsburgh, Pennsylvania

ABSTRACT

When depositing gallium arsenide on low index planes of germanium from the vapor phase by halogen transport, stacking faults are readily formed. Films free of these faults were obtained when planes that were at an angle of a few degrees with a $\{111\}$ face or curved surfaces were used as substrates. It is suggested that fast propagation of steps along the surface caused the formation of new stacking faults parallel to the existing ones, thereby completing loops and preventing the propagation of the faults. The rate of growth was much faster on curved surfaces than over the $\{111\}$ planes.

The formation of stacking faults in epitaxial films of gallium arsenide grown on low index planes of germanium substrates has been described in Part I of this series (1). Even though it is desirable to prevent the formation of faults, a method that would prevent the propagation of those faults that are formed may also be of interest. Such a method was found in the use of high index planes and of curved surfaces of germanium as substrates.

Experimental

The substrates were high index planes prepared from Czochralski-grown crystals, as-grown germanium wafers (1) (the areas connecting the flat central part of these crystals with the dendrites, the so-called "fillet regions" are curved), and both $\{111\}$ Czochralski crystals and wafers with a curvature established over part of the surface.

Wafers were cut from a Czochralski ingot at 10° to a $\{111\}$ plane in a $\langle 211 \rangle$ direction, and were then lapped, polished, and etched. Substrates 5° and 1° off the $\{111\}$ plane were obtained by angle-lapping, polishing, and etching.

Several methods were used for the preparation of concave surfaces. For example a "Kodak Photo Resist" pattern, consisting of a series of channels separating square areas was etched into a $\{111\}$ Czochralski crystal. The etching solution consisted of $\text{HF}[1] : \text{H}_2\text{O}_2[1] : \text{H}_2\text{O}[4]$. Depressions were also prepared by a jet etching technique (2). Alternatively, a Czochralski wafer was pressed against a rotating steel rod, and slurries of lapping and polishing powders were applied. In a few cases, convex surfaces were also prepared. Webs were touched with needles that were previously immersed into a solution of wax, or small, 7 mil diameter metal spheres coated with wax were made to adhere by short heating. After etching, a protrusion remained where the surface was covered with wax or with the sphere.

Details of the deposition experiments involving arsenic trichloride as the transporting agent in an open flow system have been described (1, 3). In one experiment with a web substrate, zinc chloride was used as the transporting agent in a sealed tube.

¹ Present address: Battelle Memorial Institute, Columbus, Ohio.

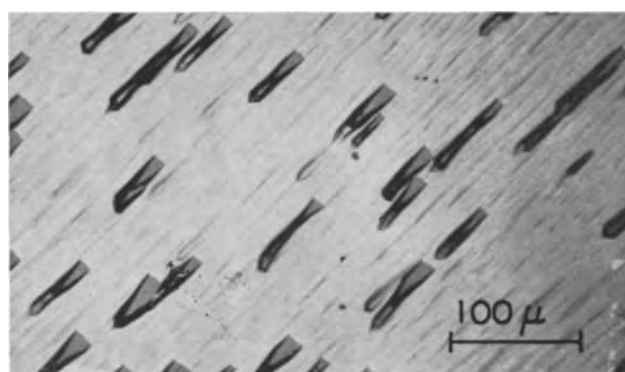


Fig. 1. Growth on substrate 10° off $\{111\}$ plane. The long axis of triangles are in $\langle 211 \rangle$ direction.

Results

Gallium arsenide films free of stacking faults could easily be grown on high index planes and on curved surfaces of germanium, even under conditions such that deposition on $\{111\}$ planes gave extremely poor films.

When using planar substrates, even though stacking faults were absent, triangular pits formed. Growth on a substrate that was cut at 10° to a $\{111\}$ plane in a $\langle 211 \rangle$ direction is shown in Fig. 1. The pits point in a $\langle 211 \rangle$ direction, and their short side is at the same level as the surrounding growth while the apex is lower. Deposition on a plane 5° off the

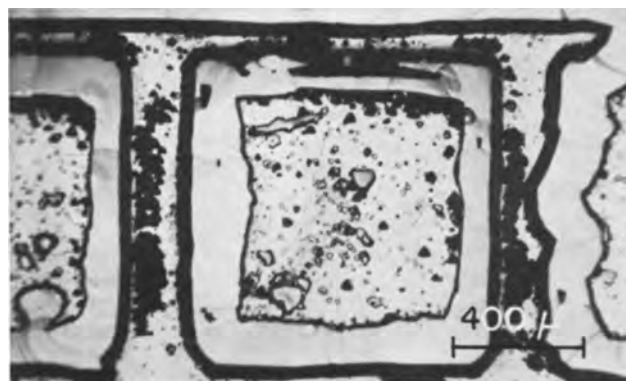


Fig. 2. Squares show $\{111\}$ planes of a Czochralski crystal. Smooth growth of GaAs on the edges of squares took place over sloping sides of channels that were etched into the crystal.

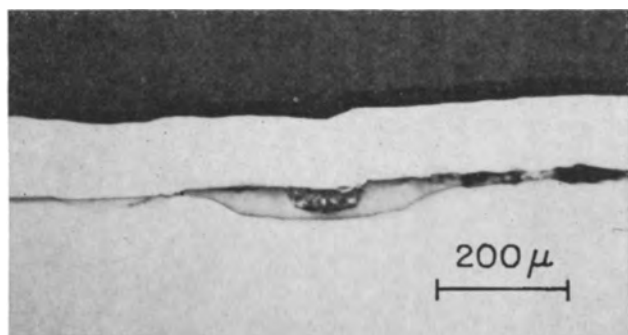


Fig. 3. Cross section through a channel and the surrounding areas of the sample shown in Fig. 2. Practically no growth took place over the $\{111\}$ planes. Light colored band is cross section of nickel coating. Dark area inside channel is probably due to deposition of polycrystalline nickel.

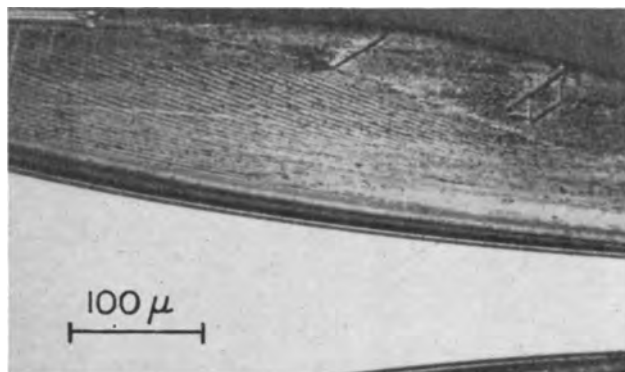


Fig. 5. Cross section in $\{211\}$ plane of sample shown in Fig. 4. Light area shows the fillet region of web, darker area with the striations the GaAs film.

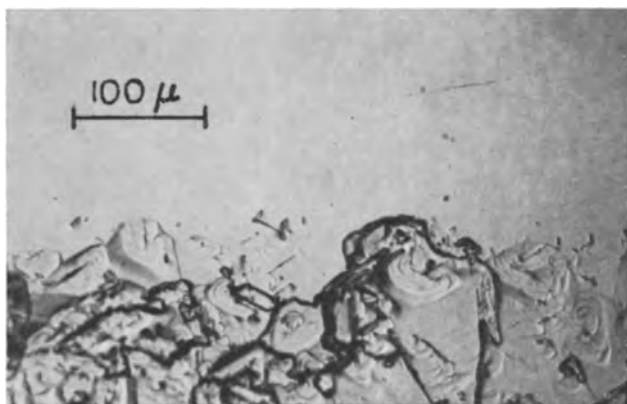


Fig. 4. Smooth area shows growth over curved fillet region of web. Poor growth shown in lower half of picture occurred over the $\{111\}$ plane.

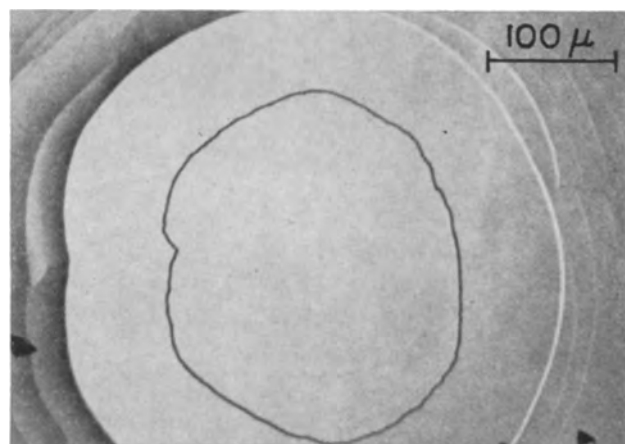


Fig. 6. Growth over protrusion on substrate

$\{111\}$ gave similar results, while stacking faults were present when a substrate 1° off the $\{111\}$ plane was used.

Only a few examples can be given of growth on curved substrates. When channels were etched into a crystal, smooth growth was obtained on the sloping sides, while there was practically no growth over the square $\{111\}$ areas (Fig. 2). A cross section over a channel and over the surrounding square areas is shown in Fig. 3.

Figure 4 shows growth over the transition area between the $\{111\}$ plane of a web and the curved fillet region. The extremely poor growth over the former was caused by a large amount of zinc chloride having been used for transport in a sealed tube. The polished and etched $(K_3Fe(CN)_6[2] : H_2O[25] : KOH[3]; 40 \text{ sec})$ cross section in a $\{211\}$ plane is shown in Fig. 5. The area below the curved line is the fillet region. The striations in the gallium arsenide may have been caused by impurity segregation. The few stacking faults that could be revealed did not originate as usual at the Ge-GaAs interface, but in an area where the growing film has already established a crystallographic plane. The same etch revealed a highly misoriented growth [presence of grains (1) throughout the whole film] over the $\{111\}$ areas. The thickness of the film over the $\{111\}$ areas was less than half of that over the curved region.

Growth obtained over a convex area is shown in Fig. 6.

Discussion

It has previously been shown (4) that the crystallographic perfection of epitaxial germanium films grown on germanium substrates was improved when the substrates were cut at an angle of a few degrees with the $\{111\}$ plane. High index planes and curved substrates both have surfaces which are composed of an infinitesimal number of atomic steps. One would expect deposition at these steps to be energetically favored, causing these steps to "flow" along the surface.

It has been suggested (1) that independent nucleations may be required for growth on the two sides of a fault; thus the propagation of a step parallel to the surface may be prevented along the intersections of stacking faults with the surface. If the rate of growth parallel to the surface is increased, as must be the case when the surface consists of an infinitesimal number of steps, there might not be sufficient time for independent nucleations to take place, so that the areas having the wrong stacking order may be overgrown by the film without the latter changing its stacking order. This corresponds to the formation of intrinsic faults parallel to extrinsic faults that may be present and vice versa. Figure 7 shows that a loop is thus created and the propagation of the fault is prevented.

The formation of pits in films grown on high index planes may be caused by the inability of the ad-

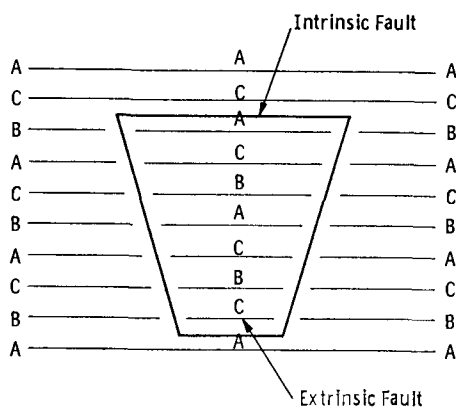


Fig. 7. Intrinsic fault generated due to fast sidewise growth of C-layer (2nd from top). Propagation of fault is prevented by loop formation.

vancing steps to overgrow all areas where there is an obstacle to growth. Once a difference in level is established between the film and the area containing the fault, the overgrowth by successive steps should be always less likely. The bottom of the pit then establishes the energetically favorable {111} surface.

We can only speculate on the reason for the presence of pits when high index planes were used as substrates and for their absence in films grown on curved surfaces. The formation of pits may be related to the relative positions of the favored growth direction and the direction of the steps.

Acknowledgment

The author thanks K. Liang for his help with this work, H. D. Larson for performing the cross sectioning and polishing operations, and H. C. Chang and W. A. Tiller for helpful discussions.

Manuscript received Oct. 23, 1963. This paper was presented at the Pittsburgh Meeting, April 15-18, 1963.

Any discussion of this paper will appear in a Discussion Section to be published in the June 1965 JOURNAL.

REFERENCES

1. T. Gabor, *This Journal*, **111**, 817 (1964).
2. G. R. Booker and R. Stickler, *Brit. J. Appl. Phys.*, **13**, 446 (1962).
3. R. R. Fergusson, T. Gabor, *This Journal*, **111**, 585 (1964).
4. H. S. Ingham, P. J. McDade, and D. M. J. Compton, *Met. Soc. Conf.*, **12**, 285 (1960).

The Oxidation Kinetics of Zirconium Diboride and Zirconium Carbide at High Temperatures

A. K. Kuriakose¹ and J. L. Margrave¹

Department of Chemistry, University of Wisconsin, Madison, Wisconsin

ABSTRACT

Kinetic studies have been made of the oxidation of zirconium diboride at 945°-1256°C, and of zirconium carbide at 554°-652°C. The ZrB_2-O_2 reaction is parabolic throughout the temperature range studied, whereas the $ZrC-O_2$ reaction is linear. In the former case ZrO_2 , together with a molten layer of boron oxide, is formed which protects against further direct attack of oxygen on the ZrB_2 , while in the latter, a rather porous film of zirconium oxide is formed which is not protective. The rate of oxidation of ZrB_2 is directly proportional to the oxygen partial pressure between 102 and 744 mm.

Because of the very refractory nature, hardness, and high tensile strengths, in general, of the borides, carbides, and nitrides of the transition metals, they are promising materials in many high-temperature applications. A knowledge of the oxidation kinetics of these materials is essential for such uses, and hence the present investigation of the high-temperature oxidation kinetics for zirconium diboride and zirconium carbide was undertaken.

The oxidation of ZrB_2 has been studied by Brown (1), Berkowitz (2), and Meerson *et al.* (3). Brown, working at atmospheric pressure in the temperature range 649°-1315°C, observed a minimum rate of oxidation around 1000°C, an accelerated rate in pure oxygen compared to dry air, and a much higher rate in moist air than in dry air. Berkowitz found a parabolic rate law to be followed after the first 40 min of oxidation at an oxygen partial pressure around 10 Torr, between 1200° and 1530°C. Brown

used porous compacts of the diboride, and there were uncertainties in the surface areas, whereas Berkowitz used electron-beam melted samples of high purity. Meerson *et al.*, from metallographic examination of the scales formed on ZrB_2 on oxidation in air at 1000°C, suggested the presence of ZrO covered by molten B_2O_3 during the initial stages of the reaction. According to them, as oxidation proceeds, B_2O_3 slowly evaporates and oxygen, while diffusing through ZrO, reacts with it to form ZrO_2 in about 10-20 hr. Berkowitz, however, found only ZrO_2 and no evidence for the presence of ZrO in the oxidation product. The resistance of ZrB_2 to scale formation was investigated also by Markevich and Markovskii (4).

Very recently, Bartlett, Wadsworth, and Cutler (5) reported an investigation of the kinetics of oxidation of ZrC powder in the temperature region 450°-580°C, and Berkowitz (2, 6) the oxidation kinetics of a zone-refined ZrC at 853°-1892°C. Watt,

¹ Present address: Department of Chemistry, Rice University, Houston, Texas.

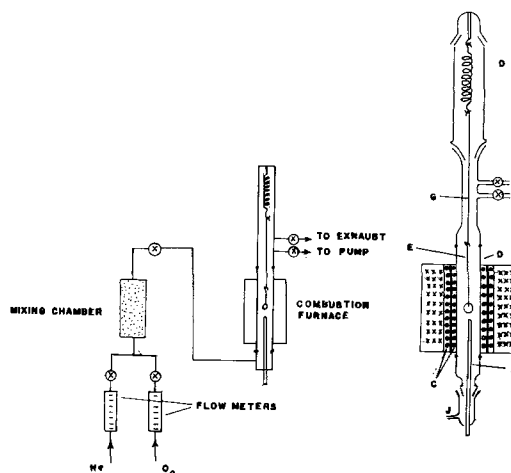


Fig. 1. Schematic diagram of the apparatus used for studying high temperature oxidation kinetics. a (left) Diagram of gas-flow system. b (right) Combustion furnace and accessories.

Crockett, and Hall (7), Thielke (8), and Hinnüber and Rüdiger (9) have also made some measurements on the oxidation of ZrC.

This investigation covers the temperature ranges 554°–652°C for ZrC and 945°–1256°C for ZrB₂, at oxygen pressures up to 744 mm Hg. The progress of reaction was derived by observing directly the weight gained by the samples with time. Electron-beam melted samples of both ZrB₂ and ZrC were used. Only specimens which did not have any apparent cracks were utilized.

Apparatus and Experimental Procedure

A schematic diagram of the gas-flow system and the apparatus is given in Fig. 1a. Figure 1b presents a detailed view of the combustion furnace and accessories. The mullite combustion tube, A, (15 in. long and 1½ in. diam) is mounted vertically and heated by two concentric furnace windings, C, of Kanthal wire. The inner winding is on the mullite itself. Pyrex tubes with standard ground-glass joints are sealed on to the mullite tube at both ends. An inlet tube, J, for the reacting gas, and a chromel-alumel thermocouple, F, are attached from the bottom, and two outlets are provided at the top, one for evacuating the system and the other for venting the gases to the hood. A helical quartz spring, D, calibrated for load vs. extension is suspended vertically as shown in the figure and the sample to be examined is attached to the lower hook of the spring by means of 0.007 in. nickel wire and a piece of quartz fiber, E, so that the sample, S, is only about 1 cm above the thermocouple bead. The proximity of the sample to the thermocouple insures accurate temperature measurement of the sample. The temperature of the heating furnace is regulated to ±2°C. When the extension of the spring is measured by means of a cathetometer, a change in weight of 0.2 mg can be determined, and with the relatively low sensitivity of the spring no vibrations were caused by the gas-flow through the system.

All the experiments were done at a total pressure of 740 ± 5 mm, and various partial pressures of O₂ were obtained by mixing it with purified helium gas. The sample was initially heated in an atmosphere

of helium to the desired temperature and the zero reading on the cathetometer taken against a fixed point (end) on the suspension wire. The system was then evacuated, O₂ gas was suddenly admitted, and the flow rate slowly adjusted. The time when oxygen was introduced was taken as zero. The readings of the cathetometer at suitable intervals of time were recorded and each run was continued until a sufficient number of points was obtained to establish the kinetics of the process.

The zirconium diboride used had a composition ZrB_{1.95} with 1.7% of Hf and a carbon content of about 200 ppm. Circular pieces of the material weighing about 0.5–0.8g were cut from zone-melted cylindrical bar and polished by grinding with fine abrasive powder. Any small cracks on the sample were visible and the cracked portions, if any, were removed by breaking them off. The specimens were then thoroughly washed with water and dried in air. The areas of the samples were calculated from the measured dimensions to the nearest 1 mm². A similar procedure was used for the zirconium carbide samples. The electron-beam melted ZrC was 99.5+ % pure with trace impurities.

The oxide films on the oxidized samples of ZrB₂ were removed by microsand blasting. The same piece could be repolished by grinding again and, thus, could be used several times. This method, apparently, did not affect the nature of the substrate material, and identical rates of oxidation within experimental error were observed (cf. section on prerun treatment). In the case of ZrC, separate pieces were used for each run.

Results and Discussion

Oxidation of Zirconium Diboride

From the extension of the spring at various intervals of time, the weight gains of the sample in milligrams per square centimeter at the respective time intervals were evaluated. The straight lines which were obtained by plotting (weight gain/square centimeter)² vs. time (Fig. 2) show that the oxidation of ZrB₂ follows a parabolic rate law. Rate

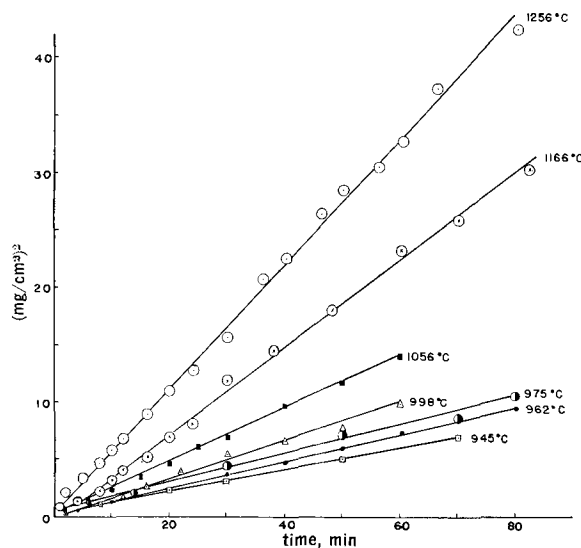


Fig. 2. Parabolic plot for the oxidation of ZrB₂ in pure oxygen at 945°–1256°C. Oxygen pressure, 1 atm.

Table I. Parabolic rate constants for the oxidation of ZrB₂ at 1056°C after various prerun treatments

Prerun treatment	Parabolic rate constant, (mg/cm ²) ^{1/2} /min
Preheated for ½ hr at the temperature of the experiment	0.2368
Oxidized sample repolished and no preheating	0.2459
Fresh sample with no preheating	0.3000

Table II. Parabolic rate constants with various flow rates of O₂ in the oxidation of ZrB₂ at 1056°C

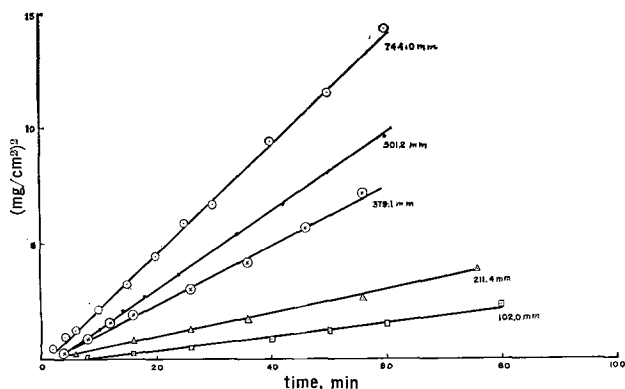
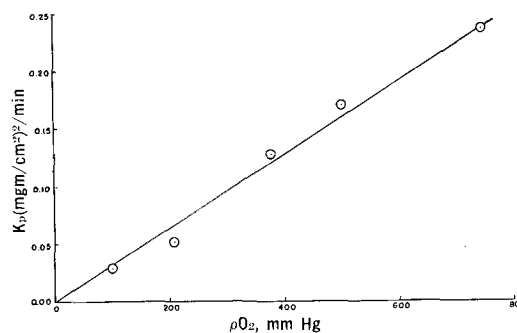
Flow rate, ml/min	Rate constant, k _p , (mg/cm ²) ^{1/2} /min
20	0.2206
50	0.2612
100	0.2459

constants were obtained from the slopes of the straight lines.

Prerun treatment.—The prerun treatment was varied in a few runs and the parabolic rate constants obtained in each case are recorded in Table I. These data indicate that there is no significant change in the rate of oxidation of ZrB₂ when the sample is preheated or when the oxidized material is repolished and used without preheating, although when a fresh piece is used without preheating, the rate constant is higher. Hence, in all the other runs the fresh sample was either preheated for ½ hr or the oxidized surface was repolished and used with no preheating. For ZrC, the sample was preheated for ½ hr for each run.

Flow rates.—Runs were done with O₂ flow rates of 100, 50, and 20 ml/min, at 1056°C in order to determine the effect of flow rate on the reaction, and the rate constants (parabolic) obtained in these cases are reported in Table II. It is evident from this table that the rate of oxidation of ZrB₂ is independent of the flow rate of O₂ in the system in the range studied, within experimental error.

Effect of oxygen partial pressure.—Figure 3 presents the parabolic plot of the results obtained at various O₂ partial pressures (102–744 mm of mercury, mixed with helium gas) for the oxidation of

Fig. 3. Parabolic plot for the oxidation of ZrB₂ at various oxygen partial pressures. Temperature, 1056°C.Fig. 4. Effect of O₂ partial pressure on the oxidation of ZrB₂. Temperature, 1056°C.

ZrB₂ at 1056°C. The oxidation rate increases with increasing partial pressure of O₂, and the increase in the parabolic rate constant is directly proportional to the partial pressure of O₂ as indicated by Fig. 4 which is a plot of the rate constants against the partial pressure.

Effect of temperature.—In order to obtain the activation energy for the reaction between ZrB₂ and O₂, experiments were carried out at various temperatures ranging from 945° to 1256°C at a pressure of 740 ± 5 mm and an O₂ flow rate of 100 ± 5 ml/min. The parabolic rate constants calculated in each case are listed in Table III. The Arrhenius plot of the results is linear with an activation energy of 19.8 ± 1.0 kcal/mole, calculated by a least-square method. Because of the volatility of boron oxide, one would expect the rate constant to fall off in the log k vs. 1/T plot at higher temperatures. This is apparently not the case, possibly, because the loss in weight by evaporation of B₂O₃ is compensated for by an increased oxidation due to less thickness in the protective oxide film. The activation energy of 19.8 kcal is in contrast to the value 66 kcal obtained by Berkowitz, although the rate constants in both this investigation and hers at about 1256°C were in excellent agreement (10). The variation in the activation energy must arise because of a change in the mechanism of oxidation. This point is further confirmed by the recent investigation of Berkowitz (11) who obtained an activation energy of 25 ± 6 kcal/mole in the temperature range below 1400°K for the oxidation of ZrB₂. The oxidation product was x-ray analyzed and was found to contain zirconium dioxide. The ethyl borate test showed the presence of boron oxide in the scales.

Table III. Parabolic rate constants for the oxidation of ZrB₂ at various temperatures
O₂ Pressure, 740 ± 5 mm; flow rate, 100 ml/min

Temperature, °C	Parabolic rate constant, (mg/cm ²) ^{1/2} /min
945	0.1019
962	0.1190
975	0.1435
998	0.1653
1056	0.2459
1056	0.2368
1166	0.3899
1256	0.5625

$$\Delta E_a = 19.8 \pm 1.0 \text{ kcal/mole}$$

Presence of water vapor in the oxygen gas.—In one of the experiments, oxygen was bubbled through distilled water and passed into the combustion tube containing ZrB_2 at $1056^\circ C$, to study the effect of moist oxygen on the reaction. A parabolic reaction rate was observed and the rate constant in this run [$0.20 \text{ (mg/cm}^2\text{)}^2\text{/min}$] was identical, within experimental error with that for dry oxygen under similar conditions [$0.24 \text{ (mg/cm}^2\text{)}^2\text{/min}$]. The slight decrease in the rate might be attributed to: (i) a reduction in the partial pressure of oxygen from 744 to 719 mm due to the presence of water vapor, and (ii) the formation of boric acid which is more volatile than B_2O_3 , which would cause a further decrease in the observed rate of weight gain. Glistening white crystals of boric acid were observed on the cooler parts of the combustion tube. It was further noticed, unlike in other cases, that the ZrB_2 became very brittle after being exposed to moist oxygen. It should be mentioned that Brown (1) reported a greater rate in moist air than in dry air.

Oxidation of Zirconium Carbide

Zirconium carbide is more susceptible to oxidation than zirconium diboride and at lower temperatures. Pieces of zirconium carbide were found to break up immediately in contact with O_2 at $1000^\circ C$ or even lower. Berkowitz (12) also has observed the same phenomenon. Gangler (13) found excessive oxidation of ZrC in air at $980^\circ C$ and Watt, Crockett, and Hall (6), rapid oxidation in air at $800^\circ C$. In order to find a workable temperature range for studying the oxidation kinetics, a piece of ZrC was heated slowly from room temperature in an atmosphere of oxygen. The sample began to crumble at about $700^\circ C$ and broke up into several pieces at about $850^\circ C$, so that the maximum workable temperature was about $650^\circ C$. Even at this temperature, samples started crumbling after about an hour of oxidation. A porous film of zirconium oxide (identified by x-ray diffraction) was formed on the sample. The results of the successful runs at 554° – $652^\circ C$ are presented graphically in Fig. 5. It is clear that the reaction follows a linear rate law at $740 \pm 5 \text{ mm}$ pressure of O_2 and a flow rate of $100 \pm 5 \text{ ml/min}$. The linear rate constants at various temperatures are given in Table IV. The activation energy calculated in this case from the Arrhenius plot is $16.7 \pm 1.7 \text{ kcal/mole}$. This activation energy is lower than the 45.7 kcal/mole reported by

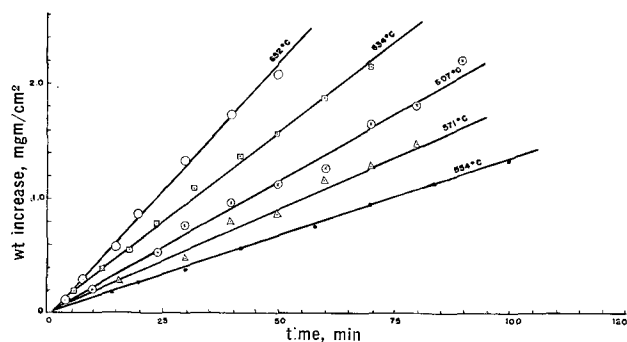


Fig. 5. Linear plot for the oxidation of ZrC at various temperatures. O_2 pressure, $740 \pm 5 \text{ mm}$; O_2 flow rate, 100 ml/min .

Table IV. Rate constants for the ZrC- O_2 reaction at various temperatures
Oxygen pressure, $740 \pm 5 \text{ mm}$

Temperature, $^\circ C$	Linear rate constant, k_1 , $\text{mg/cm}^2\text{/min}$
554	0.01371
571	0.01818
607	0.02320
634	0.03153
652	0.04444

$\Delta E_a = 16.7 \pm 1.7 \text{ kcal/mole}$

Bartlett *et al.* (5) from their study of the oxidation rate of powdered ZrC over the range 450° – $580^\circ C$. Bartlett (14), in his thesis, notes that the temperature-dependence above $580^\circ C$ is noticeably lower so that a change in reaction mechanism is again implied. One might suspect that the spalling off of flakes of ZrC or ZrO_2 as oxidation occurs could cause an apparently slow reaction, but this would have been detected by the sensitive balance used unless the particles are extremely small. An alternative suggestion is that a diffusion-controlled oxidation process through a protective Zr-O-C film predominates at low temperatures while a linear process which produces a porous ZrO_2 and gaseous CO_2 takes over in the range above $580^\circ C$.

Conclusions

The oxidation of zirconium diboride, between the temperatures 945° and $1256^\circ C$ follows a parabolic rate law over the first hour of oxidation. The oxidation products seem to be the oxides of Zr and boron, with the boron oxide present as a molten layer on the surface. Part of the boron oxide slowly vaporizes at high temperatures as indicated by a white deposit on the cooler parts of the combustion tube after several runs. Variations in flow rate of oxygen in the experimental system from 20 – 100 ml/min have practically no effect on the rate of oxidation (at $1056^\circ C$) but a direct dependence on the partial pressure of O_2 (mixed with helium) was observed. The Arrhenius plot of the rate constants for the oxidation of ZrB_2 between 945° and $1256^\circ C$ is linear and gives an activation energy of 19.8 kcal/mole .

The oxidation of zirconium carbide follows a linear rate law at 554° – $652^\circ C$, and at higher tem-

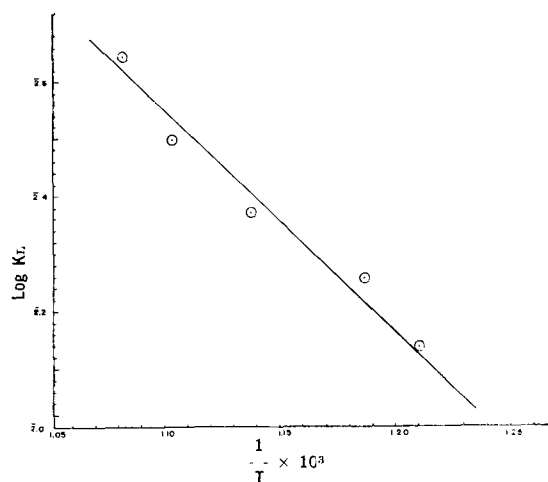


Fig. 6. Arrhenius plot for ZrC- O_2 reaction. O_2 pressure, 1 atm

peratures, a destructive oxidation of the material takes place in pure O₂. The activation energy for the oxidation of ZrC based on data at 554°-652°C is 16.7 kcal/mole.

Acknowledgments

The authors are pleased to acknowledge the financial support of this work by the United States Air Force through Contract No. AF 33(616)-7472 administered by Dr. Leslie McClaine for A. D. Little, Inc. The samples of ZrB₂ and ZrC were prepared by Dr. George Feick, of A.D. Little, Inc., and were typical high-purity zone-refined materials like those being currently used for heat of formation (15) and heat capacity studies (16, 17). Computer time and facilities of the Numerical Analysis Laboratory were made available through the Wisconsin Alumni Research Foundation.

Manuscript received March 27, 1963; revised manuscript received Nov. 1, 1963.

Any discussion of this paper will appear in a Discussion Section to be published in the June 1965 JOURNAL.

REFERENCES

1. F. H. Brown, Jr., Progress Report No. 20-252, Jet Propulsion Laboratory, Pasadena, California, February 25, 1955.
2. J. Berkowitz-Mattuck, "Thermodynamic and Kinetic Studies for a Refractory Materials Program," ASD-TDR 62-204 Part II, May 1963.
3. G. A. Meerson, G. V. Samsonov, R. B. Kotel'nikov, M. S. Voinova, I. P. Evteeva, and S. D. Krasnenkova, *Sbornik Nauch. Trudov. Nauch.-Tekh. Obshchestva Tsvetnoi Met., Moskov. Inst. Tsvetn. Metal. Zolota*, 1959, No. 29, 323-8; *C. A.*, **54**, 10781e (1960).
4. G. S. Markevich and L. Ya. Markovskii, *Zh. Prikl. Khim.*, **33**, 1008 (1960).
5. R. W. Bartlett, M. E. Wadsworth, and I. B. Cutler, *Trans. Met. Soc., AIME*, **227**, 467 (1963).
6. J. Berkowitz-Mattuck, "Kinetics of Oxidation of Refractory Metals and Alloys at 1000°-2000°C," ASD-TDR-62-203, Part II, March 1963.
7. W. Watt, G. H. Crockett, and A. R. Hall, *Metaux Corr-Ind.*, **28**, 222 (1953).
8. N. R. Thielke, WADC, TR54-467, Pennsylvania State University.
9. J. Hinnüber and O. Rüdiger, *Arch. Eisenhüttenw.*, **24**, 267 (1953).
10. Leslie A. McLaine, A. D. Little, Inc., San Francisco, California, Private communication, June 12, 1963.
11. J. Berkowitz-Mattuck, "Thermodynamic and Kinetic Studies for a Refractory Materials Program," Progress Report to Air Force Materials Laboratory, Aeronautical System Divisions, August 1963.
12. J. Berkowitz-Mattuck, "Thermodynamic and Kinetic Studies for a Refractory Materials Program," Progress Report to Aeronautical Systems Division, August 1962.
13. J. J. Gangler, Amer. Ceramic Soc. 52nd Annual Meeting, Preprint, 1950 (as cited in P. Schwartzkopf and R. Kieffer, "Refractory Hard Metals," MacMillan Publishing Co., New York, 1953) p. 195.
14. R. W. Bartlett, Ph.D. Thesis, University of Utah, 1961, p. 110.
15. G. Johnson, E. Greenberg, W. Hubbard, and J. Margrave, Abstracts, 145th American Chemical Society Meeting, New York City, September 13, 1963.
16. E. F. Westrum, Jr. and G. Feick, *J. Chem. Engr. Data*, **8**, 176, 193 (1963).
17. R. Mezaki, R. Valentine, T. Jambois, and J. Margrave, *ibid.*, (1963).

"Oxygen" Adsorption and Double Layer Capacities; Gold in Perchloric Acid

G. M. Schmid and R. N. O'Brien

Department of Chemistry, University of Alberta, Edmonton, Alberta, Canada

ABSTRACT

The "oxygen" adsorption on polycrystalline Au in 1N HClO₄ was studied between 0.4 and 1.43v vs. SCE at 5°, 25°, and 50°C, using cathodic galvanostatic stripping and rapid single pulse differential capacity measurements. A potential arrest at 0.5v is ascribed to surface Au-OH and/or Au-O formation, a plateau at 1.0v to surface oxidation to Au₂O₃, probably occurring in patches. The appearance of a maximum in the differential capacity-potential curve during the adsorption process is explained on the basis of an additional capacity, C_{ads}, of the inner double layer due to the presence of the charges of the (specifically) adsorbed species. It is shown that C_{ads} should be proportional to the slope of a plot of amount adsorbed vs. potential. The model proves satisfactory for surface "Au-OH" build-up to 1/3 of a monolayer, and on decomposition from a monolayer.

Adsorption and desorption processes on metal electrodes are frequently accompanied by a large maximum in the capacity-potential curve (1). It was shown by Lorenz (2) that the capacity maximum decreases with increasing measuring frequency but does not disappear even at 700 kc. At such frequencies the capacity can reasonably be assumed to be free of faradaic effects and to represent the capacity of the ionic double layer only.

In previous papers (3, 4) the electrical double layer (edl) differential capacities of gold in HClO₄ were reported as a function of potential. A rapid single pulse technique (5) was used to exclude the influence of the faradaic impedance. The zero point of charge was determined to be close to 0.0v on the saturated calomel electrode (SCE) scale (including a saturated KCl-HClO₄ junction potential) (4, 6). A number of maxima in the capacity-potential curve were attributed to hydrogen adsorption, some spe-

cific ClO₄⁻ adsorption, and to the adsorption of an unknown, oxygen-containing species.

An attempt to explain the behavior of the capacity of the ionic double layer on the basis of a change in dielectric constant due to the adsorbed species was made by Devanathan (7). In the present investigation the appearance of a capacity maximum on adsorption (or desorption) is attributed to the presence of the charge of the (polarized or charged) adsorbed species in the inner double layer.

The gold-"adsorbed oxygen" system was chosen because of the ease with which both the amount adsorbed (or desorbed) and the edl capacity can be measured, thus making possible a ready comparison between the two quantities.

Experimental

The electrodes were polycrystalline mint gold purchased from Engelhard Industries, Inc., Newark, New Jersey. Rods were pressure-sealed into Kel-F, cut to expose a cross-section of 0.086 cm² apparent area, and joined to a Pyrex glass holder using a Teflon washer, brass rod, and nut (Fig. 1). Before each experiment, the electrodes were abraded with 4/0 emery paper, washed with distilled water, degreased with acetone in a Soxhlet, and washed with conductivity water.

Conductivity water was prepared by redistilling tap distilled water from an alkaline permanganate solution in a Pyrex still, followed by distillation in a Heraeus two-stage quartz still. The electrolyte, 1N HClO₄ in all cases, was prepared from 70% reagent grade HClO₄ by appropriate dilution with conductivity water. Before each run it was purified by pre-electrolysis between Pt electrodes with a minimum of 35 coulombs/ml, and degassed by passing a steady stream of Grade A Helium for at least 12 hr.

The all Pyrex cell contained, in addition to the Au electrode, a cylindrical platinized Pt wire gauze as counter electrode, and two SCE's, the latter being connected to the main compartment by closed, ungreased stopcocks and capillaries. The cell had a

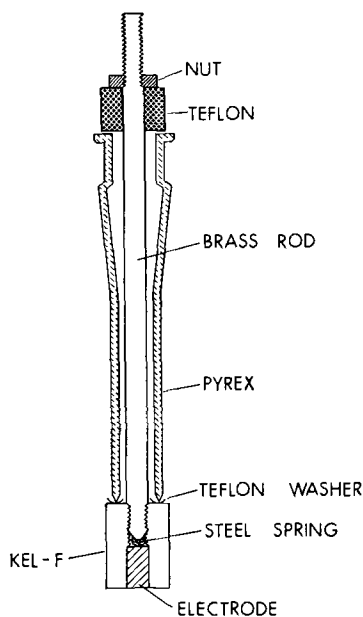


Fig. 1. Electrode assembly

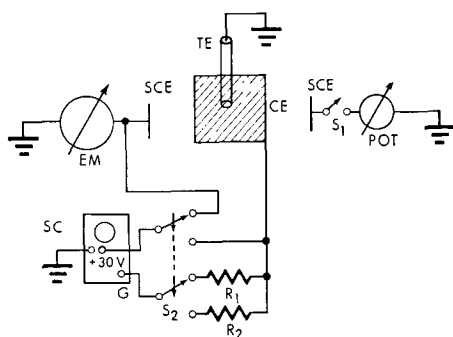


Fig. 2. Circuit diagram. TE, test electrode; CE, counter electrode; SCE, saturated calomel electrode; EM, Keithley 610A electrometer; POT, Sensitive Research Instr. Corp. PV potentiometer; SC, Tektronix 535A oscilloscope; G, gate; R_1 , R_2 , series resistor; S_1 , S_2 , switch. A stripping curve is being taken.

water jacket and was thermostated at 5°, 25°, and 50°C to $\pm 0.1^\circ\text{C}$ with a Colara Ultra Thermostat.

The test electrodes were polarized with a Hickling potentiostat (8). In the low current density region ($i < 0.1 \mu\text{a}$, +0.2 to +1.43v) the potentiostat did not give satisfactory results and was replaced by a Sensitive Research Instrument Corp. Model PV potentiometer applied between test electrode and a SCE. The potential was monitored with a Keithley 610A electrometer (input impedance 10^{14} ohms) applied between test electrode and the second SCE. The potentials are reported with respect to SCE at 25°C.

For the edl differential capacity measurements a rapid single pulse technique was used, as described elsewhere (5). The method essentially consists of measuring the slope of the potential-time curve of the test electrode at the onset, or a time very close to it, of a fast rise, rectangular current pulse. The potential-time curves were displayed on a Tektronix Type 535A oscilloscope, operated on "single sweep," with a Type D preamplifier, and connected between test and counter electrode (Fig. 2). The traces were photographed with a Tektronix Type C-12 Polaroid camera. Approximately +30v appear at the gate of the oscilloscope for the duration of the push button triggered sweep. The current pulse, of a length up to 50 μsec , was taken from this gate and dropped through a suitable resistor to give 617 μa . In the investigated potential range (0.4 to 1.4v) the potential-time curve was a straight line over at least the first 40 μsec , indicating the absence of a faradaic impedance during this period. The desired slope could be measured about 1 μsec after the onset of the pulse. The measurement thus corresponds to an a-c determination with a base frequency of more than 500 kc and represents the differential capacity of the ionic double layer only. The accuracy of the measurement is limited by the non-linearity of the oscilloscope amplifiers to $\pm 3\%$.

The coverage with oxygen-containing adsorbed species was determined by constant current cathodic stripping. For this purpose the oscilloscope was connected between test electrode and SCE, and the gate of the oscilloscope, through a series resistor, between test and counter electrode (Fig. 2). The potential of the test electrode was set to the desired value. The potentiometer was then switched off and the oscillo-

scope triggered simultaneously. All stripping was done with 121 μa . The low input impedance of the oscilloscope (1 megohm) causes an iR drop of 30 mv at 1.4v to appear between test electrode and SCE (as measured with the Keithley). A corresponding correction was applied to all potentials reported.

Reproducible results were obtained only after repeated anodic and cathodic cycling to the highest anodic potential used in this study (+1.43v) and to -0.5v. This pretreatment presumably removes oxidizable and reduceable impurities from the electrode surface (9). It also seems to introduce roughening of the surface until a constant state is reached. After cycling, capacity data were taken, beginning at about +0.4v through +1.4v and back to the starting point. The potential was changed in steps of 100 mv every 10 min, except in the vicinity of the maximum where the steps were 50 mv only. The capacity reaches a constant value after 2-5 min and does not change over a period of up to 1 hr. Stripping curves were then taken in steps of approximately 100 mv, starting from cathodic potentials through +1.43v, allowing 10 min at each potential for the adsorption to come to a steady state. The potential was then set to +1.43v for 10 min, changed to a less anodic potential, and a stripping curve taken from there 10 min later. This procedure was repeated for successively less anodic potentials, always allowing the electrode to come to a steady state at +1.43v first.

All data reported are referred to the estimated true surface area. From freshly prepared electrode to freshly prepared electrode the reproducibility of the capacity data was $\pm 15\%$. This was attributed to difficulties in reproducing a definite roughness factor. The capacity curves were normalized to an (arbitrary) capacity of 16 $\mu\text{f}/\text{cm}^2$ at the capacity minimum just before the rise to the anodic adsorption maximum. The procedure was tantamount to using a roughness factor varying between 2.1 and 2.5. The reproducibility of the capacity data was then $\pm 5\%$. The stripping data were reproducible to $\pm 10\%$ as calculated with an average roughness factor of 2.3.

Results

Figure 3a shows the coverage with "oxygen-containing" species obtained on a Au electrode in 1N HClO_4 at three different temperatures. Adsorption starts at around 0.5v and increases up to 1.43v without any indication of reaching a constant magnitude. Average values at 1.43v are 1440, 1200, and 1100 $\mu\text{coulomb}/\text{cm}^2$ for 5°, 25°, and 50°C, respectively. The adsorption is highly irreversible and this can be seen in Fig. 3b which shows the residual coverage after holding the potential at 1.43v, and then at the anodic starting potential for 10 min each. Desorption of the adsorbed species occurs in two very pronounced steps at about 1.0 and 0.5v.

The charge involved in the step at 1.0v can be separated from the charge involved in the step at 0.5v on the basis of the oscilloscope traces obtained during cathodic stripping, both for adsorption (increasing potentials) and for desorption (decreasing potentials). The duration of the plateau at 1.0v was taken from the beginning of the trace to the inflection point following the potential arrest; of the

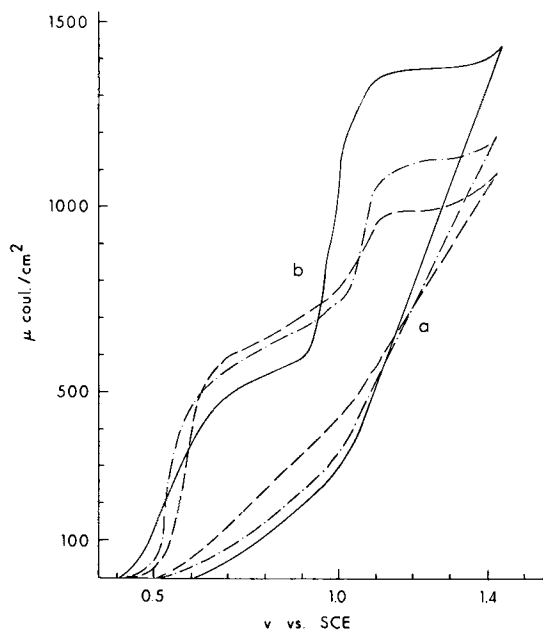


Fig. 3. "Oxygen" coverage as a function of potential. Au in 1N HClO_4 . 5°C, —; 25°C, - · -; 50°C, — — —. a. For increasing potentials; b, for decreasing potentials after steady state at 1.43v.

plateau at 0.5v from the inflection point before to the inflection point after the arrest. The potential rise to the plateau took less than 0.05 sec in most cases, the error involved in this procedure is therefore small, but may account partly for the reproducibility being $\pm 10\%$ only.

The results are shown in Fig. 4. Adsorption starts at approximately 0.5 and 1.0v respectively and shows no tendency to level off even at 1.43v (except perhaps at 5°C in Fig. 4a). The irreversibility already evident in Fig. 3 is again visible in Fig. 4. A pronounced negative temperature coefficient becomes apparent for the plateau at 1.0v, whereas the coverage causing the plateau at 0.5v increases with

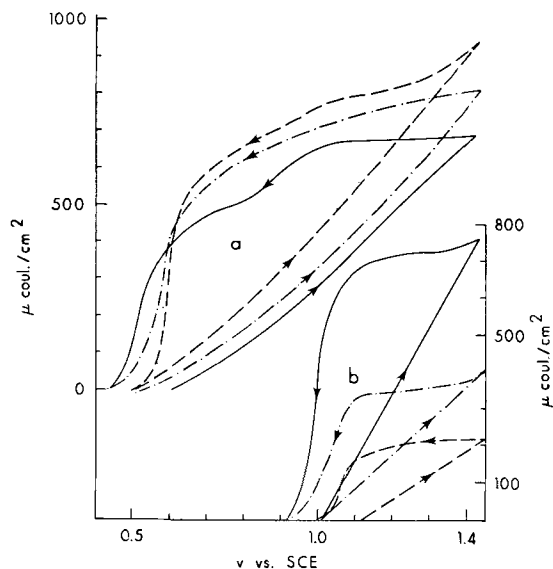


Fig. 4. "Oxygen" coverage as a function of potential. Au in 1N HClO_4 . 5°C, —; 25°C, - · -; 50°C, — — —. a, Plateau at 0.5v; b, plateau at 1.0v; both for increasing and decreasing potentials.

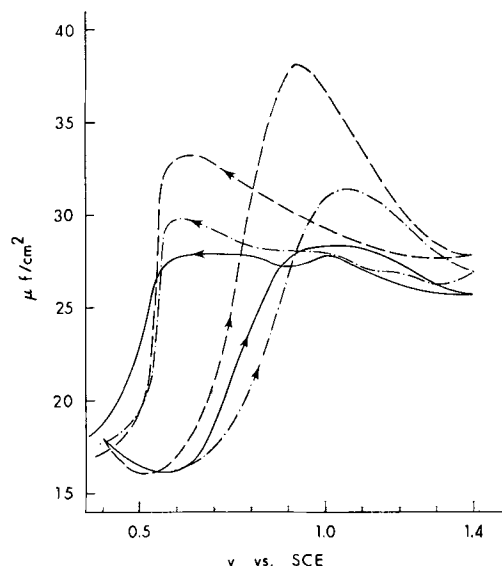


Fig. 5. Differential capacity as a function of increasing and decreasing potentials. Au in 1N HClO_4 . 5°C, —; 25°C, - · -; 50°C, — — —.

temperature. The potential plateaus on the oscilloscope traces (not shown) are displaced by about 100 mv to more cathodic values as compared to the corresponding drops in coverage shown in Fig. 3 and 4. This is due to overvoltage caused by the relatively high stripping current ($121 \mu\text{a}$, $\approx 550 \mu\text{a/cm}^2$).

Comparison of the adsorption-desorption behavior outlined above with the capacity data shown in Fig. 5 reveals that the onset of adsorption (increasing potentials) at about 0.5v closely corresponds to the beginning of the rise of the capacity to the adsorption maximum. The desorption step (decreasing potentials) at 0.5v causes a sharp drop in capacity, whereas desorption at 1.0v seems to have little or no influence on the capacity-potential behavior. After desorption is completed, at about 0.4v, the capacity returns to approximately the values encountered before adsorption. This indicates that the adsorption-desorption process leaves the surface essentially unaltered after a constant roughness factor has been achieved by cathodic-anodic cycling.

The influence of temperature on the capacity is quite pronounced, the maximum being $38.2 \mu\text{f/cm}^2$ at 50°C, and $28.3 \mu\text{f/cm}^2$ at 5°C. With increasing temperature the potential at which the maximum occurs shifts to less noble values, the maximum becoming sharper at the same time. The irreversibility in the adsorption-desorption behavior finds its expression in the capacity hysteresis. The desorption peaks (Fig. 5, decreasing potentials) are at potentials at least 300 mv more cathodic than the adsorption peaks (Fig. 5, increasing potentials).

Discussion

Adsorption-desorption behavior.—The gold-"adsorbed oxygen" system has been studied repeatedly (10). It is generally assumed that a Au-O layer is formed first which is later converted to Au_2O_3 with time and at more anodic potentials (11-14). It is then surprising that on cathodic decay only one potential arrest is reported (11, 12, 14, 15). One would

rather expect two plateaus, and this was indeed found here.

If the model outlined above is correct, the adsorption step beginning at 0.5v and causing, on desorption, the plateau at 0.5v (Fig. 4a) may be associated with the formation of Au-O, or some similar oxygen-containing species, on the surface. Perhaps the assumption of a species Au-OH (12), formed by oxidation of an adsorbed water dipole, is more reasonable since it requires the transfer of only one electron. The formation of Au-O and/or Au-OH is in agreement with the small positive temperature coefficient observed for this step, and with the strong influence on the capacity behavior (see below), which would both be expected for chemisorption-type adsorption.

The amount of "Au-OH" formed on the surface does not reach saturation even at 1.43v, although the observed value of 950 $\mu\text{coulomb}/\text{cm}^2$ at 50°C is higher than what is normally considered to be a monolayer on the basis of one electron per surface atom of Au ($\approx 500 \mu\text{coulomb}/\text{cm}^2$), even if a large error was made in estimating the roughness factor. It is interesting to note that the desorption behavior after steady state at 1.43v (Fig. 4a) shows a gradual reduction of the amount of "Au-OH" present, until, at approximately 0.65v, about one monolayer is left which is then removed within 100 mv or so. Adsorbed OH radicals in excess of one monolayer may be converted to adsorbed (atomic) oxygen, may form multilayers, and/or may be adsorbed on oxidized portions of the Au surface.

It should be pointed out that the possibility of the plateau at 0.5v being caused by adsorption of H_2O_2 could be made highly unlikely, but could not be excluded all together. H_2O_2 may be formed during pre-electrolysis, during anodic-cathodic cycling, and during the normal polarization procedures used during a run. Omission of pre-electrolysis and cycling still gave plateaus at 0.5v, although of rather irreproducible length. Also, keeping the electrolyte at 50°C for several hours should remove most of the H_2O_2 eventually present and should lead to a decrease in the amount adsorbed, whereas an increase was actually found.

The adsorption step beginning at 1.0v can be identified with oxide formation, *e.g.*, by further oxidation of "Au-OH" to Au_2O_3 . The latter is more difficult to form at higher temperatures (16), consequently a negative temperature coefficient for this adsorption step would be expected and is found. The assumption finds further support in the observation that a visible oxide film can be formed on the electrode by keeping the potential at 1.4v for 24 hr. The maximum value of 760 $\mu\text{coulomb}/\text{cm}^2$ observed at 5°C and 1.43v is too small to account even for a monolayer of Au_2O_3 . The oxidation seems to occur in patches (17), leaving a considerable part of the surface covered with OH radicals only.

The oxidation-reduction-potential behavior of the surface- Au_2O_3 resembles closely that of the adsorbed species found by Laitinen and Chao (12). These authors did not report the presence of a second adsorbate. However, as can be seen from their Fig. 3,

not all the "oxygen" adsorbed is removed at the plateau at 1.0v, the total coverage not being reduced to zero until at about 0.4v.

Differential capacity—theoretical.—The theory of the edl on metals was originally developed for ideally polarizable electrodes (1). It is generally assumed to hold for intermediate cases also, a viewpoint which will be adopted here.

The differential capacity of the edl is defined as the derivative of the (electronic) charge on the metal with respect to potential (1). Because of the electroneutrality requirement, the charge on the metal must be equal and opposite in sign to the sum of the excess charges of the anions and cations on the solution side of the interface. In the potential region in which an adsorption (or desorption) process occurs, the sum of these excess charges, considered as a function of potential, undergoes a change, as does the charge on the metal, and with it the edl capacity. It may be expected that the capacity gives a strong indication of an adsorption process only for species entering the inner double layer (specific adsorption), the capacity of the outer double layer being very large and having little influence on the total capacity of the series combination.

The differential capacity is a function of the dielectric constant in the inner double layer region and of the (effective) distance between metal surface and inner Helmholtz plane. It will be assumed in this discussion that both these parameters are constant during the adsorption process [see however (7)]. This is equivalent to assuming that the adsorbate has the same polar character and effective physical size as the water dipoles replaced. Although this assumption is open to debate, here it is perhaps not an unreasonable one. With the adsorbed water dipole already distorted to give a dielectric constant of $\epsilon < 10$ (7), due to the presence of the water-metal bond, the proton(s) missing in surface Au-O and/or Au-OH should not account for a considerable additional change in ϵ .

For an adsorption process, the differential capacity can be written as

$$\begin{aligned} C &= d(q + k'q')/dE \\ &= C_0 + C_{\text{ads}} \end{aligned} \quad [1]$$

where q represents the charge on the metal in the absence of an adsorption (or desorption) step, q' the increase in charge in the inner double layer due to adsorption, and k' the fraction of the charge q' that is reflected as an increase in charge on the metal, the fraction $1 - k'$ being compensated for by a net increase of opposite charges in the outer double layer. C_0 is the differential capacity in the absence of adsorption, C_{ads} the increase in capacity due to the adsorption process

$$C_{\text{ads}} = k'(dq'/dE) \quad [2]$$

The charge in the inner double layer due to adsorption, q' , is not easily accessible to measurement. What can be measured frequently is the charge, q_{ads} , necessary to reduce, or oxidize, the adsorbed species. If the interaction between adsorbed molecules is

negligible (for small coverage), q' is a fraction, k'' , of q_{ads}

$$q' = k'' q_{\text{ads}} \quad [3]$$

so that

$$C_{\text{ads}} = k (dq_{\text{ads}}/dE) \quad [4]$$

with

$$k = k' k''$$

The dimensionless quantity k is taken as a constant, independent of potential, although this is probably a first approximation only. It contains k' which converts the charge q' to the ensuing increase in charge on the metal. The coefficient k' will depend on the electrode material, the state of the electrode surface, and the bond established between surface and adsorbate. A determination of k' requires detailed knowledge of the components of charge of the edl which is available for some mercury systems (18), but not for solid electrodes at the present time.

One might assume that for adsorption steps accompanied by a charge transfer, q_{ads} , the magnitude of the charge present in the inner double layer, q' , and with it k' depends on the nature of the adsorbed species, that is whether they can be considered a charged species, of type M^+_{ads} , or a neutral entity, such as M_{ads} . Further discussion of k' and k'' must await a more detailed knowledge of the state of the adsorbed species and the adsorptive bonds.

According to Eq. [4], C_{ads} is proportional to the slope of a plot of q_{ads} vs. potential and will go through a maximum during the adsorption (or desorption) step. For symmetrical, S-shaped q_{ads} vs. potential curves, the capacity maximum will be established at a potential corresponding to $1/2$ of the final coverage. In potential regions where maximum adsorption has been reached, the capacity returns to C_0 , or to a new, fairly constant value, consistent with the geometrical relationships and the dielectric constant of the fully covered (or uncovered) surface (2, 19). This behavior is represented schematically in Fig. 6. An average value for k can be obtained if C_0 stays constant in the potential range involved.

The model outlined above explains the presence and position of maxima in potential-differential capacity curves caused by adsorption and desorption processes. It is assumed that the dielectric constant in the inner double layer does not change significantly in the region of the capacity maxima, and that the change in capacity is brought about by the presence of additional charged or dipolar species in the inner double layer.

Differential capacity—experimental.—The capacity data for 25°C reported here are in very good agreement with values previously found on (100) and (110) single crystal electrodes for this temperature (3). They do not agree with results obtained for polycrystalline electrodes (4), where the relative height of the anodic adsorption peaks was considerably smaller. This discrepancy is the result of the anodic and cathodic cycling used as pretreatment in the present work. The small amount of oxidation and redeposition caused by the cycling procedure leads to an increase in roughness factor, as judged

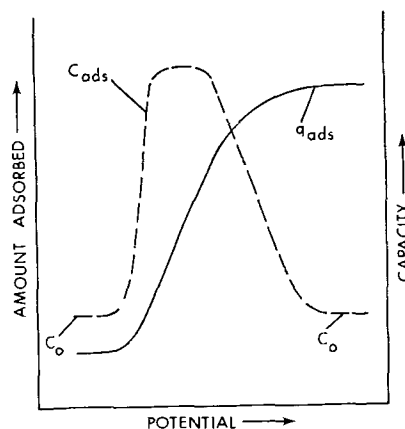


Fig. 6. Expected behavior of the capacity-potential function during an adsorption process. C_0 , differential capacity before and after the adsorption step; C_{ads} , additional capacity due to adsorption; q_{ads} , charge equivalent of amount adsorbed.

from the general increase in capacity, and also seems to lead to a surface more susceptible to adsorption, as judged from the relative height of the adsorption maximum. The latter phenomena could be caused for example by re-deposition onto preferred crystal faces leading to a preferred surface orientation (12). No x-ray analysis was performed with the electrodes used in the present work.

Although the capacities measured tended to decrease with temperature, much overlapping was caused by the irreproducibility of the roughness factor. Normalization of the capacity data to $16 \mu\text{f}/\text{cm}^2$ at the minimum just before the rise to the anodic adsorption maximum (Fig. 5) allows comparison of the capacity-adsorption (or desorption) behavior at the various temperatures used here. The $16 \mu\text{f}/\text{cm}^2$ chosen is a reasonable value for a metal surface free of adsorbed species (1).

The capacity-potential behavior during an adsorption step outlined above can be expected to hold for the formation of a surface Au-OH and/or Au-O, that is, a chemisorbed species. It will not hold for surface oxidation to Au_2O_3 . Moreover, the model is not expected to hold for adsorption exceeding a monolayer. Comparison of Fig. 4 with Fig. 5 shows that the capacity maxima are in the vicinity of beginning Au_2O_3 formation rather than at potentials with an "OH" coverage of about $250 \mu\text{coulomb}/\text{cm}^2$ ($1/2$ monolayer). Interference of Au-OH multilayer buildup and/or Au-O formation, and surface oxidation cannot be excluded. Metal oxide surfaces have an edl capacity considerably lower than "free" metal surfaces (20). The appearance of oxide patches, growing in area with potential would in itself lead to a capacity maximum. The decrease in height of the maximum with temperature is brought about by a corresponding increase in oxidation to Au_2O_3 .

Similar interference can be expected for the desorption step shown in Fig. 4 and 5. Here, coming from higher potentials, the rise in capacity is caused by a gradual conversion of a low capacity oxide into a high capacity "Au-OH" with simultaneous desorption of excess Au-OH and/or Au-O. However, the capacity maximum is positioned at or near a residual coverage with $1/2$ of a monolayer. There-

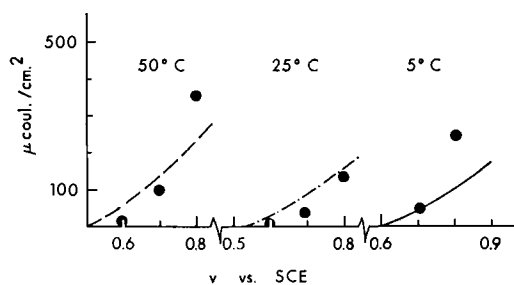


Fig. 7a. Formation of surface "Au-OH." Points calculated with Eq. [1] and [4]; $C_o = 16, \mu\text{f}/\text{cm}^2$, $k = 2.5 \times 10^{-3}$.

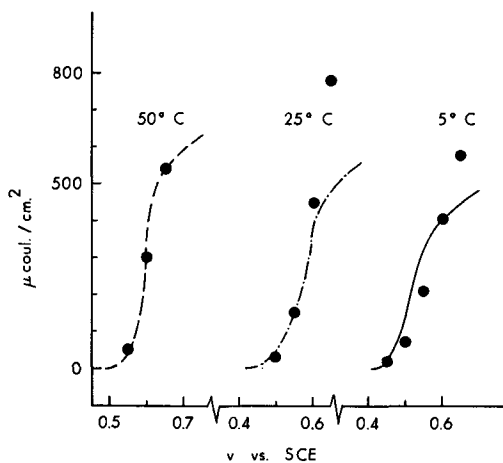


Fig. 7b. Decomposition of surface "Au-OH." Points calculated as in Fig. 7a.

fore, the capacity-adsorption model should hold for desorption of "Au-OH" from the monolayer level.

In Fig. 7 experimental coverage data are compared with values calculated from the integrated form of Eq. [1] and [4] with $C_o = 16 \mu\text{f}/\text{cm}^2$ and $k = 2.5 \times 10^{-3}$. As expected, the adsorption step is described satisfactorily only to about 1/3 of a monolayer, whereas the desorption from a monolayer is represented reasonably well.

Summary

The amount of "oxygen" adsorbed on Au in 1N HClO_4 was studied between 0.40 and 1.43v vs. SCE at 5°, 25°, and 50°C, and compared with the differential capacity of the ionic double layer. Coverage data were obtained from cathodic galvanostatic stripping curves; a rapid single pulse technique was used to measure the capacity.

The stripping curves show two potential plateaus, at 0.5v and at 1.0v. The arrest at 0.5v is attributed to surface Au-OH and/or Au-O formation on the basis of a small positive temperature coefficient, expected for chemisorption, and a pronounced influence on the capacity, expected for adsorption processes involving the inner double layer. For this species, the coverage of 950 $\mu\text{coulomb}/\text{cm}^2$ measured at 1.43v and 50°C exceeds monolayer coverage as

calculated for the transition of one electron per surface atom of Au ($\approx 500 \mu\text{coulomb}/\text{cm}^2$). This is explained by multilayer buildup or conversion of Au-OH to Au-O. The arrest at 1.0v is caused by surface oxidation to Au_2O_3 , as judged from a negative temperature coefficient of formation. The oxidation reaches 760 $\mu\text{coulomb}/\text{cm}^2$ at 1.43v and 5°C and probably occurs in patches.

The differential capacity exhibits a maximum in the "oxygen" adsorption region. The appearance of such a maximum during a (specific) adsorption process is explained on the basis of an additional capacity, C_{ads} , of the inner double layer, due to the presence of the charges of the adsorbed species, at constant dielectric constant. It is shown that C_{ads} should be proportional to the slope of a plot of "amount adsorbed" vs. potential. The capacity-adsorption model is tested for "Au-OH" adsorption and desorption. A value of $k = 2.5 \times 10^{-3}$ for the proportionality constant gives satisfactory results for adsorption up to 1/3 of a monolayer, and for desorption from a monolayer, which is the range for which the model is expected to hold.

Manuscript received Aug. 4, 1963; revised manuscript received March 2, 1964.

Any discussion of this paper will appear in a Discussion Section to be published in the June 1965 JOURNAL.

REFERENCES

1. For reviews see: D. C. Grahame, *Chem. Rev.*, **41**, 441 (1947); A. N. Frumkin, *This Journal*, **107**, 461 (1960); B. B. Damaskin, *Uspekhi Khim.*, **30**, 220 (1961).
2. W. Lorenz, *Z. physik. Chem. (NF)*, **26**, 424 (1960).
3. G. M. Schmid and Norman Hackerman, *This Journal*, **109**, 243 (1962).
4. G. M. Schmid and Norman Hackerman, *ibid.*, **110**, 440 (1963).
5. J. S. Riney, G. M. Schmid, and Norman Hackerman, *Rev. Sci. Instruments*, **32**, 588 (1961).
6. M. Green and H. Dahms, *This Journal*, **110**, 466 (1963).
7. M. A. V. Devanathan, *Proc. Roy. Soc. (London)*, **A267**, 256 (1962).
8. A. Hickling, *Electrochim. Acta*, **5**, 161 (1961).
9. S. Gilman, *J. Phys. Chem.*, **66**, 2657 (1962).
10. K. J. Vetter, "Elektrochemische Kinetik," p. 502, Springer Verlag, Berlin (1961).
11. K. J. Vetter and D. Berndt, *Z. Elektrochem.*, **62**, 378 (1958).
12. H. A. Laitinen and M. S. Chao, *This Journal*, **108**, 726 (1961).
13. J. P. Hoare, *ibid.*, **110**, 245 (1963).
14. A. Hickling, *Trans. Faraday Soc.*, **42**, 518 (1946).
15. F. G. Will and C. A. Knorr, *Z. Elektrochem.*, **64**, 270 (1960).
16. "Handbook of Chemistry and Physics," p. 1825, Chemical Rubber Publishing Co., Cleveland (1958).
17. S. Barnartt, *This Journal*, **106**, 722 (1959).
18. D. C. Grahame and B. A. Soderberg, *J. Chem. Phys.*, **22**, 449 (1954).
19. W. Lorenz and W. Mueller, *Z. physik. Chem. (NF)*, **25**, 161 (1960).
20. J. J. McMullen and Norman Hackerman, *This Journal*, **106**, 341 (1959).

Electrodialytic Demineralization Using Permselective Membranes

I. Energy Consumption and Production Rate

W. G. B. Mandersloot

Chemical Engineering Group, South African Council for Scientific and Industrial Research, Pretoria, South Africa

ABSTRACT

Equations were derived for the energy consumption and production rate in electro-dialytic demineralization, based on a simple empirical relation between the apparent compartment pair resistance and the electrolyte concentration in the desalting stream. The equations are independent of the compartment dimensions parallel to the membranes and of flow velocity. Special attention is given to the detrimental effect of water transport and an "over-all efficiency" is introduced which covers the nonideality of the membranes, salt diffusion, and water transport. The equations are compared with experimental results.

The principle of electro-dialytic demineralization (1, 2) using ion-selective membranes in a multi-compartment apparatus (Fig. 1) in which flow disturbing devices (2, 3) are placed in the compartments to combat concentration polarization (4-6) finds increasing technical application. A number of transport processes occur simultaneously in the membranes (Fig. 2), of which only counterion transport brings about the desired effect. These transport processes occur in a medium in which the concentrations of counterions and fixed ions are usually in the range of 1-6M; a good deal of interaction must therefore occur.

The optimum compartment thickness, arrived at through a balance of electrical resistance and hydraulic resistance, is approximately 1 mm. The electrolyte concentration in the brine should be high to achieve a low resistance of the compartment pair, but limitations are set by (a) the presence of precipitate forming ions; (b) the fact that the concentration difference across the membranes constitutes

the driving force for most of the detrimental processes indicated in Fig. 2; (c) electrical leakage through the brine stream.

In the design of electro-dialytic demineralization plants the cost of membrane surface area (approximately inversely proportional to the applied electric potential gradient) and the cost of electrical energy consumed (approximately proportional to this gradient) should be balanced to arrive at an economic optimum. Relations between these two variable cost-determining factors and the initial and final dialysate concentrations are therefore required. They are derived from the relation between compartment pair resistance and the dialysate concentration. For small demineralization ranges the average compartment pair resistance can be determined (7, 8) or calculated from the resistances of the component parts (9). The latter method requires an estimate of the effect of that part of concentration polarization which cannot be eliminated and of the screening effect of spacer materials and membrane potentials should be taken into account as well. A measurement of the apparent resistance of the complete assembly is, of course, much more accurate. We therefore decided on a method applicable to large desalting ranges as well, in which the relation between compartment pair resistance and dialysate concentration is determined in a laboratory size electro-dialysis apparatus with components identical to those used in a technical installation (except dimensions parallel to the membranes).

Mathematical Description of the Process

When serious concentration polarization is avoided by using an appropriate flow velocity in the compartments the apparent electrical resistance of a unit surface area of a compartment pair is a linear function of the reciprocal of the electrolyte concentration in the dialysate

$$r = a + b/C \quad [1]$$

In a given compartment pair assembly a and b are dependent on the temperature and composition of the electrolyte, and the relation is valid for the range of C for which electro-dialytic demineralization

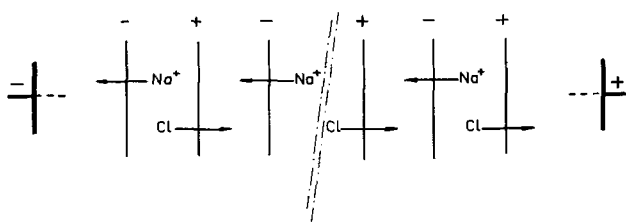


Fig. 1. Membrane arrangement in a membrane stack for electro-dialytic water demineralization. The cation and anion selective membranes are indicated by — and +, respectively.

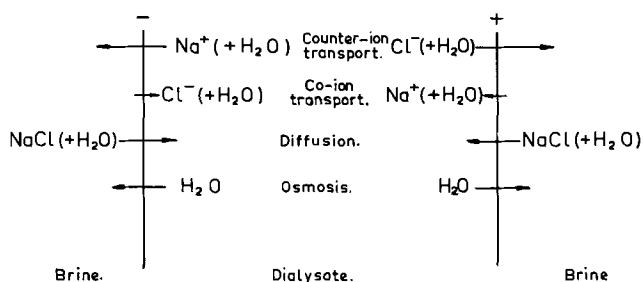


Fig. 2. Transport processes occurring simultaneously through the membranes.

is usually considered ($0.01 < C < 0.6$), provided no large variation in the brine concentration occurs. When, as usual, a constant voltage per compartment pair is applied

$$i = E/(a + b/C) \quad [2]$$

The salt transport j per square centimeter of membrane pair is then

$$j = \psi' E/F(a + b/C) \quad [3]$$

and the rate at which salt is removed from the dialysate is

$$dN/dt = -jA = -\psi' AE/F(a + b/C) \quad [4]$$

At any time

$$N = VC \quad [5]$$

and therefore

$$dN = VdC + CdV \quad [6]$$

If it is assumed that for each gram equivalent of salt removed from the dialysate the volume of the dialysate changes by H liter and that this figure includes osmotic water transport, then

$$dV = HdN \quad [7]$$

and a material balance gives:

$$V = V_T(1 - HC_T)/(1 - HC) \quad [8]$$

Combining Eq. [4], [6],[7], and [8] and taking $(1 - HC)^2 = 1 - 2HC$, the concentration change in the dialysate can be described by

$$dC/dt = -\psi' AE(1 - 2HC)/FV_T(1 - HC_T)(a + b/C) \quad [9]$$

After integration (assuming ψ' to be constant) the production rate of the process is given by

$$V_T/T = 2\psi' AEH/F(1 - HC_T) \left(a \ln[(1 - 2HC_T)/(1 - 2HC_o)] + 2bH \ln[C_o(1 - 2HC_T)/C_T(1 - 2HC_o)] \right) \quad [10]$$

and the energy consumption per liter of product of concentration C_T obtained through the integration

$$W' = AE \int_0^T idt/V_T \quad [11]$$

is

$$W' = EF(1 - HC_T) \ln[(1 - 2HC_T)/(1 - 2HC_o)]/2\psi'H \quad [12]$$

It should be noted that a and b do not appear in Eq. [12]

Simplification Using "Over-all Efficiency"

The coulomb efficiency ψ' incorporated the non-ideality of the membranes, the effect of diffusional salt transfer, and the effect of the small amount of usually unavoidable interstream leakage. We may, however, replace ψ' by the over-all efficiency ψ , which incorporates in addition the effect of water transfer. Equation [9] then changes to

$$dC/dt = -\psi AE/FV_T(a + b/C) \quad [9a]$$

the production rate is then given by

$$V_T/T = \psi AE/F(C_o - C_T)(a + b/C_{\ln \text{mean}}) \quad [10a]$$

and the energy consumption per liter of product of concentration C_T by

$$W' = EF(C_o - C_T)/\psi \quad [12a]$$

The slope of this linear relation between W' and C_T (i.e., the energy consumption per gram equivalent removed per liter) is

$$W'' = -EF/\psi \quad [13a]$$

and the energy consumption per volt per compartment pair and per gram equivalent removed per liter is

$$W = F/\psi \quad [14a]$$

Equation [14a] can be expressed in more practical units by

$$W = 2.68 \times 10^{-2}/\psi \text{ kwh/g-equiv. volt} \quad [15a]$$

In the American literature on electrodialysis reference is often made to a quantity called the Power Index, which is the energy consumption per unit volume over the production rate per unit area

$$\text{Power Index} = F^2(C_o - C_T)^2(a + b/C_{\ln \text{mean}})/\psi^2 \quad [16a]$$

Effect of Water Transport

The detrimental effect of water transport on the efficiency of the process can be shown by combining Eq. [11] and [11a]

$$\psi/\psi' = (1 - 2HC)_{\ln \text{mean}}/(1 - HC_T) \quad [17a]$$

A graphical illustration of Eq. [17a] for various values of H and C_o and for $C_T = 0.01$ (drinking water) is given in Fig. 3. Values for $H < 0.2$ are not indicated as this value corresponds with the primary hydration of the ions. Figure 3 clearly indicates that the over-all efficiency of electrodialytic demineralization can never be high when solutions of near sea water concentration are demineralized to a drinking water level.

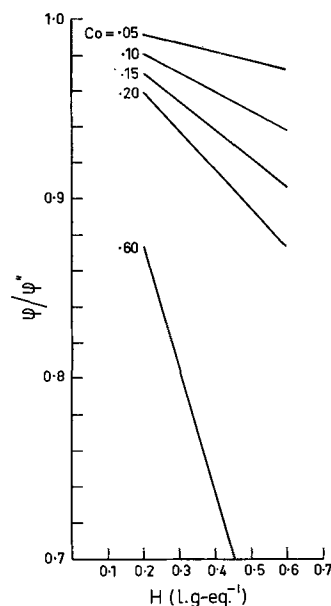


Fig. 3. The ratio ψ/ψ' , for various values of H and C_o , when $C_T = 0.01$; Eq. [17a].

Average Current Density

In electro dialytic demineralization it is often required to consider the effect of one dialysate pass through the apparatus; in some technical installations a pass length of up to several yards is used. The externally measured total current can be expressed only as an average current density \bar{i} . Making the reasonable assumption that each compartment is at one electric potential over its whole area, \bar{i} can be related to the ingoing and outgoing dialysate concentrations. If it takes the dialysate T sec to complete one pass, then

$$\bar{i} = \int_0^T idt/T \quad [18]$$

By combining Eq. [2], [9a], and [10a] we obtain

$$\bar{i} = E/(a + b/C_{\ln \text{ mean}}) \quad [19a]$$

and this equation can be used to predict the electric current in a technical installation from flow rate and a laboratory measurement of a and b .

Optimization of Cost

To optimize the cost of the process, the costs of compartment surface area and power consumption must be balanced (12, 13), and Eq. [10a] and [12a], or their more intricate equivalents, may be used to determine the optimum E with respect to cost (rather than an optimum average current density). The cost of installed compartment pair area per liter of product can be expressed as

$$S_A = qF(C_o - C_T)(a + b/C_{\ln \text{ mean}})/\psi E \quad [20a]$$

and the energy cost per liter of product by

$$S_{W'} = pEF(C_o - C_T)/\psi \quad [21a]$$

if allowance is made in the factor p for rectifying losses and also for the required pump energy. The total cost S , variable with E is

$$S = S_A + S_{W'} \quad [22]$$

and the optimum E can be obtained from $dS/dE = 0$

$$E_{\text{optimum}} = [q(a + b/C_{\ln \text{ mean}})/p]^{0.5} \quad [23a]$$

It may occur that E_{optimum} is higher than the maximum allowable value for E with respect to concentration polarization and scaling.

Experimental

The electro dialysis multicell was composed of 21 Klingerit¹ gaskets, 0.08 cm thick, with a central cut-away section 16 x 8 cm forming 11 brine and 10 dialysate compartments with a surface area of 128 cm² each. The membrane alternating with the gaskets were supported across this area by corrugated perforated spacers, the corrugations making an angle of 22° with the vertical long axis of the compartments. The assembly was clamped between Perspex² plates backed by steel plates, and a graphite cathode and a platinized titanium anode³ were placed either in or adjacent to the Perspex plates. Liquid flow was upwards in all compartments, a multislot feeding and withdrawal system being used (Fig. 4). The con-

¹ Klingerit, compressed asbestos steam jointing, Klinger & Co., England.

² Perspex, Lucite, Plexiglass.

³ Imperial Chemical Industries.

duits formed by corresponding holes in gaskets and membranes were interconnected in one of the Perspex plates on which external connections were supplied. A flow diagram is given in Fig. 5. The batch of dialysate was contained in a 10 l aspirator with a calibrated glass on top and all liquids were pumped with nonmetallic pumps. The by-pass in the dialysate system allowed quick mixing in the aspirator. A branch of this by-pass contained a conductivity cell.⁴ All lines returning to the calibrated glass with which the dialysate volume was measured ended in a length of glass tubing, the lower end of which was placed on the meniscus when a volume reading was taken.

The brine and electrode rinse systems were thermostated, which sufficed also to keep the dialysate at the required temperature, all flows being measured with rotameters.⁵ The direct current was

⁴ Radiometer, Copenhagen, type CDM2c with cell CDC114.

⁵ Fischer & Porter, flowrotors.

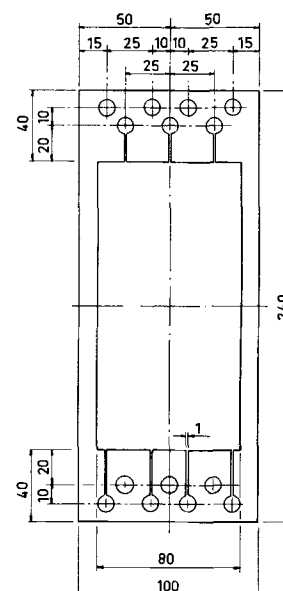


Fig. 4. Gasket to form dialysate compartments (and brine compartments by turning 180°); sizes in mm.

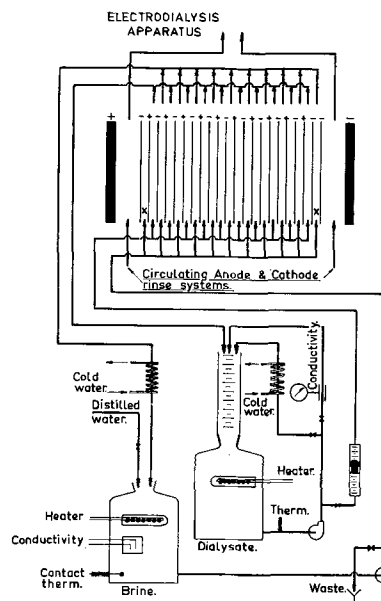


Fig. 5. Flow diagram of experimental set-up. The compartments marked "x" have a calomel probe electrode inserted.

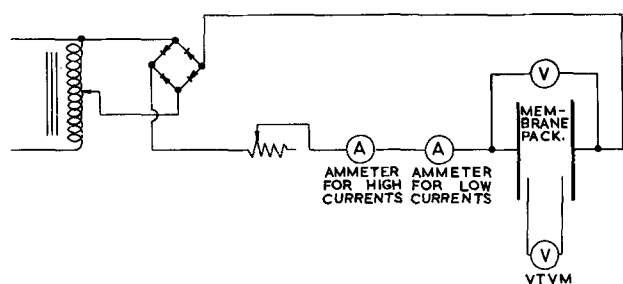


Fig. 6. Wiring diagram

obtained from a selenium rectifier;⁶ a wiring diagram is given in Fig. 6. The membrane pack voltage was measured with probe electrodes inserted in the first and last brine compartments. Best results were obtained with calomel electrodes connected to a vacuum tube voltmeter.⁷ The calomel electrodes were put under an air pressure slightly exceeding the pressure in the brine compartments.

The desalting experiments were usually carried out by selecting a temperature, brine concentration, and initial dialysate concentration and composition. By applying a constant electric potential as measured on the probe electrodes the batch of dialysate was desalted taking frequent volume, conductivity and current readings. The liquid flows were kept at 10 cm/sec in brine and dialysate compartments and 14 cm/sec in the electrode compartments. When mixed electrolytes were used intermediate samples of the dialysate were taken to determine individual ion concentrations.

Salt diffusion rates in the membrane pack were determined in a currentless experiment with the di-

⁶ Standard Telephones and Cables, Type 22JE293.

⁷ Marconi Instruments, Model TF1300.

alysate concentration at approximately 0.01N. On a number of single membranes diffusion rates were measured separately in a small stirred diffusion cell placed in a thermostat at 25°C. The low concentration was again 0.01N.

Results and Discussion

Resistance.—The validity of Eq. [2] is demonstrated in Fig. 7 and 8, in which for three constant voltages per compartment pair $1/i$ is plotted against $1/C$. The linear relations hold over large concentration ranges. Values for a and b derived from Fig. 7 and a number of similar plots are included in Table I. The spread in the values for a and b for each series of experiments (certain membrane pair, temperature, brine concentration, and electrolyte composition) illustrates the poor reproducibility of membrane pack resistance, a fact well known to workers in this field. The application of the individual values for a

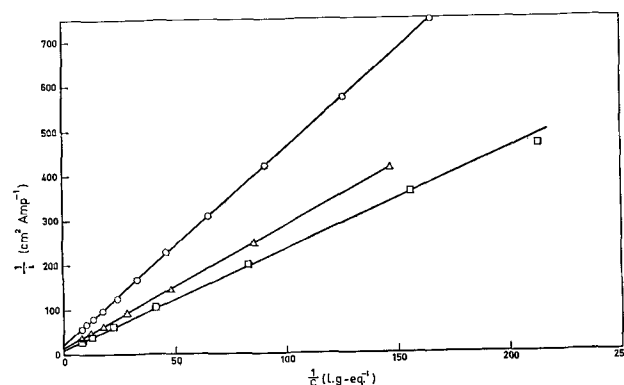


Fig. 7. Reciprocal of the current density vs. reciprocal of the concentration in the dialysate. T.N.O.-A60 and C60⁸ membranes at 25°C. ○, 0.50v; △, 0.76v; □, 1.00v.

Table I. Production rates (10^{-6} l sec⁻¹ cm⁻² volt⁻¹) calculated according to Eq. [10a], the effect of water transport

calculated according to Eq. [17a], and experimental values

Cation selective membrane	Anion selective membrane	C ₀	C _T	E	a	b	ψ	ψ'	H	ψ/ψ'		V _T /ATE		B	Temp, °C	Experiment		
										Eq. [17a]	Observed	Eq. [10a]	Observed					
3129B-56 ⁹	3129B-96 ⁹	0.152	0.012	0.50	11	2.2	0.805	0.835	0.45	0.93	0.96	1.17	1.17	1.0	35	1		
		0.146	0.010	0.75	13	1.6	0.805	0.870	0.35	0.95	0.93	1.40	1.41	1.0	35	2		
		0.167	0.010	1.00	12	1.5	0.805	0.850	0.32	0.94	0.95	1.39	1.27	1.0	35	3		
		0.163	0.010	0.50	14	2.1	0.825	0.858	0.35	0.94	0.96	1.08	1.00	0.5	35	4		
		0.154	0.010	0.75	12	2.0	0.825	0.862	0.30	0.95	0.96	1.22	1.16	0.5	35	5		
		0.100	0.005	0.70	32	2.1	0.947	1.000	0.36	0.96	0.95	1.07	1.09	0.25	20	6		
C-60 ⁸	A-60 ⁸	0.100	0.005	1.00	20	2.4	0.947	0.979	0.36	0.96	0.97	1.08	1.03	0.25	20	7		
		0.100	0.005	1.40	20	2.4	0.947	0.946	0.36	0.96	1.00	1.09	0.99	0.25	20	8		
		0.100	0.005	0.50	12	2.2	0.880	0.918	0.44	0.95	0.96	1.19	1.11	0.25	25	9		
		0.100	0.005	0.76	12	2.1	0.880	0.931	0.41	0.96	0.95	1.20	1.18	0.25	25	10		
		0.100	0.005	1.00	12	2.2	0.880	0.901	0.41	0.96	0.98	1.16	1.11	0.25	25	11		
		0.100	0.005	0.50	14	1.3	0.853	0.851	0.50	0.95	1.00	1.65	1.57	0.25	30	12		
		0.100	0.005	1.00	10	1.6	0.853	0.897	0.45	0.95	0.95	1.54	1.46	0.25	30	13		
		0.050	0.003	0.80	—	—	0.840	0.844	0.44	0.98	0.99	—	1.46	0.25	20	14		
		C-60 ⁸	TA ¹²	0.050	0.003	0.80	—	—	0.840	0.856	0.51	0.97	0.98	—	1.72	0.25	20	15
		C-20 ¹¹	A-20 ¹¹	0.250*	0.020	0.40	18	1.4	0.83	0.903	0.39	0.89	0.92	—	1.29	0.50	30	16
C-60 ⁸	A-60 ⁸	0.250*	0.020	0.80	16	1.1	0.83	0.867	0.35	0.91	0.96	—	1.24	0.50	30	17		
		0.250*	0.020	0.40	11	1.8	0.86	0.927	0.46	0.87	0.87	—	1.53	0.50	30	18		
		0.250*	0.020	0.80	12	1.2	0.79	0.854	0.39	0.89	0.89	—	1.33	0.50	30	19		
		0.250*	0.020	1.00	7	1.9	0.73	0.850	0.40	0.88	0.86	1.17	1.26	0.50	30	20		

* Initially equal equivalents of CaCl₂ and NaCl.

⁸ Central Technical Institute, T.N.O. (Netherlands); commercially available at AMFion A60 and C60 membranes from the American Machine and Foundry Company.

⁹ American Machine and Foundry Company.

¹⁰ Asahi Chemical Industry Co.

¹¹ The Permutit Co. Ltd.

¹² South African C.S.I.R.

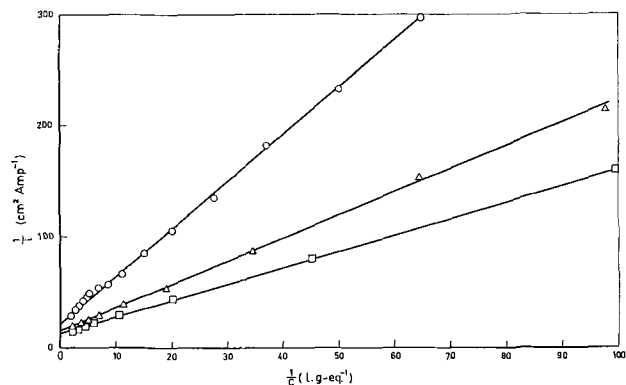


Fig. 8. Reciprocal of the current density vs. reciprocal of the concentration in the dialysate. A.M.F. 3129-B-56 and 96⁹ membranes at 35°C. ○, 0.50v; △, 0.75v; □, 1.00v.

and b in the derived equations led to good agreement with experimental values.

Salt diffusion.—In Eq. [3] it was assumed that the coulomb efficiency ψ' is constant. For most practical cases this is an acceptable approximation for the calculation of production rate and energy consumption. However, a check should always be made so that even at the end of the desalting range the back diffusion of salt from brine to dialysate remains acceptable in comparison with the current density. Practical salt diffusion rates (including a small amount of leakage) from brine towards an 0.01N dialysate appear to be proportional to the brine concentration, as illustrated in Fig. 9.

The results of diffusion measurements on single membranes are shown in Fig. 10 for a number of anion and cation selective membranes. From a simple "Donnan equilibrium" (14) it would be expected that the diffusion rates increase with the second power of the high concentration on one side of the membrane, as the amount of sorbed electrolyte in the membrane is then proportional to the square of the external concentration. The actual power, however, varies between 1.13 and 1.54 for the various membranes. Glueckauf and Watts (15) attributed the deviation from 2 to heterogeneity in the crosslinking of the resin, for which evidence was also obtained from electrolyte uptake data. The interaction of electrolyte diffusion and the simultaneously occurring osmosis in the opposite direction is the subject

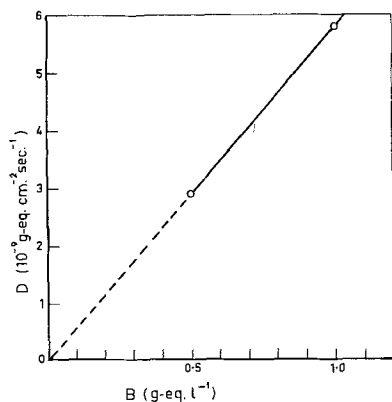


Fig. 9. Salt diffusion rate through a membrane pair at two brine concentrations; dialysate concentration approximately 0.01N; 35°C, A.M.F. 3129-B⁹ membranes.

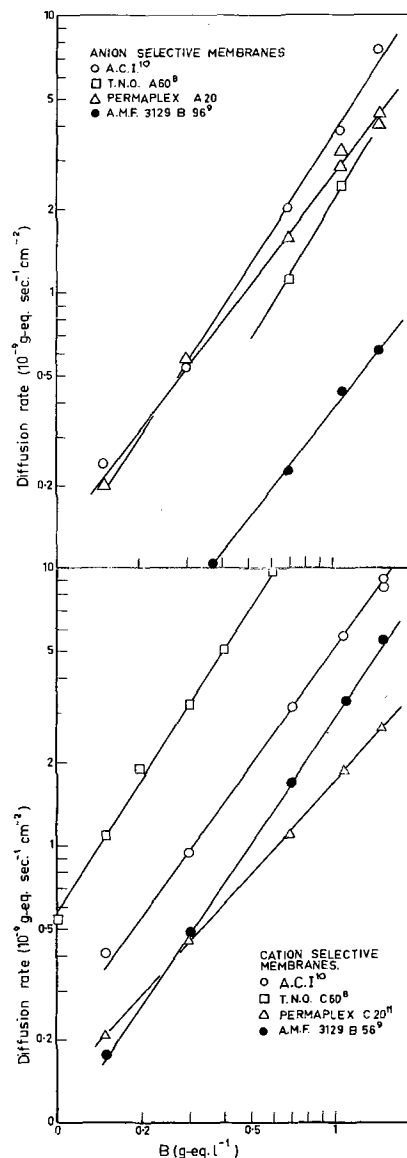


Fig. 10. Sodium chloride diffusion rate through a number of ion selective membranes; 0.01N NaCl solution on one side.

of a current investigation in this laboratory (16). It should be noted that the slopes for the data on the mechanically heterogeneous Permaplex membranes in Fig. 10 indicate lower powers than for the majority of the "homogeneous" membranes.

Water transport.—A check on Eq. [8] is presented in Table II; the experimental data were taken from experiment 20.

Production rate.—The production rates calculated according to Eq. [10] and [10a] are compared in

Table II. Calculated and experimental values for the dialysate volume; $H = 0.4$

C	V , observed	V , Eq. [8]
0.25	12.81	12.82
0.20	12.53	12.56
0.15	12.28	12.30
0.10	12.02	12.03
0.05	11.77	11.80
0.02	11.63	11.64
0.01	11.60	11.60

Table III. Production rates (10^{-6} sec $^{-1}$ cm $^{-2}$ volt $^{-1}$) calculated according to the derived equations, and experimental values

C_T	V_T/AET		Observed
	Eq. [10]	Eq. [10a]	
0.20	10.09	9.72	9.76
0.15	4.69	4.51	4.91
0.10	2.82	2.69	2.89
0.05	1.78	1.72	1.84
0.02	1.26	1.19	1.26
0.01	1.04	0.96	1.04

Table IV. Energy consumption (kwh/m 3) calculated according to Eq. [12] and [12b], and experimental values

C_T	W' , kwh/m 3	
	Eq. [12]	Eq. [12b] and experimental
0.20	1.83	1.80
0.15	3.58	3.61
0.10	5.30	5.48
0.05	7.05	7.34
0.02	8.11	8.45
0.01	8.46	8.75

Table III with experimental values from experiment 20. The following values for the constants were used in the calculations: a , 7; b , 1.92; H , 0.4; E , 1.0; A , 1280; B , 0.5; ψ' , 0.85; ψ , 0.73; F , 96,500; C_o , 0.25. Calculated and experimental values are in good agreement, even when the most simplified Eq. [10a] is used. Comparison of experimental and calculated production rates on a number of complete desalting experiments is included in Table I. The observed values for ψ/ψ' in Table I can also be compared with values in Fig. 3.

Energy Consumption.—The energy consumption calculated according to Eq. [12] and [12a] and experimental values obtained from experiment 20 are compared in Table IV. The constants used were the same as for Table III. As the concept of "over-all efficiency" originated in energy consumption data, values calculated according to Eq. [12a] and the experimental values in Table IV are the same. A separate check of the validity of Eq. [12a] can be found in a plot of energy consumption per volume of dialysate *vs.* the electrolyte concentration in the dialysate. Such plots are shown in Fig. 11 for a number of experiments on mixed NaCl/CaCl $_2$ solutions. Linear relations were obtained and the slopes of these relations have been plotted *vs.* E in Fig. 12. Again linear relations were obtained showing the validity of Eq. [13a]. In Fig. 12 the line for $\psi = 1$ is also indicated and ψ is now the ratio of the slopes of this line and of an experimental line.

Power Index.—In Eq. [16a] it has been shown that the Power Index is a complicated function of C_o . Linear plots of log P.I. *vs.* log C_o , with a slope of 1.86 have been reported (17) for desalting to drinking water concentration ($C_T = 0.01$) from $0.04 < C_o < 0.6$. It can be shown that such linear relations correspond to rather large values for the basic resistance of the compartment pair.

Conclusion

The use of the concept of "over-all efficiency" allows a mathematical description of the process with

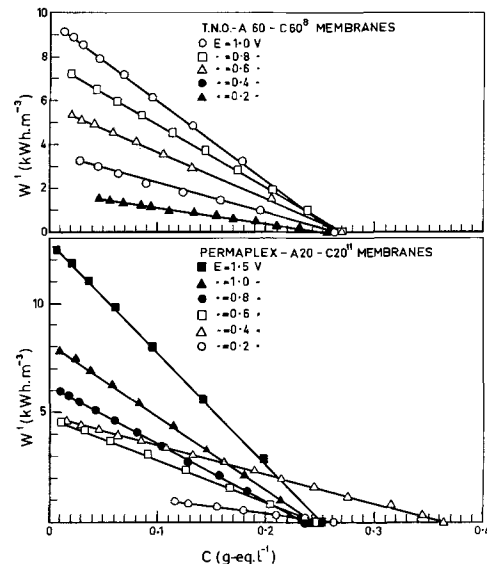


Fig. 11. Energy consumption per unit volume vs. dialysate concentration.

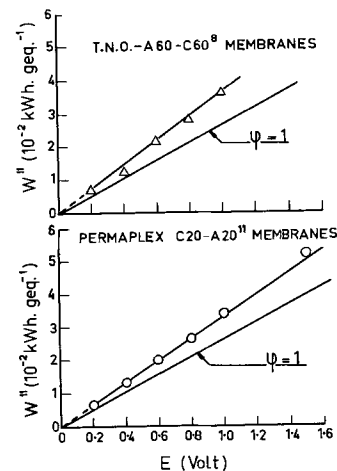


Fig. 12. Energy consumption per gram equivalent vs. compartmental voltage.

relatively simple equations which are in good agreement with experimental results and which can be used for the prediction of the operation of large scale equipment from laboratory compartment pair d-c resistance measurements because the equations are independent of the compartment dimensions parallel to the membranes. The equations can also be used for the optimization of E with respect to cost. The "over-all efficiency" incorporates the effect of water transport, which is an important detrimental factor in electrodialytic demineralization when other than short brackish desalting ranges, using reasonably high current densities, are considered.

Acknowledgment

The assistance of Mr. J. Venlet and Mr. L. R. J. van Vuuren is gratefully acknowledged.

Manuscript received July 30, 1962.

Any discussion of this paper will appear in a Discussion Section to be published in the June 1965 JOURNAL.

REFERENCES

1. "Demineralization by Electrodialysis," J. R. Wilson, Editor, Butterworths, London (1960).
2. H. J. Cohan, *Chem. & Eng. Prog.*, **57** [2], 72 (1961).

3. Ref. (1), pp. 216, 240.
4. D. A. Cowan and J. H. Brown, *Ind. & Eng. Chem.*, **51**, 1445 (1959).
5. Ref. (1), p. 13.
6. B. A. Cooke, *Electrochim. Acta*, **3**, 307 (1961); **4**, 179 (1961); **5**, 216 (1961).
7. E. Wegelin, Central Technical Institute, T.N.O. (Netherlands), Publ. 59, p. 4 (1960).
8. Ref. (1), p. 324.
9. M. van Ments, *Ind. & Eng. Chem.*, **52**, 149 (1960).
10. T. R. E. Kressman and F. L. Tye, *Trans. Faraday Soc.*, **55**, 1441 (1959).
11. W. G. B. Mandersloot, *Electrochim. Acta*, **9**, 395 (1964).
12. D. A. Cowan, *Advances in Chemistry*, Series No. 27, 224 (1960).
13. Ref. (1), p. 234.
14. F. Helfferich, "Ionenaustauscher," Vol. 1, p. 320, Verlag Chemie, Weinheim (1959).
15. E. Glueckauf and R. E. Watts, *Nature*, **191**, 904 (1961).
16. G. Eder, *Z. phys. Chem. N.F.*, **39**, 218 (1963).
17. P. M. Rapiet, W. K. Baker, and S. A. Weiner, University of California, Institute of Engineering Research, Series No. 75, Issue No. 29 (1962).

SYMBOLS

- r Resistance of 1 cm² of compartment pair, ohm-cm²
- a Constant ($a = r$ at $C = \infty$), ohm-cm²
- b Proportionality factor, ohm-cm², g-eq. l⁻¹
- C Electrolyte concentration in dialysate, g-eq. l⁻¹

- i Current density, amp cm⁻²
- E Electric potential gradient per compartment pair, volt
- j^2 Effective salt transport rate per cm², g-eq. sec⁻¹, cm²
- ψ' Coulomb efficiency
- F 96,500, coul. g-eq.⁻¹
- N Total number of g-eq. in the batch of dialysate, g-eq.
- t Time, sec
- A Available total compartment pair area, cm²
- V Volume of the batch of dialysate, liter
- H Water transport factor, l.g-eq.⁻¹
- T Time required to desalt from C_o to C_T , sec
- W' Energy consumption per liter of product, watt sec l⁻¹
- ψ Over-all efficiency
- W'' Energy consumption per g-eq. (removed per liter), watt sec g-eq.⁻¹
- W Energy consumption per g-eq. (removed per liter) and per volt applied on each compartment pair, amp sec g-eq.⁻¹
- \bar{i} Average current density, amp cm⁻²
- q (Depreciation) cost of 1 cm² of compartment pair, per sec, \$. cm⁻², sec⁻¹
- p Cost of energy, \$. Watt⁻¹, sec⁻¹
- S Cost per liter of product, \$. l⁻¹
- B Electrolyte concentration in brine, g-eq. l⁻¹
- D Salt diffusion rate through a membrane pair, g-eq. cm⁻², sec⁻¹
- Subscripts o and T refer to $t = o$ and $t = T$, respectively.
- Subscript "ln mean" indicates the logarithmic mean of the values at $t = o$ and at $t = T$.

Theoretical Calculations of the Separation Factors in the Hydrogen Evolution Reaction for the Slow Discharge Mechanism

John O'M. Bockris and S. Srinivasan

The Electrochemistry Laboratory, The University of Pennsylvania, Philadelphia, Pennsylvania

ABSTRACT

Theoretical calculations of the electrolytic separation factors (S) for the slow discharge mechanism were carried out following the lines of earlier calculations by Horiuti *et al.* Previous calculations neglected the effect on S of (i) the step following the discharge step, (ii) the real stretching frequency of the transition state, and (iii) tunneling corrections. The presently calculated S values differ from previous results mainly due to the inclusion of the real stretching frequency of the transition state. The H-T separation factors are more useful than the H-D separation factors in determining the mechanism.

Calculations of electrolytic separation factors for the slow discharge mechanism have been carried out by Keii and Kodera (1) (H/D separation factors), Conway (2) (H/D separation factors), and by Kodera and Saito (3) (H/T separation factors). The Japanese authors based their calculations on those of earlier calculations of Horiuti *et al.* (4-6) for other mechanisms. Conway carried out his calculations for various mechanisms of the evolution reactions, assuming that the isotopic effects were related in part to the difference of heats of activation measured with respect to the zero point energy levels for the isotopic reactants and products, as treated by Bockris (7). In further papers (8,9) approximate estimates of isotope effects on the energy of the transition state were made in calculations of the ratio of the hydrogen and deuterium exchange cur-

rents. The ratios of exchange currents on various metals were measured experimentally by Conway (8) and discussed in terms of calculated separation factors for the various mechanisms.

There are two important differences in these approaches. The first presents a difference in the model of the activated complex. Horiuti's calculations follow the Eyring treatment (10) in which the transition state complex is considered as a stable molecule having its own vibrational frequencies. Hence, differences of zero point energies of the isotopic activated complexes make an important contribution to the separation factor.

Conway's calculations imply that the transition state complex is transient, *i.e.*, it is sufficiently short lived so that vibrational frequencies of the activated complex do not affect the activation energy, which is

hence measured from the zero point energy of the initial state to the intersection point of the Morse curves.

A second difference is one of convenience. In Conway's calculations, the ratio of concentrations of isotopic species in the initial state is calculated from theoretical considerations of equilibrium in solution. In Horiuti's calculations it is possible to avoid these considerations by introducing an experimental equilibrium constant between isotopic species in solution and corresponding molecules in the gas phase. This latter feature of the Horiuti approach appears preferable to that of Conway's because it reduces uncertainties in calculating partition functions of species in solution.

In both treatments, the influence of the electrochemical desorption step on the separation factor for a slow discharge mechanism was neglected. Tunneling effects, which were first pointed out by Bawn and Ogden (11) were also not considered in either treatment. However, Conway (12) had previously concluded that appreciable tunneling would lead to a high dependence of S on potential and to anomalous Tafel slopes which are not observed experimentally. Nevertheless, it is the authors' opinion that calculations should include tunneling corrections, if possible, since these are certainly important in hydrogen atom and ion transfer reactions (13). In the calculation of the ratio of activities of isotopic oxonium ions ($a_{\text{H}_3\text{O}^+}/a_{\text{H}_2\text{DO}^+}$), Conway assumed incorrectly the equality of the deuteron affinity of water and the proton affinity of HDO. The slopes of Morse curves for H^+-OH_2 and D^+-OH_2 were also calculated to be different and hence to contribute to the isotope effect. This difference arose because the observed vibration frequencies of the O-H and O-D bonds were related to "a" values of the Morse equations using the usual approximate assumption (13, 14) that the H^+-OH_2 interaction could be treated by an analogous formula relevant to that for a diatomic molecule. In order to facilitate many calculations in isotope effect work, such an approximation is useful. However, its application to calculate different "a" values for the Morse curves, implies that the potential energy distance functions for the stretching of bonds exhibits isotope effects. This is not consistent with the usual opinion which is based on the consideration that in the Schrodinger equation set up in a discussion of the bond, the relevant mass is the reduced mass of the electron and the nucleus, *i.e.*, influence of nuclear mass is small (16).

Keii and Kodera and also Kodera and Saito have not included the isotope effect due to the real stretching frequency of the activated complex $\text{H}_2\text{O}---\text{H}---\text{M}$. [The H_2O molecule is treated as a pseudo atom as in previous work (14).] They also used 263 kcal mole⁻¹ (solvation energy of a proton) as the dissociation energy of the H^+-OH_2 . It is more appropriate to use the proton affinity of water. This change should also affect the Morse constant of the H^+-OH_2 molecule. In the present calculations, the Eyring assumption regarding the transition state complex (cf. Conway's transient assumption) has been used largely on grounds of the greater con-

sistency of the resultant calculations with experiment. Further, the easier way of calculating ionic concentration ratios in solution and their partition function ratios was used. The latter method is, however, more complex than that of Conway due to difficulties of evaluating potential energy surfaces of the transition state complex for calculating vibrational frequencies.

Present Calculations

Discharge Followed by Recombination

Expression for separation factor.—The H/D separation factor (S_D) is given by

$$S_D = \left(\frac{C_H}{C_D} \right)_g \bigg/ \left(\frac{C_H}{C_D} \right)_s \quad [1]$$

where $(C_H/C_D)_g$ and $(C_H/C_D)_s$ are the ratios of atomic concentrations of H to D in the gas and solution, respectively. Under the condition that $a_{\text{H}_2\text{O},l} \gg a_{\text{HDO},l}$ (where $a_{\text{H}_2\text{O},l}$ and $a_{\text{HDO},l}$ are the activities of H_2O and HDO in solution) Eq. [1] reduces to

$$S_D = \frac{1}{2} \left(\frac{C_H}{C_D} \right)_g \left(\frac{a_{\text{HDO},l}}{a_{\text{H}_2\text{O},l}} \right) \quad [2]$$

It may easily be shown (17)¹ that both for the case in which the recombination step is treated as in equilibrium or not so treated that

$$\left(\frac{C_H}{C_D} \right)_g = \frac{i_{1,H}}{i_{1,D}} \quad [3]$$

where $i_{1,H}$ and $i_{1,D}$ are the discharge currents for the isotopic reactions



respectively,

$i_{1,H}$ and $i_{1,D}$ are given by

$$i_{1,H} = k_{1,H} a_{\text{H}_3\text{O}^+} (1 - \theta_H - \theta_D) e^{-BVF/RT} \quad [6]$$

$$i_{1,D} = k_{1,D} \frac{a_{\text{H}_2\text{DO}^+}}{3} (1 - \theta_H - \theta_D) e^{-BVF/RT} \quad [7]$$

where $k_{1,H}$ and $k_{1,D}$ are the respective rate constants, when the metal-solution potential difference (V) is zero; $a_{\text{H}_3\text{O}^+}$ and $a_{\text{H}_2\text{DO}^+}$ are the activities of the H_3O^+ and H_2DO^+ ions at the double layer. The factor (1/3) in Eq. [7] arises, since it is assumed that only one out of three H_2DO^+ molecules is suitably oriented for D^+ discharge. Dividing Eq. [6] by Eq. [7], we have

$$\frac{i_{1,H}}{i_{1,D}} = \frac{k_{1,H}}{k_{1,D}} \cdot \frac{a_{\text{H}_3\text{O}^+}}{a_{\text{H}_2\text{DO}^+}} \quad [8]$$

Expressing the ratio $k_{1,H}/k_{1,D}$ in terms of the standard chemical potentials of the activated and

¹ Equation [3] follows from the equation
$$\frac{C_H}{C_D} = \frac{2(i_{2,H} - i_{2,H}) + (i_{2,D} - i_{2,D})}{C_D (i_{2,D} - i_{2,D})}$$
 and the use of the stationary state hypothesis for the intermediates, *i.e.*, adsorbed atomic hydrogen and deuterium.

initial states and ratio of the tunneling factors $(\Gamma_{1,H}/\Gamma_{1,D})^2$ for the isotopic reactions, we have

$$\frac{i_{1,H}}{i_{1,D}} = \frac{\Gamma_{1,H}}{\Gamma_{1,D}} \cdot \frac{e^{-\mu_H^{0\neq}/RT}}{e^{-\mu_D^{0\neq}/RT}} \cdot \frac{e^{-\mu_{H_2DO^+}/RT}}{e^{-\mu_{H_3O^+}/RT}} \cdot \frac{a_{H_3O^+}}{\frac{a}{3} H_2DO^+} \quad [9]$$

$$= \frac{\Gamma_{1,H}}{\Gamma_{1,D}} \cdot \frac{e^{-\mu_H^{0\neq}/RT}}{e^{-\mu_D^{0\neq}/RT}} \cdot \frac{e^{-\mu_{H_2DO^+}/RT}}{e^{-\mu_{H_3O^+}/RT}} \quad [10]$$

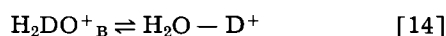
The latter Eq. [10] is obtained using the relations

$$\mu_{H_3O^+} = \mu_{H_3O^+}^0 + RT \ln a_{H_3O^+} \quad [11]$$

$$\mu_{H_2DO^+} = \mu_{H_2DO^+}^0 + RT \ln \frac{a_{H_2DO^+}}{3} \quad [12]$$

$\mu_{H_3O^+}$ and $\mu_{H_2DO^+}$ are the chemical potentials of the H_3O^+ ion and the H_2DO^+ ion (with D^+ oriented suitably for its discharge) at the double layer respectively.

Considering the following steps which are in equilibrium



we have

$$\mu_{H_3O^+_{\text{B}}} = \mu_{H_3O^+} \quad [15]$$

$$\mu_{H_2DO^+_{\text{B}}} = \mu_{H_2DO^+} \quad [16]$$

B refers to the bulk of the solution.

In addition, the following equilibrium reactions may be considered



We may thus write

$$\frac{e^{-\mu_{H_2DO^+_{\text{B}}}/RT}}{e^{-\mu_{H_3O^+_{\text{B}}}/RT}} = \frac{e^{-\mu_{HDO_g}/RT}}{e^{-\mu_{H_2O_g}/RT}} \quad [19]$$

The suffixes l and g refer to the liquid and gaseous phase, respectively.

Using Eq. [15], [16], [18], and [19], Eq. [10] may be rewritten as

$$\frac{i_{1,H}}{i_{1,D}} = \frac{\Gamma_{1,H}}{\Gamma_{1,D}} \cdot \frac{e^{-\mu_H^{0\neq}/RT}}{e^{-\mu_D^{0\neq}/RT}} \cdot \frac{e^{-\mu_{HDO_g}/RT}}{e^{-\mu_{H_2O_g}/RT}} \quad [20]$$

We also have the relations

$$\mu_H^{0\neq} = -RT \ln f_H^{\neq} \quad [21]$$

$$\mu_{H_2O_g} = -RT \ln f_{H_2O_g} + RT \ln a_{H_2O_g} \quad [22]$$

and

$$\mu_{HDO_g} = -RT \ln f_{HDO_g} + RT \ln a_{HDO_g} \quad [23]$$

Hence, the equation for $(i_{1,H}/i_{1,D})$ may be expressed in another form

$$\frac{i_{1,H}}{i_{1,D}} = \frac{\Gamma_{1,H}}{\Gamma_{1,D}} \cdot \frac{f_H^{\neq}}{f_D^{\neq}} \cdot \frac{f_{HDO_g}}{f_{H_2O_g}} \cdot \frac{a_{H_2O_g}}{a_{HDO_g}} \quad [24]$$

With Eq. [2], [3], and [24], S_D is expressed as

$$S_D = \frac{1}{2} \frac{\Gamma_{1,H}}{\Gamma_{1,D}} \cdot \frac{f_H^{\neq}}{f_D^{\neq}} \cdot \frac{f_{HDO_g}}{f_{H_2O_g}} \cdot K_D \quad [25]$$

where K_D is the equilibrium constant for reaction [18].

Similarly, the H/T separation factor (S_T) is given by

$$S_T = \frac{1}{2} \cdot \frac{\Gamma_{1,H}}{\Gamma_{1,T}} \cdot \frac{f_H^{\neq}}{f_T^{\neq}} \cdot \frac{f_{HDO_g}}{f_{H_2O_g}} \cdot K_T \quad [26]$$

where K_T is the equilibrium constant for the reaction



*Numerical calculations of separation factors (S_D and S_T).—Equilibrium constant (K_D or K_T).—*The equilibrium constant, K_D , was measured over a wide range of temperatures by Ikusima and Azakami (18). Its value at 25°C is 1.07. This value differs by only 2% from that of Horiuti and Okamoto (19).

Sepall and Mason (20) have measured K_T at temperatures ranging from 0° to 90°. Its value at 25°C is 1.093. The results of these workers are in complete agreement with that of Brown (21).

*Partition function ratio of isotopic water molecules in gas phase ($f_{HDO_g}/f_{H_2O_g}$ and $f_{HTO_g}/f_{H_2O_g}$).—*The partition function ratio ($f_{HDO_g}/f_{H_2O_g}$) is given by

$$\frac{f_{HDO_g}}{f_{H_2O_g}} = \frac{\sigma_{H_2O}}{\sigma_{HDO}} \left(\frac{m_{HDO}}{m_{H_2O}} \right)^{3/2} \frac{(I_A I_B I_C)_{HDO}^{1/2}}{(I_A I_B I_C)_{H_2O}^{1/2}} \cdot \frac{\prod_3 \sinh(h\nu_i/2kT)_{H_2O}}{\prod_3 \sinh(h\nu_i/2kT)_{HDO}} \quad [28]$$

A similar expression may be written for the ratio ($f_{HTO_g}/f_{H_2O_g}$). Using the spectroscopic data of Benedict, Gailer, and Plyer (22), $f_{HDO_g}/f_{H_2O_g}$ is 59.16 at 25°C and that of Libby (23), $f_{HTO_g}/f_{H_2O_g}$ is 289.54. Together with K_D and K_T , given in the previous subsection, we have

$$\frac{1}{2} K_D \frac{f_{HDO_g}}{f_{H_2O_g}} = 31.68 \quad [29]$$

$$\frac{1}{2} K_T \frac{f_{HTO_g}}{f_{H_2O_g}} = 158.23 \quad [30]$$

*Partition function ratio of isotopic activated complexes (f_H^{\neq}/f_D^{\neq} and f_H^{\neq}/f_T^{\neq}).—*Complete partition function ratio.—It may be assumed that the activated complex, $H_2O\text{---}H\text{---}M$ (or its isotopes) is analogous to a linear triatomic molecule, as has been done previously by Parsons and Bockris (14).

² The quantum mechanical rate constant, (k_q) is related to the classical rate constant (k_c) by the relation $k_q = \Gamma k_c$, where Γ is the tunneling correction to the classical rate.

The partition function ratio of the isotopic activated complexes is given by

$$\frac{f_{\text{H}}^{\neq}}{f_{\text{D}}^{\neq}} = \frac{f_{t,\text{H}}^{\neq}}{f_{t,\text{D}}^{\neq}} \cdot \frac{f_{r,\text{H}}^{\neq}}{f_{r,\text{D}}^{\neq}} \cdot \frac{f_{v,\text{H}}^{\neq}}{f_{v,\text{D}}^{\neq}} \quad [31]$$

where f_t^{\neq} , f_r^{\neq} , and f_v^{\neq} represent the translational, rotational, and vibrational contributions, respectively, of the indicated isotopes.

Translational partition function ratio.—The activated complex may be regarded as immobile. Under these conditions, the translational partition function ratio is unity. Even if the translational motion were treated as restricted, no isotope effect arises, since the heavy metal atom forms a part of the isotopic activated complexes.

Rotational partition function ratio.—A small isotope effect exists due to the restricted rotation of the isotopic activated complexes about the two axis through the center of gravity of the activated complex and mutually perpendicular to the axis of the molecule. The partition function ratio due to this restricted rotation is expressed as

$$\frac{f_{r,\text{H}}^{\neq}}{f_{r,\text{D}}^{\neq}} = \frac{\sinh^2 h\nu_{\text{D}}/2kT}{\sinh^2 h\nu_{\text{H}}/2kT} \quad [32]$$

Since the observed vibrational frequencies are small (e.g., for water 600 cm^{-1} at room temperature), and are inversely proportional to the square roots of the corresponding moments of inertia

$$\frac{f_{r,\text{H}}^{\neq}}{f_{r,\text{D}}^{\neq}} = \frac{I_{\text{H}}^{\neq}}{I_{\text{D}}^{\neq}} \quad [33]$$

where I_{H}^{\neq} and I_{D}^{\neq} are the moments of inertia of the H and D activated complexes, respectively, about an axis, perpendicular to the axis of the molecule and through their respective centers of gravities. The calculated rotational partition function ratios are

$$\frac{f_{r,\text{H}}^{\neq}}{f_{r,\text{D}}^{\neq}} = 0.983 \quad [34]$$

Similarly

$$\frac{f_{r,\text{H}}^{\neq}}{f_{r,\text{T}}^{\neq}} = 0.962 \quad [35]$$

Vibrational partition function ratios.—For a linear triatomic molecule, there are four degrees of vibrational freedom. Since one of these is imaginary for the activated complex, three frequencies are to be considered in calculating the vibrational partition function ratio of the isotopic activated complexes (7), which is given by

$$\frac{f_{v,\text{H}}^{\neq}}{f_{v,\text{D}}^{\neq}} = \frac{\sinh(h\nu_{\text{D}}/2kT)_s}{\sinh(h\nu_{\text{H}}/2kT)_s} \cdot \frac{\sinh^2(h\nu_{\text{D}}/2kT)_b}{\sinh^2(h\nu_{\text{H}}/2kT)_b} \quad [36]$$

The suffixes, s and b stand for stretching and bending frequencies, respectively.

The bending frequency (ν) of a linear triatomic molecule, XYZ, is given by (24)

$$\lambda = 4\pi^2\nu^2 = \frac{1}{l_1^2 l_2^2} \left[\frac{l_1^2}{m_z} + \frac{l_2^2}{m_x} + \frac{(l_1 + l_2)^2}{m_y} \right] k_s \quad [37]$$

where l_1 and l_2 are the distances of X and Z from the central atom Y; m_x , m_y , and m_z are the masses of the atoms X, Y, and Z, respectively, and k_s is the bending force constant. In the case under consideration, X = M, Y = H, D, or T, and Z = H_2O .

Assuming that force constants are invariant upon isotopic substitution and also that $m_x \gg m_y$ and $m_z \gg m_y$, it follows from Eq. [37] that

$$\frac{\nu_{\text{D}}}{\nu_{\text{H}}} = \left(\frac{m_{\text{H}}}{m_{\text{D}}} \right)^{1/2} \quad [38]$$

and

$$\frac{\nu_{\text{T}}}{\nu_{\text{H}}} = \left(\frac{m_{\text{H}}}{m_{\text{T}}} \right)^{1/2} \quad [39]$$

Generally bending frequencies are small ($< 600 \text{ cm}^{-1}$). We may hence assume that

$$\frac{\sinh^2(h\nu_{\text{D}}/2kT)_b}{\sinh^2(h\nu_{\text{H}}/2kT)_b} = \frac{\nu_{\text{D}}^2}{\nu_{\text{H}}^2} = \frac{m_{\text{H}}}{m_{\text{D}}} = \frac{1}{2} \quad [40]$$

$$\frac{\sinh^2(h\nu_{\text{T}}/2kT)_b}{\sinh^2(h\nu_{\text{H}}/2kT)_b} = \frac{\nu_{\text{T}}^2}{\nu_{\text{H}}^2} = \frac{m_{\text{H}}}{m_{\text{T}}} = \frac{1}{3} \quad [41]$$

as has been done by Melander (16)

For the calculation of the stretching vibrational frequencies, it is necessary to know the force constants of the respective bonds in the activated complex (Fig. 1). The potential energy of the system can then be expressed as a function of displacements from the saddle point by the equation

$$V = V_0 + \frac{1}{2} k_{11} (r_1 - r_1^{\neq})^2 + \frac{1}{2} k_{22} (r_2 - r_2^{\neq})^2 + k_{12} (r_1 - r_1^{\neq}) (r_2 - r_2^{\neq}) \quad [42]$$

where k_{11} is the force constant for the stretching of the bond between the water molecule and H^+ ion, k_{22} that for the stretching of the bond between the hydrogen and metal atoms, and k_{12} is a coupling constant. The kinetic energy of the system is given by

$$T = \frac{1}{2} m_1 \dot{r}_1^2 + \frac{1}{2} m_2 \dot{r}_2^2 + \frac{1}{2} m_3 \dot{r}_3^2 \quad [43]$$

where m_1 , m_2 , and m_3 are the masses of the water molecule, hydrogen, and metal atoms, respectively.

Using Lagrange's equation of motion, it can then be shown that the stretching frequencies are given by the equation

$$\lambda^2 - \lambda \left[\left(\frac{1}{m_1} + \frac{1}{m_2} \right) k_{11} + \left(\frac{1}{m_2} + \frac{1}{m_3} \right) k_{22} - \frac{2}{m_2} k_{12} \right] + \frac{m_1 + m_2 + m_3}{m_1 m_2 m_3} (k_{11} k_{22} - k_{12}^2) = 0 \quad [44]$$

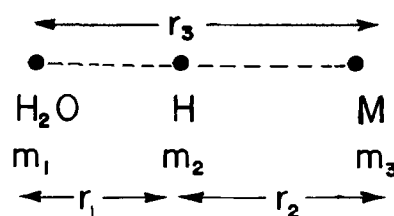


Fig. 1. Activated complex for slow discharge mechanism

where

$$\lambda = 4\pi^2\nu^2 \quad [45]$$

As pointed out earlier, one of these frequencies is imaginary for the activated complex. An absolute calculation of the partition function ratio of the isotopic activated complexes, due to the real stretching frequencies presents a number of difficulties. Two of the approximate methods used will be described in the following subsections.

Method 1, Case of low real stretching frequencies.—According to Westheimer (25), if the imaginary frequency be taken as zero, (one vibration becomes translation along reaction path), the last term in Eq. [44] can be set equal to zero.

$$\therefore k_{11} k_{22} = k_{12}^2 \quad [46]$$

Under these conditions, the real frequency of the activated complex is given by

$$\lambda = 4\pi^2\nu^2 = \frac{k_{11}}{m_1} + \frac{k_{22}}{m_3} + \frac{k_{11} + k_{22} - 2k_{12}}{m_2} \quad [47]$$

Using Eq. [46], Eq. [47] becomes

$$\lambda = 4\pi^2\nu^2 = \frac{k_{11}}{m_1} + \frac{k_{22}}{m_3} + \frac{k_{11} + k_{22} - 2\sqrt{k_{11}k_{22}}}{m_2} \quad [48]$$

If we now make the assumption that $m_1 \gg m_2$, $m_3 \gg m_2$, and $k_{11} \gg k_{22}$, Eq. [48] reduces to

$$\lambda = 4\pi^2\nu^2 = \frac{k_{11} + k_{22} - 2\sqrt{k_{11}k_{22}}}{m_2} \quad [49]$$

It is clear from Eq. [49] that the ratio of vibrational frequencies for the H to D (or H to T) activated complexes is equal to the ratio of the square roots of the masses of the D to H (or T to H) atoms. Further, if we assume that these frequencies are small, the vibrational partition function ratio of the H to D (or H to T) activated complexes is equal to the ratio of the corresponding frequencies. Thus

$$\frac{f_{V,H^\ddagger}}{f_{V,D^\ddagger}} = \frac{m_H^{1/2}}{m_D^{1/2}} = \frac{1}{\sqrt{2}} \quad [50]$$

$$\frac{f_{V,H^\ddagger}}{f_{V,T^\ddagger}} = \frac{m_H^{1/2}}{m_T^{1/2}} = \frac{1}{\sqrt{3}} \quad [51]$$

Using Eq. [34], [35], [40], and [41], the complete partition function ratio is

$$\frac{f_{H^\ddagger}}{f_{D^\ddagger}} = 0.3479 \quad [52]$$

$$\frac{f_{H^\ddagger}}{f_{T^\ddagger}} = 0.1851 \quad [53]$$

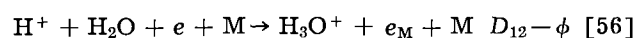
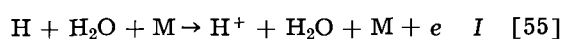
The use of this method for the calculation of the vibrational partition function ratio gives an upper limit for the separation factors.

Method 2, Case of moderate or high frequencies, the method of Eyring *et al.* (10).—In this method, the potential energy of the linear three atom system (Fig. 1, H₂O is treated as a single atom) is given by the Heitler-London expression, *viz.*

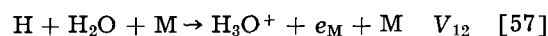
$$V = K_{12} + K_{23} + K_{31} - \left[\frac{1}{2} \{ (J_{12} - J_{23})^2 + (J_{23} - J_{31})^2 + (J_{31} - J_{12})^2 \} \right]^{1/2} \quad [54]$$

where K 's are the coulombic and J 's the exchange contributions to the total energies for interactions between H₂O and H⁺, H and M, and M and H₂O.³ As in the method of Eyring *et al.*, the reference state for the energy was taken as that of the separated atoms H₂O + H + M and Morse functions were used to express variation of potential energy with distance.

The potential energy of the initial state H₂O - H⁺ + e_{o,M} + M, expressed as a function of the distance between H⁺ ion and H₂O molecule (pseudo atom) can then be obtained by considering the following Born-Haber cycle (14)



Adding



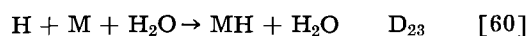
$$\therefore V_{12} = K_{12} + J_{12} = I + D_{12} - \phi \quad [58]$$

where I is the ionization energy of the H atom, ϕ is the electronic work function of the metal, D_{12} is the energy of the H⁺-OH₂ interaction as a function of the internuclear distance and is given by

$$D_{12} = D_{12}^0 [1 - e^{-a(r_1 - r_{10})}]^2 - L \quad [59]$$

L is the heat of solvation of a proton and D_{12}^0 is the proton affinity of water.

Similarly, the potential energy of the final state MH + H₂O, expressed as a function of the distance between the M and H atoms, is obtained by considering the reaction



where

$$D_{23} = D_{23}^0 [e^{-2a_2(r_2 - r_{20})} - 2e^{-a(r_2 - r_{20})}] = V_{23} = K_{23} + J_{23} \quad [61]$$

Since the metal atom and water molecule are relatively far apart for all values of r_1 and r_2 , and also because the interaction between M and H₂O is considerably less than between H and M or H⁺ and H₂O, the M-H₂O interaction was taken as zero for all distances of separation, *i.e.*

$$V_{31} = K_{31} + J_{31} = 0 \quad [62]$$

As in the method of Eyring *et al.*, a certain percentage of each of the energies V_{12} , V_{23} , and V_{31} was assumed to be coulombic and the balance exchange, for all distances of separation. Thus, the total en-

³ In a normal chemical reaction of the type $A + BC \rightarrow AB + C$, where A, B and C are atoms, all atoms maintain the same electronic state throughout the reaction path. In our case, it is necessary to treat the central particle as an ion for interaction with water and as an atom for interaction with M, since the initial state of the discharge step is H₂O - H⁺ + M + e_{o,M} and the final state is M - H + H₂O. Although not strictly correct, the approximation may be considered as satisfactory, since for small displacements from the equilibrium position of the H⁺ and H₂O, the interaction energy is mainly that of H⁺-OH₂, while the M-H interaction energy is small and vice versa for the case of small displacements of the H from the M-H equilibrium position. In the activated state, the central atom may be considered as partly neutralized, since in the initial state it is totally ionic, whereas in the final state it is an atom.

Table I. Physical constants used in calculation of potential energy of system for slow discharge mechanism

D_{12}^0	D_{23}^0	I	L	ϕ	r_1^0	r_2^0	a_1	a_2
187	57	313	263	104	1.05	1.74	1.375	1.20
	kcal · mole ⁻¹				Å		Å ⁻¹	

ergy of the system H₂O---H---M was calculated, using Eq. [54], as a function of r_1 and r_2 .

All calculations were carried out with M = Hg. The constants used in the calculation of V_{12} and V_{23} with the aid of Eq. [58], [59], and [61] are given in Table I and were obtained from the paper of Parsons and Bockris (14) except for D_{12}^0 and a_1 . Parsons and Bockris used the figure of 263 kcal mole⁻¹ for D_{12}^0 , which is the heat of solvation of a proton. D_{12}^0 represents the dissociation energy of the H₂O-H⁺ into H₂O and H⁺ and the more appropriate figure is the proton affinity for water (187 kcal mole⁻¹). Due to this change in D_{12}^0 , a_1 is also altered.

Three calculations were carried out varying the percentage coulombic energies, ρ_1 and ρ_2 , in V_{12} and V_{23} , respectively. In the first calculation, ρ_1 and ρ_2 were taken as 20%. The energy V , given by Eq. [54] was calculated as a function of the variable distances r_1 and r_2 , using an I.B.M. 7090 computer. From the table of values of V as a function of r_1 and r_2 , the reaction path and saddle point were determined. It was found that $r_1^\ddagger = 1.05\text{Å}$ and $r_2^\ddagger = 3.40\text{Å}$. This calculation also showed that the classical activation energy excluding zero point energies is 2 kcal mole⁻¹. The force constants k_{11} , k_{22} , and k_{12} , appearing in Eq. [42] were then calculated by evaluating the second derivatives of V (Eq. [54]) at the saddle point. The coupling constant, k_{12} , is zero for the present model since the interaction between M and H₂O was ignored. The stretching vibrational frequencies, calculated using Eq. [44], for the isotopic activated complexes (H, D, and T) in this

case and the subsequent two calculations are given in Table II.

In the second calculation, the percentage coulombic energy used for each interaction was reduced to 5% since the first calculation gave too small an activation energy. The activation energy increased to 6 kcal mole⁻¹ in this case. This calculation and the subsequent one were also carried out to check any variation in the vibrational partition function ratio (due to stretching) of the isotopic activated complexes.

In the last calculation, the percentage coulombic energy for the O-H⁺ bond was taken as 39% and 3% for the Hg-H bond. These figures were obtained from the relationship between percentage ionic character of a bond and the difference in electronegativities of the atoms forming the bond (26).

The results of all three calculations, including partition function ratios of the isotopic activated complexes are given in Table II. ρ_1 and ρ_2 are the percentage coulombic energies of the O-H⁺ and H-Hg bonds respectively, r_1^\ddagger and r_2^\ddagger are the O-H⁺ and Hg-H internuclear distances respectively in the activated complex, E^\ddagger is the activation energy $\frac{\sinh(h\nu_D/2kT)_s}{\sinh(h\nu_H/2kT)_s}$ and $\frac{\sinh(h\nu_T/2kT)_s}{\sinh(h\nu_H/2kT)_s}$ the partition function ratios of the isotopic activated complexes due to the real stretching frequencies.

Table II reveals that the variation in percentage coulombic energy has little influence on the real vibrational frequencies (ω_H , ω_D , ω_T) of the activated complexes. Further, the calculated activation energies are considerably less than the experimentally observed values. This discrepancy is probably due to the neglect of the H₂O-Hg interaction in the calculation of V . The real frequency for the H activated complex is of the order of the frequency of the bond O-H⁺, which is the highest possible value. This high value may be expected, since it is found that in the activated complex the O-H bond is not stretched from the equilibrium value in H₂O-H⁺ in any of the calculations. Thus, the partition function ratios, $f_{H^\ddagger}/f_{D^\ddagger}$ and $f_{H^\ddagger}/f_{T^\ddagger}$, in Table II, may be considered as the lower limits for these ratios.

Tunneling factor ratios ($\Gamma_{1,H}/\Gamma_{1,D}$ and $\Gamma_{1,H}/\Gamma_{1,T}$).—The tunneling factor ratios depend on potential. The calculations of Christov (27) refer to the reversible potential. The H/T separation factors on Hg were determined (28) at a current density of 10⁻² amp cm⁻². Hence the tunneling factor ratios are now calculated at the barrier height corresponding to this current density. The overpotential (η) at this current density is about 1v. The activation energy (E^\ddagger) may be obtained by using the relation

$$E^\ddagger = E_{o^\ddagger} - \beta\eta \quad [63]$$

where E_{o^\ddagger} is the activation energy at the reversible potential and β is the symmetry factor.

Using $E_{o^\ddagger} = 21.5$ kcal mole⁻¹ and $\beta = 1/2$, $E^\ddagger = 10$ kcal mole⁻¹.

Two proton (or isotopic ions) transfer distances are possible, depending on the model chosen. If it is assumed that the proton transfer takes place from

Table II. Force constant (k 's), stretching vibrational frequencies (ω 's), partition function ratios ($f_{H^\ddagger}/f_{D^\ddagger}$ and $f_{H^\ddagger}/f_{T^\ddagger}$) of isotopic activated complexes for the slow discharge mechanism

Parameter	Calculation number		
	1	2	3
ρ_1 (%)	20	5	39
ρ_2 (%)	20	5	3
r_1^\ddagger (Å)	1.05	1.05	1.05
r_2^\ddagger (Å)	3.40	2.92	3.30
E^\ddagger (kcal mole ⁻¹)	2	6	4
k_{11} (kcal mole ⁻¹ Å ⁻²)	688.6	635.1	654.8
k_{22} (kcal mole ⁻¹ Å ⁻²)	-3.9	-12.7	-10.6
k_{12} (kcal mole ⁻¹ Å ⁻²)	0	0	0
ω_H (cm ⁻¹)	2906	2773	2820
ω_D (cm ⁻¹)	2110	2015	2048
ω_T (cm ⁻¹)	1763	1686	1714
ω_{H^\ddagger} (cm ⁻¹)	52 i	90 i	84 i
ω_{D^\ddagger} (cm ⁻¹)	50 i	88 i	83 i
ω_{T^\ddagger} (cm ⁻¹)	50 i	89 i	81 i
$\frac{\sinh(h\nu_D/2kT)_s}{\sinh(h\nu_H/2kT)_s}$	0.1465	0.1605	0.1552
$\frac{\sinh(h\nu_T/2kT)_s}{\sinh(h\nu_H/2kT)_s}$	0.0633	0.0725	0.0672
$\frac{\sinh(h\nu_H/2kT)_s}{(f_{H^\ddagger}/f_{D^\ddagger})^{10^2}}$	7.207	7.897	7.636
$\frac{\sinh(h\nu_H/2kT)_s}{(f_{H^\ddagger}/f_{T^\ddagger})^{10^2}}$	2.030	2.325	2.155

a hydroxonium ion specifically adsorbed on the electrode, the proton transfer distance is 1.15Å. The other possible proton transfer distance follows from the model of Bockris, Devanathan, and Müller (29), where a layer of water molecules is assumed between the electrode surface and the Helmholtz plane. In this case, the proton transfer distance is 2.86Å. This distance corresponds to the width of the equivalent Eckart barrier (4.75Å) used by Christov at the reversible potential.

Tunneling factors were obtained both for the symmetrical Eckart and parabolic barriers. In the former case, they were obtained from the tunneling factors tabulated as a function of the barrier height and frequency at the top of the barrier [which can easily be related to the barrier height and width (17)] by Johnston and Rapp (30). In the latter case, the method of Bell (31) was followed, assuming in this calculation the same barrier height and curvature at the top of the barrier as the equivalent Eckart barrier.

For the smaller proton transfer distance, the tunneling factor ratios, $\Gamma_{1,H}/\Gamma_{1,D}$ and $\Gamma_{1,H}/\Gamma_{1,T}$, for a symmetrical Eckart barrier are 4.8 and 8.4, respectively. The corresponding values for a parabolic barrier are 14 and 33. It has been pointed out earlier that when the degree of tunneling is high, the use of the parabolic barrier overestimates the tunneling factor ratios.

For the higher proton transfer distance, the tunneling factor ratios, $\Gamma_{1,H}/\Gamma_{1,D}$ and $\Gamma_{1,H}/\Gamma_{1,T}$ are 1.24 and 1.35, respectively, for a symmetrical Eckart barrier. These values are in excellent agreement with the corresponding ratios of 1.25 and 1.34 obtained for a parabolic barrier.

Separation factors.—Separation factors excluding tunneling corrections (S_D^ and S_T^*).*—Excluding tunneling corrections, the separation factors⁴ were calculated for the two methods of obtaining vibrational partition function ratios due to the real stretching frequencies (cases of low and moderate/high real frequencies). For this purpose, the Eq. [25], [26], [29], [30], [52], [53] and data in Table II were made use of. The separation factors are tabulated in Table III. The first method (low real stretching frequencies) gives an upper limit whereas the second (moderate or high frequencies—Eyring's method) a lower limit for the separation factor. The values obtained by the latter method, with variation of percentage coulombic and exchange energies are consistent to within 10%.

The values of S_D^* and S_T^* , calculated here, are significantly different from the earlier values of Keii and Kodera (1) for S_D^* of 12-14, and of Kodera and Saito (3) for S_T^* of 33-37, mainly because of the inclusion of the isotope effect due to the real stretching frequency in the present work.

Separation factors including tunneling corrections.—Table III shows that if we use $2l_E = 1.90\text{Å}$ ($2l_E$ is the width of the equivalent Eckart barrier, corre-

⁴Inclusion of anharmonicity corrections in the partition function ratios of (a) isotopic water molecules in the gas phase and (b) isotopic activated complexes has an effect of less than 10% on the separation factors. The authors wish to thank one of the reviewers for pointing out the effect of anharmonicity corrections on the former partition function ratio.

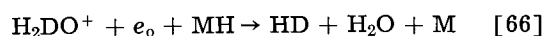
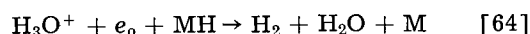
Table III. Separation factors for the slow discharge fast recombination mechanism

Separation factors excluding (S^*) or including tunneling corrections (S)	Methods of calculation of $f_H \neq f_D$ or $f_H \neq f_T$			
	Method 1	Method 2—Moderate or high real stretching frequency Calculation 1	Calculation 2	Calculation 3
S_D^*	11.0	2.3	2.5	2.4
S_T^*	29.3	3.2	3.7	3.4
$S_D(2l_E = 1.90\text{Å})$	53.0	11.1	12.0	11.6
$S_D(2l_E = 4.75\text{Å})$	13.6	2.9	3.1	3.0
$S_T(2l_E = 1.90\text{Å})$	245.2	26.8	31.0	28.5
$S_T(2l_E = 4.75\text{Å})$	39.6	4.3	5.0	4.6

sponding to a proton transfer distance of 1.15Å), the separation factors obtained including tunneling corrections for both methods of calculation of partition function ratios of activated complexes, are considerably higher than the experimental separation factors. For $2l_E = 4.75\text{Å}$, with the second method of calculation of vibrational partition function ratios due to the real stretching frequencies, S_D and S_T are in the region of experimentally determined separation factors.

It may also be added that with $2l_E = 4.75\text{Å}$ the separation factors, obtained for the case of low real stretching frequencies of the isotopic activated complexes, are considerably higher than the experimentally observed separation factors (even for the case of the linked discharge-electrochemical desorption mechanism, as seen below). We may thus conclude that the approximate method (for low real stretching frequencies) is not valid in our case.

Discharge followed by electrochemical desorption at low and intermediate overpotentials.—Expression for separation factor.—The discharge steps [4] and [5] are followed by



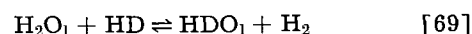
It follows from Eq. [1] and [2] that S_D is given by

$$S_D = \frac{c_{\text{H}_2}}{c_{\text{HD}}} \cdot \frac{a_{\text{HDO}_1}}{a_{\text{H}_2\text{O}_1}} \quad [67]$$

for the condition that $(c_H)_s \gg (c_D)_s \cdot c_{\text{H}_2}/c_{\text{HD}}$ is the ratio of concentrations of the electrolytic gases H_2 to HD. Since the electrochemical desorption steps may be considered to be in equilibrium at low and intermediate overpotentials, when the discharge step is rate-determining, we have from Eq. [64] and [66] the following equilibrium



In addition to this equilibrium reaction, we also have the equilibrium reactions [13], [14], and [17], from which it follows that



The ratio, $c_{\text{H}_2}/c_{\text{HD}}$, may now be expressed as

$$\frac{c_{\text{H}_2}}{c_{\text{HD}}} = K_{\text{HD}} \cdot \frac{a_{\text{H}_2\text{O}_1}}{a_{\text{HDO}_1}} \quad [70]$$

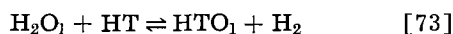
where K_{HD} is the equilibrium constant for reaction [69]. Use of Eq. [70] in [67] gives the interesting result

$$S_D = K_{HD} \quad [71]$$

and similarly we have

$$S_T = K_{HT} \quad [72]$$

where K_{HT} is the equilibrium constant for the reaction



Numerical values of separation factors (S_D and S_T).—The equilibrium constants K_{HD} and K_{HT} are 3.8 [Farkas and Farkas (32)] and 6.2 [Libby (33)], respectively, at room temperature. The calculated and experimental results of these equilibrium constants are in excellent agreement. Thus, for the case

$$\frac{\theta_D}{\theta_H} = \frac{k_{3,H_2} a_{H_3O^+} + k_{1,D} \frac{1}{3} a_{H_2DO^+} + k_{3,H,D} \frac{1}{3} a_{H_2DO^+} + k_{1,D} \frac{1}{3} a_{H_2DO^+}}{k_{1,H} a_{H_3O^+} + k_{3,D,H} a_{H_3O^+}} \quad [85]$$

of the slow discharge mechanism followed by the fast electrochemical desorption step, with the latter treated as in equilibrium, the H/D and H/T separation factors are equal to these values at room temperature.

Discharge followed by electrochemical desorption of high overpotentials.—*Expression for separation factor.*—At high overpotentials the reverse currents of the electrochemical desorption steps may be neglected. During electrolysis, the ratio $(c_H/c_D)_g$ is hence given by

$$\left(\frac{c_H}{c_D} \right)_g = \frac{2i_{3,H_2} + i_{3,HD}}{i_{3,HD}} \quad [74]$$

where i_{3,H_2} and $i_{3,HD}$ are the partial currents for H_2 and HD evolution, respectively. Since $(c_H)_s \gg (c_D)_s$, $i_{3,H_2} \gg i_{3,HD}$ and Eq. [74] reduces to

$$\left(\frac{c_H}{c_D} \right)_g = \frac{2i_{3,H_2}}{i_{3,HD}} \quad [75]$$

Using Eq. [2] and [75], we have

$$S_D = \frac{a_{HDO_1}}{a_{H_2O_1}} \cdot \frac{i_{3,H_2}}{i_{3,HD}} \quad [76]$$

$i_{3,HD}$ is composed of two further partial currents, since there are two paths [65] and [66] for HD evolution. We may, therefore, write

$$i_{3,HD} = i_{3,D,H} + i_{3,H,D} \quad [77]$$

where $i_{3,D,H}$ and $i_{3,H,D}$ are the partial currents according to paths [65] and [66] respectively. The electrochemical desorption currents may be expressed as

$$i_{3,H_2} = k_{3,H_2} a_{H_3O^+} + \theta_H e^{-\beta VF/RT} \quad [78]$$

$$i_{3,D,H} = k_{3,D,H} a_{H_3O^+} + \theta_D e^{-\beta VF/RT} \quad [79]$$

$$i_{3,H,D} = k_{3,H,D} \frac{a}{3} H_2DO^+ + \theta_H e^{-\beta VF/RT} \quad [80]$$

$$\frac{i_{3,HD}}{i_{3,H_2}} = \frac{i_{3,D,H} + i_{3,H,D}}{i_{3,H_2}} \quad [81]$$

$$= \frac{k_{3,D,H}}{k_{3,H_2}} \cdot \frac{\theta_D}{\theta_H} + \frac{k_{3,H,D}}{k_{3,H_2}} \cdot \frac{\frac{1}{3} a_{H_2DO^+}}{a_{H_3O^+}} \quad [82]$$

It is now necessary to evaluate the ratio θ_D/θ_H . Using the stationary state hypothesis for θ_H and θ_D , we have

$$k_{1,H} a_{H_3O^+} + (1 - \theta_H - \theta_D) - k_{3,H_2} a_{H_3O^+} + \theta_H - k_{3,H,D} \frac{1}{3} a_{H_2DO^+} + \theta_H = 0 \quad [83]$$

and

$$k_{1,D} \frac{1}{3} a_{H_2DO^+} + (1 - \theta_H - \theta_D) - k_{3,D,H} a_{H_3O^+} + \theta_D = 0 \quad [84]$$

Solving the simultaneous Eq. [83] and [84] for θ_H and θ_D ,

The second term in the numerator on the right hand side of Eq. [85] is very small compared to the first, since

$$a_{H_3O^+} \gg a_{H_2DO^+} \quad [86]$$

and

$$k_{3,H_2} > k_{3,H,D} \quad [87]$$

Equation [85], thus reduces to

$$\frac{\theta_D}{\theta_H} = \frac{k_{3,H_2}}{k_{1,H}} \cdot \frac{k_{1,D}}{k_{3,D,H}} \cdot \frac{\frac{1}{3} a_{H_2DO^+}}{a_{H_3O^+}} \quad [88]$$

Using Eq. [88] in [82], we have

$$\frac{i_{3,HD}}{i_{3,H_2}} = \frac{k_{3,HD}}{k_{3,H_2}} \cdot \frac{\frac{1}{3} a_{H_2DO^+}}{a_{H_3O^+}} + \frac{k_{1,D}}{k_{1,H}} \cdot \frac{\frac{1}{3} a_{H_2DO^+}}{a_{H_3O^+}} \quad [89]$$

It follows from Eq. [76] and [89] that

$$S_D = \frac{a_{HDO_1}}{a_{H_2O_1}} \cdot \frac{a_{H_3O^+}}{\frac{1}{3} a_{H_2DO^+}} \cdot \frac{1}{\left(\frac{k_{3,H,D}}{k_{3,H_2}} + \frac{k_{1,D}}{k_{1,H}} \right)} \quad [90]$$

$$= \frac{1}{\frac{1}{S_{D,E1}} + \frac{1}{2S_{D,1}}} \quad [91]$$

where

$$S_{D,1} = \frac{1}{2} \frac{k_{1,H}}{k_{1,D}} \cdot \frac{a_{H_3O^+}}{\frac{1}{3} a_{H_2DO^+}} \cdot \frac{a_{HDO_1}}{a_{H_2O_1}} \quad [92]$$

and

$$S_{D,E1} = \frac{k_{3,H_2}}{k_{3,H,D}} \cdot \frac{a_{H_3O^+}}{\frac{1}{3} a_{H_2DO^+}} \cdot \frac{a_{HDO_1}}{a_{H_2O_1}} \quad [93]$$

It may be noted that Eq. [92] is also obtained from Eq. [2], [3], [6], and [7] and is numerically

Table IV. Separation factors for the slow discharge fast electrochemical desorption mechanism at high overpotentials

Calculation (27) No. for S_{D,E_1} or S_{T,E_1}	Percentage coulombic energy (ρ)			Separation factors excluding tunneling corrections			Separation factors including tunneling corrections		
	ρ_{M-H}	$\rho_{H^+-OH_2}$	ρ_{H-H}	$S_{D,1}^*$	S_{D,E_1}^*	S_D^*	$S_{D,1}$	S_{D,E_1}	S_D
3	100	100	100	2.4	11.8	3.4	3.0	13.0	4.1
4	20	20	15	2.4	14.9	3.6	3.0	16.4	4.4
				$S_{T,1}^*$	S_{T,E_1}^*	S_T^*	$S_{T,1}$	S_{T,E_1}	S_T
3	100	100	100	3.4	27.9	5.4	4.6	29.5	7.0
4	20	20	15	3.4	34.1	5.7	4.6	39.5	7.5

equal to the separation factor worked out in an earlier subsection. It is also shown in a separate paper (33) that S_{D,E_1} is pseudo separation factor for the electrochemical desorption step according to paths [64] and [66] only.

Numerical calculation of separation factors.—Separation factors excluding tunneling corrections (S_D^ and S_T^*).—*With the average of the $S_{D,1}^*$ values, 2.4, using the second method for the calculation of the partition function ratio of the isotopic activated complexes due to the real stretching frequencies (earlier subsection) and the value of S_{D,E_1}^* (11.8) assuming a 100% coulombic energy for all interactions, Eq. [91] shows that S_D^* is 3.4. A similar calculation, using $S_{T,1}^* = 3.4$ and $S_{T,E_1}^* = 25.5$ gives a value of 5.4 for S_T^* at 25°C.

Assuming at 20% coulombic energy for the H^+-OH_2 and also for the M-H interactions and a 15% coulombic energy for the H-H interaction, in the calculation of S_{D,E_1}^* and S_{T,E_1}^* , their respective values are 14.9 and 34.1. With these values and the values used earlier for $S_{D,1}^*$ and $S_{T,1}^*$, S_D^* and S_T^* are 3.6 and 5.7, respectively.

*Separation factors including tunneling corrections (S_D and S_T).—*These values are summarized in Table IV along with the corresponding S^* values.

Conclusions

It may be seen from Table V that the separation factor for a slow discharge mechanism depends on the desorption step as well. For a desorption step by the combination of adsorbed hydrogen atoms, the separation factor is solely determined by the ratio of rate constants for the discharge step. For a de-

sorption by the electrochemical mechanism the separation factors depend on whether this step is treated as in equilibrium or not in equilibrium. In the former case, the separation factors (S_D and S_T) become the respective equilibrium constants of the H_2/HDO_1 and H_2/HTO_1 interchange reactions. In the latter case, the separation factors are the same as for a coupled discharge-electrochemical desorption mechanism.

The H/D separation factors are not sufficiently separated to be of value in determining the desorption step. The H/T separation factors may be useful for this purpose.

A slow discharge-fast electrochemical desorption mechanism cannot be distinguished from a fast discharge-slow electrochemical desorption mechanism [as seen in a subsequent paper (33)] at high overpotentials when the reverse currents of the discharge and electrochemical desorption steps may be neglected in comparison to their forward currents. The only way of distinguishing between these two mechanisms is by a determination of degree of coverage (θ) of atomic hydrogen on the electrode since $\theta \rightarrow 0$ for a slow discharge mechanism and $\theta \rightarrow 1$ for a slow electrochemical desorption mechanism.

The tunneling corrections may be somewhat overestimated. In this case, the H/T separation factors for the three cases are nearly equal.⁵ There are two possible ways of examining the tunnel effect (i) influence of potential on the separation factors [cf., Conway, ref. (11)], and (ii) influence of temperature on the separation factor at constant potential. Assuming no change of mechanism, with variation of potential, there should be no change of separation factor with current density if the desorption step is the electrochemical desorption mechanism and is treated as in equilibrium. The other mechanisms will be affected since the tunneling factors change with potential. Temperature effect of S will also distinguish the slow discharge-fast electrochemical desorption mechanism (with the latter treated as in equilibrium) from the others.

Acknowledgments

Financial support from the Aeronautical Systems Command, Air Force Systems Command, United States Air Force, Contract 33 (657)-8823, is gratefully acknowledged. The authors also wish to thank Drs. E. R. Nixon, E. R. Thornton, T. E. Sharp, H.

⁵ The authors wish to thank Mr. D. B. Matthews for making these suggestions.

Table V. Theoretical separation factors for the slow discharge mechanism

Mechanism	Separation factors excluding tunneling corrections		Separation factors including tunneling corrections	
	S_D^*	S_T^*	S_D	S_T
Slow discharge-fast recombination	2.4	3.4	3.0	4.6
Slow discharge-fast electrochemical	3.8	6.2	3.8	6.2
Linked discharge-electrochemical				
(i) Coulombic energy—100% for all interactions	3.4	5.4	4.1	7.0
(ii) Coulombic energy—20% for M-H and H^+-OH_2 , 15% for H-H interactions	3.6	5.7	4.4	7.5

Carl Michael, and K. Thormalingam, and Messrs. D. B. Matthews and R. Haynes for helpful theoretical discussions. Mathematical assistance from Mr. C. Vaseekaran and part of the computer facilities afforded by Dr. L. Nanis are also greatly appreciated.

Manuscript received Aug. 5, 1963; revised manuscript received Dec. 11, 1963. This paper is from work carried out in partial fulfillment of requirements for the degree of Ph.D.

Any discussion of this paper will appear in a Discussion Section to be published in the June 1965 JOURNAL.

REFERENCES

1. T. Keii and T. Kodera, *J. Research Inst. Cat.*, **5**, 105 (1957).
2. B. E. Conway, *Proc. Roy. Soc.*, **A247**, 400 (1958).
3. T. Kodera and T. Saito, *J. Research Inst. Cat.*, **7**, 5 (1959).
4. G. Okamoto, J. Horiuti, and K. Hirota, *Sci. Papers Inst. Phys. Chem. Research (Tokyo)*, **29**, 223 (1936).
5. J. Horiuti, T. Keii, and K. Hirota, *J. Research Inst. Cat.*, **2**, 1 (1951).
6. J. Horiuti and T. Nakamura, *ibid.*, **2**, 73 (1951).
7. J. O'M. Bockris, "Modern Aspects of Electrochemistry," vol. I, chap. IV, Butterworths, London (1954).
8. B. E. Conway, *Proc. Roy. Soc.*, **A256**, 128 (1960).
9. B. E. Conway, "Transactions Symposium on Electrode Processes," chap. 15, The Electrochemical Society, John Wiley & Sons, New York (1961).
10. S. Glasstone, K. J. Laidler, and H. Eyring, "The Theory of Rate Processes," McGraw Hill Book Co., New York (1941).
11. C. E. H. Bawn and G. Ogden, *Trans. Faraday Soc.*, **30**, 432 (1934).
12. B. E. Conway, *Can. J. Chem.*, **37**, 178 (1959).
13. H. S. Johnston, "Advances in Chemical Physics," vol. III, p. 131, Interscience Publishers, New York (1961).
14. R. Parsons and J. O'M. Bockris, *Trans. Faraday Soc.*, **47**, 914 (1951).
15. B. E. Conway, J. O'M. Bockris, and B. Lovrecek, "Proceedings C.I.T.C.E., Sixth Meeting," p. 207, Butterworths, London (1955).
16. L. Melander, "Isotope Effects on Reaction Rates," Ronald Press, New York (1960).
17. S. Srinivasan, Thesis, University of Pennsylvania (1963).
18. M. Ikusima and S. Azakami, *J. Chem. Soc. Japan*, **59**, 40 (1938).
19. J. Horiuti and G. Okamoto, *Bull. Chem. Soc. Japan*, **10**, 503 (1935).
20. O. Sepall and S. G. Mason, *Can. J. Chem.*, **38**, 2024 (1960).
21. G. Brown, Referred to in ref. (20).
22. W. S. Benedict, N. Gailer, and E. K. Plyer, *J. Chem. Phys.*, **24**, 1139 (1956).
23. W. F. Libby, *ibid.*, **11**, 101 (1943).
24. G. Herzberg, "Infra Red and Raman Spectra of Polyatomic Molecules," p. 173, Van Nostrand, New York (1945).
25. F. H. Westheimer, *Chem. Rev.*, **61**, 265 (1961).
26. L. Pauling, "The Nature of the Chemical Bond," Cornell University Press, New York (1962).
27. St. G. Christov, *Electrochim. Acta*, **4**, 194 (1961).
28. J. O'M. Bockris and S. Srinivasan, To be published in *Electrochem. Acta*.
29. J. O'M. Bockris, M. A. V. Devanathan, and K. Müller, *Proc. Roy. Soc.*, **A274**, 55 (1963).
30. H. S. Johnston and D. Rapp, *J. Am. Chem. Soc.*, **83**, 1 (1961).
31. R. P. Bell, *Trans. Faraday Soc.*, **55**, 1 (1959).
32. A. Farkas and L. Farkas, *J. Chem. Phys.*, **2**, 468 (1934).
33. J. O'M. Bockris and S. Srinivasan, *This Journal*, **111**, 853 (1964).

Theoretical Calculations of the Separation Factors in the Hydrogen Evolution Reaction for the Slow Electrochemical Desorption Mechanism

John O'M. Bockris and S. Srinivasan

The Electrochemistry Laboratory, The University of Pennsylvania, Philadelphia, Pennsylvania

ABSTRACT

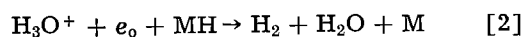
Separation factors (S) for the slow electrochemical desorption mechanism at low and intermediate overpotentials are calculated for Ni. The S values are distinctly separated from those for all other mechanisms. The results are consistent with variation of percentage coulombic energy of all interactions. The separation factor method alone cannot be used to distinguish between either of the rate-determining steps in a linked discharge electrochemical desorption mechanism. A knowledge of the degree of coverage is also required.

Calculations of electrolytic separation factors are of value in examination of mechanism of hydrogen evolution and are discussed elsewhere (1). Of the mechanisms cogent in this discussion, the electrochemical desorption mechanism is one of importance. The theoretical values, associated with this mechanism, are calculated in this paper.

In previous calculations of the separation factor for this mechanism (2), the rate of only one of the two paths for HD evolution



was compared with the rate of H_2 evolution according to



That HD evolution could occur by the two parallel paths [1a] and [1b] was considered by the author of the previous paper, who concluded however that HD evolution by step [1b] would lead to separation fac-

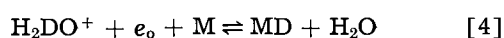
tors less than unity, which is in conflict with experimental observations. Since the total quantity of HD in the electrolytic gas is evolved according to the two parallel paths, it is necessary to compare the rates of both paths simultaneously with the rate of path [2]. Further refinements on the previous calculations are possible through inclusion of the zero point energy differences of the isotopic activated complexes (which were assumed sufficiently short lived that their vibrational frequencies do not contribute to the activation energy), and of tunneling corrections [as there is still some question as to the conditions under which these contribute significantly to the separation factors (3, 4)].

For mechanisms involving adsorbed species in the rate determining step, the ratio of adsorbed atomic hydrogen to deuterium (θ_H/θ_D) is a particularly important quantity. In the previous separation factor calculations, this ratio was worked out for a steady-state situation, allowing for isotopic differences of free energies of activation in the forward and backward directions of the discharge step. The result of assuming that θ_H/θ_D is approximately equal to the ratio of activities of the isotopic ions H_3O^+ and H_2DO^+ was also considered. Since an isotope effect exists in the primary discharge step, this latter assumption is not correct.

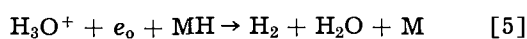
Present Calculations

Slow Electrochemical Desorption at Low and Intermediate Overpotentials

Expression for separation factor.—Under these conditions, the discharge steps may be considered to be in equilibrium. They are represented by



and are followed by [1], [2] and



If $a_{H_2O_1} \gg a_{HDO_1}$, the separation factor is given by

$$S_D = \frac{1}{2} \left(\frac{C_H}{C_D} \right)_g \cdot \frac{a_{HDO_1}}{a_{H_2O_1}} \quad [6]$$

where $(C_H/C_D)_g$ is the ratio of atomic concentrations of H to D in the electrolytic gas. During electrolysis, $(C_H/C_D)_g$ may be expressed as

$$\left(\frac{C_H}{C_D} \right)_g = \frac{2i_{3,H_2} + i_{3,HD}}{i_{3,HD}} \quad [7]$$

where i_{3,H_2} is the electrochemical desorption current according to path [5] and $i_{3,HD}$ is the total current for HD evolution according to the two parallel paths [1] and [2]. Since $i_{3,H_2} \gg i_{3,HD}$, S_D is given by

$$S_D = \frac{a_{HDO_1}}{a_{H_2O_1}} \cdot \frac{i_{3,H_2}}{i_{3,HD}} \quad [8]$$

The currents i_{3,H_2} and $i_{3,HD}$ may be represented as

$$i_{3,H_2} = k_{3,H_2} a_{H_3O^+} + a_{MH} e^{-\beta VF/RT} \quad [9]$$

$$i_{3,HD} = i_{3,H,D} + i_{3,D,H} \quad [10]$$

where

$$i_{3,H,D} = k_{3,H,D} \frac{a}{3} H_2DO^+ + a_{MH} e^{-\beta VF/RT} \quad [11]$$

$$i_{3,D,H} = k_{3,D,H} a_{H_3O^+} + a_{MD} e^{-\beta VF/RT} \quad [12]$$

$i_{3,D,H}$ and $i_{3,H,D}$ are the partial currents according to paths [1] and [2], respectively; k 's are the respective rate constants; a_{MH} and a_{MD} are the activities of the adsorbed hydrogen and deuterium atoms respectively, on the surface; and V is the metal solution potential difference.

It follows from Eq. [9] to [12] that

$$\frac{i_{3,HD}}{i_{3,H_2}} = \frac{i_{3,H,D} + i_{3,D,H}}{i_{3,H_2}} \quad [13]$$

$$= \frac{k_{3,H,D}}{k_{3,H_2}} \cdot \frac{\frac{1}{3} a_{H_2DO^+}}{a_{H_3O^+}} + \frac{k_{3,D,H}}{k_{3,H_2}} \cdot \frac{a_{MD}}{a_{MH}} \quad [14]$$

$$= \frac{\Gamma_H}{\Gamma_D} \cdot \frac{f_{H,D^\ddagger}}{f_{H_2^\ddagger}} \cdot \frac{f_{H_3O^+}}{f_{H_2DO^+}} \cdot \frac{\frac{1}{3} a_{H_2DO^+}}{a_{H_3O^+}} + \frac{\Gamma_H}{\Gamma_D} \cdot \frac{f_{D,H^\ddagger}}{f_{H_2^\ddagger}} \cdot \frac{f_{MH}}{f_{MD}} \cdot \frac{a_{MH}}{a_{MD}} \quad [15]$$

$$= \frac{\Gamma_H}{\Gamma_D} \cdot \frac{f_{H,D^\ddagger}}{f_{H_2^\ddagger}} \cdot \frac{e^{-\mu_{H_3O^+}/RT}}{e^{-\mu_{H_2DO^+}/RT}} + \frac{\Gamma_H}{\Gamma_D} \cdot \frac{f_{D,H^\ddagger}}{f_{H_2^\ddagger}} \cdot \frac{e^{-\mu_{MH}/RT}}{e^{-\mu_{MD}/RT}} \quad [16]$$

Γ , f , μ with the appropriate suffices are the tunneling factor, partition function, and chemical potential, respectively, of the indicated isotopes.

By considering the equilibrium reactions [3] and [4] and also between the isotopic oxonium ions and water molecules in the liquid phase and then in the gaseous phase (5), Eq. [16] may be written as

$$\frac{i_{3,HD}}{i_{3,H_2}} = \left(\frac{f_{H,D^\ddagger}}{f_{H_2^\ddagger}} + \frac{f_{D,H^\ddagger}}{f_{H_2^\ddagger}} \right) \frac{\Gamma_H}{\Gamma_D} \cdot \frac{e^{-\mu_{H_2Og}/RT}}{e^{-\mu_{HDOg}/RT}} \quad [17]$$

It follows from Eq. [8] and [17] that

$$S_D = \frac{\Gamma_H}{\Gamma_D} \cdot \frac{f_{HDOg}}{f_{H_2Og}} K_D \left[\frac{f_{H,D^\ddagger}}{f_{H_2^\ddagger}} + \frac{f_{D,H^\ddagger}}{f_{H_2^\ddagger}} \right]^{-1} \quad [18]$$

Equation [18] may also be expressed in the form

$$\frac{1}{S_D} = \frac{1}{S_{D,E1}} + \frac{1}{S_{D,E2}} \quad [19]$$

where

$$S_{D,E1} = \frac{\Gamma_H}{\Gamma_D} \cdot \frac{f_{H_2^\ddagger}}{f_{H,D^\ddagger}} \cdot \frac{f_{HDOg}}{f_{H_2Og}} K_D \quad [20]$$

and

$$S_{D,E2} = \frac{\Gamma_H}{\Gamma_D} \cdot \frac{f_{H_2^\ddagger}}{f_{D,H^\ddagger}} \cdot \frac{f_{HDOg}}{f_{H_2Og}} K_D \quad [21]$$

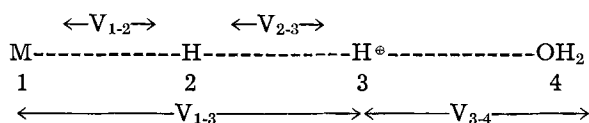
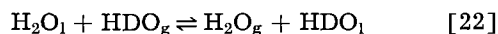


Fig. 1. Activated complex for slow electrochemical desorption mechanism.

K_D is the equilibrium constant for the reaction



The H/T separation factor for the fast discharge-slow electrochemical desorption mechanism at low and intermediate overpotentials is given by an expression, similar to [19].

Numerical Calculations of Separation Factors

Product of equilibrium constant (K_D or K_T) and partition function ratio of isotopic water molecules in the gas phase ($f_{\text{HDO}_g}/f_{\text{H}_2\text{O}_g}$ or $f_{\text{HTO}_g}/f_{\text{H}_2\text{O}_g}$).—In a previous paper (3), it was shown

$$K_D \cdot \frac{f_{\text{HDO}_g}}{f_{\text{H}_2\text{O}_g}} = 63.36 \quad [23]$$

$$K_T \cdot \frac{f_{\text{HTO}_g}}{f_{\text{H}_2\text{O}_g}} = 316.48 \quad [24]$$

Partition function ratios of isotopic activated complexes ($f_{\text{H,D}}^\ddagger/f_{\text{H}_2}^\ddagger$, $f_{\text{H,T}}^\ddagger/f_{\text{H}_2}^\ddagger$, $f_{\text{D,H}}^\ddagger/f_{\text{H}_2}^\ddagger$, and $f_{\text{T,H}}^\ddagger/f_{\text{H}_2}^\ddagger$).—It may be assumed that the activated complex has a configuration in which the centers of the metal atom, hydrogen atom, partially neutralized hydrogen ion and water molecule are collinear, as shown in Fig. 1.

For the calculation of $f_{\text{H,D}}^\ddagger/f_{\text{H}_2}^\ddagger$, isotopic substitution occurs at position 3 in Fig. 1, whereas for calculating $f_{\text{D,H}}^\ddagger/f_{\text{H}_2}^\ddagger$, isotopic substitution is at position 2. The activated complexes may be regarded as immobile, under which conditions their translational partition function ratio is unity. The contribution to the isotope effect due to restricted rotation about the two axes, mutually perpendicular to the axis of the molecule is insignificant, due to the heavy end atoms. Thus, the partition function ratios of the isotopic activated complexes reduce to

$$\frac{f_{\text{H}_2}^\ddagger}{f_{\text{H,D}}^\ddagger} = \frac{\prod_1^5 \sinh(h\nu_i/2kT)_{\text{H,D}}}{\prod_1^5 \sinh(h\nu_i/2kT)_{\text{H}_2}} \quad [25]$$

$$\frac{f_{\text{H}_2}^\ddagger}{f_{\text{D,H}}^\ddagger} = \frac{\prod_1^5 \sinh(h\nu_i/2kT)_{\text{D,H}}}{\prod_1^5 \sinh(h\nu_i/2kT)_{\text{H}_2}} \quad [26]$$

To determine the coordinates of the central atoms (or its isotopes) in the activated complex, the potential energy of the system (V) was treated as a four atom problem (6). V is given by

$$V = K_{12} + K_{23} + K_{34} + K_{13}$$

$$- \left[\frac{1}{2} \{ (\alpha - \beta)^2 + (\beta - \gamma)^2 + (\gamma - \alpha)^2 \} \right]^{1/2} \quad [27]$$

where

$$\alpha = J_{12} + J_{34} \quad [28]$$

$$\beta = J_{13} \quad [29]$$

$$\gamma = J_{23} \quad [30]$$

and

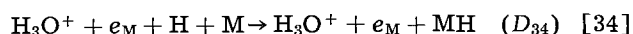
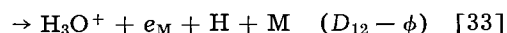
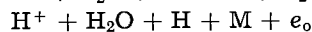
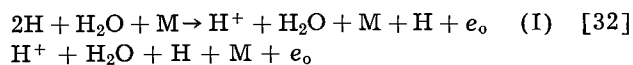
$$V_{ij} = K_{ij} + J_{ij} \quad [31]$$

according to the Heitler-London method. V_{ij} is the potential energy due to interactions between atoms i and j with varying internuclear distance; K_{ij} and J_{ij} are the respective coulombic and exchange contributions to the total energy.

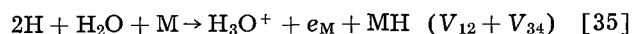
The M-H₂O and H-H₂O interactions were neglected since their respective internuclear distances are relatively far apart and also because these interactions are considerably less than the others where strong chemical bonding exists.

As in the method of Eyring *et al.*, the reference state for the energy was taken as that of the separated atoms $2\text{H} + \text{M} + \text{H}_2\text{O}$ [H_2O is treated as a pseudo atom (7)]. The sum of the energies, ($V_{12} + V_{34}$), represent the potential energy of the initial state as a function of the M-H and H⁺-OH₂ distances. For this calculation, the respective Morse functions were used.

The potential energy ($V_{12} + V_{34}$) was expressed as a function of the distance between the H⁺ ion (position 1) and H₂O molecule and also between the metal atom and H atom (position 2) by considering the following Born-Haber cycles (8).



Adding



$$V_{12} + V_{34} = I + D_{12} - \phi + D_{34} \quad [36]$$

with

$$D_{12} = D_{12}^0 [1 - e^{-a_{12}(\tau_{12} - \tau_{12}^0)}]^2 - |L| \quad [37]$$

and

$$D_{34} = V_{34} = D_{34}^0 [e^{-2a_{34}(\tau_{34} - \tau_{34}^0)} - 2e^{-a_{34}(\tau_{34} - \tau_{34}^0)}] \quad [38]$$

L and D_{12}^0 are the heat of solvation of a proton and the proton affinity for a water molecule in the gas phase, respectively, as used in the slow discharge mechanism calculations (5). V_{23} is the energy of the final state, H₂, as a function of the H-H distance and is given by the Morse function of the final state. In the absence of spectroscopic data for the M-H⁺ interaction, the Morse function of M-H was used for the V_{13} energy. (Spectroscopic data for Hg-H and Hg-H⁺ are practically the same.) As in the slow discharge mechanism calculation, the hydrogen ion is assumed to be an ion, where interactions with the water molecule are concerned and as an atom for interaction with the other hydrogen atoms. However, the energy of the electron has been accounted for through the chosen reference state. Further, when the hydrogen ion is sufficiently separated from the water molecule, the H⁺-OH₂ interaction is small and the H-H energy is predominant and it is likely that in this position the hydrogen

Table I. Physical constants in calculation of potential energy of system (V)

Parameter	Interaction		
	H-H	Ni-H	H ⁺ -OH ₂
D° kcal mole ⁻¹	109.52	60.00	187.00
a Å ⁻¹	1.94	1.60	1.375
r_e Å	0.74	1.48	1.05

ion is fully neutralized. Thus, the assumption is not seriously in error.

As in the slow recombination mechanism calculation (9), the metal atom was considered as fixed. In addition, the position of the water molecule, with respect to the metal atom, was also considered to be fixed for purposes of simplifying the calculation of vibrational frequencies. The error involved in the calculation of the vibrational frequencies, due to the latter assumption, is small since the water molecule is heavy compared to the hydrogen or deuterium atoms and also because the motion of the water molecule is restricted due to hydrogen bonding with surrounding water molecules.

The potential energy of the system was then calculated as a function of the coordinates of the two hydrogen atoms with respect to the metal atom using a computer. Four calculations were carried out for nickel. The constants, used in the calculation of V , are shown in Table I. In the first two calculations, an Ni-H₂O distance of 3.5 Å was used, as in the calculation of Conway and Bockris (8). No saddle point was obtained when the total energy was assumed to be 100% coulombic for all interactions nor for the case of 20% coulombic energy for the Ni-H, H⁺-OH₂ interactions and 15% coulombic for the H-H interaction. The results of these two calculations indicate that the electrochemical desorption mechanism can take place readily for the assumed distance between the Ni atom and water molecule.

In the third and fourth calculations, the distance between the Ni atom and water molecule was taken as 5.4 Å. This distance follows from the model of the double layer according to Bockris, Devanathan, and Müller (10) in which a layer of water molecules separates the metal surface from the first layer of ions. In the third calculation, the total energy of the system was assumed to be coulombic. In the fourth calculation 20% of the H⁺-OH₂, Ni-H interactions and 15% of the H-H interactions were assumed to be coulombic. Saddle points were obtained in the two calculations. Let the coordinates of the H atom (position 2) and H ion (position 3) at the saddle point be (x_0, D, D) and (y_0, O, O). (The axis of the activated complex is the x axis, the y and the z axis are the two axes mutually perpendicular to the x axis).

The potential energy in the neighborhood of the saddle point may be expanded by a Taylor series and is given by

$$V = V_0 + \frac{1}{2} \sum_x^{\xi} a_{xx}(x - x_0)^2 + a_{x\xi}(x - x_0)(\xi - \xi_0) + a_{y\eta}y\eta + a_{z\zeta}z\zeta \quad [39]$$

Since the activated complex is linear, the other cross terms vanish. The terms a_{xx} --- $a_{z\zeta}$ were obtained by a determination of the corresponding second derivatives ($\partial^2 V / \partial x^2$ --- $\partial^2 V / \partial z \partial \zeta$) of the potential function at the saddle point. They were then used in the secular equations

$$\begin{vmatrix} a_{xx} - 4m_1\lambda, & a_{x\xi} \\ a_{x\xi}, & a_{\xi\xi} - 4m_2\lambda \end{vmatrix} = 0 \quad [40]$$

$$\begin{vmatrix} a_{yy} - 4m_1\lambda, & a_{y\eta} \\ a_{y\eta}, & a_{\eta\eta} - 4m_2\lambda \end{vmatrix} = 0 \quad [41]$$

$$\begin{vmatrix} a_{zz} - 4m_1\lambda, & a_{z\zeta} \\ a_{z\zeta}, & a_{\zeta\zeta} - 4m_2\lambda \end{vmatrix} = 0 \quad [42]$$

where $\lambda = 4\pi^2\nu^2$, m_1 and m_2 are the masses of hydrogen (or its isotopes) at positions 2 and 3, respectively. One of the frequencies is imaginary. The bending frequencies are doubly degenerate due to the cylindrical symmetry of the potential function around the saddle point. The results of the two calculations including partition function ratios of the activated complexes are summarized in Table II.

The fourth calculation gave an activation energy (E^{\ddagger}) considerably higher than the third. The experimentally observed E^{\ddagger} for the hydrogen evolution reaction on Ni in acid solutions (11) is 7 kcal mole⁻¹ and this figure is also much less than the

Table II. Force constants (σ 's) vibrational frequencies (ω 's) partition function ratios ($f_{H_2^{\ddagger}}/f_{H,D^{\ddagger}}$, etc.) of isotopic activated complexes for the slow electrochemical desorption mechanism

Parameter	Percentage coulombic energy for Ni-H, H ⁺ -OH ₂ and H-H interactions (ρ) and calculation number in parentheses	
	$\rho_{Ni-H} = \rho_{H^+-OH_2} = \rho_{H-H} = 100$	$\rho_{Ni-H} = \rho_{H^+-OH_2} = 20$ $\rho_{H-H} = 15$
r_{12}^{\ddagger} Å*	2.40	2.74
r_{23}^{\ddagger} Å*	1.88	1.58
r_{34}^{\ddagger} Å*	1.12	1.08
E^{\ddagger} kcal mole ⁻¹ *	21.1	50.8
a_{xx} kcal mole ⁻¹ Å ⁻²	-109.52	-191.39
a_{yy} kcal mole ⁻¹ Å ⁻²	39.47	22.94
a_{zz} kcal mole ⁻¹ Å ⁻²	39.47	22.94
$a_{\xi\xi}$ kcal mole ⁻¹ Å ⁻²	448.84	298.18
$a_{\eta\eta}$ kcal mole ⁻¹ Å ⁻²	61.10	27.96
$a_{\zeta\zeta}$ kcal mole ⁻¹ Å ⁻²	61.10	27.96
$a_{x\xi}$ kcal mole ⁻¹ Å ⁻²	70.84	152.68
$a_{y\eta}$ kcal mole ⁻¹ Å ⁻²	-22.07	-14.65
$a_{z\zeta}$ kcal mole ⁻¹ Å ⁻²	-22.07	-14.65
ω for Ni - - - H - - - H ⁺	588i, 1156, 468,	829i, 999, 343,
- - - OH ₂ (cm ⁻¹)	274, 468, 274	176, 343, 176
ω for Ni - - - H - - - D ⁺	584i, 823, 387,	806i, 726, 295,
- - - OH ₂ (cm ⁻¹)	234, 387, 234	145, 295, 145
ω for Ni - - - D - - - H ⁺	418i, 1151, 440,	600i, 975, 310,
- - - OH ₂ (cm ⁻¹)	206, 440, 206	137, 310, 137
ω for Ni - - - H - - - T ⁺	571i, 675, 366,	794i, 596, 286,
- - - OH ₂ (cm ⁻¹)	202, 366, 202	124, 286, 124
ω for Ni - - - T - - - H ⁺	341i, 1149, 433,	496i, 964, 301,
- - - OH ₂ (cm ⁻¹)	171, 433, 171	116, 301, 116
$f_{H_2^{\ddagger}}/f_{H,D^{\ddagger}}$	0.1864	0.2359
$f_{H_2^{\ddagger}}/f_{D,H^{\ddagger}}$	0.4411	0.4411
$f_{H_2^{\ddagger}}/f_{H,T^{\ddagger}}$	0.08048	0.1077
$f_{H_2^{\ddagger}}/f_{T,H^{\ddagger}}$	0.2828	0.2845

* r_{12}^{\ddagger} , r_{23}^{\ddagger} and r_{34}^{\ddagger} are the Ni-H, H-H⁺ and H⁺-OH₂ inter-nuclear distances in the activated complex; E^{\ddagger} is the activation energy.

Table III. Separation factors for the slow electrochemical desorption mechanism at low and intermediate overpotentials

Calculation No.	Percentage coulombic energy (ρ) S			Separation factors excluding tunneling corrections			Separation factors including tunneling corrections		
	$\rho_{\text{Ni-H}}$	$\rho_{\text{H}^+-\text{OH}_2}$	$\rho_{\text{H-H}}$	$S_{\text{D},\text{E}_1}^*$	$S_{\text{D},\text{E}_2}^*$	S_{D}^*	S_{D,E_1}	S_{D,E_2}	S_{D}
3	100	100	100	11.8	27.9	8.3	13.0	30.7	9.1
4	20	20	15	14.9	27.9	9.7	16.4	30.7	10.7
				$S_{\text{T},\text{E}_1}^*$	$S_{\text{T},\text{E}_2}^*$	S_{T}^*	S_{T,E_1}	S_{T,E_2}	S_{T}
3	100	100	100	27.9	89.5	19.8	29.5	103.8	23.0
4	20	20	15	34.1	90.0	24.7	39.5	104.4	28.7

value obtained in the third calculation. The partition function ratios in the two calculations are, however, not significantly different. The value obtained in the third calculation is preferable since E^\ddagger in this calculation is closer to the experimental activation energy. It may be expected that the correct partition function ratios of the activated complexes may be slightly less than the values of calculation 3. The isotope effect is greater when the isotopic substitution is at position 2 rather than position 3 (see Fig. 1).

Tunneling factor ratios ($\Gamma_{\text{H}}/\Gamma_{\text{D}}$ and $\Gamma_{\text{H}}/\Gamma_{\text{T}}$).—The tunneling factor ratios were obtained for hydrogen ion or atom (or its isotopes) transfer distances of 2.13 Å [5.40 – (1.48 + 1.05 + 0.74)]. Calculations for both parabolic and Eckart barriers (5, 12) were in good agreement. $\Gamma_{\text{H}}/\Gamma_{\text{D}}$ is 1.09 for a parabolic and 1.10 for an Eckart barrier, the corresponding $\Gamma_{\text{H}}/\Gamma_{\text{T}}$ ratios being 1.13 and 1.16, respectively.

Separation Factors

Separation factors excluding tunneling corrections (S_{D}^* and S_{T}^*).—Using Eq. [19] to [21], [23], [24] and the data in Table II, S_{D}^* and S_{T}^* were calculated and are given in Table III. The values obtained in calculation 3 are closer to the correct values, since the activation energy obtained in this calculation is closer to the experimental activation energy than that of calculation 4.

Separation factors including tunneling corrections (S_{D} and S_{T}).—The separation factors including tunneling corrections are also given in Table III. It is probable that the tunneling factors are somewhat overestimated in view of the low barrier height at an overpotential of 0.4v on Ni and thus the separation factors, excluding tunneling corrections are the preferred values for this mechanism.

Table IV. Separation factors for the slow electrochemical desorption mechanism at all overpotentials

Overpotential region	Percentage coulombic energy (ρ)			Separation factors excluding tunneling corrections		Separation factors including tunneling corrections	
	$\rho_{\text{Ni-H}}$	$\rho_{\text{H}^+-\text{OH}_2}$	$\rho_{\text{H-H}}$	S_{D}^*	S_{T}^*	S_{D}	S_{T}
Low and intermediate	100	100	100	8.3	19.8	9.1	23.0
Low and intermediate	20	20	15	9.7	24.7	10.7	28.7
High	100	100	100	3.4	5.4	4.1	7.0
High	20	20	15	3.6	5.7	4.4	7.5

Slow Electrochemical Desorption Mechanism at High Overpotentials

Expression for separation factor.—At high overpotentials, the reverse currents of the discharge steps 3 and 4 may be neglected. The separation factor expression for this case was worked out previously (5) as

$$\frac{1}{S_{\text{D}}} = \frac{1}{2S_{\text{D},1}} + \frac{1}{S_{\text{D},\text{E}_1}} \quad [43]$$

where $S_{\text{D},1}$ is the separation factor expression for the discharge step and is given by

$$S_{\text{D},1} = \frac{1}{2} \cdot \frac{f_{\text{H}}^{\ddagger}}{f_{\text{D}}^{\ddagger}} \cdot \frac{f_{\text{HDOg}}}{f_{\text{H}_2\text{Og}}} \cdot K_{\text{D}} \quad [44]$$

This equation holds for a linked discharge-electrochemical desorption mechanism. However, at high overpotentials, if the coverage of the electrode with adsorbed atomic hydrogen (θ) is low, the mechanism is rate determined by the discharge step, whereas if θ is high, the electrochemical desorption step is rate-determining. Equation [43] was obtained in the general case but holds equally well for the two special cases of low and high degree of coverage, the determination of which distinguishes the alternate rate-determining steps.

Numerical values of separation factors.—The numerical values of separation factors were worked out previously and are given in Table IV, along with the S values for the slow electrochemical desorption mechanism at low and intermediate overpotentials.

Conclusions

At low and intermediate overpotentials, when the discharge step can be treated as in equilibrium, the calculated S values are distinctly separated from the corresponding values for all other mechanisms.

The theoretical separation factors, using a 100% coulombic energy for all interactions, are closer to the true S values, since the experimental activation energy is closer to the calculated activation energy for this case than for the case where the coulombic energy is taken at 20% for the Ni-H and H^+-OH_2 bonds and 15% for the H-H bond. It is not possible to reduce the calculated values any further, since the separation factors in both the presently calculated cases are not much different even though the calculated activation energies differ by as much as 30 kcal mole⁻¹.

At high overpotentials the separation factor is given by that for a linked discharge-electrochemical

desorption mechanism. Thus, the separation factor method cannot be used to distinguish between a rate-determining discharge and a rate-determining electrochemical desorption mechanism at high overpotentials. The only way of distinguishing between these two mechanisms is by a determination of the degree of coverage of adsorbed hydrogen on the electrode, since the coverage is low for a slow discharge mechanism and is high for a slow electrochemical desorption mechanism.

Some aspects of separation factor calculations.—It may be thought that there are inaccuracies in such calculations [ref. (5, 9) and this paper]. The statistical mechanical treatment of reaction rates is quite satisfactory. The only doubt arises in the calculation of vibrational frequencies of transition state which is vital. Defects of calculation are those of the semi-empirical method of Eyring *et al.* The Heitler-London treatment for H bonds is used in the present calculations as well. The inaccuracies of the calculations are much less than is thought, as has been shown by a variation of parameters: metal, M-M distance, percentage coulombic energy. In any case, many defects are present in absolute calculation of reaction rates, they are particularly useful in conjunction with isotope effects (3).

The separation factors for the slow electrochemical desorption mechanism at low and intermediate overpotentials and the slow discharge mechanism are distinctly separated, mainly due to the high real stretching frequencies in the activated complex of the slow discharge step. Thus, the separation factor method has proved useful in distinguishing between these two mechanisms on a number of metals (1) in which cases other methods (*e.g.*, stoichiometric numbers, variation of degree of coverage with potential) are inapplicable (12).

Acknowledgments

Financial support from the Aeronautical Systems Command, Air Force Systems Command, United States Air Force, Contract 33(657)-8823, is gratefully acknowledged. The authors also wish to thank Drs. E. R. Nixon and K. Tharmalingam for helpful theoretical discussions. Mathematical assistance from Mr. C. Vaseekaran and computer facilities afforded by the Physics Department are greatly appreciated.

Manuscript received Aug. 9, 1963; revised manuscript received Dec. 11, 1963. This paper is from work carried out in partial fulfillment of requirement for the degree of Ph.D.

Any discussion of this paper will appear in a Discussion Section to be published in the June 1965 JOURNAL.

REFERENCES

1. J. O'M. Bockris and S. Srinivasan, *Electrochim. Acta*, in press.
2. B. E. Conway, *Proc. Roy. Soc.*, **A247**, 400 (1958).
3. J. O'M. Bockris and S. Srinivasan, *This Journal*, **111**, 858 (1964).
4. B. E. Conway, *Can. J. Chem.*, **37**, 178 (1959).
5. J. O'M. Bockris and S. Srinivasan, *This Journal*, **111**, 858 (1964).
6. S. Glasstone, K. J. Laidler, and H. Eyring, "The Theory of Rate Processes," p. 121, McGraw Hill Book Co., New York (1941).
7. R. Parsons and J. O'M. Bockris, *Trans. Faraday Soc.*, **47**, 914 (1951).
8. B. E. Conway and J. O'M. Bockris, *Can. J. Chem.*, **35**, 1124 (1957).
9. J. O'M. Bockris and S. Srinivasan, *This Journal*, **111**, 844 (1964).
10. J. O'M. Bockris, M. A. V. Devanathan, and K. Müller, *Proc. Roy. Soc.*, **A274**, 55 (1963).
11. J. O'M. Bockris and E. C. Potter, *J. Chem. Phys.*, **20**, 614 (1952).
12. S. Srinivasan, Ph.D. Thesis, University of Pennsylvania (1963).
13. J. Bigeleisen and M. Wolfsberg, in "Advances in Chemical Physics," vol. I, chap. II, Interscience Publications, New York (1960).

Theoretical Calculations of the Separation Factors in the Hydrogen Evolution Reaction for the Slow Recombination Mechanism

John O'M. Bockris and S. Srinivasan

The Electrochemistry Laboratory, The University of Pennsylvania, Philadelphia, Pennsylvania

ABSTRACT

The theoretical calculations of H/D and H/T separation factors have been carried out on the metals Ni and Pt, following the lines of earlier calculations by Okamoto *et al.* The effect of variations in the metal-metal internuclear distances and the coulombic exchange energy ratio on the separation factor was small. Tunneling corrections were also made. The calculated H/T separation factor on Pt is in agreement with the experimentally determined value. The theoretically predicted separation factors for a slow molecular hydrogen diffusion mechanism are not distinctly separated from the values for a slow recombination mechanism. Separation factor determinations on the platinum group of metals or the temperature coefficients of separation factors on these metals should be useful to distinguish between the two mechanisms.

Earlier calculations (1-3) of the separation factors for the slow recombination mechanism are contradictory. In the original calculations (1, 2), the longer of the two possible M-M distances for Ni and

Pt surfaces were used. Recent overpotential measurements in Ni (4) showed that the most closely packed plane has the smallest overvoltage and it is hence more appropriate to use the closer M-M dis-

tances in the determination of the coordinates of the saddle point and the vibrational frequencies of the activated state therefrom. Wigner's tunneling correction was also used and this is applicable only for very small degrees of tunneling. Since hydrogen or its isotopes are the masses involved in the reaction, larger tunneling corrections are to be expected.

Considerations in the most recent calculations of the zero point energy differences of the isotopic activated complexes and of the concentration ratio of adsorbed atomic hydrogen to deuterium have been discussed in the previous paper of this series (5).

Present Calculations

Expression for Separation Factor

Under the conditions that $a_{\text{H}_2\text{O}_1} \gg a_{\text{HDO}_1}$, the H/D separation factor is given by

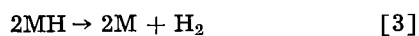
$$S_D = \frac{1}{2} \left(\frac{c_H}{c_D} \right)_g \frac{a_{\text{HDO}_1}}{a_{\text{H}_2\text{O}_1}} \quad [1]$$

where $(c_H/c_D)_g$ is the ratio of atomic concentrations of H to D in the electrolytic gas; $a_{\text{H}_2\text{O}_1}$ and a_{HDO_1} are the activities of H_2O and HDO in solution.

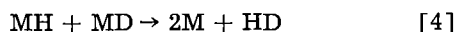
During electrolysis, the ratio $(c_H/c_D)_g$ is given by

$$\left(\frac{c_H}{c_D} \right)_g = \frac{2i_{\text{H}_2} + i_{\text{HD}}}{i_{\text{HD}}} \quad [2]$$

where i_{H_2} and i_{HD} are the recombination currents for the isotopic reactions



and



respectively. Since $i_{\text{H}_2} \gg i_{\text{HD}}$, we have

$$S_D = \frac{i_{\text{H}_2}}{i_{\text{HD}}} \cdot \frac{a_{\text{HDO}_1}}{a_{\text{H}_2\text{O}_1}} \quad [5]$$

using Eq. [1] and [2]. The currents i_{H_2} and i_{HD} may be expressed as

$$i_{\text{H}_2} = k_{\text{H}_2} a_{\text{MH}}^2 \quad [6]$$

$$i_{\text{HD}} = k_{\text{HD}} a_{\text{MH}} a_{\text{MD}} \quad [7]$$

where k_{H_2} and k_{HD} are the respective recombination rate constants for the isotopic reactions, a_{MH} and a_{MD} are the activities of H and D atoms adsorbed on the electrode.

Dividing Eq. [6] by [7], we have

$$\frac{i_{\text{H}_2}}{i_{\text{HD}}} = \frac{k_{\text{H}_2}}{k_{\text{HD}}} \cdot \frac{a_{\text{MH}}}{a_{\text{MD}}} \quad [8]$$

Expressing the rate constants in terms of statistical mechanical functions, we have

$$\frac{i_{\text{H}_2}}{i_{\text{HD}}} = \frac{\Gamma_H}{\Gamma_D} \cdot \frac{f_{\text{H}^\ddagger}}{f_{\text{D}^\ddagger}} \cdot \frac{f_{\text{MD}}}{f_{\text{MH}}} \cdot \frac{a_{\text{MH}}}{a_{\text{MD}}} \quad [9]$$

where Γ_H/Γ_D is the ratio of the tunneling factors for the isotopic reactions, $f_{\text{H}^\ddagger}/f_{\text{D}^\ddagger}$ is the ratio of partition functions of the isotopic activated complexes and $f_{\text{MD}}/f_{\text{MH}}$ is the ratio of partition functions of an MD molecule to an MH molecule.

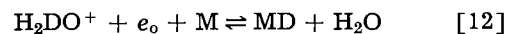
The reference state, used in the definition of partition functions for isotopic species, is the minima

of potential energy curves and not the zero point energy level.

If f , a , μ are the partition function, activity, and chemical potential of a species respectively, then $f/a = e^{-\mu/RT}$. Thus, Eq. [9] becomes

$$\frac{i_{\text{H}_2}}{i_{\text{HD}}} = \frac{\Gamma_H}{\Gamma_D} \cdot \frac{f_{\text{H}^\ddagger}}{f_{\text{D}^\ddagger}} \cdot \frac{e^{-\mu_{\text{MD}}/RT}}{e^{-\mu_{\text{MH}}/RT}} \quad [10]$$

The discharge steps



may be considered to be in equilibrium when the recombination step is rate-determining. Hence,

$$\frac{e^{-\mu_{\text{MD}}/RT}}{e^{-\mu_{\text{MH}}/RT}} = \frac{e^{-\mu_{\text{H}_2\text{DO}^+}/RT}}{e^{-\mu_{\text{H}_3\text{O}^+}/RT}} \quad [13]$$

It was shown in an earlier paper (6) that

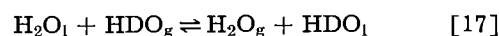
$$\frac{e^{-\mu_{\text{H}_2\text{DO}^+}/RT}}{e^{-\mu_{\text{H}_3\text{O}^+}/RT}} = \frac{e^{-\mu_{\text{HDO}_g}/RT}}{e^{-\mu_{\text{H}_2\text{O}_g}/RT}} \quad [14]$$

Using Eq. [5], [10], [13], and [14], we have

$$S_D = \frac{a_{\text{HDO}_1}}{a_{\text{H}_2\text{O}_1}} \cdot \frac{\Gamma_H}{\Gamma_D} \cdot \frac{f_{\text{H}^\ddagger}}{f_{\text{D}^\ddagger}} \cdot \frac{e^{-\mu_{\text{HDO}_g}/RT}}{e^{-\mu_{\text{H}_2\text{O}_g}/RT}} \quad [15]$$

$$= \frac{\Gamma_H}{\Gamma_D} \cdot \frac{f_{\text{H}^\ddagger}}{f_{\text{D}^\ddagger}} \cdot \frac{f_{\text{HDO}_g}}{f_{\text{H}_2\text{O}_g}} \cdot K_D \quad [16]$$

where $f_{\text{HDO}_g}/f_{\text{H}_2\text{O}_g}$ is the partition function ratio of the isotopic water molecules in the gas phase and K_D is the equilibrium constant of the reaction



The suffixes 1 and g stand for the liquid and gas phase, respectively.

The H/T separation factor is given by a similar expression.

Numerical Calculation of Separation Factors

Product of equilibrium constant (K_D or K_T) and partition function ratio of isotopic water molecules in the gas phase ($f_{\text{HDO}_g}/f_{\text{H}_2\text{O}_g}$ or $f_{\text{HTO}_g}/f_{\text{H}_2\text{O}_g}$).—In a previous paper (6) it was shown that

$$K_D \cdot \frac{f_{\text{HDO}_g}}{f_{\text{H}_2\text{O}_g}} = 63.36 \quad [18]$$

$$K_T \cdot \frac{f_{\text{HTO}_g}}{f_{\text{H}_2\text{O}_g}} = 316.48 \quad [19]$$

Partition function ratio of isotopic activated complexes ($f_{\text{H}^\ddagger}/f_{\text{D}^\ddagger}$ or $f_{\text{H}^\ddagger}/f_{\text{T}^\ddagger}$).—At low coverages, interactions between adsorbed hydrogen atoms may be neglected. The activated complex may be regarded as planar and also to have a plane of symmetry through the right bisector of the line joining the two metal

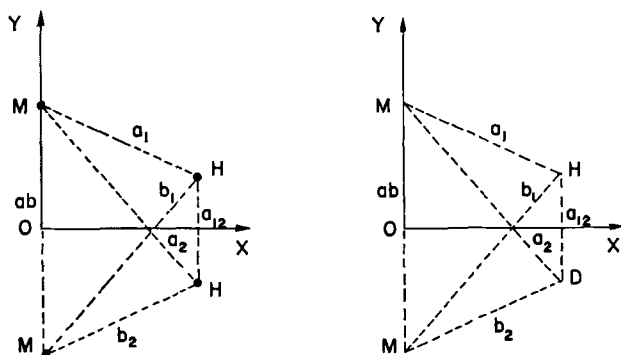


Fig. 1. Activated complex for slow recombination mechanism

atoms and perpendicular to the plane of the molecule (1, 7).

In the activated state, the hydrogen atoms may be considered to be immobile. The translational and rotational partition function ratio are unity, apart from a symmetry factor and hence

$$\frac{f_{H^{\ddagger}}}{f_{D^{\ddagger}}} = \frac{\sigma_D}{\sigma_H} \cdot \frac{\prod [\sinh(h\nu_i/2kT)]_D}{\prod [\sinh(h\nu_i/2kT)]_H} \quad [20]$$

The activated complex has five real frequencies.

To determine the coordinates of the H atoms (or its isotopes) in the activated complex, the potential energy of the system was treated as a four electron problem, cf. Eyring *et al.* (8). The potential energy of the system (V) is given by

$$V = K_{ab} + K_{12} + K_{a1} + K_{b2} + K_{a2} + K_{b1} - \left[\frac{1}{2} \{ (\alpha - \beta)^2 + (\beta - \gamma)^2 + (\gamma - \alpha)^2 \} \right]^{1/2} \quad [21]$$

with

$$\alpha = J_{ab} + J_{12} \quad [22]$$

$$\beta = J_{a1} + J_{b2} \quad [23]$$

$$\gamma = J_{a2} + J_{b1} \quad [24]$$

where K 's are the coulombic and J 's the exchange contributions to the total energies of interactions M-M, H-H and M-H (see Fig. 1).

As in the method of Eyring, a certain percentage of each interaction was assumed to be coulombic for all distances of separation.

Three calculations were carried out, two on nickel and one on platinum. The constants, used in the calculation of V , are given in Table I. In the first calculation on Ni, the physical constants used are the same as in the calculation of Okamoto *et al.* (1). In the second calculation on Ni and the one on Pt, the shorter of the two possible M-M distances was used.

As in previous work (1, 7) a fixed distance was assumed between the two metal atoms in all calcula-

tions. This assumption may be considered as valid, since the metal atoms are much heavier than the hydrogen atoms and thus the hydrogen atoms only move in the formation of the activated complex. The potential energy of the system (V) was then expressed as a function of two coordinates, the distance between the two hydrogen atoms ($2y$) and that between the centers of the two metal atoms and the two H atoms (x), in keeping with the assumption that the activated complex is symmetrical. V was calculated as a function of x and y on a computer and from the table of these V values, the coordinates of the saddle point were determined.

Following the treatment of Okamoto *et al.* (1) let the coordinates of the H atoms in any arbitrary position be (x_1, y_1, z_1) and (x_2, y_2, z_2) . [The OZ axis is perpendicular to the plane of the paper through O; Fig. 1]. Introducing a change of coordinates to simplify the subsequent treatment, we have

$$\begin{aligned} x &= \frac{x_1 + x_2}{2} & \xi &= \frac{x_1 - x_2}{2} \\ y &= \frac{y_1 + y_2}{2} & \eta &= \frac{y_1 - y_2}{2} \\ z &= \frac{z_1 + z_2}{2} & \zeta &= \frac{z_1 - z_2}{2} \end{aligned}$$

At the saddle point, $x = x_0$, $y = y_0$, and $z = \xi = \eta = \zeta = 0$. The potential energy in the neighborhood of the saddle point may be expanded by a Taylor series and is given by

$$V = V_0 + \frac{1}{2} \sum_x a_{xx} (x - x_0)^2 + a_{xy} (x - x_0) (y - y_0) + a_{\xi\eta} \xi \eta \quad [25]$$

Due to the symmetry of the activated complex, the other cross terms are zero. The terms $a_{xx} \dots a_{\xi\eta}$ were obtained by a determination of the corresponding second derivatives ($\partial^2 V / \partial x^2 \dots \partial^2 V / \partial \xi \partial \eta$) of the expression [21] at the saddle point.

$a_{xx} \dots a_{\xi\eta}$ were used in the secular equations

$$\begin{vmatrix} a_{xx}(m_1 + m_2) - 4m_1m_2\lambda, & a_{\xi\xi}(m_1 - m_2), \\ & a_{xy}(m_1 + m_2), a_{\xi\eta}(m_1 - m_2) \\ a_{xx}(m_1 - m_2), & a_{\xi\xi}(m_1 + m_2) - 4m_1m_2\lambda, \\ & a_{xy}(m_1 - m_2), a_{\xi\eta}(m_1 + m_2) \\ a_{xy}(m_1 + m_2), & a_{\xi\eta}(m_1 - m_2), \\ & a_{yy}(m_1 + m_2) - 4m_1m_2\lambda, a_{\eta\eta}(m_1 - m_2) \\ a_{xy}(m_1 - m_2), & a_{\xi\eta}(m_1 + m_2), \\ & a_{yy}(m_1 - m_2), a_{\eta\eta}(m_1 + m_2) - 4m_1m_2\lambda \end{vmatrix} = 0 \quad [26]$$

$$\begin{vmatrix} a_{zz}(m_1 + m_2) - 4m_1m_2\lambda, & a_{\zeta\zeta}(m_1 - m_2) \\ a_{zz}(m_1 - m_2), & a_{\zeta\zeta}(m_1 + m_2) - 4m_1m_2\lambda \end{vmatrix} = 0 \quad [27]$$

Table I. Physical constants used in calculation of potential energy of system for slow recombination mechanism

Parameter	Interaction and calculation number							
	H-H		Ni-Ni		Ni-H		Pt-Pt	Pt-H
	1	2 and 3	1	2	1	2	3	3
D^0 kcal mole ⁻¹	109.10	109.52	20.60	20.00	60	74.24	21.55	65.52
a Å ⁻¹	1.95	1.94	—	—	1.60	1.45	—	1.63
r_e Å	0.74	0.74	3.52	2.49	1.48	1.48	2.77	1.62
ρ	11	14	37	30	24	20	40	27

Table II. Force constants (α 's) vibrational frequencies (ω 's) and partition function ratios ($f_{\text{H}}^{\neq}/f_{\text{D}}^{\neq}$ and $f_{\text{H}}^{\neq}/f_{\text{T}}^{\neq}$) of isotopic activated complexes for the slow recombination mechanism

Parameter	Metal, $d_{\text{M-M}}$ and calculation number in parenthesis		
	Ni, $d_{\text{Ni-Ni}} = 3.52\text{\AA}$ 1	Ni, $d_{\text{Ni-Ni}} = 2.49\text{\AA}$ 2	Pt, $d_{\text{Pt-Pt}} = 2.77\text{\AA}$ 3
x_0 \AA^*	1.06	1.74	1.48
y_0 \AA^*	0.69	0.39	0.63
E^{\neq} kcal mole $^{-1}$ *	14.2	36.0	15.8
a_{xx} kcal mole $^{-1}$ \AA^{-2}	232.75	-57.55	400.06
a_{yy} kcal mole $^{-1}$ \AA^{-2}	-155.09	546.65	-393.58
a_{zz} kcal mole $^{-1}$ \AA^{-2}	0.96	0.23	1.61
$a_{\xi\xi}$ kcal mole $^{-1}$ \AA^{-2}	276.66	138.69	452.19
$a_{\eta\eta}$ kcal mole $^{-1}$ \AA^{-2}	267.09	26.65	131.79
$a_{\zeta\zeta}$ kcal mole $^{-1}$ \AA^{-2}	38.38	124.02	41.33
a_{xy} kcal mole $^{-1}$ \AA^{-2}	-193.09	194.41	-101.33
$a_{\xi\eta}$ kcal mole $^{-1}$ \AA^{-2}	-221.30	36.23	-179.70
$\omega_{\text{H}_2^{\neq}}$ cm^{-1}	1170i, 1696, 1355, 543, 473, 75.	818i, 1876, 933, 305, 850, 36.	1539i, 1762, 1551, 547, 491, 91.
$\omega_{\text{HD}^{\neq}}$ cm^{-1}	998i, 1554, 1049, 446, 406, 62.	690i, 1635, 776, 249, 737, 30.	1322i, 1663, 1166, 448, 426, 79.
$\omega_{\text{HT}^{\neq}}$ cm^{-1}	924i, 1531, 879, 390, 387, 53.	627i, 1553, 692, 216, 695, 26.	1232i, 1653, 963, 391, 392, 68.
$f_{\text{H}}^{\neq}/f_{\text{D}}^{\neq}$	0.1715	0.187	0.1550
$f_{\text{H}}^{\neq}/f_{\text{T}}^{\neq}$	0.07153	0.0827	0.05934

* x_0 and $2y_0$ are the distances of the line joining the 2 hydrogen atoms from the line joining the 2M atoms and the distance between the 2 hydrogen atoms in the activated complex; E^{\neq} is the activation energy.

where $\lambda = 4\pi^2\nu^2$. Of the six frequencies, one is imaginary, corresponding to motion along the reaction coordinate.

The results of all three calculations, including partition function ratios of the activated complexes, are given in Table II. The first calculation on nickel gives values of partition function ratios of activated complexes lower than the corresponding values of Horiuti *et al.* (1, 2), although the same input parameters were used in both calculations. The discrepancy is probably due to an inaccurate location of the saddle point in the earlier work. Further, the calculation of the force constant, a_{xx} , appears to be inexact since a negative value is reported, though it is clearly positive, as indicated in the corresponding energy map. The procedure of calculating the force constants in the present work (*viz.*, by evaluating the corresponding second derivatives at the saddle point) may also be thought to be more accurate than that carried out by Horiuti *et al.* (*viz.*, from potential energy maps).

$f_{\text{H}}^{\neq}/f_{\text{D}}^{\neq}$ and $f_{\text{H}}^{\neq}/f_{\text{T}}^{\neq}$, obtained in the second calculation on Ni, with variation of Ni-Ni distance, coulombic exchange energy ratio and Morse constants, are in reasonable agreement with the corresponding values of the first calculation.

$f_{\text{H}}^{\neq}/f_{\text{D}}^{\neq}$ and $f_{\text{H}}^{\neq}/f_{\text{T}}^{\neq}$ on Pt are also lower than the values obtained by Horiuti and Nakamura (2). In addition to the above possible explanations, this discrepancy may be due to the different Pt-Pt distances used (2.77 \AA in this work and 3.92 \AA in the former work).

Tunneling factor ratios.—The tunneling factor ratios on Ni were obtained for a hydrogen atom transfer distance of 2.48 \AA (3.52-0.74) in the first calculation and 1.75 \AA (2.49-0.74) in the second calculation. Bell's method of calculation for a parabolic barrier (9). [which gives good agreement with calculations for an Eckart barrier, when the tun-

neling corrections are small (10)] was used. This method of calculating tunneling corrections was first applied to the separation factor problem by Bawn and Ogden (10), and more recently by Conway (11).

The height of the barrier, E^{\neq} , at $\eta = 0.4v$ was calculated as 2.4 kcal mole $^{-1}$, using equation

$$E^{\neq} = E_0^{\neq} - \beta\eta F \quad [28]$$

with $\beta = 1/2$ and $E_0^{\neq} = 7$ kcal mole $^{-1}$ (13). The ratios $\Gamma_{\text{H}}/\Gamma_{\text{D}}$ are 1.07 and 1.15 according to the first and second calculations, respectively. The corresponding values of $\Gamma_{\text{H}}/\Gamma_{\text{T}}$ are 1.09 and 1.20, respectively.

For Pt, a hydrogen atom transfer distance of 2.03 \AA (2.77-0.74) was used. E^{\neq} calculated at $\eta = 0.05v$, using Eq. [28] with $\beta = 2.0$ and $E_0^{\neq} = 5.2$ kcal mole $^{-1}$ (14) is 2.9 kcal mole $^{-1}$. $\Gamma_{\text{H}}/\Gamma_{\text{D}}$ is 1.13 and $\Gamma_{\text{H}}/\Gamma_{\text{T}}$ is 1.18.

It is probable that these tunneling factors are overestimated in view of the fact that the barrier heights are small.

Separation factors.—*Separation factors excluding tunneling corrections (S_{D}^* and S_{T}^*).*—Using Eq. [18], [19], and the partition function ratios in Table II, S_{D}^* and S_{T}^* ,¹ arising in the three calculations are given in Table III. Though the H/D separation factors differ by about 10%, whereas the H/T separation factors differ by about 16% in the two calculations and both sets of results are somewhat higher than the results on Pt, we may conclude that the separation factors do not significantly depend on the metal, the interatomic distances and the coulombic-exchange energy ratios, but they de-

¹Inclusion of anharmonicity corrections in the partition function ratios of (a) isotopic water molecules in the gas phase and (b) isotopic activated complexes has an effect of less than 10% on the separation factors. The authors wish to thank one of the reviewers for pointing out the effect of anharmonicity corrections on the former partition function ratio.

Table III. Separation factors for the slow recombination mechanism

Separation factors excluding (S^*) or including tunneling (S)	Metal and calculation number		
	Ni 1	Ni 2	Pt 3
S_D^*	5.4	5.9	4.9
S_T^*	11.3	13.1	9.4
S_D	5.8	6.4	5.5
S_T	13.0	15.7	11.1

pend mainly on the mechanism. Of the two results on Ni, for both H/D and H/T separation factors, the lower values are preferable since for a Ni-Ni distance of 3.52Å, the activation energy is considerably lower than for the Ni-Ni distance of 2.49Å. This result was also reported by Okamoto *et al.* (1) but is contrary to the conclusions reached by Piontelli *et al.* from overpotential measurements on Ni single crystals. The present calculations on Pt also yield considerably lower S values than those of Horiuti and Nakamura ($S_D = 7.2$, $S_T = 16.1$ with no tunneling corrections). From the results on Ni for the two interatomic distances, we may expect still lower values on Pt for a Pt-Pt distance of 3.92Å as used by Horiuti *et al.*

Separation factors including tunneling corrections (S_D and S_T).—The separation factors, including tunneling corrections are also given in Table III. Calculations 1 and 3 give results in reasonable agreement with each other. The results of calculation 2 are somewhat higher. Due to a higher activation energy for a Ni-Ni distance of 2.49Å, as compared with 3.52Å, we may conclude that the separation factor on polycrystalline nickel is more likely to correspond to the value obtained in the first calculation for a slow recombination mechanism.

Conclusion

Due to the higher calculated activation energy for a Ni-Ni distance of 2.49Å than that for 3.52Å, it is probable that most of the reaction takes place on two adjacent Ni atoms 3.52Å apart for a slow recombination mechanism.

On Pt, it is probable that the reaction takes place on 2Pt atoms 3.92Å apart, but since the calculated activation energy for a Pt-Pt distance of 2.77Å is itself fairly low, S values for the higher Pt-Pt distance are not likely to be much different, although they may be somewhat lower (since there was a decrease in S with decrease of activation energy on Ni).

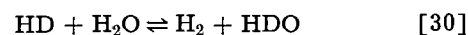
In some experimental determinations of H/T separation factors (S_T), an increasing trend or a small scatter was observed with each successive measurement (15). This variation in S_T was probably due to certain preferred sites being used up.

The values of S_T for the recombination mechanism are distinctly separated from S_T for a slow discharge or for a coupled discharge-electrochemical desorption mechanism. S_D values for a slow recombination and coupled discharge-electrochemical desorption mechanism are not markedly separated.

The H/D separation factor for a slow molecular hydrogen diffusion mechanism is

$$S_D = K_D \left(\frac{\mu_D}{\mu_H} \right)^{1/2} \quad [29]$$

where K_D is the equilibrium constant for reaction



and μ_H or μ_D is the reduced mass of an H_2 or HD and H_2O molecules (15). The H/T separation factor is given by a similar expression. With K_D as 3.8 (16) and K_T as 6.2 (17), S_D and S_T are 4.5 and 8.2, respectively. Unfortunately, these values are not distinctly separated from the corresponding values for the slow recombination mechanism on platinum. It is on the platinum group of metals that this mechanism was proposed. However, for a slow recombination mechanism, there should be a slight dependence of S on the metal, whereas for a diffusion mechanism, there should be no dependence of S on the metal. Thus, from the experimental S values on the platinum group of metals, we may be able to distinguish the two mechanisms. The temperature coefficient of the separation factors should also prove useful in distinguishing between a slow recombination and slow molecular hydrogen diffusion mechanism.

Acknowledgments

Financial support from the Aeronautical Systems Command, Air Force Systems Command, United States Air Force, Contract 33(657)-8823, is gratefully acknowledged. The authors also wish to thank Drs. E. R. Nixon, E. R. Thornton, T. E. Sharp, H. Carlmichael, and K. Tharmalingam for valuable theoretical discussions. Mathematical assistance from Mr. C. Vaseekaran and part of the computer facilities afforded by Dr. L. Nanis are also greatly appreciated.

Manuscript received Aug. 29, 1963; revised manuscript received Dec. 12, 1963. This paper is from work carried out in partial fulfillment of requirement for the degree of Ph.D.

Any discussion of this paper will appear in a Discussion Section to be published in the June 1965 JOURNAL.

REFERENCES

1. G. Okamoto, J. Horiuti, and K. Hirota, *Sci. Papers Inst. Phys. Chem. Research (Tokyo)*, **29**, 223 (1936).
2. J. Horiuti and T. Nakamura, *J. Research Inst. Cat.*, **2**, 73 (1951).
3. B. E. Conway, *Proc. Roy. Soc.*, **A247**, 400 (1958).
4. R. Piontelli, L. Peraldo Bicelli, and A. LaVecchia, *Rend. accad. naz. Lincei*, **VIII**, **27**, 312 (1959).
5. J. O'M. Bockris and S. Srinivasan, *This Journal*, **111**, 844 (1964).
6. J. O'M. Bockris and S. Srinivasan, *ibid.*, **111**, 853 (1964).
7. A. Sherman, C. E. Sun, and H. Eyring, *J. Chem. Phys.*, **3**, 49 (1934).
8. S. Glasstone, K. J. Laidler, and H. Eyring, "The Theory of Rate Processes," p. 121, McGraw-Hill Book Co., New York (1941).
9. R. P. Bell, *Trans. Faraday Soc.*, **55**, 1 (1959).

10. T. E. Sharp and H. S. Johnston, *J. Chem. Phys.*, **37**, 154 (1962).
11. C. E. H. Bawn and G. Ogden, *Trans. Faraday Soc.*, **30**, 432 (1934).
12. B. E. Conway, *Can. J. Chem.*, **37**, 178 (1959).
13. J. O'M. Bockris and E. C. Potter, *J. Chem. Phys.*, **20**, 614 (1952).
14. R. Parsons, *Trans. Faraday Soc.*, **56**, 1340 (1960).
15. S. Srinivasan, Ph.D. Thesis, University of Pennsylvania (1963).
16. A. Farkas and L. Farkas, *J. Chem. Phys.*, **2**, 468 (1934).
17. W. F. Libby, *ibid.*, **11**, 101 (1943).

The Mechanism of the Electro-Oxidation of Acetylene on Platinum

James W. Johnson, Halina Wroblowa, and John O'M. Bockris

The Electrochemistry Laboratory, The University of Pennsylvania, Philadelphia, Pennsylvania

ABSTRACT

The increasing interest in hydrocarbon oxidation reactions connected with the development of electrochemical energy conversion makes the investigation of the influence of the relations between structure of the oxidized compound and the mechanism of the reaction of primary importance. The study of oxidation reactions of several olefins has been reported elsewhere. This paper is concerned with the mechanism of acetylene oxidation.

Experimental

Cell and apparatus.—The electrolytic cell and electrical apparatus were similar to that described previously (1, 2) unless otherwise stated. The test electrode was a planar rectangle of platinized 52 mesh platinum gauze of geometric area 11.7 cm². The auxiliary electrode (cathode) was of similar platinized gauze (47 cm²). The procedure for platinization and activation of the electrodes has been reported (1, 2). The reference electrodes were saturated calomel for alkaline and 1*N* mercury-mercurous sulfate for acid solutions.

Coulombic efficiency.—*Acid solution.*—This was measured galvanostatically in a three compartment cell with closed stopcocks between the compartments. The effluent gases from the anodic compartment were passed through an absorber containing barium hydroxide solution. For a measurement, 300 ml of saturated solution (~ 30g Ba(OH)₂/liter) were initially filtered into the absorber; 50 ml were withdrawn and titrated with 0.200*N* HCl using phenolphthalein indicator. Precautions were taken so that air did not contact the solutions. All containers were nitrogen-flushed, and nitrogen was used to pass the solutions from one container to another.

The cell was first operated for a sufficient length of time at constant current to saturate the anolyte with carbon dioxide. During this time, the gases were vented to the atmosphere via a three-way stopcock and a bubbler. Immediately following, the gases were diverted through the absorber. A low flow rate of gases (~ 5 cm³ min⁻¹ at STP) and glass bead packing in the absorber were used to increase the gas-liquid contact. (A second absorber indicated no carbon dioxide was passing out of the first.)

After the carbon dioxide had been collected for the desired length of time (cell always operated at the original constant current), the absorber was disconnected from the cell. Another 50 ml sample was withdrawn and titrated as described above.

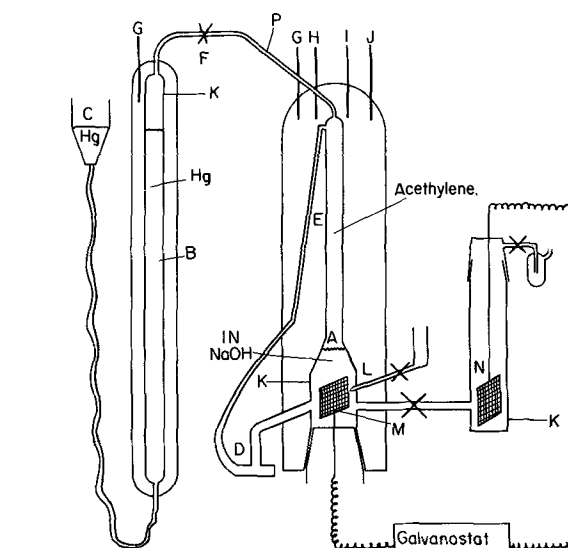


Fig. 1. Diagram of apparatus for measurement of coulombic efficiency in alkaline solution. A, anode compartment; B, gas buret; C, leveling bulb; D, circulation pump; E, water jacket; F, three-way stopcock; G, thermometer; H, thermoregulator; I, heater; J, stirrer; K, gas inlet; L, Luggin capillary; M, anode; N, cathode; P, water cooled condenser.

Separate experiments indicated that the barium hydroxide could be titrated accurately in the presence of barium carbonate.

Alkaline solution.—A diagram of the apparatus is shown in Fig. 1. The change in volume of gaseous acetylene contained in a closed anodic compartment A above the anolyte is measured at constant pressure with a mercury-filled buret B and leveling bulb C which are integral parts of the compartment. The carbon dioxide produced during the oxidation is absorbed by the alkaline anolyte. A small magnetically driven glass centrifugal pump D circulates the anolyte causing it to flow down column E (approximately 12 in. in length). This gives a sufficient gas-liquid contact area to keep the anolyte saturated with acetylene.

When making a consumption determination, the cell was filled with electrolyte and the circulation pump D started. The mercury level in the buret was raised near to the three-way stopcock F and nitrogen vigorously bubbled through the anode and cathode compartments to remove oxygen from the cell. After about 1 hr of bubbling, the nitrogen passing through the anode compartment was stopped and acetylene flow started. This was continued for 1 to 2 hr to saturate the anolyte and replace the other gases in the compartment with acetylene. Next, stopcock F was turned so as to connect the gas buret to the anode compartment and the mercury displaced by acetylene until the desired amount was contained in the buret. The system was allowed to equilibrate, the buret reading noted, and the current started at a value to keep the potential within the linear Tafel region. The run was continued (with frequent adjustment of the leveling bulb) until a desired volume of acetylene had been consumed.

Reagents.—Sulfuric acid, "Baker Analyzed" reagent; sodium sulfate, "Fisher Certified" reagent; sodium hydroxide, "Baker Analyzed" reagent; acetylene, Air Reduction Company, purified (> 99.5% purity, impurities largely water and nitrogen); nitrogen, Matheson, prepurified (99.996% purity); water-distilled; gas mixtures of acetylene and prepurified nitrogen were supplied in cylinders and analyzed by Matheson.

Results

Rest potentials.—All potentials are given on the normal hydrogen scale ($e^{\text{H}_2} = 0$ at 80°C). The correction for the reference electrode being at room temperature was made as described previously (2).

Oxygen was removed from the electrolyte by vigorously passing nitrogen through the anode and cathode compartments for 1 to 2 hr. Acetylene (or the mixtures with nitrogen) was then passed through the anolyte at a rate of 90 cm³ (STP)/min. The rest potentials were found to be -0.58 in 1N NaOH and $+0.26\text{v}$ in 1N H₂SO₄. These values were attained almost immediately after admitting the acetylene and remained constant for periods of 1-2 hr. For more prolonged periods, the potentials slowly became more positive. The rest potentials varied by 60-70 mv per unit pH (Table I) and were independent of the partial pressure of acetylene in the range 10⁻⁴ to 1 atm.

Coulombic efficiency.—*Acid solution.*—The amount of electricity q per mole of CO₂ produced during the time t by current i is

$$q = \frac{2V_s it}{N V_a (V_o - V_e)}$$

Table I. Rest potentials for acetylene at 80°C

pH	V_{rest} , v
12.6	-0.58
11.9	-0.45
8.7	-0.36
1.2	+0.19
0.3	+0.26

where V_s is the volume of samples titrated, ml; V_a the volume of barium hydroxide solution in absorber, ml; V_o the volume of hydrochloric acid for initial titration, ml; V_e the volume of hydrochloric acid for final titration, ml; and N the concentration of hydrochloric acid, mole/ml.

For acetylene oxidation in 1N H₂SO₄ (in the Tafel region), it was found that $(4.8 \pm 0.2) \times 10^5$ coulombs of electricity was produced per mole of CO₂ as compared with the theoretical value of 4.82×10^5 coulombs according to the equation: $\text{C}_2\text{H}_2 + 4\text{H}_2\text{O} \rightarrow 2\text{CO}_2 + 10\text{H}^+ + 10\text{e}^-$.

Alkaline solution.—The amount of electricity q produced per mole of acetylene consumed was directly calculated by the formula

$$q = \frac{22,400 it}{\Delta V_{\text{corr}}}$$

where ΔV_{corr} is the volume of acetylene consumed corrected to standard temperature and pressure.

For acetylene oxidation in 1N NaOH, the Faradaic equivalence was found to be $(9.1 \pm 0.5) \times 10^5$ coulombs per mole of acetylene, as compared with the theoretical value of 9.65×10^5 coulombs. The error in this determination is much higher than in the first method; it is connected with the measurement of the volume and correction for the water vapor pressure (the presence of the temperature gradient between A and B, Fig. 2) and amounts to about 5%.

Analysis of electrolyte.—An analysis¹ was made of the 1N NaOH anolyte to determine the presence of any organic substances that might be the products of branching reactions. Previous to the analysis an anodic oxidation of acetylene was carried out for approximately 100 hr in the electrolyte.

An ultraviolet spectrum of the electrolyte showed no significant absorption, indicating no conjugated unsaturation, such as might be suspected for polymerization reactions.

Infrared spectrograms of samples obtained by extracting portions of the electrolyte with benzene,

¹ Analysis performed by Sadler Research Laboratories, Philadelphia, Pennsylvania.

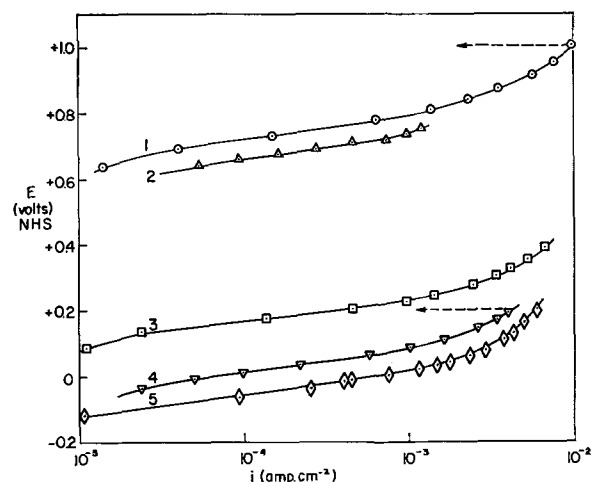


Fig. 2. Current-potential relation ($\bar{P}_A = 1$ atm) as a function of pH = curve 1, 0.3; curve 2, 1.2; curve 3, 8.7; curve 4, 11.9; curve 5, 12.6.

ethyl ether, and n-hexane revealed nothing other than sodium carbonate.

Water was removed from a sample neutralized with hydrochloric acid. The sample was then extracted with anhydrous ethyl alcohol. No organic residue could be demonstrated.

Current-potential relation.—These were determined both galvanostatically and potentiostatically. A linear Tafel region was found at potentials 450–500 mv more positive than the rest potentials (Fig. 2). This region extended over about one and a half decades of current and had a slope of 65–75 mv/decade. Below the linear region the current was quite small and nearly independent of potential. Above the linear region the slope increased rapidly, with passivation (2) occurring at potentials $V = 0.2v$ and $1.0v$ for $1N$ NaOH and $1N$ H_2SO_4 , respectively. Reproducibility of the current values at constant potential was within 10%.

Time effects and electrode activation.—The variation of current with time depended on the electrode potential as related to the linear Tafel region. At potentials below the linear region, the current decreased steadily with time and reached a quasi-steady state only after several hours at a constant potential. In the lower section of the linear region, the current increased with time reaching a steady value in 30–90 min. (The time necessary to reach the steady state decreased as the potential increased.) In the upper part of this region, steady currents were attained almost immediately. At potentials still higher by about 200 mv, a passivation region was found, but no consistent behavior noted. The electrode might passivate immediately on switching the potential to this region or it might function quite normally for periods up to 45 min before suddenly passivating. The electrode could be re-activated by interrupting the current and allowing the rest potential to be re-established. This normally required 1–2 hr. (At potentials below the

Table II. Activation energies for the anodic oxidation of acetylene on platinumized platinum electrodes

Electrolyte	Potential (V), v	Activation energy (E_A), kcal mole ⁻¹
1N H_2SO_4	0.790	21.2
1N H_2SO_4	0.740	22.4
1N NaOH	-0.005	25.4
1N NaOH	-0.055	26.7

passivation region, the rest potential was re-established rapidly after opening the circuit.) Once a steady current was attained in the linear Tafel region, it remained constant with almost no perceptible change for periods in excess of 24 hr.

pH effect.—The effect of pH at constant ionic strength is shown in Fig. 2. A linear Tafel region with the same slope ($b = 70$ mv) was found in each case over approximately the same current range. The only effect was that the lines were shifted in the positive direction along the potential axis as the pH decreased, $(dV/dpH)_i \sim -50$ mv.

Temperature effect.—The effect of temperature on current was measured potentiostatically in both $1N$ NaOH and $1N$ H_2SO_4 solutions at potentials within the linear Tafel region. Results are shown in Fig. 3. Activation energies were calculated and are shown in Table II. The shift in activation energy with potential is ~ -25 kcal/volt as compared with the theoretical value $d(E_A)/dV = \alpha F = -23.06$ kcal/v for $\alpha = 1$.

From the above values the heat of activation at reversible potential was calculated $E_{Arev} = E_{A(\eta)} + \eta F = 42$ kcal mole⁻¹ for acidic, and 48 kcal mole⁻¹ for alkaline solutions.

Pressure effect.—Acetylene of a given partial pressure (mixed with prepurified nitrogen) was passed through the cell. The electrode was held at constant potential and, after a steady state had been obtained, the pressure was changed to another value. The i - p curves thus attained in $1N$ sulfuric acid are shown in Fig. 4. For acetylene pressures between 0.04 and 1.0 atm it can be seen that the current increases inversely with pressure. The Tafel lines at various pressures are laterally shifted hav-

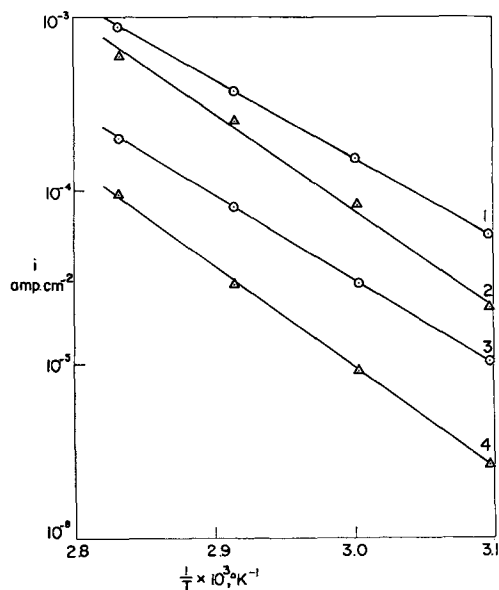


Fig. 3. Current-temperature relation as a function of potential: 1, 0.790v, $1N$ H_2SO_4 ; 2, 0.740v, $1N$ H_2SO_4 ; 3, 0.005v, $1N$ NaOH; 4, 0.055v, $1N$ NaOH.

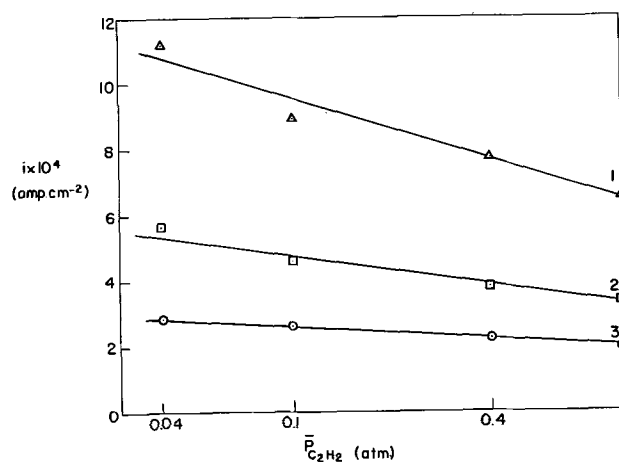


Fig. 4. Current-pressure relation ($1N$ H_2SO_4) as a function of potential: curve 1, 0.775v; curve 2, 0.750v; curve 3, 0.725v.

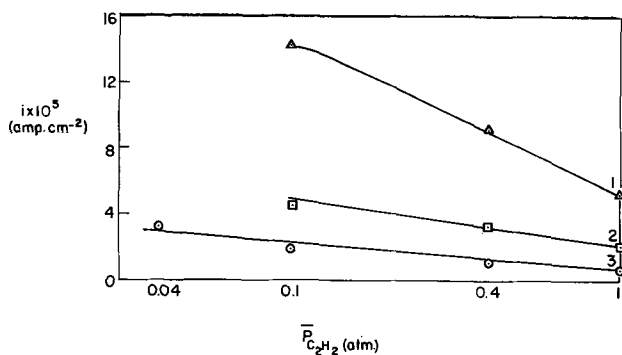


Fig. 5. Current-pressure relation (1N NaOH) as a function of potential: curve 1, 0.005v; curve 2, 0.030v; curve 3, 0.055v.

ing approximately the same slope but different intercepts. At pressures lower than 0.04 atm, limiting currents (influenced by the rate of stirring) are observed at very low current densities, and no Tafel lines could be obtained. The pressure effect in 1N NaOH is shown in Fig. 5. The effect was similar but more pronounced than in sulfuric acid.

Discussion

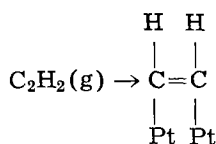
Adsorption of Acetylene

In a recent paper (2) adsorption of ethylene from aqueous solutions under anodic conditions had been discussed. The adsorption isotherm was formulated as

$$\frac{\theta_E}{(1 - \theta_E)^4} = K_{cE} c_E$$

where θ_E is the fractional coverage by ethylene, c_E the concentration of ethylene (mole cm^{-3}). The order of magnitude of K_{cE} estimated by two independent methods give a range of 10^6 – 10^8 cm^3 mole $^{-1}$. No data are available which would allow an independent evaluation of the isotherm constant K_c for acetylene adsorption on Pt from solution. The evidence from the gas phase (4) shows that the heat of adsorption of acetylene is independent of coverage. Taking this into account, as well as the fact that the coverage of acetylene is probably even higher than that of ethylene (4), which in turn is already high (2), Langmuir conditions are assumed. A very rough estimation of K_c can then be made on the following basis.

The most probable mode of acetylene adsorption is



The evidence from the gas phase adsorption suggests that acetylene forms an immobile layer (4) by means of covalent bonds with d-band electrons (5). Since one Pt atom may supply 0.5 of d-electrons, one molecule of acetylene requires 4 adjacent surface sites to adsorb. Thus, the adsorption isotherm is of the same type as in the case of ethylene, i.e.,

$$\frac{\theta_A}{(1 - \theta_A)^4} = K_{cA} c_A = K_{pA} p \quad [1]$$

The similarity of the ethylenic and acetylenic radicals allows one to assume analogous adsorption behavior of the two hydrocarbons and to calculate roughly the value of $K_{cA} \equiv Ke^{-\Delta G^\circ/RT}$, where ΔG_A° is the standard free energy of adsorption of acetylene, and the K value includes energy changes connected with the displacement of water. The free energy of adsorption of ethylene and acetylene will differ by a value which consists of the following contributions:

1. The difference connected with the energy of breaking one C—C bond in a double and a triple bond. The values of energies reported in the literature (6–8) differ; the best estimate of $\Delta G_1 = \Delta G_{c=c} - \Delta G_{c\equiv c} = 6$ kcal mole $^{-1}$ seems to be that given by Bond (4).

2. The difference in free energies of adsorption due to different adsorbate-solution interactions. This difference may be roughly estimated (9) as

$$\Delta G_2 = \Delta G^\circ_{SE} - \Delta G^\circ_{SA} = RT \ln a_E/a_A$$

where ΔG°_{SE} and ΔG°_{SA} are the standard free energies of solution of ethylene and acetylene, respectively, and a_E and a_A are the activities of saturated solutions at 1 atm partial pressure of the respective hydrocarbons. Assuming activity coefficients to be 1 and introducing $c_E \cong 0.1 c_A$,² $\Delta G_2 \cong -1.6$ kcal, thus $K_{cA} = K_{cE} e^{\Delta G_1 + \Delta G_2/RT} = 5.5 \cdot 10^8$ to $5.5 \cdot 10^{10}$ cm^3 mole $^{-1}$ and the limits of the corresponding K_{pA} values are 10^4 – 10^6 atm $^{-1}$ (K_{pA} is the adsorption constant for isotherm relating coverage to partial pressure of acetylene).

Reaction Mechanism

General nature.—(A) The efficiency of CO_2 production is $100 \pm 1\%$ in acid and $95 \pm 5\%$ in alkaline solutions. Thus, it is assumed that no branching leading to products other than CO_2 and water (or protons) occurs to an appreciable extent. The results of ultraviolet and infrared spectroscopy of the anolyte confirm this result. However, a branching reaction occurring with $< 1\%$ of the total current cannot be excluded by these measurements even in acid solution.

(B) The high value of the heat of activation $E_a \cong 40$ kcal mole $^{-1}$ precludes terminal desorption of CO_2 as a rate-determining step (1).

(C) The observed Tafel slopes, $b = 0.065 - 0.075\text{v}$ (Fig. 2) are consistent with the value of $b = 2.3 RT/F$. For a consecutive sequence of reactions, such as must exist in acetylene oxidation to CO_2 , the slope $b = 2.3 RT/F$ must be associated under Langmuir conditions with a chemical reaction following the first charge transfer, or following any later charge transfer in which the reactant is at full coverage as can easily be shown by a treatment of the consecutive reaction kinetics in the usual way (10). For the latter case, however, no pressure effect could be expected. Thus, the value of $b = 2.3 RT/F$, together with the fact that $di/dp < 0$, fix the

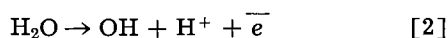
² Data were not available for determining the ratio of c_E/c_A directly for 1N H_2SO_4 at 80°C. The value $c_E/c_A \cong 0.1$ is for the ratio of the solubilities of the gases in water at 80°C. Data available at lower temperatures indicated the solubilities of each gas in 1N H_2SO_4 to be about 80% of their respective values in water.

location of the r.d.s. as one of the chemical reactions between the first and the second charge transfer.

(D) The negative pressure effect, $di/dp < 0$, shows that the r.d.s. must include a substance other than the adsorbing acetylene, or a radical derived from acetylene.

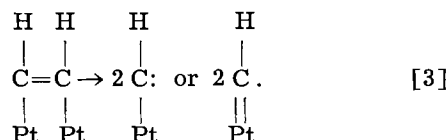
Reaction sequence and reaction rate.—The requirements listed above allow one to formulate the reaction path up to the r.d.s., and the nature of the latter.

The substance other than acetylene, or a radical derived therefrom and adsorbed on the surface, may be only OH^- or OH radical. Since all kinetic parameters are the same in acidic and alkaline solutions, the same mechanism may be assumed for both. This points to the OH radical being the entity in question. This in turn (in acidic solutions) may arise only from water discharge (2). Thus the charge transfer preceding the r.d.s. is assumed to be water discharge:



The rate-determining chemical reaction involves apart from OH either adsorbed acetylene, or a radical derived therefrom, in a chemical reaction. (Any dissociation into H atoms would involve ionization into $\text{H}^+ + \bar{e}$ and contribute to the Tafel slope.) Thus, the radical derived from acetylene can be only CH or an addition product involving acetylene and water.

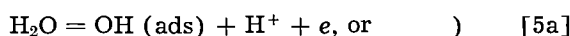
The adsorption of acetylene followed by splitting, i.e.,



would require additional energy connected with breaking of the double bond of about 146 kcal mole⁻¹. Even if each carbon atom were to form not one, but two covalent bonds with Pt, the extra energy needed would be about 80 kcal mole⁻¹.³ Therefore, the possibility of CH being the radical seems unlikely.

It is impossible to distinguish whether the radical in question is adsorbed acetylene or a product of water addition since both would give similar kinetic parameters. Absence of polymerization products and of acetaldehyde in the electrolyte indicate there is no hydrolysis in solution. Thus, the radical is assumed to be adsorbed acetylene.

The reaction path may be now formulated as



³ The energy of C-Pt bond was calculated as:

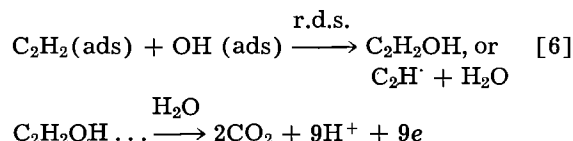
$$E_{\text{C-Pt}} = 1/2(E_{\text{C-C}} + E_{\text{Pt-Pt}}) - 23.06(X_{\text{C}} - X_{\text{Pt}})^2$$

where X = electronegativity value, $E_{\text{C-C}} = 83$ kcal mole⁻¹, $E_{\text{Pt-Pt}} = 20.3$ kcal mole⁻¹, $X_{\text{C}} = 2.5$, $X_{\text{Pt}} = 2.2$ (6).

Table III. Comparison of theoretical and experimental kinetic parameters

Kinetic parameter Tafel slope	Theoretical value $2.3 RT/F = 70$ mv	Experimental value 65-75 mv (Fig. 2)
pH dependence, assuming $\theta_A \neq 0$	$\left(\frac{\partial \log i}{\partial \text{pH}}\right)_V = 1$	0.8*
$f(\text{pH})$ at constant ionic strengths	$\left(\frac{\partial V}{\partial \text{pH}}\right)_i = -70$ mv	-50 mv (Fig. 2)
	$\left(\frac{\partial \log i_0}{\partial \text{pH}}\right) = 0$	~ 0 (See below, "Exchange current")

* The coefficient $\left(\frac{\partial \log i}{\partial \text{pH}}\right)_V$ was obtained by extrapolating the Tafel lines (Fig. 2) so that the current could be obtained at the same potential for various pH values, and by plotting $\log i$ vs. pH (Fig. 6).



From the quasi-equilibrium in reaction [5]

$$\theta_{\text{OH}} = K_5 (1 - \theta_T) a_{\text{H}^+}^{-1} e^{FV/RT}$$

where K_5 represents either $K_{5a} a_{\text{H}_2\text{O}}$ for 5a or $K_{5b} K_W a_{\text{H}_2\text{O}}$ for 5b, and K_W is the ionization constant of water.

The coverage of OH radicals is very low (11) and the coverage of all other intermediates may be neglected in comparison with θ_A , since they occur in the reaction sequence after the rate-determining step, and are not in equilibrium because of the constant removal of the final product, CO_2 . Thus the total coverage θ_T may be approximated as $\theta_T \approx \theta_A$.

The rate of anodic oxidation of acetylene may then be expressed as

$$i = nFK_5 k_6 a_{\text{H}^+}^{-1} \theta_A (1 - \theta_A) e^{FV/RT} \quad [7]$$

See Table I for a comparison of theoretical and experimental kinetic parameters.

Pressure dependence.—The dependence of the steady-state reaction rate on the acetylene pressure (Fig. 4 and 5) can be stated in terms of the coefficient $Z \equiv (\partial i / \partial \log P)$. The values of Z are given in Fig. 7. They depend on potential, $d \log Z / dV$ being

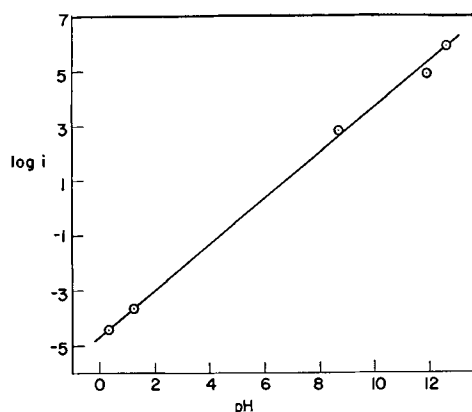


Fig. 6. Dependence of current on pH at constant potential $V = 0.40$ v.

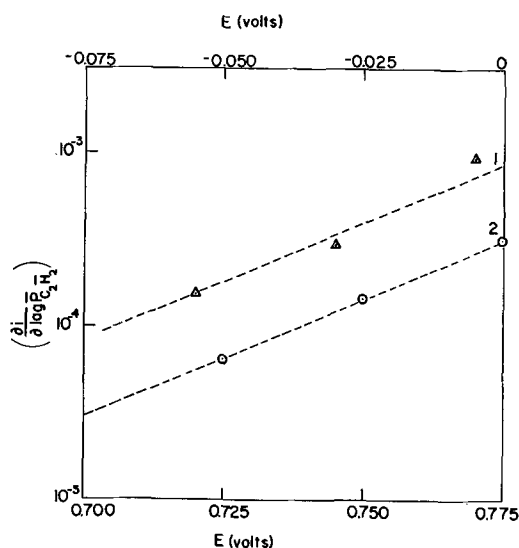


Fig. 7. Dependence of $Z \equiv \left(\frac{\partial i}{\partial \log p} \right)_V$ on potential curve 1 1N NaOH (use potential scale at top), curve 2 1N H_2SO_4 (use potential scale at bottom).

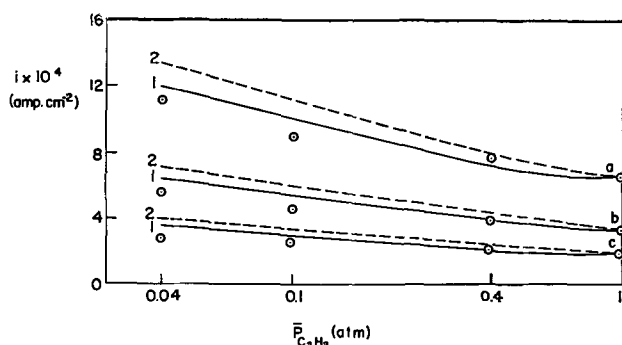


Fig. 8. Theoretical dependence of current on pressure as a function of potential: (a) 0.775v, (b) 0.750v, (c) 0.725v; curve 1 for $K_{P_A}^- = 10^4 \text{ atm}^{-1}$, curves 2 for $K_{P_A}^- = 10^6 \text{ atm}^{-1}$, \odot experimental points.

equal to $\sim 13.5 \text{ v}^{-1}$, as calculated from Fig. 7.

Qualitatively, two types of explanation may be considered for the inverse pressure effect: (i) It could be due to increasing adsorption of a poison, either present in the C_2H_2 , or produced by a side branching reaction of current efficiency too low to be detected by the methods employed. A polymerization of a reactant or product might also lead qualitatively to the effects observed. However, this explanation is not consistent with a number of facts, as discussed elsewhere (12). (ii) Acetylene blocks partly the area available for reaction. A detailed treatment of such effects, in terms of poisoning, and hydrocarbon adsorption model, is published elsewhere (12). It is shown here that the observations are consistent with the type (ii) model according to the mechanism suggested in Eq. [7].

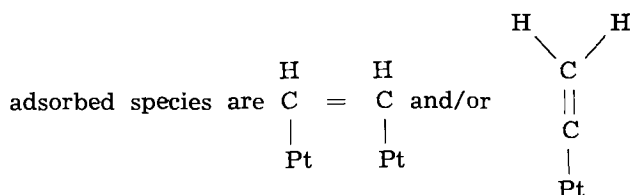
To compare the experimental data with the theoretical dependence of current on pressure at various potentials, the calculated limits of $K_p \approx 10^4 - 10^6 \text{ atm}^{-1}$ (cf. section on Adsorption of Acetylene above), were inserted in Eq. [1]. By plotting the term $\theta(1 - \theta)$ vs. p , the values of $\theta(1 - \theta)$ at any

given pressure may be read. Inserting those values into Eq. [7] and calibrating the term $ka^{-1}\text{H} + e^{FV/RT}$ for one value of current for $\bar{p}_A = 1 \text{ atm}$, the theoretical $i - \log p$ curves for 3 potential values were obtained (Fig. 7, curve 1, $K_p = 10^4 \text{ atm}^{-1}$; curve 2, $K_p = 10^6 \text{ atm}^{-1}$). The experimental results obtained in 1N H_2SO_4 for these potentials are also shown in Fig. 8. It may be seen that a better fit would be obtained for somewhat lower K_p values than 10^4 atm^{-1} . However in view of the very rough calculation of K_p , the agreement is considered satisfactory.

The theory also yields the coefficient $d \log Z/dV$ as $F/2.3 RT \approx 14 \text{ v}^{-1}$ in fair agreement with the experimental value of 13.5 v^{-1} .

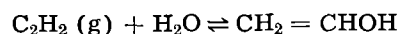
For 1N NaOH solution the change of current with pressure at constant potential is about 2-3 times higher than that predicted by theory. Variation of K_p to values considerably outside those deduced earlier does not cover the observed discrepancy. The coefficient $d \log Z/dV$ (Fig. 7) and all other kinetic parameters are in agreement with the suggested mechanism. This strongly points to a similar mechanism for the oxidation reaction in both acidic and alkaline solutions, but with a different type of adsorption isotherm, in that the amount of sites occupied by one adsorbed acetylenic radical in alkaline solution would be less than in acidic solution, since the value of $\left(\frac{d[\theta(1 - \theta)]}{d \log p} \right)_V = \left(\frac{di}{d \log p} \right)_V$ would then be higher. Two explanations of this possible difference in surface occupancy by acetylene in H_2SO_4 and NaOH solutions may be suggested:

1. In NaOH, a rearrangement occurs, so that the



giving rise to a decreased occupancy per 1 acetylenic radical.

2. Acetylene does not form covalent bonds with d-electrons as assumed above, and on the basis of steric considerations it will occupy only two adjacent sites. In H_2SO_4 , however, adsorption occurs along with hydration, according to the equation



and the resulting radical occupies an area covering approximately four surface sites.

Behavior at potentials above Tafel region.—Acetylene behaves here similarly to ethylene, and diffusion limiting currents are observed for $p_A \leq 0.4$. At higher pressures the potential of about +1v, where the current rapidly decreases to negligible value is reached earlier than the limiting current value. The observed passivation of the electrode had been interpreted elsewhere (2) in terms of accumulation of surface oxide resulting from the reaction between the OH radicals which at the above potential becomes sufficiently fast. The resulting oxide is unable to oxidize the hydrocarbon.

Exchange current.—From the thermodynamic data, the standard reversible potential of the C_2H_2/CO_2 couple is

$$E_{30}^{\circ} = - \frac{\Delta G_{25}^{\circ} - \Delta S^{\circ} (80 - 25)}{10F} = - 0.0503v$$

Taking into account the solubility of carbon dioxide [cf. ref. (1)] and the actual value of pH, the reversible potential at 1 atm acetylene partial pressure is

$$- 0.11v \text{ in } 1N \text{ H}_2\text{SO}_4 \text{ (pH} = 0.3) \\ \text{and } - 0.97v \text{ in } 1N \text{ NaOH (pH} = 12.6)$$

solutions. The exchange currents obtained by extrapolation of the Tafel lines to those potential values are

4.5×10^{-18} and 6.6×10^{-18} amp cm^{-2} (geom.), respectively. The model proposed indicates equality of i_0 in acid and alkaline solutions (cf. Table III).

Rest potentials.—The rest potential observed on Pt in presence of acetylene in solution is about 350 mv more positive than the reversible potential, for the acetylene oxidation to CO_2 . Similar differences between the rest and reversible potentials have been reported for other hydrocarbons (1-3).

It is of interest to consider the possible nature of this potential. The principal facts with which an interpretation must be consistent are the following: 1, It is linearly dependent on pH: $dE/dpH \approx - 2.3 RT/F$. 2, It is independent of the nature of the hydrocarbon used. 3, The partial pressure of hydrocarbon has no effect. 4, The potential concerned differs little from that which exists in the nitrogen saturated solution before the ingress of the hydrocarbon. The average effect of adding the hydrocarbon is to make the rest potential at the zero current flow more negative by approximately 20 mv. 5, Purification of the solution has no effect. 6, Temperature coefficient $dE/dT < 0$. 7, Stirring has no effect.

Possible interpretations of this potential are:

1. It may be a mixed potential set up between the reduction of oxygen to water on hydrogen peroxide and the oxidation of the hydrocarbon to CO_2 . This theory would agree with the sign of the dependence of rest potential on pH and with the lack of effects of hydrocarbon pressure and temperature coefficient. However, it is unlikely that the nature of the hydrocarbon would then have a small effect, because acetylene and ethylene, at least, have very largely different exchange current values. Correspondingly, for the oxygen concentration present, it can be shown that the potential would be stirring dependent.

2. It may be a mixed potential between the oxidation of the unsaturated hydrocarbon to CO_2 and its reduction to the corresponding saturated hydrocarbon. This theory might be consistent with the absence of partial pressure effects in the hydrocarbon and stirring. Although neither the exchange current densities nor Tafel slopes for the reduction of the hydrocarbons are known, consideration of a mixed potential diagram shows that a mixed potential at the constant value observed, independent of the

nature of the hydrocarbon, would require certain unlikely differences between the Tafel slopes and exchange current densities in the reduction of ethylene and acetylene. Furthermore, the small change brought about upon the introduction of the hydrocarbon into the nitrogen-saturated solution makes this theory unlikely.

3. Another possibility is the interference of the ethylene oxidation reaction by some redox process connected with the presence of impurities. This seems unlikely, however, because of the fact that calculations show that the impurities have to be present at a concentration having an order of magnitude of 10^{-5} moles/liter. If the rest potential at zero current flow is to be independent of stirring, this is an improbably high concentration of impurities to have present. A constant value independent of purification is also a strong point against this view.

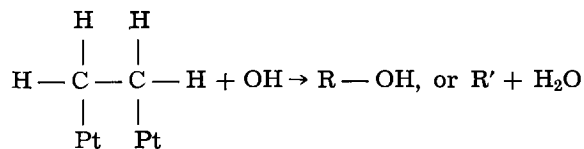
4. Last, it is possible to regard the potential as that corresponding to the reversible equilibrium of water with hydroxyl radicals according to the reaction $H_2O \rightleftharpoons OH \cdot + H^+ + e_0^-$. A reaction similar to this has been discussed by Bockris and Oldfield (13). Attempts to calculate the potential utilizing a PtOH bond, gives values which are approximately 0.5v too high. However, such calculations are uncertain. The theory would be consistent with the absence of stirring effects and with the negative temperature coefficient of the reversible potential. It might, however, be thought that the introduction of the hydrocarbon would play a large effect, for it would presumably reduce the concentration of hydroxyl radicals, on which the potential (according to this view) would be linearly dependent.

At the present time it is not possible to elucidate the mechanism of this rest potential, but the above remarks may serve as a beginning to such work.

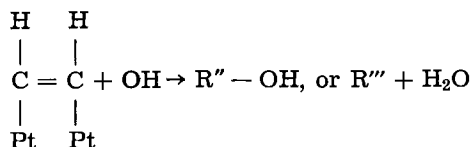
Effect of the Triple Bond

The mechanisms proposed for olefin oxidation involves a rate-determining water discharge reaction, whereas that for acetylene involves a rate determining reaction between adsorbed acetylene and OH radicals. That the systems have a difference in mechanisms arises probably from a higher value of the heat of adsorption of acetylene as compared to that of ethylene as a result of the triple bond in the former (4).

For the case of ethylene, the specific rate of the reaction



is higher than that of water discharge, whereas for acetylene, the specific rate of the reaction



is less than that of water discharge. This results in a change of the Tafel slope from $2RT/F$ to RT/F and a reduced i_0 value.

Summary

The acetylene oxidation reaction on platinized platinum has been studied at 80°C in solutions of $\text{H}_2\text{SO}_4 + \text{Na}_2\text{SO}_4$ and NaOH of constant ionic strength. Reaction rates were measured as a function of potential, pH, and partial pressure of acetylene. Coulombic efficiency was determined by measurements of CO_2 production in acidic solutions and of C_2H_2 consumption in alkaline solutions. An improved apparatus for consumption measurements is described.

The following parameters have been found

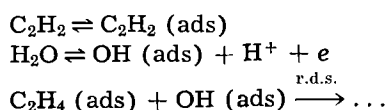
$$\left(\frac{\partial V}{\partial \log i}\right)_p = 70 \text{ mv}, \left(\frac{\partial \log i}{\partial \text{pH}}\right)_v \approx 0.8,$$

$$\left(\frac{\partial \log i_0}{\partial \text{pH}}\right) \approx 0, \left(\frac{\partial i}{\partial p}\right)_v < 0,$$

$$\frac{\partial \log \left(\frac{\partial i}{\partial \log p}\right)_v}{\partial V} \approx 13.5 \text{ V}^{-1}$$

Coulombic efficiency is $100 \pm 1\%$ in acidic and $95 \pm 5\%$ in alkaline solutions. $i_0 \approx 10^{-18} \text{ amp cm}^{-2}$ for both solutions. The heat of activation at the reversible potential, $\Delta H^\circ \approx 42 \text{ kcal mole}^{-1}$ in acidic and $\approx 46 \text{ kcal mole}^{-1}$ in alkaline solutions. At $V \approx 1 \text{ V}$ in $1 \text{ N H}_2\text{SO}_4 \approx 0.3 \text{ V}$ in 1 N NaOH , "passivation" due to oxide formation occurs.

The reaction mechanism in the Tafel range was interpreted in terms of the following sequence



over the entire pH range investigated ($\text{pH} = 0.3 - 12.6$). The inverse pressure effect observed could also be quantitatively accounted for in terms of the suggested mechanism.

Acknowledgments

The authors' thanks are due to Dr. Allan R. Day for helpful discussions, Alan Saunders for construction of the cells, and to Pratt and Whitney Division of United Aircraft Corporation for support of this work.

Manuscript received Sept. 19, 1963.

Any discussion of this paper will appear in a Discussion Section to be published in the June 1965 JOURNAL.

REFERENCES

1. M. Green, J. Weber, and V. Drazic, *This Journal*, **111**, 721 (1964).
2. H. Wroblowa, B. J. Piersma, and J. O'M. Bockris, *J. Electroanal. Chem.*, **6**, 401 (1963).
3. H. Wroblowa, B. J. Piersma, and J. O'M. Bockris, In course of publication.
4. G. C. Bond, "Catalysis by Metals," Academic Press, London, New York (1962).
5. B. M. V. Trapnell, "Chemisorption," Butterworths, London (1955).
6. C. A. Coulson, "Valence," Oxford University Press, London (1961).
7. L. Pauling, "The Nature of the Chemical Bond," Cornell University Press (1960).
8. E. A. Moelwyn-Hughes, "Physical Chemistry," Pergamon, New York, London (1961).
9. E. Blomgren, J. O'M. Bockris, and C. Jesch, *J. phys. Chem.*, **65**, 2000 (1961).
10. J. O'M. Bockris, *J. Chem. Phys.*, **24**, 1956.
11. H. Dahms and J. O'M. Bockris, *This Journal*, **111**, 728 (1964).
12. H. Wroblowa and J. O'M. Bockris, In course of publication.
13. J. O'M. Bockris and L. F. Oldfield, *Trans. Faraday Soc.*, **51**, 249 (1955).

Technical Notes



Growth Twins and Branching of Electrodeposited Copper Dendrites

Fielding Ogburn

National Bureau of Standards, Washington, D. C.

It is not unusual to see electrodeposited dendrites or trees which are branched in one plane only. That is, all the branches and the main stalk lie in the same plane, the whole dendrite being flat. Such dendrites of lead, tin, and copper were described by Wranglen (1), but he gave no explanation for the growth being restricted to one plane. From crystallographic considerations one would not predict this restricted growth if the dendrite were a single crystal. Branching would be expected to appear also

in other planes passing through the main stalk.

Faust and Johns (2) reported twinning boundaries in electrodeposited dendrites of aluminum, copper, gold, lead, and silver. They showed that twinning can play a dominant role in the electrolytic growth of dendrites and cite references showing the same dominant role for growth other than electrolytic. The twinning boundary provides a re-entrant groove, and this groove may be self-perpetuating if two or more twin planes occur close together.

Consideration of these two pieces of information leads to the proposal that branching in one plane only is directly related to the occurrence of growth twins and that at least one twinning boundary extends throughout the dendrite and is parallel to the plane of the dendrite. The reasoning is that, if the twinning boundary facilitates the growth of the deposit by providing a re-entrant groove, then the dendrite should grow fastest at or close to the re-entrant groove. Growth at a distance from the groove would proceed more slowly or not at all. Thus, a platelet would form with the twinning boundary sandwiched between two thin layers of metal. Within the plane of the dendrite, the rate of growth would be different in different crystallographic directions, and one would expect the usual dendritic pattern. The net effect is to produce a fern-like shape with a twinning boundary extending throughout the stalk and each of its branches.

To test this hypothesis, copper dendrites were selected which were branched in one plane only and examined metallographically and by x-ray diffraction. These dendrites had been grown in a solution of 2g of cuprous chloride, 15g of sodium chloride, and 1 ml of concentrated hydrochloric acid in 80 ml of distilled water. All the chemicals were reagent grade. The deposition was carried out potentiostatically with 150 mv between the cathode deposit and a reference electrode. The latter was a copper wire in a Luggin capillary with the tip of the capillary within 5 mm of the cathode. The rate of growth of the dendrite is estimated to have been about 1 mm/hr or less judging from rate measurements made under similar conditions. The dendrites were free to grow in all directions.

Figure 1 shows an x-ray Laue transmission diffraction pattern taken of a copper dendrite 1 or 2 mm long with several branches, all in one plane. The plane common to the stalk and its branches was normal to the x-ray beam in each case. The pattern shows a sixfold symmetry which is characteristic of diffraction patterns of twinned face-centered cubic metals for which the (111) twinning plane is normal to the x-ray beam. The six Laue spots nearest the center of the pattern are 311 reflections.

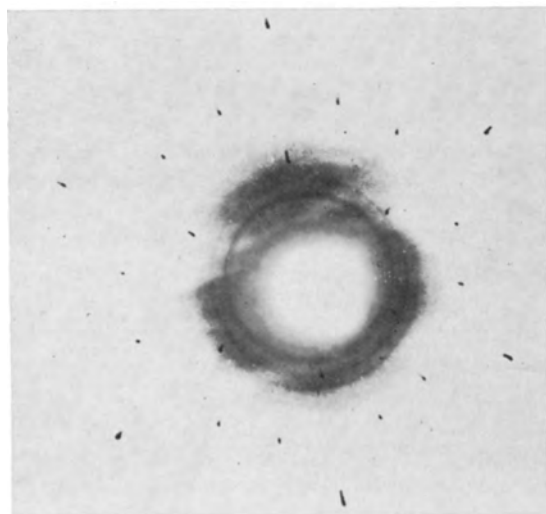


Fig. 1. Laue transmission pattern of copper dendrite. X-ray beam perpendicular to plane of dendrite.

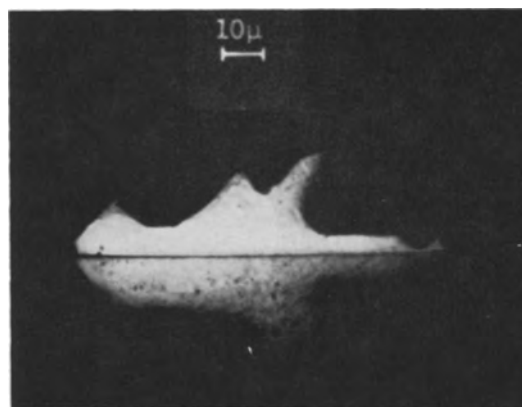


Fig. 2. Section through dendrite of Fig. 1 showing boundary between growth twins; etchant, ammonium hydroxide with hydrogen peroxide.

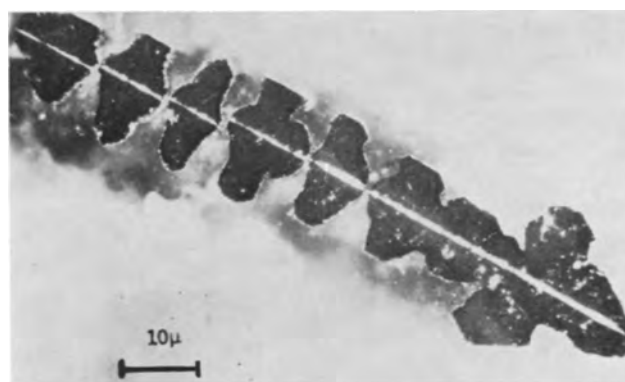


Fig. 3. Section through dendrite showing boundary between growth twins which extends through branches and main stalk. Section is perpendicular to branches and oblique to stalk. Polarized light; etchant, ammonium hydroxide with hydrogen peroxide.

The dendrite was mounted in plastic, sectioned, polished, and etched with a solution of dilute ammonium hydroxide and hydrogen peroxide. Figure 2 shows an etched section of the main stalk. It shows what appears to be the boundary between a pair of crystals in twin orientation and the plane of the twinning boundary is essentially parallel to the branches of the dendrite.

Figure 3 shows a similar section of a second dendrite grown simultaneously with the dendrite of Fig. 1 and 2. This section passes through the main stalk and the branches and is essentially perpendicular to the branches. Here again it appears that a twinning boundary extends throughout the dendrite, but with a slight displacement. Successive sections showed that the displacement disappears as the section approaches the junctions of the branches with the stalk.

To summarize, x-ray diffraction and metallographic examinations of copper dendrites which are branched in one plane only show them to be twinned with the twinning boundary extending the length of the stalks and branches. This appears to be an example of a growth twin and one which exerts a substantial influence on the growth of the dendrite. This is to be compared with the apparent influence of growth twins in polycrystalline electrodeposits of copper (3).

Acknowledgment

The author is indebted to Theodore Orem for the diffraction pattern and to the Advanced Research Projects Agency, Department of Defense, which helped support the work described.

Manuscript received Dec. 31, 1963.

Any discussion of this paper will appear in a Discussion Section to be published in the June 1965 JOURNAL.

REFERENCES

1. G. Wranglen, *Trans. Roy. Inst. Tech.*, **94** (1955).
2. J. W. Faust, Jr., and H. F. Johns, *This Journal*, **108**, 109 (1961); **110**, 463 (1963).
3. F. Ogburn and C. Newton, *ibid.*, **110**, 1148 (1963).

Evidence for Oxidation Growth at the Oxide-Silicon Interface from Controlled Etch Studies

W. A. Pliskin and R. P. Gnall

Components Laboratory, International Business Machines Corporation, Poughkeepsie, New York

The purpose of this paper is to show how a dilute selective etch can be used in the study of various glass and oxide film systems. We shall show, as an example, the details for only one specific application, in particular its usefulness for the study of silicon oxidation. Ligenza and Spitzer have shown by infrared spectroscopy using isotopic oxygen that, with high pressure steam, the oxidation occurs at the silicon-silicon dioxide interface (1). The controlled etch technique described here, is a simpler method of showing that oxidation occurs at the silicon-silicon dioxide interface with both atmospheric steam and dry oxygen oxidation. This technique depends on the ability of the selective etch, consisting of 15 parts hydrofluoric acid (49%), 10 parts nitric acid (70%), and 300 parts water, to etch various type glass and mixed oxide layers much more rapidly than silicon dioxide. The selective nature of this etch, referred to as P etch, is shown in Fig. 1. A silicon dioxide film was exposed to a phosphorus diffusion process to form a mixed $\text{SiO}_2 + \text{P}_2\text{O}_5$ layer on top of a pure silicon dioxide layer as shown on the left. The film thicknesses¹ were measured after etching for various times with P etch and plotted as shown on the right. The film thickness measurements were accurate to tens of Angstroms.

It is thus seen that the etch rate is much faster for the $\text{SiO}_2 + \text{P}_2\text{O}_5$ layer than for pure SiO_2 , and the demarcation is clearly visible. Similar results have been observed with various type glasses on silicon dioxide, and this technique has been used

¹ Thicknesses were measured with Vamfo, an interference microscope developed for accurate, nondestructive, film thickness measurements. (2).

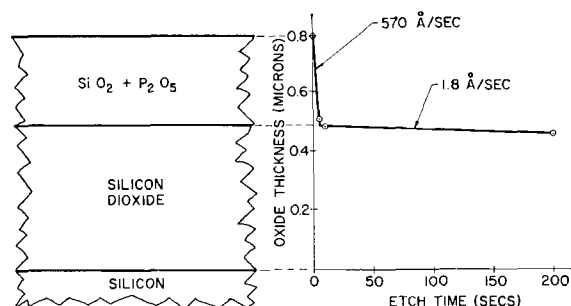


Fig. 1. Etch rates after exposure of an SiO_2 film to phosphorus diffusion.

Table I. Etch rates ($\text{\AA}/\text{sec}$) for $\text{P}_2\text{O}_5\text{-SiO}_2$ and SiO_2 (23°C)

	$\text{P}_2\text{O}_5\text{-SiO}_2$ layer		SiO_2		
	Thickness, \AA	P etch, $\text{\AA}/\text{sec}$	$\text{NH}_4\text{F-HF}$, $\text{\AA}/\text{sec}$	P etch, $\text{\AA}/\text{sec}$	$\text{NH}_4\text{F-HF}$, $\text{\AA}/\text{sec}$
After phosphorus diffusion					
A	2960	570	270	1.8	9.5
B	1940	390	110	—	—
C	1310	220	—	—	9.0
After reoxidation (steam at 970°C)					
A	3930	35.1	33.2	1.7	9.0
B	2460	27.6	—	1.8	—
C	1860	18.3	28.5	1.8	10.3

for studying the penetration of glass films and glazes into underlying silicon dioxide films. (3).

Etch data for phosphosilicate films formed on silicon dioxide after exposure to different phosphorus diffusion conditions² is shown in Table I, where we have compared the etch rate of P etch with that of an ammonium fluoride buffer etch.³ For the purpose of delineation of films, the etch rate ratio between the phosphosilicate layer and the silicon dioxide layer should be as large as possible. For P etch, this ratio is 100 to 300 after the phosphorus diffusion, whereas, with the $\text{NH}_4\text{F-HF}$ buffered solutions, it is only about 10 to 30, about one order of magnitude less. After reoxidation, the ratio for P etch is about 10-20 and for $\text{NH}_4\text{F-HF}$ it is only 3-4. Thus it is seen that the P etch is much better for delineation than is the ammonium fluoride buffer etch.

Table I also shows the thicknesses of the phosphosilicate layer on SiO_2 before and after reoxidation. This layer increases in thickness during reoxidation due to further penetration of the P_2O_5 into the SiO_2 , thus diluting the concentration of P_2O_5 and decreasing the etch rate. At the same time, a small quantity of P_2O_5 outdiffuses resulting in a slightly slower etch rate within a few hundred Angstroms of the outer surface.

Evidence that the oxidation occurs at the oxide-silicon interface is given in Fig. 2. After the phosphorus diffusion, the phosphosilicate layer extended

² The phosphorus diffusion process used P_2O_5 in nitrogen carrier gas at either 1050° or 1100°C for various times.

³ The buffer etch consists of one part hydrofluoric acid to ten parts of ammonium fluoride solution which was made by mixing 1 lb of NH_4F with 680 cc water.

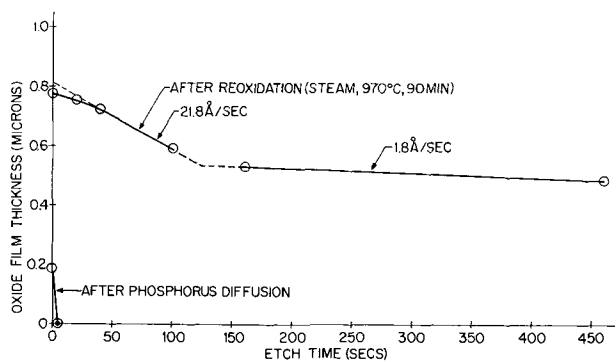


Fig. 2. P etch rate before and after steam oxidation

to the silicon as shown by the lower film thickness-etch time plot. The wafer was then oxidized in steam at atmospheric pressure for 90 min at 970°C. If the diffusing species were silicon, then Si atoms would diffuse out through the $\text{SiO}_2 + \text{P}_2\text{O}_5$ layer to form the SiO_2 layer on the outer surface. An etch rate plot of such a film should show a slow etch rate at the surface and a faster etch rate near the oxide-silicon interface. On the other hand, if the diffusing species were the oxidizing species diffusing through the phosphosilicate layer, then the new oxide would form at the oxide-silicon interface and the phosphosilicate layer would be at the outer surface. The etch rate plot would then show a fast etch rate followed by a slower etch rate corresponding to that of silicon dioxide. As shown in Fig. 2, this is exactly what is observed. It is concluded that in steam at atmospheric pressure the oxide forms at the oxide-silicon interface in agreement with the infrared isotopic studies of high pressure steam oxidation carried out by Ligenza and Spitzer.

Since in dry oxygen the oxidation rates are much slower, greater precautions are necessary. These precautions consist of limiting the phosphorus concentration and thickness of the phosphosilicate layer. This was accomplished by exposing a 1900Å SiO_2 film (on a 0.9 ohm-cm P-type wafer) to a diffusion condition which limited the phosphosilicate layer above $\sim 100\text{Å}$ of the silicon surface. The film thickness after the phosphorus diffusion was 2380Å. The wafer was then subjected to dry nitrogen at 970°C for 90 min. The etch rate of this film was found to be 100Å/sec, and it extended to the bare silicon as shown by thermal probe and infrared carrier absorption. Since this layer would be too thick for

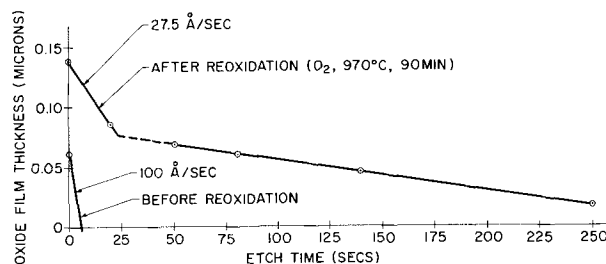


Fig. 3. P etch rate before and after dry oxygen oxidation

the subsequent reoxidation experiment, most of the phosphosilicate layer was removed by etching for 16.8 sec in P etch, leaving a 620Å phosphosilicate film as shown in Fig. 3. The wafer was oxidized in dry oxygen at atmospheric pressure at 970°C for 90 min. The upper plot was obtained by etching for various times with P etch.⁴ It shows the phosphosilicate layer on top of a 700Å SiO_2 layer thus verifying the hypothesis that dry oxygen oxidation also occurs at the oxide-silicon interface. Similar results were obtained with various phosphosilicate layers and a borosilicate layer containing approximately 10% B_2O_3 .

In conclusion, these results show how a dilute selective etch can be used in the study of film systems and, particularly, by simple techniques show that in thermally oxidized silicon by atmospheric steam or dry oxygen, oxidation occurs at the oxide-silicon interface.

Acknowledgment

The authors wish to thank Dr. J. A. Perri, Dr. J. Riseman, and Mr. H. S. Lehman for helpful discussions during the course of this work.

Manuscript received Jan. 23, 1964. This paper was presented at the Pittsburgh Meeting, April 15-18, 1963.

Any discussion of this paper will appear in a Discussion Section to be published in the June 1965 JOURNAL.

REFERENCES

1. J. R. Ligenza and W. G. Spitzer, *J. Phys. Chem. Solids*, **14**, 131 (1960).
2. W. A. Pliskin and E. E. Conrad, Paper presented at International Colloquium on the Optics of Thin Solid Layers, Marseille, France, Sept. 9, 1963; *IBM J. Res. & Dev.*, **8**, 43 (1964).
3. W. A. Pliskin, Unpublished work.

⁴ The thicknesses of thinner oxide films were obtained from the intensity of the 9.2μ SiO_2 absorption band in the infrared spectra of the silicon wafer. The oxidized wafer was compared with a comparable thickness nonoxidized wafer in a Perkin-Elmer model 221G spectrophotometer.

Note on Calcium-Orthovanadate

L. H. Brixner, P. A. Flounoy, and Keith Babcock

Pigments, Engineering Physics, and Central Research Departments,

Experimental Station, E. I. du Pont de Nemours & Company, Inc., Wilmington, Delaware

Although calcium orthovanadate $\text{Ca}_3(\text{VO}_4)_2$ has been known since 1925, when Tammann (1) obtained it by solid-state reaction between CaO and V_2O_5 , there is no publication on its structure. One reason for this may be that $\text{Ca}_3(\text{VO}_4)_2$ is isomorphic with neither the corresponding phosphate nor with

the vanadates of strontium and barium. Therefore, the lattice parameters could not readily be derived from powder patterns and required the availability of large single crystals.

We have grown single crystals of $\text{Ca}_3(\text{VO}_4)_2$ up to 10 cm long and 1.25 cm in diameter by the Czo-

chalski (2) technique, employing a 25 kw Westinghouse radio-frequency generator, 450 kc/sec. An automatic radio-frequency voltage controller, regulating to 2.5%, was used in conjunction with the generator. The melt was contained in a 60% Pt-40% Rh crucible and the temperature observed with an optical pyrometer. The apparent melting point was 1430°C. An occasional check with a Pt/Pt 13% Rh thermocouple indicated that the optical measurement was about 40°C too low; hence, the true melting point is about 1470°.

The starting material was obtained by interacting CaCO_3 with $\text{Ca}_2\text{V}_2\text{O}_7$, which had been prepared by precipitation from purified solutions of calcium nitrate and ammonium metavanadate. While $\text{Ca}_2\text{V}_2\text{O}_7$ is a distinct lemon-yellow color, $\text{Ca}_3(\text{VO}_4)_2$ in the polycrystalline state is practically colorless. The pulled single crystals always had a very light orange-yellow color, which thus far has not been associated with any specific impurity. Spectroscopic as well as x-ray fluorescence analysis, in comparison with a "glass clear" sample of CaMoO_4 , indicated only such elements as Sr and Ba present in greater quantities than in the absolutely colorless CaMoO_4 . X-ray fluorescence analysis gave: CaO, 48.20% $\text{V}_2\text{O}_5 = 52.05\%$ (calc.: CaO, 48.05; V_2O_5 , 51.95) for the composition of a grown crystal.

We suspect, therefore, that the VO_4^{-3} group may indeed be slightly colored intrinsically. In view of the decreasing intensity of color of the neighboring isoelectric anion groups, MnO_4^{-1} and CrO_4^{-2} , this conclusion appears quite reasonable.

X-ray examination by oscillation and Weissenberg methods of a section cut from a 10 cm crystal gave

the following parameters: $a_0 = 8.35\text{\AA}$; $b_0 = 10.77\text{\AA}$; $c_0 = 7.00\text{\AA}$; $\beta = 95.0^\circ$. The most probable space group is C_{2h}^6 C 2/c. The x-ray density is $3.55 \text{ g}\cdot\text{ml}^{-1}$, which checks closely with the pycnometrically determined density of $3.49 \text{ g}\cdot\text{ml}^{-1}$.

Pure $\text{Ca}_3(\text{VO}_4)_2$ does not fluoresce at room temperature in either 2537 or 3660Å ultraviolet radiation. However, when irradiated at -196°C , yellow fluorescence is observed.

Since the ionic radius of Ca^{+2} is about the same as the average of the trivalent rare earths, the latter can be readily introduced in the lattice of $\text{Ca}_3(\text{VO}_4)_2$ if electroneutrality is restored by compensation with Na^{+1} as in the typical compound $\text{Ln}_x^{+3}\text{Na}_x^{+1}\text{Ca}_{3-2x}(\text{VO}_4)_2$ or with Ti^{+4} as in a compound of the general type $\text{Ln}_{2x}\text{Ca}_{3-2x}(\text{V}_{1-x}\text{Ti}_x\text{O}_4)_2$.

Studies of the fluorescent emission of various rare earth ions in $\text{Ca}_3(\text{VO}_4)_2$ will be the subject of a future and more detailed publication. An intense fluorescence emission at 1.063μ is observed at -196°C from Nd^{3+} doped $\text{Ca}_3(\text{VO}_4)_2$ when sodium compensation is used. The emission lines are narrower and fewer in number than those observed for neodymium in CaWO_4 and CaMoO_4 . Experiments to produce laser quality crystals of $\text{Ca}_3(\text{VO}_4)_2$ are now under way.

Manuscript received March 28, 1964.

Any discussion of this paper will appear in a Discussion Section to be published in the June 1965 JOURNAL.

REFERENCES

1. G. Tammann, *Z. anorg. u. Allgem. Chem.*, **149**, 68 (1925).
2. J. Czochralski, *Z. physik. Chem.*, **29**, 219 (1917).

The Preparation of Semi-Insulating Gallium Arsenide by Chromium Doping

G. R. Cronin and R. W. Haisty

Texas Instruments Incorporated, Dallas, Texas

The preparation of high resistivity or semi-insulating¹ GaAs has been reported by several laboratories using a variety of methods (1-12). For example, it has been prepared by compensation involving copper diffusion, by addition of oxygen, by extensive purification, that is, by vertical zoning, and by doping with iron, cobalt, or nickel. These methods, however, have not been amenable to the preparation of material with resistivity as high as $10^6 \text{ ohm}\cdot\text{cm}$ by crystal pulling techniques. Attempts to pull single crystal semi-insulating GaAs by oxygen doping at this laboratory have not been entirely successful mainly due to the formation of oxides on the melt surface.

¹The term "semi-insulating" was first used by Allen (2) to describe materials whose resistivities are so high that the term "semi-conductor" seems inappropriate. For a more precise definition, we propose for the purpose of this paper to define as "semi-insulating," material whose resistivity lies in the range 10^4 - $10^{12} \text{ ohm}\cdot\text{cm}$. This range is the upper half of the 10^4 - $10^{12} \text{ ohm}\cdot\text{cm}$ arbitrary limits between conductors and insulators suggested by Spence (13).

Experimental Results

Our experiments have shown that semi-insulating GaAs with room temperature resistivity at $10^8 \text{ ohm}\cdot\text{cm}$ can be pulled consistently by doping with chromium. The minimum amount of chromium required is that concentration which just exceeds the concentration of the usual residual n-type impurities such as sulfur, tellurium, or silicon. Only on one occasion was low resistivity material obtained after the introduction of chromium. This crystal was grown before an effective segregation coefficient for chromium had been measured and was shown by spectrographic analysis to contain a higher than normal silicon content. Subsequent crystals were grown with chromium contents on the order of a few parts per million or less and have all been of the semi-insulating variety.

Table I. Properties of chromium-doped GaAs at 300°K

Crystal	Cr analysis (ppm by wt)	R_H (cm ³ /coulomb)	R_H/ρ (cm ² /v-sec)	ρ (ohm-cm)	Type	
					By Hall coefficient	By thermal probe
3-37	0.2-0.3	1.2×10^{11}	1130	1.06×10^8	n	p
3-41	0.4	2.8×10^2	2120	1.34×10^{-1}	n	n
3-42	0.2-0.5	8.8×10^{10}	256	3.43×10^8	n	p
3-44	0.4	3.5×10^{11}	630	5.61×10^8	n	p
3-45*	0.4-0.5	3.0×10^8 4.0×10^{11}	—	3.30×10^8	n	n
555-215	1.8	3.2×10^{11}	1120	2.84×10^8	n	p
555-216	3.5	2.9×10^{11}	693	4.17×10^8	n	p
3-50	360-400	1.3×10^{10}	614	2.15×10^8	n	p

* Crystal 3-45 inhomogeneous. Two values for Hall coefficient are measurements at each end of sample.

The crystals were all pulled on the (111) direction from melts compounded in the crystal puller. The details of this apparatus and its manipulation have been described previously (14). The chromium, in pellet form, was added directly to the gallium which was contained in an alumina crucible surrounded by a SiC-coated graphite susceptor. The purity of the gallium was 99.9999% while the arsenic was an equivalent grade made at Texas Instruments. The total charge weight was about 90g which included about 10% excess of arsenic over the stoichiometric quantity. The chromium content of each charge was between 100 and 200 mg.

The material was compounded slowly over a period of about 1 hr. Crystals were pulled at a withdrawal rate of 1.5 in./hr with a rotation speed of 25 rpm. The crystals tend to grow in what is approximately a tetrahedral shape and up to about 75% of the charge weight can be pulled. The crystals were cooled slowly to room temperature and their surface which was bright and shiny was apparently oxide free. Crystals grown under these same conditions but without addition of chromium have consistently been low resistivity n-type with excess carrier concentrations in the low 10^{16} cm⁻³ range.

Some data taken from a series of chromium-doped crystals are shown in Table I. The chromium content was obtained by emission spectrographic analysis. With the exception of crystal 3-41, referred to earlier, all of the crystals are semi-insulating. It is interesting to note that while sign of the Hall coefficient indicates n-type material in every case, the sign of the thermoelectric power determined by electrometer measurement indicates p-type material in all cases but one. The same result was obtained whether contact was made directly to the sample or by melting indium dots on the sample surface at about 375°C. Similar measurements on semi-insulating samples which were not doped with chromium have consistently checked n-type by thermoelectric power in agreement with the sign of the Hall coefficient. The difference in conduction type as measured by Hall coefficient and thermoelectric power for the chromium-doped samples would ordinarily be expected to occur only when the hole and electron concentrations are nearly

Table II. Cr⁵¹ in GaAs crystal 217 (300°K)

	Cr content (cm ⁻³)	R_H (cm ² /coulomb)	R_H/ρ (cm ² /v-sec)	ρ (ohm-cm)
Slice No. 5	1.03×10^{17}	9.7×10^{11}	1920	5.1×10^8
Slice No. 5	1.56×10^{17}	1.5×10^{11}	395	3.8×10^8

equal, but due to the large mobility difference between holes and electrons in GaAs there is a wider range of hole and electron concentrations over which this effect can occur, since the mobility ratio enters as the square in determining the sign of the Hall coefficient. In agreement with this possible explanation we do find that the Hall mobilities are generally low as would be predicted from this model. Another possible explanation for this anomalous behavior of conduction type would be the existence of small n-type regions in the predominantly p-type samples which influence the sign of the Hall coefficient due to the greater mobility of electrons. This seems unlikely, however, in view of the uniform distribution of chromium as shown by the autoradiograms.

In order to measure the effective segregation coefficient and the uniformity of distribution of chromium across the diameter, crystal 217 was grown with the addition of 211 mg of Cr⁵¹ enriched chromium in about 83g of material. Approximately half of the total melt was pulled. The crystal was cut perpendicular to the growth direction into 17 slices, numbered from top to bottom, and the chromium content of each slice was counted. Data from two slices near the top and bottom of the crystal are shown in Table II. Again the resistivity is in the 10^8 ohm-cm range while the chromium content varies by a factor of about 1.5 between these two slices representing total fractions solidified of 0.03 and 0.37, respectively. Autoradiograms of two of the slices in this crystal show that the distribution of chromium across the diameter of this particular crystal was very uniform with no evidence of "faceting" effects. A plot of $\log C/C_0$ vs. $\log (1-X)$, where C and C_0 refer to the chromium concentration in each slice and the initial melt respectively and X is the fraction solidified, yields an "effective segregation coefficient" of 6.4×10^{-4} .

In one instance a larger amount of chromium (about 1.5g) was added to the melt to determine whether the electrical properties would be affected. The resulting crystal, 3-50, had electrical properties similar to those containing a part per million or less chromium although, as shown in Table I, this crystal contained at least 400 ppm chromium. This high chromium concentration is difficult to reconcile with such a small segregation coefficient and therefore suggests the presence of a second phase. In this case the spectrographic analysis was checked and substantiated by wet chemical analysis. Metallographic examination of a section of this crystal disclosed the presence of small inclusions, metallic in appearance, which we believe are precipitates of chromium or a chromium compound. Attempts to confirm their identity with electron diffraction techniques have not yet been successful. Similar metal-

lographic examinations of crystals whose chromium content are in the low part per million range showed no evidence of these precipitates.

Discussion

Chromium doping is a convenient and very reliable method for producing semi-insulating GaAs. While we cannot as yet with certainty identify the mechanism by which this occurs, we can rule out some of the possible explanations.

If chromium introduced a deep donor level one should still observe low resistivity n-type material, since these crystals would have been low resistivity n-type without adding chromium. Thus the fact that chromium always produces semi-insulating material is an indication that it either introduces an acceptor or reduces the donor concentration enough to expose a deep level. To test this hypothesis further, crystal 3-59 was grown doped with both tellurium and chromium. Sufficient tellurium was added to the charge to produce a crystal whose excess n-type carrier concentration should range from 10^{16} cm^{-3} to 10^{17} cm^{-3} . The correct melt concentration had been determined from many previous tellurium-doped crystals. An amount of chromium calculated to exceed the tellurium concentration at the first to freeze portion of the crystal was also added. Most of the resulting crystal was again semi-insulating, and the electrical data shown in Table III indicate little if any difference between this crystal and those grown doped only with chromium. Near the very bottom, this crystal abruptly changed to low resistivity n-type, presumably where the tellurium concentration exceeded the chromium concentration as a result of the limited solubility of the latter. Similar attempts to counter dope with a shallow acceptor, for example, manganese or zinc, in melts containing chromium have not produced semi-insulating material (Table III), although analysis of the crystals shows that chromium was present in amounts in excess over other impurities. The hole concentrations in the p-type materials obtained were somewhat lower than expected. This effect, possibly the result of complex formation involving chromium, is under investigation and will be the subject of another paper.

There are at least three other possible explanations for the role of chromium in GaAs which should be considered.

1. Chromium, by gettering, reduces the concentration of shallow donors to expose an existing deep donor level when $N_D < N_A$ and $N_{DD} > (N_A - N_D)$.

2. Chromium is a relatively shallow acceptor which compensates the shallow donors to expose an existing deep donor level when $N_A > N_D$ and $N_{DD} > (N_A - N_D)$.

3. Chromium introduces a deep acceptor, (N_{AA}) possibly in combination with a defect or other impurity which is revealed when $N_{AA} > (N_D - N_A)$ provided that $N_D > N_A$.

At this time we feel the evidence weighs against a gettering action such as has been ascribed to tantalum in the growth of high resistivity AlSb by Shaw and McKell (15), for example. The evidence they got for this mechanism was a lowering of the hole concentration accompanied by an increase in mobility with the addition of tantalum, indicating removal of scattering centers rather than compensation. In our case the mobilities in the chromium-doped semi-insulating GaAs are much lower than expected, and in the low resistivity n-type crystal (3-41) which did contain some chromium the mobility was 2100 $\text{cm}^2/\text{v-sec}$, also a rather low value for pulled crystals with this carrier concentration.

The next two explanations involving chromium as an acceptor are somewhat more plausible. If chromium were a relatively shallow acceptor it would actually be a secondary cause of semi-insulating material, the primary cause being a deep level already present. In support of this explanation is the fact that plots of log resistivity vs. reciprocal temperature for several samples of chromium doped material show slopes corresponding to energies ranging from 0.73 to 0.80 electron volts. This is remarkably close to that reported for semi-insulating GaAs which contained no chromium (4, 5). However, calculations have shown that if the deep level already present is a donor, chromium, as a shallow acceptor must compensate the donors present rather exactly. Since we expect some variation in both shallow and deep donor concentrations, it seems unlikely that we would obtain such consistent results, unless some automatic compensation mechanism as discussed by Allen (2) were operative.

Chromium as a deep acceptor would not require such close compensation and perhaps is a more straightforward explanation. A deep level is certainly present and chromium behaves as if it were an acceptor. The exact location of the chromium level however is still uncertain and will require further investigation, possibly luminescence, photoconductivity, and infrared absorption measurements.

Regardless of the exact nature of the mechanism involved, the preparation of semi-insulating GaAs by chromium doping has several advantages:

1. The doping can be carried out easily in vertical crystal pulling equipment and thus provides a source of large single crystals of controlled orientation.

2. Under reasonable precautions which maintain purity, the doping concentration which achieves semi-insulating material is not a really critical factor, it being necessary only to exceed the concentration of the usual residual n-type impurities.

Table III. Properties of Cr-doped GaAs counter-doped with Te and Mn, at 300°K

Crys- tal	Analysis (ppm by wt)	R_H ($\text{cm}^3/\text{coulomb}$)	R_H/ρ ($\text{cm}^2/\text{v-sec}$)	ρ (ohm-cm)	$1/R_{He}$ (cm^{-3})
3-59	5Cr, 2Te*	6.5×10^{11}	1.7×10^3	3.9×10^8	
3-60	8Cr, 1Mn	6.5×10^3	1.6×10^2	4.1×10^1	9.6×10^{14}

* Te and Cr content of crystals 3-59 determined by solids mass spectrographic analysis.

Acknowledgments

The authors would like to thank the Semiconductor Physics branch of our laboratory for the Hall measurements, the Analytical branch for the chromium analyses, and G. Larrabee for the tracer work. We also acknowledge the support of the Electronic

Technology Laboratory of the Research and Technology Division, Air Force Systems Command, United States Air Force, under Contract Number AF 33(657)-9196 for part of this work.

Manuscript received Dec. 13, 1963. This paper was presented at the New York Meeting, Sept. 29-Oct. 3, 1963.

Any discussion of this paper will appear in a Discussion Section to be published in the June 1965 JOURNAL.

REFERENCES

1. J. Blanc, R. H. Bube, and H. E. MacDonald, *J. Appl. Phys.*, **32**, 1666 (1961).
2. J. W. Allen, *Nature*, **187**, 403 (1960).
3. J. Blanc and L. R. Weisberg, *ibid.*, **192**, 155 (1961).
4. R. W. Haisty, E. W. Mehal, and R. Stratton, *J. Phys. Chem. Solids*, **23**, 829 (1962).
5. C. H. Gooch, C. Hilsum, and B. R. Holeman, *J. Appl. Phys.*, **32**, 2069 (1961).
6. R. H. Bube, *ibid.*, **31**, 315 (1960).
7. F. A. Cunnell and R. Wickham, *J. Sci. Instruments*, **37**, 410 (1960).
8. J. M. Whelan and G. H. Wheatley, *J. Phys. Chem. Solids*, **6**, 169 (1958).
9. L. R. Weisberg, F. D. Rose, and P. G. Herkart, in "Properties of Elemental and Compound Semiconductors," Vol. 5, pp. 25-66, Interscience Publishers, New York (1959).
10. J. F. Woods and N. G. Ainslie, *J. Appl. Phys.*, **34**, 1469 (1963).
11. N. G. Ainslie, S. E. Blum, and J. F. Woods, *ibid.*, **33**, 2391 (1962).
12. W. J. Turner, G. D. Pettit, and N. G. Ainslie, *ibid.*, **34**, 3274 (1963).
13. E. Spenke. "Electronic Semiconductors," p. 3, McGraw-Hill Publishing Co., New York (1958).
14. G. R. Cronin, M. E. Jones, and O. W. Wilson, *This Journal*, **110**, 582 (1963).
15. D. Shaw and H. D. McKell, *Brit. J. Appl. Phys.*, **14**, 295 (1963).

Polycrystalline Silicon Films on Foreign Substrates

W. J. McAleer, M. A. Kozlowski, and P. I. Pollak

Electronic Chemicals Department, Merck Sharp & Dohme Research Laboratories, Rahway, New Jersey

Layers of silicon with crystallites up to 0.3×0.7 cm were prepared on graphite by a zone melting technique. Vapor deposition of silicon on foreign substrates by a chemical decomposition reaction (1, 2) yields layers with very small crystallites ranging from 2 to 200μ across (Fig. 1). Substantial increases in the size of the crystallites (Fig. 2) can be realized by passing a molten zone through the deposited layer and effecting a controlled recrystallization in the layer. The zone melting is accomplished using a 2.5 kw r.f. generator as power source, and the melting step is carried out in argon. Although the initial deposition step can be carried out with virtually any graphite, the melting step was much more critical in this regard. A variety of graphites were tested and found wanting, due to penetration of the molten silicon into the substrate which produced fractioning of the support. A graphite¹ with a scleroscope hardness of 72 and moderate

¹ United Carbon-UT 1.

density (1.65) was found to react with molten silicon at the graphite surface forming a SiC film. Residual silicon remained on the surface forming a semiconductor layer.

All graphites tested produced silicon layers with varying acceptor (p-type) levels undoubtedly due to group III impurities in the graphite. To produce uniformly and heavily n-doped layers the graphite slabs were pretreated with P_2O_5 in methylcellosolve. Employing this technique, layers could be produced with the following characteristics: n-type, 1-2 ohm-cm resistivity, $\mu = 190 \text{ cm}^2 \text{ v}^{-1} \text{ sec}^{-1}$ and $\tau = 0.5\text{-}1 \mu\text{sec}$. The very low mobility presumably arises from the general imperfection and contamination of the layers.

Preparation of Devices

Mesa diodes.—To the polycrystalline silicon layer was applied a solution of B_2O_3 in cellosolve (50%), and the layer was inserted into a quartz diffusion

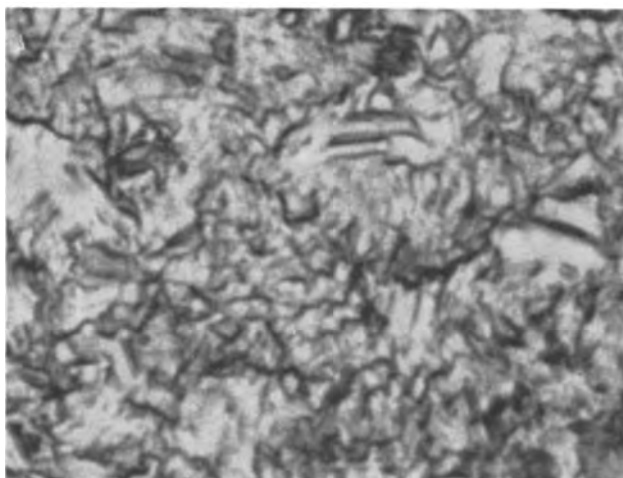


Fig. 1. Photomicrograph of surface of vapor deposited silicon layer on graphite. Magnification.

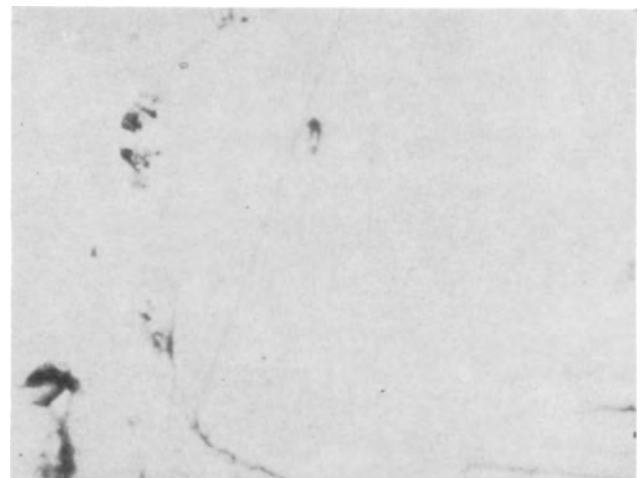


Fig. 2. Photomicrograph of zone melted silicon layer showing enlarged crystallites. Magnification.

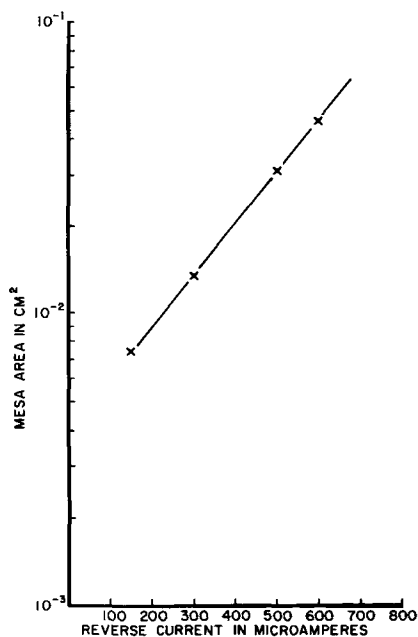


Fig. 3. Reverse currents as a function of mesa diode area

apparatus. The assembly was purged with N_2 for 15 min, closed off, and inserted into a Globar furnace set to 1523°K. Diffusion was continued for 17 hr. The assembly was removed from the furnace and allowed to cool to room temperature.

The layer was treated with hydrofluoric acid for 30 to 60 sec to remove a neutral glass-like film which forms during the diffusion operation. Following this operation the silicon was thermally probed and was found to be strongly p-type, demonstrating that boron diffusion had occurred. The freshly etched surface was covered with 1-2 mm dots of an acid resistant wax (Apiezon W) dissolved in toluene, and the layer was exposed to an IR heat lamp to drive off the solvent leaving the dry wax. The assembly was etched in modified CP-4 ($5HNO_3 : 3HF : 3HOAc$) for 1 to 2 min and immediately quenched in distilled water. The wax was removed from the etch produced mesa with toluene, and the layer was finally washed with distilled water and air dried. Reverse characteristics were measured dynamically using an oscilloscope. The mesas exhibited PIV's ranging from 40 to 90v with leakage currents as low as $100\mu a$. In the forward direction mesas 2 mm in diameter (0.03 cm^2) were found to pass 1.2 amp at 1v. This would be equivalent to $> 30\text{ amp/cm}^2$ at 1v.

The mesa area was found to affect critically the reverse characteristics of the diode. Figure 3 is a plot of reverse current (leakage) vs. area for four mesas formed on one layer of polycrystalline silicon. Leakage current varied from $150\mu a$ for a mesa of 0.0075 cm^2 to $600\mu a$ at 0.05 cm^2 . Mesas larger than 0.05 cm^2 gave progressively poorer reverse characteristics, and at an area of 0.2 cm^2 rectification was virtually eliminated.

Photovoltaic cells.—The silicon on graphite piece was placed in a quartz apparatus which was evacuated to 1 mm Hg pressure. Gaseous BCl_3 was introduced into the system pressure of 150 mm Hg, and

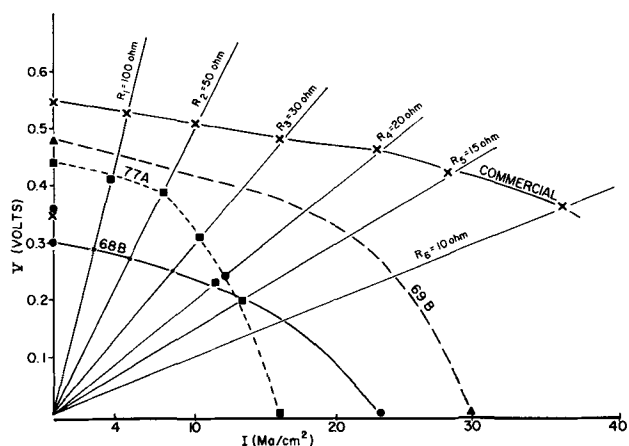


Fig. 4. Voltages and currents of photovoltaic diodes at various loads

the sealed ampule was inserted into a Globar furnace held at 1323°K. The diffusion was continued for 5 hr. Following the diffusion the assembly was removed from the furnace and allowed to cool naturally to room temperature. The piece was cut into several 1 cm^2 sections, and the edges were abraided and etched (CP-4) to avoid short-circuiting of the p-layer to the graphite contact. Edge contacts were provided to the p-layer by chemically plating nickel strips on the upper surface taking care to leave the largest portion of the layer free for illumination.

Leads were then provided from the photovoltaic cell to a Triplet multimeter (Model 630-NA) and various resistors were inserted in the circuit in parallel with the cell to enable one to examine the performance of the cells under different loading conditions. Figure 4 shows the results obtained with 3 polycrystalline cells and a standard single crystal cell ($\sim 9\%$ efficient). The current-voltage characteristics were determined at 100, 50, 30, 15, and 10 ohms resistance under identical illumination conditions (100 watt lamp mounted 12 cm from the cell). Referring to Fig. 4, it can be seen that the power output ($I \times V$) of the polycrystalline cells most closely approaches the single crystal cell at high loads (100-50 ohms) and thereafter falls off very rapidly. The maximum power output varies for each cell illustrated in Fig. 4 falling at around 15 ohms for cell No. 69B (6.5 mw/cm^2) and approximately at 30 ohms for cell No. 77A (3.1 mw/cm^2).

Acknowledgment

The authors express their thanks to Professor H. P. Kallmann for his helpful advice and discussions and to Drs. Conrad and Rosenberg for assistance in electrical and metallurgical examinations.

Manuscript received March 24, 1964.

Any discussion of this paper will appear in a Discussion Section to be published in the June 1965 JOURNAL.

REFERENCES

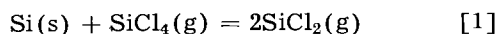
1. C. K. Teal, J. R. Fisher, and A. W. Trystow, *J. Appl. Phys.*, **17**, 879 (1946).
2. J. F. Elliott, R. E. Hysell, and C. L. Kolbe, Final Report 1/29/60-1/28/61, Contract No. DA36-039 sc 85286 ARPA Order No. 80-59, U.S. Army Signal Res. & Dev. Labs, Fort Monmouth, N. J.

A Kinetic Study of the System Si-SiCl₄

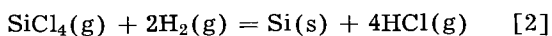
R. R. Monchamp,¹ W. J. McAleer,² and P. I. Pollak²

Electronic Chemicals Division, Merck & Company, Incorporated, Rahway, New Jersey

As an adjunct to the development of epitaxial programs several investigators have reported upon the kinetics of the hydrogen reduction of SiCl₄ (1-4) and SiCl₃H (5, 6). In all of these studies flow-type systems of one or more designs were used and, with the exception of Bylander's work, no direct study was made of the etching reaction.



Schäfer (7) has studied the SiCl₄-Si system to determine the equilibrium constant as a function of temperature by means of a manometric method. From his equilibrium experiments Schäfer concluded that the only important gaseous species in equilibrium with solid silicon were SiCl₄ and SiCl₂ over the temperature range 1125°-1300°C. No study of the equilibrium of the SiCl₄-H₂-Si system, *i.e.*, the hydrogen reduction of SiCl₄



has ever been reported. However, sufficient thermodynamic data are available to calculate equilibrium constants.

In their studies Theuerer (1) and Steinmaier (4) have shown that, as the ratio of SiCl₄/H₂ increases, the rate of deposition increases to a maximum and then decreases until the rate actually becomes negative. Considering the work of Schäfer it is reasonable to assume that the observed deposition rates are actually the net rate for two competing reactions [1] and [2]. Such a situation would explain the observed maximum and final negative rate, although no attempt has been made to modify the reduction data in these terms.

Second, because of the nature of flow systems the results of these investigations can only be interrelated by means of a system variable. Heinecke and Ing (8) in their study of the etching rates of germanium by elemental iodine found that they could not get reproducible kinetic data using an atmospheric flow type reactor. As a result they resorted to a low-pressure system from which they obtained "true kinetic data."

Similar results were obtained in this laboratory in some initial experiments. Using helium as a carrier gas for the SiCl₄ an activation energy of ~5 kcal was obtained which indicated that a mass transport phenomenon was the rate-controlling step. Furthermore, it was observed that the etch rate was significantly affected by the wafer orientation in the reactor. Therefore in order to investigate the SiCl₄-SiCl₃H-H₂ kinetics systematically, a low-pressure static system was devised to avoid the prob-

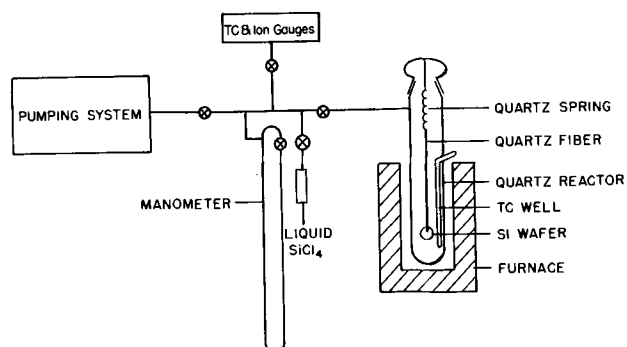


Fig. 1. Low pressure static system apparatus used to study SiCl₄-Si kinetics.

lems and variables associated with flow-type reactors. Considering all possible reactions which could be studied the simplest reaction, [1], was used as a starting point, and it is the kinetics of this reaction which are reported in this paper.

Experimental

The apparatus as shown in Fig. 1 was constructed from Pyrex glass with the exception of the reactor itself which was made of quartz. The pumping stage consisted of a fore pump, diffusion pump, and liquid nitrogen-cooled trap. The thermocouple and ion gauges were NRC types 501 and 518, respectively. The furnace was constructed from an Alundum core and heavy Nichrome winding. The temperature was measured with a Pt-Pt:13% Rh thermocouple seated in a well within the reactor and with a L&N potentiometer for reading the emf. In setting up the reactor the thermocouple was positioned opposite the center of the wafer.

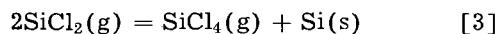
In operation silicon wafers which had been mechanically lapped with 600 mesh aluminum oxide were chemically polished with CP-4 etchant, washed, rinsed with absolute methanol, and dried in the reactor under vacuum. The wafers were 8 mils thick and 20 mm in diameter, having a 1 mm hole just off center for suspension. In this series only $\langle 111 \rangle \pm 1/2^\circ$ oriented wafers were used, and they were p-type, 89-116 ohm-cm. The wafer was suspended from calibrated quartz spring (Worden Laboratory) by means of a thin quartz fiber. The springs had sensitivities of 5-7 mg/mm. The system was evacuated to ca. 2×10^{-4} Torr and then 0.5 atm of high-purity dry hydrogen was admitted to the reactor chamber. The furnace was then raised and the wafer heated in the hydrogen atmosphere for 1 hr. The system was evacuated again to 2×10^{-4} Torr. SiCl₄ was then admitted to a pressure of 30-260 Torr, and the spring displacement was measured by means of a cathetometer as a function of time. Two sets of experiments were performed, one to

¹ Present address: Airtron, Division of Litton Industries, Morris Plains, New Jersey.

² Present address: Merck Sharp & Dohme Research Laboratories, Division of Merck & Company, Inc.

determine the pressure dependency at a particular temperature and the other to determine the temperature dependency at a particular pressure.

Since the upper part of the reactor is much colder, the reverse reaction



takes place in the cooler portions just above the furnace. By means of reaction [3] SiCl_4 is continuously being generated and can migrate to the silicon surface again to be reacted with it. As a consequence of these reactions [1] and [3] the reactor operates under steady-state conditions. The slope of the line of a plot of weight loss *vs.* time is the rate for that SiCl_4 pressure and temperature. For most of the runs only 5-10% of the total wafer weight was consumed with no reduction in wafer diameter being noted.

Discussion

Unlike the decomposition reaction of SiCl_4 , where the question has been raised as to whether or not the reaction occurs on or just near the silicon surface, the etching reaction must involve the silicon surface. The SiCl_4 pressure dependence for this reaction can be written most simply as follows

$$R = Kp^n \quad [4]$$

where R is the rate, K a constant, p the SiCl_4 pressure in the system, and n is the pseudoreaction order.

Figure 2 shows a log log plot of the pressure *vs.* rate data from which the slope of the line or n has been determined to be one-half. The equation derived from the data is

$$R = 1.41 \times 10^{17} p^{0.49} \quad (T = 1110^\circ\text{C}) \quad [5]$$

where R is expressed as $\text{at./cm}^2 \text{ sec}$ and p is in atmospheres.

An interpretation of the observed results is that the surface is partially covered by adsorbed reactant molecules since the value of n is one-half. For a zero order reaction, one which is pressure independent, n would thus equal zero indicating complete surface coverage by adsorbed reactant molecules. The

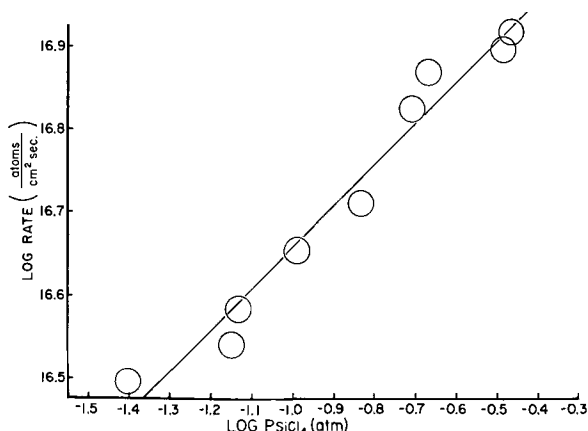


Fig. 2 Log rate *vs.* log P_{SiCl_4} plot for etching study at 1110°C ; rate = $1.41 \times 10^{17} p^{0.49}$; $T = 110^\circ\text{C}$.

other case which might have been anticipated is that the surface would be bare or sparsely covered by reactant molecules, in which case the reaction would be expected to demonstrate a first order-type pressure dependency, and the value of n would be one. Thus, the conclusion, based on an intermediate value of n , must be that the surface is partially covered by adsorbed molecules. This value of n should then vary with temperature and approach one at higher temperatures where adsorption decreases and conversely approach zero at lower reaction temperatures. An alternate interpretation of the results rests in the possibility that the reaction products, SiCl_2 molecules, may be involved in the rate-determining step. In this case the reaction is retarded by the adsorbed products strongly held on the surface.

The general rate equation which may then be written is

$$R = K \frac{P_{\text{reactant}}}{P_{\text{product}}} \quad [6]$$

If it is assumed that equilibrium conditions are approached near the surface of the wafer, then the equilibrium expression

$$K = \frac{P_{\text{SiCl}_2}^2}{P_{\text{SiCl}_4}} \quad [7]$$

may be solved for P_{SiCl_2} and this quantity substituted in the rate equation to give the following rate expression

$$R = K' P_{\text{SiCl}_4}^{1/2} \quad [8]$$

This alternate approach is in excellent agreement with the observed rate-pressure dependency.

The assumption of near equilibrium attainment close to the surface is not unreasonable when it is considered that the system is a static type in which the products must diffuse or be convected to the cold regions rather than be swept away by fresh unreacted gases.

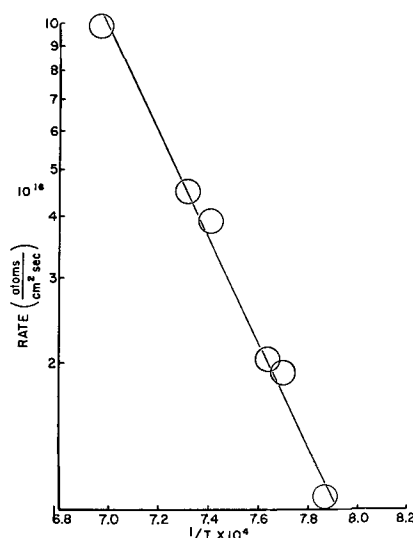


Fig. 3 Arrhenius plot of rate data at $P_{\text{SiCl}_4} = 112 \text{ Torr}$; rate = $10^{24.5} e^{-49,100/RT}$.

Figure 3 shows the rate *vs.* $1/T$ relationship from which an activation energy of 49 kcal was calculated for the reaction.

Equation [9] was calculated by the least mean square method to represent the data

$$R = 3.16 \times 10^{24} e^{-49100/RT} \quad [9]$$

The activation energy of 49 kcal when viewed in accordance with heterogeneous rate theory is in agreement with either of the proposed mechanisms. However, for a chemical reaction controlled mechanism this activation energy is on the high side (8-10), whereas a desorption controlled mechanism would be expected to have an activation energy in this range (10).

Unfortunately there is not sufficient molecular constant data in the literature for SiCl₂ to allow a theoretical calculation to be made for either of the mechanisms.

Manuscript received Dec. 20, 1963; revised manuscript received Jan. 24, 1964.

Any discussion of this paper will appear in a Discussion Section to be published in the June 1965 JOURNAL.

REFERENCES

1. H. C. Theuerer, *This Journal*, **108**, 649 (1961).
2. S. K. Tung, "The Influence of Process Parameters on the Growth of Epitaxial Silicon," in "Metallurgy of Semiconductor Materials, Metallurgical Society Conferences," J. B. Schroeder, Editor, **15**, pp. 87-102, Interscience Publishers, New York (1961).
3. E. G. Bylander, *This Journal*, **109**, 1171 (1962).
4. W. Steinmaier, *Philips Research Repts.*, **18**, 75 (1963).
5. J. M. Charig and B. A. Joyce, *This Journal*, **109**, 957 (1962).
6. R. Glang and E. S. Wajda, "Status of Vapor Growth in Semiconductor Technology," in "Metallurgy of Semiconductor Materials, Metallurgical Society Conferences," J. B. Schroeder, Editor, **15**, pp. 22-47, Interscience Publishers, New York (1961).
7. H. Schäfer and J. Nickl, *Z. anorg. allgem. Chem.*, **274**, 250 (1953).
8. W. J. Heinecke and S. Ing, Jr., *J. Appl. Phys.*, **32**, 1498 (1961).
9. J. I. Carasso and I. Stelzer, *J. Chem. Soc.*, 1797 (1960).
10. E. A. Moelwyn-Hughes, "Physical Chemistry," 2nd ed., pp. 1186-1199, Pergamon Press, New York (1961).

Epitaxial Growth of Silicon Carbide

R. W. Brander

Central Research Laboratories, The General Electric Company Limited,

Hirst Research Centre, Wembley, England

Single crystal silicon carbide is normally grown by the vapor phase sublimation technique, devised by Lely (1). This requires the use of very high temperatures, usually 2500°C, and a cavity, at least partially closed, in order to retain silicon vapor. Elaborate heat shields and accurately designed heaters are required to obtain the close control of temperature gradient necessary for the growth of flat platelets of single polytype.

Silicon carbide consists of layers of tetrahedrally bonded silicon and carbon atoms, stacked in such a way as to give cubic, rhombohedral, and/or hexagonal symmetry. The *c*-dimension of the hexagonal unit cell in the various polytypes depends on the exact number of layers necessary for the arrangement to repeat itself.

In order to obtain good quality growth it is essential to control the furnace conditions so as to produce only a slight supersaturation of the ambient, thus allowing the material striking the surface to migrate to lattice sites rather than nucleate to form new crystals. Too low a degree of saturation will allow the crystal surface to decompose. With a binary compound it is also necessary to provide the correct quantities of the two elements. An excessive quantity of one species settling on the surface will tend to result in the formation of inclusions in the grown layer.

The necessary vapors can be produced either by decomposing silicon carbide, or by cracking compounds such as SiCl₄ and CCl₄, or by vaporizing the elements silicon and carbon. The first mentioned

method resembles closely the vapor phase growth technique of Lely and has been used by Hergenrother *et al.* (2). It did not offer sufficiently variable conditions for the present experiments. The second method is similar to that used in the growth of β -silicon carbide or in silicon epitaxy and appears to require the presence of hydrogen. The third method is simpler to use and most variables can be altered independently, hence this technique was employed.

Material Preparation

Hexagonal silicon carbide crystals grown by the vapor phase technique were used throughout this work. The crystals were either obtained from the Norton Co., Arendal Co., or were grown in this Laboratory (3) by a technique similar to that described by Lely (1). Both flat parallel sided platelets and bulky crystals with one terraced face were used. Lapping, polishing, and etching were carried out as required.

The structure of silicon carbide results in opposite {0001} crystal faces being terminated in different atomic layers. It has been observed by Faust (4) and others that these opposite faces etch differently, one face exhibiting hexagonal pits while the other becomes "wormy." In this work the crystal face which exhibits the hexagonal pits will be referred to as the "p" face, and other as the "q" face. The growth on both {0001} faces was studied and the effect of substrate quality on the perfection of growth examined. Surfaces with various degrees of flatness were obtained by either lapping with 800

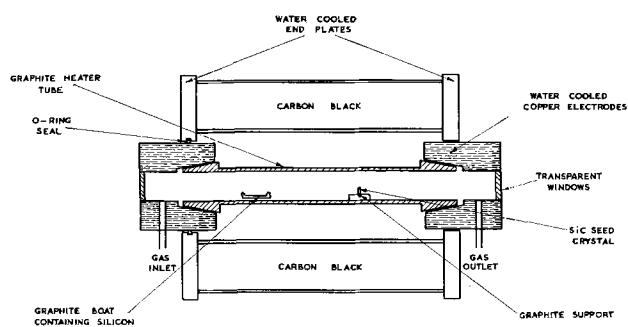


Fig. 1. Schematic diagram of furnace

Norbide, polishing with 1200 alumina or 1μ diamond, or chemically etching in 50% KOH/ KNO_3 or NaOH. The untreated surfaces of flat platelets grown by the vapor phase technique were also examined as substrates. All substrates were chemically cleaned before use to remove oxide, etc.

Crystal polytype and perfection were determined prior to growth by x-ray techniques and by etching to ascertain the etch pit density. The latter was carried out by etching in either NaOH, Na_2CO_3 or borax at temperatures in the range $800^\circ\text{--}1000^\circ\text{C}$. Two types of hexagonal pit can be observed, flat bottomed pits due to macroscopic imperfections at the surface, and tapering pits which occur where dislocations intersect the surface (5). The densities of these untruncated pits found on our seed crystals varied from 10 to 10^3 per cm^2 . The grown layers were similarly investigated for perfection.

Growing Technique

The furnace (Fig. 1) consisted of a long graphite tube of $\frac{3}{4}$ in. bore and 12 in. long heated by the passage of a high current. The crystal substrate was situated in or near the hottest part of the tube, the temperature of which could be varied up to 2700°C . The crystal surface was allowed to radiate freely to the ends or to the walls of the tube. The silicon source was contained in a boat of high density graphite situated in the cooler part of the tube in a position which could be controlled externally but was often fixed prior to the run. The vapor pressure of Si in the tube could thus be controlled within the range $10^{-4}\text{--}10^{-1}$ mm Hg.

Carbon vapor was supplied from the walls of the tube and the necessary vapor pressure above the specimen controlled by adjusting the position of the specimen and the maximum temperature of the tube. Carbon vapor pressures in the range $10^{-6}\text{--}10^{-2}$ mm Hg could be obtained in the absence of silicon. The vapors were carried over the specimen in a stream of argon at a rate of 0.05 to 1 liters/min. The degree of supersaturation above the crystal was regulated either by increasing the tube and source temperatures or by altering the position and temperature of the substrate. The exact nature of the molecular species transported was not determined, but it is most likely to consist of SiC_2 and Si_2C and Si (6).

The crystal substrates were mounted in a high density graphite holder in such a manner as to expose only one face to the vapors. In this way the

growth on individual faces could be investigated without any influence from the other face either during the run or in subsequent measurements.

A number of experiments were performed in which one single crystal was broken in two and then mounted in such a way that the same crystallographic face was turned towards the gas flow and away from it.

A similar arrangement was also employed in order to ascertain the growth rates on different crystal faces. In this case the crystal was broken and then mounted so that opposite crystallographic faces were facing the same direction with respect to the gas flow.

Results

Initial growth runs indicated that it was necessary to have the temperature of the carbon source about $600^\circ\text{--}800^\circ\text{C}$ higher than that of the silicon source in order to prevent the formation of silicon globules on the growing surface and silicon inclusions in the grown layer. It would appear from published vapor pressure data that this temperature difference ensures approximately equal vapor pressures from the two sources.

Growth rates.—The rate of growth of silicon carbide layers was found to vary with the orientation of the crystal in the furnace. Fastest growth was observed when the gas stream was directed onto the crystal face. The rate of growth fell off rapidly as the crystal was rotated towards the tube wall and was approximately 1/5th of the fastest rate when the crystal face was parallel to the direction of flow. Growth on the face shielded from the gas stream was slower still, being about 1/10th that of the fastest rate.

Growth rate could be easily varied by altering the various parameters of the system and rates from 0.05 to $5\mu/\text{min}$ were examined. Growth of $5\mu/\text{min}$ was achieved with the substrate at a temperature of 2200°C facing a gas flow of 500 cc/min, with silicon and carbon source temperature of 1800° and 2500°C , respectively. In this case the vapor pressures of the two elements would be of the order of 10^{-3} mm Hg. It was found that suitable reduction of the various temperatures and flow rate could produce any desired growth rate below this value. The above temperatures were measured optically and have not been corrected for emissivity.

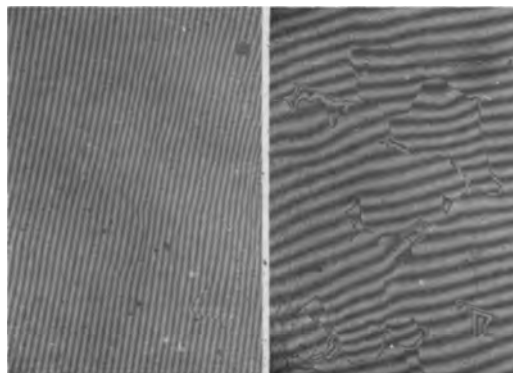


Fig. 2. Interference patterns on SiC epitaxial layer (slow growth rate). Magnification approximately 20X.

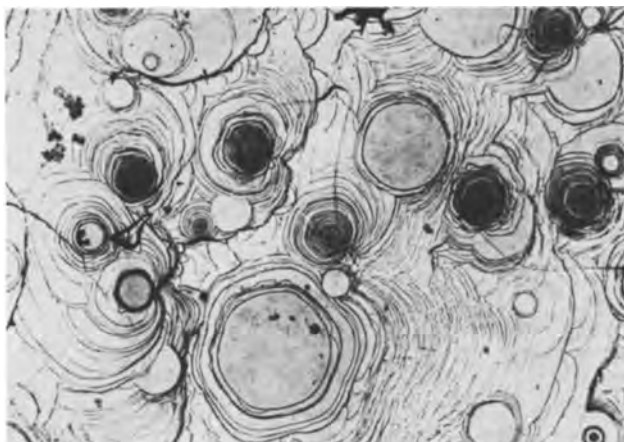


Fig. 3. Growth features on SiC epitaxial layer (fast growth rate). Magnification approximately 50X.

The above growth rates were measured on the p crystal face. The rate growth on the opposite {0001} face was also examined and this was found to be approximately half that of the growth rate on the p face under identical conditions of growth and substrate preparation. This fast growing face has also been observed to etch faster than face q (7).

Quality of growth.—Examination of the grown layers under a polarizing microscope, magnification 500X, showed that the three smooth substrates obtained with polished, etched, or untreated platelets produced layers of similar appearance when grown under similar conditions. At rates of $0.5 \mu/\text{min}$ or less it was found possible to grow layers on sheltered crystal faces which were flat to better than 1000\AA over an area of a few square millimeters (Fig. 2). Some areas had an irregular stepped structure of the type shown in Fig. 2b. Faster growth rates, exposure to the direct gas stream, or a rough substrate surface, resulted in uneven growth, an extreme example of which is shown in Fig. 3. Here the surface is composed of "hills" ranging up to 0.3 mm across and 10μ high.

The quality of growth was also investigated by etch pit studies. Observations showed that layers of the type shown in Fig. 3 had extremely large dislocation densities compared with that of the original crystal and often exceeded $10^3/\text{cm}^2$. The slowly grown flat layers showed appreciably fewer etch pits, the density being of the same order, or slightly greater than that on the seed.

X-ray examination of the grown layers showed that they were of a single polytype without any ob-

servable random stacking disorder. For growth temperatures above 1900°C the polytype was always identical to that of the seed crystal for the polytypes investigated, namely 4H, 6H, 15R, 33R, and 51R. The polytype of layers grown at lower temperatures was not so easily reproduced and a few layers of different polytype to the seed were observed. In all cases the layers were found to be single crystals over the whole area of the seed.

Conclusions

The experiments described in this paper show that good quality single crystal layers can be grown on silicon carbide seeds by a simple vapor phase technique without the need to obtain pure polycrystalline silicon carbide starting charges, or the necessity of cracking volatile compounds.

Good quality growth can be achieved at rates of $0.5 \mu/\text{min}$ as long as the vapor stream does not impinge on the growing face. With an impinging vapor stream rates of less than $0.1 \mu/\text{min}$ are necessary to produce relatively smooth surfaces.

Layers grown above 1900°C show perfect polytype reproduction of the substrate. Below this temperature the polytypism is often different to that of the seed, and if the temperature is sufficiently low polycrystalline cubic material may nucleate. Since the various crystallographic modifications are known to have different energy gaps, their controlled growth could be used as a method of producing heterojunctions.

It was also observed during these experiments that opposite {0001} faces grow at a markedly different rate under identical conditions of preparation and growth. In this case the hexagonal pitted face, which etches fastest in molten KOH/KNO_3 , was the fast growing face.

Manuscript received Aug. 12, 1963.

Any discussion of this paper will appear in a Discussion Section to be published in the June 1965 JOURNAL.

REFERENCES

1. J. A. Lely, *Ber. dent. keram. Ges.*, **32**, 229 (1955).
2. K. M. Hergenrother, S. E. Mayer, and A. I. Mlavsky, "Silicon Carbide," p. 60, Pergamon Press, New York (1960).
3. R. W. Brander and J. R. Martin, To be published by I.E.E.
4. J. W. Faust, Jr., "Silicon Carbide," p. 403, Pergamon Press (1960).
5. S. Amelinckx and G. Strumane, *ibid.*, p. 162.
6. J. Drowart and G. De Maria, *ibid.*, p. 16.
7. R. W. Brander, To be published.

Ta₂O₅ Films Formed with Nonsteady Potentials

D. A. Vermilyea

Research Laboratory, General Electric Company, Schenectady, New York

This note reports two characteristics of anodic Ta₂O₅ films formed with nonsteady potential and an observation of a new type of film formed with alternating potential. The first characteristic of films formed with nonsteady potential is observed for films formed by applying either an alternating

voltage or a pulsating direct voltage to a cell containing platinum and tantalum electrodes immersed in any of several aqueous solutions. Such films are thinner for a given peak formation voltage than films formed at a steady voltage equal to the peak voltage. For example, films were formed by apply-

ing half-wave rectified 60 cycle alternating voltage to a cell shunted by a resistance which reduced the potential to zero between pulses. The formation field (voltage applied 2 min) was 0.077 v/Å, while the corresponding value for films formed 2 min at a steady voltage was 0.0625 v/Å. If the pulsating potential was applied for 1 hr the field was 0.0726 v/Å, while for steady voltage it was 0.053 v/Å. The platinum potential measured against the saturated calomel electrode was +0.3v and did not change with either the pulsating or steady potential. With an alternating voltage of 10v maximum the field was about 0.08 v/Å. Films formed by one type of potential (for instance pulsating) to one thickness and then formed further with the other type of potential (for instance steady) had a formation field characteristic of the final type of potential.

The second characteristic is that films formed with nonsteady potential dissolve more slowly in hydrofluoric acid. For example films formed with either pulsating direct potential or alternating potential dissolved in 50% HF at about 12.5 Å/sec. Films formed one way and then another showed dissolution at a rate characteristic of the final type of formation.

Both of these characteristics, slower attack by HF and the requirement of a higher field for ion motion, are characteristic of films which have been annealed after formation (1, 2). Such annealing occurs even at room temperature and is accelerated by applied fields smaller than those required for ion motion. It is suggested that films formed with nonsteady potential are annealed during the portions of each cycle when the field is within the range of 100-75% of the maximum field.

When alternating potentials are applied in certain solutions a new type of film is formed. The solutions in which this phenomenon occurs are those containing alkali ions at fairly high concentrations. For example, with a 1M lithium chloride solution and an alternating potential of 10v maximum (20v peak to peak) the film formed on a ¼x1 in. tantalum coupon showed several orders of interference colors indicating thicknesses varying from 1000Å to 3500Å (at 10v a film formed at constant voltage was ~160Å thick). The figure shows a black-and-white photograph of the specimen; the colors indicated a thicker film at the edges where the current density was highest. Indeed, a high current density favors the effect, for in tenth molar solutions the effect was greatly reduced. Similar effects occur with lithium solutions containing other anions and is somewhat more pronounced in the order $\text{NO}_3^- <$

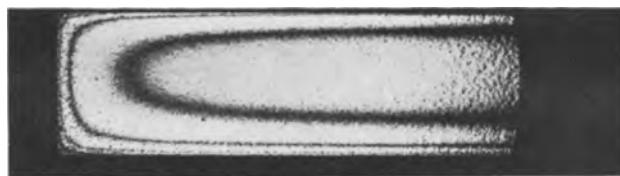


Fig. 1. Tantalum oxide film formed with an alternating potential of 10v maximum.

$\text{Cl}^- < \text{ClO}_4^-$, possibly because of differences in the conductivities of the various solutions. Greater differences exist among the alkali cations, the effect increasing in the order $\text{Rb}^+ \sim \text{K}^+ < \text{Na}^+ < \text{Li}^+$. In NH_4Cl , KCH_3COO plus 0.5M CH_3COOH , Mg_2SO_4 , $(\text{C}_2\text{H}_5)_4\text{NCl}$, and in solutions of Li^+ or K^+ at $\text{pH} < \sim 0.5$ the effect is absent. Apparently a condition for the occurrence of this phenomenon is the development of a high pH at the electrode surface during the portion of the cycle when tantalum is negative. In solutions containing buffers (NH_4^+ , acetic acid) or in solutions in which high pH cannot be reached because of precipitation of a hydroxide (Mg^{++}) or ion decomposition [$(\text{C}_2\text{H}_5)_4\text{N}^+$] the effect is absent. The capacitance of both the multicolored films and those formed in buffered solutions is the same and corresponds to a film about 160Å thick. These multicolored films dissolve completely on immersion for 2 sec in 50% HF. Underneath the multicolored film is a thin film which etches at the 12.5 Å/sec characteristic of films formed with pulsating potential. No such multicolored films were formed during pulsating direct potential formation.

Probably the anodic oxidation in the very high pH solution at the surface immediately following the half cycle in which the tantalum is negative forms soluble tantalates (3). As the pH falls these tantalates would hydrolyze to give Ta_2O_5 which would precipitate on the electrode. Such Ta_2O_5 would probably be gelatinous or porous and is evidently an electrical conductor rather than a dielectric. The properties of these multicolored films resemble strongly those of films formed during illumination with ultraviolet light (4).

Manuscript received Dec. 11, 1963.

Any discussion of this paper will appear in a Discussion Section to be published in the June 1965 JOURNAL.

REFERENCES

1. D. A. Vermilyea, *This Journal*, **104**, 427 (1957).
2. D. A. Vermilyea, *ibid.*, **104**, 485 (1957).
3. W. H. Nelson and R. S. Tobias, *Inorg. Chem.*, **2**, 985 (1963).
4. L. Young, "Anodic Oxide Films," p. 135, Academic Press, New York (1961).

Orientation of Stacking Faults and Dislocation Etch Pits in β -SiC

W. K. Liebmann

IBM-Laboratories, Boeblingen, Germany

SiC crystallizes in several modifications which exhibit either hexagonal, rhombohedral, or cubic crystal symmetry. All crystal modifications are identical with respect to their nearest neighbor arrangement and differ only with respect to the stacking sequence of SiC-tetrahedra in the direction of the hexagonal crystal axis (1). Epitaxial growth of one SiC modification on another along a plane normal to the hexagonal axis is thus possible without the incorporation of too many lattice defects at the interface.

In the preparation of SiC-single crystals by the Lely method (2) it is often found that hexagonal α -SiC crystals possess a thin epitaxial coating of cubic β -SiC. Fused salt etching (3) and subsequent optical microscopy have revealed markings in

these cubic layers which are reminiscent of the stacking faults in epitaxial Si (4, 5), and which will consequently be called stacking faults below. Figure 1 shows an example of such a stacking fault triangle on a $\{111\}$ β -SiC surface. All closed stacking fault triangles on a specific crystal are of the same size, indicating that the stacking faults nucleate at the sample depth, evidently at the α - β -interface. Aside from stacking fault triangles straight line segments are found, as shown, *e.g.*, at A in Fig. 2. These segments probably correspond to two very closely spaced extrinsic-intrinsic stacking fault pairs as found by Finch *et al.* (4) in epitaxial Si.

Triangular dislocation etch pits are formed at the corners of the stacking fault triangles and at the termination points of the straight stacking fault segments, marking the intersection points between the connecting stair-rod dislocations and the $\{111\}$ observation plane. Figure 3 demonstrates that both extrinsic and intrinsic stacking faults are possible. The two interacting stacking faults do not annihilate along their junction, but form a new fault terminating on both sides with dislocations.

It is interesting to note that the orientation of the stacking fault triangles and the triangular dislocation etch pits is reversed, even though both intersect with the $\{111\}$ observation plane along $\langle 110 \rangle$ directions. This means that either the stacking faults or the side faces of the dislocation etch pits do not consist of $\{111\}$ planes.

In the zincblende structure, the lowest energy plane which can lead to a stacking fault or an etch pit of opposite orientation from a $\{111\}$ fault is the $\{311\}$ plane. There are three sets of $\{311\}$ planes

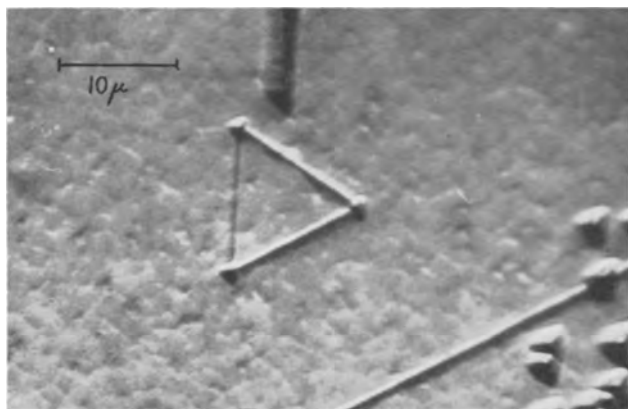


Fig. 1. Stacking fault triangle in β -SiC. Thickness of the epitaxial layer: 10μ ; etched with $\text{NaNO}_2 + 10\% \text{Na}_2\text{O}_2$ at 500°C for 10 min.

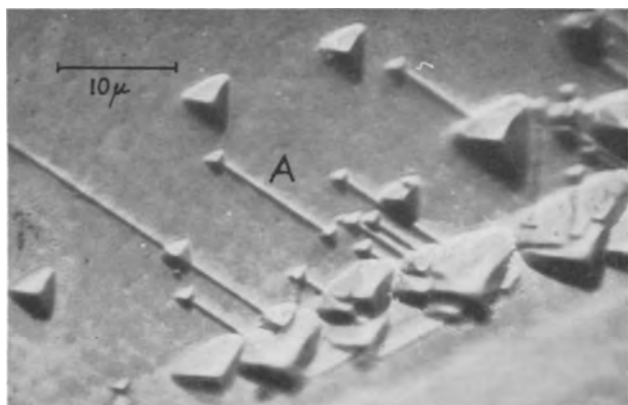


Fig. 2. Straight line stacking fault segment at A

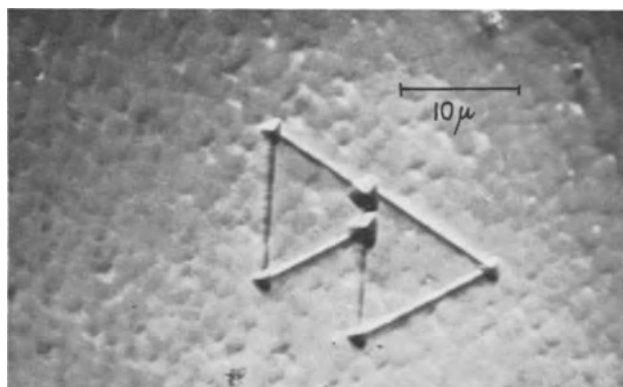


Fig. 3. Two interacting stacking fault triangles

Table I. Possible orientations of etch pits and stacking faults

	Etch pit orientation	Stacking fault orientation	h/a For stacking fault pyramids
A	{311} 29° plane	{111}	0.81
B	{311} 79° plane	{111}	0.81
C	{111}	{311} 29° plane	0.16
D	{111}	{311} 79° plane	1.6

intersecting with the {111} observation plane with intersection angles equal to 29° 30', 58° 31', and 79° 59'. Out of these three sets of planes only the 29° 30' and the 79° 59' planes are inclined opposite to the corresponding {111} plane and can thus form etch pits or stacking faults of the opposite orientation. Only these two planes intersect with the {111} plane along a $\langle 110 \rangle$ direction, while a pyramidal defect formed by three 58° planes would be slightly misoriented with respect to a {111} defect.

Assuming that the {311} plane is involved in the formation of the observed defects, the configurations listed in Table I are possible. The stacking fault orientations can be easily tested by computing the altitude "h" of the various possible stacking fault pyramids from their altitude to base ratio, h/a , and comparing it to the thickness of the epitaxial β -SiC layer. The values for (h/a) are also listed in Table I, and it can be seen that they are sufficiently different to use this method of differentiation. The thickness of the epitaxial layers was measured by angle lapping and subsequent etching, and in all cases very close agreement between the h/a ratio for a {111} stacking fault pyramid and the measured layer thickness was obtained. This establishes that the stacking fault planes are parallel to {111}, eliminating possibilities C and D. B would lead to a very steep etch pit, with a depth to side length ratio of 1.6, if the etch pit sides are not terraced. A, on the other hand, would lead to a very shallow etch pit, with a depth of side length ratio of 0.16. This ratio is actually found when measuring the depth of the etch pits by focussing a light microscope to their edge and to their bottom. This indicates that the etch pits are actually formed by three 29° {311} planes, even though electron microscope examinations will have to establish whether

the etch pit side actually corresponds to a lattice plane or whether it is terraced.

The formation of etch pits involving {311} planes can be understood if one uses the same criteria for the etching process which Sangster (6) developed to determine the most favorable growth direction. Following his arguments, the greatest etching rate will not occur in crystallographic directions normal to the most stable plane, but in directions normal to planes where the removal of individual atoms will not alter the net number of "dangling" covalent bonds, so that the formation of the first hole in a perfect crystallographic plane will not represent a serious energetic problem. In the zincblende lattice the {311} plane is the lowest energy plane where this condition is satisfied.

It is interesting to note that also in silicon thermal etching in vacuum produces triangular etch pits which are rotated 180° with respect to the orientation of stacking fault triangles (7). It thus appears that the {311} plane is of similar importance in elemental semiconductors and that also the formation of etch pits on the {111} planes of III-V compounds should receive further attention.

Acknowledgment

The author wishes to thank Dr. B. A. Unvala for suggesting the {311} plane, and Dr. H. G. Jansen for many helpful discussions.

Manuscript received Feb. 24, 1964.

Any discussion of this paper will appear in a Discussion Section to be published in the June 1965 JOURNAL.

REFERENCES

1. H. Jagodzinski and H. Arnold, Proc. Conf. Silicon Carbide Boston 1959, p. 136, Pergamon Press, New York.
2. J. A. Lely, *Ber. dtsch. Keram. Ges.*, **32**, 229 (1955).
3. J. W. Faust, Proc. Conf. Silicon Carbide, Boston 1959, p. 403, Pergamon Press, New York.
4. R. H. Finch, H. J. Queisser, G. Thomas, and J. Washburn, *J. Appl. Phys.*, **34**, 406 (1963).
5. T. L. Chu and J. R. Gavaler, in "Metallurgy of Advanced Electronic Materials," G. E. Brock, Editor, Interscience Publishers, Inc., New York (1963).
6. R. C. Sangster, in "Compound Semiconductors," Vol. I, R. K. Willardson and H. L. Goering, Editors, p. 241, Reinhold Publishing Co., New York (1962).
7. G. R. Booker and B. A. Unvala, submitted for publication to *Phil. Mag.*

The Effect of Orientation on the Electrical Properties of Epitaxial Gallium Arsenide

Forrest V. Williams

Central Research Department, Monsanto Chemical Company, St. Louis, Missouri

The anisotropic segregation of impurities in semiconductors has been well established. A dependence of the segregation coefficient on orientation has been reported for germanium by Hall (1) and by Dikhoff (2), for indium antimonide by Hulme and Mullin (3), and for gallium antimonide by Hall (4) and by Willardson (5). Apparently, the effect is general for the III-V compounds and has been re-

ported for a variety of solutes in the case of indium antimonide (6) and germanium (2). In the above cited examples the segregation being referred to is for the case of a solid-liquid interface; that is, a crystal growing in contact with its melt. In the present paper are reported some data which indicate anisotropic segregation of impurities at a solid-vapor interface.

Briefly, epitaxial layers of gallium arsenide were deposited on seed crystals of gallium arsenide oriented on $\langle 100 \rangle$, $\langle 110 \rangle$, $\langle 111 \rangle$ A, and $\langle 111 \rangle$ B planes. (The $\langle 111 \rangle$ B plane terminates with arsenic atoms.) An open tube system using hydrogen chloride as a transporting agent was employed. This method has been described in detail (7). The epitaxial layers were doped by either the use of doped gallium arsenide as a source or the use of a separate reservoir of the doping element in the vapor transport system. The chemically polished seed crystals were undoped, high resistivity ($>10^8$ ohm-cm) material which permitted the electrical properties of the epitaxial layer to be determined directly since the resistivities of the epitaxial layers were many factors smaller than the resistivity of the substrate. Wherever possible, seeds with different orientations were cut from the same high resistivity ingot. To eliminate the effect of slight run to run variations in flow rates, growth rates, and other variables, substrates with at least two different orientations were present in all experiments; four different orientations were present in some experiments.

Some representative data which have been obtained are summarized in Table I. Only net carrier concentrations are reported in this table, but the same differences are noted for the other electrical properties. This is shown for two experiments in Table II. The relative growth rates of epitaxial layers on the four orientations studied are shown in Table III. Comparison of the growth rates with the data of Table I indicates no relation between purity and the growth rate of the epitaxial layer. Thus, comparable carrier levels are obtained on epitaxial layers grown on $\langle 100 \rangle$ and $\langle 110 \rangle$ oriented substrates while the growth rates differ by a factor of about seven. On the other hand, widely different carrier levels are obtained on epitaxial layers grown on $\langle 111 \rangle$ B and $\langle 110 \rangle$ oriented substrates which

Table I. Net carrier concentration of epitaxial GaAs as a function of substrate orientation

Run	Dopant	Carrier conc, at./cc			
		$\langle 110 \rangle$	$\langle 111 \rangle$ A	$\langle 100 \rangle$	$\langle 111 \rangle$ B
1	None*	9.6×10^{15}	1.8×10^{16}	4.2×10^{16}	2.7×10^{17}
2	None*			3.0×10^{16}	3.4×10^{17}
3	S			3.7×10^{18}	5.8×10^{18}
4	Sn			3.0×10^{18}	7.6×10^{18}
5	Zn	9.0×10^{17}	2.2×10^{18}	1.5×10^{18}	5.8×10^{17}
6	Zn			7.3×10^{18}	3.2×10^{18}
7	Te	4.6×10^{16}	3.7×10^{16}	9.0×10^{16}	6.7×10^{17}
8	Te			1.4×10^{18}	1.1×10^{19}
9	Se	3.6×10^{17}		2.2×10^{17}	1.6×10^{18}

* Undoped runs gave n-type epitaxial layers.

Table II. Effect of substrate orientation on electrical properties of epitaxial GaAs

Run	Orientation	n	μ	ρ
10	$\langle 100 \rangle$	2.3×10^{16}	4420	0.062
	$\langle 111 \rangle$ B	1.7×10^{17}	3310	0.011
11	$\langle 100 \rangle$	2.7×10^{17}	3090	0.008
	$\langle 111 \rangle$ B	1.5×10^{18}	1660	0.002

Table III. Relative growth rates of epitaxial GaAs on different orientations

Orientation	Growth rate
$\langle 100 \rangle$	1.0
$\langle 111 \rangle$ A	0.9
$\langle 110 \rangle$	0.14
$\langle 111 \rangle$ B	0.10

have nearly equivalent growth rates. Clearly, the electrical properties obtained on epitaxial layers are governed by the crystal orientation of the substrate.

The following conclusions are evident from the data of Table I.

1. There is a marked difference in electrical properties of epitaxial layers grown on $\langle 111 \rangle$ B oriented substrates and layers grown on the other three orientations, $\langle 100 \rangle$, $\langle 110 \rangle$, and $\langle 111 \rangle$ A.

2. In the case of n-type doped layers, the doping level is much higher in layers grown on $\langle 111 \rangle$ B oriented substrates.

3. In the case of p-type doped layers, the doping level is lower in layers grown on $\langle 111 \rangle$ B oriented substrates than those grown on the other three orientations. Further, the magnitude of the differences between the orientations is smaller in the case of p-type dopants.

4. For n-type doped layers, the difference in doping levels on $\langle 111 \rangle$ B and $\langle 100 \rangle$ oriented substrates decreases in the order $\text{Te} > \text{Se} > \text{Sn} > \text{S}$.

These conclusions are more apparent from the data presented in Table IV which show the ratio of the carrier levels obtained in the four orientations as a function of dopant. Actually, this ratio can be viewed as the ratio of the segregation coefficients of the various impurities between the solid and vapor phase.

There are some striking similarities between the effects described here and those which have been reported for anisotropic segregation in the solid-melt systems referred to initially. These similarities are illustrated in Table V, in which some data are compared for the anisotropic segregation of impurities in crystals of InSb and GaSb grown from the melt and crystals of GaAs grown epitaxially from the vapor (data from Table IV). Anisotropic segregation of tellurium in a melt grown crystal of GaAs has been recently reported (11). The ratio of the segregation coefficient in the $\langle 111 \rangle$ facet to the segrega-

Table IV. Ratio of carrier concentrations on different orientations as a function of dopant

Dopant	n		
	$\frac{\langle 111 \rangle \text{B}}{\langle 100 \rangle}$	$\frac{\langle 111 \rangle \text{B}}{\langle 111 \rangle \text{A}}$	$\frac{\langle 111 \rangle \text{B}}{\langle 110 \rangle}$
None	11.0 (6)	15 (1)	28 (1)
Zn	0.43 (7)	0.20 (1)	0.49 (2)
Te	7.4 (8)	~ 20 (3)	~ 15 (1)
Se	6.3 (3)	—	4.4 (1)
Sn	2.3 (2)	—	—
S	1.4 (2)	—	—

Numbers in parentheses refer to the number of experimental runs.

Table V. Comparison of anisotropic segregation of impurities in crystals grown from the melt and from the vapor

Impurity	$k_{\langle 111 \rangle B / \langle 100 \rangle}$		
	InSb (melt)	GaSb (melt)	GaAs (vapor)
Zn	1.3		0.4
S	3.1		1.4
Sn	3.9		2.3
Se	5.4, 6.1, 5.7	1.5	6.3
Te	6.1, 8.9, 5.9	2.0	7.4

InSb, ref. (6); GaSb, ref. (5); GaAs, Table IV, this paper.

tion coefficient "on the surrounding material" was 2.6.

Several theories have been postulated to account for the orientation dependence of segregation coefficients. Originally, Hall (1) postulated that the incorporation of impurities into the crystal depended on specific adsorption of the impurities at the different growth interfaces. Others (6, 8) have attempted to rationalize the effect by consideration of the detailed mechanism of the growth process for the different orientations. Burton *et al.* (9) have proposed a transport theory to account for the variation of segregation coefficient with growth rate and orientation. An impurity diffusion layer at the growth interface is postulated in this theory. The segregation coefficient is a function of the thickness of this diffusion layer. Since the thickness of the impurity diffusion layer is also a function of stirring, this theory has proved useful in explaining the variation of segregation coefficients with stirring. This theory, however, has difficulty accounting for the variation of segregation coefficient with orientation. A dependence of the impurity diffusion layer on orientation is then invoked.

Gatos (10) has pointed out that adsorption phenomena alone can account for the anisotropy of segregation coefficients. The results of the experiments reported in the present paper support the original adsorption theory of Hall (1). The same general features of the phenomenon in the solid-melt interface system are observed in the solid-vapor interface system, where transport processes in the vapor should be negligible.

Of particular interest are the cases of the segregation of gallium in germanium and zinc in gallium arsenide. Dikhoff (2) found that gallium is incorporated less readily on the $\langle 111 \rangle$ planes of germanium than the other planes. As indicated earlier in this paper, zinc is less readily incorporated into the $\langle 111 \rangle B$ plane of gallium arsenide than the other orientations. These are the only reported examples of ratios of the segregation coefficient on the $\langle 111 \rangle$ to $\langle 100 \rangle$ orientation less than unity. However, there is no need, in the adsorption theory, to postulate that preferential adsorption is exhibited by the $\langle 111 \rangle B$ planes for all impurities. It is reasonable to assume that other examples will be discovered which display behavior similar to zinc and gallium.

The results of this paper imply that more pure GaAs could be prepared by the Czochralski technique if the seed crystal were oriented in the $\langle 100 \rangle$ or $\langle 110 \rangle$ direction. This result has been confirmed for the case of $\langle 110 \rangle$ oriented seeds in this laboratory.

Manuscript received Feb. 10, 1964. This paper was presented at the Toronto Meeting, May 3-7, 1964.

Any discussion of this paper will appear in a Discussion Section to be published in the June 1965 JOURNAL.

REFERENCES

1. R. N. Hall, *J. Phys. Chem.*, **57**, 836 (1953).
2. J. A. M. Dikhoff, *Solid State Electron.*, **1**, 202 (1960).
3. J. B. Mullin and K. F. Hulme, *J. Phys. Chem. Solids*, **17**, 1 (1960).
4. R. N. Hall and J. H. Racette, *J. Appl. Phys.*, **32**, 856 (1961).
5. R. K. Willardson, "Compound Semiconductors," Vol. 1, "Preparation of III-V Compounds," p. 189, Reinhold Publishing Co., New York (1962).
6. J. B. Mullin, *ibid.*, p. 378.
7. R. L. Newman and N. Goldsmith, *This Journal*, **108**, 1127 (1961); F. V. Williams and R. A. Ruehrwein, *ibid.*, **108**, 177C (1961).
8. W. P. Allred and R. T. Bate, *This Journal*, **108**, 258 (1961).
9. J. A. Burton, R. C. Prim, and W. P. Slichter, *J. Chem. Phys.*, **21**, 1987 (1953); H. E. Bridgers and E. D. Kolb, **25**, 648 (1956).
10. M. D. Banus and H. C. Gatos, *This Journal*, **109**, 829 (1962).
11. C. Z. Lemay, *J. Appl. Phys.*, **34**, 439 (1963).

A Thermal Probe for Segregation Detection

J. H. Westbrook, A. U. Seybolt, and A. J. Peat

Research Laboratory, General Electric Company, Schenectady, New York

Physical property measurement techniques which will permit detection of compositional variation over micron distances are still few in number. Some success has been achieved recently in the application of microhardness measurements for the detection of grain boundary segregation of solute elements in a variety of base materials (1-5). A limitation of this method is that for most materials the hardness indentation itself is of the order of 5-50 μ diameter and the region strained by the indenter a multiple of 2-3 times this. Thermal emf probes

have sometimes been suggested for sorting of unknown samples (6), measurement of diffusion gradients (7), or identification of inclusions (8). In the latter case several features were provided by the authors to facilitate the measurement and adapt it to problems requiring high resolution: an electrolytically sharpened tungsten probe tip, use of a microhardness tester for applying the probe to the sample, and heating one leg of the thermocouple, *i.e.*, the probe itself, rather than the test sample. The present article reports the adaptation of this

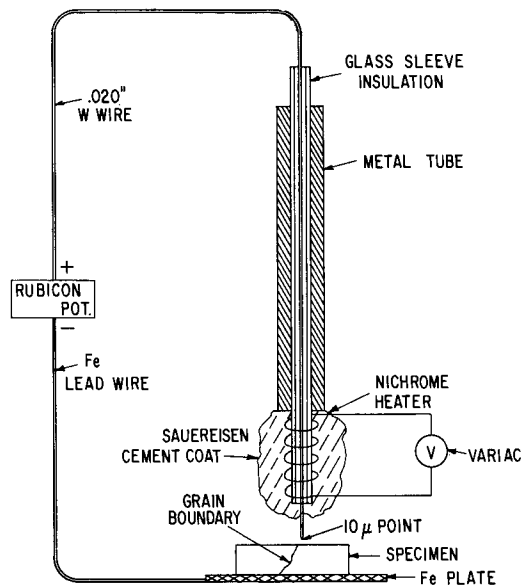


Fig. 1. Schematic drawing of thermal emf probe and associated equipment.

technique to the detection of grain boundary segregation.

Figure 1 shows a schematic drawing of the test equipment and the detail of the probe itself. The probe was formed by electrolytically etching a 0.020 in. W wire in a NaOH bath (9, 10). The wire was insulated with a woven glass sleeve, and this assembly was placed in a metal tube for rigid support. The heater was a 0.010 in. diameter Nichrome wire wound around the lower section of the insulated probe. This section of the probe was then coated with Sauereisen cement to hold the heater in place and to insulate the heater. The complete assembly was then mounted on a Kentron Microhardness Tester in place of the usual diamond indenter. Connections between probe and sample and measuring potentiometer were iron thermocouple wire. A small Variac provided variable power to the nichrome heating element.

Bicrystals, or coarse-grained polycrystals, of several intermetallic compounds (NiGa, NiAl, and AgMg) containing dissolved oxygen and dilute alloys of lead and of nickel were examined. Sample surfaces were prepared metallographically with a chemical polish or an electropolish as the final treatment. In a typical experiment a bicrystal of the compound NiGa, known to contain grain boundary segregated oxygen (3), was used as the test sample. A few preliminary experiments established that suitable experimental conditions were of the order of 10 μ probe tip diameter, 10g load on probe tip, and 5-20v on the heater. At heater voltages of this order negligible heating of the sample surface occurs since the probe temperature is estimated to be less than 200°C, and furthermore, the contact between the probe and specimen is only a few microns diameter. The sample and the thermoelectric circuit were protected from drafts by plexi-glass shields.

Typical experimental results are shown in Fig. 2a, which also presents a hardness profile for the

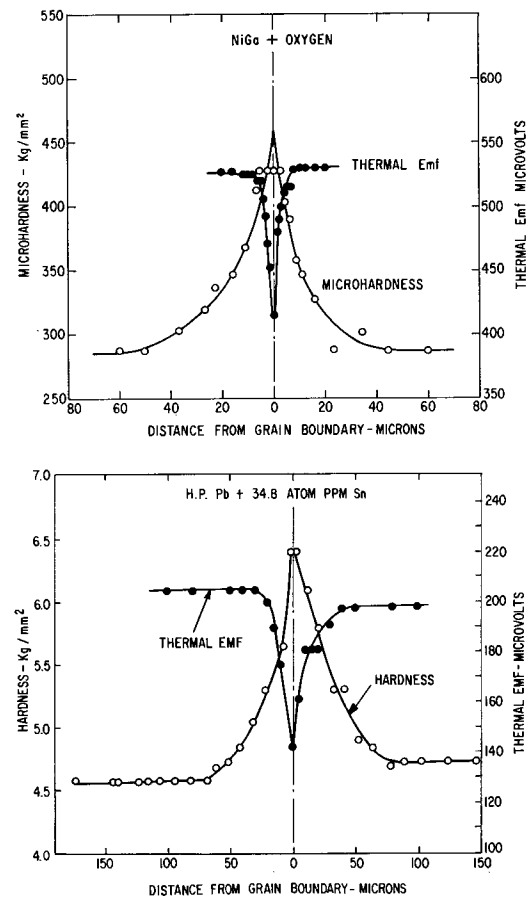


Fig. 2. Comparison of thermal emf and microhardness profiles at grain boundaries in (a) (top) NiGa (52 a/o Ga) containing oxygen and (b) (bottom) zone-refined lead with 34.8 at. ppm tin.

same specimen. The thermal emf is observed to fall about 25% in the vicinity of the grain boundary. The width of the affected region is somewhat smaller than that deduced from the hardness measurements, as would be expected from the greater resolving power of the finer probe. Figure 3 shows that the mean thermal emf increases in a regular manner as the heater voltage is increased, while

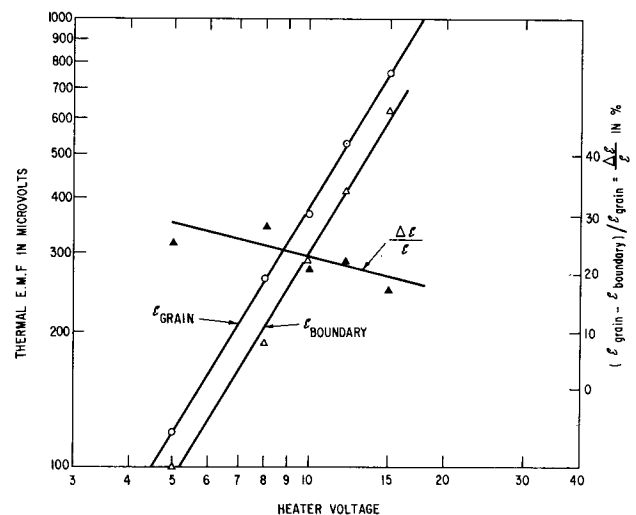


Fig. 3. Effect of temperature (heater voltage) on absolute and relative thermal emf in an oxygen contaminated grain boundary in NiGa containing 52 a/o Ga.

the relative change in thermal emf, grain *vs.* grain boundary, decreases only slightly.

Since the amount and distribution of grain boundary segregated oxygen in the intermetallic compound samples are not known, further experiments were carried out on bicrystals of zone-refined lead, some of which contained substitutional solute in parts per million concentrations. The zone-refined lead bicrystals with no added solute had previously been demonstrated to have extremely mobile grain boundaries whose microhardness was the same as that of the contiguous crystals. It is, therefore, inferred that impurity segregation in these samples is very slight. Thermal probe traverses across such a grain boundary gave an emf constant to within $\pm 5 \mu\text{v}$. On the other hand similar traverses across a bicrystal of the same zone-refined lead to which about 35 atom ppm Sn had been added exhibited sharp minima in thermal emf (about $60 \mu\text{v}$ change) and sharp maxima in microhardness as shown in Fig. 2b.

Previous investigations (2-5) have shown that quenching from a high temperature eliminates the grain boundary hardness peak, and from this it is inferred that the local gradient in the hardening agent is removed at the high temperature. Accordingly pairs of samples of the intermetallic compounds NiGa and NiAl containing oxygen at grain boundaries were both quenched and slowly cooled from high temperature. Comparison of thermal probe traverses showed that for quenched specimens the thermal emf was low and essentially constant over the length of the traverse whereas slowly cooled specimens showed a higher level of thermal emf together with a sharply cusped minimum at the grain boundary.

A peculiarity of the time dependence of thermal emf was observed in the tests. Upon initial contact of the probe with the specimen surface a certain potential could be measured almost instantaneously. This potential would then drift slowly higher for many seconds until a steady-state emf was reached of the order of 15-20% above the initial value. In surveys in which both the initial and steady-state emf were recorded as a function of distance from the grain boundary, parallel curves were obtained with both emf parameters exhibiting minima at the grain boundary.

Continued experience with this testing technique disclosed some difficulties. First, in attempts to calibrate the thermal emf with composition in a series of homogeneous specimens, no regular correlation was obtained. Next it was found that even on a single specimen the level of thermal emf was sensitively dependent on the method of preparation of the surface, on the time of exposure to room temperature air following polishing, and on the load applied to the probe. Although the regular decrease observed in room temperature thermal emf with time of exposure to air at room temperature (Pb) or elevated temperature (NiAl) suggests that oxide film thickness is of critical importance, attempts to standardize these conditions for calibration purposes were not notably successful. Nonetheless traverses

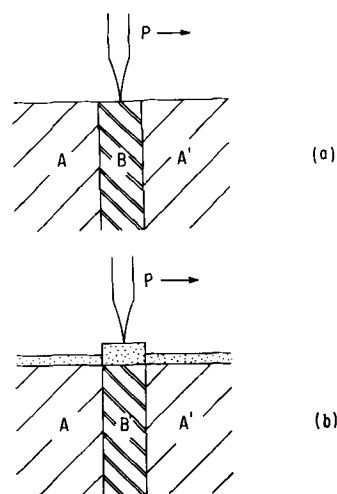


Fig. 4. Section through a grain boundary region showing schematically a composition change at the grain boundary, without (a) and with (b) oxide film formation.

on zone-refined lead or quenched intermetallics containing oxygen always showed constant emf across grain boundaries and slowly cooled specimens containing solutes always showed grain boundary minima in emf-distance curves.

Although the system is admittedly complex and the experiments inadequate to identify unambiguously the operative mechanism, an attempt will be made at least to describe the physical processes contributing to the observed results. For simplicity assume that the sample in the region of a grain boundary is a sandwich as in Fig. 4a, wherein a layer of material B at the grain boundary has one set of physical and chemical properties and the contiguous grain volumes A and A' another set of physical and chemical properties. A thermal probe, P, traversing such a region perpendicular to the grain boundaries should then develop an emf which for a number of reasons is dependent on its position.

First, this emf is primarily the Seebeck effect which will depend on the temperature difference ΔT between probe and sample and on the thermoelectric characteristics of the materials in the circuit. The temperature difference for a given power applied to the probe heater will depend on the thermal diffusivity or conductivity and the surface heat transfer coefficient. Since both these factors and the thermoelectric characteristics are expected to vary, A as against B, the over-all Seebeck emf will be expected to vary as the probe traverses the ABA' sandwich.

Since the thermal conductivity of the presumably more highly alloyed material, B, would be expected to be lower than that of A, a higher ΔT and hence a higher steady-state emf is to be expected at the grain boundary from this variable alone. The fact that only minima are observed indicates either (a) that cases are comparatively rare for which the variation in thermoelectric coefficient does not more than compensate for the effects of the variation in thermal conductivity, or (b) that some other dominating factor enters in. One such possibility is that in Fig. 4b, which illustrates schematically the for-

mation of oxide films of various thickness depending on the chemical characteristics of the substrates A and B. If B oxidizes faster than A, the film thickness at B will be greater than at A and, in accordance with the above observations on progressively oxidized surfaces, the resultant thermal emf from the probe less at B than at A. The slow increase in emf following initial contact of the probe might result from local build up of surface oxide about the tip of the hot probe insulating it and raising the effective ΔT . The model of a differential film thickness dominating the net thermal emf is also consistent with the observed difficulties in reproducibility, calibration, and deterioration.

Although it is obvious that much further work will be required to establish the details of the mechanism, the technique is attractive for several reasons. These reasons include: the fact that the measurement depends on a different group of properties than those of other grain boundary probe methods, the improved resolution, and the possibility of automated profile display on an x-y recorder.

Manuscript received Dec. 31, 1963.

Any discussion of this paper will appear in a Discussion Section to be published in the June 1965 JOURNAL.

REFERENCES

1. J. H. Westbrook and D. L. Wood, *Nature*, **192**, 1281 (1961).
2. J. H. Westbrook and D. L. Wood, *J. Inst. Metals*, **91**, 174 (1963).
3. A. U. Seybolt and J. H. Westbrook, *Acta Met.*, **12**, 449 (1964).
4. J. H. Westbrook and K. T. Aust, *ibid.*, **11**, 1151 (1963).
5. P. J. Jorgensen and J. H. Westbrook, *J. Am. Ceram. Soc.*, In press.
6. Antony Doschek, *J. Soc. Non-Destructive Testing*, **10**, 22 (1951).
7. B. I. Boltaks and V. P. Zhuze, *Zhur. Tekh. Fiz.*, **18**, 1459 (1948).
8. V. N. Novogrudskii and I. G. Fadikov, "Determination of Electromotive Force with a Modified Microhardness Tester," *Phys. Met. and Met.*, **7**, 99 (1959-1960) (Eng.) *Fiz. Met. i Met.*, **7**, 903 (1959) (Russian).
9. W. G. Pfann, U.S. Pat. No. 2,434,286 (1948).
10. F. G. Pany, Paper presented at Los Angeles Meeting, Electrochemical Society, Electronics Division Abstracts, No. 90, May 1962.

Electrode Potentials in Fused Systems

VII. Effect of Ion Size on Membrane Potentials

Kurt H. Stern and Judith A. Stiff

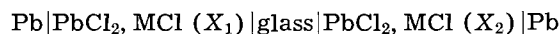
Electrochemistry Section, National Bureau of Standards, Washington, D. C.

ABSTRACT

Concentration cells exhibiting glass membrane potentials have been measured for the AgBr-NaBr, AgCl-KCl, and AgCl-CsCl systems. It is shown that cations from the melt diffuse into the glass and that sodium ion impurities in KCl and CsCl may transport a large part of the current. The possibility of anion transport through glass is suggested.

Although the literature on glass membrane potentials in aqueous systems is very large (1), virtually nothing has been published on this subject in molten salt systems. Several differences to be expected between the behavior of glass membranes in aqueous solutions and in molten salts are worth noting. In the molten salt there is no molecular solvent, and therefore the ionic concentrations are extremely high. When a glass is immersed in an aqueous electrolyte only its surface layers are in equilibrium with the solution (2). At the high temperatures usually employed for molten salt studies, glasses are considerably more permeable to ions, and it is to be expected that the glass will come to equilibrium with the melt at some approximately uniform ionic concentration in the glass. [For example, it has recently been shown (3) that even anions can migrate through fused silica under an applied potential.] This does not imply, however, that the relative ionic composition of the glass will be the same as in the melt when equilibrium is reached. Thus, sodium ions diffuse preferentially to potassium ions into the glass from a $\text{KNO}_3\text{-NaNO}_3$ melt containing only 1% NaNO_3 (4).

Studies (5) of the concentration cell



where $\text{M} = \text{Na}, \text{K}, \text{Li}$, showed that when $\text{M} = \text{Na}$ and the glass initially contained a considerable proportion of Na_2O all the charge was transported across the glass by sodium; when KCl was added no change in potential was observed, indicating that potassium ion did not penetrate into the Na glass. However, with a K glass and KCl in the melt the potential varied with melt composition although the slope was less than expected on the basis of potassium transport alone.

Recent studies (6,7) on similar concentration cells in the AgCl-NaCl system are generally consistent with the above findings, although the glasses used initially contained virtually no ($<0.04\%$) alkali metal ions. In treating the membrane region quantitatively a modification of liquid junction theory was successful.

In a simple liquid junction there are no phase boundaries and the solution composition changes smoothly and continuously from compartment A to

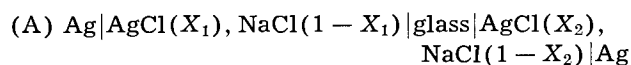
B. The general expression for the liquid junction potential is

$$E_J = (-RT/F) \int_A^B \sum_i \frac{t_i}{z_i} dl na_i \quad [1]$$

where the t_i 's are the transport numbers of the ions transported across the junction and the a_i 's are the corresponding activities. In a molten salt, e.g., in a solution of two salts with a common anion, the cation composition changes continuously from A to B in the junction and therefore the summation cannot be taken outside the integral sign. However, it has been found for a number of nearly ideal solutions (8,9) ($a_i = X_i$, the mole fraction) that $E_J \cong 0$, and that therefore $t_i = X_i$ (7,9,10).

When the liquid junction is replaced by a glass membrane it is reasonable to suppose that the latter controls ion transport so that t_i becomes largely independent of melt composition and can be taken outside the integral sign. We thus suppose that when pure silica is equilibrated with the melt all potential-determining ions migrate into the glass, but the fraction of the charge carried through it depends not only on melt composition but on some other parameter, such as ion size. Thus the ion activities in the glass need not be known since the two glass-melt interfacial potentials are of equal magnitude and opposite sign.

The above model may be regarded as a hypothesis to be tested experimentally. For example, in the cell reported previously (7)



$$E_{\text{cell}} = E_{\text{Nernst}} + E_{\text{M}} = RT/F [(1 - t_{\text{Ag}^+}) \ln (X_2/X_1) - t_{\text{Na}^+} \ln (1 - X_2)/(1 - X_1)] \quad [2]$$

where activities have been replaced by mole fractions because of the AgCl-NaCl system deviates only slightly from ideality (11,12), and the activity coefficient ratio as it would appear in Eq. [2] is nearly unity. Assuming charge transport by cations only ($t_{\text{Na}^+} + t_{\text{Ag}^+} = 1$), Eq. [2] then becomes

$$E_{\text{cell}} = t_{\text{Na}^+} (RT/F) \ln [(X_2/X_1)] [(1 - X_1)/(1 - X_2)] \quad [3]$$

Equation [3] was found to apply over the entire range of salt composition in both the AgCl-NaCl system with Vycor and fused silica glass (7) and to

the AgCl-(1:1 NaCl-KCl) system and Supremax glass (6). In these systems sodium carries 95% of the current through the glass, silver 5%. The usefulness of Eq. [3] lies in the fact that it can be applied to reference electrodes for sodium-containing melts even when nothing is known of the detailed charge transport mechanism in the glass itself, a situation not unlike that for glass electrodes in aqueous solution. In addition, the applicability of the equation provides an experimental test which theoretical models for membrane behavior must satisfy.

In the present work we examine the applicability of Eq. [3], and the model on which it is based, to the AgCl-KCl and AgCl-CsCl systems. If the glass contains only sodium ions, either present initially or carried into it by diffusion from KCl or CsCl where it is present as impurity, one might expect that Eq. [3] will no longer apply when, for example, potassium is substituted for sodium in the melt, and $(1 - X)$ represents KCl rather than NaCl. On the other hand, if the glass is merely an open Si-O network through which ions may migrate and in which a constant potassium ion concentration is set up Eq. [3] would apply. The situation may be more complicated if the glass acts as a sieve which permits ions to pass more or less easily on the basis of size, each ion carrying some of current. For example, Na^+ is smaller than Ag^+ (Pauling radii of 0.95 and 1.25Å, respectively) and Na^+ carries most of the current. Therefore, it is possible that sodium ions carry a large fraction of the current, though present only as impurity, in melts of potassium ($r_{\text{K}^+} = 1.33\text{Å}$) or cesium ($r_{\text{Cs}^+} = 1.69\text{Å}$) salts, whereas no corresponding term for sodium appears in Eq. [3]. In view of the fact that Littlewood (6) had observed the same alkali metal transport number in the AgCl-(1:1 NaCl-KCl) system as applied to the AgCl-NaCl system it seemed of interest to carry out similar measurements with varying KCl-NaCl ratios. In the present work we report on measurements with KCl:NaCl mole ratios of 12.4, 19, and 49. In addition, the AgBr-NaBr system was investigated to see if a change of anion affects the cation transport.

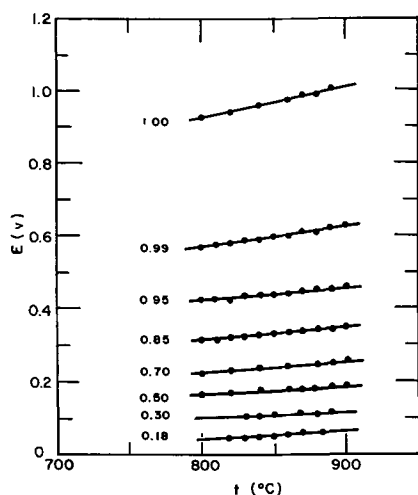


Fig. 1. Emf for the cell $\text{Ag} | \text{AgBr}(X_1), \text{NaBr}(1-X_1) | \text{Vycor glass} | \text{AgBr}(X_2), \text{NaBr}(1-X_2) | \text{Ag}$. $X_1 = 0.10$. X_2 values are shown to the left of the respective curves.

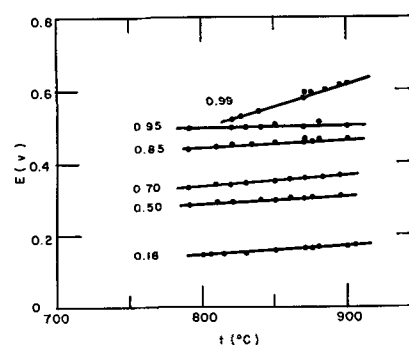


Fig. 2. Emf for the cell $\text{Ag} | \text{AgCl}(X_1), \text{KCl}(1-X_1) | \text{Vycor glass} | \text{AgCl}(X_2), \text{KCl}(1-X_2) | \text{Ag}$. $X_1 = 0.10$. X_2 values are shown to the left of the respective curves.

Experimental

Procedures were those reported previously (7). Reagent grade NaBr, KCl, and CsCl were dried at 500° under vacuum. It was noted that cells containing KCl and CsCl took considerably longer, 2 or 3 hr, than those with NaCl, before the emf-temperature curves became reproducible. Some cells containing both NaCl and KCl exhibited rapid and large (several hundred millivolt) fluctuations in emf. Since this phenomenon occurred at random, i.e., of two cells with the same melt composition one might exhibit the fluctuations while the other was quite steady, it may be associated with microscopic defects in the glass. Reproducibility of emf values for KCl-NaCl cells was also somewhat poorer (± 5 mv) than in the others.

Results

EMF data for cells B, C, D, and E are shown, respectively, in Fig. 1, 2, 3, and 4.

- (B) $\text{Ag}/\text{AgBr}(X_1),$
 $\text{NaBr}(1 - X_1)/\text{Vycor glass}/\text{AgBr}(X_2),$
 $\text{NaBr}(1 - X_2)/\text{Ag}$
- (C) $\text{Ag}/\text{AgCl}(X_1),$
 $\text{KCl}(1 - X_1)/\text{Vycor glass}/\text{AgCl}(X_2),$
 $\text{KCl}(1 - X_2)/\text{Ag}$
- (D) $\text{Ag}/\text{AgCl}(X_1),$
 $\text{CsCl}(1 - X_1)/\text{Vycor glass}/\text{AgCl}(X_2),$
 $\text{CsCl}(1 - X_2)/\text{Ag}$

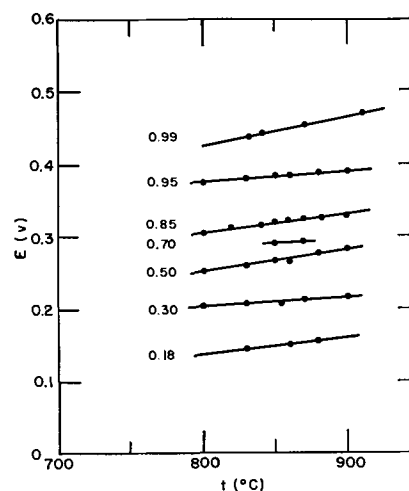


Fig. 3. Emf for the cell $\text{Ag} | \text{AgCl}(X_1), \text{CsCl}(1-X_1) | \text{Vycor glass} | \text{AgCl}(X_2), \text{CsCl}(1-X_2) | \text{Ag}$. $X_1 = 0.10$. X_2 values are shown to the left of the respective curves.

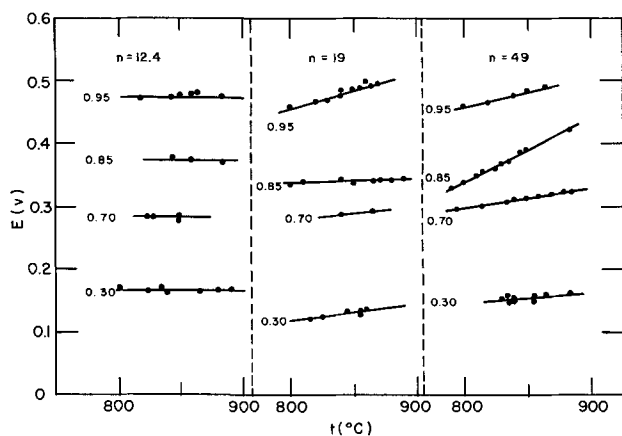
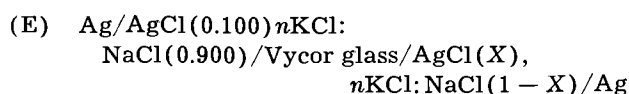


Fig. 4. Emf for the cell Ag | AgCl(0.100), n KCl:NaCl(0.900) | Vycor glass | AgCl(X), n KCl:NaCl ($1-X$) | Ag. X values are shown to the left of the curves.



for each value of n in (E) the same four values of X were used: 0.30, 0.70, 0.85, and 0.95. Only for $n = 49$ is the temperature coefficient appreciable. The analogous AgCl-NaCl and AgCl-KCl systems show only a very small temperature coefficient. In general, since transport numbers are nearly temperature-independent the cell emf would be expected to vary linearly with the temperature. Deviations from this behavior are most probably produced by the temperature dependence of ionic mobilities.

Discussion

For all of the systems the activity coefficient ratio is nearly unity (11-14) and activities can be replaced by mole fractions. If, as before, we assume charge transport by cations only and concentration-independent transport numbers in the glass

$$E_{\text{cell}} = t_+ (RT/F) \ln \left[\frac{(X_2)}{(X_1)} \frac{(1-X_1)}{(1-X_2)} \right] \quad [4]$$

where the X 's represent the mole fractions of the salts (or the cation fractions). As indicated in cells (B)-(D), $X_1 = 0.100$ and $X_2 = X$, $X_{\text{KCl}} + X_{\text{NaCl}} = 1 - X$ in cell (E). t_+ is the transport number of the alkali metal cation. Figure 5 is a plot of the log term of Eq. [4] vs. E_{cell} at 850° for the four systems with one alkali metal cation. For the AgCl-NaCl and AgBr-NaBr systems nearly the same straight line through the origin results, showing that, as expected, a change in anion does not affect the relative cation transport number. A least-square calculation yields for t_{Na^+} 0.93 in the bromide, and 0.95 in the chloride system.

The curves for the AgCl-KCl and AgCl-CsCl systems are quite different. They are not linear over the entire range of composition and apparently do not extrapolate to the origin. It follows that t_+ cannot be constant as implied in the derivation of Eq. [4]. Since the AgCl-NaCl and AgBr-NaBr plots are linear and pass through the origin the same value

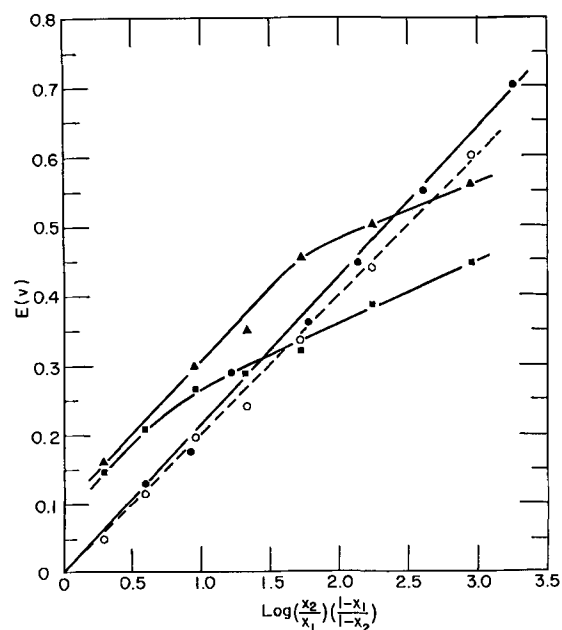


Fig. 5. Test of Eq. [1]: ●, AgCl-NaCl; ○, AgBr-NaBr; ▲, AgCl-KCl; ■, AgCl-CsCl.

of $t_+ = t_{\text{Na}^+}$ is obtained from the slope of the plot or by applying Eq. [4] to each point on it.

If t_+ is calculated for cells (C) and (D) from the individual points the results shown in Table I are obtained.

The results are in complete contrast to the Ag^+ - Na^+ systems for which a single value of $t_+ < 1$ is applicable. Moreover, the most unreasonable values of t_+ occur when the assumptions made in the derivation of Eq. [4] should hold best, i.e., at more nearly equal compositions of the two sides. These calculations imply that the alkali metal ion composition variables in Eq. [4] do not apply in any simple way to KCl and CsCl. Two possibilities are suggested: If the larger cations do not pass through the glass at all, sodium ion impurities in the salts may become potential determining; alternatively, these impurity ions carry a substantial fraction of the current, the larger ions carrying some of it also. To explore the first possibility we calculate the sodium ion ratio to be expected from the measured emf, assuming no transport by K^+ and Cs^+ (Table II).

Qualitatively the results are in a reasonable direction, i.e., as the composition of the two solutions approaches equality the Na^+ ion concentration ratios in the membrane do likewise, the higher concentration always occurring at the alkali halide rich end. If the results of, for example, cell C are to be ac-

Table I. Formal alkali metal ion transport numbers calculated from Eq. [4] ($X_1 = 0.100$) 850°

X_2	E (cell C), v	E (cell D), v	t_{K^+}	t_{Cs^+}
0.99	0.560	0.445	0.86	0.68
0.95	0.500	0.382	1.00	0.77
0.85	0.455	0.320	1.20	0.85
0.70	0.355	0.290	1.19	0.99
0.50	0.300	0.265	1.42	1.25
0.30	—	0.210	—	1.61
0.18	0.160	0.150	2.43	2.28

Table II. Sodium ion concentration ratios calculated for cells C and D from Eq. [4]

X_2	$(X_{Na^+})_1/X_{Na^+})_2,$ cell C	$(X_{Na^+})_1/X_{Na^+})_2,$ cell D
0.99	46.2	13.0
0.95	24.6	6.8
0.85	17.0	3.9
0.70	6.8	3.4
0.50	5.3	3.6
0.30	—	3.3
0.18	3.2	2.9

counted for by both sodium and potassium ion transport, we write instead of Eq. [4], (considering NaCl on both sides at sufficiently low concentration so that $X_{K^+} = (1 - X_{Ag^+})$ on both sides of the cell)

$$E_{cell} = RT/F \left[(1 - t_{Ag^+}) \ln \frac{X_2}{X_1} - t_{Na^+} \frac{X_2'}{X_1'} - t_{K^+} \ln \frac{(1 - X_2)}{(1 - X_1)} \right] \quad [5]$$

where the primed quantities refer to Na^+ . X_2' and X_1' were determined by flame photometry for $X_2=0.99$ and $X_1=0.10$, and found to be 0.73×10^{-4} and 1.1×10^{-4} , respectively. Equation [5] is then an equation in three unknowns: t_{Ag^+} , t_{Na^+} , t_{K^+} . Additional relations are provided by the definition $t_+ = 1$ and by the assumption that t_{Ag^+} is probably not altered significantly from its value of 0.05 in the AgCl-NaCl system. The results of this calculation are: $t_{Na^+} = 0.155$, $t_{K^+} = 0.795$. This is at least plausible, and suggests (within the limitations of the present model) that even when present in extremely low concentrations sodium carries an appreciable part of the cationic charge through the glass. Since sodium is appreciably smaller than all the other cations studied so far, it seems reasonable to conclude that for a given set of ions in the melt ionic size largely determines relative ion transport through the molecular structure of the glass. SiO_2 consists of a three-dimensional network of covalently bonded silicon-oxygen rings whose center is large enough to accommodate the passage of small ions. It seems reasonable to expect that the smallest ions in a melt would pass most easily through the glass.

The results of cell E may be used to gain some information on relative potassium/sodium transport. For $n = X_{KCl}/X_{NaCl}$ values of 12.4 and 19, plots of Eq. [4], (cf. Fig. 6), where $t_+ = t_{K^+} + t_{Na^+}$, lie on the AgCl-NaCl rather than on the AgCl-KCl line. However, for $n = 49$, i.e., 2% NaCl, there appears to be a shift toward the latter. This suggests that, as the sodium concentration in the melt becomes low, potassium ion begins to transport some of the current. Similar conclusions were also reached by Lengyel and Sammt (5) from their measurements in the $PbCl_2$ -KCl system and potassium glasses.

The results on cells A-D indicate that Eq. [4] must be applied cautiously, particularly in the design of reference electrodes (7); i.e., one should not assume *a priori* that the ions which are deliberately added to a cell are necessarily the ions to which the X 's

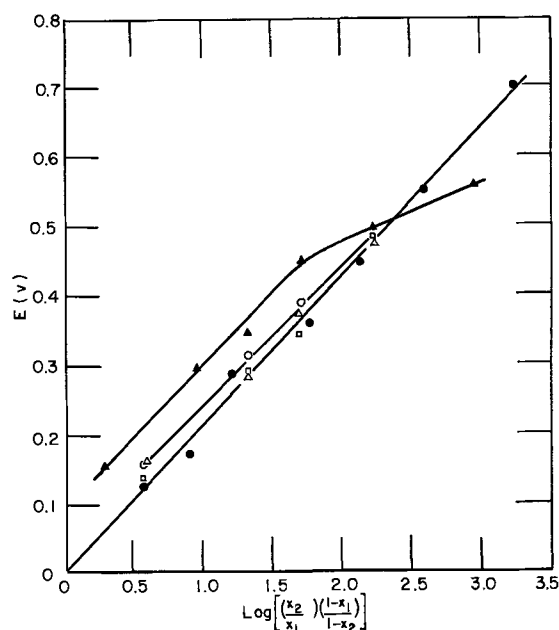


Fig. 6. Plot of Eq. [1]: Δ , $n = 12.4$, $n = 19$; \circ , $n = 49$; \bullet , AgCl-NaCl; \blacktriangle , AgCl-KCl.

apply. Thus, it is possible that an ion which does not explicitly appear as a cell constituent but is present as an impurity, e.g., sodium, is potential determining because it transports a large fraction of the current across the membrane. Such behavior was previously (7) observed in the AgCl-NaCl system where the sodium-ion impurity in reagent-grade AgCl ($X_{Na^+} \approx 10^{-4}$) is sufficient to provide for Na^+ transport across the glass membrane.

In the preceding discussion, as well as in previous studies of the AgCl-NaCl (7) and AgCl-(NaCl + KCl) (6) systems it was assumed that no charge is transported by anions. The assumption was made because, when the anion activity is equal on both sides of the cell, the term $d \ln a_- = 0$ and thus does not appear in the equation for the cell potential

$$E = (RT/F) [\ln X_2/X_1 - \sum t_i d \ln a_i] \quad [6]$$

i.e., the term in t_- does not appear explicitly. However, it does not follow that t_- is necessarily zero. Indeed, recent experiments (3) have provided direct evidence for anion transport through fused silica. For systems containing only one anion t_- may be made to appear explicitly by substituting

$$t_{Ag^+} + t_{Na^+} + t_- = 1$$

i.e.

$$1 - t_{Ag^+} = t_{Na^+} + t_- \quad [7]$$

into Eq. [2]. This gives

$$E = (RT/F) [t_+ \ln (X_2/X_1) (1 - X_1) / (1 - X_2) + t_- \ln (X_2/X_1)] \quad [8]$$

Equation [8] is an equation in two unknowns, t_+ and t_- , which can be evaluated from measurements of at least two cells. If the transport numbers are independent of composition, as assumed in the derivation, they will show a small standard deviation in a particular system.

All the data for the AgCl-NaCl and AgBr-NaBr systems are indeed well fitted by single values of t_+ and t_- as follows

	t_{Na^+}	t_-	t_{Ag^+}
AgCl-NaCl	0.985	-0.036	0.051
AgBr-NaBr	0.995	-0.236	0.241

These results, which suggest cationic halide complexes, do not appear very reasonable since these entities are very large compared with potassium and cesium ions and thus would not be expected to pass through the glass. They may be artifacts of the calculation. Studies on anion concentration cells now in progress on the AgCl-AgBr system should shed more light on the question of anion transport through glass.

At any rate, all of the results obtained so far for silver halide-alkali metal halide systems indicate that most of the charge is transported through the glass by alkali-metal cations. Although the present work does not rule out transport by such ions other than sodium it strongly suggests that sodium is far more effective in transporting charge than other ions, even when present in very low concentration.

Acknowledgment

Helpful discussions with Dr. Blanton Duncan are gratefully acknowledged.

Manuscript received Oct. 25, 1963; revised manuscript received March 12, 1964.

Any discussion of this paper will appear in a Discussion Section to be published in the June 1965 JOURNAL.

REFERENCES

- cf. G. J. Hills, Chap. 9 in "Reference Electrodes," D. J. G. Ives and G. J. Janz, Academic Press, New York (1961).
- cf. R. G. Bates, Chap. 5, in "Reference Electrodes," D. J. G. Ives and G. J. Janz, Academic Press, New York (1961).
- A. Berlin, Personal communication.
- B. v. Lengyel, *Z. phys. Chem.*, **167**, 295 (1933).
- B. v. Lengyel and A. Sammt, *ibid.*, **181**, 55 (1937).
- R. Littlewood, *Electrochim. Acta*, **3**, 270 (1961).
- K. H. Stern, *J. Phys. Chem.*, **67**, 898 (1963).
- R. W. Laity, Chap. 12 in "Reference Electrodes," D. J. G. Ives and G. J. Janz, Academic Press, New York (1961).
- K. H. Stern, *J. Phys. Chem.*, **63**, 741 (1959).
- I. G. Murgulescu and D. I. Marchidan, *Rev. Chim. Acad. de la Repub. Populaire Roumaine*, **3** [1] (1958).
- K. H. Stern, *J. Phys. Chem.*, **62**, 385 (1958).
- M. B. Panish, R. F. Newton, N. R. Grimes, and F. F. Blankenship, *ibid.*, **62**, 1328 (1958).
- J. H. Hildebrand and E. J. Salstrom, *J. Am. Chem. Soc.*, **54**, 4257 (1932).
- K. H. Stern, *J. Phys. Chem.*, **60**, 679 (1956).

Kinetics of the Anodic Dissolution of Nickel in Sulfuric Acid Solutions

Norio Sato and Go Okamoto

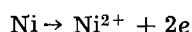
Division of Applied Chemistry, Faculty of Engineering, Hokkaido University, Sapporo, Japan

ABSTRACT

A kinetic study was made on the anodic dissolution of nickel in sulfuric acid solutions ranging in pH from 0 to 3. Rapid polarization and steady-state polarization techniques were used. The anodic polarization curve was found to change in appearance with time of polarization; the Tafel constant changed from its initial value of 0.5 to a steady-state value of 2. Increasing the pH of the solution shifted the anodic polarization curve in the direction of less noble potential, and the dissolution rate at constant potential therefore increased with the increase of OH⁻ ion concentration. The pH dependence of the dissolution rate was estimated to be $(\partial \log i / \partial \text{pH})_E = 1$ in the case of both rapid polarization and steady-state polarization.

Results analyzed in terms of electrochemical kinetics suggest the following consecutive steps for the anodic dissolution reaction: (a) Ni + OH⁻ → NiOH(ads) + e; (b) NiOH(ads) → NiOH⁺ + e; (c) NiOH⁺ → Ni²⁺ + OH⁻. The rate-determining step changes from step (a) to step (c) as NiOH⁺ ion concentration increases in the vicinity of the surface. The rate of anodic dissolution is controlled also by the amount of OH⁻ ion involved in a reaction cycle consisting of steps (a), (b), and (c).

The anodic reaction of nickel is an electrochemical reaction, and its over-all reaction is usually written as



The rate of the reaction depends on the electrode potential of nickel, and the relationship between the two can be obtained by the polarization of a nickel electrode. In polarizing nickel, however, the polarization state often varies with time, resulting

in a hysteresis of the polarization curve. This was first noted by Förster and Krüger (1) over thirty years ago, and thereafter was also found for iron (2, 3, 4) and cobalt (5). The factors controlling the rate of reaction and its time variation have been investigated by many workers (3, 4, 6). There is as yet no commonly accepted mechanism of anodic dissolution for nickel. In this investigation the polarization curve, its variation with time, and the effect of pH were measured, and the results are discussed in

terms of electrochemical kinetics leading to a mechanism for anodic dissolution in acid solution.

Experimental

Specimens of nickel sheets of 15 x 10 x 5 mm (~6 cm²) with small handles were made from electrolytic nickel melted in vacuum. After annealing at 800°C for 10 min each specimen was polished with 4/0 emery paper. The small handle was welded to a platinum lead and was sealed into a glass tube with an epoxy resin (Epilite No. 500) which required no heat-treatment to harden. Only a small surface area of the epoxy resin, less than 0.1 cm², was exposed to avoid contamination of the solution. The specimen was then degreased by swabbing with pure benzene and was etched with an equivolume mixture of concentrated H₂SO₄ and HNO₃ for about 1 min followed by washing with a jet stream of distilled water. The spectroscopic analysis of the specimen gave the following composition: Co 0.28%, Cr(-), Al 0.04, Mg(-), Mn 0.03, Ca(+), Zn(+), Ag(-), Cu(+), Sn(-), Pb(-), Fe(+), Ni balance, where the sign (+), refers to detectable elements and (-) refers to undetectable elements. Carbon and sulfur contents expected from the composition of the original electrolytic nickel are about 0.01% and 0.001%, respectively.

Solutions of various pH values up to 3 with a constant sulfate ion concentration of 0.5 mole/liter were used as the test solutions. They were prepared from redistilled water, A. R. grade sulfuric acid, and sodium sulfate.

The electrolytic cell was an air-tight container of hard glass with a capacity of about 500 ml; it had compartments for the specimen and for an auxiliary platinum electrode. A sintered glass filter was provided to connect the two compartments in order to avoid diffusion of hydrogen gas from the platinum cathode to the surface of the specimen. Dissolved oxygen and other impurities in solution were carefully removed by pre-electrolysis with a platinum cathode of 10 cm² in the specimen compartment for several hours at a current density of 5 ma/cm² and by bubbling pure nitrogen gas (O₂ < 0.001%) for one day before the experiments. All the experiments were performed in static solutions saturated with pure nitrogen gas at temperatures of 25° and 40°C.

A rapid method (4) was used to obtain polarization curves without changing the original surface conditions. In this method the polarization curve is rapidly determined by applying a successive stepwise change of current at certain fixed short time intervals using an oscillograph. The usual type of galvanostat and electronic potentiostat were used for measurements of (a) steady-state polarization curves, (b) time variation of polarization potential, and (c) time variation of anodic current. The potentiostat had a current capacity of 150 ma; the response time for potential variation was about 10⁻² sec/v.

The potential of the specimen was measured with reference to a saturated calomel electrode using a fine pointed tip Luggin capillary placed at about 0.05 cm from the specimen surface. The potential was converted to the standard hydrogen scale.

Results

In Fig. 1 the anodic polarization curves of nickel in a static solution of 1N H₂SO₄ at 40°C (obtained by the rapid method) is compared to that obtained by the steady-state method. In the rapid method a stepwise increase of the current was made in a short time (1 sec), and the potential at each current was measured about 0.2 sec after changing the current; this was long enough for charging the electrochemical double layer at each value of current. The steady-state polarization was usually attained about 30 min after applying the anodic current. In the present experiments the anodic current of nickel is equivalent to the dissolution current of nickel because of the absence of hydrogen and oxygen gases in the solution.

In comparing the two curves it is to be understood that in galvanostatic polarization the potential changes with time in two different ways. One is the change toward the noble potential in the relatively

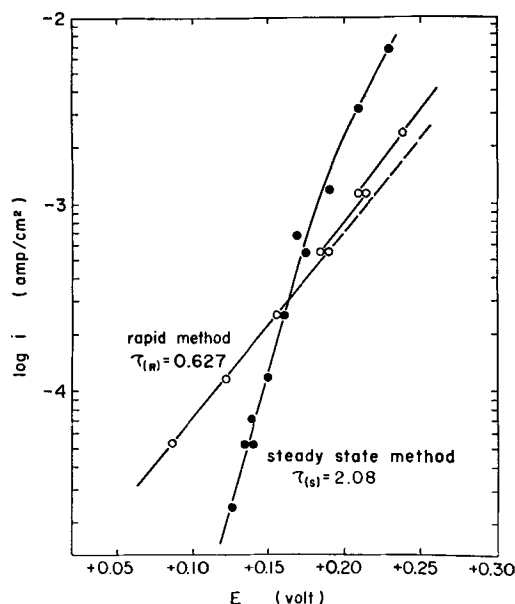


Fig. 1. Anodic polarization curves of nickel obtained by means of rapid polarization and steady-state polarization. Electrolyte, 1N H₂SO₄ saturated with N₂; 40°C; $\tau = \frac{RT}{F} \left(\frac{\partial \ln i}{\partial E} \right)$, Tafel constant.

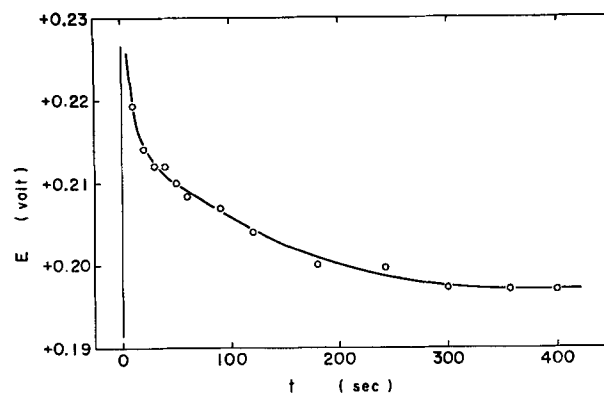


Fig. 2. Time variation of polarization potential of nickel during galvanostatic polarization at a relatively large anodic current of 2.32 ma/cm². Electrolyte, 1N H₂SO₄ saturated with N₂; 25°C; $i = 2.32$ ma/cm².

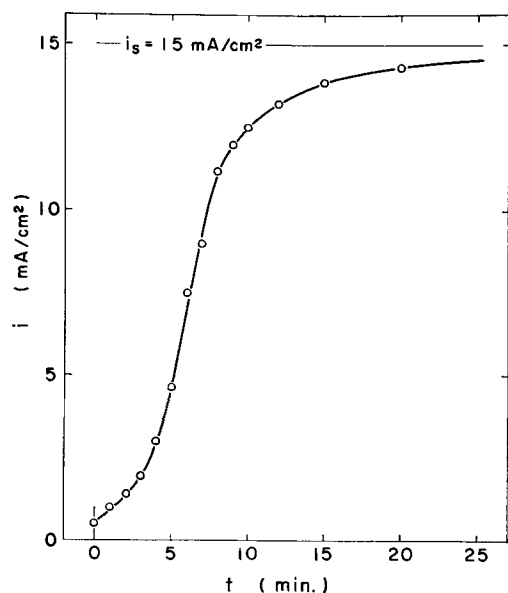


Fig. 3. Time variation of anodic dissolution current of nickel during potentiostatic polarization at a relatively noble potential of + 0.25v. Electrolyte, 1N H₂SO₄ saturated with N₂; 25°C; E = + 0.25v.

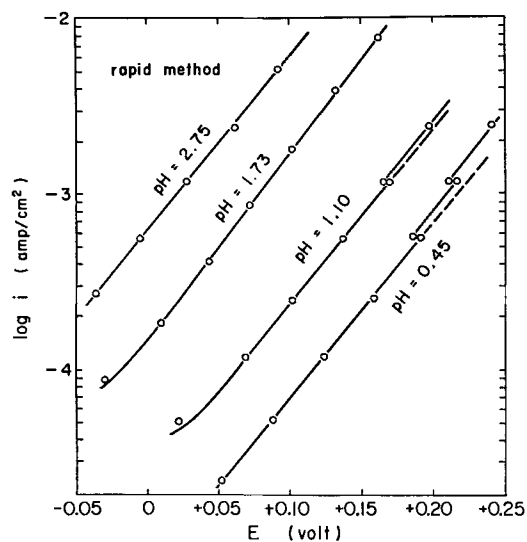


Fig. 4. Effect of pH on the rapid anodic polarization curve of nickel. Electrolyte, solutions of 0.5M SO₄²⁻/1 saturated with N₂; 40°C.

low current region, and the other toward the less noble direction in the high current region. An example of the latter is shown in Fig. 2. In potentiostatic polarization, correspondingly, the change of anodic current with time is observed. Figure 3 shows the increase in anodic current with time during the potentiostatic polarization at a relatively noble potential. In the less noble potential region, conversely, the anodic current decreases with time.

In Fig. 1 the rapid polarization curve is seen to fit the Tafel relation ($E = a + b \log i$) over a wide range of current density. This Tafel line moves with constant slope toward the less noble potential with increasing pH of the solution as shown in Fig. 4. The slope of these Tafel lines and the corresponding Tafel constant, as is seen in Table I, are almost independent of pH, and the mean values for the two are respectively as follows

Table I. Slope of the Tafel line and Tafel constant for the rapid polarization curves of Fig. 3

pH	Slope of Tafel line, 40°C $b_r = \left(\frac{\partial E}{\partial \log i} \right)$	Tafel constant $\tau_r = \frac{RT}{F} \left(\frac{\partial \ln i}{\partial E} \right)$
0.45	0.098	0.633
	0.091	0.682
	0.100	0.621
	0.109	0.570
1.10	0.092	0.674
	0.099	0.627
1.73	0.096	0.646
	0.110	0.564
2.75	0.130	0.477
	0.120	0.517

$$b_r = (\partial E_r / \partial \log i)_{40^\circ\text{C}} = 0.105\text{v} \quad [1]$$

$$\tau_r = \frac{RT}{F} (\partial \ln i / \partial E_r) = 0.60 \quad [2]$$

The pH dependence of the polarization potential at constant anodic current can be obtained from the curves in Fig. 4. Figure 5 gives a numerical value of the pH dependence

$$(\partial E_r / \partial \text{pH})_{1 \text{ ma/cm}^2} = 0.105\text{v} \quad [3]$$

This value should be independent of the anodic current because of the parallel shift of the polarization curve in Fig. 4. Accordingly, the effect of pH on the anodic current at constant potential can be estimated by combination of Eq. [1] and [3]. Thus

$$\lambda_r = (\partial \log i / \partial \text{pH})_{E_r} = 1 \quad [4]$$

Figure 6 shows the steady-state anodic polarization curves of nickel in solutions of three different pH values. It is seen that the curve obeys the Tafel relation only in a relatively narrow range of current density which depends on the pH of the solution. The

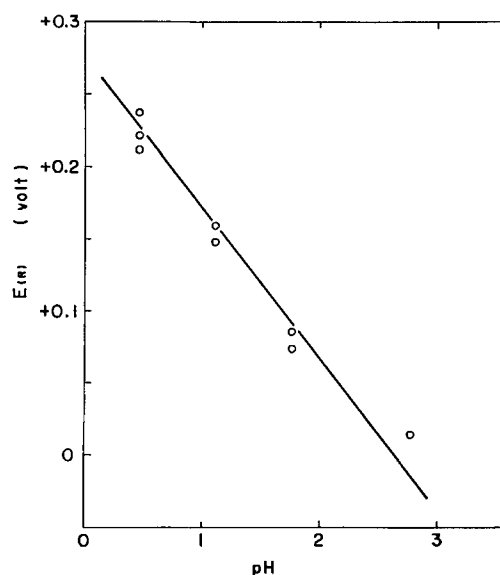


Fig. 5. Effect of pH on the rapid polarization potential of nickel at constant anodic current, derived from the curves of Fig. 4. $i = 1 \text{ ma/cm}^2$; $\left(\frac{\partial E(r)}{\partial \text{pH}} \right)_{1 \text{ ma/cm}^2} = 0.105\text{v}$.

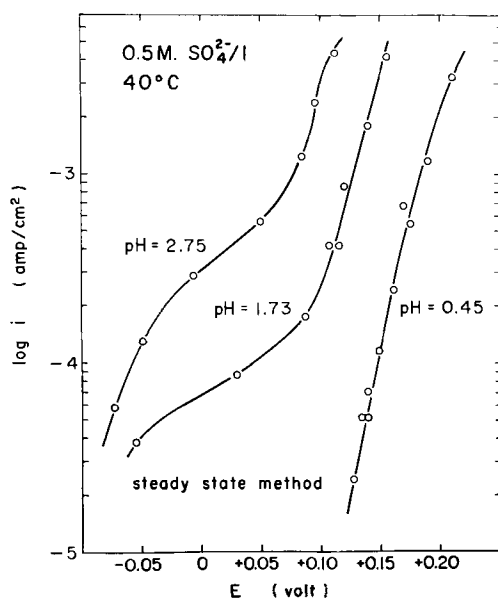


Fig. 6. Effect of pH on the steady-state anodic polarization curve of nickel. Electrolyte, solutions of 0.5M $\text{SO}_4^{2-}/\text{l}$ saturated with N_2 ; 40°C.

slope is nearly independent of pH and is close to 0.03v corresponding to a Tafel constant of 2;

$$\tau_s = \frac{RT}{F} (\partial \ln i / \partial E_s) \approx 2 \quad [5]$$

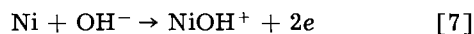
By combining both values of the slope of the Tafel line and the pH dependence of the steady polarization potential at constant anodic current shown in Fig. 7, the effect of pH on the steady anodic current at constant potential is obtained for the potential range where the Tafel relation is established

$$\lambda_s = (\partial \log i / \partial \text{pH})_{E_s} \approx 1 \quad [6]$$

Discussion

Mechanism of anodic dissolution by rapid polarization.—If the anodic dissolution of nickel is a single step reaction represented by $\text{Ni} \rightarrow \text{Ni}^{2+} + 2e$, no effect of pH on the anodic polarization curve should be observed. This, however, does not agree with the results described above.

To explain the results, a reaction involving OH^- ion is assumed for the anodic dissolution of nickel, that is



where NiOH^+ is a complex ion which has been ascertained by several workers (7). According to electrochemical kinetics (8), the rate of this reaction can be derived if the rate-determining step is established. Thus, if this reaction is a single step reaction, the rate would be given by

$$i = k'[\text{OH}^-] \exp \{2\alpha EF/RT\} \quad [8]$$

where k' is a constant, $[\text{OH}^-]$ the concentration of OH^- ion, and α the symmetry factor of the step.

From the standpoint of kinetics, reaction [7] may be divided into two elementary consecutive steps

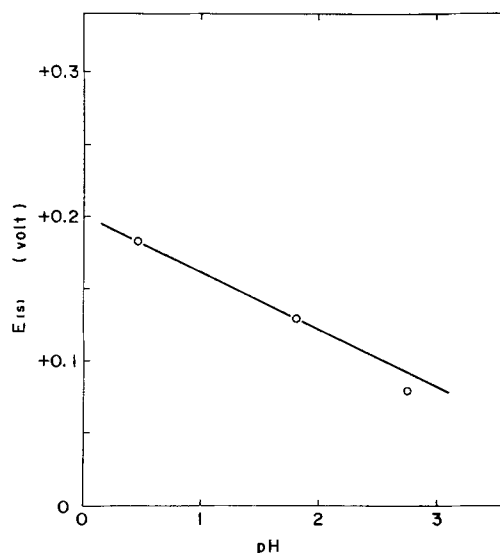
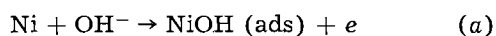


Fig. 7. Effect of pH on the steady-state polarization potential of nickel at constant anodic current. The current region is that where the Tafel relation was established (Fig. 6). $i = 1 \text{ ma/cm}^2$; $\left(\frac{\partial E(s)}{\partial \text{pH}}\right) 1 \text{ ma/cm}^2 = 0.036\text{v}$.



where $\text{NiOH}(\text{ads})$ is an activated complex adsorbed on the nickel surface. By applying the kinetics of consecutive reactions (8), the rate equation of the over-all reaction can be derived for both cases of the rate-determining step (a) and (b). Thus, for step (a), the rate of the over-all reaction is given by

$$i = k_a [\text{OH}^-] \exp \{\alpha EF/RT\} \quad [9]$$

where k_a is a constant and α the symmetry factor of step (a).

If step (b) is rate determining, the derivation of the rate equation for the over-all reaction results in two different ones depending on whether x_{NiOH} , the surface coverage of $\text{NiOH}(\text{ads})$, is much smaller than its maximum value or is nearly equal to the maximum value. The rate of step (b) is

$$i_b = k_b [\text{NiOH}(\text{ads})] \exp \{\alpha EF/RT\} \quad [10]$$

where k_b is a constant, α the symmetry factor, and $[\text{NiOH}(\text{ads})]$ is the concentration of $\text{NiOH}(\text{ads})$ on the surface. If $x_{\text{NiOH}} = K [\text{NiOH}(\text{ads})]$, then

$$i_b = k'_b x_{\text{NiOH}} \exp \{\alpha EF/RT\} \quad [11]$$

where $k'_b = Kk_b$. Since step (a) can be regarded as in quasi-equilibrium

$$[\text{NiOH}(\text{ads})] = K_a [\text{OH}^-] \exp \{EF/RT\} \quad [12]$$

where K_a is a constant. Equation [12] is valid only when $x_{\text{NiOH}} \ll 1$. Substitution of Eq. [12] into Eq. [10] or [11] gives the rate of the over-all reaction

$$i = k_b K_a [\text{OH}^-] \exp \{(1 + \alpha) EF/RT\} \quad [13]$$

When $x_{\text{NiOH}} \rightarrow 1$, Eq. [13] is no longer valid, and the rate is simply given from Eq. [11]. Thus

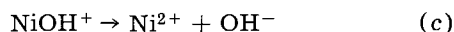
$$i = k'_b \exp \{\alpha EF/RT\} \quad [14]$$

From Eq. [8], [13], and [14] the Tafel constant and pH dependence of the reaction rate can be cal-

culated for each reaction mechanism; these are tabulated in Table II. In calculating the Tafel constant from the above rate equations, the symmetry factor α of the rate-determining step was assumed to be approximately 0.5.

Since in the rapid measurement of polarization no change of the surface conditions including the OH^- ion concentration in the vicinity is expected to occur, the rate-determining step can be inferred from the comparison between the rapid polarization curve and the rate equation derived theoretically for each reaction mechanism. It is seen that the Tafel constant τ_r and the pH dependence λ_r obtained from the rapid polarization curve are both in agreement with those calculated for rate-determining step (a). This leads to the conclusion that under the constant surface conditions the anodic dissolution proceeds according to the consecutive steps (a) and (b) in which step (a) is the rate-controlling one.

Mechanism of steady anodic dissolution.—The complex ion NiOH^+ produced by anodic dissolution tends to dissociate to Ni^{2+} and OH^- ions in acid solution by virtue of the value of the dissociation constant: $K_c = [\text{NiOH}^+]/[\text{Ni}^{2+}][\text{OH}^-] = 10^5$ (7).



This dissociation may occur in a solution layer adjacent to the surface with the rate given by

$$i_c = 2k_c F [\text{NiOH}^+]$$

where k_c is the rate constant. If the rate of dissolution is much smaller than the surface reaction (a) + (b), the concentration of NiOH^+ ion in the solution layer increases with time up to the equilibrium concentration for the surface reaction which is given by

$$[\text{NiOH}^+] = K_{(a)+(b)} [\text{OH}^-] \exp \{2EF/RT\}$$

where $K_{(a)+(b)}$ is a constant. The anodic dissolution rate for the rate-determining reaction (c) then is given as

$$i = 2k_c K_{(a)+(b)} [\text{OH}^-] \exp \{2EF/RT\} \quad [15]$$

Furthermore, if the diffusion of Ni^{2+} ion produced by dissociation (c) is controlling the anodic dissolution rate, the rate equation of the over-all anodic dissolution is written as follows, assuming the attainment of quasi-equilibrium for the surface reaction (a) + (b) and dissociation (c)

$$i = 2F(D_{\text{Ni}^{2+}}/\delta_{\text{Ni}^{2+}})(K_{(a)+(b)}/K_c) \exp \{2EF/RT\} \quad [16]$$

where $D_{\text{Ni}^{2+}}$ is the diffusion coefficient of Ni^{2+} ion, $\delta_{\text{Ni}^{2+}}$ the thickness of diffusion layer. The Tafel constant τ and pH dependence λ for the two cases of Eq. [15] and [16] are shown in Table II.

Although the concentration of NiOH^+ ion in the solution layer just over the surface increases with time, the concentration of OH^- ion may not change during the anodic polarization by virtue of the rapid diffusion of OH^- ion. A constant OH^- ion concentration at the surface may be attained in the solution of relatively large concentration of OH^- ion or in the relatively small current density region. If this

Table II. Tafel constant and pH dependence of anodic dissolution of nickel. These are derived theoretically for the various possible reaction steps listed, assuming the symmetry factor $\alpha = 0.5$

Reaction step	Tafel constant $\tau = \frac{RT}{F} \left(\frac{\partial \ln i}{\partial E} \right)$	pH dependency $\lambda = \left(\frac{\partial \log i}{\partial \text{pH}} \right)$
$\text{Ni} \rightarrow \text{Ni}^{2+} + 2e$	1	0
$\text{Ni} + \text{OH}^- \rightarrow \text{NiOH}^+ + 2e$	1	1
(a) $\text{Ni} + \text{OH}^- \rightarrow \text{NiOH}(\text{ads}) + e$	0.5	1
(b) $\text{NiOH}(\text{ads}) \rightarrow \text{NiOH}^+ + e, x_{\text{NiOH}} \rightarrow 0^*$	1.5	1
$x_{\text{NiOH}} \rightarrow 1$	0.5	0
(c) $\text{NiOH}^+ \rightarrow \text{Ni}^{2+} + \text{OH}^-$	2	1
Ni^{2+} diffusion	2	0

* x_{NiOH} designates the fraction of surface covered with $\text{NiOH}(\text{ads})$.

condition is satisfied in the regions where the Tafel relation was obtained by steady-state polarization, one can compare, for the purpose of inferring the rate-determining step, the Tafel constants τ and pH dependence λ evaluated from the steady Tafel lines with those calculated theoretically as shown in Table II. The conclusion is that the rate-determining step of anodic dissolution at the steady state is the dissociation of NiOH^+ ion in the solution layer attached to the surface.

Role of OH^- ion.—From the above discussion it appears that the decrease of anodic current observed at a relatively less noble potential (or the movement of polarization potential toward the more noble potential at a relatively small anodic current) is caused by the increase of NiOH^+ ion concentration in the vicinity of the surface. This increase results in switching over of the rate-determining step from the surface reaction to the dissociation reaction of NiOH^+ ion. The observed increase of anodic current at noble potential (or the movement of potential toward the less noble potential at large anodic current), however, cannot be explained only by the alternation of the rate-determining step. To explain this a particular role of OH^- ion must be taken into account.

In the consecutive steps of anodic dissolution, one can see a reaction cycle of the OH^- ion that consists of steps (a), (b), and (c) (Fig. 8). The OH^- ion in this reaction cycle is considered to act as a carrier (or a catalytic agent) that causes nickel ion to be transferred from the metallic phase to the solution. The rate of nickel dissolution, then, is equivalent to the rate of the reaction cycle with respect to OH^- ion. The rate can be given as follows, no matter whether step (a) or (c) is determining the rate

$$i = 2kF[\text{OH}^-]_0 \exp \{\tau EF/RT\} \quad [17]$$

where $[\text{OH}^-]_0$ denotes the OH^- ion concentration in a solution layer adjacent to the surface and both k and τ are constants closely related to the rate-determining step. This equation suggests that, even if no alternation of the rate-determining step occurs, the polarization curve should change with lapse of time when the OH^- ion concentration at the surface changes during anodic dissolution.

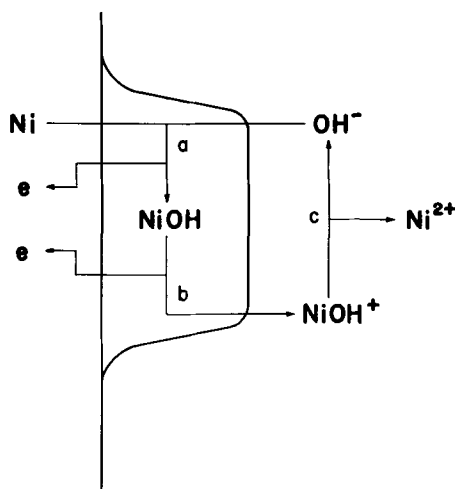


Fig. 8. Reaction cycle with regard to OH^- ion at the surface of nickel. a, $\text{Ni} + \text{OH}^- \rightarrow \text{NiOH(ads)} + e$; b, $\text{NiOH(ads)} \rightarrow \text{NiOH}^+ + e$; c, $\text{NiOH}^+ \rightarrow \text{Ni}^{2+} + \text{OH}^-$.

Since the H^+ ion is the main carrier of ionic current in acid solution, the concentration of the H^+ ion in the vicinity of the surface of anodically dissolving metals tends to decrease with lapse of time (9). The concentration gradient due to the departure of H^+ ion from the surface then gives rise to the back diffusion of H^+ ion against the migration caused by the electric field. The time variation of the H^+ ion concentration at the surface at constant ionic current of the H^+ ion can be derived theoretically under the assumption of linear diffusion of H^+ ion (10). The result of the derivation is the equation

$$\Delta[\text{H}^+] = [\text{H}^+]_s - [\text{H}^+]_0 = \frac{2in_{\text{H}^+}}{F} \sqrt{\frac{t}{\pi D_{\text{H}^+}}} \quad [18]$$

where n_{H^+} is the transport number of H^+ ion, D_{H^+} the diffusion coefficient, $[\text{H}^+]_s$ the concentration of H^+ ion in the distant solution. Combination of Eq. [17] and [18] gives the following equation for the change of the polarization potential with time at constant anodic current

$$E = A + \frac{RT}{\tau F} \ln \left(1 - \sqrt{\frac{t}{t_0}} \right) \quad [19]$$

$$A = \frac{RT}{\tau F} \ln \left(\frac{i[\text{H}^+]_s}{2kFKw} \right)$$

$$t_0 = F\sqrt{\pi D_{\text{H}^+}} [\text{OH}^-]_s / 2in_{\text{H}^+}$$

where t_0 is the time required to attain a concentration of H^+ ion negligible at the surface compared with that in the bulk of solution.

The plot of E vs. $\log(1 - \sqrt{t/t_0})$ was made based on the experimental results shown in Fig. 2, and two straight lines were obtained as is shown in Fig. 9.

In this calculation the time t_0 was taken to be 300 sec, at which the potential reached almost the stationary value. The data obtained later than $0.6 t_0$ were excluded because of this approximation. It is seen that the two straight lines intersect each other at 20 sec. This means that the Tafel constant changes around 20 sec and hence so does the mechanism of

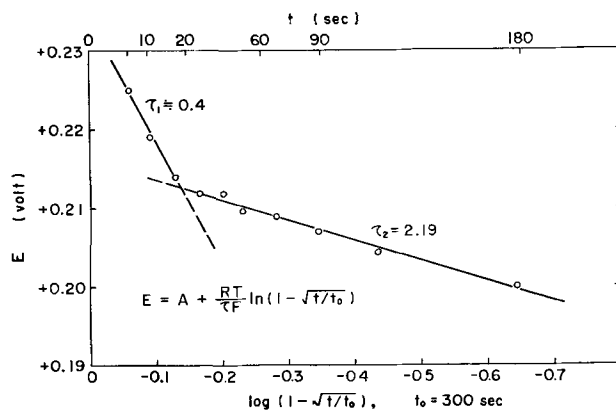


Fig. 9. Relationship between the polarization potential and $\log(1 - \sqrt{t/t_0})$ during galvanostatic polarization. The relationship was calculated from the curve of Fig. 2 using $t_0 \approx 300$ sec. $1N \text{H}_2\text{SO}_4$; 25°C ; $i = 2.32 \text{ ma/cm}^2$.

anodic dissolution. The Tafel constants calculated from the slopes of these straight lines are

$$\begin{aligned} \tau_1 &= 0.4 & (t < 20 \text{ sec}) \\ \tau_2 &= 2.19 & (t > 20 \text{ sec}) \end{aligned}$$

The Tafel constant τ_1 is very close to that obtained from the rapid polarization curve, so that step (a) determines the rate of over-all reaction in the initial period of time. On the other hand, τ_2 is close to that obtained from the steady-state polarization curve, suggesting that the dissociation reaction (c) is rate-determining in the later period of time.

The fact that two Tafel constants instead of one are obtained from the $E - \log(1 - \sqrt{t/t_0})$ curve demonstrates that not only the concentration of OH^- ion but also that of NiOH^+ ion is increased with the time of polarization. The increase in concentration of NiOH^+ ion at the surface, as mentioned in the foregoing section, finally results in the alternation of the rate-determining step in anodic dissolution.

The role of OH^- ion anodic dissolution may be gathered also from the experimental result of the potentiostatic polarization shown in Fig. 4. If the increase of anodic current during potentiostatic polarization is due mainly to the increase of OH^- ion at the surface, then $(i_s - i)$, the change of anodic current relative to a stationary value i_s , should be proportional to the concentration gradient of H^+ ion at the surface (10). Since the concentration gradient at the surface is given by (10)

$$\left(\frac{d[\text{H}^+]_x}{dx} \right)_{x \rightarrow 0} = \frac{[\text{H}^+]_s}{\sqrt{\pi D_{\text{H}^+} t}} \quad [20]$$

a linear relationship is to be realized between $(i_s - i)$ and $1/\sqrt{t}$. A check on the validity of the above inference was made based on the experimental result shown in Fig. 4. Figure 10 shows the plot of $\log(i_s - i)$ against $\log t$. A straight line with a slope of -0.5 [i.e., a linear relation between $(i_s - i)$ and $1/\sqrt{t}$] is seen during the potentiostatic polarization, except in the initial period of time in which the rate-determining step seems to be altered.

It is emphasized from the above that, although there are other factors to be taken into account in the anodic dissolution such as the nature of active

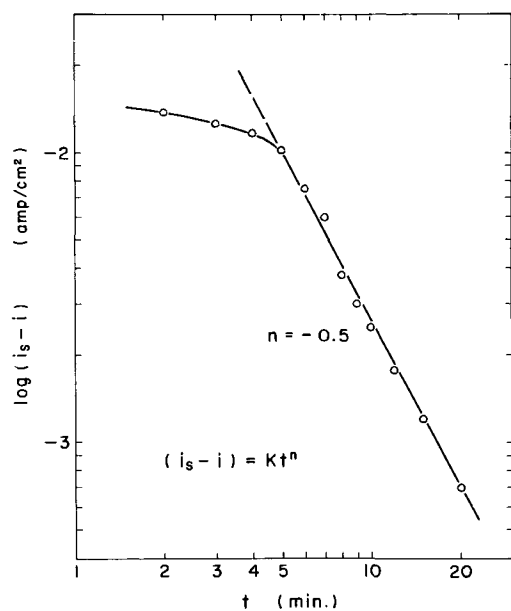


Fig. 10. Relationship between $(i_s - i)$ and time t during potentiostatic polarization. The relationship was calculated from the curve in Fig. 3 using a final anodic current of 15 ma/cm^2 for i_s . $1N \text{ H}_2\text{SO}_4$; 25°C ; $E = +0.25\text{v}$.

sites and adsorption state on the surface, OH^- ion is essential to the transfer of nickel ion from the metal phase to the solution. The role of OH^- ion is to bring the metal ion from the metal phase into the aqueous solution by producing a complex metal ion as an intermediate which may reduce the activation energy of anodic dissolution. Some other anions such as halogen ions may also have the same function in the anodic dissolution of metals. Accordingly, in studying the mechanism of anodic dissolution it seems to be of fundamental importance to know

what kind of complex ion is formed preferentially during dissolution.

Manuscript received Oct. 30, 1963; revised manuscript received March 16, 1964.

Any discussion of this paper will appear in a Discussion Section to be published in the June 1965 JOURNAL.

REFERENCES

1. F. Förster and F. Krüger, *Z. Elektrochem.*, **33**, 418 (1927).
2. S. C. Britton and U. R. Evans, *J. Chem. Soc.*, **1930**, 1780.
3. K. F. Bonhoeffer, *Z. Elektrochem.*, **55**, 152 (1951).
4. G. Okamoto, N. Sato, and M. Nagayama, Proc. Eighth Meeting of C.I.T.C.E., Madrid, p. 72 (1956); *J. Electrochem. Soc. Japan*, **25**, 116 (1957); overseas edition, **25**, E34 (1957).
5. G. Kröncke and G. Masing, *Werkstoffe u. Korrosion*, **4**, 86 (1953).
6. K. F. Bonhoeffer and K. E. Heusler, *Z. Physik. Chem. N. F.*, **8**, 390 (1956); *Z. Elektrochem.*, **61**, 122 (1957); K. E. Heusler, *Z. Elektrochem.*, **62**, 582 (1958); Ja. M. Kolotyrkin, *This Journal*, **108**, 209 (1961); J. O'M. Bockris, D. Drazic, and A. R. Despic, *Electrochim. Acta*, **4**, 325 (1961); J. O'M. Bockris and H. Kita, *This Journal*, **108**, 676 (1961); M. L. Kronenberg, J. C. Banter, E. Yeager, and F. Hovorka, *ibid.*, **110**, 1007 (1963).
7. K. H. Gayer and L. Woontner, *J. Am. Chem. Soc.*, **74**, 1436 (1952); S. Chaberek, R. C. Courtney, and A. E. Martell, *ibid.*, **74**, 5057 (1952); "Stability Constant of Metal-Ion Complexes, II," The Chemical Society, Burlington House, London (1958).
8. J. O'M. Bockris, "Modern Aspects of Electrochemistry I," p. 180, J. O'M. Bockris and B. E. Conway, Editors, Butterworths Scientific Publications, London (1954); J. O'M. Bockris, *J. Chem. Phys.*, **24**, 817 (1956).
9. L. Tronstad, *Z. Physik. Chem.*, **144**, 49 (1929).
10. I. M. Kolthoff and J. J. Lingane, "Polarography, I," p. 18, Interscience Publishers, Inc, New York, London (1952).

Growth Kinetics of Discontinuous Thermal Oxide Films; Aluminum

R. W. Bartlett

Research Laboratory, Philco Corporation, Newport Beach, California

ABSTRACT

A theory of the growth kinetics of discontinuous oxide films is formulated by coupling two dimensional phase transformation theory with the linear and parabolic rate equations in the manner of Evans. Various specific models can be constructed to conform with the kinetic data and oxide morphology of a particular system, and the theoretical weight change curves can be plotted using tables of the incomplete Γ -function. Depending on the specific model and rate constants used, the theory provides for the following anomalous phenomena often observed in oxidation studies: pseudo-logarithmic weight vs. time curves including those with knees too sharp to fit a true logarithmic plot; greater oxide accumulation than can be explained by thin film theories for logarithmic oxidation; an increase in the apparent rate of oxidation with time and sigmoidal weight change vs. time curves. An application of this method to the oxidation of aluminum is included.

The rates of many heterogeneous oxidation reactions are controlled by (a) chemical reaction, including adsorption at the gas-solid interface, or (b) steady state diffusion of one reactant species through a condensed phase oxide product. These respective

processes are described by the following isothermal rate equations

$$\frac{d(m/A)}{dt} = k_1 c_g \quad [1]$$

$$\frac{d(m/A)}{dt} = k_p t^{-1/2} \quad [2]$$

which in their integrated forms provide linear or parabolic plots of the weight change with time, respectively. In these equations, m is the mass change, A is the surface area which is assumed constant, t is time, c_g is the gas concentration at the surface, and k is the appropriate linear or parabolic rate constant designated by the subscript.

Most of the remaining oxidation reactions that have been studied are described as obeying logarithmic, inverse logarithmic, or asymptotic behavior with respect to a plot of the weight change per unit area of surface (m/A_0) vs. time. Each of these latter phenomenological laws describes a rapid initial rate of oxidation followed by a sharp and permanent rate decrease. Explanations of this behavior have been founded on models which accelerate diffusion through thin oxide films without affecting thick films. Quantum mechanical tunneling (1) and theories based on an accumulation of charge at or near one of the oxide interfaces are well known (2-4). All of these theories tacitly assume a continuous oxide film of uniform thickness and difficulties are often encountered in applying them. First, this type of rate behavior has been observed at oxide thicknesses greater than the thin film theories can account for. Second, the knee in the rate curve often has a more pronounced curvature than can be fitted by any of the thin film theories. Third, electron micrographs of thin oxide films often have shown that their thickness is not uniform and their structure is not homogeneous. Growth mounds, discrete oxide particles, apparent small crystals, and whiskers have been observed in many systems, and the role of the oxide morphology in oxidation has been considered qualitatively by Fischmeister (5).

Derivations of expressions for lateral growth of two dimensional films from nucleating sites have been given by Evans (6), Johnson and Mehl (7), and Melvin (8), and Evans briefly discussed lateral growth as a complicating factor in film thickening. The purpose of this paper is to present a more detailed discussion of the kinetics of oxidation resulting when the linear or parabolic rate processes are occurring simultaneously with lateral growth, or shrinkage, of the available surface or reaction product resulting from these processes and to apply this treatment to the oxidation of aluminum.

Theory

The following relations have been shown to govern the lateral growth of islands of two dimensional films beginning at nucleating sites (6-8). The area covered by the expanding film A_1 and the uncovered area A_2 are given in terms of the total surface area A_0 .

$$A_1 = A_0[1 - \exp(-bt^n)] \quad \text{when } t = 0, A_1 = 0 \quad [3]$$

$$A_2 = A_0 \exp(-bt^n) \quad \text{when } t = 0, A_2 = A_0 \quad [4]$$

The value of n is determined by the time dependence of the nucleation frequency. When the nucleation frequency is constant, $n = 3$; when the nuclei density is fixed at $t = 0$ and thereafter, $n = 2$; when

the nucleation frequency decreases with time, $2 < n < 3$ and when the nucleation frequency increases with time, $n > 3$.

When an oxide film is simultaneously expanding laterally on the surface and growing normal to the surface at a rate controlled by the phase boundary reaction the combined rate equation is

$$\frac{d(m/A_0)}{dt} = k_1 c_g [1 - \exp(-bt^n)] \quad [5]$$

However, when the rate of oxide growth normal to the surface is controlled by a diffusion process, the combined rate equation for an expanding oxide film is not as simple. The rate will vary depending on the thickness of the oxide diffusion barrier which has accumulated, and this is dependent on time of coverage at the point in question. Consequently, further discussion of lateral growth coupled with diffusion will be omitted.

More than one oxide phase, with or without identical chemical composition, may form on different areas of the surface simultaneously and grow at different rates. An example is nucleation and growth of a crystalline oxide phase within an amorphous oxide matrix. In this case, lateral growth of the crystalline oxide will cause a reduction in the available area for oxidation by the amorphous process, either by an amorphous to crystalline phase transformation or physical coverage of the amorphous layer by the crystalline oxide. In this situation, the accumulation of oxide by the amorphous process is described by one of the following rate equations, depending on whether the growth rate in the direction normal to the surface is controlled by a phase boundary reaction or a diffusion process, respectively. Since film shrinkage is involved, Eq. [4] can be substituted directly in Eq. [2].

$$\frac{d(m/A_0)}{dt} = k_1 c_g X_0 \exp(-bt^n) \quad [6]$$

$$\frac{d(m/A_0)}{dt} = k_p X_0 \exp(-bt^n) t^{-1/2} \quad [7]$$

where X_0 is the initial fraction of the total area A_0 covered with the contracting oxide film. In Eq. [5] through [7] only the accumulation of oxide (or removal of metal) through the respective primary oxidation processes are described. It should be noted that although changes in the available surface area due to allotropic or phase transformations are accounted for, no credit is given for the transfer of mass of one oxide allotrope to another by the phase transformations.

Combinations of expanding and contracting film behavior may occur; e.g., nucleation and expansion of a porous metastable α phase may precede subsequent nucleation and expansion of a totally impervious β phase within, and eventually consuming, the metastable α phase. In the first instance, because of porosity the growth rate normal to the surface will be controlled by a reaction at the oxide/metal phase boundary described by Eq. [5], but when the effects of the β phase growth are included, the mass

change from the phase boundary process is described by the following rate equation

$$\frac{d(m/A_o)}{dt} = k_1 c_g [1 - \exp(-b_\alpha t^n)] \exp(b_\beta t^n) \quad [8]$$

The solution of Eq. [5] through [8] and others of this type requires evaluation of the appropriate linear and parabolic integrals. For the linear case, integrals of the form $\int_0^t \exp(-bt^n) dt$ must be evaluated. These can be solved from tables of the incomplete Γ -function (9) since

$$\int_0^\infty \exp(-bt^n) dt = \frac{1}{nb^{1/n}} \Gamma(1/n) \quad [9]$$

and

$$\int_0^t \exp(-bt^n) dt = \frac{1}{nb^{1/n}} (\Gamma(1/n)) [I(1/n, bt^n)] \quad [10]$$

where I is the ratio of incomplete to complete Γ -function.

The appropriate form of the integral and its solution for the parabolic process are similar

$$\int_0^t \exp(-bt^n) t^{-1/2} dt = \frac{1}{nb^{(1/2n)}} (\Gamma(1/2n)) [I(1/2n, bt^n)] \quad [11]$$

If more than one rate controlling process is occurring simultaneously, the rate determined by the usual experimental methods will be the sum of the rates for each of these processes. An oxidation model must be constructed, using equations of the type described, to conform with the chemistry, kinetic data, and morphology of the oxide film. Thus, a complete analysis of any system with condensed phase oxides required the use of electron microscopy, electron or x-ray diffraction or other suitable methods for identifying the structure of the oxide film.

Construction and Results of General Models

Before proceeding to a specific application, it is worthwhile to construct two general models and plot the net weight *vs.* time curves for arbitrarily assigned values of the rate constants. This is done to illustrate the types of oxidation curves that can result.

Logarithmic oxidation curves.—The first curve in Fig. 1 is the result when a linear rate process with initial $A_1 = A_o$ is followed by nucleation of a second phase with a negligible growth rate normal to the surface. In this instance it is assumed that the nuclei are located at fixed points such as surface imperfections; *i.e.*, $n = 2$. Thus, from Eq. [6]

$$\frac{d(m/A_o)}{dt} = k_1 c_g \exp(-bt^2) \quad [12]$$

and

$$m/A_o = \frac{k_1 c_g (\Gamma(1/2))}{2b^{1/2}} [I(1/2, bt^2)] \quad [13]$$

The second curve of Fig. 1 is based on an initially parabolic process followed by the same phase change sequence. The constants of Fig. 1 are $k_1 c_g = 1$, $k_p = 0.2$, and $b = 2.5 \times 10^{-5}$ (in arbitrary units of t^{-2}) for both curves. The curves are similar to the "logarithmic" type of weight change curve observed for many metals.

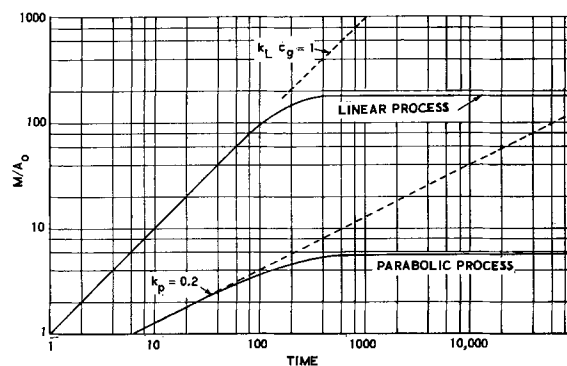


Fig. 1. Log plots of model oxidation curves resulting from a phase transformation in the oxide film limiting the available area for significant continued oxidation, Eq. [6] and [7], resulting in pseudo-logarithmic type oxidation curves.

Sigmoidal oxidation curves.—Lateral expansion of a linear process oxide starting at surface defect nuclei ($n = 2$) and a subsequent phase transformation or ordering with a negligibly slow rate process is shown in curves 2, 3, and 4 of Fig. 2. These curves are based on the integrated form of Eq. [8]

$$m/A_o = \frac{k_1 c_g (\Gamma(1/2)) [I_\beta]}{2b_\beta^{1/2}} - \frac{k_1 c_g (\Gamma(1/2)) [I_{\beta+\alpha}]}{2(b_\alpha + b_\beta)^{1/2}} \quad [14]$$

with the same rate constants used for Fig. 1. The shrinkage constant, b_β is 2.5×10^{-5} , while the expansion constant, b_α , is varied as shown. During the oxide expansion period the logarithmic plots of Fig. 2 provide slopes greater than one. This means that a rate increase with time or concave upward oxidation curve will be observed under these conditions on a linear plot of the data. This type of oxidation behavior has been observed (10) and cannot be explained by any of the continuous film theories of oxidation. Curves 2, 3, and 4 of Fig. 2 are sigmoidal oxidation curves. This is better illustrated by linear plots of these curves, which are shown in Fig. 3. Several cases of sigmoidal oxidation curves have also been observed (11).

Oxidation of Aluminum

The kinetics of the dry oxidation of aluminum above 350°C can be summarized as follows. The rate below about 450°C is parabolic (12-14). Above this temperature, the rate is approximately linear during an initial period and then diminishes sharply (12-

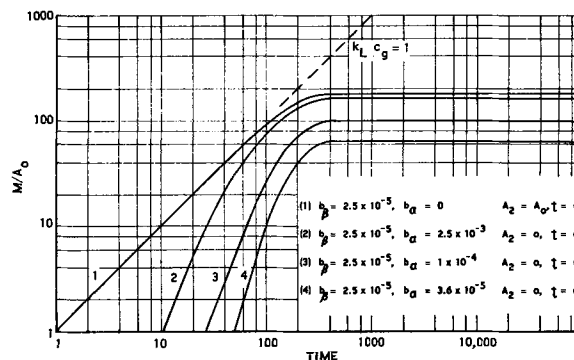


Fig. 2. Log plots of model oxidation curves similar to those of Fig. 1 with lateral expansion of the oxide film preceding phase transformation, Eq. [8], resulting in sigmoidal oxidation curves.

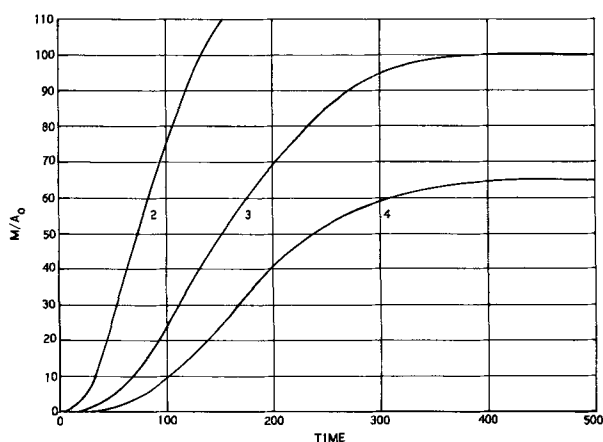


Fig. 3. Linear plots of model oxidation curves, Eq. [8] and Fig. 2, showing sigmoidal oxidation curves.

15). The magnitude of the rates and points of inflection for the high temperature oxidation curves vary considerably with surface treatment. Samples polished with 000 metallographic paper show a weight gain of 30-40 $\mu\text{g}/\text{cm}^2$ before leveling off. Chemical polishing reduces this level by an order of magnitude (15). This difference is attributed to differences in surface roughness. Otherwise, the kinetic data are reasonably consistent in form and magnitude. No variation in oxide film chemistry from Al_2O_3 has been reported, although the exact stoichiometry has not been determined.

The morphological information is summarized as follows. All of the oxide is amorphous below about 450°C . Above this temperature, gamma alumina (16) or eta alumina (17) are detected by x-ray diffraction, and small crystals are observed in the amorphous matrix using electron microscopy. They are oriented in a manner characteristic of the substrate grain which suggests an epitaxial relation with the metal (16). There is little doubt that the decorations seen with the electron microscope are gamma or eta alumina. These forms of alumina are structurally similar. The former is a defect spinel structure, $\text{Al}_{21}1/2\text{O}_{32}$, and the latter is cubic. It appears likely that these crystalline forms of alumina nucleate and grow laterally and that the rate of oxidation associated with them initially follows a linear behavior. Subsequent phase transformations or sintering may drastically lower the diffusion rate within these crystals in conformance with the observed rate curves. Both gamma and eta alumina are known to undergo several time and temperature dependent phase transformations, ending in alpha alumina. In recent studies by Doherty and Davis (18), voids have been observed between the crystal and substrate. This peculiar effect provides an alternate explanation for the apparent cessation of crystal growth.

The kinetic data of Cochran and Sleppy (15) at 50 Torr of dry oxygen are the most extensive in terms of the time and temperature span. Unfortunately, no data below 450°C were acquired. In this range, Gulbransen and Wysong's determination of the parabolic rate constant k_p was used (12).

The following model in conformance with the morphological data was postulated and put to the test

of Cochran and Sleppy's data. At all temperatures an amorphous oxide is formed by a slow diffusion controlled mechanism. At undetermined nucleation sites at the metal surface, $n = 2$, growth of gamma alumina spreads laterally and outward from the surface at a linear rate. Subsequently, a second phase transformation in the gamma to alpha series or void formation occurs, with lateral growth from nucleating sites, and the oxidation rate at the crystal becomes negligibly slow. The treatment is identical to that of Eq. [14] and Fig. 2. However, for ease of calculation a somewhat simplified treatment was made in which the nucleation and expansion of the linear oxide was neglected and the gamma crystallites were assumed to initially cover a small but finite fraction of the surface area. On this basis the perturbation of the weight contribution of the parabolic process governing the growth rate of the amorphous matrix film from that of a straight line slope of $1/2$ on a logarithmic plot is negligible. The resulting approximate rate equation is

$$\frac{d(m/A_0)}{dt} = k_1 c_g X_0 \exp(-bt^2) + k_p t^{1/2} \quad [16]$$

and the model is shown schematically in Fig. 4. Gulbransen and Wysong's integrated value for k_p was multiplied by $(0.1)^2$ to account for the tenfold decrease in effective surface area when the specimen is chemically polished rather than mechanically polished (15). On this basis the value of k_p to be used in Eq. [16] for comparison with Cochran and Sleppy's experimental data is

$$k_p = (0.1)^2 1.2 \times 10^{-7}$$

$$\exp\left(\frac{-22800}{RT}\right) [\text{g}^2 \text{cm}^{-4} \text{min}^{-1}] \quad [17]$$

Comparisons of the results from Eq. [16] with the experimental results are shown in Fig. 5a-f. The points in the isotherms of Fig. 5 represent the experimental data. They were selected randomly from the published curves. The values of the product of time independent constants, $k_1 c_g X_0$, were obtained from the intercepts of the initial part of the experimental data of Fig. 5 or from the intercepts of a tangent to the loci of data points having a slope of

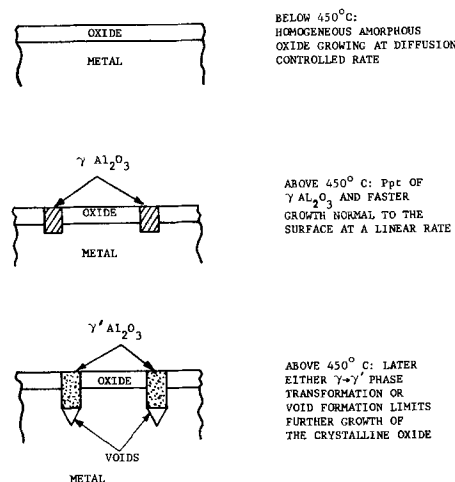


Fig. 4. Model for thermal oxidation of aluminum

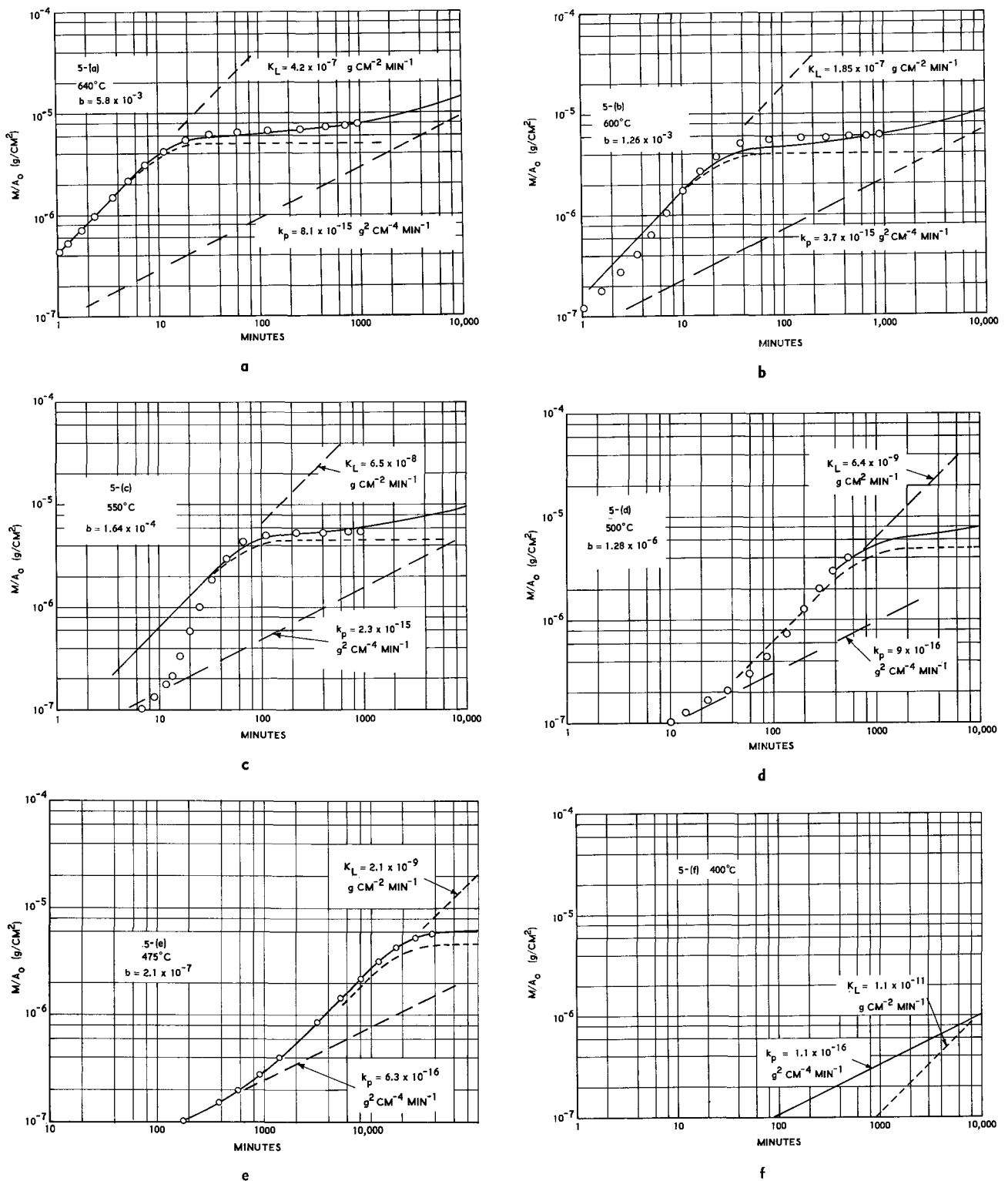


Fig. 5(a)-(f). Oxidation of aluminum by growth of (i) amorphous Al_2O_3 matrix (parabolic) and (ii) gamma Al_2O_3 crystallites (linear) with a subsequent cessation of crystal growth by a phase transformation or void formation, Eq. [16], points experimental, solid lines theoretical sum.

one. In Fig. 5 this term is abbreviated as K_L . The shrinkage constant, b , was determined from the value of m/A_0 at the end of the oxidation run and the relation

$$\left. \frac{(m/A_0)}{t} \right|_{t=\infty} = \frac{k_1 c_g X_0 \Gamma^{1/2}}{2b^{1/2}} \quad [18]$$

The curves of Fig. 5 represent the fit of Eq. [16] using these values for $(k_1 c_g X_0)$ and b and Eq. [17] for

k_p . The agreement between calculated and experimental oxidation curves is reasonably good but could be improved by the neglected lateral expansion term in the crystal growth rate equation. This refinement would account for the sigmoidal curves observed at intermediate temperatures, 500° and 475°C of Fig. 5. An Arrhenius plot of the experimental linear rate constants, K_L , is shown in Fig. 6. The conformance to expected Arrhenius behavior is good, yielding an ac-

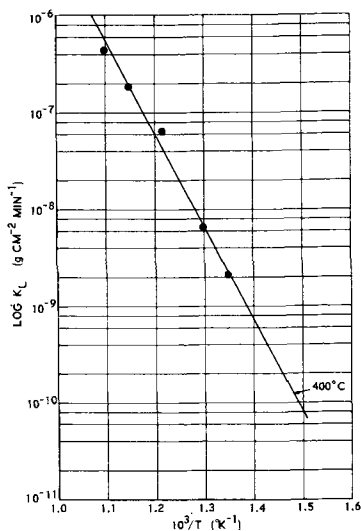


Fig. 6. Arrhenius plot of the linear rate constant (intercepts of Fig. 5) for the oxidation of aluminum. $E_{(exp)} = 44$ kcal/mole.

tivation energy of 44 kcal/mole. A more interesting aspect is the extrapolated value of the linear rate constant, K_L , at 400°C. The linear part of the oxidation curve resulting from this value of K_L is plotted in Fig. 5f with the corresponding parabolic contribution. It is seen that the parabolic contribution is larger out to beyond 10,000 min. Under these conditions, the linear rate is negligible compared to the parabolic rate. This difference will become more pronounced with decreasing temperatures. Thus, the observed transition from simple parabolic behavior below 450°C to pseudo-logarithmic oxidation above 450°C is accounted for by the model.

Summary

When the linear and parabolic rate laws are coupled with the theory of lateral growth of a two dimensional film and applied to discontinuous oxide

films, the resulting oxide growth rate equations can explain sigmoidal oxidation curves and logarithmic oxidation curves for thick films. This approach also can fit the pseudo-logarithmic oxidation curves of aluminum and account for the parabolic-logarithmic transition temperature in the thermal oxidation of this metal.

Acknowledgment

The author is indebted to Drs. J. N. Ong, S. W. Weller, and W. M. Fassell, Jr., for helpful discussions and a critical review of the manuscript.

Manuscript received Nov. 27, 1963; revised manuscript received March 11, 1964.

Any discussion of this paper will appear in a Discussion Section to be published in the June 1965 JOURNAL.

REFERENCES

1. N. F. Mott, *Trans. Faraday Soc.*, **35**, 1175 (1939).
2. N. Cabrera and N. F. Mott, *Rept. Progr. Phys.*, **12**, 163 (1948-1949).
3. H. J. Engell and K. Hauffe, *Metallk.*, **6**, 285 (1952).
4. H. H. Uhlig, *Acta Met.*, **4**, 541 (1956).
5. H. F. Fischmeister, "Reactivity of Solids," J. H. De Boer, Editor, p. 194-204, Elsevier Publishing Co., New York (1961).
6. U. R. Evans, *Trans. Faraday Soc.*, **41**, 3-5 (1945).
7. W. A. Johnson and R. F. Mehl, *Trans. Am. Inst. Mining and Met. Engrs.*, **135**, 416 (1939).
8. M. A. Melvin, *J. Chem. Phys.*, **9**, 177 (1941).
9. K. Pearson, "Tables of the Incomplete Γ -Function," Cambridge Press, Cambridge, England (1957).
10. A. Ronnquist, *J. Inst. Metals*, **91**, 89 (1962-1963).
11. R. F. Tylecote, *ibid.*, **81**, 681 (1952-1953).
12. E. A. Gulbransen and W. S. Wysong, *J. Phys. Chem.*, **51**, 1087 (1947).
13. W. W. Smeltzer, *This Journal*, **103**, 209 (1956).
14. D. W. Aylmore, S. J. Gregg, and W. B. Jepson, *J. Inst. Metals*, **88**, 205 (1960).
15. C. N. Cochran and W. C. Sleppy, *This Journal*, **108**, 322 (1961).
16. M. J. Dignam, *ibid.*, **109**, 184 (1962).
17. M. S. Hunter and P. Fowle, *ibid.*, **103**, 482 (1956).
18. P. E. Doherty and R. S. Davis, *J. Appl. Phys.*, **34**, 619 (1963).

High-Temperature Oxidation

I. A Thermal Conductivity Method for Oxidation Measurements

Joan B. Berkowitz-Mattuck

Arthur D. Little, Inc., Cambridge, Massachusetts

ABSTRACT

An apparatus employing a thermal conductivity bridge to compare the oxygen concentration in a gas stream before and after reaction with an inductively heated metallic pellet is described. The measurements are continuous and sensitive to rates of oxygen consumption of 10^{-6} g/min. The method has been used to study oxidation of silicides, borides, carbides and pure metals in the range 900°-2100°C. Results reported here on the oxidation of copper at temperatures around 1000°C are in reasonable agreement with results obtained by more conventional methods in other laboratories, and with the Wagner theory of parabolic reactions.

The oxidation of metallic conductors is conveniently studied by using a thermal conductivity cell, of the type employed in vapor phase chromatography, to compare the oxygen concentration in a gas stream before and after reaction (1, 2). The tech-

nique is particularly well-suited for investigations at high temperatures (900°-2100°C), since it is compatible with induction heating and permits direct and continuous measurement of oxidation rates at low oxygen pressures with a sensitivity of about 10^{-6}

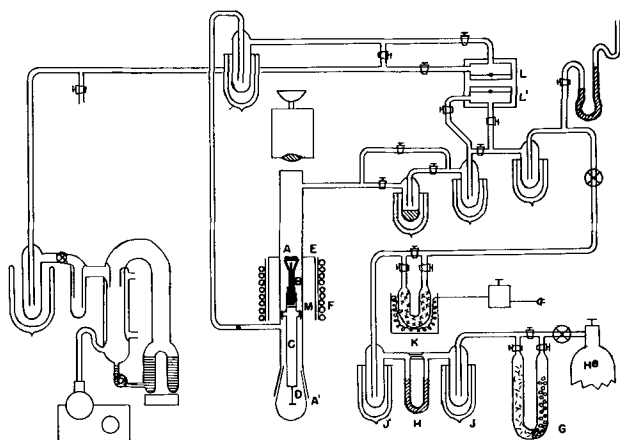


Fig. 1. Apparatus for oxidation rate measurements. A Metallic sample, B refractory oxide support rods, C aluminum holder, D positioning screw, E silver-plated copper concentrator, F r.f. coils, G purification train, H Dibutylphthalate flow meter, J, J' liquid nitrogen traps, K heated CuO, L, L' reference and sampling sides of the thermal conductivity cell.

g/min. This paper reports results on the oxidation of copper obtained by this method. These results are in good agreement with those obtained in other laboratories by conventional manometric or continuous weighing techniques. In subsequent papers studies of the oxidation of refractory silicides, borides, and carbides at temperatures up to 2100°C will be reported.

Experimental

Apparatus.—A schematic diagram of the apparatus is shown in Fig. 1. Samples are machined in the form of cylinders, 0.8 cm in diameter and 0.3 cm in height, and are mounted by point contact on three alumina or thoria rods, 3 cm in length. These in turn are fastened with gold wire to an aluminum holder. A screw at the bottom of the holder permits the optimization of the position of the pellet with respect to the concentrator and r.f. coils of a Sylvania 5 kw induction unit. The mounted pellet is enclosed in a constant pressure flow system constructed entirely of Pyrex, except for a short length of quartz tubing in the immediate neighborhood of the sample.

The flow system is of conventional design. Helium carrier gas flows through a purification train of magnesium perchlorate, Ascarite, Drierite, and glass wool. Flow rate is measured with a dibutyl phthalate capillary flow meter flanked by liquid nitrogen traps. Oxygen is introduced into the helium stream at partial pressures up to 20 Torr by allowing the helium to flow through heated CuO. The helium-oxygen mixture passes through a Dry-Ice-acetone trap and enters the reference side of a thermal conductivity cell. The stream then flows through a second cold trap and over the inductively heated sample pellet where a portion of the oxygen is removed by chemical reaction. The gas stream, depleted in oxygen, flows through another cold trap, enters the sampling side of the thermal conductivity cell, and is ultimately vented to the atmosphere. The two sides of the thermal conductivity cell are connected in a Wheatstone bridge circuit, the output of which is recorded and is proportional to the rate of change of the difference in oxygen concentration in the two

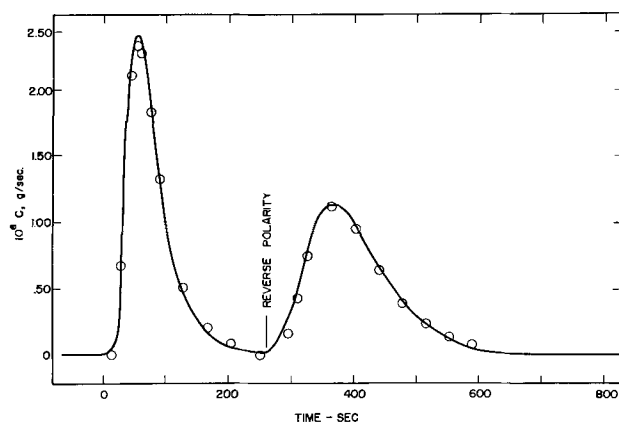


Fig. 2. Recorder tracing for a single calibration point (solid lines). Points were calibrated from Eq. [1].

sides, or equivalently, to the rate of oxygen consumption by the heated sample. The area under the experimental curve from time zero to time t is proportional to the total oxygen consumed in time t .

Calibration.—In order to calibrate the cell, measured slugs of oxygen are introduced into the helium stream by means of manometric device (3). A typical recorder tracing for a single calibration is shown in Fig. 2. The first peak occurs as the oxygen slug passes through the reference side of the thermal conductivity cell, while the sampling side is filled with pure helium. The first peak declines and a reverse peak is observed when the reference side is once more filled with pure helium and the oxygen slug passes through the sampling side. The area under either peak is proportional to the total mass of oxygen that was introduced. From the area calibration factor determined in this manner and from the measured recorder speed, signal height can be related to rate of change of oxygen concentration in the sampling cell for constant concentration in the reference cell (see below).

Figure 3 gives a calibration curve obtained with a Burrell 340-148 thermal conductivity cell operated from a 6v storage battery with a current of 300 ma and a helium flow rate of 95 ml/min.¹ The response of the cell is linear for the entire concentration range used in this work. For the conditions described, a

¹ Gow-Mac hot wire and thermistor cells have also been used successfully.

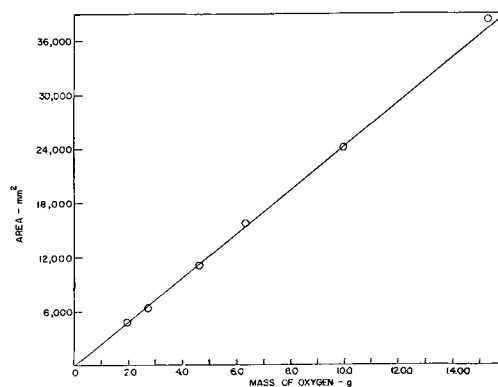


Fig. 3. Calibration curve for the thermal conductivity cell; measured area on the recorder tracing vs. total mass of oxygen introduced.

signal of 1 mv corresponds to an oxidation rate of 1.3×10^{-4} g/min. The calibration factor for a given set of conditions is reproducible to $\pm 4\%$. Separate calibrations are required for each flow rate and current setting. Sensitivity is approximately proportional to the square of the current and the reciprocal of the flow rate.

Procedure.—A sample is polished, cleaned, measured with a micrometer, weighed and mounted in position eccentrically in the quartz tube, close to the concentrator slit, with its upper surface slightly higher than the top of the concentrator. With careful positioning, surface temperatures of the inductively heated specimens are uniform to $\pm 5^\circ\text{C}$. The system is pumped down to a leak rate of less than $5 \mu/\text{hr}$, and flow of pure helium is started. The r.f. power supply is turned on and the sample pellet is degassed at a temperature slightly higher than that planned for the oxidation run. The degassing is monitored with the thermal conductivity bridge and terminated when the signal from the bridge drops to zero. The sample is reweighed, remeasured, and replaced. A stream of helium and oxygen is permitted to flow through the system, and when the bridge signal is steady, the sample is rapidly brought to temperature. If oxidation occurs, an unbalance is observed in the bridge indicative of the rate of oxygen pick-up by the sample. At the end of a run, the sample is cooled rapidly to room temperature, weighed, and measured. The highest temperature at which this apparatus has been used so far was the oxidation of HfC at 2100°C .

Analysis of the Flow System

An oxygen slug introduced into the flow system spreads as a result of diffusion and of the radial velocity distribution in the tubing. Each of the peaks of the calibration curve in Fig. 2 can be fitted approximately by a logarithmic normal distribution function of the form

$$c_i(t - t_i) = \frac{0.286 c_o}{\sqrt{2\pi t_{i \max}}} \frac{(t_{i \max} - t_i)}{(t - t_i)} \exp \left\{ - \frac{\tau}{(t_{i \max} - t)} \ln \frac{(t - t_i)}{(t_{i \max} - t_i)} - 12.2 t_{i \max} \right\}^2 / 24.5 t_{i \max} \quad [1]$$

where c_o is the known total mass of oxygen introduced into the flow system, t is a running time coordinate, t_i is the time of appearance of a signal at position i for an oxygen slug introduced at time zero, $t_{i \max}$ is the time of maximum oxygen concentration at position i . The parameters t_i and $t_{i \max}$ were measured in a series of experiments in which pulses of varying oxygen concentration were introduced into the flow system. For the first cell ($i = 0$), $t_o \approx 65$ sec, $t_{o \max} \approx 120$ sec; for the second cell ($i = 2$), $t_2 = 380$ sec, $t_{2 \max} = 532$ sec. Points calculated from [1] with these values of the parameters are superimposed on the experimental curves in Fig. 2. It is not possible to derive the observed peak shapes from simple theoretical considerations. Axial diffusion along the stream produces concentration curves which are

symmetric about the maximum; the assumption of simple laminar flow alone predicts a spread which is very much greater than that observed.

During an oxidation run, let n_o be the concentration of oxygen in the reference side of the thermal conductivity cell, n_2 the rate of arrival of oxygen gas at the detector cell, and $A(t)$ the rate of oxygen consumption by the sample pellet. The unreacted oxygen may be looked on as a continuous series of infinitesimal pulses emitted from the sample region into the flowing stream. A pulse of amplitude $n(t) = n_o - A(t)$ that leaves the vicinity of the pellet at time t will be spread by the flow and by diffusion, so that its concentration at the detector is given by an equation of the form [1]. The net rate of arrival of oxygen at the detector cell will be the sum of contributions from all pulses that have left the pellet region from the time when the experiment started to time of detection t

$$n_2(t) = \int_{t'=\tau}^{t-\tau} \frac{n(t') (t_{d \max} - \tau)}{\sqrt{2\pi t_{d \max}} (t - t' - \tau)} \exp \left[(t_{d \max} - \tau) \ln \frac{(t - \tau - t')}{(t_{d \max} - \tau)} - 12.2 t_{d \max} \right]^2 / 24.5 t_{d \max} dt' \quad [2]$$

where τ is the minimum travel time of a pulse from pellet to detector, given by the quotient of distance and linear flow velocity, ($\tau \approx 240$ sec) and $t_{d \max}$ is evaluated at the detector ($t_{d \max} < 370$ sec). It is convenient to approximate the integrand in [2] by a square pulse of amplitude $n(t')/\Delta(t_{1/e})_d$ and duration $\Delta(t_{1/e})_d$ where $\Delta(t_{1/e}) = (t_{1/e} - t'_{1/e})$. The times $t_{1/e}$ and $t'_{1/e}$ at which the concentration at any position is $1/e$ of the maximum, are given by

$$\ln t_{1/e} = \frac{+5\sqrt{t_{i \max}}}{(t_{i \max} - t_i)} + \ln (t_{i \max} - t_i) \quad [3]$$

$$\ln t'_{1/e} = \frac{-5\sqrt{t_{i \max}}}{(t_{i \max} - t_i)} + \ln (t_{i \max} - t) \quad [4]$$

With this approximation, and with the substitution $y = t - t' - \tau$ in [2], the observed signal ($n_o - n_2$) should be equal to

$$n_o - n_2 \approx \frac{1}{\Delta(t_{1/e})_d} \int_{(t_{1/e})_d}^{(t'_{1/e})_d} A(t - \tau - y) dy \quad [5]$$

If $A(t - \tau - y)$ can be expressed by a Taylor's series in y , then

$$n_o - n_2 \approx A(t - \tau) + \sum_{n=1}^{\infty} \frac{A^{(n)}(t - \tau)}{\Delta(t_{1/e})_d (n + 1)!} [(t_{1/e})_d^{n+1} - (t'_{1/e})_d^{n+1}] \quad [6]$$

where $A^{(n)}(t - \tau)$ denotes the n th derivation of $A(t - \tau)$ with respect to $(t - \tau)$. Thus, if the summation in [6] is small, the signal at the detector will be proportional to the rate of oxidation of the sample retarded by the time τ .

If the sample oxidizes according to a simple rate law, [6] can be used to estimate the magnitude of the experimental error in the detector signal. If oxidation is linear, $A(t)$ is independent of time, and the

correct oxidation rate should be observed. If oxidation is parabolic, $A(t) = k_p/t^{1/2}$ where k_p is the parabolic rate constant, and the error will be less than 1% of the signal at times $(t - \tau) > 7$ min. Similar results are obtained if the rate equation is logarithmic. Thus, with the exception of the first 10 min for the flow rates employed in this work, the observed steady state rates will be equal to the true rates and are essentially unaffected by the physical separation between reaction zone and detector.

Oxidation of Copper

The lack of precise oxidation measurements on simply behaved, well characterized systems above 1000°C makes a detailed quantitative comparison of our results with those of other workers difficult. Copper was selected as the most satisfactory standard material. The oxidation of copper was studied by Feitknecht (4) at 1020°C and 7.6 Torr, by Grünwald and Wagner (5) at 1000°C at pressures between 0.23 and 63 Torr, and by Baur, Bridges, and Fassell (6) between 900° and 1000°C at oxygen partial pressures of 5-95 Torr.

We have made measurements with the thermal conductivity apparatus at temperatures between 977° and 1044°C, and oxygen pressures between 1.7 and 10 Torr. The experiments were carried out with copper pellets machined from 99.999 + copper rod supplied by American Smelting and Refining Co., South Plainfield, N. Y., and cleaned in acetone and distilled water prior to degassing as described earlier.

The data obtained by us and in the other three investigations are plotted in Fig. 4 as total oxygen consumption or net weight gain per unit area ($\Delta m/A$) vs. time, and in Fig. 5 as $(\Delta m/A)^2$ vs. time. There is good agreement between our results at 1044°C and 7.6 Torr and Feitknecht's at 1020°C and 10 Torr; our results at 990°C and 10 Torr and Baur *et al.* (6) at 1000°C and 10 Torr; and our results at 977°C and 3.0 Torr and Grünwald and Wagner (5) at a higher temperature, 1000°C and low pres-

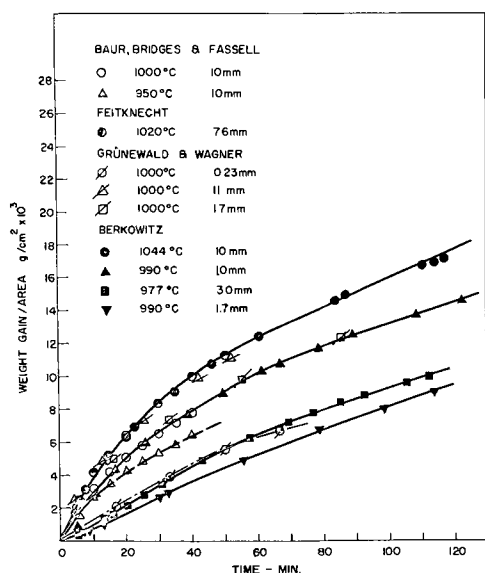


Fig. 4. Total oxygen consumption vs. time for copper, results of four investigations.

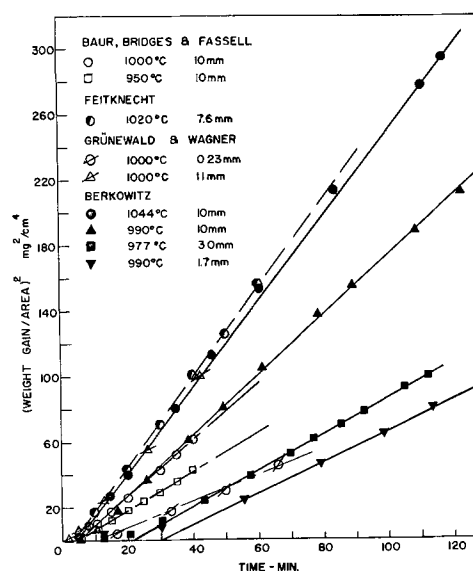


Fig. 5. Parabolic plot for the oxidation of copper, data of Fig. 4

sure, 0.23 Torr. Results from two laboratories at 1.7 Torr are in disagreement. Considering that the average precision of results from a given laboratory is $\pm 10\%$, and that errors can be expected in the measurement of weight change or oxygen consumption, in the determination of zero time, and in the measurement of temperature and pressure, agreement among the four groups is good. Discrepancies are largest at the lower oxygen pressures. However, the data support the conclusion that the rate of oxidation of copper increases with both increasing temperature and increasing pressure. All of the data can be fitted to a parabolic rate equation after times that vary between 10 and 60 min, depending upon the temperature and pressure, when a layer of $\text{Cu}_2\text{O}(c)$ 400,000-900,000Å thick has been built up on the surface of the copper.

It has been pointed out (5) that in the oxidation of copper, both interface and diffusion reactions are important until a very thick layer of Cu_2O has formed. In order to extract the diffusional rate constant from experimental weight change or oxygen consumption data, it is customary to fit the data to a relation of the form

$$\left(\frac{1}{k_p}\right) \left(\frac{\Delta m}{A}\right)^2 + \frac{1}{K} \left(\frac{\Delta m}{A}\right) = t \quad [7]$$

The parabolic rate constant is then calculated as the reciprocal of the slope of a plot of $t/(\Delta m/A)$ vs. $(\Delta m/A)$. The rate constants obtained in this way from the present results are compared with those of Grünwald and Wagner (5) and Baur *et al.* (6) in Table I. The table also gives parabolic rate constants calculated from the theoretical Eq. [8] (8-10)

$$k_p = 2\Omega \left(\frac{kT}{e^2}\right) \sigma_o t_i [p^{1/8}(\text{O}_2/\text{X}) - p^{1/8}(\text{O}_2/\text{O})] \quad [8]$$

In [8], Ω is the volume of Cu_2O per copper ion, σ_o is the electrical conductivity of Cu_2O at an oxygen pressure of 1 atm, t_i is the transference number of cations in Cu_2O at the experimental temperature, $p(\text{O}_2/\text{X})$ is the ambient oxygen pressure, $p(\text{O}_2/\text{O})$

Table I. Values of the parabolic rate constant, k_p ($\text{mg}^2/\text{cm}^4\text{-hr}$)

Reference	T, °C	P_{O_2} , mm	k_p , calculated from $\frac{1}{k_p} \left(\frac{\Delta m}{A} \right) + \frac{1}{k}$ $= t / \left(\frac{\Delta m}{A} \right)$	k_p , calculated from conductivity data
(4)	1020	7.6	—	132
This work	1044	10.0	159	145
(5)	1000	11.0	178	134
(5)	1000	1.71	123	94
This work	990	10.0	123	127
(6)	1000	10.0	143	131
(6)	950	10.0	81	102
This work	977	3.0	105	84
This work	990	1.7	132	80
(5)	1000	0.23	79	63

is the oxygen pressure calculated from the equilibrium $2\text{Cu} + \frac{1}{2}\text{O}_2 = \text{Cu}_2\text{O}$ at the absolute temperature T , k is the Boltzmann constant, and e is the charge of the electron. Conductivity values for the calculations were taken from Dünwald and Wagner (11); other values in the literature are as much as a factor of two higher (12). The transference number of Cu^+ in Cu_2O at 1000°C was found to be between 4 and 5×10^{-4} (10); the lower value was used here in calculating k_p . In view of the uncertainties in the electrical properties of $\text{Cu}_2\text{O}(c)$, the values of k_p might be as much as a factor of two higher than those given in the last column of the table.

It is seen that the results of the present investigation are in good agreement both with previously published results obtained by conventional weight change techniques and with the predicted rate constants of Wagner.

Acknowledgment

It is a pleasure to acknowledge the laboratory assistance of John Mellor, John T. Larson, and Richard F. Quigley, and many invaluable discussions with Dr. Alfred Emslie and Dr. Alfred Büchler. This research was supported in whole by the United States Air Force under Contract No. AF 33(616)-6154, monitored by the Materials Laboratory, Wright Air Development Center, Wright-Patterson Air Force Base, Ohio.

Manuscript received Dec. 13, 1963; revised manuscript received March 20, 1964.

Any discussion of this paper will appear in a Discussion Section to be published in the June 1965 JOURNAL.

REFERENCES

1. E. R. Weaver and W. G. Berl, "Physical Methods in Chemical Analysis," Vol. II, p. 382, Academic Press, New York (1951).
2. ASD Report TDR-62-203, Part II, March 1963.
3. C. Littman and J. B. Berkowitz-Mattuck, *Rev. Sci. Instruments*, **32**, 1154 (1961).
4. W. Feitknecht, *Z. Electrochem.*, **35**, 152 (1929).
5. C. Wagner and K. Grunewald, *Z. phys. Chem.*, (B) **40**, 455 (1938).
6. J. P. Baur, D. W. Bridges, and W. M. Fassell, Jr., *This Journal*, **103**, 273 (1956).
7. C. Wagner, "Kinetics in Metallurgy," M.I.T. Course 3.63 [M.I.T., Spring (1955)].
8. C. Wagner, *Z. phys. Chem.*, (B) **21**, 25 (1933).
9. O. Kubaschewski and B. E. Hopkins, "Oxidation of Metals and Alloys," Academic Press, New York (1962).
10. T. B. Grimley, Ch. 14 in W. E. Garner, "Chemistry of the Solid State," Academic Press, New York (1956).
11. H. Dünwald and C. Wagner, *Z. Phys. Chem.*, (B) **22**, 212 (1933).
12. M. O'Keefe and W. J. Moore, *J. Chem. Phys.*, **35** 1324 (1961).

Effect of Surface Preparation on Cracking and Structure of Chromium Deposits

David W. Hardesty

Research Laboratories, General Motors Corporation, Warren, Michigan

ABSTRACT

Conventional bright chromium deposits (0.02-0.05 mil thick) on buffed nickel plates often develop a directionally oriented crack pattern which may adversely affect appearance and corrosion resistance. This cracking was found to occur by interaction of polishing-induced, directional residual stress in a surface layer of the nickel with isotropic internal stress of the chromium deposit. Removal of the stress-containing layer by electropolishing or stress relief by annealing eliminates this cracking. Similar cracking can occur in bright nickel-chromium composites plated on polished steel. Chromium deposits on electropolished nickel are apparently strongly epitaxial. Observed variations in appearance, porosity, and corrosion behavior of deposits on individual grains of wrought nickel correspond to similar variations symmetrically distributed in chromium plated on spherical nickel single crystal. The significance of these observations is discussed.

The use, efficacy, and electrochemistry of micro-cracked chromium in controlling corrosion of copper-nickel-chromium plated coatings for decorative automobile trim have been discussed by a number of

authors (1-6). This type of cracking [Type M in Lindsay's (2) classification] is described by Lovell (1) as ". . . a fine network of cracks extending through the chromium and invisible to the unaided

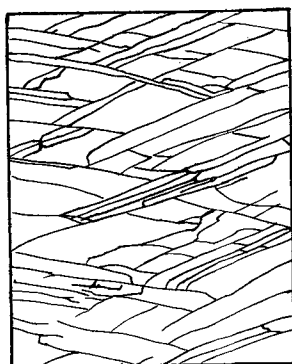


Fig. 1. Example of Type Y crack pattern in chromium plated in half-box on buffed nickel panel.

eye . . .," and is attributed to relief of the high internal (tensile) stress of electrodeposited chromium (7). It has been the subject of numerous investigations [see references cited by Fry (10) for examples].

Not all cracked deposits are equally effective in corrosion control as some forms of cracking adversely affect appearance and resistance to basis metal corrosion. One such undesirable deposit, illustrated in Fig. 1, has a system of irregularly spaced, parallel cracks [Type Y in Lindsay's (2) classification] which were found to occur consistently in chromium plated uniformly on buffed nickel panels. Virtually invisible in freshly-plated chromium, these cracks appear initially at thicknesses of 0.025-0.030 mil,¹ become more closely spaced, gradually change to Type YM, and eventually to Type M (microcracked) exclusively as the chromium thickness is increased above 0.050-0.060 mil. It has been reported (1, 2) that Type Y cracking is particularly unreliable in corrosion control. Since these cracks sometimes appear in deposits which are mainly the efficacious Type M microcracking, it seemed desirable to learn why Type Y cracking develops so that steps could be taken for its elimination.

The random directions and spacings of Type M cracks in chromium indicate that these occur when isotropic internal stresses exceed the tensile strength of the deposit. Although cracking similar to Type Y has been observed previously in chromium deposits up to 0.050 mil thick (1, 2, 11, 24-26), it appears that no serious attempt has ever been made to explain their origin other than by vague attributions to "stress." In the absence of externally applied stresses, anisotropic stress distribution in the deposit appears to be the most likely explanation of the directionality of Type Y cracking. The origin of such a stress distribution is, however, obscure. Since these cracks are quite often very difficult to detect prior to corrosion, it was suspected that they may result from a special type of stress-corrosion cracking.

There are available at least three possible hypotheses which may account for the occurrence of Type Y cracking. The first of these assumes the presence of the same isotropic stresses which account for Type M cracking and that the deposit is still essentially continuous. Thus, at deposit thicknesses

¹ 1 mil = 0.001 in.

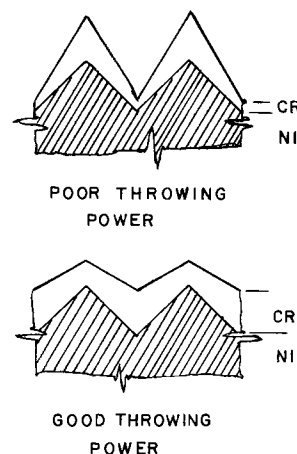


Fig. 2. Effect of "throwing power" on chromium distribution on surface asperities.

where Type Y cracking is most prevalent, the internal stress acting through the still continuous deposit (in a manner analogous to stresses induced by thermal contraction of a bi-metal sheet) is resolved vectorially into principal stresses acting in definite directions, dependent on the dimensions of the plated area. On a 3 x 4 in. area, these principal stresses would be along the diagonals, at angles of 37° to the longer sides of the rectangle, and cracking would then occur perpendicular to the diagonals at 53° angles. The cracks of Fig. 1 are at an angle of 65-70°, in only fair agreement with prediction if other factors are not operative. If dimensional stress resolution does contribute to the observed orientations of cracking, then altering plated area dimensions would result in concomitant alteration of crack patterns.

A second explanation of the orientation of Type Y cracking considers the effect of a nonuniform chromium thickness on surface asperities as shown schematically in Fig. 2, which represents local thickness variations on polished or buffed surfaces. In this event, assuming stress proportional to local chromium thickness, maximum stress would be in the direction of buffing; cracks, then, would be expected at right angles to this direction. The angle between crack direction expected and that observed, about 20°, possibly arises from scratches angled about 20° from the buffing direction due to spreading of the buffing head under pressure. In any event, buffing a portion of a panel in another direction, for example, at right angles to the original direction, would result in a radical change in crack direction, as reported but not explained by Blum, Barrows, and Brenner (11). These directional effects would be expected to be independent of the method of abrasion. Chromium plated on an absolutely smooth surface or on one free of asperities would not be expected to display directional or Type Y cracking. Such a surface could be approximated by metallographic polishing or by electropolishing.

The third possible explanation of Type Y cracking involves interaction of stresses in the chromium deposit with residual stresses in the basis metal. This hypothesis was developed only after the two previous ones had been considered and partially tested with inconclusive or negative results. Cracking very

similar to Type Y frequently has been observed on sharply curved surfaces of bumpers and other stampings in patterns which suggested that residual stresses in the basis metal were affecting the cracking of the plated coatings. Safranek (12), in exposures of "bend-stressed" plated specimens to corrosion, obtained similarly spaced cracks oriented perpendicular to the applied stress. However, the panels used in the present work are sheared from steel sheets plated with nickel and then buffed. There is, therefore, no obvious source of deformation to induce stresses, except at the sheared edges. These stresses would extend from the edge only a distance comparable to the panel thickness. Because of the plating procedure used to obtain uniform chromium deposit thickness, these areas are not plated and there is, therefore, no opportunity for interaction of basis metal-deposit stresses. Thus, it was concluded that some other source of stresses was responsible for the appearance of Type Y cracking.

As remarked above, it was suspected that Type Y cracking might develop as the result of a special case of stress-corrosion cracking of the chromium deposit. During a survey of the pertinent literature, a possible source of directional residual stresses in the basis metal was suggested by Nielsen (13) who obtained crack patterns with many of the characteristics of Type Y cracking of chromium in a study of effects of abrasion on stress-corrosion cracking of austenitic stainless steel. These cracks were attributed to tensile stresses induced in a surface layer of the metal by deformation associated with the cutting action of individual abrasive grains.

Samuels (14) has shown that all buffing, polishing, and abrasion occur by a cutting action of the abrasive particles, and that only the magnitude of the effect varies with the size of the cutting particle. There is available, therefore, a reasonable explanation for the presence in buffed nickel of directional residual tensile stress which may interact with the internal tensile stress of chromium deposited thereon to account for the occurrence of the observed Type Y cracking. The cracking directions thus observed are consistent with the direction of buffing scratches. If chromium were plated on surfaces free of such residual stresses, then Type Y cracking should not occur. Such surfaces could be prepared by electropolishing off the stress-containing layer or by appropriate stress-relief annealing. Comparison of results obtained by these two procedures would also permit evaluation of the effect of surface profile on the cracking mechanism.

In order to determine which one of the three hypotheses is primarily responsible for the occurrence of Type Y cracking, laboratory work was undertaken to test the above postulates. Interaction of stresses of bright nickel and chromium deposits on polished steel was also explored as a matter of more current interest, since there is little present commercial use of buffed nickel.

Experimental Procedures

All chromium plating was done in a "conventional" bright plating bath containing 32 oz/gal (240 g/l) CrO_3 and 0.32 oz/gal (2.4 g/l) H_2SO_4 . Bath

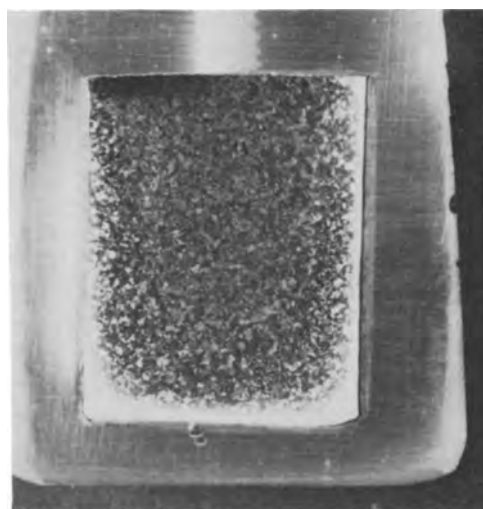


Fig. 3. Nickel bar specimen potted in epoxy resin. Electropolished and chromium plated. Magnification approximately 3X.

temperature was controlled at $110^\circ \pm 3^\circ\text{F}$. Current densities of 1.0 and 1.5 amp/in.² (144 and 216 amp/ft²) were used to obtain 0.040-mil thick chromium deposits. In the case of 3-in. wide panels, a half-box was used to insure uniform deposit thickness (8). Other specimens of large grained wrought nickel bar stock were potted in an epoxy resin² casting (see Fig. 3) to facilitate handling and to insulate all but one face. Electrical contact was made with a No. 6 screw through a tapped hole in the side of the casting. No attempt was made to control current distribution on these potted samples, since the deposit was seriously nonuniform in thickness only on the rim of the plated face.

Nickel electropolishing was done in a phosphoric-sulfuric-chromic acid bath (15) at room temperature, using current densities of 2.2 to 2.5 amp/in.². The bath composition is 65% H_3PO_4 , 15% H_2SO_4 , 6% CrO_3 [weight per cent (w/o) of anhydrous acids], balance water. Satisfactory polishing is obtained with the bath specific gravity above 1.70.

The panels used were either purchased 3 x 4 in. pre-plated panels with 1.0 mil of buffed Watts nickel (5, 8) or buffed 3 x 4 in. panels cut from 0.040-in. thick, high purity (99.9%), annealed nickel sheet.

Crack patterns were examined using a conventional metallographic microscope. Surface profile information and chromium thickness measurements were obtained by interference microscopy (16). Where deemed advisable, photomicrographs were made. Cracks were emphasized in some cases by partially stripping the chromium anodically (at 6v) in 5% potassium dichromate solution.

Additional buffing of panels was done by normal techniques of commercial hand buffing. Polishing of the mounted small samples was done with conventional metallographic equipment and techniques.

Experimental Results

Effect of dimensions of plated area on crack pattern.—Buffed 3 x 4 in. panels were used. Areas of 3 x 3 in. and 3 x 2 in. were plated by adjusting the half-box (8) position so that only the required area

² Bakelite Resin ERL 2774, 100 parts; hardener ZYL 0812, 22.5 parts by weight.

was immersed in the plating bath. One panel was cut to a 3 x 3 in. square, and another to a 3 x 2 in. rectangle before plating for comparison with deposits of similar dimensions on 3 x 4 in. panels.

Type Y cracking, oriented as in Fig. 1, was found in the deposits on all panels. The direction was not affected by dimensions.

Effect of variations in microprofile on cracking.—Verification of dependence of crack direction on buffing direction.—The buffed 3 x 4 in. panels were used. Some were buffed at right angles to the original buffing direction. On others, approximately half of the panel area was buffed at right angles to the original buffing direction. The panels were then chromium plated.

In both cases, Type Y cracking approximately perpendicular (with the normal 20° angular spread) to the last buffing direction was obtained. On the second group of panels, cracks could, in some instances, be followed through approximately 90° bends across the boundary zone between buffing directions.

Effect of large scratches (size and direction) on crack patterns.—On buffed nickel panels, a steel phonograph needle was used to scribe a number of parallel grooves (1/8 in. apart) in the direction of buffing, at 90° to, and at 45° to this direction. On another panel, the same patterns were scribed in 1 in. square patches so that all patterns were on the same basis metal. The panels were then chromium plated.

Crack patterns of varying complexity were obtained. Where grooves were parallel to the buffing direction, Type Y cracks were found at right angles to the grooves and buffing direction. The only effect noted was that cracks crossed the scribed grooves at very nearly 90° angles while the usual 70° angularity was found in the original buffed areas. Near grooves perpendicular to the buffing direction, cracking was more complex. Some cracks perpendicular to either the grooves or the buffing direction appeared to cross each other. Others could be found which crossed a groove perpendicularly, then bent through about 90° to cross buffing scratches. The over-all effect was that of a very coarse Type M cracking. Near the grooves scribed at a 45° angle to the buffing direction, Type Y cracks perpendicular to the grooves predominated but were mixed with similar but fewer cracks perpendicular to the more prominent scratches. The same cracking patterns were noted on the panel containing patches of all the groove angles.

Effect on crack pattern of abrasion with grits of many sizes.—Examination of buffed nickel surfaces with the aid of an interference microscope showed the surface contour to be a very fine (5-40 μin. deep) sawtooth profile. To determine if the peak-to-valley depth of this profile had any effect on Type Y cracking of chromium, potted nickel specimens (mounted as described above) were unidirectionally polished on water-lubricated silicon carbide grits (AB Grinding Paper, Buehler 1469 SW) and then chromium plated. Grit sizes used were 240, 320, 400, and 600. Profiles, by interferometry, were found to be similar to those of buffed nickel surfaces except for depths. Surprisingly, it appeared that most of the grooves

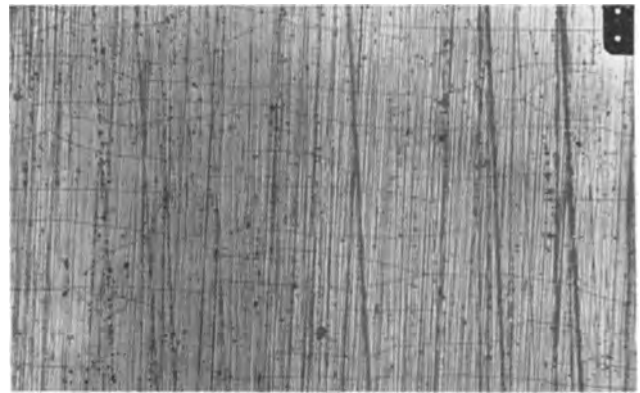


Fig. 4. Type Y cracking in chromium plated on nickel polished with 320-grit silicon carbide paper. Magnification approximately 100X.



Fig. 5. Type Y cracking in chromium plated on nickel polished on 400-grit silicon carbide paper. Magnification approximately 100X.

were only 0.01 to 0.02 mil deep; a few grooves ranged up to 0.1 mil in depth. The number and dimensions of the latter seemed to depend on the grit size and "age" of the paper used. When chromium was plated on these abraded surfaces, Type Y cracking occurred as illustrated in Fig. 4 and 5.

To complete the study of effect of scratch or groove size on chromium cracking, these specimens were also unidirectionally polished on metallographic polishing wheels (laps). A canvas cloth (Buehler AB 1592) was used with a suspension of polishing alumina No. 1 (Buehler AB 1550), and a "Kitten-ear" cloth (Buehler AB 1598) with alumina No. 2 suspension (Buehler AB 1551). Cracking, as illustrated in Fig. 6 and 7, was obtained. These cracks are more irregular in spacing and direction than those on buffed or grit polished surfaces. Conventional (nondirectional) polishing of the specimens prior to chromium plating resulted in an apparent Type M crack pattern. On closer examination of the deposit, individual cracks were found to cross the more prominent scratches at right angles, and to be independent of superficial scratches.

Effect on crack pattern of electropolishing.—Initial trials with electropolishing were made on the buffed, nickel plated panels. About 0.08-0.1 mil (of the 1.00 mil thick nickel plate) had to be removed to obliterate all traces of scratches left by the buffing. The resulting brightly reflecting surface had a smoothly undulating contour marred by considerable



Fig. 6. Type Y cracking in chromium plated on nickel polished on canvas lap using Buehler No. 1 alumina. Magnification approximately 100X.

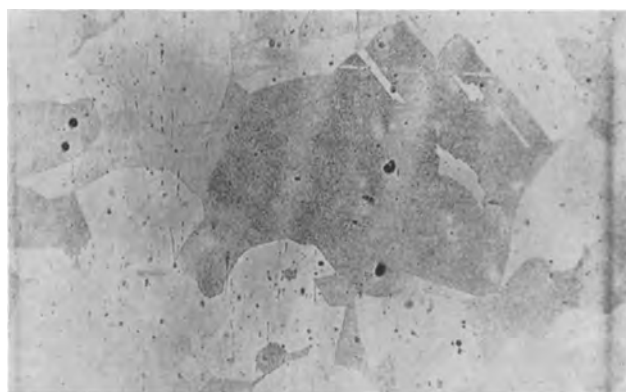


Fig. 8. Appearance of chromium deposit on electropolished rolled nickel (same material as the specimen shown in Fig. 3). Magnification approximately 100X.

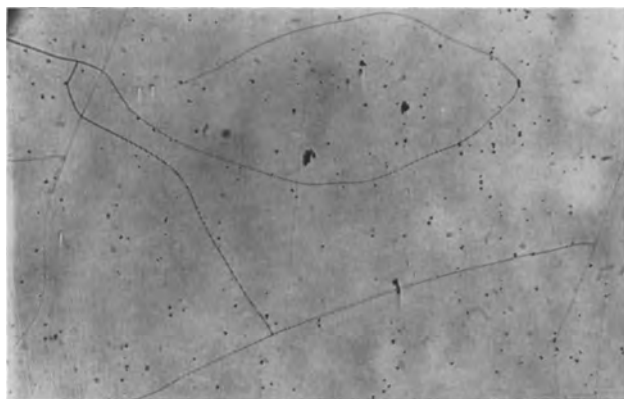


Fig. 7. Type Y cracking in chromium plated on nickel polished on "Kitten-ear" cloth lap using Buehler No. 2 alumina. Magnification approximately 100X.

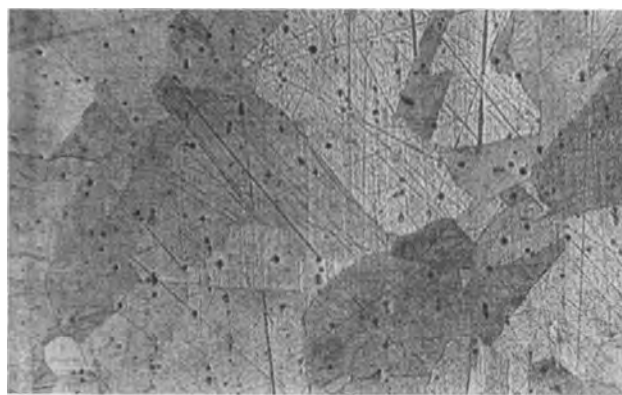


Fig. 9. Appearance of the surface of rolled nickel after metallographic polishing and etching (Marble's reagent). Magnification approximately 100X.

pitting. On chromium plating samples which had been sufficiently electropolished, no Type Y cracking was observed. Type M cracking did occur when the chromium deposit thickness was increased to about 0.06-0.08 mil. Reproducibility and quality of the surface was very poor when buffed, plated nickel was electropolished. It was found that equivalent cracking results were obtained with wrought nickel on which surfaces were of better quality and more reproducible. Mounted bar stock specimens were therefore used for further work. As expected, it was found that the electropolishing time required to eliminate all traces of sharp scratches, *i.e.*, to round out the grooves, was approximately proportional to the grit size used in polishing. In general, undulating or rippled profiles of varying periodicity, roughly comparable to those of the grit polished surface, were obtained. Startlingly, chromium plated on the bright surface of electropolished nickel (with no visible grain structure) had the appearance of a polished and etched surface prepared for metallographic examination. Figure 3 shows this effect very well and Fig. 8 is a photomicrograph of this chromium. For comparison, Fig. 9 shows the appearance of the specimen metallographically polished and etched.

Effect of annealing on crack pattern.—It was considered that Type Y cracking was prevented on electropolished nickel by removal of the abrasion-deformed surface layer containing directional residual stresses which interact with the deposit

internal stress to produce oriented cracking. In order to determine that removal of the strained layer and not the change in surface contour was the effective operation, buffed 0.040 in. thick wrought, high purity nickel panels (2 x 3 in.) were subjected to a "stress equalizing" anneal (17) (2 hr at 500°F in an all-glass apparatus at a pressure of 0.5×10^{-5} mm Hg). Surface contour was unchanged and, after chromium plating, no Type Y cracking was observed in the bright deposit.

Cracking of chromium plated on bright nickel deposits.—The results of the work described above indicated that, since directional residual tensile stresses in a surface layer of mechanically polished nickel had considerable influence on chromium cracking, it was in order to explore the effect of high internally stressed bright nickel plate as a base for chromium deposits. Bright nickel was therefore plated on 0.010 in. thick buffed brass and on 0.090 in. thick flat polished bumper stock panels. Because of contamination during previous use, the proprietary bright plating bath yielded deposits with tensile stress of about 54,000 psi [as determined by the rigid flat strip method (18)], so high that improper cleaning of the basis metal was revealed by spontaneous peeling of the nickel plate. On properly cleaned samples, no cracks were visible in the adherent nickel deposits even when viewed under a microscope.

The thin brass panels became concave toward the plated side during nickel plating and developed an

oval or elliptical crack pattern after chromium plating, presumably the result of the stress distribution in the nickel deposit. The steel bumper stock panels, when bright nickel and chromium plated, developed Type Y cracks perpendicular to the direction of flat polishing of the steel, very similar in detail to the patterns in chromium plated on abraded nickel. Only on steel which had been subjected to a 1-min electropolish (in the same bath used for electropolishing nickel) was adhesion of the nickel completely satisfactory. There was no significant change in surface contour. On conventionally cleaned steel, the plate could be peeled off, after chromium plating, by prying up with a needle at the readily visible cracks. As this suggested cracking through the nickel to the steel, an electropolished and plated panel with visible cracks was immersed in a slightly acid (pH 3.00) potassium bromide (1M) solution containing 1 g/l o-phenanthroline. Positive indication of iron (pink coloration) appeared at the cracks almost instantaneously, and upon making the panel anodic (at 1.0v against Pt), a strong red-pink color appeared immediately at the cracks. This was taken as proof that cracking through the nickel had indeed occurred.

Properties of chromium deposited on electropolished nickel.—The “metallographic etch” effect obtained by plating chromium on large-grained wrought nickel was believed to be due to variations in texture of the chromium on the individual grains of nickel (see Fig. 8). It suggested that deposit porosity might be related to structure, and that corrosion behavior would be similarly affected. An electropolished specimen of nickel was chromium plated to a thickness of 0.020 mil and then, to reveal porosity, copper plated at 0.2v for 2 min in an acid copper bath (11). Discrete nodules and lines of copper were found on the surface as illustrated in Fig. 10. After sketching the pattern of copper nodules found on a large grain, the copper was removed by scrubbing with a cotton swab and a suspension of magnesium oxide. The specimen was then made anodic (1.0v against Pt) in an acid potassium bromide solution for 5 min. After examining the same area and finding no apparent change in appearance,

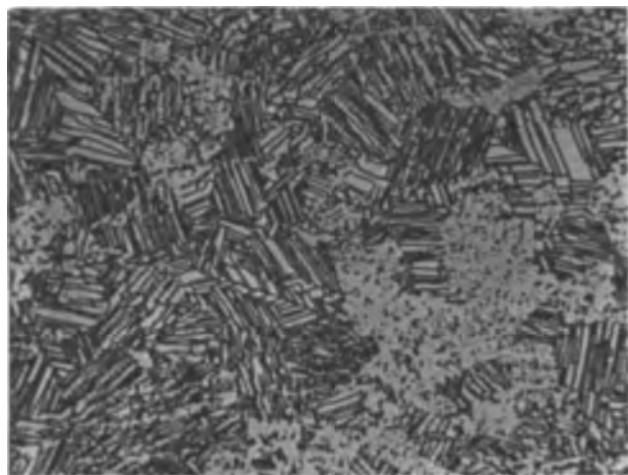


Fig. 10. Structure dependent porosity revealed by copper deposit on chromium plated on electropolished nickel. Magnification approximately 100X.

the chromium was anodically dissolved in 5% potassium dichromate. Under the microscope, a series of plane-faceted, remarkably regular pits were found which corresponded to the location of copper nodules. In individual grains, the pits varied in size but had similar shapes which were, variously triangular based pyramidal, square based, or flat-bottomed boat shaped.

Properties of chromium deposited on other metals.—Because of the striking effects obtained with chromium plated on electropolished nickel, trials were made by plating on electropolished Monel, Inconel, and copper. Results of such plating duplicated those obtained on nickel. Copper plating of the samples after chromium plating resulted in copper nodules and lines distributed much as on similarly treated nickel.

Chromium plated on spherical nickel single crystal.—The variation of chromium deposit surface character appeared to be related to structural variations on individual grains of nickel and other metals and suggested a high degree of epitaxy. To explore this, a spherical nickel single crystal³ was electropolished and chromium plated. With thin chromium deposits (plated 2 min at a nominal 1 asi), the plate seemed to be bright and smooth when the sphere was examined in diffuse light. In the beam of a flashlight, however, squares, triangles, and narrow rectangles could be seen. With thicker deposits (5-10 min), regular bright and dull areas could be seen on the sphere. Again, these could be more easily seen when examined in a flashlight beam. Examination of the sphere surface with a microscope, using a 2-circle goniometer, established, from symmetry relationships, that bright smooth squares of chromium were found at positions corresponding to cube faces; bright, regularly lined triangles at octahedral faces; and dull, nodular, roughly circular patches at dodecahedral faces. Between these figures, a regular line array of chromium nodules was found. Copper deposition indicated pore-free chromium in the cube-face squares, lines of pores in the octahedral face triangles, randomly scattered pores in dodecahedral face circles, and regular lines of pores on the remainder of the sphere surface. Anodically corroding the chromium plated sphere in acidified potassium bromide or sodium chloride solutions showed the variety and regularity of pit shapes at regularly repeated areas on the sphere as had been observed in individual grains of polycrystalline nickel. With still heavier deposits of chromium, Type M cracking occurred which was readily observed only on the bright surfaces at cube face and octahedral face positions; the nodules characteristic of thick chromium deposits tended to obscure the crack pattern in the intermediate areas.

Discussion of Results

The experimental results are largely self-explanatory in that two of the basic hypotheses tested have been rejected and the third accepted as valid. Interaction of deposit tensile stress with directional tensile stress in the substrate provides the most satis-

³Purchased in this form from Virginia Institute for Scientific Research, Richmond, Virginia.

factory explanation of the occurrence, orientation, and direction of Type Y cracks in chromium plated on abraded or buffed nickel.

These findings also permit speculation about related matters such as magnitude of polishing-induced stresses, effect of abrasive size on stresses, effect of stresses on underlying electrodeposits, basis metal finishing, and the structure of the chromium deposit.

The magnitude of the tensile stress in the uppermost layer of buffed nickel can be estimated if the following assumptions are made: (i) Stresses of base and deposit are additive. (ii) Stress of uncracked deposit is approximately proportional to thickness. (iii) Cracking occurs when internal stress equals or exceeds the tensile strength of the deposit.

Brenner (19) found, in chromium deposits plated at similar conditions, a maximum stress of about 80,000 psi. From this and the properties of heat treated deposits, he suggested 80,000 psi as the approximate ultimate tensile strength of an uncracked chromium deposit. It was found in this investigation that when 0.08-0.1 mil of buffed nickel was removed by electropolishing, or when buffed nickel was annealed, directionally oriented cracking of chromium deposits did not occur. From this, it is concluded that significant stresses are present only in the surface layer, and since directionally oriented chromium cracking occurs at deposit thicknesses about half that in which the nonoriented cracking is first observed on electropolished nickel, it is presumed that half the fracturing stress arises in the nickel substrate. At a chromium thickness of 0.025 mil, the total stress required to fracture a 1 in. wide section would be about 2 lb. The average unit stress in a 0.1 mil thick surface layer of nickel, then, must be about 10,000 psi, or in an 0.08-mil layer, 12,500 psi. This value is comparable to the 15,000 psi tensile stress found by Noble (20) near the surface of "abusively" abraded steel and very different from the 15,000-25,000 psi compressive stress induced by normal polishing and buffing procedures. (However, his method did not detect stresses in layers as thin as 0.1 mil.) A measurement of stress in buffed nickel (21) by an x-ray method gave values of 3000-6000 psi compression but, again, this is an average stress in a layer considerably thicker than 0.1 mil and probably results from the compressive deformation observed by Samuels (14) beneath abraded metal surfaces. Perhaps a more sensitive method could detect tensile stresses in such thin layers, but it appears that chromium plating and cracking afford at least a rough estimate of such stresses.

The crack spacing, and the chromium deposit thickness at which cracking is first observed, appears to be inversely proportional to the size of SiC grit used to abrade nickel surfaces, suggesting that stresses are higher in the rougher surface produced by abrasion on 240 grit than on a surface abraded on 600 grit. The reduced crack frequency in chromium plated on surfaces produced by metallographic polishing probably signifies a lower stress level in a very thin layer, with possibly some influence from stress-concentrating factors, such as failure of the

chromium to cover a nonmetallic inclusion in the base (see Fig. 7).

The above speculations are of potential value in understanding the behavior of brittle electrodeposited chromium and seem also to be substantially correct in accounting for the directionality of cracking of brittle, tensilely stressed bright nickel on polished steel when plated with chromium. The tensile stress induced by the relatively coarse "flat polishing" of the steel plus the internal stress of the bright nickel deposit were not apparently enough to cause cracking as visible cracking occurred only when the high stress of chromium was added. Since bright nickel with stress as high as 54,000 psi typically is very brittle and has ultimate tensile strengths over 150,000 psi (18), a considerable total stress must be required to crack this brittle deposit. Chromium, at the thickness used, can provide such high stress as shown by Brenner (9) and by Stareck (7) who found maximum stresses (spiral contractometer method) of 80,000 and 150,000 psi, respectively. Assuming that the chromium cracked and produced a notch in the surface of the nickel which acted as a stress riser, the nickel then probably cracked very rapidly without yielding as do other brittle, notch-sensitive materials. These results and hypotheses indicate that the problems of electrodeposit stress control and basis metal surface finish require further study if for no other reason than to confirm the existence of their interaction.

The apparent epitaxy exhibited by chromium plated on stress-free nickel suggests that "bright" chromium is bright not because of inherently small grain size (22) or decomposition of unstable hydrides of chromium (23) but because the chromium deposits epitaxially on the extremely small grains in buffed nickel or in bright nickel plate. The results of plating on a spherical nickel single crystal might perhaps have been predicted from the work of Reddy and Wilman (27) except that they reported no such textural effects in chromium plated on copper single crystal faces. Work is under way on plating of chromium on nickel single crystals which, it is hoped, will permit a better understanding of the deposition of chromium on nickel (and, perhaps, of other base-deposit combinations) and which may contribute to an understanding of the role of stresses in growth and cracking of electrodeposits.

Manuscript received May 13, 1963; revised manuscript received March 13, 1964. This paper was presented at the New York Meeting, Sept. 29-Oct. 3, 1963.

Any discussion of this paper will appear in a Discussion Section to be published in the June 1965 JOURNAL.

REFERENCES

1. W. E. Lovell, E. H. Shotwell, and J. Boyd, *Proc. Am. Electroplaters' Soc.*, **47**, 215 (1960).
2. J. H. Lindsay, W. E. Lovell, and D. W. Hardesty, *ibid.*, **48**, 165 (1961).
3. E. J. Seyb, *ibid.*, **47**, 209 (1960).
4. W. H. Safranek, R. W. Hardy, and H. R. Miller, *ibid.*, **48**, 156 (1961).
5. R. L. Saur, *Plating*, **48**, 1310 (1961).
6. W. H. Safranek, H. R. Miller, and C. L. Faust, *ibid.*, **49**, 607 (1962).
7. J. E. Stareck, E. J. Seyb, and A. Tulumello, *Proc. Am. Electroplaters' Soc.*, **41**, 209 (1954).

8. C. F. Nixon, J. D. Thomas, and D. W. Hardesty, *ibid.*, **47**, 90 (1960).
9. A. Brenner and S. Senderoff, *ibid.*, **35**, 53 (1948).
10. H. Fry, *Trans. Inst. Met. Finishing*, **32**, 107 (1955).
11. W. Blum, W. P. Barrows, and A. Brenner, *J. Research Nat. Bur. Standards*, **7**, 697 (1931).
12. W. H. Safranek, H. R. Miller, and R. W. Hardy, *Proc. Am. Electroplaters' Soc.*, **47**, 96 (1960).
13. N. A. Nielsen, "Physical Metallurgy of Stress-Corrosion Fracture," T. N. Rhodin, Editor, p. 121, Interscience Publishers, New York (1959).
14. L. E. Samuels, *Proc. Am. Electroplaters' Soc.*, **46**, 122 (1959).
15. Fedot'ev and Grilikhes, "Electropolishing, Anodizing, and Pickling," p. 119, Robert Draper, Ltd., Teddington, England (1959).
16. J. D. Thomas and S. R. Rouze, *Proc. Am. Electroplaters' Soc.*, **42**, 49 (1955).
17. "Metals Handbook," 1948 Ed., p. 1032, ASM, Cleveland, Ohio (1948).
18. W. M. Phillips and F. L. Clifton, *Proc. Am. Electroplaters' Soc.*, **34**, 97 (1947).
19. A. Brenner, P. Burkhead, and C. W. Jennings, *ibid.*, **34**, 32 (1947).
20. H. J. Noble, *SAE Spec. Publ. 181*, May 1960.
21. J. G. Roberts, Private communication (1963).
22. W. A. Wood, *Trans. Faraday Soc.*, **31**, 1248 (1935).
23. C. A. Snavely, *Trans. Electrochem. Soc.*, **92**, 537 (1947).
24. E. M. Baker and A. M. Rente, *ibid.*, **54**, 337 (1928).
25. D. J. MacNaughton and A. W. Hothersall, *Trans. Faraday Soc.*, **31**, 1168 (1935).
26. E. M. Baker and W. L. Pinner, *SAE Journal*, **22**, 331 (1928).
27. A. K. N. Reddy and H. Wilman, *Trans. Inst. Met. Finishing*, **36**, 97 (1958-1959).

A Three-Point Probe Method for Electrical Characterization of Epitaxial Films

John Brownson¹

Microwave Associates, Incorporated, Burlington, Massachusetts

ABSTRACT

A three-point probe has been devised which makes possible simple, rapid measurements of resistivity and conductivity type of epitaxial silicon films. The probe in contact with a silicon crystal is effectively a point-contact diode with ohmic base termination. The external circuitry measures this "diode's" V-I characteristics. Its peak inverse voltage is a predictable function of resistivity and hence resistivity is determined from this parameter. The advantage of the probe is that special preparation of rectifying and nonrectifying contacts is not necessary. The design, calibration, and operation of the probe are discussed in addition to some experimental results such as resistivity as a function of location within the reactor and a relatively simple method for measurement of resistivity gradient in the film. Finally, the method's limitations in measuring thin, high resistivity films are described and capability limits defined.

For measurement of resistivity of epitaxial films there have been two commonly used methods. The first method is to process a high resistivity control slice of opposite conductivity type along with a lot of substrates to be evaluated (1). Since the film on the control slice is of the opposite conductivity type from the slice itself, the film is effectively isolated by a p-n junction and direct four-point probe measurements are possible. The main disadvantage of this method is that the film on the control slice can be appreciably less doped than the films on the other substrates due to a lack of proximity to heavily doped substrate sources. Another disadvantage of the method is that it is inherently a sampling procedure with 100% inspection impossible.

The second method commonly used for measurement of resistivity of epitaxial films is to fabricate diodes from a sample of the material to be evaluated and to measure the capacitance per unit area from which the film resistivity may be calculated (2). The disadvantages of this method are that it requires relatively elaborate techniques and equipment, the method is costly and time consuming, and is also inherently a sampling procedure.

Aware of these disadvantages, we have sought a method which would provide reasonably accurate results and yet require relatively simple techniques and equipment. Accordingly, the breakdown voltage of whisker contacts on silicon has been investigated to determine whether a predictable dependence on resistivity exists. Initially, a two-point probe with a conventional curve tracer was used for this purpose. The second point used to complete the circuit did not provide an adequate ohmic contact, and since it contributed appreciable IR drop, the accuracy of apparent breakdown voltage measurements was questionable. The problem was solved simply by adding a third point to the probe as shown in Fig. 1. The third point, at which the output voltage is now detected, carries negligible current and thus contributes negligible IR drop to the output. Probe spacing has no appreciable effect on the display which represents the E-I characteristic associated with the whisker contact only. A 3.5 mil blunt tungsten wire was used for the whisker and 20 mil blunt Dumet wire for the other probe points. The tungsten whisker is a standard diode part and readily replaceable. The probe output impedance is typically 20-100 kilohms; the 9 megohm multiplier resistor reduces to

¹Present address: Department of Electrical Engineering, Massachusetts Institute of Technology, Cambridge, Massachusetts.

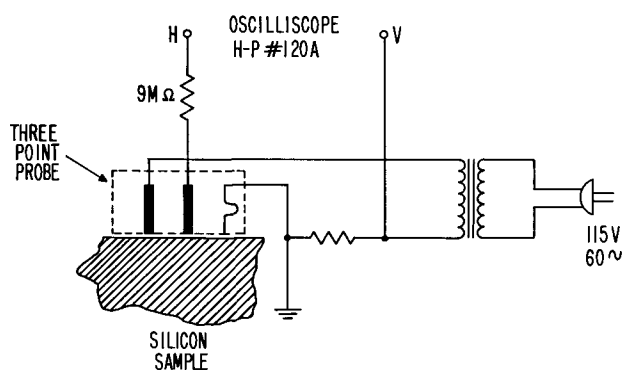


Fig. 1. Three-point probe schematic

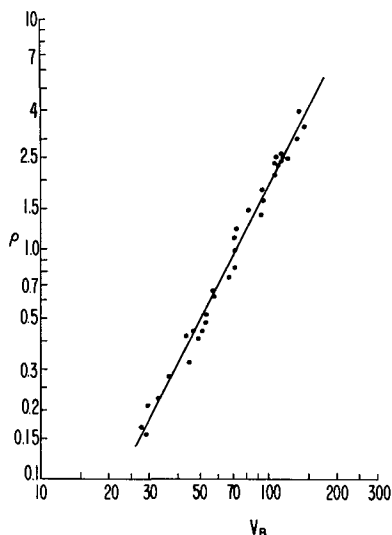


Fig. 2. Three-point probe calibration curve for homogeneous n-type silicon.

negligible proportions the loading effect of the oscilloscope input.

Calibration

In order to determine the relationship between whisker breakdown voltage and resistivity, a test group was prepared consisting of 36 samples of homogeneous n-type silicon covering the resistivity range 0.2-4 ohm-cm. The resistivity of each sample was measured several times using a four-point probe and the average value recorded. Two samples were eliminated due to resistivity inhomogeneity. The breakdown voltage for each sample was measured several times using the three-point probe and the average value recorded. Figure 2 shows a scatter diagram of the experimental results. Correlation with the indicated line of regression is sufficiently good that a useful determination of resistivity is possible.

Several general characteristics for whisker breakdown have been observed and should be mentioned. First, breakdown voltage down to about 15v may be defined by the peak value preceding a negative resistance region in the E-I characteristic. This feature makes it unnecessary to specify an arbitrary value of current for the breakdown voltage measurement. Leakage current up to breakdown voltage is typically 5-20 ma. Second, film surfaces must be free of chemical contamination in order to make reliable

measurements. Jitter, "dog-leg" breakdown, and instability are characteristic of such contamination. Slices immediately after deposition are normally quite clean and suitable for measurement. When indications of contamination have been observed, water and ammonia washes have been successfully used to achieve reproducible results. Third, leakage current increases appreciably with increased whisker pressure and apparent breakdown voltage decreases moderately. Our measurements are based on a minimum pressure touch contact. Fourth, breakdown voltage measurement reproducibility is not good enough for a single measurement to characterize a specimen accurately. We normally make several measurements and average them. If a series of measurements is made on a specimen, typically 75% of the individual measurement are within 10% of the mean value. Fifth, the cleanliness and perhaps the mechanical uniformity of the point tip seem to have an effect. When in doubt, one should replace the tungsten whisker. Sixth, breakdown voltage increases with increased temperature. In order to minimize E-I heating, we use minimum point pressure. Seventh, breakdown voltage decreases with increased point diameter. Consequently, a three-point probe must be empirically calibrated.

Using the least squares method, the line of regression for the calibration data was found to be $V_B = 73\rho^{0.51}$. This line pertains to results obtained before the 9 megohm resistor was added to the test circuit. Subsequent measurements indicate that with minimum circuit loading, the exponent may be as high as 0.56 or 0.57.

The median deviation from the line of regression in Fig. 2 is less than 10%, and this is considered the accuracy capability for the technique.

Some Typical E-I Characteristics

Figure 3 is an oscillograph of E-I characteristics using the curve tracer equipment previously described. It is a double exposure comparing the characteristics of the same n-type epitaxial silicon specimen using first a two-point probe and then a three-point probe for measurement. Calibration is 10 ma per division vertical and 20v per division horizontal. The difference between the two forward characteristics in the second quadrant is quite striking. There is less difference between the reverse characteristics

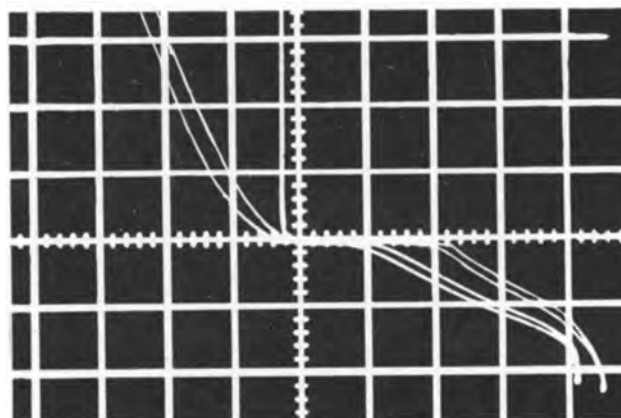


Fig. 3. Two-point vs. three-point probe

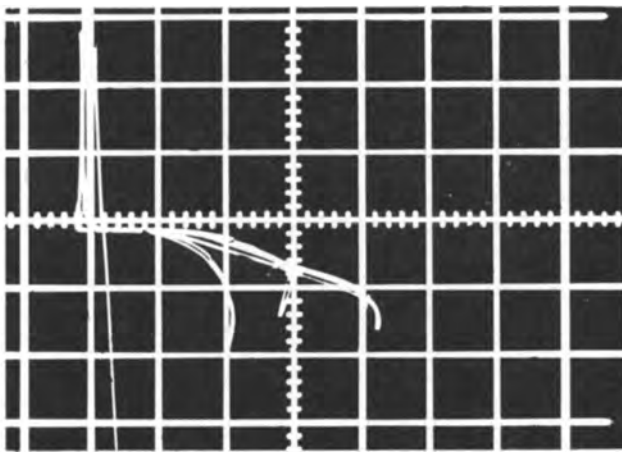


Fig. 4. Family of curves for different film resistivities

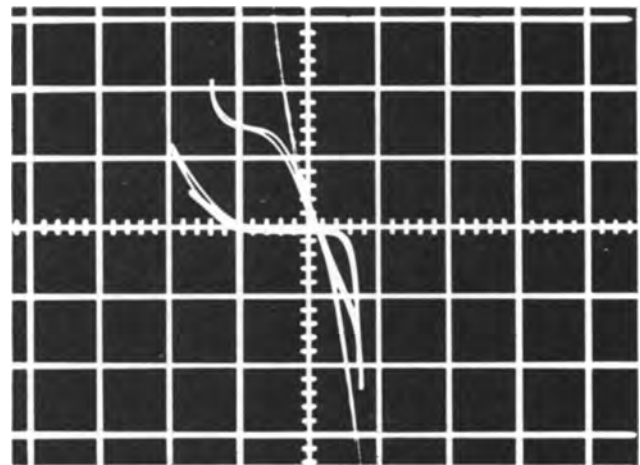


Fig. 6. Irreversible breakdown

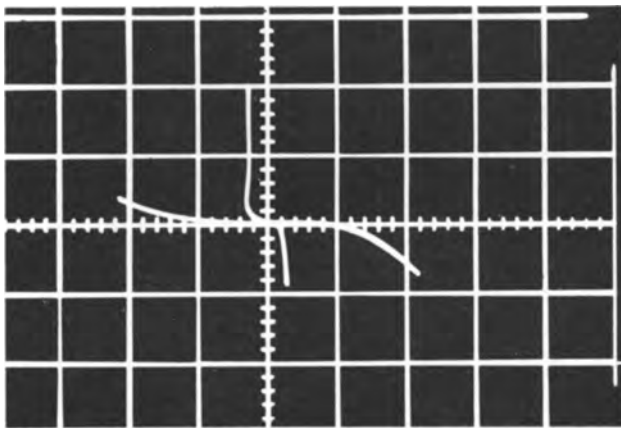


Fig. 5. N-type vs. p-type

in the fourth quadrant. Apparent breakdown voltage using the two-point probe is characteristically greater than that using the three-point probe, but the increment depends on geometry, pressure, and other variables.

Figure 4 is multiple-exposure oscillograph comparing E-I characteristics of several n-type epitaxial silicon specimens of various resistivities. The very low reverse voltage specimen is a substrate with no epitaxial film. Calibration is 10 ma per division vertical and 20v per division horizontal with the origin displaced three divisions to the left of center.

Figure 5 is a double exposure oscillograph comparing E-I characteristics of n-type and p-type films. The second quadrant contains the forward characteristic of the n-type specimen and the fourth quadrant the forward characteristic of the p-type specimen. The opposite, of course, is true of the reverse characteristics. Calibration is 10 ma per division vertical and 10v per division horizontal. There is completely unambiguous conductivity-type indication down to micron thick, low resistivity films using the three-point probe.

When relatively thin films are measured using the three-point probe, irreversible, destructive breakdown occurs at the region under the whisker. For films as thin as 0.3 mil, this occurrence is not unusual, and for those 0.1 mil and less it is characteristic. This phenomenon undoubtedly originates in excessive power dissipation at the whisker contact. A very

small discolored spot on the film surface can occasionally be seen under magnification where destructive breakdown has occurred. Figure 6 is multiple exposure oscillograph showing progressive destructive breakdown of a p-type film 0.1 mil thick. Calibration is 5 ma per division vertical and 5v per division horizontal. The localized shorts produced by this destructive breakdown would affect only a very small fraction of the number of devices fabricated on an epitaxial slice if the individual device area is small.

V_B vs. Location in the Reactor

Figure 7 shows three-point probe breakdown voltage as a function of location in the reactor for a deposition run in an early model horizontal system. The large $\frac{3}{4}$ round slices are high resistivity p-type slices, and the small $\frac{3}{4}$ round disks on top are low resistivity n-type substrates. The films on each are n-type. In general, the breakdown voltages on the p-type slices tend to be appreciably higher than those on the adjacent n-type substrates showing that the film on the substrates is doped appreciably more than on the high resistivity slices. Also, the breakdown voltages generally tend to decrease downstream indicating cumulative doping.

Resistivity Gradient Measurement

The resistivity gradient in epitaxial films may be measured, using the three-point probe, as follows: (a) measure film thickness using the infrared interference technique (3); (b) bevel lap the specimen at a small angle, say 2° ; (c) measure whisker breakdown voltage down the bevel surface as a function

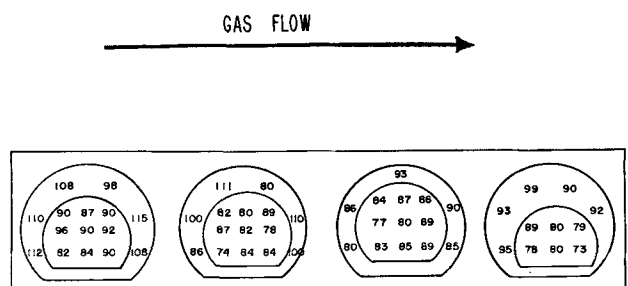


Fig. 7. Breakdown voltage as a function of location in the reactor

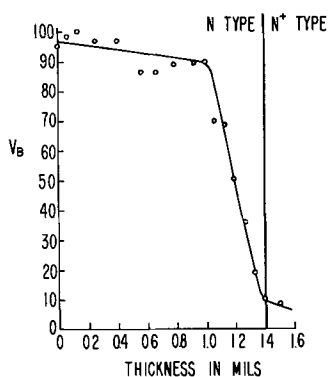


Fig. 8. "Typical" resistivity profile

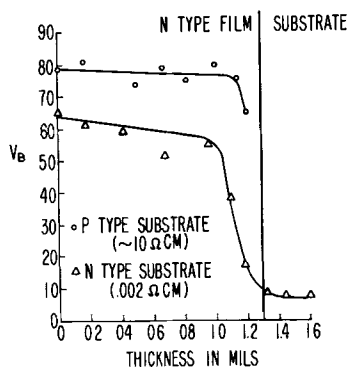


Fig. 9. Comparison of films on adjacent n+ and p substrates

of lateral displacement from the intersection of the bevel plane and the film surface; (d) convert breakdown voltage to resistivity if desired and convert arbitrary lateral displacement units to thickness units. Figure 8 is the plot of a typical profile. An abrupt change of slope at some point near the substrate is characteristic. There is some uncertainty in the measurements close to the interface due to the problem of resolving small displacements with a relatively large diameter whisker and also due to the possibility of punch-through as discussed in the Appendix.

Figure 9 compares the gradients in the films formed on adjacent high resistivity p-type and low resistivity n-type substrates. The films on each are n-type. The profiles show that the doping level at the surface of the sampling slice is appreciably lower than for the n+ substrate. This disparity between the film on the sampling slice and that on the n+ slice is characteristic of all samples we have measured.

In general, for an n on p control slice, resistivity values determined with the three-point probe are consistently greater than those resulting from four-point probe measurements. Three-point probe resistivity values range from 120% to 200% of four-point values with 140% the typical ratio. The four-point probe measures reciprocal average conductivity from surface to junction according to the law

$$\rho \text{ Avg} = \frac{x_j - x_o}{\int_{x_o}^{x_j} \sigma(x) dx}$$

The three-point probe, on the other hand, measures resistivity only in the region occupied by the deple-

tion layer at breakdown voltage. The width of this region depends on the resistivity and the resistivity gradient in the film and in many practical cases is appreciably less than the over-all film thickness. The relatively heavily doped material of initial deposition reduces the over-all average resistivity measured by the four-point probe whereas this material normally does not affect the three-point probe measurement. Thus, the disparity in the results obtained from the two measurement methods can be explained. Another contributing factor may be poor isolation between the film and the substrate in the four-point probe measurement; the more current shunted through the substrate, the lower will be the apparent resistivity.

Probe V_B vs. Device PIV

We have found a three-point probe breakdown voltage characterization of epitaxial films to be quite useful. A practical example is illustrated in Fig. 10 and 11 which compare finished device PIV's with three-point probe measurements made on the slices prior to device fabrication. For deep diffusions, PIV's correlate with V_B 's but are generally moderately greater. For shallow diffusions, there is also correlation but PIV's tend to be somewhat less than three-point probe voltages. A reliable predictability of finished device PIV has been achieved.

Conclusions

The three-point probe method characterizes epitaxial films without some of the disadvantages of the other methods. In a production situation, large quantities of material may be quickly and inexpensively evaluated. Sampling and destructive testing are not necessary. Relatively simple equipment and procedures are used. A reliable determination of

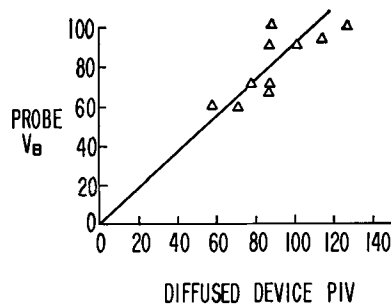


Fig. 10. Correlation of V_B with device PIV for deep diffusions

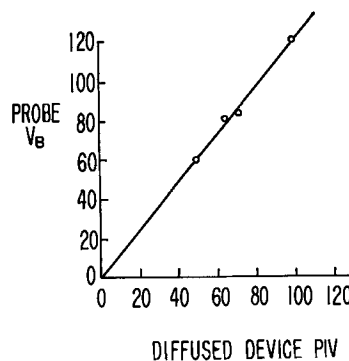


Fig. 11. Correlation of V_B with device PIV for shallow diffusions

conductivity type is obtained. Although the three-point probe does not give a complete evaluation of the layer, the information it gives is generally more relevant for device fabrication than that obtained from a four-point probe sheet resistance measurement on an n on p control slice.

Acknowledgment

The author wishes to acknowledge help from several colleagues at Microwave Associates, Inc., in particular Arthur Uhler, Jr., who suggested adding a third point to a two-point probe, and Edward Gordon, who performed the mathematical analysis.

Manuscript received Dec. 31, 1963; revised manuscript received March 16, 1964. This paper was presented at the Los Angeles Meeting, May 6-10, 1962.

Any discussion of this paper will appear in a Discussion Section to be published in the June 1965 JOURNAL.

APPENDIX

Limitations of the three-point probe.—If Poisson's equation is solved for an abrupt p-n junction and planar boundary conditions apply, the following well-known relationship may be derived

$$V = \frac{W^2}{2\epsilon\mu\rho}$$

where V is the applied potential in volts, W the depletion layer width in centimeters, ϵ the permittivity of the material in farads per centimeter, μ the majority carrier conduction mobility in volt seconds per cm^2 , and ρ the resistivity in ohm-centimeters. It is reasonable to assume that this relationship also holds for the three-point probe because (a) the distribution of free charge is sharply discontinuous at the whisker contact and (b) the contact diameter (~ 3.5 mils) is large compared to the depletion layer widths considered here.

Whenever the film thickness is equal to or greater than the depletion layer width at breakdown voltage, the probe sees the equivalent of an infinitely thick sample and the calibration curve in Fig. 2 should be applicable.

However, when the film is thinner than the depletion layer would be in a homogeneous sample, a special boundary condition is imposed, and it is believed the calibration curve does not apply. Under this condition, the depletion layer below a biased whisker contact extends through the entire film thickness at a terminal voltage less than breakdown voltage (4). In such a case, with increasing terminal voltage, the depletion layer width would increase negligibly due to the low resistivity of the substrate. On the other hand, the field strength in the depletion layer would increase at a greater rate than would be the case if the resistivity were uniform. Therefore, the critical field strength and hence breakdown voltage are reached at a lower terminal voltage than would be the case if no resistivity discontinuity existed.

For a given constant film thickness, as resistivity is increased beyond that at which this punch-through phenomenon² begins to occur, the probe breakdown voltage in theory should change relatively slowly due to accompanying changes in the electric field intensity distribution in the depletion region. Thus, the hypothesis is proposed that the breakdown voltage ($V_B = 73\rho^{0.51}$), for which the depletion layer width just equals the film thickness, represents a practical limit, V_{\max} , for three-point probe voltages for a given film thickness. For such films, and for those of yet higher resistivity, breakdown voltage is V_{\max} and should be a function of thickness only. For a given film thickness, after a certain ρ_{\min} is exceeded, V_B becomes essentially constant and loses its functional dependence on ρ . The ρ_{\min} , a function of thickness only, is that resistivity for which the depletion layer width at breakdown voltage just equals the film thickness.

² This punch-through phenomenon is a completely reversible breakdown process and should not be confused with the irreversible, destructive breakdown previously discussed.

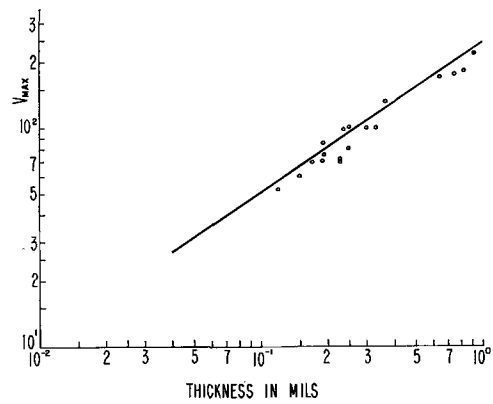


Fig. 12. Thickness vs. V_{\max}

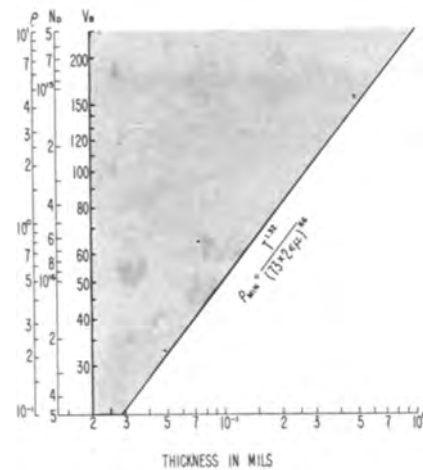


Fig. 13. Thickness vs. ρ , N_D , V_B

The functional relationships for V_{\max} and ρ_{\min} may be readily derived by applying the boundary conditions of the hypothesis to the equations already described. They are

$$V_{\max} = \frac{17.5T^{0.68}}{(2\epsilon\mu)^{0.34}}$$

$$\rho_{\min} = \frac{T^{1.32}}{17.5(2\epsilon\mu)^{0.66}}$$

where T is the film thickness in centimeters. The number 17.5 has dimensions of $\text{volt}^{0.66} (\text{ohm-cm})^{-0.34}$.

To investigate this hypothesis, a series of experimental epitaxial runs was made for which the reactants were undoped, and all possible care was taken to avoid extraneous contamination. The samples were carefully measured for thickness and three-point probe breakdown voltage. The resulting values are plotted on Fig. 12. Also plotted in Fig. 12 is the $V_{\max} = V(T)$ function of the hypothesis. Over nearly a tenfold range of thickness, experimental results conform strikingly to the theoretical prediction. The resistivity of several of the samples was measured using the differential capacitance method (5), and in each case the resistivity was many times higher than would be predicted using the calibration curve of Fig. 2.

It is thus tentatively concluded that the hypothesis is correct and that the functions relating V_{\max} and ρ_{\min} to film thickness are probably useful approximations.

In Fig. 12, the region above the curve is a domain in which three-point probe measurements cannot occur. For films of $\rho \geq \rho_{\min}$, the results will plot along the curve and for films of $\rho < \rho_{\min}$, the results will plot below the curve. Whenever a sample plots significantly below the curve it is an indication that the calibration curve of Fig. 2 is valid. Whenever a sample plots close to the curve in Fig. 12, it is an indication that the three-point probe voltage may not be a measure of film resistivity.

Figure 13 has been prepared for convenience in analyzing an epitaxial sample. Whenever the sample

plots in the unshaded portion of the graph, the three scales ρ , N_D , and V_B are equivalent. Whenever the sample is in the shaded forbidden region or along the curve, the scales are not equivalent.

REFERENCES

1. H. C. Theuerer, *This Journal*, **108**, 650 (1961).
2. *Ibid.*
3. M. P. Albert and J. F. Combs, *ibid.*, **109**, 709 (1962).
4. C. C. Allen and E. G. Bylander, "Evaluation Techniques for and Electrical Properties of Silicon Epitaxial Films," AIME Meeting, Los Angeles, August 1961.
5. D. Kahng, R. C. Manz, M. M. Atalla, and C. O. Thomas, Paper presented at Electrochemical Society Meeting, Detroit, October 1961.

Correlation of Electrical Measurements with Chemical Analysis in Zinc- and Cadmium-Diffused GaAs

J. Black

General Telephone & Electronics Laboratories, Inc., Bayside, New York

ABSTRACT

Hall effect and resistivity measurements of zinc-diffused and cadmium-diffused GaAs are compared with chemical determinations of the diffusant concentration in the samples. The form of the diffusion profile in the diffused layer was varied from near linear through a complementary error function profile to a discontinuous-type concentration-dependent diffusant distribution. The results show that, unlike sheet resistance-type measurements, Hall effect measurements are a reliable means of directly determining the average diffusant concentration regardless of the form of the penetration profile or the variation of mobility in the diffused layer. Free carrier concentrations calculated from Hall effect measurements were accurate within $\pm 20\%$ of the chemically determined diffusant concentration over a range of acceptor concentrations from greater than $10^{20}/\text{cm}^3$ to $10^{18}/\text{cm}^3$ in GaAs.

Numerous papers published over the last few years (1-5) describe methods for correlating sheet conductance (or sheet resistance) measurements with dopant concentrations in diffused semiconductor layers. Measurements of this kind are important in evaluating device fabrication procedures. In general, however, conductance-type measurements require that the dependence of mobility on the free carrier concentration and the form of the diffusion profile be known to interpret the measurement accurately in terms of the average diffusant concentration. If the mobility of the charge carriers is affected by compensating impurities or if the form of the diffusion profile is not known, then serious errors are introduced in all of the methods mentioned above. On the other hand, the Hall effect is much less sensitive to variations in mobility than is the resistivity and hence is inherently more accurate as a means of determining the free carrier concentration.

Recently, measurements of the Hall effect have been used to determine the average diffusant concentration and the surface concentration in diffused silicon wafers (6, 7). These investigations, however, considered only the case of a complementary error function (erfc) type of diffusion profile in the diffused layer.

The purpose of this paper is to present the results of measurements of the average Hall effect in zinc- and cadmium-diffused GaAs wafers in which various types of concentration profiles including erfc profiles were produced in the diffused layer. The accuracy of the Hall-effect measurement was checked directly by chemical determination of the diffusant concen-

tration in the samples. It is shown that the form of the diffusion profile in a diffused layer has little effect on the accuracy of the average Hall effect measured and that the free carrier concentration calculated from the Hall effect measurement is accurate within $\pm 20\%$ over an acceptor concentration range from greater than $10^{20}/\text{cm}^3$ to $10^{18}/\text{cm}^3$ in GaAs. Although all of the measurements reported herein were performed on samples with p^+-p diffused structures rather than the usual $p-n$ junction configuration it is shown that the measurements can be made as well on samples containing $p-n$ junctions.

Experimental Methods

Slices of n -type single-crystal GaAs of low free-carrier concentration ($n < 5 \times 10^{16}/\text{cm}^3$) were ground and lapped on both faces to a surface finish of about 1μ and were then lightly etched in $\text{NaOH-H}_2\text{O}_2$ solution. After grinding and etching, the faces of the slices were parallel to within 2% of their thickness. Groups of three or more slices of the same thickness (within 2%), along with several grams of finely powdered GaAs and a weighed quantity of pure zinc or pure cadmium, were encapsulated in evacuated quartz tubes. During evacuation, the capsule and its contents were outgassed by heating to several hundred degrees centigrade several times until the heating produced no further increase in pressure. The capsules were sealed off at 10^{-6} mm Hg pressure.

The GaAs slices, the GaAs powder, and the diffusant were arranged so that the diffusant was transported by the vapor only. The region of the capsule containing the diffusant was always the coolest

part of the capsule, (about 5°C cooler than the temperature of the GaAs during diffusion) which insured that the diffusant would not condense on the GaAs to cause alloying or melting of the samples. Before diffusion, each group of encapsulated samples was given a preliminary heating which was 2 hr at 900°C for zinc and 4 hr at 1000°C for cadmium. In preliminary tests in which this was not done, considerable surface alloying and partial melting of the samples occurred during the initial stages of diffusion. Apparently the GaAs powder absorbed a large fraction of the dopant during the preheat period, and this served to suppress surface alloying and partial melting of the slices at the subsequent higher diffusion temperature. Immediately after this pretreatment, the temperature was increased to the diffusion temperature. The temperature for zinc diffusion was 1175°C; for cadmium diffusion it was 1200°C. To prevent condensation of dopant vapors on the GaAs slices or on the powder during cooling from the diffusion temperature, the capsule was cooled so that the region containing the GaAs was always hotter than the rest of the capsule. When the capsule had cooled to about 600°C, it was quenched into water. The whole cooling and quenching procedure required no more than 3 min.

The finely powdered GaAs served to minimize surface decomposition of the slices by supplying most of the arsenic required to fill the free volume of the capsule. Since the powdered GaAs was at the same temperature as the GaAs slices, exactly the right partial pressure of arsenic was maintained. In addition, because the powder particle size was small (less than 0.001 in. diameter) compared to the diffusion depth, the concentration of dopant diffused into the powder was a good measure of the surface concentration of the dopant in the diffused slices. Since the sizes, shapes, and origins of the prepared slices were the same and since all slices in any diffusion run were diffused under identical conditions it was assumed that any slice from a given diffusion run was an exact duplicate of any other slice in that run. Thus, incremental grinding operations and chemical analysis could be carried out on different slices with the results being regarded as derived from one slice. After the capsule was cracked open and the diffused wafers were recovered, bar-shaped Hall samples were cut from one of the diffused slices. Another of the diffused slices had measured and equal increments removed from both faces by careful grinding. The powdered GaAs, the remainder of the diffused slice from which the Hall samples were cut, and the remainder of the ground slice were analyzed by a spectroscopic technique which was accurate within $\pm 20\%$. The average diffusant concentration in the layer removed by grinding was then calculated algebraically from the chemical analyses and the thickness of the diffused sample before and after grinding. The analysis data were used to plot an approximate concentration profile for each diffusion run, as shown in Fig. 1.

Although all samples were n-type of low free-carrier concentration before diffusion, the underlying insulating layers in the diffused slices, *i.e.*, those regions

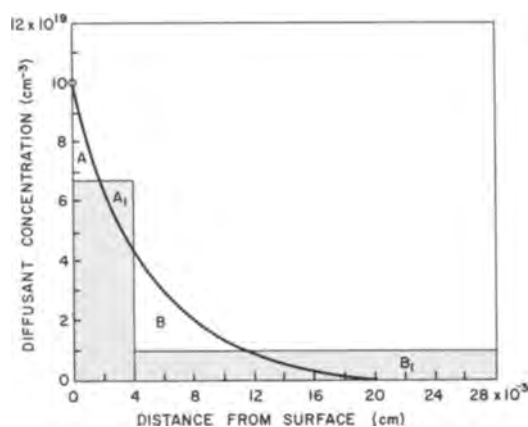


Fig. 1. Method of determining the approximate concentration profile in diffused samples. The open circle is the diffusant concentration in the diffused powder. The shaded regions denote the average diffusant concentration in the surface layer removed by grinding (0.4×10^{-3} cm) and in the remainder of the ground sample (4.28×10^{-3} cm). The profile line is drawn to cut the shaded regions so that $A_1 = A$, and $B_1 = B$. The sample is actually diffused equally from both faces, but since the diffused sample is symmetrical we need only represent the region from one face to $\frac{1}{2}$ the sample thickness to describe the concentration profile.

which were essentially free of diffusant, were converted to p-type during diffusion. This was established by monitoring the conductivity type with a thermoelectric "hot point" probe as the sample was ground to $\frac{1}{2}$ thickness to remove one of the diffused layers. These p-type central regions showed a uniform resistivity of about 1 ohm-cm which is equivalent to an acceptor concentration of about $10^{17}/\text{cm}^3$ in GaAs. Spectroscopic analysis revealed that several parts per million of copper were picked up during sample preparation and/or diffusion treatments. This contamination was sufficient to cause the conversion from n- to p-type, but its effect on the average Hall coefficient was neglected in view of the much larger average Zn and Cd concentrations present in these diffused slices. Since the entire diffused slice was of the same conductivity type, the total thickness of the Hall sample was used to calculate the Hall coefficient and resistivity.

Current contacts were formed by plating the ends of the Hall sample bars with rhodium. Hall and resistivity contacts were formed by alloying pure indium spheres onto the samples using a graphite jig to maintain good alignment of the spheres during alloying. A sketch of the prepared Hall sample is shown in Fig. 2. The Hall effect was measured by the

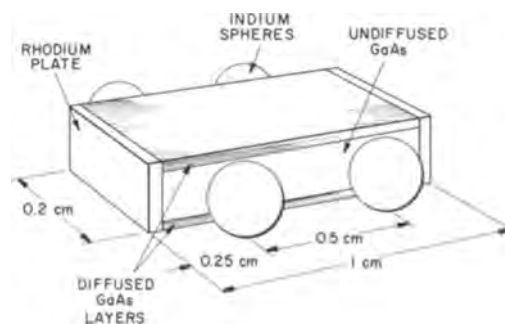


Fig. 2. Sketch of prepared Hall sample. The shaded regions near the surface represent the diffused layers.

usual d-c technique at magnetic field strengths of 4500 gauss, and the free-carrier concentration was calculated from the relation $n = 1/R_H e$. The measured Hall effect on the two sets of Hall probes on each sample agreed within 10%, while the resistivity measured on the resistance probes agreed within 5%.

Experimental Results and Discussion

The effect of inhomogeneities and gradients in the carrier concentration on the Hall effect have been investigated both theoretically (8-11) and experimentally (9-11) in recent years. These investigations considered the general case of the magnetic field dependence of galvanomagnetic effects in a semiconductor sample as affected by gradients in the carrier concentration. Essentially, for a given average free carrier concentration, gradients in the carrier concentration can cause the measured Hall coefficient to be far larger than in a homogeneous sample. Thus the calculated average free carrier concentration in a nonuniform sample can be significantly lower than the true average carrier concentration. In particular, the theory was well developed for gradients in the carrier concentration along the direction of current flow. In this investigation, however, the gradient in the carrier concentration is perpendicular to the direction of current flow. Theoretical considerations by Bate and Beer (9) indicate that gradients of the latter kind should have little or no influence on the Hall effect. In any case if the phenomena described above are of any consequence we will observe a measurable change in the Hall coefficient as the magnetic field is increased. It was determined that the Hall coefficient did not vary by more than $\pm 5\%$ (which was the precision of the Hall measurement) with magnetic field over a range of field strength from 4500 to 6500 gauss in the samples reported on herein.

The use of the simple relation $n = 1/R_H e$ to calculate the average free-carrier concentration in a diffused layer implies that the average Hall coefficient measured is independent of the carrier mobility. Tufte (6) pointed this out recently by calculations which showed that the average Hall coefficient measured in diffused silicon wafers is dependent on the mobility, but only weakly so, over the range of doping from $10^{21}/\text{cm}^3$ to $10^{16}/\text{cm}^3$. Assuming a mobility independent Hall effect, Tufte calculated the average free-carrier concentration to be in error by about -50% , at the most, in the region from $10^{20}/\text{cm}^3$ to $10^{17}/\text{cm}^3$ where the carrier mobilities in Si were varying most rapidly with the carrier concentration. The experimental data obtained in our investigation shows that the simplifying assumption of a mobility independent Hall coefficient introduces an error of less than -50% in the calculated free-carrier concentration over a doping range from greater than $10^{20}/\text{cm}^3$ to $10^{18}/\text{cm}^3$ in p-type diffused layers in GaAs.

By variation of the slice thickness, the diffusant, and the diffusion schedule, several types of diffusant concentration profiles were produced in the samples. The type of penetration profile present in each sample was determined from chemical analysis, as

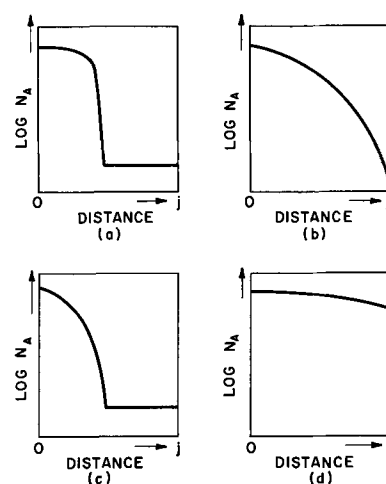


Fig. 3. The four types of concentration-penetration profiles produced in the diffused samples. See text for a description of each. The boundary j represents the limit of the diffused region which is sampled; j corresponds to the midplane in our samples, but would correspond to the p-n junction in a diode structure.

shown in Fig. 1, from electrical measurements with successive removal of thin layers by careful grinding, from examination of polished and etched transverse sections under the microscope, and from the published results of other investigations (12, 13) of the diffusion of zinc and cadmium into GaAs. There were essentially four different kinds of penetration profiles represented in the diffused layers of our samples: (a) a concentration-dependent diffusion profile superimposed on a low-level background of the same conductivity type; (b) a complementary error function profile; (c) a complementary error function diffusion profile superimposed on a low-level background of the same conductivity type; (d) a near linear diffusion profile of the type produced by diffusion into a thin slab at constant surface concentration where the diffusion depth is of the order of the slab thickness for the greater part of the diffusion period. These profiles are illustrated in Fig. 3. Diffusion profiles of type (d) could be produced by prolonged diffusion of either zinc or cadmium into GaAs. Diffusion profiles of type (a) were produced by limited diffusion of zinc into GaAs at constant surface concentration greater than $10^{19}/\text{cm}^3$, while profiles of types (b) and (c) were produced by diffusion of cadmium into GaAs. The distinct difference in the form of type (a) and (b) profiles could be

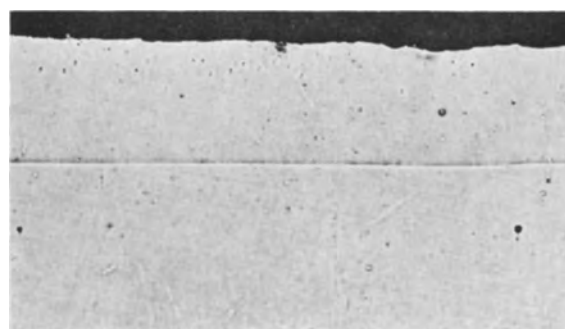


Fig. 4. Photomicrograph of etched $p^+ - p$ boundary in zinc diffused GaAs. Etched with $\text{HNO}_3 - \text{AgNO}_3 - \text{HF}$ solution. The black region is the mounting material. Magnification 100X.

Table I. Chemical analysis and Hall effect data for zinc diffused GaAs

Sample	Chemical analysis				Hall effect	Ratio of
	N_s, cm^{-3*}	N_c, cm^{-3*}	t, cm^*	\bar{N}, cm^{-3*}	$\bar{N}_H, \text{cm}^{-3*}$	\bar{N}_H/\bar{N}
33 (d)	2.3×10^{20}	4×10^{19}	0.071	7.4×10^{19}	8.3×10^{19}	1.12
31 (d)	1.5×10^{20}	7×10^{19}	0.059	1.0×10^{20}	1.0×10^{20}	1.00
36 (d)	1.5×10^{20}	5×10^{19}	0.054	8.5×10^{19}	7.8×10^{19}	0.92
35 (d)	1.5×10^{20}	3×10^{19}	0.061	7.1×10^{19}	6.4×10^{19}	0.90
32 (a)	1.3×10^{20}	$<1 \times 10^{19}$	0.079	4.3×10^{19}	4.2×10^{19}	0.98

* N_s is the surface concentration, N_c is the concentration at $\frac{1}{2}$ the sample thickness estimated from the approximate concentration profile, t is the thickness of the sample, \bar{N} is the average zinc concentration, \bar{N}_H is the average free carrier concentration determined from Hall effect measurements.

Table II. Chemical analysis and Hall effect data for cadmium diffused GaAs

Sample	Chemical analysis				Hall effect	Ratio of
	N_s, cm^{-3}	N_c, cm^{-3}	t, cm	\bar{N}, cm^{-3}	$\bar{N}_H, \text{cm}^{-3}$	\bar{N}_H/\bar{N}
9A (b)	4.0×10^{19}	$<1 \times 10^{18}$	0.037	5.6×10^{18}	6.9×10^{18}	1.23
5D (d)	3.5×10^{19}	1.3×10^{19}	0.016	1.6×10^{19}	1.9×10^{19}	1.19
3C (d)	2.3×10^{19}	9×10^{18}	0.015	1.7×10^{19}	1.5×10^{19}	0.88
9C (b)	1.5×10^{19}	$<1 \times 10^{18}$	0.035	4.9×10^{18}	4.3×10^{18}	0.88
8C (c)	1.3×10^{19}	$<1 \times 10^{18}$	0.062	2.5×10^{18}	2.3×10^{18}	0.92

N_s, N_c, t, \bar{N} , and \bar{N}_H are defined in the caption of Table I.

seen in polished and etched transverse sections of diffused samples. Figure 4 shows a photomicrograph of a zinc-diffused wafer ($c_s = 2 \times 10^{20}/\text{cm}^3$) in which a sharp p^+-p diffusion front is visible. Chemical analysis of such samples indicates that this p^+-p boundary occurs at a zinc concentration of about $1 \times 10^{19}/\text{cm}^3$ which corresponds well with the concentration that marks the characteristic knee in the penetration profile of heavily zinc-diffused GaAs (12). This is a region of a sharp gradient in the zinc concentration which is the probable cause of the appearance of a well-defined junction on etching. No sharp p^+-p diffusion front is visible in cadmium-diffused samples at the highest concentrations attainable ($c_s = 5 \times 10^{19}$ at./ cm^3).

The correlation between free-carrier concentration and chemical analysis for the diffused samples is shown in Tables I and II. The surface concentration, the concentration at the mid-plane of the sample (N_c) estimated from the concentration profile, and the thickness of the sample are included in the tables to indicate the concentration gradient in each sample. The letters after each sample indicate the type of diffusion profile. The agreement between the free-carrier concentration and the chemical analysis is, for every sample, within the limits of experimental error over the entire range of doping

covered by the two diffusants which shows that the use of the simple relation $n = 1/R_H e$ does not introduce a serious error in the calculation of the average free-carrier concentration in these samples. The good agreement between the average free-carrier concentration and the chemical analysis data indicates that the higher surface concentrations listed in Table I and Table II are lower limits of the solid solubility of the dopant at the given diffusion temperature, in accord with other measurements (12, 13).

To determine whether the symmetry of the diffused sample, i.e., whether diffused into one face or simultaneously into both faces, could have an effect on the accuracy of the electrical measurements, several samples were ground to remove completely one of the diffused p-layers. The results of electrical measurements and chemical analyses for these samples are given in Table III. The agreement between chemical analysis and free-carrier concentration confirms that the symmetry of the diffused wafer has little effect on the accuracy of the Hall effect measurement. It was noted that the contact area of the alloyed indium spheres used to measure the Hall effect and resistivity voltages did not always cover the entire thickness of the diffused sample. In fact some samples showed that only a small portion of

Table III. Chemical analysis and Hall effect data for diffused GaAs

Sample	Diffusant	Chemical analysis		t, cm	\bar{N}, cm^{-3}	Hall effect	Ratio of
		N_s, cm^{-3}	N_c, cm^{-3}			$\bar{N}_H, \text{cm}^{-3}$	\bar{N}_H/\bar{N}
8A				0.066	4.9×10^{18}	3.8×10^{18}	0.78
8B* (c)	Cd	2.5×10^{19}	$<1 \times 10^{18}$	0.034	3.8×10^{18}	3.9×10^{18}	1.03
40A				0.065	5.2×10^{19}	5.4×10^{19}	1.04
40B* (d)	Zn	8.5×10^{19}	2×10^{19}	0.030	5.7×10^{19}	6.0×10^{19}	1.05
39A				0.066	1.05×10^{20}	8.5×10^{19}	0.81
39B* (d)	Zn	1.2×10^{20}	4×10^{19}	0.034	9.9×10^{19}	8.7×10^{19}	0.88

Starred samples (*) have had one diffused layer removed by grinding. N_s, N_c, t, \bar{N} , and \bar{N}_H are defined in the caption of Table I.

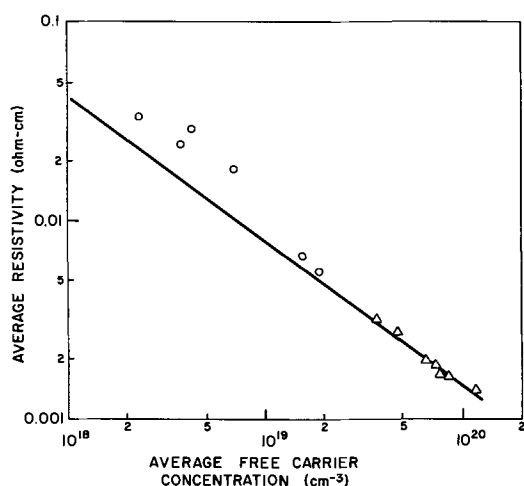


Fig. 5. Average resistivity vs. average free carrier concentration for diffused samples. The solid line represents the resistivity normally measured in GaAs melt-doped with zinc or cadmium; \circ , cadmium diffused; \triangle , zinc diffused.

one of the diffused layers was contacted by the indium spheres. This made little difference in the accuracy of the measurements, either. Thus the exact placement of the Hall and resistivity probes is not critical, which considerably simplifies the task of making satisfactory contacts to samples of this type.

Figure 5 shows the correlation obtained between the average free-carrier concentration and the average resistivity. The solid line was fitted to measurements of the resistivity and free-carrier concentration of many melt-doped samples (cadmium-doped and zinc-doped) taken from published data and was assumed to represent the resistivity one could expect from uncompensated uniformly doped single crystals. Now, depending on the form of the diffusant profile, the mobility variation with free-carrier concentration and the average free-carrier concentration in the diffused layer, the average resistivity (or average conductivity) of the layer may not be an accurate measure of the average free-carrier concentration (1-7). In order to determine accurately the average free-carrier concentration (diffusant concentration) from the average resistivity we require accurate data regarding the variation of mobility with free-carrier concentration for the sample being measured as well as an accurate mathematical description of the form of the diffusant concentration profile. Only when the mobility is known and is essentially invariant over the range of free-carrier concentration present will the average resistivity be useful as a reasonably accurate direct measure of the average free-carrier concentration in a diffused sample. The correlation between the average resistivity and the average free-carrier concentration shown in Fig. 5 is, for all zinc diffused samples and for several cadmium diffused samples, well described by the solid line. This shows that over the range of acceptor concentration present in these samples the mobility does not vary enough to cause serious deviation in the average resistivity. For most of the cadmium dif-

fused samples, however, it is evident that the average resistivity is not a good direct measure of the average free-carrier concentration. In these samples it is necessary to take into account the other factors mentioned above to correctly interpret the resistivity measurements. On the other hand the Hall effect data can be directly interpreted in terms of the average free-carrier concentration for any of the cadmium diffused samples as well as for the zinc diffused samples through the simple $1/R_{He}$ relation.

Although all of the measurements described herein were performed on samples with a diffused p^+-p configuration, samples with a diffused $p-n$ junction structure can be measured just as effectively. The essential difference between the two types of samples is that in the p^+-p samples the current flow along the length of the sample is restricted by four insulating sample-air interfaces while in the $p-n$ junction samples the current flow is restricted by three insulating sample-air interfaces and an insulating $p-n$ junction. The main difficulty in measuring diffused layers where a $p-n$ junction is formed by the diffusion lies in making electrical contacts to the diffused region without shorting across the $p-n$ junction. This can usually be accomplished by using alloy dots doped to the same conductivity type as the diffused layer so that if the dots spread across the $p-n$ junction during the alloying process, blocking or rectifying contacts will be formed that will effectively prevent shorting of the $p-n$ junction. Of course the thickness of the diffused layer (*i.e.*, the depth of the $p-n$ junction) must also be measured to calculate the correct Hall effect in the layer.

Acknowledgment

The author wishes to thank J. Daly for his assistance in various phases of the experiments and S. Weissberger for the spectroscopic analysis of the diffused samples.

Manuscript received Jan. 2, 1964; revised manuscript received March 20, 1964.

Any discussion of this paper will appear in a Discussion Section to be published in the June 1965 JOURNAL.

REFERENCES

1. G. Backenstoss, *Bell System Tech. J.*, **37**, 699 (1958).
2. R. Glang and W. B. Easton, *This Journal*, **107**, 758 (1960).
3. H. S. Veloric and W. J. Greig, *R.C.A. Rev.*, **21**, 437 (1960).
4. D. B. Cuttriss, *Bell System Tech. J.*, **40**, 509 (1961).
5. J. C. Irvin, *ibid.*, **41**, 387 (1962).
6. O. N. Tufte, *This Journal*, **109**, 235 (1962).
7. V. K. Subaschiev and S. A. Poltinnikov, *Soviet Phys. Solid State*, **2**, 1059 (1960).
8. C. Herring, *J. Appl. Phys.*, **31**, 1939 (1960).
9. R. T. Bate and A. C. Beer, *ibid.*, **32**, 800 (1961).
10. R. T. Bate, J. C. Bell, and A. C. Beer, *ibid.*, **32**, 806 (1961).
11. A. C. Beer, "Galvanomagnetic Effects in Semiconductors," Chap. X, Academic Press, New York (1963).
12. F. A. Cunnell and C. H. Gooch, *SERL Tech. J.*, **10**, 83 (1960).
13. B. Goldstein, *Phys. Rev.*, **118**, 1024 (1960).

Evaluation of Passivated Integrated Circuits Using the Scanning Electron Microscope

T. E. Everhart,¹ O. C. Wells,² and R. K. Matta

Research Laboratories, Westinghouse Electric Corporation, Pittsburgh, Pennsylvania

ABSTRACT

By examining passivated silicon integrated circuits in the scanning electron microscope, the surface contours of p-n junctions have been mapped, potential drops across integrated resistors have been observed, and physical characteristics of the oxide surface, evaporated leads, and bonded gold wires have been determined. Typical faults discovered by this method of testing include poor registration, improperly masked diffusions, harmful and nonharmful surface scratches, poor evaporated interconnections, and defective passivation oxide layers. Most junctions in a 40 mil square integrated circuit can be delineated with 1μ resolution in approximately 1 min by this technique.

In many present-day applications, integrated semiconductor circuits fabricated on a single wafer of silicon are replacing circuits made by connecting discrete electrical components together. The integrated circuit is inherently smaller and lighter than the discrete component circuit, and it is potentially cheaper and more reliable. However, its successful manufacture requires exacting control of many successive process steps; this control becomes more difficult as the size of integrated circuits decreases. Mask registration and surface structure on integrated circuits are evaluated during and after fabrication by light-microscope observation. Electrical testing of the integrated circuit is carried out by applying voltages or currents at certain of the external leads and observing the resulting voltages or currents at the remainder of these leads. This testing determines whether or not the circuit meets its design specifications; it does not determine why a given circuit (or entire production run of circuits) is faulty. Measurements at internal circuit nodes to help determine why a circuit is faulty require that electrical contact be made with needle-like probes. As integrated circuits become smaller, probe measurements become more tedious and time consuming, and the probability that the probe will mechanically damage the circuit surface increases.

The use of the scanning electron microscope to detect reverse-biased p-n junctions in germanium and gallium phosphide was demonstrated several years ago (1-3). This technique has now been extended to passivated integrated circuits. By applying appropriate potentials to an integrated circuit while it is being examined in the scanning electron microscope the surface contours of p-n junctions have been evaluated, potential drops across integrated resistors have been observed, surface inversion layers have been detected, and the physical appearance of the oxide surface, evaporated leads, and bonded gold wires has been determined. In some cases it has been possible to determine junction contours without

externally applied potentials. In these cases, it is believed that the contact potential drop which exists at p-n junctions has been detected.

The theory and operation of the scanning electron microscope has been described in detail previously (3-6). A review paper (7) has pointed out the great depth of field possible with this instrument and has described how voltage contrast between two areas at different potentials is achieved. The work described below differs from most previously reported work in that the angle between the electron beam and the specimen normal has generally been about 15° instead of 60° . This geometry minimizes image foreshortening and still yields excellent contrast between sample areas at different potentials. An accelerating voltage of either 10 or 16 kv has been used for this work, and the electron probe diameter has generally ranged between 0.2 and 0.8μ . A pressure of 10^{-6} Torr was normally obtained in the vacuum system used, which was provided with a liquid nitrogen trap, and was back-filled with dry nitrogen before opening it to atmospheric pressure.

It is worth emphasizing that the power dissipated at the sample is extremely small, ranging from several nanowatts to several microwatts. The peak power density can be high because the current is focused into a very small spot, but the average power density at the sample is quite small because this spot is continually scanned over the sample surface. In practice, no noticeable heating of the sample has been observed. Neither do the bombarding electrons damage the crystal structure of the sample, since their energy is far below the threshold value required to produce lattice defects (8). It should, however, be pointed out that the complete range of effects of the electron bombardment on the oxide-silicon system are not at present fully understood, and it may prove that these have a harmful effect on passivated transistors.

Interpretation of Scanning Electron Micrographs

The geometrical interpretation of scanning electron micrographs has been summarized by Smith

¹ Permanent address: Department of Electrical Engineering, University of California, Berkeley 4, California.

² Present address: CBS Laboratories, Stamford, Connecticut.

and Oatley (6); the contrast caused by potential differences between two adjacent areas of a semiconductor surface has been discussed by Everhart, Wells, and Oatley (3). The present paper deals almost exclusively with passivated silicon devices; the silicon surface of these devices is covered with a passivating layer which may range from a few hundred to several thousand angstrom units in thickness. Under scanning electron microscope examination, the surface of this insulator assumes very nearly the same potential as the semiconductor surface which it protects, and furthermore, this potential of the oxide surface is observed to be very stable. This relationship between the semiconductor potential and that of the oxide surface is believed due to electron-beam-induced conductivity (9-11). Energetic primary electrons generate hole-electron pairs in the oxide as well as in the silicon beneath it; these carriers are free to move through the insulator until they recombine or are trapped. In particular, if an electric field exists between the surface of the insulator and the semiconductor-insulator interface, the carriers generated by the primary beam will move to neutralize this field. This electron-beam-induced conductivity depends on many parameters, including the electron probe accelerating voltage and current, the probe diameter, the rate-of-scan, the trap density in the oxide and at the oxide-semiconductor interface, and the mobilities of electrons and holes in the oxide. While it is beyond the scope of this paper to discuss this complex subject in more detail, it should be noted that to date all experimental observations and preliminary analytical calculations support this explanation of electrostatic stabilization of the oxide surface by electron-beam-induced conductivity.

In evaluating passivated integrated circuits, it is often desirable to compare scanning electron micrographs of a given area taken under different bias conditions. Such a pair of comparison micrographs is

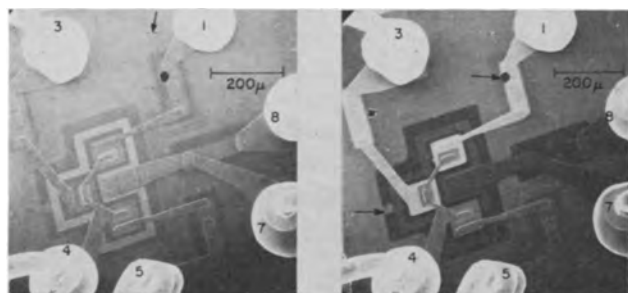


Fig. 1. Scanning electron micrographs of experimental DCTL NOR gate "A," illustrating voltage contrast between areas at different potentials. (a) (right) zero bias; (b) (left) applied bias, $V_1 = V_3 = -2v$, $V_4 = V_5 = 0v$, $V_7 = V_8 = 2v$.

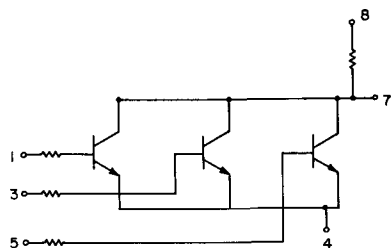


Fig. 2. Equivalent lumped-element circuit of DCTL NOR gate

shown in Fig. 1. The equivalent lumped analog of this integrated circuit is shown for reference in Fig. 2. The zero bias micrograph of Fig. 1(a) should be compared to the micrograph of Fig. 1(b), in which the collector-base junction and two of the three emitter-base junctions have been reverse biased. Note that substantial contrast is obtained between areas whose potentials differ by only 2v. Isolation junctions not shown in the equivalent circuit of Fig. 2 are also apparent in Fig. 1(b); one such junction surrounds the three transistor region, isolating it from the remainder of the silicon wafer, and another such junction similarly isolates the collector resistor.

Low magnification micrographs may be used to determine areas of surface damage or defective fabrication. These areas may then be examined at higher magnification. Two such areas of interest are immediately obvious from Fig. 1(b). The first is a black spot on the resistor of base lead one (top arrow), and the second is an irregularity in the collector-isolation junction at the lower left-hand side of the micrograph (bottom arrow). The base resistor area is shown enlarged in Fig. 3(a). The base-emitter junction has been forward biased, turning on the transistor, and producing a substantial potential drop across the collector resistor, which appears shaded. The isolation region surrounding the base resistor is also apparent in Fig. 3(a), as is the dark area of apparent surface damage. The lower left-hand quadrant of Fig. 3(a) is somewhat darker than the rest of the micrograph; this shading is caused by contamination resulting from previous scans of the darkened area by the electron beam. The irregular collector-isolation junction is magnified considerably in Fig. 3(b) and seems related to surface damage evident in this micrograph. Light-microscope examination of this area indicated that the damage originated in the silicon wafer and extended through the thermally grown oxide to the device surface.

Referring again to Fig. 1, note that the junctions which are clearly delineated by reverse bias in Fig. 1(b) are also faintly observable in Fig. 1(a). This is particularly true of the isolation junctions. This contrast is observed even when the junctions are externally short-circuited and is therefore attributed to the diffusion voltage which exists across the

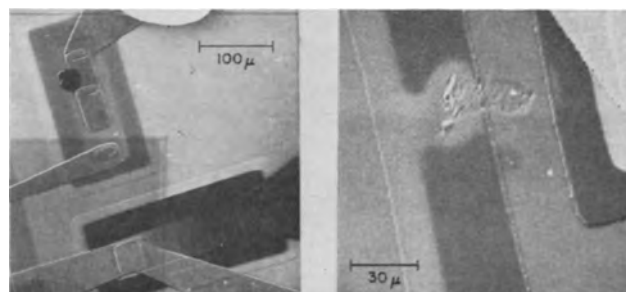


Fig. 3. Scanning electron micrographs of experimental DCTL NOR gate "A." (a) (left) Base-emitter junction forward-biased and voltage drop across the collector resistor: $V_1 = V_3 = 1v$, $V_4 = V_5 = 0v$, $V_7 = 0.2v$, $V_8 = 5v$; (b) (right) an imperfection in the collector-isolation junction, $V_1 = V_3 = -2v$, $V_4 = V_5 = 0v$, $V_8 = 5v$.

junction. Similar results have been obtained for open-circuited junctions, showing that under some conditions at least it is possible to determine junction position without having leads attached to both sides of the junction. Thus this technique is potentially useful for device inspection at intermediate stages of integrated circuit fabrication, so long as a reference potential (normally ground) is connected to at least one region of the wafer.

The micrographs discussed thus far illustrate that positive areas appear darker and negative areas appear lighter than areas which are grounded. This conclusion holds for all micrographs discussed in this paper, and is a consequence of the particular geometrical arrangement of the sample, collector, and other electrodes in the specimen chamber of the scanning electron microscope. For a different geometry, a different relationship between the applied voltage and the apparent brightness might be obtained (12).

Charging of insulating foreign particles is often observed in the scanning electron microscope; such a particle is observable near the top of the micrographs in Fig. 1 [see arrow in Fig. 1(a)]. This particle appears very bright with a dark horizontal zone on either side of it, indicating that it has been charged negatively by the electron beam. In all the micrographs shown in this paper, the beam was swept rapidly from left to right during a single slow scan from top to bottom. This particle did not charge negatively until the beam first reached it on the slow downward scan. On subsequent horizontal scans, the beam struck the particle, charging it to a negative voltage which was large enough to deflect secondary electrons generated on either side of it away from the collector. The particle itself appears bright because the secondary electrons from it were either attracted to the positive collector, or to the final lens, where they generated additional secondary electrons which were in turn attracted to the collector. After the electron beam passed below the particle, it discharged and produced no additional effect of the micrograph. Additional examples of this phenomena will be observed in subsequent micrographs.

Evaluation of Passivated Integrated Circuits

Several integrated circuits which have been examined in the scanning electron microscope will now be discussed. The evaluation of these circuits will be based on the interpretation of voltage contrast presented in the preceding section. A second experimental DCTL NOR gate is shown in Fig. 4. The transistor region of Fig. 4(a) is turned on; *i.e.*, the base-emitter junction is forward biased, turning on the transistor to saturation, which forces current through the collector resistor, and reduces the collector voltage to nearly zero. Note that no potential change is observable at the base-collector junction of Fig. 4(a), while a very distinct potential change is observable at the junction in Fig. 4(b), where the transistor is turned off; *i.e.*, the base-emitter junction is reverse biased. It is possible to determine from Fig. 4(a) and 4(b) that the base resistor is p-type silicon, surrounded by a thin shell of n-type material. Similarly, the n-p-n transistor is embedded

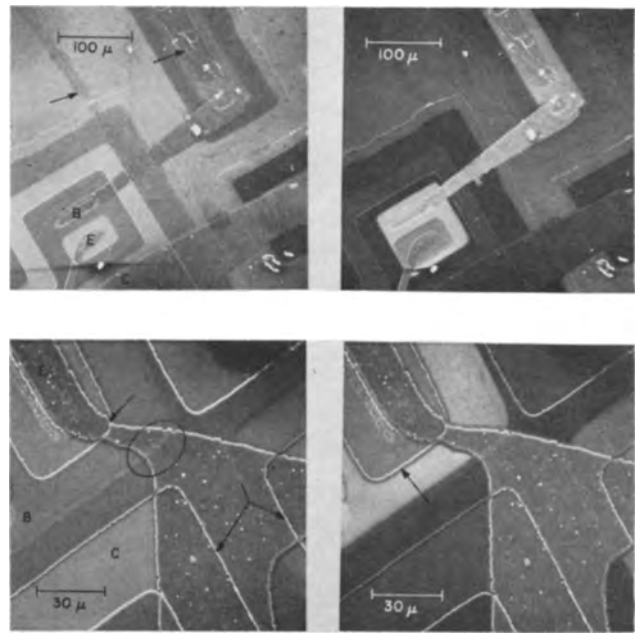


Fig. 4. Scanning electron micrographs of experimental DCTL NOR gate "B." Leads are numbered as in Fig. 1. (a) (top left) Base-emitter junction forward biased; $V_1 = V_3 = 1v$, $V_4 = V_5 = 0v$, $V_8 = 3v$; (b) (top right) base-emitter junction reverse biased; $V_1 = V_3 = -2v$, other voltages as in (a); (c) (bottom left) higher magnification at zero bias; (d) higher magnification biased as (b).

in a p-type region. Two scratches are visible on the surface of this device [see arrows in Fig. 4(a)]; the first crosses the base lead, as is clearly shown in Fig. 4(b), and the second lies along the evaporated aluminum lead to the base resistor. Neither of these scratches seem to harm the device performance; however they are imperfections which probably should be avoided when striving for maximum inherent device reliability.

Higher magnification comparison micrographs of another area of the same device are shown in Fig. 4(c) and 4(d). The base-emitter junction [see arrow in Fig. 4(d)] lies underneath the oxide layer which masked the phosphorus emitter diffusion. This transverse displacement of the junction from the edge of the oxide mask is due to lateral impurity diffusion. If the ratio of lateral junction position to junction depth is known, junction depth can be measured by this technique. The abrupt changes in oxide thickness at the emitter-base junction and at the n^+ collector diffusion boundary [see arrows on Fig. 4(c)] are another interesting feature of these micrographs. These abrupt changes in oxide thickness should be contrasted with the more normal gradual changes which are evident at the circled base-collector junction. Figure 5 shows why abrupt changes in oxide thickness underneath evaporated aluminum leads should be avoided. A thicker aluminum lead must be evaporated over an abrupt step to maintain electrical continuity; even then the cross-sectional area of the lead is greatly reduced at the step, which becomes a potential "hot-spot" and may decrease the device reliability. Conversely, a thinner evaporated aluminum lead may be used over a gradual change in oxide thickness with a much lower probability of failure.

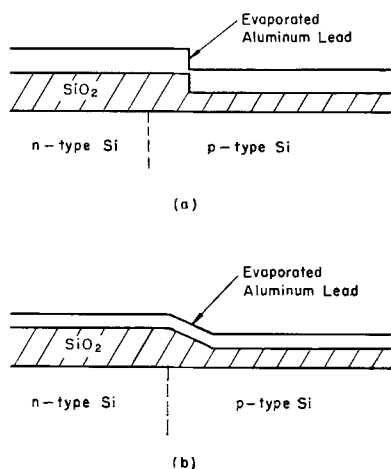


Fig. 5. Sketch of passivating oxide thickness steps which are (a) abrupt and (b) gradual.

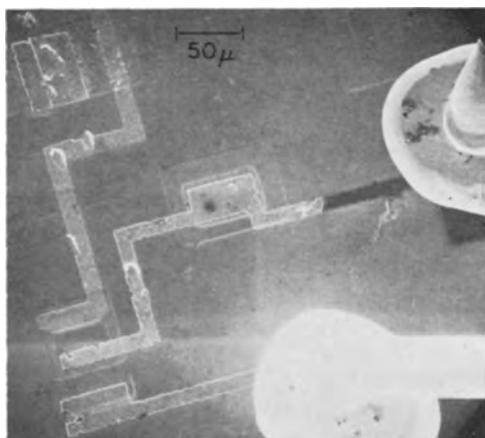


Fig. 6. A broken lead detected by potential contrast

An obvious break in an evaporated aluminum lead found through voltage contrast is shown in Fig. 6. This defect was not detected during a preliminary light-microscope examination of this device, although it was observable in the light microscope after it had been found in the scanning electron microscope. The damage apparent on this sample was caused by mechanical probes used to provide electrical contacts for testing purposes. Another area of this same integrated circuit is shown in Fig. 7. The left-hand diode (D-1) of this NAND gate was forward biased, and the right-hand diode (D-2) was reverse biased, for half of the single slow vertical scan used in recording this micrograph. The bias was off while the bottom half of the micrograph was recorded. The contrast between the top and bottom halves of both D-1 and D-2 is quite noticeable, while switching off the bias produced virtually no contrast on the zero potential surface separating the two diode areas. It can be seen that when diode D-1 is forward biased, it appears lighter than when no bias is applied. This example illustrates how the presence of potentials can be detected by comparing two differently biased areas of the same micrograph.

The minimum detectable potential drop across a p-n junction has been discussed previously (3). Figure 8 shows four comparison micrographs of the same transistor with the collector-base junction re-

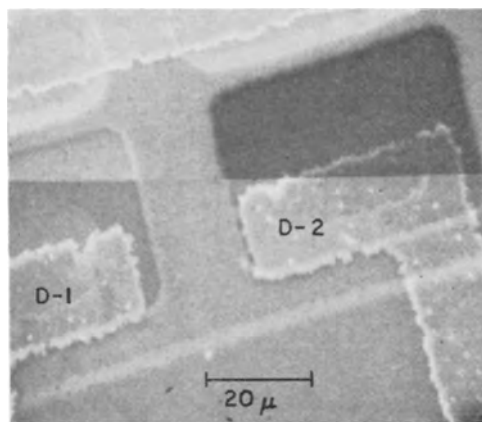


Fig. 7. Fan-in diodes of commercial NAND gate integrated circuit, showing potential contrast due to 2.5 ma forward bias current (top left) and 5v reverse bias (top right) contrasted with zero applied current and voltage (bottom half of micrograph).

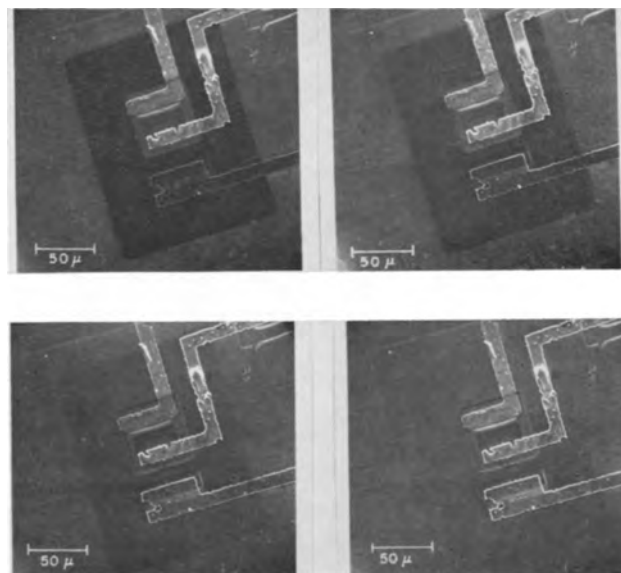


Fig. 8. Scanning electron micrographs of the transistor region of an integrated NAND gate. Collector base junction reverse biased: (a) (top left) 2v, (b) (top right) 1v, (c) (bottom left) 0.25v, and (d) (bottom right) 0v.

verse biased by two, one, one-quarter, and zero volts, respectively. The applied bias was the only parameter changed between these consecutive micrographs. These micrographs demonstrate that potential changes as small as one-quarter of a volt can be detected on passivated integrated circuits.

Micrographs of a commercial integrated circuit are shown in Fig. 9. Various biases were applied to the device terminals to determine the quality of the junction contours, as in Fig. 9(a). Figure 9(b) shows a 2v drop across the large resistor in this integrated circuit. The mask registration, oxide surface, and the junction contours all appear to be of high quality in this device.

Figure 9(c) shows the transistor region of this circuit at a higher magnification. Note that the two oxide thickness steps crossed by the emitter lead (see arrows) are quite gradual, and the evaporated lead itself appears quite smooth at these points. The foreign particles located on the base (right-hand) lead in Fig. 9(c) do not appear to adversely affect

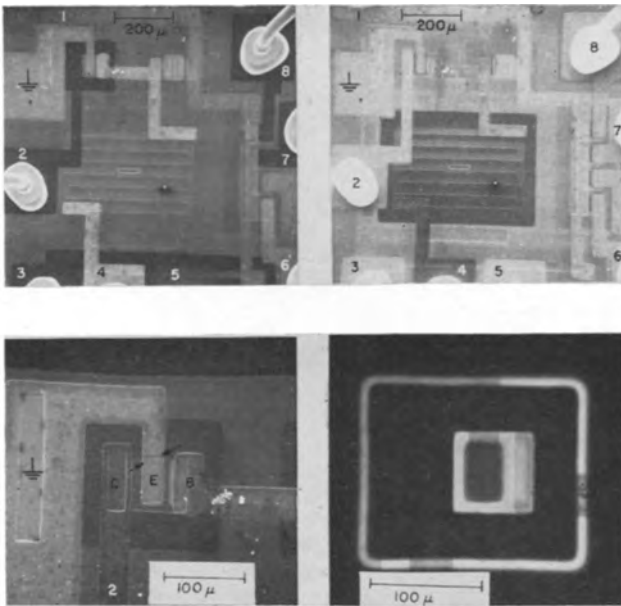


Fig. 9. Scanning electron micrographs of a commercial integrated circuit. (a) (top left) $V_1 = 0.75\text{v}$, $V_{2,3,4,8} = 4\text{v}$, $V_4 = -2\text{v}$, $V_6 = 0\text{v}$; (b) (top right) $V_4 = 2\text{v}$, all other pins grounded; (c) (bottom left) $V_1 = 2\text{v}$, $V_2 = 1.5\text{v}$, $V_4 = -6.7\text{v}$; (d) (bottom right) photovoltage micrograph $V_2 =$ video signal, beam voltage $= 20\text{ kv}$.

its performance. In Fig. 9(d), the photovoltage generated by the scanning electron beam was used as the video signal which modulates the CRT intensity. To obtain this micrograph, the normal secondary electron video signal was disconnected from the video amplifier input, and the transistor collector (left-hand) lead of Fig. 9(c) was connected in its place. The collector-isolation junction surrounding the transistor area is clearly delineated, even when it lies beneath the evaporated aluminum leads. The base region appears much brighter in this micrograph than the emitter region; this is probably due to phototransistor action, with the electron beam replacing light as the initiating energy source. The brightness in this photovoltage micrograph corresponds to the energy dissipated by the electron beam in or near the depletion layer surrounding the collector region of the semiconductor (or in the base region as noted above). Primary electrons lose more of their energy penetrating both the aluminum leads and the passivating oxide layer than they lose penetrating the oxide layer alone. This is the reason that the photovoltage is diminished where the collector-isolation junction lies underneath the aluminum leads. The foreign particles on the base lead, which are silhouetted against the bright collector isolation junction, have also absorbed energy from the primary beam.

The micrographs of integrated circuits chosen as examples up to this point have all shown major or minor defects which have been detected in the scanning electron microscope. Not all integrated circuits examined to date have had such imperfections. A production-line DCTL NOR gate with no apparent blemishes is shown in Fig. 10. The masking, registration, and junction profiles of this device appear to be of high quality.

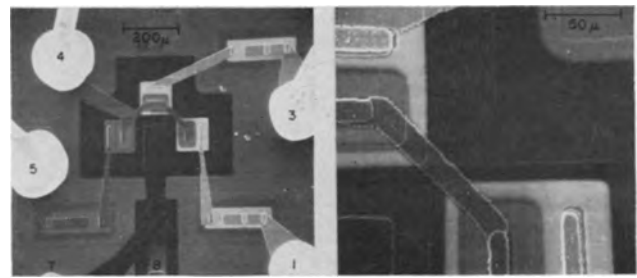


Fig. 10. Scanning electron micrographs of production DCTL NOR gate. (a) (left) $V_1 = V_3 = -2\text{v}$, $V_4 = V_5 = V_8 = 0\text{v}$, $V_7 = 4\text{v}$; (b) (right) higher magnification of (a).

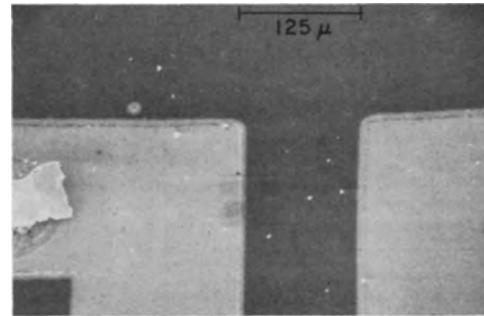


Fig. 11. Pinhole diffusion in experimental sample detected by scanning electron microscopy. Reverse bias, 2.4v.

Figure 11 shows an experimental planar device fabricated such that the p-n junction is formed some 6 or 7μ from the edge of the masking silicon dioxide. The boron diffusion (light) into the n-type base material (dark) has proceeded not only in the unmasked area, but also through pinholes which are apparent in the masking oxide. One such pinhole diffusion is made very obvious when a reverse bias of a few volts is applied across the junction. This micrograph shows that the p-type region due to this particular pinhole diffusion must be connected to the main p-type region beneath the surface, since these two regions do not seem to be connected at the surface. Similar p-type regions formed at other pinholes are not obvious because they are isolated from the applied bias by the n-type material which surrounds them.

Maximum Information per Micrograph

When evaluating large quantities of integrated circuits, the evaluation time per device should be minimized. This implies that for scanning electron microscope evaluation the information per micrograph should be maximized. Ideally, an integrated circuit should be completely evaluated with one micrograph. A photovoltage micrograph of a commercial integrated circuit is shown in Fig. 12(a). A micrograph obtained by mixing the secondary electron video signal with the photovoltage is shown in Fig. 12(b). In this micrograph the surface structure information carried by the secondary electron video signal is superimposed on the information in depth³ carried by the photovoltage video signal, increasing the information content of the micrograph. Note that the base collector junction of this device (see arrow) departs from its intended contour along

³The hole-electron pairs which produce the photovoltage are generated in the bulk material to the penetration depth of the primary electrons.

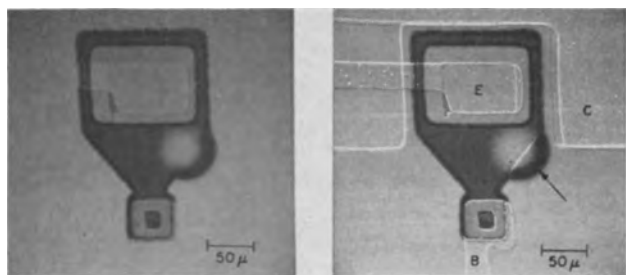


Fig. 12. Scanning electron micrographs of an imperfect transistor in a commercial integrated circuit, illustrating the increase in micrograph information content obtained by mixing the electron-beam-induced photovoltage with the secondary electron video signal. (a) (left) Photovoltage micrograph; (b) (right) photovoltage mixed with the video signal (no bias).

the oxide mask. Figure 13(a) shows a lower magnification micrograph of this device obtained by mixing the photovoltage from two transistor base leads with the secondary electron video signal, and Fig. 13(b) shows the increase in information content which results from biasing the collector positive. Not only are the base-emitter and base collector junctions delineated, but the junctions surrounding the collector and resistor regions are also depicted. A semicircular departure from the expected collector-isolation junction is noticeable in Fig. 13(b) (see arrow); this error probably has little effect on the device performance. The substandard base collector junction noted above, however, might well lead to reduced reliability. The same device is shown in Fig. 13(c) after a few hours electron bombardment of the sub-standard junction area. The resulting contamination has apparently lowered the secondary emission coefficient of this area; however, this amount of contamination cannot be detected

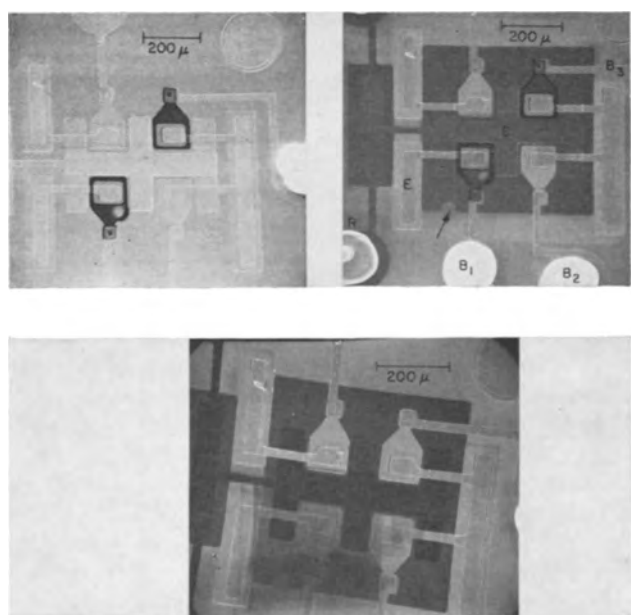


Fig. 13. Scanning electron micrographs of the commercial integrated circuit of Fig. 11, illustrating high information content and contamination effects. (a) (top left) Base photovoltage mixed with normal video signal, zero applied bias; (b) (top right) base photovoltage mixed with normal video signal, $V_C = 4v$; (c) (bottom) normal micrograph (no photovoltage), showing contamination of the imperfect transistor region after excessive electron beam bombardment, $V_C = 5v$.

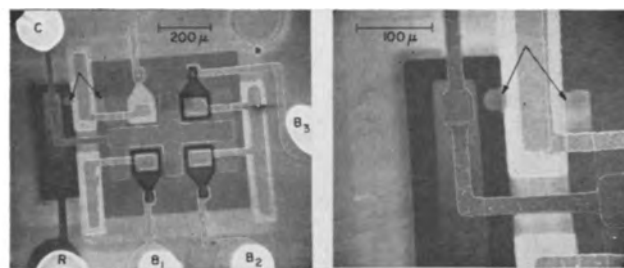


Fig. 14. Scanning electron micrographs of a commercial integrated circuit similar to that of Fig. 12 and 13. (a) (left) V_B photovoltage, $V_C = 1v$, $V_R = 3v$; (b) (right) enlarged view of (a), $V_C = 2v$, $V_R = 5v$.

by light-microscope examination. Contamination effects are discussed further below.

A similar commercial device evaluated by mixing the photovoltage with the secondary electron video signal is shown in Fig. 14(a). Not only are all junctions on the device delineated in this micrograph, but also the 2v drop across the collector resistor is clearly visible. Approximately 1 min is required to scan such a micrograph after the electron beam has been focused for best resolution. Substandard areas observed in the low magnification micrograph, such as the deviations in the isolation junctions (see arrow), can be inspected at a higher magnification, as in Fig. 14(b).

If this technique proves feasible for production-line quality control, a large number of integrated circuits could be loaded into the specimen chamber at one time for batch evaluation, or alternatively, they could be fed continuously into the specimen chamber through differentially pumped vacuum locks (13). Using an automatically focused beam, a single low-magnification micrograph similar to Fig. 14(a) could be obtained of each device in less than 1 min. These micrographs could be examined by a trained person, and thus devices could be sorted on the basis of this evaluation. This sorting could possibly be automated by comparing the video signals from the device under test with a master video signal obtained from an ideal device, and stored on magnetic tape.

Contamination Effects

The effects of contamination have been pointed out in several of the micrographs discussed above. The secondary emission coefficient of the contaminated area is generally reduced; thus contaminated areas of a sample surface appear shaded in scanning electron micrographs. To obtain a measure of the effects of contamination on device performance, the reverse current of the emitter-base junctions of the DCTL NOR gate shown in Fig. 10 were measured as a function of applied voltage before the device was inserted into the scanning electron microscope, and again after normal evaluation. The results of these tests are shown as the bottom two curves of Fig. 15.

The device was then reinserted into the microscope, and only one transistor region was bombarded intensively for a few hours. A heavy layer of contamination similar to that shown in Fig. 13(c) was observed to build up during this time. Following this bombardment, the same reverse current measure-

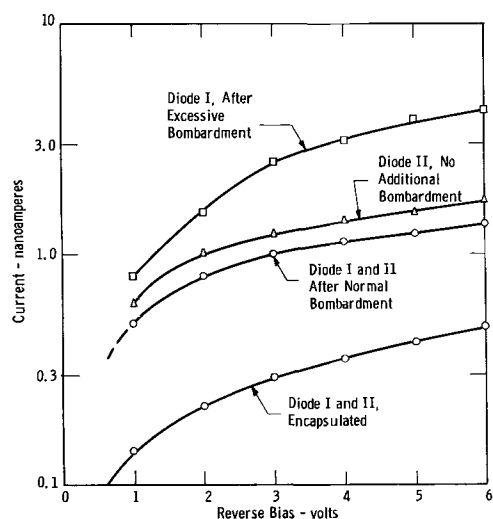


Fig. 15. Base-emitter reverse current vs. applied voltage before electron beam bombardment, after normal bombardment and after excessive bombardment.

ments were performed on the bombarded transistor, and on the control transistor which received very little, if any, additional bombardment. The results of these measurements are shown as the top two curves of Fig. 15. If the data of the bottom curve are subtracted from the data of the top curve, and the resulting data points are plotted vs. reverse bias, a linear graph is obtained. This graph indicates that the contamination layer is equivalent to a 1.5 gigaohm resistor shunting the emitter-base diode.

In this instance, contamination due to excessive bombardment has increased the emitter-base reverse-bias current by approximately one order of magnitude. It is not known at this time how this contamination will affect device reliability. However, it does seem important to understand the mechanism of contamination formation and, if possible, to devise a means of eliminating contamination itself.

Specimen contamination in the electron microscope has been studied for several years (14-17). Briefly, hydrocarbon molecules found in diffusion pump oil, O-ring seals, etc., may be adsorbed by the specimen surface. The bombarding electrons polymerize these molecules, and subsequent bombardment probably carbonizes the polymers. Hillier (14) states that the contamination is primarily amorphous carbon. An analysis by Christy (18) indicates that under the conditions pertaining to the scanning electron microscope, the rate of contamination is proportional to the partial pressure of the contaminating molecules. Leisegang (16) and Heide (17) have demonstrated that this carbon contamination can be removed during electron bombardment if the specimen is surrounded by a sufficiently cold surface, or if certain gases are admitted into the vacuum chamber. Heide (17) has postulated that electron-beam-induced chemical reactions producing gaseous products are responsible for carbon removal. He also showed that, if the specimen is surrounded by a surface cooled below -130°C , the rate of contamination is decreased by two or three orders of magnitude, to an essentially negligible value. Thus there is

every reason to believe that contamination caused by scanning electron microscope evaluation of integrated circuits can be greatly reduced and probably virtually eliminated.

Conclusions

A novel method of passivated integrated circuit evaluation has been described, which complements normal electrical testing of the external device characteristics. Not only have the physical characteristics of device surfaces been imaged with high resolution and great depth of field, but also the relative potentials between different points on device surfaces have been determined. It has also been demonstrated that by mixing the photovoltage generated by the electron beam with the secondary electron video signal, a high information content per micrograph can be obtained.

Acknowledgments

The authors have profited from technical discussions with several colleagues including H. Kanter, I. M. Mackintosh, H. C. Nathanson, J. W. Thornhill and P. M. Waters. The continuing encouragement of S. J. Angello, R. E. Davis, H. F. John, I. M. Mackintosh, P. F. Pittman, E. A. Sack and J. W. Thornhill has also been greatly appreciated. A large number of samples have been generously supplied by the Westinghouse Molecular Electronics Division. The technical assistance of H. D. Larson and J. D. Marks is also gratefully acknowledged.

Manuscript received Jan. 2, 1964. This paper was presented at the New York Meeting, Sept. 29 to Oct. 3, 1963. This work was supported by the Electronics Technology Division, Aeronautical Systems Division, United States Air Force, Wright-Patterson Air Force Base, Ohio, under Contract No. AF 33(657)-9897.

Any discussion of this paper will appear in a Discussion Section to be published in the June 1965 JOURNAL.

REFERENCES

1. C. W. Oatley and T. E. Everhart, *J. Electron.*, **2**, 568 (1956).
2. T. E. Everhart, K. C. A. Smith, O. C. Wells, and C. W. Oatley, "Proceedings of the Fourth International Conference on Electron Microscopy," Berlin, 1958, p. 269, Springer-Verlag, Berlin (1960).
3. T. E. Everhart, O. C. Wells, and C. W. Oatley, *J. Electron Control*, **7**, 97 (1959).
4. V. K. Zworykin, G. A. Morton, E. G. Ramberg, J. Hillier, and A. W. Vance, "Electron Optics and the Electron Microscope," J. Wiley & Sons, Inc., New York (1945).
5. D. McMullan, *Proc. Inst. Elec. Engrs.*, **100**, 245 (1953).
6. K. C. A. Smith and C. W. Oatley, *Brit. J. Appl. Phys.*, **6**, 391 (1955); K. C. A. Smith, "Encyclopedia of Microscopy," G. L. Clark, Editor, p. 241, Reinhold Publishing Corp., New York (1961).
7. I. M. Mackintosh, To be published.
8. J. J. Loferski and P. Rappaport, *Phys. Rev.*, **100**, 1261 (1955).
9. L. Pensak, *ibid.*, **75**, 472 (1949).
10. K. G. McKay, *ibid.*, **74**, 1606 (1948); **77**, 816 (1950).
11. F. Ansbacher and W. Ehrenberg, *Proc. Phys. Soc.*, **A64**, 362 (1951).
12. T. E. Everhart, "Contrast Formation in the Scanning Electron Microscope," Ph.D. Dissertation, University of Cambridge (1958).
13. S. S. Charschan and H. Westgaard, Paper presented at ECS Pittsburgh Meeting, Abstract No. 66 (1963).
14. J. Hillier, *J. Appl. Phys.*, **19**, 226 (1948).

15. A. E. Ennos, *Brit. J. Appl. Phys.*, **4**, 101 (1953); **5**, 27 (1954).
16. S. Leisegang, "Proceedings of the International Conference on Electron Microscopy, 1954," 184, Royal Microscopical Society, London (1956).
17. H. G. Heide, "Proceedings of the Fourth International Conference on Electron Microscopy, 1958," 87, Springer-Verlag, Berlin (1960); "Proceedings of the Fifth International Conference on Electron Microscopy, 1962," **1**, A-4, Academic Press, New York (1962).
18. R. W. Christy, *J. Appl. Phys.*, **31**, 1680 (1960).

Superconducting Thin Films of Niobium, Tantalum, Tantalum Nitride, Tantalum Carbide, and Niobium Nitride

D. Gerstenberg and P. M. Hall

Bell Telephone Laboratories, Incorporated, Murray Hill, New Jersey

ABSTRACT

Tantalum and niobium films have been examined with respect to their superconducting properties. The films were deposited both by sputtering in a high vacuum station and by electron beam evaporation in an ultra high vacuum system. The transition temperatures of sputtered films are lower than the respective values of the pure bulk metals presumably due to interstitial impurities. Reactively sputtered TaC, TaN, and NbN films were found to be superconducting, but no superconducting transition was found for Ta₂N films. Bulk Ta₂N and TaN have no superconducting transition down to 1.5°K, and the appearance of a transition in the TaN film is probably related to a new fcc crystal structure of the TaN films. Electron beam evaporated tantalum and niobium films of a few thousand angstrom thickness have superconducting transition temperatures of 4.3° and 9.1°K, respectively, which are comparable to those of the pure bulk metals of 4.5° and 9.5°K. The purest evaporated tantalum and niobium films, however, show critical fields which are an order of magnitude higher than bulk values, probably due to imperfections and strain.

Several attempts have been made to deposit tantalum and niobium films with superconducting transition temperatures close to those reported for pure samples of the bulk metals. It is well known that films of these metals react with residual gases during deposition and that their superconducting properties are very sensitive to nonmetallic impurities like oxygen, nitrogen, and carbon. Thus great care is necessary to avoid contamination by interstitial impurities. An early study (1) of evaporated and sputtered films of both metals indicated a systematic decrease of transition temperature with decreasing thickness. Generally lower values for the transition temperatures were observed in the case of sputtered films compared to evaporated ones, but no explanation was offered for the differences. Tantalum films with critical temperatures only slightly lower than the values reported for pure bulk tantalum have been evaporated at extremely low pressures (2). Superconducting niobium films have been deposited at high rates by a vacuum arc process (3), and recently the method of asymmetric a-c sputtering has demonstrated the formation of tantalum and niobium films with superconducting properties (4). One of the most successful method so far devised for producing very pure tantalum and niobium films with bulk transition temperatures has been that of "getter sputtering" (5). By varying the substrate temperature during deposition, it was shown (6) that, if the temperature is lowered, the transition temperature decreases and the critical field increases. The result that even the thickest films show higher

critical fields than the bulk metals has been interpreted in terms of the very small grain size produced by sputtering films at substrate temperatures as high as 1400°C. The method of "getter evaporation" in combination with substrate temperatures in excess of 500°C has also been successfully applied for the formation of very pure tantalum, niobium, and vanadium films with bulk transition temperature (7).

Our investigation was undertaken in the hope that the superconducting properties could provide a tool for studying the factors (impurities, defects) which affect room temperature resistivity. To this end, we have investigated the variation of the critical temperature with normal state resistivity for evaporated and sputtered tantalum and niobium films. The purest tantalum and niobium films have also been studied with respect to their critical field behavior. In addition, films of tantalum and niobium compounds formed by sputtering in argon with small additions of a reactive gas were examined with respect to their superconductivity.

Experimental

Preparation of films.—Due to the high melting temperatures of tantalum and niobium the evaporated films were deposited by heating pure samples of the bulk metals with a high energy electron beam. This technique allows one to vary the deposition rate from a few angstroms per second to several hundred angstroms per second. Figure 1 shows the all-metal system (constructed by the NRC Corporation) in which the interaction of organic vapors from the oil

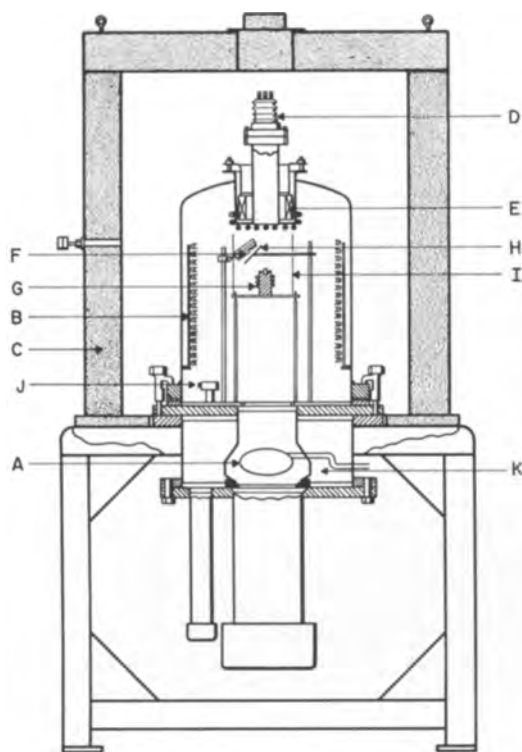


Fig. 1. Electron beam evaporator: (A) 1st cold trap; (B) Meissner trap; (C) bake-out furnace; (D) electron source; (E) focusing solenoid; (F) substrate; (G) copper post; (H) shutter; (I) radiation shield; (J) high conductance ionization gauge; (K) double pumped system to minimize leaks from feedthroughs to base plate.

diffusion pump with the metal vapor has been minimized by adding a Meissner trap. This liquid nitrogen cooled trap consists of a coil of 12 mm diameter copper tubing within 2.5 cm of the inner walls of the bell jar. A reduction of outgassing from bell jar and fixtures inside the vacuum chamber during evaporation from the molten tantalum sample can be accomplished by prebaking at 400°C. The Viton O-rings at the base of the bell jar are water cooled during the bake-out. The ultimate limit in vacuum after the bake-out cycle with liquid nitrogen being fed into both cold traps is in the 10^{-9} Torr range, while during evaporation at a rate of about 30 Å/sec a vacuum of $<2 \times 10^{-6}$ Torr can be maintained. The ratio of metal atoms to gaseous molecules impinging on the substrate is of the order of 10 to 1. The pressure before and during evaporation was measured with an NRC open ended ionization gauge located above the base plate, about 25 cm from the evaporation source. However, the pressure may be lower at the substrate than at the gauge due to the gettering action of the evaporant.

The electron source for melting and evaporating samples of the desired metal is of the self-accelerated type and is located on top of the bell jar. Its output can be continuously varied up to 150 ma at 20 kv. The focusing solenoid outside the bell jar allows the focal spot of about 0.2 cm in diameter to be positioned any place within an area of 5 cm². A 2.5 cm diameter cylinder was used as a holder for the sample to be evaporated. It was made of copper so as to have a large thermal conductivity. A helical coil of copper tubing soldered to the copper cylinder and

cooled by flowing water prevents alloying between the copper and the molten sample, e.g., tantalum or niobium. The substrates are attached to a 10 x 10 cm stainless steel plate which has a platinum wound quartz heater element on its back side. A distance of 10 cm was used between source and substrate. A shield between vapor source and substrate was operated through a rotary seal from the outside of the vacuum system. This permitted the establishment of equilibrium conditions before evaporating onto the substrate.

The sputtered films were deposited in a d-c argon glow discharge at a pressure of about 2×10^{-2} Torr and a rate of 2 Å/sec. The residual gas pressure before sputtering was about 5×10^{-6} Torr. The commercial bell jar type vacuum station used for the sputtering operation has been described previously (8). It was also shown that compounds between these metals and carbon or nitrogen can be produced while adding relatively small quantities of methane or nitrogen to the argon atmosphere (0.1-0.5% of the argon pressure).

Substrates.—All films were deposited on polished fused quartz substrates heated to 400°C, since unheated substrates frequently resulted in poor adherence of the tantalum films to the substrate for thicknesses larger than 2000Å. The quartz substrates, 3.75 x 7.5 cm, had nine fired gold terminations on each longitudinal side. Nine film strips, 2 x 0.125 cm, were deposited simultaneously through a stainless steel mask. Film thickness, necessary for evaluating the electrical resistivity, was determined with a stylus method (9) which has an accuracy of about $\pm 5\%$ for film thicknesses between 1000 and 5000Å.

Cryogenic measurements.—All of the superconducting transitions were measured resistively, T_c being defined as that temperature at which the resistance is half its normal value. Measurements below 4.2°K were made with the sample directly in the helium bath, and the temperature was measured by the vapor pressure. The temperature control was about 0.001°K, and the temperature was known to about 0.01°K. Above 4.2°K, measurements were made in a temperature controlled chamber. Here the temperature was controlled to 0.01°K, and spatial temperature variations within the chamber were no larger than 0.01°K. Above 4.2°K, the temperature was measured with a commercial calibrated germanium resistance thermometer¹ whose accuracy was better than 0.1°K in the region below 10°K.

The critical magnetic field was found to be a function of the angle between the magnetic field and the film (10). In fact, for a film in the middle of a transition, the resistance had a fairly sharp minimum as this angle went through zero (while the temperature was held constant). Therefore, all measurements reported here were made with the magnetic field parallel to the film. This maximizes the observed H_c . The magnetic fields were obtained with a superconducting solenoid, and the field was parallel to the measuring current.

¹ Texas Instruments type RT104.

Table I. Results of the electrical properties

	Resistivity $\rho_{298^\circ\text{K}} [10^{-9} \text{ ohm-cm}]$	Temperature derivative of the resistivity $\frac{d\rho}{dT} [10^{-8} \text{ ohm-cm}/^\circ\text{K}]$	Film thickness $t, \text{ \AA}$	Critical temp $T_c, ^\circ\text{K}$	Transition width $\Delta T, ^\circ\text{K}$
Pure bulk Ta	13.7#	5.05	∞	4.48*	0.002
Evaporated Ta	19.2	5.77	2500	4.30	0.07
	21.2	6.11	3460		
Sputtered Ta	21.2	6.07	1100	4.19	0.15
	52.2	5.39	1400	3.25	
Pure bulk Nb	14.6##	5.42	∞	9.46**	
Evaporated Nb	16.9	5.45	6000	9.11	0.04
Evaporated Nb	19.1	5.47	1800		
Evaporated Nb	21.6	5.86	2050	8.81	0.07
Evaporated Nb	24.2	6.31	760		
Evaporated Nb	25.4	6.18	420	8.12	0.21
Evaporated Nb (cold substrate)	25.7	6.50	3200	8.64	0.09
Evaporated Nb	28.2	6.45	340		
Sputtered Nb	62.4	6.87	1800	6.70	0.70

Ref. (9); ## ref. (10); * ref. (18); ** ref. (14).

Experimental Results

Evaporated and sputtered tantalum and niobium films.—Data are presented in Table I for films between 340 and 6000 Å thick. They indicate that the room temperature resistivity of the evaporated tantalum and niobium films ranges from 1.2 to 2.0 ρ_b , where ρ_b is the bulk resistivity. The sputtered films have values which are considerably higher (about 4 ρ_b). Electron diffraction analysis of the sputtered films revealed that they still have the structure of the bulk material with no other phase detectable.

The temperature derivative of the resistivity $d\rho/dT$, is taken from the range in which the resistivity is linearly dependent on temperature (78°–300°K). It is interesting to note that generally $d\rho/dT$ appears to go up with increasing resistivity. The increase for $d\rho/dT$ is particularly noticeable for the niobium films, both evaporated and sputtered. This variation is somewhat unexpected for the evaporated niobium and tantalum films. Matthiessen's rule should hold fairly well in this resistivity range, and it should not make any difference whether the larger resistivity values of the evaporated films are caused by interstitial impurities, strain, or crystalline imperfections (13). However, although it does not seem likely, the possibility cannot be ruled out that some of this variation in $d\rho/dT$ may be due to the purely geometrical effects due to cavities formed during deposition.

The critical temperature of the tantalum and niobium films decreases with increasing resistivity and in general the transition width ΔT becomes broader (Table I). This is reasonable if the larger values for the resistivity are assumed to be caused by a higher content of impurities. It has been shown by a number of authors that doping of bulk tantalum (14, 15) and niobium (16) with interstitial impurities leads to lower critical temperatures and broader transition widths. Usually the resistance ratio, $\Gamma = R_{300^\circ\text{K}} - R_N/R_N$, is used as a measure of the purity, where R_N is the normal resistance of the sample just above the transition to the superconducting state.

The ratio Γ is used as a measure of purity and "perfectness" of the sample because it is proportional to the low-temperature electron mean free path. This is only strictly true, however, in samples where Matthiessen's rule holds, but even in the present films, it is a fair approximation. The crystallite size in these films was found to be smaller than the thickness. Thus the electron mean free path in these films is not limited by surface scattering but rather by grain boundary or impurity scattering, just as in a bulk sample of equivalent grain size, purity, and defect concentration.

In Fig. 2 and 3 the critical temperatures T_c of the present films are plotted as a function of $1/\Gamma$, and the results are compared to studies of bulk tantalum and niobium containing interstitial impurities (15, 16). The slopes of the data for the evaporated tantalum and niobium films agree quite well with values reported on bulk tantalum doped with small amounts of nitrogen (15) and niobium doped with oxygen (16) suggesting that in the evaporated films the mean free path is limited by interstitial impurities. For the sputtered tantalum and niobium

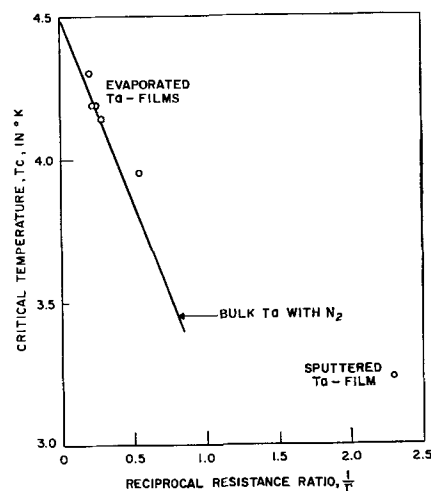


Fig. 2. Critical temperature of tantalum films as a function of the inverse resistance ratio. Solid curve: bulk tantalum with interstitial nitrogen (18).

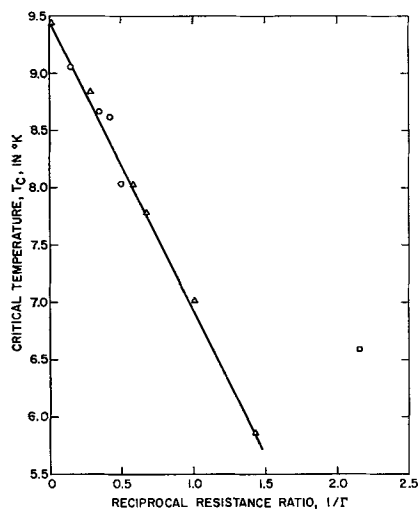


Fig. 3. Critical temperature of niobium films as a function of the inverse resistance ratio compared to bulk niobium with interstitial oxygen (16). Γ of bulk niobium has been calculated using ρ_N from DeSorbo (16) and $\rho_{300^\circ\text{K}}$ from Tottle (17) assuming the validity of Matthiessen's rule. This assumption is vindicated by the fact that $d\rho_N/dc$ from DeSorbo is very close to $d\rho_{300}/dc$ from Tottle where c is the oxygen concentration. \circ , Evaporated Nb films; \square , sputtered Nb films; \triangle , bulk Nb with O_2 .

films T_c is larger than would have been expected from the data on bulk samples.

Both ρ and Γ reflect the bulk properties of the films, while superconductivity, when measured resistively, can be caused by only a small fraction of the sample. The bulk properties, ρ and Γ , of the sputtered films imply a higher impurity and defect concentration than would be suspected from the T_c value (Fig. 2 and 3). This result suggests a nonuniform distribution of the contaminants and imperfections in the sputtered films. There is some preliminary evidence from the resistive properties of niobium and tantalum films that as the sputtering proceeds less impurities are available for reaction.

Another possible interpretation of these data can be expressed in terms of the two contributions to $1/\Gamma$; grain boundaries and impurities. Both contributions depress T_c (6, 15, 16), but the magnitude of the two effects may be quite different. Thus in the sputtered films, where a major fraction of $1/\Gamma$ probably comes from grain boundaries, the T_c depression could be considerably less than is expected from data on T_c depression due to impurities. But in the evaporated films, the grain size is considerably larger, and perhaps grain boundary scattering makes only a small contribution to $1/\Gamma$. This reasoning is consistent with the fact that for our sputtered films, if all of $1/\Gamma$ were due to nitrogen or oxygen doping, for example, we would have exceeded the solubility limits (16), and another phase would have been detectable. Thus, whereas the T_c of the evaporated films can be explained in terms of impurity scattering alone, the sputtered films cannot.

The resistance of evaporated tantalum and niobium films with the highest transition temperature has been measured as a function of magnetic field at constant temperature. H_c is arbitrarily defined as that field which restores 50% of the normal resistance, and it is plotted as a function of temperature

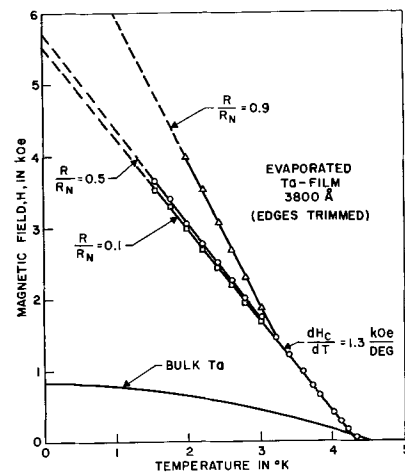


Fig. 4. Critical magnetic field of the purest evaporated tantalum film compared to bulk tantalum (19).

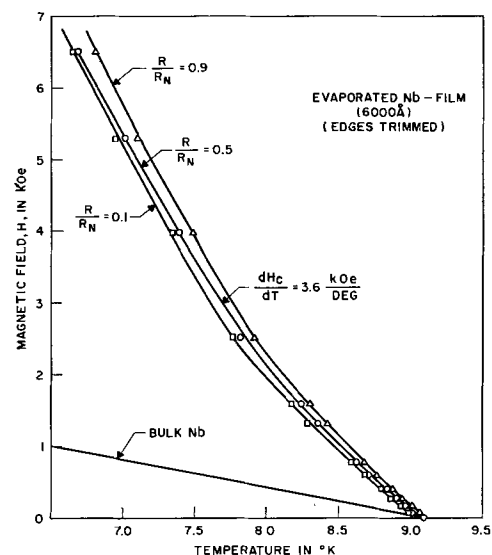


Fig. 5. Critical magnetic field of the purest, evaporated niobium film. (H_{cb}) $T \rightarrow 0 = 1.9$ KOe for bulk niobium (18).

on Fig. 4 and 5. Also shown are the fields required to restore 10% and 90% of the normal resistance. Figures 4 and 5 show that even the purest evaporated niobium and tantalum films have critical fields when linearly extrapolated to absolute zero, which are an order of magnitude or more higher than those reported for the pure bulk metals (18, 19). The measuring current density was the same as the one used for the determination of the critical temperature without magnetic field (200 amp/cm²). There are some differences to be noted between the curves for tantalum and niobium. The transition of the tantalum film remains very sharp down to 3.2°K, while the transition of the niobium film becomes less sharp at very small fields. However, below 3°K the resistance transition for the tantalum films begins to broaden, especially for the region $R/R_N > 0.5$ until the normal state resistance is restored. This behavior is in qualitative agreement with data obtained on extremely pure bulk tantalum (19). It seems likely that broadening of the resistance transition will also occur for niobium films at higher magnetic fields which, unfortunately, were not available for the present study.

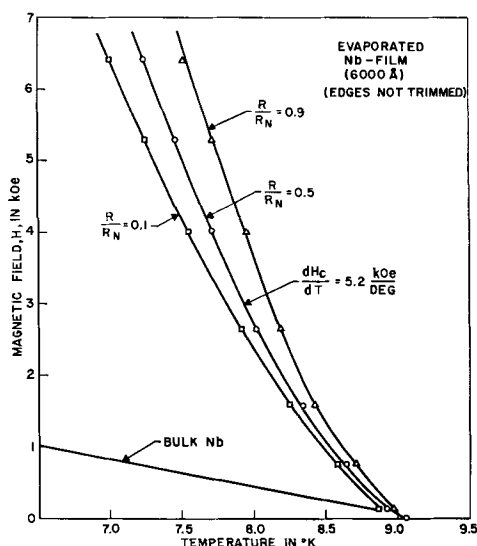


Fig. 6. Critical magnetic field of the purest, evaporated niobium film with edges not removed.

It has previously been found that tin films which have been evaporated through mechanical masks have sloping edges, resulting in broader resistance transitions and higher critical fields than those found for films with sharp edges (20). This effect was evident in the present films also. Therefore, we trimmed the edges of the films away with a special ruling engine. For comparison, in Fig. 6 the critical field of an untrimmed niobium film is plotted as a function of temperature. Although the critical temperature at zero field is identical with the value for the trimmed niobium film (Fig. 5) the critical field rises faster with decreasing temperature and the resistance transitions become much broader.

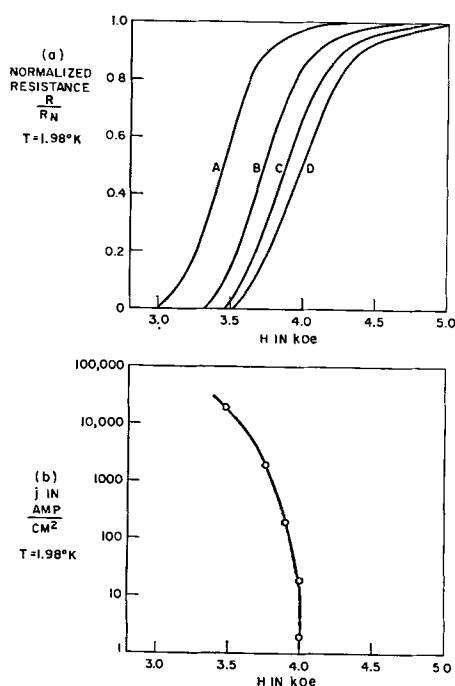


Fig. 7. (a) Resistance transitions for purest evaporated tantalum film with edges removed; (b) current dependence of the critical field ($H_c = H(0.5R_N)$). Amp/cm²: curve A, 20,000; curve B, 2,000; curve C, 200; curve D, 20 and 2.

Figure 7a shows the resistance transitions of the purest tantalum film (edges trimmed) as a function of the measuring current for $T = 1.98^\circ\text{K}$. At this temperature the transition curves were completely reversible up to 20,000 amp/cm². The general behavior was quite similar to that reported for cold rolled alloys of transition metals (21). That is, at low current densities (<100 amp/cm²) the critical field, $H_c(j)$, appears to be independent of the measuring current, while above 1000 amp/cm² the critical field begins to decrease slowly (7). The significance of these and the following results with respect to superconducting filaments will be discussed later.

Several $H_c(j)$ curves, (not shown here) above the λ -point of liquid helium, 2.2°K, had the same general shape as that of the curve presented in Fig. 7b. However, Joule heating of the sample after switching to the normal state was observed at temperatures above the λ -point for current densities >5000 amp/cm². This caused the sample to assume temperatures higher than the helium bath after the sample was switched normal. The heating resulted in discontinuously sharp transitions on increasing H , and instability and hysteresis on decreasing H . Figure 8a gives transition curves for the tantalum film before its edges had been removed. For very small current densities the transition is fairly sharp, and H_c is quite large (about $7H_{cb}$ compared to $3H_{cb}$ for the trimmed film). For the range 20-2000 amp/cm², broad transitions were obtained, but the same "upper point" can be observed for all three curves. For 20,000 amp/cm² and more, this sample also shows sharp, unstable transitions on increasing the magnetic field due to Joule heating, and instability and hysteresis on decreasing H . The H_c values above current densities of 2000 amp/cm² are comparable to

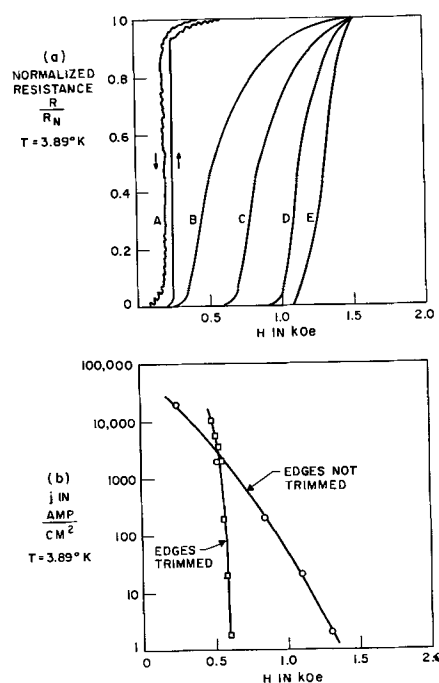


Fig. 8. (a) Resistance transitions for purest, evaporated tantalum film with edges not removed; (b) current dependence of the critical field ($H_c = H(0.5R_N)$). Amp/cm²: curve A, 20,000; curve B, 2,000; curve C, 200; curve D, 20; curve E, 2.

those measured for the trimmed films at 3.89°K (Fig. 8b).

Since magnetic fields $H > 6.5$ k Oe were not available, a study of the critical field *vs.* the measuring current for the purest niobium film below 6.6°K was not possible.

Reactively sputtered compounds of tantalum and niobium.—During the sputtering process in an argon atmosphere, impurities can be incorporated into refractory metal films. This effect has been utilized in a deliberate manner for producing tantalum and niobium compounds with carbon or nitrogen. This is done by introducing small quantities of methane or nitrogen into the inert gas glow discharge. The results on the resistive and structural properties of these compounds have been reported elsewhere (8). Structural examination of tantalum films sputtered in a partial methane atmosphere indicated only one tantalum carbide, TaC, above the solubility limit of carbon in tantalum. The tantalum carbide film has a sodium chloride structure which is identical with that reported for the bulk material (22). The bulk TaC has a wide homogeneity range (from 36.7 to 47.6 a/o [atomic per cent]) resulting in a strong dependence of the superconducting transition temperature upon the carbon concentration. Critical temperatures from 1.5 to 9.5°K have been reported previously for the bulk material (23). The results in Table II indicate that a 990Å sputtered tantalum carbide film has a T_c of 5.09°K, indicating that the carbon concentration in the film is probably well below the stoichiometric composition.

Electron diffraction analysis of tantalum films sputtered in a partial nitrogen atmosphere revealed that with increasing nitrogen concentration two stable compounds of tantalum and nitrogen were formed. The hexagonal structure of the Ta₂N film is identical with that formed for bulk Ta₂N (24). The sodium chloride structure of the higher nitride film differs from that previously described for bulk TaN (25). However, this structure is common for compounds of transition metals and nitrogen (26). Bulk hexagonal Ta₂N and TaN were found to be non-superconducting down to 1.5°K (27, 28). The same result was obtained for the sputtered Ta₂N films (Table II), which showed no superconductivity above 1.2°K. The TaN films revealed a behavior different from that of bulk TaN, as indicated in Table II. They became superconducting with a critical temperature of about 4.84°K. This value is suffi-

ciently close to the critical temperature of pure tantalum to suspect that the superconductivity of the TaN film might be caused by a small amount of tantalum. This is not very likely since the electron diffraction analysis of this sample did not indicate a second phase, and if there were a small amount of another phase present, one would expect nonsuperconducting Ta₂N rather than tantalum. The broadness of the transition suggests that the TaN films are rather impure or have a nitrogen content, similar to the TaC film, that is below the stoichiometric composition. The fact that the sputtered TaN shows superconductivity while the bulk material does not is probably related to the difference in structure found for the two materials, a behavior which has also been found for bulk NbN (29). Preliminary results indicate that niobium nitride films sputtered in a partial nitrogen atmosphere have the NaCl-type structure of NbN III and not that of the hexagonal modification of NbN I (29). The sputtered NbN films become superconducting in the range between 6° and 9°K depending on the partial nitrogen pressure during sputtering. The values for T_c are somewhat lower than those reported for bulk NbN III (30-33), but lower values have also been reported for NbN III with nitrogen deficiency (34).

Discussion and Conclusions

It has been found that tantalum and niobium films can be obtained which have critical temperatures comparable to values reported for pure samples of the bulk metals (Table I), without reducing the vacuum in the evaporator during deposition to a very low value. It seems to be sufficient to keep a favorable balance between the residual gas pressure and the deposition rate. Due to the bake-out of the electron beam evaporator the residual gas pressure during evaporation was at least one order of magnitude lower than in conventional vacuum stations (35). It appears from the higher resistivity and the lower critical temperatures observed for thinner evaporated films that in spite of the use of a shutter for establishing equilibrium conditions the films below 1000Å have a higher impurity and defect content or smaller grain size than thicker films. There is preliminary evidence that the purity of the evaporated tantalum and niobium films depends strongly on the deposition rate. Higher deposition rates than have been used for the present experiments might well result in purer films for the thickness range below 1000Å if the residual pressure can be kept low enough. Due to the slightly higher residual gas pressure during sputtering and the much slower rate of deposition the sputtered niobium and tantalum films show values for resistivity and critical temperature which are, respectively, much higher and much lower than those observed on samples of the bulk metals.

A comparison of the present T_c *vs.* $1/\Gamma$ curves with data reported for samples of the bulk metals (doped with small quantities of gaseous impurities) shown in Fig. 2 and 3 indicates that even the purest evaporated films contain a concentration of interstitial impurities of the order of 0.5 a/o. These impurities

Table II. Superconducting transition temperatures of tantalum compounds

Sample	Film thickness, t [Å]	Critical temperature, T_c [°K]	Resistivity, $\rho_{295^\circ\text{K}} \times 10^6$ ohm-cm
Bulk TaC	∞	9.5-1.5	30.0-170
Sputtered TaC	947	5.09	177.5
Bulk Ta ₂ N	∞	No s.c.	—
Sputtered Ta ₂ N	1200	No s.c.	245*
Bulk TaN (h.c.p.)	∞	No s.c.	—
Sputtered TaN (f.c.c.)	1200	4.84	245*

* The electrical resistivity of sputtered Ta₂N and TaN films was found to be identical within 10% (6).

and imperfections appear to be inhomogeneously distributed in these films since they seem to break up the samples into a network of superconducting filaments which persist at magnetic fields much higher than the bulk critical field (Fig. 4 and 5). Such a behavior is in agreement with results found on impure samples of bulk tantalum and niobium (14, 16). But it should be noted that when $1/\Gamma$ is as large as it is for the present films, superconducting filaments can be energetically favorable even without postulating inhomogeneities (36).

It is not clear at present how the filaments form and where they are located. It can be said, however, that for an untrimmed film at low current densities and large magnetic fields, the filaments are in the extreme edges (see Fig. 5, 6, and 8b). Although the critical field was not measured as a function of the current density for the niobium films, the results described in Fig. 5 and 6 for the purest niobium film before and after trimming indicate that the edges are responsible for the higher values of dH_c/dT in the untrimmed film, at $j = 200$ amp/cm². At current densities $j > 1000$ amp/cm² the tantalum film with untrimmed edges shows values for the critical field which are about the same as the ones observed on the trimmed film. This indicates a saturation of the filaments along the edges of the untrimmed film. Above 1000 amp/cm² both types of films seem to carry the superconducting current by the filamentary network in the interior. When the current density is raised by four orders of magnitude the critical field for the trimmed tantalum film decreases by only 15% at 1.98°K as well as at 3.89°K. Such a behavior suggests either a high filament density or uniform critical fields for the filaments. The broad resistance transitions (Fig. 7a) even for low current densities, however, would indicate a rather broad distribution of critical fields for the filaments in the evaporated tantalum film. It is evident that considerably more work on pure tantalum and niobium films is needed before the question about the origin of the filaments can be answered satisfactorily.

Acknowledgments

The authors are indebted to N. Schwartz and F. B. Hagedorn for valuable comments throughout the course of this work. It is a pleasure to thank J. J. Hauser for helpful discussions.

Manuscript received Jan. 27, 1964; revised manuscript received March 13, 1964. This paper was delivered before the Pittsburgh Meeting, April 15-18, 1963.

Any discussion of this paper will appear in a Discussion Section to be published in the June 1965 JOURNAL.

REFERENCES

1. Khukhareva and Shalnikov, *Doklady Akad. Nauk SSSR*, **99**, 735 (1954).
2. J. F. Marchand and A. Venema, *Phillips Research Repts.*, **14**, 427 (1959).
3. M. S. P. Lucas and D. T. Meyer, *Nature*, **193**, 766 (1962).
4. R. Frerichs, *J. Appl. Phys.*, **33**, 1898 (1962); R. Frerichs and C. J. Kircher, **34**, 3541 (1963).
5. H. C. Theuerer and J. J. Hauser, *J. Appl. Phys.*, **35**, 554 (1964).
6. J. J. Hauser and H. C. Theuerer, *Phys. Rev.*, **135**, A198 (1964).
7. C. A. Neugebauer and R. A. Ekvall, Oct. 63, Report No. 63, RL-(3482 M); see also P. Fowler, *J. Appl. Phys.*, **34**, 3538 (1963).
8. D. Gerstenberg and C. J. Calbick, *J. Appl. Phys.*, **35**, 402 (1964).
9. N. Schwartz and R. Brown, 1961 Vacuum Symposium Transactions, Vol. II, p. 836, Pergamon Press, New York.
10. This general type of behavior is expected from the flux quantization effects considered by M. Tinkham, *Phys. Rev.*, **129**, 2413 (1963) and has been observed in tin films by E. H. Rhoderick, *Proc. Roy. Soc. (London)*, **267A**, 231 (1962).
11. Landolt-Boernstein, II. Band, 6 Teil, *Elektrische Eigenschaften I*, p. 4, Springer Verlag, Berlin (1959).
12. G. K. White and S. B. Woods, *Can. J. Phys.*, **35**, 892 (1957).
13. A. N. Gerritsen, *Encyclopedia of Physics*, Vol. XIX, 207, Springer Verlag, Berlin (1956).
14. D. P. Seraphim and R. A. Connell, *Phys. Rev.*, **116**, 606 (1960).
15. D. P. Seraphim, N. R. Stemple, and D. T. Novick, *J. Appl. Phys.*, **33**, 136 (1962).
16. W. E. DeSorbo, *Phys. Rev.*, **132**, 107 (1963).
17. C. R. Tottle, *J. Inst. Metals*, **85**, 375 (1956/57).
18. American Institute of Physics Handbook, Table 4e-8, Vol. 4, p. 49, McGraw Hill Book Co., Inc., New York (1957). For $H_c(T)$, see C. Chou, D. White, and H. L. Johnston, *Phys. Rev.*, **109**, 788 (1958).
19. J. I. Budnick, *Phys. Rev.*, **119**, 1578 (1960).
20. E. T. S. Appleyard, J. R. Bristow, H. London, and A. D. Misener, *Proc. Roy. Soc. (London)*, **A172**, 540 (1939); H. L. Caswell, *J. Appl. Phys.*, **32**, 105 (1961).
21. T. G. Berlincourt and R. R. Hake, *Phys. Rev. Letters*, **9**, 293 (1962).
22. V. T. Smirnova and B. F. Ormont, *Doklady Akad. Nauk SSSR*, **96**, 557 (1954).
23. A. L. Giorgi, E. G. Sklarz, E. K. Storms, A. L. Bowman, and B. T. Matthias, *Phys. Rev.*, **125**, 837 (1962).
24. E. Rundle, *Acta Cryst.*, **1**, 180 (1948).
25. G. Brauer and H. K. Zapp, *Naturwissenschaften*, **40**, 604 (1953).
26. W. B. Pearson, "Handbook of Lattice Spacings and Structures of Metals and Alloys," Pergamon Press, New York (1958).
27. G. F. Hardy and J. K. Hulm, *Phys. Rev.*, **93**, 1005 (1954).
28. F. H. Horn and W. T. Ziegler, *J. Am. Chem. Soc.*, **69**, 2762 (1947).
29. G. Brauer and J. Jander, *Z. anorg. u. allgem. Chem.*, **270**, 160 (1962).
30. G. Aschermann, E. Friederich, E. Justi, and J. Kramer, *Phys. Z.*, **42**, 349 (1941).
31. H. Rögener, *Z. Phys.*, **132**, 446 (1952).
32. F. H. Horn and W. Ziegler, *J. Am. Chem. Soc.*, **69**, 2762 (1947).
33. F. C. Haley and D. H. Andrews, *Phys. Rev.*, **89**, 821 (1953).
34. E. Schröder, *Z. Naturforschung*, **12A**, 247 (1957).
35. R. W. Berry, Proceedings of the Third Symposium on Electron Beam Technology (1961) p. 358.
36. C. Chiou, R. A. Connell, and D. P. Seraphim, *Phys. Rev.*, **129**, 1070 (1963).

Electrical Properties of Selected Rare Earth Compounds and Alloys

F. J. Reid, L. K. Matson, J. F. Miller, and R. C. Himes

Battelle Memorial Institute, Columbus, Ohio

ABSTRACT

Rare earth elements, neodymium, gadolinium, samarium, cerium, erbium, and ytterbium, in compounds and alloys with Group V elements arsenic and antimony and Group VI elements selenium and tellurium have been studied. The properties discussed include carrier concentration and carrier mobility, electrical and thermal conductivity, and thermoelectric power as functions of temperature and composition. Several suggested applications utilizing these materials are presented.

The results of a previous exploratory investigation of the properties of rare earth intermetallic compounds indicated that certain of the compounds were semiconductors or were materials which possessed interesting and potentially useful electrical properties (1). The study of the electrical properties of rare earth intermetallic compounds has been continued with the specific objective being to investigate, systematically, the electrical properties of intermetallic compounds formed between the rare earth elements and the elements of chemical Groups VA or VIA (arsenic, antimony, selenium, and tellurium). It is intended that the basic information obtained in this investigation will make possible the ultimate development of useful solid-state electronic devices based on these materials.

Considering that there are 14 rare earth elements, that information obtained in the early work pointed to the existence of several compounds in each of the systems, and that at least four metalloid species are involved, the number of possible compounds in the systems under consideration is seen to be extremely large. To undertake investigation of all of the compounds would constitute a prohibitively large task. Therefore, a systematic survey program calling for study of selected, representative compounds was undertaken. Available information on the chemistry of the rare earth elements was utilized in the selection of representative compounds for study as is revealed in the discussion to follow. Since in the initial exploratory study (1), the more interesting electrical properties were observed for the selenides and tellurides, initial and major portions of this investigation were devoted to study of these compounds and their alloys.

Pertinent Rare-Earth Chemistry

In discussions of the chemistry of the rare earth elements, the similarity of their behavior and the predominance of the tripositive oxidation state are often stressed, thus creating popular misconceptions. As shown in Table I, other important oxidation states also are observed for a number of the elements. Conversion to the dipositive or tetrapositive state is, in fact, utilized in effecting the chemical

Table I. Oxidation states and electronic configurations of rare earth elements

Element	Known oxidation states	Corresponding 4f electronic configurations
La	3	4f ⁰
Ce	3-4	4f ¹ -4f ⁰
Pr	3-4	4f ² -4f ¹
Nd	3	4f ³
(Pm)	3	4f ⁴
Sm	2-3	4f ⁶ 4f ⁵
Eu	2-3	4f ⁷ -4f ⁶
Gd	3	4f ⁷
Tb	3-4	4f ⁸ -4f ⁷
Dy	3	4f ⁹
Ho	3	4f ¹⁰
Er	3	4f ¹¹
Tm	2-3	4f ¹³ -4f ¹²
Yb	2-3	4f ¹⁴ -4f ¹³
Lu	3	4f ¹⁴

separation of some elements from (naturally occurring) mixtures. Hence it is apparent that several types of chemical behavior of the rare earth elements must be considered if one is to study representative rare earth materials.

Among the tripositive ions, high stability is associated with the electronic configurations of the La³⁺, Gd³⁺, and Lu³⁺ ions in which the 4f levels are empty, half-filled, and filled, respectively. The dipositive and tetrapositive oxidation states of the neighboring rare earth elements (Table I) appear to arise as a result of approach to, or achievements of, the stable 4f⁰, 4f⁷, and 4f¹⁴ configurations. Among these, the dipositive states of samarium, europium, and ytterbium, and the tetrapositive state of cerium are the more important; the corresponding states of thulium, praseodymium, and terbium appear to be less stable and are observed only under special conditions.

Within a given class of compounds, it is reasonable to expect that different characteristics will be obtained as the chemical nature of the rare earth element changes. Accordingly, rare earth elements were selected from the three types noted. Neodymium, gadolinium, and erbium were chosen as representatives of the "regular" rare earth elements which ex-

hibit only the tripositive oxidation state. Samarium and ytterbium were selected for study as representatives of the elements which exhibit both dipositive and tripositive states. Compounds of cerium were also prepared and studied since this element exhibits both the tripositive and tetrapositive states.

Another factor which one might expect to warrant consideration is the possible effect of the lanthanide contraction. The decrease in atomic and ionic radii with progression through the rare earth series certainly produces an effect on properties of the elements and compounds. However, results indicate this to be of secondary importance among the effects and phenomena noted and discussed.

Experimental Procedures

Compound synthesis which has been described previously in detail (1-3) was accomplished by means of solid-vapor reaction between turnings or filings of the rare earth metals and the desired metalloid elements in vapor form. The granular materials, so prepared, were subsequently melted and directionally crystallized in tantalum containers. In the case of the rare earth arsenides, this was not possible, however, because of the high melting points encountered. Bulk specimens of these latter compounds were prepared by powder metallurgical techniques, *i.e.*, by pressing (100,000 psi) and sintering (2000°-2500°C, ½-1 hr) the granular material. Single crystal specimens of the rare earth monoselenides and monotellurides were obtained by the directional freezing technique. Specimens of rare earth selenides and tellurides with compositions in the range M_3X_4 to M_2X_3 were polycrystalline, containing crystallites with minimum dimensions of about 0.4 cm.

In general, the standard grades of rare earth metals readily available from commercial sources were utilized. In several cases, however, some further purification of the metals was accomplished.

As can be seen in Table II, where data on suppliers' typical analyses and analyses of the specific lots of metals utilized are tabulated, purity of the standard grade of rare earth metals is low (99+%),

relative to the usual standards for electronic materials. In metals as reactive as the rare earths, one might tend to be concerned first about the concentrations of oxygen and other gaseous impurities. It can be noted that oxygen concentrations are, indeed, high. However, the concentrations of several of the metallic impurities (*e.g.*, tantalum, calcium, iron, and copper) also are high, being in aggregate of comparable magnitude on an atom fraction basis. Thus, the importance of oxygen as an impurity in the compounds may not surpass that of the metallic impurities.

As is shown in the first three entries in Table III, significant purification of samarium metal was achieved by vacuum distilling the metal and condensing the product at a temperature below its melting point. Concentrations of the metallic impurities calcium, magnesium, and molybdenum were sharply reduced by the process. However, no difference was detected between the electrical properties of SmAs prepared from the as-received metal and that prepared from the purified metal. On the other hand, differences were noted between the electrical properties of Nd_2Te_3 specimens prepared from different lots of neodymium metal: Nd-I and Nd-II (see Table III). The specimens prepared from Nd-I metal were consistently p-type, presumably because of the calcium and/or tantalum present, whereas the specimens containing Nd-II metal were consistently n-type.

The selenium, tellurium, arsenic, and antimony used to synthesize the compounds were of higher purity (at least 99.99+%) than the rare earth metals. The contribution of charge carriers from these sources is, therefore, believed to be negligible with respect to (i) those from impurities present in rare earth elements, (ii) those from impurities introduced in the course of synthesis of the compounds, and (iii) those arising as results of deviations from stoichiometry.

Electrical measurements were made on specimens cut or cleaved from the various ingots. Parallelepipeds were shaped by lapping the specimens with

Table II. Typical analyses of rare earth metals^(a)

Impurity element	Impurity concentrations, ppm, in indicated metal					
	Ce	Nd	Sm	Gd	Er	Yb
Ta	~1000	800-1000	100-1000	~300	~2200	~1000
Ca	200-500	200-500	100-1000	~100	1000-2000	100-1000
Mg	300-1000	~100	10-10,000	—	—	~100
Fe	300-3000	200-500	~300	~1000	—	~300
Ni	—	~100	~200	~1000	~1000	400-1000
Cu	—	~2000	~100	~100	—	10
Al	—	~500	~100	—	—	—
Si	—	~100	~100	~100	—	—
Other rare earth elements	~1000	~250	200-1000	~700	~2000 (Tm)	~1000
O ₂	500-2000	1000-2000	500-2500	1000-2800	~1200	—
N ₂	50	—	—	20	—	—
Total	3350-8500	5250-7050	1700-6400 ^(b)	4300-6100	7400-8400	2900-4400

^(a) Results derived from supplier's typical analyses and analyses of specific lots utilized are given. Ranges of impurity concentrations given reflect variation of values from sample to sample, lot to lot, and supplier to supplier for the subject metal. Metals were obtained from Lindsay Chemical Division of American Potash and Chemical Corporation, Michigan Chemical Corporation, Nuclear Corporation of America, and Kleber Laboratories.

^(b) Excluding magnesium.

Table III. Results of spectrographic analyses of rare earth metals

Material	Impurity elements detected, ppm by weight											Total detected
	Ca	Mg	Si	Ni	Fe	Mn	Cu	Al	O ₂	Mo	Ta	
Sm, as-received	500	~10,000	5	—	5	20	10	<10	—	2000	~10 ⁴	~12,000 ^(a)
Sm, distilled, condensed as liquid	10	5	10	—	10	50	100	<10	—	20	<10 ⁵	205 ^(a)
Sm, redistilled, condensed as solid	10	10	10	—	20	10	50	10	—	10	<10 ⁴	130 ^(a)
Nd-I	300	—	—	—	500	—	—	—	1000	—	800	2600
Nd-II	ND ^(b)	—	—	—	500	—	—	—	1000	—	ND	<1700

^(a) Excluding tantalum.^(b) ND, not detected, <100 ppm.

600-grit SiC paper. Both the cutting and lapping were done in a dry state since the compounds, in general, tend to hydrolyze. Ohmic contacts were made by applying indium solder with an ultrasonic tool.

The apparatus used for high-temperature (to 1300°K) resistivity and Seebeck coefficient measurements utilized spring-loaded pressure contacts. The specimens were held between platinum end plates which served as sample-current contacts. Platinum-platinum 10% rhodium thermocouples, or Chromel-Alumel thermocouples, were utilized as current leads and to determine temperatures at the ends of the specimens. Point contacts of platinum or Chromel were pressed against a face of the specimen for resistivity-voltage measurements. All high-temperature electrical measurements were made in vacuum at residual pressures in the range 1×10^{-5} to 1×10^{-4} mm Hg. This was found to be necessary in an early stage of the study of the selenides and tellurides. At pressures greater than $\sim 10^{-4}$ mm Hg, irreversible changes in electrical properties of specimens, presumably resulting from oxidation of the materials, were observed to occur. At pressures less than $\sim 10^{-4}$ mm Hg, reproducible results were obtained.

Experimental Results and Discussion

Selenides and tellurides.—Temperature-composition relationships and crystal structures (2-5), determined in connection with studies of electrical properties of rare earth selenides and tellurides, indicate that four binary crystalline phases probably exist in each of the systems. This is in general agreement with the work of others (6-10). There are the compounds of the Types MX, MX₂, and MX₄, and the M₃X₄-M₂X₃ type, which is a single, crystalline phase persisting through the indicated composition range. The results of rather extensive work with the Gd-Te, Nd-Te, Gd-Se, Nd-Se, Ce-Te, and Ce-Se systems indicate that the four phases exist in the systems containing these rare earth elements which readily exhibit the higher (trivalent and tetravalent) oxidation states. Evidence of possible deviation from this general picture is the noted (3, 4) apparent instability of the higher selenides and tellurides (M₂X₃) of the rare earth elements, samarium and ytterbium, which exhibit a highly stable divalent oxidation state and therefore may not readily assume the higher, oxidation states. Similar behavior has been noted also in the case of the normally tri-

positive element erbium. Routine attempts to prepare the M₂X₃ compounds of samarium, ytterbium, and erbium generally have yielded polyphase specimens in which the major phase is the fcc MX compound.

In the majority of the systems, only two of the four crystalline phases have been studied intensively. These are the MX compounds and the M₃X₄-M₂X₃ phases, which exhibit good thermal stability and can be crystallized from the melt, and thus readily can be prepared and studied. In contrast, it is found that the higher selenides and tellurides (MX₂ and MX₄) evolve selenium and tellurium when heated, at temperatures well below their melting points. Because of this poor thermal stability, these compounds have been prepared in atmospheres of metalloid vapors, and studies of these materials have been restricted to the low-temperature (below $\sim 400^\circ\text{K}$) range.

Monoselenides and monotellurides (Nd, Gd, Er, Sm, and Yb).—The monoselenides and monotellurides of the rare earth elements constitute a family of refractory materials, the members of which possess a variety of electrical properties (3). It is seen that the compounds all crystallize in a fcc, NaCl structure and have melting points in the range 1700°-2100°C.

In terms of their electrical properties, these materials fall into two general classes: one class which will be referred to as type II consists of compounds of rare earth elements which normally exhibit a stable divalent oxidation state, such as samarium and ytterbium; the other class which will be referred to as type III includes compounds of rare earth elements which normally exhibit a trivalent oxidation state, such as neodymium, gadolinium, and erbium. The type II compounds exhibit relatively high resistivities (>100 ohm-cm), large negative temperature coefficients of resistance (negative TCR), and have low room-temperature free-carrier concentrations (10^{15} - $10^{17}/\text{cm}^3$). The type III compounds exhibit very low resistivities (10^{-5} to 10^{-4} ohm-cm), positive TCR's, and appear to be degenerate semiconductors, or metallic in nature.

Figure 1 shows the temperature dependence of the electrical resistivity of various SmSe specimens. This material is characterized as n-type with room-temperature resistivity of about 2000 ohm-cm and carrier concentration of about $10^{15}/\text{cm}^3$. Although samples having resistivities which deviate from the

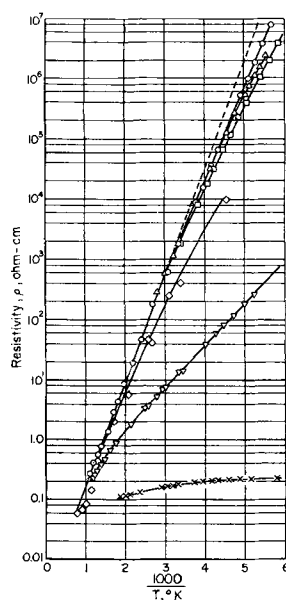


Fig. 1. Resistivity as a function of temperature for n-type SmSe samples: \circ , sample 70; \triangle , sample 75; \square , sample 72; \diamond , sample 15A; ∇ , sample 15B; \times , sample 55.

more typical values in the low-temperature range can be prepared, (e.g., specimens 15B and 55 in Fig. 1) the differences usually can be rationalized by pointing up obvious additions of impurities or defects (e.g., by deviation from stoichiometry) in substantial amounts. Single-crystal specimens exhibit electrical properties not materially different from those of polycrystalline specimens.

Hall data also indicate large temperature dependences suggesting a conduction mechanism involving the thermal activation of charge carriers. The fact that the high-temperature electrical properties are the same for so many samples prepared under a variety of conditions (e.g., with both purified and as-received samarium, with both excesses and deficiencies of samarium, and with additions of chemical impurities) suggests that the observed conductivity characteristics may be intrinsic to the material. Magnetic susceptibility studies (10) suggest that, for the compounds containing dipositive metal ions, the third valence electrons are highly localized in 4f levels. Samarium in SmSe apparently shows a +2 oxidation state because the third normally available valence electron tends to reside in a 4f level in an attempt to achieve a stable half-filled 4f⁷ configuration (see Table I). Hence, the activation energy for conduction giving rise to $\rho \propto e^{0.36 \text{ eV}/kT}$ may be associated with an electron transition from a 4f level to a 5d or 6s conduction band as suggested by McClure (11) for the rare earth monosulfides. If classical semiconductor theory is applied, the forbidden energy gap, E_g , is calculated to be about 0.72 eV for SmSe, as determined from the limiting slope in Fig. 1. However, an intrinsic conduction mechanism other than normal activation from a valence band to a conduction band may be operable.

In contrast to the n-type SmSe, the monoselenides and monotellurides of ytterbium have exhibited hole conduction presumably as a result of the presence of p-type impurities or lattice defects behaving as ac-

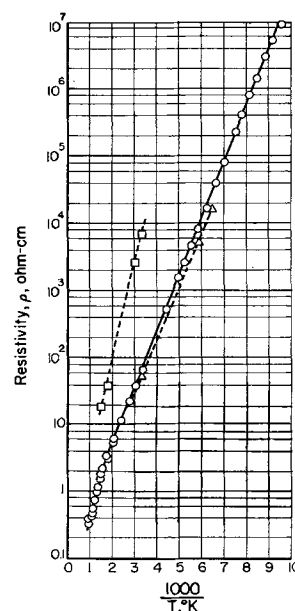


Fig. 2. Resistivity as a function of temperature for p-type specimens of YbTe and YbSe: \square , YbTe-3; \circ , YbSe-16B; \triangle , YbSe-16A.

ceptor sites. Figure 2 shows the temperature dependence of resistivity for p-type YbSe and YbTe specimens. The two YbSe specimens have carrier concentrations on the order of 4×10^{17} per cm³, with the hole mobilities being on the order of 0.3 cm²/volt-sec. Activation energies of 0.17 and 0.3 eV can be calculated from the data ($\rho \propto e^{0.17/kT}$ and $\rho \propto e^{0.3/kT}$) in the range 300°–500°K for YbSe specimen 16B and YbTe specimen 3, respectively, again assuming that classical semiconductor theory is applicable. At higher temperatures, the data indicate the possibility of approach to an intrinsic-conduction range; however, a slope is not well defined, and the specimen is still p-type at 1130°K (as determined from the sign of the thermoelectric power).

In the case of the Type III compounds, such as NdSe and the monotellurides of Nd, Gd, and Er, the above described electron transition from a 4f level to a conducting state appears to occur readily at all temperatures above 4°K. It is noted that these rare earth elements normally exhibit only the +3 oxidation state. In contrast with the Type II compounds, these Type III compounds exhibit low room-temperature resistivities, in the 10^{-5} to 10^{-4} ohm-cm range, and positive temperature coefficients of resistance, as is shown for the neodymium, gadolinium, and erbium compounds in Table IV and for GdTe in Fig. 3. Also carrier concentrations in these materials, which are all n-type, are apparently very large; estimates of the concentrations fall in the range 10^{21} to 10^{22} per cm³. The source of these carriers is believed to be the excess valence electrons contributed by the some 2×10^{22} rare earth atoms per cm³ in the lattice.

As has been noted, the Type II rare earth monoselenides and monotellurides exhibit large TCRs, coupled with good high-temperature stability. In addition, as seen in the preparation of SmSe, properties can be reproduced readily without close con-

Table IV. Room-temperature electrical properties of selenides and tellurides

Synthetic composition	Resistivity, ρ , ohm-cm	Hall coefficient, R_H , cm ³ /coulomb	Hall mobility, μ , cm ² /v-sec	Carrier concentration, n , cm ⁻³	Seebeck ^(a) coefficient, α , μ V/°K
Ce ₂ Se ₃	3.3×10^{-3}	-0.01	3.7	5.3×10^{20}	-57
Ce ₂ Te ₃	145	-315	—	—	—
Gd ₃ Se ₄	1.1×10^{-3}	Negative	—	—	-14
Gd ₂ Se ₃	1.3×10^{-3}	Negative	—	—	-7
Nd ₃ Te ₄	3.5×10^{-4}	Negative	—	—	-20
Gd ₃ Te ₄	4.6×10^{-4}	Negative	—	—	—
Er ₃ Te ₄	2.8×10^{-4}	Negative	—	—	—
Nd ₂ Te ₃	0.31	+1.15	5	4.2×10^{18}	+180
Nd ₂ Te ₃	1.2×10^{-3}	-0.008	6	8×10^{20}	-30
Nd ₂ Te ₃	22	Negative	—	—	-260
Gd ₂ Te ₃	1.9×10^{-2}	+0.34	18	1.9×10^{19}	+190
Gd ₂ Te ₃	1.5×10^{-2}	+0.16	11	4×10^{19}	+160
Gd ₂ Te ₃	2.0×10^{-3}	-0.11	55	5.7×10^{19}	-80
Gd ₂ Te ₃	8.1×10^{-3}	-0.3	40	2×10^{19}	-60
GdTe ₂ (melt-grown)	5.5×10^{-2}	Positive	—	—	—
GdTe ₂ (vapor-grown)	1.79	+2	1.3	2.7×10^{18}	—
CeSe ₂	292.0	Positive	0.4	5×10^{16}	+90

(a) Seebeck coefficient values were determined at temperatures 20°-40°C above room temperature.

trol over preparation methods. Thus, these materials are of interest as the active materials of thermistors and related devices. Potential device applications, the properties of alloys of Type II with the Type III compounds, and the electrical conduction process in the alloys have been discussed previously (12).

M_3X_4 - M_2X_3 selenides and tellurides (Nd, Gd, and Ce).—Rare earth selenide and telluride compositions ranging from M_3X_4 to M_2X_3 , in which the rare earth element is one normally exhibiting a stable +3 oxidation state, have been observed to have good thermal stability and to crystallize in either a bcc thorium phosphide structure or an orthorhombic structure. The lower atomic number rare earth elements form phases which exhibit the Th_3P_4 -type structure. For elements of higher atomic number than about 60 (neodymium), the tellurides assume the lower symmetry structure. The selenides of rare

earth elements heavier than gadolinium apparently crystallize in the orthorhombic structure. Details of observations on this subject have been given in oral presentation elsewhere (4).

Figure 3 shows the temperature dependence of resistivity for Gd_2Te_3 and Gd_3Te_4 compositions which crystallize in the orthorhombic structure. For the 2-3 composition both p- and n-type conduction are observed with carrier concentrations in the range 1×10^{19} to $6 \times 10^{19}/cm^3$. The top curve of Fig. 3 is for a specimen which is p-type at low temperatures and crosses over to n-type at about 900°K, as determined by the sign of the thermoelectric power. This sample was single phase (the orthorhombic structure) material, which by chemical analysis was found to contain ~0.9 w/o excess tellurium. Above 900°K the negative temperature coefficient of resistivity suggests the onset of intrinsic conduction with $\rho \propto e^{0.7/2kT}$, for kT expressed in electron volts.

Without exception, specimens of the 3-4 composition are n-type with free electron concentrations in the range 10^{20} to $10^{22}/cm^3$ and $R_{H\sigma}$ values < 1 cm²/volt-sec. It is noted that if the rare earth elements are present as trivalent ions, it is possible that each molecular unit could contribute a free conduction electron. At 100% ionization of the rare earth elements, about 4 to 8×10^{21} electrons/cm³ would be available for conduction.

As is shown in Fig. 3 and Table IV (in which the properties of representative specimens are given), corresponding compositions containing neodymium or other rare earth elements exhibit properties which are generally similar to those of the gadolinium compounds.

It is worthy of note that the M_2X_3 compositions exhibit rather typical semiconducting properties, being obtainable as both n- and p-type materials and possessing higher resistivities and higher carrier mobilities, and, in the case of Gd_2Te_3 at least, showing the apparent onset of intrinsic conduction at higher temperatures. On the other hand, for the

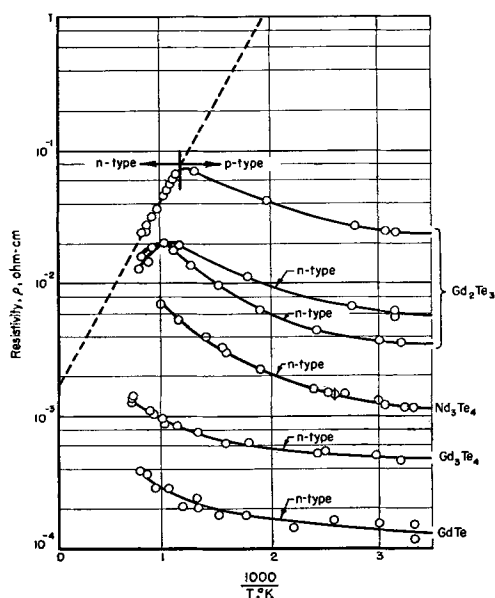


Fig. 3. Resistivity as a function of temperature for various nominal Gd-Te and Nd-Te compositions.

M_3X_4 compositions, no indication of a thermally activated conduction process has been obtained from resistivity data taken as a function of temperature in the range 77° - 1300°K ; reliable Hall data could not be obtained at the generally high carrier concentrations. Both the resistivity and Seebeck coefficient for these materials show a temperature dependence that appears similar to that of a metal.

The compounds which crystallize in the Th_3P_4 structure make up a family of materials, members of which are of interest as thermoelectric materials for power generators operated at high temperatures. The Th_3P_4 structure is body-centered-cubic with 28 at. per unit cell. The M_2X_3 compositions are considered to have a defect Th_3P_4 structure with 16 anions per unit cell and $10\frac{2}{3}$ rare earth atoms per unit cell distributed at random over 12 equivalent sites. As additional rare earth atoms are added, these vacant sites are progressively filled until the M_3X_4 composition is attained, corresponding to all sites filled.

At the 2-3 composition, formal charge balance prevails if the rare earth element assumes a tri-positive state. At the 3-4 composition, as many as 4 excess valence electrons are available per unit cell, or approximately 6×10^{21} electrons/ cm^3 .

One may adjust the carrier concentration, with a corresponding change in the vacancy concentration, by changing the composition of the compound in the range M_3X_4 to M_2X_3 . Hence, the values of electrical resistivity and Seebeck coefficient may be adjusted to optimize the thermoelectric figure of merit $Z = \alpha^2/\kappa\rho$, where α is the Seebeck coefficient and κ is the thermal conductivity. The carrier concentration also may be adjusted, without a change in the vacancy concentration, by replacing rare earth elements with divalent alkaline earth elements, such as barium or strontium.

The range of compositions of interest is shown in Fig. 4, using the Ce-Sr-Se system as an illustration. In analyzing series of specimens at points along the

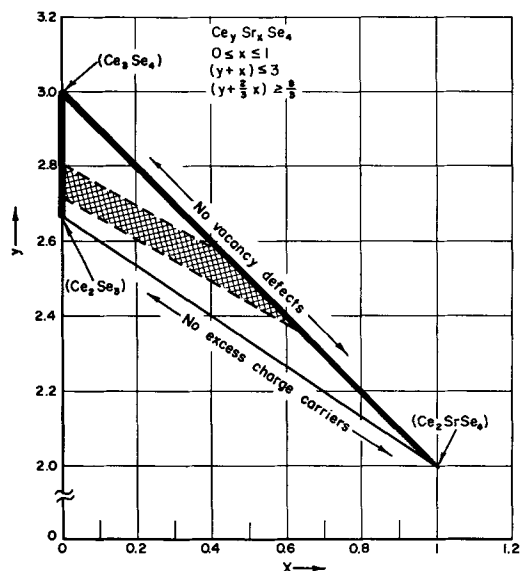


Fig. 4. Boundary conditions of interest for rare-earth compound and alloy compositions.

Table V. Thermoelectric data for representative rare earth compounds and alloys

Synthetic composition	T, °K	ρ , ohm-cm	α , $\mu\text{V}/\text{deg}$	$\kappa^{(a)}$, watt/cm-deg	ZT (est.)
$\text{Ce}_{2.72}\text{Se}_4$	298	8.0×10^{-3}		0.024	
$\text{Ce}_{2.4}\text{Sr}_{0.6}\text{Se}_4$	298	1.1×10^{-3}	-48	0.021	0.9
	1300	4.0×10^{-3}	-200	0.015	
$\text{Ce}_{2.5}\text{Ba}_{0.5}\text{Se}_4$	298	8.0×10^{-4}	-35	0.024	0.6
	1300	1.7×10^{-3}	-140	0.026	
$\text{Ce}_{2.5}\text{Sr}_{0.5}\text{Te}_4$	298	1.1×10^{-3}	-40	0.020	1.0
	1300	4.0×10^{-3}	-210	0.015	
$\text{Nd}_{2.76}\text{Te}_4$	298	1.4×10^{-3}	-40	0.014	1.1
	1300	7.5×10^{-3}	-240	0.009	

(a) Thermal conductivity, κ , at 1300°K was calculated as $\kappa = \kappa_{\text{elec}} + \kappa_{\text{ph}}$, where $\kappa_{\text{elec}} = \text{LT}/\rho$, $L = \frac{\pi^2}{3} \left(\frac{k}{e} \right)^2$, κ_{ph} (at 1300°K) = $\frac{1}{2} \kappa_{\text{ph}}$ (at 298°K), and $ZT = \alpha^2 T / \kappa \rho$.

two bold-face lines starting with the 3-4 composition and progressively replacing cerium atoms with vacancies or strontium atoms, electrical resistivity and Seebeck coefficient of the specimens increase in a regular manner. This suggests that carrier concentration decreases as the rare earth atoms are replaced or as the concentration of excess valence electrons is decreased. In the limited number of cases in which Hall effect could be measured, carrier concentrations given by $1/R_{\text{HE}}$ were in fair agreement with the calculated number of excess valence electrons. The most interesting compositions for thermoelectric applications have been found in the regions of intersection of the cross-hatched region with the two bold-face lines. Actually, interesting compositions would be expected also within the cross-hatched region in which the normally vacant sites of the 2-3 composition are filled only partially with rare earth and alkaline earth atoms.

Table V shows thermoelectric data at 298° and 1300°K for representative compositions. The high-temperature thermal conductivities were estimated by considering (i) measured electrical resistivities, (ii) the Wiedemann-Franz relationship, (iii) the measured room-temperature thermal conductivities, and (iv) high-temperature lattice thermal conductivities deduced from observed trends in this parameter for $\text{CeS-Ce}_2\text{S}_3$ compositions (10). Estimates obtained in this manner are believed to be conservative. In view of the fact that no serious attempt has yet been made to optimize the material compositions, it is encouraging that ZT values greater than unity at 1000°C have been attained. High-temperature figures of merit of this magnitude are rare. Other similar work reported (13, 14) has been limited to sulfides of rare earths with strontium or barium doping, and estimated ZT values of unity have been obtained with certain compositions. It has been observed that prevention of surface oxidation and application of contacts are more serious problems with the rare earth sulfides than with the tellurides or selenides.

Polyselenides and polytellurides.—Although compounds of the type MX_2 and MX_4 tend to dissociate

Table VI. Observed electrical properties of NdAs, GdAs, SmAs, and NdSb

Sam- ple	Syn- thetic com- position	Temper- ature, T, °K	Resis- tivity, ρ , 10^{-3} ohm-cm	Mobil- ity, μ , $\text{cm}^2/\text{v-sec}$	Carrier con- centra- tion, n , 10^{20} cm^{-3}	Seebeck coefficient, α , $\mu\text{V}/\text{deg}$
42R	NdAs	310	0.21	76	4.0	-22
		97	0.12	130	4.2	-8
42RA	NdAs	309	0.155	87	4.7	-9
		102	0.054	270	4.3	-2
29R	NdAs	304	0.142	86	5.2	-11
		106	0.087	140	5.2	-4
46R	NdAs	300	0.15	30	12	-3
30R	GdAs	305	0.12	70	8.0	-13
		110	0.076	90	8.6	-6
44R	SmAs	306	0.19	50	6	-5
		104	0.13	70	7	-2
47R	NdSb	300	0.076	40	20	
		130	0.045	70	20	

at moderate temperatures, specimens of GdTe_2 , GdTe_4 , and CeSe_2 have been prepared by crystallization of melts under atmospheres of the metalloid vapor. The GdTe_4 , so prepared, was in the form of leaflets embedded in a matrix of lower tellurides, and only crystal structure studies on this material were undertaken. However, polycrystalline specimens of GdTe_2 and CeSe_2 , large enough to permit electrical property measurements, were synthesized. In addition, sizable single crystals of GdTe_2 were prepared by a vapor growth method in which halogens were utilized to promote transport through the vapor phase.

The observed electrical properties (lower portion of Table IV) indicate that these compounds always exhibit p-type conduction, with resistivities being higher, Seebeck coefficient generally lower than those of the p-type specimens of the M_2X_3 compounds. The results for CeSe_2 show a combination of high resistivity, negative TCR, low carrier concentration, and low carrier mobility, suggesting similarity to the samarium and ytterbium monoselenides in which ionic valences are balanced. In contrast, resistivity of the ditelluride of the normally trivalent gadolinium is low, while carrier concentration is high and the TCR is positive. It is therefore suggested that ionic valences may be balanced in CeSe_2 , and that an appreciable fraction of the cerium is present in the +4 state.

Arsenides and antimonides (Nd, Sm, and Gd).—The rare earth elements form binary compounds with the elements of chemical Group V, arsenic and antimony, which contain nominally equiatomic portions of the elements and which crystallize in the fcc NaCl structure. Electrical properties of representative specimens of the compounds are shown in Table VI. All specimens measured have been n-type. If carrier concentrations are calculated using the simple $1/R_H e$ relation, where R_H is the Hall coefficient and e the charge on an electron, large free-electron concentrations in the range 4×10^{20} to $2 \times 10^{21}/\text{cm}^3$ are obtained. Nevertheless, the electron mobilities

determined from $R_H \sigma$, where σ is the electrical conductivity, are seen to be relatively large.

The electrical properties of SmAs prepared using purified samarium were found to be substantially the same as for SmAs prepared with as-received samarium metal. Thus, it appears that impurities initially present in the commercial rare earth metals are not contributing a significant portion of the free carriers. One can make the same statement (with even greater certainty) about the starting arsenic used in the preparations. However, these compounds are prepared under extremely severe conditions (e.g., at temperatures near 2500°C), and it is distinctly possible that electrically active impurities are introduced from components of the system in the course of the high-temperature preparation.

Spectrographic analysis of a SmAs specimen revealed the presence of significant levels of silicon, tantalum, and copper: concentrations of 2000, 2000, and 400 ppm (atomic), respectively, (compared with approximately 130, 400, and 60 ppm, respectively, in the starting materials). If the silicon and tantalum act as donor impurities, the concentration of each element could account for about 1×10^{20} electrons/ cm^3 , which is still somewhat smaller than the measured carrier concentration of this particular sample ($n \approx 8 \times 10^{20}/\text{cm}^3$). The source of tantalum is no doubt the tantalum tube which holds the SmAs charge. The source of silicon and copper may be the quartz envelope used in the preparation. The carbon and oxygen concentrations in this sample have not been determined. However, it appears that one must look at other possibilities in addition to chemical impurities for the origin of the high free-electron concentrations.

The results of chemical analysis of several NdAs specimens indicate that the specimens tend to be arsenic deficient. For example, analysis of Specimen 42RA, which was prepared with excess arsenic and subsequently sintered in arsenic vapor at 1 atm of pressure, gave a composition of $\text{NdAs}_{0.994}$. Specimen 46R apparently lost arsenic in preparation, going from a synthetic composition of $\text{NdAs}_{0.97}$ to a final composition of $\text{NdAs}_{0.96}$. Carrier concentrations obtained from the electrical measurements on the two specimens (see Table VI) reflect the differences between compositions of the samples, suggesting lattice defects as one possible source of the high carrier concentrations. Even up to temperatures of 1200°K , no indication is obtained from Hall effect measurements to suggest an increase in carriers due to a thermally activated process, for example, across a forbidden band gap. However, with such large free-carrier concentrations already present, this is not surprising.

Figure 5 shows the temperature dependence of $R_H \sigma$ for these materials. The large concentrations of charged carriers present suggests the possibility of large concentrations of ionized scattering centers which would suppress the mobility of electrons in these materials. However, using the simple relation $R_H \sigma$ for mobility, one sees that this is not the case. Relatively high mobilities are obtained, being on the order of $100 \text{ cm}^2/\text{volt-sec}$ for the arsenides at room

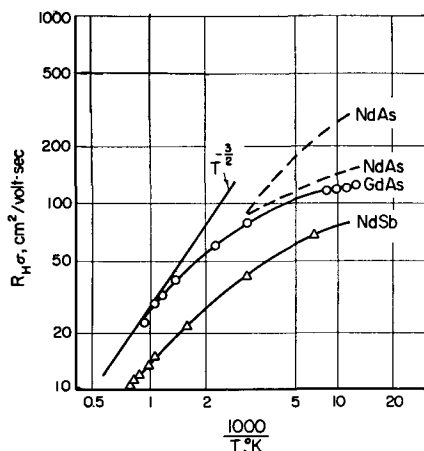


Fig. 5. Hall mobility as a function of temperature for n-type NdAs (---), GdAs (○), and NdSb (△).

temperature, with a temperature dependence suggesting that a lattice scattering mechanism dominates.

Work has been reported (15) on the rare earth nitrides indicating optical band gaps in these materials of about 2 eV. Hence, as this class of rare earth compounds, which includes the nitrides, phosphides, arsenides, and antimonides is developed, interesting refractory electronic materials for active device elements may be forthcoming.

Summary

Utilization of representative rare earth elements to form compounds and alloys with the Group VA and Group VIA elements has provided materials for which electrical characteristics range from those of high-resistivity semiconductors to those of metallic conductors, and which exhibit electronic transport properties of both practical and theoretical interest. It has been found that within a single system, MX_n , of variable selenium or tellurium content, a sequence of compounds can be formed, possessing a wide range of properties. In some ranges of composition, the transition from one type of conduction process to another appears to be gradual, thus presenting the opportunity for study of subtle differences between the extremes. When the changes in conductivity mechanism are accompanied by change in structure, the opportunity exists, within a single binary system, for a study of the effects of changes in lattice spacing, bonding, and other crystalline environmental factors, on the transport properties of a solid. Complications resulting from changing chemical species are avoided. Thus, these are attractive systems for studying interrelations between crystal structures, band structures, and transport mechanisms.

Although electronic grade rare earth metals are not yet available and problems connected with control of stoichiometry remain, the eventual utilization of rare earth compounds and alloys in electronic ap-

plications is definitely indicated. The Group VA compounds appear to be a class of refractory, moderately high-mobility semiconductors of potential interest for active device components. The M_3X_4 to M_2X_3 rare earth selenides and tellurides show distinct promise as thermoelectric materials for power generation utilizing high-temperature sources, and the high-resistivity monoselenides and monotellurides may be useful in thermistors and related devices.

Acknowledgment

This paper is based on the results of research supported by the Electronic Research Branch, Electronic Technology Division, Air Force Avionics Laboratory, Research and Technology Division, Air Force Systems Command of the United States Air Force.

Manuscript received Jan. 24, 1964; revised manuscript received March 13, 1964. This paper was presented at the Pittsburgh Meeting, April 15-18, 1963.

Any discussion of this paper will appear in a Discussion Section to be published in the June 1965 JOURNAL.

REFERENCES

1. J. F. Miller, F. J. Reid, and R. C. Himes, *This Journal*, **106**, 1043 (1959).
2. J. F. Miller and R. C. Himes, "Rare-Earth Research," E. V. Kleber, Editor, p. 232, The MacMillan Company, New York (1961).
3. J. F. Miller, L. K. Matson, and R. C. Himes, "Rare-Earth Research," C. Lundin and J. Nachman, Editors, p. 233, Gordon and Breach Science Publishers, New York (1962).
4. J. F. Miller, L. K. Matson, and R. C. Himes, "Observations on M_3X_4 - M_2X_3 Crystalline Phases of Rare-Earth Tellurides, Selenides, and Sulfides," paper presented at Third Rare Earth Conference, Clearwater, Florida (April, 1963); to be published in Proceedings of Third Rare-Earth Research Conference, Gordon and Breach Science Publishers.
5. R. C. Vickery and H. M. Muir, "Rare-Earth Research," E. V. Kleber, Editor, p. 223, The MacMillan Company, New York (1961).
6. A. Benacerraf and M. Guittard, *Compt. rend.*, **248**, 2012 (1959).
7. L. Domange, J. Flahaut, M. Pardo, A. Chirazi, and M. Guittard, *ibid.*, **250**, 857 (1960).
8. M. Pardo, J. Flahaut, and L. Domange, *ibid.*, **256**, 1793 (1963).
9. M. Pardo, J. Flahaut, and L. Domange, *ibid.*, **256**, 953 (1963).
10. A. Iandelli, "Rare-Earth Research," E. V. Kleber, Editor, p. 135, The MacMillan Company, New York (1961).
11. J. W. McClure, *J. Phys. Chem. Solids*, **24**, 871 (1963).
12. F. J. Reid, L. K. Matson, J. F. Miller, and L. K. Matson, F. J. Reid, R. C. Himes, Papers presented at the New York Meeting, Electrochemical Society, October, 1963.
13. R. C. Miller and R. W. Ure, Jr., "Energy Conversion for Space Power," N. W. Snyder, Editor, Academic Press, New York (1961).
14. S. Kurnick, R. L. Fitzpatrick, and M. F. Merriam, "Rare-Earth Research," C. Lundin and J. Nachman, Editors, p. 249, Gordon and Breach Science Publishers, New York (1962).
15. N. Sclar, *J. Appl. Phys.*, **33**, 2999 (1962).

Some Properties of GaSb-Ga₂Se₃ and GaSb-Ga₂Te₃ Alloys

J. C. Woolley¹ and K. W. Blazey²

Physics Department, University of Nottingham, Nottingham, England

ABSTRACT

The ranges of solid solution of Ga₂Te₃ and Ga₂Se₃ in GaSb at 500°C have been determined by annealing powdered samples to equilibrium and measuring lattice parameters by x-ray methods. For the Ga₂Te₃ alloys, periods of annealing of up to 12 months were required to give equilibrium conditions. The limits of solid solution at 500°C were found to be 36 mole % for Ga₂Te₃ and 10 mole % for Ga₂Se₃. Measurements of room temperature optical energy gap and Hall coefficient have been made for alloys containing up to 5 mole % chalcogenide. Starting with p-type GaSb, the alloys become n-type with addition of very small amounts of chalcogenide, and values of electron concentration of up to $4 \times 10^{17}/\text{cc}$ and $2 \times 10^{20}/\text{cc}$ were found for telluride and selenide alloys, respectively. Corresponding minima in the values of E_g due to compensation were observed. The nonstoichiometry at low concentrations of chalcogenide which results in these values is discussed and the results compared with those for GaSb heavily doped with tellurium and selenium.

A number of alloy systems formed from A^{III}B^V compounds and A₂^{III}B₃^{VI} compounds of defect zinc blende structure have been investigated (1-6). The range of solid solution of the A₂^{III}B₃^{VI} compound in the A^{III}B^V is very different for the various alloy systems, but in all cases electrical measurements show that at low A₂^{III}B₃^{VI} content the solid solution is nonstoichiometric, with a loss of some lattice vacancies. This allows some of the B^{VI} atoms in the B sublattice to act as donors, and hence the material becomes n-type with very high carrier concentration. The results under these conditions are of interest for comparison with those obtained when the A^{III}B^V compound is very heavily doped with the B^{VI} element, the difference from the mass action view point being the additional A^{III} atoms included in the A₂^{III}B₃^{VI} compound (7). In addition, in many cases the variation with composition of various parameters such as carrier concentration, optical energy gap, etc., can, by means of extrapolation, give useful data on the A^{III}B^V compound concerned (8).

A number of papers (9-11) have considered the effects of doping GaSb with selenium and tellurium, but no work has been reported on the corresponding alloy systems GaSb-Ga₂Se₃ and GaSb-Ga₂Te₃.

Preparation of Alloys and Methods of Measurement

In all cases, the compounds were prepared directly from the elements and then the alloys produced by melting together under vacuum the appropriate weights of the compounds required. The gallium and antimony used for the preparation of GaSb were each of 99.999% purity. In the case of the selenide and telluride 99.99% pure elements were used, the selenium and tellurium being purified further before use by repeated sublimation.

The alloys were initially quenched from the melt and samples x-rayed by standard powder techniques

using 9 cm cameras and copper K α radiation. All alloys were then annealed at 500°C until equilibrium conditions at that temperature were obtained. The times of annealing required to give equilibrium were determined by x-raying representative samples after various times and noting when the lines obtained were sharp and unaffected by further annealing. Lattice parameter values for the equilibrium conditions were then determined.

For the alloys which showed single phase zinc blende behavior, electrical and optical measurements were made on polycrystalline samples. For this purpose alloys were made up and annealed as above. In order to eliminate blow holes, etc., in the final ingots of these samples, the molten alloy was roughly centrifuged until it had solidified. For each alloy, measurements were made at room temperature of the Hall coefficient and optical energy gap. The methods used were the same as those described previously for similar alloys (4).

Results

X-ray data.—For the Ga₂Te₃ alloys, various samples containing up to 60 mole % Ga₂Te₃³ were investigated. Some of the alloys were initially annealed at 700°C, but those with Ga₂Te₃ content greater than 10 mole % were found to have melted, indicating the probable presence of a eutectic or peritectic horizontal at a temperature lower than 700°C. Annealed at 500°C, the alloys of higher Ga₂Te₃ content required very long annealing times to attain equilibrium, the x-ray photographs at shorter times showing blurred lines characteristic of a nonequilibrium condition. After 4 months annealing, alloys out to 20 mole % Ga₂Te₃ showed a single phase condition, but the 30 and 35 mole % alloys required further annealing, and the 35 mole % alloy was found to be single phase after

¹ Present address: Physics Department, University of Ottawa, Ottawa, Canada.

² Present address: IBM Research Laboratory, Zurich, Switzerland.

³ In calculating mole % in systems composed of one A^{III}B^V compound and one A₂^{III}B₃^{VI} compound, the molecules have been taken as A₃^{III}E₃^V and A₂^{III}B₃^{VI}, i.e., the percentage is strictly the percentage of B^V and B^{VI} atoms on the B sublattice.

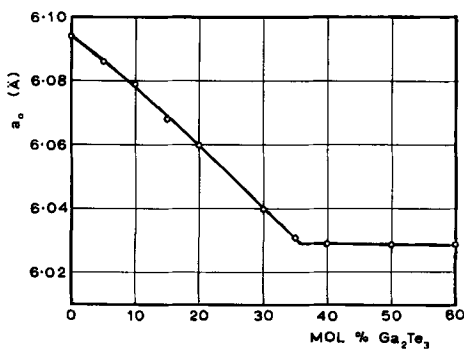


Fig. 1. Variation of zinc blende phase lattice parameter a_0 with composition for $\text{GaSb-Ga}_2\text{Te}_3$ alloys.

more than 12 months at 500°C . Alloys of Ga_2Te_3 content larger than this were found to be two phase and attained an equilibrium condition more rapidly.

The variation of lattice parameter of the zinc blende type phase as a function of composition is shown in Fig. 1. It is seen that at 500°C the range of single phase solid solution extends to 36 mole % Ga_2Te_3 .

The alloys of Ga_2Se_3 were treated in a similar way, but in this case the range of solid solution could not be determined from lattice parameter data because the variation of lattice parameter with alloy composition was too small. Hence the disappearing phase technique was used. In this system, equilibrium could be attained with one or two weeks annealing at 500°C . Alloys of 10 mole % or less Ga_2Se_3 then appeared single phase, while for alloys containing 20 mole % or more the equilibrium second phase was clearly visible. Alloys containing 12, 14, 16, and 18 mole % Ga_2Se_3 , respectively, were annealed to equilibrium and x-rayed. One of the stronger lines of the second phase was close to the 422 line of the zinc blende structure, and for each alloy the ratio of intensity of these two lines was determined with a Hilger & Watts comparator microphotometer. The graph of intensity ratio against composition is shown in Fig. 2 and extrapolation of the intensity ratio to zero indicates a limit to the single phase solid solution of between 10.0 and 10.5 mole % Ga_2Se_3 .

Electrical data.—Values of Hall coefficient R_H were determined at various compositions up to 2

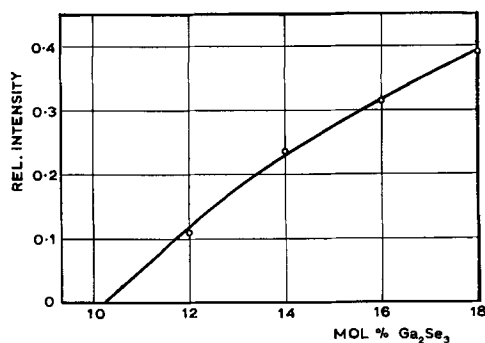


Fig. 2. Variation of intensity ratio for second phase line and 422 line of zinc blende phase as function of composition in $\text{GaSb-Ga}_2\text{Se}_3$ alloys.

mole % for the Ga_2Se_3 alloys and 5 mole % GaTe_3 . The electrical data was limited to this range of composition because (a) the main interest in the electrical work was the modification of the behavior of GaSb and (b) the electrical measurements are more sensitive than the optical work to the presence of segregations, etc., and so the compositions investigated were kept to a range in which good single phase behavior would be expected from consideration of x-ray data, etc. Since the GaSb was initially p-type and the effect of adding Ga_2X_3 (hereafter X will be used to indicate general results for both Te and Se) was to dope the material n-type, many of the alloys showed mixed conduction, and so the value of R_H could not directly give a value for carrier concentration. Also, the variation of electrical parameters with temperature would be very difficult to interpret since intrinsic behavior would not be reached even at the melting point. The variation of room temperature values of R_H with composition for both alloy systems is shown in Fig. 3. The two curves are similar in general form, but show marked differences in detail. In the case of the selenide alloys, the value of R_H changes from positive to negative at 0.1 mole % Ga_2Se_3 , and the number of conduction electrons continues to increase rapidly with Ga_2Se_3 content so that R_H shows a sharp minimum at about 0.2 mole % Ga_2Se_3 and then reapproaches zero giving a value of $0.098 \text{ cm}^3/\text{coulomb}$ at 1 mole % Ga_2Se_3 and $0.026 \text{ cm}^3/\text{coulomb}$ at 2 mole % Ga_2Se_3 . If at these values we can assume $R_H = 1/ne$, this gives an electron concentration n of $2 \times 10^{20}/\text{cc}$ for the 2 mole % alloy. In the case of the telluride alloys, R_H changes sign with the addition of only 0.05 mole % Ga_2Te_3 , but then the rate of increase in number of conduction electrons becomes small and the curve flattens out at a value of R_H corresponding to 4×10^{17} electrons/cc.

Optical data.—Values of optical energy gap E_g were determined by transmission measurements in both systems for alloys up to 10 mole % Ga_2X_3 . The samples used in the work had thicknesses in the range $100\text{-}200\mu$, and values of fractional transmission I/I_0 were determined as a function of wavelength as shown in Fig. 4. Values of E_g were determined as

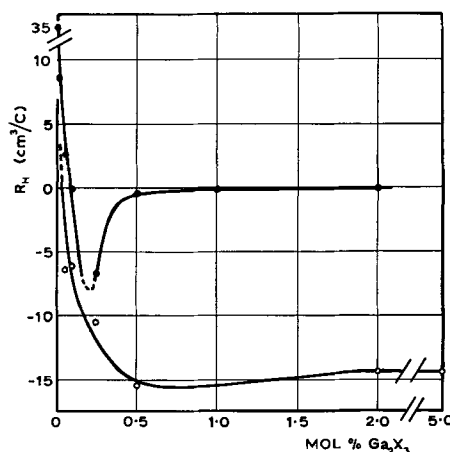


Fig. 3. Variation of Hall coefficient R_H with composition for $\text{GaSb-Ga}_2\text{X}_3$; ●, X is Se; ○, X is Te.

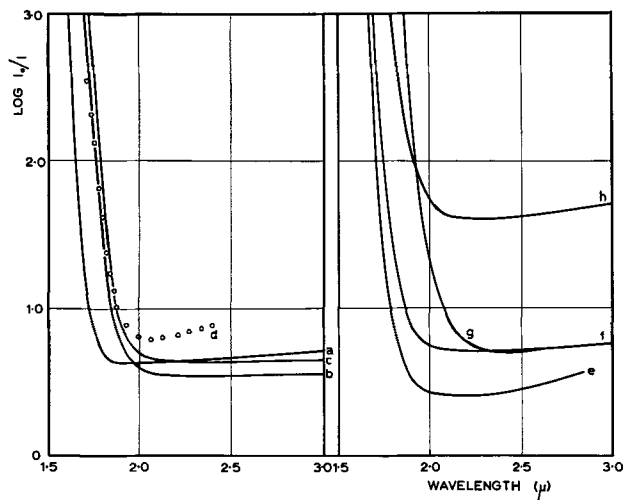


Fig. 4. Variation of $\log I_0/I$ with wavelength for various GaSb-Ga₂X₃ alloys: a, 0.05 mole % Ga₂Te₃, 99.95 mole % GaSb; b, 0.5 mole % Ga₂Te₃, 99.5 mole % GaSb; c, 2.0 mole % Ga₂Te₃, 98.0 mole % GaSb; d, 10.0 mole % Ga₂Te₃, 90.0 mole % GaSb; e, 0.01 mole % Ga₂Se₃, 99.99 mole % GaSb; f, 0.25 mole % Ga₂Se₃, 99.75 mole % GaSb; g, 1.0 mole % Ga₂Se₃, 99.0 mole % GaSb; h, 10.0 mole % Ga₂Se₃, 90.0 mole % GaSb.

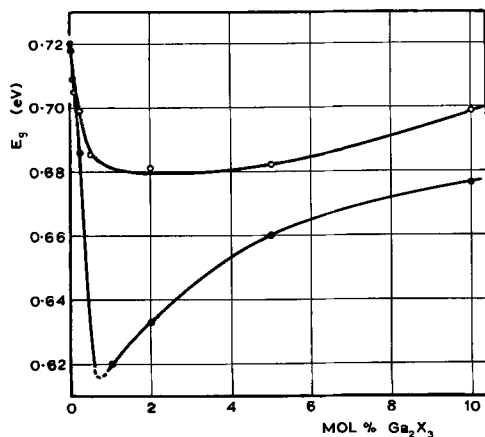


Fig. 5. Variation of optical energy gap E_g with composition for GaSb-Ga₂X₃ alloys: ●, X is Se; ○, X is Te.

described previously (4). The variation of E_g with composition for the two systems is shown in Fig. 5. Again the results for the two systems are generally similar, but differ in detail. The addition of the chalcogenide in each case causes the observed value of E_g to fall initially from that for GaSb and then to rise again, but while the minimum for the tellurides is 0.68 eV, a fall of only 0.04 eV from the GaSb value, the minimum for the selenides is much lower, being less than 0.62 eV.

Discussion

The difference in range of solid solution for the selenide and telluride alloys is similar to that for the corresponding indium compounds where the solid solution of In₂Se₃ in InSb is very limited. This is despite the fact that the replacement of antimony by selenium in both indium and gallium alloys causes very little change in the lattice parameter, so that lattice strain would not appear to be a major factor limiting solid solution.

In discussing the above electrical and optical data, it is of interest to summarize first the results obtained for heavy doping of GaSb with selenium or tellurium (9-11). The exact interpretation of R_H is difficult here, in that for materials with large electron density at room temperature there will be electrons in both (000) and <111> conduction band minima and these have different effective masses. Nevertheless a comparison of the results for addition of selenium or tellurium is possible and also the results for the addition of Ga₂Se₃ and Ga₂Te₃. Strauss (10) observed different behavior for tellurium-doped and selenium-doped material and attributed this to impurity band conduction. Bate (11) has shown that the appropriate donor level for selenium in GaSb is associated with <111> minima, being in energy below these minima but above (000) minimum. He also suggests that tellurium gives a similar donor level nearer in energy to the <111> minima. Thus when these levels are broadened into impurity bands, even if they do not overlap the conduction band at the <111> minima, they will be at energies equal to or greater than those of the (000) minimum, and electrons can be transferred from the impurity band at the (000) valley by phonon collision.

Hall and Racette (9) showed that the mobility of carriers in GaSb doped with selenium or tellurium dropped rapidly for carrier concentrations greater than $n = 4 \times 10^{18}/\text{cc}$ for tellurium doping and $n = 1.5 \times 10^{18}/\text{cc}$ for selenium. They also showed that an eightfold increase in the tellurium content of the melt beyond this limit caused the value of n to increase by a factor of 1.3 only, and that for both selenium and tellurium, crystallites of a second phase were observed in the heavily doped GaSb crystals. Thus the limiting carrier concentrations observed due to selenium and tellurium doping would be of the order $2 \times 10^{18}/\text{cc}$ and $5 \times 10^{18}/\text{cc}$, respectively.

In considering the results for the Ga₂Se₃ and Ga₂Te₃ alloys, data for these alloys must be considered in terms of the behavior shown to occur in the case of similar A^{III} B^V=A₂^{III} X₃^{VI} alloys (3-6). Thus at very low concentrations of the chalcogenide, practically no lattice vacancies occur in the material, and the effect is very similar to the doping of the A^{III} B^V compound with X. However as the concentration of A₂X₃ increases, vacancies occur in the lattice, and we have a transition toward a normal alloy behavior between two compounds A^{III} B^V and A₂^{III} X₃^{VI}. The concentration of A₂X₃ at which this transition occurs and the rate at which vacancies are included in the lattice are, of course, the factors which vary from system to system. Even in the case of A^{III} B^V compounds doped heavily with X, it appears probable that lattice vacancies tend to develop on the A sublattice as the concentration of X is increased.

In the range of composition of the Ga₂Se₃ and Ga₂Te₃ alloys considered above, the appearance of a second phase is not a factor since the x-ray data show that the alloys remain single phase to compositions well beyond the limit of the electrical

measurements. Here the limiting factor on the effective number of selenium (or tellurium) donors is the occurrence of compensating lattice vacancies (7). Considering first the alloys with very low chalcogen concentration, here the number of lattice vacancies formed is likely to be small, although previous measurements with the corresponding indium alloys (4) showed that at 0.1 mole % In_2Te_3 approximately half of the stoichiometric number of lattice vacancies do occur. For the results shown here, the rate of change of R_H can be taken as a measure of the relative number of lattice vacancies produced by addition of Ga_2X_3 , assuming the ionization energy of the donors to be zero. With the selenide, 0.1 mole % must be added before the acceptor concentration in GaSb is compensated, whereas with the telluride only 0.05 mole % is required. Thus at these low concentrations, more lattice vacancies (and hence effectively fewer donors) are occurring in the selenide alloy than in the telluride. As further chalcogenide is added, however, the behavior changes. Beyond 0.2 to 0.3 mole % Ga_2Te_3 , the number of conduction electrons (and hence of tellurium donors) changes very little with composition, the R_H curve levelling out at a value corresponding to 4×10^{17} electrons/cc. Thus it would appear that in this range, further addition of Ga_2Te_3 produces a stoichiometric number of lattice vacancies. In contrast, with the selenide alloys the R_H values show that the number of conduction electrons continues to increase rapidly with addition of Ga_2Se_3 and is still rising at 2 mole % Ga_2Se_3 where $n = 2 \times 10^{20}$ /cc. Thus even with this amount of Ga_2Se_3 added, the stoichiometric number of vacancies are not being included in the lattice. This inability to retain the stoichiometric number of lattice vacancies could be an important factor in determining the limited range of solid solution of Ga_2Se_3 in GaSb and similarly of In_2Se_3 in InSb.

The formation of lattice vacancies may also be an important factor in considering the values for limiting carrier concentrations in GaSb doped with selenium or tellurium. The limit to the effective number of donors may be either the formation of a second phase, as observed by Hall and Racette, or the occurrence of lattice vacancies as indicated above. Thus the smaller number of carriers obtained by selenium addition is consistent with the suggestion above that the tendency for lattice vacancy formation is limited in the selenium case, and hence without extra gallium being available to balance the added selenium in the zinc blende lattice, the selenium is lost to a second phase even at relatively small concentrations. In the case of tellurium addition, lattice vacancies can form in the gallium sublattice to balance the extra tellurium content, and results nearer to those for Ga_2Te_3 alloys can be obtained.

The variation of E_g for the Ga_2Se_3 and Ga_2Te_3 alloys is consistent with the electrical data discussed

above. As has been shown by Stern and Dixon (12) for InAs, the observed band gap may be reduced by the presence of large numbers of donors and acceptors, this effect being associated with the formation of impurity bands. Comparing the Ga_2Se_3 and Ga_2Te_3 alloys, the initial donor levels are lower in energy in the former case, and also many more selenium atoms act as donors as compared with tellurium. Hence a broader impurity band will be produced in the selenide than the telluride and will extend further into the band gap of GaSb. Under the conditions here the onset of absorption will correspond to transitions from valence band (or acceptor impurity band) to the bottom of the donor impurity band and hence the fall in E_g should be considerably greater for Ga_2Se_3 alloys than Ga_2Te_3 alloys, as in fact observed. The subsequent rise in E_g is due to a general increase in the band spacings as the addition of Ga_2X_3 modifies the general form of the GaSb bands. This increase in band spacing was also observed for Ga_2Se_3 alloys by measurement of the reflection spectrum of the 10 mole % Ga_2Se_3 alloy using the method described previously (13). The E_1 peak of the reflectivity spectrum, which corresponds to a $\lambda_3 \rightarrow \lambda_1$ transition between valence and conduction bands was found to occur at an energy about 0.08 eV higher than the value for GaSb itself.

Acknowledgments

The authors are indebted to Professor L. F. Bates for the facilities of his laboratory. The work described forms part of an investigation carried out for the Admiralty.

Manuscript received Dec. 24, 1963; revised manuscript received March 18, 1964.

Any discussion of this paper will appear in a Discussion Section to be published in the June 1965 JOURNAL.

REFERENCES

1. D. N. Nasledov and I. A. Fel'tin'sh, *Soviet Phys.-Solid State* (English Transl.), **2**, 755 (1961).
2. S. I. Radautsan and B. E-Sh. Malkovich, *ibid.*, **3**, 2413 (1962).
3. D. B. Gasson, P. J. Holmes, I. C. Jennings, J. E. Parrott, and A. W. Penn, *Proc. Int. Conf. on Semiconductor Phys.*, Czech. Acad. Sci., p. 1032, Prague (1961).
4. J. C. Woolley, C. M. Gillett, and J. A. Evans, *J. Phys. Chem. Solids*, **16**, 138 (1960).
5. J. C. Woolley, B. R. Pamplin, and J. A. Evans, *ibid.*, **19**, 147 (1961).
6. J. C. Woolley and P. N. Keating, *Proc. Phys. Soc.*, **78**, 1009 (1961).
7. D. B. Gasson, I. C. Jennings, J. E. Parrott, and A. W. Penn, *Proc. Int. Conf. on Physics on Semiconductors*, Exeter, p. 681 (1962).
8. J. C. Woolley and E. W. Williams, *This Journal*, **111**, 210 (1964).
9. R. N. Hall and J. H. Racette, *J. Appl. Phys.*, **32**, 856 (1961).
10. A. J. Strauss, *Phys. Rev.*, **121**, 1087 (1961).
11. R. T. Bate, *J. Appl. Phys.*, **33**, 26 (1962).
12. F. Stern and J. R. Dixon, *ibid.*, **30**, 268 (1959).
13. J. C. Woolley and K. W. Blazey, *J. Phys. Chem. Solids*, in press.

On the Anode Gas Reactions in Aluminum Electrolysis

I. The Reactivity of Dissolved Aluminum in NaF-AlF₃-Al₂O₃ Melts

Jomar Thonstad¹

*Institute of Metallurgy and Institute of Inorganic Chemistry,
The Technical University of Norway, Trondheim, Norway*

ABSTRACT

The reactions between aluminum dissolved in NaF-AlF₃-Al₂O₃ melts and CO₂, CO, and CO₂/CO mixtures have been studied by bubbling known amounts of gas through the melts followed by gas analysis. The results clearly show that CO₂ is reduced not only to CO, as commonly assumed, but a part of the CO is further reduced to carbon. The extent of both reactions is strongly dependent on the NaF/AlF₃ ratio and decreases with increasing AlF₃ content over the whole range investigated (NaF/AlF₃ molar ratio from 97/3 to 62/38). Published data indicate that the solubility of aluminum in these melts increases with increasing AlF₃ content when NaF/AlF₃ < 75/25 (cryolite); hence, it is suggested that part of the dissolved metal in these melts is present in a state which is nonreactive to CO₂/CO. The rate of reduction of CO₂ to CO increases markedly with temperature, while the rate of the subsequent reduction to carbon decreases slightly. When the inlet gas is CO instead of CO₂, the fraction of gas reduced to carbon is 7.7% as compared to 0.8% with CO₂ (at cryolite composition, t = 1000°C).

The anode gas from industrial aluminum cells consists of CO₂ together with as much as 30-50% CO. It is considered that most of the CO is formed by a reaction between CO₂ evolved at the anode and dissolved metal in the melt, and that this reaction is responsible for the loss in current efficiency in the aluminum electrolysis (1, 2). The reaction may tentatively be written



The dissolved metal, here denoted Al_f, most likely consists of subvalent ions like Al⁺ and Na₂⁺ (as free ions or in associations) (3-5), but the possibility of uncharged metal atoms or even a colloidal dispersion of metal in the melt (6) cannot be entirely rejected. (For simplicity, Al_f is regarded as uncharged in the equations.) The vapor above such melts contains sodium (7, 8) (as metal or as subhalide), so the dissolved metal seems to consist partly of sodium.

The content of dissolved metal in cryolite-alumina melt at about 1000°C has been measured by three workers (5, 7, 2), all of whom found a metal content corresponding to about 0.10 weight per cent (w/o) Al in the melt. Other measurements (5, 2) indicate that the solubility increases with either higher or lower ratios of NaF/AlF₃, thus exhibiting a minimum around the cryolite composition. The solubility also increases with increasing Al₂O₃ content (9) and with temperature (2).

The dissolved metal is formed at the interface between metal and electrolyte and is transported upwards (by diffusion and convection) to the vicinity of the anode where reaction [1] takes place. It has also been suggested that CO₂ is dissolved in the

electrolyte and transported towards the cathode but, since the solubility of CO₂ in cryolite melt is very low (7), this mechanism should be of minor importance only.

The equilibrium for reaction [1] (with Al_(l) in place of Al_f) is strongly displaced to the right ($\Delta G^\circ_{1000^\circ\text{C}} = -86 \text{ kcal}$), so it is evident that the extent of reduction of the CO₂ by the dissolved metal is controlled by kinetic effects.

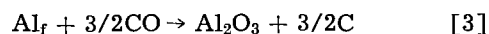
Reaction [1] can be studied by bubbling CO₂ through a cryolite melt in contact with aluminum, with subsequent gas analysis, as done by Schadinger (10) and Årseth (11), whereas Revazyan (12) passed the CO₂ over the surface of the melt only.

Revazyan's results in particular show that the amount of gas reduced per unit time does not depend on gas inlet rate or distance from the metal surface to the reaction zone, but rather depends on the aluminum activity in the metal. This author concludes that the degree of reaction is controlled by the rate of dissolution of the metal.

The reactions



and/or



have not received much attention. Beljajev (2) mentions that reduction of CO₂ to carbon may take place in overheated industrial cells. Schadinger (10) tried to study this reaction by the previously described bubbling method with CO as inlet gas. Although his curve seems to indicate a slight reduction of CO, he rejects the possibility.

The purpose of the present investigation was to study in more detail the reactions which occur between CO₂ and CO and dissolved aluminum in NaF-

¹ Present address: Department of Metallurgical Engineering, University of Toronto, Toronto, Canada.

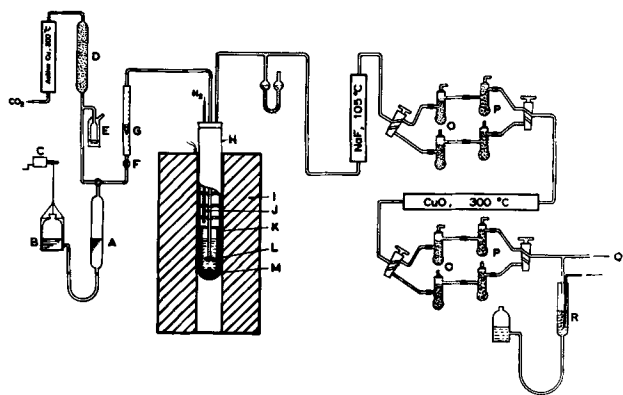


Fig. 1. Apparatus for investigation of the reactivity of dissolved aluminum. A, Gasometer; B, levelling bottle with mercury; C, gear lift; D, drying agent (Dehydrite); E, overflow; F, valve; G, rotameter, H, Pythagoras tube (500 x 41 x 35 mm); I, Kanthal furnace; J, inlet for N_2 ; K, boron nitride crucible; L, copper "anode"; M, aluminum; O, absorption bulbs with Dehydrite; P, absorption bulbs with Ascarite + Dehydrite; Q, to suction pump; R, overflow.

$AlF_3-Al_2O_3$ melts, in particular the possibility of reduction to carbon.

Experimental

The apparatus is shown in Fig. 1. Tank CO_2 was purified and led into a gasometer A (volume 1164 ml). In some preliminary experiments an aqueous solution of $Na_2SO_4 + H_2SO_4$ [Kobe's liquid (13)] saturated with CO_2 , was used as containing liquid in the gasometer. With this solution, sufficient accuracy was not obtained, however, so it was replaced by mercury. The melt was contained in a boron nitride crucible K (32 x 25 x 100 mm) placed in a Pythagoras tube H. The tube was heated in a Kanthal furnace I, which was connected to an on/off temperature regulator (millivolt-meter-controller). CO_2 , and/or CO, from the gasometer was bubbled through the melt from a copper tube with an "anode-like" copper plate L (diam 20 mm) at the end. The distance to the aluminum metal surface was 25 mm. Purified nitrogen, acting as carrier gas, was led into the Pythagoras tube above the crucible.

The effluent gas passed to the gas absorption unit. Traces of HF were absorbed by NaF at $105^\circ C$ (14). H_2O and CO_2 were absorbed in the absorption bulbs O and P, filled with Dehydrite and Ascarite + Dehydrite, respectively. H_2 and CO were oxidized to H_2O and CO_2 by copper oxide at $300^\circ C$, followed by a second set of absorption bulbs. A suction pump Q was applied at the outlet in order to keep atmospheric pressure in the Pythagoras tube.

The gas velocity was maintained at 11 ml NTP per minute. This rate corresponds to the rate of CO_2 evolution from a carbon anode of the same size as the copper plate during electrolysis at a current density of 1 amp/cm² (assuming the anode gas to be pure CO_2). Before and after each run, nitrogen was bubbled through the melt in order to prevent the bubbling device from becoming blocked.

The Al_2O_3 content in the melt was kept at 4 w/o, except in the strongly basic melts where it had to be lower because of the limited solubility of Al_2O_3 in these melts. The ratio NaF/ AlF_3 in the melt was controlled by pyrotitration (15).

The amount of inlet gas from the gasometer could easily be calculated, and the amount of effluent gas could be determined by weighing the absorption bulbs before and after each run. From these data the amount of gas reduced to carbon was evaluated by means of the following relation

$$n_{CO_2(in)} = n_{CO_2(out)} + n_{CO(out)} + n_C$$

where n denotes the number of moles of the respective species. Using this expression the determination of n_C , i.e., the amount of carbon formed, was very sensitive to errors in the measured amounts of gas. Blank runs with an empty crucible or a crucible with molten electrolyte free of metal, however, gave a reproducibility which indicated that the method should be of adequate accuracy for this purpose. A small blank correction (deficit in gas out) was found and has been applied to the measured amounts. (This discrepancy may be due in part to a slight inaccuracy in the volume calibration of the gasometer, and in part to impurities in the tank gas.)

The extent of reaction with the dissolved aluminum may be expressed as

$$1/2(n_{CO} + 2n_C)/n_{CO_2(in)} = 1/2n_O/n_{CO_2(in)}$$

where n_O denotes the number of gram atoms of oxygen which is transferred from the gas molecules to the melt. The quantity $n_O/2n_{CO_2(in)}$ may be taken to express the "total reactivity" of dissolved aluminum under the given experimental conditions. Since the gas rate is constant, this quantity can easily be converted to amount of oxygen transferred (or amount of reacted aluminum) per unit time.

In the following, the amounts of the different species will for simplicity be expressed as per cent of the inlet gas amount, i.e.

$$n_{CO}/n_{CO_2(in)} \cdot 100 = \% CO; \quad n_C/n_{CO_2(in)} \cdot 100 = \% C$$

$$n_O/n_{CO_2(in)} \cdot 100 = 1/2 (\% CO + 2\% C)$$

In addition to CO_2 and CO the effluent gas usually contained H_2O and H_2 originating from the initial water content in the melt. As these gases always occurred in very small amounts, they are of minor interest in this context and are therefore omitted in the presentation of the results.

Results

In preliminary experiments with Kobe's liquid (13) in the gasometer, the temperature dependence of the reactions at the cryolite composition was measured. While these experiments were insufficiently accurate to assess the amount of carbon formed, they gave adequate information about the reduction of CO_2 to CO. The results are presented in Fig. 2. It is evident that % CO increases rather rapidly with increasing temperature.

All other experiments were made with mercury in the gasometer. Figure 3 shows the temperature dependence measured in a basic melt, molar ratio NaF/ AlF_3 = 91/9. Here, % CO is markedly larger than in the case of cryolite, and considerable amounts of carbon are formed.

Figure 4 shows the results of runs with the molar ratio NaF/ AlF_3 varying from 97/3 to 62/38 at

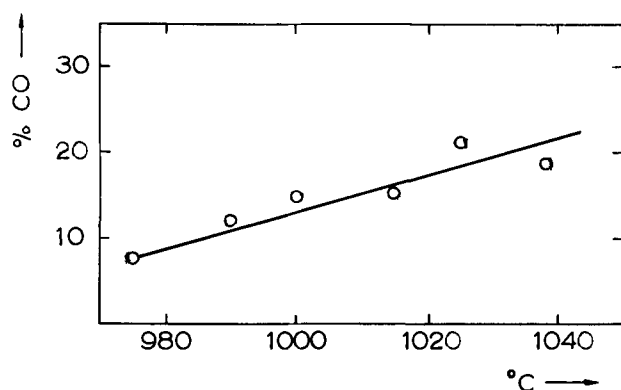


Fig. 2. Per cent CO as function of temperature. Cryolite, inlet gas CO₂.

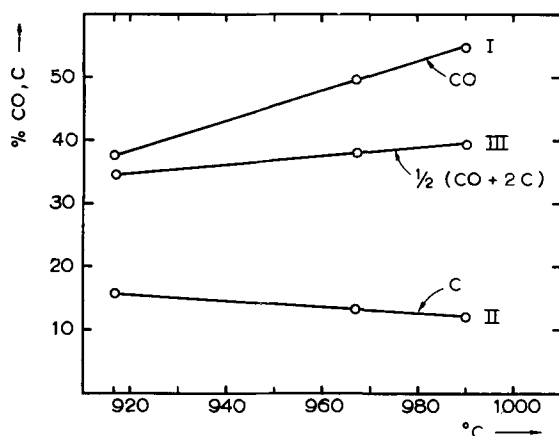


Fig. 3. Reactivity as function of temperature. NaF/AlF₃ = 91/9, inlet gas CO₂.

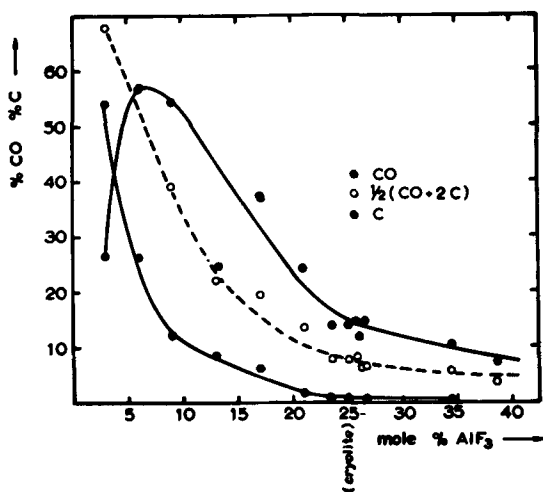


Fig. 4. Reactivity as function of NaF/AlF₃ ratio (mole per cent AlF₃), t = 1000°C, inlet gas CO₂.

1000°C. In particular % C falls off rapidly with increasing AlF₃ content. At the lowest AlF₃ content % C is even greater than % CO. Some of the results for compositions near that of cryolite are also given in Table I.

In melts in this composition range, the fraction of the gas which is reduced to carbon exhibits a fairly constant and low value.

That this indirectly measured quantity, % C, really was due to formation of carbon, was proved by examination of samples from the melt. In such

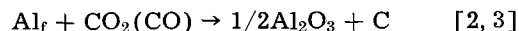
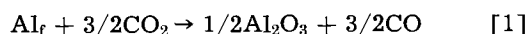
Table I. Per cent of inlet CO₂ reduced to carbon at different compositions of the melt, t = 1000°C

Mole % AlF ₃	17	20.8	23.5	25.0 (cryolite)	26.7	34.5
% C	5.9	1.5	0.8	0.8	0.8	0.6

samples black flake-like particles could be observed under a binocular microscope. The presence of carbon was established by subjecting samples of the melt to standard carbon analysis by combustion in oxygen. (After making blank corrections, the analysis indicated a carbon content in the cryolite samples of about 0.2% of the sample weight. This is too high to represent the average carbon content of the melt, since the samples were taken from the top of the melt where the carbon will accumulate.) This carbon could hardly have any other origin than CO₂ reduced by the dissolved aluminum. Treating the samples with hot water gave no indication of aluminum carbide.

The varying influence of some experimental conditions was examined using the cryolite composition at 1000°C. The distance between the metal surface and the bubbling device was increased from 2.5 cm to 3.5 cm. This caused only a slight decrease in % CO and % C. By increasing the inlet gas rate, % CO and % C decreased, but the amount reduced per unit time was nearly constant, increasing only slightly, as would be expected.

When CO₂ is the inlet gas, the reactions



will "compete for" the aluminum fog and, except in strongly basic melts, reaction [1] will predominate, as is evident from Fig. 4. In order to study reaction [3] separately, some experiments were carried out with CO as inlet gas.

In Fig. 5

$$\% \text{C} = \frac{n_{\text{C}}}{n_{\text{CO}(\text{in})}} \cdot 100 = \frac{(n_{\text{CO}(\text{in})} - n_{\text{CO}(\text{out})})}{n_{\text{CO}(\text{in})}} \cdot 100$$

is plotted vs. temperature for a cryolite melt. At 1000°C, % C = 7.7 as compared to 0.8 with CO₂ as inlet gas. The "total reactivity," however, is somewhat lower with CO than with CO₂.

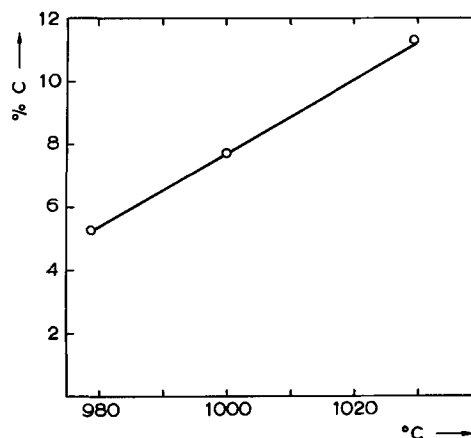


Fig. 5. Per cent of inlet gas reduced to carbon as function of temperature. Cryolite, inlet gas CO.

Table II. Reaction between CO and dissolved aluminum in NaF-AlF₃-Al₂O₃ melts, t = 1000°C

Mole % AlF ₃	% CO ₂	% CO	% C
35	0.8	95.2	4.0
25 (cryolite)	0.4	94.3	5.3

Using an acid melt, molar ratio NaF/AlF₃ = 65/35, the results presented in Table II were obtained. Again in this case, the "total reactivity" decreases with increasing AlF₃ content. The small content of CO₂ in the effluent gas is most likely due to reduction of copper oxide on the copper tube.

In Table III are presented the results obtained with CO₂/CO mixtures as inlet gas. In Fig. 6, % C is plotted as function of the CO content of the inlet gas. It is seen that % C increases nearly linearly with the partial pressure of CO, although the point at 50% CO lies somewhat above the straight line.

Discussion

The results presented in Fig. 6 strongly indicate that the reduction of CO₂ to carbon proceeds in two steps, viz., reaction [1] and then reaction [3]. This, of course, is also what would be expected.

From Fig. 3 it is seen that the importance of reaction [1] increases relative to that of reaction [3] when the temperature increases. This trend is expected from equilibrium considerations. It is, however, in disagreement with the statement of Beljajev (2), that the reduction of CO₂ to carbon would occur in overheated cells only.

As shown in Fig. 4, both % CO and % C fall off with increasing AlF₃ content in the melt, first rapidly and then more slowly as the cryolite composition is passed. The latter fact is rather surprising when compared to measurements of the aluminum losses by evaporation from NaF-AlF₃ melts in contact with aluminum made by Loshkin (2), Mashovets and Svoboda (5), and Skei (8). These measurements showed increasing aluminum losses when the AlF₃ content was increased above the cryolite composition. Likewise Mashovets (5) found that the content of dissolved metal in the melts increased with increasing AlF₃ content in these melts.

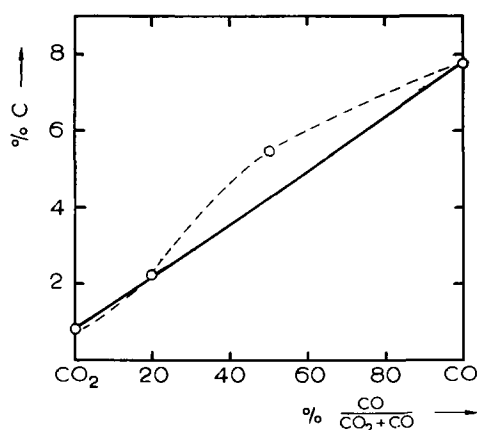
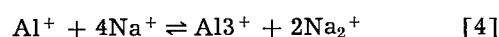


Fig. 6. Per cent of inlet gas reduced to carbon as function of per cent CO in inlet gas. Cryolite, t = 1000°C.

Table III. Reaction between CO₂/CO mixtures and dissolved aluminum in cryolite melts, t = 1000°C

Inlet gas		Effluent gas		% C
% CO ₂	% CO	% CO ₂	% CO	
100	0	85.5	13.7	0.8
80	20	64.58	33.18	2.24
50	50	32.68	61.8	5.52
0	100	0.75	91.5	7.75

The apparent inconsistency between these observations and those presented here can hardly be explained in any other way than by assuming that the dissolved aluminum in the AlF₃-rich region is partly present in a state which is nonreactive to CO₂/CO. The following hypothetical equation expresses an equilibrium between aluminum and sodium in the dissolved metal:



according to which the ratio Na₂⁺/Al⁺ varies with the NaF/AlF₃ ratio. If constituents containing monovalent aluminum are volatile so that they cause metal losses, but nonreactive to CO₂/CO, this may constitute an explanation.

As stated previously, the reaction between CO₂ and dissolved aluminum seem to be governed by the rate of dissolution of aluminum in the melt (12), at least at the inlet gas rates that have been applied. On this assumption the rate of dissolution may be calculated from the present results for the "total reactivity." For cryolite at 1000°C the calculated rate is 0.25 mg Al/cm²·min, which increases to about 0.38 mg Al/cm²·min at 1040°C in the same melt, while it is 2.35 mg Al/cm²·min at 1000°C in the melt of molar ratio NaF/AlF₃ = 97/3. In addition, if nonreactive but volatile subvalent components are present as suggested above, the true numbers will be higher.

The numerical values obtained in studies of kinetic phenomena will usually depend somewhat on experimental conditions. The negligible variations obtained in these experiments by varying the gas-metal distance and the gas rate, however, suggest a reliability of the results on which general conclusions can be safely based.

Compared to industrial electrolysis, the degree of reaction between CO₂ and dissolved aluminum seems to be much lower in the present case. Applying the Pearson and Waddington formula for electrolytic cells (1)

$$\eta = 50 + 1/2 \% \text{CO}_2 (= 100 - 1/2 \% \text{CO})$$

a current efficiency of say 87% would give 26% CO as compared to about 12.5% as found in the present experiments. Then the rate of solution of metal also should be proportionately larger. In industrial cells, convection must be assumed to have great influence on the rate of solution and transport of dissolved aluminum in the electrolyte. Second, a partial discharge of cations (e.g., Al³⁺ + 2e → Al⁺) at the cathode may speed up the rate of solution.

In conclusion, the results clearly show that CO₂ can be reduced to CO and further to carbon by dissolved aluminum in NaF-AlF₃ melts. The latter reaction is shown to be strongly dependent on the NaF/AlF₃ ratio, and also to occur to a certain extent in melts of compositions similar to the electrolyte in industrial aluminum cells. The findings therefore should be applicable to the study of secondary reactions of the anode gas during electrolysis. This will be demonstrated in a subsequent paper.

Manuscript received March 7, 1963.

Any discussion of this paper will appear in a Discussion Section to be published in the June 1965 JOURNAL.

REFERENCES

1. T. G. Pearson and J. Waddington, *Discussions Faraday Soc.*, **1**, 307 (1947).
2. A. I. Beljajev, M. B. Rapoport, and L. A. Firsanova, "Metallurgie des Aluminiums," VEB Verlag Technik, Berlin (1956).
3. K. Grjotheim, "Contribution to the Theory of the Aluminium Electrolysis," Det Kongelige Norske Videnskabers Selskabs Skrifter, Nr. 5, Trondheim (1956).
4. L. N. Antipin, *J. Phys. Chem. (U.S.S.R.)*, **29**, 1668 (1956).
5. V. P. Mashovets and R. V. Svoboda, *J. Appl. Chem. (U.S.S.R.)*, **32**, 2157 (1959).
6. R. Lorenz and W. Eitel, "Pyrosole," Akademische Verlagsgesellschaft, Leipzig (1926).
7. W. E. Haupin, *This Journal*, **107**, 232 (1960).
8. K. Skei, Thesis, NTH, Trondheim 1957.
9. A. I. Beljajev and L. N. Firsanova, *Met. i. Toplivo*, **27**, No. 5 (1959).
10. R. Schadinger, *Alluminio*, **22**, 691 (1953).
11. S. Arseth, Thesis, NTH, Trondheim 1958.
12. A. A. Revazyan, *Non-Ferrous Metals (U.S.S.R.)*, **33**, No. 8, 51 (1960).
13. G. Wagner, "Gasanalytisches Prakticum," Franz Deuticke, Wien (1946).
14. F. A. Lenfesty, Thad. D. Farr, and J. C. Brosher, *Ind. Eng. Chem.*, **44**, 1448 (1952).
15. Determination of Deficiency or Excess of Sodium Fluoride, Elektrokemisk A/S, Fiskaa Verk (1948).

On the Anode Gas Reactions in Aluminum Electrolysis, II

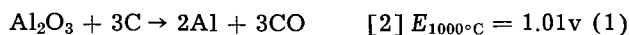
Jomar Thonstad¹

*Institute of Metallurgy and Institute of Inorganic Chemistry,
The Technical University of Norway, Trondheim, Norway*

ABSTRACT

The anode reaction and related secondary reactions in aluminum electrolysis have been studied in a small laboratory cell where the total amounts of anode gas could be analyzed. The primary anode product is found to be CO₂, at least at current densities above about 0.05 amp/cm². Assuming that CO₂ is formed with 100% current efficiency, a gas volume deficit of about 4% is actually observed. This deficit increases with increasing NaF/AlF₃ ratio in the electrolyte and with decreasing interpolar distance, and it is most likely due to a reduction of CO₂ to carbon by dissolved aluminum in the electrolyte. At normal current densities CO₂ does not react with the anode carbon to form CO. It can, however, react with the "carbon froth" formed by disintegration of the anode. A reaction between CO₂ and the anode carbon is found to occur only at very low current densities, below 0.1-0.05 amp/cm². A simple theory for the mechanism of the anode reaction is proposed.

The primary electrochemical reaction in aluminum electrolysis can be one of the following:



Under equilibrium conditions at the anode, the primary product would be about 99% CO (1). Equilibrium is not achieved, however, since kinetic effects evidently have great influence, as indicated by the rather high anodic overvoltage which occurs at normal current densities.

Pearson and Waddington (2) have found that the anode carbon consumption in a laboratory cell is only slightly higher than the theoretical amount for primary CO₂ formation. Several workers (3-6), who have measured the anode potential in various ways, also support the idea that CO₂ is the primary anode product. At low current densities, however,

other workers (7-9) claim that CO is also a primary product. Antipin (7) has suggested that at current densities below 0.1 amp/cm² only CO is formed at the anode, from 0.1 to 0.3 amp/cm² an equimolar mixture of CO and CO₂ is formed, while above 0.3 amp/cm² the anode product is predominantly CO₂.

The theory of combustion of carbon in air involves the formation of an intermediate C-O complex on the carbon surface (10, 11). If this concept is applied to the normal anode reaction in aluminum electrolysis, the process can be schematically divided in the following consecutive steps:

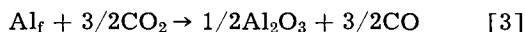
1. Discharge of oxygen: $\text{O}^{2-}(\text{in complex}) \rightarrow \text{O} + 2e^-$
2. Chemisorption of O: $\text{O} + \text{C} \rightarrow \text{C}_x\text{O}$
3. Conversion of C_xO: $2\text{C}_x\text{O} \rightarrow \text{CO}_2(\text{ads.}) + \text{C}$
4. Desorption of CO₂: $\text{CO}_2(\text{ads.}) \rightarrow \text{CO}_2(\text{g})$

Rempel and Khodak (3) and Stern and Holmes (4) assume that step 3 is the rate determining re-

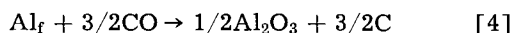
¹ Present address: Department of Metallurgical Engineering, University of Toronto, Toronto, Canada.

action responsible for the overvoltage, while Welch and Richards (6) assume that steps 1 and 2, *i.e.*, the transfer of ions through the double layer and formation of the C_xO complex, are rate determining.

The most important secondary reaction is the so-called back reaction between dissolved aluminum in the electrolyte, here denoted Al_f and CO_2 from the anode; *viz.*

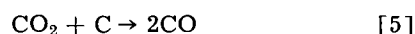


In Part I of this paper (12) it is shown that part of the CO from reaction [3] may be further reduced to carbon



These two reactions [3] and [4] are the principal causes for the loss in current efficiency during aluminum electrolysis.

Another possible secondary reaction is the so-called Boudouard reaction



This equilibrium is strongly displaced to the right at 950° – $1000^\circ C$, but it is known to be a slow reaction. The carbon reactant may be anode carbon or carbon particles floating in the melt, the so-called "carbon froth," formed by disintegration of the anode. In the former case, the result is equivalent to primary formation of CO at the anode.

Whether reaction [5] occurs in aluminum cells or not has long been a matter of dispute. Pruvot (13) assumes that it is prevented by electrostatic repulsion between the anode and CO_2 gas bubbles, and also that a suspension of solid particles in a melt, like the "carbon froth," is nonreactive to gases. In a recent work, Revezyan (14) claims that CO_2 can react with the "carbon froth" but not with the anode, because the latter is positively charged and therefore lacks free valency electrons for the formation of CO.

From reactions [1], [2], and [5] it is obvious that primary as well as secondary formation of CO (by reaction with carbon) produces twice the volume of anode gas as in the case of CO_2 . Reaction [3] which is another source of CO does not, on the other hand, affect the gas volume. This fact gives a means of determining by laboratory experiments whether CO in the anode gas is formed by reaction with carbon or with dissolved aluminum.

In the present investigation the quantity and composition of the anode gas has been measured for different current densities. On the basis of these data, the nature of the primary anode reaction is discussed as well as different possible secondary reactions, especially the Boudouard reaction.

Experimental

The laboratory cell is shown in Fig. 1. A sintered alumina tube G, 60 mm ID, is placed in a graphite crucible H, the bottom of which constitutes the electrical contact for the aluminum cathode L.

The anode K (50 mm diam) which is entirely immersed in the melt, is threaded to a tube of stainless steel B, which also serves as protection tube

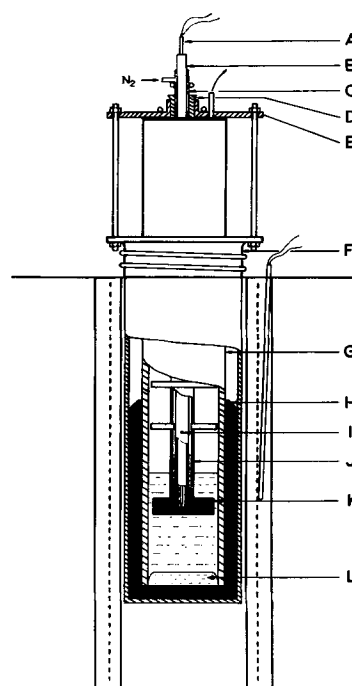


Fig. 1. Experimental electrolytic cell. A, Thermocouple; B, stainless steel tube; C, copper tube; D, rubber insulator; E, steel lid; F, heat resistant steel crucible; G, alumina tube; H, graphite crucible; I, N_2 -carrier gas inlet; J, alumina tube; K, anode; L, aluminum cathode.

for the thermocouple A. This tube is enclosed in a copper tube, and nitrogen is introduced between the two tubes. The part which dips into the melt is protected by a tube of sintered alumina J and the intervening space is packed with alundum. Because of the high thermal conductivity of the tubes, this arrangement acts as a frozen seal preventing electrolytic attack on the metal tubes. The crucible is heated in a Kanthal furnace connected to an on/off temperature controller.

The effluent gas proceeds to a gas analyzing unit similar to that described in Part I (12) for determination of the amounts of CO_2 , CO, H_2O , and H_2 .

The most important part of this apparatus is the anode. Most carbonaceous materials, including graphite, tend to disintegrate to a certain extent during electrolysis. If the "carbon froth" thus formed reacts with the anode gas, an extra reactant is introduced which will severely complicate the interpretation of the results.

The disintegration of the anodes is assumed to be due to selective oxidation of the most reactive constituents of the anode (15). In the case of industrial materials, the coke originating from the tar/pitch binder is usually more reactive than the aggregate coke. In the present case this problem was solved by Elektrokemisk A/S who produced small anodes using a pitch coke aggregate which was precalcined at only $500^\circ C$. Under these conditions the aggregate and the binder form a homogenous structure during the baking. While these anodes were rather porous, they proved to be nondisintegrating in these experiments.

When not otherwise stated, the electrolyte consisted of cryolite saturated with alumina, and the

interpolar distance was 5 cm. The temperature was kept at 1000°C during electrolysis. In runs at normal current densities, 0.4-1.0 amp/cm², 20 amp-hr were passed through the cell. By means of a copper coulometer the amount of current could be determined with an accuracy of $\pm 0.1\%$ (16). The number of moles of primary CO₂ at 100% faraday yield, denoted $n_{pr.CO_2}$, then could be easily calculated. The amounts of effluent gas absorbed in the gas analyzing unit, n_{CO_2} and n_{CO} , are presented in per cent of this number, as follows:

$$\% CO_2 = n_{CO_2}/n_{pr.CO_2} \cdot 100$$

$$\% CO = n_{CO}/n_{pr.CO_2} \cdot 100$$

where n denotes the number of moles of the respective species. As in Part I (12), the small contents of H₂O and H₂ are disregarded in presenting the results. Curves for % CO are omitted in the diagrams, but they can be obtained by subtraction.

Results and Discussion

Figure 2 illustrates the results for electrolysis with nondisintegrating anodes at three different current densities, covering the range applied in industrial cells. In these runs less effluent gas was found than the theoretical amount calculated as primary CO₂ ($n_{pr.CO_2}$). This deficit is expressed by curve C in Fig. 2, where

$$\% C = n_{pr.CO_2} - (n_{CO_2} + n_{CO})/n_{pr.CO_2} \cdot 1000 = n_c/n_{pr.CO_2} \cdot 1000$$

The reason for the gas deficit will be discussed later.

From these results it can be concluded that CO₂ is the anode product at normal current densities and that neither reaction [2] nor [5] has occurred to any measurable extent, since these reactions would give a gas excess. The CO content (% CO = 100 - % CO₂ - % C) then must be wholly due to reaction [3].

The slope of the CO₂ curve reveals that % CO decreases with increasing current density. This fact accounts for the well-known increase in current efficiency with increasing current density. The extent of reaction [3] per unit time depends on the amount of dissolved aluminum transported to the

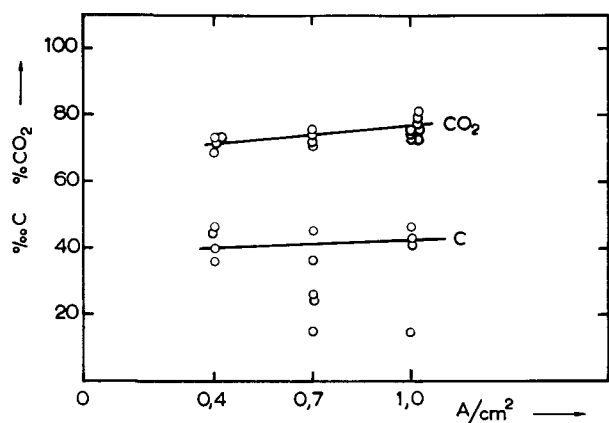


Fig. 2. % CO₂ and gas deficit (%C) as function of current density in electrolysis with non-disintegrating anodes. Cryolite, $t = 1000^\circ\text{C}$.

vicinity of the anode, which in the ideal case should be constant and independent of current density, *i.e.*, % CO should be inversely proportional to the current density. In the present experiments the amount of CO formed per unit time seemed to increase slightly with increasing current density. This may be ascribed to the influence of gas evolution on convection in the electrolyte, which may facilitate the formation and/or transport of dissolved aluminum.

In order to test Antipin's theory (7) that CO and CO/CO₂ mixtures are the primary anode product at low current densities, some runs were made with current densities from 0.05 to 0.4 amp/cm². At the lowest current densities the surprising observation was made that much less gas than theoretical ($n_{pr.CO_2}$) was evolved. This must be due to the influence of the dissolved aluminum, which either reduces most of the anode gas to carbon, or is directly oxidized anodically (e.g., $Al^+ \rightarrow Al^{3+} + 2e$).

This disturbing effect of dissolved aluminum, which occurred at low current densities where the anode gas evolution is slow, was diminished by using a cathode consisting of a liquid silver-copper alloy (40 Ag-60 Cu) containing only about 1 weight per cent (w/o) Al. With this alloy, where the aluminum activity is very low, the influence of back reactions [3] and [4] should be reduced to a tolerable degree. [Judging from available data (1) for the binary systems Ag-Al, Cu-Al, and Cu-Ag a slight negative deviation from ideality would be expected.]

The results obtained when this cathode was used, are presented in Table I. A minor excess of gas occurred at 0.1 amp/cm². At all other current densities the gas amounts are quite consistent with the theory of 100% primary CO₂, the results at higher current densities showing the previously mentioned gas deficit. The potential at the two lowest current densities was lower than the reversible decomposition potential for reaction [1], owing to the depolarization caused by the low-activity aluminum cathode. Approximate calculations show that a rather steep concentration gradient will be set up on the cathode surface at higher current densities. At 0.4 and 0.7 amp/cm² the alloy therefore approaches the behavior of a pure aluminum cathode, as indicated by the potentials and the gas analysis.

The previous conclusion that the anode product is CO₂ at normal current densities can now be extended also to lower current densities of about 0.05 amp/cm².

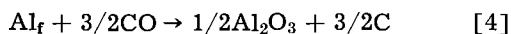
The Gas Deficit

As shown in Fig. 2, the gas deficit, expressed as per cent C, has a fairly constant value of about

Table I. Electrolysis with an Ag-Cu-Al cathode, $t = 1000^\circ\text{C}$

Current density	0.05	0.1	0.2	0.4	0.7
Potential (v-IR)	1.04	1.05	1.37	1.45	1.55
Ampere-hours	0.66	1.05	2.78	16.53	10.19
% CO ₂	15.9	41.3	56.0	79.8	82.0
% CO	84.1	64.2	41.6	17.1	15.3
% C (gas deficit)	0	-5.5	3.1	2.7	2.4

40%, although there is considerable scattering of the points, especially at 0.7 amp/cm². Blank runs excluded the possibility of faulty experimental technique, so the reason must be sought among the following possibilities: I. Electronic conductivity. II. Anode products other than CO₂ (CF₄, F₂). III. "Chemical short circuit," (a) by the dissolved aluminum (*e.g.*, Al⁺ → Al³⁺ + 2e), (b) by other multivalent ions (impurities like Fe, V). IV. Secondary reaction



V. Solubility of CO₂ in the melt.

The phenomena I-III affect the yield of primary CO₂, while IV-V describe secondary effects, each of which will be discussed below:

I. In some alkali metal-halogen salt systems electronic conductivity has been observed (17), but in the aluminum-cryolite system where the metal solubility is very low [0.1 w/o Al (18)], such a mechanism seems very unlikely.

II. Discharge of the strongly electronegative fluoride anion is most unlikely in melts saturated with Al₂O₃. A mass spectrographic analysis of anode gas from industrial cells (19) revealed no fluorine or carbon-fluorine compounds in the anode gas during normal electrolysis.

III(a). As already suggested, anodic oxidation of subvalent ions may occur at low current densities. Because of the low solubility of aluminum in the electrolyte, this reaction must have a low limiting current density. When this is exceeded, the normal oxygen discharge with subsequent CO₂ formation should start, and dissolved metal would be consumed by reactions [3] and [4] before reaching the anode.

III(b). Most cationic impurities will be reduced to metal or be volatilized as fluorides.

IV. In Part I (12) reaction [4] is shown to take place when CO₂ is bubbled through the melt without electrolysis.

V. The solubility of CO₂ in the melt will not have any influence when several runs are made in series, and the solubility is in any case very low (18).

Summing up, the total reduction of CO₂ to carbon (IV) must be regarded as the most reasonable explanation for the gas deficit, although a direct anodic oxidation of dissolved aluminum cannot be ruled out.

In an attempt to cast more light on this problem, the dependence of the gas deficit on the following variables was investigated: (i) Duration of electrolysis, (ii) aluminum activity of cathode metal, (iii) inter-polar distance, and (iv) the NaF/AlF₃-ratio.

(i) The results for three short-time experiments are given in Table II. The first two experiments

Table II. Results for short-time experiments, *t* = 1000°C

Amp/cm ²	Amp-hr	% CO ₂	% CO	% Gas deficit (% C)
1.0	6.75	80.2	19.6	0.2 (= 3 ml)
1.0	10.50	79.2	20.6	0.2 (= 4 ml)
1.0	10.23	80.0	15.7	4.3

were run in series, and the results show very good agreement with the theoretical $n_{\text{pr.CO}_2}$, the deviation being within the limits of error. The last experiment shows the "normal" deficit. These results indicate that the reaction which causes the gas deficit must be initiated in some way, and that this does not always happen. Such an explanation is reasonable for reaction [4] which requires some sort of nucleus for the formation of carbon.

(ii) Experiments with Cu-Al and Cu-Ag-Al cathodes with varying aluminum content gave somewhat confusing results, although the general trend was an increase in % CO and % C with increasing aluminum content. In these runs the previously mentioned concentration gradient of aluminum on the cathode may have disturbed the results.

(iii) By diminishing the inter-polar distance from 5 to 2.5 cm, the results presented in Fig. 3 were obtained. The curves for 5 cm are taken from Fig. 2. The diagram shows that both % CO and % C are higher when the inter-polar distance is diminished. This effect must be due to greater transport of dissolved aluminum toward the anode because of increased convection.

(iv) When the NaF/AlF₃ ratio was varied, the results presented in Fig. 4 and Fig. 5 were obtained. For the cryolite composition (25% AlF₃) the results are taken from Fig. 2. The gas deficit (Fig. 5) decreases very rapidly with increasing AlF₃ content, being close to zero in AlF₃ rich melt.

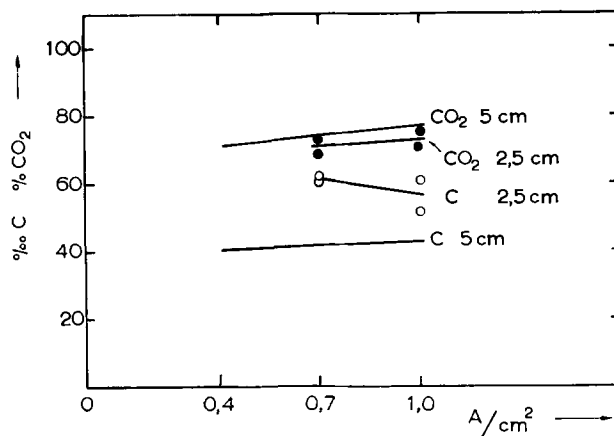


Fig. 3. Electrolysis with different inter-polar distances. Non-disintegrating anodes, Cryolite, *t* = 1000°C.

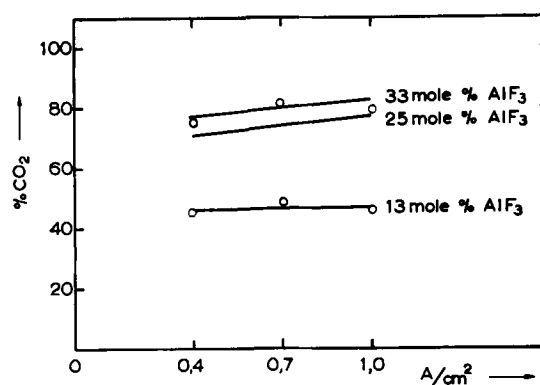


Fig. 4. Electrolysis with different bath compositions. Non-disintegrating anodes, *t* = 1000°C.

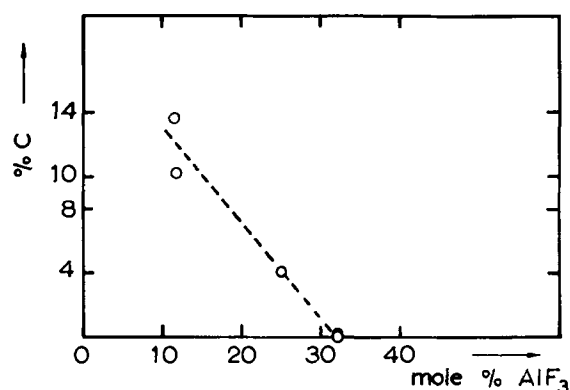


Fig. 5. Dependence of bath composition on the gas deficit (% C). Non-disintegrating anodes, $t = 1000^{\circ}\text{C}$.

The results both for % CO and % C are consistent with the findings in Part I (12). The extent of the back reactions [3] and [4] is evidently less in an AlF₃ rich melt than in cryolite. The results seem to support the assumption that reaction [4], *i.e.* the reduction of CO to carbon, is responsible for the gas deficit.

Current efficiency.—In an attempt to measure the cathodic current efficiency the cathode was made up of an Al-Cu alloy with 10 w/o Cu, whereby the increase in aluminum content during electrolysis could be determined by copper analysis. Due to several experimental difficulties involved, rather few reliable results were obtained. Furthermore the relatively wide limits of error prevented strict control of the relationship between the extent of the back reactions [3] and [4] and the current efficiency, such control being the aim of these measurements. The few results obtained, however, indicated a fairly good agreement between the metal losses calculated from reactions [3] and [4] and the measured losses.

Reaction between CO₂ and Carbon

In the foregoing it is concluded that CO₂ is the primary anode product although CO is thermodynamically preferred. The latter fact is also expressed by the Boudouard equilibrium [5] which gives CO₂/CO \approx 1/99 at about 1000°C. One might therefore expect that the primary CO₂ might react chemically with the anode or with "carbon froth" that might be present in the melt. Judging from the gas amounts, this has evidently not occurred to any measurable extent with the non-disintegrating anodes.

With graphite anodes, which disintegrate somewhat during electrolysis, an excess of gas was actually observed. Since anodes made of graphite are less reactive than the non-disintegrating type (the anodic overvoltage was found to be markedly higher on graphite anodes), it seems reasonable to assume that the gas leaving the graphite anode is CO₂, and that reaction [5] occurs only with the "carbon froth."

There will now be two different sources of CO



In the following evaluation, CO from the two reactions are designated by subscripts *f* and *c*, as indicated above, whereby

$$n_{\text{CO}_f} + n_{\text{CO}_c} = n_{\text{CO}}$$

$$n_{\text{CO}_f} + 1/2n_{\text{CO}_c} + n_{\text{CO}_2} = n_{\text{pr.CO}_2}$$

Eliminating n_{CO_f} , the following expression is obtained

$$n_{\text{CO}_c} = 2(n_{\text{CO}_2} + n_{\text{CO}}) - n_{\text{pr.CO}_2}$$

and

$$\% \text{CO}_c = n_{\text{CO}_c}/n_{\text{pr.CO}_2} \cdot 100$$

This calculation of n_{CO_c} is only approximate, as the influence of reaction [4] on the gas amount is not taken into account. When gas excess occurs, the degree of this reaction cannot be determined. It must, however, be expected to occur to the same extent as found previously, *i.e.*, % C = 4%. The two reactions should not influence each other, as [4] most likely occurs just beneath the anode and [5] mostly occurs near the surface of the melt, where the "carbon froth" is concentrated. The true values for CO_c should then be 8% larger and for CO_f 8% lower than given by the expression above.

Results and Discussion, Graphite Anodes

The results for graphite anodes are given in Fig. 6. In order to make the results comparable with those for non-disintegrating anodes

$\% \text{CO}_2 + 1/2 \% \text{CO}_c = (n_{\text{CO}_2} + 1/2n_{\text{CO}_c})/n_{\text{pr.CO}_2} \cdot 100$ is plotted. In addition

$$\% \text{CO}_2 = n_{\text{CO}_2}/(n_{\text{CO}_2} + n_{\text{CO}}) \cdot 100$$

is plotted. % CO_c decreases with increasing current density, but the amount formed per unit time is fairly constant. This is what would be expected, since [5] is known to be a slow reaction. Similar results were obtained with anodes of the same type as prebaked anodes used in industrial cells, but these measurements were made with another and less accurate apparatus and will not be reported here.

Since the formation of CO_c seemed to be caused by a reaction with "carbon froth," artificial "carbon froth" was added to the melt in some runs with non-disintegrating anodes. It was prepared by crushing and grinding pieces of the anode material, and added to the melt in the following proportions:

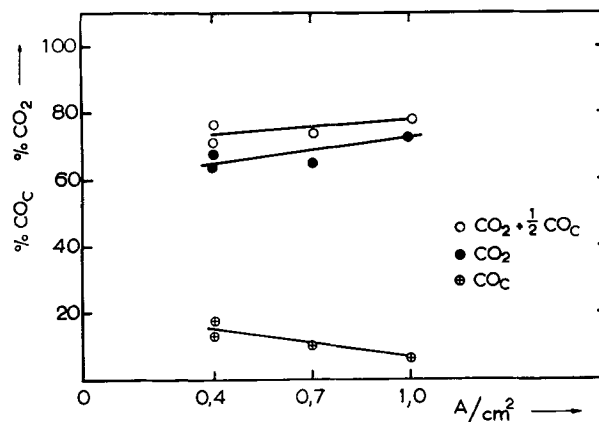


Fig. 6. Electrolysis with graphite anodes. Cryolite, $t = 1000^{\circ}\text{C}$

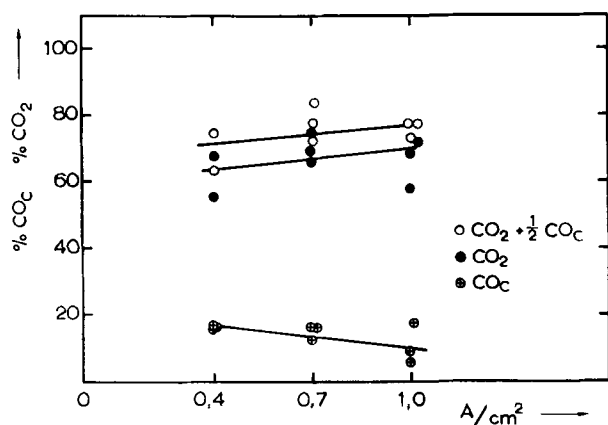


Fig. 7. Electrolysis with non-disintegrating anodes when added "artificial carbon froth." Cryolite, $t = 1000^{\circ}\text{C}$.

1.5g, 10-22 mesh; 1.5g, 100-22 mesh; 0.5g, -100 mesh.

As shown in Fig. 7, the Boudouard reaction also occurred in this case, % CO_c being even larger than with graphite anodes. These results make it clear that CO_2 can react with the "carbon froth" but not with the anode itself, at least not at normal current densities. Further support for this conclusion is given by results obtained by bubbling CO_2 under the anode during electrolysis.

Addition of CO_2 during electrolysis.—Tank CO_2 was delivered from the gasometer described in Part I (12), and bubbled under the anode from an alumina tube which passed through the middle of the anode. The gas rate was kept at 35 ml NPT/min. In order to diminish the reaction between CO_2 and dissolved aluminum, the previously mentioned Ag-Cu-Al alloy was used as cathode.

In order to see if the reactivity of the anode would have any influence, two types of non-disintegrating anodes were used, one with an addition of 0.6% H_3BO_3 and the other with 0.6% Na_2CO_3 . The former addition is known to make carbonaceous materials less reactive (at least by combustion in air), while the latter acts in the opposite direction (20). In normal electrolysis these additions had no measurable influence on the results.

The amount of inlet gas and the gas formed in electrolysis could easily be calculated, and CO_c evaluated by the same expressions as used above.

Only the results for CO_c are of interest in this context, and these are shown in Fig. 8. At zero current density the anode with H_3BO_3 addition gave 26.2% CO_c . Applying a current density of 0.00125 amp/cm² a very slight decrease, 25.3% CO_c , was observed, but this decrease is within the limits of error. The curve falls off very rapidly with increasing current density, reaching zero between 0.05 and 0.1 amp/cm². Curve II, representing the more reactive anode (with Na_2CO_3), starts at a much higher value, about 50% CO_c , but has a similar slope, though always lying above the other.

On the diagram the curves cross the abscissa giving negative values for CO_c at higher current densities. The negative values have no physical meaning referred to reaction [5], but simply indicate that a gas deficit occurs due to reaction [4] and that reaction

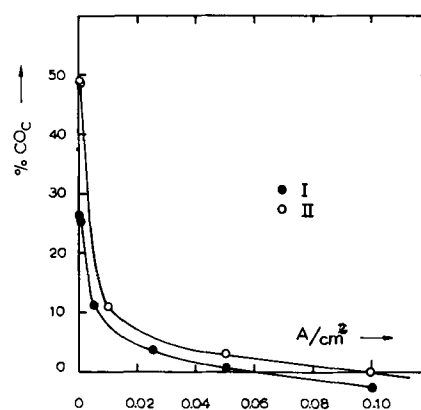


Fig. 8. Dependence of the Boudouard reaction on the anode current density when additional CO_2 is bubbled under the anode. Non-disintegrating anodes: I, with 0.6% H_3BO_3 ; II, with 0.6% Na_2CO_3 . Cryolite, $t = 1000^{\circ}\text{C}$.

[5] has ceased. In the range 0.05-0.1 amp/cm² the two reactions overlap in the calculation, and thus prevent an exact determination of the maximum current density at which reaction [5] can occur. (This maximum current density may even lie a little below 0.05 amp/cm², as the small amounts of CO_c obtained at this current density might have been formed at the sides of the anode where the current density will be lower than underneath.)

Besides, the maximum current density evidently is somewhat dependent on the reactivity of the anode, as indicated in Fig. 8. In any case, however, the results clearly show that it is far below the current densities applied in industrial cells (0.6-1.0 amp/cm²), proving that CO_2 cannot react with the anode under these circumstances.

With the present experimental technique it is not possible to identify the primary anode product at very low current densities at which the Boudouard reaction may occur at the anode. This is because primary CO_2 could react with the anode in a secondary reaction and also because of the interfering reactions with dissolved aluminum.

Reaction Mechanism

The anode reaction during electrolysis seems to block the anode surface in some way, preventing the Boudouard reaction. A reasonable explanation for this effect may be found by examining the theory of the mechanisms for such reactions.

Both the primary anode reaction and the Boudouard reaction must be assumed to proceed with chemisorbed C-O complexes as an intermediate step (3, 4, 10, 11). The two reactions will then compete for the active sites on the anode carbon surface. At a certain current density the surface may be so occupied with C-O complexes from oxygen deposition that there will be no free sites left where the Boudouard reaction may occur. Or in other words, the concentration of chemisorbed oxygen becomes so high that formation of CO_2 is preferred.

This theory will be extended below, considering the nature of the complexes. It seems to give a better explanation than the theory of Revazyan (14), according to which the positive charge of the anode is the reason for its non-reactivity to CO_2 . The latter

theory does not explain the results presented in Fig. 8, since the positive charge of the anode is nearly the same at 0.00125 amp/cm² and at 0.1 amp/cm².

In the present state of knowledge of the combustion of carbon, it is impossible to work out a detailed theory for the mechanism of the anode reaction in aluminum electrolysis. Furthermore, there is at least one major difference between combustion of carbon in air and during electrolysis, since in the latter case oxygen reaches the carbon surface as single oxygen atoms and not as molecules.

The chemisorption of oxygen will preferably occur on active sites in the carbon network, *i.e.*, at edges, holes, pores, and dislocations, where the carbon atoms will have free valences. In electrolysis at higher current densities the reaction may occur not only on active sites but it may spread over the whole surface. In that case the free conductivity π -electrons may contribute to the bonding.

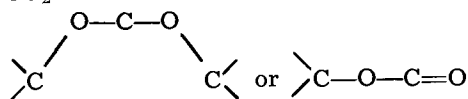
Bonds like >C-O , >C-O-C , and possibly >C-O-O may occur. For example a single

>C-O-C surface compound may be rather stable, not allowing $\text{CO}_{(g)}$ to be formed, but when also a neighbor site is occupied in the same way,

giving >C-O-C-O-C , a cleavage of the re-

maining C-C bond may occur as indicated with dotted lines, $\text{CO}_{2(g)}$ being formed.

The Boudouard reaction will involve chemisorption of CO_2 as



with subsequent breaking of C-O bonds and formation of $\text{CO}_{(g)}$. Because of the already existing C=O bonds in CO_2 , the formation of such complexes must be assumed to be less stable than the C-O complexes formed by discharge of oxygen atoms. The former then should be completely expelled if oxygen is produced at a sufficient rate, *i.e.*, if the current density is high enough. In this connection the important factor must be the rate of transition of the complex, since this will determine at which rate oxygen has to be discharged in order to prevent the formation of CO. The rate determining step should then be the conversion of the C-O complex, *i.e.*, $2\text{C}_x\text{O} \rightarrow \text{CO}_2 + \text{C}$. It is difficult to decide from this reasoning, if this also is the case at higher current densities.

Conclusion

The results obtained in this work may be summed up as follows:

I. The primary anode product is CO_2 , at least at current densities above 0.05-0.1 amp/cm². At normal current densities CO_2 seems to be formed with 100% anodic current efficiency.

II. Some of the CO_2 reacts with dissolved aluminum whereby CO and also a small amount of free carbon is formed.

III. At current densities above 0.05-0.1 amp/cm², CO_2 cannot react with the anode to form CO. It will, however, react with "carbon froth" that might be present in the bath.

IV. The extent of the reactions mentioned above cannot be measured independently by simple means, and it is therefore impossible to set up an exact formula relating anode gas composition with cathodic current efficiency.

Acknowledgment

The special anode materials, which have been quite indispensable for some of the measurements, were made by Elektrokemisk A/S Kristiansand S. Norway. Elektrokemisk has also given financial support for this work.

Helpful discussions with Professors R. Lepsøe, T. Rosenqvist, and K. Grjotheim are gratefully acknowledged.

Manuscript received March 7, 1963.

Any discussion of this paper will appear in a Discussion Section to be published in the June 1965 JOURNAL.

REFERENCES

- O. Kubaschewski and E. L. Evans, "Metallurgical Thermochemistry," Pergamon Press, London (1958).
- T. G. Pearson and I. Waddington, *Discussions Faraday Soc.*, **1**, 307 (1947).
- S. I. Rempel and L. P. Khodak, *J. Appl. Chem. (U.S.S.R.)*, **26**, 857 (1953).
- H. Stern and G. T. Holmes, *This Journal*, **105**, 478 (1958).
- V. P. Mashovets and A. A. Revazyan, "Soviet Electrochemistry," Vol. II, p. 185 (1959).
- B. J. Welch and N. E. Richards, AIME Int. Symp., Extractive Met. of Al, New York, 1962.
- L. N. Antipin and A. N. Khudyakov, *J. Appl. Chem. (U.S.S.R.)*, **29**, 985 (1956).
- S. I. Rempel, L. P. Khodak, and N. A. Anisheva, "Soviet Electrochemistry," Vol. II, p. 192 (1959).
- A. A. Revazyan, *Tsvetnye Metally*, **33**, No. 3, 51 (1960).
- A. R. Ubbelohde and F. A. Lewis, "Graphite and Its Crystal Compounds," Clarendon Press, Oxford (1960).
- H. E. Blayden, Conference on Science in the Use of Coal, Institute of Fuel, Session V, 1957.
- J. Thonstad, *This Journal*, **111**, 955 (1964).
- E. Pruvot, *Alluminio*, **22**, 721 (1953).
- A. A. Revazyan, *Metallurg*, **3**, No. 1, 101 (1960).
- O. Bowitz and O. Sandberg, *Trans. AIME*, **224**, 53 (1962).
- W. Riemann, J. Neuss, and B. Naimann, "Quantitative Analysis," McGraw Hill Book Co., New York (1951).
- H. R. Bronstein and M. A. Bredig, *J. Phys. Chem.*, **65**, 1220 (1961).
- W. Haupin, *This Journal*, **107**, 232 (1960).
- I. L. Henry and R. D. Holiday, *J. Metals*, **9**, 1384 (1957).
- G. Wranglen, *Jernkontorets Ann.*, **142**, 613 (1958).

Desalination of Sodium Halide Electrolytes by a Differential Redox Method

E. I. Onstott

Los Alamos Scientific Laboratory, University of California, Los Alamos, New Mexico

ABSTRACT

A method of differential desalination of electrolytes which utilizes electrochemical mass transport is described. Sodium chloride and/or sodium bromide electrolyte containing dissolved chlorine or bromine is electrolyzed between closely spaced parallel porous carbon electrodes with the electrolyte flowing through the pores of the electrodes to separate the electrolysis products. No membrane or barrier between the electrodes is used. At the anode, halide is oxidized to halogen (or other oxidation products) and a halide depletion region is established; at the cathode, dissolved halogen is reduced to halide, thus producing an enrichment region. As a result of the halide ion concentration gradient created by electrolysis, sodium ion migrates from the anode region to the cathode region. Desalination takes place in the flowing anolyte stream and salt enrichment occurs in the flowing catholyte stream. The electrolysis can be driven unidirectionally in steady state, since no phase change in the heterogeneous electrode reactions is effected. Electrical energy requirements are low and indicate that near reversible behavior is possible with $\text{Br}_2\text{-NaBr}$ electrolytes. The method seems to be promising for further study for possible application in practical saline water conversion processes.

Little research has been done on electrochemical methods of desalination except for electro dialysis with ion selective membranes (1). Blair and Murphy (2) have described recently an electrochemical "adsorption" method of desalination which utilizes carbon electrodes.

Electrolysis of saline waters to reduce the salt content has been a project of some interest, and a few desalination devices have been developed (3). However, methods utilizing these devices all have suffered from very high energy consumption.

Our main purposes in this paper are to demonstrate the feasibility of desalination of electrolytes by a new electrochemical mass transport method and to show that specific electrode reactions can be utilized to lower electrical energy requirements.

In a letter to Faraday in 1839, Daniell (4) described some of his experiments in which electrochemical mass transport phenomena in aqueous electrolytes were observed. Daniell used a three-compartment cell with two bladder diaphragms separating the electrodes. Hittorf (5) evidently was the first to study mass transport in a cell without a diaphragm or barrier interposed between the electrodes. He electrolyzed silver nitrate electrolytes between silver electrodes and found that the anolyte accumulated silver nitrate and the catholyte lost silver nitrate. In Hittorf's experiment, silver was oxidized at the anode and silver ion was reduced at the cathode, thus creating a concentration gradient for silver ion by enrichment-depletion at the electrodes. To compensate for the unidirectional steady-state charge transfer, it was necessary that some nitrate ion migrate from the cathode region to the anode region.

With different electrode reactions, Washburn (6) demonstrated an opposite effect of the anode compartment becoming depleted of dissolved salt on electrolysis of sodium chloride electrolytes between silver-silver chloride electrodes. In Washburn's experiments chloride ion was removed at the anode and generated at the cathode, and migration of sodium ion from the anode compartment to the cathode compartment resulted from the creation of the chloride ion gradient. Murphy (7) demonstrated some practical aspects of desalination of sodium chloride electrolytes with silver-silver chloride electrodes.

Some of our early experiments were done on electrolysis of sodium chloride electrolytes between closely spaced porous graphite electrodes with the electrolyte forced through the pores in the electrodes to prevent mixing of the anolyte and catholyte products. It was soon realized that a cathodic depolarizer (oxidant) could be added to the electrolyte to lower the driving voltage and thus diminish the energy requirement. Dissolved chlorine was an obvious choice because of the chloride content of naturally occurring saline waters. Fortunately, the use of a dissolved oxidant such as chlorine or bromine, with multiple oxidation states in aqueous solution, provides a method of unidirectional steady-state heterogeneous desalination without phase transfer with no net consumption of the oxidant (for the ideal case).

Successful execution of the redox method described in this paper evidently depends on at least three fundamental requirements. These are: (i) provision of two separated but closely positioned inert surfaces for transfer of the electrical energy

to the electrolyte reactants, (ii) a method of separating the anode and cathode reaction products, and (iii) a soluble energy transfer agent capable of existing in at least two oxidation states.

Experimental

Feed solutions were made by dissolving the appropriate reagent grade chemicals in distilled water. Chlorine was added by bubbling through distilled water prior to final dilution. Chlorine concentration was determined by solvent weight difference before and after dissolving. Polyethylene containers and tubing were used for both chlorine and bromine solutions; some coloration due to bromination was noted. Solutions containing a high concentration of bromine were made up in glass bottles to avoid localized bromination of polyethylene. Use of Tygon tubing was limited to short joint connections to minimize rapid reaction with chlorine (hypochlorite) and bromine.

Power supply.—A power supply operating from the a-c line was made with a 2.5v filament transformer, silicon diode bridge and 4000 μ f electrolytic filter capacitor. The d-c output was controlled with a manually operated variable voltage transformer ("Variac") connected to the input transformer. Conventional d-c meters were used.

Power measurements.—Currents below 120 ma were generally measured with a Weston Model 430 micrometer with a precision calibrated stepped shunt with a maximum attenuation ratio of 4000. Errors in this instrument were <0.7% for all ranges at maximum deflection. Currents larger than 120 ma were measured with conventional meters with specified error of <2%.

Driving voltages were measured at the cell terminals with an Electro-Instruments Model 3500 digital voltmeter which is specified to measure with an accuracy of 0.01% or 0.1 mv at an input impedance of 1000 megohms when measuring <10v. This instrument has features of automatic ranging and polarity, a-c filter, and a response time of a few seconds. Accuracy of the instrument was frequently checked with Weston standard cells and found to be

consistently better than 1 mv. Precision was found to be 0.1 mv at values less than 10v.

Porous carbon cell.—The cell used for most of the data collection is illustrated in Fig. 1. Electrodes were cut from National Carbon Co. grade 60 porous carbon which has a specified porosity of 50%. Size of the electrodes was 5x20x1 cm, and spacing was approximately 3 mm. Electrical connection to each electrode was made by press fitting a 0.64 cm diam type AUC graphite rod manufactured by National Carbon Co. The electrodes were sealed at the edges in polymethylmethacrylate plastic with an adhesive made from this plastic and chloroform. Polyethylene inlet and outlet tubes were sealed in the cell with an epoxy resin. Spacing between the back side of each electrode and the exterior cell wall was about 2 mm.

The cell used in obtaining current-voltage curves and steady-state current-voltage data was modified to minimize inherent ohmic resistance by connecting a nonporous graphite rod to the top of each electrode in the long dimension. The resistance of each electrode prior to cell assembly was measured to be \sim 0.03 ohm.

In desalination experiments the cell was operated with the feed countercurrent to the force of gravity and flow rates were controlled at the anode and cathode outlets with a pinch clamp on a short length of "Tygon" tubing. The electrolyte feed level was controlled manually at about 40 cm higher than the inlet level.

Experiments in which data for Fig. 2 through 8 were collected were done with the electrolyte also fed countercurrent to the force of gravity, but anolyte and catholyte flow rates were controlled with a dual acting peristaltic pump at the outlets. In these experiments a few centimeters positive pressure head was maintained. With Cl_2 -NaCl steady-state electrolyses, the evolved gas was vented frequently to prevent gas blocks between electrode faces.

A typical experiment was done as follows: After adjusting the desired current with the Variac, the flow rates of anolyte and catholyte were adjusted. On desalination runs, steady state operation was continued for 15 min to an hour prior to collecting anolyte and catholyte samples. Flow rates were averaged over the entire collection time interval, and sometimes minor adjustments in flow at anode and/or cathode were made to restore the starting power input level. Immediately after a run was completed, feed samples from the reservoir were taken for comparison with anolyte and catholyte samples. **Salt analyses.**—Salt content of electrolyte was determined by weighing the residue after evaporating electrolyte samples on a steam plate, then quantitative transfer to tared quartz beakers, evaporation again, and ignition for about 3 hr at 550°C. Electrolyte samples, which were weighed on a Mettler balance with a precision of 100 mg, were large enough so that precision of the data for the complete procedure consistently was better than 0.05%. For each run duplicate and sometimes triplicate samples of feed, anolyte and catholyte were analyzed. In determination of chloride-bromide mix-

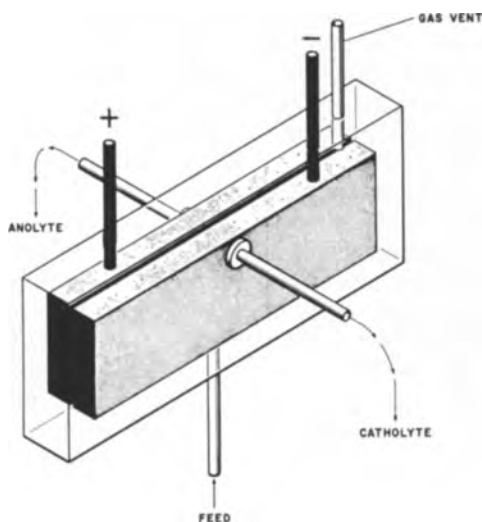


Fig. 1. Porous carbon cell with 5x20x1 cm electrodes spaced 0.3 cm

tures, the bromide was converted to chloride with chlorine water prior to the final evaporation in the tared quartz beakers. Ignition of samples was necessary to eliminate small amounts of organic material picked up from the tubing and feed electrolyte reservoir.

Experiments were done in an air conditioned laboratory at $21.8 \pm 0.2^\circ$ and relative humidity of about 50%. Before making weighings the ignited samples and/or quartz beakers were allowed to equilibrate with the atmosphere in the laboratory for at least 1 hr. Precision of taring was consistently better than 0.2 mg, and precision of the Mettler balance was better than 0.05 mg. Consequently the differential demineralization data can be regarded to be accurate to better than 1 mg, if true steady state electrolyte samples were obtained.

Results

Early experiments were done with Cl_2 -NaCl electrolytes and porous graphite electrodes. These experiments, which were mostly exploratory in nature, demonstrated conclusively that desalination was effected in the anolyte and that NaCl enrichment took place in the catholyte. Flow rates were unsatisfactory; thus no data are presented for experiments with graphite electrodes.

Porous carbon cell.—Operating conditions and data on electrolyses with Cl_2 -NaCl electrolytes are given in Tables I and II. A number designation for

Table I. Porous carbon cell operating conditions

No.	Electrolyte feed, molarity	Current, ma	Driving voltage, mv	Flow rate, ml/min	
				Anolyte	Catholyte
1	0.062 Cl_2 0.05 NaCl	8.3	56	2.11	2.02
2	0.060 Cl_2 0.05 NaCl	17.1	113	5.47	5.30
3	0.062 Cl_2 0.050 NaCl	52.1	256	1.81	1.85
4	0.062 Cl_2 0.050 NaCl	270	540	4.85*	4.96
5	0.013 Br_2 0.050 NaBr	13.9	27.5	2.08	2.00
6	0.013 Br_2 0.050 NaBr	54	104	3.44	5.38
7	0.013 Br_2 0.050 NaBr	265	370	10.0	11.4
8	0.013 Br_2 0.050 NaBr	270	291	41.0	42.4
9	0.0026 Br_2 0.010 NaBr	133	608	58.5	77.8
10	0.066 Br_2 0.50 NaBr	275	142	2.23	1.99
11	0.061 Br_2 0.067 NaCl	118	226	5.97	5.45
12	0.061 Br_2 0.067 NaCl	135	186	20.3	13.8
13	0.032 Br_2 0.050 NaCl	88	190	10.9	9.44
14	0.032 Br_2 0.050 NaCl	113	185	22.8	23.1
15	0.0079 Br_2 0.050 NaCl	86	247	9.60	10.1
16	0.0079 Br_2 0.050 NaCl	88	188	38.9	35.9

* Cell vented intermittently to remove gas formed at anode.

Table II. Porous carbon cell desalination and Faraday efficiency data

No.	Salt content, ppm			Depletion ratio*	Faraday efficiency, %		Salt depletion in anolyte, mg
	Feed	Anolyte	Catholyte		Anode	Cathode	
1	2940	2910	2926	0.982	13	21	8.9
2	2875	2857	2903	0.984	15	25	13.6
3	2924	2775	3101	0.895	14	17	67.5
4	2951	2672	3260	0.820	14	16	148.7
5	5111	4920	5259	0.936	35	33	75.1
6	5105	4750	5350	0.888	35	37	170.4
7	5071	4420	5648	0.783	38	39	293.0
8	5071	4912	5242	0.937	38	43	143.6
9	1020	961	1062	0.905	40	38	111.0
10	48590	45850	51390	0.892	34	32	363.4
11	3902	3668	4189	0.876	33	36	112.0
12	3902	3822	4097	0.933	33	50	40.5
13	2946	2835	3064	0.925	38	35	60.4
14	2946	2878	3012	0.956	38	37	31.0
15	2945	2813	3068	0.917	41	40	63.3
16	2945	2915	2979	0.979	37	38	23.3

* Anolyte/catholyte salt ratio.

experiments is used to allow correlation of the data in the two tables. The cell is illustrated in Fig. 1.

Results obtained with Br_2 -NaBr electrolytes are given in Tables I and II, entries 5-10. These data show the improvement in the Faraday efficiency. Anolyte depletion is about equal to catholyte enrichment.

The Faraday current efficiencies were computed in the same way that cation transference numbers are computed from transference experiments. The values for the Faraday efficiency are quite close to values for the cation transference numbers for NaCl electrolytes as determined by the Hittorf method (6).

The bromide-bromide couple in NaCl electrolytes was also investigated. Data are given in Tables I and II, entries 11-16. Faraday efficiencies are not significantly different from those computed for sodium bromide electrolytes.

Current-voltage data, except for steady-state operation, were taken with as little concentration polarization as possible. That is, voltage and current values were recorded as soon as the voltmeter reached a null reading, usually about 3 sec. Immediately then the power to the cell was interrupted prior to continuation of data taking. Data on the effect of electrolyte composition for three redox couples are plotted in Fig. 2-7.

The Br_2 -NaBr system seemed to behave almost ideally, but polarization and stagnation effects were observed with both the Br_2 -NaCl couple and the Cl_2 -NaCl couple. Even after 2 or 3 sec electrolysis times potentials of several millivolts magnitude were built up. These potentials did not decay for several minutes and sometimes for hours due to stagnant pockets in the porous electrodes. The scatter of the data and curvature of the plots at low input energy levels is directly attributable to the galvanic action of stored chemical energy due to prior energy

Table III. Porous carbon cell desalination rate and energy data

No.	Elec- trolysis time, min	Desalination rate millimoles/hr	Experimental	Computed	Irreversible
			electrical work	reversible work	electrical work
			Joules/millimole		
1	220	0.042	40	5.05	35
2	150	0.093	74	5.04	69
3	250	0.46	173	5.61	167
4	110	1.39	387	5.95	381
5	240	0.18	7.5	5.29	2.2
6	140	0.71	28	5.55	22.5
7	45	3.80	93	6.18	87
8	22	3.80	74	5.28	69
9	32	3.20	144	5.45	139
10	60	3.35	42	5.53	36.5
11	80	1.44	67	5.52	61
12	25	1.66	54	5.30	49
13	50	1.24	48	5.35	43
14	20	1.59	47	5.19	42
15	50	1.30	59	5.39	54
16	20	1.20	50	5.07	45

input increments. To minimize galvanic (fuel cell) effects, the low energy data were taken first.

Data on the effect of flow rates on steady-state operation are plotted in Fig. 8. These data show quite clearly that polarization voltages are diminished by higher flow rates.

Steady-state differential desalination rate values and energy values computed from data in Tables I and II are listed in Table III.

Interpretation of Results

The Faraday efficiency data show that the mass transport phenomena observed here are the same general phenomena that have been observed in other transference experiments.

In the Br_2 -NaBr system the anode reaction undoubtedly is oxidation of bromide ion to bromine, and the cathode reaction is reduction of dissolved bromine to bromide ion. No physical manifestation of any other reaction at either electrode was observed.

Fundamentally, the current through the cell is a measure of the rate of charge transfer at the elec-

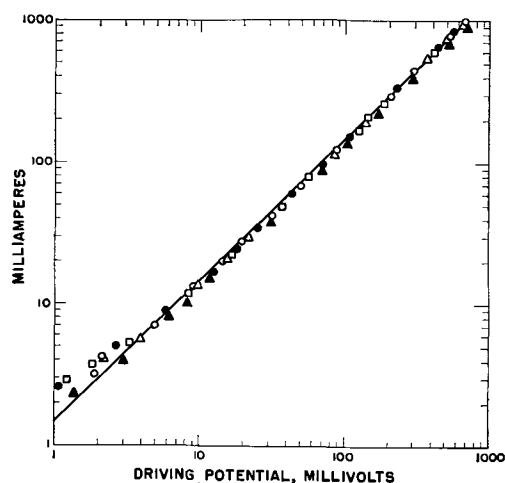


Fig. 2. Effect of Br_2 concentration with constant NaBr concentration and controlled electrolyte flow rates. The line is drawn with a slope of 1.00. 0.05M NaBr electrolyte. Anolyte flow rate 8.4-8.6 ml/min; catholyte flow rate 8.9-9.2. \blacktriangle , 0.0094M Br_2 ; \square , 0.019M Br_2 ; \bullet , 0.038M Br_2 ; \circ , 0.060M Br_2 ; \triangle , 0.075M Br_2 .

trodes. Figure 2 shows that for Br_2 -NaBr electrolytes, the rate of charge transfer is directly proportional to the driving voltage. The reaction is thus first order with respect to driving voltage since log-log plotting should give a slope of one for a first order reaction (8). Ohms law is obeyed. However, the Br_2 concentration does not alter appreciably the energy requirement for electrolysis and shows that charge transfer is not limited by the Br_2 concentration. This is a zero order effect and is typical of heterogeneous reaction wherein a species is present in such large amounts that only a fraction of it is needed to sustain the reaction.

Figure 3 shows that the NaBr concentration has a large effect on the charge transfer reaction. Thus, the resistance to the driving voltage is related to the movement of ions in the electrolyte. Such an effect is expected from well known conductivity and diffusion experiments.

Figures 4 and 5 show that the behavior of Br_2 -NaCl is quite similar to the behavior of Br_2 -NaBr, so the electrode reactions must be predominantly

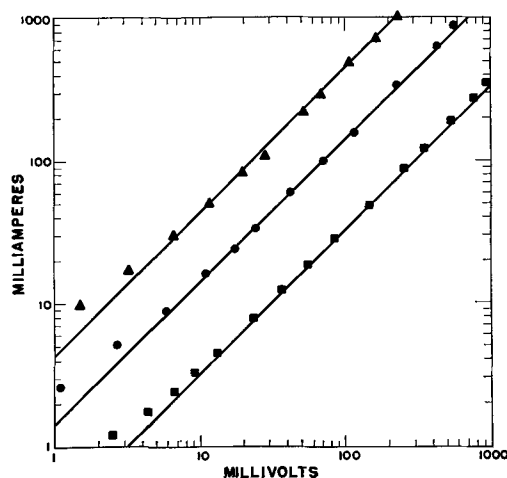


Fig. 3. Effect of NaBr concentration with constant Br_2 concentration and controlled flow rates. The lines are drawn with slopes of 1.00. 0.038M Br_2 . Anolyte flow rate 8.1-8.4 ml/min; catholyte flow rate 9.1-9.2. \blacktriangle , 0.50M NaBr; \bullet , 0.05M NaBr; \blacksquare , 0.01M NaBr.

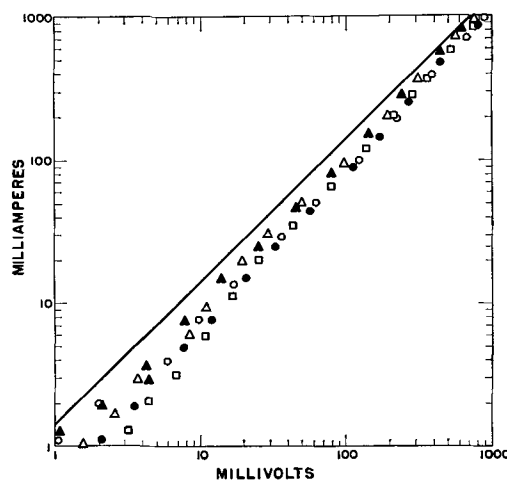


Fig. 4. Effect of Br_2 concentration with constant NaCl concentration and controlled flow rates. The line is drawn with the same coordinates as the line in Fig. 2. 0.05M NaCl. Anolyte flow rate 7.8-8.6 ml/min; catholyte flow rate 8.6-9.2. \bullet , 0.0094M Br_2 ; \square , 0.019M Br_2 ; \circ , 0.038M Br_2 ; \triangle , 0.075M Br_2 ; \blacktriangle , 0.075M Br_2 .

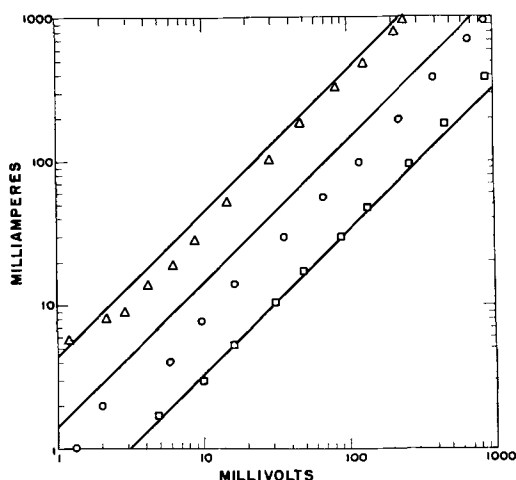


Fig. 5. Effect of NaCl concentration with constant Br₂ concentration and controlled flow rates. Lines are drawn with the same coordinates as those in Fig. 3. 0.038M Br₂. Analyte flow rate 8.3-8.6 ml/min; catholyte flow rate 9.0-9.1. Δ , 0.50M NaCl; \circ , 0.05M NaCl; \square , 0.01M NaCl.

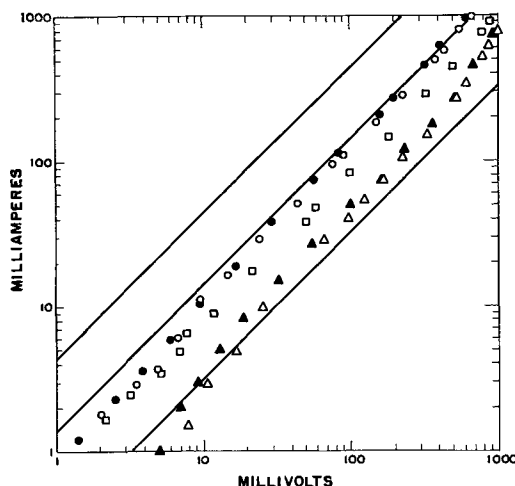


Fig. 7. Effect of NaCl concentration with high Cl₂ concentration and controlled flow rates. The lines are drawn with slopes of 1.00 and have the same coordinates as those in Fig. 3. Analyte flow rate 8.0-9.0 ml/min; catholyte flow rate 7.4-9.1. \circ , \bullet : 0.50M NaCl, 0.045M Cl₂ (sat'd); \square , 0.05M NaCl, 0.059M Cl₂; Δ , 0.01M NaCl, 0.045M Cl₂; \blacktriangle , 0.01M NaCl, 0.059M Cl₂.

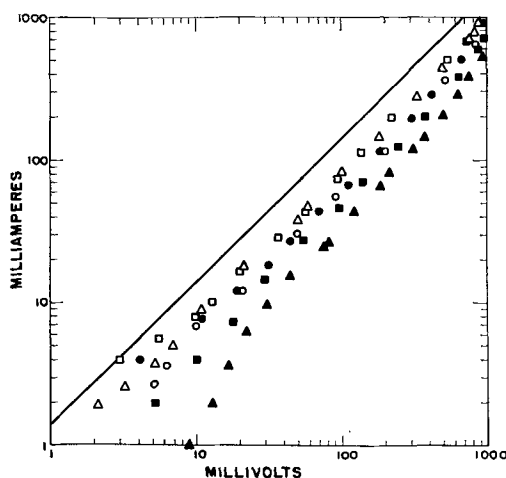
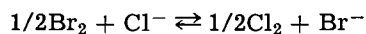


Fig. 6. Effect of Cl₂ concentration with constant NaCl concentration and controlled flow rates. The line is drawn with the same coordinates as the line in Fig. 2. 0.05M NaCl. Analyte flow rate 6.8-8.1 ml/min; catholyte flow rate 8.1-8.8. \blacktriangle , 0.0092M Cl₂; \circ , 0.015M Cl₂; \blacksquare , 0.018M Cl₂; \square , 0.030M Cl₂; \bullet , 0.037M Cl₂; Δ , 0.059M Cl₂.

the same. Evidently the supply of bromide ion for anodic oxidation comes from the chloride-bromine equilibrium



This reaction must be very fast to supply sufficient bromide ion so that the driving voltage is only about a factor of two greater than when Br₂-NaBr is electrolyzed. No gas oxidation products were observed, but the formation of bromate cannot be ruled out. In fact, the higher polarization potential required at low electrolyte flow rates, shown in Fig. 8, probably is due primarily to the build-up of bromate ion in the anolyte.

The Cl₂-NaCl system is complicated by reaction of chlorine with water to form hypochlorite. Data in Fig. 6 and 7 could not be taken fast enough to eliminate polarization effects and thus do not represent the idealized minimum energy input. The dependence of driving potential on chlorine concen-

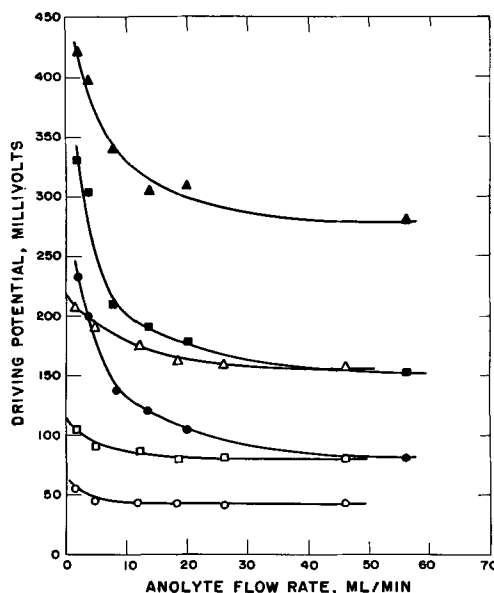


Fig. 8. Effect of flow rates on driving potential required to sustain steady-state current. Ten minutes or longer was allowed for steady-state operation. Analyte catholyte flow rate ratios were 0.9-1.0. 0.038M Br₂. \blacktriangle , 0.05M NaCl 200 ma; \blacksquare , 0.05M NaCl 100 ma; \bullet , 0.05M NaCl 50 ma; Δ , 0.05M NaBr 200 ma; \square , 0.05M NaBr 100 ma; \circ , 0.05M NaBr 50 ma.

tration shows that the charge transfer process is limited to some extent by the concentration of oxidant (s) and/or reductant(s). Conductivity in 0.5M NaCl containing Cl₂ is considerably less than in 0.5M NaCl or 0.5M NaBr containing bromine.

With Cl₂-NaCl there is considerable gas evolution from the anode (undoubtedly oxygen). Convective mixing of the electrolysis products by the gas evolution probably accounts for the lower Faraday efficiencies and the discrepancy between anode and cathode Faraday efficiencies observed.

The steady-state data in Fig. 8 show that at high electrolyte flow rates the energy required to electrolyze Br₂-NaCl is about twice as great as required to electrolyze Br₂-NaBr to get the same de-

salination rate with 0.05M electrolyte salt concentrations. Sufficient steady-state data are not available for comparison at other electrolyte salt concentrations.

An interesting consequence of electrochemical reaction and polarization is demonstrated by data in Table III. Experiments 13, 15, and 16 were done at about the same current; thus, with the same Faraday efficiency prevailing, the desalination rates should be the same in all three experiments. However, the bromine concentration for experiments 13 and 15 was about a factor 4 different, but flow rates were comparable. To compensate for the concentration deficiency, a higher driving voltage was required for the lower concentration. Experiments 13 and 16 show that the effect of the factor of 4 in bromine concentration could be compensated by flowing 4 times as much electrolyte per unit time since the energy requirements were about the same in both experiments.

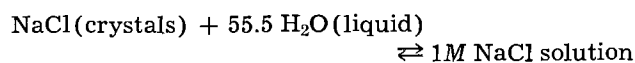
Temperature effects.—When electrical energy is pumped into an electrochemical system, only when the energy is reversibly absorbed, as in oxidation-reduction, can the process be done isothermally. Otherwise there will be localized Joule heating at the energy transfer surfaces (electrodes). The effect of Joule heating is barely perceptible in the Br₂-NaBr system, but somewhat more prominent in the Br₂-NaCl and Cl₂-NaCl systems. With increasing energy inputs the rate of charge transfer increases exponentially with voltage rather than linearly as shown by the increase in slopes of the upper portion of the data plots, especially in Fig. 4 and 6. This effect can logically be attributed to an increase in concentration of oxidant and/or reductant due to an increase in temperature in the heterogeneous reaction zones.

Energy requirements.—For this redox method the important energy requirement is the electrical energy. Thus, it is of interest to compare the experimental values of electrical energy for desalination (Table III) to the minimum energy requirement as computed for the ideal thermodynamic process.

The concept of "equilibrium" separation processes has been used somewhat indiscriminately to describe what is meant as "reversible" separation processes (9, 10). An equilibrium process is necessarily done isothermally with no net mass transport; thus, there can be no useful desalination done and no free energy change results. By contrast, a differential reversible process can be utilized to do useful desalination at low rates and a free energy change is necessary. The minimum work to do the desalination reversibly is exactly the free energy change for the process at the specified temperature.

In discussing heat of solution, Pitzer and Brewer (11) distinguish the difference between the integral heat of solution and the differential heat of solution. Here also a distinction must be made between the integral free energy change for the complete separation and the differential free energy change for depletion of a solution of specified composition.

Consider the reaction:



If the reaction is completely reversed to the left, then 1 mole of salt is obtained and a yield of 55.5 moles of water is obtained. The energy required can be computed from the standard free energy changes as defined for the components and the solution. From Latimer (12) the free energy change on dissolving NaCl according to the above reaction is -2134 cal/mole at 25°. The value of 8.93 Joules/millimole represents the minimum work that must be done for the integral process of separating 1 millimole of salt crystals from 0.0555 moles of water.

For a differential desalination process the minimum energy requirement can be computed from the partial molal free energy change.

The total free energy of solution of NaCl in 1000g of water is given by (13)

$$\frac{F - F^\circ}{2RT} = -M\phi + 2.303M \log M\gamma_{\pm}$$

where M is the NaCl molality, ϕ is the osmotic coefficient, and γ_{\pm} is the activity coefficient. Assume an ideal process wherein a millimole of NaCl is removed reversibly from a very large reservoir of 0.05M NaCl electrolyte. The desalination energy is the work of removing the NaCl from the reservoir to a second solution of the same molality as the desalinated solution. By setting ϕ and γ_{\pm} equal to unity, the free energy change at 25° is computed to be 4.96 Joules/millimole.

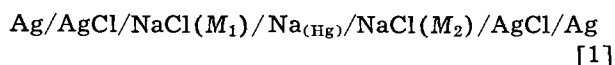
For NaBr the differential desalination energy requirement should be the same as for NaCl, again assuming ideal solution behavior.

By a different procedure the desalination energy can be computed from vapor pressure data. The minimum energy required to vaporize 1 mole of water from an infinite reservoir of NaCl solution and condense it reversibly as pure water is $-RT \ln p/p^\circ$ where p is the vapor pressure of water over the NaCl solution and p° is the vapor pressure of water over pure solvent water. The energy of desalination can be computed by considering the amount of water that must be transported in the process to obtain differential enrichment of NaCl in the remaining infinite reservoir of NaCl solution. For 0.1M NaCl p/p° is 0.99671 at 25° (14) and the energy requirement is 8.163 Joules/mole of water transported. To obtain enrichment of 1 mole of NaCl in the infinite reservoir requires that 10 kg of water be vaporized and condensed. Thus, for 1 millimole enrichment, the energy required is 8.163×0.555 or 4.53 Joules/millimole (15) of NaCl depletion in the pure product water. By a similar procedure the requirement for desalination of 0.5M NaCl was computed to be 4.54 Joules/millimole. This process is not the same as the differential process described above since the product electrolyte is completely stripped of salt.

The free energy equation above can be used to compute the additional energy necessary to desalinate against a concentration (chemical potential) gradient, but concentration cell data can be used di-

rectly and the complication of activity coefficients is avoided and the processes are more understandable in terms of the mass transfer.

Two types of cells will be considered. One type requiring phase transfer of both sodium and chlorine is



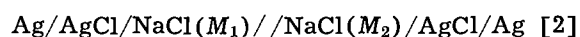
The emf of this cell is exactly the same as the external electrostatic potential which must be applied to the electrodes to establish electrochemical equilibrium and prevent net mass transport between phases. This is a condition of zero net charge transfer through the cell. In order to get desalination, a potential infinitesimally larger than the cell emf must be applied to cause charge transfer and mass transport.

The total reversible energy required to desalinate against a chemical potential gradient (neglecting the effect of the osmotic coefficient) where the electrode reactions have unity Faraday efficiency is the electrical work done against the concentration gradient plus the work of removing 1 millimole of NaCl from the anode compartment

$$\Delta F_d^1 = \frac{(\text{Cell}[1]\text{emf} \times 96,494) + 2RT}{1000} \text{ Joules/millimole}$$

It should be emphasized that the energy expended in overcoming the cell emf is not irreversible, since this energy is stored as chemical energy in the enriched electrolyte in the cathode compartment and can be extracted by operating the cell as a primary cell. By such operation the original set of conditions before desalination is restored for the ideal case.

The second type of cell to be considered is one with a liquid junction, which is the same general type of cell employed in the experiments described in this paper, except that the electrode reactions are different.



In cell [2] chlorine undergoes phase transfer but sodium does not.

The Faraday efficiency of cell [2] is not unity, but is given by the Hittorf cation transference number, t^+ . Consequently, more charge must be transferred per mole to compensate for the inefficiency. The free energy of desalination is

$$\Delta F_d^2 = \frac{\left(\frac{\text{Cell}[2]\text{emf}}{t^+} \times 96,494\right) + 2RT}{1000} \text{ Joules/millimole}$$

In Table IV are values of reversible energy of desalination computed from cell data in the literature and from transference numbers determined by the Hittorf and moving boundary methods. These data for cell [1] and cell [2] show that the reversible energy of desalination is the same when the NaCl concentration gradients in the different cells are identical.

It can be concluded that the minimum energy required to drive the desalination reaction against a

Table IV. Computed reversible energy of desalination at 25° for cell [1] and cell [2]

Cell	M_1	M_2	Depletion ratio M_1/M_2	Cell emf, mv	Faraday efficiency	ΔF_d , Joules/millimole
1	0.0500	0.0500	1.000	Infinitesimal	>0<1	4.96
1	0.0500	0.1000	0.500	32.5 ¹⁶	1.000	8.10
1	0.1000	0.5000	0.200	75.8 ¹⁶	1.000	12.27
2	0.04992	0.05994	0.833	3.37 ¹⁷	0.388 ^a	5.70
2	0.04985	0.09987	0.499	12.72 ¹⁷	0.386 ^a	8.14
2	0.04985	0.09987	0.499	12.72 ¹⁷	0.366 ^b	8.31
2	0.01002	0.04974	0.201	30.22 ¹⁷	0.388 ^a	12.48

^a Moving boundary method, ref. 18.

^b Hittorf method for 1.25M NaCl, ref. 6.

chemical potential gradient is the same whether both anion and cation make the phase transfer or whether only the anion makes a phase transfer. When Br₂ is used as the energy transfer agent, no phase transfer is required. Proper data are not available at this time to extend the hypothesis to these types of electrode reactions, but there is no reason to believe that the reversible energy requirement would differ appreciably.

Additional energy is required to drive the desalination reactions at finite rates, and evidently this additional energy manifests itself as Joule heating (or cooling) at the electrode surfaces. This energy can be considered to be irreversible, since it is not immediately available to the desalination mechanisms. Data in Table III show that most of the energy required for desalination is irreversibly lost except at low desalination rates.

Figure 2 shows that for Br₂-NaBr the rate of desalination is a first order function of the driving voltage when the desalination chemical potential gradient is essentially zero. Whether the Faraday efficiency is lower at very low driving voltages remains to be proved. An approach to reversibility is demonstrated.

There is not much hope that an energy transfer agent better than bromine will be found, since the results with bromine show that the rate of desalination is limited by the ionic charge separation processes rather than by the heterogeneous charge transfer electrode reactions. Other oxidants such as oxygen, hydrogen peroxide, and nitrogen oxides should work as energy transfer agents at one or both electrodes, but probably with reduced energy efficiency compared to bromine.

Acknowledgments

The author wishes to thank R. J. Bard and R. D. Baker for enthusiastic and unrestricted support of this research. The work was done under the auspices of the Atomic Energy Commission.

Manuscript received April 1, 1963.

Any discussion of this paper will appear in a Discussion Section to be published in the June 1965 JOURNAL.

REFERENCES

- J. R. Wilson, Editor, "Deminceralization by Electro-dialysis," Butterworth Scientific Publications, London (1960).
- John W. Blair and George W. Murphy, "Saline Water Conversion," p. 206, American Chemical

- Society Advances in Chemistry Series No. 27, Washington, D. C. (1960).
3. A. S. Behrman, *Ind. Eng. Chem.*, **19**, 1229 (1927), *J. Chem. Ed.*, **6**, 1611 (1929); Edward Bartow and R. H. Jones, *Ind. Eng. Chem.*, **22**, 1020 (1930); Jean Billiter, *This Journal*, **60**, 217 (1931), *ibid.*, **70**, 409 (1936); L. Streichter, *Civil Eng.*, **16**, 312 (1946).
 4. J. F. Daniell, *Phil. Trans. Roy. Soc.*, **129**, 97 (1839).
 5. W. Hittorf, *Pogg. Ann.*, **89**, 117 (1853).
 6. E. W. Washburn, *J. Am. Chem. Soc.*, **31**, 322 (1909).
 7. George W. Murphy, *This Journal*, **97**, 405 (1950).
 8. Sidney W. Benson, "The Foundations of Chemical Kinetics," p. 82, McGraw-Hill Book Co., New York (1960).
 9. "Desalination Research and the Water Problem," Nat. Acad. Sci., Nat. Res. Council, Publication 941 (1962).
 10. "Saline Water Conversion," American Chemical Society Advances in Chemistry Series, No. 27, Washington, D. C. (1960).
 11. K. S. Pitzer and L. Brewer, Revision of "Thermodynamics" by G. N. Lewis and M. Randall, p. 382, 388, McGraw-Hill Book Co., Inc., New York (1961).
 12. W. M. Latimer, "Oxidation Potentials," Second Ed., p. 337, Prentice-Hall, Inc., Englewood Cliffs, N. J. (1952).
 13. Ref. (11), p. 642.
 14. International Critical Tables, V.III, p. 297, McGraw-Hill Book Co., New York (1928).
 15. Sign convention used in Latimer, ref. 12.
 16. H. S. Harned and L. F. Nims, *J. Am. Chem. Soc.*, **54**, 423 (1932).
 17. G. J. Jantz and A. R. Gordon, *ibid.*, **65**, 218 (1943).
 18. L. G. Longworth, *ibid.*, **54**, 2741 (1932).

APPENDIX

Practical aspects.—These first results show some interesting possibilities with respect to practical saline water conversion. A number of tentative conclusions can be drawn:

1. An approach to the ideal differential process is demonstrated.
2. The process can be done under ambient conditions.
3. High flow rates at low pressure drops can be utilized.
4. Unidirectional steady-state operation is possible.
5. No membranes or exotic materials are needed.
6. Phase transfer of salt is not required, but cyclic phase transfer of bromine is required for steady-state differential desalination.
7. Higher desalination rates are possible with higher salt concentrations without an energy penalty or need for larger electrodes.
8. The rate of desalination is proportional to the current input, and the rate of desalination should also be proportional to the electrode volume. Thus a choice can be made between power input and plant size.
9. Bromine is present in sea water in significant concentrations and it is easily extracted; thus it is readily available.
10. Bromine behaves ideally as the energy transfer agent, and it can be easily purged from anolyte solutions to recycle to allow a fixed inventory for plant operation.

Electrical Conductivity of the Melts in the System



K. Matiasovsky

CSAV, Institute of Inorganic Chemistry, Slovak Academy of Sciences, Bratislava, CSSR

M. Malinovsky and S. Ordzovensky

Department of Inorganic Technology of the Slovak Technical University, Bratislava, CSSR

ABSTRACT

The specific conductivities of cryolite and of melts of the systems $\text{Na}_3\text{AlF}_6\text{-Al}_2\text{O}_3$, $\text{Na}_3\text{AlF}_6\text{-NaCl}$, and $\text{Na}_3\text{AlF}_6\text{-Al}_2\text{O}_3\text{-NaCl}$ have been measured at high concentrations of cryolite. It has been proved that the specific conductivity decreases with increasing concentration of Al_2O_3 in the melt composition. Further it has been found that the addition of NaCl increases the specific conductivity of cryolite and of the system $\text{Na}_3\text{AlF}_6\text{-Al}_2\text{O}_3$ as well. With regard to the technology of aluminum production it is most important that the influence of NaCl is most pronounced at low concentrations of NaCl and at higher concentrations of alumina.

Electrolytes used nowadays in the production of aluminum do not differ much from those used seventy years ago. Actually they are melts of the ternary system $\text{Na}_3\text{AlF}_6\text{-AlF}_3\text{-Al}_2\text{O}_3$, or of the quaternary system $\text{Na}_3\text{AlF}_6\text{-AlF}_3\text{-Al}_2\text{O}_3\text{-CaF}_2$. In order to improve the physico-chemical properties of the electrolyte, different additives were used. The substance that is to be used as an additive to the electrolyte must comply with certain requirements, such as: it must be resistant to heat under the conditions of electrolysis, it must not contain cations with lower precipitation potential than aluminum, and finally it must improve those physico-chemical properties

of the electrolyte which enhance the economics of electrolysis. An ideal addition should lower the temperature of the primary crystallization, the density and the viscosity of the electrolyte and increase its electrical conductivity, etc. From this point of view the influence of different additives, especially of fluorides, chlorides, and oxides of alkali metals and alkali earths has been studied.

Sodium chloride is one of these substances, which, after preliminary experiments, seems to fulfill most of the above mentioned requirements. The addition of NaCl to the system $\text{Na}_3\text{AlF}_6\text{-Al}_2\text{O}_3$ lowers the temperature of primary crystallization (1, 2), the

density (3, 4), and the viscosity (3) of these melts. According to Belyaev (3), the specific conductivity of the cryolite is increased too. The electrical conductivity is important from the practical as well as from the theoretical point of view. The increase of the conductance influences directly the intensification of the production (5), and, on the other hand, research on electrical conductance can help in studies of the structure of melts.

The measurements of electrical conductivity of fluoride melts are rather difficult; for this reason there is wide discrepancy in conductivity data of the cryolite, and of multicomponent systems of cryolite-base melts, as recorded by various authors (5, 12-17).

The present work is concerned with the measurement of the specific conductivity of the binary systems $\text{Na}_3\text{AlF}_6\text{-Al}_2\text{O}_3$, $\text{Na}_3\text{AlF}_6\text{-NaCl}$ and of the ternary system $\text{Na}_3\text{AlF}_6\text{-Al}_2\text{O}_3\text{-NaCl}$ chiefly with high concentration of cryolite, as these are most important for aluminum production. To check the measured values, the specific conductivity of cryolite was measured again as a function of temperature (7).

Experimental

Materials.—The samples were prepared with alpha-alumina containing 99% Al_2O_3 , and with reagent grade NaCl. Cryolite, whose specific conductivity was determined as a function of temperature, was used for the measurements of the specific conductivity of binary melts $\text{Na}_3\text{AlF}_6\text{-Al}_2\text{O}_3$ and $\text{Na}_3\text{AlF}_6\text{-NaCl}$. Cryolite was prepared by fusing the reagent grade NaF and vacuum sublimed aluminum fluoride containing 99.5% AlF_3 ; NaF and AlF_3 were mixed in stoichiometric ratio. It has been found by pyrohydrolytic methods (6) that the cryolite contained 54.0% F. The melting point was $1005^\circ \pm 2^\circ\text{C}$. Cryolite used for measurements of specific conductivity of molten $\text{Na}_3\text{AlF}_6\text{-Al}_2\text{O}_3\text{-NaCl}$ has been prepared from reagent grade NaF and anhydrous AlF_3 containing 65.9% F, which is equivalent to 97.2% AlF_3 . Alumina was present as impurity. In the prepared cryolite there was 53.4% F, the melting point was $1001^\circ \pm 2^\circ\text{C}$.

Method.—For conductivity measurements a modified Thompson bridge specially developed for this purpose has been used (ref. 7, Fig. 1). With this apparatus rapid balancing of the bridge could be attained as it depended only on one variable, and consequently one measurement did not last more than 30 sec. Current of 0.1 amp and frequency of 5 kc/sec was used.

Platinum electrodes of identical shape were used as in previous work (11). The cell constant of the resistance cell was determined by means of molten KNO_3 , NaCl, and Na_2SO_4 whose electrical conductivity has been determined with satisfactory accuracy (8-10). On the basis of measurements performed over a wide range of temperatures, the capacity of the cell has been found to be $0.423 \pm 0.005 \text{ cm}^{-1}$.

The cooling rate of the furnace was about $1^\circ\text{C}/\text{min}$. Since a determination could be made in 30 sec, it was not necessary to provide the furnace with a thermostat, and it was possible to work while the

melt was cooling, because the change of density and 0.5°C drop in temperature during one measurement were negligible.

A Pt-Rh/Pt (10% Rh) thermocouple, calibrated at the melting points of KCl (770.3°C), NaCl (800.4°C), Na_2SO_4 (884.7°C), K_2SO_4 (1069°C), and the eutectic $\text{Na}_2\text{SO}_4\text{-NaCl}$ (627°C) was used.

Accuracy.—The accuracy of each measurement was $\pm 1\%$.

The isotherms of the specific conductivity of the melt compositions under investigation were constructed by means of several values which had been interpolated on the conductivity polytherms of pertinent samples. One may assume that the error in measurement is smaller than the above value. Four parallel measurements were performed to determine the specific conductivity of cryolite as a function of temperature (Fig. 1). Single values differed from the arithmetic mean value maximum by 0.9%.

The accuracy of temperature measurements was $\pm 2^\circ\text{C}$.

Results

The values of specific conductivity of cryolite measured in the course of our investigations (Fig. 1) are in good accord with previous work (11-13) and are slightly higher than those of Abramov (5). The value at 1000°C had to be extrapolated, because the melting point of the cryolite used was $1005^\circ \pm 2^\circ\text{C}$. The good agreement with previous work gives confidence in the method used. Data reported in ref. (14-17) seem to be erroneous to a high degree. The errors in these measurements can be attributed, apart from the causes pointed out by Abramov (5), to the fact that the authors measured not only the ohmic resistance of the melt, but also the impedance part or all of the measuring circuit.

Analogous conclusions are valid as regards the recorded values of specific conductivity of melted $\text{Na}_3\text{AlF}_6\text{-Al}_2\text{O}_3$ (Fig. 2); these data are in relatively good agreement with some (5, 13) but differ fundamentally from others (14-17). The decrease of electrical conductivity while the concentration of alumina is being raised may be caused by a relative

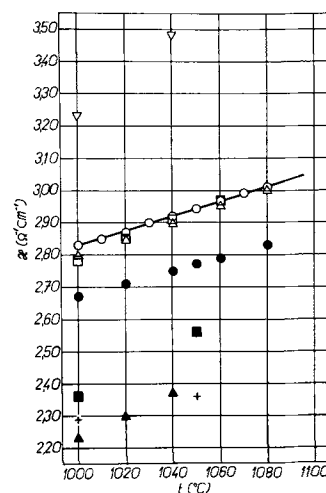


Fig. 1. Specific conductivity of cryolite vs. temperature. ○, This investigation; ▽, Batasev (15); □, Yim and Feinleib (13); △, Edwards et al. (12); ●, Abramov et al. (5); ■, Vajna (17); +, Belyaev (3); ▲, Arndt and Kalass (14).

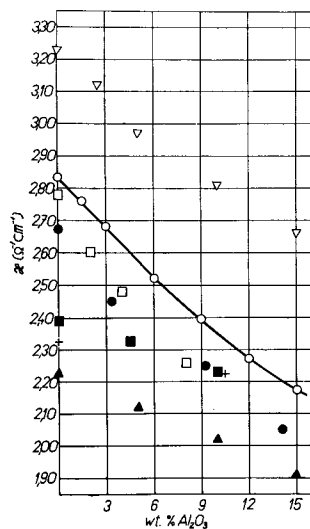


Fig. 2. Specific conductivity of melts of the system $\text{Na}_3\text{AlF}_6\text{-Al}_2\text{O}_3$ at 1000°C . \circ , This investigation; ∇ , Batasev (15); \square , Yim and Feinleib (13); \bullet , Abramov et al. (5); \blacksquare , Vajna (17); $+$, Belyaev (16); \blacktriangle , Arndt and Kalass (14).

decrease of the concentration of Na^+ ions, which according to Frank and Foster (18) contribute considerably to the conductivity of cryolite melts ($t_{\text{Na}^+} = 0.99$). The increase in activity of Na^+ ions due to the increase of sodium chloride in melts of $\text{Na}_3\text{AlF}_6\text{-NaCl}$ increases the specific conductivity (Fig. 3). The specific conductivity of the melts of this system are higher than would be expected from the pertinent additive values (11). It is possible to see on the plot that the influence of NaCl is relatively much more pronounced at low concentrations of sodium chloride. Above 20% NaCl, the specific conductivity of the melt increases very slowly. It can be assumed that NaCl is completely dissociated at low concentrations and the increase in specific conductivity is caused by Na^+ cations as well as by the rather mobile Cl^- anions. The number of free Na^+ and Cl^- ions, however, is not being increased proportionally with the increasing concentration of NaCl. This is probably caused by the formation of associated ions, e.g., of the type Na_2Cl^+ , NaClF^- , Na_2F^+ , or eventually of complex fluorochlorine-aluminum ions.

The recorded values of the specific conductivity of this system are considerably higher than reported by Belyaev (3) and the character of the dependence

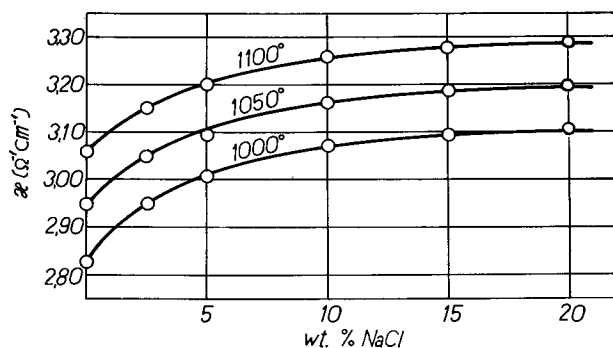


Fig. 3. Polytherms of specific conductivity of melts of the system $\text{Na}_3\text{AlF}_6\text{-NaCl}$.

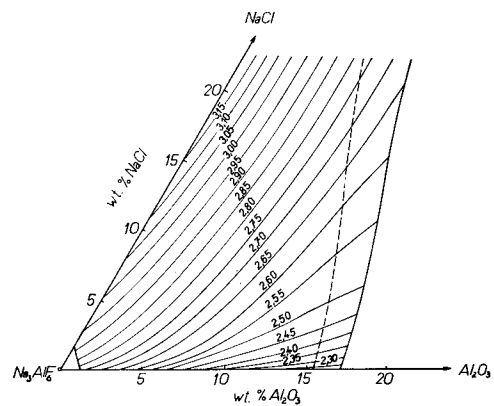


Fig. 4. Specific conductivity of melts of the system $\text{Na}_3\text{AlF}_6\text{-Al}_2\text{O}_3\text{-NaCl}$ at 1000°C .

$\kappa = f(c_{\text{NaCl}})$ as found in the present work is fundamentally different too.

The diagram of the specific conductivity of the system $\text{Na}_3\text{AlF}_6\text{-Al}_2\text{O}_3\text{-NaCl}$ at 1000°C (Fig. 4) is limited by the isotherms of the liquidus at 1000°C and by the threshold concentration 20% NaCl. The specific conductivity is influenced by the concentration of Na^+ ions in the melt. An increase in the concentration of Al_2O_3 causes a relative decrease of Na^+ ions in the unit volume and consequently the decrease of the conductivity. On the other hand, if NaCl is added, the concentration of Na^+ ions increases and owing to this the conductivity of the melt increases too. Similarly as in the binary system $\text{Na}_3\text{AlF}_6\text{-NaCl}$, the influence of NaCl is most pronounced at low concentrations, up to 5%, and at this concentration it is relatively greater at higher concentrations of Al_2O_3 . With regard to the fact that sodium chloride, like most additives, lowers the solubility of alumina in the electrolyte, viz., the liquidus of the system $\text{Na}_3\text{AlF}_6\text{-Al}_2\text{O}_3\text{-NaCl}$ (1, 2), it is very advantageous from the technological point of view that the relative increase of specific conductivity can be attained at relatively low concentrations of NaCl.

Manuscript received July 16, 1963.

Any discussion of this paper will appear in a Discussion Section to be published in the June 1965 JOURNAL.

REFERENCES

1. N. W. F. Philipps, R. H. Singleton, and E. A. Hollingshead, *This Journal*, **102**, 690 (1955).
2. K. Matiasovsky and M. Malinovsky, *Chem. zvesti*, **14**, 551 (1960).
3. A. I. Belyaev, "Elektrolit Alyuminiyevych Vann," p. 101, Metallurgizdat, Moscow (1961).
4. K. Matiasovsky, A. Jaszova, and M. Malinovsky, *Chem. zvesti*, **17**, 605 (1963).
5. G. A. Abramov et al., "Teoreticheskie Osnovy Elektrometallurgii Alyuminiya," p. 145, Metallurgizdat, Moscow (1953).
6. J. C. Warf, W. D. Cline, and R. D. Tevebaugh, *Anal. Chem.*, **26**, 342 (1954).
7. J. Bajcsy, M. Malinovsky, and K. Matiasovsky, *Electrochim. Acta*, **7**, 543 (1962).
8. P. F. Antipin et al., "Elektrokhimiya Rasplavlenykh Solei I.," p. 342, ONTI, Leningrad-Moscow (1937).
9. A. Aten, *Z. phys. Chem.*, **78**, 1 (1912).
10. W. Biltz and W. Klemm, *Z. anorg. allgem. Chem.*, **152**, 267 (1926).

11. K. Matiasovsky, S. Ordzovensky, and M. Malinovsky, *Chem. zvesti*, **17**, 839 (1963).
12. J. D. Edwards *et al*, *This Journal*, **99**, 527 (1952).
13. E. W. Yim and M. Feinleib, *ibid.*, **104**, 622, 627 (1957).
14. K. Arndt and W. Kalass, *Z. Elektrochem.*, **30**, 12 (1924).
15. K. P. Batasev, *Legkije metally*, **10**, 48 (1936).
16. A. I. Belyaev, "Fiziko-khimicheskie Processy pri Elektrolize Alyuminia," Metallurgizdat, Moscow (1947).
17. A. Vajna, *Alluminio*, **19**, 215 (1950).
18. W. B. Frank and L. M. Foster, *J. Phys. Chem.*, **61**, 1531 (1957).

The Oxidation of Aluminum by Carbon Dioxide in the Presence of Cryolitic Electrolyte

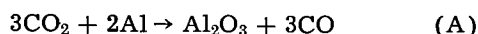
Sigbjorn Gjerstad and B. J. Welch¹

Reduction Research Division, Reynolds Metals Company, Sheffield, Alabama

ABSTRACT

The oxidation of aluminum by carbon dioxide in the two layer liquid system cryolitic melt/molten aluminum has been investigated in the temperature range 965°-1050°C. Velocities of the oxidation reaction at 980°C are compared for variations in oxygen potential, depth of electrolyte, the thermodynamic activity of aluminum, and mass transfer conditions. The comparison of the results show that the rate-determining step for the oxidation reaction is the mass transfer of the dissolved metal from the melt/metal interface to the melt/gas interface.

Increasing application of anode gas analysis as a technique for instantaneous determination of current efficiency for metal production in an alumina reduction cell (1) has focused attention on the reactions that contribute to the reduced metal production. While there have been many different reactions postulated for the metal loss (2), it is generally accepted that reaction between carbon dioxide and aluminum dissolved or suspended in the electrolyte is the most important metal consuming reaction. Indeed, all the equations (3, 4) derived to correlate anode gas composition with current efficiency have assumed that the reaction



account for all the metal loss. This assumption is supported (although not validated) by long-term metal and alumina inventories which invariably show that more than 99% of the metal in alumina is recovered (5). This correlation shows that most of the metal lost is reoxidized and returns to the reduction cell as alumina or aluminum derivatives.

While the mechanism of the reaction between CO₂ and aluminum dissolved in cryolite has received attention earlier, none of the independent sets of results (6, 7) have been in agreement. Abramov *et al.* (6) observed a dependence on depth of electrolyte using a metal loss technique to study the mechanism of the reaction. Revazyan (7) criticized these results because of the errors involved in Abramov's technique for measuring the rate of reaction. Using a gas analysis technique, Revazyan re-investigated the mechanism of oxidation of Al dissolved in the cryolitic melt. His results led him to the conclusion that the velocity of solvation of Al by the electrolyte is the rate-determining step in the oxidation reaction. However, Grjotheim, Heggelund, Krohn, and Motz-

feldt (8) have rightfully claimed that there might be other mechanisms, since Forland, Storegraven, and Urnes (9) and also Haupin (10) have shown that there is an appreciable solubility of CO₂ in the cryolitic electrolyte. The experimental technique used by Revazyan (7) is also subject to criticism since the method he employed to determine the rate of metal loss was to measure the total amount reacted in a given time for reaction. Such a method does not allow for either presaturation of the electrolyte with the metal or the case where the two liquids have had no time to equilibrate at all. Therefore, one can also be skeptical of the mechanism proposed by Revazyan.

This doubt is also supported by results of Pruvot (11), and also of Nozaki and Miyanchi (12). The observed increase in current efficiency with anode to cathode distance (11) in operating reduction cells is more consistent with the rate-determining step being mass transfer than Revazyan's proposed rate of solution. Nozaki and Miyanchi (12) analyzed electrolyte layers between the anode and the cathode in a reduction cell that had been suddenly closed down. They found that the concentration of free metal near the anode was zero, but the concentration gradually increased to a maximum value at the cathode-melt interface. Because of the resulting inherent uncertainty about the mechanism of the re-oxidation reaction in aluminum reduction cells a re-investigation of the mechanism is warranted. The results of our re-investigation are reported in this paper.

Experimental

The method employed to study the rate of the reaction in this study was to measure the change in composition of carbon dioxide that had been passed, at a controlled flow rate, over a confined surface area of reacting melt. The design of the apparatus

¹ Present address: School of Chemical Technology, The University of New South Wales, Kensington, N.S.W., Australia.

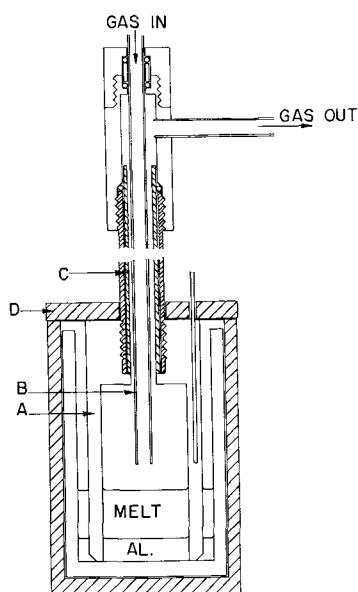


Fig. 1. Schematic view of reaction assembly. (a) Boron nitride hood; (B) alumina gas inlet tube; (C) alumina gas outlet tube; (D) graphite lid.

constructed was based on that used by Revazyan (7), but in this case the apparatus was constructed of fused recrystallized alumina and boron nitride to minimize side reactions with the CO_2 . While the boron nitride undergoes a reaction that also yields CO, this reaction is slow, and it can be compensated for as the exact velocity of it can be simultaneously determined from the nitrogen analysis. The melt-containing crucible was also of BN. The pertinent portions of the apparatus are illustrated in Fig. 1. The boron nitride hood (A) confined the reacting carbon dioxide to a fixed surface area of electrolyte. The alumina tube (B) used to bring the gas to the reacting zone was positioned so that its orifice was 1 cm above the surface of the electrolyte. The gas emerging from the reaction zone passed through an impervious tube (C) larger than, but concentric with, the gas inlet tube. This outlet tube was sealed to the boron nitride hood with alumina cement. Fluctuations in the melt level (due to occasional pressure differentials between the reacting zone and the furnace chamber) were minimized by the damping effect induced by having the bottom of the hood against the bottom of the crucible, and also by the close fitting graphite lid (D). An atmosphere of argon was maintained in the sealed Inconel furnace tube at all times.

A vertical tube Kanthal resistance furnace was used to heat the apparatus. The thermal gradient of this furnace was adjusted so that the melt surface was $2^\circ\text{--}3^\circ\text{C}$ hotter than the metal pad at the bottom of the crucible. Temperature control was maintained by a Kelvin Hughes Mark IV proportional action controller and was better than $\pm 0.5^\circ\text{C}$ during a run.

The reacting gas flow rates were both controlled and measured by calibrated Fisher and Porter Rotameter flow meters. A Loenco 15B gas chromatograph was used to analyze the reacting gas compositions. The chromatograms were recorded with a L&N

AZAR Speedomax G Recorder fitted with a Disc Instrument Company integrator. The materials used for the electrolyte were Natural Greenland cryolite, A.R. grade calcium fluoride and alumina, and C.P. aluminum fluoride. All were used without further purification. An electrolyte composition of 7.5 w/o (weight per cent) Al_2O_3 ; 7.5 w/o CaF_2 with the balance being NaF and AlF_3 in the weight ratio of 1.45 to 1 was used for all measurements in this study. The CO_2 was analyzed Mathieson grade cylinder gas.

Procedure.—The required weights of electrolyte and aluminum were placed in the crucible and the apparatus assembled in the furnace in a manner similar to that represented in Fig. 1. The necessary weights of the aluminum and also of the premixed and prefused electrolyte were determined for the required depths of each. For most of the measurements a 2 cm depth of electrolyte (95.7g) and 1 cm of metal (52.4g) were used.

The furnace was then heated to the required temperature, and when the metal and electrolyte were molten the crucible was raised until its base was against the lower end of the boron nitride hood. During this procedure, an inert atmosphere was maintained within the furnace and apparatus.

At thermal equilibrium the reaction was started by flowing carbon dioxide through the reaction zone. Samples of the off gas were chromatographed at five minute intervals. An integral gas sampling valve was used to sample the gas from its stream and introduce the sample to the chromatographic columns.

For a given set of conditions reaction rate measurements (as given by off gas compositions) were continued until a constant rate was observed over at least a 30-min period.

Results

At constant temperature and electrolyte depth, measurements were made for the determination of reaction velocity when the CO_2 flow rate, its partial pressure, the thermodynamic activity of the aluminum, and the time of contact between metal and electrolyte were each independently varied. An experiment was also conducted where the thermal gradient was reversed to introduce different mass transfer conditions. The effect of the depth of the electrolyte between the metal and reacting gas was also studied. Results were also obtained for the reaction velocity at different temperatures between 969° and 1049°C .

CO_2 flow rate and partial pressure.—For these studies an electrolyte depth of 2.0 cm was maintained over a 1 cm depth of molten aluminum. The partial pressure of CO_2 was varied by using gas mixtures. Premixed cylinders of CO_2 and CO (of known composition) were used for this purpose. Rate measurements were made at four different flow rates and three different partial pressures of CO_2 . The experimental results are summarized in Table I.

Effect of reduced aluminum activity.—Since copper alloys with aluminum but does not dissolve in the cryolitic electrolyte or react with it (13), use

Table I. Velocity of the reaction between CO₂ and dissolved aluminum as a function of CO₂ flow rate and its partial pressure

CO ₂ pressure, atm	CO ₂ flow rate, moles CO ₂ /min, × 10 ³	Temp, °C	Reaction rate, moles CO ₂ cm ⁻² min ⁻¹ , × 10 ⁶
1.00	0.665	980	7.47
1.00	1.052	980	7.75
1.00	1.763	976	7.58
1.00	2.741	978	7.64
0.54	0.424	980	7.10
0.28	0.277	1005	8.23

was made of copper aluminum alloy to reduce the thermodynamic activity of the aluminum. Measurements were made with a 50 mole % Al alloy, and the results compared with those obtained for pure aluminum. The volumes of electrolyte and metal used were the same as for the above studies. Three separate measurements were made at 980°C for the 50 mole % Al alloy. The velocity of reaction of CO₂ with the dissolved aluminum (or reacting species) was found to be $4.40 \pm 1.5 \times 10^{-6}$ moles CO₂ cm⁻² min⁻¹, as compared to $7.60 \pm 0.64 \times 10^{-6}$ moles CO₂ cm⁻² min⁻¹ for pure aluminum.

Effect of time of contact between metal and bath.—The velocity of the reaction between CO₂ and dissolved aluminum was measured as a function of time for all experiments. A typical plot of the measured reaction velocity vs. time is given in Fig. 2. In that experiment there was a lapse of approximately 120 min between melting the electrolyte and impressing the CO₂. The form of the curve indicates a definite dependence on time. To study this variable further reaction velocities were measured as a function of time after various times of contact, between melt and metal before the reacting gas was impressed. These results are tabulated in Table II. All the results reported in this table were measured at $980^\circ \pm 5^\circ\text{C}$.

Effect of thermal convection.—The velocity of the reaction as a function of time when there is thermal convection within the electrolyte is compared with the curve obtained in the absence of thermal convection but otherwise under the same conditions in Fig. 3. Thermal convection was introduced to the

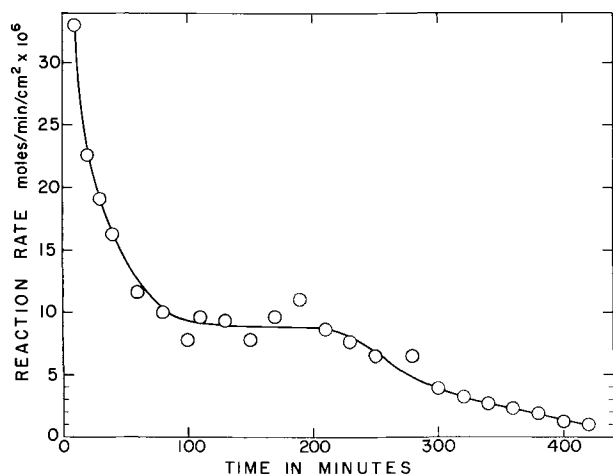


Fig. 2. Velocity of oxidation of dissolved aluminum vs. time at 980°C for 2 cm of electrolyte between pure metal and gas phases.

Table II. Velocity of the reaction between CO₂ and dissolved aluminum at 980°C as a function of time, and time of contact between aluminum and electrolyte

Time of contact before reaction, min	Time of reaction at measurement, min	Velocity of reaction, mole CO ₂ cm ⁻² min ⁻¹ , × 10 ⁶
0	10	3.13
0	50	3.60
0	100	7.00
0	200	7.11
0	250	2.51
40	5	9.0
80	5	12.5
300	5	88.6

apparatus by altering the furnace thermal gradient so that the surface of the melt was 10°C colder than that at the melt-metal interface. During experimentation the temperature of the melt-metal interface was maintained the same as the previous experiments.

Effect of depth of electrolyte.—Experiments were carried out with melt layer heights of 1, 2 and 4 cm of electrolyte while all other variables were maintained constant. Equilibrium velocities measured are represented in Fig. 4.

Temperature dependence of reaction velocity.—Reaction velocities were measured at different temperatures in the range 969°–1049°C. Results obtained for a 2 cm electrolyte depth are illustrated in Fig. 5.

Discussion

The results obtained in this study show that the velocity of the reaction is independent of the flow rate and partial pressure of CO₂ but dependent on the thermodynamic activity of aluminum. Therefore, if the reacting carbon dioxide is dissolved in the electrolyte, its rate of solution is not rate determining, and the rate of reaction is dependent on the concentration of dissolved aluminum at the reaction zone. From this, the rate of reaction could be controlled by the rate of solution of the dissolved aluminum or reacting species, the mass transfer of the reducing species from the metal-electrolyte interface to the reaction zone, or its saturation solubility. The last possibility can be rejected because of the observed dependence of velocity of reaction on the

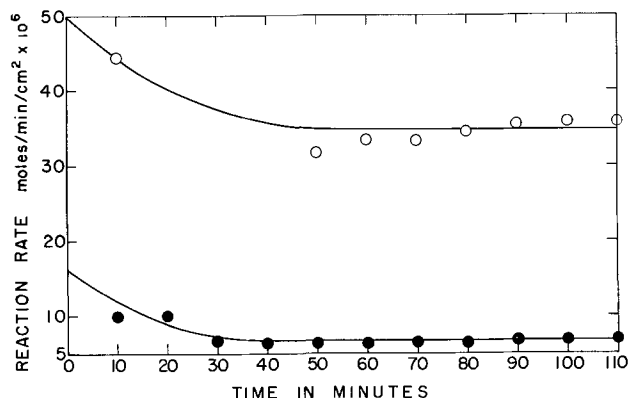


Fig. 3. Reaction rate as a function of time for different mass transfer conditions. ●, Mass transfer by diffusion only; ○, thermal convection in melt.

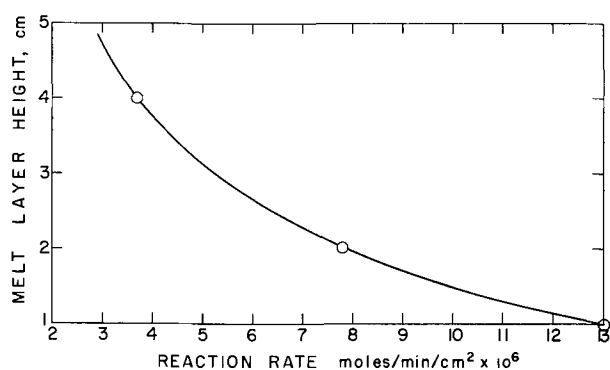


Fig. 4. Variation in steady-state reaction rate with depth of electrolyte between pure metal and gas phases.

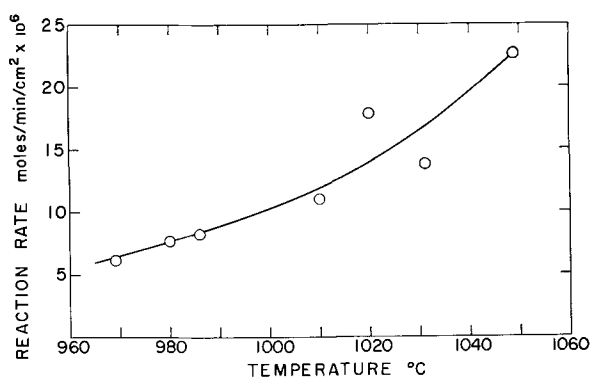


Fig. 5. Steady-state reaction rate vs. temperature for a 2 cm melt layer separating the pure aluminum and the CO₂.

time of contact between metal and molten electrolyte. Similarly, it can be seen that the rate of reaction is controlled by mass transfer of the reducing species from the melt-metal interface to the reaction zone. This is consistent with both dependence of reaction velocity on the height of electrolyte and also the increased reaction rate when there is thermal convection in the apparatus. In the latter case, the steady-state reaction velocity increased from 7.6×10^{-6} moles CO₂ cm⁻² min⁻¹ to 33×10^{-6} moles CO₂ cm⁻² min⁻¹ as a result of the thermal convection introduced by having a 10°C temperature gradient.

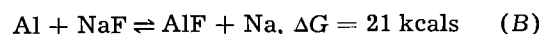
The observed rate-determining step is in disagreement with the mechanism by Revazyan (7), but is consistent with results of Abramov *et al.* and supported by the work of Nozaki and Miyanchi (12) and also of Pruvot (11).

From these results the mechanism of the reaction will involve the following steps: (a) solvation of the metal by the melt, or reaction of metal with melt (fast); (b) transfer of the dissolved metal, or reacting species, from the melt-metal interface to, or near the melt-gas interface (rate-determining step); (c) reaction with the gas or dissolved gas (fast); (d) if the oxidized species is other than aluminum, then we would have a disproportionating reaction between the melt and the oxidation product.

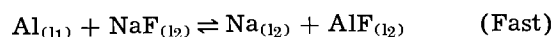
There still exists some uncertainty about the first step of the mechanism, *i.e.*, the solvation of the aluminum by the cryolitic melt. It has been pro-

posed that aluminum dissolves either as a pyrosol, or it undergoes thermodynamic reaction with the electrolyte to form a new species (such as monovalent aluminum ions or sodium). The latter possibility is favored by measurements of current efficiency as a function of electrolyte composition (14) and also Revazyan's determination of the relative extents of reaction between CO₂ and the reacting species when the aluminum fluoride content of the electrolyte is varied (7). In each study, a dependence on electrolyte composition was observed.

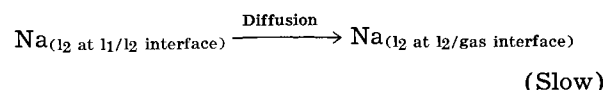
Since the mass transfer in this experimental study is by diffusion, the velocity of the reaction being studied can be correlated with the concentration of the reacting species at the melt-metal interface (by Ficks laws of diffusion). Therefore, from this, the observed dependence on electrolyte (7, 14), and applying the law of mass action, arguments can be forwarded to support the chemical reaction (or subvalent compound) theory. While one can write numerous possible reactions between the melt and metal, the following two are the most favored thermodynamically at the reaction temperature



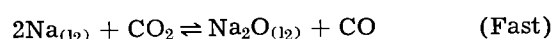
In spite of the small equilibrium constants that these reactions would have there is some experimental evidence to support them. Haupin (10) and also Schadinger (15) analyzed condensates found above molten cryolite and aluminum in an inert atmosphere. In both investigations, sodium and aluminum were detected, the amount of aluminum being in excess of that expected from normal vapor losses. The cryolite dissociation mechanism proposed by Frank and Foster (16), the above observations, and the observed decrease in velocity of reaction between CO₂ and the reacting species by increasing the aluminum fluoride content of the electrolyte (7, 13) all indicate that reaction (B) rather than (C) is the prevalent one for the solvation of aluminum. As a result there are two oxidizable species and the measured reaction velocities are for oxidation of both species. Formulating the reaction mechanisms according to reaction (B) and the steps of the reaction we have



thence



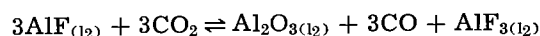
At melt/gas interface



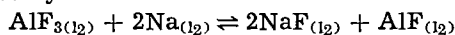
followed by



Alternately, if velocity of oxidation of Al⁺ is greater than for sodium, the third step could be



followed by



Besides these, several other possibilities could be formulated, but all equations would follow the same pattern, and the slow step would be governed by the mass transfer of dissolved reducing species.

No attempt has been made to calculate the activation energy for the rate-determining step from the temperature dependence studies (Fig. 5 of results). This is because the solubility of the aluminum, by reaction with the electrolyte, will be strongly temperature dependent, and therefore we have two variables effecting the velocity of reaction. Any activation energy derived under these conditions would be fallacious.

The variation of reaction velocity with time as illustrated in Fig. 2 shows three distinct zones. The first two zones, high reaction velocity due to pre-saturation of electrolyte, followed by a constant reaction velocity due to steady-state conditions, are readily understood, but the subsequent slow decrease in reaction velocity warrants further comment. From observations of electrolyte and apparatus immediately after experimental measurements, it was concluded that the decrease in reaction velocity after reaching steady-state conditions was due to a build-up of alumina at the melt-gas interface. In experiments where this decrease was observed, the surface of the melt appeared to have undissolved particles, while in experiments where there was considerable reaction, a high alumina content crust formed inside the reaction hood in the zone of the electrolyte surface.

Acknowledgment

The authors wish to thank Reynolds Metals Company for permission to publish this work.

Manuscript received Dec. 20, 1963.

Any discussion of this paper will appear in a Discussion Section to be published in the June 1965 JOURNAL.

REFERENCES

1. J. D. Hamlin and N. E. Richards, *Proc. AIME Symposium on Extraction of Aluminum*, John Wiley & Sons, Inc., New York, in press.
2. V. P. Mashovets and R. V. Svoboda, *J. Appl. Chem. U.S.S.R.*, **31**, 2210 (1958).
3. T. G. Pearson and J. Waddington, *Discussions Faraday Soc.*, **1**, 307 (1947).
4. T. R. Beck, *This Journal*, **106**, 710 (1959).
5. T. G. Pearson, "Chemical Background of the Aluminum Industry," Roy. Inst. Chem. Lect. Mono. Repts., No. 3 (1955).
6. G. Abramov, M. Vetyukov, *et al.*, "Theoretical Basis of Electrometallurgy of Aluminum," Moscow (1953).
7. A. A. Revazyan, *Tsvetnye, Metally*, **32** [8], 65 (1960).
8. K. Grojtheim, P. Heggelund, C. Krohn, and K. Motzfeldt, *Acta. Che. Scand.* (1960).
9. T. Forland, H. Storegraves, and S. Urnes, *Alluminio*, **22**, 631 (1953).
10. W. E. Haupin, *This Journal*, **107**, 232 (1960).
11. E. Pruvot, *Alluminio*, **22**, 721 (1953).
12. H. Nozaki and K. Miyanchi, *J. Chem. Soc. Japan (Ind. Chem. Sec.)* **51**, 3 (1948).
13. K. Grojtheim: "Contribution to the Theory of Aluminum Electrolysis," *Kgl. Norske Videnskabs Selskabs, Skrifter* 1956, No. 5.
14. Gy. Szeker, *Acta Technica*, **X**, 1-2 pp. 91 (1954).
15. R. R. Schadlinger, *Alluminio*, **22**, 691 (1953).
16. W. B. Frank and L. M. Foster, *J. Phys. Chem.*, **64**, 95 (1960).

Studies on Alternating Current Electrolysis

V. Double Layer Resistance and Electrode Area as Factors in Electrode Kinetics

Donald D. Bump¹ and A. Edward Remick

Department of Chemistry, Wayne State University, Detroit, Michigan

ABSTRACT

Impedance measurements were made on an a-c electrolytic cell composed of platinum electrodes in poised aqueous solutions of ferrocyanide and ferricyanide containing potassium sulfate as supporting electrolyte. Empirical equations were developed for the polarization resistance and capacitance of the supporting electrolyte as functions of frequency, expressing each as the sum of frequency-dependent and frequency-independent terms. The frequency-dependence of the polarization resistance proved it to be nonfaradaic in origin and hence probably a double-layer resistance. The frequency-independent term of the capacitance equation was shown to be altered by addition of the ferrocyanide-ferricyanide system, contrary to the assumption usually made. This fact was employed in altering the Bockris-Conway "v-method" of separating the faradaic and double-layer admittances. This altered method proved to be more satisfactory than the "classical method." The Bockris-Conway theory of the double-layer admittance was shown to be in accord with the experimental data in certain regards, but the value of the relaxation time calculated from these data was found to be of a different order of magnitude than that to be expected from the theory. An equation for the calculation of the rate constant for electron transfer at an electrode, without the necessity of knowing the electrode area, was derived. Values of rate constants calculated from this equation compared favorably with those of Randles and Somerton. Measurements made on a series of solutions of different depolarizer concentrations but constant ionic strength gave evidence that depolarizer adsorption is a disturbing influence only in solutions of concentrations less than 0.005*N*.

It is important to fashion an adequate equivalent circuit for an alternating current electrolytic cell in order that the faradaic parameters can be calculated. Grahame (1) has presented equivalent circuits for several "classes" of compounds. These circuits seem to be satisfactory in the absence of specific adsorption when a dropping mercury electrode is used.

The use of a solid measuring electrode introduces complications. A double layer resistance (R_d) is introduced and dispersion of both R_d and C_d (the double layer capacitance) is observed (1-11). The magnitudes of R_d and the two dispersions are greater for rough than for smooth surfaces (2, 3). C_d has been reported as dependent on (12) and, to a first approximation, independent of (8) the shape of the solid electrode. In order to represent these observations in terms of the equivalent circuit, the double-layer branch was modified by Bockris and Conway (5) by shunting C_d with a resistance, R_d .

Another complication arising with solid electrodes is the occurrence of the well-known resistance polarization. Grahame's equivalent circuit was modified to take this factor into account by Remick and McCormick (13), who added an "electrode layer resistance" (R_L) in series with the electrolytic resistance (R_T). It has been found recently that non-uniformity of the electric field between the elec-

trodes introduces a spurious resistance which appears to be added to R_T (14). It may be that this factor contributed to R_L . Fortunately, the usual method for measuring R_T will in reality give $R_T + R_L$ so that they are subtracted together, and separate measurements of the two need not be made. In this paper, therefore, the values of R_T are to be understood as including those of R_L , if any.

The obvious sequel to the establishment of the equivalent circuit is the establishment of the mathematical theory of each of the circuit elements. This problem seems to have been solved for the faradaic branch of the circuit for the simple mechanism consisting merely of a bidirectional electron transfer step in the absence of specific adsorption (1).² It would be beyond the scope of this paper to summarize the progress made in dealing with other mechanisms. The corresponding problem for the double-layer branch of the circuit has been reviewed frequently in recent years (6, 12, 15). The most recent contribution to this problem has been made by Bockris *et al.* (16, 5). They advance the theory that the relaxation time of water dipoles adsorbed on an electrode approaches that of ice and hence falls within the frequency range of measurement. The result is that these dipoles do not respond fully to the alternating potential and give rise to a frequency-dependent phase distortion which can be analyzed into capacitive and resistive

¹ Present address: Institute of Paper Chemistry, Appleton, Wisconsin.

² See ref. (1) for a summary of earlier work done on this problem.

components (R_d and C_d), both frequency dependent. This theory will be discussed more fully in the Discussion Section.

It is a well-known fact that the accurate determination of kinetic parameters of reactions at electrodes demands an accurate determination of the true electrode area. We will show in this report how electrode area can be eliminated from such calculations. We will also describe work done to test the use of the Bockris-Conway equivalent circuit and the adequacy of their theory of the double-layer resistance.

Experimental

Electrolytic cell.—An electrolytic beaker fitted with a rubber stopper served as the cell. The electrodes were sealed into glass tubing so that only one face of each came in contact with the solution. They were circular platinum disks 0.7 cm in diameter, each supported vertically and rigidly. They were parallel to each other 1.4 cm apart. Purified nitrogen gas was passed through the solution in the cell.

Cleaning electrodes.—The electrodes were cleaned by a modification of the method previously used (13). They were made alternately anodic and cathodic in an aqueous solution of potassium hydroxide, potassium cyanide, and potassium carbonate. A current of 1 amp passed through the cell for 15 min in each direction. Then the current was reduced to 0.6 amp for 10 min in each direction. This reduction of current and time was continued over a 2-hr period, after which the electrodes were tied together and made cathodic with respect to a third platinum electrode. A current of 0.1 amp was then passed through the cell for 10 min. The entire cell assembly was then washed three times with distilled water and twice with conductivity water. It was then filled with conductivity water and allowed to soak for at least 30 hr. The cell was then rinsed with the experimental solution, filled, allowed to stand for an hour, rinsed again, and finally filled for the test.

Chemicals and solutions.—Potassium sulfate, potassium ferrocyanide, and potassium ferricyanide of A.C.S. specification stock were recrystallized from water.

Nitrogen for purging the solutions was purified by passing oil-pumped nitrogen over hot copper, then through a concentrated solution of sodium hydroxide, and finally through a wash bottle containing the sample to be tested.

Temperature.—All experiments were carried out in a water bath at a temperature of $30.5^\circ \pm 0.05^\circ$.

Measuring bridge.—The bridge is shown in Fig. 1. The ratio arms were formed by two 1000 ohm ($\pm 0.25\%$) a-c resistors, R_1 and R_2 , interchangeable through switch S_1 . The resistor R_p (a series combination of a General Radio Company types 4132-K and 510 AA decade resistors, over-all accuracy $\pm 0.05\%$) and the capacitor C_p (a parallel combination of a General Radio type 219 M decade, 1,110 μf , a calibrated Cornell-Duiliier decade, 10 μf in 1 μf steps, and a calibrated L&N air capacitor having a continuous range down from 0.001 μf) constituted the balancing arm.

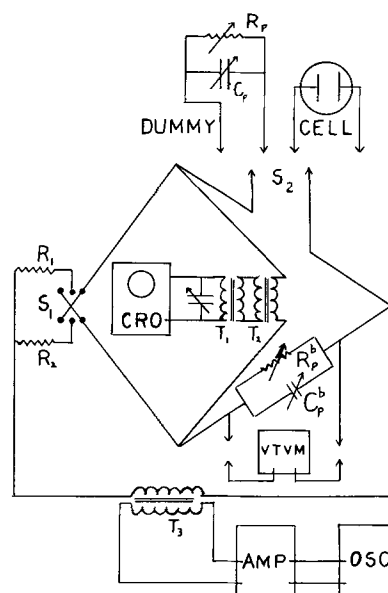


Fig. 1. Electrical circuit for impedance bridge and associated apparatus.

Balance was observed by a Dumont type 304 H cathode ray oscilloscope (C.R.O.). This was isolated from the bridge with a General Radio type 578-B shielded transformer (T_1). T_2 was a General Radio type 941-A toroidal transformer. The over-all voltage amplification by T_1 and T_2 was 64 to 1. A variable capacitor connected across the input of the C.R.O. was tuned to resonance with the bridge frequency below 3000 cps in order to cut down on the harmonics induced by nonlinearity in the cell.

The a-c source was a Jackson model 652 audio frequency oscillator driving a push-pull amplifier.

A substitution technique was used. Switch S_2 made it possible to substitute a dummy for the electrolytic cell. The dummy components, R_p and C_p , were respectively a General Radio type 602-J decade resistance box and type 219-M decade capacitor.

The potential across the cell at balance was maintained at 20 mv as read on a Ballentine model 300 electronic voltmeter (VTVM), which was connected across the balance arm at balance. This reading would be the same as though the VTVM had been connected across the cell, and it happened to be more convenient to make the connection across the balance arm.

The bridge was checked against the parallel combination of a 100 ohm standard resistor (type 500-D) and a 0.2 μF standard capacitor (type 505-V), both manufactured by the General Radio Company. The bridge reproduced the standards to within 0.01 ohm and 0.0003 μF from 150 to 6000 cps. At 10,000 cps reproduction was 0.05 ohm and 0.002 μF .

Square wave circuit.—As a matter of incidental interest, we wished to devise an oscillographic square wave method for measuring the electrolytic resistance, R_T . The circuit used is shown in Fig. 2. The square wave generator was a Dumont electronic switch, model 185-A. R_3 was an 80,000 ohm, 3-watt resistor, C_1 a 10 μF capacitor, and R_c a General Radio type 602-J resistance box. The signal traces on the oscilloscope screen were photographed with a

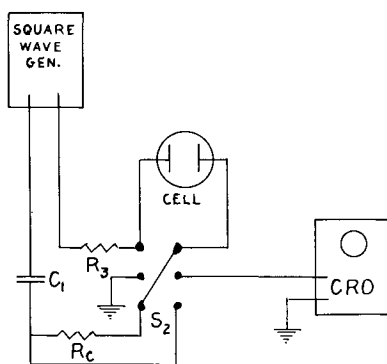


Fig. 2. Square wave circuit

Dumont oscillographic camera. These traces were from the cell when the switch S_2 was in the up position and from the calibrating resistance R_c when in the down position. Letting D_c represent the length of the vertical trace (*i.e.*, the invisible part of it) when the switch is in the down position, and D_x the length for the up position, R_T can be calculated from the equation

$$R_T = (D_x/D_c)R_c$$

Experimental data.—Bridge measurements of R_p with platinized electrodes and of R_p and C_p with smooth platinum electrodes were made on a series of aqueous solutions containing potassium sulfate as supporting electrolyte and equimolar concentrations of potassium ferrocyanide and potassium ferricyanide as depolarizer. All solutions were of the same total ionic strength, *viz.*, 0.3402 mole/liter. The decision to hold the ionic strength constant, despite the disapproval of Breiter, Kleinerman, and Delahay (17), was dictated by the experimental results of Remick and McCormick (13) who found that, at a given frequency and temperature, the faradaic capacitance of a poised solution is a function of the ionic strength of the solution, *per se*, and the depolarizer concentration, C . Since we wished to study the effect of varying C , it was necessary to hold the ionic strength constant. Representative results are given in Table I and II. The concentrations there listed are the equal concentrations of ferricyanide and ferrocyanide. The resistance values in Table I have been converted into their series equivalents. All measurements were made at a cell potential (rms) of 0.020v. This value was chosen because it was high enough to give good bridge sensitivity, low enough to minimize sufficiently the second harmonic distortion, and because measurements on 0.005N and 0.001N solutions at frequencies of 300, 1000, and 4000 cps showed no difference in the balance points of the bridge when the potential was varied from 0.005 to 0.100v.

Table I. Dispersion of series resistance, R_s , at platinized platinum electrodes

Solution	Frequency in cps			
	200	500	1000	3000
K_2SO_4 only	ohm	ohm	ohm	ohm
0.0001N	42.40	42.19	42.14	42.02
0.0001N	42.64	42.29	42.18	42.16
0.0005N	42.87	42.64	42.48	42.40
0.001N	43.18	42.92	42.84	42.77
0.005N	46.06	45.84	45.82	45.72

Table II. Bridge data with smooth platinum electrodes

Solution	Freq, cps	R_p , ohms	C_p , μF	R_s^* , ohms	$X_s^* = 1/\omega C_s^*$, ohms
K_2SO_4 only	150	137.5	10.56		
	200	98.8	8.40		
	250	80.0	6.68		
	300	70.2	5.43		
	350	64.0	4.52		
	400	59.4	3.76		
	500	54.2	2.70		
	600	51.30	2.04		
	800	47.95	1.27		
	1000	46.24	0.856		
	1500	44.51	0.415		
	2000	43.69	0.248		
	2500	43.26	0.158		
	3000	43.00	0.1123		
	3500	42.88	0.0840		
4000	42.79	0.0650			
5000	42.68	0.0413			
6000	42.60	0.0277			
8000	42.40	0.0137			
10,000	42.25	0.0064			
0.005N	150	51.46	1.53	3.21	1.875
	200	50.88	1.18	3.00	1.72
	250	50.52	0.781	2.84	1.315
	300	50.24	0.635	2.75	1.23
	350	49.99	0.527	2.665	1.145
	400	49.79	0.446	2.64	1.145
	500	49.42	0.348	2.465	0.985
	600	49.10	0.282	2.375	0.93
	800	48.70	0.204	2.29	0.84
	1000	48.36	0.158	2.21	0.79
	1500	47.80	0.097	2.105	0.625
	2000	47.42	0.0667	1.97	0.55
	2500	47.16	0.0481	1.855	0.385
	3000	46.93	0.0367	1.73	0.38
	3500	46.77	0.0294	1.69	0.335
4000	46.66	0.0194	1.615	0.29	
5000	46.50	0.0194	1.495	0.15	

The values of the faradaic series resistance (R_s^*) and reactance (X_s^*) listed in Table II were calculated from the directly measured values, R_p and C_p , by the standard methods of circuit analysis following the steps indicated diagrammatically in Fig. 3. Step 4 involves a change from parameters for the whole cell to those for half of the cell. The details of calculation beyond step 4 will be given later. R_T for each solution was obtained by extrapolation of plots of R_s vs. $\omega^{-1/2}$ to infinite frequency. R_T values are listed in Table III. Also listed in Table III are the square wave data.

Discussion

Among the methods which have been used for separation of the components of the double layer

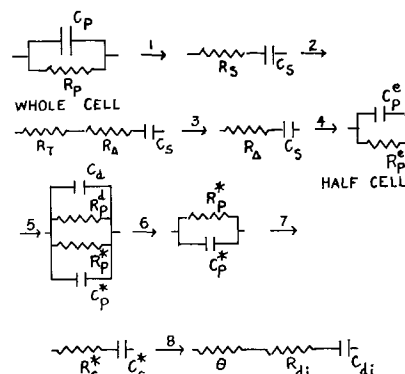


Fig. 3. Diagram of steps required to calculate Faradaic parameters

Table III. Values of R_T

Method: Electrodes: Solution	Bridge Platinized, ohm	Square wave Platinized, ohm	Square wave Smooth, ohm
K ₂ SO ₄ only	41.98	41.6	42.0
0.0001N	42.05	42.5	42.1
0.0005	42.35	42.9	41.8
0.001	42.72	42.9	42.8
0.005	45.68	45.7	45.3
0.010	49.38	—	—

from the rest of the circuit are the following three.

1. The "classical method" (5). R_d is nonexistent, and C_d is frequency-independent. Capacitance measurements are made at various frequencies on the supporting electrolyte alone and extrapolated to infinite frequency. The extrapolated value is taken as C_d . This extrapolation is meant to eliminate the influence of extraneous faradaic processes. The C_d value thus obtained is assumed to be unchanged by the addition of depolarizers to the supporting electrolyte.

2. R_d is nonexistent, and C_d is either frequency-dependent or it is frequency-independent and accompanied by a pseudocapacitance arising from an extraneous faradaic process associated with the supporting electrolyte. This particular pseudocapacitance is assumed to persist unchanged after depolarizer is added to the supporting electrolyte as is also the double-layer capacitance. The over-all capacitance of the supporting electrolyte alone is measured as a function of the frequency and its value at each frequency is subtracted from C_p^e (the equivalent parallel capacitance of the electrode layer) measured at the same frequency for the depolarizer solution (13).

3. The " ν Method" (5). The equivalent circuit used is that pictured in Fig. 3. Both R_d and C_d exist and are frequency dependent. They are calculated from measurements on the supporting electrolyte alone at a number of frequencies, and it is assumed that addition of depolarizer to the supporting electrolyte has no effect on these values. Each value is valid only at a given frequency.

The first method, although usually reliable for mercury electrodes, was rejected by Bockris and Conway (5) because they observed that the resistance and capacitance of the copper-sulfuric acid interface showed dispersion under conditions where a faradaic process is very unlikely and also because plots of R_s^* and C_s^* (obtained with copper electrodes in a sulfuric acid solution of cupric sulfate) against $\omega^{-1/2}$ were definitely more linear when the third method was used instead of the first. These dispersion data appear to be of the E_c -control, E_c -dispersion type³ and were carried out at frequencies

³ We here use a system of nomenclature previously introduced (10) and expanded by one of us. "X-control, Y-dispersion" means that the electrochemical parameter X was "controlled" (held "constant") while making the measurements at any one frequency and that Y was held constant when the frequency was changed. X and Y may be E, I, Q, etc., (respectively, meaning voltage, current and the number of coulombs per half cycle, etc.). Subscripts may be used to specify exactly the part of the equivalent circuit involved. Thus the subscripts c, d, f, etc., refer, respectively, to the whole cell, the double layer branch or the branch through which only faradaic current flows, etc. Symbols may also be printed over X or Y, thus: \bar{I} would mean a sinusoidal current of constant amplitude, and \bar{I} would mean direct current.

not exceeding 1000 cps. The mathematical theory of the faradaic admittance on which this linear dispersion relationship is based (1) assumes \bar{E}_f -dispersion with \bar{E}_f -control and, if d.c. is superimposed, \bar{E}_f -control also.

Satisfactory linear dispersion curves also obtain when the data of Remick and McCormick (13) are plotted. These data were obtained using platinum electrodes with the ferrocyanide-ferricyanide system in aqueous potassium sulfate solution; the second method of calculation was employed and the

measurements were of the \bar{I}_c -control, Q_c -dispersion type. Randles and Somerton (18) also obtained linear dispersion curves for this same system employing a method closely similar to the first method.

The examples just quoted seem to suggest that any of these three methods may be used to separate the faradaic parameters from the cell data although admittedly the work of Bockris and Conway involved more elaborate precautions than were employed by the others and hence deserves more consideration. From their observations, the first method is suspect. However, it should be pointed out that the cyanide electrode "cleaning" process used in our laboratory apparently leaves the electrodes reproducibly "dirty" and probably buffered against trace impurities. Under these conditions, it is doubtful that pre-electrolysis would be of any value, and in any event only the potassium sulfate solution could be preelectrolyzed. It is no doubt true that exceedingly great purity of materials, although necessary if the objective is the absolute values of rate constants, is not necessary to establish basic laws. This is borne out by the large number of such measurements that yield the theoretical linear relation between the faradaic parameters and $\omega^{-1/2}$.

With these ideas in mind, let us turn to the mathematical analysis of our data with the idea of testing the Bockris-Conway theory and equivalent circuit.

In the determination of the electrolytic resistance, R_T , we employed the standard procedure of platinizing the electrodes. The data in Table I show a slight dispersion, however, probably indicating that the faradaic impedance was not completely eliminated. This resistance data was therefore plotted *vs.* $\omega^{-1/2}$ and extrapolated to infinite frequency to give the "true" values of R_T listed in Table III under "Bridge" method.

The values of R_s obtained by the square wave method would be expected to be free of faradaic influence since the vertical part of the square wave path corresponds nearly to infinite frequency. Thus these R_s values should correspond to R_T . Comparison of the values in Table III indicates that this is true within the limit of error inherent in the oscillographic readings whose uncertainty ranges from about ± 0.2 ohm for the most dilute solution up to about ± 0.4 ohm for the most concentrated. This test was made merely to assure ourselves that the oscillographic method (which would be the only one applicable if distorted waves were being studied) is reliable. It is to be expected, as observed, that plati-

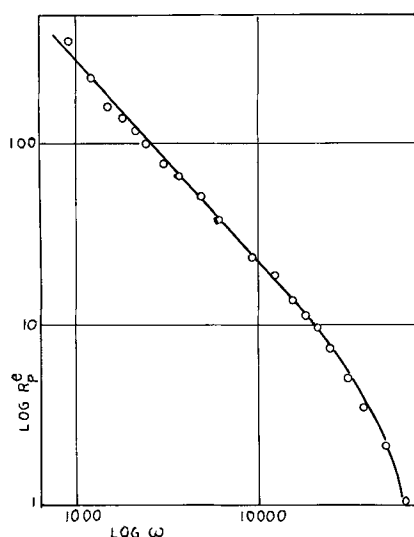


Fig. 4. Plot of $\log R_p^e$ against $\log \omega$ for supporting electrolyte alone

nization of electrodes is without effect when the square wave method is used.

The values of R_T listed in Table III are subtracted in the third step of Fig. 3. The fourth step is performed by the standard method. It was found that a plot of $\log \omega$ vs. $\log R_p^e$ for the supporting electrolyte (Fig. 4) is linear up to 4000 cps. The empirical equation for this relationship was found to be

$$\log R_p^e = 5.775 - 1.104 \log \omega \quad [1]$$

Note from Eq. [1] that the log-log plot for the supporting electrolyte has a slope of -1.104 . It can readily be shown from Grahame's equations for the faradaic admittance (1) together with a-c circuit theory that if R_p^e were faradaic in nature, said slope would be -0.5 . It is therefore evident that R_p^e for the supporting electrolyte is at least largely nonfaradaic in character. If it be assumed that no faradaic process is here involved, $R_p^e = R_p^d$ in Eq. [1].

A semi-empirical equation, whose derivation will be described later, may be written as follows for the capacitance of the supporting electrolyte at low frequencies

$$C_p^e = C_d = 39.0 - 1.624 \omega^{0.208} \quad [2]$$

In all three of the methods considered above for the separation of the various circuit elements, it was tacitly assumed that the depolarizer has no effect on the double-layer parameters. We doubted the correctness of this assumption and decided to test it. Since C_d is frequency-dependent, we do not see how we could determine its dependence on depolarizer concentration because it would have to be separated from the coexisting C_p^* , which is also frequency-dependent. We may, however, assume that only the frequency-independent part of C_d (*viz.*, C_d^0) is a function of the depolarizer concentration. Equation [2], now applied to the depolarizer solution, therefore becomes

$$C_d = C_d^0 - 1.624 \omega^{0.208}$$

Furthermore, since C_p^e for the depolarizer solution is compounded of C_p^* and C_d , we may write

Table IV. Frequency-independent portion of double-layer capacity (C_d^0) as function of depolarizer concentration

Solution	C_d^0 in μF
K_2SO_4	39.0
0.0001N	36.5
0.0005	34.0
0.001	32.8
0.005	49.1
0.01	60.0

$$C_p^e + 1.624 \omega^{0.208} = C_p^* + C_d^0 \quad [3]$$

The quantity $(C_p^e + 1.624 \omega^{0.208})$ can be plotted against $\omega^{-1/2}$ and extrapolated to infinite frequency where C_p^* is zero. The extrapolated value is C_d^0 . The values so obtained are listed in Table IV. Equation [3] can now be solved for C_p^* . R_p^* can be calculated from the equation

$$1/R_p^* = 1/R_p^e - 1/R_p^d \quad [4]$$

after getting R_p^d from Eq. [1]. R_p^* and C_p^* can be converted into their series equivalents, R_s^* and C_s^* , by the usual method (step 7). The values of R_s^* and X_s^* listed in Table II were obtained by this method, which we will call the fourth method. It is obviously based on the Bockris-Conway circuit and is a slight modification of the third method. Plots of R_s^* and X_s^* (the equivalent series capacitive reactance of the faradaic branch) against $\omega^{-1/2}$ are parallel and show the following points of interest: (A) Using the fourth method and the data for the 0.005N solution, a plot of R_s^* vs. $\omega^{-1/2}$ is linear up to ca. 2000 cps compared to ca. 1500 cps when the first method is used.⁴ This test is based on the universally accepted equation of Grahame (1)

$$R_s^* = \theta + \eta/\sqrt{\omega} \quad [5a]$$

(B) Similar plots for X_s^* are linear up to ca. 1500 cps for both methods. (C) For the 0.010N solution, similar plots for both R_s^* and X_s^* calculated by the fourth method only are linear up to ca. 1000 cps (the maximum frequency used by Bockris and Conway).

Observations (A) and (B) indicate only a slight advantage for the fourth method over the first one. Observation (C) indicates continued concordance with the theory of the faradaic admittance at concentrations greater than 0.005N. This concordance was not found in the more dilute solutions for which the resistance and reactance curves crossed. The linear portions of these curves clearly indicated greater slopes for the reactance curves for the two most dilute solutions. Matsuda (19) has stated that this would occur if specific adsorption of the reacting ions occurs at the electrode surface. This had been observed previously by Laitinen and Randles (20) and by Randles and Somerton (18) for certain other redox systems. It appears that at low concentrations specific adsorption interferes with the faradaic impedance whereas, at high concentrations, normal faradaic impedance masks the specific adsorption.

⁴ The extrapolated value of the double layer capacity used in the first method was found to be 34.0 μF .

The above comparison of methods did not necessarily involve any theory of the double-layer resistance. Let us now turn to the theory of Bockris and Conway (5). Their Eq. [11] may be written in terms of our symbol R_p^d as

$$R_p^d = \frac{1}{\Delta\epsilon C_o} \left[\frac{\tau'^{(1-\beta)}}{\omega^\beta} + \frac{\tau'^{(\beta-1)}}{\omega^{2-\beta}} \right] \quad [5]$$

in which we have corrected an obvious misprint in their equation by replacing their τ by τ' . The symbols have the following meaning: $\Delta\epsilon$ is the difference between the dielectric constant at very small and very large frequencies, C_o is a constant, τ' is the mean relaxation time for the rotation of water dipoles adsorbed on the electrode surface, and β is used in place of the empirical factor α , introduced by Cole and Cole (21), which presumably corrects for the distribution of relaxation times. Algebraic manipulation transforms Eq. [5] into

$$\log R_p^d = (\beta - 2) \log \omega + \log \frac{\tau'^{(\beta-1)}}{\Delta\epsilon C_o} [1 + (\omega\tau')^{2-2\beta}] \quad [6]$$

It is apparent that as long as $(\omega\tau')^{2-2\beta} \ll 1$, $\log R_p^d$ should be a linear function of $\log \omega$ with a slope of $\beta - 2$. Figure 4 shows that such a plot is linear up to 4000 cps, thus satisfying this particular requirement of the theory. The slope of the linear portion of this curve corresponds to a value of 0.896 for β , thus fulfilling the requirement that $0 < \beta < 1$.

The Bockris-Conway theory also leads to their Eq. [10], viz.

$$C_d^f = \frac{C_o \Delta\epsilon (\omega\tau')^{2-2\beta}}{1 + (\omega\tau')^{2-2\beta}} \quad [7]$$

where C_d^f is the frequency-dependent parallel component of C_d . It appears from Eq. [7] that when $(\omega\tau')^{2-2\beta} \ll 1$, a plot of C_d^f (or of C_d) against $\omega^{2-2\beta}$ should be linear. Using the value of β derived from our resistance measurements, a plot of C_d^f against $\omega^{0.208}$ was found to be linear up to 4000 cps in accord with the theory. Equation [2] is the semi-empirical equation derived from this plot.

Bockris and Conway used a successive approximation procedure for evaluating τ' from Eq. [5]. This quantity can be more readily obtained from Eq. [8] which we derived by multiplying R_p^d from Eq. [5] by C_d^f from Eq. [7].

$$R_p^d C_d^f = \omega^{-\beta} \tau' (1 - \beta) \quad [8]$$

Equation [8] predicts that a plot of $\omega^{-0.896}$ against $R_p^d C_d^f$ should be linear with an intercept of zero and a slope of $\tau'^{(0.104)}$. Such a plot is shown in Fig. 5 for the supporting electrolyte alone.

We took $C_d^f = 39.0 - C_p^e$ (cf., Eq. [2]). The slope is 0.92 corresponding to a value of 0.45 sec for τ' . Thus, despite the fact that the curve is linear as demanded by theory, the calculated value of the relaxation time is of a decidedly different order of magnitude than that of ice, which is 2×10^{-5} sec at -1° (26) and must, of course, be even smaller at 25° . Our high value for τ' is not of itself inconsistent with the Bockris-Conway theory if we recognize that any slow process which affects the polarization

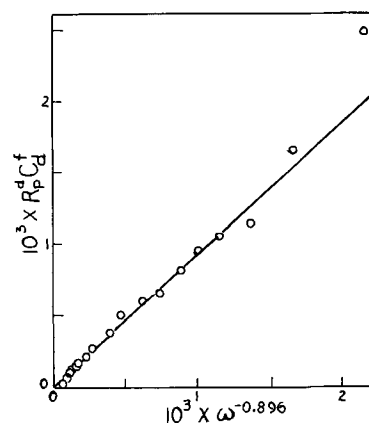


Fig. 5. Plot of $10^3 R_p^d C_d^f$ (in sec) against $10^3 \omega^{-0.896}$ (in $\text{sec}^{0.896}$) for supporting electrolyte alone.

of the dielectric would yield equations of the same form. The slow process would merely be one with a larger relaxation time than the process of adsorbing and desorbing water dipoles. In this relation it might be well to remember that Cole and Cole (21) expressed misgivings as to their own interpretation of their empirical equation in terms of a distribution of relaxation times and suggested "that a more general fundamental mechanism or process must be involved."

It is not impossible that adsorption of some impurity on the electrode surface is responsible for our surprisingly low value of τ' . If so, it is not without interest that such adsorption gives rise to a double-layer resistance that is adequately described by the equations of Bockris and Conway and therefore may be calculated and separated from the cell impedance in the calculation of the faradaic impedance. The experimental basis for this assertion is in the adequacy of the fourth method as described above.

Bockris and Conway (22) pointed out that "the physical origin of the double layer resistance is in the inertia of the adsorbed dipoles in their response to the alternating current field" and emphasized that this inertia to orientation polarization is only observed at frequencies higher than the relaxation frequency. It should, perhaps, be pointed out that the resistance so created acts like a series resistance, increasing with the frequency. They chose, however, to use the equivalent parallel resistance which decreases as the frequency is raised. Furthermore, since a distribution of relaxation times is postulated, it certainly does not follow that the series resistance is zero below the mean relaxation frequency ($1/\tau'$). Thus we found, as Bockris and Conway did also, that the series resistance is greater than zero at frequencies well below 1000 cps. For Bockris and Conway, this means well below their mean relaxation frequency; for us, it means somewhat above. In their work and to a lesser degree in ours, the measured values of τ' lay well outside the range over which experiments were performed. It should also be mentioned that our high value of τ' involves the difficulty that it is not true that $(\omega\tau')^{0.208} \ll 1$ over the linear portions of the curves as required by Eq. [6] and [7]. This theoretical deficiency need not, however, prevent us from using the

equations as empirical ones, which rather satisfactorily describe the properties of the double-layer resistance and capacitance at frequencies below 4000 cps, as was done with the fourth method.

A well-known difficulty which arises in the calculation of "apparent rate constants" (k_h) for electrode reactions is the uncertainty in the true electrode area (A). It occurred to us that this difficulty could be easily circumvented as follows. Randles (23) has given the following two equations

$$\theta = \frac{RT}{n^2 F^2 k_h A C_i} \quad [9]$$

$$\eta = \frac{RT}{\sqrt{2} n^2 F^2 A C_i} \left(\frac{1}{\sqrt{D_o}} + \frac{1}{\sqrt{D_r}} \right) \quad [10]$$

where D_o and D_r are, respectively, the diffusion coefficients of the oxidant and reductant, and C_i is the geometric mean of the depolarizer concentrations. Values of θ and η may be obtained graphically by the usual method, employing Eq. [5a]. If now we divide Eq. [10] by Eq. [9], we get the equation

$$\eta/\theta = (k_h/\sqrt{2})(D_o^{-1/2} + D_r^{-1/2}) \quad [11]$$

which is independent of the electrode area and the number of electrons (n) involved in the electron-transfer step. Equation [11] can obviously be solved for k_h .

This method of calculating k_h suffers from the disadvantage that accurate values for the diffusion coefficients must be known. In using it with our data, we have employed as a reasonably good approximation the diffusion coefficients obtained in 0.1M KCl solution at 25° by Macero and Rulfs (24): $D_o = 0.836 \times 10^{-5}$ and $D_r = 0.687 \times 10^{-5}$ cm²/sec. Table V shows the values of k_h calculated from Eq. [11] together with the values of θ and η determined graphically. The three most dilute solutions are included although they gave erratic results, as mentioned above, probably owing to adsorption.⁵ In all cases, the linear parts of the resistive dispersion curves were used to evaluate θ and η .

Figure 6 shows a plot of k_h against the depolarizer concentration and indicates clearly that the anomalous variation of k_h with concentration dies out as the concentration increases. It is interesting to compare the limiting value of our rate constant, viz., 0.14-0.15 cm/sec (at 30.5°), with those determined by Randles and Somerton (18), viz., 0.13 in 0.5M K₂SO₄ and 0.09 in M KCl, both at 20°. They gave the value of 4 kcal/mole as the activation energy, from which one can calculate the corresponding values of their rate constants at 30.5° to be 0.16 and

⁵ For a possibly related explanation, see Parsons (25).

Table V. Rate constants calculated from Eq. [11]; Ionic strength = 0.3402

Conc.	θ , ohm	η , ohm/sec ^{1/2}	k_h , cm/sec ⁻¹
0.010N	0.51	13	0.15
0.005	1.60	49.6	0.19
0.001	2.22	226	0.62
0.0005	1.67	280	1.03
0.0001	2.84	789	1.71

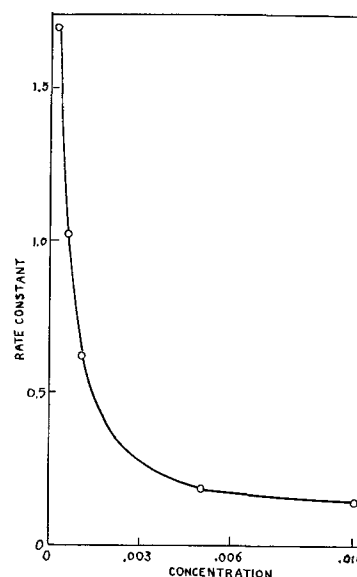


Fig. 6. Plot of the rate constant, k_h , (in cm/sec) against concentration of depolarizer (in moles/l).

0.11 cm/sec. Although at first thought one would expect their constants to be higher than ours because they used the apparent instead of the true electrode area, it must also be realized that our constants are too large because we used diffusion coefficients determined in a solution of lower ionic strength than that of our solution.

Manuscript received Jan. 27, 1964.

Any discussion of this paper will appear in a Discussion Section to be published in the June 1965 JOURNAL.

SYMBOLS

- C depolarizer concentration, moles/l.
- C_d capacity of the electrical double layer at one electrode, μF .
- C_d^f frequency-dependent part of double-layer capacity, μF .
- C_d^o frequency-independent part of double-layer capacity, μF .
- C_{di} equivalent series capacitance of the Warburg impedance (i.e., the diffusional capacitance), μF .
- C_i the geometric mean of the concentrations of Ox and Red.
- C_o a constant in Eq. [2].
- C_p equivalent parallel capacitance of cell, μF .
- C_p^e equivalent parallel capacitance of electrode layer, μF .
- C_p^* equivalent parallel capacitance of faradaic branch at one electrode, μF .
- C_s equivalent series capacitance of cell, μF .
- C_s^* equivalent series capacitance of faradaic branch, μF .
- D_o diffusion coefficient of oxidant, cm² sec⁻¹.
- D_r diffusion coefficient of reductant, cm² sec⁻¹.
- R_{di} equivalent series resistance of the Warburg impedance (i.e., diffusional resistance), ohms.
- R_{p^d} equivalent parallel resistance of the electrical double layer at one electrode, ohms.
- R_L electrode layer resistance, ohms.
- R_p equivalent parallel resistance of cell, ohms.
- R_p^e equivalent parallel resistance of electrode layer, ohms.
- R_p^* equivalent parallel resistance of faradaic branch at one electrode, ohms.
- R_s equivalent series resistance of cell, ohms.
- R_s^* equivalent series resistance of faradaic branch.
- R_T electrolytic resistance of cell, ohms.
- R_Δ the frequency-dependent part of R_s , ohms.
- T temperature, °K.
- X_{di}^* $1/C_{di}\omega$
- X_s^* $1/C_s^*\omega$
- β the factor of Cole and Cole, Eq. [2].

$\Delta\epsilon$ difference between dielectric constant at very small and very large frequencies.
 η slope of the curve of R_s^* vs. $\omega^{-1/2}$.
 θ transfer resistance.
 μ ionic strength.
 τ mean relaxation time of adsorbed water dipoles.
 ω frequency of alternating current in radians/sec.

REFERENCES

1. D. C. Grahame, *This Journal*, **99**, 370C (1952).
2. T. I. Borisova and B. Ershler, *Zhur. Fiz. Khim.*, **24**, 337 (1950).
3. D. C. Grahame, Tech. Rept. No. 22 to O.N.R., March 1956.
4. H. A. Laitinen and R. A. Osteryoung, *This Journal*, **102**, 598 (1955).
5. J. O'M. Bockris and B. E. Conway, *J. Chem. Phys.*, **28**, 707 (1958).
6. R. Parsons in "Modern Aspects of Electrochemistry," pp. 141-3, J. O'M. Bockris and B. E. Conway, Editors, Academic Press, New York (1954).
7. J. O'M. Bockris, W. Mehl, and B. E. Conway, *Tr. Chetvertogo, Soveshch. po Elektrokhim.*, Moscow, 380 (1956).
8. W. D. Robertson, *This Journal*, **100**, 194 (1953).
9. C. Chalin and E. Picard, *Compt. rend.*, **245**, 1309 (1957).
10. M. Shaw and A. E. Remick, *This Journal*, **97**, 324 (1950).
11. J. D. Ferry, *J. Chem. Phys.*, **16**, 737 (1948).
12. D. C. Grahame, *Ann. Rev. Phys. Chem.*, **6**, 337 (1955).
13. A. E. Remick and H. W. McCormick, *This Journal*, **102**, 534 (1955).
14. G. D. Kupradze, *Trudy Gruzin. Politekhn. Inst.*, No. 35, 163 (1954); Referat, *Zhur.*, *Khim.*, 1955, Abstr. No. 54716.
15. D. C. Grahame, *Chem. Rev.*, **41**, 441 (1947).
16. J. O'M. Bockris, W. Mehl, B. E. Conway, and L. Young, *J. Chem. Phys.*, **25**, 776 (1956).
17. M. Breiter, M. Kleinerman, and P. Delahay, *J. Am. Chem. Soc.*, **80**, 5111 (1958).
18. J. E. B. Randles and K. W. Somerton, *Trans. Faraday Soc.*, **48**, 937 (1952).
19. H. Matsuda, *J. Phys. Chem.*, **64**, 339 (1960).
20. H. A. Laitinen and J. E. B. Randles, *Trans. Faraday Soc.*, **51**, 54 (1955).
21. K. S. Cole and R. H. Cole, *J. Chem. Phys.*, **9**, 341 (1941).
22. J. O'M. Bockris and B. E. Conway, Proc. Intern. Comm. Electroch. Thermod. and Kinetics, 8th meeting, 170 (1958). (Discussion).
23. J. E. B. Randles, *Discussion Faraday Soc.*, **1**, 11 (1947).
24. D. J. Macero and C. L. Rulfs, *J. Am. Chem. Soc.*, **81**, 2942 (1959).
25. R. Parsons in "Advances in Electrochemistry and Electrochemical Engineering," Vol. 1, p. 41, P. Delahay and C. W. Tobias, Editors, Interscience Publishers (1961).
26. C. P. Smyth and C. S. Hitchcock, *J. Am. Chem. Soc.*, **54**, 4631 (1932).

On the Mixed Potentials Observed in the Iridium-Oxygen-Acid System

James P. Hoare

Research Laboratories, General Motors Corporation, Warren, Michigan

ABSTRACT

The rest potential of an Ir bead in O_2 -saturated 2N H_2SO_4 acid was studied as a function of the partial pressure of oxygen, pH, and the history of preparation of the test electrode. Two electrode systems are distinguished. The Ir/Ir-O system consists of an adsorbed monolayer of oxygen atoms, and the rest potential, 1020 ± 15 mv, is a mixed potential. The Ir/IrO₂ system consists of an adsorbed monolayer of oxide, IrO₂, and the rest potential, 940 ± 10 mv, is a metal-metal oxide potential. The adsorbed films are nearly reversibly formed or reduced. A discussion of the mechanisms of mixed potentials is included.

Earlier studies of the rest potential of noble metal electrodes in oxygen-saturated acid solution (1-4) indicate that these metals are not truly inert to this electrolyte. As a result, films of adsorbed oxygen about a monolayer thick (5) are formed on the metal surface. Since these layers appear to be incomplete (1-4), a mixed potential (6) is observed instead of the reversible oxygen potential. In certain cases where it is assumed that the oxygen film is complete (7), the reversible oxygen potential was observed.

There is evidence in the literature (8) from polarization measurements using a triangular-pulse (9) technique that the adsorbed oxygen layers on iridium are reversibly formed and reduced, because the oxidation peak appears at about the same po-

tential as the reduction peak. An investigation of the rest potentials of such a system seemed interesting, and a presentation of such measurements on the Ir-O-acid system is given in this report.

Experimental

The test electrodes were in the form of small beads (0.1-0.15 cm in diameter) melted at the end of iridium wires (99.9+% pure). Three of these beads, as checks, were cleaned and mounted in a prepared dual Teflon cell as described before (1-4). The potentials were measured against an α -Pd-H reference electrode (10) and reported against the normal hydrogen electrode (NHE) unless stated otherwise. All measurements were carried out at a temperature of $25^\circ \pm 1^\circ C$. The results were ob-

tained from the data recorded on 26 different Ir-bead electrodes on which the potential was determined with ± 1 mv.

Results and Discussion

Potential-time behavior.—After the Ir bead had been anodized at 1.8v, the circuit was broken and the open-circuit potential followed as a function of time. In oxygen-stirred acid solution, the potential fell to a minimum value of 800 mv in 5 hr. Now, oxygen-stirring was replaced with H₂ stirring for 15 min to destroy all peroxides formed during the pre-electrolysis procedure. The potential came to the hydrogen potential (−50 mv with respect to α -Pd-H) within 300 sec. When the system was stirred with oxygen again, the potential rose quickly (within 200 sec) to about 850 mv and came to a steady value of 1020 ± 15 mv¹ within about 10 hr. If the system was again stirred with hydrogen, it required less than 200 sec for the potential to reach the hydrogen potential.

The fact that the system responded so quickly (within 200 sec) to changes from an oxidizing to a reducing atmosphere, and the reverse, agrees quite well with Böld and Breiter's (8) observations that the adsorbed oxygen layers are formed and reduced rapidly and easily on Ir.

Potential as a function of the partial pressure of oxygen.—The partial pressure of oxygen, P_{O_2} , was varied in the same way as described before (1) by diluting the O₂ with N₂. The potential of an anodized Ir bead before the treatment with hydrogen was independent of P_{O_2} . However, after treatment with hydrogen, the potential was dependent on P_{O_2} when the system was again stirred with oxygen. Typical experimental results of three such electrodes are presented in Fig. 1. The P_{O_2} dependence was determined on two of the electrodes (curves A and B) about an hour after O₂ stirring had begun

¹The spread in potential, ± 15 mv, represents the difference in steady-state potential values (virtually ± 0 v over an 8-24-hr period) observed from one electrode to another and is meant to include electrodes exhibiting the lowest and the highest steady-state values. Similar notation was used in ref. (1)-(4).

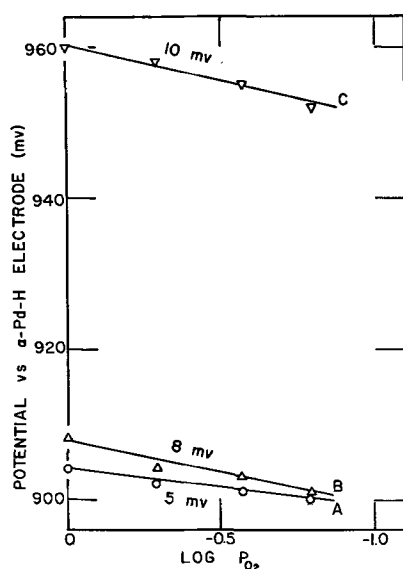
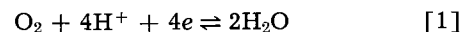


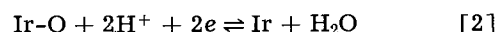
Fig. 1. A plot of the open-circuit potential as a function of the log of the partial pressure of oxygen in atmospheres.

and on one (curve C) after the steady state had been reached.

It is interesting to note the very low values of the slope of these curves, which, taken at face value, would require a potential-determining reaction involving from 6 to 12 electrons. Such a mechanism, of course, cannot be taken seriously, and some other explanation must be sought. Since similar rest potentials in the noble metal-oxygen systems (1-4) could be interpreted in terms of a mixed potential involving the O₂/H₂O reaction



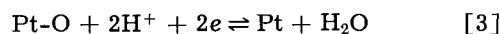
and some metal-oxygen reaction, it will be assumed that these observed mixed potentials may be explained by a local cell mechanism composed of the O₂/H₂O reaction and the Ir/Ir-O reaction



Here, the symbol, Ir-O, represents a hydrated monolayer of adsorbed oxygen atoms, and the system will be referred to as the Ir/Ir-O electrode.

Now, the large values obtained for n , the number of electrons transferred in the over-all potential-determining reaction, may be understood in terms of the local cell polarization curves. A sketch of such curves for three different cases is shown in Fig. 2 as a plot of the observed local cell potential, E , against the total local cell current, I . Since the areas of the metal surface, on which the anodic and cathodic half-reactions may occur, may be different, the current densities for the anodic and cathodic half-reactions may also be different. Therefore, two half-reactions with the same i_0 may be polarized to different extents for a given value of the local cell current, I . Where the two half-cell polarization curves intersect is the steady-state mixed potential and the local cell current.

The situation depicted in Fig. 2a may be exemplified by the Pt/Pt-O electrode. Curve A is the polarization curve for the O₂/H₂O reaction, Eq. [1], and curve B is that for the Pt/Pt-O reaction



Curves A₁, A₂, and A₃ are the polarization curves of

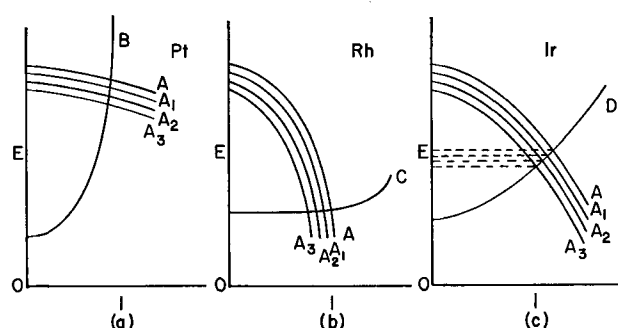
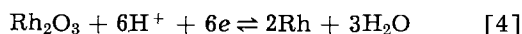


Fig. 2. A sketch of the polarization curves for the half-reactions which determine the mixed potential in the (a) Pt/Pt-O system, (b) Rh/Rh₂O₃ system, and (c) Ir/Ir-O system. The A-curves are those for the O₂/H₂O reaction for decreasing values of P_{O_2} ; the B-curve, the Pt/Pt-O reaction; the C-curve, the Rh/Rh₂O₃ reaction; and the D-curve, the Ir/Ir-O reaction. The mixed potential is the point of intersection of the curves; the E_0 value, the point of intersection of curves and the E -axis. I is the total local cell current.

Eq. [1] for different values of P_{O_2} less than unity. Since the number of bare platinum sites is relatively low (7), the current density at these sites is relatively high. It also may be that the i_0 for Eq. [1] is larger than the i_0 for Eq. [3]. These conditions would cause Eq. [3] to be polarized strongly with much less polarization of Eq. [1]. From Fig. 2a, it is seen that the difference of potential between the mixed potentials at different P_{O_2} values (points of intersection of the B-curve with the A-curves) is about the same as that between the E_0 potentials at different P_{O_2} values for the A-curves (points of intersection of the A-curves with the E-axis). Then, the mixed potential is controlled by the O_2/H_2O reaction, and a value of 4 for n may be observed (1).

The other extreme case is described by Fig. 2b and the Rh/Rh₂O₃ electrode (3) is representative of this situation. It appears that the O_2/H_2O reaction is established with difficulty on the Rh/Rh₂O₃ surface. Therefore, the i_0 for the O_2/H_2O reaction on a Rh₂O₃ surface is quite low, and the A-curves in Fig. 2b would be strongly polarized at quite low local current densities. Curve C of Fig. 2b represents the polarization curve for the Rh/Rh₂O₃ reaction



which has a relatively much higher i_0 .

In this case, the mixed potential would be determined by Eq. [4]. Since this reaction is independent of P_{O_2} , the C-curve would not vary with P_{O_2} . The A-curves cut the C-curve at about the same potential, and the mixed potential is independent of P_{O_2} , as confirmed by experiment (3).

These two cases demonstrate the behavior of the mixed potential with changes in P_{O_2} (a) when the P_{O_2} -independent half-reaction is strongly polarized (Pt case), and (b) when the P_{O_2} -dependent half-reaction is strongly polarized (Rh case).

The intermediate case where both half-reactions are moderately polarized is exemplified by the iridium-oxygen system as shown in Fig. 2c. Here the A-curves intersect the D-curve in such a way that the differences in the values of the mixed potential for different values of P_{O_2} are less than those of the E_0 potentials for these values of P_{O_2} . Although the rest potential (mixed potential) is a function of P_{O_2} , the value of n estimated from the observed potential measurements will be too large since the change in potential for a given change in P_{O_2} is too low. In this way, one may reconcile the experimental data with the suggestion that a four-electron reaction is involved in the over-all potential-determining mechanism.

Since both half-reactions in the Ir-O₂ system are polarized, the observed value for $\Delta E/\Delta \log P_{O_2}$ may vary as the shape of the polarization curve varies which, in turn, may depend on the relative anodic and cathodic local current densities. This effect is reflected in the change in slope of the curves in Fig. 1 with time because the structure of the surface is continually changing until the steady state is reached. Whenever the mixed potential is controlled by more than one reaction, as shown in Fig. 2c, reproducible potential-partial pressure meas-

urements cannot be obtained until the steady state is reached.

When the Ir/Ir-O system was stirred with purified nitrogen for about 24 hr, the potential had come to a steady value of 870 ± 20 mv. It is suggested that the standard potential for the Ir/Ir-O reaction, Eq. [2], is in the neighborhood of 870 mv.

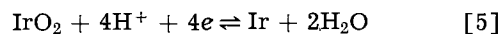
Potential as a function of pH.—The pH of the solution was varied by diluting the 2N H₂SO₄ with 2N Na₂SO₄ in order to keep the ionic strength constant. The pH was determined at the end of the run by measuring the potential difference between a saturated calomel electrode and a Pt/H₂ electrode in the same solution. It was found that the rest potential with respect to α -Pd-H was independent of pH in all cases. This means that the potential-determining reactions varied with the hydrogen ion concentration in the same way as the reaction for the α -Pd-H electrode did, i.e., for each electron transferred, a hydrogen ion was involved (11). Equations [1] and [2] satisfy this requirement.

The Ir/IrO₂ electrode.—To study the film produced on Ir by anodization without peroxides interfering, a technique using two cells was used (3, 7). The electrode was anodized in one cell and the solution prepared in the second. Then the electrode was transferred to the second cell to be studied in O₂-saturated, peroxide-free 2N H₂SO₄ solution.

Initially, the potential was in the vicinity of 1300 mv. This potential decayed slowly so that at the end of about 24 hr a steady potential of about 940 ± 10 mv was obtained. This potential with respect to α -Pd-H was independent of both P_{O_2} and pH.

According to Sidgwick (12), the only stable oxide formed by iridium is IrO₂, and this can be made by heating Ir in air. An Ir wire was cleaned in the same way as the Ir bead and heated white hot in a H₂ flame. After the wire had cooled down in air, it was plunged into oxygen-saturated, peroxide-free 2N H₂SO₄. The potential came to a steady value of 935 ± 5 mv within about 4 hr.

These observed potential values are very close to that reported by Latimer (13) for the standard potential of the Ir/IrO₂ couple



Equation [5] agrees with the P_{O_2} and pH observations. Therefore, it is suggested that the rest potential in the Ir/IrO₂ system is not a mixed potential but a metal-metal oxide potential determined by Eq. [5] with a standard potential near 930 mv.

Böld and Breiter (8) observed that, after a monolayer of adsorbed oxygen was formed, the film continued to grow for a short time with continued anodization. It appears that a monolayer of adsorbed oxygen is formed on the iridium surface first and is then converted to a thin film of IrO₂ not much thicker than a monolayer with continued anodization (14). Since this film of IrO₂ is a good electronic conductor, the film ceases to grow and the current goes into an oxygen evolution reaction. This is supported by the observation that the appearance of an iridium bead does not change with time and remains bright while it is anodized at a

potential where oxygen is being evolved (about 1.5v).

A film of IrO₂ seems to be somewhat unstable in acid solution because the potential of an Ir/IrO₂ electrode drifts from the steady-state value after about 48 hr, after which the potential is no longer independent of P_{O₂}. Apparently an Ir/IrO₂ electrode is converted to an Ir/Ir-O electrode with long standing in H₂SO₄ solution. If the E_o for Eq. [5] is 930 mv and that for Eq. [2], 870 mv, one would expect such a transformation.

When an Ir/IrO₂ electrode, which had been made either by anodization or by heating in air, was treated with H₂-stirring, it was found that the hydrogen potential was obtained within 150-200 sec. Apparently, not only the film of Ir-O but also that of IrO₂ is easily formed or reduced as noted by Böld and Breiter (8).

Polarization at low current densities.—As described before (1, 2), the beads were cathodized at very low current densities by changing the variable input impedance of the model 1230-A General Radio Electrometer. A plot of the polarization (difference between the open-circuit potential, E_{oc}, and the potential, E, at a given current density) as a function of the logarithm of the estimated apparent current density is given in Fig. 3. The polarization of the Ir/Ir-O system with oxygen-stirring is shown by curve A with N₂ stirring by curve B. Curve C is a plot of the polarization of the Ir/IrO₂ electrode with O₂ stirring and curve D, that with N₂ stirring. Each point represents the average of at least 5 independent observations.

The fact that the two sets of curves are parallel indicates that the same kinetic process is occurring on the Ir-O and the IrO₂ surface. Data obtained with O₂ stirring, but not with N₂ stirring, yield a Tafel-like curve which suggests that most of the current goes into the reduction of oxygen. The fact that the N₂ stirred curves deviate from the O₂ stirred curves at about the same potential suggests that the rate-determining step is the same on the Ir/Ir-O electrode as on the Ir/IrO₂ electrode. It is in-

teresting to note from a comparison of the two sets of curves that the Ir/IrO₂ system appears to be more highly polarized than the Ir/Ir-O system for a given apparent current density, which means that the rate-determining step is more greatly hindered in the IrO₂ case. This behavior is opposite to what is observed in the Pt-O₂ system (1) where the polarization is lowered by the presence of PtO₂ in the Pt-O layer. Sufficient data to identify the nature of the rate-determining step are not presented here.

From these studies on noble metals, it appears that their behavior is alike in that all of them initially form a very thin layer (about a monolayer thick) of adsorbed oxygen atoms in a potential range from 800 to 1000 mv. In this region, the observed rest potentials seem to be mixed potentials. With anodic polarization to higher potentials, definite oxides may be formed and a metal-metal oxide equilibrium system may be observed in certain cases such as the Au/Au₂O₃ (2), Pd/PdO₂ (4), and Ir/IrO₂ electrodes, but are not indefinitely stable in acid solutions.

Under ordinary circumstances, however, anodic polarization does not convert the Pt-O layer to a PtO₂ layer completely, and only mixed potentials are observed in the case of platinum (1). Also, Rh does not seem to form a true oxide of Rh₂O₃ with anodic polarization, but rather, a surface alloy of Rh and O atoms dissolved in one another (3). Again, only mixed potentials are observed. Since the monolayers of adsorbed oxygen on Pt and Rh are good electronic conductors and since true metal-metal oxide electrode systems are not formed on these metals, this may be a reason why it is generally known that Pt and Rh are interesting catalysts for oxygen reactions. Yet, as it is well known further, Pt surpasses all other pure metals as a material for oxygen electrodes in acid solution. This may be traced to the observation that Rh is a much poorer catalyst for the decomposition of peroxides than Pt (3).

Acknowledgment

For most helpful discussions and suggestions, the author expresses his gratitude to Dr. Raymond Thacker and Dr. John L. Griffin of the General Motors Research Laboratories.

Manuscript received Dec. 4, 1963; revised manuscript received March 23, 1964.

Any discussion of this paper will appear in a Discussion Section to be published in the June 1965 JOURNAL.

REFERENCES

1. J. P. Hoare, *This Journal*, **109**, 858 (1962).
2. J. P. Hoare, *ibid.*, **110**, 245 (1963).
3. J. P. Hoare, *ibid.*, **111**, 232 (1964).
4. J. P. Hoare, *ibid.*, **111**, 610 (1964).
5. K. J. Vetter, "Elektrochemische Kinetik," p. 502, Springer Verlag, Berlin (1961).
6. C. Wagner and W. Traud, *Z. Elektrochem.*, **44**, 391 (1938).
7. J. P. Hoare, *This Journal*, **110**, 1019 (1963).
8. W. Böld and M. Breiter, *Electrochim. Acta*, **5**, 169 (1961).
9. F. Will and C. A. Knorr, *Z. Elektrochem.*, **64**, 258 (1960).
10. D. J. G. Ives and G. J. Janz, "Reference Electrodes," p. 112, Academic Press, New York (1961); J. P. Hoare, *G. M. Eng. J.*, **9** [1], 14 (1962).

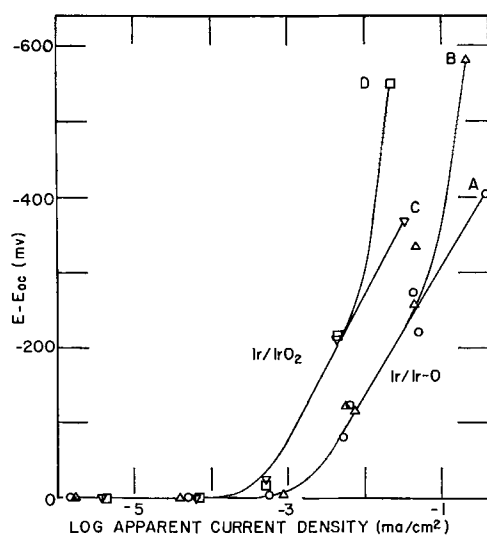


Fig. 3. Polarization data for the Ir/Ir-O and Ir/IrO₂ systems with O₂ or N₂ stirring. See text for details.

11. S. Schuldiner, G. W. Castellan, and J. P. Hoare, *J. Chem. Phys.*, **28**, 16 (1958).
12. N. V. Sidgwick, "Chemical Elements and Their Compounds," p. 1533, Oxford Press (1950).
13. W. H. Latimer, "Oxidation Potentials," p. 218, Prentice-Hall, New York (1952).
14. J. A. V. Butler and G. Drever, *Trans. Faraday Soc.*, **32**, 427 (1936).

A Study of Adsorption and Oxidation of Carbon Monoxide on Platinum Using Constant Current Pulses

Theodore B. Warner¹ and Sigmund Schuldiner

U. S. Naval Research Laboratory, Washington, D. C.

ABSTRACT

Using single anodic constant-current pulses, the steady-state concentration of carbon monoxide already adsorbed on the surface of a bright Pt electrode in 1M H₂SO₄ and the additional amount of CO adsorbed during the application of the pulse has been determined. At potentials of 0.3-0.4v (NHE), surface coverage of one molecule of CO per surface Pt atom was observed at very low CO partial pressures; for CO partial pressures up to 1 atm the coverage increased to about 1.06 CO molecules per Pt atom, indicating that additional CO physically adsorbs on the base chemisorbed layer. At 1.0-1.3v the rate of adsorption of CO was slower than the rate of diffusion (25°C), and indirect evidence suggests that CO is not adsorbed at potentials above 1.3v. The mechanism of oxidation of CO appears to be an electrochemical oxidation of water to form chemisorbed oxygen atoms, which then rapidly react with chemisorbed CO to form CO₂.

The amount of CO that is adsorbed on Pt has been studied in the past under varying conditions. Most evidence is indirect, and results are strongly dependent on the substrate. In the gas phase evidence has been found for one-site (1), two-site (2a), and mixed (2b) adsorption. Gilman (3-5) has studied the adsorption and oxidation of CO on a Pt wire in aqueous solutions using a potentiostatic method. He concluded that there was evidence of mixed linear and bridged adsorption.

The purpose of the present work was (a) to determine the extent of equilibrium surface coverage of a bright Pt electrode as a function of partial pressure of CO in aqueous acidic solution, (b) to study the mechanism of oxidation of such adsorbed CO, and (c) to determine if the rate of transfer of CO from solution, during anodic charging, to an electrode partially covered with CO was diffusion- or adsorption-controlled.

Experimental

The cell, electrodes, helium and hydrogen purification systems, and general method have been described elsewhere (6, 7). The cell contained a Pt (99.99%) bead working electrode (6), a 90% Pt-10% Rh gauze electrode (6), an L&N miniature glass reference electrode (6), a palladium tube electrode (7, 8), and a 5 cm long platinum wire electrode (99.99%, 0.064 cm diameter) not previously described, that, like the others, was mounted in Teflon and inserted into the cell through a glass nipple. Platinum bead electrodes with true areas of 0.177 and 0.289 cm² were used. True areas were defined using the method previously reported (7, 9), which is based on a determination of the number of

oxygen atoms deposited on the surface as a monolayer during anodic oxidation of water.

The electrolyte was 1M H₂SO₄ (triply distilled water) maintained at 25° ± 1°C. The electrolyte was pre-electrolyzed periodically, while being stirred with either helium or hydrogen, by making the Pt bead and gauze electrodes anodic (about 100 ma) relative to the Pt wire. At the end of the pre-electrolysis period (24-48 hr) the Pt wire electrode was removed from the cell (without disconnecting the current), dipped into concentrated nitric acid, then heated white hot in a hydrogen flame and replaced in the cell. The solution was stirred with hydrogen until the potential between all pairs of platinum electrodes was equal to zero. At the same time the glass electrode was calibrated against a Pt/H₂ electrode (NHE) (-0.660 ± 0.002v). The hydrogen flow was then replaced with helium.

After purification, the solution was stirred continuously with either helium or an appropriate gas mixture containing CO; a very slow stirring rate was maintained during application of charging pulses, except in the experiments on rate of diffusion of CO. Prior to each polarization pulse, rest potentials (*vs.* the glass reference electrode) of all the electrodes were determined with Keithley 603 Electrometer. After the electrodes had attained the rest potential, they were allowed to remain exposed to the CO-containing solution long enough to assure equilibrium adsorption of CO at each given CO partial pressure.

The Pt bead was anodized with single constant-current pulses (7) using an Electro-Pulse Model 3450 D pulse generator; the counter electrode was, at first, the Pt-Rh gauze electrode. It was found, however, that under some conditions significant

¹ National Academy of Sciences Resident Research Associate.

amounts of the hydrogen produced at this electrode would migrate to the Pt bead. To avoid this, the Pd tube electrode was substituted as counter electrode. In this case, hydrogen produced on the surface of the Pd tube would migrate into the metal and be oxidized by oxygen in the air-space inside the tube (8).

Using the Pt wire as a reference electrode, the anodic charging curve of the Pt bead was photographed from the display on a carefully calibrated Tektronix 535 oscilloscope, which was recalibrated (voltage and time) before each series of measurements. To evaluate possible transport effects, pulse current densities were varied from 56.1 to 2540 ma/cm². (All current densities reported here are on the basis of true electrode areas.)

To investigate the relative importance of the rate of diffusion of CO *vs.* the rate of adsorption, charging curves were obtained in unstirred solution and in solutions stirred vigorously by bubbling in gas at rates well over 1000 ml/min; this rate of stirring was sufficient to cause the working electrode to vibrate rapidly. Tank carbon monoxide (C. P. grade) was introduced into the cell through a separate inlet after passing through a flowmeter, a dry ice-ethylene glycol monoethyl ether trap, and a water saturator. The gases used were (a) pure CO, (b) 9.89% CO in N₂ (henceforth referred to as 0.1 atm partial pressure CO), (c) 0.0037% CO in He (referred to as 0.0037 atm partial pressure CO), (d) purified He, and (e) pure H₂. The first two gases were analyzed mass spectrometrically and showed, respectively, 10 ± 10 ppm H₂ and < 10 ppm H₂. The 0.0037 atm CO was prepared by mixing 0.1 atm CO with He. Total cell pressure was slightly above atmospheric.

Cleanliness of the Pt bead was checked from time to time, under CO-free conditions, by an anodic charging test (9). To prepare electrodes covered with adsorbed CO in solutions for which the CO partial pressure was zero, CO was admitted for varying periods of time (from 1 min to many hours), after which the cell was flushed with pure helium for 0.5 to 170 hr.

Results

Anodic charging curves.—Typical anodic charging curves for the Pt bead are shown in Fig. 1. The form of the curve was remarkably consistent over wide ranges of CO partial pressure and current densities.

A typical charging curve is sketched in Fig. 2, where potential changes in the CO oxidation region have been exaggerated to show fine detail. When a constant-current pulse is applied, the anode potential rises abruptly as the double layer capacitance is charged. After an initial potential overshoot (right-hand side of figure), the potential increases slowly to a rather constant value, which is maintained until the CO oxidation region ends (middle of figure). These details are apparent in low current density pulses, but tend to be obscured in rapid sweeps made with high c.d. pulses. After adsorbed CO has been oxidized, the potential rises linearly as the Pt surface becomes covered with a monolayer of adsorbed oxygen atoms; upon completion of this

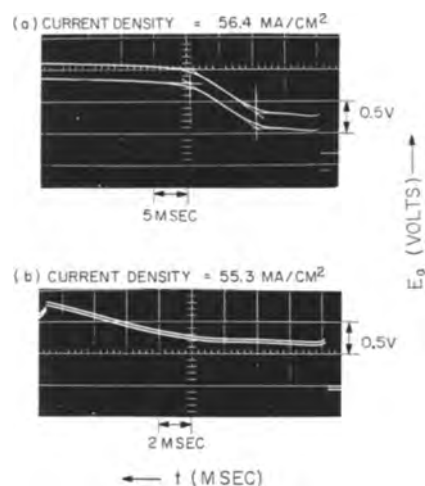


Fig. 1. Representative anodic charging curves for the Pt bead showing oxidation of carbon monoxide. In oscillogram (a) $p_{\text{CO}} = 0.1$ atm, in (b) $p_{\text{CO}} = 0.0037$ atm. In each oscillogram the top trace was made in vigorously stirred solution, and the bottom trace was made in quiescent solution. Because of the faster sweep speed used in (b), the curve is expanded to show the lower CO plateau in more detail. E_a is the anodic potential.

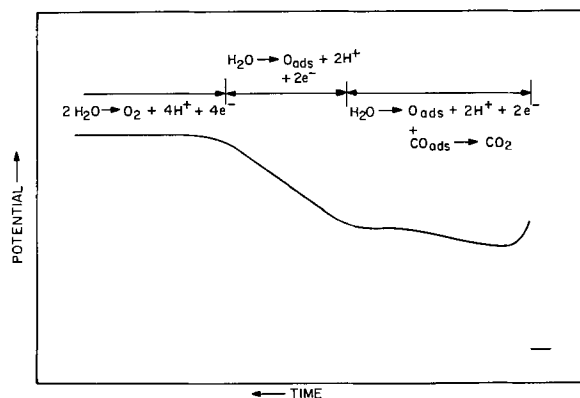


Fig. 2. Sketch of a typical constant-current anodic charging curve obtained with a bright platinum electrode in 1M H₂SO₄ solution containing dissolved CO. The characteristics of the curve in the CO oxidation plateau region have been exaggerated to show fine detail.

monolayer, a new plateau (left-hand side of figure), which indicates the generation of molecular oxygen, is reached.

Potentials observed on open circuit and in the various portions of the charging curve are summarized in Table I (the latter potentials were obtained from measurements made on oscillograms). The solution IR drop has been subtracted from all polarization potentials. The errors indicated are estimated limits of errors. The rather large error limits shown for the potentials at the start of the CO and O regions are partially due to the fact that these potentials were dependent on current density; they increased slightly with increasing current density.

Quantities of charge consumed in the CO oxidation region and in the oxygen adsorption region.—The amount of charge transferred in the CO oxidation region and in the oxygen adsorption region (O_{ads}) was calculated by taking the product of current density and charging time (the time required to complete the particular oxidation process, as

Table I. Platinum bead potentials observed on open circuit and during anodic pulses

Measured potentials,* v	Partial pressure of CO			
	1.0 atm	0.1 atm.	0.0037 atm	0 atm
Open-circuit rest potential	0.36 ± 0.02	0.36 ± 0.03	0.36**	0.29 ± 0.04
Potential at start of CO oxidation, E_{CO}	1.25 ± 0.13	1.18 ± 0.11	1.03**	1.00 ± 0.11
Difference between potential at start of CO oxidation and minimum potential during oxidation	0.10 ± 0.01	0.08 ± 0.01	0.07**	0.0 to 0.05
Potential at start of O atom adsorption region	1.25 ± 0.13	1.25 ± 0.14	1.03**	1.09 ± 0.11
Potential at start of O ₂ evolution region	1.81 ± 0.08	1.79 ± 0.08	1.69**	1.67 ± 0.08

* With reference to the N.H.E.

** Too little data to allow estimation of uncertainty.

measured on charging curve oscillograms). The amount, q_{CO} , of carbon monoxide oxidized in the lower plateau region was calculated by taking the total number of coulombs per square centimeter transferred and subtracting the number of coulombs per square centimeter used to charge the double layer. In this case, although the potential was approximately constant over the entire CO region, the double layer capacitance changed as the layer of adsorbed CO was removed. The charge consumed, $q_{d.l.}$, in charging the double layer was thus given by the relation

$$q_{d.l.} = E\Delta C \text{ (}\mu\text{coul/cm}^2\text{)} \quad [1]$$

where E is the potential in volts and ΔC is the change in capacitance in $\mu\text{fd/cm}^2$. Based on relatively few measurements, the double layer capacitance of a Pt bead covered with CO is about $8 \mu\text{fd/cm}^2$. The capacitance at the end of the CO region should be that of a clean Pt electrode, i.e., $40 \mu\text{fd/cm}^2$ (7). (This assumes that the CO₂ formed during the oxidation of CO either is not chemisorbed or, if sorbed, leaves the surface rapidly.) Hence, $\Delta C = 32 \mu\text{fd/cm}^2$.

The amount of charge, q_0 , used in oxidation processes in the O atom formation region was calculated similarly, with the charge going to the double layer being subtracted from the total charge transferred. In this case, the double layer capacitance, C , was taken to be $40 \mu\text{fd/cm}^2$ over the potential range transversed and thus

$$q_{d.l.} = C\Delta E \text{ (}\mu\text{coul/cm}^2\text{)} \quad [2]$$

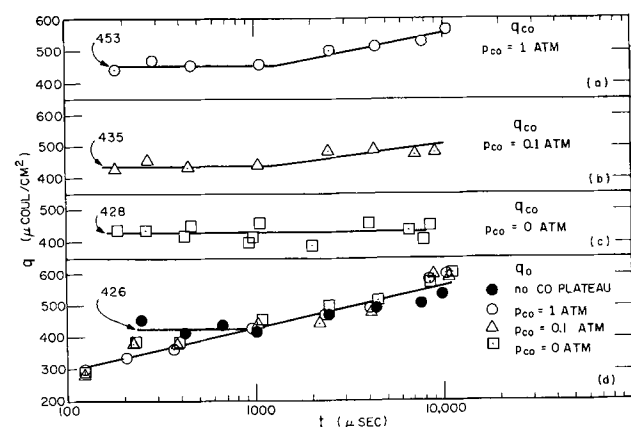


Fig. 3. Amount of charge, q_0 or q_{CO} , transferred in each region of the anodic charging curves is plotted against the time required to complete the process in that region.

Values of q_{CO} and q_0 obtained with different CO partial pressures, p_{CO} , are plotted in Fig. 3 vs. charging time t ; the shortest charging times correspond to the highest current densities. Each point plotted in curves (a), (b), and (d) represents the average of 4 to 16 determinations and is uncertain by about $20 \mu\text{coul/cm}^2$ (estimated standard deviation) for the plots of q_{CO} , and $30 \mu\text{coul/cm}^2$ for the plot of q_0 . Each point in curve (c) represents an individual determination. The arithmetic mean of the first four points of curves (a), (b), and (d) [the solid black circles only], and of all the points of curve (c) are represented by horizontal lines; the numbers appearing above the lines are these mean values in microcoulombs per square centimeter.

Mechanism of Carbon Monoxide Oxidation

During the oxidation of CO, the amount oxidized was primarily that amount already chemisorbed on the anode; for the lower current density pulses a slight additional amount of CO migrated to the electrode and was also oxidized. The fact that the electrode potential changed relatively little as CO coverage was reduced to zero suggested that direct electrochemical oxidation of CO was not taking place, for if it were, the potential would be expected to rise more sharply as the CO coverage decreased. The results suggest that the following processes may be taking place at the platinum surface:

- I. $\text{Pt} + \text{H}_2\text{O} \rightarrow \text{Pt}-\text{O} + 2\text{H}^+ + 2e^-$
- II. $\text{Pt}-\text{O} + \text{Pt}-\text{CO} \rightarrow \text{Pt}_2-\text{CO}_2^*$
- III. $\text{Pt}_2-\text{CO}_2^* \rightarrow 2\text{Pt} + \text{CO}_2$ [3]
- IV. $\text{CO}_b \rightleftharpoons \text{CO}_{d.l.}$
- V. $\text{Pt} + \text{CO}_{d.l.} \rightarrow \text{Pt}-\text{CO}$

where Pt- signifies a species adsorbed on Pt, the subscript b is for the species in the bulk of the solution, and the subscript d.l. is for the species in the double layer. It should be remembered that essentially all of the Pt sites are normally covered with CO before application of an anodic pulse.

Experimental results indicate that the rate of step I is evidently equal to or slower than step II; otherwise, the oxygen concentration would increase with time, especially for the faster high-current sweeps, and the potential would steadily rise. [Previous work (7) has demonstrated that the potential of Pt in this region will be affected by the amount of adsorbed O on the surface.] The flatness of the CO

oxidation region at all sweep speeds indicates that the number of adsorbed oxygen atoms remains effectively constant until all of the CO is removed. In addition, if step I were faster than II, an excess of adsorbed O could be formed at high current densities, which would result in more coulombs being consumed than at low current density pulses. This is directly contrary to the experimental results obtained.

Carbon monoxide oxidation took place at about 1.0-1.2v, depending on CO partial pressure. This potential is near the low end of the oxygen atom adsorption region (0.88-1.76v) and supports the view that a small concentration of atomic oxygen is generated, which reacts with CO present on the electrode surface as fast as water is oxidized (step I). The fine structure of the charging curve in the CO region also supports this mechanism. For a dynamic system involving a sequence of several interdependent reactions, it is quite reasonable (10) that at the start of the reaction the concentration of a species may actually overshoot its ultimate steady-state concentration. After the double layer is charged by the pulse, the anode potential, which is believed to be a function of the atomic oxygen concentration on the surface of the electrode, overshoots and falls rapidly to some lower value. This shows an instantaneous excess of oxygen atoms on the surface. The oxygen atom concentration then falls to a lower steady-state value as the various reactant and product concentrations adjust themselves. Subsequently, when the degree of surface coverage, θ , of CO on the electrode is reduced to about 2/3, the anode potential rises a little. This may represent a slight increase in the concentration of atomic oxygen which is required to maintain the oxidation reaction at the required rate as the CO coverage falls toward zero.

Another interpretation of the initial overshoot is that, because of the high electrode surface coverage with CO, a small amount of adsorbed CO is initially electrochemically oxidized. This will make bare a sufficient number of Pt sites so that the oxidation of water to adsorbed oxygen atoms then occurs, with subsequent chemical reaction with adsorbed CO. This latter reaction would then be favored because it goes at a somewhat lower potential.

Surface Coverage of Platinum with Carbon Monoxide

Figure 3 shows that for a charging time longer than about 1000 μsec , as t increased (*i.e.*, as current density decreased), q_{CO} increased. At times shorter than about 1000 μsec , q_{CO} remained constant. The value of q_{CO} obtained at the shortest charging times represents the charge required to oxidize the CO that was adsorbed on the electrode before the anodic pulse was applied. The increased q_{CO} observed at longer charging times is due to oxidation of not only the initially adsorbed CO but also of the additional CO reaching the surface from the surrounding solution.

The numerical values given in Fig. 3 for the charge required to oxidize adsorbed CO are given in $\mu\text{coul}/\text{cm}^2$. Because of the method used to define surface area, however, the quantities actually compared in determining the surface coverage of Pt

with CO are the coulombs required to cover the surface with oxygen atoms [420 $\mu\text{coul}/\text{cm}^2$, based on the method used in ref. (7)] *vs.* the coulombs required to oxidize CO adsorbed on the same surface. Since the same apparatus was used to measure both quantities, any instrumental errors will tend to cancel out, and the ratio of the two values should be much more accurate than either one individually.

The solid circles plotted in Fig. 3(d) represent values of q_0 obtained from charging curves of clean platinum (*i.e.*, with no CO adsorbed on the surface) in pure sulfuric acid solution. The amount of charge transferred remains constant for charging times up to 1000 μsec and represents the charge required to cover the surface of the Pt bead with oxygen atoms. At longer charging times, q_0 increases as some process removes oxygen atoms from the surface during the time of the pulse. This process could be the combination of oxygen atoms to form oxygen molecules, which could then diffuse into solution, or it could be the dissolution of adsorbed atoms into the bulk of the platinum. Since analysis of charging curves in quiescent solution and in rapidly stirred solution show no significant difference in q_0 , the second process is probably dominant.

The area of the Pt bead was originally defined on the assumption that for each 420 μcoul transferred (after correction for d.l. charging) in the oxygen atom adsorption region, 1 cm^2 of Pt area was covered. The average of a number of later measurements, shown in Fig. 3(d), is 426 $\mu\text{coul}/\text{cm}^2$; this shows the reproducibility of such measurements.

Curves (a), (b), and (c) in Fig. 3 show that the amount of CO initially adsorbed on the surface of the anode increases somewhat with increasing CO partial pressure, and additional oxidizable material reaches the electrode at charging times longer than about 1000 μsec . In Fig. 3(c), for the case $p_{\text{CO}} = 0$, the charge required to oxidize CO adsorbed at open-circuit rest potentials of 0.3 to 0.4v was essentially the same as that required to deposit a monolayer of O atoms on the Pt bead when clean (428 $\mu\text{coul}/\text{cm}^2$ as compared to 426 $\mu\text{coul}/\text{cm}^2$); in this case CO coverage is evidently unity (one CO molecule per surface Pt atom). The charge q_{CO} , is independent of charging time because there is virtually no additional CO in the solution to be adsorbed on the electrode during the charging pulse.

For CO partial pressures of 0.1 and 1.0 atm [Fig. 3(a) and (b)], surface coverage increased to about 1.02 and 1.06 CO molecules per Pt atom, respectively, indicating that additional CO physically adsorbs on the base chemisorbed layer. The relationship between the physically adsorbed CO and CO partial pressure is, within experimental error, in accordance with Henry's law. At these partial pressures, q_{CO} is larger at longer charging times because significant transport of CO from solution occurs.

The total amount of CO oxidized during a charging time of 10,000 μsec when $p_{\text{CO}} = 1$ atm is 550 $\mu\text{coul}/\text{cm}^2$; the excess over the initial surface coverage which must have migrated to the surface during the charging pulse is 97 $\mu\text{coul}/\text{cm}^2$. The corresponding excess for $p_{\text{CO}} = 0.1$ atm and 0.0037 atm is 68 and 12 $\mu\text{coul}/\text{cm}^2$, respectively.

To determine whether diffusion or adsorption of CO in solution was the slow process limiting the rate of increase of q_{CO} as the charging time increased, charging curves were obtained for both quiescent and vigorously stirred solution. Since the rate of diffusion could be independent of rate of stirring if the diffusion layer were sufficiently thin, 0.0037 atm CO was used in these experiments to confirm the results obtained with higher CO pressures. While the thickness of the diffusion layer is an uncertain quantity, particularly under the conditions of this experiment, it was most certainly thick enough to be affected by the stirring rate used. At 0.0036 atm CO, the volume of solution that contains enough CO to contribute the excess of q_{CO} observed ($12 \mu\text{coul}/\text{cm}^2$) may be computed, and from this the thickness of a reasonable diffusion layer may be computed. The layer was calculated to be about 1.4 mm thick in this, the most dilute solution used.² This result is substantially larger than the value usually assumed (about 0.2 mm in a system with natural convection and a vertical electrode) (12).

To minimize experimental errors, charging curves were alternately obtained for stirred and unstirred solution. Under no conditions did the average values of q_{CO} in stirred and unstirred solution show significant differences, nor were the average values consistently higher in stirred solutions than those in unstirred solution. Figure 1 shows typical results. In each of these oscillograms the bottom curve was taken in quiescent solution, and the top curve was taken in solution which was stirred with gas flow rates well in excess of 1000 ml/min. The fact that the rate of transfer of CO to the electrode is independent of stirring rate, even in very dilute solutions, shows that some process is slower than diffusion of CO (step IV, Eq. [3]). The most probable rate-controlling step is the adsorption of CO (step V, Eq. [3]) on the surface of the electrode.

The diffusion coefficient, D_{CO} , for CO would be expected to be close to that of N_2 , $2.25 \times 10^{-5} \text{ cm}^2/\text{sec}$ at 25°C (13). Using this value for D_{CO} and assuming, as a first approximation, that the conditions of semi-infinite linear diffusion (3-5, 14) prevail, then the amount of CO which can diffuse to the electrode in the time of a charging pulse, q_{diff} , may be calculated. Expressed in terms of coulombs and for the case where $p_{CO} = 1.0 \text{ atm}$, this quantity becomes

$$q_{diff} = 0.96 \times 10^{-3} t^{1/2} \text{ coul}/\text{sec}^{-1/2}/\text{cm}^{-2} \quad [4]$$

Equation [4] can give only a rough approximation of q_{diff} , however, because one of the assumptions underlying its use is that the concentration of the oxidizable substance at the electrode is equal to zero as soon as electrolysis has started. In our case, this is not true until the end of the CO region. Thus surface coverage, θ_{CO} , will be varying between 1 and 0 as the CO region is traversed, and because the

amount of extra CO being adsorbed on the electrode is small compared to the amount initially present, θ_{CO} will vary almost linearly with t/t_{CO} , where t is the time elapsed after the start of CO oxidation and t_{CO} is the total charging time for the CO oxidation plateau. On the average, then, during the time of the charging pulse in the CO oxidation region θ_{CO} will be about $1/2$, and to a first approximation the amount of CO which would diffuse to the electrode under these conditions might be about $(1/2) q_{diff}$ as calculated from Eq. [4] or $48 \mu\text{coul}/\text{cm}^2$ for a charging time of $10^4 \mu\text{sec}$ when $p_{CO} = 1 \text{ atm}$. The actual Δq_{CO} observed was $97 \mu\text{coul}/\text{cm}^2$, and since this was shown to be adsorption limited, the rate of diffusion must be even larger. Therefore, in order to fit Eq. [4] to the experimental results, one would have to assume that the diffusion coefficient of CO in 1M H_2SO_4 is appreciably higher than the value used. The alternate, and more likely possibility, is that this adaptation of the semi-infinite linear diffusion equation to this system is not valid.

The Oxygen Atom Adsorption Region

The number of coulombs per square centimeter transferred in the oxygen atom adsorption region is given in Fig. 3(d). For a clean Pt surface in H_2SO_4 and for charging times less than 1000 μsec , q_0 is constant and represents the charge required to deposit a single monolayer of O atoms on the surface, giving at 1:1 correspondence between O and Pt surface atoms. The values of q_0 for solutions containing CO is independent of CO partial pressure, suggesting that the increase in q_0 at long charging times is not due to adsorption and oxidation of additional CO on the surface. This is confirmed by the fact that q_0 is independent of stirring rate, which strongly indicates that in the potential range of 1.3 to 1.8v, CO is not adsorbed on Pt. The increase in q_0 to over $426 \mu\text{coul}/\text{cm}^2$ at times longer than 1000 μsec is attributed to absorption of some of the O atoms formed into the surface layers of Pt (15), freeing fresh surface for the oxidation of additional water.

For charging times less than 1000 μsec , q_0 decreases steadily to values indicating formation of less than one monolayer of oxygen atoms. It is suggested that this is due to blocking of part of the surface by CO_2 , which is formed in the CO oxidation region, and which has not had time to diffuse away from the surface. The fact that the q_0 equivalent to a full monolayer is obtained at charging times of about 1000 μsec indicates that by this time removal of CO_2 must be essentially complete.

Acknowledgments

The authors are indebted to Dr. J. C. White of the Naval Research Laboratory and Professor P. H. Emmett of Johns Hopkins University for helpful discussions concerning this work.

Manuscript received Jan. 3, 1964; revised manuscript received March 23, 1964. This paper was presented at the Toronto Meeting, May 3-7, 1964.

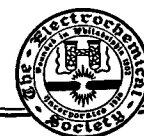
Any discussion of this paper will appear in a Discussion Section to be published in the June 1965 JOURNAL.

²This assumes that the concentration of CO in the saturated 1M H_2SO_4 solution under 1 atm partial pressure is $9 \times 10^{-7} \text{ mole}/\text{cm}^3$ (11), that the concentration of CO under 0.0037 atm can be calculated by Henry's law, that the Pt bead is a sphere whose true area is twice its geometric area, that the concentration gradient in the diffusion layer is linear, and thus that the thickness of the diffusion layer is twice the thickness of the layer which holds sufficient CO to account for the excess q_{CO} observed.

REFERENCES

1. M. A. H. Lanyon and B. M. W. Trapnell, *Proc. Roy. Soc.*, **A227**, 387 (1955).
2. (a) D. Brennan, M. J. Graham, and F. H. Hayes, *Nature*, **199**, 1152 (1963); see additional references in (3-5); (b) R. P. Eischens and W. A. Pliskin, in "Advances in Catalysis," Vol. 10, Academic Press, Inc., New York (1958).
3. S. Gilman, *J. Phys. Chem.*, **66**, 2657 (1962).
4. S. Gilman, *ibid.*, **67**, 78 (1963).
5. S. Gilman, *ibid.*, **67**, 1898 (1963).
6. S. Schuldiner and R. M. Roe, *This Journal*, **110**, 1142 (1963).
7. S. Schuldiner and R. M. Roe, *ibid.*, **110**, 332 (1963).
8. S. Schuldiner, *ibid.*, **106**, 440 (1959).
9. S. Schuldiner and T. B. Warner, *J. Phys. Chem.*, **68**, 1223 (1964).
10. R. M. Lago, J. Wei, and C. D. Prater, *J. Chem. Ed.*, **40**, 395 (1963).
11. "Handbook of Chemistry and Physics," 43rd Ed., Chemical Rubber Publishing Co., Cleveland, 1961; A. Christoff, *Z. Phys. Chem.*, **55**, 622 (1906).
12. N. Ibl, *Chemie-Ing.-Techn.*, **33**, 69 (1961).
13. R. E. Smith, E. T. Friess, and M. F. Morales, *J. Phys. Chem.*, **59**, 382 (1955).
14. P. Delahay, "New Instrumental Methods in Electrochemistry," p. 61, Interscience Publishers, Inc., New York (1954).
15. T. V. Kalish and R. Kh. Burshtein, *Doklady Akad. Nauk, S.S.S.R.*, **88**, 863 (1953); *C.A.*, **48**, 56a (1954).

Technical Notes



Constancy of a Modified Weston Standard Cell over Long Periods

W. C. Vosburgh

Department of Chemistry, Duke University, Durham, North Carolina

and Roger G. Bates

National Bureau of Standards, Washington, D. C.

In 1937 it was shown that the combination of two alterations in the construction of the saturated Weston cell gave a cell with a temperature coefficient between a quarter and a third of that of the saturated Weston cell and opposite in sign (1). The two alterations were the saturation of the electrolyte with $\text{CdSO}_4 \cdot \text{Na}_2\text{SO}_4 \cdot 2\text{H}_2\text{O}$ as well as $\text{CdSO}_4 \cdot 8/3\text{H}_2\text{O}$ (with excess of both salts) and the addition of enough Bi to the Cd amalgam to give a three-phase amalgam (2). The cells were reproducible and were of satisfactory constancy over a period of 2-2.5 years (3). When 4 of the cells were mounted in wooden boxes and maintained at variable room temperature (20-28°C) over a period of 8 months no variation larger than 0.01% (0.1 mv) of the emf was observed (3).

Some of the experimental cells have been used as practical standards without special temperature regulation for over 20 years. The records of 5 cells are available and show very satisfactory constancy. Cells 749 and 754 were used in the Analytical Chemistry Division of the National Bureau of Standards, and cell 756 was kept there unused and in an unmounted condition. Cells 752 and 753 were used in the Chemistry Department of Duke University. The variation of emf over a period of 26 years is shown in Table I. In columns 2 and 3 is given the emf measured at Duke University in 1937 and in

Table I. Constancy of emf for 26 years

Cell No.	Emf at 25°C, v				
	1937	1943	1961	1963	1963
749	1.01875	1.01873	1.01880	1.01871	1.01874
752	1.01875	—	—	1.01875	1.01873
753	1.01875	1.01873	—	1.01876	1.01874
754	1.01873	—	1.01872	1.01876	1.01876
756	1.01872	1.01868	1.01863	1.01866	1.01871

1943 at 25°C against carefully controlled standards. Values of the emf in "international volts" recorded prior to 1948 have been converted to "absolute volts" by multiplying by the factor 1.00033. Measurements in 1961 by direct comparison with the standards of the National Bureau of Standards gave the data in column 4, and similar measurements in 1963 gave the data in column 5. Values in column 6 were obtained in the Analytical Chemistry Division with respect to laboratory reference cells certified in terms of the NBS standards and are included to give an idea of the short-time variability under such conditions as fluctuating room temperature, mechanical disturbances due to moving, and the like.

The modified Weston cell containing Na_2SO_4 and Bi is much more nearly constant in emf over long periods than the unsaturated cell, whose emf has been found to decrease by 20-85 μv per year (4).

The temperature coefficient of the modified Weston cell is only $+0.013 \text{ mv deg}^{-1}$ over the room temperature range, or about one-quarter that of the Weston normal cell at 25°C . Special temperature regulation is therefore unnecessary for many purposes.

Manuscript received February 21, 1964.

Any discussion of this paper will appear in a Discussion Section to be published in the June 1965 JOURNAL.

REFERENCES

1. W. C. Vosburgh, M. Guagenty, and W. J. Clayton, *J. Am. Chem. Soc.*, **59**, 1256 (1937).
2. W. C. Vosburgh and H. C. Parks. *ibid.*, **61**, 652 (1939).
3. W. C. Vosburgh, P. F. Derr, G. R. Cooper, and B. Pettengill, *ibid.*, **61**, 2687 (1939).
4. W. C. Vosburgh, *J. Opt. Soc. Amer.*, **11**, 59 (1925); G. W. Vinal, D. N. Craig, and L. H. Brickwedde, *Trans. Electrochem. Soc.*, **68**, 139 (1935); G. D. Vincent, *IRE Trans. Instr.*, **1-7**, 221 (1958).

Alkali Metal Voltaic Cells

D. C. Hamby, B. W. Steller,¹ and J. B. Chose²

Linfield Research Institute, McMinnville, Oregon

The utilization of the alkali metals Na and Li as anodic reactants in voltaic cells has long been of interest to the electrochemist (1-8). Among the reasons cited for not exploiting the favorable properties of these materials in practical cells are: (a) the difficulty of preventing undesirable side reactions; and (b) the difficulty of restricting the reactions of the alkali metal to the anode (9). A proposed solution to these problems is to use cells of the type

Alkali Metal Alloy Anode	Nonporous Membrane	Molten Salt Electrolyte	Cathode
(charge transport by alkali metal ions)			

This paper describes several cells of this type which have been constructed and tested in this laboratory. Cell characteristics and resistivity data on membrane materials are given.

Experimental

The outer cell envelope consisted of two parts, a closed-end Vycor tube and a Pyrex top (Fig. 1). The Vycor tube was 64 mm in diameter, 45-60 cm long, and flanged at the open end; the Pyrex top, also fashioned from 64 mm tubing, had a matching flange and tubular openings through which electrodes, thermocouple tubes, and sampling tubes could be introduced into the cell. When assembled, the glass flanges were separated by a Tygon gasket and clamped together by metal clamps. The various cell components, which entered through the cell top, were coupled by means of rubber tubing of appropriate sizes to the tubular openings in the Pyrex top. Thus the cell was air tight during operation.

An inner crucible of Vycor, 51 mm in diameter and 10-15 cm high, contained the electrolyte. This inner crucible was used as a safety factor and because of the fact that solidification of the melt usually caused cracking of the electrolyte container. An additional feature which proved useful was the

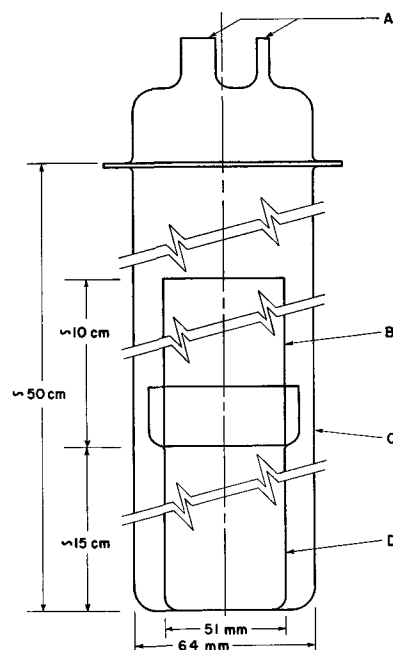


Fig. 1. Cell envelope: A, openings in Pyrex top for cell components; B, Vycor tube; C, outer Vycor envelope; D, Vycor container for melt.

independent Vycor tube, labeled B in Fig. 1. Because the Vycor envelope was immersed in the main furnace only to a depth of 10 cm evaporated salt condensed on the inside of tube B, this salt could be returned to the crucible, D, by raising the cell temperature and/or utilizing auxiliary heating coils around B.

All salts used in electrolyte preparation were reagent grade. The salts CaCl_2 , NaCl , KCl , and LiCl were vacuum oven dried and stored in screw-cap bottles until used. NiCl_2 required further drying treatment; HCl was passed over the oven dried powder for several hours at 400°C . Final dehydration of each melt was carried out after mixing the oven dried salts by chlorinating the molten salts in the presence of carbon for at least 1 hr (10). In the cases where Ni was used as a cathode grid material, dry, oxygen-free argon was used to purge chlorine from the envelope and to maintain an inert atmosphere in the envelope and over the anode alloy during cell operation.

¹ Present address: Tektronix, Inc., Beaverton, Oregon.

² Present address: Lawrence Radiation Laboratory, Livermore, California.

Table I. Membrane materials

Sample No. or name	Practical composition, w/o		Actual analysis, w/o		Fabrication (procedure)	Firing temp, °C
8	Spodumene	74.2	SiO ₂	57.9	Wet milled, slip cast	1000
	Edgar Plastic		Al ₂ O ₃	30.7		
	Kaolin	7.0	Li ₂ O	7.7		
	Tenn. No. 1		Fe ₂ O ₃	2.0		
	Ball Clay	7.0	F	4.1†		
9	LiF	11.8			Wet milled, slip cast	1065
	Glass F, Fritted	69.5	SiO ₂	50.5		
11	Tenn. No. 1				Sintered, wet milled, spray dried, pressed	1100
	Ball Clay	17.1	Al ₂ O ₃	41.6		
	Georgia Kaolin	13.4	Na ₂ O ₃	6.6		
	LiCO ₃	38.0	Li ₂ O	20.2		
	Georgia Kaolin	62.0	SiO	42.5		
			Al ₂ O	35.5		
12	Spodumene	80.0	Fe ₂ O ₃	0.3	Wet milled, spray dried, pressed	1150
	Glass E, Fritted	20.0	TiO ₂	0.8		
Glass E	SiO ₂	76.1	Na ₂ O	0.2	Dry milled, fired, pulverized for frit	1200
	Al ₂ O ₃	8.1	K ₂ O	0.3		
	Li ₂ O	15.8				
Glass F	Na ₂ SiO ₃	26.8			Dry milled, fired, pulverized for frit	1250
	Al ₂ O ₃	22.4				
	SiO ₂	24.5				
	Tenn. No. 1					
	Ball Clay	11.3				
Penberthy Glass	Georgia Kaolin	14.9	SiO ₂	78.6	Drawn from melt	
			Na ₂ O	19.4		
			Al ₂ O ₃	0.9		
			K ₂ O	0.1		
			CaO	0.0		
		Fe ₂ O ₃	0.08			
Labrie and Lamb††						

† Fluorine was determined in a second and independent analysis.
 †† Procedure for preparation given in original reference (11).

Tubular anode membranes, closed at one end, were used in all cells. Fabrication information for the membranes is given in Table I, wall thicknesses are included in Table II. When possible, the membrane tubes were fused directly to glass tubes which allowed positioning of the membranes from outside the envelope. In cases in which a membrane could not be sealed to glass because of difficulty in

matching coefficients of expansion, a Vycor basket attached to a Vycor tube was used to support the membrane (see Fig. 2). Soft glasses used as membrane materials were supported by both a Vycor basket and a porous crucible (Norton, RA98 99% aluminum oxide, particle retention 20 μ) which prevented sagging of the glass membrane during the experiment (see Fig. 3).

Table II. Cell Data

Cell No.	Anode alloy	Membrane	Electrolyte, mole %		Cathode	Operating temp, °C	Open-circuit voltage, v	Cell life
III	Na(Sn)	Sodium aluminosilicate (Labrie and Lamb), 1 mm wall	NaCl 46 CaCl ₂ 45 NiCl ₂ 9		Ni	730	1.85 (1.3 a/o Na)	3 hr
VI	Li(Sn)	Lithium aluminosilicate, Sample No. 8, 2 mm wall	LiCl 45 KCl 45 NiCl ₂ 10		Ni	500 to 900	1.5 (730°C and 1 a/o Li)	22 hr intermittently over 5 day period
XV	Li(Sn)	Lithium aluminosilicate, Sample No. 12, 2 mm wall	LiCl 100		Cl ₂ , C	720	2.43 (1 a/o Li)	26 hr
XII	Na(Sn)	Penberthy soda glass, 1 mm wall	NaCl 100		Cl ₂ , C	820	2.35 (1 a/o Na)	15 hr
VII	Na(Sn)	Sodium aluminosilicate, Sample No. 9, 1 mm wall	NaCl 45 KCl 45 NiCl ₂ 10		Ni	680	1.6 at (1 a/o Na)	11 hr

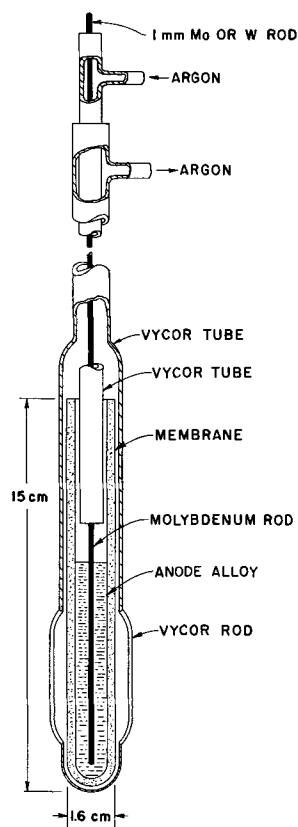


Fig. 2. Design of hard membrane electrode; used only in cases in which the hard membrane could not be sealed to glass.

Each anode was prepared by placing a weighed quantity of tin in the membrane tube before cell assembly. The alloy was then prepared *in situ* by electrolysis after the cell had reached operating temperature. Alloy concentrations were calculated by Faraday's law. Electrical contact was made to the anode by means of 1 mm diameter molybdenum or tungsten rod. No mechanical stirring was attempted in the anode compartment.

Nickel grids consisted of cylindrical sheet or screen placed symmetrically around or near the anode tube. Electrodes consisting of porous carbon tubes threaded and cemented to nonporous graphite tubes served as chlorine cathodes. Under the high temperature and corrosive conditions of cell operation no coating of the chlorine cathodes was attempted. Both Speer Carbon Company No. 7716 and National Carbon Company, grade No. 60, porous carbon were used to construct chlorine electrodes.

The resistivities of various membrane materials listed in Table I were measured under an inert atmosphere. Solid cylindrical samples were coated on the ends with graphite and placed between carbon steel electrodes. Chromel-Alumel thermocouples placed in contact with the sample surface were used to control and record the sample temperature. Resistances were measured with an ESI 1000-cycle resistance bridge.

Cell characteristics which were measured were (a) open-circuit voltage, (b) instantaneous polarization, (c) time dependent polarization, (d) energy efficiency, (e) utilization of anode reactant, and (f)

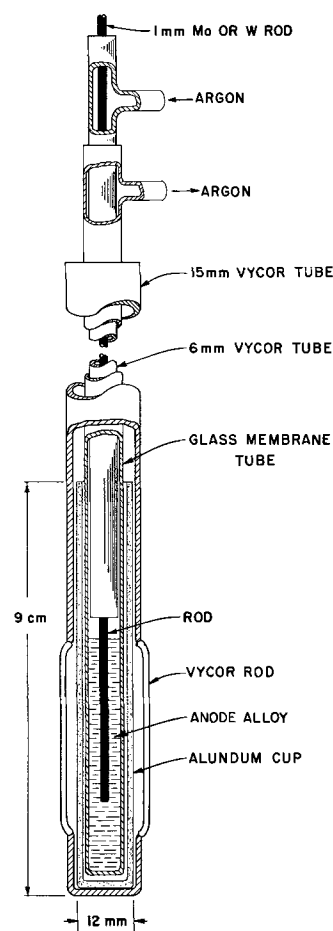


Fig. 3. Design of soft glass membrane electrode

cell life. Energy efficiency and reactant utilization as used in this paper are defined as follows

$$\text{Energy efficiency (\%)} = \frac{\int I(t) \text{ discharge } V(t) dt}{\int I(t) \text{ charge } V(t) dt} \times 100$$

$$\text{Utilization (\%)} = \frac{\int I(t) \text{ discharge } dt}{\int I(t) \text{ charge } dt} \times 100$$

where $I(t)$ is cell current, $V(t)$ is terminal potential difference, and t is time.

The procedure used in determining energy efficiency and utilization may be discussed with reference to Fig. 4. The cell was first cycled through several charge and discharge cycles. Each charging cycle was carried out at constant current for a definite period of time, 500 ma for 10 min for cell VI. During each discharge cycle the cell current was decreased stepwise from 250 ma to 100 ma to 50 ma as the anodic reactant was depleted; however, each cycle was terminated when the terminal potential had reached 0.5v at 50 ma cell current. Thus, after establishing a cycle, data such as that shown in Fig. 4 and 6 were recorded. The assumption was made that the alloy concentration was uniquely determined by the electrode potential at a particular current density. Current densities were calculated on the basis of apparent surface areas of the electrodes.

Results and Discussion

Selected cell data are given in Table II and in Fig. 4 through 6; both solid (sodium or lithium

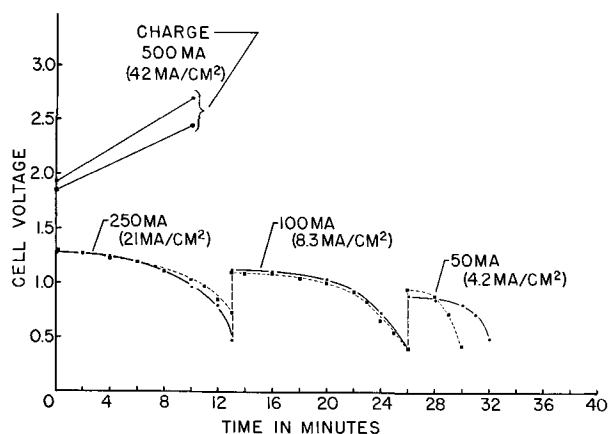


Fig. 4. Time dependent polarization data for cell VI. Both total cell currents and apparent anodic current densities are given. Two complete cycles are shown. The straight lines indicate the charging process and the lower curves the discharge process. Efficiencies and utilizations are stated for each individual cycle: utilization, ●, 97%, ■, 95%; energy efficiency, ●, 45%, ■, 50%; temperature, 610°C.

aluminosilicate ceramics) and semi solid (glass) membrane materials are represented. Resistivities of the membrane materials described in Table I are plotted in Fig. 7 as functions of $1/T^{\circ}K$. Resistivities estimated from instantaneous polarization data for cell VI as given in Fig. 5 were in essential agreement with the data of Fig. 7 in the range 720°-840°C.

The maximum continuous anodic current density recorded at a terminal potential difference greater than 1v, 42 ma/cm², was observed during the testing of cell III which utilized a sodium aluminosilicate membrane fabricated by Labrie and Lamb¹¹. Wall thickness of this membrane was 1 mm.

The lithium aluminosilicate ceramics, used in cells VI and XV were of interest because of their low resistivity (see Fig. 7) and good mechanical strength at temperatures up to 900°C. Furthermore, it was observed that the lithium ceramics were less subject to chemical attack by the lithium anode alloys than were the sodium ceramics by the corresponding sodium alloys. The effect of chemical attack on the sodium ceramics was a surface blackening which was observed in one case to have

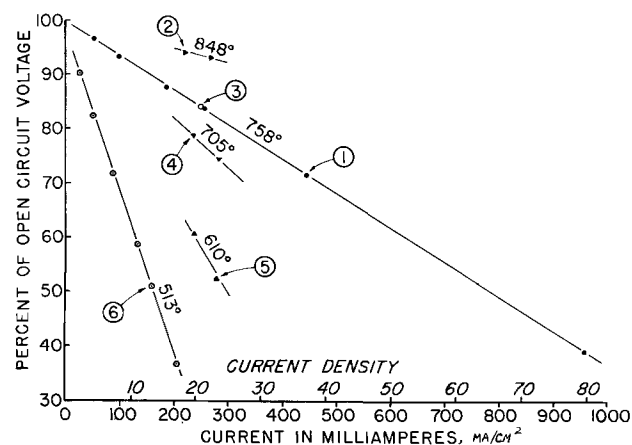


Fig. 5. Instantaneous polarization for cell VI. The circled numbers indicate the chronological sequence of data taking.

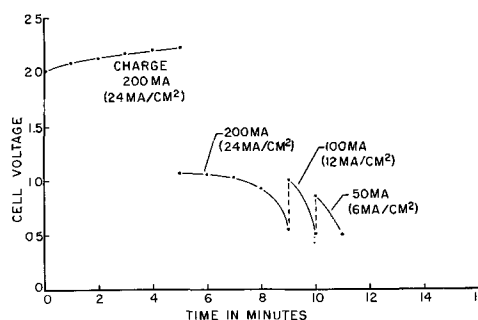


Fig. 6. Time dependent polarization data for cell VIII. Both total cell current and apparent anodic current density are given. Utilization, 95%; energy efficiency, 40%; temperature, 690°C.

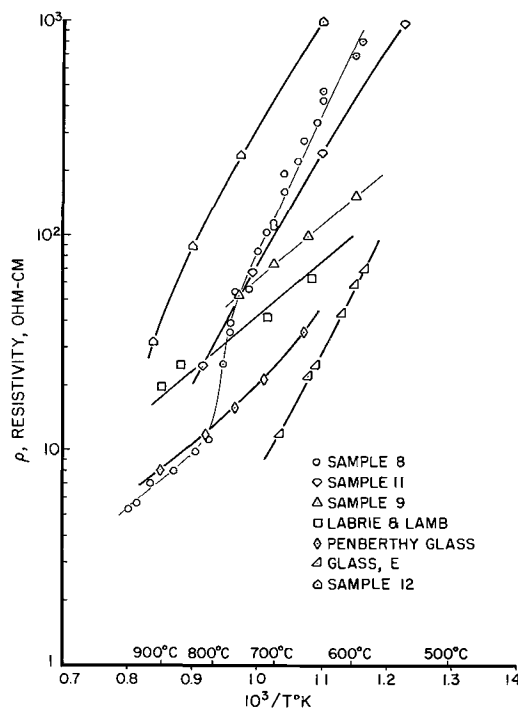


Fig. 7. Resistivity data for the materials listed in Table I

penetrated to a depth of 0.1 mm after being exposed to a 1 a/o (atom per cent) Na in Sn alloy for 11 hr at 680°C. Similar blackening was not observed with the lithium ceramic materials at comparable alloy concentrations and temperatures. Chemical attack was extreme in the case of the Penberthy glass membrane used in cell XII at 820°C. The glass was blackened throughout its 1 mm wall thickness after 15 hr of cell operation and cell resistance had increased to five times its initial value.

No direct measurement of ceramic or glass membrane porosities was attempted; however, observation of the depth of penetration of Ni⁺⁺ ions into the membrane offered a qualitative means of judging porosity. In the case of the glass membranes and the sodium ceramic membranes penetration was negligible and caused only a light surface coloration. The lithium aluminosilicate membrane of cell IV was observed to have been penetrated to a depth of approximately 1/2 mm of the 2 mm wall in 26 hr. The result was typical for membranes of this type.

The life termination mechanism for ceramic membrane cells was, in every case, cracking of the membrane. Cracking was indicated experimentally by failure of the cell to charge properly or to hold charge; in most cases, close examination of the membranes after dismantling the cells disclosed visible cracks. Cracking was observed both in the presence and in the absence of ions foreign to the membrane in the melt, and the lifetime before cracking varied widely. The exact cause for membrane cracking remains undetermined. Although the glass membranes did not crack, an increase in resistivity with time was observed, leading to limited lifetime.

The deviation of cell reactant utilization from 100% is attributed to (a) volatilization, (b) side reactions with the membrane materials, (c) reaction of the alkali metal with residual reducible gases in the membrane tube, and (d) lack of stirring in the anode compartment.

It is concluded that further improvements of the life and performance of membrane cells of the type described depend primarily on improvement of the resistivity and mechanical stability of the conducting membrane material. The results of this work demonstrate that hard ceramic membranes having resistivities of 20 ohm-cm or less can be fabricated and that these membranes can be utilized in high temperature alkali metal voltaic cells. It remains to be demonstrated whether or not membranes of this type can be fabricated which remain mechanically stable under the severe conditions of cell operation.

Acknowledgments

The research reported in this paper has been sponsored by the Electronics Research Directorate of the Air Force Cambridge Research Laboratories, Office of Aerospace Research, under contract AF19(604)-7395.

The authors wish to express their thanks to Robert Johnson of Tektronix who assisted in ceramic fabrication and to R. J. Labrie, N.B.S., who generously contributed several porcelain membrane tubes.

Manuscript received Jan. 3, 1964; revised manuscript received April 6, 1964.

Any discussion of this paper will appear in a Discussion Section to be published in the June 1965 JOURNAL.

REFERENCES

1. E. F. Uhler and G. A. Lozier, Air Force Systems Command, Technical Documentary Report No. ASD-TDR-62-4, AD 277197, April, 1962.
2. T. P. Dirkse, Naval Research Lab., Report No. P-2503, 1945.
3. E. A. Schumacher, Terminal Technical Report, National Carbon Company, ONR Contract Nonr 1785(00), ASTIA 301978.
4. E. Yeager, *et al.*, Western University, OWR Contract Nonr-581(00). February, 1955, AD 75335.
5. J. Gyuris, U. S. Pat. 2,081,926 (June 1, 1937).
6. J. Gyuris, U. S. Pat. 2,102,701 (Dec. 21, 1937).
7. G. S. Lozier, Proc. 15th Annual Power Sources Conf., p. 80 (1961).
8. R. D. Weaver, S. W. Smith, and N. L. Willman, *This Journal*, **109**, 653 (1962).
9. M. A. Bredig, J. W. Johnson, and W. T. Smith, *J. Am. Chem. Soc.*, **77**, 307 (1955).
10. D. L. Maricle and D. W. Hume, *This Journal*, **107**, 354 (1960).
11. R. J. Labrie and V. Lamb, *ibid.*, **106**, 895 (1959).

Electrolytic Cell for X-Ray Diffraction Studies of Electrode Phenomena

Jeanne Burbank and C. P. Wales

U. S. Naval Research Laboratory, Washington, D. C.

The identification of materials taking part in an electrochemical reaction is a necessary part of characterizing fundamental electrode processes. Measurements of a purely electrochemical nature are not definitive of themselves and must be augmented by analytical data to identify the species acting in an electrode system. In many instances side reactions are possible, and it is of interest to know whether and under what conditions side reactions actually take place. When solid crystalline phases are involved, x-ray diffraction may be used for their identification. Usually the electrode is removed from the electrolytic cell for separate x-ray diffraction examination; however, some investigators (1-5) have used electrolytic cells in place on x-ray machines under various conditions.

Briggs (1) used a wire electrode oscillating partly out of the electrolyte, registering the x-ray diffrac-

tion pattern from the upper part of the wire. When an unstable product was being formed there could be self-discharge on the upper part of this wire, where the effective current density was lower than the average value for the wire as a whole (2). Falk (3) sealed a pair of electrodes in a thin polyethylene bag. Before x-ray examination the surface of the test electrode facing the counter electrode was moved to the edge of the plastic to minimize electrolyte thickness. The resulting pattern included polyethylene peaks. Salkind and Bruins (4) used plastic cells with horizontal electrodes on a vertical circle x-ray goniometer. The test electrode did not face the counter electrode directly, and the patterns were corrected for minor displacement of the sample from the rotation axis of the goniometer.

This report describes a cell designed for use on a General Electric horizontal circle x-ray spectro-

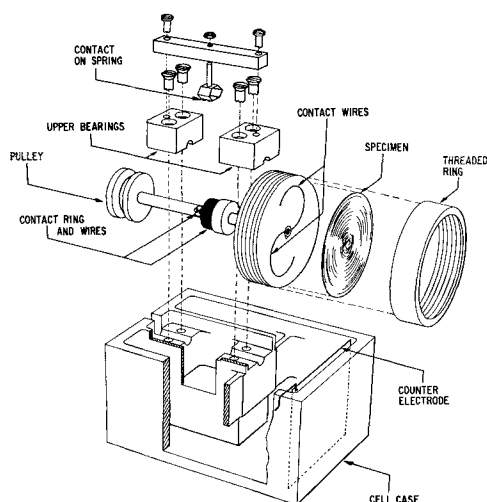


Fig. 1. Expanded view of electrolytic cell. Portions of outer and inner walls of the cell case are omitted for clarity, as indicated by the hatching.

goniometer, permitting the x-ray examination to be made simultaneously with electrochemical measurements and visual observations.

Cell Design

The cell is shown in Fig. 1. All parts are made of Teflon except the screws, the pulley, and the electrical contact system. An electrode of the specimen material, a disk 57 mm diameter and any thickness up to 6 mm, is mounted vertically in the cell so that it is always half submerged in electrolyte. The specimen disk is held tightly against platinum contact wires by a threaded retainer ring. The inner edge of the specimen disk can be coated with an inert stopcock grease to prevent any electrolyte that might leak past the retainer from reaching the back side of the sample. Platinum contact wires pass through a hole in the drive shaft and are connected to the contact ring by a small screw. This contact ring is machined from brass and plated with successive layers of nickel-cobalt, gold, and finally rhodium to prevent corrosion. The moving contact is made through platinum or two small buttons of Palinay which are fastened onto a gold-plated beryllium-copper spring.

The horizontal x-ray beam passes above the cell case and is reflected from the upper portion of the rotating electrode which is not submerged. A counter electrode faces the submerged part of the specimen disk in the same compartment of the cell. A reference electrode can be put in one of the other compartments where it does not interfere with the x-ray beam path.

A synchronous motor with appropriate reduction gears rotates the specimen disk by a belt drive to the pulley. The specimen rotates continuously and remains wet with a film of electrolyte. The current need not be interrupted during the x-ray examination because the electrode is always partially submerged. The rotation rate may be varied so that the time elapsing between total submersion and registration of the x-ray pattern may be made quite short and is limited only by the onset of splash or by the build-up of an electrolyte film sufficiently

thick that adsorption of the x-ray beam becomes excessive. In the latter case an air jet can be blown at the reflecting area to thin the electrolyte film. Rotation speeds of 10 and 60 rpm have been used. An increased speed of rotation minimizes both unevenness in the diffraction pattern due to lack of sample flatness and decomposition of any unstable material formed during electrolysis. At 60 rpm the x-ray pattern was registered 0.25 sec after the sample left the meniscus, and the total drain time was 0.5 sec.

As the sample rotated the electrolyte gradually reached the inner cell compartment and, if this compartment filled, the electrolyte could then spill from the rear of the cell case. An airlift pump prevented this. The pump consisted of plastic tubing leading from a drainage well drilled partway into the bottom of the inner compartment. A slow air stream entered the tubing near its bottom. As air bubbles rose in the tube the electrolyte was carried along over the inner wall and was dumped back into a side compartment of the cell.

On a spectrogoniometer the pattern is recorded from only those crystals lying in the sample surface in the reflecting positions within the area covered by the impinging x-ray beam. In using the cell described here a larger-than-normal area of the sample is scanned by the beam as different sectors move into position during registration of the patterns. This same principle is used in the flat sample spinners available for study of medium and large grained specimens. The success of the diffractometer technique depends on having a sufficient number of crystals in the correct orientations in the sample surface to give satisfactory signal intensity. The rotating specimen will tend to insure maximum intensity for the diffraction peaks because more crystals contribute to the diffracted rays. This increase will tend to offset the loss in intensity caused by absorption of the beam in the thin film of the electrolyte coating the sample.

The cell is shown in place on the spectrogoniometer in Fig. 2. The cell is aligned on the spectrogoniometer by eye, and the final adjustment may be achieved conveniently by optical means. The vertical rotating specimen and the spectrogoniometer comprise a two-circle goniometer and the alignment



Fig. 2. Cell mounted on spectrogoniometer. Electrical wiring and part of the shielding were removed for this photograph.

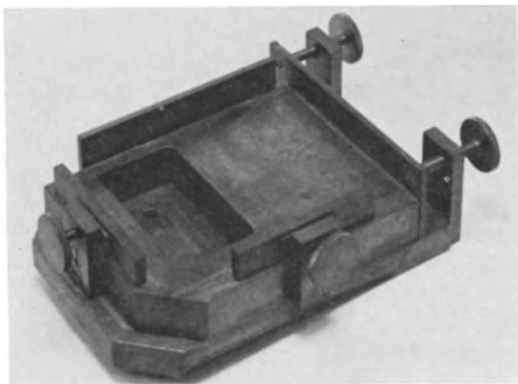


Fig. 3. Cell base

is performed in an analogous fashion. The cell mounting, Fig. 3, provides horizontal adjusting screws for bringing the sample surface into position at the axis of rotation of the horizontal circle. Shim stock may be used under the cell to bring the surface into vertical position. The axis of rotation of the horizontal circle must lie in the sample surface, and this is readily ascertained by using a telescope with cross hairs to view the stationary sample as it is swung through the arc of the spectrogoniometer. When in correct position the sample image lying on the cross hair will not move during rotation of the spectrogoniometer. Satisfactory diffraction patterns may usually be obtained from the specimen after this adjustment.

More precise alignment may be obtained by having a light beam traverse from the detector to the specimen to the source slit, the reverse of the path traversed during registration of the diffraction patterns. Two standard detector slits are mounted upside-down on the detector slit bracket using the holes and bolts that normally carry the detector and soler slits. A small light bulb placed between the detector tube housing and the first slit gives a collimated beam for alignment. The specimen surface is then brought into position so that the reflected slit image impinges on the x-ray source slit. When horizontal and vertical alignments are achieved, the slit image will not move during rotation of the specimen nor in swinging the spectrogoniometer through its full arc.

For studies requiring the absence of air, the cell may be enclosed in a flexible bag of plastic material to form a gas tunnel in which a positive pressure of the special atmosphere is maintained. Connections to the gas supply and to the source and detector slits may be made with elastic bands. Submersion heating or cooling coils may be placed in the electrolyte for varying or controlling temperature.

Two diffraction patterns obtained using this cell are shown in Fig. 4. The top pattern was made after an abraded Ag sample was anodized in 20% KOH for one day at an apparent current density of 0.05 ma/cm² until O₂ evolution began, then the current was increased to 0.1 ma/cm², and gassing continued for a second day. The sample showed a strong pattern for poorly crystallized AgO with the only other pattern being that of metallic Ag, probably coming from the substrate since the original strong Ag pattern was greatly obscured. This result agreed with

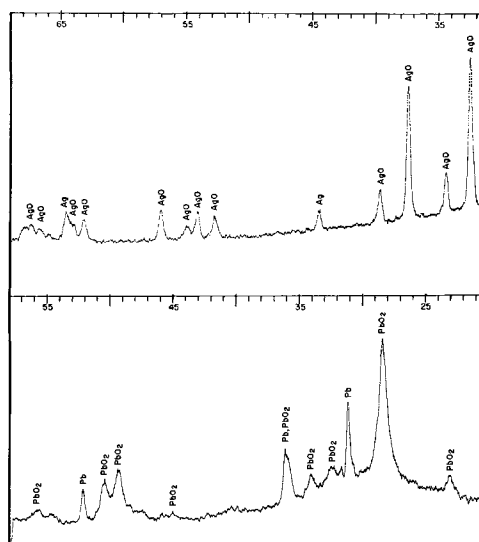


Fig. 4. Spectrogoniometer CuK α x-ray diffraction patterns. Top, Ag anodized to O₂ evolution in 20% KOH forming AgO. Bottom, Pb anodized to O₂ evolution in 1% KOH forming α -PbO₂. Both patterns made with sample rotating at 60 rpm and current flowing. Numbers at top of patterns give degrees 2 θ .

earlier work in which a silver anode was removed from a cell, and examined by x-ray diffraction after rinsing in water and blotting dry (6).

The bottom pattern of Fig. 4 is that of α -PbO₂ formed on metallic lead on anodizing in 1% KOH for 7 hr at an apparent current density of 2 ma/cm² followed by anodization at 1 ma/cm² overnight. The appearance of this polymorph of PbO₂ as the anodic product in alkali was earlier identified by x-ray diffraction on specimens removed from electrolytic cells and examined after drying (7). Following the recording of the bottom pattern in Fig. 4 the sample was discharged in the same electrolyte, and x-ray examination showed that the α -PbO₂ discharged directly to tetragonal PbO, again verifying earlier work (7). Thermodynamically, the higher oxide might be expected to discharge to one of the intermediate oxides, Pb₃O₄ or PbO_x, and if permitted to stand in contact in alkali, the higher and lower oxides do react chemically to form Pb₃O₄, but Pb₃O₄ did not appear as an anodic product directly.

During registration of the bottom diffraction pattern in Fig. 4 a jet of air was used to thin the electrolyte layer and increase the peak height relative to the background intensity. The specimen was not blown dry by this air jet, which was directed at the area scanned by the x-ray beam, so the surface remained wet with electrolyte for the entire 0.5 sec it was above the solution.

Many questions associated with electrode phenomena involving crystalline phases lend themselves to investigation by application of this technique. The cell was designed to study electrochemical processes of a widely varied nature including active material transformations in primary and secondary battery electrodes, electrolytic deposition, and corrosion processes. The use of this cell greatly lowers the possibility of an unstable crystalline compound being present but undetected by x-ray

diffraction, since the pattern may be registered at any time without interrupting the flow of current.

Manuscript received March 30, 1964.

Any discussion of this paper will appear in a Discussion Section to be published in the June 1965 JOURNAL.

REFERENCES

1. G. W. D. Briggs, *Electrochim. Acta*, **1**, 297 (1959).

2. G. W. D. Briggs, I. Dugdale, and W. F. K. Wynne-Jones, *ibid.*, **4**, 55 (1961).
 3. S. U. Falk, *This Journal*, **107**, 661 (1960).
 4. A. J. Salkind and P. F. Bruins, *ibid.*, **109**, 356 (1962); A. J. Salkind, Thesis, Polytechnic Institute of Brooklyn, 1958.
 5. E. J. Ritchie, Private communication.
 6. C. P. Wales and J. Burbank, *This Journal*, **106**, 885 (1959).
 7. J. Burbank, *ibid.*, **106**, 359 (1959).

Anodic Oxidation of Titanium in Formic Acid Electrolytes

D. M. Cheseldine

Sprague-TCC (Canada) Ltd., Toronto, Ontario, Canada

Data relating to the anodic oxidation of titanium are limited and much are conflicting, *e.g.*, values for the product of capacity and voltage (CV) ranging from 5 to 13 $\mu\text{f}\cdot\text{v}/\text{cm}^2$ have been reported (1-3). This may be due to the relatively few electrolyte systems which can be used to form thick insulating (>100v) uniform films on the metal.

The present study was conducted in formic acid with various additions. Piggott and Shreir (4) used formic acid/water mixtures to investigate the conditions under which the metal corroded or formed oxide films. In the present investigation it appeared that the limiting voltage in such solutions was about 60-70v, but with certain essential additions this range could be extended to 250v. The films formed up to this voltage have bright uniform interference colors.

Experimental

Titanium films were deposited on Pyrex cover glass slides by evaporation from tantalum boats under a vacuum of 10^{-4} to 10^{-5} Torr. Five charges, each in separate boats, were used for each deposition cycle. The first charge was evaporated in a position screened from the substrate to "getter" the vacuum chamber. The remaining four charges were evaporated in quick succession without breaking the vacuum. To minimize alloying, boat temperatures were held to the minimum consistent with most of the charge being evaporated in 30 sec. The deposit pattern was obtained by metal masking, the anodizable metal area on each substrate being about 2 cm^2 . The area for formation was defined by stopping off with either an air curing silicone rubber or a silicone varnish.

Formation was at constant current (values ranging from 0.1 to 3.0 ma/cm^2) at room temperature in a stirred solution using a platinum foil cathode. Voltage was measured across the cell, and allowance was made for the IR drop in the solution as measured using a very high impedance volt meter between the cathode and a platinum probe placed near the anode.

B.D.H. analar reagent formic acid (98-100%) was used to make up the electrolytes. It had a specific resistance of about 5500 ohm-cm at 25°C.

Capacity and dissipation factor measurements were made at 120 cycles in the formation electro-

lyte. Film colors were compared with a tantalum optical step gauge (2v steps) which was used as an arbitrary measure to compare the optical thicknesses of the titanium oxide films. All optical thicknesses are recorded in terms of a tantalum formation voltage.

Results

With little or no water present in the electrolyte the films have a low capacity, appear optically thinner, and require less coulombs for their formation than films formed to the same voltage in more aqueous electrolytes. There is an optimum water content between about 5 and 10% in which films showing maximum capacity are formed. With higher water concentrations some "graying" of the film occurs at higher voltages.

Up to 100v (Table I), the coulomb expenditure and optical thickness are proportional in either electrolyte to the voltage increment, indicating that

Table I. Anodic oxidation of titanium deposits in electrolytes 1 and 2

Formation at 1 ma/cm^2 constant current								
Formation, v	Capacity, $\mu\text{f}/\text{cm}^2$		Equivalent optical thickness, v (Ta)		Ratio 1/2	Charge/volt, coulombs/ $\text{v}/\text{cm}^2 \times 10^3$		Ratio 1/2
	1	2	1	2		1	2	
20	0.62	0.59	23	19	1.21	2.60	1.90	1.37
60	0.21	0.16	68	56	1.22	2.72	2.00	1.36
100	0.11	0.081	112	93	1.20	2.69	1.95	1.37
140	0.073	0.045	150	120	1.25	2.78	1.78	1.56
180	0.056	0.028	192	148	1.30	2.72	1.65	1.65
220	0.044					2.69		
260	0.036					2.70		
Electrolyte compositions								
			1	2	3	4	5	
Phosphorous acid, g			1.7	1.7	1.7	1.7	1.7	
Hydrogen fluoride, ppm			400	400	720	720	720	
Formic acid, g			95	95	95	95	95	
Water, g			5.3	0.8				1.0
To adjust specific resistance to: (ohm-cm at 25°C)						365	840	
Triethylamine								
To adjust specific resistance to: (ohm-cm at 25°C)					840		365	365
Specific resistance, ohm-cm at 25°C					840			

film growth increases regularly with voltage. Films grown in 1 have a higher capacity. Their optical thickness is about 20% greater and the charge to form unit voltage increment is about 37% higher. The fact that the optical thickness difference is less than the charge-to-form difference is probably due to differing formation efficiencies and refractive indices of the two films. A partial breakdown of the film in 2 is indicated above 100v. This process is characterized by a reduction in CV and in the coulomb expenditure per voltage increment. Above 180v the breakdown becomes catastrophic resulting in a crazing of the film.

Capacity and Equivalent Series Resistance

Plots of reciprocal capacity against voltage give lines with up to four changes of slope. The changes in slope are abrupt giving the appearance of break points in the $1/C$ vs. V curve. One break point was observed between 20 and 70v for current densities within the range 0.1 to 3.0 ma/cm². A second break point occurs at about 10v. Both break points are shown in Fig. 1. The ESR curve shows two maxima, one coincident with each break point. The maximum CV occurs below the 10v break point and is about 20 $\mu\text{f-v/cm}^2$ measured in the formation electrolyte. There is no significant change in charge-to-form detectable at either break point. A third break point occurs at about 100v for films formed in low water concentration electrolytes. This point precedes the breakdown of the film which is characterized by crazing or graying. Between this third break point and the complete breakdown of the film, the formation shows a rapidly decreasing coulomb expenditure per voltage increment.

The position of the first break point (20-70v) is influenced by the formation current density and water content of the electrolyte. The slopes of adjacent regions of the capacity curves are also influenced by these factors (Table II). Electrolytes 3, 4, and 5 contain decreasing amounts of water in that order. The intersection voltage of the two curves increases with increasing water concentration (Table II) and with current density. The slope of the $1/C$ line above the break point is sensitive

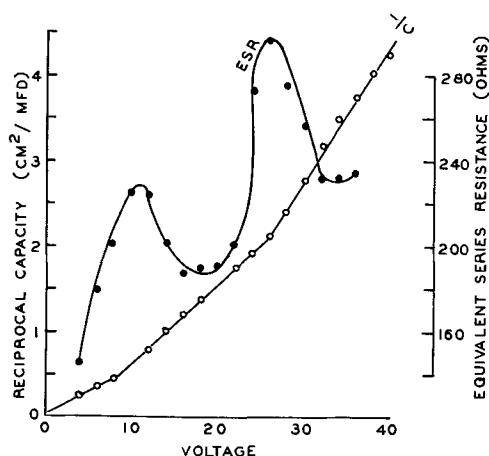


Fig. 1. Reciprocal capacity and equivalent series resistance curves in electrolyte 5.

Table II. Variation of $1/C$ curves with current density and electrolyte

Electrolyte	Current density, ma/cm ²	Reciprocal Slope 1, low voltage, CV ($\mu\text{f-v/cm}^2$)	Reciprocal Slope 2, high voltage, CV ($\mu\text{f-v/cm}^2$)	Approximate intersection voltage
3	3.0	12.4	10.4	70
	1.0	11.3	10.1	42
	0.3	12.1	7.9	25
	0.1	12.3	7.4	25
4	3.0	11.5	9.0	64
	1.0	11.2	8.0	52
	0.3	11.0	8.3	30
	0.1	10.4	6.9	20
5	3.0	10.5	6.9	52
	1.0	10.4	7.3	38
	0.3	10.3	7.1	30
	0.1	9.6	7.0	20

to current density changes only in the electrolytes with high water concentrations.

To illustrate how the current density affects the final films, anodic films were formed as follows in electrolyte 4. One film was formed at a constant current of 0.1 ma/cm² to 70v. It gave a capacity of 0.11 $\mu\text{f/cm}^2$ and a color which corresponded to 92v on the tantalum step gauge. A second film formed at 3 ma/cm² to 70v and then at 70v to 0.1 ma/cm² gave a capacity of 0.13 $\mu\text{f/cm}^2$ and a color corresponding to 87v tantalum.

When films are formed successively in electrolytes of different water content it is found that the voltage increment per coulomb adjusts immediately to the value characteristic of the new electrolyte. The capacity of the final film, however, varies according to the formation sequence. The capacity was 0.23 $\mu\text{f/cm}^2$ when formation in 3 containing relatively more water preceded formation in 5. When carried out in the reverse order the capacity was 0.18 $\mu\text{f/cm}^2$. The latter sequence gave a slightly higher optical thickness and a charge/voltage increment which was about 4% higher in 3.

The anomalies of the capacity and ESR curves were also observed with sheet titanium (99.6%), and the shape of the curves was found to be essentially the same as those obtained with the vacuum deposited films.

Discussion

Two factors affecting the capacity of these oxide films are the current density of formation and the water concentration of the organic electrolyte. Lack of recognition of these factors is probably the reason for the divergence of CV values reported, since most of the values were obtained in predominantly organic electrolytes.

The films obtained in this work bear a striking resemblance to those found on tantalum when formed in similar organic electrolytes (5) which suggests that in both cases the formation mechanism is determined by the electrolyte. Within the variation of water concentrations employed the film characteristics changed in the same manner as those of tantalum, i.e., in relatively more organic electrolytes the films had lower capacity, lower optical thickness, and required less coulombs for their formation.

There are also some differences in the anodic behavior of the two metals. There is first the difficulty in forming films on titanium in aqueous solution. Also the capacity and ESR anomalies are more accentuated with titanium, and the low dielectric constant of the film is less compensated by increasing field strength, giving a considerable range of CV values. Further, increased current density gives a reduced optical thickness, as for tantalum, but a higher break point and in some cases a higher slope of the $1/C$ curves which is the opposite of tantalum behavior.

It was suggested that breaks in the capacity curve for tantalum were attributable to a multiplication of the void structure of the outer part of the film. The effects observed with increasing current density were also ascribed to a higher void structure caused, in this case, by less trapping of ions within the film. If a similar explanation can be applied to titanium it must be inferred that a certain degree of void structure is preferable in the outer film and results in a higher capacity. This is unlikely unless, for some reason, the more dense type of film is unable to grow. It is possible that stresses, due perhaps to incompatibility of ion sizes, disrupt the dense type of film after it has reached a certain thickness. Such a situation might produce gross voids, giving rise to a lower capacity film than would result from a film into which small voids are deliberately introduced to relieve the

stresses. The nature of the electrolytes found most successful in this work gives some support for the idea that a film with pores may grow preferably on titanium. Such films grow in electrolytes which are able to partially dissolve the films and in the present work the presence of HF in the electrolyte was found to be essential. HF is commonly used in precleaning solutions and contamination of the surface may often be a possibility since as little as 50 ppm HF in the forming bath is effective.

Acknowledgment

The work was carried out under contract DRB 715-00124(DGS) from the Canadian Defence Research Board to whom thanks are due for permission to publish. It was under the general direction of Dr. F. J. Burger to whom the author is indebted for consultation, encouragement, and valuable discussions throughout its course.

Manuscript received May 4, 1964.

Any discussion of this paper will appear in a Discussion Section to be published in the June 1965 JOURNAL.

REFERENCES

1. F. Huber and J. Bloxom, *IRE Trans. on Component Parts*, **8**, 80 (1961).
2. H. G. Rudenberg, J. R. Johnson, and L. C. White, *Proc. Electronics Components Conference*, **90**, (1962).
3. M. E. Sibert, *This Journal*, **110**, 65 (1963).
4. R. A. Piggott and L. L. Shreir, *Nature*, **189**, 216 (1961).
5. D. M. Cheseldine, To be published.

Use of Index of Refraction Liquids for the Measurement of the Refractive Index of Thin Transparent Films on Silicon

Arthur E. Lewis

Fairchild Semiconductor, A Division of Fairchild Camera and Instrument Corporation, Palo Alto, California

The use of liquids of known refractive index has long been common for the determination of the index of refraction of transparent materials. The unknown solid is immersed in a known liquid, the closeness of the match in index is estimated from the relief, and the solid is determined to have a smaller or larger index by observation of the effect of light on the interface using the method of central illumination or oblique illumination (1). This process is repeated until a match is obtained and the interface is no longer visible. For this condition the index of the solid is the same as that of the liquid.

The use of liquids to determine the index of thin films is somewhat different. Thin films are defined for this purpose as those showing recognizable interference colors. Interference colors are produced in an oxide of silicon by the interference of white light reflected from the air-oxide interface and the oxide-silicon interface when the thickness of the oxide is of the order of the wavelength of visible light or a few multiples thereof. The brightness of the colors is determined by the reflectivity of both

interfaces, the brightest colors being obtained when the reflectivities of the interfaces are large and equal. The air-oxide interface has a lower reflectivity than the oxide-silicon interface. Dielectric films of index greater than silicon dioxide, such as TiO_2 , SiO , and Pb-doped oxide, show more intense colors because the reflectivity of the air-dielectric interface is increased over that of ordinary silicon oxide.

In the oil immersion technique the air-oxide interface is replaced by an oil-oxide interface. If a thick film of oil with an index of refraction equal to that of the silicon dioxide film is applied over a film step, the interface between the oil and the silicon dioxide disappears optically, eliminating the interference colors and causing the film edge to become invisible.

As long as the index of the oil is greater than air and less than that of the film, the conditions for maxima and minima in the film are the same as for an air-film interface, and the interference color is the same but reduced in intensity. If the index of the oil is greater than that of the film, the light reflected from the oil-film interface is 180° out of

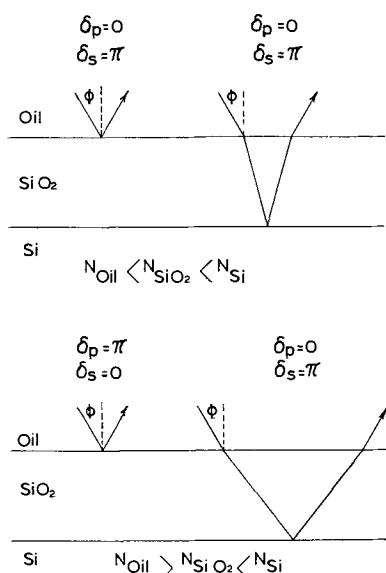


Fig. 1. Phase changes at low angles of incidence for reflection from various interfaces between Si, SiO₂, and oil. The phase change of the components parallel and normal to the plane of incidence are given by δ_p and δ_s , respectively.

phase with the light reflected from the film-silicon interface, and the conditions for maxima and minima are reversed (Fig. 1). In white light the complements of the original interference colors appear. This effect is most striking if liquid with an index much higher than that of the film is used, and the effect is accompanied by an illusion of the original color on the oil-silicon side of the step. If the re-

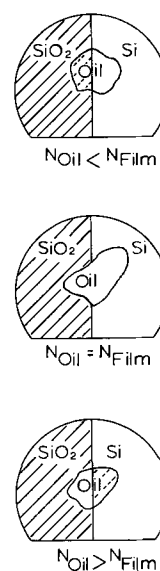


Fig. 2. Appearance of film edge observed under oils of various indices of refraction when the indices of the film and the oil are only slightly different.

fractive indices of the oils are only slightly different from that of the film, as is the case when a match is being sought, the effect is observed as an apparent change in intensity rather than a distinct color change, with the darker side on the oil-silicon side of the step (Fig. 2).

The refractive index of oxide films on silicon may be determined with an accuracy of 0.001-0.006 using this method. The best accuracy is obtained

Table I.* SiO₂ on silicon, index of refraction

n	$T, ^\circ\text{C}$	Atm	$d, \text{\AA}$	Conductivity type	Resistivity, ohm-cm	Sample No.
1.462 ± 0.003	800	Wet O ₂	1030	N	0.5	PF 24
1.457 ± 0.002	800	Wet O ₂	1340	N	0.5	PF 3
1.466 ± 0.003	920	Dry O ₂	~900	N	0.01	W Wh
1.466 ± 0.003	1000	Wet O ₂	455	N	0.5	PF 67B
1.462 ± 0.003	1000	Wet O ₂	610	N	0.5	PF 67C
1.451 ± 0.001	1000	Wet O ₂	850	N	0.5	PF 67E
1.488 ± 0.001	1000	Wet O ₂	1050	N	0.5	PF 67D
1.468 ± 0.005	1000	Wet O ₂	2525	N	0.5	72
1.461 ± 0.003	1000	Wet O ₂	10620	N	0.5	73
1.461 ± 0.005	1000	Wet O ₂	17200	N	0.5	74
1.467 ± 0.004	1200	Wet O ₂	2420	P	1.4	BD 29D
1.461 ± 0.002	1200	Wet O ₂	4900	P	1.2	BD 33D
1.460 ± 0.002	1200	Wet O ₂	5020	P	1.2	BD 37D
1.460 ± 0.003	1200	Dry O ₂	5210	P	1.4	BD 32D
1.456 ± 0.002	1200	Wet O ₂	5270	P	1.4	BD 30D
1.462 ± 0.003	1200	Dry O ₂	4800	N	9	W Wh
1.460 ± 0.003	1200	Wet O ₂	715	P	0.01	AL 44
1.457 ± 0.003	1200	Wet O ₂	880	P	0.01	AL 43
1.462 ± 0.003	1200	Wet O ₂	905	P	0.01	AL 42
1.459 ± 0.004	1200	Wet O ₂	1025	P	0.01	AL 41
1.458 ± 0.003	1200	Wet O ₂	1240	P	0.01	AL 39
1.459 ± 0.004	1200	Wet O ₂	3360	P	0.01	AL 21
1.460 ± 0.003	1200	Wet O ₂	5320	P	0.01	AL 12
1.461 ± 0.004	1200	Wet O ₂	7275	P	0.01	AL 6
1.461 ± 0.004	1200	Wet O ₂	9110	P	0.01	AL 1
1.459 ± 0.004	1300	Wet O ₂	3495	N	0.5	PF 83
1.460 ± 0.005	1300	Wet O ₂	7160	N	0.5	PF 84
Pyrolytic oxide**						
1.443 ± 0.002	Pyrolytic oxide		500-4500	N	1.5	GT
1.446 ± 0.005	Pyrolytic oxide		~4500	N	1.2	A

* Wet oxygen means oxygen bubbled through water at approximately 98°C.

** Pyrolytic oxide—SiO₂ formed by the decomposition of ethyl silicate on a hot substrate (750°C) at reduced pressure.

on films with the greatest color contrast relative to silicon.

The useful range of indices that may be measured by this method is determined by the availability of standard index of refraction liquids. A set of oils in the range of 1.300-1.700 with intervals of 0.002 and accurate to 0.0002 is available and easy to use. Oils with a refractive index as high as 2.11 are obtainable, but are less stable, somewhat toxic, and therefore less convenient to use in the high end of this range (2).

Some of the results of measurements on oxides grown on silicon are shown in Table I. The small variations of index observed are probably only apparent variations resulting from the dispersion of the films inasmuch as the measurements were made in white light. The refractive index of silica glass varies from 1.470 at a wavelength of 4000Å to 1.455 at 7000Å (3). The index of refraction of thermally grown oxide on silicon appears to be relatively independent of the temperature or water content of the atmosphere in which the oxide was grown and of the resistivity of the silicon. A mean value of the refractive index of thermally grown oxide is about 1.460, the same as for fused quartz.

Because the oil-film interface disappears optically when the indices of the oil and the film are equal, the index of refraction determined is that of the material near the oil-film interface. The question of whether the index of the film varies through its thickness may be answered by etching

away increments of the film and determining the index of each newly exposed surface. The AL Series was obtained by oxidizing a number of wafers from the same silicon crystal to a thickness of 9100Å and then etching these to obtain a set of samples of different thicknesses. Measurements on these wafers indicate that the index of refraction is relatively constant through the film, at least from 700 to 9000Å for films grown in wet oxygen at 1200°C.

Pyrolytic oxide has a lower refractive index than thermal oxide. This index does not appear to vary as a function of oxide thickness.

The method described in this paper for the determination of the index of refraction of silicon oxide on silicon using liquids of known index of refraction is applicable to any nonabsorbing film on a reflecting substrate that shows interference colors, providing that the film is insoluble in the liquid used.

Manuscript received April 2, 1964.

Any discussion of this paper will appear in a Discussion Section to be published in the June 1965 JOURNAL.

REFERENCES

1. E. S. Larsen and H. Berman, Bull. 848, U. S. Geological Survey, pp. 11-18 (1934).
2. The index of refraction liquids used in this study were obtained from R. P. Cargille Laboratories, Inc., 33 Village Park Rd., Cedar Grove, N. J.
3. G. W. Morey, "The Properties of Glass," p. 371, Reinhold Publishing Corp., New York (1954).

Doping of Alkaline Earth Halide Single Crystals

P. F. Weller and J. E. Scardefield

Watson Research Center, International Business Machines Corporation, Yorktown Heights, New York

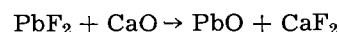
In recent years alkaline earth halides, when doped with rare earths and uranium, have become important for use as optically pumped lasers (1). This has necessitated the growth of large, optically clear, single crystals reproducibly doped with various concentrations and oxidation states of rare earths and uranium. The most widely used method of crystal preparation is Bridgman-Stockbarger growth in a graphite crucible using an oxygen "scavenger" such as PbF₂ to obtain crystal clarity. However, when doping with rare earths or uranium, it can be shown that Pb⁺² functions not only as a "scavenger" but also as an effective oxidizing agent yielding trivalent rare earths and tetravalent uranium. These results can be generalized and used to indicate other possible hosts for divalent rare earths and trivalent uranium.

Crystal Growth

Apparatus and procedure.—Doped, single crystals of CaF₂, SrF₂, BaF₂, and SrCl₂ were grown in a Bridgman-Stockbarger furnace with two separately controlled temperature zones maintained at 50°-100°C above and below the melting point of the

host material with a gradient of about 100°C/in. between the zones. A cylindrical, graphite crucible with a 60° cone was lowered through the furnace at about 1/3 in./hr in an argon atmosphere flowing at about 2 liters/min. Grown crystals ranged from 1/8 to 1 in. in diameter and were 1 to 6 in. in length. A number of the Sm⁺² and U⁺³ doped CaF₂ and SrF₂ crystals worked as optically pumped lasers.

Oxide contamination.—As reported previously (2, 3) oxide contamination arising from impure starting materials or hydrolysis at high temperatures is the major growth problem for alkaline earth halides. The easiest and most successful method of eliminating cloudiness caused by oxide precipitation has been the addition of a chemical "scavenger" such as PbF₂ (2).



This purification procedure works quite well when the host materials are doped with stable species such as trivalent rare earths. However, when a dopant is desired in an unusual, low oxidation state, as with Sm⁺², PbF₂ can exhibit unwanted oxidizing properties, as is shown below.

Table I. Chemical oxidation potentials in various solvents. E°_{H} designates standard oxidation potentials for which the hydrogen electrode is arbitrarily chosen as a zero reference (H^+ at unit activity) and E°_{Na} the fused salt potentials at 700°C for which the sodium electrode is defined as the zero reference (Na^+ at unit activity)

	E°_{H} Aqueous	E°_{H} Fused chlorides	E°_{Na} Fused chlorides	E°_{Na} Fused fluorides	E°_{Na} Fused NaF
$\text{Ba} \rightarrow \text{Ba}^{+2} + 2e^-$	2.90	2.60	0.31	0.47	
$\text{Sr} \rightarrow \text{Sr}^{+2} + 2e^-$	2.89	2.52	0.21	0.40	
$\text{Ca} \rightarrow \text{Ca}^{+2} + 2e^-$	2.87	2.36	0.060	0.29	
$\text{Na} \rightarrow \text{Na}^+ + e^-$	2.71	2.39	0.00	0.00	0.00
$\text{Sm} \rightarrow \text{Sm}^{+3} + 3e^-$	2.41		-0.41		
$\text{U} \rightarrow \text{U}^{+4} + 4e^-$	1.50		-1.31		
$\text{Cd} \rightarrow \text{Cd}^{+2} + 2e^-$	0.403	0.26	-2.0		-0.93
$\text{Pb} \rightarrow \text{Pb}^{+2} + 2e^-$	0.13	0.10	-2.17		-1.19
$\text{H} \rightarrow \text{H}^+ + e^-$	0.00	0.00			

Doping Problems

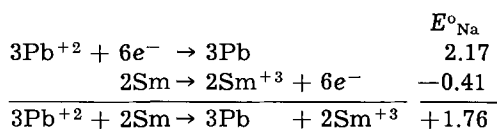
Divalent samarium.—That the presence of PbF_2 is undesirable when doping with Sm^{+2} is illustrated by the following experiments.

Crystals of CaF_2 doped with Sm^{+2} were prepared by adding SmF_3 to CaF_2 and crystallizing in the presence of PbF_2 . This procedure gave low, nonreproducible Sm^{+2} concentrations. To improve reproducibility and obtain higher Sm^{+2} concentrations, a reducing agent of Sm metal was added to the sample mixture so that the following reaction would occur.



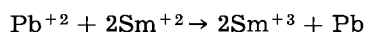
The resulting crystals, however, showed no increase in Sm^{+2} concentration.

This can be expected to happen if the appropriate oxidation potentials are considered. Table I gives some comparisons between aqueous solution (4) and fused salt values (5) and between fluoride and chloride fused salts. (Since the chloride data are most extensive and probably most reliable, they have been used in the discussion that follows. It should be noted, however, that the relative positions in the electrochemical series are quite constant in various fused salt systems.) The following reaction can then be written with its corresponding oxidation potential (a positive value indicating that the reaction is favored as written).



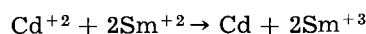
E°_{Na} designates the standard oxidation potential for which the sodium electrode is defined as the zero reference (Na^+ at unit activity). It is seen, then, that divalent lead oxidizes samarium, and other rare earth metals, to the trivalent state.

That Pb^{+2} also oxidizes divalent rare earths according to the following reaction



can be inferred indirectly, in the absence of the necessary thermodynamic data. In doping CaF_2 crystals with samarium a $\text{Sm}^{+2}/\text{Sm}^{+3}$ ratio of about 1/100 is always obtained. However, when the CaF_2

is co-doped with CdF_2 and SmF_3 , no Sm^{+2} is obtained. We conclude from this that the following reaction takes place

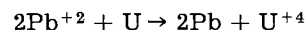


Thus a positive oxidation potential exists for the reaction. Since Pb^{+2} is a better oxidizing agent than Cd^{+2} , as can be seen in Table I, Sm^{+2} would also be oxidized by Pb^{+2} .

Divalent lead, therefore, oxidizes the divalent rare earths and metals to the trivalent state. Consequently, when divalent rare earth doping of alkaline earth halides is required, the "oxygen scavenger," PbF_2 , cannot be added to the sample mixture. Starting materials must, of course, be purified prior to the doping crystallization. Rather large divalent rare earth concentrations can be obtained in this way. For example, we have grown single crystals of CaF_2 containing about 0.5 mole % Sm^{+2} with a 1% total samarium content.

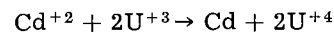
Trivalent uranium.—A similar case can be stated for the doping of alkaline earth halide crystals with uranium by adding uranium metal to the sample mixture of host plus scavenger, PbF_2 .

Consideration of the appropriate oxidation potentials yields the following equation



with a standard oxidation potential of + 0.86 at 700°C in fused chlorides. Here Pb^{+2} acts as a necessary oxidizing agent, yielding only U^{+4} . This has been shown by melting a sample charge and crystallizing rapidly by furnace quenching. Under these conditions only U^{+4} is formed (6). U^{+3} can then be obtained by remelting and holding the melt temperature for an extended period, 15 hr or more. Decomposition of UF_4 to UF_3 at the melt temperature, then, might be the predominant mechanism of U^{+3} production.

If trivalent uranium is added directly to the sample, in the form of UF_3 for example, PbF_2 should not be used. This can again be shown indirectly, as above, by co-doping CaF_2 with UF_3 and CdF_2 . In this case only U^{+4} is obtained indicating that the following reaction has a positive oxidation potential.



A similar reaction with divalent lead is probable since Pb^{+2} is a better oxidizing agent than Cd^{+2} .

It seems evident, then, that uranium is oxidized to U^{+4} by Pb^{+2} at the high crystallization temperatures. If uranium metal is used as the dopant source, this is a necessary and desirable function. However, when UF_3 is added to the sample charge, no oxidant such as PbF_2 should be present.

Conclusions

1. When doping alkaline earth halides with divalent rare earths, easily reduced species such as Pb^{+2} must be absent.

2. U^{+3} doping is obtained from uranium metal by using long melt times along with the PbF_2 oxidizing agent. If U^{+3} is added directly to the host, as UF_3 for example, PbF_2 should not be used.

3. Other ionic host materials for divalent rare

earths and/or U^{+3} can be chosen or eliminated on the basis of an oxidation potential argument. For example, alkaline earth and alkali metal halides as well as La, Y, and Sc halides can be doped with divalent rare earths, whereas halides of In, Tl, Bi, Pb, or Cd, in general, cannot.

Manuscript received March 27, 1964.

Any discussion of this paper will appear in a Discussion Section to be published in the June 1965 JOURNAL.

REFERENCES

1. L. F. Johnson, *J. Appl. Phys.*, **34**, 897 (1963).
2. D. C. Stockbarger, *J. Opt. Soc. Am.*, **39**, 731 (1949).
3. D. C. Stockbarger, *Discussions Faraday Soc.*, **5**, 294 (1949).
4. W. M. Latimer, "Oxidation Potentials," 2nd ed., Prentice-Hall, Inc., Englewood Cliffs, N. J. (1952).
5. I. U. K. Delimarskii and B. F. Markov, "Electrochemistry of Fused Salts," The Sigma Press, Publishers, Washington, D. C., 1961.
6. R. S. Title *et al.*, *Phys. Rev.*, **128**, 62 (1962).

Small Particles in Silicon

G. R. Booker

Cavendish Laboratory, University of Cambridge, Cambridge, England

and R. Stickler

Research and Development Center, Westinghouse Electric Corporation, Pittsburgh, Pennsylvania

Silicon grown by Czochralski or float-zone techniques occasionally gives anomalously low yields of p-n junction devices, even though the resistivity, minority carrier lifetime, and dislocation density are within the normally acceptable ranges. We have investigated such material by the transmission electron microscope method.

Slices parallel to the (111) plane were cut from a number of such ingots from different sources, lapped and chemically polished with CP4¹ from both sides in order to remove the lapping damage. These specimens were then jet chemically thinned from alternate sides using an HNO_3/HF solution (1) until a small hole appeared. Many of the specimens did not then exhibit the smooth, mirror-like surfaces usually resulting from such a preparation, but showed irregular, pitted surfaces. When the thin areas of such specimens were examined in transmission in the electron microscope,

¹ 200 ml HNO_3 : 120 ml HF : 120 ml CH_3COOH .

large numbers of small particles embedded in the Si matrix were observed.

A bright field transmission electron micrograph of a Si specimen which gave poor devices is shown in Fig. 1a. Numerous small defects (A) and several large defects (B) are present. The small defects (A) are shown again in Fig. 2 at higher magnification. These defects consist in most instances of an approximately circular gray area up to 1000Å across containing sharply defined black centers. The black centers are thought to be small particles, and the surrounding gray areas to be regions of either high strain or high segregation. The extinction contrast thickness fringes (C) show that the surface is irregular, especially in the regions immediately surrounding many of the defects.

Selected-area transmission electron diffraction patterns from regions containing such defects showed the single crystal (111) Si spots, and sometimes in addition extra weak spots. A dark field transmission electron micrograph taken with one of these weak spots is shown in Fig. 1b. This micro-

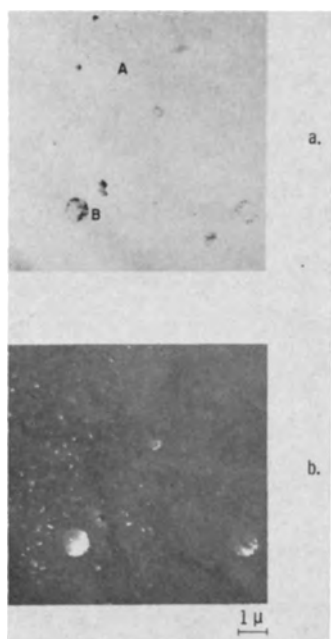


Fig. 1. (a) Bright field transmission electron micrograph of "poor" Si; (b) dark field transmission electron micrograph of the same area. Magnification approximately 4000X.

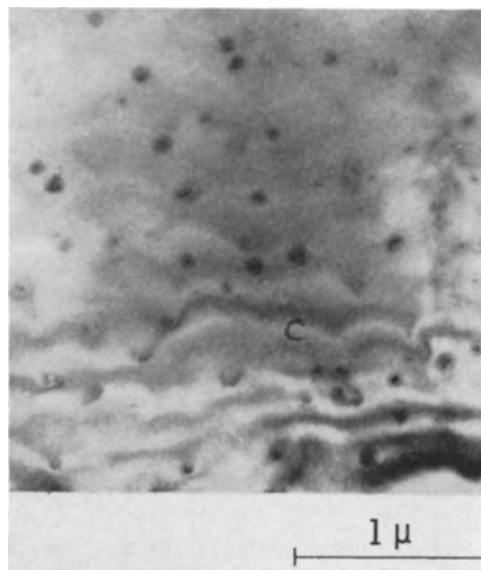


Fig. 2. Bright field transmission electron micrograph of "poor" Si. Magnification 25,000X.

graph may be compared with Fig. 1a, which is the same region in bright field. The dark field micrograph shows many of the large defects and the small defects as sharply defined bright images. This observation confirms that the defects are not surface effects arising from the jet chemical thinning, but are definite structural defects within the interior of the specimen. Some of the extra weak spots in the electron diffraction patterns were streaked, indicating the presence of strains and/or faulting in the defects and/or surrounding regions. None of the patterns enabled an unambiguous identification of the particles to be made.

Hence, the results show that the Si specimens which gave poor devices possess local regions containing large numbers of small particles. The presence of these particles and/or their associated strains could account for the low device yields. They undoubtedly account for the irregular surfaces resulting from the jet chemical thinning. The origin and identity of the particles has not yet been ascertained. One possibility is that the particles are silicon carbide and that the carbon was picked up during the growth process. Newman and Wakefield (2) have demonstrated that carbon can be picked up readily by silicon. They have also studied the diffusion of carbon into silicon and have shown that dislocations and precipitation effects result from

this diffusion; however, these effects were of sufficient size to be observed by conventional microscopy and infrared transmission.

A large number of Si specimens from ingots not exhibiting anomalous properties were also examined by transmission electron microscopy. Many of these specimens contained particles similar in appearance to those observed in the Si which gave poor devices, although they were of course much more sparsely distributed. Nevertheless, their presence was somewhat surprising. They may be responsible for the degradation of the electrical characteristics of p-n junction devices which sometimes occur even with "good" Si material. Moreover such particles could act as dislocation sources and/or initiate fracture when the material is mechanically deformed.

Manuscript received Jan. 6, 1964; revised manuscript received April 24, 1964.

Any discussion of this paper will appear in a Discussion Section to be published in the June 1965 JOURNAL.

REFERENCES

1. G. R. Booker and R. Stickler, *Brit. J. Appl. Phys.*, **13**, 446 (1962).
2. R. C. Newman and J. Wakefield, *Solid State Physics in Electronics and Telecommunications*, **1**, 318 (1959); also "Carbon in Silicon," in "Metallurgy of Semiconductor Materials," J. Schroeder, Editor, Interscience Publishers, New York (1962).

Brief Communication



Transmitted Phonon Drag Measurements in Epitaxial Silicon

R. Gereth and C. Stephens

Shockley Research Laboratory, Clevite Corporation, Palo Alto, California

Transmitted phonon drag (1) has been measured previously in diffused npn silicon structures (2-6). In all cases the three layer structures were prepared from crucible pulled or float zone silicon crystals. So far no results have been reported of transmitted phonon drag measurements in epitaxial silicon films. Since thick layers of epitaxial silicon (7) are now easily available, investigations were initiated to explore the transmitted phonon drag in epitaxial layers.

Epitaxial films used in the present work were grown by thermal decomposition of SiCl_4 (or an admixture of SiCl_4 and B_2H_6) in hydrogen (8). The substrates were [111] oriented high resistivity n-type slices. After the growing process the substrate layers were completely lapped away leaving epitaxial layers with thicknesses between 40 and 140 μ . In this way epitaxial silicon layers were prepared

having boron concentrations of 6×10^{14} , 6.5×10^{16} , and 2.5×10^{17} at./ cm^3 , respectively.

Symmetrical npn structures had to be made to observe the transmitted phonon drag in epitaxial silicon. The structures were fabricated by exposing the cleaned epitaxial slices to a 30 min phosphorus predeposition at 800°C with a subsequent diffusion for 60 min at 1300°C. After the phosphorus diffusion, rectangular samples (10 × 1 mm) were cut and electrical contacts were applied to the n-layers by the thermocompression bonding of 0.003 in. diameter gold wires. The geometry of the finished test samples is shown in Fig. 1 ($x = 10$ mm, $y = 1$ mm).

The transmitted phonon drag in the epitaxial npn structures was observed by means of the same technique as described earlier (2-6). An electric field \vec{E}_1 applied to the top n layer (see Fig. 1) disturbs the thermal phonon equilibrium. This disturbance of

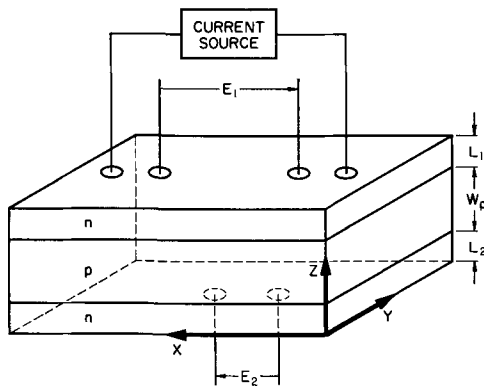


Fig. 1. Geometry of test sample

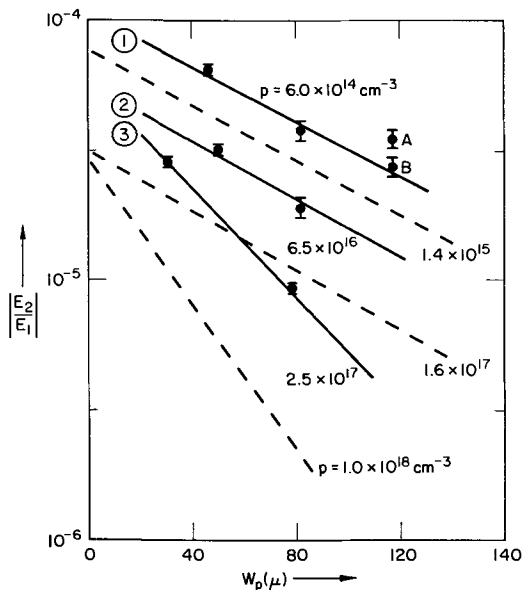


Fig. 2. Dependence of the transmitted phonon drag on impurity concentration in the intermediate p-layer. —, Epitaxial material; - - - Czochralski crystal; $T = 77^\circ\text{K}$.

the relevant phonons propagates through the middle p-layer, and phonons reaching the bottom n-layer drag electrons along with them, thus setting up an electric field \vec{E}_2 . Plotting the logarithm of the ratio $|E_2/E_1|$ as a function of the width W_p of the middle p-layer allows the mean free path of the relevant phonons to be determined (2, 6). This method was applied to the case of the epitaxial samples. The measurements were carried out with the samples immersed in liquid nitrogen.

Results are shown in Fig. 2. The solid straight lines labelled 1, 2, and 3 in Fig. 2 approximate the experimental points obtained from epitaxial silicon with the different boron concentrations. For $W_p = 117\mu$ two different sets of data are shown, labelled A and B. The values A for $|E_2/E_1|$ represent the actual measured points which were corrected¹ to yield the values B.

The dotted lines in Fig. 2 are taken from similar measurements reported by Hubner and Shockley

¹ The samples with $W_p = 117\mu$ exhibit an n-layer sheet resistance of 17 ohms per square compared to 13 ohms per square present in the remaining epitaxial samples. This causes a relatively larger efficiency (3, 6) of the receiving n-layers in the samples with $W_p = 117\mu$. Therefore, the measured values A were corrected accordingly (6).

(3) for the case of crucible grown silicon. Hubner and Shockley concluded from their results that in silicon samples with low boron concentration, the mean free path L_ϕ depends only on phonon-phonon scattering. L_ϕ drops, however, as soon as phonon-hole scattering becomes dominant (see the dotted line in Fig. 2 referring to $p = 1 \times 10^{18} \text{ cm}^{-3}$). The lines 1 and 2 in Fig. 2 were drawn through the experimental points and parallel to the dotted curve corresponding to a boron concentration of $p = 1.4 \times 10^{15} \text{ cm}^{-3}$. The slope of this particular curve is well established, being the result of measurements of a large number of specimens (3).

In conclusion it can be said that the mean free path L_ϕ of the relevant thermal phonons at 77°K due to pure phonon-phonon scattering is $80 \pm 10\mu$ in epitaxial silicon with a boron concentration between 6×10^{14} and $6.5 \times 10^{16} \text{ at./cm}^3$. This result is in very good agreement with the data published for crucible grown silicon crystals of equivalent low boron concentrations, and it shows that under these conditions there is apparent equality in crystal perfection for melt-grown vs. vapor-grown silicon. In addition, Fig. 2 shows that L_ϕ drops to 40μ in epitaxial slices with a boron concentration of $2.5 \times 10^{17} \text{ cm}^{-3}$ while in Czochralski crystals with a boron concentration of $1.0 \times 10^{17} \text{ cm}^{-3}$ pure phonon scattering ($L_\phi = 80\mu$) is still dominant. The difference in L_ϕ indicates that more highly doped epitaxial silicon is structurally less perfect (9, 10) than corresponding crucible grown material, as also suggested by the more pronounced brittleness of the highly doped epitaxial slices observed during the course of the experiments described in this communication.

Acknowledgments

The authors are grateful to R. H. Finch for growing the epitaxial layers. This work was supported by the Advanced Research Project Agency through the Office of Naval Research of the United States Navy.

Manuscript received April 27, 1964.

Any discussion of this paper will appear in a Discussion Section to be published in the June 1965 JOURNAL.

REFERENCES

1. W. Shockley, "Structure and Properties of Thin Films," pp. 306-326, C. A. Neugebauer, J. B. Newkirk, and D. A. Vermilyea, Editors, John Wiley & Sons, Inc., New York (1959).
2. K. Hubner and W. Shockley, *Phys. Rev. Letters*, **4**, 504 (1960).
3. K. Hubner and W. Shockley, "Proc. International Conference on Semiconductor Physics," Prague, p. 229 (1961).
4. K. Hubner and W. Shockley, *Advanced Energy Conversion*, **1**, 93 (1961).
5. K. Hubner and W. Shockley, Report of International Conference on Physics of Semiconductors, Exeter, p. 157 (1962).
6. R. Gereth and K. Hubner, *Phys. Rev.*, **134**, A235 (1964).
7. R. H. Finch and H. J. Queisser, *Electrochem. Technol.*, **2**, 114 (1964).
8. H. C. Theuerer, *This Journal*, **108**, 649 (1961).
9. H. J. Queisser, R. H. Finch, and J. Washburn, *J. Appl. Phys.*, **33**, 1536 (1962).
10. G. H. Schwuttke, *ibid.*, **33**, 1538 (1962).

A High Performance Propane Fuel Cell Operating in the Temperature Range of 150°-200°C

W. T. Grubb and C. J. Michalske

Research Laboratory, General Electric Company, Schenectady, New York

ABSTRACT

High performance and complete electro-oxidation of propane have been achieved in fuel cells operating in the range 150°-200°C. The cells contain platinum catalyzed electrodes and concentrated phosphoric acid electrolytes. For best performances the electrolyte concentration and operating temperature are selected so that the partial pressure of water vapor over the electrolyte is in the vicinity of 600 mm. Observing this condition, complete propane-oxygen fuel cells produced 50 ma/cm² at 0.5v cell potential (with ohmic resistance losses included) at 200°C. The mechanism of the electro-oxidation of propane is discussed.

It is generally felt that the broad impact of fuel cells as a class of power sources will only be felt if they can be made to operate on inexpensive, easily stored fuels, of which the saturated hydrocarbons represent a notable class. Recently a high performance fuel cell for saturated hydrocarbons was announced (1). The present paper presents more detailed information about performance of such cells on propane. A brief communication on propane-oxygen cell performance at 150°C with some comments on cell structure has already been published (2).

Most investigators have expected saturated hydrocarbons to be inert electrochemically except at high temperatures (in the range of operation of fuel cells with fused salt or ceramic electrolytes).

In this temperature region hydrocarbons do not react directly but are converted in the cell by reaction with water into other electrochemically reactive species, usually hydrogen and carbon monoxide (3-5). More recently, cells with aqueous sulfuric acid electrolyte operating below 100°C have directly oxidized some hydrocarbons at low current densities (6-10), and it has even been observed that oxidation of propane is complete to CO₂ and water as low as 65°C (11).

A survey of many saturated hydrocarbon anode systems (7-11) showed empirically that certain factors are conducive to high reactivity. These are the following: (i) Use of platinum as the electrocatalyst, (ii) use of strong acid as the electrolyte, (iii) use of propane as the fuel, and (iv) operation at high temperature within the range of stability of the electrolyte, cell, and electrode structure. Aside from reactivity considerations the use of acid electrolyte is desirable also from the point of view of rejection of CO₂ (which would be converted into carbonate in a cell with a strongly alkaline electrolyte).

The present paper describes the results of increasing the temperature of operation of fuel cells that conform to the criteria listed above. Oxidizing acids are not stable in fuel cells at elevated temperatures, and phosphoric acid was selected as the

electrolyte because of its known ability to resist direct reduction. It has not previously shown particular promise as a fuel cell electrolyte, for example, in the work of Vaucher and Bloch (12, 13) with propane at 200°C, or in the work of Elmore and Tanner (14) with hydrogen-oxygen cells at 150°C. Furthermore, Tarmy (15) found that the performance of an oxygen cathode was poorer in phosphoric acid than in sulfuric acid at 80°C.

Despite the above, under selected operating conditions, propane-oxygen fuel cells employing phosphoric acid electrolytes show both high performance and complete fuel oxidation in the range of about 150°-200°C. The paper reports on the performance of such cells particularly as a function of temperature and electrolyte concentration.

Experimental

The propane fuel gas was Matheson Company Instrument Grade 99.5% min. purity. This was selected for convenience over Phillips Petroleum Company Research Grade. The two grades gave identical performance in fuel cells. A typical tank analysis of the instrument grade propane was as follows (volume per cents) propane 99.5, air (O₂, N₂, A) 0.1, methane below 0.002, ethane 0.01, and *n*-butane, 0.3. The air content was often lower than 0.1% and did not affect performance up to that value.

The oxygen used was 99+% O₂ from liquid air distillation. Substitution of electrolytic grade had no effect on cell performance.

Several sources of phosphoric acid electrolyte were employed with no observable effect on performance, as follows: (i) Mallinckrodt Analytical Reagent Grade (85% by weight H₃PO₄), (ii) Monsanto Food Grade (75% by weight, H₃PO₄), (iii) Monsanto Phospholeum (105% by weight H₃PO₄). Concentrations above 85% were prepared by boiling off (i) in Pyrex or Teflon beakers, or by mixing (iii) with (i) or (ii). The concentrations were determined by potentiometric titration or by density determination employing a Fisher-Davidson Gravimeter. The latter method is especially convenient

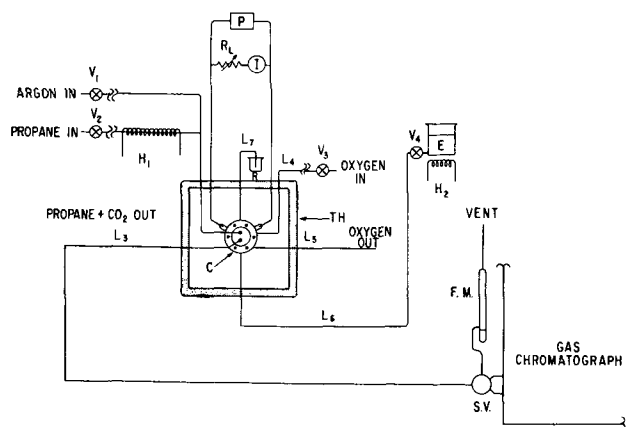


Fig. 1. System for investigating propane-oxygen phosphoric acid fuel cells at elevated temperatures.

after calibration against values determined by titration.

Platinum black, the electrocatalyst in all electrodes used in the present work, was Engelhard Industries 100% platinum black. The surface area of the black was $20 \text{ m}^2/\text{g}$ as determined using a Perkin-Elmer Shell Sorptometer.

The cell structure has been previously described (2). It was investigated in the system shown in Fig. 1. An air thermostat, TH, enclosed the fuel cell, C, and controlled the cell ambient temperature to $\pm 1^\circ\text{C}$. The electrolyte was fed to the cell by gravity from a reservoir E heated to about 110°C (using heater H_2) for the purpose of outgassing. A Teflon needle valve stopcock, V_4 controlled the flow rate to the cell so that the electrolyte chamber volume of 2.6 ml was changed approximately every 10 min. Samples of electrolyte for analysis after passing through the cell were collected in the small reservoir R. The use of a once-through system for supplying electrolyte to the cell was entirely a matter of convenience. The electrolyte was crystal clear and uncolored on emerging from the cell. It could be reused in the cell with no loss in performance if the water concentration was adjusted back to the initial value. Oxygen was fed to the cell at a flow rate representing at least a 2-fold excess over that required to supply the cell. Propane was supplied at a flow rate giving 20% or less conversion under the heaviest load currents employed (about 2 amp maximum). Argon sweep gas was used as necessary to avoid the presence of air-propane mixtures in the anode chamber of the cell. Various gas flows were controlled by the brass needle valves $V_1 - V_3$. The inlet and outlet tubings for electrolyte (L_6 and L_7) and gases ($L_1 - L_5$) were made of Teflon "spaghetti." The propane was in some cases preheated to the temperature of TH by the line heater H_1 . This had an affect on performance only at high flow rates of propane.

Electrical measurements were performed as follows (symbols in parentheses refer to items in Fig. 1). Cell potential was measured using a Rubicon Model 2730 potentiometer (P), cell load current was measured using a Sensitive Instrument Co. Polyrange (I), and cell load resistance was varied using a General Radio Co. Decade Resistance Box (R_L). The cell acted as the sole source of emf in

the system. Cell performance free of ohmic resistance loss was obtained by subtracting the iR loss based on internal cell resistance measured on open circuit using a General Radio Model 650 A impedance bridge at 1000 cps. A second method using a Kordesck Marko bridge (16) to obtain the iR free cell emf gave current density-emf curves superimposable on those obtained by the above method.

A Perkin-Elmer Model 154B gas chromatograph was used for analysis of both the fuel input and product gas streams. The components of this system (referring to symbols in Fig. 1) are, besides the chromatograph itself, a gas sampling valve with a 1.25 ml standard sample volume (S.V.), and a 10 ml soap film flow meter (F.M.) which was calibrated by weight of mercury to 0.1%. The transit time of gas through S.V. was determined using a calibrated stop watch.

The conditions for the chromatograph operation were: temperature, 104°C ; column, 2 meter silica gel; and carrier gas, helium at 55 ml/min exit flow rate. The calibration of the chromatograph was performed using Matheson known gas mixtures and using mixtures prepared by combining gas streams at measured flow rates. The accuracy of the gas analysis for the volume fraction of a component was approximately $\pm 1.5\%$ of the value.

In common with most work on complete fuel cells, only the ambient temperature was controlled. Two types of steady state data could be obtained: (i) steady state with respect to the overvoltages at the electrodes or electrical steady state, and (ii) steady state with respect to temperature rise at the anode (the cathode has a negligible temperature coefficient). The results in this paper correspond to condition (i) and not to condition (ii) except where indicated. The temperature rise at the anode was determined in a few cases, and it becomes greater than 5°C at current densities above $100 \text{ ma}/\text{cm}^2$.

A further condition on the results reported is the following. The concentration of phosphoric acid in various cells for which data are reported is the nominal H_3PO_4 concentration or $1.3804 \times$ the P_2O_5 content as measured on the electrolyte fed into the cell. In passage through the cell, the concentration of the electrolyte increased by approximately 2% (e.g.,

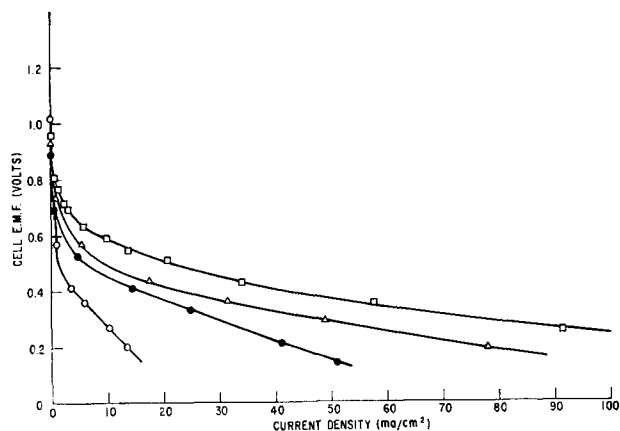


Fig. 2. Cell emf vs. current density curves for propane-oxygen cells at 150°C with phosphoric acid electrolytes of various concentrations. \square 85% H_3PO_4 , \triangle 96% H_3PO_4 , \bullet 101% H_3PO_4 , \circ 105% H_3PO_4 .

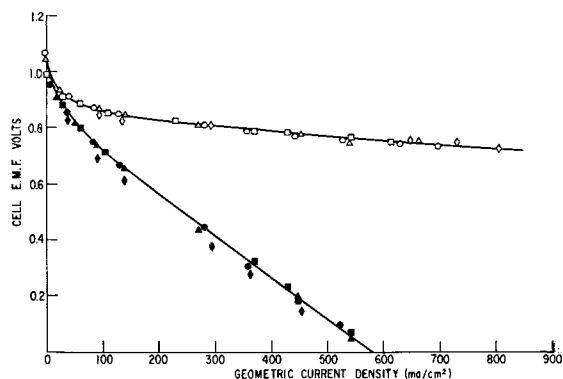
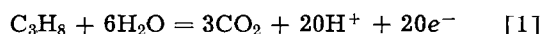


Fig. 3. Cell emf vs. current density curves for hydrogen-oxygen cells at 150°C with phosphoric acid electrolytes of various concentrations. ○ ● 85% H_3PO_4 , □ ■ 96% H_3PO_4 , △ ▲ 101% H_3PO_4 , ◇ ◆ 105% H_3PO_4 . (Solid points are cell potential, open points are iR free cell potential.)

from 85 to 87% H_3PO_4) under the conditions employed.

Results

The effect of the electrolyte concentration variable was examined by measuring cell emf vs. current density at various constant temperatures for cells containing phosphoric acid electrolyte of various concentrations. Such results are presented in Fig. 2 for cells operating at 150°C. The effect of increasing the H_3PO_4 concentration is to decrease performance. The effect might be due to higher iR drop or to increased overvoltages at either the cathode or the anode. The first two possibilities are eliminated by measuring the performance of the same cells with hydrogen and oxygen. These results are depicted in Fig. 3. In separate experiments the hydrogen anode used in these cells had an overvoltage linear with current density with a value of only 7 mv at 200 ma/cm^2 . Therefore, the drop in emf in the curves of Fig. 3 is for practical purposes due to iR drop and/or oxygen cathode overvoltage. Neither is significantly affected by the electrolyte concentration changes in the range of those used here. Therefore, the predominant effect is at the propane anode. It has been shown that the over-all reaction at the propane anode is



Hence water is consumed in the reaction. The present results suggest that water is involved in one or more rate determining steps in the electro-oxidation of propane.

The approximate anode overvoltage vs. current density may be obtained by subtracting the lower curve of Fig. 3 (including iR loss) from each of the curves of Fig. 2.

The effect of electrolyte concentration was explored at other temperatures, and the results are summarized in the graph of Fig. 4. Here the current density at 0.2v of cell potential (iR loss included) is plotted against nominal H_3PO_4 electrolyte concentration for several temperatures. The concentration is not an extremely critical variable. Especially at the lower temperatures, the water vapor pressure over the electrolyte may vary con-

siderably without substantially affecting performance. The vapor pressure of water over the phosphoric acid electrolyte at various concentration-temperature points is indicated in Fig. 4 (in mm Hg) by numbers in ellipses. These values were obtained from the data of Brown and Whitt (17). At the higher temperatures changing water vapor pressure above the entering electrolyte has a pronounced effect even near the approximate optimum value of 600 mm.

In order to study the effect of temperature on performance, it was elected to adjust the electrolyte concentration and temperature so as to keep the water vapor pressure over the electrolyte constant at about 600 mm. This corresponded to operating the cell about 8°C below the boiling point of the electrolyte. Thus, 150°C and 85% (14.6M) H_3PO_4 electrolyte was a typical operating point. The variation of the operating temperature and concentration was as shown in the graph of Fig. 5. The boiling line and the 600 mm water vapor pressure line were interpolated from data cited by Van Wazer (18).

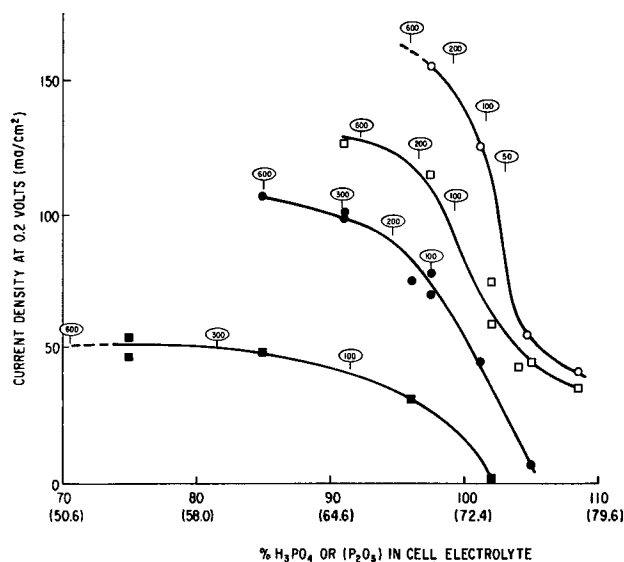


Fig. 4. Current density of propane-oxygen cells at 0.2v cell potential at several temperatures as a function of concentration of H_3PO_4 electrolyte. ■ 120°C, ● 150°C, □ 175°C, ○ 200°C. Numbers in ellipses are water vapor pressures in millimeters over the electrolytes from the data of Brown and Whitt (17).

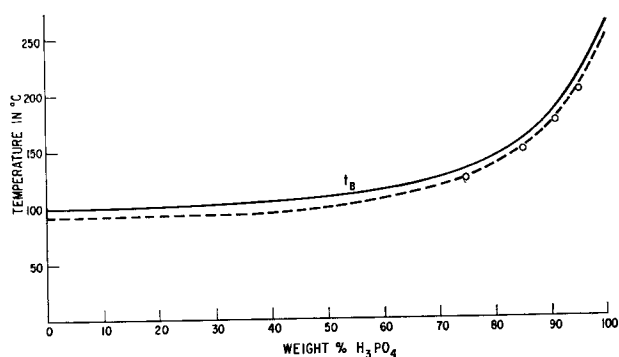


Fig. 5. H_3PO_4 composition-temperature diagram with boiling line —, 600 mm water vapor pressure line - - -, and some approximately optimum operating points for propane-oxygen fuel cells ○.

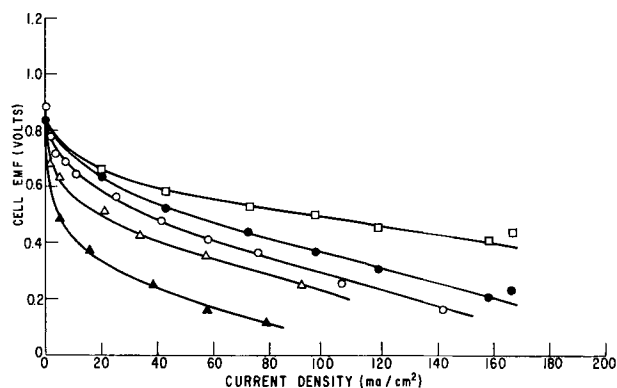


Fig. 6. Cell emf vs. current density curves for propane-oxygen cells at the operating points shown on Fig. 5. \blacktriangle 75% H_3PO_4 120°C, \triangle 85% H_3PO_4 150°C, \circ 91% H_3PO_4 175°C, \bullet 95% H_3PO_4 200°C, \square 95% H_3PO_4 200°C, *iR* free.

Cells operating at the 4 open circle points on Fig. 5 gave the current density-emf curves shown in Fig. 6. It is found that there is a sizeable improvement with temperature. Internal ohmic loss is removed from the 200°C curve for the purpose of comparing on this basis with many other fuel cell data reported in this way and to give an idea of the ohmic loss found for the cells. The 1000 cycle resistance of the cells was 0.12 ± 0.01 ohm over the range of temperatures employed. This was divided into lead resistance of 0.04 ohm and cell internal resistance of 0.08 ohm. A typical electrolyte resistivity was 1.760 ohm·cm for 85% by weight H_3PO_4 (19), which, with the cell constant (area/length) having a value 28, yields a value for internal ohmic resistance of 0.06 ohm. Thus the ohmic loss in the cell is largely in the electrolyte.

The effect of temperature on propane-oxygen fuel cell performance has been compared with a process of constant activation energy by plotting the logarithm of current density at a fixed *iR* free cell potential of 0.45v as a function of reciprocal absolute temperature. This plot is shown in Fig. 7. It is apparent that improvement with increasing tem-

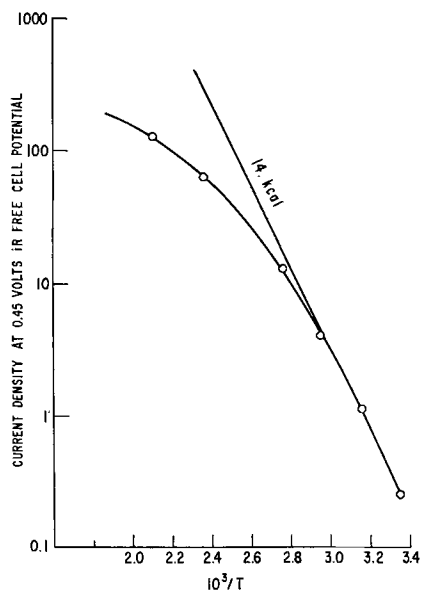


Fig. 7. Log of current density at 0.45v *iR* free cell potential vs. $10^3/T$ for propane-oxygen cells.

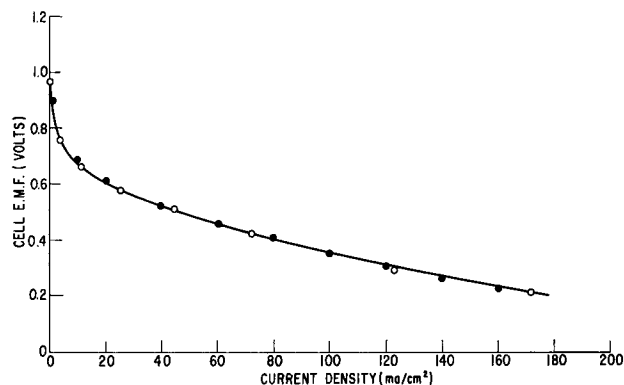


Fig. 8. Cell emf vs. current density for propane-oxygen cell at 200°C. \circ Experimental points, \bullet calculated from three constant equation (see text).

perature falls off at the higher temperatures. This might be attributed to the onset of diffusion control; however, the form of the current density vs. emf curves shows no effect of this kind.

In fact, at 200°C, the polarization emf-current density curve for a cell which was allowed to reach thermal steady state on each point is presented in the plot of Fig. 8. The curve is expressed within experimental error by a three constant equation

$$E = 0.900 - 0.200 \log i - 0.0015i$$

This is to be considered an entirely empirical situation as the temperature of the anode is rising at the heavy load currents. However, at least there is no apparent onset of diffusion limitation. It has been shown elsewhere (20) that this occurs at a current density above 500 ma/cm².

Carbon dioxide yield data have been obtained for propane-oxygen cells under a variety of conditions of temperature and electrolyte concentration. There is no discernible trend of the CO_2 yield as a function of these variables. The CO_2 yield is defined here as 100 times the ratio of the CO_2 production rate to that which would be produced at a given electron production rate (cell current) by reaction [1]. At 150°C, forty-four such CO_2 yield determinations were made. They were found to be normally distributed about a mean value of 99.3% with a standard deviation of 2%. It is concluded that the CO_2 yield from propane in the fuel cells investigated here at 150°C is $99.3 \pm 4\%$ with 95% confidence limits.

Discussion and Results

The over-all steady state rate of anodic oxidation could be influenced by several factors including: (i) rate of mass transport of the fuel or water to the electrocatalyst sites, (ii) rate and extent of adsorption of the fuel or water on the electrocatalyst, and (iii) rate of surface reactions, (iv) rate of mass transport of carbon dioxide away from the reaction sites. All of the present work is in the region of the polarization curve well removed from that of limiting current, and (i) and (iv) above will therefore not be rate determining. While either or both of (ii) and (iii) will be rate determining, little detailed information concerning them is available. The adsorption of propane on the platinum

electrocatalyst is undoubtedly dissociative (21). Furthermore, both C-C and C-H bonds dissociate (22). At steady state many different species are expected to be reacting concurrently and the situation is extremely complex in detail. In light of this the simple result that the only carbonaceous product of the reaction is carbon dioxide is very surprising.

The completeness of oxidation may be simply explained by the following hypothesis. If the intermediates are more strongly adsorbed on the anode than the initial fuel molecules, then if steady-state electro-oxidation occurs, it will proceed to completion. Steady-state electro-oxidation would occur only if none of the intermediates is both strongly adsorbed and inert to further electrochemical oxidation. This also means that the final oxidation product is not strongly adsorbed on the anode, and this is surely the case with CO₂. The results of this paper therefore indicate that propane does in fact compete poorly with the surface intermediates for reaction sites. This would be expected for all probable partly oxidized and/or dehydrogenated species that would be formed from propane on the fuel cell anode. The observation of good steady state performance indicates that intermediates inert to further oxidation do not form. The nature of those that are formed is not as yet established.

The competitive adsorption hypothesis to explain complete electro-oxidation of propane also predicts that more strongly adsorbed fuels might be less completely oxidized. This may explain why in previous work (11) the CO₂ yields from propylene and cyclopropane were only 82% and 91%, respectively, while that from propane was 99+% from fuel cells operating at 90°C.

Summary

High performance of propane-oxygen fuel cells has been observed in the temperature region of about 150°-200°C. Propane is oxidized completely in the cells. The concentration of the H₃PO₄ electrolyte is a variable important to performance but not requiring extremely close control. The effect of temperature has been established under conditions which maintain the vapor pressure of water over the electrolyte approximately constant at 600 mm. Between 25° and 200°C the current density at a constant overpotential shows a diminishing improvement with increasing temperature (compared to a process of constant activation energy) as the temperature reaches higher values. The current density vs. emf (polarization) curves show no evidence of limiting currents suggesting that mass transport steps are not rate determining in the region up to about 200 ma/cm². A typical polarization curve is well fitted by a three constant equation of the form

$$E = a - b \log i - c i$$

It is proposed that complete oxidation of the propane takes place because propane molecules compete unsuccessfully for reaction sites on the electrocatalyst surface with the intermediates that are

formed in the course of the electrochemical oxidation reaction.

Acknowledgment

This work was supported in part by the Advanced Research Projects Agency through a contract with the United States Army Engineer Research and Development Laboratories, Ft. Belvoir, Virginia.

Manuscript received Feb. 24, 1964. This paper was presented at the New York Meeting, Sept. 29-Oct. 3, 1963.

Any discussion of this paper will appear in a Discussion Section to be published in the June 1965 JOURNAL.

REFERENCES

1. General Electric Research Laboratory Press Release, April 23, 1963.
2. W. T. Grubb and L. W. Niedrach, *This Journal*, **110**, 1086 (1963).
3. G. J. Broers and J. A. A. Ketelaar, "High Temperature Fuel Cells," in "Fuel Cells," G. J. Young, Editor, p. 78, Reinhold Publishing Corp., New York (1960).
4. H. H. Chambers, *Trans. North East Coast Inst. of Engineers and Shipbuilders*, **77**, 379 (1961).
5. E. B. Shultz, Jr., K. S. Vorres, L. G. Marianowski, and H. R. Linden, "High Temperature Methane Fuel Cells," in "Fuel Cells," G. J. Young, Editor, Vol. 2, p. 24, Reinhold Publishing Corp., New York (1963).
6. R. P. Buck, L. R. Griffith, R. T. MacDonald, and M. J. Schlatter, *Proc. 15th Annual Power Sources Conference*, Atlantic City, New Jersey, May 1961, p. 16.
7. W. T. Grubb, *Proc. 16th Annual Power Sources Conference*, Atlantic City, New Jersey, May 1962, p. 31.
8. M. J. Schlatter, "Fuel Cell Intermediates and Products," in "Fuel Cells," G. J. Young, Editor, Vol. 2, p. 190, Reinhold Publishing Corp., New York (1963).
9. G. J. Young and R. B. Rozelle, "Low Temperature Electrochemical Oxidation of Hydrocarbons," in "Fuel Cells," G. J. Young, Editor, Vol. 2, p. 216, Reinhold Publishing Corp., New York (1963).
10. L. W. Niedrach, *This Journal*, **109**, 1092 (1962).
11. W. T. Grubb and L. W. Niedrach, *Proc. 17th Annual Power Sources Conference*, Atlantic City, New Jersey, May 1963, p. 69.
12. R. Vaucher and O. Bloch, *Compt. rend.*, **254**, 3676 (1962).
13. O. Bloch, P. Degobert, M. Prigent, and J. C. Balaceanu, 6th World Petroleum Congress, Frankfurt-Main, June 1963, Section VI, Paper No. 3.
14. G. V. Elmore and H. A. Tanner, *This Journal*, **108**, 669 (1961).
15. B. L. Tarmy, *Proc. 16th Annual Power Sources Conference*, Atlantic City, New Jersey, May 1962, p. 29.
16. K. Kordes and A. Marko, *This Journal*, **107**, 773 (1960).
17. E. H. Brown and C. D. Whitt, *Ind. Eng. Chem.*, **44**, 615 (1952).
18. J. R. van Wazer, "Phosphorus and Its Compounds," Vol. I, pp. 484, 773, Interscience Publishers, Inc., New York (1958).
19. R. A. Munson and M. E. Lazarus, To be published.
20. W. T. Grubb, *Nature*, **201**, 699 (1964).

Zirconium Dioxide-Oxygen Reactions

I. Molecular Oxygen Adsorption with Electron Transfer

Tennyson Smith

North American Aviation Science Center, Canoga Park, California

ABSTRACT

The rates and amounts of oxygen pickup by samples of powdered zirconium dioxide have been measured as a function of temperature (400°-900°C), oxygen pressure (10^{-5} to 760 mm Hg), and particle size. Many experiments, performed to correlate oxygen pickup with the mass of oxide and with the oxide surface, indicate that oxygen pickup is primarily a surface phenomenon. After complete reduction of the ZrO_2 adsorbed surface oxygen, approximately one atomic monolayer of oxygen will adsorb irreversibly, and about 5% of the total adsorbed oxygen can be reversibly adsorbed and desorbed as molecules. The apparent activation energy for the adsorption of molecular oxygen is about 35 kcal/mole and for desorption about 53 kcal/mole, as compared to about 58 kcal/mole for adsorption of atomic oxygen. From theoretical calculations it was concluded that electron transfer must occur (*e.g.*, oxygen adsorbs as O_2^-), and this molecular oxygen anion adsorbs as a mobile layer.

The mechanism of the interaction of a gas with a solid surface is important to the understanding of the oxidation of metals and many catalytic processes. A study of the reaction of oxygen with zirconium dioxide powder was initiated in the hopes of discovering something about the reactions at the gas-oxide interface during the oxidation of zirconium. Of particular interest is the oxygen species (O , O^- , $O^=$, O_2 , O_2^- , or $O_2^=$) that adsorbs on the surface. The effect of oxygen adsorption on the electrical properties of semiconductors (1) suggests that electron transfer occurs and that oxygen is adsorbed as a negative ion. Judging from the electronegativities of the above species in the gas phase, the most probable adsorbed oxygen species would be O^- and O_2^- . It is shown in this paper that electron transfer probably does occur and that oxygen molecules are adsorbed as O_2^- .

Part I is concerned with the primary adsorption of molecular oxygen on zirconium dioxide and the thermodynamic and kinetic evidence relating adsorption to the semiconducting properties of the oxide. Part II will treat the secondary adsorption of atomic oxygen which is fed by the primary adsorption.

Experimental

Material, apparatus, and procedure.—Table I lists the source and the physical characteristics of each

Table I. Zirconium dioxide powder characteristics

Batch	Source	Color	Specific surface area, m^2/g
I	Decomposed zirconyl nitrate dihydrate, Fisher Co.	White	5.0
II	W. P. Kieth Co.	Yellow	1.2
III	Reactor grade, Carborundum Corp.	Cream	1.16
IV	Nuclear grade, Zirconium Corp. of America Zircoa A-H (—325 mesh)	White	10.5

batch of zirconium dioxide powder. Spectrographic analysis of samples revealed the greatest impurity in batch I was Na; in batch II, Ca; in batch III, Fe; and in batch IV, Si.

Tank hydrogen was purified by passing it through a train consisting of a deoxo unit, a bed of platinumized asbestos at 300°C, a tube of P_2O_5 , and a liquid nitrogen trap. High-purity research grade oxygen (obtained from the Matheson Company) was used as-received. The maximum limits of possible impurities were listed in mole per cent as $CO_2 < 0.1$, $CO < 0.01$, $Ar < 0.01$, $N_2 < 0.01$, and $H_2 < 0.01$.

A constant-volume system with a thermistor pressure manometer was used for low-pressure work (10^{-5} to 1 mm Hg). This same system contained a strain gauge pressure transducer for work in the pressure range 1-1000 mm Hg. A constant-temperature bath was built into the system to control the temperature of the thermistor and transducer to $\pm 0.02^\circ C$.

Some of the experiments were carried out in a BET apparatus; some were carried out in a Sartorius vacuum microbalance.

Samples of the zirconium dioxide were weighed into a Vycor sample holder and placed in the apparatus. The system was evacuated and the sample was outgassed at temperature. The sample could alternately be exposed to hydrogen and oxygen and the pressure changes recorded with time as a function of temperature, gas, pressure, etc.

A number of control experiments were made under conditions identical to the oxidation-reduction experiments, but without a sample. In every instance, pressure changes for the constant-volume system were negligible compared to those in the experiments with samples, and no appreciable weight change was noted with the microbalance.

Results and Discussion

Surface vs. lattice phenomenon.—When zirconium dioxide powder is reacted with hydrogen or oxygen,

the question arises as to whether the reaction (a) is a surface reaction, (b) a reaction in the lattice interior, or (c) involves a combination of these phenomena.

A direct experiment can be made to test these possibilities by measuring the effect of specific area (m^2/g) on the total quantity of gas that will react, holding all other conditions constant. That is, the amount reacted should be directly proportional to the specific surface area of the powder, if the surface reaction is predominant, or proportional to the mass of the powder, if the lattice reaction is predominant.

In either case, the rate of the reaction should be proportional to the specific surface area. In the case of a powder with small surface area, care must be taken not to mistake a very slow lattice diffusion reaction for a surface reaction approaching saturation. It is because of this last problem that it is sometimes difficult to determine conclusively which phenomenon is predominant.

An experiment to determine the predominant mechanism was performed by exposing a powder sample to hydrogen until no further reaction occurred, then exposing it to oxygen and recording the pressure change (constant volume system) or weight change (microbalance) as a function of time. The specific surface areas of the powder samples were measured by the BET method. The total equilibrium amount of oxygen pickup by different ZrO_2 samples is given in Table II. It is seen in the table that for many samples of different weights (0.091–1.67g) and at various temperatures (530° – 900°C), the total weight of oxygen pickup varies over a wide range on a mass basis (65 – $1750\mu\text{g O}_2/\text{g}$) but is almost constant on a specific area basis ($0.021 \pm 0.005 \mu\text{g O}_2/\text{cm}^2$). It is important to note (bottom of Table II) that the average value for total oxygen pickup ($0.021 \mu\text{g O}_2/\text{cm}^2$) is very close to the weight per unit area ($0.019 \mu\text{g O}_2/\text{cm}^2$) of 1 at. monolayer. The monolayer calculation was made with the estimate of approximately 0.7×10^{15} zirconium sites per cm^2 of ZrO_2 using the data of McCullough and Trueblood (2). These two facts, plus information that will be given later, indicate that the predominate oxygen pickup reaction is surface adsorption rather than bulk diffusion.

Table III. Mass spectrographic analysis of gases that outgas from ZrO_2 powder from batch III (Table I)

Gas sample	ZrO_2 history As-received	Out-gassing temp, $^\circ\text{C}$	Per cent by volume of gas sample			
			H_2O	CO_2	H_2	O_2
1	Evacuated system above as-received ZrO_2 sam- ple at room temp. Closed system and col- lected outgassing sam- ple at	170	30	70		
2	Continued outgassing	440	35	65		
3	Continued outgassing to Evacuated the system then took a sample at	900	7	93		
After exposing the ZrO_2 to 20 mm Hg of H_2 at 600°C						
4	Outgassed ZrO_2 for 20 min and took sample	600	36	36	29	
5	Continued outgassing at	800	15	49	36	
6	Continued outgassing at	900	10	74	16	
After exposing to H_2 at 900°C						
7	Evacuated the system then took a gas sam- ple at	900	6	2	92	
After outgassing then exposing a new sample (batch IV, Table I) to oxygen at 900°C						
1	Evacuated system then took a sample	900	(A, N_2) 1, 3	3	93	

Outgassing ZrO_2 powder samples.—In the study of hydrogen or oxygen pickup by samples of ZrO_2 powder, it is essential to distinguish between gases that are initially present on the as-received ZrO_2 and gases that come from the sample after exposure to the reactants H_2 or O_2 .

Table III has been prepared from mass spectrographic analysis of gases evolved from ZrO_2 at various temperatures before and after exposure to hydrogen and oxygen.

The results in Table III indicate two important things: (A) some oxygen can be removed from the ZrO_2 sample by evacuation after reaction, and (B) some hydrogen remains either on the sample surface, in the sample, or both, after reduction.

Equilibrium experiments.—After a sample of ZrO_2 has been outgassed to remove H_2O and CO_2 and reduced with hydrogen to ensure that surface ox-

Table II. Oxygen pickup by ZrO_2 powders after reduction with hydrogen

ZrO_2 batch	Systems	Temp, $^\circ\text{C}$	Sample wt. g	Specific surface area, m^2/g	Total O_2 pickup	Total O_2 pickup
					(μgO_2) g	(μgO_2) cm^2
I	Const. vol*	550	0.903	5.0	880	0.017
	Microbalance	530	0.125	5.0	1100	0.022
III	Const. vol	(700–900)	0.322	1.16	245	0.021
	Microbalance	811	0.091	1.16	440	0.038
IV (–325 mesh)	Const. vol	900	0.838	10.5	1750	0.017
	Microbalance	790	0.096	10.5	1660	0.016
IV (–48 mesh)	Const. vol	900	0.887	0.93	170	0.019
IV (–4 mesh)	Microbalance	807	0.267	0.26	100	0.038
IV (–200 + 250 mesh)	Const. vol	900	1.672	0.33	65	0.019
Weight per gram, equivalent to one monolayer						avg = 0.021 ± 0.005 ~ 0.019

* Const. vol refers to the constant volume system.

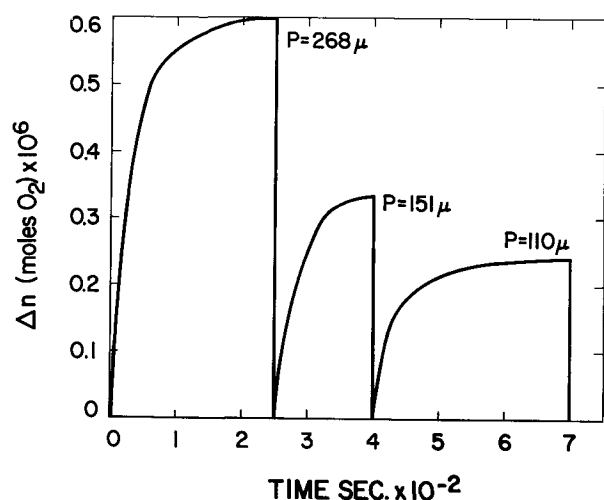


Fig. 1. Equilibrium desorption of oxygen from ZrO_2 powder; temperature, $900^\circ C$; $N_s = 3.2 \times 10^{-6}$ moles O_2 .

xygen has been removed, oxygen will be adsorbed irreversibly to form approximately one atomic monolayer. However, about 5% of the oxygen can be reversibly adsorbed and pumped off. Although the data are more difficult to interpret for the reversible adsorption because of the small amount and because of the more dominant irreversible reaction, the rest of this paper will be primarily concerned with the reversibly adsorbed oxygen. Part II will be concerned with the irreversibly adsorbed oxygen.

Figure 1 illustrates desorption of reversibly adsorbed oxygen after oxidation to completion at $900^\circ C$. After evacuating the system, it was closed off, and the pressure increase was measured as a function of time. The number of moles of gas that have desorbed (calculated from the pressure increase and the perfect gas law) are shown in Fig. 1. When the gas pressure approached the equilibrium pressure (e.g., 286μ at 250 sec) the system was evacuated and closed again, this being repeated as shown in Fig. 1. It is estimated that less than 5% of the oxygen desorbed was removed during the evacuation processes (which took < 3 sec), and this has been neglected in the calculations. A number of such experiments revealed that the total amount of oxygen that could be reversibly adsorbed and desorbed (N_s) was 3.2×10^{-6} moles.

The number of moles of oxygen, n_s , that desorbed at equilibrium is given as a function of the equilibrium pressure P in Table IV. The fraction of N_s that remains adsorbed for a given value of n_s is θ and is calculated from $\theta = (N_s - n_s)/N_s$. Values for θ and equilibrium constants (to be defined later) are also given in Table IV.

Kinetic experiments.—An experiment was carried out on a freshly reduced ZrO_2 sample, at low oxygen pressure, to test the effect of temperature on the rate of oxygen pickup. The results of this experiment are recorded in Fig. 2. The pressure was allowed to drop as oxygen was adsorbed until equilibrium was attained (at 600° and $650^\circ C$, 240 – 35μ), the system was evacuated, and then the pressure was increased for the next experiment. It is seen (Fig. 1 and 2) that at these low pressures the oxy-

Table IV. Values for θ and theoretical equilibrium constants as a function of the equilibrium oxygen pressure. (The correct equilibrium constant should be constant at constant temperature with variation in P and n_s)

Sample from batch IV, wt = 1.44g, $N_s = 3.2 \times 10^{-6}$ moles O_2

Experiment	P , atm $\times 10^4$	n_s , mole $\times 10^6$	θ	$b_a \times 10^{-2}$	$b_m \times 10^{-3}$	$b_L' b_e \times 10^{-4}$	$b_L \times 10^{-4}$	$b_m' b_e \times 10^{-4}$
1 ($900^\circ C$)	0.92	0.47	0.855	5.8	19	38	6.4	11
	1.05	0.37	0.885	7.1	17	55	7.1	12
	1.84	0.25	0.926	9.3	10	85	6.8	12
2 ($900^\circ C$)	1.84	1.15	0.645	1.4	7.0	1.8	0.99	1.3
	2.50	0.95	0.706	1.5	5.6	2.3	0.96	1.4
	4.47	0.64	0.800	1.9	3.6	3.5	0.89	1.4
3 ($900^\circ C$)	1.45	1.00	0.691	1.9	9.5	3.4	1.5	2.2
	2.00	0.81	0.750	2.1	7.5	4.5	1.5	2.2
	3.53	0.53	0.836	2.7	4.7	7.5	1.4	2.4

P is the equilibrium oxygen pressure, i.e., the limiting pressure caused by desorption from the sample; n_s is the number of moles of gas desorbed, as calculated from the constant volume of the system and the equilibrium pressure P ; N_s is the total oxygen that can desorb (about 5% of that which can adsorb); $\theta = (N_s - n_s)/N_s$.

gen pickup is definitely a function of the pressure as well as the temperature. This experiment, as well as others, showed that the rate of oxygen pickup, for about the first 5%, was dependent on the oxygen pressure. However, it was found that after the first 5% was adsorbed the rate became independent of the oxygen pressure. One example of this is shown in Fig. 3, where it is seen that the rate remains constant as the pressure is increased from the range 2.0 to 6.8 to the range 13 and 20 mm Hg at the indicated times. The sample had adsorbed 26μ moles of oxygen prior to the experiment recorded in this figure. The different mechanism for the first 5 or 10%, as compared to the remainder, is shown in Fig. 4 (compare curves 3 and 6, and 4 and 7) and in the Arrhenius plot, curves 4, 5, and 6 (in squares) Fig. 5. It is seen that up to curve 4 (Fig. 4 and 5) the sample had adsorbed about 12μ moles of oxygen ($\sim 10\%$ of total). At this point, the Arrhenius plot changes slope, indicating a change in mechanism. The absolute values of the data at the beginning of the transition (curves

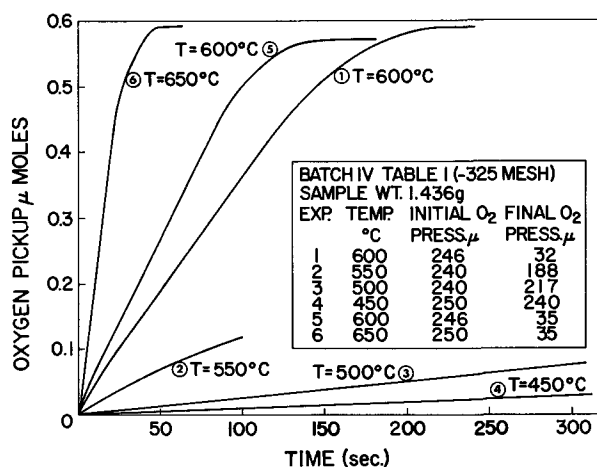


Fig. 2. Oxygen pickup by ZrO_2 as a function of temperature at low pressures. Shows the effect of temperature and pressure.

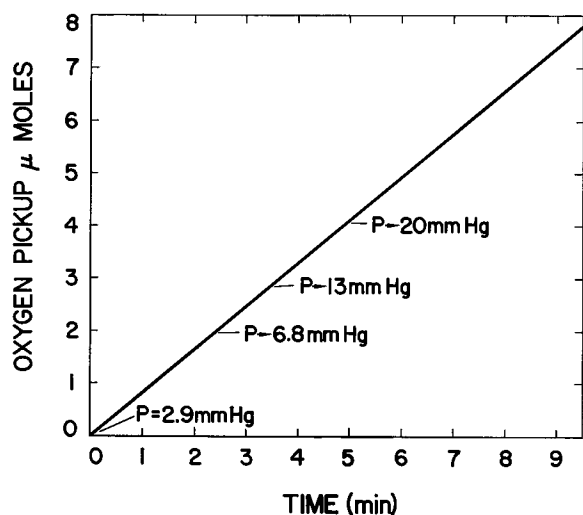


Fig. 3. Oxygen pickup by ZrO_2 that had $26 \mu\text{moles } O_2$ to start with. The rate of oxygen pickup during the first $26 \mu\text{moles}$ was a function of pressure. The rate is independent of pressure for more than $26 \mu\text{moles}$. Batch IV, Table I (-325 mesh); sample weight, 1.436g; temperature, 600°C .

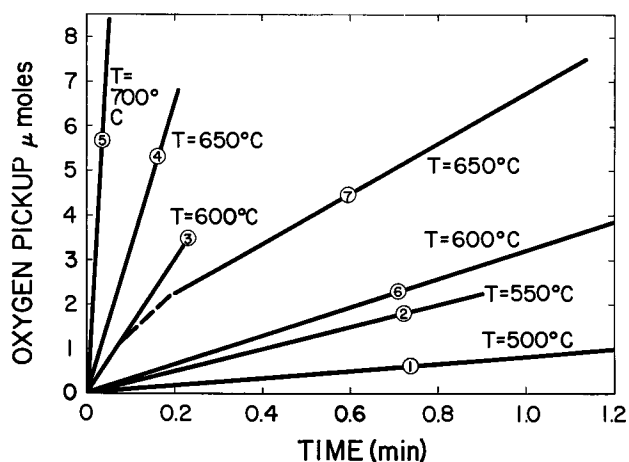


Fig. 4. Oxygen pickup on the surface of ZrO_2 as a function of temperature at constant pressure. The numbers indicate the experimental sequence. Batch IV, Table I (-325 mesh); sample weight, 1.436g; oxygen pressure, 19 mm Hg.

5, 6, and 7, Fig. 4 and 4, 5, and 6 in squares, Fig. 5) only give an order of magnitude value for E_{app}^\ddagger (64 kcal/mole) of the second mechanism because the transition is not complete.

Theoretical Interpretation and Discussion of Results

Adsorption Models

Equilibrium experiments.—From a consideration of the electron affinity for various oxygen species (e.g., O_2 , O , O^- , $O^=$, O_2^-) and the large effect of oxygen adsorption on the electrical properties of semiconductors, others (3) have suggested that oxygen would first adsorb as O_2^- by attracting an electron from the solid and then dissociate and adsorb as O^- .

These species may adsorb on localized sites or as a mobile layer (approaching a two-dimensional gas). Concerning the reversibly adsorbed oxygen, it should be of interest to identify which of the above-mentioned species exists and whether a mobile or localized adsorption is involved. To do this, we

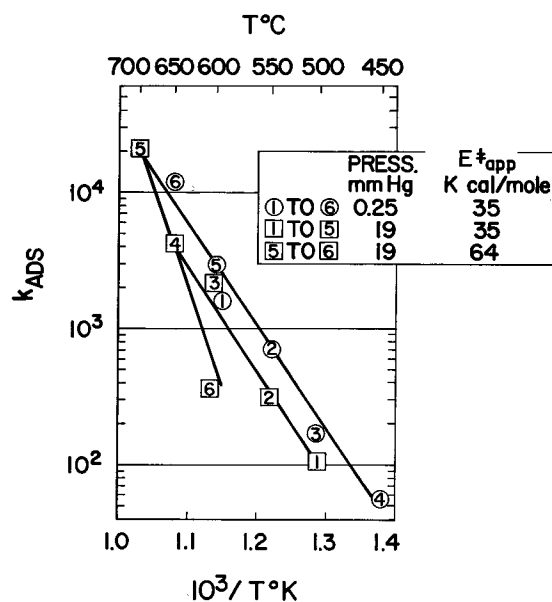
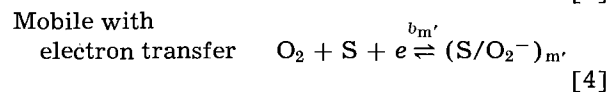
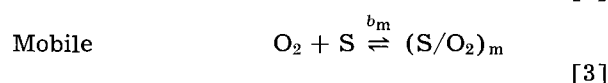
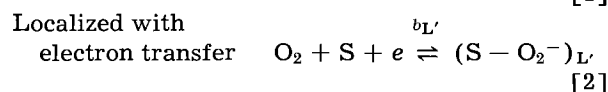
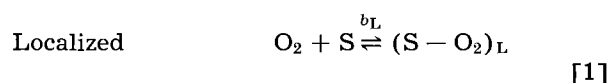


Fig. 5. Arrhenius plot for the rate of reversible adsorption of molecular oxygen on a ZrO_2 surface. Numbers in the open circles indicate the sequence of the experiments at low pressure (0.25 mm Hg). Numbers in the squares indicate the sequence for experiments at 19 mm Hg of oxygen.

next derive the equations for different models involving molecular oxygen. The models that will be considered are localized adsorption without electron transfer, localized adsorption with electron transfer, mobile adsorption without electron transfer, and mobile adsorption with electron transfer. The reactions can be expressed as follows



The equilibrium constants can be expressed in terms of the activities, represented by a 's in the equation

$$b' = (a_{s-o_2^-}) / (a_{o_2} a_s a_e) \approx b/a_e \quad [5]$$

with the appropriate L or m subscript.

At this point we wish to evaluate a_e as a function of temperature and also to account for the experimental observation that only 5-10% of the total oxide surface is occupied by reversibly adsorbed oxygen at equilibrium. Let us assume that the source of electrons is the conduction band of the oxide and that these electrons are promoted from donor levels with average energy, w , below the conduction band.

Since the average particle radius ($\sim 5 \times 10^{-6}$ cm) was of the order of the width of the exhaustion layer ($\sim 10^{-4}$ to 10^{-6} cm for most semiconductors)

we will assume that all donor sites could be ionized.

The number of moles of donor levels is just

$$N_T = N_D + N_e + N_s \theta \quad [6]$$

where N_D , N_e and $N_s \theta$ represent the number of moles of electrons at un-ionized sites, in the conduction band and on adsorbed oxygen, respectively. We will consider ionization of a donor site for the first electron only, due to the large energy usually associated with ionization for the second electron. When essentially all of the electrons from donor levels have been promoted to adsorbed oxygen, N_D and N_e approach zero, and θ approaches unity, so that from Eq. [6]

$$N_s \sim N_T \quad [7]$$

That is, the amount of reversibly adsorbed oxygen is limited by the number of available electrons rather than the total number of adsorption sites at the surface. Since about 5% of the surface was covered with reversibly adsorbed oxygen at saturation and since the total number of surface sites, $N_o \approx 1.5 \times 10^{-4}$ mole, it follows that the approximate number of donor levels is

$$N_T \sim 7.5 \times 10^{-6} \text{ moles} \quad [8]$$

or in concentration units (1.44g sample with a density of 5.83 g/cm³)

$$C_T \sim 3 \times 10^{-5} \text{ mole/cm}^3 \quad [9]$$

These donors may be anion vacancies with trapped electrons or impurity centers in the oxide.

The ionization process can be expressed



where D , D^+ , and e represent un-ionized donor sites, ionized donor sites, and electrons in the conduction band, respectively.

It follows that

$$b_e = (a_{D^+} a_e) / a_D \quad [11]$$

In addition to Eq. [6] we have the mass balance equations

$$N_T = N_{D^+} + N_D \quad [12]$$

$$N_{D^+} = N_e + N_s \theta \quad [13]$$

We assume $a = N/N^o$, where N^o is the standard state (Henries law obeyed and activity coefficients unity) and choose $N_{D^+}^o = N_{D^+}$. Then from Eq. [6], [7], [11], [12], and [13] we get

$$a_e = [(1-\theta)/\theta] b_e \quad [14]$$

if $N_e \ll \theta N_s$. We choose the standard state for adsorbed oxygen to be $N_s/2$, and for localized adsorption we choose the standard state of the surface sites to also be $N_s/2$ (both correspond to $\theta^o = 1/2$). The standard state of oxygen gas is chosen to be 1 atm. The equation for b_L becomes

$$b_L = [\theta/(1-\theta)] P^{-1} \quad [15]$$

The equations for equilibrium adsorption take a different form if the molecules adsorb as a two-dimensional gas. For the two-dimensional gas model

we can assume the fugacity of the surface, f_s , to be independent of coverage and choose the surface standard state fugacity f_s^o such that $f_s^o = f_s$ and therefore $a_s = \text{unity}$. The activity of the adsorbed molecules is $a (s/O_2) = F/F^o$, where F and F^o are the spreading pressure, dynes/cm, at equilibrium and in the standard state, respectively.

The spreading pressure, F , can be related to the area per mole, A , by the perfect gas law, $F = RT/A$, if A is large enough. Since only 5% of the surface is covered by reversibly adsorbed oxygen, this relation should be valid. Thus for mobile adsorption without electron transfer

$$b_m = (A^o/A) / (P/P^o) \quad [16]$$

where A^o is the area per mole of adsorbed molecules in the standard state and P^o is the oxygen pressure in the standard state. The area available per mole of adsorbed molecules can be expressed as

$$A = [(N_o - n)/n] A_M \quad [17]$$

where $n = (N_s - n_s)$ is the moles of O₂ adsorbed, and A_M is the effective cross-sectional area per mole. Since $N_s \approx 0.05 N_o$, and $n/N_s = \theta$, it follows from Eq. [16] and [17] that

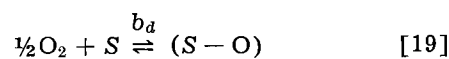
$$b_m \approx 2 \theta / P \quad [18]$$

if we choose $\theta^o = 1/2$ as before.

From Eq. [5], [14], [15], and [17] we obtain the following set of equations.

	Localized adsorption	Mobile adsorption
without electron transfer	$b_L = \left(\frac{\theta}{1-\theta} \right) \frac{1}{P}$	$b_m \approx 2 \theta / P = 2(1-\theta) b_L$
with electron transfer	$b_L' b_e = \left(\frac{\theta}{1-\theta} \right)^2 \frac{1}{P}$	$b_m' b_e \approx \frac{2\theta^2}{(1-\theta)P}$
	$= \left(\frac{\theta}{1-\theta} \right) b_L$	$= 2 \theta b_L$

If the reversibly adsorbed oxygen dissociates upon adsorbing, we can represent the reaction by



and obtain

$$b_d = \left(\frac{\theta_o}{1-\theta_o} \right) \frac{1}{P^{1/2}} \quad [20]$$

The equilibrium constants should be constant and independent of θ or P at constant temperature. Values for b_d , b_m , $b_L' b_e$, b_L and $b_m' b_e$ are recorded in Table IV for three experiments. It is seen that for a given experiment b_L and $b_m' b_e$ give fairly constant results while b_d , b_m , and $b_L' b_e$ do not, even though the absolute values between experiments do not agree very well. (Experiment 1 yields values much larger than Experiments 2 and 3.)

Adsorption enthalpy.—Now, expressing b_e as a function of temperature we get

$$b_e = e^{(\Delta \bar{S}_e^o)/R} e^{-W/RT} \quad [21]$$

Let $\Delta\bar{H}_L^\circ$ and $\Delta\bar{H}_m^\circ$ be the enthalpy change for reaction [1] and [3], respectively, and $\Delta\bar{H}_L^{\circ'}$ and $\Delta\bar{H}_m^{\circ'}$ be the enthalpy change for reactions [2] and [4], respectively. It follows that a plot of the natural logarithm of b_L' , $b_L b_e$, b_m , and $b_m' b_e$ vs. $1/T$ should yield values for $\Delta\bar{H}_L^\circ$, $(\Delta\bar{H}_L^{\circ'} + w)$, $\Delta\bar{H}_m^\circ$ and $(\Delta\bar{H}_m^{\circ'} + w)$, respectively, only one of which will be correct. Since the activation energy for the adsorption of molecular oxygen is probably very small or zero, $\Delta\bar{H}_L^\circ$, $\Delta\bar{H}_L^{\circ'}$, $\Delta\bar{H}_m^\circ$ or $\Delta\bar{H}_m^{\circ'}$ (whichever the case may be) should be equal to the negative of the activation energy for desorption. From measurements of the rates of desorption at 800° and 900°C, the desorption activation energy is about 53 kcal/mole. It is shown in the next section on kinetics that, if electron transfer is involved, w should be just the apparent activation energy for molecular oxygen adsorption (*i.e.*, approximately 35 kcal/mole; see Fig. 5). Therefore the predicted values of $\Delta\bar{H}_L^\circ$, $(\Delta\bar{H}_L^{\circ'} + w)$, $\Delta\bar{H}_m^\circ$ and $(\Delta\bar{H}_m^{\circ'} + w)$ are -53, -18, -53, and -18 kcal/mole, respectively. Plots of the natural logarithm of b_L , $b_L' b_e$, b_m , and $b_m' b_e$ vs. $1/T$ (at 400°, 520°, 600°, 700°, 800°, and 900°C) yielded the approximate values of -12, -17, -9, and -14 kcal/mole for $\Delta\bar{H}_L^\circ$, $(\Delta\bar{H}_L^{\circ'} + w)$, $\Delta\bar{H}_m^\circ$ and $(\Delta\bar{H}_m^{\circ'} + w)$, respectively. It is concluded from Table IV and this information that the most probable mechanism involves mobile adsorption of molecular oxygen with electron transfer.

Adsorption entropy.—The experimental entropy change should correlate with the theoretical entropy change for the correct model. If we can establish an order of magnitude theoretical value for the entropy change of the adsorption process and if their values differ for different models, it should be possible to determine the correct model.

At 400°C and standard state of 1 atm, $\bar{S}_{g, tr}^\circ = 40$ e.u. for oxygen. The surface sites are fixed in space and have approximately the same vibrational entropy before and after adsorption so that the vibrational part of the entropy change is approximately zero. For localized adsorption with standard state of $\theta^\circ = 1/2$ the configurational entropy is zero. For mobile adsorption with $\theta^\circ = 1/2$, (keeping in mind that at $\theta = 1/2 = (N_s - n_s)/N_s$ where N_s is only 0.05 N_o) about 2.5% of the surface is covered, and the entropy is calculated to be about 23 e.u. It is difficult to estimate the entropy of the adsorbed oxygen ions and the entropy of the electrons in the case of electron transfer. However from the above information the theoretical entropy change for reaction [1] is of the order of -40 e.u. and for reaction [3] about -17 e.u. The experimental entropy change calculated from the intercepts of plots of $\ln b_L$, $\ln b_L' b_e$, $\ln b_m' b_e$, and $\ln b_m$ vs. $1/T$ is of the order of zero (± 5 e.u.), and we conclude on this basis that if one of the reactions [1], [2], [3], or [4] is correct, reactions [2] and [4] with electron transfer are more likely. This supports the previous conclusion that reaction [4] is the most probable mechanism. Although absolute values for the equilibrium constants are not very accurate, they would have to

be off by a factor of about 10^3 to account for a discrepancy of 17 e.u. and about 10^8 to account for a discrepancy of 40 e.u.

Kinetic Experiments

Adsorption rates for Eq. [1], [2], [3], and [4] are

$$\text{Localized} \quad r_L = k_L N_g (N_s - n) \quad [22]$$

$$\text{Localized with} \\ \text{electrons transfer} \quad r_L' = k_L' N_e N_g (N_o - n) \quad [23]$$

$$\text{Mobile} \quad r_m = k_m A N_g \quad [24]$$

$$\text{Mobile with} \\ \text{electron transfer} \quad r_m' = k_m' A N_e N_g \quad [25]$$

where the k 's are the appropriate rate constants.

For the limiting case, where $t \rightarrow 0$, $N_s \gg n$, Eq. [22] and [25] can be integrated to yield

$$n = k_{ads}' N_g t \quad [26]$$

If the pressure is held constant, n should increase linearly with time and this is seen to be the case, in Fig. 4, for experiments at 500°-700°C. These experiments were carried out with a freshly reduced surface of ZrO_2 at 19 mm Hg oxygen pressure. N_s for this sample was 2.7×10^{-5} mole O_2 . The fact that the rate constants for experiments at 19 mm Hg fall below those at 0.25 mm Hg (see Fig. 5) is attributed to some factor, other than pressure, interfering (such as heat treatment mentioned later). The repeat of experiment one (curve 5, Fig. 2) was made to see if curve 1 would be reproduced. If the same correction is made to curves 2, 3, 4, and 6 as is needed to make curve 5 correlate with curve 1, almost all of the data, in Fig. 5, fall on the same curve.

The equation for the rate of desorption should be the same for all of the models, *viz.*

$$r_{des} = k_{des} n \quad [27]$$

The amount of oxygen desorbed as a function of time (as given in Fig. 1) should be predicted by integration of the net desorption ($r - r_{des}$) equation. Such an analysis shows that Eq. [22] and [24] do not predict the experimental results. Equations [23] and [25] (with electron transfer) cannot be tested since values for N_e are not accurately known. However, we can make an order of magnitude estimate of N_e as follows.

For initial adsorption experiments, such that n is small, it follows from Eq. [22], [23], [24], and [25] that $k_L \approx r/N_g N_s$, $k_L' \approx N_s k_L/N_e N_o$, $k_m \approx k_l N_s/A$, and $k_m' \approx k_L N_s/AN_e$, respectively. Experimental values for the adsorption rate constant k_{ads} (expressed as $r/N_g N_s$) from initial rates are shown in Fig. 5.

A theoretical derivation of r can be made in terms of the gas-surface collision rate [$\nu = P/(2\pi MRT)^{1/2}$] and the probability that the molecule will stick.

For initial adsorption the theoretical equations are

$$r_L \approx S\nu A (N_s - n)/N_o \approx SAN_g (RT/2\pi M)^{1/2} N_s/N_o V \quad [28]$$

$$r_L' \approx S\nu A (N_o - n) N_e/N_o N_T \approx \\ SAN_g (RT/2\pi M)^{1/2} N_e/N_T V \quad [29]$$

Table V. Comparison of experimental (Fig. 5) and theoretical values for the adsorption rate constants at 500°C

 $A \approx 1.5 \times 10^6 \text{ cm}^2$, $N_s \approx 2.7 \times 10^{-5}$ mole O_2 , $N_o \approx 5.4 \times 10^{-4}$ mole sites, $N_T \approx N_s$, $V \approx 16 \text{ cm}^3$, $S \sim 1$

Theoretical	Experimental
$k_L \approx (SA/N_oV) (RT/2\pi M)^{1/2} \sim 3.4 \times 10^{11}$	$k_L \approx k_{ads} = \tau/N_g N_s \sim 10^2$
$k_L' \approx (SA/N_o N_T V) (RT/2\pi M)^{1/2} \sim 10^{16}$	$k_L' \approx N_s k_{ads}/N_e N_o \sim 5/N_e$
$k_m \approx (S/V) (RT/2\pi M)^{1/2} \sim 1.2 \times 10^3$	$k_m \approx N_s k_{ads}/A \sim 2 \times 10^{-8}$
$k_m' \approx (S/N_T V) (RT/2\pi M)^{1/2} \sim 4 \times 10^7$	$k_m' \approx N_s k_{ads}/N_e A \sim \frac{2 \times 10^{-8}}{N_e}$

$$r_m \approx SvA \approx SAN_g (RT/2\pi M)^{1/2}/V \quad [30]$$

$$r_m' \approx SvA N_e/N_T \approx SAN_g (RT/2\pi M)^{1/2} N_e/N_T V \quad [31]$$

where $(N_s - n)/N_o$ is the probability that an active adsorption site is empty, $(N_o - n)/N_o$ is the probability that a site is empty (all sites available), N_e/N_T is the probability that an electron is in the conduction band, and S (condensation coefficient) is the probability that the gas molecule will stick if N_e/N_T is unity. S will be less than unity if elastic collisions with the surface are possible, but we will assume that S is unity for our experiment.

It is seen from Fig. 5 that at 500°C, $k_{ads} \sim 100$. Values for k , calculated from the theoretical Eq. [28] and [31] are given in Table V. The theoretical values for adsorption without electron transfer differ by a factor of 10^{10} from the experimental values. With electron transfer the theoretical values for k_{ads} correspond with the experimental values if $N_e \sim 5 \times 10^{-16}$ mole. A distinction between localized and mobile adsorption cannot be made with the kinetic results.

The concentration of electrons in the oxide conduction band is estimated to be

$$C_e \sim 2 \times 10^{-15} \text{ mole/cm}^3 \quad [32]$$

since the sample volume was 0.246 cm³. The concentration of electrons in the conduction band is related to the conductivity, σ , the charge per electron, q , and the electron mobility R_e , by the expression

$$C_e = \sigma/q R_e \quad [33]$$

Although the mobility for electrons in ZrO₂ is not known, it has been shown to vary from about 10^2 (at about 400°C) to about unity (at about 900°C) for other n-type oxides and sulfides (4) (units of cm²/volt sec). The conductivity (ohm⁻¹ cm⁻¹) of ZrO₂ is estimated to range from about 10^{-4} (at 400°C) to about 10^{-2} (at 900°C) (5).

If q is expressed in the proper units ($q = 1.6 \times 10^{-19}$ coulombs) the conduction electron concentration is estimated as

$$C_e \text{ (mole/cm}^3\text{)} \sim 10^{-11} \text{ (400°C)} \text{ to } 10^{-7} \text{ (900°C)} \quad [34]$$

The correlation between C_e in Eq. [32] and [34] is considered satisfactory considering the approximations that are made. The correlation would be considerably improved however if we had assumed $S \sim 10^{-4}$ rather than unity.

It is concluded that the kinetic data also support the electron transfer model.

Temperature effect.—Assuming Eq. [31] is the correct equation, we obtain the relation between k_{ads}

and the temperature from Eq. [11] and [21]

$$k_{ads} = k_o' N_e^o e^{\Delta \bar{S}_e^o/R} e^{-w/RT} \quad [35]$$

where $k_o' = SA (RT/2\pi M)^{1/2}/N_s N_T V$. The concentration of N_e is so low that even at the lowest measurable coverage, $a_{D+} \approx a_D$. The empirical equation for k_{ads} as a function of temperature is

$$k_{ads} \approx k_o - E^{\ddagger}_{app}/RT \quad [36]$$

where E^{\ddagger}_{app} is the apparent activation energy. It is seen from Eq. [35] and [36] and Fig. 5 that $w \equiv E^{\ddagger}_{app} \approx 35$ kcal/mole and

$$k_o = k_o' N_e^o e^{\Delta \bar{S}_e^o/R} \quad [37]$$

Entropy of conduction electrons.—Equation [37] provides another theoretical check on the electron transfer model since $\Delta \bar{S}_e^o$ can be calculated from statistical mechanics. $\Delta \bar{S}_e^o = \bar{S}_e^o - \bar{S}_D^o$ where \bar{S}_e^o is the standard state entropy of the electrons in the conduction band and \bar{S}_D^o is the standard state entropy of the electrons in the localized donor levels. \bar{S}_D^o has little translational, vibrational or configurational contribution at $\theta = 1/2$ and is therefore approximately zero. \bar{S}_e^o will depend on the choice of standard state N_e^o , and we will choose this to be the actual electron density at $\theta = 1/2$ and $T = 500^\circ\text{C}$ (i.e., $N_e^o = N_e$ at $\theta = 1/2$ and 500°C). We can consider the conduction band electrons to obey classical statistics rather than Fermi-Dirac statistics (6) since at the low electron concentrations

$$\Lambda^3 N/V^o \sim 2 \times 10^{-11} \ll 1 \quad [38]$$

where the de Broglie wavelength

$$\Lambda = \left(\frac{2\pi m kT}{h^2} \right)^{-1/2} \quad [39]$$

N is Avagadro's number and V^o is the electron gas volume per mole in the standard state ($V^o = 1/C_e^o \approx 5 \times 10^{14}$ cm³/mole). The standard state entropy change for promoting electrons from localized donor levels to a free electron gas is expressed

$$\Delta \bar{S}_e^o \approx \bar{S}_e^o \approx R \ln \left(\frac{2\Lambda^{-3} V^o e^{5/2}}{N} \right) \sim 56 \text{ eu} \quad [40]$$

The terms in Eq. [37] have the following order of magnitude theoretical values

$$\begin{aligned} k_o' &\sim 2 \times 10^{17} \\ N_e^o &\sim 5 \times 10^{-16} \\ e^{\Delta \bar{S}_e^o/R} &\sim 10^{12} \end{aligned}$$

The theoretical value for k_o is therefore

$$k_o \sim 10^{14}$$

as compared to the experimental value of

$$k_o (\text{exp}) \sim 10^{12}$$

from Fig. 5. This correlation is well within the uncertainty of N_e and S and is considered to support the electron transport mechanism.

Summary and Conclusions

The rates and amounts of oxygen pickup by samples of powdered zirconium dioxide have been measured as a function of temperature (400°-900°C), oxygen pressure (10^{-5} to 760 mm Hg), and particle size. Many experiments, performed to correlate oxygen pickup with the mass of oxide and with the oxide surface, indicate that oxygen pickup is primarily a surface phenomenon. After complete reduction of the ZrO_2 adsorbed surface oxygen, approximately one atomic monolayer of oxygen will adsorb irreversibly, and about 5% of the total adsorbed oxygen can be reversibly adsorbed and desorbed as molecules. The apparent activation energy for the adsorption of molecular oxygen is about 35 kcal/mole, and for desorption about 53 kcal/mole, as compared to about 58 kcal/mole (see Part II) for adsorption of atomic oxygen.

The equilibrium adsorption of oxygen was analyzed on the basis of five models, *viz.*, localized adsorption, mobile adsorption, localized adsorption with electron transfer, mobile adsorption with electron transfer, and localized adsorption with dissociation. It was concluded that the experimental data favored mobile adsorption with electron transfer. Comparison of experimental and theoretical enthalpy and entropy of adsorption favors the electron transfer process, but did not distinguish between localized or mobile adsorption. Analysis of

the adsorption kinetics revealed that the electron transfer was probable, but could not distinguish between localized and mobile adsorption.

It is concluded that the most probable mechanism involves adsorption of molecular oxygen which is stabilized by receiving an electron from the conduction band of the oxide. The apparent activation energy for this adsorption process is actually the energy required to promote electrons from donor levels (probably anion vacancies) to the conduction band. The molecular adsorption is fast with respect to the subsequent dissociation and adsorption as atomic oxygen, so that equilibrium is essentially established with respect to O_2^- which feeds the dissociation process. The amount of O_2^- adsorbed at equilibrium is determined by the number of donor sites in the oxide particles. For the material used in this study this proved to be about 3×10^{-5} mole/ cm^2 , and this may be the anion vacancy concentration. This paper has been concerned with the 5% that adsorbs as O_2^- . Part II will be concerned with the dissociation and adsorption of the other 95% to complete a monolayer as atomic oxygen.

Manuscript received Oct. 22, 1963.

Any discussion of this paper will appear in a Discussion Section to be published in the June 1965 JOURNAL.

REFERENCES

1. J. T. Law, "Semiconductors," p. 676, N. B. Hannay, Editor, Reinhold Publishing Corp., New York (1959).
2. J. D. McCullough and K. N. Trueblood, *Acta Cryst.*, **12**, 507 (1959).
3. E. R. S. Winter, "Advances in Catalysis," Vol. X, p. 214, Academic Press, Inc., New York (1958).
4. A. R. Hutson, "Semiconductors," p. 541, N. B. Hannay, Editor, Reinhold Publishing Corp., New York (1959).
5. J. M. Dixon *et al.*, *This Journal*, **110**, 276 (1963).
6. T. L. Hill, "An Introduction to Statistical Thermodynamics," p. 441, Addison-Wesley Publishing Co., Inc., Reading, Mass. (1960).

Zirconium Dioxide-Oxygen Reactions

II. Chemisorption of Atomic Oxygen

Tennyson Smith

North American Aviation Science Center, Canoga Park, California

ABSTRACT

The chemisorption of oxygen on zirconium dioxide has been studied in the temperature range 400°-900°C and oxygen pressure range 10^{-5} to 760 mm Hg. Analysis of the kinetic data indicates that except for about 5-10% the oxygen adsorbs as an atomic monolayer. The proposed mechanism involves primary adsorption of molecular oxygen which then dissociates and becomes adsorbed as atoms. The temperature coefficient for the primary molecular adsorption and secondary atomic adsorption is 35 and 58 kcal/mole, respectively. The primary adsorption is oxygen pressure dependent; whereas, the secondary adsorption is not.

The previous paper was concerned with the primary adsorption of molecular oxygen on the surface of zirconium dioxide and related this process with electron transfer and the semiconducting properties of the oxide. This paper will treat the kinetics and

mechanism of the dissociation of the primary oxygen molecules and their subsequent chemisorption.

Aronson (1) studied the mechanism of oxygen and hydrogen reaction with zirconium dioxide powders. He concluded that, during hydrogen reduction,

oxygen was removed from the lattice positions interior to the zirconium dioxide to form nonstoichiometric oxide, and that subsequent oxidation was controlled by diffusion of oxygen into lattice anion vacancies.

There are a number of important points which Aronson mentioned that were inconsistent with his proposed mechanism. For example, he found that the activation energy for the oxygen-oxide reaction was about 58 kcal/mole which is much larger than found from zirconium metal oxidation studies (20-35 kcal/mole). He also found from his interpretation that the heat of the oxygen-oxide reaction was positive instead of negative as expected. In favor of his mechanism, the correlation between oxidation kinetic data and the theoretical diffusion equation was excellent.

It was shown in the previous paper that the reaction of oxygen with zirconium dioxide in the temperature range 400°-900°C is primarily an adsorption process. Recently Kofstad and Ruzicka (2) attempted to reproduce Aronson's results, but contrary to Aronson they found the range of nonstoichiometry too low to measure with their thermogravimetric technique. They concluded that nonstoichiometry for zirconium dioxide was at least a factor of ten smaller than Aronson concluded. Since Kofstad and Ruzicka used sintered specimens with presumably very low surface area, whereas Aronson used powders of approximately 4 m²/g, it is safe to conclude that a surface rather than a bulk process was measured in Aronson's work. Furthermore, in this paper we show that the correlation between experimental data (ours and Aronson's) and the theoretical adsorption equation is as good as for the diffusion equation. It will be shown in a future paper, concerning the reaction of ZrO₂ with hydrogen, that by interpreting the oxygen-oxide reaction as an adsorption process, Aronson's data yield a negative heat of reaction. Finally, for an adsorption process a correlation between the activation energy for oxidation of zirconium and oxygen reaction with a reduced zirconium dioxide surface is not expected.

The experimental materials, apparatus, and procedure is described in the previous paper.

Experimental Results and Discussion

A number of experiments were carried out, in the temperature range 400°-900°C, in which the ZrO₂ samples were exposed to pure oxygen after they had been exposed to hydrogen. The hydrogen exposure continued until no further reaction occurred in each case, then the system was evacuated. The subsequent oxygen exposure was allowed to continue until no further reaction would occur. Examples of the results of oxygen pickup *vs.* time at 600°, 700°, and 800°C are given in Fig. 1. The reduction of total oxygen pickup from 160 μmoles to about 130 μmoles at 700° and 800°C indicates the reduction in surface activity due to heat treatment. All of the experiments in Fig. 1 were with the same sample.

As was pointed out in Fig. 3 of the previous paper, the reaction is independent of the oxygen pressure except for the first 5-10%.

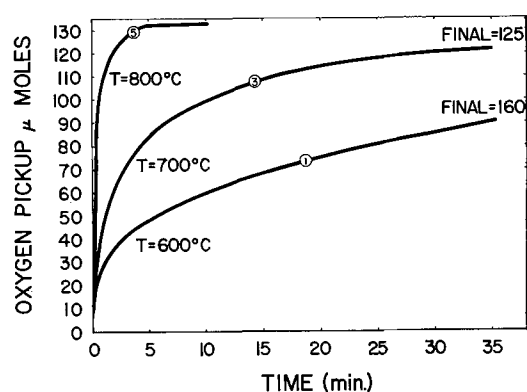


Fig. 1. Oxygen pickup by a ZrO₂ powder (that had been surface reduced) as a function of temperature.

Sample weight is 1.436g, Batch IV, Table I (-325 mesh).

Exp. (Table IV)	Temp, °C	Initial O ₂ press., mm Hg	Final O ₂ press., mm Hg
1	600	127	54
3	700	150	94
5	800	140	81

Chemisorption of Atomic Oxygen

After the surface has become saturated with respect to molecular oxygen, consider the slower reaction in which the molecules dissociate and become adsorbed as atoms. The rate of reaction can be expressed as

$$\left(\frac{dn_o}{dt}\right)_{s-o} = k_{s-o} \theta N_s (N_o - n_o)^2 \quad [1]$$

where $(dn_o/dt)_{s-o}$ represents the rate of adsorption of oxygen atoms, k_{s-o} represents the rate constant for this process, N_o represents the total number of moles of available adsorption sites, and n_o represents the number of moles of atomic oxygen adsorbed at time t . Except at very low pressure θ for molecular oxygen is unity. Integration of Eq. [1] yields

$$\frac{\theta_o}{1 - \theta_o} = k_{s-o} N_s N_o t = k_o' t \quad [2]$$

if $n_o = 0$ at $t = 0$, $\theta_o = n_o/N_o$, and $k_o' = k_{s-o} N_s N_o$.

Data in Fig. 1, where oxidation was allowed to completion, are plotted in Fig. 2 utilizing Eq. [2]. It is seen that fairly straight lines result, in accord with the proposed mechanism. Data from Aronson's (1) Fig. 2 were re-analyzed with respect to the mechanism of adsorption rather than to that of diffusion. The plot of his data, (his C corresponds to θ_o for adsorption) in Fig. 3, shows that the experimental data and theoretical curves correlate as well as for the diffusion model. Consequently, the choice of model must rest on other experimental evidence such as that illustrated in Table II of the previous paper.

Values for the rate constant k_o' from the data in Fig. 2 and 3 are given in an Arrhenius plot of k_o' *vs.* reciprocal temperature in Fig. 4. Values for k_o' (open circles in Fig. 4), calculated from Aronson's

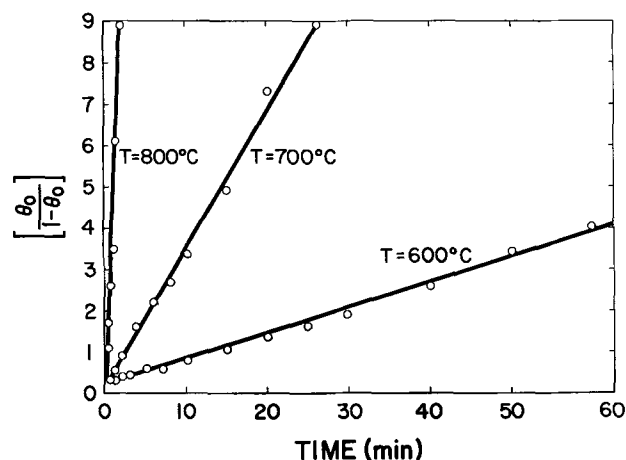


Fig. 2. Plot of the integrated rate equation for chemisorbed oxygen atoms. Batch IV, Table I (—325 mesh), sample weight is 1.436 g.

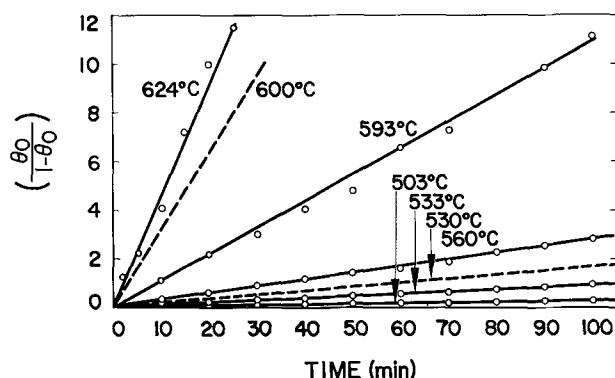


Fig. 3. A plot of $\theta_0 / 1 - \theta_0$ vs. time, to test the equation $dn/dt = k_0 \theta_{O_2} N_{O_2} (N_{O_2} - n)^2$ for the data in Aronson's Fig. 2. The points were calculated from Aronson's data, the lines are a visual fit of these points. The dashed lines are for data of this work at 530°C on a microbalance and 600°C in the constant volume system.

data, yield an activation energy of 58 kcal/mole, just as he obtained for the diffusion analysis. Our datum at 530°C (solid point at 530°C, Fig. 4) was obtained from the dashed line in Fig. 3. This experiment was carried out on the microbalance, as were Aronson's experiments. The datum at 600°C on curve A of Fig. 4 was obtained from the dashed line in Fig. 3 at this temperature. The experiment for this curve was carried out in the constant volume-variable pressure system with a different sample. All of Aronson's data were obtained by using a different sample of ZrO_2 for each experiment. It is believed that curve A in Fig. 4 reflects the true temperature effect for samples that had not been recycled. Curve B in Fig. 4 shows the results from Fig. 2 for experiments on the same sample; that is, this sample had undergone oxidation-reduction experiments a number of times. The deviation of curve B from curve A indicates the effect of heat treatment on the surface activity. At a particular temperature, the effect of repeated recycling is to decrease the number of sites and the rate of adsorption.

It should be mentioned that analysis of our data as a diffusion process as was done by Aronson

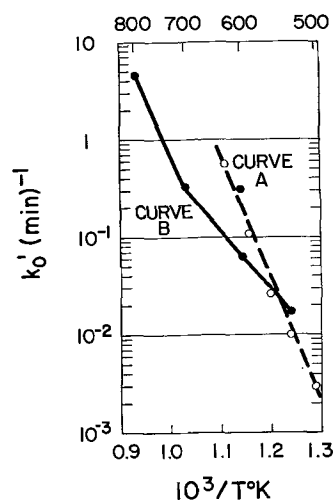


Fig. 4. Arrhenius plot of data for the rate of chemisorption of oxygen on ZrO_2 . \circ , 58 ΔH^\ddagger from Aronson's data; \bullet , 28.5 ΔH^\ddagger , this work 550°-700°C; \bullet , 58 ΔH^\ddagger , this work 700°-800°C.

yielded diffusion coefficients (which should have been constant with time) that decreased by a factor of three between 10 and 100 min for each temperature. However, average values for these diffusion constants proved to be close to the values obtained by Aronson.

Aronson did not expect a pressure effect for oxidation rates in his proposed model but did find it between 20 and 100 mm Hg. A pressure effect was found in this work for only very low pressures. It can be seen from Eq. [15-18] of the previous paper and Eq. [1] of this paper that such an effect would depend on θ , i.e., for $\theta < 1$, it is expected. However, θ depends on b , and b would in turn be a function of the heat of adsorption on the oxide surface. It might well be that b for Aronson's powder was much smaller than it was for the powder in this work, due to the different treatment.

Theoretical rate constant.—The experimental value for k'_0 in Eq. [2] can be compared with a theoretical value with the following equation

$$k'_0 = \frac{kT}{h} e^{-\frac{\Delta S^\ddagger}{R}} e^{-\frac{\Delta H^\ddagger}{RT}} N_s N_{O_2} \quad [3]$$

Since equilibrium data for atomic oxygen adsorption was not obtained, it cannot be decided, as for molecular oxygen, that electron transfer takes place. The fact that Eq. [1] and [2] hold up to $\theta = 0.9$ (note Fig. 2) may indicate that the adatoms are not negatively charged. If electron transfer occurred for adsorption of each oxygen atom, one would expect strong interaction between anions except at low coverage and Eq. [1] would have to take this into account. The reaction is visualized as O_2^- giving up an electron and dissociating into two atoms. The oxygen atoms then bond with surface sites by sharing electrons that were previously unshared due to the surface structure.

It is expected that the activated complex would have even greater freedom on the surface than the reactants O_2^- and unshared surface electrons, and therefore, ΔS^\ddagger would be positive. It would be difficult to calculate ΔS^\ddagger or ΔH^\ddagger from first principles, but

they can be estimated from the experimental data. For example, for $\Delta H^\ddagger = 58$ kcal/mole and at 600°C

$$\frac{e^{-\frac{\Delta H^\ddagger}{RT}}}{h} = 3.7 \times 10^{-15}$$

$$N_s = 3.2 \times 10^{-6}$$

$$N_o = 1.5 \times 10^{-4}$$

$$\frac{kT}{h} = 1.8 \times 10^{13}$$

so that

$$\frac{e^{-\frac{\Delta S^\ddagger}{R}}}{h} = k_o' \times 3.1 \times 10^{10}$$

After converting to reciprocal seconds, k_o' from Fig. 4 (curve A) is about 5×10^{-3} . From Eq. [3], the activation entropy change proves to be $\Delta S^\ddagger \cong 38$ e.u. This suggests that the activated complex has a great deal of freedom. It is not known how much of this freedom is retained (*i.e.*, localized or mobile layer) when the oxygen atoms complete the reaction and become adsorbed.

Summary and Conclusions

Many experiments performed to correlate oxygen pickup with the bulk oxide or the oxide surface, indicate that the oxygen pickup is primarily a surface phenomenon. After complete reduction of the ZrO_2 surface, approximately one atomic monolayer of oxygen will adsorb irreversibly on the surface. About 5% of the total adsorbed oxygen can be reversibly adsorbed and desorbed. From equilibrium and kinetic data, it was concluded that the 5% is reversibly adsorbed as molecular oxygen and the remainder as atomic oxygen.

The apparent activation energy for the adsorption of molecular oxygen proved to be about 35 kcal/mole and for desorption about 53 kcal/mole, as compared to about 58 kcal/mole for adsorption of atomic oxygen. The rate of adsorption of molecular oxygen was a function of oxygen pressure at low pressures, while the chemisorption process of atomic oxygen was independent of pressure.

Mechanism.—The mechanism of the adsorption of oxygen on freshly reduced ZrO_2 powder is schematically illustrated in Fig. 5. The actual reaction is considered to follow the solid line in Fig. 5, although it is not suggested that the distance coordinate is linear. It is postulated that as oxygen molecules approach the ZrO_2 surface the surface-oxygen energy relation would follow the dashed line 1, as repulsive forces become effective. However, an electron from the conduction band of the solid is trapped by the approaching oxygen and stabilizes the adsorption. The apparent activation energy for this process, about 35 kcal/mole, is actually the energy w needed to promote electrons from donor levels into the lowest level of the conduction band. The system forms a stable bond ($\text{S} - \text{O}_2^-$) of $\Delta\bar{H}^\circ \cong -50$ kcal/mole. Once the molecules have entered this potential energy well, they can either approach the surface along curve 2 or desorb. The thermodynamic relations predict the desorption activation energy, E_{des}^\ddagger , to be just equal to $-\Delta\bar{H}^\circ$, about 50 kcal/mole,

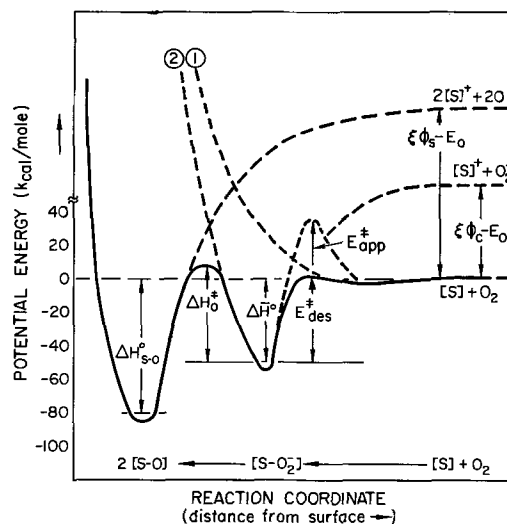


Fig. 5. A schematic potential energy diagram illustrating the energy relationships during oxygen adsorption on ZrO_2 . ($e\psi$ is the work function and E is the energy to place an electron on oxygen.)

as compared to the experimental value of about 53 kcal/mole. As O_2^- approaches the surface, it forms bonds with unshared electrons associated with surface atoms and dissociates into two atoms. The atomic oxygen surface bond ($\text{S} - \text{O}$) is estimated to be about -40 kcal/mole from equilibrium hydrogen reduction studies.

The adsorption of molecular oxygen is much more rapid than the dissociation process, because of the low activation energy, and adsorbed molecular oxygen becomes saturated before appreciable amounts have dissociated. As a consequence the concentration of adsorbed molecular oxygen feeding the dissociation process is constant, and the dissociation process is independent of the oxygen pressure. On the other hand, the adsorption of molecular oxygen is a function of the oxygen pressure. The surface becomes saturated with respect to O_2^- when only 5 to 10% of the sites (from BET measurement) are occupied, and this is attributed to the depletion of electrons from the donor sites of the oxide. It is predicted then, that the amount of molecular adsorption will depend on the concentration of donor levels in the oxide and should change from sample to sample or for different oxides. The atomic oxygen atoms occupy essentially all available sites.

By analyzing the equilibrium adsorption of molecular oxygen without electron transfer, the experimental entropy is unreasonably low (approximately zero or even positive). By analyzing the process with electron transfer, experimental and theoretical values for the entropy change are close. This is taken as new evidence in favor of charge transfer for such a process. It was concluded that molecular oxygen adsorbs as a mobile layer on the surface.

Electrical properties.—According to the mechanism above, the electrical conduction of the bulk oxide should decrease as molecular oxygen is adsorbed (electrons removed from conduction band) and the surface conductivity of the oxide should increase due to the mobile nature of the O_2^- . The

adsorption of atomic oxygen may increase the surface conductivity due to the formation of an electrical double layer while the bulk oxide conductivity may not be changed much.

Experiments to measure the effect of oxygen adsorption on the electrical conductivity of our ZrO_2 have been carried out¹ between 400° and 800°C. The results indicated that as predicted the surface conductivity does increase and the bulk conductivity does decrease when the oxide is exposed to oxygen.

Experiments have been reported for the O_2 -NiO systems (3), at 400°C. It was found that the surface conductivity was dramatically increased by a pulse of oxygen in the gas stream that passed the oxide and that reduction with hydrogen reversed the effect. The bulk conductivity was much less affected.

It should also be noted (4) that oxygen adsorbs on NiO as molecular oxygen until about 1-2% of

¹ These experiments were carried out by Saltsburg and Snowden at the General Atomic Laboratory, San Diego, California, (see ref. 3).

the surface is covered and with an apparent activation energy of 35 kcal/mole.

The theoretically calculated values of W , N_e , and N_D for the semiconducting properties of ZrO_2 are predicted order of magnitude values and must await experimental verification from electrical experiments. The consistency of the theoretical calculations is in favor of the proposed mechanism.

Manuscript received Oct. 22, 1963.

Any discussion of this paper will appear in a Discussion Section to be published in the June 1965 JOURNAL.

REFERENCES

1. S. Aronson, *This Journal*, **108**, 312 (1961).
2. P. Kofstad and D. J. Ruzicka, *ibid.*, **110**, 181 (1963).
3. D. P. Snowden and H. Saltsburg, ARPA Fuel Cell Conference, Whiting Research Laboratory, American Oil Company, Whiting, Indiana, Feb. 13-14, 1962. (Advanced Research Projects Agency, Washington, D. C.) Appendix XV, p. 141.
4. E. R. S. Winter, "Advances in Catalysis," vol. X, p. 214, Academic Press, Inc., New York (1958).

Mechanical Stresses during the Oxidation of Copper and Their Influence on Oxidation Kinetics. III*

W. Jaenicke,¹ S. Leistikow, and A. Stadler

Institute of Physical Chemistry, Technische Hochschule, Karlsruhe, Germany

ABSTRACT

Bending and oxygen uptake of a helix of copper or of gold-copper alloys, protected at one side by layers of silver and gold, were measured simultaneously between temperatures of 220° and 400°C and with oxygen pressures up to 140 mm Hg. The oxidation mostly showed an induction period and then followed a logarithmic law. In all cases dilatation of the oxide-covered side of the helix was first observed, followed by a strong contraction. Finally, dilatation was found again. The effects increased if the oxidation rate was lowered, which was possible by change of temperature, oxygen pressure, or pretreatment of the metal. The stresses within the oxide were calculated as greater than $\pm 12,000$ kp/cm² ($= 1.7 \cdot 10^5$ psi), if related to layer thickness. They influenced oxidation kinetics and under special conditions were connected with whisker formation. The site of the stresses could be located experimentally. Epitaxy, hole formation within the metal, oxygen penetration through a porous layer, and transformation of the oxides into one another were found to be the factors which successively caused stresses, during oxidation.

During the oxidation of a metal two solid phases are in contact; one is formed by consumption of the other. Therefore, one has to expect mechanical forces in the system metal-oxide (1) if there is no plastic flow (3), that is, if the oxidation temperature is not too high. The components of forces, which are directed parallel to the surface of the oxide layer, are able to bend a thin metal strip which is oxidized at one side and protected against oxidation at the other side (4-6). Equilibrium is reached if, along the cross section of the strip, all longitudinal forces and, simultaneously, the internal bending moments are compensated. If those forces are related to a suitable area on which they work, they are called stresses.

* I, II see ref. (4), (5).

¹ Present address: Institute of Physical Chemistry, University of Erlangen Nuremberg, Germany.

In Fig. 1 some examples of bent strips in equilibrium are shown. Resulting compressive stresses between layer surface and axis of zero stress give a convex equilibrium shape of the initially straight oxide layer (Fig. 1a, b), resulting tensile stresses a concave shape (Fig. 1c, d). The bending which is observed therefore is an integral phenomenon; it gives no information on the distribution of stresses along the cross section.

If a compressive stress is observed, the oxide layer may be compressed, the metal below it expanded (Fig. 1a), but it is quite as possible that compression is within the metal and tensile stress within the layer (Fig. 1b). The same alternative is valid if tension is predominant (Fig. 1c, d).

The source of the observed effects, therefore, can be situated in the layer, at the phase boundary, or

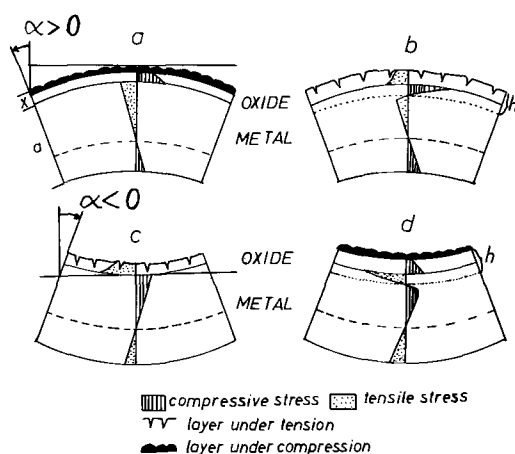


Fig. 1. Bending of a straight metal beam caused by stresses of different distribution within an oxide layer and the underlying metal (schematically); h , area of stress generation; - - - -, axis of zero stress.

inside the metal (4): stresses within the layer occur if oxides of different composition and molar volume are transformed into one another, if crystal growth or recrystallization is directed along the surface, or if oxygen penetrates the layer and forms oxide within pores. In the phase boundary epitaxial stresses often are possible; within the metal one can observe stresses if oxygen is dissolved or if, during the consumption of the metal, defects of atomic size are formed which can agglomerate or be deposited at dislocations.

Experimental Procedure and Results

We measured such effects during the oxidation of copper and of copper-gold alloys between 220° and 400°C with oxygen pressures between 2 and 140 mm Hg (7).

The sample was a strip of electrolytic copper with thickness of 5×10^{-3} cm and an area of 1 cm x 20 cm. It was annealed first in high vacuum at 400°C for 1 hr. After annealing the orientation of the surface was found to be mostly (100) [001] and the average grain diameter reached 17μ . It remained constant during the oxidation experiments. A protective layer of 3μ of silver and 3μ of gold then was electro-deposited on one side of the specimen, and it was formed to a helix of 1 cm diameter, in most cases with the layer at the inner side.

The sample was heated inside a silica tube which was connected to a differential manometer (Taylor Instruments Company, Rochester, N. Y., type 339 RF5) (5). At the end of the helix a glass thread was attached. It reached to the lower, cooled part of the furnace and could be observed by means of a microscope. The helix was mounted on the axis of a high vacuum rotating joint (Fig. 2). The angular deflection of the system during oxidation was measured by turning the axis and keeping the thread in a fixed position. At the same time the oxygen uptake was recorded. Before (not especially dried) oxygen was admitted into the evacuated and heated reaction vessel, one had to wait several minutes, until the initial creep of the helix under its own weight had finished.

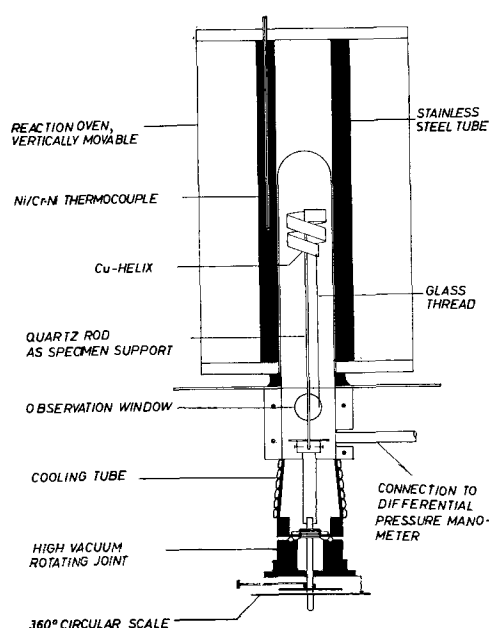


Fig. 2. Reaction tube and measuring system

Sign and magnitude of the angular deflection measure the direction and quantity of the resulting bending moment. Its origin has to be located by special experiments.

In any case it seems reasonable to relate the mechanical effects to the amount of oxide formed. Therefore in most cases the results are discussed in terms of α/m , the ratio of angular deflection and consumed oxygen. A positive value of α/m stands for a bending toward more convex shape, that means a compression in the oxide-layer side of the specimen (cf. Fig. 1a, b).

From α/m the stress within a surface layer of a curved beam can be calculated, using Stoney's approximation formula (8)

$$S = \frac{E \cdot a^2}{6h} \cdot \Delta \left(\frac{1}{r} \right) \quad [1]$$

(S is the maximal stress within a layer of thickness h (cm) on a beam of thickness a (cm); E is Young's modulus of the metal, r the radius of curvature. S and E are measured in kp/cm^2 ; $1 \text{ kp/cm}^2 = 14.22$ psi. This formula is valid within a few per cent error for different stress distributions across the layer, as long as $h/a < 0.01$. This was the case in our experiments. The radius of the curvature may be calculated from the strip length L (cm), the helix angle γ and the angular deflection α (°)

$$\Delta \left(\frac{1}{r} \right) = \frac{2\pi\alpha}{360 L \cos \gamma} \quad [2]$$

To get an impression of the order of magnitude of the effects, h can be taken as the oxide-layer thickness x . In this way a stress S [kp/cm^2] within the oxide is calculated from [1] and [2]. For the reasons mentioned above, this method is not exact. More suitable, however, to the system should be the instantaneous stress (9) which relates differential change of stress with increment of layer thickness x . It is defined by the equation

$$\int_0^h \sigma d\xi = S \cdot h \quad [3]$$

Sometimes it is preferred to compare the angular deflection and the amount of oxide separately as a function of time.

Influence of Pretreatment of Specimens on Measured Effects

First of all it has to be stated that all quantitative results strongly depend on the pretreatment of the metal. The method of surface finishing or the time and temperature of annealing can change the rate of oxidation and the angular deflection to a great extent (6). For example an annealed and abraded sample oxidized faster at 400°C than another sample did at the same temperature, which after being annealed previously was oxidized for 1 hr at 300°C, reduced, and abraded. The angular deflections also differed considerably. A similar difference was observed, if the specimen before oxidation was heated either in contact with hydrogen or in high vacuum for 10 min and then reduced with hydrogen. In the latter case the remainder of oxygen can form some oxide, which is then reduced giving a rough copper surface, while in the former case no oxidation is possible. Thus the oxidation rate is slower and the angular deflection reaches its negative maximum later. Also the shape of the curves is different; therefore there remain differences also in the stresses (Fig. 3, solid and dotted lines).

The oxidation rate further increases and the stresses diminish if the specimen is oxidized and

reduced several times without smoothing the surface. The behavior, however, is reproducible and the samples can be used several times if either the formed oxide or the metal remaining after the reduction of the oxide is abraded with 6/0 emery paper. In this way one can remove only the oxide layer or the loose metal remaining after the reduction of the oxide as was found by the loss in weight. Both pretreatments, however, show different results (Fig. 3, solid and dashed lines): while the oxidation rate is not much changed (Fig. 3a), the angular deflection (Fig. 3b) is greater if the oxide was abraded before without reduction. Therefore in this case the curves of stress are shifted to more negative values (compare in Fig. 3c the solid and dashed lines).

All the experiments reported below were made with the pretreatment, marked by solid lines in Fig. 3.

Oxidation Kinetics

The specimens so treated always oxidized initially with a small rate constant. After an induction period the rate suddenly increased, as was observed by Cabrera and Mott (10) at lower temperatures (see Fig. 10b). The induction period t_i depends on pretreatment and oxygen pressure. Between 2 and 25 mm Hg, one finds $t_i \approx k \cdot p^{-3/2}$. After the induction period, the measured weight gain m can be expressed by a logarithmic law (Fig. 4)

$$m = A \log [B(p)(t-t_i) + C]$$

A is independent of pressure, B is obtained by extrapolation of the linear parts of the curves to $m = 0$. We found that it was approximately proportional to the pressure p .

One has to be cautious stating and interpreting oxidation laws, but in this connection an idea of Davies, Evans, and Agar (11) in their work about the oxidation of iron is interesting. If oxygen penetrates a porous layer and if the oxide formed inside the pores is compressing other pores in the neighborhood, the pores diminish proportional to their frequency N and to the amount of oxygen

$$-dN = (N/A) dm$$

In addition, the amount of oxygen penetrating is proportional to the time, the pore frequency, and the oxygen pressure (2)

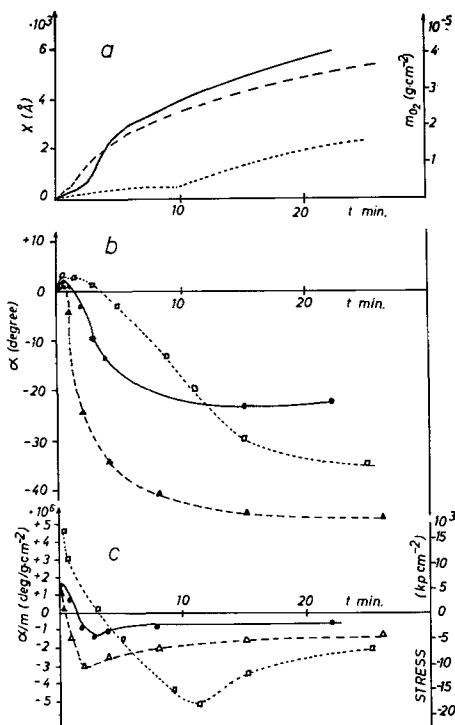


Fig. 3. Influence of copper pretreatment: (a) on weight gain m (layer thickness x) vs. time; (b) on angular deflection α vs. time; (c) on stress (α/m) vs. time. Samples annealed at 400°C and pre-oxidized at 300°C, then . . . layer reduced with H_2 , abraded, heated in hydrogen before oxidizing; — layer reduced with H_2 abraded, heated in vacuum before oxidizing; - - - layer abraded, heated in vacuum for 10 min, then treated with H_2 before oxidizing; after pretreatment: oxidized at 300°C, $p_{\text{O}_2} = 6$ mm Hg.

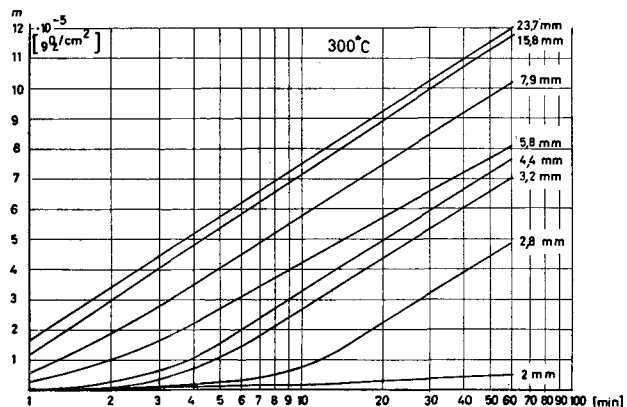


Fig. 4. Weight gain m of the specimen as function of time; ($T = 300^\circ\text{C}$) parameter: oxygen pressure.

$$dm = BpNdt$$

From the first equation it follows that $N = N_o \exp(-m/A)$ and by substituting this expression in the second equation, remembering that $m = m_o$ for $t = t_i$, one can write

$$m = a \log [Bp(t-t_i) + C]; \quad B = BN_o/A \\ C = \exp(m_o/A) \quad [4]$$

This is exactly the relation which was found experimentally.

One can assume, therefore, that at the time t_i a first dense oxide layer breaks down to give a porous structure; then oxygen is built in and closes the pores, giving compressive stresses inside the layer.

Before it is shown that our stress measurements confirm and refine this view, it may be demonstrated by some electron micrographs that the layer structure actually is changed at time t_i . In Fig. 5 the smooth surface during the induction period is given. After the increase of the oxidation rate one suddenly observes a structure which appears to be dug up (Fig. 6). Often with those layers interference colors are still observed, but they soon assume a dull red appearance. At this time cuprous oxide seems to be the major constituent of the layer. Later black cupric oxide is formed (Fig. 7), which finally covers the whole surface.

Stresses during Oxidation

In Fig. 8 the dependence of α/m vs. m is given, which is equivalent to the stress as a function of oxide layer thickness (Eq. [1]). The temperature was 300°C , and the oxygen pressure was varied between 3 and 20 mm Hg. The sign of the stress is taken as discussed above for Fig. 1.

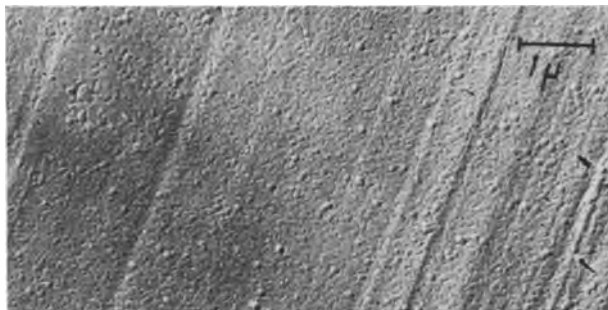


Fig. 5. Surface of cuprous oxide during the induction period; $T = 300^\circ\text{C}$; $p_{\text{O}_2} = 3.2$ mm Hg; $t = \text{ca } 6$ min.

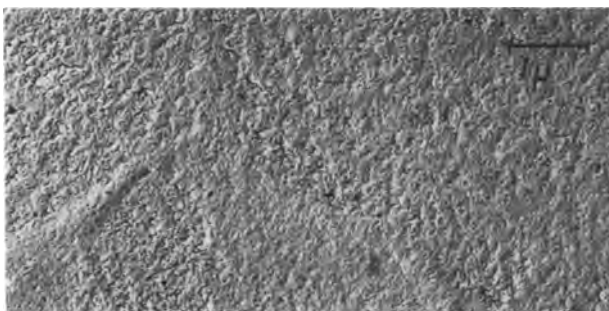


Fig. 6. Surface of cuprous oxide after the induction period; $T = 300^\circ\text{C}$; $p_{\text{O}_2} = 3.2$ mm Hg; $t = \text{ca } 8$ min.



Fig. 7. Surface of cuprous oxide, partially covered with cupric oxide (right side); $T = 300^\circ\text{C}$; $p_{\text{O}_2} = 15.8$ mm Hg.

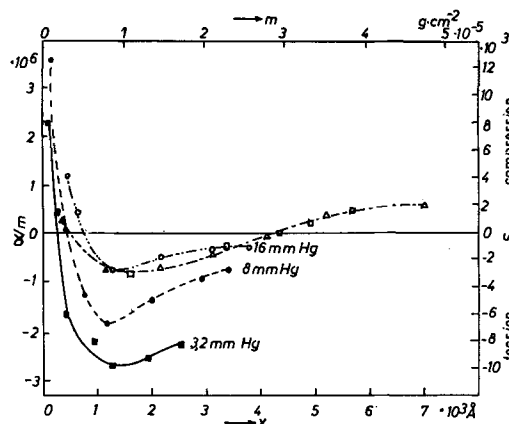


Fig. 8. Stress (α/m [$\text{deg/g} \cdot \text{cm}^{-2}$]) and S [kp/cm^2]) in the system $\text{Cu}/\text{Cu}_2\text{O}$, CuO as a function of oxygen uptake (layer thickness) parameter: oxygen pressure: $T = 300^\circ\text{C}$; \square , 140 mm Hg; Δ , 20 mm Hg.

All curves have the same shape. Initially the system is highly compressed. If related to the oxide-layer thickness,² the stress reaches $12,000 \text{ kp/cm}^2$ ($1.7 \cdot 10^5 \text{ psi}$). This is about the ultimate compressive strength of hard ceramic material and should cause plastic flow. Either the initial oxidation rate exceeds the reciprocal relaxation time or the compressive forces are effective up to a greater depth, perhaps by some oxygen diffusion. The elastic limit of the basis metal, however, is not exceeded. Its maximum stress at the metal-oxide interface is approximately given by (9) $S_{\text{met}} = S_{\text{layer}} \cdot (x/a)$ and therefore $S_{\text{met}} < 25 \text{ kp/cm}^2$.

The stress decreases during the growth of the layer, changes its sign, and goes through a negative maximum at a layer thickness of about 1500\AA . The tensile stress at this point increases as the oxygen pressure is lowered, i.e., as the oxidation rate decreases. If oxidation is continued, the stress increases again in a nearly linear manner until at last a compression inside the layer is reached. This happens, particularly, if cupric oxide is formed.

If the oxygen pressure is kept constant and the temperature is varied between 220° and 400°C , one obtains the curves in Fig. 9 for the dependence of stress on layer thickness. Compressive stress in thin layers can be measured only below 300°C . At 220°C , the initial oxidation rate is low enough to make it possible to observe that the stress goes through a maximum at a layer thickness of about 100\AA . At

² For all calculations the whole oxide was considered to be Cu_2O .

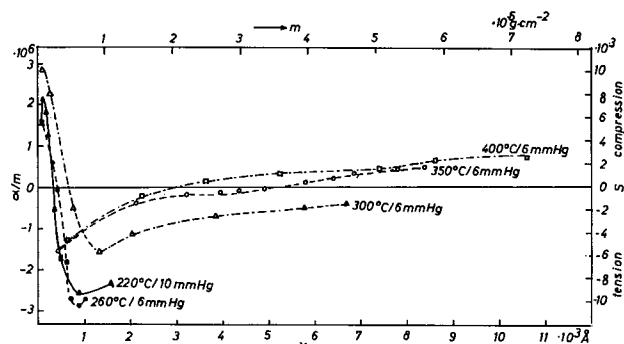


Fig. 9. Stress (α/m [$\text{deg/g}\cdot\text{cm}^{-2}$] and S [kp/cm^2]) in the system $\text{Cu/Cu}_2\text{O}$, CuO as a function of oxygen uptake (layer thickness) parameter: temperature.

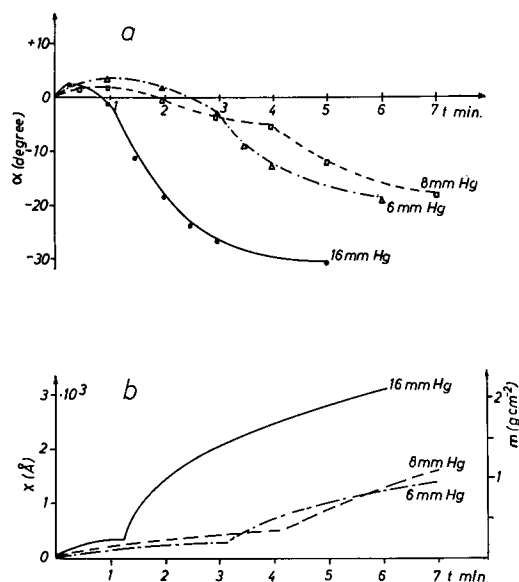


Fig. 10. Comparison of the dependence of (a) the angular deflection α and (b) the oxygen uptake m (oxide layer thickness x) on time; $T = 300^\circ\text{C}$, parameter: oxygen pressure.

300°C , a short stop of the angular deflection is just visible at the beginning. One can conclude therefore that also at this temperature the stress is initially positive. Only at 400°C the initial oxidation rate is so high that no sign of compression can be observed. In the whole temperature range tensile stress occurs at layer thicknesses above 500\AA . They reach a negative maximum, which is shifted to greater values if the temperature is lowered. It is of the same order of magnitude as the first compressive stress. The range of layer thickness, in which tensile stress occurs, diminishes with higher temperatures. If the oxidation is continued, one gets compression ultimately.

A comparison of stress curves at different pressures and different temperatures shows that an increase of oxidation rate shifts the curves in about the same way, whether it is produced by pressure or by temperature.

It is difficult to conclude from the curves of stress a connection with the induction period of oxidation, because the angular deflection and the layer thickness at this point are changed in the same manner. Therefore their ratio is not much varied. If, however, both values are compared separately as a

function of time, as in Fig. 10, their dependence is evident. During the induction period the angular deflection goes through a flat maximum and always reaches small negative values. At the moment when the rate of oxidation increases, the angular deflection also changes unsteadily.

One may argue from these experiments that there is a tensile stress within the layer at time t_i . Therefore to explain the effects it is necessary to know the origin of the forces inside the system. We tried to find it by reduction experiments. Unfortunately, it is not possible to record the reduction manometrically as it was done for the oxidation, because hydrogen is replaced by the same molar quantity of water vapor. Therefore we have weighed the samples after different times of reduction (12) and compared the loss in weight with the change of the angular deflection. It was found that after 1 min about 90% of the oxide was reduced. At this time the remainder had acquired a loose structure. Therefore the whole stress inside the layer should disappear within 1 min.

In Fig. 11 the angular deflection is given as a function of time for two experiments, during which the oxidation was stopped at different states of stress.

If hydrogen is admitted when the total stress nearly reached its negative maximum, the angular deflection becomes still more negative during the reduction of the layer (Fig. 11, curve 2). The tensile stress is greater in absence of the layer. Therefore it must be situated in the metal near the phase boundary. As a consequence the layer is under high compression when the total stress is negative.

However, if the reduction begins when a thick layer has grown and the system shows compressive stress, the compression disappears immediately and the system returns to its initial position (curve 1).

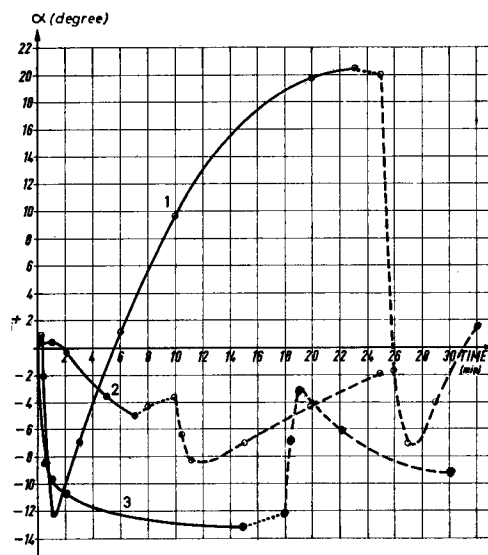


Fig. 11. Variation of the angular deflection α during oxidation and reduction. Curve 1, Cu , 350°C , $p_{\text{O}_2} = 6 \text{ mm Hg}$; curve 2: Cu 300°C , $p_{\text{O}_2} = 6 \text{ mm Hg}$; curve 3: Cu , 60 a/o Au , 350°C , $p_{\text{O}_2} = 8 \text{ mm Hg}$; —, oxidation; . . ., high vacuum; - - -, reduction.

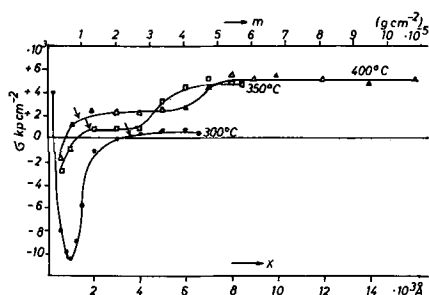


Fig. 12. Instantaneous stress σ (kp/cm^2) in the system $\text{Cu}/\text{Cu}_2\text{O}$, CuO as a function of oxygen uptake m (oxide layer thickness x), parameter: temperature, $p_{\text{O}_2} = 6 \text{ mm Hg.}$ \rightarrow Begin of blackening of the layers.

This experiment demonstrates that the compressive stress which is found at longer oxidation times is situated within the layer. The metal, however, is first under tension and finally becomes free of stress. Therefore, when the oxide layers are thinner than 1μ , one temporarily observes tensile stress (see curve 1), which is not found if thick layers are reduced. The compressive stress which is localized within the oxide was found to be independent of layer thickness over a rather large range of thicknesses. Therefore it is effective inside the whole layer. This is shown by calculating the instantaneous stress, as given for 3 temperatures in Fig. 12. In the area of compression they first reach small constant values, which suddenly change into higher constant values. The first step is connected with the blackening of the layers.

Discussion

All of our experimental results give a self-consistent view of copper oxidation between 220° and 400°C forming layer thicknesses up to about 10^{-4} cm .

On smooth (abraded) surfaces cuprous oxide is first spread, which is formed under very high epitaxial (19) stress as in Fig. 1a. If only those stresses were effective, further oxide would soon be formed in an unstrained condition. Therefore the observed angular deflection should attain a constant limiting value and α/m , which is assumed to be proportional to the stress should diminish asymptotically. This is not the case because holes are soon formed in the metal at the phase boundary $\text{Cu}/\text{Cu}_2\text{O}$. Those holes seem not to be annihilated by condensation at the oxide-metal interface and inward movement of the oxide by means of plastic flow, but they diffuse into the bulk of the metal and are precipitated at inner defects.

This mechanism was first proposed by Schottky (13). Experimental support was given by Heumann (14), who investigated the formation of copper-antimony alloys by interdiffusion. For the holes he found a very high diffusion constant of about $2 \cdot 10^{-7} \text{ cm}^2 \text{ sec}^{-1}$ at 350°C . This is understandable, because it is only necessary to spend that part of the activation energy which is due to hole migration.

In this way a high tension will occur in the metallic phase, by which an increasing pressure is exerted on the layer (see Fig. 1d). That is the reason why Borie, Sparks, and Cathcart (15) using

x-ray diffraction found tangential compression inside the oxide at temperatures and thicknesses at which we already measured a negative total stress (e.g., 400\AA thickness at 250°C).

Because of the high pressure of about $15,000 \text{ kp/cm}^2$ which is exerted on the layers, their disorder and their growth rate are diminished.

As soon as the ultimate compressive strength is exceeded, the layer breaks down. It gets a porous structure as long as its plasticity is comparatively low. This happens at the end of the induction period. The resistance, which the layer exerts to the bending of the system, then disappears, and the angular deflection quickly reaches its negative maximum. In competition with this relaxation, oxygen penetrating the porous layer is forming new oxide within the whole layer, causing constant instantaneous stress of positive sign as formulated by Davies, Evans, and Agar (11).

The reaction at last proceeds by a rate-determining growth of Cu_2O , while a CuO -layer of constant thickness remains at the outer surface (7). Therefore during oxidation CuO is continuously transformed into Cu_2O at the phase boundary $\text{Cu}_2\text{O}/\text{CuO}$ by means of the reaction $\text{Cu} + \text{CuO} \rightarrow \text{Cu}_2\text{O}$, while at the outer surface new CuO is formed. The reaction at the inner phase boundary is a permanent source of instantaneous stresses which have the same value throughout the newly formed Cu_2O -layer (see Fig. 12, horizontal part of the curves).

Those stresses seem to cause the growth of CuO -whiskers. This can be concluded from a paper of Albert and Jaenicke (16) about statistics of needle population. It was found that whisker growth is a rapid process, which is stopped statistically and is independent of the respective length of the needles. The whisker formation, however, takes place during the entire layer growth with a probability, inversely proportional to the layer thickness, if a parabolic oxidation law is valid. From that it was concluded that the extrusion of whiskers was induced by dislocations which are formed during the conversion of CuO into Cu_2O (3).

During oxidation, the inner phase boundary $\text{Cu}/\text{Cu}_2\text{O}$ moves into the bulk of the metal, and the disordered part of the metal is consumed. Due to the decrease of the oxidation rate and the high diffusion coefficient of the holes, the average concentration of newly formed holes is lowered. As a consequence of these effects the tensile stress inside the metal disappears. This can cause the second step in the curve of instantaneous stress (Fig. 12), but it is also possible that it depends on the transformation of CuO into Cu_2O which is enhanced if the surface is fully covered with a CuO layer of sufficient thickness.³

³ Note added in press: In a recent paper of Pawel, Cathcart, and Campbell (17) which was published after this communication was presented, it was observed that, during the oxidation of Ta, bending was approximately proportional to the square root of time, while the oxygen uptake showed no simple law (perhaps as a result of a cracking mechanism). The stress was attributed to oxygen, whose diffusion in the metal also followed a square root law. The calculated stress therefore remained constant and showed no dependence on the weight gain of the specimen. It was of the same order of magnitude as the instantaneous stress, which we have found in thicker layers on Cu (Fig. 12). In the case of copper, however, a diffusion mechanism is not suitable to explain the experiments.

Stress during Oxidation of Cu-Au Alloys

Experimental results with copper-gold alloys of 60 and 75 atomic per cent (a/o) gold are in agreement with the view of the copper oxidation mentioned above. The alloys oxidize at a much lower rate than the pure metal (18). When the temperature was increased to 350°C, the rate was still small enough so that effects at layer thicknesses of about 100Å could be observed. Nevertheless compressive stress at the beginning of oxidation was never found. High negative stress always occurred; the angular deflection kept its negative value nearly constant for a long time (Fig. 11, curve 3). The stress changed its sign only at 400°C and after very long oxidation times.

If the alloy of 75 a/o Au is oxidized instead of pure Cu, the misfit between the lattices of Cu₂O and the base metal in the (100) direction diminishes from 15 to 8%. It is concluded, therefore, that epitaxial stress is of less importance in the case of the alloys. There is no question, however, about the existence of holes in the alloys during the oxidation, for all the metal which composes the layer must be supplied by diffusion from the bulk of the alloy phase. At the same time the annihilation of vacancies as voids at the oxide-metal interface should be made more difficult. Therefore the argument, that tensile stresses are caused by holes inside the metal, gains in probability.

If the oxide on copper-gold alloys is reduced, the tensile stress decreases immediately (Fig. 11, curve 3), but later it begins to rise. This, however, does not prove the existence of tensile stress inside the layer. It is possible that the reduced copper diffuses quickly into the holes near the surface, the stress being over-compensated here. Some of this metal then migrates slowly into the bulk of the alloy, giving new tensile stress.

Acknowledgments

The authors are indebted to Dr. L. Albert, Technische Hochschule, Karlsruhe, who has made numerous electron micrographs, and they also would like to give credit to the "Deutsche Forschungsgemeinschaft" for two scholarships and to the "Landesgewerbeamt Baden-Württemberg" and the "Fonds der Chemie" for financial support.

Manuscript received Oct. 14, 1963. This paper was presented at the Colloque international de chimie minérale, Paris, June 14, 1963.

Any discussion of this paper will appear in a Discussion Section to be published in the June 1965 JOURNAL.

REFERENCES

1. The first direct observations were made by P. D. Dankov and P. V. Churaev, *Doklady Akad. Nauk. SSSR*, **73**, 1221 (1950). The authors explained their results in terms of the Pilling-Bedworth rule, which is not valid in this case (2). For a more probable interpretation of their results see ref. (2). An indirect evidence of stresses was given, e.g., by experiments of U. R. Evans, *Trans. Electrochem. Soc.*, **91**, 547 (1947).
2. W. Jaenicke in H. Fischer, K. Hauffe and W. Wiederholt, "Passivierende Filme und Deckschichten," p. 160, Springer, Berlin, Göttingen, Heidelberg (1956).
3. cf. J. A. Sartell, R. J. Stokes, S. H. Bendel, T. G. Johnson, and C. H. Li, *Trans. Met., Soc. AIME*, **215**, 420 (1959).
4. W. Jaenicke and S. Leistikow, *Z. phys. Chem. N.F.*, **15**, 175 (1958).
5. S. Leistikow, Thesis, Karlsruhe 1961; experimental details are given here.
6. A. Stadler, Diplomarbeit, Karlsruhe (1963).
7. Recent review articles about copper oxidation: R. F. Tylecote, *J. Inst. Metals*, **78**, 259 (1950-51); **81**, 681 (1952-53); R. Rönnequist and H. Fischmeister, **89**, 65 (1960-61).
8. G. G. Stoney, *Proc. Roy. Soc. London*, **A82**, 172 (1909).
9. A. Brenner and S. Senderoff, *J. Research Nat. Bur. Standards*, **42**, 89, 105 (1949).
10. N. Cabrera and N. F. Mott, *Rep. Progr. Phys.*, **12**, 163 (1949).
11. D. E. Davies, U. R. Evans and I. N. Agar, *Proc. Roy. Soc.*, **225**, 443 (1954).
12. cf. R. F. Tylecote, *Metallurgia*, **53**, 191 (1956).
13. W. Schottky, *Z. Elektrochem.*, **63**, 784 (1959).
14. Th. Heumann, *ibid.*, **63**, 789 (1959); Th. Heumann, O. v. Franqué, Unpublished work.
15. B. Borie, C. J. Sparks, and J. V. Cathcart, *Acta Met.*, **10**, 691 (1962).
16. L. Albert and W. Jaenicke, *Naturwissenschaften*, **46**, 491 (1959); *Z. Naturforschung*, **14a**, 1040 (1959); **15a**, 59 (1960).
17. R. E. Pawel, J. V. Cathcart, and J. J. Campbell, *This Journal*, **110**, 551 (1963).
18. For theoretical discussion of the oxidation of copper-gold alloys see C. Wagner, *This Journal*, **99**, 369 (1952).
19. For the epitaxy of Cu₂O on Cu see K. R. Dixit and V. V. Agashe, *Z. Naturforschung*, **10a**, 152 (1955); **11a**, 41 (1956); **12a**, 96 (1957).

The Oxide Films Formed on Copper Single Crystal Surfaces in Water

III. Effect of Light

Jerome Kruger and Joan P. Calvert

Metallurgy Division, National Bureau of Standards, Washington, D. C.

ABSTRACT

Studies of the effect of illumination on the growth of oxide films on copper single crystal surfaces immersed in water containing different amounts of dissolved oxygen reveal that, while illumination has little effect on the oxidation process when the water is in equilibrium with a 100% oxygen atmosphere, it does lower the rate of film formation when the water is in equilibrium with 1% oxygen. For both the (111) and (100) planes illumination causes a departure from the rate law observed for oxidation in the dark. At intensities of $290 \mu\text{w}/\text{cm}^2$ or higher the film formed on the (111) plane never grows beyond a limiting thickness of 100Å. The behavior observed can be explained on the basis of a competition between growth and dissolution reactions, the dissolution reaction being promoted by illumination.

This is a continuation of a study of the growth of oxide films on copper single crystal surfaces in water containing varying amounts of oxygen. The previous work (1, 2) investigated the nature of the films formed and the rate of film growth. Early in these studies (3) it was noted that light has an influence on the formation of oxide films on copper in water, retarding the growth or decreasing the thickness of already existing films. The effect of illumination on the growth of Cu_2O films on copper was related to the photocurrent produced in this p-type semiconductor material. Since the flow of electrons and ions are all important in the growth processes of oxide films, this study of the effect of illumination on the kinetics of film formation was undertaken with the hope that by affecting the flow of electrons using light we could obtain valuable insights into the oxidation process.

A number of other works on photo effects in cuprous oxide and the existence of potentials between illuminated and dark cuprous oxide covered copper electrodes has appeared in the literature (4-6). All this work has dealt with quite thick oxide films and has been concerned with electrical or electrochemical effects rather than film growth. This preliminary study is concerned with the effects of light on the kinetics of growth of the initial thin ($<200\text{Å}$) film.

Experimental

The method and apparatus used for studying the growth of oxide films on copper surfaces immersed in water using ellipsometry has been described elsewhere [2]. The copper crystals used in this study were grown from 99.999+% pure copper by the Bridgeman technique, cut into shape using spark-erosion machining, annealed, the desired faces polished flat using an acid wheel technique [7] and finally electropolished, washed, and annealed in H_2 in place as described before (2). It was possible to study four crystallographic planes, (111), (110),

(100), and (311), immersed in water in equilibrium with either pure oxygen or $\text{O}_2\text{-He}$ mixtures.¹

Illumination was provided by a slide projector whose radiation was focused on a 0.5 cm diameter spot on the specimen using the arrangement shown in Fig. 1. With the exception of a hole for admitting the light to the part of the specimen to be illuminated and the windows used for ellipsometric measurements, the rest of the apparatus was masked off with aluminum foil. The experiments were carried out in a dark room.

The intensity of the light used was measured by a foot candle meter. It was not possible to use intensities higher than those given later on in this paper without effecting a rise in the temperature of the water ($25^\circ \pm 1^\circ\text{C}$).

In all of the experiments discussed only the (100) and (111) planes (the fastest and the slowest) will be compared. This was done for the sake of simplicity and because, as recent work by Cathcart, Epperson, and Peterson (8) has shown, the strain in the oxide films formed on these two planes does not introduce the optical anisotropy which compli-

¹ The system was assumed to be in equilibrium after the oxygen or $\text{O}_2\text{-He}$ mixture had been bubbled through the water slowly until the pressure in the system was built up from the vapor pressure of water to 1 atm.

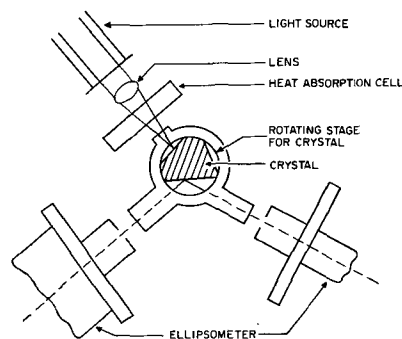


Fig. 1. Apparatus for studying the effect of light on the formation of oxide films on copper single crystals immersed in water.

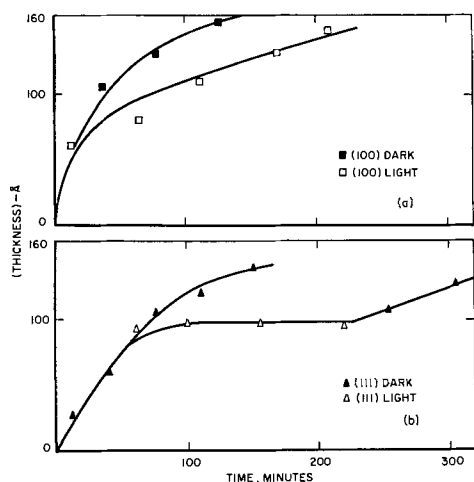


Fig. 2. Effect of illumination by white light on the growth of oxide films on copper single crystals immersed in water in equilibrium with 99% He 1% O_2 gas mixture. (a) (100) Surface, (b) (111) surface.

cates the ellipsometric measurements made on (110) and (311) surfaces.

Results

Studies in the dark of the oxidation of copper in water in equilibrium with 100% oxygen showed that when the thickness of the initial Cu_2O had reached a limiting value after 70 to 120 min depending on the orientation of the surface, a second component of the film, CuO , started to form. This coincided with a build-up in concentration of $Cu(II)$ ions to a value where the solubility product of CuO was exceeded. When the crystal was illuminated by a 500 watt tungsten lamp, the interval of time required to observe the formation of CuO was not appreciably affected.

When, however, the water in which the copper crystal was immersed was in equilibrium with an atmosphere containing 1% O_2 , the rest helium, illumination did have a marked influence on the film formation process. It has been shown earlier (2) that when the partial pressure of oxygen is lowered, Cu_2O is the only oxide observed because at lower oxygen pressures and at pH 7 this is the thermodynamically stable oxide (9). It is under these conditions that most of our experiments were carried out.

Figure 2 a and b show by time-thickness curves for the oxidation of (100) and (111) crystallographic planes how the film growth is affected by illumination of white light of an intensity of approximately $290 \mu W/cm^2$ for the (100) and 370 for the (111). In Fig. 2b it can be seen that for white light of this intensity that the growth apparently stops at a limiting thickness of 100 Å on the (111) but that when the light is removed the film starts to grow again at approximately the same rate as that in the absence of illumination.

Figure 3 a and b show the effect of illumination at different intensities for both the (100) and the (111) crystallographic planes. By means of least square approximations it was found that the thickness-time data could be said to obey a cubic rate equation somewhat better than the parabolic one

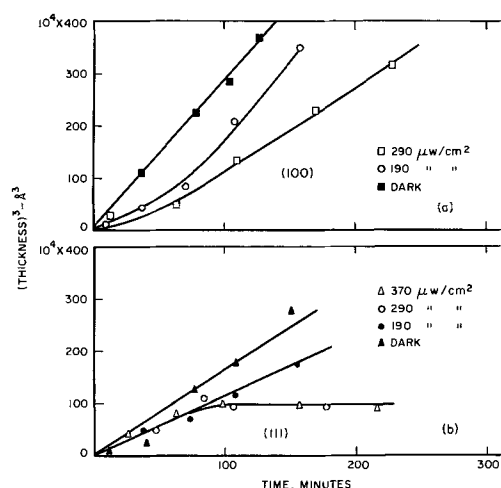


Fig. 3. Cubic plot showing the effect of illumination of different intensities on the growth of oxide films on copper single crystals immersed in water in equilibrium with 99% He 1% O_2 gas mixture. (a) (100) Surface, (b) (111) surface.

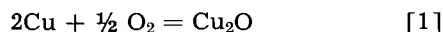
reported earlier (2). In fact, it was found that the earlier results also gave a lower standard deviation from a cubic law than that from a parabolic law. Therefore, the data in Fig. 3 are presented as cubic plots (X^3 vs. t) from which can be seen that for oxidation in the dark and perhaps for some of the lower intensities a cubic rate law may best describe the process. This is the sort of behavior predicted by one theory (10). It should be stressed, however, that the fit of the data to a cubic law was only somewhat better than that to a parabolic law; therefore our agreement with this theory may not be significant.

It should be pointed out that the rates observed in the dark shown here are higher than those obtained in the previous study of this system (2). This is probably due to the fact that no great care was taken to exclude light in the earlier studies. Another possible reason for this difference in rate may be that the earlier studies were carried out using less pure copper than the present study. Since the effect of impurities on the oxidation rate of metals such as copper forming more than one oxide is complicated and unpredictable (11), either an increase or a decrease in rate due to their presence is possible.

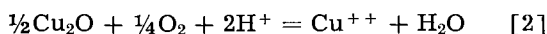
We were not able to detect any significant differences in oxidation behavior when the wavelength of the radiation was varied using filters. However, since all the filters used let through radiation which included the long wavelength end of the absorption spectrum of Cu_2O , which is the region of the spectrum where illumination increases the photoconductivity (12), we cannot say that the oxidation rate has no dependence on the wavelength of the radiation. Attempts were made to use a monochromator to irradiate with light of a wavelength (5700 Å) which was lower than the absorption edge for Cu_2O , where strong absorption takes place; but the intensity of the light was too low for us to be able to decide if there was any effect due to the wavelength of the radiation.

Discussion

The results just described can best be explained in terms of two competitive reactions taking place. One of these reactions is the Cu_2O film growth reaction



and the other is a film dissolution reaction



The latter which actually involves the oxidation of Cu(I) ions to Cu(II) ions is called a dissolution reaction because the Cu(II) ions when formed can go into solution. That this dissolution reaction undoubtedly takes place was shown in the earlier work (3) where a thick ($>1000\text{\AA}$) film of Cu_2O could be reduced in thickness on illumination. This plus the recent work of Ives and Rawson (6), which showed that illumination increased the rate of Cu(II) ion build-up in solution, indicates that the light promotes the removal of the Cu_2O film and oxidation of the Cu(I) ions to Cu(II) ions which then enter the solution. This is just the dissolution-oxidation reaction [2].

Illumination promotes this reaction in a way that can be inferred from the physics of a copper- Cu_2O photocell. As treated by Mott (13) many years ago, when this $\text{Cu-Cu}_2\text{O}$ couple is illuminated, an emf is developed because the electrons produced by the light flow through the blocking layer (stoichiometric Cu_2O) next to the copper from the cation deficient Cu_2O on the outside. They flow from the p-type Cu_2O against the existing field (see Fig. 4). Since the Cu_2O is a p-type material, it is on the minority carriers, the electrons, that the illumination will have its biggest effect (14). This effect as Miller (15) has shown studying the illumination of copper single crystal surfaces immersed in CuSO_4 solution whose orientation and surface preparation were essentially the same as those used in this work, shifted the potential in a noble (more positive) direction. Other workers have also shown the photo potential developed is a positive one (4). On this basis then, the effect of the light as shown in the schematic picture (Fig. 4), based on some ideas of

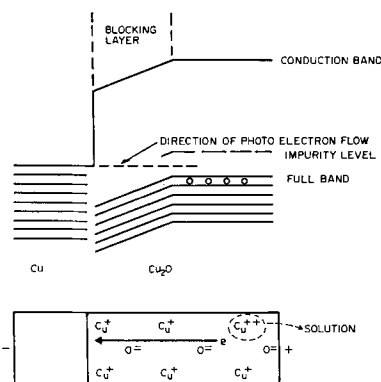


Fig. 4. Energy level diagram of cuprous oxide in contact with copper, after Mott (13), showing direction of photo electron flow. Lower diagram shows the effect of this flow on the cuprous oxide film.

Williams (16), would be to enhance the dissolution of Cu(II) ions if the free energy change for this were favorable. As Ives and Rawson (17) have calculated, it is -25.7 kcal. Thus, illumination enhances the reaction and one can even consider the concentration of electrons as contributing to the over-all chemical potential of the reaction as Brattain and Garrett (14) have done for Ge.

According to the Pourbaix diagram for the system copper-water (9), two ways in which the film oxidation-dissolution reaction can be made to take place are by either raising the partial pressure of oxygen (which tends to raise the potential) or lowering the pH. In the experiments reported here the pH was kept at approximately 7. At this pH another way to bring about dissolution at a low oxygen partial pressure is to increase the potential of the copper, while it is oxidizing, in the positive direction by illumination. When 1 atm of oxygen is in equilibrium with the system, it was shown that the influence of light on the dissolution of Cu_2O , though perhaps present, is undetectable. Apparently the partial pressure of oxygen was high enough to yield a maximum rate of Cu(I) ion oxidation and dissolution, the addition of illumination not being able to enhance further the rate of dissolution. Under the conditions of film formation with a 100% oxygen atmosphere in equilibrium with the water, the higher limiting film thickness for the (100) plane as compared to the (111) indicates that either the rate of growth of the film on (100) was greater or the rate of dissolution of this film slower than that of the film on the (111). It is reasonable to expect that the former is more likely on the basis of studies of the gaseous oxidation of copper (18) which found that the (100) has a higher oxidation rate than the (111).

The same order of oxidation rate for the above two planes is observed when a 1% oxygen atmosphere is in equilibrium with water and a copper surface. Here, however, illumination is important in promoting the oxidation-dissolution reaction because the low oxygen partial pressure favors the formation of Cu_2O (9). The results described show that this is so. For illumination by white light of intensities above $190 \mu\text{w}/\text{cm}^2$, a limiting thickness of $\sim 100\text{\AA}$ can be observed. The film thickness remains constant at this value for as long as illumination is continued. Since an increase in intensity does not change this limiting thickness on the (111), it appears that there exists a saturation current for the photo-electrons as that found, for instance, by Williams for CdS (16). The attainment of a limiting thickness after a certain level of light intensity indicates that for this intensity the rate of growth must be equal to the rate of dissolution. It is thus possible to calculate roughly this rate of dissolution assuming that the rate of growth is not changed from that observed for copper oxidizing in the dark.

This assumption is probably not completely valid since as Cabrera (10) has shown illumination increases the field across very thin n-type films, increasing their rate of formation. The effect would

probably be in the opposite direction for p-type semiconductors such as Cu_2O . Since it is difficult in these experiments involving oxidation in solution to separate the effects of illumination on growth from those on dissolution, the rate of dissolution calculated based on the assumption above is probably an upper limit. The value obtained is approximately 3.6×10^{-8} g/l-min. This is of the same order of magnitude as that which can be estimated for the oxidation of the (111) plane in water in equilibrium with 100% oxygen, if it is assumed that the concentration of Cu(II) ions builds up uniformly from the beginning of the oxidation process. From earlier work (2) this was a concentration of 0.04 mg/l in 70 min. In the early stages of the process (the first 10 min or so) most of the copper ions produced probably remain in the film so that the rate of dissolution is probably greater than that estimated on the basis that dissolution occurs uniformly throughout the whole process.

Thus the rate of dissolution of films on a (111) plane due to high oxygen partial pressure is probably somewhat larger than the maximum rate possible using white light.

Such a limiting thickness was not observed for the oxidation of a (100) surface using the intensities described. Higher intensities were not used because of solution heating problems which gave erratic results. For the range of intensities used, however, the light lowered the rate of film growth and caused, as in the case of the (111), a departure from a cubic rate law. This indicates that the lower rate is not due to a lowering of the rate of the growth reaction alone which would result in a lower but still cubic rate. Instead the dissolution reaction is also taking place.

For both the (111) and the (100) planes earlier work (2) has shown that where oxidation took place in the dark no limiting film thickness was reached for times exceeding 18 hr, indicating that the rate of dissolution in the dark when the water is in equilibrium with a 1% oxygen atmosphere is very low.

In order to gain a more quantitative picture of the growth and dissolution of copper oxide films on copper in solution, it would be desirable to measure and control electrochemical parameters,

potential and current density, while measuring film thickness. This sort of experiment combined with future studies of the nature of the films can possibly explain the differences observed on the different crystallographic planes studied, for electrochemical considerations undoubtedly play a profound role. Such studies can be more readily carried out in solutions more highly conductive than water containing only oxygen. This is the direction that will be followed in subsequent studies.

Acknowledgments

The authors wish to thank Joseph M. Cameron of the Statistical Engineering Section of NBS for assistance in the statistical treatment of some of the data.

Manuscript received Jan. 27, 1964; revised manuscript received March 24, 1964. This paper was presented at the Boston Meeting, Sept. 16-20, 1962.

Any discussion of this paper will appear in a Discussion Section to be published in the June 1965 JOURNAL.

REFERENCES

1. J. Kruger, *This Journal*, **106**, 847 (1959).
2. J. Kruger, *ibid.*, **108**, 503 (1961).
3. J. Kruger, *J. Appl. Phys.*, **28**, 1212 (1957).
4. V. P. Barton, *Phys. Rev.*, **23**, 337 (1924).
5. A. D. Garrison, *J. Phys. Chem.*, **27**, 601 (1923).
6. D. J. G. Ives and A. E. Rawson, *This Journal*, **109**, 477 (1962).
7. L. D. Dyer, *Rev. Sci. Instruments*, **34**, 1114 (1963).
8. J. V. Cathcart, J. E. Epperson, and G. F. Peterson, *Acta Met.*, **10**, 699 (1962).
9. M. J. N. Pourbaix, "Thermodynamics of Dilute Aqueous Solutions," p. 59, Edward Arnold and Co., London (1949).
10. N. Cabrera, *Phil. Mag.*, **40**, 175 (1949).
11. O. Kubaschewski and B. E. Hopkins, "Oxidation of Metals and Alloys," Second ed., p. 145, Butterworths, London (1962).
12. A. V. Ioffe and A. F. Ioffe, *Zhur. Eksptl. i Teoret. Fiz.*, **6**, 737 (1936).
13. N. F. Mott, *Proc. Roy. Soc. (London)*, **171A**, 281 (1939).
14. W. H. Brattain and C. G. B. Garrett, *Bell Syst. Tech. J.*, **34**, 129 (1955).
15. G. T. Miller, Jr., Dissertation, Ph.D., Univ. of Virginia (1958).
16. R. Williams, *J. Chem. Phys.*, **32**, 1505 (1960).
17. D. J. G. Ives and A. E. Rawson, *This Journal*, **109**, 458 (1962).
18. F. W. Young, Jr., J. V. Cathcart, and A. T. Gwathmey, *Acta Met.*, **4**, 145 (1956).

Electrode Reactions and Mechanism of Silicon Anodization in N-Methylacetamide

E. F. Duffek, C. Mylroie, and E. A. Benjamini

Fairchild Semiconductor, A Division of Fairchild Camera and Instrument Corporation, Palo Alto, California

ABSTRACT

The electrochemical processes occurring during anodization of low resistivity silicon were studied to determine the effect of electrolysis conditions on the rate and quality of oxide production. The rate of anodic SiO_2 formation vs. water content in N-methylacetamide (NMA) + KNO_3 solutions was studied by means of ionic current efficiency, weight and analysis of silicon oxide. Current efficiencies of oxide production up to 3.0% were observed and the best oxides were formed at the lowest values of 1.6-1.8%. The oxide formed corresponded within experimental error of method ($\pm 15\%$) to SiO_2 when Si was anodized in NMA solutions containing from about 0.5-3.5% H_2O . At higher water content, the film weight increased with respect to stoichiometric SiO_2 as determined by silicon in oxide analysis. Thermally grown oxides showed a stoichiometric ratio (with some scatter); however, weight measurements of the silicon before and after thermal oxidation indicated that about 12% of the silicon consumed did not appear in the oxide formed. The mechanism proposed at this time suggests anodization of Si depends on the water formed during electrolysis of NMA. Hydrogen at the cathode is accompanied by KOH formation. Oxygen containing electrolytes such as KNO_3 are not involved in the mechanism and are necessary only to increase solution conductivity. A solid secondary amide may be considered as the main anodic electrolysis product.

The formation of dense oxide films by anodization of silicon in nonaqueous systems of N-methylacetamide (NMA) has been studied. Advantages such as room temperature oxidation, control of thickness, and possible incorporation of ions for useful electrical characteristics has indicated a study of the mechanism of anodization was needed for better understanding of the process.

The electrochemical processes occurring during anodization of low resistivity silicon were therefore examined to determine the effect of electrolysis conditions on the rate and quality of oxide production. Past work on the anodization of silicon in N-methylacetamide (NMA) has been presented by Schmidt and other workers (1-4). Water was observed to cause an increase in the rate of anodization. Couch and Brenner have reported on the electrolysis of simple amides (5).

Experimental

Two series of experiments were carried out; one to separate and analyze the electrolysis products of NMA, and the other to study some of the effects of water in the NMA on the quality of the SiO_2 formed.

Anodizations were performed using a regulated d-c power supply capable of delivering 0-600v and 0-200 ma. The electrolysis cell for product separation consisted of a "U"-type split cell separated by a Pormax, polyvinyl chloride membrane as shown in Fig. 1. An open 600 ml beaker was used for the water studies. Agitation was done by means of ultrasonics carried out by suspending the cell in the transducer tank. Eastman Kodak white label NMA (M. P. 29-31°C, 98.5% assay, 0.05-0.1% H_2O) was

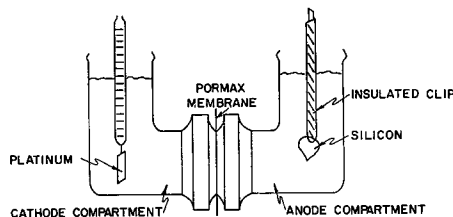


Fig. 1. Cell for non-rigid membranes

used in all cases. Salts added to the NMA included KNO_3 , KNO_2 , NH_4F , Li_2SO_4 , NaF , $\text{Na}_2\text{SO}_4 \cdot 10\text{H}_2\text{O}$, all of reagent grade purity. The current density was 10-15 ma/cm². No special precautions were taken in regard to illumination of silicon.

High purity single-crystal silicon, 1-2 ohm-cm p- and n-type were used. Prior to anodization, the silicon was etched in CP-6 (1:5 HF:HNO₃) or CP-8 (6:10 HF:HNO₃), dipped in HF for several seconds, rinsed in deionized water, and dried. The HF and HNO₃ were 49 and 70%, respectively. Electrical contact to the silicon crystals was made by means of an insulating pressure clip (6). This allowed over 90% of the wafer area to be introduced in the solution in a quick manner.

Electrolysis products were separated and analyzed after anodization of 20-30 p-type silicon slices in the same solution containing KNO_3 as the electrolyte, each to about 350v using the cell shown in Fig. 1. IR drop between electrodes was about 200v. The temperature was held as close to 35°C as possible. The surfaces of the silicon initially anodized were bright, smooth, and even. The later anodized silicon crystals showed a surface similar to that of thermal etching of silicon. This is shown in Fig. 2. The total

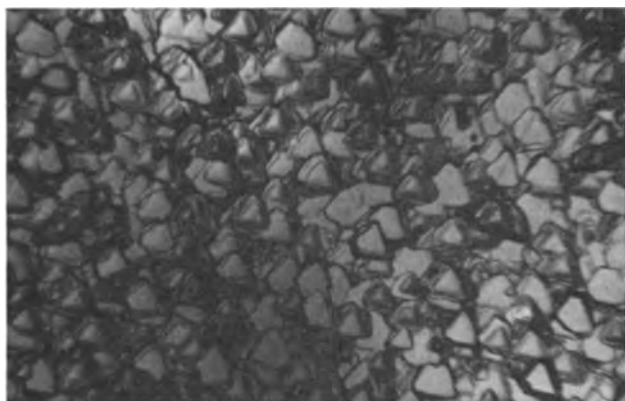


Fig. 2. Silicon surface produced after anodization in "used" N-methylacetamide + 0.04 KNO₃ solution. Anodic oxide removed from lightly shaded areas. Magnification 151.2X.

amount of electricity passed through NMA was about 0.02 Faraday/mole NMA. Anode electrolysis products were examined principally by fractional distillation, solvent extraction, infrared and class tests.

In the second series of experiments using open beakers, anodic oxides on 1.3-1.5 ohm-cm, p-type silicon crystals were formed in solutions of NMA + 0.04N KNO₃ with added water contents varying from 0 to 8.4%. Freshly prepared, unused solutions were selected for each water content determination. The original and final water contents were estimated by Karl Fischer titration. Oxides were formed to 200v net at about 10 ma/cm² in about 15 min. This gave an oxide thickness of 1040 ± 50Å. Karl Fischer titrations after anodization showed a slight, but negligible, amount of water pick-up. The films formed were weighed to ± 3 μg with a Cahn electrobalance and chemically analyzed for silicon by a modified poly-blue method (7) to ± 1 μg. Results were compared with oxides of 1000 ± 100Å formed in steam plus oxygen at 1000°C for 6-7 min on twelve 1.5 ohm-cm, p-type wafers. Oxide thickness determinations were made by the Tolansky multiple beam interferometric (8) and color comparison (9) techniques. Measurements were based on a refractive index of 1.46 for SiO₂.

Nitrate utilization studies by electrolysis of NMA with various arrangements of anhydrous KNO₃, KNO₂, Li₂SO₄, NaF, NH₄F, the hydrate, Na₂SO₄ · 10H₂O as electrolytes were carried out to show mode of the anodization process. Anodization was found to occur in NMA-"dry" NH₄F solutions bubbled with dry nitrogen.

Experimental Results

Electrolysis product analyses.—Hydrogen, formed cathodically, was determined by gas chromatography and accounted for at least 90% of the cathode current. A solid precipitate produced in the cathode compartment during electrolysis was determined to be KOH. Reduction of nitrate ion to nitrite was observed using the sulfanilic acid, 2-naphthylamine Griess test (10).

Fractional distillation under 1 mm Hg pressure, solvent extraction and infrared analysis indicated the presence of H₂O, an amide (not NMA), and

traces of other compounds not definitely classed or identified. Pot residue examinations by extractions with ethanol and chilling resulted in very small amounts of crystalline solid. A melting point could not be obtained. However, Couch and Brenner (5) in their studies on the electrolysis of NMA with platinum electrodes have reported the isolation of a secondary amide, 3,5 diaza-2,6 heptanedione (CH₃CONHCH₂NHCOCH₃). Their electrolysis was carried out in 10% by volume of 1M H₂SO₄ and crude yields of 13 g/Faraday were obtained. If our reaction were similar we would expect about 0.26g of solid products from our 0.02 Faraday. Our actual yield was much less. It is suggested that the production of this compound accounts for much of the anodic electrochemical current.

Various electrolytes in NMA.—Early experiments were concerned with the effect of anhydrous electrolytes on the anodizing process. Various combinations of 0.04N solutions of KNO₃ and KNO₂ in the electrode compartments showed anodization took place immediately as long as each compartment had an electrolyte. The sulfanilic acid, 2-naphthylamine test showed nitrate reduction to nitrite readily occurred but nitrite oxidation to nitrate did not occur. Anodization of silicon also occurred with 0.02N solutions of NaF, and 0.04N solutions of Li₂SO₄ and NH₄F. In the last case the NH₄F was dried at 110°C and anodization immediately carried out while bubbling nitrogen through NMA before and during electrolysis. This indicates NMA, electrolysis products or contaminants are involved in anodization and an oxygen containing electrolyte is not essential to the process. NaCl or KCl will not anodize silicon and produces only an etched surface.

Water studies.—The hygroscopic nature of NMA explains the presence of the majority of the H₂O observed in the distillations of the first experimental series. Titrations with the Karl Fischer reagent indicated 25 ml of stirred NMA at 30°C in a 400 ml beaker will absorb about 40 mg H₂O under room conditions of 50-70% relative humidity.

Several determinations using the split cell with a Pb/PbSO₄ cathode, silicon anode, and CsNO₃ electrolyte in a nitrogen flushed dry box were carried out to determine the presence and site of water production during electrolysis. The Pb/PbSO₄ electrode permitted the reduction of PbSO₄ rather than evolution of H₂, and the CsNO₃ was considered less apt than KNO₃ to transport H₂O from one compartment to the other. Electrolysis of NMA for 30 min at 75 ma and subsequent Karl Fischer titration for two runs produced 0.010 and 0.015g H₂O. A blank was carried along to indicate the hygroscopic pick-up of H₂O. According to Faraday's laws, electrolysis would produce 0.013g H₂O assuming an equivalent weight of 9 for H₂O. Attempts to determine site of product formation including isopropyl titanate for water and phenolphthalein for KOH were not successful. It is suggested further work be carried out in closed glass apparatus to determine the site of H₂O production. However, the main point from this work is that H₂O will generally be present in NMA solutions and will therefore cause a great effect on

Table I. Results of silicon analyses of oxides formed to 200v in N-methylacetamide with various H₂O contents

No.	H ₂ O, %	Oxide weight, μg	Oxide weight, μg/cm ²	Si (analyzed), μg/cm ²	Si (calc), μg/cm ²	Si consumed, μg/cm ²
1	0	98	30.4	10.8	13.3	12.8
2	0.1	85	22.7	9.3	10.0	8.8
3	0.4	94	24.5	8.8	10.7	11.0
4	0.8	80	19.4	8.0	8.5	9.4
5	1.2	94	22.0	8.9	9.6	9.3
6	2.4	89	21.6	8.5	9.5	7.8
7	3.6	95	21.0	8.2	9.2	13.1
8	4.8	81	22.4	7.7	9.8	9.4
9	7.2	118	26.8	8.4	11.7	8.4
10	8.4	145	35.2	12.6	15.4	12.1
4A	0.8	77	18.6	8.5	8.7	8.8
	0.8	71	19.0	8.8		
5A	1.2	89	20.9	9.4		
	1.2	94	29.2	11.5	10.5	11.7

Table II. Current efficiencies of anodic oxides formed to 200v in N-methylacetamide with various H₂O contents

No.	% H ₂ O	$\frac{It}{F} \cdot \frac{60.06}{4}$, μg	Wt oxide produced, μg	Current efficiency, %
1	0	3360	98	2.9
2	0.1	3180	85	2.7
3	0.4	5210	94	1.8
4	0.8	4550	80	1.8
5	1.2	6040	94	1.6
6	2.4	5180	89	1.7
7	3.6	5590	95	1.7
8	4.8	4080	81	2.0
9	7.2	4430	118	2.7
10	8.4	4910	145	3.0

results obtained and particularly the quality of oxide formed.

Effect of Water on the anodic oxides formed in NMA.—Visual observation during silicon anodization to 200v net in NMA showed that cloudy oxides with nonuniform thicknesses were produced in solutions containing about 7% or more water.

The effect of H₂O was further evaluated by means of weight of oxide and silicon analysis measurements. The results of these data are given in Tables I and II and Fig. 3-7. Figure 3 and Table I show the weights of oxide formed to 200v are constant from 0.5-5% H₂O. Increased weights of silicon oxides were obtained above 5% H₂O. Analysis of the silicon in the oxide was within experimental error of the calculated silicon in produced oxide up to about 5% H₂O. Beyond 5% H₂O the difference increased significantly. Measurements on oxides formed in NMA solutions containing less than 0.8% H₂O suggested an initial process occurring, limited by the amount of water present for reaction at the silicon anode. Attempts to dry the NMA with molecular sieves and other drying agents for zero water content anodization were not successful.

The variation of total silicon consumed compared to analysis of the oxide is shown in Fig. 4. The difference was not significant and suggests a barrier type film was formed.

Figure 5 further illustrates the nature of the anodization process. At constant current density, the

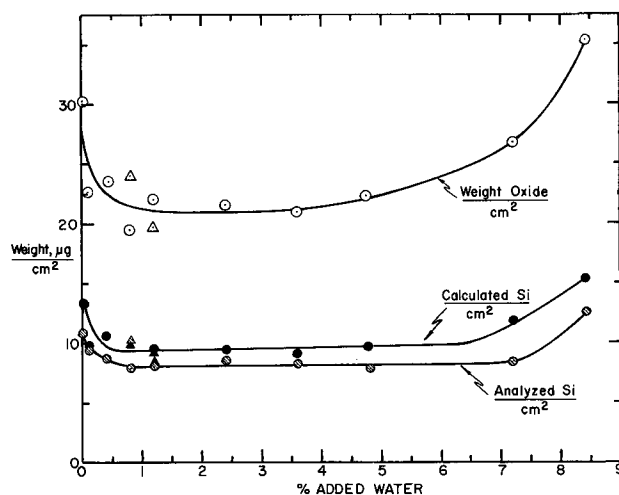
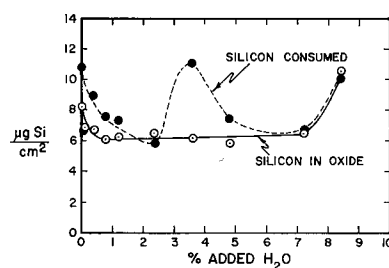
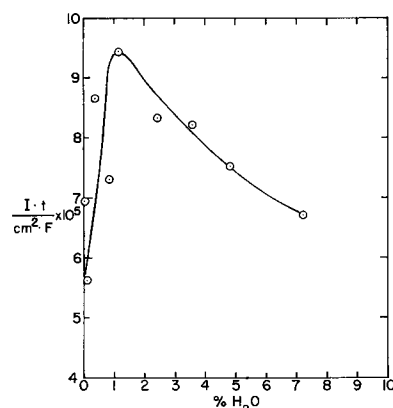
Fig. 3. Weight gain of oxides and silicon in oxides formed to 200v vs. H₂O content in N-methylacetamide.

Fig. 4. Variation of silicon consumed and analyzed silicon in oxide with water content for oxides formed to 200v.

Fig. 5. Total equivalents vs. H₂O content for oxides formed to 200v.

time to reach 200v net goes through a maximum. That is, beyond 0.8-1.2% H₂O the rate of anodization increased with increased water contents. Below 0.8% H₂O water for the anodization may not be available, and increased anodization rates were not observed. An uneven oxide was obtained at 7.2% H₂O and above.

Estimations of the ionic current efficiency of oxide production are given in Table II and Fig. 6. On the basis of the analytical study and visual observations the most suitable oxides were produced along the minimum of the current efficiency plot. Thus, although ionic current efficiency increased with water content, the surface quality of the oxide deteriorated markedly.

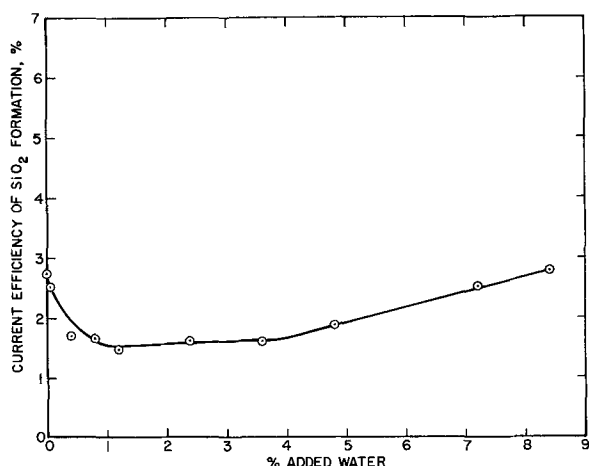


Fig. 6. Current efficiency vs. water content for oxides formed to 200v.

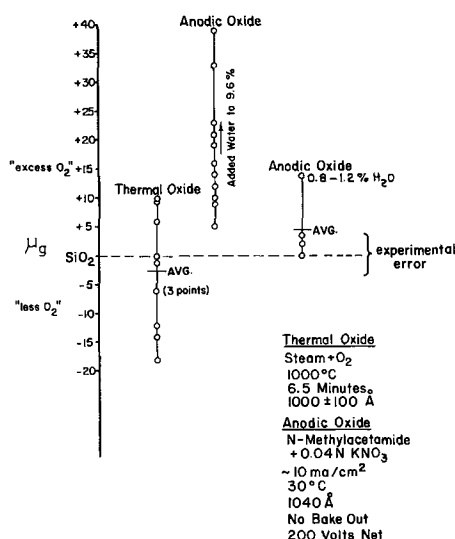


Fig. 7. Comparison of thermal and anodic oxides based on silicon in oxide analyses. Thermal oxide: steam + O₂, 1000°C, 6.5 min, 1000 ± 100Å; anodic oxide: N-methylacetamide + 0.04N KNO₃, ~10 ma/cm², 30°C, 1040Å, no bake out, 200v net.

Figure 7 and Table III compare the results of silicon analyses of oxides anodically grown with added water contents up to 8.4% with "dry" NMA (0.8-1.2% water) and steam grown at 1000°C. The actual weights of oxide produced are plotted as deviations from the chemically estimated silicon calculated as SiO₂. "Excess O₂" and "less O₂" denote the difference in micrograms between total weight of oxide produced experimentally minus weight of SiO₂ as calculated from silicon analysis. The ratio of Si:O₂ is also given. Except for the anodization in NMA with residual H₂O, the measurements showed an increase in oxide weights produced with increased H₂O content. Additional anodization experiments with 0.8-1.2% H₂O in NMA and thermal oxidation of silicon gave SiO₂ weights which were within the experimental error of ±4 μg. Weight loss measurements and the amount of silicon in the oxide also showed that 12% (5.6 μg out of 44.3 μg) of the total weight loss of silicon was lost to the atmosphere during thermal oxidation.

Oxide film thickness measurements vs. net forming voltage at 5 ma/cm² and with 0.1-0.5% water

Table III. Results of silicon analysis of anodic and thermal oxides to determine the silicon to oxygen ratio

Anodic oxides formed to 200v				Thermal oxides grown to 1000Å				
H ₂ O, %	Oxide wt, μg	Si (anal), μg	(Oxide formed minus SiO ₂ calc), μg	Ratio Si:O ₂	Oxide wt, μg	Si (anal), μg	(Oxide formed minus SiO ₂ calc), μg	Ratio Si:O ₂
0	98	35	+23	1:3.18	67	37	-12	1:1.44
0.1	85	35	+10	1:2.52	87	36	+10	1:2.49
0.4	94	35	+19	1:2.98	97	48	-6	1:1.79
0.8	80	33	+9	1:2.51	93	44	-1	1:1.95
1.2	94	38	+12	1:2.59	72	40	-14	1:1.40
2.4	89	35	+14	1:2.73	88	38	+6	1:2.32
3.6	95	37	+16	1:2.77	87	36	+10	1:2.43
4.8	81	28	+21	1:3.31	72	42	-18	1:1.25
7.2	118	37	+39	1:3.86	79	37	0	1:2.01
8.4	145	52	+33	1:3.14	80	40	-6	1:1.75
0.8	77	35	+2	1:2.12	76	38	-6	1:1.76
0.8	71	33	0	1:2.02				
1.2	89	40	+3	1:2.14				
1.2	77	37	+14	1:2.65				

in NMA are given in Fig. 8. The data show a straight line relationship corresponding to 5.3 Å/v from 100-425v net. The error of the thickness determinations is ± 50Å. However, previous workers (1-4) have observed a break in the curve of voltage vs. time measurements.

P-type silicon anodized almost immediately after electrical contact was made. N-type required photo-illumination for immediate anodization. However, we have found that initial illumination was not necessary even with freshly cleaned Si wafers (HF dip); that often a short time (seconds to minutes) the voltage drops and then steeply rises regularly with oxide growth. This sort of behavior was also shown in Fig. 8 of Schmidt and Michel's paper (1).

Discussion

On the basis of these results the following electrode processes are proposed for the electrolysis of NMA and anodization of silicon.

Cathode

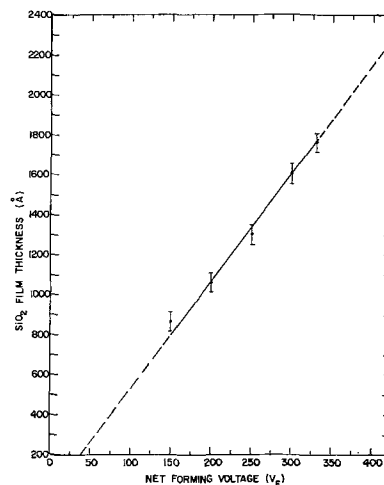
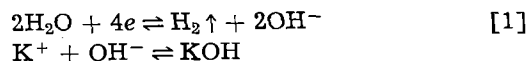
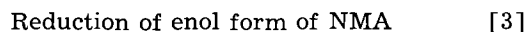
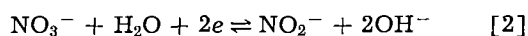
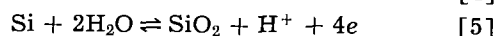
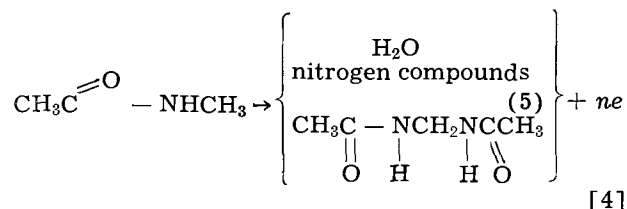


Fig. 8. SiO₂ film thickness as a function of forming voltage. Electrolyte: N-methylacetamide with 0.04N KNO₃; substrate: mechanically polished, 0.01 ohm-cm, p-type Si; current density, 5 ma/cm².



Anode



The mechanism proposed at this time suggests the anodization of silicon depends on the water obtained from the oxidation of NMA, or water otherwise present. Hydrogen formation at the cathode is accompanied by KOH formation in the cathode compartment. Charge balance is maintained by migration of $[\text{K}(\text{H}_2\text{O})]^+$ through the membrane into the cathode compartment. Due to the hygroscopic nature of NMA sufficient water will generally be present to anodize the silicon in the manner shown.

Oxygen containing electrolytes as KNO_3 or Li_2SO_4 are not essential for the anodization process. Oxides have also been formed by anodizing silicon in $\text{NMA} + \text{H}_2\text{O}$ solutions.

The technique of weighing and analyzing the anodic oxide has shown the extent to which water as a contaminant or by-product influences the nature of the oxide and suggests other contaminants

and properties of anodic oxides may be critically evaluated in a similar manner.

Acknowledgments

The authors wish to thank W. Waring and K. E. Lemons for their suggestions in carrying out this work.

Manuscript received July 16, 1963; revised manuscript received April 2, 1964. This paper was delivered before the Pittsburgh Meeting, April 15-18, 1963.

Any discussion of this paper will appear in a Discussion Section to be published in the June 1965 JOURNAL.

REFERENCES

1. P. F. Schmidt and W. Michel, *This Journal*, **104**, 230 (1957).
2. P. F. Schmidt, U.S. Pat 2,909,470, Oct. 20, 1959.
3. T. M. Donovan, Thesis, Stanford University, Dept. of Chemistry, August 1961.
4. W. Hass, *This Journal*, **109**, 1192 (1962).
5. D. E. Couch and A. Brenner, (*This Journal*, **106**, 202C, Paper No. 65), talk presented at Columbus, Ohio, Electrochemical Society Meeting, October 1959; private communication.
6. E. A. Benjamini and E. F. Duffek, *Rev. Sci. Instruments*, **35**, 237, No. 2, (1964).
7. A. B. Carlson and C. V. Banks, *Anal. Chem.*, **24**, 472 (1952).
8. P. S. Flint, Private communication; S. Tolansky, "Multiple-Beam Interferometry of Surfaces and Films," Clarendon Press, Oxford (1948).
9. A. E. Lewis, To be published.
10. Fritz Feigl, "Spot Tests in Inorganic Analysis," 5th ed., pp. 328-331, Elsevier Publishing Co., New York (1958).

The Effect of Annealing on the Microstructure and Hardness of Some Nickel Electrodeposits

R. Weil, W. N. Jacobus, Jr., and S. J. DeMay¹

Department of Metallurgy, Stevens Institute of Technology, Hoboken, New Jersey

ABSTRACT

The effects of annealing on the microstructure and hardness of nickel electrodeposits from six different plating baths were studied. The structural changes of the bulk as observed by transmission electron microscopy occurred in the same annealing-temperature range as the major decreases in hardness. The first change in the surface structure occurred 200°C higher. The annealing process appears to consist of the migration of grain boundaries, which in most cases seemed to carry impurities along with them. A mechanism for this process in electroplated metals is proposed.

The changes in the microstructure and mechanical properties which electrodeposited metals experience when they are annealed, have been studied by Gardam and Macnaughton (1), Roehl (2), and Zentner, Brenner, and Jennings (3) among others. Conventional metallographic methods were used to study alterations in the microstructure. Within recent years, transmission electron microscopy has been successfully employed by Bollmann (4), Bailey and Hirsch (5), and Hu (6) to elucidate the structural changes which occur during annealing of cold-worked metals. An electron-microscopic study of

the behavior of electroplated metals when they are heated was therefore indicated and became the subject of this investigation.

The earlier work, mentioned above, which employed conventional metallographic techniques dealt primarily with electrodeposited nickel. The as-plated structures of this metal have also been extensively studied by electron microscopy. For these reasons, nickel was selected for this investigation. As the products resulting from the codeposition of plating-bath additions, especially those containing sulfur, have a great effect on the structure and mechanical properties of nickel, bath compositions

¹ Present address: Grumman Aircraft Corp., Bethpage, New York.

were selected particularly to reveal their role in the annealing processes. Five of the baths had deliberate additives and only one was sulfur-free.

Experimental Procedure

Nickel was deposited to a thickness of 150μ on electropolished copper substrates from the baths listed in Table I. The copper was subsequently dissolved in the manner previously described (7). The center sections of the nickel plates was cut into pieces 2.5×1.5 cm. Two pieces from deposits from each bath were placed in a Vycor tube which was evacuated to better than 10^{-5} mm of Hg and then inserted in the constant-temperature region of a tube furnace. The samples were annealed for 1 hr at temperatures between 200° and 1200°C in 100° intervals. In the temperature intervals in which major structural changes were found to occur, additional runs at 50° intervals were made. Samples from bath D were annealed at 200°C for 15 min, 30 min, 2 hr, and 4 hr in addition to the 1-hr-long test. Two-stage carbon replicas were produced from the surfaces of the as-plated and annealed specimens by the technique described earlier (8). The replicas were examined in a Hitachi HU-11 electron microscope at 5000 magnifications.

The hardness of the samples was measured on a metallographically polished cross section with a Leitz Durimet Microhardness Tester using a 100g load. Other pieces of the annealed and as-plated samples were electrolytically thinned by the Bollmann (9) technique for transmission electron-microscopic examination. All nickel deposits, which were studied, were initially very fine grained. In deposits from some baths, the grain size increased with plating thickness up to about 50μ and then became constant. Therefore, the initial 50μ were not used for hardness measurements or for transmission electron microscopy.

Experimental Results

It is evident from Table I that the nickel deposits have two types of structure, relatively coarse grained and very fine grained. The variation of hardness with annealing temperature for the three coarse-grained deposits is plotted in Fig. 1 and for the three fine-grained ones in Fig. 2. The coarse-grained deposits are initially much softer than the

**Table I. Basic bath composition: 400 g/l $\text{NiSO}_4 \times 6\text{H}_2\text{O}$, 45 g/l $\text{NiCl}_2 \times 6\text{H}_2\text{O}$, 45 g/l H_3BO_3
Plating conditions: temperature, $55^\circ\text{C} \pm 2^\circ$; current density, 5 amp/ dm^2 ; pH, 4**

Bath	Addition agents	Type of structure
A	None	Relatively coarse grained
B	0.1 g/l Coumarin	Relatively coarse grained
C	0.07 g/l Thiourea	Relatively coarse grained
D	Proprietary bright nickel	Very fine grained
E	0.2 g/l 1-5 Naphthalene disulfonic acid (Na Salt)	Very fine grained with crevices
F	0.8 g/l 1-5 Naphthalene disulfonic acid + 1.0 g/l zinc	Very fine grained with crevices

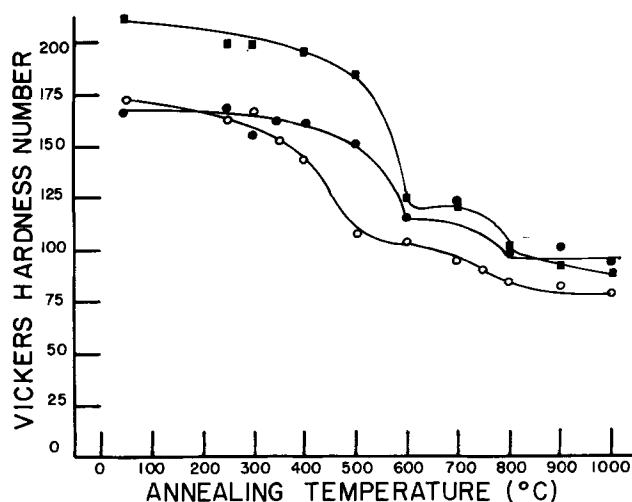


Fig. 1. Hardness-annealing temperature graphs for samples from coarse-grained deposits. ●, 0.1 g/l Coumarin; ○, no additives; ■, 0.07 g/l thiourea.

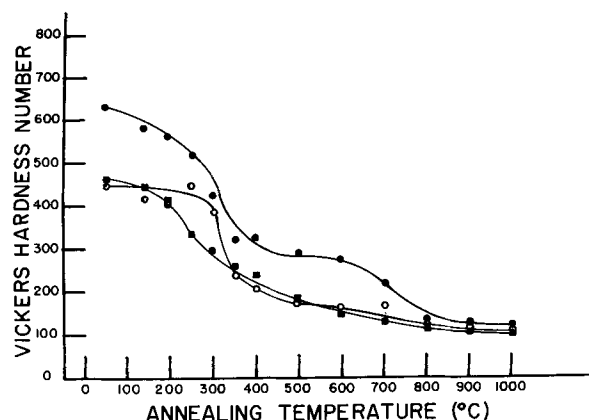


Fig. 2. Hardness-annealing temperature graphs for samples from fine-grained deposits. ○, 0.8 g/l Naphthalene disulfonic acid and 1.0 g/l zinc; ●, proprietary bright nickel; ■, 0.2 g/l naphthalene disulfonic acid.

fine-grained ones and the major reduction in hardness occurs at a higher temperature in the former than in the latter.

The first noticeable change in the structure of the surfaces as revealed by replica examination takes place about 200°C above the temperature of the major decreases in hardness. The deposits from bath A are typical of the behavior of the relatively coarse-grained deposits. The variation of the surface structure with annealing temperature is shown in Fig. 3. The as-plated structure shown in Fig. 3a persists to 700°C . A few areas of the deposits annealed at 700°C exhibit the change shown in Fig. 3b. A few grain boundaries (B) deepen, some new ones (C) form and in some areas (A) the surface becomes smoother and the steps become more distinct. With increasing annealing temperature, this trend continues as seen in Fig. 3c. It is evident that remnants of the pyramidal shapes from the as-plated structure can still be recognized (P). Annealing at temperatures above 900° results in some vacuum etching as seen in Fig. 3d. In samples annealed at these temperatures, spirals are also frequently observed. The effect of annealing on the surface structures of the deposits from baths B and

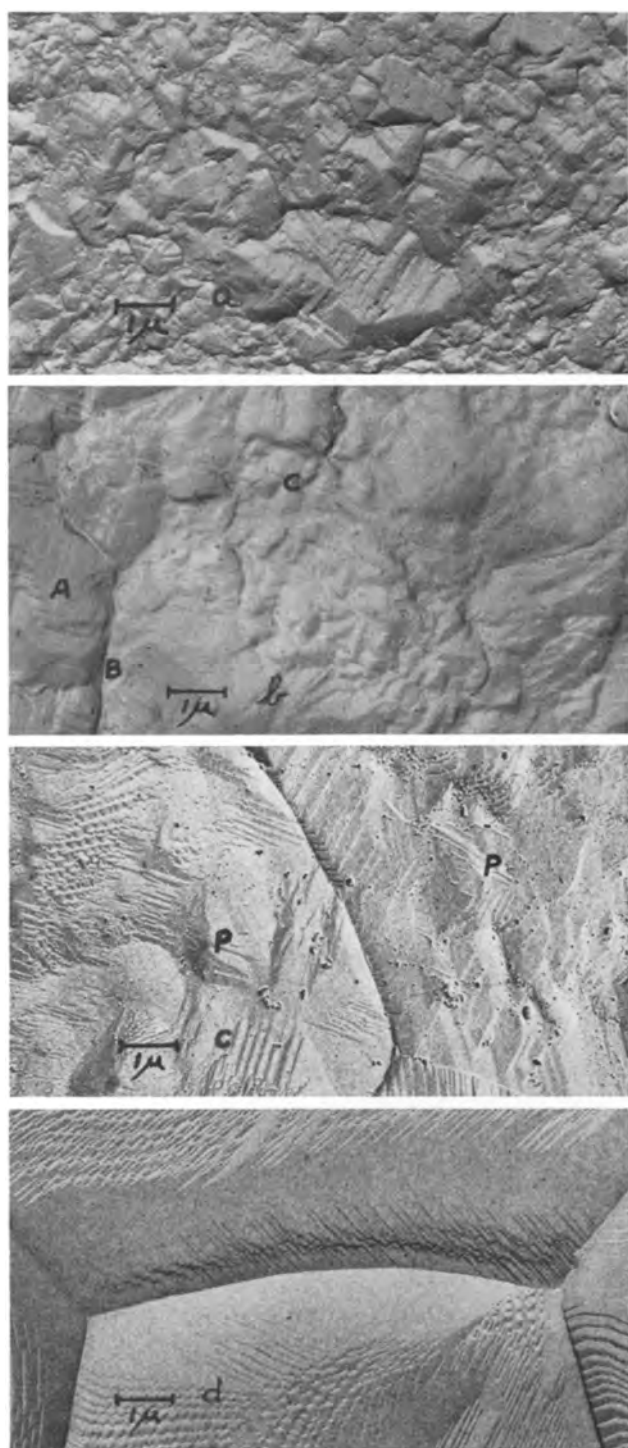


Fig. 3. Effect of annealing on surface structure of coarse-grained deposits from bath A. a, As-plated structure; b, annealed at 700°C; c, annealed at 850°C; d, annealed at 1100°C.

C is essentially like that shown in Fig. 3. The first change in structure in the deposits from bath B, however, is observed at 800°C. In an earlier study (8) deposits plated in a solution with the same addition of thiourea as bath C yielded a much finer grained structure. As pointed out at that time, the structures are not always reproducible.

Some features of the behavior of the fine-grained deposits are shown in Fig. 4. The as-plated structure of the deposit from the proprietary bath is uniformly smooth. The grain size is not resolved in the replica. The surfaces of the deposits plated in baths

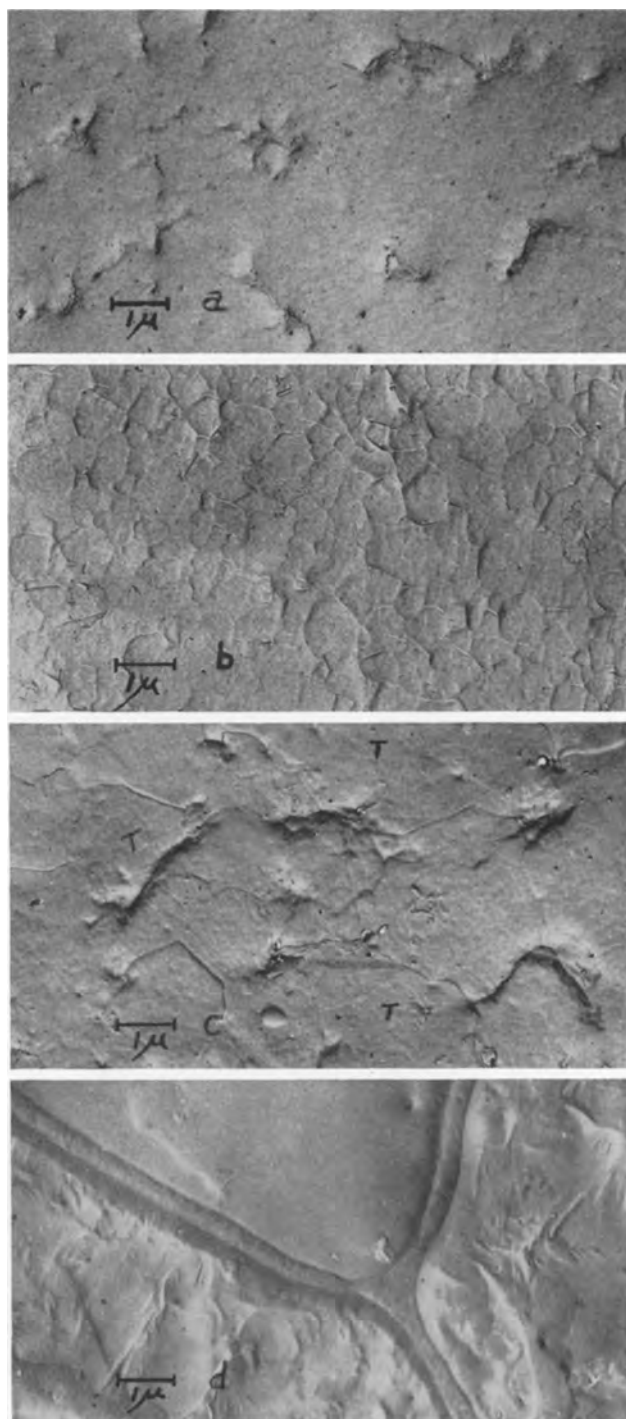


Fig. 4. Effect of annealing on surface structure of fine-grained deposits. a, As-plated structure from bath F; b, sample from bath D annealed at 600°C; c, sample from bath F annealed at 700°C; d, sample from bath D annealed at 700°C.

E and F show crevices between groups of grains as seen in Fig. 4a. The structure from the proprietary bath looks like the areas between the crevices in Fig. 4a. The first structural changes are noted in samples annealed at 500°C. Grains about 1μ in diameter become visible, but fainter than seen in Fig. 4b. The crevices, when they are present in the as-plated structure, always contain a grain boundary. This can be seen in Fig. 4c, which shows the structure of a sample annealed at 700°C. At this temperature the grains have grown larger than 1μ . Evidence of twin boundaries (T) can also be

seen in Fig. 4c. Samples from bath D annealed at 700°C and from bath F annealed at 850°C show the formation of broad grain-boundary regions as seen in Fig. 4d. In some areas the constituent responsible for these regions is not continuous, but consists of individual particles. Annealing at higher temperatures results in a structure with normal grain boundaries like that shown in Fig. 3d.

The first structural changes as revealed by transmission electron microscopy of thin films taken

from the bulk of the deposit occurs in the same temperature range as the major decreases in hardness. Figure 5 shows the effect of annealing on the structure of thinned films from deposits having the relatively large grain size in the as-plated condition. Figures 5a and 5b show the as-plated structures of deposits from baths A and C, respectively. The structure of the deposit from bath B closely resembles that shown in Fig. 5a. Some twins (T) and regions of misorientation within a grain, as manifested by diffraction-contrast variations, are seen in both Fig. 5a and 5b. Individual dislocations can be seen in Fig. 5a only. The structure in Fig. 5b shows variations in the intensity of the transmitted electron beam indicative of strong lattice distortions within the grains.

No noticeable changes are found in samples from bath A annealed up to 350°C. Very slight alterations may have occurred, which would have been only noticeable by comparing the same area before and after annealing. The experimental condition precluded such an observation. The major hardness drop occurs between 400° and 500°C in the samples from bath A. The structure also changes in this temperature range. Figure 5c shows that annealing at 450°C results in more twins (T), some of which are associated with the elimination (E) of regions of misorientation within a grain. The number of small grains also decreases from that seen in Fig. 5a. Samples held at 500°C have the structure pictured in Fig. 5d. This figure shows many twins, sharp orientation contrast between grains, and practically no misalignment within a grain. Above 500°C the grain size only increases with increasing temperatures. The sequence of events which occurs during the hardness drop in the samples from bath A is also found in specimens from bath B at corresponding temperatures. Samples from bath C annealed in the temperature range where the major hardness decrease occurs and up to about 900°C show an increasing tendency for grain-boundary attack during electropolishing. At the same time the contrast within the grains becomes more uniform.

The structure of the deposits from baths D, E, and F consists of grains 100-500Å in diameter. These grains are randomly oriented in the plane of the deposit because complete and uniformly intense rings are obtained by electron diffraction. The relative intensity of the rings from the various reflecting planes indicates that no strong fibering is present perpendicular to the surface of the deposit. The samples with crevices on the surface, show the structural feature pictured in Fig. 6a. The areas corresponding to the crevices have been preferentially dissolved during the electrolytic thinning of the specimens with only an extremely fine-grained sliver remaining. A few samples not thinned so as to dissolve the crevice areas show that the grain size there is finer than in the rest of the sample. Selected-area-diffraction patterns of the regions containing a crevice and those adjacent on either side show no difference in orientation; all areas yield complete rings with no arcs of varying intensities.

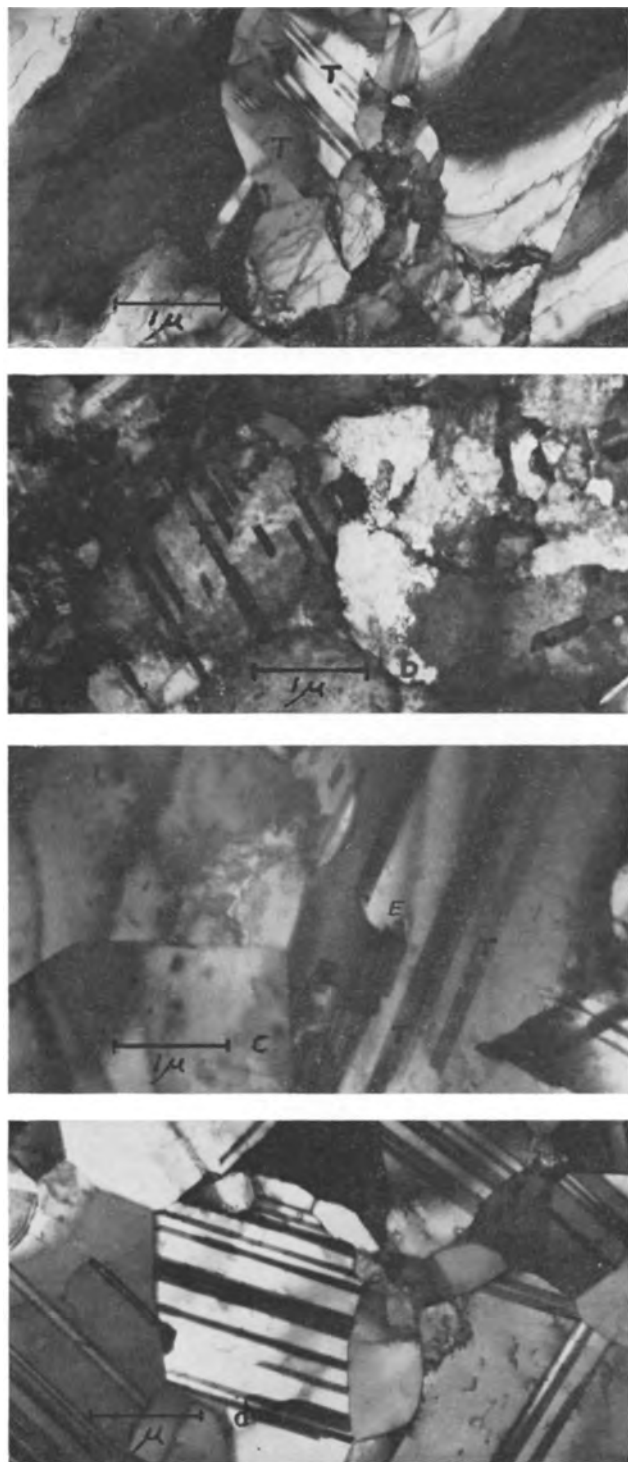


Fig. 5. Structural changes on annealing in coarse-grained thin film. a, As-plated structure from bath A; b, as-plated structure from bath C; c, sample from bath A annealed at 450°C; d, sample from bath A annealed at 500°C.

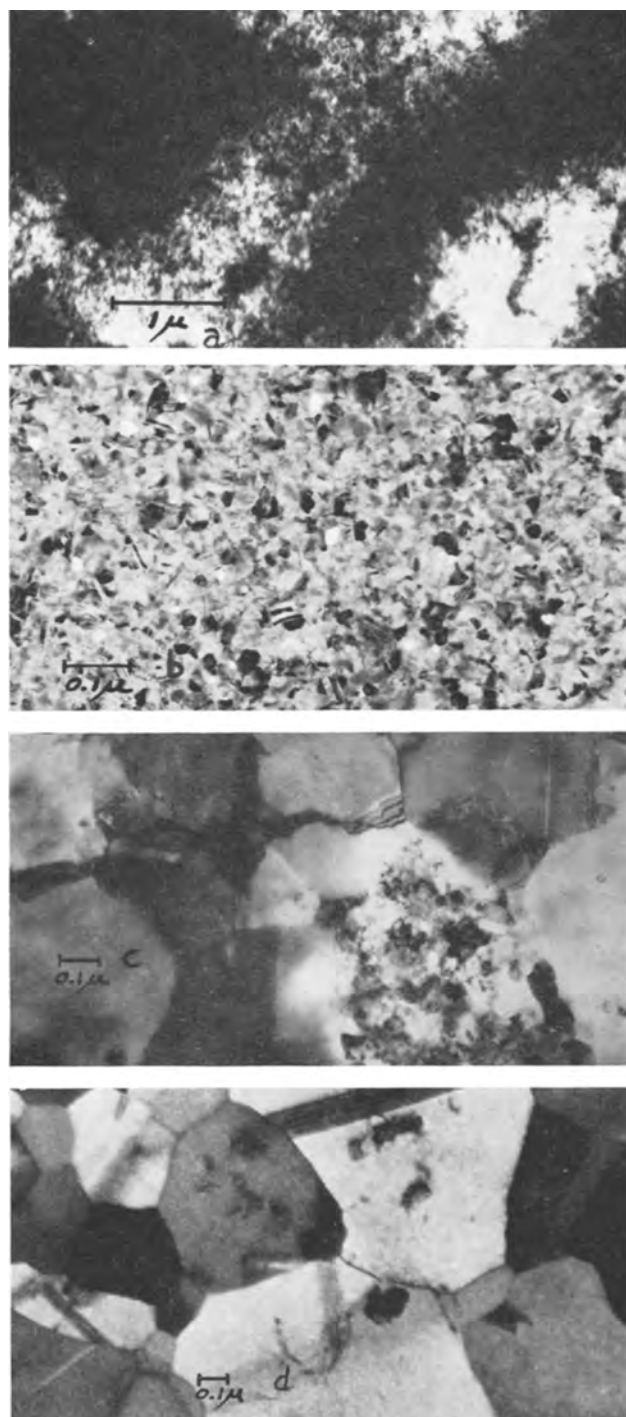


Fig. 6. Structural changes in annealing in fine-grained thin films. a, As-plated structure from bath F; b, beginning of recrystallization; c, later stage during recrystallization in sample from bath E; d, later stage in recrystallization in sample from bath D.

The first structural changes on annealing of the samples are shown in Fig. 6b. A few grains have become larger than the original ones. A sample, which originally shows crevices, annealed at a higher temperature is shown in Fig. 6c. The distribution of the still fine-grained regions corresponds to the crevices in the as-plated structure. Figure 6d shows the structure in a sample from bath D which has no crevices. Electron-diffraction patterns from the larger-grained regions in Fig. 6c and 6d show Kikuchi lines. Annealing at temperatures between about 250° and 900°C results in

an increased tendency for the preferential dissolution of the grain boundaries during electrolytic thinning. Above 900°C there is no discernible preferential attack.

The samples from bath D, annealed at 200°C for various times, reveal the existence of an incubation period of between 15 to 30 min prior to the formation of the larger grains seen in Fig. 6d. After 15 min there is no noticeable change from the as-plated structure. The structure which results from a half-hour annealing treatment consists of grains which are about 10 times larger than the original ones.

Discussion

The difference in temperature at which structural changes occurred on annealing on the surface and in the bulk of the electrodeposits were probably due to oxides, adsorbed material, and other surface impediments. A similar phenomenon was reported by Bailey (10) and by Hu (6), who found that recrystallization in thin films occurred at higher temperatures than in bulk. It was also observed in a few experiments conducted as part of this investigation in which as-plated deposits were thinned and then heated in the electron microscope. As the brightness of electrodeposits was shown (7) to depend on the surface structure, alterations in this property should occur at considerably higher annealing temperatures than changes in the mechanical properties, which are related to the structure of the bulk. It was found to be so experimentally.

Annealing of the initially relatively coarse-grained deposits from baths A, B, and C in the temperature range of 400°-600°C, where the major decrease in the hardness occurred, resulted in the migration of grain and subgrain boundaries, as is evident from Fig. 5. As a result of this boundary movement, misorientations within certain grains and a number of small grains were eliminated. In samples of baths A and B a noticeable decrease in the number of dislocations occurred which can be seen by comparing Fig. 5d with 5a. It is generally agreed that recrystallization is associated with an incubation period. Experiments to determine if there was such a period have not yet been conducted. It was therefore not positively established that recrystallization rather than spontaneous grain-boundary migration occurred.

As previously indicated, few individual dislocations were seen in the as-plated samples from bath C. There were, however, strong indications of lattice distortions, which can be seen in Fig. 5b. These distortions were probably due to stresses around codeposited impurities. After annealing, these distortions were virtually eliminated. It is suggested that this occurred because the moving boundaries absorbed the impurities, which caused the stresses. In this way, the boundaries became regions of high impurity concentrations. In the samples from the bath containing thiourea, the impurities were undoubtedly rich in sulfur, which is well known to make nickel more susceptible to corrosion. Therefore, the grain boundaries tended to be preferentially attacked during electropolishing. The mech-

anism of moving grain boundaries absorbing sulfur-rich impurities in nickel was suggested by Olsen, Larkin, and Schmitt (11) to account for the embrittlement of nickel, containing about 9 ppm of sulfur, after annealing between 400° and 600°C. Such embrittlement was also found by Zentner, Brenner, and Jennings (3) in nickel which was electrodeposited in baths with sulfur-containing addition agents and then annealed.

The hardness drop which was observed between 200° and 400°C in samples from baths D, E, and F was associated with recrystallization because the previously mentioned requirement for such a process, namely, the incubation period was observed. The recrystallization temperatures were somewhat lower than those which Bollmann (4), for example, reported for cold-worked nickel. There were also other important differences between cold-worked and fine-grained, electrodeposited nickel. The grain size of the electroplated nickel was considerably smaller than the regions which Bollmann (4) and Bailey and Hirsch (5) have shown to be the nuclei for recrystallization in cold-worked metals. Bailey and Hirsch have proposed an equation for the minimum size (L) of the boundary which can bulge out for migration.

This equation is

$$L > \frac{2\gamma}{E} \quad [1]$$

where γ is the grain-boundary surface energy and E the difference in stored energy across the boundary. In cold-worked silver with a value of $E \approx 4$ cal/g-atom and $\gamma \approx 400$ ergs/cm², a value of $L > 5 \times 10^{-5}$ cm was obtained. Steidel, Li, and Spencer (12) quoted a value of $\gamma \approx 200$ ergs/cm² for a boundary in nickel containing sulfur. Substituting this in the above equation it is evident that a much higher value of stored energy would be required if regions of the same size or smaller than the fine grains of the electrodeposited nickel were to grow by the grain-boundary movement as indicated in Fig. 6b. Some of the grains in Fig. 6b had the qualifications which Bollmann (4) gave for recrystallization nuclei. The smallest of these was about 100Å in diameter. Substituting the appropriate quantities in Eq. [1], a value of $E \approx 65$ cal/g-atom was obtained as the minimum energy necessary to cause a grain boundary to move. Binder and Fischer (13) have reported stored-energy values in very fine-grained, electrodeposited copper of 1.3 kcal/g-atom due to internal stresses of Type II and III (those stresses which cause line broadening in x-ray diffraction patterns). These stresses were shown to be associated with codeposited impurities. It is, of course, doubtful if a stored-energy difference of 1.3 kcal/g-atom actually existed across a boundary, as this required a region completely free of impurities on one side and a region with a high impurity concentration on the other. However, a value of E of 65 cal/g-atom could result if a region of low internal stress, due to a low impurity concentration, existed on one side of a boundary. Such regions may have been present in the as-plated structure

or they could have formed by the gathering of the impurities into a type of zone. The time needed for the latter process could account for the incubation period. It is therefore suggested that the recrystallization nuclei were regions of low internal stress, and that the driving force for the process was the relief of these stresses.

Based on the above hypothesis, there was then another important difference between pure, cold-worked, and fine-grained, electrodeposited nickel. In the electroplated nickel the stresses could only have been relieved by the redistribution of the impurities, which caused them. The moving grain boundary thus became a sink for physical entities, impurities rather than structural ones, dislocations. It is well known that impurities impede grain-boundary movements. For this reason, the regions corresponding to the crevices in deposits from bath E and F remained fine grained as shown in Fig. 6c and finally became part of the grain boundary as seen from Fig. 4c. The regions corresponding to the crevices are believed (14) to be caused by locally high concentrations of impurities. Therefore these regions must have had the highest internal stresses and their edges fulfilled the conditions for nucleation. However, the growth of recrystallization nuclei into these regions must have been very difficult because the large amount of impurities which the boundaries absorbed, anchored them.

The formation of the grain-boundary constituent seen in Fig. 5a can be explained by the ability of the grain boundaries containing increasing impurity concentrations to continue to move because of the higher temperature. When the concentration of impurities in the boundary was sufficiently high, the constituent formed. At still higher annealing temperatures, as suggested by Olsen, Larkin, and Schmitt (11), the impurities again tended to become more uniformly distributed because of diffusion. Therefore the grain-boundary constituent disappeared and small particles were seen throughout the grains. In all samples, the grain size was very large after annealing at high temperatures.

It appears that transmission electron microscopy can be usefully applied to study the annealing phenomena in electroplated metals. However, more work is needed in such areas as measuring stored-energy releases, the cause of internal stresses and the location of impurities. Some of this work is presently in progress and it is hoped that in subsequent papers a clearer picture of the involved mechanisms can be developed.

Conclusions

1. The structural changes on the surface of the electrodeposited nickel occurred at higher annealing temperatures than in the bulk.
2. In initially relatively coarse-grained deposits movement of boundaries resulted in the elimination of misorientations within a grain and of small grains.
3. In deposits that had a very fine-grained structure in the as-plated conditions, recrystallization

occurred probably by the growth of small regions of low internal stress.

4. Recrystallization in fine-grained, electrodeposited nickel was different from that in pure, cold-worked nickel because in the former, the nuclei were smaller and their growth required the absorption of impurities in the boundaries which tended to impede their further movement.

5. After annealing at high temperatures the structures of all electrodeposits, which were studied, consisted of very large grains. In some deposits there were particles distributed throughout the grains.

Acknowledgments

This project was supported by the Undergraduate Science Education Program of the National Science Foundation. The proprietary nickel deposits, Superlume were supplied by the Hanson-Van Winkle-Munning Corp., Matawan, N.J. Some suggestions by other members of the staff of the Department of Metallurgy, Stevens Institute of Technology, are gratefully acknowledged.

Manuscript received Jan. 31, 1964. This paper was presented at the New York Meeting, Sept. 29-Oct. 3, 1963.

Any discussion of this paper will appear in a Discussion Section to be published in the June 1965 JOURNAL.

REFERENCES

1. G. E. Gardam and D. J. Macnaughton, *Trans. Faraday Soc.*, **29**, 755 (1933).
2. E. J. Roehl, *Monthly Rev. Am. Electroplaters' Soc.*, **34**, 1129 (1947).
3. V. Zentner, A. Brenner and C. W. Jennings, "Physical Properties of Electroplated Metals," p. 96, American Electroplaters' Soc., Newark, N. J. (1952).
4. W. Bollmann, *J. Inst. Metals*, **87**, 438 (1958-9).
5. J. E. Bailey and P. E. Hirsch, *Proc. Roy. Soc., London*, **A267** 11 (1962).
6. H. Hu, *Trans. Metallurgical Soc., AIME*, **224**, 75 (1962).
7. R. Weil and R. Paquin, *This Journal*, **107**, 87 (1960).
8. R. Weil and H. C. Cook, *ibid.*, **109**, 295 (1962).
9. W. Bollmann, "Electron Microscopy, Proc. of Stockholm Conference, 1956," p. 316, Almqvist and Wiksell, Stockholm (1957).
10. J. E. Bailey, *Phil. Mag.*, **5**, 833 (1960).
11. K. M. Olsen, C. F. Larkin, and P. H. Schmitt, Jr., *Trans. ASM*, **53**, 349 (1961).
12. C. Steidel, C. Li, and C. W. Spencer, Paper presented at AIME Meeting, Dallas, February 1961.
13. H. Binder and H. Fischer, *Z. Metallkunde*, **53**, 161 (1962).
14. R. Weil and H. Tsourmas, *Plating*, **49**, 624 (1962).

Phase Equilibria and Manganese-Activated Luminescence in the Systems $\text{CdO-P}_2\text{O}_5$ and $\text{Zn}_2\text{P}_2\text{O}_7\text{-Cd}_2\text{P}_2\text{O}_7$; Summary for the System $\text{ZnO-CdO-P}_2\text{O}_5$

Jesse J. Brown and F. A. Hummel

Department of Ceramic Technology, The Pennsylvania State University, University Park, Pennsylvania

ABSTRACT

The equilibrium relationships in the system $\text{Zn}_2\text{P}_2\text{O}_7\text{-Cd}_2\text{P}_2\text{O}_7$ and a portion of the system $\text{CdO-P}_2\text{O}_5$ were constructed from quench, D.T.A., and high-temperature x-ray data. The compatibility and solid solution relationships in the system $\text{ZnO-CdO-P}_2\text{O}_5$ are summarized. The pyrophosphate join is a simple eutectic-type binary system with a maximum of 28 mole % $\text{Cd}_2\text{P}_2\text{O}_7$ soluble in $\beta\text{-Zn}_2\text{P}_2\text{O}_7$ and 34 mole % $\text{Zn}_2\text{P}_2\text{O}_7$ soluble in $\text{Cd}_2\text{P}_2\text{O}_7$ at 947°C. Beta zinc pyrophosphate is stabilized to room temperature by the addition of a minimum of 7 mole % $\text{Cd}_2\text{P}_2\text{O}_7$ in solid solution. In addition to the meta-, pyro-, and orthophosphate, a fourth stable cadmium phosphate compound, $\text{Cd}_4\text{P}_2\text{O}_9$, was found to exist. Cathodoluminescence emission data are presented for the pyrophosphate solid solutions and for $\text{Cd}_4\text{P}_2\text{O}_9$ using molar substitutions of divalent manganese as an activator. The stabilized $\beta\text{-Zn}_2\text{P}_2\text{O}_7$ solid solution phosphors emit in the range 6620-6420Å with low brightness values and the $\text{Cd}_2\text{P}_2\text{O}_7$ solid solution phosphors emit near 6200Å with considerably higher brightnesses. Tetracadmium phosphate was only weakly responsive to cathode ray excitation.

In two previous papers (1,2) the phase relationships and cathodoluminescence of manganese-activated compounds and solid solutions in the zinc-cadmium orthophosphate and metaphosphate binary joins were reported. This concluding paper, in addition to reporting the equilibrium relationships and cathodoluminescence data for manganese-activated phases on the pyrophosphate join, is intended to present a comprehensive summary of the solid solution phases in the $\text{ZnO-CdO-P}_2\text{O}_5$

ternary system. Special attention is given to those phases that were found to be phosphor host lattices.

The equilibrium relationships in the $\text{ZnO-P}_2\text{O}_5$ system were determined by Katnack and Hummel (3), and the existence of high- and low-temperature modifications of the ortho-, pyro-, and metaphosphate compounds was established. In a related paper Hummel and Katnack (4) presented cathodoluminescence emission data for the manganese-activated zinc phosphate polymorphs.

Table 1. Compositions, heat treatments, and phase analyses used to construct the phase diagram for the system Zn₂P₂O₇-Cd₂P₂O₇. Also tabulated are the refractive indices of glasses and d-values for selected reflections of the solid solution phases

No	Zn ₂ P ₂ O ₇	Mole % Cd ₂ P ₂ O ₇	Temp/time, °C	Phases	Remarks**
1	100	0	1125/20 min 800/48 hr	G α-Z ₂ P*	n _D = 1.615
2	97	3	800/48 hr 75/15 min† 68/15 min† 60/15 min†	α-Z ₂ P _{ss} * β-Z ₂ P _{ss} α-Z ₂ P _{ss} + β-Z ₂ P _{ss} α-Z ₂ P _{ss}	
3	93	7	800/48 hr	β-Z ₂ P _{ss}	
4	90	10	1004/15 min 994/15 min 981/15 min 800/48 hr	G G + β-Z ₂ P _{ss} β-Z ₂ P _{ss} β-Z ₂ P _{ss}	d = 1.696Å
5	80	20	1125/20 min 974/15 min 965/15 min 961/15 min 800/48 hr	G G G _{tr} + β-Z ₂ P _{ss} G _{tr} + β-Z ₂ P _{ss} β-Z ₂ P _{ss}	n _D = 1.633 d = 1.703Å
6	70	30	968/15 min 957/15 min 947/15 min 800/48 hr	G G (28.0) + C ₂ P _{ss} β-Z ₂ P _{ss} + C ₂ P _{ss} β-Z ₂ P _{ss} + C ₂ P _{ss}	d = 1.709Å
7	60	40	1125/20 min 800/48 hr	G β-Z ₂ P _{ss} (28.0) + C ₂ P _{ss} (71.0)	n _D = 1.650
8	50	50	982/15 min 964/15 min 940/48 hr 800/48 hr 650/48 hr	G (37.5) + C ₂ P _{ss} G _{tr} + C ₂ P _{ss} (73.0) β-Z ₂ P _{ss} (28.0) + C ₂ P _{ss} (66.0) β-Z ₂ P _{ss} (28.0) + C ₂ P _{ss} (71.0) β-Z ₂ P _{ss} (28.0) + C ₂ P _{ss} (75.0)	
9	40	60	1125/20 min 1010/15 min 800/48 hr	G G (51.0) + C ₂ P _{ss} β-Z ₂ P _{ss} (28.0) + C ₂ P _{ss} (71.0)	n _D = 1.666
10	30	70	1040/15 min 1000/15 min 800/48 hr	G (65.0) + C ₂ P _{ss} G + C ₂ P _{ss} (79.0) C ₂ P _{ss}	d = 1.817Å
11	20	80	1125/20 min 1079/30 min 1051/30 min 800/48 hr	G G (78.0) + C ₂ P _{ss} G + C ₂ P _{ss} (89.0) C ₂ P _{ss}	n _D = 1.680 d = 1.828Å
12	10	90	800/48 hr	C ₂ P _{ss}	d = 1.841Å
13	0	100	1127/30 min 1116/30 min 800/48 hr	G C ₂ P C ₂ P	n _D = 1.692 d = 1.856Å

† These data were obtained by use of a high-temperature furnace mounted on an x-ray diffractometer unit.

** The data tabulated in this column were used to construct Fig. 2.

* The stable phase at the indicated temperature is β-Z₂P (or β-Z₂P_{ss}) which reverts rapidly to α-Z₂P (or α-Z₂P_{ss}) upon quenching.

Ropp and Mooney (5) investigated the dehydration behavior of numerous cadmium phosphate and cadmium ammonium phosphate compounds. Ropp, Mooney, and Hoffman (6) presented x-ray powder data for ten cadmium ortho- and pyrophosphates. Ropp (7) described the effects of preparation on the fluorescence excitation and emission spectra of manganese-activated cadmium ortho- and pyrophosphates.

Experimental Procedure

The raw materials and experimental techniques used were the same as those described previously (1). The compositions listed in Tables I, II, III, and IV were used to determine respectively the

equilibrium relationships in the Zn₂P₂O₇-Cd₂P₂O₇ and CdO-P₂O₅ binary systems, the solid solubility in the ZnO-CdO system, and the compatibility relationships in the ZnO-CdO-P₂O₅ ternary system.

X-ray diffraction data were obtained using CuK_α radiation (λ = 1.5418Å) from a Norelco diffractometer operating at 40 kv and 15 ma. Precise lattice spacings were obtained using silicon powder (a₀ = 5.4305Å) as an internal standard and a diffractometer scanning rate of ¼° - 2θ/min. High temperature x-ray diffraction data were obtained using a platinum wound furnace similar to that manufactured by Tem-Pres, Inc. Temperature was controlled automatically with a West instrument. Petro-

Table II. Quench and D.T.A. data used to construct the phase equilibrium diagram for the system CdO-P₂O₅

No.	Mole %		Temp, °C	Time	Phases
	CdO	P ₂ O ₅			
1	90	10	850	48 hr	CdO + C ₄ P
			1000-1200	—	dissociates (D.T.A.)
2	85	15	850	48 hr	CdO + C ₄ P
			1000-1200	—	dissociates (D.T.A.)
3	80	20	850	48 hr	C ₄ P
			1000-1200	—	dissociates (D.T.A.)
4	77.5	22.5	850	48 hr	C ₃ P + C ₄ P
			—	—	solidus (D.T.A.)
6	70	30	1068	10 min	C ₃ P + C ₂ P
			1080	10 min	C ₂ P + G
			1090	10 min	C ₂ P + G
			1107	10 min	G
			1151	—	—
8	60	40	988	10 min	C ₂ P + G
			1027	10 min	C ₂ P + G
			1054	10 min	C ₂ P + G
			1070	5 min	G
			854	20 min	β-CP + C ₂ P
			860	20 min	β-CP + C ₂ P
9	55	45	868	20 min	C ₂ P + G
			871	20 min	C ₂ P + G
			908	15 min	C ₂ P + G
			932	15 min	C ₂ P + G
			942	15 min	C ₂ P + G
			952	15 min	G
			—	—	—

Table III. Lattice Parameters for ZnO and CdO

Composition, mole %		Axial parameters (Å)			
ZnO	CdO	a	c	a	c
		1000°C		800°C	
100	0	3.249	5.205	3.249	5.205
97	3	3.261	5.217	—	—
94	6	3.262	5.222	—	—
90	10	3.262	5.219	3.252	5.206
80	20	3.262	5.220	3.252	5.206
0	100	4.695	—	4.695	—
3	97	4.687	—	—	—
6	94	4.687	—	—	—
10	90	4.687	—	4.690	—
20	80	4.687	—	4.690	—

Table IV. Compositions, heat-treatments, and phase analysis of ZnO-CdO-P₂O₅ mixtures

Sample No	ZnO	Mole % CdO	P ₂ O ₅	Temp, °C	Time, hr	Phases
1	35.25	35.25	29.50	800	48	B _{ss} + β-Z ₂ P _{ss} + C ₂ P _{ss}
2	24.00	48.00	28.00	800	48	C _{ss} + C ₂ P _{ss}
3	48.00	24.00	28.00	800	48	B _{ss} + β-Z ₂ P _{ss}
4	27.25	54.50	18.25	800	48	ZnO + C ₃ P
5	54.50	27.25	18.25	800	48	ZnO + C _{ss}
6	25.00	60.00	15.00	800	48	ZnO + C ₄ P
7	42.85	42.85	14.30	800	48	ZnO + C ₃ P
8	20.00	70.00	10.00	800	48	ZnO + CdO + C ₄ P

graphic microscope determinations of refractive indices of glasses were accurate to ±0.003 using immersion oils which had been calibrated with an Abbé refractometer. Cathodoluminescence spectral distributions were determined on a demountable television tube using an electron beam with a current density of 1.0 μa/cm² and an accelerating potential of 15 kv. Brightnesses under these conditions were measured with an eye-corrected foot-lambert meter.

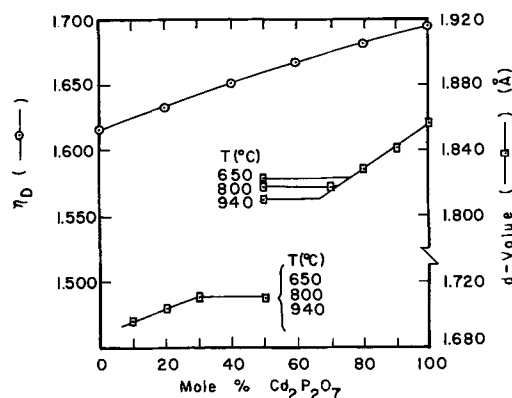


Fig. 1. Refractive indexes of pyrophosphate glasses and d-values of selected reflections of the β-Zn₂P₂O₇ and Cd₂P₂O₇ solid solutions.

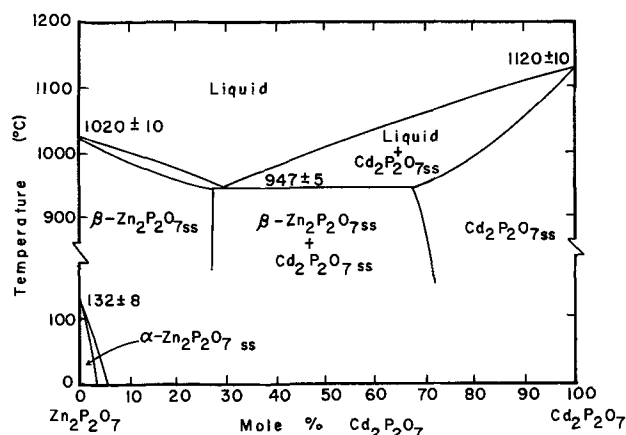
Results and Discussion

Phase relationships in the Zn₂P₂O₇-Cd₂P₂O₇ system.—The refractive index plot for the pyrophosphate glasses is shown by the top curve in Fig. 1. This curve was used to determine the composition of the glass phase in those quench samples that consisted of glass + crystal phase assemblages. Similarly the composition of the crystalline phase (s) in glass + crystal or crystal + crystal phase assemblages were determined from the two d-value curves¹ shown in Fig. 1. As an example of this procedure consider the 50Zn₂P₂O₇-50Cd₂P₂O₇ composition quenched from 940°, 800°, and 650°C. The equilibrium phase assemblages were found to be β-Zn₂P₂O_{7 ss} + Cd₂P₂O_{7 ss}. In all 3 quenches the d-spacing for the β-Zn₂P₂O_{7 ss} phase was 1.709Å indicating that the β-Zn₂P₂O_{7 ss} to β-Zn₂P₂O_{7 ss} + Cd₂P₂O_{7 ss} phase boundary was isoplethal (within experimental accuracy) between 940° and 650°C. From the lower left curve in Fig. 1 the composition of this phase boundary was determined to be 28±2 mole % Cd₂P₂O₇. On the other hand the d-spacing for the Cd₂P₂O_{7 ss} phase was found to change from 1.810Å at 940°C to 1.822Å at 650°C. From the lower right curve in Fig. 1 it can be seen that these measurements indicate a decrease in the solubility of Zn₂P₂O₇ in Cd₂P₂O₇ from 34 mole % Zn₂P₂O₇ at 940°C to 25 mole % at 650°C.

A complete tabulation of the data used to construct the phase relationships in the Zn₂P₂O₇-Cd₂P₂O₇ system is shown in Table I. The values in parenthesis indicate compositions in mole % Cd₂P₂O₇. Solid-state reactions in this system were found to be essentially completed in 24-48 hr; however, those reactions involving a liquid phase were greatly accelerated and, for all practical purposes, attained equilibrium in 15-30 min.

The Zn₂P₂O₇-Cd₂P₂O₇ phase equilibrium diagram (Fig. 2) is a simple eutectic-type (eutectic at 947°C) system with end members Zn₂P₂O₇ and Cd₂P₂O₇ melting congruently at 1020° and 1120°C, respectively. The temperature of the rapid reversible Zn₂P₂O₇ transformation, previously established at 132°C (3), was found by high-temperature x-ray

¹The d-values used correspond to the 54.0°-2θ reflection of β-Zn₂P₂O₇ and the 49.0°-2θ reflection of Cd₂P₂O₇ (CuKα radiation). Higher angle reflections could not be obtained due to the low symmetry (probably monoclinic or triclinic) of these structures.

Fig. 2. Phase equilibrium diagram for the system Zn₂P₂O₇-Cd₂P₂O₇

experiments to decrease with the addition of Cd₂P₂O₇. A minimum of 7 mole % Cd₂P₂O₇ in solid solution was sufficient to stabilize the high (β) Zn₂P₂O₇ structure to room temperature.

Table V lists the powder x-ray diffraction data for the α-Zn₂P₂O₇, β-Zn₂P₂O₇, and Cd₂P₂O₇ structures.

Phase relationships in the CdO-Cd(PO₃)₂ System.

—Four stable cadmium phosphate compounds were found to exist: Cd(PO₃)₂, Cd₂P₂O₇, Cd₃(PO₄)₂, and

Table V. X-ray diffraction data of Cd₄P₂O₉ and of phases in the zinc-cadmium pyrophosphate system

α-Zn ₂ P ₂ O ₇ d I/I ₀	β-Zn ₂ P ₂ O ₇ ss (Zn _{10,80} , Cd _{0,20}) ₂ P ₂ O ₇ d I/I ₀	Cd ₂ P ₂ O ₇ ss (Zn _{0,20} , Cd _{0,80}) ₂ P ₂ O ₇ d I/I ₀	Cd ₂ P ₂ O ₇ d I/I ₀	Cd ₄ P ₂ O ₉ d I/I ₀					
4.37	15	4.38	25	4.35	5	4.37	10	5.04	25
4.17	15			4.15	35	4.20	35	4.37	25
				3.92	10	3.99	10	4.06	10
3.75	5	3.71	5					3.72	10
3.60	5	3.29	—	3.31	20	3.36	25	3.66	10
				3.23	35	3.28	15	3.43	15
3.09	5	3.21	5	3.20	30	3.26	25	3.38	10
3.03	60			3.09	50	3.13	20	3.31	10
						3.13	60	3.16	10
3.01	100	3.04	100	3.05	100	3.09	100	3.12	25
2.87	5	2.97	70	2.97	20	2.96	20	3.08	25
2.85	10			2.92	70	2.95	60	3.04	90
2.81	—			2.81	65	2.84	60	2.97	100
2.72	5			2.74	5	2.80	5	2.84	55
2.59	—			2.72	10			2.81	75
				2.63	—	2.66	10	2.78	55
2.54	45	2.56	35	2.59	15	2.61	15	2.76	35
2.48	—			2.47	10	2.49	5	2.72	40
2.36	—			2.41	10	2.39	20	2.67	30
2.30	10	2.23	5	2.32	20	2.32	20	2.53	10
2.19	5			2.27	20	2.29	10	2.50	20
2.11	20	2.13	10	2.15	15	2.17	15	2.49	15
2.09	45							2.46	30
other re- flections	other re- flections	other re- flections	other re- flections					2.40	—
								2.36	—
								2.30	10
								2.28	10
								2.25	10
								2.18	10
								2.12	15
								2.00	—
								1.961	15
								1.918	15
								1.892	15
								other re- flections	

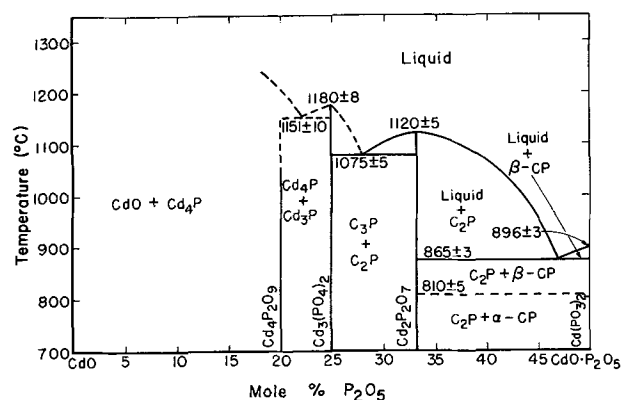
Cd₄P₂O₉. The cadmium meta-, pyro-, and orthophosphate compounds are well-known and have been characterized previously. A search of the literature did not reveal any reference to a 4CdO·P₂O₅ compound.

By comparing the x-ray powder diffraction pattern of Cd₄P₂O₉ with that of Ca₄P₂O₉ it was found that these two structures appear to be isostructural. A D.T.A. of Cd₄P₂O₉ did not show any heat effects up to 1300°C; however, a marked drift in the background was observed at 1000°C and above. X-ray diffraction examination of the sample after the D.T.A. run indicated a predominance of Cd₃(PO₄)₂ with a trace of CdO and no Cd₄P₂O₉. Based on these strictly qualitative data, it was concluded that Cd₄P₂O₉ is stable in air up to 1000°C above which temperature it dissociates to CdO (vapor) + Cd₃(PO₄)₂ (solid). It should be noted that none of the other cadmium phosphate compounds indicated any decomposition or vaporization tendencies up to their melting points. However, since chemical analyses were not obtained for these samples, slight vaporization could have occurred without being detected.

The CdO-P₂O₅ equilibrium relationships shown in Fig. 3 were constructed from the D.T.A. and quench data listed in Table II and the previously established melting points and inversion temperature of the cadmium phosphate compounds. Compositions on the CdO side of 70 CdO:30 P₂O₅ ratio were nonglass forming. The solidus and liquidus boundaries in this region are shown by dashed lines due to the poorer accuracy obtainable, relative to that which can be expected and obtained for glass forming regions.

Simple eutectic relations exist between the various cadmium phosphate compounds. It was impossible to examine the equilibrium relationships on the P₂O₅ side of Cd(PO₃)₂ due to excessive vaporization of P₂O₅.

The ZnO-CdO system.—The ZnO-CdO system was explored to ascertain the existence of stable binary compounds and to determine the extent of solid solubility. Although no compounds were found, small regions of solid solubility of Cd²⁺ in ZnO and Zn²⁺ in CdO were detected. These solid solution compositions were examined in detail at 800° and

Fig. 3. Phase equilibrium diagram for a portion of the system CdO-P₂O₅.

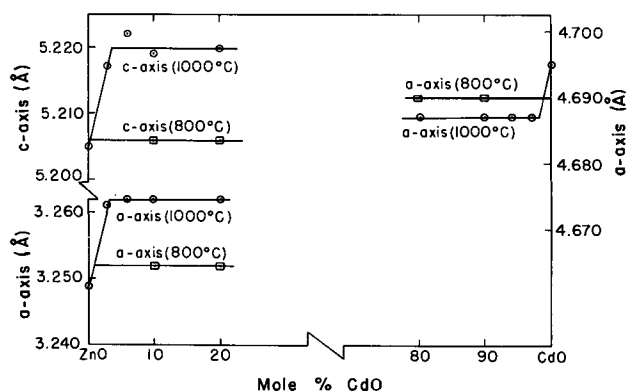


Fig. 4. Plot of axial parameters showing ZnO and CdO inter-solubility at 800° and 1000°C.

1000°C using high angle x-ray diffraction techniques with silicon powder as an internal standard. The reflection used for cubic CdO ($a_0 = 4.6953\text{Å}$) were:

$$[511], d = 0.9036\text{Å}$$

and for hexagonal ZnO ($a_0 = 3.249$ and $c_0 = 5.205\text{Å}$)

$$[213], d = 0.9069\text{Å}$$

$$\text{and } [302], d = 0.8826\text{Å}.$$

The axial parameters were calculated by employing the appropriate crystallographic equations for cubic and hexagonal symmetry. The experimental results shown in Table III and Fig. 4 indicate a solid solubility of less than 1 mole % CdO in ZnO at 800°C and 3 mole % at 1000°C. On the other hand, approximately 1 mole % ZnO is soluble in CdO at 800°C and 2 mole % at 1000°C.

Luminescence

The compositions shown in Table VI were activated with 1.0 mole % divalent manganese (substituted for either Zn^{2+} or Cd^{2+}) and heat treated at 850°C for 48 hr.

These results show that the $\beta\text{-Zn}_2\text{P}_2\text{O}_7$ solid solution phosphors have better "redness" but poorer brightness than the N.B.S. red $\beta\text{-Zn}_3(\text{PO}_4)_2\text{:Mn}$ phosphor. Substitution of Cd^{2+} for Zn^{2+} in this structure shifts the emission peak from 6620 to 6420Å and increases the brightness from 6.1 to 10.8 ft-L.

Table VI. Compositions, heat-treatments, phase analyses, and manganese-activated cathodoluminescence emission data for compounds and solid solutions in the $\text{Zn}_2\text{P}_2\text{O}_7\text{-Cd}_2\text{P}_2\text{O}_7$ system and for $\text{Cd}_4\text{P}_2\text{O}_9$

No.	Composition, mole % $\text{Zn}_2\text{P}_2\text{O}_7$ $\text{Cd}_2\text{P}_2\text{O}_7$	Temp/time, °C/hr	Phases	Peak wave-length, Å	Brightness, ft-L
1	100 0	850/48	$\alpha\text{-Z}_2\text{P}$	6850	7.1
2	90 10	850/48	$\beta\text{-Z}_2\text{P}_{\text{SS}}$	6620	6.1
3	80 20	850/48	$\beta\text{-Z}_2\text{P}_{\text{SS}}$	6520	7.4
4	70 30	850/48	$\beta\text{-Z}_2\text{P}_{\text{SS}}$	6420	10.8
5	30 70	850/48	$\text{C}_2\text{P}_{\text{SS}}$	6210	28.8
6	20 80	850/48	$\text{C}_2\text{P}_{\text{SS}}$	6230	27.6
7	10 90	850/48	$\text{C}_2\text{P}_{\text{SS}}$	6200	34.5
8	0 100	850/48	C_2P	6190	33.6
9	$\text{Cd}_4\text{P}_2\text{O}_9$	850/48	$\text{Cd}_4\text{P}_2\text{O}_9$	—	2.4
	NBS (red)	—	$\beta\text{-Z}_3\text{P}$	6380	21.0

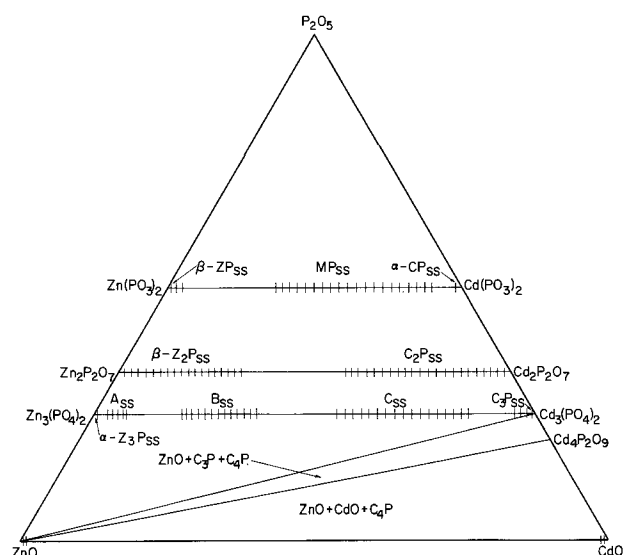


Fig. 5. Subsolidus solid solution and compatibility relationships in the ZnO-CdO- P_2O_5 ternary system ($800 \pm 25^\circ\text{C}$ isothermal plane).

As Cd^{2+} is substituted for Zn^{2+} in the $\text{Cd}_2\text{P}_2\text{O}_7$ solid solution series, the emission peak changes from 6210 to 6190Å and the brightness increases from approximately 28 to 34 ft-L.

It was shown by Ropp (7) that $\text{Cd}_2\text{P}_2\text{O}_7\text{:Mn}$ fired in air was weakly responsive to 2537Å ultraviolet radiation with an emission peak at 6180Å. It is noteworthy that this emission peak is not appreciably changed when the excitant is cathode rays; however, cathode radiation appears to produce a marked increase in the brightness of the phosphor.

Manganese-activated $\text{Cd}_4\text{P}_2\text{O}_9$ is an extremely weak red-emitting cathode ray phosphor.

Summary for the System ZnO-CdO- P_2O_5

The compatibility relationships and solid solution regions in the $800^\circ \pm 25^\circ\text{C}$ isothermal plane in the ternary system ZnO-CdO- P_2O_5 are shown in Fig. 5. These relationships were determined using data contained in this investigation and those in ref. (1-4). Supplementary data are provided in Table IV to establish compatibility relationships which were not previously determined. The region of the system above the metaphosphate join was not investigated because of excessive loss of P_2O_5 in air. Glasses can be easily formed in this system from all compositions which contain more than about 30 mole % P_2O_5 .

The cathodoluminescence emission properties of the manganese-activated phosphors prepared in the ZnO-CdO- P_2O_5 system are summarized in Table VII. It has been noted throughout this investigation that the emission characteristics of these phosphors are dependent on method of preparation, heat-treatment, and activator concentration.

With the increasing interest in crystal structure analyses, it can be anticipated that eventually it will be possible to correlate these emission data, at least qualitatively, with the lattice environment associated with the activator ion. Calvo has started a significant trend in this direction by examining the crystal structures of $\alpha\text{-}$ and $\beta\text{-Zn}_3(\text{PO}_4)_2$ (9)

Table VII. Cathodoluminescent emission data for phosphors in the system ZnO-CdO-P₂O₅

Host lattice	Composition	Activator, mole % Mn ²⁺	Heat-treatment, °C/hr	Emission peak, Å	Brightness, ft-L	Remarks
	metaphosphates					
α-ZP	α-Zn(PO ₃) ₂	1.0	600/96	6240	12.9	
β-ZP	β-Zn(PO ₃) ₂	1.0	750/24	5880 and 6300	19.1	two emission peaks
MP _{ss}	(Zn _{0.65-0.10} , Cd _{0.35-0.90})(PO ₃) ₂	1.0	750/24	5820-5660 and 6290-6410	27.6-12.1	two emission peaks
α-CP	α-Cd(PO ₃) ₂	1.0	800/24	5580	46.1	
β-CP	β-Cd(PO ₃) ₂	1.0	835/10	5850	16.1	
	pyrophosphates					
α-Z ₂ P	α-Zn ₂ P ₂ O ₇	1.0	850/48	6850	7.1	
β-Z ₂ P _{ss}	β-(Zn _{1.00-0.75} , Cd _{0-0.25}) ₂ P ₂ O ₇	1.0	850/48	6620-6420	6.1-10.8	pure β-Zn ₂ P ₂ O ₇ :Mn was not examined
C ₂ P _{ss}	(Zn _{0.30-0} , Cd _{0.70-1.00}) ₂ P ₂ O ₇	1.0	850/48	6200	30.0	
	orthophosphates					
α-Z ₃ P	α-Zn ₃ (PO ₄) ₂	1.1	805/5	5510	8.7	data obtained from reference (4)
β-Z ₃ P _{ss}	β-(Zn _{1.00-0.85} , Cd _{0-0.15}) ₃ (PO ₄) ₂	1.0	950/48	6370-6340	23.6-20.2	
A _{ss}	(Zn _{0.98-0.93} , Cd _{0.02-0.07}) ₃ (PO ₄) ₂	1.0	800/48	6300	20.2	only one phosphor was prepared in this region
B _{ss}	(Zn _{0.80-0.63} , Cd _{0.20-0.37}) ₃ (PO ₄) ₂	1.0	850/48	6150-6340	25.0	
C _{ss}	(Zn _{0.44-0.20} , Cd _{0.56-0.80}) ₃ (PO ₄) ₂	1.0	850/48	6540-6510	13.5	
C ₃ P _{ss}	(Zn _{0.06-0} , Cd _{0.94-1.00}) ₃ (PO ₄) ₂	1.0	950/48	6110	26.0	
C ₄ P	Cd ₄ P ₂ O ₉	1.0	850/48	6000	2.4	
N.B.S.	zinc orthophosphate:Mn			6380	21.0	

and "γ-Zn₃(PO₄)₂" (10). His conclusions on the coordination of Zn²⁺ (and Mn²⁺) in these structures have strengthened the postulate of Linwood and Weyl (11) that green emission can be attributed to Mn²⁺ in tetrahedral coordination and red emission to Mn²⁺ in octahedral coordination. However, with the exception of these three structures, none of the other zinc-cadmium phosphate compounds or solid solution crystal structures appear to have been analyzed.

Acknowledgment

Emission data were obtained through cooperation of Marjorie Brines of the Chemical Products Plant, General Electric Company, Cleveland, Ohio. This investigation was made possible through the financial assistance of the International Lead Zinc Research Organization.

Manuscript received Jan. 9, 1964; revised manuscript received April 10, 1964. This is Contribution No. 63-61 from the College of Mineral Industries, The Pennsylvania State University, University Park, Pennsylvania.

Any discussion of this paper will appear in a Discussion Section to be published in the June 1965 JOURNAL.

REFERENCES

1. J. J. Brown and F. A. Hummel, *This Journal*, **110**, 128 (1963).
2. J. J. Brown and F. A. Hummel, *ibid.*, **111**, 660 (1964).

3. F. L. Katnack and F. A. Hummel, *ibid.*, **105**, 24 (1958).
4. F. A. Hummel and F. L. Katnack, *ibid.*, **105**, 528 (1958).
5. R. C. Ropp and R. W. Mooney, *J. Am. Chem. Soc.*, **82**, 4848 (1960).
6. R. C. Ropp, R. W. Mooney, and C. W. W. Hoffman, *Anal. Chem.*, **33**, 1687 (1961).
7. R. C. Ropp, *This Journal*, **109**, 569 (1962).
8. ASTM Data Files, Card No. 11-1232, American Society for Testing Materials, Philadelphia, Pa.
9. C. Calvo, Private communication.
10. C. Calvo, *J. Phys. Chem. Solids*, **24**, 141 (1963).
11. S. H. Linwood and W. A. Weyl, *J. Opt. Soc. Amer.*, **32**, 443 (1942).

SYMBOLS

G,	glass
α-CP,	α-Cd(PO ₃) ₂
β-CP,	β-Cd(PO ₃) ₂
C ₂ P,	Cd ₂ P ₂ O ₇
C ₃ P,	Cd ₃ (PO ₄) ₂
C ₄ P,	Cd ₄ P ₂ O ₉
α-ZP,	α-Zn(PO ₃) ₂
β-ZP,	β-Zn(PO ₃) ₂
α-Z ₂ P,	α-Zn ₂ P ₂ O ₇
β-Z ₂ P,	β-Zn ₂ P ₂ O ₇
α-Z ₃ P,	α-Zn ₃ (PO ₄) ₂
β-Z ₃ P,	β-Zn ₃ (PO ₄) ₂
MP,	(Zn _{0.65-0.10} , Cd _{0.35-0.90})(PO ₃) ₂
A,	(Zn _{0.98-0.93} , Cd _{0.02-0.07}) ₃ (PO ₄) ₂
B,	(Zn _{0.80-0.63} , Cd _{0.20-0.37}) ₃ (PO ₄) ₂
C,	(Zn _{0.44-0.20} , Cd _{0.56-0.80}) ₃ (PO ₄) ₂
ss,	solid solution
tr,	trace

Semiconducting Behavior of Substituted Tungsten Diselenide and Its Analogues

W. T. Hicks

*Pigments Department, Experimental Station,
E. I. du Pont de Nemours & Company, Incorporated, Wilmington, Delaware*

ABSTRACT

Tantalum substitutions up to 5 atomic per cent (a/o) of the cations have been made in the three Group VIB dichalcogenides, WSe_2 , $MoSe_2$, and $MoTe_2$. Tantalum-substituted p-type WSe_2 had the best thermoelectric properties with a figure of merit about $0.5 \times 10^{-3} \text{ deg}^{-1}$ from 500°-1000°C. Substitution of a number of other elements was attempted in the compounds WSe_2 and $MoSe_2$, but only the Group VB metals were sufficiently soluble to give p-type materials with electrical conductivities at useful levels. Hall coefficient measurements were made on all three of the above-mentioned compounds, and WSe_2 was shown to have the highest carrier mobility ($100 \text{ cm}^2/\text{v-sec}$); this explains its superior thermoelectric properties. An excellent correlation is shown between Seebeck coefficient measurements and Hall coefficient measurements for the family of compositions $W_{1-x}Ta_xSe_2$ in the range $x = 0$ to $x = 0.05$ for an effective mass ratio of 1.0 with the assumption of an ionic lattice scattering mechanism.

Brixner (1) has shown that when 1-3% of the metal in WSe_2 is substituted with tantalum or niobium, p-type materials with useful thermoelectric properties are obtained. Recent measurements of the electrical properties of the particular composition $W_{0.99}Ta_{0.01}Se_2$ up to 1000°C indicate a figure of merit of approximately $0.5 \times 10^{-3} \text{ deg}^{-1}$ from 500°-1000°C, which is comparable to p-type germanium-silicon alloys in this temperature range (2).

In the present study, the substitution of tantalum was also made in the analogous Group VIB compounds, $MoSe_2$ and $MoTe_2$. Tungsten ditelluride has considerably different electrical properties and crystal structure from the other compounds and is not considered here. In addition, the substitution of a number of other elements was attempted in these compounds.

This investigation showed that the original system studied by Brixner, tantalum-substituted WSe_2 , has the best thermoelectric properties of these Group VIB dichalcogenides. Therefore, measurements of Hall coefficient as a function of temperature were undertaken to elucidate the conductivity mechanism of this compound.

Experimental Procedure

Preparation of samples.—High-purity tungsten powder having a particle size of 2-5 μ was obtained from the Wah Chang Corporation and used for preparation of most of the samples described here. According to their analysis, iron was the most serious metallic impurity, at a concentration of 30 ppm. The oxygen level was 230 ppm. The tantalum used in these experiments was a high-purity (99.5+%) powder from Fansteel Metallurgical Corporation. The molybdenum was a 325 mesh powder purchased from Fansteel Corporation and had a purity of about 99.9%. The selenium and tellurium were from the American Smelting and Refining Company and had a purity of 99.999+%.

Appropriate amounts of the elements were weighed accurately into a quartz tube which was then evacuated and sealed. Initial reaction was carried out at 550°C for a period of about 15 hr. A loose powder product resulted, having a considerably greater volume than the reacting elements, and this was well mixed by shaking the sealed tube on a mechanical vibrator for about 30 min. Subsequently, a final reaction was carried out at temperatures above 1000°C in the same sealed tube. A lustrous powder resulted which was pressed into $\frac{1}{4} \times \frac{1}{4} \times 2$ in. bars at room temperature with a pressure of 40 tsi (yielding samples having 92-93% of theoretical density) for the electrical measurements.

Measurements of these pressed powder bars were necessary since these compounds do not melt at temperatures below 1400°C and probably decompose before melting at atmospheric pressure. Tungsten diselenide decomposes to give an appreciable selenium pressure ($40\mu \text{ Hg}$) at 1000°C (3).

Electrical measurements.—The Seebeck coefficients and resistivities were measured with conventional d-c equipment with a small temperature gradient imposed on the sample (25° at 600°C). The thermocouples were closely fitted into holes in the sample $\frac{1}{8}$ in. deep and 3 cm apart. Considerable trouble arose from thermocouple-sample reactions; this was finally solved at temperatures of 600°C and below by using sheathed Megapak chromel-alumel thermocouples. Seebeck coefficient values measured at 600°C with these thermocouples, wire chromel-alumel thermocouples, and wire platinum *vs.* platinum-10% rhodium thermocouples, gave good agreement when new thermocouples were used in the latter two cases for each measurement.

Hall effect measurements.—Conventional d-c equipment was used to measure Hall coefficients on samples of dimensions $\frac{1}{4}$ in. wide x 1 in. long x $\frac{1}{16}$ to $\frac{1}{8}$ in. thick, cut from the compacted bars

with a precision diamond saw. For the high-temperature measurements, a water-cooled, stainless steel furnace was built which incorporated a boron-nitride sample holder and platinum electrode contacts. Measurements were possible up to 600°C without severe reaction of the samples with the electrodes. With this 1 in. diameter furnace a magnetic field of 12,000 gauss was available from the d-c electromagnet. For the high-temperature measurements a grounded silver foil shield was used around the sample holder to prevent stray pickup from rectified signals coming from the a-c resistance heater.

Lattice parameter measurements.—X-ray diffraction patterns were made using the as-reacted powder in a Debye-Scherrer camera. In order to calculate accurate lattice parameters Cohen's least squares method for hexagonal crystal structures (4) was carried out on five resolved high-angle lines using an IBM 7070 Computer.

Anisotropy.—Due to the hexagonal platelike crystal structures of these compounds considerable orientation of the crystallites takes place during the compaction operation, and this results in a considerable degree of anisotropy with respect to direction of pressing in both the electrical and thermal conductivities. Brixner found that conductivities measured normal to the pressing direction had values approximately three times the values measured parallel to pressing direction. However, the Hall coefficient is virtually isotropic according to measurements on several pressed samples of $W_{1-x}Ta_xSe_2$. The Seebeck coefficient may be somewhat anisotropic; Brixner (1) reports a 30% higher value normal to the pressing direction than parallel to the pressing direction. He indicates, therefore, a higher figure of merit in this direction. As a result of these effects all electrical measurements described in this paper were made in the direction normal to the direction of pressing, which corresponds to the preferred direction of orientation for the a-axes of the crystals. In the Hall measurements presented here the magnetic field was aligned parallel to the direction of pressing, and the current and voltage measurements were made in directions mutually perpendicular to each other and to the direction of pressing. Thus the Hall mobility values are characteristic of the direction normal to pressing.

Results and Discussion

Comparison of WSe_2 , $MoSe_2$, and $MoTe_2$.—The Seebeck coefficient, α , resistivity, ρ , and α^2/ρ are summarized for doped and undoped compositions of the three compounds WSe_2 , $MoSe_2$, and $MoTe_2$ as measured at 100° and 600°C in Table I. The undoped compounds ($x = 0$) are characterized by low electrical conductivities even at temperatures as high as 600°C. The Seebeck coefficients of all three of the undoped compounds are high at 100°C but are somewhat lower at 600°C. Both $MoSe_2$ and $MoTe_2$ are n-type materials at 100°C, but $MoSe_2$ converts to p-type at 500°C. When all three compounds are substituted to the extent of 2% with tantalum, they remain p-type over the whole temperature range, 100°-600°C. Furthermore, they all show approxi-

Table I. Thermoelectric properties of WSe_2 , $MoSe_2$, and $MoTe_2$

Compound	x	100°C		600°C		$\frac{\alpha^2}{\rho}$, w/deg ² -cm · 10 ⁸
		α , μ v/deg	ρ , ohm-cm	α , μ v/deg	ρ , ohm-cm	
$W_{1-x}Ta_xSe_2$	0	+560	0.570	+527	0.780	0.04
	0.02	+104	0.003	+213	0.005	0.93
$Mo_{1-x}Ta_xSe_2$	0	-900	20.0	+190	1.0	0.004
	0.02	+112	0.009	+242	0.011	0.53
$Mo_{1-x}Ta_xTe_2$	0	-360	25.0	-104	0.1	0.01
	0.02	+108	0.04	+200	0.025	0.16

mately the same value of Seebeck coefficient at a given temperature indicating a common value of Fermi level. The resistivities, however, increase by a factor of approximately two as one proceeds from WSe_2 to $MoSe_2$ and from $MoSe_2$ to $MoTe_2$ at 600°C. As previously mentioned, none of these compositions has appreciable thermoelectric value at temperatures below 600°C. The thermal conductivities as measured by Brixner are of the same order for all three of these compounds, but are slightly higher for $MoSe_2$ and $MoTe_2$ (5). Therefore, it was concluded that tantalum-doped WSe_2 provided the best thermoelectric properties of the Group VIB dichalcogenides.

Cation Substitutions in WSe_2 and $MoSe_2$.—A number of attempts were made to substitute some of the metal in either WSe_2 or $MoSe_2$ with metals other than tantalum. In each case the solubility of these elements was established by determining the lattice parameters as a function of the doping concentration. These substitutions were attempted in the composition range $x = 0.01$ to $x = 0.05$ for the solution $A_{1-x}B_xSe_2$, where A is either tungsten or molybdenum and B is the doping metal. Figure 1 shows the lattice parameters as a function of x for the

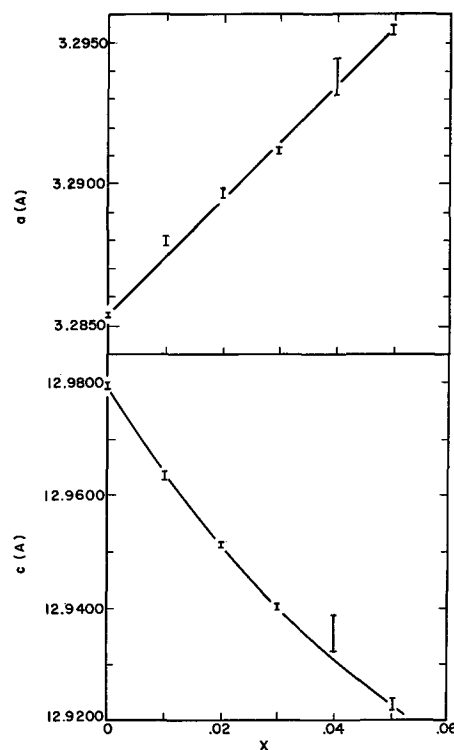


Fig. 1. Lattice parameters vs. x for $W_{1-x}Ta_xSe_2$

system $W_{1-x}Ta_xSe_2$. It is apparent from this figure that tantalum is soluble to a higher value of x than 0.05. Indeed, Brixner (1) has shown that the solubility limit lies at $x = 0.38$ where there is a crystal structure change. The most precise lattice parameters measured for the undoped material ($x = 0$) at 25°C are $a = 3.2860 \pm 0.0002\text{\AA}$ and $c = 12.978 \pm 0.001\text{\AA}$ for this hexagonal structure. The uncertainties given here are the 50% probability limits, i.e., standard deviation. These values are in good agreement with those given by Brixner: $a = 3.286\text{\AA}$ and $c = 12.976\text{\AA}$ (1).

Room temperature lattice parameters and resistivity measured at 600°C are shown as functions of x in Fig. 2 for the system $W_{1-x}Ti_xSe_2$. In this case the lattice parameters indicate the presence of a second phase at a composition above $x = 0.01$, which correlates with a constant resistivity above this composition. Thus, we may conclude that although titanium is very effective in increasing the electrical conductivity of WSe_2 , its solubility is less than $x = 0.01$, and therefore it is not capable of bringing the electrical conductivity of WSe_2 into a range of interest for thermoelectric applications.

A third example is shown for the case of $Mo_{1-x}Re_xSe_2$ by Fig. 3 where the lattice parameter a and the resistivity measured at 25°C are shown as functions of x . For this series the lattice parameter c of the hexagonal structure could not be determined with as great an accuracy as those shown for the WSe_2 series. For undoped $MoSe_2$ ($x = 0$), $a = 3.2898 \pm 0.0003\text{\AA}$ and $c = 12.921 \pm 0.001\text{\AA}$. Brixner (5) gives $a = 3.288\text{\AA}$ and $c = 12.900\text{\AA}$. It is apparent from Fig. 3 that the solubility limit for rhenium in $MoSe_2$ lies at a value of x between 0.02 and 0.03. Correspondingly, doping with rhenium at levels of x higher than 0.02 has little effect in increasing the electrical conductivity as shown in Fig. 3.

The results of attempts to make acceptor-type substitutions in p-type WSe_2 by substitutions with

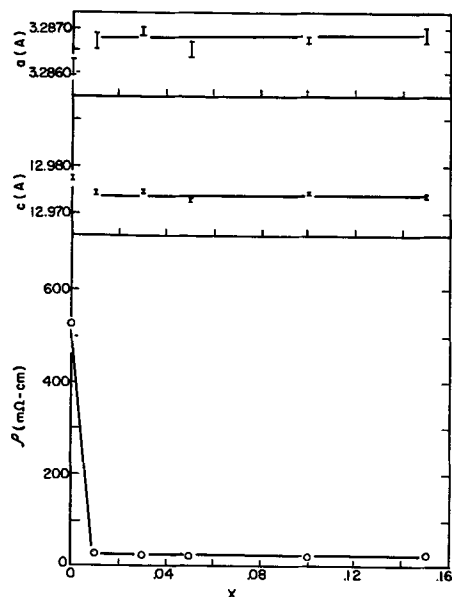


Fig. 2. Lattice parameters and resistivity (600°C) vs. x for $W_{1-x}Ti_xSe_2$.

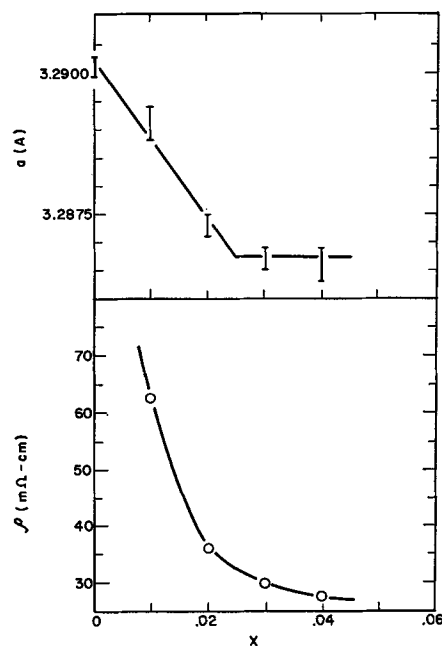


Fig. 3. Lattice parameters and resistivity (25°C) vs. x for $Mo_{1-x}Re_xSe_2$.

elements of Groups III, IVB, and VB, which have fewer electrons than Group VIB metals, are summarized in Table II. Here the minimum resistivity obtained when the doping elements were substituted up to a value of $x = 0.05$ and the solubility limits as determined from lattice parameter measurements are tabulated. It is seen that only Group VB metals are soluble to a sufficient extent to decrease the resistivities to desirable levels. Goldschmidt quadrivalent ionic radii are also tabulated in Table II to show any correlation existing between the size of the atom and its solubility. Zirconium and hafnium should be less soluble than titanium in WSe_2 and this is shown by the resistivity values in the table. However, similarity in chemical character seems to be more important than radii in determining solubility, as seen from the fact that the neighboring Group VB elements are the most soluble despite their size. For example, vanadium is more soluble in WSe_2 than titanium, even though there is a greater disparity between its radius and that of tungsten.

Table II. Acceptor substitutions in $W_{1-x}Me_xSe_2$

Me	ρ min, mohm-cm ^a	x at solubility limit	Goldschmidt quadrivalent ionic rad, Å
W	250-1000	—	0.68
V	4	>0.05	0.61
Nb	4	>0.05	0.67
Ta	4	>0.05	0.67
Ti	25	<0.01	0.64
Zr	410 ^b	not det.	0.87
Hf	720 ^b	not det.	0.87
Al	250 ^c	<0.01	<0.57

^a Minimum resistivity obtained when x was varied from 0 to 0.05 in measurements at 600°C.

^b Room temperature values from L. H. Brixner.

^c Room temperature value.

Table III. Donor substitutions in Mo_{1-x}Me_xSe₂

Me	ρ min, ohm-cm*	x at solubility limit	Goldschmidt quadrivalent ionic rad, Å
Mo	10-10 ⁴	—	0.68
Mn	0.6	<0.01	0.48
Re	0.03	0.02-0.03	0.59
Ru	1.6	<0.01	0.65
Pt	0.7	<0.01	0.63

* Minimum resistivity obtained when x was varied from 0 to 0.05 in measurements at 25°C.

A number of donor-type substitutions, *i.e.*, elements having more electrons than molybdenum, were attempted in n-type MoSe₂. These substitutions are summarized in Table III where again the lowest resistivity obtained with values of x ranging from 0.01 to 0.05 are tabulated with the solubility limit x determined from lattice parameter studies and the Goldschmidt quadrivalent ionic radius for each element. In this case of the two elements available in Group VIIIB, which is the next highest group from that of molybdenum, only rhenium had appreciable solubility, apparently because its ionic radius is closer to that of molybdenum than that of manganese. Unfortunately, although an n-type material of relatively high conductivity is obtained with rhenium as shown in Fig. 3, the resistivity is still rather high for thermoelectric applications. Since no additional rhenium can be dissolved, a maximum figure of merit of the order of only 10⁻⁴ deg⁻¹ is obtained from rhenium substitutions in MoSe₂ even at higher temperature. Brixner (1) attempted rhenium substitutions in WSe₂, but here the solubility was apparently even lower, and although an n-type material resulted over a part of the temperature range, the resistivity of this substituted material was even higher than that of undoped material. Ruthenium and platinum from Group VIII of the periodic table are less soluble than rhenium in MoSe₂ even though they have radii which are closer to molybdenum's than that of rhenium, apparently because they are too far removed from molybdenum in chemical nature.

Thus a general rule may be derived for solubility and hence effective doping in WSe₂ and MoSe₂. Not only must the doping element have an ionic radius close to that of the host metal, but also it must come from an adjacent group of the periodic table.

Anion substitutions.—An attempt was made to replace some of the selenium in MoSe₂ with iodine to make a donor-type substitution. However, for the most dilute solution attempted, MoSe_{1.98}I_{0.02}, considerable iodine vapor was observed in the quartz tube while it was still warm after the initial reaction at 600°C. Therefore it appeared that this composition would not be stable enough for the final reaction at 1000°C. A bar pressed from this incompletely reacted powder did show some increase in electrical conductivity, but it was not sufficient to be of thermoelectric interest.

An acceptor-type substitution was attempted by replacing selenium with antimony according to the formula WSe_{2(1-y)}Sb_{2y}. Although some increase in electrical conductivity was observed, lattice param-

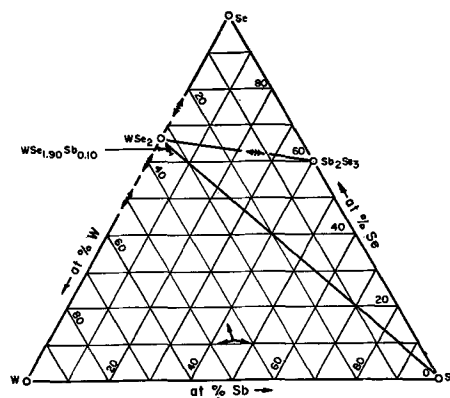


Fig. 4. Tungsten-selenium-antimony phase diagram

eter measurements showed that a second phase was being formed; a preliminary study of the tungsten-selenium-antimony ternary equilibrium phase diagram was made to ascertain what second phase was present and causing this increase in conductivity. A number of samples of varying composition in this system were reacted at final temperatures of 1150°C and furnace cooled. Two compositions containing more than two atoms of selenium per atom of metal, however, were not reacted above 700°C, the boiling point of selenium. X-ray diffraction patterns were obtained on all these samples and the phases detected by this method are shown by the arrows radiating from the points representing sample compositions in Fig. 4. This work indicated that the ternary equilibrium diagram may be divided into three three-phase regions consisting of (i) W + WSe₂ + Sb, (ii) WSe₂ + Sb + Sb₂Se₃, and (iii) WSe₂ + Sb₂Se₃ + Se. No indication of the compound WSe₃ mentioned by Hansen (6) was found in this work, and in fact this composition gave an x-ray diffraction pattern indicating the presence of two phases, WSe₂ and elemental Se. Also no selenides of tungsten lower than WSe₂ were found. The antimony-substituted compound of interest in this study, WSe_{1.90}Sb_{0.10}, thus contains metallic tungsten and metallic antimony in addition to WSe₂, which explains its higher conductivity.

Interstitial substitution.—An attempt was made to dissolve carbon into the WSe₂ lattice according to the formula WSe₂C_x. Lattice parameter measurements showed that the solubility was less than $x = 0.01$, and there was no enhancement of the electrical conductivity.

Effects of stoichiometry.—Several compositions were made up with varying tungsten-to-selenium ratios according to the formula WSe_{2(1+y)} and the room-temperature properties of these compositions are summarized in Table IV. The lattice parameter

Table IV. Effects of stoichiometry on room temperature properties of WSe_{2(1+y)}

y	a , Å	unc, Å*	C , Å	unc, Å*	ρ , mohm-cm
-0.02	3.2860	0.0003	12.978	0.001	289
-0.01	3.2858	0.0002	12.980	0.001	263
0	3.2860	0.0003	12.979	0.001	227
+0.01	3.2864	0.0002	12.978	0.001	304
+0.02	3.2862	0.0002	12.978	0.001	132

* Uncertainty for 50% probable error.

Table V. Hall effect measurements at room temperature on WSe_2 , $MoSe_2$, and $MoTe_2$

Compound	x	ρ , mohm-cm	R_{H1} , $cm^3/coul$	n , cm^{-3}	μ , $cm^2/v\text{-sec}$	$\frac{n}{n_a}$
$W_{1-x}Ta_xSe_2$	0	780	78	$8.0 \cdot 10^{16}$	99	—
	0.005	30.2	$3.9 \cdot 10^{-1}$	$1.6 \cdot 10^{19}$	12.9	0.2
	0.01	11.7	$7.4 \cdot 10^{-2}$	$8.4 \cdot 10^{19}$	6.3	0.6
	0.02	4.3	$2.5 \cdot 10^{-2}$	$2.5 \cdot 10^{20}$	5.8	0.9
	0.03	3.2	$1.8 \cdot 10^{-2}$	$3.5 \cdot 10^{20}$	5.6	0.8
	0.04	2.4	$1.5 \cdot 10^{-2}$	$4.2 \cdot 10^{20}$	6.2	0.7
$Mo_{1-x}Ta_xSe_2$	0	7600	-110	$5.6 \cdot 10^{16}$	15	—
	0.01	24.8	$1.1 \cdot 10^{-1}$	$6 \cdot 10^{19}$	4	0.4
$Mo_{1-x}Ta_xTe_2$	0	7000	-85	$7.3 \cdot 10^{16}$	12	—
	0.03	37.8	$2.4 \cdot 10^{-2}$	$2.6 \cdot 10^{20}$	0.6	0.7
$Mo_{1-x}Re_xSe_2$	0.02	43.1	$-1.4 \cdot 10^{-1}$	$4.5 \cdot 10^{19}$	4	0.15

measurements show that the homogeneity region for the compound WSe_2 must be extremely narrow; that is, it lies between the values of $y = -0.01$ and $+0.01$, for if any appreciable excess of tungsten or selenium were incorporated into the lattice one would expect a significant change in lattice parameters. As a result very little change in conductivity is noted. There is some tendency for the compacts containing an excess of tungsten to have a lower density, apparently due to the kinetics of the reaction of the elements.

Room temperature Hall measurements on the substituted compounds WSe_2 , $MoSe_2$, and $MoTe_2$.—Room-temperature Hall effect and resistivity measurements are summarized in Table V for the compounds WSe_2 , $MoSe_2$, and $MoTe_2$, pure, substituted with tantalum, and for $MoSe_2$ substituted with rhenium. From these values the carrier concentrations and carrier mobilities were calculated and are also tabulated. In addition the last column shows the carrier concentration divided by concentration of acceptor atoms, i.e., the contribution of carriers per acceptor atom. As one might expect, since tanta-

lum has one less electron than tungsten or molybdenum, it contributes approximately one positive carrier per atom to the host lattice for all three of the compounds, WSe_2 , $MoSe_2$, and $MoTe_2$. However, rhenium, which has one more electron than molybdenum, does not contribute a full negative carrier to the host lattice. An increase in values of n/n_a for the system $W_{1-x}Ta_xSe_2$ is noted as x increases from 0.005 to 0.05; this is probably due to a compensating impurity contribution which is more apparent at lower doping levels.

The carrier mobility for the system $W_{1-x}Ta_xSe_2$ decreases from about $100 \text{ cm}^2/\text{volt-sec}$ for the undoped material to a value of about $6 \text{ cm}^2/\text{volt-sec}$ for the range $x = 0.01$ to $x = 0.04$ and decreases to about $4 \text{ cm}^2/\text{volt-sec}$ at $x = 0.05$. At equivalent doping levels the mobilities of both $MoSe_2$ and $MoTe_2$ are lower than that of WSe_2 , thus explaining their poor thermoelectric properties. Interestingly enough the mobility for negative carriers in $MoSe_2$ is approximately the same as that of positive carriers in this compound.

Hall measurements as a function of temperature.—Figure 5 shows a plot of logarithm of $1/eR$ plotted against the reciprocal temperature as determined from Hall measurements between 25° and 600°C . Here R is the Hall coefficient and e is the electronic charge; $1/eR$ is equal to the carrier concentration for extrinsic material. One notes that for the composition $x = 0$ the carrier concentration remains relatively constant up to a temperature of about 400°C , indicating extrinsic behavior. Above 400°C the carrier concentration appears to increase indicating the onset of intrinsic behavior. An approximate energy gap value of 1.9 eV may be derived from the slope of the highest temperature points of this curve. Recently Frindt (7) measured the optical transmission of WSe_2 and found an absorption edge at 7800\AA (7). The latter value leads to an energy gap value of 1.6 eV in good agreement with the above Hall measurements.

The doped compositions, $x = 0.01$ and 0.03 , show a constant carrier concentration from 25° to 600°C and therefore appear to be in an extrinsic region.

From the resistivities measured on these samples and the carrier concentrations shown in Fig. 5 the carrier mobilities of these compositions were calculated as functions of temperature and are shown in Fig. 6. Here the logarithm of the mobility is

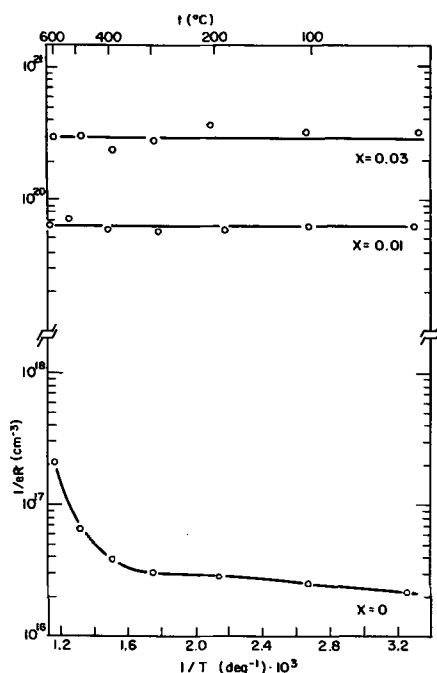


Fig. 5. Carrier concentration vs. reciprocal temperature for $W_{1-x}Ta_xSe_2$.

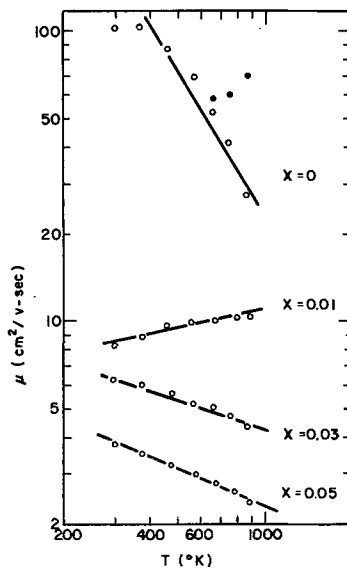


Fig. 6. Carrier mobility vs. absolute temperature for $W_{1-x}Ta_xSe_2$: \circ , assumed hole conductivity only; \bullet , assumed mixed carrier conductivity.

plotted vs. the logarithm of the absolute temperature to show the dependence of the mobility on temperature.

The mobility values shown by the solid points in Fig. 6 were calculated from the formula $\mu = \sigma/ep$. Here μ is the carrier mobility, p is the carrier concentration, e is the electronic charge, and σ is the conductivity of the material. The carrier concentration was calculated from the Hall coefficient. Thus for all the solid points shown it was assumed that conduction was by positive hole carriers only and conduction by electrons was neglected.

From the slopes of the lines the power dependence of the mobility on temperature may be derived. For the composition $x = 0.01$, the mobility varies as $T^{+0.2}$, for the composition $x = 0.03$ the mobility varies at $T^{-0.3}$ and for the composition $x = 0.05$ the mobility varies at $T^{-0.4}$. In the case of impurity scattering the mobility has a large positive power dependence on the temperature while for ionic scattering the mobility should vary at $T^{-0.5}$ according to Ioffe (8). Thus it appears that as the doping level is increased the scattering mechanism varies from one intermediate between impurity scattering and ionic lattice scattering at $x = 0.01$ to almost pure ionic lattice scattering at the composition $x = 0.05$.

For the composition $x = 0$ the solid circles show a power dependence of -1.7 while according to Ioffe an atomic lattice should have a mobility dependence of $T^{-1.5}$. Actually for this composition we have already shown in Fig. 5 that an intrinsic contribution sets in above $600^\circ K$. Thus for this particular composition the slope derived from solid circles may be misleading. Corrected values for the mobilities (open circles) were calculated at the highest temperatures taking into account the contribution of electrons in the intrinsic region through the use of several assumptions: (a) At lower temperatures where the material is extrinsic the electron contribution to the conductivity may be neglected; (b) above these temperatures it was assumed

that equal numbers of positive hole carriers and negative electron carriers are produced as the temperature is increased, and in the case of the hole carriers this addition is added to the relatively constant impurity contribution which occurred below this temperature; (c) it was assumed that the mobility of the electrons in WSe_2 would be equal to the mobility values of the positive hole carriers. This last assumption receives some support from the fact that in $MoSe_2$, where both highly conducting n-type and p-type materials may be achieved by doping, the mobilities for both types of extrinsic materials are equal as seen in Table V. It is seen that for the composition $x = 0$ a line through the solid circles at low temperatures and the open circles at high temperatures shows considerable departure from a straight line in a log-log plot, but this may result from the oversimplification of the above assumptions. In any case when the intrinsic contribution to the conductivity is considered the power dependence no longer conforms to the $T^{-1.5}$ power dependence of an atomic lattice but conforms more closely to the $T^{-0.5}$ power of an ionic lattice, and the scattering mechanism conforms more closely to that shown by the doped compositions $x = 0.01$ to $x = 0.05$.

Correlation between variations of Seebeck coefficient and Hall coefficient with temperature.—Johnson (9) indicates that for a p-type impurity semiconductor the Seebeck coefficient is in general given by the following expression:

$$\alpha = \alpha' + \frac{E_G + E_F}{eT} \quad [1]$$

where E_G is the width of the forbidden energy gap and E_F is the Fermi energy level measured with respect to the conduction band. For semiconductors in the classical region the first term α' is a constant which depends on the scattering mechanism but is independent of the Fermi level. Thus for classical statistics a simple relationship is obtained which directly relates the Seebeck coefficient to the carrier concentration, p , which in turn is determined from the Hall coefficient measurements

$$\alpha = \frac{k}{e} \left[A + \ln \frac{2(2\pi mkT)^{3/2}}{ph^3} \right] \quad [2]$$

In this expression, k is the Boltzmann constant, e is the electronic charge, h is the Planck constant, and m is the effective mass of the charge carriers.

At higher carrier concentrations where semiconductors become degenerate Fermi-Dirac statistics prevail and the first term, α' , in Eq. [1] becomes a complex function of the Fermi level and involves a quotient of Fermi-Dirac integrals. For this region Johnson (9) gives curves showing the relationship between α' and the Fermi level, E_F , for different scattering mechanisms. Since the carrier concentration as determined by Hall coefficient measurements is related to the Fermi level by the following expression for a p-type material

$$p = \frac{4\pi}{h^3} (2mkT)^{3/2} F_{1/2}(-E_F^* - E_G^*) \quad [3]$$

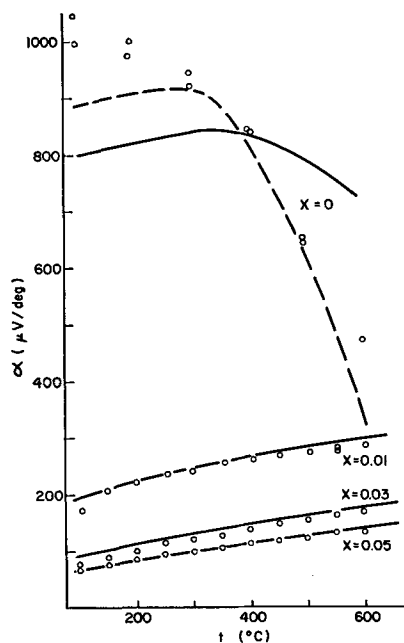


Fig. 7. Seebeck coefficient vs. temperature for $W_{1-x}Ta_xSe_2$: —, calculated assuming positive carriers only; - - -, calculated assuming mixed carrier conductivity.

Hall and Seebeck coefficient measurements may be correlated in this region also. In Eq. [3] $F_{1/2}(-E_F^* - E_G^*)$ is a Fermi-Dirac integral whose values are given as a function of $(-E_F^* - E_G^*)$ by McDougall and Stoner (10). Here E_F^* equals E_F/kT and E_G^* equals E_G/kT .

For the family $W_{1-x}Ta_xSe_2$ the effective mass is most decisively evaluated by using the Hall coefficients and Seebeck coefficients measured for the composition $x = 0.05$, since as shown by Fig. 6 the mobility of this composition conforms most exactly to the $T^{-0.5}$ law expected of ionic scattering. This scattering mechanism corresponds to a value of $A = 3$ in Eq. [2]. For the composition $x = 0.05$ the Fermi level was derived from the Seebeck coefficient value measured at 350°C and the α vs. E_F^* curves presented by Johnson. Then through the use of Eq. [3] and the carrier concentration determined for this composition by the Hall measurements an effective mass was calculated. In this way the ratio of the effective mass of the carriers to the mass of a free electron, $m/m_0 = 1.0$ was obtained. With the same values for the effective mass ratio and for A the Seebeck coefficient was then calculated as a function of temperature, and this is shown by the solid line in Fig. 7 for the composition $x = 0.05$. The circles show the experimental values of Seebeck coefficient vs. temperature for this composition. An excellent agreement is shown between the temperature coefficient of the measured and calculated Seebeck coefficient.

Subsequently assuming the same scattering mechanism and effective mass ratio the Seebeck coefficient as a function of temperature was also calculated for the compositions $x = 0.01$ and $x = 0.03$, and these are shown in Fig. 7. Excellent agreement is found between the experimentally meas-

ured values and the calculated values without any re-evaluation of effective mass ratios or scattering constant for these compositions.

The composition $x = 0$ has carrier concentrations in the classical region, and thus Eq. [2] was used to calculate its Seebeck coefficient as a function of temperature and this is shown by the solid curve in Fig. 7. Here the same effective mass ratio of 1.0 was used with the value of $A = 2$ derived from the dependence of the carrier mobility of this composition on temperature. It is seen that the average value of the Seebeck coefficient calculated in this way agrees with the experimental points, but there is considerable disagreement with the temperature variation of the Seebeck coefficient. Agreement is improved, however, if corrections are made for the electronic contribution to the Seebeck coefficient in the intrinsic region for this composition. As previously mentioned when this contribution is taken into effect, the power dependence of the mobility on temperature as shown in Fig. 6 changes from $T^{-3/2}$ ($A = 2$) to correspond more closely with the behavior for the doped compositions $T^{-0.5}$ ($A = 3$). This increases the calculated Seebeck coefficient at lower temperatures where there is no electronic contribution to the conductivity assumed. Expressions in Johnson (9) may be used to calculate Seebeck coefficient as a function of temperature for regions of mixed carrier conductivity, and these expressions were used above the temperature of 300°C where the material becomes intrinsic. In addition to the assumptions made to correct the mobilities shown in Fig. 6 the additional assumption was made that the effective mass of the hole and electron carriers are equal. The curve calculated using these assumptions is shown by the dashed line in Fig. 7, and indeed this curve shows much closer agreement with the experimental points.

Acknowledgment

A number of helpful suggestions were received from Dr. L. H. Brixner of this department. Dr. W. J. Siemons of the Central Research Department of this company contributed substantially to the theoretical correlations involved in this work.

Sample preparation and electrical measurements were carried out by Mr. A. R. Sohodski. X-ray diffraction patterns and film readings were made by Mr. A. T. Weinmann.

This work was partially supported by the Bureau of Ships, Department of the Navy (Contract NObs 84824) and their permission to publish these results is gratefully acknowledged.

Manuscript received July 24, 1963; revised manuscript received March 17, 1964. A portion of this paper was presented at the Pittsburgh Meeting, April 15-18, 1963.

Any discussion of this paper will appear in a Discussion Section to be published in the June 1965 JOURNAL.

REFERENCES

1. L. H. Brixner, *This Journal*, **110**, 289 (1963).
2. B. Abeles, D. S. Beers, G. D. Cody, and J. P. Dismukes, *Phys. Rev.*, **125**, 44 (1962).
3. H. Valdsaar, Private communication.

4. H. P. Klug and L. E. Alexander, "X-Ray Diffraction Procedures," p. 485, John Wiley & Son, Inc., New York (1954).
5. L. H. Brixner, *J. Inorg. & Nuclear Chem.*, **24**, 257 (1962).
6. M. Hansen, "Constitution of Binary Alloys," p. 1192, McGraw-Hill Book Co., Inc., New York (1958).
7. R. F. Frindt, *J. Phys. Chem. Solids*, **24**, 1107 (1963).
8. A. F. Ioffe, "Semiconductor Thermoelements and Thermoelectric Cooling," p. 29, Infosearch Ltd., London (1957).
9. V. A. Johnson in "Progress in Semiconductors," Vol. 1, pp. 65-95, A. F. Gibson, Editor, Heywood & Co., Ltd., London (1956).
10. J. McDougall and E. C. Stoner, *Phil. Trans. Roy. Soc. London*, **237**, 67 (1938).

Polarography in Acetonitrile of Titanium Tetrachloride and Tetraiodide in Various Supporting Electrolytes

I. M. Kolthoff and F. G. Thomas

School of Chemistry, University of Minnesota, Minneapolis, Minnesota

ABSTRACT

Current-potential curves of titanium tetrachloride in acetonitrile (AN) with tetraethylammonium perchlorate as supporting electrolyte have been determined at the dropping mercury electrode. The effect of chloride, bromide, iodide, and thiocyanate ions has been investigated. In general, only two well defined reduction waves were obtained corresponding to the reduction of Ti(IV) to Ti(III) and Ti(0), respectively. With tetraethylammonium chloride as supporting electrolyte, three reduction waves corresponding to the reduction of Ti(IV) to Ti(III), Ti(II), and Ti(0), respectively, were observed. The valence states of these reduced titanium species was verified by constant potential electrolysis experiments. Titanium tetrachloride in AN reacts with mercury to produce mercurous chloride and Ti(III). The latter reacts slowly with perchlorate if present. No reaction with mercury occurs in the presence of excess chloride ions, or if the water content is 0.03M or greater. Water at this concentration slowly hydrolyzes titanium tetrachloride in AN. Titanium tetrachloride is strongly solvated in AN and conductance data indicate that the solvate dissociates according to $2\text{TiCl}_4(\text{CH}_3\text{CN})_2 \rightleftharpoons \{\text{TiCl}_3(\text{CH}_3\text{CN})_3\}^+ + \{\text{TiCl}_5\text{CH}_3\text{CN}\}^-$ with a dissociation constant of 7×10^{-4} at 25°C. Titanium tetraiodide in AN with tetraethylammonium perchlorate as supporting electrolyte gives a single reduction wave at the dropping mercury electrode corresponding to the reduction of Ti(IV) to Ti(0). In the presence of excess chloride ions replacement of the iodide occurs and three reduction waves are observed, similar to those obtained with titanium tetrachloride. Solutions of titanium tetraiodide in AN are extremely sensitive to traces of oxygen, except in the presence of excess chloride ions.

In dilute, acidic, aqueous media Ti(IV) is only reduced to Ti(III) at the dropping mercury electrode (D.M.E.) (1). In the absence of complexing agents, the reduction of $\text{TiO}^{2+}_{\text{aq}}$ to $\text{Ti}^{3+}_{\text{aq}}$ is irreversible. In the presence of complexing agents such as oxalate, citrate, sulfate, chloride, phosphate, thiocyanate, ethylenediaminetetraacetic acid, etc. (1-9), the reduction of Ti(IV) at the D.M.E. may become reversible, provided that the pH of the solution is sufficiently low to prevent the formation of hydroxy complexes. In general it appears that the greater the tendency for Ti(IV) to exist as a hydroxy complex in the system, the less reversible and more difficult is its reduction to Ti(III). In the present paper, a study of the polarography of titanium tetrachloride and titanium tetraiodide in acetonitrile is reported. In solvents which are much stronger bases than water, the "Lewis" acid-base reaction between the acid titanium tetrachloride and the basic solvent yields such a stable neutralization product that only reduction to Ti(III) occurs. For example, the polarograms of titanium tetrachloride in the basic solvent morpholine (10) using

tetrabutylammonium iodide as supporting electrolyte show only a single reduction wave corresponding to the reduction of Ti(IV) to Ti(III). In the much weaker base dimethylsulfoxide as solvent (11) only one reduction wave was observed in the polarogram of titanium(IV) dicyclopentadienyldichloride but the derivative polarogram exhibited three ill-defined peaks, indicating that reduction of Ti(IV) to Ti(III), Ti(II), and Ti(0) may occur.

Since the solvated proton in acetonitrile has a dissociation constant of the order of 10^5 times that in water (12), acetonitrile is a considerably weaker base than water, (at least with respect to the proton); nevertheless, it reacts with titanium tetrachloride to form a stable Lewis neutralization product (13). Polarograms have been determined in tetraethylammonium perchlorate, chloride, bromide, iodide, and thiocyanate, as supporting electrolytes. The effect of small amounts of water added to solutions of titanium tetrachloride has also been determined. The interpretation of the data has been substantiated by the results of constant potential electrolysis experiments at a mercury pool cathode

and also by conductance data of titanium tetrachloride solutions in AN in the absence of a supporting electrolyte. Difficulties were experienced in reproducing polarograms of titanium tetrachloride in the presence of tetraethylammonium perchlorate and iodide supporting electrolytes. In the former medium it was found that a reaction occurs between titanium tetrachloride and mercury. This reaction also occurs in the absence of any other salts in solution. In iodide medium oxidation by traces of oxygen of the titanium tetrachloride-iodide complex formed in solution was found to be responsible. In order to interpret the effect of iodide on polarograms of titanium tetrachloride a preliminary study of the polarography of titanium tetraiodide in AN using various supporting electrolytes was undertaken. Titanium tetraiodide is a weaker "Lewis" acid than titanium tetrachloride and forms a less stable neutralization product with AN (13).

Experimental

Cells.—Two polarographic cells were used in these studies. Cell A has been described previously (14). Cell B was a modification of cell A. The flanged end of an "s" bend made from 1 mm diameter capillary was sealed through the base of the cell, the external end being connected to a sealed polyethylene tube. This arrangement enabled the drops of mercury from the D.M.E. to be removed from contact with the solution under investigation (and hence virtually prevent reaction between mercury and titanium tetrachloride in solution) and prevented the solution from draining out of the cell. The capillary and polyethylene tube were filled with nitrogen prior to adding the solution to the cell. A pinch clip on the polyethylene tube was continually released during an experiment to prevent nitrogen displaced by the mercury forming bubbles and stirring the solution. The resistance of these cells containing 0.1M tetraethylammonium perchlorate in AN and the associated circuit was 1800 and 1950 ohms, respectively.

Controlled potential electrolyses were carried out in a cell similar to that employed by Coetzee (15) but using all-Pyrex glass fittings. A take-off tube, sealed through the lid and connected to a calibrated buret enabled samples of the electrolyzed solution to be transferred to a titration cell under a nitrogen atmosphere. All electrolyses in this cell were carried out using a Fisher Controlled Potential Electroanalyzer.

A conductivity cell with a cell constant of 0.0366 cm^{-1} (calibrated with 10^{-3}M aqueous potassium chloride) was used and the resistances of solutions in this cell were measured with an a-c bridge with an accuracy of $\pm 1\%$.

Electrodes.—The dropping mercury electrode used in the majority of the studies reported here had the following characteristics: $m = 1.469 \text{ mg sec}^{-1}$ with a mercury height of 53.7 cm (corr.), $t = 3.95 \text{ sec}$ in 0.1M tetraethylammonium perchlorate in AN at zero applied voltage. The capillary constant was thus $1.621 \text{ mg}^{2/3} \text{ sec}^{-1/2}$. A saturated calomel electrode (SCE) served as reference electrode.

Polarograph.—A Leeds and Northrup Electrochemograph Type E was used to record current-potential curves.

Materials. Solvent.—Acetonitrile (Eastman-Kodak practical grade) was purified by the method of Coetzee (16), and distilled through a fractionating column 1 m long by 2 cm diameter packed with glass helices. After the initial fractionations over phosphorous pentoxide and calcium hydride the solvent was further fractionated four times from 1g lots of phosphorous pentoxide and finally by itself, B. P. $81.0^\circ\text{C} (\pm 0.2^\circ\text{C})$ at $750 \pm 5 \text{ mm Hg}$. The final product gave the following assay: water (Karl Fischer) 0.8-2.0 millimole (mM), ammonia (picric acid test) not detectable, residual current of various batches with 0.1M tetraethylammonium perchlorate supporting electrolyte $0.6\text{-}1.2 \mu\text{a}$ at -2.5v [due to acrylonitrile (16)], specific conductivity $(1.5\text{-}2.5) \times 10^{-7} \text{ ohm}^{-1} \text{ cm}^{-1}$.

Titanium tetrachloride.—Fisher "purified" grade was redistilled under nitrogen, B.P. $135^\circ\text{-}136^\circ\text{C}$ at 753 mm Hg. Analysis; titanium (as TiO_2) 25.35% (theoretical 25.25%). Because of the vigorous reaction between acetonitrile and titanium tetrachloride at room temperature, stock solutions were prepared at -25°C . The resulting solutions of $\text{TiCl}_4(\text{CH}_3\text{CN})_2$ (13, 17) were bright yellow at concentrations above 10 mM.

Titanium tetraiodide.—A K and K Laboratories product was used without further purification. Analysis: titanium [spectrophotometrically (18) after removing iodide by evaporation with sulfuric acid] 8.85%; iodide (Volhard's method) 91.24%. Theoretical for TiI_4 : titanium 8.62%, iodide 91.38%. Titanium tetraiodide readily dissolves in AN without vigorous reaction, to give deep yellow-brown solutions (10 mM). The extreme sensitivity of titanium tetraiodide toward oxygen necessitated that all work with it and its solutions be carried out in a nitrogen filled glove-box.

Tetraethylammonium perchlorate.—This was prepared as previously described (19).

Tetraethylammonium thiocyanate.—It was prepared from the bromide by a method analogous to that used by Krauss and Fuoss (20) to prepare tetraisoamylammonium thiocyanate. The crude product was recrystallized twice from a chloroform-petroleum ether mixture and dried under vacuum at 65°C for 3 days. The current-potential curve of M/10 solution in AN had no discernable wave at -1.95v showing that $[\text{K}^+] < 0.05 \text{ mM}$; the residual current at -2.5v was $1.6 \mu\text{a}$ c.f. $1.2 \mu\text{a}$ in 0.1M tetraethylammonium perchlorate at -2.5v .

Tetraethylammonium chloride.—This was prepared by passing 2 l. of 0.1M aqueous tetraethylammonium bromide solution slowly through a column of Dowex 1X8 anion exchange resin in the chloride form (total column capacity = 0.5 mole). The resulting solution was concentrated until syrupy and allowed to dry at room temperature. The product was recrystallized twice from an ethanol (5%)-ethyl acetate mixture. The residual current of a 0.1M solution of the product in AN was the same

as that of 0.1M tetraethylammonium perchlorate from -0.5 to -2.0 v and was $2.0 \mu\text{a}$ at -2.5 v.

Tetraethylammonium bromide and tetraethylammonium iodide.—These were Eastman-Kodak reagents, recrystallized from water.

Anhydrous ferric chloride.—Prepared by the chlorination of iron, this was obtained from Dr. D. Britton of the Inorganic Chemistry Department.

Anhydrous methanol.—It was prepared by distilling Fisher A.R. grade methanol from magnesium (21). A solution of anhydrous ferric chloride in this solvent served as oxidant in the determination of Ti(II) produced by electroreduction of titanium tetrachloride in AN in the presence of excess chloride ions.

Nitrogen.—Linde 99.9% purity was used and when necessary, was further purified by passing it through a 1 m long by 3.5 cm diameter column of activated copper at 200°C . The resultant nitrogen is reported to contain only $\sim 4 \times 10^{-5}\%$ oxygen (22).

Technique.—Current-potential and current-time curves using the D.M.E. were determined as previously described (14, 19). All measurements were made at $25.00 \pm 0.02^\circ\text{C}$. All potentials reported are relative to the SCE and have been corrected for iR drop and all currents for residual current. Nitrogen was saturated with AN at 25°C before being passed through the polarographic cell. Electrolysis experiments at constant potential at a mercury cathode were carried out in the usual manner (15). A 25 ml aliquot was removed at the completion of the electrolysis via the enclosed buret and transferred to the titration cell. An excess of anhydrous ferric chloride in anhydrous methanol was added and the solution stirred for 2 hr at -15°C under nitrogen (23). After acidifying this solution with 25 ml 5M aqueous sulfuric acid, the Fe(II) produced by the reduction of Fe(III) by Ti(III) and/or Ti(II) was determined with 0.01M ceric sulfate using ferroin indicator. For the determination of total titanium in the aliquot, iron, cerium, and titanium were precipitated as hydroxides, the precipitate filtered and dissolved in 5M sulfuric acid. Titanium was determined spectrophotometrically (18) after 5 ml of 2M phosphoric acid had been added to mask the Fe(III).

A precipitate formed on electrolysis at a constant potential of -2.2 v was filtered, washed with AN, dissolved in 0.5M sulfuric acid, and analyzed for titanium (with hydrogen peroxide), mercury (with dithizone), chloride (with silver nitrate), and perchlorate (with silver nitrate after addition of acidified titanium (III) sulfate). The mercury of the cathode after electrolysis at -2.2 v was dissolved in nitric acid, converted to the chloride with hydrochloric acid and analyzed for titanium with hydrogen peroxide.

Heat of solution.—Heat of solution of titanium tetrachloride in AN was determined in the usual manner (24) using a 500 ml Dewar flask as calorimeter ("water equivalent" $29.5 \pm 1.0 \text{ cal deg}^{-1}$). Approximately 0.5g titanium tetrachloride was dissolved in 200 ml (= 155.7g at 23.568°C) of AN and the initial and final temperatures measured with a

high precision thermometer. The amount of titanium tetrachloride added to the AN was accurately determined by gravimetric and spectrophotometric analysis of the resulting solution.

Results

The limiting current at -1.8 v observed in polarographic cell A, containing solutions of titanium tetrachloride in AN with 0.1M tetraethylammonium perchlorate as supporting electrolyte decreased on prolonged electrolysis at the D.M.E. The diffusion current was 70% of its initial value after 50 min electrolysis indicating that reducible Ti(IV) was being depleted in the bulk of the solution. In the absence of mercury the solutions were stable. By adding acrylonitrile in various concentrations it was shown that this impurity in the solvent was not responsible for the decrease in the current in the presence of mercury. The following experiments show that the mercury collecting in the base of cell A reacts with the solute. An oxygen-free, 5.52 mM solution of titanium tetrachloride in AN (40 ml) was shaken with mercury (2g) in a sealed vessel for 60 min and allowed to stand overnight. The resulting solution was light indigo-blue in color [due to Ti(III)] and a white precipitate of mercurous chloride was formed. Analysis showed that all the titanium remained in solution, 65% being present as Ti(III). Similar experiments in the presence of 0.1M tetraethylammonium perchlorate yielded a precipitate consisting of a mixture of mercurous chloride and a titanium compound. The resulting colorless solution contained 67% of the original amount of Ti(IV), but no Ti(III), while only 1.89 moles of chloride per 1 mole of titanium remained

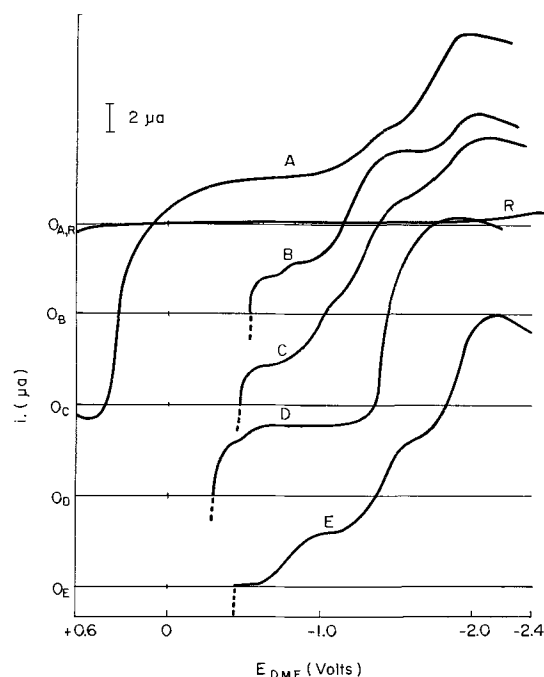


Fig. 1. Current-potential curves of 1.00 mM titanium tetrachloride in acetonitrile with various supporting electrolytes. A, 0.1M tetraethylammonium perchlorate; B, 0.1M tetraethylammonium iodide; C, 0.1M tetraethylammonium bromide; D, 0.05M tetraethylammonium perchlorate + 0.05M tetraethylammonium thiocyanate; E, 0.1M tetraethylammonium chloride; R, residual current in 0.1M tetraethylammonium perchlorate.

in solution. Evidently, the Ti(III) formed in the absence of perchlorate reduces perchlorate with the formation of TiO^{2+} , part of which is in the precipitate. The total chloride content in the solution plus precipitate was 3% greater than that corresponding to the concentration of titanium present in the tetrachloride initially present, indicating that perchlorate was reduced to chloride.

In order to eliminate the above interfering reaction in the polarography of titanium tetrachloride with tetraethylammonium perchlorate as supporting electrolyte cell B was used. With this cell the current at -1.8v was found to remain constant.

Current-Potential Curves of Titanium Tetrachloride in AN

In 0.1M tetraethylammonium perchlorate as supporting electrolyte.—The current-potential curves of solutions of titanium tetrachloride in the concentration range 0.24 to 1.81 mM were determined using 0.1M tetraethylammonium perchlorate as supporting electrolyte and polarographic cell B. The current-potential curve for 1 mM titanium tetrachloride is shown in Fig. 1, curve A, and the characteristics of the anodic and two principal cathodic waves are listed in Table I. The limiting current of the total cathodic wave at -2.0v (*vs.* SCE) is well developed, the diffusion current at this potential being proportional to the concentration of titanium tetrachloride (Fig. 2, curve B). The value of the diffusion current constant, $I_D = 8.29 \mu\text{a mole}^{-1} 1.\text{mg}^{-2/3} \text{sec}^{1/2}$, at -2.0v corresponds to a four electron transfer of Ti(IV) to Ti(0). This reduction is irreversible. The first cathodic diffusion current is poorly defined, the plot of $i_d t^{-1/6}$ *vs.* concentration at -0.6v (Fig. 2, curve A) not being linear, the slope increasing with increasing concentration. (In Fig. 2 $i_d t^{-1/6}$ and not i_d is plotted in order to relate all currents to the same drop time.) At the higher concentrations the slope of this plot approaches a value which is $1/4$ of the slope of the plot for the total cathodic wave at -2.0v (Fig. 2, curve B). Also, at

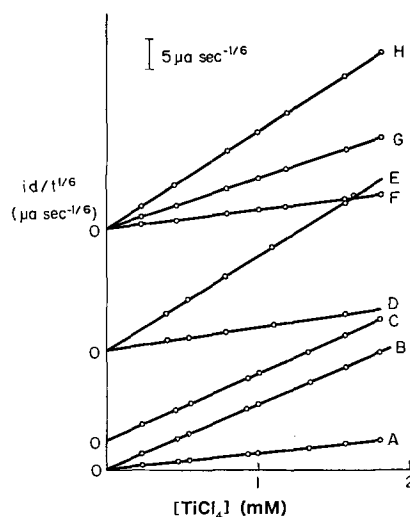


Fig. 2. Relation between diffusion current (corrected for drop time effects) and concentration of titanium tetrachloride in various supporting electrolytes. A, B, and C, 0.1M tetraethylammonium perchlorate: currents measured at -0.6 , -2.0 , and $+0.55\text{v}$, respectively; D and E, 0.05M tetraethylammonium perchlorate $+0.05\text{M}$ tetraethylammonium thiocyanate; currents measured at -0.8 and -1.9v , respectively; F, G, and H, 0.1M tetraethylammonium chloride; currents measured at -1.1 , -1.65 , and -2.2v , respectively.

higher concentrations the first cathodic diffusion current becomes more clearly defined. From the drawn-out shape of this wave it appears that the reduction of Ti(IV) to Ti(III) is irreversible. The second cathodic wave with $E_{1/2}$ of about -1.3v is small and poorly defined. It indicates a reduction of Ti(III) to Ti(II), but it overlaps with the third wave corresponding to the reduction to Ti(0).

The anodic wave in 1 mM titanium tetrachloride has an $E_{1/2}$ of $+0.34\text{v}$ and is composite with the first cathodic wave. The slope of the plot of $\log i$ *vs.* $E_{D.M.E.}$ between $+0.4$ and $+0.5\text{v}$ is equal to 0.025, indicating a reversible oxidation of mercury to mercurous chloride in this voltage range. The diffusion current at $+0.55\text{v}$ is not as well defined as that of the total reduction wave at -2.0v , nevertheless,

Table I. Characteristics of polarographic waves of acetonitrile solutions of titanium tetrachloride

Supporting electrolyte	Reaction at D.M.E.	I_D , ($\mu\text{a mM}^{-1} 1.\text{mg}^{-2/3} \text{sec}^{1/2}$)	$E_{1/2}$, <i>v vs.</i> S.C.E.
0.1M $(\text{C}_2\text{H}_5)_4\text{NClO}_4$	$\text{TiCl}_4 + 4\text{Hg} \rightarrow 2\text{Hg}_2\text{Cl}_2 + 4e$	8.35	$+0.34^b$
	$\text{Ti(IV)} + e \rightarrow \text{Ti(III)}$	2.05^a	Composite with anodic wave
	$\text{Ti(IV)} + 4e \rightarrow \text{Ti(0)}$	8.29	-1.75^b
0.1M $(\text{C}_2\text{H}_5)_4\text{NCl}$	$\text{Ti(IV)} + e \rightarrow \text{Ti(III)}$	2.29	-0.80^c
	$\text{Ti(IV)} + 2e \rightarrow \text{Ti(II)}$	6.23	-1.39^d
	$\text{Ti(IV)} + 4e \rightarrow \text{Ti(0)}$	12.32	-1.92^d
0.1M $(\text{C}_2\text{H}_5)_4\text{NBr}$	$\text{Ti(IV)} + e \rightarrow \text{Ti(III)}$	1.70	Composite with anodic wave
	$\text{Ti(IV)} + 4e \rightarrow \text{Ti(0)}$	12.15	?
	$\text{Ti(IV)} + e \rightarrow \text{Ti(III)}^g$	1.55	Composite with anodic wave
0.1M $(\text{C}_2\text{H}_5)_4\text{NI}$	$\text{Ti(IV)} + e \rightarrow \text{Ti(III)}^h$	2.13	-0.77^e
	$\text{Ti(IV)} + 4e \rightarrow \text{Ti(0)}^i$	6.78	-1.20^e
	$\text{Ti(IV)} + 4e \rightarrow \text{Ti(0)}^k$	8.70	-1.86^e
	$\text{Ti(IV)} + e \rightarrow \text{Ti(III)}$	2.79	Composite with anodic wave
	$\text{Ti(IV)} + 4e \rightarrow \text{Ti(0)}$	11.90	-1.46^d

^a Value for 1.81 mM titanium tetrachloride; I_D is lower at lower concentrations.

^b $E_{1/2}$ constant in the concentration range 0.9 to 1.81 mM.

^c At 1 mM $E_{1/2}$ decreases with increasing concentration from -0.81 at 0.236 mM to -0.76 at 1.81 mM.

^d $E_{1/2}$ independent of concentration.

^e At 1mM.

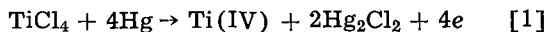
^g First part of split one-electron reduction wave.

^h Total one-electron wave.

ⁱ First part of split four-electron reduction wave.

^k Total four-electron wave.

from the average values of the diffusion current constants at these two potentials (Table I) it is clear that the anodic wave is the result of a four electron transfer, corresponding to the over-all reaction



The zero current potential at +0.1v is a mixed potential. At this potential the reduction current due to $\text{Ti(IV)} + e \rightarrow \text{Ti(III)}$ is equal to the anodic current (Eq. [1]).

Effect of water.—Small amounts of water, up to 4 mM have no effect on the current-potential curves. Larger amounts of water result in the hydrolysis of the solute. The current-potential curve of a freshly prepared solution, 31 mM in water, 1.00 mM in titanium tetrachloride, and 0.1M in tetraethylammonium perchlorate is given in Fig. 3, curve A. Comparison of this curve with Fig. 1, curve A shows that in the presence of 31 mM water the half wave potential of the anodic wave is shifted from +0.34 to +0.22v, the anodic and cathodic waves are no longer composite, the first cathodic wave is more drawn out, there is no evidence of a $\text{Ti(IV)}/\text{Ti(II)}$ reduction wave, the $\text{Ti(IV)}/\text{Ti(0)}$ wave occurs at about 0.3v more positive, and the total diffusion current at -2.0v is 10% less than in water-free solution. On standing for 24 hr the solution became cloudy and after three days titanium had precipitated as titanium dioxide. The precipitate, after washing with AN and dissolving in 5M sulfuric acid, gave a negative test for chloride with silver nitrate. From the current-potential curve of the resulting solution (Fig. 3, curve B) it is clear that most of the titanium has precipitated from solution as a result of the slow hydrolysis of the tetrachloride.

Effect of chloride.—Solutions of titanium tetrachloride containing 0.1M tetraethylammonium chloride exhibit three well defined waves as shown in Fig. 1, curve E. The first wave is no longer composite with the anodic chloride current. In agree-

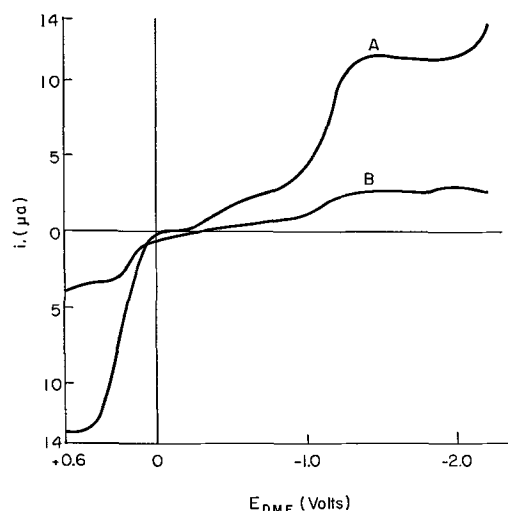


Fig. 3. Effect of 31 mM water on the polarogram of 1.00 mM titanium tetrachloride with 0.1M tetraethylammonium perchlorate as supporting electrolyte. A, Freshly prepared solution; B, solution aged 72 hr.

Table II. Effect of chloride ion on the characteristics of the total wave of 1 mM titanium tetrachloride in acetonitrile

Added [Cl ⁻] (mM)	i_d at -2.15v (μa)	Drop time (sec)	I_D	$-E_{1/2}$	Color of solution
101	18.00	2.07	12.32	1.92	Colorless
50	17.98	2.08	12.30	1.91	Colorless
25	17.83	2.17	12.11	1.90	Colorless
12	17.48	2.20	11.87	1.87	Colorless
8	17.30	2.20	11.72	1.86	Very faint yellow
4	16.94	2.19	11.52	1.84	Pale yellow
2	15.48	2.20	10.51	1.79	Yellow
1	14.63	2.17	9.97	1.78	Yellow
0	12.20	2.18	8.29	1.75	Pale yellow

ment with this behavior is the fact that chloride containing solutions of titanium tetrachloride in AN do not react with mercury. The characteristics of the three cathodic waves are given in Table I. The limiting diffusion currents of the three waves (at -1.1 , -1.65 , and -2.2v vs. SCE) are proportional to the concentration of titanium tetrachloride in the concentration range 0.236 to 1.81 mM (Fig. 2, curves F, G, and H). The ratio of the values of the diffusion current constants for the three waves are 1:2.72:5.37 with the ratio for the second and third waves of 1:1.98. Although the diffusion current constant for the first wave is low compared with the other two, these ratios, together with the magnitude of the diffusion current constants indicate that the three waves correspond to the reduction of Ti(IV) to Ti(III) , Ti(II) , and Ti(0) , respectively. The waves are well defined, but all are drawn out and the reductions are irreversible. As is seen in Table I, the diffusion current for the four electron reduction in the presence of chloride is about 50% larger than in the presence of perchlorate. The effect of various chloride concentrations on the characteristics of the total wave of 1.00 mM titanium tetrachloride is summarized in Table II. The total ionic strength was maintained at 0.1M by means of tetraethylammonium perchlorate. The pale yellow color of the solution in the absence of added chloride becomes more intense at low chloride concentrations; probably as a result of formation of $\text{TiCl}_5(\text{CH}_3\text{CN})^-$. At higher chloride concentrations the solutions are colorless; apparently, all the titanium is then present as TiCl_6^{2-} . The formation of these complex ions also accounts for the increase in the diffusion current constant for the four electron reduction.

Controlled potential electrolysis.—The results obtained from these experiments substantiate the above interpretation of the current-potential curves, in particular, that Ti(II) is stabilized in AN in the presence of chloride. Ninety five milliliters of 5.52 mM titanium tetrachloride in AN with 0.5M tetraethylammonium chloride as supporting electrolyte, was electrolyzed at -1.11v (vs. SCE) at a mercury cathode. Electrolysis was complete after passage of 50.4 coulombs of current [theoretical 50.5 for reduction to Ti(III)] and the solution which was initially colorless, was an extremely pale bluish-green color. An aliquot (10 ml) of this solution was added to 50 ml of 2M sulfuric acid containing an excess of

Fe(III). The Fe(II) produced by the reduction of Fe(III) by Ti(III) was titrated with $10^{-2}M$ Ce(IV) and it was found that all the titanium was present as Ti(III). Thus, at $-1.1v$ the reduction in the presence of chloride is to Ti(III) and the current efficiency is 100%. After removing a further 6 ml sample for tests, the remainder was electrolyzed at a constant potential of $-1.67v$ (*vs.* SCE). Electrolysis was complete after passage of 44.8 coulombs of current (theoretical 42.0) and the final solution was purple-black with some material in very fine suspension. A 25 ml aliquot of this solution was transferred under nitrogen to the titration cell and analyzed for Ti(II) and Ti(III) (see experimental section) and found to contain 97% of the titanium as Ti(II) and 3% as Ti(III). Thus, at $-1.67v$ the reduction of titanium tetrachloride in AN in the presence of chloride is to Ti(II) with a current efficiency of 91%. Attempts to separate Ti(0), *i.e.*, titanium metal or amalgam, were not successful. In all instances electrolysis at $-2.2v$ was completed after passage of 4.2 to 4.3 equivalents of current per mole of titanium tetrachloride and a pale yellowish precipitate was formed which contained 34.6 to 37.0% titanium by weight and about half of the total added titanium. This solid was freely soluble in dilute aqueous (0.1M) sulfuric acid, giving a pale yellow solution. The final solution in the electrolysis cell was yellow, it contained the balance of the titanium, had a strong odor like that of aliphatic amines, and the vapor evolved with the nitrogen (which was passed through the solution during electrolysis) was alkaline to litmus.

When solutions of titanium tetrachloride containing both tetraethylammonium perchlorate and tetraethylammonium chloride as supporting electrolyte were electrolyzed at $-1.67v$ reduction of Ti(IV) to Ti(III) was first observed. After this reduction was complete a grayish-blue precipitate was formed and no Ti(II) was detected in solution. Apparently Ti(II) reacts with perchlorate, both in the absence and presence of chloride. On addition of perchlorate under oxygen-free conditions to a solution of Ti(II), prepared by electrolysis in the presence of excess chloride, a grayish-blue precipitate formed, confirming that perchlorate is reduced by Ti(II). Electrolysis at $-2.0v$ in the presence of perchlorate resulted in the formation of the yellowish precipitate. Neither chloride nor perchlorate was found to be a constituent of this precipitate. On completion of reduction at $-2.0v$ (perchlorate) or $-2.2v$ (chloride) the mercury of the cathode was collected and analyzed for titanium. In all instances the test was negative, indicating the absence of titanium in the mercury.

Although the constant potential electrolysis experiments do not give any indication of the formation of titanium amalgam or metal, it seems fairly certain that the final stage of the reduction of titanium tetrachloride in AN at the D.M.E. is to Ti(0). This apparently reacts with the surrounding system to produce an aliphatic amine together with a slightly soluble complex of titanium in a higher

valence state which is very stable to electrochemical reduction.

Effect of bromide.—Solutions of titanium tetrachloride (1.00 mM) in AN containing small amounts of tetraethylammonium bromide (1-8 mM) are colored orange-yellow, but in the presence of higher concentrations of bromide are colorless. As with chloride these observations are accounted for by the formation of various complex ions. Curve C, Fig. 1 shows a typical polarogram of titanium tetrachloride in 0.1M tetraethylammonium bromide as supporting electrolyte; the characteristics are recorded in Table I. The first cathodic wave is fairly well defined and is composite with the bromide anodic wave. The limiting current of this wave appears to be less than that which corresponds to a one electron reduction. Apparently the one electron reduction of Ti(IV) in the various complexing solutions occurs at different potentials. The first wave is followed by three poorly defined waves, only the limiting current for the total four electron reduction is well defined and can be measured with any accuracy. The presence of various titanium(IV) chloride-bromide complexes of the form $\{TiCl_xBr_{(6-x)}\}^{2-}$ probably accounts for the complicated nature of the current-potential curves. Solutions of titanium tetrachloride in AN containing bromide, either in the presence or absence of oxygen, are quite stable as shown by the reproducibility of the current-potential curves on aging the solutions for 24 hr.

Effect of Iodide.—Solutions of titanium tetrachloride containing iodide are very sensitive to oxygen, the initial yellowish-brown air-saturated solution rapidly becoming red-brown in color, deepening in intensity on standing, and finally yielding a precipitate of titanium oxide. On the other hand, addition of solid tetraethylammonium iodide to an oxygen-free solution of titanium tetrachloride produces a yellow solution which is quite stable (as shown by the reproducibility of the current-potential curves) for several weeks, provided air is rigorously excluded. The current-potential curve of a 1.00 mM solution of titanium tetrachloride in 0.1M tetraethylammonium iodide is shown in Fig. 1, curve B and its characteristics are recorded in Table I. An interpretation of the polarogram is presented in the discussion section.

Effect of thiocyanate.—In a supporting electrolyte 0.05M in tetraethylammonium perchlorate and 0.05M in tetraethylammonium thiocyanate, two well developed reduction waves are observed (Fig. 1, curve D) which correspond to a one and a four electron reduction, respectively. The characteristics of the current-potential curves are listed in Table I, the diffusion currents being proportional to the concentration of titanium tetrachloride (Fig. 2, curves D and E). The second reduction wave is irreversible, while the first wave is composite with the anodic thiocyanate wave, *i.e.*, the zero current potential is a mixed potential, at which the following reactions occur simultaneously

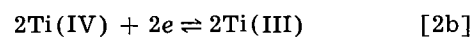


Table III. Characteristics of polarographic waves of acetonitrile solutions of titanium tetraiodide

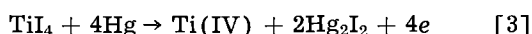
Supporting electrolyte	Reaction at D.M.E.	I_D , ($\mu\text{a mM}^{-1}$ $\text{l.mg}^{-2/3} \text{sec}^{1/2}$)	$E_{1/2}$, v vs. S.C.E.
0.1M (C ₂ H ₅) ₄ NCIO ₄	TiI ₄ + 4Hg → 2Hg ₂ I ₂ + 4e	8.07 ^a	+0.22
	Ti(IV) + 4e → Ti(0)	10.29	-0.34
0.1M (C ₂ H ₅) ₄ NCl	Ti(IV) + e → Ti(III) ^b	1.13	Composite with anodic wave
	Ti(IV) + e → Ti(III) ^c	2.59	
	Ti(IV) + 2e → Ti(II)	6.07	
	Ti(IV) + 4e → Ti(0)	12.40	
0.1M (C ₂ H ₅) ₄ NI	Ti(IV) + 4e → Ti(0)	8.09	Composite with anodic wave
	Ti(IV) + 4e → Ti(0)	10.38	

All $E_{1/2}$ values for 1.00 mM titanium tetraiodide solutions.
^a III defined. ^b First part of split one-electron reduction wave. ^c Total one-electron wave.

The diffusion current constants are in the ratio of 1:4.26 and are considerably greater in the presence of thiocyanate than in the presence of perchlorate alone. This indicates that a complex is formed between titanium tetrachloride and thiocyanate ions which has a larger diffusion coefficient than does TiCl₄(CH₃CN)₂. Solutions of titanium tetrachloride in AN containing thiocyanate are sensitive to oxygen as are solutions containing iodide. In oxygen-free solutions the color is bright yellow. Such solutions are stable for several days but on standing for more than three days begin to deepen in color and finally an orange precipitate is formed. In the presence of oxygen, solutions immediately become orange in color and an orange precipitate forms within 2 or 3 hr. Current-potential curves of the resulting solutions show that most of the titanium is in the precipitate. Thus titanium(IV)-thiocyanate systems in AN are similar to titanium(IV)-iodide systems in that air oxidation of the anion occurs with the formation of titanium(IV)-oxygen compounds.

Current-potential Curves of Titanium Tetraiodide in AN

0.1M tetraethylammonium perchlorate as supporting electrolyte.—The current-potential curve of 1.00 mM titanium tetraiodide in the presence of 0.1M tetraethylammonium perchlorate is shown in Fig. 4, curve A, and the characteristics of the two waves are given in Table III. Contrary to the behavior of titanium tetrachloride in this supporting electrolyte only one reduction wave is observed with titanium tetraiodide, and the value of the diffusion current constant at -0.7v ($I_D = 10.29$) indicates that a four electron reduction of Ti(IV) to Ti(0) occurs in one irreversible step with a half-wave potential of -0.34v. A poorly defined anodic wave is also observed indicating that a reaction similar to Eq. [1] occurs



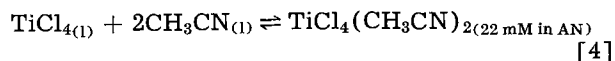
In contrast to the behavior of titanium tetrachloride, the anodic and cathodic waves do not appear to be composite, although a reaction between mercury and the solute was observed.

Effect of chloride.—The current-potential curve of 1.00 mM titanium tetraiodide using 0.1M tetraethylammonium chloride as supporting electrolyte is given in Fig. 4, curve B, and its characteristics

are listed in Table III. An interpretation of the polarogram is presented in the discussion section.

Effect of iodide.—Figure 4, curve C illustrates the current-potential curve of 1.00 mM titanium tetraiodide in the presence of 0.1M tetraethylammonium iodide, and its characteristics are recorded in Table III. Two cathodic waves are observed. The first is composite with the anodic iodide wave with an I_D value of 8.09 at -1.0v, while the second wave has an I_D value of 10.38 at -1.7v which is almost the same as that obtained with perchlorate supporting electrolyte. This indicates that in 0.1M iodide only partial replacement of the AN ligands by iodide in the co-ordination sphere of the titanium(IV) occurs. The ratio of the two wave heights is close to 3:4. Without further study it cannot be concluded whether the first wave corresponds to a three electron reduction or, which is more likely, whether there are two species of Ti(IV) in solution, which cause the four electron reduction wave to be split.

Heat of solution.—The heat of solution of titanium tetrachloride in AN



was found to be $\Delta H_s = -24 \pm 1 \text{ kcal mole}^{-1}$ at 24°C.

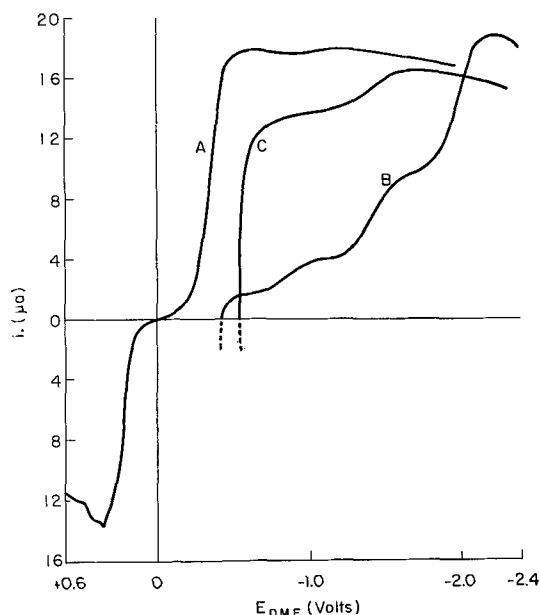


Fig. 4. Current-potential curves of 1.00 mM titanium tetraiodide in acetonitrile with various supporting electrolytes. A, 0.1M tetraethylammonium perchlorate; B, 0.1M tetraethylammonium chloride; C, 0.1M tetraethylammonium iodide.

Table IV. Conductivity of titanium tetrachloride in acetonitrile

[TiCl ₄] (mM)	Specific conductivity (ohm ⁻¹ cm ⁻¹)	Molar conductivity, L (ohm ⁻¹ cm ² mole ⁻¹)	L/L ₀ *
118.0	4.39 × 10 ⁻⁴	3.72	0.022
15.8	7.08 × 10 ⁻⁵	4.48	0.026
9.21	3.62 × 10 ⁻⁵	3.93	0.023
4.61	2.13 × 10 ⁻⁵	4.62	0.027
2.30	1.03 × 10 ⁻⁵	4.48	0.026
1.15	4.93 × 10 ⁻⁶	4.29	0.025

* L₀, the molar conductivity at infinite dilution and 100% dissociation was taken to be 170 ohm⁻¹ cm² mole⁻¹ (see text).

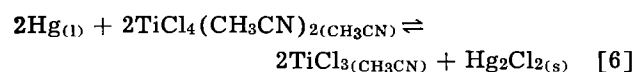
Conductivity measurements.—The molar conductivities of solutions of titanium tetrachloride in AN in the concentration range 1.15 mM to 0.118M are given in Table IV.

Discussion

From data reported in the literature (25, 26) it is found that the enthalpy change for the reaction between mercury and titanium tetrachloride in their standard states

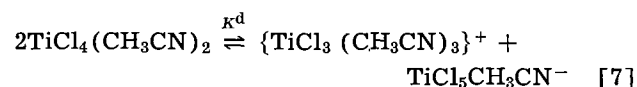


is $\Delta H^\circ_{298} = -22.3$ kcal mole⁻¹ and the free energy change of this reaction is $\Delta G^\circ_{298} = -9.7$ kcal mole⁻¹, thus the reduction of titanium tetrachloride by mercury is favored. Since the heat of solution of titanium tetrachloride in AN (Eq. [4]) is $\Delta H_s = -24 \pm 1$ kcal mole⁻¹ and the reaction



is known to proceed from left to right, then neglecting entropy changes which probably will be very similar in reactions [5] and [6], it is possible to make an estimate of the heat of solution of titanium trichloride in AN. This is estimated to be ≥ 13 kcal mole⁻¹ (exothermic). From the measured concentrations of Ti(IV) and Ti(III) in AN which are in equilibrium in the presence of mercury, the free energy change of reaction [6] is calculated to be $\Delta G^\circ_{298} = -0.7$ kcal mole⁻¹.

The molar conductivity of titanium tetrachloride in AN is independent of concentration in the concentration range 0.001 to 0.118M. This indicates that disproportionation rather than simple dissociation of the solute occurs. An estimate of the equilibrium constant, K^d , for the reaction

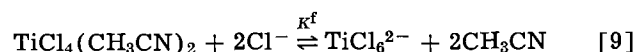


can be obtained from the conductivity data if one assumes that the total molar conductivity of these two ions at infinite dilution and 100% disproportionation is of the same order as that of the alkylammonium chlorides, *i.e.*, 170 ohm⁻¹ cm² mole⁻¹ (15). Hence the degree of dissociation, α , in this concentration range is 0.026 and

$$K^d = \frac{[\{\text{TiCl}_3(\text{CH}_3\text{CN})_3\}^+][\{\text{TiCl}_5\text{CH}_3\text{CN}\}^-]}{[\text{TiCl}_4(\text{CH}_3\text{CN})_2]^2} = \alpha^2/(1-\alpha)^2 = 7 \times 10^{-4} \quad [8]$$

From conductance data, Longworth and Plesch (27) concluded that the above type of disproportionation also occurs in solutions of titanium tetrachloride in ethylchloride and methylene dichloride. Using the same units as used above their values for K^d in these solvents correspond to 10⁻¹⁰ and 10⁻¹², respectively. As is to be expected, K^d decreases with decreasing dielectric constant, that of AN is 37, of ethyl chloride 12.3, and of methylene dichloride 9.9.

In the presence of excess chloride ions Ti(IV), Ti(III), and Ti(II) are all stabilized by complex formation, particularly Ti(IV) as its reduction potential is shifted more than 1v more negative in the presence of 0.1M chloride. From the variation in the value of the diffusion current constant, I_D , with chloride ion concentration (Table II) it is possible to make an estimate of the stability constant of TiCl_6^{2-} , formed by the reaction



where K^f is the over-all stability constant for the formation of TiCl_6^{2-} from titanium tetrachloride in AN. If it is assumed that in 1.00 mM titanium tetrachloride solution, 0.101M in chloride, the only species present is TiCl_6^{2-} with an I_D of 12.32 and in 0.1M perchlorate only $\text{TiCl}_4(\text{CH}_3\text{CN})_2$ is present with an I_D of 8.29, then it is calculated that in a solution containing 25 mM added chloride where I_D is 12.11 $[\text{TiCl}_6^{2-}] = 0.948$ mM, $[\text{TiCl}_4(\text{CH}_3\text{CN})_2] = 0.052$ mM and $[\text{Cl}^-] = (25 - 2 \times 0.948)$ mM. Thus

$$K^f = \frac{[\text{TiCl}_6^{2-}][\text{TiCl}_4(\text{CH}_3\text{CN})_2][\text{Cl}^-]^2}{= 3.5 \times 10^4 \text{ l}^2 \text{ mole}^{-2}}$$

In this calculation it has been assumed that in the presence of 25 mM chloride the concentration of $\text{TiCl}_5\text{CH}_3\text{CN}^-$ is negligible compared with the other two Ti(IV) species in solution.

The higher diffusion current constant observed in 0.1M chloride supporting electrolyte compared with that in 0.1M perchlorate is accounted for by the fact that the size of TiCl_6^{2-} is smaller than that of $\text{TiCl}_4(\text{CH}_3\text{CN})_2$, the species present in perchlorate medium. Using the modified Ilkovic equation (28)

$$i_{av.} = 607 nD^{1/2} C m^{2/3} t^{1/6} (1 + 25D^{1/2} m^{-1/3} t^{1/6}) \quad [10]$$

a diffusion coefficient, D , at 25°C of 2.1×10^{-5} cm² sec⁻¹ is calculated for TiCl_6^{2-} and of 1.0×10^{-5} cm² sec⁻¹ for $\text{TiCl}_4(\text{CH}_3\text{CN})_2$ from $i_{av.}$, the average diffusion current. A rough estimate of the diffusion coefficients of these two species can be obtained from the Stokes-Einstein relationship (29). Using the co-valent and Van der Waals' radii as determined in the crystalline state for the atoms involved (30, 31), the radius of the octahedral TiCl_6^{2-} ion is found to be 4.2Å, while $\text{TiCl}_4(\text{CH}_3\text{CN})_2$, which exists almost exclusively in the symmetrical trans form (32), has a semi-major axis of 6.7Å and two semi-minor axes of 4.2Å. From these values the diffusion coefficients are calculated to be 1.6×10^{-5}

$\text{cm}^2 \text{sec}^{-1}$ for TiCl_6^{2-} and $1.2 \times 10^{-5} \text{ cm}^2 \text{sec}^{-1}$ for $\text{TiCl}_4(\text{CH}_3\text{CN})_2$. These calculations ignore the effects of solvation and, in the case of TiCl_6^{2-} , charge. Also, for $\text{TiCl}_4(\text{CH}_3\text{CN})_2$ the weighted root mean square radius was used. Nevertheless, fair agreement is noted between the values of diffusion coefficient calculated by the two methods, indicating that the assumptions made about the titanium(IV) species present in chloride and perchlorate solutions are reasonable.

The behavior of titanium(IV) solutions in AN is quite involved in the presence of iodide (either present as supporting electrolyte or as titanium tetraiodide), this will be the subject of a subsequent publication. The preliminary results reported here give some information regarding the relative stabilities of the halide complexes of titanium(IV) in AN. The current-potential curve of 1.00 mM titanium tetrachloride in 0.1M iodide, Fig. 1, curve B, indicates that there are two species present in solution, each being reduced at different potentials from Ti(IV) to Ti(III) and then to Ti(0). The ratios of the diffusion current constants at -0.68v (1st wave) and -0.9v (2nd wave) to those at -1.6v (3rd wave) and -2.05v (4th wave), respectively, are 1:4.37 and 1:4.08. Thus, the limiting current at -0.9v corresponds to the reduction of all the Ti(IV) species to Ti(III) while that at -2.05v corresponds to the reduction of all the Ti(IV) species to Ti(0). The value of $E_{1/2}(-1.20\text{v})$ for the third wave suggests that the predominant species is most likely $\{\text{TiCl}_4\text{ICH}_3\text{CN}\}^-$ (c.f., $E_{1/2} = -1.75\text{v}$ in 0.1M perchlorate), while the second species may be either $\text{TiCl}_4(\text{CH}_3\text{CN})_2$ or $\text{TiCl}_4\text{I}_2^{2-}$. The fact that the total diffusion current constant is only 8.70 (Table I) as compared to 8.29 in 0.1M perchlorate indicates that iodide does not replace the chlorides and only partially replaces the solvent molecules in the coordination sphere of the titanium(IV) cation.

From the current-potential curve of 1.00 mM titanium tetraiodide in 0.1M chloride (Fig. 4, curve B) it appears that the first wave is part of the total one-electron wave and is composite with the anodic chloride wave. The second part of the split first wave is similar to the first one-electron wave of titanium tetrachloride in 0.1M chloride (Fig. 1, curve E). Thus Ti(IV) is present in two forms in this system, and since the two and four electron reduction waves (third and fourth waves, respectively) are very similar to the corresponding reduction waves of titanium tetrachloride in 0.1M chloride, and the total diffusion current constant of titanium tetraiodide in 0.1M chloride is 12.40 (Table III) as compared to 10.29 in 0.1M perchlorate and to 12.32 for titanium tetrachloride in 0.1M chloride (Table I), it may be concluded that one of these species is TiCl_6^{2-} , i.e., chloride has replaced iodide and AN in the coordination sphere of the titanium(IV) cation with the formation of four iodide ions. As the first reduction wave is split, this replacement has not occurred quantitatively, and the second species, probably $\text{TiCl}_5\text{I}^{2-}$, is reduced to Ti(III) at a more positive potential than is TiCl_6^{2-} , although the two and four electron reductions of both species occur at the same potentials.

It appears then that in AN chloride replaces iodide in titanium tetraiodide. This conclusion is substantiated by the fact that, in the presence of a large excess of chloride, titanium tetraiodide is no longer sensitive to oxygen.

Thus the bonds between titanium(IV) and chloride are much stronger than those with iodide. The titanium(IV)-bromide bond appears intermediate in strength between that of chloride and iodide. The current-potential curves of titanium tetrachloride in 0.1M tetraethylammonium bromide have several waves, indicating that the AN ligands and some of the chlorides in the coordination sphere of titanium(IV) have been replaced by bromide to give a mixture of $\{\text{TiCl}_n\text{Br}_{(6-n)}\}^{2-}$ species. The order of relative bond strengths, namely $\text{Ti-Cl} > \text{Ti-Br} > \text{Ti-I}$, is the same as that observed in aqueous and other media (17, 33). This order is also the same as the order of the bond strengths in the titanium tetrahalides as calculated from the data in the literature (34) using Pauling's relationship between bond energies and the electronegativity difference of the elements involved (30), i.e., $E(\text{Ti-Cl}) = 102 \text{ kcal mole}^{-1}$ (34), $E(\text{Ti-Br}) = 82 \text{ kcal mole}^{-1}$, and $E(\text{Ti-I}) = 57 \text{ kcal mole}^{-1}$ where $E(\text{Ti-X})$ is the mean Ti-X bond energy in TiX_4 .

Acknowledgment

This work was supported by the Directorate of Chemical Sciences' Air Force Office of Scientific Research, under Grant AF-AFOSR-28-63.

Manuscript received Jan. 14, 1964.

Any discussion of this paper will appear in a Discussion Section to be published in the June 1965 JOURNAL.

REFERENCES

1. I. M. Kolthoff and J. J. Lingane, "Polarography," Vol. II, Interscience Publishers Inc., New York (1952).
2. R. L. Pecsok, *J. Am. Chem. Soc.*, **73**, 1304 (1951).
3. M. Kalousek, *Collection Czech. Chem. Commun.*, **11**, 592 (1939).
4. G. M. Habashy, *Z. anorg. allgem. Chem.*, **306**, 312 (1960).
5. E. I. Krylov, V. S. Kolevatova, and V. A. Samarina, *Dokl. Akad. Nauk. S.S.S.R.*, **98**, 593 (1954); *C.A.*, **49**, 1445f (1955).
6. G. M. Habashy, *Collection Czech. Chem. Commun.*, **25**, 3166 (1960).
7. J. J. Lingane and J. H. Kennedy, *Anal. Chim. Acta*, **15**, 294 (1956).
8. M. Blumer and I. M. Kolthoff, *Experientia*, **8**, 138 (1952).
9. D. I. Kurbatov, *Izv. Sibirisk. Otd. Akad. Nauk S.S.S.R.*, (1958), No. 10, 35; *C.A.*, **53**, 7828a (1959).
10. V. Gutmann and E. Nedbalek, *Monatsh. Chem.*, **88**, 320 (1957).
11. V. Gutmann and G. Schöber, *Z. anal. Chem.*, **171**, 339 (1959).
12. I. M. Kolthoff, S. Bruckenstein, and M. K. Chantooni, Jr., *J. Am. Chem. Soc.*, **83**, 3927 (1961).
13. H. J. Emeleus and G. S. Rao, *J. Chem. Soc.*, 4245 (1958).
14. L. A. Knecht and I. M. Kolthoff, *Inorg. Chem.*, **1**, 195 (1962).
15. J. F. Coetzee, Ph.D. Thesis, University of Minnesota, 1955.
16. J. F. Coetzee, G. P. Cunningham, D. K. McGuire, and G. R. Padmanabhan, *Anal. Chem.*, **34**, 1139 (1962).
17. Gmelin's "Handbuch der anorganischen Chemie," No. 41, Titan (1951).

18. E. B. Sandell, "Colorimetric Determination of Traces of Metals," 2nd ed., p. 576, Interscience Publishers Inc., New York (1950).
19. I. M. Kolthoff and J. F. Coetzee, *J. Am. Chem. Soc.*, **79**, 870 (1957).
20. C. A. Krauss and R. M. Fuoss, *ibid.*, **55**, 21 (1933).
21. H. Lund and J. Bjerrum, *Ber.*, **64B**, 210 (1931).
22. F. R. Meyer and G. Ronge, *Z. angew. Chem.*, **52**, 637 (1939).
23. L. Giuffre and F. M. Capizzi, *Ann. Chim.*, **50**, 1150 (1960).
24. A. Findlay, "Practical Physical Chemistry," 7th ed., Longmans, London (1941).
25. D. Altman, M. Farber, and D. M. Mason, *J. Chem. Phys.*, **25**, 531 (1956).
26. "Selected Values of Chemical Thermodynamic Properties," N.B.S. Circular 500 (1952).
27. W. R. Longworth and P. H. Plesch, *J. Chem. Soc.*, **1959**, 1887.
28. For discussion see I. M. Kolthoff and K. Izutsu, *J. Am. Chem. Soc.*, In press.
29. I. M. Kolthoff and J. J. Lingane, "Polarography," Vol. I, Interscience Publishers Inc., New York (1952).
30. L. Pauling, "Nature of the Chemical Bond" 3rd ed., Cornell University Press, Ithaca, N.Y. (1960).
31. "Handbook of Chemistry and Physics," 42nd ed., Chemical Rubber Publishing Co., Cleveland (1960).
32. G. S. Rao, *Z. anorg. allgem. Chem.*, **304**, 351 (1960).
33. S. Ahrland, J. Chatt, and N. R. Davies, *Quart. Rev.*, **12**, 265 (1958).
34. T. L. Cottrell, "Strengths of Chemical Bonds," Butterworths, London (1958).

The Dissociation Pressures of Iron-Nickel Oxides

G. A. Roeder and W. W. Smeltzer

Department of Metallurgy and Metallurgical Engineering,
McMaster University, Hamilton, Ontario, Canada

ABSTRACT

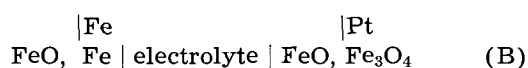
Electromotive force determinations are reported of solid galvanic cells consisting of a ZrO_2 -CaO electrolyte with iron-nickel-oxygen electrodes. To test the design of cells containing embedded electrodes of the reaction metals, dissociation pressures for wustite, magnetite, and nickel oxide were determined and compared with reported values. The standard molar free energy change of the reaction between nickel oxide and wustite and the dissociation pressures of wustite equilibrated with iron-nickel alloys containing nickel to 47.2 a/o were determined at temperatures in the range 800°-1000°C.

Solid state properties such as the dissociation pressures of metal oxides (1-4) and the metal activities for binary alloys (5) may be determined by the galvanic cell technique, the electrolyte being a solid. Following the methods developed by Kiukkola and Wagner (1), investigators have employed a ZrO_2 -CaO electrolyte exhibiting oxygen anion conductivity over a wide range of oxygen pressures and temperatures (6). Since the variation of the dissociation pressure of an oxide with metal composition in the alloy-oxide region of a ternary system has not been investigated by this technique, the dissociation pressures have been determined of wustite containing nickel in solid solution.

The Galvanic Cells

Measurements were made on cells containing binary oxides to test a design wherein the electrode compartments consisted entirely of the reaction metals. The suitability of the cells was proven and it was then possible to determine the dissociation pressure of a ternary oxide equilibrated with an alloy.

Cells of the first classification were as follows



The symbols above the cell designation represent the metals used for the electrodes. Potentials of cells (A) and (B) were known functions of electrochemical and thermochemical data thus establishing criteria of accuracy. In addition, cell (B) plus (C) was equivalent to cell (A) in magnitude of electromotive force produced giving a check of procedures.

Since the reaction is transfer of oxygen from the cathode to the anode, the electromotive force is

$$E = \frac{RT}{4F} \ln (\text{PO}_2)'' / (\text{PO}_2)' \quad [1]$$

Here $(\text{PO}_2)''$ and $(\text{PO}_2)'$ are the dissociation pressures of the oxides in the cathode and anode compartments respectively.

Cells belonging to the alloy classification were as follows



Here x and y represent the atomic fractions of iron and nickel in the alloys. The potentials of these cells may be used under specific restrictions to evaluate the dissociation pressures of wustite containing different amounts of nickel by means of equations (1).

The electrochemical theory for galvanic cells containing ternary oxides has been presented by Carter (2). For reversible potentials, the compositions of the oxides in the electrode compartments must remain unchanged. Such restrictions apply to the ternary cell of this investigation. The displacement reaction accompanying the transfer of a small in-

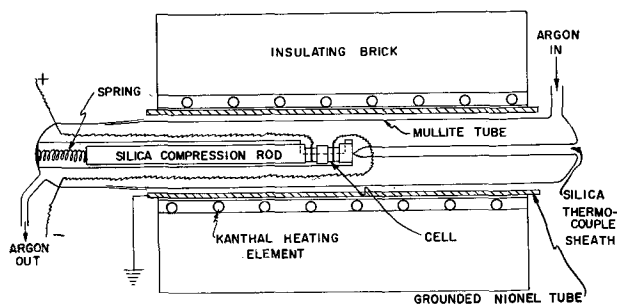
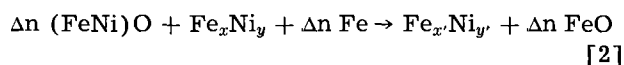


Fig. 1. Galvanic cell assembly for measurements of potentials at elevated temperatures.

crement. Δn , of oxygen from the cathode to anode compartment in cell (D) is



where x, x' and y, y' are the initial and final atom fractions of iron and nickel in the alloy, respectively. Accordingly, the change in the composition of the alloy resulting from transfer of oxygen across the electrolyte and its loss to the environment must be negligible during the experimental exposures. A criterion adopted for this condition was the establishment of steady potential values on cycling the cells between the two temperatures of interest, 900° and 1000°C.

Experimental

The apparatus used for potential determinations of the galvanic cells in flowing argon is illustrated in Fig. 1. The desirability of mounting the cell independently from the furnace assembly dictated that the compression spring governing electrode-electrolyte contacts be an integral part of the Pyrex cap enclosing the exit end of the reaction tube. A glass vacuum and gas purification system permitted the achievement of 10^{-6} mm Hg or the flow of argon through the reaction tube. This train contained an unreduced copper catalyst held at 150°C, anhydrous magnesium perchlorate, ascarite, and reduced catalyst held at 150°C. In order to reduce the oxygen content in argon to less than 0.1 ppm, the load ratio of gas to catalyst never exceeded the recommended ratio 20:1. Temperatures in the cell zone were controlled within $\pm 1^\circ\text{C}$ and potentials were determined to a precision of 10^{-3} mv with a Leeds and Northrup K-3 potentiometer.

All metal and oxide powders were Fisher C. P. reagents. Sintered electrolyte tablets, $\text{Zr}_{0.85}\text{Ca}_{0.15}\text{O}_{1.85}$, were made from zirconium and calcium oxides (1). The metal-oxide tablets placed into the cell assembly unsintered consisted of metal and oxide mixtures with M/O ratios of 2, and they were made by pressing a powder of pre-determined proportions in a compression jig at 10 tons/cm². Alloy-oxide tablets with this M/O ratio consisted of iron, nickel, and magnetite of proportions for alloy compositions of 10, 20, 30, 40, 47.5, and 55 weight per cent (w/o) nickel under the assumption that the equilibrated oxide would be wustite containing negligible dissolved nickel.

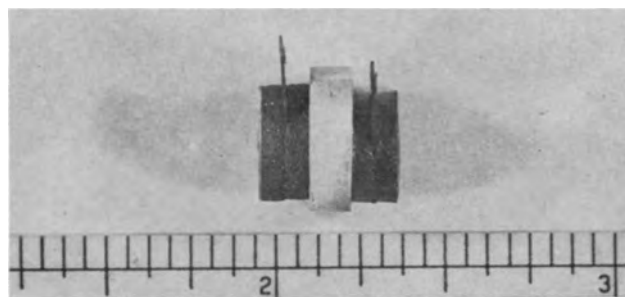


Fig. 2. Galvanic cell: $\text{FeO}, \text{Fe} | \text{electrolyte} | \text{Ni}, \text{NiO}$

It was decided to use electrodes of the alloy or metal being studied in a cell because platinum exhibits almost complete solubility of iron and nickel at high temperatures which could cause concentration gradients in the electrode compartments. A cell is illustrated in Fig. 2. The electrodes of tear drop shape, with a thickness of 0.01 in. or less and of the metals or alloys being investigated, were embedded in the anode and cathode compartments by sandwiching between two tablets of the reactants. Due to sintering processes, the metal-oxide compacts were intimately bonded to the metal electrodes. These electrodes, which were spot welded to the platinum lead wires, were discarded after each run.

As illustrated in Fig. 2, the electrolyte tablet (0.4 in. diameter and 0.15 in. thick) was larger than the metal-oxide tablets (0.3 in. diameter and 0.1 in. thick). This construction prevented short-circuiting of the electrolyte, as was found for smaller electrolyte tablets, by the iron-wustite constituents due to their flow around the electrolyte tablet.

In a typical run the pumping down period on a cell at room temperature lasted for at least 15 hr whereupon argon was admitted and adjusted to a flow rate of 2 liters/hr. The furnace was then heated to a predesignated equilibration temperature. Potentials of the cell containing binary oxides were determined at time increments until a steady value was attained and a single run consisted of voltage determinations at several temperatures. Since fine powders of iron, nickel, and magnetite were used to give the desired alloys, cells of type (D) were annealed for at least two days at 1000°C. Microscopic examinations of electrode cross-sections illustrated that metal particles actually bonded together and these particles were intimately sintered to the oxide during these exposures. These cells were annealed for two days between potential readings at 1000° and 900°C.

Alloy-oxide tablets were analyzed for the nickel content of the oxide. In a series of experiments tablets were sintered in argon for four days at 1000° and 900° and quenched in air by rapidly removing the cell assembly from the reaction tube. The tablets were crushed and the metal dissolved by a 7 hr exposure to a 15% bromine and ethyl acetate solution in a Soxhlet apparatus. Nickel contents of the oxide were then determined by the dimethyl-glyoxime method based on the assumptions that the residual oxide was wustite and that its formula was

Table I. Potentials for cells (A, B, and C) with electrode compartments of pure metals and binary oxides

	Cell (A), E (mv)	Cell (B), E (mv)	Cell (C), E (mv)	Virtual cell (A = B + C), E (mv)	Cell (A) (ref. (1)), E (mv)
730	258 (1)				259
782	268 ± 4 (4)				264
800		73 ± 2 (4)	189 ± 1 (4)	262 ± 3	266
833	272 ± 3 (4)				270
882	275 ± 4 (4)				274
900		103 ± 1 (4)	171 ± 1 (6)	274 ± 2	276
937	280 ± 4 (3)				280
950		118 (1)	162 (1)	280	281
1000		134 (2)	151 ± 1 (6)	286 ± 2	286

(FeNi)_nO where n was defined by the iron-oxygen phase diagram.

Results

Cells (A), (B), and (C).—Potentials produced by the cells containing pure metals and binary oxides at temperatures in the range 700°–1000° are recorded in Table I. (In all tables, the bracketed number after each potential value represents the number of determinations.) The potentials for the cells with FeO, Fe and NiO, Ni compartments (cell A) were reproducible to ±4 mv and, as shown in Table I, agreed with those reported by Kiukkola and Wagner (1). Iron and platinum embedded electrodes were employed in the cells with FeO, Fe and FeO, Fe₃O₄ compartments (cell B) and the potentials were consistent with values previously reported (1, 2). Platinum and nickel embedded electrodes were employed in the cells with FeO, Fe₃O₄, and NiO, Ni compartments (cell C). Potentials have not been determined previously for this cell.

Virtual cell (A).—It was possible to check the cell design employing reaction metal electrodes by a summation of the previously determined potentials for cells (B) and (C). These values, Table I, are in agreement with values reported for cell (A). Accordingly it was feasible to use cells with alloy electrodes to determine properties of the ternary Fe–Ni–O system.

Table II. Potentials of cell FeO, Fe | electrolyte | Fe_xNi_y, (FeNi)O

Alloy electrode compartment Initial Ni content of alloy (w/o)	E (mv)	
	900°C	1000°C
10	0 (1)	1.8 (1)
20	1.8 ± 0.8 (3)	4.8 ± 0.5 (3)
30	10.7 ± 0.9 (3)	19.8 ± 0.3 (3)
40	21.4 ± 2 (3)	26.9 ± 2 (3)
47.5	26.4 ± 1 (2)	36.7 ± 1 (2)
55.0	55.7 ± 1 (2)	83.7 ± 1 (2)

Table III. Analyses for nickel in the wustite phase

Initial nickel content of alloy (w/o)	T (°C)	Ni content of wustite (w/o)	Equilibrium
			Fe–Ni alloy comp. (w/o Ni)
55	1000	1.9 ± 0.6 (3)	48.4
47.5	1000	2.7 ± 0.6 (2)	44.8
40	900	2.74 (1)	38.0
40	1000	1.8 ± 0.5 (2)	38.4
30	900	1.0 ± 0.3 (2)	29.2
30	1000	<0.2 (2)	29.7

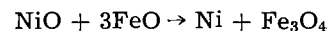
Cell (D).—Potentials produced at 900° and 1000° by the cells consisting of FeO, Fe and (FeNi)O, Fe_xNi_y, the initial compositions of the alloys being between 10–55 w/o Ni, are recorded in Table II. The potentials were larger for alloys of larger nickel contents.

Structures of the electrode tablets containing alloys of nickel contents in the range 30–50 atomic per cent (a/o) after an air quench were examined by means of metallographically prepared cross-sections. All structures exhibited large amounts of wustite with minor amounts of the spinel oxide possibly resulting from precipitation during the quench. The nickel contents of the oxide residues after dissolution of the metal by bromine and the nickel contents of the equilibrated alloys based on these analyses are recorded in Table III. X-ray analyses of two oxides residues indicated no free metal and wustite to spinel proportions in excess of 85%.

Discussion

Galvanic cells with embedded electrodes of the reaction metals exhibited two distinct advantages: first, the interfacial bonding of the electrode to the metal of a metal-oxide compact by sintering minimized any influence of oxygen from the atmosphere at this interface and, second, metal concentration gradients in a compact were avoided as the alloy was of the same composition throughout the electrode compartment. Consequently, the dissociation pressures of a ternary oxide equilibrated with an alloy could be determined from such cells.

With the exception of cell (C), earlier workers have determined the standard molar free energies for the cell reactions with the binary oxides and pure metals. The displacement reaction in this cell is



Values of the standard molar free energy change are recorded in Table IV and are shown along with

Table IV. Potentials of cell FeO, Fe₃O₄ | electrolyte | Ni, NiO and standard free energy ΔF° of the reaction NiO + 3FeO → Ni + Fe₃O₄

T (°C)	E (mv)	Standard molar free energy change (kcal/mole)		
		This investigation	Ref. (1) and (7)	Ref. (7) and (8)
800	189 ± 1 (4)	–17.43	–17.84	–19.32
900	171 ± 1 (6)	–15.77	–16.04	–17.72
950	162 (1)			
1000	151 ± 1 (6)	–13.96	–13.96	–15.98

Table V. Dissociation pressures of wustite equilibrated with iron-nickel alloys

Equilibrium Fe-Ni alloy comp. (a/o Ni)	Ni content of wustite (w/o)	Dissociation pressure (atm)			
		900°C		1000°C	
		This investigation	Ref. (7) and (10)	This investigation	Ref. (7) and (10)
0	0		1.89×10^{-17}		1.32×10^{-15}
9.6		1.89×10^{-17}	2.38×10^{-17}	1.41×10^{-15}	1.74×10^{-15}
19.2		2.02×10^{-17}	2.71×10^{-17}	1.57×10^{-15}	2.17×10^{-15}
28.5	0.6	3.44×10^{-17}	3.58×10^{-17}	2.72×10^{-15}	2.72×10^{-15}
37.0	2.1	4.40×10^{-17}	4.5×10^{-17}	3.52×10^{-15}	3.5×10^{-15}
43.6	2.7	5.37×10^{-17}		5.03×10^{-15}	
47.2	1.9	1.71×10^{-16}		2.79×10^{-14}	

comparative values determined from values for the free energies of formation of nickel oxide, wustite, and magnetite (1, 7, 8). The values are in best agreement with those determined from data given by Kiukkola and Wagner (1) and they are approximately 2 kcal smaller than those values determined from data recommended by Coughlin (8) for the standard free energy of formation of nickel oxide.

In studies on phase equilibria at 1050° in the Fe-Ni-O system, Brabers and Birchenall (9) found that wustite may be equilibrated with alloys containing nickel to approximately 55 a/o. Wustite, essentially free of nickel, and a spinel, $\text{Fe}_{2.6}\text{Ni}_{0.4}\text{O}_4$, co-existed with this alloy of critical nickel content. Since the potentials of cell (D) yield the dissociation pressures of wustite containing different amounts of nickel in solid solution (Eq. [1]), one may compare these pressures to those for wustite equilibrated with iron. Moreover, one may conclude from the variation of the oxygen pressure that the oxides equilibrated with alloys of different nickel contents are in either the variant two phase, wustite-alloy, or the invariant three phase, wustite-spinel-alloy, regions at the temperatures of 900° and 1000°.

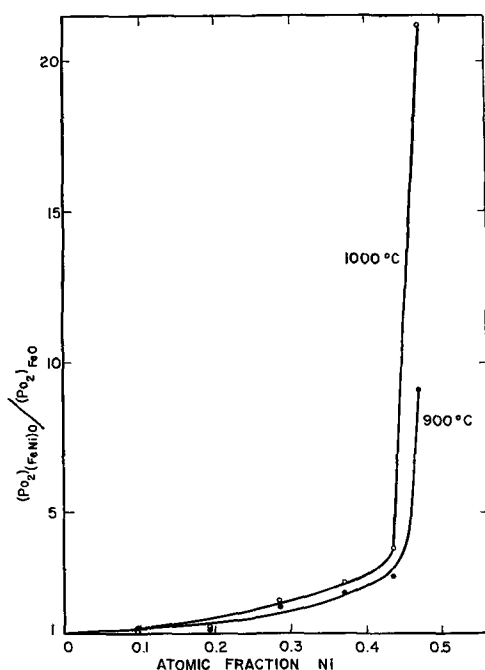


Fig. 3. Comparison of dissociation pressures of wustite containing different amounts of dissolved nickel to wustite at 900° and 1000°C.

The dissociation pressures, Table V, are compared to those of wustite in Fig. 3. Analyses for the nickel contents in the quenched compacts were only qualitatively acceptable, and points along the abscissa of Fig. 3 are average compositions of the alloys. Because the dissociation pressure of wustite continually increased with larger nickel contents in the alloy, the cathode compartment contained only two phases, the oxide being wustite with small amounts of dissolved nickel. Accordingly the small amounts of spinel found in the compacts were precipitated during the quench.

In Table V, the dissociation pressures of wustite equilibrated with alloys to 40 a/o are compared to values calculated from data given by Oriani (10) for equilibration of wustite with iron-nickel alloys in water-hydrogen atmospheres. The values from this investigation to 19.2 a/o nickel, where the electrochemical measurements were least reliable, were smaller than those pressures determined from gas equilibria measurements. At larger nickel contents in the alloys, the values from both methods showed good agreement. As the values of the dissociation pressures were much larger on equilibration of wustite with alloys containing more than 30 a/o nickel, the invariant oxygen pressure for the wustite-spinel-alloy region of the Fe-Ni-O ternary phase diagram is much larger than the dissociation pressure of wustite equilibrated with iron.

Summary

Galvanic solid cells with embedded electrodes of the reaction metals in the metal-oxide compartments were employed for determinations of oxygen dissociation pressures of binary and ternary oxides. The standard molar free energy change of the reaction between nickel oxide and wustite and the dissociation pressures of wustite equilibrated with alloys containing nickel to 47.2 a/o were determined for temperatures in the range 800°-1000°C. Application of this method to the ternary Fe-Ni-O system was limited by the precision of the determinations for the nickel contents of wustite.

Acknowledgments

This contribution is based on a thesis submitted by G. A. Roeder to the School of Graduate Studies, McMaster University, in partial fulfillment of the requirements for the M.Eng. degree. He wishes to acknowledge the award of a Cominco Fellowship. This work forms part of a research project sponsored by the U. S. Air Force Office of Scientific Research,

Office of Aerospace Research and the Defence Research Board, Ottawa, Canada.

Manuscript received Nov. 22, 1963.

Any discussion of this paper will appear in a Discussion Section to be published in the June 1965 JOURNAL.

REFERENCES

1. K. Kiukkola and C. Wagner, *This Journal*, **104**, 379 (1957).
2. R. E. Carter, *J. Am. Ceram. Soc.*, **43**, 448 (1960).
3. R. Benz and H. Schmalzried, *Z. physik. Chemie N.F.*, **29**, 77 (1961).
4. R. A. Rapp, *Trans. AIME*, **227**, 2 (1963).
5. R. A. Rapp and F. Maak, *Acta Met.*, **10**, 63 (1962).
6. W. D. Kingery, J. Pappis, M. E. Doty, and D. C. Hill, *J. Am. Ceram. Soc.*, **42**, 393 (1959).
7. L. S. Darken and R. W. Gurry, *J. Am. Chem. Soc.*, **67**, 1398 (1945).
8. J. P. Coughlin, *U. S. Bur. Mines Bull.*, 542 (1954).
9. M. J. Brabers and C. E. Birchenall, *Corrosion*, **14**, 179t (1958).
10. R. A. Oriani, *Acta Met.*, **1**, 448 (1953).

Mechanism of the Hydrogen Gas Diffusion Electrode

Raymond P. Iczkowski¹

Research Division, Allis-Chalmers Manufacturing Company, Milwaukee, Wisconsin

ABSTRACT

Equations were formulated for the electrolyte film mechanism, in which H_2 diffuses through a film of electrolyte covering the surface of the pores in the electrode. The polarization characteristics at high and low currents were obtained analytically. The equations were solved numerically on a computer using data for H_2 on Ni with an NaOH electrolyte for various values of the surface roughness, pore radius and length, temperature, concentration of electrolyte, and film thickness. A similar computer solution was made of Justi's equations for the surface diffusion mechanism, and the results of the two calculations were compared. The results show that the electrolyte film mechanism has a maximum current 300 times larger, and a slope of the polarization curve at low currents, which is 45 times less than that for the surface diffusion mechanism.

The hydrogen gas diffusion electrode consists of a porous metal plate in contact with a solution of electrolyte, such as NaOH, on one side and hydrogen gas on the other. As a working approximation it is considered that the pores in the electrode may be represented by an array of right circular cylinders each of which passes completely through the electrode. There are two theories of the mechanism by which reaction takes place in a single pore: the surface diffusion mechanism (1), and the electrolyte film mechanism (2).

According to the surface diffusion theory, the electrolyte forms a sharp circular three-phase boundary along the wall of the pore (see Fig. 1A).

¹ Present address: Xerox Corporation, Webster, New York.

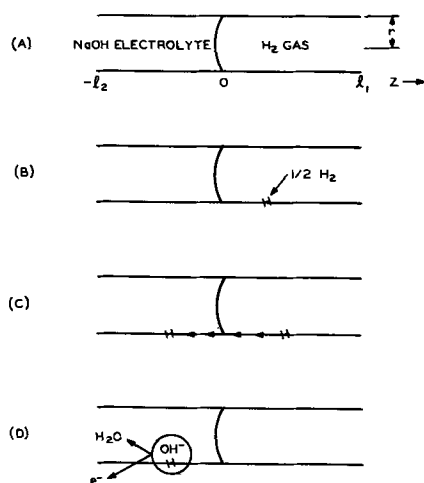


Fig. 1. Stages in the surface diffusion mechanism

The reaction proceeds by means of the following sequence of steps:

1. Hydrogen from the gas phase is adsorbed as atoms on the surface of the pore (see Fig. 1B).

2. Hydrogen atoms (a) diffuse along the walls from the point of adsorption toward the part of the pore containing the electrolyte, and (b) diffuse under the meniscus to the part of the pore in contact with electrolyte (see Fig. 1C).

3. Hydrogen atoms on the wall react with hydroxide ions from the electrolyte to form water and give up an electron to the electrode (see Fig. 1D). The equations for the surface diffusion mechanism were formulated, but not solved by Justi *et al.* (1). The surface diffusion mechanism was first considered assuming that there is no film of electrolyte adhering to the walls of the pores. Later it was shown how the results would be affected if an electrochemically inert film of liquid coated the walls on the gas side of the pore. The equations for the case of the inert film are the same as those for the case without the film except that the rate of adsorption of hydrogen is multiplied by a scale factor which is proportional to the thickness of the film.

According to the electrolyte film mechanism, the pore is considered to be covered by a layer of electrolyte which separates the hydrogen gas from the metal surface (see Fig. 2A).

The reaction proceeds by means of the following steps:

1. Hydrogen dissolves in the outermost layer of the film (see Fig. 2B).

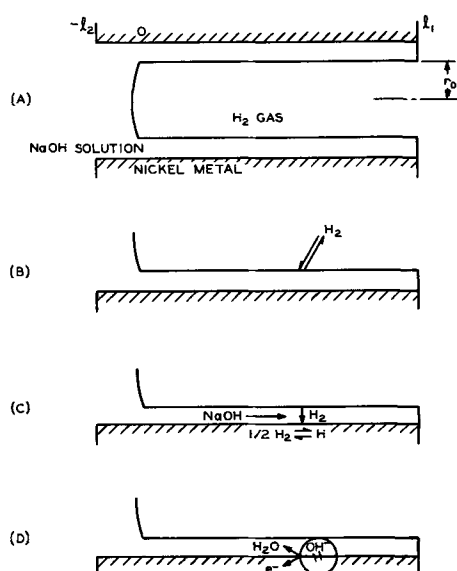


Fig. 2. Stages in the electrolyte film mechanism

2. Hydrogen diffuses radially through the film, and sodium hydroxide diffuses and migrates along the film to various points along the wall (see Fig. 2C).

3. Reaction occurs at points along the wall, forming water and an electron, which goes into the metal (see Fig. 2D). The concentrations of hydrogen and sodium hydroxide vary from point to point along the wall and depend on the rates of reaction at various points along the wall and the rate of transport by diffusion and migration.

It is of interest to formulate the equations for the electrolyte film mechanism and to solve the equations for both mechanisms to determine which one more appropriately describes the operation of the nickel-hydrogen gas diffusion electrode.

Equations for the Surface Diffusion and Electrolyte Film Mechanisms

The equations for the surface diffusion mechanism are (1)

$$\frac{d^2 a_H(z)}{dz^2} = \frac{j(z)}{FD_H} \quad [1]$$

$$\frac{d^2 \eta(z)}{dz^2} = \frac{2\rho j(z)}{r} \quad [2]$$

and

$$j(z) = sj_o \left[\frac{a_H(z)}{a_H^0} e^{\alpha \xi \eta(z)} - e^{-(1-\alpha)\xi \eta(z)} \right] \quad [3]$$

where z is the position along the wall of the pore in Fig. 1; $a_H(z)$ is the activity of hydrogen atoms adsorbed on the wall of the pore at z ; a_H^0 is the activity of adsorbed hydrogen atoms corresponding to a pressure of hydrogen of 1 atm; $\eta(z)$ is the polarization at z ; $j(z)$ is the current density at z ; D_H is the coefficient of surface diffusion for hydrogen atoms; ρ is the specific resistance of the electrolyte; r is the radius of the pore; s is the ratio of the true surface area of the pore to the apparent surface area, due to surface roughness; j_o is the exchange current density appropriate to the given bulk concentration of NaOH; $\xi = F/(RT)$.

The solutions to these equations are subject to the boundary conditions (1)

$$\left. \frac{d\eta}{dz} \right|_{z=0} = 0 \quad \left. \frac{d\eta}{dz} \right|_{z=-l_2} = -\frac{\rho J}{\pi r^2}$$

$$\frac{a_H(0)}{a_H^0} = \cos \theta - \sqrt{3} \sin \theta,$$

$$\text{where } \theta = \frac{1}{3} \cos^{-1} [1 - (J/J_{\max})^2]$$

$$\left. \frac{dC_H}{dz} \right|_{z=-l_2} = 0$$

where J is the total current delivered by the pore; J_{\max} is the maximum current which could be delivered by the pore.

The equations for the electrolyte film mechanism are similar to those for the surface diffusion mechanism. The hydrogen which dissolves in the outermost layer of the electrolyte film will be assumed to be in equilibrium with the hydrogen in the gas phase and its concentration to be given by the equilibrium concentration: $C_{H_2}(r_o - t)$ will be used to denote this concentration (in eq/cm³) at the hydrogen gas-solution interface which is at $r_o - t$ for a film of thickness t , in a pore of radius r_o . Hydrogen diffuses through the electrolyte film according to the equation

$$\frac{d}{dr} \left(r \frac{dC_{H_2}(r)}{dr} \right) = 0$$

with the boundary conditions

$$C_{H_2}(r_o - t) = \text{equilibrium solubility}$$

$$D_h \frac{dC_{H_2}(r_o)}{dr} = -\frac{j(z)}{F}$$

The solution of this equation is

$$\frac{C_{H_2}(r_o)}{C_{H_2}(r_o - t)} = 1 - \sigma j(z) \quad [4]$$

where $C_{H_2}(r_o)$ is the concentration of hydrogen at r_o , the nickel-electrolyte interface.

σ represents the collection of constants

$$\frac{r_o}{FD_h C_{H_2}(r_o - t)} \ln \frac{r_o}{r_o - t}$$

D_h is the diffusion coefficient of hydrogen in the solution. It will be assumed that D_h may be taken independent of the concentration of sodium hydroxide. Since the process of dissociation of hydrogen molecules to hydrogen atoms precedes the electrochemically rate-determining step, it may be taken to be in equilibrium

$$K = \frac{(a_H^0)^2}{a_{H_2}(r_o - t)} = \frac{[a_H(r_o)]^2}{a_{H_2}(r_o)} \quad [5]$$

The activity of hydrogen a_{H_2} will be taken to be equal to the concentration of hydrogen, C_{H_2} , since the solubility is very small. The electrochemical reaction rate on nickel is governed by the slow discharge mechanism [3] and the current density at z is given by [4]

$$j(z) = sj_0 \left[\frac{a_{\text{H}}(r_0)}{a_{\text{H}}^0} \frac{a_{\text{OH}^-}(z)}{a_{\text{OH}^-}(0)} e^{\alpha\xi\eta(z)} - \frac{a_{\text{H}_2\text{O}}(z)}{a_{\text{H}_2\text{O}}(0)} e^{-(1-\alpha)\xi\eta(z)} \right] \quad [6]$$

Equations [4], [5], and [6] may be combined to give the current density as a function of the polarization and the activities of NaOH, and water

$$j(z) = sj_0 [U_2(1 + \nu U_1 + \frac{1}{4}\nu^2 U_2^2)^{1/2} - U_1 - \frac{1}{2}\nu U_2^2] \quad [7]$$

$$\text{where } U_1 = \frac{a_{\text{H}_2\text{O}}(z)}{a_{\text{H}_2\text{O}}(0)} e^{-(1-\alpha)\xi\eta}, \quad U_2 = \frac{a_{\text{OH}^-}(z)}{a_{\text{OH}^-}(0)} e^{\alpha\xi\eta},$$

and $\nu = sj_0\sigma$. The potential distribution along the film is governed by Ohm's law which takes the form

$$\frac{d\eta(z)}{dz} = -\frac{\rho}{t(1-\frac{1}{2}tr_0^{-1})} \int_z^{l_1} j(z) dz \quad [8]$$

The flow of OH^- ions at point z in the pore due to the interdiffusion of NaOH and water is

$$-D_{\text{OH}^-} \frac{dC_{\text{OH}^-}(z)}{dz}$$

and the flow due to migration of ions in the electric field is

$$\frac{T_{\text{OH}^-}}{Ft(1-\frac{1}{2}tr_0^{-1})} \int_z^{l_1} j(z) dz \left(\frac{\text{eq}}{\text{cm}^2\text{sec}} \right)$$

The sum of these flows is equal to the total current passing the point z , divided by the cross sectional area and the Faraday. The variation in the concentration of NaOH at various points along the wall of the pore is therefore given by

$$\frac{dC_{\text{OH}^-}(z)}{dz} = -\frac{T_{\text{Na}^+}}{Ft(1-\frac{1}{2}tr_0^{-1})D_{\text{OH}^-}} \int_z^{l_1} j(z) dz \quad [9]$$

where $C_{\text{OH}^-}(z)$ is the concentration of sodium hydroxide at z ; D_{OH^-} is the diffusion coefficient of sodium hydroxide in water; T_{Na^+} is the transference number of sodium ion in NaOH. D_{OH^-} and T_{Na^+} are functions of the activity and concentration of sodium hydroxide at z . The solution of these equations is subject to the boundary conditions $C_{\text{OH}^-}(0) = \text{bulk concentration of sodium hydroxide}$

$$J = 2\pi r_0 \int_0^{l_1} j(z) dz \quad [10]$$

Limiting Behavior at High Polarization

The maximum current obtainable from the surface diffusion mechanism at one atmosphere was shown (1) to be

$$J_{\text{max}} = \frac{4\pi r F}{\sqrt{3}} \sqrt{D_{\text{H}} v_0 C_e} \quad [11]$$

where v_0 is the maximum flow density between the gas phase and the adsorbed phase. C_e is the activity of hydrogen atoms present on the surface of the pore in the absence of electrochemical reaction, at one atm.

In the electrolyte film mechanism, if the thickness of the film, the bulk concentration of NaOH, and r_0 are large and l_1 is small, then the maximum

current will be determined by the diffusion of H_2 and not by the transport of NaOH. In that case, $\rho \approx \text{const}$, and the condition $j(z) \leq j(0)$ will be required by Eq. [8]. As $\eta \rightarrow \infty$, then $j(0) \rightarrow 1/\sigma(0)$, and the total current delivered by the pore from Eq. [10] becomes

$$J_{\text{max}} = \frac{2\pi r_0 l_1}{\sigma(0)} = -\frac{2\pi F D_{\text{H}} C_{\text{H}_2}(r_0-t) l_1}{\ln(1-tr_0^{-1})} \quad [12]$$

If t , $C_{\text{OH}^-}(0)$, and r_0/l_1 are small, the maximum current will be influenced by the transport of NaOH.

Limiting Behavior at Low Polarization

The behavior of the solutions to the differential equations for the surface diffusion and electrolyte film mechanisms can be evaluated analytically at $z = 0$, in the limit as the polarization approaches zero for the gas diffusion electrode by a method analogous to that used by Perskaya and Zaidenman (5) for liquid diffusion electrodes. In this method, the activities are equated to the concentrations, $j(z)$ is expanded in series, and high order terms in η and z are eliminated in subsequent limiting processes.

In the surface diffusion mechanism, $j(z)$ may be eliminated between the two differential equations to yield

$$\frac{d^2 C_{\text{H}}(z)}{dz^2} = \frac{r}{2\rho F D_{\text{H}}} \frac{d^2 \eta(z)}{dz^2}$$

which can be integrated

$$C_{\text{H}}(z) = C_{\text{H}}(0) + \frac{r}{2\rho F D_{\text{H}}} [\eta(z) - \eta(0)] + \frac{1}{2\pi r F D_{\text{H}}} J z$$

If, in the expression for $j(z)$ in Eq. [3], the exponential function is expanded in series, and only the first order terms in η are retained, the limiting behavior for small polarization becomes

$$\frac{d^2 \eta(z)}{dz^2} = \frac{2\rho s j_0}{r} \{Q_{\text{H}}(z) - 1 + [\alpha(Q(z)-1) + 1]\xi\eta(z)\}$$

where $Q_{\text{H}} = C_{\text{H}}/C_e$. For a sufficiently deep penetration of electrolyte, $w_s l_2 \gg 1$, the solution of this equation to first order in η and z is

$$\eta(z) = \frac{A^{1/2} B J e^{w_s z}}{\gamma (s j_0 \nu^{1/2} [AB + \xi(1 + \alpha P)])^{3/2}} - \frac{P + B J z / \gamma}{AB + \xi(1 + \alpha P)}$$

where $A = \frac{1}{2} r / \rho$, $B = (F D_{\text{H}} C_e)^{-1}$, $\gamma = 2\pi r$, $P = Q_{\text{H}}(0) - 1 - AB\eta(0)$, $w_s = \{s j_0 [B + A^{-1}\xi(1 + \alpha P)]\}^{1/2}$.

Differentiating with respect to J , and taking the limits as $z \rightarrow 0$: $Q_{\text{H}}(0) \rightarrow 1$, $\eta(0) \rightarrow 0$

$$\left. \frac{d\eta(0)}{dJ} \right|_{J=0} = \frac{1}{\xi} \left[\frac{1}{\gamma} \sqrt{\frac{B}{s j_0}} - \left. \frac{dQ_{\text{H}}(0)}{dJ} \right|_{J=0} \right]$$

and

$$\left. \frac{dQ_{\text{H}}(0)}{dJ} \right|_{J=0} = -\sqrt{\frac{2}{3}} \frac{1}{J_{\text{max}}}$$

Therefore, the initial slope of the polarization curve is given by

$$\left. \frac{d\eta(O)}{dJ} \right|_{J=0} = \frac{RT}{F} \left[\frac{1}{2\pi r (s j_0 F D_H C_e)^{1/2}} + \sqrt{\frac{2}{3}} \frac{1}{J_{\max}} \right] \quad [13]$$

The slopes $\left. \frac{d\eta(O)}{dJ} \right|_{J=0}$ and $\left. \frac{d\eta(-l_2)}{dJ} \right|_{J=0}$ will differ by less than $\rho l_2 / \pi r^2$. The lengthier and more precise equation may be derived in the same way by excluding the approximation $w_s l_2 \gg 1$.

Proceeding in an analogous manner for the thin film mechanism, the change in the activity of water with changing concentration of NaOH is neglected and $a_{\text{OH}^-}(z)/a_{\text{OH}^-}(O)$ is approximated by $C_{\text{OH}^-}(z)/C_{\text{OH}^-}(O)$. When $j(z)$ is eliminated between Eq. [8] and [9], and the resulting equation is solved to first order in $\eta(z)$, the result is

$$C_{\text{OH}^-}(z)/C_{\text{OH}^-}(O) = 1 + G[\eta(z) - \eta(O)] + O(J, z)$$

where $G = T_{\text{Na}^+}/[\rho F D_{\text{OH}^-} C_{\text{OH}^-}(O)]$; T_{Na^+} , ρ , and D_{OH^-} are the values corresponding to the concentration $C_{\text{OH}^-}(O)$, and $O(J, z)$ is a term which becomes negligible in the subsequent limiting processes for J and z . By expanding the exponential term in Eq. [7] and retaining only first order terms, $j(z)$ can be put into the form

$$j(z) = j_1 + j_2 \eta(z), \text{ where } j_1 = - (1 + \frac{1}{2}\nu) + \frac{1}{2}G^2\eta^2(O) + [1 - G\eta(O)][(1 + \frac{1}{2}\nu)^2 + \frac{1}{2}G\nu^2\eta(O)(\frac{1}{2}G\eta(O) - 1)]^{1/2} \text{ and } j_2 \text{ is a similar, but more complex term.}$$

To terms in first order, Eq. [8] becomes

$$\frac{d\eta}{dz} = - \frac{\rho}{t(1 - \frac{1}{2}tr_o^{-1})} \int_z^{l_1} (j_1 + j_2\eta) dz$$

the solution of which is

$$\eta(z) = \frac{\rho J}{2\pi r_o t(1 - \frac{1}{2}tr_o^{-1})w} \frac{e^{w(l_1-z)} + e^{-w(l_1-z)}}{e^{wl_1} - e^{-wl_1}} - \frac{j_1}{j_2}$$

where $w = [\rho j_2 / t(1 - \frac{1}{2}tr_o^{-1})]^{1/2}$. Differentiating with respect to J , and taking the limits as $z \rightarrow 0$, and as $J \rightarrow 0$, yields the equation

$$\left. \frac{d\eta(O)}{dJ} \right|_{J=0} = \frac{1 + G\xi^{-1}}{2\pi r_o} \left[\frac{\rho(1 + \frac{1}{2}\nu)}{t(1 - \frac{1}{2}tr_o^{-1})s j_0(\xi + G)} \right]^{1/2} \coth \left[\frac{\rho s j_0(\xi + G)}{t(1 - \frac{1}{2}tr_o^{-1})(1 + \frac{1}{2}\nu)} \right]^{1/2} l_1 \quad [14]$$

If l_2 is not zero, then

$$\left. \frac{d\eta(-l_2)}{dJ} \right|_{J=0} = \left. \frac{d\eta(O)}{dJ} \right|_{J=0} + \frac{\rho l_2}{\pi r_o^2}$$

It is of interest to obtain the behavior of the pore when electrochemical polarization is absent, and only the concentration polarization of H_2 and NaOH and the ohmic polarization remain. This behavior can be found by assuming the exchange current, j_0 , or alternatively, the surface roughness factor, s , to be infinite. As $(s j_0) \rightarrow \infty$, then

$$\left. \frac{d\eta(O)}{dJ} \right|_{J=0} = \frac{1 + G\xi^{-1}}{2\pi r_o} \left[\frac{\rho\sigma}{2t(1 - \frac{1}{2}tr_o^{-1})(\xi + G)} \right]^{1/2} \coth \left[\frac{2\rho(\xi + G)}{\sigma t(1 - \frac{1}{2}tr_o^{-1})} \right]^{1/2} l_1 \quad [15]$$

In addition, the effect of the concentration polarization of NaOH may be eliminated by assuming the diffusion coefficient of NaOH to be infinite. As $D_{\text{OH}^-} \rightarrow \infty$, then $G \rightarrow 0$ in Eq. [15]. Will (6) derived a similar formula in which the electrochemical polarization and the concentration polarization of electrolyte were ignored. However, Will used the term, t , which corresponds to a flat film, or one which is infinitesimally thin rather than the more precise terms $r_o \ln [r_o / (r_o - t)]$, which occurs in σ in Eq. [4], and $t(1 - \frac{1}{2}tr_o^{-1})$ in Eq. [7] and [8]. As $t \rightarrow 0$, these terms approach t , and $\sigma \rightarrow t / [F D_h C_{\text{H}_2}(r_o - t)]$. When these substitutions are made, Eq. [15] reduces to Eq. [15] of Will's paper in the form in which the MacLaurin expansion is used.

Representation of Input Data

Input data, such as D_{OH^-} , ρ , D_h , j_0 , $C_{\text{H}_2}(r_o - t)$, etc., were taken from previously published experimental results and were represented mathematically by curve fitting. The data subprograms were compiled for use on an IBM 704 computer independent of the main program for integrating the differential equations so that the subprograms could be altered in the light of new data or made to apply to a different electrolyte without changing the main program.

Data used in both mechanisms.—Specific resistance of NaOH, ρ , ($\text{ohm}^{-1} \text{cm}^{-1}$).—Values (7) at 323°K were curve fitted by a ratio of two fifth order polynomials in the concentration. Interpolation according to the formula $e^{A(1/T - 1/323.16)}$ was made for the temperature dependence, where A is a fifth degree polynomial in the concentration.

Exchange current and α for the reaction of H_2 on Ni (8), j_0 , (amp/cm^2).—Values of j_0 were represented by the formula (1, 5)

$$j_0 = 0.0562 e^{-(3055/T)} a_{\text{OH}^-}^{0.58} a_{\text{H}_2\text{O}}^{0.42} P^{0.29} \text{H}_2$$

Alpha (8) was taken to be 0.42.

Apparent partial molal volume of NaOH, Φ_v , (cm^3/mole).—Values of the apparent partial molal value are given by empirical equations (9) as a function of T and m_{OH^-} , where m is the molal concentration.

Concentration scales were converted by means of

$$C = m / (1 + 10^{-3} m \Phi_v)$$

$$\frac{dm}{dC} = \frac{(1 + 10^{-3} m \Phi_v)^2}{1 - 10^{-3} m^2 d\Phi_v/dm}$$

Activity of NaOH and H_2O in sodium hydroxide solutions, a_{NaOH} , $a_{\text{H}_2\text{O}}$.—Values of the activity coefficient of NaOH and the activity of H_2O are given in terms of empirical equations (10) as a function of T and m_{OH^-} for concentrations up to 17M. Values of $d \ln \nu / dm$ were obtained by differentiating the empirical formulas.

Data used in the electrolyte film mechanism.—Diffusion coefficient of hydrogen in NaOH solution

(11) D_h , (cm²/sec).—The diffusion coefficient of hydrogen in solutions of varying concentration of NaOH was taken to be the same as the value for pure water. These values were represented by the equation

$$D_h = 4.62 \cdot 10^{-2} e^{-2140/T}$$

Transference number of Na⁺ in NaOH, T_{Na^+} .—Data (7) for concentrations above 10^{-5} eq/cm³ were curve fitted to the equation

$$T_{Na^+} = 0.1043 - 0.00855 \ln C_{OH^-}$$

The transference numbers of hydroxides do not vary appreciably with temperature between 18° and 65°C (23).

Diffusion coefficient of NaOH in water, D_{OH^-} , (cm²/sec).—Data on the diffusion coefficient at infinite dilution (12) were curve-fitted by the equation

$$D_o = 3.08 \cdot 10^{-2} e^{-2190/T}$$

The concentration dependence was given by (13)

$$D_{OH^-} = D_o \left(1 + C \frac{d \ln y_{\pm}}{dC} \right)$$

where

$$\frac{d \ln y_{\pm}}{dC} = \left[\frac{d \ln \gamma}{dm} + \frac{10^{-3}(\Phi_v + m d\Phi_v/dm)}{1 + 10^{-3} m \Phi_v} \right] \frac{dm}{dC}$$

Solubility of hydrogen in NaOH solutions, C_{H_2} , (eq/cm³).—Data (14) on the solubility of hydrogen in water (in ml/cm³) may be expressed by the equation

$$\beta = 0.0214(1 - 10^{-2}T_c) + 1.837 \cdot 10^{-10}(10^4 - T_c^2)T_c^2$$

where T_c is the centigrade temperature.

The concentration dependence of the solubility was expressed by the Setschenow equation (15), and the temperature dependence of the Setschenow coefficient was obtained from the internal pressure theory of salt effects (15). The final equation was

$$C_{H_2}(\tau_o - t) = 0.0243 \frac{\beta}{T} P_{H_2} e^{-[0.323 - 0.00272(T - 298)]C_{OH^-}}$$

Data used in the surface diffusion mechanism.—The data for the surface diffusion mechanism cannot be obtained with the same precision as the data for the electrolyte film mechanism. The most important data which are lacking are the coefficient of surface diffusion, and the activity of adsorbed hydrogen as a function of the concentration of hydrogen, and the manner in which these quantities are affected by sodium hydroxide solutions. Accordingly, the activities of hydrogen and sodium hydroxide were approximated by their respective concentrations.

Maximum flow density between the gas phase and the adsorbed phase, v_o , (g-atoms/cm² sec).—This quantity may be calculated from the transition state theory for desorption with association (16), assuming that hydrogen atoms and the activated complex are free to move within the boundaries of the site of adsorption and that the activated complex is free to rotate (16). The resulting expression is

$$v_o = \frac{4\pi r_e^2 RT}{h} e^{-\Delta E_o^\ddagger/RT} C_e^2$$

where r_e is the internuclear distance in the H₂ molecule, ΔE_o^\ddagger is the activation energy for desorption, and C_e is the surface concentration of hydrogen (g-atoms/cm²).

Activation energy for desorption, ΔE_a^\ddagger , (kcal/mole).—This quantity varies with surface coverage, as do the heat of adsorption, ΔH_{ads} and the heat of activation of adsorption, ΔH_{ads}^\ddagger . However, ΔH_{ads} at full coverage (17) is 18 kcal/mole and ΔH_{ads}^\ddagger is approximately zero. The activation energy for desorption is approximately the difference between these two quantities, or 18 kcal/mole.

Surface concentration of hydrogen atoms, C_e , (g-atoms/cm²).—If we assume that the (100) crystalline face of nickel is representative of the surface of the mixed crystals actually present and that each hydrogen atom is surrounded by four nickel atoms (17, 18), the concentration of sites is $2/a^2$, where a is the lattice constant. The concentration of hydrogen atoms is essentially equal to the number of sites, $2.684 \cdot 10^{-9}$ (g-atoms/cm²).

Coefficient of surface diffusion, D_H , (cm²/sec).—At low pressures, such as 1 atm, there is only one form of hydrogen adsorbed on nickel, and that form is strongly bonded (18). Therefore, the correct model for surface diffusion of H on Ni is activated diffusion rather than two-dimensional gas flow.

The surface diffusion coefficient can be calculated from the formula (19)

$$D = \frac{1}{4} \bar{v} \delta e^{-E_a^\ddagger/RT} \quad [17]$$

where δ is the distance between hydrogen atom sites, $2.487 \cdot 10^{-8}$ cm and \bar{v} is the average velocity of the hydrogen atom within the site, $(\frac{1}{2}\pi RT)^{1/2}$.

Activation energy for surface diffusion, E_a^\ddagger , (kcal/mole).—The activation energy for surface diffusion at zero surface coverage, $E_a(\theta = 0)$, of hydrogen atoms on Ni was found to be 7 ± 1 kcal/mole from low-temperature electron field microscopy measurements (20). To correct this activation energy to a value appropriate to higher surface coverages $E_a(\theta > 1)$, the rule (20)

$$\frac{E_a}{E_b} = \text{const}$$

may be used, where E_b is the binding energy of the adsorbed atom (the energy required to desorb the hydrogen as gaseous hydrogen atoms), and const is a constant, approximately equal to 0.1. Therefore we can obtain for various surface coverages, θ

$$\frac{E_a(\theta = 0)}{E_b(\theta = 0)} = \frac{E_a(\theta)}{E_b(\theta)}$$

The value $E_a(\theta = 1)$ is 5.68 ± 1 kcal/mole; E_a increases somewhat with decreasing surface coverage, but for the purpose of this calculation it will be treated as a constant, and equal to the value at $\theta = 1$.

Method of Solution

Equations [8] and [9] are difficult to solve because the term $\int_z^1 j(z) dz$ can only be evaluated by means of the expression $(J/2\pi r_o) - \int_0^z j(z) dz$; but J

is not known at the beginning of the calculation. Therefore an iterative technique must be used in which (a) an estimate of J is made, (b) Eq. [7]-[9] are solved simultaneously, and (c) the results of the calculations are used to make a new and better estimate of J . The procedure is repeated many times until the estimated value of J and the value of J calculated from the boundary condition, Eq. [10], are equal.

Equations [8] and [9] for the electrolyte film mechanism were reduced to three simultaneous first order differential equations and were integrated numerically by means of a double precision Runge-Kutta method (21, 22). At $z = 0$, the term $C_{\text{OH}^-}(\text{O})$ is set equal to the concentration of NaOH outside of the pore, $\eta(\text{O})$ is given a value, and a value of J is estimated as being between $2\pi r_o j(\text{O}) l_1$ as an upper limit, and zero as a lower limit. At intervals between $z = 0$, and $z = l_1$, the values of a_{OH^-} , $a_{\text{H}_2\text{O}}$, D_{OH^-} , ρ , and j were calculated from the values of C_{OH^-} and η appropriate to that point, and the values of C_{OH^-} , η , and $2\pi r_o \int_0^z j dz$ were found for the adjacent interval, from the differential equations. At any point for which $z < l_1$, the integration was begun over again from $z = 0$ with a larger estimated value of J , if $2\pi r_o \int_0^z j dz > J$ (and the previous value of J was taken as the new lower limit), or with a smaller estimated value of J , if $C_{\text{OH}^-}(z) < 0$, (and the previous value of J was taken as the new upper limit to J), but if neither of these conditions apply, the integration was continued. When the point $z = l_1$ was reached, the new estimated value of J was made larger or smaller depending on whether the calculated J was larger or smaller than the previous estimated value. The process was terminated after calculated and estimated values of J agreed to 0.01%. Calculations using 100 intervals were performed on an IBM 704 computer for a range of values of $\eta(\text{O})$ between 0 and 1v, and for various values of the parameters s , r_o , l_1 , T , $C_{\text{OH}^-}(\text{O})$, and t . Equations [1]-[3], for the surface diffusion mechanism were treated in a similar manner.

Results

All calculations presented here for the electrolyte film mechanism were made for a pore having a radius, r_o , of 5μ , a length, l_1 , of 0.05 cm, and a depth of penetration of the electrolyte, l_2 , taken to be zero. The pressures of hydrogen was 1 atm. Results

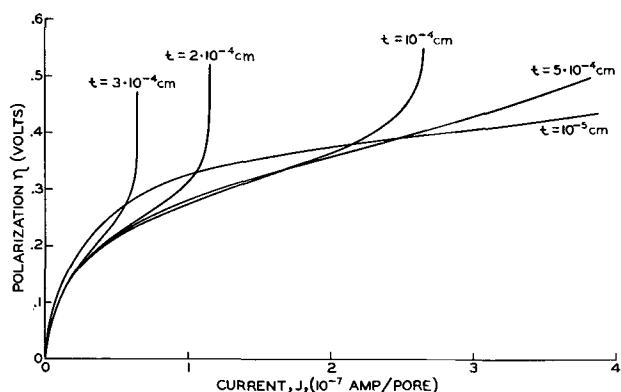


Fig. 3. Polarization curves for the electrolyte film mechanism

are presented graphically in Fig. 3 for various values of the film thickness, t , chosen as 3, 2, 1, 0.5, and 0.1μ , and for the conditions, $s = 1$, $T = 298.16^\circ\text{K}$, and $C_{\text{OH}^-}(\text{O}) = 0.01$ moles/cm³. Figures 4, 5, 6, and 7 show $j(z)$, $\eta(z)$, $C_{\text{OH}^-}(z)$, and $C_{\text{H}_2}(r_o)$ as a function of z for a film thickness of 1μ (full curves) and 0.5μ (dashed curves) at polarizations of 0.1, 0.3, 0.4, and 0.5v. In Fig. 3, the maximum current which can be produced by a pore decreases with increasing film thickness, which is attributable to the term, $1/\ln [r_o/(r_o-t)]$ in Eq. [12]. Figure 4 shows how $j(z)$ approaches the limiting value, $1/s$, as J is increased. Because a high bulk concentration of NaOH was used in the calculation, the dilution of NaOH inside the pore was relatively small (see Fig. 6). When the bulk concentration of NaOH

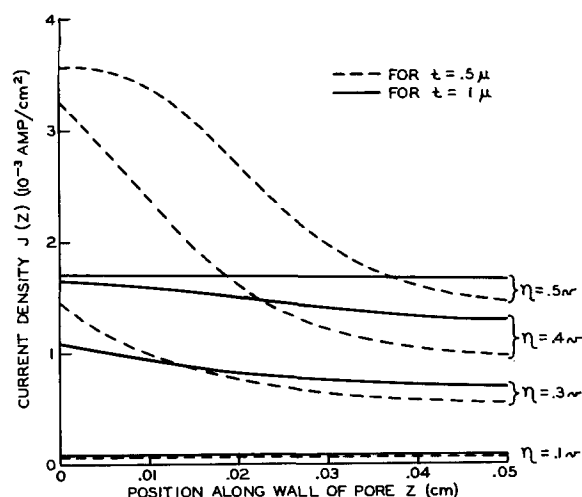


Fig. 4. Current density on the wall of the pore

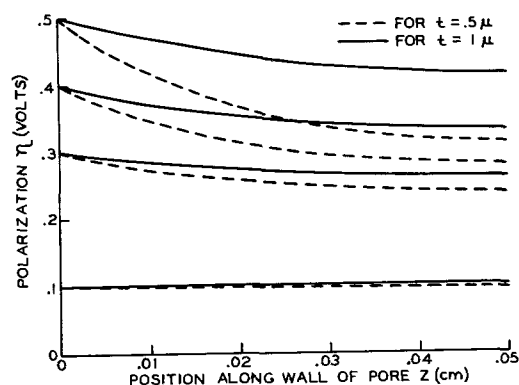


Fig. 5. Polarization of points along the wall of the pore

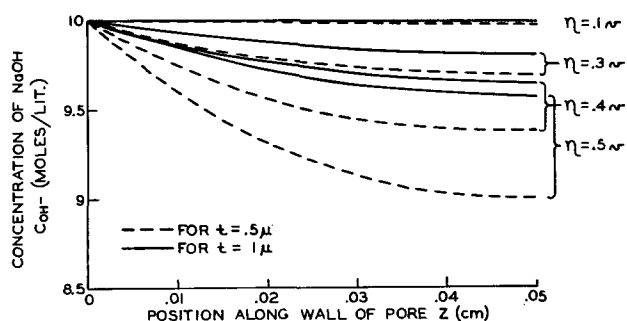


Fig. 6. Concentration of NaOH in various parts of the pore

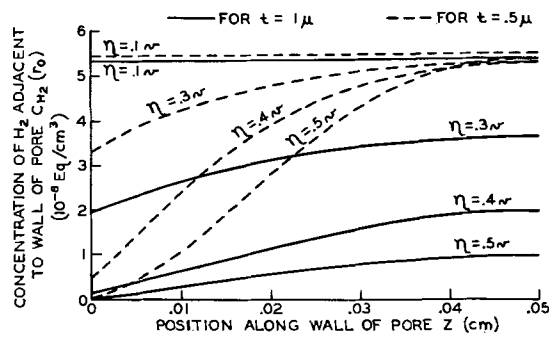


Fig. 7. Concentration of H_2 in solution adjacent to the wall of the pore.

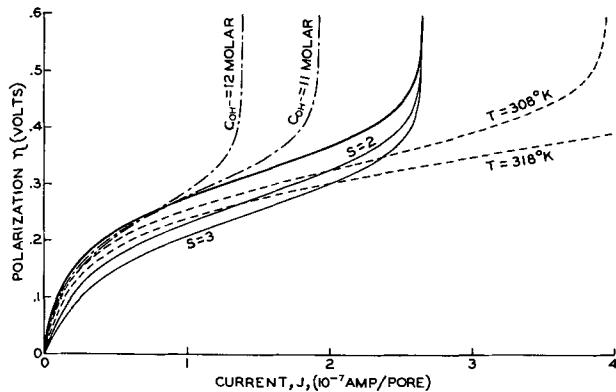


Fig. 8. Changes in the polarization curves with changing temperature, surface roughness, and concentration of NaOH, for the electrolyte film mechanism.

is 10M, the values of J_{max} given in Table I from the computer calculations agree with the values of J_{max} from Eq. [12] for films with a thickness of 0.5μ or larger.

This agreement shows that the maximum current is limited solely by the diffusion of hydrogen in these cases, since Eq. [12] was derived on the assumption that the transport of NaOH was negligible, and the limiting current was determined entirely by the diffusion of H_2 . Dilution of the NaOH solution plays a role in making J_{max} less than that given by Eq. [12] when the film thickness is less than 0.5μ . At a lower bulk concentration of NaOH, the transport of NaOH would be a more important factor in determining the limiting current. Figure 7 shows an increase in the concentration of H_2 adjacent to the metal surface as z becomes larger. This increase is partly due to the greater solubility of hydrogen in those parts of the solution which have a lower electrolyte concentration (see Fig. 6) and partly because the current density is smaller in those parts of the pore (see Fig. 4).

In Table I, values of $d\eta/dJ|_{J=0}$ calculated from Eq. [14] are compared with the slope at $J=0$ of

Table II. Effect of various sources of polarization on the slope of the polarization curve at $J=0$, for $t=1\mu$ and $s=1$

Source of polarization	$\frac{d\eta}{dJ} \Big _{J=0}$ (10 ⁶ ohm pore)		
	$s=1$	$s=10$	$s=20$
All sources included	13.055	1.546	0.9010
All except NaOH concentration polarization	13.053	1.544	0.8985
All except H_2 concentration polarization	13.001	1.50	0.852
All except electrochemical polarization	0.182	0.182	0.182
Resistance of NaOH electrolyte is zero	12.78	1.33	0.687
Electrode is infinitely thick	2.96	0.951	0.685

the polarization curves obtained from the computer calculations. Polarization at vanishingly small currents is a minimum at a film thickness near 2μ . The value of $d\eta/dJ|_{J=0}$ is not sensitive to the value of t , if t is in the range of $3\mu > t > 1\mu$. Table II shows how the slope of the polarization curve at $J=0$ would change if the sources of polarization were eliminated one by one. Electrochemical polarization is seen to be the most important factor.

Figure 8 shows the effect on the polarization curve for the conditions $T=298^\circ K$, $C_{OH^-}=10M$, $t=1\mu$, and $s=1$, (shown as the dark full curve) which is due to increasing the temperature to 308° and $318^\circ K$ (dashed curves), increasing the concentration of NaOH to 11 and 12M (partly dotted curves), and increasing the surface roughness factor to 2 and 3 (light full curves) while keeping all other factors constant. The effect of increasing the temperature is to decrease the initial slope of the curve and to increase the maximum current. The reason that J_{max} increases with increasing temperature can be seen from Eq. [12] and can be ascribed primarily to its effect of increasing the diffusion coefficient of H_2 in the solution. An increase in the concentration of NaOH decreases the polarization at low currents, but raises the polarization at higher currents, and decreases the maximum current due to decreasing the solubility of hydrogen in the solution. The effect of increasing the surface roughness is to lower the initial slope, and to shift the rest of the curve to lower polarization without affecting the maximum current.

The full curve in Fig. 9 is the polarization curve obtained from the equations for the surface diffusion mechanism for a pore having a depth of penetration by the electrolyte, l_2 , equal to 50μ , and a surface roughness ratio, s , equal to 1. The radius, length, l_1 , temperature, and concentration of NaOH are the same as those for the electrolyte film mech-

Table I. Accuracy of J_{max} calculated from Eq. [12] and $d\eta/dJ|_{J=0}$ from Eq. [14]

Film thickness, t (10^{-4} cm)		3	2	1	0.5	0.1
Maximum current, J_{max} (10^{-7} amp/pore)	from Eq. [12]	0.6469	1.160	2.656	5.626	29.34
	from computer calculations	0.6469	1.161	2.657	5.596	7.39
Slope at $J=0$	from Eq. [14]	1.308	1.302	1.306	1.323	1.479
	from computer calculations	1.308	1.303	1.306	1.324	1.498

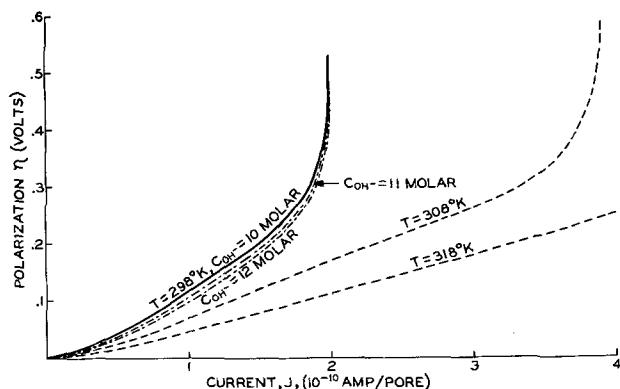


Fig. 9. Changes in the polarization curves with changing temperature and concentration of NaOH, for the surface diffusion mechanism.

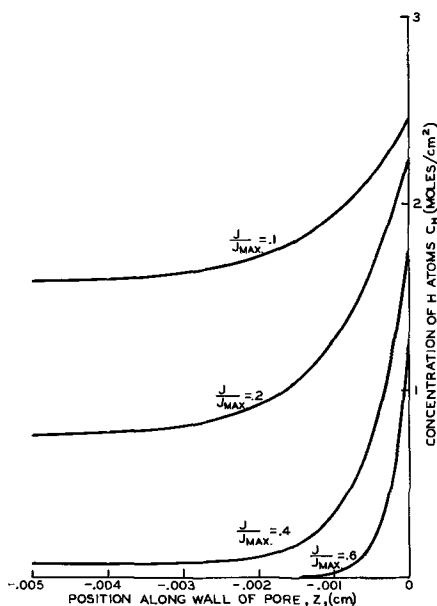


Fig. 10. Concentration of hydrogen atoms as a function of position along the wall of the pore.

anism. Figure 10 shows how the concentration of hydrogen atoms on the wall decreases after the atoms cross the meniscus boundary into the part of the pore filled with electrolyte, when the total current delivered by the pore is 0.1, 0.2, 0.4, and 0.6 of the maximum current. Figure 11 shows that the corresponding local current density on the walls of the pore, $j(z)$, drops to very low values within a distance of 20μ from the meniscus. The polarization, η , is nearly the same in all parts of the pore filled with electrolyte; at any current, $\eta(-l_2)$ and $\eta(0)$ differ by less than 0.0065%. The effect of increasing the temperature to 308° and 318°K is shown by the dashed curves in Fig. 9, while the effect of increasing the concentration of NaOH to 11 and 12M is shown by the dotted curves. The effects are similar to those for the electrolyte film mechanism, except that J_{\max} is independent of the NaOH concentration.

Comparison of the Two Mechanisms

The two mechanisms may be compared by determining the polarization curves for each mechanism for pores of equal radii (5μ) and surface

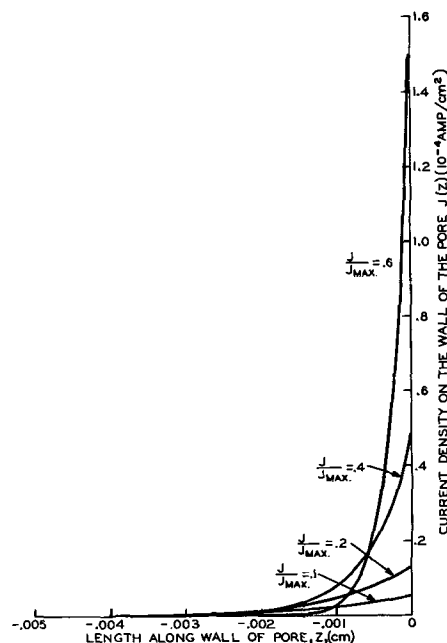


Fig. 11. Current density as a function of position along the wall of the pore.

roughness (l) and at the same concentration of sodium hydroxide (0.010 moles/cm³) and temperature (25°C). The electrolyte film thickness will be taken as 3μ , which is close to the optimum value. The maximum current and initial slope of the polarization curve are $6.47 \cdot 10^{-8}$ amp/pore and $1.31 \cdot 10^7$ ohm pore, respectively, for the electrolyte film mechanism, while the corresponding quantities for the surface diffusion mechanism are $2.00 \cdot 10^{-10}$ amp/pore and $5.96 \cdot 10^8$ ohm pore. Since the initial slope for the electrolyte film mechanism is 45 times less and the maximum current is 300 times larger than the corresponding quantities for the surface diffusion mechanism, the electrolyte film mechanism offers the more likely explanation for the operation of the hydrogen gas diffusion electrode. The calculations for the two mechanisms are not of the same order of precision mainly because the surface diffusion coefficient is difficult to estimate. However, even if the value given by Eq. [17] was too small by a factor of ten, the maximum current and the initial slope of the polarization curve would only be changed by a factor of the square root of ten. In addition, experimental studies by Will (6) on a single "inverse" pore made of platinum are in agreement with the theoretically calculated currents from the electrolyte film mechanism. It is of interest to note that even with a surface roughness factor equal to one, the polarization curves of the surface diffusion mechanism are not concave downward at very low currents, as are many experimental curves for electrodes in which electrochemical polarization is predominant. These points of comparison imply that the electrolyte film mechanism more appropriately describes the operation of the hydrogen gas diffusion electrode.

Manuscript received May 7, 1963; revised manuscript received March 20, 1964.

Any discussion of this paper will appear in a Discussion Section to be published in the June 1965 JOURNAL.

REFERENCES

1. E. Justi and A. Winsel, "Kalte Verbrennung," Chap. 3, Franz Steiner Verlag, Wiesbaden (1962); E. Justi, M. Pilkuhn, W. Scheibe, and A. Winsel, "Hochbelastbare Wasserstoff-Diffusions-Elektroden für Betrieb bei Umgebungstemperatur und Niederdruck," Chap. 3, Abh. d. Math. Nat. Kl. d. Akad. d. Wiss. u. d. Lit. Nr. 8, Komm.-Verlag, Steiner, Wiesbaden (1959).
2. H. C. Weber, H. P. Meissner, and D. A. Sama, *This Journal*, **109**, 884 (1962).
3. J. O'M. Bockris and E. C. Potter, *ibid.*, **99**, 169 (1952).
4. M. Breiter and R. Clamroth; *Z. Electrochem.*, **58**, 493 (1954).
5. R. M. Perskaya and I. A. Zaidenman, *Proc. Acad. Sci. USSR*, **115**, 548 (1957).
6. F. G. Will, *This Journal*, **110**, 145, 152 (1963).
7. International Critical Tables, Vol. VI, pp. 254, 309, McGraw-Hill Publishing Co., New York (1933).
8. B. E. Conway, "Electrochemical Data," p. 342, Elsevier Publishing Co., New York (1952).
9. G. Akerlof, and G. Kegeles, *J. Am. Chem. Soc.*, **61**, 1027 (1939).
10. G. Akerlof and G. Kegeles, *ibid.*, **62**, 620 (1940).
11. G. Tamman and V. Janssen, *Z. anorg. u. allgem. Chem.*, **179**, 125 (1929).
12. International Critical Tables, Vol. V., p. 66.
13. H. S. Harned and B. B. Owen, "Physical Chemistry of Electrolytic Solutions," p. 247, Reinhold Publishing Co., New York (1958).
14. A. Seidell and W. F. Linke, "Solubilities of Inorganic and Metal Organic Compounds," Vol. 1, p. 1078, D. Van Nostrand and Co., New York (1941).
15. F. A. Long and W. F. McDevit, *Chem. Rev.*, **51**, 119, (1952).
16. B. M. W. Trapnell, "Chemisorption," pp. 91, 99, Butterworths, London (1955).
17. O. Beek, "Advances in Catalysis," Vol. 2, p. 151, Academic Press, New York (1950).
18. W. A. Pliskin and R. P. Eischens, *Z. physik. Chem.*, **24**, 22 (1960).
19. P. C. Carman, "Flow of Gases Through Porous Media," p. 120, Academic Press, New York (1956).
20. R. Wortman, R. Gomer, and R. Lundy, *J. Chem. Phys.*, **27**, 1099 (1957).
21. H. Margenau and G. M. Murphy, "The Mathematics of Physics and Chemistry," pp. 490, 491, D. Van Nostrand, Princeton, N. J. (1956).
22. Copies of these computer programs may be obtained from the Research Division of Allis-Chalmers Mfg. Co.
23. P. T. Merenkov, *Chem. Abs.*, **57**, 13613i (1962).

Technical Notes

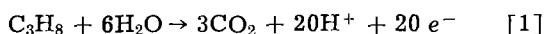


On the Reactions of Propane at the Surface of a Working Fuel Cell Anode

W. T. Grubb

Research Laboratory, General Electric Company, Schenectady, New York

The surface of a hydrocarbon fuel cell anode must perform the dual function of catalyzing dissociative adsorption of a fuel molecule and of promoting the electrochemical oxidation of the dissociated surface species. The latter process has often been called electrocatalysis (1, 2). Both electrochemical and gas phase side reactions that are undesirable from the fuel cell point of view may occur. For instance, the electrocatalyst may undergo self oxidation as has been previously noted for hydrocarbons on nickel (3). In addition, the cracking of aliphatic hydrocarbons to form gaseous methane and carbon-rich species on catalyst surfaces is well known and is thermodynamically favored in the operating temperature range of most fuel cells. This note presents information on the competitive reactions of cracking and electrooxidation of propane which have been investigated in a propane-oxygen fuel cell with platinum electrodes operating at 65°C. In such a cell, the yield of CO₂ based on rate of electron production (cell current) corresponded closely (4) to that required by the reaction



This result would not be expected if cracking of propane was a prominent side reaction since then the electrons would be produced from the oxidation of carbonaceous surface residues and for a given cell current the rate of CO₂ production would be higher than that corresponding to reaction [1].

It was the purpose of the present work, therefore, to study the cracking reaction of propane at the anode of a working fuel cell to determine what part it plays as a probable side reaction.

Experimental

The fuel cell and electrode structure employed in this work have been described previously (5, 6). The electrolyte in the cell was a heterogeneous ion-exchange membrane saturated with 6N H₂SO₄. The cell was maintained at 65° ± 0.2°C by means of an air thermostat. The area of the platinum black catalyst in the anode was determined to be 4.0 m² by nitrogen adsorption using a Perkin-Elmer Shell Sorptometer. This area was measured on the wet-proofed catalyst (6).

The propane fuel gas was Matheson Instrument Grade 99.5% minimum purity. It was found by gas

chromatographic analysis to contain less than 20 ppm of methane, about 80 ppm of ethane, and 1000 ppm of air. The choice of Instrument Grade was dictated by the very low content of methane and ethane as compared with several Research Grade tanks that were analyzed.

The gas chromatograph system consisted of a Perkin-Elmer 154B chromatograph operated isothermally at 104°C with a two meter silica gel column and helium carrier gas at a flow rate of 55 ml/min.

Because chromatograph retention time is not entirely unique for a particular molecule, a methane peak from one cracking experiment was caught in a stopcock trap at the exit from the chromatograph and was identified as methane using a mass spectrometer.

The experimental procedure was as follows. The anode chamber initially filled with air was swept with helium then with hydrogen, and then with about 50X the chamber volume of propane. Flow was stopped and timing began on the first 30-min reaction period. After 30 min the gas from the anode chamber was swept with helium into the gas sampling valve of the chromatograph and analyzed. A fresh charge of propane was admitted by sweeping through at least 50X the anode chamber volume in a few seconds and starting timing on the second 30-min interval after stopping the flow. This procedure was repeated for all analyses.

In the results reported below, the methane formation rate was measured as the per cent of methane present in the 2.6 ml anode compartment. It was assumed that the anode chamber was homogeneous in composition so that a representative sample of its contents was obtained by displacement with helium.

A conversion point is given for determining the 30-min average rate of methane production in terms of molecules per square centimeter per second based on the total surface area of platinum black in the anode. A conversion point is also given for the equivalent cell current which would have been produced if the methane formed by cracking had been oxidized electrochemically to CO₂ and water instead.

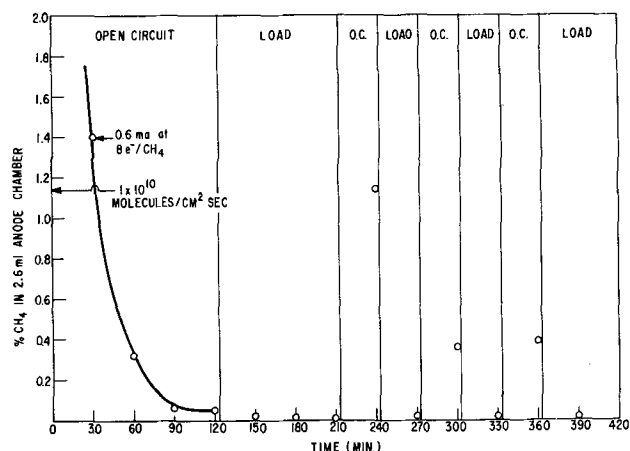


Fig. 1. Formation of methane in propane-oxygen fuel cell anode chamber in successive 30-min intervals.

Table I. Numerical CO₂ and CH₄ percentages

Cumulative time, min	Cell condition	% CO ₂ ** in anode compartment	% CH ₄ ** in anode compartment
0*	—	0	0
30	Open circuit	0.5	1.4
60	Open circuit	1.2	0.32
90	Open circuit	1.4	0.060
120	Open circuit	1.5	0.050
150	Under load 13.7 ma 0.47v	29	0.020
180	Under load 13.8 ma 0.47v	30	0.018
210	Under load 13.6 ma 0.46v	27	0.006
240	Open circuit	0.9	1.14
270	Under load 13.5 ma 0.45v	32	0.020
300	Open circuit	4.3	0.36
330	Under load 13.5 ma 0.45v	20	0.016
360	Open circuit	4.8	0.39
390	Under load 13.5 ma 0.45v	26	0.016

* Propane input.

** Volume percentages.

Results and Discussion

The results of the investigation are summarized in Fig. 1. The rate of formation of methane was highest during the first 30-min open-circuit period. It fell off to lower values in succeeding intervals of the open-circuit period. After 120 min the rate of methane formation was about 1/25 of its initial value, and appeared to be approximately constant. At this point, the cell was placed under load such that about 13.7 ma of anodic current was drawn from the anode at 0.47v of cell potential (0.5v positive to the reversible hydrogen potential in the same electrolyte). Under this condition, the methane production rate fell to 1/70 of its initial value.

After remaining on approximately the above steady load current for 90 min the cell was returned to open-circuit condition, and it was found that the 30-min rate of methane production returned to 82% of its initial value. Returning to load condition, methane formation was again suppressed, and after ½ hr on load, rose on open circuit to 32% of its initial value. This could be repeated through as many cycles as desired.

In Table I are presented the numerical CH₄ and CO₂ percentages found in the anode compartment of the cell at various points plotted in Fig. 1. Except for the trace of methane, CO₂ was the only gaseous product detected from the cell under load.

The interpretation of the suppression of methane formation under load might be that it is formed but is electrochemically oxidized. This is considered highly unlikely not only because it is present in low concentration in the presence of the more reactive propane, but also because methane did not oxidize at the same potentials as did propane in the fuel cell at this temperature as shown in the cell performance curves of Fig. 2.

All of the observations to date are consistent with the mechanism for the propane cracking reaction

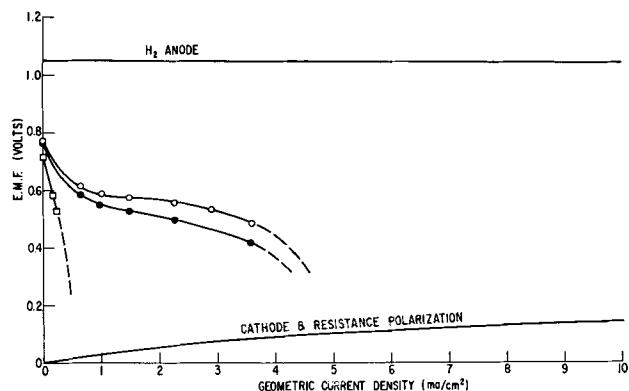
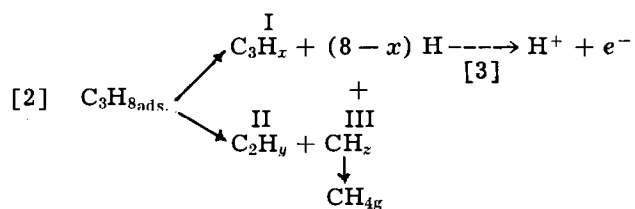


Fig. 2. Performance curves for propane, methane, and hydrogen in a fuel cell with platinum electrodes at 65°C: ○, propane anode; ●, propane total cell; □, methane total cell.

proposed by McKee (7, 8) which takes the following form



The accumulation of species I, II, and III strongly adsorbed on the surface accounts for the initial fall off in methane production rate with time which was also observed in McKee's investigations.

The recovery of the methane formation after loading the fuel cell is ascribed to the electrochemical oxidation of species I, II, and III with the formation of CO_2 .

The suppression of methane formation rate under load, e.g., at the 270 min point of Fig. 1, is attributed to the electrochemical removal of hydrogen from the surface by reaction [3] with the formation of hydrogen ions. Hydrogen is much more electrochemically reactive than the carbonaceous fuels as shown in Fig. 2, and further it is known to be present at extremely low surface coverages at

the potentials prevailing under load in these experiments.

The present open-circuit cracking experiments are thus consistent with the results of McKee. At higher temperatures, McKee found that the methane formation rate increased sharply and ethane was also formed in significant amounts. Fuel cells operating at 150°C form both methane and ethane on open circuit. The rate of formation falls with time as expected and is suppressed below the detection limit under load condition. The cell again produced a quantitative yield of CO_2 for the complete oxidation of propane at 150°C (9).

Acknowledgment

The author thanks Carol J. Michalske for technical assistance, Dr. F. J. Norton for mass spectrometer analyses, and Drs. D. W. McKee, H. A. Liebhafsky, and L. W. Niedrach for some interesting and valuable discussions. This work was made possible by the financial support of the U.S. Army Engineer Research and Development Laboratories under Contract No. DA-44-009-ENG-4909.

Manuscript received Feb. 17, 1964; revised manuscript received May 18, 1964. This paper was presented at the Pittsburgh Meeting, April 15-18, 1963.

Any discussion of this paper will appear in a Discussion Section to be published in the June 1965 JOURNAL.

REFERENCES

1. H. A. Liebhafsky and E. J. Cairns, *Proc. 1962 Pacific Energy Conversion Conf.*, San Francisco, Calif. (Dec. 1962).
2. W. T. Grubb, *Nature*, **198**, 883 (1963).
3. W. T. Grubb, *Proc. 16th Annual Power Sources Conf.*, p. 31, Atlantic City, N. J. (May 1962).
4. W. T. Grubb and L. W. Niedrach, *Proc. 17th Annual Power Sources Conf.*, p. 69, Atlantic City, N. J. (May 1963).
5. J. S. Bone, S. Gilman, L. W. Niedrach, and M. D. Read, *Proc. 15th Annual Power Sources Conf.*, p. 47, Atlantic City, N. J. (May 1961).
6. W. T. Grubb and C. J. Michalske, *This Journal*, **111**, 477 (1964).
7. D. W. McKee, *J. Am. Chem. Soc.*, **84**, 4427 (1962).
8. D. W. McKee, *J. Phys. Chem.*, **67**, 841 (1963).
9. W. T. Grubb and C. J. Michalske, *This Journal*, **111**, 1015 (1964).

The Oxidation of Pyrolytic Graphite at Temperatures of 1400°-1800°F and at Air Velocities of 25-100 cm/sec

Milton Levy and Philip Wong

U. S. Army Materials Research Agency, Watertown, Massachusetts

Graphite has been considered for many high-temperature applications because of its high refractoriness, low density, low coefficient of thermal expansion, and high mechanical strength which is retained at high temperatures, even under load.

Recently, emphasis has been placed on pyrolytic graphite, a specialized, polycrystalline form of graphite. Pyrolytic graphite has greater strength than normal graphite and exhibits a greater degree

of anisotropy in its thermal and electrical properties than single-crystal natural graphite.

Although many papers are available on the reactions of graphite with oxidizing gases (1-6, 8, 10) little or no data have been reported on the oxidation of pyrolytic graphite at air velocities above 1 cm/sec.

Horton (7) presented kinetic data for oxidation of pyrolytic graphite between 1137° and 2854°F at

low air velocities (0.27-0.50 cm/sec). Neither gas velocity nor diffusion affected the observed rates which were one-half order with respect to oxygen concentration. An activation energy of about 35 kcal/mole was calculated. Levy (9) studied the oxidation of pyrolytic graphite in quiescent air between 1250° and 1850°F. A break in the plot of reciprocal of temperature *vs.* log of reaction rate occurred at 1550°F. This break may have been due to a change in controlling mechanism, but could not be ascertained in a quiescent system.

This paper presents a gravimetric study of the oxidation kinetics of pyrolytic graphite between 1400° and 1800°F at air velocities of 25-100 cm/sec and atmospheric pressure. Under these conditions valid conclusions may be drawn regarding chemical and diffusion processes. The anisotropic behavior of pyrolytic graphite as reflected in its oxidation behavior was also studied.

Apparatus and Experimental Procedure

An automatic weighing and recording reaction system (Aminco Thermograv) was used for obtaining the rates of oxidation of pyrolytic graphite. The weight sensitivity of the system was between 1.0 and 4.0 mg for a 200 mg full range of deflection. The furnace temperature was regulated by a calibrated chromel-alumel furnace thermocouple which controlled the power input to the furnace. An additional calibrated chromel-alumel thermocouple placed directly below the sample was used to maintain the desired temperature within $\pm 3.5^\circ\text{F}$ during the oxidation runs. This assured that the difference between the temperature of the sample and the furnace would be minimized as much as possible under the experimental conditions.

Air was introduced at the bottom of the reaction chamber, measured with flowmeters, and dried with Drierite.

According to the supplier (High Temperature Materials Department, Raytheon Company, Waltham, Massachusetts), the pyrolytic graphite was deposited from methane on a synthetic graphite substrate at 3812°F and has a density of 2.20 g/cc. Specimens were 0.925 cm² and 0.318 cm thick and were rinsed with ethyl alcohol and dried to constant weight. The specimen surface area was 3.024 cm².

The oxidation of pyrolytic graphite was studied as a function of time, temperature and air velocity. Runs were made at 1400°, 1500°, 1600°, 1700°, 1800°F at flow rates of 25, 50, 75, and 100 cm/sec for each temperature. Runs were terminated at 200 mg weight loss of samples to minimize dimensional changes. Thermocouples placed below the specimens may not be adequate to describe the surface temperature of pyrolytic graphite reacting with air. The experimental set-up precluded temperature measurements by optical or radiation pyrometry. In lieu of calculating approximate surface temperatures, duplicate runs were made at each temperature and velocity and actual measurements taken by imbedding a calibrated thermocouple in the graphite specimen. These data are contained in Table I. Temperature increases due to oxidation were found

Table I. Difference between furnace temperature and specimen temperature

Air velocity, cm/sec	Furnace temperature, °F	Specimen temperature, °F	Difference between furnace and specimen temperature, °F
25	1400	1418	18
25	1500	1526	26
25	1600	1625	25
25	1700	1736	36
25	1800	1836	36
50	1400	1418	18
50	1500	1528	28
50	1600	1629	29
50	1700	1735	35
50	1800	1836	36
75	1400	1416	16
75	1500	1528	28
75	1600	1629	29
75	1700	1736	36
75	1800	1834	34
100	1400	1416	16
100	1500	1527	27
100	1600	1630	30
100	1700	1736	36
100	1800	1836	36

to be less than 36°F. For the anisotropism study, disk-like specimens 1.588 cm in diameter by 0.064 cm thick were machined from a 1 in.-thick pyrolytic graphite plate, both parallel and perpendicular to the plane of deposition. Thus specimens were prepared which exposed primarily the basal plane ("c" direction) or the edges ("a" direction) in a 12-1 ratio (surface area). Runs were made with both types of specimens at temperatures between 1400° and 1800°F in a quiescent atmosphere.

Results and Discussion

Effect of time and temperature.—Figure 1 shows oxidation curves at an air velocity of 50 cm/sec for temperatures between 1400° and 1800°F. Generally, the oxidation may be considered to proceed in two stages. The first stage represents the time necessary for the graphite to reach a relatively uniform oxidation temperature, approximately 5 min. The second stage is characterized by the most constant temperature, although there is a relatively slight increase in oxidation rate with increasing time (prob-

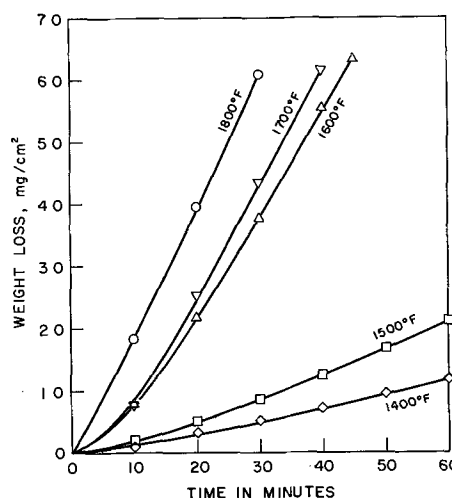


Fig. 1. Effect of temperature on oxidation of pyrolytic graphite 1400°-1800°F. air velocity 50 cm/sec.

ably due to a gradual increase in surface area). A large increase in the rate of oxidation occurs between 1500° and 1600°F. Similar results were obtained for air velocities of 25, 75, and 100 cm/sec. A major change in the mechanism occurs in this region. This suggests a transition from chemical to diffusion control. The existence of a change in mechanism of reaction at approximately 1600°F was reported for normal graphite by Tu, Davis, and Hottel (10), Kuchta, Kant, and Damon (8), Blyholder and Eyring (2, 3), Gulbransen (5), and for pyrolytic graphite by Levy (9). Gulbransen (5) found that the transition between chemical and diffusion control depends on pressure, sample size, and the nature of the reaction system. Since earlier investigators also reported transition temperatures near 1600°F, their reaction system, specimen areas, and oxidation conditions were probably similar.

Temperature dependence and energy of activation.—A plot of reaction rate vs. $1/T$ for several air velocities is shown in Fig. 2. Limiting tangents at the longer exposure times were employed for the determination of reaction rate constants. The temperature of oxidation was then at constant value for each exposure. The initial portion of the curves between 1400° and 1600°F clearly represents a region in which the chemical resistance is controlling, since the effect of velocity is overshadowed by that of temperature. For this region an energy of activation of 43 kcal/mole was calculated. Additional runs were made at 1550°F to define the plots more accurately. At 1600°F and above, a change is observed in oxidation kinetics at all gas velocities. In this region an energy of activation of 8 kcal/mole was calculated. These data are in fair agreement with that reported by Gulbransen *et al.* (5).

Dependence on air velocity.—The effect of velocity for several temperatures is shown in Fig. 3, both scales of which are logarithmic. Below 1600°F the curves are nearly parallel to the velocity axis, showing a lack of dependence of rate on air velocity because of the predominant effect of chemical resistance at the surface. The slopes of the isotherms increase at 1600°F and above, where it is substantially independent of temperature. The substantial parallelism of the curves for this temperature region

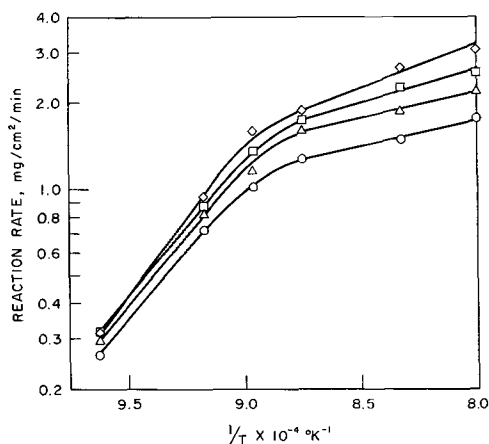


Fig. 2. Log reaction rate vs. $1/T$ oxidation of pyrolytic graphite at air velocities of 25—○, 50—△, 75—□, 100—◇ cm/sec.

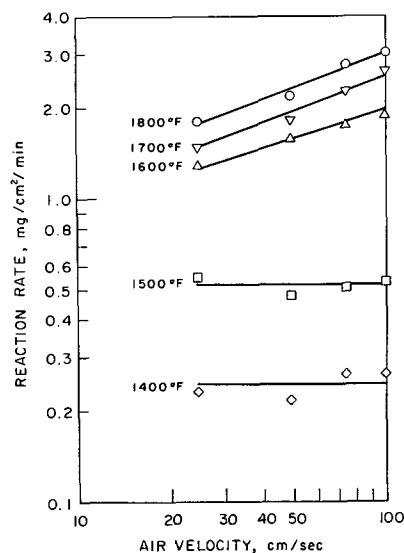


Fig. 3. Effect of air velocity, log reaction rate vs. log air velocity at 1400°-1800°F.

indicates that chemical resistance appears to have no importance between 1600° and 1800°F when the combustion rate (10) is defined as containing two additive terms, the first of which corresponds to a diffusional resistance and the second to a chemical resistance.

If the reaction is in the diffusion-controlled region, one would expect the reaction rate to increase with increasing air velocity. This was the case for the reactions at 1600°, 1700° and 1800°F.

Figure 3 also shows that the reaction rate constant in the 1600°-1800°F temperature range is proportional to $V^{0.4}$ where V is the gas velocity expressed in cm/sec. This agrees with the work of Smith and Gudmundsen ($V^{0.42}$), Hottel ($V^{0.4}-V^{0.7}$), Kuchta *et al.* ($V^{0.45}$), and Chukino and Karzhavina ($V^{0.4}$). In the first three works, electrode carbon was used, while in the other charcoal was used. This velocity effect is in good agreement with theoretical calculations in which diffusion is assumed to be the controlling effect. Kuchta *et al.* (8) defined the rate of a diffusion-controlled process by

$$N = \phi \frac{D_0 P_2}{RT^{0.25}} \frac{V^{1/2}}{d} \quad [1]$$

At relatively high air velocities, the rate is theoretically almost independent of temperature and proportional to the square root of the velocity in the diffusional region of burning.

Anisotropic behavior.—Figure 4 illustrates the columnar structure of pyrolytic graphite. The c-axis

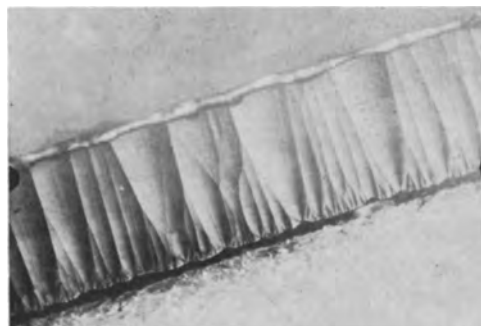


Fig. 4. Columnar structure of pyrolytic graphite (100X)

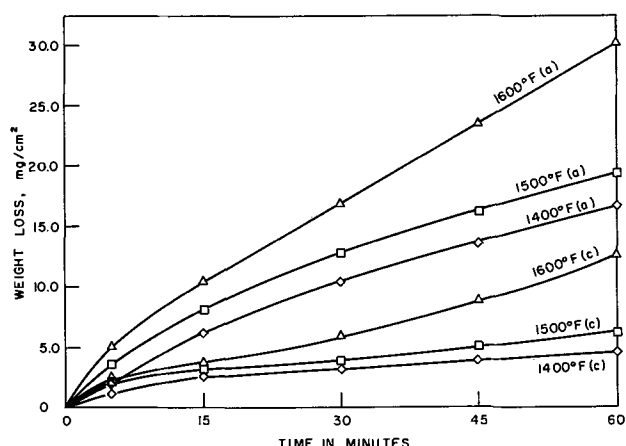


Fig. 5. Anisotropic behavior of pyrolytic graphite, 1400°-1800°F. (a) = "a" Direction; (c) = "c" direction.

lies parallel to the cone axis, the apex of the cone being nearest to the deposition face. The "a" direction is perpendicular to the axes of these cones. These are probably planar surfaces of low chemical activity, because they bond foreign substances with only Van der Waals forces. The edge atoms of the carbon planes should be more active because of their residual valence bonds; thus, oxidation should proceed preferentially along the direction perpendicular to the cone axis ("a" direction). The apparent greater porosity of the edges may also be a contributing factor. Figure 5 shows weight loss of pyrolytic graphite as a function of time and temperature when exposed in the "a" direction and the "c" direction. Temperatures between 1400° and 1600°F only were considered because chemical activity is the controlling mechanism in this region. Above 1600°F gas diffusion is rate controlling and anisotropy should have no effect. Oxidation is more rapid for specimens exposed in the "a" direction. The reaction-rate constants for the "a" and "c" direction runs at temperatures between 1400° and 1600°F are contained in Table II. In this temperature range, oxidation proceeds about twice as rapidly in the "a" direction, and this ratio increases with increasing temperature.

In a prior study, Levy (9) reported that oxidation appeared to proceed preferentially in the "c"

Table II. Reaction rate constants for "a" and "c" direction specimens at temperatures between 1400° and 1800°F

Temperature, °F	Reaction rate constant "a" direction (Ra), mg/cm ² /min	Reaction rate constant "c" direction (Rc), mg/cm ² /min	Ra/Rc
1400	0.388	0.248	1.56
1500	0.700	0.420	1.67
1600	0.993	0.466	2.13

direction which was contrary to expectation. However, this was based on a visual examination of oxidized specimens, rather than controlled experimentation. The present study demonstrates that oxidation of pyrolytic graphite occurs preferentially in the "a" direction.

Manuscript received Dec. 2, 1963; revised manuscript received May 14, 1964.

Any discussion of this paper will appear in a Discussion Section to be published in the June 1965 JOURNAL.

NOMENCLATURE

Equation [1]	
N	specific reaction rate moles/cm ² /sec
ϕ	constant
D_0	diffusivity of O ₂ at 273°K, cm ² /sec
d	diameter, cm
V	velocity of fluid, cm/sec
R	molar gas constant, ml-atm/degree/mole
P_2	partial pressure of O ₂ in ambient air stream, atm
T	absolute temperature °K

REFERENCES

1. T. H. Blakely, Carbon Proceedings, 4th Conf., Symposium Publications Division, pp. 95-105, Pergamon Press, New York (1960).
2. G. Blyholder and H. Eyring, *J. Phys. Chem.*, **61**, 682 (1957).
3. G. Blyholder and H. Eyring, *ibid.*, **63**, 1004 (1959).
4. E. A. Gulbransen and K. F. Andrew, *Ind. Eng. Chem.*, **44**, 1034 (1952).
5. E. A. Gulbransen, K. F. Andrew, and F. A. Brassart, *This Journal*, **110**, 476, Section I (1963).
6. R. A. Heindl and N. F. Mohler, *J. Am. Ceram. Soc.*, **38**, 89 (1955).
7. W. S. Horton, General Electric Co. Report No. 60GL218, Jan. 6, 1961.
8. J. M. Kuchta, A. Kant, and G. H. Damon, *Ind. Eng. Chem.*, **44**, 1559 (1952).
9. M. Levy, *Ind. Eng. Chem.*, Product Research and Development, **1**, 19 (1962).
10. C. M. Tu, H. Davis, and M. C. Hottel, *Ind. Eng. Chem.*, **26**, 749 (1934).

Cadmium Halophosphate Phosphors

R. C. Ropp¹

Sylvania Electric Products Inc., Towanda, Pennsylvania

A previous paper (1) outlined a detailed study of Cd₅Cl(PO₄)₃:Mn. The substitution of other halides for chloride in Cd₅X(PO₄)₃:Mn leads not only to expected but to unexpected results. The fluorapatite (2) requires both Pb and Mn to obtain strong response to 2537Å irradiation. The bromapatite, on the other hand, resembles the chlorapatite in that strong response to excitation by

¹ Present address: Westinghouse Electric Corporation, Bloomfield, New Jersey.

2537Å is obtained with manganese alone, but several other differences were noted. No previous studies of the bromophosphate phosphors have appeared in the literature.

The preparation of raw materials was described previously (3). The work was carried out concurrently with the preceding study (1), and the methods of preparation and measurement were similar.

Two phases were found for the bromophosphate, each having a distinctive x-ray diffraction pattern, chemical composition, and fluorescence spectrum. One phase was stable only at low temperatures ($\sim 650^\circ$), converting to the other at higher temperatures.

Chemical analysis of the phosphors gave the following experimental formulas

High-temperature phase: $(\text{Cd}+\text{Mn})_{5.1}\text{Br}_{1.1}(\text{PO}_4)_{3.0}$

Low-temperature phase: $(\text{Cd}+\text{Mn})_{5.1}\text{Br}_{2.2}(\text{PO}_4)_{3.0}$

Because of the difficulty in obtaining washed phosphors completely free from CdBr_2 , these experimental calculations represent the average of several determinations. Thus, the best chemical formulas for the high- and low-temperature phases were found to be $\text{Cd}_5\text{Br}(\text{PO}_4)_3:\text{Mn}$ and what was thought to be $\text{Cd}_5\text{HBr}_2(\text{PO}_4)_3:\text{Mn}$, respectively. The latter formula is a curious one, in that a monovalent atom is required for electrical neutrality. In this instance, because of the raw materials employed, only hydrogen was thought to be present. The compound could be $\text{Cd}_2\text{PO}_4\text{Br}$, $\text{Cd}_4\text{Br}(\text{PO}_4)_3$, the octaphosphate, or even $\text{Cd}_4\text{H}(\text{PO}_4)_3 \cdot \text{CdBr}_2$.

The similarity between the x-ray powder patterns of the high-temperature phase and $\text{Cd}_5\text{Cl}(\text{PO}_4)_3:\text{Mn}$ confirms that the former is an apatite. The patterns are nearly identical in spacings for all but one or two lines. However, the low-temperature phase

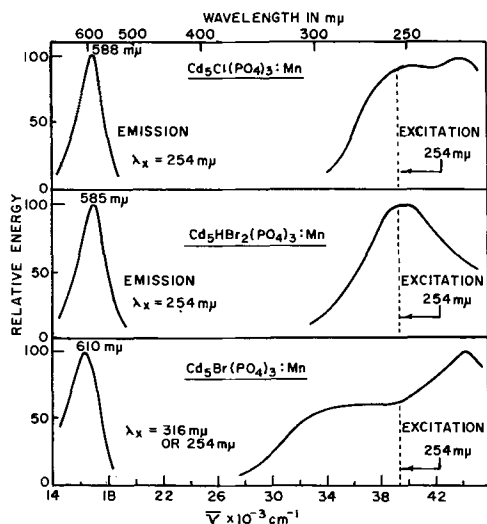


Fig. 1. Spectral properties of some cadmium halophosphates

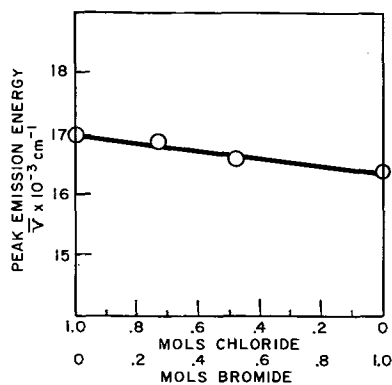


Fig. 2. Correlation of peak emission energy with chloride to fluoride ratio

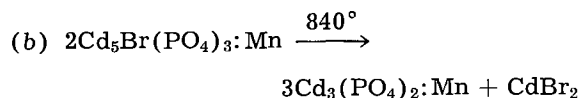
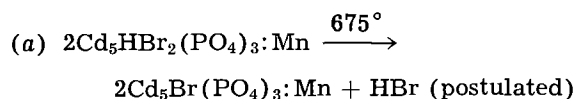
Table I. Relative brightnesses of cadmium halophosphate phosphors

Phosphor	Emission color	% Red plaque, 2537Å excitation
$\text{Cd}_5\text{Cl}(\text{PO}_4)_3:\text{Mn}$	Orange	100
$\text{Cd}_5\text{Br}(\text{PO}_4)_3:\text{Mn}$	Dull red	34
$\text{Cd}_5\text{HBr}_2(\text{PO}_4)_3:\text{Mn}$	Yellow	92
$\text{Cd}_3(\text{PO}_4)_2:\text{Mn}$	Dull red	39

does not resemble any cadmium phosphate studied previously (3).

The spectral properties of these phosphors, as shown in Fig. 1, vary considerably. $\text{Cd}_5\text{Cl}(\text{PO}_4)_3:\text{Mn}$ is an efficient orange-emitting phosphor ($\lambda_{\text{max.}} = 588 \text{ m}\mu$), whereas $\text{Cd}_5\text{Br}(\text{PO}_4)_3:\text{Mn}$ is a dull red-emitting phosphor ($\lambda_{\text{max.}} = 610 \text{ m}\mu$), similar to $\text{Cd}_3(\text{PO}_4)_2:\text{Mn}$ (4). By way of contrast, the postulated compound, $\text{Cd}_5\text{HBr}_2(\text{PO}_4)_3:\text{Mn}$, although not an apatite, most resembles the chloroapatite in its spectral properties. The yellow emission at $585 \text{ m}\mu$ is efficiently excited by 2537\AA radiation. The plaque intensities are given in Table I.

The stability of these phases, as determined by the products of thermal decomposition, is an interesting aspect that leads to several intuitive deductions concerning the nature of the original materials. The relationship was ascertained both by x-ray diffraction and by observation of the emission colors, which identified structures and reaction paths, but not specific compositions. As a result, the following equation may be written



There is a similarity in chemical behavior between the low-temperature phase, $\text{Cd}_5\text{HBr}_2(\text{PO}_4)_3:\text{Mn}$, or $\text{Cd}_4\text{H}(\text{PO}_4)_3 \cdot \text{CdBr}_2:\text{Mn}$, and an analogue in the calcium phosphate system, i.e., the octacalcium phosphate, $\text{Ca}_4\text{H}(\text{PO}_4)_3$. It has been hypothesized (5) that the latter is a form of the stoichiometric apatite which decomposes to a defect hydroxy apatite. Further reaction then gives $\text{Ca}_3(\text{PO}_4)_2$ plus a trace of $\text{Ca}_2\text{P}_2\text{O}_7$. Such a mechanism may be applicable to the present case.

When the Br:Cl ratios are changed by varying the formula, as established in the previous paper (1), mixed apatites are formed. The low-temperature phase of the bromophosphate is never observed. The preparation conditions required are the same as those for the chloroapatite.

$\text{Cd}_5\text{Br}(\text{PO}_4)_3:\text{Mn}$ is dull, but as chloride is incorporated, replacing bromide in increasing and equivalent amounts, the resulting phosphors become more efficient. At a 0.40Cl:0.43Br ratio, the red emission color of $\text{Cd}_5\text{Br}(\text{PO}_4)_3:\text{Mn}$ is maintained, but the intensity is increased 250%, as shown in Table II. As more chloride is added, the emission color approaches the orange emission of $\text{Cd}_5\text{Cl}(\text{PO}_4)_3:\text{Mn}$.

Table II. Analysis of cadmium haloapatite phosphors

Moles added*		Retained moles calculated**		Retained moles found			Color	% Red plaque, 2537Å excitation
CdCl ₂	CdBr ₂	CdCl ₂	CdBr ₂	CdCl ₂	CdBr ₂	Total		
0.75	—	1.00	—	1.01	—	1.01	Orange	100
0.65	0.10	0.87	0.13	0.76	0.17	0.93	Orange	88
0.55	0.20	0.73	0.27	0.73	0.28	1.01	Red-orange	79
0.45	0.30	0.60	0.40	0.68	0.32	1.00	Orange-red	90
0.25	0.50	0.33	0.67	0.40	0.43	0.83	Red	96
—	0.75	—	1.00	—	1.14	1.04	Red	41

* See ref. (1) for actual formula.

** Calculated, assuming a constant loss as found for Cd₅Cl(PO₄)₃:Mn in ref. (1).

Analysis of these phosphors was made by x-ray fluorescence techniques, using gravimetrically analyzed phosphors as comparison standards. The data were used to correlate brightness and emission color with composition.

These phosphors have double emission peaks, at 585 and 588 mμ. There is considerable difference in response to 2537Å in the mixed haloapatites even though the peak wave length is about the same. This is shown by comparing the plaque response of the Cd₅Cl_{0.40}Br_{0.43}(PO₄)₃:Mn phosphor to Cd₅Br(PO₄)₃:Mn. Note that the former does not contain a stoichiometric amount of halide, but that the latter does. Since plaque response has been shown to be a function of halide incorporation (1), it may be surmised that the plaque brightness might be improved by incorporation of more halide. This was borne out by the experimental data in which plaque brightnesses up to 98% of standard Cd₅Cl(PO₄)₃:Mn were achieved at an added 50-50 mole ratio of bromide of chloride (i.e., 0.375 mole Cl to 0.375 mole Br).

Using the data in Table II, a comparison between the stoichiometric ratio and the peak emission energy may be made, e.g., 0.40 Cl per 0.43 Br = 0.48 Cl per 0.52 Br. This result shows a linearity between $\bar{\nu}$ and halide content as given in Fig. 2. One is thus led to believe that the bromo- and chloroapatites form solid solutions, an observation made previously from x-ray data.

In 40w fluorescent lamps, the chloroapatite had excellent lumen output, giving 3380 lumens at zero hours, but the maintenance was poor, 3016 lumens at 100 hours, as has been noted previously. In contrast, the bromophosphates were very unstable to lehring, giving a mottled lamp of red, yellow, and blue striations of about 600 lumens.

As a final comment, in a previous work (1) it was shown that the most likely mechanism of excitation and emission would involve a charge-transfer complex to give an absorbing species similar to Cd⁺. In all of the phosphors studied, the emission spectra are similar enough to ascribe the slight differences noted to the effect of changes in crystal-field strength upon Mn⁺² emission, as a function of composition. The emission intensity is, however, a function of the presence of chloride. In Cd₅Cl_{0.5}Br_{0.5}(PO₄)₃:Mn, the emission bands include two bands, that of Cd₅Br(PO₄)₃:Mn and that of Cd₅Cl(PO₄)₃:Mn, but the emission intensity of the chlorobromoapatite phosphor is nearly three times that of the bromoapatite phosphor. In the compound believed to be Cd₅HBr₂(PO₄)₃:Mn, the emission intensity is nearly identical to that of Cd₅Cl(PO₄)₃:Mn.

It is apparent that only one halide atom would be necessary to form the charge-transfer species, Cd⁺, in Cd₅Cl(PO₄)₃:Mn or in the mixed apatites, e.g., Cd⁺⁺ + Cl⁻ → (CdCl)⁺, whereas in Cd₅HBr₂(PO₄)₃:Mn, two bromide atoms were found experimentally to be necessary to produce intense fluorescence under 2537Å irradiation.

The alternate suggestion, that the two bromide atoms are not equivalent in the compound believed to be Cd₅HBr₂(PO₄)₃:Mn, cannot be proved or disproved because of the lack of structure data. However, in Cd₅Br(PO₄)₃, the effect under 2537Å excitation does not occur, although the apatite structure is present.

In the fluoroapatite, a separate sensitizer is required to obtain strong emission intensity with 2537Å irradiation (2). Thus, for formation of the absorbing center (Cd,X)⁺, where X is a halide, a series may be derived for the number of halide atoms required to form the charge-transfer complex: F — 0; Cl — 1; Br — 2. The significance of this series is not clear and more work is required.

Manuscript received Jan. 15, 1964.

Any discussion of this paper will appear in a Discussion Section to be published in the June 1965 JOURNAL.

REFERENCES

1. R. C. Ropp, *This Journal*, **110**, 113 (1963).
2. R. W. Wollentin, *ibid.*, **103**, 17 (1956); R. W. Wollentin, U. S. Patent 2,865,863 (1958); J. S. Prener, U. S. Patent 2,636,010 (1953).
3. R. C. Ropp, *J. Am. Chem. Soc.*, **82**, 4848 (1960).
4. R. C. Ropp, *This Journal*, **109**, 569 (1962).
5. L. Winand and H. Brasseur, *Naturwissen*, **49**, 299 (1962).

A Technique for Examining the Luminous Activity of Individual Phosphor Particles in a Functioning Electroluminescent Lamp

J. I. Gedney

Research Laboratories, American Cyanamid Company, Stamford, Connecticut

The majority of the depictions of electroluminescence in ZnS which we have noted have been those connected with studies of individual crystals. Most of these studies have been made under carefully con-

trolled conditions where good electrical contacts were possible and the individual phosphor particles were not confined in permanent resin matrices of the type used in commercial lamps. We have yet to

find a description of the visible luminous activity of ZnS under working conditions in a dry, commercial-type electroluminescent lamp.

A commercial lamp consists basically of three parallel layers; of these, the outer two represent the electrodes and the inner layer contains the phosphor particles held in a solid matrix. It was the purpose of this study to examine the phosphor particles in a cross section of this type of lamp in order to determine what proportion of the particles exhibited visible luminous activity and to see if this activity was influenced by the distance of the particles from the electrodes. Additionally, we wished to determine whether the visible activity under such conditions was similar to that described by other investigators in studies of individual luminescing crystals.

Construction of Lamp

As a part of this study, it was necessary to construct a lamp of suitable dimensions to allow it to be mounted on the stage of our Bausch & Lomb metallograph. The selected ZnS phosphor, a green variety, of British manufacture, was mixed with an epoxy resin in a proportion of 1:1 by volume, and the resin was then catalyzed with triethylenetetramine. The phosphor-epoxy mixture was placed between two 2-in. square glass plates, each of which had been covered on one side with a conducting film of tin oxide. The glass plates, arranged with the conducting layers facing inward, were offset slightly to allow electrical connections to be made to the conducting layers. Pressure was applied to the glass so that a phosphor layer approximately 5 mils thick was obtained before complete polymerization of the epoxy resin occurred.

Since the chance of a short circuit was found to increase with the degree of nonuniformity of separation of the electrodes, the use of tin oxide-coated glass was advantageous because it provided reasonably plane, conducting surfaces which proved to be able to withstand relatively high voltages without shorting. Electrical connections could be clamped directly to the conducting layer without damage, thus avoiding conductivity problems. The epoxy resin for the matrix was resistant to the solvents employed in the subsequent polishing procedure and exhibited excellent adherence qualities. By locating the phosphor layer between two sheets of glass, polishing relief and plucking were minimized, since the glass served as a polishing support.

To allow the lamp to be conveniently studied in cross section on the metallograph, the lower portion of the lamp was first coated with epoxy resin. After the resin had polymerized, the coated portion of the lamp was placed in a mold (2 x 1 x ½ in.) and embedded in a block of the same resin. Precoating of the lamp was found to be necessary to eliminate the stress created by contraction of the molding resin as it polymerized. This contraction tended to produce separations between the glass layers and the mounting resin, which created subsequent difficulties during polishing of the cross section. The embedded lamp was then cross-sectioned and polished on a low-nap cloth lap with a diamond abrasive. A dia-

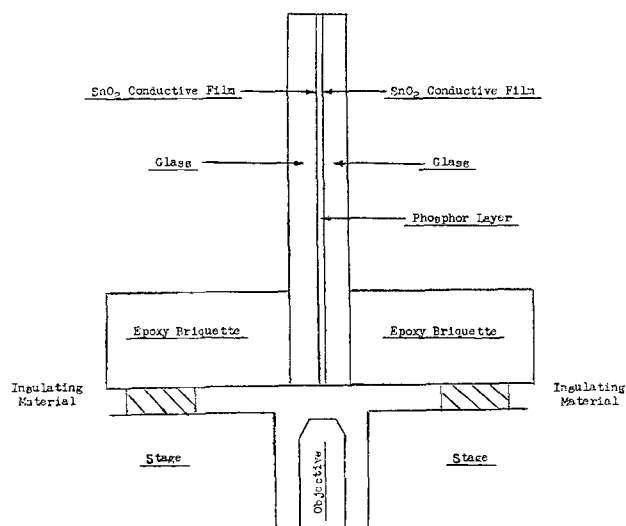


Fig. 1. Diagrammatic sketch of electroluminescent lamp mounted for microscopical examination.

grammatic sketch of the lamp is shown in Fig. 1.

For microscopical examination this assembly was clamped on the stage of the metallograph after insulators had been placed between the stage and the conductive parts of the lamp. The lamp was then connected to a standard 110v wall outlet with a transformer interposed to control the voltage.

Microscopical Examination of the Lamp

The lamp was first examined microscopically with bright-field, reflected light and then with cross-polarized, reflected light. When an area of interest was located, the external illumination was turned off and the lamp itself was lighted. The same field was then studied using only the light emitted from the particles in the field of view. By altering the voltage it was possible to obtain maximum brightness from any particular area of the lamp being examined.

Examination of the lighted lamp when operating at 300v revealed that many particles were apparently inactive, *i.e.*, were not emitting luminous energy in the visible range. Irregular luminous streaks, bright single points, and straight, dashed, or dotted lines of light were observed in the larger particles. In some instances appreciable areas with no definite boundaries were also visibly active, although usually not very bright. It should be emphasized that these observations were made while the lamp was operating at 300v, the maximum it could tolerate without short-circuiting.

The positioning of particles with respect to the electrodes did not seem to have any bearing on luminous activity. The active particles appeared to be distributed fairly uniformly between the two conductive tin oxide films. Although some of the more active particles made direct contact with one of the electrodes, many others were located at some distance from either electrode. Thus, no correlation was evident between particle location and either the type or intensity of the luminous activity exhibited.

Petrographic examination of the phosphor indicated that it was probably a mixture of the spher-

erite and wurtzite varieties of ZnS. These two phases are not readily distinguishable by reflected light on the metallograph, and it was therefore not possible to identify each electroluminescent particle observed with this instrument nor to determine whether one of these phases was more frequently active than the other.

The parallel, rectilinear orientation of many of the electroluminescent streaks suggested that they originated from structural planes within the crystals, but whether these represented open cleavage planes, zones of crystallographically oriented inclusions, or imperfections on the atomic level could not be ascertained. In some cases it appeared that certain cleavages or fractures (which were detectable as internal reflections between crossed polars) served to concentrate some of the electroluminescence, but a perfect correlation of all active spots in a crystal with the visible flaws was never possible. Undoubtedly some of the electroluminescent light is reflected and scattered as it traverses flaws in the crystals, and this must often result in irregular areas of luminosity which are not directly traceable to visible imperfections.

A brief review of recent literature on the microscopy of electroluminescent phosphors reveals that some of the electroluminescent phenomena mentioned here have also been observed (under specialized, experimental conditions) by other research workers in this field (1-6). Insofar as we have been able to discover, however, none of these investigators has published photomicrographs at high magnification, showing the "spotty" activity which individual phosphor particles exhibit under actual working conditions in a dry lamp of the commercial type.

Three regions of the lamp were selected for illustration (see Fig. 2-11). The appearance of each region by brightfield, reflected light, between crossed polars, and by electroluminescent light is presented in a series of photomicrographs made at magnifica-

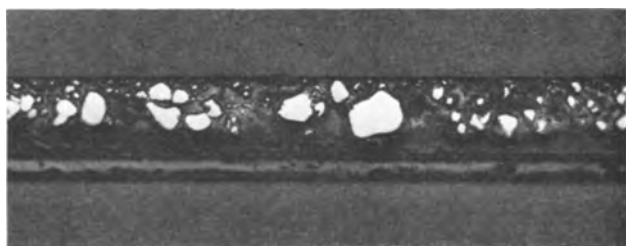


Fig. 2. Brightfield, reflected light; top and bottom, glass; center, phosphor layer; layer designation is the same in Fig. 2-11. Magnification approximately 200X.

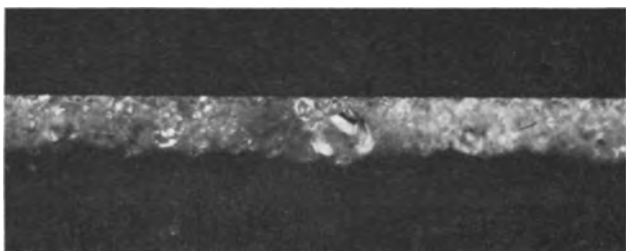


Fig. 3. Cross-polarized, reflected light; Magnification approximately 200X.

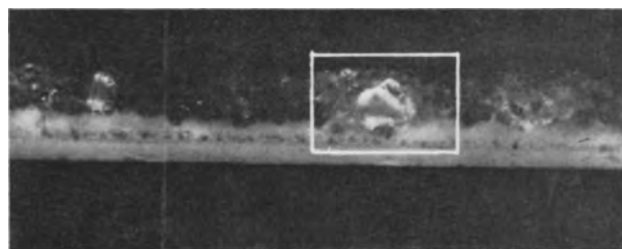


Fig. 4. Electroluminescent (300v); Magnification approximately 200X.

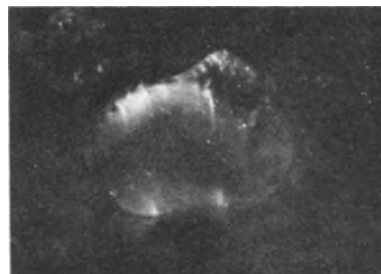


Fig. 5. Detailed view of marked area of Fig. 4. Magnification 675X.

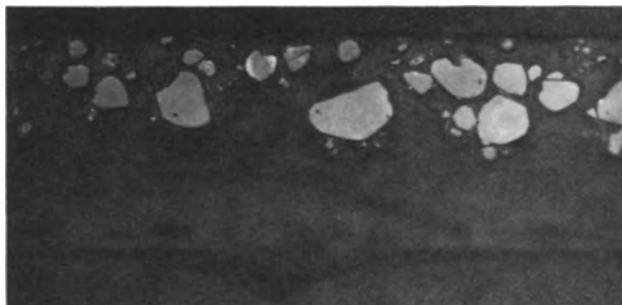


Fig. 6. Brightfield, reflected light. Magnification 400X

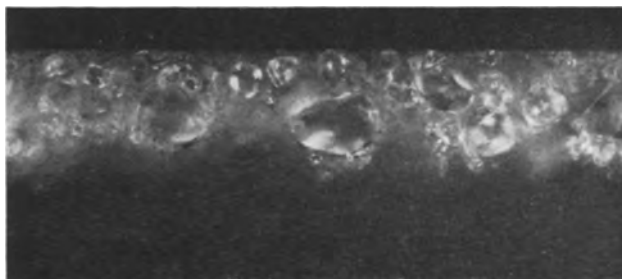


Fig. 7. Cross-polarized, reflected light. Magnification 400X

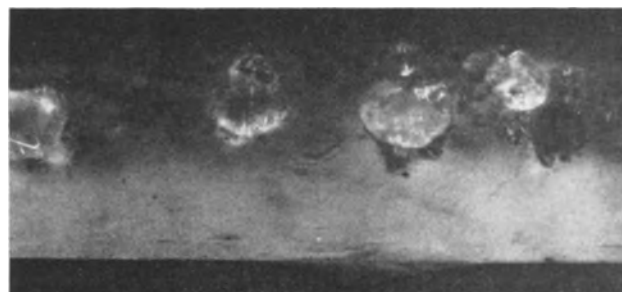


Fig. 8. Electroluminescent (300v). Magnification 400X

tions of 200X to 675X. All photomicrographs were made with an ultraviolet filter in the system, since the film used was sensitive to ultraviolet light. The spectral transmission characteristics of this filter are shown in Fig. 12.

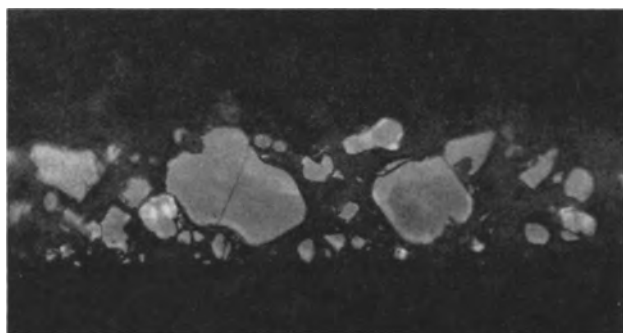


Fig. 9. Brightfield, reflected light. Magnification 600X

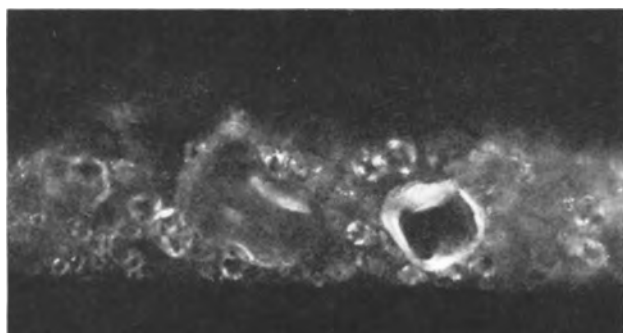


Fig. 10. Cross-polarized, reflected light. Magnification 600X



Fig. 11. Electroluminescent (300v). Magnification 600X

Summary

After cross-sectioning an electroluminescent lamp, observations were made on the polished surface of the cross-sectioned phosphor particles using external illumination as well as the particles' own electroluminescence. The sectioning and polishing of the phosphor particles did not appear to interfere with the emission of visible luminosity.

The examination of the electroluminescent lamp (operating at 300v) at 500 to 1000X magnification indicated that many of the ZnS phosphor particles did not emit luminous energy in the visible range. At substantially higher voltages more particles would probably have become active, however. The active particles encountered appeared to be scattered at random throughout the lamp, and their intensity was not noticeably affected by their distance from either electrode. The particles were not luminous

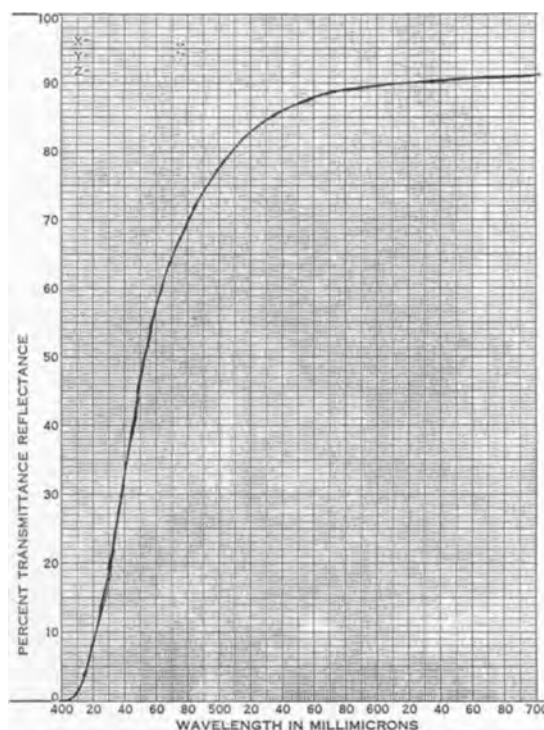


Fig. 12. Spectral transmission characteristics of u.v. filter

over their entire cross section, but exhibited three types of discontinuous activity: (i) bright, single points or clusters, (ii) straight, dotted or dashed lines of light, and (iii) irregular areas of variable intensity. The luminous regions could sometimes be directly correlated with visible imperfections in the active crystals. It also seemed quite probable that many of the luminous areas which were not associated with observable flaws were the result of internal reflection or scattering of light by cleavages, inclusions, or other optical discontinuities in the active phosphor particles.

Although these observations agree with those reported by other investigators (1-5), they were made on particles which were performing under dry conditions similar to those in which they would be commercially applied. This technique offers a relatively simple procedure by which such observations can be made at high magnifications to study the performance of the phosphor particles in a working lamp.

Manuscript received Jan. 16, 1964.

Any discussion of this paper will appear in a Discussion Section to be published in the June 1965 JOURNAL.

REFERENCES

1. W. Lehmann, *This Journal*, **107**, 22, 657 (1960).
2. A. Kremheller, *ibid.*, **107**, 8 (1960).
3. Short, Steward, and Tomlinson, *Nature*, **117**, 240 (1956).
4. A. G. Fischer, *This Journal*, **109**, 1043 (1962).
5. J. L. Gillson, Jr., and F. J. Darnel, *Phys. Rev.*, **125**, 149 (1962).
6. A. G. Fischer, *This Journal*, **110**, 733 (1963).

Multiple Slice Epitaxial Deposition of Silicon in Resistance Heated Furnace

B. A. Lombos and T. R. Somogyi

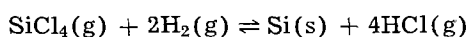
Research and Development Laboratories, Northern Electric Company Limited, Ottawa, Ontario, Canada

Much interest has been shown recently in the simultaneous production of uniformly deposited epitaxial silicon on several slices (1-7). Various methods have been used to attain layer uniformity. These were based mainly on controlled variations in the flow pattern of the reacting gas mixture, while keeping the temperature uniform across the pedestal. This paper deals with a method utilizing the variation in the equilibrium constant with temperature.

Discussion

In a uniform temperature reaction tube the yield of the reaction decreases in the direction of the gas flow because of changes in the concentrations of reactants and products. To counteract such decrease in the yield of deposition, two different approaches can be used. One is the attempt used by earlier investigators (2-3) to keep the concentration of reactants and products constant in the direction of the gas flow by arranging the inlet of the gas mixture at different locations. The other approach, described in this paper, is to shift the equilibrium of the reaction. This can be achieved by adjusting the temperature profile of the furnace according to the desired change in equilibrium to keep the deposition rate constant along the reaction tube.

Using the results of Miller *et al.* (7), the equilibrium constant, K , of the idealized reaction



will be given by

$$\log K = 18.8 - 3.28 \log T - 1.32 \times 10^4 T^{-1} + 2.69 \times 10^{-4} T + 2.91 \times 10^4 T^{-2}$$

Hence K increases with increasing temperature within the practical range for single crystal growth (approximately 1400°-1700°K). The evaluation of a temperature gradient, yielding uniform deposition, using a tubular reaction chamber could be done in the following way.

Assume that the deposition rate, r , can be expressed in the form

$$r(x, T, a_i) = f(x) g(T) h(a_i)$$

where x is the distance along the tube in the direction of the gas flow, T is the absolute temperature, and the a_i 's are other experimental variables, such as the saturator temperature, the geometry of the apparatus, etc. Here, f , g , and h depend exclusively on x , T , and the a_i 's, respectively.

The condition for uniform deposition is

$$dr = 0$$

Hence for constant a_i 's, the desired temperature gradient will be given by

$$\frac{dT}{dx} = - \frac{\frac{\partial r}{\partial x}}{\frac{\partial r}{\partial T}} = - \frac{\frac{d \ln f(x)}{dx}}{\frac{d \ln g(T)}{dT}} \quad [2]$$

Thus, if the functions $\ln f(x)$ and $\ln g(T)$ can be determined, the desired temperature profile, for uniform deposition, can be found from Eq. [2].

Experimental Results

The equipment used consists essentially of a fire brick furnace, with an embedded Kanthal A-1 heating element. Alternatively, an R.F. heating coil was also used for the experimental determination of $\ln f(x)$ and $\ln g(T)$. A clear fused quartz reaction tube, about 125 cm long and 40 mm in diameter, is inserted horizontally into the cylindrical furnace element (Fig. 1) and is connected to the saturator and to a by-pass line. The latter supplies the excess hydrogen. The apparatus was purged before each run with helium, and then the slices situated horizontally along the length of the tube were introduced into the hot zone. This was followed by a 15-min cleaning period, during which 6-8 l/min hydrogen was maintained in the bypass line. After that, deposition was started with a flow rate of 0.2 l/min through the saturator and again 6-8 l/min through the by-pass line. The saturator temperature was kept at -18°C (mole fraction of silicon tetrachloride, 0.03).

By the Arrhenius equation, we have

$$\frac{d \ln g(T)}{dT} = \frac{\text{constant}}{T^2} \quad [3]$$

where the constant incorporates the activation energy (q_A) of the reaction. Three different values for q_A were considered:

1. The experimental value obtained in this laboratory with resistance heated apparatus ($q_A = 60$ kcal/mole).

2. The experimental value given by Theuerer (4) ($q_A = 37$ kcal/mole).

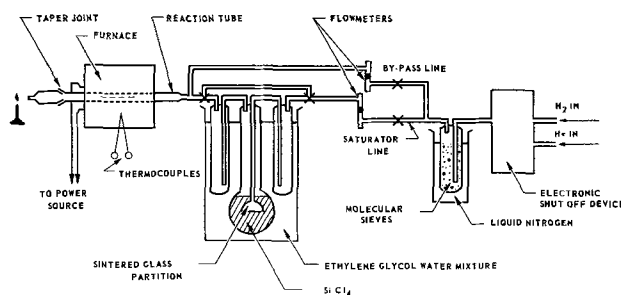


Fig. 1. Schematic of resistance heated epitaxial growth apparatus

3. The experimental value obtained in this laboratory with an R.F. heated apparatus ($q_A = 24$ kcal/mole).

The discrepancies in the values of g , as well as in the f functions given later, can be explained by differences in SiCl_4 mole fraction and furnace geometry.

To obtain the function $\ln f(x)$, the slices were placed in a uniform temperature section of the reaction tube in the resistance heated furnace at 1215°C , and the deposition rate was measured as a function of distance. A similar experiment was conducted in an R.F. heated reaction chamber, resulting in a different set of values for $\ln f$. Assuming (somewhat arbitrarily) a linear relationship between $\ln f(x)$ and x , the two sets were fitted to obtain empirical expressions, using the method of least squares. The functions representing the experimental results were found to be

$$\ln f(x) = 6.5307 \times 10^{-1} - 2.4804 \times 10^{-1}x$$

(standard deviation = 3.915×10^{-2})

for the resistance heated tube, and

$$\ln f(x) = 1.5048 - 5.2600 \times 10^{-1}x$$

(standard deviation = 3.542×10^{-2})

for the R.F. heated tube.

These results, combined with the above three values for the activation energy, give a total of six distinct curves for the temperature profile (Fig. 2). In practice, the most uniform deposition was achieved with a temperature gradient closest to curve 1 of Fig. 2. The results of two typical runs using this profile are given in Fig. 3. The substrates (arsenic doped; carrier concentration: 4×10^{19} at./ cm^3) were placed on a quartz holder spreading over 8 cm along the length of the tube. The temperature range was $1200^\circ\text{--}1300^\circ\text{C}$. The deposition parameters for the two runs are given in Fig. 3.

The relatively small change of flow rate and saturator temperature did not have any noticeable influence on the deposition.

The thickness of the deposited epitaxial layer was measured by means of infrared interference fringes (8). The measurement is based on the refractive index difference which in turn relates to the difference in carrier concentration between the epitaxial layer and the substrate material. This is used as a somewhat arbitrary definition of the thickness of the epitaxial layer. The standard deviation from a mean layer thickness of 8μ was 0.4μ , over a length of 8 cm, for a batch of 4 slices treated simultaneously.

The carrier concentration in the epitaxial layer was determined using the diode technique (9). In a depth from the surface of the epitaxial layer of approximately 0.5μ , the average negative charge carrier density was found to be 9×10^{16} at. cm^{-3} with a standard deviation of 30% measured on two slices of one run and three slices of another run.

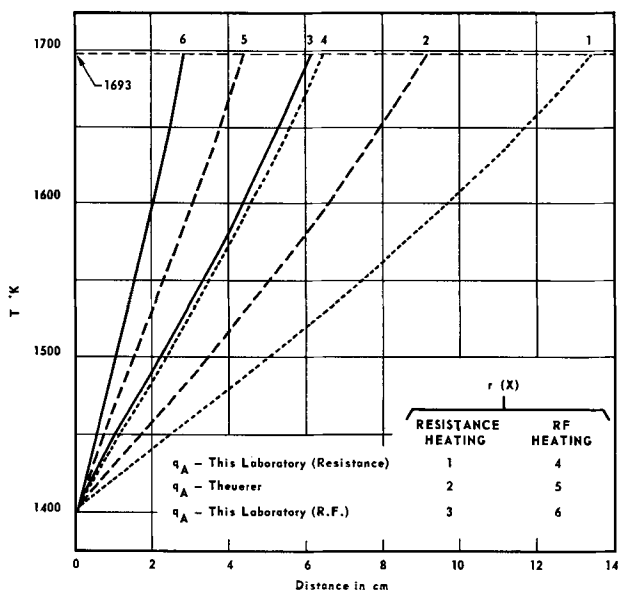


Fig. 2. Calculated temperature gradient in resistance heated apparatus.

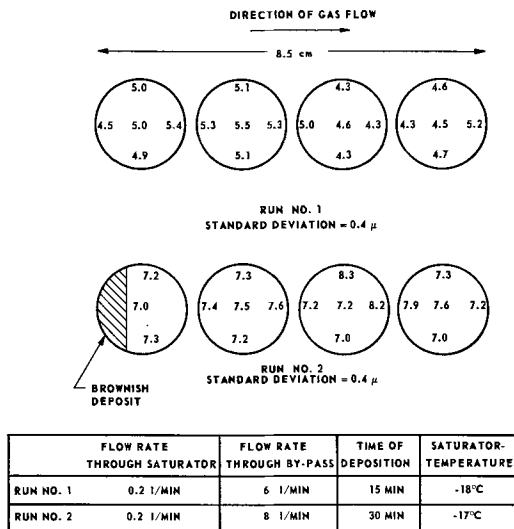


Fig. 3. Typical thickness variation along furnace

Acknowledgment

The authors would like to thank Dr. F. S. Eadie for his helpful suggestions and interest. Thanks are also due to Mr. G. Sarfi for his help in the preparation of the various fused silica ware required for the experiments.

This work has been supported in part by the Canadian Defence Research Board.

Manuscript received Oct. 11, 1963. This paper was presented at the New York Meeting, Sept. 29-Oct. 3, 1963.

Any discussion of this paper will appear in a Discussion Section to be published in the June 1965 JOURNAL.

REFERENCES

1. C. H. Li, *This Journal*, **109**, 952 (1962).
2. B. E. Deal, *ibid.*, **109**, 514 (1962).
3. A. Mark, *ibid.*, **108**, 880 (1961).
4. H. C. Theuerer, *ibid.*, **108**, 649 (1961).
5. H. C. Theuerer, H. Loar, J. Kleimack, and H. Christensen, *Proc. I.R.E.*, **48**, 1642 (1960).

6. J. M. Charig and B. A. Joyce, *This Journal*, **109**, 957 (1962).
 7. K. J. Miller, R. C. Manz, and M. J. Grieco, *ibid.*, **109**, 643 (1962).
 8. W. G. Spitzer and M. Tannenbaum, *J. Appl. Phys.*, **32**, 744 (1961).
 9. C. O. Thomas, D. Kahng, and R. C. Manz, *This Journal*, **109**, 1055 (1962).

A Study of HCl-H₂ and GeCl₄-H₂ Etching of Germanium Substrates for Epitaxial Deposition

K. J. Miller and M. J. Grieco

Bell Telephone Laboratories, Incorporated, Murray Hill, New Jersey

As part of an investigation of *in situ* etching of germanium substrates in a reaction chamber, prior to epitaxial deposition, a study was made of the kinetics and reaction chemistry of the Ge-HCl and Ge-GeCl₄ etch reactions taking place in flowing hydrogen. Recent work has been reported on the *in situ* gas phase etching of silicon and germanium samples by Bean and Gleim (1), Lang and Stavish (2), and Amick *et al.* (3). The latter authors have reported in detail on the substrate texture obtained by gas phase etching prior to epitaxial deposition.

Experimental Procedure

The apparatus used for substrate etching and epitaxial deposition was similar to that previously reported (4, 5). The HCl gas used for etching was prepared in the laboratory by dropping chemically pure concentrated aqueous HCl into chemically pure concentrated H₂SO₄ (6). The HCl gas was subsequently passed through a H₂SO₄ trap and two alcohol-dry ice traps maintained at -80°C. A mass spectrographic analysis showed that, for O₂, CO₂, and hydrocarbons, laboratory-prepared HCl was purer than that commercially available.

Germanium substrate samples were single crystal slices, approximately 0.01 ohm-cm resistivity, p-type, oriented in the (111) plane and were electrochemically polished (7). Prior to etching, the substrates were cleaned in boiling 3% H₂O₂ for 30 sec.

The HCl gas flow rate used for kinetic studies was 36 cc/min with a 2 liters/min hydrogen flow rate. Temperature measurements were taken with a Micro Optical Pyrometer and a Thermodot Radiometer.¹ Samples were heat treated in the flowing hydrogen approximately 30 min before HCl etching. Surfaces etched with HCl appeared microscopically to be smooth, and have a high degree of crystalline perfection comparable to those pre-cleaned in flowing hydrogen.

Etch rates were determined by masking an area of the surface with a quartz chip on the germanium substrates and subsequently measuring the depth of etching with an interferometer. The interferometer used was manufactured by Carl Zeiss Company and used thallium radiation.

Germanium slices were also etched using relatively high GeCl₄/H₂ mole ratios. The etch rates in

this case were determined by weight measurements. The GeCl₄/H₂ mole ratio was varied by changing the temperature of the GeCl₄ saturator (8).

Results and Discussion

The hydrogen-diluted products of the HCl-Ge etch reaction between 700° and 880°C were sampled under flowing gas conditions and analyzed at room temperature by infrared spectrophotometry. Only the absorption bands attributed to GeHCl₃ (9) and HCl were detected. The 858 cm⁻¹ and 461 cm⁻¹ GeCl₄ absorption bands (9) and those of GeH₂Cl₂ (10) were not observed. The infrared spectrum obtained, when the germanium was etched at 880°C and the HCl/H₂ mole ratio was approximately 0.018, can be seen in Fig. 1. The GeHCl₃ observed to be a product gas can be formed by the following idealized etch reactions (11, 12)

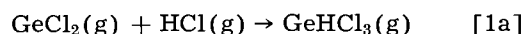


Figure 2 shows the temperature relation of the estimated (13-18)² standard state free energy change, ΔG° calculated for reactions [1] and [1a]³ and for the over-all reaction



² For GeHCl₃(g) ΔH°_{f298} was estimated from bond energies (17) with an uncertainty of ± 3 kcal/mole and ΔS°_{f298} was estimated by an empirical equation for S°_{298} (15). ΔG° values for GeHCl₃(g) were approximated from the relation

$$\frac{\partial(-\Delta G^\circ)}{\partial T} = \Delta S^\circ$$

assuming constancy of ΔH° and ΔS° (18).

³ The state of GeCl₂ is dependent on temperature. The changes in slope in Fig. 2 are reflections of these changes of state.

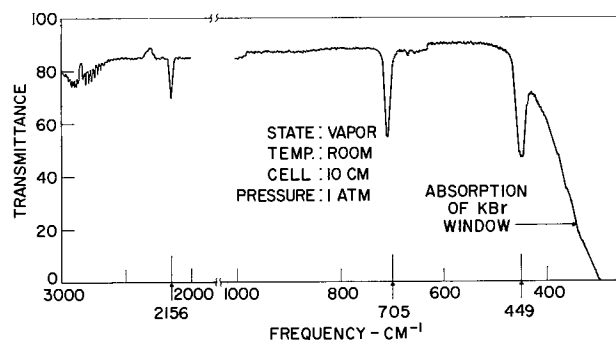


Fig. 1. Infrared spectrum of product gases from HCl etch reaction with germanium. Germanium temperature 880°C, HCl/H₂ mole ratio 0.018, 2 liter/min H₂ flow rate. Absorption at 449, 705, and 2156 cm⁻¹ frequencies attributed to GeHCl₃.

¹ Model TD-6B, supplied by Infrared Industries, Inc., Santa Barbara, California, was used for temperatures below 800°C.

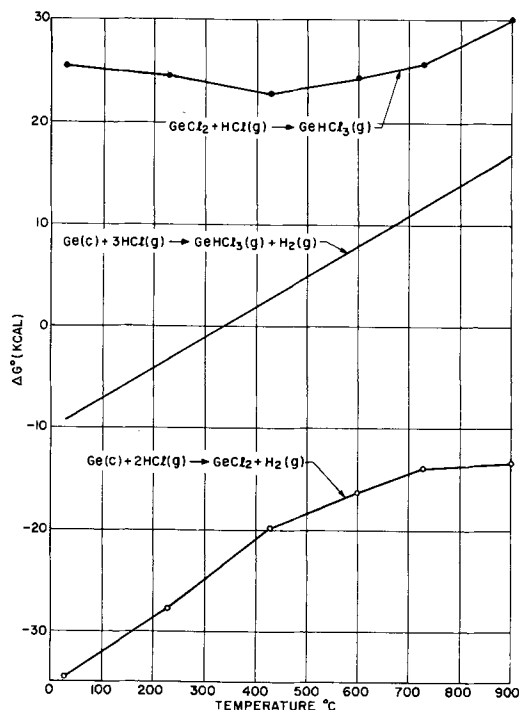


Fig. 2. ΔG° (estimated) as a function of temperature for some proposed germanium predeposition reactions.

The partial pressures of GeCl_2 obtained from the ΔG° values for reaction [1] at equilibrium used with the experimental partial pressures of HCl and H_2 , in the equation

$$\Delta G^\circ = -RT \ln \left[\frac{p_{\text{GeCl}_2} p_{\text{H}_2}}{p_{\text{HCl}}^2} \right] \quad [2]$$

show that calculated etch rates agree in general magnitude with those observed experimentally. This agreement indicates that reaction [1] is the significant etch reaction. It can be seen from Fig. 2 that ΔG° is negative for etch reaction [1] over the temperature range of interest but becomes more positive with increase in temperature. Reaction [1a] has positive ΔG° values but, because of the experimental nonequilibrium conditions which exist, particularly when the initial partial pressure of GeHCl_3 is zero, the free energy change, ΔG , for this reaction can also be expected to become negative; the formation of GeHCl_3 should not therefore be an unexpected product.

Figure 3 shows the etch rate of HCl on germanium as a function of temperature for a mole ratio $\text{HCl}/\text{H}_2 \cong 0.018$. Between $800^\circ\text{--}885^\circ\text{C}$, Fig. 3 shows that etch rates were 0.11 to 0.27 ± 0.01 μ/min and the apparent activation energy was 27 kcal/mole. In the $600^\circ\text{--}750^\circ\text{C}$ temperature range the average etch rate was 0.08 ± 0.02 μ/min . In the lower temperature range the etch rates suggested that a change in reaction mechanism from that of the higher temperature range may have taken place.

The favorable thermochemistry of the disproportionation reaction (11) below suggests that for relatively high GeCl_4/H_2 mole ratios etching also takes place with the formation of GeCl_2

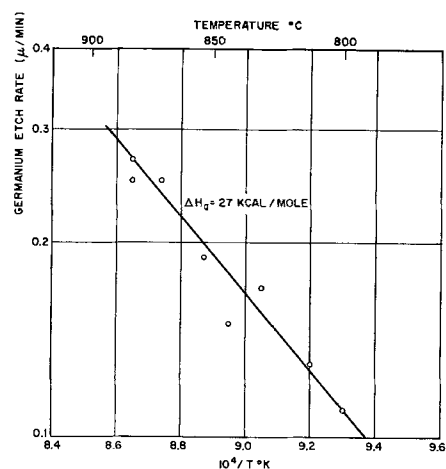
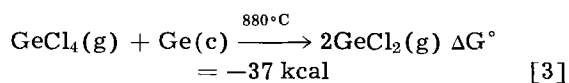


Fig. 3. Temperature dependence of germanium etch rate for 0.018 mole ratio HCl/H_2 mixtures; HCl flow rate $36 \text{ cm}^3/\text{min}$; H_2 flow rate 2 liter/min.

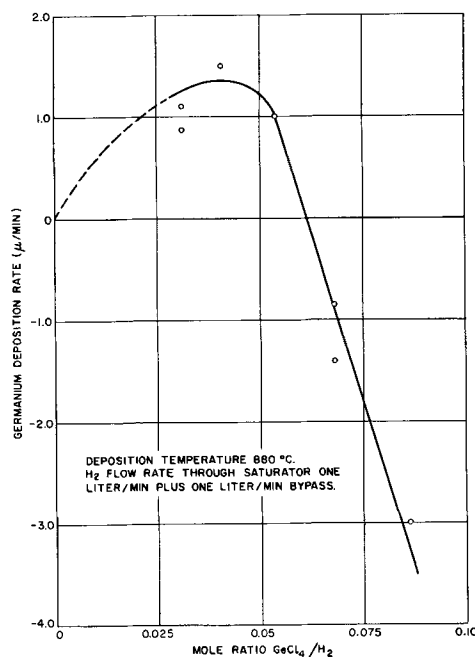


Fig. 4. Germanium deposition and dissolution rates as a function of GeCl_4/H_2 mole ratio at 880°C .

Figure 4 shows the deposition and dissolution rate as a function of GeCl_4/H_2 mole ratio, indicating that etching proceeds at > 0.06 mole ratio at 880°C . Figure 4 further indicates the limiting mole ratio which can be used for deposition of germanium.

Acknowledgment

It is a pleasure to acknowledge helpful discussions with B. Schwartz and C. D. Thurmond. The infrared spectrum was determined by Mrs. L. B. Jassie and the mass spectrometric analysis was made by D. L. Malm and A. L. Beach.

Manuscript received April 14, 1964. This paper was presented at the New York Meeting, Sept. 29–Oct. 3, 1963.

Any discussion of this paper will appear in a Discussion Section to be published in the June 1965 JOURNAL.

REFERENCES

1. K. E. Bean and P. S. Gleim, paper presented at the Electrochemical Society New York Meeting, Sept. 30–Oct. 3, 1963.

2. G. A. Lange and T. Stavish, *RCA Rev.*, **24**, 488 (1963).
3. J. A. Amick, E. A. Roth, and H. Gossenberger, *ibid.*, **24**, 473 (1963).
4. H. C. Theuerer, *This Journal*, **108**, 649 (1961).
5. K. J. Miller and M. J. Grieco, *ibid.*, **109**, 643 (1962).
6. H. S. Booth, Editor, "Inorganic Synthesis," Vol. 1, p. 197, McGraw-Hill Book Company, New York (1939).
7. M. V. Sullivan, D. L. Klein, R. M. Finne, L. A. Pompliano, and G. A. Kolb, *This Journal*, **110**, 412 (1963).
8. K. J. Miller and M. J. Grieco, *ibid.*, **110**, 1252 (1963).
9. L. P. Lindeman and M. K. Wilson, *Spectrochimica Acta*, **9**, 47 (1957).
10. T. N. Srivastava, J. E. Griffiths, and M. Onyszchuk, *Can. J. Chem.*, **41**, 2101 (1963).
11. L. M. Dennis, W. R. Orndorff, and R. L. Tabern, *J. Phys. Chem.*, **30**, 1049 (1926).
12. O. H. Johnson, *Chem. Rev.*, **51**, 441 (1952).
13. JANAF, Interim Thermochemical Tables, Vols. 1 and 2, Thermal Laboratories, Dow Chemical Co.
14. A. Glassner, "The Thermochemical Properties of the Oxides, Fluorides and Chlorides to 2500°K," ANL-5750, Argonne National Laboratory.
15. O. Kubaschewski and E. LL. Evans, "Metallurgical Thermochemistry," p. 195, Pergamon Press, London (1958).
16. S. R. Gunn and L. G. Green, *J. Phys. Chem.*, **65**, 779 (1961).
17. T. L. Cottrell, "The Strengths of Chemical Bonds," 2nd. ed., Butterworth's Scientific Publications, London (1958).
18. J. D. Fast, "Entropy," p. 102, McGraw-Hill Book Co., Inc., New York (1962).

Determination of Nitrogen in Silicon by Solid Source Mass Spectrometry

Philip R. Kennicott

Research Laboratory, General Electric Company, Schenectady, New York

The purpose of this note is to report an analysis of nitrogen in silicon in the low parts per million range making use of a solid source mass spectrograph.¹

An ingot of silicon grown in argon gas by the floating zone technique, in such a manner as would be expected to produce a single crystal, was found to be polycrystalline. Such polycrystalline growth is likely to be due to one or more impurities, and these impurities could be expected to be concentrated in one or the other end of the ingot.

Upon etching the last-to-freeze end of the ingot, a region was found which was resistant to the etch (Fig. 1). Infrared transmission micrographs showed impurities to be precipitated in this region (Fig. 2). A section was taken from the ingot containing these bands and electrodes were prepared.

The spectrum produced by the mass spectrograph consists of lines whose spacing is proportional to the square root of mass/charge. It is a characteristic of the spark source that large numbers of multiply charged ions are produced. Thus, in a matrix such as silicon (mass 28), impurities at 14, 7, etc. AMU (atomic mass units) will tend to be obscured by the much heavier lines due to the matrix. It is this fact that makes the analysis of nitrogen in silicon so difficult. Fortunately, the intensity of multiply

¹ MS-7 produced by Associated Electrical Industries.

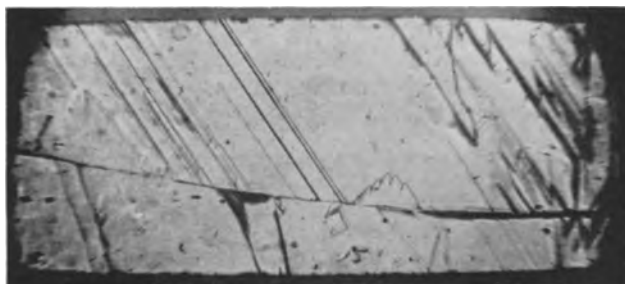


Fig. 1. Etched portion of last-to-freeze end of ingot

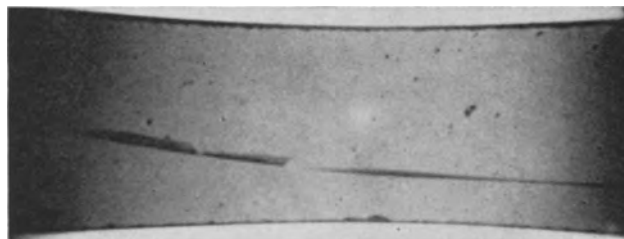


Fig. 2. Infrared transmission of last-to-freeze end

charged ions falls off rather rapidly with increasing charge. Therefore, one might expect to find some multiply charged silicon line which does not quite obscure the associated nitrogen line.

The rate at which the number of multiply charged ions decreases with increasing charge depends strongly on the electrical conditions used to produce the spark. The conditions used in this study are given in Table I.

A doublet at nominal mass 4-2/3 appeared on the plate produced from the electrodes taken from the last-to-freeze region (Fig. 3). A doublet was not present in material taken from neighboring regions in the ingot. The doublet spacing and nominal mass were consistent with identification as nitrogen ¹⁴N⁺³ and silicon ²⁸Si⁺⁶. The intensity of the nitrogen component of the doublet gave a concentration of nitrogen of 10 ± 3 ppm atomic. Since the electrodes sampled much more material than the precipitates themselves, this value must be regarded as an average value for the entire electrode.

Table I. Spark conditions

Spark voltage	20 kv
Pulse length	25 μsec
Pulse repetition rate	3000 cps
Accelerating potential	20 kv
Source pressure	1.3 × 10 ⁻⁷ Torr

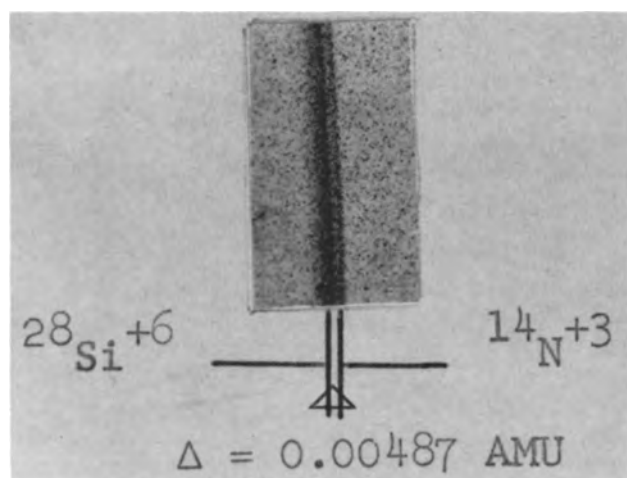


Fig. 3. Portion of mass spectrograph plate at mass 4-2/3. $\Delta = 0.00487$ AMU.

It is estimated that the ultimate sensitivity for nitrogen on these plates is 1 ppm. Thus, nitrogen from neighboring regions of the ingot must have been below this level. The source of the nitrogen was found to be an undetected contaminant in the argon used as a protective gas when the ingot was grown.

The estimations were made visually by comparing the optical density of the nitrogen line with that of $^{28}\text{Si}^{+6}$. The total exposure giving silicon an optical density equal to that of the nitrogen was determined. The concentration of nitrogen was then determined by making appropriate corrections for relative total exposure and isotopic abundance. The

method of estimation depends on the assumption that the ratio of triply charged nitrogen to singly charged nitrogen ions is equal to the similar ratio for silicon. This assumption is probably justified to within the accuracy stated above.

When this analysis was begun, it was not known what contaminant was preventing single crystal growth. Indeed, carbon was suspected. The contaminant causing the formation of the precipitates and thus preventing single crystal growth was readily shown to be nitrogen. At the same time a value for the total average concentration of nitrogen in the region of the ingot containing the precipitates was obtained. It must be realized that this value represents the level of nitrogen present after having been concentrated by the zone refining process. The upper limit for the concentration of nitrogen, which can be tolerated if single crystal growth is to be assured, lies considerably below this value.

An infrared analysis of the type described by Kaiser and Thurmond (1), if it could be placed on a quantitative basis, would give a value for the concentration of dissolved nitrogen. A lower limit for the concentration of nitrogen necessary to prevent single crystal growth might be obtained in this manner.

Manuscript received April 15, 1964.

Any discussion of this paper will appear in a Discussion Section to be published in the June 1965 JOURNAL.

REFERENCE

1. W. Kaiser and C. D. Thurmond, *J. Appl. Phys.*, **30**, 427 (1959).

Etching of Gallium Arsenide with Nitric Acid

D. F. Kyser and M. F. Millea

Aerospace Corporation, El Segundo, California

Recently Yeh and Blakeslee (1) reported the formation of etch figures on GaAs after prolonged etching with small drops of dilute nitric acid. The work reported in this note shows that these etch figures are due to the formation of As_2O_3 crystals on the GaAs during nitric acid etching.

In this study, wafers of single-crystal GaAs were etched one at a time in 50 ml of HNO_3 acid solution at room temperature. The wafers were etched while standing on edge in a slotted Teflon boat, without agitation or stirring. The GaAs was n-type (111) Czochralski grown with a tellurium doping density of $1.6 \times 10^{17}/\text{cm}^3$. Before etching, both faces of the

wafer were mechanically polished to a mirror finish, with the final polishing compound being 0.3μ alumina abrasive.

Examination of the wafer after etching revealed that foreign crystals precipitated on the surface, depending on the concentration of the acid solution used. To determine the composition of the crystals, a wafer sample was etched for 5 min in concentrated nitric acid to form a dense layer of crystals on the As {111} face. This surface layer was identified as As_2O_3 by x-ray diffraction techniques. In addition the crystals were observed to sublime at the sublimation temperature of As_2O_3 (193°C) (2).

Listed in Table I are the effects of various nitric acid concentrations on the formation of As_2O_3 crystals. An example of the As_2O_3 crystals that formed on the Ga and As {111} faces of sample 2 is shown in Fig. 1. It can easily be seen that the preferential effect of the etch on the Ga and As (111) faces is still preserved, as reported by Abrahams and Ekstrom (3). This effect enables one to identify the two faces, since etch pits form only on the Ga {111} face. The As_2O_3 crystals take a pyramidal shape and have a random orientation. Many of the crystals have flat tops which are coplanar and parallel to

Table I. Effect of nitric acid concentration on crystal formation

Sample No.	Etch time, min	Etch solution $\text{HNO}_3:\text{H}_2\text{O}$ by volume	Results
1	5	Concentrated HNO_3	Many crystals form on both faces, but more densely on As (111)
2	10	1:1	Same as above, but relatively less dense
3	10	1:2	No crystals form on either side
4	30	1:2	Same as above

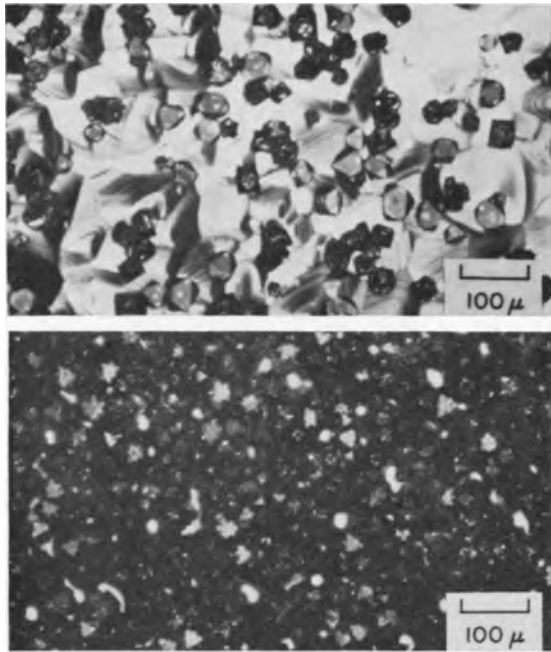


Fig. 1. As_2O_3 crystals on GaAs wafer after nitric acid etching: (a) Ga {111}; (b) As {111}.

the original surface of the wafer. The crystals adhere to the surface by means of a raised pyramidal base of GaAs which can be observed through the transparent crystals. There is a much higher density of crystals on the As {111} face than the Ga {111} face. The crystals also form on the {110} cleavage planes as well as the {111} planes.

It is believed that the nitric acid dissolves the GaAs by forming As_2O_3 and a soluble gallium compound. However, As_2O_3 is not soluble in nitric acid but is soluble in H_2O to the limit of 2.04 g/100 ml at 25°C (2). Hence, if the localized generation rate of As_2O_3 by HNO_3 exceeds the localized dissolution rate of As_2O_3 by H_2O , then the As_2O_3 concentration in solution will increase until the solubility limit is reached. At that point, the As_2O_3 in solution will precipitate out to form crystalline As_2O_3 . The crystals will attach themselves to the surface of the wafer and grow with further etching action. The surface of the wafer beneath the crystal is then protected from the etch, which explains why the crystals are supported by a raised pyramidal base of GaAs. The failure of the crystals to form with dilute nitric acid solution can be explained by the fact that the generated As_2O_3 dissolves as rapidly as it is generated.

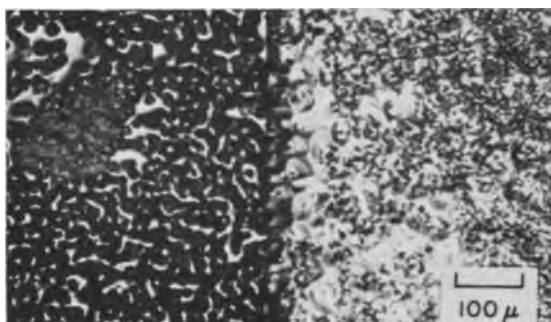


Fig. 2. GaAs wafer with twin plane revealed by nitric acid etching

A striking example of the etching rate on the formation of these As_2O_3 crystals is shown in Fig. 2. The GaAs wafer contained a twin plane intersecting the surface at an angle of 54.7°, where in the zinc-blende structure of GaAs the twinning operation must be considered as a 180° rotation about the [111] directions (4). The wafer was etched for 4 min in one part HNO_3 to one part H_2O solution by the method described previously. To the right of the plane is the Ga {111} surface with its As_2O_3 crystals and identifying etch pits. To the left of the twin plane is a {110} surface with a much higher density of As_2O_3 crystals. The etch pits do not form on the {110} surfaces. The faster etching rate of the {110} plane resulted in larger and denser As_2O_3 crystals relative to the Ga {111} surface. This is in agreement with Gatos and Lavine (5) who showed that the relative dissolution rates of low-index planes in InSb are

$$\text{Sb}\{111\} \cong \{110\} > \{110\} > \text{In}\{111\}$$

Thus, the etching rate determines the relative density of As_2O_3 crystals on the various crystallographic planes.

Additional experiments were performed to determine if As_2O_3 crystals would form on GaAs wafers etched in various other chemical solutions. No As_2O_3 crystals were observed on GaAs specimens etched in large volumes of (a) 1HF: 1 HNO_3 : 2 H_2O ; (b) concentrated H_2SO_4 ; (c) concentrated H_2O_2 ; and (d) concentrated HCl. A large density of As_2O_3 crystals were observed on a GaAs specimen etched in 1HF: 1 HNO_3 : 2HAc.

The etch figures obtained by Yeh and Blakeslee (1) can now be explained by the formation of As_2O_3 crystals. An example of As_2O_3 crystals formed in this manner is shown in Fig. 3. A small drop of 1 HNO_3 :2 H_2O solution was placed on the surface of a polished GaAs wafer, and the As_2O_3 crystals

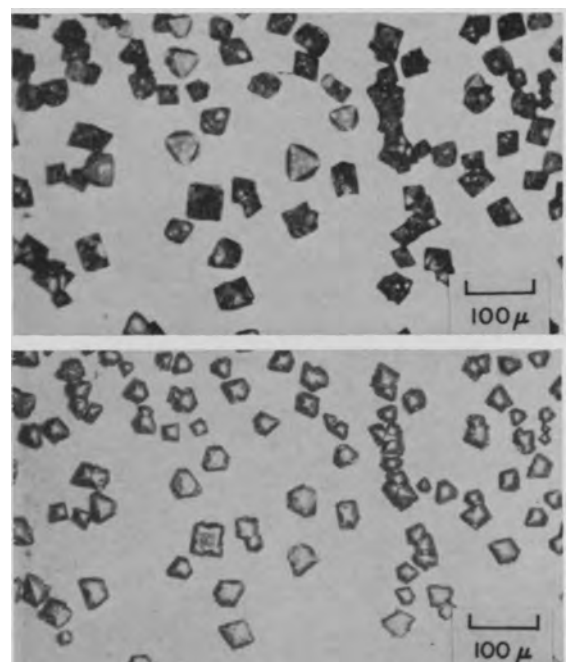


Fig. 3. As_2O_3 crystals on GaAs wafer etched with small drop of dilute nitric acid: (a) after etching; (b) after sublimation of crystals.

formed within 5 min. Also shown in Fig. 3 are the raised pyramidal GaAs bases after the As_2O_3 crystals were removed by sublimation. These results show that the As_2O_3 crystals can be formed with dilute nitric acid solutions when very small volumes of etch are used. The small volume of etch can easily become saturated with dissolved As_2O_3 , and then the crystalline precipitates of As_2O_3 can form as described previously.

Manuscript received Jan. 13, 1964; revised manuscript received April 17, 1964. This paper was prepared under U. S. Air Force Contract No. AF 04(695)-169.

Any discussion of this paper will appear in a Discussion Section to be published in the June 1965 JOURNAL.

REFERENCES

1. T. H. Yeh and A. E. Blakeslee, *This Journal*, **110**, 1018 (1963).
2. "Handbook of Chemistry and Physics," 31st ed., C. D. Hodgman, Editor Chemical Rubber Publishing Co., Cleveland (1948).
3. M. A. Abrahams and L. Ekstrom, "Properties of Elemental and Compound Semiconductors," H. C. Gatos, Editor, p. 225, Interscience Publishers, Inc., New York (1959).
4. O. Lindberg and J. W. Faust, Jr., "Compound Semiconductors," R. K. Willardson and H. L. Goering, Editors, Vol. I, Chap. 34, Reinhold Publishing Corp., New York (1962).
5. H. C. Gatos and M. C. Lavine, *This Journal*, **107**, 433 (1960).

The Transition Time of Electrode Reactions without Supporting Electrolytes

P. Bro

Laboratory of Physical Science, P. R. Mallory & Company, Inc., Burlington, Massachusetts

The effects of supporting electrolytes on the transition time of electrode reactions have been discussed recently by Morris and Lingane (1), who presented a rigorous derivation of the transition time equation for solutions without supporting electrolytes. Their experimental data agreed well with the predicted transition times for several cathodic reactions.

In connection with our studies of nonaqueous battery systems we have had occasion to examine the same problem, and Dr. Selim of our laboratory has obtained data which test the validity of the revised transition time equation under quite general conditions which have not yet been reported in the literature.

Hydrochloric acid was particularly interesting among the solutions tested since it could be used to obtain both anodic and cathodic transition times under identical conditions. Furthermore, the discharge of hydrogen ions provided as severe a test of the diffusion model as may be expected in practical systems. The experimental data are given in Table I, and they are compared with the predicted values in Table II. Equation [27] of Morris and Lingane was used to obtain the predicted values in conjunction with published diffusion data (2). It may be seen that the experimental and theoretical

Table I. Anodic and cathodic transition times in hydrochloric acid at 25°C

HCl, M	NaNO_3 , M	NH_4ClO_4 , M	Anodic $IT^{1/2}$, ma sec ^{1/2}	Cathodic $IT^{1/2}$, ma sec ^{1/2}
0.00247	—	—	3.2 ± 0.1	15.7 ± 0.5
0.00247	1.0	—	2.2 ± 0.1	4.2 ± 0.2
0.0037	—	—	5.1 ± 0.1	20.4 ± 1.8
0.0037	—	1.0	passivates	5.7 ± 0.2
0.0069	—	—	passivates	42 ± 1.5
0.0069	—	1.0	passivates	11.2 ± 0.2

* Hg electrodes supported on platinum foil, 2 cm² electrode area.

Table II. Comparison of experimental and theoretical transition time ratios

HCl concentration, M	Reaction	Experimental $(IT^{1/2}) / (IT_s^{1/2})$	Theoretical
0.00247	Anodic	1.45	1.57
0.00247	Cathodic	3.74	3.35
0.0037	Cathodic	3.58	3.35
0.0069	Cathodic	3.75	3.35

values agree within 10% which confirms that the equation given by Morris and Lingane adequately describes the behavior of electrode reactions in solutions without supporting electrolytes when no complications are present.

Our analysis of the problem included the integration of an equation equivalent to Eq. [21] of Morris and Lingane which led to an explicit expression for the concentration profile in the stagnant solution. For the discharge of cations the concentration profile becomes

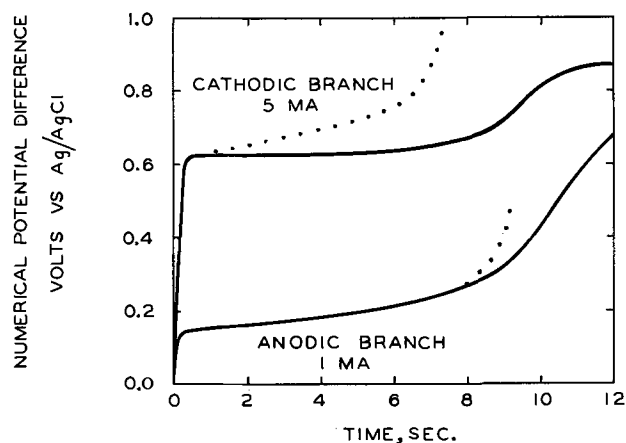


Fig. 1. Comparison of experimental and theoretical chronopotentiograms; . . . , theoretical curve; —, experimental data, 0.00247M HCl.

$$c_1(x,t) = c_0 - \frac{bI}{a(a+b)FD_1} \left[2 \left(\frac{Dt}{\pi} \right)^{1/2} \exp\left(-\frac{X^2}{4Dt}\right) - X \operatorname{erfc} \frac{X}{2(Dt)^{1/2}} \right]$$

Where the cationic current is taken as positive. This equation was used with Eq. [34] of Morris and Lingane to calculate the anodic and cathodic chronopotentiograms of hydrochloric acid shown in Fig. 1. The theoretical curves are compared with the experimental chronopotentiograms, and it may be seen that the anodic behavior can be predicted quite well, whereas the cathodic behavior is less satisfactory. The theoretical chronopotentiograms can probably be improved by the use of concentration dependent transport parameters although there is no simple, rigorous way of doing so at the present time. The discrepancies between the slopes of the curves in the transition regions are quite large, and they may be attributed to electrode reactions not allowed for in the single reaction model.

It appears, then, that the transition time formalism can be used in analyzing the behavior of elec-

trodes in solutions without supporting electrolytes, but that caution must be exercised in quantitative predictions of chronopotentiograms based on simple models.

Manuscript received Feb. 5, 1964; revised manuscript received May 11, 1964.

Any discussion of this paper will appear in a Discussion Section to be published in the June 1965 JOURNAL.

REFERENCES

1. M. D. Morris and J. J. Lingane, *J. Electroanal. Chem.*, **6**, 300 (1963).
2. R. A. Robinson and R. H. Stokes, "Electrolyte Solutions," 2nd ed., p. 158, p. 463, Butterworths, London (1959).

SYMBOLS

a	cationic charge, dimensionless
b	anionic charge, dimensionless
c_0	initial electrolyte concentration, mole/cm ³
c_1	concentration of cation, mole/cm ³
D	diffusion coefficient of electrolyte, cm ² /sec
D_1	diffusion coefficient of cation, cm ² /sec
F	the Faraday, coulombs
I	current density, amp/cm ²
t	time, sec
T	transition time, sec
T_s	transition time in presence of supporting electrolyte, sec
X	position coordinate, cm

Electrochemical Chlorination of n-Dodecane

F. N. Ruehlen, G. B. Wills, and H. M. Fox

Research Division, Phillips Petroleum Company, Bartlesville, Oklahoma

ABSTRACT

Dodecane was efficiently chlorinated at a porous carbon anode in an electrolytic cell containing a 20% hydrochloric acid electrolyte. The dodecane flowed continuously through the porous anode, and chlorinated products were continuously withdrawn. Voltametric studies on small-scale electrodes indicated that the reaction mechanism involves chlorine evolution followed by a chlorination reaction which takes place in a thin film adhering to the electrode. The distribution of products, *i.e.*, the ratio of monochlorododecanes to dichlorododecanes produced were correlated on the basis of a calculated statistical distribution assuming a free radical mechanism. The pronounced deviations from this statistical distribution at low current densities are explained on the basis of a competing reaction which involves the diffusion of free radical inhibitors into the reaction film.

Monochlorination of paraffin hydrocarbons is a growing route to olefins, alcohols, amines, amides, nitriles, alkyl benzenes, and many other alkyl products. Chlorine is substituted for hydrogen by direct action of chlorine in either light-activated or thermally activated reactions. This study considers still another technique, electrochemical chlorination. A specific objective of the study was to determine if n-dodecane can be continuously and efficiently monochlorinated at the anode of an electrolytic cell containing an aqueous hydrochloric acid electrolyte.

The experimental work was directed primarily toward two aspects of the problem: (i) determination of the effect of cell operating characteristics on products, specifically in respect to reduction of polychlorides, and (ii) understanding the mechanism of the reactions. Most of the work was conducted in a chlorination cell which was equipped to provide dodecane continuously at the surface of a porous carbon anode and to skim products and unreacted dodecane continuously from the cell. Voltametric studies were also made using small cells and specially constructed electrodes.

Experimental

Chlorination cell.—The anode of the chlorination cell (Fig. 1) was a porous carbon cylinder with one end closed and the open end tapped to receive a 1/4-in. Teflon pipe nipple. This nipple served as the hydrocarbon feed entry as well as a support for the anode. The anode was 3.7 cm long with an outside diameter of 2.5 cm and a wall thickness of 0.7 cm. A coating of porcelain cement restricted the working surface to the vertical perimeter below the end of the Teflon nipple. Electrical connection to the anode was made by means of a copper wire extending downward through the hydrocarbon feed tube.

Hydrocarbon feed to the cell was monitored by a small flow meter, but the actual quantities of dodecane fed were determined from volume changes in a calibrated feed cylinder. The hydrocarbon feed was purged with nitrogen to expel dissolved oxygen. The electrolyte was 20% hydrochloric acid and fresh acid was introduced continuously to the cell at a rate of 60 to 100 ml/hr depending on the current density. Current densities in the range 15 to 180 ma/cm² were used, and the cell temperature was maintained between 93° and 102°C. The cell terminal voltage ranged from 1.5 to about 2.0v depending on current density and dodecane feed rate. Samples were collected for analysis after several hours of operation at constant current and hydrocarbon feed rate. These samples

were analyzed for mono- and dichlorododecanes by gas-liquid chromatography.

National Carbon Grade 60 (NC-60) porous carbon was used as anode material. This carbon is reported to have a void volume of about 0.2 cm³/g in pores ranging from 10 to 60μ in diameter. Phillips pure-grade dodecane was the feed.

Voltametric cells.—Graphite-paste electrodes similar to those described by Adams (1) were constructed for the voltametric studies. The conductive pastes were prepared by mixing either dodecanes or unreactive binders with fine graphite powder. Holders were prepared from glass tubing. The lead wire extended through the glass tubing and was immersed in the paste which was packed in the end of the tubing. The electrode surface was the exposed area at the end of the tubing. Carbon or platinum counter electrodes were used. Reference electrodes were either saturated calomel or silver-silver chloride electrodes. The electrode potential was increased linearly with time relative to a reference electrode by a potentiostat based on operational amplifiers. Similar potentiostats are described in detail elsewhere (2). The cell current as a function of anode-to-reference voltage was plotted

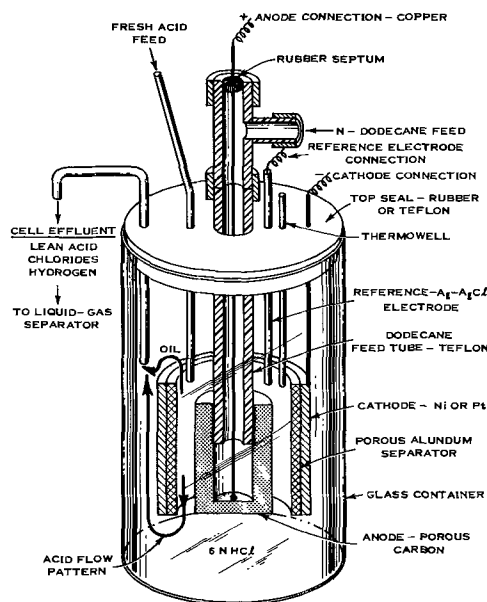


Fig. 1. Chlorination cell

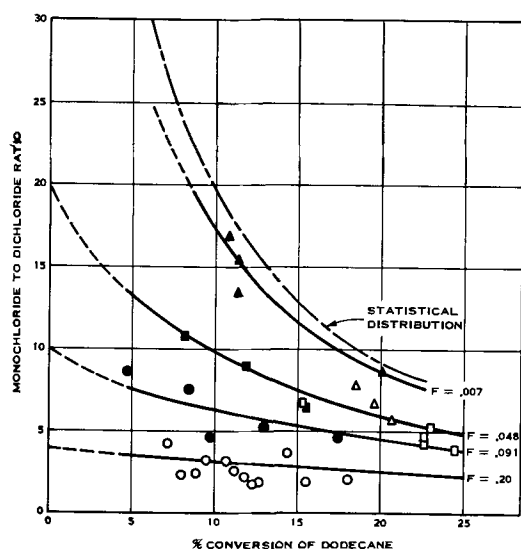


Fig. 2. Effect of current density and conversion on product distribution; current density, mA/cm^2 : \circ , 17; \bullet , 50; \square , 67; \blacksquare , 90; \triangle , 120; \blacktriangle , 70-180 with peroxide additive.

by an x-y recorder with a 2-sec pen and a $4\frac{1}{2}$ -sec chart. The voltage axis may also be considered a time axis by virtue of the linear sweep voltage.

Except as indicated the electrolyte was a 20% solution of hydrochloric acid. Some of the voltametric traces on paste electrodes were obtained in electrolyte containing 4 g/liter of potassium iodide. Consequently, oxidation peaks corresponding to the formation of iodine and iodine monochloride were noted in addition to the final upswing associated with chlorine evolution (Fig. 3). The purpose of this multiple oxidation was to show that different electrodes were comparable. It was found that paste electrodes varied in the chloride oxidation potential depending on the ratio of binder to substrate, the type of substrate, or even the mechanics of forming the electrodes. By demonstrating identical response to other reactions than the chloride oxidation confirmed that the analysis was not affected by compositional and mechanical variations in the electrodes.

Results and Discussion

Product distribution.—Products recovered in the continuous chlorination of dodecane were monochlorododecanes, dichlorododecanes, and higher chlorododecanes. One of the objectives of the product studies was to maximize the yield of monochlorododecane, which was considered to be the most important product from a commercial standpoint. Conversions were limited in this study to about 25% to minimize the yield of dichloro- and higher chlorododecanes. At conversions of 25% and less, the yield of higher chlorododecanes (primarily trichlorododecanes) was negligible. Therefore, the trichlorododecanes and higher are omitted from further discussion.

The product distribution obtained on dodecane chlorination is summarized by Fig. 2. This figure shows the monochloride-to-dichloride ratio as a function of dodecane conversion. It gives, in effect, selectivity to the two major products *vs.* conversion as affected by current density. At the highest current densities evaluated, the yields of monochlorododecane approached a calculated statistical distribution. This calculation assumed a simple model in which chlorine is evolved at the electrode and then substituted for hydrogen on the dodecane on a strictly statistical basis. For such a model the product composition is dependent only on conversion and the ratios of the rate constants for the various species present. Here, these ratios were taken to be equal to the ratio of hydrogen atoms in the respective species. Thus the ratio of reactivity of dodecane to monochlorododecane was

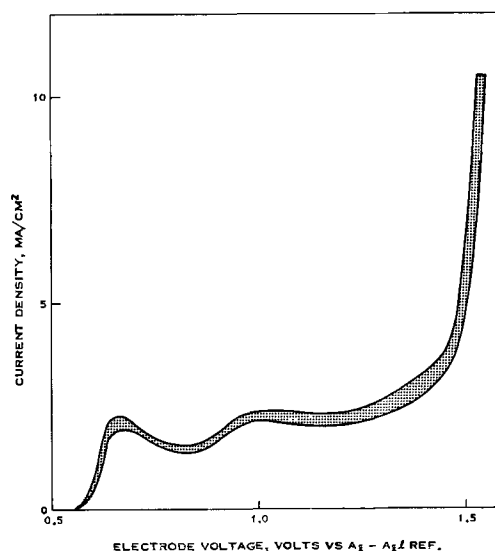


Fig. 3. Anodic voltage scans of several paste electrodes in 20% HCl containing 4 g/l potassium iodide; sweep rate, 0.32 v/min; temperature, 25°C; substrate, No. 38 Acheson graphite; binders: 36.5 w/o dodecane, 58.8 w/o carbon tetrachloride, 62.5 w/o trichlorobromo-methane.

taken to be 26/25. To a very good approximation the expected ratio of monochlorododecane to dichlorododecane can be related to extent of conversion as follows

$$R_1/R_2 = -(52 + \text{Ln } X) / 25 \text{Ln } X \quad [1]$$

where R_1 is moles of monochlorododecane/mole of dodecane feed, R_2 moles of dichlorododecane/mole of dodecane feed, and X moles of unreacted dodecane/mole of dodecane feed.

The curve labeled "statistical distribution" on Fig. 2 is a graphical representation of Eq. [1]. Under favorable conditions this ratio was closely approached but in no case was the curve exceeded. The lines drawn through the experimental points on Fig. 2 were calculated from the statistical distribution on the assumption that a certain fraction, F , of the reacting dodecane molecules converted directly to dichlorododecanes by an alternate nonradical reaction mechanism.

The pronounced dependence of the product distribution on current density is thought to be a result of inhibition of the postulated radical mechanism by transport of trace amounts of free radical inhibitors from the bulk electrolyte into the reaction zone. At high current densities this inhibition effect could be overwhelmed by the increased chlorine concentration in the reaction zone. This reasoning also explains the beneficial effect of the benzoyl peroxide, which decomposes to produce radicals that could scavenge the inhibitors and, thus give much the same effect as an increase in current density. Another observation that substantiates the foregoing was the observed change in current efficiency and selectivity to monochlorododecanes that takes place during the first two or three hours of operation with a new anode. During this initial period there was a steady and significant improvement in current efficiency and selectivity to monochlorododecanes. It is postulated that a fresh carbon anode contains adsorbed oxygen or other impurities which consume chlorine or otherwise inhibit the formation of free radicals. Once these impurities were consumed, the electrodes were operated for several days with no change in performance. Current efficiencies were in the range of 80 to 100% and were substantially independent of current density, dodecane feed rate, and conversion level. The appearance of the surface of an anode was usually changed after it was used for chlorination, and the extent of the change appeared to depend on the cur-

rent-density history of the electrode. Extensive change in appearance was not observed except at current densities much beyond those reported.

Electrode reaction mechanism.—The results in Fig. 3 show that the reaction of chlorine and dodecane does not lead to significant electrode depolarization. Dodecane and fully halogenated binders gave equivalent traces. Similar results were obtained with a small NC-60 porous carbon electrode at several temperatures in the range of 25°–95°C. For example at a current density of 5 ma/cm² an electrode saturated with dodecane gave the same voltage as a similar electrode completely free of dodecane. In light of these findings, it seems reasonable to conclude that the chlorination of dodecane does not take place on the electrode surface to any significant extent at least at current densities in excess of 5 ma/cm².

Properties of the dodecane film on the anode and the dependence of these properties on feed rate, density differences, electrode geometry, and viscosity were not investigated by direct experiment. It is believed that under the conditions evaluated the dodecane film was continuous. Likewise, reaction rates were not directly studied. However, the rates were sufficiently fast to give essentially complete utilization of the evolved chlorine.

Conclusions

1. Utilizing a cell such as described, normal dodecane is continuously and efficiently chlorinated to dodecane monochlorides. Under favorable conditions, the product distribution approaches but never exceeds a calculated statistical distribution.

2. Approach to the statistical distribution is favored by high current density or free radical promoters in the feed.

3. There is no significant depolarization due to presence of dodecane on the anode.

4. The mechanism of the reaction is believed to be chlorine evolution followed by liquid-phase chlorination reaction, which is essentially complete before the dodecane breaks away from the anode.

Manuscript received Oct. 17, 1963.

Any discussion of this paper will appear in a Discussion Section to be published in the June 1965 JOURNAL.

REFERENCES

1. C. Olson and R. N. Adams, *Anal. Chim. Acta*, **22**, 582 (1960).
2. G. L. Booman, *Anal. Chem.*, **31**, 10 (1959).

New Methods of Obtaining Fuel Cell Electrodes

I. Aluminum-Nickel Mixed Powder Hydrogen Electrode

A. R. Despić, D. M. Dražić, C. B. Petrović, and V. Lj. Vujčić

Faculty of Technology, University of Beograd, and the Institute for Chemistry, Technology, and Metallurgy, Beograd, Yugoslavia

ABSTRACT

A new method of obtaining Raney nickel hydrogen electrodes was evaluated, in which the electrodes were made by pressing aluminum-nickel powder mixture, followed by simultaneous sintering of Ni skeleton and alloying of the surface layer of the formed Ni skeleton with aluminum present in its pores. The best results were obtained with a mixture of 10% (by weight) Al and 90% Ni, followed by sintering and alloying at 660°C for ½ hr. Such electrodes, with slopes of the anodic polarization curves of 0.8–1 cm² v/amp, and limiting current densities of ca. 250 ma/cm² were similar to those made of Ni and Raney-Ni powder of the same quality, according to the method of Justi. Microscopic investigation revealed that during the heating reaction between Ni and Al took place yielding Ni₂Al₃, which is electrochemically the most active type of Raney nickel alloy. In the case of double layer electrodes, made by this method, the extent of the active layer did not substantially influence the electrochemical characteristics of the electrodes down to 0.5 mm thickness. The major advantages of this type of electrode lie in the simplicity of their preparation as well as in their mechanical strength.

Catalytic activity, or sufficiently high working current density of a hydrogen fuel cell electrode at low polarization, can be achieved in two ways. One is that of impregnation of the inactive porous bodies [e.g., made of porous carbon (1) or sintered Ni or Fe powders (2)] by an active component exhibiting a catalytic influence on the electrochemical reaction at the electrode (e.g., platinum). The other way is that of mixing an electrochemically active component in the form of powder (e.g., Raney nickel) with an inactive powder (e.g., nickel), and then pressing and sintering this powder mixture into an active hydrogen electrode (3). In the latter case the role of the inactive component is to form a sufficiently strong metal skeleton, in the pores of which the particles

of active Raney nickel alloy are situated. The particles of the Raney alloy themselves are not able to give sufficiently strong mechanical structure to the electrode.

The impregnation method has two major disadvantages. The first one is the high price of the catalytically active materials used in it (Pt, Pd, etc.) while the second one is the sensitivity of these catalysts to poisoning by very small amounts of impurities which can be present in the hydrogen used. Therefore, the danger of poisoning the electrodes implies the use of adequately purified hydrogen, increasing the cost of the fuel.

The Raney-type electrodes are known not to have both of the disadvantages mentioned above. How-

ever, the process of their preparation is considerably more involved, comprising the preparation of the Raney alloy, its disintegration into a powder of uniform particle size, mixing of Raney alloy powder with the corresponding Ni powder, pressing and sintering of this mixture into a compact body to be activated, and finally rendering the electrode active.

The purpose of this communication is to estimate the value of the ideas developed by Petrović, Despić, Jancić, and Džazić (4) that an active hydrogen electrode may be obtained by the formation of the Raney alloy at the pore-walls inside the inactive Ni porous body by the reaction of the surface layer of Ni with Al brought into the pores by a suitable method. This work is concerned with the investigation of the Raney nickel electrodes obtained by pressing and heating a mixture of aluminum and nickel powders. This process yielded simultaneous sintering of Ni particles and formation of Raney nickel by the reaction between Ni and Al.

Experimental

Two kinds of electrodes were used. For the first set of experiments the electrodes were made of a mixture of carbonyl nickel powder (Mond Nickel Co. nonfractionated Grade A) and an aluminum powder (Carlo Erba, with grain size ranging between 1 and 90μ). The percentage of Al in the mixture was varied between 0 and 15% (by weight). Such a mixture was homogenized manually in a porcelain mortar (homogenization in a mechanical homogenizer was inefficient because of the large difference in specific gravities of Ni and Al). An amount of this mixture was put into a die and pressed with a force of 50 tons to form a disk shaped electrode 40 mm in diameter and 1 mm thick.

In the second set of experiments double layer electrodes were made of the same shape as were the previous ones, but with a varying thickness of the active (coarse) layer (0.2-0.5 mm). Coarse layers were made of the same Ni-Al powder mixture with 10% Al, as used above. The fine layers were made of pure Ni powder (4-5 μ grain size) and were 0.25 mm thick.

The sintering of such pressings was done at temperatures between 600° and 700°C, in an atmosphere of purified and dried hydrogen for ½ hr. The removal of oxygen from technical hydrogen was done with Deoxo equipment after which the gas was dried in a column with NaOH pellets. In the process of sintering, the double layer electrodes showed a tendency to bend because of different shrinking properties of the fine and coarse layers. This difficulty was overcome by applying an appropriate holder in which the electrodes were sintered while under slight pressure.

After cooling, the electrodes were placed into 6N KOH solution warmed to 80°C, in order to dissolve Al from the formed Raney alloy, so as to obtain the active form of the electrode. When hydrogen bubbles stopped evolving, the electrodes were taken out of the solution and were mounted in a special holder, enabling contact between one side of the electrode and hydrogen gas under a pressure of several atmospheres, as well as contact of the other side with 6N KOH solution (warmed to 60°C). The whole assembly was gas tight.

Prior to electrochemical investigations, an additional electrochemical activation was done in the usual manner by means of anodic polarization (3).

The investigation of electrochemical behavior of the electrodes was done in a thermostated cell in 6N KOH at 60°C by observing anodic polarization at varying current density. The electrode potentials were measured against a Hg/HgO reference electrode dipped into the same solution. All the values of the electrode potentials quoted below refer to the normal hydrogen scale, taking the potential of the mentioned reference electrode as + 0.057v (5). The ohmic

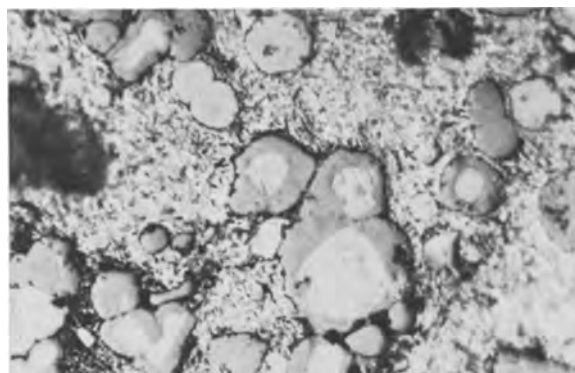


Fig. 1. Photomicrograph of Al-Ni mixture sintered at 680°C. Bright surfaces, Ni; gray surfaces, Ni_2Al_3 ; background, Al powder. Magnification 750X.

voltage drops between the tip of the Luggin capillary and the electrode were evaluated by means of the galvanostatic oscillographic method and it was found that even for the highest current densities they were less than 10 mv. Hence, in the subsequent course of measurements they were neglected.

The mechanical properties of the electrodes were examined by determining the bending strength of 10 mm wide strips cut out of the electrodes according to the standard method.

Results and Discussion

At the outset of this work there was little doubt that both alloying between Al and Ni powders and sintering of nickel particles could be achieved as separate processes (7). However, in order to get an electrochemically active and mechanically strong porous nickel electrode it was essential that under a given set of conditions sintering be effected before alloying took place to any noticeable extent.

In the course of preliminary studies a microscopic investigation was undertaken and a typical picture obtained is shown in Fig. 1 for a sample pressed and sintered at 680°C. This revealed that on one hand nickel particles could be joined together prior to their reaction with aluminum, and on the other hand that considerable alloying had taken place resulting in bluish-gray zones of newly formed phase at the surface of nickel particles. The new phase was found to be Ni_2Al_3 (6), which according to Justi *et al.* (4) is catalytically the most active type of Raney nickel alloy.

The effect of alloying of Al and Ni on the catalytic activity of electrodes can be seen from the results of the following experiments.

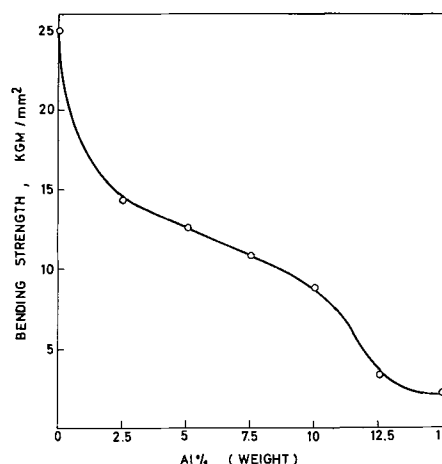


Fig. 2. Dependence of bending strength of sintered electrodes on percentage of Al.

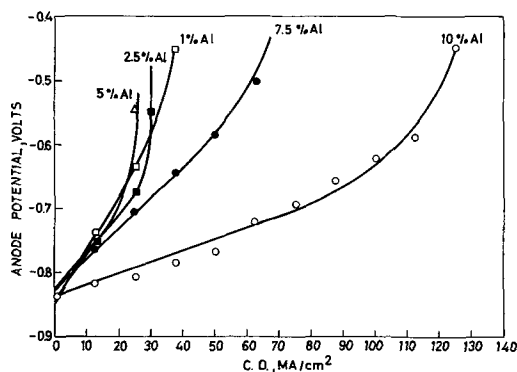


Fig. 3. Plots of electrode potential vs. current density for electrodes with varying Al content. *m*-the slopes of straight parts of the curves in cm^2 (volt/amp).

In the set of experiments with a varying ratio of Al and Ni in the mixture the intention was to find the optimal content of Al, giving both good electrochemical characteristics and sufficient mechanical strength to sustain the pressure of the gas. Therefore the electrodes with various quantities of Al from 0 to 15%, sintered at 640°C , were first examined, both mechanically and electrochemically. The results of the mechanical tests are given in Fig. 2, in which the bending strength is plotted as a function of aluminum content. The bending strength of such electrodes was always lower than that of those made of pure Ni powder. However, up to 10% of Al, it was sufficiently high to give mechanically strong electrodes. Further increase in Al content resulted in a sharp decrease of the bending strength, and the electrodes made of such powder compositions were of no practical use in electrochemical examinations.

The results marking 10% as a critical content of Al can be considered as a support to the view that the aluminum particles, being relatively soft, deform under the applied force during pressing and fill the free space between the Ni particles. One can calculate that in order to fill with Al an ideal free space remaining between close packed Ni spheres of uniform diameter, irrespective of the sphere size, 15% of Al would be required. Taking into account that the Ni powder used in these experiments was a polydisperse system with grain sizes ranging from 1 to 40μ , it is obvious that smaller spheres of Ni could fill the pores in the same way as Al. This results in a smaller quantity of Al being necessary to fill the real free space between the adjoining Ni particles.

The results of the electrochemical investigations of the electrodes with various contents of Al are presented in Fig. 3. The slope (*m*, $[\text{cm}^2 \text{ v/amp}]$) of the straight part of the polarization curve and the limiting current density were taken as criteria of the electrode quality. It can be seen that the increase in the Al content of the powder mixture resulted in increasingly better electrochemical properties of the obtained electrodes, i.e., decreased the value of the slope and increased the limiting current density.

Since the sintering process is competitive to the process of formation of the Raney alloy, sintering temperature was expected to have an influence on the properties of the electrodes. The effect of temperature on mechanical properties of electrodes is presented in Table I, for electrodes with 10% Al content. The increase of the sintering temperature resulted in an increase of the bending strength, prob-

Table I. Effect of sintering temperature on the bending strength

Temperature	640°	660°	680°	700°
Bending strength, kg/mm^2	9.9	10.3	11.0	13.2

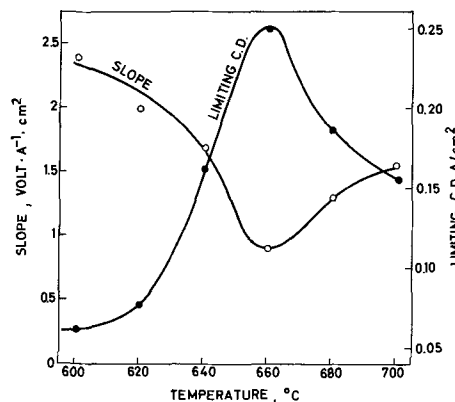


Fig. 4. Mean values of the slopes and limiting current densities as functions of the sintering temperature.

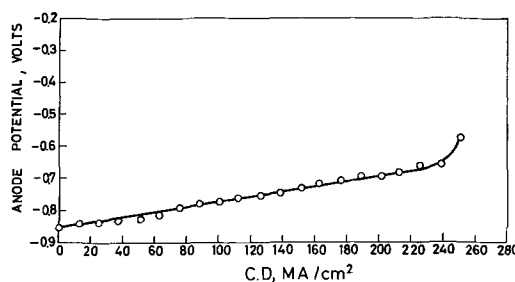


Fig. 5. Typical anodic polarization curve for an electrode sintered at 660°C . Pressure of H_2 -2 atm.

ably because of a more pronounced sintering between the Ni particles giving a more compact Ni skeleton.

The effect of temperature on electrochemical properties is presented in Fig. 4. The graphs represent the dependence of the slopes and the limiting current densities of the tested electrodes on temperature. Each point represents a mean value of 1-3 electrodes. Under the given experimental conditions it appears that *ca.* 660°C was the most appropriate temperature for obtaining optimal electrochemical behavior of the electrodes. A graph representing a typical current-potential relation for one of the electrodes sintered at 660° is given in Fig. 5.

It was also observed that the optimal sintering temperature depends on the quality of the hydrogen purification. With hydrogen deoxygenated in a column filled with Pd asbestos heated at 300°C , dried in silica-gel columns and with the final traces of humidity removed by a trap dipped into liquid air, the electrodes sintered at 660° showed the effects of over-sintering. They were mechanically stronger but their electrochemical behavior was worse.

The effect of thickness of the active layer of the double layer electrodes on their electrochemical behavior has been studied on the electrodes sintered at 640° . The thickness of the coarse (active) layer has been varied between 0.2 and 0.5 mm. The current-potential dependences for these electrodes are presented in Fig. 6, together with the corresponding graph for a 1 mm thick single layer electrode. These data indicate that the thickness of the active layer has a profound influence on the electrochemical properties below 0.5 mm, while above that it does not have any marked influence, the results being similar to those for 1 mm thick electrodes. One should point out here that similar results were obtained in this Institute earlier with 3 mm thick electrodes (5) made of the same Ni powder and a separately prepared Raney alloy according to the method used by Justi *et al.* (3).

Since both Ni and Al powders used in these experiments had wide spectra of grain sizes, homogeneous porosity has not been achieved in our experiments, although this is known to be an important factor in

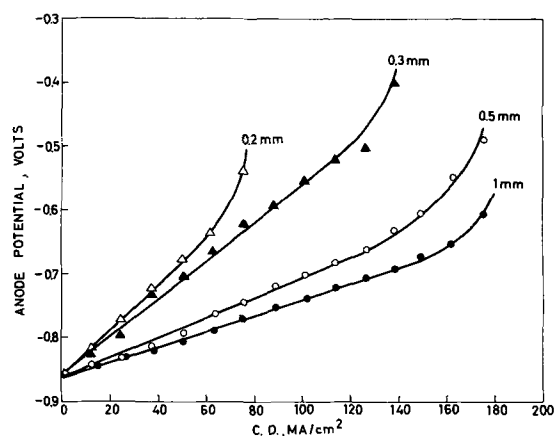


Fig. 6. Effect of thickness of the active layer of double layer electrodes on the polarization curves.

obtaining highly active hydrogen electrodes. It can be expected that by carefully selecting proper particle sizes of Ni and Al powders one should be able

to obtain much better electrochemical properties of the electrodes made according to the given method.

Manuscript received Jan. 22, 1964.

Any discussion of this paper will appear in a Discussion Section to be published in the June 1965 JOURNAL.

REFERENCES

1. K. Kordes, "Fuel Cells," G. Young, Editor, p. 11, Reinhold Publishing Co., New York (1960).
2. *Chem. and Eng. News*, **41**, No 38, 60 (1963).
3. E. Justi and A. Winsel, "Kalte Verbrennung," F. Stein. Wiesbaden (1962).
4. C. B. Petrović, A. R. Despić, M. Dj. Jancić, and D. M. Džazić, Method of obtaining fuel cell electrodes by reacting in situ a metal powder mixture forming Raney alloy. Yug. pat. appl.
5. Fuel cell research team, Project Report. Institute for Chemistry, Technology, and Metallurgy. Beograd, 1962.
6. M. Z. Malcev, T. A. Barsunova, and F. A. Borin, "Metallografya cvetnih metallov i splavov," Metalurgizdat, Moscow, 1960.
7. T. Yamanaka, *Repts. Sci. Research Inst. (Japan)*, **31**, 58 (1955).

The Role of Antimony in Positive Plate Behavior in the Lead-Acid Cell

Jeanne Burbank

United States Naval Research Laboratory, Washington, D. C.

ABSTRACT

Antimonial and antimony-free lead-acid cells of similar construction were examined together in a shallow cycle routine. The presence of antimony in the positive grid alloy caused depolarization of the plate in the float condition. It did not affect the discharge potential of the plate. The positive plate active material became progressively softer in the antimony-free cells which failed after short test duration. The antimonial cell maintained its capacity and the active material remained firm. The active material of both successful and failing positive plates was examined by electron microscopy and x-ray diffraction. The active material in the antimonial cell contained many complex prismatic crystals, whereas the antimony-free cell was characterized by nondescript nodular masses. The active material in the antimonial cell contained a large amount of α PbO_2 while the antimony-free positive contained very little of this polymorph. Because both kinds of cell were pasted and formed by the same manufacturer with the same paste formulation, it is concluded that the difference in paste morphology and composition is caused by the presence of antimony in the positive grid. It is also concluded that success or failure in float cycle tests is determined by the morphology of the positive paste.

The lead acid cell normally is fabricated with grids of lead alloyed with 5-12% antimony. This antimony has long been known to affect cell behavior in several ways, but the benefits resulting from its use have outweighed its deleterious effects, and today only special purpose cells are manufactured without antimony. The antimonial alloys are easier to cast than the antimony-free metals, lower casting temperatures are required, better castings are the rule because molds are readily filled by the melt, and the strength of the alloy makes it possible to handle and fabricate the castings immediately. In addition, antimony minimizes grid growth by distributing the corrosion attack across the body of the grains, relieving attack at the grain boundaries. All these factors combine to promote continuation of the use of antimony in the lead acid cell.

The hydrogen overvoltage on antimony is lower than on lead, and this causes spontaneous self-discharge of the negative plate. As antimony accumulates on the negative plate during operation of the cell, the efficiency of charge decreases because of the low hydrogen overvoltage on the antimony, and increasing portions of the charging current are wasted in generation of hydrogen gas. It is possible to scour the negative plate of antimony by overcharging, when it is driven off as stibine, but stibine is a poisonous gas, and charging in confined spaces may present a health hazard.

It has been shown that antimony is leached from the positive grid during charge of the battery and radioactive isotopes have been used to trace the migration of antimony in the cell. Antimony does accumulate to some extent in the positive active ma-

terial, and self-discharge of this plate has been investigated; however, the effect of antimony on the positive plate of the lead acid cell is not usually considered detrimental. Nevertheless, antimony initially in the positive will eventually find its way to the negative and cause the major deleterious side reaction, interference with charging of the plate.

In some recent studies with antimony-free lead-calcium cells, it has been shown that in certain cells the positives were failing through rapid softening of the positive active material which resulted in 80-90% loss in ampere-hour capacity. These studies showed that the positive active material of the failing cells was made up of nondescript nodular particles of PbO_2 , whereas successful antimony-free lead-calcium cells contained prismatic crystalline particles. The difference in performance of these positive plates was attributed to this difference in morphology of the PbO_2 (1-18).

The paste used in fabricating the failing lead-calcium cells was the same as normally used in the manufacturer's production of antimonial cells, and these, in turn, were performing satisfactorily in normal service. Therefore, the studies with the antimony-free lead-calcium cells that failed by softening of the positive paste presented a unique opportunity to study the effects of antimony on cell behavior because it was possible to obtain the same paste in an antimonial grid and thus directly compare antimonial and antimony-free cells, identical in all respects except for the positive grid alloy.

Experimental

The plates used in this investigation were all obtained from a single manufacturer, and the only difference between them was that one positive grid was a standard antimonial lead alloy, whereas the other grids were lead calcium alloy. The pasting and forming were carried out by the manufacturer under reputedly identical conditions, and the positives were

"formed but not charged" when the cells were assembled for this study. Lead calcium alloy negative plates were used in all cells.

Four small cells were assembled, each having one positive and two negative plates, with standard glass mat retainers and microporous rubber separators. Two sets of two cells each were run in series. The power supply, controller, and auxiliary electrode circuit of the battery analyzer of Work and Wales (19) were used to test the cells. A mercury, mercurous sulfate reference electrode in each cell was used to measure plate potentials, with the plate and cell voltage and the current monitored continuously.

The cells were assembled in plastic cell cases and filled with 1.200 sp gr H_2SO_4 . Charging was carried out according to the manufacturer's standard instructions. Following the initial charge, the specific gravity was adjusted to 1.250-1.260.

The cells, which were all positive-plate limited, were given several cycles to develop capacity and then placed on the float cycle routine known to produce rapid failure in the lead-calcium cells (17, 18). These tests are summarized in Table I.

During the tests, the positive plates were inspected visually at intervals, and before and after the tests the positive active material was examined by electron microscopy. For the electron microscopic examination, samples of the paste were extracted with saturated ammonium acetate solution to remove any divalent lead compounds present. Drops of the slurry of extracted material were gently touched to the surface of distilled water in a 10-in. crystallizing dish. The particles floated out across the surface and were picked up on parlodion covered specimen screens of the electron microscope. After drying, the particles were replicated with evaporated carbon (20).

Following replication, the parlodion supporting films were removed by solution in acetone. The PbO_2 was dissolved in dilute HNO_3 containing H_2O_2 , and the carbon replica was rinsed by floating on water. After air drying, the replicas were photographed in the electron microscope, model RCA EMU-2B.

The active materials from both kinds of positive plate were examined by x-ray diffraction using a General Electric XRD-5 X-Ray unit and copper radiation. The pastes were examined before and after the float cycle tests.

Table I. Summary of tests and results

Capacity cycle No.	Charge, amp-hr	Number of float cycles	Discharge capacity, amp-hr	
Calcium cells 1 & 2				
1	—	—	Cell 1	Cell 2
2	10.57	10	>8.47	8.47
3	8.05	7	>8.37	8.37
4	7.53	9	>7.65	7.65
5	7.25	5	>7.15	7.15
6	7.25	7	>7.13	7.13
			4.73	6.23
Calcium cell 3				
7	—	—		8.00
8	8.40	8		6.30
9	7.36	9		6.27
10	7.92	14		5.03
11	8.37	12		3.56
12	3.69	9		1.53
13	4.53	9		0.80
Antimonial cell				
14	—	—		8.00
15	8.40	8		7.60
16	9.17	9		7.60
17	7.92	14		7.50
18	8.37	12		7.40
19	7.36	9		7.40
20	7.70	9		7.30

Notes: Each capacity cycle in this series of tests comprised a constant voltage charge followed by a series of shallow daily float cycles for 5 to 14 days with continuous float at 2.24v per cell during the intervals. Capacity discharges were given every two weeks with constant voltage recharge at 2.24v.

In capacity cycles 2, 11, and 13 the cells were given constant current overcharges. Capacity cycles 1, 7, and 14 show the initial cell capacities prior to the start of the tests.

Each float cycle in the tests of calcium cells 1 and 2 comprised a discharge of 1 amp-hr at 2 amp, and recharge by float with interim float. One float cycle was given each work day until the next succeeding capacity discharge. Calcium cell 3 and the antimonial cell were in series for these tests, and cell 3 was used as control for float and the constant voltage charges. The effect of antimony on the cell and plate voltages could be followed by direct comparison with the antimony-free calcium cell. When required, these two cells were separated and handled individually; for example, for capacity discharges 8 to 13 and 15 to 20, it was necessary to run the capacity discharges and recharges individually.

At capacity cycles 6 and 13 the positive plates of the calcium cells were soft and mushy, whereas at capacity cycle 20 the antimonial cell positive was firm and in good condition.

Results and Discussion

Table I shows the capacities obtained from the cells, and also indicates that the antimony-free cells with lead-calcium alloy grids failed after relatively short test duration. The 90% fall in cell capacities, curve B, Fig. 1, illustrates a typical failure of these antimony-free cells. Failure was due to the positive plate in every case.

In contrast to this, the capacity of the antimonial cell, curve A, Fig. 1, changed hardly at all despite

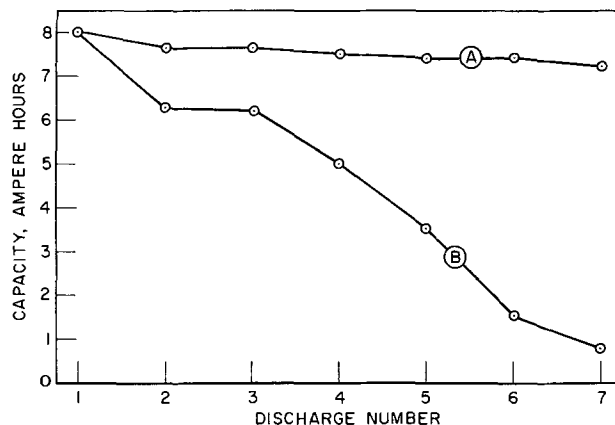


Fig. 1. Change in cell capacity in shallow cycle test. Curve A, antimonial cell; curve B, lead calcium cell.

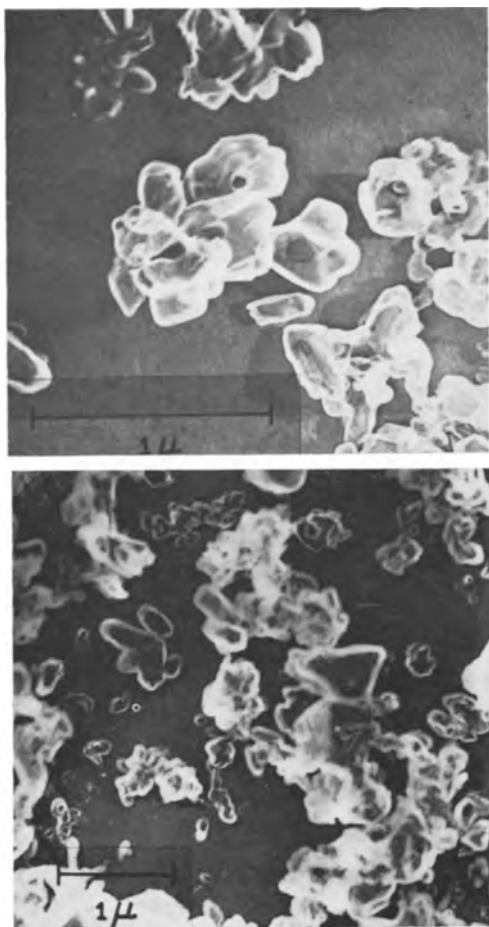


Fig. 2. Typical examples of nondescript nodular PbO_2 particles. These particles were taken from lead calcium cells that consistently failed in float installations and in float cycle tests. See also ref. (17), (18), (31).

the fact that it did not receive the overcharge normally used to maintain antimonial cells. This satisfactory behavior of the antimonial cell was not unexpected in light of earlier work (22).

It had not been known with certainty whether the identical paste would stand up in an antimonial cell in a similar test, but the results of the tests reported here show that the same paste in an antimonial cell did not fail as rapidly as in the lead-calcium cells, and it gave no indication of incipient failure at the time the tests were terminated.

When the cells were opened for inspection, the calcium positives were very messy to handle: PbO_2 smeared readily over glass mats, paper towels, and

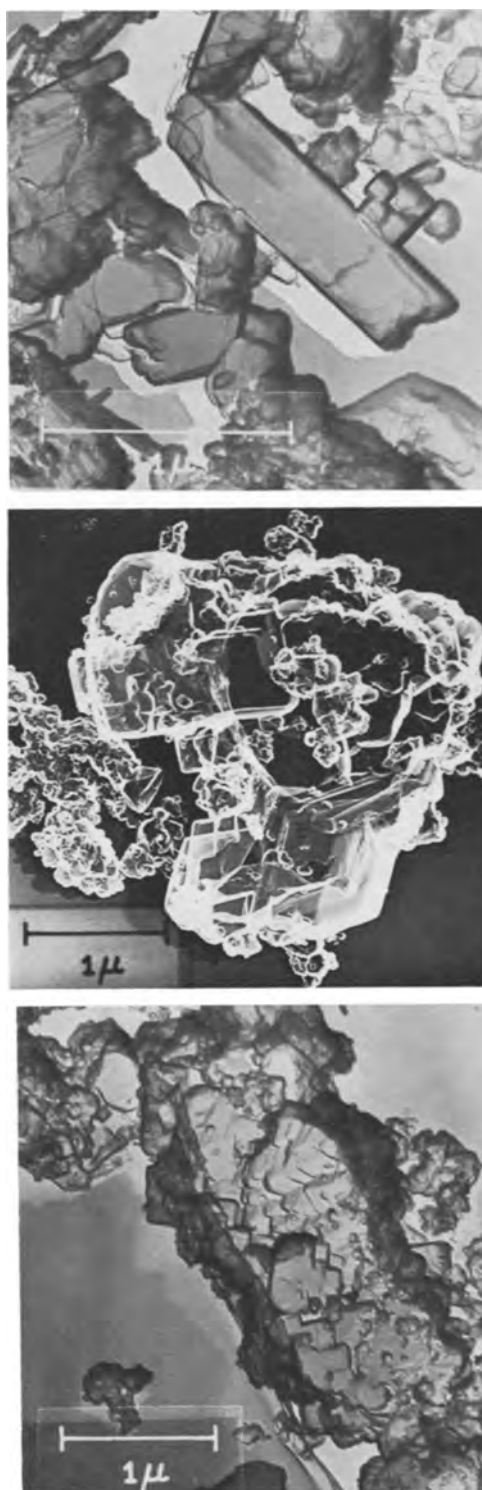
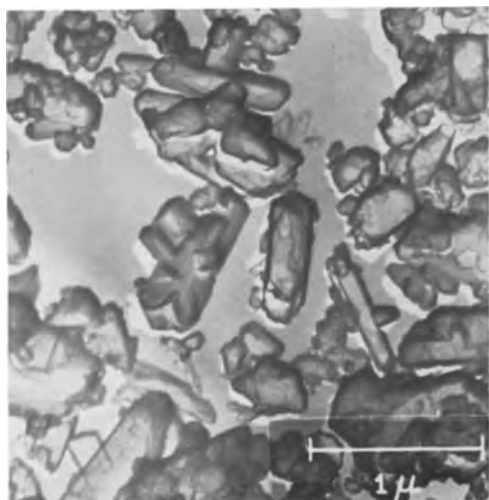


Fig. 3. (left and above) Typical examples of prismatic PbO_2 particles from lead antimony positive plates. The positive plate containing particles such as shown here was successful in the shallow cycle test, in normal service life, and cycle life test, and maintained its firm texture and capacity. See also Fig. 6, ref. (31).



glass rods used as probes, and enough washed off to discolor the electrolyte heavily. In contrast, the antimonial positives were much cleaner, the glass mats were white and clear, some PbO_2 wiped off on paper towels used to handle the wet plates and the glass probes, but not enough floated away to cause even a noticeable discoloration of the electrolyte. To be sure, the wet working positive plate of any lead cell is softer than the same plate dried, and PbO_2 can usually be smeared from the surface; however, the totally mushy condition of the failing calcium positive is

much more pronounced, and the softening proceeds through the thickness of the plate until the entire active mass may be washed out with a stream of water (17, 18).

The sole difference between the positives in these cells was the presence of antimony in the grid metal. It is concluded that the presence of antimony in the grid inhibited or prevented the softening of the paste and the resulting loss in capacity.

In this work with the antimonial and calcium cells, the calcium cell was used for voltage control in order to determine the electrochemical effects of the antimony. The well-known depolarization of the negative plate, in itself, prevents an antimonial negative from controlling float as the negative does in antimony-free cells (7, 16, 18, 21, 23, 24). The presence of antimony in the positive grid caused 20-70 mv depolarization in overcharge at constant current. However, the positive plate voltages relative to the mercury, mercurous sulfate reference electrode of both the antimonial and calcium cells were identical during charge and discharge, and no electrochemical effect of the antimony was observed when the cell was in either of these conditions.

Electron micrographs of the positive active material showed that, in the failing lead-calcium cells, the individual particles were nondescript globules both before and after failure (17, 18) and some typical examples are shown in Fig. 2. In contrast to this, the same positive paste from the antimonial cell was found to contain large amounts of prismatic material and some typical electron micrographs are shown in Fig. 3. It is concluded that the presence of antimony has affected the morphology of the PbO_2 particles formed in the paste. The electron micrographs indicate that the prismatic material takes the form of extensive complex clusters that appear to be multiple twins or parallel growths. It is believed that these crystalline formations impart mechanical stability to the positive active material. This prismatic morphology observed by electron microscopy is believed to be required in order to maintain the firm texture of the positive plates in the lead cell.

On the basis of these results, it is concluded that the antimony exerts the direct and beneficial influence of causing prismatic PbO_2 formation in the positive active material. The mechanism of this action remains to be studied; however, it appears likely that preferential adsorption of a soluble antimony species on the growing surface of the PbO_2 crystal may control the morphology. Antimony forms the ions SbO_2^+ and SbO_3^- at positive plate potentials (25). X-ray diffraction showed that metallic antimony itself becomes passivated by a heavy layer of Sb_2O_5 at this potential when anodized in H_2SO_4 solution, but this oxide is rather soluble, and the determinative influence of soluble species on electrodeposits is well known (26). The work described here indicates that the presence of antimony in the grid metal influences the morphological development of electrochemically formed PbO_2 in the positive plate of the lead acid cell, but the precise mechanism of this action remains to be clarified.

In nonantimonial cells where a prismatic PbO_2 morphology was previously observed by electron microscopy (16, 18), it was accompanied by a sponge-like network of harder material, visible in the magnification range of the optical microscope (27); however, in the antimonial and nonantimonial positive plates used in this work, no such network was visible in the formed plate when examined optically prior to testing, and none was present in the nonantimonial plate at the conclusion of the tests (28). The intricate shapes of the submicroscopic crystals in the antimonial positive, Fig. 3, suggest that it may be possible for them to form an interlocking network, but, of course, this would not be observable by optical means.

X-ray diffraction examination of the positive active materials showed that the paste from the antimonial

cell contained appreciable amounts of both α and β PbO_2 , whereas the paste from the lead-calcium cell contained a very large preponderance of β PbO_2 and only a very small amount of α PbO_2 . At the conclusion of the tests, the amount of α PbO_2 in both types of plate had decreased, but a considerable amount was still present in the antimonial positive. Simultaneously, the amount of β PbO_2 had increased in both plates.

It is concluded from this study that antimony in the grid metal acts to promote the deposition of α PbO_2 in the active material during plate formation, possibly by the same mechanism as cobalt ion (26).

Variations in the α PbO_2 content of positive pastes have been studied, and, in SAE overcharge tests, it extends the life of the plates (29, 30). It has also been suggested that there may be a relation between α PbO_2 and positive paste retention in the lead acid cell (27). The presence of a large amount of α PbO_2 in the antimonial active material and the performance of the antimonial cell in the tests reported here lend some credence to this speculation.

Conclusions

On the basis of the results of this study, it is concluded that the beneficial effects of having antimony in the positive grid are: (a) development of significant amounts of α PbO_2 during plate formation, (b) retention of a firm paste texture and cell capacity in shallow cycle tests, and (c) prismatic crystallization of the PbO_2 particles making up the paste. Without antimony, only a small amount of α PbO_2 was present initially, the paste softened and lost capacity in the shallow cycle tests, and the paste contained few, if any, prismatic crystals. These conclusions are in agreement with those of earlier studies that showed that success or failure in float cycle tests was related to the morphology and texture of the positive paste (16-18).

Manuscript received March 26, 1964.

Any discussion of this paper will appear in a Discussion Section to be published in the June 1965 JOURNAL.

REFERENCES

1. G. W. Vinal, "Storage Batteries," 4th ed., John Wiley & Sons, Inc., New York (1955).
2. L. Jumau, *Eclairage electrique*, **16**, 133 (1898).
3. Strasser and Gahl, *Z. Elektrochem.*, **7**, 11 (1900).
4. J. T. Crenell and A. G. Milligan, *Trans. Faraday Soc.*, **27**, 103 (1931).
5. G. W. Vinal, D. N. Craig, and C. L. Snyder, *Bur. Standards J. Research*, **10**, 795 (1933).
6. H. E. Haring and K. G. Compton, *Trans. Electrochem. Soc.*, **68**, 283 (1935).
7. H. E. Haring and U. B. Thomas, *ibid.*, **68**, 293 (1935).
8. J. W. R. Byfield, *ibid.*, **79**, 259 (1941).
9. A. C. Zachlin, *ibid.*, **82**, 365 (1942).
10. A. C. Zachlin, *ibid.*, **92**, 259 (1947).
11. J. J. Lander, *This Journal*, **99**, 339 (1952).
12. J. J. Lander, *ibid.*, **99**, 467 (1952).
13. J. B. Burbank and A. C. Simon, *ibid.*, **100**, 11 (1953).
14. W. Herrmann and G. H. Proepstl, *Z. Elektrochem.*, **61**, 1154 (1957).
15. W. Herrmann, W. Ilge, and G. H. Proepstl, "The Migration of Antimony in the Grid of a Lead Storage Cell Studied Using a Radioactive Tracer Method" in "United Nations Peaceful Uses of Atomic Energy," Proceedings of the Second International Conference, Geneva, September 1958, p. 272, Pergamon Press, New York (1959).
16. J. Burbank and C. P. Wales, "The Lead Calcium Battery, Part 2. Small Portable Cells," Naval Research Lab. Report 5770, May 2, 1962.
17. J. Burbank and C. P. Wales, "The Lead Calcium Battery, Part 3. Submarine Cells," Naval Research Lab. Report 5773, May 29, 1962.
18. J. Burbank, "Positive Plate Characteristics in the Floating Lead-Calcium Cell" in "Batteries," Proceedings of the 3rd International Symposium,

- Bournemouth, October 1962, p. 43, D. H. Collins, Editor, Pergamon Press, New York (1963).
19. G. W. Work and C. P. Wales, *This Journal*, **104**, 67 (1956).
 20. D. E. Bradley, *J. Appl. Phys.* **27**, 1399 (1956).
 21. J. Burbank and C. P. Wales, "The Lead Calcium Battery, Part 1, Introduction and Background," Naval Research Lab. Report 5693, Nov. 22, 1961.
 22. J. J. Lander, "Life Tests of Thin Plate Lead Acid Cells under Cycle, Stand, and Float Routine," Naval Research Lab. Memorandum Report 556, January 1956.
 23. U. B. Thomas, F. T. Forster, and H. E. Haring, *Trans. Electrochem. Soc.*, **92**, 313 (1947).
 24. R. C. Shair, *AIEE Trans.*, Pt. II (Applications and Industry) **79**, 1 (1960).
 25. M. Pourbaix, et al., "Atlas D'Equilibres Electrochimiques," p. 524 ff. Gautier-Villars & Co., Paris (1963).
 26. I. I. Astakhov, I. G. Kiseleva, and B. N. Kabanov, *Doklady Akad. Nauk USSR*, **126**, 1041 (1959).
 27. A. C. Simon and E. L. Jones, *This Journal*, **109**, 760 (1962).
 28. A. C. Simon, Private communication.
 29. V. H. Dodson, *This Journal*, **108**, 401 (1961).
 30. V. H. Dodson, *ibid.*, **108**, 406 (1961).
 31. J. Burbank, *ibid.*, **111**, 765 (1964).

Corrosion of Steels and Nickel Alloys in Superheated Steam

W. E. Ruther and S. Greenberg

Metallurgy Division, Argonne National Laboratory, Argonne, Illinois

ABSTRACT

The corrosion behavior of the 18-8 stainless steels and some nickel alloys in superheated steam was found to be dependent on the surface preparation. Those treatments which left a severely cold worked surface resulted in reduced corrosion attack in subsequent exposure to steam as compared with annealed metal surfaces. The corrosion rate of electropolished annealed type 304 stainless steel in oxygenated (30 ppm) steam rose rapidly as the temperature increased from 540° to 650°C. At 600° and 650° the measured rate decreased with increasing time during 80 day static tests. The corrosion appeared more linear with time in dynamic tests at 650°C (~7 mg/dm²-day). In these tests there appeared to be no effect of velocity (30-91 m/sec) or oxygen and hydrogen content on the corrosion rate. Flaking and loss of the outer corrosion coating was severe in the dynamic tests. The corrosion rate of type 406 was too small to be precisely measured in all of the tests, static and dynamic, in which it was simultaneously exposed with type 304. A coating equivalent to about 2×10^{-4} cm metal penetration was formed on the initial exposure of 406. No flaking of the outer coating was evident in 80 day tests. The corrosion attack of the 400 series steels in static oxygenated steam went down with increasing chromium content, particularly above about 13 w/o Cr. Both type 430 (16 w/o Cr) and 446 (25 w/o Cr) exhibited greater short term corrosion resistance than type 304 to 650°C, 42 kg/cm² steam. The nickel based alloys, particularly Inconel 625, were also more corrosion resistant than type 304 in short static and dynamic tests in 650°C, 42 kg/cm², superheated steam.

The cycle efficiency of a boiling water nuclear electric power plant can usually be improved substantially by incorporating a nuclear steam superheater before the turbogenerator. Special environmental conditions are encountered in such a superheater as compared with typical fossil fuel installations. For example, oxygen concentrations of 20-30 ppm and stoichiometric amounts of hydrogen might be expected in steam passing through the intense radiation field. The requirement for thin protective fuel element cladding (to reduce neutron losses) introduces serious corrosion penetration problems.

Spalaris and co-workers (1) have reviewed the available nonnuclear steam corrosion literature. They concluded that much of the data, typically obtained from weight gains and/or scale thickness, did not permit calculation of precise corrosion rates. Furthermore, these data were obtained in steam of very low oxygen content since that is the normal operating condition for nonnuclear boilers.

Recently, several of the laboratories associated with nuclear power plant design have been re-evaluating commercial alloys in simulated reactor steam environments in static autoclaves and dynamic test facilities (2, 3). Much of the effort has been concentrated

on corrosion cracking since the serious nature of that problem became apparent in early in-reactor experiments (4). While it was not the intent to minimize the potential cracking hazards, this laboratory chose initially to study other variables. The effects of steam temperature, pressure, oxygen and hydrogen content, and velocity on the general corrosion rate were investigated. Since the work was performed in support of a specific reactor superheater, the major fraction of the data involved the design temperature and pressure for that reactor (650°C, 42 kg/cm²)¹. For the same reason first 304 and later 406 stainless steel received particular attention.

Experimental

The static testing of corrosion coupons was performed in constantly refreshed type 347 stainless steel autoclave systems of about 1.5 liter capacity. Deionized, distilled water was vacuum degassed in storage carboys and then charged with the desired gas. A flow of about 5 ml/min of this water was pumped into the high-pressure system. A boiler and superheater preheated the stream prior to its entering the

¹ One kg/cm² equals 14.2 psi.

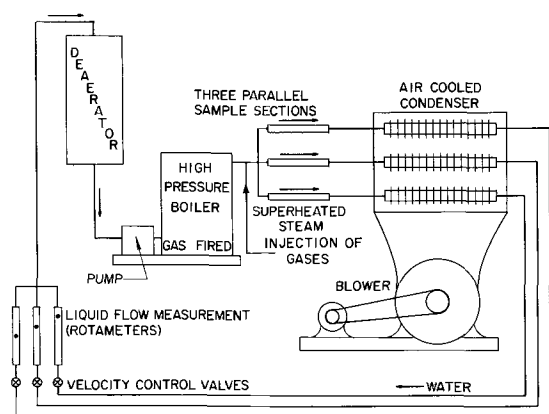


Fig. 1. Schematic diagram of dynamic test facility. Maximum test conditions: 650°C; 1000 psi; 300 ft/sec.

test autoclave. The outgoing steam was condensed in an air cooler, and the condensed water left the system via a back pressure regulator. Care was taken to provide open space around each specimen in the autoclave sufficient to prevent local depletion of oxygen in the slowly moving steam.

The high velocity testing was accomplished in a recirculating system shown schematically in Fig. 1. Type 318 stainless steel tubing and type 316 Swagelok fittings were used in the high-temperature section. Condensate water flow rates were converted to steam flows through the use of steam tables. Although 270 kg/hr of deionized distilled water were converted to steam and condensed, the steam channels were necessarily small to permit corrosion studies at velocities up to 91 m/sec past the specimens. Dimensions of the flat samples were 5 x 1.2 x 0.16 cm. Oxygen and hydrogen were introduced directly in the steam through high-pressure gas rotameters. The oxygen content of the condensate was determined using an Industrial Instruments oxygen analyzer. This analyzer depends on the specific reaction between thallium metal and dissolved oxygen in deionized water. The amount of reaction, hence the dissolved oxygen content, is measured by the conductivity of the effluent solution of thallium hydroxide.

Except as specifically noted, the specimens were corrosion tested in the annealed condition. The General Electric Company supplied the Rene' 41 alloy and the International Nickel Company supplied the other nickel alloys used in this investigation. Chemical compositions are given in Table I.

Electropolishing of all of the alloys was accomplished in a 12.5% phosphoric acid, 65% sulfuric acid, 22.5% water (per cent by volume of the concentrated acids) bath at 85°C. Current densities (0.3-0.6 amp/cm²) were varied from one alloy to another to obtain good polishing. The bath was not too satisfac-

tory for 403 and 410 steels due to acid attack, and Rene' 41 did not polish as brilliantly as did most of the other alloys. In one instance a 10% perchloric acid, 90% acetic acid mixture was used on the 300 series stainless steels.

Surface preparations, other than electropolishing, consisted of acid etching (dilute nitric-hydrofluoric acid mixture), grinding (metallographic wheels—Durite paper), grit blasting (50 μ SiO₂ particles), and machining.

Since an unknown portion of the corrosion coating was lost to the test environment, weight gains could not be used to determine the average corrosion rate. A rather lengthy, but effective, defilming process was evolved. First the sample was made the cathode at about 0.3 amp/cm² in 1 w/o (weight per cent) dibasic ammonium citrate solution at about 85°C. The current was alternately applied and interrupted for 30 sec intervals by an automatic timer. After about 15 min in this bath, the outer layer of the corrosion coating could be brushed off. The inner layer was removed by a defilming process developed at the Knolls Atomic Power Laboratory (5). This consisted of 2 hr in gently boiling alkaline permanganate solution (20 w/o NaOH, 3 w/o KMnO₄), a hot rinse, and 2 hr in 20 w/o dibasic ammonium citrate solution. The samples were brushed at the conclusion of this treatment with a nylon hand brush to remove the loosely adherent smut. A second run through the last two solutions was necessary in the case of some stubborn films. Blank losses for this defilming technique were very low compared with the typical amounts of total corrosion for the 300 series stainless steels (*i.e.*, 0.02 mg/cm² for 304) and the nickel alloys. While the blank losses were higher for the ferritic steels, the process was still satisfactory for 406 and 446.

Data and Results

Surface preparation effects.—In the initial steam corrosion experiments a wide range of total attack was noted for type 304 and 347 samples obtained from different sources. Some specimens acquired only a thin colored temper film during an exposure which resulted in heavy corrosion product coatings on other coupons of the same nominal composition. In one case the machined edges of a sample corroded much less than the as-received faces of the same specimen. It was obvious that these large surface effects had to be investigated before meaningful corrosion rates could be measured.

In the first series of experiments only two types of sample preparation were tested for a number of different alloys. The oxygen content of the superheated steam was varied with the results shown in Table II.

The surface effect was much more pronounced in the case of low oxygen content steam and was noted for all the alloys except Inconel 625 and Rene'41.

Table I. Chemical compositions of alloys

Alloy	Percentage by weight										Other
	Al	Cr	C	Fe	Mo	Mn	Ni	P	Si	S	
304		18.2	0.07	R		1.68	8.76	0.026	0.85	0.01	
316		17.5	0.05	R	2.50	1.62	13.45	0.025	0.49	0.021	0.20 Cu
321		18.0	0.04	R	0.30	1.38	9.62	0.019	0.88	0.013	0.53 Ti
347		18.6	0.078	R		1.82	10.8	0.028	0.82	0.010	(Cb + Ta) 0.90
403		12.3	0.12	R		0.46		0.015	0.27	0.013	
405 ¹	0.2	12.5	0.08	R							
406	4.48	13.1	0.11	R		0.44	0.36	0.019	0.46	0.007	
410		12.5	0.13	R		0.44		0.013	0.25	0.009	
410 (E2)		11.6	0.03	R					0.5		0.50 Ti
430		16.3	0.08	R		0.40		0.021	0.50	0.011	
446		24.7	0.09	R		0.62		0.023	0.35	0.010	
Incoloy 800		20.0	0.04	45.2		0.85	33.0		0.40	0.007	0.41 Cu
Inconel 600		16.3	0.04	7.24		0.17	75.9		0.29	0.007	
625	0.17	22.0	0.03	1.86	3.75	0.12	62.3		0.25	0.007	[(Cb + Ta) 4.24, Ti] 0.23
X750	0.74	15.13	0.04	6.87		0.45	72.5		0.25	0.007	(Cb + Ta) 0.98, Ti 2.62
Rene' 41	1.52	19.05	0.07	0.3	9.83		R		0.05	0.005	3.21 Ti 10.95 Co

R—Remainder. ¹ Nominal analysis.

Table II. Corrosion in static refreshed superheated steam at 650°C, 42 kg/cm² (600 psig)

Alloy	Defilmed metal loss, mg/cm ²			
	0.03 ppm Oxygen		30 ppm Oxygen	
	Wet ground	Electro-polished	Wet ground	Electro-polished
304	0.15	6.96	6.63	7.45
316	0.15	11.7	1.74	9.16
321	0.16	9.10	0.34	9.04
347	0.16	10.2	3.87	11.2
Inconel 600	0.45	3.21	0.22	0.44
Inconel 625	0.11	0.12	0.10	0.16
Inconel X750	0.25	1.96	0.19	0.20
Incoloy 800	0.13	4.67	0.21	8.30
GE Rene' 41	0.13	0.20	0.14	0.15

7.0 Days exposure, 3-hr start-up.

Table III. Corrosion of type 304 stainless steel in 650°C, 42 kg/cm² steam

Surface preparation	Defilmed metal loss, mg/cm ²	
	30 ppm O ₂	0.2 ppm O ₂
Grit blast (50μ SiO ₂)	2.3	1.0
Machined	3.6	0.06
Wet grind 80 grit	8.4	0.45
Wet grind 240 grit	13.8	0.25
Wet grind 600 grit	11.8	0.72
Mechanically polished (Linde B)	11.5	15.6
Electropolished	8.0	13.1
Acid pickled	12.8	14.2

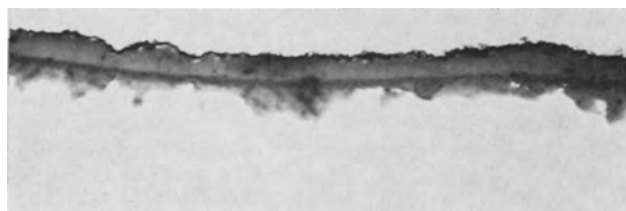
Tested 7.0 days, 3-hr start-up.

Other stainless steel samples were electropolished in a perchloric-acetic bath and corrosion tested with those prepared in the usual phosphoric-sulfuric solution. The same corrosion behavior was observed for both sets of samples, indicating that the poor corrosion resistance was characteristic of the polished surface and was not due to a residual phosphate or sulfate film.

Investigating other surface preparations for type 304, it was observed (Table III) that essentially strain-free surfaces resulted in a maximum metal loss during the one week corrosion test. Again, this was particularly noticeable in the results from the experiments with lower oxygen concentration.

Two further series of experiments were performed to test this tentative conclusion. In the first, samples were vacuum annealed after preparing them in several ways which had previously resulted in low metal loss values on exposure to steam. The result of annealing in each case was to increase the corrosion loss significantly (Table IV).

Since a cold worked disturbed layer apparently provided improved corrosion resistance, a second series of experiments was performed with 304 sheet that had been cold rolled 50%. The sheet became ferromagnetic as a result of the rolling. For this material the metal loss (Table V) values on corrosion were lower than for the original sheet for all surface preparations, although some differences were still

Fig. 2. Two layered structure of corrosion film on type 304; 7 days; 650°C; 42 kg/cm²; 0.03 ppm O₂. Top layer, mounting foil; center layer, oxide; bottom layer, stainless steel. Magnification 320X.Table IV. Effect of annealing on the corrosion of type 304 stainless steel in steam¹

Surface preparation	Defilmed metal loss, mg/cm ²
Grit blast (50μ SiO ₂)	1.0
Grit blast + anneal ²	9.2
Wet ground (80 grit)	0.45
Wet ground + anneal	10.0

¹ 7.0 days, 650°C; 42 kg/cm²; 0.2 ppm O₂.² Annealed 5 min, 1100°C, vacuum.Table V. Effect of cold work on the corrosion of type 304 stainless steel in steam at 650°C, 42 kg/cm²

Surface preparation	Defilmed metal loss, mg/cm ²	
	30 ppm O ₂	0.2 ppm O ₂
As-received before cold rolling	10.1	10.1
As cold rolled (CR)	1.4	0.16
CR + wet ground	0.79	0.05
CR + acid pickled	2.9	4.0
CR + electropolished	3.7	1.3

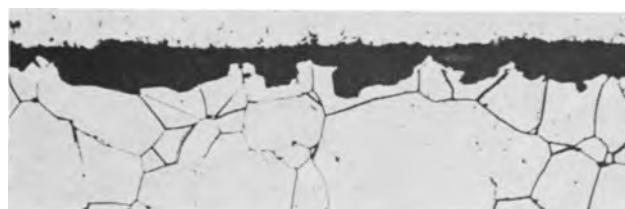
Tested 7.0 days, 3-hr start-up.

noted. Presumably, increased cold working would tend to further reduce the differences.

Those specimens in Table II with low metal losses had thin temper films after their corrosion exposure. Those samples with large metal losses were covered with a heavy dark coating. Microscopic examination of the corrosion interface of the latter on 304 indicated two layers of corrosion product of about equal thickness (Fig. 2). The attack on the metal was not uniform, and numerous pockets of oxide were noted deeper than the average penetration. It was interesting to note that the grain boundaries and the adjacent metal were more resistant than the central portion of the grains (Fig. 3).

In oxygenated steam much of the outer oxide layer had spalled off the electropolished specimens, leaving a brilliant black surface similar in smoothness to the original electropolished surface. Wet ground specimens in the same test did not spall appreciably, but a microsection of the metal-oxide interface on 304 was similar to that of the electropolished specimen. Spalling of the outer oxide coating was not thoroughly investigated, but it was related to thickness, mechanical keying with the inner coating and was triggered by temperature changes in these low velocity tests.

Tests for periods of several days indicated that even in oxygenated steam, the wet ground specimens passed through a temper film stage. This film subsequently broke down and the corrosion increased. This two-step process caused a considerable variation in the amount of metal corroded in one week. If the thin temper film broke down early in the test, the metal corroded value was high. If the particular sample retained the temper film during most of the exposure, the amount of metal loss was much lower. Samples exposed in the electropolished condition suffered this variability in metal loss values to a less extent.

Fig. 3. Grain center attack of type 304 stainless steel; 7 days; 650°C; 42 kg/cm²; 30 ppm O₂. Top layer, mounting foil; center layer, oxide; bottom layer, stainless steel. Magnification 320X.

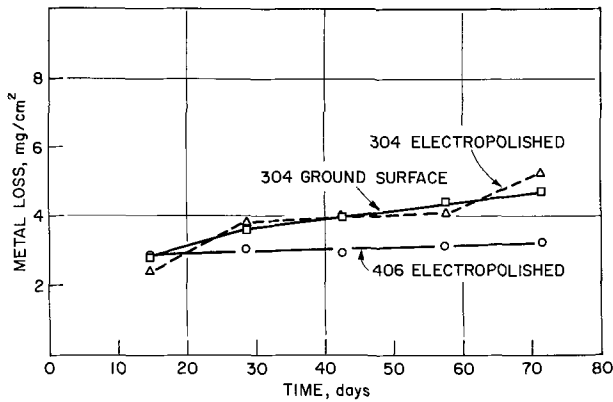


Fig. 4. Corrosion of stainless steels in static oxygenated steam, 600°C; 42 kg/cm².

The microstructures of the corrosion interface of wet ground specimens after temper film breakdown was similar to that of initially electropolished specimens. This suggested that the corrosion observed on the electropolished surfaces represented the intrinsic corrosion resistance of the alloys. If the correct interpretation has been made, the improved corrosion resistance noted for worked surfaces would represent a temporary effect. For this reason the electropolished surface preparation was chosen for measuring the corrosion rates of the various alloys. However, as will be shown later, the improvement in corrosion behavior for grit blasted surfaces has been observed to persist for relatively long periods of time.

Static corrosion testing.—Temperature.—Only two temperatures, 600° and 650°C, have been investigated in any detail. However, in a preliminary experiment, etched specimens of 304 and 347 were exposed to superheated steam (~0.2 ppm O₂) at 540°C for 374 days. The samples acquired a dulling tarnish film with isolated areas of gray film and rust colored spots. Metallographic examination after 117 days indicated carbide precipitation but no intergranular attack. Weight gains of only 0.2 mg/cm² for the type 304 and 0.1 mg/cm² for the type 347 were recorded at 374 days in this experiment. The combination of these data with the temper film observations indicated that the corrosion rate was quite low at this temperature.

At 600°C the corrosion data for 304 and 406 are presented in Fig. 4 for oxygenated steam (30 ppm) at 42 kg/cm². In this figure, as in subsequent ones, each point represents one defilmed specimen. Of the two specimen preparations tried, the grinding seemed to result in a somewhat more reproducible surface, judging from the relative smoothness of the corrosion curves. No significant difference in corrosion rate could be distinguished for the two preparation techniques under these test conditions.

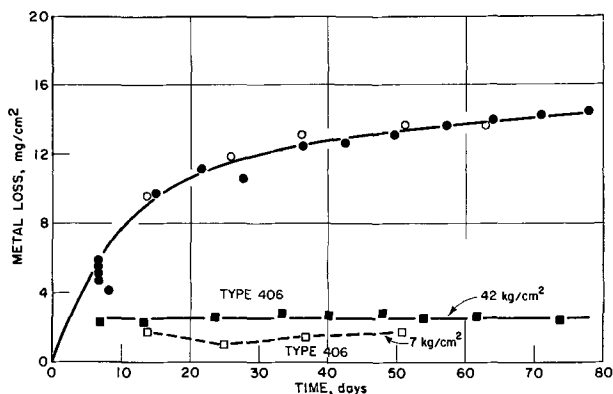


Fig. 5. Corrosion of electropolished stainless steels in oxygenated (30 ppm O₂) steam at 650°C. Type 304; ●, 42 kg/cm²; ○, 7 kg/cm².

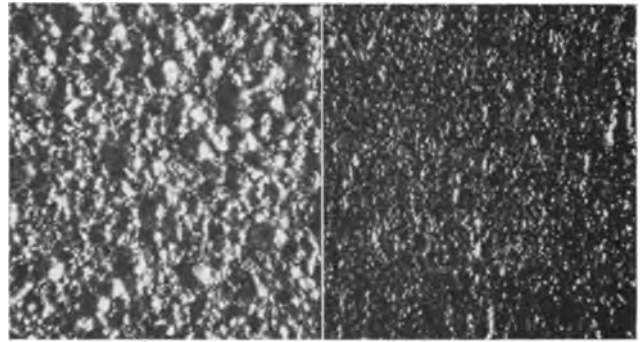


Fig. 6. Appearance of defilmed corroded samples, exposed at 650°C; 42 kg/cm²; 30 ppm O₂. Left, type 304 stainless steel, 87.9 days; right, type 406 stainless steel, 82.5 days. Magnification approximated 60X.

Type 406 steel samples were electropolished for testing in this environment. After the first exposure only very slight changes in metal loss values were obtained, almost within the normal defilming uncertainty. The average metal loss corresponded to a metal penetration of about 4×10^{-4} cm.

An unscheduled equipment shutdown at 58 days subjected the samples in one experiment to cool oxygenated water for about 20 hr. The previously smooth gray coating of type 304 was severely pitted by this low-temperature exposure while the 406 coating was not attacked. The pits noted on the 304 were rust colored and penetrated through the outer layer of corrosion coating and into the inner layer. When the samples were defilmed some slight evidence of the cold water pitting attack was noted on the underlying metal.

A corrosion rate measurement was also made at 650° (42 kg/cm²) using electropolished samples (Fig. 5). Both the total corrosion and the instantaneous corrosion rate (slope) for 304 were greater at this temperature than at 600°C for similar exposure times. Arbitrarily drawing a straight line through the longer exposure data for 304 resulted in a slope of ~5 mg/cm²-day (mdd).

Type 406 again corroded rapidly at the start with no measurable corrosion thereafter. Slightly less total corrosion was noted at this higher temperature. A sample exposed for 89 days was bent 180° around a 1 cm bar to check for embrittlement. None was evident in this simple test.

Defilmed samples of 304 acquired a deeply etched surface with increasing time (Fig. 6). Some of the pit bottoms were 0.006 cm below the average surface for the 88 day specimen. Type 406 alloy had a much smoother surface texture after defilming than did 304. No attempt was made to estimate the shallow pit depths on the specimen of 406 exposed 83 days.

Pressure.—Several steam pressures have been investigated at a temperature of 650°C. Early in the program two tests were performed in a tube furnace at atmospheric pressure. In the first, samples of the 300 series stainless steels were exposed to gently flowing dried oxygen (100 ml/min) at 650°C. The second test in this furnace used the same oxygen flow to which about 0.5 cc/min of water was added as steam. Data from these experiments are compared with a test at 42 kg/cm² total pressure (30 ppm O₂) in Table VI.

A comparison of the metal loss values for 1 atm wet oxygen and for 42 kg/cm² steam suggested only a small effect of pressure once adequate moisture was present. A surface preparation effect was noted even at 1 atm.

A longer experiment was performed in oxygenated (30 ppm) steam at 7 kg/cm², using electropolished samples of 304 and 406 (Fig. 5). The attack on 304 at 7 kg/cm² was quite similar to that obtained at 42 kg/cm². However, type 406 samples at the lower

Table VI. Effect of steam pressure on the corrosion of stainless steel

Sample, Preparation	Defilmed metal loss, mg/cm ²		
	1 atm Dry O ₂	1 atm Wet O ₂	42 kg/cm ² Steam (30 ppm O ₂)
304 Wet ground	0.19	3.6	6.6
Electropolished	0.16	5.9	7.5
321 Wet ground	0.27	1.2	1.8
Electropolished	0.16	6.5	9.2
316 Wet ground	0.15	1.8	0.34
Electropolished	—	6.6	9.0
347 Wet ground	0.24	2.3	3.9
Electropolished	0.36	6.4	11.2

* 7 Days exposure.

Table VII. Corrosion of electropolished alloy specimens in 650°C, 42 kg/cm² (30 ppm O₂) steam

Alloy	Defilmed metal loss, mg/cm ²	
	7 Days	14 Days
Incoloy 800	9.7	11.0
Type 403	13.5	a
405	18.9	23.9
410	11.4	a
410 (E ₂)	14.8	16.0
430	5.0	5.1
446	0.34	0.42

a. Very heavy coating; could not be completely removed in defilming.

pressure were still partially covered with temper film at the end of the test. The partial covering accounts for the variation in metal loss from one specimen to another, since the area per cent coverage by the heavier gray coating was not the same for each sample. At 42 kg/cm², the 406 samples were completely coated with the heavier gray film after one week exposure.

Miscellaneous alloys.—During the course of the investigation a number of different alloys were tested in static autoclaves for relatively short periods of time. Some of these tests were presented in Table II to illustrate the effect of surface preparation. Results of other tests are shown in Table VII.

Type 446 was clearly the most resistant alloy tested during these relatively short exposures. Among these 400 series alloys the corrosion resistance increased greatly as the chromium content was increased from 12 to 25%.

Dynamic testing.—Steels.—Five week experiments were performed to determine the effect of velocity (30-91 meters/sec) and the oxygen content on the corrosion of types 304 and 406 steels at 650°C, 42

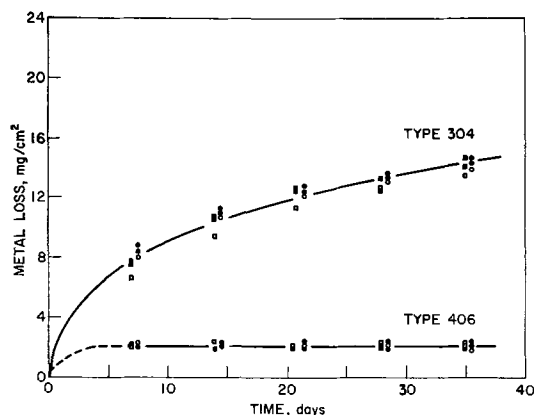


Fig. 7. Corrosion of stainless steel in flowing steam at 650°C; 42 kg/cm². Oxygen content, 0.05 ppm: Open circle, 30 meters/sec; solid circle, 61 meters/sec; circle with vertical line, 91 meters/sec. Oxygen content, 30 ppm: open box, 30 meters/sec; solid box, 61 meters/sec; box with vertical line, 91 meters/sec.

kg/cm². The two oxygen levels were 0.04-0.08 ppm and 30 ppm. As shown in Fig. 7 the data for the two experiments may be nearly superimposed, suggesting that oxygen content and velocity were not important variables in the range investigated. Comparison of Fig. 5 and 7 did show that the high velocity steam was more corrosive to type 304 than static steam. Type 406 did not show this dependence.

One additional longer test at the same temperature and pressure has been run with simultaneous gas addition of 30 ppm oxygen and 3.8 ppm hydrogen into the flowing steam. A test velocity of 61 m/sec was chosen. Again, (Fig. 8) varying the gas content of the steam had very little effect on the corrosion behavior of the electropolished specimens.

In this test, as in all of the other high velocity experiments, severe flaking of the outer corrosion coating occurred after only one week for the type 304 specimens (Fig. 9). As the test continued further loss was noted. For example, at 123 days a 304 specimen had lost an estimated 14 mg/cm² of corrosion coating, assuming a composition of Fe₃O₄. This was nearly half of the total coating produced. The same estimate performed for type 406 indicated that 95-98% of the coating was retained on the specimen at 123 days.

A smaller number of grit blasted samples were also tested. As might be expected from the results described earlier, the total metal losses were smaller (about half) for this surface preparation. The corrosion rate also appeared to be lower for these specimens.

Other alloys.—Five of the alloys frequently used for high-temperature applications were exposed to oxygenated (30 ppm) flowing steam at 650°C, 42 kg/cm². A test velocity of 61 m/sec was maintained past the electropolished specimens. Results are presented in Fig. 10. The earlier corrosion results of type 304 and 406 steel are included to establish reference levels. Of the five alloys tested, Inconel 600 and Inconel X750 were the poorest in corrosion resistance. The other three alloys (Inconel 625, Incoloy 800, and Rene' 41) all had metal losses less than type 406 at

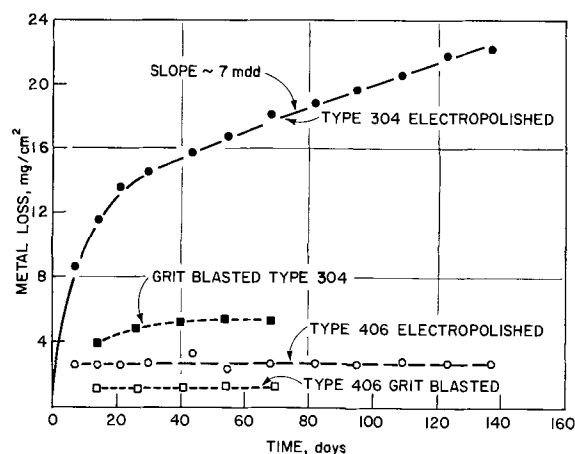


Fig. 8. Corrosion of stainless steels in flowing steam. Temperature, 650°C; pressure, 42 kg/cm²; steam velocity, 61 meters/sec; oxygen, 30 ppm; hydrogen, 3.8 ppm.

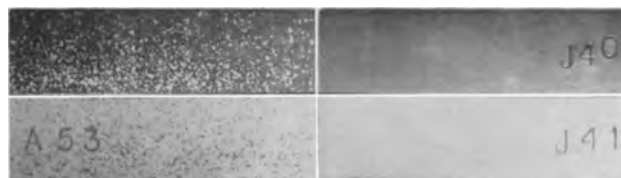


Fig. 9. Appearance of corrosion specimens after exposure to flowing steam at 650°C, 42 kg/cm²; oxygen and hydrogen added. Upper left, one-week exposure; upper right, one-week exposure; bottom left, two-week exposure; lower right, two-week exposure. Left, type 304 stainless steel; right, type 406 stainless steel.

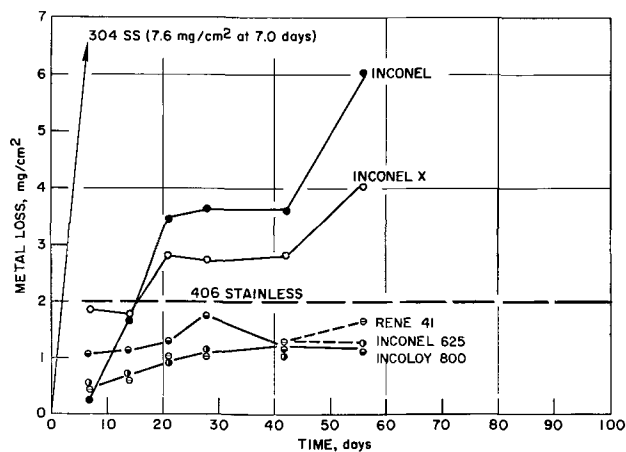


Fig. 10. Corrosion of nickel alloys in flowing steam; 650°C, 42 kg/cm², 61 meters/sec velocity, 30 ppm oxygen.

56 days, but with the possible exception of Incoloy 800, the metal losses were increasing with time.

Incoloy 800 had a low metal loss in this test, but in repeated static tests it exhibited a strong surface preparation effect and large metal losses. The static tests come to pressure and temperature much more slowly than the dynamic test (3 hr vs. about 5 min), suggesting that the method of starting the test may have played an important role in the corrosion behavior of this alloy.

Discussion

Surface.—The marked improvement in the corrosion resistance to deoxygenated steam of samples with machined surfaces had been previously noted (5) but was attributed to the removal of mill scale by the machining. In the current investigation the improvement could be reproduced on carefully cleaned surfaces and appeared to be a result of cold working the surface. It would appear likely that the oxide film formed on the cold worked metal differed in physical and electrical properties as well as in protective qualities from that formed on an annealed surface, but no extensive study was made.

It should be emphasized that the dependence of corrosion behavior on surface preparation varies from one environment to another and from one alloy to another. At temperatures of the order of 300°C in water, annealed or electropolished surfaces have been observed to corrode less rapidly than worked surfaces (7, 8) while at 400°C in steam the converse has been noted (8).

In oxygenated steam, the environment of particular interest in this study, the different surface preparations caused different corrosion behavior, but to a smaller extent than in steam of low oxygen content. Electropolishing was chosen as the primary surface preparation for the corrosion rate measurements. It appeared to represent most nearly the intrinsic corrosion resistance of the material as deduced from metallographic examinations of corroded samples. However, for many practical applications it would be advisable to reduce corrosion losses by using a final preparation which resulted in cold worked surfaces for the initial exposure.

Type 304.—The corrosion rate of type 304 in oxygenated steam rose rapidly as the temperature increased from 540° to 650°C. At 600° and 650°C the measured rate decreased with increasing time during the 80 day static tests. The rate was higher by a factor of about 1.5 in a dynamic test at 650°C. In rapid flow tests there appeared to be no effect of varying velocity or oxygen and hydrogen content on

the corrosion rate. Flaking and loss of the outer corrosion coating was particularly severe in these dynamic tests. In a nuclear superheater these particles of oxide would be radioactive. Their deposition in the turbine and condenser would present a serious contamination problem.

Even if it were not susceptible to stress corrosion cracking, it would appear that type 304 is unsuitable at 650°C and higher for the thin wall nuclear fuel element cladding discussed earlier.

Type 406.—The corrosion rate of type 406 was too small to be precisely measured in all of the tests, static and dynamic, in which it was exposed simultaneously with type 304. It did, however, rapidly form a protective coating at the onset of the tests which amounted to an average metal penetration of about 2 to 4×10^{-4} cm. No flaking of the outer corrosion coating was noted in tests of over 100 days duration. No embrittlement due to the high temperature was detected in one simple bending test.

Since alloys of approximately the same chromium content as 406, but without aluminum, suffered considerably more corrosion attack, it was assumed that the aluminum content was responsible for the low corrosion rate of this alloy.

Miscellaneous alloys.—The corrosion of the 400 series steels in static oxygenated steam went down with increasing chromium content, particularly above about 13 w/o Cr. Both type 430 (16% Cr) and type 446 (25% Cr) exhibited short term corrosion attack lower than the 18-8 austenitic stainless steels at 650°C.

The high nickel alloys, particularly Inconel 625, were also more corrosion resistant than the 18-8 steels in short static and dynamic tests at 650°C. Inconel 600 and Inconel 750X were the poorest of the high nickel alloys in extended testing in high velocity steam. Rene' 41, a cobalt bearing alloy, had very satisfactory corrosion resistance. This alloy had been included in the study for general interest although its use in a nuclear reactor was not contemplated.

Type 406 steel appears to offer advantages in general corrosion resistance, lower cost and neutron capture cross section over most of the high nickel alloys tested, but is inferior in high temperature strength and in some fabrication aspects. It appears to be an interesting material for high temperature steam applications.

Acknowledgment

The authors gratefully acknowledge the technical assistance of Messrs. D. Dorman, R. Lee, and R. Schlueter in performing many of the experiments described. Work was performed under the auspices of the United States Atomic Energy Commission.

Manuscript received Jan. 13, 1964. This paper was presented at the New York Meeting, Sept. 29-Oct. 3, 1963.

Any discussion of this paper will appear in a Discussion Section to be published in the June 1965 JOURNAL.

REFERENCES

1. C. N. Spalaris, F. A. Comprelli, D. L. Douglass, and M. B. Reynolds, GEAP 3875, (1962).
2. H. J. Pessel, Proc. Nuclear Superheat Meeting No. 8, March 1963 (COO-267).
3. G. G. Gaul and W. L. Pearl, *Nuc. Sci. and Eng.*, **17**, 30 (1963).
4. C. N. Spalaris, R. F. Boyle, T. F. Evans, and E. L. Esch, GEAP 3796.
5. M. T. Jones, Reactor Technology Report No. 14, KAPL 2000-11 (1960).
6. R. C. Ulmer, H. A. Grabowski, and R. C. Patterson, *Trans. ASME*, **82**, (A) 264-271.
7. H. R. Copson and W. E. Berry, *Corrosion*, **18**, 21t (1962).
8. Societe d'Etudes, de Recherches et d'Applications pour l'Industrie; EURAEC 704 (1963).

Surface Oxidation of Gold Electrodes

S. B. Brummer and A. C. Makrides

Tyco Laboratories, Inc., Waltham, Massachusetts

ABSTRACT

The surface oxides formed on electropolished gold by potentiostatic anodization in the range 1.2-1.85v *vs.* H^+/H_2 have been studied by galvanostatic reduction at current densities between 10 and 1000 $\mu a/cm^2$. Molar perchlorate solutions of pH 0.06 to 2.8 were employed. The extent of oxide formation is determined by the potential of anodization; the charge increasing linearly with the potential of formation in the range of 1.45-1.8v. Cathodic chronopotentiograms show that reduction of the oxide occurs at a definite potential which depends on the cathodic current density. Current-potential curves, constructed from the chronopotentiograms, follow a Tafel relation with a slope of 41 mv. The electrochemical order of the reduction reaction is -1.4 with respect to pH. Ease of reduction of the oxide, as measured by its rate of reduction at a fixed potential at any given pH, decreases with increase of potential of formation of the oxide. A mechanism for reduction is suggested in which it is assumed that the reduction of an intermediate (Au^{II}) is the slow step in the over-all process.

The formation and reduction of surface oxides on metal electrodes are of major importance in determining the kinetics of basic electrochemical reactions, for example, of the reactions involving the O_2/H_2O couple. Of particular interest are noble metals, often used as oxygen electrodes, where the absence of dissolution reactions facilitates the interpretation of current-potential relations for surface oxidation. The present study deals mainly with the kinetics of reduction of surface oxides formed on gold, a metal which is unusual in its stability toward oxidation at low temperatures.

The oxidation of gold has not received as much attention as that of platinum and is not, at present, well characterized. A number of studies have been made using chronopotentiometry (1-7). Of particular interest is the work of Laitinen and Chao (1) who combined potentiostatic techniques with galvanostatic measurements and established the steady-state concentration of oxide as a function of potential. The final surface species is believed to be Au_2O_3 (perhaps hydrated) [e.g., (7)], but there is disagreement concerning the presence (5) or absence (1, 4) of lower valent oxides. Although the surface coverage with oxidized species during galvanostatic oxidation has frequently been examined (2-8), apparently no attempt has been made to examine the kinetics of the reduction of the oxides of gold. In the present work, the kinetics of reduction of films formed potentiostatically have been studied over a range of pH.

Experimental

The principal experimental technique involved the potentiostatic oxidation of the electrode surface followed by reduction with constant current. Potential-time measurements were also made during anodic charging and during free decay from various surface oxidation conditions.

A three-compartment electrolytic cell constructed of Pyrex glass contained the working electrode in the central compartment and had sufficient volume to minimize concentration changes during an experiment. A Haber-Luggin capillary led to the reference electrode which was a platinized platinum cylinder immersed in a solution saturated with purified hydrogen. The counterelectrode was a roughened gold cylinder and was connected to the main compartment via a coarse fritted disk. All electrodes were mounted in

such a way that only glass and Teflon came in contact with solution (9).

Gold electrodes, of "spectroscopically standardized" material (Johnson, Matthey and Co.), were in the form of cylinders of area ~ 0.8 cm^2 . Immediately before use, the electrodes were electropolished in a cyanide bath (10) using a current density of ~ 6 amp/cm^2 . The specimens were polished until they showed no evidence of surface marking when viewed under a low power microscope. They were then washed in chromic-sulfuric acid, triply distilled water, and finally with the test solution. The electrodes usually retained their luster at the completion of a series of oxidation experiments, and only rarely did polishing affect the measured roughness factor of the electrodes after the first couple of treatments. Geometric areas were estimated immediately after the experiments, using a micrometer. All results are given in terms of the geometric area of the electrodes.

Solutions were made up with triply distilled water (one from alkaline permanganate) and were molar with respect to ClO_4^- . Different acidities were obtained using appropriate quantities of $HClO_4$ (Baker Analyzed Reagent) and $NaOH$ (Baker Analyzed Reagent). The pH was varied from 0.06 (N $HClO_4$) to 2.8. The working and counter electrode chambers were flushed with a continuous slow stream of N_2 , which had first passed through traps packed with glass beads cooled in liquid N_2 . Connections were made with Teflon tubing and all stockcocks, required to control the rate of gas flow, had Teflon barrels. The experimental results were not affected by stirring during the anodization or during the subsequent reduction of the film.

Potential control was maintained with a Wenking fast-rise potentiostat. Switching to a galvanostatic circuit was performed with a mercury-wetted relay (Western Electric 275C). Constant current was supplied by batteries in series with large resistances and was measured with a Greibach microammeter (type 510) to a precision of $\frac{1}{2}\%$. The potential during forced decay was measured on a Tektronix type 561A oscilloscope with a type 2A63 vertical amplifier and a type 2B67 time base.

Potentials could be read to 1 mv using a sensitive scale on the oscilloscope and a L&N potentiometer to back off most of the potential developed between the working and reference electrodes. Potential measure-

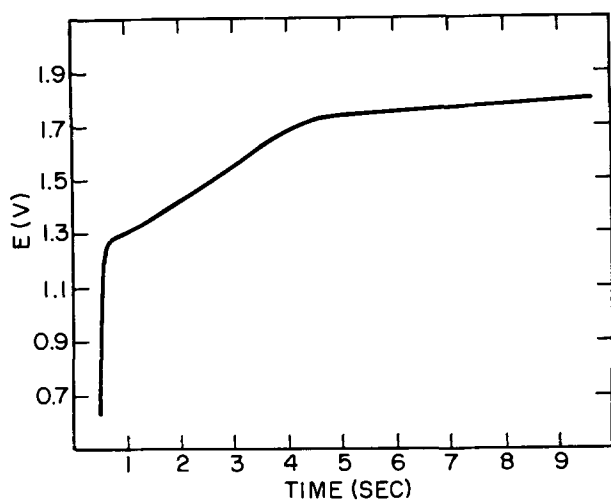


Fig. 1. Typical anodic chronopotentiogram in 1N HClO₄

ments during free decay were made with a L&N direct reading pH meter (input impedance $\sim 10^{12}\Omega$).

Reproducibility of charge with a given electrode during a run was usually $\pm 2\%$, but between different experiments scatter up to $\pm 5\%$ was observed, probably because of differences in the surface roughness of the electrode. The reproducibility of the potential during reduction was usually within the precision of measurement (± 1 mv) during a given experiment, and often was as good between different experiments. More usually, a variation of ± 2 mv was observed between different experiments. All potentials are referred to the reversible H⁺/H₂ potential in the same solution unless otherwise noted.

All observations were made at room temperature, $23^\circ \pm 2^\circ\text{C}$.

Results and Discussion

Anodic charging curves.—In Fig. 1, a typical charging curve is presented. It is seen that the potential rises steeply at first and then at about 1.28v, the exact value depending on the applied current density, a sharp break occurs. This is followed by a short region (20-30 mv) during which the potential rises quite slowly with time and then a much longer range (~ 1.3 -1.75v) where the potential increases more rapidly with time. The potential becomes steady at about 1.8v and this, no doubt, corresponds to steady-state oxygen evolution. The anodic charge during the period from the first break to 1.8v is $630 \mu\text{C}/\text{cm}^2$ which is somewhat less than the charge which is measured cathodically after potentiostatic pretreatment (for 5 min, see below) at 1.8v. However, the general shape of the charge vs. potential curves found from anodic curves is the same as that obtained by cathodic reduction after potentiostatic oxidation. The anodic charging curves are similar to those reported by Hickling (4), but differ in some respects from those reported by Laitinen and Chao (1). Hickling found that the total charge preceding oxygen evolution is equivalent to a monolayer of Au₂O₃ (perhaps hydrated). Our results and those of Laitinen and Chao (1) show that the amount of oxide on the surface increases smoothly with potential without any breaks corresponding to various stoichiometries. In particular, there are no arrests corresponding to the formation of Au^I or Au^{II} oxides.

Reduction curves.—Galvanostatic reduction curves of films formed potentiostatically at potentials ranging from 1.2 to 1.85v were determined at various cathodic current densities. Measurements were not extended above 1.85v to avoid permanent damage to the electrode (1) resulting in part, perhaps from extensive oxidation at the grain boundaries (11). A series of runs in which the time of anodization was varied showed that the charge obtained after 5 min

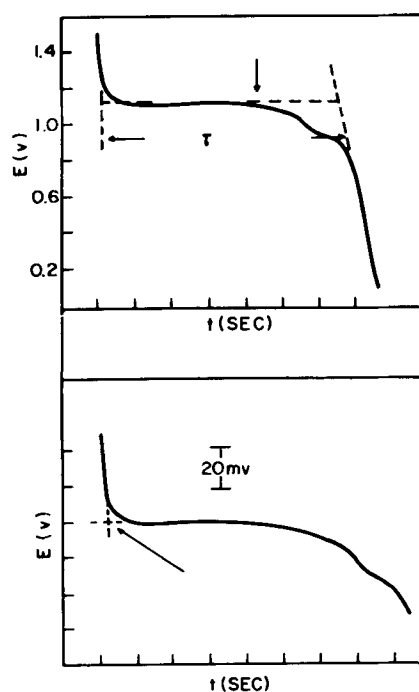


Fig. 2. Typical cathodic chronopotentiogram in 1N HClO₄ after 5 min of anodization at controlled potential. Arrow in upper figure indicates ~ 0.8 monolayer of O²⁻ remaining on surface. Arrow in lower figure indicates the potential corresponding to the reduction of the oxide.

and after 20 min of anodic oxidation differed by less than 0.5%. Since the reproducibility of the charge determinations was no better than this, all oxidations were carried out for 5 min.

In Fig. 2 are presented two typical cathodic chronopotentiograms. These were determined after the electrode had been oxidized potentiostatically at 1.55v for 5 min. It is seen that, in contrast to anodic curves, a clear and initially, well-defined arrest is observed corresponding to the onset of the reduction of the film. After a time, (indicated by the arrow in the top diagram in Fig. 2), corresponding to reduction to less than about 0.8 of a monolayer of adsorbed O²⁻, the potential falls rapidly. Then, almost at the end of the arrest, a slight "kink" is observed. Eventually, the rate of change of potential corresponds to double layer charging, and this is followed by an arrest, not shown, where H₂ is evolved.

The method of calculating the transition time, τ , is indicated on the first curve of Fig. 2 and the method of estimating the potential of reduction is shown in the second, magnified, trace. If the reduction were commenced from less than about 1.45v, the arrest corresponding to the reduction of adsorbed oxygen was less distinct and the calculation of the charge, q , less exact. Also, it was no longer possible to determine with any precision the initial potential of reduction. If reduction were started from 1.65v or above, a slight (2-5 mv) overshoot (less positive values) of the potential was observed. In this case, the potential of reduction was estimated both at the overshoot and at the arrest. The latter, while perhaps more valid, was more difficult to estimate accurately, so that there was more scatter in the current-potential curves for reduction. The results reported related to the overshoot.

At pH of 1 and above, the charge is independent of the cathodic current density, which is expected if impurity effects are negligible (no effect of stirring) and if the dissolution rate of the film is also negligibly small. However, in more acid solutions the charge decreased linearly with increase in τ (Fig. 3). The equivalent rate of loss of charge is about $3 \mu\text{a}/\text{cm}^2$ at pH 0.06. This zero order decay is suggestive of a

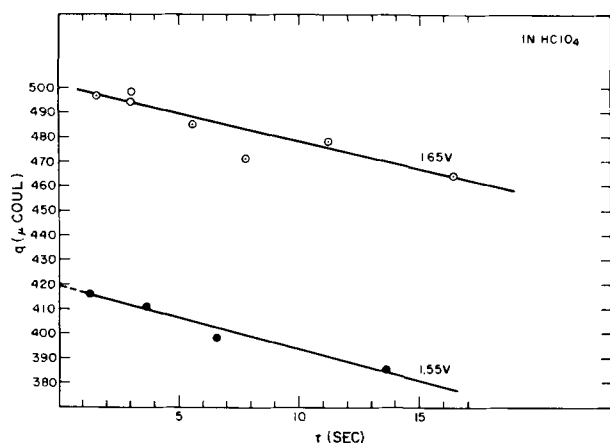


Fig. 3. Variation of the cathodic charge with time of reduction in 1N HClO₄.

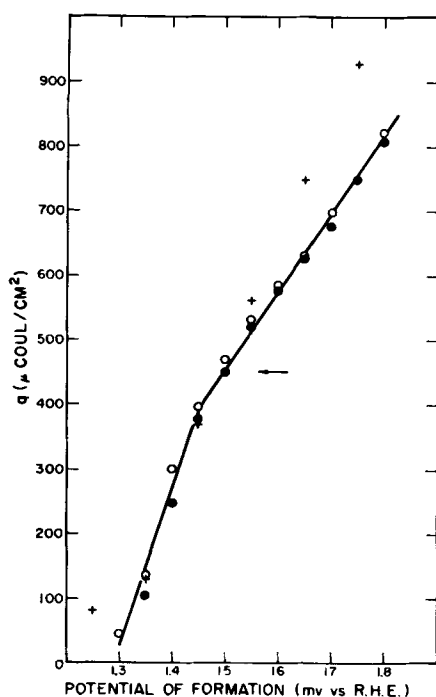


Fig. 4. Variation of cathodic charge with the potential of anodization in 1N HClO₄. Open and closed circles are from different experiments in the present study. Crosses are from the results of Laitinen and Chao (1). The arrow indicates a monolayer.

dissolution reaction, whereby the oxide disappears nonelectrochemically (no charge transfer) into solution. That this could not have been the case was shown by direct measurement of the rate of dissolution of the oxide. The electrode was left at open circuit for various times after anodization, and the oxide remaining at the end of this time was reduced galvanostatically. A dissolution rate of about $0.3 \mu\text{a}/\text{cm}^2$, determined in this way, is in good agreement with the results of Laitinen and Chao (1) and of Vetter and Berndt (6). Thus, the q vs. τ relation at $\text{pH} < 1$ is not caused by simple chemical dissolution, but must be due to the decomposition of some active intermediate produced during electrochemical reduction. In solutions where q varied with τ the reported steady-state charges were estimated by extrapolating the q vs. τ line ($i \sim 30$ to $600 \mu\text{a}/\text{cm}^2$) to $\tau = 0$.

Variation of charge with potential and pH.—The cathodic charge in 1N HClO₄ is shown as a function of potential of anodization in Fig. 4. It is seen that above $\sim 1.45\text{v}$ the charge increases almost linearly with potential. The charge at 1.45v is close to that for a monolayer, $450 \mu\text{c}/\text{cm}^2$ according to Hickling

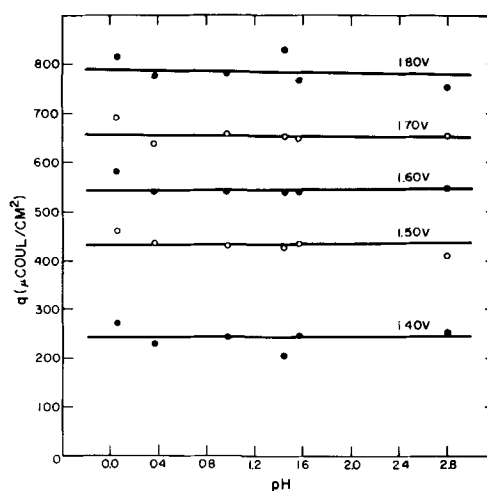


Fig. 5. Charge vs. pH at various potentials of formation

(4). In fact, if we regard the charge at the transition point in the q vs. E curve as corresponding to a monolayer, we would suggest that a monolayer of adsorbed oxygen (*i.e.*, one atom per metal atom) would be equivalent to ~ 400 rather than $450 \mu\text{c}/\text{cm}^2$. The agreement with the results of Laitinen and Chao (1) is only moderate. Below about 1.35v , Laitinen and Chao found a long slow fall in the amount of surface oxidation as a function of the potential of anodization whereas we find that below $\sim 1.45\text{v}$ q falls rapidly to zero, becoming too small to measure at $\sim 1.3\text{v}$.

Above $\sim 1.45\text{v}$, their results diverge systematically from ours. At 1.75v , this disagreement is about 15%. It may be that the discrepancy arises from a difference in the grain size of the gold specimens. Laitinen and Chao (1) report permanent damage to their electrodes after anodization above 1.75v , whereas we found that anodization up to $\sim 2.1\text{v}$ (in 1N HClO₄) does not cause appreciable permanent damage. Permanent damage would almost certainly be worst in a small-grained sample. Although the measurement is very difficult to make and is inaccurate once the charge is less than about $300 \mu\text{c}/\text{cm}^2$, the shape of the cathodic curves is substantiated at other pH's and is also similar to that of the anodic charging curves. Therefore, we conclude that no significant amount of oxide or of adsorbed oxygen is present on Au below 1.3v .

From the charge-pH relationships shown in Fig. 5 it is evident that the main factor which determines q is the formation potential vs. reversible hydrogen in the same solution (or possibly against the H₂O/O₂ potential). There appears to be a slight decrease in the charge at any given potential vs. the H⁺/H₂ couple in the same solution as the pH is raised from 0 to 2.8, but the effect is small and its magnitude is within the reproducibility of the experiments.

Kinetics of oxide reduction.—A typical series of reduction curves for gold oxide formed at different anodic potentials is shown in Fig. 6. Usually, the current potential curves were determined in the current density range 20 – $1000 \mu\text{a}/\text{cm}^2$ and, in general, the deviations from the Tafel plots were ± 1 mv. Above ~ 1 ma/cm², the Tafel lines deviate slightly in the direction of greater polarization. Reasonable assumptions about iR losses lengthen the validity of the Tafel region to at least 20 ma/cm².

Tafel lines at the highest pH's tend to curve over rapidly at current densities substantially below those corresponding to the diffusion-limited current for hydrogen ion. At pH 2.1, the current-potential lines were so curved as to vitiate any simple analysis of their slopes. The following discussion is mainly concerned with the linear Tafel plots obtained from pH 0.06 to pH 1.6.

The slope of the Tafel lines, 39 – 42 mv, was independent of the potential of formation, as indicated in

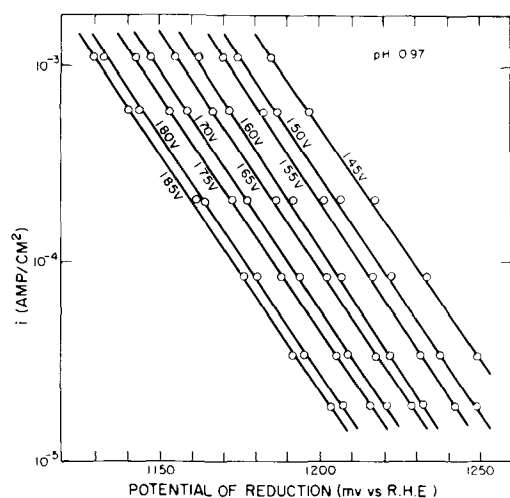


Fig. 6. Current-potential curves for reduction of films formed at various potentials.

the figure. The slope was also independent of pH in the range 0.06-1.60. In order to estimate an exchange current, i_0 , for reduction, we must know the reversible potential for the reaction, and this presupposes that we have some knowledge of the composition of the oxide. The charge vs. potential curves are smooth, once a monolayer of oxide has been put down, and give no indication of the composition of the oxide. However, the reversible potential for the reaction



is given by Latimer (12) as 1.45v (reduction potential), and experimentally (5, 13, 14) it has been found to be about 1.36v. Laitinen and Chao (1) observed rest potentials, after oxide formation, of about 1.30v and state that this results from a potential-determining reaction whose reversible potential is sufficiently close to 1.36v to assume that the oxide is very similar to $\text{Au}(\text{OH})_3$. In fact, they find it reasonable to consider the surface oxide as AuOOH [$\text{Au}_2\text{O}_3 \cdot \text{H}_2\text{O}$, see Jirsa and Buryanek (15)].

The most stable normal oxide of gold is Au_2O_3 (in its various hydrated forms) and even this is thermodynamically unstable and decomposes relatively readily (7). Lower oxides are known, *viz.*, AuO (16, 17), but it has been shown (7) that experiments (3, 5, 18) suggesting the anodic formation of lower oxides are incorrect and are probably the result of base metal impurities, probably Fe. Thus, there is no *a priori* reason for assuming any well-defined stoichiometry. Certainly, it is not found for platinum [Feldberg, Enke, and Bricker (19)] and indeed it has been suggested (19) that the similarity in the anodic behavior of various noble metals may best be understood by considering the process as essentially the oxidation of water with the products being stabilized by adsorption on the metal. However, platinum and gold adsorb oxygen (or form surface oxides) at potentials which differ by nearly 0.5v, so that it is doubtful whether such a "simplification" is particularly useful.

Although there is no clear justification for assuming any stoichiometry for the oxide, it is apparent that the potential of the oxide-gold couple is close to the potential of the $\text{Au}(\text{OH})_3/\text{Au}$ couple. For the purpose of estimating i_0 's, it will be assumed that the reversible potential is that of the $\text{Au}/\text{Au}(\text{OH})_3$ couple, *i.e.*, 1.36v, although the surface oxide may not be as completely hydrated as this. Exchange currents, obtained in this way, vary from about 5×10^{-8} to 2×10^{-9} amp/cm², and depend on the potential at which the oxide is formed (*vide infra*).

The ease of reduction of the oxide depends on the potential at which it is formed, although it is not clear at first whether this is a direct effect of the po-

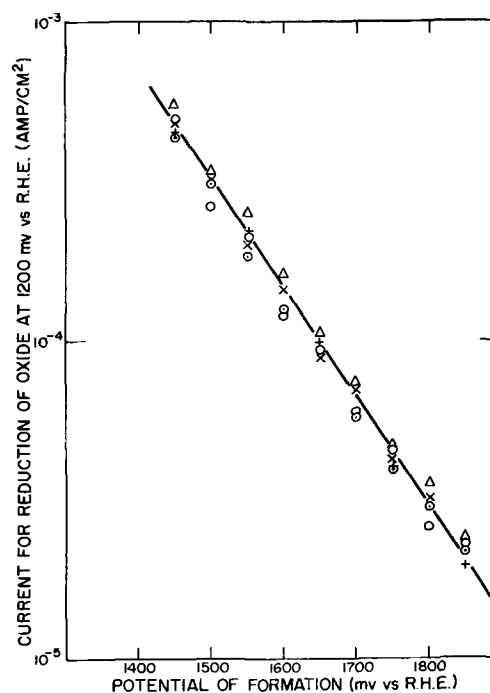


Fig. 7. Oxide reduction rate at 1200 mv as a function of potential of formation and pH. pH: \circ , 0.07; \times , 0.37; \circ , 0.97; $+$, 1.45; \triangle , 1.57.

tential, or a result of differences in thickness. The following experiment was performed to answer this question. The metal was oxidized at a certain potential and then left on open circuit. Observations were made of the charge left on the oxide from about 1.4 monolayers to about 0.7 monolayers, and, also of the potential of reduction of the oxide at a given current density as a function of time on open circuit. If the determining factor is the thickness, we expect the potential of reduction to become more positive (in the reported experiment, by about 40 mv) as the charge on the electrode decays away. Otherwise, we do not expect much change. The reduction potential became slightly (5 mv) more negative, which clearly shows that the potential of formation and not the thickness of the oxide controls the reduction kinetics.

The ease of reduction of the oxide, as a function of the potential of formation, is demonstrated in terms of the reduction current at fixed potential (1200 mv vs. R.H.E.), in Fig. 7. It is found that the reduction current decreases semilogarithmically with the increase in the potential of formation.

The pH dependence of the current at a fixed potential vs. the standard hydrogen electrode is shown in Fig. 8. $\log i$ varies linearly with pH according to $(\partial \log i / \partial \text{pH})_E = 1.39 \pm 0.02$. No significant variation in $(\partial \log i / \partial \text{pH})_E$ is found with changes of either q or of the potential of formation.

General Discussion

To describe the mechanism of the reduction of gold oxide, we should in all, have to account for the following facts: (A) Most of the oxide is reduced at a fixed potential. (B) A Tafel slope of 41 mv is observed independent of thickness or potential of formation. (C) $(\partial \log i / \partial \text{pH})_E$ is -1.39 independent of thickness or potential of formation. (D) The oxide becomes harder to reduce the higher the potential of formation. (E) In more acid solutions, the charge decreases linearly with increase in the transition time, at a rate in excess of that observed for simple dissolution of the oxide.

For the present we will assume, after Laitinen and Chao (1), that the oxide is essentially AuOOH ($\text{Au}_2\text{O}_3 \cdot \text{H}_2\text{O}$). A simple way of accounting for a Tafel slope of about 40 mv is to assume a three-electron reduction. However, aside from the inherent im-

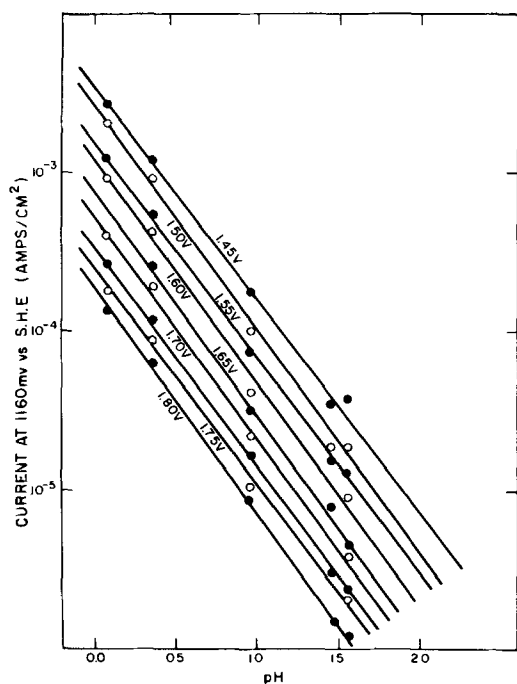
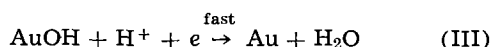
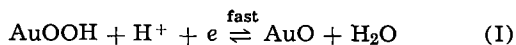


Fig. 8. Rate of reduction of oxides formed at various potentials as a function of pH.

probability of such a step, the pH dependence of the reduction rate rules out this mechanism.

A mechanism which partially satisfies (B) and (C) above is given by the following sequence of reactions



where AuO is written as the Au^{II} oxidation state and AuOH as the Au^I oxidation state, but either of these may be hydrated. The rate equation is

$$i = 3k_{\text{II}}(\text{AuO})(\text{H}^+) \exp - \frac{\alpha\phi F}{RT} \quad [1]$$

where α , the transfer coefficient, is ~ 0.5 , and ϕ is the potential. We can solve for (AuO) by assuming that reaction (I) is fast and is in equilibrium at all potentials. Then

$$\overline{k_1}(\text{AuOOH})(\text{H}^+) \exp - \frac{\beta\phi F}{RT} = \overline{k_1}(\text{AuO})(\text{H}_2\text{O}) \exp - \frac{(1-\beta)\phi F}{RT} \quad [2]$$

and

$$(\text{AuO}) = K(\text{AuOOH})(\text{H}^+) \exp - \frac{\phi F}{RT} \quad [3]$$

where K is a constant equal to $\overline{k_1}/\overline{k_1}(\text{H}_2\text{O})$. Then the final rate equation is

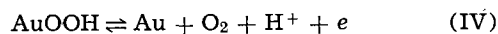
$$i = 3k_{\text{II}}K(\text{AuOOH})(\text{H}^+)^2 \exp - \frac{(1+\alpha)\phi F}{RT} \quad [4]$$

If the surface oxide (AuOOH) is thought of as a well-defined and essentially homogeneous solid, its activity will remain constant although its concentration declines during reduction. This would account for the initial flatness of the galvanostatic reduction curve. If α , in Eq. [4], is 0.5, the Tafel slope is 39 mv, in good agreement with experiment.

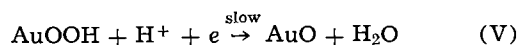
The pH dependence, $(\partial \log i / \partial \text{pH})_E$, as given by Eq. [4] is -2 . This result is only in moderate agreement with the experimental observation of $(\partial \log i / \partial \text{pH})_E = -1.39$.

A disadvantage of the above mechanism is the assumption that the reduction of Au^{II} is the slow step. Sidgwick (20) expresses the opinion that Au^{II} compounds are really complex molecules containing equal proportions of Au^I and Au^{III}. Although the evidence for this view is not strong, one has some doubts about postulating this form of gold as being so relatively stable. However, the large and unusual force field in a thin adsorbed layer could alter the relative stabilities of the various oxidation states.

An alternative to this scheme which yields the same Tafel slope and pH dependence can be constructed if it is assumed that the concentration of AuOOH is fixed by the equilibrium



and that the rate-limiting step is



Reaction (V) is followed by reactions (II) and (III), which are now assumed to be fast. This mechanism assumes that reaction (IV) is fast and reversible at potentials of $\sim 1.2\text{v}$ in 1N HClO₄, i.e. it requires that the reduction of oxygen on gold proceed at a rate greater than 1000 $\mu\text{a}/\text{cm}^2$ (the observed reduction rate of the oxide) at these potentials. This is contrary to what is known about the reduction of oxygen on gold (21). In addition, this mechanism predicts a substantial effect for oxygen while, in fact, no difference was observed either in the reduction potentials or in the amount of oxide present on the surface when oxygen was bubbled over the electrode. These findings rule out this alternative mechanism.

The variation of the reduction current at fixed potential (of reduction) is expressed by Eq. [5]

$$i \propto \exp - \frac{0.20 F E_a}{RT} \quad [5]$$

where E_a is the potential of formation of the oxide against the reversible hydrogen electrode in the same solution.

Comparison of Eq. [4] and [5] shows that the activity of (AuOOH) depends on the potential of formation according to $(\text{AuOOH}) \propto \exp -0.20 F E_a/RT$. This relation essentially expresses the qualitative observation made above, that the ease of reduction of the oxide decreases with the potential of formation, and suggests that the structure of the oxide (e.g., concentration of defects) depends on the potential of its formation. There is, unfortunately, no direct evidence bearing on the comparison or structure of very thin gold oxides formed anodically, so that it is not possible to deduce from the kinetics the structural changes which might take place (22).

An alternative explanation of the pH dependence is possible in terms of cation adsorption in the inner part of the double-layer on metals covered with oxide (23). Thus, for example, the potential of zero charge of oxide-covered platinum is in excess of 2.2v (23). The unusual pH dependence of the reduction rate may result from competition between (slightly) adsorbed Na⁺ and H⁺ ions whose ratio changes with pH. Because of the low Tafel slope of 41 mv, small changes in the potential distribution in the vicinity of the electrode could be very important. This notion received some substantiation from experiments in concentrated Mg(ClO₄)₂ solutions. The object, here, was to preserve the structure of the double layer (with a high concentration of divalent cations) while changing the pH. In the main, the results were similar to those reported above. However, at pH 0.2 or less the current potential curves were much more closely spaced than we have reported above and the pH dependence, especially at high potentials of formation ($\geq 1.7\text{v}$) was -2.0 . Further experiments, with variation of the cation are in progress and will be reported later.

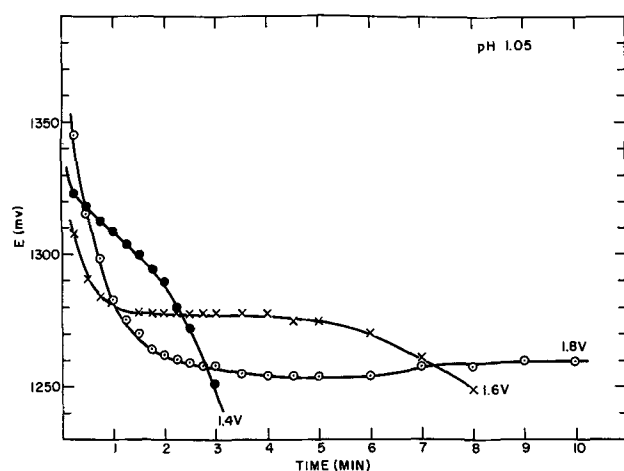


Fig. 9. Decay curves of oxides formed at various potentials

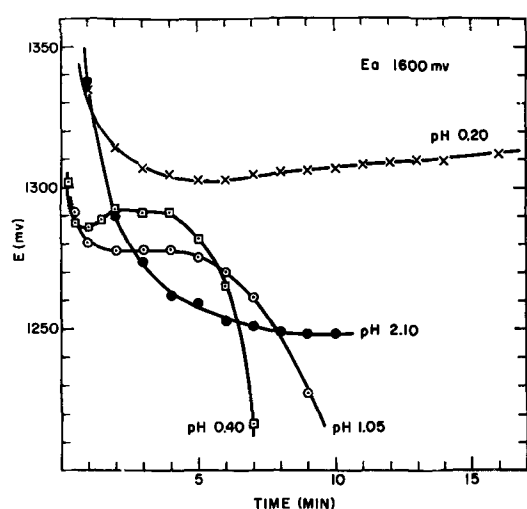


Fig. 10. Decay curves of oxides formed at 1.6v as a function of pH

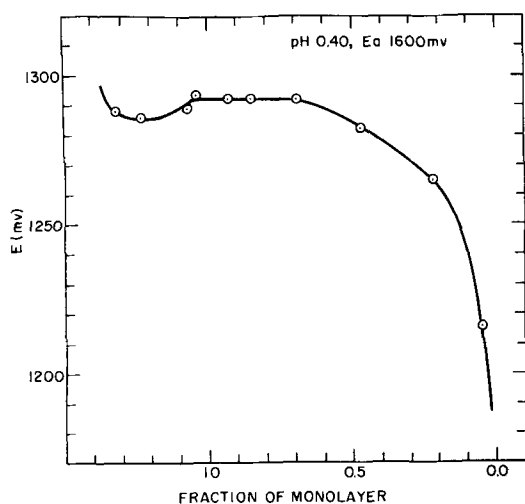


Fig. 11. Open-circuit potential as a function of the amount of oxide on the surface.

The rest potential.—Decay curves (Fig. 9-11) show (a) that the “rest” potential is a function of the potential of formation, (b) that this potential varies with pH (Fig. 10), and (c) that frequently there is an overshoot in the decay curve (Fig. 11). Since there is little doubt that the ultimate anodic product is Au^{III}

oxide (7), one expects that the higher the potential of formation, the closer to 1.36v would be the rest potential. In fact, the opposite is true. We may recall that the higher the potential of formation of the oxide, the harder it is to reduce. These observations, taken together, suggest that the rest potential is a mixed potential.

If the rest potential is a mixed potential involving an impurity couple, and if the reduction rate of the impurity is essentially controlled by its rate of diffusion to the electrode, then we expect the rest potential to vary by about 95 mv per pH unit, which is in fair agreement with the observed pH dependence (85 mv vs. S.H.E.). The overshoot phenomenon (Fig. 11) is similar to the overshoot observed in forced decay and probably arises from the same cause, i.e., from an additional potential drop within the oxide.

The observed variation of q with the reduction current in the more acid solutions is not easily accounted for. As shown above, the dependence of q on τ cannot be explained in terms of dissolution of the oxide, but must be attributed to the decomposition of an intermediate formed during forced reduction. According to the proposed mechanism, Au^{III} and Au^{II} are in equilibrium at all potentials and, therefore, also at the potential established during free decay. Consequently, any decomposition reaction involving these species must be present during both forced and free decay, and cannot, therefore, give rise to the much higher rate of dissipation of charge during forced decay. This argument implies that Au^I is the unstable species. The reaction in question is obviously not the disproportionation to Au and Au^{III}, which is a well-known reaction (24), since such a process does not dissipate charge but merely alters the kinetics of reduction. A likely path for charge dissipation is, then, reaction of Au^I with H₂O to yield O₂, which diffuses away.

Summary and Conclusions

1. The kinetics of reduction of anodic oxide films formed on gold electrodes at potentials between 1.45 and 1.85v follow a Tafel relation with a slope of 41 mv. The exchange current (determined by extrapolation to a potential of 1.36v vs. H⁺/H₂ in the same solution) is in the range of 10⁻⁷ to 10⁻⁹ amp/cm²; it decreases with increasing anodic potentials of formation of the film and is almost independent of pH.

2. The electrochemical reaction order for reduction is -1.39 with respect to pH.

3. A mechanism for reduction is suggested in which it is assumed that Au^{II} and Au^{III} are in equilibrium at all potentials and that the electrochemical reduction of Au^{II} is the slow step. This reaction scheme accounts approximately for the main experimental results.

Acknowledgment

The authors are grateful to Miss Maryjane MacLaren for her skillful assistance in the experimental part. This work was supported by the Office of Naval Research under Contract Nonr 3765(00).

Manuscript received Nov. 13, 1963. This paper was presented at the New York Meeting, Sept. 29-Oct. 3, 1963.

Any discussion of this paper will appear in a Discussion Section to be published in the June 1965 JOURNAL.

REFERENCES

1. H. A. Laitinen and M. S. Chao, *This Journal*, **108**, 726 (1961).
2. G. Armstrong, F. R. Himsworth, and J. A. V. Butler, *Proc. Roy. Soc. (London)*, **A134**, 89 (1934).
3. G. Deborin and B. Ershler, *Acta Physicochim.*, **13**, 347 (1940).
4. A. Hickling, *Trans. Faraday Soc.*, **42**, 518 (1946).
5. S. E. S. El Wakkad and A. M. Shams El Din, *J. Chem. Soc.*, **1954**, 3098.
6. K. J. Vetter and D. Berndt, *Z. Elektrochem.*, **62**, 378 (1958).

7. D. Clark, T. Dickinson, and W. N. Mair, *Trans. Faraday Soc.*, **55**, 1937 (1959).
8. F. G. Will and C. A. Knorr, *Z. Elektrochem.*, **64**, 270 (1960).
9. M. Stern and A. C. Makrides, *This Journal*, **107**, 782 (1960).
10. W. J. McG. Tegart, "The Electrolytic and Chemical Polishing of Metals," p. 62, Pergamon Press, New York (1959), (first method given).
11. H. A. Laitinen and C. G. Enke, *This Journal*, **107**, 773 (1960).
12. W. H. Latimer, "Oxidation Potentials," 2nd ed., Prentice-Hall Publishing Co., New York (1952).
13. R. H. Gerke and M. D. Rourke, *J. Am. Chem. Soc.*, **49**, 1855 (1927).
14. T. F. Buehrer and W. E. Roseveare, *ibid.*, **49**, 1989 (1927).
15. F. Jirsa and O. Buryanek, *Z. Elektrochem.*, **29**, 126 (1923).
16. F. Schottlander, *Ann.*, **217**, 337 (1883).
17. G. Krüss, *ibid.*, **237**, 296 (1887).
18. J. K. Lee, R. N. Adams, and C. E. Bricker, *Anal. Chim. Acta*, **17**, 321 (1957).
19. S. W. Feldberg, C. G. Enke, and C. E. Bricker, *This Journal*, **110**, 826 (1963).
20. N. V. Sidgwick, "The Chemical Elements and Their Compounds," Oxford University Press (1962).
21. G. Bianchi, G. Caprioglio, S. Malaguzzi, F. Mazza, and T. Mussini, Air Force Office of Scientific Research, Technical Report 60-299, May, 1960.
22. For work on this topic with other systems see, for example, M. Nagayama and M. Cohen, *This Journal*, **109**, 781 (1962); *ibid.*, **110**, 670 (1963).
23. A. N. Frumkin, *Electrochim. Acta*, **5**, 265 (1961).
24. T. F. Buehrer, F. S. Wartman, and R. L. Nugent, *J. Am. Chem. Soc.*, **49**, 1272 (1927).

Anodic Oxidation of Tantalum in Formic Acid Electrolytes

D. M. Cheseldine

Sprague-TCC (Canada) Ltd., Toronto, Ontario, Canada

ABSTRACT

Duplex films formed anodically on tantalum in formic acid and other organic electrolytes have both low capacity and low optical thickness per unit formation voltage. $1/c$ vs. V curves show a "break point," CV values being lower at higher voltages. The film adjacent to the metal has the characteristics of normal Ta_2O_5 and grows simultaneously with the outer more rapidly soluble film suggesting oxygen ion mobility in this outer film. Evidence from sequential formations in organic and aqueous electrolytes indicates also tantalum ion mobility and the growth of some new oxide in the pre-existing outer layer. Conditions at the electrolyte interface may exert some control on the number of oxygen ions entering the film. Other anions influence the film structure which is thought to contain voids.

It has been observed that the film produced on tantalum in organic or concentrated electrolytes differs in certain characteristics from that formed in dilute aqueous solution. Vermilyea (1) noticed that with films formed to the same voltage, those formed in organic electrolytes were optically thinner (absolute values varying with electrolyte composition) yet showed normal capacity. The film consisted of two portions; an outer part which dissolved rapidly in HF and an inner part which dissolved at a rate similar to that of films produced in aqueous solution. Also the efficiency of the formation process in organic electrolytes was greater than 100% assuming all the charge to be used in the production of oxide.

Young (2) made measurements of overpotential and capacity of films formed in various concentrations of H_2SO_4 and found the product CV to be approximately constant. Masing, Orme, and Young (3) showed the outer part of the film formed in concentrated H_2SO_4 to be optically absorbing. The refractive index of the film was found to be a few per cent less than that of the normal oxide.

In the present investigation formic acid with various additions has been used as the basis of a number of organic electrolyte systems in which the anodic oxidation of tantalum has been studied.

Experimental

Capacitor grade tantalum foils 0.0003 in. thick, having a surface area of 950 cm^2 were prepared by cleaning for 2 min ultrasonically in 1% alconox solution at room temperature, rinsed, then dried at 120°C in a forced draught oven. A surface area of 50 cm^2 was used for capacity measurements.

Foils were anodized in about 250g of electrolyte which was surrounded by a water bath maintained at 20°C . Most of the anodizing was carried out at a con-

stant current density of 0.095 ma/cm^2 . Voltage was measured between the anode and cathode, and the electrolytes were adjusted to have similar resistivities. Most of the work was carried out in an electrolyte consisting of 2.8g dibasic ammonium phosphate dissolved in 100g formic acid. This electrolyte had a specific resistance of 46 ohm-cm at 25°C . The aqueous electrolyte consisted of H_2SO_4 diluted to the same resistivity. The reagents were 'ANALAR' grade and were not further purified.

The tantalum oxide film was dissolved in HF. For most of the work approximately 35% HF was used, but for some experiments concentrated HF (48% or 55%) was used, the latter giving a more defined end point at which all oxide was removed. Formed foils were cut into eight equal lengths for easier manipulation in HF solution. A large volume of HF was made up and a fresh portion (approximately 200 cc) was used for each immersion interval, used acid being collected for recirculation. Acid strength was checked at intervals by measuring the solution rate of normal tantalum oxide formed in dilute H_2SO_4 .

Capacity and dissipation factor measurements were made at 120 cycles in the formation electrolyte. Optical thickness measurements were made by comparing the colors with a tantalum optical step gauge formed in dilute H_2SO_4 at 2v increments. The step gauge was used as an arbitrary scale of optical thickness, thus all thicknesses are given in terms of tantalum formation voltage.

Results

A comparison of films formed to the same voltage in formic acid electrolytes and in dilute H_2SO_4 shows that the former are optically thinner, require less coulombs for their formation, and have a slightly lower capacity. The film consists of an outer and an

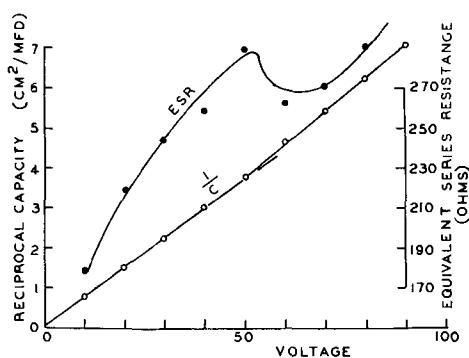


Fig. 1. Reciprocal capacity and equivalent series resistance in electrolyte 1; current density 0.3 ma/cm².

inner region with differing rates of solution in HF. Also the formation in formic acid electrolytes proceeds with greater than 100% efficiency.

Capacity and equivalent series resistance.—A typical reciprocal capacity vs. voltage plot is shown in Fig. 1 for formation in a formic acid electrolyte (composition 1).

The low voltage curve has a reciprocal slope (CV) of 13.5 $\mu\text{f}\cdot\text{v}/\text{cm}^2$ compared with 12.2 $\mu\text{f}\cdot\text{v}/\text{cm}^2$ for the high voltage curve. Increasing the current density from 0.3 to 1.0 ma/cm² reduced the low voltage reciprocal slope to 11.6 $\mu\text{f}\cdot\text{v}/\text{cm}^2$ and the high voltage to 9.4 $\mu\text{f}\cdot\text{v}/\text{cm}^2$. The break point occurred approximately 5v lower at the higher current density. The E.S.R. curve also shown in Fig. 1 exhibits a maximum.

Similar reciprocal capacity curves are found in other nonaqueous electrolytes. For instance in an electrolyte consisting of 8% concentrated H₂SO₄ and 1% water in ethylene glycol, the reciprocal slopes at low and high voltages were found to be 14.7 $\mu\text{f}\cdot\text{v}/\text{cm}^2$ and 9.4 $\mu\text{f}\cdot\text{v}/\text{cm}^2$, respectively. At 0.3 ma/cm² the break point in this electrolyte was found to occur at 35v.

Solution of films.—Both inner and outer films dissolve uniformly in HF but with differing solubility rates. Depending on the acid concentration the solubility rate of the metal also differs from that of the oxide. Therefore the weight of either film or of the total film can be determined.

Solution of the oxide was first applied to the whole film in an attempt to determine why the oxide forms with apparently greater than 100% current efficiency. Excess weight could be gained in either an electrochemical, chemical, or physical process which might occur in addition to the normal oxide formation.

The total film weight resulting from normal electrochemical formation of oxide and an electrochemical

process involving some ion other than oxygen is given by [1]

$$W_F = W_G + C \cdot EW_{\text{Ta}^{5+}} \quad [1]$$

where W_F is the total weight of film in grams, W_G is the weight gain after anodizing in grams, C is the "charge to form" in faradays, and EW is the equivalent weight.

The total film weight resulting from a chemical reaction, in addition to the normal electrochemical formation of oxide, is given by [2]

$$W_F = C \cdot EW_{\text{Ta}_2\text{O}_5} + W_E \left(1 + \frac{EW_{\text{Ta}^{5+}}}{EW_A} \right) \quad [2]$$

where the symbols are as above. W_E is the excess weight gain in grams, and A is an anion in a tantalum compound formed by a chemical process. Values can be calculated by making assumptions regarding the nature of A .

A possible type of physical process which might occur is one in which some neutral species is occluded in the oxide film. The total weight of film is then given by [3] which gives the same value for the film weight as is given by the electrochemical process

$$W_F = C \cdot EW_{\text{Ta}_2\text{O}_5} + W_E \quad [3]$$

Some typical results and figures showing the film weights to be expected for different processes are given in Table I. Of the three processes considered the electrochemical or physical give closest agreement with observed values.

The accurate determination of the point where all the film has been dissolved is difficult because the results appear to vary somewhat depending on the strength of HF used to dissolve the film and the parameter measured. To avoid this difficulty the total weight of film has been calculated in a number of instances from Eq. [1] or [3], i.e., assuming either an electrochemical or physical process in addition to electrochemical formation of oxide. This calculation gives a result very close to the film weight determined by solubility rate in concentrated HF (Table I).

The weight and solubility rate of the outer, more rapidly dissolving film have been determined at different formation voltages. It was found that the weight of the outer part of the film is directly proportional to the formation voltage and represents a fixed fraction (about 60%) of the total weight of film present (Table II), i.e. both films grow simultaneously. The inner film can only grow simultaneously with the outer film if it either grows out of the latter, i.e., if a conversion takes place, or if oxygen ions are supplied to the growth site. The latter appears more

Table I. Solution of tantalum anodic films

Electrolytic composition	1	2	3	Dilute H ₂ SO ₄
Charge to form to 100v (coulombs/meter ²)	1570	1530	1520	3000
Weight increase	130	127	126	248
Calculated from charge	185	183	178	255
Measured	55	56	52	—
Excess	48%	48%	35%	48%
HF concentration				
Parameter measured	weight	weight	capacity	weight
Weight of film dissolved	770	740	710	1350
Charge (faradays) $\times EW_{\text{Ta}_2\text{O}_5} \times 10^3$	720	705	700	1370
Calculated weight of film:				
(a) Electrochemical process	775	760	750	
(b) Chemical process				
1. Formate	820	806	794	
2. Phosphite	851	838	824	
3. Hydroxide	892	880	862	
4. Oxide	1024	1015	987	
(All weights in mg/meter ²)				
Electrolyte Compositions:	1		2	3
Phosphorus acid	1.5		1.7	—
Diammonium hydrogen phosphate	—		—	2.8
Formic acid	90.0		100.0	100.0
Water	0.75		—	—
Triethylamine	—	To give specific resistance	—	—
Specific resistance ohm-cm at 25°C	50		60	48.0

Table II. Solubility rate in 35% HF of films formed in electrolyte 3. Current density 0.095 ma/cm²

1. Formation voltage	20	40	60	80	100
2. Weight of outer film, mg/meter ²	94	170	255	345	427
Ratio 2/1	0.47	0.42	0.42	0.43	0.43
Solubility rate, mg/meter ² /sec	9.4	9.4	8.9	8.2	7.1
Weight of outer film					
Weight of total film ^(a)	0.74	0.61	0.60	0.59	0.59
Coulomb efficiency, %	148	144	135	136	142
Optical thickness, Ta voltage	—	21	31	43	60

(a) Calculated.
(All weights in mg. Solubility rate of Ta₂O₅ formed dilute H₂SO₄ = 3.6 mg/meter²/sec).

likely and implies mobility of oxygen ions in the outer film since these must originate in the electrolyte before passing through the outer film.

The formation efficiency values in Table II are typical of those obtained under controlled temperature conditions. The variations with voltage are within the reproducibility at any voltage and therefore not significant. The mean value obtained for the efficiency at 20°C from all (eight) determinations made at this temperature was 144%, all values falling within ±6% of the mean. In earlier experiments without temperature control 19 out of 30 determinations fell within this range.

For films formed above a certain voltage the solubility rate decreases with increasing voltage. An increase in the formation current density causes a marked increase in the solubility rate of the outer film. At 0.76 ma/cm² (i.e., an eightfold increase of current density) a 60v film showed a solubility rate double that for a film formed at the lower current density. The relative proportion of fast dissolving oxide remained at approximately 60% of the total film. The optical thickness of the film, however, was about 7% thinner than the film formed at the lower current density. The formation efficiency at the higher current density was 152% which is slightly higher than the highest value of 148% observed at the lower current density.

Changes in capacity, weight, and optical thickness during solution of films are shown in Fig. 2 and 3. Reciprocal capacity variations with both weight and optical thickness differ widely for the inner and outer regions of the film. For solution of equal weights of film the change in reciprocal capacity is greater by a factor of 2.7 in the outer film. Variation of reciprocal capacity with optical voltage gives a value of 14.0 μf-optical volts/cm² for the inner film, which is of the order to be expected for normal Ta₂O₅. By comparison

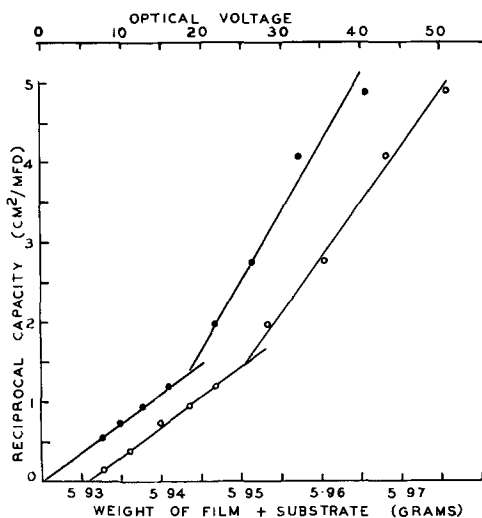


Fig. 2. Variations of reciprocal capacity with: weight of oxide + substrate, ○ - - - ○ - - - ○; optical thickness, ● - - - ● - - - ●; during solution in electrolyte 3.

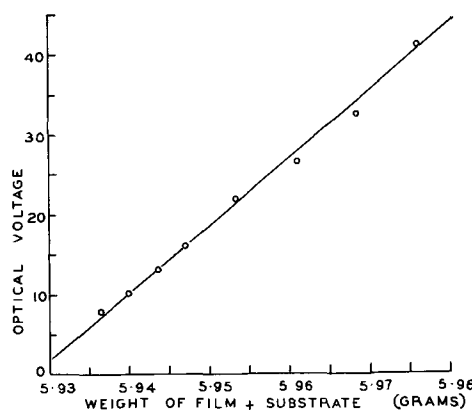


Fig. 3. Variations of optical voltage with weight of film + substrate during solution of a film formed in electrolyte 3.

the outer film gives a value of 6.2 μf-optical volts/cm². The relationship between weight and optical thickness for both films appears to be similar since no change of slope is discernible in this curve (Fig. 3).

While considering the relationship between weight and optical thickness it is interesting also to compare the formation charge required for unit increase in optical thickness. Formation in electrolyte 3 gives a value of 27 coulombs/optical volt/meter² compared with a value of 29 coulombs/optical volt/meter² for a film formed in dilute H₂SO₄. Actually the nonaqueous formation gives a composite film of which about 40% is normal Ta₂O₅. After making allowance for this it appears that the outer film grows with a coulomb expenditure/optical volt of about 12% less than normal Ta₂O₅. This difference, while significant, is quite small.

Some very interesting results are obtained when formation in a nonaqueous electrolyte is interrupted and the formation continued in an aqueous electrolyte. This type of sequential oxidation has been used by other investigators in an attempt to determine which ions carry the current through the oxide film (1, 4), the final position of the films being determined by their differing solubility rates.

If the formation is carried out first in dilute H₂SO₄ and then in a nonaqueous electrolyte the results are as might be anticipated. The outer part of the final film dissolves more rapidly in HF, this outer part amounting to about 60% of the weight of film formed in formic acid electrolyte. The remainder of the film dissolves at a uniform slower rate. This is consistent with the theory that only tantalum ions move in normal Ta₂O₅ but does not constitute proof of this theory unless it is established that all of the film formed in nonaqueous electrolyte lies above that formed in dilute H₂SO₄. This cannot be established from solubility experiments since the solubility rate of the lower film formed in nonaqueous electrolyte is the same as that of the film formed in dilute acid.

When oxidation is carried out in the reverse order it is found that the rapidly dissolving part of the film is in the middle sandwiched between two layers of less soluble oxide. This is qualitatively what might be expected still assuming only tantalum ion mobility. However, the fast dissolving part of the film is too near the air interface for this assumption to be correct, i.e., when the formation is continued in dilute acid considerable growth of normal Ta₂O₅ takes place below the rapidly dissolving film formed in nonaqueous electrolyte. Also some dispersion of the fast dissolving part of the film appears to take place because the weight of this film increases. Its solubility rate also is lower than expected. Some further anomalies are noticed in the anodizing. For instance the coulombs/voltage increment in the dilute H₂SO₄ are initially exceptionally high; also the optical thickness is greater than would be expected. Figures for formations car-

Table III. Formation in electrolyte 3 followed by formation in dilute H₂SO₄

	[I]	[II]	[III]
Formation voltage			
Electrolyte 3	30	30	30
Dilute H ₂ SO ₄	60	100	—
Optical voltage			
Electrolyte 3	16.5	16.5	16.5
Dilute H ₂ SO ₄	54	98	—
Excess coulomb expenditure in dilute H ₂ SO ₄ , coulombs/meter ²	180	175	—
Weight of film, mg/meter ²			
Outer	188	366	132
Middle	211	388	—
Inner ^(a)	288	465	81
Solubility rate of film in 35% HF, mg/meter ² /sec			
Outer	4.9	4.3	9.4
Middle	6.6	5.5	—
Inner	3.4	3.4	3.4
Weight of film formed in dilute H ₂ SO ₄ [following electrolyte 3], mg/meter ²			
Beneath existing outer film ^(b)	207	384	—
Within existing outer film	79	256	—
Above existing outer film	188	366	—
Total	474	1006	—

^(a) By difference from the calculated weight of the total film.

^(b) The inner film formed in electrolyte 3 dissolves at the same rate as the film formed in dilute acid and must be deducted to determine the weight of film added in dilute acid.

ried out first in electrolyte 3 and then in dilute H₂SO₄ are shown in Table III, [I and II] and for comparison some figures for a 30v formation in electrolyte 3 only are included [III].

These figures show that following the formation of a film in electrolyte 3, most of the oxide growth in dilute H₂SO₄ occurs above and below the outer region of the first film. Also some growth takes place within the film.

Film growth at any location indicates both anion and cation transport to that location. Therefore the sequential formation experiment is further evidence for the mobility of both ion species in the more rapidly soluble film.

Knowing the relative proportions of ions trapped in the oxide film and of ions penetrating to either interface, the proportion of charge carried by either anion or cation species can be deduced. It is assumed that the inner film is formed by anion migration and the outer film by cation migration. (When growth occurs within the film the charge must be divided equally between anion and cation transport.) For the two examples in Table III it is found that the proportion of charge carried by oxygen ions is 52% and 51% of the total for cases [I] and [II]. This agreement supports the suggested mechanism and indicates that under given formation conditions the rate at which either ion species enters the film remains constant. In this case approximately half the charge is carried by oxygen ions.

Addition of water to electrolytes.—Addition of water to a formic acid electrolyte increases the relative proportion of the inner film and also decreases the solubility rate of the outer film (Table IV).

Whereas in electrolyte 3 without any addition of water 60% of the film has a high solubility rate, with the addition of 40% water to the electrolyte this is reduced to 45%. The solubility rate is also reduced to a value very close to that of the normal oxide.

Table IV. Effect of water additions to electrolyte 3, 100v formation

Per cent water added	2	5	10	20	40
1. Weight of total film ^(a) , mg/meter ²	830	910	990	1040	1160
2. Weight of outer film, mg/meter ²	470	503	516	483	525
Ratio 2/1	0.57	0.55	0.52	0.46	0.45
3. Solubility rate of outer film, mg/meter ² /sec	5.9	5.1	4.3	4.3	3.7
Efficiency, %	136	129	119	119	112
Optical voltage	70	77	82	84	89

^a Calculated.

In considering the transport of ions through the film a complicating factor is that anions other than oxygen ions appear to enter the film. In particular the phosphate or phosphite ions present in the electrolytes so far considered play an important role. Without such additions the formation is characterized by increasing voltage increments per coulomb and break down at low voltages preceded by a decreasing product of capacity and voltage. The formation efficiency is still greater than 100%, and the outer part of the film has a very high solubility rate. For instance, with the addition of 5% water to an electrolyte consisting of triethylamine and formic acid (specific resistance 46 ohm-cm at 25°C) the voltage increment/coulomb increased from a value of 465 v/coulomb/cm² at 10v to a value of 975 v/coulomb/cm² at 100v. The outer film dissolved in 35% HF at a rate of 41 mg/meter²/sec compared with a rate of 5.1 mg/meter²/sec for a film formed in a similar electrolyte containing phosphate ions.

Further evidence of the effect phosphate ions in nonaqueous electrolytes have in decreasing the solubility rate of the formed films is obtained by forming in concentrated phosphoric acid (85% H₃PO₄). Under these conditions a film formed to 60v has an optical thickness of 40v and requires only 62% of the coulombs required to form a film to the same voltage in dilute H₂SO₄, i.e., the film has the characteristics of a film formed in a nonaqueous electrolyte including a high formation efficiency. The film, however, dissolves at a uniform rate of 2.5 mg/meter²/sec which is even lower than the rate of 3.6 mg/meter²/sec normally observed for films formed in dilute H₂SO₄.

It therefore seems likely that some phosphate or phosphite ions are taken up by the film during formation in formic acid electrolytes containing these ions. Formate ions may also be taken up since the solubility rates of the outer films are still much greater than those of films formed in concentrated H₃PO₄.

Discussion

The experimental evidence indicates that these films consist of two regions; that both cations and anions are mobile in the outer region; and that growth can occur within this outer region. The high coulomb efficiencies indicate that some ions other than oxygen are taken up by the film, and there is evidence that such a film has a higher field strength than normal. Both coulometry and optical measurements indicate that the field strength is almost double that of a normal film. While both these methods are limited by lack of knowledge of the nature of the film there are indications that this may not differ grossly from that of oxide formed in dilute solution. Also a direct weight comparison indicates that the film formed in organic electrolyte is only about 75% of the weight of one formed to the same voltage in aqueous solution. Therefore the former must be thinner unless the density changes by an equal or greater amount. Further, in spite of the low CV values of the outer film (Fig. 2) the CV values of the duplex film are only slightly lower than those of the normal oxide indicating that the duplex film must be thinner to compensate for its lower dielectric constant.

It is thought that these phenomena can best be explained by assuming that the outer film formed in organic electrolytes has some type of voids in its structure. Film growth with pores is possible when the anion is mobile. In this case, since the cation is also mobile, growth at the neck of the pore would eventually cut it off, leaving a void embedded in the film.

Vermilyea (5) found the average field strength of films formed on contaminated surfaces to be higher than normal due to the interruptions in the ion conduction paths. In this case the voids were between the metal and the oxide film. Such voids affected growth above them due to the reduced availability of tantalum ions. Thus a tendency exists for voids to reproduce. Since they are probably being continually

created in a film growing in an organic electrolyte, they may multiply giving rise to low capacities and other effects.

Films formed in formic acid electrolytes not containing ions such as phosphate or phosphite exhibit a very rapid CV drop with increasing voltage after a certain voltage has been reached. Such behavior may be due to the rapid multiplication of voids. The accompanying increase in voltage increment per coulomb provides corroborating evidence. This latter behavior is not observed when phosphate or phosphite ions are added to the electrolyte. It is thought that this may be because these ions enter the film and collapse its structure (6), thus maintaining sufficiently uniform ion conductivity to prevent the excessive generation of voids. (The decreased solubility of films formed in electrolytes with phosphorous containing ions is in accord with the idea that these films are more dense.) The break in the CV curve would then be interpreted as a measure of their failure to completely achieve this. The maximum in the ESR curves suggests that the growth form induced by these ions is strained and that at the break point the film reverts to a slightly modified growth form.

Voids would provide a site for the further growth which occurs within the film. Such growth could restore some of the conduction paths in the film thus lowering its field strength. The excess coulombs required to form a film in aqueous solution on top of a film formed in an organic electrolyte could then be explained by the decreasing field strength of the latter.

The filling of voids also offers an explanation of the decreasing solubility rate of the outer film as it grows (Table II) or as formation is continued in an aqueous electrolyte (Table III).

The absence of voids in films grown in aqueous solution is not surprising. The conditions for their origin, e.g., foreign ion inclusions, may be absent. Another possibility is that the large excess of oxygen ions present in dilute solution may fill in the voids almost as soon as they are produced. There are indications that the amount of growth within the oxide is controlled by the availability of oxygen ions at the interface. For example, in organic electrolytes an increase in current density produces less growth within the film, presumably due to slow replenishment of oxygen ions at the interface. Also, the addition of water to organic electrolytes (Table IV) is seen to give increasing growth within the outer films indicated by their decreasing solubility rates. Therefore the transition of mechanism from organic to aqueous electrolytes may be continuous. If so, one might expect to find on films grown in aqueous electrolytes, only a thin outer film containing voids which had not yet filled in. A thin surface film, showing light absorption, has in fact been observed by Young (7) during optical measurements on films formed in dilute H₂SO₄.

Summary

The following phenomena have been observed in the anodic oxidation of tantalum in formic acid electrolytes:

1. The films have many of the general features found by Vermilyea (1) for films formed in other

nonaqueous media, i.e., at the same voltages they are optically thinner and require less coulombs for formation than films formed in dilute aqueous electrolytes. The formation in nonaqueous media is characterized by an efficiency greater than 100%. Also the film consists of two regions, the outer part being more soluble in HF than the inner region.

2. Films formed in formic acid electrolytes have a slightly lower capacity than those formed in dilute solution, and the reciprocal capacity vs. voltage curve shows a break point with a lower reciprocal slope (CV) at voltages above the break point. A maximum in the ESR curve occurs at approximately the same voltage as the break point.

3. The inner and outer films grow at a constant rate provided the formation conditions are not varied.

4. Above a certain voltage the solubility rate of the outer film decreases with increasing formation voltage.

5. If formation in aqueous electrolyte follows formation in a formic acid electrolyte, it is found on dissolving the film that new oxide has been formed above and below the rapidly dissolving part of the film. Also this rapidly dissolving part has increased in weight with an accompanying decrease in solubility rate.

6. Increasing the formation current density increases the solubility rate of the outer film.

7. Increasing the water content of the electrolyte increases the proportion of the inner region of the film and decreases the solubility rate of the outer part of the film.

8. For equivalent weight or optical thickness the outer film has lower capacity than the inner film.

9. The addition of phosphate or phosphite ions to the electrolytes decreases the solubility rate of the outer region of films formed in such electrolytes. The additions also establish conditions under which films grow with uniform voltage increments for unit charge.

Acknowledgment

The work was carried out under contract DRB 715-00124(DGS) from the Canadian Defence Research Board to whom thanks are due for permission to publish. It was under the general direction of Dr. F. J. Burger to whom the author is indebted for consultation, encouragement, and valuable discussions throughout its course.

Manuscript received Jan 17, 1964; revised manuscript received May 5, 1964.

Any discussion of this paper will appear in a Discussion Section to be published in the June 1965 JOURNAL.

REFERENCES

1. D. A. Vermilyea, *Acta. Met.*, **2**, 482 (1954).
2. L. Young, *Proc. Roy. Soc.*, **A244**, 41 (1960).
3. L. Masing, J. E. Orme, and L. Young, *This Journal*, **108**, 428 (1961).
4. R. W. Franklin [see L. Young—Anodic Oxide Films A.P. (1961) p. 71].
5. D. A. Vermilyea, *This Journal*, **110**, 250 (1963).
6. R. A. U. Huddle and R. T. Anderson, *Advances in Catalysis*, **9**, 393.
7. L. Young, "Anodic Oxide Films," pp. 83-86, A. P. (1961).

Dielectric Loss Spectra of Corrosion Films on Zirconium

P. J. Harrop and J. N. Wanklyn

Metallurgy Division, A.E.R.E., Harwell, Berkshire, England

ABSTRACT

A technique has been developed for examining the bulk electrical properties of dry zirconium dioxide films. It has been used to determine the dielectric loss spectra of films formed by steam corrosion, and by anodization of Van Arkel zirconium. The most marked feature is a loss peak found for thermal films grown on pickled surfaces. This does not occur with anodized specimens or electropolished specimens and is postulated to be due to a fluorine-containing dipole. The dipole relaxes with an activation energy of 0.72 ± 0.04 ev. An interpretation of the data suggests a lower limit of concentration of 1×10^{20} fluorine ions per cubic centimeter in films of about 1500Å thickness. Anodic films show low loss curves consistent with near-stoichiometric structure.

Several workers (1-3) have attempted to make electrical measurements on dry oxide films, but they have seldom obtained reproducible results. Consequently, this work began with a study of the effective resistance of various electrode materials on flame polished platinum. A layer of unbaked colloidal graphite was found to give a variable resistance of up to 1000 ohms and was therefore rejected. Evaporated gold-palladium alloy and silver suspension in methyl isobutyl ketone were both found to be satisfactory in this respect, having less than 0.1 ohm resistance, and were tested side by side on oxidized zirconium specimens. Figure 1 shows that they gave the same loss values at all frequencies after 3 days evacuation, the time taken for the silver paint to dry out. Some specimens were measured several weeks later and these also gave the same values.

The main series of measurements reported here were made with either of the latter two electrode materials applied to the oxide face. Measurements on anodic films gave a frequency-independent dielectric constant of 22, in good agreement with wet measurements (4), indicating that significant electrode polarization did not occur.

The dielectric loss of a specimen, $\tan \delta$, is given by $\tan \delta = 1/\omega R_p C_p$, with the usual notation. The variation of loss with temperature or frequency can reveal relaxation peaks and these have been studied ex-

tensively for the case of the alkali halides (5). When they exhibit the shape and behavior of Debye relaxations, they can usually be ascribed to point defect dipoles situated in the bulk material. One such peak has been found here for steam corrosion films on pickled zirconium.

Experimental

Apparatus.—The apparatus used was similar to that used by McMullen and Pryor, who measured the dielectric loss of anodized aluminum (6). Added precautions were the provision of a thermocouple buried in one electrode and a guard ring to prevent surface conduction across glassware. The specimen was examined under 10^{-6} Torr kinetic vacuum.

Electrical measurements were made with a Wayne Kerr Universal Bridge supplied by a Muirhead D890A Decade Oscillator and balanced by a Wayne Kerr Waveform Analyser. The equipment was checked with precision standard resistors and the complete rig was checked by loss measurements over the whole range of frequencies (100 to 20,000 cps $\pm 0.2\%$) on Cd-doped NaCl single crystals. These revealed a peak at 7800 cps, 104°C which shifted to 4600 cps at 94°C in precise agreement with the work of Haven (7).

The temperature was monitored with a chromel-alumel thermocouple, a thermostat cold junction and a Pye Universal Precision Potentiometer. This arrangement was checked at the carbon dioxide sublimation and ice points.

Materials.—Samples were prepared by the oxidation of 1×2 cm annealed Van Arkel zirconium specimens which then had one side scratched clean and silver painted. Electrodes were either evaporated or painted onto the oxide film on the other side, each electrode having an area of a few square millimeters, and the specimen as a whole was gripped between glass surfaces covered with platinum foil. Platinum wires welded to this foil were led out of the rig to the measuring apparatus.

Initial electropolishing was done on previously pickled specimens at $15^\circ \pm 5^\circ\text{C}$ in a continuously stirred solution containing 9 parts by volume of acetic acid to one part of perchloric acid with a current density of 12 amp/dm² for a minimum of 5 min. Pickling was done in 45 parts of concentrated nitric to 5 parts of hydrofluoric acid (48% solution) plus 50 parts of redistilled water. Samples were then briefly rinsed in redistilled water and washed in warm running tap water for half an hour. They were then rinsed in redistilled water and methanol and dried. Variations from this treatment are described in the text. In both cases only visually immaculate surfaces were accepted. Anodizing was done at a few ma cm⁻² in saturated ammonium borate.

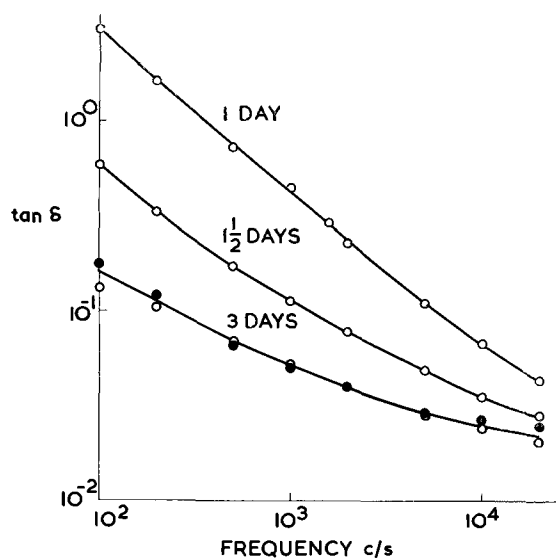


Fig. 1. Loss tangent vs. frequency for two adjacent electrodes on the same sample. O, Silver paint, ●, evaporated AuPd.

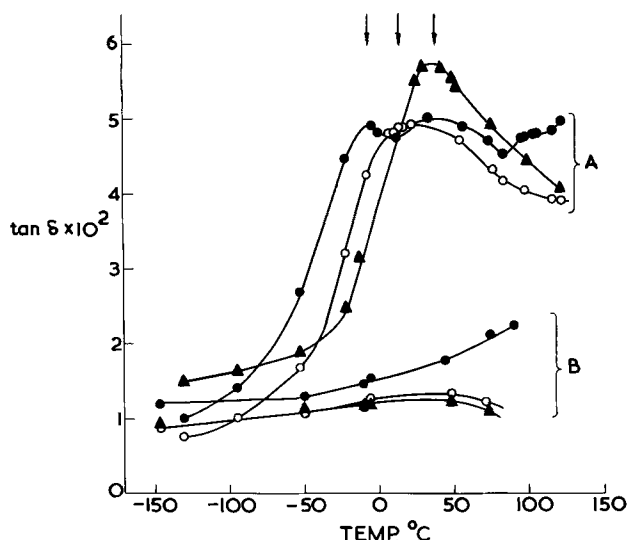


Fig. 2. Loss tangent vs. temperature comparing a typical steam corrosion film on a pickled surface (A), with a typical anodic film (B). ●, 159.2 cps; ○, 1592 cps; ▲, 15,920 cps. The main peak positions are indicated.

Results

It was found that the pressure with which the specimen was gripped did not affect the reproducibility of results, provided it was below a certain maximum, at which the film tended to short out.

All measurements were made with 0.19v r.m.s. applied to the specimen. For a typical sample, doubling this voltage only caused 3% deviation from Ohm's law. Measurements made with both increasing and decreasing temperature showed that the rate of temperature change employed did not cause a significant thermocouple temperature lag.

The "background" loss curves (*i.e.*, those outside any dispersion region) measured between +150° and -150°C could be expected to be due to structure-sensitive extrinsic conductivity and therefore to be not reproducible between specimens but reproducible between different areas of the same specimen. This was found to be so.

A large loss peak, that moved to higher temperatures with increase in frequency, was found with four pickled specimens corroded separately for about 60 min in 500°C, 1 atm steam. It did not alter in height or position over several weeks at room temperature. An electropolished specimen from the same batch corroded for the same time [and, as has recently been shown (8), to a much smaller thickness] did not show the peak, nor did two other electropolished specimens corroded for 5 and 7 hr, respectively, to produce films of comparable thickness. Two anodic films grown to about 2000Å (comparable thickness), one on an electropolished and one on a pickled surface, did not give the above loss peak but merely a low loss curve. Typical examples of the three distinct types of behavior are shown in Fig. 2 and 3. The capacitance variation with temperature for a sample showing a peak is presented in Fig. 4.

The thermal films on pickled surfaces show what is strictly a set of peaks for each frequency, characterized in each case by a main peak at the low temperature end. It is this main peak that will now be analyzed. It can be seen that its shift with frequency, which gives the activation energy of dipole orientation, can be accurately determined. Mean positions for five samples are -6.6°, 13.5°, and 39.6°C for $\omega = 10^3$, 10^4 , and 10^5 rad sec⁻¹, respectively. In contrast, the main peak heights are difficult to estimate due to uncertainty in interpolation of the background losses. It appears that the peaks in tan δ found for the four specimens corroded for about 60 min are all about

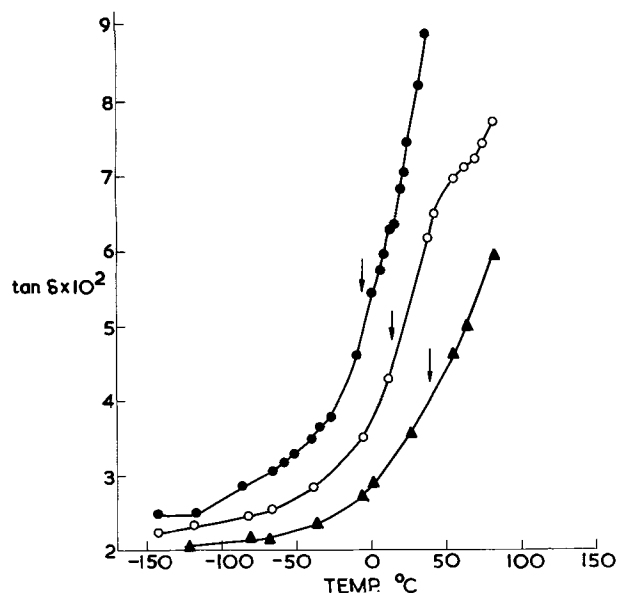


Fig. 3. Loss tangent vs. temperature for a typical steam corrosion film on an electropolished surface. ●, 159.2 cps; ○, 1592 cps; ▲, 15,920 cps. The mean peak positions for similar films on pickled surfaces are indicated.

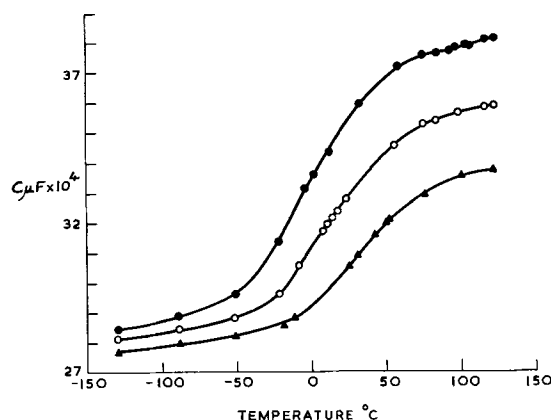


Fig. 4. Capacitance vs. temperature for a typical steam corrosion film on a pickled surface. ●, 159.2 cps; ○, 1592 cps; ▲, 15,920 cps.

0.03 in height, when subtracted from interpolated background losses. The peak heights were the same, within this accuracy, for a pickled specimen corroded for 3 hr, and consequently to twice the mean thickness of a 1 hr specimen (10).

At this stage, the dipole was ascribed to either (a) an element from the pickling treatment which entered the oxide either substitutionally or interstitially, or (b) some property of the highly nonstoichiometric regions in the oxide related to the enhanced thermal oxidation rate of pickled surfaces. Experiments were undertaken to resolve this.

Two electropolished samples were copper-contaminated by dipping in copper sulfate solution. It has been found (8) that such treatment can give accelerated initial corrosion, followed by a measure of long-term inhibition, in a similar way to alloying with copper (9). Consequently, when the samples were placed in 500°C 1-atm steam for 1 hr, their corrosion rate was much greater than for the uncontaminated case, although pickling contamination was absent. Such films did not exhibit the main dielectric loss peak, but this observation was inconclusive because the loss values were found to drift markedly with time. As a further trial of a fast growing film, a clean electropolished specimen corroded at a higher tem-

perature, 600°C, in 1-atm steam for 15 min gave steady loss values and no peak.

To identify the element from the pickling treatment responsible for the loss peak, two electropolished specimens were dipped in dilute hydrofluoric acid and corroded in 500°C 1-atm steam for 1 hr. Although they corroded at a high rate, their loss values were too high for a peak of the anticipated order of magnitude to be observed. One electropolished specimen was therefore dipped for 30 sec in a pickle solution that did not contain the hydrofluoric acid component and corroded in 500°C 1-atm steam for 2 hr. It corroded at a rate similar to that for a clean electropolished surface and did not exhibit a loss peak, despite having a low background loss. It therefore seemed that either the hydrofluoric acid, or possibly the washing treatment, was responsible for the peak.

An electropolished sample was pickled in another solution consisting of equal volumes of 15 weight per cent (w/o) ammonium fluoride aqueous solution (redistilled water) and concentrated nitric acid (sp gr 1.420), washed for one half hour in cold tap water, and corroded in 500°C, 1-atm steam for 1 hr. It exhibited a peak of the same height as that in Fig. 2.

Discussion

The above examination of surfaces prepared in a variety of ways suggests that the loss peak is only present when fluoride is present, although some contribution from the washing treatment may also occur. It therefore seems that the peak is due to substitutional or interstitial fluorine ions in the oxide film, and it is, at first sight, puzzling that the peak height, giving dipole concentration, should not alter when the mean film thickness is doubled.

The explanation could be that the fluorine lies in an outer layer of oxide. However, it is instructive to note that these measurements are, in any case, relatively insensitive to mean oxide thickness, because the thin oxide grains, which grow slowly, shunt the thicker grains. With simple assumptions, the grain growth data of Wanklyn *et al.* (10) can be used to show that these thin grains increase in thickness by a factor of 1.4 when corroded to 3 hr, when the mean thickness is doubled. The corresponding decrease in peak height might not have been detected. Only about one in three grains are "seen," and these represent a thickness of about 2.2 mg/dm² (1500Å).

For a freely orienting dipole, the oscillation frequency ν obeys the relation $\nu = \nu_0 \exp -Q/kT$ where ν_0 is a constant and Q is the activation energy of orientation. In this case, $Q = 0.72 \pm 0.04$ eV, if all possible combinations of the mean positions of the peaks at the 3 frequencies are used. This compares with the energy of motion of an anion vacancy in monoclinic zirconia of 1.45 eV (11), a value supported by direct diffusion measurements on the cubic phase (12). Therefore, as expected, the dipolar orientation energy is less than that of free vacancy conduction.

The dipole could be composed of an interstitial fluorine ion coupled to a substitutional fluorine ion. Such a dipole would tend to occur in the nonstoichiometric oxide only, as an interstitial fluorine ion is difficult to fit into the stoichiometric zirconia lattice. This would explain why anodic films, which can be taken as near-stoichiometric, do not exhibit the peak even when grown on pickled surfaces.

The dielectric loss of a substance is defined by $\tan \delta = \epsilon''/\epsilon'$ where the complex permittivity ϵ^* is expressed by $\epsilon^* = \epsilon' - j\epsilon''$. The contribution to $\tan \delta$ of a dipolar relaxation is now considered.

The dipoles are probably present in low concentration randomly distributed throughout the solid. Their mutual interaction will undoubtedly give rise to 'internal field' effects in the dielectric properties. However, the usual form of Lorentz internal field correction used by some workers (6, 14) is only applicable for point dipoles each of which is localized at a lattice point (13). Extended dipoles, of the kind

postulated here, give rise to smaller internal field effects (15), which depend on the detailed structure of the dipole. In the absence of the necessary detailed knowledge we shall omit internal field effects entirely.

The Debye equations can be applied for the case of a freely orienting dipole (16) to give, in MKS units

$$\tan \delta = \frac{(\epsilon_s - \epsilon_\infty) \omega \tau}{\epsilon_s + \epsilon_\infty \omega^2 \tau^2} = \frac{N \mu^2}{3 \epsilon_0 k T} \left(\frac{\omega \tau}{\epsilon_s + \epsilon_\infty \omega^2 \tau^2} \right)$$

where ϵ_s and ϵ_∞ are the relative dielectric constants away from the relaxation to lower and higher frequencies respectively, τ is the dipolar relaxation time, N is the concentration of dipoles per cubic meter, μ is the dipole moment, and ϵ_0 the dielectric constant of free space.

In this case, $\epsilon_s \simeq \epsilon_\infty^1$ and $\tan \delta$ is a maximum when $\omega \tau = 1$. Thus

$$\tan \delta_{\max} = \frac{N \mu^2}{6 \epsilon_\infty \epsilon_0 k T}$$

The dipole moment can be expressed as $\mu = zea$ where z and a are the effective dipole charge and length, respectively.

Taking the values $\tan \delta_{\max} = 0.03$, $T = 287^\circ\text{K}$, $\epsilon_\infty = 22$, $z = 1$, and $a = 2.7 \text{ \AA}$ results in a value of N of about 7×10^{19} dipoles per cubic centimeter. Since a few of the fluorine ions may not be paired, twice this figure must represent a lower limit of fluorine concentration. If this relates to the slower growing grains, then the relevant oxide thickness is about 1500Å.

An interesting comparison can now be made with the work of Beg and Brown (17). They used a radio-tracer technique to show that pickling left a considerable amount of fluoride on Zircaloy surfaces. When the metal was corroded for 15 min in 500°C, 1 atm steam, no remaining fluoride was detected. If their lower limit of detection was about $0.1 \mu\text{g}/\text{cm}^2$ then less than 3.2×10^{15} fluoride ions per square centimeter remained. This figure, related to a 1500Å film, gives an upper limit of fluoride concentration of about 2×10^{20} ions per cubic centimeter which is just above the dielectric loss figure.

The loss values for anodic films are much lower than for thermal films of comparable thickness. The former therefore constitute more perfect dielectrics and must be more nearly stoichiometric. This supports other spectroscopic evidence, as it has been found that similar anodic films scarcely absorb at all between the ultraviolet eigenabsorption (18), through the optical, to 12μ in the infrared region (19). In contrast, corrosion films absorb at several frequencies (19).

Conclusions

1. Oxide films grown by corrosion of Van Arkel zirconium in 500°C, 1-atm steam apparently contain fluorine ions if the metal has been previously pickled but not if it has been electropolished in acetic/perchloric acid solution. A concentration of about 1×10^{20} fluorine ions per cubic centimeter can be calculated for films of about 1500Å thickness grown on immaculate pickled surfaces. Since only fluorine in dipoles would be detected by this method, and a few fluorine ions may be unpaired, this can be taken as a lower limit of fluorine concentration in such films.

2. For anodic oxide films, grown to about 2000Å on Van Arkel zirconium in saturated ammonium borate at medium current densities, the much lower loss values found indicate that they are near-stoichiometric.

Acknowledgments

We are indebted to Mr. C. F. Britton for help with specimen preparation, to Dr. A. B. Lidiard for considerable help with the theory of dielectric loss and to other colleagues for criticism.

¹ It can be verified that this is true, within the accuracy of the calculation, by appropriate interpolation in Fig. 4.

Manuscript received Nov. 4, 1963; revised manuscript received April 26, 1964.

Any discussion of this paper will appear in a Discussion Section to be published in the June 1965 JOURNAL.

REFERENCES

1. R. D. Misch, "Electrical Resistance Studies of Anodic and Corrosion Oxide Films Formed on Zirconium," Report No. ANL6259, Argonne National Laboratory, May 1961.
2. P. H. G. Draper, Thesis, Metallurgy Department, University of London, 1958.
3. D. H. Bradhurst, Thesis, Metallurgy Department, University of London, 1963.
4. L. Young, "Anodic Oxide Films," p. 262, Academic Press Inc. (1960).
5. G. D. Watkins, *Phys. Rev.*, **113**, 91 (1959).
6. J. J. McMullen and M. J. Pryor, "1st International Congress on Metallic Corrosion," London, April 1961, Butterworths and Co. (1962).
7. Y. Haven, *J. Chem. Phys.*, **21**, 171 (1953).
8. N. J. M. Wilkins, Private communication.
9. J. N. Wanklyn *et al.*, "The Corrosion of Zirconium and Its Alloys by High Temperature Steam. Part I." Report No. AERE R 3655, March 1961.
10. J. N. Wanklyn *et al.*, *This Journal*, **110**, 856 (1963).
11. D. L. Douglass, "Corrosion of Reactor Materials," Conference, Saltzburg, 1962, I.A.E.C., Vienna, 1962, Vol. II.
12. W. D. Kingery, *et al.*, *J. Am. Ceram. Soc.*, **42**, 393 (1960).
13. A. B. Lidiard, Private communication.
14. R. G. Breckenridge, "Imperfections in Nearly Perfect Crystals," W. Shockley Editor, John Wiley and Sons Inc., New York (1952).
15. P. Ninomiya, *J. Phys. Soc. Japan*, **14**, 30 (1959).
16. H. Frohlich, "Theory of Dielectrics," p. 70, Oxford University Press Ltd. (1948).
17. F. Brown, Private communication.
18. R. E. Salomon, W. M. Graven, and G. J. Adams, *J. Chem. Phys.*, **32**, 310 (1960).
19. N. J. M. Wilkins, *Corrosion Science*, **4**, 17 (1964).

Kinetics of Anodic Dissolution of Germanium

P. J. Boddy

Bell Telephone Laboratories, Murray Hill, New Jersey

ABSTRACT

A study has been made of the potential distribution at germanium (100), (110), and (111) surfaces undergoing anodic dissolution. The data for (100) and (110) were shown to be consistent with the dissolution mechanism proposed by Beck and Gerischer. For (111) complications arise because the potential distribution over the surface may be nonuniform. The morphology of extensively etched surfaces has been examined and shown to be generally consistent with the kinetics.

The behavior of a semiconductor (sc) differs markedly from that of a metal in that a considerable portion of any potential difference (p.d.) applied across the sc-aqueous electrolyte interface generally occurs within the space charge region of the electrode. This is in distinct contrast with a metal electrode in contact with a concentrated aqueous electrolyte where practically all of the applied p.d. occurs within the Helmholtz double layer in the absence of a diffusion controlled process in the solution and is frequently of primary kinetic significance for any process involving transfer of charged species across that region. In the case of dilute aqueous solutions, it is necessary to take into account the p.d. across the diffuse part of the double layer in the solution and its influence on the concentration of charged species close to the electrode surface (1).

The sc problem is similar in principle to that of a dilute aqueous solution. For the simplest case of no change in adsorbed species (e.g., ions or oriented dipoles) or in the charge trapped in surface states it has been calculated (2, 3) for moderate space charge p.d. (ψ_s) that the p.d. across the Helmholtz double layer due to free charge on a germanium electrode is a negligibly small fraction of the p.d. across the sc space charge region. In view of this the kinetic significance of the overvoltage at a sc electrode (in the concentrated electrolyte case) must be quite different from that at metal electrodes since most of the potential change occurs across the sc space charge region, not the Helmholtz double layer. Germanium, the most investigated sc electrode, does not behave exactly according to this simple model. It has been concluded on the basis of measurements of interfacial capacity (4, 5) and surface photovoltage (6) that the steady overvoltage at a germanium anode in neutral sulfate solutions is distributed between the sc space charge and the Helmholtz double layer. No evidence of changes in the occupancy of fast surface states

sufficient to explain the observed potential change (ΔV_H) across the Helmholtz double layer is found in the experiments. Slow surface states in the surface physics sense are considered unlikely due to the absence of thick oxide films (7), hence ΔV_H has been tentatively ascribed to changes in the density of oriented dipoles adsorbed at the interface (5).

Since the detailed separation of the overvoltage can now be made it was considered of interest to re-examine the anodic dissolution of germanium to determine the relative significance of the sc space charge and Helmholtz double layer p.d.'s to the kinetics. The data suggest that the mechanism for anodic dissolution of germanium (100) proposed by Beck and Gerischer (8) (B and G) is correct and that (110) dissolution proceeds by a similar mechanism at low c.d. The (111) exhibits behavior that cannot be simply interpreted, but is believed to be due to the complexity of the nucleation process or to complications arising because of the detailed morphology of the dissolving surface.

Experimental

Electrodes were single crystal n- or p-type germanium polyhedra with all faces of each particular electrode oriented to the same plane, either (100), (110), or (111). Electrical connection was made by means of a soldered copper wire protected by a wax-filled glass tube. The solution was M/10 K_2SO_4 , phosphate buffered to pH 7.4, gettered with germanium crushed *in situ*. The electrodes were polished in CP4 and then partially immersed in the solution and anodized at ca. $400 \mu a cm^{-2}$ for 15 min before measurements were commenced. The solution contacted only germanium.

The experiments were conducted in the dark at $25^\circ C$ in an atmosphere of purified helium, which was also used to deoxygenate the solution prior to use. A separate cathode compartment with a diffusion barrier was used since the electrode potential of germanium

at low anodic current densities is sensitive to dissolved hydrogen (9). The electrode potential was determined at high impedance about 10 min after the imposition of a constant current. The interfacial capacity was calculated from the voltage response to a short duration (1-5 μ sec) current pulse (10). The true surface area was deduced from the minimum value of the interfacial capacity (4).

Results

Typical plots of overvoltage *vs.* current density for the three low index planes of p-type electrodes are shown in Fig. 1. The curves for n-type were very similar. The tendency to saturation at the highest current densities on n-type was slight ($\sim 400 \mu\text{A cm}^{-2}$) since the electrodes were close to intrinsic. A capacity *vs.* electrode potential curve taken simultaneously with some of the data in Fig. 1 is shown in Fig. 2. By analysis of the capacity, ψ_s may be deduced (11). The relationship previously used by us (5) and similar to that given by Green (12)

$$\Delta V_E = \Delta V_H - \Delta \psi_s \quad [1]$$

where ΔV_E is the change in electrode potential, is assumed to apply since changes in potential across the diffuse layer in the solution should be negligible (the capacity of the sc space charge is two to three orders of magnitude smaller than that of the solution space charge). We have previously discussed this equation in more detail (19). In this way each curve in Fig. 1 can be separated into two parts, overvoltage across the sc space charge (η_s) and overvoltage across the Helmholtz double layer (η_H) *vs.* current density. This is shown in Fig. 3, 4, and 5 for the three faces of n- and p-type electrodes.

The overvoltages are defined as follows.

$$\eta_s = \psi_s - o\psi_s \quad [2]$$

where $o\psi_s$ is the value at the reversible potential (which is not observed in practice) and

$$(\eta_H + \text{constant}) - (\eta_s + \text{constant}) = V_E \quad [3]$$

where V_E is the electrode potential *vs.* SCE. Since $o\psi_s$ is not known, $(\eta_s + \text{constant})$ is taken arbitrarily as the measured value of $\psi_s - (RT/F)\ln\lambda$, $\lambda = p/n_i$, p being the hole concentration in the sample and n_i the intrinsic electron concentration. The term $(\eta_H + \text{constant})$ is chosen to numerically balance Eq. [3], *i.e.*, $(\eta_H + \text{constant}) = V_E + \psi_s - (RT/F)\ln\lambda$ in Fig. 3-5. It should be noted that only changes in p.d. are involved in the final analysis.

Discussion

(100) Surface.—A proposed mechanism (8) for the anodic dissolution of (100) is shown in Fig. 6. The rate-determining process is assumed to be the breaking of a surface bond (step 3) after a hole has been

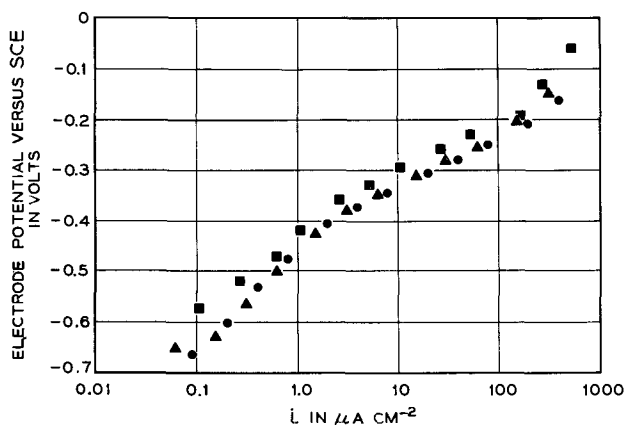


Fig. 1. Tafel curves for (100) (●) 35.6 ohm-cm, (110) (▲) 41.3 ohm-cm, and (111) (■) 38.65 ohm-cm, all p-type.

trapped in it (step 2) by coulombic interaction with the negative end of the dipole created by ionization of a surface hydroxyl group (step 1). Thus it may be seen from steps 2 and 3 that the rate-determining process is first order in the surface concentration of holes.

Considering the general case of a positively charged surface species which is subsequently transferred across the Helmholtz double layer into solution [as-

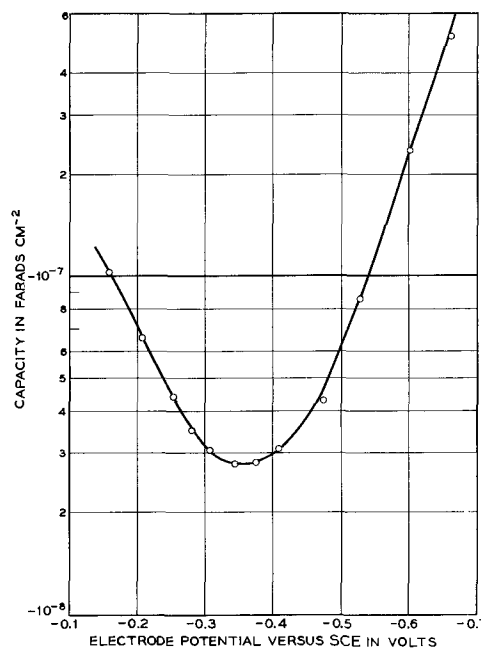


Fig. 2. Capacity taken simultaneously with Tafel curve in Fig. 1 for (100) electrode.

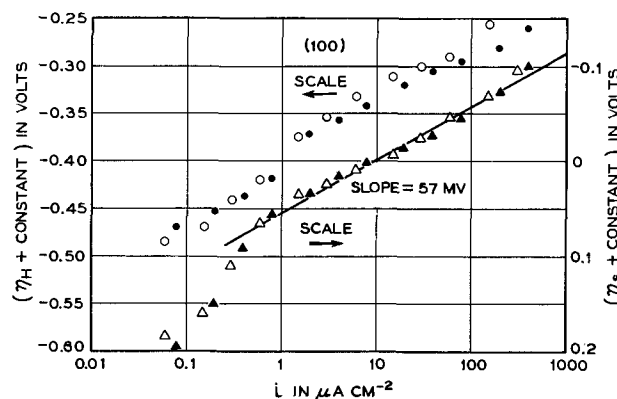


Fig. 3. Separation of overvoltage for (100) into components across Helmholtz region (○,●) and semiconductor space charge (△,▲). Open points p-type, filled points n-type 34.05 ohm-cm.

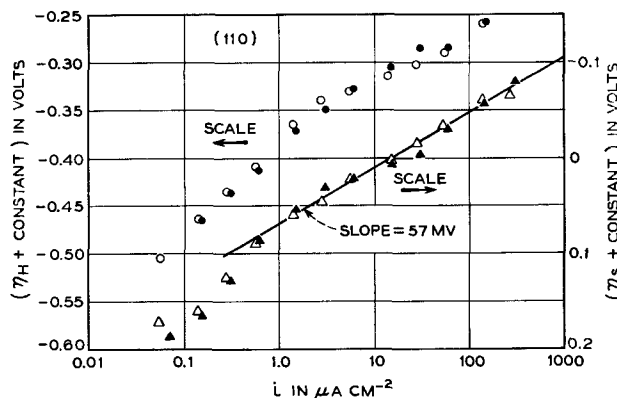


Fig. 4. Same as Fig. 3 but for (110) and n-type 28.7 ohm-cm

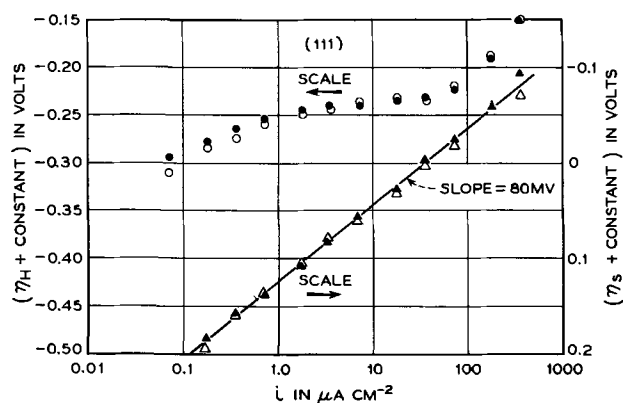


Fig. 5. Same as Fig. 3 but for (111) and n-type 38.8 ohm-cm

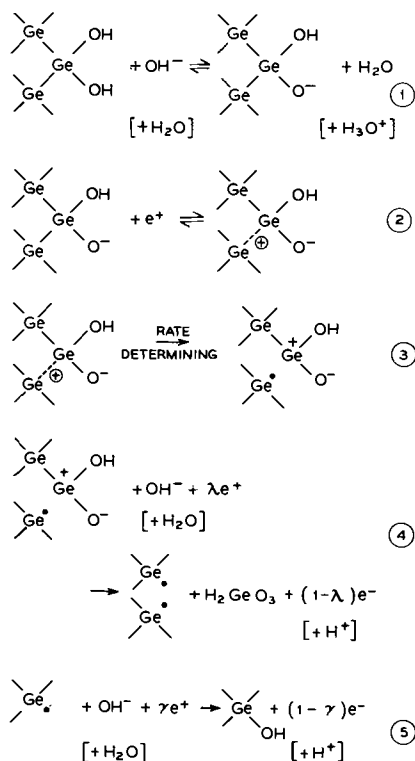
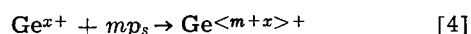
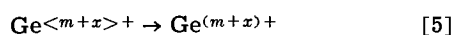


Fig. 6. Beck and Gerischer's mechanism for the anodic dissolution of germanium in alkaline solutions. Alternatives for acid solution in parentheses.

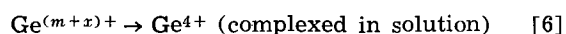
suming, as indicated by a large body of experimental evidence (13, 14), that holes are the carriers involved in the formation of the surface species], we may write



where Ge^{x+} is a surface atom in the $(+x)$ oxidation state, p_s is a hole close to the surface, and $\text{Ge}^{<m+x>}$ is the species on the RHS of step 2 in Fig. 6, followed by



and



where $\text{Ge}^{(m+x)+}$ is the species on the RHS of step 3 in Fig. 6. From Eq. [4]

$$[\text{Ge}^{<m+x>}] \propto [p_s]^m \quad (7)$$

It is assumed that in step 5 of Fig. 6 the steady state lies very far to the right and also that $\theta_{\text{Ge}^{<m+x>}}$ and

$\theta_{\text{Ge}^{(m+x)+}}$ are small, hence $\theta_{\text{Ge}^{x+}} \approx \text{constant}$.

From Eq. [4]

$$v_4 - v_{-4} = k_4 \theta_{\text{Ge}^{x+}} [p_s]^m - k_{-4} \theta_{\text{Ge}^{<m+x>}} \quad (8)$$

and since

$$[p_s] = [p_o] \exp\{-F\psi_s/RT\} \quad (9)$$

where $[p_o]$ is the hole concentration in the bulk, then combining k_4 and $\theta_{\text{Ge}^{x+}}$ into k'_4 we have

$$v_4 - v_{-4} = k'_4 [o p_s]^m \exp\{-m\eta_s F/RT\} - k_{-4} \theta_{\text{Ge}^{<m+x>}} \quad (10)$$

From Eq. [5]

$$v_5 - v_{-5} = k_5 \theta_{\text{Ge}^{<m+x>}} - k_{-5} \theta_{\text{Ge}^{(m+x)+}} \quad (11)$$

From Eq. [6] neglecting the reverse reaction when $\eta_H > 2RT/F$

$$v_6 = k_6 \theta_{\text{Ge}^{(m+x)+}} \exp\{\alpha(4-m-x)\eta_H F/RT\} \quad (12)$$

In the steady state

$$v_4 - v_{-4} = v_5 - v_{-5} = v_6 = i/4F \quad (13)$$

Eliminating $\theta_{\text{Ge}^{<m+x>}}$ and $\theta_{\text{Ge}^{(m+x)+}}$ we obtain

$$\begin{aligned}
 i = (4Fk'_4 [o p_s]^m \exp\{-m\eta_s F/RT\}) & \\
 (k_5 k_6 \exp\{\alpha(4-m-x)\eta_H F/RT\}) \dots & \\
 \dots (k_5 k_6 \exp\{\alpha(4-m-x)\eta_H F/RT\}) & \\
 + k_{-4} [k_{-5} + k_6 \exp\{\alpha(4-m-x)\eta_H F/RT\}]^{-1} & \quad (14)
 \end{aligned}$$

Since [5] is assumed to be slow we may put

$$k_6 \exp\{\alpha(4-m-x)\eta_H F/RT\} \gg k_{-5} \quad (15)$$

and also

$$k_{-4} \gg k_5 \quad (16)$$

whence Eq. [14] simplifies to

$$i = 4Fk'_4 k_{-4}^{-1} k_5 [o p_s]^m \exp\{-m\eta_s F/RT\} \quad (17)$$

and

$$d\eta_s/d \log i = -2.303 RT/mF \quad (18)$$

Equation [17] indicates that the rate is dependent on the space charge overpotential and independent of the Helmholtz overpotential. This arises because we have assumed that the rate-determining step (Eq. [5]) takes place outside the region where the Helmholtz overpotential occurs.

On a germanium (100) surface the atoms are already in the $(+2)$ oxidation state, *i.e.*, $x = +2$. The possible choices of values for m then become zero, one, or two. The observation that $(d\eta_s/d \log i)_{(100)}$ in Fig. 3 is close to -59 mv implies that $m = 1$ in Eq. [18] and is consistent with B and G's mechanism, but does not prove it. It is clear that there is also a variation in η_H of approximately equal magnitude to the variation in η_s . More complex models could possibly be constructed in which changes in η_H assumed kinetic significance. No analysis of this kind will be made here.

(110) Surface.—From Fig. 3 and 4 it is clear that the data for the (110) dissolution are very similar to those for (100). The atoms on the (110) surface are triply bonded to the lattice (*i.e.*, $x = +1$) and hence should not undergo dissolution as readily as the doubly bonded atoms on the (100) surface. This difference is illustrated two-dimensionally in Fig. 7. However, the (110) surface may readily be nucleated to undergo dissolution through the removal of doubly bonded atoms simply by breaking one bond between surface atoms. The atoms at each end of this broken bond are only doubly bonded to the lattice (*i.e.*, $x = +2$) and may be removed by B and G's mechanism. The process can propagate along a given row of atoms entirely across the crystal. Provided the rate of supply of such nuclei is sufficient that their concentration is not noticeably decreased by the current flow, and that dissolution takes place only through these doubly

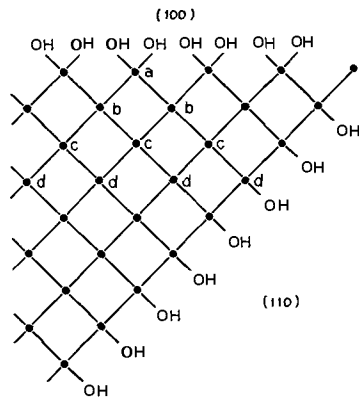


Fig. 7. Two-dimensional representation of (100) and (110) surfaces

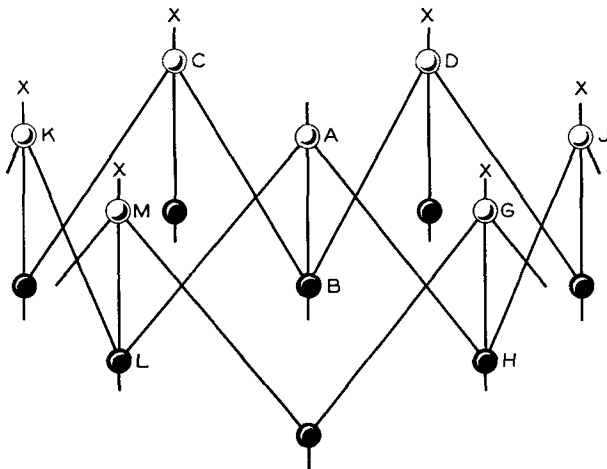


Fig. 8. Perspective view of part of a (111) surface. Atoms of one color are in one plane.

bonded atoms, then the (110) should exhibit similar kinetics to the (100). The nucleation process may occur by thermal generation of broken bonds in the surface plane, or by intersection of vacancies or appropriate impurity atoms in the surface plane. Differences between Tafel slopes for (100) and (110) have been observed at higher current densities (16, 17) and in other aqueous solutions (18).

(111) Surface.—The bonding on the (111) surface is shown in Fig. 8, and as before we will base our argument on the assumption of atomically perfect surfaces.

The mechanism of dissolution for (111) is not established. A possible scheme involves nucleation by breaking one bond between a surface and subsurface atom, or alternatively a dislocation may intersect the surface. The surface atom is now doubly bonded to the lattice and may be removed by B and G's mechanism. This constitutes the initial step in the formation of an etch pit, and the atoms along the sides of this pit are essentially in (110) orientation. Removal of one side wall can be nucleated by the breaking of any bond made by any of the three atoms in that wall to another germanium atom.

It might be expected if the rate-determining step were nucleation of the (110) oriented atoms that kinetics similar to (100) and (110) faces would be observed. The data in Fig. 5 show $(d\eta_s/d \log i)_{(111)}$ to be about 80 mv and hence seen to imply (from Eq. [13]) that the reaction is of fractional order in the surface hole concentration.

Dewald has suggested reasons for apparent fractional order hole kinetics. The dissolution reaction may take place through the participation of surface states (i.e., localized holes) distributed exponentially in the energy (3), or alternatively discrete bound states for

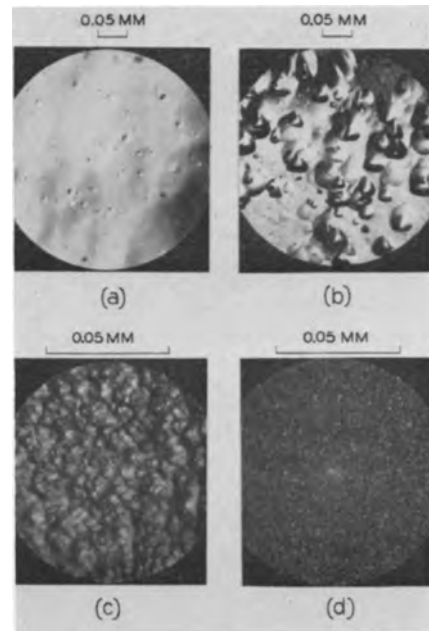


Fig. 9. (a) (100) surface after CP4 etch; (b) (111) surface after 1 ma cm^{-2} for 24 hr; (c) p-(100) surface, same treatment; (d) n-(100) surface, same treatment (with illumination).

carriers near the surface may occur if the field in the germanium space charge region is sufficiently high (20). The first suggestion requires that we postulate surface states at a (111) surface but not at (100) and (110) surfaces in approximately the same energy range. Although this is not impossible, our measurements of capacity give no indication of fast surface states on any face in this energy region. The second explanation is ruled out by the fact that our data are obtained in the region of small bending of the bands (i.e., $+200 \text{ mv} > \psi_s > -100 \text{ mv}$).

A much more likely explanation, since the dissolution takes place with the formation of etch pits with sides of orientation different from (111) (as we will discuss later), is that the nonuniformity of the potential distribution over the surface precludes any exact analysis of these data.

Morphology of Anodized Germanium Surfaces

In a further series of experiments we have examined the nature of the surfaces produced after extensive anodic dissolution at constant current in neutral K_2SO_4 solution. The behavior of the three surfaces is quite distinctly different, but for any one face both n- and p-type behave similarly indicating that the observed effects are actually due to orientation. Figure 9(a) shows the typical appearance of a CP4 etched surface before anodizing. Currents of about 1 ma cm^{-2} were passed for about 24 hr, after which the surfaces were examined by optical microscopy. Results are shown in Fig. 9(b), (c), and (d) for p-(111), p-(100), and n-(100) surfaces. The (110) is not illustrated since no features were developed. On p- and n-type (111) surfaces distorted triangular etch pits were observed. On p-type (100) hillocks formed, and on n-type (100) we saw a finer structure that could not be resolved.

The probable role of dislocations is illustrated in Fig. 10. Figures 10(a) and 10(b) show areas of a p-type (111) surface after CP4 etching and the same area after anodizing. It is clear that dissolution has occurred primarily from around pits, presumably marking emerging dislocations, on the original CP4 etched surface.

The p-type (100) surface had fewer and smaller pits when CP4 etched, but in one case we located an area where the lines of pits shown in Fig. 10(c) were observed. This pattern was sufficiently distinctive that

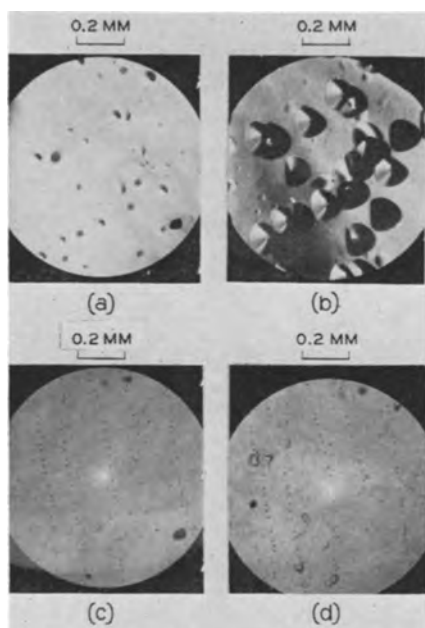


Fig. 10. (a) Area of CP4 etched (111) surface; (b) same area after anodic etching; (c) area of CP4 etched (100) surface; (d) same area after same anodic etching as in (b).

it could be located after anodizing. This (100) crystal was anodized at the same current density for the same length of time as the (111) surface in Fig. 10(b). The result is shown in Fig. 10(d). There appears to have been no preferential dissolution from the etch pits in this case. The absence of structure similar to Fig. 9(c) is due to the lower magnification and the different illumination, which was optimized to reveal the pits.

(110) Surface.—Anodic etching of this surface produced no obvious features on either n- or p-type electrodes. The surfaces retained the same polished but somewhat undulating appearance produced by the original CP4 etch. This fact is consistent with both the mechanism of anodic dissolution previously discussed and with the surface geometry. Since the number of atoms dissolved per nucleation is large [rather than a few localized at the site of the nucleation as on (111)] etch pits would not be expected. Also any blocking effect (discussed in the next section) due to slow dissolving impurities would not propagate through the lattice as on (100), since each surface atom is bonded to only one atom in the plane below (see Fig. 7) and neither of the atoms in the surface plane bonded to a blocked atom is itself blocked.

(100) Surface.—Prolonged anodizing of a (100) surface (1 ma cm⁻² for 24 hr) resulted in a surface with a matte appearance which under high magnification has the structure shown in Fig. 9(c). The features are square pyramidal etch hillocks, the largest being $\sim 5\mu$ on a side and oriented with respect to the crystal as shown in Fig. 11. If only low index planes are involved, the sides of the hillock may be of (110) orientation. The sides cannot be (111) since then the hillocks would be rotated 45° about an axis perpendicular to the plane of the paper.

The formation of hillocks can be understood if it is postulated that there are impurity atoms in the lattice which undergo dissolution considerably less rapidly than germanium. Consider that atom marked (a) in the surface (100) plane of Fig. 7. If it remains behind after the rest of that plane has dissolved, it will inhibit the dissolution of atoms (b) in the second plane since they are now triply bonded to the lattice (*i.e.*, +1 oxidation state). The process is repeated in the next plane where the dissolution of four atoms is blocked. [Since Fig. 7 is a two-dimensional representation only three are shown. The center (c) atom

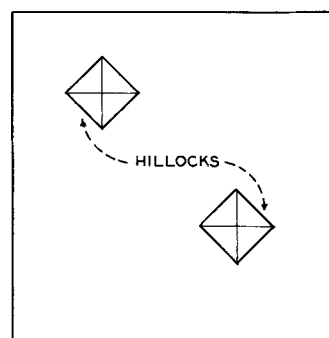


Fig. 11. Orientation of hillocks on the (100) surface. The large square represents one face of a cube having all (100) faces.

is actually two atoms superimposed. Similarly the two center (d) atoms are actually two atoms superimposed, etc.] In this way a square pyramid with (111) sides is generated as the blocking effect propagates through the lattice. Eventually the sides of all such pyramids intersect, and no (100) surface remains. On the line between the apex and the corners of these pyramids the atoms are in (110) orientation. Further dissolution of the crystal (which must occur due to the constant current imposed) is much more likely to do so from these (110) regions than from the (111) faces for the kinetic reasons described previously. Consequently the (110) faces appear at the expense of the (111) and the pyramid eventually attains the observed orientation. Figure 9(c) represents a case where the dissolution was sufficiently prolonged that the surface was entirely covered with hillocks and no (100) surface was left exposed.

The formation of such hillocks on a p-type sample was found to be reproducible. With an n-type sample at the same current density the behavior was also reproducible but different from p-type. In this case the surface was hazy rather than matte and the microscope revealed a fine granularity which was not resolved at the highest available magnification [Fig. 9(d)]. A possible explanation is that a greater density of hillocks formed before their sides intersected and converted the surface to a convoluted (110). Since the hillocks would intersect sooner they would be smaller.

We may make a rough estimate of the reasonableness of our postulate that the hillocks are caused by impurity atoms. Referring to Fig. 9(c), since the largest hillocks are about 5μ on a side at the base and assuming (110) orientation (*i.e.*, angle between opposite faces at the apex equals 90°) the maximum height is $\sim 2.5\mu$. Assuming that the peaks of all the observed pyramids occur within this depth and making an estimate of the average dimensions at the base as 1μ we then calculate a density of impurity atoms (at the peaks) of 4×10^{11} cm⁻³. If this mechanism is correct it implies that we have detected by electrochemical means some impurity present at approximately one part in 10^{11} .

(111) Surface.—The (111) surfaces [Fig. 9(b)] exhibited distorted triangular pits, all oriented in the same direction as shown in Fig. 12.

The orientation of the walls of the pits has not been determined, but they are definitely not (100) as had been previously suggested (21) since in this case the pits would be rotated by 60° from their observed orientation. If the vertical nucleation were rate determining, then the pits would tend to be flat bottomed or very shallow. Some features of this type do occur in Fig. 9(b) and may be due to this cause or possibly to dislocations which intersected the original surface but which have terminated at a relatively small depth into the crystal. The rounded shape of the pits could be due to inhibition of dissolution in the corners by concentration polarization. This causes the solution to become more acid in these regions, and

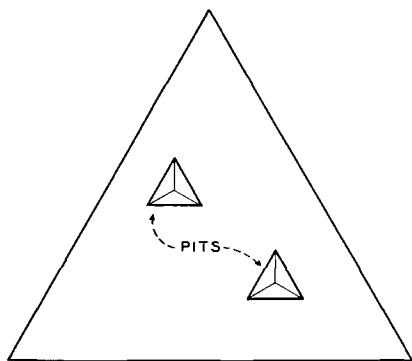


Fig. 12. Orientation of pits on the (111) surface. The large triangle represents one face of a regular tetrahedron having all (111) faces.

as a consequence the p.d. across the Helmholtz region will change in such a direction as to include an increased fraction of the total anodic overvoltage (22, 5), thus reducing the space charge overvoltage and hence the rate of dissolution.

Many of the pits appear to have sides of different slope. This may be due to the dislocation line being at some angle other than normal to the surface of the crystal (e.g., 60° dislocations) assuming that the three walls grow equally rapidly from the nucleation point.

Conclusions from Anodic Etching Experiments

The effect of the morphology of the surfaces on these and other measurements we have made is as follows. For the (111) surface in the early stages of dissolution the pits are quite small so that we are very largely dealing with a macroscopic (111). Consequently measurements of interfacial capacity refer principally to the (111) so that our previous conclusions based on capacity of this surface still hold. The measurement of overvoltage, as pointed out above, is likely to be incorrect since the potential measurements refer to (111) while dissolution takes place from the sides of the pits [possibly (110)], but may in any case be subject to concentration polarization within the pits.

Since the (110) surface does not develop any obvious features it is assumed that our measurements on (110) oriented crystals are correct.

On the (100) it is clear that after extensive anodizing we are dealing with a convoluted surface, possibly (110). In fact as we have observed both in capacity measurements and in dissolution kinetics the (100) and (110) oriented crystals behave similarly. This could be due to the fact that even on a sample which has been CP4 etched and then only mildly anodized the surface consists of microscopic (110) facets. The results on (100) may be open to the question as whether they are truly representative of a (100) surface or are affected by (110) faceting. However, some of our earlier measurements on mildly anodized surfaces (4, 6) indicate quite low values (~ 1.3) for the roughness factor. This suggests that under these circumstances faceting is not a problem.

Summary

The kinetics of anodic dissolution of germanium (100) have been shown to be consistent with Beck and Gerischer's mechanism. The (110) surface behaved similarly to the (100) at low c.d. The (111) sur-

face showed more complex behavior which was ascribed to the requirements of a nucleation process or to nonuniform distribution of potential. The morphology of anodized surfaces has been discussed with respect to the dissolution kinetics.

Acknowledgment

It is a pleasure to acknowledge continuing cooperation and advice from Dr. W. H. Brattain. The author is also indebted to Dr. W. W. Harvey of the Kennecott Copper Corporation for discussion of his results on anodic etching of germanium prior to publication, to Dr. P. C. Milner for discussion of electrode kinetics, and to Mr. W. J. Sundburg for technical assistance.

Manuscript received Nov. 20, 1963; revised manuscript received April 16, 1964. This paper was presented at the Pittsburgh Meeting, April 15-18, 1963.

Any discussion of this paper will appear in a Discussion Section to be published in the June 1965 JOURNAL.

REFERENCES

1. A. N. Frumkin, *Z. physik. Chem.*, **164**, 121 (1933).
2. M. Green in "Modern Aspects of Electrochemistry," J. O'M. Bockris, Editor, Butterworths Scientific Publications, London (1959).
3. J. F. Dewald in "Semiconductors," N. B. Hannay, Editor, Reinhold Publishing Co., New York (1959).
4. W. H. Brattain and P. J. Boddy, *This Journal*, **109**, 574 (1962).
5. P. J. Boddy and W. H. Brattain, *ibid.*, **110**, 570 (1963).
6. P. J. Boddy and W. H. Brattain, *Ann. N. Y. Acad. Sci.*, **101**, 683 (1963).
7. M. Lasser, C. Wysocki, and B. Bernstein in "Semiconductor Surface Physics," R. H. Kingston, Editor, University of Pennsylvania Press (1957).
8. F. Beck and H. Gerischer, *Z. Elektrochem.*, **63**, 500 (1959).
9. (a) W. W. Harvey, "Quarterly Progress Report Solid-State Research," Lincoln Laboratory, Lexington, Mass. (November 1958); (b) P. J. Boddy and W. H. Brattain, Unpublished results.
10. P. J. Hillson and E. K. Rideal, *Proc. Roy. Soc.*, **199A**, 225 (1949).
11. C. G. B. Garrett and W. H. Brattain, *Phys. Rev.*, **99**, 376 (1955).
12. M. Green, *J. Chem. Phys.*, **31**, 200 (1959).
13. W. H. Brattain and C. G. B. Garrett, *Bell System Tech. J.*, **34**, 129 (1955).
14. Yu. V. Pleskov, *Doklady Akad. Nauk S.S.S.R.*, **126**, 111 (1959).
15. B. Lovrecek and J. O'M. Bockris, *J. Phys. Chem.*, **63**, 1368 (1959).
16. W. Mehl, reported in "Advances in Electrochemistry and Electrochemical Engineering," P. Delahay, Editor, p. 184, Interscience Publishers, New York (1961).
17. J. A. Harrison and H. Gerischer, *Z. Elektrochem.*, **66**, 762 (1962).
18. P. J. Boddy and W. H. Brattain, Extended Abstracts of the Theoretical Division of the Electrochemical Society, **1**, 16 (1963).
19. W. H. Brattain and P. J. Boddy, *Proc. Nat. Acad. Sci.*, **48**, 2005 (1962).
20. J. F. Dewald, *Ann. N. Y. Acad. Sci.*, **101**, 872 (1963).
21. H. Gerischer in "Advances in Electrochemistry and Electrochemical Engineering," P. Delahay, Editor, Interscience Publishers, New York (1961).
22. M. Hoffman-Perez and H. Gerischer, *Z. Elektrochem.*, **65**, 771 (1961).

Preparation of InAs-InSb Alloys

J. C. Woolley¹ and J. Warner²

Department of Physics, University of Nottingham, Nottingham, England

ABSTRACT

The preparation of solid samples of InAs-InSb alloys suitable for optical transmission and electrical measurements is considered. Cross sectional slices of ingots produced by slow directional freezing and slow zone recrystallization have been investigated by x-ray powder photograph techniques, and results are given for the variation of composition with position along ingot and for homogeneity of the slice. Annealed powder samples have been used to check the previous data for the variation of lattice parameter with composition. Specimens have also been observed by photomicrograph methods and by use of an electron probe microanalyzer. The x-ray, photomicrograph, and microanalyzer data are compared for various samples with different degrees of homogeneity.

Very little information is so far available on InAs-InSb alloys. It has been shown that single phase solid solution can be obtained at all compositions (1), but compressed powder specimens need to be annealed at temperatures very close to the solidus curve for periods of six months or more before such conditions are approached. Similar annealing of solid samples needs very much longer times. The data obtained by annealing compressed powders gave the variation of lattice parameter with composition and the solidus curve shown in Fig. 1 and 2. The liquidus curve in Fig. 2 was obtained by Shih and Peretti (2) using normal cooling methods. Here the preparation of samples of InAs-InSb alloys in solid form suitable for optical and electrical work is discussed. The investigation of the semiconductor parameters of the alloys is discussed elsewhere (3).

Methods of Preparation of Solid Specimens

Two methods of preparation have been considered, viz., (a) slow directional freezing, and (b) slow zone recrystallization of suitable ingots. All of the ingots were produced by melting together appropriate amounts of high purity InAs and InSb. Both of the compounds were from zone refined ingots to give good purity and both were n type with approximate carrier concentrations of $2 \times 10^{16}/\text{cm}^3$ for InAs and $1.5 \times 10^{16}/\text{cm}^3$ for InSb.

Preparation by powder annealing.—In the case of both the directionally frozen and the zone recrystal-

¹ Present address: Physics Department, University of Ottawa, Ottawa 2, Canada.

² Present address: R.R.E., Great Malvern, England.

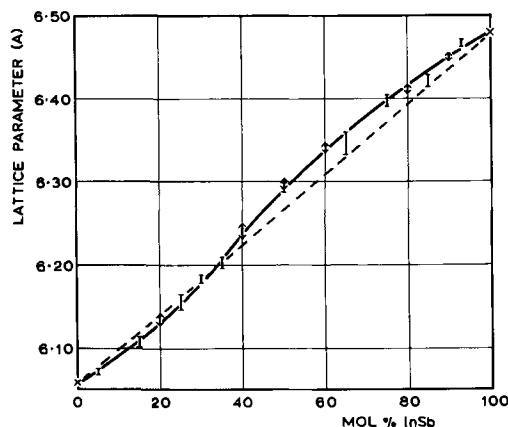


Fig. 1. Variation of lattice parameter with composition for InAs-InSb alloys. | Woolley and Smith (1), \circ present work.

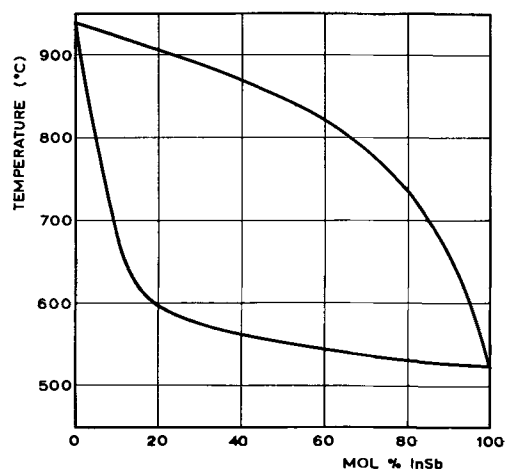


Fig. 2. Phase diagram of InAs-InSb system. Liquidus curve, Shih and Peretti (2); solidus curve, Woolley and Smith (1).

lized ingots, the composition of any cross sectional slice was to be determined by finding the lattice parameter and using the data in Fig. 1 to give the corresponding composition. Therefore, as some powdered samples were to be used in the optical work (to be published elsewhere), these were used to check the data of Fig. 1. Small samples were made by melting together under vacuum appropriate amounts of the two compounds, quenching in water, and coarsely powdering the resultant ingots. (Coarse powdering was required, since a further powdering had to be carried out in the equilibrium condition to give new surfaces necessary for the optical diffuse reflection measurements.) The powders were then compressed and sealed under vacuum as described previously (1) and annealed for some six months at closely controlled temperatures chosen to be 10° - 15°C below the relevant solidus temperature as given in Fig. 2. Even after this time of annealing, the powders were not in good equilibrium condition, the higher order x-ray reflections being blurred. Nevertheless values of lattice parameter accurate to $\pm 0.007\text{\AA}$ could be obtained, and these are shown in Fig. 1 together with the previous results for which the lattice parameter determination was less accurate. The agreement between the two sets of data is good, confirming the results of Fig. 1 and also therefore the solidus data in Fig. 2 obtained by the use of lattice parameter values.

Preparation by slow directional freezing.—In the case of GaSb-InSb and GaAs-InAs alloys, it has been found (4) that homogeneous polycrystalline samples of the alloys can be obtained by a slow directional

freezing of an ingot some 15-20 cm in length. In these cases, ingots cooled in a temperature gradient of the order $10^{\circ}\text{C}/\text{cm}$ and at a rate of $5^{\circ}\text{C}/\text{day}$ were found to be reasonably homogeneous over their whole length. This method of preparation is very convenient for the initial investigation of the semiconductor properties of an alloy system in that the variation of the composition of cross sectional slices with length gives a wide range of sample composition and hence the properties across the whole composition range can be investigated using, at the most, two or three ingots of different mean composition. It was decided therefore to try a similar method of preparation for the InAs-InSb alloys.

The ingots used were of an equimolar mean composition, had a mass of approximately 40g, and were 15-20 cm long. Initially a furnace with a temperature gradient of $10^{\circ}\text{C}/\text{cm}$ over about 20 cm was used and the temperature controlled by a switched control unit, so that the time required to completely freeze the ingot was approximately 2-3 months. In an attempt to improve the homogeneity of the material, a second ingot was cooled in the same furnace at $5^{\circ}\text{C}/\text{day}$, while a third similar ingot was cooled in a furnace having a temperature gradient of $7^{\circ}\text{C}/\text{cm}$ and controlled by a continuous control unit so that the short term temperature fluctuations at 600°C were less than $\pm 0.2^{\circ}\text{C}$. The rate of cooling in this last case was $4^{\circ}\text{C}/\text{day}$ and the freezing process required approximately 6 months to complete. The variation of composition of a cross sectional slice with distance along the ingot for the case of the third ingot is shown in Fig. 3. It was found that each end of the ingot was in good single phase condition, the Cu- $K\alpha$ doublet being well resolved in the x-ray photographs, and that the composition varied from 3 to 12 mole % InSb at one end and 88 to 98 mole % InSb at the other. In between these regions, however, there was some 3 cm of the ingot where there was a very rapid change in composition with position and where the material was not in an equilibrium condition, being two phase with each phase showing considerable broadening of the high angle x-ray reflections. The corresponding spread in composition is indicated by the vertical lines in Fig. 3.

Comparison of the three ingots showed that the third was the best of the three in that the single phase regions of this ingot were more homogeneous than for the previous ones, and at each end the composition range of the single phase region was a few mole per cent greater. In addition, electrical measurements showed that single phase samples from the third ingot had lower carrier concentrations and higher mobility values. These improvements can be attributed to the use of a slower movement of the freezing surface and to the better control of the furnace temperature. From a knowledge of the variation of temperature profile of the furnace in the temperature range concerned, the composition variation along the ingot in Fig. 3 and

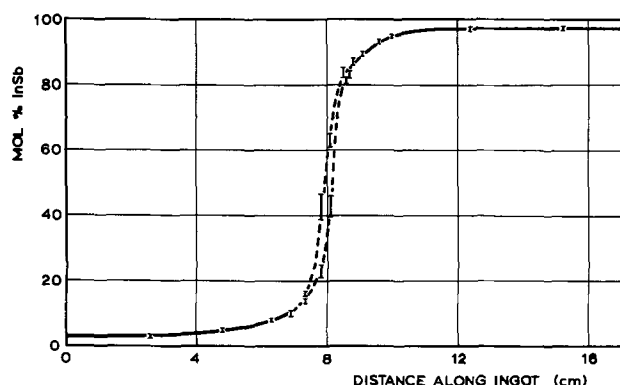


Fig. 3. Variation of composition of cross sectional slice as a function of position in a directionally frozen ingot (DF3).

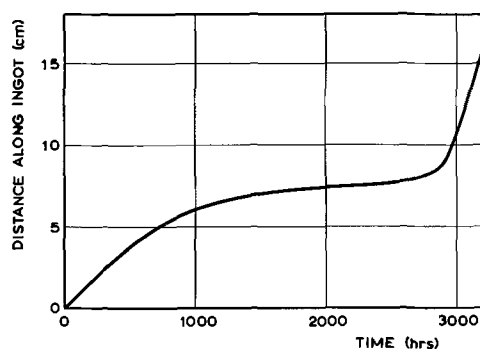


Fig. 4. Position of freezing surface as a function of time in a directionally frozen ingot (DF3).

the solidus curve of Fig. 2, the movement of the freezing surface with time can be calculated. This curve is shown in Fig. 4. This is only approximate in the two phase region where an average composition must be assumed. In the ranges where single phase material was obtained, it is seen that the rates of movement of the freezing surface are $0.2\text{ cm}/\text{day}$ at the beginning of the ingot and $0.65\text{ cm}/\text{day}$ at the end. The temperature control of $\pm 0.2^{\circ}\text{C}$ will give fluctuations in freezing surface position larger than this, and so a slower rate of cooling is of no use unless more accurate temperature control is used.

The rate of movement of the freezing surface was much slower in the central region ($\sim 0.02\text{ cm}/\text{day}$). Here, however, the inhomogeneity was similar for all ingots, and the different cooling conditions produced little difference in homogeneity. It is apparent that other effects, *e.g.*, constitutional supercooling (5), become important. This is supported by the fact that the composition of the solid at which inhomogeneity begins to occur corresponds to a point on the liquidus where the slope of the liquidus changes rapidly and becomes much steeper, as is seen in Fig. 2. Thus with the small temperature gradients used in these directional freeze techniques, constitutional supercooling is always likely to occur. Hence this particular method is not suitable for alloys in the center of the composition range.

Preparation by slow zone recrystallization.—An alternative method for preparing ingots of these alloys is the zone recrystallization technique. Here larger temperature gradients are used so that constitutional supercooling should be less of a problem, and the rate of movement of the freezing surface is directly controlled by the movement of the heater relative to the ingot. The ingots used here were of equimolar mean composition and the same dimensions as in the previous case. Two background furnaces were used to maintain an over-all temperature of the ingot at about 550°C , and the hot zone was produced by two "Crusilite" heater rods placed between the background furnaces, one above and one below the ingot. To reduce the width of the hot zone, two water cooled copper plates were placed between the heater rods and the backing furnaces. The resulting molten zone of the ingot was of the order 5 cm in length. This is considerably wider than that used for normal zone recrystallization work with compounds, *etc.*, but it was hoped with this method to obtain some advantage of the directional freeze method, *i.e.*, the variation in composition along the ingot which would provide samples over a range of alloy compositions. The molten zone was moved along the ingot by holding the ingot stationary and moving the whole furnace system along the ingot length. The velocity of the zone along the ingot was approximately $0.5\text{ cm}/\text{day}$.

The ingots produced showed little difference one to another and the variation of composition with length for one case is shown in Fig. 5. Again the ingot is homogeneous at the two ends but is inhomogeneous in the center. The beginning section of the ingot ex-

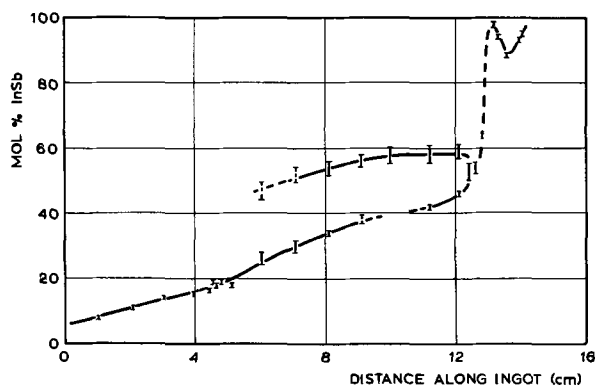


Fig. 5. Variation of composition of cross sectional slice as a function of position in a zone recrystallized ingot (ZL2).

tended the available range of homogeneous alloys out to 20 mole % InSb, but beyond this again the cross sectional slices were two phase, each phase showing some blurring of the high angle x-ray lines. However the intensity of the x-ray lines showed that the amount of second phase was small in some places (shown by dotted vertical lines in Fig. 5) and occasionally, as at a point 10 cm from the beginning of the ingot, only one phase is observed. Thus by careful selection, single phase alloy samples over a considerable range of composition could be obtained.

Again it is seen that this preparation is not satisfactory for alloys in the center of the composition range. One problem is the initial width of the molten zone and, second, the fact that the zone width and hence the temperature gradient at the freezing surface varies considerably with the composition of the zone.

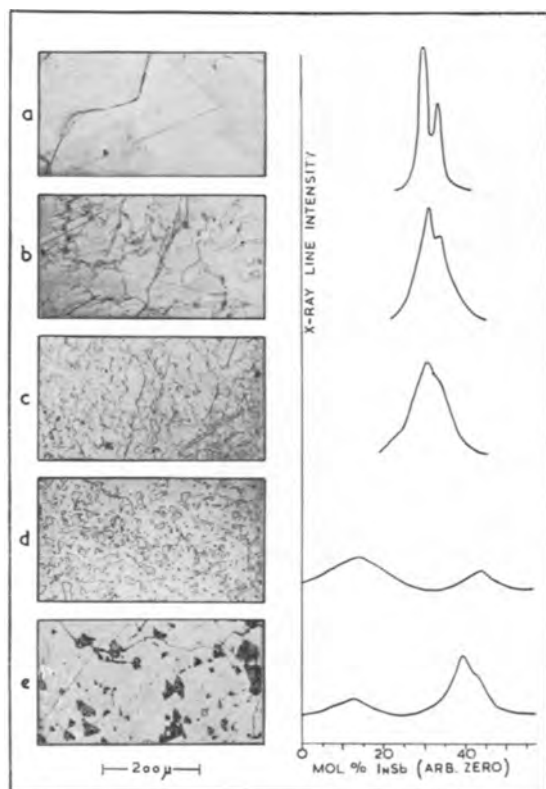


Fig. 6. Photomicrographs and x-ray line profiles of representative specimens of InAs-InSb alloys. (a) Composition 4 mole % InSb, 4 sec etch, x-ray reflection 553 and 731. (b) Peak composition 89 mole % InSb, 4 sec etch, x-ray reflection 553 and 731. (c) Peak composition 68 mole % InSb, 6 sec etch, x-ray reflection 553 and 731. (d) Peak compositions 34 mole % and 64 mole % InSb, 5 sec etch, x-ray reflection 620. (e) Peak compositions 26 mole % and 49 mole % InSb, 6 sec etch, x-ray reflection 620.

It would appear that to improve this, a different means (e.g., R.F. heating) is needed to produce the zone, and careful programming of the heating as a function of position along the ingot is required.

Comparison of X-Ray and Metallurgical Data

Samples of varying degrees of homogeneity taken from the ingots described above have been studied by x-ray powder photography and by optical photomicrography, and in certain cases Metals Research Ltd., Cambridge, have studied the samples with an electron probe microanalyzer. The aim here was to observe how the inhomogeneity as seen by metallurgical techniques could be correlated with the x-ray data and to see whether the broadening of the x-ray reflections was associated with any inhomogeneity easily observed under the microscope.

To present the x-ray data, a suitable x-ray reflection was chosen (the choice had to be varied to some extent because of accidental coincidence of lines from different phases) and the intensity profile of the line on the x-ray film determined using a Hilger and Watts comparator microphotometer. The position on the film can be correlated with Bragg angle, hence with lattice parameter, and so with composition of the alloy. Hence the line profiles given here have been plotted as intensity vs. mole per cent InSb.

The specimens for the photomicrographs were produced by embedding suitable samples in an epoxy resin and polishing with various powders down to 0.1μ γ alumina. The samples were then etched in an etchant consisting of equal volumes of nitric acid, hydrofluoric acid, and distilled water.

The results with typical samples are shown in Fig. 6, where specimens a, b, and c were single phase but with increasingly broadened x-ray lines, and d and e were two phase specimens. It is seen that for d and e the presence of two phases is easily observed on the photomicrograph, while for a the photomicrograph shows a single phase condition with grain boundaries, etc. In samples b and c the trend toward inhomogeneity can be observed, but the interpretation of the photomicrograph would be difficult without the help of the x-ray line profile.

Specimens b, c, and d were investigated by Metals Research Ltd. using a Cambridge Instruments Co.

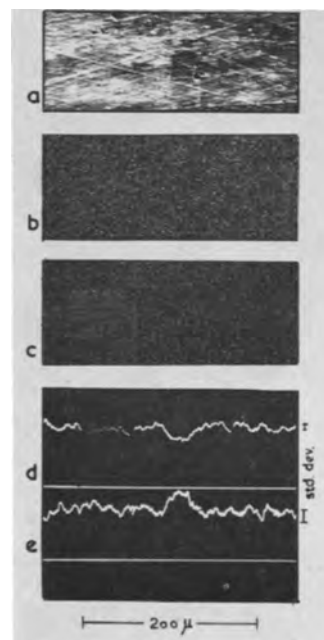


Fig. 7. Electron probe microanalysis results for specimen d (see legend of Fig. 6). (a) Electron image. (b) Antimony $K\alpha$ image. (c) Arsenic $K\alpha$ image. (d) Antimony $K\alpha$ line scan trace. (e) Arsenic $K\alpha$ line scan trace.

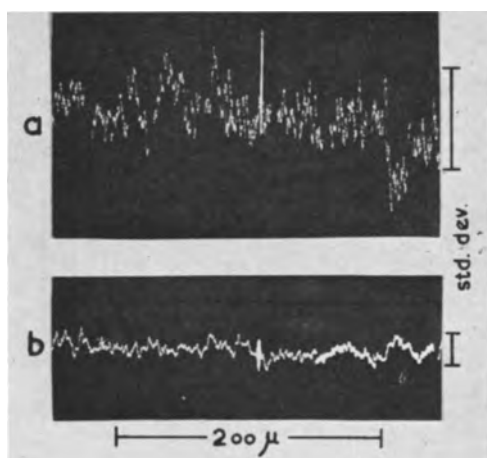


Fig. 8. Electron probe microanalysis results for specimen c (see legend of Fig. 6). (a) Arsenic $K\alpha$ line scan trace. (b) Antimony $K\alpha$ line scan trace.

electron probe microanalyzer, a Microscan. The results for specimen d are shown in Fig. 7. Figure 7a is the electron image of a region of the specimen, showing polishing scratches at this higher magnification and a dark area near the center of the photograph. Figures 7b and c are x-ray images of the same region of the specimen with the x-ray spectrometer tuned to the characteristic radiations of antimony and arsenic, respectively. A careful observation of these photographs shows that the density of spots in the area corresponding to the dark area of Fig. 7a is greater than average in Fig. 7c and smaller than average in Fig. 7b, indicating that this region of the sample is arsenic rich. This is confirmed by the curves in Fig. 7d and e which give a scan of the intensity along the line XX' with antimony and arsenic radiation, respectively. The standard deviation, taken as the square root of the number of quanta observed, is shown at the right of the curve. It is seen that the deviation at the area concerned is considerably larger than the standard deviation, confirming that this area is arsenic rich and antimony deficient.

Similar results were taken with specimen c. Here the electron image and x-ray images appeared quite uniform and no inhomogeneity could be observed.

Figures 8a and b show the results for a line scan taken with arsenic and antimony radiation, respectively. Here the standard deviation for arsenic radiation is larger because of the small mean percentage of arsenic for the specimen. However the deviations in the line scan are not significantly larger than the standard deviation and give no indication of inhomogeneity on any appreciable scale. With specimen b similar results were obtained.

It is seen that the use of x-ray powder diffraction is the most sensitive method for observing inhomogeneities in composition in the case of alloys of this system. Thus by either electron probe method or standard photomicrograph techniques the presence of inhomogeneities is clear only for samples where the x-ray photograph shows two distinct phases. Alloys such as specimen c above appear reasonably homogeneous to the electron probe and photomicrograph even though the x-ray data indicates an effective spread in composition of the order of 10 mole %. This confirms that the inhomogeneity is on a considerably smaller scale than that observed by normal microscope work and is probably due to clustering effects in the atomic lattice.

Acknowledgments

The authors are indebted to Professor L. F. Bates for the facilities of his laboratory and to Metals Research Ltd., Cambridge, for the electron probe data. The work described forms part of an investigation carried out for the Admiralty.

Manuscript received March 23, 1964; revised manuscript received May 1, 1964.

Any discussion of this paper will appear in a Discussion Section to be published in the June 1965 JOURNAL.

REFERENCES

1. J. C. Woolley and B. A. Smith, *Proc. Phys. Soc.*, **72**, 214 (1958).
2. C. Shih and E. A. Peretti, *J. Am. Chem. Soc.*, **74**, 608 (1953).
3. J. C. Woolley and J. Warner, In press *Can. J. Physics*.
4. J. C. Woolley, "Preparation of III-V Compounds," R. K. Willardson and H. L. Goering, Editors, Reinhold Publishing Co., New York (1963).
5. W. G. Pfann, K. M. Olsen, and B. Sawyer, "Transistor Technology, Volume I," H. E. Bridgers, J. H. Scaff, and J. N. Shive, Editors, Van Nostrand & Co., New York.

Germanium-Silicon Alloy Heterojunctions

J. Shewchun¹ and L. Y. Wei

University of Waterloo, Waterloo, Ontario, Canada

ABSTRACT

Germanium-silicon heterojunctions have been prepared by an alloy process. By controlling the impurity concentrations, abrupt junctions having widths from 6000Å to as low as 80Å have been realized. Forward and reverse bias characteristics of several typical heterojunctions are presented. No Esaki effect was observed for thin heterojunctions (<100Å). This is attributed to masking by an abnormally high excess current. This excess current is a tunneling current *via* defect states caused by the large dislocation densities present in the junction.

Interest in heterojunction devices was stimulated in the late 1950's by the work of Kroemer. The concept of quasi-electric and magnetic fields for variable energy-gap semiconductors was first posed by him (1, 2), and shortly thereafter he presented the theory for the wide band-gap emitter transistor (3). In the following

¹ Present address: Interdisciplinary Fellow in Materials Sciences, Brown University, Providence, Rhode Island.

years, a number of articles by other investigators were published (4-6), which dealt with similar considerations. An unsuccessful attempt to fabricate a wide band-gap emitter transistor by the diffusion of phosphorus into gallium arsenide was reported by Jenny (7). The interest in heterojunctions has also spread to the field of solar energy converters (8, 33). Theoretical considerations by Emtage (9) have shown that

it might be possible to incorporate a heterojunction type structure into a photovoltaic converter which could give an efficiency as high as 40%.

With the advent of epitaxial vapor growth techniques (10), considerable interest was stimulated in heterojunctions where one crystal was vapor deposited upon another. The first such heterojunctions were reported by Marinace (electrical properties) (11) and Anderson (analysis) (12). In a series of papers (12-14), Anderson proposed an energy-band model for these heterojunctions which included energy discontinuities in the conduction and valence band edges at the junction interface. More recently, a group consisting of Messrs. Perlman, Oldham, Williams, Feucht, and Milnes have carried out a more intensive investigation into the Ge-GaAs system originally studied by Anderson and extended the work to other systems as Ge-Si and InP-GaAs. In a series of papers (15-19, 34), the general conclusion reached seems to be that there are a large number of unexplained discrepancies which make uncertain the complete validity of the discontinuous energy-gap model. Continuing work by Howard and Fang (20, 21) on n-n Ge-GaAs diodes has shown that these heterojunctions have subnanosecond switching times but suffer the disadvantage of having a low reverse breakdown voltage.

In this paper, we wish to report our experimental investigations on the germanium-silicon system by means of alloy heterojunctions. The evidence that such a system should yield reasonably good junctions is based on the work on germanium-silicon "alloy" crystals. That germanium and silicon show good alloying affinity was demonstrated as far back as 1939 by Stohr and Klemm (22). It was noted that the lattice constant varied monotonically from that of silicon (5.43Å) to that of germanium (5.66Å) depending on the percentage of germanium in the silicon (0 → 100%). Both silicon and germanium are diamond-type crystals. A germanium-silicon substitutional alloy can be formed where the germanium and silicon atoms are arranged at random at lattice sites of a diamond-type lattice. More recent work on "single crystals" of such alloys has been carried out by a number of people at Radio Corporation of America (23, 24). Herman has considered such alloy crystals on a theoretical basis (25). Since an alloy is not a perfect crystal but disordered, it does not have an energy-band structure in the strict sense, but rather regions of high density allowed states (allowed bands) and regions of low density allowed states (forbidden bands). The transition from an allowed to a forbidden band is not as sharp as in a perfect crystal, at least theoretically. However, experimental evidence has shown that such tailing of the band edges is negligible for the Ge-Si system. Present work on the Ge-Si system seems to be concentrated on an accurate determination of the energy-band structure (26, 27). Since the lattice constants of germanium and silicon do differ by a few per cent, it is expected that the alloy crystal would have irregularities. It has been shown (28) that such lattice mismatches can be accommodated through a dislocation formation mechanism. Experimental observations by Goss, Benson, and Pfann (29) tend to confirm this. There is, on the basis of the work just described, every reason to believe that an alloy type p-n heterojunction between germanium and silicon is possible.

Fabrication

Germanium-silicon heterojunction diodes were made, as mentioned, by the alloying technique. The starting materials consist of single crystal silicon and germanium wafers. The silicon is prepared by first mechanically lapping it with suitable silicon-carbide abrasives, and then etching it to a mirror finish in CP4 (4 parts HNO₃, 3 parts CH₃COOH, 3 parts HF). After rinsing and drying, the wafer is broken or cut into small pieces suitable for the alloy process. The germanium is similarly treated and crushed into very small chips from which are extracted small particles

being more or less spheroids of diameter between 5 and 20 mils. The alloying apparatus consists of a high current strip heater with an electrical timer for the control of the temperature cycle.

The alloying is carried out by placing a silicon wafer of thickness between 10 and 20 mils on the heater with a selected spheroid of germanium on top. The area of the junction is approximately determined by the size of the germanium used. The alloy cycle consists of an abrupt heating to a temperature between 950° and 1200°C for periods of 3-15 sec, followed by a similar abrupt cooling. Short alloy times have been deliberately employed in an effort to form thin abrupt junctions and to minimize the diffusion of the doping elements in the germanium and the silicon. In order to obtain good wetting between the germanium and silicon, the alloying is carried out in an atmosphere of dry hydrogen.

After the junction has been formed, a second alloy is carried out in which a gold wire is attached to the body of the silicon to form one of the ohmic contacts. In some cases this is replaced by a gold plate on the silicon undersurface which can then be soldered. The unit is lightly etched, washed, dried, and then mounted on a standard header and a second ohmic contact of the pressure type is made to the germanium side.

In order to determine some of the physical properties of the junction, several units were cross-sectioned by mounting them in a holding jig and lapping with silicon carbide paper abrasives followed by an etch to remove surface damage. Since the luster of polished germanium is noticeably different from that of silicon, and the rate of attack of the etch on the two semiconductors also differs considerably, it was hoped that this would contribute to a relatively easy visual location of the junction. Figure 1 shows a cross-section. The polyphase region of germanium and single crystal wafer of silicon can be easily identified. The junction region appears as a dark line. Some surface irregularities present are due to the non-uniform attack of the etch. The junction region is approximately 10μ wide, but this does not represent the regrowth layer. The diameters of the junctions range from 300 to 500μ. Figure 2 also shows a cross-section. Care has been taken to control the attack of the etch so that a

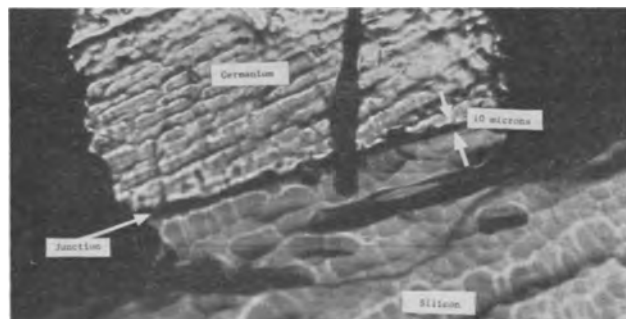


Fig. 1. Cross-section of a germanium-silicon heterojunction magnified approximately 65X.

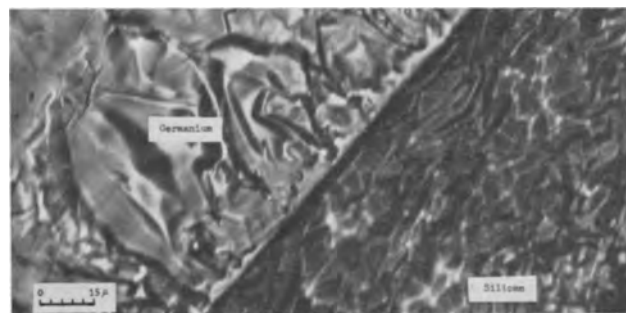


Fig. 2. Cross-section of a germanium-silicon heterojunction magnified approximately 170X.

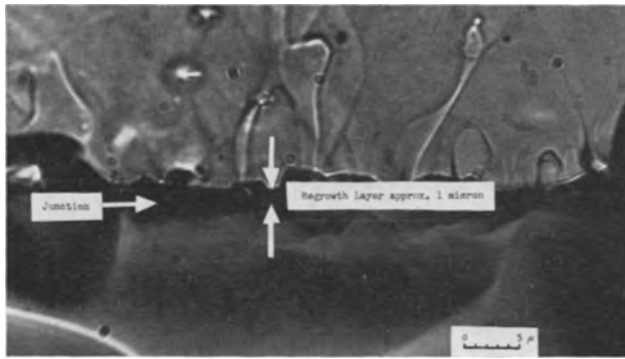


Fig. 3. Cross-section of a germanium-silicon heterojunction magnified approximately 465X.

more uniform surface is obtained on which the junction features are more clearly visible.

The junction itself is believed to consist of an abrupt transition from silicon to germanium through a germanium-silicon regrowth layer. Higher magnifications of the junction region, as in Fig. 3, show a demarcation line between the two regions. The actual regrowth layer is less than 1 μ wide.

Junctions were formed using both p and n silicon wafers of 0.001, 0.01, and 1 ohm-cm resistivity. The silicon doping agent was phosphorus for the n-type and boron for the p-type. The small single-crystal spheroids of germanium were of 0.001, 0.01, 0.1, and 1 ohm-cm. For the germanium the p-type doping agent was gallium and the n-type agent was either antimony or phosphorus. The various germanium-silicon structures that were fabricated are listed in Table I. The grouping according to types will be explained in the next section.

The quantity in the brackets indicates the resistivity of the starting material. There is no *a priori* reason for assuming that the germanium side of the junction will have the same impurity concentration (resistivity) as that of the starting material, especially since the germanium must be melted in the process of junction formation. Direct resistivity measurement is not possible since the junction areas are so small. The indirect technique of junction capacitance measurement was used to determine the impurity concentration on the germanium side of the junction.

Over 250 diodes have been made with the reproduction (essentially similar electrical characteristics) of any one type in the above list being quite good.

Electrical Characteristics

In order to examine the various germanium-silicon structures that were produced, a grouping as shown in Table I was used. The symbol + is used to indicate that

Table I. Fabricated germanium-silicon structures

Type 1 nSi-pGe pSi-nGe	n(1)Si-p(1)Ge
	n(1)Si-p(0.01)Ge
	p(1)Si-n(1)Ge
	p(1)Si-n(0.01)Ge
Type 2 n+Si-pGe p+Si-nGe	n(0.01)Si-p(1)Ge
	n(0.01)Si-p(0.01)Ge
	p(0.01)Si-n(1)Ge
	p(0.01)Si-n(0.1)Ge
	p(0.01)Si-n(0.01)Ge
	n(0.001)Si-p(0.001)Ge
Type 3 nSi-p+Ge pSi-n+Ge	n(0.001)Si-p(0.01)Ge
	n(0.001)Si-p(1)Ge
	p(0.001)Si-n(0.001)Ge
	p(0.001)Si-n(0.01)Ge
	p(0.001)Si-n(0.1)Ge
	p(0.001)Si-n(1)Ge
Type 4 n+Si-p+Ge p+Si-n+Ge	p(0.01)Si-n(0.001)Ge
	n(0.01)Si-p(0.001)Ge
	p(1)Si-n(0.001)Ge
	n(1)Si-p(0.001)Ge
	n+(0.001)Si-p+(0.001)Ge
	p+(0.001)Si-n+(0.001)Ge

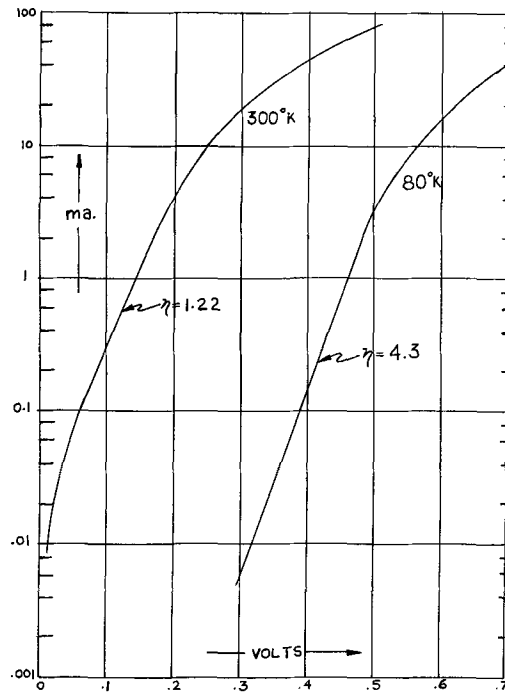


Fig. 4. Forward bias characteristics for a typical n(0.01)Si-p(0.01)Ge diode, unit AUG 8-10-63.

the Fermi level is either above (or extremely close to) the conduction band edge, or below (or extremely close to) the valence band edge.

Figure 4 shows the forward bias current-voltage characteristics of a typical type 1 heterojunction, n(0.01)Si-p(0.01)Ge, at room and liquid air temperatures. At room temperature, the characteristic exhibits an exponential region between approximately 10⁻⁴ and 10⁻² amp., with a slope $e/\eta kT$, where e is the electronic charge, k is Boltzmann's constant, T is temperature, and $\eta = 1.22$. Since the normal theory for rectification in a homogeneous diode leads to an expression

$$J_D = J_S \left[\exp \left(\frac{e V_A}{\eta k T} \right) - 1 \right]$$

where J_S is the saturation current, $\eta = 1$, and V_A is the applied bias, an increase in the slope of a plot of $\log J$ vs. V_A with decreasing temperature is expected.² From Fig. 4, it is clear that the expected behavior is not followed with η taking a value of 4.3 at liquid air temperatures. This type of behavior has been observed by Chynoweth and McKay (30) in narrow silicon p-n junctions where field emission is prevalent. For the other Type 1 structures η was generally lower, the lowest value being 1.09 for n(1)Si-p(0.01)Ge heterojunctions.

The characteristics for type 2 and type 3 heterojunctions were much the same as those just described, except for those heterojunctions where the junction width was less than about 800 \AA . (Junction widths were determined using the formula for an abrupt impurity distribution (3). Impurity concentrations were obtained from junction capacitance measurements and were checked against the observed heterojunction diffusion potentials.) In these cases, the log plot of current vs. voltage showed several distinct inflections, as in Fig. 5 for a typical p(0.001)Si-n(0.001)Ge diode. This wobble about a straight line was very reproducible from diode to diode and can be qualitatively ac-

² While the above equation cannot be applied directly to a heterojunction, our analysis (publication to appear in the *Physical Review*) indicates that the rectification equation for a heterojunction can be reduced to a similar form, where J_S and η are functions of the physical properties of the two materials employed in the heterojunction. The temperature variation is still properly described by this simple equation.

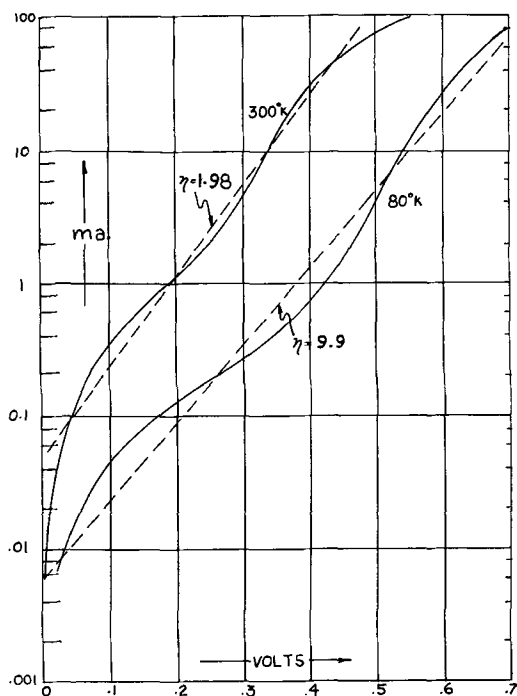


Fig. 5. Forward bias characteristics for a typical p(0.001)Si-n(0.001)Ge diode, unit OCT 22-3.

counted for by the inclusion of an additive saturation current term of the form

$$J = A(V_D - V_A)^n \exp\left(-\frac{B}{V_D - V_A}\right)$$

to the rectification equation (30). In this expression V_D is the diffusion potential, V_A the applied voltage, and A , B , n are dimensional constants. This additive saturation current represents the internal field emission process occurring in the junction due to its "thinness." At liquid air temperatures this characteristic wobble becomes more pronounced indicating an enhancement of tunneling.

Capacitance measurements on a large number of n(0.001)Si-p(0.001)Ge and p(0.001)Si-n(0.001)Ge diodes showed that impurity concentrations on the germanium side were sufficiently high to cause the Fermi level to lie above the conduction band edge for n material and below the valence band edge for p material. These type 4 diodes were expected to exhibit the Esaki effect in the forward bias direction, provided no complicating effects interfered. The experimental units did not show any negative resistance regions but rather an abnormally high current at low bias levels. In addition, these diodes had "apparent" diffusion potentials which were much lower than expected. It is believed that all Ge-Si heterojunctions contain large numbers of defect states in the forbidden band gap and tunneling can occur via these states in thin tunneling junctions, giving rise to a very large excess current J_X . The total current for junction is

$$J = J_t + J_X + J_D$$

where J_D is the diffusion current, as before. If J_X is very large, it will mask J_t (normal tunneling current) completely. This appears to be the case for the type 4 heterojunctions. The defect states by which tunneling takes place are undoubtedly the regions of fairly large dislocation densities mentioned earlier.

Since the junction width depends on the donor and acceptor impurity concentrations on both sides of the heterojunction and the reverse bias characteristic depends strongly on the junction width, a large variation in the form of the reverse bias characteristic was observed in the process of examining the different

structures listed in Table I. Figures 6-11 show typical characteristics that were observed for several diode types. The junction widths for the n(1)Si-p(1)Ge and n(1)Si-p(0.01)Ge heterojunctions in Fig. 6 and 7 were estimated to be 5900Å and 3100Å, respectively. Both units have "hard" characteristics with a soft knee prior to a sharp breakdown. This sharp breakdown is a characteristic feature of avalanche breakdown (31), along with the observation that the breakdown voltage decreases considerably on lowering of the heterojunction temperature to 80°K. The softness prior to breakdown is not normally found in homogeneous junctions, but our analysis indicates that is an inherent feature of a heterojunction. For thinner junctions such as the p(0.01)Si-n(0.01)Ge unit shown in Fig. 8 at 1200Å, there is a possibility of field emission or tunneling across the junction. When the temperature is lowered, the reverse current drops somewhat at moderate values of bias, but then increases more rapidly and crosses over the room temperature characteristic, thus leading to a lower breakdown voltage. The slight lowering of reverse current at moderate values of bias indicates field emission, while the drop in breakdown voltage indicates avalanche breakdown. This heterojunction represents transition region behavior where ionization and field emission occur simultaneously. At sufficiently high current densities, a "second" breakdown occurs (32) which will be discussed in a subsequent publication. This breakdown consists of the formation of a negative resistance region along with a hysteresis loop.

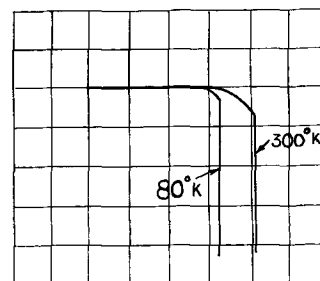


Fig. 6. Reverse characteristics for a typical n(1)Si-p(1)Ge diode, unit JUL 23-2-63. Scale: 20 v/div. horiz., 1 ma/div. vert.

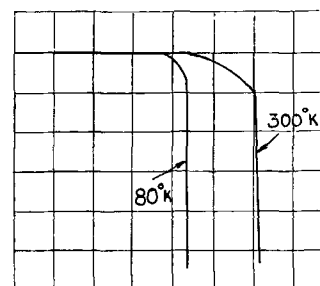


Fig. 7. Reverse characteristic for a typical n(1)Si-p(0.01)Ge diode, unit AUG 8-10-63. Scale: 10 v/div. horiz., 1 ma/div. vert.

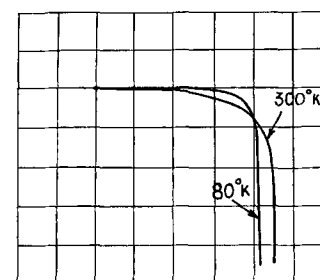


Fig. 8. Reverse characteristic for a typical p(0.01)Si-n(0.01)Ge diode, unit JUL 24-4-63. Scale: 2 v/div. horiz., 20 ma/div. vert.

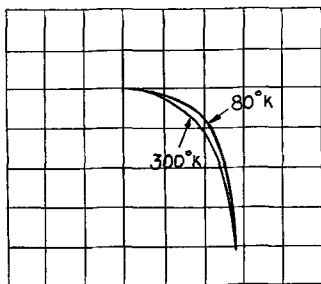


Fig. 9. Reverse characteristic for a typical $n(0.01)\text{Si-p}(0.01)\text{Ge}$ diode, unit FEB 21-5. Scale: 2 v/div. horiz., 20 ma/div. vert.

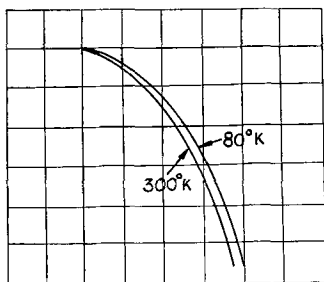


Fig. 10. Reverse characteristic for a typical $n(0.001)\text{Si-p}(0.001)\text{Ge}$ diode, unit JUL 6-2. Scale: 1 v/div. horiz., 10 ma/div. vert.

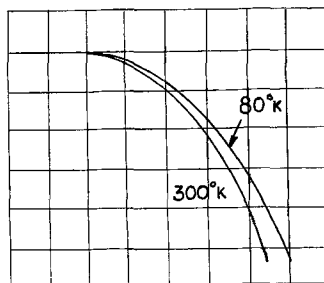


Fig. 11. Reverse characteristic for a typical $p(0.001)\text{Si-n}(0.001)\text{Ge}$ diode, unit FEB 12-3. Scale: 0.5 v/div. horiz., 20 ma/div. vert.

Figures 9, 10, and 11 show how the reverse characteristic gets progressively softer as the junction width decreases (to about 300\AA for the $n(0.001)\text{Si-p}(0.001)\text{Ge}$ and $p(0.001)\text{Si-n}(0.001)\text{Ge}$ heterojunctions), and the complete reversal in breakdown voltage shift with decreasing temperature.

Additional evidence was obtained to show that the electrical junction occurred at the material interface and not in either the silicon or the germanium. First, the measured diffusion potentials were in agreement with the calculated ones based on the appropriate heterojunction model. Second, reverse bias breakdown radiation in the form of microplasma spots was observed at the material interface, and the spectral distribution of the radiation indicated that both germanium and silicon were playing an active role in forming a true heterojunction.

Conclusions

Germanium-silicon heterojunctions have been successfully fabricated by an alloy process. A wide variety of structures were formed in which the impurity concentrations on either side of the junction were determined by the resistivity of the single crystal germanium or silicon that was employed.

The forward bias characteristics tend to resemble those of normal homogeneous junctions except when "thin" junctions are encountered. Theoretically, type 4 diodes were expected to show the Esaki effect, but, experimentally, no such effect was observed. Instead, an abnormally high current was found which was attributed to tunneling *via* defect states caused by the large dislocation densities present in the junction. This excess current was sufficiently large to mask out the negative-resistance region that was expected.

The reverse bias characteristics of germanium-silicon heterojunctions were also examined. For sufficiently large junction widths (low impurity concentrations), a heterojunction was expected to show normal avalanche breakdown with a soft knee rather than a sharp knee. The degree of softness was found to depend on the tunneling and image effects. For thin junctions (high impurity concentrations), Zener or field emission "breakdown" was predominant. A continuous transition of characteristics from hard to extremely soft was observed as the junction width of the heterojunctions varied from a few thousand angstroms to less than 100\AA .

Manuscript received Feb. 24, 1964; revised manuscript received April 15, 1964.

Any discussion of this paper will appear in a Discussion Section to be published in the June 1965 JOURNAL.

REFERENCES

1. H. Kroemer, *Bull. Am. Phys. Soc.*, **2**, 143 (1956).
2. H. Kroemer, *R.C.A. Rev.*, **18**, 1332 (1957).
3. H. Kroemer, *Proc. I.R.E.*, **45**, 535 (1957).
4. J. Tauc, *Rev. Mod. Phys.*, **21**, 307 (1957).
5. A. Armstrong, *Proc. I.R.E.*, **46**, 1307 (1958).
6. T. K. Lakshmanan, *ibid.*, **48**, 1646 (1960).
7. D. A. Jenny, *ibid.*, **46**, 959 (1958).
8. M. Wolf, *ibid.*, **48**, 1246 (1960).
9. P. R. Emtage, *J. Appl. Phys.*, **33**, 1950 (1962).
10. R. Ruth, J. C. Marinace, and W. Dunlap, *ibid.*, **31**, 995 (1960).
11. J. C. Marinace, *I.M.B. J. Res. & Dev.*, **4**, 280 (1960).
12. R. L. Anderson, *ibid.*, **4**, 283 (1960).
13. R. L. Anderson, *Solid-State Electronics*, **5**, 341 (1962).
14. R. L. Anderson, *Trans. I.R.E.*, ED-9, 509 (1962).
15. S. S. Perlman, D. L. Feucht, and R. M. Williams, *ibid.*, ED-9, 509 (1962).
16. W. S. Oldham and A. G. Milnes, *ibid.*, ED-9, 509 (1962).
17. W. S. Oldham and A. G. Milnes, *Solid-State Electronics*, **6**, 121 (1963).
18. S. S. Perlman, *Trans. I.R.E.*, ED-10, 335 (1963).
19. W. S. Oldham and A. G. Milnes, *ibid.*, ED-10, 335 (1963).
20. F. Fang and W. E. Howard, Conference Paper, 1962 Electron Devices Meeting in Washington, D. C.
21. W. E. Howard and F. Fang, *Trans. I.R.E.*, ED-10, 336 (1963).
22. H. Stohr and W. Klemm, *Z. anorg. allgem. Chem.*, **241**, 305 (1939).
23. E. R. Johnson and S. M. Christian, *Phys. Rev.*, **95**, 846 (1954).
24. A. Levitas, C. C. Wang, and B. H. Alexander, *ibid.*, **95**, 846 (1954).
25. F. Herman, *Proc. I.R.E.*, **43**, 1703 (1955).
26. R. Braunstein, *Phys. Rev.*, **130**, 869 (1963).
27. R. Braunstein, *ibid.*, **130**, 879 (1963).
28. F. C. Frank and J. H. Van der Merwe, *Proc. Roy. Soc. London*, **A198**, 205 (1949).
29. A. J. Goss, K. E. Benson, and W. G. Pfann, *Acta Met.*, **4**, 332 (1956).
30. A. G. Chynoweth and K. G. McKay, *Phys. Rev.*, **106**, 418 (1957).
31. K. G. McKay, *ibid.*, **94**, 877 (1954).
32. L. Y. Wei and J. Shewchun, *I.E.E.E.*, **5**, 946 (1963).
33. K. Lehovec, *Proc. I.R.E.*, **40**, 1408 (1952).
34. W. G. Oldham *et al.*, *This Journal*, **110**, 536 (1963).

Diffused Junction Diodes of PbSe and PbTe

J. F. Butler

Lincoln Laboratory,¹ Massachusetts Institute of Technology, Lexington, Massachusetts

ABSTRACT

A technique is described for producing diffused p-n junctions in Pb salt single crystals which utilizes an interdiffusion mechanism to introduce controlled deviations from stoichiometry, excess Pb giving rise to n-type and excess Se and Te to p-type PbSe and PbTe, respectively. An analysis of the p-n junction depths on the basis of Fick's law of diffusion results in the following effective interdiffusion constants: $D_{\Delta} = 4 \times 10^{-8} \text{ cm}^2 \text{ sec}^{-1}$ for producing a p-layer on n-type PbSe at 600°C; $D_{\Delta} = 9 \times 10^{-9} \text{ cm}^2 \text{ sec}^{-1}$ for an n-layer on p-type PbSe at 650°C; $D_{\Delta} = 6 \times 10^{-7} \text{ cm}^2 \text{ sec}^{-1}$ for an n-layer on p-type PbTe at 650°C. In the first case the diffusion has been studied as a function of time, and the results show that the assumption of Fick's law of diffusion was valid. As expected the interdiffusion constants are two to three orders of magnitude larger than the self-diffusion constants. Electrical characteristics of the diffused diodes are presented and can be explained as resulting from a combination of diffusion and tunneling current components.

Diodes of the Pb salt semiconductors have been the subject of a number of papers (1-9). It is of historical interest that PbS was one of the first materials with which the phenomenon of rectification was observed (1) and that the galena crystal detector was one of the earliest semiconductor devices (2). The evaluation of interdiffusion constants in these materials from the penetration distances of p-n junctions has been carried out to a limited degree (10-12).

This paper describes the electrical properties of diffused junction diodes of PbSe and PbTe, gives the fabrication procedures followed in making these diodes, and presents values for the effective interdiffusion constants near 600°C. The diffusion technique which is described below for diffusing an n-layer into single crystal p-type PbSe and PbTe and for diffusing a p-layer into n-type single crystal PbSe has the advantage of using an isothermal closed system and of consequent simplicity.

The diffusion method was suggested by the work of Brebrick and Gubner (13,14) and of Brebrick and Allgaier (15) who measured stability limits as functions of temperature for PbSe and PbTe by introducing deviations from stoichiometry into crystals of these semiconductors. Their method was to bring a small single crystal of the material into equilibrium through the vapor phase with a two-phase ingot of the same material rich in one or the other of the constituents. The equilibrium conditions were "frozen in" by quenching the crystals to room temperature, and the concentration of the excess constituent at the equilibrium temperature was assumed equal to the measured concentration of extrinsic charge carriers. The field of stability of PbSe was found to be roughly symmetric about the stoichiometric composition and that of PbTe to be predominantly on the p-type, Te rich side [other work (16) shows the field of stability of PbS to be predominantly on the n-type, Pb rich side]. According to Brebrick (17) the approach to equilibrium in these experiments proceeds by a mechanism of interdiffusion and may be described in terms of concentration gradient by an effective interdiffusion constant. Thus, the diffusive flow of deviation from stoichiometry

$$J_{\Delta} = J_C - J_A = -(D_C^* + D_A^*) (S/kT) \text{ grad } \mu_C \quad [1]$$

can be written as

$$J_{\Delta} = -D_{\Delta} \text{ grad } \Delta \quad [2]$$

¹ Operated with support from the U.S. Air Force.

where D_C^* and D_A^* are the cation and anion self-diffusion constants, S is the concentration of cation or anion lattice sites, μ_C is the chemical potential of the cation, $\Delta = N_C - N_A$ is the deviation from stoichiometric composition and

$$D_{\Delta} = (D_C^* + D_A^*) (S/kT) (d\mu_C/d\Delta) \quad [3]$$

is the effective interdiffusion constant. As shown by Brebrick (17) the factor $(1/kT) (d\mu_C/d\Delta)$ is of the order of the reciprocal of the total concentration of lattice point defects and the interdiffusion constant is therefore 10^2 - 10^6 times as large as the larger of the self-diffusion constants. For the case of conversion from one conductivity type to another, the process may be visualized as a plane between p and n material moving inward from the surface. For this case, quenching the crystal before equilibrium is attained will result in a p-n junction. The diffusion method described in detail below, then, consists of heating a single crystal of material of one conductivity type in a sealed container with a two phase ingot of the same material of opposite conductivity type and quenching the system before equilibrium is attained.

Fabrication Procedures

The two phase ingots used as the source of excess Se or Te were prepared by chemically combining the elements in sealed quartz tubes. Quartz tubes were etched in a 1-1 solution of nitric and hydrofluoric acids, rinsed in distilled water, drained dry, and vacuum baked at 1100°C until the final pressure was less than 10^{-6} mm Hg. The elements (99.999% pure Se and Te, 99.9999% pure Pb) were weighed out individually to the nearest milligram so that the combined weight was about 10g and the composition was either 49 or 51 atomic per cent Pb. The Pb was cut from the interior of a bar. The materials were loaded into a tube which was then outgassed at 150°C for 3 hr and sealed off at a pressure less than 10^{-6} mm Hg. The sealed tube was exposed to a carefully controlled torch flame long enough to bring about partial reaction of the contents and was then heated for 3 hr at 950°C for PbTe and 1050°C for PbSe and quenched in water. The resulting two phase ingot was removed from the tube and ground to a coarse powder. Such a ground ingot could be used with predictable results for four or five diffusions.

Most of the single crystal PbSe used in these experiments was obtained from a larger crystal grown from a near stoichiometric melt by the Bridgman tech-

nique by Dr. A. J. Strauss of Lincoln Laboratory. This crystal contained substantial portions of both p and n material with 77°K carrier concentration and Hall mobility of approximately $3 \times 10^{18} \text{ cm}^{-3}$ and $15,000 \text{ cm}^2 \text{ v}^{-1} \text{ sec}^{-1}$, respectively. The PbTe, taken from an undoped p-type single crystal obtained from Battelle Memorial Institute, had a room temperature hole concentration and Hall mobility of approximately $3 \times 10^{18} \text{ cm}^{-3}$ and $750 \text{ cm}^2 \text{ v}^{-1} \text{ sec}^{-1}$, respectively. Rectangular parallelepipeds approximately 1 mm thick and several millimeters in the other two dimensions were cleaved from the crystals. The wafers were cleaned by scrubbing with boiling high purity methanol. The diffusions were performed with the crystal and source ingot in separate, open compartments of a quartz ampoule which was etched and vacuum baked immediately before use in the manner described above for quartz tubes. The ampoule and contents were out-gassed at 120°C for 1 hr, sealed off at about 10^{-6} mm Hg, and placed in the uniform temperature zone of a furnace which had been preheated to the desired temperature. The temperature was usually 600°C for the diffusion of excess Se into n-type PbSe and 650°C for the diffusion of excess Pb into p-type PbSe or PbTe. At the end of a run, the sealed ampoules were quenched in water. On freshly cleaved surfaces junctions were often directly observable under magnification as faint white lines or discontinuities in the general appearance, and junction depths were measured by visual observations in conjunction with thermoelectric micro-probing.

Figure 1 shows junction depth plotted against the square root of time for four diffusions at 600°C of excess Se into n-type PbSe. The electron concentration of the wafer used in the 3 hr run was determined by Hall measurements to be $3.0 \times 10^{18} \text{ cm}^{-3}$; the remainder of the wafers were taken from the same portion of the parent crystal and probably had nearly the same concentration. The same complete source ingot was used in all four runs. For the diffusion of excess Pb into p-type PbSe, a representative set of values is a junction depth of $8.9 \times 10^{-3} \text{ cm}$ for a 1 hr run at 650°C and an initial hole concentration of $1.9 \times 10^{18} \text{ cm}^{-3}$. The diffusion of excess Pb at 650°C for 1 hr into p-type PbTe with an initial hole concentration of $3.0 \times 10^{18} \text{ cm}^{-3}$ produced a junction depth of $8.9 \times 10^{-3} \text{ cm}$.

The diffused junction material was usually cleaved into dice with linear dimensions of 0.1-1.0 mm and alloyed to standard metal base tabs. An artist's sketch of a diode is shown in Fig. 2. Ohmic contacts to p-type regions were generally made with pure Au or a Au-Tl alloy and to n-type regions with pure Pb or a Pb-In alloy. In general, Se, Te, Ag, Au, and Tl have been found to behave as acceptors and Pb, In, Sn, and Bi as donors. Alloying was performed on a carbon resistance heating strip enclosed in a gas tight volume of about 1 liter into which could be introduced a reducing atmosphere. The system was purged with a 5 min gas flow before each heating step and the semiconductor surface was cleaned with boiling methanol after each step. Relative temperatures were recorded for reproducibility of operations, but precise alloying tempera-

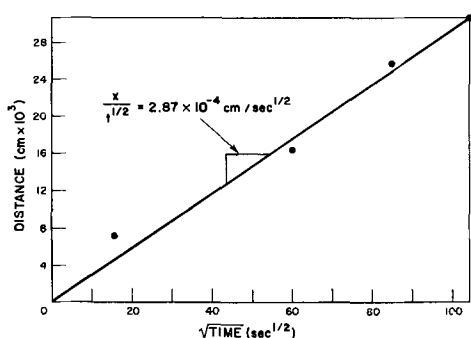


Fig. 1. Junction depths for diffusions in n-type PbSe

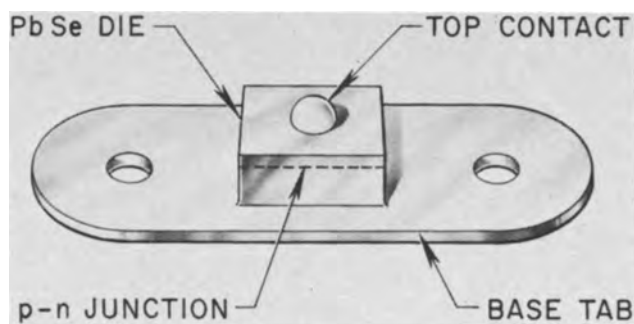


Fig. 2. Artist's sketch illustrating fabrication of diffused junction diodes.

tures were not determined. Alloying times were generally less than a minute. In some cases, a mesa structure was formed on material with a shallow junction depth by etching with a solution of potassium hydrochloride, ethylene glycol, and hydrogen peroxide as described by Coates, Lawson, and Prior (18). This etch has been found to be most effective on cleaved surfaces. The finished diodes were mounted on transistor headers with In plated Ag wires soldered to the top contacts.

Electrical Characteristics

Figures 3 and 4 show the current-voltage characteristics at three temperatures for a typical PbSe diode. The p-n junction resulted from a diffusion of excess Pb into p material at 600°C and was $3 \times 10^{-3} \text{ cm}$ deep. The surface was etched to a mesa structure with a junction area of about 10^{-3} cm^2 . The reverse current for the room temperature characteristic shows saturation near 50 ma. The reverse characteristics of PbSe diodes were found to be extremely dependent on previous surface treatment. The diode of Fig. 3 and 4 was vacuum baked and had been stored in a desiccator for a week before its characteristics were measured. No attempt was made to develop a surface treatment for optimum performance. Measurements of capacitance as a function of voltage at 77°K were made on a $5 \times 10^{-4} \text{ cm}^2$ area PbSe diode from the same diffusion run as that of Fig. 3 and 4, using a radio frequency bridge at 50 megacycles. Accuracy of these measurements was limited by breakdown effects which became evident at reverse biases greater than about 0.5v and by large reverse currents. The results show voltage proportional to the square of reciprocal capacitance and the data are plotted in this manner in Fig. 5.

The current-voltage curves of a PbTe diode are presented in Fig. 6 and 7. The junction, formed by a

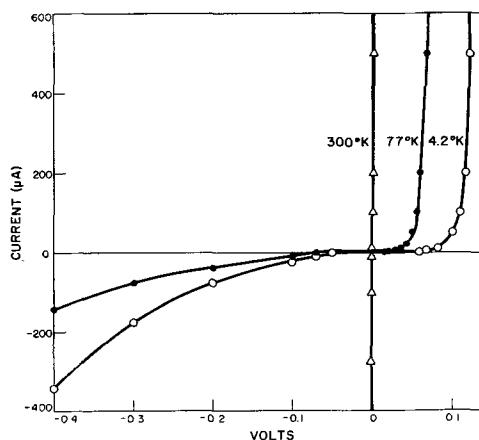


Fig. 3. Current-voltage characteristics of a diffused junction PbSe diode at various temperatures.

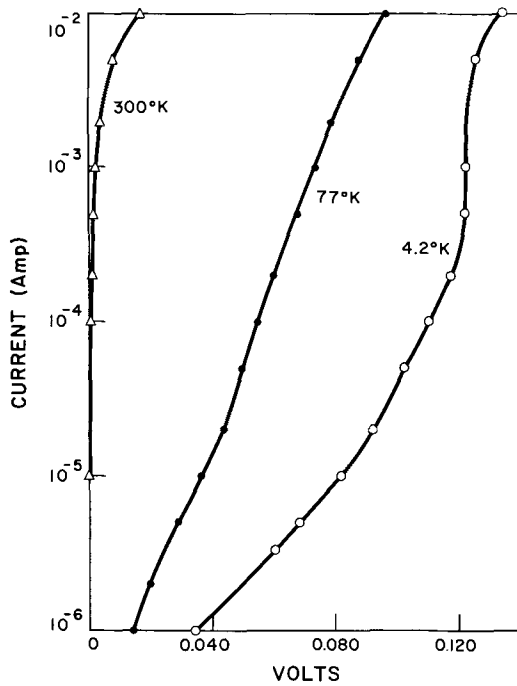


Fig. 4. Forward current-voltage characteristics on a semi-logarithmic scale of diffused junction PbSe diode of Fig. 3 at various temperatures.

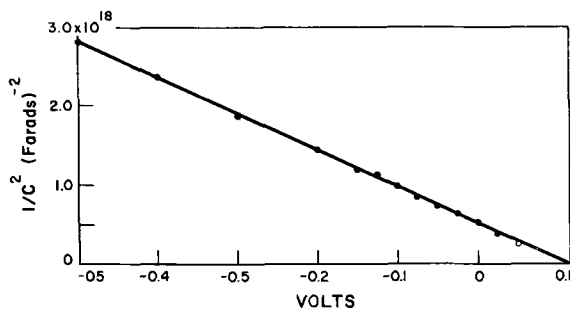


Fig. 5. Diode capacitance as a function of voltage for a PbSe diffused junction diode at 77°K.

diffusion of excess Pb into p material at 650°C, was 8.9×10^{-3} cm deep and about 10^{-2} cm² in area. The reverse current at room temperature shows saturation near 50 ma. The reverse characteristics of this diode were less sensitive to surface conditions than those of the PbSe diode.

Discussion

The linear relation between junction depth and the square-root of time evident in Fig. 1 implies that the interdiffusion process can be described by a simple constant. In order to obtain a value for D_{Δ} , it is assumed that the quantity $\Delta(x, t) = N_C(x, t) - N_A(x, t)$ diffuses into an initially homogeneous semi-infinite slab with a constant surface concentration. The initial deviation from stoichiometry within the slab, Δ_0 , can be determined from the initial carrier concentration if the semiconductor is in the exhaustion range. It is assumed that the surface deviation Δ_s due to the source is given by the stability limit at the diffusion temperature of the component in question. Under these conditions, the solution of [2] is

$$\Delta(x, t) = (\Delta_s - \Delta_0) \operatorname{erfc}(x/2\sqrt{D_{\Delta}t}) + \Delta_0 \quad [4]$$

It will be assumed that the p-n junction occurs where $\Delta(x, t) = 0$.

Substituting $x/t^{1/2}$ from the slope of the curve in Fig. 1 and $\Delta_s = 6.0 \times 10^{18}$ cm⁻³ from the data of Brebrick and Gubner (13) into [4] and assuming an ex-

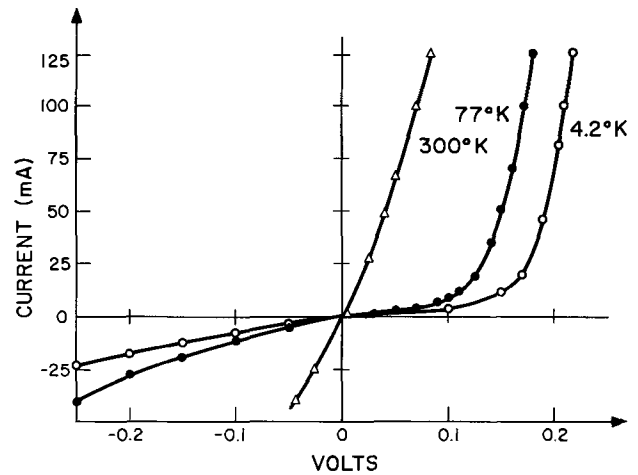


Fig. 6. Current-voltage characteristics of a diffused junction PbTe diode at various temperatures.

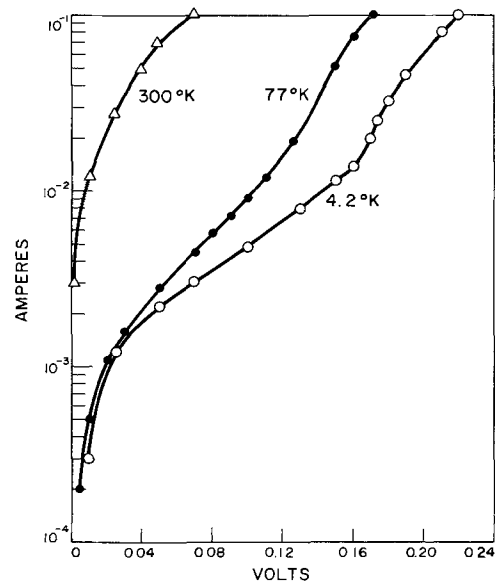


Fig. 7. Forward current-voltage characteristics on a semi-logarithmic scale of δ diffused junction PbTe diode of Fig. 6 at various temperatures.

haustion range semiconductor, gives $D_{\Delta} = 4 \times 10^{-8}$ cm² sec⁻¹ for excess Se in n-type PbSe at 600°C. It is instructive to compare this value with a diffusion constant of 10^{-12} cm² sec⁻¹ for the self-diffusion of Se in 10^{18} cm⁻³ n-type PbSe at 600°C, as extrapolated from the data obtained by radioactive tracer diffusion by Boltaks and Mokhov (19). For the diffusion of an excess Pb layer in p-type PbSe at 650°C, the measured values of junction depth, time and initial concentration, and $\Delta_s = 5.5 \times 10^{18}$ from the data of Brebrick and Gubner (13) give $D_{\Delta} = 9 \times 10^{-9}$ cm² sec⁻¹. Seltzer and Wagner (20), using Pb-210 diffusion, obtained a diffusion constant of approximately 1.5×10^{-10} cm² sec⁻¹ for the self-diffusion of Pb in 10^{18} cm⁻³ p-type PbSe at this temperature. Taking $\Delta_s = 6 \times 10^{17}$ cm⁻³ from the data of Brebrick and Gubner (14) and using measured values in [4] results in $D_{\Delta} = 6 \times 10^{-7}$ cm² sec⁻¹ for the diffusion of an excess Pb layer in p-type PbTe. Boltaks (11) has obtained diffusion constants for excess Pb in 10^{17} cm⁻³ p-type PbTe over a range of temperatures by using a delta function source and measuring junction depths. The conditions of his experiments were such that his "self-diffusion" constant corresponds approximately to the interdiffusion constant discussed here. Extrapolated to 650°C, his values give $D_{\Delta} = 2 \times 10^{-8}$ cm²/sec, in rather poor agreement with the value given above.

Two points are of interest in connection with the effective interdiffusion constants obtained in the present work. They were 2-3 orders of magnitude larger than the self-diffusion constants, in agreement with prediction (17). Second, the average interdiffusion constant for the movement of an n-p junction into p-type PbSe is smaller than that for the movement of a p-n junction into an n-type crystal for comparable values of $\Delta_s - \Delta_0$. Intuitively, this is what is to be expected if, as Seltzer and Wagner propose (20), the predominant point defects in PbSe are Frenkel defects in the Pb sub-lattice with the interstitial Pb possessing a much larger mobility than the Pb vacancy.² An alternative explanation is that p-type PbSe contains electrically inactive Se as a dislocation precipitate which acts as a sink for diffusing Pb. This is consistent with results of experiments on p-type PbTe (14) and with the fact that it is difficult to quench in the high temperature state of p-type PbSe (13).

Figure 4 shows that the low temperature forward current-voltage curves of the PbSe diode are characterized by a low bias region in which current rises slowly with voltage, followed by a middle region of rapid rise and a high bias region dominated by series resistance. In the 77°K curve the middle region shows an $\exp(qv/nkT)$ dependence of current on voltage with $n = 1$ between about 20 and 100 μa and $n = 1.25$ between 150 and 5000 μa . The 4.2°K curve has a middle region between 500 and 1500 μa with $n = 1.5$ over most of the range. The forward current at room temperature shows a rapid non-exponential rise from zero and is dominated by series resistance at a low bias. The low temperature reverse currents increase with voltage, that at 4.2°K rising the most rapidly. The reverse current at 300°K rapidly reaches a definite saturation value. These features can be explained in a qualitative manner as resulting from a combination of diffusion controlled and tunneling current components. In view of the nonparabolicity of the band edges (21), and the uncertainty in values of energy gap and lifetime, no attempt will be made here to verify the explanation quantitatively. At the carrier concentrations of this material, one would expect degeneracy near room temperature. Strong evidence that the low temperature reverse current is due primarily to tunneling is supplied by the fact that its magnitude increases with decreasing temperature (the energy gap of PbSe is known to increase linearly with temperature over most of the range under consideration). The occurrence of tunneling probably also explains the large low-bias forward currents at low temperatures.

The current-voltage characteristics of the PbTe diode show the same general behavior as those of the PbSe diode, but the large low bias currents override most of the rapidly rising middle region. The reverse current has been observed with an oscilloscope to increase in magnitude with decreasing temperature between about 250° and 77°K in the same manner as the PbSe diode and probably results from tunneling. The fact that the reverse current at 4.2°K is less in magnitude than that at 77°K is of interest and not readily explained.

Extending the linear regions of the 77° and 4.2°K semilogarithmic curves of Fig. 4, one finds the resulting straight lines to intersect at a voltage about 20% lower than the energy gap deduced by extrapolating the optical data of Gibson (22) to 0°K. Although less clear, a similar result can be obtained from the PbTe curves of Fig. 7. Furthermore, the capacitance data indicate an energy barrier in the PbSe diode at 77°K approximately 30% lower than the measured optical energy gap (22). For a degenerate semiconductor, one would expect the barrier height and optical energy gap to more nearly coincide. Any explanation for these discrepancies based on a "Burstein shift" (23) tends to be ruled out by the facts that the PbSe used in the experiments described above had about the same car-

rier concentration as that used by Gibson and, second, that Gibson observed no dependence of the position of the absorption edge on concentration. These differences could arise from the occurrence of an indirect minimum energy gap. According to experimental results of Ellett and Cuff (21), however, the valence and conduction band extremes of PbSe occur at identical points in the Brillouin zone. Another mechanism resulting in a difference between thermal and optical energy gaps is the redistribution of ionic charge associated with the intrinsic ionization process (24). This mechanism would give rise to a difference energy approximately proportional to $(\kappa_s - \kappa_0)/\kappa_s \kappa_0$, where κ_s and κ_0 are the static and optical dielectric constants, respectively, of the material. As pointed out by Scanlon (25) this effect may be important in polar semiconductors such as the Pb salts.

Summary

A method has been developed for producing diffused p-n junctions in PbSe and PbTe which utilizes an interdiffusion mechanism to introduce controlled deviations from stoichiometry. The method should be applicable to any compound semiconductor whose conductivity type can be determined by deviations from stoichiometry and for which the vapor pressure of at least one component is large enough to provide the necessary mass transfer. It could certainly be applied to PbS. The measured electrical properties of the PbSe and PbTe diffused diodes are consistent with those resulting from a current flow comprised of both diffusion and tunneling components.

Acknowledgments

The author wishes to thank Dr. R. F. Brebrick and Mr. A. R. Calawa for valuable suggestions and discussions, and Mr. R. H. Hancock for technical assistance in all phases of fabrication.

Manuscript received February 11, 1964.

Any discussion of this paper will appear in a Discussion Section to be published in the June 1965 JOURNAL.

REFERENCES

1. F. Braun, *Ann. Phys. Chem.*, **153**, 556 (1874).
2. J. C. Bose, U.S. Pat 755, 840 (1904).
3. H. K. Henisch and J. W. Granville, "Semiconducting Materials" (Report of Reading Semiconductor Conference, (1950) 87, Butterworth (1953).
4. A. F. Gibson, *Proc. Phys. Soc., London*, **B65**, 196, 214 (1952).
5. P. C. Banbury, H. A. Gebbie, and C. A. Hogarth, "Semiconducting Materials" (Report of Reading Semiconductor Conference, 1950) 87, Butterworth (1951).
6. C. A. Hogarth, *Proc. Phys. Soc., London*, **B65**, 958; *ibid.*, **B66**, 216 (1953).
7. R. H. Rediker and A. R. Calawa, *J. Appl. Phys.*, **32** (suppl.), 2189 (1961).
8. Y. Kanai and K. Shono, *Jap. J. Appl. Phys.*, **2**, 6 (1963).
9. M. F. Kimmitt and A. C. Prior, *This Journal*, **108**, 1034 (1961).
10. R. F. Brebrick and W. W. Scanlon, *Phys. Rev.*, **96**, 598 (1954).
11. B. I. Boltaks, "Diffusion in Semiconductors," p. 293, Academic Press, New York (1963).
12. E. J. Brady, *This Journal*, **101**, 466 (1954).
13. R. F. Brebrick and E. Gubner, *J. Chem. Phys.*, **36**, 170 (1962).
14. R. F. Brebrick and E. Gubner, *ibid.*, **36**, 1283 (1962).
15. R. F. Brebrick and R. S. Allgaier, *ibid.*, **32**, 1826 (1960).
16. J. Bloem and F. O. Kroeger, *Z. Phys. Chem. (Frankfurt)*, **7**, 1 (1956).
17. R. F. Brebrick, *J. Appl. Phys.*, **30**, 811 (1959).
18. D. G. Coates, W. D. Lawson, and A. C. Prior, *This Journal*, **108**, 1038 (1961).
19. B. I. Boltaks and Y. N. Mokhov, *Soviet Phys. Tech. Phys.*, **28**, 1045 (1958).
20. M. S. Seltzer and J. B. Wagner, Jr., *J. Chem. Phys.*, **36**, 130 (1962).
21. M. R. Ellett and K. F. Cuff, *American Physical*

²The author is indebted to Dr. R. F. Brebrick for bringing this point to his attention.

- Society Meeting, Pasadena (Dec. 19-21, 1963):
 Abstract in *Bull. Am. Phys. Soc.*, **8**, 601 (1963).
 22. A. F. Gibson, *Proc. Phys. Soc., London*, **B65**, 378 (1952).
 23. E. Burstein, *Phys. Rev.*, **93**, 632 (1954).

24. F. Seitz, "Modern Theory of Solids," ch. 13, McGraw-Hill Book Co., New York (1940).
 25. W. W. Scanlon in "Solid State Physics," **9**, p. 112, F. Seitz and D. Turnbull, Editors, Academic Press, New York (1959).

Thermodynamic Analyses of Open Tube Germanium Disproportionation Reactions

A. Reisman and S. A. Alyanakyian

Thomas J. Watson Research Center, International Business Machines Corporation, Yorktown Heights, New York

ABSTRACT

In order to define conditions most suitable for iodine transport of pure or gallium doped germanium, the equilibria that obtain when these elements, singly or together, are mixed with iodine or hydrogen iodide in the presence of hydrogen and/or inert gases were analyzed using computer techniques. It was found that Ge in the presence of an inert carrier gas should transport via a hot to cold process at all iodine pressures studied. These results are markedly perturbed when H₂ is substituted for the inert gas due to the establishment of a competing equilibrium whose enthalpic change is opposite in sign to that of the equilibrium responsible for semiconductor transport. The effects of the competing equilibrium in turn may be modified by using a mixture of H₂ and He. Under certain sets of conditions, in fact, temperature insensitive regions develop which appear to be suitable as semiconductor source and seed sites. The results for the gallium-iodine equilibrium are to a good first approximation independent of the nature of the carrier gas and indicate that hot to cold transport is to be expected over a wide range of iodine concentrations. Analyses of the three phase equilibrium in Ge-Ga-halogen systems show them to also be independent of the nature of the carrier gas.

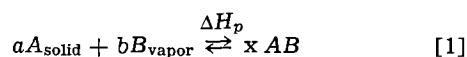
The lack of fundamental information has hindered the controlled optimized use of open tube systems for Ge transport via a disproportionation mechanism. Where such information is available, as is the case for Ge-I₂ (1) interactions, it is not readily employed because of the difficulty in putting it into usable form. When competing reactions due to the presence of reactive carrier gases and/or impurities are involved in the transport process, the problem becomes even more formidable.

To provide a firmer basis for studying the parameters affecting Ge transport via disproportionation mechanisms, it appeared worthwhile to attempt thermodynamic analyses of several potentially interesting systems. While in practice the kinetics of the vapor transport and solid-vapor reactions, not the equilibrium boundaries, represent the limiting factors in a transport process, it is evident that these boundaries at least define upper limits for a set of specified conditions.

This report is concerned with an evaluation of the equilibria that obtain when Ge and/or Ga are mixed with iodine, hydrogen iodide, hydrogen and/or inert gases in systems subject to a constant total pressure constraint.

General Considerations

Effects of simultaneous equilibria.—Given a simple equilibrium of the type represented by Eq. [1], the direction of reaction with increasing or decreasing temperature is readily deduced. Thus, if for Eq. [1]

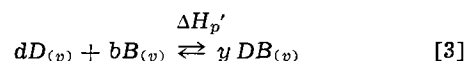


the enthalpic change for the process as written, ΔH_p , is positive, the van't Hoff expression, Eq. [2],

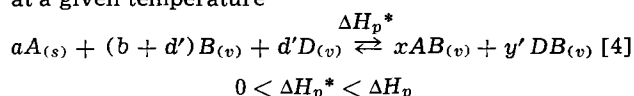
$$K_2/K_1 = e^{-\Delta H_p/R(1/T_2 - 1/T_1)} \quad [2]$$

where the K 's refer to the ratios $(p_{AB})^x/(p_A)^a(p_B)^b$ at the temperatures T_2 and T_1 , leads to the following conclusion: With ΔH_p positive and $T_2 \geq T_1$, $K_2 \geq K_1$. Con-

sequently, with increasing temperature, the reaction as written is driven to the right. In order to effect a vapor phase transport of the solid A via the model specified by Eq. [1], it is necessary that the source temperature of solid A be greater than the sink temperature for this material. With introduction of secondary reactions which tend to compete for one or more of the main transport reaction components, the prediction of transport direction in a temperature gradient is not as readily discernible. For example, in addition to the reaction described by Eq. [1], where for simplicity we will assume the coefficients a , b , and x are unity, in which event ΔH_p is the molar enthalpy of formation of AB , consider the simultaneously occurring equilibrium depicted by Eq. [3] where $\Delta H'_p$ is similar in magnitude to ΔH_p but has a negative sign, and again represents a molar enthalpy of formation.



Suppose that to a container in which one mole of A , and one mole of B have been placed we add a small fraction of a mole of D and an equal quantity of B . The ΔH^*_p for the complete process represented by Eq. [4] at a given temperature



will be positive in sign but slightly less in magnitude than ΔH_p . If subsequent experiments are performed in which the quantity of D is increased, a point will be reached ultimately at which reaction [1] now represents a perturbation on reaction [3], and ΔH^*_p will be negative in sign and transport will occur from the cold to hot regions of the system. Since the coefficients a and b may have any value, *viz.*, Eq. [1] may be multiplied by any number, it is evident that depending on the quantities of A and B initially present and

the relative magnitudes of ΔH_p and $\Delta H_p'$, the effect of addition of a defined quantity of D on both the magnitude, and more important the sign of ΔH_p^* for a given set of conditions will be different. Thus for increasing quantities of A and B the direction of transport will be less likely to change when a specified quantity of D is added. If in addition to all of the above, a vaporous species AD tends to form, the problem is further amplified. Because, as shown above, ΔH_p^* can have an infinite number of values depending on the set of experimental conditions imposed, a knowledge of its sign rather than its absolute value is of greater interest in designing a transport experiment. The sign of ΔH_p^* can be readily obtained by visual inspection of plots of semiconductor/halogen component vapor phase ratios as a function of temperature, as proposed by Lever (1).

Assumptions.—In order to enable analytical treatment of the multispecies systems of interest, it was necessary to involve such commonly employed assumptions as those pertaining to vapor phase ideality and the constancy of enthalpic changes accompanying each reaction with varying temperature. For the temperature and pressure ranges considered neither of these assumptions appears unreasonable. In addition, it was assumed that all pertinent vapor phase species were known and that halogens and halogen compounds were confined solely to the vapor phase in the temperature interval of practical interest. No attempt was made to discontinue analyses below dew point temperatures for the semiconductor halides, all analyses arbitrarily being performed in the temperature interval 0°–800°C. In practice, the data for all, except the highest halogen source pressures, are not affected by dew point considerations above 300°C.

As will become evident, it was necessary to assume that the species pressures of halogens and halogen acids bear a simple relationship to the hypothetical component pressures of halogens and halogen acids at sources of the latter. In other portions of the system this assumption was not required. Based on the available thermodynamic data for iodine and hydrogen iodide dissociation at the temperatures considered this assumption is not unreasonable.

All equilibrium data are based on a standard state choice of 1 mm Hg with species pressures specified with the same dimensions.

Finally, all systems were considered for a total pressure constraint of 760 mm Hg.

Symbols and system representations.—Each of the systems to be discussed is represented by component designations considered most appropriate for the reactions involved. Thus, in some systems, counting of iodine is based on the designation I . In other systems the molecular conservation of this halogen is based on the designation I_2 . Description of a system for example by the notation $Ge-I_2-He$ indicates that component counting is based on moles of diatomic iodine, etc.

Table I presents a list of symbols employed throughout the following discussions.

Table I. Explanation of symbols employed

P	= total pressure in mm		
p_x	= the partial pressure of the vapor phase species x where x has values from 1-12 inclusive, each number referring to a different species		
P_x	= the hypothetical pressure of the component x whose designations coincide with those for p_x		
M_x	= the component mole quantity		
m_x	= the species mole quantity		
x	=	1— I	7— He
		2— I_2	8— Ge
		3— HI	9— GeI
		4— H_2	10— GeI_2
		5— GeI_2	11— Ge
		6— GeI_4	12— H

* An asterisk superscript to one of the above, such as P_x^* , refers to the pressure at the first point considered in the system.

' A prime superscript to one of the above, such as P_x' , refers to the pressure at the second point considered in the system.

Analyses of Systems

The System $Ge-I_2-He$

Experimentally, the treatment relates to a transport apparatus in which an inert gas, He , is transpired through an iodine source bed at some temperature, T , necessary to provide an equilibrium component pressure of iodine, P_2^* . The saturated gas, in which $P_2^* + P_7^* = 760$ mm, is then carried through a germanium source with which the iodine reacts and with which the resulting vapor phase species equilibrate. Since the component I_2 is assumed to be confined to the vapor phase, the component ratio He/I_2 , X , established at the iodine source remains constant thereafter.

From the phase rule it is seen that two parameters are necessary to completely define the isobaric system comprised of three components coexisting in two phases. For convenience, the temperature and the component ratio X , defined above, were chosen. Values of this ratio may be experimentally established at the iodine source bed. At this point in the system, the constant total pressure constraint together with the assumption of the relation between component and species pressures at halogen sources requires that

$$P_7^* = 760 - P_2^* = 760 - p_2^* \quad (I-1)$$

Since

$$p_7^* = m_7^* RT/V \quad (I-2)$$

and

$$p_2^* = m_2^* RT/V \quad (I-3)$$

we obtain after dividing (I-2) by (I-3) for the value of X

$$X = \frac{760 - p_2^*}{p_2^*} \quad (I-4)$$

For specified values of X and T , therefore, the complete system $Ge-I_2-He$ will possess unique values of the partial pressures of the species assumed present. These species are I , I_2 , GeI_2 , GeI_4 , and He , and the five independent relationships employed to calculate their partial pressures at given values of X and T are:

$$I_{2(v)} \rightleftharpoons 2I_{(v)}; K_1 = p_1^2/p_2; \log_{10} K_1 = 8.362 - 7991/T \quad (2) \quad (I-5)$$

$$Ge_{(s)} + I_{2(v)} \rightleftharpoons GeI_{2(v)}; K_3 = p_5/p_2; \log_{10} K_3 = 2.45 + 434/T \quad (1) \quad (I-6)$$

$$Ge_{(s)} + GeI_{4(v)} \rightleftharpoons 2GeI_{2(v)}; K_4 = p_5^2/p_6; \log_{10} K_4 = 12.56 - 7936/T \quad (1) \quad (I-7)$$

$$P = p_1 + p_2 + p_5 + p_6 + p_7 \quad (I-8)$$

$$X = P_7/P_2 = p_7/(1/2 p_1 + p_2 + p_5 + 2p_6) \quad (I-9)$$

The values of the species partial pressures, p_x , were then used to compute the ratio $(Y)_X = f(T)$ where

$$(Y)_X = \frac{P_{11}}{P_2} = \frac{p_5 + p_6}{1/2 p_1 + p_2 + p_5 + 2p_6} \quad (I-10)$$

The ratio $(Y)_X$ is an efficiency factor which shows the number of moles of Ge carried in the vapor phase for each mole of the component I_2 present. Since the component I_2 is confined to the vapor phase, it is evident that if $(Y)_X$ increases with increasing T , the concentration of the component Ge in the vapor must be increasing with increasing T . Consequently, the transport process is a hot to cold one. This implies, therefore, that the sign of ΔH_p^* for the combined processes (I-5)–(I-7) is positive.

In the temperature interval treated, 0°–800°C, Ge deposition occurs primarily as a result of the disproportionation reaction (I-7). The species responsible for this deposition is GeI_2 , the GeI_4 being a disproportionation product. The efficiency factor $(Y)_X$, however, does not discriminate between the disproportionation product GeI_4 and the effective species GeI_2 . A Ge availability factor which may be used in place of Y in the temperature region in question is defined by

$$(Y')_X = p_5/(1/2 p_1 + p_2 + p_5 + 2p_6) \quad (I-11)$$

which to a reasonable first approximation is given in simplified form by

$$(Y')_X \sim p_5/(p_5 + 2p_6) \sim \frac{(Y)_X - 0.5}{0.5} \quad (\text{I-12})$$

It is to be noted that the values of Y' vary between 0 and 1 in distinction to the values of Y which vary between 0.5 and 1. In the temperature interval in which the quantities p_1 and p_2 are not trivial and in which as a matter of fact Ge may be deposited via (I-6) and (I-7), the ratio $(Y')_X$ is no longer valid. If one considers both temperature ranges, then the initial ratio $(Y)_X$ must be employed. This ratio will then encompass the range 0-1. The $(Y)_X$ data provide a family of constant total pressure curves each curve being at constant X , and the family being projected on the Y - T plane.

The System Ge-I₂-H₂

In this system the iodine component value is again based on the I₂ molecule. Experimentally the physical system is that defined in I above. Chemically the systems differ in that a reactive gas also functions as a carrier. For the three component-two phase equilibrium under a constant pressure constraint, two degrees of freedom are again required to fix the state of the system. Those chosen are the temperature and the H₂/I₂ component ratio, X . The species assumed present are I, I₂, HI, H₂, GeI₂, and GeI₄ requiring specification of six independent relations in order to solve for the several species pressures, p_x , at specified values of T and X . The independent set utilized includes (I-5)-(I-7) as well as

$$\text{H}_{2(v)} + \text{I}_{2(v)} \rightleftharpoons 2\text{HI}_{(v)}; K_2 = p_3^2/p_2p_4; \log_{10} K_2 = 0.834 + \frac{622.4}{T} \quad (\text{II-1})$$

$$P = \sum_{x=1}^6 p_x \quad (\text{II-2})$$

$$X = \frac{P_4}{P_2} = \frac{760 - p_2^*}{p_2^*} = \frac{p_4 + 1/2 p_3}{1/2 p_1 + p_2 + 1/2 p_3 + p_5 + 2p_6} \quad (\text{II-3})$$

The partial pressures as a function of T for specified values of X were used to compute values of $(Y)_X = f(T)$ where

$$(Y)_X = P_{11}/P_2 = (p_5 + p_6)/(1/2 p_1 + p_2 + 1/2 p_3 + p_5 + 2p_6) \quad (\text{II-4})$$

The System Ge-I₂-H₂-He

Experimentally, the physical system conforms to one in which He and hydrogen sources are used to provide a carrier mixture having a H₂ mole fraction F . This mixed gas is then transpired through an iodine source supply where setting of the pressure of iodine fixes the ratio H₂/I₂, X . The four component system coexisting in two phases possesses three degrees of freedom. These have been chosen as F , X , and T . The seven species, I, I₂, HI, H₂, He, GeI₂, and GeI₄ are assumed present in the complete system. For specified values of F , X , and T the partial pressures of these species were obtained by simultaneous solution of (I-5)-(I-7), (II-1) and

$$P = \sum_{x=1}^7 p_{x,s} \quad (\text{III-1})$$

$$F = \frac{P_4}{P_4 + P_7} = \frac{1/2 p_3 + p_4}{1/2 p_3 + p_4 + p_7} \quad (\text{III-2})$$

$$X = \frac{P_4}{P_2} = \frac{1/2 p_3 + p_4}{1/2 p_1 + p_2 + 1/2 p_3 + p_5 + 2p_6} \quad (\text{III-3})$$

Experimentally, values for F and X are established at the points of mixing of hydrogen and helium and at the iodine source, respectively. Since the compo-

nents H₂, He, and I₂ are always confined to the vapor phase, these ratios once established remain constant thereafter. At the point of mixing of H₂ and He it is the case that

$$F = \frac{P_4^*}{P_4^* + P_7^*} = \frac{P_4^*}{760} \quad (\text{III-4})$$

Since the system is constrained by the total pressure being equal to 1 atm, and since the gas behavior is assumed to be ideal, it is seen that at the point of mixing of He and H₂

$$\frac{\text{Flow rate of H}_2}{\text{Total flow rate}} = F \quad (\text{III-5})$$

In transpiring this mixture F through the iodine source the sum of the pressures of hydrogen and helium $p'_4 + p'_7$ no longer = 760 mm since p'_2 will account for part of the total. The ratio X may be defined experimentally as follows. As the combined pressure of He + H₂ at the iodine source is given by

$$(P'_4 + P'_7) = (760 - P'_2) \quad (\text{III-6})$$

and the mole fraction of H₂ relative to He and H₂ must remain constant everywhere in the system, we see that dividing (III-6) by P_4 and rearranging leads to

$$P'_4 = F(760 - P'_2) \quad (\text{III-7})$$

Thus, X can be specified by

$$X = \frac{F(760 - P'_2)}{P'_2} \quad (\text{III-8})$$

in the region of the iodine source.

Solutions to the several $p_{x,s}$ as a function of T were obtained for specified values of X and F . These p_x data were then used to compute families of Y curves, each curve in a family representing the variation of Y with T at constant F and X , and each family being specified at constant P'_2 . The expansion of $(Y)_{F,X}$ has the same form as (II-4). It is evident that in order to obtain finite and physically significant solutions it is necessary that $0 < F < 1$ and $0 < P'_2 < 760$ mm Hg.

The System Ge-HI-H

This case is thermodynamically equivalent to that defined in (II) above insofar as the same species are assumed present, and the equilibrium relationships employed are the same. The treatment is, however, based on a different choice of component stoichiometries, more consistent with the experiment in mind. It is to be noted that the hydrogen species content in the present instance cannot independently be brought to zero. As implied by the system designation, component counting is accomplished in terms of Ge, HI, and H, a differentiation being made between hydrogen derived from a source tank and from the halogen acid. In addition, hydrogens are counted singly. As before, two degrees of freedom exist at constant total pressure. These were chosen as the temperature and the component ratio H/HI, X^+ . In an experiment, X^+ is established as follows: At the point of mixing of HI and H₂ the mole fraction of the component HI, k , is fixed for the entire system. At this mixing point, therefore, we may write

$$k = \frac{P_3^*}{760} = \frac{\text{Flow rate of HI}}{\text{Total flow rate}} \quad (\text{IV-1})$$

Since at this same point

$$X^+ = \frac{P_{12}^*}{P_3^*} = \frac{2P_4^*}{P_3^*} = \frac{2(760 - P_3^*)}{P_3^*} \quad (\text{IV-2})$$

it is seen from (IV-1) and (IV-2) that

$$X^+ = \frac{2(1-k)}{k} \quad (\text{IV-3})$$

Solutions for the six species partial pressures were obtained from (I-5)-(I-7), (II-1), (II-2), and

$$X^+ = \frac{P_{12}}{P_3} = \frac{2p_4 - 2p_2 - p_1 - 2p_5 - 4p_6}{p_1 + 2p_2 + p_3 + 2p_5 + 4p_6} \quad (\text{IV-4})$$

The partial pressures were then used to compute values of the efficiency factor $(Y^+)_{X^+} = f(T)$ with $(Y^+)_{X^+}$ defined by

$$(Y^+)_{X^+} = \frac{P_{11}}{P_3} = \frac{p_5 + p_6}{p_1 + 2p_2 + p_3 + 2p_5 + 4p_6} \quad (\text{IV-5})$$

The System Ge-HI-H-He

This system is thermodynamically equivalent to that described in case (III), and makes use of the same equilibrium relationships. The three degrees of freedom for the system at constant pressure were chosen as the temperature, the component ratio $1/2\text{H}/(1/2\text{H} + \text{He})$, F^+ , and the component ratio H/HI , X^+ .

At the point of mixing of hydrogen and helium, the ratio F^+ is given by

$$F^+ = \frac{1/2 P_{12}^*}{760} = \frac{\text{Flow rate of H}_2}{\text{Total flow rate}} \quad (\text{V-1})$$

At the point of mixing of the hydrogen-helium mixture with HI, the mole fraction of HI in the total gas mixture is given by

$$k = \frac{P'_3}{760} = \frac{\text{Flow rate of HI}}{\text{Total flow rate}} \quad (\text{V-2})$$

Since the pressure of the component H at this point is given by

$$P_{12} = 2F^+ (760 - P'_3) \quad (\text{V-3})$$

it is seen that

$$X^+ = \frac{P_{12}}{P_3} = \frac{2F^+ (1 - k)}{k} \quad (\text{V-4})$$

In the system containing all of the components, the equations for F^+ and X^+ used in addition to (I-5)-(I-7), (II-1), and (III-1), for obtaining simultaneous solutions for the seven species partial pressures are

$$F^+ = \frac{p_4 - 1/2 p_1 - p_2 - p_5 - 2p_6}{p_4 - 1/2 p_1 - p_2 - p_5 - 2p_6 + p_7} \quad (\text{V-5})$$

and

$$X^+ = \frac{P_{12}}{P_3} = \frac{2F^+ (1 - k)}{k} = \frac{2p_4 - p_1 - 2p_2 - 2p_5 - 4p_6}{p_1 + 2p_2 + p_3 + 2p_5 + 4p_6} \quad (\text{V-6})$$

Families of curves $(Y^+)_{F^+, X^+} = f(T)$ were computed, each family derived at constant total P and P'_3 , with the expanded form of $(Y^+)_{F^+, X^+}$ equal to that shown in Eq. (IV-5).

The System Ga-I-He

The treatment follows that for case (I), excepting that iodine counting is based on a monatomic stoichiometry. In addition to Eq. (I-5), the following were employed to obtain partial pressures for the six species I, I₂, Ga, GaI, GaI₃, and He.

$$P = p_1 + p_2 + \sum_7^{10} p_x \quad (\text{VI-1})$$

$\text{Ga}_{(l)} = \text{Ga}_{(v)}$; $K_5 = p_8$;

$$\log_{10} K_5 = -\frac{14,900}{T} - 0.515 \log_{10} T + 10.22 \quad (\text{VI-2})$$

$2\text{Ga}_{(l)} + \text{GaI}_{3(v)} = 3\text{GaI}_{(v)}$; $K_6 = \frac{p_9^3}{p_{10}}$;

$$\log_{10} K_6 = -\frac{11,000}{T} + 18.6 \quad (\text{VI-3})$$

$\text{Ga}_{(v)} + \frac{3}{2} \text{I}_2(v) = \text{GaI}_{3(v)}$; $K_7 = \frac{p_{10}}{p_2^{3/2} p_3}$;

$$\log_{10} K_7 = -9.565 \log_{10} T + \frac{24,780}{T} + 15.78 \quad (\text{VI-4})$$

The variable X^o is defined by

$$X^o = \frac{P_7}{P_1} = \frac{760 - P_2^*}{2P_2^*} = \frac{p_7}{p_1 + 2p_2 + p_9 + 3p_{10}} \quad (\text{VI-5})$$

Derived data were used to compute a family of curves of $(R^o)_{X^o} = f(T)$ where

$$(R^o)_{X^o} = \frac{P_8}{P_1} = \frac{\sum_8^{10} p_x}{p_1 + 2p_2 + p_9 + 3p_{10}} \quad (\text{VI-6})$$

The System Ga-HI-H

This Ga analog of system (IV) is defined on the basis of the seven species model, I, I₂, HI, H₂, Ga, GaI, and GaI₃ and makes use of the variables X^+ and T in addition to the equilibrium statements (I-5), (II-1) and (VI-2)-(VI-4). The total pressure constraint is given by

$$P = \sum_1^4 p_x + \sum_8^{10} p_x \quad (\text{VII-1})$$

and X^+ in expanded form by

$$X^+ = \frac{P_{12}}{P_3} = \frac{2(1 - k)}{k} = \frac{2p_4 - p_1 - 2p_2 - p_9 - 3p_{10}}{p_1 + 2p_2 + p_3 + p_9 + 3p_{10}} \quad (\text{VII-2})$$

The ratio $(R^+)_{X^+} = f(T)$ was derived, providing a family of curves all at constant total P . $(R^+)_{X^+} = f(T)$ is defined by

$$(R^+)_{X^+} = \frac{P_8}{P_3} = \frac{\sum_8^{10} p_x}{p_1 + 2p_2 + p_3 + p_9 + 3p_{10}} \quad (\text{VII-3})$$

The System Ga-HI-H-He

The species assumed present were I, I₂, HI, H₂, He, Ga, GaI, and GaI₃. The same degrees of freedom were utilized as in case (V). As in the previous Ga treatments (I-5), (II-1), and (VI-2)-(VI-4) were employed. P is defined by

$$P = \sum_1^4 p_x + \sum_7^{10} p_x \quad (\text{VIII-1})$$

F^+ by

$$F^+ = \frac{\frac{1}{2} P_{12}^*}{760} = \frac{p_4 - \frac{1}{2} p_1 - p_2 - \frac{1}{2} p_9 - \frac{3}{2} p_{10}}{p_4 - \frac{1}{2} p_1 - p_2 - \frac{1}{2} p_9 - \frac{3}{2} p_{10} + p_7} \quad (\text{VIII-2})$$

and X^+ by

$$X^+ = \frac{P_{12}}{P_3} = \frac{2F^+ (1 - k)}{k} = \frac{2p_4 - p_1 - 2p_2 - p_9 - 3p_{10}}{p_1 + 2p_2 + p_3 + p_9 + 3p_{10}} \quad (\text{VIII-3})$$

values of $(R^+)_{F^+, X^+} = f(T)$ were derived providing families of curves each at constant total P and P'_3 .

$(R^+)_{F^+, X^+}$ is defined by (VII-3).

The System Ge-Ga-I-He

This analysis was attempted in order to define conditions for maximum incorporation of Ga in an epitaxial Ge film. Consequently, it is based on a treatment for the three-phase equilibrium Ge (solid solu-

tion)-liquid-vapor. Two approaches were utilized. The first assumed that the solubility of Ga in Ge is small enough so that $p_{\text{Ge}}/p^{\circ}_{\text{Ge}} = 1$, and the liquid in equilibrium with solid Ge is for all practical purposes pure liquid Ga. The second approach makes use of the first assumption but not the second. In its place the assumption is made that if the solid-liquid curve for Ge solid is ideal, the liquid-vapor equilibrium obeys Raoult's law. In either case the systems are such that experimentally they are approximated by having a mixed bed of liquid Ga saturated with Ge, and Ge solid saturated with Ga, all in transpiration with a vapor stream. Species assumed present were I, I₂, GeI₂, GeI₄, He, Ga, GaI, and GaI₃. The two degrees of freedom chosen were T and the ratio He/I , X° .

Approach 1.—The equilibria used were (I-5)-(I-7) and (VI-2)-(VI-4) along with

$$P = \sum_1^2 p_x + \sum_5^10 p_x \quad (\text{IX-1})$$

$$X^{\circ} = \frac{P_7}{P_1} = \frac{760 - p_2^*}{2p_2^*} = \frac{p_7}{p_1 + 2p_2 + 2p_5 + 4p_6 + p_9 + 3p_{10}} \quad (\text{IX-2})$$

Values of $(Y^{\circ})_{X^{\circ}} = f(T)$ and $(R^{\circ})_{X^{\circ}} = f(T)$ were derived providing two families of curves. The expanded forms of these efficiency factors are given by

$$(Y^{\circ})_{X^{\circ}} = \frac{P_{11}}{P_1} = \frac{p_5 + p_6}{p_1 + 2p_2 + 2p_5 + 4p_6 + p_9 + 3p_{10}} \quad (\text{IX-3})$$

and

$$(R^{\circ})_{X^{\circ}} = \frac{P_8}{P_1} = \frac{\sum_8^{10} p_x}{(p_1 + 2p_2 + 2p_5 + 4p_6 + p_9 + 3p_{10})} \quad (\text{IX-4})$$

An indication of the final state, that is, whether the deposit is richer or poorer than the source in Ge or Ga, can be discerned from a consideration of $(R^{\circ}/Y^{\circ})_{X^{\circ}} = f(T)$. Where this ratio increases with decreasing temperature, it is the case that the bulk deposit is poorer in Ga than the source. Similarly, when the ratio decreases, the bulk deposit is richer in Ga.

Approach 2.—Everything specified in 1 above with the exception of (VI-2) is utilized. In place of (VI-2) a modified relation based on the following argument is used. Thurmond and Kowalchick (7) have indicated that to a good first approximation the solubility of Ge in liquid Ga is predicted by the simple van't Hoff relationship, and that at temperatures not too far removed from the melting point of Ge, $\Delta H_{\text{fusion Ge}}$ can be considered constant. With this information and the assumption that the liquid-vapor equilibrium obeys Raoult's law when the solid-liquid equilibrium is ideal, the vapor pressure curve along the Ge liquidus may be deduced.

Let the vapor pressure of pure liquid Ga at any temperature T be designated p°_{Ga} . For the equilibrium (VI-2) we write

$$K_5 = p^{\circ}_{\text{Ga}} \quad (\text{VI-2})$$

Along the ideal liquidus we may then write

$$p_{\text{Ga}} = N_{\text{Ga}} \cdot p^{\circ}_{\text{Ga}} \quad (\text{IX-5})$$

for the equilibrium

$$\text{Ga}_{\text{liquid solution}} \rightleftharpoons \text{Ga}_{\text{vapor}} \quad (\text{IX-6})$$

where p_{Ga} = the partial pressure of Ga over the solution and N_{Ga} = the mole fraction of Ga.

Since

$$N_{\text{Ga}} = 1 - N_{\text{Ge}} \quad (\text{IX-7})$$

in the liquid, and

$$N_{\text{Ge}} = -\frac{\Delta H_{\text{Ge}}}{R} \left(\frac{1}{T} - \frac{1}{T_{\text{Ge}}} \right) \quad (\text{IX-8})$$

ΔH_{Ge} being the heat of fusion of Ge and T_{Ge} being the melting point of Ge, we may substitute for p°_{Ga} and N_{Ga} in (IX-5), the equivalencies given by (VI-2) and (IX-7). Thus

$$p_{\text{Ga}} = N_{\text{Ga}} K_5 = K_9 \quad (\text{IX-9})$$

$$\log K_9 = \log K_5 + \log N_{\text{Ga}} \quad (\text{IX-10})$$

As

$$N_{\text{Ge}} = 10 \left(-\frac{1770}{T} + 1.46 \right) \quad (7) \quad (\text{IX-11})$$

it is seen that

$$\log_{10} N_{\text{Ga}} = \log_{10} \left[1 - 10 \left(-\frac{1770}{T} + 1.46 \right) \right] \quad (\text{IX-12})$$

and finally that

$$\log_{10} K_9 = -\frac{14,900}{T} - 0.515 \log_{10} T + 10.22 + \log_{10} \left[1 - 10 \left(-\frac{1770}{T} + 1.46 \right) \right] \quad (\text{IX-13})$$

The same data were extracted as in Approach 1.

The System Ge-Ga-HI-H

As in the preceding analysis two approaches were employed using the identical assumptions.

Approach 1.—In addition to (I-5)-(I-7), (II-1) and (VI-2)-(VI-4), the two chosen degrees of freedom were the temperature and the ratio X^+ . The expansions for P and X^+ were as follows:

$$P = \sum_1^6 p_x + \sum_8^10 p_x \quad (\text{X-1})$$

$$X^+ = \frac{P_{12}}{P_3} = \frac{2(1-k)}{k} = \frac{2p_4 - p_1 - 2p_2 - 2p_5 - 4p_6 - p_9 - 3p_{10}}{p_1 + 2p_2 + p_3 + 2p_5 + 4p_6 + p_9 + 3p_{10}} \quad (\text{X-2})$$

Solutions were as usual obtained for the p_x 's and the efficiency factors. These are

$$(Y^+)_{X^+} = \frac{P_{11}}{P_3} = \frac{p_5 + p_6}{p_1 + 2p_2 + p_3 + 2p_5 + 4p_6 + p_9 + 3p_{10}} \quad (\text{X-3})$$

$$(R^+)_{X^+} = \frac{P_8}{P_3} = \frac{p_8 + p_9 + p_{10}}{p_1 + 2p_2 + p_3 + 2p_5 + 4p_6 + p_9 + 3p_{10}} \quad (\text{X-4})$$

The ratios $(R^+/Y^+)_{X^+} = f(T)$ were also obtained.

Approach 2.—Equation (VI-2) is replaced by (IX-13), everything else remaining unchanged.

The System Ge-Ga-HI-H-He

This final system containing 10 species and three degrees of freedom was treated using two approaches, one making use of (VI-2)-(VI-4) plus the appropriate Ge equations and (II-1), and the other using (IX-13) instead of (VI-2). Both make use of (XI-1)-(XI-3). Solutions were obtained for $(Y^+)_{X^+,F^+}$ and $(R^+)_{X^+,F^+}$ both as a function of T , defined by (X-3) and (X-4) and the ratio $(R^+/Y^+)_{X^+,F^+} = f(T)$.

$$P = \sum_1^{10} p_x \quad (\text{XI-1})$$

$$F^+ = \frac{1/2 P_{12}^*}{760} = \frac{p_4 - 1/2 p_1 - p_2 - p_5 - 2p_6 - 1/2 p_9 - 3/2 p_{10}}{p_4 - 1/2 p_1 - p_2 - p_5 - 2p_6 - 1/2 p_9 - 3/2 p_{10} + p_7} \quad (\text{XI-2})$$

$$X^+ = \frac{P_{12}}{P_3} = \frac{2F^+(1-k)}{k}$$

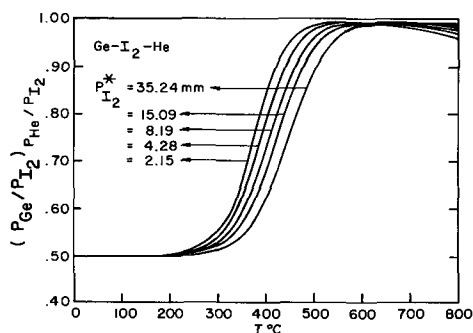


Fig. 1. Efficiency curves for the system Ge-I₂-He at varying iodine source bed pressures.

$$= \frac{2p_4 - p_1 - 2p_2 - 2p_5 - 4p_6 - p_9 - 3p_{10}}{p_1 + 2p_2 + p_3 + 2p_5 + 4p_6 + p_9 + 3p_{10}} \quad (\text{XI-3})$$

Results and Discussion

The System Ge-I₂-He

Figure 1 graphically depicts the variation of the component ratio $\text{Ge}/\text{I}_2 = Y$ as a function of temperature. Each projected curve represents a different He/I_2 ratio, X , consequently each coincides with a different iodine source bed temperature. The curves all exhibit the same general shape and are indicative of hot to cold transport over most of the temperature range surveyed. At the low temperature end of the scale plateaus develop at approximately 220° and a Y value of 0.5, the proper value for a vapor phase species stoichiometry of GeI_4 . The 220° plateaus are experimentally unimportant since this temperature lies below the dew points of both GeI_4 and GeI_2 for the iodine pressures considered. At the high temperature end of the scale plateaus also develop, the highest X curve flattening at 550°C and the lowest at 600°C. These plateaus, as will be discussed below, are experimentally significant.

It is significant that the efficiency of forming GeI_2 (higher Y values) decreases with increasing I_2 source bed pressure (decreasing X values) over most of the temperature range. This conclusion is most clearly focused upon by a consideration of Table II which lists calculated values of the pressures of GeI_2 and GeI_4 at different germanium and iodine source bed temperatures. It is seen that, while the absolute value of GeI_2 increases with increasing I_2 source bed pressure, excepting at high Ge source bed temperatures, a disproportionate percentage of the vapor phase Ge content is present as the product of the disproportionation process and therefore unavailable as a deposition species.

The large slopes in the temperature interval in which seeds might be placed indicate that extremely close tolerance seed temperature control would be required in order to effect reproducible deposition rates. On the

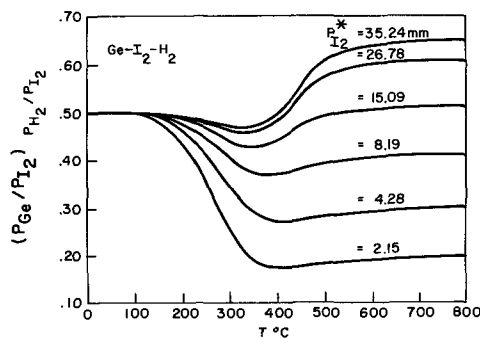


Fig. 2. Efficiency curves for the system Ge-I₂-H₂ at varying iodine source bed pressures.

other hand if Ge source temperatures are made coincident with the high-temperature plateau intervals, close temperature control tolerance at the Ge source sites is not very critical. Furthermore, use of these plateaus would obviate the efficiency question discussed above. In all the systems discussed it is evident that even when transpiration conditions are attained at source beds, control of flow rates will represent a critical factor in achieving reproducible deposition rates, all other factors remaining constant.

The System Ge-I₂-H₂

Figure 2 shows an equivalent plot to that given in Fig. 1 for the case where the carrier gas is also a reactive component. It is noted on comparison of Fig. 1 and 2 that whereas the Ge/I_2 ratio never drops below 0.5 in the nonreactive carrier gas system it does so when H_2 is present. This is believed due to the competition for iodine between Ge and H_2 . Since the heat of formation of HI is negative [Eq. (II-1)] the effects of this competition decrease with increasing temperatures and are greatest at low iodine pressures and low temperatures. In the present analysis, two other marked perturbations are evident. First, the efficiency in terms of formation of GeI_2 increases with increasing iodine source bed temperature and, second, the competition for iodine results in the occurrence of low temperature cold to hot transport regions which generate minima in the curves. These minima fall in convenient temperature regions for seed locations providing less temperature sensitive sites. Aside from the higher pressure curves, however, the utility of the system in its described form is questionable since the system is inefficient, the Y ratio not approaching one at any temperature due to the large quantity of HI present. This is seen by examination of Table III which presents several $P_{\text{I}_2}^*$ source values and the resulting pressures of GeI_2 , GeI_4 , and HI in the thermodynamic system.

A comparison of Fig. 1 and 2 raised the interesting possibility of developing low-temperature minima in usable seed site temperature intervals by employing mixtures of H_2 and He as carrier gases. Thus, it is

Table II. Selected data for the Ge-I₂-He System

T _{Ge} source, °C	P* _{I₂} mm	pGeI ₂ mm	pGeI ₄ mm
350	35.24	3.308	16.34
400	35.24	8.920	13.47
450	35.24	18.29	8.665
500	35.24	27.65	3.865
550	35.24	32.67	1.284
350	15.09	2.096	6.562
400	15.09	5.382	4.901
450	15.09	9.975	2.578
500	15.09	13.30	0.895
550	15.09	14.56	0.255
350	2.154	0.698	0.729
400	2.154	1.446	0.354
450	2.154	1.954	0.099
500	2.154	2.105	0.022
550	2.154	2.136	0.005

Table III. Source values and pressures

T _{Ge} source, °C	P* _{I₂} mm	pGeI ₂ mm	pGeI ₄ mm	pHI mm
350	35.24	3.042	13.82	10.38
400	35.24	7.686	9.998	16.02
450	35.24	14.28	5.281	21.25
500	35.24	19.39	1.901	24.21
550	35.24	21.57	0.560	25.07
350	15.09	1.775	4.704	8.001
400	15.09	3.974	2.673	11.64
450	15.09	6.117	0.970	14.10
500	15.09	7.120	0.256	14.91
550	15.09	7.448	0.067	14.99
350	2.154	0.287	0.123	3.242
400	2.154	0.355	0.021	3.512
450	2.154	0.377	0.004	3.539
500	2.154	0.389	0.001	3.525
550	2.154	0.398	0.000	3.507

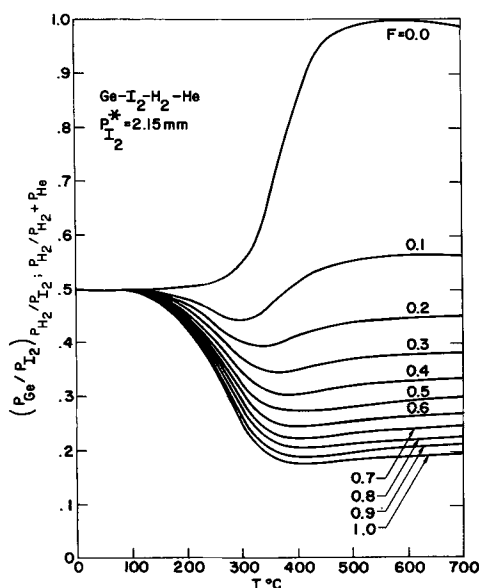


Fig. 3. Efficiency curves for the system Ge-I₂-H₂-He at an iodine source bed pressure of 2.15 mm and varying H₂/(H₂ + He) fractions.

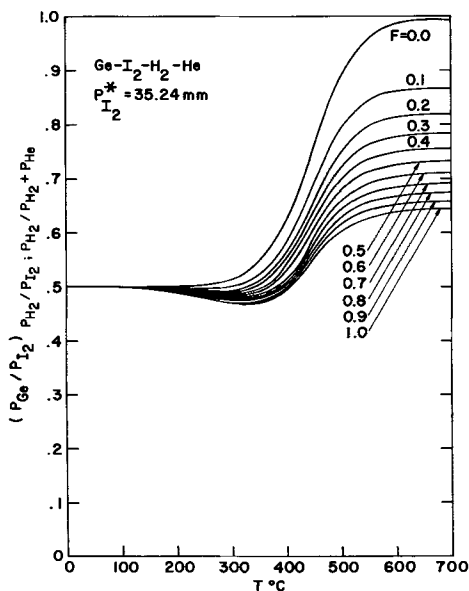


Fig. 4. Efficiency curves for the system Ge-I₂-H₂-He at an iodine source bed pressure of 35.24 mm and varying H₂/(H₂ + He) fractions.

observed that the minima in Fig. 2 for a particular iodine source temperature lie at higher temperatures than the low-temperature plateaus of Fig. 1. It was reasoned that if the H₂ carrier is diluted with He, the competitive action of H₂ would decrease causing the minima to shift to lower temperatures and to become more shallow in the process. This possibility occasioned the analysis of the following system.

The System Ge-I₂-H₂-He

Figures 3 and 4 show the variations of Ge/I₂ ratio with temperature for two families of curves, each family being at constant P_{I₂}* and each curve in a family representative of a different H₂-He mixture. Thus, the data for a given curve depicts (Y)_{F,X} = f(T). Present in each family are reiterations of the curves derived from the analysis of systems I and II to provide a complete picture. Figures 5 and 6 present some of the data in a different fashion, namely, with constant H₂/(He + H₂) mole fractions, where the values of Y are plotted as a function of T, each curve depicting a different iodine source temperature. Figure 1 repre-

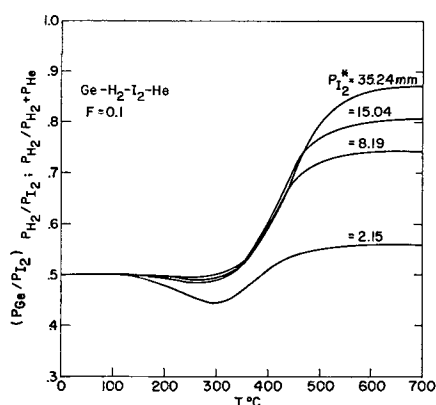


Fig. 5. Efficiency curves for the system Ge-I₂-H₂-He at a H₂/(H₂ + He) fraction of 0.1 and varying iodine source bed pressures.

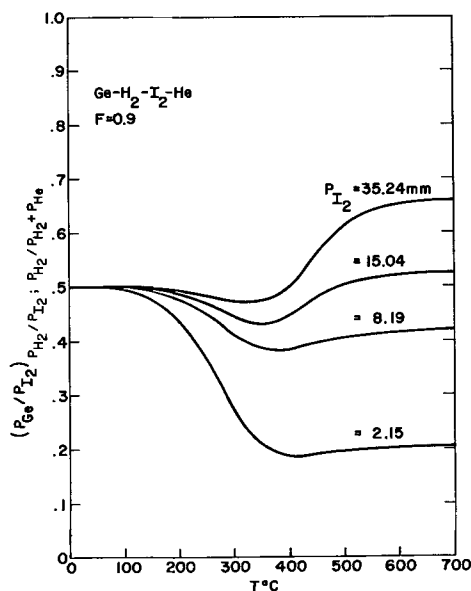


Fig. 6. Efficiency curves for the system Ge-I₂-H₂-He at a H₂/(H₂ + He) fraction of 0.9 and varying iodine source bed pressures.

sents the case of F = 0 and Fig. 2 the case for F = 1.

As seen from Fig. 3 and 4 the perturbation of the pure He curves increases with increasing H₂/(He + H₂) mole fraction (increasing F), the higher I₂ source pressure curves being most efficient over-all and providing what appear to be the least temperature sensitive seed site regions, coupled with high relative GeI₂ formation efficiency.

The System Ge-HI-H

The data for this system (Fig. 7) are presented in the form of Ge/Hi ratios, a value of 0.25 now coincident with pure GeI₄ and 0.5 coincident with pure GeI₂. The range of iodine pressures covered, 1.9 mm I₂-361 mm I₂, is larger than those treated in the I₂ systems previously discussed. It is seen that as found in system II, the efficiency of GeI₂ formation increases with increasing iodine pressure. Furthermore, at the highest P_{HI}* pressures the minima give way to low temperature plateaus with relative temperature insensitivity up to 400°.

The System Ge-HI-H-He

The data for this system are depicted in a manner similar to those of system III. Thus, Fig. 8-14 present families of curves each family at constant component HI mole fraction k and Fig. 15 and 16 depict two families of curves at constant H₂ mole fraction relative to H₂-He mixtures. From the first set of graphs it is seen that as the P_{HI}* values increase, the effect of varying H₂/(H₂ + He) mole fraction diminishes, finally result-

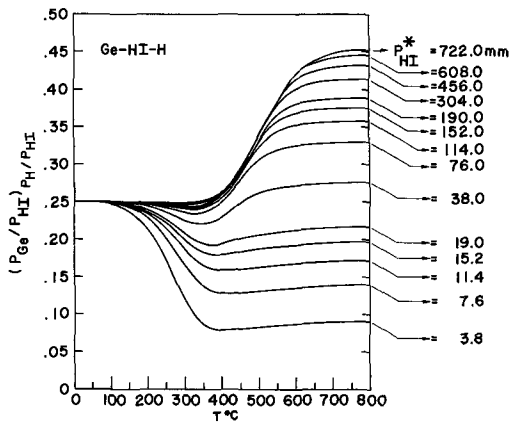


Fig. 7. Efficiency curves for the system Ge-HI-H at varying hydrogen iodide source pressures.

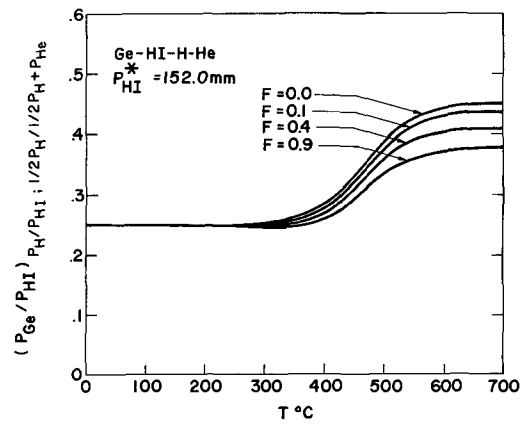


Fig. 11. Efficiency curves for the system Ge-HI-H-He at an HI source pressure of 152.0 mm and varying $H_2/(H_2 + He)$ fractions.

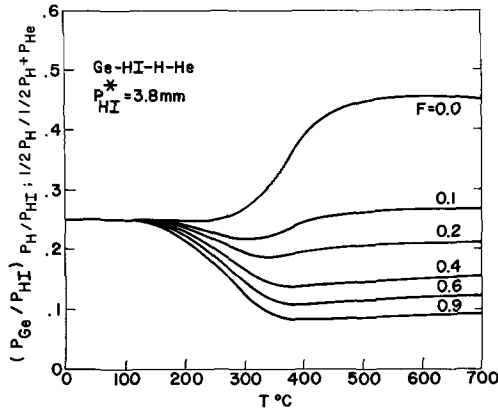


Fig. 8. Efficiency curves for the system Ge-HI-H-He at an HI source pressure of 3.8 mm and varying $H_2/(H_2 + He)$ fractions.

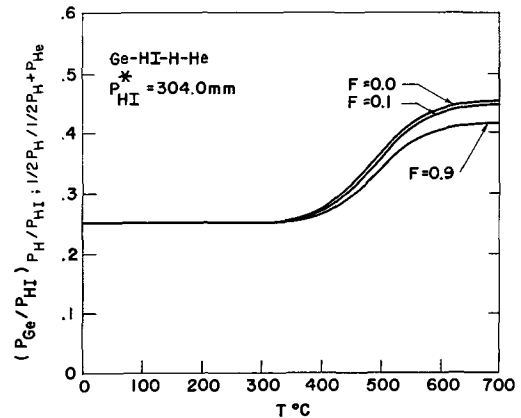


Fig. 12. Efficiency curves for the system Ge-HI-H-He at an HI source pressure of 304.0 mm and varying $H_2/(H_2 + He)$ fractions.

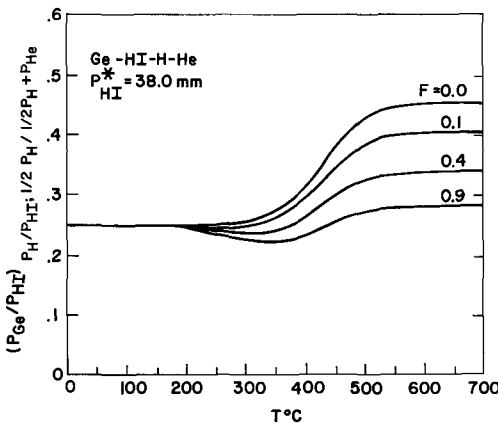


Fig. 9. Efficiency curves for the system Ge-HI-H-He at an HI source pressure of 38.0 mm and varying $H_2/(H_2 + He)$ fractions.

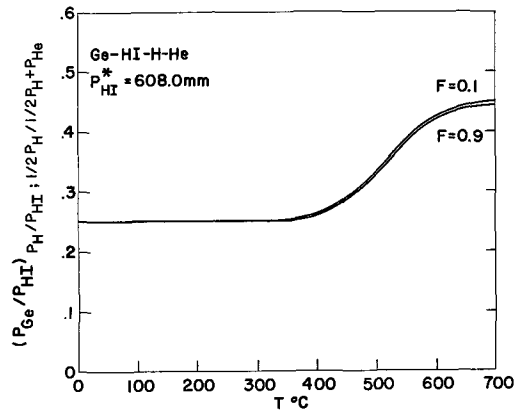


Fig. 13. Efficiency curves for the system Ge-HI-H-He at an HI source pressure of 608.0 mm and varying $H_2/(H_2 + He)$ fractions.

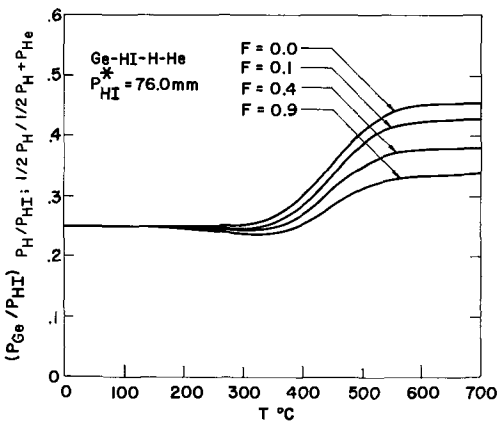


Fig. 10. Efficiency curves for the system Ge-HI-H-He at an HI source pressure of 76.0 mm and varying $H_2/(H_2 + He)$ fractions.

ing in data at 722 mm P_{HI}^* in which the curves for $F = 0.1$ and 0.9 are indistinguishable. Since the minimum component pressure value of hydrogen possible in these systems coincides with the partial pressure of component iodine, the Y^+ values are always less efficient than the Y values of system I. At low $H_2/(H_2 + He)$ mole fractions it is the case that over appreciable temperature regions the high P_{HI}^* curves are more efficient than the lower pressure ones. However, the slopes and temperatures of plateau or minima occurrence appear more usable in the lower pressure cases.

It is to be pointed out that the figures include data for $F = 0$. These were obtained from a separate partial analysis of the system Ge-HI-He, arguments for which are not presented, but whose format is similar

to the related systems. A constraint was employed setting the H/I ratio = 1.

The System Ga-I-He

Figure 17 shows the results for this system. In essence the data are quite similar to those for the Ge analog, system I, and need not be discussed further.

The System Ga-HI-H

The data for this system, Fig. 18, are completely unlike those for the Ge analog, systems II and IV. First, the efficiency in formation of the transporting species GaI is greater at lowest P_{HI}^* pressures. Second, no minima develop. These results are not unexpected in view of the large values for the Ga-I equilibrium constants which preclude any competition for iodine by

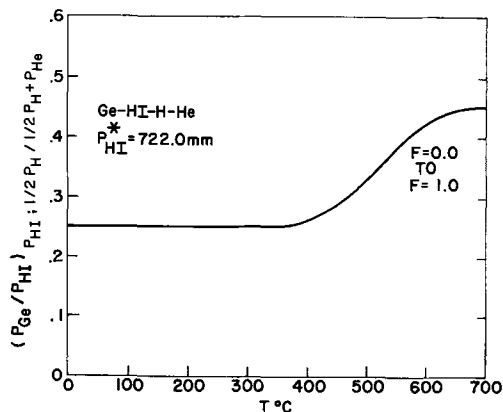


Fig. 14. Efficiency curves for the system Ge-HI-H-He at an HI source pressure of 722.0 mm and varying $H_2/(H_2 + He)$ fractions.

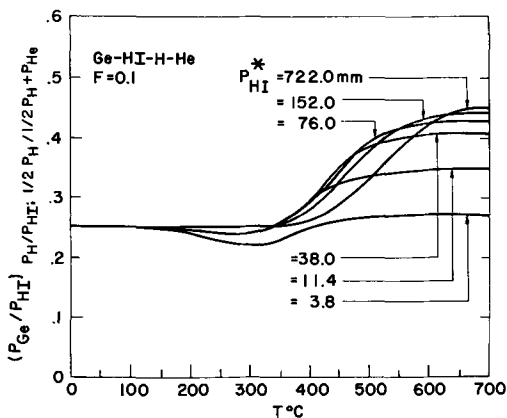


Fig. 15. Efficiency curves for the system Ge-HI-H-He at a $H_2/(H_2 + He)$ fraction of 0.1 and varying hydrogen iodide source pressures.

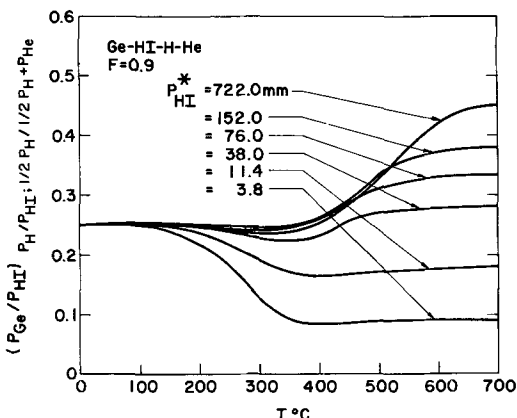


Fig. 16. Efficiency curves for the system Ge-HI-H-He at a $H_2/(H_2 + He)$ fraction of 0.9 and varying hydrogen iodide source pressures.

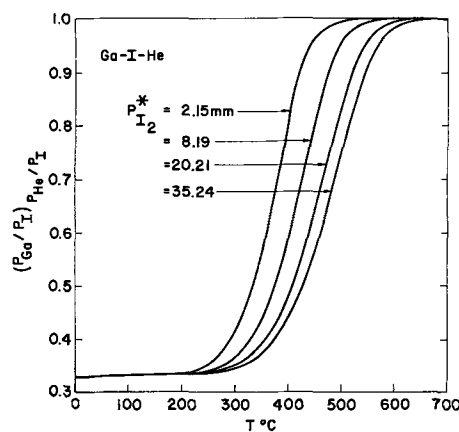


Fig. 17. Efficiency curves for the system Ga-I-He at varying iodine source bed pressures.

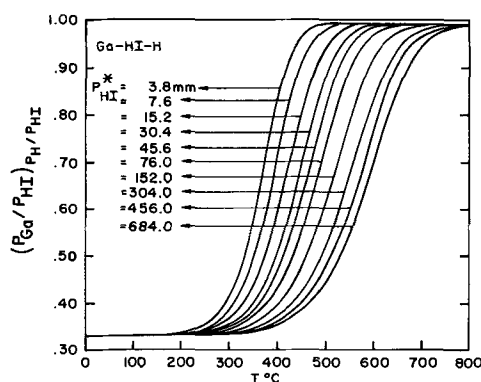


Fig. 18. Efficiency curves for the system Ga-HI-H at varying hydrogen iodide source pressures.

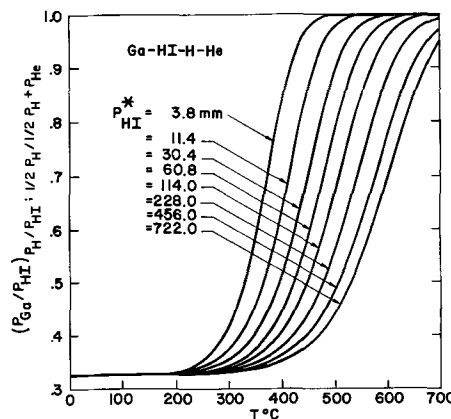


Fig. 19. Efficiency curves for the system Ga-HI-H-He at varying hydrogen iodide source pressures, and representing all $H_2/(H_2 + He)$ fractions between 0.1 and 0.9.

hydrogen. This system represents a clear case where one reaction dominates all others, independent of the signs of the ΔH_p 's, and remains essentially unperturbed in the presence of a reactive carrier gas.

The System Ga-HI-H-He

The data are presented in the form of a single family of curves at constant F^+ value, Fig. 19. Again, because of the domination of competing equilibria by the primary one, the effect of inert-reactive carrier gas mixtures is undetectable. Thus, depending on P_{HI}^* alone, the $(R^+)_{X+,F^+}$ values appear to be determined, the system behaving as one of only three components.

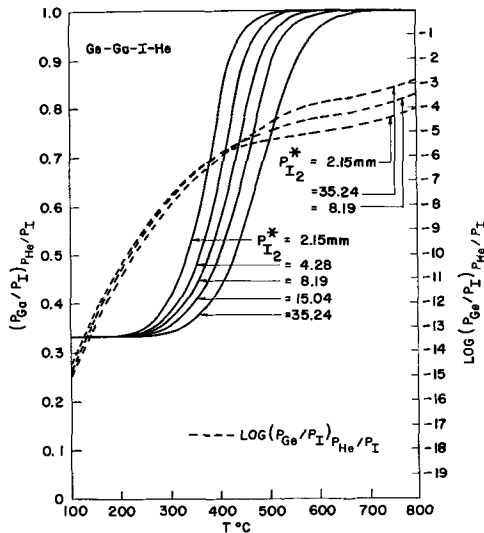


Fig. 20. Efficiency curves for the system Ge-Ga-I-He at varying iodine source bed pressures.

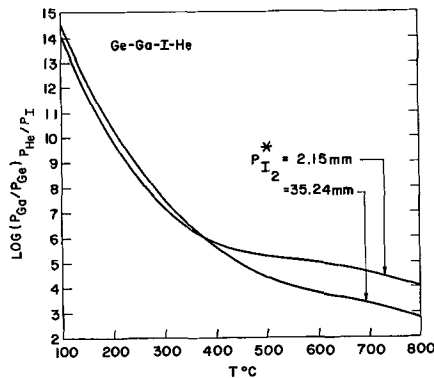


Fig. 21. Variation of Ga/Ge vapor phase content in the system Ge-Ga-I-He at two different iodine source bed pressures.

The System Ge-Ga-I-He

As discussed previously, two approaches were employed. These led to sets of data essentially indistinguishable from one another and as a consequence only one set of results, Fig. 20, is presented, that from the second approach. In Fig. 20 $(R^0)_{X_0}$ and $\log_{10}(Y^0)_{X_0}$ values are plotted as a function of T . It is to be noted that while the R^0 data vary in the range 0-1, the Y^0 data vary in the range 10^{-22} - 10^{-4} . This implies that in the mixed transport, the quantity of Ge moved from the source is many orders of magnitude smaller than the quantity of Ga transported. Also, while the R^0 curves follow the same general contours as where no Ge is present, the Y^0 curves exhibit no plateaus. It is also to be observed that an efficiency cross-over occurs in the Y^0 data. Figure 21 shows a $\log_{10}(R^0/Y^0)_{X_0}$ plot vs. temperature. It is seen that starting at a source temperature of 800° , the vapor is some 2-4 orders of magnitude richer in Ga, but that this value increases to between 5 and 6 orders of magnitude at 400° . Thus, the removal of Ge from the vapor at a potential seed site appears fairly efficient in a hot to cold transport process.

The System Ge-Ga-HI-H

The data for this system, Fig. 22 and 23, are similar to those in the previous system not being perturbed to any great extent by either of the approaches employed or the use of H_2 as a carrier. The noticeable effects are that the high-temperature plateau for the R^+ curves develop at slightly lower temperatures and the amount of Ge in the vapor phase is somewhat greater in the present system.

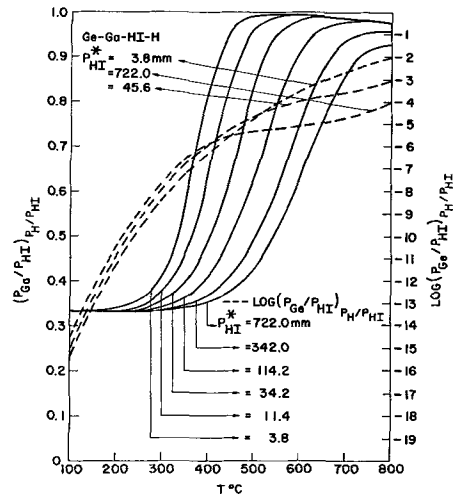


Fig. 22. Efficiency curves for the system Ge-Ga-HI-H at varying hydrogen iodide source pressures.

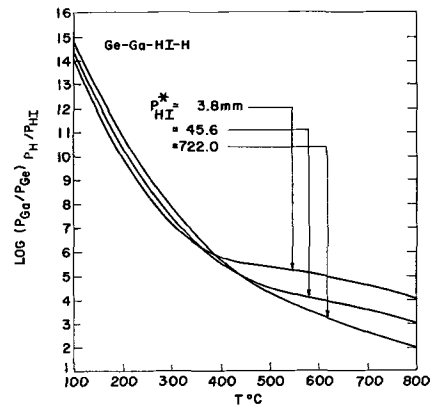


Fig. 23. Variation of Ga/Ge vapor phase content in the system Ge-Ga-HI-H at three different hydrogen iodide source pressures.

The System Ge-Ga-HI-H-He

The data for this system are equivalent to those of system X and need not be repeated.

Acknowledgment

The authors are indebted to the following IBM Research personnel: Dr. R. P. Kelisky of the Mathematical Sciences Department for his continued efforts, during the entire course of this work, toward developing mathematical treatments amenable for computer analyses (8). They also wish to thank Miss A. G. Kuhlke, J. Reinke, Mrs. E. Smith, Mrs. J. K. Somorjai, and R. A. Stevens of the Computing Center for their tireless efforts in carrying the analyses to successful conclusions. In addition, the authors are grateful to G. Cheroff, R. F. Lever, and M. Berkenblit of the Solid State Science Department for their many stimulating discussions and invaluable suggestions concerning the chemical implications of the several systems considered.

Manuscript received Nov. 12, 1963; revised manuscript received March 2, 1964. This paper was presented in part at the New York Meeting, Sept. 29-Oct. 3, 1963 and the work was supported in part by A.F.C.R.L. Contract No. AF19(628)-2468.

Any discussion of this paper will appear in a Discussion Section to be published in the June 1965 JOURNAL.

REFERENCES

1. R. F. Lever, Private communication. Certain of his data were presented at the Los Angeles Meeting of the Society, May 6-10, 1962, Electronics Division Abstracts Vol. 11, p. 240.
2. Selected Values of Chemical Thermodynamic Prop-

- erties, Natl. Bur. Standards Circ. 500, Series III, Washington, D. C. (1952).
- G. M. Murphy, *J. Chem. Phys.*, **4**, 344 (1936).
 - C. N. Cochran and L. M. Foster, *This Journal*, **109**, 144 (1962).
 - V. J. Silvestri and V. J. Lyons, *ibid.*, **109**, 963 (1962).
 - Calculated from data from L. L. Quill, "The Chemistry and Metallurgy of Miscellaneous Materials, Thermodynamics," University Microfilms, Ann Arbor, Mich. (1961); W. Fischer and O. Jübermann, *Z. anorg. u. allgem. Chem.*, **227** (1936).
 - C. D. Thurmond and M. Kowalchick, *Bell System Tech. J.*, **39**, 169 (1960).
 - The mathematical techniques used for computer analyses are described in "Numerical Methods and Fortran Programming" by D. D. McCracken and W. S. Dorn, John Wiley & Sons, Inc., New York (1964).

Incorporation of Zinc in Vapor Grown Gallium Arsenide

V. J. Silvestri and F. Fang

Thomas J. Watson Research Center, International Business Machines Corporation, Yorktown Heights, New York

ABSTRACT

A vertical sealed tube configuration has been used to deposit epitaxially Zn doped GaAs on Te doped substrates. The vapor grown junctions were characterized through capacitance measurements. Linearly graded, nonuniform, and abrupt impurity profiles were observed. The nature of these junctions is shown to correlate with the zinc dopant concentrations present in the vapor. The distribution of zinc between the vapor phase and solid GaAs were determined for the junction growth conditions, and this distribution was found to follow Henry's law for the range investigated. The results of these investigations indicate that autodoping phenomena are involved in producing the variety of junctions observed.

The epitaxial growth of GaAs using various transporting agents has become well established among many investigators (1-6). Little has been reported, however, on the nature of incorporation of impurities during the growth process. The recent interest in the electroluminescence of GaAs p-n junctions has created a renewed interest in these doping aspects during the growth process, particularly in connection with junction fabrication.

In this investigation the incorporation of zinc in vapor grown GaAs has been examined through variation of vapor dopant concentrations, and the effects which these variations produced in junctions are discussed. In addition, the zinc in solid (Zn_s)-zinc in vapor (Zn_v) distribution was determined from Hall measurements of grown layers doped to various concentrations.

1 Provided by S. E. Blum of this laboratory.

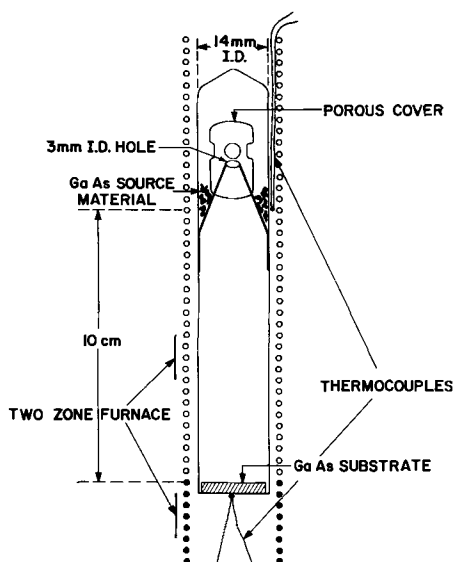


Fig. 1. Vertical tube configuration employed for depositing gallium arsenide.

Experimental

Figure 1 shows the vertical closed tube configuration which was employed for the depositions. Temperatures in the source and seed regions were independently controlled at 800° and 630°C, respectively. Iodine was introduced at a concentration of 2 mg/cm³ to effect transport via the GaAs-I reaction (7). In a first series of experiments carried out to obtain p-n junctions the substrates used were from pulled crystals which were doped with Te to carrier concentrations of $5 \times 10^{17}/\text{cc}$.¹ These substrates were oriented in the $\langle 111 \rangle$ direction, and the depositions were on the gallium side.

Zinc was incorporated in the deposits primarily through the introduction of $ZnAs_2$, but the effects of using Zn doped source material were also evaluated. When using $ZnAs_2$ as a dopant, the source consisted of vapor grown GaAs which had been synthesized at 750°C from high purity Ga and As using the iodine reaction. In depositing the junctions, the amounts of dopant added were varied such as to supply different ZnI_2 overpressures. From thermodynamic considerations (8) ZnI_2 is more stable than the gallium iodides, and in separate experiments it was shown that the reaction between $ZnAs_2$ and iodine goes virtually to completion to form ZnI_2 . The amounts of dopant were chosen such that at the transport temperatures no condensed phase of ZnI_2 was present. Even at the highest zinc concentration used, the formation of ZnI_2 did not significantly deplete the iodine hence there was always sufficient iodine available for the transport of GaAs.

In this first series the epitaxial layers were used for junction evaluation and were grown to thicknesses of from 1-4 mils. Most depositions were completed within 5 hr and from these structures diodes were fabricated. Initially through electrical probing it was determined that the junctions were located within the grown region in some instances being closer to the physical interface than others. Through subsequent etching it was found that the junction locations varied depending on the experimental conditions employed. The etching solution used to indicate junction positions relative to the physical interface consisted of 10 H₂O : 1 HF, 1, 30% H₂O₂. Figure 2 is a photograph of a stained cross section taken through a physical interface and junction

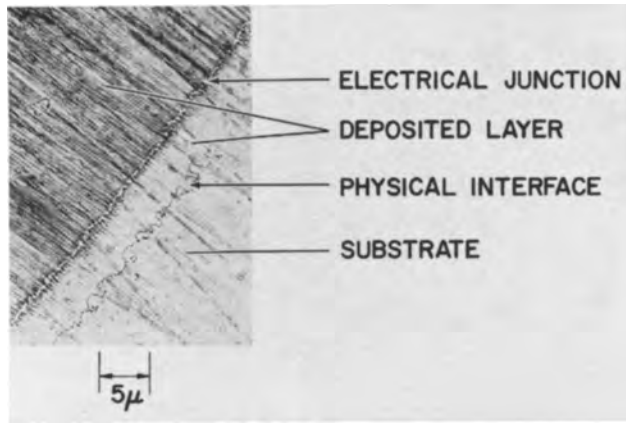


Fig. 2. Microphotograph of a stained cross section through the physical interface and vapor grown electrical junction.

which was lapped on a 3° angle block prior to etching. In addition to staining, the junctions also were electrically probed to determine conductivity type and gave results consistent with the etching delineations.

A second series of depositions was also conducted in which ZnI_2 vapor content was varied over a range similar to that of series one under which the junctions were grown. The purpose of this second study was to determine the distribution of Zn between the vapor phase and solid GaAs. These layers were deposited on $\langle 111 \rangle$ high purity substrates to thicknesses of from 12-22 mils. From these more thickly grown regions Hall samples were sectioned and electrically characterized.

The diodes fabricated from series one were characterized through capacitance measurements. It is well known that the differential capacitance of a junction is a result of the electrical dipole double layer of the space charge region. In particular, it is a measure of the fixed charge density near the edge of the space charge region. These fixed charges are ionized impurity centers of the semiconductor. It can be readily shown (9) that for an abrupt junction with a uniform impurity concentration N_a and N_d in both p and n type materials, the differential capacitance per unit area is given by

$$C = \left[\frac{KqN}{8\pi(V_D + V_A)} \right]^{1/2} \quad [1]$$

where K is the absolute dielectric constant, q the electronic charge, V_D the diffusion potential of the junction, V_A the applied voltage and $1/N = 1/N_a + 1/N_d$.

For an unsymmetrical junction, i.e., N_a and N_d differ appreciably, N approaches the smaller of the two. Most of the experimental junctions reported here are highly unsymmetrical. The substrates are heavily doped. Thus, the N 's determined from the voltage dependence of the junction capacitance are in general indicative of the lightly doped vapor grown side. It can be shown quite generally that for this type of unsymmetrical junction if N is a function of the distance x_1 from the junction, then

$$N(x_1) = \frac{8\pi}{Kq} \frac{dV_A}{d(1/C^2)} \quad [2]$$

where x_1 is given by

$$x_1 = \frac{K}{4\pi C} \quad [3]$$

analogous to the parallel plate capacitors.

Finally, if the composite impurity profile is a linear function of the distance from the junction, i.e., $|N_a - N_d| = ax$ where a is the impurity gradient, the junction capacitance becomes

$$C = \left[\frac{K^2 qa}{192 \pi^2 (V_D + V_A)} \right]^{1/3} \quad [4]$$

Table I. Representative data for junctions grown under various ZnI_2 concentrations

ZnI_2 concentration in vapor (moles/cc)	P_{ZnI_2} (Torr)	Impurity gradient classification	Width of space charge region over which gradient is found (mm)	Gradation (atoms/cm ⁴)
7.8×10^{-10}	0.043	Nonuniform	5.8×10^{-4}	
5.2×10^{-9}	0.29	Linearly graded	3.2×10^{-4}	2.7×10^{21}
4.2×10^{-8}	2.34	Linearly graded	1.3×10^{-4}	3.3×10^{22}
4.2×10^{-7}	23.7	Abrupt	2.9×10^{-5}	
4.2×10^{-6}	236.0	Abrupt	1.8×10^{-5}	

Using a Zn doped GaAs source (2×10^{17} atoms/cc)

4.2×10^{-10} * 0.023 Nonuniform 5.5×10^{-4}

* This value represents an upper limit for Zn vapor content.

In what follows, the grown junctions are conveniently classified into three categories, namely, abrupt, linearly graded, and nonuniform. The abrupt junctions are those whose capacitances have bias dependence as shown in Eq. [1]. The impurity concentration in these junctions is uniform beyond the zero bias space charge width. The linearly graded junctions have voltage dependent capacitance shown in Eq. [4]. The "nonuniform" junctions are those whose impurity profiles found by [2] are nonlinear functions of x . In the vapor grown nonuniform junctions reported here, they were usually found to be either superlinear, i.e., $|N_a - N_d| \propto x^n$ where $n > 1$ or exponential, where $|N_a - N_d| \propto \exp. x$.

Results

In Table I representative results for these measurements of series one are shown. All three types of junctions have been produced depending on the growth conditions. The data indicate that the space charge region over which the impurity distribution occurs narrows, and that there is a corresponding steepening of the impurity gradient with increasing Zn vapor content.

At the low ZnI_2 concentration (7.8×10^{-10} moles/cc), experimentally produced by either the addition of small quantities of $ZnAs_2$ or the use of Zn doped source, "nonuniform" impurity gradients occurred. In addition, at these low concentrations the formation of a second junction was sometimes found to occur if the layer was allowed to grow sufficiently thick.

Experimentally, with increase of vapor phase dopant concentrations, the electrical junctions were found to occur closer to the physical interface. At the very highest ZnI_2 concentration (4.2×10^{-6} mole/cc) the grown junctions were found to be abrupt. In such cases staining confirmed that the physical interface and junction were not observably separated.

The data obtained from series two are given in Fig. 3. Since information concerning carrier concentration

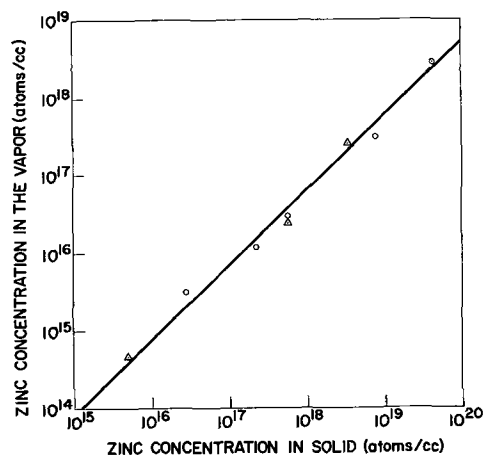


Fig. 3. Distribution of zinc between the vapor phase and solid gallium arsenide as determined from Hall and capacitance measurements; temperature, 630°C; O, Hall samples; Δ, capacitance data.

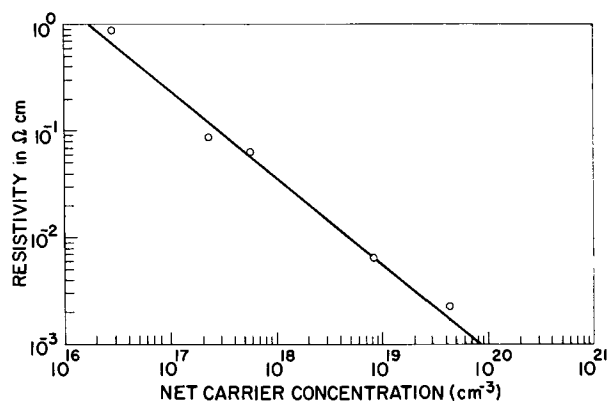


Fig. 4. Plot of resistivity as a function of carrier concentration for zinc in vapor grown gallium arsenide.

was also derivable from some of the capacitance measurements these values have been included and show good agreement. The distribution of Zn experimentally observed between vapor and solid may be represented by the equation

$$\log C_V = \log C_S - 1.16$$

where C_V , the concentration in the vapor, is proportional to C_S , the concentration in the solid (Henry's law). In Fig. 4 the variation of resistivity with net carrier concentration for the deposited Hall samples is also shown.

Discussion

From the material control aspects these variety of junction characteristics are of some interest. The junctions were found to change consistently from nonuniform through linearly graded to abrupt profiles in the order of increasing ZnI_2 overpressures. Staining experiments in both the linearly graded and nonuniform junctions confirmed that they were always found in the grown region at some distance from the physical interface. In addition it was noted that the degree of displacement of these electrical junctions diminished with increasing zinc overpressures. These experimental observations indicated that process effects were involved.

Autodoping phenomena in vapor grown Ge have been reported previously (10). These process effects in junction growth have also been examined in Si. The effect of vapor contamination as introduced by the substrate and system were described in producing a "junction lag" effect (11-13). The basic observation made in both investigations was that the impurities present in the substrate contaminate the vapor and are then redistributed in the growing layer at a constantly decreasing concentration as growth continues. It appears that a similar model can be used to describe the junction displacements reported here. It might in fact be expected that autodoping effects would be even more pronounced in a sealed system.

It is believed that the vapor etching which occurs initially from the reaction of GaAs with iodine facilitates the introduction of seed impurities to the vapor.

If one now considers a model such as described by Kahng, Thomas, and Manz for the autodoping process in silicon (11-13) which involves, namely, repetitive etching, mixing, and growth steps, one can see that the Te introduced from the initial substrate etching undergoes dilution such that the Te content (N_D) approaches zero as the layer grows. The Zn concentration (N_A), however, simultaneously is approaching a value determined by the particular zinc overpressure used. Under such conditions a compensating process would ensue and the electrical junction would occur within the grown region at some distance from the physical interface. Such a descriptive model fits the experimental data. In Fig. 5a and b the impurity profiles for two linearly graded junctions grown under dissimilar ZnI_2

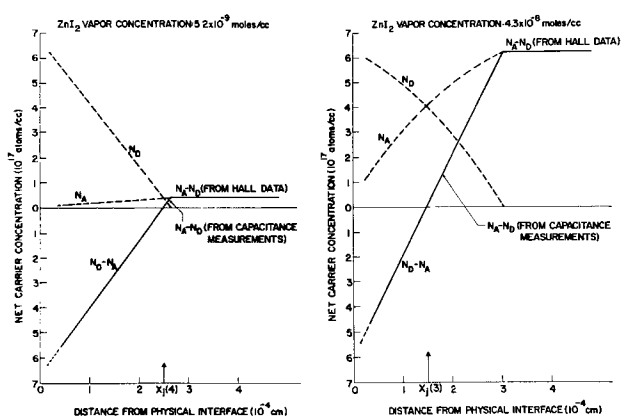


Fig. 5(a, left; b, right). Impurity profiles for two linearly graded junctions grown under dissimilar ZnI_2 overpressures. Solid lines indicate experimentally determined impurity concentrations. Broken lines indicate hypothetical profiles for substrate impurity (N_D) and vapor dopant (N_A) in the grown layers.

overpressures are shown. Through the junction positions $x_j(3)$ and $x_j(4)$ (determined through staining and electrical probing) the impurity profiles have been plotted. Extrapolations of this capacitance data have been made both to the physical interface and to the expected final Zn doping level for the conditions of growth as obtained from the distribution data (Fig. 3).

Diffusion effects were considered; however, calculations based on reported diffusion constants (14) indicated that for the experimental conditions used such effects could not contribute significantly to junction positioning. Under different growth conditions diffusion effects could become important. However, the junction displacements reported here appear to result primarily from an autodoping effect.

At very low Zn concentrations, one has the special case in which the depletion of Zn from the vapor phase is significant and in combination with the autodoping effects is important in shaping the impurity profiles. In Fig. 6 a descriptive representation of this depletion effect is shown. The first junction, $x_j(1)$, originates from the autodoping effects described above. In cases in which a significant background donor level was present in the source material a second junction could also be formed. This second junction, $x_j(2)$ resulted from the Zn vapor depletion which produced an impurity profile for N_A of the type shown. An example of this n-p-n structure is shown in Fig. 7.

In using Zn doped source material similar depletion effects were observed since the Zn vapor content was

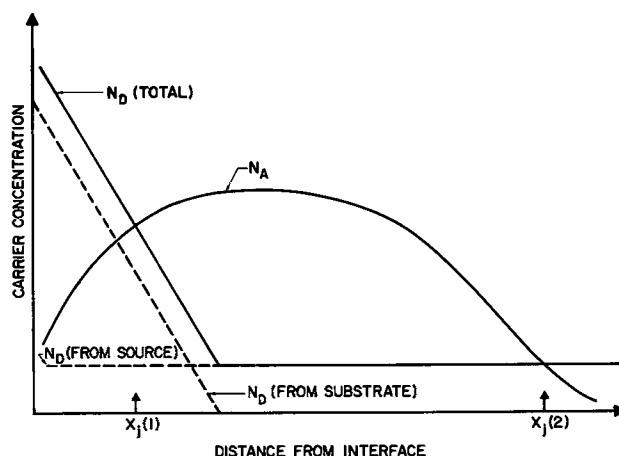


Fig. 6. General type of impurity distribution found when using low ZnI_2 overpressures combined with a source GaAs containing a background donor level.

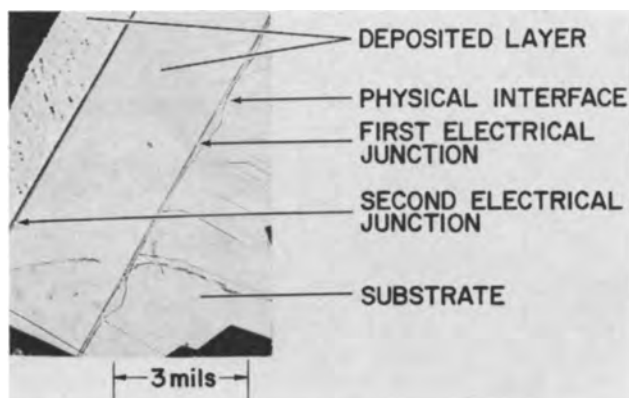


Fig. 7. Microphotograph of a cleaved cross section showing a double junction formation.

always in the low concentration range. The specific impurity profiles in such cases however, depend on factors such as the Zn diffusion rate from the source, the rate of source etching, and the depositing layer depletion rate. Generally, it was found that the impurity profiles for junctions grown using Zn doped source material were not readily reproduced.

With increasing vapor dopant, the per cent perturbation of Zn vapor content due to incorporation is insignificant, and no depletion effects are observed. The impurity profile is then primarily the result of redistribution of substrate impurity.

Similar autodoping effects have been observed in depositing Cd doped layers on Te doped substrates and Zn doped layers on Si doped substrates.

Summary

In the formation of junctions in sealed tubes through deposition of GaAs by vapor transport autodoping phenomena were found to influence both junction location and impurity distributions. The junction variations in the system employed appear to result from (i) the time required for the arrival of ZnI_2 to the vapor, (ii) the distribution which is established between $(Zn_S)-(Zn_V)$, and (iii) the reincorporation of

the vapor contaminant initially introduced through seed etching.

Acknowledgments

The authors wish to acknowledge the helpful discussions with Drs. H. Leonhardt and A. Reisman. We also wish to thank Dr. J. F. Woods and Mr. S. R. Baliozian for the Hall measurements and Mr. M. E. Cowher for his experimental assistance.

Manuscript received Feb. 25, 1964. This paper was presented at the New York Meeting, Sept. 30-Oct. 3, 1963.

Any discussion of this paper will appear in a Discussion Section to be published in the June 1965 JOURNAL.

REFERENCES

1. V. J. Lyons and V. J. Silvestri, *This Journal*, **108**, 177C (1961), Abstract 140.
2. R. R. Moest and B. R. Shupp, *ibid.*, **108**, 178C (1961), Abstract 143.
3. F. V. Williams and R. A. Ruehrwein, *ibid.*, **108**, 177C (1961).
4. N. Holonyak, Jr., D. C. Jillson and S. F. Bevacqua, *Proc. AIME* (1961); Conf. on the Met. of Semiconductor Materials, Los Angeles, Aug. 1961, vol. 15, p. 49, John Wiley and Sons, Inc., New York (1962).
5. R. L. Newman and N. Goldsmith, *This Journal*, **108**, 1127 (1961).
6. C. J. Frosch and C. D. Thurmond, Abstracts of "Recent News" Papers, Electrochemical Society Meeting, Sept. 16-20, 1962.
7. V. J. Silvestri and V. J. Lyons, *This Journal*, **109**, 963 (1962).
8. L. L. Quill, "The Chemistry and Metallurgy of Miscellaneous Materials, Thermodynamics," McGraw Hill Book Co., Inc., New York (1950).
9. See for example: W. Ehrenberg, "Electric Conduction in Semiconductors and Metals," Oxford Press (1958).
10. E. Matovich and R. J. Andres, *This Journal*, **108**, 177C (1961), Abstract 137.
11. D. Kahng, R. C. Manz, M. M. Atalla, and C. O. Thomas, *ibid.*, **108**, 177C (1961), Abstract 135.
12. C. O. Thomas, D. Kahng, and R. C. Manz, *ibid.*, **109**, 1055 (1962).
13. D. Kahng, C. O. Thomas, and R. C. Manz, *ibid.*, **110**, 394 (1963).
14. B. Goldstein, *ibid.*, **118**, 1024 (1960).

The Determination of the Density of Ta, Nb, and Anodically Formed Ta_2O_5 and Nb_2O_5

A. J. Schrijner and A. Middelhoek

N. V. Philips Gloeilampenfabrieken, Zwolle, The Netherlands

ABSTRACT

By refining a method used by Young we have determined the density of Ta, Nb, Ta_2O_5 , and Nb_2O_5 . It has been found that the forming electrolyte has some influence on the density of the Ta_2O_5 formed by anodizing. This can be interpreted by assuming that some electrolyte has been built in.

In investigations of the anodic oxidation of metals the density of the oxide film plays an important role, e.g., it can be used to determine the thickness of the oxide layer.

In an article by Young (1) a method is given to determine the density of anodically formed Ta_2O_5 without separating the oxide layer from the base metal. The method consists of weighing a piece of Ta foil in air and under water before and after forming of the oxide layer.

A disadvantage of Young's method is that a small surface area (~ 100 cm² foil) is used which results in a low accuracy. This article describes a variation on this

method which gives a greater accuracy as a sintered slug with a larger surface area is employed.

Experimental Procedure

The Ta and Nb anodes listed in Table I were used. The surface area of such a Ta anode is about 400 cm² and of the Nb anode about 450 cm². To enlarge the surface area five anodes were welded to a common Ta wire. This assembly is called a group. The following groups were used: 4 groups of Ta anodes (I, II, III, IV), 4 groups of Nb anodes (V, VI, VII, VIII), and combinations of groups I+II, III+IV, V+VI, and VII+VIII.

Table I. Ta and Nb anodes used

	Ta	Nb
Powder weight, g	3.00	2.00
Diameter (pressed), mm	6.6	6.6
Length (pressed), mm	10.2	13.0
Green density, g/ml	8.7	4.6
Wire diameter, mm	0.8	0.8
Sintering conditions	1 hr 2000°C	30 min 1700°C

The determinations mentioned below were made by means of a Mettler B6 balance with a reproducibility of 0.03 mg. The groups were degreased and then dried to a constant weight. After the determination of the "dry" weight the groups were impregnated in water to a constant weight. The "wet" weight determinations were made by suspending the groups to the balance by means of a thin nylon wire, so that the groups did not at all emerge from the water. After impregnation all the groups remained under water.

To determine the density of the water during the wet weighings it is necessary to measure the temperature of the water.

Forming Procedure

In the case of Ta, two different electrolytes were used, *viz.*, a very dilute type (0.01% HNO₃) and a concentrated type (50% H₂SO₄).¹ The purpose was to detect whether the density of the Ta₂O₅ films depends on the type of electrolyte.

In the literature no value has been published for the density of anodically formed Nb₂O₅; it is the purpose of this paper to determine this value.

The groups were formed with a constant current to 100v resp. 150v, thereupon they were formed at a constant voltage to a final current of 8 ma/group resp. 15 ma/group.

After forming the anodes were rinsed for 15 hr in deionized water and dried to a constant weight. Hereafter the dry and wet weighing process was repeated.

List of Symbols

A	"Dry" weight of a Ta or Nb group.
B	"Wet" weight of a Ta or Nb group.
a	"Dry" weight of a (Ta + Ta ₂ O ₅) (Nb + Nb ₂ O ₅) group. c.q.
b	"Wet" weight of a (Ta + Ta ₂ O ₅) (Nb + Nb ₂ O ₅) group. c.q.
ρ _{Ta}	density of Ta.
ρ _{Nb}	density of Nb.
ρ _w	density of water.
M _{Ta₂O₅}	molecular weight of Ta ₂ O ₅ .
M _{Nb₂O₅}	molecular weight of Nb ₂ O ₅ .
M _O	atomic weight of oxygen.
M _{Ta}	atomic weight of Ta.
M _{Nb}	atomic weight of Nb.

The density of Ta or Nb can be calculated by means of the formula

$$\rho_{Ta\ Nb} = \frac{A\rho_w}{A - B}$$

The formula for the calculation of ρ_{Ta₂O₅} c.q. ρ_{Nb₂O₅} is somewhat more complicated. It can be derived in the following way

$$\rho_{Ta_2O_5} = \frac{\text{weight Ta}_2O_5}{\text{volume Ta}_2O_5}$$

The weight of Ta₂O₅ can be found from the difference in dry weight of a group before and after forming:

¹ Weight per cent.

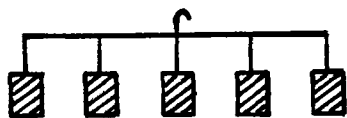


Fig. 1. Assembly of anodes

Table II. Forming conditions

	Ta anodes		Nb anodes
Numbers of the groups	I + II	III + IV	V + VI + VII + VIII
Forming electrolyte and concentration	HNO ₃ 0.01%	H ₂ SO ₄ 50%	H ₃ PO ₄ 0.1%
Forming current per group	35 ma	35 ma	100 ma
group temperature of the forming bath	17°-20°C	17°-20°C	17°-20°C
Formed with constant current to	100v	100v	150v
Formed to final current	8 ma/group	8 ma/group	15 ma/group

a - A. This difference equals the weight of the oxygen in the oxide film. Assuming that the oxide is Ta₂O₅ we find for the weight of the Ta₂O₅

$$\frac{M_{Ta_2O_5}}{5M_o} (a - A)$$

The volume of the Ta₂O₅ is equal to the volume of (Ta + Ta₂O₅) minus the initial volume of Ta, and plus the volume of Ta which has been transformed in Ta₂O₅. So we find

$$\text{Volume Ta}_2O_5 = \frac{a - b}{\rho_w} - \frac{A - B}{\rho_w} + \frac{(a - A) 2M_{Ta} / 5M_o}{A/A - B \rho_w}$$

Hence, the density of Ta₂O₅ is

$$\rho_{Ta_2O_5} = \frac{\frac{M_{Ta_2O_5}}{5M_o} (a - A)}{\frac{a - b}{\rho_w} - \frac{A - B}{\rho_w} + \frac{(a - A) (A - B) 2M_{Ta}}{A \rho_w 5M_o}}$$

To calculate ρ_{Nb₂O₅} the same formula is used, except that M_{Ta₂O₅} is replaced by M_{Nb₂O₅} and M_{Ta} by M_{Nb}.

Corrections

The wet weight B and b have to be corrected for the weight of the nylon wire. The dry weight of the nylon wire was subtracted from all wet weights, which in turn necessitates a correction x for that portion of the wire which was immersed in the water.

The correction x consists of two parts p and q. The correction for the buoyancy of the part of the nylon wire which is immersed in the water is called p. In the experiment this part is kept as small as possible. The physical interpretation of q is more complicated; it is connected with the creeping up of the electrolyte on the nylon wire. Therefore

$$B = B_1 + (p + q)$$

where B₁ is the wet weight of a group and the dry weight of the nylon wire.

$$B^I = B_1^I + (p + q)$$

$$B^{II} = B_1^{II} + (p + q)$$

and

$$B^{I+II} = B_1^{I+II} + (p + q)$$

in which I and II denote the group number. Thus

$$B^I + B^{II} - B^{I+II} = B_1^I + B_1^{II} - B_1^{I+II} + (p + q)$$

Now it is clear that

$$B^I + B^{II} - B^{I+II} = 0$$

Further, we define x as follows

$$x = B_1^I + B_1^{II} - B_1^{I+II}$$

Therefore:

$$0 = x + (p + q)$$

$$x = - (p + q)$$

so:

$$B = B_1 - x$$

Table III. Density of Ta, Nb, Ta₂O₅, and Nb₂O₅

Group	Density Ta	Density Ta ₂ O ₅	Group	Density Nb	Density Nb ₂ O ₅
I	16.596	8.034	V	8.576	4.750
II	16.594	8.049	VI	8.577	4.743
I + II	16.596	8.034	V + VI	8.576	4.752
III	16.599	7.853	VII	8.578	4.734
IV	16.600	7.892	VIII	8.578	4.735
III + IV	16.600	7.861	VII + VIII	8.577	4.734
Mean	16.598	8.039* 7.869†	Mean	8.577	4.741

* Density of Ta₂O₅ formed in 0.01% HNO₃.
† Density of Ta₂O₅ formed in 50% H₂SO₄.

Table IV. Standard deviations and standard deviations of the mean calculated from the results

	Density Ta	Density Ta ₂ O ₅ 0.01% HNO ₃	Density Ta ₂ O ₅ 50% H ₂ SO ₄	Density Nb	Density Nb ₂ O ₅
S	0.003	0.009	0.021	0.001	0.008
S _m	0.001	0.005	0.012	0.0005	0.003

As it appeared from the experiment that x is positive, q has to be negative and $-q > p$.

Results

The results of the experiment are collected in Table III. It appears that the density of Ta₂O₅ formed in 0.01% HNO₃, differs appreciably from the density of Ta₂O₅ formed in 50% H₂SO₄. The densities of Ta and Nb metal, determined in this manner, are in good agreement with those found in literature.

The calculated standard deviations (S) of these series and the standard deviation of the mean (S_m) are reported in Table IV. The standard deviations of the density of the metals are lower than those of the oxides. This is so because the weight of the oxide is found as a small difference of two large weights. To increase the accuracy it is necessary to take a large surface area with respect to the metal volume. The standard deviations are in good agreement with the standard deviations which can be calculated from the weighing results.

Conclusions

1. For the density of Ta we find 16.598 ± 0.001 g/ml which is in good agreement with literature data mentioned below. So we may say that the porous anodes are totally impregnated in the case of the wet weighings.

2. It appears that the density of anodically formed Ta₂O₅ depends on the forming electrolyte. For dilute electrolytes we find:

Ta formed in 0.01% HNO₃: $\rho_{Ta_2O_5} = 8.039 \pm 0.005$ g/ml
Ta formed in 0.1% H₃PO₄: $\rho_{Ta_2O_5} = 8.03 \pm 0.04$ g/ml
Ta formed in 1% H₂SO₄: $\rho_{Ta_2O_5} = 8.01 \pm 3\%$ g/ml²

For Ta formed in a concentrated electrolyte (50% H₂SO₄) we find

$$\rho_{Ta_2O_5} = 7.87 \pm 0.01 \text{ g/ml}$$

This shows that in concentrated H₂SO₄ the density is much lower than in dilute solutions which can be interpreted by assuming that some electrolyte has been "built in" when forming takes place in concentrated sulfuric acid. Additional evidence can be found in an article by Vermilyea (9) which states that in concentrated H₂SO₄ the apparent Faraday efficiency is much higher than 100%.

² Measured by Young.

3. For the density of Nb₂O₅ we find 4.741 ± 0.003 g/ml. This is much higher than the literature value mentioned below for amorphous Nb₂O₅ which has been prepared by hydrolysis of NbCl₅ in water and drying at 100°C.

Literature Data

A wide range of values for the density of Ta₂O₅ and Nb₂O₅ is found in literature.

1. In Gmelin-Kraut's Handbook (2) a broad spectrum of values is reported for the density of chemically prepared Ta₂O₅. The values given vary from 7.028 to 8.257 and concern amorphous, glassy, and crystalline oxides.

2. The "Handbook of Chemistry and Physics" (3) gives: $\rho_{Ta} = 16.6$ g/ml; $\rho_{Ta_2O_5} = 8.735$ g/ml (rhombic). Waber *et al.* (4) and Vermilyea (5) both used this value for the density of Ta₂O₅ in their studies on thermal and anodic oxide films. The source of this number is unknown but we found it in the International Critical Tables (6) from 1926 without further reference.

3. Güntherschulze (7): $\rho_{Ta_2O_5} = 8.27$ g/ml.

4. Reisman *et al.* (8): $\rho_{Ta_2O_5}(\beta) = 8.18$ g/ml; $\rho_{Ta_2O_5}(\alpha) = 8.37$ g/ml.

5. Young (1): $\rho_{Ta_2O_5} = 7.95$; 7.82; 8.25; 8.01 g/ml; or averaged $\rho_{Ta_2O_5} = 8.01$ g/ml. Young himself neglected the value 8.25 g/ml, hence his average is $7.93 \pm 3\%$ g/ml. He formed the Ta₂O₅ layer in approximately 1% H₂SO₄. This was the first time the density of anodically formed Ta₂O₅ was measured directly.

6. In an earlier experiment we found for Ta₂O₅ formed in 0.1% H₃PO₄: $\rho_{Ta_2O_5} = 8.03 \pm 0.04$ g/ml (estimated error).

7. Holtzberg *et al.* (10) give for Nb₂O₅: amorphous oxide, $\rho_{Nb_2O_5} = 4.36$ g/ml; crystalline oxide (γ), $\rho_{Nb_2O_5} = 5.17$ g/ml; crystalline oxide (α), $\rho_{Nb_2O_5} = 4.55$ g/ml.

8. The "Handbook of Chemistry and Physics" (3): $\rho_{Nb} = 8.55$ g/ml, $\rho_{Nb_2O_5} = 4.47$ g/ml (rhombic).

9. Kirk Othmer (11): $\rho_{Nb} = 8.57$ g/ml.

10. Gulbransen and Andrew (12): $\rho_{Nb_2O_5} = 4.95$ g/ml (crystalline).

The above data for $\rho_{Nb_2O_5}$ are commonly used for the density of the anodic oxide films.

Acknowledgment

The authors are greatly indebted to Mr. M. Vogels and Mr. A. Meyer for carrying out the experiments and part of the calculations and also for helpful discussions.

Manuscript received Dec. 20, 1963.

Any discussion of this paper will appear in a Discussion Section to be published in the June 1965 JOURNAL.

REFERENCES

- L. Young, *Proc. Roy. Soc.*, **A244**, 41 (1958).
- Gmelin-Kraut's "Handbuch der anorganischen Chemie," Band VI, Abteilung 1, pp. 291, 292 (1928).
- "Handbook of Chemistry and Physics," C. D. Hodgman, Editor, 41st ed., pp. 617, 667, Chemical Rubber Publishing Co., Cleveland (1959).
- J. T. Waber, G. E. Sturdy, E. M. Wise, and C. R. Tipton, Jr., *This Journal*, **99**, 121 (1952).
- D. A. Vermilyea, *Acta Met.*, **1**, 282 (1953).
- International Critical Tables, Vol. I, p. 135, McGraw-Hill Book Co., Inc., New York (1926).
- A. Güntherschulze and H. Betz, "Elektrolytkondensatoren," 2nd ed., p. 89, Technischer Verlag Herbert Cram, Berlin (1952).
- A. Reisman, F. Holtzberg, M. Berkenblit, and M. Berry, *J. Am. Chem. Soc.*, **78**, 4514 (1956).
- D. A. Vermilyea, *Acta Met.*, **2**, 482 (1954).
- F. Holtzberg, A. Reisman, M. Berry, and M. Berkenblit, *J. Am. Chem. Soc.*, **79**, 2039 (1957).
- "Encyclopedia of Chemical Technology," vol. IV, R. E. Kirk and D. F. Othmer, Editors, p. 318, The Interscience Encyclopedia, Inc., New York (1954).
- E. A. Gulbransen and K. F. Andrew, *This Journal*, **105**, 4 (1958).

Torsion Effusion Study of the Vapor Pressure and Heat of Sublimation of Gallium

Zuhair A. Munir and Alan W. Searcy

Department of Mineral Technology and Lawrence Radiation Laboratory,
Inorganic Materials Research Division, University of California, Berkeley, California

ABSTRACT

The vapor pressure of gallium was measured by the torsion effusion method between 1174° and 1603°K. The pressure, in atmospheres, is given by the expression: $\log P = 5.5458 - (13\ 743/T)$ in that temperature range. The heat of sublimation of gallium is calculated by the third-law method to be 65.4 kcal. A second-law determination is in reasonable agreement.

Harteck (1) in 1928 and Speiser and Johnston (2) in 1952 measured the vapor pressure of gallium by the Knudsen effusion method with quartz effusion cells. However, more recently a mass spectrometric study (3) showed that gallium reacted with quartz, giving a considerable concentration of $\text{Ga}_2\text{O}(g)$ above 865°C. This evidence suggested that the reported gallium vapor pressures might be too high. To clarify the situation, Cochran and Foster (4) investigated the apparent vapor pressures of gallium in alumina Knudsen cells with and without added silica or magnesia. Apparent pressures obtained with silica added agreed well with the pressures of Speiser and Johnston, but pressures measured when only gallium was present were four- to fivefold lower. Cochran and Foster concluded that the previous studies in quartz cells were in error because the reaction $2\text{Ga}(l) + \text{SiO}_2(c) = \text{SiO}(g) + \text{Ga}_2\text{O}(g)$ yielded higher weight losses than did the direct vaporization of gallium.

At the time that the paper of Cochran and Foster appeared, we were engaged in a redetermination of the vapor pressure of gallium by the torsion effusion method (5-8) with use of a graphite cell. A mass spectrometer study by Drowart and Honig (9) had demonstrated that atomic gallium is the only major vapor species when gallium is heated in graphite. Nonetheless, the pressures measured in our research are in good agreement with the average of the data of Harteck and of Speiser and Johnston and thus are four

to five times the pressures reported by Cochran and Foster.

Experimental

Figure 1 shows a schematic diagram of the torsion effusion apparatus. The vacuum chamber is a cylinder about 35 cm in diameter and about 46 cm long. In the center a 7.8 cm diameter cylinder of 0.5 mm tantalum sheet forms the heating element. Several layers of tantalum radiation shields are wrapped around this element. A glass tube of approximately 10 cm diameter and 92 cm length forms the upper part of the apparatus. Above this tube a goniometer acts as the anchor point for the suspension system by means of an aluminum rod which enters the top of the glass tube through an O-ring seal. A 0.05 mm diameter annealed tungsten wire 28 cm long hangs from the aluminum rod. To the lower end of the tungsten wire, a second aluminum rod is attached. A 1.3 cm diameter circular mirror is glued to this rod directly in front of a window which has an optically flat surface. An aluminum disk attached to the rod serves as a damper when a permanent magnet is placed near it. A 0.25 cm diameter tantalum rod is joined to the aluminum one, and the graphite torsion cell is rigidly attached to the bottom of this rod. During a run the cell hangs free in the center of the heating element.

The exterior cell dimensions were 2.5 x 1.3 x 1.3 cm. Two sets of orifices, one set of 6.3 mm² cross-sectional area and the other of 1 mm² area, were used.

Angular deflections resulting from the force of the effusing vapors were determined by returning the suspension system to its original (null) position. Measurements were made by sighting through a telescope on the mirror that reflects a scale placed outside the vacuum system just below the telescope. After returning the suspension assembly to its original position, deflection angles were read from the goniometer. With this arrangement, it was possible to measure angles to the nearest 0.01°. A vacuum of better than 10⁻⁵ mm Hg was maintained by means of an oil diffusion pump and a liquid nitrogen trap.

A 30-kva transformer supplied the power at a maximum of 10v. Temperature measurements were made by means of a calibrated 0.5 mm Pt-Pt + 10% Rh thermocouple. The thermocouple bead was inserted in a small hole in the bottom of a "dummy" graphite cell located 1.3 cm below the effusion cell. The freezing points of gold, silver, copper, and aluminum measured in the dummy cell in the furnace were used as standard points in the calibration of the thermocouple.

In order to verify the assumption that the temperature of the dummy cell was the same as that of the effusion cell for a given power setting, the dummy cell was moved up and down over a distance of 8 cm in the middle portion of the heating element. The temperature remained constant to within 3°. This experiment was repeated at different power inputs, and

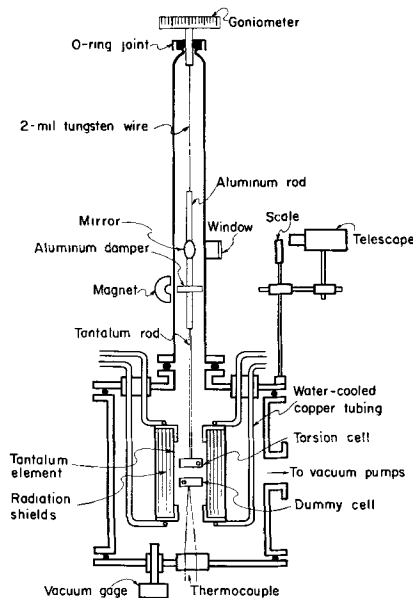


Fig. 1. Schematic diagram of torsion apparatus

Table I. Torsion cell constants

Cell	Orifice diameters, cm		Mount arms, cm		Orifice correction factors		Orifice length-to-radius ratio	
	d_1	d_2	q_1	q_2	f_1	f_2	l/r_1	l/r_2
1	0.2563	0.2436	1.2626	1.1216	0.840	0.827	0.539	0.589
2	0.1016	0.1001	1.1242	1.1221	0.7726	0.7359	1.05	0.985

the results were all identical. The thermocouple leads were led through a Kovar seal to the outside and were protected with alumina tubes. A mixture of ice and distilled water formed the cold junction, and the emf was measured by a potentiometer. The output of the thermocouple was fed to a strip chart recorder. Measurements were made only after the temperature had reached a constant value.

The gallium used was 99.97% pure material obtained from the Aluminum Company of America.

As a test of the apparatus, the vapor pressure of tin was redetermined. Results are described in the discussion section.

Results

Pressures were calculated from the equation

$$P = 2D\phi / (q_1 a_1 f_1 + q_2 a_2 f_2) \quad [1]$$

where P is the vapor pressure, atm; D the torsion constant of the wire, dyn-cm; ϕ the angle of deflection, radians; q_1, q_2 perpendicular distances from the center of the effusion hole to the axis of rotation, cm; a_1, a_2 areas of effusion holes, cm²; f_1, f_2 correction factors for finite orifice lengths (10, 11).

Constants for the two sets of cells used and for the torsion wire are summarized in Table I. A 2-mil tungsten wire with $D = 3.416$ was used for all runs. Figure 2 shows the agreement between pressures calculated with the two orifices. Data collected below 1200°K are clearly seen from Fig. 2 to be unreliable because the force of effusing vapor is too low for accurate measurement, and these data were not used in subsequent calculations.

The heat of sublimation ΔH_s was determined by using both the second- and third-law methods (12). Apparent pressures less than 10^{-6} atm were not used in making these calculations because background torsional effects obscured the lower pressure readings. An experimental investigation by Schulz (15) has shown that Eq. [1] can be used up to pressures for which the ratio of mean-free-path to orifice diameter becomes unity. From the diameters of the orifices and the van

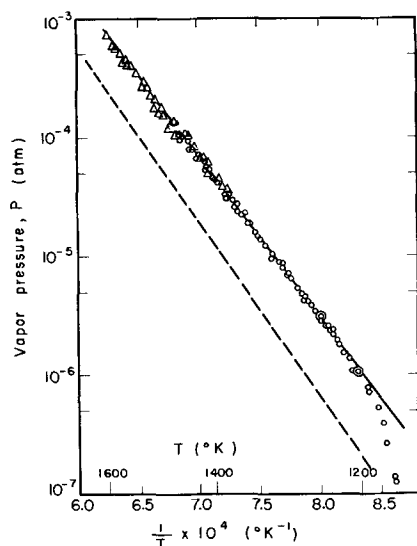


Fig. 2. Vapor pressure of gallium (l): \circ , this work, orifice $d \approx 2.5$ mm; \triangle , this work, orifice $d \approx 1.0$ mm; —, Hultgren *et al.*, selected values (13); - -, Cochran and Foster (10).

Table II. Third law heats of sublimation of gallium (l)

T, °K	$-\ln P$, cal/deg	ΔH_s^{298} , cal	T, °K	$-\ln P$, cal/deg	ΔH_s^{298} , cal
A. Cell 1					
1204	27.308	65 452	1326	22.414	65 392
1204	27.286	65 425	1326	22.429	65 412
1211	27.244	65 749	1333	22.281	65 552
1213	26.784	65 296	1336	22.089	65 429
1213	26.869	65 399	1340	21.909	65 388
1221	26.559	65 438	1350	21.594	65 430
1227	26.217	65 330	1352	21.569	65 488
1229	26.088	65 275	1355	21.152	65 070
1234	25.859	65 243	1360	21.269	65 451
1234	25.652	64 987	1366	21.139	65 563
1236	25.652	65 192	1367	20.812	65 154
1241	25.544	65 217	1370	20.964	65 507
1243	25.544	65 318	1374	20.707	65 335
1249	25.280	65 252	1382	20.381	65 248
1250	25.205	65 245	1384	20.572	65 602
1250	25.205	65 245	1386	20.406	65 462
1257	24.948	65 261	1390	20.203	65 374
1261	24.721	65 195	1398	19.848	65 256
1262	24.721	65 252	1403	19.631	65 442
1266	24.548	65 233	1405	19.636	65 536
1270	24.491	65 359	1410	19.453	65 224
1270	24.385	65 225	1416	19.408	65 422
1275	24.239	65 280	1418	19.473	65 514
1281	24.056	65 330	1419	19.195	65 258
1289	23.741	65 330	1429	19.134	65 482
1290	23.703	65 337	1429	18.934	65 334
1294	23.501	65 271	1435	19.037	65 740
1295	23.565	65 396	1440	18.710	65 493
1303	23.256	65 395	1446	18.724	65 770
1304	23.101	65 234	1448	18.404	65 393
1305	23.065	65 242	1455	18.225	65 437
1314	22.836	65 379	1459	18.416	65 900
1316	22.755	65 268	1465	18.223	65 887
1318	22.957	65 729	1466	17.879	65 417
B. Cell 2					
1380	20.260	64 991	1491	17.361	65 716
1391	20.192	65 396	1495	17.041	65 403
1394	19.858	65 073	1498	17.253	65 852
1411	19.546	65 391	1508	16.787	65 493
1416	19.213	65 146	1508	17.044	65 961
1421	19.073	65 143	1513	16.579	65 471
1427	19.093	65 459	1519	16.299	65 287
1432	19.010	65 564	1529	16.246	65 620
1437	18.624	65 233	1530	16.047	65 363
1448	18.219	65 125	1544	15.730	65 446
1453	18.192	65 305	1556	15.433	65 486
1466	17.823	65 335	1561	15.411	65 654
1469	18.210	66 023	1566	15.263	65 626
1471	17.861	65 593	1567	15.350	65 794
1473	17.611	65 325	1575	15.034	65 622
1477	17.711	65 638	1585	14.824	65 690
1482	17.908	66 146	1588	14.770	65 729
1485	17.321	65 393	1603	14.310	65 588

der Waals radius for gallium (13), this pressure is calculated to be about 10^{-2} atm. The highest pressure measured in this work was 8×10^{-4} atm.

Second-law calculation by the least-square method gave $\Delta H_T = 61.96$ kcal with a standard deviation of 0.24 kcal and $\Delta S_T = 24.34$ eu with a standard deviation of 0.17 eu. From this $\Delta H_s, 298 = 64.2$ kcal/mole. Third-law calculations based on free-energy functions selected by Hultgren (14) are given in Table II. The average value calculated for the heat of sublimation of gallium at 298°K from data collected with 2.5 mm diameter orifices is 65.39 kcal/mole and with 1.0 mm orifices is 65.50 kcal. The over-all average $\Delta H_s, 298$ is 65.44 kcal/mole with an average deviation of 0.23 kcal. The third-law evaluation gave the following expression for the vapor pressure of gallium, in atmospheres, between 1174° and 1603°K:

$$\log P = 5.458 - 13 743/T \quad [2]$$

Discussion

Recent studies by Cochran and Foster (4) appeared to demonstrate conclusively that any studies of the vapor pressure of gallium that were carried out in the presence of silica are in error because of extensive reaction to yield volatile oxides. But the vapor pressures measured for gallium in the present investigation are higher by about a factor of four, than the vapor pressures reported by Cochran and Foster, and the heats of sublimation calculated from the data of the present research are in excellent agreement with the heat reported by Hultgren *et al.* (14) from analysis of the results of the two studies made with silica effusion cells.

The possibility of errors that could make the apparent pressures of the present investigation higher than the true pressures by a factor of four will be discussed, and then evidence for the possibility of error in the work of Cochran and Foster will be examined.

The factors that might cause systematically high apparent pressures in the present investigation are contribution to the vapor of products of reaction of gallium with the graphite effusion cell, faulty temperature calibration, faulty pressure calibration, and leakage of vapor through the cell wall. Strong evidence can be adduced that none of these factors caused the observed discrepancy.

The possibility that gaseous products of some reaction of gallium with the graphite of the effusion cell were formed in significant concentration is disproved by the mass spectrometer study by Drowart and Honig of the effusion of gallium from a graphite cell (9). No ions other than Ga^+ , Ga_2O^+ , and Ga_2^+ were observed. The GaO^+ and Ga_2^+ intensities rapidly decayed to negligible levels, indicating that these ions were produced from oxides that were introduced with the initial sample, but that were soon removed by heating.

The possibility of a temperature error in this work of more than 5° at most appears excluded by the calibration of the readings of the dummy cell against the melting points of four metals measured in the actual furnace in which the vapor pressure measurements were made. Furthermore, the furnace was demonstrated to have a uniform hot zone over the region in which the dummy cell and torsion effusion cell were placed. A temperature error of 90° would be required to introduce an error of a factor of four in the pressure measurements at the midpoint of the experimental range.

Evidence that the apparatus was calibrated correctly is provided by agreement to within 10% of the vapor pressure plot obtained for tin with this apparatus and the "best" vapor pressure curve for tin as selected by Hultgren *et al.* (14). From nineteen separate measurements of the vapor pressure of tin with two different wires that had torsion constants which differed by a factor of 18, the heat of sublimation of tin at 298°K is calculated to be 72.4 kcal compared to 72.2 kcal calculated by Hultgren *et al.* from previous work and compared to 71.8 kcal which was obtained by Schulz in an extensive study of the reliability and limitations of the torsion-effusion method for vapor pressure determinations (15).

To test the reliability of their apparatus and techniques, Cochran and Foster also studied the vapor pressure of tin. Their three pressure measurements lie considerably lower than the pressures calculated by Stull and Sink (16) or Hultgren *et al.* from evaluation of the data in the literature. We calculate from the Cochran and Foster data a heat of sublimation of tin at 298°K of 74.0 ± 0.6 kcal/mole.

Cochran and Foster commented that the vapor pressure data accepted by Stull and Sinke as the most reliable are probably in error because of unrecognized leakage through walls of the graphite crucibles that were used for the pressure studies.

There certainly is evidence that the quantity of metal that escapes from a graphite cell may sometimes be comparable to the quantity that escapes through an orifice of the dimensions normally employed in effusion studies (17). However, in the torsion-effusion method, if the cell side walls are uniform in thickness, the escape of molecules by leakage through the walls will contribute no net torque to the assembly. As part of his investigation Schulz heated tin in cells in which no orifices were drilled and found that no measurable torque was produced by any leakage that may have taken place (15).

While the present investigation of gallium did not include measurement of the torque produced when a sample was heated in a cell that had no orifices, the study did include measurement of the pressure with sets of orifices that had areas that differed by more than a factor of six. The calculated pressures agree within the small random scatter in data. If leakage contributed significantly to the torque, this excellent agreement between the pressures calculated with these two sets of orifices would not have been obtained.

The heat of sublimation for tin calculated from the data of Cochran and Foster is thus 1.8-2.2 kcal higher than the heats calculated from the best available studies. Similarly the heat of sublimation of silver calculated from three pressure measurements by Cochran and Foster is 0.9 kcal higher than the selected value of Hultgren *et al.* (14).

Gallium is more volatile than tin and less volatile than silver. The heat of sublimation for gallium calculated from the Cochran and Foster data can be expected to be subject to a systematic error in pressure determination that would contribute an error in the derived heat of sublimation of +1 to +2 kcal. Their heat of sublimation is 3.6 kcal higher than that found in the present work, so about half the discrepancy in results for gallium remains unaccounted for.

Furthermore, a systematic error in the measurements of Cochran and Foster would not invalidate their conclusion that in the presence of silica the weight loss is increased by a factor of four or five because of volatile oxide formation. Remaining to be explained, therefore, is the question of how the studies of Harteck (1) and of Speiser and Johnston (2) which were both conducted in silica cells, could agree with the results of the present investigation in graphite.

A possible explanation is that the surface area at which the heterogeneous reaction between the gallium and silica could occur in silica Knudsen cells is much smaller than the surface provided for reaction by the coarse silica powder added to the cells in the experiments of Cochran and Foster. As a result, although some reaction must have occurred in the silica cells, the extent of reaction may well have been considerably less than was measured in the experiments of Cochran and Foster.

This hypothesis is substantiated by the results of the mass spectrometer study of gallium vaporization from a silica cell. The observed intensity ratio $\text{Ga}^+/\text{Ga}_2\text{O}^+$ was about 10/1 at 1140° to 1300°K (3). From the assumptions normally applied to calculate pressures from ion intensities and usually claimed to be correct to within a factor of two (18), these intensities would yield a $\text{Ga}/\text{Ga}_2\text{O}$ pressure ratio of 22/1. The heat of sublimation calculated for gallium by a third-law method from weight losses measured at 1300°K and with the assumption that the total weight loss was of elemental gallium would be low only by about 0.3 kcal because of neglect of Ga_2O and SiO effusion.

The heat of formation calculated by Cochran and Foster from effusion studies with gallium-silica mixtures is in good agreement with the heats calculated from another study (19). This fact implies that their effusion studies were not subject to significant systematic errors. The possibility remains, therefore, that their results for gallium are more nearly correct than ours, but we conclude that the heat of sublimation of gallium obtained by the third-law method in the present investigation, 65.4 kcal/mole is probably correct to within ± 1 kcal.

Acknowledgment

Dr. Lies N. Finnie provided valuable help and counsel during the preparation of this manuscript. The research was supported by the U.S. Atomic Energy Commission.

Manuscript received Nov. 4, 1963.

Any discussion of this paper will appear in a Discussion Section to be published in the June 1965 JOURNAL.

REFERENCES

1. P. Harteck, *Z. physik. Chem.*, **134**, 1 (1928).
2. R. Speiser and H. L. Johnston, *J. Am. Chem. Soc.*, **75**, 1469 (1952).
3. S. Antkiw and V. H. Dibeler, *J. Chem. Phys.*, **21**, 1890 (1953).
4. C. N. Cochran and L. M. Foster, *This Journal*, **109**, 144 (1962).
5. M. Volmer, *Z. physik. Chem. (Bodenstein Festband)*, **1931**, 863.

6. K. Neumann and E. Völker, *Z. physik. Chem.*, **161A**, 33 (1932).
7. A. W. Searcy and R. D. Freeman, *J. Am. Chem. Soc.*, **76**, 5529 (1954).
8. J. L. Margrave, "Vapour Pressure," Chap. 10 in "Physico-Chemical Measurements at High Temperatures," J. O'M. Bockris, J. L. White, and J. D. Mackenzie, Editions, Butterworths Scientific Publications, London (1959).
9. J. Drowart and R. E. Honig, *Bull. Soc. Chim. Belges*, **66**, 411 (1957).
10. R. D. Freeman and A. W. Searcy, *J. Chem. Phys.*, **22**, 762 (1954).
11. D. A. Schulz and A. W. Searcy, *ibid.*, **36**, 3099 (1962).
12. R. Ackerman and R. Thorn, *Progr. Cer. Sci.*, **1**, 39 (1961).
13. L. Pauling, "Nature of the Chemical Bond," 3rd ed., Cornell University Press (1960).
14. R. Hultgren, R. L. Orr, P. D. Anderson, and K. K. Kelley, "Selected Values of Thermodynamic Properties of Metals and Alloys," John Wiley & Sons, Inc., New York (1963).
15. D. A. Schulz, Ph.D. Thesis, University of California, Berkeley, 1961 (unpublished).
16. R. D. Stull and G. Sinke, "Thermodynamic Properties of the Elements," American Chemical Society, Washington, D. C. (1956).
17. R. K. Edwards and J. H. Downing, *J. Phys. Chem.*, **59**, 1079 (1955).
18. J. W. Otvos and D. P. Stevenson, *J. Am. Chem. Soc.*, **78**, 546 (1956).
19. C. J. Frosch and C. D. Thurmond, *J. Phys. Chem.*, **66**, 877 (1962).

Methods for the Calculation of Polarization in Porous Electrodes

F. A. Posey

Chemistry Division, Oak Ridge National Laboratory, Oak Ridge, Tennessee

ABSTRACT

Solutions in closed form are presented for the polarization behavior and the distribution of current and potential in idealized, one-dimensional porous electrodes in the case of a simple oxidation-reduction reaction under pure activation control. Exact solutions are derived for transfer coefficients of 1/3, 1/2, and 2/3 for electrodes of finite length, while solutions for semi-infinite electrodes are given for transfer coefficients of 1/4, 1/3, 1/2, 2/3, and 3/4. An approximate method for calculating current and potential distributions in porous electrodes is proposed which is valid for any value of the transfer coefficient, and exact and approximate solutions are compared.

Studies on the distribution of current and potential in porous electrodes have received considerable stimulus from the intensive development of fuel cells in recent years (1,2). Porous electrodes are also widely used in battery technology and in the chemical process industries. The theory of electrochemical reactions at simple, planar electrodes having a well-defined interface has been developed extensively, and a comprehensive monograph is available (3). In contrast, the theory of the polarization behavior of porous electrodes is relatively less advanced because a number of factors which are unimportant or easily treated in the case of planar electrodes greatly complicate the calculation of reaction rates in porous electrodes. These factors include parameters pertaining to the physical structure of the electrode, such as the porosity, specific surface area, and conductivity of both solid and electrolyte phases.

A number of authors have reported solutions to the problem of the distribution of current and potential in porous or tubular electrodes (4-33). The generality of these solutions depends on the model adopted and on the assumptions or approximations made for each special case in order to obtain solutions in closed form. A one-dimensional model of porous electrodes is most frequently used; this choice avoids considerable mathematical difficulty and at the same time provides solutions which are in reasonable agreement with experiment. The one-dimensional model assumes a system of idealized, liquid-filled pores in an electronically conducting matrix together with uniform, average values of parameters such as porosity, specific surface area, resistivity, etc. The current or reaction rate, the interfacial potential difference, and the concentrations of reactants then vary throughout the length of the electrode in a manner determined by the physical parameters, the rate law for reaction at the interface, mass transfer conditions, and initial and boundary conditions.

The fundamental differential equation governing the distribution of potential in porous electrodes was de-

rived by Daniel'-Bek (4). This equation, a Poisson-type relation, has since been integrated for a number of important cases occurring in the operation of porous electrodes. In the case of constant reactant concentrations throughout the length of the porous electrode, solutions for the polarization characteristics and for the distribution of current and potential may be classified according to the type of electrochemical reaction rate law assumed and the type of electrode, *i.e.*, whether the electrode is finite or semi-infinite. In general, the boundary conditions for semi-infinite electrodes are simpler than those for electrodes of finite length, and the solutions are correspondingly simpler in form. The reaction rate law, or the relation between the current density of the interfacial electrochemical reactions and the interfacial potential difference at any point in the electrode, has been used in three different forms: (a) current density depends linearly on potential difference (or overpotential), the linear law; (b) current density depends exponentially on potential difference, the exponential (or Tafel) law; and (c) current density is a more general function of overpotential, the general or exact law. Cases (a) and (b) are special cases of the general law (c) which considers both forward and reverse rates of the partial processes in the usual manner (3). For the linear law, solutions for the semi-infinite electrode are given by Frumkin (5), Buvet, Guillou, and Warszawski (21), and Guillou and Buvet (30), while solutions for the finite electrode are due to Daniel'-Bek (4), Euler and Nonnenmacher (16), and Newman and Tobias (20). In the case of the exponential law, the semi-infinite electrode is treated by Ksenzhek (17) for the case of diffusion supply of reagents, and solutions for the finite electrode are given by Daniel'-Bek (4) and Newman and Tobias (20). General solutions, those valid for both large and small values of polarization for reactions under pure activation control, are reported only for the case of a symmetrical polarization law, *i.e.*, the transfer coefficient equals 1/2. General solutions of this type for the semi-infinite electrode are given by Frumkin (5) and

Ksenzhek and Stender (8,9), while general solutions for the finite electrode are due to Ksenzhek (18) and Winsel (19).

In addition to the previous work, other solutions for special cases in the operation of porous electrodes are available. The polarization resistance of finite electrodes with a linear polarization law and forced solution flow is given by Perskaya and Zaidenman (11,13,14). Tubular electrodes are specifically considered by Frumkin (5), Ksenzhek and Stender (9), Mueller (27), and Blaedel, Olson, and Sharma (33). Operation of porous electrodes in a steady state with diffusion supply of reagents and with forced supply is treated by Ksenzhek (17) and Gurevich and Bagotskii (24,25,26). Potentiostatic and galvanostatic transient discharge characteristics of porous electrodes are treated according to special models by Euler (22) and Winsel (19). Response of porous electrodes to alternating current is considered by Ksenzhek and Stender (9), Winsel (19), and de Levie (31). The determination of the specific surface area of porous electrodes by measurement of interfacial capacity using a-c and d-c methods is treated by Ksenzhek and Stender (7), Ksenzhek (28), and de Levie (31). Ksenzhek (10) gives an interpretation of the meaning of activation energy measurements on porous electrodes. Euler (29) and de Levie (31) discuss the influence of diffusion. Euler and Müller (32) consider the accuracy to which distributions of current and potential can be calculated. Winsel (19) reports a general method for the calculation of potential and current distribution in idealized, cylindrical pores which considers the effect of cylindrical symmetry. Mueller (27) employs the equations for current and potential distribution in tubes to calculate the throwing power in anodic and cathodic protection of pipes.

This paper presents solutions to the problem of the distribution of current and potential in porous electrodes for the case of unsymmetrical rate laws having certain values of the transfer coefficient.¹ Solutions in closed form are given for transfer coefficients of 1/3, 1/2, and 2/3 for an electrode of finite length, while solutions for the semi-infinite electrode are given for transfer coefficients of 1/4, 1/3, 1/2, 2/3, and 3/4.² Dimensionless parameters are used for economy of notation and ease in the comparison of solutions. In addition, an approximate method for calculating current and potential distributions in porous electrodes is proposed which is valid for any value of the transfer coefficient.

Fundamental Equations and Transformation to Dimensionless Form

A schematic diagram of an idealized, one-dimensional porous electrode is shown in Fig. 1. The total current, i , flows from the polarizing electrode into the pores of the porous electrode of length, l . Because of the finite conductivity of the solution phase, the passage of current introduces a gradient of the potential in the solution phase, $\phi_s(x)$, throughout the length of the pores. As a consequence, the interfacial potential difference, $\Delta\phi(x) = \phi_M - \phi_s(x)$, varies and with it the current density of the electrochemical reactions occurring at the interface between solid and liquid phases, $j(x)$. Since the resistivity of the metallic

¹ It is assumed throughout this paper that the resistivity of the metallic phase is negligible compared to that of the liquid phase. Situations where the resistivities of the phases are comparable are discussed by Daniel'-Bek (4), Ksenzhek and Stender (8), Euler and Nonnenmacher (16), Newman and Tobias (20), and Euler (22). The effects of concentration polarization and of changes of reactant concentrations with time are not considered. These solutions therefore apply most directly to two situations: (a) the distribution of current and potential in a porous electrode during the first moments following the application of a current, before significant changes in reactant concentrations occur; (b) the distribution obtained with a flow of solution through the electrode so large that concentration changes due to the electrochemical reaction are negligible.

² The solutions for a transfer coefficient of 1/2 are the same or alternative forms of those of Frumkin (5), Ksenzhek and Stender (8,9), Ksenzhek (18), and Winsel (19). They are included here for the sake of completeness and for comparative purposes.

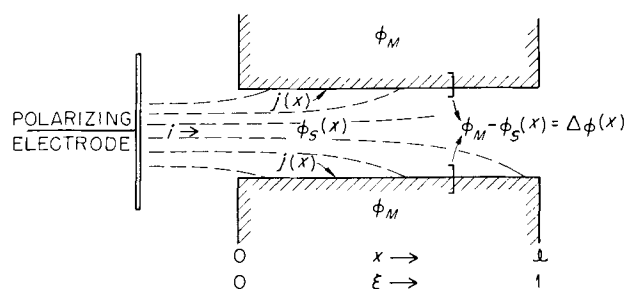


Fig. 1. Schematic diagram of idealized, one-dimensional porous electrode.

phase is assumed negligible, ϕ_M is constant and $j(x)$ is largest near $x = 0$.

The rate law for reaction at the interface is assumed to be given by Eq. [1], which is of the conventional form for a simple oxidation-

$$j(x) = j_0 \left\{ \exp \left[+ \frac{\beta F \eta(x)}{RT} \right] - \exp \left[- \frac{(1-\beta) F \eta(x)}{RT} \right] \right\} \quad [1]$$

reduction reaction under pure activation control (3). In Eq. [1], j_0 is the exchange current density of the reaction at the reversible potential ($\Delta\phi_0$), β is the transfer coefficient ($0 < \beta < 1$), RT/F is the thermal volt equivalent, and $\eta(x) = \Delta\phi(x) - \Delta\phi_0$ is the overpotential. The total current is obtained by integrating the current density over the length of the electrode, according to Eq. [2]. In Eq. [2], S is the surface area

$$i = S \int_0^l j(x) dx \quad [2]$$

of the porous electrode per unit length. The gradient of potential in the solution phase and the gradient of the overpotential are given by Eq. [3]

$$\frac{1}{A} \left[i - S \int_0^x j(x) dx \right] = \sigma \frac{d\phi_s(x)}{dx} = -\sigma \frac{d\eta(x)}{dx} \quad [3]$$

obtained from Ohm's law, in which A is the average cross-sectional area of the electrolyte in the electrode and σ is the specific conductance of the solution. Differentiation of Eq. [3] leads to Eq. [4], which is

$$\frac{d^2\eta(x)}{dx^2} = \frac{S}{\sigma A} j(x) \quad [4]$$

Daniel'-Bek's fundamental relation (4) for the distribution of potential in porous and tubular electrodes.

A simplified notation is obtained if some of the parameters in the preceding equations are converted to dimensionless form. A reduced length is defined by $\xi = x/l$ (cf. Fig. 1); a relative or reduced current density or reaction rate is defined by $\rho(\xi) = j(\xi)/j_0$; a reduced total current is given by $I = i/i_0$, where $i_0 = S l j_0$ is the exchange current of the electrode; $\kappa = (i_0 l F) / (\sigma A R T)$ is a resistance parameter which is essentially a ratio of solution impedance to interfacial impedance; and $\phi(\xi) = [F \eta(\xi)] / RT$ is a reduced overpotential. In this notation, the fundamental relations of Eq. [1]-[4] are replaced by Eq. [5]-[8].

$$\rho(\xi) = e^{+\beta\phi(\xi)} - e^{-(1-\beta)\phi(\xi)} \quad [5]$$

$$I = \int_0^1 \rho(\xi) d\xi \quad [6]$$

$$\frac{d\phi(\xi)}{d\xi} = -\kappa \left[I - \int_0^\xi \rho(\xi) d(\xi) \right] \quad [7]$$

$$\frac{d^2\phi(\xi)}{d\xi^2} = \kappa \rho(\xi) \quad [8]$$

The distribution of potential is obtained by integration of Eq. [8] subject to the boundary conditions

$$\left(\frac{d\phi(\xi)}{d\xi}\right)_{\xi=0} = -\kappa I; \left(\frac{d\phi(\xi)}{d\xi}\right)_{\xi=1} = 0$$

The distribution of (relative) current density is then calculable from Eq. [5] and the total current follows from Eq. [6] or by use of the boundary condition at $\xi = 0$.

A first integration of Eq. [8] leads to Eq. [9], where the

$$\frac{d\phi(\xi)}{d\xi} = -(2\kappa)^{1/2} \left\{ \frac{1}{\beta} [e^{+\beta\phi(\xi)} - e^{+\beta\phi(1)}] + \frac{1}{(1-\beta)} [e^{-(1-\beta)\phi(\xi)} - e^{-(1-\beta)\phi(1)}] \right\}^{1/2} \quad [9]$$

boundary condition for $\xi = 1$ is used to evaluate the integration constant. Equation [9] and the boundary condition at $\xi = 0$ lead to Eq. [10], an expression

$$I = \left(\frac{2}{\kappa}\right)^{1/2} \left\{ \frac{1}{\beta} [e^{+\beta\phi(0)} - e^{+\beta\phi(1)}] + \frac{1}{(1-\beta)} [e^{-(1-\beta)\phi(0)} - e^{-(1-\beta)\phi(1)}] \right\}^{1/2} \quad [10]$$

for the (reduced) total current. For large anodic polarization, if $\phi(0) \gg \phi(1)$, Eq. [10] reduces to Eq. [11], which is the equation for the anodic Tafel

$$I = \left(\frac{2}{\beta\kappa}\right)^{1/2} e^{+\beta\phi(0)/2} \quad [11]$$

line of porous electrodes having a highly nonuniform current distribution. The slope of the Tafel line, $d\phi(0)/d \ln I$, equals $2/\beta$, or twice the slope of the Tafel line for the same reaction on a planar electrode. The intercept at $\phi(0) = 0$ is a function of both the transfer coefficient (β) and the resistance parameter (κ).

Evaluation of the potential distribution is accomplished by integration of Eq. [9], which may be rearranged into the form of Eq. [12].

$$\frac{d\phi(\xi)}{\left\{ \frac{1}{\beta} [e^{+\beta\phi(\xi)} - e^{+\beta\phi(1)}] + \frac{1}{(1-\beta)} [e^{-(1-\beta)\phi(\xi)} - e^{-(1-\beta)\phi(1)}] \right\}^{1/2}} = -(2\kappa)^{1/2} d\xi \quad [12]$$

Expressions equivalent to Eq. [12] were solved by Ksenzhek (18) and Winsel (19) for $\beta = 1/2$, the case of the symmetrical rate law. Solutions in closed form may also be obtained for certain other values of β , and these are presented below.

The Finite Electrode

The substitutions, $y = \exp \{1/2[\phi(\xi) - \phi(1)]\}$ for $\beta = 1/2$, or $y = \exp \{1/3[\phi(\xi) - \phi(1)]\}$ for $\beta = 1/3$ or $2/3$, transform Eq. [12] into integrable expressions. Integration of the resulting equations is accomplished by use of Jacobian elliptic functions and integrals (34). Table I presents equations derived in this manner for the potential distribution in finite electrodes for the cases, $\beta = 1/3, 1/2$, and $2/3$. Elliptic functions used in Table I and elsewhere are defined below in the list of Symbols. Alternative forms of Eq. [13] are given by Ksenzhek (18) and Winsel (19). In order to compute potential distributions, values of u , the incomplete elliptic integral of the first kind, and of k , the modulus, are obtained from the expressions in the third and fourth columns of Table I as a function of $\phi(1)$. Values of $\phi(\xi)$ may then be calculated from the formulas in the second column, with the aid of tables of the Jacobian elliptic functions (35).

The total current may be calculated from Eq. [10] and values of $\phi(0)$ and $\phi(1)$ obtained from Eq. [13], [14], or [15] of Table I, or from the formulas of Table II. Three types of polarization curves may be computed from the equations of Table II; I may be evaluated as a function of $\phi(0)$, of $\phi(1)$, or of $\phi(0) - \phi(1)$. A family of curves corresponding to Eq. [16] is presented below.

The Semi-Infinite Electrode

Relations for the potential distribution in semi-infinite porous electrodes may be derived from the equations presented above with a modified notation. On replacing the length variable for finite electrodes, ξ , by the distance, x , Eq. [5]-[8] are transformed into Eq. [19]-[22]. The resistance parameter κ' in Eq. [21] and [22] replaces κ of

$$\rho(x) = e^{+\beta\phi(x)} - e^{-(1-\beta)\phi(x)} \quad [19]$$

$$I' = \int_0^\infty \rho(x) dx \quad [20]$$

$$\frac{d\phi(x)}{dx} = -\kappa' \left[I' - \int_0^x \rho(x) dx \right] \quad [21]$$

$$\frac{d^2\phi(x)}{dx^2} = \kappa' \rho(x) \quad [22]$$

Eq. [7] and [8]; $\kappa' = (j_o S F) / (\sigma A R T)$ is a resistance parameter for semi-infinite electrodes. The (reduced) total current [$I' = i / (S j_o)$] has the dimensions of a

Table I. Equations for the calculation of potential distributions in porous electrodes of finite length for transfer coefficients of 1/3, 1/2, and 2/3

β	y (Potential Distribution)	u	k^2	Equation No.
1/2	$\exp\{1/2[\phi(\xi) - \phi(1)]\} = \frac{dn^2(u, k)}{cn^2(u, k)}$	$\frac{(1-\xi)\kappa^{1/2}}{2} e^{+\phi(1)/4}$	$e^{-\phi(1)}$	[13]
1/3	$\exp\{1/3[\phi(\xi) - \phi(1)]\} = \frac{1 - \gamma sn^2(u, k)^*}{cn^2(u, k)}$	$\frac{(1-\xi)\kappa^{1/2}}{2k\sqrt{3}} e^{-\phi(1)/3} (1 + 8e^{+\phi(1)})^{1/4}$	$\frac{2e^{-\phi(1)} [1 + 8e^{+\phi(1)}]^{1/2}}{4 - e^{-\phi(1)} [1 - [1 + 8e^{+\phi(1)}]^{1/2}]}$	[14]
2/3	$\exp\{1/3[\phi(\xi) - \phi(1)]\} = \frac{dn^2(u, k)^*}{1 - \delta sn^2(u, k)}$	$\frac{(1-\xi)\kappa^{1/2}}{2\sqrt{3}} e^{+\phi(1)/3} (1 + 8e^{-\phi(1)})^{1/4}$	$\frac{4e^{-\phi(1)} - 1 + [1 + 8e^{-\phi(1)}]^{1/2}}{2[1 + 8e^{-\phi(1)}]^{1/2}}$	[15]

* $\gamma = (1/4) e^{-\phi(1)} [1 + [1 + 8e^{+\phi(1)}]^{1/2}]$; $\delta = \frac{3 + [1 + 8e^{-\phi(1)}]^{1/2}}{2[1 + 8e^{-\phi(1)}]^{1/2}}$.

Table II. Equations for the calculation of polarization curves of porous electrodes of finite length for transfer coefficients of 1/3, 1/2, and 2/3

β	Polarization Equation*	Equation No.
1/2	$I = \frac{2}{(\kappa)^{1/2}} e^{+\phi(0)/4} \frac{(k')^{2t} n(u_0, k)}{dn(u_0, k)}$	[16]
1/3	$I = \frac{\sqrt{3} e^{+\phi(0)/6}}{\sqrt{2} (\kappa)^{1/2}} \{4 - e^{-\phi(0)} (1 - [1 + 8e^{+\phi(0)/2}]^{1/2})\}^{1/2} (1 - \gamma) tn(u_0, k) dn(u_0, k)$	[17]
2/3	$I = \frac{\sqrt{3} e^{+\phi(0)/3}}{(\kappa)^{1/2}} [1 + 8e^{-\phi(0)}]^{1/4} \frac{(\delta - k^2) sd(u_0, k) cn(u_0, k)}{1 - \delta sn^2(u_0, k)}$	[18]

* Values of u_0 and k are given by the formulas in Table I for $\xi = 0$; γ and δ are defined in the footnote to Table I.

length and is equal to the current divided by the exchange current per unit length of electrode. The potential distribution is obtained on integration of Eq. [22] with the revised boundary conditions

$$\left(\frac{d\phi(x)}{dx}\right)_{x=0} = -\kappa' I'; \phi(\infty) = 0$$

A first integration of Eq. [22], with use of the boundary condition, $\phi(\infty) = 0$, leads to Eq. [23], which is similar in form to Eq. [9].

$$\frac{d\phi(x)}{dx} = -(2\kappa')^{1/2}$$

$$\left\{ \frac{1}{\beta} [e^{+\beta\phi(x)} - 1] + \frac{1}{(1-\beta)} [e^{-(1-\beta)\phi(x)} - 1] \right\}^{1/2} \quad [23]$$

Use of the boundary condition at $x = 0$ with Eq. [23] leads to Eq. [24]

$$I' = \left(\frac{2}{\kappa'}\right)^{1/2}$$

$$\left\{ \frac{1}{\beta} [e^{+\beta\phi(0)} - 1] + \frac{1}{(1-\beta)} [e^{-(1-\beta)\phi(0)} - 1] \right\}^{1/2} \quad [24]$$

for the total current. This equation is quite general for the polarization behavior of the semi-infinite electrode having the rate law of Eq. [19]; it is valid for any value of the transfer coefficient β ($0 < \beta < 1$). An equation for the anodic Tafel line of the semi-infinite electrode is obtained from Eq. [24] for large $\phi(0)$. This relation is given in Eq. [25]

$$I' = \left(\frac{2}{\beta\kappa'}\right)^{1/2} e^{+\beta\phi(0)/2} \quad [25]$$

which is of the same form as Eq. [11]. Separation of the variables in Eq. [23] leads to Eq. [26], the counterpart of Eq. [12]. Relations

$$\frac{d\phi(x)}{\left\{ \frac{1}{\beta} [e^{+\beta\phi(x)} - 1] + \frac{1}{(1-\beta)} [e^{-(1-\beta)\phi(x)} - 1] \right\}^{1/2}} = -(2\kappa')^{1/2} dx \quad [26]$$

corresponding to Eq. [26] were integrated by Frumkin (5) and Ksenzhek and Stender (8,9) for the case of the symmetrical rate law ($\beta = 1/2$). Other solutions in closed form for different values of β are given below.

The substitutions, $y = \exp[(1/2)\phi(\xi)]$ for $\beta = 1/2$, $y = \exp[(1/3)\phi(\xi)]$ for $\beta = 1/3$ or $2/3$, or $y = \exp[(1/4)\phi(\xi)]$ for $\beta = 1/4$ or $3/4$, transform Eq. [26] into integrable expressions. The resulting potential distributions may be calculated from the equations of Table III. Equation [27] is equivalent to the solutions reported by Frumkin (5) and Ksenzhek and Stender (8,9). Polarization curves for these and other cases of the semi-infinite electrode may be calculated directly from Eq. [24]. The function $\pi\{u, \alpha^2/(\alpha^2 - 1)\}$ in Eq. [30] and [31] is Legendre's incomplete elliptic integral of the third kind (34, 36). The symbols $u_{1,0}$, $u_{2,0}$, and f_0 denote values of the functions given in the footnote to Table III for $x = 0$.

An Approximate Method

The formulas presented in the previous sections provide exact solutions in closed form to the problem

Table III. Equations for the calculation of potential distributions in semi-infinite porous electrodes for transfer coefficients of 1/4, 1/3, 1/2, 2/3, and 3/4

β	Potential distribution function	Equation No.
1/2	$\tanh[\phi(x)/8] = \tanh[\phi(0)/8] \exp[-(\kappa')^{1/2} x]$	[27]
1/3	$\frac{(2 \exp[\phi(x)/3] + 1)^{1/2} - \sqrt{3}}{(2 \exp[\phi(x)/3] + 1)^{1/2} + \sqrt{3}} = \frac{(2 \exp[\phi(0)/3] + 1)^{1/2} - \sqrt{3}}{(2 \exp[\phi(0)/3] + 1)^{1/2} + \sqrt{3}} \exp[-(\kappa')^{1/2} x]$	[28]
2/3	$\frac{\exp[\phi(0)/3] - 1}{\exp[\phi(x)/3] - 1} = \frac{2 \exp[\phi(0)/3] + 1 - \sqrt{3} \exp[\phi(0)/6] (2 + \exp[\phi(0)/3])^{1/2}}{2 \exp[\phi(x)/3] + 1 - \sqrt{3} \exp[\phi(x)/6] (2 + \exp[\phi(x)/3])^{1/2}} \exp[-(\kappa')^{1/2} x]$	[29]
1/4	$(u_1 - u_{1,0}) + [1/(\alpha - 1)] [\pi\{u_1, \alpha^2/(\alpha^2 - 1)\} - \pi\{u_{1,0}, \alpha^2/(\alpha^2 - 1)\} + \alpha(f - f_0)] = \mu x^*$	[30]
3/4	$(u_2 - u_{2,0}) + [1/(\alpha - 1)] [\pi\{u_2, \alpha^2/(\alpha^2 - 1)\} - \pi\{u_{2,0}, \alpha^2/(\alpha^2 - 1)\} - \alpha(f - f_0)] = -\mu x^*$	[31]

$$* cn u_1 = \frac{\sqrt{3} \exp[\phi(x)/4] - 1}{\sqrt{3} \exp[\phi(x)/4] + 1}; \quad cn u_2 = \frac{\exp[\phi(x)/4] - \sqrt{3}}{\exp[\phi(x)/4] + \sqrt{3}}; \quad \alpha = \frac{\sqrt{3} + 1}{\sqrt{3} - 1}; \quad k^2 = \frac{\sqrt{3} - 1}{2\sqrt{3}};$$

$$\mu = \frac{\sqrt{3} + 1}{3^{1/2}\sqrt{2}} (\kappa')^{1/2}; \quad f = \frac{1}{2} \left[\frac{\alpha^2 - 1}{k^2 + (k')^2 \alpha^2} \right]^{1/2} \ln \left[\frac{(\alpha^2 - 1)^{1/2} dn u + \{k^2 + (k')^2 \alpha^2\}^{1/2} sn u}{(\alpha^2 - 1)^{1/2} dn u - \{k^2 + (k')^2 \alpha^2\}^{1/2} sn u} \right]$$

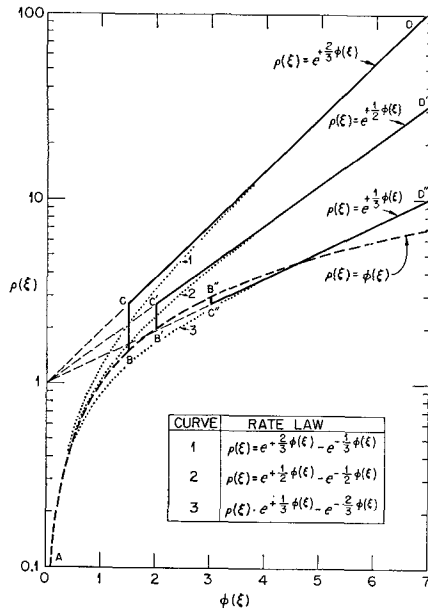


Fig. 2. Comparison of exact and approximate reaction rate laws for $\beta = 1/3, 1/2, \text{ and } 2/3$.

of the distribution of current and potential in porous electrodes for several values of the transfer coefficient (β) in the rate laws of Eq [5] and [19]. Although these exact solutions should be useful for calculations on the operation of porous electrodes in the special cases for which they are valid, the computations are tedious. An approximate method of calculation is presented below which circumvents a great part of the arithmetical difficulty, but which provides approximate solutions which are in good agreement with the exact solutions.

The nature of the approximation is shown in Fig. 2 for $\beta = 1/3, 1/2, \text{ and } 2/3$. Curves 1, 2, and 3 show the exact rate laws for $\beta = 2/3, 1/2, \text{ and } 1/3$, respectively. The corresponding approximate rate laws are given by curves ABCD, AB'C'D', and AB''C''D''. The approximate rate law follows the linear polarization relation, $\rho(\xi) = \phi(\xi)$, up to the potential, $\phi(\xi_0)$, where a discontinuity transition (BC, B'C', and B''C'') occurs to the exponential rate law, $\rho(\xi) = \exp[\beta\phi(\xi)]$. At $\phi(\xi_0)$, the slopes of both linear and exponential rate laws in the plot of Fig. 2 are equal, and $\phi(\xi_0) = 1/\beta$. Equations for the polarization behavior and the distribution of current and potential in both finite and semi-infinite porous electrodes according to this approximation are presented below.

The Finite Electrode.³—Three special cases arise in the application of the approximate method to the finite electrode: (a) $\phi(\xi_0) = 1/\beta \cong \phi(0) > \phi(1) \cong 0$ (for anodic polarization), so that in this case the entire electrode operates with the linear rate law, $\rho(\xi) = \phi(\xi)$; (b) $\infty > \phi(0) > \phi(1) \cong \phi(\xi_0) = 1/\beta$, where the rate processes everywhere in the electrode follow the exponential law, $\rho(\xi) = \exp[\beta\phi(\xi)]$; and (c) $\phi(0) > \phi(\xi_0) > \phi(1)$, a transition region where $0 < \xi_0 < 1$ and ξ_0 is a function of $\phi(0)$.

For case (a), when $\phi(\xi_0) = 1/\beta \cong \phi(0) \cong 0$, integration of Eq. [8] with the linear rate law, $\rho(\xi) = \phi(\xi)$, leads to Eq. [32] and [33] of Table IV for the potential distribution and the polarization curve. The value of $\phi(0)$ when $\phi(1) = \phi(\xi_0) = 1/\beta$ may be determined from:

$$\phi(0) = \frac{2}{\beta} \ln \frac{\exp(1/2)}{\cos(\beta\kappa e/2)^{1/2}} \quad (\xi_0 = 1)$$

Therefore when $\phi(0)$ is greater than this value, Eq. [8] may be integrated with $\rho(\xi) = \exp[\beta\phi(\xi)]$ to give the potential distribution and polarization curve for case (b), Eq. [34] and [35] of Table IV.

The potential distribution functions and the polarization curve of case (c), when $0 < \xi_0 < 1$ and $\phi(0) > \phi(\xi_0) = 1/\beta > \phi(1)$, are given by Eq. [36], [37], and [38] of Table IV. The distribution of Eq. [36] holds in the region $0 < \xi < \xi_0$, while Eq. [37] gives the distribution in the region $\xi_0 < \xi < 1$. The parameter ξ_0 may be computed from the relation given in Table IV as a function of $\phi(0)$. Once ξ_0 is known, Eq. [36] and [37] are used to calculate $\phi(\xi)$ and the total current is calculated from Eq. [38].

The effect of the discontinuity in the rate law is averaged out to a considerable extent, so that potential distributions calculated in this manner are quite close to those found with the exact methods discussed previously. This averaging effect may be utilized further to calculate more precise values of the (reduced) reaction rate, $\rho(\xi)$, than would result from the use of the exact rate law of Eq. [5] is used with values of the potential, $\phi(\xi)$, calculated from Eq. [36] and [37]. By use of this technique, the major effect of the use of a discontinuous rate law appears in the calculated polarization curves rather than in the calculated potential and current distributions.

The Semi-infinite Electrode.³—The boundary conditions are somewhat simpler in the case of the semi-infinite electrode than for the finite electrode, and only

³ Nearly all parameters used in this section and the next are defined above in the sections dealing with the exact treatment of the finite and semi-infinite electrodes; others are defined as they occur. The equations are derived for the case of anodic polarization; cathodic polarization may be treated similarly.

Table IV. Equations for the approximate calculation of potential distributions and polarization curves of porous electrodes of finite length

Case	Potential distribution	Equation No.	Polarization equation	Equation No.
(a) Linear law $1/\beta \cong \phi(0) > \phi(1) \cong 0$	$\phi(\xi) = \phi(0) \frac{\cosh[(\kappa)^{1/2}(1-\xi)]}{\cosh[(\kappa)^{1/2}]}$	[32]	$I = \frac{\phi(0)}{(\kappa)^{1/2}} \tanh(\kappa)^{1/2}$	[33]
(b) Exponential law $\infty > \phi(0) > \phi(1) \cong 1/\beta$	$\cos^{-1}[\exp(-\beta/2[\phi(\xi) - \phi(1)])] = \cos^{-1}[\exp(-\beta/2[\phi(0) - \phi(1)])] - [(\beta\kappa/2) e^{-\beta\phi(1)}]^{1/2} \xi$ [34] where: $\exp[(\beta/2)\phi(0)] = \frac{\exp[(\beta/2)\phi(1)]}{\cos[\beta\kappa/2 e^{-\beta\phi(1)}]^{1/2}}$	[34]	$I = \{(2/\beta\kappa) [e^{-\beta\phi(0)} - e^{-\beta\phi(1)}]^{1/2} / [(2/\beta\kappa) e^{-\beta\phi(1)}]^{1/2} \tan [(\beta\kappa/2) e^{-\beta\phi(1)}]^{1/2}$	[35]
(c) Transition region ($0 < \xi_0 < 1$)	$\cos^{-1}[Qe^{-\beta\phi(\xi)}]^{1/2} = \cos^{-1}[Qe^{-\beta\phi(0)}]^{1/2} - \left[\frac{\beta\kappa Q}{2} \right]^{1/2} \xi$ [$0 < \xi < \xi_0$] where: $Q = e^{+1} - \frac{\tanh^2[(\kappa)^{1/2}(1-\xi_0)]}{2\beta}$ $\phi(\xi) = \frac{\cosh[(\kappa)^{1/2}(1-\xi)]}{\beta \cosh[(\kappa)^{1/2}(1-\xi_0)]}$ [$\xi_0 < \xi < 1$]	[36] [37]	$I^2 = \frac{\tanh^2[(\kappa)^{1/2}(1-\xi_0)]}{\beta^2 \kappa} + (2/\beta\kappa)(e^{-\beta\phi(0)} - e^{-1})$ [38] ξ_0 is computed from: $e^{-\beta\phi(0)} = \frac{Q}{\cos^2[\cos^{-1}[Q/e]^{1/2} + (\beta\kappa Q/2)^{1/2} \xi_0]}$	[38]

Table V. Equations for the approximate calculation of potential distributions and polarization curves of semi-infinite porous electrodes

Case	Potential distribution	Equation No.	Polarization equation	Equation No.
(a) Linear law $1/\beta \cong \phi(0) > 0$	$\phi(x) = \phi(0) \exp[-(\kappa')^{1/2}x]$	[39]	$I' = \phi(0)/(\kappa')^{1/2}$	[40]
(b) General case $\infty > \phi(0) > 1/\beta$	$\cos^{-1}[Q' e^{-\beta\phi(x)}]^{1/2} = \cos^{-1}[Q' e^{-\beta\phi(0)}]^{1/2} - \left(\frac{\beta\kappa'Q'}{2}\right)^{1/2} x$ [$0 < x < x_0$] where: $Q' = e^{+1} - 1/2\beta$ $\phi(x) = 1/\beta \exp[-(\kappa')^{1/2}(x-x_0)]$ [$x_0 < x < \infty$]	[41] [42]	$(I')^2 = \frac{1}{\beta^2\kappa'} + \frac{2}{\beta\kappa'} (e^{+\beta\phi(0)} - e^{+1})$ x_0 is computed from: $x_0 = \left(\frac{2}{\beta\kappa'Q'}\right)^{1/2} \cos^{-1}[Q' \exp\{-1/2[1 + \beta\phi(0)]\}] + \{(1-Q'e^{-\beta\phi(0)})(1-Q'e^{-1})\}^{1/2}$	[43]

two special cases arise in the application of the approximate method. For case (a), when $\phi(x_0) = 1/\beta \cong \phi(0) > 0$, the linear rate law is a good approximation everywhere in the electrode, and integration of Eq. [22] for $\rho(x) = \phi(x)$ leads to Eq. [39] and [40] of Table V for the potential distribution and the polarization curve in this region.

For case (b), when $\infty > \phi(0) > \phi(x_0) = 1/\beta$, the potential distribution functions and the polarization curve are given by Eq. [41], [42], and [43] of Table V. The distribution of Eq. [41] holds in the region $0 < x < x_0$, while Eq. [42] gives the distribution in the region $x_0 < x < \infty$. The parameter x_0 may be computed from the relation given in Table V as a function of $\phi(0)$. Once x_0 is known, Eq. [41] and [42] are used to calculate $\phi(x)$ at any point in the electrode. An approximate polarization curve may be calculated by use of Eq. [40] and [43], or the exact polarization curve may be computed by use of Eq. [24].

Discussion

A family of polarization curves for the finite porous electrode is shown in Fig. 3. These curves were computed for the case of the symmetrical rate law ($\beta = 1/2$) by use of Eq. [13] and [16] in Tables I and II and tables of the Jacobian elliptic functions (35). The solid line in Fig. 3 is the polarization curve of finite porous electrodes when the reaction is distributed uniformly throughout the electrode; it is identical to the polarization curve of a planar electrode of the same surface area. As the resistance parameter (κ) increases, the potential and current distributions be-

come increasingly nonuniform at constant total current (I). For sufficiently large κ , the polarization curve consists of a single Tafel line of slope, $d\phi(0)/d\ln I = 2/\beta$, and $\phi(1)$ is quite small compared to $\phi(0)$. For sufficiently small κ , two Tafel lines may be observed in the polarization curve of the finite porous electrode. At small currents, $\phi(0)$ is not much different from $\phi(1)$, the reaction distribution is essentially uniform, and the polarization behavior of a planar electrode is obtained. At large currents, $\phi(0)$ eventually becomes large compared to $\phi(1)$, the reaction distribution becomes highly nonuniform, and a typical porous electrode polarization curve is obtained. The dashed lines in Fig. 3 correspond to Eq. [11]. At large I , $\phi(1)$ approaches a limiting value which depends only on κ . The value of this limiting potential is determined by the equation, $u_0 = K$, where $K(k)$ is the complete elliptic integral of the first kind (34) and u_0 is defined in Eq. [13] of Table I for $\xi = 0$. Curves similar to those in Fig. 3 are discussed by Winsel (19).

The distribution of potential and current in the finite electrode as a function of the polarization is shown in Fig. 4 and 5 for the case of symmetrical rate law ($\beta = 1/2$) and $\kappa = 1$. The parameter Φ of Fig. 4 is a relative potential function which is useful for plotting potential distributions on a convenient scale. For small currents, the relative potential distribution is essentially independent of I (cf. curve A). This limiting potential distribution occurs when the linear rate law is a good approximation, and an expression for the limiting distribution is given by Eq. [44], which is obtained from Eq. [32] of

$$\Phi = \frac{\phi(\xi) - \phi(1)}{\phi(0) - \phi(1)} = \frac{\cosh[(\kappa)^{1/2}(1-\xi)] - 1}{\cosh[(\kappa)^{1/2}] - 1} \quad [44]$$

Table IV. With increasing current, the potential distribution becomes more nonuniform. The relative reaction rate function, $\rho(\xi)/\rho(0) = j(\xi)/j(0)$, of Fig. 5

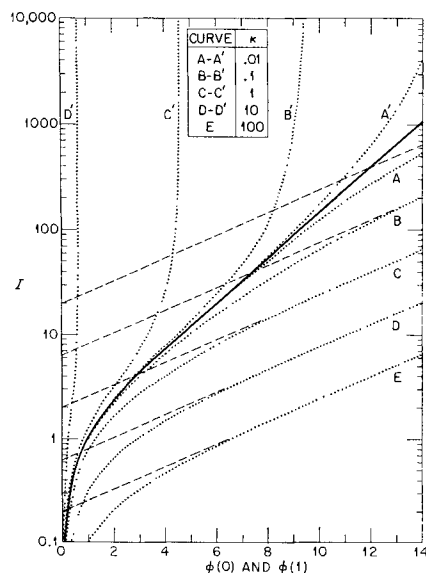


Fig. 3. Polarization curves for the finite porous electrode as a function of the resistance parameter, κ , for the case of the symmetrical rate law ($\beta = 1/2$). Curves A-E plot $\phi(0)$ vs. I ; curves A'-D' plot $\phi(1)$ vs. I ; dashed lines are extrapolations of the Tafel lines.

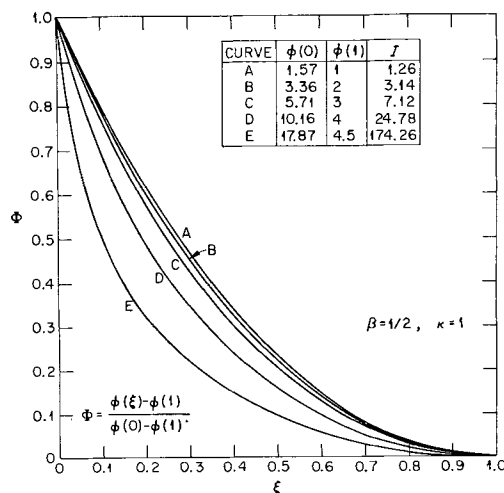


Fig. 4. Plot of the relative potential function, Φ , against ξ

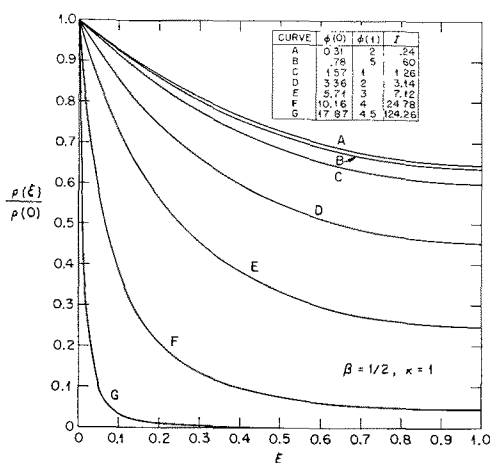


Fig. 5. Plot of the relative reaction rate function, $\rho(\xi)/\rho(0)$, against ξ .

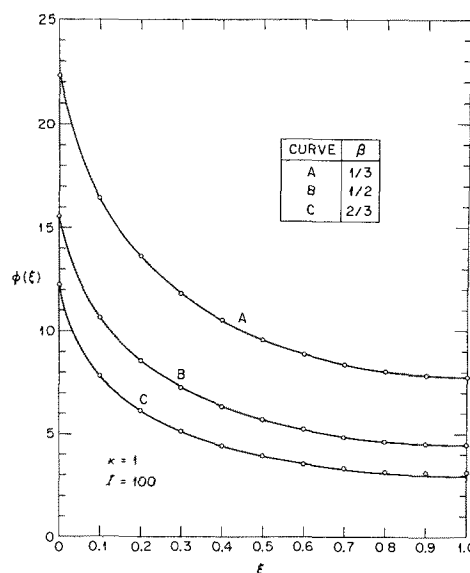


Fig. 7. Potential distribution in the finite porous electrode as a function of the transfer coefficient (β) at constant current (I). Solid lines are calculated with exact equations, open circles with approximate method.

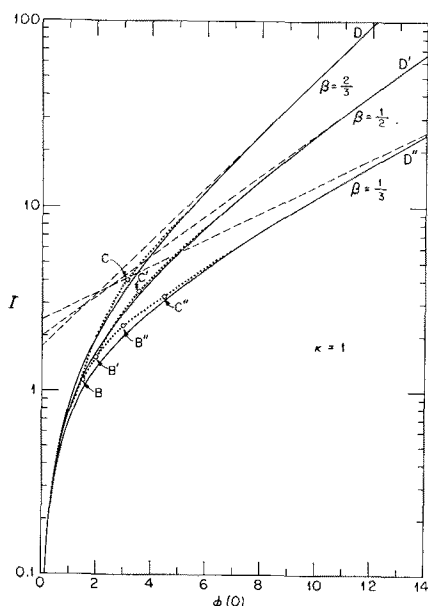


Fig. 6. Comparison of exact and approximate methods for the calculation of polarization curves of the finite porous electrode. Solid lines are the exact solutions; dotted lines are the approximate solutions; dashed lines are extrapolations of the Tafel lines.

also shows a limiting behavior for small polarization. Equation [45] is an expression for this limiting behavior. The

$$\frac{\rho(\xi)}{\rho(0)} = \frac{\cosh[(\kappa)^{1/2}(1 - \xi)]}{\cosh[(\kappa)^{1/2}]}$$
 [45]

distributions of Fig. 4 and 5 correspond to points on curves C and C' of Fig. 3. Polarization curves and potential and current distributions in the case of $\beta = 1/3$ and $2/3$ are quite similar to those shown in Fig. 3-5.

A comparison of polarization curves for the finite electrode calculated by use of both exact and approximate methods is shown in Fig. 6. The solid lines are exact solutions computed from Eq. [16], [17], and [18] of Table II for $\kappa = 1$. Sections AB, AB', and AB'' of the approximate solutions were calculated from Eq. [33] of Table IV; points B, B', and B'' correspond to the condition $\phi(0) = 1/\beta$. Sections BC, B'C', and B''C'' were calculated with Eq. [38] of Table IV and represent the transition region between operation of the entire electrode with a linear reaction rate law and operation with an exponential law. Sections CD, C'D', and C''D'' were calculated from Eq. [35] of Table IV; points C, C', and C'' correspond to the condition, $\phi(1) = 1/\beta$. The correspondence between exact and

approximate solutions decreases in the sequence: AB'C'D', ABCD, AB''C''D''. Reference to Fig. 2 shows that this sequence might have been anticipated from the relative behavior of the exact and approximate rate laws. The major effect of the assumption of a discontinuous rate law as an approximation to the more exact law is exhibited in the calculation of the polarization curve of the finite electrode. As shown below, the effect of the discontinuity in the rate law is averaged out over the length of the electrode, and exact and approximate methods for the calculation of potential and current distributions agree well.

Potential and reaction rate distributions in the finite electrode, computed by use of both exact and approximate methods, are shown in Fig. 7 and 8 as a function of the transfer coefficient. Curves A, B, and C in Fig. 7 and 8 were calculated from Eq. [14], [13], and [15] of Table I, with $\kappa = 1$ and $I = 100$; the open circles were calculated from Eq. [34] of the approximate method. The agreement between exact and approximate methods is very good. Since the total current (I) is constant, the reaction rate curves of Fig. 8 intersect.

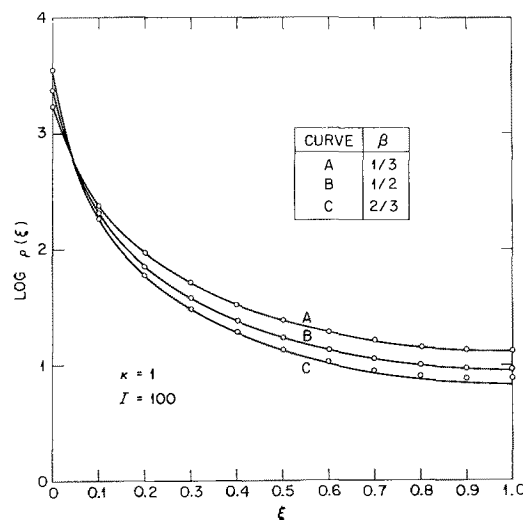


Fig. 8. Reaction distribution in the finite porous electrode as a function of the transfer coefficient (β) at constant current (I). Solid lines are calculated with exact equations, open circles with approximate method.

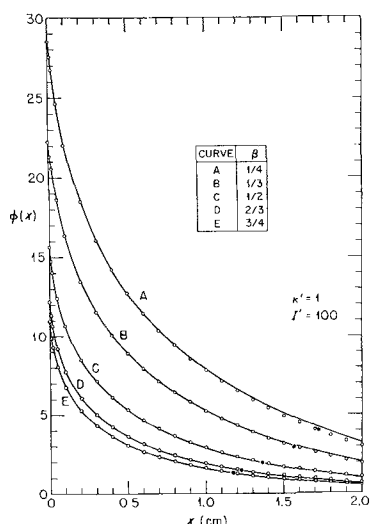


Fig. 9. Potential distribution in the semi-infinite porous electrode as a function of the transfer coefficient (β) at constant current (I'). Solid lines are calculated with exact equations, open circles with approximate method; filled circles denote x_0 , where $\phi(x_0) = 1/\beta$ and the rate law changes from $\rho(x) = \exp[\phi(x)]$ to $\rho(x) = \phi(x)$.

Potential distributions for the semi-infinite electrode are shown in Fig. 9 as a function of the transfer coefficient for the parameters $\kappa' = 1$ and $I' = 100$. The exact distributions were calculated from Eq. [27] to [31] of Table III. Values of incomplete elliptic integrals of the third kind occurring in Eq. [30] and [31] were computed by use of tables (36). The approximate distributions were calculated by use of Eq. [41] and [42] of Table V. The locus of the point x_0 was calculated in each case from the formula in Table V. Since x_0 represents the transition point between linear and exponential rate laws, it is a useful measure of the degree of penetration of the reaction into the porous electrode. As for the case of the finite electrode, the agreement between exact and approximate methods is good. The best agreement is found for the case of the symmetrical rate law ($\beta = 1/2$). The distributions of reaction rates corresponding to the potential distributions of Fig. 9 are similar in form to those of Fig. 8.

In contrast to the calculation of polarization curves for the finite electrode (cf. Fig. 6), calculation of the potential profile using the approximate method proposed here shows little effect of the assumption of a discontinuous rate law. Furthermore, as shown in Fig. 7-9, both exact and approximate methods provide essentially the same distributions. Figures 7 and 9 show that the potential distribution in porous electrodes is a rather sensitive function of the value of the transfer coefficient in the reaction rate law. Although the exact solutions reported above should be useful for computational purposes in special cases, their utility is somewhat limited for arbitrary values of the transfer coefficient which are likely to occur with practical porous electrodes. The approximate method outlined above then affords a much easier and still relatively exact technique for the calculation of polarization behavior and potential and current distributions in porous electrodes under pure activation control.

Acknowledgment

The author wishes to express grateful appreciation to K. A. Kraus and F. Nelson of this Laboratory for illuminating discussions of their observations on phenomena occurring in porous electrodes and for continued interest and encouragement of this work.

Manuscript received Nov. 8, 1963; revised manuscript received March 31, 1964. This paper was presented at the Toronto Meeting, May 3-7, 1964. This paper is based on work performed for the Office of

Saline Water, U. S. Department of the Interior, at the Oak Ridge National Laboratory, Oak Ridge, Tennessee, operated by the Nuclear Division, Union Carbide Corporation, for the U. S. Atomic Energy Division.

Any discussion of this paper will appear in a Discussion Section to be published in the June 1965 JOURNAL.

SYMBOLS

A	Average cross-sectional area of electrolyte in porous electrode, cm^2
$cn(u, k)$	Jacobian elliptic function, cosine amplitude u
$dn(u, k)$	Jacobian elliptic function, delta amplitude u
f, f_0	Functions occurring in exact treatment of semi-infinite electrode for $\beta = 1/4$ or $3/4$; defined in Table III
i	Total current of porous electrode, amp
i_0	Total exchange current of finite porous electrode, amp
I	Dimensionless reduced total current of finite electrode; $I = i/i_0 = i/Sj_0$
I'	Reduced total current of semi-infinite electrode; $I' = i/Sj_0$, cm
$j(\xi), j(x)$	Current density of electrochemical reactions occurring at the interface between solid and liquid phases in finite and semi-infinite porous electrodes, respectively, amp/cm^2
j_0	Exchange current density of porous electrode, amp/cm^2
k	Modulus of Jacobian elliptic functions and integrals
k'	Complementary modulus: $k' = (1 - k^2)^{1/2}$
K	Complete elliptic integral of the first kind
l	Length of finite porous electrode, cm
Q, Q'	Dimensionless integration constants occurring in the approximate treatments of finite and semi-infinite electrodes, respectively; defined in Tables IV and V
RT/F	Thermal volt equivalent, volts
$sd(u, k)$	$sd(u, k) = sn(u, k)/dn(u, k)$
$sn(u, k)$	Jacobian elliptic function, sine amplitude u
S	Surface area of porous electrode per unit length, cm
$tn(u, k)$	$tn(u, k) = sn(u, k)/cn(u, k)$
u	Incomplete elliptic integral of the first kind
u_0	Value of u when $\xi = 0$ or $x = 0$
x	Distance parameter of semi-infinite porous electrode, cm
x_0	Point of transition between linear and exponential rate laws in approximate treatment of semi-infinite electrode, cm
y	Convenient functions used in exact treatments of finite and semi-infinite porous electrodes
α	Parameter occurring in exact treatment of semi-infinite electrodes for $\beta = 1/4$ or $3/4$; defined in Table III
β	Transfer coefficient of the anodic reaction ($0 < \beta < 1$)
γ	Parameter occurring in exact treatment of finite electrode for $\beta = 1/3$; defined in Table I
δ	Parameter occurring in exact treatment of finite electrode for $\beta = 2/3$; defined in Table I
$\eta(\xi), \eta(x)$	$\eta(\xi) = \Delta\phi(\xi) - \Delta\phi_0$; $\eta(x) = \Delta\phi(x) - \Delta\phi_0$; overpotential in finite and semi-infinite electrodes, respectively, volts
κ, κ'	$\kappa = (i_0 l F)/(\sigma A R T)$; $\kappa' = (j_0 S F)/(\sigma A R T)$; resistance parameters occurring in treatment of finite and semi-infinite electrodes, respectively ($\kappa' = \text{cm}^{-2}$)
μ	Parameter occurring in exact treatment of semi-infinite electrodes for $\beta = 1/4$ or $3/4$; defined in Table III
ξ	Dimensionless distance parameter of finite porous electrodes

ξ_0	Point of transition between linear and exponential rate laws in approximate treatment of finite electrode
$\pi\{u, \alpha^2/(\alpha^2-1)\}$	Legendre's incomplete elliptic integral of the third kind; occurs in Eq. [30] and [31] of Table III
$\rho(\xi), \rho(x)$	$\rho(\xi) = j(\xi)/j_0$; $\rho(x) = j(x)/j_0$; dimensionless reduced reaction rates in finite and semi-infinite electrodes, respectively.
σ	Specific conductance of solution, $\text{ohm}^{-1} \text{cm}^{-1}$
ϕ_M	Potential of the metallic phase of porous electrodes, here assumed constant, volts
$\phi_s(\xi), \phi_s(x)$	Potential of the solution phase of finite and semi-infinite porous electrodes, respectively, volts
$\phi(\xi), \phi(x)$	$\phi(\xi) = F\eta(\xi)/RT$; $\phi(x) = F\eta(x)/RT$; dimensionless reduced overpotentials in finite and semi-infinite electrodes, respectively
$\phi(0)$	Dimensionless reduced overpotential at $\xi = 0$ or $x = 0$
$\phi(1)$	Dimensionless reduced overpotential at $\xi = 1$
$\phi(\xi_0), \phi(x_0)$	$\phi(\xi_0) = \phi(x_0) = 1/\beta$; dimensionless reduced potential of transition between linear and exponential rate laws in approximate treatments of finite and semi-infinite electrodes, respectively
$\Delta\phi(\xi), \Delta\phi(x)$	$\Delta\phi(\xi) = \phi_M - \phi_s(\xi)$; $\Delta\phi(x) = \phi_M - \phi_s(x)$; interfacial potential difference in finite and semi-infinite porous electrodes, respectively, volts
$\Delta\phi_0$	Reversible interfacial potential difference, volts
Φ	$\Phi = [\phi(\xi) - \phi(1)] / [\phi(0) - \phi(1)]$; relative potential function

REFERENCES

- G. J. Young, Editor, "Fuel Cells," Reinhold Publishing Co., New York (1960).
- G. J. Young, Editor, "Fuel Cells," Vol. II, Reinhold Publishing Co., New York (1963).
- K. J. Vetter, "Elektrochemische Kinetik," Springer-Verlag, Berlin (1961).
- V. S. Daniel'-Bek, *Zhur. Fiz. Khim.*, **22**, 697 (1948).
- A. N. Frumkin, *ibid.*, **23**, 1477 (1949).
- J. J. Coleman, *This Journal*, **98**, 26 (1951).
- O. S. Ksenzhek and V. V. Stender, *Doklady Akad. Nauk S.S.S.R.*, **106**, 487 (1956).
- O. S. Ksenzhek and V. V. Stender, *ibid.*, **107**, 280 (1956).
- O. S. Ksenzhek and V. V. Stender, *Zhur. Fiz. Khim.*, **31**, 117 (1957).
- O. S. Ksenzhek, *Ukrain. Khim. Zhur.*, **23**, 443 (1957).
- R. M. Perskaya and I. A. Zaidenman, *Doklady Akad. Nauk S.S.S.R.*, **115**, 548 (1957).
- E. Justi, M. Pilkuhn, W. Scheibe, and A. Winsel, "Hochbelastbare Wasserstoff-Diffusions-Elektroden für Betrieb bei Umgebungstemperatur und Niederdruck," *Akad. Wiss. u. Lit.*, Nr. 8, Komm. Verlag Steiner, Wiesbaden, 1959.
- I. A. Zaidenman and R. M. Perskaya, *Zhur. Fiz. Khim.*, **33**, 50 (1959).
- I. A. Zaidenman, *ibid.*, **33**, 437 (1959).
- J. Euler and L. Horn, *Elektrotech. Zeit.*, **81**, 566 (1960).
- J. Euler and W. Nonnenmacher, *Electrochim. Acta*, **2**, 268 (1960).
- O. S. Ksenzhek, *Zhur. Fiz. Khim.*, **36**, 243 (1962).
- O. S. Ksenzhek, *ibid.*, **36**, 633 (1962).
- A. Winsel, *Z. Elektrochem.*, **66**, 287 (1962).
- J. S. Newman and C. W. Tobias, *This Journal*, **109**, 1183 (1962).
- R. Buvet, M. Guillou, and B. Warszawski, *Electrochim. Acta*, **6**, 113 (1962).
- J. Euler, *Electrochim. Acta*, **7**, 205 (1962).
- J. C. Sohm, *ibid.*, **7**, 629 (1962).
- I. G. Gurevich and V. S. Bagotskii, *Inzhenerno-Fiz. Zhur.*, **6** (2), 60 (1963).
- I. G. Gurevich and V. S. Bagotskii, *ibid.*, **6** (3), 69 (1963).
- I. G. Gurevich and V. S. Bagotskii, *ibid.*, **6** (5), 75 (1963).
- W. A. Mueller, *This Journal*, **110**, 698 (1963).
- O. S. Ksenzhek, *Zhur. Fiz. Khim.*, **37**, 2007 (1963).
- J. Euler, *Electrochim. Acta*, **8**, 409 (1963).
- M. Guillou and R. Buvet, *ibid.*, **8**, 489 (1963).
- R. de Levie, *ibid.*, **8**, 751 (1963).
- J. Euler and K. N. Müller, *ibid.*, **8**, 949 (1963).
- W. J. Blaedel, C. L. Olson, and L. R. Sharma, *Anal. Chem.*, **35**, 2100 (1963).
- P. F. Byrd and M. D. Friedman, "Handbook of Elliptic Integrals for Engineers and Physicists," Springer-Verlag, Berlin (1954).
- G. W. Spenceley and R. M. Spenceley, "Smithsonian Elliptic Functions Tables," Smithsonian Institute, Washington, 1947.
- R. G. Selfridge and J. E. Maxfield, "A Table of the Incomplete Elliptic Integral of the Third Kind," Dover, New York (1958).

Transport Numbers in Pure Molten AgNO_3 and AgCl by a Simplified Weighing Method

Paul Duby¹ and Herbert H. Kellogg

Department of Mineral Engineering, Columbia University, New York, New York

ABSTRACT

A very simple technique is described for measuring transport numbers in pure fused salts. The transport of matter due to ionic electromigration is determined by recording continuously during electrolysis, the weight change of a movable half-cell, which consists merely of a vertical tube closed at its lower end by a coarse-fritted Pyrex plug. A small but significant decrease of the silver transport number with increasing temperature is found in both molten AgNO_3 and AgCl .

A number of techniques have been used for measuring transport numbers in pure molten salts. Most of these techniques have been criticized because of experimental limitations. More recently, the principle of the measurement itself has been questioned, and doubts have been expressed about the concept of the

transport number (1). Devising new independent methods of measurements has therefore a twofold purpose. First, it will make possible the selection of the most appropriate technique in each case, and it will improve the reliability of presently available data. Second, each new measurement brings more facts to support theories about the experimental significance of the transport number concept.

¹ Present address: School of Metallurgical Engineering, University of Pennsylvania, Philadelphia, Pa.

The present paper describes a very simple technique for measuring transport numbers, which is directly derived from the weighing method previously reported by the authors (2,3). Both techniques are based on the measurement of the equivalent mass transport due to electromigration. The first one records the displacement of the center of gravity of a horizontal cell when the electrical current passes through it. The second one measures directly the weight change of one electrode compartment while the electrolysis proceeds. This is done by suspending a half-cell from a recording balance so that it dips into the vessel containing the melt and the other electrode.

This simplified weighing technique does not yield results with as high precision as the more elaborate one, but in this respect it is still as good or better as recently reported radiotracer experiments (4). The apparatus is quite simple and the procedure is very fast. It is recommended for rapid measurement of transport numbers within a few per cent.

Let us consider a molten salt MX , being electrolyzed between two electrodes of the metal M , separated by a porous membrane which defines the two electrode compartments. An equivalent mass M_t is transferred per faraday from the anode toward the cathode

$$M_t = T_M M_M - T_X M_X \quad [1]$$

where M_M , M_X are the equivalent masses of components M and X , and T_M , T_X are the transport numbers measured with respect to the porous plug.

A volume change of the melt in the electrode compartments also takes place. It produces a level difference between the electrode compartments, from which a mechanical flow results. It has been shown (3) that the total rate of weight change due to both the electromigration and the return flow is a function of time,

$$\frac{d}{dt} W(t) = M_t \frac{I}{F} g - (V_t + V_e) \frac{I}{F} \rho g (1 - e^{-at}) \quad [2]$$

where $W(t)$ is the weight of the moving half-cell; I , the electrical current; F , the faraday constant; g , the gravitation constant; V_t and V_e , the volume changes due to electromigration and to the electrode reaction; ρ , the density of the melt; a , a time constant which defines the rate of hydraulic flow through the porous membrane; t , the time.

For the system described above

$$V_t + V_e = T_X V_{MX} - V_{M^0} \quad [3]$$

where V_{MX} is the equivalent volume of the salt and V_{M^0} is the equivalent volume of the metal in the electrode.

The rate of weight change per unit of electric current depends only on the transport number and the hydraulic characteristics of the plug. If the duration of the run is small compared with $1/a$, the second term vanishes in Eq. [2] and the initial weight change is a direct measurement of the equivalent mass transport and hence the transport number

$$T_M = \frac{M_t + M_X}{M_M + M_X} \quad [4]$$

With coarse fritted disks, $1/a$ is rather small and the last term of Eq. [2] cannot be neglected. The magnitude of this term can be evaluated from a measurement of the time constant, a . In the experiments reported below, the measured weight change was always corrected in this manner in order to compute the equivalent mass transport. This correction amounted to about 0.01 on the transport number.

Experimental

The apparatus is represented in Fig. 1. The electrolysis cell consists of a 30 mm-diameter Pyrex vessel containing the molten salt. Inside hangs the movable half cell. The latter consists merely of a 8 mm-diameter Pyrex tube closed at its bottom by a coarse porosity

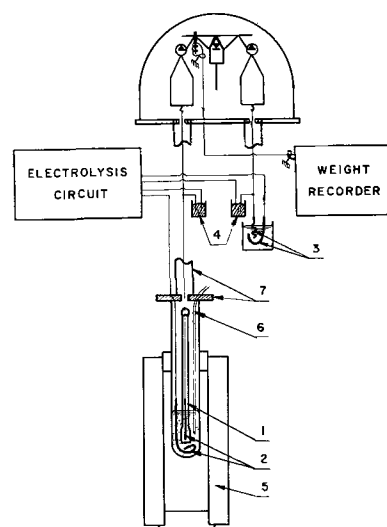


Fig. 1. Diagrammatic sketch of apparatus. 1, movable half-cell with porous membrane; 2, silver electrodes in molten salt; 3, silver electrodes in aqueous silver nitrate solution; 4, mercury contacts; 5, furnace; 6, chromel-alumel thermocouple; 7, heat and draft shields (not completely shown).

fritted plug. The two electrodes are made of silver wire ($\frac{1}{8}$ in. diameter). One hangs inside the half-cell, the other is exterior to it and is formed into a loop at the bottom of the outer vessel. A thermocouple, protected by a Pyrex tubing also dips into the melt.

The cell is contained in a small resistance furnace with a viewport, so that the free motion of the half-cell can be observed. The temperature is controlled by a proportional controller, receiving its signal from a thermocouple located under the cell. The temperature is constant to about 2°C over a length of 4 cm around the porous membrane.

The movable electrode compartment hangs from the left pan of an Ainsworth semimicro recording balance. The fine nichrome suspension wire (B + S No. 36) also serves to carry the electrical current to the electrode.

With such an experimental set-up, the force acting on the balance, F , equals the weight of the half-cell, W , minus the buoyancy, B , plus the resultant of surface tension forces, S . If one assumes that the surface tension forces remain constant, then a change of weight of the half-cell, ΔW , produces a displacement of the left pan ΔX , and accordingly a change of buoyancy, ΔB . The resulting change of the force acting on the balance is, ΔF , given by

$$\Delta F = \Delta W - \Delta B = \Delta W - \rho g A \Delta X \quad [5]$$

where A is the cross-section of the movable electrode compartment. If k is the proportionality constant of the automatic balance mechanism which relates ΔX to ΔF , then

$$\Delta F = \frac{\Delta W}{1 + kA\rho g} \quad [6]$$

In the conditions of our experiments the expression $1 + kA\rho g$ is approximately equal to 20, which means that the sensitivity of our apparatus is reduced to about $1/20$ the nominal sensitivity of the balance. One division of the chart ($1/10$ in.) represents accordingly 2 mg instead of the nominal 0.1 mg.

A first series of measurements were made with the apparatus as described so far. The system was calibrated by changing weights on the right pan. Allowing for some oscillation of the balance, which was probably due to thermal convection currents above the cell, the readability was found equal to half a division or 1 mg. The reproducibility of the calibration, however, was uneven and seemed to depend on the

speed with which the weights were applied. This was attributed to a change of the surface tension forces on the movable half cell as a function of the speed or acceleration of its motion. To take care of that, another calibration procedure was adapted, as follows:

From the right pan of the balance hangs a piece of silver wire ($\frac{1}{8}$ in. diameter) dipping into an aqueous solution of 10% silver nitrate. A second silver electrode is fixed into the vessel containing the solution so that the whole cell constitutes a silver coulometer. The calibration of the balance is done by passing a known electrical current through the coulometer in order to cause a rate of weight change roughly equal to the expected rate of weight change due to electrolysis of the molten salt. In this manner, the very same displacement occurs during the calibration and the actual run.

By this method the rate of weight change is, indeed, calibrated. The measurement is then merely the comparison of two slopes on the weight vs. time plot recorded by the balance: one for current through the cell, the other for current through the coulometer.

The same apparatus can be used also as a zero-method, by passing simultaneously two different current intensities through the cell and through the coulometer and varying one of them until the balance beam is maintained in equilibrium. The result is then computed from the ratio of electrical currents. This method has also been applied successfully.

Results and Discussion

The experimental procedure is very similar to the one used by Harrington and Sundheim (5) to measure leakage rates through porous diaphragms in order to evaluate their possible use for transport experiments. We have, however, improved this technique in two ways. First, the use of a recording balance makes the experiment easier and more reliable. Second, the use of the silver coulometer improves the calibration since it makes possible the actual calibration of the rates of weight change.

Measurements have been made first with molten silver nitrate in order to evaluate the technique by comparison with the results obtained with the horizontal cell. Figure 2 shows all the data. They are somewhat more scattered than the other ones but the general agreement is quite good. The two values obtained by Laity and Duke with their bubble cell (6) are also indicated. The following temperature dependence has been obtained by the least square technique

$$T_{\text{Ag}} = 0.798 - 5.6 \cdot 10^{-4} (\theta - 200)$$

with a standard deviation 0.006.

A series of measurements have been made with molten AgCl . Figure 3 shows the results. A small but significant temperature dependence is found. It is very similar to the one observed for silver nitrate. The best line obtained by a least square calculation is

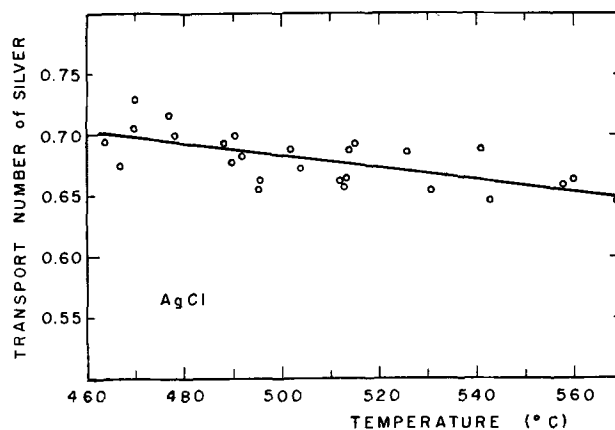


Fig. 3. Temperature dependence of transport number in molten silver chloride.

$$T_{\text{Ag}} = 0.682 - 4.8 \cdot 10^{-4} (\theta - 500)$$

with a standard deviation 0.016. The two other measurements of transport number in molten silver chloride, which we know of, disagree among themselves and with our results. We have so far no explanation for those differences. First, Duke and co-workers (7) found $T_{\text{Cl}} = 0$, and accordingly $T_{\text{Ag}} = 1$, in the 500°-600°C temperature range, by means of a radiotracer technique in a Pyrex cell. It must be recalled, however, that Lunden (8) concludes from his own experience with the radiotracer technique that "it seems wise always to check the results by using both anion and cation tracers." Accordingly, Duke and co-workers' value should eventually be checked by a more thorough investigation. Second, Murgulescu and Marta (9) found an average value of $T_{\text{Ag}} = 0.54$ by weighing the anodic compartment after passing the current. Their results, however, are scattered between a lower value 0.45 and an upper one 0.68. Taking this scattering into account, those data seem no longer very different from ours.

Summarizing, this simplified weighing method gives quick and reproducible transport number measurements. The slight temperature dependences of transport numbers in both silver nitrate and silver chloride appear significant. It is to be compared with the dependence on temperature found by Fisher and Klemms (10) for zinc chloride and thallium chloride and the one already reported (3) for lead bromide.

Acknowledgment

The authors wish to acknowledge the generous support of the National Science Foundation under contract NSF-G-20879.

Manuscript received Feb. 3, 1964.

Any discussion of this paper will appear in a Discussion Section to be published in the June 1965 JOURNAL.

REFERENCES

1. R. W. Laity, *J. Chem. Ed.*, **39**, 67 (1962).
2. H. H. Kellogg and P. DUBY, *J. Phys. Chem.*, **66**, 191 (1962).
3. P. DUBY and H. H. Kellogg, *J. Phys. Chem.*, **68**, 1755 (1964).
4. E. D. Wolf and F. R. Duke, *This Journal*, **110**, 311 (1963).
5. G. Harrington and B. S. Sundheim, *J. Phys. Chem.*, **62**, 1454 (1957).
6. R. W. Laity and F. R. Duke, *This Journal*, **105**, 97 (1958).
7. F. R. Duke, M. L. Bowman, E. Wolf, and H. Garfinkel, *Ann. N. Y. Acad. Sc.*, **79**, 1023 (1960).
8. I. G. Murgulescu and L. Marta, *Acad. rep. populare Romine, Studii cercetari chim.*, **8**, 375 (1960).
9. A. Lunden, *This Journal*, **109**, 260 (1962).
10. W. Fisher and A. Klemm, *Z. Naturforsch.*, **16a**, 563 (1961).

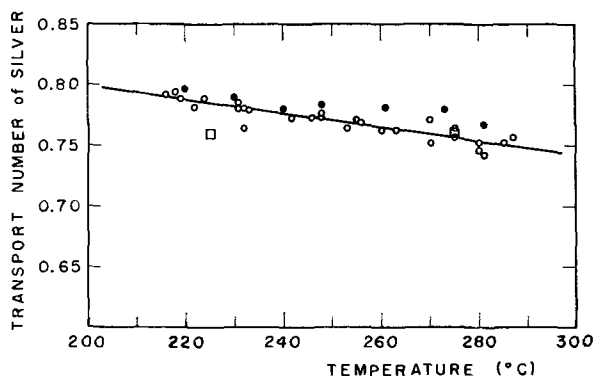


Fig. 2. Temperature dependence of transport number in molten silver nitrate. AgNO_3 : \circ , vertical half-cell; \bullet , horizontal cell (3); \square , Laity and Duke (6).



Some Observations on the High-Temperature Oxidation of Lanthanum

W. L. Phillips

Engineering Materials Laboratory, Engineering Research Division, Engineering Department,
E. I. du Pont de Nemours & Company, Inc., Wilmington, Delaware

Loriers (1) showed that lanthanum is attacked by dry air until a constant weight increase of 0.45 mg/cm^2 was reached after 25 min at 300°C . More recently Vorres and Eyring (2) reported that this element oxidizes in a parabolic manner. Above 300°C lanthanum transforms from hcp (hexagonal-close-packed) to fcc (face-centered-cubic). The volume ratio of the oxide to the fcc phase is 1.11 (3).

Testing was carried out in an Ainsworth aperiodic milligram analytical balance. The balance was modified to accommodate a 12-in. long sapphire rod supporting a zirconia crucible in a vertical furnace (4). Samples of 99.5% pure lanthanum were purchased from the American Chemical and Potash Company. Since lanthanum oxidizes readily at room temperature, the paraffin-protected ingots were cut under oil into samples approximately $0.1 \times 0.2 \times 1 \text{ cm}$. Each sample was then dried under vacuum at 100°C for 5 hr prior to oxidation. Density measurements showed that the samples were 100% dense. The lack of oxidation before testing was indicated by the absence of white La_2O_3 . The time of transfer from the vacuum chamber to the oxidation apparatus was $\sim 25 \text{ sec}$.

Representative weight-gain vs. time plots for lanthanum at 700°C are shown in Fig. 1. The initial linear weight gain is constant at the same rate in repetitive tests. At times varying from 750 to 1200 sec, the weight gain discontinuously jumps to a constant value of $32 \pm 1.0 \text{ mg/cm}^2$. Figure 2 is a plot of the weight gain vs. time for samples tested at temperatures of 600° to 850°C . In the temperature range of 600° to 700°C , the samples obeyed a single linear law until a time varying from 810 to 2150 sec when the weight gain jumped

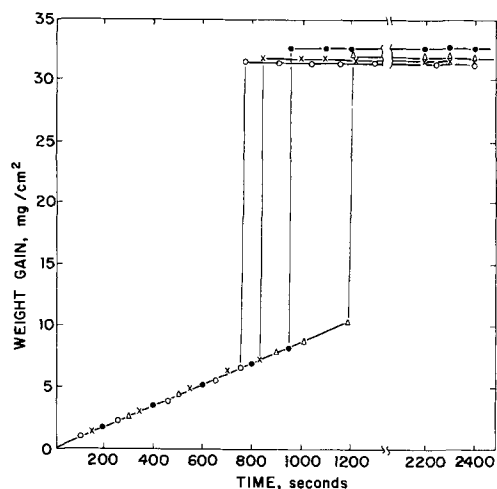


Fig. 1. Weight gain vs. time for lanthanum oxidized at 700°C :
●, No. 1; X, No. 2; ○, No. 3; △, No. 4.

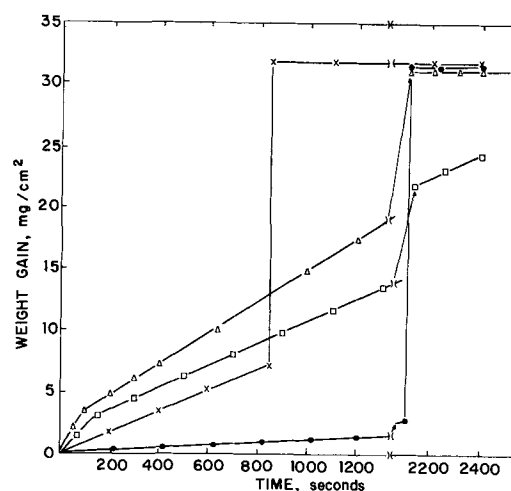


Fig. 2. Weight gain vs. time for lanthanum oxidized at the temperatures indicated: ○, 600°C ; X, 700°C ; △, 800°C ; □, 850°C .

to $32 \pm 1 \text{ mg/cm}^2$. Above 700°C two distinct linear regions were observed. In the times investigated, 2400 sec, no discontinuities were observed until the samples reached a weight gain of $32 \pm 1.0 \text{ mg/cm}^2$. At this weight no further gain was observed. The initial linear-weight-gain constant reached a maximum at 810°C . Figure 3 is a plot of the initial linear-weight-

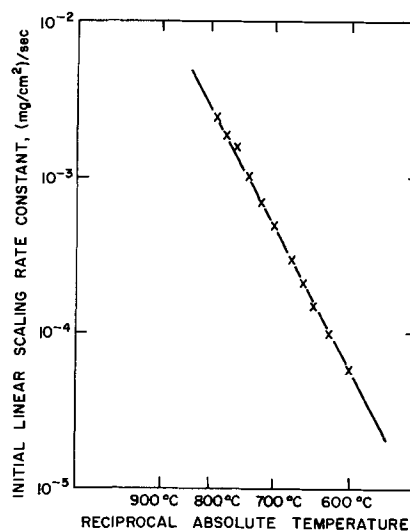


Fig. 3. Initial linear scaling rate constant vs. reciprocal absolute temperature.

gain constant in the temperature range of 600°-810°C as a function of reciprocal absolute temperature. The activation energy was ~32.8 kcal/mole. X-ray examination indicated that La₂O₃ was the only oxidation product at all temperatures.

These results demonstrate that lanthanum oxidizes linearly in the temperature range of 600°-850°C. This is in disagreement with the results of Vorres and Eyring (2). No reason is advanced for this discrepancy.

The weight gain of the samples used in the present investigation, if all the lanthanum were oxidized to lanthanum oxide, would be ~35 mg/cm². This agrees within experimental limits with the observed value of 32 mg/cm². Lories used samples which, if completely oxidized, would gain 0.42 mg/cm². This is also in agreement with the observed value of 0.45 mg/cm². These observations and x-ray data indicate that lanthanum oxidizes completely to lanthanum oxide by either a continuous or discontinuous mechanism.

The observation of a discontinuity in the weight-gain-vs.-time plots and the decrease in the initial rate as the temperature increases has been observed in

columbium by Kolski (5). The discontinuity is much sharper in lanthanum. Although the phenomena observed in the two metals may be related, normal metallographic practices are unsuitable for studying lanthanum because of its instability even at room temperature.

Manuscript received April 15, 1964.

Any discussion of this paper will appear in a Discussion Section to be published in the June 1965 JOURNAL.

REFERENCES

1. J. C. Lories, *Acad. Sci. Paris*, **229**, 547 (1949); **231**, 522 (1950).
2. K. S. Vorres and L. R. Eyring, "High Temperature Oxidation of Rare Earth Metals," p. 119-23. Rare Earth Research Seminar, Lake Arrowhead, Calif. (1960).
3. O. Kubaschewski and B. E. Hopkins, "Oxidation of Metals and Alloys," p. 7, Academic Press, New York (1953).
4. W. L. Phillips, Jr., *J. Less Common Metals*, **5**, 97 (1963).
5. T. L. Kolski, *Trans. ASM*, **55**, 119 (1962).

Diffusion of Oxygen in Hafnium

J. P. Pemsler

Ledgemont Laboratory, Kennecott Copper Corporation, Lexington, Massachusetts

Some years ago I first reported on the determination of the diffusion coefficient of oxygen in hafnium (1). The technique was one used previously to measure the diffusion of oxygen in zirconium (2) and consisted of observations of the dissolution rate of anodically deposited interference colored oxide films. At the time of the hafnium study no data were available regarding the hafnium-oxygen phase diagram, and since calculations based on this technique required a knowledge of the solubility limit of oxygen in hafnium, the diffusion coefficient was reported for each of three assumed solubility limits. Since this publication there have been three papers by other authors concerned with this subject. Gadd and Evans (3) report measurements of the diffusion coefficient of oxygen in hafnium in the temperature range 700°-1200°C based on microhardness measurements made on oxidized samples. Wallwork and Smeltzer (4) report values for the diffusion coefficient at temperatures of 800° and 950°C based on microhardness indentations on oxidized samples and calculated on the basis of a theory involving a steady-state solution for the oxygen gradient in the metal phase during linear oxidation. Rudy and Stecher (5) in a determination of the hafnium-oxygen phase diagram report a value of the solubility limit of oxygen in hafnium as 20.5 at. % at 1350°C and almost independent of temperature.

In recent studies I have shown that the concentration gradient of oxygen beneath the oxide/metal interface in oxidized samples of zirconium (6) and hafnium (7) can be accurately predicted by a theoretical expression involving diffusivity, time, and oxide thickness. This enables the diffusivity of oxygen in the metal to be calculated when the other parameters are accurately known. In addition, the depth of penetration of oxygen was found to increase with time during protective oxidation and, on the onset of linear oxidation, begins to decrease. Zones of constant hardness at high oxygen concentration probably due to ordered hafnium-oxygen alloys were reported.

It is the purpose of this communication to review the data concerning the diffusion of oxygen in hafnium in the light of the subsequent publications and some additional studies carried out in this Laboratory.

Experimental and Results

In conjunction with the aforementioned study (7) the diffusion coefficient of oxygen in hafnium was re-

determined by the anodization technique, this time performing measurements within a single grain of hafnium to avoid the necessity of estimating average colors, and hence average thicknesses, of interference films on a large number of grains in a polycrystalline sample. The new measurements were performed at 575°, 614°, and 655°C. The diffusion coefficient D may be expressed as

$$D = \frac{(x')^2}{4b^2t}$$

where b satisfies the equation

$$b(1 + \operatorname{erf} b) = \frac{C_o}{m_o \sqrt{\pi}} e^{-b^2}$$

Here in time, t , there is a displacement of the oxide/metal boundary, x' , which is related to the observed decrease ΔL in thickness of oxide film by the following expression involving the respective molecular volumes

$$x' = \frac{V_{\text{Hf saturated}}}{V_{\text{HfO}_2}} \Delta L$$

The quantity C_o is the difference between the saturated concentration, C_s , and initial concentration of oxygen in the metal, and m_o represents the weight of oxygen removed from the HfO₂ consumed in the generation of unit volume of saturated hafnium (HfO_{0.25s}). Values for the constants used are $\rho_{\text{HfO}_2} = 10.13 \text{ g/cm}^3$ (8), $\rho_{\text{Hf saturated}} = 13.29 \text{ g/cm}^3$, $C_s = 0.300 \text{ g/cm}^3$ (5), $m_o = 2.03 \text{ g/cm}^3$, $x' = 0.661 \Delta L$, and $b = 0.0764$.

In order to determine whether extrapolation of the low-temperature diffusion data to high temperatures is justified, 3/4 in. diameter hafnium spheres were oxidized at 950°C for 111 hr and 1050°C for 64 hr. The sample was sectioned through the center, polished metallographically, and photographed at 400X and 800X magnifications at each of sixteen equidistant positions around the perimeter. The thickness of the oxide was determined with a planimeter and used to calculate the total quantity of oxygen contained in the oxide scale. This value when subtracted from the total weight gain gives the quantity of oxygen in solution in the metal substrate. In the case under consideration about 50% of the oxygen absorbed was contained in the metal substrate. These data were then used to calculate the diffusion coefficient.

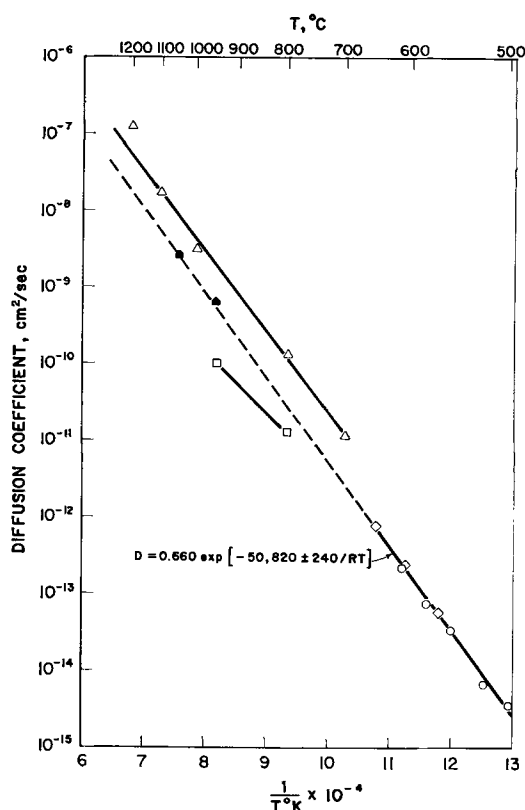


Fig. 1. Temperature dependence of the diffusion coefficient of oxygen in hafnium. Open triangle, Gadd and Evans (3); Open square, Wallwork and Smeltzer (4); Open circle, Pemsler (1); Open diamond, this work, anodic dissolution; Solid pentagon, this work, weight gain.

cient of oxygen in hafnium at 950° and 1050°C according to equations derived previously (6, 7).

Results of the investigations to date are summarized in Fig. 1.

The excellent agreement of the point at 950° and 1050°C with an extrapolation of the low-temperature data indicates that hafnium, like zirconium, conforms to an Arrhenius plot over many decades in values of the diffusion coefficient. A least square solution of the data from anodic dissolution measurements gives a value for the diffusion coefficient as

$$D = 0.660 \exp [-50,820 \pm 240/RT]$$

A variation in the diffusion coefficient of a factor of about two among the differently oriented grains was reported in my initial study (1). A more precise re-determination indicates that the variation with orientation is a factor of about 1.4 and that in a polycrystalline sample relatively few grains show this extreme; the large majority vary by a factor of no more than 1.1. Studies on single crystal material are planned to further clarify the orientation dependence.

Discussion

The work of Gadd and Evans may be criticized from several viewpoints. First, their oxidations were carried out in air so that in addition to the development of a hafnium-oxygen gradient in the metal they must have had a superimposed hafnium-nitrogen gradient. Although the diffusion of nitrogen in hafnium is undoubtedly much slower than that of oxygen, it would be expected to penetrate to a significant depth at the temperatures of their investigation. In addition, the anomalous microhardness of concentrated hafnium-oxygen alloys were not taken into account.

Since Wallwork and Smeltzer worked in pure oxygen and obtained microhardness readings as an average of five hardness scans, their data may represent adequate approximations to the diffusion gradient. However, I am in disagreement with their interpretation of a steady-state gradient during the course of linear oxidation, and the disagreement between our diffusion coefficients may be ascribed to these differences in interpretation.

Manuscript received May 18, 1964.

Any discussion of this paper will appear in a Discussion Section to be published in the June 1965 JOURNAL.

REFERENCES

1. J. P. Pemsler, *This Journal*, **106**, 1067 (1959).
2. J. P. Pemsler, *ibid.*, **105**, 315 (1958).
3. J. D. Gadd and E. B. Evans, *Corrosion*, **17**, 441t (1961).
4. G. R. Wallwork and W. W. Smeltzer, *This Journal*, **110**, 943 (1963).
5. E. Rudy and P. Stecher, *J. Less-Common Metals*, **5**, 78 (1963).
6. J. P. Pemsler, *This Journal*, **111**, 381 (1964).
7. J. P. Pemsler, *ibid.*, to be published.
8. J. Adam and M. D. Rogers, *Acta Cryst.*, **12**, 951 (1959).

Growth of As_2O_3 on GaAs

M. E. Straumanis and C. D. Kim

Department of Metallurgical Engineering, School of Mines and Metallurgy,
University of Missouri at Rolla, Rolla, Missouri

It was frequently observed that on polished sections of GaAs, if etched with diluted HNO_3 (1:10 by volume), crystallites (not etch pits) were produced. These crystallites were a product of growth because of their slight elevation above the surface of GaAs. The same observation was made by Yeh and Blakeslee (1).

If GaAs is etched with concentrated HNO_3 , the process of growth of the salt-like compound is very fast, as the surface becomes whitish dull in a short time. The microscope revealed clearly that on the surface of the GaAs a deposit is formed, with the black matrix of the arsenide still shining through (Fig. 1). By careful scratching of the surface with a blade tiny amounts of a white substance could be removed, of which very good x-ray powder patterns were obtained. They turned out to be clear patterns of As_2O_3 . Evidently the latter was formed by oxidation of As with HNO_3 , while the $\text{Ga}(\text{NO}_3)_3$ went into solution

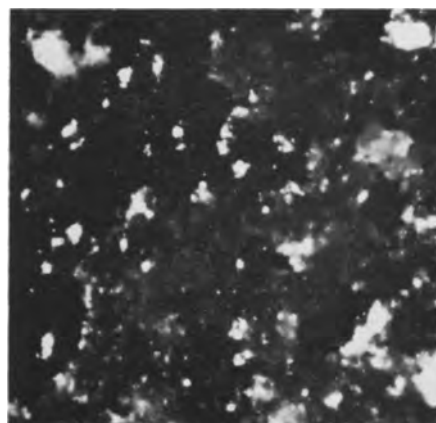


Fig. 1. GaAs etched with concentrated HNO_3 ; white deposit on the black matrix. Magnification 60X.

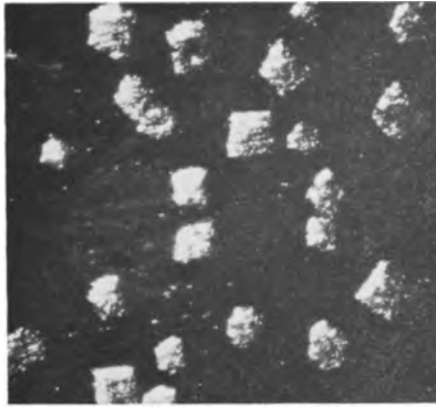


Fig. 2. As_2O_3 platelets, formed on GaAs in 3 hr, 10% HNO_3 , lateral illumination. Magnification 60X.

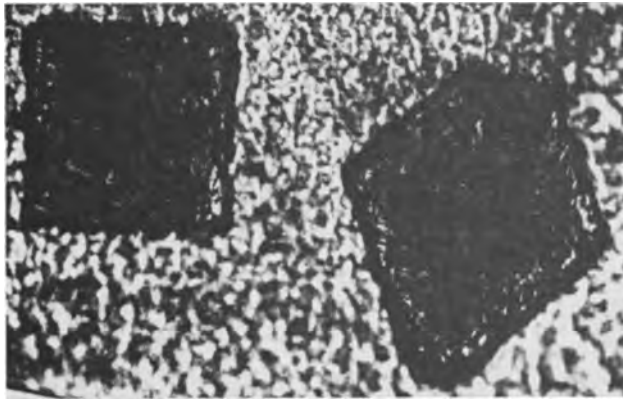


Fig. 3. As_2O_3 platelets, 10μ thick, $[110]$ and $[001]$ perpendicular to the GaAs surface, vertical illumination, 10% HNO_3 . Magnification 320X.



Since the solubility of As_2O_3 in water is not very good (2.1g in 100 ml of H_2O at 25°C), the oxide crystallized out on the surface of GaAs.

The process of As_2O_3 crystallization was much slower in dilute HNO_3 (1:10). But in such a case thin, crystal platelets on the GaAs surface (Fig. 2) were formed. The orientation of these crystals, as can be seen, is at random (1), on the large monocrystalline grains of GaAs. However, many of them, if observed under a larger magnification, appeared as beautiful platelets having two preferred orientations: with the direction $[110]$ or $[001]$ nearly perpendicular to the GaAs surface (Fig. 3), while their orientation in the surface itself was random. The rhomb-shaped crystals appeared most frequently.

If instead of HNO_3 , aqua regia ($\text{HNO}_3 : \text{HCl} = 1:3$) is used, in about 20 min very beautiful thick As_2O_3 crystals, sticking well to the GaAs surface are obtained (Fig. 4).

All these crystals were combinations of cubic, rhombic, and octahedral planes [the latter are typical for As_2O_3 (2)], with two preferred orientations relatively to the substrate, as already mentioned (see Fig. 3). The growth of such crystals is explained on Fig.

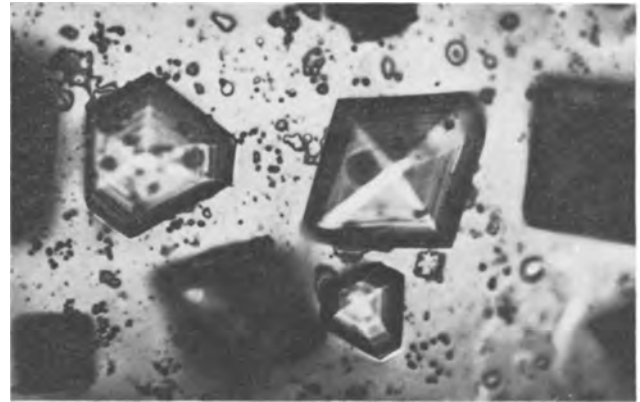


Fig. 4. As_2O_3 crystals on GaAs. Steps are discernible on the planes; etchant: aqua regia. Magnification 580X.

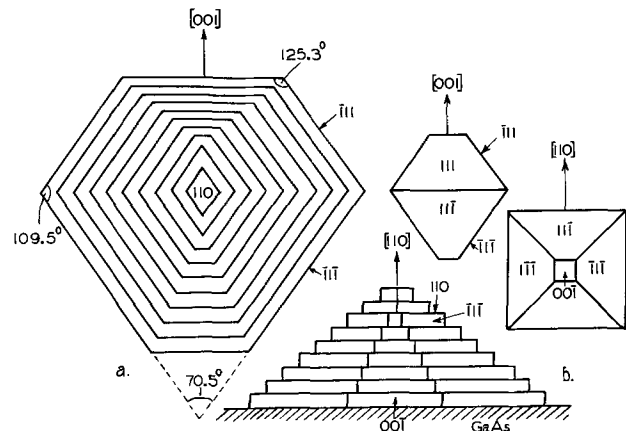


Fig. 5. Schematized growth of As_2O_3 crystals on GaAs: a, top view; b, front view.

5a and b. First, thin crystal platelets are formed (Fig. 3) with the direction $[110]$ approximately perpendicular to the dissolving GaAs surface, and the $[001]$ in the surface. Then the same kind of layers with the same orientation grow on each other stepwise, as can be seen from Fig. 4 and is shown schematically in Fig. 5. The angles of the rhomb-shaped crystals (Fig. 3 and 4), as drawn in Fig. 5a, are close to the theoretical angles between two $\langle 111 \rangle$ planes and between the (100) and (111) planes. Of course, it cannot be said whether or not the square on Fig. 3 is a cube plane or a top view of an octahedron. An ideal cubo-octahedron in two projections is shown on Fig. 5.

Acknowledgment

The authors thank the Office of Naval Research for support.

Manuscript received June 4, 1964.

Any discussion of this paper will appear in a Discussion Section to be published in the June 1965 JOURNAL.

REFERENCES

1. T. H. Yeh and A. E. Blakeslee, *This Journal*, **110**, 1018 (1963).
2. G. A. Wolff, *Amer. Mineral.*, **41**, 60 (1956).

Silicon Phosphide Precipitates in Diffused Silicon

P. F. Schmidt and R. Stickler

Westinghouse Research and Development Center,
Pittsburgh, Pennsylvania

The presence of a silicon phosphide phase in the surface layers of heavily phosphorus-diffused silicon was suggested by the results of tracer experiments. Investigation of suitably thinned silicon specimens then led to the direct observation of the precipitate by transmission electron microscopy, and to its crystallographic identification by means of electron diffraction.

Tracer Work

The occurrence of a steep spike in the phosphorus concentration at the Si/SiO₂ interface, extending into the silicon for a distance of only 1-2,000 Å, as detected by tracer techniques has been reported before (1). Figure 1 shows the profile of such a spike, obtained by step-wise dissolution of the phosphorus-doped anodic oxide film which had been used as the diffusion source (1), subsequent multiple anodization of the silicon, and dissolution of the anodically formed oxide in HF between each step. The sloping of the phosphorus concentration in the oxide from left to right is due to the fact that the doped oxide was not protected by a nondoped SiO₂ layer, and that the diffusion was carried out in a sealed quartz tube. Under these conditions initially a large quantity of phosphorus was lost from the doped anodic oxide to the surroundings, but did not diffuse deeply into the quartz walls because of the density of the latter. During the later stages of these long-time diffusion runs the oxide became depleted of phosphorus, and eventually some of the phosphorus from the walls diffused back into the anodic oxide. The activity of the P³² contained in the silicon layer which was converted to oxide by anodization, was determined after evaporating the HF solution to dryness in a Teflon tray. The reproducibility of the magnitude of the spike as determined in this fashion was poor, whereas the adjoining portion of the diffusion profile could be reproduced quite accurately from run to run. This fact suggested that the phosphorus in the region of the spike might be present either as elemental phosphorus, precipitated at dislocations, or as silicon phosphide. The existence of a silicon phosphide phase (and its gettering properties for gold), has been suggested by Kooi (2).

In the tracer experiments reported here the P-32 tagged silicon wafers were counted: (a) after anodization in the radioactive solution; (b) after diffusion;

(c) after stripping of the original oxide; (d) after anodization in nontracer solution (pyrophosphoric acid in tetrahydrofurfuryl alcohol); (e) after stripping of the oxide formed by anodization. In addition, the activity of the HF used for stripping the oxide was also determined. It was found that the activity lost from the system when stripping the oxide in HF could be accounted for by the activity of the HF solution, within the somewhat high limit of error of determining the activity in the tray; apparently the distribution of the residue in the tray is not uniform, leading to uncertainties in the analysis.

A large loss of activity from the silicon samples occurred during the first anodizing step, i.e., the phosphorus contained in the surface layer of the silicon was not all incorporated into the oxide, but was largely lost to the anodizing solution. Table I presents the normalized count from two wafers during the various steps described above. The anodization was to 200v at constant current only. On less highly doped silicon, this voltage would correspond to a surface layer of silicon of 332 Å ± 5% converted to oxide. In the present case, due to the heavy loss of phosphorus originally contained in the silicon, the increment could be somewhat larger than 332 Å.

It is noteworthy that the phosphorus surface concentration, determined after the first anodization from junction depth and sheet resistance, assuming an erfc distribution and using Irvin's data (3), was only 5.2 × 10¹⁹/cc on one sample (see Table I).

The assumption of very heavy doping of the outermost layers of the silicon is in agreement with infrared transmission measurements performed on another set of phosphorus diffused wafers. After stripping the original anodic oxide source, these wafers showed a strong structureless absorption, increasing approximately with the square of the wavelength in the region between 2 and 9 μ. The strong absorption disappeared completely after the first three anodizations.

The outstanding feature in Table I is the large drop in activity after the anodization step. It is, however, not entirely clear whether any phosphorus is also leached out of the silicon itself when the oxide source is dissolved in HF. The shape of the phosphorus diffusion profile in the oxide (Fig. 1) suggests that this should only be a second order effect, if present at all. The observed behavior, loss of phosphorus from the silicon during anodization, but no or little loss during removal of the oxide in cold HF, is in agreement with the reported chemical properties of

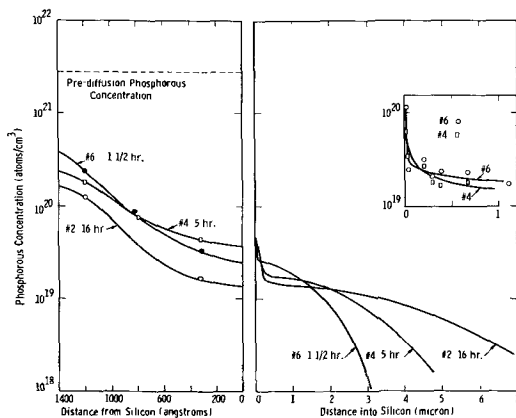


Fig. 1. (left) Phosphorus concentration profile in anodic oxide source after diffusion; (right) phosphorus concentration profile in silicon after diffusion from anodic SiO₂(P) source; parameter: diffusion time at 1175°C.

Table I. Normalized count above background from 2 phosphorus-32 diffused silicon wafers

(a) Diffused for 54 min at 1050°C in sealed quartz tube with argon backfilling;
(b) Diffused for 14 min at 1250°C in sealed quartz tube with argon backfilling.

	1	2	3	4	5
After anodization in tracer solution		After diffusion	After stripping original oxide	After anodization in nontracer solution	After stripping anodic oxide
(a)	226	163	100	36.4	33.5
(b)	201	126	100	52.1	44.6

	Sheet resistance after step 5, ohms/square	Junction depth, μ	Phosphorus surface conc. assuming erfc
(a)	29	1.07	1.2 × 10 ²⁰ /cc
(b)	18	3.47	5.2 × 10 ¹⁹ /cc

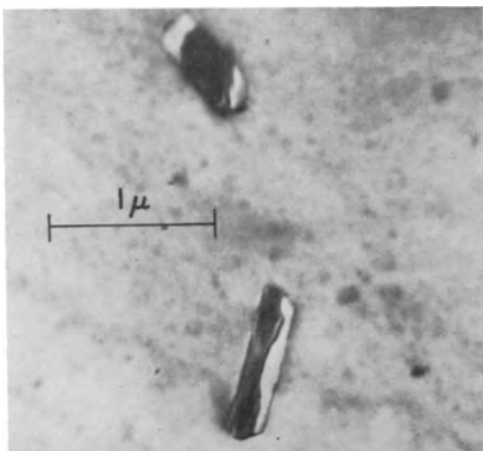


Fig. 2. SiP precipitates in (110) oriented silicon. Transmission electron micrograph.

silicon phosphide (4). SiP is rather resistant to cold dilute acids, whereas its anodization behavior may be expected to be similar to that of (p-type) silicon carbide. Anodization of silicon carbide results in the formation of a dense oxide film, composed presumably entirely of SiO_2 (5).

In order to differentiate between a silicon phosphide phase and elemental phosphorus precipitated at dislocations, the diffused silicon wafers were stripped of the original oxide and were then examined by electron microscopy in transmission.

Electron Microscopic Work

For the examination by direct transmission in the electron microscope, portions of the Si-wafer must be prepared to be transparent to the electron beam (less than 1μ for Si). Small pieces of the Si-wafer were thinned in the central portion by a chemical jet polishing technique (6). By thinning the wafer from one side only, a surface layer approximately 1μ thick can be examined, while carefully timed polishing from the top side and final thinning from the other side allows the examination of layers approximately 1μ thick at any desired distance from the surface (accurate to within $\pm 1\mu$).

The examination of the surface layer of the p-diffused Si-wafers revealed the presence of numerous rod-shaped particles (Fig. 2) oriented along $\langle 110 \rangle$ directions, as determined by electron diffraction. Selected area electron diffraction yielded patterns consisting of the reflections from the particle superim-

posed on that of the $\langle 110 \rangle$ pattern of the Si-matrix. The electron diffraction pattern of the particle could be indexed according to structure data reported by Schubert *et al.* (7) for SiAs which is isomorphous with SiP. A detailed report on the structure of SiP and SiAs determined by x-ray diffraction and electron diffraction will be published elsewhere (8), it is briefly summarized here. Contrary to the monoclinic structure of SiAs suggested by Schubert (7) the results of our investigation indicate that SiP has an orthorhombic structure ($a = 6.90$, $b = 9.40$, $c = 7.68$). It precipitates in the Si-matrix with following orientation relationship

$$[010]_{\text{SiP}} // [111]_{\text{Si}}$$

$$[001]_{\text{SiP}} // [110]_{\text{Si}}$$

Precipitates, however, could not be detected at other levels below the surface of the Si in accordance with the tracer studies. Thus, the transmission electron microscope observation gives proof of the presence of SiP in the outer regions of the diffused wafer, explaining the anomalous diffusion profile revealed by the tracer experiments. It should be noted that the observations reported here do not exclude the simultaneous presence of phosphorus precipitated in other forms.

Acknowledgment

This work was supported jointly by the Electronics Development Laboratory, Aeronautical Systems Division, Wright-Patterson Air Force Base, Dayton, Ohio, and by Westinghouse Electric Corporation. Thanks are due to Drs. T. W. O'Keeffe and T. J. Phillips for help in the evaluation of the results and to Mr. N. Roney for help with the tracer work.

Manuscript received April 29, 1964.

Any discussion of this paper will appear in a Discussion Section to be published in the June 1965 JOURNAL.

REFERENCES

1. P. F. Schmidt and A. E. Owen, *This Journal*, **111**, 682 (1964).
2. E. Kooi, Recent News Paper, Electrochemical Society Meeting, Pittsburgh, 1963.
3. J. C. Irvin, *Bell System Tech. J.*, **41**, 387 (1962).
4. B. Giessen and R. Vogel, *Z. Metallkunde*, **50**, 274 (1959).
5. P. F. Schmidt, Unpublished data.
6. G. R. Booker and R. Stickler, *British J. Appl. Phys.*, **13**, 446 (1962).
7. K. Schubert, E. Dörre, and E. Günzel, *Naturwissenschaften*, **41**, 448 (1954).
8. T. Phillips and R. Stickler, to be published.

The Effect of Lithium Ion on the Mechanism of the Polarographic Reduction of Benzil in Dimethylformamide

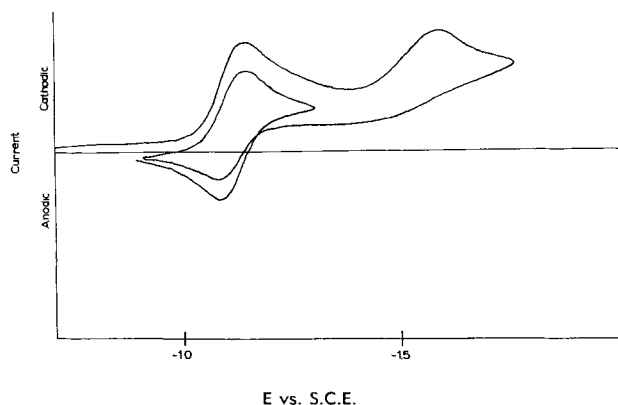
Robert H. Philp, Jr.,¹ Thomas Layloff, and Ralph N. Adams

Department of Chemistry, The University of Kansas, Lawrence, Kansas

The polarographic reduction of benzil in dimethylformamide (DMF) proceeds via a reversible one electron transfer at ca. -1.0v vs. SCE followed by an irreversible one electron transfer at ca. -1.6v vs. SCE with tetrabutylammonium iodide as the supporting electrolyte (1). The cyclic voltammetry of benzil in DMF with 0.1M tetraethylammonium perchlorate (TEAP) proceeds in a similar fashion at a hanging mercury drop (Fig. 1). The primary reduction wave is found to have $|E_{\text{P anodic}} - E_{\text{P cathodic}}| = 59\text{ mv}$ which

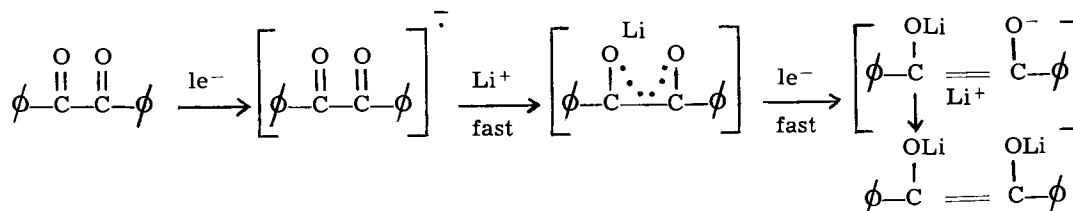
is in good agreement with the theoretical value of $58/n\text{ mv}$ given by Matsuda and Ayabe for a reversible one electron process (2). An irreversible second reduction wave is observed at -1.6v vs. SCE. The one electron transfer step of the primary reduction wave was verified by obtaining the Electron Paramagnetic Resonance (EPR) spectrum of benzil (Fig. 2) by applying a potential just beyond the primary wave employing standard electrochemical *in situ* generation techniques (3). The coupling constants obtained were $a_o = a_p = 1.03\text{ gauss}$ and $a_m = 0.35\text{ gauss}$ which is in good agreement with the coupling constants found by

¹Present address: Department of Chemistry, University of South Carolina, Columbia, South Carolina.

Fig. 1. 10^{-3} M benzil with 0.1 TEAP in DMF

Luckhurst and Orgel via sodium and potassium reduction in tetrahydrofuran (4).

The cyclic polarogram of benzil in the presence of 0.05M lithium perchlorate with 0.1M TEAP in DMF proceeds via a quasi-reversible electrode reaction at a potential corresponding to the primary reduction wave with no lithium ion present. This reduction appears to involve the transfer of two electrons since $i_p(\text{LiClO}_4)/i_p(\text{TEAP}) = 2.03$ and can proceed either by two consecutive one electron transfers occurring in rapid succession or a one-step two-electron transfer. No EPR spectrum could be obtained with this system by applying a potential just beyond the reduction wave. Thus the EPR experiment did not clarify the electron transfer mechanism of this reaction. In view of the work of Bauld and references therein (5) we suggest the following mechanism



where the follow up reaction of the benzil radical is too fast to obtain its EPR spectrum.

Acknowledgment

This work was supported by the Atomic Energy Commission through contract AT(11-1)-686-40, and this support is gratefully acknowledged.

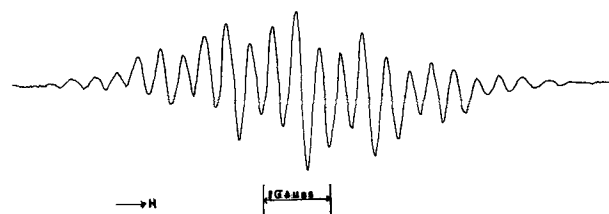
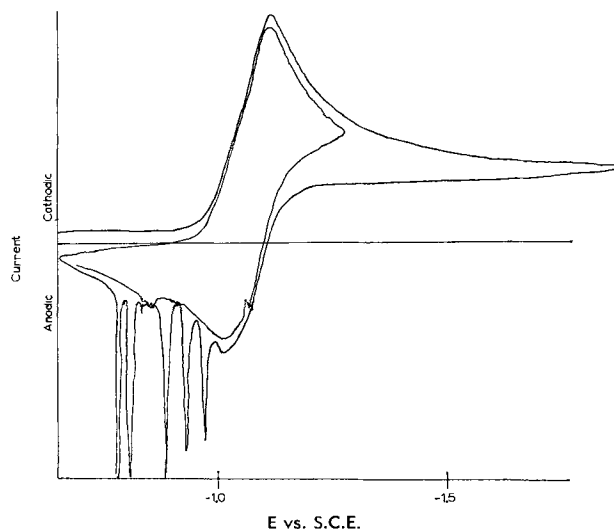


Fig. 2. EPR spectrum of benzil with 0.1M TEAP in DMF. Field increasing toward the right.

Fig. 3. 10^{-3} M benzil, 0.05M LiClO_4 , and 0.1M TEAP in DMF
Manuscript received May 18, 1964.

Any discussion of this paper will appear in a Discussion Section to be published in the June 1965 JOURNAL.

REFERENCES

1. R. H. Philp, Jr., R. L. Flurry, and R. A. Day, Jr., *This Journal*, **111**, 328 (1964).
2. H. Matsuda and Y. Ayabe, *Z. Electrochem.*, **59**, 494 (1955).
3. L. H. Piette, P. Ludwig, and R. N. Adams, *Anal. Chem.*, **34**, 916 (1962).
4. G. R. Luckhurst and L. E. Orgel, *Mol. Phys.*, **7**, 297 (1964).
5. N. L. Bauld, *J. Am. Chem. Soc.*, **84**, 4345 (1962).

A Correlation of Electrochemical Oxidation Potential of Organic Compounds with Photoionization Potential

W. C. Neikam, Glenn R. Dimeler, and M. M. Desmond

Sun Oil Company, Marcus Hook, Pennsylvania

In studies of electrochemical oxidation of organic substances by polarographic techniques, it has been found in previous work from this laboratory (1) that there is an indication of a linear relation between the half wave potential, $E_{1/2(\text{ox})}$, for oxidation of seven mono- and dinuclear aromatic hydrocarbons, and their ionization potential determined spectroscopically. This relation has been confirmed and extended to include five other hydrocarbon compounds in a more recent paper using photoionization and electron impact ionization potentials (2). Theoretical relations between

$E_{1/2(\text{ox})}$ and the energy of the highest occupied molecular orbital have been proposed by Hoijtink (3). The energy factors determining $E_{1/2(\text{ox})}$ for a single electron reaction such as $R \rightarrow \text{O}^+ + e_m$ involving a molecule R and its resulting oxidized ionic form O^+ will be given by an equation of the form

$$E_{1/2(\text{ox})} = aI + \Delta E_{\text{soln.}} - \beta EA -$$

$$\frac{T\Delta S^\circ}{F} - \frac{RT}{F} \ln \frac{f_{\text{O}^+} D_R}{f_R D_{\text{O}^+}} + C$$

The energy terms are: (i) the ionization potential I modified by a factor α to apply to ionization at the electrode-solution interface, i.e., it corrects I for effects of adsorption on the electrode and the presence of solvent; (ii) the change of heat of solvation ΔE_{solv} between R and O^+ expressed as a potential; (iii) the electron affinity EA of the metal m , (i.e., the negative of the relevant work function) modified by a coefficient β to apply to the electrode-solution interface where EA may be perturbed by the effect of the solvent and by oxide film formation; (iv) the term ΔS° is the sum of entropy changes associated with change of solvation of R to O^+ and effects associated with the temperature dependence of EA due to adsorbed species (mainly solvent) at the metal surface; (v) the logarithmic term involves the activity coefficient f and diffusion coefficient D of reduced and oxidized species in the reaction; (vi) the constant C is determined by the potential of the reference electrode used in the evaluation of $E_{1/2(\text{ox})}$.

In a series of electrochemical oxidations for a range of compounds, changes in the ΔS° terms and activity coefficient ratio will be expected to be small compared with changes in I . These terms may hence be grouped with C as a combined constant C' and $E_{1/2(\text{ox})}$ may be written

$$E_{1/2(\text{ox})} = \alpha I + \Delta E_{\text{solv}} - \beta EA + C'$$

Hence, for a given electrode metal where βEA may be assumed constant, $E_{1/2(\text{ox})}$ will be proportional to I and will involve any change in solvation energy ΔE_{solv} involved in the reaction $R \rightarrow O^+ + e_m$.

In the present paper, the above relations are tested for a series of 23 widely different compounds including both aromatic hydrocarbons and their halogen derivatives, together with olefins. The relation is extended to cover, in addition, $E_{1/2(\text{ox})}$ data for 12 polycyclic hydrocarbons in relation to ionization potential obtained from charge transfer spectra and absorption spectra.

Experimental

The $E_{1/2(\text{ox})}$ data reported here were measured in 0.50N NaClO₄, 0.10N AgClO₄, 3 CH₃CN (4) acetonitrile solution against a Ag, Ag⁺ reference electrode. The anode was a platinum wire, 0.50 cm in length and 0.08 cm in diameter, rotated at 600 rpm. The repeatability

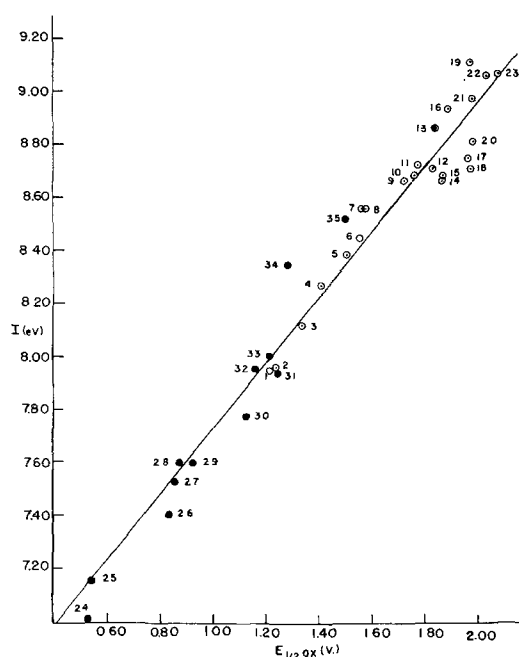


Fig. 1. Plot of photoionization potential (ev) against $E_{1/2(\text{ox})}$ (v) vs. the Ag, 0.1N Ag⁺ reference electrode: O, ref. (5), (6); ●, ref. (4), (9). Numbers refer to compounds listed in Table I.

Table I. Oxidation potentials and photoionization potentials for organic compounds

No. in Fig. 1	Organic compound	$E_{1/2(\text{ox})}$, V vs. Ag, Ag ⁺	I^c , ev photoionization
1	2-Methylnaphthalene	1.22	7.95
		1.15 ^a	
2	1-Methylnaphthalene	1.24	7.96
		1.13 ^a	
3	Naphthalene	1.34	8.12
		1.24 ^a	
		1.31 ^b	
4	1,2,4-Trimethylbenzene	1.41	8.27
5	1,3,5-Trimethylbenzene	1.51	8.39
		1.50 ^a	
6	p-Xylene	1.56	8.445
		1.47 ^a	
7	o-Xylene	1.57	8.56
		1.59 ^a	
8	m-Xylene	1.58	8.57
		1.61 ^a	
9	p-Bromotoluene	1.72	8.67
10	p-Chlorotoluene	1.76	8.69
11	Iodobenzene	1.77	8.73
12	2,3-Dimethyl-1,3-butadiene	1.83	8.72
13	2-Methyl-1,3-butadiene	1.84	8.87
14	t-Butylbenzene	1.87	8.67
15	Isopropylbenzene	1.87	8.69
16	Cyclohexene	1.89	8.94
17	Ethylbenzene	1.96	8.75 ^d
18	n-Propylbenzene	1.97	8.72
19	2-Methyl-1-butene	1.97	9.12
20	Toluene	1.98	8.82
		1.68 ^a	
		1.93 ^b	
21	Bromobenzene	1.98	8.98
22	1,3-Butadiene	2.03	9.07
23	Chlorobenzene	2.07	9.07

^a Data of ref. (2).

^b Data of ref. (4).

^c Data of ref. (5).

^d Data of ref. (6).

of $E_{1/2(\text{ox})}$ values on a Sargent Model XXI polarograph was within 0.02v. Corrections for the resistance of the solution was found to be negligible. The concentration of the organic depolarizer was 1.00 mM in all cases. Further details have been described in a previous article from this laboratory (1) and by Lund (4).

Results and Discussion

In Fig. 1 is shown a plot of photoionization potential (5, 6) vs. $E_{1/2(\text{ox})}$ for the 23 compounds of Table I¹ (open circles). Also plotted in Fig. 1 (closed circles) is the experimental data from Table II for 12 compounds whose ionization potentials have been de-

¹ The numerical data used in constructing Fig. 1 are recorded in Table I to provide a record for other workers in this field.

Table II. Comparison of I calculated polarographically with I calculated from charge transfer spectra and from absorption spectra

No. of Fig. 1	Organic compound	I , ev charge transfer spectra	I^a , ev, adsorption spectra	I , ev, polarographic	$E_{1/2(\text{ox})}$, V vs. Ag, Ag ⁺
24	Tetracene	6.98 ^b	6.94	7.15	0.54 ^e 0.47 ^f
25	Perylene	7.13 ^c	7.10	7.17	0.55 ^{e,f}
26	Anthracene	7.42 ^b	7.42	7.52	0.84 ^e 0.79 ^f 0.83 ^{e,f}
27	Pyrene	7.50 ^c	7.70	7.55	0.86 ^{e,f}
28	1,2-Benzanthracene	7.55 ^b	7.52	7.57	0.88 ^{e,f}
29	Coronene	7.63 ^d	7.64	7.63	0.93 ^{e,f}
30	Chrysenes	7.71 ^b	7.82	7.88	1.13 ^e 1.05 ^f 1.10 ^g
31	Hexamethylbenzene	7.95 ^d	—	7.92	1.16 ^g
32	Phenanthrene	8.11 ^c	8.07	8.01	1.23 ^e 1.20 ^f
33	Triphenylene	7.95 ^d	—	8.04	1.25 ^{e,f}
34	1,2,4,5-Tetramethylbenzene	8.35 ^d	—	8.09	1.29 ^g
35	Styrene	8.53 ^d	—	8.34	1.50 ^g

^a From the data of ref. (8).

^b Average value of the data from ref. (9-11).

^c Average value of data from ref. (9-12).

^d Data of ref. (9).

^e Data of ref. (4). These data and that from this laboratory were used to calculate I .

^f Data of ref. (2).

^g Data from this laboratory.

terminated from charge transfer spectra. Included in Table I and Table II are the values of $E_{1/2(\text{ox})}$ obtained by Pysh and Yang, and by Lund. The agreement is not as good as is expected considering the precision with which polarograph oxidation potentials can be obtained. The $E_{1/2(\text{ox})}$ values obtained in this laboratory utilized the same reference electrode and electrolyte concentration as was used by Lund. Pysh and Yang used 2M NaClO₄ electrolyte solution rather than the 0.5M solution used in this laboratory and by Lund.

However, experiments conducted in this laboratory, in efforts to duplicate Pysh and Yang's work, with 2M NaClO₄ but using the Ag, Ag⁺ reference gave the same results as in 0.5M NaClO₄. The source of discrepancy must be with the reference electrode used. Pysh and Yang used an aqueous calomel electrode with a KCl agar bridge to the electrolyte solution. It has been our experience that this reference causes considerable experimental difficulty in obtaining $E_{1/2(\text{ox})}$ values apparently due to salt precipitation at the agar acetonitrile interface and contamination of the electrolyte solution with water from the agar bridge. The Ag, Ag⁺ reference used in this laboratory, and by Lund, avoids difficulties due to junctions or contamination by water. It has the added advantage that it may be made quite large and placed very near the working electrode thus avoiding large corrections for IR drop across the test solution. For these reasons, we believe it is much to be preferred over aqueous references, and we suggest that results obtained with the Ag, Ag⁺ reference are more reliable.

The data reported by Pysh and Yang for p-xylene, toluene, and the naphthalenes differ substantially from those from this laboratory and that reported by Lund; we have tried to resolve this difficulty by careful repetition of experiments with American Petroleum Institute standards. We can discover no experimental basis for doubting the validity of our results and the discrepancy must lie in the choice of reference electrode. In this regard, it should be noted, however, that the values obtained by Pysh and Yang for toluene and p-xylene are nearer those expected, from a M.O. consideration of the inductive effect of the methyl group, than are ours.

The least squares equation based on the data represented by the 23 open circles in Fig. 1 is

$$E_{1/2(\text{ox})} = 0.827 I - 5.40\text{v}$$

The values of I predicted by the above equation for the hydrocarbons of Table II are compared with experimental values in Table II; the agreement is good.

The value of the constant 5.40v in the above empirical equation should involve the work function of platinum. The corresponding constant for oxidation at a

palladium anode obtained on 16 compounds at this metal is 5.04v. This value differs from that for the platinum electrode by 0.36v which is in good agreement with the difference of the average values of the electron work function for platinum, [5.29 (7)] and palladium [4.82 (7)] viz., 0.47v.

The fact that a very satisfactory straight line is obtained (Fig. 1) must indicate that either (i) the $\Delta E_{\text{solv.}} - T\Delta S_{\text{solv.}}^{\circ}$ (i.e., the free energy change in solvation of R as it is oxidized to O⁺) term is constant for the whole series of compounds and largely independent of their structure. This implies that ionization produces a localized charge which interacts with solvent with a constant energy independent of the structure of the whole ion, the remainder of which is then solvated with the same energy as that of the neutral reduced form R. In the solvent used this localized charge is probably an ion pair involving interaction with the anion of the electrolyte. The behavior observed indicates that effects associated with delocalization of the charge on the ion (which would be specific for the various molecules involved in the series) are not significant or (ii) the solvation free energy from $\Delta E_{\text{solv.}} - T\Delta S_{\text{solv.}}^{\circ}$ changes in proportion to the value of I (2) and is thus included in the value of the proportionality constant 0.827.

As long as a unit electric charge is involved, it does not seem that the latter supposition would be the reason for the behavior observed so that the explanation suggested in (i) must be preferred.

Acknowledgment

The authors are indebted to Dr. Brian Conway for helpful discussions during the course of this research.

Manuscript received March 17, 1964.

Any discussion of this paper will appear in a Discussion Section to be published in the June 1965 JOURNAL.

REFERENCES

1. J. West Loveland and G. R. Dimeler, *J. Anal. Chem.*, **33**, 1196 (1961).
2. E. S. Pysh and N. C. Yang, *J. Am. Chem. Soc.*, **85**, 2124 (1963).
3. G. J. Hoijsink, *Rec. trav. chim.*, **77**, 555 (1958).
4. H. Lund, *Acta Chem. Scand.*, **11**, 1323 (1957).
5. K. Watanabe, *J. Chem. Phys.*, **26**, 542 (1957).
6. W. C. Price, *Chem. Rev.*, 257 (1947).
7. H. B. Michaelson, *J. Appl. Phys.*, **21**, 536 (1950).
8. Haruo Kuroda, *Nature*, **201**, 1214 (1964).
9. C. Briegleb and J. Czekalla, *Z. Elektrochem.*, **63**, 6 (1959).
10. H. Kuroda, K. Yoshihara, and H. Akamatu, *Bull. Chem. Soc. Japan*, **35**, 1604 (1962).
11. M. Kinoshita, *ibid.*, **35**, 1609 (1962).
12. H. Kuroda, M. Kobayashi, M. Kinoshita, and S. Takemoto, *J. Chem. Phys.*, **36**, 457 (1962).

A Technique for Studying Oxygen Diffusion and Locating Oxide Inclusions in Metals by Using the Proton Radioactivation of Oxygen-18

Ralph H. Condit and J. Birch Holt

Lawrence Radiation Laboratory, University of California, Livermore, California

Numerous techniques have been described for the activation analysis of oxygen (1). In view of the importance of oxygen diffusion in many materials and effects of oxygen on the properties of metals, we have been adapting these activation techniques along with autoradiographic methods to locate oxygen, particularly the oxygen-18 tracer. The most generally applicable procedure appears to be that which starts with

the proton bombardment of a specimen, wherein the O¹⁸ (p, n) F¹⁸ reaction gives fluorine-18. This emits a 0.6 Mev positron and has a half-life of 112 min. Since oxygen-18 is present in 0.2% concentration in normal oxygen, oxide inclusions may be identified in a metallographic section. Also, the use of enriched oxygen-18 together with this activation procedure allows the study of grain boundary and volume diffusion in the

same way as is frequently done using radioactive tracers. Some of the factors of importance in these types of procedures have been discussed in studies of photosynthesis (2) and in the measurement of the thickness of oxide layers on metals (3).

In our procedure we bombard the specimen with 2.7 Mev protons. The reaction is endothermic with a Q of -2.45 Mev (4). Under these conditions, the recoil in most solids will be less than 0.1μ (5). For the purposes of this experiment, therefore, it may be stated that the activity is produced in the same place as the inclusion or the tracer. The neutrons from this reaction will have energies up to 130 kev. Neutrons may also be produced by proton reactions with other elements in a specimen, and these may have higher energies. The additional activation which these neutrons induce in most specimens will be less than a few per cent of the reactions generating them, and the amount of this second-step activation can be minimized by using relatively thin specimens, a few millimeters being a convenient size in many studies. If a specimen is not chemically homogeneous, this activation may not be uniform, and in such cases a control experiment would be required. A zirconium foil partly oxidized in oxygen-18 and placed over the specimen can serve as a convenient neutron source while shielding it from the proton beam.

The protons will activate other elements than the oxygen, but a large fraction of these will yield half-lives short compared with the fluorine-18, and these can be permitted to die out before starting an autoradiograph exposure. Other products will have a sufficiently long half-life that their specific activity will be well below that of the fluorine. In addition, the nuclear coulomb repulsion of an incoming proton increases with atomic number, and the cross section for p,n and p,γ reactions of a 2.7 Mev beam will begin dropping off rapidly above atomic number 40 (6). The degree to which specific elements will obscure the activity due to oxygen activation is currently being investigated. On the basis of literature references [see ref. (3)] and our measurements it is clear that the following elements will cause little if any interference: Be, C, N, F, Mg, Na, Al, Si, P, K, Mn, Co, As, Y, Nb, and those elements above atomic number 50. A few parts per million of oxygen in the presence of these elements or their compounds should be detectable. Others in which some background activity will be generated are: Cr, Fe, Cu, Zr, Rb, and Pd. More serious difficulty will be encountered with Li, B, Ca, Ti, Ni, Ge, Sr, Zn, Cd, Se, and Ag listing them in approximate order of decreasing ease of activation. It might be noted that the energy spread of the available proton beam may vary from one laboratory to another, and the amount of unwanted activation due to the high energy tail on the distribution may differ.

A principal experimental consideration on the use of this technique is the problem of specimen heating in the vacuum of an ion accelerator. For example, a typical 5μ proton beam put 14w of energy into the sample. It must be ascertained that the diffusion of oxygen during this heating will be negligible. Another difficulty in studies of very small amounts of oxygen in a metal arises from the fact that residual air in the target chamber may react with the hot surface to form a small additional oxide layer.

One reason for using a 2.7 Mev beam is that this energy is low enough to minimize unwanted activation. Another is that while it is only 0.11 Mev above the reaction threshold of 2.59 Mev for the oxygen activation this energy spread includes the first resonance peak at about 2.65 Mev with a cross section of about 40 millibarns (7-8). The essential point is that protons impinging on a typical solid will lose this excess energy after passing about 5μ into it, and the activation will be confined to this surface region. Thus, even though the fluorine-18 positrons might have a range up to 0.1 cm, the surface features of oxygen distribu-

tion can be fairly well resolved by autoradiograph film without interference from subsurface activity. In order to take advantage of the fact that this active layer is about 5μ , the film used should have an emulsion of similar thickness, and such stripping films are commercially available.

A diffusion specimen may be beveled in the manner of Kurtz *et al.* (9, 10) before irradiation, and from the distribution of activity along the surface cut at a small angle to the original diffusion interface the oxygen penetration profile may be determined. We are using this procedure to study the grain boundary diffusion of oxygen, and Fig. 1 is an autoradiograph which illustrates the type of result which may be obtained. It was taken on a magnesium oxide bicrystal in which the boundary is roughly a 10° tilt boundary superimposed on a 15° twist. The specimen was annealed in 60% oxygen-18 at 1610°C for 17 hr. The irradiated region is not completely circular, since two collimator shields in the cyclotron beam were not in perfect alignment. The important features of the autoradiograph are the beveled portion in which the grain boundary may be seen, the initial surface below this in the picture and the initial surface in the bottom portion which has a partial cover of platinum. This platinum deposits on the surface during the high-temperature anneal as a result of the usual small amount of vaporization of the platinum crucible in which the specimen was supported. It does not seem to inhibit the exchange of oxygen between the gas and the magnesium oxide. The bevel angle is 0.23° so that on the irradiated spot having a radius of 0.5 cm the new surface at the edge is about 20μ below the original surface. Thermal grooving at the grain boundary which may have occurred during the high-temperature anneal was less than 1μ , so the darkening along it must be due to oxygen diffusion. On the basis of single crystal oxygen exchange measurements (11) the mean penetration of oxygen into the bulk of the specimen should be about 2μ . A microdensitometric inspection of the autoradiograph indicates penetration of oxygen at the grain boundary to the full 20μ depth with the likelihood that it went yet deeper. This activation technique is being applied to further study of diffusion.

Acknowledgment

The authors wish to thank the staff of the 90-in. cyclotron at the Lawrence Radiation Laboratory,

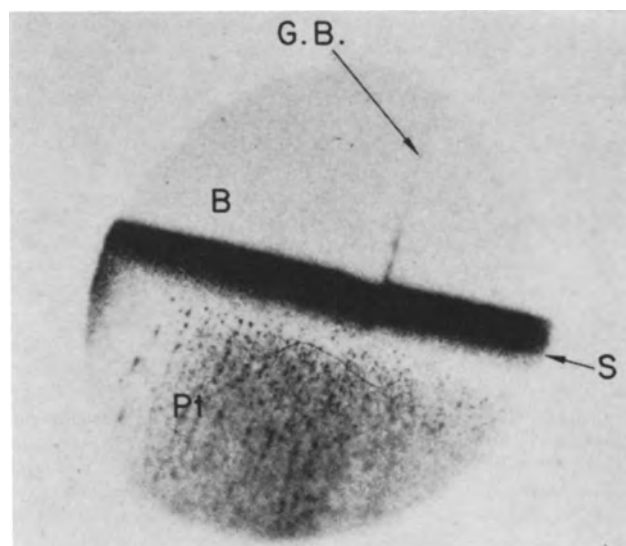


Fig. 1. Autoradiograph of proton irradiated MgO bicrystal: S, initial surface of the specimen; Pt, region of the crystal where surface remained covered with platinum during proton activation; B, beveled region of the crystal, the bevel angle is 0.23° , and the right edge is 20μ below the initial interface; G.B., position of the grain boundary.

Livermore, for their help in carrying out these experiments. Professor C. E. Birchenall of the University of Delaware has also made valuable suggestions in the course of this work. This work was performed under the auspices of the U.S. Atomic Energy Commission.

Manuscript received March 26, 1964.

Any discussion of this paper will appear in a Discussion Section to be published in the June 1965 JOURNAL.

REFERENCES

1. R. C. Koch, "Activation Analysis Handbook," Academic Press, New York (1960).
2. I. Fogelstrom-Fineman, O. Holm-Hansen, B. M. Tolbert, and M. Calvin, *Intern. J. Appl. Radiation and Isotopes*, **2**, 280 (1957).
3. B. A. Thompson, *Anal. Chem.*, **33**, 583 (1961).
4. V. J. Ashby and H. C. Catron, "Tables of Nuclear Reaction Q Values," University California Radiation Laboratory Report No. 5419 (1959).
5. B. G. Harvey, "Annual Review of Nuclear Science," E. Segre, Editor, **10**, 235 (1960).
6. J. Mattauch, "Nuclear Physics Tables," Interscience Publishers, Inc., New York (1946).
7. H. Mark and C. Goodman, *Phys. Rev.*, **101**, 768 (1956).
8. J. M. Blair and J. J. Leigh, *ibid.*, **118**, 495 (1960).
9. A. D. Kurtz, B. L. Averbach, and M. Cohen, *Acta Met.*, **3**, 442 (1955).
10. H. C. Gatos and A. D. Kurtz, *J. Metals*, **6**, 616 (1954).
11. Y. Oishi and W. D. Kingery, *J. Chem. Phys.*, **33**, 905 (1960).

The Phase Diagram of Cobalt Monoxide at High Temperatures

Bertina Fisher and D. S. Tannhauser

Department of Physics, Technion-Israel Institute of Technology, Haifa, Israel

In the course of measuring the electrical properties of CoO, we determined the phase diagram, i.e., the region of existence of the material and the dependence of the ratio Co/O on temperature and pressure, in the range $920 < T < 1350^\circ\text{C}$ and the range of pressures $10^{-12} \leq P(\text{O}_2) \leq 1$ atm. This was done by a combination of gravimetric and electrical measurements. The results are described by the parameter x in the formula CoO_{1+x} , and appear in Fig. 3 in the form $T = f[P(\text{O}_2)]$ at $x = \text{constant}$.

Two samples of cobalt metal sheet (Johnson-Matthey spectrographically standardized, 0.1 mm thick) were suspended in the furnace on platinum wires attached by spotwelding. One sample with four wires was used for electrical measurements, the other one was hung by a single wire from a balance with a sensitivity of about 0.05 mg. The two samples were very close to each other, and a Pt/PtRh thermocouple measured their temperature. A mixture of either O_2 and CO_2 or CO_2 and CO flowed through the furnace, and the partial pressures of oxygen were calculated from the equilibrium constants given by Kassel (1). Oxidation to equilibrium was complete in less than 10 min at 1350°C , and the samples kept their shape. The upper limit of the working range was given by the start of rapid evaporation of both platinum and cobalt-monoxide, and the lower limit by the long time the sample took to reach equilibrium below 900°C . The weight of the metallic cobalt in the weighing sample was determined accurately on a microbalance and was about 1000 mg, so that a change of 3×10^{-4} in x could be detected.

Figure 1 shows the relation between x and the conductance $\Sigma = 1/R$ at various temperatures; it is seen to be linear over most of the range. Since the balance used for weighing in the furnace had a small range and could therefore only measure changes in x , we determined the zero point on the abscissa, i.e., the point of stoichiometric weight, by extrapolating the straight portion of the Σ vs. x plot to zero conductance. This zero point was checked independently by the quenching in air of some samples which were oxidized in $P(\text{O}_2) = 1$ atm at various temperatures, and by direct weighing on a microbalance of the total oxygen uptake during oxidation. The agreement was better than 5×10^{-4} in x . Values of x in Fig. 1 appear in Fig. 3 as lines of constant composition for $x \cong 2 \cdot 10^{-3}$.

The curves for $x < 2 \cdot 10^{-3}$ were determined as follows: the plot of $\log \Sigma$ vs. $\log P(\text{O}_2)$ (Fig. 2) gave two distinct regions, region A with slope 1/4 at higher oxygen pressures, corresponding essentially to the range $x > 1 \cdot 10^{-3}$, and region B with slope 1/6 at

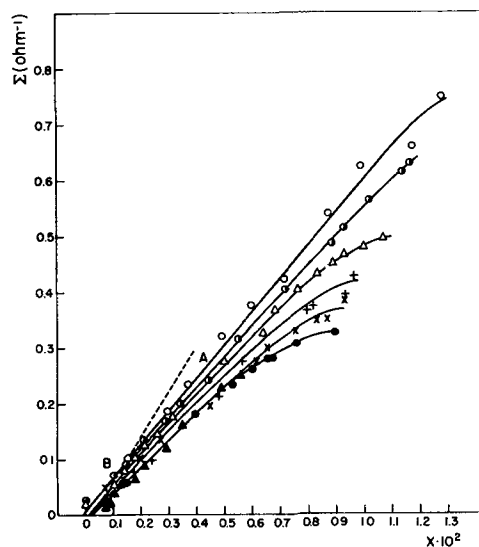


Fig. 1. Conductance vs. excess oxygen in cobalt monoxide. x is defined by the formula CoO_{1+x} ; A is the region of $\log \Sigma = 1/4 [\log P(\text{O}_2)] + \text{const}$; B is the region of $\log \Sigma = 1/6 [\log P(\text{O}_2)] + \text{const}$ (see Fig. 2). Symbols, T, $^\circ\text{C}$: Open circle, 1347; half dark circle, 1285; open triangle, 1191; +, 1129; X, 1094; dark circle, 1035; dark triangle, 986.

lower pressures. To explain this behavior we shall assume that the dominant defects in the lattice are metal vacancies which can be singly and doubly ionized. Following the terminology of Kroeger and Vink (2) we can write

$$\frac{[\text{V}_M]}{P(\text{O}_2)^{1/2}} = K_{x0} \exp\left(-\frac{\Delta H_v}{kT}\right) \equiv K_x \quad [1]$$

$$\frac{p [\text{V}_M']}{[\text{V}_M]} = K_{10} \exp\left(-\frac{E_1}{kT}\right) \equiv K_1 \quad [2]$$

$$\frac{p [\text{V}_M'']}{[\text{V}_M']} = K_{20} \exp\left(-\frac{E_2}{kT}\right) \equiv K_2 \quad [3]$$

$$[\text{V}_M'] + 2[\text{V}_M''] = p \quad [4]$$

$$[\text{V}_M] + [\text{V}_M'] + [\text{V}_M''] = x \quad [5]$$

where $[\text{V}_M]$ is the molar fraction of un-ionized vacancies in the lattice, $[\text{V}_M']$ is the molar fraction of singly ionized vacancies, $[\text{V}_M'']$ is the molar fraction of

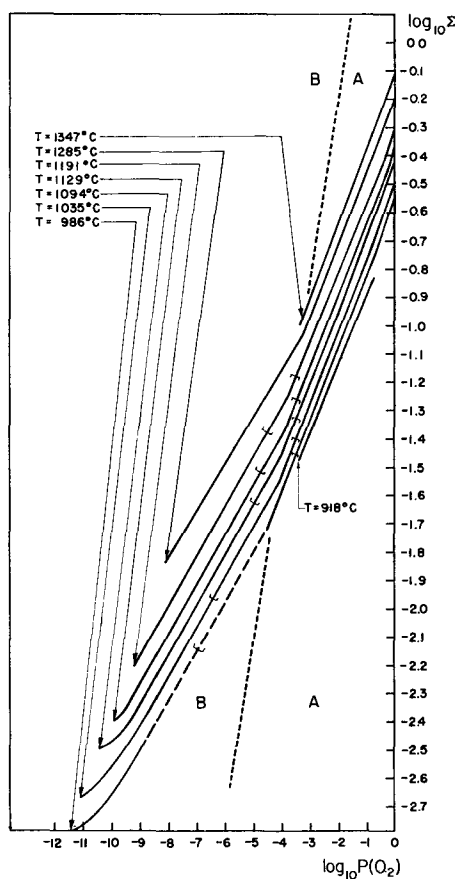


Fig. 2. Logarithm of conductance of cobalt monoxide vs. logarithm of partial pressure of oxygen at various temperatures; the conductance is measured in ohm^{-1} and the pressure in atmospheres. The brackets indicate the range where $P(\text{O}_2)$ may contain a large error because of the finite purity of CO_2 and the high mixing ratios in this range.

doubly ionized vacancies, p is the molar fraction of free holes and $K_x K_1 K_2$ are equilibrium constants which depend on the temperature in the manner indicated. Equation [5] is exact only for small molar fractions. These equations give, when $[\text{V}_M'] \gg [\text{V}_M'']$

$$\Sigma = C_{\mu} e p = C_{\mu} e (K_x K_1)^{1/2} P(\text{O}_2)^{1/4} \quad [6]$$

and when $[\text{V}_M''] \gg [\text{V}_M']$

$$\Sigma = C_{\mu} e p = C_{\mu} e (2K_x K_1 K_2)^{1/3} P(\text{O}_2)^{1/6} \quad [7]$$

where μ is the mobility, e is the electronic charge, and the constant C contains the geometry of the sample as well as the conversion factor from molar fraction to the number of charge carriers per cm^3 .

When μ is independent of the concentrations we get two linear ranges of $\log \Sigma = f[\log P(\text{O}_2)]$ with slopes of $1/4$ and $1/6$, i.e., the observed behavior.

The linear relation between Σ and x in range A of Fig. 1 shows that $[\text{V}_M] \ll [\text{V}_M']$, and therefore according to Eq. [4] and [5] $p = x$ and $\Sigma = C_{\mu} e x$. At the highest values of oxygen pressure x rises faster than Σ , this indicating that we are getting into the range where $[\text{V}_M]$ and $[\text{V}_M']$ are of the same order of magnitude. In range B the slope of $\Sigma = 2C_{\mu} e x$ vs. x should be twice as large as in range A, but this range is so short in terms of x that the difference in slopes is not noticeable.

Figure 1 shows that $C_{\mu} e$, which is given by the slope of Σ vs. x , is practically independent of temperature in the range of temperatures studied. Taking an average value of $C_{\mu} e$ we can then calculate p from the curves of Fig. 2, and from that the molar fraction of

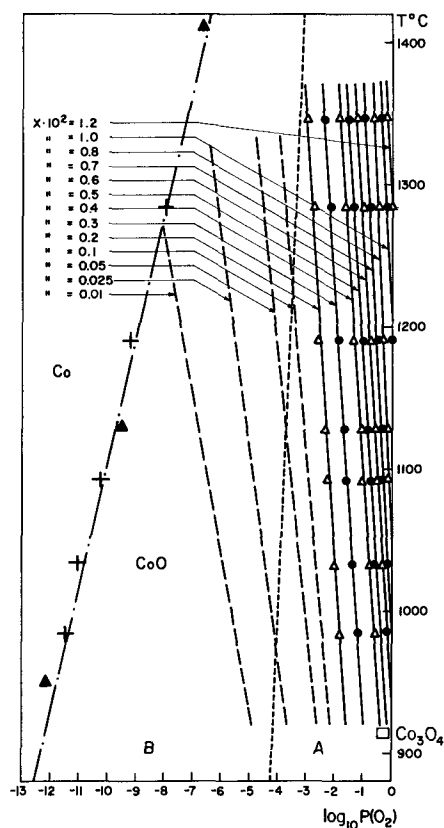


Fig. 3. Phase boundary Co-CoO and lines of constant composition of CoO_{1+x} in the range of temperatures 920°C - 1350°C . The pressure is measured in atmospheres; +, points on the phase boundary in the present work; \blacktriangle , points on the phase boundary given in the literature (4); \square , point on the boundary $\text{CoO-Co}_3\text{O}_4$; —, measured compositions; — — —, compositions calculated from conductance measurements; - - -, boundary between regions A and B (see Fig. 2).

metal vacancies $x = p$ or $x = \frac{1}{2}p$, respectively. Results appear in Fig. 3 as curves for $x < 2 \cdot 10^{-3}$. It should be noted that we have neglected $[\text{V}_M]$ in this range, this being permitted because $[\text{V}_M] < p$ already in most of range A, and $[\text{V}_M]$ decreases much faster with $P(\text{O}_2)$ than p . Naturally the curves for lowest x rely on the assumption that the intrinsic defect structure is negligible, i.e., that no oxygen vacancies appear at these values of x . The analysis of the results assumes that the mobility is independent of charge carrier concentration. This seems to be a reasonable assumption since otherwise the dependence of the conductance on $P(\text{O}_2)$ would not give straight lines on a log-log plot.

The results agree with previous measurements of Carter and Richardson (3) at $P(\text{O}_2) = 1$ atm and $P(\text{O}_2) = 0.005$ atm within their limit of error.

The phase boundary between the CoO and Co phases was determined essentially by the sudden break in the conductance at the boundary. It agrees with results given in "Cobalt monograph" (4). Only one point on the $\text{CoO-Co}_3\text{O}_4$ boundary could be determined, since Co_3O_4 is not stable in $P(\text{O}_2) < 1$ atm above 920°C . The point agrees with the literature (5).

A full account of the electrical properties of CoO will be published later.

Manuscript received Jan. 27, 1964; revised manuscript received June 15, 1964. This work constitutes part of the thesis to be submitted by one of the authors (B.F.) to the Senate of the Technion in partial fulfillment of the requirements for the D.Sc. degree.

Any discussion of this paper will appear in a Discussion Section to be published in the June 1965 JOURNAL.

REFERENCES

1. L. S. Kassel, *J. Am. Chem. Soc.*, **56**, 1838 (1934).
2. F. A. Kroger and H. J. Vink, "Solid State Physics," Seitz and Turnbull, Editors, Vol. 3, p. 310, Academic Press Inc., New York (1956).
3. R. E. Carter and F. D. Richardson, *Trans. AIME*, **200**, 1244 (1954).
4. "Cobalt Monograph," Edited by Centre d'Information du Cobalt, Brussels, 1960, Table 14, p. 159.
5. C. R. Johns and W. M. Baldwin, *Trans. AIME*, **185**, 720 (1949).

Thin Silicon Film Growth on Polycrystalline Alumina Ceramic

V. Y. Doo

Components Division, International Business Machines Corporation, Poughkeepsie, New York

Epitaxial growth of thin films by vapor deposition on a single crystal substrate of the same material has been carried out on various semiconductor materials, such as germanium, silicon, gallium arsenide, silicon carbide, etc. In those cases where the single crystal substrate material differed from the film material and their physical properties such as the crystal structure, lattice parameter, coefficient of expansion, etc., were compatible, successful epitaxial growth has been reported, e.g., GaAs on Ge and GaP on GaAs (1, 2). However, when the substrates were of polycrystalline material which differed from the film material to be grown and their physical properties were grossly different, it was rather difficult, if not impossible, to grow large crystal films.

Epitaxial growth of silicon on silicon substrate has been in production during the last few years. However, the growth of large crystal silicon film on polycrystalline alumina substrate has involved great difficulties. Rasmanis (3) reported that large-grain sili-

con films have been grown on alumina substrates which were coated with a glassy layer prior to the film growth. The purpose of this paper is to report a different technique to grow large-grain silicon films on alumina.

Experiment and Results

The substrate material was mostly of 96% Al_2O_3 and some 99% Al_2O_3 alumina ceramic slides, about $\frac{1}{2} \times \frac{1}{2} \times 40$ in./1000 in dimensions. These ceramic slides were rather porous and their grain size was about 1μ in diameter. A thin film of silicon, (approximately $12\text{-}15\mu$ thick) was deposited on the substrate by the reduction of silicon tetrachloride by hydrogen at elevated temperature. The as-grown silicon film is shown in Fig. 1. The grain size of the silicon film was about the same as that of the substrate. The x-ray Laue back-reflection pattern showed that the silicon crystals were randomly oriented and their size was quite uniform (Fig. 2).

Annealing at temperatures near the melting point of silicon or at the incipient fusion temperature caused limited grain growth. Figures 3 to 5 show

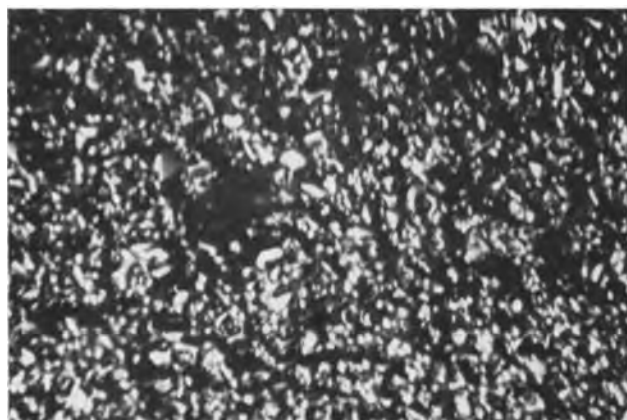


Fig. 1. Polycrystalline silicon film grown on 96% Al_2O_3 ceramic, silicon crystallites of $1\text{-}3\mu$ diameter. Magnification 520X.

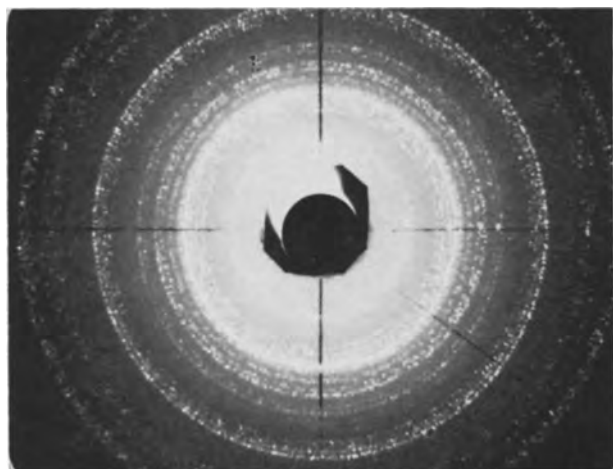


Fig. 2. Laue back-reflection x-ray pattern of polycrystalline silicon film shown in Fig. 1. Crystallites are randomly oriented.



Fig. 3. Polycrystalline silicon film annealed 30 min at about $5^\circ\text{-}10^\circ\text{C}$ below the melting point of silicon. Magnification 520X.



Fig. 4. Same as Fig. 3. except the annealing temperature was very close to, or at, the incipient fusion point. Magnification 520X.

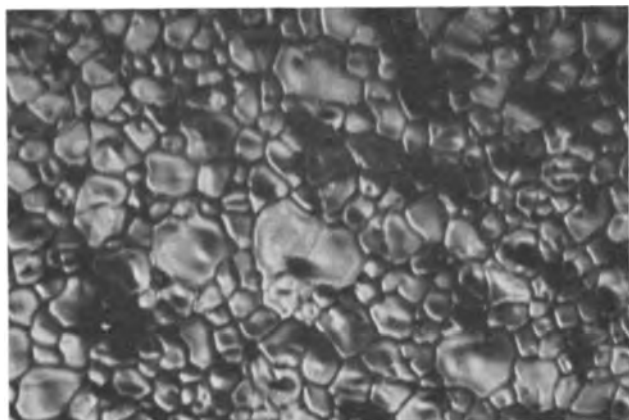


Fig. 5. Same as Fig. 3, except the annealing temperature was at the incipient fusion point. Magnification 520X.

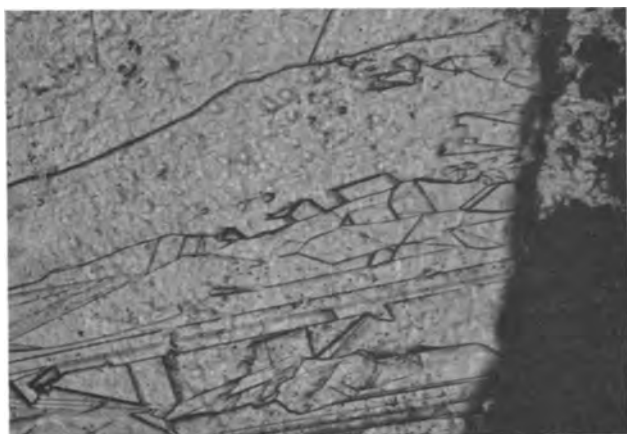


Fig. 6. Film crystals grown by the melt-regrowth method, near the border of molten zone. Magnification 37X.

the silicon film after 30 min annealing at a few degrees below the melting point of silicon, very close to the incipient fusion temperature, and at the incipient fusion temperature, respectively. It is apparent that only the region annealed at the incipient fusion temperature had some degree of growth (from 1μ to about $10\text{--}25\mu$). The region annealed only a few degrees below the melting point of silicon shows very little grain growth. For practical purposes, however, even grains annealed at the incipient fusion temperature are too small to have much value in device application.

A melting and regrowth technique was used to obtain large grain silicon films. A polycrystalline silicon film of about $12\text{--}15\mu$ thick was first deposited on the alumina substrate. It was followed by heating to about $5^\circ\text{--}15^\circ\text{C}$ above the melting point of silicon until a large part of the silicon film was completely melted. Then the temperature was rapidly lowered to about $30^\circ\text{--}50^\circ\text{C}$ below the melting point until the molten silicon film was crystallized, and finally, the sample was slowly brought down to room temperature. Figure 6 shows the regrown silicon crystals near the border of the molten zone. Since the neighboring unmelted crystallites could act as the nuclei in regrowth, some of the grains were relatively small. However, further away from the border, much larger crystals were observed. Figure 7 shows part of a large silicon crystal. Many crystals of about $500\mu \times 3000\mu$ have been observed. Figure 8 shows the x-ray Laue back-reflection pattern of a large silicon crystal. The orientation of this crystal was [201]. All the silicon films grown on alumina substrate by the melt-regrowth technique were p-type and the resistivity of the film grown on the 96% Al_2O_3 substrate was ranged from $0.0005\text{--}0.009$ ohm-cm, and that on the 99% Al_2O_3 substrate was about $0.05\text{--}0.10$ ohm-cm. The samples were then cleaned by light acid etch and subsequently used as the substrate for epitaxial

growth. About 5 to 8μ silicon film was grown on the large grain silicon substrate by the conventional vapor growth technique (the reduction of SiCl_4 by hydrogen at elevated temperature). No dopant was intentionally added to the epitaxial film. The epitaxial film remained p-type, and the surface resistivity of the films grown on 96% Al_2O_3 ceramic was about $0.03\text{--}0.07$ ohm-cm and that on 99% Al_2O_3 was about $0.5\text{--}1.0$ ohm-cm.

A p-n junction was formed in the epitaxial films by phosphorus diffusion. It was followed by masking and mesa etch. Figure 9 shows a single crystal mesa, whose dimension is about $250 \times 375\mu$. Figure 10 shows another mesa, which has a line cutting across the mesa.



Fig. 7. Same as Fig. 6 except it is about 6-7 mm away from the border of molten zone. Magnification 37X.

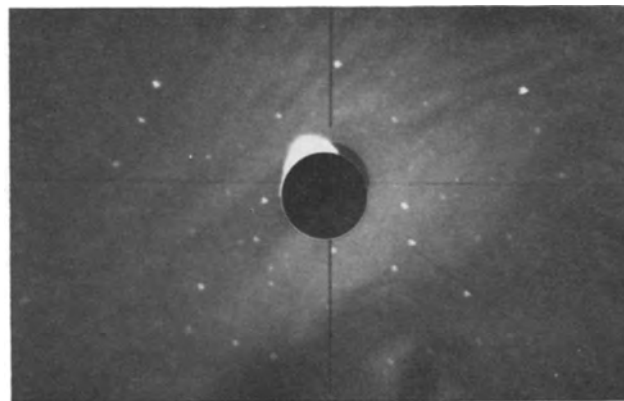


Fig. 8. Laue back-reflection x-ray pattern of a large crystal. Presence of some substructure is indicated and the misorientation is not more than a few minutes.

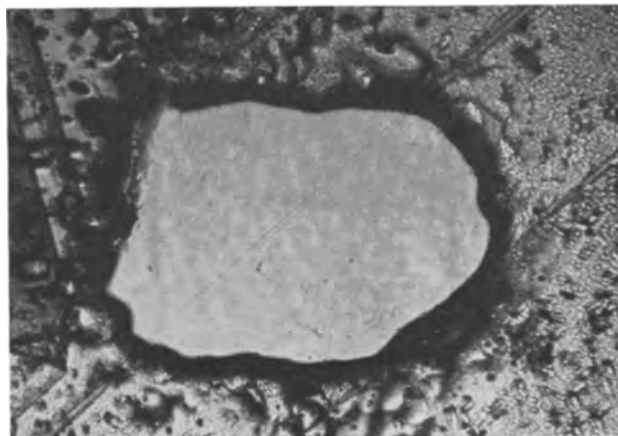


Fig. 9. Single crystal mesa after melt-regrowth, epitaxial growth, phosphorus diffusion, and mesa etch. Magnification 97X.

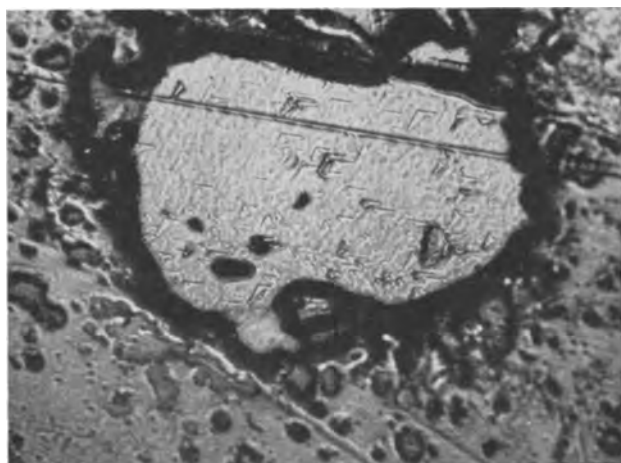


Fig. 10. Same as Fig. 9. The oriented surface defects indicate very small misorientation across the small angle boundary. Magnification 97X.

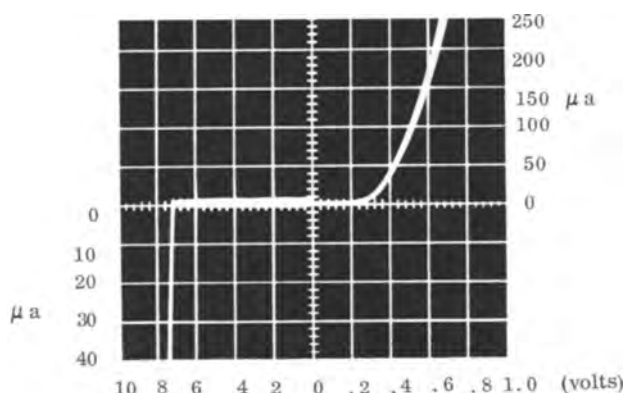


Fig. 11. Forward and reverse bias characteristics of diode made from the silicon film grown on alumina ceramic.

The line appears to be a grain boundary. However, the oriented surface defects observed on both sides of the line indicate that the crystal orientation of one side is not much different from the other. The x-ray pattern shown in Fig. 8 does indicate the presence of some substructures. The misorientation among the substructures is no more than a few minutes.

The electric characteristics of the mesa diodes were measured by point contact-probe which was linked to a micromanipulator. The typical I-V relation of the diodes grown on 96% Al_2O_3 ceramic under both forward and reverse bias is shown in Fig. 11. The high forward-voltage drop is caused primarily by the contact resistance. The reverse bias breakdown voltage is about 7v in Fig. 11. The breakdown voltages of other diodes made on the sample ranged from 6 to 10v. Even

though the substrate silicon film was highly contaminated during the melt-regrowth process, the diode made from the epitaxial film grown on it showed sharp breakdown. Also, the current leakage is quite low (in the order of 10^{-8} amp). The breakdown voltage of the diodes made from the epitaxial films grown on the 99% Al_2O_3 ceramic was in the range of 100-150v.

Discussion

As mentioned earlier, the coefficient of expansion of silicon is greatly different from that of alumina, being about a factor of 2.5 smaller than that of alumina. When two different materials in juxtaposition which differ greatly in coefficient of expansion go through large temperature changes severe stress developed at the interface could cause the cracking of the weaker material. However, no cracks have ever been observed on the silicon films grown on alumina substrates. This indicated that between the silicon and alumina, some materials of intermediate coefficient of expansion could be present. At the temperatures above 1400°C , it would not be unexpected that the molten silicon might attack the Al_2O_3 to form a thin film of possibly $\text{Al O}_x\text{-Si O}_y$, where x and y are arbitrary constants. This postulation is based on the high electronegativity of silicon over aluminum. This new film situated between Al_2O_3 and silicon might act as a buffer zone which is the analogue of the graded seal in the Pyrex-quartz seal.

The resistivity of the silicon epitaxial films grown on 96% and 99% Al_2O_3 without intentional doping was 0.03-0.07, and 0.5-1.0 ohm-cm (p-type), respectively. It is believed that epitaxial films of various resistivity could be grown on the alumina substrates by adjusting the film thickness and external doping. As has been experienced in growing epitaxial films on heavily doped substrates, the surface resistivity of the film in case of no external doping is a function of the film thickness, i.e., the thicker the film the higher the resistivity. By introducing proper amounts of dopant into the growth chamber, one should be able to compensate or reinforce the impurities from the substrate material.

Manuscript received Feb. 21, 1964.

Any discussion of this paper will appear in a Discussion Section to be published in the June 1965 JOURNAL.

Acknowledgment

The author wishes to thank D. W. Boss and W. H. White for their help in growing film crystals.

REFERENCES

1. N. Holonyak, Jr., D. C. Jillson, and S. F. Bevacque, *AIME Proc. of Tech. Conf.*, **15**, 49 (1961).
2. H. M. Manasevit and W. I. Simpson, "Single Crystal Silicon on a Sapphire Substrate." Late-News Paper Reported at American Physical Society Summer Meeting, August 1962, Edmonton, Ala., Canada.
3. E. Rasmanis, Paper presented at Pittsburgh Meeting of the Electrochemical Society, April 15-18 (1963).



Radiotracer Studies on the Incorporation of Phosphorus in Epitaxially Grown Silicon

S. Nakanuma

Semiconductor Division, Nippon Electric Company, Kawasaki, Japan

The incorporation of phosphorus into silicon epitaxial films grown by the hydrogen reduction of silicon tetrachloride has been reported by Theuerer (1), Corrigan (2), and Nuttall (3). The radio isotope tracer technique was applied to obtain information about the transfer of phosphorus from gas phase to solid phase and the ratio of Hall mobility to conductivity mobility, μ_H/μ_c , which is an important parameter in the determination of impurity concentrations in semiconductors from the Hall coefficient R_H . That is

$$R_H = - \left(\frac{\mu_H}{\mu_c} \right) \frac{1}{ne}$$

but little experimental data exist for this ratio for phosphorus in silicon.

The radioactive phosphorus trichloride used as the dopant in this experiment was synthesized by the carbon reduction of phosphoric acid, which contained β -emitting phosphorus P^{32} , to yellow phosphorus in a nitrogen stream, followed by chlorination and reduction to phosphorus trichloride. Using silicon tetrachloride doped with the radioactive phosphorus trichloride, silicon epitaxial films were grown at 1250°C with a hydrogen flow of 1 l/min at a mole fraction of 0.02. The films were about 30μ thick.

Phosphorus concentrations in the films were determined from the measurements of volume, and activity by a gas flow counter, which gives a high geometrical efficiency. The self-absorption effect was neglected in these experiments, because the energy of β particles from P^{32} is high enough to penetrate through the epitaxial films. Phosphorus concentration in the gas phase was calculated from Raoult's law and the preliminary determination of phosphorus concentration in the silicon tetrachloride solutions. Hall samples were prepared by the evaporation of Au containing Sb for ohmic contacts and mesa-etch as shown in Fig. 1. The

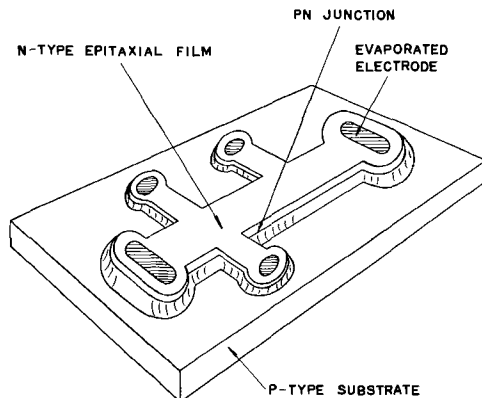


Fig. 1. Hall sample

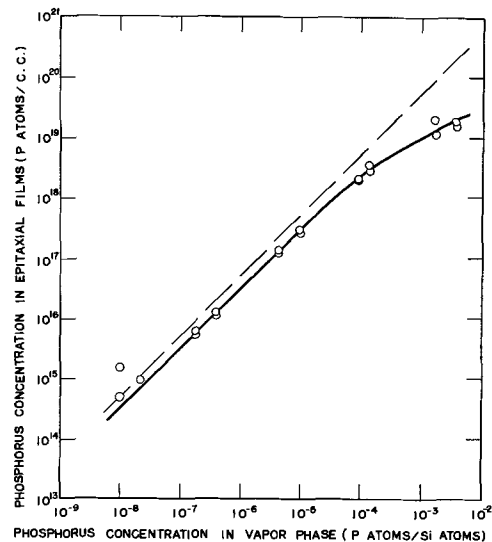


Fig. 2. Phosphorus transfer from vapor phase to films

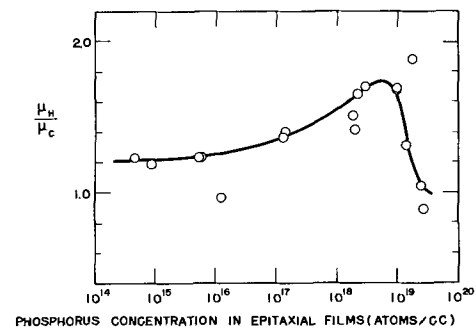


Fig. 3. The ratio of Hall mobility to conductivity mobility

measurements of Hall coefficient and conductivity were made over a temperature range from 77° and 300°K under a magnetic field of 5350 gauss.

Figure 2 shows the phosphorus concentration in the epitaxially grown silicon films as a function of that in gas phase. The dashed line is the curve calculated assuming a transfer ratio of unity as defined by the following formula

$$\text{transfer ratio} = \frac{(\text{P atoms/Si atoms})_{\text{in solid}}}{(\text{P atoms/Si atoms})_{\text{in gas}}}$$

The transfer ratio remains constant at about 0.8 over the range of phosphorus-silicon atom ratio in the gas phase between 10^{-8} - 10^{-4} , but a relatively large de-

crease in this ratio is observed at higher concentrations. This might be due to the effect of repulsive forces between phosphorus in the gas phase and that adsorbed on the growing surface, or the effect of having reached the solubility limit of phosphorus in silicon.

Figure 3 shows the ratio of Hall mobility to conductivity mobility as a function of phosphorus concentration at 300°K. The theoretical treatment of this ratio in semiconductors has been discussed by several authors (4) and gives a ratio greater than unity in the nondegenerate case and a ratio of unity in the degenerate case. This is in good agreement with the present results. The Hall mobilities observed are close to the values reported by Morin and Maita (5). It is concluded from these results that the phosphorus atoms in silicon epitaxial films grown by the hydrogen reduction of silicon tetrachloride doped with phosphorus trichloride are incorporated substitutionally in the silicon lattice in spite of much lower growth temperature than from a melt; that is, there is no exist-

ence of electrically inactive phosphorus atoms in these films up to phosphorus concentrations of 3×10^{19} at./cc.

Acknowledgment

The author wishes to extend his appreciation to Mr. K. Ohta for laboratory assistance, Mr. S. Ohtani for isotope handling guidance, and Dr. H. Osafune and Y. Matsukura for helpful discussions.

Manuscript received May 18, 1964; revised manuscript received July 2, 1964.

Any discussion of this paper will appear in a Discussion Section to be published in the June 1965 JOURNAL.

REFERENCES

1. H. C. Theuerer, *This Journal*, **108**, 649 (1961).
2. W. J. Corrigan, *Metallurgy of Semiconductor Materials*, **15**, 103 (1962).
3. R. Nuttall, *This Journal*, **111**, 317 (1964).
4. F. J. Blatt, *Phys. Rev.*, **105**, 1203 (1957).
5. F. J. Morin and J. P. Maita, *ibid.*, **96**, 28 (1954).

Bromine-Zinc Secondary Cells

Sidney Barnartt and David A. Forejt

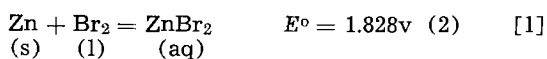
Research Laboratories, Westinghouse Electric Corporation, Pittsburgh, Pennsylvania

ABSTRACT

Secondary bromine-zinc cells were made with aqueous $ZnBr_2$ electrolyte and carbon plate electrodes separated by a multiple diaphragm. A layer of activated charcoal over the positive electrode was provided as a bromine sorbent. Data are given on discharge and cycling characteristics, open-circuit potentials, polarization, internal resistance, temperature effects, self-discharge, and the mechanism of failure. Outputs as high as 2.4 watt min/g (18 watt hr/lb) were observed and could be increased appreciably by minimizing cell weight. Electrode polarization was low, self-discharge rates high.

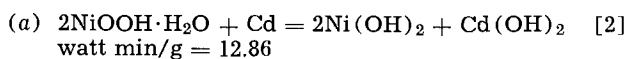
The bromine-zinc storage battery is old in general concept (1), but there is little published information on it. The present study was undertaken to obtain realistic data on energy density, optimum power density, cycling characteristics, and electrode polarization.

The system is attractive because of the high theoretical energy of the reactants.

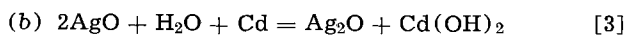


$$2FE^\circ \text{ per mole } ZnBr_2 = 26.11 \text{ watt min/g}$$

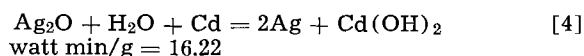
Compared with secondary alkaline systems, bromine-zinc has considerably higher voltage and specific energy than nickel-cadmium or silver-cadmium, and is equivalent to silver-zinc.



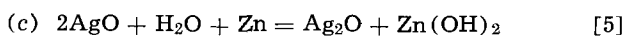
$$E^\circ = 1.327v \quad (3)$$



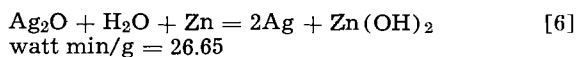
$$E^\circ = 1.413v \quad (4)$$



$$E^\circ = 1.151v \quad (5)$$



$$E^\circ = 1.849v$$



$$E^\circ = 1.587v$$

The general formulation of a bromine-zinc secondary cell is simply an aqueous $ZnBr_2$ solution and two inert electrodes with a porous diaphragm separating the electrode compartments. In horizontal cells liquid bromine is deposited at the lower electrode during charging, zinc at the upper (1, 6). Vertical electrodes may be used if the surface of the positive electrode is covered with an immobilized porous sorbent (1, 7). The latter holds the bromine in place; it also slows diffusion of bromine to the zinc surface, thus improving charge retention.

The cells described below were based on the vertical arrangement, with two carbon electrodes and a layer of activated charcoal held against the surface of the positive.

Experimental

Cells.—The basic cell design is shown in Fig. 1. Two flat carbon electrodes *a*, 15 cm square, were sealed to a methyl-methacrylate frame *b*. One edge of each carbon plate protruded and was cemented to a carbon bar with conducting cement. A layer of activated charcoal particles *d*, 200-400 mesh, was held against the positive electrode by a multi-layered diaphragm *c*. The latter was cemented around its edges to insulator *b*, which carried a planar network of window frames

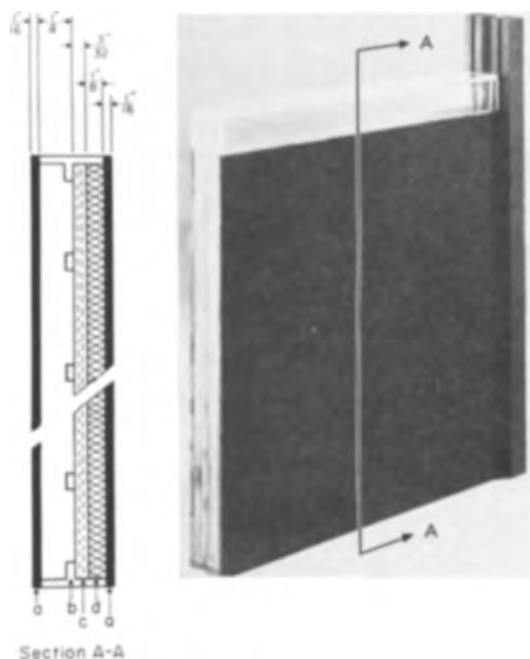


Fig. 1. Two-electrode bromine-zinc cell: *a*, carbon electrodes; *b*, insulator; *c*, multilayer diaphragm; *d*, activated charcoal.

intended as a support for the diaphragm. The porous diaphragm consisted of a finely woven glass cloth, facing the activated charcoal, which was backed by three layers of open glass screening and finally by a sheet of polyvinyl chloride (1.3 mm thick, pore diameter 5-10 μ).

Each compartment of the cell was vented by means of small holes in the top of the insulating frame and in the cap above it. One larger hole was used for connecting a saturated calomel reference electrode, by means of a glass tube filled with the electrolyte which terminated in a capillary tip close to the negative electrode. The surface of the negative electrode was scored in order to improve the adhesion of zinc deposited during charging. Because the carbon plates were not entirely impermeable to bromine and some early cells developed leaks at the edges, the cells described below were partially encased in a potting compound. The weight of the latter was not included, however, in calculations of output per unit weight.

The principal features of the 2-electrode cell, Fig. 1, were retained in the design of a 3-electrode cell. A central positive electrode in the latter had half of its activated charcoal on either side of it, and with two negative electrodes formed two chemically isolated parallel cells each having the general construction of Fig. 1. Besides the thinner activated charcoal layer, the

$$E_{Br} = 1.065 + 0.0296 \log a_{Br_2} - 0.0592 \log a_{Br^-} \quad [9]$$

decayed somewhat more rapidly (30 mv in 24 hr).

Open-circuit potential measurements on cell 2-IC after 18 amp-hr charge showed similar potential decay. The bromine potential followed closely the curve for 3-MC, but the zinc potentials were displaced to values 17 mv more positive (higher concentration of Zn^{++}). The fact that the bromine potential was not changed appreciably indicated that the increase in a_{Br^-} was offset by a larger value of a_{Br_2} (Eq. [9]), since 18 amp hr was sufficient to saturate the bromine electrode of cell 2-IC but not that of 3-MC.

Internal resistance.—Measurements were made periodically during discharge across a 1-ohm load by switching for 1 min from the load circuit to that of Fig. 2. Data for cells 2-IC and 3-MC are given in Fig. 5. The former cell, with half the electrode area of the latter, was expected to have somewhat less than double the internal resistance because it contained a solution of higher conductivity, and this was observed. The internal resistance tended to remain constant during discharge although cell 2-IC, which had the thicker activated charcoal layer, showed increasing resistance towards the end of discharge.

Electrode polarization.—Figure 6 presents two sets of polarization curves for cell 3-MC. The first set was taken after a charge input of 18 amp-hr, with constant current maintained at each point for 10 min. During this interval the zinc and bromine potential readings remained constant within ± 1 mv. Both electrodes gave linear polarization curves over the whole range of apparent current density i_a (based on geometrical electrode area). The return curve (decreasing currents) was displaced slightly in each case, the shift being related to the open-circuit potential decay (Fig. 4).

The exchange current density $(i_o)_a$ may be estimated from the slope of the polarization curve, using the theoretical equation based upon activation overpotential (8) as the major contribution

$$(i_o)_a = \frac{RT}{F} \left(\frac{\nu}{n} \right) \left(\frac{\partial i_a}{\partial \eta} \right)_{\eta \rightarrow 0} \quad [10]$$

Here n is the number of electrons in the over-all electrode process as arbitrarily written, and ν is the stoichiometric number.

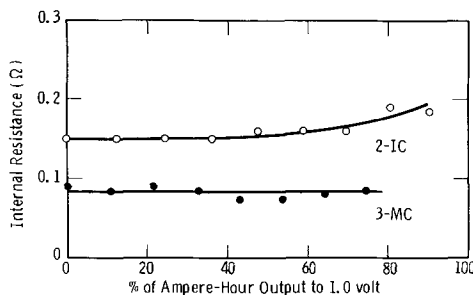


Fig. 5. Internal resistance of cells 2-IC and 3-MC during discharge.

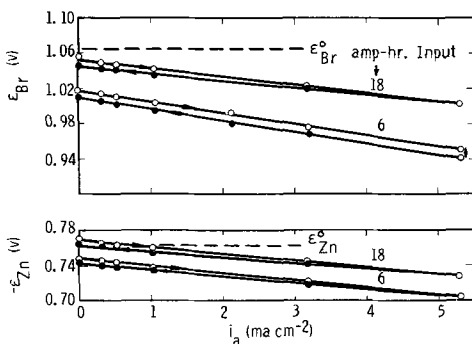


Fig. 6. Electrode polarization in cell 3-MC

chiometric number. Since the rate-determining step has not been established for the discharge reactions in the bromine-zinc cell, evaluation of $(i_o)_a$ was based on the assumption $\nu = n$, which yields for 25°C

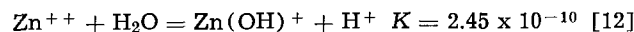
$$(i_o)_a = 0.0257 \left(\frac{\partial i_a}{\partial \eta} \right)_{\eta \rightarrow 0} \quad [11]$$

Equation [11], applied to the return curves (decreasing currents) in Fig. 6, gives $(i_o)_a$ values of 3.9 ma/cm² for the zinc electrode reaction and 3.3 ma/cm² for bromine reaction. Thus the apparent exchange currents are relatively high for both electrode processes, so that the bromine-zinc system is of interest for battery application even when the bromine is adsorbed on activated charcoal.

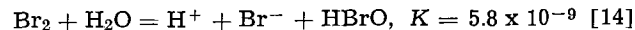
The second set of polarization curves in Fig. 6, taken after 6.0 amp-hr input (29% of theoretical design capacity), demonstrated that both electrode reactions remain fast under conditions of partial charge. The data were obtained at a rate of 5 min/point, so that only 11% of the input was discharged during the polarization measurements. The zinc potentials remained constant with time, but the bromine potentials, stable at low currents, drifted 11 mv at the highest current density. Both the initial and final values of the latter reading are plotted in Fig. 6 to show that most of the displacement of the polarization curve resulted from this drift. The slopes of the polarization curves after the 6 amp-hr charge are seen to be only slightly larger than those after the 18 amp-hr charge.

Self-discharge.—During charging, dissolved bromine in the anolyte diffuses through the porous separators to the other electrode and reacts with the depositing zinc. This shortens shelf life. Delayed-discharge measurements on cell 2-IC indicated a half-life for charge retention of 2.7 days. Self-discharge of cell 3-MC was expected to be even faster since this cell had double the electrode area and decreased electrode separation, and this was confirmed. It would be possible to reduce the self-discharge rate with separators of finer porosity, with an accompanying increase in internal cell resistance.

The rate of the self-discharge reaction at the zinc electrode will increase as the pH of the solution decreases. Zinc bromide hydrolyzes to form a slightly acid solution and generates complex ions (9), and at 25°C



During charging, bromine diffuses into the zinc compartment and its hydrolysis produces HBrO as well as hydrogen ions (10)



The low value of K (25°C) from Eq. [14] shows that little acid can be generated by diffusing bromine when the concentration of zinc bromide is relatively high. Similarly any pH change resulting from the chemical reaction of bromine and zinc will be small.

Larger pH changes could be produced if hydrogen codeposits cathodically with zinc (efficiency < 100%), whence the solution pH in the zinc compartment would increase during charging. This effect was observed. Measurements of catholyte pH in cell 2-IC, initially containing 3M $ZnBr_2$ at pH 4.3, showed a pH rise to 5.1-5.2 during a 24 amp-hr charge (cycles 40, 41). During discharge the solution pH near the zinc anode fell slowly to a minimum of 3.7 ± 0.1 , and then rose to 4.3 after complete discharge to zero cell voltage (cycles 37, 40, 41). Hence the self-discharge rate should increase to a maximum during the discharge portion of the cycle, when the concentration of dissolved bromine in the zinc compartment is still relatively high and the pH is approaching or has reached the minimum value.

The anodic liberation of bromine is accompanied by the formation of Br_3^- , and to a smaller extent Br_5^- .

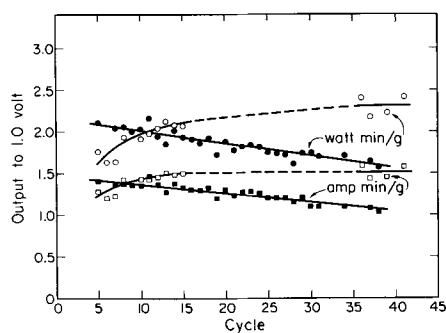
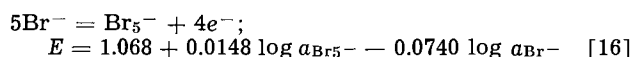
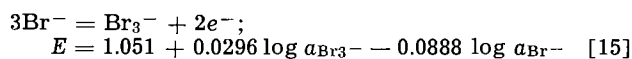


Fig. 7. Coulombic and energy yields for cells 2-IC and 3-MC; ○, □, cell 2-IC; ●, ■, cell 3-MC.

The concentrations of these ions in the anolyte will increase continuously during the charging process. The reversible potentials at 25°C are given by (11)



During charging the anions Br_3^- and Br_5^- diffuse with the dissolved Br_2 from the bromine compartment to the zinc compartment, because of the concentration gradient, and all three species contribute to corrosion of the depositing zinc. Electrical migration of these two anions in the applied field is in the opposite direction, however, and near the end of charging migration of Br_3^- and Br_5^- to the bromine electrode will occur to a significant extent. During discharge these ions migrate toward the zinc electrode and tend to accelerate the nongalvanic loss in capacity of the negative electrode, particularly during the initial part of the discharge.

Cycling.—The discharge data for optimum load are shown in Fig. 7. Cell 2-IC was cycled with a 24 amp-hr charge and a 2 ohm discharge. Cell 3-MC was cycled with 30 amp-hr charge and 1 ohm discharge. The latter cell yielded approximately 90% of the theoretical design capacity in the early cycles. The output decreased gradually and linearly up to 38 cycles. Within the next three (nonstandard) cycles the cell failed abruptly.

The two-electrode cell exhibited an initially increasing coulombic output, which stabilized within 15 cycles at 1.5 amp min/g (90% of theoretical). After an additional 14 (nonstandard) cycles this cell failed also, but it was reactivated by a treatment described below and again yielded 1.5 amp min/g (cycles 36 to 41). After reactivation its average voltage was somewhat higher, and its final energy output was 2.4 watt min/g (18 watt hr/lb).

Since the cells were not designed to minimum weight in this study, it is evident that appreciably higher specific energy output would be possible with optimized cell design.

Cell deterioration and reactivation.—Examination of several cells which failed revealed zinc dendrites which had grown from the negative electrode and penetrated the polyvinyl chloride separator sheet.

During charging, zinc dendrites growing into the three layers of glass screening would be exposed to a relatively high concentration of dissolved bromine which may limit their penetration. The failed cells, however, also exhibited settling of the activated charcoal layer and bulging of the open-grid retainer (b in Fig. 1, openings 3.1 cm square). This structural weakness resulted in some of the activated charcoal particles penetrating the glass separator layers and reaching the surface of the polyvinyl chloride sheet. Internal shorting, caused by contact of the migrating charcoal particles with zinc dendrites which penetrated the polyvinyl chloride, appeared to be the most probable cause of cell failure.

On this basis an attempt was made to reactivate cells 2-IC and 3-MC after failure by dissolving out the shorting dendrites. Cell 2-IC was successfully reactivated by replacing the electrolyte with 1M HBr, heating to 40°C for 24 hr, then refilling the cell with 3M ZnBr_2 after flushing it three times with this solution. The reactivated cell yielded high outputs (Fig. 7). Two similar acid treatments, however, failed to reactivate cell 3-MC.

Effect of temperature.—Cycling of other cells was carried out at 0° and 50°C. The ampere-hour outputs obtained at 0°C were approximately equal to the theoretical design capacities, but the average discharge voltage was about 10% less than that at 25°C. The coulombic outputs obtained at 50°C were much lower, usually under 60% of the theoretical design capacities, and the average voltage was also lower. The higher temperature accelerated both the corrosion reaction at the zinc surface and bromine diffusion to it, thus increasing the self-discharge rate during the entire charge-discharge cycle.

Acknowledgment

The authors are indebted to R. Zito, D. G. Hargreaves, and R. M. Lowy for their work on cell construction and for very useful measurements on preliminary cells.

Manuscript received Feb. 21, 1964. This paper was presented at the Washington Meeting, Oct. 11-15, 1964.

Any discussion of this paper will appear in a Discussion Section to be published in the June 1965 JOURNAL.

REFERENCES

1. C. S. Bradley, U. S. Pat. 312,802 (1885); 409,448 (1889).
2. G. Jones and S. Baekström, *J. Am. Chem. Soc.*, **56**, 1524 (1934).
3. P. L. Bourgault and B. E. Conway, *Can. J. Chem.*, **38**, 1557 (1960).
4. J. F. Bonk and A. B. Garrett, *This Journal*, **106**, 612 (1959).
5. W. J. Hamer and D. N. Craig, *ibid.*, **104**, 206 (1957).
6. H. E. R. Little, U. S. Pat. 870,973 (1907).
7. W. Morrison, U. S. Pat. 950,861 (1910); 1,006,494 (1911).
8. R. Parsons, *Trans. Faraday Soc.*, **47**, 1332 (1951).
9. W. M. Latimer, "Oxidation Potentials," 2nd ed., Prentice Hall, New York (1952).
10. G. Jones and S. Baekström, *J. Am. Chem. Soc.*, **56**, 1517 (1934).
11. M. Pourbaix, "Atlas d'Equilibres Electrochimiques," p. 604, Gauthier-Villars, Paris (1963).

A Methanol Fuel Cell with an Invariant Alkaline Electrolyte

E. J. Cairns and D. C. Bartosik

Research Laboratory, General Electric Company, Schenectady, New York

ABSTRACT

The inconvenience and expense of using hydrogen as a fuel for fuel cells have prompted interest in inexpensive liquid fuels such as methanol. The chief difficulties encountered by workers in the field of methanol cells have been lack of electrolyte invariance, incomplete fuel oxidation, and deactivation of the cathode by dissolved fuel in the electrolyte.

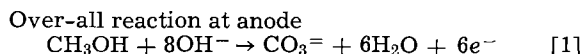
Feasibility has been shown for an intermediate temperature methanol fuel cell using a cesium carbonate electrolyte and Teflon-bonded platinum electrodes at an optimum temperature of 115°-130°C, which is free from all of the above-mentioned problems. Performance has been studied as a function of temperature, electrolyte composition, fuel composition, and other variables. Material balances have been performed showing complete electrochemical oxidation of the fuel to CO₂ and H₂O. At an operating point of 0.55v at 20 ma/cm², the comparative thermal efficiency is 42%. The conversion of the fuel to electricity in one pass through the cell is 75 to 85%. Power densities of 40-45 milliwatt/cm² can be drawn from the cell. An endurance test of over 560 hr has shown a gradual increase in performance with time, and no change in the electrolyte. Performance on carbon monoxide is also reported.

For several reasons, methanol has come under consideration as an attractive liquid fuel for fuel cells. First, the difficulty of handling and storing gaseous fuels such as hydrogen has made it increasingly important to investigate liquid fuels. Second, tank hydrogen is expensive compared to more conventional fuels, largely because of shipping and handling costs for the bulky gas cylinders. Other reasons for methanol being an interesting fuel are its high reactivity at fuel cell anodes, and the fact that it is an organic fuel, presenting many of the characteristics of even less expensive (but less reactive) saturated hydrocarbon fuels. Therefore, methanol may be regarded not only as an organic fuel of immediate interest and usefulness, but also as an interim fuel for use while more difficult problems with the saturated hydrocarbons are being solved.

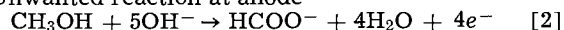
The fact that methanol is electrochemically active in both acidic and alkaline electrolytes even at ambient temperatures and pressures has been known for some time. As early as 1922, Müller (1) reported on fairly detailed studies of the electrochemical oxidation of methanol and other organic compounds at platinum anodes in aqueous electrolytes. Later, Tanaka (2) presented results for methanol on Pt, Pd, Rh, and Au in a sodium hydroxide electrolyte. During the last few years, interest has revived in the determination of the adsorption of methanol on platinum anodes (3, 4) and the details of its anodic oxidation process, particularly in acidic electrolytes (5-8).

The present great surge in fuel cell activity throughout the world has resulted in a varied array of development programs for methanol anodes (9-14), as well as considerably more limited work on complete methanol-oxygen fuel cells (15-20). One of the reasons for the fact that the work on complete methanol-oxygen cells is so limited is the lack of invariance of the cell components, particularly the electrolyte and the cathode, whose performance is greatly reduced by dissolved methanol in the electrolyte.

The majority of the methanol cells reported have used hydroxide electrolytes (KOH or NaOH) over the temperature range 20°-100°C. In such a system, the electrolyte is consumed in the main cell reaction, as well as in various unwanted reactions. Examples are



Unwanted reaction at anode



Note that in reaction [1], eight equivalents of hydroxyl ion are consumed in the production of only six Faradays of electricity. In reaction [2], five equivalents of hydroxyl ion are consumed, while only four Faradays of electricity are produced. In addition, the electrolyte is contaminated by carbonate and formate ions (15-20).

Obviously, it is necessary to have an electrolyte which allows complete oxidation of the methanol to CO₂ and H₂O, and which will reject the reaction products completely. Strong acids reject the CO₂, but only allow nearly complete oxidation of the methanol under certain current density conditions (21). In addition, complete cells with acid electrolytes have shown that the methanol, which is soluble in the electrolyte, diffuses to the cathode, drastically reducing the performance of the cathode (17, 21, 22).

The experiences of previous investigators have pointed out the need for an electrolyte which will support complete electrochemical oxidation of methanol at useful current densities and overvoltages, while rejecting CO₂ and preventing access of the CH₃OH to the cathode. A strong aqueous solution of Cs₂CO₃ or Rb₂CO₃ is such an electrolyte, particularly when operated in the temperature range 100°-140°C.

The general properties of cesium and rubidium carbonates and bicarbonates which are of particular importance to the operation of fuel cells on organic fuels have already been discussed by one of us (23). The very high solubility of Cs₂CO₃ and Rb₂CO₃ in water allows fuel cell operation up to at least 200°C. In addition, the instability of bicarbonates above about 100°C allows for simple, direct CO₂ rejection by the carbonate electrolyte.

It was the object of this work to overcome the difficulties encountered in previous methanol-cell work by developing a high performance, intermediate temperature methanol fuel cell by using an aqueous Cs₂CO₃ or Rb₂CO₃ electrolyte. It was necessary to establish that the cell was invariant and that the stoichiometry was such that CO₂ and H₂O were the only products of the anode reaction. In addition, none of the fuel was to be consumed by diffusion through the electrolyte to the cathode, or by any side reactions.



Fig. 1. Photograph of Teflon cell and auxiliary apparatus

Experimental

The fuel cell and some auxiliary equipment used in these investigations are shown in Fig. 1. The Teflon cell itself (A) is shown in the center of the photograph and is held together by stainless steel end-plates and bolts. The identical cell to the left (B) contains two reversible H_2 reference electrodes. The reservoir at the upper right (C) fed the aqueous Cs_2CO_3 electrolyte by gravity to both cells through Teflon tubing and platinum connectors. Electrolyte from the cells was collected in the receiver at the lower front (D) and returned to the upper reservoir by an all-Teflon pump. The electrolyte flow rate was set by the valve on the fuel cell exit. The electrodes were platinum black and Teflon bonded to a platinum screen, of the general type described by Niedrach and Alford (24), having 11.38 cm^2 of active area. They ". . . consist of a Teflon-catalyst mix that is pressed and sintered onto a suitable supporting screen . . ." (24). The electrolyte chamber thickness (distance between the electrodes) could be varied from 3 to 9.5 mm as desired. No membranes or separators other than the electrodes themselves were used. The cell was operated in an apparatus shown schematically in Fig. 2.

The fuel cell and the cell containing H_2 reference electrodes were connected via the electrolyte stream so that individual anode *vs.* reference and cathode *vs.* reference voltages could be measured. The methanol or methanol-water fuel mixture was fed at a steady, accurately known flow rate to the fuel gas compartment by a syringe drive. When the liquid methanol entered the air thermostat (usually above $100^\circ C$), the methanol vaporized and entered the fuel cell as a gas. Oxygen was metered into the oxygen compartment through a water bubbler (not shown).

The exit gas from the fuel compartment passed through a trap (E in Fig. 1) to catch any electrolyte that might have leaked through the anode, then out of the thermostat, through a condenser to collect un-

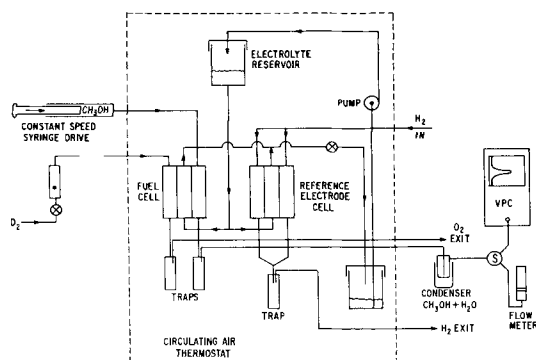


Fig. 2. Schematic drawing of fuel cell test apparatus

reacted CH_3OH and product H_2O , and finally through a sampling valve to a flow measuring device and a vapor phase chromatograph for analysis of the non-condensables (CO_2). The condensed CH_3OH-H_2O mixture was analyzed by microdensity techniques using samples in the range 25-100 microliters. The oxygen exit stream followed a similar path and could be analyzed as desired. All of the apparatus inside the air thermostat was made of either Teflon or platinum in order to prevent contamination and to simplify analysis of the results.

The electrical measurements were carried out using a Kordes-Marko interrupter (25) with suitable modifications in the circuitry. The over-all cell voltage was recorded continuously, while the anode *vs.* reference, cathode *vs.* reference, and anode *vs.* cathode voltages (without *IR* losses) were measured periodically with the Kordes-Marko interrupter and a potentiometer.

Several types of experiments were performed: (i) electrical performance of the cell as measured by the current density-voltage curves; (ii) limited endurance tests up to about 570 hr; (iii) rate of fuel consumption at constant current density; (iv) rate of CO_2 production at constant current density; (v) fraction of fuel converted to electricity in a single pass through the anode compartment (conversion per pass); (vi) analysis of electrolyte samples for possible intermediates or by-products.

Using the above experimental approach, the following variables were studied: (i) temperature of cell operation ($25^\circ-180^\circ C$); (ii) fuel composition, (a) methanol and water vapors carried in nitrogen, (b) methanol or methanol-water mixtures fed directly to the cell by syringe drive as shown in Fig. 2; (iii) electrolyte composition [50 to 95 weight per cent (w/o) Cs_2CO_3].

Results and Discussion

Electrical Performance

Typical current density-voltage curves for $CH_3OH(Pt)/Cs_2CO_3(aq)/O_2(Pt)$ cells operating at $125^\circ-130^\circ C$ are shown in Fig. 3. The performance is presented on an *IR*-free basis in order to facilitate comparisons among cells which did not have the same internal resistance due to differences in the thickness of the electrolyte chamber. The open-circuit voltage for one of these cells was somewhat lower than the value of about 1.0v usually found on open circuit for cells of this type. The data points shown are for "steady" operation, that is, no voltage changes in excess of ~ 10 mv took place at the given current density for at least an hour. Usually, readings were taken at least 5 min after changing the current density to the next higher value.

The propinquity of the two curves in Fig. 3 indicates the degree of reproducibility which can be obtained for cells prepared in the same manner and operated under the same conditions. The good reproducibility obtained at current densities below 100 ma/cm^2 is difficult to maintain at much higher current densities.

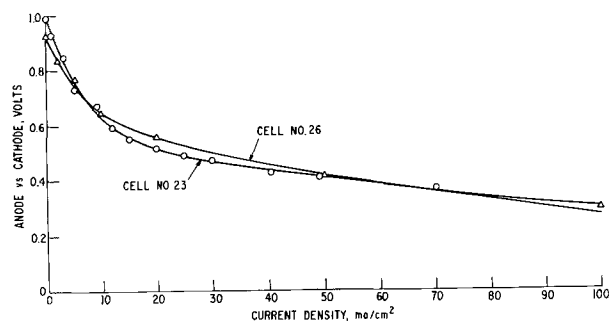


Fig. 3. Methanol-oxygen fuel cell. Cs_2CO_3 electrolyte, $t = 130^\circ C$ (does not include *IR* losses).

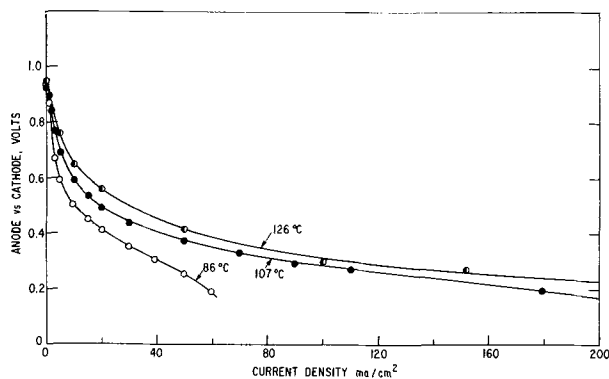


Fig. 4. Effect of temperature on cell performance. $\text{CH}_3\text{OH}_{(g)}(\text{Pt})/\text{Cs}_2\text{CO}_3/\text{O}_2(\text{Pt})$, cell No. 26.

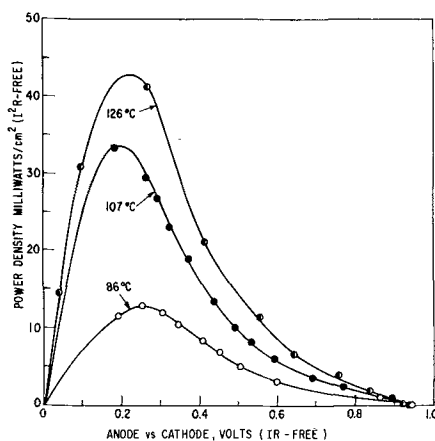


Fig. 5. Effect of temperature on power output. $\text{CH}_3\text{OH}_{(g)}(\text{Pt})/\text{Cs}_2\text{CO}_3/\text{O}_2(\text{Pt})$.

Effect of temperature on performance.—The effect of temperature on performance is shown in Fig. 4 for a cell operated on pure methanol vapor. Heating the cell has its most beneficial effect from room temperature up to about 125°C . Further temperature increases only improve the performance by marginal amounts. Data were collected at 126°C out to 400 ma/cm^2 , where the anode vs. cathode voltage was reduced to less than 0.1v .

The power density is plotted against anode vs. cathode voltage for various temperatures in Fig. 5. The curves in Fig. 5 were constructed from the data shown in Fig. 4. The power loss due to I^2R heating of the electrolyte has been eliminated from the curves shown.

The polarization of the individual electrodes (anode vs. reversible H_2 and cathode vs. reversible H_2 in the same electrolyte) is shown in Fig. 6 as a function of temperature over the range 86°C – 126°C . The effect of temperature is most pronounced at the anode; the cathode showed only a minor performance increase with temperature. Notice that the open-circuit anode voltage was always within about 80 mv of the reversible potential for the oxidation of methanol to carbon dioxide and water ($-0.03\text{v vs. rev H}_2$ at 127°C). At high current densities, the polarization of both anode and cathode increased very slowly with increasing current density. At 130°C , up to 400 ma/cm^2 could be drawn from the cell before the anode vs. cathode voltage was reduced to nearly zero. Increases in temperature beyond 140°C did not significantly enhance the performance of either the anode or the cathode.

The shape of the anode vs. reference and cathode vs. reference curves nearly follows a Tafel relationship, with deviations indicative of possible mass transport limitations at high current densities. At the anode, the escaping CO_2 could cause such an effect, while at the cathode, small amounts of inerts from the oxygen

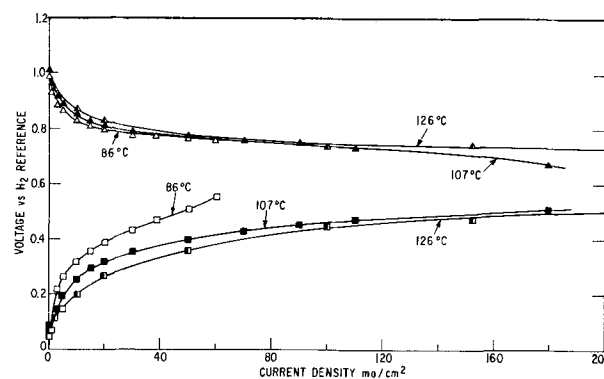


Fig. 6. Effect of temperature on electrode performance. $\text{CH}_3\text{OH}_{(g)}(\text{Pt})/\text{Cs}_2\text{CO}_3/\text{O}_2(\text{Pt})$.

could collect in the pores of the electrode. No clear-cut effects of concentration polarization in the electrolyte have been found.

Effect of fuel composition on performance.—The main effect of the mode of introduction of methanol is its partial pressure in the fuel stream. Therefore, the lower the partial pressure of methanol, the lower the limiting current density at the anode. When the methanol was introduced to the cell at a partial pressure of 0.1 atm (with water present at about 0.05 atm and nitrogen at 0.85 atm), the limiting current density at the anode was 20 to 30 ma/cm^2 at 130°C . On increasing the methanol partial pressure to 0.4 atm (by supplying a $\text{H}_2\text{O}-\text{CH}_3\text{OH}$ mixture to the air thermostat), current densities of over 200 ma/cm^2 could be supported. Finally, at nearly 1 atm of methanol, over 400 ma/cm^2 could be drawn without encountering a diffusion limitation. Below the limiting current corresponding to a given methanol partial pressure, the performance of the cell is nearly independent of methanol partial pressure in the range 0.1 – 1.0 atm .

Electrolyte composition effects.—The composition of the electrolyte *per se* has only a small effect on electrode performance in the range 50 – $95\text{ w/o Cs}_2\text{CO}_3$. Since the electrolytic conductivity is a reasonably strong function of electrolyte concentration, the internal resistance of the cell is affected accordingly. The concentration for maximum conductivity is about 5 normal (about $46\text{ w/o Cs}_2\text{CO}_3$; boiling point, 106°C). Therefore, in order to minimize I^2R losses, a minimum concentration of electrolyte consistent with the operating temperature will give minimum internal resistance at operating temperatures above 106°C .

A more subtle effect than electrolyte concentration is the activity (or chemical potential) of the water at the anode. The chemical potential of water at the anode determines whether or not carbon will deposit from the fuel at chemical equilibrium. The water activity in the electrolyte was controlled at or above the value corresponding to carbon deposition for the fuel being used in order to avoid the conditions under which carbon might deposit.

The carbon deposition boundaries for the CHO system have been computed and are available, together with gas phase compositions and explanatory calculations (26–29). Following the methods outlined previously (29), the partial pressure of water necessary to suppress carbon deposition from methanol at a total pressure of 1 atm and 130°C is about $2/3$ of an atmosphere. Therefore, the electrolyte should operate at a temperature not lower than about 15° below its boiling point. In addition, the methanol-water composition for most of the longer runs was made up such that on evaporation the water would have a partial pressure of about $2/3$ of an atmosphere. From the practical standpoint of maximizing performance, the best results are obtained when the electrolyte is operated about 5° – 10°C below its boiling point. Since several factors are important in setting the water activity in the fuel

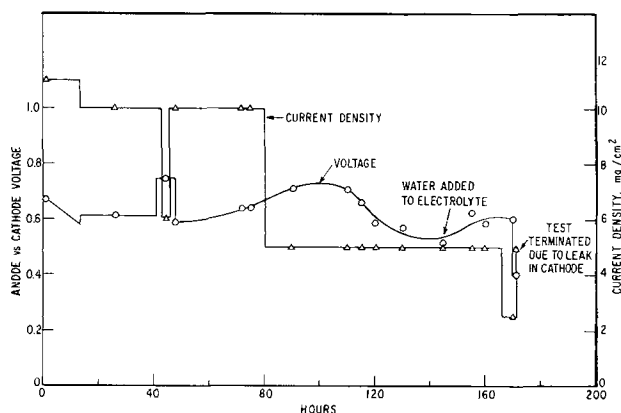


Fig. 7. Endurance test No. 1. CH_3OH in $\text{N}_2(\text{Pt})/\text{Cs}_2\text{CO}_3/\text{O}_2(\text{Pt})$, cell No. 19, $t = 128^\circ\text{C}$.

cell, and at 130°C , all of them indicate a necessity for a water partial pressure of about $2/3$ of an atmosphere, it is not a simple task to separate those which have the strongest relation to cell performance.

In any case, a set of experiments was performed at a constant temperature, while varying the water activity at the anode in order to determine if the above conclusions were reasonable. The water partial pressure was varied from 200 to 600 mm Hg at 130°C by varying the composition of the fuel mixture. The effect of the water partial pressure on the current density for a given anode overvoltage was determined in the range

$$\eta = (E_{\text{anode}} - E_{\text{rev CH}_3\text{OH}}) = 0.4 \text{ to } 0.65\text{V}$$

For all η , it was found that

$$i_{\eta=\text{const}} = \alpha p_{\text{H}_2\text{O}}^{0.4} + \beta$$

where α and β are constants.

Since the current density at a constant anode overvoltage was a relatively weak function of water partial pressure, it can be concluded that the water does not enter directly in any simple manner as a reactant into the over-all rate-determining process at the anode. Since the anodic oxidation of methanol may involve a combination of rate-limiting steps, it is not possible to draw any simple conclusions about the role of water at the anode.

Endurance Tests

Only two significant endurance tests were performed. Figure 7 shows a test lasting 171 hr on a cell that was fed with CH_3OH and H_2O vapors carried in N_2 gas, and operated at 128°C . The current density (shown on right-hand ordinate) was regulated and the anode vs. cathode voltage was measured as a function of time. During the test, no special attempt was made at holding the water activity absolutely constant. Since the test shown in Fig. 7, it has been determined that better performance is maintained throughout cell life if the water activity is maintained at a high level. Note that after the single water addition, the cell voltage did improve. The run was terminated at 171 hr due to a pinhole in the cathode, which allowed seepage of the electrolyte.

A second endurance test using a cell fed with $1/3$ CH_3OH and $2/3$ H_2O vapor at 130°C was carried out for over 560 hr. The water activity was maintained by adding 10 cc of H_2O to the upper electrolyte reservoir every 4 hr. The electrolyte was circulated at about 2 cc/min. The results of the test are shown in Fig. 8. Notice that there was a slight upward trend in the anode vs. cathode voltage at a constant current density. The electrolyte in the cell was not changed. It remained crystal clear after over 560 hr of operation.

Electrochemical Efficiency

Before discussing the fuel cell efficiency in detail, it is desirable to consider the over-all electrode and

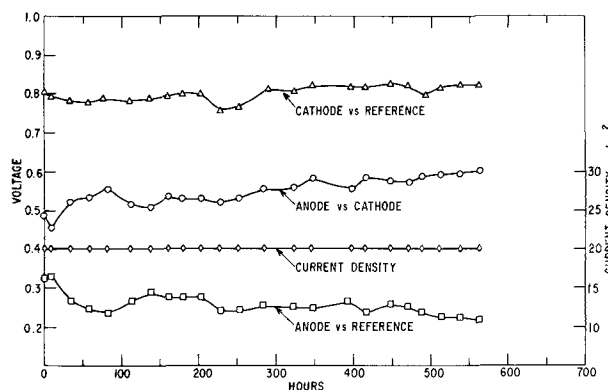


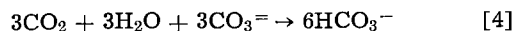
Fig. 8. Endurance test No. 2. $\text{CH}_3\text{OH}_{(\text{g})}(\text{Pt})/\text{Cs}_2\text{CO}_3/\text{O}_2(\text{Pt})$, cell No. 66.

cell reactions. In this carbonate fuel cell system, it has been shown by electrolyte analysis that during operation on CH_3OH there is usually no detectable hydroxyl ion present, but there is about 10% (on an equivalent basis) of bicarbonate present at 130°C . It is almost certain that the carbonate ion carries the current in the electrolyte and is a reactant at the anode. If carbonate is a reactant at the anode, the over-all anode reaction probably is

Anode reaction (over-all)



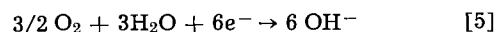
There is a consumption of carbonate in reaction [3]. If this process were to continue unchecked, the electrolyte would not be invariant, since no CO_2 is supplied to the cathode from an external source. It is postulated that CO_2 is reabsorbed by the electrolyte at the anode yielding bicarbonate



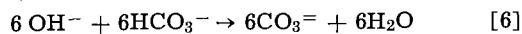
Reaction [4] was written using only three of the CO_2 molecules of reaction [3], allowing the fourth CO_2 molecule to be rejected from the system in the anode exit gas. The bicarbonate ions produced in reaction [4] are free to diffuse to the cathode.

At the cathode, there are two reasonable possibilities for the over-all electrode reaction

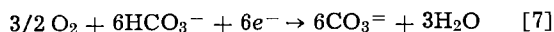
Cathode reaction (over-all):



followed by

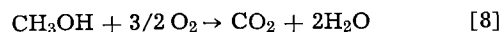


which could take place in the electrolyte phase adjacent to the cathode. In any event, the over-all reaction in the vicinity of the cathode is probably



The six carbonate ions are then free to recycle to the anode, where three of them may react according to reaction [3] and the other three according to reaction [4].

The over-all cell reaction is the sum of reactions [3], [4], and [7]



Current Efficiency.—Reaction [8] serves as a starting point for efficiency measurements and calculations. The current efficiency (30)

$$\text{Eff}_i = \frac{i}{NF \left(\frac{dn}{dt} \right)} \quad [9]$$

is a measure of the extent to which the conditions of only CO_2 and H_2O as oxidation products, and the absence of side reactions, are met.

The current efficiency was determined at a constant current density (usually 20–50 ma/cm^2) while feeding the methanol-water fuel mixture to the cell

at a constant, accurately known rate, and analyzing the exit gas from the cell.

The analyses were of two kinds: (a) Microdensity determination of condensed $\text{CH}_3\text{OH}-\text{H}_2\text{O}$ from the exit gas, combined with a weighing of the collected sample for a known time interval (methanol consumption material balance). (b) Gas phase (noncondensables) analysis on a chromatograph combined with accurate flow rate measurements (CO_2 production material balance).

As a sample of the methanol material balance: $\text{CH}_3\text{OH}/\text{Cs}_2\text{CO}_3/\text{O}_2$ fuel cell at 130°C ; current drawn = 500 ma = 44 ma/cm²; fuel feed rate: 0.012656 cc/min; fuel density: 0.914 g/cc; methanol content : 52 w/o; equivalents per mole of CH_3OH : 6; \therefore 0.012656 cc/min \times 0.914 g/cc = 0.011562 g/min; 0.011562 \times 0.520 = 0.0601g $\text{CH}_3\text{OH}/\text{min}$; $\frac{0.0601 \times 96,493 \times 6}{32.04 \times 60} = 1.813$

coul/sec in. Condensation rate at fuel cell exit: 0.3312g in 27 min = 0.01227 g/min; analysis of condensate: density = 0.9435 g/cc or 35.8 w/o CH_3OH ; this corresponds to 1.324 coul/sec out.

Therefore, the fuel consumed was 1.813 - 1.324 = 0.489 coul/sec which corresponds to the denominator of Eq. [9]. Thus

$$\text{Eff}_i = \frac{0.500}{0.489} = 1.023$$

Many other material balance runs indicate that the current efficiency is 1.00 ± 0.08 . The principal error results from the difficulty in performing precise microdensity determinations.

The carbon dioxide material balances show that

$$\frac{i}{NF \left(\frac{dn}{dt} \right)} = 0.98 \pm 0.03$$

where N is the theoretical number of coulombs of electricity produced per mole of CO_2 produced (six in this case).

The above material balance results indicate that no side reactions, diffusion of methanol to the cathode (or anywhere else) or incomplete oxidation reactions (formation of unconsumed intermediates) are taking place within the precision of the measurements.

Voltage Efficiency.—The voltage efficiency (30) of the cell during endurance tests was usually held at about

$$\text{Eff}_E = \frac{E}{E_{130^\circ\text{C}}} = \frac{0.55}{1.200} = 0.46 \quad [10]$$

Gibbs free energy efficiency.—The above results may be used to calculate a Gibbs free energy efficiency of

$$\text{Eff}_G = \text{Eff}_E \cdot \text{Eff}_i = 1.0 \times 0.46 = 0.46 \quad [11]$$

Comparative thermal efficiency (30).—The comparative thermal efficiency allows comparison of the fuel cell to heat engines. The value is

$$\text{Eff}_{CT} = \text{Eff}_G \cdot \frac{\Delta G_{400^\circ\text{K}}}{\Delta H_{\text{comb}, 298^\circ\text{K}}} = 0.46 \frac{-164,841.2}{-182,606.6} = 0.42 \quad [12]$$

Conversion per pass.—An important parameter related to the fuel cell efficiency is the fraction of the fuel fed to the cell which is converted to electricity in one pass through the anode compartment

$$\text{Conversion per pass} = \frac{i}{NF \left(\frac{dn'}{dt} \right)} \quad [13]$$

where (dn'/dt) is the fuel feed rate, rather than the fuel consumption rate (dn/dt) of Eq. [9]. The experimentally determined conversion per pass at 130°C in the neighborhood of 50 to 60 ma/cm² using a 52 w/o

Table I. Methanol cell electrochemical efficiencies

Representative operating point: 0.55v a-c, 20 ma/cm ²	
Current efficiency	1.00 \pm 0.08
CO_2 material balance	0.98 \pm 0.03
Voltage efficiency (at 0.55v)	0.46
Gibbs free energy efficiency	0.46
Comparative thermal efficiency	0.42
Conversion per pass	0.75-0.85

methanol-water mixture as fuel is 75 to 85%. This means that in a fuel battery system, very little fuel recovery and recycling is necessary.

Table I summarizes the various efficiency values for a methanol fuel cell operating at 120° - 130°C .

Product Removal

The removal of gaseous products from a gaseous fuel can be a difficult task, especially when high efficiency is desired. The products can form a diffusion barrier at the anode which may severely limit the current capability of the cell if they are not removed continuously and efficiently. Purging excess fuel through the anode compartment may accomplish the desired result, but can be very wasteful. Fortunately, in this particular system there are two alternate and complementary ways of removing CO_2 and H_2O and separating them from the methanol.

Carbon dioxide removal can be accomplished either by condensing the fuel away from the fuel cell exit stream and recycling the methanol, or by absorbing the carbon dioxide in the circulating electrolyte and allowing it to be desorbed from the electrolyte at another point in the system, e.g. an electrolyte reservoir. It was found experimentally that at a current density of 50 ma/cm² at 130°C , about 60-70% of the carbon dioxide was removed by the slowly circulating electrolyte. If the electrolyte was not circulated, all of the CO_2 was found in the anode compartment. Figure 9 shows the fraction of the theoretical carbon dioxide production found in the anode exit gas for flowing and nonflowing electrolyte. The flow rate when on was about four cell volumes per minute.

The removal of CO_2 by the electrolyte can be an important method for preventing the establishment of a diffusion layer of carbon dioxide in the pores of the anode. This mechanism may be unique to carbonate electrolyte systems.

Water removal can take place by means of the anode exit gas or the cathode exit gas if the electrolyte is not circulated, or by evaporation from the reservoir if a circulating electrolyte is used. In most of the present experiments, the electrolyte was circulated, and a small amount of makeup water was required (1 to 2 cc/hr).

Performance on Other Fuels

Cells were briefly tested on several fuels other than methanol. Only CO showed performance equivalent to that of methanol. The results are shown in Fig. 10 as

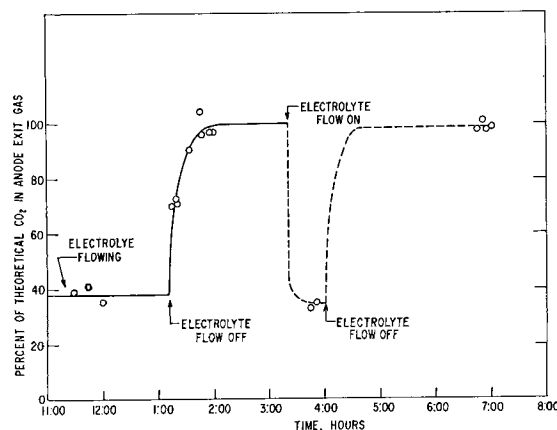


Fig. 9. Carbon dioxide production and removal. $\text{CH}_3\text{OH}_{(g)}$ (Pt)/ $\text{Cs}_2\text{CO}_3/\text{O}_2$ (Pt), cell No. 63; 50 ma/cm², 130°C .

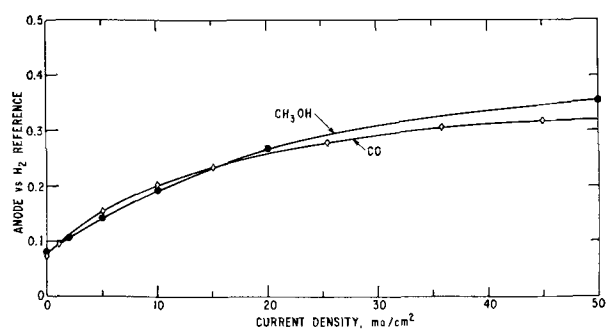


Fig. 10. Performance on carbon monoxide fuel (Pt)/Cs₂CO₃/O₂(Pt), $t = 130^{\circ}\text{C}$.

anode vs. reference H₂ voltages as a function of current density for direct comparison. No attempt was made to optimize operating conditions or electrode preparation for any of the fuels except methanol.

Electrolyte Invariance

It is difficult to prove electrolyte invariance by any single set of experiments. Various approaches have been taken, and all seem to indicate that the cell performance and electrolyte composition do not change over operating times of at least hundreds of hours. All material balances have shown that the fuel is consumed at only the rate required by the current drawn, and CO₂ is produced at the theoretical rate. This means that within the experimental error shown in Table I no fuel is reacting with or dissolving in the electrolyte. No fuel or CO₂ is transported across the electrolyte to the cathode. No CO₂ was ever found in the oxygen compartment. No partial oxidation products are left in the electrolyte.

Electrolyte samples have been analyzed for oxidizable organic material, and none has been found beyond experimental error of the analytical procedure (tenths of milli-equivalents per cell volume). Samples of electrolyte taken after 200 and 500 hr of continuous running on CH₃OH have been crystal clear and show no accumulation of colored material. The analyses of these samples showed no oxidizable organic material. Certainly it is likely that nothing which causes performance degradation accumulates in the electrolyte as is evidenced by endurance test No. 2, Fig. 8.

Conclusions

1. An intermediate temperature methanol fuel cell using an aqueous Cs₂CO₃ electrolyte has been shown feasible for power densities of 40 to 45 milliwatts/cm², on an I²R-free basis.
2. Material balances showed complete conversion of CH₃OH to CO₂ and H₂O.
3. Endurance tests exceeding 560 hr of continuous performance at 20 ma/cm² have been performed with steady (or slightly increasing) performance.
4. Electrolyte invariance has been shown.
5. Methanol does not migrate to the cathode causing performance decreases.
6. Carbon monoxide performance was found to be good, leading to the suggestion that a cell running on H₂ + CO fuel mixtures from a simple steam reformer, with Cs₂CO₃ electrolyte might be of interest.

Acknowledgments

The authors wish to thank S. Gilman for the use of some Teflon parts used in this work. They are grateful for the helpful discussions of A. D. Tevebaugh, L. W. Niedrach, and W. T. Grubb. D. W. McKee's aid with some of the gas analyses and his helpful comments are appreciated. They wish to thank G. J. Holm, A. Breitenstein, and Miss C. J. Michalske for their aid in various phases of this work. The encouragement of H. A. Liebhafsky is appreciated.

Manuscript received Feb. 6, 1964; revised manuscript received May 20, 1964. This paper was presented at the Washington Meeting, Oct. 11-15, 1964. In part this work was made possible by the support of the Advanced Research Projects Agency (Order No. 247) through the United States Army Engineer Research and Development Laboratories under Contract No. DA-44-009-ENG-4909.

Any discussion of this paper will appear in a Discussion Section to be published in the June 1965 JOURNAL.

REFERENCES

1. E. Müller, *Z. Elektrochem.*, **28**, 101 (1922).
2. S. Tanaka, *ibid.*, **35**, 38 (1929).
3. M. W. Breiter and S. Gilman, *This Journal*, **109**, 622 (1962).
4. M. W. Breiter, *Electrochim. Acta*, **7**, 533 (1962).
5. T. O. Pavla, *Ann. Acad. Sci. Fennicae, Ser. A*, **II**, No. 59 (1954).
6. S. Gilman and M. W. Breiter, *This Journal*, **109**, 1099 (1962).
7. W. Vielstich, Paper presented at Electrochemical Society Meeting, Indianapolis, May 1961, Abstract No. 113.
8. D. E. Icenhower and A. P. Bond, Paper presented at Electrochemical Society Meeting, Detroit, October 1961, Abstract No. 19.
9. R. P. Buck and L. R. Griffith, *This Journal*, **109**, 1005 (1961).
10. M. Shaw, W. Subcasky, and G. Frick, Paper presented at Electrochemical Society Meeting, Detroit, October 1961, Abstract No. 17.
11. D. B. Boies and A. Dravnieks, Paper presented at Electrochemical Society Meeting, Boston, September 1962, Abstract No. 48.
12. O. Bloch, M. Prigent, and J. C. Balanceanu, Paper presented at Electrochemical Society Meeting, Indianapolis, May 1961, Abstract No. 116.
13. G. Cohn, *Proc. 15th Ann. Power Sources Conf.*, Atlantic City (1961), p. 12.
14. B. L. Tarmy, *Proc. 16th Ann. Power Sources Conf.*, Atlantic City (1962), p. 29.
15. H. Krupp, H. Rabenhorst, G. Sandstede, G. Walter, and R. McJones, *This Journal*, **109**, 553 (1962).
16. H. G. Hunger, *Proc. 14th Ann. Power Sources Conf.*, Atlantic City (1940), p. 55.
17. J. F. Yeager, Paper presented at Electrochemical Society Meeting, Indianapolis, May 1961, Abstract No. 109.
18. P. G. Grimes, B. Fiedler, and J. Adam, *Proc. 15th Ann. Power Sources Conf.*, Atlantic City, 1961, p. 29.
19. J. E. Wynn, *Proc. 14th Ann. Power Sources Conf.*, Atlantic City, 1960, p. 52.
20. M. J. Schlatter, Paper presented at American Chemical Society Meeting, Chicago, September 1961.
21. O. J. Aldhart, Final Report of Englehard Industries to USASRD for period July 1, 1960—June 30, 1962.
22. B. L. Tarmy, E. L. Holt, D. G. Levine, A. W. Moerekofer, J. A. Shropshire, and C. H. Worsham, Final Report of Esso Research and Eng. Co. to USAELRDL for the period Jan. 1, 1962—Dec. 31, 1962.
23. E. J. Cairns and D. I. Macdonald, Paper presented at Electrochemical Soc. Meeting, New York, October 1963, Abstract No. 30; also, *Electrochem. Tech.*, **2**, 65 (Mar.-Apr. 1964).
24. L. W. Niedrach and H. R. Alford, Paper presented at Electrochemical Society Meeting, Washington, D. C., Oct. 1964.
25. K. Kordes and A. Marko, *This Journal*, **107**, 480 (1960).
26. E. J. Cairns and A. D. Tevebaugh, G. E. Research Lab. Rept. No. 63-RL-3222C (February 1963).
27. A. D. Tevebaugh and E. J. Cairns, G. E. Research Lab. Rept. No. 63-RL-3246C (February 1963).
28. E. J. Cairns and A. D. Tevebaugh, G. E. Research Lab. Rept. No. 63-RL-3281C (April 1963).
29. E. J. Cairns, A. D. Tevebaugh, and G. J. Holm, *This Journal*, **110**, 1025 (1963).
30. H. A. Liebhafsky and E. J. Cairns, Fuel Cells Manual, Published by Amer. Inst. Chem. Engrs. (1963).

Corrosion of Iron and Steel in $\text{NH}_4\text{NO}_3\text{-NH}_3\text{-H}_2\text{O}$ Solutions

G. Schick and H. H. Uhlig

Corrosion Laboratory, Massachusetts Institute of Technology, Cambridge, Massachusetts

ABSTRACT

Iron corrodes in aqueous $\text{NH}_4\text{NO}_3\text{-NH}_3$ solutions at high rates (over 2 in. per year) depending on NH_3 concentration and on certain metallurgical factors. The corrosion product by analysis is found to be $[\text{Fe}(\text{NH}_3)_6](\text{NO}_3)_2$ in presence of NH_3 , and Fe_3O_4 in its absence. Cold-rolled iron corrodes more rapidly than annealed or quenched iron. The cause is related to orientation during rolling of the (001) face of iron parallel to the surface. This face is the one that apparently corrodes most rapidly. Orientation is partially destroyed by annealing or quenching. Such effects are marked only when rate of complex formation is controlling; when other reactions control, the effect of cold work is not pronounced. The corrosion rate is sensitive to alloyed nitrogen but not to alloyed carbon. Zone-refined iron corrodes at a rate comparable to that of annealed mild steel. Iron containing 0.04% nitrogen corrodes at a lower rate, or about $\frac{1}{4}$ that of zone-refined iron. Inhibitors such as SCN^- appear to interfere with the cathodic reduction of NO_3^- to NH_3 .

The first observations on a high rate of attack of iron in $\text{NH}_4\text{NO}_3\text{-NH}_3$ solutions were apparently reported by Haber (1) and his students who described streaming yellow corrosion products from an iron cathode during electrolysis at 0.02 amp/dm² of saturated NH_4NO_3 at 0°C. Employing a Pt cathode instead, the resulting catholyte was also corrosive to iron, apparently forming an iron-ammonium complex. Surprisingly, they reported no attack of iron in $\text{NH}_4\text{NO}_3\text{-NH}_3$ solutions without current flow. The latter situation, however, as subsequent investigators showed, turned out to be an instance of passivity which cathodic polarization destroyed, rather than an inherent lack of reactivity. Weitz and Muller (2) described the preparation of ferrous ammonium complexes of the general formula $[\text{Fe}(\text{NH}_3)_6]^{++}$. The corresponding solid nitrate crystallized as green octahedra. When dissolved, and heated slowly, the compound on reaching 90°C quickly decomposed, depositing black Fe_3O_4 . They ascribed the oxide $\text{FeO}\cdot 2\text{Fe}_2\text{O}_3$ obtained earlier through decomposition of solutions employed in experiments by Kaufmann (3) similar to those of Haber, as being caused by presence of nitrite. Nilsson (4) found that iron could become passive in aqueous $\text{NH}_4\text{NO}_3\text{-NH}_3$ solutions without appreciable corrosion. On the other hand, iron when activated electrolytically, such as by galvanic contact with zinc, or mechanically, or chemically, resulted in a high rate of attack. Haber's observation on lack of reactivity in $\text{NH}_4\text{NO}_3\text{-NH}_3$ solutions was thereby explained.

This general subject is of interest to corrosion science because of the phenomenally high reaction rates of iron (over 2 in. penetration per year) in contact with nitrate-ammonia mixtures and the need to understand the mechanism of such high rates. It is also of practical interest to the fertilizer industry which employs aqueous solutions of this kind for supplying available nitrogen to the soil. Several papers have been published on the corrosion characteristics of nitrate-ammonia solutions, including the use of inhibitors to reduce rate of attack (5-8). The effect of metallurgical factors, identification of corrosion products and a plausible corrosion mechanism have been treated in previous publications; the present investigation explores and extends these studies in further detail.

Experimental

Materials investigated included a commercial 0.10% C mild steel (0.005% N, 0.36% Mn, 0.03% Ni, 0.04% Cu, 0.01% P, 0.03% S, 0.004% As) a pure 0.094% C steel (0.006% N), a pure 0.043% N steel (0.001% C) and zone-refined iron (<0.001% C, 0.0003% N). The

pure steels were prepared in vacuum in alumina crucibles by induction melting of electrolytic iron and spectroscopic graphite in the case of carbon steel, and by melting under a purified nitrogen atmosphere in the case of nitrogen steel. In either instance, castings were obtained from the melt by drawing into 9 mm Vycor tubing and water quenching (employing a helium atmosphere in the case of the carbon steel). Ingots were homogenized in vacuum at 1050°C for 18 hr and air cooled. They were subsequently cold-rolled to 0.040 in. (0.10 cm) strip.

Heat-treatment when required was carried out in helium purified over copper at 450°C employing a liquid nitrogen cold trap. Specimens, contained in a quartz tube, were air-cooled from furnace temperatures, the specimens remaining in helium during cooling. Quenching was accomplished by placing specimens in a vertical furnace at 950°C for 30 min in helium and dropping them directly into ice water.

Cold rolling of mild steels was carried out to the extent of 70% reduction in thickness; for 0.094% C and 0.043% N steels it was 85%; and for zone-refined iron 50%.

Specimens measured 3.8 x 2.5 x 0.1 cm; they were abraded, finishing with No. 600A emery paper. They were then pickled in 1:1 HCl at 60°C for 5 min and washed in water followed by successive immersion in acetone and benzene. Specimens of zone-refined iron were cut from the original ingot and, in order to save material, were not trimmed to standard size.

Corrosion rate measurements were carried out in 250 ml glass containers with specimens suspended from glass frames, similar to the arrangement used by Hackerman *et al.* (7). The bottles were sealed by means of a Bakelite screw cap with a polyvinyl gasket to prevent loss of NH_3 . During tests, the bottles were placed in a 25°C thermostated room. The ratio of specimen area to solution volume was in the order of 1 dm²/liter. After 48 hr exposure, specimens were washed and brushed under water, then immersed in acetone followed by benzene. In the $\text{NH}_4\text{NO}_3\text{-NH}_3\text{-H}_2\text{O}$ solutions, washing alone produced clean and bright surfaces. In $\text{NH}_4\text{NO}_3\text{-H}_2\text{O}$ solutions a black adherent corrosion product was removed by immersing specimens in boiling 10% NaOH containing 100g Zn powder per liter.

Potential measurements were carried out using mild steel electrodes partially immersed in solution, employing a salt bridge containing the same electrolyte. The reference electrode was Ag-AgCl in 0.1N KCl. Polarization measurements were conducted in an all-glass cell arranged so that a Luggin capillary con-

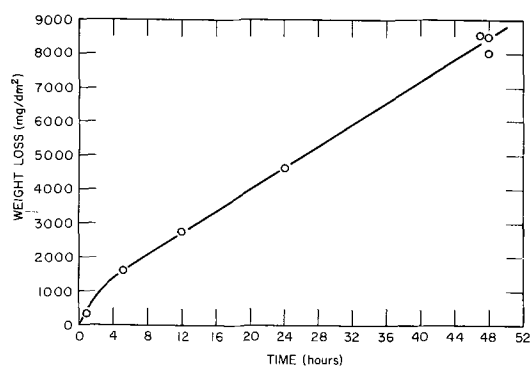


Fig. 1. Weight loss of 0.06% C mild steel vs. time in 44.4% NH_4NO_3 + 11.1% NH_3 , balance H_2O , 25°C.

taining the same solution as the electrolyte of the test was located near a mild steel electrode. Steady-state potentials at a given current density were usually achieved within 1 hr or less.

Results

Corrosion rates became constant after an initial higher rate lasting for 1 or 2 hr. Figure 1 shows data for cold rolled 0.06% C mild steel exposed for periods up to 48 hr, each point of which is the average for 3 specimens. The steady-state corrosion rate is 4000 mdd (mg/dm²/day) or 0.73 ipy (inch penetration per year). This steel, the supply of which ran out, was replaced by the 0.10% C mild steel described earlier. The mild steel of Fig. 1 contained 0.003% N, 0.11% Cu, 0.012% As, and amounts of other listed elements comparable to the 0.10% C steel. Its corrosion rate in 44.4% NH_4NO_3 -5.9% NH_3 was 60% that of the 0.10% C steel illustrating the effect of minor composition variations. This matter is discussed later. Response to heat-treatment after cold work was similar for both steels, but differed in detail. Data for the 0.06% C steel are given in Fig. 2 for two different composition NH_4NO_3 - NH_3 - H_2O solutions. Each point is the average for 3 specimens, maximum deviation from the average being 10% or less. The steel immersed in 40.0% NH_4NO_3 , 20.0% NH_3 showed almost no response to annealing whereas in the solution containing 11.1% NH_3 , mild steel annealed at 900°C (pearlite plus ferrite), corroded at a rate about 1/2 that of the cold-rolled steel. This difference provides evidence that the mechanism of attack changes with composition of the solution.

Effect of heat-treating cold-rolled 0.10% C mild steel is shown in Fig. 3 for a solution containing 44.4% NH_4NO_3 , 5.9% NH_3 , and also for 44.4% NH_4NO_3 in absence of free NH_3 . Each point is the average for 3 specimens, maximum deviation being 5% or less for the first solution and 10% for the second. The effect

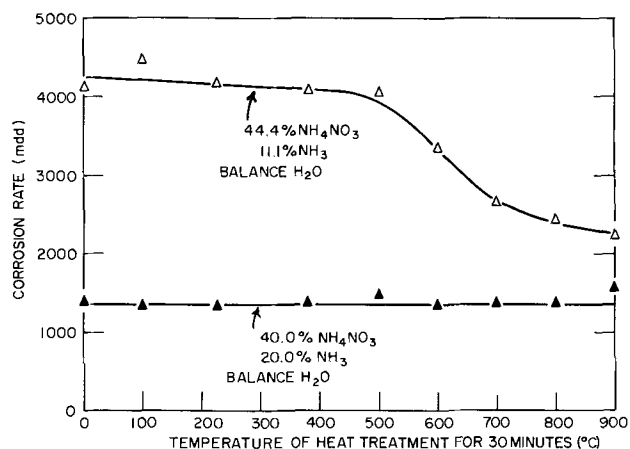


Fig. 2. Corrosion rates of cold rolled and heat treated 0.06% C mild steel, 25°C, 48-hr exposure.

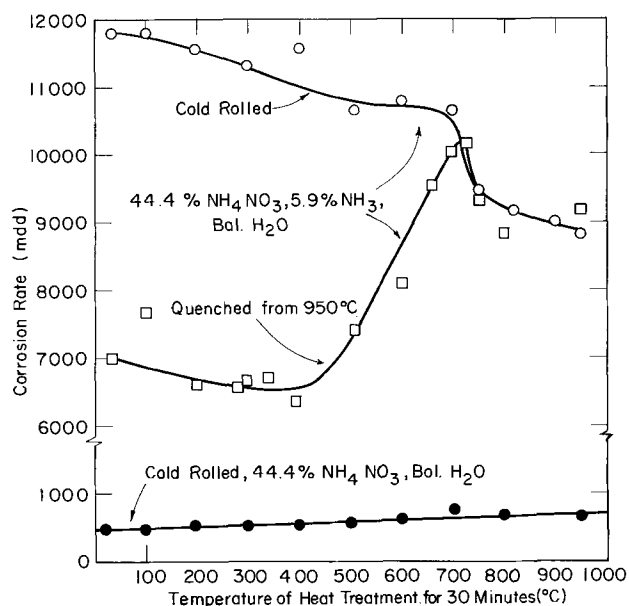


Fig. 3. Corrosion rates of cold rolled and quenched 0.10% C mild steel, 25°C, 48-hr exposure.

of heat-treatment is appreciable for the first solution, the annealed steel corroding at a rate which is 75% that of the cold-rolled steel. The corrosion rate is much less in NH_4NO_3 solution, and heat-treatment increases the rate. The corrosion product in NH_4NO_3 was in the form of a thin black, firmly adherent layer. This proved by x-ray to be mostly Fe_3O_4 . In the 5.9% NH_3 solution, the product was voluminous yellow-green, nonadherent and water soluble. Exposed to air, it became red-brown and insoluble.

Figure 3 also contains data for quenched mild steel (in ice water from 950°C), subsequently heat treated in helium at various temperatures for 30 min. Specimens were pickled in 1:1 HCl before immersion. Each point represents an average of 3-5 specimens. Maximum deviation from the average was 25% for specimens heat treated at 200°C; they were within 15% for specimens heat treated at 600°C and were less than 10% for all other conditions. The data show that quenched steel (martensite and ferrite) corrodes at a lower rate, or at about 60%, that of cold-rolled steel. Surprisingly, heat-treatment at temperatures near the critical temperature (723°C) increases the rate by 45% over that of the quenched steel. The rate for the pearlitic structure resulting from heat-treatment above the critical temperature remains high and is the same or slightly lower than for specimens heat treated at 700°-720°C. Corrosion of specimens was uniform and showed no evidence of pitting or of preferred grain boundary attack.

Effect of carbon and nitrogen.—The steels discussed above frequently became passive in the corrodent and had to be activated by brief contact with a piece of zinc, the galvanic action serving to disrupt the passive state in accord with Nilsson's description (4). This factor undoubtedly entered as an explanation for the lack of reactivity of quenched mild steel in 66.6% NH_4NO_3 , 16.7% NH_3 , 16.7% H_2O as reported by Hackerman *et al.* (7). We found that tendency to passivate was even more pronounced with zone-refined iron and the pure steels. These materials almost always became passive remaining without evidence of attack for a period of at least five days which was the maximum period of observation. They had to be activated by brief contact with zinc before the start of each corrosion experiment.

The pure 0.094% C steel corroded in 44.4% NH_4NO_3 , 5.9% NH_3 solution at the highest rate when cold rolled, 17% less as quenched, and 10% less as annealed (Table I). The rate for cold-rolled material was lower than

Table I. Comparative corrosion rates of pure iron, pure C and N steels, and commercial mild steel in 44.4% NH_4NO_3 , 5.9% NH_3 , Bal. H_2O , 25°C, 48 hr exposure

Specimen	Average corrosion rate								
	Cold rolled	Max. dev.	% Thickness red.	Cold rolled, annealed 800°C, 30 min	Max. dev.	Quenched from 950°C	Max. dev.	Quenched, heat-treated 800°C, 30 min	Max. dev.
Zone-refined Fe (1 spec.)	6990 mdd	—	50	8770 mdd	—	—	—	—	—
0.094% C steel (3 spec.)	8770	425 mdd	85	7940	208 mdd	7270	93	7870	780
0.043% N steel (2-3 spec.)	3280	1220	85	2170	310	1770	250	1420	50
0.10% C mild steel (3 spec.)	11700	115	70	9210 (820°C, 30 min)	140	7010	380	8870	720

for cold-rolled 0.10% C mild steel, but with less difference for the quenched or annealed steels.

Zone-refined iron when cold rolled corroded at a somewhat lower rate than when annealed. However, its rate cold-rolled was lower than for cold-rolled mild steel and also lower, although with less difference, than cold-rolled 0.094% C steel. In the annealed state the reverse situation applied, zone refined iron corroding slightly higher than 0.094% C steel and at about the same rate as annealed mild steel. Grain orientation was found to have a large effect on the rate as was clearly visible in the case of the large grain size zone-refined iron (Fig. 4). Levels of attacked grains differed by fractions of a millimeter. It is probable, therefore, that differences in crystal orientation also entered into accounting for rates of cold-rolled and annealed specimens, with soft zone-refined iron being oriented less through 50% cold reduction than the harder mild steel cold reduced 70%.

Perhaps unexpected is the much lower rate observed for 0.043% N steel which in all cases was lower than for any of the other steels including zone-refined iron. Nitrogen in iron behaves quite differently from carbon with respect to the corrosive media presently considered.

Effect of NH_3 concentration.—Cold-rolled 0.10% C mild steel was exposed to 44.4% NH_4NO_3 containing NH_3 varying from 1 to 20% by weight. Corrosion rates are plotted in Fig. 5, each point of which represents the average for 3 specimens. Maximum deviation of individual specimens from the average was 5% or less, but data at 5.9% NH_3 differ from Fig. 3 by 15%, perhaps because of the difficulty of maintaining free NH_3 concentration at the prescribed level. The corrosion rate is relatively low in solutions free of NH_3 , reaches a maximum about 30 times higher than the initial low rate between 5 and 11% NH_3 , and then falls to 6 times the initial rate at 15–20% NH_3 . Corrosion products were black-green in 1–3% NH_3 and yellow-green in 5–20% NH_3 with adherence being noticeably greater between 14 and 20% NH_3 . Some pitting occurred in the 15–20% NH_3 solution; otherwise attack was uniformly distributed. The weight-loss results are similar to those reported earlier by Goodrich and Hackerman (8).

Effect of inhibitors.—Various inhibitors are effective for reducing the corrosion rate. Hackerman, Hurd, and Snavely (7) found 0.04% or more NH_4SCN , 0.1% thiourea, and 0.05% mercaptoethanol plus 0.05% so-



Fig. 4. Specimen of zone-refined iron after 48 hr in 44.4% NH_4NO_3 , 5.9% NH_3 solution, 25°C, showing unequal attack of grains.

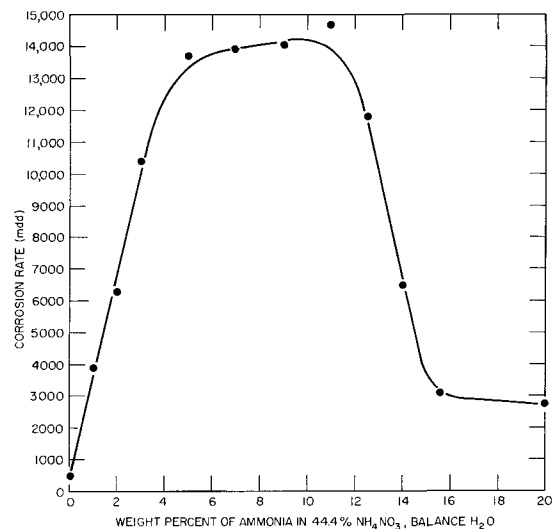


Fig. 5. Effect of NH_3 on the corrosion rate of cold-rolled 0.10% C mild steel, 25°C, 48-hr exposure.

dium arsenite to be among those that were most efficient. Our tests using cold-rolled 0.10% C mild steel in 44.4% NH_4NO_3 , 5.9% NH_3 solution are reported in Table II. Other than these results, it was also found that one commercial pickling inhibitor was excellent. The most effective inhibitor in our series was mercaptobenzothiazol.

Discussion

Information on the mechanism of attack was obtained through experiments on galvanic coupling, polarization, and analysis of corrosion products. Both cold-rolled and annealed 0.10% C mild steel specimens were coupled to an equal area of Pt, cementite, or nitrated electrolytic iron and immersed, as before, in 44.4% NH_4NO_3 , 5.9% NH_3 , balance H_2O . The specimens were initially activated by contact with zinc. No changes in corrosion rate, beyond the experimental error, were observed compared with rates for steel specimens uncoupled. Corrosion, therefore, in the above solution is largely anodically controlled.

This conclusion was confirmed by polarization measurements employing annealed mild steel specimens immersed in the same solution. The corrosion poten-

Table II. Effect of inhibitors on corrosion of cold-rolled 0.10% C mild steel in 44.4% NH_4NO_3 , 5.9% NH_3

Inhibitor	% Inhibition
	$\frac{\text{Wt. loss (no inhib.)} - \text{wt. loss (inhib.)} \times 100}{\text{wt. loss (no inhib.)}}$
0.5% Na_3PO_4	35%
0.05% $(\text{NH}_4)_2\text{HPO}_4$	44
0.1% Guanilurea	37
0.05% Na_3AsO_3	96.8
Diphenylthiourea (sat'd)	97.5
0.5% 1-3 Diethylthiourea	99.8
0.5% NH_4SCN	99.8
Mercaptobenzothiazol (sat'd)	99.9

Table III. Corrosion potentials of 0.10% C mild steel, 25°C, 24 hr immersion

Condition of electrode	% NH ₄ NO ₃	% NH ₃	Pot. H ₂ Scale
Annealed 950°C, 30 min	44.4	0.0	-0.34 volt
Annealed 950°C, 30 min	44.4	5.9	-0.50
		+0.5% NH ₄ SCN	-0.69
Annealed 950°C, 30 min	44.4	11.1	+0.03 (passive)
Annealed 950°C, 30 min	40.0	20.0	-0.52 (active)
Cold rolled	44.4	5.9	-0.59
Quenched from 950°C	44.4	5.9	+0.05 (passive)
			-0.49 (active)
			-0.49

tial at 25°C on the hydrogen scale several minutes after immersion was -0.49v. At current densities of 3.6, 11.4, and 22.8 ma/cm², mild steel as cathode was polarized 13, 33, and 50 mv, respectively, whereas as anode it was polarized 1580, 1630, and 1660 mv, respectively.

Annealed mild steel in 44.4% NH₄NO₃ behaved similarly. At current densities of 3.6, 11.4, and 22.8 ma/cm², mild steel as cathode polarized 9, 125, and 150 mv; and as anode 2090, 2150, and 2180 mv, respectively. However, both in this solution and in the previous solution, anodic polarization induced passivity so that polarization measurements are more properly an index of reactions occurring in the passive state. On the other hand, the foregoing galvanic coupling experiments, in view of the fact that corrosion rates remained high, reliably indicated anodic control in the active state.

Previous investigators have proposed that NH₃ forms a complex with Fe⁺⁺ accounting for the high corrosion rates in NH₄NO₃-NH₃ solutions. This is confirmed by corrosion potentials listed in Table III. Potentials of mild steel annealed at 950°C and immersed in 44.4% NH₄NO₃ solution become more active in the order of 160-250 mv through additions of NH₃. This shift is accounted for by reduced Fe⁺⁺ activity of the complex. At 20% NH₃, the potential remains active despite a falling off of the corrosion rate and is slightly more active compared to potentials in the 5.9% NH₃ solution. This behavior indicates that the complexing tendency continues at the higher NH₃ concentrations and suggests that the decrease in corrosion rate is caused by an inhibiting effect of NH₃ on the cathodic reaction. For example, increased adsorption of NH₃ on cathodic surfaces of iron could exert such an effect by impeding reduction of NO₃⁻.

Analysis of the corrosion product also confirmed that a complex is formed. Formation of a complex, although surmised by earlier investigators, had never been confirmed by actual analyses. The product obtained by exposing 0.10% C mild steel to 44.4% NH₄NO₃, 5.9% NH₃ solution after 48 hr immersion was dried in a helium atmosphere. In order to avoid oxidation, manipulations were carried out by and large in a dry box through which helium passed continuously. The dried product was transferred to weighed test tubes and stoppered. After dissolving the product in HCl, iron was determined colorimetrically using the ortho-phenanthroline method. Samples of product for ammonia and nitrate analysis were dissolved in dilute H₂SO₄, and then 33% NaOH in proper amount introduced, whereupon NH₃ was distilled into 0.02N HCl which was back titrated. To include NO₃⁻, the procedure was repeated after boiling the acid solution with an excess of iron powder in order to reduce nitrates to ammonia. Final results are given in Table IV. They also include chemical analysis of the black product obtained from 44.4% NH₄NO₃ solution, qualitative analysis of which showed absence of NH₃ or NO₃. X-ray analysis confirmed that the black product was largely Fe₃O₄.

Data of Table IV show that the water-soluble yellow-green product has the general composition [Fe(NH₃)₆](NO₃)₂. The product was not found to contain nitrites, contrary to reports by Goodrich and Hackerman (8). Treatment of the corrosion prod-

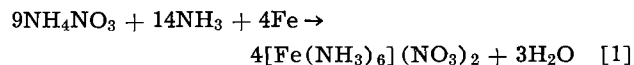
Table IV. Analysis of mild steel reaction products

Corrodent	Analysis of dried corrosion product		
	% Fe	% NH ₃	% NO ₃
44.4% NH ₄ NO ₃ + 5.9% NH ₃	18.58	35.69	44.00
As calculated for [Fe(NH ₃) ₆](NO ₃) ₂	19.80	36.20	44.00
	% Fe ⁺⁺	% Fe ⁺⁺⁺	Ratio Fe ⁺⁺⁺ /Fe ⁺⁺
44.4% NH ₄ NO ₃	18.02	48.63	2.7
As calculated for Fe ₃ O ₄	24.15	48.30	2.0

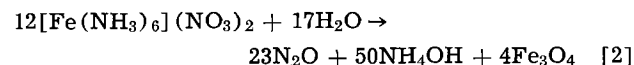
uct with 1:1 HCl did not produce evidence of NO or NO₂ evolution as would have been the case if NO₂⁻ were a component. It is concluded, therefore, that NO₃⁻ during the corrosion reaction is reduced at cathodic areas directly to NH₃. This was also the conclusion of Libinson *et al.* (5).

Heating the yellow-green corrosion product to 90°C produced gas evolution and a black precipitate, a reaction which had also been observed earlier by Haber (1) and by Kaufmann (3). A piece of burning wood glowed when inserted in the gas, indicating the presence of N₂O. The black precipitate according to Weitz and Muller (2) is Fe₃O₄.

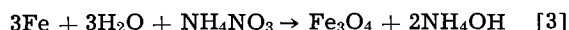
The corresponding over-all reaction which accompanies corrosion of iron, forming the observed complex is the following



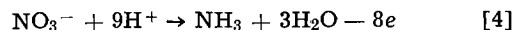
The complex decomposes on heating, presumably as follows



On the other hand, when iron corrodes in NH₄NO₃ in absence of NH₃, the reaction is



The action of inhibitors is probably one of adsorbing on the iron surface but with preferential adsorption on cathodic areas. They thereby increase cathodic polarization and impede the corrosion reaction. In the case of 0.5% NH₄SCN, the corrosion potential is shifted correspondingly in the active direction by 190 mv. This agrees with similar potential data of Goodrich and Hackerman (8) who found that other inhibitors also induce a more active potential. This change of potential suggests that the cathodic reaction



is the reaction that is largely inhibited by adsorbed SCN⁻.

Passivity of iron in this system appears to be no different than in other solutions. The potential of passive iron, cold rolled or annealed, is 540-550 mv more noble than active iron. Potentiostatic polarization curves (8) are typical of passive metals in general. Activation can be induced electrochemically and mechanically precisely as can activation of passive iron in other aqueous media. No unique reason exists, therefore, for believing that a protective Fe₂O₃ film forms in NH₄NO₃-NH₃ solutions. The passive film, as in the case of nitric acid, chromate, or nitrite passivation, may also be considered to be a chemisorbed oxygen-OH or oxygen-H₂O complex.

The effect of cold work is to increase corrosion in the 5.9% NH₃ solution, but with rather small effect on the corrosion potential. Hence, both the anodic and cathodic reactions are affected. Increase in carbon content seems to increase the rate in accord with greater cathodic area provided by the corresponding cementite. The effect is not marked, however, as is seen by the prevailing high corrosion rate of zone-refined iron which contains <0.001% C. Goodrich and

Hackerman (8) also found that the effect of carbon in steels was not large. Their lower result for zone-refined iron may have been caused by passivity over part of the exposure test. Similarly Libinson (5) reported that cast iron normally containing high carbon corrodes at a rate only slightly higher than that of ordinary iron.

Present evidence favors grain orientation as the important factor in accounting for differences between cold-worked and quenched mild steel. Cold rolling orients the (001) face of iron parallel to the rolled surface and it is this face which presumably corrodes most rapidly. Quenching produces a more random orientation of crystals which exhibit, on the average, a lower corrosion rate. The extent of preferred orientation existing after a given reduction of thickness probably depends on grain size and composition so that all steels respond qualitatively but not necessarily quantitatively to a given process of cold rolling. On this basis, zone-refined iron appears to be oriented less by cold rolling than the other steels.

Heat-treatment of cold-rolled and quenched mild steel above the critical temperature (723°C) re-oriens the grains, and the corrosion rate then becomes the same for both cold-rolled and quenched steels (Fig. 3). The increase in rate for the quenched steel just before reaching the critical temperature may be caused by recrystallization with some preferred orientation dictated by past rolling history. It is not caused by Fe_3C precipitation from martensite because this should produce the highest corrosion rate at 400°C , as is observed in the corrosion of quenched carbon steel exposed to sulfuric acid (9). Instead, the rate climbs for heat-treatment temperatures above 400°C and increases until the critical temperature is reached.

The effect of grain orientation is most pronounced when rate of complex formation controls the corrosion process. In NH_4NO_3 solutions free of NH_3 , the complex does not form, the corrosion rate is lower, and heat-treatment and cold work no longer have as large an effect. The higher rate in this medium for annealed compared to cold-rolled steels suggests that the reaction in NH_4NO_3 is influenced by different crystal faces than in NH_4NO_3 - NH_3 solutions. Similarly in 40% NH_4NO_3 , 20% NH_3 solution, in which corrosion control is apparently shifted to cathodic areas, effects of heat-treatment and cold work are not important. From this

observation, reduction of NO_3^- to NH_3 is apparently not greatly sensitive to crystal face.

Lack of potential difference between cold-rolled and annealed steel also supports crystal orientation as cause of the altered corrosion rate. The most reactive crystal faces corrode first, regardless of crystal orientation, leaving behind the least reactive face and a rougher surface (10). The increased surface area leads to a higher corrosion rate, but has no effect on potential which is always measured for the same least reactive face regardless of crystal orientation.

Iron containing nitrogen corrodes much less than any of the other materials whether cold-worked, annealed, or quenched. A possible reason is that reaction products of alloyed nitrogen such as amines form in appreciable amounts as a result of the corrosion reaction. These products may adsorb on iron and inhibit the anodic or cathodic reaction.

Acknowledgment

The authors are indebted to the Shell Companies Foundation Inc. for support of the program. Zone-refined iron was made available by courtesy of the American Iron and Steel Institute and the mild steels through courtesy of the United States Steel Corporation.

Manuscript received March 26, 1964. This paper was presented at the Washington Meeting, Oct. 11-15, 1964.

Any discussion of this paper will appear in a Discussion Section to be published in the June 1965 JOURNAL.

REFERENCES

1. "Grundriss der Tech. Elektrochem. auf Theoret. Grundlage," by F. Haber, p. 504-5, Munich and Leipzig (1898).
2. E. Weitz and H. Muller, *Ber.*, **58**, 363 (1925).
3. A. Kaufmann, *Z. Elektrochem.*, **7**, 733 (1901).
4. G. Nilsson, *Chem. Tech.*, **9**, 479 (1957).
5. I. Libinson, I. Kukushkin, and A. Morozova, *Zhur. Kim. Prom. (Moscow)*, **12**, [6], 590 (1935).
6. D. Vreeland and S. Kalin, *Corrosion*, **12**, 569t (1956).
7. N. Hackerman, R. Hurd, and E. Snavely, *ibid.*, **14**, 203t (1958).
8. J. Goodrich and N. Hackerman, *This Journal*, **108**, 1092 (1961); **109**, 795 (1962).
9. "Corrosion and Corrosion Control," H. H. Uhlig, p. 109, John Wiley & Sons, Inc., New York (1963).
10. H. H. Uhlig, *Corrosion*, **19**, 231t (1963).

The Mechanism of the High-Temperature Oxidation of Iron-Chromium Alloys in Water Vapor

C. T. Fujii and R. A. Meussner

Physical Metallurgy Branch, Metallurgy Division, U. S. Naval Research Laboratory, Washington, D. C.

ABSTRACT

Oxidation studies of Fe-Cr alloys show that a characteristic layered scale is formed on alloys containing 15 w/o (weight per cent) Cr or less when oxidized in atmospheres of Ar- H_2O ($p_{\text{H}_2\text{O}} \leq 0.1$ atm) in the temperature range 800° - 1100°C . Though the outer wüstite layer is extensively detached from the inner wüstite-spinel layer, a linear oxidation rate is observed. For the continued high rate of oxidation a dissociative mode of scale development is necessary, and hydrogen appears to play an important role in this process as an oxygen carrier in the internal voids. Since the oxidation rate is linear, is virtually independent of Cr content, is approximately proportional to $(p_{\text{H}_2\text{O}})^{1/2}$, and shows a modest activation energy of 22 kcal/mole, the rate-controlling process occurs at the gas:oxide interface.

Previous studies of the oxidation of alloys in atmospheres containing water vapor show that water, even in very small amounts, may be a particularly aggressive oxidizer for some alloys. Foley (1) at-

tributed the poor reproducibility of the oxidation rates of Fe-Ni alloys to the day-by-day changes in the humidity of the laboratory air. Cohen and Caplan (2) reported anomalous effects of moisture in the oxidation

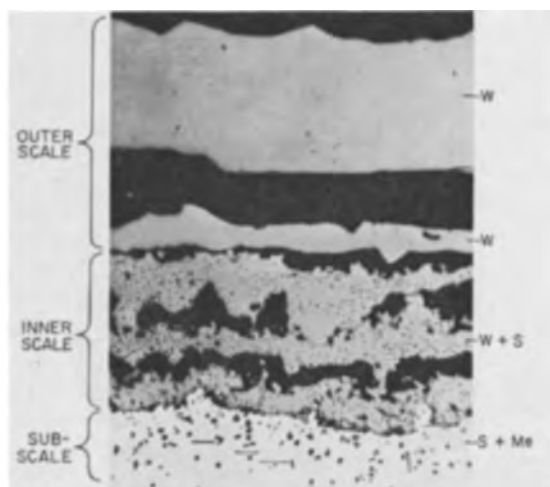


Fig. 1. Microstructure of an Fe-5Cr alloy oxidized in a 0.1 H₂O-0.9 Ar atmosphere at 1100°C for 20 hr. Magnification 80X.

of a number of commercial steels in dry and humid air at temperatures between 870° and 1093°C. They showed that water vapor accelerated the oxidation of Type 302 stainless, decelerated that of Type 446, and had a negligible effect on others, such as 410 and 430. Cohen and Caplan indicated that the effect of water vapor depended sensitively on the alloy composition, which in turn determined the scale composition. Because water vapor is a common contaminant of service atmospheres, an understanding of its role in oxidation is of practical significance as well as scientific value. The present study of the oxidation of Fe-Cr alloys in atmospheres containing only water vapor as an oxidizer indicates the importance of a dissociative process in the oxidation mechanism and suggests a role for hydrogen in addition to those reviewed by Cohen and Caplan (2).

Oxidation of Fe-Cr alloys in water vapor produces simple, reproducible structures and simple (for alloy oxidation), reproducible kinetics over a broad range of conditions. The characteristic structure of the scale, illustrated in Fig. 1, contains three distinct zones: (i) an outer scale of one or more layers of wüstite, which converts on cooling to room temperature to wüstite plus a precipitate of magnetite, (ii) an inner porous scale containing wüstite and an Fe-Cr spinel phase, and (iii) a subscale of the Fe-Cr spinel, and at times

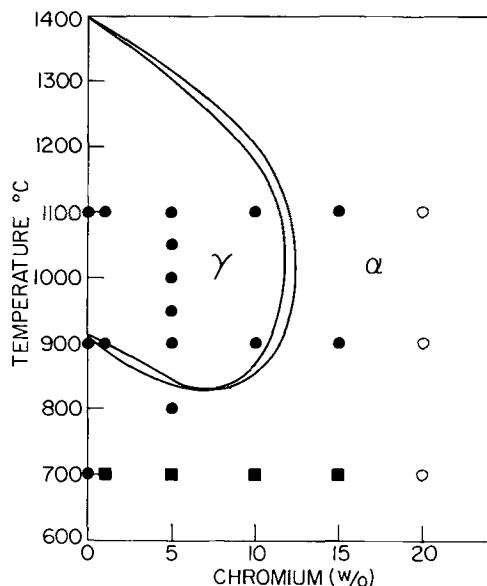


Fig. 2. Oxide characteristics of the Fe-Cr alloys: ●, FeO surface; ○, chromium rich oxides; ■, Fe₃O₄-Fe₂O₃.

higher chromium oxides, in the unoxidized alloy. A detailed description of this scale structure has been presented previously (3).

The range of temperatures and alloy compositions giving this scale structure in 0.1 H₂O-0.9 Ar is indicated by the filled circles of Fig. 2. The discussion of the oxidation mechanism will be largely confined to this area, i.e., 0-15 w/o Cr at temperatures from 800° to 1100°C. Under these conditions structurally analogous scales were produced on all specimens, and the weight gain data can be compared directly. The oxides produced on the iron were naturally free of the iron-chromium spinel phase and the subscale was absent, but the scale showed the same two-layer form characteristic of the alloys. However, the inner scale was less porous than for the alloys.

At chromium contents higher than 15 w/o, or at lower temperatures, the generation of the scale was less regular. The 20 w/o Cr alloy initially formed a chromic oxide layer which, for a time, was protective. This layer broke down as the oxidation time was extended, and the rapid oxidation process characteristic of the lower chromium alloys was achieved gradually. However, since the growth of the areas participating in the rapid oxidation process was erratic, the gravimetric measurements were meaningless. At temperatures below 800°C the formation of magnetite, and at times hematite, on the outer surface of the scale altered the rate-controlling process from that of the normal oxidation mechanism.

Experimental

The iron and the alloys, listed in Table I, were prepared from high-purity electrolytic metals by vacuum melting and casting. One-inch diameter rods, forged and rolled hot from these ingots, were shown to be homogeneous by chemical analysis of samples obtained from different radial and longitudinal portions of the rods. The chromium content of the samples varied by less than $\pm 0.1\%$ for each of the alloys. Metallographic examination of a cross section from each rod revealed no microsegregation, few chromic oxide particles, and no appreciable surface oxidation. Confirmation of the microhomogeneity of the alloys was obtained with an electron beam microanalyzer (3).

The specimens were one-quarter segments of 0.16-cm-thick disks with a surface area of 2.56 cm². After surface grinding both faces and drilling a 1-mm-diameter suspension hole in the apex of each specimen, the specimens were vacuum annealed (10^{-5} mm Hg) for 24 hr at 1050°C.

During the oxidation experiments the weight changes of the specimens were automatically and continuously recorded to ± 0.5 mg on a spring balance. The entire balance assembly, described in (4), was heated above the dew point of the water vapor atmosphere. In a typical experiment, the annealed specimen was chemically cleaned in a sulfuric-hydrochloric acid mixture for 5 min (1:1:18 by volume H₂SO₄:HCl:H₂O) and rinsed successively in a 5% sodium cyanide solution, water, and acetone. Immediately following this treat-

Table I. Chemical analysis of Fe-Cr alloys

Element	Weight per cent of element in the alloy						
	Fe*	Fe-1Cr	Fe-5Cr	Fe-10Cr	Fe-15Cr	Fe-20Cr	Fe-25Cr
Cr	—	0.99	5.0	9.9	14.8	19.5	24.3
S	—	0.007	0.010	0.010	0.008	0.008	0.007
P	—	0.004	0.004	0.006	0.007	0.003	0.007
Si	—	0.02	0.04	0.05	0.04	0.05	0.03
Mn	—	0.01	0.04	0.06	0.08	0.07	0.08
O**	0.037	—	0.027	0.024	0.031	0.035	0.043
N**	0.0013	—	0.0010	0.0019	0.0028	0.0037	0.0055
C	0.0012	—	—	—	—	—	—

* The analysis of the iron included only O, N, C. This iron was the same electrolytic material used in preparing the alloy.

** The oxygen and nitrogen contents were determined by vacuum fusion. The amount of these elements in the Fe-1Cr alloy were not determined.

ment, the specimen was dried and suspended from the spring balance by a fine platinum wire. The system was then purged with purified, dried argon¹ for 1 hr before the vertical furnace, at the desired temperature, was pulled up into place around the oxidation chamber. The dry argon atmosphere was maintained while the furnace recovered its initial temperature. No weight gain was detected ($\Delta W < 0.5$ mg) during the recovery periods of approximately 5, 10, and 15 min at 700°, 900°, and 1100°C, respectively, indicating that the purified argon was nonoxidizing.

Zero time was taken as the moment water vapor was introduced into the system. A rapid rate of weight gain was immediately recorded. The water vapor atmosphere was produced by passing purified argon through two water-filled fritted disk bubblers immersed in a constant-temperature bath. For the principal oxidation experiments a water vapor pressure of 0.1 atm was provided by operating the saturators at $46.2^\circ \pm 0.1^\circ\text{C}$, i.e., $0.1 \text{ atm} \pm 0.5\%$. The argon flow rate, 175 ± 10 ml/min for all experiments, was shown to be adequate in a preliminary series of experiments (see below). The experiments were terminated by quickly lowering the furnace and cooling the specimen to room temperature in dry argon. In all cases the furnace temperature was controlled to within $\pm 2^\circ\text{C}$.

Studies of the surface oxide structures, metallographic examinations of sections of the specimens, powder x-ray diffraction analyses of the inner and outer oxide layers, and chemical analyses of a few outer scale samples were performed. Data from similar studies have been reported (3), and only conclusions derived from these observations are cited here to define the oxidation mechanism.

Oxidation Kinetics

Curves of the weight gain per unit geometric area of the original specimen, constructed from the continuously recorded weight gain data, are presented in Fig. 3 and 4. The curves representing the studies at the two higher temperatures show very similar characteristics. For all of the specimens containing less than 20 w/o Cr, the high initial rate of weight gain gradually decreased to a constant value. While the data for the iron specimen oxidized at 1100°C conforms to a parabola for the first 2-3 hr without serious deviation, all the other specimens show an early departure from this behavior. At 1100°C (Fig. 3) a linear weight gain was established in 3-4 hr for all specimens and persisted throughout

¹The argon purification train consisted of a fritted glass bubbler containing chromous sulfate solution for oxygen removal, two dry ice-acetone traps, and an Anhydron-Ascarite drying tower for removal of residual water and carbon dioxide.

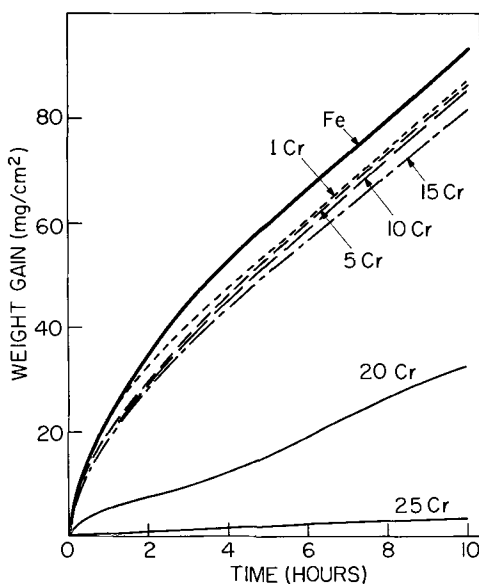


Fig. 3. Weight gain vs. time curves for experiments in a 0.1 H₂O-0.9 Ar atmosphere at 1100°C.

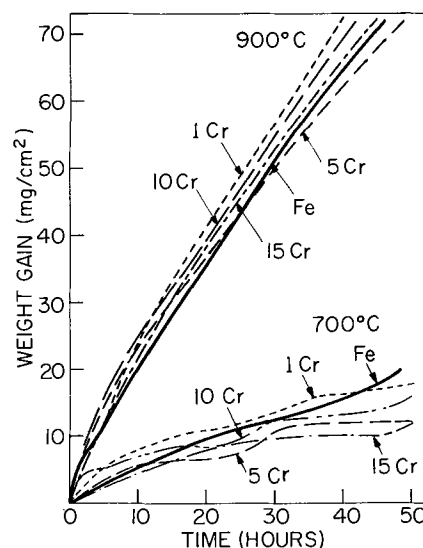


Fig. 4. Weight gain vs. time curves for experiments in a 0.1 H₂O-0.9 Ar atmosphere at 900° and 700°C.

the remainder of the experiments, i.e., for an additional 6-7 hr. During this period the rate of weight gain was $6.2 \text{ mg/cm}^2\text{-hr}$, and each specimen gained approximately 50 mg/cm^2 . The transient protection afforded by the chromic oxide initially formed on the higher chromium alloys is illustrated in this figure by the curves for the 20 and 25 w/o Cr specimens. However, in these cases the calculated weight gain per unit area is not a true measure of the rate since oxidation did not occur uniformly over the surface.

At 900°C (Fig. 4) the period of linear oxidation extends from 10 to 30 or 40 hr, and again all of the specimens from Fe to Fe-15 Cr display approximately the same oxidation rate ($1.5 \text{ mg/cm}^2\text{-hr}$). After 30 or 40 hr of oxidation the rate of weight gain for some of these specimens gradually decreased. This is believed to be caused by random nucleation and growth of a thin magnetite layer on the external surface of the scale. Very thin layers of magnetite were observed metallographically on some of these specimens. However, the general precipitation of magnetite within the wüstite adjacent to this surface during cooling makes it difficult to determine whether the magnetite surface layer was formed during oxidation or during cooling.

At 700°C, there is no doubt that magnetite, and even hematite, layers are formed on specimens oxidized for prolonged periods in an atmosphere of 0.1 H₂O-0.9 Ar. The weight-gain data from such specimens (Fig. 4) show very irregular behavior, with periods of accelerated weight gain interspersed with periods of very limited weight gain. Such complicated behavior obviously cannot be used in the study of the oxidation mechanism. The irregularities in the rate of weight gain can be ascribed to a variety of factors, e.g., non-uniform initiation and growth of the external scale, local detachment of this wüstite layer from the inner scale and the possibility of fracture at these sites, and the formation of magnetite and hematite layers on the external surface—preferentially at the sites of local detachment. The curve for a 5 w/o Cr alloy oxidized at 800°C and included in Fig. 7 (a figure discussed in a later section) shows that these disrupting factors are greatly attenuated at this temperature, restoring the normal linear oxidation rate.

Effect of chromium concentration.—As indicated in Fig. 3 and 4, the over-all weight gain of specimens containing from 0² to 15 w/o Cr at 900° and 1100°C are

²The impurities in the electrolytic iron appear to play an important role in the generation of the detached scales observed on the iron specimens. A few recent experiments in which spectrographically pure iron was oxidized in this atmosphere produced quite dense wüstite scales and a near parabolic rate of weight gain for rather long oxidation periods. The impure electrolytic iron, however, is a more representative base composition for the comparisons of this study.

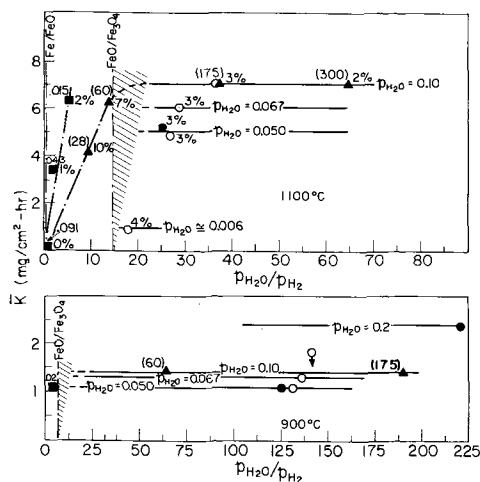


Fig. 5. Effect of the effective water vapor to hydrogen ratio in the atmosphere on the oxidation rate at 1100° and 900°C.

similar, and in the period of linear weight gain the chromium content of the alloys has a negligible effect of the rate.

Metallographic studies and x-ray diffraction data have shown that the effects of the changes in the chromium content of the alloy are largely confined to alterations of the structure of the inner scale and the subscale (3). The population of spinel particles in the subscale, and ultimately the inner scale, increases with increasing chromium content. As a consequence, local detachment of the scale from the metal, and outer scale from the inner scale, increases with increasing chromium content. While these effects alter the progress of the oxidation process in the initial period, they have little effect on the rate during the subsequent linear growth period. For all specimens, the outer scale was nearly pure FeO (a maximum of 0.1-0.3 w/o Cr was detected by chemical analyses) of almost identical composition ("oxygen rich" wüstite, $a_o = 4.28$ kx). Thus the insensitivity of the oxidation rate to the chromium content of the alloys suggests that the processes occurring in the outer scale are rate determining.

Effect of atmosphere.—The effects of flow rate, water vapor partial pressure, and small hydrogen additions on the oxidation at 900° and 1100°C are shown in Fig. 5. Table II indicates the significance of the symbols used in these graphs and defines the nature of the

Table II. Key to symbols used in Fig. 5, 6, and 8

Symbol*	System and experimental conditions
\bar{K} K_1	
(XX)	Flow rate studies: Conducted in a 1-in.-diameter silica tube equipped with a preheat coil for the gas stream. Flow rate, ml/min, indicated in parenthesis. $p_{H_2O} = 0.1$ atm.
▲	
0.000	Hydrogen additions: Same equipment as above. p_{H_2} in gas stream indicated. Flow rate was constant at 175 ml/min. $p_{H_2O} = 0.1$ atm.
■	
●	Variation in partial pressure of water vapor: Same equipment as above. p_{H_2O} in gas stream indicated. Flow rate was constant at 175 ml/min.
○	
⊙	Variation in partial pressure in water vapor: Recording balance (1.5-in.-diameter silica tube). p_{H_2O} in gas stream indicated. Flow rate constant at 175 ml/min.
X%	Calculated percentage depletion of water vapor as a consequence of the reaction. (At 900°C the depletion is less than 1% for all data and this notation has been omitted.)

* \bar{K} Average rate of weight gain in a 20-hr experiment (mg/cm²-hr).
 K_1 Linear rate of weight gain (mg/cm²-hr).

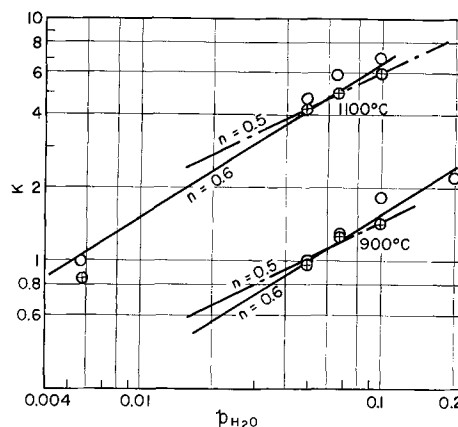


Fig. 6. Effect of water vapor partial pressure on the oxidation rate at 1100° and 900°C.

experiments involved. Since the apparatus used in the auxiliary studies on flow rate and hydrogen addition effects was not equipped with a weighing mechanism, the oxidation rate constants derived from these experiments are indicated as \bar{K} , the average for a 20-hr oxidation period. From the shape of the curves of Fig. 3 and 4 it is evident that \bar{K} is greater than the true linear rate constant, but as shown in Fig. 6 the difference is small. Thus \bar{K} is accepted as an adequate measure of the reaction rate for these auxiliary studies. The ratio, p_{H_2O}/p_{H_2} , is calculated from the composition of the gas stream admitted to the reaction chamber, the volume flow rate, the reaction rate (\bar{K}), and the reaction area (the original specimen surface area). This calculated composition is an adequate measure of the gas surrounding the specimen since a steady state is achieved in the system during the prolonged period of constant reaction rate. It is recognized that the actual p_{H_2O}/p_{H_2} ratio is somewhat lower at the reacting surface. Although all of these data are from experiments with Fe-15 Cr, the results in Fig. 3 and 4 show that they apply to all alloys studied.

The flow rate data of Fig. 5 are particularly informative. At 900°C the reaction rate was insensitive to changes in flow rate which altered the p_{H_2O}/p_{H_2} ratio from 65 to 190. In fact, in an initial experiment in which a series of alloy specimens were simultaneously oxidized for 20 hr, a \bar{K} of 1.4 mg/cm²-hr was obtained with a gas ratio of 10 to 20. At 1100°C, where the reaction rate is five times greater, a similar plateau was observed at high flow rates. At reduced flow rates (60 ml/min or less) the reaction rate decreased, the depletion of water vapor became appreciable, and the calculated gas ratio fell below the equilibrium value for FeO/Fe₃O₄.

The graphs of Fig. 5 have been divided into two areas by hatched zones based on the p_{H_2O}/p_{H_2} of the FeO/Fe₃O₄ equilibrium. This value defines the lower limit of atmospheres in which the full range of composition of the FeO phase can be attained in the kinetic system. A zone of increasing width with increasing \bar{K} has been indicated to recognize that the calculated gas ratio is greater than that at the reacting surface. To the right of this zone the surface reactions are rate controlling. To the left, where the calculated gas ratio restricts the range of composition of the FeO phase, the effects of the atmosphere on the reaction rate are complicated and have not been fully investigated. As the ratio of water vapor to hydrogen is decreased, either by decreased flow rate or hydrogen addition, the reaction is retarded. However, a moderate hydrogen addition (0.015 atm H₂ at 1100°C or 0.02 atm H₂ at 900°C) which restricts the FeO composition range and thus lowers the defect concentration at the outer surface, produces only a small decrease in the reaction rate. These results suggest that the rate-controlling reaction

is not greatly dependent on the defect concentration of the FeO surface and that hydrogen is not extensively adsorbed from the gas phase.

In the area of primary interest in these studies, the area to the right of the FeO/Fe₃O₄ limit, the data are supported by continuous weight gain curves and the results are uncomplicated. The data from the 900° and 1100°C experiments in an atmosphere containing 0.1 atm of water vapor show that the reaction rate is independent of the flow rate and hence independent of the $p_{\text{H}_2\text{O}}/p_{\text{H}_2}$ ratio of the atmosphere. The data points from oxidation studies at reduced water vapor pressures, at flow rates of 175 ml/min, all remain within this area. These data show that the linear oxidation rate is independent of the $p_{\text{H}_2\text{O}}/p_{\text{H}_2}$ ratio but that it is rather strongly dependent on the partial pressure of water vapor suggesting that the rate-controlling reaction is occurring at the oxide:gas interface.

A logarithmic plot of these data, Fig. 6, indicates a pressure dependence of the form $K_1 = k(p_{\text{H}_2\text{O}})^n$, where $n = 0.5$ to 0.6 . This dependence is not unlike those observed by Hauffe and Pfeiffer (5) in the oxidation of iron in CO₂/CO ($K_1 \propto [p_{\text{CO}_2}/p_{\text{CO}}]^{0.7}$) and Pfeiffer and Laubmeyer (6) at very low oxygen pressure ($K_1 \propto [p_{\text{O}_2}]^{0.7}$). Pettit, Yinger, and Wagner (7) and Smeltzer (8) have also studied the CO₂/CO oxidation of iron and concluded that the linear oxidation rate is a linear function of the mole fraction of CO₂ and the sum of the partial pressures of CO₂ and CO (7), or directly proportional to the partial pressure of CO₂ (8) in these respective studies. Each of these treatments of the complex problem of heterogeneous surface reactions has merit for each provides an excellent correlation with the experimental data. However, the data are not detailed enough to assure the validity of the set of assumptions introduced in each of these investigations.

Halsey's (9) treatment of catalysis on nonuniform surface appears to offer an alternative explanation for the observed pressure dependence in the present study. By considering the variations in the activation energies for the adsorption of the reactant and the desorption of the product after rearrangement (which might be enlarged to mean reaction with the oxide) among the sites on a nonuniform surface, Halsey showed that the over-all rate of unimolecular reactions is proportional to the square root of the Langmuir isotherm of the reactant, i.e., $(L_A)^{1/2}$. This result is halfway between the case where the desorption of the product has no effect on the reaction rate, $(L_A)^1$, and the case where the desorption of the product is rate controlling, $(L_A)^0$. Halsey (9) points out the unreasonableness of attempting to define a single process as rate determining when the process occurs on a nonuniform surface.

In view of these considerations it may be suggested that the reaction of water vapor with FeO is occurring on a nonuniformly reactive surface and that if the fraction of the surface occupied by adsorbed water vapor is not too great, $L_{\text{H}_2\text{O}}^{1/2}$ reduces to $p_{\text{H}_2\text{O}}^{1/2}$. The temperature coefficient of the reaction rate then represents not the activation energy of a single process but the average of several.

Effect of temperature.—The weight-gain data for Fe-5 Cr oxidized at four intermediate temperatures, together with bands summarizing the data for the full range of alloy compositions, are shown in Fig. 7. The extended linear growth period has been delineated for each curve in this figure. The temperature dependence of the linear rate constants for the Fe-5 Cr from Fig. 3, 4, and 7 is shown in Fig. 8 and the small spread in the measured rate constants for the entire composition range, 0-15 w/o Cr, is indicated at 900° and 1100°C. Although only two data points are available for each of the lower water vapor pressures, these define lines which parallel the line at $p_{\text{H}_2\text{O}} = 0.10$. The apparent activation energy of 22 ± 1 kcal/mole for the over-all oxidation process is significantly lower than the 29-30

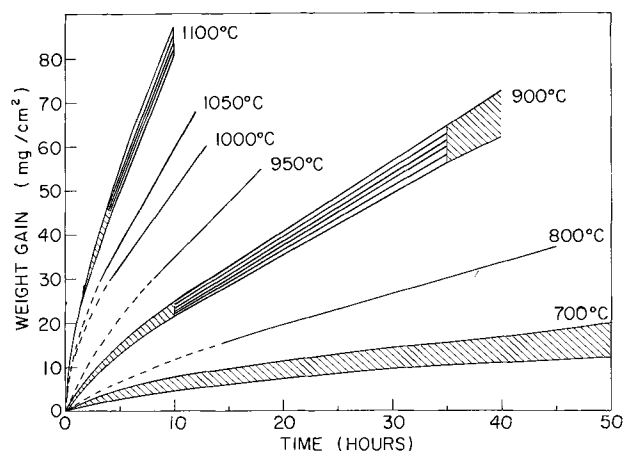


Fig. 7. Summary of weight gain vs. time curves for experiments in a 0.1 H₂O-0.9 Ar atmosphere. The bands at 1100°, 900°, and 700°C include the weight gain curves for all alloy compositions between 1 and 15 w/o Cr; the curves at the four other temperatures are for the Fe-5Cr alloy.

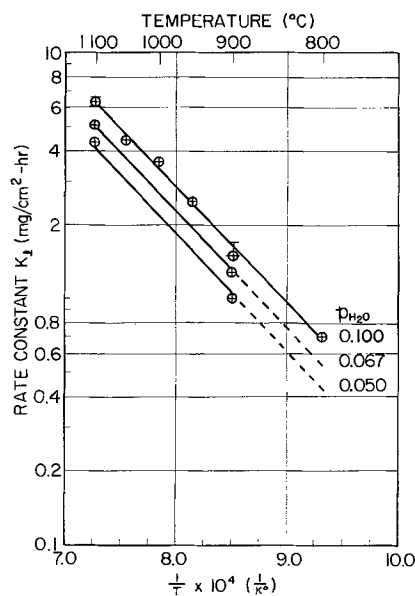


Fig. 8. Effect of temperature on the oxidation rate at 0.10, 0.067, and 0.050 atm water vapor partial pressure.

kcal/mole activation energy reported for iron diffusion in wüstite (10).

The linear kinetics indicate that the rate-controlling process with low activation energy is an interface reaction and the strong pressure dependence indicates that the process occurs at the gas:oxide interface. However, as proposed in the preceding section, the 22 kcal/mole activation energy is probably an average of the processes occurring on sites of different reactivities.

Oxidation Mechanism

Figure 9 depicts schematically the processes involved in the growth of the outer wüstite and inner porous wüstite-spinel layers. Although the lattice transfer of iron (from the metal to the outer oxide:gas interface) is restricted to the narrow oxide bridges connecting the two oxide layers, it is the surface reaction and not the diffusional transport that is rate controlling. The linear oxidation rates are rates of incorporation of oxygen from the water vapor into the wüstite lattice at the outer oxide:gas interface.

From the measured rates and the dimensional changes in the scale it was concluded (3) that a dissociative process operates within the voids separat-

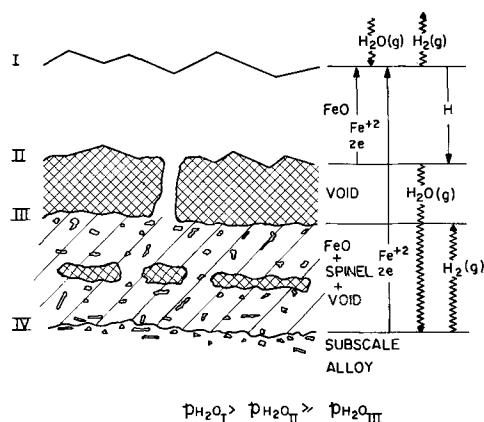


Fig. 9. Proposed mechanism for the oxidation of Fe-Cr alloys in water vapor at high temperatures.

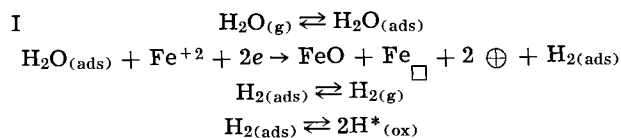
ing the two scale layers. This process supplied oxygen for the growth of the inner layer and released iron ions for the maintenance of the outer surface reaction. From studies of these structures it was estimated (3) that a substantial part of the iron ion flux in the outer scale was derived from this dissociative process, i.e., 10-30% at 900°C and 30-50% at 1100°C, the proportion being higher for the high chromium alloys. However, as Dravnieks and McDonald concluded previously (11), a simple calculation based on gas kinetics shows that at the expected dissociation pressure of FeO (10^{-15} to 10^{-11} atm) only 10^{-8} to 10^{-4} mg/cm²-hr of oxygen impinge on the walls of the voids. Obviously a vapor species which contains oxygen and can exist at moderate pressures while maintaining a low oxygen potential is required to accomplish the observed transfer rate of 2-3 mg/cm²-hr at 1100°C. Water vapor is a logical candidate for this important role. Although the recent findings (given below) do not identify water vapor as the carrier species directly, they provide evidence that hydrogen, and thus water vapor, can be present in the voids. Recognizing that the partial pressure of hydrogen within the voids can be no greater than that at the exterior of the scale, i.e., of the order of 10^{-3} atm for these experiments, and assuming the above dissociation pressures for FeO, the equilibrium pressure of water vapor at 1100°C is 10^{-4} to 10^{-1} atm. This is much greater than the 10^{-7} atm required to provide an impingement rate equal to the observed oxygen transfer rate. These water vapor pressures thus appear to be sufficient to support the suggested dissociative process even with a low number of effective impingements.

The possibility that wüstite is permeated by hydrogen was indicated by the results of Flint (12). While investigating the effects of oxide surface layers on the hydrogen permeation of stainless steels, he observed a marked reduction in the hydrogen permeation when a surface layer of chromium-rich oxide formed but no reduction when the experimental conditions were such that a wüstite scale developed. The case for the diffusion of hydrogen through wüstite, and the generation of a hydrogen and water vapor atmosphere within the voids of the scale, was further strengthened by the results of auxiliary experiments in the present research.

In these experiments, thin walled thimbles of an Fe-5 Cr alloy were threaded to a nickel support tube and oxidized at 1100°C in a 0.1 H₂O-0.9 Ar atmosphere. A small diameter nickel tube inserted in the support tube permitted the internal cavity of the specimen to be swept rapidly with argon. An outer silica envelope, of small volume so that the exit gas stream was representative of the gas surrounding the oxide surface of the specimen, enclosed the specimen. The exit gas stream (Ar-H₂O) and that sweeping the internal cavity (Ar only) were periodically analyzed for hy-

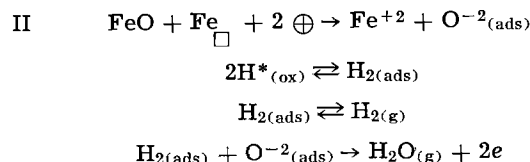
drogen in a gas chromatograph. No hydrogen was detected in either gas streams while the specimen was heated to the oxidation temperature in argon. During the first 30 hr of oxidation 3-5% of the hydrogen generated in the oxidation process penetrated the oxide and metal and appeared in the gas swept from the internal cavity. By the time the experiment had proceeded for 33 to 36 hours almost all of the metal in the thin walls of the thimble had been consumed and magnetite was being generated on the external oxide surface. The hydrogen content of the exit stream of oxidizing gas dropped gradually as the oxidation process was retarded. When this source of hydrogen was reduced by 30% or more, hydrogen was no longer detected in the inner cavity gas stream (less than 0.1 μl in a 0.5-ml gas sample). The correlation of the change in the hydrogen concentrations and the changes in the structure of the specimen, indicated above, were determined by metallographic examinations of a series of these specimens oxidized for different periods of time. These results show that wüstite exhibits a substantial permeability for hydrogen, while magnetite is sufficiently impermeable that a thin surface layer of this phase effectively blocks the passage of hydrogen.

The reactions occurring during the growth of this characteristic layered scale, indicated in Fig. 9, require little comment. At the outer interface, I, water vapor is adsorbed and reacts with iron ions derived from reactions at interfaces II and IV generating FeO, defects in the oxide, and adsorbed hydrogen. Most of the hydrogen desorbs, but some dissolves in the oxide.



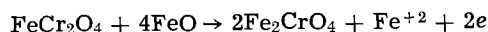
In these expressions the symbols Fe_□ and ⊕ have their usual meanings of a vacant iron ion site and an electron defect. The symbol for hydrogen dissolved in the oxide, H*, is intentionally ambiguous. While it is likely that this species is ionized, no proof of this can be offered. The nature of this reaction appears to be unimportant since this process is reversed at II and the electron balance is maintained.

At the inner interface, II, iron oxide dissociates and an oxide ion appears as an adsorbed species (lattice defects are consumed in this process). The permeating hydrogen permits these adsorbed species to react to form the carrier gas for oxygen transport in the void.



Succeeding wüstite layers of the outer scale are produced in this resulting atmosphere by the reactions defined for interfaces I and II. Thus, reactions similar to those at interface I also occur at interface III.

Within the inner scale there is probably some small change in the composition of the spinel phase. A reaction of the type



accounts for this change. The compositions of the spinel phase in this equation are not significant but only indicative of the enrichment of this phase in iron.

The processes occurring at the metal:oxide interface are complicated by the partition of iron and chromium between the wüstite and spinel phases. The predominant reaction is the production of metal ions with the release of electrons and the elimination of defects in the oxide. In addition some oxygen must be removed from the oxide and dissolved in the metal

to continuously generate the oxide particles of the subscale. Similarly hydrogen must be transferred to the metal until an "equilibrium state" is reached. These several processes lead to the generation of a highly irregular interface with local separations at the scale:metal interface.

Summary

The water vapor oxidation of Fe-Cr alloys containing 0-15 w/o Cr is linear in the temperature range 800°-1100°C after the establishment of a duplex scale structure. For a continued high rate of oxidation a dissociative mode of scale development is necessary, and hydrogen appears to play an important role in this process as an oxygen carrier between the separated inner and outer scale layers.

While the processes which occur in the void between the inner and outer scale layers are critical for the maintenance of a sustained linear rate of oxidation, the very small influence of the alloy chromium content, the significant effect of water vapor pressure on the oxidation rate, and the modest activation energy of 22 kcal/mole, all suggest that the rate-determining process occurs at the oxide:gas interface.

Acknowledgment

The assistance of Mr. C. D. Carpenter in the design and construction of the experimental apparatus is

gratefully acknowledged. One of the authors (CTF) served as a NAS-NRC Postdoctoral Research Associate at the U. S. Naval Research Laboratory during a portion of the research.

Manuscript received Jan. 27, 1964.

Any discussion of this paper will appear in a Discussion Section to be published in the June 1965 JOURNAL.

REFERENCES

1. R. T. Foley, *This Journal*, **109**, 278 (1962).
2. D. Caplan and M. Cohen, *Corrosion*, **15**, 141t (1959).
3. C. T. Fujii and R. A. Meussner, *This Journal*, **110**, 1195 (1963).
4. C. T. Fujii, C. D. Carpenter, and R. A. Meussner, *Rev. Sci. Inst.*, **33**, 362 (1962).
5. K. Hauffe and H. Pfeiffer, *Z. Metallk.*, **44**, 27 (1953).
6. H. Pfeiffer and C. Laubmeyer, *Z. Elektrochem.*, **59**, 579 (1955).
7. F. Pettit, R. Yinger, and J. B. Wagner, Jr., *Acta Met.*, **8**, 617 (1960).
8. W. W. Smeltzer, *ibid.*, **8**, 377 (1960).
9. G. D. Halsey, Jr., *J. Chem. Phys.*, **17**, 758 (1949).
10. L. Himmel, R. F. Mehl, and C. E. Birchenall, *Trans AIME*, **197**, 827 (1953).
11. A. Dravnieks and H. J. McDonald, *J. (and Trans.) Electrochem. Soc.*, **94**, 139 (1948).
12. P. S. Flint, USAEC Report KAPL 659, Dec 14, 1951.

The Mechanism of Oxidation of Zirconium in the Temperature Range 400°-850°C

R. J. Hussey¹ and W. W. Smeltzer

Department of Metallurgy and Metallurgical Engineering, McMaster University, Hamilton, Ontario, Canada

ABSTRACT

A study of the oxidation mechanism for zirconium in the temperature range 400°-850°C, based on examination of the oxide scale growth and oxygen gradients in the metal substrate, is reported. The oxidation kinetics at long times obeyed a parabolic rate equation which was best described in terms of a diffusion model for oxygen diffusion in both the oxide and metal. From the determination of the oxygen gradients, the diffusion constant was evaluated for oxygen diffusion in alpha-zirconium.

In previous studies (1, 2) on the oxidation of zirconium in oxygen at temperatures in the range 400°-850°C, the kinetics was best described by a parabolic rate relationship, and the mechanism of oxidation was considered to be the same over the temperature range investigated with an initial deviation at the lower temperatures. The amount of oxygen present in the metal during the region of parabolic behavior varied from 14% to 62% over the temperature range 500°-850°C.

This investigation covers the study of the solid-state processes and the mechanisms involved, when the oxidation kinetics conform to a parabolic rate equation. Accordingly zirconium was oxidized in oxygen at a pressure of 10 cm Hg over the temperature range for periods extending to several hundred hours.

Experimental

The 0.030 in zirconium sheet, the same as used in the previous investigations (1, 2), was cut into specimens 1.5 x 1 cm. The oxygen was purified as before, and prior to oxidation the samples were chemically polished and annealed (1).

Individual specimens were suspended in a quartz reaction tube and oxidized for successively increasing

times over the temperature range 500°-600°C. After oxidation sections of the specimens were prepared (1) and metallographically examined. In order to prepare the oxide for film thickness determinations such that the outer edge of the scale was not rounded, the specimens were abraded to 600 mesh SiC wet papers and then polished for 1 min on a napless cloth impregnated with 1 μ diamond.

Hardness profiles in the metal substrate beneath the oxide layer were determined with a Vickers microhardness indenter using the standard 124° diamond under a 10g load. Measurements of the oxide scale thickness were made using a filar micrometer eyepiece on normal sections of the polished specimens.

Results

Effect of temperature.—Separate zirconium specimens were oxidized in oxygen at a pressure of 10 cm Hg at temperatures of 500°, 550°, and 600°C for increasing lengths of time. The maximum periods of oxidation varied from 260 hr at 600°C to 550 hr at 500°C. The variation of the total weight gains giving the total oxygen consumption with time is shown in Fig. 1. A comparison of these data with the continuous kinetic curves obtained with a vacuum microbalance technique (1) shows that over the time interval studied there is reasonable agreement between the two sets

¹ Present address: School of Metallurgy, University of New South Wales, Kensington, Australia.

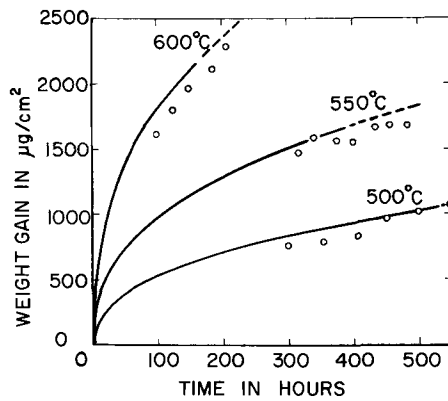


Fig. 1. Oxidation of zirconium at 500°-600°C in oxygen at 10 cm Hg pressure. The present data (individual points) are compared with corresponding kinetic curves (full lines), which are extrapolated (dashed lines) to the maximum times at each temperature.

of data. An additional zirconium sample was oxidized at a temperature of 750°C for 96 hr at a pressure of 40 cm Hg.

Metallographic examination.—Examination of the oxide scale formed on the metal under polarized light showed it to be dense, gray, and adherent to the metal and columnar in structure; at the specimen edges the oxide had thickened and exfoliated (1, 2).

In all specimens a thin dark wavy line was observed beneath the scale at a depth which coincided with a hardness of approximately 300 D.P.N. It is considered that this line was due to differential polishing rates associated with the differences in hardness due to oxygen solution. The region or band of hardened metal was roughly the same thickness over the flat surface of the specimens, but at the edges beneath the exfoliated oxide scale it was thinner and rounded.

Twenty measurements of oxide thickness were made on each sectioned specimen oxidized for a given time at each of the temperatures 500°, 550°, and 600°C, and the mean of these values were determined. Variation of scale thicknesses with time and the mean error in the determination at each temperature are given in Table I. Taking the density of zirconia to be 5.826 g/cm³ (3),

Table I. Influence of temperature on the amount of oxygen in zirconium oxidized at a pressure of 10 cm Hg

Temp. °C	Time, hr	Film thickness, μ	% Oxygen in metal			
			(a)	(b)	(c)	
400	644	1.2 ± 0.5	29 ± 24	—	4	
	500	300	4.6 ± 0.5	8	12	—
		358	4.6	11	—	—
		409	4.6	15	12	—
		450	5.9	7	—	—
		500	5.7	15	10	10
		550	6.3	10	—	—
Average = 11 ± 9			Average = 11 ± 4		—	
550	316	7.9 ± 1.0	19	—	—	
	341	8.7	17	11	—	
	377	8.9	13	—	—	
	402	8.1	21	11	—	
	435	8.5	23	—	—	
	457	8.9	19	—	—	
	486	8.9	20	14	17	
	Average = 19 ± 8			Average = 12 ± 3		—
600	100	8.3 ± 1.0	22	—	—	
	125	9.5	20	14	—	
	150	10.1	22	—	—	
	186	10.7	23	13	—	
	209	11.9	21	—	—	
	259	12.7	22	14	22	
	Average = 22 ± 7			Average = 14 ± 2		—
750	96	26.7 ± 1.4	32 ± 4	41 ± 2	39	
850	6	10.0 ± 2.0	51	—	—	
	16	21.0	42	—	—	
	24	23.0	57	—	—	
	48	33.0	53	58 ± 10	68	
Average = 51 ± 6			—			

(a) From film thickness measurements.
 (b) From area beneath hardness gradients.
 (c) From values of the diffusion constant derived from the present data.

the weight of oxygen in the scales was determined in each case from the mean oxide thickness. From the oxygen combined as oxide and the total oxygen consumption the amount of oxygen in the metal was determined as a function of time and temperature. It is seen that the mean value varies from 11% at 500°C to 22% at 600°C. Further the relative amount of oxygen in the metal shows no variation with time within the experimental precision.

Three microhardness traverses were made on each of three sectioned specimens oxidized for different times at temperatures in the range 500°-600°C. The gradients, given in terms of the diamond pyramid number (10g) vs. the distance in microns from the metal/oxide interface, are shown in Fig. 2-4. It is evident that the hardness gradients penetrated further into the metal with increasing time and moved more slowly with decreasing temperature. Moreover the penetration distance, that is, the distance from the metal/oxide interface where the hardness number becomes equal to the hardness of pure metal, increased from 10 μ at 500°C after 300 hr to 44 μ at 600°C after 260 hr.

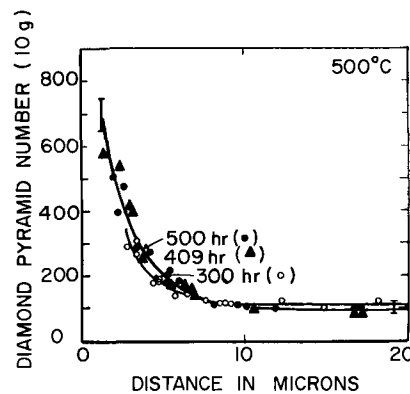


Fig. 2. Hardness gradients in specimens oxidized at 500°C

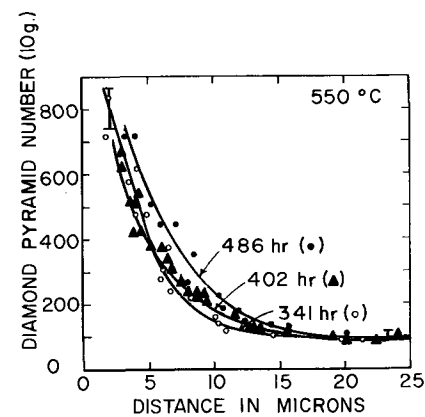


Fig. 3. Hardness gradients in specimens oxidized at 550°C

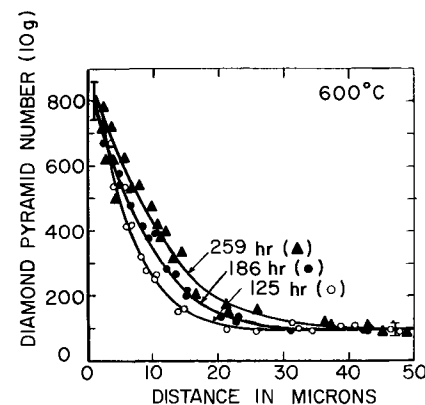


Fig. 4. Hardness gradients in specimens oxidized at 600°C

The amount of oxygen in the metal was also determined by measuring the area beneath the hardness profiles with the substitution of hardness for concentration; it was assumed that the hardness at the metal/oxide interface was 1100 D.P.N. and for the pure metal was 100 D.P.N., and that the terminal solubility of oxygen in zirconium was 28.6 at % (4). The values (Table I) showed no trend with time, but increased with temperature from a mean value of 11% at 500°C to a mean value of 14% at 600°C.

Evidence for oxygen solution in the metal at 400°C was shown in a 1:5 taper section of a specimen oxidized for 644 hr by the presence of a band of hardened metal immediately adjacent to the metal/oxide interface. It was very thin in comparison to the oxide film thickness of 1.2 μ and was estimated to be of the order of 0.2 μ . From a specimen oxidized at 750°C for 96 hr the amount of oxygen in the metal was determined from both scale thickness measurements and by measuring the area beneath the hardness gradient. The values obtained were 32% and 41%, respectively, and lie between those values determined for 600° and 850°C (2).

From the amounts of oxygen in the metal, as determined from scale thickness measurements and from determinations of the areas beneath the oxygen concentration gradients (Table I), it is evident that the values obtained in the temperature range 500°-850°C were in agreement with one another within the precision of the measurements.

Discussion

Oxidation of zirconium proceeds by diffusion of oxygen in both oxide and metal and, in carrying out the analysis for the oxidation mechanism of a polycrystalline metal aggregate, the assumption is made that average values of the diffusion constants for oxygen may be utilized for an oxide and a metal of monoclinic and hexagonal crystalline structures, respectively. This assumption appeared reasonable for the polycrystalline oxide layer as it was uniform and showed no variation of thickness with grain orientations in the metal. Also, there were no discontinuities in the hardness gradients in the metal due to crystallographic orientations of grains although nonuniformity of hardness within grains due to ordering of oxygen in the metal-oxygen solid solution has been shown (5). However, it is emphasized that these latter measurements give an average value of the hardness because the indentations were relatively large compared to any possible local changes in hardness.

For the growth of a superficial oxide layer and concurrent solution of oxygen in the metal substrate, the oxygen concentration at a distance x from the original edge position after time t is (6, 7)

$$C(x) = C_0 + B_1 (1 - \operatorname{erf}x/2\sqrt{D_1t}) \quad [1]$$

Here, C_0 is the initial oxygen content of the metal, D_1 is the diffusion constant, and B_1 is an arbitrary constant. Accordingly the gradients for different times become coincident on a normalized graph of $C(x)$ vs. x/\sqrt{t} . By assuming that the concentration of oxygen in the metal was proportional to its hardness (8), a test was made of this relationship. The position of the original surface of the metal was established by converting the measured thickness of oxide to the corresponding thickness of metal consumed using the densities of both phases. Plots of the data for 500°, 550°, and 600°C showed that the gradients were coincident, and thus it was concluded that oxygen solution in the metal at long times approximated to a parabolic relationship. A plot for the data at 600°C is shown in Fig. 5.

For additional confirmation of Eq. [1], values were determined for the diffusion constants of oxygen in zirconium from the hardness gradients in normalized form on probability paper, H_x vs. x/\sqrt{t} . The best straight line through the data was determined by least squares. From this, two pairs of values for H_x and x/\sqrt{t} were

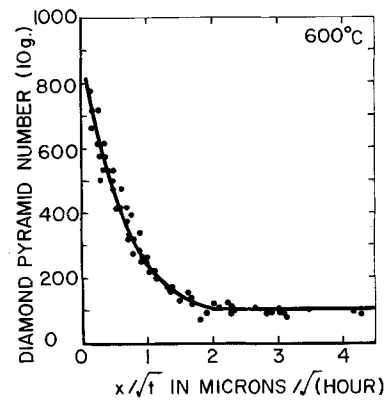


Fig. 5. Hardness gradients in specimens oxidized at 600°C normalized with respect to time.

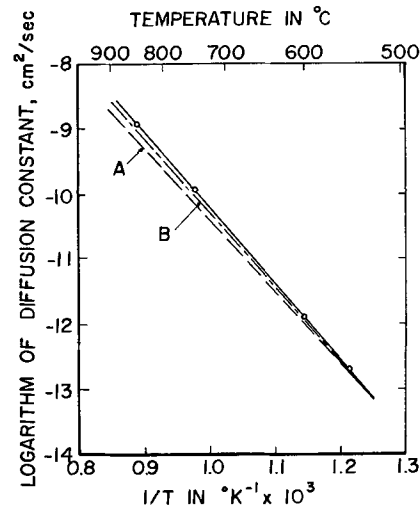


Fig. 6. Arrhenius plots for the diffusion coefficient for oxygen in zirconium: full line, this investigation; dashed line A, Kearns and Chirigos (8); dashed line B, Pemsler (9).

chosen to solve the simultaneous equations for the value of the diffusion constant. The values of the diffusion constants calculated from the data of this investigation and values calculated from reported oxygen concentration gradients at 850°C for the time of 6, 16, 24, and 48 hr (2) are shown in Fig. 6 in Arrhenius form. Utilizing least squares, the diffusion constants in the temperature range 550°-850°C may be expressed by the equation,

$$D_1 \text{ (cm}^2\text{/sec)} = 28.8 \exp(-53,400/RT) \quad [2]$$

The value of 53.4 kcal/mole for the activation energy is in excellent agreement with the values of 56.2 and 50.8 kcal/mole reported by Kearns and Chirigos (8), and Pemsler (9), respectively. Moreover, the plots in Fig. 6 demonstrated that the magnitudes of the diffusion constants at each temperature were in good agreement with the values previously reported. Thus, values of the diffusion constants for oxygen in zirconium determined from thermally oxidized specimens in the range of parabolic oxidation agree with those determined from diffusion anneal experiments. The amount of oxygen in the metal was calculated for the maximum time at each temperature in the range 550°-850°C from Eq. [1] and [2]. In addition, calculations were made of the amount of oxygen in the metal at 400° and 500°C using values of the diffusion constant obtained from the extrapolation of the Arrhenius plot (Fig. 6). These results were in good agreement with those determined experimentally (Table I) and show that a parabolic model describes the diffusion of oxygen in the metal substrate for long times in the range 400°-850°C.

In the present investigation of the solid-state processes occurring during the oxidation of zirconium, it has been shown that in the temperature range 500°-600°C the oxygen consumption of the individual specimens on oxidation for a specified time is consistent with that determined by the vacuum microbalance technique (Fig. 1). If the present data be plotted in parabolic form, the parabolic rate constant has a value of $2.14 \times 10^4 (\mu\text{g}/\text{cm}^2)^2/\text{hr}$ at 600°C, which is in good agreement with the value of $2.33 \times 10^4 (\mu\text{g}/\text{cm}^2)^2/\text{hr}$ from the kinetic data (1). Also, if the data for the rate of oxide scale growth at 600°C (Table I) are plotted in parabolic form, a good approximation to this rate relation is obtained. Representative parabolic rate constants could not be determined from the present data giving the total oxygen consumption and variation of scale thicknesses with time at temperatures of 550° and 500°C, however, due to the more pronounced scatter in the data.

In a previous investigation (2), Wallwork *et al.* have demonstrated that the parabolic oxidation kinetics of zirconium at 850°C may be adequately described by a diffusion model advanced by Wagner (6). The parabolic constant for the uptake of oxygen per unit area due to growth of the superficial oxide layer by oxygen diffusion and to oxygen solution in the metal substrate was expressed as

$$K_p = (C_{\text{II}}^{\text{I}} - C_{\text{I}}^{\text{II}}) 2\gamma\sqrt{D_{\text{II}}} + 2B_1\sqrt{D_{\text{I}}/\pi} \exp\left(-\frac{\gamma^2 D_{\text{II}}}{D_{\text{I}}}\right) \quad [3]$$

or

$$K_p = \{K_p(\text{oxide}) + K_p(\text{metal})\} \quad [4]$$

In this equation, C_{II}^{I} and C_{I}^{II} are the concentrations of oxygen from the zirconium-oxygen phase diagram in the oxide and the metal at the metal/oxide interface, respectively, D_{II} and D_{I} are the diffusion constants of oxygen in the oxide and metal, γ and B_1 are constants.

It was possible to analyze the oxidation data for 600°C according to Eq. [3] by making the assumptions that the parabolic constants for oxygen uptake and scale growth could be determined from the limiting tangents of the kinetic data at long times when plotted in parabolic form, and from the evaluation of the oxygen diffusion constant in the metal from the hardness profiles. The parabolic oxidation relationship was determined to be

$$K_p (\mu\text{g}\cdot\text{O}/\text{cm}^2\text{hr}^{1/2}) = (76.00 + 43.77) = 1.20 \times 10^2 \quad [5]$$

upon substitution of the following values in Eq. [3]: C_{II}^{I} and C_{I}^{II} = 1.514 and 0.439 g·O/cm³, respectively, $2\gamma\sqrt{D_{\text{II}}} = 7.07 \times 10^{-5}$ cm/ $\sqrt{\text{hr}}$, $B_1 = 0.768$ g·O/cm³ and $D_{\text{I}} = 1.24 \times 10^{-12}$ cm²/sec. This value was in

agreement to that of $1.33 \times 10^2 \mu\text{g}\cdot\text{O}/\text{cm}^2\text{hr}^{1/2}$ found experimentally and it is apparent that, in spite of the initial deviation, the mechanism of oxidation at long times can be explained in terms of the proposed oxidation model.

Unfortunately the applicability of this analysis to the data at lower temperatures could not be determined because the accuracy of the determinations of scale thicknesses (Table I) was not sufficient to permit a reliable value for the rate of movement of the metal/oxide interface. Nevertheless, all the evidence from measurements of scale thicknesses and oxygen gradients in the metal at long times is consistent with the model for oxygen diffusion in both the oxide and the metal leading to a parabolic rate equation.

Conclusions

The oxidation mechanism for zirconium in the temperature range 400°-850°C was consistent with an oxidation model for oxygen diffusion in the oxide, and the metal and the kinetics for long times were best expressed in terms of a parabolic rate equation. Determinations of oxygen diffusion constants in the metal from oxidation data over the above temperature range were in good agreement with reported data.

Acknowledgments

The authors were indebted to J. S. Kirkaldy, G. R. Purdy, and G. R. Wallwork for helpful discussions. This work forms part of a research project sponsored by the U. S. Air Force Office of Scientific Research, Office of Aerospace Research and the Defence Research Board, Ottawa, Canada.

Manuscript received Feb. 3, 1964.

Any discussion of this paper will appear in a Discussion Section to be published in the June 1965 JOURNAL.

REFERENCES

1. R. J. Hussey and W. W. Smeltzer, *This Journal*, **111**, 564 (1964).
2. G. R. Wallwork, W. W. Smeltzer, and C. J. Rosa, *Acta Met.*, **12**, 409 (1964).
3. J. D. McCullough and K. N. Trueblood, *Acta Cryst.*, **12**, 507 (1959).
4. B. Holmberg and T. Dagerhamn, *Acta Chem. Scand.*, **15**, 919 (1961).
5. J. P. Pemsler, *This Journal*, **111**, 381 (1964).
6. C. Wagner, "Diffusion in Solids, Liquids and Gases," p. 71, W. Jost, Academic Press, New York (1952).
7. J. Crank, "The Mathematics of Diffusion," p. 113, Oxford (1957).
8. J. J. Kearns and J. N. Chirigos, U. S. Atomic Energy Commission Rept. WAPD-TM-306 (1962).
9. J. P. Pemsler, *This Journal*, **105**, 315 (1958).

Electrochemical Calorimetry

IV. Measurement of the Reversible Heat Effect Attending the Passage of an Electric Current Across a Liquid Junction

Abner Brenner and S. L. Catey

National Bureau of Standards, Washington, D. C.

ABSTRACT

Measurements of the temperature changes resulting from the passage of current across the interface of two electrolytes were made at various distances from the junction so as to yield a temperature profile of the effect. The total heat effect was calculated from the area under the curve of the temperature profile. The coefficient obtained by dividing the total heat effect by the charge is reported as a voltage-equivalent. The following values were obtained for three systems of electrolytes and are probably correct to within about 7 mv: 0.04M hydrochloric acid and 0.4M hydrochloric acid, 30 mv; 0.90M hydrochloric acid and 3.0M potassium chloride, 80 mv; 1.15M hydrochloric acid and 1.21M lithium chloride, 80 mv. A hypothesis is advanced to relate the voltage-equivalent of the heat effects to the diffusion liquid junction potentials and to the Peltier effect.

This research is one phase of a continuing program of electrochemical calorimetry dealing with the broad aspects of the heat effects attending the passage of the electric current across interfaces involving electrolytes. Previous papers (1-3) in this series have dealt with the reversible heat effects attending the passage of current between a metal electrode and an electrolyte. This paper deals with the reversible heat effects attending the passage of current across the boundary of two electrolytes.

The reversible heat effect attending the passage of an electric current across the boundary of two metals is known as the Peltier effect. The heating produced at a junction by the passage of charge in one direction is equal to the cooling produced when charge flows in the opposite direction. The Peltier effect is reversible in this sense, but this should not be confused with thermodynamic reversibility. The Peltier coefficient is obtained by dividing the heat effect, expressed in joules, by the charge expressed in coulombs. Although joules per coulomb has the dimensions of voltage, it is a moot point as to whether this voltage actually exists at the interface of two metals at constant temperature.

The passage of an electric current across the interface of an electrolyte and a metal or across the junction of two different electrolytes also gives rise to reversible heat effects. The phenomenon involving electrolytes has also been called a Peltier effect, and sometimes an electrolytic Peltier effect. For reasons given in the Discussion, it is the authors' opinion that this designation is a misnomer and leads to confusion in the interpretation of the phenomenon.

To avert preconceived ideas in the explanation of these reversible heat effects, the term reversible electrothermal effect will be used in the case of electrolytes. As with the Peltier effect, the coefficient which characterizes this phenomenon will be expressed in joules per coulomb and will be called the voltage-equivalent.

Bagard (4) made qualitative measurements of the reversible electrothermal effect and asserted that the phenomenon had been demonstrated as early as 1870. The early work showed that the flow of current from a solution of electrolyte of one concentration to a similar solution of lower concentration produced heating at the junction of two salt solutions and cooling at the junction of two acid solutions. Planck (5) made a mathematical analysis of the production of heat resulting either from free interdiffusion or from the passage

of an electric current between two dilute electrolytes in contact, but did not mention the electrothermal effect. According to his theory, a temperature difference, which should be readily detectable, occurs near the boundary of two electrolytes which are freely diffusing into each other. No such effect was detected in our experiments.

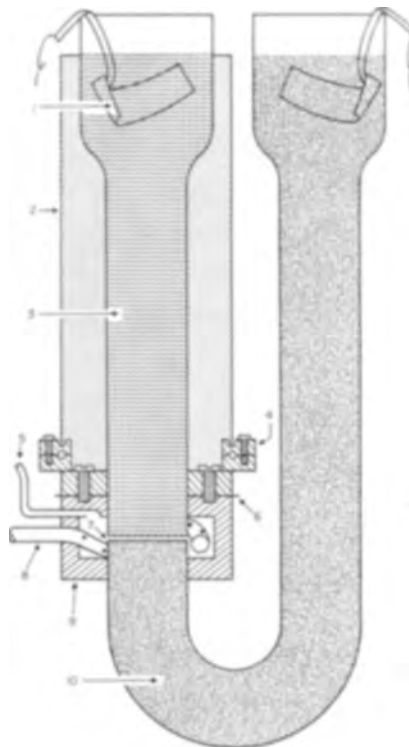


Fig. 1. U-tube used for measurement of thermoelectric effect at liquid junctions. Schematic drawing of U-tube: 1, Ag-AgCl electrode; 2, glass cylinder containing powder for thermal insulation; 3, less dense electrolyte; 4, brass flange for holding glass cylinder; 5, tube for removing air from chamber; 6, spacer for adjusting width of slit; 7, slit at the boundary, 0.25 mm wide; 8, plastic tube with small perforations for removing electrolytes through the slit, thus forming a sharp junction between the electrolytes; 9, Lucite housing to hold the two parts of the U-tube; 10, denser electrolyte.

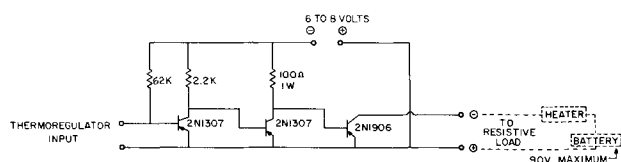


Fig. 2. Circuit of solid-state relay: 1, the input terminals are activated by a column of mercury and an electrical contact in a thermoregulator; 2, shorting the input terminals turns off the power to the load; 3, output current to Resistive Load should not exceed 1 amp.

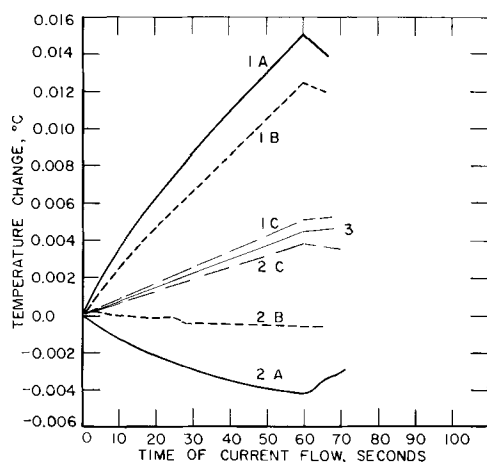


Fig. 3. Temperature changes occurring in the vicinity of the junction of 0.9M HCl and 3.0M KCl as a result of the passage of current, 13.3 ma/cm², for 60 sec. Curves were directly produced with a recording potentiometer. The designations A, B, and C indicate the position of the thermistor bead with respect to the junction: A indicates the interface of the junction; B and C distances of 2 and 10 mm from the junction, respectively. 1 and 2 denote the direction of passage of current. Curve 1, current passed from hydrochloric acid to potassium chloride; curve 2, current passed in the opposite direction; curve 3, temperature effect caused by Joule heat alone. Result obtained by placing thermistors 4 cm from boundary.

Our interest in the measurement of the reversible electrothermal effect arose in the course of our experiments on electrochemical calorimetry. Naively, it seemed possible to measure the diffusion liquid junction potential between two electrolytes from the reversible heat developed by the passage of charge across their junction. In the Discussion, we show that this was not easy to accomplish.

Apparatus and Procedure

A large U-tube contained the two electrolytes forming the liquid junction. The U-tube and associated equipment are shown in Fig. 1-2.

The procedure used for measuring the reversible electrothermal effect is only briefly mentioned here. Experimental details are given in the appendix.

For a typical experiment, current was passed across the boundary of two different electrolytes; for example, hydrochloric acid and potassium chloride, for 30 sec. The resulting change of temperature was detected at the end of the period with small, sensitive thermistors, located at a specific distance from the boundary. The experiment was repeated with the current flowing in the opposite direction. Typical graphs of the variation of temperature with time are shown in Fig. 3. The difference between the two temperature measurements gave the temperature change due only to the reversible heat effect. A series of these dual experiments were made at the junction of the electrolytes and at various distances in each electrolyte up to 2 cm from the junction, at which distance the reversible electrothermal effect was negligible. The temperature profile of the reversible electrothermal effect is obtained by

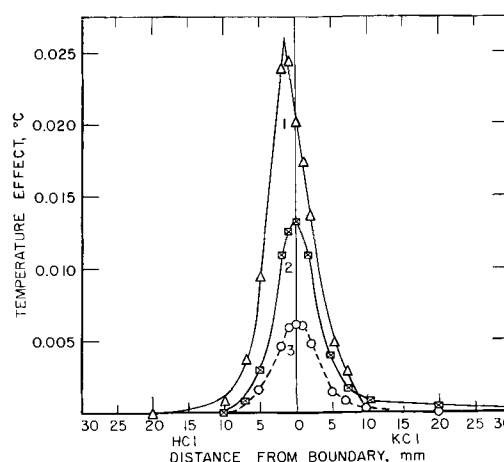


Fig. 4. Effect of current density on the temperature profile of the thermoelectric effect obtained in the vicinity of the junction of 0.9M HCl and 3.0M KCl. Current was passed for 30 sec. Curves 1, 2, and 3 represent, respectively, current densities of 26.6, 13.3, and 6.7 ma/cm².

plotting the temperature change against distance normal to the junction. The voltage-equivalent for the junction is then readily calculated from the temperature profile. This type of calorimetry, referred to as the method of temperature profile, has not been previously applied to aqueous solutions.

Results

Effect of Variables on the Voltage-Equivalent

It was important to know whether the current density, the period of current passage, and the sharpness of the junction affected the value of the voltage-equivalent measured by the temperature profile method.

The study of these variables was made with two electrolytes chosen to produce the same temperature rise from the Joule heat effect (when a common current passed through them). This choice reduced the amount of Joule heat that would flow across the junction in the course of an experiment. The solutions were 3M potassium chloride and 0.9M hydrochloric acid, with specific resistivities, respectively, 2.98 ohm-cm and 3.5 ohm-cm.

Figure 4 shows temperature profiles at current densities of 6.7 ma/cm², 13.4 ma/cm², and 27 ma/cm². The electrothermal effect was approximately proportional to the current densities. The range of the voltage-

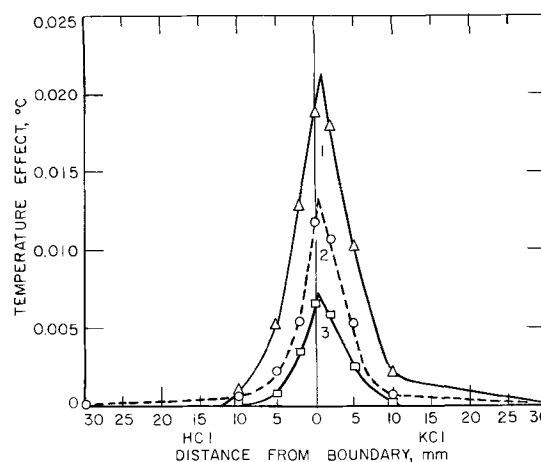


Fig. 5. Effect of period of current flow on the temperature profile of the thermoelectric effect obtained in the vicinity of the junction of 0.9M HCl and 3.0M KCl. Current density was 13.3 ma/cm². Curves 1, 2, and 3 represent periods of current flow of 60, 30, and 15 sec, respectively.

equivalent, 72-88 mv, was probably within the experimental error.

The effect of the period of current passage was investigated using intervals of 15, 30, and 60 sec. These data were obtained with a recording potentiometer. The temperature profiles are shown in Fig. 5. The voltage-equivalent ranged from 70 to 91 mv. Deviations from the average are probably within the experimental error.

Another variable is the time at which the temperature measurement is made after cessation of current flow. The temperature reading may be taken immediately after the cessation of current flow or a short time afterwards. Even though heat flowed from one region of the U-tube to another, the total amount of heat obtained by graphically integrating the area under the temperature profile should remain constant. The voltage-equivalents based on readings taken 0, 30, and 60 sec after cessation of current flow had no definite trend, and the differences were within the probable experimental error. An example of experimental data is shown in Fig. 6.

In the preliminary work, measurements at the junction between two electrolytes were not reproducible, in some instances varying by a factor of 3. The cause of the poor reproducibility was traced to lack of sharpness of the junction. Qualitatively, this was demonstrated by a series of measurements starting with a diffuse junction and then progressively sharpening the junction by drawing off successive increments of electrolyte. The electrothermal effect was found to increase in magnitude and become constant when the junction was sharp.

In one series of measurements, readings for each position of the thermistors were taken within 10 min after a new junction had been established. This was the time required for the temperature to become stable after each withdrawal of solution. In another series of measurements, readings were taken after the electrolytes had stood 2 hr, and the junction had become diffused. Figure 7 shows that the temperature profile for the diffuse junction was much flatter than the other. However, the voltage-equivalents agreed within about 7% which is within experimental error. The small effect of the sharpness of the junction on the voltage-equivalent is consistent with its small effect on the junction potential.

If two electrolytes had an appreciable heat of mixing, the precision of measurement of the reversible electrothermal effect would be limited. Hamer (6) noted the disturbing effect of heat produced at a liquid junction on the measurement of the emf of concen-

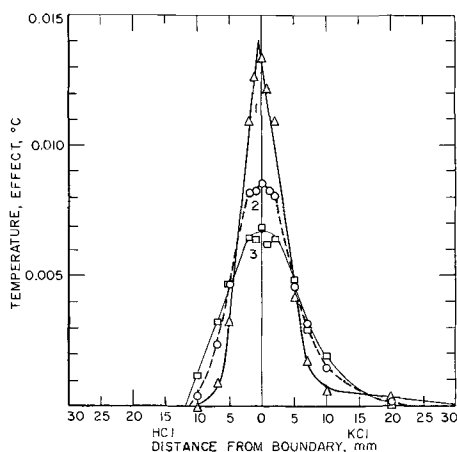


Fig. 6. Effect of interval of time after cessation of current flow on the temperature profile of the thermoelectric effect obtained in the vicinity of the junction of 0.9M HCl and 3.0M KCl. Current density, 13.3 ma/cm²; period of current flow, 30 sec. Curves 1, 2, and 3 represent, respectively, measurements taken immediately after cessation of current flow, 30 sec and 60 sec later.

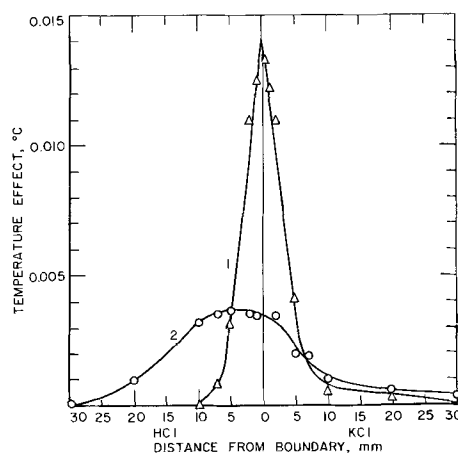


Fig. 7. Effect of sharpness of junction between 0.9M HCl and 3.0M KCl on the temperature profile of the thermoelectric effect. A current density of 13.3 ma/cm² was passed for 30 sec across the junction. Curves 1 and 2 represent readings taken, respectively, within 10 min after establishment of a sharp junction and 2 hr later.

tration cells containing sulfuric acid. The effect was smaller than 0.01 mv for solutions having a difference in partial molal heat content of less than 800 cal and only 0.15 mv for solutions having a difference of 2000 cal. The solutions with which we were dealing had a small heat of mixing. For example, we found that the partial molal heat of mixing of 1.2M LiCl with 1.1M HCl was only about 100 cal. In our measurements, we did not observe any heat effect caused by the spontaneous diffusion of the solutions, hence, it must have been less than 0.0005 degree/min.

Measurements on Other Pairs of Electrolytes

The following pairs of electrolytes were studied: 3.0M KCl and 0.9M HCl; 0.04M HCl and 0.40M HCl; and 1.15M HCl and 1.21M LiCl. The first pair of electrolytes has been discussed in the preceding section.

Measurements on hydrochloric acid solutions having concentrations of 0.04M and 0.4M were more difficult to obtain than those of the potassium chloride-hydrochloric acid systems, because the high resistivity of the 0.04M solution caused the generation of a large amount of Joule heat which tended to obscure the electrothermal effect. The difficulty was partly resolved by working at lower current densities of 3.5-7 ma/cm². Since the Joule heat falls off as the square and the electrothermal effect as the first power of the current, decreasing the current produced a net gain in discrimination. However, the current must be sufficient to yield an electrothermal effect greater than the statistical, accidental fluctuations. The voltage-equivalent for the hydrochloric acid system was about 30 mv.

No particular difficulty was encountered with 1.15M HCl and 1.21M LiCl solutions. The voltage-equivalent was about 80 mv.

Direction of the Electrothermal Effect

Since the current across a junction can cause either heating or cooling, the direction of the current must be correlated with the temperature effect. For our purposes, it was convenient to specify the direction of the current (that is, the impressed current being regarded as flowing from a positive toward a negative electrode) that produced cooling.

The arrow in the following chart gives the direction of current flow according to the above convention as well as the heat effect produced by passage of a faraday of electricity across the junction. This is derived from the voltage-equivalent by multiplying by 23,000 which is approximately the number of calories in a volt-faraday.

System	Voltage-equivalent	Electrothermal heat per faraday, cal
0.4M HCl:→:0.04M HCl	0.030	700
1.21M LiCl:→:1.15M HCl	0.080	1800
3.0M KCl:→:0.90M HCl	0.080	1800

Discussion

In a study of the reversible electrothermal heat effect of a silver-silver chloride electrode in chloride electrolytes, Lange (7) and Sherfey (2) concluded that the effect was a composite one. The major component of the heat effect was associated with the entropy change of the electrochemical reaction. An additional effect was inferred from the unexpected result that the heat effect for the lithium chloride solution differed from that for the hydrochloric acid solution, although both had the same chloride ion activity. Lange proposed that the additional effect was an entropy of transport, and Brenner (2, p. 218) suggested that it was a contact voltage or Peltier coefficient similar to that which occurs at the interface between two metals.

Lange referred to the reversible heat effect as a Peltier effect, whereas Sherfey referred to it as a half-cell entropy. The appellation of "Peltier" to the experiments in this paper could lead to confusion, since the reversible electrothermal effect does not possess the same characteristics as the "Peltier." For example, the emf at uniform temperature of a complete circuit composed of metals is zero, but the emf of a circuit consisting of metals dipping into electrolytes is not zero, witness the concentration cell. In the case of the silver-silver chloride electrode immersed in a chloride electrolyte, Sherfey found that the voltage-equivalent of the junction obtained by calorimetric measurements was closely equal to $T \cdot dE/dT$,¹ as is characteristic of the Peltier effect, but this was not true for a silver electrode immersed in a solution of silver perchlorate. Furthermore, the summation of the $T \cdot dE/dT$ for all the junctions in a complete electrolytic circuit is not necessarily equal to zero as is characteristic of the Peltier effect.

Similarly, the reversible electrothermal effect at liquid junctions is not a true Peltier effect, since it has been demonstrated that a complete circuit of liquid junctions can have an appreciable emf at uniform temperature. Data to be reported in a future paper will show that the voltage-equivalent of a liquid junction, as determined by the method of temperature profile, is not equal to $T \cdot dE/dT$.

We suggest that the electrothermal effect of liquid junctions is also a composite phenomenon. The voltage-equivalent must include the conventional liquid junction potential² as one component, as the following argument shows. If the liquid junction potential is V_{pd} , then it must be capable of generating energy equal to $V_{pd} F$ per faraday, F , of electricity. The source of this energy must be the entropy change that occurs at the junction. It cannot come from a change in internal energy since the heat of mixing of the electrolytes was not significant. Therefore, according to the first law of thermodynamics, the energy furnished by the liquid junction must come from the absorption of heat which is changed into electrical energy. Phenomenologically, it makes no difference to the changes at the junction whether the electric current is generated internally or passed through from an external source. Hence, a current passed through the junction in the direction of the spontaneously generated current should cause an absorption of heat equal to $V_{pd} F$ and, if passed in the opposite direction, should cause the evolution of an equal amount of heat.

¹ dE/dT is the change in the interface potential with absolute temperature.

² This refers to the diffusion liquid junction potential calculated by the following relations: $V_{pd} = \frac{-RT}{F} \int_1^{II} \sum \frac{t_i}{Z_i} d \ln a_i$, where t_i is the transference number of the various ions, Z_i the valence, and a_i the activities.

If the junction should happen to be a thermodynamically reversible system, then the Gibbs-Helmholtz law should apply, $E = \Delta H/F - T \cdot dE/dT$. Since ΔH is not significant, then the emf of the junction should be given by $T \cdot dE/dT$. Data which will be presented in a forthcoming publication will show that this last relation is not followed.

If the conventional liquid junction potential were the only source of the electrothermal effect, then the determination of the latter would afford a means of measuring the junction potential. However, our data showed that another source of voltage must be superimposed. For example, the experimental voltage-equivalent for the 1.21M LiCl solution in contact with 1.15M HCl was found to be 80 mv. However, the calculated liquid junction potential was 33 mv, and its direction was opposite to that of the measured voltage-equivalent. Therefore, the latter must include a component that was not only larger than the liquid junction, but also of opposite polarity.

The second component of the voltage-equivalent, V_{pc} , perhaps can be interpreted as Lange did for the metal-electrolyte system, as an entropy of transport. However, the authors prefer at this point not to give an ultimate explanation of the effect. They consider the second component to be phenomenologically the same as the Peltier coefficient that exists between two different metals in contact at uniform temperature, because this component appears to have the same characteristics. The basis for this opinion is contained in data on hand which will be published in the near future, but is summarized here. The component V_{pc} does not appear to contribute to the emf of a complete cell at uniform temperature. This is consistent with the law of thermocouples, which states that the sum of the Peltier coefficients of a circuit of metals is zero. Furthermore, the component appears to be given by the Kelvin relation, $V_{pc} = T dE/dT$, where dE/dT is the change in the potential of a liquid junction with temperature. The conventional liquid junction potential, V_{pd} , does not appear to have an appreciable temperature coefficient.

The results of this discussion can be summarized by three equations:

$$V_p = V_{pc} + V_{pd} \quad [1]$$

where V_p is the voltage-equivalent that is determined experimentally, V_{pd} is the liquid junction potential (see footnote No. 2) and V_{pc} is the Peltier coefficient.

$$\Sigma V_{pc} = 0 \quad [2]$$

for a complete circuit or cell.

$$V_{pc} = T \cdot dE/dT \quad [3]$$

where dE/dT is the temperature coefficient of the liquid junction.

In work to be reported later, values of V_{pc} were obtained by means of the Kelvin relation of Eq. [3], for the three systems of electrolytes reported here. V_p was determined by the method of temperature profile calorimetry. The liquid junction potential, V_{pd} , should be obtainable from Eq. [1]. The data are given in the following table:

System	V_p , mv	V_{pc} , mv	V_{pd} , mv	Liquid junction potential, approx.
0.4M HCl: :0.04M HCl	30	6	24	35
	→	→	→	→
1.21M LiCl: :1.15M HCl	80	93	13	33
	→	←	←	←
3.0M KCl: :0.90M HCl	80	103	23	30
	→	←	←	←

The arrows indicate the direction of each voltage across the junction, for current flowing across the junction from left to right. Values for V_{pd} may not be precise, since there may be other phenomena than the two noted. However, the values are of the right order of magnitude and have the right polarity.

Temperature Profile Method of Calorimetry

Electrochemical reactions and phenomena occur at interfaces and, consequently, the method of temperature profile which in a measure isolates the heat effects at an interface should be peculiarly applicable to electrochemical investigations. This investigation has shown that calorimetry by the method of temperature profile is an alternative to conventional calorimetry, as described by Sherfey and Brenner (1) for studying electrochemical reactions.

The one advantage of the conventional type of electrochemical calorimetry is that the system under study can be stirred and is, therefore, of a uniform temperature. However, the small heat effects which occur at the electrodes are dissipated through a volume of electrolyte so that the temperature rise is small.

The advantage of the method of temperature profile is that the heat effects are temporarily immobilized, as it were, and can be measured readily, even though of small magnitude. Whereas, the conventional type of electrochemical calorimetry might involve the production of a few hundred calories, the method of temperature profile requires the production of only a tenth or a hundredth of a calorie, a quantity smaller by a factor of 10^2 or 10^3 . For example, in an experiment by the method of temperature profile, a current of 0.05 amp was passed for 30 sec across a junction having a voltage-equivalent of 0.03v. The reversible heat in such an experiment was about 0.01 cal. The advantage of small electric currents is that a system in equilibrium is disturbed very little. Also, polarization is less of a problem.

The method of temperature profile described in this report is a first, crude attempt and should be capable of many refinements. These would improve the present rather low precision and extend the method to shorter periods of current passage. For example, the heat effects on the passage of a pulse of current of millisecond duration could be picked up by a recording oscillograph.

Acknowledgment

The authors wish to acknowledge the assistance of J. M. Sherfey and Albert Brown in the early phases of the work and also to Jean Connor for measuring the temperature coefficients of the emf's. Thanks also go to the Division of Research, Chemistry Branch, Atomic Energy Commission, for the financial support of this investigation.

APPENDIX**Apparatus, Experimental Details, and Calculations**

U-tube and thermistors.—The experiments were conducted with a large U-tube in which the junction between the two electrolytes was formed approximately in the middle of one limb. The general nature of the U-tube is shown in Fig. 1. It has two large bells at the top for containing extra solution. The rest of the U-tube had a uniform diameter of 4.5 cm. The U-tube was 45 cm long and 15 cm across the narrow part of the limbs. The size of the tube was arbitrary. A tube with a large cross section minimizes heat leakage from the interior of the solution, and the system is essentially adiabatic. Heat leakage was reduced further by insulating the limb containing the junction. The functional limb of the U-tube was constructed in two pieces having ground, parallel ends spaced about 0.25 mm apart by a lucite housing. The lucite housing contained a plastic tube perforated with many small holes which surrounded the slit. The free end of the tube was attached to a water aspirator. To form the junction, both electrolytes were drawn simultaneously from the inner part of the U-tube, through the slit between the two glass tubes, into the perforation in the plastic tube and from there to waste. One of the electrolytes was colored with a dye to make the position of the junction more easily discernible. This device gave a sharp junction.

Silver-silver chloride electrodes, through which a current was introduced into the U-tube, were placed in the bell-shaped upper ends.

Temperatures were measured with thermistors, since thermocouples were not sensitive enough. The

average temperature at any horizontal plane above or below the junction was measured by four thermistors rigidly fastened together in the same horizontal plane and connected in parallel. The thermistors were mounted on a screw device and could be raised or lowered readily. Their distance from the junction was read on a scale calibrated in millimeters.

Since the local temperature in the electrolyte had to be measured with a time lag of less than 1 sec, the thermistor beads had to be small. They were about 0.15 mm in diameter and had a resistance of about 1000 ohms. They were connected to platinum-iridium lead wires about 0.1 mm thick. The beads were fused into the end of a glass proboscis, 0.5 mm in diameter and about 6 mm long, which was connected to a glass shaft about 50 cm long.

The thermistor beads were more than 1 cm from the wall of the U-tube and there was no indication that heat flow from this point to the wall was a factor during measurement. The total cross section, about 0.3 cm², of the glass supports and guards was only a small fraction of the cross section of the U-tube, which was 15 cm². It is not likely that these supports caused an appreciable error in the measurement of temperature.

Measurements of temperature were made with a bridge circuit. At the beginning of an experiment, the bridge was balanced; at the end of the experiment, the reading of the null detector, a microvoltmeter, gave the change of temperature. About $1 \mu\text{v}$ corresponded to a temperature change of about 0.001°C.

The current passing through each thermistor was about 100 μa . Larger currents caused heating and a consequent slow drift of the reading on the microvoltmeter.

A uniform, constant temperature in the U-tube was desirable, but it could not be attained by stirring without disrupting the junction. The U-tube was immersed in an oil thermostat and allowed to equilibrate until fluctuations fell below a certain acceptable value; for example, 0.5 $\mu\text{v}/\text{min}$. The uniformity of temperature was improved by placing a layer of mineral oil over the electrolyte in the bells to decrease evaporation.

The thermostat temperature ($\sim 30^\circ\text{C}$) was maintained to within 0.002° as indicated by a Beckman thermometer, but thermistors revealed short-time fluctuations around the average value which amounted to perhaps twice this amount. The thermostat contained oil instead of water, as the conductivity of the latter sometimes permitted parasitic currents to enter the measuring system.

Suppression of convection currents.—*Experimental details.*—The most important single factor for making quantitative measurements was the suppression of convection currents, which, if present, completely vitiated attempts to measure heats. The difficulty was simply overcome by making the electrolyte about 20 or 30 times more viscous than water.

The only thickening agent which we found to be satisfactory for both neutral and acid solutions was a polyacrylamide.³ It did not hydrolyze and was non-ionic. In a concentration of about 2% by weight it increased the viscosity of solutions about 20- to 30-fold, but did not affect the conductivity.

Details of procedure.—The two electrolytes were introduced into the U-tube with care to prevent mixing. A cork disk placed at about the position of the junction was helpful. Next, a set of four thermistors was placed with their beads in the horizontal plane of the slit between the two portions of the U-tube, and the pointer on the scale of the screw mechanism which raised or lowered the thermistors was set to zero. A sharp junction was produced by applying a slight vacuum to the side tube attached to the plastic housing and drawing off both electrolytes simultaneously. The volume of electrolyte drawn off varied from 50 ml to a few hundred milliliters. After each measurement (or pair of measurements) the junction was renewed. Typical diagrams of recordings of temperature against time are shown in Fig. 3. The use of a recording potentiometer appeared to offer no advantage over direct reading of the microvoltmeter.

Calculations.—Each measurement of a local reversible heat effect involved at least two passages of current in opposite directions through the U-tube. The electrochemical effect, P , is reversible, and one direc-

³ The polyacrylamide, Cyanamer P250, is a product of American Cyanamid Company.

tion of current flow produces heating and the other cooling, both effects being of equal magnitude. This property of the effect enables it to be differentiated from the Joule heat, which is of the same sign and magnitude regardless of the direction of the current flow. The electrothermal effect at any locality is equal to one-half the difference between the two heat effects, and the Joule heat effect is equal to one-half of the sum, as the following equations show

$$\begin{aligned} J + P &= \Delta T_1 & [1] \\ J - P &= \Delta T_2 & [2] \end{aligned}$$

$$\begin{aligned} 2P &= \Delta T_1 - \Delta T_2 & [1] [-2] \\ P &= \frac{1}{2}(\Delta T_1 - \Delta T_2) \\ J &= \frac{1}{2}(\Delta T_1 + \Delta T_2) & [2] [+2] \end{aligned}$$

where J and P are temperature changes contributed by the Joule and the electrochemical heat effects, respectively, and ΔT_1 and ΔT_2 are the measured temperature changes of the environment resulting from passing the current in a forward and reverse direction.

To convert the readings, which were in microvolts, into numbers representing energy, it was necessary to establish the relation between the increase in temperature of an electrolyte and the electrical energy expended. First, the specific resistance of each electrolyte was measured. Then a calibration was made by passing current ranging from about 7 ma/cm² to about 34 ma/cm² through the U-tube with the thermistor beads at least 3 cm from the junction, so that the reversible heat was not included. The relation between the reading of the microvoltmeter and the energy developed per cubic centimeter of electrolyte is: $I^2Rt = kv$ or $k = I^2Rt/v$ where I is the current in amperes per square centimeters of junction, R is the specific resistance of each electrolyte in ohm-cm, t is seconds, and v is microvolts. The proportionality factor k is then the number of Joules required to change the temperature of 1 cm³ of electrolyte by a value equivalent to 1 μ v.

To obtain the reversible electrothermal heat, a plot of P (the local electrothermal effect) was made with microvolts as ordinates against distance from the junction as abscissa. The area under the curve was obtained with a planimeter. The area was converted into an energy term, P_j , of Joules/cm² of junction by means of the constant k determined as above. The voltage-equivalent, V_p , was equal to P_j/It .

Validation of calorimetry by temperature profile.— Since the reversible electrochemical heat of solutions has not been measured previously by the temperature profile method, the procedure needed to be validated. In order to do this, a metallic lamella was substituted for the liquid junction and heat was generated by passing current in the plane of the lamella. The rate of heat evolution was within the range of that produced by the electrothermal effect. The heat output calculated from the temperature profile agreed within about 5% with the heat calculated from the current, voltage, and time. This agreement was adequate for the present state of development of temperature profile calorimetry.

Manuscript received Nov. 18, 1963; revised manuscript received May 22, 1964.

Any discussion of this paper will appear in a Discussion Section to be published in the June 1965 JOURNAL.

REFERENCES

1. J. M. Sherfey and A. Brenner, *This Journal*, **105**, 660 (1958).
2. J. M. Sherfey, *ibid.*, **110**, 213 (1963).
3. W. H. Metzger, Jr., and J. M. Sherfey, *Electrochemical Technology*, To be published.
4. Henri Bagard, *Ann. chim. phys.*, **3**, 7th series, 83 (1894).
5. Max Planck, *Ann. Physik*, [3] **39**, 161 (1890).
6. W. J. Hamer, *J. Am. Chem. Soc.*, **57**, 662 (1935).
7. E. Lange and Th. Hesse, *Z. Elektrochem.*, **39**, 374 (1933).

Electron Microscope Observations of the Crystallization of Anodically Formed Tantalum and Niobium Oxide Films¹

R. E. Pawel and J. J. Campbell

Metals and Ceramics Division, Oak Ridge National Laboratory, Oak Ridge, Tennessee

ABSTRACT

Anodic oxide films ranging in thickness from about 200 to 1000 Å were formed on electropolished surfaces of tantalum and niobium by conventional techniques. The films were then stripped from the metal, given a variety of thermal treatments in vacuum, and examined directly in the electron microscope. Crystallization of the amorphous films was induced by high-temperature annealing or in the microscope itself by increasing the beam intensity. The distinguishing features of each type of crystallization process are discussed and illustrated with appropriate micrographs.

The characteristics of anodically formed amorphous oxide films on the so-called valve metals, particularly tantalum, have been investigated intensively for a number of years (1,2). The changes in the dielectric properties of the films as their environment is altered are of particular interest from a practical standpoint, and considerable understanding of this behavior has evolved from continuing research.

Most previous work has been concerned with the nature of the films as they exist in intimate contact with the substrate metal; examination of the stripped films by transmission electron microscopy has been included as a tool in only a few investigations. Harvey and Wilman (3) used electron diffraction to characterize the crystallization of stripped tantalum pentoxide films heated at temperatures up to 750°C. Their

method of stripping the anodic oxide film made use of the fact (4, 5) that films formed on chemically polished tantalum are not strongly adherent and, thus, small pieces could be removed by a cathodic treatment subsequent to anodizing the specimens. These investigators found that crystallization occurred above 700°C although some regions of the films crystallized at slightly lower temperatures. Their data also indicated that the amorphous, as-stripped oxide crystallized first to a hexagonal structure, then to an orthorhombic structure when annealed at higher temperatures or for longer times. Calvert and Draper (6) found that the nominal crystallization temperatures for films in place on the metal varied with the forming electrolyte, the highest crystallization temperature observed being about equivalent to that of Harvey and Wilman's stripped films. The structure, determined from glancing-angle x-ray diffraction techniques, was found

¹ Research sponsored by the U.S. Atomic Energy Commission under contract with the Union Carbide Corporation.

to be orthorhombic with some pattern anomalies which were explained by assuming varying degrees of disorder in the a and b axes.

Vermilyea (5, 7-9) investigated the crystallization of films in place on tantalum by both thermal and electric-field stimuli. The thermal crystallization spectrum was found to lie between 500° and 800°C, and the x-ray pattern from a thin specimen held for 1 hr at 800°C and examined in transmission indicated β -Ta₂O₅ as the product. "Field crystallization" (5) was found to occur at temperatures between 0° and 100°C, providing a strong electric field was present in the film. It should be emphasized, however, that this process is probably not one of crystallization in the usual sense and is not necessarily similar to thermal crystallization. In the case of field crystallization, growing regions of crystalline oxide mechanically displace the overlying amorphous film.

The electrochemical behavior of niobium, as well as the properties of the anodic film, are qualitatively similar to those of tantalum (1, 2, 10). However, the processes leading to crystallization of the amorphous, as-formed anodic niobium oxide film appear to require less activation. As with tantalum, the part played by impurities and imperfections is recognized as large, but is not well understood.

This paper reports results of one phase of an investigation dealing with the effects of anodically formed oxide films on the subsequent thermal oxidation characteristics of tantalum and niobium. Although we are more concerned with the properties of the film as it exists on the metal, some interesting phenomena are associated with the stripped films which revealed themselves rather spectacularly in the electron microscope. Through these observations, it is possible to infer some of the expected events for a film in contact with the metal.

Experimental Procedure

Specimens for the electron microscope were prepared by mechanical stripping of the anodic oxide films formed on electropolished surfaces. Because of high absorption, it was impractical to use transmission microscopy with specimens thicker than about 1000Å. Most of the films were in the 200-400Å range.

Tantalum and niobium (nominal analysis of tantalum and niobium is about 99.7-8% with Ta, Nb, Fe, W, and Si being major metallic impurities; interstitial content after vacuum anneal is 200-300 ppm) coupons were cut from 0.020-in. sheet and annealed in vacuum for 2 hr at 1600° and 1000°C, respectively. These coupons were mechanically polished through 0.3 μ alumina and electropolished in a 90% H₂SO₄-10% HF solution. A length of 0.020-in. tantalum wire was lightly discharge-welded to one end of each specimen to serve as support and electrical contact during anodization.

Anodization at a given voltage was accomplished through a series of decreasing resistances for a time sufficient to ensure a good reproducibility of thickness. The oxide thickness-voltage calibration in the electrolytes given below was determined to be 16.7 Å/v for tantalum and about 26.7 Å/v for niobium. These figures agree reasonably well with previous measurements (2).

In order to strip large areas of anodic oxide film from the electropolished specimens, it was desirable to anodize the specimens in a solution containing a small amount of fluoride ion. This is the basis of a previously reported, very sensitive sectioning technique for these metals (11). Films formed in 0.5% Na₂SO₄ to which two drops of HF per 100 cc had been added were found to strip easily when pulled off with plastic tape. Later it was found that several dilute fluoride salts worked equally as well, and we are now using a 0.2% KF solution as the anodizing bath.

Specimens for transmission microscopy were prepared by flooding the surface of the anodized specimen with a 2% solution of Parlodion in amyl acetate.

The solution was allowed to dry and the resulting film peeled off, removing with it the underlying oxide film. The Parlodion was then dissolved by several washings with amyl acetate and small pieces of the film were then picked up on standard 1/8-in. microscope screens. Copper or stainless steel screens were used when the specimens were annealed prior to observation in the microscope.

Results and Discussion

There were few distinguishing features of as-stripped tantalum and niobium anodic films when viewed in the electron microscope at 100 kv. Since the anodic film is essentially an unshadowed replica of the electropolished surface, little structure is observed. However, the film stripped from freshly electropolished tantalum did show an array in the background which was a remnant of the "bubble-raft" texture (12) (a series of shallow depressions about 100Å deep with 700-800Å separation) existing on the surface prior to anodizing. This structure was not observed in thick anodic films when viewed by transmission or surface replication, in contrast to what has been reported for thermal oxidation (12). This observation is consistent with the prevailing concept that anodic growth involves primarily tantalum ion migration while thermal oxidation places a greater importance on oxygen diffusion. In transmission electron diffraction, the broad halos which indicate very fine crystallite size or amorphous material were observed.

Beam crystallization.—If the intensity of the electron beam in the microscope was increased, particularly near a crack or edge of the film, the amorphous film could be induced to crystallize. The crystallized region was characterized by increased electron transmission and a very high density of extinction contours which moved about as the region grew or as the direction of the beam was changed. Figure 1 shows crystalline (on the left) and amorphous regions in a tantalum oxide film 250Å thick, the crystallization having been initiated by the action of the beam. The rate of growth of the interface could be controlled by varying the intensity of the electron beam at the interface. Thus it was possible to stop the action, take a picture, and then continue the process by increasing the beam intensity. The size of the crystallites depended heavily on the speed of the growth front or on the intensity and position of the beam with respect to the front. It is difficult to say whether the trigger for crystallization in this case was entirely thermal, or if other factors such as strain or impurities were involved.

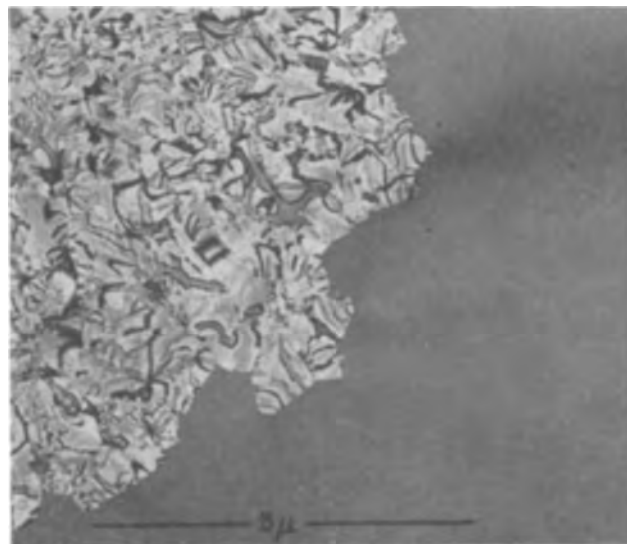


Fig. 1. Electron micrograph showing beam-crystallized region growing in amorphous tantalum oxide film; anodic film 250Å thick.



Fig. 2. Electron micrograph showing crystalline regions of widely different grain size, beam-crystallized; anodic tantalum oxide film 250Å thick.

It was possible in some instances to increase the beam intensity in a crystallized region and cause grain growth and rearrangement to occur. An example of such an occurrence is shown in Fig. 2 where large grains, defined by the extinction contour boundaries, grew into a region of finer grains under the influence of the beam. This behavior is a graphic illustration of a fundamental metallurgical phenomenon. It should be pointed out that the extinction contours seen in the figures do not indicate film structure, but merely show that the film is crystalline and wrinkled on a very fine scale.

Stripped anodic films from niobium behaved similarly, although it was more difficult to control the growth rate of a crystallizing region with beam intensities also suitable for viewing.

Thicker films seemed to crystallize even more easily in the microscope. In a large number of cases, crystallization commenced with a "burst" as the beam intensity was increased. A "nucleus" formed in this manner sometimes had several cracks, presumably because of the volume decrease associated with the product plus the more efficient constraint system of its thicker amorphous oxide surroundings. An example



Fig. 3. Electron micrograph of crystallized region in thick anodic film, beam-crystallized; anodic tantalum oxide film 1000Å thick.

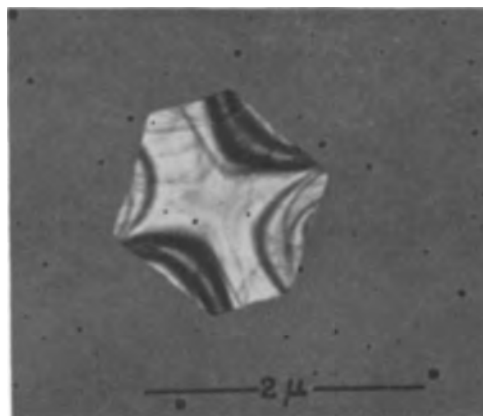


Fig. 4. Electron micrograph of small crystallite formed in anodic film. 250Å anodic tantalum oxide film annealed in vacuum for 30 min at 600°C.

of such a region is shown in Fig. 3. Most of the detail visible in this figure is also via extinction effects, although at higher magnification (especially in thermally crystallized films) dislocation networks and other structure were observed. Frequently, however, very large areas of film crystallized to a fine-grain network without any trace of cracks. It was almost impossible to control the crystallization of the thicker films in the microscope due to poor visibility and the speed at which the action proceeded; the crystallized regions were also subject to considerable rearrangement in the beam.

Thermal crystallization.—Amorphous stripped films can be crystallized by conventional annealing in vacuum at elevated temperatures. For tantalum oxide films about 250Å thick, the first evidence of thermal crystallization was observed on specimens annealed for 30 min at 600°C. Small regions, having mostly hexagonal or rectangular symmetry, were inferred as crystalline by the presence of extinction contours. The crystallites were too small at this stage to be identified by selected area diffraction. Figure 4 is an example of such a small crystal observed in a specimen annealed for 30 min at 600°C. Specimens annealed up to 16 hr at 600°C exhibit larger crystallites of the same description from which electron diffraction patterns were obtained, confirming the fact that they were single crystals. For the films studied, two basic symmetries of single-crystal diffraction patterns were observed. Patterns having hexagonal symmetry were usually associated with nuclei having hexagonal shape, while patterns having two- or fourfold symmetry were associated with either small rectangularly shaped crystals or larger leaf-shaped crystals like those shown in Fig. 5. The latter type of crystal predominated during crystallization of thin 250Å films at 600° and 700°C. However, especially for the case of thicker films annealed at higher temperatures, the completely crystallized oxide showed large areas with hexagonal symmetry in their diffraction patterns which were now complicated by Moiré and/or superlattice reflections.

Figure 5 illustrates the process of crystallization as observed in the electron microscope after annealing for short times at temperatures from 600° to 900°C. When the annealing temperature was low, single nuclei could grow relatively large before interfering with each other. Each "leaf" of the crystals shown in Fig. 5a and 5b was a single crystal; generally, the misorientation between "leaves" was one of rotation in the plane of the film. On increasing the annealing temperature, the average crystallite size decreased and the manner in which the crystals resisted impingement was revealed (Fig. 5c). A completely crystallized film is shown in Fig. 5d. Obviously, some of the structural details of the film were obscured because of the high density of extinction contours.

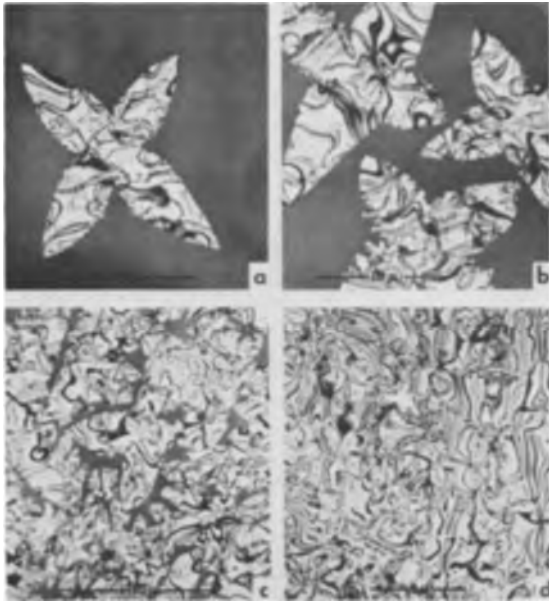


Fig. 5. Electron micrographs illustrating thermal crystallization sequence in 250 Å thick anodic tantalum oxide film. (a) 8 hr at 600°C; (b) 18 hr at 600°C, note the mutual interference of the crystals to growth; (c) 1 hr at 700°C; (d) 30 min at 900°C, completely crystallized.

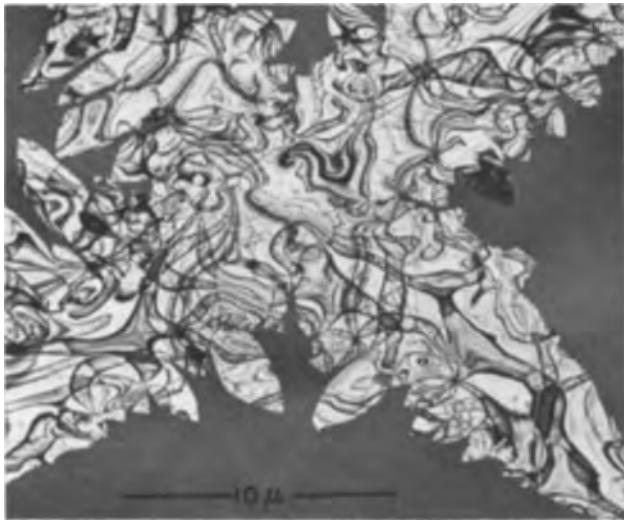


Fig. 6. Electron micrograph of a large crystallite in an anodic tantalum oxide film 275 Å thick. Multiple-branching into a "two-dimensional dendrite" is observed. Annealed in vacuum 18 hr at 600°C.

The growth sequence illustrated in Fig. 5 is similar in several respects to a two-dimensional dendritic crystallization process. When a crystallite grew comparatively large, secondary and even tertiary branches (characteristic of dendritic growth) were associated with each leaf. Such a structure is shown in Fig. 6. In analogy to processes involving dendritic growth it becomes all the more important in attempting to give a complete description of the crystallization process for the anodic film to consider such variables as the energy of crystallization, the heat transfer characteristics of the film (and its support), impurities, directional stresses in the film, and surface and interfacial energy considerations. Undoubtedly, as a result of these variables, differences are to be expected in the morphology of the crystallized regions depending on the initial condition of the metal surface, the anodizing solution, and the manner of washing, handling, and annealing the stripped films. While such variations were indeed observed, the results presented are typical for the conditions of our experiments.

In the thicker (1000 Å) films, there was less severe wrinkling and, as a consequence, more true structure of the films could be observed although the resulting micrographs were very dark and reproduced poorly. When annealed at temperatures of 900°-1000°C, crystal boundaries and dislocation arrays were seen in the film, and occasionally what appeared to be a fine Moiré pattern was noticed. Moiré diffraction effects were also observed. Annealing the 1000 Å film at 600°-700°C resulted in small crystallites being formed in the amorphous matrix. These crystallites did not consistently have the geometric shapes observed in the 250 Å films, nor did they behave in the same fashion. Many crystals as large as 10 μ in diameter were observed which apparently had not yet grown through the whole thickness of the film. This phenomenon, implying surface nucleation, is probably general to all film thicknesses.

The process of thermal crystallization of films stripped from niobium specimens was qualitatively the same as that for tantalum oxide films. The first stages of crystallization, consisting mostly of the generation of small rectangular regions of crystalline oxide, were observed after annealing 200 Å films for 30 min at 500°C. Crystallization was complete for such a film annealed for 30 min at 600°C.

X-ray studies.—Although a structure analysis of the crystalline oxide is certainly beyond the scope of the present paper, the x-ray results on tantalum oxide prepared under different conditions are useful in interpreting some of the electron-optical observations. Specimens for x-ray analysis were prepared by crystallizing stripped anodic films at 600° and 1000°C in both oxygen and vacuum environments. For comparison, specimens of tantalum metal were completely oxidized in dry oxygen at these temperatures, and samples of each were then held in vacuum for extended periods at the temperature of oxidation.

The anodic film specimens were obtained by stripping large 1 x 4 cm areas in the manner described earlier. These films were removed from the amyl acetate bath with a fine quartz fiber, the film being manipulated so that it coiled itself around the fiber. Thus, the specimen presented many thicknesses of film to the x-ray beam. A comparison of the Debye-Scherrer films for such specimens yielded the following general conclusions: (i) No significant difference was detected in the patterns from crystallized anodic films and those from thermally oxidized tantalum. (ii) No significant difference was detected in the pattern from the specimens prepared in oxygen and those annealed

Table I. Diffraction data for β -Ta₂O₅ (Cu-K α radiation)

Interplanar spacing <i>d</i> , Å	Intensity	Interplanar spacing <i>d</i> , Å	Intensity
3.34	w	1.332	s-
3.87	s+	1.317	m+
3.31	w+	1.306	m-
3.11	s+	1.298	m
3.06	s	1.226	m
2.98	w-	1.214	m-
2.721	w	1.199	s-
2.643	w+	1.180	m-
2.534	w+	1.145	m
2.441	s+	1.133	w-
2.416	s	1.117	w
2.360	w	1.094	w-
2.098	w	1.074	w
2.031	w+	1.060	w+
1.940	s	1.052	w
1.826	m+	1.044	w
1.800	m+	1.032	w+
1.764	m	1.022	w+
1.677	w	1.015	w-
1.652	s+	1.000	w+
1.647	s-	0.997	w-
1.633	m	0.984	w-
1.604	m-	0.973	w+
1.574	m	0.939	w-
1.543	m	0.929	m
1.502	w+	0.916	w-
1.485	w+	0.893	w+
1.462	m+	0.882	w+
1.440	m+	0.859	m
1.403	m	0.829	m
1.385	m		

in vacuum after crystallization or oxidation, although the vacuum treatments produced a gray cast to the normally chalk-white bulk oxide. Thus it appears that the slight variation of stoichiometry did not produce a noticeable modification of structure. (iii) Several broad diffraction lines from the low-temperature specimens were observed as doublets after 1000°C anneals. A noticeable intensity increase also occurred for many high index lines. Such behavior is consistent with the interpretation of Calvert and Draper (6) who suggested that ordering processes occur during extended or high-temperature annealing. The x-ray diffraction data taken from a specimen held in oxygen at 1000°C is presented in Table I. Reasonably good agreement exists between the stronger lines of this pattern and literature data for β -Ta₂O₅ (13, 14). In this regard, it should be re-emphasized that crystallized anodic oxide films, and perhaps thermally formed crystalline oxide films as well, can exist in a rather pronounced fiber texture. Such a condition could affect the direct comparison of x-ray data obtained by the many techniques which are commonly applied.

Conclusions

The anodic oxide films formed on tantalum and niobium surfaces can be easily stripped from the metal if they are formed in electrolytes containing fluoride ion. The amorphous, as-stripped film can be crystallized in the electron beam of an electron microscope or by annealing at elevated temperatures in air or vacuum. The crystallized regions of thin films are usually characterized by a high density of well-defined extinction contours. For stripped films, thermal crystallization is initiated in short times above 600°C for tantalum oxide and above 500°C for niobium oxide. If thermal crystallization is allowed to take place at lower temperatures, the growth of single-crystal nuclei can be observed. It appears that crystallization results in a limited number of preferred orientations existing in the plane of the film. This pronounced fiber-like texture may account for some anomalies of the structure of oxides crystal-

lized from anodic film specimens. This texture in the crystallized films may also lead to other directional properties.

Acknowledgments

The authors would like to thank J. V. Cathcart and J. O. Stiegler of the Metals and Ceramics Division, Oak Ridge National Laboratory, for helpful discussions. In addition, appreciation is extended to R. M. Steele of this Laboratory for the x-ray data.

Manuscript received May 13, 1964. This paper was presented at the New York Meeting, Sept. 29-Oct. 3, 1963.

Any discussion of this paper will appear in a Discussion Section to be published in the June 1965 JOURNAL.

REFERENCES

1. For example, see references contained in L. Young, "Anodic Oxide Films," Academic Press, New York (1961), particularly the work of Young, Vermilyea, Dewald, and Guntherschulze and Betz.
2. L. Young, *Proc. Roy. Soc., A-244*, 41 (1958); *Can. J. Chem.*, **38**, 1141 (1960).
3. J. Harvey and H. Wilman, *Acta Cryst.*, **14**, 1278 (1961).
4. L. Young, *Trans. Faraday Soc.*, **53**, 841 (1957).
5. D. A. Vermilyea, *This Journal*, **102**, 207 (1955).
6. L. D. Calvert and P. H. G. Draper, *Can. J. Chem.*, **40**, 1943 (1962).
7. D. A. Vermilyea, *Acta Met.*, **1**, 282 (1953).
8. D. A. Vermilyea, *ibid.*, **5**, 113 (1957).
9. D. A. Vermilyea, *This Journal*, **104**, 485 (1957).
10. D. M. Lakhiani and L. L. Shreier, *Nature*, **188**, 49 (1960).
11. R. E. Pawel and T. S. Lundy, *J. Appl. Phys.*, **35**, 435 (1964).
12. J. V. Cathcart, R. Bakish, and D. R. Norton, *This Journal*, **107**, 668 (1960).
13. ASTM Powder Diffraction File, ASTM-STP-48-M2 (1963), card 8-255 (Battelle Memorial Institute).
14. L. K. Frevel and H. W. Rinn, *Anal. Chem.*, **27**, 1329 (1955).

The Interaction of Electrophoretic and Dielectrophoretic Forces

William F. Pickard

Division of Engineering and Applied Physics, Harvard University, Cambridge, Massachusetts

ABSTRACT

The effect of ionic space charge on dielectrophoretic forces in dielectric fluids is examined both theoretically and experimentally. Two new theoretical results are presented. The alteration of dielectrophoretic force by a space charge is illustrated experimentally by exhibiting the frequency dependencies of the Pellat-Greinacher method of determining the electric susceptibility of liquids. Finally, a new method is developed for measuring the electrical conductivity of liquids.

Since the investigations of Pohl (1) several years ago, it has been customary to divide electrical force effects in dielectric fluids into two classes: dielectrophoretic for those which arise from the action of the applied electric field on the charge-free dipolar molecules which constitute the bulk of the fluid and electrophoretic for those which arise from the action of the field on charged particles in the fluid.

That it is difficult in practice to achieve a force effect which is purely dielectrophoretic or purely electrophoretic has been recognized at least since the dielectrophoresis experiments of Geyman (2), and has been discussed by a number of authors: Andrade and his co-workers (3, 4) investigated the electrophoretic masking of the viscoelectric effect; Pohl (5) and Horgan and Edwards (6), for example, have discussed their

interaction in force effects observed in systems with air-liquid interfaces; Pohl (7) has presented a theoretical analysis of their relationship from a molecular point of view; Ogawa (8) and Pickard (9) have discussed their interrelationship in a fluid acted upon by a rotating electric field; and, finally, Pohl (1) and Pickard (10) have discussed methods for distinguishing between electrophoretic and dielectrophoretic forces.

However, while the interrelationship of these forces has been recognized, discussed from a molecular point of view, and even used to explain various experimental observations (3, 4, 9, 11), it appears not to have been given a quantitative formulation from a macroscopic viewpoint. In this paper two relatively general results about the effect of interelectrode space charge on di-

electrophoretic forces will be proved. Some simple experiments which support the theory will be described.

Theory

The electric force per unit volume acting on a dielectric fluid is given to good approximation by (12)

$$\vec{F} = \vec{F}_e + \vec{F}_d \quad [1]$$

where the electrophoretic force \vec{F}_e is

$$\vec{F}_e = \rho \vec{E} \quad [1a]$$

and the dielectrophoretic force \vec{F}_d is

$$\vec{F}_d = \frac{1}{2} (\epsilon - \epsilon_0) \text{grad} (\vec{E} \cdot \vec{E}) \quad [1b]$$

Here ρ is the volume density of charge, \vec{E} is the electric field in the fluid, ϵ is the permittivity of the fluid, and ϵ_0 is the permittivity of free space. It can be shown (13) that the electrical energy \mathcal{E} stored in a volume Γ , which is delimited by a finite number of surfaces Σ_i ($i = 1, 2, \dots$) of known potential, is

$$\mathcal{E} = \frac{1}{2} \int \epsilon E^2 d\Gamma \quad [2]$$

It is difficult to predict the variation of \vec{F}_e , \vec{F}_d , and \mathcal{E} as ρ is varied and the electrode voltages held fixed. Some mathematical analysis is given in an Appendix to this paper, and only two results will be quoted here.

I. The introduction of space charge into a fluid near a convex (or planar) electrode alters the dielectrophoretic force in such a manner that the electrophoretic force is aided.

II. The effect of adding an arbitrary space charge to an initially charge free volume, which is bounded by surfaces of fixed potential, is to increase the electrostatic energy associated with the volume.

The Sumoto effect (11) is thought to provide an experimentally observable example of Theorem I. Theorem II will be applied in the next section.

The Pellat-Greinacher Experiment

It was suggested by Pellat (14), verified by himself (15) and Fortin (16), and later rediscovered by Greinacher (17) that the dielectrophoretic force tending to suck a dielectric liquid upward between the plates of a vertically oriented condenser could be used to measure the permittivity of the liquid. In a related experiment Gyemant (2) studied the height to which a dielectric liquid of known permittivity would rise between the plates of a condenser; he recognized the necessity of using an alternating applied voltage to reduce space charge effects, although he did not study the variation of height of rise with frequency.

The basic apparatus for a permittivity determination by the Pellat-Greinacher method is a vertical glass pipe of known cross sectional area s which is connected via a suitable U-tube to a two-electrode condenser into which a liquid can be sucked by an applied field. This apparatus is filled with liquid to a level at which the condenser is partially filled. Let the cross sectional area of the condenser be S and let the height of rise of the liquid within it be H . Then, neglecting possible changes in the shape of the liquid surface due to the action of the electric field, the change in the stored electrical energy will be

$$P_E = \frac{(\epsilon - \epsilon_0)}{2} H \int_S E^2 dS \quad [3]$$

which can be rewritten as

$$P_E = \frac{(\epsilon - \epsilon_0)}{2} H \nu I_0 \quad [4]$$

where I_0 is the value which the integral in [3] would have in the absence of space charge and ν is a proportionality factor which takes space charge into account; by Theorem II ν will never be less than unity. A rise H in the condenser will necessitate a lowering h ($=S/s H$) of the liquid in the glass pipe; it is the level h which is commonly observed in experiments. The mechanical potential developed by this shift in heights will be

$$P_M = \frac{1}{2} \delta g h^2 \frac{(s + S)}{S} s \quad [5]$$

where δ is the density of the liquid and g is the acceleration of gravity. The equilibrium height in the glass tube is readily found by determining the extremum of $P_M - P_E$

$$h = \nu(\epsilon - \epsilon_0) \frac{1}{S + s} \frac{I_0}{2\delta g} \quad [6]$$

For a parallel plate condenser of plate separation l the formula for the relative electric susceptibility $\chi_r = (\epsilon - \epsilon_0)/\epsilon_0$ becomes, from [6]

$$\nu \chi_r = \left[\frac{2\delta g}{\epsilon_0} \left(\frac{s + S}{S} \right) l^2 \right] h / V_{\text{eff}}^2 \quad [7]$$

where V_{eff} is the voltage across the liquid. Two facts about [7] should be pointed out. First, that while it is generally assumed that $h(V_{\text{eff}}^2)$ curves determine χ_r , it is seen here that they actually determine an "effective" relative susceptibility $\nu \chi_r$. Second, h is not exactly a measure of H but is rather a measure of the increase of the volume of liquid in the condenser: in practice, ν may contain a small component arising from a change in meniscus shape due to the applied electric field.

In the apparatus used for the experiments to be described the glass pipe was a length of precision-bore Pyrex tubing of 1.26 cm ID; liquid height was measured to 1/50 mm using a cathetometer. The condenser was made of a thin ($\sim 1/2$ cm) piece of Teflon (duPont brand polytetrafluoroethylene) with a rectangular slot (approximately 2 by 5 cm) milled into it and two metal plates which were pressed against the Teflon spacer; the plates considerably overlapped the edges of the rectangular slot so that fringing field in liquid would be reduced as much as possible. Liquid was admitted to the condenser by way of a hole drilled through from the bottom edge of the Teflon spacer into the bottom edge of the rectangular slot; air escaped through a similar hole drilled into the top of the spacer. The appropriate constants of the condenser were $S = 0.976 \text{ cm}^2$ and $l = 0.503 \text{ cm}$. The liquid used for these experiments was acetone; its purification has been described elsewhere (18). All measurements were corrected to 25°C using the $d\epsilon/dT$ values of Cole (19);¹ at this temperature acetone has a relative permittivity (20) of 20.76.

Two types of condenser plates were used. The basic plates were made of 0.03 in. molybdenum which had been cleaned in a strong solution of sodium hydroxide; this metal was chosen since it was known to produce a large space charge in acetone (11, 18). For some experiments these plates were used with a thin coating ($\sim 1/2$ mil) of Teflon. The variation of h with the mean-square applied voltage V^2 was linear with either type of plate. The variation of h with frequency f , or angular frequency $\omega = 2\pi f$, for some fixed voltage was radically different for the two types of plates.

For the coated plates one would expect $h(f)$ curves

¹ The proper temperature to use for correcting the permittivity of the acetone to 25°C was that of the acetone itself and not that of the room which was available; as a result of ohmic heating, the room temperature could be lower than that of the acetone. To minimize this effect the voltage was applied only long enough to set the cross-hairs of the cathetometer telescope on the liquid meniscus in the glass pipe; it was left off while the cathetometer was read, frequency reset, etc.

to show, for constant V , a superposition of two effects. First, since the liquid itself can ideally be represented as an impedance Z composed of a resistance R and a capacitance C in parallel and since the Teflon coatings on the plates can be considered to be capacitances C_T in series with Z , the effective voltage across the liquid will not be the applied voltage V but can be approximated by

$$V_{\text{eff}} = V \frac{\left(\frac{R}{1 + j\omega CR} \right)}{\left(\frac{R}{1 + j\omega CR} \right) + \frac{2}{j\omega C_T}} \quad [8]$$

The limiting forms of [8] are

$$V_{\text{eff}} \doteq \frac{V}{1 + 2 \frac{C}{C_T}} \quad \omega CR \rightarrow \infty \quad [9a]$$

$$V_{\text{eff}} \doteq V \frac{j\omega C_T R}{2} \quad \omega CR \rightarrow 0 \quad [9b]$$

h should tend to zero with the applied frequency and should approach an asymptotic value somewhat less than the theoretical bare plate value as the frequency becomes large. If the second effect to be discussed is not too large, it should be possible to obtain a good estimate of the conductivity from the $h(f)$ curve. The second effect for the coated plates is caused by the charge between them. By Theorem II and Eq. [6] this will result in an increase in h ; however, since the space charge will decrease with increasing f , this effect should be most pronounced at low frequencies and die out at higher ones. These two effects make possible two types of curves: (i) monotone increasing toward the high frequency asymptote, and (ii) increasing to a maximum at some frequency and then decreasing toward the high frequency asymptote. The latter form is to be expected whenever space-charge effects persist into the frequency range where [9a] obtains. In the experiments performed with acetone both forms were observed, thus pointing up the pre-

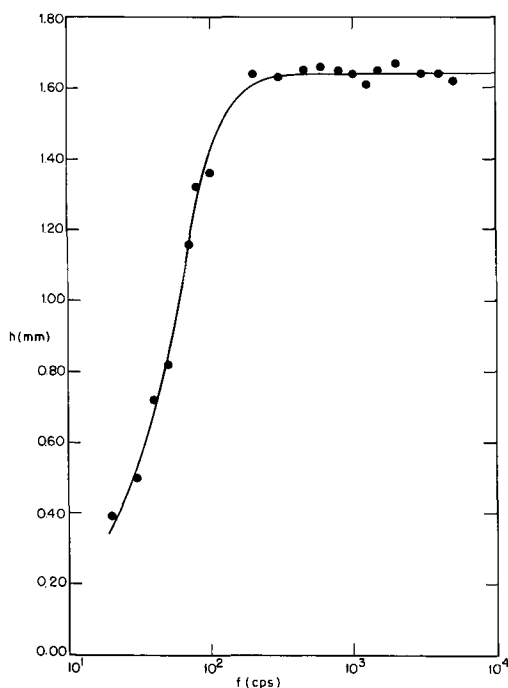


Fig. 1. Typical $h(f)$ curve for cell with Teflon coated plates. $V = 3.05$ kv. The asymptotic value of $h(1.64$ mm) yields a susceptibility which, when corrected for temperature and, by Eq. [9a], for a Teflon layer 0.5 mil thick on each plate, gives a relative permittivity of 20.5.

viously noted fact that, in acetone at least, the conductivity is not strongly correlated with the space charge (18). A typical curve of the first kind is shown in Fig. 1. It should be noted that the rising portion of the curve, while representative of those commonly encountered, is by no means unique, since the frequency range over which it rises is controlled by the conductivity of the acetone, and this tends to drop slowly over a series of runs, presumably due to ionic cleanup of the sample in use. By suitable conditioning of the acetone one could obtain a conductivity less than 3×10^{-7} mho/meter, which is about an order of magnitude less than those which have been reproducibly obtained by electrochemists (21) using metallic electrodes. The $h(f)$ curve obtained using Teflon coated electrodes seems to offer a new method of measuring conductivities without electrodes in the range 10^{-9} - 10^{-3} mho/meter. For example, neglecting the space charge, the curve of Fig. 1 yields, from [7], [8], [9], and a Teflon coating 0.5 mil thick on the plates, a series of conductivity values which decrease slowly from about 1.3×10^{-6} mho/meter at 150 cps to 1.2×10^{-6} mho/meter at 70 cps to 1.0×10^{-6} mho/meter at 20 cps; R , C , and C_T were calculated using the formulas for a parallel plate geometry. This variation is roughly what one would expect if a space charge which damped out with increasing frequency were present: if the true value of σ were 1.35×10^{-6} mho/meter, the data of Fig. 1 would imply, for instance, $\nu = 1.9$ at 20 cps and $\nu = 1.1$ at 50 cps. The example points up a general property of this method that, as long as space-charge effects damp out somewhat below the high frequency asymptote, a moderately accurate value of the conductivity can be obtained.

For uncoated molybdenum condenser plates, one would expect the $h(f)$ curves to decrease monotonically with frequency as the space charge was progressively damped out. This was normally observed except that there was occasionally a tendency for the falling portion of the curve to undershoot the asymptote slightly and, in violation of one's expectation on the basis of Theorem II, to approach it from beneath. This anomaly was probably caused by a modification of the air-liquid interface by the applied field. As in the coated-plate case, the nonasymptotic portion of the $h(f)$ curve was subject to some shift from run to run; this reflected once again the unstable character of space charge in organic liquids. A typical $h(f)$ curve is shown in Fig. 2.

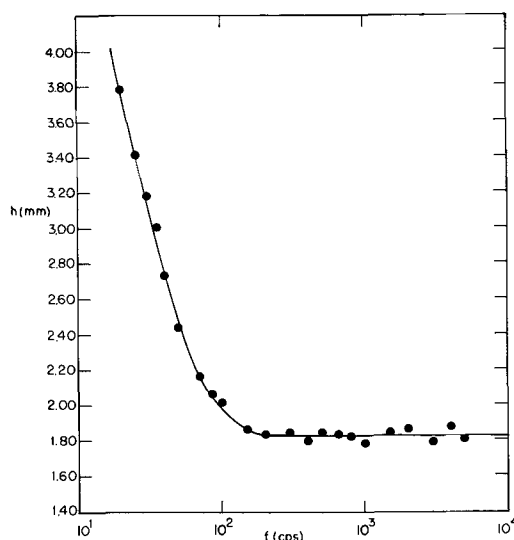


Fig. 2. Typical $h(f)$ curves for cell with bare molybdenum plates. $V = 3.05$ kv. The asymptotic value of $h(1.82$ mm) gave a temperature corrected relative permittivity of 20.8. The ν variation here is slightly larger than that inferred from the $h(f)$ curve of Fig. 1 for the coated-plate case. This suggests that, as might be expected, space-charge effects are more pronounced in a liquid in contact with the driving electrodes.

The values of permittivity obtained for both the coated and uncoated plates are in excellent agreement with the "accepted" value. The agreement obtained here is primarily due to the simple precaution of going to a frequency high enough to annul space-charge effects. The measurements, for example, of Greinacher (17) using the Pellat technique, or of Quincke (22) and Clark (23) using a slightly different dielectrophoretic technique, gave high values of permittivity for virtually all the liquids tested; this discrepancy can be explained by their failure to use a sufficiently high frequency.

Conclusions

It has been shown that the effect of a space charge near a convex electrode immersed in a dielectric fluid is, for space charges of importance in conduction phenomena, always such that the change in the dielectrophoretic force due to the space charge reinforces the electrophoretic force associated with the space charge. An illustration of this rule is provided by the Sumoto effect (11).

It was further shown that the effect of adding space charge to a dielectric bounded by surfaces of fixed potential was, if the system was initially uncharged, always to increase the electrical energy in the system. This result was applied to explaining the frequency-dependent behavior of the rising up of a dielectric liquid between a pair of condenser plates. The experimental data obtained were in accord with the predictions made.

In addition, a new method was described for electrodelessly measuring the conductivity of liquids of intermediate conductivity (10^{-9} - 10^{-3} mho/meter).

Acknowledgment

The author wishes to thank Miss Jennifer H. Smith for her assistance in taking the measurements reported here.

APPENDIX

To investigate \vec{F} consider an equipotential surface Σ which is in contact with a homogeneous fluid of permittivity ϵ . Assume that the frequency of the voltage applied to the system is such that the electric field is derivable from a scalar potential ϕ in the form

$$\vec{E} = -\text{grad } \phi \tag{10}$$

Choose an orthogonal coordinate system (u, v, w) such that $u = 0$ represents the surface Σ and such that, at any point on the surface, \hat{u} , a unit vector along u , is normal to Σ while \hat{v} and \hat{w} are tangential to it. Then, ϕ can be expanded about the point $(0, v_0, w_0)$ in the series

$$\phi = f + (uf_u + Vf_v + Wf_w) + \frac{1}{2}(u^2f_{uu} + V^2f_{vv} + W^2f_{ww} + 2uVf_{uv} + 2uWf_{uw} + 2VWf_{vw}) + \dots \tag{11}$$

where $V = (v - v_0)$, $W = (w - w_0)$, $f = \phi(0, v_0, w_0)$,

$$f_u = \left. \frac{\partial \phi}{\partial u} \right|_{(0, v_0, w_0)}, \text{ etc. Since the surface is an equipotential, } f_v = f_w = f_{vv} = f_{ww} = f_{vw} = 0. \text{ Thus, over distances which are small compared to the surface's radii of curvature}$$

$$\phi = f + uf_u + \frac{1}{2}(u^2f_{uu} + 2uVf_{uv} + 2uWf_{uw}) \tag{11}$$

In such an orthogonal coordinate system (13)

$$\text{grad } \Psi = \hat{u} \left[\frac{1}{e_1} \frac{\partial \Psi}{\partial u} \right] + \hat{v} \left[\frac{1}{e_2} \frac{\partial \Psi}{\partial v} \right] + \hat{w} \left[\frac{1}{e_3} \frac{\partial \Psi}{\partial w} \right] \tag{12a}$$

$$\nabla^2 \Psi = \frac{1}{e_1 e_2 e_3} \left[\frac{\partial}{\partial u} \left(\frac{e_2 e_3}{e_1} \frac{\partial \Psi}{\partial u} \right) + \frac{\partial}{\partial v} \left(\frac{e_1 e_3}{e_2} \frac{\partial \Psi}{\partial v} \right) + \frac{\partial}{\partial w} \left(\frac{e_1 e_2}{e_3} \frac{\partial \Psi}{\partial w} \right) \right] \tag{12b}$$

$e_1, e_2,$ and e_3 are the distance metrics associated with the coordinate system and are non-negative. For $u, V,$ and W sufficiently small it follows, from [10], [11], [12a] and [12b], that

$$\vec{E} = - \left[\hat{u} \frac{1}{e_1} (f_u + uf_{uu} + Vf_{uv} + Wf_{uw}) + \hat{v} \frac{1}{e_2} (uf_{uv}) + \hat{w} \frac{1}{e_3} (uf_{uw}) \right] \tag{13a}$$

$$\text{grad } E^2 = f_u^2 \text{grad} \left(\frac{1}{e_1^2} \right) + \frac{2f_u}{e_1^2} \left[\hat{u} \frac{f_{uu}}{e_1} + \hat{v} \frac{f_{uv}}{e_2} + \hat{w} \frac{f_{uw}}{e_3} \right] \tag{13b}$$

$$\nabla^2 \phi = \frac{1}{e_1 e_2 e_3} \left[\frac{e_2 e_3}{e_1} f_{uu} + f_u \frac{\partial}{\partial u} \left(\frac{e_2 e_3}{e_1} \right) \right] \tag{13c}$$

By using the Poisson equation and [13c], by neglecting appropriate higher order terms, and by assuming that the variation of ϕ is much faster normal to the surface than tangential to it, it is possible to simplify [13a] and [13b] still further

$$\vec{E} = - \hat{u} \frac{f_u}{e_1} \tag{14a}$$

$$\text{grad } E^2 = f_u^2 \text{grad} \left(\frac{1}{e_1^2} \right) - \hat{u} \frac{2}{e_1^3} f_u \left[\frac{\rho_0}{\epsilon} e_1^2 + f_u \frac{\partial}{\partial u} \log \left(\frac{e_2 e_3}{e_1} \right) \right] \tag{14b}$$

where ρ_0 is the value of ρ near $(0, v_0, w_0)$. If it is further assumed that e_1 is sensibly constant near Σ , it is possible to reduce [1a] and [1b] to

$$\vec{F}_e = - \hat{u} \frac{\rho_0}{e_1} f_u \tag{15a}$$

and

$$\vec{F}_d = - \hat{u} \frac{(\epsilon - \epsilon_0)}{e_1} \left[\frac{\rho_0}{\epsilon} f_u + \frac{f_u^2}{e_1^2} \frac{\partial}{\partial u} \log \left(\frac{e_2 e_3}{e_1} \right) \right] \tag{15b}$$

The major assumptions made in deriving these two equations are that the curvature radii of Σ were large compared to $u, V,$ and W and that the variations of ϕ were much larger and more rapid normal to Σ than they were tangential to it. To interpret these expressions for the force it is necessary to deduce also the variation of f_u with ρ_0 . Let f be fixed and let $f_u^{(0)}$ denote the value of f_u in the absence of space charge. Then, sufficiently near Σ

$$f_u^{(0)}/f_u < 1 \quad \rho_0 f < 0 \tag{16a}$$

$$f_u^{(0)}/f_u > 1 \quad \rho_0 f > 0 \tag{16b}$$

where it has been assumed that the boundary conditions have been chosen in such a way that f will have a sign opposite to that of the charges which would be electrostatically attracted to Σ . These equations can be given a simple justification by noting that $\rho_0 f < 0$ represents, in effect, electrostatic shielding which will cause ϕ to vary more quickly and that $\rho_0 f > 0$ represents the opposite. Further, since ϕ is harmonic for $\rho_0 = 0$

$$f_u^{(0)} f \leq 0 \tag{16c}$$

Finally, in problems of conduction that involve force effects in dielectric liquids it invariably turns out that

$$f_u^{(0)} f_u \geq 0 \tag{16d}$$

With the Eq. [15] and [16] it is possible to discuss the several ways in which the electrophoretic and dielectrophoretic forces can vary when the potentials of the

system's electrodes are fixed and the space charge is permitted to change.

For \vec{F}_e there are two simple cases: as $|\rho_0|$ increases from zero, $\hat{u}\vec{F}_e$ becomes increasingly negative (force toward electrode) for $\rho_0 f < 0$, and increasingly positive (force away from electrode) for $\rho_0 f > 0$. However, as a result of the variation of f_u with ρ_0 , this variation is greater for $\rho_0 f < 0$ and less for $\rho_0 f > 0$ than would be expected from a consideration of $\rho_0 f_u^{(0)}$ alone. An interesting consequence of this is that a fluid containing a relatively steady space charge, maintained for example by diffusive forces or by photoemission into the fluid, should, in an alternating electric field, experience a net electrophoretic force toward the electrode.

For \vec{F}_d there are four possible cases as ρ_0 increases from zero

$$(i) \quad \rho_0 f < 0 \text{ and } \frac{\partial}{\partial u} \log \left(\frac{e_2 e_3}{e_1} \right) \cong 0.$$

Force toward electrode increased.

$$(ii) \quad \rho_0 f > 0 \text{ and } \frac{\partial}{\partial u} \log \left(\frac{e_2 e_3}{e_1} \right) \cong 0.$$

Force toward electrode decreased and possibly reversed.

$$(iii) \quad \rho_0 f < 0 \text{ and } \frac{\partial}{\partial u} \log \left(\frac{e_2 e_3}{e_1} \right) < 0.$$

Force away from electrode varied in unpredictable manner.

$$(iv) \quad \rho_0 f > 0 \text{ and } \frac{\partial}{\partial u} \log \left(\frac{e_2 e_3}{e_1} \right) < 0.$$

Force away from electrode varied in unpredictable manner.

Cases (i) and (ii), which correspond to a nonconcave electrode, are most common. Theorem I follows from

them and the results for \vec{F}_e .

To prove Theorem II for the case in which ϵ is a continuous function of position within Γ , split the total electric scalar potential into two parts Ψ and ϕ such that

$$\text{div}(\epsilon \text{ grad } \Psi) = -\rho \quad \text{over } \Gamma \quad [17a]$$

$$\Psi = 0 \quad \text{on } \Sigma_i (i = 1, 2, \dots) \quad [17b]$$

and

$$\text{div}(\epsilon \text{ grad } \phi) = 0 \quad \text{over } \Gamma \quad [18a]$$

$$\phi = \phi_i \quad \text{on } \Sigma_i (i = 1, 2, \dots) \quad [18b]$$

Equation [2] then becomes

$$\mathcal{G} = \frac{1}{2} \int_{\Gamma} \epsilon [\text{grad}^2 \phi + \text{grad}^2 \Psi] dV + \int_{\Gamma} \epsilon \text{ grad } \phi \text{ grad } \Psi dV \quad [19]$$

The proof can be completed by showing that the second term of [19] is identically zero; it must be since it equals

$$\int_{\Gamma} \{\text{div}[\Psi(\epsilon \text{ grad } \phi)] - \Psi \text{ div}(\epsilon \text{ grad } \phi)\} dV$$

which, by the divergence theorem, [17b] and [18a], vanishes. A proof for the case in which Γ has been split into a number of subregions, over each of which the permittivity is constant, has been given elsewhere (24); the extension to many subregions over each of which the permittivity is merely continuous is trivial. It should be noted that an increase in \mathcal{G} does not depend on the introduction of a net charge into Γ : any nonzero ρ , whatever its integral over Γ , will effect an increase.

Manuscript received Dec. 24, 1963; revised manuscript received May 25, 1964.

Any discussion of this paper will appear in a Discussion Section to be published in the June 1965 JOURNAL.

REFERENCES

- H. A. Pohl, *J. Appl. Phys.*, **22**, 869 (1951).
- A. Gyemant, *Wiss. Veröff. Siemens-Konz.*, **5**, No. 2, 55 (1926).
- E. N. Da C. Andrade and C. Dodd, *Proc. Roy. Soc. (London)*, **A197**, 296 (1946).
- E. N. Da C. Andrade and C. Dodd, *ibid.*, **A204**, 449 (1951).
- H. A. Pohl, *J. Appl. Phys.*, **32**, 1784 (1961).
- J. D. Horgan and D. L. Edwards, *J. Appl. Phys.*, **32**, 1784 (1961).
- H. A. Pohl, *This Journal*, **107**, 386 (1960).
- T. Ogawa, *Repts. Sci. Research Inst. Japan*, **36**, 408 (1960).
- W. F. Pickard, *Nuovo Cimento*, **21**, 316 (1961).
- W. F. Pickard, *J. Soc. Electronic Engineers (India)*, **7**, 45 (1963).
- W. F. Pickard, *J. Appl. Phys.*, **33**, 941 (1962).
- W. F. Pickard, *Progress in Dielectrics*, **6**. To be published.
- R. W. P. King, "Fundamental Electromagnetic Theory," Dover Publications, Inc., New York (1963).
- H. Pellat, *Compt. rend.*, **119**, 675 (1894).
- H. Pellat, *ibid.*, **123**, 691 (1896).
- C. Fortin, *ibid.*, **140**, 576 (1905).
- H. Greinacher, *Helv. Phys. Acta*, **21**, 261 (1948).
- W. F. Pickard, *J. Appl. Phys.*, **34**, 251 (1963).
- R. H. Cole, *J. Chem. Phys.*, **9**, 251 (1941).
- J. Timmermans, A. M. Piette, and R. Philippe, *Bull. soc. chim. Belges*, **64**, 5 (1955).
- J. F. J. Dippy and S. R. C. Hughes, *J. Chem. Soc.*, 953 (1954).
- G. Quincke, *Ann. Physik*, **19**, 705 (1883).
- A. L. Clark, *Phys. Rev.*, **6**, 120 (1898).
- W. F. Pickard, Cruft Laboratory Technical Report No. 423, Harvard University, Cambridge (1963).

The Dielectric Properties of Cyanoethylated Polyvinyl Alcohol

Leonard C. Flowers and Daniel Berg

Research Laboratories, Westinghouse Electric Corporation, Pittsburgh, Pennsylvania

ABSTRACT

Polyvinyl alcohol was reacted with acrylonitrile (*i.e.*, cyanoethylated) to obtain a series of polymers differing in degree of cyanoethylation (D.S.). Dielectric constants (ϵ') and $\tan \delta$'s of these cyanoethylated polyvinyl alcohols were measured from 60 cps to 300 kcps and -50° to 75°C ; d-c volume resistivities (ρ) were measured at 25°C . Unusually high dielectric constants were observed; however, the losses did not develop dispersion peaks within the frequency range studied even on cooling the polymers to -50°C . In general, ϵ' and $\epsilon'' = \epsilon' \tan \delta$ first decreased slightly with increasing cyanoethylation, then increased and reached plateaus or maxima at 30 to 40% D.S. Cross linking the polymer had little effect on dielectric properties when the D.S. was high, but lowered ϵ' and ϵ'' and increased ρ when the D.S. was low; these changes were greatest with unmodified polyvinyl alcohol (D.S. = 0). Polar group substitution presumably accounts for the observed variations in dielectric properties.

The dielectric constant (ϵ') of polyvinyl alcohol is about 15 at 60 cycles per second (cps) and 25°C . This is an unusually high dielectric constant even for a polar polymer. Most organic polymers exhibit dielectric constants in a range from about 3 to perhaps 7 or 8 when measured at 60 cps and room temperature.

However, unmodified polyvinyl alcohol (PVA) is readily soluble in water, and the lack of moisture resistance has generally been a deterrent to the use of this polymer for dielectric purposes. By combining PVA with acrylonitrile in a base-catalyzed reaction called cyanoethylation, it is possible to transform the original material into a series of new polymers, cyanoethylated polyvinyl alcohols (CEPVA's), which dissolve less and less easily in water and eventually become virtually insoluble in this medium. Moreover, it is also possible to add cross-linking agents to these new materials in subsequent operations, thus extending their solvent resistance to include many organic solvents in addition to water, as well as improving physical properties. In general, the new polymers possess dielectric constants as high, or in many instances even higher, than are observed with unmodified PVA. Cross linking, as expected, stiffens and hardens the structure; however, when the polymer has been highly cyanoethylated the cross linking and increased rigidity seemingly have little or no effect on dielectric properties. For these reasons, it has been of interest to study the electrical behavior of a series of these CEPVA polymers.

A wide variety of CEPVA polymers can be made by controlling the cyanoethylation reaction. As is indicated in Fig. 1, hydroxy (OH) groups on the long polyvinyl alcohol chains (these chains being represented by X repeating units of the dimer formula in the brackets) are gradually replaced by cyanoethyl ether linkages ($-\text{OCH}_2\text{CH}_2\text{CN}$) derived from acrylonitrile. The rate of replacement is reasonably slow. Hence the reaction can be stopped at appropriate time intervals short of completion to yield a series of homologous polymers which range from 0 to 100% in (OH) groups replaced. The per cent substitution, ($\text{OCH}_2\text{CH}_2\text{CN}$) groups for (OH) groups, is conveniently termed the degree of cyanoethylation. In more general terms, this percentage figure is frequently called the degree of substitution (D.S.) and to avoid unnecessary symbols, the same abbreviation (D.S.) will be used in this paper to denote the more specific term, "degree of cyanoethylation." These polymers and especially the 100% D.S. variety have been designated by the chemical name of polyvinyl β -cyanoethyl ether (1, 2). However, the generic name, cyano-

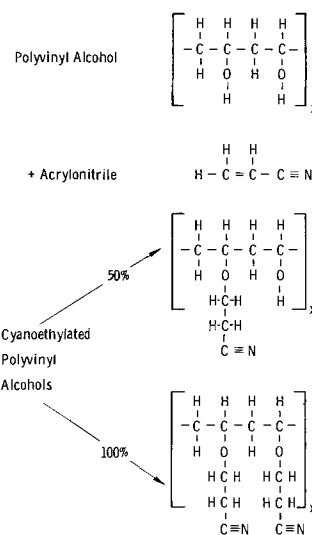


Fig. 1. Cyanoethylation of polyvinyl alcohol

ethylated polyvinyl alcohol or its simpler abbreviation, CEPVA, seems better suited to the partially reacted varieties in view of their structural complexities. Figure 1 illustrates only two of the many CEPVA's that could be produced; these are the half-substituted or 50% D.S. polymer and the fully substituted or 100% D.S. polymer. All of the dimer formulas shown in Fig. 1 are, of course, purely constitutional and have no significance in respect to steric configurations.

Measurements of (ϵ') and loss index (ϵ'') for completely cyanoethylated polyvinyl alcohol (D.S. = 100%) have been reported previously by Lewis and Hogle (1). These measurements indicated strong polarization; for example, ϵ' was found to be approximately 21 at 60 cps and 25°C . To account for the polarization, the authors postulated a rotation of ($-\text{CH}_2\text{CN}$) dipoles about the central C-C bond in the ($-\text{OCH}_2\text{CH}_2\text{CN}$) linkages branching off the main chain. However, they also reported that their evidence for rotation (large loss index peaks at high frequencies) could not be considered conclusive since the polymer was rubbery and polar rubbers commonly exhibit this type of behavior. Moreover, the low frequency losses were extremely high. The authors attributed these high losses to ionized impurities which were retained by the gummy and rubbery polymer, in spite of repeated attempts at purification.

Table I. CEPVA polymers

Nitrogen content, %	Degree of cyanoethylation, %	Soluble in	Preparation method	Reaction time, hr
0	0	Water	(Original PVA as supplied*)	
1.52	4	Water	DePauw (3)	0.5
2.7	9	Water	DePauw (3)	1.1
7.2	29	Water**	DePauw (3)	3.0
10.8	57.5	Acetone	DePauw (3)	20.0
13.2	83	Acetone	Houtz (2)	3.0

* ELVANOL 71/30, supplied by E. I. du Pont de Nemours & Company, Inc.

** Slowly soluble in water, more soluble in ethanol, insoluble in acetone.

Lewis and Hogle had limited their studies on CEPVA to the 100% D.S. polymer (polyvinyl β -cyanoethyl ether). One purpose of the present study has been to measure the dielectric properties at lower degrees of cyanoethylation and, so far as possible, to relate the variation in dielectric properties to the percentage of (OH) groups replaced. The effect of increased polymer rigidity on dielectric properties has also been considered; first, by measuring the properties at temperatures ranging downward to -50°C , whereas the lowest temperature employed by Lewis and Hogle was $+25^{\circ}\text{C}$; and second, by measuring and comparing the properties of three representative polymers after stiffening their structures by cross linking.

Experimental

Five CEPVA polymers were prepared, each with a different degree of cyanoethylation and were analyzed for nitrogen (N) content. A nitrogen analysis provides a convenient measure of the D.S. of the polymer, the basis being polyvinyl β -cyanoethyl ether (D.S. = 100%) for which the theoretical N-content is 14.42%. Table I lists the original PVA and the five prepared polymers in order of increasing N-content and corresponding degrees of cyanoethylation.

The first four of the partially cyanoethylated polymers in Table I, up to and including 10.8% N, were prepared in aqueous media by a procedure published by DePauw (3). Acetic acid was added to stop the alkaline catalysis at the time intervals listed in the fifth column of the table. The final polymer in the group, 13.2% N, was made by modifying a method described by Houtz (2) since DePauw's procedure was considered inappropriate for the high D.S. desired.

DePauw's procedure, where applicable, was followed exactly as given by the author. The Houtz method, however, was modified as follows:

One hundred grams of PVA, 890g of acrylonitrile, 74 ml of ammonium hydroxide (28-30%), and 185 ml of aqueous sodium hydroxide solution (3% by weight) were stirred together and heated under reflux for approximately 3 hr. The reaction mixture was then cooled and filtered, and the crude CEPVA polymer was precipitated from solution by pouring into 9.25 liters of an alcoholic solution consisting of equal volumes of ethanol and water. The ethanol used was specially denatured alcohol containing 5 gal methanol per 100 gal ethyl alcohol (Formula No. 1; U.S. Department of Internal Revenue). The precipitated polymer was then dissolved in 1.3 liters of methyl ethyl ketone (MEK), and the resulting solution was extracted (or washed) in a separatory funnel three times with an immiscible solvent mixture consisting of 1.8 liters of distilled water and 0.84 liter of MEK. After the final wash the polymer was reprecipitated in 16 liters of distilled water, squeezed between Teflon covered rolls to remove most of the occluded water, and dried in a vacuum oven below 50°C . The yield was approximately 80% based on the computed D.S. of 83%.

None of the polymers in Table I were considered very pure. The same difficulty reported by Lewis and

Hogle was experienced in purification, i.e., finely divided precipitates that could be properly washed were never obtained even though the polymers were redissolved and reprecipitated many times. The coagulated gummy masses that actually separated on precipitation would, therefore, be expected to retain appreciable amounts of occluded impurities.

The transition from water soluble to organic soluble polymers is shown in the third column of Table I. The nitrogen content at which this change occurred lies between 7.2 and 10.8%, probably closer to the lower figure than the higher. The 7.2% N polymer dissolved only very slowly in water and also differed from all others in the list by being appreciably soluble in alcohol. As will become evident later, a change in dielectric properties also appears in the neighborhood of 7-8% nitrogen.

The dielectric test specimens were made in the form of small, thin capacitor-type elements. The dielectric films in these elements were formed by casting the polymer solutions on aluminum foil or electrically conducting glass plate which thus became one electrode of the capacitor. Six sets of specimens were prepared in duplicate, five from the CEPVA polymers and one from the original PVA. Three additional sets were prepared with cross-linking agents added to the polymer solutions; these included the original PVA, a low D.S. CEPVA (2.7% N), and a high D.S. CEPVA (13.2% N). The films were baked 30 min at 150°C to remove solvent and also to effect a "cure" if cross-linking agents had been added. Each element was completed by evaporating aluminum metal over a circular area 0.500 in. in diameter on the exposed side of the film, thus forming a second electrode. The thickness of the polymer films sandwiched between the electrodes ranged from 0.0007 to 0.006 in.

In preparing the cross-linked films, appropriate chemical agents were mixed with the polymer solutions just before casting the film. The water soluble varieties, namely, the original PVA and the 2.7% nitrogen CEPVA, were cross-linked with hexamethoxymethyl melamine (CYMEL 300 obtained from the American Cyanamid Company), approximately two parts by weight of cross-linking agent per five parts of solid polymer in solution. The organic soluble polymer (13.2% nitrogen) was cross-linked on a 5% by weight basis with a blocked trifunctional polyisocyanate ester supplied by Mobay Chemical Company under the commercial name of MONDUR-S. The cured films after baking were no longer soluble in their former solvents whereas their unmodified counterparts could always be redissolved, usually quite easily. For this reason, solvent resistance was generally used as a quick test for effectiveness of cross linking and cure.

Measurement of Dielectric Properties

Dielectric constants (ϵ') and dissipation factors ($\tan \delta$) were measured by substitution methods on a General Radio Schering bridge (Type 714C). The dielectric loss index (ϵ'') was calculated from the relation $\epsilon'' = \epsilon' \tan \delta$. Each polymer specimen was tested at six different frequencies ranging from 60 cps to 300 kcps and at six different temperatures ranging from -50° to $+75^{\circ}\text{C}$.

Since some of the polymers were hygroscopic it was standard practice to condition the test specimens for at least 24 hr in a closed chamber containing a desiccant (phosphorus pentoxide) and then perform a complete series of measurements without reopening the chamber. In testing at different temperatures the chamber was submerged in a bath maintained at the approximate temperature desired and the exact temperature was measured by means of a thermocouple located inside the chamber near the test specimens. A minimum time of 3 hr at constant temperature was allowed after each temperature change before a new series of measurement was started.

D.C. volume resistivities (ρ) were also measured while the specimens were in the dry chamber but only at one temperature, 25°C. The instrument used was a General Radio D.C. Amplifier and Electrometer Type 1230A. Readings were taken at 1- and also at 2-min time intervals after applying a potential difference of 9.1v to the electrodes.

The dielectric constants and loss indices of the polymers listed in Table I are plotted against frequency and temperature in Fig. 2 and 3, and also against nitrogen content and frequency in Fig. 4 and 5. The d-c resistivities at 25°C are plotted for different N-contents in the bar graph of Fig. 6. The effects of cross linking on dielectric properties are shown in Fig. 7 and 8.

Discussion

In Fig. 2, the variation in ϵ' with frequency and temperature is shown in six separate graphs, one for each polymer composition. All of the polymers including the original PVA exhibit a typical decrease in ϵ' with increasing frequency and also with decreasing temperature. However, the very high values shown, especially at low frequencies and high temperatures, should not be accepted uncritically. These extremely

high dielectric constants were always associated with losses that were also extremely high. High losses, of course, would affect the measured capacitance, and in that case the apparent values of ϵ' cannot be trusted. In some instances, for example, in the graph for the original PVA at 75°C, no points are shown below 10 kcps since at lower frequencies the losses were so high that the bridge could not be balanced.

Similar separate graphs for the loss indices are plotted in Fig. 3. From these data it is apparent that the measurements were not carried into a frequency range high enough for definite loss index peaks to occur. However, it can also be seen in the graphs for the nitrogen-containing polymers that the ϵ'' values almost always increase with frequency in the upper ranges approaching the 300 kcps limit. This may indicate the early stages of the anomalous dispersion region. Moreover, the rising trend seems most pronounced for the polymer containing the most nitrogen.

On the other hand, the failure of the original PVA to show any ϵ'' peaks or even a rising trend below

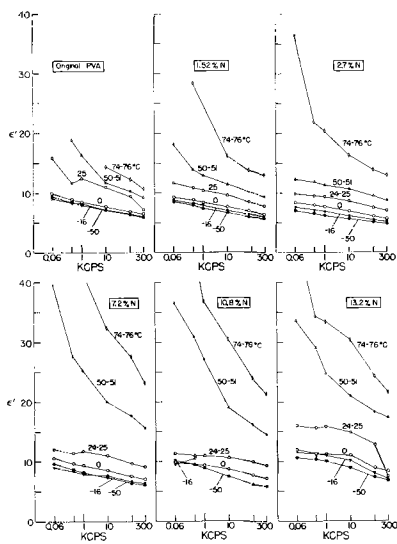


Fig. 2. Variation of dielectric constants (ϵ') of CEPVA polymers with frequency and temperature.

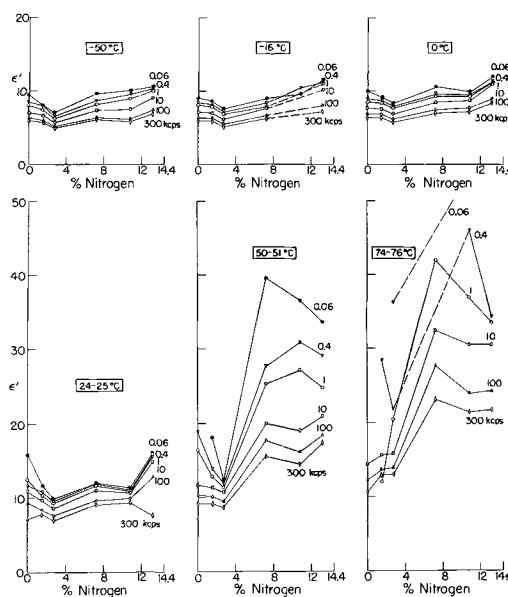


Fig. 4. Variation in dielectric constant (ϵ') with N-content of CEPVA polymers.

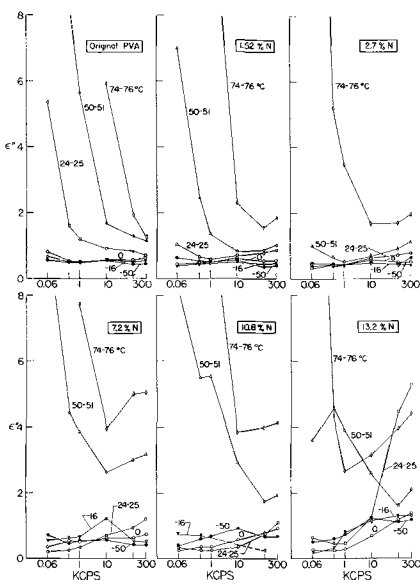


Fig. 3. Variation of loss indices (ϵ'') of CEPVA polymers with frequency and temperature.

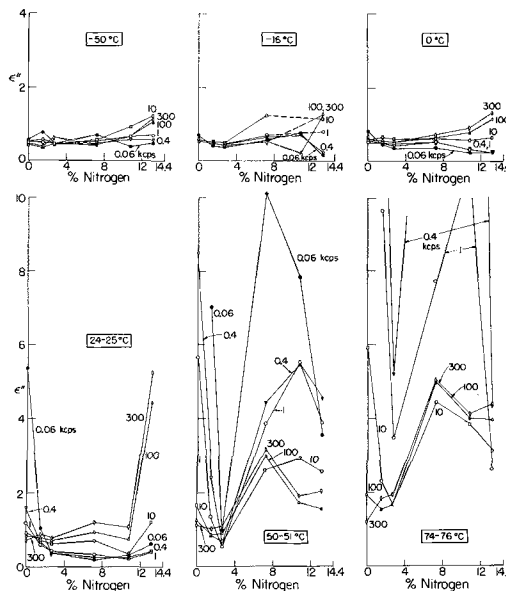


Fig. 5. Variation in loss index (ϵ'') with N-content of CEPVA polymers.

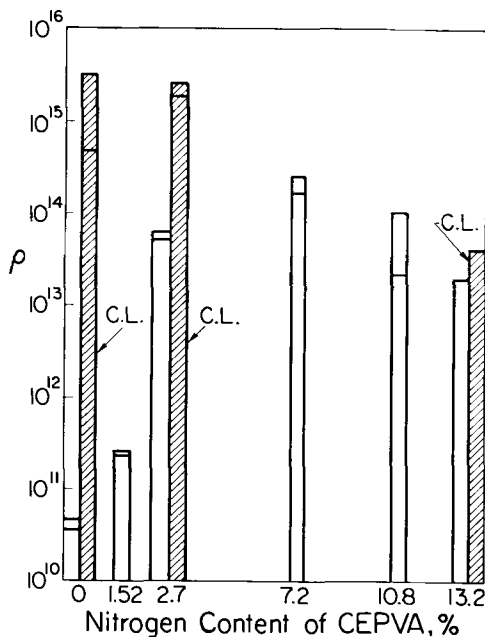


Fig. 6. D-C resistivities (ρ) of CEPVA polymers at 25°C. C.L. = cross-linked.

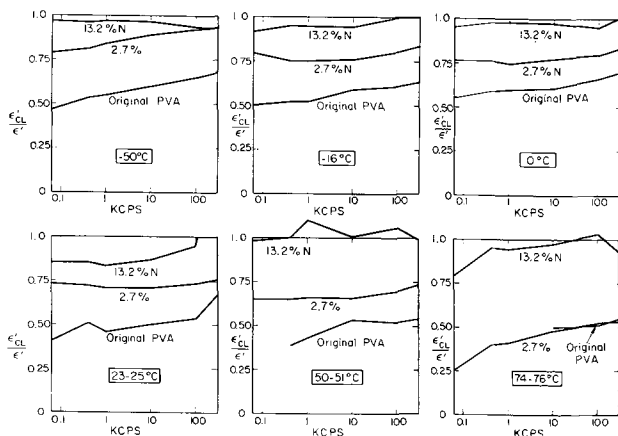


Fig. 7. Effect of cross linking on dielectric constant of PVA and two varieties of CEPVA.

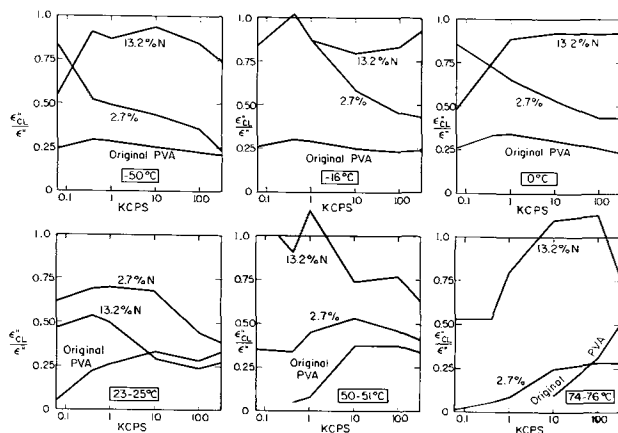


Fig. 8. Effect of cross linking on loss index of PVA and two varieties of CEPVA.

300 kcps is somewhat puzzling. The data in this respect are inconsistent with the observations of Kurosaki and Furomaya (4) who reported loss peaks for polyvinyl alcohol in the vicinity of 10-100 kcps at temperatures ranging from -16.8° to $+16.8^\circ\text{C}$. Other than to suggest a possible difference in polymer samples, no

explanation can be given for the apparent lack of agreement.

The failure to find ϵ'' peaks at temperatures of 25°C and higher was not surprising, especially where the high nitrogen content polymers were concerned. It is true that Lewis and Hogle had found a loss peak around 30 megacycles/sec for completely cyanoethylated CEPVA at 25°C , but the present measurements were not carried above 300 kcps. However, in the present measurements the temperature was dropped to -50°C where it might be expected that increased rigidity of the polymer structure would retard dipole rotation sufficiently for dispersion peaks to occur at frequencies below 300 kcps. The absence of such dispersion peaks at such a low temperature lends further support to the Lewis and Hogle theory of a high degree of freedom for the rotating ($-\text{CH}_2\text{CN}$) dipole. Moreover, the failure to reach a loss peak below 300 kcps when the polymers are cooled to -50°C indicates that the rotation apparently has a relaxation time shorter than a microsecond even at this low temperature.

It was also no surprise to see in most instances very high losses at low frequencies instead of negligibly low losses as predicted by the Debye theory. In some instances the measured losses were greater than calculated by the Debye equation even if one assumes the rotational frequency maximum in the calculation. Ionic conductance presumably accounts for a large proportion of the low-frequency loss since; as was mentioned earlier, it was virtually impossible to rid the gummy polymers of all ionized impurities.

The influence of cyanoethylation on dielectric properties becomes apparent in the composition based graphs of Fig. 4 and 5. In general, the dielectric constants first decrease with increasing nitrogen contents (or equally increasing degrees of cyanoethylation), then increase and at higher temperatures seem to reach plateaus or maxima at 7-8% nitrogen. These changes are only slight at temperatures below 25°C . The loss index curves in Fig. 5 show similar trends and even more pronounced maxima, again at about 8% nitrogen. Behavior of this type is not unique; a similar maximum in ϵ'' depending on composition was observed by Scott, McPherson, Curtis, and Cummings (5) in studying the effect of sulfur in vulcanized rubber. However, it is a curious coincidence that the maxima in ϵ' and ϵ'' of the CEPVA polymers occur at just about the same nitrogen content as marked the transition from water soluble to water insoluble materials. A plausible inference, though certainly not too well established, is that the maxima are in some manner associated with structural changes also indicated by the change in solubility.

The distinctive pattern of the dielectric property vs. nitrogen content curves suggests a relation to the substitution that occurs during the cyanoethylation reaction. The mentioned work of Kurosaki and Furomaya (4) indicated that the oxygen-hydrogen dipoles contributing most to PVA polarization are located in the more accessible, amorphous regions of the polymer. If these dipoles are the first to be removed by reaction with acrylonitrile, it is then plausible that ϵ' and ϵ'' should show an initial decrease, as was observed. However, the continued introduction of easily rotatable ($-\text{CH}_2\text{CN}$) groups should soon dominate the electrical behavior and ϵ' and ϵ'' should rise accordingly. This was likewise observed. But as the ($-\text{CH}_2\text{CN}$) dipoles increase in number and percentage, they also become crowded more closely together. At some point, presumably 8% nitrogen which corresponds to about 35% cyanoethylation, the restriction to rotation by crowding would be expected to balance the effect of new dipoles entering, and beyond that point ϵ' and ϵ'' should remain stationary or even decrease. This, too, was observed. Moreover, if one now returns to the frequency based graphs of Fig. 3 and compares the trends of the ϵ'' curves as they approach the 300 kcps limit, the earliest and strongest upward trend is shown

by the polymer containing the most nitrogen (13.2%). One would thus assume that this polymer would have been the first to reach a loss index peak if the measurements had been extended beyond the present limit into the anomalous dispersion frequency range. If so, this would also be consistent with the view that rotational freedom begins to diminish at high N-contents.

The bar graph in Fig. 6 portrays the d-c resistivities (ρ at 25°C) for all the polymer specimens, including the cross-linked varieties. Open bars are shown for the polymers without cross-linking, cross-hatched bars labeled C. L. for those with cross-linking, and the basis for comparison in each case is the N-content. The range of ρ in the case of the unmodified polymers is roughly four orders of magnitude; from, say 5×10^{10} (ohm-cm) for the original PVA to about 5×10^{14} ohm-cm for the 7.2% N-content CEPVA. The last named value is a maximum for the unmodified polymers; this again presents a curious parallel to the ϵ' and ϵ'' maxima seen in Fig. 4 and 5. Whatever may be the reason for the increase in ϵ' and ϵ'' leading to these maxima, it is presumably not an increase in ionic conductance. Such an explanation would be tenable if higher values of ϵ' and ϵ'' had been accompanied by lower values of ρ ; however, the opposite was observed.

Cross linking has increased the resistivity of the three polymer films that were tested. The greatest effect is seen for the original PVA where the increase is about four orders of magnitude. A lesser increase, about two orders of magnitude, appears to have occurred in cross linking the low N-content CEPVA, and a very much smaller increase, perhaps negligible, in cross linking the high N-content CEPVA.

In similar fashion, the nitrogen content of the polymer also seems to determine whether cross linking will have a large or small effect on dielectric constant and loss. In the six constant temperature graphs of Fig. 7, a direct comparison of the effect on dielectric constant is obtained by pairing the measurements on cross-linked specimens ($\epsilon'_{C.L.}$) with the corresponding measurements on their unmodified counterparts (ϵ'), and plotting the ratio $\epsilon'_{C.L.}/\epsilon'$ against frequency. Fractional ratios, of course, indicate a reduction in dielectric constant in proportion to their departure from unity. Hence the lower the position of the $\epsilon'_{C.L.}/\epsilon'$ line on a graph, the more the dielectric constant of that particular polymer has been reduced as a result of cross linking. Similar graphs of loss index ratios, $\epsilon''_{C.L.}/\epsilon''$, are shown in Fig. 8.

A quick glance at the positions of the lines in these two sets of graphs reveals that cross linking has in most instances affected the dielectric properties of the polymers in reverse order of their nitrogen contents. Thus, the high N-content CEPVA (13.2% N) shows little, if any, change in dielectric constant on cross linking, and the lines plotted for this polymer in Fig. 7 are closest to unity. On the other hand, the cross-linked specimens of the other two polymers show substantial decreases in dielectric properties, the reduction in ϵ' and ϵ'' being in the order of 25-50% with the low N-content CEPVA (2.7% N) and 50-75% or more with the original PVA (0% N). The changes in loss index on cross linking as seen in Fig. 8 generally show the same trend as the changes in dielectric constant but seem to be more erratic. At 25°C, for example, the $\epsilon''_{C.L.}/\epsilon''$ ratios for the high nitrogen content polymer appear in an intermediate to lowest position whereas at all other temperatures these ra-

tios normally occupy a top position. The lack of harmony is unexplained and, of course, must be viewed with suspicion.

However, it appears to be true in general that the dielectric properties are most strongly affected by cross linking when the PVA has not been cyanoethylated, less strongly affected when the polymer has been given a minor degree of cyanoethylation, and only mildly affected when cyanoethylated to the maximum extent employed in these experiments. The inference, therefore, is that the ($-\text{CH}_2\text{CN}$) dipoles have considerable rotational freedom which is not destroyed nor even appreciably diminished by joining the polymer chains together via the cross-linking isocyanate group. This cross-linking agent apparently interacts very little, if at all, with the ($-\text{CH}_2\text{CN}$) dipole.

From the known reactions of the agents used, it is more reasonable to assume that the actual cross-linking sites in all three polymers are positions on the polymer chain still occupied by (OH) groups. According to this view, when the polarity of the polymer is reduced by cross linking it is because easily rotatable oxygen-hydrogen dipoles have been converted to nonrotatable oxygen bridges between the chains. If this is so, the extent to which the polarity is reduced depends on the degree of cyanoethylation before cross linking. The number of (OH) groups per polymer unit is, of course, greatest in the original PVA where none have been replaced and least in the 13.2% N content CEPVA where 83% of the (OH) groups have been replaced. Cross linking through the hydroxy groups should, therefore, produce the greatest reduction of ϵ' and ϵ'' in the case of the original PVA, a lesser reduction in the case of the low N-content CEPVA, and the least reduction in the case of the high N-content CEPVA, as was observed.

It is interesting to note for the high nitrogen content material that cross linking can produce striking physical changes with no commensurate effect on dielectric constant and loss. After cross linking, the films cast from this polymer not only became insoluble in the usual solvents as was mentioned earlier, but also were no longer rubbery. Although the present study did not include actual physical property measurements, it could be easily seen that the cross-linked films were often quite rigid and glassy. It was, therefore, most surprising to find so little change in their dielectric properties in spite of the increased rigidity.

Acknowledgment

It is a pleasure to acknowledge the skillful assistance of David Marschik and Donald G. Martin in performing the experiments described in this paper.

Manuscript received March 18, 1964.

Any discussion of this paper will appear in a Discussion Section to be published in the June 1965 JOURNAL.

REFERENCES

1. C. W. Lewis and D. H. Hogle, *J. Polymer Sci.*, **21**, 411 (1956).
2. R. C. Houtz, U.S. Pat. 2,341,553; Feb. 15, 1944.
3. A. DePauw, *Ind. chim. belge*, **20**, Spec. No. 1955, p. 563-6.
4. S. Kurosaki and T. Furumaya, *J. Polymer Sci.*, **43**, 137 (1960).
5. A. H. Scott, A. T. McPherson, H. L. Curtis, and A. D. Cummings, *Bur. Standards J. Research*, **11**, 173 (1933).

Cobalt-Nickel Electrolytes Containing Phosphite or Benzoate Additive Developed for Magnetic Plating

G. V. Elmore and P. Bakos

GPD-Manufacturing Research Laboratory, International Business Machines Corporation, Inc., Endicott, New York

ABSTRACT

Two cobalt-nickel electroplating baths were developed for magnetic plating with coercivities in the range from 200 to 400 oe. One bath contained phosphite as the additive (and active agent) for control of coercivity; the other bath contained benzoate as the additive. Both electrolytes had long plating life and coercivities were relatively unaffected by small changes in temperature, pH, and current density such as would be normally encountered in operation of the baths. Two phases are present in the plate. One phase, containing the additive, is a very fine grained amorphous-phase which is resistant to attack by acid and is nonmagnetic; the other phase is crystalline and is more readily attacked by acid. The coercivity of the plate is controlled by the particle size of the crystalline component in the amorphous matrix.

The use of electroplated ferromagnetic metals for memory storage purposes has had increasing application. A great many of the electrolytes used have been developed from the work of Brenner (1) who used hypophosphite or phosphite salts as brightening agents for cobalt-nickel alloy plating. Bonn and Wendell (2) patented the use of hypophosphite in a cobalt-nickel electrolyte to produce plated magnetic tapes. A number of recent investigations are based on the use of hypophosphite salts in a cobalt or cobalt-nickel electrolyte to produce platings with coercivities varying from 250 to 1000 oersteds.

This work indicated that coercive forces of 200-400 oe could be produced in plating from a cobalt-nickel electrolyte containing approximately 0.3 g/liter of $\text{NaH}_2\text{PO}_2 \cdot \text{H}_2\text{O}$. The use of this low concentration of hypophosphite is undesirable because frequent addition of hypophosphite is required to maintain constant coercive force platings.

This study describes the characteristics of two cobalt-nickel electrolytes, one containing a phosphite additive and one containing a benzoate additive. Both electrolytes had a much longer life before rejuvenation by addition of active agents than the hypophosphite additive electrolyte. A study was also made of the correlation between the physical properties of the plating and its coercivity.

Experimental

The electroplating experiments were performed in rectangular plastic cells (14 x 8.9 x 11.4 cm) of 1-liter capacity. The standard brass Hull-cell plates used as the plating substrates were prepared for plating by reverse-current cleaning followed by treatment with ammonium persulfate solution. The anodes, an alloy of 80% cobalt-20% nickel, for the cobalt-nickel electrolytes and 100% cobalt for the cobalt electrolyte, are of 99% purity and all chemicals are C.P. grade. Agitation was accomplished with a Hull-cell agitator operating at 50 strokes per min with the wiper blade located 0.6-cm from the cathode plate. All substrates (Hull-cell plates) except those intended for x-ray analysis, were plated to a thickness of 0.4-0.5 μ . The substrates intended for x-ray examination were plated to a thickness of 1.5 μ . Thickness measurements were made with a Kocour tester or by a Talysurf profilometer after suitable etching. The magnetic properties were measured by a 60-cycle hysteresigraph (1000-4000 gauss drive) that was calibrated and adjusted for the thickness of each plate. The hysteresigraph is a modified version of the instrument described by Howling (3).

Table I. Nickel-cobalt electroplating solution (phosphite additive)

Conditions of operation: temperature, 25°C;
pH, 4.5; current density, 5 ma/cm²

Composition	G/liter
$\text{NiCl}_2 \cdot 6\text{H}_2\text{O}$	110
$\text{CoCl}_2 \cdot 6\text{H}_2\text{O}$	50
NH_4Cl	25
$\text{Na}_2\text{SO}_4 \cdot 10\text{H}_2\text{O}$	50
$\text{Na}_2\text{HPO}_3 \cdot 5\text{H}_2\text{O}$	Variable

Results

Preliminary investigations of the electrolyte containing phosphite established the acceptable concentrations of the various constituents. This basic composition is described in Table I. The initial study was an examination of the behavior of the phosphite electrolyte during long plating periods. In this study 6 g/liter of $\text{Na}_2\text{HPO}_3 \cdot 5\text{H}_2\text{O}$ were used. One liter of solution was used and plated an area of 77 cm². Throughout this testing, samples were taken at periodic intervals with dummy plating between samples. All plates were heat treated at 55°C for 20 min prior to the measurement of the coercivity. This heat treatment was used because the initial coercivity decreased, on standing at room temperature, by 40-60 oe, before a stable value was reached. Plates with stable coercivities were produced after 5 min of heat treatment at 55°C. Sallo and Carr (4) have previously observed similar decreases in coercivity of Co-Ni-P and Co-P platings on heating.

The results of the life testing are illustrated in Fig. 1. Three per cent of phosphorus in the plating caused the concentration of phosphite in the electrolyte to decrease slowly as plating continued. The initial coercivity in this test was 400 oe. After 48 hr of plating time, the coercivity decreased to 320 oe; 2 g/liter of $\text{Na}_2\text{HPO}_3 \cdot 5\text{H}_2\text{O}$ were added to the electrolyte and the

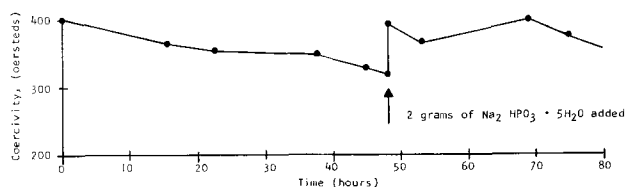


Fig. 1. Effect of continuous electrolysis on coercivity (nickel-cobalt electrolyte with phosphite additive); temperature, 25°C; current density, 5 ma/cm².

coercivity increased to 396 oe. As the plating operation continued, the coercivity decreased by 50 oe. The average ratio of remanence to saturation induction (B_r/B_s) for the entire test was 0.74 and the average value for the vertical angle (θ) was 77° . [The vertical angle (θ) may be defined as the angle between the abscissa and the demagnetization portion of the hysteresis loop when the hysteresigraph is adjusted to 5000 gauss/cm on the ordinate and 200 oe/cm on the abscissa. The value of B_r/B_s is the ratio between the remanence at zero driving field and the flux density at saturation.]

To study the effects of variation in temperature, pH, and current density, the composition described in Table I was used with 5.5 g/liter of $\text{Na}_2\text{HPO}_3 \cdot 5\text{H}_2\text{O}$. All samples were heat treated at 55°C for 20 min before the coercivity was measured. The effect of variation of temperature on coercivity is illustrated in Fig. 2. The coercivity was reduced approximately 100 oe as temperature was increased from 25° to 50°C . Figure 3 illustrates the effect of pH on coercivity; as the pH increased from 4.0 to 6.0, the coercivity increased from 300 to 550 oe. Figure 4 illustrates the effect of current density on coercivity; as the current density was increased from 4.0 to 8.0 ma/cm², the coercivity was reduced from 340 to 325 oe. In the range of conditions described above the B_r/B_s ratio and θ were approximately constant except when the pH was increased from 5.0 to 6.0. With the increased pH the B_r/B_s ratio rapidly decreased to 0.66 and θ decreased to 66° .

For the development of the benzoate additive electrolyte, the basic concentrations and conditions were established by preliminary testing. The concentrations of the various constituents and conditions of

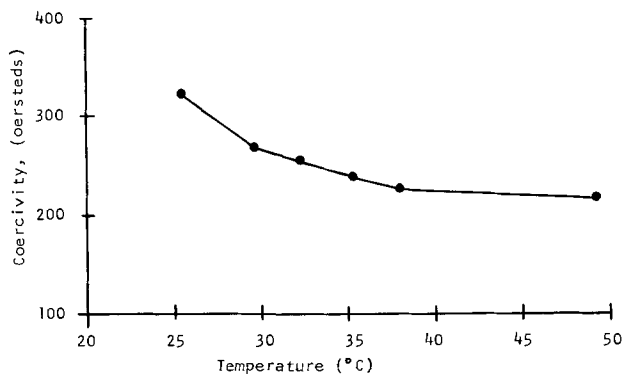


Fig. 2. Effect of temperature on coercivity (nickel-cobalt electrolyte with phosphite additive): pH, 4.5; current density, 5 ma/cm²; $\text{Na}_2\text{HPO}_3 \cdot 5\text{H}_2\text{O}$, 5.5 g/liter.

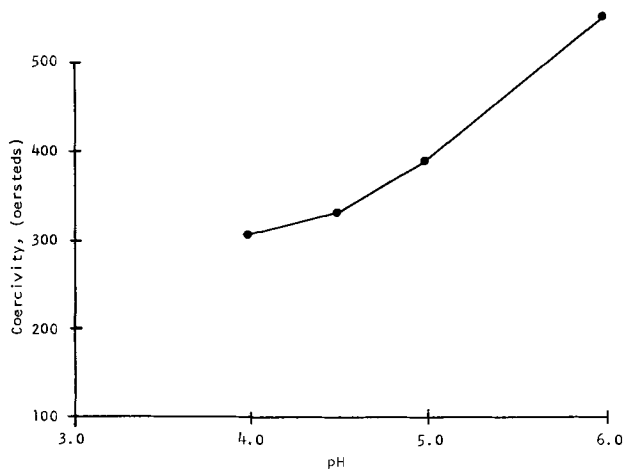


Fig. 3. Effect of pH on coercivity (nickel-cobalt electrolyte with phosphite additive): temperature, 25°C ; current density, 5 ma/cm²; $\text{Na}_2\text{HPO}_3 \cdot 5\text{H}_2\text{O}$, 5.5 g/liter.

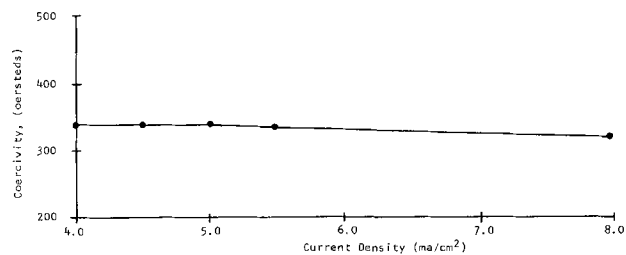


Fig. 4. Effect of current density on coercivity (nickel-cobalt electrolyte with phosphite additive): temperature, 25°C ; pH, 4.5; $\text{Na}_2\text{HPO}_3 \cdot 5\text{H}_2\text{O}$, 5.5 g/liter.

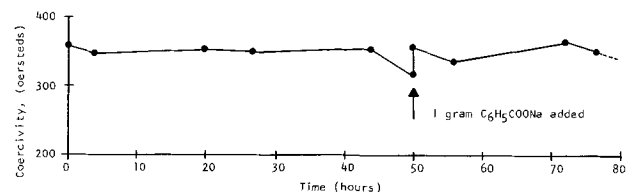


Fig. 5. Effect of continuous electrolysis on coercivity (nickel-cobalt electrolyte with benzoate additive): temperature 43°C ; current density, 15 ma/cm²; pH, 5.5.

operation are described in Table II. This composition with 4 g/liter of $\text{C}_6\text{H}_5\text{COONa}$ was used to study the behavior of the benzoate additive on the electrolyte during extended plating periods, in a similar manner to the study of the phosphite additive. The results are illustrated in Fig. 5. It was observed that the plating absorbed organic material (analysis indicated approximately 1% of carbon in the plate), therefore, the concentration of benzoate in the electrolyte decreased as plating continued. After 50 hr of operation, the initial coercivity of 360 oe had decreased to 320 oe, and 1 g/liter of $\text{C}_6\text{H}_5\text{COONa}$ was added. The coercivity immediately increased to 355 oe and then slowly decreased as the plating operation continued. The 50-hr period before rejuvenation of the benzoate additive electrolyte is the equivalent of 150 hr of the phosphite additive electrolyte operation, because the current density of the benzoate additive electrolyte is three times larger than the phosphite additive electrolyte.

The coercivity of the plates from the benzoate additive electrolyte did not change on standing at room temperature or after heat treating at 55°C . The average B_r/B_s ratio for the testing was 0.72 and the average θ was 79° .

The effect of temperature, pH, and current density on coercivity was studied. The composition described in Table II, with 2 g/liter of $\text{C}_6\text{H}_5\text{COONa}$, was used. Figure 6 illustrates the effect of a temperature increase from 25° to 60°C ; the coercivity increased from 170 to 440 oe. Figure 7 illustrates the effect of a pH increase from 4.0 to 5.5; the coercivity increased from 170 to 300 oe. As illustrated in Fig. 8, a current density increase from 5 to 15 ma/cm² caused the coercivity to be reduced from 400 to 270 oe. The B_r/B_s ratio and θ demonstrated very little variation as temperature, pH, and current density were varied within the specified range.

Table II. Nickel cobalt electroplating solution (benzoate additive)

Conditions of operation: temperature, 43°C ;
pH, 5.5; current density, 15 ma/cm²

Composition	G/liter
$\text{NiCl}_2 \cdot 6\text{H}_2\text{O}$	120
$\text{CoCl}_2 \cdot 6\text{H}_2\text{O}$	40
NH_4Cl	25
$\text{Na}_2\text{SO}_4 \cdot 10\text{H}_2\text{O}$	50
$\text{C}_6\text{H}_5\text{COONa}$	Variable

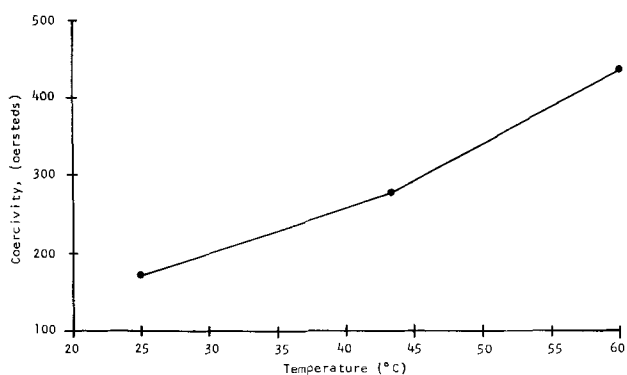


Fig. 6. Effect of temperature on coercivity (nickel-cobalt electrolyte with benzoate additive): pH, 5.5; current density, 15 ma/cm²; C₆H₅COONa, 2 g/liter.

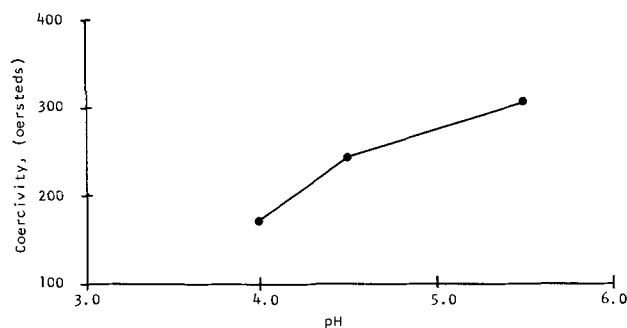


Fig. 7. Effect of pH on coercivity (nickel-cobalt electrolyte with benzoate additive): temperature, 43°C; current density, 15 ma/cm²; C₆H₅COONa, 2 g/liter.

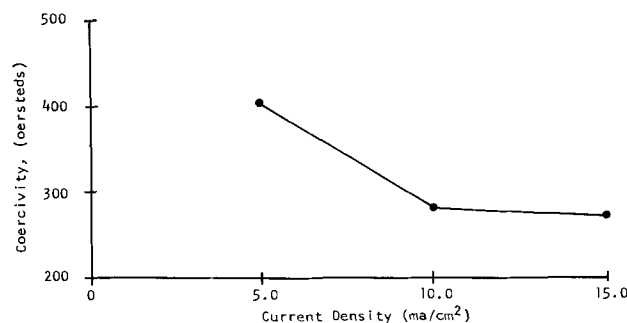


Fig. 8. Effect of current density on coercivity (nickel-cobalt electrolyte with benzoate additive): temperature, 43°C; pH, 5.5; C₆H₅COONa, 2 g/liter.

The relation between the physical properties and the magnetic properties of electroplated magnetic materials was sought. For these investigations, a study was made of the electrolyte containing hypophosphite. Hypophosphite in comparison to phosphite has a wider range of coercivities and has a greater solubility in the electrolyte. Nickel was eliminated from the electrolyte because it was determined that as the current density was varied in the cobalt-nickel-hypophosphite electrolyte, the ratio of cobalt to nickel also varied. Thus the interpretation of the current density *vs.* coercivity measurements were unnecessarily complicated. The composition of the electrolyte is described in Table III. This composition was used to study the effect of current density variation on coercivity when the electrolyte contained 5 and 10 g/liter of NaH₂PO₂·H₂O. The results are illustrated in Fig. 9. A similar curve for nickel-cobalt-sodium hypophosphite electrolyte has been published by Kaznachei and Zhogina (5).

To determine if the variation of coercivity with current density occurred with other additives of a

Table III. Cobalt electroplating solution

Conditions of operation: temperature, 25°C; pH, 4.5

Composition	G/liter
CoCl ₂ · 6H ₂ O	50
Na ₂ SO ₄	25
NH ₄ Cl	25

similar type, measurements were made with the same electrolyte and three different concentrations of sodium arsenite which is chemically similar to hypophosphite. The results, illustrated in Fig. 10, produced curves similar to those in Fig. 9. Phosphite and benzoate also produced similar curves except the peaks of the curves are not as sharp or as high. Since the coercivity-current density curves were flatter, changes in current density caused less change in coercivity than when current density was changed in the hypophosphite containing electrolyte.

When plates were produced at very low current densities for electrolytes containing either hypophosphite or arsenite, the plates were nonmagnetic and had crystal sizes less than 40Å (by x-ray diffraction analysis). As the current density increased, the x-ray diffraction pattern indicated an increasing amount of hexagonal crystalline material. Low current density, low coercive-force plates were predominantly (0002) plane oriented (easy axis [0001] perpendicular to plate); those in the approximate range from 270 to 800 oe were predominantly (1010) plane oriented (easy axis parallel to plate) while those of 800 oe and above were predominantly (1120) plane oriented (easy axis parallel to plate).

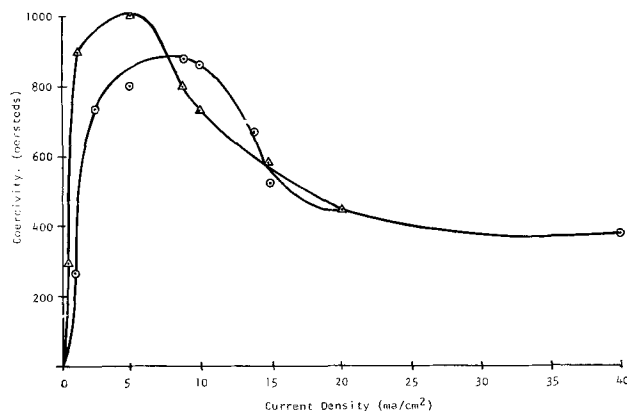


Fig. 9. Effect of current density on coercivity (cobalt electrolyte with hypophosphite additive). Δ , 5 g/l NaH₂PO₂·H₂O; \circ , 10 g/l NaH₂PO₂·H₂O.

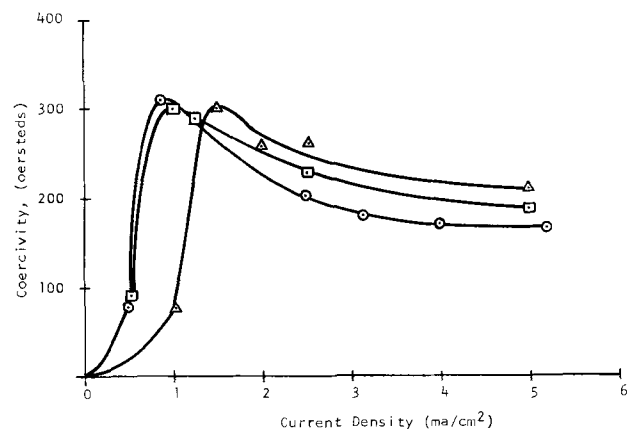


Fig. 10. Effect of current density on coercivity (cobalt electrolyte with arsenite additive). Δ , 0.5 g/l NaAsO₂; \square , 0.3 g/l NaAsO₂; \circ , 0.2 g/l NaAsO₂.

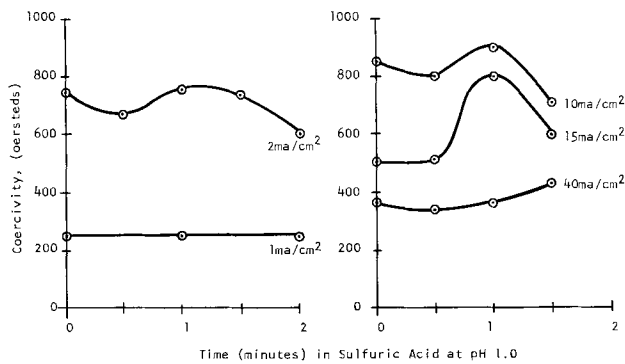


Fig. 11. Effect of acid treatment on coercivity (cobalt electrolyte with hypophosphite additive).

When treated with sulfuric acid at pH of 1.0, the plates with crystal sizes less than 40Å were not attacked; however, plates produced at higher current densities were attacked. The effect of the acid treatment on coercivity is illustrated in Fig. 11. For the acid treatment, plates deposited from the electrolyte containing 10 g/liter of $\text{NaH}_2\text{PO}_2 \cdot \text{H}_2\text{O}$ at different current densities were used. As each plate was treated with acid for increasing periods of time, the coercivity changed in a characteristic manner depending on the original current density at which it was plated. Starting from its original position on the current density vs. coercivity curve, progressive acid treatment caused the plate to progressively change in coercivity as if it had been plated at progressively lower current densities. Thus a plate that was originally deposited at a current density greater than that producing the maximum coercivity was treated with acid. It initially increased in coercivity until the maximum was reached and then decreased as treatment continued. A plate that was originally deposited at a current density lower than that producing the maximum coercivity, decreased in coercivity with acid treatment. Plates made at a current density of 1 ma/cm² were very slowly attacked by the acid and did not change during the sulfuric acid treatment. The plate produced at 40 ma/cm² became too thin for measurement on the hysteresigraph before the maximum coercivity was reached.

Because the plates with crystal sizes less than 40Å (nonmagnetic) produced at low current densities were not attacked by sulfuric acid, and plates produced at higher current densities containing crystalline material were attacked, the mechanism of the acid reaction could be a preferential removal of crystalline material with particle sizes greater than 40Å in size.

X-ray examination of samples before and after treatment, for 10 min with sulfuric acid at pH of 1.0, were made to determine the effect of the treatment on the ratio of crystalline material, with particle sizes greater than 40Å, to total metal and on the ratio of additive to total metal. All samples for x-ray examination were plated to a thickness of approximately

1.5μ. The total metal and additive analyses were obtained by x-ray fluorescence and the crystalline metal analysis by x-ray diffraction. The results are illustrated in Table IV. The comparison of relative ratios, in counts per minute, from x-ray data before and after treatment of the same sample obviated problems in the calibration of intensity of the three diffraction peaks with actual concentration. Therefore, in Table IV, a comparison should only be made of a sample before and after treatment but not between samples that have different orientations. Thus, in Table IV, the first three samples are oriented with the (0002) plane parallel to the plate; the last two samples are (1010) oriented. It is significant that, in every case, the sulfuric acid treatment has produced a decrease in the ratio of crystalline material, with size above 40Å, to total metal and an increase in the ratio of additive to total metal in the case of the electrolyte containing hypophosphite. This effect of sulfuric acid upon the two ratios was also evident in the cobalt electrolyte containing sulfite or in a cobalt electrolyte containing arsenite. If the sulfuric acid treatment is continued until reaction stops, a black deposit (with crystallite size less than 40Å) remains such as determined by Brenner and co-workers (6). Through the use of electron diffraction, two faint lines of Co_2P can be detected; when the black residue is heated to the melting point, strong x-ray diffraction lines of Co_2P are obtained.

Examination of replicas of the surface by electron microscopy, before and after acid treatment, revealed a removal of crystalline material. Figure 12 illustrates the surface before acid treatment. The surface is quite similar to that illustrated by Sallo (7). Figure 13 illustrates a replica of a section of the same plating after a treatment of the plate with H_2SO_4 at pH of 1.0.

Discussion

The results of this study indicate that two phases are present in the magnetic plates, a crystalline phase and an acid-resistant phase of crystalline size less than 40Å. Sallo and Carr (4) also found evidence of two phases from studies of effects of annealing. Comparison of the current density vs. coercivity curve for hypophosphite additive in cobalt electrolyte (Fig. 9) with the curve obtained by Luborsky (8) who plotted the logarithm of particle size against coercivity for cobalt plated in a mercury matrix; indicates that Luborsky's curve rises sharply to a maximum coercivity of 1000 oersteds as particle size is increased and then slowly decreases. The similarity indicates, for this study, that as current density is increased, the particle size is increased for the crystalline material larger than 40Å in a matrix of crystals with size less than 40Å.

The mechanism of formation of the crystalline fraction with size less than 40Å, which also contains the additive, is probably a chemical reduction of cobalt ions rather than a direct electrochemical action. Ther-

Table IV. Effect of treatment with sulfuric acid pH of 1.0 on composition and coercivity

Relative ratio of crystalline metal (counts per minute) to total metal (counts per minute)		Relative ratio of additive (counts per minute) to total metal (counts per minute)		Coercivity (oersteds)	
Before treatment	After treatment	Before treatment	After treatment	Before treatment	After treatment
0.0111	0.00816	0.00241	0.00638	120	40
0.0104	0.00828	0.00226	0.00911	140	100
0.0114	0.00952	0.00202	0.00626	260	40
0.0743	0.00443	0.00139	0.0246	800	760
0.0322	0.0112	0.00169	0.0124	960	1260

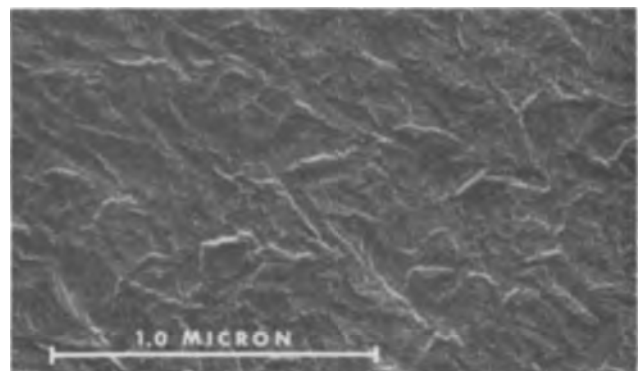


Fig. 12. Electron microscope photograph of surface before sulfuric acid treatment.

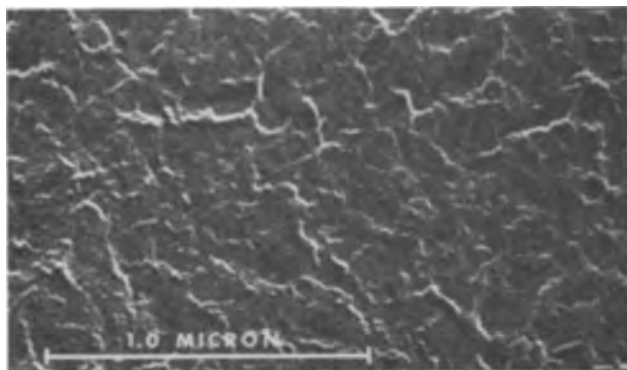


Fig. 13. Electron microscope photograph of surface after sulfuric acid treatment.

modynamically, hypophosphite can reduce the cobalt ions to metal; however, the reaction rate in acid solutions at room temperature is quite slow. Arsenite is not capable of reducing Co^{++} ; therefore, it seems likely that neither hypophosphite nor arsenite is directly involved in the chemical reduction of Co^{++} . A more active intermediate of the additive formed at the cathode by electrochemical reduction is probably involved. The rate of the chemical reduction phase in proportion to the electrochemical reduction would vary with the type of additive and would therefore affect the range of particle sizes of the electrochemical crystalline-material that could be obtained with each additive.

Summary

Two electroplating baths, one containing a phosphite additive and the other containing a benzoate additive were developed for use in magnetic plating.

In a study of the correlation between the physical

properties of the plate and the coercivity, two metallic phases were observed in the plating. One phase is composed of crystals smaller than 40\AA and contains the additive, the other phase is composed of crystals greater than 40\AA . It appears that a balance exists between the rates of reactions leading to the two phases that control the particle size of the larger crystals and, thus, control the coercivity.

Acknowledgment

The authors wish to acknowledge R. B. Overfield and M. A. Sanborn of our laboratory for contributions to the initial development of the phosphite electrolyte and all x-ray analysis; acknowledgments are also due to J. D. Kresge for magnetic evaluation, T. C. Ku and R. A. Schumacher of Physical Technology for electron microscopy and diffraction pattern studies.

Manuscript received March 12, 1964; revised manuscript received May 20, 1964. This paper was presented at the New York Meeting, Sept. 29-Oct. 3, 1963.

Any discussion of this paper will appear in a Discussion Section to be published in the June 1965 JOURNAL.

REFERENCES

1. A. Brenner, "Electrodeposition of Alloys," Academic Press, New York (1963).
2. T. H. Bonn and D. C. Wendell, Jr., U.S. Pat. 2,644,787 (1953).
3. D. H. Howling, *Rev. Sci. Instr.*, **27**, 952 (1956).
4. J. S. Sallo and J. M. Carr, *J. Appl. Phys.*, **34**, 1309 (1963).
5. B. YaKaznachei and V. M. Zhogina, *Trudy Vsesoyuz. Nauch.-Issledovatel. Inst. Zhukozapisei*, No. 6, 119 (1959).
6. A. Brenner, D. E. Couch, and E. K. Williams, *J. Research Natl. Bur. Standards*, **44**, 109 (1950).
7. J. S. Sallo and H. H. Olsen, *J. Appl. Phys.*, **32**, 2035 (1961).
8. F. E. Luborsky, *J. Appl. Phys.*, **33**, 1909 (1962).

Reactions of Gallium Arsenide with Water Vapor and Hydrogen Chloride Gas

M. Michelitsch, W. Kappallo, and G. Hellbardt

IBM Laboratories, Boeblingen, Germany

ABSTRACT

Thermal etching and deposition experiments on gallium arsenide using water vapor/hydrogen and hydrogen chloride/hydrogen as reaction gas mixtures have been performed. It will be shown that the experiments take place near thermodynamical equilibrium, although open tube systems are used. The thermodynamically calculated enthalpies of the respective reactions are in good agreement with the measured ones.

For successful epitaxial growth it is desirable to know about the chemism of the special system as much as possible. Especially thermal etching rate experiments and deposition rate experiments give an indication which reactions take place in particular cases. The experiments allow to determine the respective enthalpies of reactions. Because of the simplicity of this method, it can also be applied to similar tasks in different growth systems.

Experimental

The GaAs/H₂O/H₂ system.—The apparatus used is shown in Fig. 1. It consists of a vertical double walled quartz tube of 20 mm outer and 13 mm inner diameter, which is sealed by a quartz window at the lower end. The upper part is provided with a gas inlet and outlet and the fixture of the wafer holder. The wafer holder consists of a quartz tube of 7 mm diameter and a flat, polished lower end with a 1 mm hole. The wafer to be held, is sucked onto this end by vacuum. Thus there

is thermal etching or deposition on one side only. The source material basket is located at the lower part of

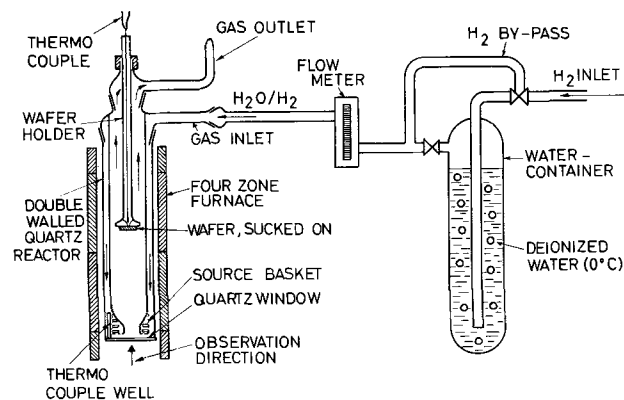


Fig. 1. The GaAs/H₂O/H₂ system

the reaction tube. The wafer can be observed during the run through the quartz window and a central opening of the source material basket by a long focus microscope. This is advantageous, because immediate changes can be observed after varying different parameters during the run.

Highly purified hydrogen as carrier gas bubbles through a water bath of constant temperature (here 0°C), where it is saturated with water vapor. There is a by-pass, if only dry hydrogen is desired, *e.g.*, during the heat-up or cool-down period. The flow rate is measured by a "Rotameter" flow meter. Then the reaction gas mixture enters the reaction vessel.

The reactor is heated by a wire-wound four-zone quartz furnace of low heat capacity. Thus the desired wafer and source temperatures are reached quickly (5-10 min). The cool-down time is also short, about 20 min. The temperatures are measured by chromel-alumel thermocouples.

Prior to each etching run, [111]-oriented wafers (Ga-side, about 7 mm in diameter), mechanically polished to a mirror-like finish are chemically polished in a 0.8% NaOCl-solution (1) at 90°C for 10 to 15 min. This is done to clean the wafer and to remove the mechanically damaged surface layer. Then the wafer is rinsed three times in deionized water and in methanol and dried in a hot hydrogen stream. Before it is inserted into the reactor, it is weighed on a micro-balance, the average weight being between 50 and 70 mg. After the insertion, the whole system is flushed with dried hydrogen for about 15 min at room temperature and heated up to operation temperature of 600°-1000°C within 10 min. When the operation temperature is reached, hydrogen is allowed to bubble through the water bath of 0°C. This bath yields a water vapor partial pressure in the gas low enough to prevent the formation of the higher oxide Ga₂O₃ (2). One single run takes 30-60 min. During the cooling cycle of the run, only dried hydrogen is allowed to enter the reactor to prevent further etching. After each run, the wafers are weighed again.

The orientation and the preparation of the wafers for vapor growth experiments are the same as mentioned before. The polycrystalline GaAs source material is etched in CPI, rinsed in deionized water several times, dried, weighed prior to each run, and inserted in the source material basket. The whole assembly is heated up to the respective temperatures simultaneously with dry hydrogen running. The source temperatures are 50°-100°C higher than the wafer temperatures. Further treatment is the same as mentioned above.

The GaAs/HCl/H₂ system.—Figure 2 shows the experimental arrangement. The reaction tube design is essentially the same as described before. Only the dimensions are changed. The outer diameter of the reaction tube is 38 mm, the inner 25 mm. The hydrogen chloride is generated by dehydration of hydrochloric acid (37%) with sulfuric acid (96%). It passes a fur-

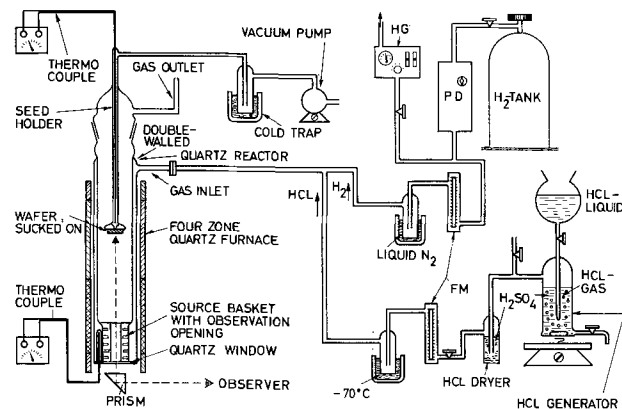


Fig. 2. The GaAs/HCl/H₂ system (PD: H₂ puridryer, HG: hygrometer, FM: flow meters).

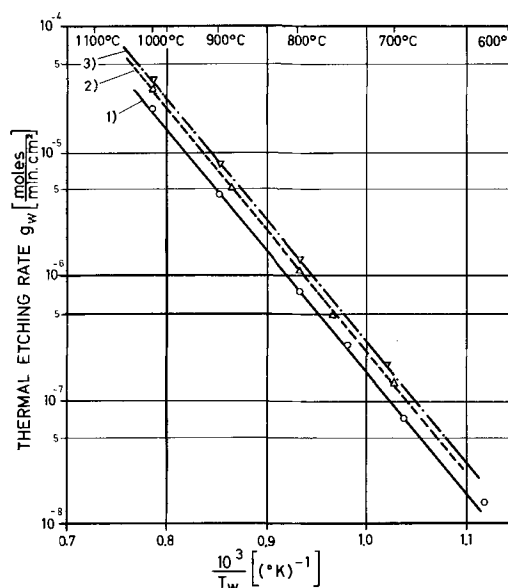


Fig. 3. Thermal etching rate g_w as a function of the reciprocal wafer temperature and different H₂ flow rates (GaAs/H₂O/H₂ system. H₂ flow: 1, 166 cc/min; 2, 245 cc/min; 3, 315 cc/min ($P_{\text{H}_2\text{O}} \approx 6.1 \times 10^{-3}$ atm).

ther sulfuric acid bubbler and a flow meter. Before it reaches the reactor, it is mixed with purified dried hydrogen (water content less than 5 ppm) and then allowed to enter the reactor. The wafer preparation and orientation is the same as described earlier. Also all the other steps are analogous to those mentioned above (etching runs).

Results

Experiments in the GaAs/H₂O/H₂ system.—**Thermal etching.**—We used three different H₂ flow rates f_{H_2} namely, 166, 245, and 315 cc/min, the partial pressure of water always being 6.1×10^{-3} atm. The temperature range was 600°-1000°C. The weight loss of the wafers Δw_w per unit area is proportional to the thermal etching rate g_w

$$g_w = \frac{\Delta w_w}{M \cdot t \cdot A_w} \quad [\text{moles GaAs/min cm}^2] \quad [1]$$

where M is the molecular weight of GaAs, t the duration of the run, and A_w the wafer surface area. A plot of $\log g_w$ vs. the reciprocal wafer temperature T_w is shown in Fig. 3. We find a straight line with a slope of about 48 kcal/mole GaAs for each H₂ flow rate. Furthermore, the etching rate g_w is proportional to the H₂ flow rate f_{H_2} .

Vapor growth deposition.—All deposition experiments were performed with a H₂ flow rate of 315 cc/min and a water vapor partial pressure of 6.1×10^{-3} atm. The source material was kept at constant temperature T_s , which was either 950°, 900°, or 850°C. The weight loss of the source Δw_s is proportional to the source etching rate g_s

$$g_s = \frac{\Delta w_s}{M \cdot t} \quad \text{moles GaAs/min} \quad [1a]$$

The number of moles of water vapor $(n/t)_{\text{H}_2\text{O}}$ transported per unit time follows from the ideal gas law. The ratio of gallium to oxygen in the vapor $[\text{Ga}]/[\text{O}]$ is given by

$$[\text{Ga}]/[\text{O}] = g_s / (n/t)_{\text{H}_2\text{O}} \quad [2]$$

This ratio depends on the source temperature. We get experimentally, according to Eq. [3] with $(n/t)_{\text{H}_2\text{O}} = 8.5 \times 10^{-5}$ moles/min, results shown in Table I.

The weight of the polycrystalline source material varied between 0.8 and 1.1g from batch to batch. Despite this relatively large variation, a plot of \log

Table I. Ratio of gallium to oxygen

$T_s, ^\circ\text{C}$	$[\text{Ga}]/[\text{O}]$
950	0.110 ± 0.005
900	0.053 ± 0.005
850	0.030 ± 0.005

$([\text{Ga}]/[\text{O}])$ vs. the reciprocal source temperature T_s exhibits a straight line relationship with an average slope of 42 ± 6 kcal/mole GaAs (Fig. 4). This is in good agreement with the value reported above. Furthermore, this result shows that the slope is independent of the crystal orientation within the experimental errors.

By varying the wafer temperature from 720° to 860°C , we get the dependence of the deposition rate on the wafer temperature and the $[\text{Ga}]/[\text{O}]$ ratio. For each $[\text{Ga}]/[\text{O}]$ ratio a straight line can be drawn (Fig. 5), the slope of which has the same value as for the etching rate experiments, but the reverse sign. Furthermore, we find that the deposition rate for $T_w = \text{constant}$ is proportional to the square of the $[\text{Ga}]/[\text{O}]$ ratio

$$\left(\frac{g_{wi}}{g_{wj}}\right)_{T_w=\text{const}} = \left\{ \frac{[\text{Ga}]/[\text{O}]_i}{[\text{Ga}]/[\text{O}]_j} \right\}^2 \quad [3]$$

Table II shows some experimental results, exhibiting a good agreement with Eq. [3].

Relatively good epitaxial growth was found to occur if the temperature difference between source and wafer is up to 100°C . If it is larger, polycrystalline precipitation on the wall of the reactor will be found

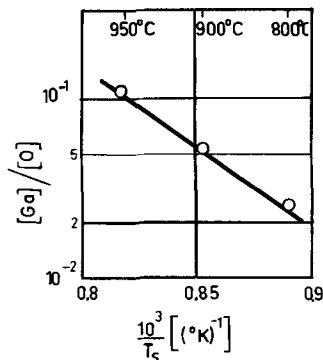


Fig. 4. Gallium-to-oxygen ratio as a function of the reciprocal source temperature T_s (GaAs/ $\text{H}_2\text{O}/\text{H}_2$ system).

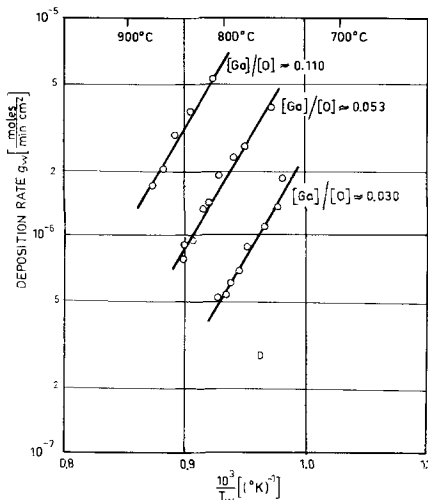


Fig. 5. Deposition rate g_w as a function of the reciprocal wafer temperature and different $[\text{Ga}]/[\text{O}]$ ratios.

Table II. Experimental results

$T_w, ^\circ\text{C}$	$[\text{Ga}]/[\text{O}]$	$g_w \times 10^3$ moles/ min cm^2	$\frac{[\text{Ga}]/[\text{O}]_i}{[\text{Ga}]/[\text{O}]_j} = x$	x^2	$\frac{g_{wi}}{g_{wj}}$
760	0.0530	3.7	$\frac{0.0530}{0.0282} \approx 1.88$	3.5	$\frac{3.7}{1.05} \approx 3.5$
760	0.0282	1.05			
800	0.0282	0.52	$\frac{0.0612}{0.0282} \approx 2.16$	4.6	$\frac{2.23}{0.52} \approx 4.3$
800	0.0612	2.23			
800	0.0435	1.1	$\frac{0.0612}{0.0435} \approx 1.41$	2	$\frac{2.23}{1.1} \approx 2$
800	0.0318	0.56	$\frac{0.0435}{0.0318} \approx 1.37$	1.9	$\frac{1.1}{0.56} \approx 1.9$
810	0.1152	5.2	$\frac{0.1152}{0.0365} \approx 3.16$	10	$\frac{5.2}{0.52} \approx 10$
810	0.0365	0.52			
840	0.0560	0.78	$\frac{0.0560}{0.0482} \approx 1.16$	1.35	$\frac{0.78}{0.53} \approx 1.45$
840	0.0482	0.53			

before the position of the wafer. This changes the $[\text{Ga}]/[\text{O}]$ ratio in an unknown manner. These runs were not taken into consideration here.

Etching experiments with the GaAs/HCl/ H_2 system.—For these experiments a constant HCl and H_2 flow rate was chosen ($f_{\text{H}_2} = 500$ cc/min and $f_{\text{HCl}} = 4.5$ cc/min, corresponding to a HCl partial pressure of 9×10^{-3} atm). The thermal etching rates, g_w , of the wafers were determined according to Eq. [1]. The experiments were performed in the temperature range of 600° – 800°C . Figure 6 shows the plot of $\log g_w$ vs. the reciprocal wafer temperature, T_w . The slope determined is 25 ± 3 kcal/mole GaAs.

Preliminary deposition experiments exhibit similar results as mentioned for the GaAs/ $\text{H}_2\text{O}/\text{H}_2$ system, especially the slope of the $\log g_w - 1/T$ curve is the same as for the etching experiments, but with the reverse sign.

Etching rate experiments below 600°C were also performed, but probably we had no chemical equilibrium in the system.

Thermodynamics and Discussion

In this section we will give an interpretation of the measured g -values and slopes. There are the following questions to be answered: Do the etching and deposition rate reactions happen at chemical equilibrium?

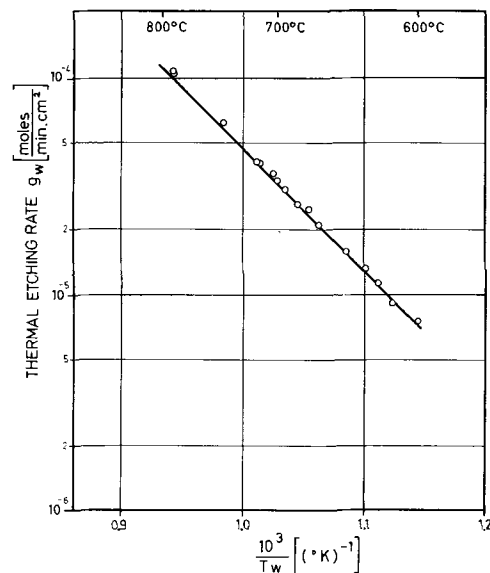


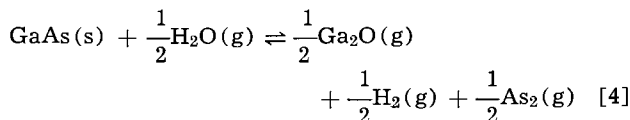
Fig. 6. Thermal etching rate g_w as a function of the reciprocal wafer temperature T_w (GaAs/HCl/ H_2 system).

Table III. Results

T, °K	p _{Ga₂O} , atm	K _p [5]	α	$\left(\frac{1-\alpha}{1+\alpha}\right)^{1/2}$
903	2.5 × 10 ⁻⁷	3.5 × 10 ⁻⁷	0.38	0.67
973	2.2 × 10 ⁻⁶	3.5 × 10 ⁻⁶	0.27	0.76
1073	2.1 × 10 ⁻⁶	7.4 × 10 ⁻⁵	0.18	0.84
1173	1.7 × 10 ⁻⁴	8.4 × 10 ⁻⁴	0.13	0.88
1273	8.5 × 10 ⁻⁴	7.0 × 10 ⁻³	0.09	0.92

Is it possible to deduce the measured energies from the reaction enthalpies of the proposed reactions?

The GaAs/H₂O/H₂ system.—According to [2] and [3] we have to consider only the formation of Ga₂O and no higher gallium oxides



together with the equilibrium of As₂ and As₄



The partial pressures of Ga₂O are obtained from the ideal gas law

$$p_{\text{Ga}_2\text{O}} = \frac{RT_0 \cdot \Delta w_w}{2Mt \cdot f_{\text{H}_2}} \quad [6]$$

With these values we can calculate the ratio of the partial pressures of As₂ and As₄ from

$$p_{\text{Ga}_2\text{O}} = 2p_{\text{As}_4} + p_{\text{As}_2} \quad [7]$$

and

$$\alpha = \frac{p_{\text{As}_4}}{p_{\text{As}_4} + p_{\text{As}_2}} = \frac{p_{\text{As}_4}}{p_{\text{As}}} \quad [8]$$

and

$$K_p[5] = \frac{p_{\text{As}_2}^2}{p_{\text{As}_4}} = p_{\text{As}} \frac{(1-\alpha)^2}{\alpha} \quad [\text{see (4)}] \quad [9]$$

where p_{As} is the total arsenic pressure. Results are shown in Table III.

This shows that the major part of the total arsenic pressure consists of As₂, which is in agreement with (3). The mass action constant for reaction [4] is

$$K_p[4] = \left\{ \frac{p_{\text{Ga}_2\text{O}} \cdot p_{\text{As}_2} \cdot p_{\text{H}_2}}{p_{\text{H}_2\text{O}}} \right\}^{1/2} \quad [10]$$

or

$$K_p[4] = \frac{p_{\text{Ga}_2\text{O}} \cdot \left(\frac{1-\alpha}{1+\alpha}\right)^{1/2}}{(p^0_{\text{H}_2\text{O}} - p_{\text{Ga}_2\text{O}})^{1/2}} \quad [10a]$$

following from the assumption

$$p_{\text{H}_2} = \text{const.} \approx 1 \text{ atm}^1$$

and from the relation

$$p_{\text{H}_2\text{O}} = p^0_{\text{H}_2\text{O}} - p_{\text{Ga}_2\text{O}}$$

(p⁰_{H₂O} is the initial water vapor pressure), together with Eq. [7] and [8].

Table IV contains K_p[4] values calculated from Eq.

¹The atmospheric pressure of 720 Torr has been set equal to 1 atm. This approximation does not cause any serious error.

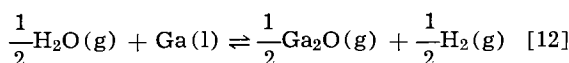
Table IV. K_p [4] values calculated from Eq. [10a]

T, °K	K _p [4] _{exp.}	K _p [4] _{calc.}
903	2.10 × 10 ⁻⁶	6.1 × 10 ⁻⁷
973	2.05 × 10 ⁻⁵	5.4 × 10 ⁻⁶
1073	2.20 × 10 ⁻⁴	6.8 × 10 ⁻⁵
1173	1.91 × 10 ⁻³	6.7 × 10 ⁻⁴
1273	1.06 × 10 ⁻²	5.0 × 10 ⁻³

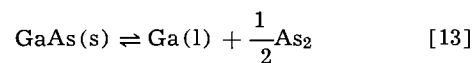
[10a] and those calculated from the free energy function of reaction [4].

$$-\left(\frac{\Delta F_T - \Delta H_{298}}{T}\right) = -\frac{1}{2}\left(\frac{F_T - H_{298}}{T}\right)_{\text{Ga}_2\text{O}} - \frac{1}{2}\left(\frac{F_T - H_{298}}{T}\right)_{\text{H}_2} - \frac{1}{2}\left(\frac{F_T - H_{298}}{T}\right)_{\text{As}_2} + \left(\frac{F_T - H_{298}}{T}\right)_{\text{GaAs}} + \frac{1}{2}\left(\frac{F_T - H_{298}}{T}\right)_{\text{H}_2\text{O}} \quad [11]$$

The free energy functions of Ga₂O, H₂O, H₂, and As₂ are given in the literature (2, 4). The corresponding values for GaAs have been calculated from available data of the enthalpy H_T and the entropy S_T (5). We used for reaction [4] ΔH₂₉₈ = 62 kcal/mole. This is obtained by combining the following reaction enthalpies:



with ΔH[12]₂₉₈ = 19.1 kcal/mole according to (2) and



with ΔH[13]₂₉₈ = 43 ± 1 kcal/mole according to (6, 7).

A plot of K_p[4] vs. 1/T is shown in Fig. 7. K_p[4]_{calc.} is smaller than our experimental values by a factor 2 to 3. This is not surprising since a change of a few kcal in ΔF results in a change of about an order of magnitude in K_p. From the slope of the log K_p[4] - 1/T - curves we get the enthalpy of reaction [4] in this temperature range

$$\Delta H_{T\text{exp.}} = 54 \pm 3 \text{ kcal/mole}$$

and

$$\Delta H_{T\text{calc.}} = 57 \pm 3 \text{ kcal/mole}$$

The agreement is good.

An estimate of ΔH_T can be made from the slope of the log g_w - 1/T - curves (Fig. 3). For temperatures below 1000°K p_{Ga₂O} << p_{H₂O} and it becomes

$$\Delta H_T = RT^2 \cdot \frac{\partial \ln K_p}{\partial T} \approx RT^2 \cdot \frac{\Delta \ln g_w}{\Delta T} \quad [14]$$

This estimate yields ΔH_T ≈ 48 kcal/mole. The deviation from the correct value of 54 kcal/mole is due to the

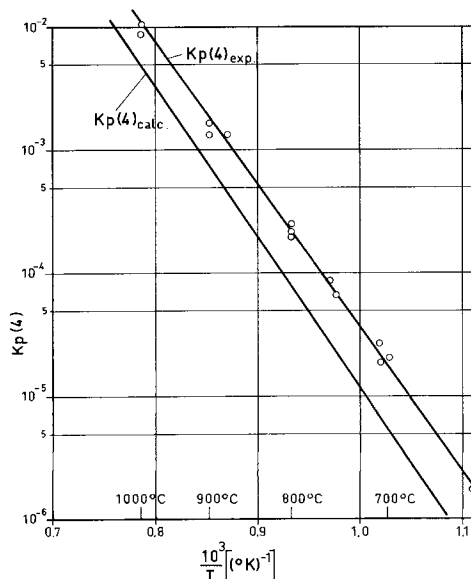


Fig. 7. Mass action constant of reaction [4] vs. 1/T

factor $[(1-\alpha)/(1+\alpha)]^{1/2}$ which has been omitted in the approximation of Eq. [14].

The GaAs/HCl/H₂ system.—Using data given by Fergusson and Gabor (5), it was possible to calculate the enthalpies and entropies of the following reactions by using the H_T and S_T value of the different species. For it is

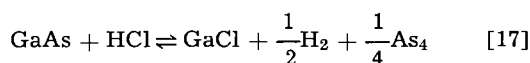
$$H_T = \sum_i v_i H_T^i \quad [15]$$

$$S_T = \sum_i v_i S_T^i \quad [15a]$$

(right side positive, left side negative) and we also obtain K_p by

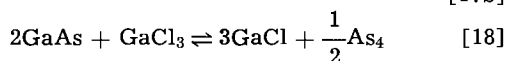
$$\ln K_p = \frac{T\Delta S - \Delta H}{RT} = -\frac{\Delta F}{RT} \quad [16]$$

For the reactions to be considered, we get



$$\Delta H = (32.2 - 1.09 \times 10^{-3}T) \text{ kcal} \quad [17a]$$

$$\ln K_p = 17.4 - 0.55 \ln T - 16200/T - 0.805 \times 10^{-3}T \quad [17b]$$



$$\Delta H = (108.1 - 6.4 \times 10^{-3}T) \text{ kcal} \quad [18a]$$

$$\ln K_p = 69.5 - 3.20 \ln T - 54400/T - 1.61 \times 10^{-3}T \quad [18b]$$

It might be mentioned that the data given by (5) are in agreement with the reaction enthalpy for



$\Delta H_{\text{exp.}} = 50$ kcal/mole, measured by Zuegel (8).

The following estimate shows that the partial pressure of As₂ is small. From the weight loss of the wafer Δw_w the total amount of Ga and As in the vapor phase (p_{Ga} and p_{As}) can be calculated.

$$p_{\text{Ga}} = \frac{RT_0 \cdot \Delta w_w}{M_t \cdot f_{\text{H}_2}} \quad [20]$$

with

$$p_{\text{Ga}} = p_{\text{GaCl}} + p_{\text{GaCl}_3} = 4p_{\text{As}_4} + 2p_{\text{As}_2} \quad [21]$$

and

$$p_{\text{As}} = p_{\text{As}_4} + p_{\text{As}_2} \quad [22]$$

From Eq. [8], [9], and [22] the fraction α can be calculated (Table V).

An analogous reasoning shows that the partial pressure of GaCl₃ can be totally neglected in this temperature range. We define the fraction

$$\beta = \frac{p_{\text{GaCl}}}{p_{\text{Ga}}}$$

Together with Eq. [20], [21], and K_p [18] we arrive at

$$K_p[18] = \frac{p_{\text{GaCl}}^3 \cdot p_{\text{As}_4}^{1/2}}{p_{\text{GaCl}_3}} = \frac{\beta^3 \cdot p_{\text{Ga}}^{5/2}}{2(1-\beta)} \quad [24]$$

Inserting the calculated K_p [18] and the experimental p_{Ga} for temperatures between 873° and 1073°K yields $0.98 \leq \beta < 1$ (Table VI)

Therefore the reaction in question is reaction [17]. For K_p [17] together with the definition of α we get

Table V. Calculations of fraction α

T, °K	p_{Ga} , atm	K_p [5]	α
873	1.4×10^{-4}	1.1×10^{-7}	0.95
923	2.8×10^{-4}	7.4×10^{-7}	0.88
973	6.2×10^{-4}	4.0×10^{-6}	0.83
1063	1.7×10^{-3}	5.4×10^{-6}	0.75

Table VI.

T, °K	K_p [17] _{calc.}	K_p [18] _{calc.}
873	3.5×10^{-3}	1.2×10^{-7}
973	2.2×10^{-2}	4.6×10^{-6}
1073	9.7×10^{-2}	7.5×10^{-3}

Table VII

T, °K	p_{GaCl} , atm	$\left(\frac{\alpha}{2(1+\alpha)}\right)^{1/4}$	K_p [17] _{exp.}
873	1.4×10^{-4}	0.704	1.15×10^{-3}
923	2.8×10^{-4}	0.695	3.16×10^{-3}
973	6.2×10^{-4}	0.691	7.95×10^{-3}
1063	1.7×10^{-3}	0.677	3.15×10^{-2}

$$K_p[17] = \frac{p_{\text{GaCl}} \cdot p_{\text{H}_2}^{1/2} \cdot p_{\text{As}_4}^{1/4}}{p_{\text{HCl}}} = \frac{p_{\text{GaCl}}^{5/4} \left(\frac{\alpha}{2(1+\alpha)}\right)^{1/4}}{p_{\text{HCl}}^0 - p_{\text{GaCl}}} \quad [25]$$

assuming again $p_{\text{H}_2} \approx 1$ atm. p_{HCl}^0 is the initial vapor pressure of HCl.

The quantity $\left(\frac{\alpha}{2(1+\alpha)}\right)^{1/4}$ becomes $\left(\frac{1}{4}\right)^{1/4}$, if As₄

is predominant. In the worst case (1063°K) the ratio

$$\left\{ \frac{\alpha}{2(1+\alpha)} \middle/ \frac{1}{4} \right\}^{1/4}$$

becomes 0.96. For K_p [17], Eq. [25], we obtain the figures given in Table VII.

A plot of K_p [17] vs. $1/T$ is shown in Fig. 8 K_p [17]_{exp.} differs from K_p [17]_{calc.} by a factor of about 3, which is not a serious deviation. The reaction enthalpy for reaction [17] becomes

$$\Delta H_{T_{\text{exp.}}} = 32 \pm 2 \text{ kcal/mole}$$

and

$$\Delta H_{T_{\text{calc.}}} = 31 \text{ kcal/mole}$$

The agreement is very good.

As before, an estimate of ΔH_T can be made from the slope of the $\log g_w - 1/T$ curve (Fig. 6), if $p_{\text{GaCl}} \ll p_{\text{HCl}}$. We obtain

$$\Delta H_T = RT^2 \cdot \frac{\partial \ln K_p}{\partial T} \approx \frac{5}{4} RT^2 \frac{\Delta \ln g_w}{\Delta T} \quad [26]$$

which yields $\Delta H_T \approx 31$ kcal/mole.

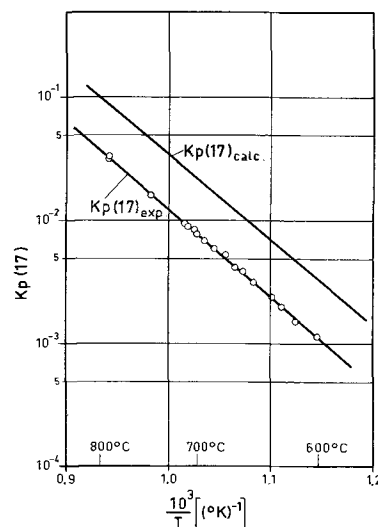
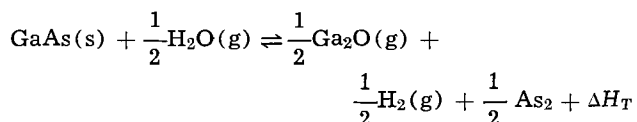


Fig. 8. Mass action constant of reaction [17] vs. $1/T$

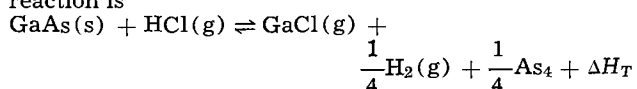
Summary

Vapor etching as well as vapor growth experiments in an open tube GaAs/H₂O/H₂ system and vapor etching experiments in an open tube GaAs/HCl/H₂ system revealed straight line relationships between the logarithm of the etching deposition rates g_w and $1/T_w$, respectively, at temperatures between 600° and 1000°C. By calculating the mass action constants of the respective reactions from experimental data, we are able to determine the respective reaction enthalpies. They are compared with reaction enthalpies calculated from data given in the literature.

For the GaAs/H₂O/H₂ system the reaction is



with $\Delta H_{T_{\text{calc.}}} = 57 \pm 3$ kcal/mole and $\Delta H_{T_{\text{exp.}}} = 54 \pm 3$ kcal/mole. For the GaAs/HCl/H₂ system the reaction is



with $\Delta H_{T_{\text{calc.}}} = 31$ kcal/mole and $\Delta H_{T_{\text{exp.}}} = 32 \pm 2$ kcal/mole.

The agreement between experimental and thermodynamically calculated K_p values is satisfying; the deviation is about a factor of 3.

All this gives good reason to assume that the above mentioned reactions are appropriate and that the etching reactions take place close to equilibrium.

Deposition experiments revealed also a relationship between the growth rate at a constant wafer temperature and the square of the gallium-to-oxygen ratio.

Acknowledgments

The authors wish to thank Dr. M. Zuegel for furnishing them with the thermodynamical data from his experiments prior to publication, and Miss H. Leistikow and Mr. H. Treiber for helping with the experiments.

Manuscript received Dec. 24, 1963; revised manuscript received May 25, 1964.

Any discussion of this paper will appear in a Discussion Section to be published in the June 1965 JOURNAL.

REFERENCES

1. M. Zuegel, Private communication.
2. C. N. Cochran and L. M. Foster, *This Journal*, **109**, 144 (1962).
3. G. E. Gottlieb and J. F. Corboy, *RCA Rev.*, **24**, 585 (1963).
4. D. R. Stull and G. C. Sinke, "Thermodynamic Properties of the Elements" (1956).
5. R. R. Fergusson and T. Gabor, Scientific Paper 63-166-452-P3 Westinghouse Research Lab.
6. V. J. Silvestri and V. J. Lyons, *This Journal*, **109**, 963 (1962).
7. H. Gutbier, *Z. Naturforschg.*, **16a**, 268 (1961).
8. M. Zuegel, To be published.

SYMBOLS

A_w	wafer area, cm ² .
f_x	flow rate of the gas x at room temperature, cc/min.
F_T	free energy at the temperature T , kcal.
g_s	thermal etching rate of the source material, moles/min.
g_w	thermal etching or deposition rate of the wafer, moles/min cm ² .
$[\text{Ga}]/[\text{O}]$	gallium-to-oxygen ratio.
H_T	enthalpy at the temperature T , kcal/mole.
ΔH_T	reaction enthalpy at the temperature T kcal/mole.
K_p	mass action constant.
M	molecular weight (of GaAs), g
$(n/t)_x$	moles of transported vapor of species x per unit time, moles/min.
p_i	partial pressure of the species i , atm.
R	gas constant, cal/deg mole or atm cm ³ /deg mole.
S_T	entropy at the temperature T , cal/deg.
t	duration of run, min.
T	temperature, °C or °K.
T_0	room temperature, °K.
Δw_s	weight loss of the source material, g .
Δw_w	weight loss of the wafer, g .
α, β	fraction of the total pressure produced by a certain gaseous species.

The Fluorescence of the Europium and Terbium Dibenzoylmethides

Max Metlay

Advanced Technology Laboratories, General Electric Company, Schenectady, New York

ABSTRACT

Data on the fluorescence spectra, fluorescence lifetimes, and the temperature dependence of these quantities for the dibenzoylmethane chelates of europium and of terbium in a variety of environments are presented. The effect of the environments studied on the europium chelate is much more pronounced than on the terbium chelate. Lewis bases cause a decrease in temperature dependence of fluorescence in the europium chelate. Quenching of fluorescence takes place through vibronic interaction with the lowest excited (triplet) state of the ligand.

The recent resurgence of interest (1,2) in the spectroscopic properties of rare earth chelates first discussed by Weissman (3) has led to the prediction (2) of laser action in these compounds and to the demonstration (4, 5) of such action in two chelates of europium, the benzoylacetate and the thenoyltrifluoroacetate. The pertinent spectroscopic properties include a broad, intense absorption in the ultraviolet, characteristic of the organic portion of the molecule, and a relatively sharp line fluorescence, at the energies characteristic of the rare earth. The path of intramolecular energy transfer leading to the fluorescence

process has been the subject of considerable study. The absorption of an ultraviolet photon raises the molecule to an excited singlet state, from which the excitation energy is rapidly transferred to the resonance levels of the lanthanide. This transfer has been presumed to take place via a triplet state (1, 2, 6) but the extreme rapidity of the process ($<10^{-7}$ sec) casts doubt on this explanation (7, 8).

This paper presents data on the fluorescence spectra, fluorescence lifetimes, and on the temperature dependence of fluorescence lifetime and of peak fluorescence intensity of the dibenzoylmethane chelates of

europium and terbium (EuD_3 and TbD_3) in a variety of environments. Such measurements are a first step in an understanding of the interactions of the chelates with their chemical environment and lead in the present case to an hypothesis on the mechanism of fluorescence quenching in these systems.

Experimental

The chelates were prepared and purified by the method described by Whan and Crosby (2) as giving the tris-chelated materials, EuD_3 and TbD_3 . In addition, a sample of the europium chelate (here called EuD_4) was not subjected to the final step of vacuum heating normally done to drive off piperidine and excess dibenzoylmethane. The apparent composition of EuD_4 , as determined by thermogravimetric analysis, consists of four dibenzoylmethanes and one piperidine per europium atom.¹

The solvents used included EPA (ether, 3-methylpentane, alcohol, 5:5:2), styrene (subsequently thermally polymerized to polystyrene after vacuum outgassing), and Bisphenol A (Dow Epoxy Resin 332) subsequently polymerized by one of the catalysts triethylenetetramine (A), diethylaminopropylamine (B) and imidazole (C).

Fluorescence spectra were obtained at 77° and at 300°K. A G.E. H100A4/T 100 watt mercury lamp, filtered by a Corning CS 7-54 filter, provided excitation. The fluorescence radiation passed through a Kodak Wratten No. 2B filter, to eliminate scattered source radiation below 3900Å, which would interfere in the second order with the fluorescence spectrum. It was then analyzed by a Bausch and Lomb grating monochromator which had been provided with a motor driven wavelength scan, and with slits set to give 10Å dispersion. The output of the monochromator was monitored by a 1P22 photomultiplier tube, the output of which was recorded by a Brown potentiometric recorder.

The variation with temperature of the intensity of the fluorescence peak of each of the solid samples was followed by inserting a chromel-alumel thermocouple into each sample and recording its output as one coordinate for an X-Y recorder, while the output of the photomultiplier monitoring the peak intensity activated the other coordinate.

¹ The formula $\text{EuD}_3 \cdot \text{HD} \cdot \text{pip}$ has gained considerable acceptance as showing the structure of this material. While this is the most probable structure, it has not been demonstrated definitively.

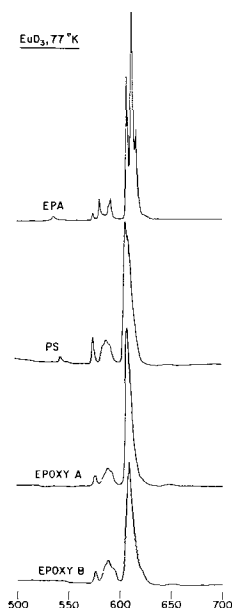


Fig. 1. Fluorescence spectrum of EuD_3 in various solvents at 77°K. Ordinate is fluorescence intensity, abscissa is wavelength in millimicrons.

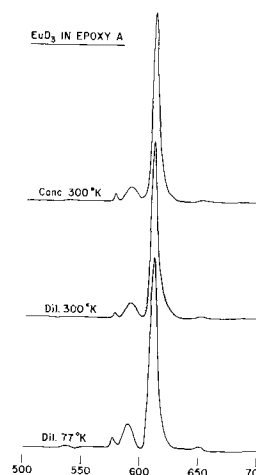


Fig. 2. Fluorescence spectrum of EuD_3 in epoxy A. Concentrations: conc. = 2.1 mg/cc, dil. = 0.8 mg/cc.

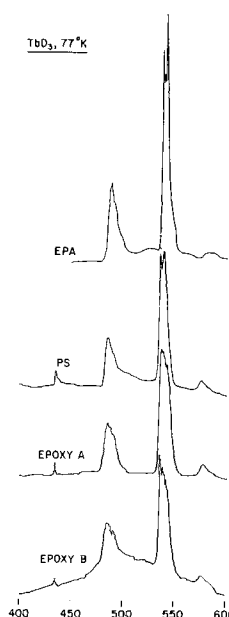


Fig. 3. Fluorescence spectrum of TbD_3 in various solvents at 77°K.

Fluorescence lifetimes were measured for each sample at 77°K and at 300°K, as described previously (9). These measurements were also performed on the microcrystalline chelates and on the hydrated rare earth chlorides, for comparison with literature values.

Results and Discussion

The fluorescence spectra of the europium samples are shown in Fig. 1 and 2. The main peak is due to the $^5\text{D}_0 \rightarrow ^7\text{F}_2$ transition. As can be seen in Fig. 1, the fluorescence spectra of EuD_3 in various hosts show differences in detail, with greater resolution of the main peak in EPA than in the polymeric solvents. Figure 2 illustrates the invariance of the spectrum in one epoxy matrix with concentration and with temperature. Figure 3 illustrates the fluorescence spectra of the terbium samples at 77°K. The major peak here is the $^5\text{D}_4 \rightarrow ^7\text{F}_5$ transition. The broad band underlying the spectrum in epoxy B is due to an impurity in the diethylaminopropylamine catalyst. The spectra have not been corrected for the spectral sensitivity of the photomultiplier.

The fluorescence lifetimes of the europium samples are listed in Table I and those of the terbium samples in Table II. As is apparent from Table I, the lifetimes of EuD_3 and EuD_4 are not the same (9).

Table I. Fluorescence lifetime, europium compounds

Material	Lifetime, μsec	
	300°K	77°K
$\text{EuCl}_3 \cdot 6\text{H}_2\text{O}$	120	120
EuD_3	80	369
EuD_3 in EPA, 1.0 mg/cc	—	360
EuD_4	533	533
EuD_4 in EPA, 1.3 mg/cc	—	451
EuD_3 in polystyrene, 1.5 mg/cc	—	404
EuD_3 in polystyrene, 4.3 mg/cc	—	458
EuD_3 in epoxy A, 0.8 mg/cc	342	332
EuD_3 in epoxy A, 2.1 mg/cc	317	339
EuD_3 in epoxy B, 0.8 mg/cc	485	568
EuD_3 in epoxy B, 2.1 mg/cc	451	549
EuD_3 in epoxy C, 2.1 mg/cc	462	510

Table II. Fluorescence lifetime, terbium compounds

Material	Lifetime, μsec	
	77°K	
$\text{TbCl}_3 \cdot x\text{H}_2\text{O}$	450	
TbD_3	54	
TbD_3 in epoxy A, 0.9 mg/cc	587	
TbD_3 in epoxy B, 0.9 mg/cc	648	
TbD_3 in epoxy C, 0.9 mg/cc	450	
TbD_3 in polystyrene, 1.5 mg/cc	566	
TbD_3 in polystyrene, 5.0 mg/cc	400	

The temperature variation of the intensity of the major fluorescence line of several of the samples is illustrated qualitatively in Fig. 4.

The EuD_3 samples can be divided into two groups, according to the behavior of these properties. In Group I, containing microcrystalline EuD_4 , and the epoxy samples, fluorescence lifetime and intensity are relatively independent of temperature. In all of these samples an electron donor molecule, either a dibenzoylmethane molecule, a piperidine or one (or more) of the amine molecules used to catalyze the epoxy polymerization, is associated with EuD_3 . In Group II, containing microcrystalline EuD_3 , the polystyrene and the EPA samples, fluorescence intensity is relatively much more dependent on temperature.

The data suggest a mechanism for quenching the EuD_3 fluorescence. As pointed out by Whan and Crosby (2), quenching normally takes place by vibronic coupling of the central ion to the ligands, and of the ligands to the surrounding matrix. For this to occur at low temperatures, ligand states must exist at energies below that of the central ion. As the temperature increases, the rate of phonon assisted transitions to higher energy states will increase exponentially, although the rate may remain low if the dif-

ference in energy between states is sufficient. The lowest lying ligand state is the triplet, lying some 3500 cm^{-1} above the Eu^{3+} resonance level in EuD_3 , and $\sim 100 \text{ cm}^{-1}$ above the Tb^{3+} resonance level in the TbD_3 (1). At temperatures around 77°K , these energy differences are sufficient to prevent transitions to the triplet. At higher temperatures, the rate of the quenching interaction in the TbD_3 samples becomes large. At higher temperatures still, the EuD_3 samples of Group II behave similarly. The samples of Group I, however, show comparatively little change in lifetime or intensity up to room temperature. In these samples, the Lewis base interacts with the ligand, presumably through charge transfer complex formation, increasing the electron density in the chelate, and simultaneously increasing its stability. We postulate that this interaction results in a raising of the energy of the triplet state. In the complex, the lowest excited state will differ in configuration from the triplet state of the uncomplexed EuD_3 , but we retain the triplet designation for convenience. If the "triplet" associated with the complex is higher in energy than that in the uncomplexed material, vibronic interaction between resonance and triplet states are less frequent, sufficiently so that quenching in the complexed EuD_3 samples is suppressed. In TbD_3 , however, the original separation between triplet and resonance levels is small, and the increase in triplet energy is apparently not sufficient to suppress quenching.

A detailed study of the fluorescence intensity of a series of Eu^{3+} and Tb^{3+} doped molybdates and tungstates (10, 11) show some parallels to the results of the present work. Van Uitert showed that the temperature dependence of fluorescence intensity in an alkali-terbium molybdate is much greater than the corresponding tungstate, or than the corresponding europium molybdate. Intensity in the europium doped tungstates increases with bond energy between europium and its neighboring oxygen atoms. Increase in coupling with the surroundings decreases intensity in terbium molybdates by increasing energy losses to lattice processes, and increases intensity in the terbium tungstates where lattice processes are less important. The significance of Van Uitert's results for the present study lies in the experimental demonstration that the fluorescence properties of europium and terbium, in inorganic as well as the organic media discussed in this paper, are extremely dependent on environment, and more particularly on the details of the modes of energy transfer to and from the lanthanide.

Acknowledgment

Helpful discussions during the progress of this work with Drs. G. P. Brown, J. Gaynor, and W. S. Horton are hereby gratefully acknowledged.

Manuscript received April 16, 1964. Portions of this paper were presented at the Pittsburgh Meeting, April 15-18, 1963.

Any discussion of this paper will appear in a Discussion Section to be published in the June 1965 JOURNAL.

REFERENCES

- G. A. Crosby, R. E. Whan, and R. M. Alire, *J. Chem. Phys.*, **34**, 743 (1961).
- R. E. Whan and G. A. Crosby, *J. Molecular Spectroscopy*, **8**, 315 (1962).
- S. I. Weissman, *J. Chem. Phys.*, **10**, 214 (1942).
- A. Lempicki and H. Samelson, *Phys. Lett.*, **4**, 133 (1963).
- N. E. Wolff and R. J. Pressley, *Appl. Phys. Lett.*, **2**, 152 (1963).
- J. J. Freeman and G. A. Crosby, *J. Phys. Chem.*, **67**, 2717 (1963).
- M. Kleinerman, R. J. Hovey, and D. O. Hoffmann, Abstract No. 33, *This Journal*, **110**, 53C (1963).
- M. Kleinerman, Abstract HA3, *Bull. Am. Phys. Soc. Ser. II*, **9**, 265 (1964).
- M. Metlay, *J. Chem. Phys.*, **39**, 491 (1963).
- L. G. Van Uitert, *ibid.*, **37**, 981 (1962).
- L. G. Van Uitert, *This Journal*, **110**, 46 (1963).

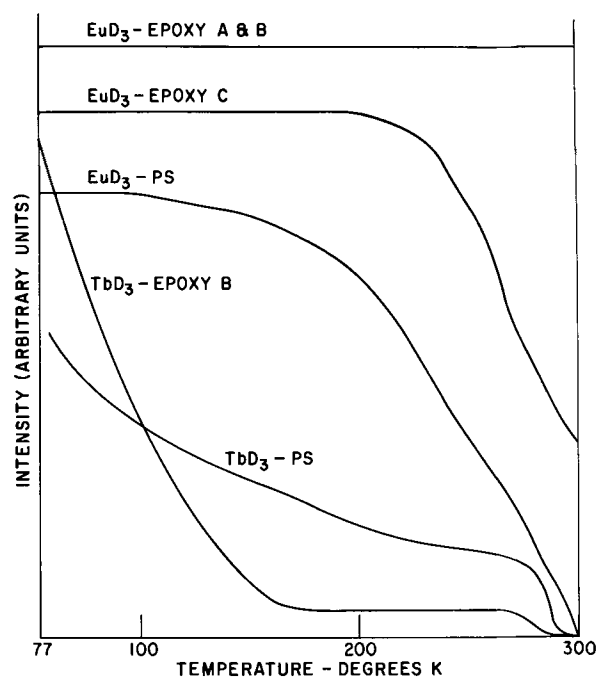


Fig. 4. Temperature dependence of fluorescence peak intensity

Luminescence during the Anodic Oxidation of Silicon

Worden Waring¹ and E. A. Benjamini²

Fairchild Semiconductor, A Division of Fairchild Camera and Instrument Corporation,
Palo Alto, California

ABSTRACT

Silicon wafers were anodized in ethylene glycol containing KNO_3 . Luminescence, measured with a photomultiplier, began with oxide growth and, at constant current, increased with some low power of the voltage, the power depending on the type and resistivity of the silicon. When anodization was interrupted on low resistivity silicon and the voltage and current were decreased, then increased again, the luminescence was exponential with the voltage and linear with the current during this excursion. Initially, both the luminescence and the oxide growth on n-type silicon of moderate or high resistivity were patchy; the patches gradually came together to form a uniform layer. With p-type material the light emission was uniform even at the start. At the highest voltages, breakdown occurred with the appearance of "sparks," which involve electrical discharge from the wafer into the solution

When a silicon wafer is anodically oxidized at constant current, a bluish-white glow from the material can be seen in a darkened room. The glow increases in brightness as anodization continues, until at some high voltage gas evolution from the wafer becomes very noticeable, and soon thereafter bright points of light, "sparks," appear and disappear in succession, initially at the edge of the wafer, then also on the flat surfaces. The voltage becomes erratic, levelling off, or even decreasing somewhat. Later examination of the oxide shows it is cloudy and nonuniform; a "breakdown" region has been reached when the "sparks" appear.

The emission of light on anodization has long been known for aluminum and for a number of other metals such as Ta, Zn, Mg, W; it has been called "galvanoluminescence" (1, 2). In an attempt to learn more about where the photoemission occurs, whether or not there is a minimum voltage required before photoemission starts, and what the relations are between the intensity of light emission and the electrical variables during anodization, the following experimental work with silicon was undertaken.

Anodization Procedure

Anodization was carried out at constant current (corresponding to about 7 ma/cm^2 of wafer surface) in an electrolyte of ethylene glycol with $0.04N \text{ KNO}_3$. Silicon wafers of (111) orientation, of both types and several resistivities, were used. After being lapped and chemically polished, they were held vertically in a special clip (3). In general no stirring or ultrasonic agitation was used. Experiments were at room temperature, but there was some resistive heating of the solution during the longer runs to higher voltages.

Light from the silicon wafer being anodized was picked up by a photomultiplier having a Dumont 6292 tube with an S11 photocathode and operated at 1200v. The output from this was fed to a Kin-Tel meter, model 202B, whose output in turn went to the Y-axis of a Moseley X-Y recorder Model 135. Different amplifications were used as needed. The X-axis of the recorder was driven by the voltage applied to the anodization cell. In this manner relative light intensity could be recorded automatically as a function of voltage. A separate strip chart recorded voltage across the cell as a function of time.

In most runs the power source was turned on at constant current, and the recording was continued up

to a high voltage, but stopped before the "sparks" began to appear. When the power was turned on, the applied voltage jumped immediately to a value around 30 to 60v with lower resistivity material, or around 100v for the higher (10 ohm-cm p-type or 2 ohm-cm n-type). This initial voltage was subtracted from the later readings to obtain the net voltage, V_f . A reference value for the output millivolts of the photomultiplier with zero luminescence from the wafer was obtained at this start, or when available from the voltage down-and-up runs (discussed below), wherein the luminescence disappeared at the lowest voltages, but all other conditions on the photomultiplier assembly were the same. Luminescence values (L) were corrected for this small reference value, in each run.

Luminescence at Constant Current

In most runs the voltage and luminescence were allowed to climb at constant current without interruption. In a few of the later runs, the growth was interrupted and the voltage was run down and up as described below. Data read from the X-Y recorder charts were plotted in various ways. Figure 1 shows the results in one of the later runs, with 0.002-0.003 ohm-cm n-type Si. The general procedure is evident from the arrows: an initial jump to about 30v (which was sub-

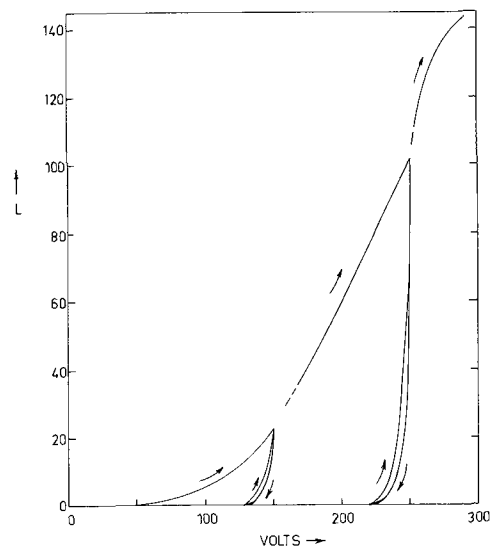


Fig. 1. Luminescence and total voltage run, 0.002-0.003 ohm-cm n-type Si.

¹ Present address: Rancho Los Amigos Hospital, Downey, California.

² Present address: Signetics Corporation, Sunnyvale, California.

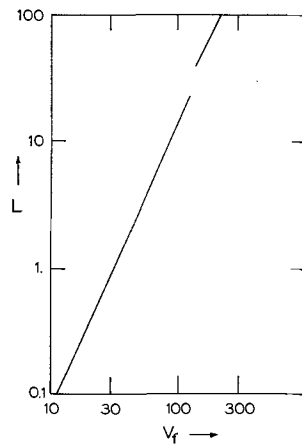


Fig. 2. Luminescence and net voltage at constant current; run of Fig. 1.

tracted to give V_f values), then a steady increase, with (in this run) two interruptions for the down-and-up excursions. In this run, the curvature at the highest voltages is typical of the appearance when gas generation becomes significant: many fine bubbles form and leave the wafer surface, and scatter the light.

Graphs of the data from oxide growth at constant current, plotted as $\log L$ vs. $\log V_f$ were linear (with the possible exception of the lowest, least certain values). Figure 2 shows this plot for the run of Fig. 1 up to about 200v. The interruption corresponds to the excursion at 150v ($V_f = 120v$). Slopes of such lines for various runs were as shown in Table I. Runs with the lowest resistivity material gave values of the slope always between 2 and 3, but somewhat lower after than before the down-and-up voltage excursion. Data from runs with the 1 ohm-cm p-type could be accurately fitted algebraically by a parabola. In addition, one run with 10 ohm-cm p-type showed a slope of 1 before the down-and-up excursion and about 2.8 afterward.

The results showed that the luminescence increased with a power of the voltage (linear, parabolic, or almost cubic). Semilogarithmic plots ($\log L$ vs. V_f) could not be made linear by the addition to L of a small constant, as was done successfully with aluminum, thus showing exponential increase (4). The luminescence apparently began concurrently with film growth; there seemed to be no initial oxide thickness (no significant "threshold" voltage) required after oxide growth began before luminescence appeared. This was shown even more clearly with the n-type material, as discussed next.

A significant difference between n- and p-type silicon of intermediate resistivities (1-2 ohm-cm) should be noted. The p-type material started anodizing readily at a reasonable current density such as used here: turning on the constant current power source (in the dark, for runs with either type material) gave an initial jump to the starting voltage, then a steady rise in voltage and increase in luminescence (accurately parabolic, as we have noted). The first visible luminescence was uniform across the wafer. If, however, the constant current power source was turned on with n-type material, there was a jump to a starting voltage, then a brief decrease in voltage as the luminescence increased, and finally an increase again

Table I. Slopes for various runs

Resistivity, ohm-cm	Type	Exponent
0.002-0.003	p, n	2 to 3
1	p	2
2	n	1

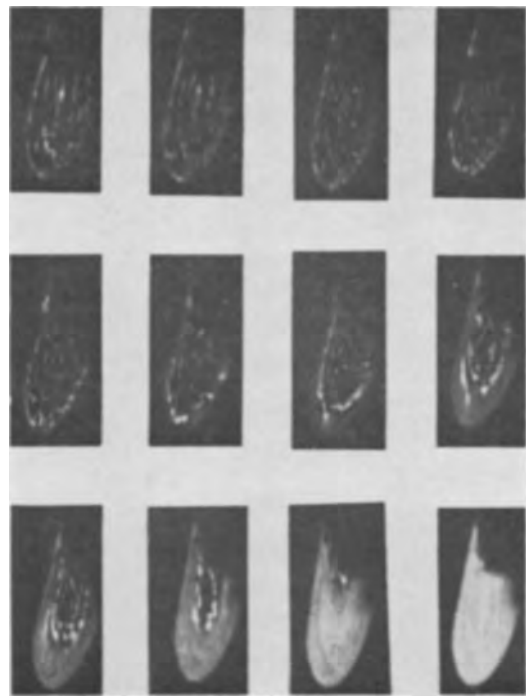


Fig. 3. Growth of luminescence and oxide layer on 2 ohm-cm, n-type Si.

with smooth growth of luminescence with voltage (linear, rather than parabolic). A similar behavior of the voltage was observed earlier by Schmidt and Michel (5).

With this n-type silicon the glow started at a number of isolated bright spots (on edges and flat surfaces), then consolidated and expanded in from the edges to develop the uniform sheet glow over all the wafer surface, initially dimmer than the isolated spots had been. The isolated areas were areas of initial thin oxide growth, as was made evident by photographing the glow, then stopping the run and comparing the wafer surface to the photographs. Figure 3 shows the sequence on one wafer, set at an angle to the camera.

We noticed previously (6) that anodization of n-type silicon can be started readily either by illumination (generating holes, needed for the reaction) or by waiting. In either case, when anodization has begun it runs smoothly without further illumination being required. It may be that after a very thin layer of oxide has formed (from the residual holes available or from the Cabrera-Mott mechanism) the concurrent luminescence itself serves to generate more holes for the continuing reaction. In agreement with this, we have found illumination is useful also in starting with high resistivity p-type silicon, but it contributes less at the higher voltages, i.e., later in the run. That is, there is then less jump in voltage if the illumination (a Sylvania Sun-Gun) is turned off. This autocatalysis seems also related to our power law increase of L with V_f whereas van Geel and co-workers (4) found an exponential increase with aluminum, which is presumably not affected by illumination.

Luminescence at Constant Oxide Thickness

In a few runs the constant-current oxide growth was interrupted as shown in Fig. 1. The voltage was decreased in steps until the total current had fallen to less than 0.1 ma and the luminescence had disappeared (a constant, low, reference level of the photomultiplier was reached for each particular run). Different wafers had exposed areas of 6-10 cm², but in each case the photomultiplier minimum reference level was reached. Simultaneous values of voltage, current, and luminescence were read and recorded at each step both during the voltage decrease and during the

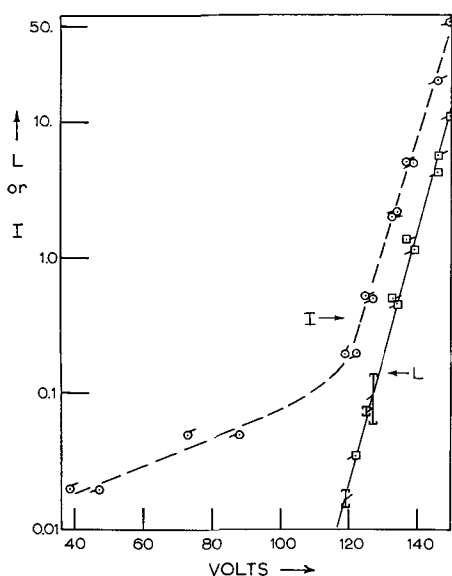


Fig. 4. Luminescence, current, and voltage at constant oxide thickness; run of Fig. 1.

increase again to the same constant current for continuing the oxide growth.

With 0.002-0.003 ohm-cm material, both p- and n-type, the current and luminescence fell extremely rapidly with voltage, dropping two or three decades with only 20-30v decrease. The data for $\log I$ or $\log L$ against voltage seemed to fall on straight lines, at least down to the lowest levels where the data were least accurate. Figure 4 shows data from the 150v excursion of the run in Fig. 1; I is in milliamperes and L in arbitrary units. Tags to the left show data with decreasing current; to the right, with increasing. These data suggest there may be some levelling off with a small leakage current without luminescence. The luminescence also seemed to vary linearly with the current, as indicated by the approximately 45° slope on a $\log L$ vs. $\log I$ graph, and the proportionality constant was greater for the higher voltage excursions.

However, in such an excursion during a run with 10 ohm-cm p-type silicon the luminescence fell much less rapidly with voltage: one decade for 60-v decrease. In this case, L and I were apparently linear (not exponential) with the voltage; L was, as before, linear with I .

Small loops are seen in Fig. 1; these may be experimental scatter, but the direction was consistent in the several excursions made. This, together with the fact that the slope of the line for $\log L$ vs. V_f was sometimes somewhat different after an excursion, indicated that some oxide growth or structure rearrangement ("forming") may have been going on during the excursion. It is not strictly correct to consider these phenomena as occurring with constant oxide thickness and structure.

Spectrum

An attempt was made to obtain the spectrum of the luminescence. However, when dispersed through a monochromator, the light was too faint to be registered by the photomultiplier.

Location of Photoemission

It seemed that the light might be generated in any of several regions: at the oxide-electrolyte interface, within the oxide layer, at the oxide-silicon interface, or within the silicon. As a simple test for the first of these, neon gas was bubbled over 1 ohm-cm p-type wafers during anodization, to see if the characteristic red-orange glow of neon would appear in bubbles brushing along the surface of a wafer.

When the only light emission from the wafer was the uniform bluish-white glow, no neon bubbles showed

their orange discharge color, whether they bubbled up past and struck the edge of a vertical wafer, or slid along the under surface of a wafer tilted somewhat from the vertical. However, as soon as "sparks" began to appear on the edge of the wafer, neon bubbles passing near individual sparks gave brilliant red-orange flashes. The striking color bursts, contrasting with the background glow and the sparks, were photographed in color with some success.

These experiments indicated that the sparks are associated with a discharge through the oxide layer and a strong field then extending into the solution. Unfortunately, this does not give any convincing evidence as to the location of the uniform glow. We found that sparks drawn between two platinum electrodes in a beaker of the electrolyte did not cause the neon bubbles to flash bright red-orange, even up to 100v between the electrodes. Hence there could be some field at the oxide-electrolyte interface without the neon indicating its presence. However, since the voltage V_f has been shown to be proportional to the oxide thickness, at least, below the breakdown voltages, then there is very little voltage that can be allocated to this interface, except perhaps some of the initial starting voltage jump.

It seems unlikely that the glow occurs within the silicon itself, because of the bluish-white color. Light coming out through a layer of silicon will be yellowish or reddish unless it is generated within a fraction of a micron of the surface (7). With other oxides, it has been considered that the light is generated at trapping centers within the oxide; for example, with aluminum whose oxide glow is greatly affected in intensity and color by impurities in the aluminum, and hence in the oxide grown from it (8-10).

There is another question of some interest. Since the thickness of the oxide is proportional to the voltage V_f (about 6 Å/volt according to measurements in this laboratory), the field is therefore constant during the growth, and there seems no reason to anticipate a limiting voltage, or breakdown. We have, however, noted the increase in bubbling just before breakdown, and interpret this, with other observations, as indicating that with the thickest oxide layers, the current efficiency (usually about 2% goes to oxide formation) decreases somewhat so that with more gas evolution there is less oxide growth and hence the field increases. Since the field during growth is about 1.6×10^7 v/cm and therefore near the breakdown limit anyway, this increase is enough to cause the weaker spots in the oxide to give way, thus showing the sparks.

Discussion

Since most of the studies of galvanoluminescence have used aluminum rather than other metals, our results will be compared to the behavior of aluminum except where specifically noted otherwise. In some electrolytes (such as aqueous borate or boric acid, citrate or phosphate) aluminum forms thin, dense, anodic oxide films; in others (such as aqueous sulfuric, phosphoric, or oxalic acid) it forms thicker, porous, more easily conducting films (4, 11). But even in the latter case there is a thin, dense layer of oxide next the aluminum. The luminescence occurs in well-formed, dense oxide only (4, 12).

The most extensive study of the luminescence seems to be that of van Geel, Pistorius, and Bouma (4). They found an exponential increase of L with V at constant current; that is, $\log(L + a)$, where a is a small constant, is linear with V . Then a curve of $\log L$ against $\log V$ would be convex toward V . Our own results give a straight line on such a log-log plot, and the slope depends on the characteristics of the silicon. Our data do not seem to fit an exponential relation even with the addition of a reasonable, small constant to L . This shows a definite difference between the behavior of aluminum and that of silicon.

An earlier study with aluminum (13) gave a curve of $\log L$ against $\log V$ concave toward the V axis. In this work a citric acid solution was used, so presumably the increasing luminescence in the thin, non-porous oxide layer was partially absorbed in the thickening porous oxide layer, and this caused the curvature found (cf. 4).

van Geel, Pistorius, and Bouma also found that at constant film thickness the luminescence was linear with the current, and the slope of the line was greater at the higher forming voltages. Our own results agree with this. Smith (10) also found this proportionality, but only at the higher field strengths, and only for washed, not electropolished, aluminum. Forrest (14), too, observed a linearity of luminescence with current over a range, although his results were admittedly not of high precision.

Güntherschulze and Betz (13) found a minimum voltage was required before the emission of visible light began. This ranged from a very few volts with aluminum (depending on the electrolyte) to 55v for tungsten in nitric acid. Gee (15) using silicon, found that about $\frac{1}{2}$ -1v was required before a glow appeared, but he grew an oxide layer chemically before he began anodization. He noted a faint reddish glow appeared and then disappeared at about 1v, with no continuing luminescence. His conditions, especially having the previously formed layer, were different from those of other investigators. We found with silicon that the voltage jumps to an initial value, which includes a drop through the resistance of the electrolyte, the space charge within the silicon and at the silicon-electrolyte interface, some drop through the wafer itself at the higher resistivities, and any contact potentials (and cathode drop) there may be. All these we included in an initial voltage, assumed constant, and subtracted from the total voltage to obtain the voltage drop across the growing oxide. With this definition, we found no additional voltage required before luminescence began; it seemed to start with the onset of film growth. This was particularly striking with n-type silicon, as described above. If there were an additional very few volts required, however, we could not detect it clearly with the procedures we used, and it could provide a strong field across the thin initial oxide.

In our down-and-up runs, we found a rapid disappearance of the luminescence with decreasing voltage and a significant voltage was required before its reappearance. This agrees with Forrest (14) who found that some 60v were required before luminescence was observable with previously formed aluminum anodes. (The forming voltage was not stated, but sparks appeared at about 150v and breakdown at 200 v.)

Anderson (16) noted that luminescence occurs only with metals whose oxides may be considered as n-type semiconductors; intensive search failed to reveal its presence with a metal whose oxide is p-type (such as Cu, Ni, Fe). That an oxide layer is not uniform in composition, at least under some conditions of forming, has been shown by van Geel (17) and by Duffek *et al.* (18) with silicon. Migration of ions in the high fields during oxide growth may change the charge distribution and field, and hence the luminescence. We have shown (19) that silicon moves through the oxide. The behavior of completely formed oxide is somewhat different from growing oxide (20), and our own curves at "constant thickness" seem to have permitted some growth or redistribution of ions, as judged by the appearance of small loops (Fig. 1 and 4) and some-

times a change in slope of the $\log L$ vs. $\log V_f$ line after a down-and-up run.

Conclusions

The experimental work reported here indicates that when silicon is anodized (in ethylene glycol containing KNO_3), the following occur:

1. At constant current, the luminescence increases with some power of the net voltage. The precise value, from 1 to 3, depends on the type and resistivity of the silicon.
2. At constant thickness of the oxide layer on low resistivity silicon, the luminescence is exponential with the voltage and is linear with the current. A minimum voltage (or field) is required before luminescence appears.
3. After oxide growth begins, with constant current, there seems to be no significant minimum voltage or thickness before luminescence appears.
4. On n-type silicon of moderate or high resistivity, oxide growth and luminescence start at a number of discrete areas, which soon merge into a uniform layer. On p-type material, the light emission is uniform even at the start of anodization.
5. "Spark" discharges penetrate into the solution.
6. When "sparking" begins, the general glow decreases; the current and luminescence are concentrated in these limited, intense, breakdown locations.

Manuscript received March 16, 1964.

Any discussion of this paper will appear in a Discussion Section to be published in the June 1965 JOURNAL.

REFERENCES

1. N. Harvey, *J. Phys. Chem.*, **33**, 1456 (1929).
2. H. F. Ivey, *I.R.E. Trans. on Electron Devices ED-6*, 203 (1959); *This Journal*, **108**, 590 (1961); *Electrochem. Technol.*, **1**, 42 (1963); "Electroluminescence and Related Effects," pp. 161 ff, Academic Press, New York (1963).
3. E. A. Benjamini and E. F. Duffek, *Rev. Sci. Inst.*, **35**, 237 (1964).
4. W. Ch. van Geel, C. A. Pistorius, and B. C. Bouma, *Philips Res. Repts.*, **12**, 465 (1957).
5. P. F. Schmidt and W. Michel, *This Journal*, **104**, 230 (1957).
6. E. F. Duffek, C. Mylroie, and E. Benjamini, Paper presented at E.C.S. Meeting in Pittsburgh, April 1963 (Abstract No. 178).
7. H. K. Henisch, "Electroluminescence," p. 179, Pergamon Press, New York (1962).
8. H. Betz, *Z. Physik*, **95**, 189 (1935).
9. A. W. Smith, *Can. J. Phys.*, **35**, 1151 (1957).
10. A. W. Smith, *ibid.*, **37**, 591 (1959).
11. L. Young, "Anodic Oxide Films," p. 193, Academic Press, London and New York (1961).
12. K. Guminski, *Bull. intern. acad. polon. sci., Classe sci. math. nat. (Bulletin Internat. Polska Akademia)* **8-9A**, 457 (1936).
13. A. Güntherschulze and H. Betz, *Z. Physik*, **74**, 681 (1932).
14. J. S. Forrest, *Phil. Mag.*, **10**, 1003 (1930).
15. A. Gee, *This Journal*, **107**, 787 (1960).
16. S. Anderson, *J. Appl. Phys.*, **14**, 601 (1943).
17. W. Ch. van Geel, in "Halbleiterprobleme," pp. 299 ff, Friedr. Vieweg & Sohn, Braunschweig (1954).
18. E. F. Duffek, E. A. Benjamini, and C. Mylroie, Paper presented at the E.C.S. Meeting in Toronto, May 1964.
19. E. A. Benjamini, E. F. Duffek, C. A. Mylroie, and F. Schulenburg, Paper presented at E.C.S. Meeting in New York, October, 1963.
20. R. R. Sullivan and R. T. Dufford, *J. Opt. Soc. Amer.*, **21**, 513 (1931).

The Removal of Copper and Nickel from Germanium by Vacuum Annealing with Tin and Chlorinated Hydrocarbons

G. Conrad,¹ J. Friedman,² H. Meriwether, and C. Rosenblum

Research Laboratories, Merck Sharp & Dohme, Rahway, New Jersey

ABSTRACT

The removal of copper and nickel from germanium by annealing in vacuum with a remotely placed tin melt and frozen chlorinated hydrocarbons has been studied. The results of Albers have been confirmed and extended to higher copper concentrations and to nickel removal. It has been found, by radiotracer methods, that copper and nickel, removed from the bulk, are bound to the surfaces of the germanium, and that indiffusion of copper from the germanium surface is inhibited if the undoped germanium has previously been exposed to the gettering process.

Levi (1) has shown that it is possible to remove copper from germanium by thermal cycling, in vacuum, in the presence of a tin-germanium melt, and CCl_4 at liquid N_2 temperatures. He conjectured that copper reacted at the germanium surface with chlorine or other pyrolysis products of the CCl_4 vapor and was transferred to the melt.

Albers (2, 3) simplified the thermal cycle to a 650° anneal to maximize the surface to bulk distribution ratio of the dissolved copper. He made no attempt to determine the fate of the copper so removed. The process is unique in its independence of contact between the germanium and a getter in a condensed phase. Of course, dissolved copper and other metals can be precipitated and inactivated by annealing at a temperature corresponding to a low solubility and appreciable diffusion coefficient, but this is not removal.

In this work, the experiments of Albers have been extended nearly to the maximum solubility of copper in germanium, to the gettering of nickel, and to the use of radiotracers to determine the fate of the metal atoms removed from the germanium.

Experimental

The apparatus is shown in Fig. 1. A similar apparatus, lacking the extra cold trap, was used for much of the early work. Before each run, the tube was cleaned with aqua regia, rinsed in D.I. water and methanol and then heated in air at over 1000°C . The germanium samples, which were cut from high resistivity, boat-grown crystals, were prepared by dipping etched wafers (0.5-1 mm thick) into an aqueous solution of CuSO_4 or $\text{Cu}(\text{NO}_3)_2$, and heated in H_2 for $\frac{1}{2}$ hr or

more at a temperature suitable for attaining the desired copper doping level (about 800° for 10^{16} Cu/cc, 830° - 840° for 2×10^{16}). After air-quenching and bromineless CP4 etching, a four-point probe resistivity measurement was made. The wafers were etched again in two steps, replacing the etchant, and turning over the sample between steps. Several mils were removed at each step. The wafers, which were usually two in number, each about 2 cm^2 in area, were placed on a silica or carbon flat, near a boat containing about 50-100g of pure tin, or were placed on a quartz grid directly over the tin.

The system was then closed and pumped down to the 10^{-5} mm Hg range, and a furnace at 650° was slid into position around the germanium and tin. With both traps cold, the vacuum usually reached the range 10^{-6} - 10^{-5} mm Hg. The process was usually run for $3\frac{1}{2} \pm 1$ hr. After this time the furnace was removed and cooling under vacuum permitted until the tin solidified, after which the apparatus was opened. Four-point probe measurements of resistivity were made after etching. The resistivity was converted to an impurity concentration using a curve due to Prince (4). The copper acceptor concentration was converted to atom concentration by dividing by the number of ionized acceptor levels per atom, obtained from a calibration curve drawn from the data of Fuller and Wolfstirn (5). These concentrations are only approximate since the resistivities do not take into account mobility variations.

Results

Table I shows the results of a series of runs, obtained only after considerable experience, during

Table I. Gettering of copper

Sample No.	Copper concentration atoms/cc $\times 10^{-15}$	
	Initial	Final
84)	12	0.09
85)	12	0.02
86)	12	0.002
87)	11.3	0.09
88)	12.6	0.05
89)	12.6	0.02
90)	13.4	0.05
91)	13.4	0.09
92)	12.6	0.039
93)	13.4	1.3
96)	13.5	0.0088
97)	13.4	0.085
101)	13.7	0.048
102)	13.7	0.044
103)	12.9	0.001
104)	11.9	0.062

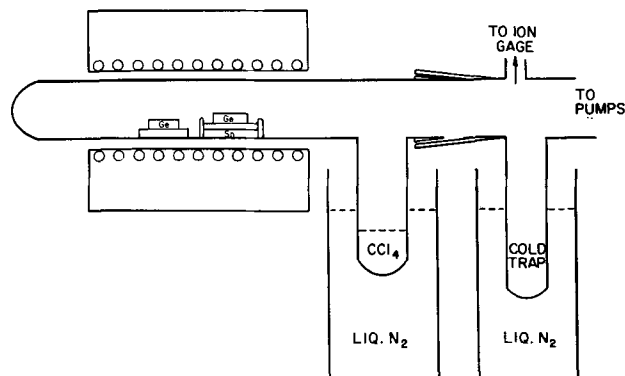


Fig. 1. Experimental arrangement, schematic

¹ Present address: The Glidden Company, 3901 Hawkins Point Road, Baltimore, Maryland.

² Present address: Physics Department, Polytechnic Institute of Brooklyn, 333 Jay Street, Brooklyn, New York.

which the final copper concentration was about an order of magnitude higher than that shown in the table, and very variable. The samples shown all had about 9×10^{13} acceptors per cubic centimeter and were run with some variation in amount of tin (two or three, instead of one boat-load); vacuum range (2×10^{-6} mm Hg, with two traps cold, or 2×10^{-5} mm Hg with only one trap); or chlorinated hydrocarbon (pure CCl_4 or mixture of similar compounds). The effects of these variations were inconclusive. The curly brackets represent pairs of samples in each run, one supported directly over the tin melt, and the other more remote. The former are distinguished by lower residual copper in every case but sample 84. The starting copper concentrations on the table are about ten times that for Albers' sample.³

The process has been successfully applied to samples doped to 2×10^{16} Cu/cc (near saturation), with the residual copper comparable to that shown in Table I. Considerable difficulty was experienced in reproducing these results. Conversely, some experiments with starting copper concentrations of zero to 7×10^{14} Cu/cc gave results similar to those in Table I, rather uniformly.

The variability in the final copper concentrations prevented a critical study of the effects of the obvious variables. The only fairly clear relations appear, as already indicated, to be the effect of initial copper concentration and the effect of location of the sample with respect to the tin melt.

In the case of initial copper concentration, the lower final concentration is purely statistical; as noted above, processing a copper-free sample caused it to dissolve 3×10^{13} Cu/cc.

The situation suggests a copper contamination problem at one or more stages of processing. The most likely sources are the reagents used to "clean" samples and apparatus. The degree of reproducibility shown in Table I may be the result of a transiently favorable situation with respect to some uncontrolled source of contamination. Despite early recognition of contamination as a potentially serious problem, little could be done, since all sanitary precautions were in use. Deliberate contamination experiments were instructive; one of these was carried out with the usual pair of samples doped to 10^{16} Cu/cc.

One of the samples was dipped in 0.01% aqueous CuSO_4 just before the run. Afterward, this had 1.4×10^{15} Cu/cc, and the control, though over the tin melt, had 8.2×10^{14} Cu/cc. Both were rerun, over the tin melt, without significant reduction in the residual copper concentrations. This suggests persistent migratory behavior of copper contamination in the apparatus.

Fate of the Removed Copper

In view of the retrograde solubility of copper in germanium, the possibility existed of precipitation during the 650° annealing of some of the copper originally dissolved at a higher temperature. An attempt was made to check this in a gettering run using four samples originally doped to 8×10^{15} Cu/cc. Two of these were etched respectively in hot HNO_3 and CP4. Along with a third, as a control, they were returned to the gettering apparatus and processed for 20 min during which the temperature was held at 840° to redissolve any copper precipitate. The fourth sample was measured as gettered and showed 10^{14} Cu/cc. The etched samples, after 840° reheat, had 4.8 and 6.3×10^{14} Cu/cc, respectively. The unetched sample had 9.5×10^{14} Cu/cc after reheat. To the extent that these data are significant, they suggest that most copper is not precipitated, but leaves the bulk of the sample and some at least may remain on its surface.

More informative experiments were run with radioactive Cu^{64} . Germanium wafers were dipped in 9%

Table II. Gettering of Cu^{64} from germanium

Sample No.	By gamma count			By resistivity	
	Nanograms initial Cu	Cu/gram Ge final Cu		initial Cu	final Cu
		Before etch	After etch		
R 15)	280	260	$\leq 0.2^*$	13	0.0081
R 16)	260	240	≤ 0.2	13	0.0039
R 17)	280	260	1.5	13	0.068
R 19)	43	30	≤ 0.7	1.65	0.015

* Near detection limit.

solution of $\text{Cu}(\text{NO}_3)_2$ in dilute HNO_3 containing 10–20 millicuries of Cu^{64} , and furnaceed. Most of the radioactivity measurements were made in a well-type gamma-ray scintillation counter equipped with a NaI-Tl crystal. A limited number of beta-ray measurements were performed by dispersing ground-up wafers in a 3-in. stainless steel planchet and counting. Quantitation was achieved by comparison with known amounts of the doping solution. The most significant results are shown in Table II. The column headed "After Etch" gives the results of gamma-counting on the samples just as they come from the gettering apparatus. The succeeding columns refer to the sample after a CP4 etch. It seems clear that most of the copper is removed to within a few mils, or much less, of the surface. In one trial, the lightest controllable etch, about 1μ , was sufficient to remove the activity.

Table II and other measurements indicate a small net loss of activity from the unetched samples. This is of the order of the measurement precision, but could represent the transfer of some copper to one or more sinks in the apparatus.

Surface Effects of the Process

As might be expected, it was found that the germanium surface was altered by the gettering process. Point contact tests always showed an n-type surface which was unaltered by HCl , HF , or H_2O_2 but required a light etch to show true conductivity type.

In addition, the exposed germanium surface grows hemispherical structures ("dots") $2\text{--}3\mu$ in diameter numbering thousands to perhaps millions per square centimeter. Careful study, if a low-power microscope is used, is required to see them in the lower concentrations; the higher concentrations appear as a haze on the crystal surface.

Repeated observation strongly suggested that good gettering is accompanied by high dot concentrations, although no quantitative correlation was obtained. It was found possible to have a dot-free surface and still getter effectively. This was done by covering the upper surface of a sample supported over the melt with a quartz plate. The dots showed no response to an overnight soak in HCl and other nonetching reagents. This suggests that they are not tin, or tin-rich, and bears on the question of whether the process mechanism is not simply gettering by a metallic phase (6). In this case, there is the possibility of tin-transport, by direct vacuum evaporation or a tin-halogen transport reaction. Evidence against gettering by a metallic phase is: (a) no visible appearance of tin or tin-alloying after processing, and no evidence of reaction with non-etching acids; (b) no weight change (to about 0.1 mg) due to processing; (c) resistivity of processed wafers is essentially the same when measured after processing, and after a thorough etch; (d) the extreme sensitivity to copper contamination described above is not consistent with gettering by a metallic phase.

Pertinent to this problem is the stability of the copper on the processed germanium surface. The radio-tracer experiments suggest that substantially all the copper is removed to that surface. However, in the

³ The 800° copper doping temperature in Albers' work is apparently a misprint as indicated by the relatively high resistivity after doping in Fig. 6 (ref. 2) and Fig. 2 (ref. 3). Dr. Albers, in correspondence, has stated that he copper-doped at 650° .

Table III. Copper diffusion into processed germanium

Sample No.	Copper source	Final copper concentration; atoms/cc $\times 10^{-15}$
ST-1) C-1)	Copper-doped Ge, dipped in Cu ⁺⁺ soln.; 2×10^{-6} mm Hg vacuum	0.049 11
ST-2) C-2)	Same; 3×10^{-6} mm Hg, 2 boatloads of tin present	0.59 0.81
ST-3) C-3)	Copper-contaminated quartz tube; H ₂ atmosphere	0.043 1
ST-4) C-4)	Both samples dipped in 0.01% Cu ⁺⁺ soln.	0.08 11
ST-5) C-5)	Same	9 14
ST-7) C-7)	Same; ST-7 previously processed at 800°	2.6 12

four-sample experiment described in the preceding section, the control sample, originally doped to 8×10^{15} Cu/cc redissolved less than 10^{15} Cu/cc on reheating to 840°. This result suggested that germanium samples without copper-doping in advance be gettered and tested for sensitivity to surface copper, in comparison with ungettered controls. This was done by heating for 45 min at 800° in the environment described in Table III. All samples originally contained 10^{14} acceptors/cc.

It is clear that processed germanium sample surfaces ("ST") can inhibit the indiffusion of copper relative to the controls ("C"). This is, of course, characteristic of metallic-phase gettering, although the negative evidence on this point, described above, still applies. The processed germanium showed dots, and the inhibition of copper pickup was correlated with the dot concentration.

Gettering of Nickel

The effect of nickel on the electrical properties of germanium is similar to that of copper (7). It has less effect on the resistivity, since it lacks a shallow acceptor level, but it has a greater effect in lowering the minority carrier lifetime.

The results of a series of gettering runs on nickel-doped samples, originally containing 10^{14} acceptors per cc, are summarized in Table IV. In all runs, 15 ml of CCl₄ and 2 or 3 boatloads of tin were used. The double cold-trapped system of Fig. 1 was operated at $4-8 \times 10^{-6}$ mm Hg for 3 to 4 hr. The samples were nickel-doped by firing at 900° in H₂, after dipping in a nickel-salt solution. In most cases no serious copper or other contamination was observed. Samples 111, 112, and 114 might be exceptions, however.

The nickel concentrations were calculated from four-point probe measurements, using corrections for partial ionization of both nickel acceptor levels. As the table shows, more than 99% of the nickel is removed from the germanium bulk. However, the equilibrium solubility of nickel is more than an order of magnitude below that of copper (8), so that most of the nickel could have annealed out at the 650° processing temperature. Samples 115 and 116 were run at 750°. This temperature is near the nickel-germanium eutectic (775°). Since 650°C coincides with the copper-germanium eutectic, and is suggested as an optimum (2, 3, 8) for surface-gettering processes, 750° was tried for nickel. The solubility of nickel in germanium at 750° is about ten times the residual nickel in samples 115 and 116; so apparently gettering occurred.

The fate of the nickel was checked by a radio-tracer experiment. Germanium wafers were doped by dipping into a 2.85% aqueous NiCl₂ solution containing about 1.2 millicuries of Ni⁶³, and heating for ½ hr at 900° in H₂. The electrical measurements showed results similar to Table IV, except that the samples dissolved 1.5×10^{16} Ni/cc. Possibly some of this is copper.

Table IV. Gettering of nickel

Sample No.	Nickel concentration		Notes
	Before	After	
107) 108)	2×10^{16} /cc 3.9	0.31×10^{13} /cc 2.2	1 1
109) 110)	8.0 8.0	3.7 8.4	1
111) 112)	9.8 10.5	1.7 2.5	1
113) 114)	8.0 7.8	0.44 3.2	1, 2
115) 116)	6.4 6.4	5.0 4.2	1, 3 3

Notes: 1, Supported over tin melt; 2, upper surface covered with quartz plate; 3, run at 750°.

Table V. Distribution of Ni⁶³ after gettering

Etch No.	Sample RN4		Sample RN7	
	Ge etched	Ni ⁶³ counted	Ge etched	Ni ⁶³ counted
1	3.6 mg	1.71 μ g (γ)	4.8 mg	0.42
2	75.3	0.022	52.2	0.016
3	52.5	0.00	54.0	0.00
4	74.2	0.00	87.0	0.00
5	132.8	0.00	74.0	0.00
6	50.8	0.00	—	—

Note: Detection limit $\approx 0.09 \mu$ g Ni/g Ge.

Radioactivity measurements were performed by successive etching and counting. Etch solutions were assayed by liquid scintillation counting, using the method of Gleit and Dumot (9). Table V shows clearly that the activity is mostly within about 10μ or so of the surface, with no sign of a residue in the bulk of the germanium, although the samples were etched, in steps, to destruction.

Summary and Discussion

It has been shown that gettering of nickel and copper from germanium by a variant of Albers' process can remove, typically, 99.5% of concentrations in the 10^{16} /cc region. Even smaller, as well as larger, residues are found depending apparently on the level of contamination of the germanium sample surface by these metals, during the experiment. Radiotracer methods indicate that virtually all the copper and nickel are concentrated within 10μ or less of the germanium surface, after processing. This surface appears n-type by contact rectification, and is covered with micron-sized mounds of unknown structure and composition. The concentration of these "dots" increases with the effectiveness of gettering, so that they are involved directly or concomitantly in the gettering process. It appears, nevertheless, possible to prevent dot formation on one germanium surface, and still have good gettering (sample 113, Table IV).

Copper-free germanium which has been subjected to the gettering process resists subsequent copper doping, presumably due to the very stable binding of copper to the gettered surface. The effect is related to "dot" concentrations also.

The mechanism of the process is unknown. The process did not demonstrate a critical dependence on many of the obvious variables, although this probably exists; this has been discussed above. Unless due to metallic tin transferred to the germanium surface, the process may be an example of gettering by an "active" surface such as that shown by Kikuchi and Izima (9). Another example is gettering by Group V element diffusion (10). It has been found in our laboratory that a 1μ diffused layer of arsenic can remove 90% or more of

the copper from a germanium wafer originally doped to 10^{16} Cu/cc. This leads, apparently, to copper concentrations in the arsenic-doped layer higher than expected, in the absence of ion-pairing effects (11). Finally, it has been observed that during the epitaxial deposition of germanium under certain conditions, considerably less copper is taken up by the germanium substrate, than by controls cycled without deposition; typical data are $1-1.5 \times 10^{14}$ Cu/cc vs. $1-2 \times 10^{15}$ Cu/cc (12).

Acknowledgments

The aid of Dr. R. Rosenberg for surface microscopy, Dr. G. W. C. Davis for spectroanalysis and H. J. Powers for general assistance is gratefully acknowledged. Dr. P. I. Pollak is thanked for encouragement and helpful discussions.

Manuscript received Dec. 20, 1963; revised manuscript received June 19, 1964.

Any discussion of this paper will appear in a Discussion Section to be published in the June 1965 JOURNAL.

REFERENCES

1. Levi, AIEE-IRE Semiconductor Device Research Conference, Boulder, Colorado, 1956.
2. W. Albers, *J. Electronics and Control*, **10**, 197 (1961).
3. W. Albers, *Solid State Electronics*, **2**, 85 (1961).
4. M. B. Prince, *Phys. Rev.*, **92**, 681 (1953).
5. K. Wolfstirn and C. S. Fuller, *J. Phys. Chem. Solids*, **7**, 141 (1958).
6. Logan and Schwartz, *J. App. Phys.*, **26**, 1287 (1955).
7. Burton, Hull, Morin, and Severiens, *J. Phys. Chem.*, **57**, 853 (1953).
8. F. A. Trumbore, *Bell System Tech. J.*, **39**, 205 (1960).
9. M. Kikuchi and S. Izima, *J. Phys. Soc. Japan*, **12**, 824 (1957).
10. K. Lehovc and C. Pihl, *J. Electrochem. Soc.*, **108**, 552 (1961).
11. R. N. Hall, Final Report, Contract AF19 (604)-6623, May 31, 1962, has reported solubilities of copper in arsenic-doped germanium at 600° of 25 times theoretical. Our data suggest still higher concentrations.
12. E. Schaarschmidt and R. Connell, Private communication.

Degradation of Planar Junctions during Reoxidation

F. Barson, W. J. Armstrong, and W. E. Mutter

Components Division, International Business Machines Corporation, Poughkeepsie, New York

ABSTRACT

Planar junctions in silicon can be degraded electrically by the growth of an oxide on the surface, particularly if the oxidation is carried out at low temperatures and at rapid rates. It is suggested here that the mechanism of degradation involves the formation of shallow dislocation loops due to dopant pile-up at the surface as the oxide grows, followed by the precipitation of fast-diffusing impurities about these defects. High-temperature oxidation, especially at low growth rates, minimizes this problem.

In the fabrication of npn silicon planar transistors, the collector junction is commonly formed by diffusing boron through oxide masking patterns. This step is followed by a reoxidation of the exposed areas for subsequent emitter masking.

It has been found that the electrical quality of the collector junctions so produced are sometimes degraded during this postboron reoxidation. The degradation is observed as a decreased breakdown voltage or softening of the reverse junction characteristic, usually accompanied by visible light emission at discrete points as avalanche occurs (1, 2). These "microplasmas" are occasionally red in appearance, indicating that they occur on that part of the junction lying below the surface, but most often they are whitish in color, occurring at the periphery where the planar junction comes to the surface. If the reverse bias applied to a degraded junction is less than that which causes conduction through the microplasmas, the leakage current remains low, usually in the nanoampere or fractional nanoampere range.

The problem of junction degradation had been observed to some extent in this laboratory in connection with a two-zone, open tube B_2O_3 diffusion process (3), the subsequent oxidation cycle consisting of a steam oxidation at $970^\circ C$ for 90 min, followed by a dry oxygen heating cycle of 60 min more at $970^\circ C$. When work was undertaken on a new capsule boron diffusion process, employing the same subsequent reoxidation cycle, the problem of junction degradation became acute and prompted a more detailed study of this phenomenon.

In the work reported here, the effects of various temperatures and rates of reoxidation were investigated with respect to the electrical quality of reoxidized

junctions. Based on these results and related experimental observations, a physical model is proposed for the mechanism by which the degradation occurs.

Experimental Results

Since junctions formed by the capsule boron diffusion process are particularly susceptible to damage during reoxidation, this process was convenient for a study of the phenomenon. The capsule technique consisted of heating the wafers to be diffused in an evacuated, sealed quartz capsule together with a boron-doped silicon powder as a source. Diffusion temperatures in the range of $1100^\circ-1200^\circ C$ were commonly used. A single-zone furnace was employed, the boron surface concentration for the diffusion being determined by the boron concentration in the powdered silicon source, and the diffusion depth being fixed by the time and temperature of diffusion. For the work reported below, planar junctions with depths in the range of 0.08-0.11 mils were formed in n-type (phosphorus doped) silicon wafers of 0.3 ohm-cm resistivity. The surface concentration for the diffusions was approximately $5 \times 10^{18} \text{ cm}^{-3}$.

Oxidation of these junctions was carried out at various temperatures between 950° and $1250^\circ C$. Steam or wet oxygen was used as the oxidizing ambient, so that the oxidation rate could be varied both by temperature and by ambient control. The moisture content of the oxygen was regulated by bubbling it through a water bath at a fixed temperature prior to passing it over the silicon wafers in a tube furnace.

Figure 1 shows the results of these oxidations. The figure is primarily an indication of the oxidation rates vs. temperature for the following ambients, respectively: steam, oxygen bubbled through $80^\circ C$ water,

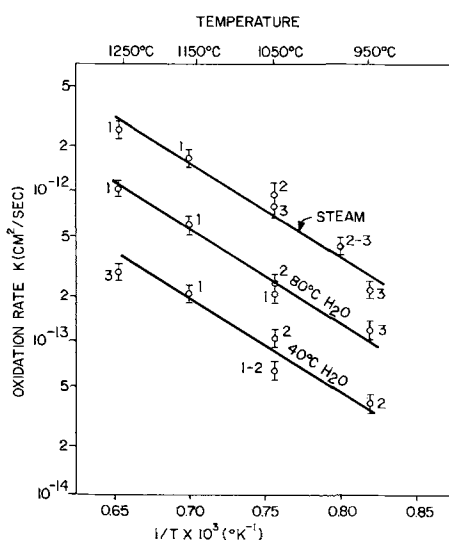


Fig. 1. Rates of oxidation in steam, O_2 bubbled through $80^\circ C$ water and O_2 bubbled through $40^\circ C$ water, respectively. Points 1, $> 75\%$ good junctions; points 2, $\sim 50\%$ good junctions; points 3, $< 10\%$ good junctions.

and oxygen bubbled through $40^\circ C$ water. The rate constant K plotted on the ordinate is defined by the equation for parabolic growth:

$$x^2 = Kt$$

where x is the oxide thickness in centimeters, and t is the time of growth in seconds. A number has been placed near each data point to indicate semi-quantitatively the electrical quality of junctions oxidized under the indicated conditions. A "good" junction is defined as one with a sharp breakdown and with avalanche occurring within 5v of the value anticipated for the resistivity of the silicon used. The number "1" indicates over 75% yield of good junctions, "2" indicates approximately a 50% yield, and "3" is the catastrophic case of about 10% or less yield of good junctions. Each data point represents the measurement of some fifty junctions on a wafer, with a minimum of two wafers oxidized under each of the indicated conditions. With the exception of only one anomalous point at $1250^\circ C$, it is seen that junction degradation is minimized by oxidizing at high temperatures and relatively slow oxidation rates.

In other experiments, similar capsule diffused junctions were heat-treated in nonoxidizing atmospheres before or after oxidation, and the effect of such heat treatments on junction quality was noted. The most significant result here is the fact that actual oxide growth was necessary for this type of junction degradation. Most junctions are of good quality as diffused (prior to reoxidation) and remain good if heated in a nonoxidizing ambient such as nitrogen through a heat cycle comparable to a harmful oxidation. A pyrolytic oxide was also deposited over diffused junctions without harm. It was only under conditions of oxide growth involving oxidation of the wafer surface itself that junction damage was caused.

Following junction degradation by steam oxidation, it was found that junctions could often be improved once more, or even completely restored, by sufficient heating in a nonoxidizing atmosphere. This might require heating for an hour or more at $1050^\circ C$ - $1100^\circ C$, for example. A limited amount of work was done on heating with P_2O_5 in contact with the wafer, as might occur during an emitter diffusion in transistor fabrication. There was some evidence here that the healing process is hastened by the presence of P_2O_5 , and that junctions so treated are slightly less prone to degradation on further reoxidation. This suggests that a gettering action by the P_2O_5 may be involved.

Table I. Junction quality as a function of diffusion and reoxidation processes

Diffusion Method	Good junctions, %
Capsule diffusion, $970^\circ C$ steam reoxidation	20
Two-zone B_2O_3 diffusion, $970^\circ C$ steam reoxidation	75
Capsule diffusion, $1150^\circ C$ reoxidation in wet oxygen ($80^\circ C$ H_2O)	95

In order to compare the quality of junctions produced by various boron diffusion processes, some typical junction yields are compiled in Table I. The first two diffusion methods are the capsule diffusion and the open tube diffusion, as described early in this paper, both employing a $970^\circ C$ steam reoxidation. The third process is one suggested by the preceding experiments and consists of a capsule diffusion followed by oxidation at $1150^\circ C$ in oxygen wet by bubbling through $80^\circ C$ water, and finally heating for 45 min more in dry oxygen at $1150^\circ C$. An oxide about 5000\AA thick was grown in all three cases. Table I illustrates not only the improved junction quality with high-temperature oxidation, but also the peculiar susceptibility of the capsule diffusion process to degradation during low temperature steam oxidation.

Discussion

Since the junction quality prior to reoxidation is generally good, we may discount the original wafer oxidation and the boron diffusion as principal causes of poor junctions and concern ourselves here with the reoxidation process itself. In attempting to postulate a mechanism for junction degradation, we note from the preceding section the importance of both oxidation rates and temperatures together. This suggests that impurity segregation at the oxide-silicon interface may be involved. Attala and Tannenbaum (4) have discussed this effect in detail. If an impurity is rejected by the oxide as it is grown, its concentration will be enhanced at the surface of the silicon. However, this results in a concentration gradient, so that at high temperatures there is a competing process, that of diffusion, which tends to redistribute the impurities once again and reduce any pile-up at the surface. Thus, fast oxide growth rates and low temperatures favor a build-up of impurities under the oxide film, while slower growth rates and higher temperatures minimize this effect. Quantitatively, it can be shown that the ratio K/D determines the increase in concentration of rejected impurities at the oxide interface. Here K is the oxidation rate, as previously defined, and D is the diffusion coefficient of the impurity. High K/D ratios correspond to oxidation conditions which result in greater impurity pile-up. For example, applying the equations of Attala and Tannenbaum (4), the enhancement in surface concentration of phosphorus due to a steam reoxidation at $970^\circ C$ would be over sevenfold, while a wet oxygen oxidation ($80^\circ C$ water) at $1150^\circ C$ would approximately double its surface concentration.

We have implied that it is phosphorus, and not boron, which is involved in causing degradation, since boron is reportedly depleted from the surface during oxidation rather than piled up (5, 6). Hence we are led to assume that phosphorus from the bulk doping in the original silicon wafer is concentrated at the surface to such an extent that shallow, localized flaws result in the crystal.

In Fig. 2, the oxidation rates and junction quality data of Fig. 1 are reproduced, but with the addition of several dashed lines denoting the K/D ratios for various conditions of temperature and oxidation rate. The diffusion coefficient values for phosphorus, used in plotting these lines, are taken from the work of Mackintosh (7) and Maekawa (8), and from confirming results obtained in this laboratory. It can be seen in Fig. 2 that the correlation of junction quality with

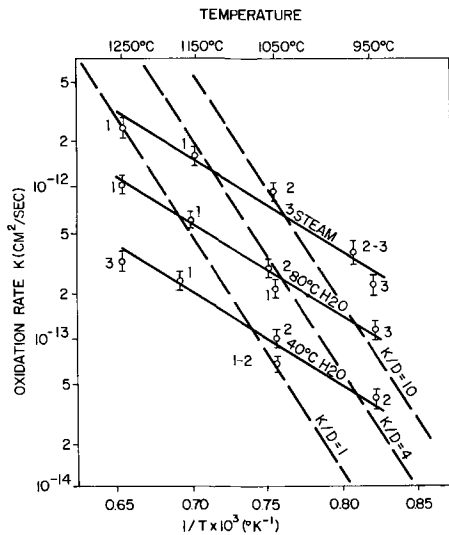


Fig. 2. Rates of oxidation of steam, O₂ bubbled through 80°C water and O₂ bubbled through 40°C water, respectively. Points 1, > 75% good junctions; points 2, ~ 50% good junctions; points 3, < 10% good junctions.

K/D is better than that with either the oxidation rate or the temperature alone.

In a separate experiment designed to support the proposed model, phosphorus-doped wafers of various resistivities were simultaneously capsule diffused and reoxidized in steam at 970°C. If one thinks of a certain minimum phosphorus build-up at the surface as being necessary to cause local damage, then junction quality should be worst on the highly doped wafers and best on those of highest resistivity. Experimental results are listed in Table II. The range of breakdown voltages are given after diffusion and also after the subsequent reoxidation. Some fifty junctions were probed on each wafer, and the lowest 10% and the highest 10% were discarded in order to indicate the range of the majority of the junctions, rather than anomalous values. It can be seen that the steam reoxidation caused disastrous results on highly doped samples, up to about 0.2 ohm-cm, but less so on the higher resistivity ones. On the 9.0 ohm-cm wafers, relatively few junctions were much under the anticipated breakdown (for planar junctions) and visible microplasmas were few. The highest breakdown voltages recorded are still well below that which a mesa junction would have. This is a familiar observation and probably indicates some phosphorus pile-up, or other surface effect, which is insufficient to result in highly localized defects or microplasmas. The variation of junction depth (shown in Table II) is a natural consequence of the variation of bulk doping. However, an experiment conducted on 0.3 ohm-cm material indicated that junctions with 0.11 mil depth were no better than those with 0.08 mil depth, and the differences shown in Table II are felt to be due to doping levels rather than to junction depths.

Table II. Junction quality as a function of bulk wafer resistivity

Resistivity, ohm-cm	Reverse junction breakdown, v		Junction depth, mils
	Diffused	Reoxidized	
0.07	13-26	1-4	0.06
0.07	11-26	1-4	0.065
0.1	15-26	1-4	0.075
0.1	21-26	1-6	0.08
0.2	29-36	3-6	0.085
0.2	25-37	5-38	0.085
0.5	31-48	5-54	0.09
0.5	35-48	7-50	0.095
1.0	47-62	15-69	0.10
1.0	55-64	24-69	0.105
9.0	85-90	109-120	0.11
9.0	85-90	48-120	0.115

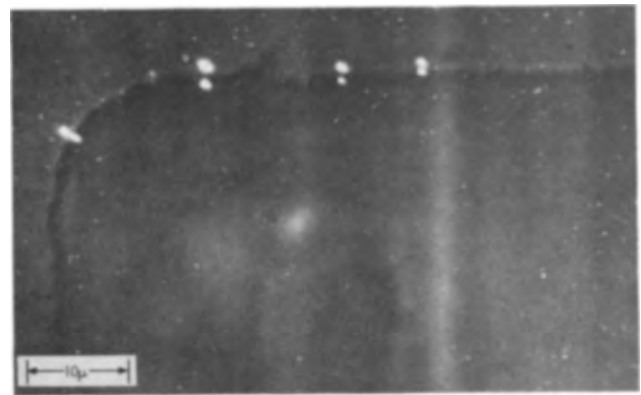


Fig. 3. Microphotograph of light spots occurring at microplasmas when avalanche breakdown occurs. The boron-diffused region is in the lower right-hand portion of the figure.

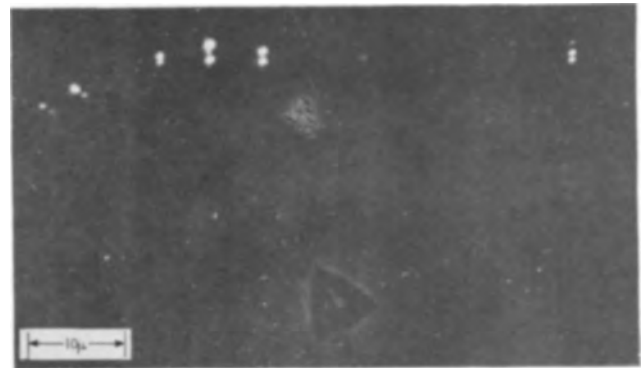


Fig. 4. Double exposure of microplasmas and etch pit, demonstrating orientation of the microplasmas relative to crystal directions.

Some insight into the type of physical defect produced may be gained by examining the visible light emission, or microplasmas, which can be seen when avalanche breakdown occurs in degraded junctions. White light spots appearing in pairs around the periphery of the junction are very commonly found. The photomicrograph shown in Fig. 3 illustrates this phenomenon. It will be noticed that the pairs of microplasmas are oriented in certain specific directions. These are crystallographic directions, as is demonstrated in Fig. 4. This photomicrograph is a double exposure which superposes the microplasmas over an etch pit elsewhere on the same wafer. Care was taken to translate the wafer without rotation in making the two superposed photographs. The wafer surface corresponds to a (111) plane, and the microplasma pairs lie in $\langle 110 \rangle$ directions, parallel to the edges of the triangular etch pit shown in the figure. From the appearance of the pairs of microplasmas, it is reasonable to identify them with shallow dislocation loops. Previous investigators (2, 9) have also found that microplasmas can in some instances be associated with dislocations.

In order to propose a complete model for junction degradation, it is still necessary to explain the extreme susceptibility of capsule-diffused junctions to steam reoxidation, as opposed to the less severe effect on two-zone B₂O₃ diffused junctions (see Table I). Dislocations are known to act as points of condensation for impurities (10, 11). However, if one thinks of dislocations alone, or even of phosphorus precipitation about dislocations, as being the source of microplasmas, it is difficult to explain a difference in junction quality between two boron diffusion processes in which the reoxidations are identical. If, however, it is postulated that some unidentified fast-diffusing impurity precipitates on the dislocations, then it can be expected that junction degradation will be severe only if this unknown impurity, as well as dislocations, is actually

present in the wafer. In the open-tube diffusion process, a B_2O_3 glass is formed on the wafer surface. Since B_2O_3 is a getter for certain impurities at diffusion temperatures (12, 13) it is to be expected that wafers diffused from such a source would be relatively free of these impurities. In the capsule diffusion process, where a doped silicon powder serves as the source, no B_2O_3 glass is formed and no gettering action occurs. A model involving fast-diffusers as the offending impurity is also consistent with the experimental observation that degraded junctions seem to be improved more readily by heating in the 1050°-1100°C range when P_2O_5 is present, than by similar heating without P_2O_5 . It is well known that P_2O_5 acts as a getter for impurities at these temperatures.

Summarizing, it is proposed that the surface pile-up of phosphorus during low temperature, relatively fast reoxidations results in shallow dislocation loops which act as sites for the precipitation of fast-diffusing impurities from the bulk. Such defects, if they occur at the periphery of a planar junction, where the junction comes to the surface, cause microplasmas and a corresponding degradation of the electrical characteristics of the junction. Such junction damage can be minimized by the use of high-temperature oxidations, particularly at low oxide growth rates, for this reduces the amount of surface pile-up of the phosphorus. The degradation is also reduced to some extent by the use of getters in the process, which tend to remove fast-diffusing impurities.

Manuscript received Feb. 21, 1964; revised manuscript received April 30, 1964. This paper was presented at the New York Meeting, Sept. 29-Oct. 3, 1963.

Any discussion of this paper will appear in a Discussion Section to be published in the June 1965 JOURNAL.

REFERENCES

1. A. G. Chynoweth and K. G. McKay, *Phys. Rev.*, **102**, 369 (1956).
2. B. D. James and P. S. Flint, "Localized Breakdown in Diffused Silicon Junctions," Paper presented at the Chicago Meeting of the Electrochemical Society, May 4, 1960.
3. T. H. Yeh and W. J. Armstrong, "Diffusion of Boron in Silicon," Paper presented at the Indianapolis Meeting of the Electrochemical Society, May 3, 1961.
4. M. M. Atalla and E. Tannenbaum, *Bell System Tech. J.*, **39**, 933 (1960).
5. T. H. Yeh, *J. Appl. Phys.*, **33**, 2849 (1962).
6. W. J. Armstrong, Thesis, Rensselaer Polytechnic Institute, June 1962.
7. I. M. Mackintosh, *This Journal*, **109**, 392 (1962).
8. S. Maekawa, *J. Phys. Soc. Japan*, **17**, 1952 (1962).
9. A. G. Chynoweth and G. L. Pearson, *J. Appl. Phys.*, **29**, 1103 (1958).
10. W. C. Dash, *J. Appl. Phys.*, **27**, 1193 (1956).
11. W. J. Shattis and H. A. R. Wegener, *ibid.*, **29**, 866 (1958).
12. A. Goetzberger and W. Shockley, *ibid.*, **31**, 1821 (1960).
13. S. W. Ing, Jr., R. E. Morrison, L. L. Alt, and R. W. Aldrich, *This Journal*, **110**, 533 (1963).

Influence of Vapor Composition on the Growth Rate and Morphology of Gallium Arsenide Epitaxial Films

R. E. Ewing and P. E. Greene

—hp associates—, Palo Alto, California

ABSTRACT

An apparatus was constructed to permit control and sampling of the vapor phase in the deposition zone during the vapor transport of GaAs with hydrogen-hydrogen chloride mixtures at atmospheric pressure. Gallium-arsenic ratios were determined by conventional analytical methods on aqueous solutions of the gallium and arsenic species condensed and scrubbed from gaseous samples. The data show that excess gallium in the vapor phase suppresses growth on the (111) surface and promotes growth of the $(\bar{1}\bar{1}\bar{1})$ surface. Similarly, excess arsenic in the vapor phase suppresses growth on the $(\bar{1}\bar{1}\bar{1})$ surface and enhances growth on the (111) surface. The studies show further that slight variations in the gallium-arsenic ratio in the vapor phase can result in differences in the surface morphology. Excellent growth rates on the (100) surface were obtained for transport conditions which were favorable for either of the two (111) surfaces. The film morphologies for the (100) and $(\bar{1}\bar{1}\bar{1})$ surfaces were best when transport was made with a gallium-arsenic ratio of 3 to 1.

The vapor transport of gallium arsenide from a polycrystalline source to form an epitaxial layer on a single crystal substrate in open tube systems has been described by several investigators (1-3). Preliminary experiments in this laboratory indicated that the morphology and growth rate of the film were determined, in part, by the substrate temperature and, in part, by the vapor phase composition. The purpose of this investigation was to determine the influence of the gallium-arsenic ratio in the vapor phase in the deposition zone on the morphology and growth rate of the deposited layer.

Experimental

Materials.—The gallium arsenide, polycrystalline, or single crystal source material and single crystal sub-

strates were obtained from Monsanto Chemical Company and Texas Instruments, Inc. Gallium, 99.999%, was obtained from the Eagle Picher Company. Commercial grade hydrogen passed through a hot palladium-silver alloy purifier was used without further treatment. The arsenic trichloride used as the source of hydrogen chloride was reagent grade which had been distilled once through a 24 in. packed distillation column and had a boiling point of 130.1°C.

All the substrates used in this investigation were first mechanically polished. The $(\bar{1}\bar{1}\bar{1})$ and (100) substrates were chemically polished to insure complete removal of all mechanical damage using a solution composed of 1 part water, 1 part 30% hydrogen peroxide, and 3 parts concentrated sulfuric acid. Since

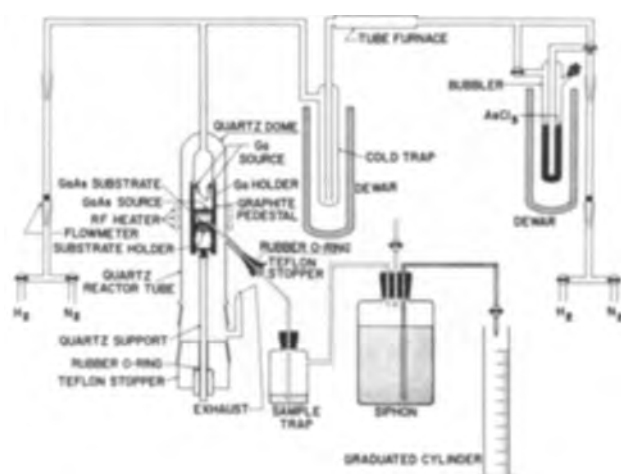


Fig. 1. Apparatus for transport of GaAs using RF heating and vertical flow of transporting gases with vapor phase sampling line.

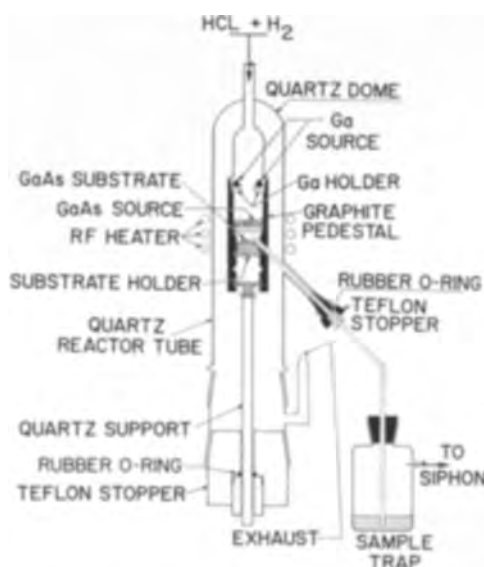


Fig. 2. Enlarged view showing graphite susceptor

the (111) surface is difficult to chemically polish, these substrates were etched 2 min in the same solution for a final surface cleaning.

Apparatus.—The apparatus used in this investigation is shown in Fig. 1 and 2. The design was made with RF heating to eliminate the hot wall quartz tube as a source of contamination, particularly Si and O₂. The specially constructed graphite susceptor, shown in Fig. 2, was made from spectroscopic grade graphite obtained from United Carbon Products Company and was further treated at 1200°C with hydrogen-hydrogen chloride gaseous mixture before using. The incoming gases, hydrogen and hydrogen chloride, were confined inside the graphite susceptor and passed over the source and substrate. Additional gallium was introduced as desired by filling the upper ring of the graphite susceptor with high purity gallium. Additional arsenic was introduced by allowing the AsCl₃ from the bubbler to enter the main gas stream.

Procedure.—After purging the apparatus with nitrogen followed by pure hydrogen, the flow of hydrogen was adjusted to 300 cc/min. The RF coil was positioned such that the temperature of the substrate was 780°–790°C with the hottest zone around the source at 875°–885°C. After reaching the operating temperature, hydrogen at 20–30 cc/min saturated with AsCl₃, 20°C, was introduced into the main hydrogen stream initiating transport under conditions of excess arsenic. For all other conditions, the AsCl₃-H₂ mix-

Table I. Growth rates of epitaxial layers at various Ga-As ratios in the vapor phase

Substrate temp, °C	Ga-As mole ratio	Growth rate, μ/min			Surface photomicrograph
		(111)	(111)	(100)	
780	0.1	0.02			4A
780	0.2	0.06	0.6		4A
780	0.3	0.07	0.33		4A
780	0.72	0.06		0.26	6A (100)
780	0.94	0.03			4B
780	1.1	0.06	0.35	0.59	4B (111)
780	1.4	0.07	0.37	0.59	4B
780	2.1	0.1			4C
780	2.95	0.25	0.09	0.34	
780	3.04	0.16		0.27	4D (111) 6B (100)
780	3.64	0.18		0.37	
780	3.92	0.22	0.07	0.33	
780	5.9	0.05			4E (111)
780	10.0	0.02		0.02	4F
825	0.47	0.05			5A
825	1.32	0.07			5B
825	4.7	0.14			5C
825	5.9	0.12			5D
825	80	0.007			5E
825	173	0			5F

ture was prereacted in a tube furnace converting the AsCl₃ to HCl and As₄. The latter was removed by a cold trap. In all of the experiments reported, a constant hydrogen chloride concentration of 1.45 × 10⁻⁷ mole/cc or its equivalent as AsCl₃ was maintained within experimental limits. For conditions requiring excess gallium, gallium metal was placed in the annular ring at the top of the graphite pedestal. A very large excess of gallium was obtained by adding 0.1g of gallium metal to the gallium arsenide source in addition to the gallium in the annular ring. Experience proved that reproducible gallium-arsenic ratios could be obtained with gallium in the annular ring at a given temperature.

After the epitaxial run was started, a sample of the vapor phase consisting of hydrogen, arsenic, hydrogen chloride, and gallium chlorides was removed at the rate of 15 cc/min. The gaseous mixture was bubbled through a trap containing 20 ml of 6M H₂SO₄ and 1 ml of 30% H₂O₂. Upon completion of the run, the gallium compounds and arsenic which condensed on the inside surface of the sampling line were carefully washed out with the acid mixture. The resulting aqueous solution was analyzed for arsenic volumetrically by the method of Kolthoff and Amder (5) and for gallium colorimetrically with hematoxylin as used for aluminum (6) but standardized for gallium.

Results

Growth of GaAs on the (111) surface.—Epitaxial layers were prepared at two substrate temperatures and several gallium-arsenic ratios on the arsenic surface. The results are shown in Table I and in Fig. 3 for 780°C substrate temperature. The data show that maximum growth on the (111) surface occurred with a gallium-arsenic ratio near 3 to 1 in the vapor phase. When the gallium-arsenic ratio in the vapor phase was near unity, or less, the growth rate was lower. Previous investigators (3, 4) observed slower growth rates on the (111) surface than on the (111) or (100) surfaces. Their results are in agreement with this investigation where the operating conditions are comparable, *i.e.*, with a gallium-arsenic ratio in the vapor phase near unity, or less.

Surface defects were obtained at both substrate temperatures. The nature of the defects varied with the gallium-arsenic ratio as shown in Fig. 4 and 5. Comparing the photomicrographs 4A with 5B, 4B with 5C, 4C with 5D, the defects are greater in number or larger in size at the higher temperature. All films obtained at the higher growth temperatures had growth defects indicating that the expected increased surface mobility at the higher temperature did not improve the surface structure.

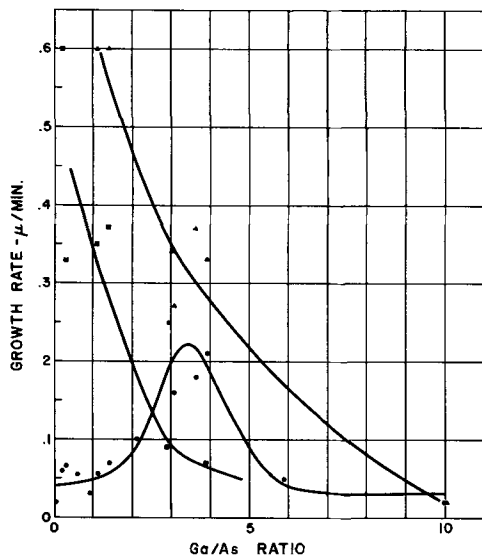


Fig. 3. Growth rate of GaAs epitaxial layers at various Ga-As ratios in the vapor phase. ●, $(\bar{1}\bar{1}\bar{1})$ surface; ■, (111) surface; ▲, (100) surface.

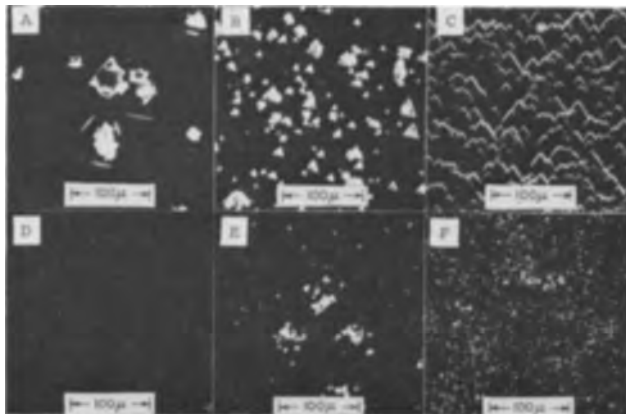


Fig. 4. Photomicrographs of GaAs epitaxial layers prepared by vapor transport with various Ga-As ratios in vapor phase and using 100° temperature difference between source and substrate (200X, dark field illumination), $(\bar{1}\bar{1}\bar{1})$ surface.

Growth of GaAs on the (111) surface.—All epitaxial layers grown on the (111) surface had many surface defects. The conditions for eliminating these defects were not evident in these experiments. Growth rates at various gallium-arsenic ratios are given in Table I and plotted in Fig. 3. The data show that the growth rate on the (111) surface increases as the gallium-arsenic ratio in the vapor phase decreases. At gallium-arsenic ratios above unity where the growth rate on the $(\bar{1}\bar{1}\bar{1})$ surface was greatest, the growth rate on the (111) surface decreased.

Growth of GaAs on the (100) surface.—The growth rates of epitaxial layers on the (100) surface for various gallium-arsenic ratios in the vapor phase are given in Table I and are shown graphically in Fig. 3. The results show that higher growth rates are observed on the (100) surface than on either of the (111) surfaces. The highest growth rates on the (100) surface were obtained with a gallium-arsenic ratio of less than unity corresponding to the conditions giving the highest growth rate on the (111) surface. However, the film had many surface defects, as shown in Fig. 6A. Using a gallium-arsenic ratio in the vapor phase of 3/1, the film had fewer growth defects, as shown in Fig. 6B. The growth defects on the (100)

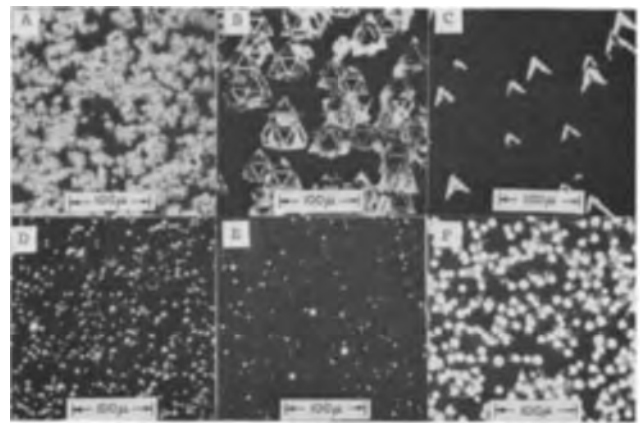


Fig. 5. Photomicrographs of GaAs epitaxial layers prepared by vapor transport with various Ga-As ratios in vapor phase and using 50° temperature difference between source and substrate (200X, dark field illumination), $(\bar{1}\bar{1}\bar{1})$ surface.

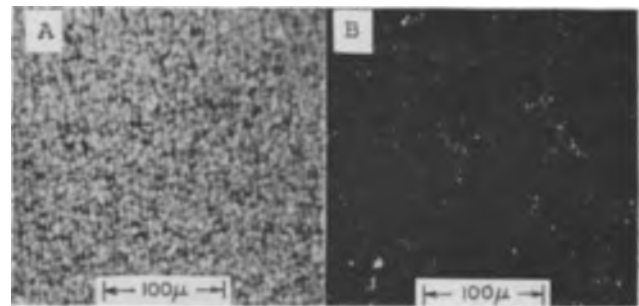


Fig. 6. Photomicrographs of GaAs epitaxial layers prepared by vapor transport at two Ga-As ratios in vapor phase and using 100° temperature difference between source and substrate (200X, dark field illumination), (100) surface.

surface have been eliminated for all gallium-arsenic ratios ranging from 3/1 to 1/3 by reducing the total flow rate in the system from 300 to 250 cc/min. This change did not affect the results for the (111) surfaces.

Discussion and Conclusions

These experimental results have shown that the epitaxial growth rates of GaAs by vapor transport onto the (111) surfaces of the host crystal are dependent on the gallium-arsenic ratio in the vapor phase. The growth rates for these surfaces are enhanced by providing excess gallium in the vapor phase during growth on the As surface and excess arsenic in the vapor phase when growing on the Ga surface. The data suggest that nucleation on the (111) surfaces is the slow step in the growth rate of the depositing layer, i.e., nucleation of Ga on the arsenic surface and As on the gallium surface. Sangster (9), in discussing crystal growth of III-V compounds, characterizes the (111) surfaces as having poor nucleation properties whereas the (100) surface has good nucleation properties. In the "atom by atom" approach to crystal growth, the high gallium in the vapor phase on the arsenic surface for example would lead to the increased probability of forming a seed nucleus such as the one proposed by Sangster, *loc. cit.* Hence, the growth rate of the crystal would be enhanced by a high gallium-arsenic ratio in the vapor phase for growth on the $(\bar{1}\bar{1}\bar{1})$ surface and correspondingly by a low gallium-arsenic ratio for growth on the (111) surface. In the case of crystals growing from a vapor phase, there are also the etching reactions which occur and which tend to decrease the rate of crystal growth. However, the experimental data do not permit the separate evaluation of the etching rate or the nucleation rate and their individual influence on measured growth rate and morphology.

Growth studies on the $(\bar{1}\bar{1}\bar{1})$ and the (100) surfaces show that high arsenic concentrations tend to introduce more surface defects. Part of the improved film morphology for the (100) surface at the high gallium concentrations in the vapor phase could be attributed to the slower growth rate. However, the slower growth rate at high arsenic concentrations in the vapor phase on the $(\bar{1}\bar{1}\bar{1})$ and (100) surfaces produced more surface imperfections. Therefore, the occurrences of imperfections are more closely related to vapor composition than net growth rate. The excess arsenic could serve as an impurity which, when adsorbed on the growing crystal, induced defect growth. It is probable that, under conditions of transport without excess gallium or arsenic, the arsenic partial pressure in the vapor phase over the substrate exceeded the equilibrium partial pressure of arsenic over gallium arsenide at the substrate temperature by a factor of 10^3 .

Acknowledgments

The authors wish to thank N. Spilling who performed most of the experiments described and G. Marshall for his assistance in establishing the analytical procedures.

This work was sponsored by the Electronic Technology Laboratory of the Aeronautical Systems Division under Contract No. AF33 (657)-9772.

Manuscript received April 9, 1964.

Any discussion of this paper will appear in a Discussion Section to be published in the June 1965 JOURNAL.

REFERENCES

1. C. J. Frosch, *This Journal*, **111**, 180 (1964).
2. F. V. Williams and R. A. Ruehrwein, *ibid.*, **108**, 177C (1961).
3. R. L. Newman and N. Goldsmith, *ibid.*, **108**, 1127 (1961).
4. T. Akada, *Japan J. Appl. Phys.*, **2**, 206 (1963).
5. I. M. Kolthoff and K. Amder, *Ind. Eng. Chem., Anal. Ed.*, **12**, 177 (1940).
6. N. H. Furman, Editor, "Standard Methods of Chemical Analysis," 6th ed., p. 41, D. Van Nostrand Co., Inc., New York (1962).
7. R. C. Sangster, "Model Studies of Crystal Growth Phenomena in the III-V Semiconducting Compounds," "Compound Semiconductors," R. K. Willardson and H. L. Goering, Editors, Vol. I, pp. 241-253, Reinhold Publishing Corp., New York (1962).

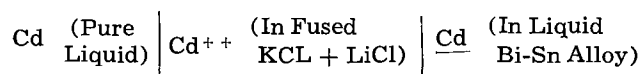
Galvanic Cell Measurement of the Thermodynamic Interaction between Cadmium and Tin in Liquid Bismuth

W. M. Boorstein and R. D. Pehlke

Department of Chemical and Metallurgical Engineering, The University of Michigan, Ann Arbor, Michigan

ABSTRACT

The interaction parameter between cadmium and tin in dilute solution has been measured in molten bismuth. Measurements were made in the temperature range 400°-600°C in a galvanic cell of the type



The influence of tin on the activity coefficient of cadmium was measured in the dilute ternary system and the influence of cadmium on its own activity was measured in the dilute binary system. The data were extended to concentrated solutions to show that the present activity coefficient measurements are consistent with those previously reported on the binary cadmium-bismuth system.

Thermodynamic interactions among solutes in metallic solutions have been shown to have great practical engineering importance as well as basic theoretical significance. It is therefore of twofold interest that these intersolute effects or interaction parameters be ascertained.

In order to organize and transform laboratory data from the present interaction study into a convenient and usable form, the expression for the thermodynamic interaction parameter as derived by Wagner (2) will be employed. This expression can be written as

$$(\epsilon_i^j)_k = \left(\frac{\partial \ln \gamma_i}{\partial x_j} \right)_{k(x_i=x_j=0)} \quad [1]$$

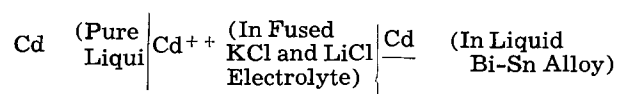
The term γ_i is the thermodynamic activity coefficient of component i in alloy solution and x represents mole fractions of the solutes.

Experimental Method

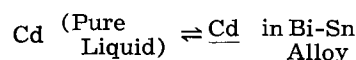
Electromotive force measurements to determine the thermodynamic properties of metallic alloys were first reported by Taylor (3) in 1923. Since that time many such investigations have been carried out on various

metallic systems using only slightly modified techniques. However, these investigations, conducted in solutions having approximately 10 mole % or more solute, are not suitable for the evaluation of interaction at infinite dilution. For this purpose data must be taken in the dilute regions of the ternary system where Henry's law is more closely obeyed and extrapolations to zero solute concentrations can be made with confidence.

The measurement of thermodynamic properties by the emf technique is carried out in a galvanic cell. A representation of the cell used in this work is



The emf produced by the cell reaction, if reversible, is also a measure of the free energy change or driving force for the net cell reaction,



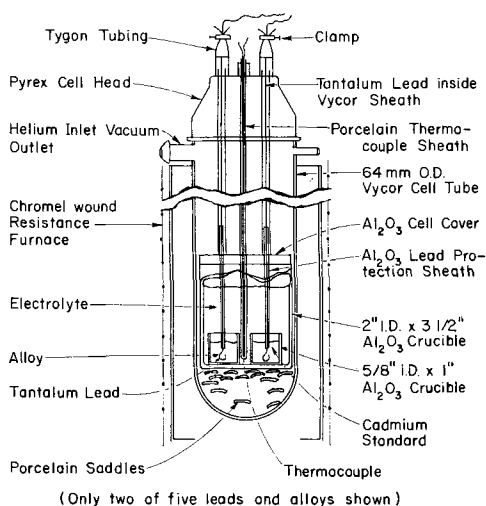


Fig. 1. Diagram of cell

at constant temperature and pressure. Selecting pure liquid cadmium at the temperature under immediate consideration as the standard state, this relationship can be expressed in a form of the Nernst equation

$$-nFE = \Delta F = \bar{F}_{Cd} - F^{\circ}_{Cd} = RT \ln a_{Cd} = RT \ln \gamma_{Cd} X_{Cd} \quad [2]$$

where n is the valency state of the cadmium ion in the electrolyte ($=2$), F is the Faraday equivalent ($=23,066$ calories/v), E is the emf of the cell, \bar{F}_{Cd} is the partial molal free energy of cadmium in solution in the bismuth-tin alloy, and F°_{Cd} is the molal free energy of pure liquid cadmium. Therefore, the activity coefficient of cadmium in solution, γ_{Cd} , can be calculated directly from the emf of the cell. The interaction parameter can then be evaluated by graphic extrapolation of the logarithm of the activity coefficient to infinite dilution of both solutes.

Experimental Technique

The cell assembly used in this investigation is illustrated in Fig. 1.

The cell electrolyte was a mixture of approximately 53% KCl, 42% LiCl, and 5% CdCl₂ by weight. All three salts were Baker Chemical Company Reagent Grade. The metals were 99.998+ % pure (Bi and Cd, ASARCO; Sn, Vulcan Material Company).

The data were obtained by emf measurements on 15 cells using pure liquid cadmium as a standard electrode. The four alloys in each run had mole fractions of cadmium and tin ranging from 0.025 to 0.075. The pure metals were weighed to one ten-thousandth of a gram and placed in the individual crucibles. Each metallic mixture was then liquified for 2 hr at 450°C in a purified helium atmosphere to accomplish both partial homogenization and insertion of the tantalum lead wires.

Eight hours before its use, 250g of the eutectic mixture of potassium chloride and lithium chloride was fused under a vacuum at 450°C in an effort to remove any moisture (LiCl being highly hygroscopic). The third salt of the electrolyte, cadmium chloride, is volatile and was dried separately at atmospheric pressure and charged directly to the cell.

The cell was then assembled as shown in Fig. 1, and lowered into the unheated cell furnace which could be controlled to within $\pm 2^{\circ}\text{C}$ at the location of the experimental cells. With the vacuum and inert gas system connected, the cell tube was flushed five times with purified helium before energizing the furnace coils. The electrode leads protruding from the cell tube head were attached to a multipole switch which permitted the connection of each individual electrode with the standard cadmium electrode across

the measuring potentiometer circuit. The cell was allowed to equilibrate at 500°C for 12 hr before the first readings were taken.

The emf was measured by a L&N No. 8687 volt potentiometer and recorded every 20 min over a 2-hr period. These potential measurements were made over the temperature range of 400°-600°C at 50° intervals. After each change in temperature, approximately 3 hr were allowed for equilibration before readings were again taken. Caution was exercised during each reading that the circuit was not closed for more than a fraction of a second to prevent polarization and mass transport in the cell. Most runs lasted for at least a 72-hr duration.

Results

Comparison of numerical data.—It was desired to compare the results of these measurements with studies on this system by other investigators, especially those who have employed other experimental techniques. A review of the literature revealed no investigations of the cadmium-tin-bismuth ternary nor the cadmium-bismuth binary systems by other than emf methods. Mellgren's emf study of the cadmium-tin-bismuth ternary (4) was made using mole ratios of tin to bismuth on the order of 1:1 and could not be correlated with the measurements of this investigation. The cadmium-bismuth binary system has been studied independently by Taylor (3), Mellgren (4), Elliott and Chipman (5,6), and Nikol'skoya and Gerassimov (7) in the approximate range of 0.10-0.90 mole fraction cadmium, and all results were in very close agreement. Activity values obtained from the binary data of the present study are in agreement with the work of Elliott and Chipman in the more dilute solution regions as shown in Fig. 2.

Interaction parameter calculation.—The thermodynamic activities and respective activity coefficients of cadmium in alloy solution (with respect to pure liquid cadmium) were calculated from the emf data for each cell utilizing Eq. [2].

The determination of the thermodynamic interaction parameter (2)

$$\epsilon_{Cd}^{Sn} \equiv \left(\frac{\partial \ln \gamma_{Cd}}{\partial x_{Sn}} \right)_{x_{Cd}=x_{Sn}=0} \quad [3]$$

can be achieved by either of two means. Using the values of activity coefficients calculated from electromotive force data, a plot of γ_{Cd} vs. x_{Sn} was constructed for each isotherm investigated. Values of γ_{Cd} at various mole fractions of tin were read from each individual curve representing constant mole fraction of cadmium in the alloy solutions. This information allowed the plotting of a second set of curves, $\ln \gamma_{Cd}$ vs. x_{Cd} at constant mole fractions of tin, which were then extrapolated to zero mole fraction of cadmium. These intercept values

$$(\ln \gamma_{Cd})_{x_{Cd}=0} \text{ for } x_{Sn} = 0, 0.025, 0.050, \text{ and } 0.075$$

were subsequently plotted vs. the corresponding mole

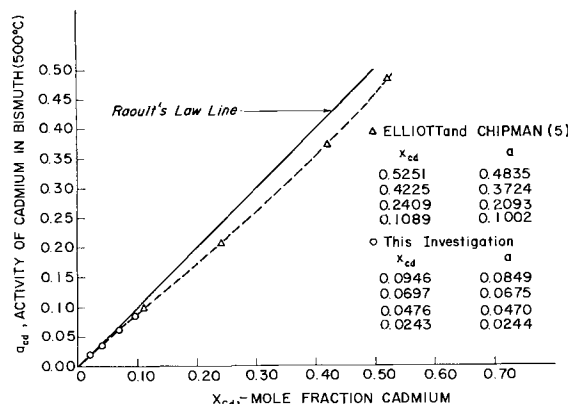


Fig. 2. Activities in cadmium-bismuth binary at 500°C

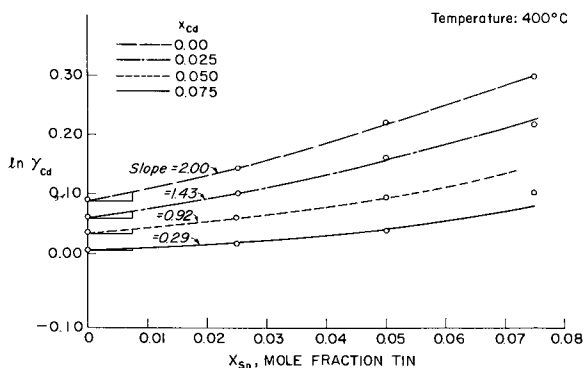


Fig. 3. Logarithm of cadmium activity coefficient vs. mole fraction tin.

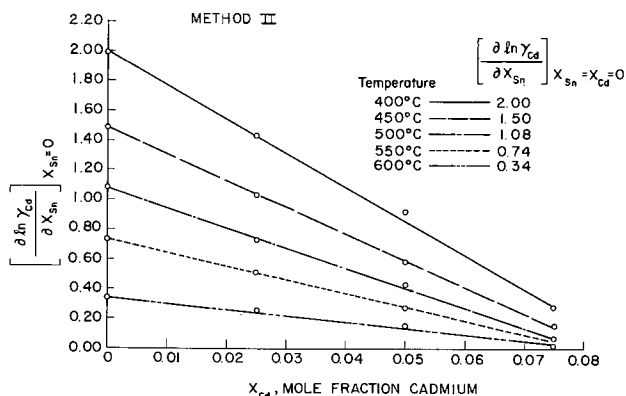


Fig. 4. Slope of cadmium activity coefficient-tin relation at infinite tin dilution vs. mole fraction cadmium.

fraction of tin. The interaction parameter is given by the slope of the resulting curve at zero mole fraction tin

$$\text{Slope (at } x_{Sn} = 0) = \left[\frac{\partial \ln \gamma_{Cd}}{\partial x_{Sn}} \right]_{x_{Cd} = 0, x_{Sn} = 0} = \epsilon_{Cd}^{Sn} \quad [4]$$

The interaction parameter may be calculated by a second method which consists of plotting $\ln \gamma_{Cd}$ vs. x_{Sn} for constant mole fractions of cadmium as shown in Fig. 3 for the 400°C isotherm. The slopes of the curves were evaluated at zero mole fraction tin. These slope values were then plotted on a graph which has the ordinate

$$\left[\frac{\partial \ln \gamma_{Cd}}{\partial x_{Sn}} \right]_{x_{Sn} = 0}$$

and the abscissa x_{Cd} as seen in Fig. 4. The value of the resulting curve at zero mole fraction cadmium is

$$\left[\frac{\partial \ln \gamma_{Cd}}{\partial x_{Sn}} \right]_{x_{Cd} = 0, x_{Sn} = 0}$$

which is the Wagner interaction parameter ϵ_{Cd}^{Sn} . Excellent agreement was obtained for the two methods. The resulting parameter values are shown in Fig. 4.

The cadmium-bismuth binary data were used to determine the self interaction of cadmium ϵ_{Cd}^{Cd} in molten bismuth. The parameter values and graphic analysis at the five temperatures studied are presented in Fig. 5.

Discussion

Cell reversibility.—Without a sound basis for assuming that the cell has functioned reversibly for the reaction studied, the potential measurements obtained cannot justly be applied to the calculation of equilibrium thermodynamic properties. Many factors must be taken into consideration in connection with the construction of the galvanic cell employed to prevent

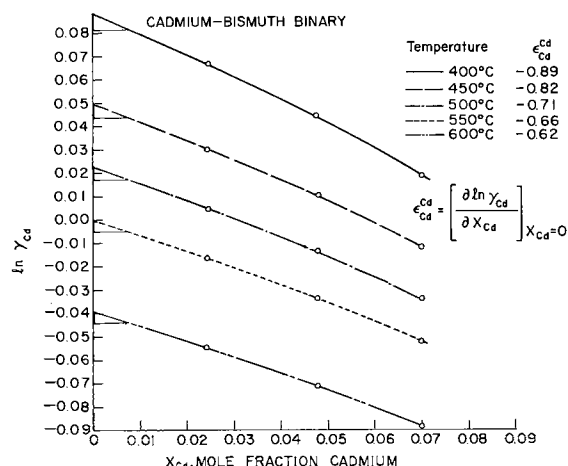
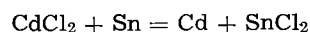


Fig. 5. Logarithm of cadmium activity coefficient vs. mole fraction cadmium for cadmium-bismuth binary.

extraneous reactions which generate spurious potentials and cause irreversibility within the cell. These considerations, among which are included (a) the relative positions of the alloy components in the electromotive force series; (b) the relative stabilities, valency states, and electronic conduction characteristics of the electrolyte components at the temperatures of cell operation; and (c) possible side reactions between the molten electrolyte or alloy solutions and the cell materials or the cell atmosphere, were taken into account in the present study.

A means for quantitatively estimating the error caused by exchange reactions in galvanic cells has been developed by Wagner and Werner (8). Dealy and Pehlke (9) have extended this analysis to ternary systems permitting an estimate to be made of the error caused by exchange reactions between the active solute ion in the electrolyte and the solvent metal, and the active solute ion in the electrolyte and the third component in the metallic solution. Using this analysis, criteria for the relative stability of the chlorides were developed based on the possible reactions:



The concentration of $CdCl_2$ in the electrolyte was maintained at 1.6 mole % (5 wt %) for all cells. This concentration represented a compromise between lower concentrations where small interferences could become significant and higher concentrations which favor the forementioned exchange reactions.

On this basis, the possible error in the cell potential was shown to be much less than 1%, even in the most unfavorable cases of minimum cadmium and maximum tin or bismuth concentration in the electrode. Alloys having cadmium contents at or below 0.010 mole fraction showed a tendency toward continuously drifting cell potentials. This observation is in qualitative agreement with the theoretical analysis described above.

Reversibility can most readily be inferred from the behavior of the cell potentials. A cell which is not reversible will show a drift in the readings and yield potential values which are not reproducible. The cells from which the accepted data were obtained displayed extremely steady and reproducible behavior. When corrected for temperature fluctuations, the potentials at any constant temperature did not vary more than ± 0.2 mv or approximately $\pm 0.2\%$ in any 2-hr measurement period or in excess of ± 0.5 mv in the average 72-hr life of a cell.

Estimate of error in parameter.—Whereas the two graphic methods described yield almost identical values for the interaction parameter, it must be noted that

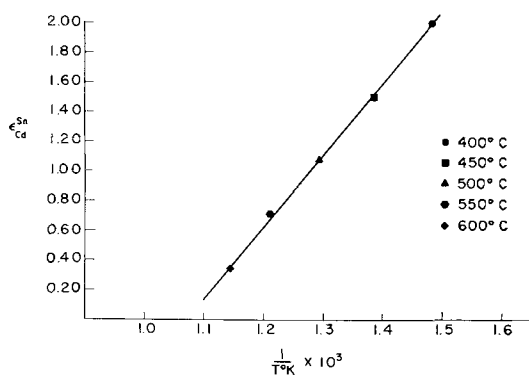


Fig. 6. Cadmium-tin interaction parameter vs. reciprocal temperature.

they are not independent of one another. Furthermore, it was necessary to evaluate graphically the activity coefficients at specific solute concentrations by interpolation. It is not believed that any substantial error was introduced by this approach.

Temperature fluctuations which are less than 2° were found to give small corresponding changes in the cell potential. The activity calculations were corrected for these variations. The influence of a small temperature error is not significant as indicated by the slope of interaction parameter-reciprocal temperature curve shown in Fig. 6.

A confidence limit of ± 0.10 placed on each parameter value is believed to be a conservative estimate of the total error introduced through use of the graphic technique and inherent in the experimental cell operation.

Reciprocal relationship.—From the definition of the partial molar free energy

$$\bar{F} = \left(\frac{\partial F}{\partial n_i} \right)_{p, T, n_j, \dots} \quad [5]$$

where F is the molal free energy of the solution and n_i the number of moles of i th component, it can be shown (2) that

$$\frac{\partial \ln \gamma_i}{\partial x_j} = \frac{\partial \ln \gamma_j}{\partial x_i} \text{ for } x_i = x_j = 0, \text{ or } \epsilon_i^j = \epsilon_j^i \quad [6]$$

In view of this result, each value of $\epsilon_{\text{Cd}}^{\text{Sn}}$ presented in Fig. 4 is also equal to ϵ^{SnCd} .

Temperature dependence.—Dealy and Pehlke (10) derived the relationship

$$\frac{d(\epsilon_i^j)}{d(1/T)} = \frac{1}{R} \left(\frac{\partial^2 H}{\partial x_i \partial x_j} \right)_{x_i = x_j = 0} \quad [7]$$

to show that the variation of the interaction parameter with the reciprocal of the absolute temperature will be

linear if the derivative of the enthalpy with respect to the mole fractions of the two dilute solutes is not a strong function of temperature.

This linear dependency is obeyed by the alloy system under present consideration as shown in Fig. 6 where the results of this investigation are plotted against the reciprocal of absolute temperature. Thus, accurate interpolations and extrapolations can be made to determine interaction parameter values at temperatures not directly investigated.

Conclusions

1. The emf technique has been shown to be a feasible method for acquiring the thermodynamic data essential to accurate determination of interaction parameters.

2. The presence of small quantities of tin will tend to increase the activity of cadmium in dilute solution with molten bismuth as indicated by the positive sign of the interaction parameter.

3. Cadmium tends to decrease its own activity coefficient with increasing concentration in dilute solution in molten bismuth.

4. The interaction parameters $\epsilon_{\text{Cd}}^{\text{Sn}}$ and $\epsilon_{\text{Cd}}^{\text{Cd}}$ are small positive and negative numbers, respectively; both exhibit a linear relationship with reciprocal absolute temperature and tend toward zero with increasing temperature.

Acknowledgment

This work was supported in part by the Atomic Energy Commission under Contract No. AEC-AT(11-1)-979.

Manuscript received Oct. 9, 1963; revised manuscript received May 4, 1964.

Any discussion of this paper will appear in a Discussion Section to be published in the June 1965 JOURNAL.

REFERENCES

1. John Chipman, *J. Iron and Steel Inst.*, **180**, 97 (1955).
2. Carl Wagner, "Thermodynamics of Alloys," p. 52 Addison-Wesley Press, Inc., Cambridge (1952).
3. N. W. Taylor, *J. Am. Chem. Soc.*, **45**, 2865 (1923).
4. Svante Mellgren, *J. Am. Chem. Soc.*, **74**, 5037 (1952).
5. John Elliott and John Chipman, *Trans. Faraday Soc.*, **47**, 138 (1951).
6. John Elliott and John Chipman, *J. Am. Chem. Soc.*, **73**, 2682 (1951).
7. A. V. Nikol'skoya and Ya. I. Gerassimov, *Zhur. Fiz. Khim.*, **28**, 713, (1954).
8. C. Wagner and A. Werner, *This Journal*, **110**, 326 (1963).
9. John Dealy and Robert Pehlke, "Electrochemical Determination of Interaction Parameters," Paper presented at AIME Annual Meeting, New York, Feb. 1964.
10. John Dealy and Robert Pehlke, *Trans. Met. Soc. AIME*, **227**, 88 (1963).

The Transmission of Electrolytically Deposited Hydrogen through a Palladium Membrane Electrode

I. The Rate Equations

Gilbert W. Castellan

Department of Chemistry, The Catholic University of America, Washington, D. C.

ABSTRACT

A sequence of elementary steps is postulated to describe the transport of hydrogen through a palladium membrane electrode. The amount of hydrogen transmitted per square centimeter of the membrane is described by a current density, $-j$, while the rate of deposition of hydrogen per square centimeter is described by a polarization current density, $-i$. It is shown in general, without reference to the particular mechanism, that j is a linear function of i at low values of i , and that the derivative, $(di/dj)_{i=0}$, is a linear function of the membrane thickness L , provided only that Fick's law in simple form holds; the slope of the plot of $(di/dj)_{i=0}$ vs. L is independent of conditions on the exit side of the membrane. It is also shown in general that if conditions are the same on both sides of the membrane at equilibrium, no more than one-half of the hydrogen deposited can be transmitted. The postulated mechanism predicts that the rate of transmission should reach a limiting value, $-j_m$, at high values of $-i$. For thin membranes, $1/(-j_m)$ should be a linear function of L . The slope of $1/(-j_m)$ vs. L depends on the diffusion coefficient of hydrogen atoms in palladium and is independent of the rates of the surface reactions, although in some instances it depends on θ_0 , the equilibrium coverage of the surface by hydrogen atoms. In Parts II and III some experimental data are treated in terms of this mechanism.

We have studied the transmission of electrolytically deposited hydrogen through palladium. In this paper, a mechanism is postulated and the rate equations are arranged in a form suitable for graphical treatment of the data. (The side of the membrane on which hydrogen atoms are deposited will be called the entrance side, or side 1; the other side will be called the exit side, or side 2.) In Part II (1) data are presented on the transmission of hydrogen if the exit side of the foil is in contact with a solution of a strong oxidizing agent, e.g., Ce^{+4} , and if it is in contact with hydrogen gas. In Part III (2) the effects of varying the temperature and the hydrogen pressure on the exit side of the foil are described.

Experimental

The experiment may be described as follows. Two compartments are separated by a palladium foil. The compartment on the entrance side contains a sulfuric acid solution and a platinum anode; the entrance side of the palladium foil is the cathode. The compartment on the exit side was filled in different ways; we have used $Ce(SO_4)_2$ solution, H_2SO_4 solution, gaseous hydrogen, and water. A current, i (amp/cm²), is passed in the entrance compartment between the palladium membrane cathode and the platinum anode. The rate of deposition of hydrogen atoms on the entrance side of the foil is $-i$. The amount of hydrogen transmitted to the compartment on the exit side is measured and expressed as an equivalent current density, $-j$.

The problem is to determine the dependence of j on the parameters of the system, particularly on the polarization current density, i , and the membrane thickness, L .

Some General Properties

The sum of the rate of evolution of H_2 on the entrance side, $-i_{ev}$, and the rate of transmission through the membrane, $-j$, is equal to the rate of deposition on the entrance side, $-i$. After changing signs, this relation becomes

$$i = i_{ev} + j \quad [1]$$

Differentiating Eq. [1] with respect to the overvoltage η , we obtain

$$\frac{di}{d\eta} = \frac{di_{ev}}{d\eta} + \frac{dj}{d\eta} \quad [2]$$

But the derivatives, $di_{ev}/d\eta$ and $dj/d\eta$, are reciprocals of the effective resistances to evolution of H_2 and transmission, respectively. In the limit as $\eta \rightarrow 0$, these resistances become independent of η and depend only on the equilibrium conditions in the system. Thus, we write $(di_{ev}/d\eta)_0 = 1/R_{ev}$ and $(dj/d\eta)_0 = 1/R_{tr}$, in which the subscript zero denotes the limiting value at $\eta = 0$ (or $i = 0$), and R_{ev} and R_{tr} are the limiting resistances to evolution and transmission which are independent of η . Then at $\eta = 0$, if we divide Eq. [2] into the definition of R_{tr} we obtain

$$\frac{(dj/d\eta)_0}{(di/d\eta)_0} = \frac{1/R_{tr}}{(1/R_{ev}) + (1/R_{tr})}$$

which becomes

$$\left(\frac{dj}{di}\right)_0 = \frac{R_{ev}}{R_{ev} + R_{tr}} \quad [3]$$

From Eq. [3], it is clear that the initial slope, near $i = 0$, of the curve of j vs. i must be less than unity. This simply means that all the hydrogen cannot be transmitted.

The resistance to transmission is made up of a sum of terms: the resistance to penetration from the surface of the entrance side to the bulk of the metal, R_p ; the resistance due to diffusion through the bulk metal, R_D ; the resistance to exit from bulk to surface on the exit side, R_{ex} ; and the resistance to H_2 evolution on the exit side, R'_{ev} . Thus

$$R_{tr} = R'_{ev} + R_p + R_{ex} + R_D \quad [4]$$

These resistances depend only on the equilibrium conditions in the system and except for R_D which is proportional to L , are independent of the thickness of the membrane. Using Eq. [4] in Eq. [3] we obtain

$$\left(\frac{dj}{di}\right)_0 = \frac{R_{ev}}{R_{ev} + R'_{ev} + R_p + R_{ex} + R_D} \quad [5]$$

An interesting consequence of Eq. [5] is that if the conditions are the same on both sides of the mem-

Table I. Elementary reactions and rates

Reaction	Rate equation
Entrance side:	
1. $H(\text{ads}) = H^+ + e^-$	$i_1 = i_{10}e^{\alpha s} \left[\frac{\theta_1}{\theta_0} - \left(\frac{1-\theta_1}{1-\theta_0} \right) e^{-s} \right]$
2. $2H(\text{ads}) = H_2(\text{surf})$	$i_2 = i_{20} \left[\left(\frac{\theta_1}{\theta_0} \right)^2 - \left(\frac{1-\theta_1}{1-\theta_0} \right)^2 \left(\frac{c_1}{c_0} \right) \right]$
3. $H_2(\text{surf}) = H_2(\text{bulk})$	$i_3 = i_{30} [(c_1/c_0) - 1]$
4. $H(\text{ads}) = H(\text{bulk M})_1$	$i_4 = i_{40} \left[\frac{\theta_1}{\theta_0} \left(\frac{1-u_1}{1-u_0} \right) - \frac{u_1}{u_0} \left(\frac{1-\theta_1}{1-\theta_0} \right) \right]$
Diffusion through the metal:	
5. $H(\text{bulk M})_1 = H(\text{bulk M})_2$	$i_5 = i_{50} (u_1 - u_2)/u_0$
Exit side:	
6. $H(\text{bulk M})_2 = H(\text{ads})$	$i_6 = i'_{40} \left[\frac{u_2}{u_0} \left(\frac{1-\theta_2}{1-\theta_0} \right) - \frac{\theta_2}{\theta_0} \left(\frac{1-u_2}{1-u_0} \right) \right]$
7. $2H(\text{ads}) = H_2(\text{surf})$	$i_7 = i'_{20} \left[\left(\frac{\theta_2}{\theta_0} \right)^2 - \left(\frac{1-\theta_2}{1-\theta_0} \right)^2 \left(\frac{c_2}{c'_0} \right) \right]$
8. $H_2(\text{surf}) = H_2(\text{bulk})$	$i_8 = i'_{30} [(c_2/c'_0) - 1]$

brane at equilibrium, then $R_{ev} = R'_{ev}$ and $(dj/di)_0 < 1/2$; that is, no more than half the hydrogen can be transmitted. This is physically reasonable since if penetration, exit, and diffusion are extremely fast compared to evolution, then the hydrogen deposited will be distributed equally on the two sides of the membrane and half of it will be evolved on each side. If any of these processes are slow then less than $1/2$ will be transmitted.

If Fick's law is obeyed in simple form, that is, if D is constant and the rate of diffusion is proportional to the concentration gradient of H atoms in the metal, then R_D will be proportional to L . We can invert Eq. [5] and obtain

$$\left(\frac{di}{dj} \right)_0 = 1 + \frac{R'_{ev} + R_p + R_{ex}}{R_{ev}} + \frac{R_D}{R_{ev}} \quad [6]$$

Therefore, $(di/dj)_0$, the reciprocal of the initial slope of j vs. i , is a linear function of L . The slope of this function is R_D/LR_{ev} and is consequently independent of conditions on the exit side of the membrane. The intercept, on the other hand, depends on conditions on both sides of the membrane. These conclusions are independent of the mechanism of transmission and evolution so long as the system is in equilibrium when no current flows. In Part II we examine one case (Ce^{+4} on the exit side) in which the system is not at equilibrium when $i = 0$; hence these conclusions do not apply.

The Elementary Reactions

The elementary reactions chosen and the corresponding rates expressed as electrical currents are given in Table I. In every case the rate expression includes the rates of both the forward and the reverse reactions. The symbols are defined in Table II.

The form of the rate equations for reactions 1, 2, and 7 is that used by Gerischer (3) and Vetter (4) in their discussions of hydrogen overvoltage. The rate equation for reactions 4 and 6 is a rearrangement of an equation used by Barrer (5) who has treated the

Table II. Symbols

$H(\text{ads})$, adsorbed hydrogen atom on the metal surface.
$H_2(\text{surf})$, H_2 molecule in the phase outside the metal, but adjacent to the metal surface.
$H_2(\text{bulk})$, H_2 molecule in the bulk phase outside the metal.
$H(\text{bulk M})$, hydrogen atom in the bulk metal.
i_k , rate of k -th reaction as an electrical current.
i_{k0} , i'_{k0} , exchange currents on side 1 and side 2.
s , overpotential ($s = F\eta/RT$) on side 1.
α , transfer coefficient for the oxidation reaction.
θ , fraction of the surface covered by adsorbed H atoms.
c, c' , concentration of H_2 adjacent to the surface in the phase outside the metal on side 1, side 2.
u , fraction of holes in the metal which are occupied by H atoms.
Subscript zero refers to the equilibrium value.
Subscripts 1 and 2 refer to values on sides 1 and 2.
i , polarization current density passed into the membrane.
j , H atom flow through the membrane expressed as an equivalent current density.
D , diffusion coefficient for H atoms in palladium (cm^2/sec).
L , membrane thickness (cm).
c_m , concentration of metal atoms (or holes) in palladium (moles/cc).

analogous gas-to-vacuum problem in detail. The rate equation for reaction 5 is an obvious algebraic modification of Fick's first law of diffusion, under the assumptions that D is a constant and that the rate of diffusion is proportional to the concentration gradient of H atoms in the alloy. This implies that the Pd-H alloy is homogeneous, either entirely α -phase or entirely β -phase. The exchange current for reaction 5 is given by

$$i_{50} = FDu_0c_m/L \quad [7]$$

Exchange currents for the same reaction on different sides of the membrane have been distinguished by primes to provide for the possibility that conditions may differ on the two sides of the membrane. The treatment is restricted to cases in which no oxidizing agent (except possibly H^+ in equilibrium with H_2) is present on the exit side and no electrical current is drawn from the exit side.

The rate equations involve the assumptions: (a) that the adsorption of hydrogen atoms follows a Langmuir isotherm, and (b) that the mixture of vacancies and occupied sites in the metal is ideal. Nonetheless, it is possible to show by a method used elsewhere (6) that the result for the initial slope of j vs. i is independent of the form of the adsorption isotherm and the law of the solution. Thus, Eq. [16], which is obtained below, although still restricted by the elementary reactions chosen, has somewhat more generality than the derivation given here would indicate.

The mechanism postulated here does not include anything which would account for an effect, observed by Hoare and Schuldiner (7) and by Clamroth and Knorr (8), which indicates that at $\eta = -0.050\text{v}$ a process with an enormous exchange current makes its appearance on a palladium surface. In this connection it should be noted that Hoare and Schuldiner (9) do not always observe this effect on palladium membrane electrodes.

The Steady-State Conditions

The steady-state conditions are:

$$i_1 + i_2 + i_4 = 0; \quad i_2 = i_3; \quad i_4 = i_5 = i_6 = i_7 = i_8$$

By definition we have $i = i_1$ and $j = -i_5$. Using these definitions, the steady-state conditions are written in detail and in their functionality.

Detail	Functionality
$i = i_{10}e^{\alpha s} \left[\frac{\theta_1}{\theta_0} - \left(\frac{1-\theta_1}{1-\theta_0} \right) e^{-s} \right]$	$i = f_1(s, \theta_1)$ [8]
$i - j = i_{20} \left[\left(\frac{1-\theta_1}{1-\theta_0} \right)^2 \left(\frac{c_1}{c_0} \right) - \left(\frac{\theta_1}{\theta_0} \right)^2 \right]$	$i - j = f_2(\theta_1, c_1)$ [9]
$i - j = i_{30} [1 - (c_1/c_0)]$	$i - j = f_3(c_1)$ [10]
$j = i_{40} \left[\left(\frac{1-\theta_1}{1-\theta_0} \right) \frac{u_1}{u_0} - \frac{\theta_1}{\theta_0} \left(\frac{1-u_1}{1-u_0} \right) \right]$	$j = f_4(\theta_1, u_1)$ [11]
$j = i_{50} (u_2 - u_1)/u_0$	$j = f_5(u_1, u_2)$ [12]
$j = i'_{40} \left[\frac{\theta_2}{\theta_0} \left(\frac{1-u_2}{1-u_0} \right) - \frac{u_2}{u_0} \left(\frac{1-\theta_2}{1-\theta_0} \right) \right]$	$j = f_6(u_2, \theta_2)$ [13]
$j = i'_{20} \left[\left(\frac{1-\theta_2}{1-\theta_0} \right)^2 \left(\frac{c_2}{c'_0} \right) - \left(\frac{\theta_2}{\theta_0} \right)^2 \right]$	$j = f_7(\theta_2, c_2)$ [14]
$j = i'_{30} [1 - (c_2/c'_0)]$	$j = f_8(c_2)$ [15]

Solution of the Equations

Considering only the functionality we conclude from Eq. [8], [9], and [10] that s can be expressed as a function of i and $i - j$ only. Successive elimination of c_2 , θ_2 , u_2 , u_1 , c_1 , and θ_1 from Eq. [15] to [9] yields a relation between i and j and the exchange currents. The labor involved in this procedure is great and the result obtained is so complicated as to be almost useless. The experimental data (II and III) show that j as a function of i begins as a straight line, in agreement with the general discussion given above, then flattens to a limiting value, j_m . The treatment here is limited to the calculation of the initial slope and the limiting value of the curve of j vs. i .

The Initial Slope

Since quantities with zero subscripts, the equilibrium values, are constant as the current and overpotential vary, there is only one independent variable which we choose as s . To obtain the initial slope, each of the Eq. [9] through [15] is differentiated with respect to s . The resulting equations are reduced to their limiting forms at $s = 0$. Quantities such as $(d\theta_1/ds)_0$, $(du_1/ds)_0$, etc., are then eliminated between these equations. The calculation is simplified considerably if parameters of a type described earlier (10) are introduced in place of $(d\theta_1/ds)_0$, etc. We obtain finally

$$\left(\frac{di}{dj}\right)_0 = 1 + \frac{\frac{1}{2i'_{20}} + \frac{1}{2i'_{30}} + \frac{1}{i_{40}} + \frac{1}{i'_{40}}}{\frac{1}{2i_{20}} + \frac{1}{2i_{30}}} + \frac{\left(\frac{1}{2i_{20}} + \frac{1}{2i_{30}}\right) u_0(1-u_0) F D c_m}{L} \quad [16]$$

This equation corresponds to Eq. [6] above. For this mechanism, $R_{ev} \propto (1/2i_{20}) + (1/2i_{30})$; $R_p \propto 1/i_{40}$; $R_{ex} \propto 1/i'_{40}$; and $R_D \propto L/F D u_0(1-u_0) c_m$. The discussion of Eq. [6] also applies to Eq. [16].

If, in addition to the reactions used above, we include the reaction, $H_2(\text{surf}) = H(\text{ads}) + H^+ + e^-$, on both sides of the membrane with exchange currents i_{60} and i'_{60} , then it must be that i_{60} is much smaller than i_{10} . Otherwise hydrogen would not enter the membrane when it is made cathodic. If i_{60} were larger than i_{10} the palladium would have to be anodic for hydrogen to enter (10). Vetter (11) quotes the two possible values of 10.1 or 0.099 for the ratio, i_{60}/i_{10} , which were determined by Knorr (12) from the mixed potential of a supersaturated Pd-H alloy in 2N H_2SO_4 . Of these two values, only $i_{60}/i_{10} = 0.099$ can be correct. Under the condition, $i_{60} \ll i_{10}$, the reciprocal of the initial slope of the transmission, $(di/dj)_0$, is given by an equation having the same form as Eq. [16] except that $2i_{20}$ and $2i'_{20}$ are replaced by $i_{00} + 2i_{20}$, and $i'_{00} + 2i'_{20}$, respectively, where $4/i_{00} = 1/i_{10} + 1/i_{60}$, and similarly for i'_{00} .

The Limiting Transmission Current

The simplest and most direct assumption is that the limiting atom current is attained when the entrance side of the membrane is completely covered by hydrogen atoms; that is, when $\theta_1 = 1$, we assume that $j = j_m$. Under this condition, Eq. [11] through [15] become

$$j_m \theta_0(1-u_0)/i_{40} = u_{1m} - 1 \quad [17]$$

$$j_m u_0/i_{50} = u_{2m} - u_{1m} \quad [18]$$

$$j_m/i'_{40} = \frac{\theta_{2m}}{\theta_0} \left(\frac{1-u_{2m}}{1-u_0}\right) - \frac{u_{2m}}{u_0} \left(\frac{1-\theta_{2m}}{1-\theta_0}\right) \quad [19]$$

$$j_m/i'_{20} = \left(\frac{1-\theta_{2m}}{1-\theta_0}\right)^2 \left(\frac{c_{2m}}{c'_0}\right) - \left(\frac{\theta_{2m}}{\theta_0}\right)^2 \quad [20]$$

$$j_m/i'_{30} = 1 - (c_{2m}/c'_0) \quad [21]$$

By successive elimination of u_{1m} , u_{2m} , c_{2m} , and θ_{2m} from these equations, a cubic equation in j_m is obtained. We consider only the special cases of interest.

Case I: Penetration and exit (steps 4 and 6) are very fast compared to the other steps.

Expansion of $-1/j_m$ in powers of L yields for the first two terms, that is, for thin membranes

$$-1/j_m = \theta_0^2/i'_{20} + (2K_4/F D c_m) L \quad [22]$$

where $K_4 = u_0(1-\theta_0)/\theta_0(1-u_0)$ is the equilibrium constant for reaction 4 (or 6). Since K_4 and θ_0^2/i'_{20} are independent of pressure, the maximum transmission in this case should be independent of the hydrogen pressure in the two compartments. The slope of the line, $-1/j_m$ vs. L , depends on θ_0 in this case.

Case II: Atom combination (steps 2 and 7) is very fast compared to the other steps.

Case IIA: Transport of H_2 from the exit surface (step 8) is also very fast.

In this case, $\theta_{2m} = \theta_0$, and we have

$$-1/j_m = (\theta_0/i_{40} + u_0/i'_{40}) + [1/(1-u_0) F D c_m] L \quad [23]$$

In this case the slope of $-1/j_m$ vs. L is determined by bulk properties, D and u_0 , only. Both the slope and the intercept are pressure dependent.

Case IIB: Transport of H_2 from the exit surface (step 8) is slow.

In this case we have, approximately,

$$-1/j_m = (4\theta_0^2 u_0^2/i_{40}^2 i'_{30})^{1/3} + (2/3 F D c_m) L \quad [24]$$

Here again the slope is determined by bulk properties only. The intercept is pressure dependent, but the slope is not.

The Over-all Exchange Current

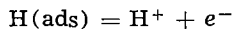
The over-all exchange current, $i_0 = (di/ds)_0$, is easily calculated by differentiating Eq. [8], [9], and [10]. We obtain

$$\frac{1}{i_0} = \frac{1}{i_{10}} + \frac{1}{2i_{20}} + \frac{1}{2i_{30}} - \left(\frac{dj}{di}\right)_0 \left(\frac{1}{2i_{20}} + \frac{1}{2i_{30}}\right) \quad [25]$$

For an electrode which does not transmit hydrogen, the reciprocal of i_0 is given by the first three terms on the right of Eq. [25]. Thus, Eq. [25] shows that, if the electrode transmits hydrogen, the exchange current may be larger than on an ordinary electrode. However, if primary discharge is much slower than combination and the subsequent transport of molecular hydrogen from the surface, then $i_0 = i_{10}$ and the transmission does not affect the value of i_0 . Physically, rapid combination of H atoms and rapid transport of H_2 from the surface imply that θ_1 remains at its equilibrium value; hence s depends only on i and i_{10} .

The "Transferred" Overvoltage

Even though no electrical current is drawn from the exit side of the membrane, an overvoltage, η' , sometimes called the "transferred" overvoltage, can be observed on the exit side [see, for example, ref. (9)]. This is a result of the reaction 9 on the exit side:



$$i_9 = i'_{10} e^{\alpha' s'} \left[\frac{\theta_2}{\theta_0} - \left(\frac{1-\theta_2}{1-\theta_0} \right) e^{-s'} \right]$$

where $s' = F\eta'/RT$. Since no current is drawn, $i_9 = 0$, and hence

$$\frac{\theta_2}{\theta_0} - \left(\frac{1-\theta_2}{1-\theta_0} \right) e^{-s'} = 0 \quad [26]$$

Equation [26] in connection with Eq. [14] and [15] determines the value of s' as a function of j . If $i'_{20} \ll i'_{30}$, then

$$(4t'/j)^{1/2} = (1/i'_{20})^{1/2} [1 + (1-2\theta_0)t']$$

while if $i'_{20} \gg i'_{30}$, then

$$(4t'/j)^{1/2} = (1/i'_{30}) (1+t')$$

in which $t' = \tanh(s'/2)$.

Acknowledgment

This research was supported by the Air Force Office of Scientific Research. The author wishes to express his thanks to the referee who suggested inclusion of the general proof of the form of the initial slope and other revisions which have improved the paper considerably.

Manuscript received May 31, 1963; revised manuscript received Feb. 4, 1964.

Any discussion of this paper will appear in a Discussion Section to be published in the June 1965 JOURNAL.

REFERENCES

1. R. LaPietra and G. W. Castellan, *This Journal*, **111**, 1276 (1964).

2. P. L. Damour and G. W. Castellan, *ibid.*, **111**, 1280 (1964).
3. H. Gerischer, *Z. Elektrochem.*, **55**, 98 (1951); *Z. physik. Chem.*, **202**, 292 (1953).
4. K. J. Vetter, *Z. Elektrochem.*, **59**, 435 (1955).
5. R. M. Barrer, *Phil. Mag.*, **28**, 148 (1939). R. M. Barrer, "Diffusion In And Through Solids," pp. 178ff, The Cambridge University Press (1951).
6. G. W. Castellan, *This Journal*, **108**, 686 (1961).
7. J. P. Hoare and S. Schuldiner, *ibid.*, **102**, 485 (1955).
8. R. Clamroth and C. A. Knorr, *Z. Elektrochem.*, **57**, 399 (1953).
9. J. P. Hoare and S. Schuldiner, *This Journal*, **103**, 237 (1956); **104**, 564 (1956).
10. G. W. Castellan, *ibid.*, **108**, 277 (1961).
11. K. J. Vetter, "Elektrochemische Kinetik," p. 491, Springer-Verlag, Berlin (1961).
12. C. A. Knorr, *Z. Elektrochem.*, **57**, 599 (1953).

The Transmission of Electrolytically Deposited Hydrogen through a Palladium Membrane Electrode

II. Experimental. Oxidizing Agents and Hydrogen Gas on the Exit Side

Richard A. LaPietra¹ and Gilbert W. Castellan

Department of Chemistry, The Catholic University of America, Washington, D. C.

ABSTRACT

Hydrogen is deposited electrolytically on one side (the entrance side) of a palladium membrane at a rate $-i$ (amp/cm²). The amount of hydrogen transmitted is measured by noting the change in normality of a solution of a strong oxidizing agent, e.g., Ce⁺⁴ or S₂O₈⁼, on the other side (the exit side), and in other experiments by measuring the hydrogen evolved on the exit side volumetrically. The results with hydrogen on the exit side are apparently capable of description by the equations developed in Part I of this series, but the value of the diffusion coefficient obtained is lower than Barrer's value at 25°C by a factor of two to three. Possible reasons for this discrepancy are discussed briefly.

Recent measurements of the transmission of electrolytically deposited hydrogen through palladium show some discrepancies. Wahlin and Naumann (1) find no dependence of the transmission rate on thickness, L , of the metal using foils 5, 10, and 15 mil thick. Heath (2) finds that the transmission rate is inversely proportional to L , as does Barrer (3) who calculated a value of D , the diffusion coefficient. Devanathan and Stachurski (4) have measured the value of D for hydrogen in the α -alloy. The work here was inspired by an investigation of Schuldiner and Hoare (5) in which they report that the rate of transmission is inversely proportional to $L^{1/2}$. A true dependence on $L^{-1/2}$ cannot be rationalized on the basis of a simple Fick's law (constant D ; flow proportional to concentration gradient) regardless of what phase boundary reactions may occur. We therefore decided to reinvestigate the experiment of Schuldiner and Hoare.

In brief, the experiment consists in depositing hydrogen electrolytically on one side, the entrance side, of a palladium membrane cathode at a rate $-i$. The other side, the exit side, of the membrane is in contact with a solution of a strong oxidizing agent, such as Ce⁺⁴. Any hydrogen which passes through the membrane is presumably oxidized by the Ce⁺⁴ solution. By measuring the rate of change of the normality of the ceric solution the rate of transmission of hydrogen, $-j$, can be calculated. For convenience we express j as an equivalent electrical current density. Values of j are measured as a function of i , the polarizing current density, and L , the membrane thickness.

Apparatus and Materials

All the experiments were done in the Teflon cell shown in Fig. 1. The anode consists of a piece of bright platinum gauze, 6 in. x 1.25 in., folded several times to form a thick, narrow band; this gauze is mounted on a heavy platinum wire which extends through the cell wall. The reference electrode is a square of bright platinum gauze, 1 cm on a side, mounted about midway between anode and cathode.

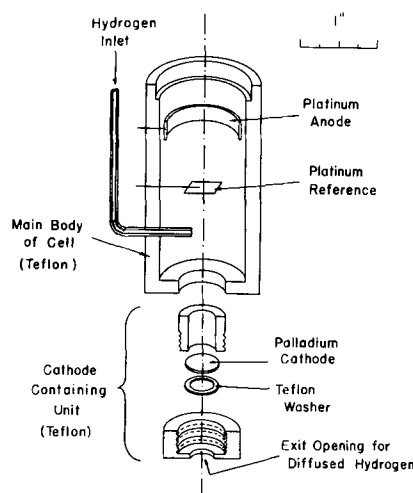


Fig. 1. The cell

¹ Present address: Marist College, Poughkeepsie, New York.

The membrane cathode is a circular disk cut from a sheet of 99.8% palladium (Baker & Company, Inc.). When installed in the Teflon cathode unit, Fig. 1, the surface area of palladium exposed to the electrolyte in the cell is 0.72 cm². The Teflon surfaces in direct contact with the palladium membrane were covered with a very thin layer of melted polyethylene. After assembly, the cathode unit was heated in an oven to 110°C whereupon the polyethylene became sticky. The unit was then screwed tight and allowed to cool, thus producing a leakproof seal. A thin platinum wire covered with polyethylene provided electrical contact with the palladium cathode from the outside of the cell.

The polarizing current was provided by a 300v d-c regulated power supply in series with appropriate resistors and was measured by a Weston Model 901 milliammeter and was measured by a Weston Model 901 milliammeter. Potential differences were measured by an L&N pH Indicator, Model 7664-A1, and recorded by an L&N Speedomax H recorder, Model S. The potential of the palladium cathode was measured relative to the platinum reference electrode.

Triply distilled water, two distillations in a quartz still, was used for preparing all solutions and for rinsing and cleaning the cell. The water and the solutions were stored in aged polyethylene bottles and later in quartz flasks. Electrolytic grade hydrogen was bubbled through the entrance compartment of the cell. The hydrogen purification train contained: a De-Oxo unit, silica gel, copper turnings at 400°C, Ascarite, silica gel, palladized asbestos, and a liquid nitrogen trap. Mass spectrometric analysis of the hydrogen issuing from the train showed the presence of hydrogen and water only.

After each experiment the cell was disassembled and rigorously cleaned. The Teflon parts were scraped free of polyethylene and cleaned in hot nitric acid. A fresh piece of palladium, cleaned by flaming in a Meker burner, was used in each experiment. After assembly the cell was rinsed several times with triply distilled water over a period of 1-2 hr. Finally the cell was rinsed with 2N H₂SO₄ and filled with about 25 cc of 2N H₂SO₄. The solution and electrodes were then cleaned by pre-electrolysis at 50 ma for a period of 12 hr. A removable platinum gauze electrode served as the pre-electrolysis cathode.

Experiments with Oxidizing Agents

In the experiments with ceric ion on the exit side of the membrane, the base of the cell was submerged in a shallow dish containing 0.05M Ce(SO₄)₂ solution in 2N H₂SO₄. The air bubble trapped in the cavity was removed, and the ceric solution was stirred rapidly with a magnetic stirrer. The vertical arrangement of the two-compartment cell has the advantage over that used by Schuldiner and Hoare in that hydrogen bubbles escape easily from the entrance face of the diaphragm.

Schuldiner and Hoare observed an increase in permeation rate with polarization current density, then a slight decrease at higher current densities of the order of 100 ma/cm². We observe something similar but rather more dramatic. The results are shown in Fig. 2, which plots $-j$ vs. $-i$; the signs of j and i are taken as negative for mathematical convenience. We also observe that at the high current densities where the fall off in transmission occurs, gaseous hydrogen is evolved rapidly on the exit side of the cathode. Since the transmission rate is calculated from the change in normality of the ceric solution, this gaseous hydrogen is not counted and there is an apparent decrease in rate of transmission.

The first results we obtained were highly erratic. (Schuldiner and Hoare mention an average error of $\pm 35\%$ in consecutive titrations of the ceric solution at 1000 sec intervals; their average error was $\pm 5\%$ in check runs over the total time period at one current density.) After observing trapped hydrogen bubbles on the exit side we added cerous ion to the ceric solution

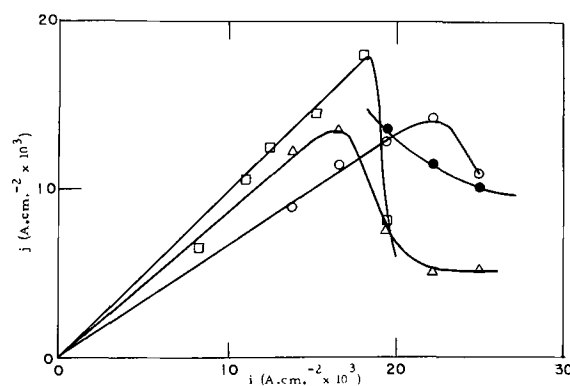


Fig. 2. j vs. i with oxidizing agents on the diffusion side. $L = 0.003$ in.; \square , \bullet , Ce⁴⁺; \circ , \triangle , S₂O₈⁼.

to see if the accumulation of cerous ion inhibits the oxidation of the hydrogen. It appears not to have such an effect. We then devised a simple pump using a hypodermic syringe operated by a solenoid controlled by a timing device. This pump could supply ceric ion from the body of the solution to the face of the membrane at the rate of 1-2 cc in 10 sec. We also used a saturated solution of ceric sulfate in 2N H₂SO₄. Under these conditions the experiment is much more reproducible, and much higher transmission rates are obtained. It is these results which are shown in Fig. 2. We used a stronger oxidizing agent, persulfate ion, in some cases. The result is substantially the same. The differences in Fig. 2 we attribute to the crude design of our hypodermic pump which did not function with the same effectiveness in all the runs.

Since we find that the transmission rate which we measure depends essentially on the rate at which ceric ion can be supplied to the palladium surface, we are forced to the conclusion that this experiment does not tell us anything about the transmission of hydrogen through palladium except that it is too rapid to be measured in this way. And we believe that the same conclusion must be drawn from the results of Schuldiner and Hoare. Figure 2 shows that for a 0.003 in. foil at 23°C essentially all of the deposited hydrogen is transmitted up to a current density of 20 ma/cm² at which point the transport of ceric ion to the membrane surface, even with our very effective stirring, cannot keep up with the hydrogen transport through the membrane, and hydrogen gas commences to be evolved. In Schuldiner and Hoare's experiments the maximum transmission through a thinner (0.001 in.) membrane at 37°C was only 12.8 ma/cm². This suggests that their method of stirring (a "moderate" flow of helium) was not as effective as ours, and that molecular hydrogen escaped unnoticed from the exit face. In their cell it would be difficult to notice hydrogen evolution from the exit face of the foil, while in our arrangement the gas is trapped and could not escape notice. Consequently, we suggest that the dependence they report of the transmission rate on $L^{-1/2}$ is an accidental result of a systematic error in their experiment.

Schuldiner and Hoare rule out the possibility that a limiting diffusion current of ceric ion is operative in their experiment, since if it were the maximum transmission should not depend on thickness. This is quite true; however, the thickness effect which they observe is a peculiar one and forces them to conclude that Fick's law does not hold and that the diffusion constant depends on the thickness of the membrane. Our experiments, described below and in Part III, indicate that Fick's law does apply.

Experiments with Hydrogen Gas on the Exit Side

To measure the transmission of hydrogen through the foil, a short glass capillary delivery tube was sealed with molten polyethylene to the exit opening of the cell on the exit side. The bottom of the cell was

immersed in a reservoir of triply distilled water; a water-filled, thermostated ($32.2 \pm 0.1^\circ$) gas buret was inverted over the opening of the delivery tube. This allowed the measurement of the diffused hydrogen to be made volumetrically. No attempt was made to thermostat the cell itself because of the heating effect of the current and the poor thermal conductivity of the Teflon. The average temperature of the cell was about 23°C .

Immediately following the interruption of the pre-electrolysis current, the palladium diaphragm was made the cathode at a current density of 10 ma/cm^2 . Hydrogen was bubbled vigorously through the cell, and the recorder trace of the potential difference between the platinum reference electrode and the palladium membrane was observed. At first the trace drifts smoothly and very slowly in a negative direction. Finally, at about the same time as hydrogen first appears in the delivery tube, the potential-time trace becomes a jagged line, indicating the formation and release of bubbles on the entrance side. From then on, immediately following release of the bubble from the cathode the potential remained at very nearly the same value. The time required to reach this steady state varied from an average of 3 hr for the 0.003-in. foils to 13 hr for the 0.020-in. foils. Measurements were not begun until this steady state had been reached.

At the instant of release of a bubble from the delivery tube a stopwatch was started. Before the evolution of the next bubble, the buret volume, the water levels in the buret and reservoir, and the atmospheric pressure were measured. In the time interval required for the evolution of about 1 cc of gas, the polarization current and the overpotential were recorded. The stopwatch was stopped, again at the instant of release of a bubble. The buret volume and the water levels in buret and reservoir were recorded. From these data the hydrogen transmission in the time interval could be expressed as an equivalent current density, $-j$. Four successive measurements of this sort were taken at each current density. The mean deviation in most cases was within $\pm 5\%$.

Then the polarization current was increased and a period of about 30 min allowed to establish the new steady state. By the end of this period the overpotential had been steady for at least 20 min.

In company with earlier investigators we were plagued by lack of reproducibility in successive measurements on the same foil. If, after measuring $-j$ at a series of polarization current densities, one attempts to begin again at low current densities and repeat the series on the same foil, the reproducibility is not good. Nor does the behavior appear to approach a limit after a number of repetitions of the series of measurements. Anodic activation of the entrance side of the foil between series of measurements appears to activate the foil in an irreproducible way.

Reasonably reproducible results were obtained by using a fresh palladium disk for each series of measurements. The disk was flamed in a Meker burner, then sealed in the cathode unit and treated in the manner described for the measurements with ceric sulfate. Even with this consistent method, about one run in four behaved differently. The overvoltage was substantially higher at low current densities and the

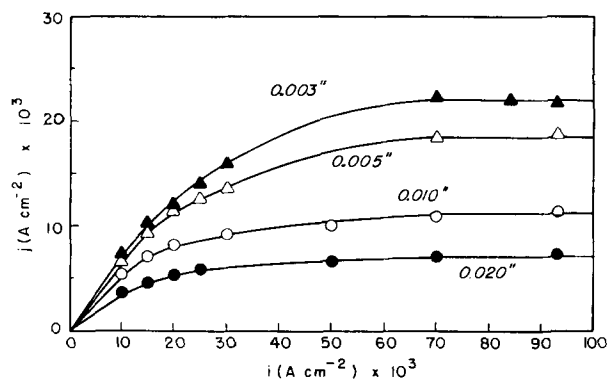


Fig. 3. j vs. i with hydrogen gas on the diffusion side

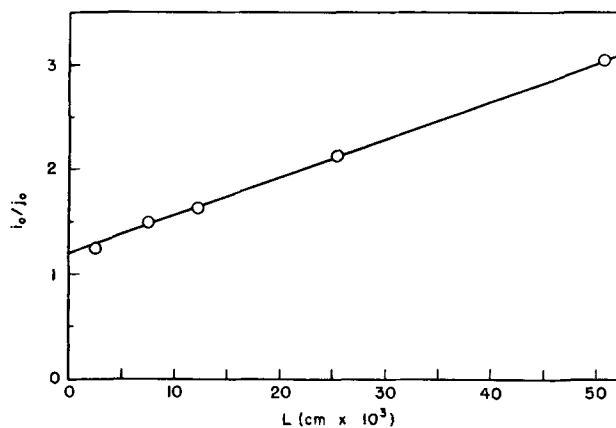


Fig. 4. $(di/dj)_0$ vs. L . $(di/dj)_0 = 1.20 + 36.3L$

transmission was substantially lower. Using the overvoltage at the lowest current density as a criterion of the surface condition, measurements were rejected if the overvoltage at the lowest current density did not lie between 80 and 90 mv. (Since the measured overvoltage contained an IR drop we do not attempt to interpret it theoretically.)

Results are given in Table I and in Fig. 3. In Fig. 3 the points are the average values of the three measurements in the table. At high current densities, a sustained plateau value of j is attained. We do not observe any decrease in j at high current densities as in the experiments with ceric sulfate. The initial portion of the curve is not too well defined because of comparatively large relative errors, but appears to be linear. Both the initial slope, $(dj/di)_0$, and the plateau value, j_m , decrease with increasing foil thickness, L .

From the treatment in Part I we expect the reciprocal of the initial slope and the reciprocal of $-j_m$ to be linear functions of the diaphragm thickness. These plots are shown in Fig. 4 and 5. In both cases the linearity is good. The equations of the lines in Fig. 4 and 5, determined by a least squares fit, are

$$(di/dj)_0 = 1.20 + 36.3L \quad [1]$$

Table I. Transmission rate, $-j(\text{ma/cm}^2)$, as a function of the polarization current density, $-i(\text{ma/cm}^2)$, and of $L(\text{in.})$.

$-i \setminus L$	0.003 in.			0.005 in.			0.010 in.			0.020 in.		
10.0	7.1	6.7	6.4	6.2	5.6	6.3	5.0	4.0	5.3	3.8	3.5	2.0*
15.0	10.3	10.5	9.2	9.9	8.4	9.6	6.9	6.3	7.8	4.8	4.5	4.2
20.0	12.3	11.4	12.0	11.8	10.4	11.9	7.6	7.8	9.0	5.2	5.1	5.4
25.0	13.7	14.3	14.0	13.2	11.2	—	—	—	10.1	—	—	5.8
30.6	15.4	18.1	14.8	14.9	12.1	—	8.0	9.1	10.8	—	—	—
50.0	—	—	—	—	—	—	—	9.8	12.3	6.7	6.0	6.8
70.0	20.6	26.2	20.1	19.1	16.7	19.0	9.3	10.8	12.5	7.6	6.4	7.2
93.0	19.7	25.5	20.0	18.5	18.8	19.3	9.3	11.1	13.6	7.8	6.7	7.3

* Value rejected in the average.

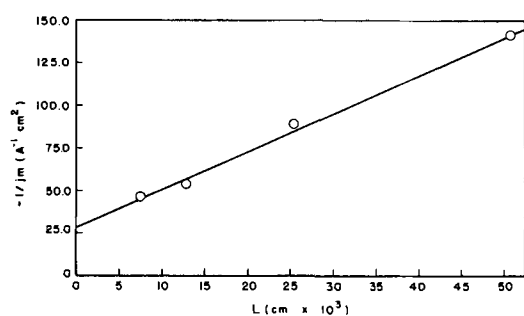


Fig. 5. $-1/j_m$ vs. L . $-1/j_m = 28.4 + 2.24 \times 10^3 L$ (cm^2/amp)

$$-1/j_m = 28.4 + 2.24(10^3) L \quad [2]$$

in which i and j are in amp/cm^2 and L is in cm .

To interpret Eq. [1] and [2] in terms of the equations developed in Part I, we first use the fact that the hydrogen evolved on the exit side pushes the water out of the capillary tube and hence the exit face of the membrane is in contact with hydrogen gas. (This is also demonstrated by the absence of any electrical contact between the water in the collecting buret and the palladium membrane.) Consequently, the transport of molecular hydrogen from the surface of the exit face should be very rapid and therefore we set $1/i_{30} = 0$. Next we take in account evidence from overvoltage measurements (6) and from the rate of absorption of hydrogen by palladium in sulfuric acid (7), that the rate of combination of hydrogen atoms is very fast on the entrance side; this enables us to set $1/i_{20} = 0$. These assumptions applied to Eq. [16] of Part I, reduce it to

$$\left(\frac{di}{dj}\right)_o = 1 + \frac{i_{30}}{i'_{20}} + \frac{2i_{30}}{i_{40}} + \frac{2i_{30}}{i'_{40}} + \frac{2i_{30}L}{u_o(1-u_o)FDc_m} \quad [3]$$

We next examine two cases in order.

Case 1: Penetration and exit are much faster than combination on the exit side.

In this case we may neglect the third and fourth terms on the right of Eq. [3] and it becomes

$$\left(\frac{di}{dj}\right)_o = 1 + \frac{i_{30}}{i'_{20}} + \frac{2i_{30}L}{u_o(1-u_o)FDc_m} \quad [4]$$

Comparing this equation with Eq. [1], we obtain the two relations:

$$i_{30}/i'_{20} = 0.20 \quad \text{and} \quad 8.65(10^{-4})i_{30}/D = 36.3$$

in which the equilibrium H/Pd ratio, $u_o = 0.69$, and the values $c_m = 0.112$ moles/cc, $F = 96,500$ coulombs/equiv have been used. Comparison of Eq. [22] in Part I, which gives the value of $-1/j_m$, with Eq. [2] above yields the two relations

$$\theta_o^2/i'_{20} = 28.4 \quad \text{and} \quad 4.13(10^{-4})(1-\theta_o)/\theta_o D = 2.24(10^3)$$

These four relations yield the values: $\theta_o = 0.68$; $D = 0.87(10^{-7}) \text{ cm}^2/\text{sec}$; $i'_{20} = 16 \text{ ma}/\text{cm}^2$; $i_{30} = 3.2 \text{ ma}/\text{cm}^2$. Of these values we may say that the value of θ_o is not unreasonable; the value of i_{30} is probably too large by at least a factor of 5 to 10 if it represents a diffusion current but is probably much too small if it can represent transfer in the presence of bubble formation. The value of D is a factor 3 smaller than Barrer's (1) value of $2.74(10^{-7}) \text{ cm}^2/\text{sec}$ at 25°C ; the value of i'_{20} may or may not be reasonable. It is certainly much smaller than the value, $280 \text{ ma}/\text{cm}^2$, which can be calculated assuming $\theta_o = 0.68$ from the expression given by Kazanskii *et al.* (8) for the dissociation velocity constant.

Case 2. Penetration and exit are slow compared to combination on the exit side.

In this case, if we assume $i_{40} = i'_{40}$, Eq. [3] becomes

$$\left(\frac{di}{dj}\right)_o = 1 + \frac{4i_{30}}{i_{40}} + \frac{2i_{30}L}{u_o(1-u_o)FDc_m} \quad [5]$$

Comparing this equation with Eq. [1] above, we obtain the relations

$$4i_{30}/i_{40} = 0.20 \quad \text{and} \quad 8.65(10^{-4})i_{30}/D = 36.3$$

Comparing Eq. [23] in Part I with Eq. [2] above, we obtain the relations

$$(\theta_o + u_o)/i_{40} = 28.4 \quad \text{and} \quad 2.98(10^{-4})/D = 2.24(10^3).$$

These four relations yield immediately: $D = 1.3(10^{-7}) \text{ cm}^2/\text{sec}$; $\theta_o = 2.49$; $i_{40} = 112 \text{ ma}/\text{cm}^2$; $i_{30} = 5.6 \text{ ma}/\text{cm}^2$. Again, the value of i_{30} seems too large. The value of D is half of Barrer's value at 25°C . The value of i_{40} may well be correct. The value of θ_o is, of course, preposterous. However, θ_o depends critically on the intercept in Eq. [1] minus unity. Since this intercept is not greatly different from unity, and since the initial slopes are not too well defined anyway, the experimental errors will tend to make rather large errors in θ_o . Without damaging the fit with the data, the line in Fig. 4 could be rotated slightly (clockwise) and θ_o brought into the realm of reality. In other words, the data are not inconsistent with $\theta_o = 1.0$; $i_{40} = 60 \text{ ma}/\text{cm}^2$; $i_{30} = 4.5 \text{ ma}/\text{cm}^2$; and the same value of D as above.

Without a study of the pressure dependence of the slopes and intercepts of the lines in Fig. 4 and 5, it is not possible to choose between these two cases. The data even seem to suggest that neither is correct, but a situation intermediate between the two exists in the system. Both types of behavior, in different experimental circumstances, have been observed by Wagner (9). The pressure and temperature dependence of the transmission are presented in Part III.

Acknowledgment

This research was supported by the Air Force Office of Scientific Research. This work was completed while one of the authors (G.W.C.) was a National Science Foundation Postdoctoral Fellow at the Max Planck Institut für physikalische Chemie, Göttingen.

Manuscript received May 31, 1963; revised manuscript received Feb. 4, 1964. This paper was delivered at the Los Angeles Meeting, May 6-10, 1962, and was taken in part from a dissertation submitted by one of the authors (R.A.L.) to the Faculty of the Graduate School of Arts and Sciences of the Catholic University of America in partial fulfillment of the requirements for the Ph.D. degree.

Any discussion of this paper will appear in a Discussion Section to be published in the June 1965 JOURNAL.

REFERENCES

- H. B. Wahlin and V. O. Naumann, *J. Appl. Phys.*, **24**, 42 (1953).
- H. R. Heath, *Brit. J. Appl. Phys.*, **3**, 13 (1952).
- R. M. Barrer, *Trans. Faraday Soc.*, **36**, 1235 (1940).
- M. A. V. Devanathan and Z. Stachurski, *Proc. Roy. Soc.*, **270A**, 90 (1962).
- S. Schuldiner and J. P. Hoare, *This Journal*, **103**, 178 (1956); See also: NRL Report 5333, July 1959.
- G. W. Castellan, *This Journal*, **108**, 282 (1961).
- R. J. Fallon and G. W. Castellan, *J. Phys. Chem.*, **64**, 4 (1960).
- V. B. Kazanskii, R. E. Mardaleishvili, V. P. Strunin, and V. V. Voevodskii, *Zhur. Fiz. Khim.*, **30**, 821 (1956).
- C. Wagner, *Z. physik. Chem.*, **159A**, 459 (1932).

The Transmission of Electrolytically Deposited Hydrogen through a Palladium Membrane Electrode

III. Pressure and Temperature Dependence

Paul L. Damour¹ and Gilbert W. Castellan

Department of Chemistry, The Catholic University of America, Washington, D. C.

ABSTRACT

An investigation of the pressure and temperature dependence of the maximum rate of transmission of hydrogen through palladium is described. The pressure dependence in the range from 0.329 to 1 atm indicates that the penetration-exit reaction, $H_{(ads)} = H_{(bulk)}$, is the slowest surface reaction, but is nonetheless very fast having an exchange current density of about 0.8 amp/cm² at 1 atm pressure. From the temperature dependence it is found that at temperatures slightly below room temperature the diffusion coefficient can be represented by $D = 0.0260 \exp(-6800/RT) \text{ cm}^2/\text{sec}$.

The investigations reported in Parts I and II, (1, 2), show that it is necessary to measure the rate of transmission of hydrogen as a function of the hydrogen pressure on the exit side of the membrane to obtain a more complete characterization of the mechanism. In this paper, the dependence of the rate of transmission on pressure and temperature as well as on membrane thickness is described. In the experiments described here, the entrance compartment of the cell contains 2*N* H₂SO₄ saturated with hydrogen gas at 1 atm pressure. The exit compartment contains hydrogen gas at arbitrary pressures (below 1 atm).

Apparatus and Materials

The cell used here was similar to that used in the work described in Part II. The palladium membrane was held in the unit shown in Fig. 1. This unit fits into the position of the cathode unit of the cell described in Part II. In this arrangement the palladium disk is clamped between two pieces of Teflon by a brass fitting. The palladium is cut large enough so that it makes electrical contact with the brass. The lower piece of brass is soldered to a Kovar metal-to-glass seal which is in turn connected to a constant pressure system by a Teflon O-ring connection. This arrangement provides tight enough seals to hold a vacuum of 10⁻³ mm over the period of a day or more. The entire cell is immersed in a thermostat controlled to $\pm 0.1^\circ\text{C}$.

The constant pressure system on the exit side contained a manometer, a thermostated 12 liter ballast bulb, a thermostated gas buret, appropriate arrangements to change mercury levels to keep the pressure constant, and a dry ice-acetone trap to prevent access of mercury vapor to the palladium. The system could be evacuated. From the measured change of volume of

hydrogen at the constant pressure in a specified time interval, the rate of transmission can be calculated.

The other instruments used were the same as those described in Part II. However, the potential of the membrane was not measured. In addition, a thermocouple well (made of thin-walled Teflon tubing) was placed in the cell with its tip near the palladium disk to permit the measurement of the temperature in the cell near the disk.

The materials used and the precautions taken were the same as those described in Part II with the following exceptions. The membrane was flamed in a hydrogen-oxygen flame (not a gas flame as in II) before insertion in the holder. The sulfuric acid used was pre-electrolyzed in an exterior quartz flask for 12 hr at 50 ma. The entrance face of the membrane was not pre-electrolyzed but was anodized (see below).

Experimental

A fresh palladium disk was used for each series of experiments. After flaming the disk in a hydrogen-oxygen flame, it was inserted in the holder which was placed in the cell. The exit compartment was evacuated and then filled with hydrogen at 1 atm pressure. The disk was anodized at 100 ma for 30 min using a platinum dummy cathode, which was then removed. Hydrogen was bubbled through the entrance compartment at a rate of 300 ml/min. Then the palladium was made cathodic using a current density of 250 ma/cm², which is sufficiently high to insure that the transmission through the foil has reached its maximum value, $-j_m$, even for the thinnest foils used.

About 8 hr were allowed for the establishment of the steady state. After this period the amount of gas passing in a specified time interval was measured volumetrically, meanwhile keeping the pressure constant by adjusting the mercury levels in the manometer and buret.

After completing the measurement at 1 atm, the pressure on the exit side was lowered. Thirty minutes were allowed for the establishment of the steady state at the lower pressure, then the measurement was made. In this way measurements were made at four pressures: 760, 540, 380, and 250 mm. These pressures are not low enough to permit the formation of the α -Pd-H alloy. After measurements at the four pressures were completed, the temperature of the cell thermostat was raised, the pressure returned to 1 atm, and the entire procedure repeated at the higher temperature. Ninety minutes were allowed for the equilibration at the new temperature. Measurements were made at four temperatures: 3.6°, 6.7°, 12.2°, and 15.3°.

Because of the passage of the current and the insulating qualities of Teflon it was not possible to keep

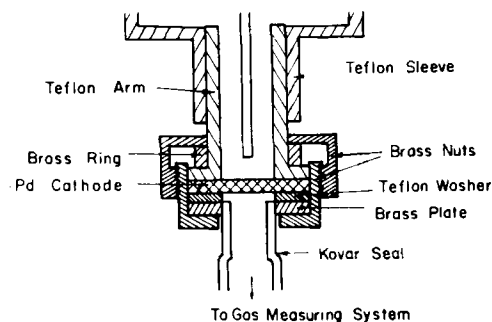


Fig. 1. Cathode unit

¹ Present address: St. Anselm's College, Manchester, New Hampshire.

Table I. Maximum transmission rate, $-j_m$ (ma/cm²), and $-1/j_m$ (cm²/amp)

$p^{1/2}$ (atm ^{1/2})		1.00		0.840		0.707		0.573	
Thick- ness, in.	Temp, °C	j_m	$1/j_m$	j_m	$1/j_m$	j_m	$1/j_m$	j_m	$1/j_m$
0.003	3.6	62.2	16.1	69.4	14.4	76.5	13.1	81.9	12.2
	6.7	70.9	14.1	78.4	12.8	86.3	11.6	92.5	10.8
	12.2	87.0	11.5	95.6	10.5	104.9	9.5	112.3	8.9
0.005	3.6	39.9	25.1	44.0	22.7	47.2	21.2	52.4	19.1
	6.7	45.3	22.1	50.1	20.0	53.9	18.6	60.2	16.6
	12.2	56.1	17.8	62.5	16.0	66.9	14.9	73.2	13.7
0.010	3.6	19.5	51.3	21.4	46.7	23.2	43.1	25.7	38.9
	6.7	22.3	44.8	24.7	40.5	26.9	37.2	29.5	33.9
	12.2	28.2	35.3	31.3	31.9	34.0	29.4	37.3	26.8
	15.3	32.5	30.8	36.0	27.8	38.9	25.7	42.5	23.5

the operating temperature in the cell, which we take as the temperature of the palladium, equal to that in the thermostat. Consequently, when the measurement of the rate was made, the operating temperature in the cell was noted. The operating temperature was different in otherwise duplicate experiments. We find that under the same external conditions, a plot of $\log j$ vs. the reciprocal of the operating temperature is linear. We therefore extrapolate this line to the temperature of the thermostat and use the extrapolated value of j_m as the value at the thermostat temperature. In Table I are the average values obtained in this way from measurements on three different foils. The maximum deviation from the average of any value in Table I is 5.7% and the average deviation from the average over the entire table is 2.4%.

The characteristic curves of j vs. i obtained in Part II in which j reaches a sustained plateau value were not observed by Wahlin and Naumann (3). At high current densities (they used currents up to 2.5 amp in a constricted tube) they observed a continued increase in transmission rate with increase in current density. We attribute this continued increase to the increase in temperature resulting from the passage of the current. We observe similar behavior at current densities greater than 100 ma/cm².

Results

The values of $-j_m$ and $-1/j_m$ are displayed as functions of temperature and pressure, $p^{1/2}$, in Table I.

Preliminary experiments showed that the value of j_m depended on $p^{1/2}$, where p is the pressure on the exit side of the membrane. This indicates that the system falls under Case IIA described in Part I. In this case, measurement of the initial slope would only contribute a value for the transport rate of molecular hydrogen from the electrode to the solution on the entrance side so it is unnecessary to measure the entire curve of j vs. i . The value of j_m suffices to describe the interesting parameters of the system.

Discussion

To find the dependence of j_m on the pressure on the exit side when the pressure on the entrance side is kept at 1 atm, it is convenient to rewrite Eq. [15], [16], and [17] of Part I in terms of the rate constants rather than the exchange currents. We further assume that i'_{30} and i'_{20} are infinitely fast. This has the consequence that $\theta_{2m} = \theta'_o$, where θ'_o is the "equilibrium" value of the coverage on the exit side under the pressure p . We use u'_o for the fraction of holes in the metal which are occupied by hydrogen atoms at "equilibrium" under the pressure p . This amounts to assuming that the surface and the bulk of the metal near the exit side of the foil are in equilibrium with the gas under the pressure p on the exit side. The equations become

$$j_m/k_4 = u_{1m} - 1 \tag{1}$$

$$j_m L / F D c_m = u_{2m} - u_{1m} \tag{2}$$

$$j_m / k_4 = \theta'_o (1 - u_{2m}) - (k_{-4} / k_4) (1 - \theta'_o) u_{2m} \tag{3}$$

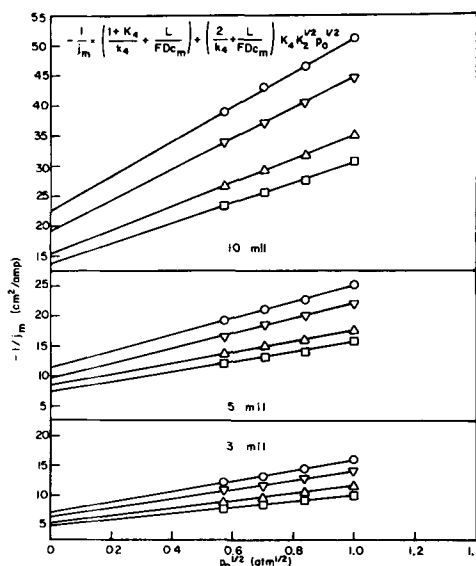


Fig. 2. — $1/j_m$ vs. $p^{1/2}$. \circ , 3.6°C; ∇ , 6.7°C; \triangle , 12.2°C; \square , 15.3°C

In addition we have the equilibrium relations

$$K_4 = (k_4/k_{-4}) = u'_o(1 - \theta'_o) / (1 - u'_o)\theta'_o \tag{4}$$

$$\theta'_o / (1 - \theta'_o) = K_4 K_2^{1/2} p^{1/2} \tag{5}$$

Elimination of u_{1m} and u_{2m} from these equations yields the final result

$$-\frac{1}{j_m} = \left(\frac{1 + K_4}{k_4} + \frac{L}{F D c_m} \right) + \left(\frac{2}{k_4} + \frac{L}{F D c_m} \right) K_4 K_2^{1/2} p^{1/2} \tag{6}$$

which we abbreviate to $-1/j_m = I_1 + S_1 p^{1/2}$. At constant temperature and membrane thickness, the plot of $-1/j_m$ vs. $p^{1/2}$ should be linear (Fig. 2). The values of I_1 and S_1 are listed in Table II.

According to Eq. [6] both I_1 and S_1 should be linear functions of L at constant temperature (Fig. 3a, b). We write

$$I_1 = (1 + K_4)/k_4 + (1/F D c_m)L \tag{7}$$

$$S_1 = 2K_4 K_2^{1/2}/k_4 + (K_4 K_2^{1/2}/F D c_m)L \tag{8}$$

From the slope of I_1 vs. L , Eq. [7], we evaluate D directly. From the ratio of the slope of S_1 vs. L to that of I_1 vs. L , we obtain the value of $K_4 K_2^{1/2}$. These values are displayed in Table III along with the values of the intercepts of Eq. [7] and [8].

The diffusion constants in Table III exhibit a temperature dependence, Fig. 4, which can be represented by

$$D = 0.0260 e^{-6800/RT} \text{ (cm}^2\text{/sec)} \tag{9}$$

The activation energy obtained, 6800 cal, is identical with that calculated by Barrer (4) by averaging the data from both high- and low-temperature measurements; since the data Barrer used were rather discordant and since our temperature range is so narrow, and the activation energy is obtained from a third

Table II. Slope and intercept of Eq. [6] as functions of L and T

L Temp, °C	0.003 in.		0.005 in.		0.010 in.	
	S_1	I_1	S_1	I_1	S_1	I_1
3.6	9.20	6.77	13.76	11.29	28.76	22.54
6.7	7.81	6.32	12.79	9.47	25.44	19.20
12.2	6.24	5.20	9.43	8.23	19.78	15.40
15.3	5.43	4.70	8.51	7.16	16.97	13.71

I_1 in cm²/amp; S_1 in cm²/amp-atm^{1/2}.

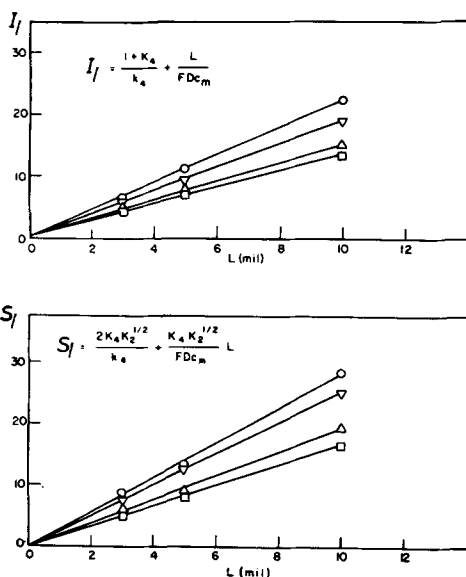


Fig. 3. (top) I_1 vs. L . (bottom) S_1 vs. L . \circ , 3.6°C; ∇ , 6.7°C; \triangle , 12.2°C; \square , 15.3°C.

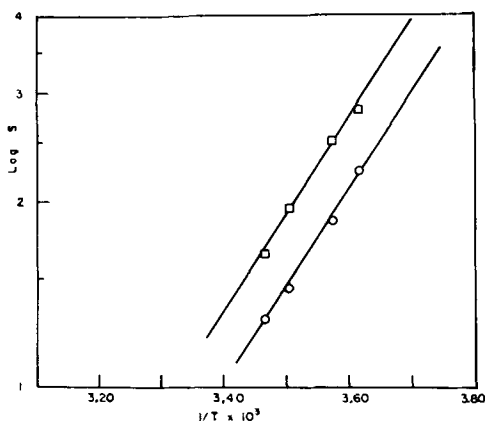


Fig. 4. Temperature dependence of D and $K_4K_2^{1/2}$. \circ , $S = 1/FDC_m$; \square , $S = K_4K_2^{1/2}/FDC_m$.

differentiation the agreement can only be regarded as fortuitous. More recently, Toda (5) found an activation energy of 5650 cal from a gas phase experiment in the range from 170° to 290°C.

The value of the composite equilibrium constant, $K_4K_2^{1/2}$, shows no consistent temperature dependence and is very nearly constant (Fig. 4). For purposes of argument we take the average value, 1.31, as independent of temperature.

The evaluation of k_4 , k_{-4} , K_4 , and $K_2^{1/2}$, individually requires the use of the values in the last two columns of Table III. These values are scattered and show no consistent temperature dependence. Since they are obtained from a second differentiation of the data they are highly inaccurate; the data fit nearly as well if all the entries in the last two columns of Table III are taken as zero. If we use the average values to attempt to gain a rough estimate of the general magnitude of the constants, we obtain: $k_4 = 12$ amp/cm²; $K_4 = 5.2$; $K_2^{1/2} = 0.25$ atm^{-1/2}. Using these values in Eq. [4] and [5], we calculate at 1 atm pressure: $\theta_0 = 0.20$; $u_0 = 0.57$; and $i_{40} = 0.8$ amp/cm². The value of θ_0 seems low but is not impossible. At 1 atm and 25°C the measured value of $u_0 = 0.69$; this would correspond to a value of $K_4K_2^{1/2} = 2.22$, indicating an error of about 40% in the value, 1.31, obtained here. The average standard deviation of the slopes of Eq. [7] is about 1/2 that of the slopes of Eq. [8]. Using this fact and the error of 40% in the value of $K_4K_2^{1/2}$ we estimate the error in the diffusion coefficient at about 17%.

Table III. Slope and intercept of D and $K_4K_2^{1/2}$

Temp, °C	$D \times 10^7$, cm ² /sec	$K_4K_2^{1/2}$, atm ^{-1/2}	$(1 + K_4)/k_4$, cm ² /amp	$2K_4K_2^{1/2}/k_4$, cm ² /amp-atm ^{1/2}
3.6	1.05	1.26	0.02	0.24
6.7	1.26	1.35	0.40	0.22
12.2	1.62	1.35	0.89	0.05
15.3	1.82	1.28	0.77	0.38
25.0	2.76*			
Average values:		1.31	0.52	0.22

* Extrapolated value; Eq. [9].

The value, $i_{40} = 0.8$ amp/cm², although only a crude estimate is probably lower than the true value, since we can fit the data fairly well with i_{40} infinitely large. The data do show, through the pressure dependence, that this penetration-exit reaction, $H_{ad} = H$ (bulk M), is slower than the combination reaction, $2H_{ad} = H_2$ (surf). In our experiments the rate of transmission is almost completely limited by the diffusion through the metal.

Poisoning

The work in Part II has been criticized privately on the grounds that flaming the metal in a gas flame (Meker burner) poisons the surface. Consequently, we used the hydrogen-oxygen flame in the work reported here. For comparison we did some experiments on pressure dependence with foils flamed in the Meker burner. In Fig. 5 the dependence of $-1/j_m$ on $p^{1/2}$ is shown for 0.005 in. foils. The slope of the line for the gas-flamed foils is about 1/2 that for the hydrogen-oxygen flamed foils; and the transmission is 15-25% less for the gas-flamed foils. Our results for the temperature dependence are fragmentary but indicate that the temperature dependence is approximately the same for both methods of preparation.

We also observed some instances of poisoning of foils which had been flamed in the hydrogen-oxygen flame in which the transmission was extremely low indicating a highly poisoned surface. In some of these cases the amount of hydrogen transmitted was immeasurably small. There was evidence that the unit holding the foil had leaked and permitted contamination of the foil from the brass fittings. The pressure dependence of the transmission for these cases (0.003 in. foils) is also shown in Fig. 5, the curves labeled "Poisoned." In these cases the rates of transmission are about half the value ordinarily observed (curves labeled "Nonpoisoned") and are nearly independent of pressure indicating that the combination reaction is slower than the penetration-exit reaction. Since the

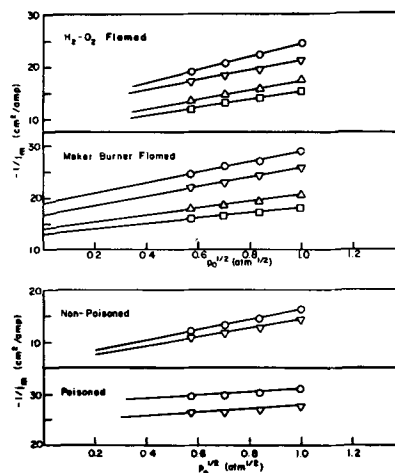


Fig. 5. Effect of poisoning. \circ , 3.6°C; ∇ , 6.7°C; \triangle , 12.2°C; \square , 15.3°C.

exchange current for the combination reaction is proportional to θ^2 and that for the penetration-exit reaction is proportional to θ , poisoning (which decreases θ) slows the combination reaction more than it does the penetration-exit reaction. Thus poisoning may make the rates of these two reactions comparable to each other or may even make the combination reaction much slower than the penetration-exit reaction.

In view of the results obtained here, we believe that the results obtained on gas-flamed foils in Part II are not correctly interpreted by either of the extreme choices, slow combination or slow penetration-exit, but probably represent an intermediate case in which these two reactions have comparable values of their exchange currents.

Acknowledgments

This research was supported by the Air Force Office of Scientific Research, and was completed while one of the authors (G.W.C.) was a National Science Founda-

tion Postdoctoral Fellow at the Max Planck Institut für physikalische Chemie, Göttingen.

Manuscript received May 31, 1963; revised manuscript received Feb. 4, 1964. Taken in part from a dissertation submitted by one of the authors (P.L.D.) to the Faculty of the Graduate School of Arts and Sciences of The Catholic University of America in partial fulfillment of the requirements for the Ph.D. degree.

Any discussion of this paper will appear in a Discussion Section to be published in the June 1965 JOURNAL.

REFERENCES

1. G. W. Castellan, *This Journal*, **111**, 1273 (1964).
2. R. A. LaPietra and G. W. Castellan, *ibid.*, **111**, 1276 (1964).
3. H. B. Wahlin and V. O. Naumann, *J. Appl. Phys.*, **24**, 42 (1953).
4. R. M. Barrer, "Diffusion in and through Solids," p. 221, Cambridge (1951).
5. G. Toda, *J. Res. Inst. Cat., Hokkaido Univ.*, **6**, 13 (1958).

Cathodic Action of the Uranyl-Malate Complexes at the Dropping Mercury Electrode

Tsai-Teh Lai and Song-Jey Wey

Department of Chemical Engineering, Cheng Kung University, Tainan, Taiwan, China

ABSTRACT

The uranyl ion in malic acid solution has been investigated by polarography and conductometry. Evidence has been presented for the existence of three kinds of chelate species, $\text{UO}_2(\text{HA})_2$, $\text{UO}_2(\text{A})_2^{-2}$, and $\text{UO}_2(\text{OH})\text{A}_2^{-3}$. Their structures and electrode reactions at various pH values have been established. In the temperature range from 9.1° to 21.5°C the chelates exist as a dimer. On raising the temperature to 28.5°C the depolymerization takes place completely to form a monomer.

Feldman, Havill, and Neuman (1, 2) have investigated the uranyl-malate complexes by titrimetric and spectrophotometric methods and have shown that at pH 3.5-4.5 a dimer having 1:1 and 1:2 molar ratio was produced, and at slightly alkaline pH these dimers reacted completely to form trinuclear complexes.

As a part of polarographic studies on the complexes of uranyl ion with carboxylic acids, the present paper describes the uranyl-malate system. The uranyl-lactate and uranyl-glycolate systems have been studied previously (3, 4).

Experimental

Polarograms were taken at $30^\circ \pm 0.1^\circ\text{C}$ using a capillary having a flow rate of 1.641 mg/sec and a drop time of 4.65 sec at -0.44 v vs. S.C.E. The apparatus and procedure have been reported elsewhere (3, 4).

An Industrial Instruments conductivity bridge Type RC with a cell having a cell constant of 0.13 was used for the conductometric titration.

A 0.9786M stock solution of malic acid was prepared by dissolving 66.95g of malic acid (Kanto Chemical Company, Inc., special grade) in recently boiled distilled water to 500 ml and was standardized by titration with carbonate-free sodium hydroxide solution.

Triton X-100 (0.002%) was used as a maximum suppressor and 0.2M sodium perchlorate solution was used as supporting electrolyte.

Results and Discussion

It is evident from Table I that reversibility holds for a wide range of ligand concentration (from 0.05 to 0.40M at pH lower than 5.7). The values of $E_{1/4}$ — $E_{3/4}$ and slopes of the conventional log plots averaged -0.057 and -0.059 v, respectively. They are in excel-

lent agreement with the theoretical values for a reversible one-electron reduction.

The value of $id/h^{1/2} = 0.667 \pm 0.004$ and the temperature coefficient of diffusion current, 0.3% per °C,

Table I. Half-wave potential dependence on pH and $C_{\text{H}_2\text{A}}$ and test for reversibility of electrode reaction $1.0 \times 10^{-3}\text{M UO}_2(\text{ClO}_4)_2$, 0.2M NaClO_4 , and 0.002% Triton X-100 (at $30^\circ \pm 0.1^\circ\text{C}$)

$C_{\text{H}_2\text{A}}$ (M)	pH	$-E_{1/2}$ vs. S.C.E.	$E_{1/4} - E_{3/4}$	Slope of log plot	i_d , μa
0.05	1.50	0.180	0.059	0.059	2.76
	2.05	0.200	0.060	0.059	3.20
	2.68	0.280	0.059	0.059	4.10
	3.36	0.357	0.059	0.059	4.57
	4.11	0.397	0.055	0.057	4.55
	4.95	0.457	0.055	0.056	3.70
	5.71	0.484	0.056	0.058	3.30
	5.80	0.503	0.056	0.055	2.18
	2.00	0.220	0.058	0.058	3.81
	2.97	0.334	0.057	0.058	4.60
0.10	3.26	0.356	0.058	0.058	4.55
	3.47	0.385	0.055	0.056	4.80
	4.20	0.426	0.055	0.057	4.34
	4.91	0.465	0.057	0.059	3.25
	5.50	0.499	0.057	0.056	2.96
	1.40	0.191	0.060	0.060	4.20
	2.05	0.250	0.059	0.058	4.50
	2.78	0.329	0.060	0.059	4.55
	3.09	0.374	0.057	0.058	4.40
	3.72	0.414	0.058	0.059	3.90
0.20	4.43	0.453	0.059	0.058	3.40
	5.01	0.484	0.056	0.055	3.20
	5.61	0.510	0.054	0.055	2.10
	1.85	0.264	0.056	0.059	4.30
	2.05	0.302	0.058	0.058	4.30
	2.26	0.322	0.056	0.058	4.20
	3.15	0.401	0.060	0.058	3.85
	3.65	0.445	0.059	0.058	3.75
	4.50	0.488	0.055	0.058	3.00
	5.05	0.508	0.055	0.057	2.40

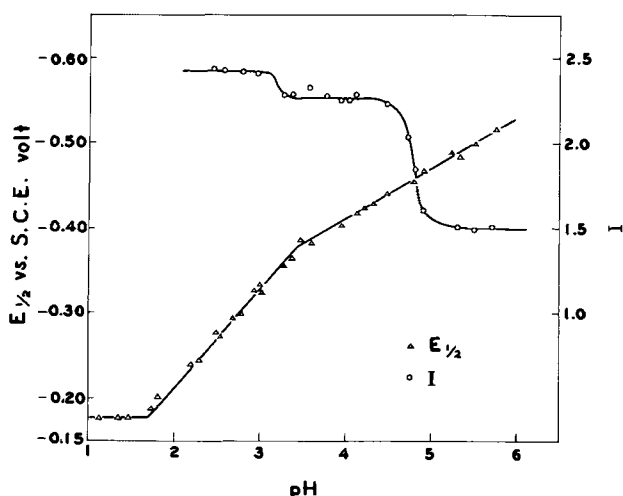


Fig. 1. Effect of pH on half-wave potential and diffusion current constant. 1.0 mM $\text{UO}_2(\text{ClO}_4)_2$, 0.1M malic acid, 0.2M NaClO_4 , and 0.002% Triton X-100.

indicated that the limiting current was diffusion controlled.

Effect of pH.—The effect of pH on the half-wave potential and diffusion current constant of uranyl-malate complexes was investigated with the results shown in Fig. 1. At pH lower than 1.78 the half-wave potentials remain constant at $-0.175\text{v vs. S.C.E.}$. This value is equal to the first half-wave potential of the simple uranyl ion (5), showing that no chelate was formed. In the pH range 1.78-3.26 the slope of the straight line is -0.012 , indicating that two hydrogen ions per uranyl ion participate in the reduction. In the pH range 3.26-5.75 the slope of the line, -0.060 , gives a value of 1.0 for the number of hydrogen ions involved or for the number of hydroxyl ions produced in the electrode reaction.

Effect of malate.—The composition of the uranyl-malate complexes was studied by measuring the variation of half-wave potential with malic acid concentration in solution at various pH values (Fig. 2).

It has been shown (6) that if the half-wave potentials of the complexes are plotted against the logarithm of chelating agent concentrations, the slope of straight line should be $-(p - q)0.060$, where $(p - q)$ is the difference in number of ligands attached between U(VI) and U(V) chelate.

As shown in Fig. 2 the slopes of straight lines are 0.00, -0.12 , -0.06 , and -0.06 corresponding to values of 0, 2, 1, and 1, respectively, for $p - q$.

Metal-ligand ratio.—The conductometric titration method was employed to determine the metal-ligand ratio of the uranyl-malate complexes. In Fig. 3 curves 1 and 2 show results of conductometric titration of the

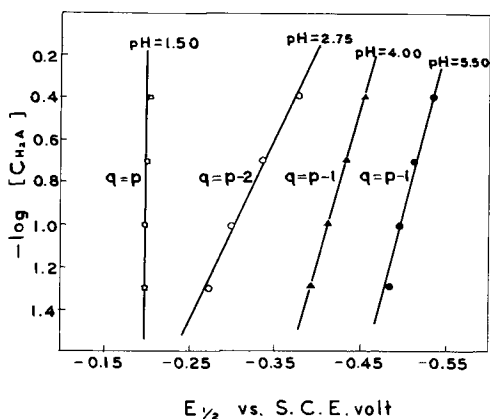


Fig. 2. Effect of ligand concentration on half-wave potential

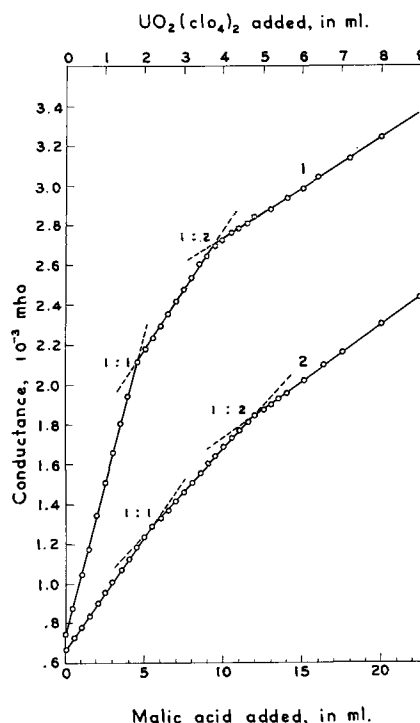


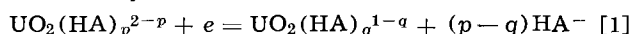
Fig. 3. Conductometric titration. Curve 1, 5.0 ml of 10 mM $\text{UO}_2(\text{ClO}_4)_2$ + 160 ml of H_2O + x ml of 10.71 mM malic acid; curve 2, 5.0 ml of 10.71 mM malic acid + 200 ml of H_2O + x ml of 10 mM $\text{UO}_2(\text{ClO}_4)_2$.

uranyl ion against malic acid and malic acid against uranyl ion, respectively.

Two well-defined breaks corresponding to a 1:1 complex when the uranyl ion is in excess and a 1:2 complex when the malate ion is in excess were obtained. This result is in good agreement with that of Feldman which was obtained by a spectrophotometric method (1, 2).

Chelate species and electrode reactions.—As shown in Fig. 1 the diffusion current constants are 2.43 for the pH range 1.78-3.26, 2.25 for the pH range 3.26-4.68, and 1.50 for the pH range 4.68-5.75. This shows that three kinds of chelate species exist at the respective pH region.

If the ligand is hydrogen malate anion, the general equation for the reduction of uranyl hydrogen malate chelate may be written



The half-wave potential for the above reaction can be expressed as (6)

$$(E_{1/2})_c = \text{const.} - 0.060(p - q) \log C_{\text{H}_2\text{A}} - 0.060(p - q) \log \frac{[\text{H}^+]}{[\text{H}^+]^2 + K_1[\text{H}^+] + K_1K_2} \quad [2]$$

where $C_{\text{H}_2\text{A}}$ is the total concentration of added malic acid.

We may distinguish three cases according to the pH value of the solution: (a) $\text{pH} < \text{p}K_1$ (3.26) (7), (b) $\text{p}K_1 < \text{pH} < \text{p}K_2$ (4.68) (7), and (c) $\text{pH} > \text{p}K_2$. In these cases Eq. [2] simplifies to

$$(a) (E_{1/2})_c = \text{const.} - 0.060(p - q) \log C_{\text{H}_2\text{A}} - 0.060(p - q)\text{pH} \quad [3]$$

$$(b) (E_{1/2})_c = \text{const.} - 0.060(p - q) \log C_{\text{H}_2\text{A}} \quad [4]$$

$$(c) (E_{1/2})_c = \text{const.} - 0.060(p - q) \log C_{\text{H}_2\text{A}} + 0.060(p - q)\text{pH} \quad [5]$$

These equations reveal that the plots of $(E_{1/2})_c$ vs. pH should break at $\text{p}K_1$ and $\text{p}K_2$, and that the slopes of each line should be $-0.060(p - q)$, zero, and $+0.060(p - q)$ for (a), (b), and (c), respectively.

If the ligand is the malate ion rather than the hydrogen malate anion, the slope would be -0.120

Table II. Experimental summarized

pH	$\Delta E_{1/2}/\Delta pH$	H ⁺ or OH ⁻ involved	$\Delta E_{1/2}/\Delta \log C$	$p - q$	Theoretical value of $\Delta E_{1/2}/\Delta pH$ $UO_2(HA)_2$	Theoretical value of $\Delta E_{1/2}/\Delta pH$ $UO_2(A_2)^{-2}$	Ligand species
1.78	0	0	0	0			
3.26-1.78	-0.12	2	-0.12	2	-0.060 $\times (p - q)$	-0.120 $\times (p - q)$	HA ⁻
4.68-3.26	-0.06	1	-0.06	1	0	-0.060 $\times (p - q)$	A ⁻²
5.75-4.68	-0.06	1	-0.06	1	+0.060 $\times (p - q)$	0	A(OH) ⁻³

($p - q$), $-0.060 (p - q)$, and zero for the same three pH conditions.

From Fig. 1 and 2, in the pH range 1.78-3.26, the value of $\Delta E_{1/2}/\Delta pH$ is -0.012 and $p - q = 2$, corresponding to a slope of $-0.060 (p - q)$. This proves that the ligand is the hydrogen malate anion. In the pH range 3.26-4.68, the value of $\Delta E_{1/2}/\Delta pH$ is -0.060 and $p - q = 1$, corresponding to a slope of $-0.060 (p - q)$. Therefore, the ligand is the malate ion. Beyond pH 4.68, the hydroxylation of ligand species was identified by the sudden drop of the diffusion current constant.

Results based on the foregoing data and discussion are summarized in Table II. Thus, the presence of the three chelate species of $UO_2(HA)_2$, $UO_2(A)_2^{-2}$, and $UO_2(OH)A_2^{-3}$ are identified, and the electrode reactions can be formulated as

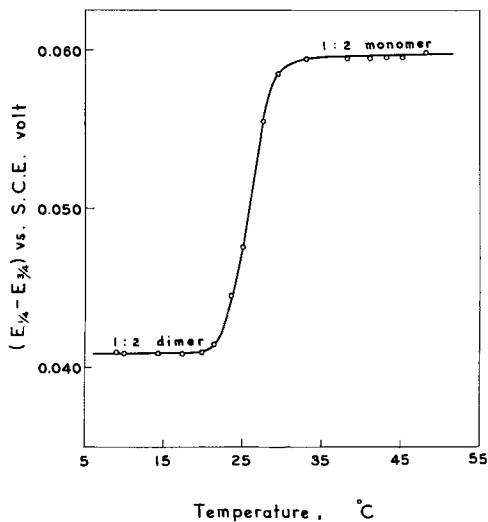
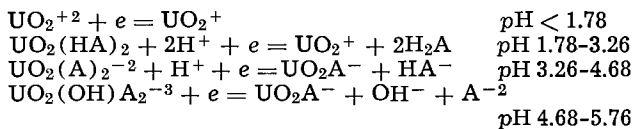
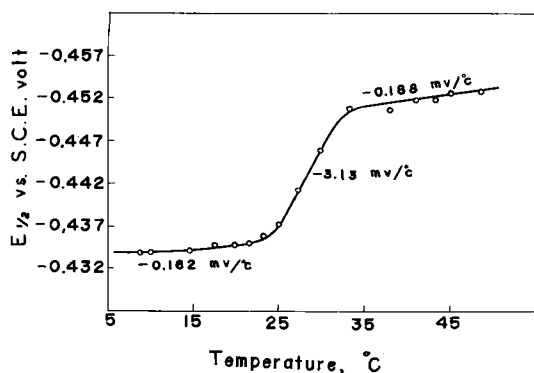
Fig. 4. Plot of $E_{1/4} - E_{3/4}$ as a function of temperature

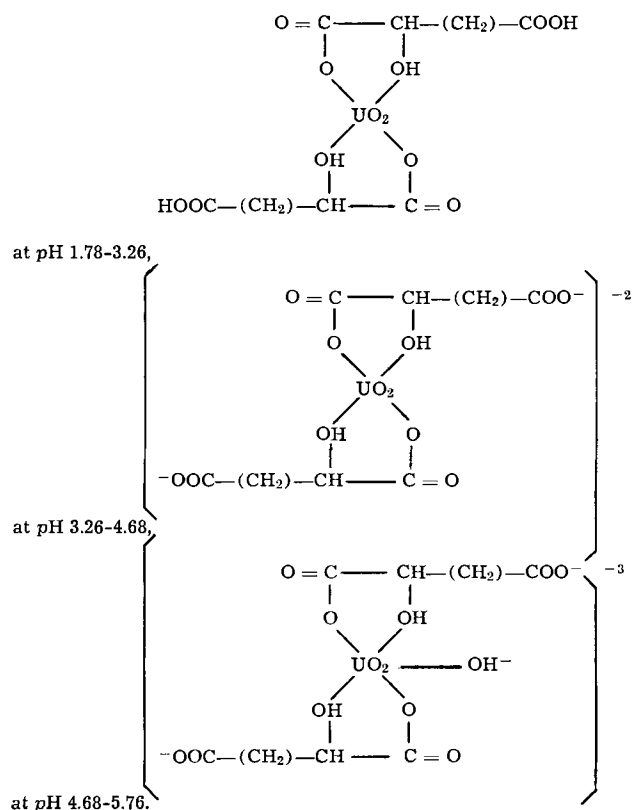
Fig. 5. Plot of half-wave potential against temperature

Probable structure.—Since malic acid is a tridentate ligand with two carboxyl and one hydroxyl groups, the uranyl-malate chelate may be either a five-membered ring or a six-membered ring.

Pfeiffer (8) has shown that, in general, a five-membered ring is more stable when the ring is entirely saturated, but that a six-membered ring is favored when one or more double bonds are present.

In considering the statistical effect of two carboxylate groups in each malate anion being available to a uranyl ion, the chelation of UO_2^{+2} with hydroxyl and γ -carboxylate groups would introduce a six-membered ring and results in a decrease in stability. Thereby, a five-membered ring was considered as the most probable structure of uranyl-malate chelate.

The evidence presented above suggests that the structures of 1:2 mononuclear uranyl-malate chelates at different pH ranges are



Effect of temperature.—The effect of temperature on the value of $E_{1/4} - E_{3/4}$ and the half-wave potential was investigated polarographically on a solution of 1.0 mM uranyl perchlorate solution in 0.1M malic acid, 0.2M sodium perchlorate, and 0.002% Triton X-100 at pH 4.5, and varying the temperature from 9.1° to 48.5°C (Fig. 4 and 5).

As shown in Fig. 4, in the temperature region 9.1°-21.5°C, the mean $E_{1/4} - E_{3/4}$ value of the polarograms is $0.041 \pm 0.01v$. It was presumed to be a reversible process by the temperature coefficient of half-wave potential, $-0.162 \text{ mv}/^\circ\text{C}$, in Fig. 5. The deviation of $E_{1/4} - E_{3/4}$ value from the theoretical value of 0.057v

Table III. Estimation of polymerization degree

Temperature, °C	$\frac{E_{1/2} - E_{7/8}}{E_{1/8} - E_{1/2}}$	$E_{1/4} - E_{3/4}$	a	b
9.1	1.00	0.040	1.43	1.43
10.0	1.03	0.041	1.27	1.40
14.5	1.03	0.041	1.27	1.40
17.5	1.00	0.040	1.43	1.43
20.0	0.97	0.041	1.37	1.37
21.5	1.02	0.042	1.44	1.45

for one electron reduction was no doubt due to the polymerization effect which arose from the asymmetry of the polarograms (3).

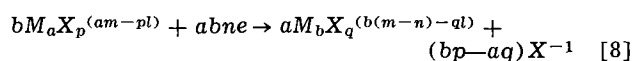
The degree of polymerization can be evaluated by application of Eq. [6] and [7] as derived by authors (3)

$$\frac{E_{1/2} - E_{7/8}}{E_{1/8} - E_{1/2}} = \frac{243 + 602(b/a)}{243(b/a) + 602} \quad [6]$$

and

$$E_{1/4} - E_{3/4} = \frac{1}{b} 0.028 \left(1 + \frac{b}{a} \right) \quad [7]$$

Here a and b are the values in the electrode reaction



The results obtained are illustrated in Table III. It can be seen that in the temperature region 9.1°-21.5°C a partial polymerization occurred forming a dimer. This result is in excellent agreement with that of the spectrophotometric studies of Feldman and his co-workers (2).

When the temperature is increased from 21.5° to 28.5°C, the value of $E_{1/4} - E_{3/4}$ increases from 0.042 to 0.056v and the shape of wave becomes more sym-

metrical. This indicates that the depolymerization of the chelates from dimer to monomer takes place in this temperature region. The abrupt increase of the temperature coefficient of half-wave potential to -3.13 mv/°C reflects the irreversible nature of the waves. This large change is quite reasonable in the transition temperature region from dimer to monomer.

Finally, on raising the temperature from 28.5° to 48.5°C, the depolymerization of chelates from dimer to monomer becomes complete, and the irreversible process becomes a reversible one. This is evidenced by the constant value of $E_{1/4} - E_{3/4}$ of 0.058 ± 0.01 v, and the symmetry of the waves. In addition, the decrease of the temperature coefficient of half-wave potential from -3.13 to -0.188 mv/°C provides another proof of this change.

Acknowledgment

The authors thank the National Council on Science Development, which supported the work described.

Manuscript received Jan. 15, 1964; revised manuscript received May 11, 1964.

Any discussion of this paper will appear in a Discussion Section to be published in the June 1965 JOURNAL.

REFERENCES

1. I. Feldman and J. R. Havill, *J. Am. Chem. Soc.*, **76**, 2114 (1954).
2. I. Feldman, J. R. Havill, and W. F. Neuman, *ibid.*, **76**, 4726 (1954).
3. T. T. Lai and B. C. Wang, *Anal. Chem.*, **35**, 905 (1963).
4. T. T. Lai and B. C. Wang, *ibid.*, **35**, 1531 (1963).
5. W. E. Harris and I. M. Kolthoff, *J. Am. Chem. Soc.*, **67**, 1484 (1945).
6. I. M. Kolthoff and J. J. Lingane, "Polarography," Interscience Publishers, Inc., New York (1952).
7. R. K. Cannon and A. Kirbrick, *J. Am. Chem. Soc.*, **60**, 2314 (1938).
8. P. Pfeiffer, *Angew. Chem.*, **53**, 93 (1940).

Preparation and Surface Area Measurements of Platinized-Platinum Electrodes

M. J. Joncich¹ and Norman Hackerman

University of Texas, Austin, Texas

ABSTRACT

Platinized-platinum electrodes were prepared under varying conditions of geometry, composition of the plating solution, time of plating, and current density. Surface areas of the platinized electrodes were measured by krypton adsorption using the BET method as well as by a modification of the method of Bowden-Rideal. Good agreement between the two methods was observed. The measured values of the specific surface areas of the platinum deposits were functions of all of the variables considered.

Because of a need for platinized-platinum electrodes of known absolute surface areas for use in catalytic-electrochemical studies, a number of electrodes were prepared under a variety of conditions, and the surface areas were measured using two different and independent methods. Although some studies have been carried out on the surface areas of electrodes of this type (1-5), no systematic investigations involving the preparation of such electrodes are known. We wished to prepare platinized-platinum electrodes reproducibly and, if possible, to determine the factors governing the specific surface areas (cm²/g) of the deposits. Although the methods discussed are well known, recent interest in surface area measurements of porous

electrodes has led to the encouragement of publication of these results.

Surface Area Measurements

Since physical adsorption of gases is well established as the "primary standard" of surface area measurement as given by Brunauer, Emmett, and Teller (6), this method as modified by the use of krypton for the adsorbate (7) was the primary means of surface area determination. Beebe *et al.* (7) used a McLeod gauge for the pressure measurements, while Rosenberg (8) developed a thermistor method for measurement of the krypton pressures. In the work described here an especially designed, small-volume McLeod gauge was used for pressure measurements and was found to give very satisfactory results. The advantages of using

¹ Present address: Department of Chemistry, Northern Illinois University, DeKalb, Illinois.

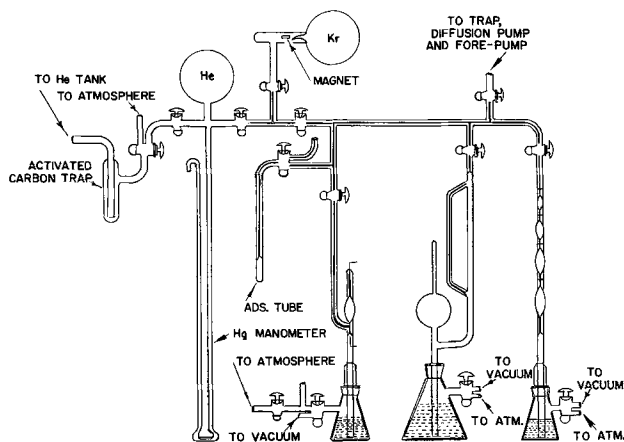


Fig. 1. Krypton adsorption apparatus showing traps, gas storage vessels, adsorption tube, McLeod gauges, and calibrated bulbs.

krypton as the adsorbate for small total surface area samples are well known (7-12), and the impracticality of attempting to determine nitrogen adsorption by pressure measurements when the total surface area is less than 1000 cm² is well established.

The adsorption apparatus is shown in Fig. 1. Two McLeod gauges were used; the larger to measure pressure during evacuation of the system and the smaller, designed to read accurately pressures in the range 0.01-2.0 mm Hg, for pressure readings before and after adsorption. Tungsten leads, which were part of a circuit that caused a light to come on when mercury touched both contacts, were introduced in the smaller McLeod gauge (13), and the mercury level was followed by a traveling microscope. A series of four accurately calibrated bulbs were used to change the pressure of the krypton in going from adsorption at lower pressure to higher pressure. The total volume of the system was 17 ml in a typical run. Total surface areas as small as 50 cm² could be measured. Corrections for adsorption on the glass of the system (10-20 cm²) were also necessary. Adsorptions at two to four pressures were carried out for each surface area determination.

Since 2 mm ID capillary tubing was used throughout, the effect of thermal transpiration (8, 14) had to be considered. The corrections are greatest at the lowest pressures used (0.1 mm) and became negligible at the upper limit of adsorption measurements (1.0 mm). Neglect of this factor introduced errors as large as 5% at the lower pressures for this particular system.

Helium gas (highest grade, U. S. Bureau of Mines) was used in the degassing process preceding the surface area measurements. Krypton gas was obtained in a sealed glass bulb from the Lamp Division of the General Electric Corporation and was said to be free of active gases and to contain less than 0.1% xenon. The krypton was used as is; the helium was passed through an activated charcoal trap surrounded by liquid nitrogen prior to use. An oxygen vapor pressure thermometer (15) was used to measure the temperature of the liquid nitrogen surrounding the adsorption tube.

Mercury cut-offs were not required. Good grade vacuum stop-cocks were used throughout and gave satisfactory results. Equipment used but not shown in Fig. 1 are liquid nitrogen traps, mercury diffusion pump, oil pump, oxygen vapor pressure thermometer, and traveling microscope.

The form of the BET equation applied to the data is given by Eq. [1]

$$\frac{P}{V(P_0 - P)} = \frac{1}{V_m C} + \frac{C-1}{V_m C} \frac{P}{P_0} \quad [1]$$

where V is the quantity of gas at STP which is adsorbed at the pressure P , V_m is the quantity of gas

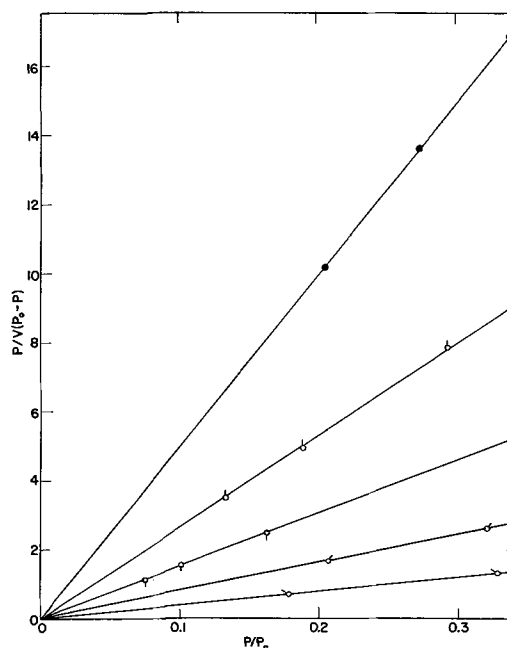


Fig. 2. BET plots for samples of total areas of 0.57, 0.82, 3.3, 6.4, and 8.7 m² (top to bottom).

(STP) which forms a monolayer on the surface, P_0 is the vapor pressure above the condensed phase of the adsorbate (krypton) at the adsorption temperature, and C is a constant related to the energetics of the adsorption process.

Plots of $P/V(P_0 - P)$ as a function of P/P_0 resulted in straight lines with rather small intercepts. Some typical plots are shown in Fig. 2 for platinized-platinum electrodes ranging in specific surface area from 0.11 to 1.6 m²/g. The straight lines were drawn visually since the deviation from linearity was very small and great accuracy was not required. On the basis of a rather large number of surface area determinations it was established that the system used is suitable, that reproducibility is good (<5% deviation on different determinations of the same sample), and that small total surface areas as obtained in platinized-platinum deposits could be measured accurately if the total area were greater than 50 cm².

Since the BET method is laborious (3-4 hr per determination) and is limited in so far as minimum surface area that can be measured is concerned, an attempt was made to apply an electrochemical method which would be more convenient, simple and capable of measuring extremely small (1-50 cm²) total surface areas. The method of Bowden-Rideal (16) as modified by Wagner (17) and Pegues (18) served as the basis for some limited experiments in the rise of polarization capacity as a means of surface area measurement. The method is based on the principle that the surface area of an electrode is related to the rate of change of cathodic potential and constant current. More refined determinations have subsequently been carried out (2, 4, 5) which yielded better results at the expense, however, of requiring more complex equipment.

One additional means was attempted, namely, correlation of the rate of dissolution of platinized-platinum electrodes in aqua regia with the surface area. This was unsuccessful, however, since the dissolution ability of the aqua regia changed rapidly with time.

Preparation of Platinized-Platinum Electrodes

Figure 3 shows schematic drawings of the various systems that were used to prepare samples of platinized-platinum. Each was designed in an attempt to remove limitations which existed in previous systems. Figure 3A and 3B show Lucite supports that were used to space rectangular pieces of platinum foil during the

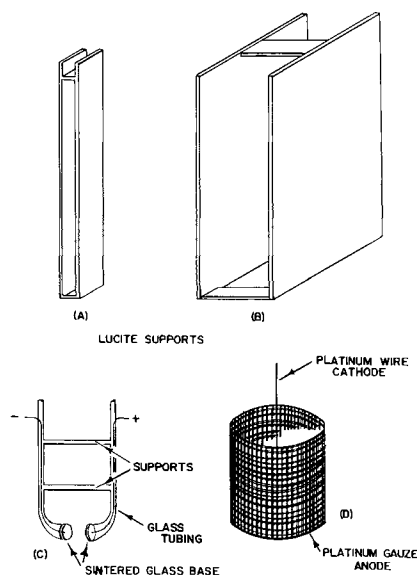


Fig. 3. Plating systems used for preparing platinized-platinum electrodes.

electrodeposition process. In Fig. 3A platinum foils of 0.85 x 7.6 cm were attached to the Lucite supports with Ucilon and platinum wire. Separation was 0.65 cm and no stirring other than bubbling gas evolved was used. A bank of lead storage batteries was used for the current source in all plating experiments. In all cases the temperature was maintained at $30^\circ \pm 1^\circ\text{C}$. Total surface areas of the samples were too small to be measured by the means used (nitrogen adsorption).

Using the supports shown in Fig. 3B, larger electrodes were prepared and the surface area was measured by krypton adsorption. The system shown in Fig. 3C was used primarily for measurements of surface area by the Bowden-Rideal method. Disks of 1.27 cm diameter wire were used with a separation between the disk of 1 cm. The system shown in Fig. 3D was the most satisfactory, since electrodes of the desired shape were prepared and the effect of edges (except for the bottom point) were eliminated. The anode used was 5 cm in diameter; the cathode was 37 mil platinum wire, 5 cm in length.

The system shown in Fig. 3B was used to prepare a number of platinized-platinum electrodes at various current densities and from solutions of differing composition. A paddle stirrer rotating at 25 rpm was used to agitate the plating solution. The apparent surface area of each electrode was 29 cm²; the solution was 0.86N HCl; the temperature was $30^\circ \pm 1^\circ\text{C}$; and the current densities ranged from 0.034 to 0.33 amp/cm². The platinized platinum electrodes were polarized cathodically until hydrogen was evolved. The surface area measurements were then carried out to a 0.1N H₂SO₄ solution at $25^\circ \pm 1^\circ\text{C}$.

Figure 4 summarizes the results obtained. The upper curve shows the values of specific surface areas as a function of current density for deposits obtained from 10.0% by weight chloroplatinic acid. The weights of the deposits ranged from 1 to 23g. The bottom curve shows the results obtained keeping all factors the same except that the chloroplatinic acid concentration was reduced to 4.39% by weight. To check the reproducibility of the surface area measurements, one point was repeated. Values of 0.41 m²/g and 0.40 m²/g were obtained. The reproducibility of the deposition process was determined using solution containing 4.4% chloroplatinic acid solution at an apparent current density of 0.15 amp/cm². The two surface areas were measured and values of 0.20 m²/g and 0.15 m²/g were obtained. In terms of roughness factors (true area divided by apparent area) the values are 620 and 350, respectively. The largest roughness factors were

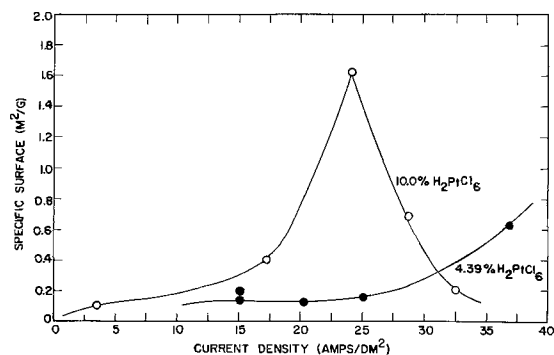


Fig. 4. Specific surface areas of platinized-platinum electrodes (m²/g) as a function of apparent current density (amp/cm²) at which electrodes were prepared.

slightly in excess of 3000. Large roughness factors were obtained only when large deposits were prepared (in excess of 20g of platinum); most values were considerably lower than the range of values (3900-20,000) reported by Brodd and Hackerman (2) and are more consistent with the values of roughness factors for platinized-platinum reported by Will (5). Most roughness factor values were in the range of 200-400.

There was considerable difference in the appearance of the electrodes prepared. Those deposits formed at the lower current densities were adherent. The deposits with the largest values for the roughness values were bright and nonadherent.

A direct comparison of the BET method and the Bowden-Rideal method was carried out using the electrode prepared at the lowest current density (Fig. 4). The BET and Bowden-Rideal values were 0.11 and 0.10 m²/g, respectively.

Using the system shown in Fig. 3C, three samples of platinized-platinum were prepared for which surface area values of 0.18, 0.18, and 0.13 m²/g were obtained by the Bowden-Rideal method. The current density was 0.24 amp/cm² and a solution identical to the one discussed previously (bottom curve, Fig. 4) was used. An indication of the reproducibility of the plating experiments can be obtained from these results. The agreement between the Bowden-Rideal surface area values and the value of the specific surface as obtained by gas adsorption (0.15 m²/g) is satisfactory.

During the course of this work it was noted that pure chloroplatinic acid solutions do not yield deposits of platinum that are black and adherent. Instead, using pure solutions, one obtains silvery-gray deposits which have a tendency to flake off the electrode. Similar results have been noted previously (19-21) and x-ray diffraction studies (22) have shown that some impurities (lead, mercury, thallium, cadmium) are incorporated into the lattice causing a widening of the crystal lattice, while other impurities (chromium, manganese, iron, cobalt, nickel, copper, zinc, palladium) are incorporated into the deposit and lead to diffraction lines indicating a contraction of the crystal lattice. Addition of salts of antimony, tin, bismuth, arsenic, and gold although modifying the nature of the deposit, did not alter the position of the diffraction lines.

Using the system shown in Fig. 4D a solution of 2.42% chloroplatinic acid solution modified by the addition of 0.001% lead acetate served as the plating solution. The deposits formed from this solution were black and adherent. The addition of the lead acetate, however, reduced the reproducibility of the plating process in terms of the specific surface areas as determined by krypton adsorption. At a current density of 0.21 amp/cm² and a plating time of 120 min, samples of specific surface areas of 0.29 and 0.68 m²/g were obtained. At 30 min plating time, deposits of 0.89 and 1.5 m²/g specific surface area were obtained. These results indicate extremely poor reproducibility even though

plating conditions for the different electrodepositions were maintained as constant as possible.

Conclusions

The experiments conducted lead us to the following generalizations regarding the measurements of surface areas and preparation of platinized-platinum electrodes:

1. BET and Bowden-Rideal surface area measurements can be used effectively for platinized-platinum electrodes. Agreement between the two methods is good.

2. The platinum deposits obtained in the initial stages of plating are of higher specific surface area than the material plated later.

3. In general, higher values of specific surface are obtained from solutions of higher chloroplatinic acid concentration.

4. Without addition agents (impurities such as lead acetate) the deposits obtained are not black or adherent. In solutions containing lead acetate the deposits are black, adherent, and generally of high specific surface area, but the reproducibility in terms of surface areas is poor.

5. Specific surface areas of platinized-platinum deposits prepared by electrodeposition are complex functions of a number of variables including geometry of the plating system, composition of the plating solution, time of plating, and current density. It appears, however, that for a particular system and solution there is an optimum current density at which deposits of maximum specific surface area are obtained.

Acknowledgment

The authors are grateful to the Naval Ordnance Laboratory for its financial support of this work and to R. J. Brodd for his assistance.

Manuscript received March 5, 1964. This paper was presented at the Boston Meeting, Sept. 16-20, 1962.

Any discussion of this paper will appear in a Discussion Section to be published in the June 1965 JOURNAL.

REFERENCES

1. E. B. Maxted, K. L. Moon, and Overgagge, *Discussions Faraday Soc.*, **8**, 135 (1950).
2. R. J. Brodd and N. Hackerman, *This Journal*, **104**, 704 (1957).
3. A. K. Wiebe and C. A. Winpler, *Can. J. Chem.*, **31**, 665 (1953).
4. J. J. McMullen and N. Hackerman, *This Journal*, **106**, 341 (1959).
5. F. G. Will, *ibid.*, **110**, 145 (1963).
6. S. Brunauer, P. H. Emmett, and E. Teller, *J. Am. Chem. Soc.*, **60**, 309 (1938).
7. R. A. Beebe, J. B. Beckwith, and J. M. Honig, *ibid.*, **67**, 1554 (1945).
8. A. J. Rosenberg, *ibid.*, **78**, 2929 (1956).
9. J. M. Haynes, *J. Phys. Chem.*, **66**, 182 (1962).
10. G. L. Gaines, Jr., and P. Cannon, *ibid.*, **64**, 997 (1960).
11. R. A. Pierotti and G. D. Halsey, Jr., *ibid.*, **63**, 680 (1959).
12. R. A. W. Haul, *Angew. Chem.*, **68**, 238 (1956).
13. C. Kenty, *Rev. Sci. Instruments*, **22**, 217 (1951).
14. M. J. Bennett and F. C. Tompkins, *Trans. Faraday Soc.*, **53**, 185 (1957).
15. A. Farkas and H. W. Melville, "Experimental Methods in Gas Reactions," p. 104, McMillan Co., London (1939).
16. F. P. Bowden and E. K. Rideal, *Proc. Roy. Soc. (London)*, **120A**, 59 (1928).
17. C. Wagner, *This Journal*, **97**, 72 (1950).
18. B. Pegues, M. A. Thesis, University of Texas (1951).
19. W. M. MacNevin and M. Levitsky, *Anal. Chem.*, **24**, 973 (1952).
20. H. T. Beans and L. P. Hammett, *J. Am. Chem. Soc.*, **47**, 1215 (1925).
21. L. P. Hammett and A. E. Lorch, *ibid.*, **55**, 70 (1933).
22. G. Bianchi, *Ann. Chim. (Rome)*, **40**, 222 (1950).

Kinetics of Recombination of Frenkel Defects in Anodic Oxide Films on Tantalum

L. Young

Department of Electrical Engineering, The University of British Columbia, Vancouver, B. C., Canada

ABSTRACT

The changes with time in the ionic conductivity of anodic oxide films on tantalum have been investigated. The results are discussed in relation to the theory that Frenkel defects are present in the films and that they recombine due to the electrostatic attraction between the vacant cation sites and the interstitial ions.

In the ionic conduction process which occurs during the growth of anodic oxide films (1) on tantalum, the fields are high enough for an exponential rather than an ohmic dependence of current on field, and the transient behavior indicates that the concentration of mobile ions is a function of the applied field, taking up its new value relatively slowly when the field is suddenly changed. The probable explanation of the transients [Bean, Fisher, and Vermilyea (2), Dewald (3)] is that the high fields produce Frenkel defects by pulling ions out of network positions and depositing them in interstitial positions where they are mobile. The recombination process which occurs during the passage of current is probably the extraction of ions from the current by the vacancies in a capture cross-section process. In the present work the mechanism of recombination was studied with zero field applied, that is, no ionic current. In these circumstances recombination is still expected but due to a different mechanism.

The electrostatic attraction between the positively charged mobile tantalum ions and the cation vacancies (which may be assumed, in the usual way, to have a negative charge) is expected to cause interstitial ions to migrate toward neighboring vacancies. Previous work includes papers by Vermilyea (4, 5) and some unpublished experiments by the late J. F. Dewald, formerly at Bell Telephone Laboratories. The changes in dielectric properties with time (6, 7) are evidently associated with related structural changes in the films.

Experimental Procedure

Anodic oxide films were grown either at constant current or at constant applied potential on chemically polished electrodes immersed in approximately 1 weight per cent H₂SO₄. When the voltage and current were, say, V₁ and i₁, respectively, (V₁ being 50 to 150v, i₁ from a few μa cm⁻² to a few ma cm⁻²), the tantalum electrodes were short circuited to a large

platinized platinum subsidiary electrode. The solution was kept saturated with hydrogen, so that this electrode took up the hydrogen potential in the given solution. The field in the oxide was thus maintained at effectively zero (so far as normal ionic conduction is concerned) for a definite time ranging from a few milliseconds to a few hours. A voltage V_2 (usually equal to V_1) was then reapplied. After the large capacitor-charging current had died away, the ionic current could be observed to be increasing with time. By back extrapolation to the time at which the voltage was applied, an estimate was obtained of the instantaneous value i_2 of the ionic current. The new ionic current was always less than that flowing at the same voltage before the period at zero field, since, as it is supposed, the concentration of mobile ions decreases because of the recombination process. It is postulated that i_2/i_1 is equal to the ratio of the concentration of defects remaining after time t to that initially present.

The principal difficulty is in the extrapolation. As has been noted previously (8) the capacitor-charging current tends to be anomalously prolonged. This limits the accuracy of the extrapolation, which is, nevertheless, sufficiently good to show the main features of the recombination process. Possibly this effect is related to the space charge effects studied by Dreiner (9).

A timing device was built for this work by E. M. Edwards. The currents were recorded either on a Sanborn recorder or by oscilloscope photography. At the higher current densities an apparatus previously described (10) was used to control the initial formation and to supply a trigger voltage to the timer. At lower current densities manual control was employed.

Results

The typical behavior is shown in Fig. 1. With the initial formation at $25 \mu\text{a cm}^{-2}$, one-tenth of the Frenkel defects (if the theory is correct) had disappeared in 10 msec but three-tenths remained after a period of hours. Evidently, if the process is represented as a relaxation process, with relaxation times a function of the separation of the components of the Frenkel defects, then there is a wide range of relaxation times. This wide range is doubtless related to the lack of a peak at any frequency in the dielectric losses at audio frequencies, since it is probable that ionic movement is involved in the dielectric loss process (1).

The second feature is illustrated by Fig. 2 and 3. The higher the initial current density at a given temperature, the greater the proportion of Frenkel defects that recombine in a given time. This effect seems to be expected for the model, since, as will be shown, the evidence is that more Frenkel defects are present the higher the current density, so that the average separation of the components of the defects is smaller.

Since the recombination process involves ionic movement, it is to be expected that a set of activation energies exists corresponding to the relaxation times,

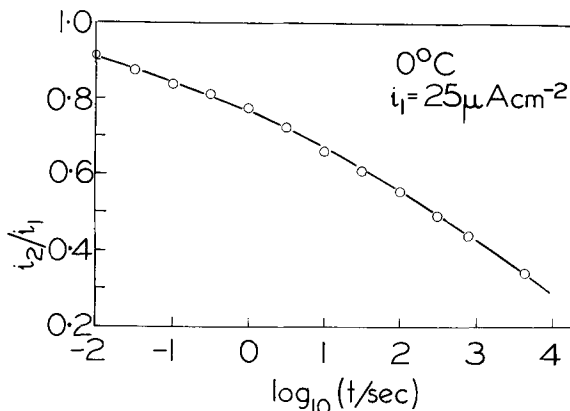


Fig. 1. Typical recombination plot. Proportion of defects remaining after time t at zero field.

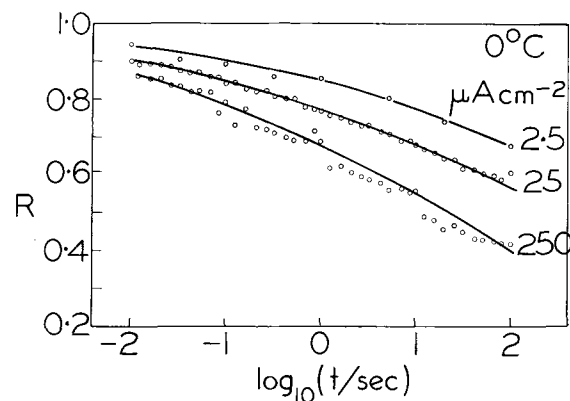


Fig. 2. Dependence on initial current density at 0°C

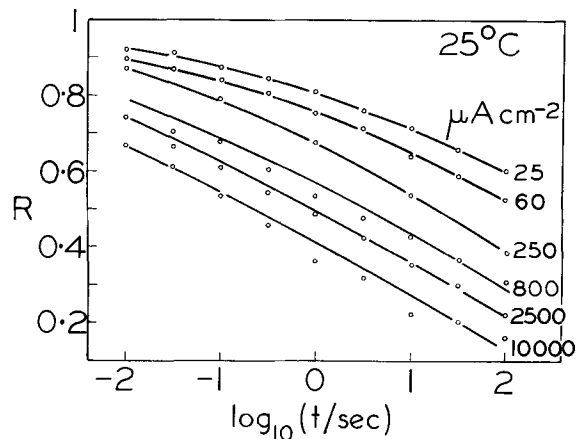


Fig. 3. Dependence on initial current density at 25°C

and that the process should be faster the higher the temperature for the same initial concentration and spatial distribution of defects. For a given current density it appears that the increased ionic mobility associated with higher temperature is roughly cancelled over the 0° - 100°C range by the effects of fall in the concentration of defects, so that the curves of the type shown in Fig. 1 are almost independent of temperature.

To find a set of initial currents at various temperatures corresponding to the same concentration of defects, recourse has to be made to the theory of the ionic conduction process as applied to experimental data on steady state and transient kinetics. There is some doubt of the validity of the theory, particularly since only the metal ions are assumed to be mobile, and recent experiments by Graham, Brown, Davies and Pringle (11) [see also, Amsel and Samuel (12)] have indicated that the situation is more complicated than previously assumed. It has not yet been made clear what changes will be required in the model to account for these new experiments. Previous difficulties regarding the lack of the expected temperature dependence of the steady state and transient Tafel slopes ($dE/d \log i$) have received an explanation (13), which requires the dependence of free energy of activation on field to be extended to include the quadratic term in the expansion in powers of E , the physical model being that the condenser pressure is large and is dependent on the square of E . Experimentally, the steady state current (10) was found to be given by $i = i_0 \exp\{-(W - qE(\alpha - \beta E))/kT\}$, where i_0 , W , α , and β are constants, $q = 5|e|$, $E = \text{field}$. This includes the dependence of concentration n of defects on the field. Transient experiments (8) give the mobility of the defects

$$i = A n \exp\{-(W_2 - qE(\alpha_2 - \beta_2 E))/kT\}$$

where A is a constant whose numerical value is not known. Hence, using the numerical values of the constants given in the above references, $n = n_1 \exp(-0.9$

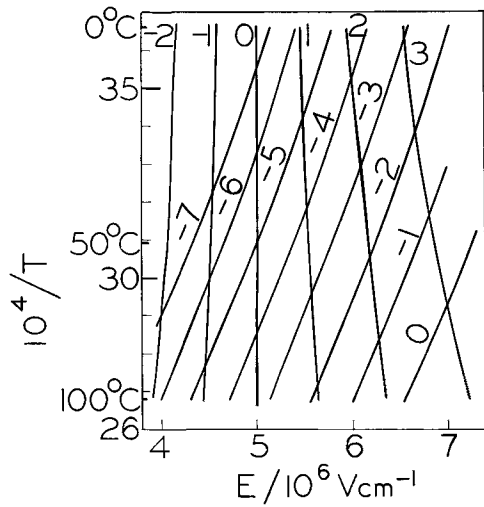


Fig. 4. Contours of i (as $\log_{10}(i/A\text{ cm}^{-2})$) and of concentration of defects (as $\log_{10}(n/\text{constant})$) as functions of field and temperature.

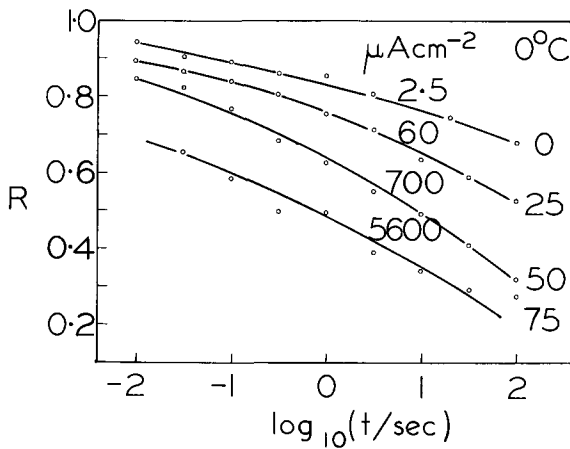


Fig. 5. Recombination curves for initial conditions corresponding to the same concentration of defects.

$eV/kT) \exp\{q(4.8\text{\AA} - 0.23(\text{\AA}/10^6\text{V cm}^{-1})E)E/kT\}$, where n_1 is an unknown constant.

A plot of contours of n and of steady state current i as functions of $1/T$ and E is given in Fig. 4. The concentration of defects is predicted to be a function of E almost independent of temperature.

Figure 5 shows data for a set of initial currents at various temperatures such that the initial concentration of defects should be the same for all. Figure 6 shows $\log_{10}(t/1\text{ sec})$, where t is the time for the first 0.3 or so of the defects to recombine, as a function of $1/T$. The slope indicates a mean activation energy of about 0.9 eV, which may be compared with the experimental value 1.3 eV for the activation energy for ionic movement at zero field (8).

The recombination process may also be studied by reapplying a constant current instead of a constant voltage (Fig. 7). (This method was used by Dewald in his unpublished work.) The electrode potential then goes through a maximum. The excess field ΔE at the maximum is an exponential measure of the amount of recombination. Neglecting the increase in concentration of defects during the build-up to the maximum field ΔE ($d \log i/dE \approx -\log(R)$ where $d \log i/dE$ refers to sudden changes of field and R is the proportion of defects unrecombined. Qualitatively, the method shows the same dependence on temperature and initial current. Quantitatively, the agreement with the other method was rather poor.

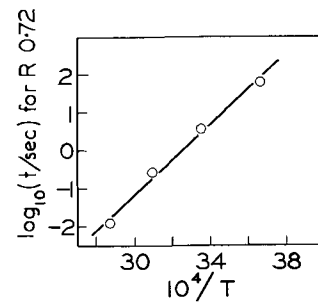


Fig. 6. Activation energy plot for data of Fig. 5

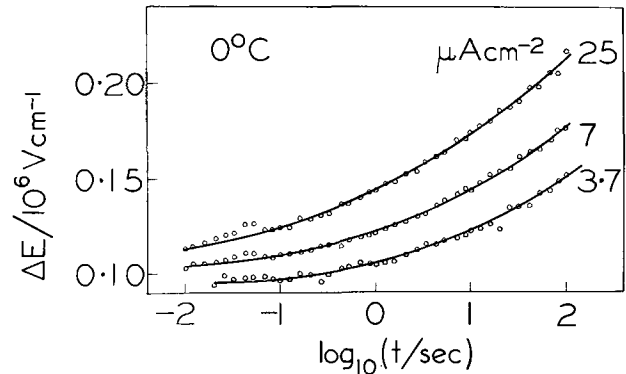


Fig. 7. Constant current method

Discussion

The discussion below follows an approach due to Dewald (unpublished).

It is assumed that each interstitial ion may be paired with a vacancy with which it would eventually recombine given sufficient time. Since the spacial distributions will be largely random, a given ion may start moving toward the wrong vacancy. Neglecting this and other complications, the distribution may be described by a function giving the concentration of pairs separated by 1, 2, . . . r unit atomic jumps. Let these concentrations be y_1, y_2, \dots, y_r .

It is assumed that the concentration of mobile ions effective when the field is reapplied is simply the sum corresponding to all unrecombined ions, that is, variations in bulk mobility associated with variations in the distance from nearby vacancies are neglected. The field acting on a given interstitial during recombination will be roughly $E = q/\epsilon(2ra)^2$, where q is the charge on the vacancy (assumed equal in magnitude to that on the ion), ϵ is the dielectric constant, r is the number of jumps for recombination to occur, and $2a$ is the spacing between successive interstitial sites. It is assumed that the rate of jumping is proportional to $\exp\{-(W - qaE)/kT\}$. A chain of equations is obtained similar to that for a sequence of radioactive decays

$$dy_i/dt = -\lambda_i y_i + \lambda_{i+1} y_{i+1}$$

where $\lambda_i = \lambda_0 \exp\{-(W - qaE_i)/kT\}$. It may be assumed that separations greater than some given value may be neglected. The solution is standard and takes the form of a set of terms in $\exp(-\lambda_i t)$ with coefficients functions of the initial values of the y_i (say N_i) and the λ_i . The initial concentrations will be of the form obtained from the probability that a vacancy has its nearest interstitial i sites away: $(n/N) g_i \prod_{r<i} (1 - ng_r/N)$,

where n is the concentration of interstitials, N that of all interstitial sites, and the g_r are geometrical factors. For big separations this goes over into a continuous distribution: $\exp(-nV) n 4\pi(2ra)^2 d(ra)$, where $V = (4/3)\pi(2ra)^3$.

A numerical investigation of this model is hardly worthwhile at present. A few qualitative features are

significant. The work done by the local field as an ion jumps successive barriers increases very rapidly as the ion approaches within a few steps of the vacancy. With the rough expression for the field given above, the contributions for the jumps in reverse order are in the ratio 1, 1/6, 1/15, 1/28. It would seem that if recombination is appreciable for larger separations it will be practically instantaneous for closer separations. This supports the capture cross-section model for the recombination during the formation of the films. Presumably, the closest separations simply do not occur in the present experiments and the recombinations observed refer to more widely spaced pairs. The observed wide spread of relaxation times is evidently not inconsistent with the model. The observed dependence on initial concentration of defects is shown in qualitative fashion. A point of interest here is that the spacial distribution produced by forming the film under given conditions and then holding at zero field till a concentration n is produced is not to be expected to be the same as that obtained directly by formation under conditions such that the concentration is n before any recombination has occurred. The problem is to decide whether this model is basically adequate or whether as Vermilyea has suggested (4,5), some more subtle

change in the structure of the films must be postulated to explain the transient and other phenomena.

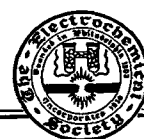
Manuscript received Feb. 10, 1964. This paper was presented at the Pittsburgh Meeting, April 15-18, 1963.

Any discussion of this paper will appear in a Discussion Section to be published in the June 1965 JOURNAL.

REFERENCES

1. L. Young, "Anodic Oxide Films," Academic Press, London and New York (1961).
2. C. P. Bean, J. C. Fisher, and D. A. Vermilyea, *Phys. Rev.*, **101**, 551 (1956).
3. J. F. Dewald, *J. Phys. Chem. Solids*, **2**, 55 (1957).
4. D. A. Vermilyea, *Acta Met.*, **5**, 113 (1957).
5. D. A. Vermilyea, *This Journal*, **104**, 485 (1957).
6. L. Young, *Acta Met.*, **4**, 101 (1956).
7. D. M. Smyth, G. A. Shirn, and T. B. Tripp, *This Journal*, **110**, 1264 (1963).
8. L. Young, *Proc. Roy. Soc.*, **A263**, 395 (1961).
9. R. Dreiner, *This Journal*, **111**, 27 (1964).
10. L. Young, *Proc. Roy. Soc.*, **A258**, 496 (1960).
11. R. L. Graham, F. Brown, J. A. Davies, and J. P. S. Pringle, *Can. J. Phys.*, **41**, 1686 (1963).
12. G. Amsel and D. Samuel, *J. Phys. Chem. Solids*, **23**, 1707 (1962).
13. L. Young, *This Journal*, **110**, 589 (1963).

Technical Notes



The Disintegration of Iron and Steel while Dissolving in Acids

M. E. Straumanis, G. E. Welch, and W. J. James

Departments of Metallurgical Engineering and of Chemistry, The University of Missouri at Rolla, Rolla, Missouri

It is known that very pure carbonyl iron dissolves in dilute H_2SO_4 at a faster rate than in HCl of the same concentration (1); the same was confirmed recently working with zone-refined Fe and with steel samples (2). In studying the latter metals and trying to explain the faster rates obtained in H_2SO_4 , suspicion arose that metallic disintegration in the form of particles might have proceeded at a faster rate in H_2SO_4 than in HCl.

The phenomenon of disintegration was observed previously while the metals Be (3, 4), Mg (5), Ga (6), In (7), and Al (8) were anodically dissolving in acids. It also occurred during self-dissolution of Be. Remarks on disintegration of Fe can be found in the article of Marsh and Schaschl (9).

Could disintegration of Fe be observed in the same way as for the other metals mentioned above? High-purity Fe and carbon steel were used for the disintegration observations. The zone-refined Fe and the steel had the compositions shown in Tables I, II, and III. As starting material for zone refining, electrolytic iron was used (Table II), the composition of which remained essentially the same after refining.

Since zone-refined iron dissolved only very slowly in HCl and H_2SO_4 (1) there was no hope of observ-

ing disintegration of the metal during self-dissolution. A Fe electrode was, therefore, made and used as an anode for dissolution in H_2SO_4 and HCl. However, at current densities up to 1 amp/cm² in less than 1N H_2SO_4 the solutions remained clear. When the current density in 1N H_2SO_4 was increased to 2.4 and more (amp/cm²), a black dispersion in the form of very fine particles was observed at the anodic surface. Unfortunately the dispersion (the solid phase having a very large active surface) dissolved before it could be washed free of acid. It is very probable that the dark dispersion consisted of metallic Fe particles (9). Larger black particles were also observed in the solution, but could not be isolated for optical examination.

Table II. Metallic impurity content in ppm detected in the electrolytic Fe

Al	15	Cr	5	Mn	0.5
Be	<0.2	Co	5	Ni	20
Cd	5	Cu	7	P	9
Ca	<10	Mg	>5	Si	10

Table III. Analyses (in % by weight) of the steel sample (balance-Fe), obtained from U.S. Steel Corporation, E. C. Bain Laboratory, Monroeville

Admixture	Steel sample
C	0.44
Mn	0.86
P	0.027
S	0.035
Si	0.20

Table I. Nonmetallic impurities of the zone-refined Fe-bar (obtained from Battelle Memorial Institute) in ppm (= 0.0001% by weight)

O	1.7	H	0.2
C	9 ± 4	S	5 ± 3
N	0.2		

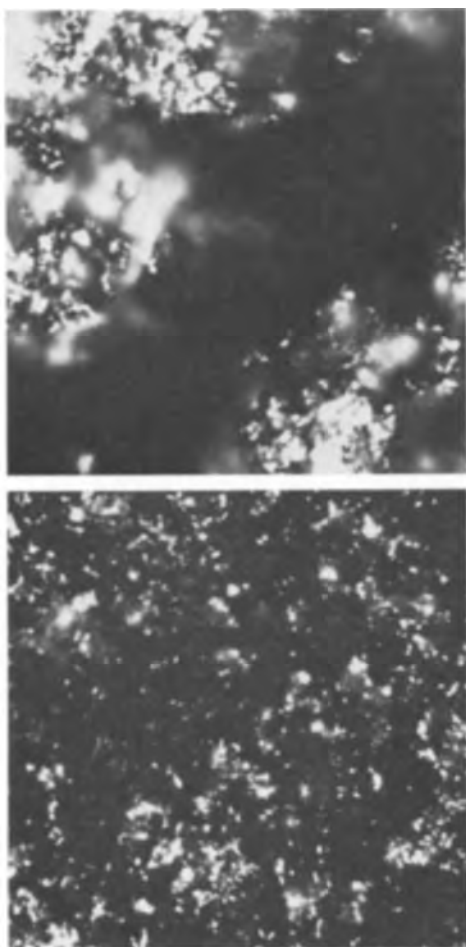


Fig. 1, a and b. Bright particles (iron chunks) of metallic luster formed as a result of attack of steel (Table III) by 5.0N H_2SO_4 ; above, larger chunks; below, smaller particles. Magnification 1430X.

In HCl a fluffy brown precipitate could be seen falling from the anode. However, there was no microscopic evidence for the presence of metallic particles in this substance.

The steel sample (Table III) exhibited quite a different behavior. In the absence of current, a black deposit was noticed to have formed on the surface of the steel samples in both H_2SO_4 and HCl acids after a short period of exposure. This deposit formed more readily in H_2SO_4 than in HCl. After a period of about 1 hr the H_2SO_4 itself started to discolor and then the solution became dull gray. In HCl, even after 6 hr, the solution remained clear.

It was suspected that the discoloration of H_2SO_4 arose from the carbon of the metal (see Table III). To collect larger amounts of the dispersion (which slowly settled), 2 x 3 cm pieces of the sample were placed in 5.0N H_2SO_4 . After 1/2 hr the solution became gray and a black deposit was observed on the bottom of the reaction vessel. The acid was decanted from the deposit, rinsed with distilled water, and finally washed with acetone. Then the dry deposit was examined in the reflecting light of an optical microscope at high magnification (1430X, oil immersion). A number of specks exhibited a metallic luster (see Fig. 1, a and b). Some of them were dispersed in a brown-pink substance. In transmitted light the shiny par-

ticles appeared as opaque spots, characteristic of particles of higher density. X-ray powder pictures of the black deposit showed the definite presence of lines of free iron. The black particles consisted, therefore, of iron and were observed in all instances to come from the surface of the steel samples.

Formation of black particles during dissolution of the steel sample in HCl was not observed. In order to check the surface of the dissolving metal for the presence of Fe chunks, the surface was washed using a soft rubber policeman. Some single particles were collected in this way, and the microscope revealed that they had the same general appearance as those formed in H_2SO_4 .

Thus, it was shown that steel and Fe have the property to disintegrate into very small particles while dissolving in H_2SO_4 and to a smaller extent when reacting with HCl. Since the particles dissolve separately, it is understandable why the rate of dissolution observed in H_2SO_4 is faster than in HCl. The experimental conditions do not permit one to assume that the Fe particles were produced as a consequence of disproportionation of Fe^{+1} to Fe^0 and Fe^{2+} , as was erroneously assumed in the case of the disintegration of Be (10, 3, 4). Fe^{2+} (a normal oxidation state) is produced directly, as is observed for Zn disintegrating anodically (11). Disintegration is in all probability a surface phenomenon connected with the breakdown of oxide and other protective layers from the metal during attack by corrosive agents: evidently these layers separate from the bulk metal taking small parts of the metal with them. Thus, the degree of disintegration will depend on the adherability of the layers to the metal, the rate of production of new layers, and the undermining ability of the corrosive. As can be seen from this example of Fe and steel, the admixtures present increase the rate of disintegration, as, e.g., for Al (8).

Acknowledgments

The authors wish to thank the Office of Naval Research for support of this work. The authors are also thankful to Dr. O. T. Marzke, Vice President of the U.S. Steel Corporation, Pittsburgh, and to Dr. G. W. P. Rengstorff, Research Associate at Battelle Memorial Institute, Columbus, for the donation of the iron and steel samples.

Manuscript received May 4, 1964; revised manuscript received June 29, 1964.

Any discussion of this paper will appear in a Discussion Section to be published in the June 1965 JOURNAL.

REFERENCES

1. M. Centnerszwer and M. Straumanis, *Z. physik. Chem.*, **A162**, 94 (1932).
2. M. E. Straumanis, W. J. James, and G. E. Welch, ONR Tech. Rep. No. 6, Feb. 1964.
3. M. E. Straumanis and D. L. Mathis, *J. Less-Comm. Met.*, **4**, 213 (1962).
4. M. E. Straumanis and D. L. Mathis, *This Journal*, **109**, 434 (1962).
5. M. E. Straumanis and B. K. Bhatia, *ibid.*, **110**, 357 (1963).
6. M. E. Straumanis and K. Poush, *ibid.*, **111**, 795 (1964).
7. M. E. Straumanis and R. Martin, *Z. anorg. Chem.*, In press.
8. B. Roald and M. A. Streicher, *This Journal*, **97**, 283 (1950).
9. G. A. Marsh and E. Schaschl, *ibid.*, **107**, 960 (1960).
10. B. J. Laughlin, J. Kleinberg, and A. W. Davidson, *J.A.C.S.*, **78**, 559, 560 (1956).
11. W. J. James and G. E. Stoner, *ibid.*, **85**, 1354 (1963).

Photoluminescence and Polytypism in Boron Doped Silicon Carbide

Arrigo Addamiano

Lamp Research Laboratory, General Electric Company, Nela Park, Cleveland, Ohio

It is well known that silicon carbide exists in a large number of different but closely related crystal structures, usually referred to as "polytypes." Knippenberg (1) lists 44 such polytypes, and a few more have been reported recently (2, 3). As the band gaps of some at least of the polytypes (4) correspond to visible emission a large family of SiC phosphors with interesting structural relationships can be expected to exist. We were able to obtain some of these phosphors in the form of powders as a continuation of previous work on the room temperature luminescence of SiC (5). It was found that group III elements are activators and group V elements coactivators of the luminescence in silicon carbide. In particular, room temperature luminescence was found in silicon carbide containing controlled amounts of boron as activator and nitrogen as coactivator. Preparations at temperatures below the "transition point" $\beta\text{-SiC} \rightarrow \alpha\text{-SiC}$ (2200°-2300°C) resulted in homogeneous phosphors with red and infrared emission. High-temperature reactions (above 2300°C) always led to mixtures of phosphors with different colors of luminescence and different relative abundances. The yellow fluorescing phosphor was usually the most abundant. Orange and orange-red particles were present in substantial amounts, while green and particularly red fluorescence was limited to very few particles. Due to these differences in emission colors a mechanical separation of the different phosphors and the collection of their x-ray powder patterns and emission spectra was possible. It was found that green fluorescing SiC:B,N has the 4H structure, while particles with the 6H structure have yellow emission. As for the orange, orange-red, and red emitting phosphors a great deal of time had to be spent to obtain them in a relatively pure state. Even though the particles were very small and only those of simple geometry, usually flat platelets, were selected, the x-ray photographs indicated the presence of minor

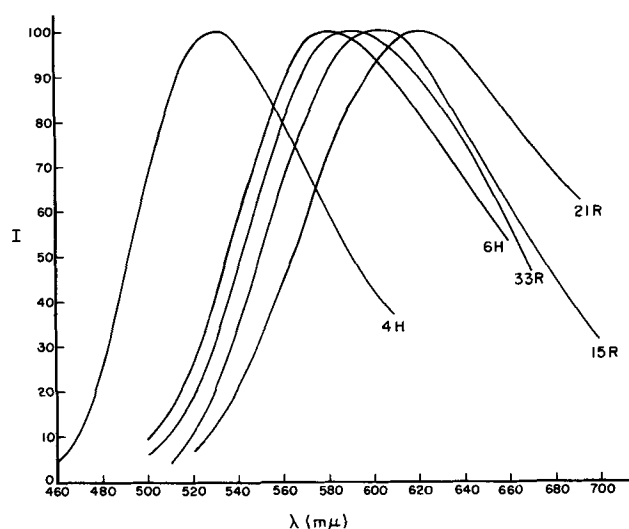


Fig. 1. Emission spectra of SiC:B,N phosphors at room temperature ($\lambda_{\text{exc}} = 3650\text{\AA}$).

Table I. Relationships between room temperature luminescence ($\lambda_{\text{exc}} = 3650\text{\AA}$), crystal structures, and energy gaps in some SiC:B,N phosphors

Emission color	E_{peak} , ev	Structure	E_{Gx} , ev	$E_{\text{Gx}} - E_{\text{peak}}$, ev
Green	2.317	4H	3.263	0.95
Yellow	2.137	6H	3.023	0.89
Orange	2.101	33R	3.01	0.91
Orange-red	2.049	15R	2.986	0.94
Red	1.983	21R	2.86	0.88
—	(1.89)*	8H	2.80	—
—	(1.48)*	3C	2.390	—

* Predicted for $E_{\text{Gx}} - E_{\text{peak}} = 0.91$ ev.

components along with the predominant polytype. In spite of these difficulties there is no doubt that the bulk of the material with orange, orange-red, and red fluorescence has the structure 33R, 15R, and 21R, respectively.

In Fig. 1 we give the emission spectra of the different phosphors isolated. The exciting radiation used was that of a General Electric A-H6 lamp filtered through Corning 7-37 filters and through a copper sulfate-cobalt sulfate solution. The emission data were recorded with a grating spectrophotometer in connection with a 1P22 phototube detector and were corrected to take into account the detector response as a function of wavelength. Table I gives, in the order, (a) color of luminescence, (b) energy of the photon at the emission peak, E_{peak} , in ev, (c) crystal structure, (d) exciton energy gaps E_{Gx} (4), and (e) $E_{\text{Gx}} - E_{\text{peak}}$.

It will be seen that, except for the blue region, luminescence over all the visible spectrum does occur. The emission is different for different polytypes, more precisely, it shifts in the same direction as the energy gap of the host lattice and in such a way that the difference $E_{\text{Gx}} - E_{\text{peak}} \approx 0.9$ ev. More work is in progress to arrive at a detailed description of the luminescence centers in these SiC:B,N phosphors.

Acknowledgments

The author wishes to thank R. M. Potter, F. J. Studer, and Miss J. R. Cooper for helping in the collection of the optical and x-ray data and for discussions.

Manuscript received July 1, 1964. This paper was presented at the Toronto Meeting, May 3-7, 1964.

Any discussion of this paper will appear in a Discussion Section to be published in the June 1965 JOURNAL.

REFERENCES

- W. F. Knippenberg, *Philips Research Repts.*, **18**, 161 (1963).
- P. Krishna and A. R. Verma, *Proc. Roy. Soc.*, **A272**, 490 (1963).
- K. Azuma, K. Ohta, and T. Tomita, *J. Phys. Soc. Japan*, **18**, 1097 (1963).
- W. J. Choyke, D. R. Hamilton, and L. Patrick, *Phys. Rev.*, **133**, A1163 (1964).
- A. Addamiano, R. M. Potter, and V. Ozarow, *This Journal*, **110**, 517 (1963).

Epitaxial Growth of Homogeneous Solid Solutions of GaAs-GaP

Edward M. Hull

Thomas J. Watson Research Center, International Business Machines Corporation, Yorktown Heights, New York

The recent discovery of lasing activity in diodes made of GaAs (1,2) has stimulated renewed interest in solid solutions of GaAs and GaP which are known to exhibit injection luminescence at shorter wavelengths depending on the composition of the solution. Alloys for use in fabricating injection luminescence devices must exhibit a very high degree of homogeneity of composition and dopant concentration if predictable and reproducible characteristics are to be obtained from the devices.

Crystals grown from molten solutions of the two compounds are generally inhomogeneous due to such effects as constitutional supercooling and segregation during growth. Melt growth techniques also require rather elaborate equipment due to the high temperatures and dissociation pressures involved when compositions containing more than a few per cent of GaP are melted.

Several methods have been published (3-5) by which solid solutions of these compounds may be epitaxially deposited on single crystal substrates by vapor transport techniques. These methods appear to allow some degree of variation in the composition of the deposit during the course of a run. This arises from the fact that simple mechanical mixtures of the crushed starting compounds were used for source material. The composition of the vapor phase and hence of the deposit was governed by the relative surface areas of the particles of the two compounds exposed to the etching vapor at any given time during the run. Curve 1 of Fig. 3 illustrates this effect. In this case the variation in composition of the deposit ranged from about 6% to about 16% GaP during the course of the run. The variation in composition was enhanced by the fact that very coarsely crushed materials were used as starting materials, but even where finely divided materials are used, it seems apparent that variations may occur.

In this note, a rather simple method is described by which mixed crystal epitaxial deposits can be produced whose composition can be accurately predicted beforehand and in which the composition cannot vary during the course of a run. There may be a very thin region at the interface between the deposit and the substrate which could show some variation in composition due to the nonsteady-state condition which exists during the initial heating of the system. However, this effect has not been verified by the author.

A closed tube iodide disproportionation transport reaction, conducted under the conditions described below, was employed in all vapor depositions. Figure 1 shows the physical aspects of the system schematically with a typical temperature profile. The reactions which are believed to govern the transport are

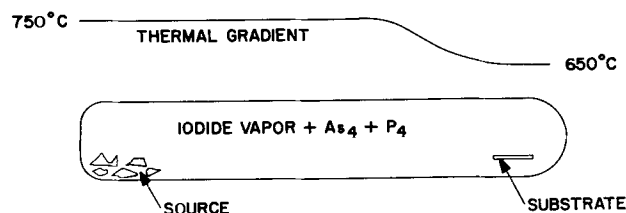
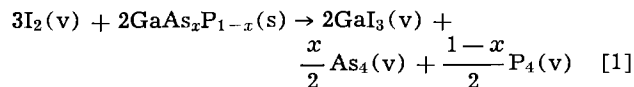
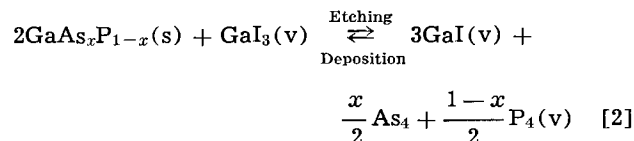


Fig. 1. Generalized physical aspects of the system



and



Reaction [1] occurs during the initial heating of the system as elemental iodine reacts with the source materials. The temperature dependence of equilibrium [2] in which the ΔH , as written, is positive results in transport occurring from the hot to the cold portions of the sealed tube.¹

Homogeneous epitaxial deposits were obtained when the starting compounds were first homogenized via a vapor transport process to form a single phase source. By this method, mixed crystal epitaxial deposits were produced whose homogeneity was adequate for the fabrication of lasers having reproducible characteristics.

The homogenization of the source materials was carried out in the following manner. The two compounds, in pieces as large as could be conveniently weighed, were placed in a clean fused silica tube in the proportions calculated to yield a solution of the composition desired. Dopant elements were added either as a constituent of one or both of the compounds, or in elemental form. The tube was evacuated, and iodine from a preweighed, break sealed ampoule was introduced by sublimation. The tube was then sealed by collapsing it onto a silica plug contained within it. Iodine quantities of 2-3 mg/cm³ of tube volume were used. The tube was placed into the vertical two zone furnace shown schematically in Fig. 2. The temperature conditions employed, with the hotter source region below the cooler deposition region, resulted in

¹ As₄ and P₄ were chosen to represent the free arsenic and phosphorus in the vapor phase in these reactions since, under the conditions employed, they are present in much larger concentrations than other arsenic or phosphorus species.

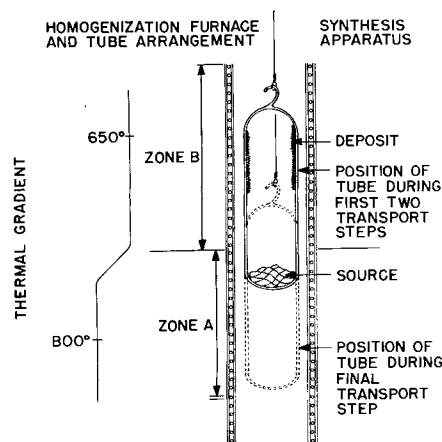


Fig. 2. Apparatus used for homogenization of source materials

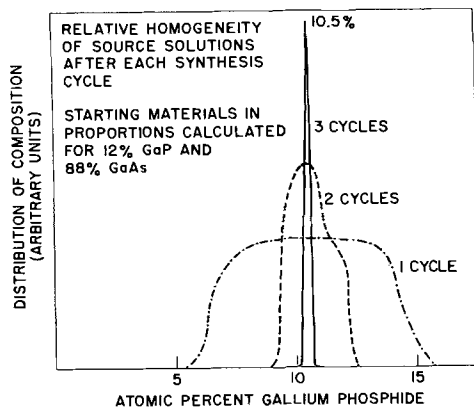


Fig. 3. Graphic representation of the effect of successive homogenization steps.

high transport rates due to enhanced convective circulation of the vapor.

The transport reaction was allowed to continue until the source materials were completely exhausted. The tube was then removed from the furnace, cooled, and replaced with the ends reversed from the previous position. The long length of the tube residing in the cooler region of the furnace during the first two transport cycles provides a relatively large surface on which nucleation may occur. This encourages the formation of a finely divided deposit, which on cooling the tube between transport cycles, falls away from the tube due to differential thermal contraction. The large number of small crystallites formed in this manner afford a more nearly homogeneous source for the next transport cycle.

The reaction was run three times in this manner with the source being completely exhausted each time. For the third and final cycle, the length of the tube residing in the cooler region of the furnace was reduced to encourage the formation of a massive deposit with minimum surface area for contamination upon exposure to the atmosphere. Upon completion of the final transport cycle, the hot tube was quenched at a point remote from the deposit to avoid condensing the vapor species on the deposit. The transport rate under the conditions described was found to be of the order of 150 mg/hr.

The variation of solution homogeneity with successive transport cycles is shown in Fig. 3. The data were obtained by comparing the line width and density variation within the lines produced by x-ray diffraction of filtered Cu radiation. The line width shown for the solution after three cycles is comparable to that of pure GaAs. The samples for x-ray analysis were prepared by pulverizing and mixing a large sample from the reaction mixtures after each transport cycle.

Epitaxial deposits of these alloys were produced in a sealed tube apparatus depicted schematically in Fig. 4. The temperature gradient shown is produced by two independently controlled windings of nichrome wire wound on a quartz cylinder and enclosed in another cylinder held concentric to the first by insulating material. The source is contained in the upper end of the tube by an inverted funnel arrangement, covered by a perforated silica cap to prevent crystallites, which form in the source region, from falling on to the seed wafer. Iodine quantities of 2-3 mg/cm³ of tube volume were used.

Growth rates in this apparatus were of the order of 4 μ /hr on GaAs substrates of approximately 1 cm² in

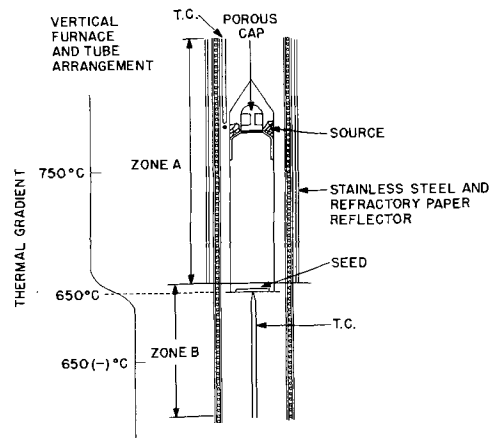


Fig. 4. Apparatus used for epitaxial deposition of homogeneous mixed crystal.

area. The (111) plane terminated by gallium atoms was found to be a satisfactory growth direction, yielding deposits of uniform thickness whose terminal surfaces exhibited an over-all shallow pyramidal pattern which could be easily removed by lapping. Care was required during the initial heating of the epitaxial deposition apparatus to avoid etching of the substrate by the iodine since this reaction would alter the initial arsenic to phosphorus ratio in the vapor leading to a variation in the composition of the deposit near the interface.

The usefulness of some of the deposits for fabrication of injection luminescence devices was investigated. Injection laser diodes were fabricated by a Zn diffusion technique (6) from several deposits with net carrier concentrations in the 5×10^{17} electrons per cubic centimeter range, and gallium phosphide content of 20% and 30%. These exhibited line narrowing from the initial spontaneous emission band width of about 150Å down to about 6Å at a threshold current density of approximately 9000 amp/cm². The width of the spontaneous emission band is not much greater than that observed for GaAs diodes which typically exhibit spontaneous band widths of about 120Å. This is probably the best indication of the level of homogeneity of the deposits in the region of the junction.

Acknowledgment

The author gratefully acknowledges the advice and assistance of H. Leonhardt, V. J. Lyons, and A. Reisman during the course of this work and preparation of the manuscript.

Manuscript received May 19, 1964, revised manuscript received Aug. 6, 1964. This paper was presented at the New York Meeting, Sept. 29-Oct. 3, 1963.

Any discussion of this paper will appear in a Discussion Section to be published in the June 1965 JOURNAL.

REFERENCES

1. M. I. Nathan, W. P. Dumke, G. Burns, F. H. Dill, Jr., and G. J. Lasher, *Appl. Phys. Lett.* **1**, 62 (November 1962).
2. R. N. Hall, C. E. Fenner, J. D. Kingsley, T. J. Soltys, and R. O. Carlson, *ibid.*, **9**, 366 (November 1962).
3. F. A. Pizzarello, *This Journal*, **109**, 226 (1962).
4. S. M. Ku, *ibid.*, **107**, 991 (1963).
5. N. Holonyak, D. C. Jillson, and S. F. Bevaqua in "Metallurgy of Semiconductor Materials," **15**, pp. 49-59, Interscience Publishers, New York (1962).
6. J. C. Marinace, *This Journal*, **110**, 11 (1963).

Critical Phenomena with Thorium Adsorbed on Single Crystal Tungsten

J. Anderson and W. E. Danforth

Bartol Research Foundation of The Franklin Institute, Swarthmore, Pennsylvania

We have studied the work function variation and thermal desorption for the adsorbed monolayer system thorium-on-tungsten.

The substrate specimen was produced from a rolled 1-mil tungsten ribbon recrystallized into a small number of large grains by the moving temperature gradient method. Ninety per cent of the emitting area under study, 6 x 1 mm, in the middle of the 2-in. ribbon was oriented to within 2° of the (411) plane, the remainder being small crystallites at the edge of the ribbon. The effects reported here are taken to be characteristic of the larger area. The ribbon surface was slightly wavy due to residual die marks, but there was no visible microscopic structure at the limits of optical resolution.

The ribbon was cleaned chemically, using no solution which might etch it preferentially, and mounted in a glass tube which was then evacuated to about 10⁻¹⁰ Torr. The ribbon was cleaned repeatedly throughout the course of the experiment by heating to 1900°C. The stability of the emission current and the absence of any pressure rise on flashing the filament indicated the virtual absence of any adsorbable gases.

In this and a number of similar systems it has been found that the work function ϕ varies with adsorbate density in a characteristic way (1). Beginning with the work function of the substrate material, ϕ decreases with increasing adsorbate coverage, passes through a well-defined minimum, and then rises to a value which then appears to remain constant.

A convenient notation for adsorbate coverage is the variable f , proportional to the coverage and so defined that f equals unity at the minimum in ϕ . Thorium, the adsorbate, is supplied to the ribbon by evaporation from a heated tungsten crucible. The rate of deposition is measured by observing the emission from a second ribbon, adjacent to the one under study, for which the coverage at minimum ϕ is known to be 4.2 x 10¹⁴ at./cm². For further information on the general experimental procedure and the method of calibrating the second ribbon see ref. (1) and (3).

Work functions quoted here are effective work functions obtained by substituting measured thermionic current density into the Richardson equation and setting A equal to 120 a/cm²deg². We assign an error of 0.02 ev to these values, largely due to temperature uncertainties.

The phenomena we are concerned with are, for $f > 1$, the variation of work function with thorium coverage, $\phi(f)$, the thermal desorption of thorium from the surface, and the surface migration of thorium atoms (observable only qualitatively). We calculate the ϕ vs. f curve from the dependence, at constant temperature, of the emission current on f . Thermal desorption is observed by holding the specimen at a convenient high temperature and, from periodic emission measurements, deducing the variation of coverage with time. For coverages at which ϕ does not change ($f > 1.7$), an average desorption rate could be obtained by depositing a large quantity of thorium (to a coverage $f=150$) and measuring the time necessary to desorb to a determinable coverage, i.e., f equal to some value less than 1.7.

In order to have confidence that the ϕ vs. f curves were accurate, it was necessary to determine the magnitude of any effects due to migration of thorium atoms to the back of the ribbon. This was done by

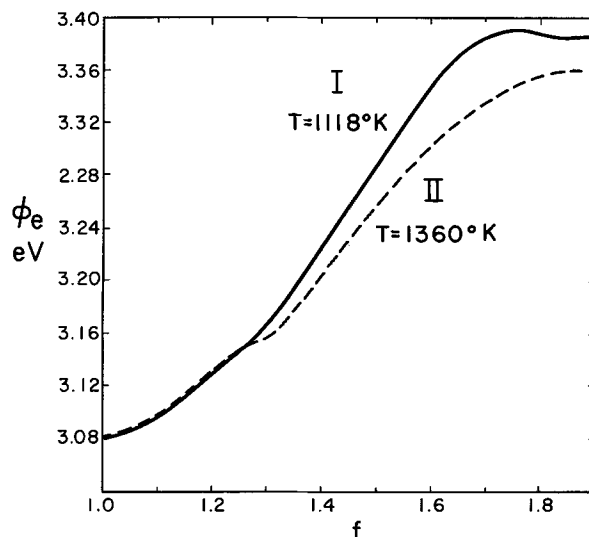


Fig. 1. Variation of effective work function with thorium coverage. Curve I, low-temperature behavior; curve II, high-temperature behavior.

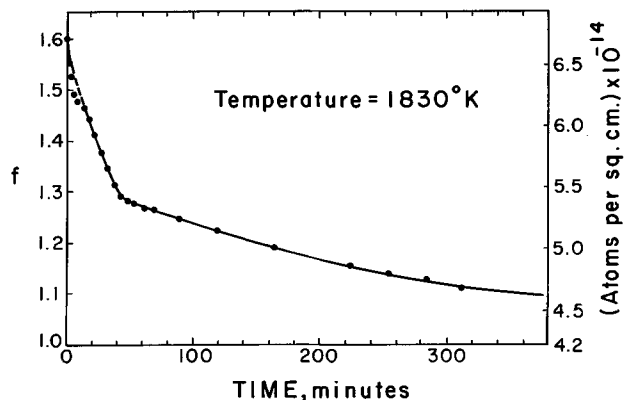


Fig. 2. Desorption of thorium from the tungsten surface for the range of coverage under study, showing the decrease of coverage with time at the desorbing temperature, 1830°K.

the shutter method wherein we interrupt the flux of thorium vapor and note any increase in emission due to removal of thorium from the front of the ribbon and its accumulation on the back.

Our experimental results are as follows. From a ϕ of 4.42 ev (essentially constant over the temperature range involved, 1100°-1360°K) ϕ decreases to a minimum (ϕ_{min}) of 3.08 ev at a thorium coverage of 4.2 x 10¹⁴ at./cm². The value of ϕ_{min} is in agreement with that of Brattain and Becker (2) and the coverage is that which produces ϕ_{min} in polycrystalline tungsten (3) and polycrystalline rhenium (1). Referring to the "low" temperature solid curve of Fig. 1, we find a change in slope between two linear portions of the ϕ vs. f curve at $f=1.3$. At this same coverage Fig. 2 shows an essential discontinuity in the desorption rate. Assuming a homogeneous surface, we conclude that these phenomena reflect a change in the nature of the binding of the thorium atoms to the surface. Both

the binding energy and dipole moment per additional adatom change at that point. Whether this is simply the occupation of different fixed binding sites or the rearrangement of the geometric configuration of the layer as a whole it is impossible at this time to say. Again referring to the solid curve of Fig. 1, we find that ϕ attains a value of 3.39 eV at $f=1.7$ and thereafter is constant to the limits of experimental accuracy. As was the case for thorium on rhenium, this value is very close to the ϕ of pure thorium ($\phi=3.35$ eV). By the shutter method we found that the thorium migrates very rapidly at $f \geq 1.65$ for all temperatures in the range. Below $f=1.65$ no such migration could be detected at all at low temperatures ($T < 1250^\circ\text{K}$). For this reason we believe curve I expresses the true variation of ϕ with f . Some migration could be detected for f as low as 1.5 at the highest temperatures, and we believe that such migration, below the level of detection by the shutter method, is responsible for the modified shape of the upper part of the high temperature ϕ vs. f curve (dashed line). It does not appear, however, that the pronounced shoulder on this latter curve at $f=1.3$ is due to migration; yet the shoulder seems to be a time dependent phenomenon

for it tends to disappear at high deposition rates. For the present we must regard it as an enigma.

We have found, by the method elucidated above, the average desorption rate for concentrations greater than $f=1.7$ to be approximately 1 f -unit in 10 min, fifteen times as great as the rate at $f=1.4$. Because of the different emissivity associated with a thick thorium layer, the desorbing temperature was slightly less than the nominal 1830°K . This last result must, therefore, be regarded as a conservative approximation. Thus we have another critical coverage, $f=1.7$, at which several properties of the system change simultaneously, and we interpret this coverage as constituting a monolayer.

Manuscript received Feb. 24, 1964.

Any discussion of this paper will appear in a Discussion Section to be published in the June 1965 JOURNAL.

REFERENCES

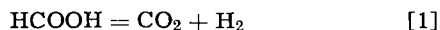
1. J. Anderson, W. E. Danforth, and A. J. Williams, III, *J. Appl. Phys.*, **34**, 2260 (1963).
2. W. H. Brattain and J. A. Becker, *Phys. Rev.*, **43**, 428 (1933).
3. W. E. Danforth and D. L. Goldwater, *J. Appl. Phys.*, **31**, 1715 (1960).

On the Oxidation Mechanism of Formic Acid on Platinum at Low Potentials in Acidic Solutions

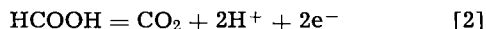
M. W. Breiter

Research Laboratory, General Electric Company, Schenectady, New York

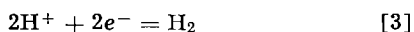
There has been considerable controversy about the mechanism of the decomposition of formic acid on platinum in recent years. The catalytic decomposition



and the anodic oxidation of formic acid



have been studied (1-12) repeatedly on platinum. The open-circuit decomposition and the low-potential oxidation occur in the potential region $U \leq 0.3\text{v}$, the potential being referred to a hydrogen electrode in the same solution as the test electrode. Hydrogen atoms are adsorbed there to some extent as can be seen at sufficient resolution from potentiostatic current-potential curves taken under the conditions of cyclic voltammetry at low speed in acidic solutions with additions of formic acid up to 1M. A monolayer of adsorbed HCOOH molecules does not occupy (9) the surface area which is available to hydrogen adsorption in the absence of formic acid. This fact suggests a participation of the net reaction of hydrogen evolution



and of the Volmer reaction



in the decomposition and, possibly, in the low-potential oxidation of formic acid. Indeed Müller's concept (1) already assumed hydrogen atoms as intermediates of the mentioned processes. The idea that the open-circuit potential of a platinum electrode in acidic solutions in the presence of oxidizable fuels is a mixed potential determined by the anodic oxidation reaction of the fuel and by the cathodic hydrogen reaction has been expressed (13, 14) recently. It was discussed (12) in detail for formic acid. A re-evaluation of this concept is presented below.

Steady-state current-potential curves of reaction [3] are represented in Fig. 1. The current densities

refer to the geometric surface area of the electrodes throughout this note. Curves a and b were measured at anodically activated electrodes in 1N H_2SO_4 under vigorous gas stirring. The gas was purified nitrogen for curve a and a nitrogen-oxygen mixture for curve b. Curves c, d, e were taken from ref. (12) and were obtained under vigorous N_2 -stirring in 1N H_2SO_4 (curve c), in 1N $\text{H}_2\text{SO}_4 + 0.1\text{M}$ HCOOH (curve d), and in 1N $\text{H}_2\text{SO}_4 + 1\text{M}$ HCOOH (curve e). The I-U curve a obeys a Tafel equation over a large range of current densities with a slope of 29 mv/decade and

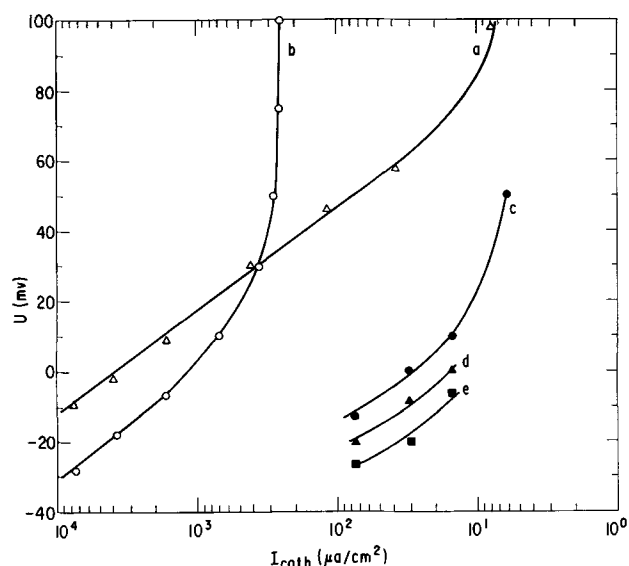
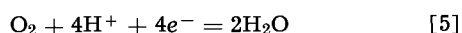


Fig. 1. Steady-state current-potential curves under vigorous gas stirring: curve a, N_2 , 1N H_2SO_4 ; curve b, $\text{N}_2 + \text{O}_2$, 1N H_2SO_4 ; curve c, N_2 , 1N H_2SO_4 ; curve d, N_2 , 0.1M HCOOH + 1N H_2SO_4 ; curve e, N_2 , 1M HCOOH + 1N H_2SO_4 ; curves c, d, and e from ref. (12).

an intersection with the abscissa of 1.7 ma/cm². The rate-controlling step is the diffusion (15) of molecular hydrogen. A hindrance of the combination step could also explain the experimental slope of 29 mv/decade. However, the value of the current-density at the intersection depends strongly on stirring, and it is not likely that vigorous stirring decreases the thickness of the diffusion layer sufficiently to make the limiting H₂-diffusion current density much larger than the exchange current densities of the other steps of reaction [3]. Curve a is representative for an electrode of large activity (minimal overvoltage at a given current-density) while curves c, d, e correspond to electrodes of lesser activity. The maximum rate I_{H_2} at which reaction [3] occurs at anodic potentials can be estimated with the aid of curve a under the assumption that no side-reactions like the O₂-reduction interfere. Thus I_{H_2} is equal to about $2 \cdot 10^{-8}$ amp/cm² at 0.145v, and $I_{H_2} = 2 \cdot 10^{-9}$ amp/cm² at 0.174v. These are maximum values not only because of the large activity of the electrode but also because the current-density might decrease more rapidly with potential than according to a Tafel law at $U > 0.1v$.

In reality, however, curves a, b, and c in 1N H₂SO₄ tend toward a limiting cathodic current density at $U > 0.05v$. The limiting current density is ascribed to the reduction of traces of molecular oxygen in the solution. As expected the limiting current density increases if oxygen is added to the nitrogen (curve b). Its value is about 6 $\mu a/cm^2$ for curve a and 5 $\mu a/cm^2$ for curve c. The same magnitude can be predicted for curves d and e which lie below curve c. The limiting O₂-current density is larger than the estimated maximum rate I_{H_2} of reaction [3] at $U > 0.1v$ under regular conditions when no extreme precautions (16) are undertaken to avoid traces of oxygen. Therefore the reduction of molecular oxygen according to the net reaction



is more likely to be the cathodic reaction of a mixed potential process for the open-circuit oxidation of fuels than the hydrogen reaction [3]. The maximum rate of the open-circuit oxidation of fuels is determined by the limiting O₂-diffusion current density under the assumption of a mixed potential process which involves the cathodic reaction [5] and an anodic reaction of the type of reaction [2]. This is a general criteria which allows one to distinguish between a mixed potential process and a catalytic reaction in certain cases.

The experimental evidence as discussed subsequently is not in agreement with the conclusions of a mixed potential process in the case of formic acid. Gottlieb (12) found a rate of about 0.05 ma/cm² for the open-circuit oxidation of HCOOH on platinized platinum in 1N H₂SO₄ at room temperature. This rate is too large to be accounted for solely by reaction [5] since his curves d and e in the presence of formic acid suggest a limiting O₂-current density of less than 0.01 ma/cm². Schwabe (5) observed an increase of the rate of the open-circuit oxidation of formic acid with the oxygen pressure, but the increase was much smaller than proportional to the oxygen partial pressure. Thus a

catalytic reaction (5) appears a better interpretation. The observation (12) that the rate of CO₂-formation at low anodic current densities is equal to that produced on open circuit plus that calculated from the current means that the low-potential oxidation is superimposed as an independent process to the catalytic reaction. A mechanism similar to the one in ref. (9) is suggested for the low-potential oxidation.

It may be pointed out at the end of this note that the Volmer reaction [4] is considered potential-determining at $0 < U < 0.3v$ for the catalytic decomposition and the low-potential oxidation of formic acid on platinum in acidic solutions by the author. Its exchange current-density $I_o(U)$ which is nearly independent of potential between 0 and 0.2v decreases by 10^{-2} to 10^{-3} if 0.1M HCOOH is added to 1N H₂SO₄. This decrease was estimated from the variation of the initial potential change of cathodic charging curves started (9) at $U = 0.4v$ during the anodic sweep of voltammetric $I-U$ curves. $I_o(U=0)$ has values (17, 18) of 0.1-1 amp/cm² on active Pt-electrodes. The equilibrium of reaction [4] can be considered established even in the presence of formic acid at $0.05 \leq U \leq 0.3$, since the actual current densities are much smaller than $I_o(U) \approx 1$ ma/cm². The possibility of an established equilibrium of the Volmer reaction during the anodic oxidation of fuels was also considered by Frumkin and Podlovchenko (19).

Manuscript received May 21, 1964.

Any discussion of this paper will appear in a Discussion Section to be published in the June 1965 JOURNAL.

REFERENCES

1. E. Müller, *Z. Elektrochem.*, **28**, 307 (1922); **29**, 395 (1923); **30**, 493 (1924).
2. C. Paal and W. Poethke, *Ber.*, **59**, 1511 (1926); see older references there.
3. E. Müller and K. Schwabe, *Z. Elektrochem.*, **34**, 170 (1928).
4. E. Müller and S. Tanaka, *ibid.*, **34**, 256 (1928).
5. K. Schwabe, *ibid.*, **61**, 743 (1957).
6. G. A. Bogdanovsky and A. I. Sklygin, *Zhur. fiz. Khim.*, **34**, 57 (1960).
7. R. P. Buck and L. R. Griffith, *This Journal*, **109**, 1005 (1962).
8. W. Vielstich, *Z. Instr.*, **71**, 29 (1963).
9. M. W. Breiter, *Electrochim. Acta*, **8**, 447, 457 (1963).
10. R. Munson, *This Journal*, **111**, 372 (1964).
11. J. Giner, *Electrochim. Acta*, **9**, 63 (1964).
12. M. H. Gottlieb, *This Journal*, **111**, 465 (1964).
13. W. Vielstich, Paper presented at the Indianapolis Meeting of The Electrochemical Society, April 30-May 3, 1961.
14. M. W. Breiter and S. Gilman, *This Journal*, **109**, 622 (1962).
15. M. Breiter and R. Clamroth, *Z. Elektrochem.*, **58**, 493 (1954).
16. B. Ershler, *Acta Physiochim. U.R.S.S.*, **7**, 327 (1937).
17. M. Breiter, C. A. Knorr, and W. Völkl, *Z. Elektrochem.*, **59**, 681 (1955); M. Breiter, H. Kammermaier, and C. A. Knorr, *ibid.*, **60**, 37 (1956).
18. C. H. Presbrey, Jr., and S. Schuldiner, *This Journal*, **108**, 986 (1961).
19. A. N. Frumkin and B. I. Podlovchenko, *Doklady Akad. Nauk. S.S.S.R.*, **150**, 349 (1963).

The Use of the Motion Picture Camera in Interferometric Electrochemical Investigations

Robert N. O'Brien

Department of Chemistry, University of Alberta, Edmonton, Alberta, Canada

Interferometry (1) has been used in electrochemical investigations for a considerable time because it is a simple, accurate, nondestructive method of detecting refractive index changes; the use of a motion picture camera as a recording instrument is, however, new.

In simple systems, that is where the concentration of only one ion is changing as in the electrolysis cell $\text{Cu}/\text{CuSO}_4/\text{Cu}$, refractive index change may be related directly to the concentration with an error of about $\pm 0.1\%$. Refractive index determinations by interferometric means can also be used to determine rate of thermal conductivity and to locate pressure waves, or, in fact to study any process in which the effective light path changes due to a density or concentration change in a region of fixed geometry. Interferometry can also supply information on processes which indirectly affect the refractive index such as the onset and extent of natural and forced convection on diffusion gradients. It is in studies of rapidly changing effects such as the latter two that the motion picture recording technique offers an advantage.

The author has applied the technique with varying degrees of success to the following research problems: the kinetics of concentration polarization and the time of onset of natural convection with the electrodes oriented differently in the earth's gravitational field; single ion diffusion constants; the specific activity of small areas on an electrode; the throwing power of a solution; concentration polarization in galvanic cells; electroorganic reactions, and the thermal conductivity of transparent liquids.¹

The technique is limited by optical considerations to solution depths of 2-3 mm or less although in some solutions, at low current densities, useful results are possible at depths up to 1 cm. Fizeau-type fringes have been found to be the most useful, although fringes of equal chromatic order and Rayleigh-type fringes have been used. Tolansky has given exhaustive accounts of the uses of these types of fringes (4). The Fizeau fringes are really multiple beam wedge fringes (formed as shown in Fig. 1) with a limited number of reflections. The reflections occur at the solution glass interfaces, or more accurately, at the interface between the solution and the reflecting coating on the flats. The shaded rectangles are the electrodes and when no current is passing, the wedge angle, which has its apex directed out of the page (the electrodes are decreasing

¹Qualitative results only are available for the last five topics. These were discussed at the Pittsburgh Meeting (1963). About 500 ft of 16 mm film was shown on all topics listed.

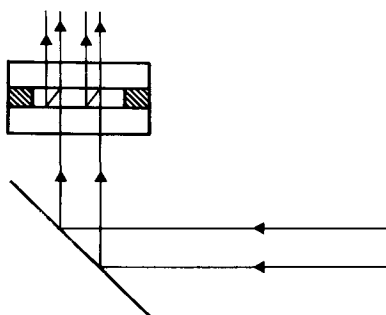


Fig. 1. Schematic light path

in height out of the page), gives a series of equally spaced equal thickness light and dark fringes at 90° to the electrode (parallel to the plane of the page). When current flows, the solution at the cathode in say a $\text{Cu}/\text{CuSO}_4/\text{Cu}$ cell becomes less concentrated and the fringes bend so that $2\mu t = \text{a constant}$, the constant being $n\lambda$ where μ is refractive index (here equated to concentration), t is thickness of the cell (here height of the electrodes), n is an integer (about 8000 in the most commonly used cell), and λ is the wavelength of the monochromatic light. Since μ is decreasing, t must increase, or the fringe shifts up wedge producing a concentration contour. A sample computation has been previously published (3), but in all interferograms one fringe shift = $1.129/\text{concentration change}$. Figure 1 shows the path of the collimated, monochromatic light. The beams shown next enter the motion picture camera lens and form an image of the fringes and the electrodes on the film as can be seen in Fig. 2-4. Since there is some energy input in electrolysis it is fair to ask what effect a temperature change might have. The effect of temperature on fringe shift is a recognizably different phenomenon; an illustration of this already has been published (2), and compilation of data for a paper on thermal conductivity in water is well along. The low energy input and relatively high thermal conductivity of water prevents any measurable thermal gradient in the experiments.

The glass flats were obtained from Liberty Mirror Division, Libby-Owens Ford Glass Company. True multiple beam fringes cannot be used because the long optical path resulting from the many successive passages through regions of changing refractive index gives a nonuniform dispersion resulting in a blurred effect. For this reason flats with 70% reflecting coatings were used. The 70% reflection is changed, of course, when water solution is substituted for air, and from the relative thickness of the dark and light fringes it is de-

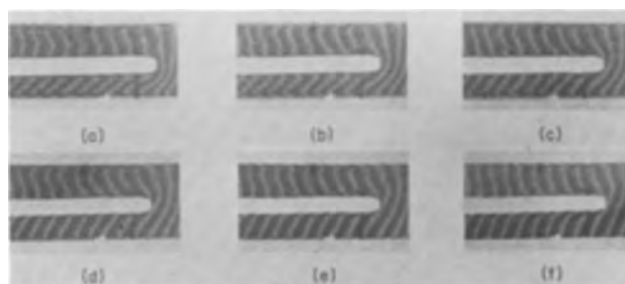


Fig. 2. A series of interferograms of the cell $\text{Fe}/\text{CuSO}_4/\text{Cu}$ where Fe is the center electrode and the fringes appear in the $0.5N$ CuSO_4 solution. The copper electrodes are 1.62 mm deep and the Fe wire is 0.7 mm diameter. The various frames show decay from a dead short by an exterior copper wire connecting the Fe to the top Cu electrode, hence maximum polarization in (a) with attendant very steep diffusion gradients which are affected by convection in the cell as shown by the gross fringe curvatures. Frames (b) to (f) show the relaxation process at varying times after the external circuit is opened. In (b) 5.4 sec have elapsed since open circuit and the concentration gradient next to the side copper electrodes is less steep and more easily visible. In (c) a further 3.3 sec has elapsed, and the process has progressed further so that the fringe pattern now closely resembles that seen in an electrodeposition cell. The successive elapsed times for (d), (e), and (f) are 6.1, 6.1, and 7.8 sec, respectively.

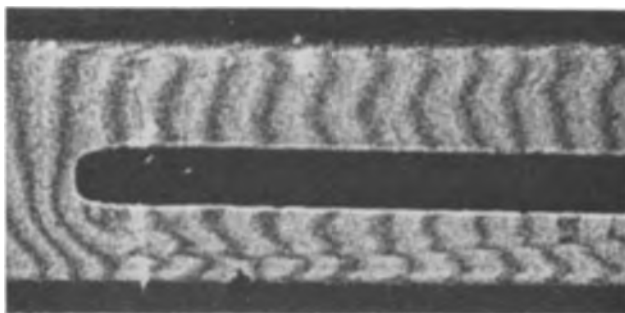


Fig. 3. Detached diffusion layer. The cell is the same as in Fig. 2. The iron wire was suddenly moved (while externally shorted to the copper electrode at the top of the frame) leaving behind its diffusion layer.

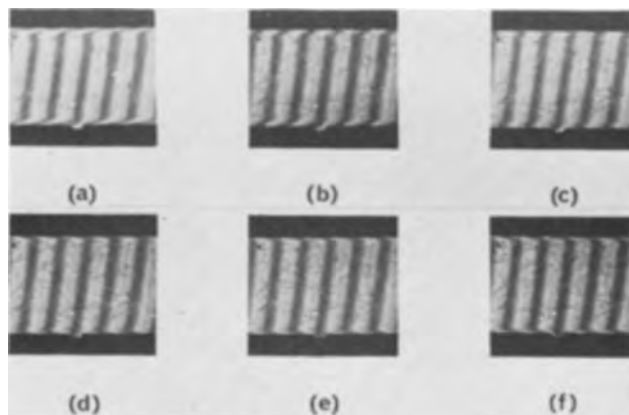


Fig. 4. Reversal of polarization in the shallow vertical position. The cell is $\text{Cu}/\text{CuSO}_4/\text{Cu}$, with 1.98 mm deep vertical electrodes at 3.28 mm separation. Frame (a) shows steady-state polarization in 0.0315N CuSO_4 at 0.68 ma/cm^2 and 0.4 impressed voltage. Frames (b) to (f) show various elapsed times after reversal of current. The successive elapsed times are (b) 5 sec, (c) 3.85 sec, (d) 4 sec, (e) 5 sec, (f) 6.25 sec. The notched electrode is the anode.

duced that the effective number of reflections is about 2.

The accuracy of the refractive index contour found depends on the precision of measurement of the distance between fringes, which depends on the location of the center of a fringe. Simple wedge fringes have a $(\cosine)^2$ distribution of intensity across a light fringe. An increased number of reflections raises the power to which the cosine is raised and thus sharpens the intensity peak and as do special photographic techniques. The maximum photographic density which occurs at the center of a fringe is not determined very accurately by eye. Accuracies approaching those of the multiple beam technique can be obtained by using a sodium vapor light as the monochromatic source and allowing interference to occur between the two lines in the doublet at 5890 and 5896Å since the center of these split fringes can be found with almost the same accuracy as that of the narrow fringes obtained in multiple beam interferometry. For refractive indices around 1.35 this will occur at odd multiples of about 0.097 mm depth of solution. 70% reflective coatings have been found to give the best fringe splitting. By adjusting the thicknesses carefully very thin center lines with sharp peak densities can be obtained in the "split" fringe system. These have been successfully replotted on cartesian coordinates using a Photovolt spot-photometer Model 501-A. Individual 16 mm frames were printed and enlarged to 5 x 7 in. or projected by use of a 45° mirror onto a large ground glass table.

The light intensity is the limiting factor. The light must be monochromatic and at such long optical paths only a minimum of pressure broadening can be tolerated. Only low-pressure Hg vapor lamps can be used,

and with filters give resultant light intensities which sodium vapor lamps can equal. Water-cooled Hg vapor lamps could be used of course. Even with a good optical train collimation is wasteful of amplitude and film with ASA ratings of about 600 is needed. Since Super Hypan² is about ASA 200, at 5893Å which is the fastest film commercially available, overdevelopment by factors of from 2-4 are necessary. A 16 mm Paillard Bolex H16 Reflex is a suitable camera if run by a synchronous motor. When equipped with an f50 mm Switar lens of about 4 cm diameter attached by a suitable length of spacer tubes, the camera can be focussed directly on the cell without further intervening optics. An obvious improvement in light sources would be a uniphase-output gas laser, with a frequency in the visible region. Such a laser has been ordered for use in this laboratory.

Four examples of work done using the technique are shown in Fig. 2-4. The variation in contrast in the reproduced frames is the result of varying depth and concentration of the solution. Frames of much less contrast than those reproduced here can be successfully analyzed by projecting them through a ground glass table top and using the densitometer head mounted on a micrometer screw carriage. All frames shown were made at room temperature (22°-24°C).

Figure 2 is a series of interferograms reproduced from individual 16 mm frames taken of the cell $\text{Fe}/\text{CuSO}_4/\text{Cu}$ where the center electrode is a 0.7 mm diameter iron wire. The cell was dead-shortened by connecting the iron wire externally to the top copper electrode. Maximum concentration polarization is very quickly obtained. The external connection was broken, and the decay of the concentration polarization followed for about 3 min or 100 ft of film at 24 frames/sec. Frame (a) shows the dead short condition, with steep concentration gradients close-in to all electrodes. The fringes are closer together than the resolution of the instrumentation will allow so that only light lines are seen next to the electrodes. Frames (b)-(f) show the relaxation of the concentration polarization at 5.4, 8.7, 14.8, 20.9, and 28.7 sec, respectively. At less than

² Trade-Mark of Ansco Corporation.

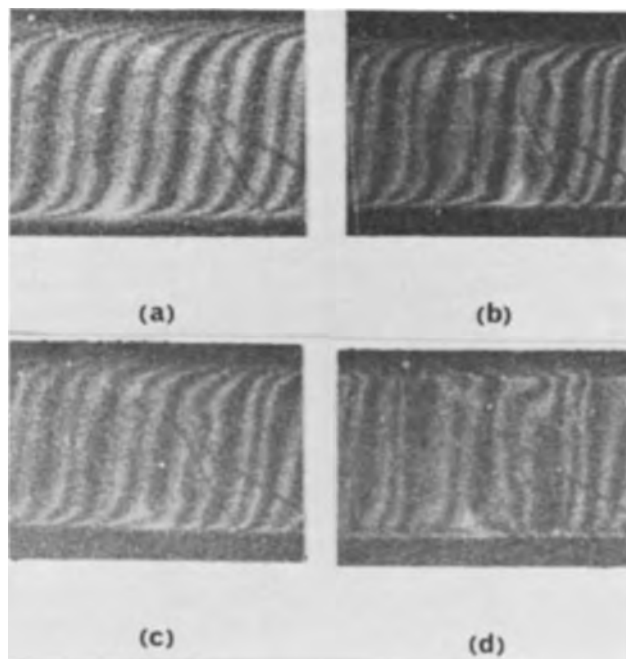


Fig. 5. Reversal of polarization in the cathode-over-anode position. Steady-state polarization in the cathode-over-anode position with the same cell as in Fig. 4. Frames (b) to (d) show the results of reversing the polarization. The successive elapsed times are (b) 16 sec, (c) 15.3 sec, (d) 12.1 sec. Pure diffusional transport is shown in (a) and the change-over to turbulent convective transport in (b) to (d).

8.7 sec the resolution of the fringes at the top copper electrode becomes possible, and at 28.7 sec the concentration gradients have become small and erratic, showing differences in activity of small areas on the electrodes.

Figure 3 shows the diffusion layer left behind in the bulk of the solution when the center electrode is moved quickly in the same cell as shown in Fig. 2. Several back and forth traverses of the center electrode were necessary to "stir up" the solution and cause the disappearance of this detached concentration gradient in less than 5 sec. Unstirred decay times were of the order of 15 sec.

Figure 4 shows several key frames from a sequence in which the electrodes were in the shallow vertical position (as shown in Fig. 1) with 0.68 ma/cm^2 current passing with an impressed voltage of 0.4v when the polarization was suddenly reversed. Frame (a) shows steady-state polarization in the cell Cu/CuSO₄/Cu containing 0.0315N CuSO₄ at 25°C and with 1.98 mm deep electrodes separated by 3.28 mm. Frames (b) to (f) were taken at elapsed times after reversal of current of 5, 8.85, 12.85, 17.85, and 24.10 sec, respectively. They show reversal of the concentration contours over the elapsed time (about 25 sec) to be essentially complete. The notch in the bottom electrode was cut for identification of the electrode, but the penetration of the concentration contour into the notch can be related to the throwing power of the solution.

Figure 5 is a sequence of frames selected to show the same phenomenon, reversal of polarization, with horizontal electrodes. Frame (a) shows the same cell as

that in Fig. 4 under the same conditions after about 5 min of electrolysis. Frames (b) to (d) were taken after reversal of current (to anode-over cathode position) at elapsed times of 16, 31.3, and 43.4 sec, respectively. Pure diffusional transport is evident in frame (a) and the change over to mainly turbulent convective transport occurs in frames (b)-(d).

A roughly 3-min sequence of the electrolysis of a cell having copper electrodes and a saturated solution of CuSO₄ (anhydrous) in methanol for electrolyte was recorded. About 1 ma/cm² passed at 36v for about 2 min produced white flecks which could be seen to move back or forth between the electrodes and to grow in size. It was impossible to tell at which electrode the reaction was taking place.¹

Manuscript received Nov. 4, 1963; revised manuscript received March 26, 1964. This paper was presented at the Pittsburgh Meeting, April 15-18, 1963.

Any discussion of this paper will appear in a Discussion Section to be published in the June 1965 JOURNAL.

REFERENCES

1. A. G. Samarcev, *Z. physik. Chem.*, **A168**, 45 (1934); N. Ibl and R. Müller, *Z. Elektrochem.*, **59**, 671 (1955).
2. R. N. O'Brien, W. F. Yakymyshyn, and J. Leja, *This Journal*, **110**, 820 (1963); R. N. O'Brien, *Nature*, **201**, 74 (1964).
3. R. N. O'Brien and C. Rosenfield, *J. Phys. Chem.*, **67**, 643 (1963).
4. S. Tolansky, "Multiple Beam Interferometry," Oxford University Press (1948).

Brief Communications



On the Nature of Burned Anodic Coatings

A. E. Hultquist

Materials Sciences Laboratory, Lockheed Missiles & Space Company, Palo Alto, California

While many studies of the growth of anodic films on aluminum have been made, there is still some disagreement on the details. One of these details is the observation of "burning" of the coating. "Burning" is the development of brown to black areas which under some condition can be enlarged until the whole coating is brown to black. The density of this discoloration can be varied so that the coating can vary from translucent to opaque. The process conditions that encourage burning are very close to those used in the hard coat processes and are generally controlled by close control of bath temperature, agitation, and current density. Since the composition of burnt coatings has not been reported previously, the data obtained in analyzing these coatings should be of interest.

Spencer (1) noted the appearance of brown to black spots in anodic coatings formed at high current densities in baths containing 5% H₂SO₄ and held at 10°C. He concluded that the burning was produced in a series of steps. Initially, a high-resistance film formed over the anode which was followed by a thickening of the film at many scattered points. The majority of the current followed paths through the film at these points. The end result was a very uneven coating.

More recently Hollo (2) in an electron-optical investigation of the pore structure of anodic films on aluminum described the growth of the oxide in similar terms. The coatings formed nonuniformly by growing primarily at scattered active centers. These centers persist despite further anodization and are in general

more active chemically and electrically than the rest of the film. While it was suggested that the reactivity of these centers could be due to the presence of metallic aluminum, the actual identification of aluminum metal at these centers was not verified.

Recent descriptions (3-6) of the preparation and properties of a black aluminum oxide suggested another explanation of the burned appearance. The black alumina can be prepared by heating a large surface area amorphous alumina in a vacuum. Additional treatment, such as mechanical compression prior to vacuum heating, must be used on crystalline material in order to produce the black alumina. The black alumina has been described as an oxygen deficient alumina. The oxygen loss is primarily a surface phenomenon.

Experimental

Samples of 40 mil 1100 Al-O-temper were cleaned and degreased in hot NaOH and then brightened in a H₂SO₄-HNO₃-H₂O solution. A final etch was made in an 11% HF solution for 3 min. The area to be anodized was taped off. Samples were anodized in a bath consisting of 49.50, 50.00, and 0.50% by weight of water, ethylene glycol, and H₂SO₄, respectively. A bath temperature of 5°C and a current density of 3.7 amp/dm² (34.4 amp/ft²) were used. Similar results were obtained in aqueous H₂SO₄ baths. The coatings formed under these conditions are black in appearance. The coatings were stripped by dissolving the aluminum substrate in bromine-methanol. One of the stripped

Table I. X-ray analysis of anodic coatings

ASTM value for AlO(OH)		Unsealed coating		Sealed coating		ASTM value for aluminum		ASTM value for boehmite	
α Value	Relative strength	d Value	Relative strength	d Value	Relative strength	d Value	Relative strength	d Value	Relative strength
3.99	100	2.33	Strong	2.34	Strong	2.34	100	6.11	100
2.32	56	2.02	Weak	2.02	Medium	2.02	47	3.16	65
2.13	52	1.43	Medium	1.85	Weak	1.43	22	2.35	53
		1.22	Weak	1.43	Medium	1.21	24	1.86	32
		0.928	Very weak	1.22	Medium	1.17	7	1.85	27
				0.925	Weak	0.93	8		
				0.905	Very weak	0.90	8		

NOTE: Halos observed at approximately 3.30 and 1.40 d values in both sealed and unsealed samples.

samples was sealed by immersing in boiling H₂O for 30 min. Both the sealed and unsealed coatings were ground in an agate mortar and analyzed by x-ray diffraction using CuK α radiation. The film was exposed for 1 hr. The results are shown in Table I and compared to the ASTM file card data for aluminum metal boehmite and AlO(OH). These last hydrated oxides are the most frequently mentioned crystallization products of amorphous anodic coatings.

As can be seen from the table, the d values and intensities agree very well with those assigned to aluminum metal. It thus follows that under certain anodizing conditions particles of aluminum metal can be incorporated into the anodic coating. If the particles are of appropriate size, they will act as pigmentation and give the coating a black color. The presence of a non-stoichiometric amorphous oxide would not be detected by the analytical methods used so that its presence is neither confirmed or denied. However, it is not impossible that a nonstoichiometric oxide could be present in anodic films formed at these or less severe anodizing conditions.

Acknowledgment

The author would like to acknowledge Mr. J. C. Robinson for the preparation and indexing of the x-ray patterns.

Manuscript received July 8, 1964.

Any discussion of this paper will appear in a Discussion Section to be published in the June 1965 JOURNAL.

REFERENCES

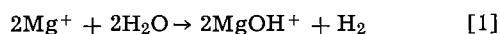
1. R. C. Spooner, *This Journal*, **102**, 156 (1955).
2. M. G. Hollo, "First International Congress on Metallic Corrosion," p. 45, Butterworths, London (1961).
3. F. Juillet, M. Prettre, and S. Teichner, *Compt. rend.*, **t248**, 555 (1959).
4. F. Juillet, M. Prettre, and S. Teichner, *ibid.*, **t249**, 356 (1959).
5. B. Arghiropoulos, J. Elston, F. Juillet, and S. Teichner, *ibid.*, **t249**, 2549 (1959).
6. A. J. Hegediis and J. Kiirthy, *J. Prakt Chem.*, **14**, 113 (1961).

Formation of Dissolved Atomic Hydrogen by Electrochemical Polarization

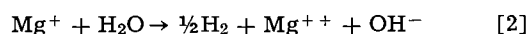
H. H. Uhlig and R. Krutenat

Corrosion Laboratory, Massachusetts Institute of Technology, Cambridge, Massachusetts

Magnesium enters solution when made anode in an electrolyte, and it is stated that the corresponding anolyte is able temporarily to reduce small amounts of KMnO₄ or AgNO₃. This was ascribed by Petty, Davidson, and Kleinberg (1), who first observed this reduction, to the presence of univalent Mg ions. These unusual valence ions, according to their viewpoint, are also able to reduce H₂O to H₂ in accord with



or



The above reactions account for liberation of H₂ gas at the anode during electrolysis, and an apparent valence of Mg ions between 1 and 2 as measured coulometrically. Other metals such as Al and Be also showed evidence of behavior analogous to Mg, and corresponding unusual valence ions were proposed such as Al⁺ and Be⁺ (2-5).

The reducing property of the anolyte appeared to rule out the possibility that local action corrosion at the metal surface was the source of an apparent unusual valence. On the other hand, other investigators proposed that the source originated from aggregates of metal atoms dislodged from the anode, perhaps as colloidal particles, and that these subsequently reacted with water after leaving the anode (6-8). Further experiments appeared to be necessary in order to resolve the matter.

Accordingly, we examined the reducing properties of the anolyte in further detail and also determined the half-life of the reducing species. This was done by anodically polarizing magnesium for 5 min at 4.4 ma/cm² in H₂-de-aerated 0.1N NaCl buffered with sodium borate to pH 10 and thermostated at 25°C. The anolyte, which remained at pH 10 during electrolysis, was then quickly transferred by means of H₂ pressure to a measuring cell made up of a large area Ag-AgCl cathode (6.9 cm²) and a small Pt anode sealed in glass, the exposed apparent area of which was 0.00283 cm². The excess diffusion current at the platinum anode was used to measure the concentration of reducing species. For this purpose, the Pt electrode was maintained at a constant potential of -0.21v (IUPAC sign) on the H₂ scale by impressing 500 mv across the Ag-AgCl and Pt cell. The diffusion current reached up to about 500 μ a/cm² immediately following transfer of the anolyte, and then largely decayed within 20-30 min. A similar increase of current was not observed if the electrolyte was transferred omitting contact with magnesium. This confirmed that a reducing species was produced during anodic dissolution of magnesium and that it was present only temporarily. A typical current-time plot is shown in Fig. 1 which also includes comparative data for the H₂-saturated electrolyte that had not been in previous contact with magnesium. The initial higher current for the H₂-saturated solution corresponds to the time

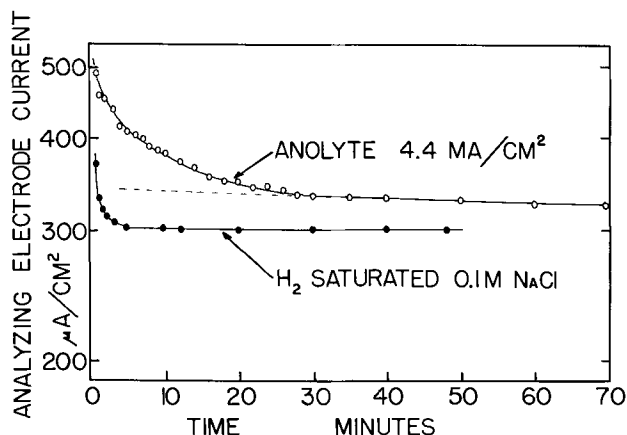


Fig. 1. Semi-log plot of diffusion current vs. time for anolyte of Mg electrolysis at 4.4 ma/cm² and for H₂ saturated electrolyte (0.1M NaCl, pH 10) 25°C.

following transfer required to eliminate turbulence and to build up the steady-state surface diffusion layer. These effects were present for all the runs, but their contribution to the measured diffusion currents after the first few minutes was negligible. The first portion of the upper curve of Fig. 1, omitting points taken previous to 4 min, corresponds to current generated by the reducing species plus the oxidation of dissolved H₂ to H⁺. The current for the latter portion of the curve corresponds to the oxidation of dissolved H₂ alone. These values, it will be noted, lie characteristically above the base-line for H₂-saturated solution. The higher values and a usual slight continuing decrease in slope after the initial current decay are discussed later. By taking the difference between total diffusion current (current between about 4-30 min, upper curve, Fig. 1) and the latter stages of the diffusion current corresponding solely to H₂ → 2H⁺ + 2e at 1 atm, the latter being extrapolated linearly to zero time (dashed upper curve, Fig. 1) the diffusion current equivalent to oxidation of the reducing species was obtained. Currents of this kind are plotted semilogarithmically in Fig. 2 showing that the reducing species follows a first order reaction and has a half-life of about 6 min.

If the reducing species were Mg⁺, it was thought possible to control its concentration by either cathodic or anodic polarization of metallic Mg at various current densities. Surprisingly, cathodic polarization also produced the reducing species, and the amount was not less than when magnesium was polarized anodically. When Ni was substituted for Mg, the reduc-

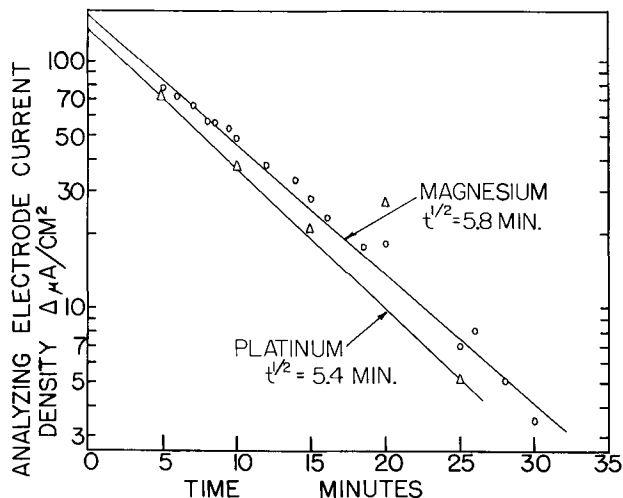


Fig. 2. Decay of reducing species in Mg anolyte and platinum catholyte. Data from Fig. 1 and 3.

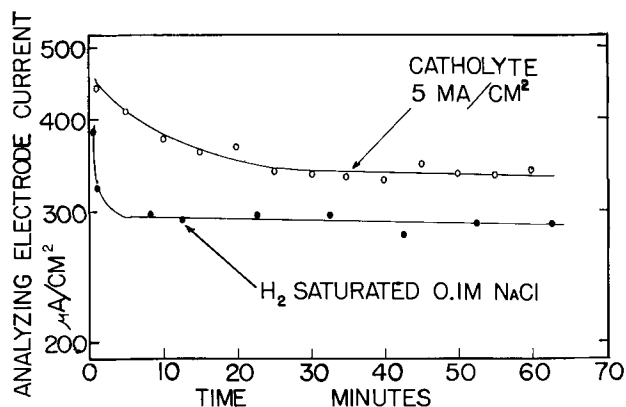


Fig. 3. Semi-log plot of diffusion current vs. time for catholyte of Pt electrode, 5 ma/cm² and for H₂ saturated electrolyte (0.1M NaCl, pH 10) 25°C.

ing species also formed with Ni as cathode, but much less so or not at all as anode, contrary to the situation for Mg. When Pt or Sn was used as cathode, the reducing species also formed (Fig. 3). For Pt cathodes, similar results were obtained in acid 0.1N NaCl of pH 2. In all instances, the measured half-life was about 5-6 min.

These experiments suggested that some form of active hydrogen forms at the cathodes, and that this very likely is atomic hydrogen. The nature of the reducing species was checked by producing atomic hydrogen in the gas phase and passing the gas into the same electrolyte, then analyzing it as before by electrochemical oxidation at the small Pt anode. The atomic hydrogen was produced by a high voltage arc discharge between two Pt wires located in H₂ at 1 atm just above the electrolyte surface. This gas was bubbled continuously through the electrolyte with simultaneous cooling to counteract a temperature rise above 25°C. Temperature variations limited the accuracy with which diffusion current measurements could be made. In these runs, a measured half-life of 3.5-4.9 min was similar within experimental limitations to the half-life measured for the reducing species produced cathodically in aqueous solution.

These experiments suggested, therefore, that a portion of the atomic H formed by reduction of H⁺ at a cathode dissolves in the surrounding catholyte to form H(aq). In turn H(aq) rapidly combines to form dissolved molecular hydrogen, H₂(aq). It is the atomic species, therefore, that apparently accounts for the temporary reducing properties preceding the time all dissolved H combines to form H₂.

The fact that a diffusion current for H(aq) → H⁺(aq) + e is measured over and above the current ascribed to H₂-saturated electrolyte, means that H(aq) diffuses more rapidly than H₂(aq). This follows because the foregoing reaction requires the same number of electrons per gram atom as does H₂(aq) → 2H⁺ + 2e. The limiting diffusion current for the first reaction is $k[\text{conc. H(aq)}]$ whereas it is $2k'[\text{conc. H}_2(\text{aq})/2]$ for the second reaction, with $k > k'$. The term k refers to DF/δ , where D is the diffusion coefficient, F is the Faraday, and δ is the equivalent thickness of the stagnant diffusion layer at the electrode surface. Since k is not known, it is not possible to assess the concentration of H(aq). However, an estimate can be made from the difference of the latter portion of diffusion current curve for the catholyte and for H₂-saturated electrolyte. Atomic hydrogen of short half-life combines to form molecular hydrogen, and since the solution is already saturated, the reaction supersaturates the electrolyte with H₂. For this reason, the latter portion of the upper curve in Fig. 3 lies above the lower curve. Neglecting dissolved H₂ that may be lost in 20 or 30 min from the super-saturated solution, and noting that the value of D for H₂(aq) is approximately 4×10^{-5} cm²/sec and $\delta =$

0.05 cm, the difference of 20-40 $\mu\text{a}/\text{cm}^2$ in diffusion current between upper and lower curves corresponds to an initial concentration of $\text{H}(\text{aq}) = 2.5\text{-}5 \times 10^{-4}$ g-at./liter.

The question might be asked—is not all of the upper curve of Fig. 3 caused by supersaturated $\text{H}_2(\text{aq})$ rather than in part by $\text{H}(\text{aq})$? This is not likely as was demonstrated by supersaturating the electrolyte with H_2 at 1.4 atm, passing the supersaturated electrolyte into the measuring cell at 1 atm and noting the decay of diffusion current with time. For this experiment, the resultant decay time was much longer than for $\text{H}(\text{aq})$, corresponding to an apparent half-life of about 300-400 min and a slight slope similar to latter portions of curves like that shown in Fig. 3. A further experiment that discounts supersaturation as total cause consisted of cathodically polarizing Pt in N_2 -saturated electrolyte with continuous bubbling of purified N_2 during electrolysis. Despite the fact that the 0.1N NaCl catholyte was undersaturated with H_2 at any time, a diffusion current was observed that decayed as before, corresponding to a half-life of about 6 min.

The reaction $2\text{H}(\text{aq}) \rightarrow \text{H}_2(\text{aq})$ occurs within the body of the electrolyte as well as at the glass and electrode surfaces. Supersaturation with respect to $\text{H}_2(\text{aq})$ indicated by the diffusion current curves was also clearly observed by formation of numerous small bubbles of H_2 in the measuring cell after transfer of catholyte. It is this phenomenon which has contributed to statements in the literature that hydrogen formed at a cathode is supersaturated.

Yeager *et al.* (9) ascribed H_2 supersaturation at a Pt cathode to pressures higher than 1 atm in small size bubbles and to lack of suitable nuclei for gas evolution. This explanation was used to account for observed reduction of measured hydrogen overvoltage in 0.107N H_2SO_4 in the order of 6 mv when the stagnant solution was agitated. Schuldiner (10) found a 15 mv reduction of hydrogen overvoltage for Pt when the electrolyte was stirred by bubbles of H_2 . Earlier, Kandler, Knorr, and Schwitzer (11) observed a similar effect of stirring for Pt or Pd cathodes in either acid or alkaline electrolytes. They ascribed the effect to concentration polarization caused by slow diffusion of molecular H_2 away from the cathode surface. Platonova and Levina (12) observed that the potential of platinized Pt located close to an Fe cathode in 0.4N KOH at which H^+ was discharging was moved to a potential 14 mv more active than the reversible hydrogen electrode. They ascribed the effect to supersaturation of the electrolyte with H_2 in accord with Kandler *et al.*'s explanation. They also pointed out that supposed supersaturation occurred with Ni cathodes and was still more marked in 10.5N KOH. Bockris and Azzam (13) reported hysteresis for cathodic polarization curves of Pt electrodes in 5N HCl which they thought might be due to trace impurities in solution, but which further purification procedures nevertheless did not eliminate.

Our experiments, on the other hand, indicate that $\text{H}(\text{aq})$ is the primary cause of both hysteresis and an effect of stirring on hydrogen overvoltage measurements, and it is also the cause of observed supersaturation of catholyte with hydrogen. The thermodynamic effect of $\text{H}(\text{aq})$ according to $\text{H}(\text{aq}) \rightleftharpoons \text{H}^+ + e$ is the same as that of increased hydrogen pressure for the equilibrium: $\text{H}_2 \rightleftharpoons 2\text{H}^+ + 2e$, namely, that of producing a more active potential. Hence when the solution is stirred, the concentration of $\text{H}(\text{aq})$ at the cathode surface decreases and the potential changes in the more noble direction corresponding to an apparent reduction of overvoltage. Similarly, series of polarization measurements made with systematic decrease of current density occur in presence of higher concentrations of $\text{H}(\text{aq})$ than with increase of current density, giving rise to an observed hysteresis. The presence of $\text{H}(\text{aq})$ very likely also enters

the explanation for some aspects of the decay characteristics of hydrogen overvoltage.

It would normally be assumed that the reaction $\text{H}(\text{aq}) \rightarrow 1/2\text{H}_2(\text{aq})$ is second order. The fact that a first order reaction is followed instead suggests that the reaction proceeds only on some surface on which atomic hydrogen first adsorbs, and that subsequent reaction depends on the concentration of $\text{H}(\text{aq})$ which diffuses to the adsorbed H. Presumably dust in the electrolyte can act as a suitable surface in addition to the glass or metal surfaces within the cell.

The supposed formation of dissolved atomic H was actually announced by Kobosev and Nekrassov (14) in 1930. They reported that a suspension of small particles of yellow WO_3 in 1N H_2SO_4 catholyte was reduced to blue W_2O_5 during electrolysis. The reduction was greater the higher the overvoltage of the cathode metal. Their results, however, were not confirmed by Bagotsky and Jofa (15) using 0.2N H_2SO_4 and a Hg cathode. The latter investigators found that particles of WO_3 were reduced only if in physical contact with the mercury surface; those particles 0.1-0.2 mm distant were not affected by the cathodic current. Bockris (16) thought that formation of $\text{H}(\text{aq})$ at a cathode was excluded on kinetic considerations, and that the results of Kobosev and Nekrassov must have been the result of contact of WO_3 particles with the cathode surface.

We also could not confirm visible reduction of WO_3 or MoO_3 by $\text{H}(\text{aq})$. Instead, in accord with conclusions of Bagotsky and Jofa, only when the oxide particles actually touched a Pt cathode at which H^+ discharged did we find a color change; otherwise not. Apparently surface reactions of $\text{H}(\text{aq})$, such as formation of $\text{H}_2(\text{aq})$, take place in preference to reduction of the oxide.

From the preceding discussion, the reducing properties of the anolyte when magnesium is polarized as anode is due presumably to $\text{H}(\text{aq})$ and not to an unusual valence Mg ion. Atomic hydrogen may be produced, therefore, by local action cathodes during exposure of the corroding magnesium anode to the electrolyte. However, $\text{H}(\text{aq})$ may also be produced by reaction of Mg^+ with H_2O , in accord with reaction [2], on substituting $\text{H}(\text{aq})$ for $1/2 \text{H}_2$ on the right-hand side. There is some question whether colloidal Mg could equally be the source of $\text{H}(\text{aq})$. In such an event, the complete reaction of colloidal Mg with H_2O must of necessity consume almost no time (high reaction rate) in order to account for an observed half-life for resulting $\text{H}(\text{aq})$ of 6 min, similar to the half-life observed in absence of colloidal Mg. This is unlikely. The ionic reaction involving Mg^+ , on the other hand, could conceivably be rapid enough to account for similar half-lives. The possible formation of Mg^+ during anodic dissolution of Mg, therefore, deserves further study.

Although the above discussion relates all observed effects to $\text{H}(\text{aq})$, it is possible, of course, that H reacts with H^+ to form species like H_2^+ , and it may be such species that also enter the observed reactions. The possible existence of H_2^+ was discussed briefly by Ives (17).

Further details of the above experiments will be described in a subsequent paper.

Acknowledgment

This research was supported jointly by the General Motors Research Laboratory and by the Corrosion Research Council of the Engineering Foundation to whom the authors express their appreciation.

Manuscript received April 28, 1964; revised manuscript received Aug. 20, 1964.

Any discussion of this paper will appear in a Discussion Section to be published in the June 1965 JOURNAL.

REFERENCES

1. R. Petty, A. Davidson, and J. Kleinberg, *J. Am. Chem. Soc.*, **76**, 363 (1954).

2. E. Raijola and A. Davidson, *ibid.*, **78**, 556 (1956).
3. B. Laughlin, J. Kleinberg, and A. Davidson, *ibid.*, **78**, 559 (1956).
4. K. Heusler, *Z. Elektrochem.*, **65**, 192 (1961).
5. J. Greenblatt, *This Journal*, **103**, 539 (1956); *Corrosion*, **18**, 125t (1962).
6. G. Hoey and M. Cohen, *ibid.*, **105**, 245 (1958).
7. G. Marsh and E. Schaschl, *ibid.*, **107**, 960 (1960).
8. M. Straumanis and B. Bhatia, *ibid.*, **110**, 357 (1963).
9. E. Yeager, T. Oey, and F. Hovorka, *J. Phys. Chem.*, **57**, 268 (1953); E. Yeager in "Trans. Symp. on Electrode Processes," E. Yeager, editor, p. 145, John Wiley & Sons, Inc., New York (1961).
10. S. Schuldiner, *This Journal*, **99**, 488 (1952).
11. L. Kandler, C. Knorr, and C. Schwitzer, *Z. physik. Chem.*, **180A**, 281 (1937).
12. I. Platonova and J. Levina, *J. Phys. Chem. (USSR)*, **21**, 331 (1947).
13. J. Bockris and A. Azzam, *Trans. Faraday Soc.*, **48**, 145 (1952).
14. N. Kobosev and N. Nekrassov, *Z. Elektrochem.*, **36**, 529 (1930).
15. V. Bagotsky and S. Jofa, *Compt. rend. (Doklady), Acad. Sci. (URSS)*, **53**, 439 (1946).
16. "Modern Aspects of Electrochemistry," J. O'M. Bockris, Editor, pp. 219-20, Academic Press, New York (1954).
17. D. Ives, *Can. J. Chem.*, **37**, 213 (1959).

Water Vapor as an Etchant for Silicon

T. L. Chu and R. L. Tallman

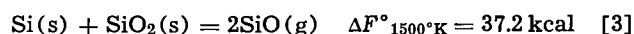
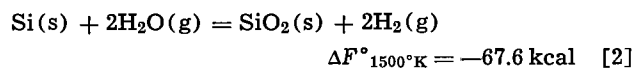
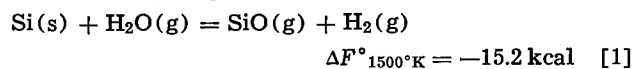
Research Laboratories, Westinghouse Electric Corporation, Pittsburgh, Pennsylvania

Clean silicon surfaces are important in device technology for such purposes as epitaxial growth, growth of silica films, diffusion, etc. For example, when the surface of silicon substrates is free from mechanical damage, the structural imperfections in the epitaxial silicon are caused mainly by the foreign impurity particles on the substrate surface (1). In the growth of silica films, impurity particles on the silicon surface could produce discontinuities in the film and may also affect the interface characteristics (2). Since clean surfaces are not readily obtained by the usual etching and cleaning operations (3), it is preferable that silicon surfaces be chemically etched in the apparatus in which further processes will be carried out. Anhydrous hydrogen chloride has been used as an etchant for silicon substrates used in the epitaxial growth process, and the etching is carried out in the growth apparatus immediately prior to the deposition process (4, 5). Clean, structureless surfaces can be obtained in this manner. The epitaxial silicon grown on these surfaces by the thermal reduction of silicon tetrachloride with hydrogen was found to have stacking fault concentrations less than 200/cm² and dislocation densities no greater than that of the substrate.

In spite of its success, hydrogen chloride is not an entirely satisfactory etchant for silicon substrates in the epitaxial growth process. In this process, the silicon substrates are supported and heated by an rf susceptor which frequently has a silicon surface. Since the reaction between silicon and hydrogen chloride is chemically reversible, silicon and its dopants can be transported between the susceptor and the substrate. Thus, unless the substrate and the susceptor are of very high purity, the electrical resistivity of the grown layer is not readily controllable. For example, when heavily doped p-type substrates are subjected to hydrogen chloride treatment, the susceptor may become so contaminated as to influence strongly the resistivity of the subsequently grown layer. It is therefore preferable to eliminate this transport process by the use of etchants which react irreversibly with silicon. We have used water vapor at low partial pressures in hydrogen or inert atmospheres for this purpose, and the results are summarized in this communication. The use of water has the further advantage that it can be readily purified in contrast to the variable quality of "pure" hydrogen chloride available commercially.

At low partial pressures of water in a hydrogen or inert atmosphere, silicon is presumably oxidized to a mixture of silicon monoxide and silicon dioxide. Silicon monoxide is volatile at high temperatures, and

silicon dioxide reacts with silicon to form the volatile monoxide. The free energy changes of these reactions at 1500°K, calculated from the JANAF thermochemical data (6), are given below



These reactions are rapid at the temperatures under consideration. In spite of its large positive free energy change, reaction [3] takes place readily because of the high volatility of silicon monoxide. Furthermore, carbonaceous impurities on the substrate may also react with water vapor to form volatile products.

The epitaxial growth of silicon was carried out by the conventional method, i.e., the thermal reduction of a silicon chloride with hydrogen on heated substrate surfaces in a flow system. The silicon substrates were of {111} orientation, mechanically lapped with American Optical Company No. 305 abrasive, and chemically etched with CP₄. Prior to the growth process, the substrates were heated to about 1270°C in hydrogen containing 0.02-0.1% water, at a flow rate of 6-20 l/min, for 15-30 min. Depending on the experimental conditions, silicon may be removed at a rate of up to 5 μ/hr. This water vapor etch appears to be nonpreferential, and the resulting silicon surface resembles the original surface when examined with an optical microscope.

The structural perfection of the epitaxial silicon grown in the above manner was evaluated using chemical etching and optical microscope techniques (1). The commonly observed imperfections in epitaxial silicon are stacking faults, dislocations, and polycrystalline inclusions. They are easily revealed by etching the specimen with the Sirtl etch (7) for 30-60 sec while removing 0.5-1 μ of the grown material. The Sirtl etch is superior to other etchants for this purpose. Specimens from many experiments all exhibited considerably lower concentrations of stacking faults, dislocations, and polycrystalline inclusions as compared to similar experiments in which no water treatment was used. In general, the concentration of the stacking faults originating at the interface was reduced from approximately 10³ cm⁻² to less than 10 cm⁻² as a result of the water treatment. In a thick grown layer, say 200 μ, these faults would be small in number relative to the stacking faults generated in the grown layer. The dislocation density in the grown layer be-

came similar to that in the substrate when the water treatment was used. Furthermore, the probability of obtaining inclusion-free specimens was greatly enhanced.

In conclusion, the water vapor treatment of silicon substrate just prior to the growth process can reduce the number of structural imperfections originating at the interface of the epitaxial silicon. Silicon surfaces prepared in this manner may also be useful for other device purposes.

Manuscript received Aug. 7, 1964. This paper was presented at the Washington Meeting, Oct. 11-15, 1964.

Any discussion of this paper will appear in a Discussion Section to be published in the June 1965 JOURNAL.

REFERENCES

1. T. L. Chu and J. R. Gavaler, in "Metallurgy of Advanced Electronic Materials," G. E. Brock, Editor, p. 209, (Metallurgical Society Conferences, Vol. 19), Interscience, New York (1963).
2. M. M. Atalla, E. Tannenbaum, and E. J. Scheibner, *Bell Syst. Tech. J.*, **38**, 749 (1959).
3. R. Stickler and J. W. Faust, Jr., Paper presented at the Toronto Meeting of The Electrochemical Society, May 1964.
4. K. Bean and P. Gleim, *This Journal*, **110**, 265C (1963).
5. G. A. Lang and T. Stavish, *RCA Rev.*, **24**, 488 (1963).
6. JANAF Interim Thermochemical Tables, The Dow Chemical Co., Midland, Mich., Dec. 31, 1960.
7. E. Sirtl and A. Adler, *Z. Metallk.*, **52**, 529 (1961).

Manuscripts and Abstracts for Spring 1965 Meeting

Papers are being solicited for the Spring Meeting of the Society, to be held at the Sheraton Palace in San Francisco, Calif., May 9, 10, 11, 12, and 13, 1965. Technical sessions probably will be scheduled on: Electric Insulation, Electronics (including Luminescence and Semiconductors and a Symposium on Optical Masers), Electro-Organic (including a Symposium on Industrial Organic Chemistry and a Symposium on Elucidation of Electro-Organic Electrode Processes jointly with the Theoretical Electrochemistry Division), Electrothermics and Metallurgy (including joint Symposium on Molten Salts jointly with the Theoretical Electrochemistry Division, and, also, a Symposium on Strengthening Mechanisms in Nonmetallics), Industrial Electrolytic (including a Symposium on Electrolytic Diaphragms and Battery Separators jointly with the Battery Division and, also, a Symposium on the Production of Chlorine without Caustics).

To be considered for this meeting, **triplicate copies of the usual 75-word abstract, as well as of an extended abstract of 500-1000 words** (see notice on page 1308 of this issue), must be received at The Electrochemical Society, 30 East 42 St., New York, N. Y., 10017, *not later than December 15, 1964. Please indicate on 75-word abstract for which Division's symposium the paper is to be scheduled, and underline the name of the author who will present the paper.* No paper will be placed on the program unless one of the authors, or a qualified person designated by the authors, has agreed to present it in person. Clearance for presentation of a paper at the meeting should be obtained before the abstract is submitted. An author who wishes his paper considered for publication in the JOURNAL or ELECTROCHEMICAL TECHNOLOGY should send triplicate copies of the manuscript to the Managing Editor of the appropriate publication 30 East 42 St., New York, N. Y., 10017. Concerning papers to be published in JOURNAL, see notice on per page charges on page 263C of this issue.

Presentation of a paper at a technical meeting of the Society does not guarantee publication in the JOURNAL or ELECTROCHEMICAL TECHNOLOGY. However, all papers so presented become the property of The Electrochemical Society, and may not be published elsewhere, either in whole or in part, unless permission for release is requested of and granted by the Editor. Papers already published elsewhere, or submitted for publication elsewhere, are not acceptable for oral presentation except on invitation by a Divisional program Chairman.

Galvanostatic and Volumetric Studies of Hydrocarbons Adsorbed on Fuel Cell Anodes

L. W. Niedrach

Research Laboratory, General Electric Company, Schenectady, New York

ABSTRACT

The reactions of C_1 through C_4 hydrocarbons, both saturated and unsaturated, on platinum-black fuel cell anodes have been followed with the aid of volumetric and galvanostatic techniques. Gas chromatography has been employed to provide supplementary information. Both acidic and alkaline electrolytes have been included in the studies. The hydrocarbons fall into three groups with regard to surface coverage with C_n species: low for methane, intermediate for saturated hydrocarbons, and high for unsaturates (including cyclopropane). Cracking, polymerization, and self-hydrogenation are among the reactions occurring on fuel electrodes; evidence is presented for the formation of C_1 , C_2 , C_3 , and C_4 species on electrodes equilibrated with ethylene. Significant amounts of species as high as C_8 are formed from propylene and cyclopropane. The oxidation of the adsorbed carbonaceous species from all of the hydrocarbons requires high overvoltages which can be reduced by raising the temperature.

In the oxidation of hydrocarbons at fuel cell anodes, the reaction sequence involves many successive steps. Concurrent with the necessary steps for complete oxidation, many side reactions can occur. It was the purpose of this investigation to identify some of the processes occurring in the complex environment of a representative fuel cell anode.

Galvanostatic and volumetric techniques including gas chromatography were employed. Measurements were made with acidic and alkaline low-temperature cells, and information was obtained relating to open circuit as well as load conditions. Included in the studies was a broad variety of hydrocarbons in order to uncover any important structural effects. Where possible the observations have been correlated with the literature on heterogeneous catalysis as well as with fuel cell operating data obtained with cells of related structure (1, 2).

Galvanostatic curves were employed in these studies because their structures often permit deductions about the reactions and species that are involved. Furthermore, a considerable literature exists pertaining to the galvanostatic and related behavior of hydrogen, the simplest fuel, on platinum electrodes (3-7). Prior examination of the present electrodes (Teflon-bonded platinum black) in the presence and absence of adsorbable hydrogen had shown that they gave galvanostatic curves in agreement with those previously reported for conventional smooth platinum and platinized platinum electrodes. Thus, the reversible hy-

drogen region, the "clean" double layer region, the oxide film region, and the oxygen evolution region are found. The curves obtained with hydrogen then served as a convenient basis of reference for interpretation of the curves obtained with the other fuels.

Experimental

Cell and procedures.—The cell used in the studies is shown in the cross-sectional diagram in Fig. 1. The 3.8 cm (1.5 in.) diameter test electrodes were prepared from 0.20g platinum black (Fisher Lot No. 701,281) using 0.027g Teflon as the binder. They were heated for 2 min at 350°C under a pressure of 78 kg/cm² (1100 psi) in order to sinter the Teflon binder. The reference electrode was a 1.27 cm square of the same material. For the counterelectrode a 3.8 cm diameter circle of 80 mesh platinum screen was employed.

The electrolyte was incorporated into a suitable matrix by equilibration. A Zerolit C-20 cation exchange membrane was used as the matrix for the sulfuric acid. Zerolit A-20 membranes were used with the potassium bicarbonate and potassium hydroxide electrolytes. In addition, some experiments were performed in which the potassium hydroxide was retained in a matrix of asbestos cloth. In all cases the matrices were thoroughly rinsed with frequent changes of the equilibrating electrolytes for a period of several days before use.

A matrix and the associated electrodes were assembled into the housing which consisted of a glass face-plate on the side of the test electrode and a Lucite plate on the opposite side. Teflon-100 gaskets were used with the glass plate and silicone rubber with the Lucite. Platinum screens, which pressed against the electrodes and the faceplates, held the electrodes in good contact with the membrane matrix.

In general, new cells (electrodes, matrix, and electrolyte) were assembled when the electrolyte or temperature was changed.

The reference electrode was fed continuously with pure hydrogen. A slow flow of helium was generally maintained on the counterelectrode, but during long equilibrations of the test electrode with a fuel gas, the counterelectrode was flooded with electrolyte.

In performing a series of experiments with a cell, a galvanostatic oxidation curve was first obtained for the test electrode after saturating its surface with hydrogen. This was done by admitting hydrogen into chamber II and allowing equilibration for about 30 min. Chamber II was then completely flooded by forcing in additional electrolyte from a reservoir up to the vent. With the electrode thus "drowned," a current

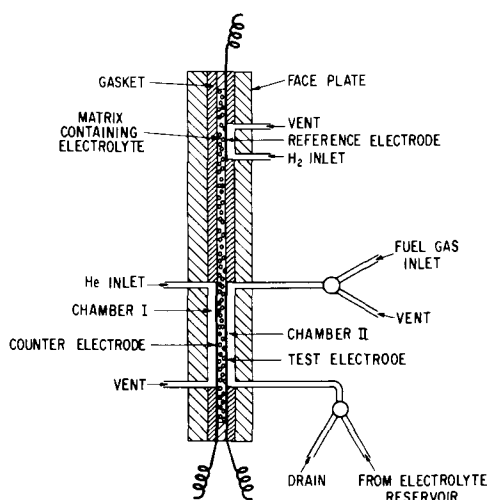


Fig. 1. Cross section of test cell

of 30 ma (2.63 ma/cm²) was then forced through the cell in a direction to oxidize the adsorbed gas. Electrolysis was continued through oxygen evolution. This initial galvanostatic curve served as a convenient reference against which frequent checks were made throughout the life of the electrode. Even after several weeks' use no changes in the general shape of the hydrogen curve were ever detected. The lengths of the hydrogen breaks showed a very gradual decrease which at most represented a change of about 15%. This occurred with a cell that had been used over a period of several weeks.

After allowing oxygen evolution for 3-4 min the current was interrupted and the free electrolyte was drained from the chamber. Fresh electrolyte was then admitted from the reservoir, and all gas bubbles were eliminated. The current was then reversed to reduce the oxide film on the platinum surface. When the potential had reached a value well within the "double-layer" region [*i.e.*, the region where, with the low sweep speeds employed, the electrode surface is essentially free of oxide and hydrogen films (4,7)] the current was again interrupted. In the acidic systems the reductions were stopped at a potential of 0.40v *vs.* the hydrogen reference electrode; in the alkaline and bicarbonate systems at potentials of 0.3-0.5v.

With the electrode clean, the "drowning" liquid was withdrawn from the cell, and the gas to be adsorbed was simultaneously drawn into the chamber through the fuel gas inlet at the top. When volumetric adsorption data were to be obtained the adsorbant gas was contained in a thermostated gas buret attached to the fuel gas inlet at the top of the cell. A 2 ml glass Luer syringe was then used in withdrawing the drowning liquid so that a zero correction could be applied to the readings obtained with the gas buret. The system was then allowed to equilibrate for the desired time. During this period the potential of the test electrode *vs.* the hydrogen reference was recorded as was the change in volume of the gas in the buret.

At the end of an equilibration the gas was forced from the cell chamber by reflooding with electrolyte. In some cases the vented gas was forced into the graduated collector tube shown in Fig. 2. Similarly residual gas in the buret could be transferred to the collector. After measuring the volumes, aliquots were taken through the rubber septa with Hamilton gas-tight syringes. These samples were subsequently analyzed with a Perkin-Elmer Fractometer.

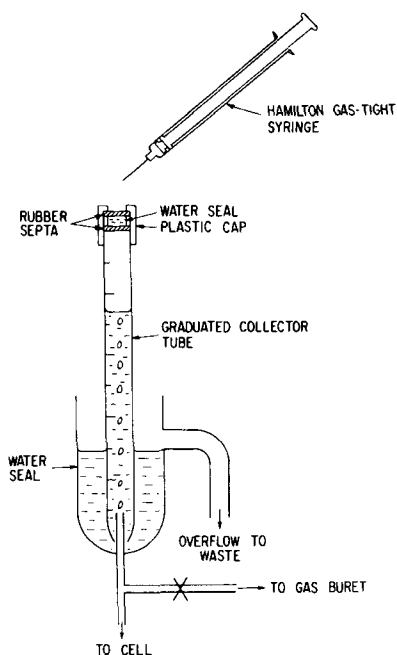


Fig. 2. Collecting system for gas samples

The gases adsorbed on the electrode were then removed by galvanostatic oxidation or reduction while the potential was recorded against the hydrogen reference. Oxidations were continued until oxygen had evolved for 3-4 min. Because of the high solubility of CO₂, the major oxidation product, in aqueous solutions it was not possible to obtain meaningful volumetric data during oxidations.

During reductions fully hydrogenated hydrocarbons were desorbed. These gases, along with excess hydrogen produced at the electrode, displaced the acid in the cell chamber where they were allowed to accumulate. They were then transferred rapidly to the collector by forcing them from the cell chamber with acid without interrupting the current. Three such displacements having volumes of 1.5 cc each were made during the cathodic treatments. Suitable aliquots of the measured volumes were taken for chromatographic analysis. Because of the relatively low solubilities of the gases in acid (8,9) and water (10,11), and the rapidity of the transfer steps, including the withdrawal of syringe samples, losses were low and 80-90% of the initially adsorbed hydrocarbons were accounted for.

Anodic oxidations were always carried through to oxygen evolution for several minutes so that all oxidizable materials were removed. Cathodic evolutions were regularly followed immediately by an oxidation to oxygen evolution to determine whether residual oxidizable species remained on the electrode.

Following a run the electrode was regularly exposed to hydrogen (with or without a volumetric measurement of its uptake) and after an equilibrium time of 30 min or more, an oxidation curve was run. This treatment served a dual purpose of detecting spurious oxidation waves from residual materials and of indicating any changes in electrode surface area by changes in the length of the breaks for hydrogen oxidation and oxygen coverage. [As noted above over a period of several weeks it was found that the surface area of the electrode gradually declined by at most 15%. This can probably be attributed to changes resulting from slow platinum dissolution as a result of the repeated rigorous treatment involving oxygen evolutions for extended periods of time. Indeed a small amount of platinum (~8 mg) was found to be deposited on the membrane facing the counterelectrode in one case.] When the hydrogen wave was found to be satisfactory, generally in the run immediately following an oxidation, the electrode was reflooded in preparation for potential adjustment to the "double layer" region for another run.

In addition to the static equilibrations on open circuit a number of runs were performed in which the electrode was operated continuously as a fuel anode before it was flooded and the remaining surface species were removed cathodically. In these runs the electrode was kept on load during flooding to prevent readorption of gases. As soon as it was flooded (within 3-5 sec) the current was interrupted. Subsequent treatment was as above.

Materials.—The hydrogen used in these experiments was electrolytic grade. With the exception of the cyclopropane, which was Matheson C.P. grade, all of the hydrocarbons were Phillips Research Grade.

Reagent chemicals were used throughout without further purification. Dissolved oxygen was, however, removed from the electrolytes by purging with helium.

The platinum black used in the experiments had a surface area of 37 m²/g as determined by the BET method employing krypton as the adsorbant. Galvanostatic charging curves obtained for this black in the absence of the Teflon binder gave a value of 1.03 x 10¹⁵ H atoms/cm² which is in reasonable agreement with the values one calculates for several of the major

¹ The author has obtained similar values from galvanostatic and BET data for two other Fisher platinum blacks and one Engelhard black; *viz.*, 0.98, 1.11, and 1.12 x 10¹⁵ H at/cm² for blacks having BET areas of 37, 35, and 32 m²/g, respectively. Vacuum annealing for 60 hr at 150°C resulted in only a 2% loss of hydrogen sites.

Table I. Packing densities of platinum atoms in the major planes of face-centered cubic platinum

$a_0 + 3.913\text{\AA}$	
Plane	Pt at./cm ²
100	1.30×10^{15}
110	0.93×10^{16}
111	1.51×10^{15}

crystal faces of platinum, cf. Table I, and is consistent with previous suggestions that one hydrogen atom is adsorbed on each platinum site (4-6).

It is of interest to note that in applying a similar calculation to the hydrogen break associated with the platinum in the Teflon bonded electrodes 0.95×10^{15} H atoms/cm² were found. This indicates that 93% of the original sites are accessible for electrochemical action.

Results and Discussion

Effect of Electrolyte and Fuel Structure

Because of the dearth of information available, it was of immediate importance to examine the behavior of a series of hydrocarbons in the presence of a variety of electrolytes to determine whether the electrolyte or the structural characteristics of the fuel would have an important influence on the adsorption and oxidation characteristics. In the initial experiments, galvanostatic oxidation curves were obtained for a variety of hydrocarbons adsorbed on the test electrodes after equilibration times of 30 or 60 min. In general the shorter equilibrations were used for the unsaturates and the longer for the saturates. The series of saturated hydrocarbons ethane, propane, and isobutane (with primary, secondary, and tertiary carbon-hydrogen bonds, respectively) were examined in cells employing sulfuric acid, potassium hydroxide, and potassium bicarbonate as electrolytes.

Additional tests were run with methane, cyclopropane, and ethylene in some cases in order to uncover other differences in structure that might have bearing on performance. Data were obtained at 25° and 65°C. In each cell, a series of gases was run in the order hydrogen, methane (acid system only), ethane, propane, and isobutane. Following the initial tests with hydrogen and these saturated hydrocarbons, additional tests were run with the same materials and in some cases with ethylene and cyclopropane so that replicate and comparison data would be available.

Representative data showing the changes in the working electrode potentials with time during equilibration at 25°C are shown in Fig. 3 through 5. In Fig. 6 galvanostatic oxidation curves are shown for the adsorbed materials after 30 or 60 min equilibra-

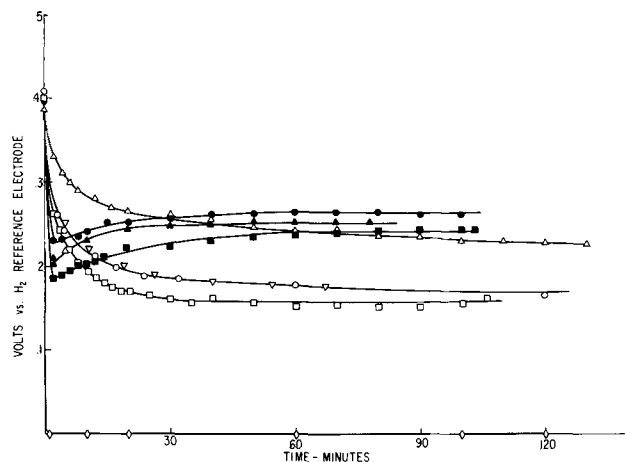


Fig. 3. Change in electrode potential with time during gas adsorption with acidic electrolyte. \diamond , hydrogen; \triangle , methane; \circ , ethane; \square , propane; ∇ , isobutane; \bullet , ethylene; \blacktriangle , propylene; \blacksquare , cyclopropane. $5N$ H_2SO_4 , 25°C, cells LFC 348 and 235.

tions. The galvanostatic curves in each family are superimposed in such a way that the oxygen evolution regions overlap. Similar oxidation curves were ob-

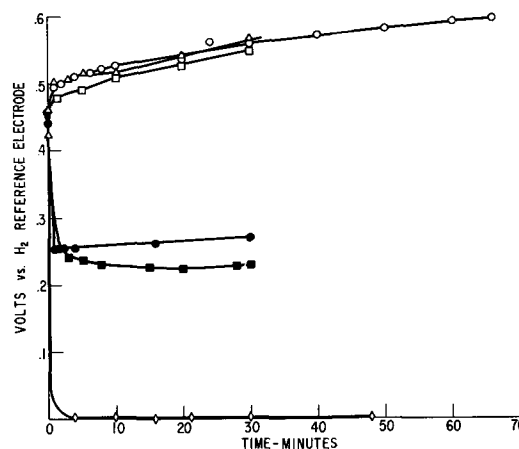


Fig. 4. Change in electrode potential with time during gas adsorption with $KHCO_3$ electrolyte. \circ , Ethane; \square , propane; \triangle , isobutane; \bullet , ethylene; \blacksquare , cyclopropane; \diamond , hydrogen. $3M$ $KHCO_3$, 25°C, cell LFC 239.

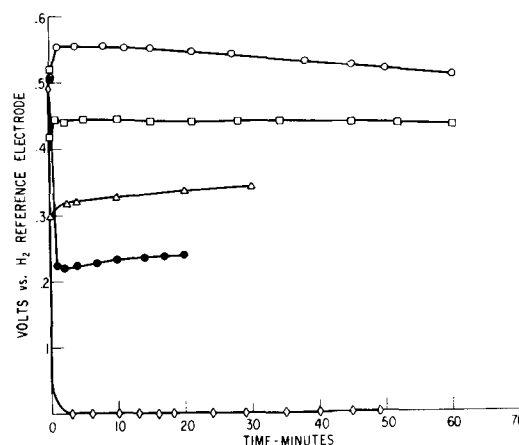


Fig. 5. Change in electrode potential with time during gas adsorption with caustic electrolyte. \diamond , Hydrogen; \circ , ethane; \square , propane; \triangle , isobutane; \bullet , ethylene. $6M$ KOH , 25°C, cell LFC 237.

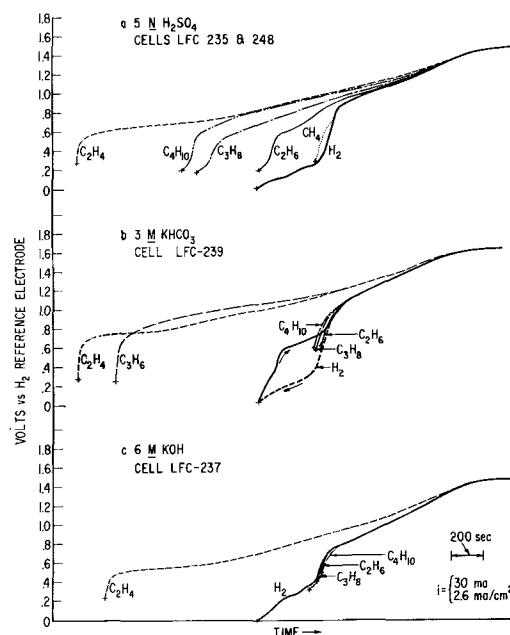


Fig. 6. Galvanostatic oxidation curves for hydrocarbons adsorbed on platinum black electrodes at 25°C.

tained with higher and lower current densities, the major differences being in the magnitude of the overvoltages associated with the plateaus on the curves.

In each family of galvanostatic curves one for hydrogen as the fuel is included for reference. It is to be noted in this connection that the curve for the oxidation of adsorbed hydrogen obtained with the bicarbonate electrolyte is irregular in that a high overvoltage is required. This appears to result from a reaction of adsorbed hydrogen with the carbonate to form CO or a related species on the electrode surface. The galvanostatic curve for the electrodeposition of hydrogen on the electrode is shown as a dashed curve. It is seen that a pronounced hysteresis loop is obtained for the cycle. This is in sharp contrast to the behavior of hydrogen in the presence of acid and base, when the oxidation and deposition curves superimpose.²

In examining the data in Fig. 3-6 several features are striking. One is the similarity of behavior among all of the saturated hydrocarbons regardless of whether they contain primary, secondary, or tertiary carbon-hydrogen bonds. Second is the vast difference in behavior of the saturated hydrocarbons in the acidic and the other media. Third is the marked difference between the saturated and the unsaturated hydrocarbons. In related fuel cell studies Grubb (1) has found that ethylene performed well on platinum black electrodes in both acidic and alkaline low-temperature fuel cells while saturated hydrocarbons gave steady load currents only in the acidic cells. In this connection, it should be noted that others employing platinized carbon electrodes have reported obtaining performance from saturated hydrocarbons in alkaline cells (14, 15). While their results were obtained at somewhat higher operating temperatures than those used by Grubb, they could indicate an important influence of the support on the performance.

One sees from the curves in Fig. 6 that, while well developed oxidation waves appear for ethane, propane, and isobutane (and to a lesser extent for methane) in the acidic system, evidence for adsorbed oxidizable material is essentially lacking for the bicarbonate and caustic electrolytes after similar periods of equilibration. The slow changes in the electrode potentials with time during adsorption in the latter media further indicate that adsorption is, at best, exceedingly slow. Similar results were obtained for both 25° and 65°C equilibrations.

In contrast, the length of the ethylene oxidation wave remained essentially constant in all media, and cyclopropane, with considerable strain energy in the ring, gave a wave of similar length in the bicarbonate cell. Again, the lengths of the breaks were not found to be highly temperature sensitive. In fact in the case of both the saturated and unsaturated hydrocarbons the effect of increasing the temperature was mainly the lowering of the oxidation voltages (overvoltage) and a sharpening of the breaks in the oxidation curves, i.e., a noticeable enhancement of the rate of the oxidation step itself.

The marked effect of the electrolyte on the adsorption behavior of the saturated hydrocarbons in contrast to the absence of a detectable effect with ethylene was not anticipated, and an explanation is not now at hand. However, because of the use of the anion exchange membrane as the matrix material it was felt that some decomposition products from the resin (amines, for example) might be a cause of the effect. To eliminate such a possibility an additional cell was constructed using asbestos cloth as the matrix for KOH. Tests with ethane verified that adsorption was slow in the presence of KOH and negligible over a period of an hour. After equilibration times of 4 and

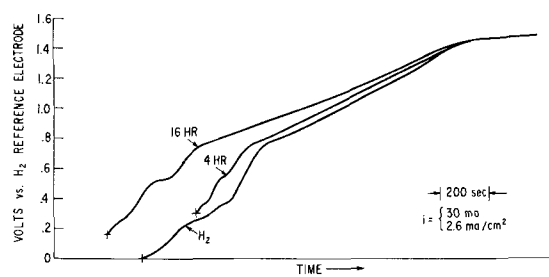


Fig. 7. Galvanostatic oxidation curves for ethane on platinum black after long equilibrations in the presence of KOH. Electrolyte, 6M KOH in asbestos matrix, cell LFC 238, 25°C.

16 hr, however, adsorption did occur, and oxidation waves similar to those observed with the acidic medium were obtained. These are shown in Fig. 7. Similar results were obtained with propane.

Further work will be required before the slow adsorption in alkaline systems can be explained. It is possible that the double layer structure interferes with an equilibrium involving a preliminary weak physical adsorption of the saturated hydrocarbon and thereby reduces the rate of a subsequent chemisorption step that results in a higher equilibrium coverage and that is also essential as a prerequisite to oxidation. The preliminary physical adsorption of an unsaturated might be less affected in this way since stronger attractions would exist between the hydrocarbon and the surface as a result of less shielding by hydrogens in the molecule.

It is now of interest to compare the galvanostatic oxidations of the different hydrocarbons in the acidic medium where all are adsorbed to appreciable extents. Several stages are encountered during these oxidations. With methane, ethane, propane, and isobutane an initial break is observed at potentials between 0.2 and 0.3v. (A similar break is evident in the curves in Fig. 7 for ethane equilibrated for longer periods in the caustic cell with the asbestos matrix.) Since this potential region overlaps a portion of the break observed for hydrogen, it is reasonable to assume that it corresponds to the oxidation of some hydrogen on the surface resulting from dissociation of the adsorbed hydrocarbons. It would then appear that the open-circuit potentials of these fuel electrodes are determined by the equilibrium amounts of hydrogen that are formed by dissociative adsorption.

Following this initial "hydrogen" break there is a sharp rise in potential before a second break is observed in the oxidation curves for the saturates. The sharp rise is associated with charging of the double layer to potentials at which oxidation of the carbon containing species can occur on the new plateau that is reached at about 0.5-0.6v in all cases. In the acidic medium evolution of CO₂ already occurs as the potential rounds the bend into the plateau. Following the period on the plateau the potential of the electrode gradually rises with continuing gassing. This rise eventually blends in with the rise associated with the formation of a surface oxygen layer on the platinum. Eventually a final plateau is reached when oxygen evolution occurs. While the shapes of the oxidation curves for all the saturates are similar, the over-all lengths become longer in the series ethane, propane, and isobutane. This, of course, is in the order of their increasing molecular weights and, as a corollary, in the order of increasing number of coulombs required per mole of adsorbed gas to be oxidized. (Similar volumes of these gases adsorb; cf. next section.)

The deviations of the slopes of the curves in the oxygen film region from that observed when hydrogen is the fuel become greater with the increasing weight of the hydrocarbon. These deviations are in all likelihood associated with concurrent formation of the oxide layer and the oxidation of carbonaceous intermediates that accumulate on the surface of the elec-

² It is of interest to note that a similar hysteresis loop can be obtained with an acid electrolyte cell if the test electrode is "smothered" with CO₂ instead of "flooded" with electrolyte during the electrodeposition of hydrogen. In this and the case of the bicarbonate electrolyte the plateau on the oxidation wave corresponds with that seen when CO is adsorbed directly on the electrode (12). Recently this reduction of CO₂ by hydrogen at a platinum electrode has been studied in some detail (13).

trode during the early stages of the oxidation. It would not be unreasonable for larger fractions of intermediates to accumulate with the higher molecular weight materials.

A major difference between the curves for the saturated hydrocarbons and those for ethylene and cyclopropane is the absence of the preliminary hydrogen break in the latter cases. As discussed below this appears to result from the removal of surface hydrogen by self-hydrogenation reactions which are also in accord with observations in heterogeneous catalysis.

Apart from this difference and the obvious greater length of the breaks (indicative of more extensive coverage) the general shape of the curves for ethylene and cyclopropane parallel those for the saturates. This would imply that the carbonaceous species on the surface are similar for the saturates and unsaturates and that the mechanisms of their oxidations are also similar.

A few remarks are in order about the potentials plotted in Fig. 4-6. Those for the saturated hydrocarbons are reasonable for surfaces that are gradually being covered by dissociative adsorption. In such a system the amount of hydrogen on the surface would be expected to increase with coverage, and it is reasonable to expect that the open-circuit potential is established by the hydrogen-hydrogen ion couple.

With the unsaturated hydrocarbons the open-circuit potential is probably again determined by the hydrogen-hydrogen ion couple, but the amount of free hydrogen on the surface is too small to detect by present methods. The initial overshoot in potential, *i.e.*, to values closer to the reversible hydrogen potential, could be caused by the transient presence of an excess of hydrogen on the surface as a result of dissociative adsorption of the unsaturate during the early stages. As this hydrogen is slowly removed by self-hydrogenation, the electrode potential rises to an equilibrium value. This hypothesis receives support from the fact that a galvanostatic oxidation curve obtained after a 1-min equilibration with ethylene showed a small hydrogen wave similar to those obtained with saturated hydrocarbons. This is in sharp contrast to the initial abrupt rise in potential in the oxidation curves obtained after longer equilibrations.

Additional Studies with the Acidic Electrolyte

Following the broad survey described in the previous section, more detailed attention was given to electrodes in contact with a 5*N* H₂SO₄ electrolyte. These studies included measurements of the volumes of the gases adsorbed, identification and measurement of gaseous reaction products, and partial identification and measurement of species formed on the electrode surface. This path was elected because of the greater reactivity seen with the acid electrolyte. Acids are also attractive for practical hydrocarbon fuel cells because of their ability to reject carbon dioxide. Since the earlier observations indicated that the C₂ hydrocarbons appear to be representative of the general behavior of the homologous series, major emphasis was placed on ethane and ethylene. In addition, a few experiments were performed with the C₃ hydrocarbons, propane, propylene, and cyclopropane.

In these studies the type of reactions observed parallel those of heterogeneous catalysis in the absence of electrolytes. That is, in addition to the adsorption, evidence was found for self-hydrogenation, cracking, and polymerization.

Volumetric measurements of gas adsorption.—Volumetric data obtained during equilibrations of platinum black electrodes with representative fuels at 25°C are shown in Fig. 8; corresponding changes in electrode potentials appear in Fig. 3. All volumetric data have been normalized to standard temperature and pressure, and blank corrections obtained from the cell in the absence of the test electrode have been applied. The blanks amounted to about 15% of the total volumes adsorbed. In addition, volumes have been cor-

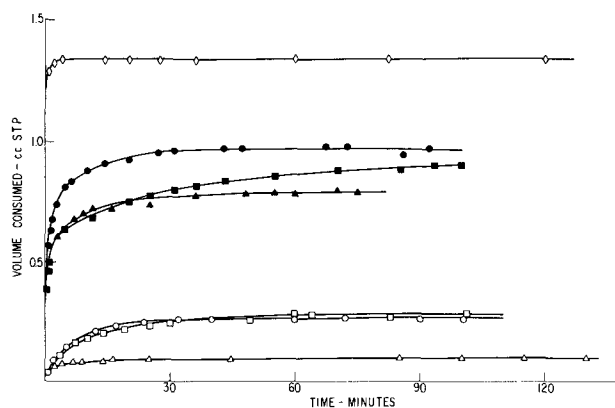


Fig. 8. Gases consumed during equilibrations. \diamond , Hydrogen; \triangle , methane; \circ , ethane; \square , propane; \bullet , ethylene; \blacktriangle , cyclopropane. 5*N* H₂SO₄, 25°C cell LFC 348.

rected for the methane and ethane that were formed by cracking during the equilibrations; *cf.* next section. Corrections have not been applied for the volumes of fuel that would be consumed in charging the double layer capacity as the potential changed from the initial 0.4v to the final rest potential because appropriate data are not available. It is not to be expected, however, that the volumes would be affected greatly because of the small potential changes.

From the data in Fig. 8 it is apparent that the hydrocarbon fuels fall into several groups when considered in the light of surface coverage with C_n species. Thus we see that methane is in a class by itself with very little adsorbing. The higher molecular weight saturated hydrocarbons adsorb to a greater extent and relatively large amounts of the unsaturates (including cyclopropane) adsorb. In all cases the gross volumes are less than that of hydrogen which, as described above, is close to a monolayer.

The behavior of the methane and other saturated hydrocarbons is consistent with related behavior in the absence of electrolytes when less than complete monolayers also adsorb (16). In these cases dissociative adsorption occurs with the formation of hydrogen atoms and probably both ethyl radicals and 1,2 diadsorbed ethane (17). These observations are consistent with the galvanostatic oxidation curves in Fig. 6 in which breaks attributable to dissociated hydrogen are found.

In the case of the unsaturated hydrocarbons, the final coverage of the catalyst surface with C_n groups is much higher. This is again consistent with "dry" studies in which it has also been found that hydrogen formed in an initial dissociative step is subsequently removed by self-hydrogenation of additional unsaturated gas so that sites become available for coverage by more C_n groups (18,19). Similar self-hydrogenation occurs under the present conditions; *cf.* next section. The net result is a surface more fully covered with Pt-C linkages and very little adsorbed hydrogen. This too is consistent with the galvanostatic curves in Fig. 6 in which no wave attributable to hydrogen appears in the oxidation curves for adsorbed ethylene and cyclopropane.

The surface species resulting from the self-hydrogenation reaction are hydrogen poor. This may result in the formation of additional bonds to the metal, say four-point attachment, or compensation may be accomplished through the formation of double bonds between carbons with only two bonds to the metal. There is evidence for both in the literature of heterogeneous catalysis (20). Were two bonds to the metal involved, saturation coverage from ethylene would require the adsorption of a volume equal to that for saturation coverage with hydrogen. Steric effects would undoubtedly result in a somewhat lower coverage. Conversely, four bonds to the surface would call for adsorption of a volume one-half that of hydrogen.

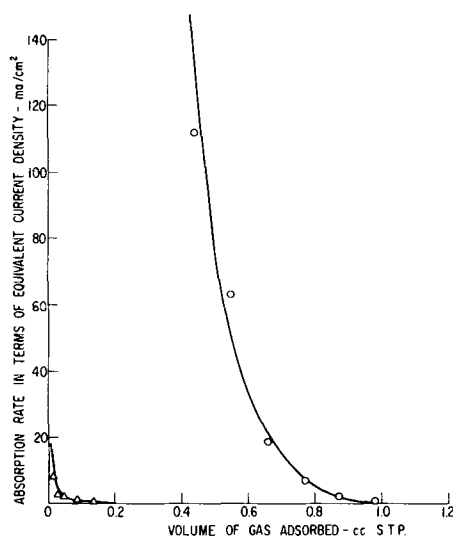


Fig. 9. Adsorption rates as a function of amount adsorbed. Δ , Ethane; \circ , ethylene. $5N$ H_2SO_4 , $25^\circ C$, cell LFC 345 (assuming complete oxidation to CO_2 and H_2O).

The actual volume adsorbed is intermediate and in all probability points to mixed species on the surface.

In Fig. 9 adsorption rates are plotted for ethane and ethylene against the amount adsorbed. The data for this figure were derived from the slopes of large scale plots of data similar to those in Fig. 8. The ordinate is expressed in terms of the current that could be supported if the adsorbing gas were immediately oxidized completely to CO_2 and water. A current density of 1 ma/cm^2 is equivalent to a volumetric adsorption rate for ethane on the 11.4 cm^2 electrode of 0.0113 cc/min and for ethylene, 0.0132 cc/min .

Because of the thickness of the electrodes, about 0.007 cm , slow diffusion to underlying sites could be an important rate-determining step during some stages. It is nevertheless clear that there is a marked difference in the rates for the unsaturated ethylene and the saturated ethane. While an exact relationship between these rates and fuel cell performance is not yet apparent, it appears clear that much lower limiting currents are to be anticipated in the case of saturated than unsaturated fuels. It is therefore not unreasonable to suspect that the limiting currents (*i.e.*, regions of unstable performance) observed with low temperature fuel cells operating on saturated hydrocarbons (1, 21, 22) is associated with slow adsorption kinetics. This conclusion is further strengthened by the observations in the previous section that adsorption of saturated hydrocarbons on platinum black electrodes is markedly slower in alkaline media, and cell performance is similarly poorer with the saturates in these media (1). Before a rigorous correlation between fuel cell performances and rates of adsorption is possible, however, less ambiguous data will be required. This can probably best be obtained with micro electrodes in well stirred solutions using some of the modern transient techniques.

It is appropriate to comment on the exceedingly rapid adsorption of hydrogen. This appears to result from an electrochemical transfer of hydrogen from the sites readily accessible to gas to those in the underlying flooded regions of the electrode. This type of transfer can occur with the hydrogen because its electrode reactions are highly reversible and there is an abundant supply of the oxidized form in the electrolyte, as protons in the acidic system and as water in all of the systems. The only other gas which meets either requirement is oxygen, for which an abundant supply is available in the water of the electrolyte. In this case, however, the electrode reaction is highly irreversible and the electrochemical transfer step does not occur as readily as with hydrogen. Adsorption

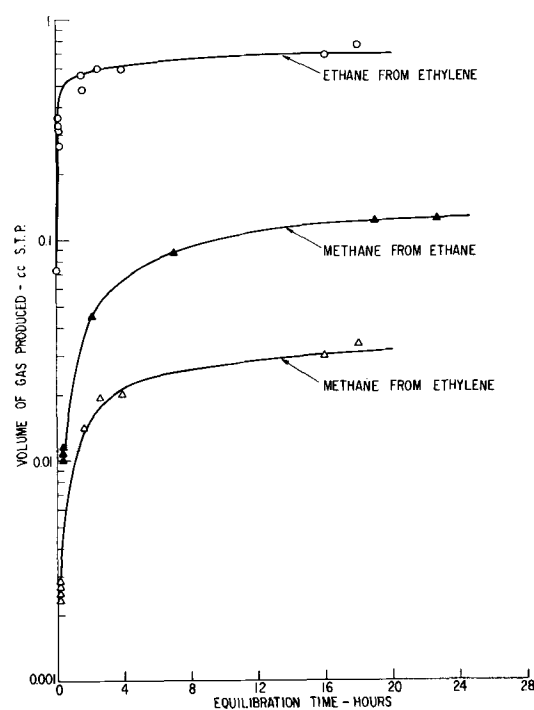


Fig. 10. Gaseous products formed during equilibrations. $5N$ H_2SO_4 , $25^\circ C$, cell LFC 345.

rates for oxygen are accordingly much slower than for the hydrogen.

Gaseous products formed during equilibrations.—The adsorptions of hydrocarbons on fuel anodes are somewhat beclouded by superimposed side reactions. These include reactions which introduce gaseous products into the system, and others which result in products which remain on the electrode surface. The former will be considered here.

As mentioned above, self-hydrogenation of ethylene during its adsorption on metals is well known. A similar behavior is found in the presence of the acidic electrolyte and ethane is seen to grow into the gas phase, Fig. 10. During equilibrations of propylene and cyclopropane, propane was found in the gas phase in both cases, which is in agreement with the ethylene.

In addition to the saturated hydrocarbons from self-hydrogenation, lower molecular weight materials are also found in the gas phase. This parallels the methane production that has been observed from ethylene and ethane adsorbed on rhodium (23), nickel (24), and other metals (31) and the methane and ethane from propane in gas phase studies at low pressures with nickel (25) and platinum (26). It also parallels the observations of Grubb on related fuel cell systems (27).

It is seen that the amount of gaseous methane produced from ethane is considerably higher than that for ethylene. A similar relationship holds among the limited data shown for the C_3 hydrocarbons in Table II. This is not surprising in view of the more limited

Table II. Gaseous products formed during 100 min equilibrations with several gases

Cells LFC-345 and 348

Gas adsorbed	Amount adsorbed cc S.T.P.	Amount self-hydrogenated cc S.T.P.	Cracking products in gas phase cc S.T.P.	
			CH_4	C_2H_6
Ethane	0.26	—	0.039	—
Ethylene	0.97	0.58	0.014	—
Propane	0.28	—	0.018	0.017
Propylene*	0.79	0.34	0.003	0.008
Cyclopropane	0.91	0.36	0.003	0.0023

* 75-min equilibration.

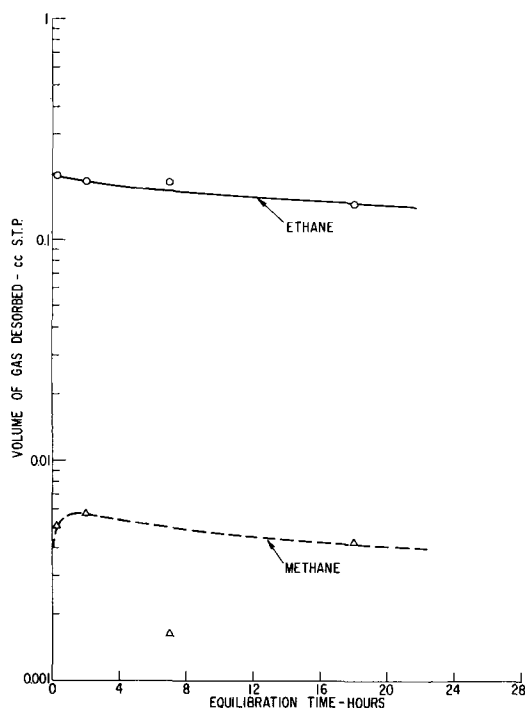


Fig. 11. Gases desorbed during cathodic hydrogenation after ethane equilibrations. 5N H_2SO_4 , 25°C, cell LFC 345, current 30 ma.

amounts of hydrogen available from the unsaturated hydrocarbons. Since formation of methane (and ethane in the C_3 systems) requires hydrogen, the residues must be stripped in the process. Similarly Grubb has reported that if one further reduces the availability of hydrogen by electrochemical means (e.g., by drawing current from the electrode), the gas phase methane concentration from propane is reduced even further (27).

Surface species formed during equilibrations.—With regard to electrode performances in fuel cells, the nature of the materials that accumulate on the elec-

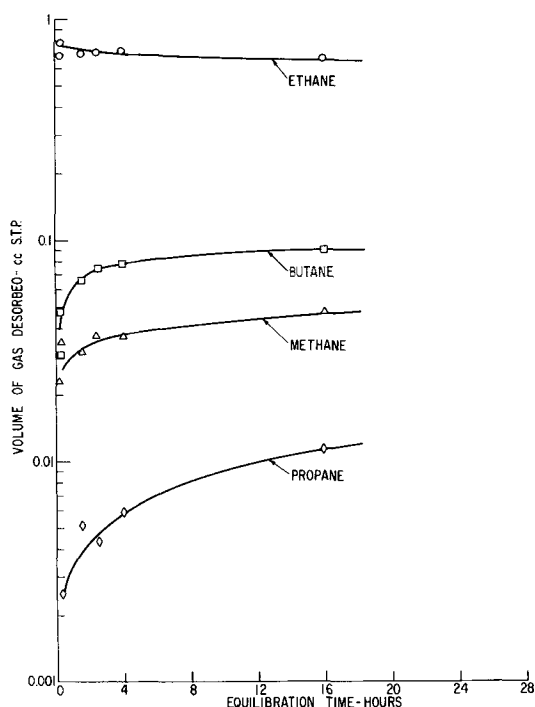


Fig. 12. Gases desorbed during cathodic hydrogenations after ethylene equilibrations. 5N H_2SO_4 , 25°C, cell LFC 345, current 30 ma.

Table III. Species released on cathodic hydrogenation after 100-minute equilibrations

Cells LFC-345 and 348

Gas adsorbed	Products from surface cc S.T.P.				
	CH_4	C_2H_6	C_3H_8	C_4H_{10}	C_6H_{14}
Ethane	0.0058	0.19	<0.001	<0.001	—
Ethylene	0.033	0.72	0.004	0.063	—
Propane	0.009	0.018	0.33	<0.001	—
Propylene*	0.007	0.003	0.73	<0.001	Present
Cyclopropane	0.018	0.010	0.81	<0.001	Present

* 75-min equilibration.

trode surface are of perhaps greater immediate interest than the gaseous products which are eventually released. There is abundant evidence in the literature that a variety of species are formed on catalyst surfaces during equilibrations with hydrocarbons. Thus Beeck has reported the formation of polymers (28), Stephens found evidence for C_3 and C_4 species after equilibrations with ethylene (19), and ample evidence has been presented for the formation of C_1 residues (23, 31). Such materials have been deduced from the products of hydrogenation of the surfaces following equilibrations. Little information has been published concerning similar reactions on fuel cell catalysts, but Holman (29) has found propane among the products of hydrogenation of platinum fuel electrodes after exposure to ethylene. Holman did his hydrogenations by exposing the electrode to gaseous hydrogen after operation on load. In the present work the hydrogenations were performed electrolytically by cathodic treatment of the electrodes after the equilibrations.

Hydrogenated products obtained from electrodes following equilibrations with ethane are shown in Fig. 11 and for ethylene in Fig. 12. It is evident that appreciable cracking occurred in both cases. In the case of ethylene, however, a depletion of hydrogen on the surface limited desorption to the gas phase and large concentrations of C_1 species accumulated on the surface.

The tendency toward polymerization was much greater in the case of ethylene. Indeed in the case of ethane no C_3 or C_4 polymer was detected. The tendency toward polymerization in the case of ethylene does not seem unreasonable in view of the high surface concentrations of relatively unsaturated C_2 species. Similar trends are evident for the C_3 hydrocarbons, but to a lesser extent, cf. Table III.

One other aspect of the experiments with ethane and ethylene is of particular interest. This relates to the gradual decline in the amount of C_2 hydrocarbon recovered from the surface of the catalyst with increasing equilibration time. While this can be partially explained in the case of ethylene on the basis of C_3 , C_4 , and possibly higher hydrocarbon formation, a similar balance is not evident in the case of ethane. An explanation may be forthcoming from the oxidation curves for electrodes after the cathodic treatment. Examples in the case of ethane are shown in Fig. 13. Invariably a break is found at a potential of about 0.6v,

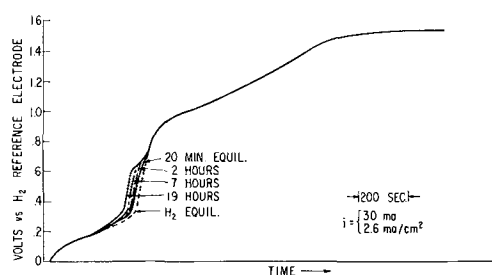


Fig. 13. Galvanostatic oxidation curves after ethane equilibrations and cathodic hydrogenations. Electrolyte, 5N H_2SO_4 , cell LFC 345, 25°C.

the length of the break becoming longer as the equilibration time increases. The buildup of this break has, in fact, been found to continue for times as long as 70 hr. Actually a similar effect was observed with the ethylene though to a less significant extent.

In the absence of even C_3 and C_4 hydrocarbons among the desorption products from ethane, it is difficult to attribute this wave to a high polymer on the surface. A much more reasonable alternative is CO or a related species which could be formed by reaction of the hydrocarbon with water. Furthermore, adsorbed CO produces an oxidation wave at the required potential, and it is not displaced by cathodic hydrogenation. This was shown by cathodic generation of hydrogen on a CO covered surface. Another possibility is a tightly bonded carbon residue. Nothing is known about the electrochemical behavior of such a species.

Operation on load.—In addition to the equilibrations on open circuit, a number of runs were made at 25°C in which the test electrode was operated continuously on load before it was flooded for a cathodic desorption. Such experiments were performed with slowly flowing ethane and ethylene as fuels.

With the ethylene, current densities of 0.26, 0.88, and 2.6 ma/cm² were employed, and only a slow drift in potential was evident. At all current densities the electrode potential was in the neighborhood of 0.7–0.9v vs. the hydrogen reference. Sustained operation was possible with ethane only with current densities of 0.18 ma/cm² or less. Attempts to operate at higher current densities rapidly resulted in complete polarization to eventual oxygen evolution. Because of the poor performance of the ethane, attempts were not made to identify residual surface species from ethane after continuous operation on load. In the case of ethylene several analyses were made of the species desorbed cathodically after such operation.

Composition of the desorbed gases collected after operation with ethylene are shown in Fig. 14. The general trends are of considerable interest in that the amount of material on the surface declined quite markedly during operation. The decrease in the amount of C_2 species resulted in a concomitant decline in the amount of C_4 polymer. As the surface became depleted the amount of C_1 species increased with a concomitant increase in the amount of the C_3 species

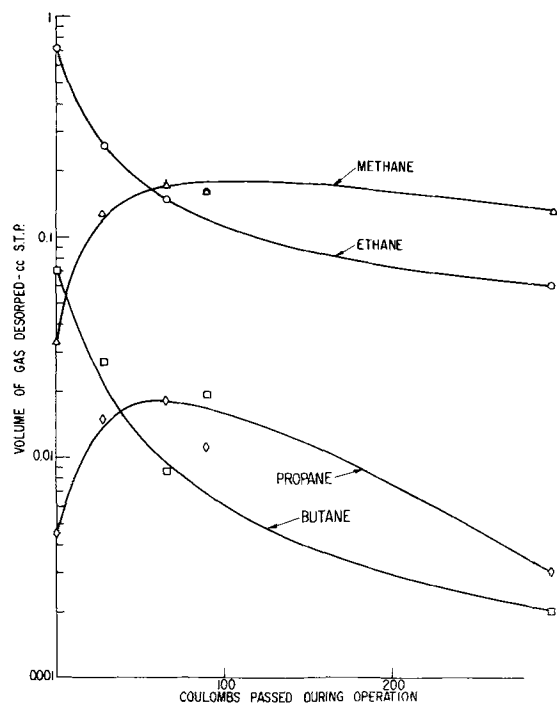


Fig. 14. Gases desorbed cathodically after operating on load with ethylene. 5N H₂SO₄, 25°C, cell LFC 345.

(formation obviously dependent on C_1 and C_2 surface concentration).

These preliminary measurements provide an indication of some important surface reactions occurring on working electrodes. In part they are encouraging in that they indicate a reduction in the amounts of higher molecular weight materials during operation on load. This may well imply that tendencies toward tar formation will be minimal on fuel electrodes.

Summary and Conclusions

The behavior of hydrocarbons at platinum black fuel cell electrodes is dependent on the hydrocarbon structure and the electrolyte. In the presence of a dilute sulfuric acid electrolyte all of the low molecular weight aliphatic hydrocarbons show some adsorption even at room temperature, although that of methane is slight. Surface coverage falls into three categories: low for methane, intermediate for the saturated hydrocarbons, and high for unsaturates. Rates of adsorption are also reasonably high with the acidic electrolyte, and no appreciable effects seem to be associated with the presence of primary, secondary, or tertiary carbon-hydrogen bonds in the fuel molecule.

The adsorption of saturated hydrocarbons is exceedingly slow in the presence of alkaline and carbonate electrolytes. In contrast, the adsorption of the unsaturated hydrocarbons is affected but little by the electrolyte. The performance of these hydrocarbons as fuel gases in low-temperature cells appears to reflect the observed differences in adsorption properties.

During equilibration on open circuit many surface reactions including dehydrogenation, hydrogenation, cracking, and polymerization occur. These appear to be preceded by dissociative chemisorption with the formation of some hydrogen on the surface. Subsequently low molecular weight, saturated cracking products are released, and highly unsaturated carbonaceous residues can accumulate on the surface. While the dissociated hydrogen oxidizes readily, high overvoltages are required for the oxidation of the carbonaceous surface species. These overvoltages are lowered if the temperature is increased.

At present it is not possible to predict with certainty the importance of the surface reactions with regard to actual cell performance on load. It is likely, however, that some will be of great significance. In particular it would seem likely that the cracking reaction resulting in the formation of C_1 species would be of direct concern as a step in the over-all oxidation of a hydrocarbon to CO₂. The apparent ease of hydrogen dissociation probably has direct bearing on the frequent observations that hydrocarbon oxidations in fuel cells proceed almost quantitatively to CO₂ (2, 14). Such dissociation coupled with the ease of oxidation of the hydrogen means that the surface species on a working anode must be hydrogen poor. Such species should therefore be multiply bonded to the catalyst so that their desorption as reaction intermediates would be difficult and highly unlikely.

This behavior of the hydrocarbons is in marked contrast to that of many partially oxygenated hydrocarbons such as alcohols and aldehydes in which cases oxidation frequently stops far short of complete oxidation (30). While it is well known that such materials are not as strongly adsorbed as the hydrocarbons it would also seem to suggest a different mechanism of adsorption that does not lead to the formation of strong multiple bonds to the metal such as suggested above for the hydrocarbons. It would seem likely that in these cases dissociative chemisorption involving the breaking of C-H bonds would not be involved or we would again see the tendency toward complete oxidation. This strongly suggests that a weaker adsorption through an oxygen bond may be involved with such materials.

Acknowledgments

The author is particularly indebted to H. R. Alford for assistance with many of the measurements and to

W. T. Grubb for the use of his gas chromatography equipment. He is also indebted to Miss C. Michalske for her assistance with the chromatographic analyses and to G. L. Gaines, Jr., for the surface area measurements on the platinum black samples. In addition he wishes to acknowledge helpful discussions with S. Gilman, W. T. Grubb, H. A. Liebhfasky, and D. W. McKee.

This work was made possible by the support of the Advanced Research Projects Agency (Order No. 247) and the United States Army Engineer Research and Development Laboratories under Contract DA44-009-ENG-3771 and 4909.

Manuscript received April 30, 1964; revised manuscript received July 23, 1964. This paper was presented at the New York Meeting, Sept. 29-Oct. 3, 1963.

Any discussion of this paper will appear in a Discussion Section to be published in the June 1965 JOURNAL.

REFERENCES

1. W. T. Grubb, Proceedings 16th Annual Power Sources Conference, Atlantic City, N. J., p. 31 (1962).
2. W. T. Grubb and L. W. Niedrach, Proceedings 17th Annual Power Sources Conference, Atlantic City, N. J., p. 69 (1963).
3. A. Slygin and A. Frumkin, *Acta physicochim. URSS*, **3**, 791 (1935).
4. B. Erschler, *Discussions Faraday Soc.*, **1**, 269 (1947).
5. M. Becker and M. Breiter, *Z. Elektrochem.*, **60**, 1080 (1956).
6. M. Breiter, C. A. Knorr, and W. Völkl, *ibid.*, **59**, 681 (1955).
7. A. N. Frumkin, Chap. 5 in "Advances in Electrochemistry and Electrochemical Engineering," Vol. 3, p. 287, P. Delahay, Editor, Interscience Publishers (1963).
8. L. R. Griffith and D. R. Rhodes, "Fuel Cells," p. 32, Am. Inst. of Chem. Engrs., New York (1963).
9. M. A. Kerdivarenko, P. K. Migal, and M. Kh. Kishinevsky, *J. Appl. Chem. USSR (English Trans.)*, **28**, 441 (1955).
10. T. J. Morrison and F. Billett, *J. Chem. Soc.*, **1952**, 3819.
11. W. F. Claussen and M. F. Polglase, *J. Am. Chem. Soc.*, **74**, 4817 (1952).
12. L. W. Niedrach, Unpublished results.
13. J. Giner, *Electrochim. Acta*, **8**, 857 (1963).
14. M. J. Schlatter, "Fuel Cells," p. 190, G. J. Young, Editor, Reinhold Publishing Co., New York (1963).
15. G. J. Young and R. B. Rozelle, *ibid.*, p. 216.
16. B. M. W. Trapnell, *Trans. Faraday Soc.*, **52**, 1618 (1956).
17. G. C. Bond, "Catalysis by Metals," p. 184, Academic Press, New York (1962).
18. G. I. Jenkins and E. Rideal, *J. Chem. Soc.*, **1955**, 2490.
19. S. J. Stephens, *J. Phys. Chem.*, **62**, 714 (1958).
20. G. C. Bond, *loc. cit.*, p. 232 ff.
21. L. W. Niedrach, *This Journal*, **109**, 1092 (1962).
22. M. J. Schlatter, Preprints of Papers, Am. Chem. Soc., Div. of Fuel Chem., **7**, No. 4, 234 (1963).
23. R. W. Roberts, *Trans. Faraday Soc.*, **58**, 1159 (1962).
24. D. W. McKee, *J. Am. Chem. Soc.*, **84**, 1109 (1962).
25. D. W. McKee, *ibid.*, **84**, 4427 (1962).
26. D. W. McKee, *J. Phys. Chem.*, **67**, 841 (1963).
27. W. T. Grubb, *Nature*, **198**, 883 (1963).
28. O. Beeck, *Rev. Mod. Phys.*, **17**, 61 (1945).
29. J. Holman, Unpublished results.
30. H. Binder *et al.*, Preprints of Papers, Am. Chem. Soc., Div. of Fuel Chem., **7**, No. 4, 232 (1963).
31. R. W. Roberts, *Brit. J. Appl. Phys.*, **14**, 485 (1963).

A Thermal Battery Based on the Reaction of Cadmium and Liquid Iodine

Klaus Otto

Scientific Laboratory, Ford Motor Company, Dearborn, Michigan

ABSTRACT

A thermal battery consisting of a cadmium anode, a solution of potassium iodide in liquid iodine, and an inert cathode was studied at 125°C. The solubilities of KI and CdI₂ as separate components and as mixtures in liquid iodine, the conductivities of these solutions, and their corrosion behavior toward cadmium were investigated. The conductivity of polycrystalline CdI₂ follows the expression $\sigma = 0.14 \exp(-12350/RT) + 5.2 \times 10^{-8} \exp(-1990/RT)$ in the range between 0° and 200°C. Current-voltage dependence of the cell, efficiency and the importance of the formation of the complex salt K₂CdI₄ are discussed. The cell exhibits a fairly flat discharge curve. It was not possible to recharge it. Corrosion of the cadmium anode was negligible at current densities above 35 ma/cm².

There are several properties which made it attractive to investigate the possibility of utilizing solutions of KI in liquid iodine as an electrolyte in thermal batteries (1,2): (i) the electrolyte has a high conductivity (up to 0.35 ohm⁻¹ cm⁻¹ at 125°C); (ii) liquid iodine is used as a solvent and a reactant at the same time; (iii) an inert cathode is used; (iv) the battery can be operated at relatively low temperatures (115°-185°C).

Cadmium was chosen as anode material for a detailed study, after testing Ag, Mg, Zn, Cd, Hg, Al, Sn, and Pb for this purpose. Platinum, graphite, and molybdenum are equally suitable as material for the cathode. The emf of the system Cd/liquid iodine/C is about 1v.

The potassium iodide in the electrolyte serves two purposes: it increases the conductivity of the electrolyte considerably and dissolves the reaction product CdI₂ off the anode by forming a complex salt K₂CdI₄

which is soluble in iodine. CdI₂ is practically insoluble in pure iodine and exhibits a high resistivity; it would choke the current within a short time, if it were not removed continuously from the anode.

Conductivity measurements of iodine solutions containing KI, CdI₂, and mixtures of these iodides furnished information that K₂CdI₄ is formed by the reaction of KI and CdI₂ in iodine, and that the conductivity of this complex salt in iodine is only about a factor 2 smaller than the conductivity of the corresponding solutions of KI in iodine. This fact explains the relatively small changes of the inner resistance of the cell during normal operation.

Measurements of the solubilities of KI, CdI₂, and mixtures of KI and CdI₂ in liquid iodine furnished additional information about the formation of the complex salt.

Corrosion rates of iodine solutions on cadmium at various concentrations of KI were measured.

The chemical attack on platinum, molybdenum, and graphite by solutions of KI in iodine was investigated.

The temperature dependence of the conductivity of the reaction product CdI_2 in the temperature range between 0° and 200°C showed that CdI_2 is a typical ionic conductor. The conductivity was used to calculate the thickness of the CdI_2 layer on the anode, which depends on the concentration of KI in the electrolyte and on the current density. The right thickness of the CdI_2 layer is considered to be important for the proper functioning of the cell.

Voltage-current curves were measured under various conditions.

Conductivities of Iodine Solutions Containing KI and CdI_2

A thermostat containing glycerin as a heating liquid, an electronic temperature controller with heater and stirrer, which kept the temperature of the bath constant within $\pm 0.1^\circ\text{C}$, and a calibrated chromel-alumel thermocouple were used for temperature control. Resistances were measured by a commercial a-c bridge, which had a range from 0.2 to 2.5×10^6 ohms; on some occasions these limits had to be extended by putting a standard resistor in series or parallel to the unknown resistor. A standard conductivity vessel contained platinum electrodes, the cell constant being 0.1 . Another conductivity vessel consisted of a U-shaped Pyrex tube (length 20 cm, I.D. 1.8 cm), containing about 150 g of iodine. The electrodes were graphite rods of 0.6 cm diameter; they were sealed into glass tubes, leaving only about 1 cm of the graphite protruding into the liquid. These tubes were fitted into the U-tube by ground joints. Only Mg and Si could be detected spectrographically as impurities in these graphite rods.

The freezing point of iodine (A. C. S. reagent) was found in three separate runs to be $113.4^\circ \pm 0.1^\circ\text{C}$. The specific conductance of pure iodine at 140°C gave values between 2.0×10^{-5} and 4.0×10^{-5} ohms $^{-1}$ cm $^{-1}$. These data agree with values given in the literature: Lewis and Wheeler (3) state a conductivity of 2.16×10^{-5} ohms $^{-1}$ cm $^{-1}$ at this temperature. Rabinowitsch (4) found 4.48×10^{-5} ohms $^{-1}$ cm $^{-1}$ at 138.2°C , and Plotnikow *et al.* (5) published 1.68×10^{-4} and 0.92×10^{-5} ohms $^{-1}$ cm $^{-1}$ as a maximum and minimum value of the specific conductance at 140°C . The temperature coefficient of the conductivity was found to be negative in the temperature interval between 114° and 145°C , i.e., there is a decrease of 3.50×10^{-7} ohms $^{-1}$ cm $^{-1}$ per degree with increasing temperature. Measurements upon heating up and cooling down of the iodine resulted in the same value. The temperature coefficient calculated from the data of Rabinowitsch (4) between 113° and 155°C is -3.34×10^{-7} ohms $^{-1}$ cm $^{-1}$ deg $^{-1}$.

The first detailed investigation concerning the conductivity of nonaqueous iodine solutions containing KI was done by Lewis and Wheeler (3). Plotnikow *et al.* (5,6) executed further measurements using RbI, NaI, LiI, SnI $_4$, SbI $_5$, HgI $_2$, PI $_3$, and AlI $_3$; but only the alkali iodides, with the exception of NaI, increased the conductivity of iodine considerably; e.g., a saturated solution of KI in iodine has a specific conductance of about 0.35 ohms $^{-1}$ cm $^{-1}$ at 125°C which is a factor 3×10^4 higher than the conductivity of pure iodine. During the present investigation it was found that the addition of K_2CO_3 shows the same effect as KI does. Probably the reaction $\text{K}_2\text{CO}_3 + \text{I}_2 \rightarrow 2\text{KI} + \text{CO}_2 + \frac{1}{2}\text{O}_2$ takes place because oxygen and carbon dioxide have been found to be set free.

Conductivity measurements of iodine solutions containing KI and CdI_2 were executed in a U-shaped cell with graphite electrodes, as described above. A Teflon covered magnet (1.5 cm long) in the solution acted as an effective stirrer by means of a rotating magnet on the outside of the thermostat. Only A.C.S. reagents were used as chemicals. Results are depicted in Fig. 1. The upper curve represents the specific conductance of

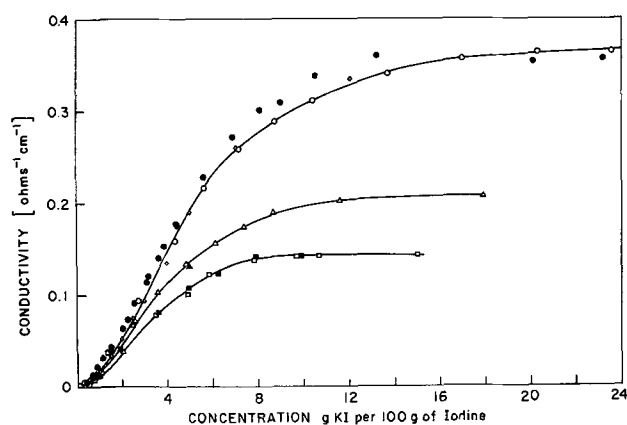


Fig. 1. Conductivity of mixtures of KI and CdI_2 in iodine. KI in iodine: \diamond , run 1; \circ , run 2; \bullet , data of Lewis and Wheeler. Three moles KI per mole CdI_2 : \triangle , run 1; \blacktriangle , run 2. Two moles KI per mole CdI_2 : \blacksquare , excess CdI_2 as sediment present; \square , KI and CdI_2 added at the same time.

a solution of KI in iodine at 125°C . The concentration is given in grams of KI per 100 g of iodine. Two series of measurements have been plotted together with the data given by Lewis and Wheeler (3) at 140°C which have been reduced to 125°C by extrapolation, using the temperature coefficients which are given as a function of the concentration by these authors. The horizontal course of the curve at higher concentrations is due to the limit of solubility of KI in iodine.

CdI_2 is practically insoluble in pure iodine and has a negligible effect on the conductivity of pure iodine. However, if CdI_2 is added to an iodine solution which contains KI, a noticeable change of the conductivity takes place. For the first series of experiments a mixture of 2 moles KI and 1 mole CdI_2 was prepared and the conductivity of this salt in iodine was determined as a function of the concentrations (grams of KI per 100 g of iodine). The results are represented in the lowest curve of Fig. 1 by open squares. For the second series, 17.311 g CdI_2 were added to the iodine (152.7 g) from the beginning, and the conductivity was measured while KI was added successively. These measurements (filled squares) agree with the previous series. The formation of a complex salt K_2CdI_4 is indicated by this result. Two more runs were made with a mixture containing 3 moles of KI per mole CdI_2 . These conductivities are represented by triangles in Fig. 1.

Solubilities of KI and CdI_2 in Liquid Iodine

The formation of the complex salt K_2CdI_4 was confirmed by measuring solubilities of KI and CdI_2 in iodine. Several solutions of iodine which were supersaturated with KI were sealed into glass tubes and kept in a thermostat at 125°C for several hours. The samples were quenched in ice water, and several parts of them were analyzed by subliming off the iodine and weighing the residue. The top parts of the samples were not considered because the excess KI was floating on top of the solutions. A solubility of 0.1788 ± 0.0005 g KI per gram of iodine was found.

The solubility of CdI_2 in iodine was determined in an analogous way. The bottom parts of the samples were not analyzed, as the excess of CdI_2 was settled as a sediment. The solubility was found to be only 0.135×10^{-3} g of CdI_2 per gram of iodine at 125°C (average of 3 samples). However, in the presence of KI much more CdI_2 is distributed homogeneously in liquid iodine, confirming the formation of a complex salt.

To determine the composition of the complex salt, 13.1922 g CdI_2 and 3.0078 g KI, corresponding to a mole ratio of 2 moles CdI_2 to 1 mole KI, were put into 29.8232 g of iodine at 125°C . The top part of the quenched sample was analyzed. Under the assumption that the KI was distributed homogeneously in the

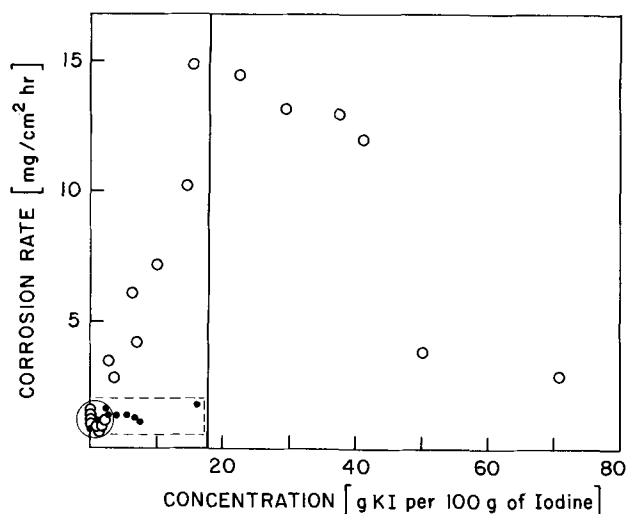


Fig. 2. Corrosion of cadmium in solutions of KI and liquid iodine: \circ , iodine + KI; \bullet , iodine + KI + CdI_2 .

iodine, 0.10085g KI should be present per 1g of iodine; the amount of salt found per gram of iodine was 0.2098g, leaving 0.1090g CdI_2 . This result corresponds to a ratio 2.04 moles of KI to 1 mole of CdI_2 , which is in agreement with the formula K_2CdI_4 .

Corrosion of Cadmium by Electrolyte

Cadmium corrodes in iodine on open circuit. This corrosion, which consumes cadmium without contributing to the current, was measured as a function of the KI concentration in the electrolyte. Rectangular plates measuring $2.5 \times 1.25 \times 0.1 \text{ cm}^3$, were cut from cadmium sheets and cleaned in ethyl alcohol. The weighed cadmium samples were sealed into test tubes, containing 30g of iodine and between 0 and 16g of KI, and were kept at 125°C . The cadmium specimens were removed from the solutions after 22 hr, cleaned with ethyl alcohol, and the weight loss was determined. In some cases a considerable change of the surface area (up to 20%) and likewise in the concentration of KI took place during the reaction. The corrosion rates were adjusted for these surface changes and concentration changes by taking the arithmetic means of the original and final surface areas and averaging the concentrations the same way. These corrected rates (milligrams of cadmium consumed per cm^2 per hour) have been plotted in Fig. 2 vs. the concentration of KI in the solution (open circles). In spite of the fact that these corrosion rates show considerable scattering, the diagram indicates clearly a continuous increase of the corrosion with increasing concentration of KI up to the limit of solubility (indicated by a vertical solid line). The reaction rate keeps constant on adding more KI, but declines rather rapidly for solutions which contain considerably more KI than soluble (40-50g KI per 100g of iodine). The reaction rate for an iodine solution saturated with KI is 0.014 g/hr cm^2 , that of pure iodine is 0.0013 g/hr cm^2 .

The influence of KI on the corrosion is reduced by adding CdI_2 to the solution, due to the formation of K_2CdI_4 . Ten samples were prepared as described above; however, KI was added as a mixture of KI and CdI_2 in a mole ratio 2:1. In Fig. 2 all these points (filled circles) are located within the rectangle which is limited by dash lines. These corrosion rates are only as high as those which have been obtained for pure iodine.

Corrosion of Cathode Materials by Electrolyte

Quantitative results as to how badly platinum is attacked by iodine solutions at 125°C are given in Table I. The data indicate a very slow attack of pure iodine on platinum, probably due to a compound which passivates the surface. The higher reaction rates in

Table I. Pt corrosion

Time of exposure, hr	Concentration of solution, grams KI per gram iodine	Reaction rate, grams Pt per cm^2 per hour
22	0.70	5.6×10^{-4}
26	0.25	4.9×10^{-4}
24	0	9.7×10^{-6}

the presence of potassium iodide can be explained by the formation of a soluble complex, similar to the behavior of cadmium.

Graphite and molybdenum showed practically no corrosion in solutions of KI and iodine. The potential difference between a platinum anode and a graphite cathode in KI-iodine solutions was found to be smaller than 0.002v, while a molybdenum anode showed less than 0.0005v against a graphite cathode.

Conductivity of Solid CdI_2

Samples for measuring the conductivity of polycrystalline CdI_2 were prepared as follows. A clean copper tube was dipped into a CdI_2 melt. A graphite rod bearing two pieces of glass tube as spacers was put into the melt concentric with the copper electrode. After the CdI_2 had solidified, the sample was put into a snug-fitting glass tube together with a thermocouple and placed in the thermostat. The resistance was measured at 60 cps, one time going from room temperature to 200°C , and then on cooling down to room temperature again.

At least two terms are needed to describe ionic conductivity of solids (7). One expression takes care of the conductance by lattice defects, characterized by a relatively low energy of activation E' ; the second expression describes the migration of the normal ions through the lattice, impeded by an energy barrier E , i.e., $\sigma(T) = A \exp(-E/RT) + A' \exp(-E'/RT)$. To represent the data by a formula of this kind, the measured resistance values were converted into conductivities, and an iteration process was exercised. The best fit was obtained for $\sigma = 0.14 \exp(-12350/RT) + 5.2 \times 10^{-8} \exp(-1990/RT)$ [$0 \leq T \leq 200^\circ\text{C}$]. In Fig. 3 both members of this equation are drawn on a logarithmic scale as straight lines; addition of these partial conductivities furnishes the curve, to which the straight lines are asymptotes. The maximum deviation of the measured values from this curve is about $\pm 5\%$. Different samples showed a reproducibility within 0.5

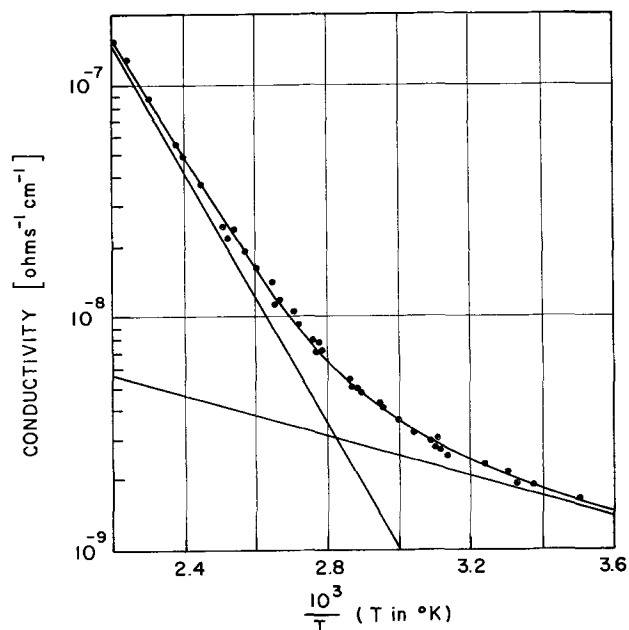


Fig. 3. Conductivity of polycrystalline CdI_2

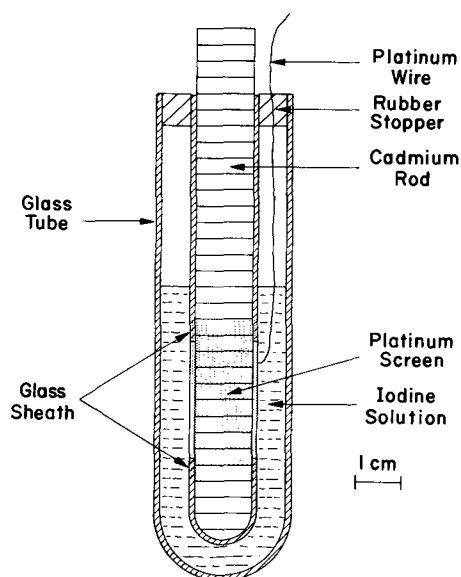


Fig. 4. Cell with concentric electrodes

kcal/mole for the energies of activation $E = 12.35$ kcal/mole and $E' = 1.99$ kcal/mole, while the absolute conductivity values are reliable only within a factor 2 which is probably due to differences in contact between the polycrystalline CdI_2 and the electrodes and to other effects, which were created by the pretreatment of the samples. The data which are given here are those obtained from the sample which furnished the highest conductivity values.

Voltage-Current Relationships

For these measurements U-shaped or H-shaped conductivity vessels were used; if a low inner resistance was desired for an experiment, a cell with concentric electrodes, as shown in Fig. 4, was employed. If pure iodine is used as electrolyte, an open-circuit voltage of 0.98v (as measured by a potentiometer) builds up after the cadmium has been in the liquid for several minutes. A high concentration of KI in the electrolyte favors high currents due to the increased conductivity; however, it also causes the emf of the cell to drop. The voltage recovers if CdI_2 is added, which is accompanied by an increase of the inner resistance. If a clean cadmium anode is dipped into a KI-iodine solution, a voltage builds up instantaneously (about 0.55v within the first second, 0.80v within 1 min). It was observed repeatedly that the voltage decreased more or less if no current was drawn, but recovered if a high enough current passed the cell. These phenomena were investigated by determining the relationship between current and voltage for several compositions of the electrolyte. A temperature of 125°C was chosen, as there is no pronounced temperature dependence of the emf.

A U-shaped vessel, which contained a graphite rod and a cadmium rod as electrodes, was used. The circuitry included a potentiometer, a sensitive ammeter, a variable-load resistor, and an auxiliary voltage source. The resistance of the electrodes plus their leads was small (<0.5%) compared to the whole resistance of the cell.

Curve I in Fig. 5 was obtained with an iodine solution containing 5g KI per 100g of iodine. A current of 1 ma corresponds approximately to a current density of 0.5 ma/cm². Open circles represent measurements with increasing voltage, squares mark a decreasing voltage. Positive currents were produced by the emf of the cell and a variable load resistor; negative currents were furnished by an adjustable countervoltage (Cd cathode). At negative and small positive currents a linear relationship between voltage and current was found, but the slope changed above 5 ma (dash

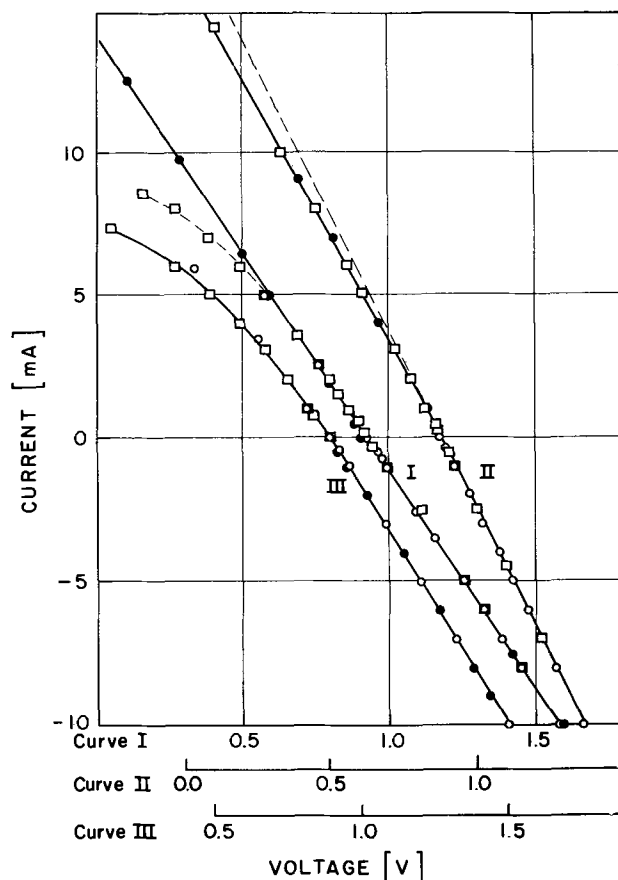


Fig. 5. Voltage/current relationship of the system Cd/liq. iodine + KI/C. These solutions contain per 100g iodine: (I) 5g KI; (II) 10g KI; (III) 15g KI and 17g CdI_2 .

curve). The current increased on stirring the solution resulting in a value of 12.6 ma at 0.10v which coincides with the straight line at the lower part of curve I. This straight line was confirmed by measuring again at increasing voltage while stirring continuously (filled circles).

The linearity between current and voltage could be improved, without stirring the electrolyte, by adding more KI to the solution. Solution II contained 10g KI per 100g of iodine (curve II). The voltage values have been displaced by 0.3v in Fig. 5 to avoid overlapping with curve I. The open circles again represent an increasing voltage, the squares indicate a decreasing voltage. The values are not exactly located on a straight line (which is made plain by the course of the dash branch). No difference was noticed when the solution was stirred (filled circles). The inner resistance which is calculated from the positive branch is $R(+)$ = 54 ohms, while the negative branch corresponds to $R(-)$ = 50 ohms. A typical example for pairs of values $R(+)$ and $R(-)$, which were measured by an a-c bridge, is given for various concentrations of the electrolyte, in Table II.

Table II. Dependence of OCV and R on concentrations of electrolyte

Concentration, g KI/100g iodine	$R(-)$, ohms	$R(+)$, ohms	$R(+)-R(-)$, ohms	Open-circuit voltage, v
0.17	130	200	70	0.965
0.34	43	155	112	0.976
0.59	22	60	38	0.960
0.96	11	60	49	0.967
1.54	8	50	42	0.969
2.19	7.3	46	38.7	0.968
2.98	6.3	20	13.7	0.960
3.80	5.0	15	10.0	0.908
4.63	2.5	2.8	0.3	0.892
5.72	1.70	1.75	0.05	0.897
7.02	1.15	1.40	0.25	0.890
8.60	0.85	0.96	0.11	0.875
11.06	0.75	0.85	0.10	0.870

The (+) sign designates a cadmium anode, the reversed voltage (Cd cathode) is marked by the (-) sign. Typical for this series is: It is always $R(+)$ > $R(-)$. The difference $\Delta R = R(+)$ - $R(-)$ becomes smaller with increasing concentration of KI. The decrease of ΔR is accompanied by a decrease of the open circuit voltage. The voltage decreases slowly at low concentrations, but the voltage drop becomes more pronounced at higher concentrations (above 3g of KI per 100g of iodine). These three statements have been found to be true for all iodine cells containing either cadmium or mercury as an electrode.

Curve III in Fig. 5 finally shows how an excess of CdI_2 in the solution influences the voltage-current dependence. A solution of 15g (0.090 moles) KI and 17g (0.046 moles) CdI_2 in 100g of iodine was used. Again the voltage has been displaced in the plot for reasons of clarity. This time the curvature at positive currents could not be avoided by stirring. The deviation from a linear relationship between current and voltage at positive currents, which was observed when the mole ratio of CdI_2 to KI exceeded 0.5, has been pursued to higher voltages.

A solution containing 16g (0.044 moles) CdI_2 and 1g (0.008 moles) KI per 100g of iodine was used. Two cadmium strips served as electrodes. Each current reading was taken about 2 min after the voltage had been changed, when a rather constant value had been established (Fig. 6, open circles). A smoother curve, resembling a hysteresis loop (filled circles), was obtained as follows:

The voltage was increased in small steps and current readings were taken. As soon as the current started falling off (at 1.35v) the voltage was increased swiftly to keep a constant current of 2.4 ma. At 15.5v the current started again to increase with further increase of the voltage. The voltage was then decreased in an analogous way. Replacing the cadmium cathode by a graphite rod did not change the shape of the hysteresis loop, while replacement of the cadmium anode resulted in a linear relationship between current and voltage (measured up to 4v). The hysteresis loop disappeared if more KI was added. This finding means that there is passivation occurring at the anode if too much CdI_2 is present.

Cells which contain an excess of CdI_2 show a considerable decrease of the current with time, as the reaction product cannot go into solution by the formation of K_2CdI_4 . The next experiment elucidates this point: A U-shaped vessel with a cadmium anode and a graphite cathode contained 25g (0.15 moles) KI, 30g (0.12 moles) CdI_2 , and 150g of iodine. A load resistor was continuously adjusted to keep the external resistance equal to the inner resistance of the cell. Table III lists the time dependence of the current together with the changing inner resistance R_i .

There is a linear decrease of the current with time, after a relatively constant current has been flowing for a certain time. This change is due to a linear increase of the inner resistance, because the open-circuit voltage of the cell remained constant. These measurements were reproduced by replacing the anode by an equal piece of cadmium which had just been polished with emery paper.

Cell Performance

The current of a U-shaped cell with an inner resistance of about 50 ohms has been kept constant within 1% for more than 24 hr at the maximum power output (inner resistance equal to load resistance). The power output for a cell with a low inner resistance (Fig. 4) is about 0.01 w/cm². For one typical sample, using a solution of 10g KI and 100g of iodine and a cadmium rod with 9.4 cm² of its surface exposed to the liquid, a constant current of 245 ma at 0.45v was obtained for 1 hr; after 2 hr the current was still 240 ma (125°C, solution not stirred). This current corresponds to a power output of $0.45 \times 0.245 = 0.11\text{w}$ or 0.012 w/cm². With another cell, which had been

Table III. Dependence of current with time

Time, <i>t</i> , min	Current, <i>i</i> , ma	$-\frac{\Delta i}{\Delta t} \left(\frac{\text{ma}}{\text{min}} \right)$	Inner resistance, R_i , ohms
0	1.1	0.00	409
5	1.0	0.02	450
17	1.0	0.00	450
32	0.95	0.003	474
37	0.87	0.016	517
42	0.72	0.03	625
45	0.62	0.03	726
48	0.52	0.03	865
52	0.38	0.03	1184
55	0.28	0.03	1607
57	0.21	0.03	2140
60	0.09	0.04	5000

stirred, up to 0.026 w/cm² were obtained for a short time (10-15 min).

It was not possible to recharge the cell. The plating out of cadmium on the Cd-cathode was always over-compensated by corrosion.

Losses of Current and Voltage

The corrosion of cadmium in iodine may be described in terms of a localized current, i_c , (difference effect). The total anodic current, i_a , is given by the sum of current i_e which is delivered to the external circuit and i_c . The total anodic current, i_a , is proportional to the total weight loss of the cadmium anode Δm . The amount $\Delta m'$ of cadmium which supports the current in the external circuit is proportional to i_e . Thus the current efficiency is given by

$$E_f = \frac{i_e}{i_c + i_e} = \frac{i_e}{i_a} = \frac{\Delta m'}{\Delta m}$$

The experimental results, which were obtained with three different cells, are given in Table IV. Current i_e was measured by the silver deposit in a coulometer. The concentration of the electrolyte was at least 15g KI per 100g of iodine during all these measurements. Table IV shows that the current efficiency is proportional to the current density up to 35 ma, where corrosion becomes negligible and an optimum current efficiency has been reached.

There are not sufficient thermodynamic data available to calculate the exact emf which is provided by the reaction of cadmium and iodine to form CdI_2 at 125°C. The standard free enthalpy¹ (at 25°C) ΔG_f° for this reaction is -48.0 kcal/mole (8), and the standard emf is given according to Nernst's equation by

$$E_o = -\frac{\Delta G_f^\circ}{23.04 \times n_e} [\text{volts}] (\Delta G_f^\circ \text{ in kcal/mole})$$

This value corresponds to $48.0/23.04 \times 2 = 1.04\text{v}$. The emf at 125°C for this reaction is expected to differ only slightly from this value. This assumption can be supported by a corresponding calculation for the mercury-iodine system, which also has been investigated, and was found to behave analogous to the cadmium-iodine cell:

The standard free enthalpy for the formation of the red modification of HgI_2 is $\Delta G_f^\circ = H_f^\circ - T\Delta S_f^\circ = -24.0 \text{ kcal/mole}$ (at 25°C) (9, 10) and thus $E_o = 0.520\text{v}$. It was evaluated from the heat capacities c_p

¹The magnitude $G = H - TS$ is designated as "free enthalpy" in conformity with a suggestion of the Commission for Nomenclature and Electrochemical Definitions of C.I.T.C.E.

Table IV. Experimental current efficiencies

Cell No.	Average current passed, ma	Total time, hr	Current efficiency, %	Current density, ma/cm ²
I	24.8	19.5	24.4	6.9
I	15.1	26.0	17.2	4.8
I	125	2.8	100	34.7
II	160	3.0	41.4	12.8
II	195	1.5	46.0	15.6
II	290	1.5	65.3	23.4
II	367	4.0	82.3	29.6
III	10	24.0	24.5	4.35

of the components: $\Delta G_f^\circ(125^\circ\text{C}) = -23.8$ kcal/mole or $E = 0.516$ v. This voltage differs only slightly from the value at 25°C . Experimentally an emf of 0.51v has been found for the system Hg/liquid iodine/Pt at 125°C .

Several other metals, e.g., Ag, Mg, Zn, Al, Sn, and Pb, were tested for the ability to produce electricity by their reaction with liquid iodine. The voltages which were obtained with a platinum cathode for these metals at 125°C were found in reasonable agreement with the theoretical values, which were calculated from the free enthalpies of formation at 25°C .

Therefore, considering the standard emf, $E_0 = 1.04$ v, the theoretical value for the formation of CdI_2 at 125°C should be in agreement with the voltage of 0.98v which has been measured with pure iodine and iodine solutions containing low concentrations of potassium iodide.

The following experiment was done to determine whether the voltage drop due to an increase of KI in the electrolyte is caused at the anode or at the cathode. A conductivity vessel was used in which the anode and cathode limbs had been separated by plugging the connecting tube between the compartments with glass wool.

- (I) At first pure iodine was used as electrolyte; for this system Cd/liquid iodine/C a voltage $E_0 = 0.98$ v was obtained.
- (II) To the cathode compartment 10g KI per 100g of iodine were added which caused the voltage to drop 0.02v. Thus the voltage for this system Cd/liquid iodine//liquid iodine + KI/C is equal to $E_1 = E_0 - 0.02 = 0.96$ v.
- (III) Exchanging Cd- and C-electrode (or adding KI to the Cd-compartment from the beginning) resulted in a voltage of $E_2 = 0.79$ v.
- (IV) Changing back the electrodes to position (II) did not result in regaining the corresponding voltage E_1 ; only the lower voltage $E_2 = 0.79$ v was sustained. However, the voltage started to increase slowly (faster, if a current was drawn) and within 90 min a voltage of 0.96v had been re-established. Reversing the electrodes afterwards to position (III) resulted again in the lower voltage of 0.79v.

The following potentials have to be considered for describing these systems:

1. $E_0 = 0.98$ v is the voltage which has been observed for pure iodine; it is given by the standard potential in Nernst's equation.
2. E' is described by the concentration dependent part of Nernst's equation:

$$E = E_0 - \frac{RT}{2F} \ln [\text{I}^-]^2 [\text{Cd}^{++}] = E_0 - E'$$

Thus the addition of KI to the homogeneous solution causes the potential to decrease at the cathode due to the increased concentration of iodide ions. The iodide can be higher associates, e.g., I_3^- . The formation of the complex ions $(\text{CdI}_4)^{--}$ increases the potential E' according to the relationship

$$[\text{Cd}^{++}] = k \frac{[\text{CdI}_4^{--}]}{[\text{I}^-]^4}$$

3. If the anode and cathode compartments contain different concentrations of KI, a concentration potential E'' is superimposed.

E_0 , E' , and E'' do not suffice to account for the observed potential changes. A potential drop from 0.98 to 0.96v as described under (I) and (II) can be explained by concentration differences in the electrolyte; however, a decrease from 0.96 to 0.79v [cf. (III)] and the slow recovery of the voltage [cf. (IV)] cannot be attributed to concentration potentials. Changes at the graphite (or platinum) cathode which behaves like an iodine-iodide electrode can be ruled out, too. It seems reasonable that a layer of CdI_2 on the anode

is necessary to maintain the standard potential $E = E_0 - E'$, preventing a short circuit caused by a local cell action.

As CdI_2 is a typical ionic conductor (cf. Fig. 3), it is permeable for at least one kind of reacting ions, presents a high resistance to electrons, and keeps neutral iodine molecules off the cadmium surface. If the CdI_2 layer becomes too thin, uncharged iodine molecules may reach the cadmium surface via cracks in the CdI_2 deposit, or electrons may leak through by the tunnel effect, causing the reaction $\text{I}_2 + 2e \rightarrow 2\text{I}^-$ near the anode. The anode provides the electrons for this reaction which causes the anodic potential to decrease.

It cannot be decided whether the current through the CdI layer is carried by Cd^{++} or by I^- ; both possibilities are given:

1. Cd-cations move through the CdI_2 lattice and react with iodide ions at the boundary between CdI_2 and the electrolyte.

2. I-anions move through the CdI_2 layer and react with cadmium at the surface of the anode.

The formation of a CdI_2 deposit on the anode which varies its thickness according to the given conditions can be illustrated by the data given in Table II. The change of the inner resistance $\Delta R = R(+)-R(-)$ which is found upon reversal of the current direction can be attributed to the CdI_2 layer on the Cd electrode. This deposit is dissolved more or less if the cadmium is used as a cathode because negative iodide ions move out of the CdI_2 into the electrolyte, and at the same time Cd cations move toward the cadmium cathode, resulting in the destruction of the ion conducting membrane.

The equilibrium between the build-up of the CdI_2 layer on the anode and its dissolving by the formation of soluble K_2CdI_4 depends on the concentration of KI near the anode. A higher concentration of KI enhances the dissolution of the CdI_2 deposit, causing the difference between the inner resistances $R(+)$ and $R(-)$ to diminish. The open-circuit voltage is reduced with the decrease of $R(+)$ according to the above given explanation.

The same reason can be applied to explain why the bend at the upper curve I in Fig. 5 is straightened, when the electrolyte is stirred: The process of dissolving CdI_2 is accelerated, as the transport of the reagent KI to the anode as well as the transport of the final product K_2CdI_4 from the anode occur faster than it is possible by mere diffusion. The bend of curve III in Fig. 5 is not influenced by stirring because

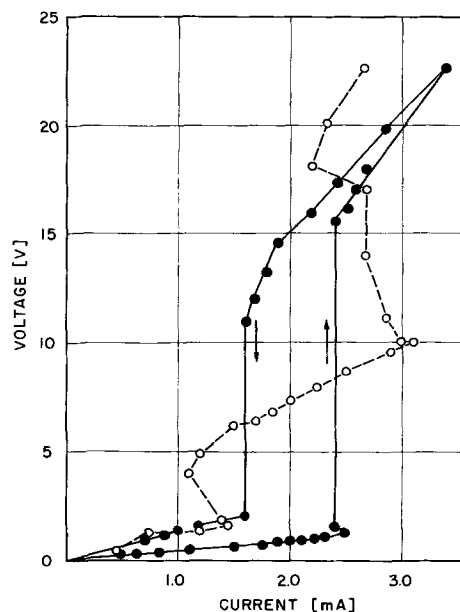


Fig. 6. Anodic passivation of cadmium in iodine

no free KI is available in the electrolyte to form the soluble complex salt.

Some calculations were made to determine the thickness of the CdI_2 deposit on the anode. There are the results of two measurements available, for which the CdI_2 was not removed by the formation of K_2CdI_4 due to the lack of KI in the solution.

In Fig. 6 the increase of the voltage from 1.2 to 15.5v at a constant current of 2.4 ma is attributed to a growing CdI_2 deposit. The inner resistance R_i of the cell is composed of the variable resistance R_f of the CdI_2 film and a constant resistance R_o (electrolyte plus leads). From Ohm's law $R_f = E/i - R_o$ and with numerical values taken from Fig. 6

$$R_f = \frac{15.5}{2.4 \times 10^{-3}} - \frac{1}{2.2 \times 10^{-3}} \approx 6000 \text{ ohms}$$

With an effective anode surface of 12 cm^2 and the specific conductance of CdI_2 at 125°C ; $\sigma = 2.5 \times 10^{-8} \text{ ohms}^{-1} \text{ cm}^{-1}$ the average thickness of the layer is $12 \times 6000 \times 2.5 \times 10^{-8} = 1.8 \times 10^{-3} \text{ cm}$.

The data in Table III show that there was a linear increase of the resistance with time after the current started to decline. If this increase of 4550 ohms is produced by a CdI_2 deposit on a anode surface of 10 cm^2 the average thickness follows to be $10 \times 4550 \times 2.5 \times 10^{-8} = 1.1 \times 10^{-3} \text{ cm}$. This result is in agreement with the first value, which was obtained independently.

An approximate value, how thick the CdI_2 film has to be in order to support the emf, can be calculated from the data in Table II. The difference between $R(+)$ and $R(-)$ is considered as the resistance of the CdI_2 film. For high concentrations of KI in iodine it was found $R(+)-R(-) = 0.1 \text{ ohm}$. With an estimated surface area of 20 cm^2 a film thickness of $0.1 \times 20 \times 2.5 \times 10^{-8} = 5 \times 10^{-8} \text{ cm}$ is calculated. As CdI_2 is hexagonal with $a = 4.249\text{\AA}$, $c = 6.854\text{\AA}$ (11) the stated film corresponds within the limits of error to one monolayer of CdI_2 . This result agrees with values which have been obtained in aqueous solutions: Protective films which have been produced after the

anodic polishing of metals, were found to be between one monolayer and 100\AA thick (13).

Acknowledgments

The author is indebted to Dr. J. T. Kummer for valuable suggestions and comments during all phases of this work, and to Dr. M. Dzieciuch for helpful discussions. The critical reading given this manuscript by Dr. J. V. Petrocelli is gratefully acknowledged.

Manuscript received April 27, 1964; revised manuscript received July 23, 1964.

Any discussion of this paper will appear in a Discussion Section to be published in the June 1965 JOURNAL.

REFERENCES

1. R. B. Goodrich and R. C. Evans, *This Journal*, **99**, 207C (1952).
2. S. M. Selis, L. P. McGinnis, E. S. McKee, and J. T. Smith, *ibid.*, **110**, 469 (1963).
3. G. N. Lewis and Plumer Wheeler, *Z. phys. Chem.*, **56**, 179 (1906).
4. Mark Rabinowitsch, *ibid.*, **119**, 79 (1926).
5. W. A. Plotnikow, J. A. Fialkow, and W. P. Tschalij, *ibid.*, **A172**, 304 (1935).
6. V. A. Plotnikov, Ya. A. Fialkov, and V. P. Chalii, *J. Gen. Chem. (USSR)*, **6**, 273 (1936).
7. A. Smekal, *Z. techn. Phys.*, **8**, 561 (1927).
8. "Handbook of Chemistry and Physics," The Chemical Rubber Publishing Co., p. 1882-1915, Cleveland, Ohio, 44th ed. (1962).
9. Landolt-Börnstein, *Eigenschaften der Materie in ihren Aggregatzuständen*, Springer Verlag, Berlin (1961).
4. Teil, kalorische Zustandsgrößen, page 247.
10. Selected Values of Chemical Thermodynamic Properties, Circular of the National Bureau of Standards 500 (1952).
6. Teil, elektrische Eigenschaften I, page 245.
11. Konrad Sagel, *Tabellen zur Röntgenstrukturanalyse*, p. 42, Springer Verlag, Berlin (1958).
12. J. O'M. Bockris, "Modern Aspects of Electrochemistry," Vol. 2, p. 313-323, Butterworths Scientific Publications, London (1959).

Anodic Oxidation of Lead at Constant Potential

P. Ruetschi¹ and R. T. Angstadt

Electric Storage Battery Company, C. F. Norberg Research Center, Yardley, Pennsylvania

ABSTRACT

Lead and lead alloys were subjected to anodic oxidation in sulfuric acid solution under potentiostatic conditions. The current-time transients reveal that, as a result of inhibited ionic diffusion across the corrosion film, a secondary corrosion reaction takes place below the lead sulfate layer built up in the primary phase. The experimental findings are explained in terms of a high local pH in the interior of the corrosion film. This hypothesis is shown to be in accord with self-depassivation phenomena and cathodic constant-current stripping experiments. The potential-determining reactions in the corrosion film are discussed in the light of new pH-potential diagrams, constructed under consideration of the formation of basic lead sulfates. A model for the composition of the corrosion film is developed which conforms to all experimental findings, including the phenomena relating to the ohmic resistance of the film.

Much work has been done in the past on anodic corrosion of lead in sulfuric acid solution using the constant current technique (1-10). This method is particularly suitable for the investigation of the corrosion processes at high anodic potentials in the region of oxygen evolution. The electrode potential is then forced rapidly through the initial transient, and the electrode is exposed to lower potentials only over short periods of time. It is difficult to study the corro-

sion behavior at relatively low electrode potentials with constant current techniques because certain phases of the film-formation process involve relatively large quantities of electricity, while others require only minute coulometric current flow, resulting in correspondingly widely different time periods which are difficult to manage experimentally.

Investigations using constant potential techniques largely avoid these problems and allow a particularly clear resolution of the different phases during the ini-

¹ Present address: Leclanché S.A., Yverdon, Switzerland.

tial transients of the film-formation process. Also with this technique, the corrosion of lead can be studied conveniently at low potentials, e.g., at potentials near or below the reversible $\text{PbSO}_4/\text{PbO}_2$ couple.

Film-formation on lead in sulfuric acid at constant potential was first studied by Lander (11,12), and later Burbank (13-15) and Maeda (16). However, the experimental techniques applied by these authors were crude, compared with present-day standards, because they did not have available to them automatically regulating electronic potentiostats. Instead, the potentials were controlled by using a large counterelectrode and by manually adjusting the externally applied voltage between counterelectrode and working electrode, whereby it was presumed that the counterelectrode did not change its own potential during the course of the experiment. Lander states that the half-cell potentials were controlled to within ± 10 mv, while Burbank and Maeda do not reveal their error limits. The named authors also were not able to record initial current-time transients accurately because of the limited response time of their voltage-recording equipment.

Electronic potentiostats for the study of anodic film-formation and anodic precipitation processes were used by Fleischmann, Thirsk, and co-workers. The current-time traces obtained by Fleischmann and Thirsk for anodic oxidation of lead (17) and silver (18) in sulfuric acid, and mercury (19) in hydrochloric acid are similar to results presented in this paper. The present investigation has, however, revealed a new phenomenon, not previously described. It becomes apparent only if the current-time curves are recorded with high sensitivity over prolonged periods of time. The effect to be described is related to changes in the corrosion film due to inhibited mass transport phenomena.

The present paper points out the importance of ionic diffusion processes in corrosion films and demonstrates that a second corrosion product may be formed, beneath a protecting layer, as a result of depletion effects.

Constant Potential Experiments

The experimental cell used in these investigations is illustrated in Fig. 1. Cells of this type, machined of Lucite or Teflon, or made of Pyrex glass, comprised a reference electrode compartment connected through a capillary in the side wall to a working electrode compartment. The test electrode was clamped tightly against a circular hole of 1 cm² area in the bottom of the cell. O-rings of neoprene or Teflon were used as gaskets. $\text{Hg}/\text{Hg}_2\text{SO}_4$ reference electrodes, which were carefully equilibrated with the acid in the test cell, were used throughout the investigation. The auxiliary electrode was foil of platinum. The whole cell was in-

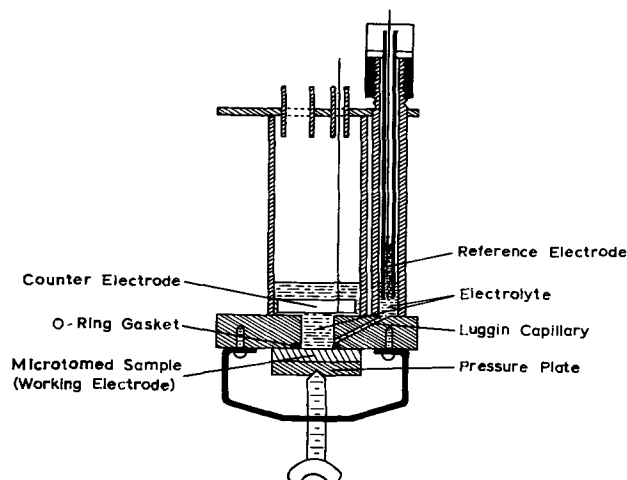


Fig. 1. Schematic drawing of corrosion cell

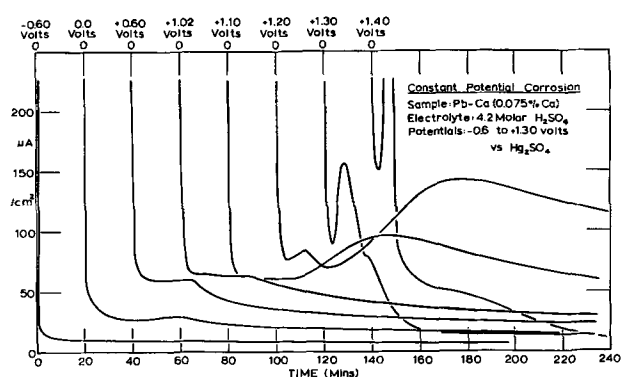


Fig. 2. Constant potential corrosion curves, showing current vs. time for Pb-Ca samples corroded at eight potentials from -0.60 to $+1.40$ v vs. $\text{Hg}/\text{Hg}_2\text{SO}_4$.

serted into a nickel or plastic can which was in turn immersed into a constant temperature water bath at $30^\circ \pm 0.1^\circ\text{C}$. The electrolyte was prepared from triple distilled water and CP sulfuric acid. The surface of the test, or working, electrode was carefully microtomed to a mirror-finish. The anodizing potential was applied immediately after filling the cell with electrolyte.

In total, five cells were used simultaneously, connected to five electronic potentiostats. These had response times of better than 10^{-4} sec and were specially designed for low drift. The drift was 1 mv or smaller over a 24-hr period. The potential of the test electrodes was thus kept at a constant value within 1 mv. Each experiment was normally carried out over 24 hr, but longer anodization periods were also studied.

Typical initial current-time transients at constant potential are presented in Fig. 2. The origin of the different traces is shifted along the abscissa to make a clear presentation. For this set of experiments, the electrolyte was 4.20M H_2SO_4 and the temperature $30^\circ \pm 0.1^\circ\text{C}$. The potential expressed against a $\text{Hg}/\text{Hg}_2\text{SO}_4$ reference electrode in the same solution is given at the top of each curve. The test electrode was a Pb-Ca alloy containing 99.925% Pb and 0.075% Ca. Several other lead alloys were also studied, but in the present paper only the results with 0.05 and 0.075% Pb-Ca alloys will be presented because of their increasing technical importance in the manufacture of batteries. Results similar to the ones given below were obtained with pure lead. The curve for -0.6 v in Fig. 2 exhibits one sharp initial peak only, whose ascending branch is not shown since the initial rise was extremely fast. All other corresponding curves taken at voltages above -0.9 v and below -0.4 v, which are not given in Fig. 2 for lack of space, also exhibited only one sharp initial peak. This first peak, lasting in the order of 1-2 min, can readily be interpreted as due to the formation of PbSO_4 layer. The current peak is followed by a gradual decay towards a steady value of the corrosion current as the sulfate layer increases in thickness. Only the first 180 min are plotted here; all the experiments were continued over 24 hr, however, and the final corrosion currents were determined at this point.

At constant potentials above -0.4 v vs. $\text{Hg}/\text{Hg}_2\text{SO}_4$, one observes the emergence of what ultimately becomes a broad second peak, apparent in Fig. 2 in the curve for $+0.0$ v. This hump slowly increases in height and breadth as the potential is increased. As discussed below, the authors believe that this second hump is caused by a new electrochemical corrosion process, occurring beneath the lead sulfate layer formed initially.

At a potential of $+1.20$ v vs. $\text{Hg}/\text{Hg}_2\text{SO}_4$, a third current peak appears in the current-time transient. This peak starts to become visible at a potential of 1.14 v, and the corresponding curve is shown in Fig. 3. It is positioned between the first and second peak. As

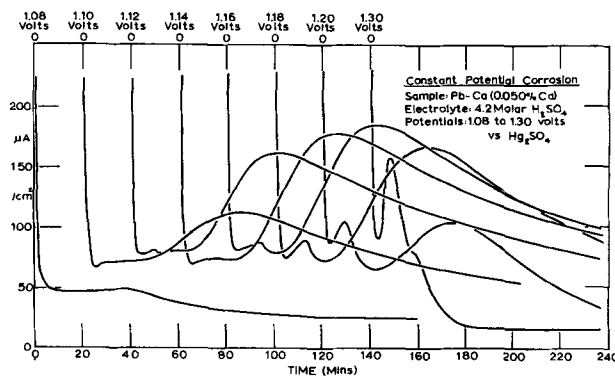


Fig. 3. Constant potential corrosion curves, showing current vs. time for Pb-Ca sample corroded at eight potentials from +1.08 to +1.30v vs. Hg/Hg₂SO₄.

discussed below, this new peak stems from oxidation of PbSO₄ to β-PbO₂ in the outer, acidic part of the corrosion layer. With increasing potential this peak becomes more and more pronounced. At the same time, the broad hump gradually disappears. Above 1.3v only the new peak remains. It is this peak which was investigated by Fleischmann and co-workers, who limited their investigations to relatively high potentials and short times. Thus, they did not observe the broad hump discovered in the present study.

The broad hump reaches its maximum height and breadth at that critical potential where the third peak first appears, and thus where PbSO₄ is beginning to be oxidized to β-PbO₂ in acidic milieu. At increasingly higher potentials, the oxidation of PbSO₄ to β-PbO₂ becomes increasingly fast because the nucleation process is facilitated (17, 20). Finally, the oxidation of PbSO₄ to β-PbO₂ becomes so fast that alkaline conditions in the interior are largely avoided and restricted to relatively short times.

The critical region is illustrated in greatest detail in Fig. 3, which displays a series of corrosion curves taken at 20 mv intervals for the 0.05% Ca-Pb alloy. The data demonstrate the excellent reproducibility of these experiments. Each curve was obtained with a newly microtomed sample surface, using the same alloy casting throughout the series.

The corrosion currents reached a nearly constant value after 10-20 hr. After this, there was only a very slight decrease in current which continued uniformly over many days. The currents at 24 hr were selected to obtain quasi-steady-state corrosion behavior. The corrosion currents at 24 hr are plotted vs. potential in Fig. 4. The curve shows a characteristic peak at 1.10v and a minimum at 1.20v. A similar curve was first obtained by Lander (11) and others (21) from weight loss measurements.

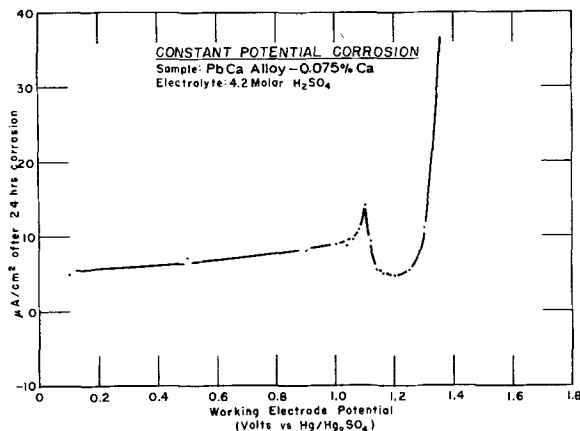


Fig. 4. Quasi-steady-state current after 24 hr constant potential corrosion for the potential range 0 to +1.40v vs. Hg/Hg₂SO₄.

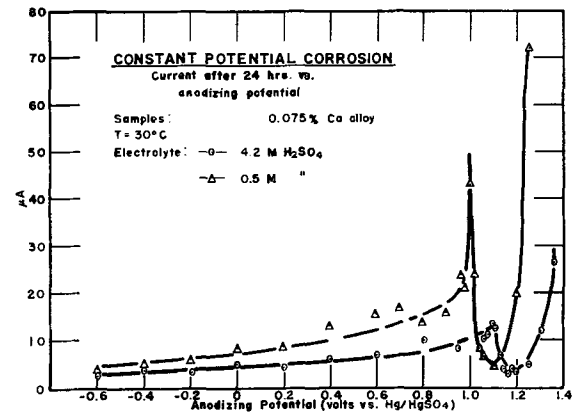


Fig. 5. Quasi-steady-state current after 24 hr constant potential corrosion for the potential range 0 to +1.40v vs. Hg/Hg₂SO₄, comparing corrosion in 0.5 and 4.2M H₂SO₄.

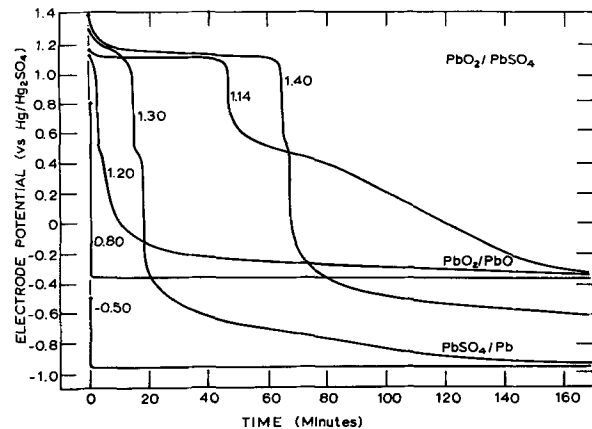


Fig. 6. Self-depassivation of Pb-Ca electrodes after corrosion at constant potential in the range -0.5 to +1.40v vs. Hg/Hg₂SO₄ for 24 hr.

Figure 5 shows a comparison of the quasi-steady-state corrosion currents after 24 hr for the same alloy in 4.20 and 0.5M H₂SO₄. With decreasing acid concentration the corrosion peak is increased in height and shifted to lower electrode potentials. This was already pointed out by Lander (12) who also recognized the importance of the corrosion peaks with respect to the life of positive grids in lead acid storage batteries (12, 22).

Depassivation

After subjecting the test electrodes to a constant potential for 24 hr, they were disconnected from the potentiostat and were permitted to self-depassivate on open circuit. The electrode potential was recorded as a function of time using an electrometer-voltmeter with recorder output. The input impedance of the electrometer-voltmeter was better than 10¹³ ohms. A high input impedance is required to prevent discharge of the corrosion film through the recording voltmeter. Earlier investigators (13) used voltmeters with much lower input impedance, which might have caused errors in observing the voltage plateaus during decay. Typical decay curves obtained in 4.2M H₂SO₄ are given in Fig. 6. Hundreds of decay curves were actually taken with samples held for 24 hr at constant potentials in 20 mv intervals. Four voltage plateaus are readily apparent; they occur at about 1.1, 0.5-0.6, -0.4, and -0.9v.

Electrodes which were held for 24 hr at potentials between -0.9 and -0.4v vs. a Hg/Hg₂SO₄ electrode in the same solution returned instantly to the -0.9v level after the potentiostat was disconnected. This is the voltage of a Pb/PbSO₄ electrode in this solution. This confirms the fact that in this voltage range the only

corrosion product is PbSO_4 . The thickness of the PbSO_4 layer increases almost linearly with potential, as is evident from the linearly increasing ohmic drop.

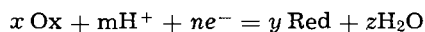
All electrodes which had been held for 24 hr at a constant voltage between -0.4 and $+0.8$ v showed a rapid voltage decay to a voltage plateau at -0.4 v vs. $\text{Hg}/\text{Hg}_2\text{SO}_4$. This voltage plateau was well-defined and was maintained for many hours, or sometimes even days, before the voltage decayed further to the Pb/PbSO_4 potential at -0.9 v. Only the curve for the potential of 0.8 v is shown in Fig. 6 but the decay curves for all potentials below 0.8 v and above -0.4 v were alike. As shown below, the voltage level at -0.4 v corresponds to that of a PbO_2 electrode in an alkaline electrolyte. Electrodes anodized at potentials above $+0.8$ v exhibited an ill-defined, vague plateau during decay at $+0.6$ v. This plateau is identified as corresponding to a PbO_2 electrode in slightly acidic medium at pH 2 which corresponds to the pK of the dissociation of bisulfate ions $\text{HSO}_4^- \rightarrow \text{H}^+ + \text{SO}_4^{--}$. Sulfuric acid thus shows a buffer action at this pH since, according to Latimer (25), one calculates $\log [a_{\text{SO}_4^{--}}/a_{\text{HSO}_4^-}] = -1.90 + \text{pH}$. Finally, electrodes held for 24 hr at constant potentials above 1.10 v maintained, during decay, a well-defined plateau at 1.1 v which is readily identified as that of a PbO_2 electrode in strong sulfuric acid.

Therefore, all voltage plateaus of Fig. 6 in the voltage range between the $\text{PbO}_2/\text{PbSO}_4$ electrode and the PbSO_4/Pb electrode are here explained as due to couples of PbO_2 in various pH environments. This is in contrast to previous interpretations of the voltage plateaus observed during self-depassivation, since earlier investigators assigned the intermediate voltage plateaus to couples between basic divalent lead compounds and metallic lead (9-11, 13)

pH-Potential Diagrams

To illustrate clearly the present analysis of the electrochemical process during constant potential corrosion and during subsequent depassivation, it appears advantageous to use pH-potential diagrams. For the $\text{Pb}-\text{H}_2\text{O}$ system, the pH-potential diagram has been reported by Pourbaix and co-workers (23) and for the $\text{Pb}-\text{H}_2\text{O}-\text{H}_2\text{SO}_4$ system, by Delahay, Pourbaix, and Van Rysselberghe (24). These authors, however, did not include the formation of basic lead sulfates, which results in a considerable alteration of the diagram. In order to discuss the formation of such products in corrosion films it was decided to reconstruct the pH potential diagram of lead, using the best available data, including the free energy of formation of the basic lead sulfates.

In constructing the pH-potential diagram, the potential E corresponding to the equilibrium



is calculated from the equation

$$E = (1/23.07n) (x\Delta F^\circ_{\text{Ox}} - y\Delta F^\circ_{\text{Red}} - z\Delta F^\circ_{\text{H}_2\text{O}}) - 0.0591(m/n)\text{pH} + (0.0591/n) \log (a^x_{\text{Ox}}/a^y_{\text{Red}})$$

in which the ΔF° 's are the standard free energies of formation at 25°C , and the a 's the activities of the corresponding species.

The standard free energies (in kcal/mole) (Table I) were used for the various reactants and products. References are given in brackets.

The equilibria between the various solid phases are determined by the reactions listed in Table II.

The pH-potential diagram was calculated for a total sulfate activity ($a_{\text{HSO}_4^-} + a_{\text{SO}_4^{--}}$) of 1 and also of

Table I. Standard free energies

SO_4^{--}	(25)	-177.34	PbSO_4	(25)	-193.89
HSO_4^-	(25)	-179.94	$\text{PbO} \cdot \text{PbSO}_4$	(26)	-243.2
H_2O	(25)	-56.69	$3\text{PbO} \cdot \text{PbSO}_4 \cdot \text{H}_2\text{O}$	(26)	-397.3
Pb_3O_4	(25)	-147.60	$5\text{PbO} \cdot 2\text{H}_2\text{O}$	(26)	-336.35
Pb_2O_3	(23)	-98.417	PbO	(23)	-45.05
$\alpha\text{-PbO}_2$	(27)	-51.94	$\beta\text{-PbO}_2$	(23)	-52.34

Table II. Equilibria between solid phases

- $\text{PbSO}_4 + \text{H}^+ + 2e^- \rightarrow \text{Pb} + \text{HSO}_4^-$
 $E = -0.302 - 0.0295 \text{pH} - 0.0295 \log a_{\text{HSO}_4^-}$
- $\text{PbSO}_4 + 2e^- \rightarrow \text{Pb} + \text{SO}_4^{--}$
 $E = -0.356 - 0.0295 \log a_{\text{SO}_4^{--}}$
- $\text{PbO} \cdot \text{PbSO}_4 + 2\text{H}^+ + 4e^- \rightarrow 2\text{Pb} + \text{SO}_4^{--} + \text{H}_2\text{O}$
 $E = -0.099 - 0.0295 \text{pH} - 0.0148 \log a_{\text{SO}_4^{--}}$
- $3\text{PbO} \cdot \text{PbSO}_4 \cdot \text{H}_2\text{O} + 6\text{H}^+ + 8e^- \rightarrow 4\text{Pb} + \text{SO}_4^{--} + 4\text{H}_2\text{O}$
 $E = 0.037 - 0.0443 \text{pH} - 0.0074 a_{\text{SO}_4^{--}}$
- $5\text{PbO} \cdot 2\text{H}_2\text{O} + 10\text{H}^+ + 10e^- \rightarrow 5\text{Pb} + 7\text{H}_2\text{O}$
 $E = 0.260 - 0.0591 \text{pH}$
- $\text{PbO}_2 + \text{HSO}_4^- + 3\text{H}^+ + 2e^- \rightarrow \text{PbSO}_4 + 2\text{H}_2\text{O}$
 $E = 1.628 - 0.0886 \text{pH} + 0.0295 \log a_{\text{HSO}_4^-}$
- $\text{PbO}_2 + \text{SO}_4^{--} + 4\text{H}^+ + 2e^- \rightarrow \text{PbSO}_4 + 2\text{H}_2\text{O}$
 $E = 1.685 - 0.1182 \text{pH} + 0.0295 \log a_{\text{SO}_4^{--}}$
- $2\text{PbO}_2 + 6\text{H}^+ + \text{SO}_4^{--} + 4e^- \rightarrow \text{PbO} \cdot \text{PbSO}_4 + 3\text{H}_2\text{O}$
 $E = 1.422 - 0.0886 \text{pH} + 0.0147 a_{\text{SO}_4^{--}}$
- $4\text{PbO}_2 + 10\text{H}^+ + \text{SO}_4^{--} + 8e^- \rightarrow 3\text{PbO} \cdot \text{PbSO}_4 \cdot \text{H}_2\text{O} + 4\text{H}_2\text{O}$
 $E = 1.285 - 0.0739 \text{pH} + 0.0074 a_{\text{SO}_4^{--}}$
- $5\text{PbO}_2 + 10\text{H}^+ + 10e^- \rightarrow 5\text{PbO} \cdot 2\text{H}_2\text{O} + 3\text{H}_2\text{O}$
 $E = 1.070 - 0.0591 \text{pH}$
- $3\text{PbO}_2 + 4\text{H}^+ + 4e^- \rightarrow \text{Pb}_3\text{O}_4 + 2\text{H}_2\text{O}$
 $E = 1.127 - 0.0591 \text{pH}$
- $2\text{PbO}_2 + 2\text{H}^+ + 2e^- \rightarrow \text{Pb}_2\text{O}_3 + \text{H}_2\text{O}$
 $E = 1.090 - 0.0591 \text{pH}$
- $\text{Pb}_2\text{O}_3 + 2\text{SO}_4^{--} + 6\text{H}^+ + 2e^- \rightarrow 2\text{PbSO}_4 + 3\text{H}_2\text{O}$
 $E = 2.270 - 0.177 \text{pH} + 0.0591 a_{\text{SO}_4^{--}}$
- $\text{Pb}_2\text{O}_3 + \text{SO}_4^{--} + 4\text{H}^+ + 2e^- \rightarrow \text{PbO} \cdot \text{PbSO}_4 + 2\text{H}_2\text{O}$
 $E = 1.750 - 0.1182 \text{pH} + 0.0295 \log a_{\text{SO}_4^{--}}$
- $2\text{Pb}_2\text{O}_3 + \text{SO}_4^{--} + 6\text{H}^+ + 4e^- \rightarrow 3\text{PbO} \cdot \text{PbSO}_4 \cdot \text{H}_2\text{O} + 2\text{H}_2\text{O}$
 $E = 1.480 - 0.0886 \text{pH} + 0.0147 a_{\text{SO}_4^{--}}$
- $3\text{Pb}_2\text{O}_3 + 2\text{H}^+ + 2e^- \rightarrow 2\text{Pb}_3\text{O}_4 + \text{H}_2\text{O}$
 $E = 1.230 - 0.0591 \text{pH}$
- $\text{Pb}_3\text{O}_4 + 3\text{SO}_4^{--} + 8\text{H}^+ + 2e^- \rightarrow 3\text{PbSO}_4 + 4\text{H}_2\text{O}$
 $E = 2.790 - 0.236 \text{pH} + 0.0886 \log a_{\text{SO}_4^{--}}$
- $2\text{Pb}_3\text{O}_4 + 3\text{SO}_4^{--} + 10\text{H}^+ + 4e^- \rightarrow 3[\text{PbO} \cdot \text{PbSO}_4] + 5\text{H}_2\text{O}$
 $E = 2.010 - 0.148 \text{pH} + 0.0443 \log a_{\text{SO}_4^{--}}$
- $4\text{Pb}_3\text{O}_4 + 3\text{SO}_4^{--} + 14\text{H}^+ + 8e^- \rightarrow 3[3\text{PbO} \cdot \text{PbSO}_4 \cdot \text{H}_2\text{O}] + 4\text{H}_2\text{O}$
 $E = 1.605 - 0.1035 \text{pH} + 0.0222 a_{\text{SO}_4^{--}}$
- $5\text{Pb}_3\text{O}_4 + 10\text{H}^+ + \text{H}_2\text{O} + 10e^- \rightarrow 3[5\text{PbO} \cdot 2\text{H}_2\text{O}]$
 $E = 0.960 - 0.0591 \text{pH}$

10^{-7} . This latter value was chosen to indicate the conditions at the lower limit. Bode and Voss (26) have calculated the activity of sulfate ions in lead acid battery pastes to be $\log a_{\text{SO}_4^{--}} = -6.8$. A similarly low activity might be expected to prevail in the interior of corrosion films at locations of complete acid exhaustion and in the presence of alkaline corrosion products such as PbO , Pb_3O_4 , and $\alpha\text{-PbO}_2$. The diagrams are not changed noticeably if $5\text{PbO} \cdot 2\text{H}_2\text{O}$ is replaced by PbO .

From the pH-potential diagrams, presented in Fig. 7 and Fig. 8 (potential vs. STP H_2), the following interesting conclusions must be drawn:

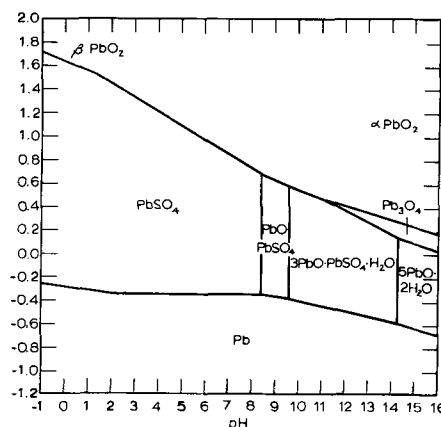


Fig. 7. Potential-pH diagram of the system $\text{Pb}-\text{H}_2\text{O}-\text{H}_2\text{SO}_4$ for ($a_{\text{HSO}_4^-} + a_{\text{SO}_4^{--}} = 1$) (potential vs. STP H_2).

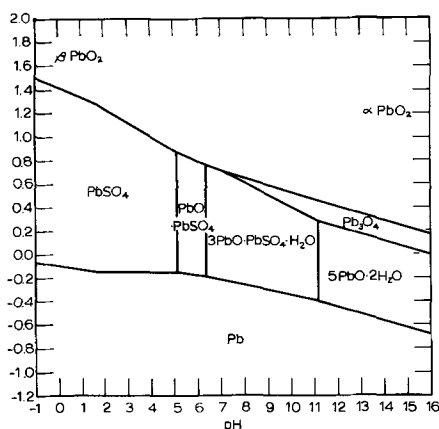


Fig. 8. Potential-pH diagram of the system Pb-H₂O-H₂SO₄ for ($a_{\text{HSO}_4^-} + a_{\text{SO}_4^{--}} = 10^{-7}$ (potential vs. STP H₂).

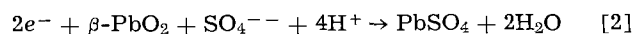
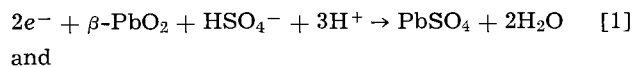
1. Above potentials of 0 volts vs. STP H₂, (this is about -0.6v vs. Hg/Hg₂SO₄) the only electrochemical oxidation or reduction processes are those involving PbO₂ or Pb₃O₄ as the oxidized species.

2. The solid phase Pb₂O₃ does not appear in the diagram, since the equilibria Pb₂O₃/PbO and Pb₂O₃/PbO₂ are not thermodynamically stable with respect to the equilibria Pb/PbO, PbO/PbO₂, PbO/Pb₃O₄, and Pb₃O₄/PbO₂. Thus, Pb is more easily oxidized to PbO than to Pb₂O₃, and PbO₂ is more easily reduced to PbO than to Pb₂O₃. According to the data of Table I Pb₂O₃ can be formed from PbO and PbO₂. The "domain" of Pb₂O₃ in the pH-potential diagram is thus "inside" that of PbO.

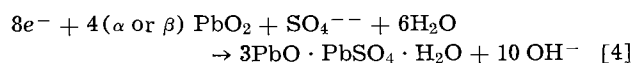
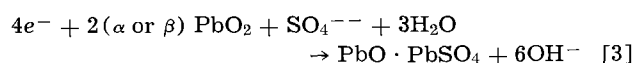
3. Electrode couples between metallic lead and any divalent lead compound, including PbO, have electrode potentials below -0.1v vs. STP H₂. Electrode couples between Pb and basic sulfates or lead monoxide exhibit more negative potentials than the Pb/PbSO₄ couple in acid solution.

These diagrams then indicate that any voltage plateaus between the potentials of the Pb/PbSO₄ and the PbSO₄/PbO₂ couple must be ascribed to electrode couples of PbO₂ or Pb₃O₄ in electrolytes of elevated pH. This fact is properly considered in the present interpretation of the corrosion and depassivation phenomena, but has not been recognized by earlier investigators.

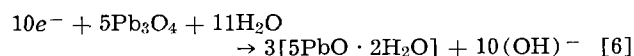
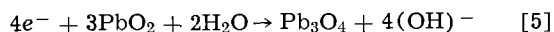
According to the present theory, the self-depassivation process must be formulated as follows: At the surface of the film nearest the electrolyte, β -PbO₂ is electrochemically reduced in acid medium according to



As the surface becomes covered with PbSO₄, further reduction of β -PbO₂ and underlying α -PbO₂ to PbSO₄ is inhibited because of slow diffusion of H₂SO₄ into the film. Thus, instead of reactions [1] and [2] the electrode passes rapidly through the sequence of the following transitory reactions

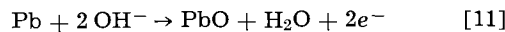
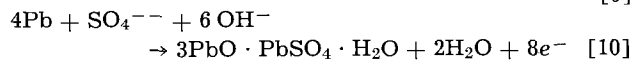
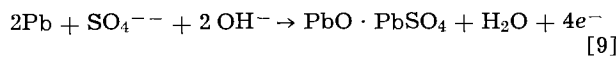
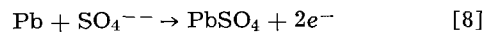
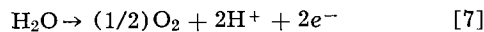


which probably occur over a very limited time period, such that no significant quantities of basic sulfates are produced. Finally, PbO₂ will be reduced in alkaline solution to Pb₃O₄ and the latter to PbO.



Here, and in the following, 5PbO · 2H₂O also stands for PbO and Pb(OH)₂ or other hydrated forms.

Electrons for reactions [1] to [6] are supplied during self-depassivation by either one or a combination of the following reactions



In addition, electrons may be delivered for reactions [1] and [2] by further oxidation of the divalent lead compounds generated by [9], [10] and [11], to Pb₃O₄ or α PbO₂, that is, by the reverse of reactions [3] to [6].

During self-decay, or self depassivation, the mixed potential of the electrode is largely determined by reactions [1], [2], [6], and [8] since it is plausible that these can proceed faster and with less restrictions than the other reactions which must be associated with large reaction and diffusion overvoltages. These reactions then determine the four respective voltage plateaus observed during self-passivation.

The length of the plateaus corresponding to Eq. [1], [2], and [6] depends on the relative speed at which electrons are delivered by reactions [7] to [11], as well as the rate at which sulfuric acid is able to penetrate into the corrosion film. The first condition determines the current at which PbO₂ is reduced, the second determines the quantity of any particular reaction product formed.

The experiments illustrated in Fig. 6 were repeated in several different acid concentrations and the dependence of the voltage level of each plateau on acid concentration was established. In order to correlate the data, the electrode potentials were expressed vs. a standard hydrogen electrode at unit pressure and unit hydrogen ion activity, at 25°C (STP H₂). This correlation was established by calculating first the potential of the Hg/Hg₂SO₄ reference electrode vs. a hydrogen electrode in the same solution from Hamer's data (28), and then computing the potential difference between this hydrogen electrode and a STP H₂ electrode, using pH values reported by Delahay (24), and the relation $-\log a_{\text{H}^+} = \text{pH}$. The reference-electrode data obtained in this manner are presented in Table III, in which the potentials have been corrected to 30°C.

Using these reference electrode data, the experimentally observed voltage plateaus during self-depassivation were compared with theoretically calculated voltage levels. The corresponding results are summarized in Table IV. Here, column 4 lists the experimental voltage of the plateaus, expressed with respect to a STP H₂ electrode, using the figures of the last column in Table III for the reference electrode potential.

Theoretical plateau potentials were calculated assuming a plausible potential-determining electrode process on the basis of the pH-potential diagram, using compatible pH values and sulfate ion activities in the corrosion film. All the data of Table IV relate to 30°C.

Table III. Reference-electrode data

Sulfuric acid concentration moles/liter	moles/1000g H ₂ O	pH	Electrode potential at 30°C	
			Hg/Hg ₂ SO ₄ vs. H ₂ in the same solution	Hg/Hg ₂ SO ₄ vs. STP H ₂ in pH 0
0.01	0.01	1.8	0.785	0.679
0.10	0.10	1.03	0.737	0.676
0.50	0.51	0.48	0.696	0.668
1.00	1.04	0.20	0.674	0.662
4.20	5.05	-0.48	0.592	0.620
10.0	17.9	-1.2	0.467	0.538

Table IV. Results

Plateau	Acid concentration, moles/liter	Experimental plateau, v		Electrode process	Conditions at potential-determining site		Theoretical plateau potential, v			
		vs. Hg/Hg ₂ SO ₄	vs. STP H ₂		pH	SO ₄ activity	vs. H ₂ in same solu.	vs. STP H ₂		
I	0.1	0.830	1.51	PbO ₂ + HSO ₄ ⁻ + 3H ⁺ + 2e ⁻ → PbSO ₄ + 2H ₂ O	1.03	as in bulk	1.561	1.50		
	0.5	0.940	1.61		0.48		1.604	1.58		
	1.0	0.960	1.62		0.20		1.626	1.61		
	4.2	1.120	1.74		-0.48		1.714	1.74		
	10.0	1.380	1.92		-1.2		1.790	1.86		
II	0.1	0.6	1.3	PbO ₂ + SO ₄ ²⁻ + 4H ₂ + 2e ⁻ → PbSO ₄ + 2H ₂ O	2	a _{SO₄²⁻} = 10 ⁻²	—	1.4		
	0.5	0.6	1.3					1.4		
	1.0	0.6	1.3					1.4		
	4.2	0.6	1.2					1.4		
	10.0	0.6	1.1					1.4		
III	0.1	-0.50	0.18	Pb ₂ O ₄ + H ₂ O + 2e ⁻ → 3PbO + 2(OH) ⁻	13.2	a _{SO₄²⁻} = 10 ⁻⁷	—	0.18		
	0.5	-0.46	0.21					12.7	0.21	
	1.0	-0.47	0.19					13.0	0.19	
	4.2	-0.38	0.24					12.2	0.24	
	10.0	-0.2	0.30					11.2	0.30	
IV	0.1	-0.970	-0.29	PbSO ₄ + 2e ⁻ + H ⁺ → Pb + HSO ₄ ⁻	1.03	as in bulk	-	-0.234		
	0.5	-0.960	-0.29					0.48	-0.276	-0.30
	1.0	-0.955	-0.29					0.20	-0.287	-0.30
	4.2	-0.960	-0.34					-0.48	-0.377	-0.35
	10.0	-0.965	-0.42					-1.2	-0.405	-0.34

The theoretical potentials of plateaus I and IV vs. hydrogen in the same solution were interpolated from the data of ref. (29) and (30), except the values for the most concentrated solution (17.9M) which were calculated from the water activity and mean molal sulfuric acid activity coefficient reported by Glueckauf and Kitt (31). The electrode potentials calculated for this relatively concentrated solution are less accurate. The potential vs. STP H₂ was obtained from the potential vs. H₂ in the same solution by

$$E(\text{vs. STP H}_2) = E(\text{vs. H}_2 \text{ in same solution}) - 0.0591 \text{ pH}$$

For plateaus II and III the theoretical potential vs. STP H₂ was obtained from Eq. 7 and 20 in Table II, using the particular pH values and sulfate ion activities specified for the interior of the corrosion film in Table IV.

Excellent agreement is obtained between experimentally observed and theoretically calculated potential levels of plateaus I and IV. For the intermediate levels II and III, theoretical potentials calculated on the basis of plausible conditions in the corrosion film conform well with the experimentally observed values.

Composition of the Corrosion Film

The present analysis indicates that the following processes take place on anodization of lead in sulfuric acid. Initially, a PbSO₄ film is formed, and as this film grows to a critical thickness, accompanied by a corresponding critical ohmic drop, SO₄²⁻ and H⁺ ions are no longer able to readily penetrate it. Any depletion of SO₄²⁻ ions is accompanied by an equivalent depletion of H⁺ ions, and *vice versa* because of the tendency of the electrolyte to maintain electrical neutrality. The very high electric field established in the dense PbSO₄ layer, manifested by the large ohmic drop, will tend to repel positive H⁺ ions from the microcavities of the inner part of the film and attract SO₄²⁻ ions and OH⁻ ions generated by dissociation of H₂O molecules. This latter effect tends to enhance the alkalinity in the interior of the corrosion film and to stabilize the high local pH.

The increase in pH must be rather abrupt once the ionic diffusion is sufficiently impaired and the reaction mass-transport limited. Thus the pH will rise quickly to the point where OH⁻ ions will be available to oxidize lead to PbO or hydrated forms, such as 5PbO · 2H₂O. These divalent lead compounds are readily oxidized further to α-PbO₂. According to the pH-potential diagrams and the data of Table IV, the oxidation of PbO to α-PbO₂ in the corrosion film may take place above about + 0.3v vs. STP H₂ or above -0.4v vs. Hg/Hg₂SO₄. On applying increasingly higher electrode potentials, the outer sulfate layer and the PbO layer

increase in thickness as higher ohmic drops are now accommodated. Finally, at sufficiently high potentials, lead sulfate may be oxidized to PbO₂ in the more acidic, outer portions of the corrosion layer. At a pH of 2 in the interior of the film, *e.g.*, lead sulfate could be oxidized to PbO₂ at a potential of about + 0.7v vs. Hg/Hg₂SO₄. At anodizing potentials above this voltage, β-PbO₂ is present in the corrosion film, and a corresponding voltage plateau is observed during subsequent open-circuit self-depassivation. The fact that the outermost, acidic portions of the film are oxidized last is in agreement with Feitnecht's observation (9) that the PbO₂ formation starts in the interior, below the PbSO₄ film, and grows toward the electrolyte side.

All phenomena relating to the corrosion process and self-depassivation may be thus properly accounted for by postulating the existence of a pH gradient in the corrosion film. The part nearest the sulfuric acid electrolyte is effectively acidic; the inner part nearest the metal is effectively alkaline. This confirms an earlier discussion of this subject by the authors (32, 33).

The alkaline milieu at the electrode interface may be maintained during self-depassivation over prolonged periods of time, extending often over many hours and sometimes over days. The diffusion of acid into the interior must therefore be extremely slow under these conditions. If, however, the surface of the electrode is scratched with a glass rod or a tantalum wire, the electrode potential drops immediately to -0.9v vs. Hg/Hg₂SO₄, corresponding to the Pb/PbSO₄ couple. The damage in the film may heal since the exposed lead may be oxidized electrochemically to PbSO₄ and PbO, whereby a corresponding amount of α-PbO₂ is reduced to the divalent state of lead.

Integration of the current-time curves of Fig. 2 and 3 theoretically yields the number of coulombs of electricity expended in each phase of the film-formation process. Figure 9 shows the integrated quantity of current which was accepted by the corroding electrode in 24 hr as a function of potential. Integration was carried out graphically using a compensating polar planimeter. The values determined in this manner agree well with the total amount of electricity (current x time) required for complete reduction of the corrosion film to metallic lead, after corrections for utilization-factor effects. Attempts to divide this total current input into contributions made by the various corrosion processes are met with difficulties. As shown in Fig. 2 and 3, the various peaks overlap considerably; in other words, there is always present a large "background" current. Also, the broad second hump represents, as already pointed out, the sum of

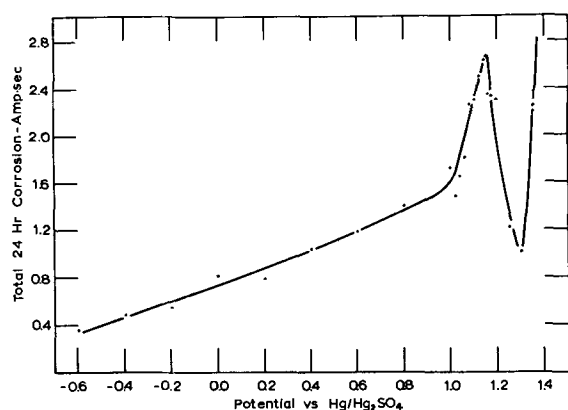


Fig. 9. Total integrated current input over 24 hr at constant potential of Pb-Ca vs. Hg/Hg₂SO₄.

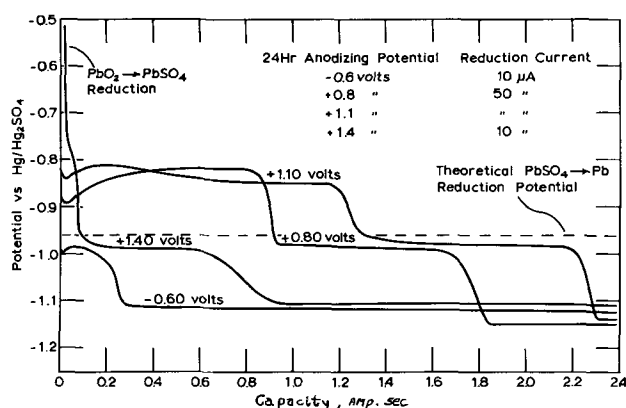
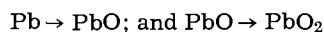


Fig. 10. Constant current reduction curves for corrosion films previously formed by constant potential corrosion in the potential range -0.60 to $+1.40$ v vs. Hg/Hg₂SO₄ for 24 hr.

all the basic corrosion processes, including in particular the reactions



In order to gain a more quantitative insight into the structure of the corrosion film, a number of galvanostatic stripping experiments were carried out. Corrosion films produced by constant potential anodization for 24 hr were reduced at constant current and the voltage-time curves recorded. The constant currents used were chosen sufficiently small such that polarization effects did not severely obscure the voltage-time curves and utilization factors were close to unity, and the currents were sufficiently large that self-depassivation entered the measurements only in a minor and defined manner. Self-depassivation effects were largely eliminated by reducing several identical films at several different currents and extrapolating the amount of electricity required to reduce the film to zero discharge time, as described in earlier work relating to constant current studies (7, 8).

Some results obtained at constant current are illustrated in Fig. 10 where the potential during cathodic stripping is plotted against capacity. For corrosion films formed below -0.4 v vs. Hg/Hg₂SO₄ only one step is observed in the curve, namely, the one corresponding to the reduction of PbSO₄ to Pb at -0.96 to -0.99 v vs. Hg/Hg₂SO₄. The steady voltage reached below -1.10 v is due to hydrogen evolution. Films formed between -0.4 and $+0.8$ v showed two plateaus, of which the first is attributed to the reduction of α -PbO₂ to PbO and the second to the reduction of PbSO₄ to Pb. Finally, for films formed above $+0.8$ v vs. Hg/Hg₂SO₄, the PbO₂/PbSO₄ plateau is obtained first, but its level is too high to be visible in Fig. 10.

The capacity obtained at the PbO₂/PbO plateau (-0.8 v) in Fig. 10 was almost independent of the discharge current, while the capacity of the PbO₂/PbSO₄ plateau ($+1$ v) increased with increasing discharge current (7, 8). This indicates a higher self-discharge rate at the PbO₂/PbSO₄ plateau than at the PbO₂/PbO plateau, which is not unexpected, since the reactions of the latter are strongly inhibited by diffusion effects.

The PbSO₄/Pb potential is indicated in Fig. 10 by the dotted line. The fact that defined quantities of electricity can be withdrawn above this potential is proof for the existence of corrosion products with a valency larger than two.

From data of the type illustrated in Figs 2, 3, and 10 a schematic diagram of the composition of the corrosion film as a function of the potential at which it was formed was computed. The result of this analysis, which refers to films produced at constant potential during 24 hr in 4.2M H₂SO₄ at 30°C, is shown in Fig. 11.

The capacity obtained at constant current reduction at the first plateau of Fig. 6, that is above 0.8v vs. Hg/Hg₂SO₄ (after proper consideration of self-discharge) was taken as a measure for the quantity of β -PbO₂ in the outer part of the corrosion film, accessible to an acidic medium during discharge. No significant quantity of electricity was obtained during constant current reduction from the second plateau of Fig. 6. In fact, even at currents as small as 1 μ A/cm² this plateau tended to disappear. The third plateau in Fig. 6, corresponding to the PbO₂/PbO couple in alkaline milieu, was polarized from its level at -0.4 v to about -0.8 v at the currents used for the reduction experiments. The amount of electricity from this plateau could be determined quite accurately, as illustrated in Fig. 10, and allowed the determination of α -PbO₂ in the inner part of the corrosion film.

Finally, constant current reduction of the plateau at about -1.0 v vs. Hg/Hg₂SO₄ (corresponding to the reduction of PbSO₄ to Pb) yielded the total amount of lead attacked by anodic corrosion, as expressed in terms of the two-valent state. The actual amount of two-valent lead compounds present in the corrosion film prior to constant current reduction was determined by the difference between the total electricity expended and the electricity accounted for by the sum of the acidic and alkaline PbO₂ plateaus plus the reduction of a corresponding amount of sulfate. The quantity of each corrosion product present was expressed in terms of a layer thickness by using standard bulk densities for the various compounds. Figure 11 thus presents the theoretical model of the composition of the corrosion film in the absence of micro-porosity, which may be presumed to be relatively unimportant in view of the fact that only a semi-quantitative analysis is possible at all. Figure 11 re-

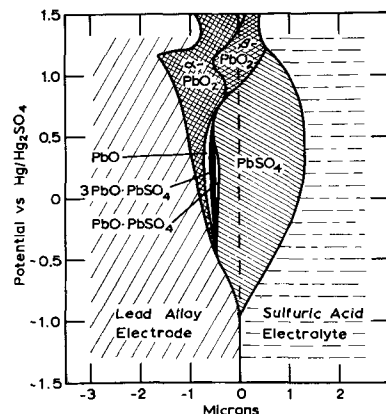


Fig. 11. Schematic diagram of the composition of the corrosion film as a function of potential.

veals several characteristic features as to the dependence of the structure of the corrosion film on the potential at which it was formed. First, in agreement with the self-depassivation experiments illustrated in Fig. 6, there are four regions with respect to the potential determining interface. Throughout the potential range, the electrode potential is determined by the interface between the electronically conducting phase and the electrolyte adjacent to it. Thus, between -0.9 and -0.38 v the Pb surface constitutes the electronically conducting phase. It is in contact with PbSO_4 and H_2SO_4 , and the potential is therefore that of the PbSO_4/Pb couple. In the potential range between -0.38 and $+0.8$ v the $\alpha\text{-PbO}_2$ constitutes the electron conductor, and, in contact with PbO and basic solution, it forms the $\alpha\text{-PbO}_2/\text{PbO}$ couple. Finally, above $+0.8$ v the electronic conductor $\beta\text{-PbO}_2$ is in contact with PbSO_4 and H_2SO_4 , forming the $\text{PbO}_2/\text{PbSO}_4$ couple.

Second, there is a large region of potential, where PbO is underlying a PbSO_4 film. The interior of the film is thus protected from acidic electrolyte and alkaline conditions prevail therein.

Each corrosion product in the film, as depicted in Fig. 11, is formed and exists only in an electrolyte of compatible pH. This self-supporting explanation of the present hypothesis overcomes a major weakness of the previous interpretations, which presumed the formation and existence of corrosion products such as PbO , basic lead sulfates, and $\alpha\text{-PbO}_2$ in acid media. Moreover, these products were thought to create potential-determining couples in acid media, to which the various voltage plateaus during self-depassivation were ascribed. On the basis of the present analysis, all experimental facts can be explained logically in terms of a pH gradient in the corrosion film. This pH gradient is the result of inhibited ionic diffusion in the dense corrosion layer.

As shown in Fig. 4 and 5, the corrosion rate of lead in sulfuric acid reaches a peak at or just below the potential corresponding to the $\text{PbO}_2/\text{PbSO}_4$ couple. The high corrosion rate at this potential is due to the development of a high pH in the interior of the corrosion film with insufficient protection by either PbSO_4 or PbO_2 . This corrosion process takes place below a weak PbSO_4 film which acts as a semipermeable membrane, keeping H^+ ions and SO_4^{--} ions away. It is probable that water may partly penetrate the film, dissociate to form OH^- ions, which are attracted to the electrode by the anodic potential, while H^+ ions are repelled by the high electric field in the film.

The corrosion mechanisms at potentials below the $\text{PbO}_2/\text{PbSO}_4$ level where a heavy covering layer of PbSO_4 exists, and at highly anodic potentials in the region of active oxygen evolution where the film consists entirely of $\alpha\text{-}$ and $\beta\text{-PbO}_2$, still show a certain similarity. In both cases the diffusion of an oxygen carrying species, H_2O , OH^- , O^{--} , or $[\text{O}]$, into the interior of the corrosion film, is involved (34). However, the species need not be the same in both instances. Moreover, the influence of foreign anions such as NO_3^- , Cl^- , or ClO_4^- may be different in the two cases due to the different composition and permeability of the corrosion films.

Finally, the model of Fig. 11 explains the high resistance of the corrosion films apparent in the depassivation experiments of Fig. 6 for certain potential ranges. The resistance is due to a build-up of divalent corrosion products, probably largely PbSO_4 . It increases almost linearly with potential and reaches a maximum at about $+0.7$ v vs. $\text{Hg}/\text{Hg}_2\text{SO}_4$ in 4.2M

H_2SO_4 , which is 0.4v below the reversible $\text{PbO}_2/\text{PbSO}_4$ potential. Above $+0.8$ v the resistance decreases rapidly due to the formation of highly conductive PbO_2 , confirming earlier results (35) obtained with another experimental technique involving d-c superimposed square-wave current.

Manuscript received April 28, 1964; revised manuscript received July 20, 1964. This paper was presented at the New York Meeting, Sept. 29-Oct. 3, 1963.

Any discussion of this paper will appear in a Discussion Section to be published in the June 1965 JOURNAL.

REFERENCES

1. W. Feitknecht and A. Gümman, *J. chim. phys.*, **49C**, 136 (1952).
2. E. V. Krivolapova and B. N. Kabanov, *Trudy Soveshchaniya Elektrokhim. Akad. Nauk. SSSR*, **1950**, 539 (1953).
3. W. H. Beck, R. Lind, and W. F. K. Wynne-Jones, *Trans. Faraday Soc.*, **50**, 147 (1954).
4. P. Jones, R. Lind, and W. F. K. Wynne-Jones, *ibid.*, **50**, 972 (1954); P. Jones, H. R. Thirsk, and W. F. K. Wynne-Jones, *ibid.*, **52**, 1003 (1956).
5. K. Nagel, R. Ohse, and E. Lange, *Z. Elektrochem.*, **61**, 795 (1957).
6. M. Maeda, *J. Electrochem. Soc. Japan*, **25**, 197 (1957).
7. P. Ruetschi and B. D. Cahan, *This Journal*, **104**, 406 (1957).
8. P. Ruetschi and B. D. Cahan, *ibid.*, **105**, 369 (1958).
9. W. Feitknecht, *Z. Elektrochem.*, **62**, 975 (1958).
10. R. W. Ohse, *Werkstoffe u. Korrosion*, **11**, 220 (1960).
11. J. Lander, *This Journal*, **98**, 213 (1951).
12. J. Lander, *ibid.*, **103**, 1 (1956).
13. J. Burbank, *ibid.*, **103**, 87 (1956).
14. J. Burbank, *ibid.*, **104**, 693 (1957).
15. J. Burbank, *ibid.*, **106**, 369 (1959).
16. M. Maeda, *J. Electrochem. Soc. Japan (overseas Suppl. Ed.)*, **26**, E-21 (1958).
17. M. Fleischmann and H. R. Thirsk, *Trans. Faraday Soc.*, **51**, 71 (1955).
18. I. Dugdale, M. Fleischmann, and W. F. K. Wynne-Jones, *Electrochim. Acta*, **5**, 229 (1961).
19. A. Bewick, M. Fleischmann, and H. R. Thirsk, *Trans. Faraday Soc.*, **58**, 2200 (1962).
20. M. Fleischmann and M. Liler, *ibid.*, **54**, 429 (1958).
21. E. Voss, Transactions of the Second International Symposium on Batteries, Inter-Departmental Committee on Batteries, Bournemouth, Oct., 1960, Sydenham and Co. Ltd. Oxford Road, Bournemouth, England.
22. J. Lander, *This Journal*, **105**, 289 (1958).
23. M. Pourbaix, "Atlas d'Equilibres Electrochimiques," p. 485, Gauthier-Villars, Paris (1963).
24. P. Delahay, M. Pourbaix, and P. Van Rysselberghe, *This Journal*, **98**, 57 (1951).
25. W. M. Latimer, "Oxidation Potentials," Prentice Hall, Inc., Englewood Cliffs, N. J., (1959).
26. H. Bode and E. Voss, *Electrochim. Acta*, **1**, 318 (1959).
27. R. T. Angstadt, C. J. Venuto, and P. Ruetschi, *This Journal*, **109**, 177 (1962).
28. H. S. Harned and W. J. Hamer, *J. Am. Chem. Soc.*, **57**, 27 (1935).
29. W. Hamer, *ibid.*, **57**, 9 (1935).
30. H. S. Harned and W. J. Hamer, *ibid.*, **57**, 33 (1935).
31. E. Glueckauf and G. P. Kitt, *Trans. Faraday Soc.*, **52**, 1074 (1956).
32. P. Ruetschi and B. D. Cahan, *This Journal*, **106**, 1079 (1959).
33. P. Ruetschi, J. Sklarchuk, and R. T. Angstadt, *Electrochim. Acta*, **8**, 333 (1963).
34. B. N. Kabanov, E. S. Weisberg, and I. L. Romanova, Paper presented at the 14th CITCE conference, Moscow, Aug., 1963.
35. P. Ruetschi and B. D. Cahan, *This Journal*, **106**, 543 (1959).

The Heat-Treatment of Anodic Oxide Films on Tantalum

III. The Conductivity Profile

D. M. Smyth, G. A. Shirn, and T. B. Tripp

Research Center, Sprague Electric Company, North Adams, Massachusetts

ABSTRACT

Dielectric measurements have been used to study the distribution of the conductivity which is introduced into the anodic oxide film on tantalum by heat-treatment in air. The temperature and frequency dependences of capacitance indicate that the conductivity distribution is exponential with position in the oxide. The combination of these dependences yields an activation energy of 0.6 ev for the conduction process. The temperature and frequency dependences of $\tan \delta$ for films which have been partially reanodized after heat-treatment also yield an activation energy of 0.6 ev.

In the first two papers of this series, it was shown that during the heat-treatment of anodized tantalum at 200°-500° the tantalum extracts oxygen from the oxide, thus creating a distribution of oxygen deficiency across the oxide film (1, 2). The oxygen deficiency, which is assumed to consist of oxygen vacancies, is frozen-in when the sample is cooled and results in a distribution of conductivity across the oxide film. Evidence has been presented which indicates that the conductivity is highest at the metal-oxide interface and decreases across the film when the heat-treatment takes place in an oxygen-containing atmosphere.

In this paper the frequency and temperature dependences of the capacitance and dielectric losses are analyzed to determine the shape of the conductivity profile and the activation energy of conduction.

Experimental

Samples having about 18 cm² surface area and narrow tabs were stamped from 0.010 in. Fansteel sheet and cleaned as previously described, except that all samples were electropolished instead of chemically polished (1). The anodization was performed in 0.01M H₂SO₄ held at 34° as described. All of the data in this paper are for samples anodized to 75v which seems to be suitably typical.

Results

In the previous two papers of this series it was shown that the dielectric properties of anodized tantalum which has been heated above 200° in air are determined by a gradient of conductivity, related to a gradient of stoichiometry, across the oxide film. Figure

1 is a schematic representation of the conductivity profile across the oxide at three different temperatures, $T_1 > T_2 > T_3$. (The stoichiometry profile, i.e., distribution of oxygen vacancies, is quenched-in when the sample is allowed to cool after heat-treatment; this discussion is concerned with the reversible change of conductivity with temperature.) σ_0 is a conductivity level defined such that the observed capacitance is the parallel capacitance expected for the oxide thickness for which $\sigma \leq \sigma_0$. It is apparent that, as the temperature decreases, the effective dielectric thickness will increase as the intersection between the conductivity profile and σ_0 moves toward the tantalum. Below the temperature at which the conductivity equals σ_0 at the Ta-Ta₂O₅ interface, the effective dielectric thickness is equal to the full Ta₂O₅ thickness. Thus one can anticipate a large decrease in capacitance with decreasing temperature down to some characteristic temperature below which the temperature dependence of capacitance decreases. The experimental observation of this behavior is demonstrated in Fig. 2 and has been previously discussed in detail (2).

If it is assumed that the conductivity arises from the first ionization of oxygen vacancies which normally contain two electrons, and if the extent of ionization is small, the mass-action expression and the condition of charge neutrality yields

$$n_x = [V_x]^{1/2} K^{1/2} e^{-E_1/2kT} \quad [1]$$

where n_x is the local concentration of conduction electrons, $[V_x]$ is the local concentration of oxygen va-

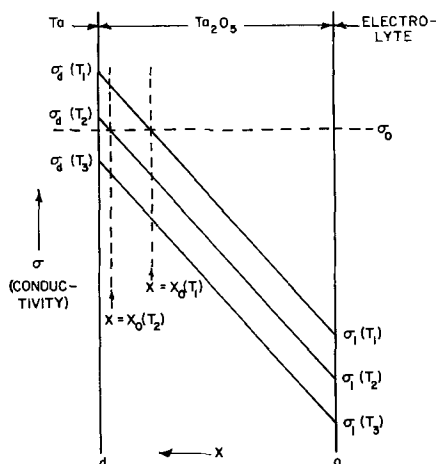


Fig. 1. Schematic representation of the conductivity profile across heat-treated, anodized tantalum at three temperatures, $T_1 > T_2 > T_3$.

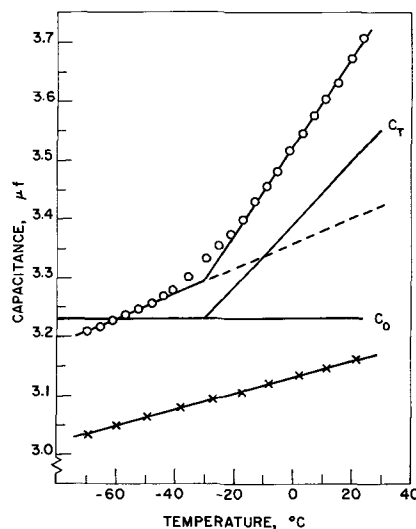


Fig. 2. Temperature dependence of capacitance at 50 cycles for anodized tantalum: \times , unheated, 75v anodization; \circ , heated 30 min, at 500°, in air.

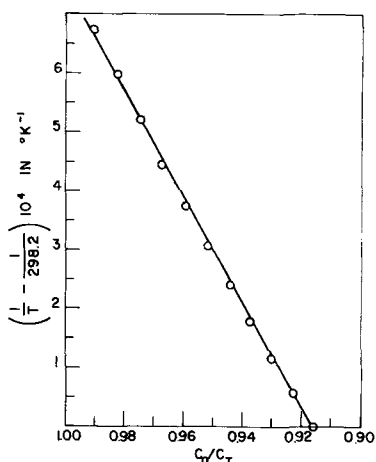


Fig. 3. Relative shape of the conductivity profile for heat-treated, anodized tantalum (see Eq. [2]) (from data shown in Fig. 2).

cancies, K is the pre-exponential portion of the mass-action constant, and E_1 is the ionization energy. If the temperature dependence of the mobility of conduction electrons can be neglected compared with the temperature dependence of their concentration, then Eq. [1] is proportional to the conductivity. Referring again to Fig. 1, the conductivity at T_2 is known, by definition, to be equal to σ_0 at the point $x_0(T_2)$, which is determined by the measured capacitance at T_2 . As the temperature is raised to T_1 , the conductivity at $x_0(T_2)$ will rise to the value at that position on the T_1 line. The relative change of conductivity from any temperature, T , to some reference temperature, T_1 , is given by Eq. [1], for T_1 and the position $x_0(T)$, divided by the same equation for T . This can be expressed as

$$\ln \frac{\sigma(T_1)}{\sigma_0} = \frac{E_1}{2k} \left(\frac{1}{T} - \frac{1}{T_1} \right) \quad [2]$$

In this way, data taken at a series of temperatures can be normalized to a single reference temperature, T_1 . Thus a plot of $(1/T - 1/T_1)$ vs. position in the film as determined by C_0/C , where C_0 is the capacitance of the system without conduction in the oxide, and C is the capacitance of the sample at T , gives the relative shape of the conductivity profile.

Such an analysis has been carried out on the data shown in Fig. 2. C_0 has been arbitrarily defined as the observed capacitance at -60° . In order to remove the effects of the temperature dependence of dielectric constant and of variable immersion depth due to thermal expansion of the electrolyte, the difference between the extrapolated low temperature slope and C_0 has been subtracted from the capacitance at each temperature to give the corrected line, C_T , which should include only the effect of conductivity. Thus $(1/T - 1/298.2)$ has been plotted against C_0/C_T in Fig. 3. The linearity of the result indicates that the conductivity varies exponentially with position in the region which is controlling the dielectric properties. No indication of the absolute values of conductivity are possible since neither E_1 nor σ_0 are known at this point.

Young has derived an expression for the series capacitance of a dielectric which has an exponential gradient of resistivity (3). In terms of conductivity this can be expressed as

$$\frac{1}{C_s} = \frac{1}{2aA\epsilon\epsilon_0} \ln \left[\frac{1 + \left(\frac{\omega\epsilon\epsilon_0}{\sigma_1} \right)^2}{1 + \left(\frac{\omega\epsilon\epsilon_0}{\sigma_d} \right)^2} \right] \quad [3]$$

where

$$\sigma(x) = \sigma_1 e^{ax} \quad [4]$$

σ_1 is the conductivity at the poorer conducting side, σ_d is the conductivity at the better conducting side (see Fig. 1), ω is 2π times the frequency, a is the exponential slope of the conductivity gradient, and the other symbols have their conventional significance. By definition σ_0 at a position x is

$$\sigma_0 = \sigma_1 e^{-\frac{C_0 d}{C}} \quad [5]$$

where d is the geometric oxide thickness and $\frac{C_0 d}{C}$ thus equals x . Substituting

$$C_0 = \frac{\epsilon\epsilon_0 A}{d} \quad [6]$$

and [3] into [5] gives

$$\sigma_0 = \sigma_1 \left[\frac{1 + \left(\frac{\omega\epsilon\epsilon_0}{\sigma_1} \right)^2}{1 + \left(\frac{\omega\epsilon\epsilon_0}{\sigma_d} \right)^2} \right]^{1/2} \quad [7]$$

If

$$\left(\frac{\omega\epsilon\epsilon_0}{\sigma_1} \right)^2 \gg 1 \text{ and } \left(\frac{\omega\epsilon\epsilon_0}{\sigma_d} \right)^2 \ll 1 \quad [8]$$

then [7] reduces to

$$\sigma_0 = \omega\epsilon\epsilon_0 \quad [9]$$

Thus within the limitations of [8], which will be discussed later, σ_0 is directly proportional to the frequency of measurement and can be easily calculated from [9].

One can also consider that there is a critical level of conductivity, σ_c , where the incremental resistance equals the incremental reactance, i.e.,

$$R = \frac{1}{\sigma_c} \frac{dx}{A} = \frac{dx}{\omega\epsilon\epsilon_0 A} = X \quad [10]$$

It is seen that $\sigma_c = \sigma_0$ within the region of validity for [8]. This is the natural dividing line between predominantly capacitive and predominantly resistive behavior. It is also the point where, by definition, $\tan \delta = 1.00$; this is good justification for neglecting the normal, background, dielectric losses compared with the losses due to conduction, since the former are usually in the range $\tan \delta = 0.01-0.02$.

Equation [10] implies that Eq. [9] is a very general relationship, although the latter was specifically derived for an exponential conductivity profile. An examination of the case of a hypothetical linear distribution of conduction gives, however,

$$\sigma_0 = \frac{\pi}{2} \omega\epsilon\epsilon_0 \text{ (linear)} \quad [11]$$

It appears that σ_0 will be proportional to $\omega\epsilon\epsilon_0$ for all distributions of conductivity, but that the proportionality constant will depend on the nature of the distribution. For any new case, [9] can be used to obtain the shape of the distribution, and the appropriate proportionality constant can then be derived to give a quantitative relationship.

The frequency dependence of capacitance can thus be used to obtain the conductivity as a function of position for dielectric films. The frequency determines the conductivity through [9] and the capacitance determines the location in the oxide. Figure 4 shows an example of such results where the profile has been determined at several temperatures. C_0 has been taken as the capacitance of the fully reanodized sample at each particular frequency and temperature. The conductivity is seen to vary exponentially with position over the experimentally accessible region which includes about 15% of the film thickness. The points taken at a combination of high frequency and low temperature have been corrected for deviations from

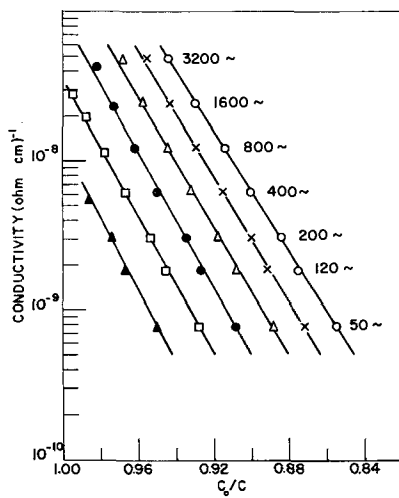


Fig. 4. Distribution of conductivity in heat-treated, anodized tantalum at several temperatures (75v anodization, heated 30 min, at 400°, in air). \circ , 30°; \times , 20°; \triangle , 10°; \bullet , 0°; \square , -10°; \blacktriangle , -20°.

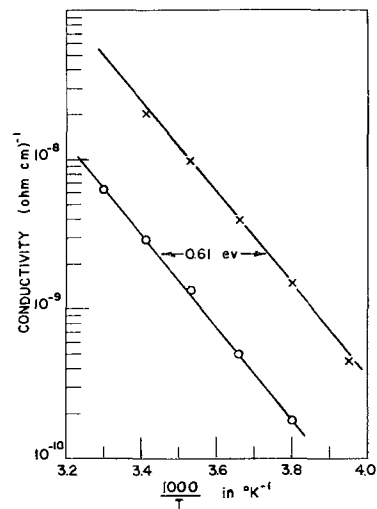


Fig. 5. Temperature dependence of conductivity at $C_0/C = 0.90$ (\circ) and 0.94 (\times) from Fig. 4.

the assumption of Eq. [8], and this causes the apparent decrease in conductivity for points taken at the same frequency as C_0/C approaches unity. The details of this correction are discussed later.

The activation energy of conduction can be obtained from the temperature dependence of conductivity at a given position in Fig. 4. This is shown for two positions in Fig. 5. The activation energy is found to be 0.6 eV, and, according to our hypothesis, this corresponds to one half of the ionization energy of the more weakly bound electron from an oxygen vacancy. There is no indication that the ionization energy depends on the position and, hence, the vacancy concentration in the oxide.

An expression for the series resistance of a dielectric having an exponential resistivity gradient has also been given by Young (3). Modified to our symbolism this is

$$R_s = \frac{1}{aA\omega\epsilon\epsilon_0} \left(\tan^{-1} \frac{\sigma_d}{\omega\epsilon\epsilon_0} - \tan^{-1} \frac{\sigma_1}{\omega\epsilon\epsilon_0} \right) \quad [12]$$

Since $\tan \delta = \omega R_s C_s$, an expression for $\tan \delta$ can be obtained from [3] and [12]

$$\tan \delta = \frac{2 \left[\tan^{-1} \frac{1}{\gamma} - \tan^{-1} \frac{1}{\gamma e^{ad}} \right]}{\ln \frac{1 + \gamma^2 e^{2ad}}{1 + \gamma^2}} \quad [13]$$

where γ is a normalized frequency parameter defined as

$$\gamma = \frac{\omega\epsilon\epsilon_0}{\sigma_d} \quad [14]$$

$\gamma = \sigma_0/\sigma_d$ when [8] is valid.

As previously described, reanodization of the heat-treated oxide results in a stepwise removal of the oxygen deficiency and its related conductivity from the oxide-electrolyte interface inward (2). This situation is idealized in Fig. 6 which shows two stages of reanodization, $\alpha = 0.8$ and 0.9 , where α is the fraction of the film rendered nonconducting by the reanodization. The $\tan \delta$ for this situation, based on the assumption that $\sigma = 0$ for $C_0/C < \alpha$, is

$$\tan \delta = \frac{2 \left[\tan^{-1} \frac{1}{\gamma} - \tan^{-1} \frac{e^{ad(\alpha-1)}}{\gamma} \right]}{2ad + \ln \frac{1 + \gamma^2 e^{-2ad(\alpha-1)}}{1 + \gamma^2}} \quad [15]$$

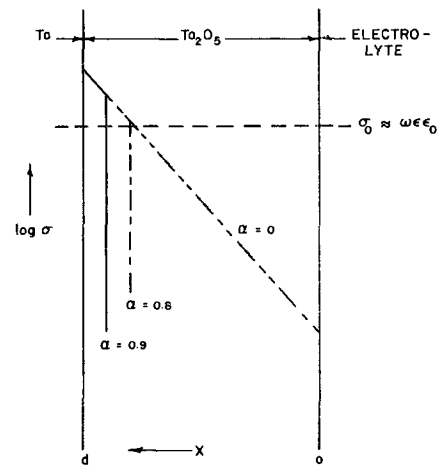


Fig. 6. Schematic representation of the conductivity gradient of heat-treated, anodized tantalum at various stages of reanodization.

which reduces to [13] for no reanodization, i.e., $\alpha = 0$. A plot of $\tan \delta$ vs. γ is shown in Fig. 7 for $\sigma_d/\sigma_1 = 10^{20}$ and $\alpha = 0, 0.6, 0.8, \text{ and } 0.9$, and for $\sigma_d/\sigma_1 = 10^5$ and $\alpha = 0$.

The case of the steeper conductivity gradient shown in Fig. 7 approximates the situation found for heat-treated, anodized tantalum. For the case of no reanodization, it is seen that there is a broad region in which $\tan \delta$ changes very little with frequency as is

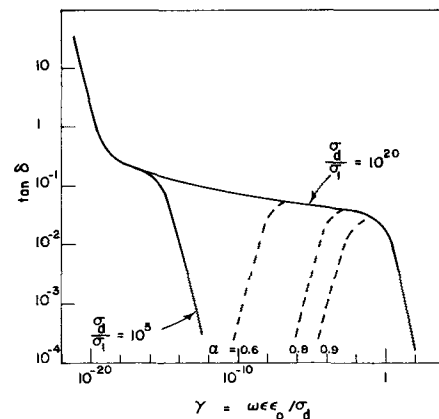


Fig. 7. Theoretical frequency dependence of $\tan \delta$ for a dielectric having an exponential conductivity gradient.

typically observed for anodic oxide dielectrics. At higher frequencies, however, $\tan \delta$ drops linearly with increasing frequency. As reanodization proceeds, the low-frequency end of $\tan \delta$ bends downward to an increasing extent until, for $\alpha > 0.8$, a reasonably sharp maximum appears which moves toward higher frequencies with additional reanodization. For a particular conductivity gradient and extent of reanodization, the maximum value of $\tan \delta$ appears at a specific γ . γ is a function of both frequency and temperature since σ_d is temperature-dependent, and γ can be expressed as

$$\gamma = \frac{\omega \epsilon \epsilon_0}{A(d)} e^{E_1/2kT} \quad [16]$$

Thus one can obtain a family of $\tan \delta$ curves as a function of frequency at constant temperature, or vice versa. In each case the position of the maximum value of $\tan \delta$ will depend on the parameter since [16] must be satisfied. Experimentally the sharpest maxima are obtained when $\tan \delta$ is plotted against temperature.

The same sample which was analyzed for E_1 by the temperature dependence of capacitance was reanodized for various times at the anodization voltage. Figure 8 shows $\tan \delta$ vs. temperature at 50 cycles for the unheated, heat-treated, and partially reanodized sample. The data have been corrected for the contribution of electrolyte resistance by the method of Bernard (4). This plot represents a mirror image of the right-hand side of Fig. 7 for a fixed conductivity gradient and various degrees of reanodization. The movement of the maxima toward lower temperatures by the further bending-down of the high temperature end as reanodization proceeds is clearly shown. In Fig. 9, $\tan \delta$ has been plotted against temperature for a series of frequencies after the sample had been reanodized for 30 min at the formation voltage. These data were not corrected for electrolyte resistance which accounts for both the increase of the maximum value of $\tan \delta$ as the frequency increases, and the upsweep at low temperatures. The positions of the maxima must satisfy [16] so a plot of log frequency vs. the reciprocal of the temperature at which $\tan \delta$ has its maximum value will yield E_1 , the activation energy of conduction. Two such plots are shown in Fig. 10 and the value $E_1/2 = 0.6$ eV is in excellent agreement with the value obtained from the capacitance measurements.

The $\tan \delta$ maxima lie in a region which is readily accessible at normal frequencies and temperatures. The frequency range of conventional bridges covers a spread in γ values of only about a factor of 10^4 . About 10-15% of the oxide film is rendered significantly conducting by heat-treatment in air, so an amount of reanodization which has a detectable effect is sufficient to give a sharp maximum value of $\tan \delta$. These coincidental factors were essential to the experimental detection of the phenomena just described.

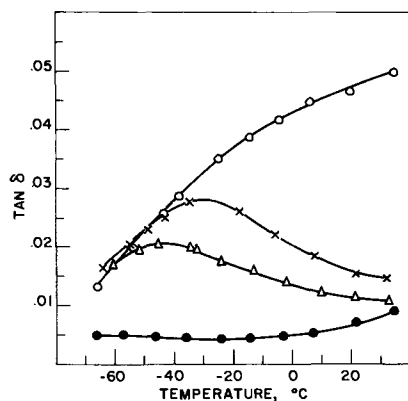


Fig. 8. Temperature dependence of $\tan \delta$ at 50 cycles for anodized tantalum: \bullet , unheated (75v anodization); \circ , heated 400°, 30 min, in air; \times , reanodized 30 min at 75v; \triangle , reanodized 120 min at 75v.

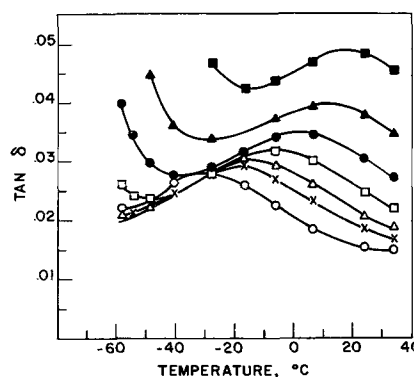


Fig. 9. Temperature dependence of $\tan \delta$ for partially reanodized, heat-treated Ta-Ta₂O₅ (75v anodization, heated 30 min, at 400°, in air, reanodized 30 min at 75v): \circ , 50 cycles; \times , 120 cycles; \triangle , 200 cycles; \square , 400 cycles; \bullet , 800 cycles; \blacktriangle , 1600 cycles; \blacksquare , 3200 cycles.

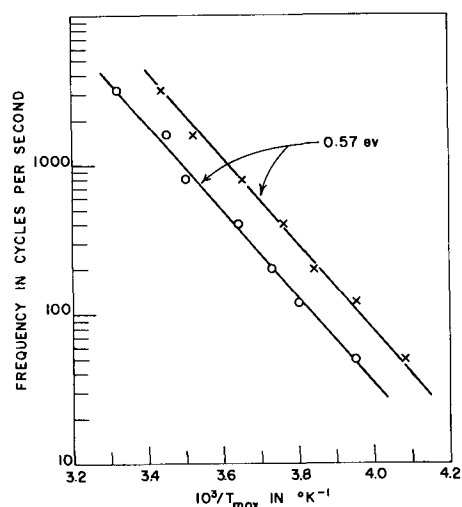


Fig. 10. Temperature dependence of the maxima of $\tan \delta$ at various frequencies: \circ , reanodized 15 min; \times , reanodized 30 min.

Discussion

The results presented here are consistent with the following picture for the heat-treated anodic oxide on tantalum. The oxide has a position-dependent conductivity which decreases exponentially from a maximum value at the Ta-Ta₂O₅ interface. The slope is such that the conductivity would change by about a factor of 10^{20} - 10^{25} over the entire film thickness if such an extrapolation were valid. The conductivity is associated with an oxygen deficiency and is assumed to result from the partial ionization of the more weakly bound electrons from oxygen vacancies which normally contain two trapped electrons. As shown in Eq. [1] this picture leads to an ionization energy equal to twice the observed activation energy of conduction. The ionization energy is thus taken to be 1.2 eV. These results were derived solely from an analysis of dielectric properties; no technique has been devised which would permit a direct measurement of the conductivity.

Measurements on oxide films of various thicknesses indicate that the slope of the conductivity adjusts to maintain an extrapolated change of 20-25 decades of conductivity across the oxide film, except at the lower anodization voltages, i.e., ≤ 50 v, where the gradients become somewhat steeper as the thickness decreases. These experimental results indicate that the conductivities at the Ta-Ta₂O₅ and Ta₂O₅-air interfaces, σ_d and σ_1 , respectively, are determined only by the conditions of heat-treatment. Thus the exponential slope of the conductivity profile decreases with increasing film thickness. The adjustment of the conduc-

tivity slope with film thickness results in the percentage increase of capacitance due to heat-treatment and the percentage change of capacitance with frequency and temperature being independent of film thickness, except for the thinner films where the percentage changes are somewhat less.

The frequency dependence of capacitance has been used previously to determine the distribution of conduction in dielectrics. Rose (5) and Pfozter (6) have investigated Cu_2O rectifiers by this technique. Rose derived the equivalent of our Eq. [9] by equating the resistance and reactance as shown in our Eq. [10]. He attributes this approach to some unpublished work of K. Lehovec. Pfozter presents derivations for several possible conductivity profiles including the exponential case which is formally similar to our Eq. [3]-[9]. Scholte and van Geel have studied anodic oxide films on aluminum by a related technique (7). They consider their treatment to be more rigorous than previous methods since they take specific account of the regions which make both resistive and reactive contributions, whereas the use of (9) implies a distinct boundary between such regions. Their method is mathematically cumbersome, however, and an analysis of their data by means of [9] gives the same results as their more involved calculation.

As pointed out in all of the references just cited, this general method of analysis does not yield an unequivocal distribution of conductivity. Any arrangement of the various increments of thickness with their appropriate conductivities would give the same dielectric properties. Other evidence indicates, however, that in the present case the major portion of the conduction lies near the Ta-Ta₂O₅ interface (1, 2). This does not exclude a small contribution from the other side of the film.

Breckenridge has determined the activation energy for relaxation processes involving pairs of ionic defects in ionic crystals from the temperature dependence of the maximum value of $\tan \delta$ as a function of frequency, and *vice versa* (8). The treatment is formally identical to that used here, but the physical situation is completely different. The work of Breckenridge is concerned with an ionic process, homogeneously distributed throughout a crystal, and is essentially a Debye relaxation process. In our case, the measurements are believed to involve the interaction between ionic and electronic defects, and an inhomogeneous distribution of defects, achieved by partial reanodization, is required before a maximum value for $\tan \delta$ is observed. Moreover, the positions of the maxima are a function of the extent of reanodization. This is more closely related to a Maxwell-Wagner type of dielectric structure.

In the range $0.01 \sigma_d \cong \sigma_0 \cong 100 \sigma_1$ Eq. [13] reduces to

$$\tan \delta = \frac{\pi}{2 \ln \gamma \frac{\sigma_d}{\sigma_1}} \quad [17]$$

Thus $\tan \delta$ is independent of film thickness insofar as σ_d/σ_1 is independent, *i.e.*, for anodization voltages greater than 50v. For 50 cycles, 34°C, and $\sigma_d/\sigma_1 = 10^{21}$, as shown in Fig. 4, $\tan \delta = 0.038$. The observed value is shown in Fig. 8. If the losses of the unheated sample are subtracted from those of the heated sample, the contribution due to the conductivity gradient is 0.040, which is close to the calculated value.

In an individual sample having a complex distribution of conductivity, such as a partially reanodized sample, the magnitude of the $\tan \delta$ is determined by the slope of the gradient where it crosses σ_0 . This can be seen from Eq. [17] if it is considered that the effective values of σ_d and σ_1 are those obtained by extrapolation of the conductivity slope in the vicinity of σ_0 . Where the gradient is steep, and the effective σ_d/σ_1 is high, the transition from good dielectric to good conductor is sharp, and the dielectric losses are

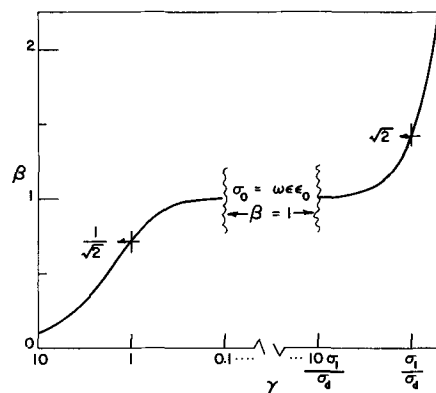


Fig. 11. Correction factor β from Eq. [18]

$$\text{vs. } \gamma = \frac{\omega \epsilon \epsilon_0}{\sigma_d}$$

low. This qualitative analysis leads, for example, to a nonmathematical explanation for the maximum values of $\tan \delta$ observed as a function of frequency or temperature for partially reanodized films.

A correction can be applied for deviations of [9] from [7] in the region where the assumptions of [8] are not valid, by defining a correction factor, β ,

$$\beta = \frac{\sigma_1}{\gamma \sigma_d} \left(\frac{1 + \left(\gamma \frac{\sigma_d}{\sigma_1} \right)^2}{1 + \gamma^2} \right)^{1/2} \quad [18]$$

such that $\beta \omega \epsilon \epsilon_0$ equals σ_0 as defined by [7]. Figure 11 shows a plot of β vs. γ . The correction is less than 10% for $\gamma < 0.5$ and $\gamma > 5\sigma_1/\sigma_d$. The latter region is of no practical interest since it concerns the profile near the poorer conducting end which is not experimentally accessible. The correction factor is $1/\sqrt{2}$ at $\gamma = 1$ or $\sigma_d = \omega \epsilon \epsilon_0$. Thus the use of [9] is valid over most of the dielectric with acceptable accuracy. The data shown in Fig. 4 have been corrected with values of β taken from Fig. 11.

Kofstad has investigated the electrical properties of ceramic Ta₂O₅ as a function of temperature and oxygen pressure (9). He finds a region at low oxygen pressures and low temperatures, where the conductivity seems to be controlled by the partial ionization of the more weakly bound electrons from oxygen vacancies. This corresponds to the conduction mechanism we have proposed for the heat-treated, anodic oxide films. For Ta₂O₅ samples cooled in 1 atm oxygen Kofstad found an activation energy of resistance of 40 kcal/mole down to 800°. Between 800° and 600°, equilibrium was attained very slowly, and below 600° an activation energy of 14 kcal/mole or 0.61 eV was observed. It was suggested that the latter value might be related to conduction due to impurities. It seems equally likely that the mobility of oxygen in the Ta₂O₅ is decreasing to the extent that no further change in stoichiometry occurs below 600°, and that the lower activation energy represents the ionization energy of a charge carrier from a defect. Two factors complicate the identification of this ionization energy with the one reported here, however. Kofstad's measurements were made on sintered samples which may be assumed to be crystalline, whereas our samples involve amorphous, anodic films; and, according to Kofstad's interpretation, his samples should have been strongly p-type for the particular conditions used for this experiment, whereas our results refer to n-type conduction. If the ionic defect in the p-type oxide is interstitial oxygen, as Kofstad proposes, then the defect can be considered as a helium-like center with two holes associated with the two negative charges of the interstitial ion. This would be formally similar to

an oxygen vacancy with two trapped electrons, and the ionization energies might be very similar. The similar ionization energies for substitutional donors and acceptors in germanium and silicon may be considered as a precedent for this argument. Moreover, the ionization energy will be determined by the immediate environment of the defect, and even the short-range order of the amorphous oxide may be sufficient to create a crystalline environment for the defect. Thus the correspondence of the activation energy reported by Kofstad and that reported here may be more than coincidence.

A recent paper by Pavlovic describes the dielectric behavior of ceramic α - and β - Ta_2O_5 and of samples cut from a boule of α - Ta_2O_5 (10). For some of these samples the temperature and frequency dependences of the dielectric constant and dissipation factor are extremely large and are analogous to the behavior reported here for heat-treated, anodized tantalum. Pavlovic attributes this behavior to a high degree of ionic polarization. It is apparent from the work of Kofstad (9) that these samples must have been non-stoichiometric and probably inhomogeneous. It seems probable that the reported dielectric properties were strongly influenced by the conductivity of the non-stoichiometric samples. It is of particular interest that Pavlovic found an activation energy of about 0.6 eV for the relaxation effects.

The work described here on heat-treated, anodized tantalum raises some interesting questions about the properties of the unheated system. It cannot be doubted that a sharp interface between tantalum metal and stoichiometric Ta_2O_5 is unstable. Any adjustment on the part of the oxide in the direction of thermodynamic equilibrium at the interface will result in

oxygen deficiency and semiconduction in the oxide. Young has pointed out that the frequency dependences of capacitance and series resistance of anodic oxides, and the observed relationship between them, can be explained on the basis of a very steep, exponential gradient of conductivity within the oxide (3). Winkel and de Groot have proposed an alternative explanation based on a wide distribution of relaxation times (11), and this seems to have gained favor over the Young hypothesis in recent years (12). The results reported in this paper lend some support to Young's original interpretation.

Manuscript received May 20, 1964.

Any discussion of this paper will appear in a Discussion Section to be published in the June 1965 JOURNAL.

REFERENCES

1. D. M. Smyth, G. A. Shirn, and T. B. Tripp, *This Journal*, **110**, 1271 (1963).
2. D. M. Smyth and T. B. Tripp, *ibid.*, **110**, 1277 (1963).
3. L. Young, *Trans. Faraday Soc.*, **51**, 1250 (1955).
4. W. J. Bernard, *This Journal*, **108**, 446 (1961).
5. F. Rose, *Ann. Phys., Lpz.*, **9**, 97 (1951).
6. G. Pfozter, *Z. Naturforschung*, **4A**, 691 (1949).
7. J. W. A. Scholte and W. Ch. van Geel, *Philips Research Repts.*, **8**, 47 (1953).
8. R. G. Breckenridge in "Imperfections in Nearly Perfect Crystals," W. Shockley *et al.*, Editors, p. 219, John Wiley & Sons, New York (1952).
9. P. Kofstad, *This Journal*, **109**, 776 (1962).
10. A. S. Pavlovic, *J. Chem. Phys.*, **40**, 951 (1964).
11. P. Winkel and D. G. de Groot, *Philips Research Repts.*, **13**, 489 (1958).
12. L. Young, "Anodic Oxide Films," p. 163, Academic Press, London (1961).

Conductance during Anodic Oxidation of Tantalum and Niobium Films

C. L. White and W. E. Patterson

Texas Instruments Incorporated, Dallas, Texas

ABSTRACT

Conductance of tantalum and niobium films at room temperature is considered as a function of the forming potential of the anodic oxidation process. From elementary principles an equation is derived to relate metal film conductance to formation voltage. The equation indicates a linear relationship, and experimental measurements generally verify the linearity. Deviations of the characteristic from linear behavior are interpreted in terms of film sample and deposition parameters. Theoretical and experimental results suggest that the conductance-formation potential characteristic provides a fundamental tool for studying metal and oxide film parameters.

The behavior of the conductance of metal films has been studied as film thickness is decreased by anodization. The effect of decreasing thickness is seen implicitly by relating conductance to formation potential. Since the latter is a variable capable of being highly controlled, metal thickness and conductance may also be closely controlled. The conductance-formation voltage relationship thus forms a vehicle for studying an electrical parameter of the metal film as "layers" of metal are removed. This "peeling off" of layers is then essentially the reverse of the original deposition process. Consequently, the conductance characteristic has been especially valuable in adjusting films to preselected values of sheet resistivity.

A simple model based on the usual conductance-thickness relation shows that conductance is linearly related to forming potential. This model shows quantitatively that the characteristic depends on several parameters: (a) initial metal film thickness, (b) metal film density, (c) oxide film density, and (d)

oxide growth factor in the anodization process. Results of experimental measurements of the characteristic for sputtered niobium and tantalum films are discussed and these results used to determine initial thicknesses of the metal films. A comparison is made of initial metal film thickness for a niobium sample as determined by interferometer methods and by using the conductance characteristic. The nonlinear regions of the experimental curves are discussed qualitatively, as are observations made in using the conductance characteristic over an extended period of time.

Theoretical

To show that a linear relationship between metal film conductance (or sheet conductivity) and formation voltage is expected, it is necessary to examine briefly the metal-oxygen reaction. Tantalum is used to illustrate the required relationships.

In the tantalum-oxygen reaction one would expect 1.22g of Ta_2O_5 to be formed anodically for each gram

of tantalum, if the reaction goes to completion. For a two-layer film structure consisting of Ta_2O_5 over a layer of deposited Ta, this mass ratio can be equated with the ratio of the density-volume products

$$\frac{M(Ta_2O_5)}{M(Ta)} = \frac{d(Ta_2O_5) V(Ta_2O_5)}{d(Ta) V(Ta)} \quad [1]$$

If equal areas of metal film and oxide film are considered, and t is used to denote thickness, the ratio of oxide film thickness to metal film thickness becomes

$$\frac{t(Ta_2O_5)}{t(Ta)} = 1.22 \frac{d(Ta)}{d(Ta_2O_5)} \quad [2]$$

If anodizing conditions are such that a linear oxide growth factor exists, this factor may be used to develop the final equation. The term "linear oxide growth factor" is used here to mean that oxide thickness is directly proportional to the forming potential. With v signifying this formation voltage, [2] can be inverted and multiplied by the oxide growth factor, $t(Ta_2O_5)/v$, to yield the (voltage) rate of conversion of metal film to oxide film

$$m = \frac{t(Ta_2O_5)}{v} \frac{t(Ta)}{t(Ta_2O_5)} = \frac{t(Ta)}{v} \quad [3]$$

where m is this metal-to-oxide conversion rate. If the subscript o is used to denote initial metal film thickness, i.e., before anodization, the metal thickness remaining after anodization to v volts is the difference between the initial thickness and the thickness lost by conversion to oxide

$$t(Ta) = t_o(Ta) - mv \quad [4]$$

If metal film conductance, g , is proportional to film thickness, as in the bulk material conductance expression

$$\frac{g}{g_o} = \frac{t}{t_o} \quad [5]$$

If this equation is used in [4] and the parenthetical expressions are dropped, the final result becomes

$$\frac{g}{g_o} = 1 - \frac{m}{t_o} v \quad [6]$$

This equation relates the ratio of final metal film conductance to initial conductance and forming potential in a particularly simple way. The form of the equation, representing a normalized conductance, is convenient for comparing films of differing initial conductances (or resistances). On a graph of normalized conductance, g/g_o vs. v , the last equation represents a straight line of negative slope m/t_o and unity intercept corresponding to $v = 0$.

The quantities most easily measured are g_o , g , and v . Since

$$m = \frac{t(Ta_2O_5)}{v} \frac{d(Ta_2O_5)}{1.22d(Ta)} \quad [7]$$

for tantalum, the metal and oxide densities are required and the (linear) oxide growth factor must be known. If these last three quantities have been determined, they may be used with the conductance characteristic to yield a value for t_o , the remaining unknown. Conversely, if t_o has been determined, by optical measurement for example, any one of the other quantities can be determined. The inclusion of temperature as an experimental variable also suggests several possibilities for obtaining information on the anodic growth process and properties of film samples.

Implicit in the above model are the assumptions that: (a) the oxide has perfect stoichiometry, (b) the metal-oxygen reaction goes irreversibly to completion, (c) the substrate and oxide are perfect insulators, (d) metal and oxide densities are constants, (e) the resistance equation for bulk material is valid, (f)

the oxide is insoluble in the electrolyte used, and (g) the "metal" film consists of a pure metal.

In applying [6] and [7] to an experimental situation, suitable numerical values are often hard to determine. Metal film density, for example, may approach the bulk metal value in an asymptotic way only (1). This decreased density may be caused by agglomeration of the initially deposited particles or by structural defects, which often appear in greater concentration in films than in bulk material. The conductance characteristic might be used to determine such quantities.

Experimental

Experimentally, it has been found that the linear form of the normalized conductance expression is generally followed. Figure 1 shows the room temperature direct current normalized conductance of typical sputtered tantalum film samples anodized at approximately 5 ma/cm² in room temperature aqueous solutions of 100 ohm-cm resistivity. Figure 2 indicates the characteristics of typical sputtered niobium films under the same conditions. Each curve represents a single film, which was deposited on a glass microscope slide and selectively etched to form a film resistor. Several different patterns have been used; typical film line width is 5 mils. All samples were anodized by using a constant-voltage-rise program of 2 v/min. The voltage program was stopped periodically during its course, and the sample was removed from solution, rinsed, and dried. After drying, sample resistance was measured with L&N model 4735 guarded wheatstone bridge. In each case resistance of the leads and contacts was subtracted, so that only the area of metal undergoing anodization was included in the measurement. Table I indicates the conditions used for each sample.

Discussion of Results

In Fig. 1 sample C shows linear behavior of the characteristic above a formation potential of about 20v. The remaining two tantalum samples show a greater deviation from linearity, although the center portion of the curves suggests a linear relationship. The curves for niobium in Fig. 2 are similar in shape,

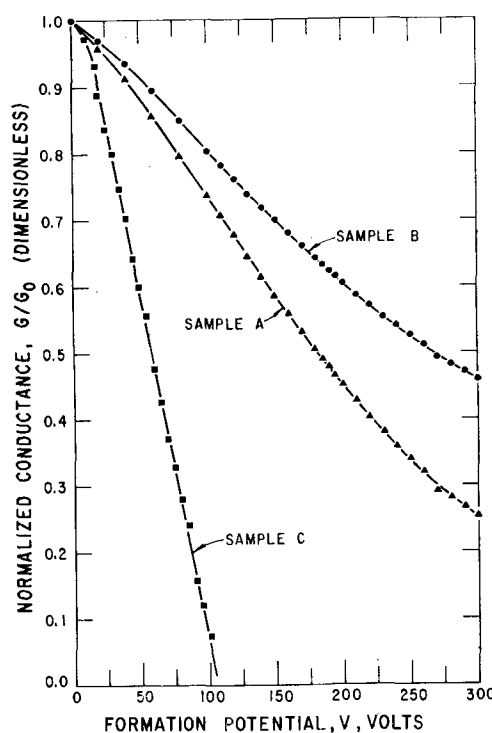


Fig. 1. Normalized room temperature conductance characteristic of typical tantalum film samples.

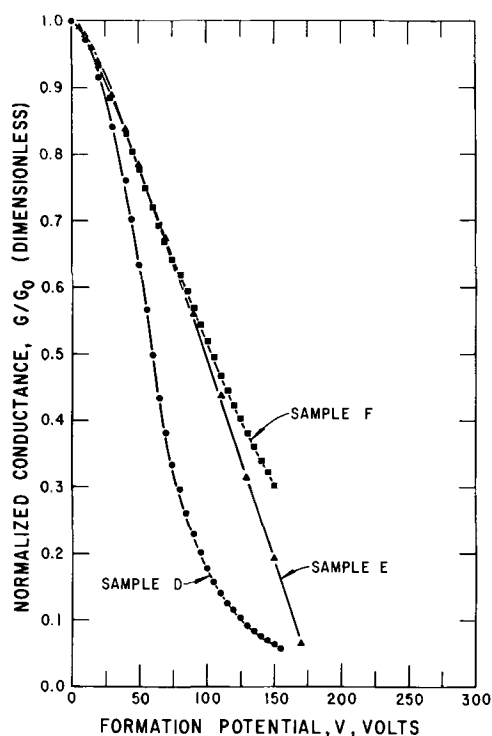


Fig. 2. Normalized room temperature conductance characteristic of typical niobium film samples.

with departures from linearity particularly pronounced at the low voltage ends.

In an effort to compare experimental results with [6], certain numerical values have been used for the parameters which enter this expression. Using $t(\text{Ta}_2\text{O}_5)/v = 15.3 \text{ \AA}/v$,¹ a value determined in this laboratory for sputtered tantalum, one finds from [7] that $m = 6.2 \text{ \AA}/v$. That is, 6.2 \AA of tantalum are converted to oxide for each volt applied. To arrive at this value a bulk tantalum density of 16.6 g/cm^3 and an oxide density of 8.2 g/cm^3 (2) were used in [7]. If $m = 6.2 \text{ \AA}/v$ is used and the slope of a line drawn through the characteristic of sample C is estimated, one finds the initial metal thickness of the sample to be 600 \AA . Since the characteristics of samples A and B are somewhat less linear, the center portion of the curves can be used, and the original metal thickness of these samples is estimated to be 2200 and 3100 \AA , respectively.

¹ Anodizing conditions essentially identical to those cited except dilute H_3PO_4 was the only solution used.

Table I. Anodization conditions for tantalum and niobium films

Sample No.	Initial resistance, ohms	Voltage program, v/min	Solution composition	Solution temp, °C	Initial metal film thickness, Å
A	5550.3	2	phosphoric acid ethylene glycol water	25	2200
B	3947.7	2	phosphoric acid ethylene glycol water	25	3100
C	60.1	2	phosphoric acid water	room temp	600
D	39.903K	2	phosphoric acid water	25	800
E	4720.7	2	methyl alcohol phosphoric acid water	28	1500
F	19.070K	2	phosphoric acid water	25	1800

Table I indicates the initial metal film thicknesses for the niobium samples, D, E, and F, as determined from the anodizing characteristic. The values shown are considered somewhat less reliable than those for tantalum because it was necessary to rely on literature values for metal density, oxide density, and oxide growth factor. Using 8.6 g/cm^3 for niobium density, 4.36 g/cm^3 for Nb_2O_5 density (3), and $22 \text{ \AA}/v$ for the growth factor of Nb_2O_5 (4, 5), one finds $m = 9.2 \text{ \AA}/v$.

Initial metal film thickness has been optically determined for only sample F. Multiple-beam interferometer techniques showed an initial thickness of 2730 \AA for sample F, compared with the 1800 \AA result from the conductance characteristic. The discrepancy could be the result of one or more deviations from the assumptions used in the equations. In addition, the optical measurement was taken in a single small area (of the order of 100 mils^2) of the metal film and may not adequately represent an average initial metal film thickness.

The curves in Figs. 1 and 2, as well as those of all samples not shown here, have a typical bend at low forming voltages. The curves generally start their linear behavior around $20v$, however. In this low voltage region the nonlinear behavior probably results from two factors. (A) There is often a thin, transparent film on the surface of sputtered tantalum films. These transparent films are $50\text{--}70 \text{ \AA}$ thick and are probably oxides and/or nitrides of the metal formed after deposition. The presence of these films reduces the electric field in the oxide to values insufficient for tantalum ion motion until several volts are reached in the voltage program. The constant value for m is thus in error in the low voltage region. (B) The linear behavior predicted by [6] incorrectly assumes that oxide overpotential and forming potential are equivalent over the entire voltage range. The error in this assumption is pronounced in the low voltage region. Because of effects (A) and (B), then, the conductance shows little change with increasing voltage until several volts have been reached.

Several of the samples in Figs. 1 and 2 show a decreasing slope in the high voltage region of the curves. Since the metal film becomes thinner as the forming voltage increases, it is thought that in the high voltage region of these curves "layers" may exist that are metal oxides or nitrides, formed by gettering action during deposition. Such a variation in composition alters conductance by altering the specific conductivity. Oxides and nitrides thus formed from residual gas in the sputtering system generally have lower specific conductivity than the metal, so that the magnitude of the slope decreases. Usually one would expect gettering to occur during the early stages of metallic film deposition. However, the fact that the characteristic starts leveling out at values as large as $g/g_0 \cong 0.6$ (for sample B) suggests that reaction of metal and residual gas may occur throughout deposition. The linear characteristic of niobium sample E and tantalum sample C suggests little gettering during deposition, particularly for the initially deposited particles, since the samples are nearly completely converted to oxide in the region $g/g_0 < 0.1$.

In addition to the bending of the curves in the low and high voltage regions, a third bending effect, not shown in the figures, has been observed. This bending occurs in certain samples in the high voltage region and is opposite in direction from the previously mentioned high voltage bending. It consists of a rapid fall-off from linear behavior such that the conductance drops substantially for a small increase in voltage. This behavior can be interpreted in two ways. First, deposition conditions could have been such that the initially deposited particles formed agglomerates which caused a discontinuous film structure. In a region of "island" structure of a very thin metallic film ($< 100 \text{ \AA}$) a different conduction mechanism is involved, one which has been discussed recently in the film literature (6-11). The discontinuous nature

of the film in this region may cause anodization to cease as a result of the loss of a "driving" potential, while the metal agglomerates remain. In the samples in which this effect occurs the characteristic might thus be used to detect the onset of this critical region, if this first interpretation is correct. A second interpretation of this drastically dropping conductance is that the metal film has become so thin that electron scattering in the thickness dimension increases. This is the third term in Matthiessen's rule for the resistivity of a thin metal film (6).

Qualitatively, several features were seen when the conductance characteristic was used as a monitoring technique. For example, although small variations exist, the slope of the characteristic tends to be essentially constant between samples deposited simultaneously in the same sputtering system. Samples sputtered at different times in the same system have different slopes, although deposition conditions are presumably identical. The first observation merely indicates good uniformity in thickness between samples, but the second suggests different residual gas contents in the system and differing impurity content in the resulting film. In comparing sputtered tantalum and niobium, the tendency for greater gettering by niobium can be seen by comparing slopes of the conductance characteristic for niobium samples from different deposition runs. On the other hand, tantalum shows good consistency, with less variation between slopes. This is, then, indirect evidence concerning relative purity of the sputtered films, and it is concluded that in comparing tantalum and niobium films, the anodizing characteristic offers one means of determining relative purity of a family of samples.

In conclusion, the normalized conductance-formation voltage characteristic relates parameters of a metal film to a dynamic variable of the oxidation process. In a fundamental sense it provides a tool for studying metal and oxide film parameters as the metal is converted to oxide. It also offers a most suitable means

for trimming metal films to preselected values of conductance, resistance, or thickness.

Acknowledgments

The authors wish to express their appreciation to D. Patterson and S. Hughey for making many of the measurements, to C. Jones for ellipsometer measurements, to D. Simpson and J. Hatcher for suggesting the utility of the method, and to J. Van Tassel and G. Larrabee for their suggestions concerning the text.

Manuscript received Feb. 17, 1964. This work was performed in part by contract DA 36-039-SC-90745, U.S. Army Electronics R&D Laboratory, Fort Monmouth, New Jersey.

Any discussion of this paper will appear in a Discussion Section to be published in the June 1965 JOURNAL.

REFERENCES

1. M. S. Blois, Jr. and L. M. Rieser, Jr., *J. Appl. Phys.*, **25**, 41 (1958).
2. L. Young, "Anodic Oxide Films," p. 76, Academic Press, New York (1961).
3. L. Young, *op. cit.*, p. 188.
4. L. Young, *op. cit.*, p. 189.
5. R. B. Hand, H. W. Ling, and T. L. Kolski, *This Journal*, **108**, 1023 (1961).
6. H. Mayer in "Structure and Properties of Thin Films," C. A. Neugebauer, J. B. Newkirk, and D. A. Vermilyea, Editors, John Wiley & Sons, Inc., New York, 1959).
7. C. A. Neugebauer, 1962 Transactions of the Ninth National Vacuum Symposium, American Vacuum Society.
8. C. A. Neugebauer and M. B. Webb, *J. Appl. Phys.*, **33**, 74 (1962).
9. C. Feldman, Paper presented at the 1962 Thin Film Conference, Glenwood Springs, Colorado; *ibid.*, **34**, 1710 (1963).
10. L. Y. Wei, Paper presented at the Canadian Electronics Conference, Toronto, Sept. 30-Oct. 2, 1963.
11. A. J. Learn and R. S. Spriggs, *ibid.*, **34**, 3012 (1963).

Studies on the Oxygen Gradients in Oxidizing Metals

II. Hafnium

J. P. Pemsler

Ledgemont Laboratory, Kennecott Copper Corporation, Lexington, Massachusetts

ABSTRACT

Coarse grained hafnium samples were oxidized for times up to 432 hr. A remarkable anisotropy of the oxidation rate was observed which persisted to the thick film region. This effect is associated with a variation in the stoichiometry of the oxide films covering the differently oriented grains. The oxygen gradient beneath the oxide film was measured using a technique involving the rate of dissolution of interference colored oxide films. Experimentally determined gradients are in good agreement with a theoretical expression involving the diffusivity, time, and oxide film thickness.

The oxidation of Groups IV A and V A metals differs from that of other metals in that during oxidation significant quantities of oxygen dissolve in the metal substrate simultaneously with the growth of oxide, so that a metal zone rich in oxygen forms beneath the oxide layer. This paper represents a continuation of the investigation into the nature of the oxygen gradient and the role that oxygen solution plays in the oxidation mechanism.

Wallwork and Jenkins (1) studying the oxidation of the Group IV A metals propose an initial parabolic rate associated with the formation of an oxygen diffusion gradient in the metal, followed by a linear rate associated with the establishment of a constant oxygen gradient in the metal. Smeltzer and Simnad (2) studied the oxidation of hafnium in the temper-

ature range 350°-1200°C. Their results are represented by logarithmic, parabolic, and linear rate equations. The persistence of the logarithmic rate decreased with increasing temperature, and no logarithmic rate was found above about 700°C. Logarithmic rates gave way to parabolic kinetics after an induction period. At longer times the parabolic rate transforms to a linear rate, simultaneous with the formation of a duplex scale of inner compact and outer porous oxides. In a previous paper (3) I measured the diffusion coefficient of oxygen in hafnium in the temperature range 500°-620°C. At the time of this study the phase diagram of hafnium-oxygen had not been determined, and the results were reported in terms of estimates of the terminal solubility of oxygen in alpha hafnium. Combining these data with the subsequent deter-

mination of the solubility limit of oxygen in hafnium by Rudy and Stecher (4), the diffusion equation may be expressed by D , $\text{cm}^2/\text{sec} = 0.66 \exp [(-50, 820 \pm 240)/RT]$. This equation has been re-evaluated in the light of subsequent publications by other investigators. The results are in excellent agreement with my initial work, and a critical evaluation of the literature concerning the diffusion of oxygen in hafnium is reported in a separate communication (5).

Theory.—Calculation of the oxygen gradient beneath the film on oxidized metals necessitates the solution of a moving interface diffusion problem with the oxidation rate as a boundary condition. The solution to this problem for the analogous case of zirconium has been derived previously (6). The oxygen concentration C at a distance x' from the oxide/metal interface is given by the expression

$$C = C_s \frac{\text{erfc}(x/2\sqrt{Dt})}{\text{erfc}(s/2\sqrt{Dt})} \quad [1]$$

where C_s is the oxygen concentration in hafnium co-existing with HfO_2 , D is the diffusion coefficient of oxygen in hafnium at the experimental temperature, s is the distance of the oxide/metal interface from the position of the initial surface, and $x = x' + s$.

Integration of Eq. [1] gives M , the total quantity of oxygen per unit area of surface present in the metal beneath the oxide film

$$M = 2C_s\sqrt{Dt} \left[\frac{\exp(-s^2/4Dt)}{\sqrt{\pi}\text{erfc}(s/2\sqrt{Dt})} - \frac{s}{2\sqrt{Dt}} \right] \quad [2]$$

Anodically deposited interference colored oxide films have been used by me to determine the diffusion coefficient of oxygen in zirconium (7) and hafnium (3) and to determine the oxygen gradient in oxidized zirconium (6). The oxygen gradient beneath an oxide film may be obtained by measuring the rate of diffusion of anodically deposited films into the metal substrate on a sample polished normal to the oxide film. The rate of decrease in thickness of the anodic film is proportional to the fraction unsaturation of the metal on which it is deposited.

Experimental

A coarse grained hafnium rod was prepared by zone melting crystal bar hafnium with three traverses of the rod. Analysis of the zone-refined stock indicated a zirconium content of less than 100 ppm and oxygen, nitrogen, and carbon contents of 120, 16, and 37 ppm, respectively. Disks 1.3 cm in diameter by about 0.3 cm thick were cut from the rod, polished with emery paper to 4/0, etched for 30 sec in an aqueous solution of 50% nitric and 5% hydrofluoric acids, and exposed to oxygen at 900°C and 1 atm for different periods of time. After cooling, the samples were cut in half through a diameter and polished normal to the oxide film. Care was taken to prevent fracture of the oxide and the embrittled metal zone adjacent to the oxide. Anodization took place at constant current in a saturated solution of sodium borate with the sample as anode and a platinum screen as cathode. Interference colored oxide films either 700 or 2000Å thick were produced. Samples with a 2000Å film were heated in vacuum for 4 hr at 615°C at pressures less than 10^{-5} Torr. This treatment did not significantly alter the gradient in the metal substrate. About 1300Å of oxide diffused into the metal in the oxygen-free zone. In the region of the oxygen gradient in the metal there existed a rainbow of color reflecting the difference in thickness of the remaining anodic film. The thickness at varying distance from the oxide/metal interface was determined by comparing the sample with a step gauge made by anodizing zirconium foil. Thus, the distances from the oxide/metal interface at which the color in the gradient matched that of the zirconium step gauge was recorded.

Samples which were anodized to 700Å film thickness were given each of three vacuum diffusion treatments in a consecutive manner. Samples were held for total times of 50 min, 2 hr, and 6 hr at 615°C. Subsequent to each of the vacuum annealing treatments, gradients were compared with color standards in an identical manner to that described above.

In order to calibrate the method and compare it with the theoretical equations relating decrease in film thickness to concentration of oxygen in the metal substrate, a series of hafnium-oxygen alloys were prepared by arc melting and analyzed by the chloride-volatility technique (8). These hafnium-oxygen alloys were then anodized to either 700 or 2000Å and diffused in a manner identical to that of the sample with a 700Å film as described above.

Results

Oxidation.—The oxidation of the large grained hafnium samples revealed a remarkable orientation effect on the oxidation rate. While it is common to observe anisotropic growth of oxide films on metals in the thin film region, hafnium exhibits an unusual persistence of this anisotropy to thick films ($\sim 25\text{--}75\mu$). Figure 1 shows the external appearance of the oxide film on a coarse grained hafnium sample oxidized for 65 hr at 900°C as it appears in bright light. The marked variation in the color of the oxide film on different grains is readily visible. The little "chicken" scurrying across the center of the picture consists of black lustrous oxide, while in other areas the oxide

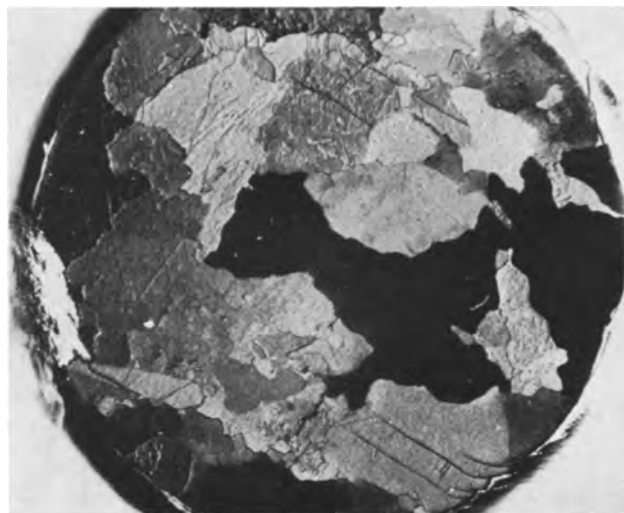


Fig. 1. External appearance of oxide film on coarse grained hafnium oxidized for 65 hr at 900°C. Magnified 10X; bright light.

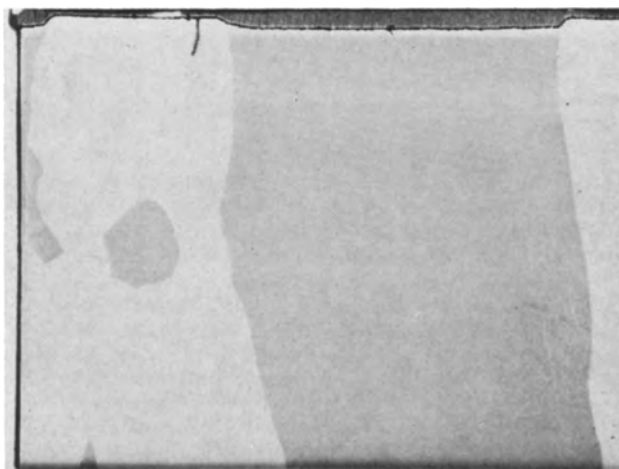


Fig. 2. Cross section of coarse grained hafnium oxidized for 250 hr at 900°C. Magnified 65X; polarized light.

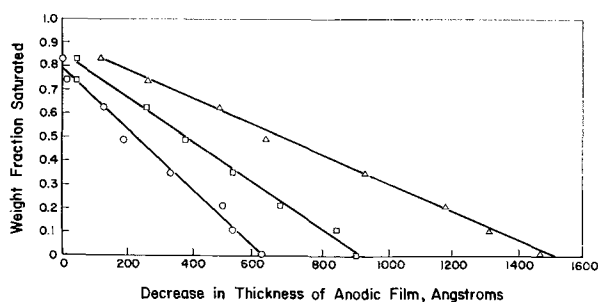


Fig. 3. Dissolution rates of 2000Å anodic films on hafnium oxygen alloys. \circ , 50 min; \square , 2 hr; \triangle , 5 hr, 45 min.

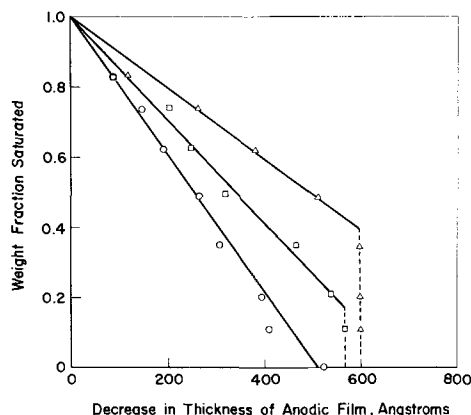


Fig. 4. Dissolution rates of 700Å anodic films on hafnium-oxygen alloys. \circ , 50 min; \square , 2 hr; \triangle , 5 hr, 45 min.

has a much lighter appearance. With the exception of a small area of spalling white oxide on the left edge of the picture, the film appears to be dense, adherent, and nonporous. It is reasonable to assume that the dark black oxide consists of material having the widest deviation from stoichiometry; whereas, the lighter oxide represents compositions closer to $\text{HfO}_{2.00}$. If this is the case, then the dark oxide should grow at the most rapid rate and the lightest oxide at the slowest rate. Sections polished normal to the oxide films confirmed the fact that the black oxide was indeed the thickest and the lighter colored the oxide film, the thinner it was. Differences in oxide thickness by as much as a factor of 2 were observed on grains of a sample oxidized for 250 hr at 900°C (Fig. 2). In cross section oxide films on both coarse grained and fine grained material exhibited a pronounced columnar structure consisting of a large number of fine parallel grains.

Gradient.—Data obtained from the diffusion of anodic films into the synthesized hafnium-oxygen alloys are shown in Fig. 3 and 4. Data from diffusion anneals of alloys with a 2000Å anodic deposit are in good agreement with the theory (6) and extrapolate linearly to values for the decrease in oxide film thickness at zero initial oxygen content which are in excellent agreement with the diffusion coefficient (3). However, the data does not conform well to theory at high oxygen contents and short diffusion times. This is probably due to residual water and cations remaining in the film after anodization. The residual water may serve further to oxidize the samples slightly during the initial vacuum annealing period, or on removal, to change the index of refraction and hence color of the hafnium film.

Data from diffusion of the hafnium-oxygen alloys with a 700Å anodic film are in poor agreement with the theory. Extrapolation to oxygen-free material should give values for the thickness of film dissolved equal to those of the alloys with the 2000Å deposit as in Fig. 3. In addition, a residual color equivalent to a film about 100Å thick persists on the samples for

some time beyond the time necessary for complete dissolution of the film. This effect may be due to a nonlinearity in the voltage-thickness relationship for anodic deposits on hafnium in the thin film region. An independent method of film thickness measurement such as ellipsometry in the zero to 100Å region would be desirable to explain these discrepancies. These thin film anomalies were not observed with zirconium where dissolution rates on 1000Å films gave data in good agreement with theory (6). In any case, the data in Fig. 3 and 4 may be used empirically to obtain an accurate measure of the oxygen gradient beneath the oxide film on the hafnium samples.

Experimentally determined gradients obtained on hafnium oxidized at 900°C for 138.7, 231.5, and 432 hr are shown in Fig. 5 and 6. The solid lines indicate the theoretical gradients as calculated from Eq. [1]. The data points in Fig. 5 were obtained from dissolution measurements of a 2000Å thick film. The two solid lines for the 432-hr samples represent calculated gradients for grains with greatly different oxide film thicknesses. The closeness of the curves for the two oxide thicknesses shows the relative insensitivity of the gradient to oxide thickness so long as the oxide remains adherent and protective. Data from dissolution measurements on samples with an initial anodic film of 700Å are shown in Fig. 6. The three sets of data points represent information obtained after each of the three vacuum annealing treatments (50 min, 2 hr, and 6 hr). The fit of the experimental points to the theoretical equation is excellent. The total quantity of oxygen dissolved in the metal as calculated from Eq. [2] and measured experimentally was found

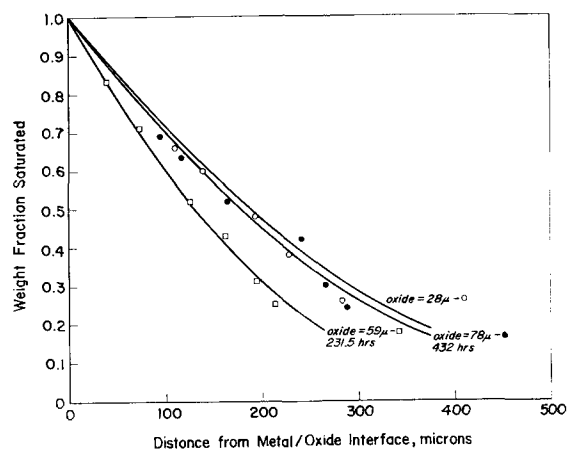


Fig. 5. Oxygen gradients in hafnium oxidized at 900°C determined by dissolution of 2000Å anodic films.

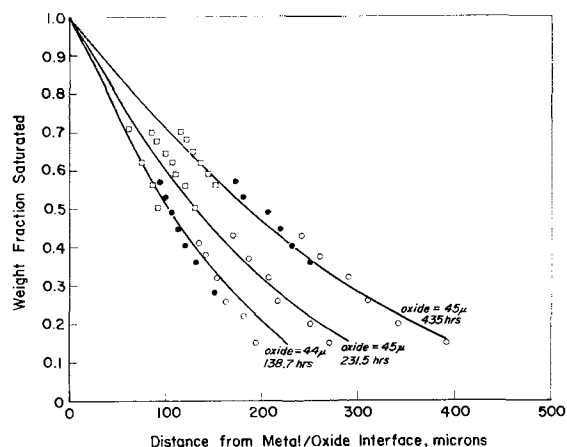


Fig. 6. Oxygen gradients in hafnium oxidized at 900°C determined by dissolution of 700Å anodic films. \circ , 50 min; \bullet , 2 hr; \square , 5 hr, 45 min.

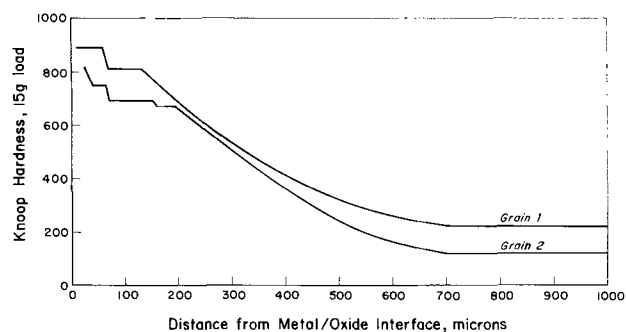


Fig. 7. Microhardness of coarse grained hafnium oxidized for 470 hr at 900°C.

to increase linearly with $t^{1/2}$ as demanded by diffusion theory.

Metallographic examination of polished samples indicated zones of optical activity in the metal substrate, but much less pronounced than those observed for zirconium (6). Hardness traverses were obtained within two different grains on the same sample using a Knoop indenter with a 15g load. Data for the two grains are presented in Fig. 7. Hardness was found to be orientation-dependent, and zones of anomalous constant hardness in the vicinity of the oxide/metal interface were observed similar to those found in zirconium (6).

Discussion

Oxidation.—The strange persistence of the oxidation anisotropy of hafnium to the thick film region appears to be without parallel in the literature. Zirconium, for example, has been observed to oxidize in the thin film region in an anisotropic manner (7, 9, 10); however, oxidation of coarse grained material to the thick film region demonstrates that the anisotropy does not persist and that grains growing side by side do not exhibit oxide differences of more than several per cent. The behavior of hafnium therefore poses some important questions concerning the nature of the oxidation process. Most theories advanced to account for anisotropic growth of oxide films are applicable to the thin film region. Mechanisms involving electron tunneling, nucleation, misfitting monolayers, etc., are clearly not applicable to the thick film region where ionic and normal electronic conductivities are considered to be the rate-controlling steps in the oxidation process. The oxidation of hafnium, like zirconium, is believed to occur by the diffusion of anion vacancies through the nonstoichiometric oxide lattice. One is then led to the over-all conclusions that the anisotropy of oxidation of hafnium is determined by the nonstoichiometry properties of the oxide throughout the oxidation process and that the mechanism of development of anisotropic-dependent nonstoichiometry is not as yet clear. Further studies using single crystal hafnium are being initiated in order to clarify the picture and to attempt to determine the general applicability of the anisotropic nonstoichiometry observation to the explanation of the anisotropic oxidation of other metals.

Gradient.—Examination of Fig. 5 and 6 indicates an excellent agreement of the observed gradient with the theoretical equation involving a moving boundary and fixed interface composition. These data indicate the absence of zones of constant concentration in the neighborhood of the oxide/metal interface and steady-

state gradients, both of which had been proposed in the literature (1, 11). It is interesting to note the agreement of the gradient with the theory in the case of the 432-hr sample on two grains of widely different oxide thicknesses which are nevertheless both adherent protective oxides. The description of the gradient by Eq. [1] holds true only in situations where the oxide remains adherent and protective. When the oxide film cracks and allows oxidation to proceed at an accelerated rate, the oxygen gradient is consumed at a rate more rapid than it can replenish itself. Under these circumstances the depth of oxygen penetration will decrease with time. When the oxide consists entirely of white, spalling, nonprotective oxide, the depth of penetration of oxygen beyond the oxide/metal interface shrinks to very small values. It is thus considered that the oxygen gradient in the metal beneath the oxide film is the effect rather than the cause of the oxidation behavior of the metal. The oxygen will contribute to the over-all weight gain in a magnitude dependent on the diffusion coefficient of oxygen in the metal and the time of exposure, but apparently has little connection to the rate of film formation, since there is only a slight difference in gradients on grains growing oxide at greatly different rates. Transition from protective to nonprotective kinetics may be associated mechanically with an embrittled oxygen-containing metal zone beneath the oxide/metal interface, but conclusive evidence of this is lacking in the literature.

The appearance of zones of anomalous hardness and optical activity is similar to that observed for titanium and zirconium and is presumed to be due to an ordered structure in the metal-oxygen solution such as those which have been observed for zirconium-oxygen and titanium-oxygen (12, 13).

Acknowledgment

The author expresses thanks to J. K. Litchfield for assistance and valuable suggestions throughout the course of the experimental work.

Manuscript received May 4, 1964. This paper was presented at the Washington Meeting, Oct. 11-15, 1964.

Any discussion of this paper will appear in a Discussion Section to be published in the June 1965 JOURNAL.

REFERENCES

- G. R. Wallwork and A. E. Jenkins, *This Journal*, **106**, 10 (1959).
- W. W. Smeltzer and M. T. Simnad, *Acta Met.*, **5**, 328 (1957).
- J. P. Pemsler, *This Journal*, **106**, 1067 (1959).
- E. Rudy and P. Stecher, *J. Less-Common Metals*, **5**, 78 (1963).
- J. P. Pemsler, *This Journal*, **111**, 1185 (1964).
- J. P. Pemsler, *ibid.*, **111**, 381 (1964).
- J. P. Pemsler, *ibid.*, **105**, 315 (1958).
- E. B. Read and L. P. Zopatti, "Determination of Oxygen in Zirconium Metal," Report AECD-2798, (1950).
- A. E. Bibb and J. R. Fascia, *Trans. AIME*, **230**, 415 (1964).
- J. N. Wanklyn, "Recent Studies of the Growth and Breakdown of Oxide Films on Zirconium and Zirconium Alloys," Presented at American Nuclear Society Meeting, New York, November 1963.
- P. Kofstad, P. B. Anderson, and O. J. Krudtaa, *J. Less-Common Metals*, **3**, 89 (1961).
- B. Holmberg and T. Dagerhamn, *Acta Chem. Scand.*, **15**, 14 (1961).
- B. Holmberg, *ibid.*, **16**, 1245 (1962).

Steel Corrosion Mechanisms

The Growth and Breakdown of Protective Films in High-Temperature Aqueous Systems: 15% NaOH at 316°C

M. C. Bloom, G. N. Newport, and W. A. Fraser

United States Naval Research Laboratory, Washington, D. C.

ABSTRACT

This paper summarizes what is known regarding the reaction of steel in high-temperature water as affected by sodium hydroxide additions and presents results of a detailed study of the reaction of 15% sodium hydroxide at 316°C by the hydrogen effusion method. The corrosion rates are correlated with microscopic study of the growth and breakdown of the protective magnetite films. It is shown that two different corrosion-rate-governing mechanisms are involved prior to the onset of pitting: a large decrease of the initial rate controlled by the build-up of a protective film on the metal surface and a subsequent smaller decrease in corrosion rate possibly controlled by penetration of the magnetite film by the corrosive solution. The pitting is apparently due to the genesis of cracks in the magnetite film after it reaches a critical thickness.

The effect of alkali on the corrosion rate of steel in high-temperature water, originally studied by Berl and Van Taack (1) in 1930, has recently been the subject of a number of investigations (2-8). Berl and Van Taack, who heated small samples of steel powder in a static autoclave for 7.5 hr at 310°C, obtained data indicating a minimum in the corrosion rate at a concentration of 0.7 g/l which corresponds to a pH of 12.24. Some measurements at 316°C by the authors using a more precise static technique, the hydrogen effusion method (9), showed a drop in total corrosion in the region of pH 12.24, and more recent measurements (Table I) confirm the actual minimum in total corrosion at this pH as reported by Berl and Van Taack. Both of these recent studies, however, show that the phenomenon is transitory, and after 25 days the corrosion rate increases monotonically with pH (10). It is of interest to note that in dynamic systems improvement in corrosion resistance seems to be obtained by alkalization to a pH of 9-12 (4, 11). This is probably due to the fact that the crystallite size of the magnetite film developed in neutral solutions (as determined by x-ray line broadening) is in the colloidal range (< about 1000Å) and the film is subject to erosion in flowing streams. Increasing the alkalinity produces an increase in crystallite size (10) and avoids erosion of the protective film in flowing streams [as shown in ref. (11)].

More recently attention has been given to more concentrated solutions. Potter and Mann (5) reported results on the corrosion of mild steel block specimens exposed in mild steel autoclaves containing 5-20% by weight of sodium hydroxide at 250°-355°C, and two of the authors (6) published a hydrogen effusion study of the reaction of 40% sodium hydroxide solution

with mild steel at 316°C. Most recently, in two papers (7, 8) presented at the 2nd International Conference on Metallic Corrosion, March 11-15, 1963, Potter and Mann extended their studies with block specimens to 500°C and Field, Stanley, Adams, and Holmes using similar specimens studied the reactions of mild steel with 15% NaOH at 315°C. The extensive work of Potter and Mann using block specimens yielded a double-layered scale which the authors interpreted as due to counter-current diffusion of oxygen-bearing ions and metal ions through the oxide film, the former producing a finely divided oxide in contact with the metal and the latter going into solution and then producing some coarsely crystalline oxide by redeposition and recrystallization at the oxide-solution interface. The general morphology of this double layer was confirmed by the work of Field, Stanley, Adams, and Holmes, but these authors gave evidence of sufficient porosity in the film to allow penetration of solution and reaction at the metal-oxide interface to account for the finely divided inner layer.

In the authors' study of 40% NaOH solutions at 316°C using the hydrogen effusion technique (9) it was shown that mild steel tubing in contact with this concentrated alkali is subject to a drastic pitting attack. The pits appeared to grow underneath substantial masses of oxide. Each pit gave the appearance of having been initiated at a single point and of having grown in all directions from this point as a nucleus. Crack formation in the oxide film allowing access of the solution to the metallic surface at the apex of the crack seemed a plausible mechanism, but while cracks in the oxide film were discovered on polished sections under the microscope, none was found which clearly penetrated to the metallic surface and was associated with pit generation. In order to obtain possible additional light on the corrosion mechanisms involved, a series of experiments was undertaken in which the hydrogen effusion technique was applied to the reaction of mild steel with 15% NaOH at 316°C.

Experimental

The hydrogen effusion technique employed has been previously described (6, 9). It uses as a specimen a small metal capsule filled with the corrosive medium. The capsule is heated in an evacuated chamber; hydrogen formed during corrosion effuses through the capsule wall into the chamber, where hydrogen pressure is measured continuously as a function of time. Rate of pressure change (hydrogen effusion rate) is

Table I. Recent corrosion measurements

pH	Total corrosion after 7.5 hr		Corrosion rate (mg/dm ² -mo) after	
	Berl and Van Taack, mg-O/g	NRL, mg-Fe/dm ²	7.5 hr	25 days
7.00	17	7	330	16
10.6		10	580	22
11.5		11	680	37
11.70	16			
12.00	16	23	970	52
12.18	11			
12.24		5	220	55
12.32	11			
12.40	18	12	810	81

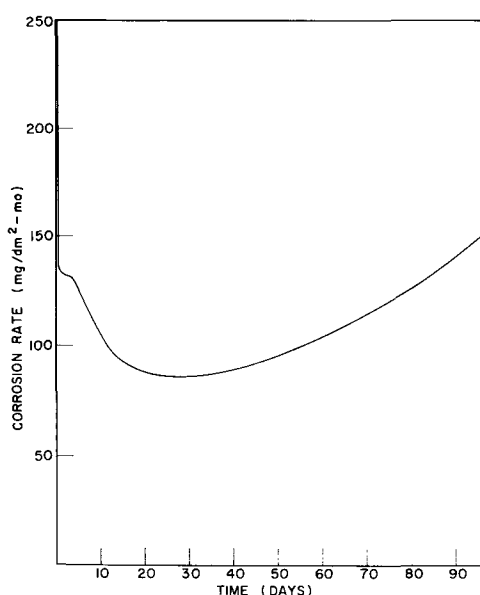
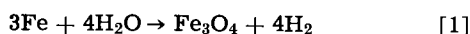


Fig. 1. Corrosion rate as a function of time for the reaction of mild steel with 15% NaOH at 316°C.

used as a measure of corrosion rate. From rate of hydrogen effusion, rate of iron consumption is calculated using stoichiometry based on the equation:



The steel used was from the same batch used for the 40% NaOH experiments (6). All procedures were the same. All solutions were prepared either in alkali-resistant glass or in polyethylene.

Results

Rate data for the reaction of steel with 15% NaOH at 316°C averaged for three representative capsules are shown in Fig. 1. The maximum deviation of individual measurements from this average was of the order of 15%. In Fig. 2, these averaged data are compared with analogous data for other alkaline solutions.

It may be noted that just as in the case of the 40% NaOH solutions, the corrosion rate in 15% NaOH reaches a minimum and then rises at an accelerating rate. Apparently, analogous phenomena are involved

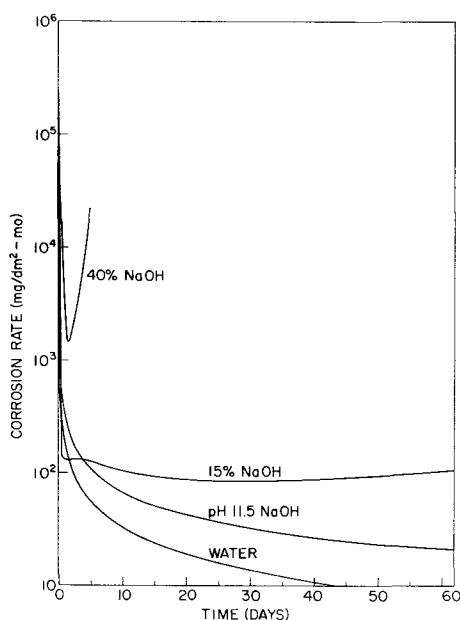


Fig. 2. Corrosion rate as a function of time for the reaction of mild steel with water and with NaOH solutions at 316°C.

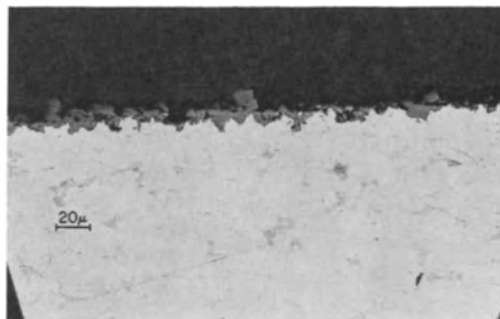


Fig. 3. Section perpendicular to inside surface of steel capsule containing 15% NaOH solution after 3.7 days at 316°C, 1% Nital etch. Original magnification 500X.

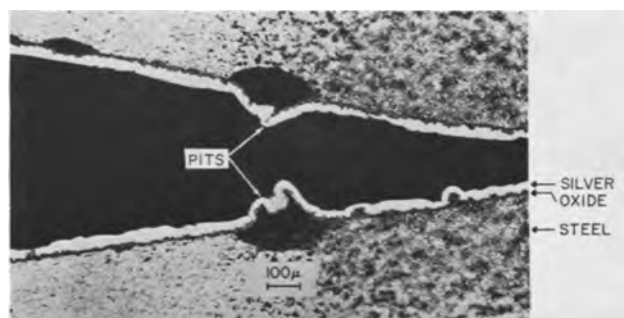


Fig. 4. Section perpendicular to inside surface of steel capsule containing 15% NaOH solution after 68 days at 316°C, 1% Nital etch. Original magnification 100X.

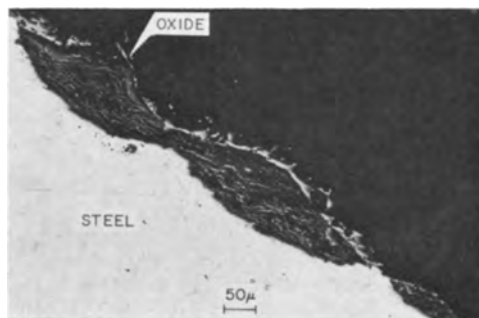


Fig. 5. Section perpendicular to inside surface of steel capsule containing 15% NaOH solution after 119 days at 316°C, 1% Nital etch. Original magnification 200X.

except that in the case of the 15% NaOH it requires about thirty days to reach the minimum and the rate increase is much more gradual. The appearance of the protective film generated as a result of general corrosion prior to reaching the minimum is shown in Fig. 3, which exhibits a representative cross section after 3.7 days of exposure.

In addition to the general corrosion, pits appeared. Quite analogous to the observations made with 40% NaOH, these pits were readily observable after the rate data passed the minimum. In this case, however, the attack was not so drastic, and it was possible to follow the course of pit development over considerable periods of time. Figures 4-7 show typical pit cross sections after various periods of time. In Fig. 4, 6, and 7 the specimens were silver plated on the oxide surface prior to mounting and polishing.

Discussion and Conclusions

The 316°C exposure of mild steel capsules containing 15% NaOH in the hydrogen effusion apparatus has revealed several phenomena of special interest from the standpoint of corrosion mechanisms. First, the corrosion rate-time curve shows a rapid drop to a plateau during the first few days of operation and

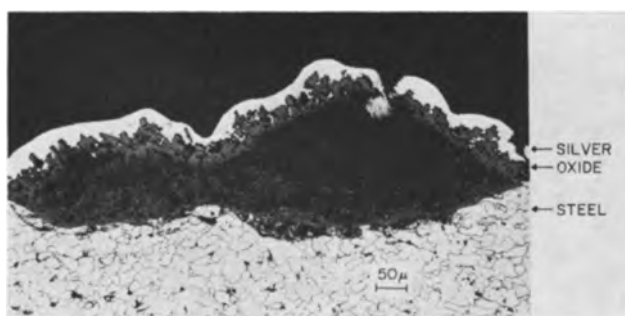


Fig. 6. Section perpendicular to inside surface of steel capsule containing 15% NaOH solution after 180 days at 316°C, 1% Nital etch. Original magnification 200X.

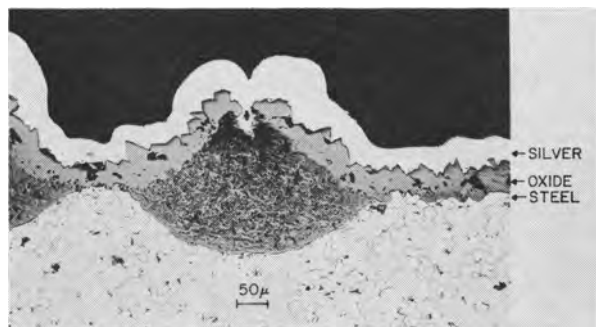


Fig. 7. Section perpendicular to inside surface of steel capsule containing 15% NaOH solution after 1 year at 316°C, 1% Nital etch. Original magnification 200X.

then a further drop to a minimum after approximately 28 days followed by an increasingly accelerating rate of attack. Second, the increase in corrosion rate following the minimum was accompanied by the development of pits. These data would seem to indicate that at least two mechanisms of general attack are involved, even before the onset of pitting. It is interesting to note in this connection in Fig. 2 that in the early stages of corrosion a 15% NaOH solution develops a more protective film than pure water. This is undoubtedly due to the more rapid development of magnetite in the 15% NaOH solution within the first few days. It may be noted in Fig. 8 that at the end of one day 240 mg/dm² of iron have been consumed. In pure water, approximately 10 mg/dm² would have been consumed in this time period. If all the corrosion went to protective film development, this would have produced a protective film of the order of 6μ from the 15% NaOH solution and 0.25μ from the water. The fact that subsequently the sodium hydroxide solution produced higher corrosion rates than the water despite the thicker magnetite films (Fig. 3) is consistent with the general effects in these alkaline systems.

In their original study using block-type specimens enclosed in autoclaves, Potter and Mann (5) concluded that attack of magnetite by high-temperature alkaline solutions takes place by a mechanism involving transfer of oxygen-bearing anions from the solution through the oxide film to the metal-oxide interface and the formation there of additional oxide, while an approximately equivalent number of metal ions diffuse away from the metal and toward the oxide-solution interface where they enter the solution and reprecipitate in part in gross crystalline form. This mechanism permits oxide growth at the metal-oxide interface without substantial stress despite the approximately 2/1 Pilling and Bedworth ratio (12). It also accounts for the double-layered oxide structure consisting of finely divided crystallites covered at the oxide-solution interface by a thinner layer of crystals of substantial size. These authors interpreted their data in terms of parabolic

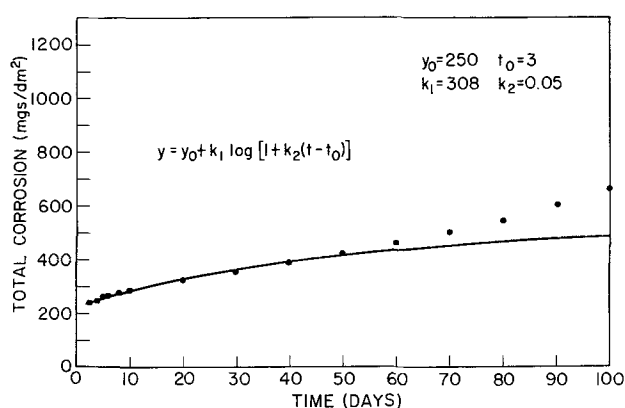
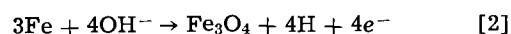


Fig. 8. Corrosion of mild steel capsules containing 15% NaOH solution at 316°C.

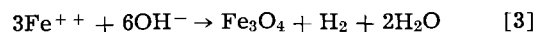
rate constants and calculated an activation energy of approximately 15 kcal/mole. They attribute the increase of corrosion rate with increase in hydroxide concentration to the increased driving force for oxide ion penetration of the magnetic lattice as the OH⁻ at the magnetite-solution interface increases.

In the discussion following the presentation of this paper, A. M. J. Adams pointed out that the activation energy seems too low to account for a lattice diffusion process.

In a discussion of the mechanism of general corrosion in these alkaline systems (6), it was pointed out by two of the present authors that the explanation of the effect of increased alkalinity in increasing the corrosion rate might be due to one of two alternative processes, depending on whether the films were sufficiently porous to allow access of the solution to the metallic surface or not. In the case where they are sufficiently porous, we would expect a gradual filling of the pores with magnetite as a result of an anodic reaction such as



where the OH⁻ would be rate-controlling. In the case where they are not sufficiently porous to allow access of the solution to the metallic surface, the corrosion would have to proceed by diffusion of ionic or atomic species through the film, and the controlling effect of OH⁻ would have to be attributed either to its control of the diffusion of oxygen-bearing species from the solution to the metallic surface as postulated by Potter and Mann, if diffusion were rate-controlling, or to its effect on a surface reaction at the oxide-water interface such as



if the surface reaction were rate-controlling. Precise measurements in less alkaline systems [see discussion section of (10)] have not been consistent with the parabolic kinetics to be expected from diffusion control, and Field, Stanley, Adams, and Holmes (7) in their exploration of the reaction of 15% NaOH on steel block specimens in autoclaves at 315°C found evidence that porosity is present. They also obtained data which was interpreted as consistent with a pore-blocking mechanism. These authors in agreement with Potter and Mann (5) present evidence for the development of a two-layered scale over the entire surface of the specimens, an inner layer of extremely fine crystallites generated *in situ* from the steel and a coarsely crystalline outer layer perhaps generated by recrystallization from solution. Their evidence of a pore-blocking mechanism was based on examination of the thickness of their "inner layer" as a function of time. They found that for the first 40 days this was consistent with an equation of the type $y = k_1 \ln(1 + k_2 t)$ where y is total corrosion, t , is time,

and k_1 and k_2 are constants. This is a type of equation (13) consistent with a pore-blocking mechanism. Beyond about 40 days, substantial deviations in the direction of increased corrosion were obtained. The period of 40 days is not far from the time that substantial rate increases and significant pit formation were observed in the hydrogen effusion experiments reported herein. Analysis of the hydrogen effusion results (total corrosion) on the basis of an equation of this type, starting after 3 days when the processes dominating the initial corrosion were apparently complete (Fig. 1), yields a fair fit from 3-40 days (Fig. 8).

Microscopic examination of the oxide films developed in this study (Fig. 3) did not reveal evidence of a two-layered scale, and the corrosion rates observed were much lower than those found with block specimens. Perhaps the two-layered scale is related to the fact that hydrogen is generated on all sides of the block specimens and any generated at the metal-oxide interface by such a reaction as Eq. [2] would have to penetrate the growing oxide scale to escape. Interference with crystal growth under these conditions may produce the finely divided "inner layer" which has been observed. In the hydrogen effusion capsules, however, hydrogen thus generated can escape through the capsule walls, and an apparently uniform compact film of oxide is formed. The appearance of this film, and the fact that it is much more protective in equivalent thickness than the double-layer films under discussion, would indicate that the films produced in the hydrogen effusion capsules are less porous. The further possibility that these films may be sufficiently less porous as to be nonpermeable to the solution cannot yet be discarded.

With regard to pitting, the postulate of crack formation after the achievement of a critical film thickness receives some support from Fig. 4-7 which show pit development after 69 days, 119 days, 180 days, and 1 year of exposure. Figure 4 which is a photomicrograph of a cross section of capsule tubing after 68 days of exposure shows pit formation at a stage corresponding to a time when the corrosion rate had passed the minimum and was rising at a substantial rate. The appearance of Fig. 4-7 is suggestive of film breakdown at a localized area allowing solution access to the metal and causing rapid build-up of a mound of finely divided corrosion product which, either by itself or with the aid of corrosion-generated hydrogen, elevated the original protective film producing a volcano-like structure. The general appearance of the attack after 68 days (Fig. 4) is similar to that exhibited by samples attacked by 40% NaOH after 46 hr (6). It may be noted that for the attack by 40% NaOH 46 hr represents a position on the corrosion rate-time curve when the rate has passed the minimum and is rising rapidly, quite analogous to the position of the 68-day samples on the corrosion rate-time curve for 15% NaOH. The attack started at the same sensitive area, the area of major plastic deformation in the welded ends. The slower action of 15% NaOH allows the progress of the attack to be more clearly seen. Figures 5, 6, and 7 show analogous sections after 119 days, 180 days, and 1 year, respectively. Although the initial attack was observed in the weld-heat-affected zone (Fig. 4), the attack subsequently spread beyond this zone (Fig. 5, 6, and 7). Figure 9, which exhibits a capsule surface after a year of exposure, shows the spread of the cracking phenomenon over the entire surface of the capsule.

If crack formation after the achievement of a critical thickness is the cause of this pitting phenomenon, it is of interest to ask (a) what is the magnitude of this critical thickness, and (b) what causes crack formation at this thickness? Some indication of the answer to the first of these questions is obtained by examination of Fig. 4-7. If we assume that the thickness of the observable oxide which forms the external

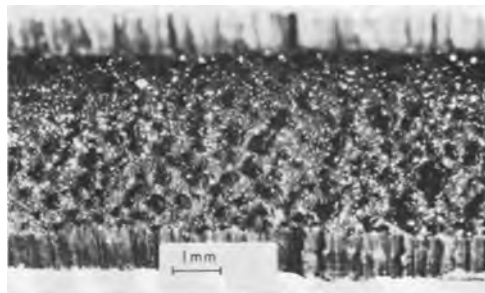


Fig. 9. Section parallel to axis of steel capsule containing 15% NaOH after 1 year at 316°C. Original magnification 16X.

surface of the volcano-like structure represents the thickness of the deposit in contact with the metal at the time of crack development, we obtain from Fig. 4, the 68-day exposure, a value of about 20μ , from Fig. 5 and 6, the 119-day and the 180 day exposures, $20-50\mu$, and from Fig. 7, the 1-year exposure, $40-60\mu$. Since in the case of the 1-year exposure, practically the entire surface is cracked, one might take the thickness of $40-60\mu$ as a maximum achievable without crack development. It may be of significance in this connection that Field, Stanley, Adams, and Holmes (8) report the loss of ability to distinguish two distinct layers on their block specimens when the film thickness reaches the neighborhood of 60μ and they present photomicrographic evidence which seems consistent with the postulate of film cracking and recrystallization of smaller crystals to larger ones inside the film.

With regard to the second question, it is suggested that crack formation is probably due to compressive stresses developing in the magnetite as it thickens. Analogous cracking phenomena have been observed in the dry oxidation of titanium (14), niobium and tantalum (15, 16), and these cracking phenomena have been related to compressive stress development in oxide films growing at the metal-oxide interface. Pawel, Cathcart, and Campbell (16) found evidence of stresses in the oxide of sufficient magnitude to create deformation lines in the metal surrounding the cracked areas. Maldy (17) using x-ray techniques has recently demonstrated that oxidation of iron in a mixture of water and hydrogen at $800^{\circ}-850^{\circ}\text{C}$ gives rise to analogous stresses in the iron of considerable magnitude but that these stresses appear only after a critical thickness of oxide has been exceeded. Perhaps some phenomenon of this kind is responsible for the fact that Field, Adams, Stanley, and Holmes (7) did not observe curvature of thin foils of iron gold-plated on one side and treated in 15% NaOH at 315°C . It should perhaps be pointed out also that the very porous "inner layers" generated, under their conditions of operation, without appreciable dimensional change might not produce stresses at the same magnitude as the relatively compact films under discussion.

Another phenomenon which may deserve mention is the striated appearance of the corrosion product within the pits. It is perhaps indicative of alternating protective film formation and breakdown. Such striated deposits within pits are found in pitted steam-generator tubes of power boilers (18).

One might summarize the most significant conclusions as follows:

1. The corrosion of mild steel capsules containing 15% NaOH at 316°C reveals the successive operation of three different mechanisms: (a) the initial rapid build-up of a protective film; (b) a continuation of the corrosion at a decreasing rate by a mechanism involving penetration and thickening of the protective film; and, (c) film breakdown at local areas resulting in pit development and increasing corrosion rates.

The quantitative rate data following the build-up of the initial film and prior to the onset of pitting can be fitted by logarithmic kinetics. This seems inconsistent with a diffusion-controlled process. It is con-

sistent with a porosity mechanism, but the films produced in these capsules appear quite compact, and the possibility that they may be sufficiently compact to be impermeable to the solution cannot yet be discarded.

Films produced on block specimens exposed in autoclaves under similar conditions appear more porous and are less protective. This is probably due to the fact that hydrogen generated at the metal-oxide interface of such specimens cannot escape except by penetration of the growing oxide film and interference with its growth. In capsule systems hydrogen generated at this interface can escape through the capsule wall.

Microscopic observations of capsule specimens over extended periods correlated with data from other systems where oxide growth takes place at the metal-oxide interface (Ti and Nb) support the thesis that pit formation is the result of crack development in the oxide film, after reaching a limiting thickness, allowing local access of the solution to the metallic surface and producing the small anode-large cathode relation conducive to pit formation.

Acknowledgments

The authors wish to acknowledge their debt to D. H. Price for aid in metallography, to O. R. Gates for chemical analyses, to R. A. Meussner for stimulating discussion, and to the Bureau of Ships for financial support.

Manuscript received April 6, 1964; revised manuscript received July 23, 1964. This paper was presented at the New York Meeting, Sept. 29-Oct. 3, 1963.

Any discussion of this paper will appear in a Discussion Section to be published in the June 1965 JOURNAL.

REFERENCES

1. E. Berl and F. Van Taaack, *Forsch, Gebiete, Ingenieurw*, **330**, 1 (1930).
2. M. C. Bloom, M. Krulfeld, W. A. Fraser, and P. N. Vlannes, *Corrosion*, **13**, 297t (1957).
3. D. L. Douglas and F. C. Zyzyes, *ibid.*, **13**, 361t (1957).
4. D. E. Tackett, P. E. Brown, R. T. Esper, Westinghouse Atomic Power Div. Report WAPD-LSR (C)-134 October (1955).
5. E. C. Potter and G. M. W. Mann, First International Congress on Metallic Corrosion, p. 417, London, 10-15 April 1961.
6. W. A. Fraser and M. C. Bloom, *Corrosion*, **18**, 163t (1962).
7. E. M. Field, R. C. Stanley, A. M. Adams, and D. R. Holmes, Paper presented at the 2nd International Congress on Metallic Corrosion, New York City, March 11-15, 1963. In press.
8. E. C. Potter and G. M. W. Mann, *ibid.*
9. M. C. Bloom and M. Krulfeld, *This Journal*, **104**, 264 (1957).
10. M. C. Bloom, Paper presented at the 21st Annual Water Conference Engineers Society of Western Pennsylvania, Pittsburgh, October 1960.
11. J. M. Decker and J. C. Marsh, *Proc. Am. Power Conf.*, **16**, 569 (1954).
12. N. B. Pilling and R. E. Bedworth, *J. Inst. Met.*, **29**, 534 (1923).
13. U. R. Evans, "Corrosion and Oxidation of Metals," p. 834, St. Martin's Press (1960).
14. J. Markali, *Research*, **10**, 366 (1957).
15. J. V. Cathcart, J. J. Campbell, and G. P. Smith, *This Journal*, **105**, 442 (1958).
16. R. E. Pawel, J. V. Cathcart, and J. J. Campbell, "Columbium Metallurgy Proceedings of Symposium of AIME," p. 667, Interscience Publishers, New York (1961).
17. Jacques Maldy, *Compt. rend.*, **256**, 5562 (1963).
18. Comments of G. M. W. Mann and E. C. Potter in Discussion of ref. (6), *Corrosion*, **18**, 451t (1962).

An Electrochemical Technique for Removing Thin Uniform Layers of Gold

J. L. Whitton and J. A. Davies

Chalk River Nuclear Laboratories, Atomic Energy of Canada Limited, Chalk River, Ontario, Canada

ABSTRACT

A reproducible and accurate electrochemical technique for the removal of extremely thin (20Å-4000Å) uniform layers of gold has been developed. The removal was achieved by anodizing at constant current in 1M H₂SO₄ and subsequent stripping in 5N HCl. An extension of the technique allows the relatively rapid (25 μm/hr) removal of gold from single crystals in a strain-free manner. Calibration curves are shown and experimental details described.

Techniques for removing thin uniform layers from metals have been used extensively in studying the range of energetic ions in solids (1, 2) and also in investigating the effects of short range diffusion (3). For range measurements, the most reliable and sensitive technique has been the two-step process of anodic oxidation at constant voltage, followed by subsequent dissolution of the oxide. So far, this technique has been satisfactorily applied to aluminum (1), tungsten (2), and silicon (4). In each case, the protective oxide film thickness is determined mainly by the voltage and can be varied from 1000 to less than 10 atomic layers of metal. With gold, however, the same technique cannot be used, as the oxide film formed during anodizing is not protective and its final thickness therefore is not controlled by the voltage.

Barnartt (5) in a study of the oxygen-evolution reaction at gold anodes showed that gold can be oxidized in dilute H₂SO₄, but with a rather low current efficiency; the oxidation process at constant current proceeds linearly with time and is dependent on current density. He interpreted this behavior as resulting from

a "blister" mechanism in which local separation continually occurs at the oxide-metal interface, thus allowing the electrolyte to contact the exposed metal surface. Earlier attempts in this laboratory (6) to use Barnartt's method for peeling thin uniform layers from gold were not too successful. This was attributed, at least in part, to the use of a horizontal anode whose surface rapidly became coated with bubbles of oxygen during the electrolysis, thus preventing uniform attack by the electrolyte.

Recently, considerable interest has been aroused in the possibility of measuring the penetration of energetic ions in clean monocrystalline metal targets (i.e., targets that are not covered by an air-formed oxide layer). Since gold is an obvious choice for such an experiment, a reinvestigation of its anodizing behavior was undertaken in an attempt to obtain more reproducible results.

Experimental

Polycrystalline gold.—For the present study, preliminary calibrations were first carried out to determine the rate of anodic oxidation of polycrystalline

disks. A simple anode-cathode geometry, shown in Fig. 1, was used. Prior to anodizing, the disks in the as-rolled condition were cleaned by Barnartt's method of (a) degreasing, (b) cathodic cleaning in 3N NaOH at 70°–80°C at 30 ma for 10 min, and (c) immersion in 9N HNO₃ for 1 min. The cleaned gold disk was supported in a Teflon holder which fitted tightly in a 200 ml crystallizing dish containing 1M H₂SO₄. Space was left under the holder to allow room for a glass-covered magnetic stirrer, and slots were cut in the base of the holder to increase the efficiency of the stirring action. Two large gold cathodes, one on either side, were mounted against the walls of the dish and parallel to the anode. Electrical contact to the anode was made by a pointed tungsten rod which was cleaned between runs in 2N NaOH and then washed in distilled water.

The resulting oxide layer was then removed by immersion in 5N HCl and the equivalent metal thickness was determined by weight loss. All weighings were made on a microbalance to an accuracy of $\pm 2 \mu\text{g}$, using an identical gold disk as a tare in order to eliminate buoyancy corrections. Accurate weighing is necessary because, unlike tungsten and aluminum, there is no voltage control on the layer thickness: i.e., both the voltage and current remain constant throughout the anodizing. Duplicate runs on separate disks agreed within the estimated experimental error of $\pm 5\%$. A calibration curve of weight of gold removed (or weight converted to oxide) vs. anodizing time at constant current, was obtained by anodizing the gold for different periods of time at a current density of 1 ma/cm². The results (Fig. 2) show that the weight of gold removed at constant current increased linearly with anodizing time. The slope of this line is equivalent to a current efficiency of 1.7%. An increase in current density to 5 ma/cm² produced a five-fold increase in the rate of anodizing and is equivalent to an oxidation rate of 3.4 μg gold/cm²/min (17A/min).

To determine the amount of gold that dissolved in the electrolyte during anodizing, several disks were irradiated in the NRX reactor. After anodizing,

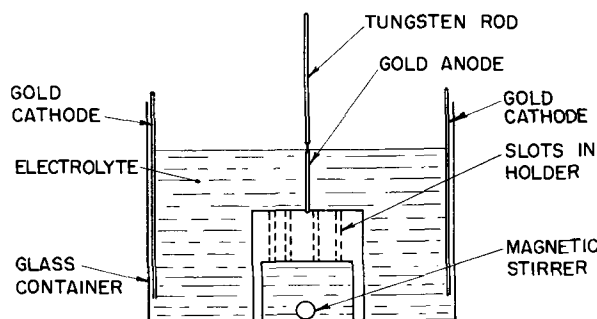


Fig. 1. Anodizing cell for polycrystalline gold disks

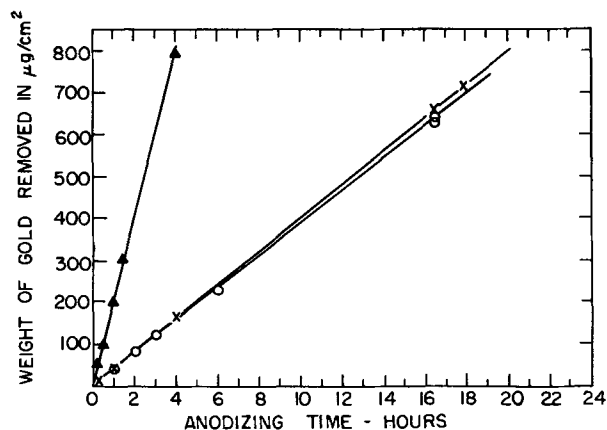


Fig. 2. Calibration of the anodizing and stripping procedure for polycrystalline gold in 1M H₂SO₄. ○X, 1 ma/cm²; ▲, 5 ma/cm².

aliquots of the electrolyte were measured for Au¹⁹⁸ content and compared with the Au¹⁹⁸ activity of the dissolved oxide layer. The fraction dissolving in the anodizing solution was found to be 1.5% of the total amount oxidized. To determine the amount of gold dissolving in 5N HCl during the dissolution of the oxide, an irradiated disk was immersed in the acid for 10 min and the activity of an aliquot was measured. No measurable activity was found. Similarly, it was found that no activity was deposited on the cathodes during the anodizing process.

In some cases the rate of anodizing gradually decreased with increasing time, but this was later found to be due to depletion of the electrolyte. It was established that about 2 μg of gold could be oxidized per milliliter of electrolyte before the 1M H₂SO₄ solution became sufficiently depleted to reduce significantly the anodizing rate.

Monocrystalline gold.—Since our interest in studying range penetrations in gold was concerned chiefly with crystal structure effects, it was necessary to extend this investigation of anodic oxidation to single crystals. For this purpose, a slightly different design of anodizing cell was required.

Monocrystalline gold rods, 0.6 cm diameter and up to 10 cm in length, were grown from 99.999% purity gold by the Bridgman method, and disks were then cut by spark machining to the desired orientation. Palatnik *et al.* (7) have shown that spark machining can produce an excess of dislocations in Bi, Sb, and Zn even at distances up to 0.25 mm from the sparked surfaces. Since it was essential in our work that the crystal faces be as strain-free as possible, it was necessary first of all to remove a thick layer, preferably 0.50 mm in order to ensure an undamaged surface. The obvious technique for doing this, namely electropolishing, has the disadvantage of being extremely slow for gold and would have required several days to remove a 0.50 mm layer.

Instead, a modified anodizing-stripping procedure was developed in which, by increasing both the concentration of H₂SO₄ and the current density, it was possible to reduce the time required to less than one day. This anodizing-stripping technique, of course, could itself be considered as a sort of electropolishing process, but one in which the oxidation and dissolution steps have been split into separate operations.

The experimental arrangement used for this purpose is illustrated in Fig. 3. The single crystal disk is fixed in the L-shaped Teflon holder by a spring-loaded tungsten rod which also provides electrical contact.¹ Such a holder allows the crystal to be mounted and demounted out of the electrolyte, which makes for easier and safer handling. The parallel gold cathodes are suspended from the top cover plate and 5 cm from each other. The gold crystal, when placed in the elec-

¹ There is no noticeable effect due to the pressure of the spring-loaded contact. This possibility was considered so the point was made as small, and the pressure as light, as possible.

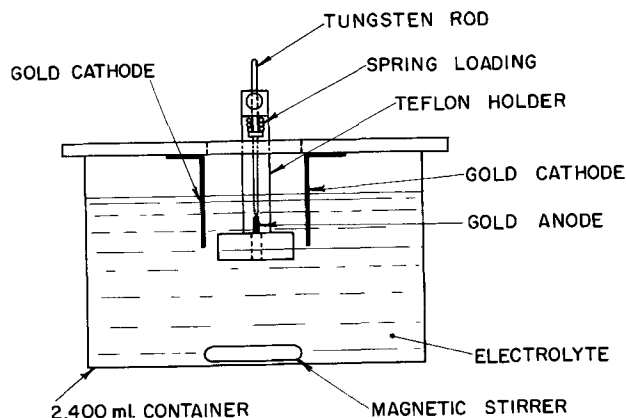


Fig. 3. Anodizing cell for monocrystalline gold rods

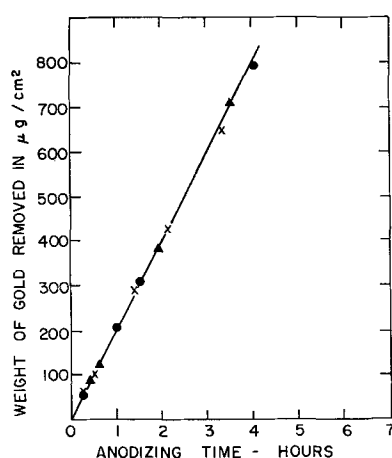


Fig. 4. Anodizing rate of: ●, polycrystalline gold, X, single crystal $\langle 112 \rangle$, and ▲ single crystal $\langle 110 \rangle$ gold in 1M H_2SO_4 at 5 ma/cm².

trolyte, is situated midway between the cathodes with the oriented faces parallel to them. The capacity of the container is 2400 ml, and the electrolyte is 10M H_2SO_4 which is constantly stirred. By using a current of 200 ma/cm², it was possible to oxidize the gold surface at the rate of 25 $\mu\text{m/hr}$. At this high current density, the oxide formed, continually flaked off the gold surface so that immersion of the specimen in HCl to dissolve the oxide layer was not necessary. After 0.50 mm of gold had been removed by this rapid anodizing treatment, the surface, although bright, was still somewhat rough, and so a brief electropolishing treatment was required.

The electropolishing was carried out in a water-cooled double-walled glass container using the same anode-cathode geometry described above. The cathode in this case was stainless steel and the current density 0.6 amp/cm² at 4v. The electrolyte was that used by Silcox and Hirsch (8), but diluted twofold. Seven hours polishing under these conditions was required to produce the desired surface finish. Electron microscopy showed that subsequent anodizing at 5 ma/cm², in 1M H_2SO_4 , did not adversely affect the electropolished surface and, in fact, actually improved it by removing the whorl-like structure which is a feature of many electropolished surfaces.

It was found that the current efficiency of the anodizing process increased from 1.7% at 5 ma/cm² in 1M H_2SO_4 to 7.9% at 200 ma/cm² in 10M H_2SO_4 , in qualitative agreement with the work of Barnartt (5) and of Jirsa and Buryanek (9). Barnartt reported a slight increase in current efficiency with increasing

current density: namely, from 0.5% at 10^{-4} amp/cm² to 1.0% at 10^{-3} amp/cm² in 0.1M H_2SO_4 . Jirsa and Buryanek investigated the effect of electrolyte concentration at 1 amp/cm² and found a significant increase: from 1.0% in 0.5M H_2SO_4 to ~30% in 18M H_2SO_4 .

The final peeling of layers for range penetration measurements in single crystals was done in 1M H_2SO_4 at either 1 ma/cm² or 5 ma/cm² in order that the calibration curves in Fig. 2 could be used. The anodizing cell arrangement was the same as that shown in Fig. 3.

As a check on the possibility of a change in the rate of anodizing with change of orientation of single crystals, disks with surfaces parallel to $\{112\}$ and disks with surfaces parallel to $\{110\}$ were anodized and calibration curves determined. These are compared with the polycrystalline calibration curve in Fig. 4 and show that the change, if any, in rate of anodizing as a function of orientation is within the estimated experimental error.

Summary

A technique for removing reproducible layers 20-4000Å thick from either polycrystalline or monocrystalline gold has been developed and calibrated. An extension of the technique to high current density enables the gold surfaces to be removed at a rate of ~25 $\mu\text{m/hr}$ without disturbing the underlying metal. This is considerably more rapid than that produced by ordinary electropolishing and is therefore a better method for obtaining a damage-free metal surface.

Manuscript received May 27, 1964; revised manuscript received July 13, 1964.

Any discussion of this paper will appear in a Discussion Section to be published in the June 1965 JOURNAL.

REFERENCES

1. J. A. Davies, J. Friesen, and J. D. McIntyre, *Can. J. Chem.*, **38**, 1526 (1960).
2. M. McCargo, J. A. Davies, and F. Brown, *Can. J. Phys.*, **41**, 1231 (1963).
3. R. E. Pawel and T. S. Lundy, U.S.A.E.C. Report ORNL-TM-575 (1963)
4. J. A. Davies, G. C. Ball, F. Brown, and B. Domeij, *Can. J. Phys.*, **42**, 1070 (1964).
5. S. Barnartt, *This Journal*, **106**, 722 (1959).
6. J. Blake, Chalk River Nuclear Labs., Private communication (1961).
7. L. S. Palatnik, A. A. Levchenko, and V. M. Kosevitch, *Dokl. Akad. Navk. S.S.S.R.*, **138**, 96 (1961). English translation in *Soviet Physics-Doklady*, **6**, 418 (1961).
8. J. Silcox and P. B. Hirsch, *Phil. Mag.*, **4**, 72 (1959).
9. F. Jirsa and O. Buryanek, *Z. Elektrochem.*, **29**, 126 (1923).

The Temperature Dependence of the Field Coefficient for the Anodization of Tantalum

R. Dreiner

Research Laboratories, Sprague Electric Company, North Adams, Massachusetts

ABSTRACT

The temperature dependence of the field coefficient B in the relation for the high field ionic current, $i = i_0 \exp[BF - (W/kT)]$, has been investigated for the anodic oxidation of tantalum. Results from constant voltage and constant current anodizations demonstrate that B is inversely proportional to the absolute temperature as expected for a barrier theory which predicts $B = a \cdot q / kT$. For the half jump distance, a , an average value of about 1.5Å was found when q was assumed to be equal to the charge on the five valent Ta-ion.

The relation between the ionic current and the field during the anodic growth of oxide films on valve metals is

$$i = i_0 \exp[BF - (W/kT)] \quad [1]$$

with k the Boltzmann constant, T the absolute temperature, and F the field across the oxide. The factor i_0 , the barrier height W , and the field coefficient B depend in their interpretation on the proposed mechanism (1), *e.g.*, whether the rate-determining barrier for the ionic motion is at the metal-oxide interface or within the oxide. Several theories agree (2) that the temperature dependence of B should be

$$B = qa/kT \quad [2]$$

with q the charge on the moving ion and a half the width of the barrier W . Adams and Kao (3) studied the formation of very thin oxide films on niobium at constant current and found agreement between the measured temperature dependence of B and Eq. [2]. Much experimental research (4) of the steady state and the transient kinetics has been reported for the anodization of tantalum which fails to show the temperature dependence of B as expressed in Eq. [2]. It was observed that plots of $\log i$ vs. field were not straight lines but very slightly curved. The curvature was such that B decreased with temperature at a constant field. To account for this, Young (5) introduced a field dependent B by making the activation distance a in Eq. [2] a linear function of the field, $a = \alpha + \beta F$. The earlier observation of a temperature independent B or Tafel slope at different fields (the inverse of B is referred to as the Tafel slope) was explained (5) by a field effect compensating the temperature effect. Later (6) the effect of condenser pressure was discussed as a possible explanation of the field dependence of coefficient B . In this paper Eq. [1] is once more applied to the anodic oxidation of tantalum at different formation fields with particular interest focused on the temperature dependence of the field coefficient B . New evaluations are presented which are based on the current decay during constant voltage formations (see Results) and on temperature changes during constant current anodizations (see Results).

Experimental

Specimens of about 18.8 cm² area and with a narrow tab were punched from 10 mil tantalum sheet (Fan-steel, impurities less than 0.1%). The samples were degreased, chemically polished for 15 sec in 5:2:2 conc H₂SO₄:conc HNO₃:48% HF, leached in boiling deionized water for 10 min, and then vacuum annealed (<10⁻⁴ Torr) at 2100°C. The tabs of the foils were anodized to a potential of about 150v to confine the area. A new foil was used for each run. Just prior to the start of the experiment the specimens (not the tabs) were etched for 20 to 30 sec in 40% HF and briefly rinsed in deionized water. Bright platinum was

used for the counterelectrode in the cell. The electrolyte was 0.1% H₂SO₄, and a pump circulated the solution through the cell and temperature baths. A two-way stopcock made it possible to circulate the electrolyte through either of two baths which were held at different temperatures. The flow rate was such that the cell was filled in three seconds.

In the earlier part of the investigations, specimens were anodized at the constant current of 1 ma/cm² to a preset voltage. At this voltage a relay switched to a constant voltage supply and the formation continued for 60 min at that constant voltage. The conditions of the constant current anodizations are described later. Currents and potentials were measured and recorded by a Keithley 610A electrometer in combination with an Esterline-Angus recorder. After formations were terminated the samples were transferred into another cell containing the same electrolyte and also bright platinum as a counterelectrode. The electrolyte was not stirred or circulated and was kept at a constant temperature of 0°C. Immediately after anodization the capacitance drops slowly with time (7) and therefore the system Ta/Ta₂O₅/electrolyte/Pt was externally shorted for 15 min before the capacitance (at 120 cps) was measured.

The charge, which had passed through the cell during the constant voltage anodization, was obtained by approximating the area of the current-time recordings by rectangles of appropriate time intervals or by approximating only the transition region in this way and by integrating.

Results

Constant voltage formations.—It is well known that the current decreases inversely proportional to time when, after a chosen formation potential has been reached, an anodization is continued at that potential. van Geel and Emmens (8) and Charlesby (9) derived an inverse time relation to explain this phenomenon. In the following an alternative derivation is given.

The oxide thickness, d , is assumed to be proportional to the total charge passed during anodization, Q

$$d = \alpha \cdot \lambda \cdot Q \quad [3]$$

where α is a current efficiency which can be temperature dependent, and λ is equal to the ratio of the equivalent weight of tantalum oxide over the product of the Faraday number times the density of Ta₂O₅ times the area of the sample. A time dependence of α may arise from the fact that the current density drops by orders of magnitude during the constant voltage part of a formation. Whether the current efficiency α is a time dependent or not was investigated by measuring the capacitance and the charge simultaneously during the constant voltage part of the formation. This was possible using a General Radio Comparator, Type 1605-A, which permits continuous capacitance recordings by comparing the unknown to a standard. The

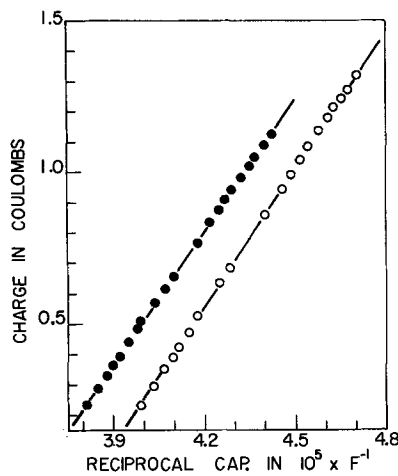


Fig. 1. Charge vs. reciprocal capacitance; charge and capacitance simultaneously measured during constant voltage anodizations; formation temperature, ●, 20°, ○, 60°C.

measuring frequency was 1 kc. Young (10) determined the density of anodic tantalum oxide, $\rho = 7.93 \text{ g/cm}^3$, which is consistent with a dielectric constant of $\epsilon = 27.6$ at 1 kc.

Substituting the expression for the parallel plate capacitor into Eq. [3] yields

$$Q = (1.48 \times 10^{-5}/\alpha) \times (1/C) \quad [4]$$

The constant is calculated with Young's (10) data. (The constant λ in Eq. [3] is $3.07 \times 10^{-6} \text{ cm/coul.}$)

Figure 1 is a plot of charge vs. $1/C$ for runs at 20° and 60°C and a linear relation is obvious which indicates that α is not a function of time. This is in agreement with results reported by Bernard and Cook (11) who studied the constant voltage formation of aluminum. The charge is counted from the start of the constant voltage formation. The first points were measured at 20 sec after the switch to constant voltage anodization and the last ones at 6000 sec. Only these constant voltage formations were extended to 100 min. During this period the current dropped from $\sim 400 \mu\text{a/cm}^2$ to $\sim 2 \mu\text{a/cm}^2$. The equations for the regression lines of Fig. 1 are

$$20^\circ\text{C}: Q = (-5.33 \pm 0.01) + (1.46 \pm 0.01) \times 10^{-5} \times 1/C \quad [5]$$

$$60^\circ\text{C}: Q = (-5.84 \pm 0.01) + (1.52 \pm 0.01) \times 10^{-5} \times 1/C \quad [6]$$

with the correlation coefficients better than [0.9996]. By definition the correlation coefficient (12) is |1| when a functional relation between two variables is perfectly linear. The intercepts are -0.77 coul (5) and -0.65 coul (6) when the charge passed at constant current is added. From the slopes the α values were calculated to be 1.01 for the 20°C and 0.97 for the 60°C formation. Besides a temperature influence, the magnitude of α depends on the constant in Eq. [4] and on the experimental conditions for the capacitance measurement. The slopes of Fig. 1 are independent of constant additive quantities of the charge and the reciprocal capacitance (the latter would arise if a constant capacitor were in series). The effect of a bias potential, here the formation potential, on the capacitance is not straightforward. Smyth *et al.* (13) reported that with the bias close to the formation potential the capacitance was not only influenced by the bias voltage but by the time the potential was applied. This effect was unrelated to oxide growth. It is known that the capacitance is a function of frequency, and the constants of this relation depend on film-thickness. Young (14) pointed out that the percentage change in reciprocal capacity for a given change in log (frequency) tends to be independent of thickness. Therefore, the slopes of Fig. 1 would be affected by a change in measuring

Table I.

Form. temp, °C	Time, sec	Q_{total} , coul.	i , ma	$i^2 \Delta(1/Q^2)$, $10^{-11} \text{ amp}^2/\text{coul}^2$	$(2i/Q^2) \cdot \Delta i$, $10^{-11} \text{ amp}^2/\text{coul}^2$	Ratio, %
13.5	1200	5.37	0.123	1.43	45.0	3.2
	3600	5.53	0.042			
	1800	5.43	0.084	0.52	17.6	2.9
	3600	5.53	0.042			
	2400	5.48	0.062	0.19	7.03	2.7
	3600	5.53	0.042			
80.0	1200	6.60	0.179	2.16	63.0	3.4
	3600	6.84	0.061			
	1800	6.69	0.122	0.75	24.4	3.1
	3600	6.84	0.061			
	2400	6.76	0.093	0.29	10.5	2.8
	3600	6.84	0.061			

frequency since the oxide thickness increased during the constant voltage part of the formation by about 20%. Furthermore, the dielectric constant increases (15) while densities decrease with temperature. The first dependency would cause the slope, $\partial Q/\partial(1/C)$, to be larger at higher temperatures and the latter would affect it in the opposite way. The discussion leads to the conclusion that the different slopes of Eq. [5] and [6] can only be tentatively assigned to a temperature dependence of the current efficiency.

With $F = V/d$ and Eq. [1] and [3], one obtains for constant V, T , and time independent α ,

$$\partial i/\partial t = -(B \cdot V \cdot \alpha \cdot \lambda/d^2) \cdot i^2 \quad [7]$$

If the variation of $(1/d^2)$ with time is sufficiently small with respect to the change in i^2 , integration becomes possible since $(1/d^2)$ could be considered a constant. To be more specific, it has to be shown that $i^2 \cdot \Delta(1/Q^2)$ is small with respect to $(2i/Q^2) \cdot \Delta i$, which is the case as seen from Table I in which the thickness is replaced by the charge. For the comparison the current efficiency is of no importance. Integration of Eq. [7] on this basis yields

$$1/i = (B \cdot V \cdot \alpha \cdot \lambda/d^2) \cdot t + \text{const} \quad [8]$$

Thus the slopes of reciprocal current vs. time plots are proportional to the field coefficient B . Figure 2 is a plot of the reciprocal current vs. time. The data in Table I and in Fig. 2 are from the same runs at 13.5° and 80°C. In both cases the time origin is the switch from constant current to constant voltage. The equations for the regression lines at 80° and 13.5°C are

$$1/i = (2.4 \pm 0.7) \cdot 10^2 + (4.41 \pm 0.02) \cdot t \quad [9]$$

$$1/i = (-1.6 \pm 1) \cdot 10^2 + (6.72 \pm 0.03) \cdot t \quad [10]$$

The correlation coefficient is in both cases better than [0.998]. A slight curvature, which one might have expected from the approximation for the integration, was not detected.

The thickness d in Eq. [8] was replaced in two ways since d is proportional to the charge and to the reci-

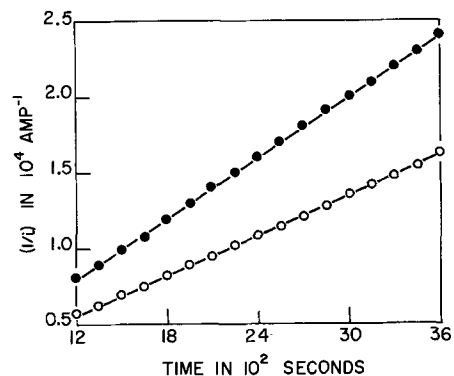


Fig. 2. Reciprocal current as a function of time; the time origin is the switch from constant current to constant voltage anodization.

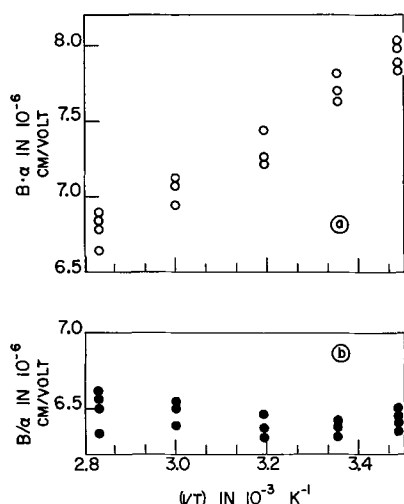


Fig. 3. Product of field coefficient B times current efficiency α , (a), and ratio of B over α , (b), as a function of the reciprocal absolute temperature; oxide thickness determined by: ●, charge and, ○, capacitance measurements.

procal capacitance. If the capacitance is measured (here always at 120 cps; 0°C; capacitor shorted 15 min after anodization) and the formula for the parallel plate capacitor is applied, Eq. [8] changes to

$$1/i = [B \cdot V \cdot \alpha \cdot \lambda \cdot C^2 / (\epsilon \epsilon_0 A)^2] \cdot t + \text{const} \quad [11]$$

Thus from slopes and capacitance measurements of runs at different temperatures, values for the product $B\alpha$ as a function of temperature were obtained, Fig. 3a. Substituting Eq. [3] in Eq. [8] yields

$$1/i = (BV/\alpha \cdot \lambda \cdot Q^2) \cdot t + \text{const} \quad [12]$$

and as seen, values for the ratio B/α can be calculated from the slopes and charge measurements, Fig. 3b. Values for the slopes $\partial(1/i)/\partial t$ were always determined over the time range 1200-3600 sec, Fig. 2. During this time the charge and, therefore, the oxide thickness increased slightly, Table I. A constant slope $\partial(1/i)/\partial t$ would imply that the field coefficient B is a function of thickness. Such a conclusion is objectionable since the detection of a slight curvature in a plot like Fig. 2, which would compensate an apparent thickness dependence of B , appeared to be beyond the experimental accuracy.

The data for current efficiency, α , which are listed in Table II, were calculated from the least square lines of Fig. 3a, b.

Table II confirms the earlier result that the current efficiency is a function of temperature. It may be considered surprising that α turns out to be larger than 1. Basically α is determined from the ratio $[\epsilon \epsilon_0 \cdot A^2 \cdot 96500 \cdot \rho] / [(equiv \text{ wt } Ta_2O_5) \cdot Q \cdot C]$ after measuring the charge, Q , the capacitance, C , and the area, A . An error in these quantities and in the choice of the dielectric constant, ϵ , and the density, ρ , may well account for α -values larger than one. After correcting for α the final values for the field coefficient B were plotted vs. the inverse of the absolute temperature in Fig. 4. The least square line is

$$B = (4.5 \pm 0.1) \times 10^{-6} + (0.75 \pm 0.11) \times 10^{-3}/T \quad [13]$$

So far all the data which have been discussed were obtained from anodizations to 97v. Data from formations

Table II. Data for current efficiency

Temperature, °C	α
13.5	1.11
25	1.09
40	1.07
60	1.04
80	1.02

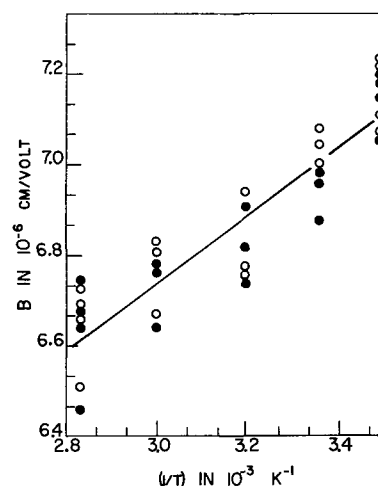


Fig. 4. Temperature dependence of field coefficient B ; oxide thickness determined from: ●, charge and, ○, capacitance measurements.

to 77v were evaluated in the same way and the regression line of a graph like Fig. 4 is

$$B = (3.6 \pm 0.1) \times 10^{-6} + (1.0 \pm 0.1) \times 10^{-3}/T \quad [14]$$

The correlation coefficients which should be 1 for a linear relation are 0.94, Eq. [13], and 0.98, Eq. [14]. Equations [13] and [14] demonstrate that the field coefficient B is inversely proportional to the absolute temperature as predicted by theory. However these equations differ strongly from Eq. [2] as far as the zero intercept, $1/T \rightarrow 0$, is concerned. If the fivefold ionized tantalum ion is the only current carrier, an assumption which is not necessarily justified (16), then half jump distances can be calculated from the slopes of Eq. [13] and [14]. Half the distances between equilibrium positions of the moving ion are 1.3Å for formations to 97v and 1.7Å for anodizations to 77v. Since the uncertainties of the slopes, $\partial B/\partial(1/T)$, almost overlap, no significance is seen in the different distances.

Constant current formation.—It is well known that the voltage increases linearly with time during a constant current anodization. From Eq. [1], [2], [3] and $F = (V_0 + V)/(d + d_0)$, where V_0 and d_0 are the electrochemical reaction potential (assumed to be independent of temperature) and the thickness of an initial oxide layer, the voltage build-up rate during constant current formations is

$$(1/\alpha) (\partial V/\partial t) = \frac{\lambda \cdot i \cdot W}{q \cdot a} + \frac{\lambda \cdot i \cdot k \cdot \ln(i/i_0)}{q \cdot a} \cdot T \quad [15]$$

Thus the voltage build-up rate should be a linear function of temperature if, as assumed for the derivation, the field coefficient B is related to temperature as expressed in Eq. [2]. If B , however, is independent of temperature, then it can be shown that the build-up rate should be proportional to the reciprocal absolute temperature.

From all the experiments which led to Eq. [13] and [14], the voltage-time recordings of the part of anodization which occurred at constant current were evaluated. Straight lines were fitted to the data using the least square method. Here the correlation coefficients were all better than |0.9995| which confirms that the voltage increases linearly with time during a constant current formation.

The equations for the regression lines of plots $(1/\alpha) (\partial V/\partial t)$ vs. temperature, Fig. 5, and vs. reciprocal absolute temperature are

$$(1/\alpha) \partial V/\partial t = (0.488 \pm 0.002) - (4.94 \pm 0.13) \times 10^{-4} \times T \quad [16]$$

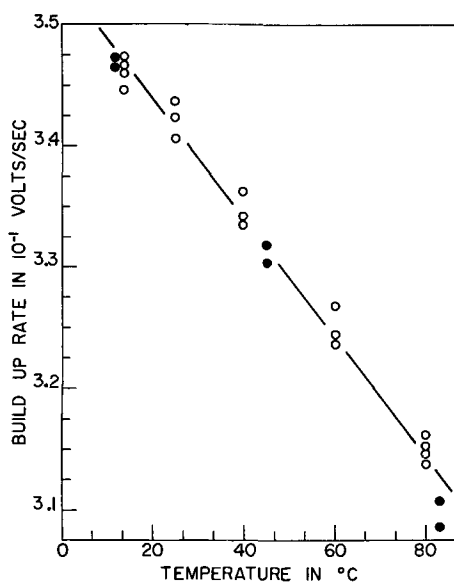


Fig. 5. Voltage build-up rate of constant current anodizations, 1 ma/cm², as a function of temperature; samples anodized to, ○, 97v and, ●, 77v.

$$(1/\alpha) \partial V/\partial t = (0.174 \pm 0.002) + (4.98 \pm 0.17) \times 10^{-1} \times 1/T \quad [17]$$

The correlation coefficient for the build-up rate as a function of temperature is |0.993| and |0.988| for $(1/\alpha) \partial V/\partial t = f(1/T)$. Although this is slightly in favor of the first case, which would imply that field coefficient B is inversely proportional to the absolute temperature, the difference is not decisive enough to discard the possibility that B is independent of temperature. However, these findings, obtained from the constant current part of the formations, at least do not contradict the earlier results from the constant voltage part of the anodizations, namely, that B is a function of temperature.

The voltage build-up rate ($\partial V/\partial t$) is not affected by a constant electrochemical reaction potential or an initial air oxide film, whereas the field is. Disregarding these uncertainties, which is permitted for thicker films, the voltage build-up is directly proportional to the field (divide Eq. [15] by $(\lambda \cdot i)$ and the left side becomes the field). If field coefficient B is independent of temperature, it can be shown that a plot field *vs.* the reciprocal absolute temperature should be a straight line with a slope independent of the formation current density. Bray *et al.* (17) observed this for the anodization of tantalum and concluded that B is not a function of temperature. Very recently Draper and Jacobs (18) reported that the field is directly proportional to temperature when tantalum samples were anodized in 0.1N H₂SO₄. However deviations from this relation were observed at higher temperatures (75° and 90°C) for formations in 40% H₂SO₄.

It was decided to try another approach rather than to repeat the experiments leading to Fig. 5 and to find out whether intercept and slope of Eq. [15] depend on current density in the right way. Assuming again that B is related to temperature, as expressed in Eq. [2], then with Eq. [1] and $F = (V + V_o)/(d + d_o)$ follows for the derivative of the voltage with respect to temperature during constant current anodization

$$\partial V/\partial T = \frac{(\alpha \cdot \lambda \cdot Q + d_o) \cdot k}{q \cdot a} \ln(i/i_o) \quad [18]$$

Here film thickness d was replaced by Eq. [3]. As seen, the voltage change due to a given temperature rise or drop should be a linear function of the total charge with the slope depending on the current den-

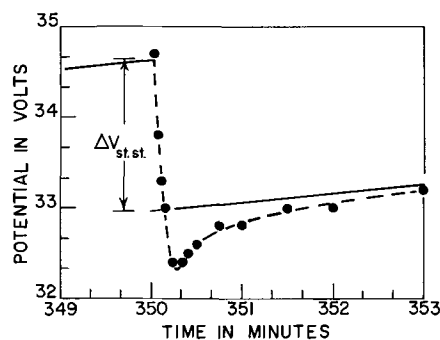


Fig. 6. Potential transient due to an abrupt temperature rise from 25.5° to 40.0°C during a constant current ($\sim 5.3 \mu\text{a}/\text{cm}^2$) anodization; solid lines are regression lines of the steady-state voltages.

sity and the intercept depending on d_o and the current density. A necessary assumption is that the thickness remains constant during the temperature change. This is the case if the current density is low and the temperature change fast enough.

In the experimental part it was mentioned that a pump circulated the electrolyte through the cell and a temperature bath with a flow rate such that the cell was filled up in 3 sec. Therefore, 10 sec is considered a very safe estimate for the transition period from T_1 to T_2 . The chosen anodization currents were 10⁻³ amp ($\sim 53 \mu\text{a}/\text{cm}^2$) and 10⁻⁴ amp ($\sim 5.3 \mu\text{a}/\text{cm}^2$). With the higher current the change in thickness is less than about 3Å (Eq. [3]; α taken as 1). The temperature was changed between 25.5° and 40°C. Over this temperature range an influence of the temperature dependence of the current efficiency should be small and is, therefore, neglected (see Table I).

Figure 6 is a plot of voltage *vs.* time of an anodization at constant current ($\sim 5.3 \mu\text{a}/\text{cm}^2$) during which the temperature was raised from 25.5° to 40°C at about 350 min of anodization. The solid lines are the regression lines of the steady state. When the temperature increased, the potential dropped rapidly to a minimum and then approached the new steady state. Overshoots were observed when the formation current density was abruptly varied during the anodization of tantalum (19). Figure 6 demonstrates a similar effect which was caused by a rapid temperature change. The difference between the steady-state voltages at the moment of the temperature change is plotted *vs.* the total charge passed in Fig. 7. ΔV was always calculated from regression lines of the steady-state voltage build-up. The magnitude of ΔV was independent of the sign of ΔT ; i.e., whether the temperature was raised from 25.5° to 40°C or dropped from 40° to 25.5°C. The temperature was changed back and forth during some of the runs; 3.3 coul and 3.9 coul were passed at a current of 10⁻³ amp in order to decrease the formation times of the runs yielding the last three points of the upper curve. The equations for the least square lines of the upper and lower curve are

$$\Delta V = (0.05 \pm 0.1) + (0.71 \pm 0.02) \cdot Q \quad [19]$$

$$\Delta V = (0.2 \pm 0.09) + (0.58 \pm 0.01) \cdot Q \quad [20]$$

with the correlation coefficients of |0.996| in both cases. These linear relations again point out that the field coefficient B of Eq. [1] is a function of temperature.

From the ratio of the slopes of Eq. [19] and [20], i_o is calculated to be 29 amp ($\sim 1.5 \text{ amp}/\text{cm}^2$). i_o is very sensitive to the ratio of the slopes. A 5% drop, which is almost within the standard deviations, would increase i_o to about 10² amp/cm². Combining either slope $\partial(\Delta V)/\partial Q$ of Eq. [19] or [20] with the ratio of these slopes leads to an activation distance of $a \simeq 1.46\text{\AA}$. This value is in very good agreement with the average half jump distance of 1.5Å derived from con-

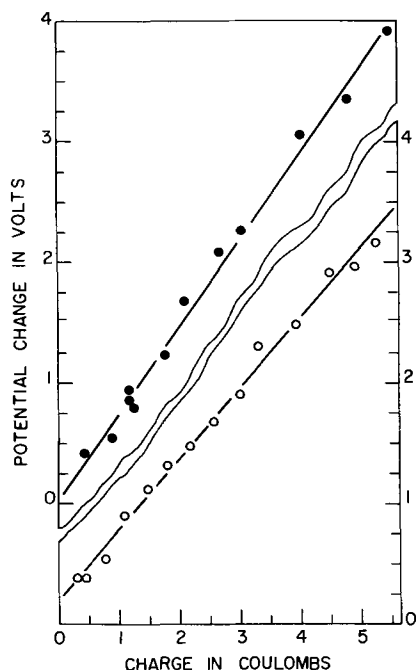


Fig. 7. Change in steady-state voltage as a function of total charge passed during constant current (●, $\sim 5.3 \mu\text{a}/\text{cm}^2$; ○, $\sim 53 \mu\text{a}/\text{cm}^2$) anodizations; potential change caused by a rapid temperature rise or drop between 25.5° and 40.0°C .

stant voltage formations. These values for the pre-exponential factor and the half jump distance may be compared with data already reported in ref. (1).

All of the experimental evidence of this work points out that the field coefficient B is inversely proportional to the absolute temperature and therefore Eq. [16] represents the right relation between the voltage build-up rate at constant current and temperature. From the combinations of the slopes of Eq. [15], [16] with the slopes of expressions [18], [19] and [18], [20] one gets $i_0 \approx 25 \text{ amp}$ ($\approx 1.4 \text{ amp}/\text{cm}^2$), $a \approx 1.44 \text{ \AA}$ and $i_0 \approx 19.5 \text{ amp}$ ($\approx 1 \text{ amp}/\text{cm}^2$), $a = 1.38 \text{ \AA}$. These half jump distances are again in good agreement with the above reported values. With an average $a = 1.43 \text{ \AA}$ from the constant current experiments and the value for the intercept, $T = 0$, of Eq. [16], the activation energy is determined to be $W \approx 0.61 \text{ ev}$.

From the current change at constant field due to a stepwise temperature variation and from Eq. [1] and [2] it follows that

$$W = q \cdot a \cdot F - \frac{K \cdot \ln(i_2/i_1)}{(1/T_2) - (1/T_1)} \quad [21]$$

where i_1 , T_1 and i_2 , T_2 are the respective quantities before and after (but at the moment of) the temperature variation. With a , the half jump distance, taken as 1.5 \AA and the data of several experiments, an average activation energy of $W \approx 1.2 \text{ ev}$ was calculated. The field was determined by the charge. Above, an activation energy of about 0.6 ev was calculated which was obtained from a value for the intercept, $T = 0$, of Eq. [15]. This latter method is identical with a determination of W from only the first right side term of Eq. [21]. But this term depends on the field, and therefore the difference between $W \approx 0.6 \text{ ev}$ (from the intercept of Eq. [15]) and $W \approx 0.4 \text{ ev}$, obtained from the first term of Eq. [21] and the field at the moment of temperature change in Fig. 8, is not surprising.

An "overshoot" was observed, as demonstrated in Fig. 6, when a rapid temperature variation altered the field across the oxide while the anodization current was kept constant. The effect of an almost identical temperature change on the current while the field across the oxide was kept constant is shown in Fig. 8. A sample was anodized at a constant current

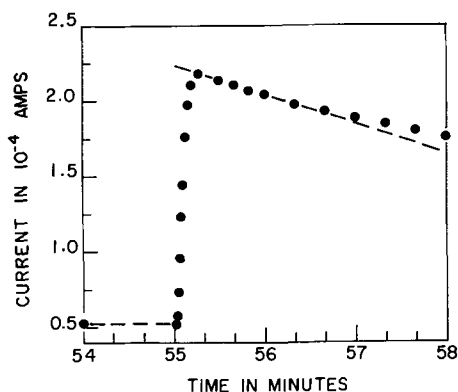


Fig. 8. Current change due to an abrupt temperature rise from 25.5° to 40.3°C during a constant voltage (97v) formation.

of $1 \text{ ma}/\text{cm}^2$ to 97v and then the formation continued at that potential. The current was measured as a potential drop across 10^2 ohms in series with the cell and the time origin is the switch from constant current to constant voltage anodization. At $t = 55 \text{ min}$ the temperature was rapidly changed from 25.5° to 40.3°C and, as seen from Fig. 8, the current increased quite substantially and then decreased slowly. However, the current-time curve does not exhibit any transient or "overshoot." It was found that this lack of overshoot cannot be attributed to the different oxide thicknesses on the samples used for Fig. 6 and 8. Another possibility, the stepwise current variation, which also changes the field across the oxide, was investigated by Dewald (20) during the anodic oxidation of tantalum at constant temperature and an overshoot was observed. It is, therefore, concluded that the mechanism of the overshoot is related to rapid changes of the field across the oxide layer.

Summary

A linear relation between the reciprocal current and the time was derived for the current decay during constant voltage anodizations. It was shown that the current efficiency was independent of time. The field coefficient B was determined from slopes of $1/i$ vs. time plots and values for the film thickness. The film thickness was obtained both from charge and capacitance measurements. The two methods led to different slopes for the temperature dependence of B . This discrepancy was due to the temperature dependence of the current efficiency, and corrections for this yielded B as a linear function of the reciprocal absolute temperature.

The voltage build-up as a function of temperature and the change in the steady-state voltage due to a given variation of temperature as a function of oxide thickness were investigated during constant current anodizations. The results confirmed that B is a function of temperature as predicted by theory. Except for the overshoots, demonstrated in Fig. 6, the data are compatible with a single barrier mechanism at the metal-oxide interface. Assuming that the five valent Ta-ion is the principal current carrier, the barrier height and half of the barrier width were calculated to about 1.2 ev and about 1.5 \AA which is close to the ionic radius of oxygen ($\text{O}^{2-} = 1.40 \text{ \AA}$) (21).

Acknowledgment

The author is grateful for valuable discussions with Dr. K. Lehovc, Dr. G. Shirn, Dr. D. Smyth, and J. R. Schimmel of these laboratories.

Manuscript received April 9, 1964; revised manuscript received July 12, 1964. This paper was presented at the Toronto Meeting, May 3-7, 1964.

Any discussion of this paper will appear in a Discussion Section to be published in the June 1965 JOURNAL.

REFERENCES

1. L. Young, "Anodic Oxide Films," Academic Press, London and New York (1961).
2. See ref. (1), p. 25.
3. G. B. Adams and T. Kao, *This Journal*, **107**, 640 (1960).
4. For specific references, see ref. (1), p. 115.
5. See ref. (1), p. 101.
6. L. Young, *This Journal*, **110**, 589 (1963).
7. L. Young, *Acta Met.*, **4**, 100 (1956).
8. W. Ch. van Geel and H. Emmens, *Z. Phys.*, **87**, 220 (1933).
9. A. Charlesby, *Proc. Phys. Soc.*, **66**, 317 (1953).
10. L. Young, *Proc. Roy. Soc.*, **A244**, 41 (1958).
11. W. J. Bernard and J. W. Cook, *This Journal*, **106**, 643 (1959).
12. E. L. Crow, F. A. Davis, and M. W. Maxfield, "Statistics Manual," Chapt. 6, Dover Publications, New York.
13. D. M. Smyth, G. A. Shirn, and T. B. Tripp, *This Journal*, **110**, 1264 (1963).
14. L. Young, *Trans. Faraday Soc.*, **51**, 1250 (1955).
15. R. W. Berry and D. L. Sloan, *Proc. IRE*, **47**, 1070 (1959).
16. J. A. Davies and B. Domeij, *This Journal*, **110**, 849 (1963).
17. A. R. Bray, P. W. M. Jacobs, and L. Young, *Proc. Phys. Soc.*, **71**, 405 (1958).
18. P. H. G. Draper and P. W. M. Jacobs, *Trans. Faraday Soc.*, **59**, 2895 (Dec. 1963).
19. See ref. (1) p. 102.
20. J. F. Dewald, *J. Phys. Chem. Solids*, **2**, 55 (1957).
21. L. Pauling, "The Nature of the Chemical Bond," 3rd ed, p. 514, Cornell University Press (1960).

The Density and Surface Tension of Molten Fluorides

II. The System NaF-LiF-ZrF₄

G. W. Mellors and S. Senderoff

Development Department, Parma Research Laboratory, Union Carbide Corporation, Parma, Ohio

ABSTRACT

Earlier studies of the surface tension of the system KF-LiF-ZrF₄ have been extended to the system NaF-LiF-ZrF₄. As was noted previously, plots of surface tension vs. log concentrations of ZrF₄ give a series of straight lines with inflection points at concentrations corresponding to the stoichiometry of complex compounds in the liquid. The strength of complexes in the latter system is found to be less than that in the former, and the complex ion [ZrF₅]⁻¹, while present in the former, is not observed in the latter. The ZrF₇⁻³ ion exists in solution in both systems.

In a recent publication (1) the densities and surface tensions of a number of molten fluoride systems were described. This report describes further work carried out with ZrF₄ dissolved in the eutectic mixture of NaF and LiF (mole ratio = 2:3) and compares and contrasts the results now obtained with those of the KF-LiF-ZrF₄ system.

Experimental

Materials.—NaF and LiF (ACS specification) were obtained from Harshaw Chemical Company. ZrF₄ was obtained from General Chemical Division, Allied Chemical and Dye Company. Argon was obtained from Linde Division, Union Carbide Corporation.

Apparatus.—This was similar to that described previously (1).

Temperature and measurements.—These were made as before using "Chromel-Alumel" thermocouples.

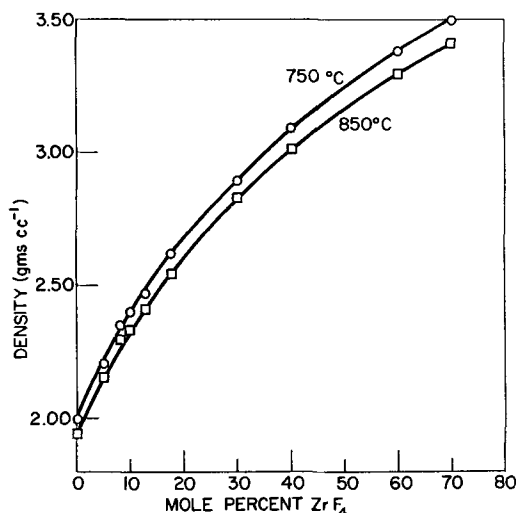


Fig. 1. Density vs. composition, NaF-LiF-ZrF₄

The general procedure, method of calculation and accuracy of the methods for determination of density and surface tension have been discussed earlier (1).

Results

Density.—The plots of density vs. temperature were in all cases straight lines while density as a function of composition has the form shown in Fig. 1.

Surface tension.—Figure 2 shows typical plots of surface tension as a function of temperature. In all cases these are straight lines and the temperature coefficient, $d\gamma/dT$ varies from -0.08 to -0.11 dyne $\text{cm}^{-1} \text{deg}^{-1}$. In Fig. 3 the surface tension is plotted against composition for the system at 800°C. It is a reasonably smooth curve up to 60 mole % ZrF₄ above which composition excessive volatility precluded further measurements.

Discussion

Surface tension is a thermodynamic property and the analogy between the various thermodynamic

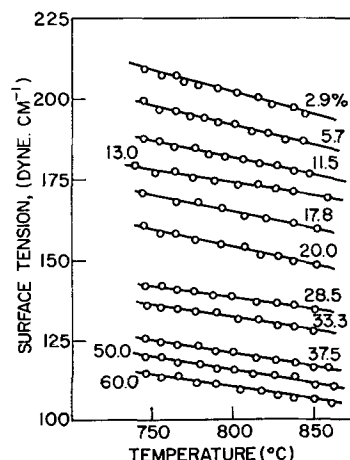


Fig. 2. Surface tension vs. temperature, NaF-LiF-ZrF₄

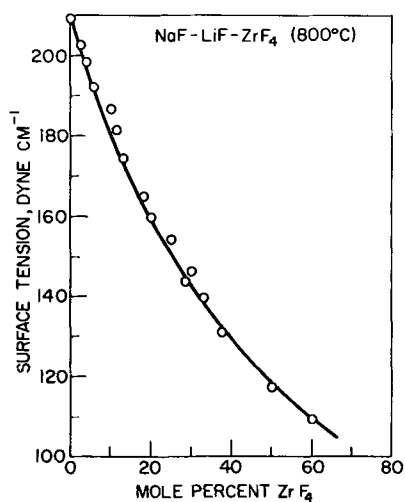


Fig. 3. Surface tension vs. composition

measurements designed to yield activity coefficient data has been discussed previously (1). It was noted, for instance, that the Gibbs adsorption equation

$$\frac{d\gamma}{d \ln n \alpha} = -RT\Gamma \quad [1]$$

[where γ is the surface tension (or surface free energy), n is the bulk concentration, α is the activity coefficient, and Γ is the surface excess (or deficiency) concentration of a species] is identical in form to the usual equations involving the free energy, such as

$$\frac{dF}{d \ln n \alpha} = -RT \text{ used with vapor pressure, cryoscopy}$$

or similar measurements, or $\frac{dE}{d \ln n \alpha} = RT$ used with

emf measurements, except for the term Γ . Since both α and Γ are unknown variables in Eq. [1], α cannot be directly determined from a measurement of the surface free energy, γ , as it can from measurements of a colligative property of the system. However, if sudden changes at significant compositions are observed in the plot of surface tension, γ , vs. log of the concen-

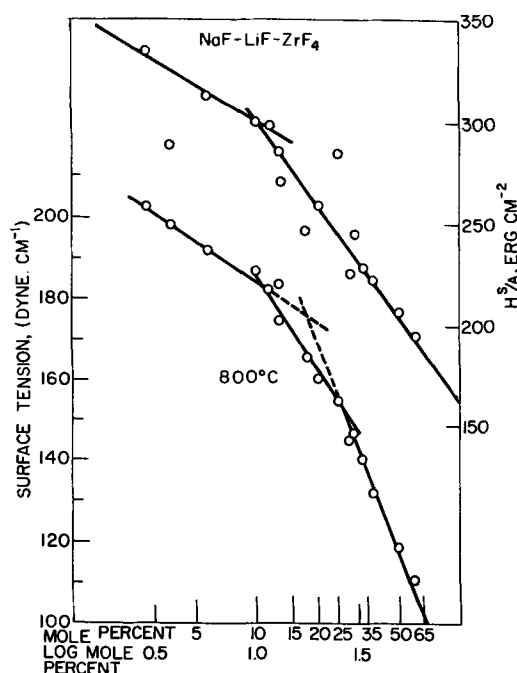
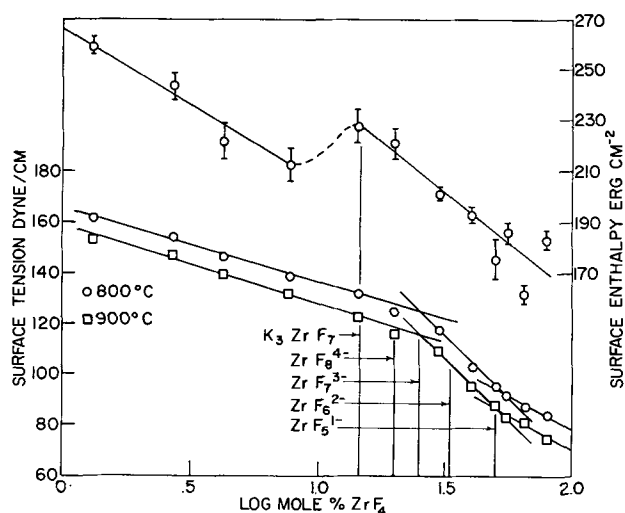


Fig. 4. Surface tension and surface enthalpy vs. log mole composition.

Fig. 5. Surface tension and surface enthalpy vs. log mole composition (KF-LiF-ZrF₄).

tration one may use these discontinuities to draw inferences regarding complex species, just as one uses sudden changes in the activity coefficient (rather than its actual value) for the same purpose. In Fig. 4 this plot is shown for the NaF-LiF-ZrF₄ system at 800°C. Although the measurements could not be carried out at concentrations greater than 60 mole % ZrF₄, the linear logarithmic extrapolation to pure ZrF₄ gives a value of 80 dynes cm⁻¹ which is identical with that obtained in the extrapolation of the KF-LiF-ZrF₄ system reported earlier (1). In the latter case experimental values were obtained up to 80 mole % ZrF₄.

The breaks in Fig. 4 occur at 10.7 mole % ZrF₄ and 26.3 mole % ZrF₄. The latter is believed to arise from $3M^+ [ZrF_7]^{-3}$ (25 mole % ZrF₄). To account for the former one notes that Na₃ZrF₇ (~11.7 mole % ZrF₄) is a solid phase found in equilibrium with the melt (3) at the 604° eutectic temperature. It was suggested in the earlier paper (1) that the effect of such a stable compound on the liquid considerably above its liquidus suggests a nonrandom distribution of the cations around the $[ZrF_7]^{-3}$ anions. While no un-ionized Na₃ZrF₇ exists, some clustering probably occurs at temperatures well above its solidification. Also shown in Fig. 4 is a plot of surface enthalpy vs. the logarithm of the concentration. The surface enthalpy, H^s/a , is calculated from the relation

$$H^s/a = \gamma + T \frac{d\gamma}{dT}$$

The variation of H^s/a with concentration is similar to that of the surface tension with inflections at approximately the same values.

For comparison, Fig. 5 shows the surface tension and the surface enthalpy plotted against the logarithm of the concentration for the KF-LiF-ZrF₄ system. In that system sharp breaks at 25 mole % (M_3ZrF_7) and 50 mole % ($M^+ [ZrF_5]^{-1}$) occurred in the surface tension curve, whereas a large inflection assigned to K_3ZrF_7 at 14 mole % occurred in the H^s/a vs. logarithm composition curve. It is noteworthy that no inflection appears at 50 mole % ZrF₄ in the NaF-LiF-ZrF₄ system. This would indicate the absence of any strongly bound $[ZrF_5]^{-1}$ complex in this system which is consistent with the findings of Sense who deduced that a vapor-phase complex with a mole ratio of NaF:ZrF₄ smaller than 1.38 exists in the NaF-ZrF₄ binary system (2a). He at first thought it might be NaZrF₅ (2a), but later suggested that it was more probably NaZr₂F₉ (2b). The study of the surface tension above 60 mole % ZrF₅, however, was prevented by the high volatility of the system. It is also interesting to note that

Na_3ZrF_7 , K_3ZrF_7 , and KZrF_5 are congruently melting compounds in the appropriate binary systems while NaZrF_5 is not a congruently melting compound in the NaF-ZrF_4 system (3). Also, Sense *et al.* (2a) have noted a constant boiling mixture in the NaF-ZrF_4 binary corresponding in composition to Na_3ZrF_7 .

Since a sharp break at 14 mole % in the KF-LiF-ZrF_4 system appears in the enthalpy curve with little or no inflection at that point in the free energy curve, then it must be concluded that both the surface entropy and enthalpy change rapidly near this composition, whereas in the sodium-containing system it follows that since both H^s/a and γ curves inflect at around 10~11 mole % ZrF_4 , then there must be virtually no sudden change in the entropy. This suggests that the distribution of solvent cations in the vicinity of the $[\text{ZrF}_7]^{-3}$ is more random in the NaF-LiF solvent than in the KF-LiF system.

In a series of investigations of the effect of alkali halide dilution of cerium chloride (4,5) it was found that the strongest complexes, as measured by negative deviations from ideality, were found in KCl-CeCl_3 systems, sodium chloride diluent led to weaker complexes, while calcium chloride solvent resulted in nearly ideal behavior with possibly some slight positive deviation. This effect was related to the quantity Z/r^3 of the solvent cation, where Z is the charge and r the (Pauling) ionic radius (6). The strength of the chlorocerium complexes decreased with increasing values of Z/r^3 of the solvent cation.

The same would be expected to hold in the present case where an average Z/r^3 can be derived for both solvents from the formulas

$$[Z/r^3]_{A/B} = N_A (Z/r^3)_A + N_B (Z/r^3)_B$$

$$[Z/r^3]_{\text{KF/LiF}} = 2.53 [Z/r^3]_{\text{NaF/LiF}} = 3.246$$

On this basis the complexing of ZrF_4 in the KF-LiF solvent would be greater than in the NaF-LiF solvent; this is borne out by the γ and H^s/a data. Also if one calculates the deviation from so-called ideality by the method of Guggenheim, it appears that the plot of γ vs. composition for NaF-LiF-ZrF_4 is more nearly ideal than that for KF-LiF-ZrF_4 .

According to Guggenheim (7) for an equimolar mixture

$$\gamma_G = \bar{\gamma} - \frac{\Delta^2 a}{\gamma k T}$$

where $\bar{\gamma} = (\gamma_1 + \gamma_2)/2$, $\Delta = \gamma_1 - \gamma_2$, a is the area per single molecule, k the Boltzmann constant, and T temperature, °K.

γ_G is 125.8 dyne⁻¹ cm⁻¹ for NaF-LiF-ZrF_4 at 800°C compared with 118 dyne cm⁻¹ measured experimentally, or a negative deviation of 6%. For the KF-LiF-ZrF_4 system $\gamma_G = 112.8$ dyne cm⁻¹ compared

with the experimental value of 98 dyne cm⁻¹, or a negative deviation of 13%.

It must be noted that the basis of this equation is the interaction of two ideal liquids, a condition which is somewhat far removed from the present systems under investigation.

Neither system studied shows any $[\text{ZrF}_6]^{-2}$ ions in the liquid state although the hexafluoro-zirconate is the compound most easily obtained in the solid. This would suggest that the most stable coordination number increases on melting, although it is possible that surface tension measurements are insufficiently sensitive to resolve the breaks due to intermediate structures.

The higher volatility of ZrF_4 from the NaF-LiF solvent than from the KF-LiF solvent is another factor supporting the theory of less tight complexing in the former case.

Conclusions

1. Sharp variations of surface thermodynamic properties are observed in the liquid at concentrations corresponding to the most stable congruently melting compounds in the system. Since this is observed as much as 100°C above the melting point considerable ordering in the liquid state is indicated.

2. The $[\text{ZrF}_7]^{-3}$ ion exists in solution in both the KF-LiF and the NaF-LiF solvents.

3. $[\text{ZrF}_5]^{-1}$ is observed in the KF-LiF solvent but not in NaF-LiF .

4. $[\text{ZrF}_6]^{-2}$, the most stable configuration in the solid, is not found in either liquid system.

5. Complexes and ordering appear stronger in the KF-LiF than in the NaF-LiF solvents further corroborating the solvent cation effects observed in other systems.

Manuscript received March 19, 1964.

Any discussion of this paper will appear in a Discussion Section to be published in the June 1965 JOURNAL.

REFERENCES

1. G. W. Mellors and S. Senderoff, Proceedings of the First Australian Conference on Electrochemistry, p. 578 Pergamon, New York (1964).
- 2a. K. A. Sense, C. A. Alexander, R. E. Bowman, and R. B. Filbert, Jr., *J. Phys. Chem.*, **61**, 337 (1957).
- 2b. K. A. Sense and R. W. Stone, *ibid.*, **62**, 1411 (1958).
3. "Phase Diagrams of Nuclear Reactor Materials," R. E. Thoma, Editor, Oak Ridge National Laboratory, Nov. 20, 1959, ORNL 2548.
4. S. Senderoff, G. W. Mellors, and R. I. Bretz, *Ann. N. Y. Acad. Sci.*, **79**, 878 (1960).
5. S. Senderoff, G. W. Mellors, and R. I. Bretz, *This Journal*, **108**, 93 (1961).
6. L. Pauling, "The Nature of the Chemical Bond," 3rd ed., p. 514, Cornell University Press, Ithaca, N. Y. (1960).
7. E. A. Guggenheim, "Mixtures," p. 177, Oxford University Press (1952).

Correlation of Limiting Currents; Electrodeposition of Copper in Microelectrolytic Cells

R. N. O'Brien and L. M. Mukherjee

Chemistry Department, University of Alberta, Edmonton, Alberta, Canada

ABSTRACT

Limiting currents have been measured using microelectrolytic cells of the type: Cu/CuSO₄ or CuSO₄ + H₂SO₄ (or Na₂SO₄)/Cu. Good agreement with existing theory of the correlation of limiting current densities under free convective conditions was obtained for relatively thick (5 mm) electrodes confirming that convection does occur in microcells. For thin electrodes a correlating factor, which is assumed to be related to "edge effect," is evaluated.

Free or natural convection in an electrochemical cell results from density changes caused by concentration changes in the vicinity of the electrode (1). A spontaneous laminar flow of fluid sets in due to the density difference between the solution at the electrode/solution interface and the bulk. From a consideration of mass transfer under free convection conditions Tobias and co-workers (1a) were able to explain the dependence of limiting currents on electrode dimensions, bulk concentration, etc., in the deposition of copper at vertical cathodes from unstirred copper sulfate-sulfuric acid solutions. Such a correlation, however, has not yet been attempted in the type of microcell assembly recently used in optical interferometric studies of electrolysis (2). Any indication of free convection in such a microset-up will prove useful in correctly interpreting the interference patterns. In view of this, examination of the current-voltage relationship in the electrolysis of copper sulfate solutions in microcells with fixed copper electrodes of known dimensions has been undertaken.

Theory

On the basis of the combined effects of diffusion, electrical migration and free convection the average limiting current density, I was quantitatively expressed as follows (1a)

$$I = \frac{0.673nF\Delta C_o}{x_o(1-t_{Cu^{2+}})} \cdot \left[\frac{gx_o^3 D^3 \rho \Delta C_o (\alpha_{CuSO_4} - \alpha_{H_2SO_4} t_{H^+} + [D_{CuSO_4}/D_{H_2SO_4}]^{3/4})}{\mu} \right]^{1/4} \quad [1]^1$$

where $\Delta C_o = C_o - C_i$, C_o and C_i being, respectively, the concentration of Cu²⁺ ion in the bulk and that at the electrode-solution interface; D is the diffusion constant of Cu²⁺ ion while D_{CuSO_4} and $D_{H_2SO_4}$ denote the same for the species indicated; ρ is the average density of the solution; α_{CuSO_4} and $\alpha_{H_2SO_4}$ are the densification coefficients of CuSO₄ and H₂SO₄, respectively, and are related to the fluid density and concentration of each species in the bulk and at the electrode/solution interface; μ is the viscosity of the solution; x_o , the height of the cathode used; n , the number of electrons involved in the electrochemical process; $t_{Cu^{2+}}$ and t_{H^+} , the transference numbers of Cu²⁺ and H⁺ ions present in the system; F and g have their usual significance. Equation [1] is analogous to those derived by Levich (3), Wagner (4), Agar (5), and Keulegan (6) based on similar physical models.

Since C_i is practically equal to zero at the limiting current conditions, ΔC_o can be replaced by C_o . Further, since the diffusion constants, viscosity, densification coefficients, and density depend on the composition, they can be regarded as practically constant for electrolytes of comparable compositions. Therefore

¹ Apparently, the original equation, viz., Eq. [21] in ref. (1a), was misprinted; the expression presented in this paper is correct.

they can all be combined in one constant K resulting in

$$I_t = \frac{kx_o^{3/4} l C_o^{5/4}}{1 - t_{Cu^{2+}}} \quad [2]$$

provided one also assumes t_{H^+} is constant and it also is included in k . I_t is now the total limiting current and l and x_o the width and height of the cathode.

According to Eq. [2] the total limiting current should vary with (a) the 5/4 power of the bulk concentration of the electroactive species, i.e., Cu²⁺ ion in the present case; and (b) the 3/4 power of the cathode height.

The above predictions are well substantiated by the investigations of Tobias and co-workers (1a). In their experiments solutions containing copper sulfate (0.01-0.74M) and sulfuric acid (1.38-1.57M) were electrolyzed in a relatively large rectangular cell using copper cathodes having surfaces of heights, x_o , equal to 0.634 cm, 2.54 cm, 3.75 cm, and 7.6 cm and width, l , of 7.6 cm. Evidently, the dimensions of the electrodes and the size of the cell used were widely different from those recently employed in interferometric study of electrodeposition (2) where a narrow thin layer of solution was electrolyzed in a cell (2.5 cm x 3 mm x 2 mm) between a pair of vertical electrodes about 3 mm apart.

The applicability of Eq. [2] requires that the cathode dimensions remain unchanged during electrodeposition. This requirement may be roughly fulfilled in the case of large electrodes. However, for small cathodes surface distortion, nucleation around edges (the "edge effect") and related effects (7) will be pronounced. Because of this, it is very doubtful if the area (0.05 cm² or less) of the small cathodes used in the present study will remain unaffected while the current-voltage measurement is in progress. In fact, at the limiting stage, a net increase in area of such small cathodes is definitely anticipated, and this effect should be time-dependent. Accordingly, the limiting current may also be expected to be higher than that predicted from Eq. 2 on the basis of x_o and l . A precise correction for the increase in surface area would require a detailed knowledge of the phenomenon. At present, no satisfactory theory is available for any quantitative evaluation. However, assuming as a first approximation that the area will increase by a finite amount at the limiting current, Eq. [2] can be tentatively written as follows

$$I_t = \frac{k}{1 - t_{Cu^{2+}}} x_o^{3/4} l C_o^{5/4} f \quad [3]$$

where $f > 1$ is an empirical factor. It is related to the per cent increase in surface area of the cathode, and its magnitude is expected to be governed by the actual values of x_0 and l besides other factors. Equation [3] is by no means exact; it merely illustrates the gross effect of possible increase of electrode area on the limiting current.

Assuming $t_{\text{Cu}^{2+}} = 0$ Eq. [3] yields

$$I_t = k x_0^{3/4} l C_0^{5/4} f \quad [4]$$

or

$$\log I_t - \frac{3}{4} \log x_0 - \log l = \log k + \log f + \frac{5}{4} \log C_0 \quad [5]$$

The plot of left side of Eq. [5] vs. $\log C_0$ should be linear having a slope of 1.25 and the intercept would be given by $\log k + \log f$. Assuming the area of thin cathodes to increase if $l \gg x_0$ the relative variation in l will be negligible compared to that of x_0 , and f will be largely determined by x_0 , becoming greater as x_0 decreases.

In the present work several cells with (rectangular) copper electrodes of heights (x_0) equal to 0.005 cm, 0.021 cm, or 0.41 cm and widths (l) approximating to 1.15 cm, 1.80 cm, or 2.35 cm were used. Details of cell construction have been given in the experimental section.

Limiting currents were measured in copper sulfate-sulfuric acid mixtures of compositions comparable to those used by Tobias and co-workers (1a). Plain copper sulfate solutions and mixtures containing a suitable "neutral" electrolyte were also included in the present study in order to ascertain roughly the transference number of the electroactive ion *i.e.*, $t_{\text{Cu}^{2+}}$. Preliminary experiments with copper sulfate solutions to which potassium nitrate was added to act as a neutral electrolyte yielded erratic results presumably due to superimposed chemical and/or electrochemical reduction of nitrate ions (8) on copper under the present experimental conditions. Copper sulfate-sodium sulfate mixtures, on the other hand, gave fairly consistent and reproducible limiting currents. Because of this, copper sulfate-potassium nitrate systems were excluded from the present study. The molarity of copper sulfate used varied between 0.05 and 0.50 for the pure solutions as well as in the mixtures containing sulfuric acid or sodium sulfate.

The present investigation, carried out under conditions similar to those of optical interferometric study of electrodeposition (2), is aimed at showing that the equations of Tobias *et al.* are obeyed and, since they depend on the occurrence of free convection, the free convection occurs in microcells of the type Cu/CuSO_4 or $\text{CuSO}_4 + \text{H}_2\text{SO}_4$ (or Na_2SO_4) Cu.

Experimental

Chemicals.—Twice recrystallized B.D.H. ("Analar") copper sulfate was used to prepare a 1M stock solution which was standardized by the iodine-thiosulfate method. Pure copper sulfate solutions used in the study were obtained by diluting the stock solution with water while the mixtures were prepared from known volumes of stock solutions of copper sulfate and standard reagent grade sulfuric acid (or sodium sulfate) with subsequent dilution, if necessary.

Cell assembly.—The cell assembly and the holder unit were essentially the same as those used in the interferometric study (2). A schematic representation has been given in Fig. 1a. The cell actually comprises three detachable portions. The portions marked G are two glass flats which, in the interferometric measurements, are required to have a particular reflectance-transmittance ratio: in the present study, such requirement is, however, immaterial. The portion R is made of epoxy resin; it contains the electrodes and has a slot which provides a well for the electrolyte when mounted on one of the glass flats.

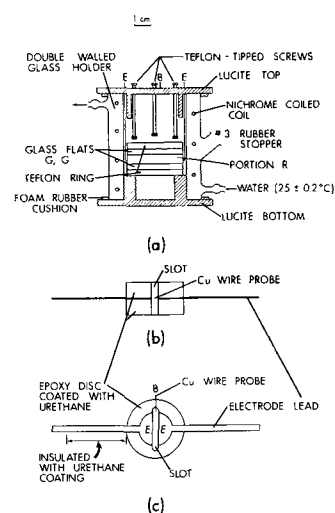


Fig. 1. The cell and its components: (a) cell-holder assembly; (b) section through the "sandwich"; (c) top view of the portion R.

Construction of the portion R (Fig. 1b).—A copper (99.5–100% purity) strip of desired thickness was "sandwiched," using epoxy resin glue, between two circular disks of cast epoxy resin. The "sandwich" was left under pressure in an air-oven ($\sim 130^\circ\text{C}$) for about 3 hr to cure fresh resin used as glue and ensure a good metal-disk contact. By choosing a suitable thickness for the upper and the lower epoxy disks the over-all thickness of the metal-disk combination was kept between 5.5 and 6.5 mm; this, also, made it possible to vary the relative position of the metal strip in the sandwich. A slot about 3.5 mm wide was then milled through the body of the sandwich in the position indicated (see Fig. 1c); this divided the central circular portion of copper and produced two rectangular cross sections of the metal embedded in the opposite walls across the width of the slot so formed. The two metal surfaces thus obtained served as the two electrodes (E, E), *viz.*, the cathode and the anode. The x_0 value for the electrodes (*i.e.*, after pretreatment and polishing) was determined by the original thickness of the metal strip used; the width, l , approximated to the diameter of the circular section of the sandwiched copper strip. By using a slide calliper l was subsequently measured to ± 0.02 cm. A probe electrode (B) of 18 gauge copper wire of the same purity was cemented to R through the side (Fig. 1c); about 1 mm of the wire actually remained within the slot half-way between and on the same plane as the electrodes. Interference patterns (2) suggested no change in concentration was to be anticipated at this location of the probe electrode, giving a stable potential throughout an electrolysis run. This probe electrode was used as a "reference" for measuring the cathodic polarization in all runs. Also, it was believed that the probe electrode would not interfere with the natural convection, if any.

The portion R for the cell with $x_0 = 0.41$ cm was similar in all the essential features to the ones described before, except that in place of using a copper strip two flat well-machined semicircular slabs of copper were sandwiched with faces; $x_0 = 0.41$ cm and $l = 2.31$ cm aligned opposite each other across a gap of about 3.5 mm.

The resin part of R was coated with a thin layer of urethane plastic to make it hydrophobic; also, urethane coating was used as an insulation for those parts of the leads of the probe electrode and the electrodes (E, E) which might come in contact with the electrolyte. The special holder designed for the cell assembly was a cylindrical glass unit with water ($25^\circ \pm 0.2^\circ\text{C}$) circulating through the outer jacket which contained a spiral of coiled nichrome wire to secure greater thermal uniformity (see Fig. 1a). The cylinder rested

on a Lucite base. A similar Lucite piece with three adjustable Teflon-tipped screws and openings for the electrode leads was mounted on the top of the cylinder and clamped to the base. The Teflon-tipped screws were adjusted to hold the G-R-G assembly placed inside the cylinder horizontal and snugly in position. No leakage was detected.

Pretreatment of the electrodes.—Prior to an actual run the electrodes (E,E) were short-circuited to form a cathode which was then plated with copper from a dilute copper sulfate-sulfuric acid mixture using the probe reference as the anode. The electrodes were later carefully polished with fine emery paper to secure uniformity in surface condition. Finally, the electrodes were scrubbed with filter paper soaked in acetone, rinsed with water and air-dried.

Limiting current measurement.—The limiting current was ascertained from the height of the plateau in the plot of I_t vs. the cathodic polarization. Usually, increasing voltages from a K-type potentiometer were applied to the electrodes (E,E), and the corresponding currents were measured by a calibrated ultrahigh sensitivity Simpson (model No. 269) multimeter; the cathodic polarization (vs. the probe reference) at each point was determined with the help of a Beckman Zeromatic pH meter. For large currents, as in the case of the electrode with $x_0=0.41$ cm, an arrangement similar to that of Tobias and co-workers (1a) was used; that is, batteries in conjunction with a variable resistance were substituted for the potentiometer as the source and the actual emf's applied between the cathode and the anode were measured with a vacuum tube voltmeter.

A period of approximately 1 min proved satisfactory for reaching a steady state in the current-potential measurement.

Results and Discussion

The general relationship between the current and the cathodic polarization observed in the present series of experiments is illustrated by the two plots given in Fig. 2. (The actual compositions and the cell dimensions have been indicated in the figure.) The half-wave potentials for pure copper sulfate solutions and the mixtures lie around 0.200v; the observed shifts in the half-wave potentials do not suggest any definite trend which could be related to the concentration of copper sulfate or the nature of the added electrolyte.

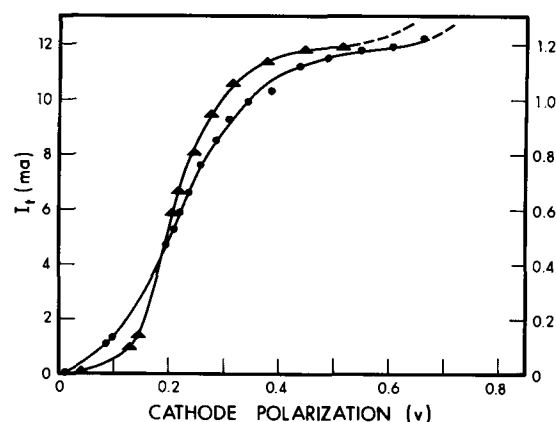


Fig. 2. Typical current vs. cathodic polarization plots. \blacktriangle , 0.005 cm; 1.8 cm; 2.81/2.27; 0.1998M CuSO_4 + 1.56M H_2SO_4 ; $I_t = 1.18$ ma; \bullet , 0.021 cm; 2.33 cm; 3.00/2.20; 0.5010M CuSO_4 ; 1.372M + H_2SO_4 ; $I_t = 11.9$ ma.

The experimental results obtained for the different systems are summarized in Tables I to IV. The first three columns in each table refer to the dimensions of the cell used in the respective cases: x_0 represents the height and l the width of the electrodes, whereas the third column lists the thickness of the epoxy disks used in making the portion R described above. The value recorded on the left of the oblique stroke refers to the upper disk and that on the right to the lower one. Since the depth (5.5-6.5 mm) of the cell is determined by the total thickness of the portion R, a knowledge of the thickness of the upper and the lower disks gives the position of the electrodes from the cell floor.

The observed limiting currents, $I_{t(\text{obs.})}$, are the best estimates from the height of the plateau of the current vs. cathodic polarization plots, the average reproducibility being $\pm 5\%$. In agreement with previous observation (1a) the position of the electrode plane with respect to the floor of the cell (or to the liquid surface) has no significant effect on the limiting current. The values listed as $I_{t(\text{calc.})}$ represent limiting currents calculated for the different copper sulfate-sulfuric acid runs according to Eq. [4] assuming $t_{\text{Cu}^{2+}}$ to be zero as before (1a); the numerical values of k used for such calculations (c.f. footnote to Tables I

Table I. Electrolysis of $\sim 0.50\text{M}$ copper sulfate systems

x_0 , cm	l , cm	Disk thickness, mm	CuSO_4 molarity	H_2SO_4 molarity	Na_2SO_4 molarity	$I_{t(\text{obs.})}$, ma	$I_{t(\text{calc.})}$,* ma	$f = \frac{I_{t(\text{obs.})}}{I_{t(\text{calc.})}}$
0.005	1.80	2.81/2.27	0.4995	—	—	4.2	—	—
0.005	2.36	2.80/2.30	0.5010	—	—	5.0	—	—
0.021	1.80	2.10/2.30	0.4995	—	—	9.0	—	—
0.021	2.36	2.80/2.30	0.5010	—	—	10.4 ₅	—	—
0.41	2.31	0.75/0.75	0.5010	—	—	73.2	—	—
0.005	1.15	4.30/0.80	0.5010	1.37 ₂	—	2.4	1.3 ₇	1.75
0.005	1.15	0.80/4.30	0.4995	1.56	—	2.4 ₅	1.3 ₆	1.80
0.005	1.80	4.30/0.75	0.4995	1.56	—	3.9	2.1 ₃	1.83
0.005	1.80	0.75/4.30	0.5010	1.37 ₂	—	3.8	2.1 ₄	1.77
0.005	1.80	2.81/2.27	0.499 ₅	1.56	—	3.8 ₅	2.1 ₃	1.81
0.005	2.35	4.30/1.00	0.499 ₅	1.56	—	4.8	2.7 ₅	1.73
0.005	2.35	1.00/4.30	0.499 ₅	1.56	—	5.1	2.7 ₅	1.83
0.005	2.36	2.30/2.80	0.5010	1.37 ₂	—	5.0	2.80	1.78
0.021	1.80	4.30/0.80	0.499 ₅	1.56	—	9.0	6.2 ₅	1.44
0.021	1.80	0.80/4.30	0.5010	1.37 ₂	—	9.3	6.2 ₅	1.48
0.021	1.80	2.10/2.30	0.4995	1.56	—	9.5	6.2 ₅	1.52
0.021	2.33	3.00/2.20	0.5010	1.37 ₂	—	11.9	8.1 ₂	1.47
0.021	2.36	4.01/0.77	0.4995	1.56	—	12.2	8.20	1.49
0.021	2.36	0.77/4.01	0.4995	1.56	—	12.0	8.20	1.46
0.021	2.36	2.30/2.80	0.5010	1.37 ₂	—	12.6	8.2 ₅	1.53
0.41	2.31	0.75/0.75	0.5010	1.37 ₂	—	72.6	74.8	0.97
0.005	1.15	4.30/0.80	0.5010	—	1.01	2.5	—	—
0.005	1.15	0.80/4.30	0.4995	—	1.05	2.3	—	—
0.005	1.80	4.30/0.75	0.4995	—	1.05	3.5	—	—
0.005	1.80	0.75/4.30	0.5010	—	1.01	3.4	—	—
0.021	1.80	4.30/0.80	0.4995	—	1.05	8.9	—	—
0.021	1.80	0.80/4.30	0.5010	—	1.01	9.4	—	—
0.021	2.33	3.00/2.20	0.5010	—	1.01	11.9 ₅	—	—
0.41	2.31	0.75/0.75	0.5010	—	1.01	75.0	—	—

* Equation [4]: $k = 150$; $t_{\text{Cu}^{2+}} = 0$.

Table II. Electrolysis of ~0.33M copper sulfate systems

x_0 , cm	l , cm	Disk thickness, mm	CuSO ₄ molarity	H ₂ SO ₄ molarity	Na ₂ SO ₄ molarity	I_t (obs.), ma	I_t (calc.),* ma	$f = \frac{I_t(\text{obs.})}{I_t(\text{calc.})}$
0.005	2.36	2.80/2.30	0.333	—	—	3.0	—	—
0.021	2.36	2.30/2.80	0.333	—	—	7.5	—	—
0.41	2.31	0.75/0.75	0.333	—	—	48.5	—	—
0.005	1.80	4.30/0.75	0.333	1.56	—	2.3	1.28	1.77
0.005	1.80	0.75/4.30	0.333	1.56	—	2.2	1.28	1.69
0.005	2.36	2.80/2.30	0.333	1.56	—	2.9	1.68	1.74
0.021	1.80	2.10/2.30	0.333	1.56	—	5.7 ₅	3.77	1.52
0.021	2.36	2.30/2.80	0.333	1.56	—	7.3	4.94	1.47
0.41	2.31	0.75/0.75	0.333	1.56	—	47.2	44.90	1.05
0.005	2.36	2.80/2.30	0.333	—	1.05	2.8 ₅	—	—
0.021	1.80	2.10/2.30	0.333	—	1.05	6.0	—	—
0.021	2.36	2.30/2.80	0.333	—	1.05	7.5	—	—
0.41	2.31	0.75/0.75	0.333	—	1.05	45.8	—	—

* Equation [4]: $k = 150$; $t_{Cu^{2+}} = 0$.

Table III. Electrolysis of ~0.2M copper sulfate systems

x_0 , cm	l , cm	Disk thickness, mm	CuSO ₄ molarity	H ₂ SO ₄ molarity	Na ₂ SO ₄ molarity	I_t (obs.), ma	I_t (calc.),* ma	$f = \frac{I_t(\text{obs.})}{I_t(\text{calc.})}$
0.005	2.36	2.80/2.30	0.1998	—	—	1.70	—	—
0.021	2.36	2.30/2.80	0.1998	—	—	4.20	—	—
0.41	2.31	0.75/0.75	0.1998	—	—	23.70	—	—
0.005	1.80	4.30/0.75	0.1998	1.56	—	1.18	0.70	1.68
0.005	1.80	0.75/4.30	0.1998	1.56	—	1.15 ₅	0.70	1.65
0.005	1.80	2.81/2.27	0.1998	1.56	—	1.18	0.70	1.68
0.005	2.36	2.80/2.30	0.1998	1.56	—	1.64	0.92	1.78
0.021	1.80	2.10/2.30	0.1998	1.56	—	2.88	2.06	1.40
0.021	2.36	2.30/2.80	0.1998	1.56	—	4.00	2.70	1.48
0.41	2.31	0.75/0.75	0.1998	1.56	—	22.60	24.51	0.92
0.005	2.36	2.80/2.30	0.1998	—	1.05	1.72	—	—
0.021	1.80	2.10/2.30	0.1998	—	1.05	2.65	—	—
0.021	2.36	2.30/2.80	0.1998	—	1.05	4.30	—	—
0.41	2.31	0.75/0.75	0.1998	—	1.05	23.00	—	—

* Equation [4]: $k = 155$; $t_{Cu^{2+}} = 0$.

to IV) are the averages of the temperature-corrected values obtained from the previous data (1a) for comparable systems. The last column lists values of the factor f , given by the ratio $I_t(\text{obs.})/I_t(\text{calc.})$ for the copper sulfate-sulfuric acid solutions. It is evident that these values are characterized by the corresponding x_0 values of the electrode used, the average value of f being 1.76, 1.48₅, and 1.01 for x_0 equal to 0.005, 0.021, and 0.41 cm, respectively. This observed relationship between f and x_0 conforms to the idea of edge effects mentioned above for cases where $l \gg x_0$. However, any specific comment on the actual size of the f value requires a more systematic study.

The fact that good limiting current plateaus could be obtained in all cases suggest that the rate of increase of the electrode area must decrease with time and the rate of change must be slow as the maximum current density is approached. Thus, any dependence of f on time is not apparent from the present set of measurements. Moreover, the direct dependence of f on the magnitude of x_0 was further demonstrated by interchanging the dimensions of x_0 and l . This was accomplished by rotating one of the cells ($x_0=0.021$ cm, and $l=2.33$ cm in 0.0501M CuSO₄+1.37₂M H₂SO₄) through 90° from its usual horizontal alignment so that the electrode height was now l rather than x_0 .

Table IV. Electrolysis of ~0.5M copper sulfate systems

x_0 , cm	l , cm	Disk thickness, mm	CuSO ₄ molarity	H ₂ SO ₄ molarity	Na ₂ SO ₄ molarity	I_t (obs.), ma	I_t (calc.),* ma	$f = \frac{I_t(\text{obs.})}{I_t(\text{calc.})}$
0.005	1.15	4.30/0.80	0.0501	—	—	0.20	—	—
0.005	1.15	0.80/4.30	0.0499 ₅	—	—	0.25	—	—
0.005	1.80	4.30/0.75	0.0499 ₅	—	—	0.29	—	—
0.005	1.80	0.75/4.30	0.0501	—	—	0.31	—	—
0.005	2.36	2.30/2.80	0.0501	—	—	0.40	—	—
0.021	1.80	4.30/0.80	0.0499 ₅	—	—	1.10	—	—
0.021	1.80	0.80/4.30	0.0501	—	—	1.04	—	—
0.021	2.33	3.00/2.20	0.0501	—	—	1.22	—	—
0.021	2.36	2.30/2.80	0.0501	—	—	1.25	—	—
0.41	2.31	0.75/0.75	0.0501	—	—	6.95	—	—
0.005	1.15	4.30/0.80	0.0501	1.37 ₂	—	0.13 ₅	0.08 ₂	1.65
0.005	1.15	0.80/4.30	0.0499 ₅	1.56	—	0.14 ₅	0.08 ₂	1.77
0.005	1.80	4.30/0.75	0.0499 ₅	1.56	—	0.25	0.12 ₅	1.95
0.005	1.80	0.75/4.30	0.0501	1.37 ₂	—	0.22	0.12 ₅	1.72
0.021	1.80	4.30/0.80	0.0499 ₅	1.56	—	0.52	0.37 ₅	1.39
0.021	1.80	0.80/4.30	0.0501	1.37 ₂	—	0.58	0.37 ₆	1.55
0.021	2.33	3.00/2.20	0.0501	1.37 ₂	—	0.75	0.48 ₇	1.54
0.021	2.36	2.30/2.80	0.0501	1.37 ₂	—	0.75	0.49 _a	1.52
0.41	2.31	0.75/0.75	0.0501	1.37 ₂	—	4.95	4.49	1.10
0.005	1.15	4.30/0.80	0.0501	—	1.01	0.14	—	—
0.005	1.15	0.80/4.30	0.0499 ₅	—	1.05	0.13 ₅	—	—
0.005	1.80	4.30/0.75	0.0499 ₅	—	1.05	0.25	—	—
0.005	1.80	0.75/4.30	0.0501	—	1.01	0.20	—	—
0.021	1.80	4.30/0.80	0.0499 ₅	—	1.05	0.55	—	—
0.021	1.80	0.80/4.30	0.0501	—	1.01	0.60	—	—
0.021	2.33	3.00/2.20	0.0501	—	1.01	0.76	—	—
0.41	2.31	0.75/0.75	0.0501	—	1.01	4.80	—	—

* Equation [4]: $k = 160$; $t_{Cu^{2+}} = 0$.

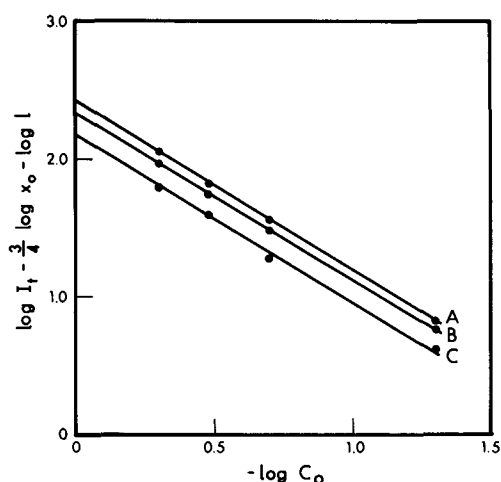


Fig. 3. Plot of Eq. [5]: $x_o = 0.005$ cm (A); 0.021 cm (B); and 0.41 cm (C).

and the width was x_o instead of l . It was observed that quite reasonable agreement with theory (the calculated and observed limiting currents were, respectively, 0.27 and 0.33 ma) was obtained using the appropriate f value (1.76).

Although the interactions of closely spaced electrodes will have some effect on one another especially in determining the configuration of convective flows, experience in this laboratory has shown that, if the over-all cell dimensions are constant, the change in size of electrodes is not important. Specifically one would expect that the dependence of the limiting current density on height of the electrode would fall below the theoretical value of the x_o exponent (1.25) which it does. Further, that since the convection flow patterns in this geometry of cell are known to consist of two convective whorls with under and over-flow between them, that the extra frictional force caused by the small dimension of the whorl (the extra viscous drag per volume of solution moving in a small space) the smaller heights of electrode should produce lower convective velocities and a more circular whorl and therefore should approach theory more closely which they do as shown in Tables I and IV.

The data on the various copper sulfate-sulfuric acid runs when plotted according to Eq. [5] yield three straight lines characteristic of the three different x_o values used (see Fig. 3). (Each solid circle in the plots A and B contains a cluster of points each of which represents a particular set of $I_{t(obs.)}$, l , and C_o). The results of a least squares treatment together with the probable error of the relevant quantities are given in Table V. The slopes corresponding to the three different x_o values, viz., 0.005 , 0.021 , and 0.41 cm, are, respectively, 1.23 , 1.22 , and 1.174 in fair agreement with the theoretical value 1.25 ; the intercepts given by $\log k + \log f$ are 2.415 , 2.34 , and 2.14 . Taking the average value of k as 155 , the values of f calculated from the intercepts are found to be 1.68 , 1.41 , and 0.89 for x_o equal to 0.005 , 0.021 , and 0.41 cm, respectively. The agreement of the data obtained in copper sulfate-sulfuric acid solutions with Eq. [5] indicated that little or no electrical migration is involved in this system. Apart from the consideration of electrical migration, Eq. [5] is based essentially on the same physical model which was adopted in deriving Eq. [1]. The apparent validity of Eq. [5] would, therefore, suggest that free convection also operates in the vicinity of microelectrodes of the type used for optical interferometric study of electrodeposition (2).

It is interesting to note that for the same electrode

Table V. Least squares results using Eq. [7]

x_o , cm	Slope	δ^{**}	Intercept	δ^{**}	f	b
0.005	1.23	0.0075	2.415	0.005	1.76	1.68
0.021	1.22	0.006	2.34	0.0045	1.485	1.41
0.41	1.174	0.030	2.14	0.020	1.01	0.89

** δ = the probable error of the quantity in the preceding column; a from $I_{t(obs.)}/I_{t(calc.)}$ (see Tables I-IV); b from intercept using $k = 155$.

dimensions the observed limiting currents for 0.20 , 0.33 , and $0.50M$ copper sulfate solutions and for all the mixtures containing $1M$ sodium sulfate are about the same as those obtained in the corresponding copper sulfate-sulfuric acid runs (Tables I-IV). The solution of $0.05M$ copper sulfate, on the other hand, is an exception, the observed limiting currents in this case being about twice as high as the corresponding values for the mixtures containing sulfuric acid or sodium sulfate (Table IV).

A thorough analysis of the behavior of the different systems necessitates an examination of the characteristic mass-transfer mechanisms. However, it would appear that electrical migration is of minor importance in the copper sulfate-sodium sulfate mixtures and also in the copper sulfate solutions of higher concentrations, e.g., 0.20 , 0.33 , and $0.50M$, containing no added electrolyte. On the contrary, the higher limiting currents observed in $0.05M$ copper sulfate solution are possibly due to a substantial contribution from the electrical migration effect. On this assumption a rough estimate of the transference number of Cu^{2+} ion in $0.05M$ copper solution can be obtained from Eq. [3] using the appropriate f values. The average number 0.36 so derived is comparable to the limiting transference number of Cu^{2+} ion, 0.39 calculated from the mobilities of Cu^{2+} and SO_4^{2-} ions only (9). Since the application of Eq. [3] to pure copper sulfate solutions is not truly justifiable no great importance can, however, be attached to the present value of the transference number.

Manuscript received Dec. 13, 1963; revised manuscript received July 16, 1964. This paper was presented at the Western Regional Conference of C.I.C., Trail, B. C., September 1963 and in part at the Annual Meeting of C.I.C., Edmonton, May 1962.

Any discussion of this paper will appear in a Discussion Section to be published in the June 1965 JOURNAL.

REFERENCES

- (a) C. R. Wilke, M. Eisenberg, and C. W. Tobias, *This Journal*, **100**, 513 (1953); (b) N. Ibl and R. Muller, *ibid.*, **105**, 346 (1958).
- R. N. O'Brien and C. Rosenfield, *J. Phys. Chem.*, **67**, 643 (1963).
- B. Levich, *Acta Physicochim. U.R.S.S.*, **19**, 117 (1944).
- C. Wagner, *J. (and Trans.) Electrochem. Soc.*, **95**, 161 (1949).
- J. N. Agar, *Discussions Faraday Soc.*, **26** (1937).
- G. H. Keulegan, *J. Research Natl. Bur. Standards*, **47**, 156 (1951).
- J. A. V. Butler, Editor "Electrical Phenomena at Interfaces," p. 202, Methuen and Co. Ltd., London (1961); J. O'M. Bockris, "Transactions Symposium on Electrode Process," Ernest Yeager, Editor, p. 165, John Wiley & Sons, Inc., New York (1961); V. G. Levich and A. N. Frumkin, *Zhur. Fiz. Khim.*, **15**, 748 (1941).
- S. Glasstone and A. Hickling, "Electrolytic Oxidation and Reduction," pp. 186-87, 223, D. Van Nostrand and Co., Inc., New York (1936).
- B. B. Owen and R. W. Gury, *J. Am. Chem. Soc.*, **60**, 3074 (1938)

Fluorescent Properties of Some Europium-Activated Phosphors

A. Bril and W. L. Wanmaker

N. V. Philips' Gloeilampenfabrieken, Eindhoven, Netherlands

ABSTRACT

The following europium-activated phosphors were prepared: gadolinium oxide, gadolinium borate, gadolinium phosphate, lanthanum borate, and europium phosphate. The phosphors show an emission spectrum characteristic of the europium. From the excitation spectrum of some phosphors it is deduced that energy absorbed by gadolinium ions can be transferred to the europium ions. Most phosphors have a relatively high brightness at elevated temperatures. Gd_2O_3 -Eu has a rather high luminous efficiency with cathode-ray excitation.

Activation of phosphors by rare earth elements has been known for a long time. Kröger (1), for example, listed in his book as many as 35 phosphors activated with trivalent europium and 19 phosphors with divalent europium. In recent years there has been a growth of interest in the preparation of phosphors activated by rare earths or with rare earths as host lattice constituents, especially in connection with the possible use of these phosphors as laser materials. We will confine ourselves here mainly to europium-activated phosphors.

Van Uitert (2,3) studied the preparation of compounds like $M^{II}_{0.98}Na_{0.01}Eu_{0.01}WO_4$ where M^{II} may be Cd, Ca, Sr, Pb, or Ba. MacDonald, Vogel, and Brookman (4) described the fluorescence of europium tungstate. Borchardt (5) prepared the tungstates of all rare earth elements. The same author (6) prepared europium-activated tungstates and molybdates, such as $(Y_{0.9}Eu_{0.1})_2O_3 \cdot WO_3$, $(Gd_{0.8}Eu_{0.2})_2O_3 \cdot MoO_3$, $(La_{0.6}Eu_{0.4})_2O_3 \cdot 3WO_3$, and $(Gd_{0.7}Eu_{0.3})_2O_3 \cdot 3MoO_3$. These phosphors show a high quantum efficiency, *viz.*, quantum efficiencies in excess of 80% have been observed. Some of them showed a relatively high brightness at elevated temperatures, *e.g.*, $(Y_{0.9}Eu_{0.1})_2O_3 \cdot WO_3$. Chang (7) investigated the properties of europium-activated yttrium oxide for which also laser action on crystals was found. Wickersheim and Lefever (8) studied both the latter phosphor and also europium-activated gadolinium oxide. Y_2O_3 -Eu shows a high fluorescence intensity at elevated temperatures. Under high-pressure mercury excitation the brightness increases from room temperature and reaches a maximum value at 650°C, the relative brightness at this temperature being about twice the brightness measured at room temperature. In a recent paper Ropp (9) described the spectral properties, especially the excitation and emission spectra of rare earth oxide phosphors activated by other rare earth elements. The most efficient phosphors found were: Y_2O_3 -Eu; La_2O_3 -Eu; Gd_2O_3 -Eu; La_2O_3 -Tb, and Gd_2O_3 -Tb. The phosphors were prepared by first precipitating the required rare earth oxalates; after drying the precipitate at 110°C, they were fired in air at 1000°C.

Much work has also been done on organic Eu-complexes both in the solid state and dissolved in suitable solvents. Examples are the Eu-chelates, Eu-dibenzoyl-methane, Eu-thenoyl trifluoroacetate, and other compounds (10). Lempicki and Samelson (11) found laser action in a liquid, namely, Eu-benzoylacetate dissolved in ethyl- or methyl alcohol.

In this paper we present some measurements on the properties of Eu-activated gadolinium oxide, Gd-borate, Gd-phosphate, La-borate, and also of europium phosphate. Gd_2O_3 -Eu was already described in 1909 by Urbain (12), and $EuPO_4 \cdot 4H_2O$ was investigated by Lange (13).

For use as laser materials the phosphor should have a high efficiency, a small number of narrow emission lines, and in some cases, *e.g.*, low-level excitation, a long decay time. Further the wavelength dependence

of the absorption and the efficiency are important for the choice of the exciting pumping source.

Experimental

Method of phosphor preparation.—The ingredients used in the firing mixtures were reagent grade H_3BO_3 and $(NH_4)_2HPO_4$; the rare earth oxides Gd_2O_3 and Eu_2O_3 were obtained from the Lindsay Chemical Division of American Potash and Chemical Corporation in purities of 99.9%. For some preliminary experiments use was made of Gd_2O_3 with a purity of 99%; this ingredient proved, from the red fluorescence, to be contaminated with europium. We used La_2O_3 , supplied by Auer Remy (Hamburg) of a purity of 99.9%.

The required amounts of the dry materials were thoroughly mixed and subsequently fired. For the phosphates and borates the mixtures were pre-fired at a temperature of 300°-700°C. Samples of 3-10g were fired twice for 2 hr in small quartz crucibles in air at a temperature of 1000°-1400°C. For preparing Gd_2O_3 -Eu, a small amount of NH_4F (0.10-0.30 mole per mole Gd_2O_3) was added to the firing mixture in order to promote the incorporation of the activator into the host lattice.

Excitation spectra, absorption spectra, and efficiency.—The fluorescent output was determined as a function of wavelength, giving the so-called relative excitation spectrum of the light output. This was done with the aid of a Perkin-Elmer 13U double beam automatically recording spectrophotometer with quartz prism, while a hydrogen lamp was used as a source. For measuring the excitation spectrum the instrument was used in the single beam mode. An attachment made in our laboratory was placed behind the exit slit of the monochromator (see Fig. 1-1a), so that the phosphors were excited monochromatically. The fluorescent radiation was incident on suitable filters, which absorbed the reflected uv radiation and passed the fluorescence to a photomultiplier tube (EMI 9558 having a tri-

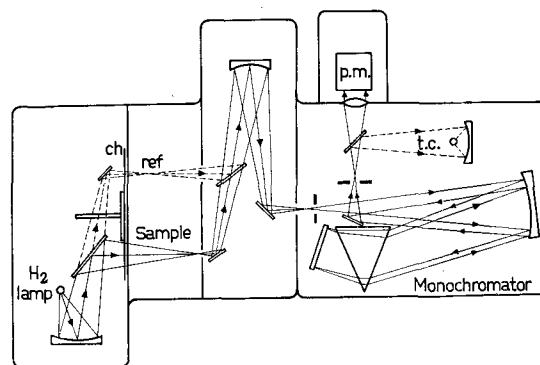


Fig. 1. Optical diagram of the spectrophotometer used for the measurement of the excitation- and the reflection spectra. ch, chopper (13 rps); p.m., photomultiplier tube; t.c., thermocouple; ref., reference beam; sample, sample beam.

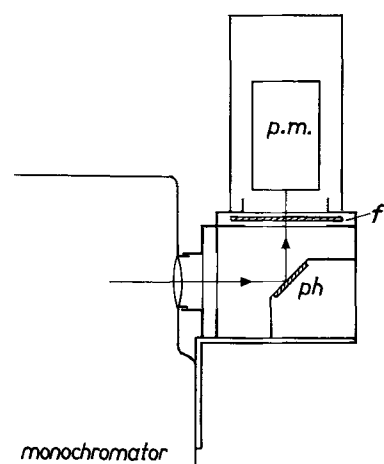


Fig. 1a. Attachment at the exit slit of the monochromator used for the excitation spectra: p.m., photomultiplier tube; ph, phosphor sample; f, filter.

alkali photocathode with good red sensitivity). The filters used in our case were 4 mm Schott WG 1 + 4 mm OG 1, the latter being placed between WG 1 and photomultiplier in order to avoid fluorescence produced by the OG 1 filter due to reflected exciting radiation. The output of the phosphor was compared with the fluorescent output of sodium salicylate, which was measured in the same way. The sodium salicylate was assumed to have a constant quantum efficiency (14). In this way the relative fluorescent output in quanta could be determined as a function of wavelength. No correction was made for the reflected uv radiation.

The excitation spectrum generally consists of a continuous part and of a number of lines. If narrow excitation lines occur, the width of these lines will generally be determined by the resolving power of the instrument. The intensities of the lines were normalized to a width of 5 nm.

Emission spectra.—The spectral distribution of the emission of the phosphors was measured with the aid of a Jarrel-Ash grating scanning monochromator with a focal distance of 50 cm. A grating blazed at 500 nm and 30,000 lines/in. was used, being capable of a resolution of 0.02 nm in first order. The actual resolution was 0.05–0.1 nm corresponding to a slit width of 0.03–0.06 mm, which was generally used.

The phosphors were excited by the uv radiation of a Philips SP 500 mercury discharge lamp or a spectral lamp No. 93109, both with a Schott UG5 and a nickel sulfate filter placed in front of it in order to isolate the short-wave uv. As detector a photomultiplier with tri-alkali photocathode and quartz window was used (EMI 9558 Q).

Decay.—The decay times with cathode-ray excitation were measured by a method described by Brill and Klasens (15). For uv excitation a pulsed cathode-ray tube was used with a fast uv-emitting phosphor [ZrP_2O_7 with a broad emission band, maximum 290 nm so that pulses of uv radiation were obtained (16)].

Efficiency.—The absolute efficiencies were determined for excitation in the wavelength region of 250–270 nm, as described by Brill and Hoekstra (17). The phosphors were measured with respect to one of the standard phosphors issued by the N.B.S. (18), viz., magnesium arsenate activated with manganese (sample No. 1030). As detector for the fluorescence and reflected radiation a thermopile was used. No correction has been applied for the small absorption by the phosphor for its own emission.

Diffuse reflection.—The reflections of the powders were determined with the Perkin-Elmer 13U in the double beam mode provided with a diffuse reflection attachment. A sample of gently pressed magnesium oxide powder was placed in the reference beam. In

this way the ratio of the reflections of sample and MgO were directly recorded. For MgO a value of 91% was assumed [see ref. (17)].

Results and Discussion

Emission spectra.—All the phosphors investigated show emission lines characteristic of europium (19). The main emission peaks are located near 580–590 nm and 610–625 nm, being transitions from the 5D_0 level to the 7F_1 and 7F_2 levels, respectively. The spectra at room temperature are given in Fig. 2 and 3.

In the curves of the emission spectra the recorded photocurrent is given as a function of wavelength. Thus no correction has been applied for the changes

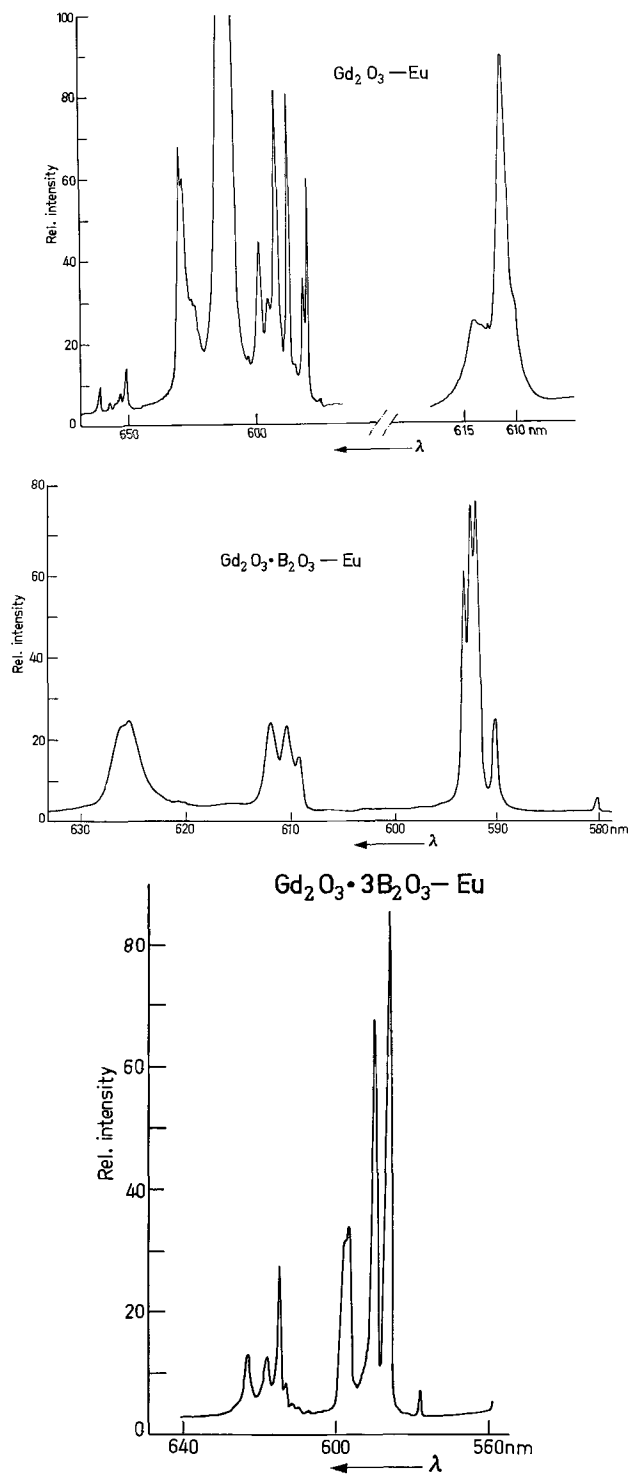


Fig. 2. Spectral emission, short wavelength uv excitation: (a) $Gd_2O_3 \cdot Eu$; left part: 13X amplified; (b) $Gd_2O_3 \cdot B_2O_3 \cdot Eu$; (c) $Gd_2O_3 \cdot 3B_2O_3 \cdot Eu$.

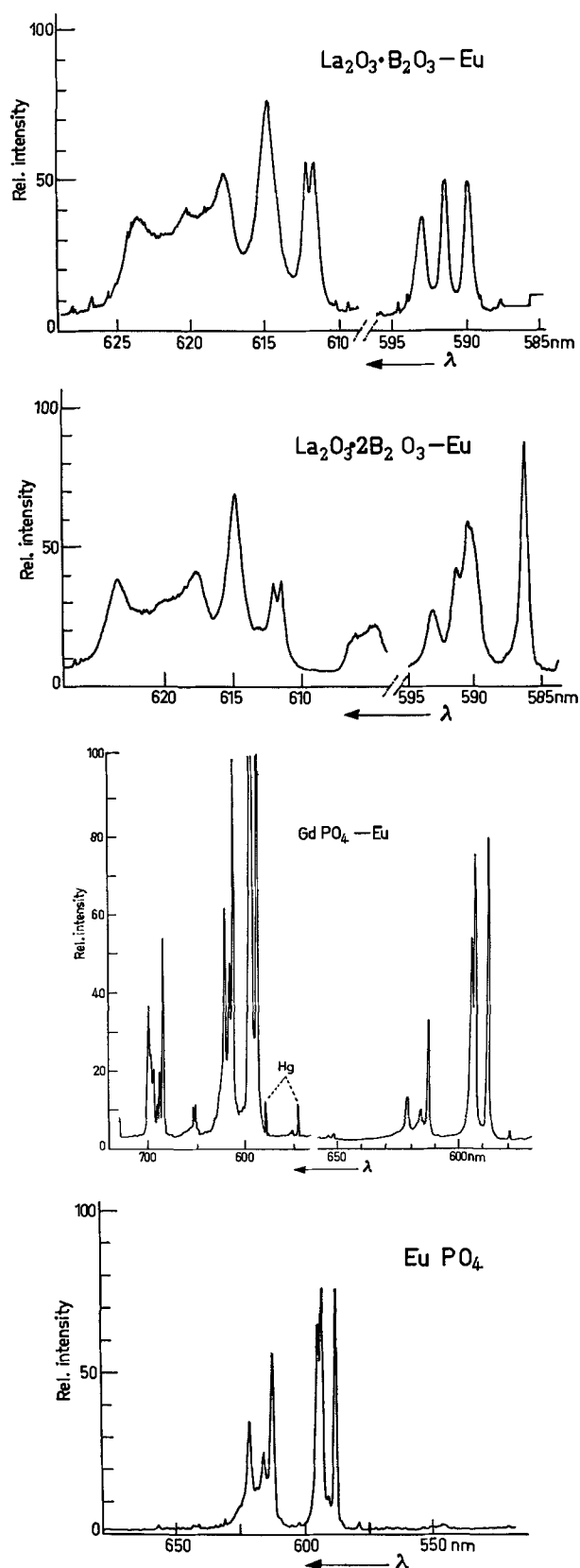


Fig. 3. Spectral emission, short wavelength uv excitation: (a) $\text{La}_2\text{O}_3 \cdot \text{B}_2\text{O}_3\text{-Eu}$; (b) $\text{La}_2\text{O}_3 \cdot 2\text{B}_2\text{O}_3\text{-Eu}$; (c) $\text{GdPO}_4\text{-Eu}$; (d) EuPO_4 .

in sensitivity of the setup within the spectral region considered. In order to get the irradiated power considered as a function of wavelength the curves have to be corrected, due to the wavelength dependence of the photomultiplier sensitivity and the transmission of the monochromator. To determine the correction factor as a function of wavelength, the output of a

standard tungsten ribbon lamp (for which the emitted power as a function of wavelength was known at the filament temperature used) was measured as a function of wavelength. With reference to 590 nm, the factors with which the output of the phosphors given in the figures have to be multiplied are at 610, 650, and 700 nm 1.3, 2.3, and 7.5, respectively. Probably due to the influence of the crystal field of the particular lattice on the Eu-ion, the relative intensities of the various Eu-emission lines differ considerably from one type of phosphor to another. For instance in $\text{Gd}_2\text{O}_3\text{-Eu}$ the most pronounced emission peak is located at 611 nm, the half-value width being 1.05 nm, whereas in $\text{Gd}_2\text{O}_3 \cdot \text{B}_2\text{O}_3\text{-Eu}$ the lines in the 590 nm region are the most intense. The emission spectra of $\text{GdPO}_4\text{-Eu}$ and EuPO_4 are quite similar (Fig. 3). Both compounds have the same crystal structure (see x-ray analysis and Table III), as might be expected from the fact that both ions have nearly the same ionic radius, viz., Eu 1.13Å and Gd 1.11Å.

Excitation and absorption spectra.—The wavelength dependence of the quantum output of the Eu-fluorescence was determined for $\text{Gd}_2\text{O}_3\text{-Eu}$, $\text{Gd}_2\text{O}_3 \cdot \text{B}_2\text{O}_3\text{-Eu}$, $\text{La}_2\text{O}_3 \cdot \text{B}_2\text{O}_3\text{-Eu}$ and EuPO_4 . Figure 4 gives examples of uncorrected recorded curves, from which the data in Fig. 5 and 6 are calculated. The excitation spectrum of $\text{Y}_2\text{O}_3\text{-Eu}$ was studied by Chang (7), Wickersheim and Lefever (8), and also by Ropp (9). The latter author also investigated, among many other rare earth oxides, the excitation spectra of $\text{La}_2\text{O}_3\text{-Eu}$

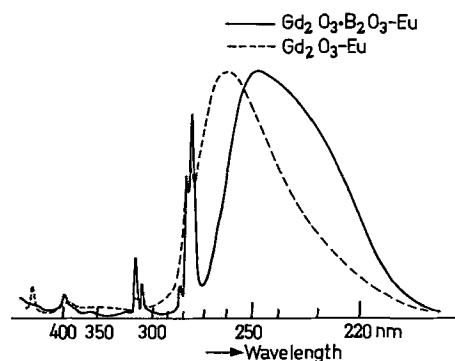


Fig. 4. Relative excitation spectra of the Eu fluorescence; uncorrected recorder curves.

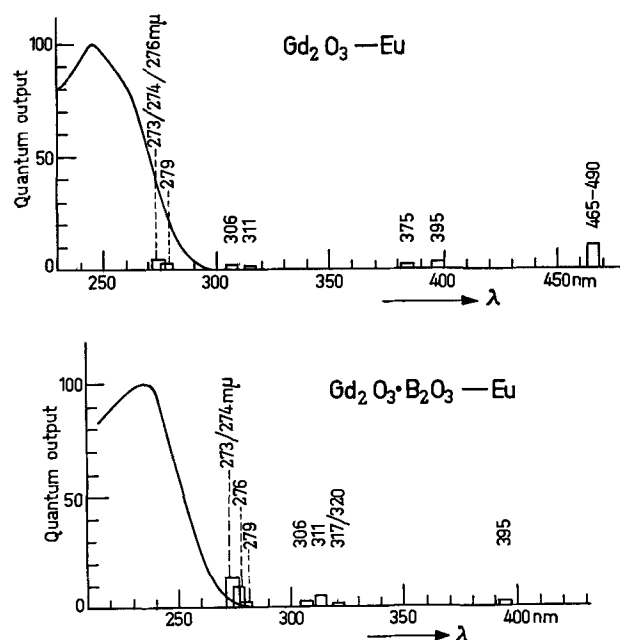


Fig. 5. Relative excitation spectra of the Eu fluorescence; quantum output: (a) $\text{Gd}_2\text{O}_3\text{-Eu}$; (b) $\text{Gd}_2\text{O}_3 \cdot \text{B}_2\text{O}_3\text{-Eu}$.

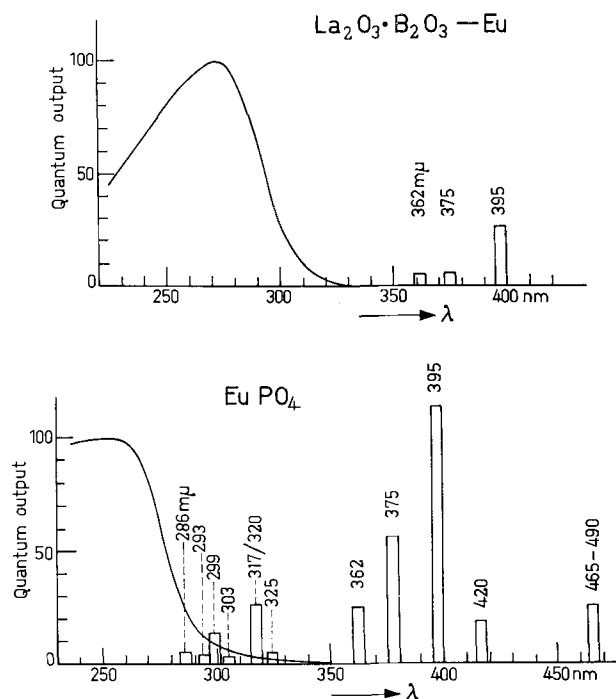


Fig. 6. Relative excitation spectra of the Eu fluorescence; quantum output: (a) $\text{La}_2\text{O}_3 \cdot \text{B}_2\text{O}_3\text{-Eu}$; (b) EuPO_4 .

and $\text{Gd}_2\text{O}_3\text{-Eu}$. In $\text{Y}_2\text{O}_3\text{-Eu}$ a broad excitation maximum was located at about 250 nm and also a maximum beyond the limits of measurement (200 nm). The excitation spectrum of $\text{Gd}_2\text{O}_3\text{-Eu}$ as described by us closely resembles that found by Ropp. It consists of a broad band at about 260 nm and a number of narrow peaks. Many of the narrow peaks can be attributed to transitions within the 4f configuration, while according to Ropp, the broad band will be due to host lattice excitation (host sensitization) or excitation in a broad energy band probably related to a perturbed level of the activator. Some of the narrow bands need some further explanation. Ropp mentions one peak at about 270 nm which he correlates with an excitation of the $^6\text{I}_j$ levels of the Gd^{3+} ions. We find two peaks between 270 and 280 nm, probably due to a higher resolving power of the instrument. This is illustrated in Fig. 4 for $\text{Gd}_2\text{O}_3\text{-Eu}$ and also for $\text{Gd}_2\text{O}_3 \cdot \text{B}_2\text{O}_3\text{-Eu}$, where the peaks are much more pronounced. These Eu emission peaks in the excitation spectrum are always found when Gd is present in the lattice. Moreover, characteristic Gd absorption lines are found at about the same wavelength as the peaks in the excitation spectrum. This may be concluded from a comparison of the excitation spectra with the reflection spectra of the powders and with data on the absorption of the rare earth ions. El'Yashevich (20) for instance gives the following wavelengths for the absorption of Gd ions: 244/246 nm, 252 nm, 273/274/276/279 nm and 306/311 nm. In Fig. 7 we give the reflection curves of $\text{Gd}_2\text{O}_3\text{-Eu}$ and $\text{Gd}_2\text{O}_3 \cdot \text{B}_2\text{O}_3\text{-Eu}$. The group of 273-279 nm absorption lines are clearly shown. The width of the lines is determined by the resolving power of the instrument (slit width), which is about 0.5 nm at 300 nm.

Considering the excitation spectra of the gadolinium salts, it can be seen that the excitation peaks are found at wavelengths corresponding closely to the Gd absorption lines. Thus the energy absorbed by the gadolinium ions is transferred to the europium ions, giving rise to the red europium fluorescence. The Eu emission due to the characteristic Gd absorption lines is only found in cases where the host lattice absorption is weak with respect to that of the Gd ions. Excitation lines due to Eu absorptions are also weakly present; this can be seen, e.g., in $\text{Gd}_2\text{O}_3 \cdot \text{B}_2\text{O}_3\text{-Eu}$.

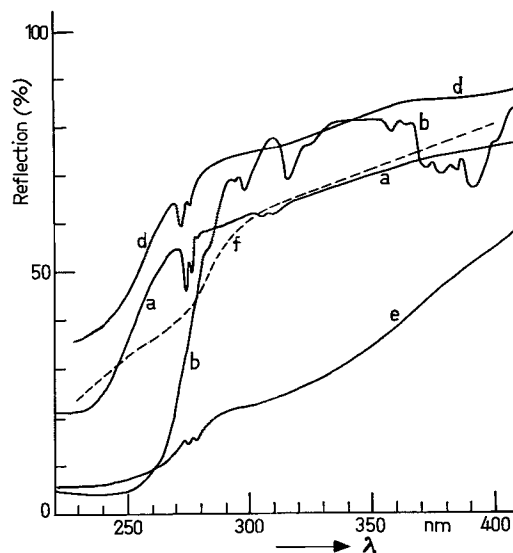


Fig. 7. Diffuse reflection spectra: (a) $\text{Gd}_2\text{O}_3 \cdot \text{B}_2\text{O}_3\text{-Eu}$; (b) EuPO_4 ; (c) $\text{Gd}_2\text{O}_3\text{-Eu}$; (d) $\text{Gd}_2\text{O}_3 \cdot \text{B}_2\text{O}_3\text{-Eu}$; (e) $\text{GdPO}_4\text{-Eu}$; (f) $\text{La}_2\text{O}_3 \cdot 2\text{B}_2\text{O}_3\text{-Eu}$.

It is not yet clear in what way the energy is transferred from gadolinium to europium. Radiative transfer is not very probable because the unactivated Gd_2O_3 does not show the 310 nm Gd emission when excited with the 250-270 nm radiation. It may be that the energy transfer is due to a quantum mechanical resonance process, analogous to that occurring in tungstates and molybdates activated with samarium. This process has been studied by Botden (21). Energy transfer from one rare earth ion to another was already reported by Van Uitert and Soden (22), dealing with alkali metal ion rare earth tungstates, like $\text{Li}_{0.5}\text{Tb}_{0.5-x}\text{Eu}_x\text{WO}_4$ where the Eu^{3+} emission is greatly enhanced by the incorporation of Tb^{3+} . The matter is extensively discussed by Van Uitert (23), referring also to measurements by Garrett and Kaiser (24) who found an enhancement of the Tb^{3+} emission in CaF_2 when Ce^{3+} ions were incorporated. When, however, Ce^{3+} and Tb^{3+} are incorporated into tungstates, the Ce^{3+} strongly quenches the Tb^{3+} emission. All these phenomena are accounted for by considering the relative situation of the Tb^{3+} and Eu^{3+} levels involved in the former case and the Ce^{3+} and Tb^{3+} levels in the latter case.

This explanation is in accordance with our case of Eu-activated Gd compounds, where the excited Gd levels are lying higher than the $^5\text{D}_0$ level of the Eu so that transfer from Gd to Eu is possible. Holloway, Kestigian, and Newman (25) observed energy transfer from terbium to europium in $(\text{Tb}_{0.8}\text{Eu}_{0.2})_2(\text{WO}_4)_3$. The mechanism of the transfer was not elucidated.

In EuPO_4 the excitation lines due to Eu absorption are of course very strong, caused by the large amount of Eu present in the lattice. The excitation and reflection spectra are shown in Fig. 6 and 7.

Efficiency.—In Table I the efficiencies of the Eu emission of the phosphors at room temperature are given for excitation in the 250-270 nm region. These efficiencies are corrected for the reflection of the ex-

Table I. Efficiencies

Sample no.	Excitation	Reflection, %	250-270 nm Radiant efficiency, %	Quantum efficiency, %
1	$\text{Gd}_2\text{O}_3\text{-0.06 Eu}$	13	22	52
2a	$0.83 \text{ Gd}_2\text{O}_3 \cdot \text{B}_2\text{O}_3\text{-0.02 Eu}$	59	21	48
2b	$0.80 \text{ Gd}_2\text{O}_3 \cdot \text{B}_2\text{O}_3\text{-0.20 Eu}$	34	24	55
3	$\text{Gd}_2\text{O}_3 \cdot 2\text{B}_2\text{O}_3\text{-0.02 Eu}$	48	11	25
4	$0.83 \text{ La}_2\text{O}_3 \cdot \text{B}_2\text{O}_3\text{-0.02 Eu}$	16	10	23
5	$\text{La}_2\text{O}_3 \cdot 2\text{B}_2\text{O}_3\text{-0.02 Eu}$	34	15	35
6	$\text{GdPO}_4\text{-0.06 Eu}$	46	12	28
7	EuPO_4	12	6	14

citing radiation (17). In this way the quantum efficiency (the ratio of the number of emitted quanta and the number of absorbed quanta) is obtained.

From the table it can be seen that Gd_2O_3 -Eu and $Gd_2O_3 \cdot B_2O_3$ -Eu are efficient phosphors for uv excitation in the neighborhood of 250 nm.

Partial substitution of Gd by La (up to 20 mole %) results in a less efficient phosphor, whereas substitution by yttrium (also investigated to a percentage of 20 mole %) does not affect the brightness of the fired phosphor. The last phenomenon is in accordance with the fact that Y_2O_3 -Eu is an efficient phosphor, too (7, 8). We measured this phosphor and found a reflection of 32% and a quantum efficiency of about 50% at 210 nm. The spectral emission consists of a narrow line at 611 nm while the lines in the neighborhood of 590 nm are weak as is the case with Gd_2O_3 -Eu.

The quantum efficiency curve of Y_2O_3 -Eu was already given by Chang (7), who finds a maximum excitation at a wavelength of about 240 nm and a quantum efficiency of 40% at this wavelength. In this connection it is important to note that the luminescent efficiency of phosphors, even with a given composition, strongly depends on factors such as purity and reactivity of the starting materials and also the firing conditions. Up to now these factors were not studied by us in detail. So the values given in Table I still might rise and cannot be used for definite comparisons for the various phosphors investigated.

In the preparation of gadolinium borates-Eu, about 0.20g atom Eu per mole of the host lattice is required to give the phosphor a high brightness.

Concerning the phosphates it follows from Table I that the quantum efficiency of $GdPO_4$ -Eu is much higher than that of $EuPO_4$. When the Eu content in $GdPO_4$ was increased from 0.06g atom per mole $GdPO_4$ to 0.10g atom, the uv absorption increased and an increase in brightness of nearly 70% was found.

Decay.—In the literature some data are already to be found on the life times of rare earth fluorescence. In particular much work has been carried out by Dieke and associates (26).

In most cases the decay curves are exponential. The time which the intensity takes to fall to $1/e$ of the original value is given for some of the phosphors investigated in Table II. Chang (7) found in Y_2O_3 -Eu, which phosphor is similar in performance to Gd_2O_3 -Eu, a decay time of 0.87 msec at room temperature and at the temperature of liquid nitrogen. Wickersheim and Lefever (8) give a lifetime of the 5D_0 state in Y_2O_3 -Eu of 0.90 msec, the principal emission being a transition from the 3D_0 to one of the 7F_2 levels. These values are very close to the lifetime found by us in Gd_2O_3 -Eu, viz., 0.8 msec at room temperature and 0.65 msec at $-196^\circ C$. In many cases the decay times are about equal at room temperature and at the temperature of liquid nitrogen, indicating that the efficiency for lower temperatures does not increase appreciably. For Gd-borate-Eu the decay is faster at low temperature. For Eu-phosphate, which shows a non-exponential decay, the decay with cathode-ray excitation at liquid nitrogen temperature is about 10 times slower than at room temperature.

Table II. Decay times in milliseconds

Sample no.	Phosphor	U.V. excitation		C.R. excitation	
		20°C msec	-196°C msec	20°C msec	-196°C msec
1	Gd_2O_3 -0.06 Eu	0.8	0.65	0.85	
2a	0.83 $Gd_2O_3 \cdot B_2O_3$ -0.02 Eu	2.0	0.5	2.8	
3	$Gd_2O_3 \cdot 2B_2O_3$ -0.02 Eu			2.7	
4	0.83 $La_2O_3 \cdot B_2O_3$ -0.02 Eu	1.6	1.7	1.8	
5	$La_2O_3 \cdot 2B_2O_3$ -0.02 Eu			0.75	
6	$GdPO_4$ -0.06 Eu			3.0	
7	$EuPO_4$	0.6	0.5	0.675	0.8

The samples investigated are the same as given in Table II.

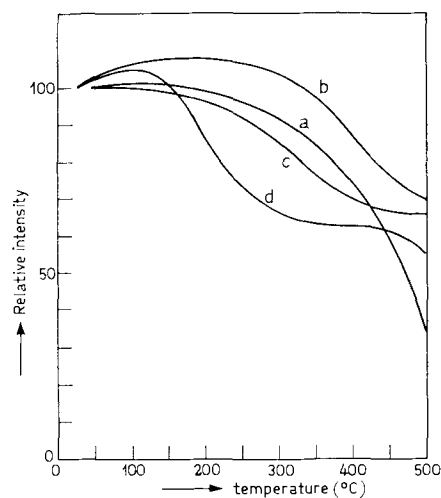


Fig. 8. Variation of brightness with temperature, excitation by germicidal lamp (mainly 254 nm radiation): (a) Gd_2O_3 -Eu; (b) $Gd_2O_3 \cdot B_2O_3$ -Eu; (c) $GdPO_4$ -Eu; (d) $EuPO_4$.

Dieke and Hall concluded from their measurements on rare earth salts that the decay times would be approximately the same for the same rare earth ion in various compounds. We found, however, much longer lifetimes, viz., up to 2.0 msec than they found for $EuCl_3$ (0.120 msec). In our opinion it is difficult to understand why the lifetimes should be the same, as the lifetime is dependent on the occurrence of radiationless transitions originating from the same level as the fluorescent transitions. The natural lifetime of the excited level is of the order of 10 msec. Apparently the number of radiationless transitions in our phosphors is smaller, leading also to higher efficiencies.

Temperature dependence.—The temperature dependence of the phosphors investigated was determined by irradiating a phosphor plaque with a low-pressure mercury discharge quartz lamp, mainly emitting 254 nm radiation, with a Bäckström filter ($NiSO_4 \cdot CoSO_4$ solution) placed between the lamp and the phosphor plaque and a selenium photocell corrected for the eye sensitivity with the aid of a filter.

It may be seen from Fig. 8 that the phosphors show a relatively high brightness at elevated temperatures.

X-ray analysis.—The x-ray diffraction of the phosphors was determined by conventional x-ray diffraction techniques, using $CuK\alpha$ radiation from a Philips Norelco Unit.

Table III gives x-ray diffraction patterns of $EuPO_4$ and $GdPO_4$ -Eu. It may be seen that the diagrams are nearly identical. Concerning the borates, in addition

Table III. X-ray diffraction patterns

$Eu_2O_3 \cdot P_2O_5$		$Gd_2O_3 \cdot P_2O_5$ -Eu	
d, Å	Int.	d, Å	Int.
5.13	5		
4.70	5	4.72	5
4.57	9	4.57	12
4.11	20	4.11	18
4.00	7	4.00	8
3.47	5	3.50	4
3.44	5	3.45	7
3.24	24	3.23	22
3.04	39	3.04	40
2.92	8	2.92	6
2.814	35	2.814	32
2.564	10	2.564	9
2.398	8	2.398	7
2.146	9	2.146	9
2.104	12	2.104	13
2.080	8	2.080	8
1.926	13	1.926	10
1.838	10	1.838	6
1.827	8	1.827	8
1.734	9	1.734	6
1.704	11		

to the preparations with a molar ratio $R_2O_3/B_2O_3 = 1$, preparations were also made in which the molar ratio was 2 and 3, respectively. In general this resulted in less crystallized products, probably due to an excess of B_2O_3 . The x-ray diagrams of the preparation made with $R_2O_3/B_2O_3 = 1, 2, \text{ and } 3$, respectively, are nearly identical. This is in accordance with Felten (27) who concluded that there would exist only one type of rare earth borate, *viz.*, RBO_3 . However, the spectral emission of the fluorescence for $Gd_2O_3 \cdot xB_2O_3$ -Eu with $x = 1$ is different from that with $x = 2$ and 3, and the same holds for $La_2O_3 \cdot xB_2O_3$ -Eu. The difference is especially noticeable in the lines with F_1 as lower state (see Fig. 2 and 3).

$LaBO_3$, $PrBO_3$, and $NdBO_3$ are isomorphous with aragonite (28), whereas Felten found that the borates of yttrium and the remainder of the rare earth series (including Gd) have a unit cell similar to that of vaterite, a third polymorph of $CaCO_3$.

The x-ray diffraction data found in our Gd borate preparations are similar to those given for yttrium borate (29).

Applications.— Gd_2O_3 -Eu is very suitable as a laser material for short-wavelength uv excitation, owing to the narrow emission line at 611 nm in which most of the emitted power is concentrated.

The phosphors offer further possibilities for application in high-pressure mercury discharge lamps (color correction) because of the good temperature dependence. The sharpness of the lines is then of course a disadvantage.

Some of the phosphors investigated might be interesting for application as a red component in color television tubes. Only those phosphors are suitable which have their main emission peak at 611-614 nm with only weak emission at shorter wavelengths, *e.g.*, Gd_2O_3 -Eu. The color coordinates of this emission correspond closely to what is required for the red component in color television tubes.

The radiant efficiencies of these phosphors are not so high with cathode-ray excitation, but the lumen equivalent has a value of more than 300 lm/w, as compared with 75 lm/w and 140 lm/w for the conventional red phosphors (0.2 Zn 0.8 Cd) S-Ag and $Zn_3(PO_4)_2$ -Mn. This high lumen equivalent is due to the small widths of the emission lines. This will be considered in more detail elsewhere.

Acknowledgments

The authors wish to express their thanks to Mr. J. G. Verlijndonk and Mr. A.A.L. Sleutjes for preparing the phosphors; to Mr. J.A.A. Bertens, Mr. C.D.J.C. de Laat, and Mr. C. J. Loyen for carrying out the measurements on the phosphors investigated and to Mr. W. Parchen for the x-ray diffraction analysis.

Manuscript received May 1, 1964; revised manuscript received July 7, 1964. This paper was prepared for delivery before the Toronto Meeting, May 3-7, 1964.

Any discussion of this paper will appear in a Discussion Section to be published in the June 1965 JOURNAL.

REFERENCES

1. F. A. Kroeger, "Some Aspects of the Luminescence of Solids," p. 291, Elsevier Publishing Co., Amsterdam—New York (1948).
2. L. G. Van Uitert, *J. Chem. Phys.*, **37**, 981 (1962).
3. L. G. Van Uitert, *This Journal*, **110**, 1 (1963).
4. R. E. MacDonald, M. J. Vogel, and J. W. Brookman, *I.B.M.J. Res. Develop.*, **6**, 363 (1962).
5. H. J. Borchardt, *J. Chem. Phys.*, **39**, 504 (1963).
6. H. J. Borchardt, *ibid.*, **38**, 1251 (1963).
7. N. C. Chang, *J. Appl. Phys.*, **34**, 3500 (1963).
8. K. A. Wickersheim and R. A. Lefever, *This Journal*, **111**, 47 (1964).
9. R. C. Ropp, *ibid.*, **111**, 311 (1964).
10. E. Nardi and S. Yatsiv, *J. Chem. Phys.*, **37**, 2333 (1962); M. L. Bhaumik and C. L. Felk, *J. Opt. Soc. Amer.*, **53**, 1346 (1963).
11. A. Lempicki and H. Samelson, *J. Chem. Phys. Letters*, **4**, 133 (1963).
12. G. Urbain, *Ann. Chim. Phys.*, **18** [8], 293 (1909).
13. H. Lange, *Ann. Phys.*, **32**, 361 (1938).
14. K. Watanabe and E.C.Y. Inn, *J. Opt. Soc. Amer.*, **43**, 32 (1953).
15. A. Brill and H. A. Klasens, *Philips Res. Repts.*, **7**, 421 (1952).
16. A. Brill, H. A. Klasens, and P. Zalm, *ibid.*, **8**, 393 (1953).
17. A. Brill and W. Hoekstra, *ibid.*, **16**, 356 (1961).
18. *Nat. Bur. of Stand. Techn. News Bull.*, **42**, 145 (1958).
19. L. B. DeShazer and G. H. Dieke, *J. Chem. Phys.*, **38**, 2190 (1963); J. D. Kingsley and J. S. Prener, *Phys. Rev.*, **126**, 458 (1961).
20. M. A. El'Yashevich, "Spectra of the Rare Earths," Book 2, p. 527, translated from Russian by United States Atomic Energy Commission, Washington (1961).
21. Th. P. J. Botden, *Philips Res. Repts.*, **6**, 425 (1951); **7**, 197 (1952).
22. L. G. Van Uitert and R. R. Soden, *J. Chem. Phys.*, **36**, 1289 (1962).
23. L. G. Van Uitert, *Metallurgy of Advanced Electronic Materials*, **19**, 305 (1962).
24. C. G. B. Garrett and W. K. Kaiser, U.S. Pat. 3,079,347 (1963).
25. W. W. Holloway, M. Kestigian, and R. Newman, *Phys. Rev. Letters*, **11**, 458 (1963).
26. G. Dieke and L. A. Hall, *J. Chem. Phys.*, **27**, 465 (1957).
27. E. J. Felten, *J. Inorg. & Nuclear Chem.*, **19**, 61 (1961).
28. E. M. Levin, R. S. Roth, and J. B. Martin, *Am. Mineralogist*, **46**, 1030 (1955).
29. R. E. Newnham, M. J. Redman, and R. P. Santoro, *J. Am. Ceram. Soc.*, **46**, 253 (1963).

Plasma Anodized Aluminum Oxide Films

George J. Tibol and Robert W. Hull¹

Applied Research Laboratory, General Instrument Corporation, Newark, New Jersey

ABSTRACT

A low-pressure gas plasma of oxygen ions has been used as the electrolyte for anodizing evaporated aluminum films on glass substrates. The oxide film grows at 22Å/v at low voltages, while above 50v, the growth rate is somewhat less. Films have been anodized up to 90v. Capacitors formed of such plasma anodized aluminum films with aluminum counterelectrodes are almost entirely free of pinholes and other faults so that they exhibit very low and nearly nonpolar leakage currents. Capacitors anodized at 50v have shown excellent electrical and life performance when operated at 20v, even at temperatures of 150°C.

Electrochemical oxidation at the anode of an electrolytic cell is well known as a process for the formation of thin insulating oxides on aluminum, tantalum, etc., for capacitor dielectrics. Such anodization is

¹ Present address: Weston Instruments, Newark, New Jersey.

customarily performed in a liquid electrolyte, usually aqueous, containing a dissolved ionized salt. However, the electrolyte providing the oxygen ions to the anode need not be a liquid. Miles and Smith (1) recently

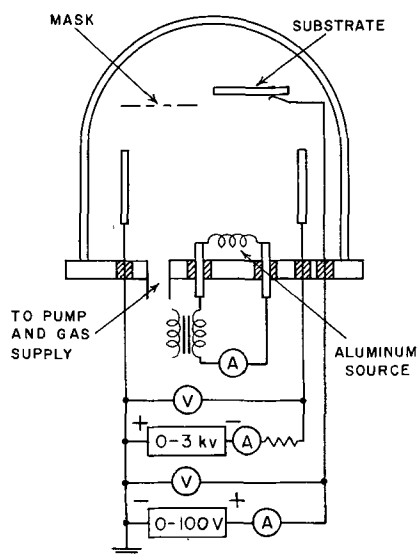


Fig. 1. Schematic plasma anodizing system

reported the use of a plasma of oxygen ions for anodizing. The plasma is generated by a low-pressure glow discharge in oxygen gas. Part of the ions are extracted from the discharge by the anodizing potential for oxide formation at the surface of the third electrode, as shown in Fig. 1. The plasma itself, outside the region of the cathode dark space, is very nearly at the potential of the plasma anode. Thus, the anodizing cathode is the glow discharge anode.

Miles and Smith reported near perfect films of Al_2O_3 about 20Å thick, and accordingly the plasma anodizing process was investigated as a means of forming thick dielectric films suitable for capacitors. Evaporated aluminum was chosen as the metal to be oxidized because thin films of aluminum have good conductivity and are adherent to the glass substrate on which they are deposited. A thin film circuit can thus be prepared using aluminum conductors, Al_2O_3 capacitor dielectric, and resistors of nichrome or other refractory material.

Capacitors formed by plasma anodizing aluminum were operable at 20v when anodized at 50v. They are essentially nonpolar when made with aluminum counterelectrodes and exhibit a leakage current which increases with voltage only gradually until breakdown occurs suddenly at nearly the anodizing voltage. The oxide film forms at a rate of approximately 22Å/v below about 50 v.

Experimental Procedure

A bell jar vacuum system with a liquid nitrogen trap was used for these experiments. Pressures of $1-2 \times 10^{-6}$ Torr were obtained. The capacitors were formed on soft glass slides by deposition of evaporated aluminum, anodization, and deposition of aluminum counterelectrodes in one continuous cycle without opening the vacuum system. The system was equipped with a series of masks and tungsten evaporation filaments for depositing the appropriate test patterns as shown in Fig. 2. A glow discharge electrode was provided for anodizing, with potentials as in Fig. 1. Purified oxygen was passed through a liquid nitrogen trap (some O_2 liquifies) before being admitted during the anodizing cycle at a pressure of 50μ directly over the surface of the slide. The local partial pressure of water vapor was thus kept to a minimum.

Particular attention was given to contamination by dust, pump oil, or unintended oxidation. Slides were cleaned ultrasonically in detergent and in hot chromic-sulfuric acid solution and immediately transferred to the vacuum system. They were further cleaned by ion bombardment before evaporating the base electrode. The evaporant was 99.999% Al. Previous outgassing

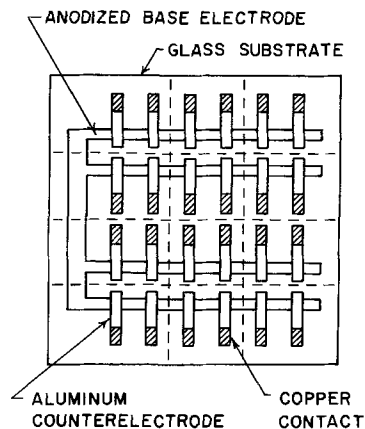


Fig. 2. Anodizing test pattern. Cutting along the dotted lines provides double-unit capacitors; typical crossover is 0.060 in. square.

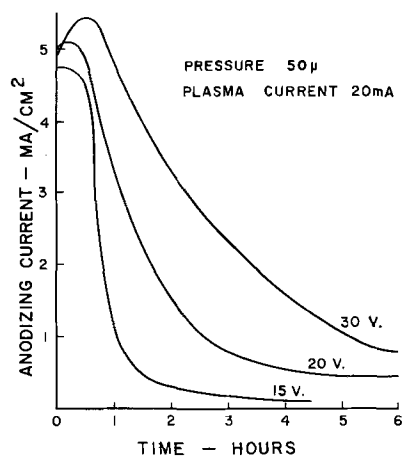


Fig. 3. Anodizing curves. Current held constant at start, then voltage held constant at indicated value.

made it possible to keep the pressure at 2×10^{-6} Torr during evaporation. As soon as possible after this evaporation, oxygen was admitted, and both anodizing and glow discharge potentials were applied. Anodizing voltage was raised in steps such that the current density did not exceed 5 ma/cm² (30 ma total). It was not possible to draw more than this without seriously disturbing the glow discharge which operated at 50 ma. The anodizing current fell to a low value, as shown in Fig. 3, in a manner similar to that observed with wet electrolytes. Anodizing was continued until the current diminished to a few per cent of the initial value. Voltages up to 90 were used. Connection to the substrate was made by a previously anodized aluminum wire so the observed current was entirely that flowing to the substrate.

After anodizing, the oxygen was pumped out and aluminum counterelectrodes evaporated. Copper contact areas, not over the capacitor element, were finally evaporated over the counterelectrodes to act as lands for lead attachment. Cleanliness of the various interfaces was indicated by the excellent adhesion between layers. Copper lead wires, soft soldered to the copper pads, could not be pulled free without breaking either the glass, the solder, or the wire.

The plasma anodized capacitors are stable as produced, but are usually protected from mechanical damage during handling by coating with silicone varnish or epoxy resin.

Discussion

Various investigators have established the fact that anodization in liquid electrolytes proceeds by ionic diffusion of aluminum through the Al_2O_3 layer to the surface where more oxide is formed [see, for example,

the work of Amsel and Samuel (2)]. Ionic diffusion can occur only so long as the applied field strength is sufficient. The available field diminishes as the oxide film grows. At constant voltage, the anodizing current will therefore decrease. A similarly diminishing current is observed in plasma anodization as shown by the curves of Fig. 3.

The electrolytic efficiency of the gas anodizing process was poor in these experiments, perhaps owing to the presence of a large electron population in the plasma of the particular discharge used. Oxide thickness and capacitance was dependent on anodizing voltage and not significantly dependent on the anodizing time up to 24 hr. The major growth appeared to stop after the anodizing current had fallen to a small value, using both capacitance and interference color as a growth indicator.

Oxide thickness measurement

Determination of the thickness of the oxide film is not straightforward since there is no *a priori* assurance that the film has the density of crystalline Al_2O_3 . Thus neither index of refraction nor dielectric constant are known.

The oxide grows partly above and partly below the original aluminum surface since the aluminum removed is converted to Al_2O_3 of larger volume. Multiple beam interferometry can be used to determine the oxide thickness step above the aluminum surface at an oxide edge. However, the depth of oxide penetration below the original aluminum surface (*i.e.*, aluminum removed by ionic diffusion) cannot be measured readily as there are no convenient solvents for removing only the oxide layer. A computation of total oxide thickness from the height of oxide above the original aluminum surface would require the assumption of uniform structure throughout the film thickness.

If a single crystal sample is to be destroyed in the process of oxide thickness measurement, the vacancy pit technique of Doherty and Davis (3) can be used to remove flakes of oxide. These flakes are deposited on glass flats, silvered, and their thickness measured by the multiple beam. Alternately, the flakes may be supported on collodion, angle shadowed, and examined by transmission electron microscopy. This technique is not useful for evaporated films.

When many samples are to be examined nondestructively we have found the following procedure useful and of adequate precision. If we consider a transparent dielectric film of less than the density of the crystalline solid, it will exhibit an index of refraction which is given by $n = (n_1 - 1)f + 1$

$$n = 1.75 \text{ for } \text{Al}_2\text{O}_3 \text{ at } 4900\text{\AA}$$

where f is the fraction of full density of material of index n_1 . The dielectric constant follows the series capacitor law so that $k = 1/(1-f) + f/k_1$, where f is again the fraction of material of dielectric constant k_1 .

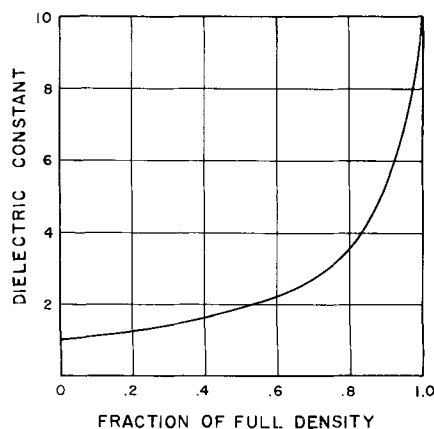


Fig. 4. Dielectric constant of Al_2O_3 . An average value of $K = 10$ for crystalline Al_2O_3 is assumed.

Such a curve is shown in Fig. 4 for Al_2O_3 of $k = 10$ (an average value for unoriented crystalline Al_2O_3). Two measurements are now made on the unknown film: (a) capacitance per unit area; and (b) optical thickness as judged by the peak of the interference color observed by light transmitted down and back through the film. A semitransparent overcoating enhances the interference color. Use of the interpolation curves provides that value of film density whose n and k satisfy the two measurements.

The optical set-up for the above process consists simply of a diffuse white light source illuminating the sample, a low power microscope to observe the sample in half of the field, and a narrow band filter covering the other half as a visual spectral comparison. The sample may be tilted on a graduated circle to change the optical path length in the film. A polarizer reduces specular reflection at the front surface of the film when observing beyond the Brewster angle. The film thickness then is $t = \lambda / (2n \cos r)$ where r is the angle of refraction and λ is the spectral comparison wavelength.

This procedure can be used for Al_2O_3 films thicker than about 1000Å. For very thick films the method of Pliskin and Conrad (5), using three wavelengths, provides an extension of this simple nondestructive method into the micron range.

All thicknesses reported here were measured by multiple beam interferometry and for films above 50v, by the optical spectral matching procedure. In both cases the measured thickness depends on an assumed value of n so that the curves of Fig. 4 are used. The interferometric measurement is subject to considerable error as two thickness measurements must be subtracted. Fringes were of the order of $\lambda/10$ wide. Estimated errors are indicated in the figures.

Results

Data on a number of plasma anodized films are presented in Fig. 5. Most films were formed with the substrate at the local ambient temperature in the vacuum system, estimated to be nearly 200°C. Under these conditions anodizing was carried out up to 90v. Anodizing times were sufficient to reduce the anodizing current to a few per cent of the initial value; at 90v, times were as long as 20 hr.

The Al_2O_3 films were examined for thickness by both multiple beam interferometry and by refracted ray color matching as described above. The observed thicknesses have been corrected by the use of Fig. 4 for densities of less than 100%. Capacitance values for use in this correction were obtained by measurement at 1000 cycles of the 0.060x0.60 in. crossovers. The lowest observed Al_2O_3 density was 92% and the highest 98% (k between 6 and 8.5).

The oxide growth shows a linear rate at low voltages of about 22Å/v. The rate found by Miles and Smith (1) up to 9v was 23Å/v. The rate above about

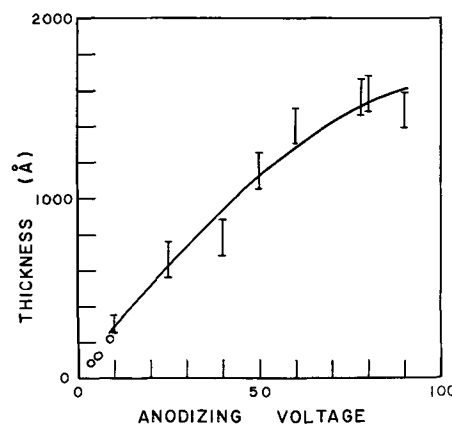


Fig. 5. Plasma anodized film growth: a, I, this work; b, O, Miles and Smith (1).

50v diminishes and may reach a limiting value of thickness near 1600Å for 80-90v. One may expect that voltages sufficient to establish a glow discharge to the sample will prevent further anodization by preventing the establishment of the proper anodizing field.

The plasma anodizing growth rate should be compared to the liquid electrolyte anodizing growth rate of 14.4 Å/v for a quite completely anodized aluminum foil reported by Bernard and Cook (4). Lower rates occurred for less complete anodization. Density of 98% Al₂O₃ was obtained ($k = 8.4-8.5$). The explanation for the higher growth rate of the plasma oxide is not clear at present.

Anodization of Other Metals

The plasma anodization process is applicable to those metals whose oxides are insulators and have sufficiently high ionic mobility. Oxide films that would be soluble in liquid electrolytes may be produced by the gaseous process. For application to electronic circuits those oxides of high dielectric constant are of interest. Accordingly both titanium and tantalum have been anodized up to 60v. Preliminary results lead one to expect that capacitors so made will be satisfactory. In both cases k was found to be in the region of 20.

Capacitor Characteristics

The detailed characteristics of gas anodized aluminum capacitors will be reported elsewhere (6) so that only a survey need be given here. In all cases the capacitors were formed from 0.060 in. wide evaporated aluminum electrodes with aluminum counterelectrodes crossing at right angles, also 0.060 in. wide. Substrates were 0.010 in. thick soft glass, cut by scribing to separate the array into individual units for

testing. Since external contact to the anodized bottom electrode was difficult to make through the oxide, the finished capacitor was frequently arranged to consist of two adjacent counterelectrodes each with capacitance to a common floating section of the base electrode (e.g., with two capacitors in series). The surface of the capacitors was mechanically protected with Teflon spray, silicon varnish, or epoxy resin.

Test results are shown in Fig. 6 on a group of 25 units anodized at 50v and held at 20v d.c. at 150°C. There is a 2% reduction in capacitance during the first 100-150 hr, during which time all evidence of leakage current pulses has ceased. Capacitance change during the next 500 hr is about 1%. The individual units in the test showed a spread in data of about 0.2%, approximately the bridge reproducibility. The accelerated ageing represented by the 150°C data has not yet been compared to room temperature ageing rates.

The characteristics of capacitors made from films plasma-anodized to 50v are shown in Fig. 7. The capacitors have been operated over the temperature range of -65° to +175°C. The temperature coefficient of capacitance is about 300 ppm/°C near room temperature. Dissipation factor at 1000 cycles is about 0.5% at room temperature, rising to 1% at 150°C.

Leakage current through the oxide varies exponentially with inverse temperature in the manner shown in Fig. 8. Current-voltage data on several typical single capacitors, Fig. 9, show ohmic behavior up to about 10v (ca. 10⁶ v/cm) with the current above this

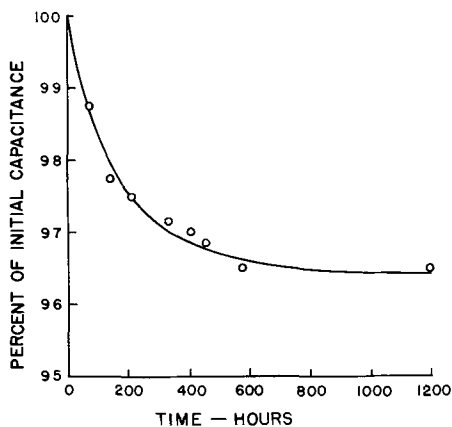


Fig. 6. Life test of plasma anodized capacitors: Anodization voltage, 50v; operating conditions, 150°C, 20v d.c.; average of 25 units (no failures observed).

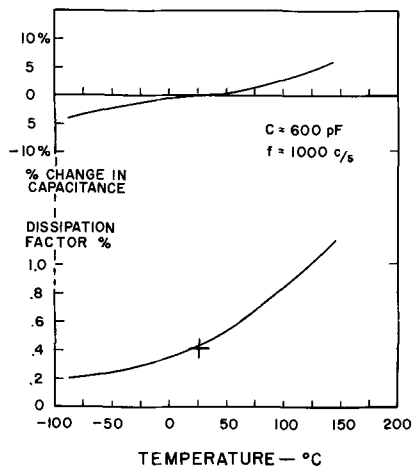


Fig. 7. Capacitance and dissipation vs. temperature. Plasma anodization voltage 50v, aged 120 hr, 150°C, 0.060 x 0.060 in. double units.

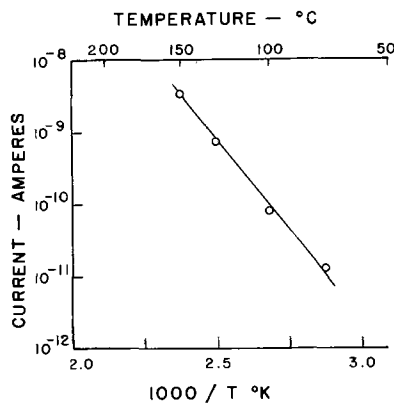


Fig. 8. Leakage current vs. temperature. Plasma anodization voltage 50v, aged 120 hr, 150°C, test voltage, 7.5v; 0.060 x 0.060 in. double units.

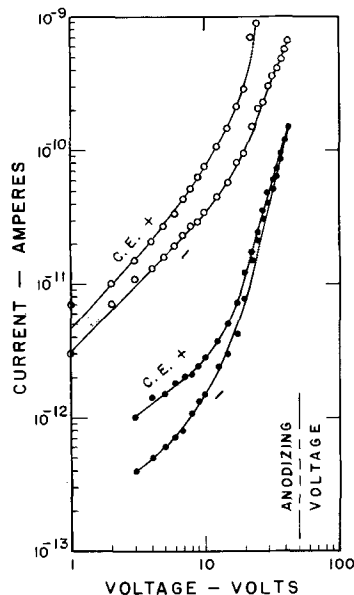


Fig. 9. Volt-ampere characteristics of plasma anodized capacitors. Anodizing voltage 50v, aged 120 hr, 150°C; 0.060 x 0.060 in. single units. Counterelectrode voltage polarity as shown: ●, one typical unit; ○, one of the highest leakage units.

rising slightly faster than $i \propto v^2$. This same slope extends nearly to the voltage at which anodization was done. Currents are higher by a factor of only about two for positive instead of negative polarity of the counterelectrode.

Summary

The experiments reported here show that plasma anodization may be used to produce exceptionally high quality thin film capacitors suitable for microcircuit applications. The complete circuit may be produced in a single pass through the vacuum system. The process parameters may be readily controlled to produce the desired characteristics at high yield. While the reported work has been confined largely to the anodization of aluminum, preliminary experiments with both tantalum and titanium indicate the potential scope of the process.

The Al_2O_3 films produced have an average dielectric constant between 6 and 8 and grow at the rate of 22 Å/v. Films up to 90v have been produced with no indication that the anodizing voltage could not be raised even higher.

Acknowledgment

The authors wish to thank the staff of the Applied Research Laboratory for their extensive assistance, without which this program would have been impossible.

Manuscript received May 11, 1964; revised manuscript received July 27, 1964.

Any discussion of this paper will appear in a Discussion Section to be published in the June 1965 JOURNAL.

REFERENCES

1. J. L. Miles and P. H. Smith, *This Journal*, **110**, 1240 (1963).
2. G. Amsel and D. Samuel, *J. Phys. Chem. Solids*, **23**, 1707 (1962).
3. P. E. Doherty and R. S. Davis, *J. Appl. Phys.*, **34**, 619 (1963).
4. W. J. Bernard and J. W. Cook, *This Journal*, **106**, 643 (1959).
5. M. A. Pliskin and E. E. Conrad, *IBM J. Research*, **8**, 43 (1964).
6. G. J. Tibol and W. M. Kaufman, *Proc. IEEE*, **52** [12] (1964).

Transmission Electron Microscope Investigations on Diffused Silicon Wafers with Relation to Electrical Properties of Controlled Rectifiers

A. N. Knopp

Semiconductor Division, Westinghouse Electric Corporation, Youngwood, Pennsylvania

and R. Stickler

Research Laboratories, Metallurgy Department, Westinghouse Electric Corporation, Pittsburgh, Pennsylvania

ABSTRACT

Uncontrollable variations of electrical properties of controlled rectifiers are considered to be caused by relatively small concentrations of undesired impurities in the semiconductor material. Transmission electron microscope investigations on diffusion zones of silicon wafers showed that a correlation between the electrical properties of controlled rectifiers and microheterogeneities in various diffusion zones exists. Due to mass spectrometric analysis, it seems very reasonable to correlate these microheterogeneities with the desired diffusion product and with heavy metals.

It is known that the electrical characteristics of semiconductor devices can vary considerably, although all measurable processing parameters are held constant. These uncontrollable variations are considered to be caused by impurities, the concentration of which is so small that they cannot be detected by conventional analytical methods. They are frequently referred to as "poisoning effects." The variations of some of the electrical parameters, *e.g.*, increased leakage currents, "soft" avalanche breakdown, and increased forward voltage drops, may result from the presence of heavy metal atoms in the vicinity of the p-n junctions. Such effects have already been described in the literature (1, 2).

The purpose of this paper is to show the existence of a correlation between the presence of certain microheterogeneities in the diffusion zones of the silicon wafers and the electrical characteristics of devices fabricated from such slices. These microheterogeneities could be related to traces of heavy metal atoms in the diffused zone.

Experimental Procedure

(111) silicon wafers sliced from high-purity float-zone ingots were lapped to a final thickness of 250 μ . It can be assumed that the damage resulting from the slicing operation had been removed by lapping. After

lapping, the slices were subjected to a short chemical polishing treatment to remove most of the lapping damage. Subsequently, the slices were carefully washed and dried in a vacuum oven. They were inserted into a quartz tube system, sealed off, and gallium diffused for 40 hr at 1215°C. All precautions were taken to exclude any undesired impurities during the diffusion process.

Several diffusion runs were carried out in the described way. To our best knowledge, the only varying parameters were the silicon wafers and the quartz parts needed as diffusion ampules and as seal-off parts. After diffusion, the majority of the diffused wafers were alloyed to form rectifying and nonrectifying con-

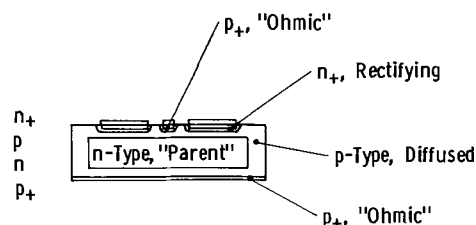


Fig. 1. Controlled rectifier device after diffusion and alloying (schematic cross-section).

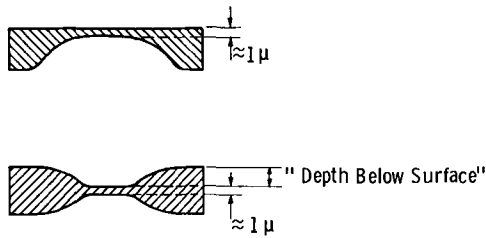


Fig. 2. and 2a. Thinning of diffused silicon specimen for electron microscope investigation (schematic cross-section).

tacts for controlled rectifying devices as shown in Fig. 1. The alloying was carried out at the same cycle with the same thickness of foils except as indicated further below. Furthermore, the geometry of all devices within question was held constant. The diffused junctions were then isolated and protected. The units were finally encapsulated and electrical characteristics measured. The blocking data were taken on an a-c tester while the forward voltage drop was determined by a d-c supply. In order to eliminate or at least to minimize surface effects the units were temperature cycled for many times prior to testing.

The remaining diffused wafers were used for junction depth measurements, impurity distribution by successive lapping, and for microstructure examination by transmission electron microscopy (3). For this investigation, specimens of approximately 1μ thickness were required in order to be transparent to the electron beam. Such specimens were prepared by a jet-chemical polishing process (3). To examine the layers immediately below the specimen surface, an impression was formed from the other side of the specimen until the required thickness was obtained (Fig. 2a). To examine layers at various depths below the specimen surface, the thinning process was carried out from both sides of the specimen (Fig. 2b). By carefully controlling the time for polishing from one side, and final thinning from the other side, approximately 1μ thick layers could be obtained at different distances from the surface. The depth below the surface was determined by focusing with an optical microscope; the obtained values are accurate to $\pm 2\mu$.

After the electron microscope examination, some of the samples were analyzed in a spark source mass spectrometer (4) to obtain information about the presence of a higher concentration of impurity elements in the surface layers. In this type of instrument, only a small area of the specimen surface (approximately 50μ in diameter) is attacked by a high-frequency spark, which causes evaporation and ionization of the elements present to a depth of only several microns. Thus, a semiquantitative chemical analysis is obtained from only a small sample volume.

Results

Electrical measurements.—The silicon wafers of two different diffusion runs were physically evaluated as noted above. The surface concentration of one group, below, designated as Group B, was found to be slightly lower than the other group, designated as Group A; in both cases, the junction depth was 43μ . This can be expected for deep diffusion. Its influence on leakage variation should be negligible since the doping gradient is virtually the same. The variation could affect the forward voltage drop in the opposite direction of the observed results and will be discussed later.

Figures 3a through 3c list results of electrical measurements obtained from two groups of units, the wafers of which stemmed from the above-mentioned Group A and Group B diffusions. These particular runs were chosen due to significant deviations in their reverse blocking capability and forward characteristics, although essentially no differences in diffusion and alloying parameters were apparent except the one which was already mentioned.

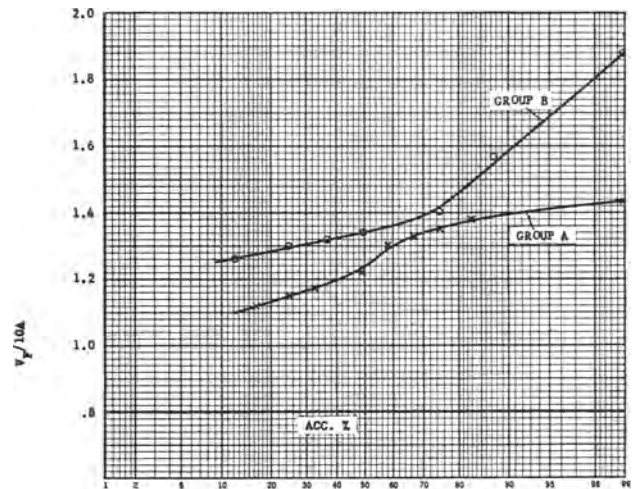


Fig. 3a. Distribution of V_F .

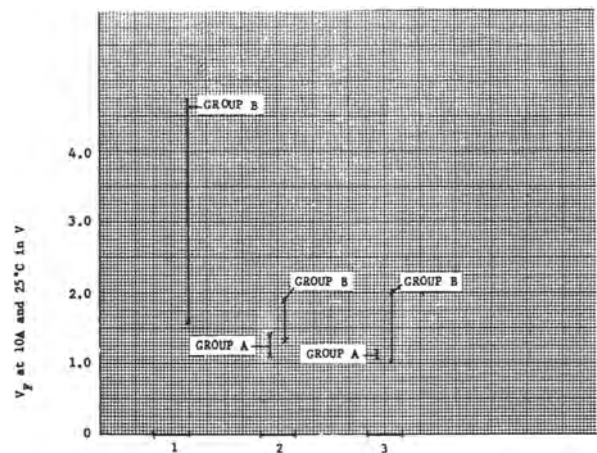


Fig. 3b. Lower and upper limits of V_F as a function of alloying depth. 1, shallow alloyed; 2, standard alloyed; 3, deep alloyed.

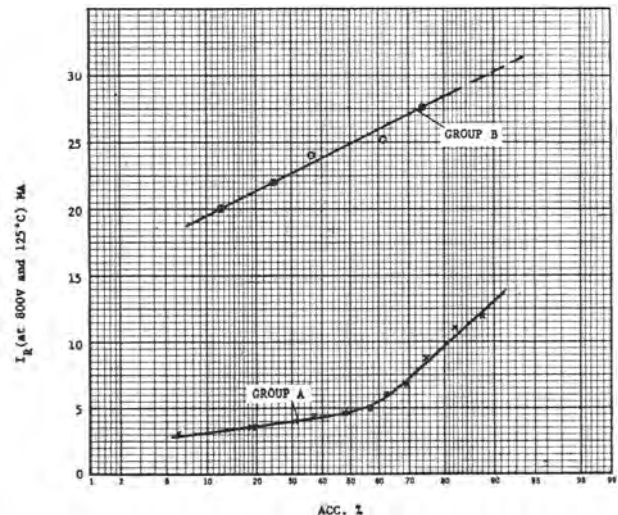


Fig. 3c. Distribution of I_R .

Figure 3a shows the forward voltage drop distribution of both groups. The average value of Group B is about two-tenths of a volt higher than that of Group A; peak values of Group B are about five-tenths of a volt higher as compared to Group A. In Fig. 3b, we have plotted some results of alloying. The fluctuations in the voltage drop of Group A are considerably less than those of Group B, independent of deeper or shallower penetration of the alloying front. As can be seen from Fig. 3c, Group A shows a considerably

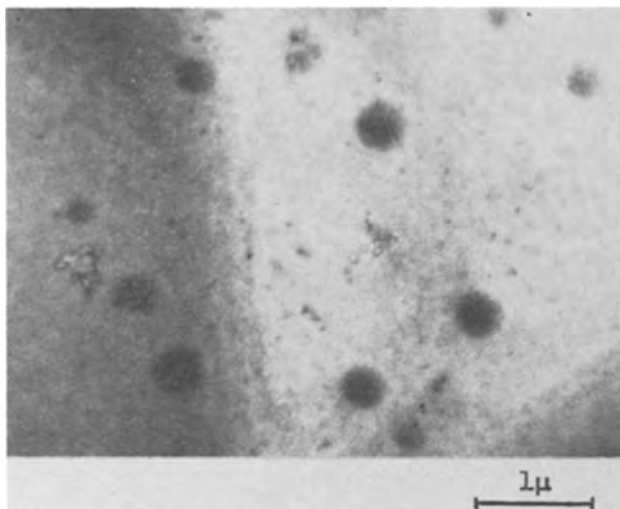


Fig. 4. Ga-diffused silicon group A, transmission electron micrograph of layer 1μ below surface.

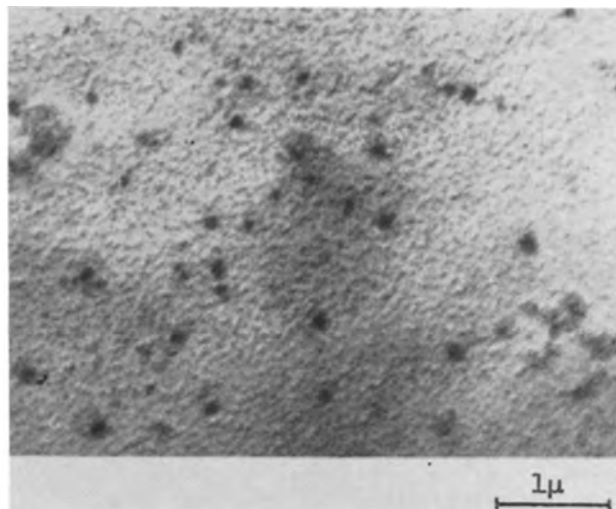


Fig. 6. Ga-diffused silicon group A, transmission electron micrograph of layer 15μ below surface.

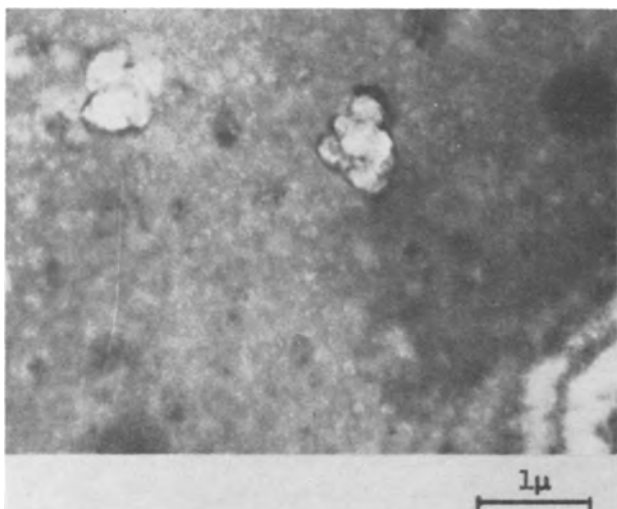


Fig. 5. Ga-diffused silicon group A, transmission electron micrograph of layer 1μ below surface.

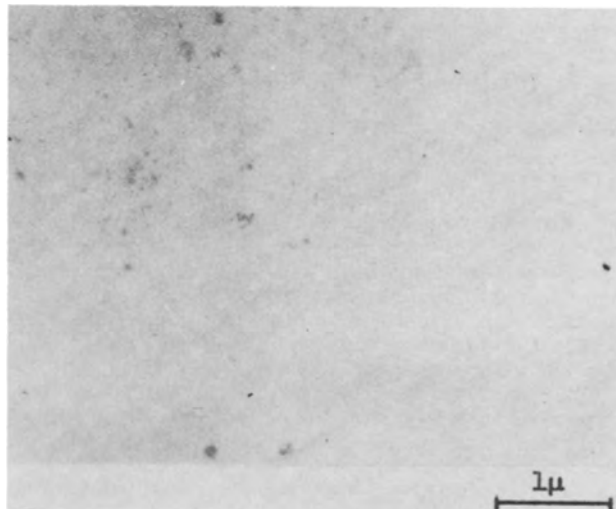


Fig. 7. Ga-diffused silicon group A, transmission electron micrograph of layer 50μ below surface.

smaller leakage current compared to Group B. The distribution of Group A exhibits a concave trend while the curve of Group B does not show this trend.

Transmission electron microscope investigation.—Representative micrographs of the observed microstructure at various depths of the diffused wafers from Group A are shown in Fig. 4 to 7; micrographs of the wafers from Group B are shown in Fig. 8 to 12.

1. *Group A.* Layers at 1μ , 15μ , and 50μ below the surface were investigated. In the surface layer, a large number of dark particles can be seen (Fig. 4) which vary considerably in size and number in different areas. When observed in the electron microscope under a high-intensity beam, these dark particles reacted to form bubble shaped bright zones, probably voids, as shown in Fig. 5.

At a depth of 15μ below the surface, dark particles again are visible (Fig. 6). However, they are smaller in size than those in the surface layer. At a depth of 50μ below the surface, no dark particles are detectable (Fig. 7). In these areas, the specimen looks exactly like an undiffused silicon specimen.

2. *Group B.* Layers at 1μ , 5μ , and 18μ below the surface were examined. In the surface layer, two kinds of irregularly shaped small spots or particles are visible, one kind exhibiting strong contrast and the other a light gray appearance. Very often several dark particles are surrounded by a gray patch (Fig. 8). Occasionally, larger dark particles can be seen.

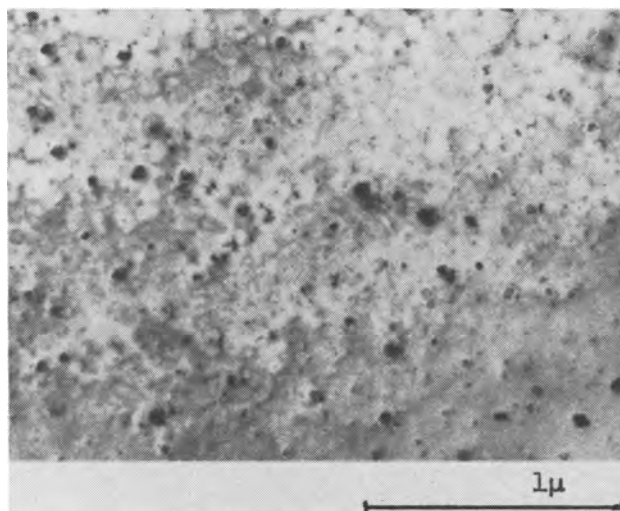


Fig. 8. Ga-diffused silicon group B, transmission electron micrograph of layer 1μ below surface.

In layers 5μ below the surface, clusters of globular dark particles, similar in size to that observed in the Group A specimen, can occasionally be observed (Fig. 9). However, in most areas of the Group B specimen, only fine dark particles are visible which are embedded

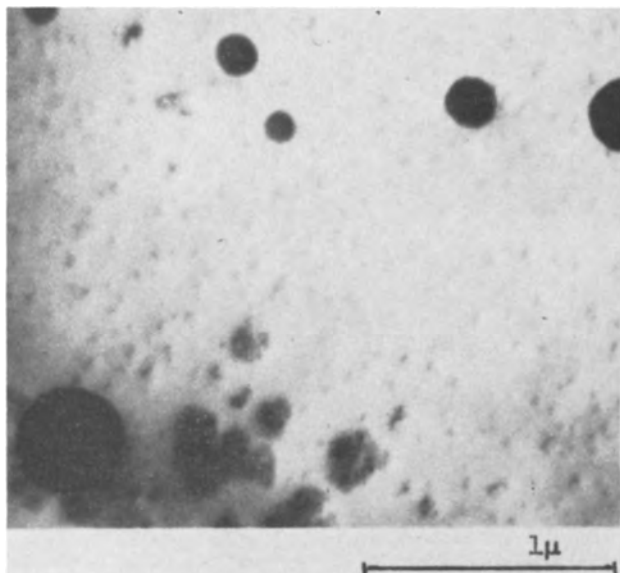


Fig. 9. Ga-diffused silicon group B, transmission electron micrograph of layer 5μ below surface.

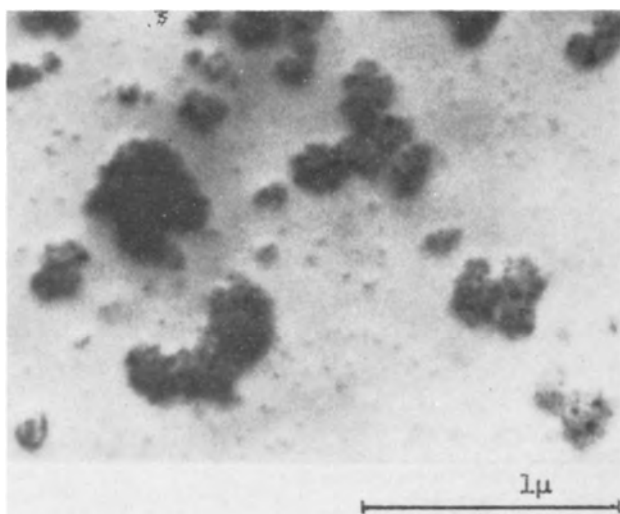


Fig. 10. Ga-diffused silicon group B, transmission electron micrograph of layer 5μ below surface.

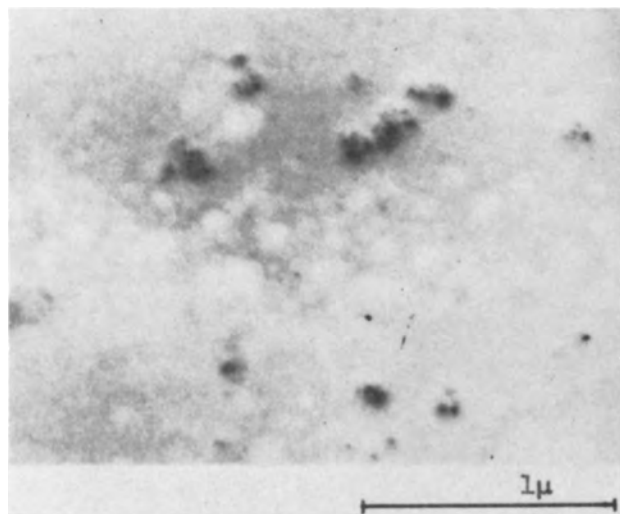


Fig. 11. Ga-diffused silicon group B, transmission electron micrograph of layer 18μ below surface.

in relatively large, gray, irregularly shaped patches (Fig. 10). These patches decrease in size with increasing distance from the specimen surface. At 18μ below

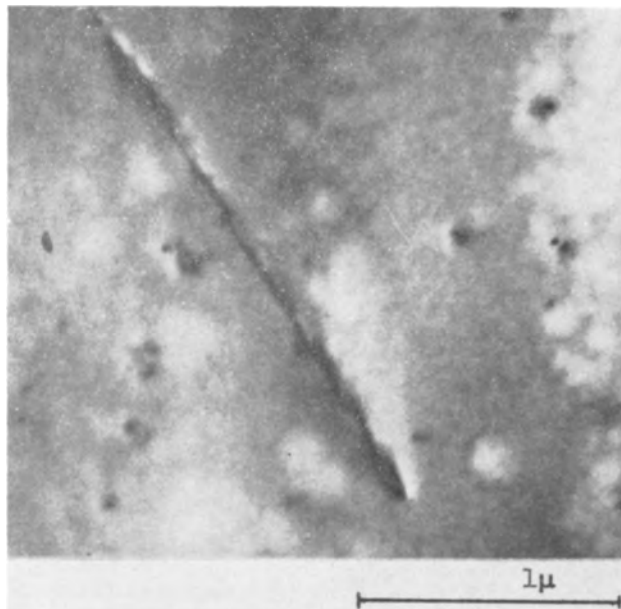


Fig. 12. Ga-Diffused silicon group B, transmission electron micrograph of layer 18μ below surface.

the surface, only small patches with a few dark particles inside are visible (Fig. 11). Dislocations in these areas show a streaked contrast, most probably due to segregation of impurity atoms (Fig. 12).

Mass spectrometric chemical analysis.—The results obtained from several samples of diffused wafers are combined in Table I. It can be seen that samples from Group A contained only the diffused element gallium (apart from traces of alkaline elements and phosphorus which seem not to affect the electrical characteristics), while samples of Group B invariably contained traces of copper, sometimes in concentrations up to 0.5 ppm. No information concerning the presence of traces of iron can be obtained by this method because of coincidence of the iron-spectral line with high order silicon lines.

Discussion

Electrical properties.—From Fig. 3a through 3c, it is obvious that the leakage and forward drop of the devices made of Group A wafers are superior to those made of Group B wafers. One of the possibilities for the fluctuations in the forward voltage drop is due to variations in the concentration of undesired impurity elements being present in the different slices (Fig. 3a and 3b). Although forward voltage drop data of Group A devices were incomplete (Fig. 3b), we nevertheless may conclude, that they scatter relatively little for that group. Deeper alloying seems to narrow the width of fluctuation while Group B appears to be affected very little in this respect. The drastic differences observed at Group B are probably due to the presence of undesirable impurities in the voltage drop determining layers. The higher voltage drop of this group can be given even more weight since the doping level of the gallium was lower in all regions compared to Group A units. Normally, the junction formed on the lower gallium doping level should yield lower V_f .

Quantitative comparison of the leakage current to calculation from recombination theory was not attempted especially in view of the nature of the aggregate revealed by this study. However, qualitatively, the variation of the leakage currents may be ascribed

Table I. Mass spectrograph analysis

Group	Detectable elements
A	Si, Ga, Na, P, K, Ca
B	Si, Ga, Cu, Na, K, Ca

to varying numbers of recombination centers (trap centers) (5) in the devices, which probably originate from the same contamination responsible for the forward voltage drop characteristics (Fig. 3c). The upward trend of the Group A curve may be attributed to some failures different from those described in this investigation.

Microstructure and chemical composition.—Although it was not possible to identify positively the nature and composition of all spots, particles, and patches, it seems reasonable to correlate these with products resulting from the diffusion operation. Thus, the dark particles close to the surface of Group A wafers may be products of the Ga diffusion (the thermal instability could be explained by Ga-rich zones, the Ga evaporating under the high-intensity electron beam leaving voids in the specimen). A very rough estimation has shown that the ratio of the concentrations of the dark particles at the various depths from the specimen surface can be correlated to the ratio of the Ga concentrations at the same depths. The distribution of these "Ga-clusters" in the layers close to the surface appears not to be as uniform as in layers located well within the diffusion zone. The absence of the dark particles in layers more than 50μ below the surface is a further indication that these resemble Ga-clusters.

The globular dark spots and particles which are revealed at shallower depths from the surface of Group B wafers are similar to those shown in micrographs of Group A wafers; thus they, too, may be correlated with Ga-clusters. The irregularly shaped gray patches shown in the micrographs of Group B wafers very probably can be correlated with the presence of the detected heavy metals; e.g., Cu and Fe, which cluster in preferential regions of the crystal. Although by mass spectrometry, only Cu could be detected positively, it is strongly suspected that Fe is present, too. This assumption is further supported by recent results from the analysis of the SiO deposits which were distilled off the silicon wafers during a heat-treatment at elevated temperatures (6) which will be reported elsewhere, and from studies on gettering effects (7). A gettering treatment of Group B wafers utilizing thermally grown oxides, subsequent to diffusion considerably improved the electrical characteristics. Transmission electron microscope investigation of such wafers showed still the presence of dark globular particles while the irregularly shaped gray patches are missing (Fig. 13; compare with Fig. 9 and 10). This appears to be a further indication that the gray patches represent microheterogeneities of heavy metal impurities which are removed by the gettering process. The presence of Na, K, Ca, or P does not seem to have any major influence. Different Si-crystals were used in the diffusion runs evaluated in this study. The evaluation according to well-defined specifications did not show any significant difference. Therefore, it is assumed that the observed variations do not result from the single crystal material itself.

Conclusion

Owing to its lengthy and delicate manner of analysis, the results appear to be limited. However, it seems reasonable to infer that the electrical characteristics of the diffused junctions can be correlated to the presence of microheterogeneities in diffused silicon layers and the heavy metals. The latter can be removed by the known gettering methods and thereby improving the electrical characteristics. It is important to determine the source of undesired contamination of the crystal surface and in the crystal itself. It is highly

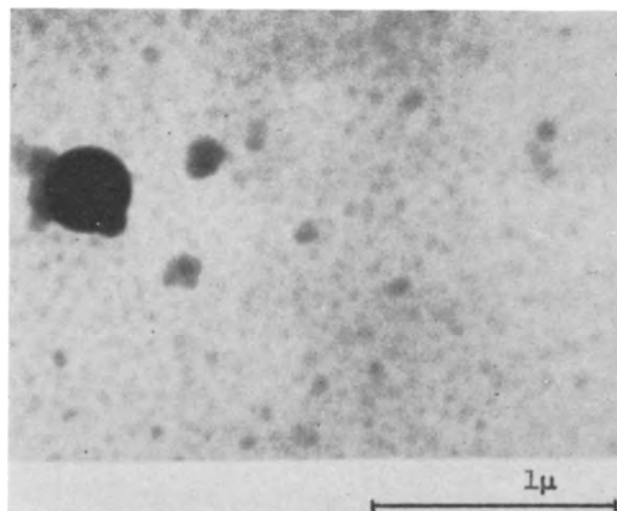


Fig. 13. Ga-diffused silicon group B, after gettering treatment, transmission electron micrograph of layer 6μ below surface (compare with Fig. 9 and 10).

possible that impurities are introduced during the mechanical processing such as slicing, lapping, and polishing treatments. Since the impurities are very difficult to remove completely by known cleaning and etching procedures (8), extreme care has to be exercised to avoid or minimize any contact with the contaminating media (9). Ultimately, new techniques under development to eliminate mechanical processing over and above the more effective cleaning procedures should be adopted. In the meantime, gettering methods can be employed for recovering the desired junction characteristics.

Acknowledgments

The authors wish to thank W. M. Hickam for mass spectrographic analysis; T. C. New and J. W. Faust, Jr., for helpful discussions; R. Kuehn and R. Roth for processing and testing; and R. J. Engle and W. Hughes for specimen preparation for electron microscope investigation.

The present work was partially supported by Westinghouse-Semiconductor Division and the Metallurgy Department of the Westinghouse Research and Development Center, but supplemented by the Navy Department, Bureau of Ships, Electronics Division, in connection with Contract No. N0bsr-87647, Project No. SR-0080301, Task No. 9348.

Manuscript received May 28, 1964. This paper was presented at the Toronto Meeting, May 3-7, 1964.

Any discussion of this paper will appear in a Discussion Section to be published in the June 1965 JOURNAL.

REFERENCES

1. A. Goetzberger and W. Shockley, *J. Appl. Phys.*, **31**, 1821 (1960).
2. J. Prussin, *ibid.*, **32**, 1876 (1961).
3. G. R. Booker and R. Stickler, *Phil. Mag.*, **8** [89], 859 (1963).
4. W. M. Hickam and G. G. Sweeney, *Rev. Sci. Instr.*, **34** [7], 783 (1963).
5. C. T. Sah, R. H. Noyce, and W. Shockley, *Proc. IRE*, **45**, 1228 (1957).
6. A. Knopp, *This Journal*, **110** [1], 82 (1963).
7. S. W. Ing, Jr., R. E. Morrison, L. L. Alt, and N. W. Aldrich, *ibid.*, **110** [6], 533 (1963).
8. J. W. Faust, Jr., *ASTM-STP No. 246*, p. 66 (1958).
9. P. F. Schmidt, Private communication.

Gold in Silicon: Effect on Resistivity and Diffusion in Heavily-Doped Layers

W. R. Wilcox

Aerospace Corporation, El Segundo, California

and T. J. LaChapelle and D. H. Forbes

Autonetics Research Center, North American Aviation, Inc., Anaheim, California

ABSTRACT

Resistivity changes caused by gold diffusion into silicon were studied in detail. The results did not agree with previous theoretical calculations. Radio-tracer studies also showed that previously diffused n^+ (phosphorus) layers greatly retard the diffusion of gold into silicon and increase its solubility. p^+ (boron) diffused layers do not retard gold diffusion but cause a more ideal type of diffusion. Autoradiographs showed lateral nonuniformity of gold concentration unless oxide formation is prevented during pretreatment, plating, and diffusion.

The diffusion of gold into silicon and its effects on the properties of silicon are of great fundamental and practical importance. Collins (1) found that gold has two ionization energy levels in silicon, a donor level at 0.35 eV and an acceptor level at 0.62 eV from the valence band. Because of this gold can compensate both p-type and n-type silicon. Since the levels are deep-lying, however, the compensation is not, in general, one for one. In addition, gold lowers the mobility of current carriers in silicon, which also tends to increase the resistivity. Boltaks (2) made theoretical calculations of resistivity vs. gold concentration for various starting resistivities. He assumed a constant value for mobilities and made approximate calculations for the fraction of gold ionized. Unfortunately, little experimental data are available with which to test his conclusions. Consequently, an extensive set of experiments were required to determine resistivity changes for a number of useful concentration-temperature combinations.

Because of device applications the characteristics of the diffusion of gold into silicon are of considerable importance and interest. This diffusion has been found to be complex and sensitive to the perfection of the silicon (3). A second purpose of the present paper was to investigate the effect of heavy boron or phosphorus doping on gold diffusion. Effects of various other diffusion parameters on the diffusion were also studied.

Experimental Procedure

Radiotracers Au^{198} and Au^{199} were used in the studies of gold plating and diffusion. Known quantities of stable gold and the radiotracer (as dilute gold chloride solutions) were mixed together and displacement plated from dilute HF solutions onto 0.2-in. thick wafers of approximately 0.5-in. diameter. The plating solution (0.1g Au/liter in 0.1M HCl + 0.5M HF) was confined to the top of the wafer so that the exact quantity of gold was known. The wafers were then counted with a thin end-window Geiger-Muller counter. The wafers were heated in vacuum in quartz tubes and then encapsulated in sufficient argon to produce approximately 1 atm at the diffusion temperature.

Autoradiographs of plated and diffused wafers showed that strict avoidance of oxide is necessary to assure lateral uniformity of gold concentration. This includes an initial rinse of the wafer in concentrated HF and diffusion in a reducing or neutral atmosphere (4).

For the resistivity measurements, thin (0.010-0.015 in.) silicon wafers were diffused with gold from both sides for 1 to 12 days and from 700° to 1300°C. After diffusion, a thickness of about 0.001 in. was removed

from each side by lapping, and resistivity measurements were taken by use of the four point probe technique at 20°-25°C.

Diffusion concentration profiles were obtained by counting the wafers, as described in detail in ref. (3) and (4). The counting rates were converted to concentrations by means of the equation derived in the Appendix.

For the study of prior doping effects, wafers with n^+ - and p^+ -diffused layers were initially produced from both Czochralski and floating-zone silicon. Excess red phosphorus was used in sealed quartz capsules at 1225°C for 3 to 6 days to produce the n^+ layers. Using Irvin's curves (5), the surface concentration was calculated to be about $5 \times 10^{20} \text{ cm}^{-3}$. Decaborane ($B_{10}H_{14}$) was used as the volatile diffusant for the boron p^+ diffusion in a quartz capsule adjacent to the above phosphorus run, resulting in a calculated surface concentration of about $2 \times 10^{21} \text{ cm}^{-3}$. Several uniformly doped wafers of lower concentration were also used.

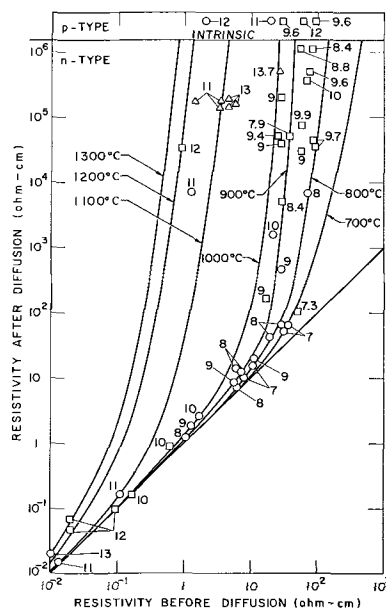


Fig. 1. Resistivity change caused by gold diffusion of n-type silicon. Numbers represent diffusion temperatures in 100°C. Points above the horizontal line represent silicon converted to p-type (final resistivities not indicated). Circle with dot, thin wafer results with long diffusion periods; square with dot, results from tracer experiments on thick wafers; triangle with dot, Boltaks' results (2).

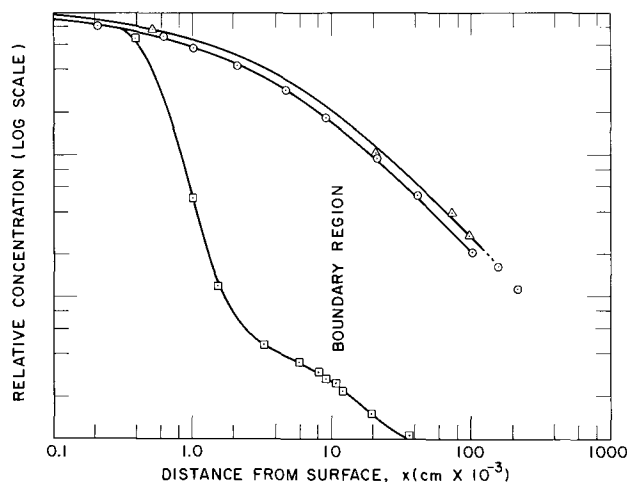


Fig. 6. Comparison of gold diffusion concentration profiles for normal silicon and n^+ -diffused silicon. Triangle with dot, diffused with gold for 330 min at 1000°C , dislocation-free, 0.02 ohm-cm n -type silicon; circle with dot, diffused with gold for 360 min at 1000°C , dislocation-free, 0.005 ohm-cm n -type silicon; square with dot, diffused with gold for 300 min at 1000°C ; n^+ -phosphorus-diffused surface layer as described in text.

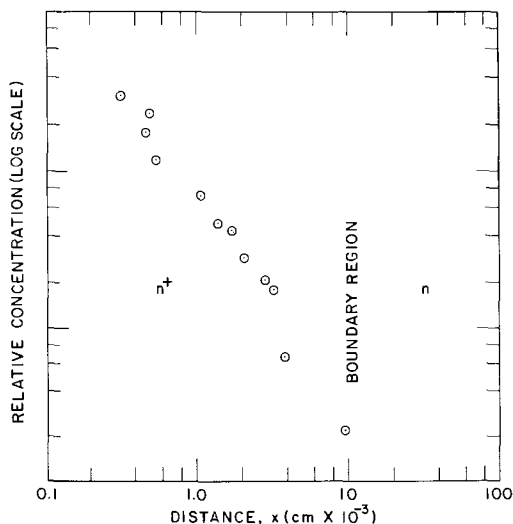


Fig. 7. Concentration profile for gold-diffusion at 900°C for 16 hr into n^+ -phosphorus-diffused surface layer described in text. This is to be compared with Fig. 9 obtained with p^+ layer in the same gold diffusion run.

Above 900°C , no resistivity effect on diffusion was noted for uniformly doped p -type materials above 0.06 ohm-cm or for n -type material above 0.02 ohm-cm . Above this resistivity and temperature range no differences in gold diffusion rate or distribution were detected between n - and p -type silicon. At 900° and 1000°C , the value of K for 0.005 ohm-cm n -type silicon was only about 20% of that given in Table I for higher resistivities.

At 1000° , 975° , and 900°C , n^+ -diffused layers greatly slowed down the gold diffusion. This action led to diffusion concentration profiles of the type shown in Fig. 6 and 7. As can be seen from these figures, the gold concentration for diffused silicon can be as much as two decades lower than for nondiffused material. The effect was qualitatively the same as that observed for uniformly doped silicon. The solubility of gold was higher in heavily doped n -type regions,¹ that is, in the degenerate n^+ region, as shown in Fig. 8.

At 1200°C , the p^+ -diffused layer caused no detectable change in the diffusion rate or concentration profile. At 900°C , it brought about a higher diffusion rate

¹ Adamic has reported an identical observation (6).

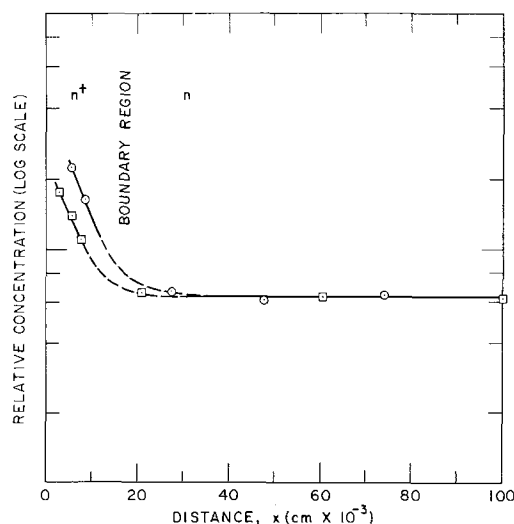


Fig. 8. Concentration profile for gold diffusion at 975°C for 96 hr into previously phosphorus-diffused silicon. Circle with dot, floating-zone silicon. ($\sim 10^4\text{ disl./cm}^2$); square with dot, dislocation-free, Czochralski silicon.

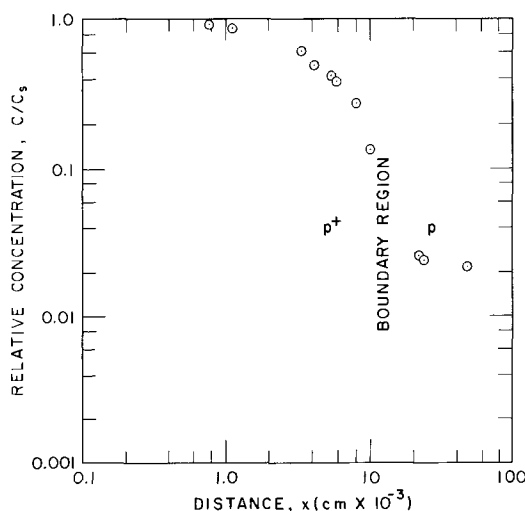


Fig. 9. Concentration profile for gold diffusion at 900°C for 16 hr into previously boron-diffused silicon.

and an ideal error-function complement concentration profile, as shown in Fig. 9. The diffusion coefficient in the p^+ layer was $3.3 \times 10^{-10}\text{ cm}^2/\text{sec}$ at 900°C . The gold solubility appeared to be the same as in non-diffused silicon.

At 900° , 1000° , and 1200°C no effects other than those described above were observed for p - n junctions.

Discussion of Gold Diffusion Experiments

Effects of crystal perfection on gold diffusion have already been explained (3). In confirmation of those results we have observed that quenching before gold diffusion causes an error-function complement diffusion at 1000°C with $D = 3.3 \times 10^{-7}\text{ cm}^2/\text{sec}$. Such quenching at 1000°C into glycerine shatters or cracks roughly one out of every three wafers so treated, thus demonstrating the large magnitude of the stresses so generated.

The phenomena responsible for the effects of heavy prior doping with boron and phosphorus on the diffusion and solubility of gold in silicon are not known. The most probable explanation for the increased gold diffusion rate in a p^+ layer at 900°C is the great number of dislocations generated in the boron diffusion (7). A very high dislocation density has been found to cause a rapid and more ideal gold diffusion at this temperature (3). Some possible mechanisms for the

greatly reduced diffusion rate and increased solubility caused by phosphorus doping are as follows:

1. The effect of the built-in electric field (8, 9).
2. Interaction between gold and phosphorus ions because of ion pairing (10) or their effect on the free electron concentration (11).
3. Some sort of vacancy interaction could account for the observed behavior. It is known that vacancies act as acceptors; they would therefore attain a negative charge in heavily doped n-type material. The positively charged (12) interstitial gold atoms would be attracted to the negative vacancies and tend to combine with them. This would increase the equilibrium concentration of substitutional gold and probably also decrease the equilibrium interstitial concentration. This alone would decrease the diffusion rate of the gold (3), even if the association between negative vacancy and gold does not itself slow down the diffusion. In the case of boron-doped silicon, the number of negative vacancies would not be decreased enough on an absolute scale to appreciably affect the gold solubility and diffusion.

4. Compound formation. Phosphorus and gold form a compound Au_2P_3 with a vapor pressure of 640 mm Hg at 697°C (13). Formation of this compound during gold diffusion could possibly account for higher apparent solubility and lower diffusion rates. Since the compound dissociates readily, an equilibrium would be established, and segregation or precipitation would probably not occur. Because gold is not known to form a compound with boron (14), this explanation conforms with the p^+ diffusion results.

The first mechanism can be ruled out by the observation of reduced gold diffusion in uniformly doped 0.005 ohm-cm n-type silicon. The first two possibilities are eliminated by virtue of the fact that phosphorus is a positive ion and gold diffuses as a positive ion (12). Experimental distinction between the latter two mechanisms might be achieved by gold diffusion into both aluminum-doped silicon and arsenic-doped silicon. Aluminum is an acceptor similar to boron but forms a gold compound $AuAl_2$ that has a melting point of 1060°C (14). Conversely, arsenic is a donor similar to phosphorus, but forms no gold compound (14). Therefore, if the gold diffusion is slowed down in the aluminum-doped silicon but not in the arsenic-doped silicon, then compound formation is probably the cause. If the reverse is true, then a vacancy interaction is more likely. If either, both, or neither is slowed down, then some other explanation must be found.

Summary

The effect of gold on the resistivity of silicon under wide conditions was studied. The results differed significantly from those predicted theoretically (2).

The presence of high concentrations of phosphorus was found to decrease greatly the diffusion of gold into silicon and to increase its solubility. Prediffused layers of boron increase the diffusion rate and make it more ideal. Two equally possible explanations for the effects of phosphorus were given along with proposed experiments for selecting the most valid one. The effects of boron were explained by the increase of dislocation density caused by prediffusion and the effects of such imperfections on gold diffusion.

A proper plating technique, a small quantity of plated gold, and a nonoxidizing diffusion atmosphere were all found necessary to obtain good alloying into silicon and to ensure uniform cross-sectional gold concentrations. Avoiding an oxide layer between gold and silicon is also important.

Acknowledgments

The authors performed the experimental portion of this paper while affiliated with Pacific Semiconductors, Inc. Permission of PSI to publish this work is gratefully acknowledged. The authors wish to thank M. Millea for helpful discussions and I. G. Hudson for

silicon specimen preparation and assistance with the counting.

Manuscript received March 17, 1964; revised manuscript received June 26, 1964. Parts of this paper were delivered before the Los Angeles Meeting, May 6-10, 1962.

Any discussion of this paper will appear in a Discussion Section to be published in the June 1965 JOURNAL.

APPENDIX

Conversion of Counting Rate to Concentration: Residual Activity Method

In the residual activity technique, the specimen is counted after increments are removed from the surface. This gives the wafer counting rate, I , as a function of the depth, x , of material which has been removed by lapping. A relation is now derived to convert this to concentration.

First, it is assumed that the absorption of the radiation obeys Beer's law, i.e., $I = I_0 e^{-\mu d}$, where I is the radiation penetrating an absorber of thickness d from an incident radiation density of I_0 , and μ is the absorption coefficient of the radiation (cm^{-1}) (determined separately with aluminum and silicon absorbers on standard samples). With this, the wafer counting rate after thickness x has been removed by lapping is

$$I = \frac{SAW}{N} \int_x^\infty C(z) \exp[-\mu(z-x)] dz$$

$$= \frac{SAW}{N} \exp(\mu x) \int_x^\infty C(z) \exp(-\mu z) dz \quad [1]$$

where z is the distance from the original surface; C is the concentration at x in at./cm^3 ; N is Avogadro's number (6.023×10^{23} atoms/mole); S is specific activity X counting efficiency, or the counting rate before diffusion per gram of original gold deposited on the wafer (counts/min/g); A is the top surface area of the wafer (cm^2); and W is the atomic weight of gold (g/mole).

Taking the derivative by parts of I with respect to x and substituting from Eq. [1], we obtain

$$\frac{dI}{dx} = \frac{SAW}{N} \left[\mu \exp(\mu x) \int_x^\infty C(z) \exp(-\mu z) dz - \exp(\mu x) C(x) \exp(-\mu x) \right] = \mu I - \frac{SAW}{N} C(x) \quad [2]$$

Rearrangement of this equation gives

$$C(x) = \frac{N}{SAW} \left[\mu I - \frac{dI}{dx} \right] \quad [3]$$

which is the desired relation.

REFERENCES

1. C.B. Collins, R. O. Carlson, and C. J. Gallagher, *Phys. Rev.*, **105**, 1168 (1957).
2. B. I. Boltaks, G. S. Kulikov, and R. S. Malkovich, *Soviet Phys.-Solid State* (English Transl.), **2**, 167 (1960).
3. W. R. Wilcox and T. J. LaChapelle, *J. Appl. Phys.*, **35**, 240 (1964).
4. W. R. Wilcox, T. J. LaChapelle, and D. H. Forbes, "Factors Affecting Gold Diffusion Rates in Silicon," ATN-64 (9236)-8, Aerospace Corp., El Segundo, Calif. (1964).
5. J. C. Irvin, *Bell Syst. Tech. J.*, **41**, 387 (1962).
6. J. W. Adamic, Jr., Private communication.
7. S. Prussin, *J. Appl. Phys.*, **32**, 1876 (1961).
8. K. Lehovec, *Solid State Electr.*, **2**, 260 (1960).
9. F. M. Smits, *Proc. I.R.E.*, **46**, 1049 (1958).
10. H. Reiss, C. S. Fuller, and F. J. Morin, *Bell Syst. Tech. J.*, **35**, 535 (1956).
11. K. Lehovec and A. Slobodskoy, *This Journal*, **111**, 65 (1964).
12. B. I. Boltaks, G. S. Kulikov, and R. S. Malkovich, *Soviet Phys. Solid State* (English Transl.), **2**, 2134 (1961).
13. H. Haraldsen and W. Blitz, *Z. Elektrochem.*, **37**, 502 (1931).
14. M. Hansen, "Constitution of Binary Alloys," McGraw-Hill Book Co., Inc., New York (1958).

Analysis of the Hydrogen Reduction of Silicon Tetrachloride Process on the Basis of a Quasi-Equilibrium Model

T. O. Sedgwick

Thomas J. Watson Research Center, International Business Machines Corporation, Yorktown Heights, New York

ABSTRACT

The process for the growth of silicon single crystals by the hydrogen reduction of silicon tetrachloride has been described using a model which assumes that chemical equilibrium obtains at the silicon deposition site. The thermodynamic calculations by Lever for the equilibrium gas phase composition in the Si-Cl-H system (primarily H_2 , HCl , $SiCl_2$, $SiHCl_3$) were used to calculate the growth rate of silicon as a function of mole fraction silicon tetrachloride input and temperature in an open tube system. Some of the features of the experimental results reported in the literature are predicted by the equilibrium model. The results are discussed in relation to similar calculations by Steinmaier who did not take the species $SiHCl_3$ into account.

Recently, considerable attention has been given to studies of the hydrogen reduction of $SiCl_4$ for the preparation of both pure bulk and epitaxial Si for device fabrication. As a result, considerable data relating Si growth rate and/or yield to experimental parameters has appeared in the literature (1-5). Certain general features of these results have been interpreted by the various authors as evidence for particular models of the reaction mechanism. For example, Bylander (1) and Theurer (2) noted that log of growth rate increased linearly with decreasing $1/T$ and suggested that the slope of these curves was a measure of the activation energy of a rate limiting activated adsorption or diffusion process. Bylander interpreted the observed leveling out of growth rate at the highest temperatures as due to a mass transfer rate limiting process. On the other hand, Wolf and Teichmann (3) and Steinmaier (4) have compared experimental results with calculations based on a model which assumes that thermodynamic equilibrium obtains in the reaction zone.

Recently Lever (6) has made a complete thermodynamic analysis of the Si-Cl-H system by calculating the partial pressures of the species H_2 , HCl , $SiCl_4$, $SiHCl_3$, $SiCl_2$, SiH_2Cl_2 , SiH_3Cl , $SiCl$, and SiH_4 in equilibrium with solid Si as a function of total pressure, over-all Cl/H ratio, and temperature. These calculations are more complete than either Steinmaier's or Wolf's, since the concentration of $SiHCl_3$ was considered in the calculations and found to be a major constituent of the vapor phase under the experimental conditions of practical interest.

It will be shown in the following that some of the main features of the experimental results reported in the literature may be explained by using a simple quasi-equilibrium model without assuming any specific kinetic or mass transfer reaction limitations.

Quasi-Equilibrium Model

In the hydrogen reduction of $SiCl_4$, a mixture of H_2 and $SiCl_4$ gas at about 1 atm total pressure is passed over a heated Si substrate where reduction occurs and Si is deposited. If all of the $SiCl_4$ - H_2 gas mixture comes into complete chemical equilibrium with the solid Si phase present in the heated reaction zone, the Si deposition rate, D , in g/min is

$$D = J \cdot \alpha \quad [1]$$

where J is the flux of Si in g/min into the reaction tube and α is a theoretical efficiency factor equal to the fraction of Si atoms in the input gas stream which will be deposited as a result of chemical equilibration. The flux J is given by

$$J = n \cdot M \cdot F \cdot X_{SiCl_4} \quad [2]$$

where n is the density of the input gas in moles/liter,

M is the molecular weight of Si in g/mole, F is the flow rate in liters/min, and X_{SiCl_4} is the mole fraction of $SiCl_4$ in the input gas.

The theoretical efficiency factor α , which is the fractional change of the Si content of the gas phase, is a function of both X_{SiCl_4} and the temperature of the reaction zone. In terms of the quantities discussed by Lever (6),

$$\alpha = \frac{\eta \text{ input} - \eta \text{ equi.}}{\eta \text{ input}} \quad [3]$$

where, in general, η is the ratio of the total density of Si atoms in the gas phase divided by the total density of Cl atoms in the gas phase summed over all species. In particular, η input refers to the input gas, and for an input gas consisting of $SiCl_4$ and H_2 it equals 0.25. The ratio η equi. refers to the gas phase in the heated reaction zone and is obtained from Lever's calculations. The factor α may change from 1 through 0 to negative values thus encompassing the case where a net etching of Si in the reaction zone occurs.

It must be noted, however, that in a typical epitaxial growth system, the actual geometry of the heated deposition zone is not particularly favorable for achieving intimate gas-solid contact and hence equilibrium. The Si substrate upon which deposition occurs is usually placed on a heater element (inductive or resistive) which is the heat source for both substrate and impinging gas stream. Both the Si substrate and heater usually do not occupy more than one half the cross-sectional area of the quartz tube through which the $SiCl_4$ - H_2 gas mixture passes (1, 2, 4). Let it be assumed, then, that only a fraction, β , of the incoming gas equilibrates with the Si substrate and that the remaining fraction $1 - \beta$ streams by unreacted. This may be described as a quasi-equilibrium condition and the deposition rate in this case would be,

$$D = J \cdot \alpha \cdot \beta \quad [4]$$

Equation [4] will only have practical significance if either $\beta \approx 1$ and essentially complete chemical equilibrium obtains, or if β is at least constant and therefore independent of some of the experimental parameters. Unfortunately, there is insufficient data in the literature to enable a reliable calculation of β . However, Bylander found an almost linear dependence of growth rate on flow rate up to at least 2 liters/min which implies that β is, in fact, constant under some conditions. The calculated results in Fig. 1 and 2 were made assuming a β equal to unity, a flow rate of 1 liter/min and A equal to 20 cm².

Before making a comparison between experimental and calculated results, it will be noted that the growth parameter usually cited in the literature is the so-called "growth-rate," G , or actual thickness of planar

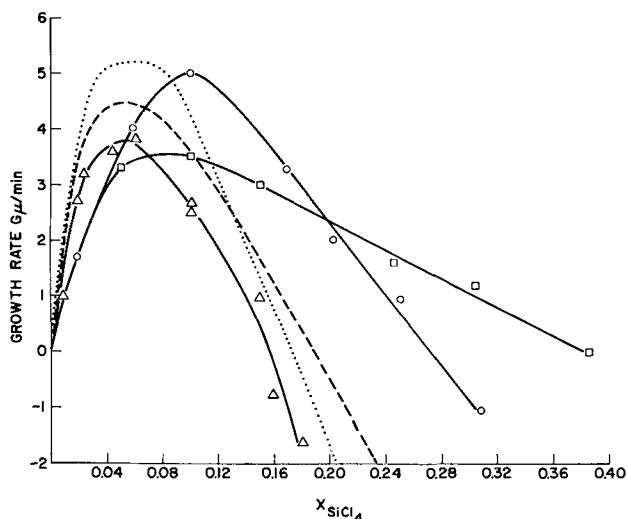


Fig. 1. Comparison of experimental and calculated growth rates of Si as a function of mole fraction SiCl_4 input. Δ , Bylander, 1523°K; \circ , Theuerer, 1550°K;, calculated, 1550°K; \square , Steinmaier, 1423°K; — — —, calculated, 1450°K.

deposit growth on a wafer per unit time. This growth rate G in μ/min is related to the deposition rate D by

$$G = \frac{D}{d_{\text{Si}} A} \times 10^4 \quad [5]$$

where d_{Si} is the density in g/cm^3 of Si and A is the area in cm^2 of deposit.

Comparison of Calculated and Experimental Results

Experimental and calculated growth rates G as a function of X_{SiCl_4} are displayed in Fig. 1. A comparison of the relative heights of both experimental and calculated curves show a growth rate maximum and a cross over to etching at high concentrations of SiCl_4 . Although the present calculated curves are similar to those calculated by Steinmaier (his calculated curves are not shown), the maxima and cross over points of the present curves occur at considerably lower concentrations of SiCl_4 than do his. The difference is due to the fact that SiHCl_3 has been accounted for in the present calculations. For example, when the input SiCl_4 concentration is greater than 0.12, the reduction products at equilibrium are both SiHCl_3 and SiCl_2 . At high temperatures SiCl_2 is the primary product, while SiHCl_3 predominates at lower temperatures.

In Fig. 2 experimental and calculated values of the log of growth rate vs. the reciprocal of the absolute temperature are displayed. Both calculated and experimental curves show an increase in growth rate with temperature at relatively low temperatures and finally a leveling out of growth rate at high temperatures. There is particularly good agreement between Bylander's data at 2 liters/min flow rate and the appropriate calculated curve. On the other hand, the leveling out of growth rate at high temperatures was not found by Theuerer and may indicate that his experiments were carried out under conditions not described by this model. An additional indication of this is the fact that Theuerer made his measurements at a flow rate high enough so that growth rate was no longer linearly dependent on flow rate.

In order to make a quantitative comparison between calculated and experimental results, i.e., an evaluation of β , it is necessary to know the area A on which the Si is deposited. On the basis of Si substrate surface areas in the cited experimental results, β ranges from ca. 0.03-0.30. The actual area on which deposition occurs is presumably considerably larger than the area of the Si wafer substrate alone. Hornberger (7), for example, found in the $\text{GeCl}_4\text{-H}_2$ system that typically

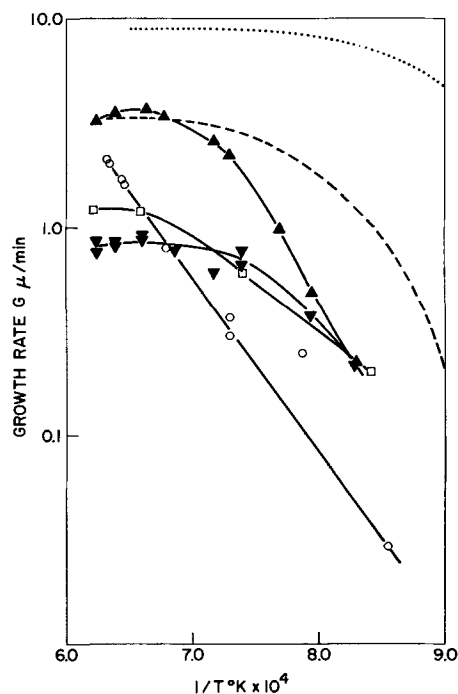


Fig. 2. Comparison of experimental and calculated growth rates of Si as a function of reciprocal temperature.

Source	X_{SiCl_4}	Flow rate, l/min
\blacktriangle , Bylander	0.02	16
\blacktriangledown , Bylander	0.02	2
\circ , Theuerer	0.02	1
— — —, Calculated	0.02	1
\square , Steinmaier	0.004	1
., Calculated	0.004	1

10 times as much Ge is deposited on the heater pedestal as on the wafer in a similar deposition apparatus, which suggests that the actual β in the experiments cited is much closer to unity than the numbers 0.03-0.30 suggest.

Discussion

Although the postulated quasi-equilibrium model is only approximate, it is, in fact, capable of explaining some of the main features of the experimental results. Unfortunately, in most of the experiments to date, there is little or no information regarding gas composition either in the reaction region or in the effluent gas. Likewise a material balance, i.e., quantitative accounting of input SiCl_4 in terms of total deposited Si and by-products, in an epitaxial growth system has not been reported in the literature to this author's knowledge. If a material balance revealed that β were constant, or even more important if it were close to unity, considerable weight would be given to the above arguments.

It is most probable that a more rigorous experimental and theoretical investigation of this process would reveal that, in general, the Si growth rate is dependent variously on mass transport, kinetic and/or equilibrium factors depending on experimental conditions, and reactor geometry. The value of an equilibrium approach to describing the process is that it will presumably describe the process at sufficiently low flow rates, and it will provide a thermodynamic basis for discussing possible reactions in this obviously complex system.

It is clear that thermodynamic properties per se do not provide information regarding the actual mechanism of a reaction system. However, in this complex multi-reaction process, the thermodynamic analysis does yield information which suggests meaningful kinetic experiments and aids in the interpretation of

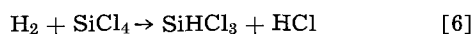
kinetic results. For example, the reduction of SiCl₄ by H₂ to Si may be considered (although somewhat arbitrarily) as a three-stage process:

1. Heating of H₂ and SiCl₄ to about 800°C with possible reactions in the gas phase.

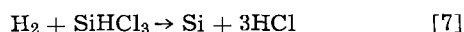
2. Further heating of the gas mixture to say 1250°C with reaction at the Si surface to produce Si and by-products.

3. Cooling of the by-products to room temperature with possible chemical re-equilibration.

It is perhaps of most interest to investigate the kinetic details of the actual deposition reaction [2]. Obviously, the details of this process will be obscured if there is appreciable reaction at stage 1 to produce unknown chemical intermediates which are the actual reacting species at 2. It is not uncommon to find rate determining steps in a reaction preceded or followed by fast reactions which result in the re-equilibration (8) of products or reactants especially when a temperature change is involved. To the extent that equilibrium is achieved in the present system, the thermodynamic analysis indicates that a gas stream containing initially 1 mole % SiCl₄ in H₂ is essentially reduced¹ to SiHCl₃ and HCl at 800°C, i.e., 1,



Further increase of the temperature of the gas to 1250°C, i.e., 2, in intimate contact with the Si surface results in the reduction¹ of SiHCl₃ to Si

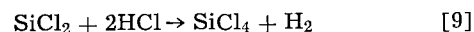


Whether or not the reduction of SiCl₄ actually proceeds via an intervening gas phase reduction to SiHCl₃ could be established experimentally by measuring the homogeneous gas phase reaction rate of H₂ with SiCl₄ to determine if the rate is fast compared to the residence time of SiCl₄ in the high-temperature zone of a specific reaction apparatus. Certainly, the possibility of such a pre-equilibration of reactants must be taken into consideration in a kinetic analysis of the reaction.

Finally, at the exit side of the deposition region, i.e., 3, the equilibrium calculations predict that the major by-products are HCl and SiCl₂ at 1250°C. Equilibrium considerations predict, however, that at lower temperatures the HCl and SiCl₂ will re-equilibrate to produce SiHCl₃ and to a lesser extent SiCl₄.



¹Equations [6] and [7] express the net change in the gas phase concentration of the major chemical species as a result of re-equilibration with increasing temperature. These equations should not be considered as detailed steps in a mechanism nor do they take into account other species which are present in small concentrations (<0.1%). It should be pointed out that under different conditions, i.e., input concentration SiCl₄ and temperature, the major species and hence net changes of gas phase composition with temperature could be quite different.



The fact that SiHCl₃ and SiCl₄ are the primary silicon containing by-products found at room temperature experimentally (2, 5) indicates that the re-equilibration according to [8] must be quite rapid in the post deposition zone.

From a practical standpoint, it is desirable to minimize the formation of the high molecular weight solid (or possibly liquid) reaction products which occurs to at least some extent (1, 2) in the reaction and post reaction zones. Schafer (9) points out that compounds of the form (SiCl₂)_n H₂ and (SiCl₂)_n Cl₂ are probably formed from the reaction of SiCl₂ with SiCl₄, SiCl₂ and others under thermal quench conditions. The results of the previous paragraph would suggest that a Si deposition reactor should be designed (geometry and reactor cooling technique) so that the reaction gases are not too quickly cooled in the reaction and post reaction zones so that the re-equilibration according to Eq. [8] is favored rather than rapid thermal quenching which tends to produce high molecular weight products. This effect becomes more acute as the mole fraction SiCl₄ input is increased and/or the temperature is raised since these conditions tend to favor increased amounts of by-product SiCl₂.

Acknowledgments

The author wishes to thank Dr. A. Reisman and Mr. R. Lever for a critical reading of the manuscript and for many helpful suggestions regarding this work. He is particularly indebted to Mr. Lever for allowing him to use his calculations before their publication.

Manuscript received May 26, 1964; revised manuscript received July 17, 1964. This work was supported in part by AFCRL No. AF19(628)-2468.

Any discussion of this paper will appear in a Discussion Section to be published in the June 1965 JOURNAL.

REFERENCES

1. E. G. Bylander, *This Journal*, **109**, 1171 (1962).
2. H. C. Theuerer, *ibid.*, **108**, 649 (1961).
3. E. Wolf and R. Teichmann, *Z. f. Chem.*, **2**, 343 (1962).
4. W. Steinmaier, *Philips Research Repts.*, **18**, 75 (1963).
5. M. Nakagawa, *J. Chem. Soc. (Japan)*, **65**, 466 (1962).
6. R. F. Lever, *IBM J. Res. & Develop.*, **8**, 460 (1964).
7. W. P. Hornberger, Private communication.
8. A. A. Frost and R. G. Pearson, "Kinetics and Mechanism," Chap. 8, John Wiley & Sons, New York (1953).
9. H. Schafer, *Z. anorg. allgem. Chem.*, **274**, 265 (1953).

Formation and Composition of Surface Layers and Solubility Limits of Phosphorus During Diffusion in Silicon

E. Kooi

Philips Research Laboratories, N. V. Philips' Gloeilampenfabrieken, Eindhoven, Netherlands

ABSTRACT

A neutron activation analysis was used to study the behavior of phosphorus during its diffusion into silicon and silicon dioxide films. Certain correlations were found between the compositions of the oxide layers formed during the diffusions and the existing phase diagram of the system SiO₂-P₂O₅. In several experiments the concentration of phosphorus in silicon had reached the solubility limit, and a layer with very high phosphorus content was found to be present between the oxide film and the silicon substrate.

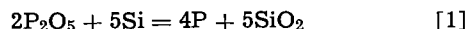
It has been shown by several authors (1-3) that diffusion of phosphorus in silicon cannot be described by a single diffusion coefficient. Tannenbaum (2) and more recently Maekawa (3) found a difference between the actual diffusion patterns and those obtained

from resistivity measurements. The results can be explained in terms of an extra fast diffusion mechanism at high phosphorus concentrations. This may be due to diffusion of interstitial phosphorus atoms. Their presence may also affect the electron mobility in dif-

fused layers. Both Tannenbaum and Maekawa found that phosphorus-doped silicon had a lower limit of resistivity of about 0.00035 ohm-cm.

These conclusions are in agreement with the results of our experiments in which the diffusion of phosphorus into silicon and the masking effects of SiO₂ layers were studied by a neutron activation analysis. P₂O₅ was applied as a source for the diffusion. Different P₂O₅ pressures were used, and the temperature of the silicon was varied from 920° to 1310°C.

The phosphorus which diffuses into the silicon can be supposed to be formed according to the reaction



A certain amount of oxygen will also diffuse into the silicon, but because the solubility is low compared to that of phosphorus, this will be neglected. The oxide layer which forms at the surface is not a pure SiO₂ layer, because it will react with phosphorus oxide from the vapor. Assuming that the average composition of the oxide can be given by γ SiO₂·P₂O₅, the value of γ could be determined by activation analysis. When the diffusions are carried out in an oxygen ambient the picture is somewhat more complicated because more SiO₂ will form than corresponds with reaction [1].

Reaction of P₂O₅ with SiO₂ can also be supposed to occur when the silicon surface has been provided with a SiO₂ layer before the diffusion starts. Diffusion of phosphorus (-oxide) through SiO₂ films has been studied by Sah *et al.* (4) and Allen *et al.* (5). In both cases p-type silicon underneath the oxide films was used as a phosphorus detector to check cases in which the masking conditions were fulfilled. Sah *et al.* concluded that a glassy layer of unknown composition was built up at the top of the oxide films so that a sharp boundary existed between the glassy layer and the oxide. This conclusion was confirmed by our analysis in which the phosphorus distribution in the oxide layers was measured directly.

In several cases the compositions of the oxide layers could be correlated with the phase diagram of the system SiO₂-P₂O₅ as given by Tien and Hummel (6). This was especially the case in two stage processes, both for oxide layers formed during diffusion in silicon and formed at the top of a masking SiO₂ film.

If the diffusion of phosphorus in silicon is not fast enough to carry off all the phosphorus formed by reduction of phosphorus oxide, the phosphorus concentration in silicon will reach a saturation value and a new phase may form. In several cases we found indeed a layer with very high phosphorus concentration just at the interface between the silicon and the oxide layer formed during the diffusion. This enabled us to determine the solid solubility of P in Si.

Experimental Procedure

Silicon wafers were cut perpendicular to the <111> direction of a float zone single crystal of 5 ohm-cm p-type silicon. After lapping with fine alundum powder, the slices were etched in a mixture of 2 parts HF (50%) and 5 parts HNO₃ (65%), so that 60 μ were removed from each side. The final thickness of the slices was about 250 μ . The diffusions were carried out in a two zone furnace, supplied with a quartz tube of 2.5 cm diameter. A quartz boat filled with P₂O₅ was placed in the low temperature zone (either 210° or 300°C). The temperature of the silicon slices was varied between 920° and 1310°C. Dry nitrogen or oxygen was used as carrier gas (gas flow 0.2 l/min). Heating of the silicon slices occurred by pushing them into the hot furnace, cooling by pulling them into a cold region of the quartz tube.

In a number of cases the diffusions were carried out in two stages, a pre-diffusion at 920°C followed by diffusion at a higher temperature in a second quartz tube, the walls of which had been exposed previously to P₂O₅ vapor at the diffusion temperature. However,

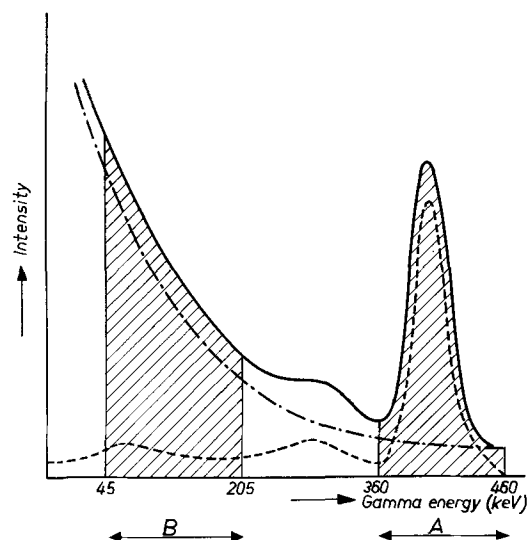


Fig. 1. Gamma spectrum of an irradiated silicon sample containing both phosphorus and gold (recorded after decay of Si³¹). — — —, Au¹⁹⁸; - · - ·, P³²; —, total.

before the silicon slices were inserted, the tubes were heated for a few hours at this temperature, without supply of P₂O₅. Under these conditions the amount of phosphorus per silicon slice did not change noticeably during the heat-treatments.

After the diffusion the silicon slices together with a phosphorus standard (about 40 mg (NH₄)₂HPO₄) were irradiated in a neutron flux of 5×10^{11} neutrons/cm²/sec for a period of 5-10 days.¹ Except activity due to P³² (half-life 14.3 days), we found always some activity due to Au¹⁹⁸ (half-life 2.7 days), which had also been formed during the neutron activation process. This gold had been introduced during handling, etching, washing, and subsequent heat-treatment of the slices. The also formed Si³¹ has a relatively short half-life (2.6 hr) and decays practically completely in a few days.

If P³² as well as Au¹⁹⁸ activity was present, the measurements were done with NaI(Tl) well-type scintillation detector coupled with a gamma spectrometer. In those cases we measured both the distribution of phosphorus and of gold in the silicon and in the oxide film. The gamma radiation spectrum of Au¹⁹⁸ with a peak at 412 keV is superposed on the bremsstrahlung spectrum of P³² (Fig. 1). The amount present of both Au and P was determined by counting in two channels A and B according to the method of Elleman *et al.* (7). Comparisons were made with irradiated standards. The conditions of measurement for samples and standards were made as alike as possible by pipetting some of the standard solution onto nonirradiated silicon-slices of the same thickness as the samples.

In the cases in which we were not interested in the behavior of gold, we waited until the Au¹⁹⁸ had disintegrated to a very low amount and measured the activity simply with a Geiger Müller counter. The lowest amount of phosphorus which could be detected in this way was 10¹³ atoms.

Results

Oxide-layer compositions.—One stage processes.—The activity of the silicon slices was counted before and after removal of the oxide layer (by a quick dip in an aqueous HF solution). The average composition of the layers could then be calculated by correlating the weight decrease with the decrease in activity.

If no oxygen was present, a second method could be used. After the oxide layer had been removed, the

¹ For the irradiations we had the help of the Centre d'Etudes de l'Energie Nucléaire at Mol in Belgium. The samples were irradiated in the reactor BR I.

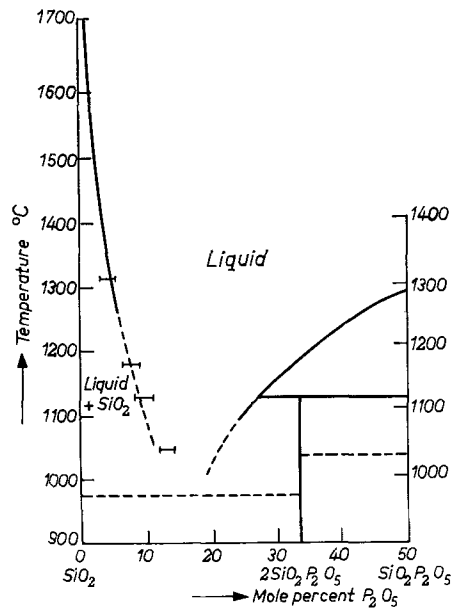


Fig. 2. Saturation values of oxide layer compositions in two-stage diffusion processes, plotted in the phase diagram of $\text{SiO}_2\text{-P}_2\text{O}_5$.

residual activity gave the number of reduced P-atoms and so according to Eq. [1] also the number of SiO_2 molecules in the oxide layers. Both methods gave the same results within 10%.

The oxide layers formed during the diffusion did not always show a "glassy" appearance. In some cases a crystalline structure was present; in other cases only very minor structure differences could be seen. According to the phase diagram of the system $\text{SiO}_2\text{-P}_2\text{O}_5$ given by Tien and Hummel (6) compounds with compositions $\text{SiO}_2\cdot\text{P}_2\text{O}_5$ and $2\text{SiO}_2\cdot\text{P}_2\text{O}_5$ exist (Fig. 2). Whether one or both of these compounds were present in the oxide layers could not be ascertained, but the presence of crystallites certainly occurred more frequently when the amount of P_2O_5 in the oxide layers was higher.

Using diffusion temperatures of 920° , 1050° , 1180° , and 1310°C , a P_2O_5 temperature of 210°C , nitrogen as carrier gas, and diffusion period of 15 and 60 min, the compositions of the oxide layers varied from $2\text{SiO}_2\cdot\text{P}_2\text{O}_5$ to $4\text{SiO}_2\cdot\text{P}_2\text{O}_5$. When the source was held at 300°C , the P_2O_5 content was sometimes higher, but effects of nonconstant P_2O_5 pressures due to aging of the source were of more influence in this case. It was found that a new source of P_2O_5 held at 210°C could give a larger amount of deposited phosphorus than a source held at 300°C , which had already been heated for a few hours.

When oxygen was used as carrier gas instead of nitrogen, the phosphorus contents of the oxide layers were lower, especially when the temperature of the silicon was relatively low and the diffusion time short. With a diffusion period of 15 min, the average oxide composition ranged from $10\text{SiO}_2\cdot\text{P}_2\text{O}_5$ for experiments at 920°C to $4\text{SiO}_2\cdot\text{P}_2\text{O}_5$ at 1310°C . For diffusion times of 60 min the difference between oxygen and nitrogen ambients became much less pronounced. Variations between $2\text{SiO}_2\cdot\text{P}_2\text{O}_5$ and $4\text{SiO}_2\cdot\text{P}_2\text{O}_5$ were found, depending on the state of the source. The large effect of the presence of oxygen in the short diffusion runs is explained by the fact that the oxidation velocity of silicon depends on diffusion through the oxide layer, which grows thicker during the experiment.

Two-stage processes.—The prediffusion was done at 920°C for 15 or 60 min in a nitrogen ambient. In the second stage the silicon slices were heated separately at a higher temperature for varying periods, using either a nitrogen or oxygen ambient. During the first stage oxide layers formed with a composition of

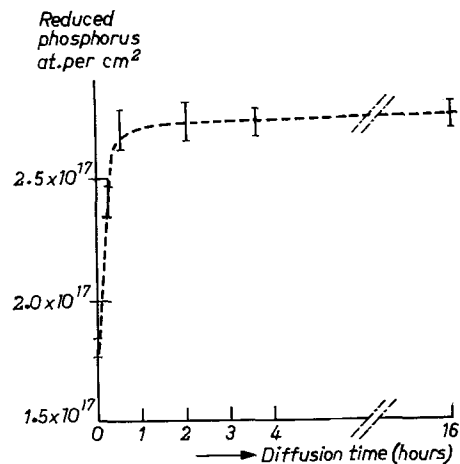
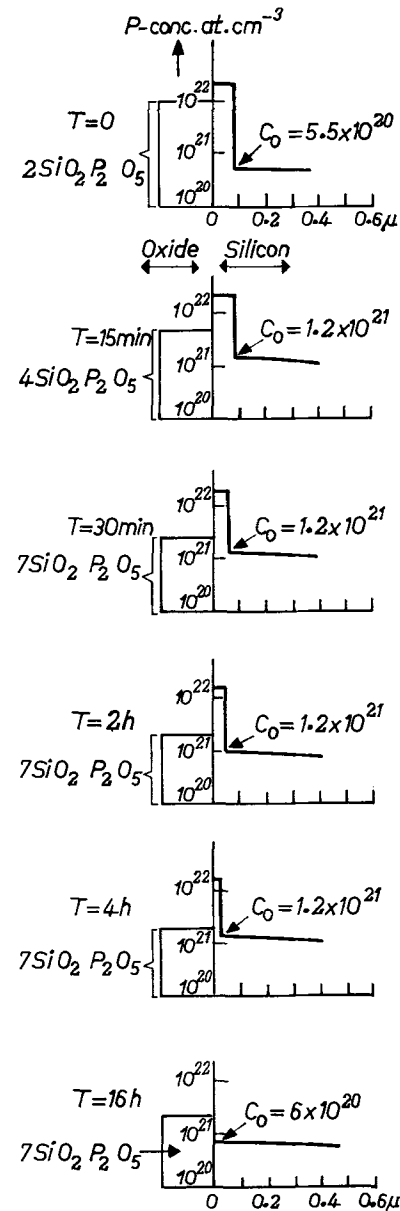


Fig. 3. Behavior of P-concentrations in oxide layers, silicon, and interface layer during the second stage of a two-stage process, consisting of a prediffusion at 920°C for 30 min followed by a diffusion at 1050°C for a variable time T . 3a. The oxide layer obtains a constant composition, the surface concentration of P in Si remains constant as long as the interface layer is present; 3b. The total amount of phosphorus in silicon and interface layer goes to a constant value.

about $2\text{SiO}_2 \cdot \text{P}_2\text{O}_5$. During the second stage their compositions altered, owing to further reaction of P_2O_5 and Si resulting in SiO_2 and P. The changes of the oxide layer compositions as function of time have been given in Fig. 3a for a diffusion in N_2 at 1050°C . In the beginning the phosphorus content decreases rapidly, but then seems to become more or less constant at a lower limit ($7\text{SiO}_2 \cdot \text{P}_2\text{O}_5$). This means also that the amount of reduced phosphorus reaches a nearly constant value after some time (Fig. 3b). The limiting composition of the oxide layers appeared to vary with temperature. Less phosphorus remained present when the temperature was higher. The values found at 1060° , 1120° , 1180° , and 1310°C have been plotted in Fig. 2. They appear to coincide more or less with the limiting solubility of SiO_2 in the phosphorus-containing liquid, as given in the phase diagram of Tien and Hummel.

A possible explanation can be obtained if one assumes that the reduction of phosphorus oxide occurs at the interface between the silicon and the oxide layer. As the reduction of phosphorus oxide goes together with oxidation of silicon, one can understand that the reaction stops more or less as soon as a thin SiO_2 layer forms at the interface. This will occur when the oxide layer has reached such a composition that SiO_2 can no longer remain dissolved. The presence of a SiO_2 layer between the phosphorus-containing oxide layer and silicon could be shown clearly in the case where the second stage of the diffusion process was carried out in oxygen instead of nitrogen. By removal of successive layers of the oxide films, we could demonstrate the presence of a SiO_2 film between the phosphorus-containing oxide layer and the silicon substrate. This SiO_2 film may have contained some phosphorus, but we could not detect any, which means that it contained less than 10^{19} phosphorus atoms/cm³. These oxidation experiments prove also that the species diffusing through the (phosphorus-containing) oxide layers was oxygen and not silicon.

Using the same procedure a sharp boundary between a phosphorus-containing glass and underlying SiO_2 could also be demonstrated in samples on which thermally grown SiO_2 films had been used as masks against the diffusions. In two-stage processes again an equilibrium composition of the glassy layer was found, if the diffusion period was sufficiently long. In these cases the second stage of the process was carried out at 1120°C . The final glass composition was calculated to be between $8\text{SiO}_2 \cdot \text{P}_2\text{O}_5$ and $12\text{SiO}_2 \cdot \text{P}_2\text{O}_5$, again showing a reasonable correspondence with the solubility of SiO_2 in the glassy phase at this temperature.

Solubility limits and diffusion profiles of P in Si.—If at a certain temperature the concentration of P in Si reaches the maximum solubility, one would expect the formation of a second phase of the diagram Si-P. Indeed in several cases we found that after removal of

the oxide layer by a quick dip in an HF solution, a thin layer with a high P-content remained present at the surface. In our experiments this layer was always thinner than 0.1μ . It could be removed by heating the slices in hot water or acid solutions, for example, immersion in an aqueous HF-solution for several minutes. It was also possible to remove successive parts of the layer by anodic oxidation in a solution of KNO_3 in N-methyl acetamide and subsequent rinsing in an HF solution. The concentration of phosphorus in these layers was between 2×10^{22} and 4×10^{22} atoms/cm³ in experiments below 1100°C . In diffusion experiments at 1180° and 1310°C the concentration appeared to be somewhat lower, although still of the order of 10^{22} atoms/cm³. This is in agreement with the phase diagram of the system Si-P as given by Giessen and Vogel (8), partly given in Fig. 4. In this system a compound SiP can be in equilibrium with silicon saturated with phosphorus, as long as the temperature is below 1131°C . Above that temperature equilibrium can exist between silicon saturated with phosphorus and a melt with a rather high phosphorus content. It seems probable that the interface layers which were found in several of our experiments are due to formation of one of these phases, although some oxygen may have been incorporated. When a "Si-P" phase was present at the surfaces, the surface concentration of the phosphorus diffusion was found to be determined only by the temperature of the heat treatment. Therefore we were able to determine the solubility limits of phosphorus in silicon for a few temperatures. Results are given in Fig. 5. Our results show a higher solubility of phosphorus in silicon than reported by Abrikosov *et al.* (9), whose values were obtained from microhardness measurements in the system Si-P. The results are very close to the lower limits of solubility found by Mackintosh (10). This agreement is rather fortuitous however because Mackintosh's results were obtained from measurements of sheet resistance and PN junction depth.

In a way similar to that described by Tannenbaum (2) and Maekawa (3) we measured both the diffusion profiles and the distribution of electrical conductivity in the diffused layers. Good agreement with their measurements was found, such as a minimum in resistivity of 3×10^{-4} ohm-cm for phosphorus doped silicon. We found that this minimum corresponded to a phosphorus concentration of 6.5×10^{20} per cm³. The minimum in resistivity did not necessarily occur at the silicon surface, as the solubility of phosphorus in silicon can be higher.

The surface concentration of phosphorus found in a two-stage process is often lower than corresponds with the solid solubility. However as long as a silicon phos-

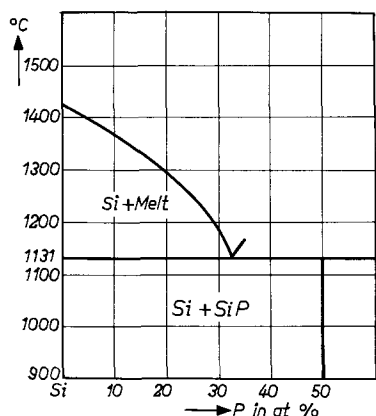


Fig. 4. The system Si-P (according to Giessen and Vogel)

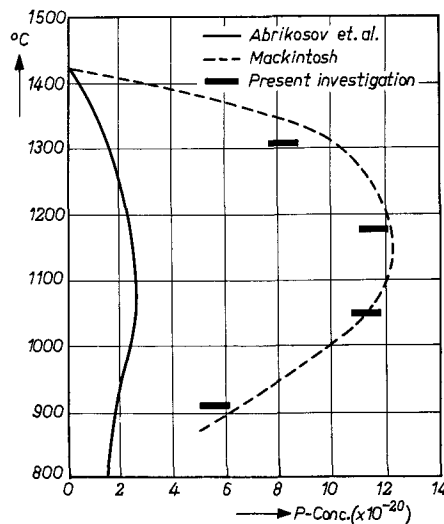


Fig. 5. Solubility limits of P in Si.

phide phase is present at the surface, the surface concentration of phosphorus will have its maximum value at the given temperature. As an example of the behavior of P-concentration in the oxide, interface layer, and silicon in a two-stage process a schematic picture has been given in Fig. 3a. In this case both diffusion steps were carried out in nitrogen; in the first step the silicon was held at 920°C for 30 min with P₂O₅ at 220°C and in the second step at 1050°C for various times.

Formation of surface films with phosphorus concentrations as high as 10²² cm⁻³ has been reported neither by Tannenbaum nor by Maekawa. Also in our experiments such a layer was not always found to be present. Obviously the experimental conditions play an important role. We found that the presence of these surface layers was less pronounced if the P₂O₅ content of the oxide layers was decreased and the temperature of the silicon increased. This can be understood if one considers that the formation of a Si-P phase will be enhanced when more P₂O₅ can be reduced and when the diffusion into silicon is not fast enough to carry away the reduced phosphorus atoms from the surface. As discussed before the P₂O₅ content of the oxide layers depends on many factors such as the presence of oxygen. It may well be that in Tannenbaum's experiments the highly doped layers were not found because the silicon was preheated at the diffusion temperature for 10 min in oxygen before admitting the P₂O₅ (private communication). In Maekawa's experiments the source was H₄P₂O₇, so that comparison is more difficult.

It is known that phosphate glasses, such as formed in phosphorus diffusions, can have gettering action for metal impurities present in the silicon (11). Due to the fact that we always found some presence of Au¹⁹⁸ after the irradiations, we could demonstrate the gettering action of the glassy layers directly. We found

however, that also the "Si-P" phase plays an important role in this gettering behavior, especially at the higher temperatures, when this phase can be supposed to be molten.

Acknowledgments

The experiments described in this paper were carried out in cooperation with Mr. A.B.D. van der Meer. Mr. M. L. Verheijke assisted in the measurements of the activity of irradiated samples.

Manuscript received Jan. 3, 1964; revised manuscript received June 22, 1964. This paper was presented at the Pittsburgh Meeting, April 15-18, 1963.

Any discussion of this paper will appear in a Discussion Section to be published in the June 1965 JOURNAL.

REFERENCES

1. V. K. Subashiev, A. P. Landsman, and A. A. Kukharskii, *Sov. Phys. Solid State*, **2**, 2406 (1961).
2. E. Tannenbaum, *Solid State Electronics*, **2**, 12 (1961).
3. S. Maekawa, *J. Phys. Soc. Japan*, **17**, 1592 (1962).
4. C. T. Sah, H. Sello, and D. A. Tremere, *J. Phys. Chem. Solids*, **11**, 288 (1959).
5. R. B. Allen, H. Bernstein, and A. D. Kurtz, *J. Appl. Phys.*, **31**, 334 (1960).
6. T. Y. Tien and F. A. Hummel, *J. Am. Ceram. Soc.*, **45**, 422 (1962).
7. T. S. Elleman, J. E. Howes, Jr., and D. N. Sunderman, *Int. J. Appl. Rad. and Isotopes*, **12**, 142 (1961).
8. B. Giessen and R. Vogel, *Z. Metallkunde*, **5**, 174 (1959).
9. N. K. Abrikosov, V. H. Glazov, and L. Chên-Yian, *Russ. J. Inorg. Chem.*, **7**, 429 (1962).
10. F. A. Trumbore, *Bell Syst. Tech. J.*, **39**, 205 (1960).
11. R. Goetzberger and W. Shockley, *J. Appl. Phys.*, **31**, 1821 (1960).

Preparation and Properties of Thin Barium Titanate Films

A. E. Feuersanger, A. K. Hagenlocher, and A. L. Solomon

General Telephone & Electronics Laboratories Inc., Bayside, New York

ABSTRACT

Thin films of barium titanate were synthesized by the simultaneous deposition of the barium and titanium oxides evaporated by electron bombardment. The oxides were reacted on a substrate to form barium titanate during deposition. The reaction was carried out in an oxygen atmosphere at a substrate temperature in excess of 600°C. Experiments were performed to determine the range of conditions under which barium titanate was formed during deposition and to evaluate the potential of the films for electronic applications. The thickness of the films was in the range from 0.1 to 1 μ . Effects of heat treatment on films deposited at room temperature are given. X-ray spectroscopy and x-ray diffraction were used to determine the composition and structure of the films. The maximum dielectric constant at room temperature is 1330, close to the value for polycrystalline barium titanate. Leakage current and frequency dependence of the dielectric properties are given. Films with high structural order show the characteristic phase transition, indicated by a peak in capacitance at 120°C.

The unique dielectric properties of barium titanate make this material particularly attractive for a variety of electronic components. In recent years a number of attempts have been made to produce layers of this high-dielectric-constant material for microelectronic thin-film capacitors. This paper describes a technique for the deposition of these thin-film dielectrics that overcomes some of the major difficulties encountered in obtaining control over the dielectric properties of these films.

Barium titanate films have been prepared by direct evaporation (1-4) and dielectric constants as high as 1500 were reported (4). Direct evaporation methods, however, present problems. When barium titanate is evaporated as a single component, it can

decompose on heating into barium oxide and titanium oxide. When this occurs, the barium oxide tends to evaporate faster and produces a barium-rich layer. This form of decomposition can be overcome by a flash evaporation technique (2-5) in which one grain is evaporated completely before evaporation of another is started, so that it is possible to stay close to the stoichiometric ratio. The technique is difficult to perform and does not circumvent another form of decomposition, the loss of oxygen by the titanate or the TiO₂ possibly formed during evaporation. To restore oxygen to the titanate or to react the barium and titanium oxides formed as a result of decomposition, the film deposits are often heat-treated in an oxygen-containing atmosphere (1, 3, 4).

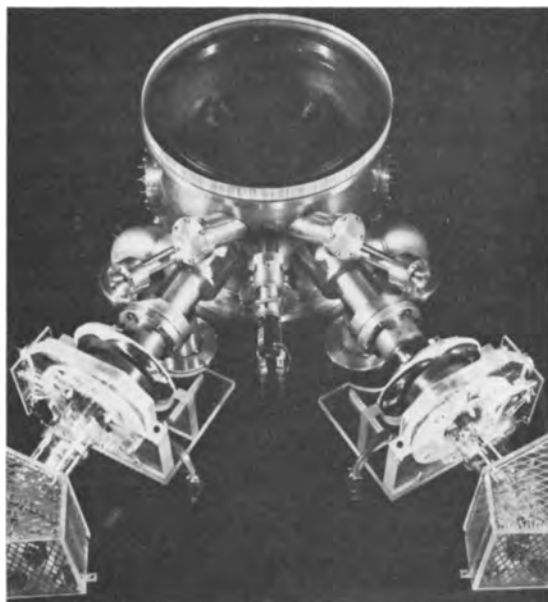


Fig. 1. Top view of evaporation system (the two electron guns are located in front).

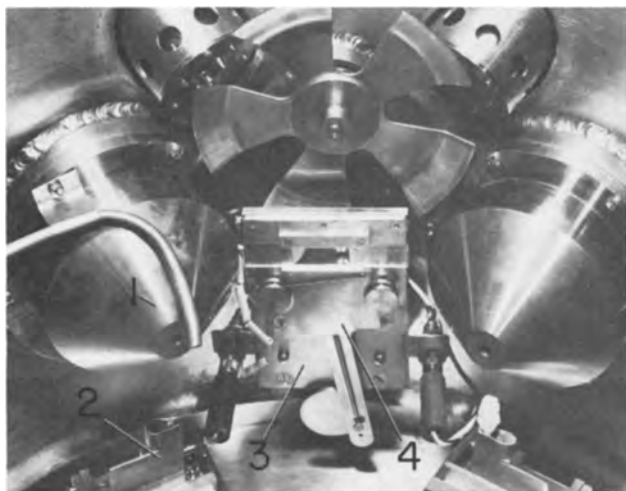


Fig. 2. Inside view of evaporation chamber. 1. Nozzle through which the electron beam enters the system. Oxygen is supplied through tube attached to nozzle. 2. Target holder, movable in the plane perpendicular to the electron beam. 3. Substrate holder. 4. Shutter.

Green (6) has attempted to form BaTiO_3 by evaporating layers of BaO and TiO_2 consecutively and then heat treating the deposit at 1150°C . Only a low dielectric constant resulted. In the technique described in this paper, BaO and TiO_2 are evaporated simultaneously from two independent electron-beam-heated sources at individually controlled rates. The evaporated oxides are reacted on a heated substrate to form BaTiO_3 . Loss of oxygen is prevented by performing the evaporation in an oxygen atmosphere. Films prepared by this technique showed high dielectric constant with relatively low dissipation.

Equipment, Materials and Techniques

Evaporation system.—A specially designed evaporation system was constructed for the preparation of barium titanate by this simultaneous evaporation technique. Details of the design of this evaporation system have been reported previously (7). The system, shown in Fig. 1 and 2, incorporates the following features: (I) Each of the evaporation sources is heated in its own "crucible" by striking a target of the evaporant material with an electron beam of 30 kv

at 1 to 2 ma. This technique prevents any contamination by heater or crucible materials that would otherwise be required. (II) A means for maintaining a controlled pressure of oxygen in the evaporation chamber while maintaining an adequate vacuum at the electron guns is provided by passing each electron beam through a two-stage differential pumping system between the gun and the evaporation chamber. With a pressure of 10^{-2} Torr in the evaporation chamber, a vacuum of 10^{-5} Torr is obtained at the electron gun. (III) The evaporants are deposited on a substrate whose temperature is controlled by resistance heating.

Evaporant sources.—The source of barium oxide used most frequently in this work was the metal, electron-beam-heated in a stream of oxygen. The metal is readily available and the oxide is generated at a sufficiently high rate. Other materials that are less susceptible to oxidation or hydrolysis before they are placed in the system, have been used successfully. For example a 1:1 Ba-Ti (TAM Division of National Lead Company) was employed. Over 90% barium oxide and less than 10% titanium oxide was evaporated because barium oxidizes and evaporates at a lower temperature than titanium. A 90% Ti-10% Ba alloy resulted in a deposit with a 3:1 Ba/Ti ratio. Barium titanate itself heated in an oxygen stream gave a deposit substantially of barium oxide.

The source of titanium oxide was also the metal heated in an oxygen stream. When TiO_2 was similarly heated by electron bombardment, a molten crater was formed in the oxide. Small particles that appeared in the melt were ejected and deposited on the substrate. Reaction of these deposited particles with barium oxide at the substrate to form BaTiO_3 proved difficult and was effected only by a post-deposition heat treatment at higher temperatures and for longer times than those used during deposition.

Conditions for barium titanate deposition.—Films were initially deposited on unheated substrates at evaporation rates of 1 to 5 Å/sec; the oxygen pressure was varied between 10^{-5} and 10^{-2} Torr for different films. Barium titanate was not found by either x-ray or electron diffraction, and dielectric constants were smaller than 100, although x-ray spectroscopy showed that the BaO-TiO_2 stoichiometric ratio was close to unity. Barium titanate was detected by x-ray diffraction, however, when films deposited on platinum-rhodium foil at any oxygen pressure of 10^{-3} Torr or greater were post-deposition heat treated in helium. Heating the sample in a high-temperature x-ray camera in steps of 100°C showed that a significant amount of the constituents reacted when the substrate temperature was maintained at 950°C for several hours. This result showed that all constituents were present in the deposit when the oxygen pressure was sufficiently high and that it was necessary only to supply thermal activation energy to react the oxides to form BaTiO_3 .

In further post-deposition heat-treatment experiments, microscopy revealed that the thin BaTiO_3 films were broken into crystallites after heating for extended periods. The degree of crystallization depends on the composition and size of the particles. A film approximately 1200 Å thick which had been heated to 940°C for 18 hr in argon is shown in Fig. 3(a). Under such treatment films grow some sizeable crystallites by depleting their surroundings. As might be expected, after counter-electroding, these films showed electrical shorts. Continuous barium titanate films suitable for forming capacitor dielectrics resulted when the simultaneously evaporated constituent oxides were reacted by heating the substrate during deposition. No post-deposition heat treatment was required to react the oxides. Figure 3(b) shows the surface micrograph of a film on a 60 Pt-40 Rh substrate held at 935°C during deposition in oxygen. The lines are substrate grain boundaries. The films prepared this way are continuous and were successfully

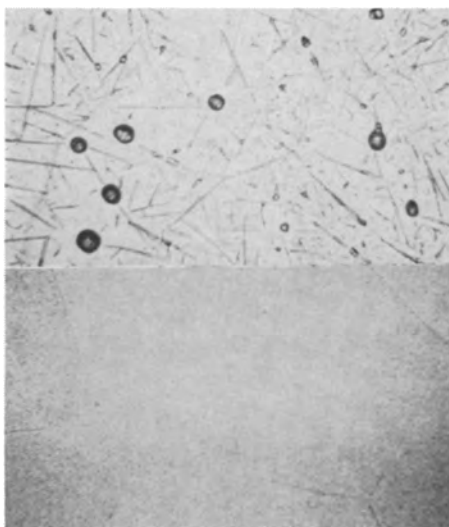


Fig. 3. Surface micrograph of thin BaTiO_3 films. (a) (top) After heating in argon for 18 hr at 940°C ; (b) (bottom) film synthesized at 935°C . Magnification 225X.

counter-electroded for measurements without experiencing electrical shorts.

The minimum substrate temperature required to supply sufficient activation energy for reacting the simultaneously evaporated oxides depended upon the nature of the evaporant sources and the oxygen pressure. When the oxides were generated from barium and titanium metal, barium titanate was formed at temperatures as low as 600°C . With ceramic TiO_2 and BaTiO_3 as sources for TiO_2 and BaO , the lowest substrate temperature required was 800°C . In either event, the reaction of the oxides took place at lower temperatures and in shorter times when it was effected during deposition rather than during a post-deposition heat treatment. For film deposition rates from 2 to 8 Å/sec performed for periods ranging from 10 to 40 min, reaction took place on the heated substrates during deposition at the temperatures described. Films similarly prepared on room temperature substrates required heat treatments (in argon or oxygen at atmospheric pressure) at temperatures in excess of 900°C for times exceeding 15 hr.

In no case was it possible to form barium titanate at an oxygen pressure lower than 10^{-3} Torr at a temperature below 900°C . Barium titanate films prepared at a substrate temperature of 800°C and an oxygen pressure of 5×10^{-3} Torr did not show the strong x-ray diffraction pattern of films prepared at higher temperatures under the same oxygen pressure. When films were prepared at the same temperature with the oxygen pressure increased to 10^{-2} Torr, x-ray diffraction patterns showed they possessed a degree of crystallinity equal to or higher than that of films prepared at substrate temperatures 200°C higher. At an oxygen pressure of 10^{-2} Torr, BaTiO_3 was formed as low as 600°C , although it was not possible to obtain films with the same degree of crystallinity as those prepared under the same pressure at 800°C .

Preparation of substrates.—Several materials were studied for applicability as substrates. Among these, polished 60 Pt-40 Rh substrates which were vacuum fired at 1400°C , lapped and diamond polished provided the most suitable surfaces. Defects could be reduced to small dimensions relative to the thickness of the deposited dielectric film. The material was relatively unreactive to the effects of high temperature, oxygen atmosphere, and the film deposit. These substrates also contributed only a simple line structure in its x-ray diffraction pattern and presented a highly conductive base electrode for test capacitors.

Firing at 1400°C in vacuum was employed to increase the grain size and stabilize the substrate dur-



Fig. 4. Surface of a prepared 60-40 Pt-Rh substrate after heating to deposition temperature. (a) (top) Interference contrast micrograph. Magnification 35X; (b) (bottom) interferogram of grain boundary. Magnification 225X.

ing subsequent heating. Although the grain boundaries could not be seen after this treatment, subsequent reheating at 950°C in the deposition system caused them to reappear on the highly polished surface. The interference contrast micrograph, Fig. 4(a), illustrates the grain structure and indicates that the grains are slightly shifted against one another. The interferogram, Fig. 4(b), shows that steps are of the order of 300Å at the grain boundaries. These grain boundaries, however, did not appear to affect the dielectric properties of the films deposited on these substrates.

Measurements of Film Properties

Composition and structure.—The BaTiO_3 films were examined by x-ray spectroscopy to determine the relative composition of Ba and Ti. The technique was to measure the BaL_α to TiK_α intensity ratio and to compare this with bulk BaTiO_3 samples. To determine the crystalline phases and their structure, conventional x-ray diffraction analysis of the films was made. All of the films revealed the cubic Perovskite-type structure at room temperature, except for some of the thicker film where tetragonality was indicated by the appearance of the (110) line splitting. These measurements showed further that BaTiO_3 appeared when the Ba/Ti spectroscopic intensity ratio was in the range from 0.4 to 0.8, with the strongest diffraction patterns for a ratio of 0.6. The Ba/Ti intensity ratio from measurements on barium titanate powders and

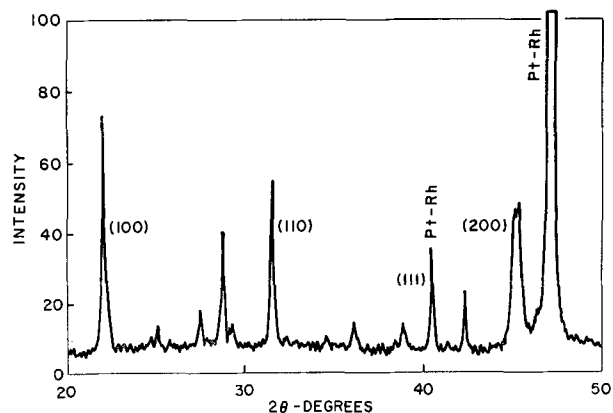


Fig. 5. X-ray diffraction pattern of mixed barium titanate film (BaTiO_3 -indexed peaks, Ba_2TiO_4 -unmarked peaks and Pt-Rh substrate peaks.) BT 82; Ba/Ti = 1.1.

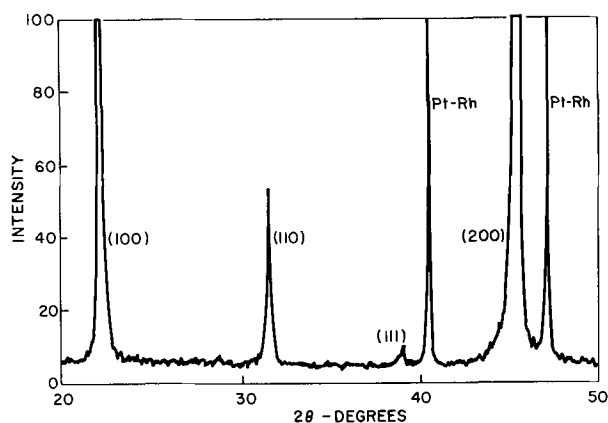


Fig. 6. X-ray diffraction pattern of barium titanate film; BT 94; Ba/Ti = 0.62.

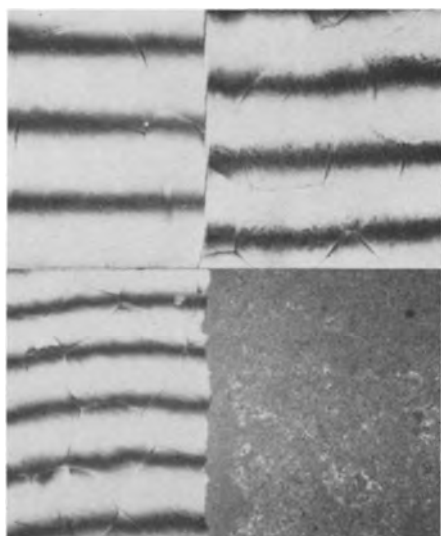


Fig. 7. Dual-beam interferograms taken (a) (top) on a smooth film, (b) (bottom) on a rough film. (Note the film is removed on the left.)

single crystals gave an average intensity ratio of 0.87. The discrepancy is probably due to the presence of a Ti-rich phase of low order (as TiO_{2-x} and BaTi_2O_5) which has poor diffracting power and does not show up in the diffraction pattern. For ratios above 0.8, the appearance of the Ba-rich orthotitanate (Ba_2TiO_4) as a minor phase was observed. In Fig. 5 the diffraction pattern of a film with the Ba/Ti intensity ratio of 1.1 is shown in the range from 20° to 50° , where the main diffraction peaks occur. The ortho- and meta-titanates are distinguishable and also the peaks for the Pt-Rh substrate. The diffraction pattern of a film with an x-ray spectrographic Ba/Ti ratio of 0.62 is shown in Fig. 6. The pattern is strong and shows a preferential orientation in the (200) plane; the Ti-rich phase does not appear in the pattern.

Film thickness.—It has been the practice to determine an average film thickness by weighing (1, 2, 4, 5). In our measurements, film thickness was determined by dual-beam interferometry in the region close to a test capacitor. The film was partially removed by HF-etching after masking with a wax solution, and the step was then metallized by silver evaporation. An example of an interferogram for thin films with a smooth surface is shown in Fig. 7(a). For some thick films, or when the films are Ba-rich, the surface was usually rough, see Fig. 7(b), and the interference pattern was then washed out. When the measurements of the thick films could not be made by use of white light fringes, a stylus micrometer was used.

Table I. Properties of synthesized BaTiO_3 films

Sample No.	C/A ^a ($\mu\text{F}/\text{cm}^2$)	d ^b (μ)	ϵ' ^c (23°C)	D ^d (%)	Ba/Ti ^e avg	Structure ^f
BT-27	0.25	0.11	31	7.9	0.65	A
BT-29	0.085	0.22	21	4.7	1.05	A
BT-67	0.91	0.14	140	2.7	0.73	B
BT-69	1.32	0.37	550	3.2	0.45	B
BT-71	1.61	0.73	1330	17.6	0.45	BT
BT-77	0.44	0.54	270	6.0	0.88	B, B ₂
BT-81	1.58	0.46	820	4.1	0.13	B
BT-82	0.80	0.75	680	8.3	1.87	B, B ₂
BT-85	0.76	1.04	900	5.5	0.57	B
BT-96	1.87	0.57	1200	25.7	0.55	B, B ₂

^a C/A is the capacitance per unit at 1 kc.

^b d is film thickness.

^c ϵ' is the dielectric constant at room temperature.

^d D is the dissipation factor.

^e Ba/Ti is the average x-ray spectroscopic peak intensity ratio.

^f Structure: A, amorphous; B, BaTiO_3 ; BT, BaTiO_3 tetragonal; B₂, Ba_2TiO_4 .

Dielectric properties.—To carry out electrical measurements, a pattern of 18 to 36 thin-film aluminum counter electrodes (1-mm diameter) was evaporated over the 1×2 cm BaTiO_3 film area. The leakage resistance was measured with a voltage divider circuit using a Keithley 610 electrometer (input resistance of 10^{14} ohms) and a Keithley 241 voltage supply. Capacitance and dissipation factors in the range from 50 cps to 300 kc were measured with a General Radio 716-C capacitance bridge.

Results and Discussion

For each film, measurements were made of capacitance and dissipation factor at 1 kc. Film thickness, the average Ba/Ti intensity ratio and crystal structure by x-ray diffraction were also determined. These data, with dielectric constants and specific capacitances, are compiled for some films in Table I. Samples BT-27 and 29 are amorphous films deposited on 304 stainless steel before the crystallization conditions were established. The dielectric constants are low, together with relatively high dissipation factors. In the other films prepared at higher substrate temperatures, low-field dielectric constants from 820 to 1330 are found. Although dissipation factors tend to be high in films with high dielectric constant, values as low as 3% are obtained for a film with a dielectric constant of 550. Dielectric constant and dissipation factor do not depend on the substrate temperature in the range from 770° to 1025°C .

The d-c leakage current was measured as a function of the applied voltage for several films. The breakdown voltage was determined in the same measurement. In Fig. 8 the measurement for a crystalline BaTiO_3 film is shown. This particular film did not show breakdown with the applied 14v. In most films, however, a relatively sharp upturn in the current was observed, indicating the onset of breakdown between 4 and 10v. The relatively high leakage was probably caused by a slight oxygen deficiency. The dielectric constant and dissipation factor were also measured over the frequency range from 50 cps to 300 kc; both showed a monotonic decrease in this frequency range. The capacitance decreases by 13% and the dissipation factor from 7.9 to 2% for the sample measured.

The appearance of a minor phase of the orthotitanate reduced the dielectric constant. For a film of the orthotitanate (Ba_2TiO_4) the dielectric constant was found to be approximately 30. In addition to the dependence of the dielectric constant on composition, a dependence of the dielectric constant on film thickness appeared in thin barium titanate films. There was a trend to lower dielectric constant, the thinner the film.

The dependence of capacitance and dissipation factor on temperature is of interest for finding the temperature coefficient of capacitance, and in this case particularly to determine whether there exists a phase

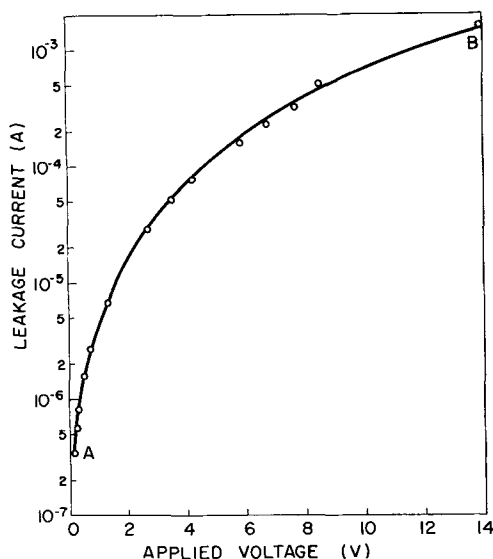


Fig. 8. Leakage current as a function of applied voltage for a BaTiO_3 film. J, (amp/cm²); E (v/cm). Point A, J 4.00×10^{-5} ; E 2.27×10^3 . Point B, J 1.76×10^{-1} ; E 1.90×10^{-5} .

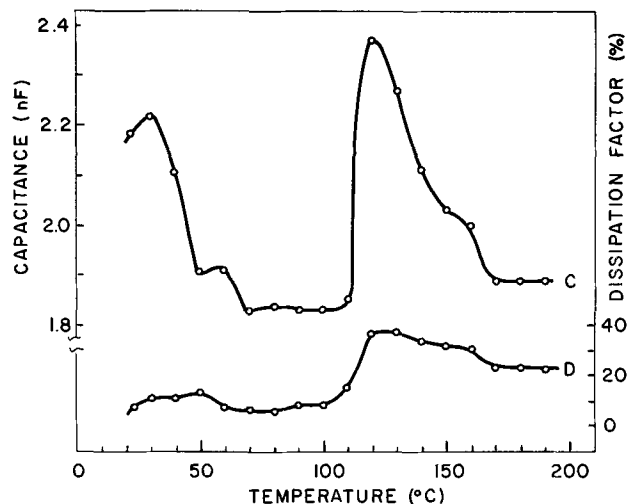


Fig. 9. Capacitance and dissipation factor as a function of temperature for a BaTiO_3 film. BT 94-21; $f = 1$ kc.

transition indicated by a sharp peak in capacitance near 120°C . Usually, only a monotonic increase in capacitance and dissipation factor was found. Several films, however, have shown anomalies at 120°C . One film, which showed higher order of crystallization by x-ray diffraction, also showed maxima in C and D, indicating a phase transition for some of the material. In Fig. 9 the capacitance and dissipation factor vs. temperature are shown for a test capacitor on initial heating. A clear peak in capacitance at 120°C may be observed. None of the electron beam deposited films, however, exhibited a ferroelectric hysteresis loop. This may be expected since a predominantly cubic structure is found in most of the films.

Conclusions

Barium titanate films 0.1 to 1μ thick were synthesized by the simultaneous evaporation of its constituent oxides and reacting them during deposition on a

heated Pt-Rh substrate in a low pressure atmosphere of oxygen. At formation temperatures above 800°C , sufficient energy was supplied to react the constituents, BaO and TiO_2 . BaTiO_3 was detected by x-ray diffraction in films prepared at temperatures as low as 600°C . The formation temperature for BaTiO_3 in films heated during deposition was approximately 200°C less than for films deposited on substrates at room temperature which were heat treated after oxide deposition.

At room temperature the thicker films had dielectric constants above 1000. They did not, however, exhibit spontaneous polarization. This is compatible with the cubic structure found in most films. The tetragonal phase was observed at room temperature only for films that are of the order of 1μ thick. The highest dielectric constant was 1330, measured at 1 kc. A specific capacitance of $1.6 \mu\text{F}/\text{cm}^2$ with a loss tangent of 0.041 was obtained. Although a specific capacitance of $2 \mu\text{F}/\text{cm}^2$ was approached the losses were higher.

The experiments described have shown that the method of simultaneous deposition of oxides is well suited for the preparation of barium titanate films. In contrast to previous work, the stoichiometry indicated by the Ba/Ti ratio can be controlled, but further work is required to prepare single phase (metatitanate) films reproducibly. The technique is promising for the preparation of thin film capacitors; however, there are limitations imposed by the available choice of substrate materials in the preparation of barium titanate films for application in microcircuitry. These limitations are common to all methods of preparation and lie in the high temperature ($>600^\circ\text{C}$) necessary to form barium titanate and in the reactivity of barium compounds with substrate materials at such elevated temperatures.

Acknowledgments

The assistance of W. Kmety, O. Hedquist, and J. deSantis with the film preparation and measurements is gratefully acknowledged. The authors are indebted to Paul Lublin for the x-ray experiments, the interpretation of x-ray diffraction data with regard to the structure of the films, and valuable discussions. They also would like to thank Dr. H. J. Degenhart and I. H. Pratt, of the U.S. Army Electronics Laboratories, for their continued support and guidance in this investigation.

This research was supported by the U.S. Army Electronics Laboratories, Fort Monmouth, New Jersey, under Contract No. DA 36-039-sc-87302.

Manuscript received May 21, 1964; revised manuscript received July 7, 1964. This paper was delivered at the New York Meeting, Sept. 30-Oct. 3, 1963.

Any discussion of this paper will appear in a Discussion Section to be published in the June 1965 JOURNAL.

REFERENCES

1. C. Feldman, *Rev. Sci. Instruments*, **26**, 463 (1955).
2. A. Moll, *Z. angew. Phys.*, **10**, 410 (1958).
3. O. Roder, *Z. angew. Phys.*, **12**, 323 (1960).
4. E. Sekine and H. Toyoda, *Rev. Comm. Lab. (Japan)*, **10**, 457 (1962).
5. E. K. Müller, B. J. Nicholson, and M. H. Francombe, *Electrochem. Techn.*, **1**, 159 (1963).
6. J. P. Green, Jr., Tech. Memo ESL-TM-105, MIT, Cambridge, Mass. (April 1961).
7. D. R. Frankl, A. Hagenlocher, E. D. Haffner, P. H. Keck, A. Sandor, E. Both, and H. J. Degenhart, Proceedings 1962 Electronic Components Conference, Washington, D. C.

Anodic Reactions of Simple Phenolic Compounds

Frederick J. Vermillion, Jr.,¹ and Irwin A. Pearl

The Institute of Paper Chemistry, Appleton, Wisconsin

ABSTRACT

A study of the anodic reactions of phenols was made using the techniques of voltammetry, coulometry, and controlled potential electrolysis. It was shown that two entirely different anodic reactions are possible with phenolic compounds. The first is an electrophilic attack on the aromatic nucleus of the nonionized phenol with the irreversible removal of two electrons to give a mesomeric phenoxonium ion. As an example of this process an electrolysis of 2,6-di-*tert*-butyl-*p*-cresol in acetonitrile at a platinum anode resulted in the addition of methanol to form 2,6-di-*tert*-butyl-4-methyl-4-methoxy-cyclohexadienone in 65% yield. The second possible electrode reaction is the reversible removal of one electron from the phenoxide anion to give a phenoxy free radical. This process was illustrated by the electrolysis of the vanillinate anion in acetonitrile at a platinum anode to give dehydrodivanillin in 65% yield. It was found that half-wave potentials for both electrode reactions could be correlated by Hammett-type equations. Brief voltammetric experiments in 50% aqueous isopropanol on a carbon electrode indicated that both reactions could also occur in this system, depending on the pH and on the pK_D of the phenol being investigated.

Because of the importance of the phenolic hydroxyl group in the field of wood chemistry, an investigation of the anodic reactions of phenols was made using the techniques of voltammetry, coulometry, and controlled potential electrolysis. The literature on the voltammetry of phenols was reviewed recently by Suatoni *et al.* (1). Although a number of workers have made investigations of the anodic voltammetry of phenolic compounds, only a few papers have attempted to explain the mechanism of the primary electrode reaction, and these revealed two conflicting theories.

The first theory, advanced by Hedenberg and Freiser (2), and supported by Ginzberg (3), is that the primary reaction involves the loss of one electron to form a phenoxy free radical. The second theory, proposed by Gaylor *et al.* (4, 5) is that the primary reaction involves the loss of two electrons to give an unspecified intermediate. The latter authors based their admittedly tentative conclusions on the assumption that the reaction of hydroquinone on a graphite electrode in buffered 50% aqueous isopropanol was a two-electron process. However, more recent studies have indicated a strong possibility that, under these conditions, hydroquinone undergoes a one-electron transfer (6, 7). If this is the case, the results of Gaylor *et al.* should be reinterpreted as indicating a one-electron primary electrode reaction in agreement with the results of Hedenberg and Freiser. Nevertheless, the data of Nash, Skauen, and Purdy (8) reveal variations between different phenolic compounds which would seem to preclude the possibility of a single simple mechanism.

Experimental

Apparatus.—The polarograph, voltammetric cell, apparatus for constant potential electrolysis, and their use were described in detail in a previous paper (9). Platinum electrodes used in this study had the following areas: A, 0.029 cm²; and B, 0.0058 cm².

The carbon paste of Olsen and Adams (10) was used in a rotating electrode. The paste was contained in a 1/8 in. hole which was bored in the end of a Teflon rod. Electrical contact was made to the paste through a brass rod which was press fitted into the Teflon. The brass rod was insulated from the synchronous rotator by a nylon sleeve. A small nylon cup at the top held mercury for external electrical connection. Contact between the mercury and the brass was achieved with a platinum pin through the bottom of the nylon cup. The carbon paste was formulated from Acheson Grade

No. 38 graphite, kindly donated by National Carbon Company, and mineral oil (Nujol). The paste was packed into the end of the electrode, and the surface was smoothed to give a disk-shaped surface.

For the electrolysis of 2,6-di-*tert*-butyl-*p*-cresol (2,6-DTBC) the Potentiostat (9) was used to supply a constant current by controlling the potential drop across a fixed resistor in series with the electrolysis cell. The methanolic solution of tetraethylammonium hydroxide was added dropwise at 20-35 sec intervals with a timing device which was adjusted manually at intervals throughout the electrolysis so that the rate was maintained at one equivalent per faraday of electricity.

Chemicals.—Unless otherwise stated, reagent-grade chemicals were employed. Chemicals not available commercially were prepared by methods in the literature (11-18). When necessary, phenols were purified by recrystallization or vacuum distillation until a melting point close to that reported in the literature was obtained. It was noted that 3,5-di-*tert*-butyl-4-hydroxybenzoic acid prepared by the method of Yohe *et al.* (18) melted at 205°-207° and remelted at 215°-217°, whereas the original authors reported a melting point of 217°-218°. However, the present product had an infrared spectrum identical with that of an authentic sample kindly provided by Dr. Yohe (19).

Voltammetric procedure.—Samples were weighed in a dry box maintained below 20% (usually 7-10%) relative humidity. The weighed sample of phenol was dissolved and diluted with supporting electrolyte to 10 ml in a volumetric flask. The resulting stock solution was subsequently diluted with a solution of supporting electrolyte to prepare the test sample.

The phenoxide anions in acetonitrile were prepared by adding tetraethylammonium hydroxide (as 10% aqueous solution) to the solution of the phenol.

For the experiments in 50% aqueous isopropanol, buffer stock solutions were prepared in water with an ionic strength of 1M. Five milliliters of the buffer, 20 ml of distilled water, and the phenol dissolved in isopropanol were placed in a 50-ml volumetric flask and diluted to the mark with isopropanol to give a solution of 0.1M ionic strength. The buffers used and their apparent pH after dilution are given in Table I.

Test solutions were deaerated for at least 15 min before running a voltammogram. The span voltage and cell resistance were measured frequently, the usual procedure being to measure the span voltage with a L&N Student potentiometer before each experiment, and the cell resistance after each experiment. Residual

¹Present address: West Virginia Pulp and Paper Company, Charleston, South Carolina.

Table I. Buffer solutions

Main buffer components	Apparent pH after dilution with isopropanol
HCl, KCl	1.4
Potassium acid phthalate	3.7
HCl, sodium acetate	5.8
NH ₄ OH, NH ₄ Cl	8.1
H ₂ BO ₃ , NaOH	9.8
NaOH, Na ₂ HPO ₄	11.8

current curves were run frequently to check the purity of the system. The direction of polarization was $-$ to $+$ and the rate of polarization was 2.94 mv/sec.

Experiments were conducted on both oxidized and reduced platinum electrodes. The oxidized electrode was achieved by a half-minute treatment in hot chromic acid. The reduced electrode was obtained by cathodically pretreating the electrode at about -0.5 v vs. the SCE. In some cases where a polymer film was indicated on the electrode surface, the cathodic pretreatment was preceded by a half-minute treatment with hot chromic acid, but in the case of 2,6-DTBC and its derivatives no such cleaning was needed.

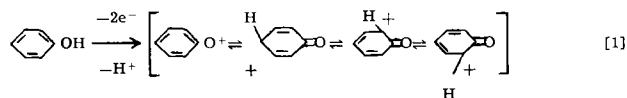
Analysis of Voltammetric Data

Potentials are reported as measured vs. the SCE. The curves were evaluated with a computer program which corrected for residual current and iR drop, and selected i_D as the value which gave the best least squares fit to a straight line in a plot of $\log i/(i_D-i)$ vs. E . The program gave values of i_D , $E_{1/2}$, and βn_{β} .

The trial and error basis for the selection of i_D would not be applicable in the case midway between "reversible" and "totally irreversible" voltammetric behavior, nor in the case of kinetic or catalytic behavior. In these cases the computed value of βn_{β} would have no significance. However, since the waves of interest in this study did give a reasonably good fit to a straight-line plot, the calculated values of βn_{β} have a practical use since they at least describe the wave shape empirically.

Phenoxonium Ion Mechanism in Acetonitrile

Initial voltammetric studies with a number of phenols gave diffusion currents which by comparison with hydroquinone indicated approximately a two-electron transfer.² Since the phenolic hydroxyl is practically undissociated in acetonitrile, it was presumed that the nonionized phenol was reacting to form a mesomeric phenoxonium ion according to Eq [1]. The



calculated values of βn_{β} ranged from 0.48 to 0.72 depending on the condition of the electrode surface and the concentration. This indicated an irreversible electrode process. The effect of an oxide film on the surface of a platinum electrode was pronounced, an oxidized surface giving a half-wave potential as much as 0.1v lower than a reduced electrode. There was also a decrease in the apparent reversibility of the reaction on an oxidized surface, but no significant effect on the diffusion current. With isoeugenol, severe filming was encountered, but with the hindered phenols and other phenols which had two or more of the reactive ortho and para positions blocked, no filming was encountered.

Detailed studies on 2,6-Di-tert-butyl-p-cresol.—2,6-DTBC was selected for intensive study because the reactions of this compound with chemical oxidizing agents are quite well known. All of the voltammetric studies in this section were conducted on platinum

²The results of Lund (21) and Geske (13) have indicated indirectly that the anodic reaction of hydroquinone in acetonitrile involves a two-electron transfer.

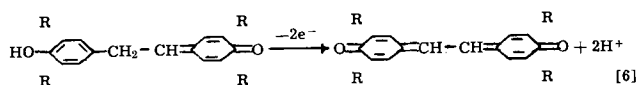
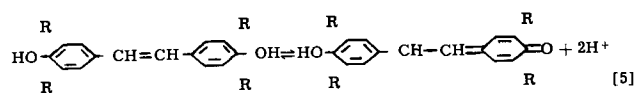
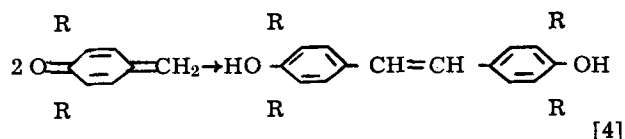
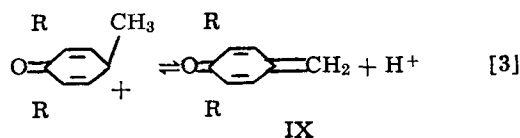
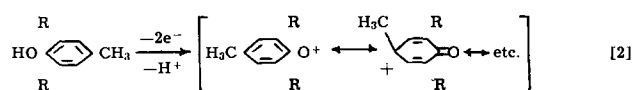
Table II. Effect of concentration on the voltammetry of 2,6-Di-tert-butyl-p-cresol

Concn., mM	(Electrode B, reduced surface)					
	Wave I			Wave II		
	$-i_D/C$, $\mu\text{A}/\text{mM}$	$E_{1/2}$, (v vs. SCE)	βn_{β}	$-i_D/C$, $\mu\text{A}/\text{mM}$	$E_{1/2}$, (v vs. SCE)	βn_{β}
0.0210	9.5	1.21	—	—	—	—
0.0416	10.6	1.19	—	—	—	—
0.106	12.1	1.25	0.61	—	—	—
0.528	13.3	1.25	0.62	1.6	1.63	0.50
1.06	14.6	1.26	0.54	3.0	1.63	0.60
3.64	14.6	1.24	0.70	6.3	1.60	0.43
6.68	14.5	1.22	0.83	8.3	1.53	0.51
9.66	13.7	1.21	0.86	9.4	1.54	0.47

electrode B with a reduced surface, using 0.5M tetraethylammonium perchlorate as a supporting electrolyte. Representative data in the concentration range from 0.021 to 9.66 mM are given in Table II.

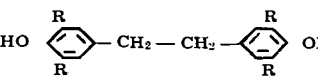
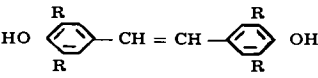
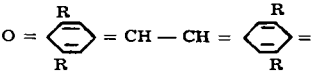
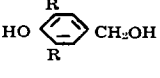
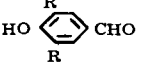
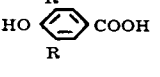
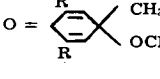
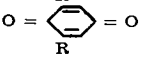
Two points of interest will be noted in these data. First, the diffusion current constant for the main wave increases numerically from a value indicating a two-electron reaction at low levels of concentration to a value indicating a three-electron reaction at high levels of concentration. Second, there is a second wave which is absent at very low levels of concentration, but occurs at intermediate levels of concentration and becomes more pronounced at high levels of concentration. The values of the diffusion current constant for the main wave would suggest a limiting two-electron reaction at the lowest level of concentration, and a three-electron reaction at the highest level of concentration. Both the increased diffusion current constant and the second wave can be explained by the reoxidation of a product of reaction after some kinetic process which follows the primary electron transfer.

A postulated sequence of reactions which would give limiting n values of two and three at the low and high extremes of concentration, respectively, is given by Eq. [2]-[6].³ This reaction sequence was supported (R = *t*-Butyl)



³This reaction sequence was chosen because of the work of Fujisaki (23-26) who has given evidence for the methylenequinone, IX, as an intermediate in this type of reaction.

Table III. Voltammetry of products from chemical oxidations of 2,6-DTBC

		(Electrode B, reduced surface)				
Compound (R = t - Bu)	Concn, mM	Wave I		Wave II		
		i_D/C , $\mu\text{A}/\text{mM}$	$E_{1/2}$, (v vs. SCE)	i_D/C , $\mu\text{A}/\text{mM}$	$E_{1/2}$, (v vs. SCE)	
I 	1.23	19.7	1.23	5.8	1.51	
II 	0.77	9.1	0.77	9.1	1.53	
III 	^a	—	—	^a	1.53	
IV 	0.174 1.00	14.3 13.2	1.25 1.24	— 3.2	— 1.72	
V 	1.10	—	—	11.0 ^b	1.68 ^b	
VI 	0.586	—	—	7.3 ^b	1.68 ^b	
VII 	No wave observed.					
VIII 	No wave observed.					

^a This compound was sparingly soluble in acetonitrile and its concentration was not known with certainty. However, there is little doubt that this was a two electron wave, i.e., $i_D/C \sim 9 \mu\text{A}/\text{mM}$.

^b The waves for these compounds occurred so close to the decomposition point of the solvent supporting electrolyte system that a precise evaluation of i_D/C and $E_{1/2}$ was impossible.

by the fact that of the known oxidation products of 2,6-DTBC only the dimeric products, I, II, and III in Table III give waves at approximately the same potential as the second wave of 2,6-DTBC.

Since it was known that an electrolysis of 2,6-DTBC in acetonitrile would result in the generation of hydrogen ions in solution, voltammetric experiments were

performed with anhydrous perchloric acid in glacial acetic acid added to the test solution. The results of typical experiments are given in Fig. 1. Although there is little effect on the observed voltammogram at hydrogen ion concentrations up to 1 mM, at a concentration of 11.4 mM the wave shape is altered entirely, thus indicating a changed reaction path. Voltammetric experiments with the dimers II and III in the presence of excess hydrogen ion gave new waves at low potentials which indicated that a destructive oxidation of the stilbenequinone was occurring.

These experiments with excess hydrogen ion were significant because they indicated that unless the hydrogen ion was consumed as it was liberated in the electrode reaction and following processes, destructive oxidation of the initial products of reaction could be expected in a controlled potential electrolysis. One method of overcoming this difficulty would have been to introduce a suitable buffer into the reaction mixture. However, preliminary voltammetric studies with pyridine, tetraethylammonium acetate-acetic acid, and tetraethylammonium nitrate-nitric acid quickly revealed that none of these would be suitable as a buffer for the anodic reaction of 2,6-DTBC in acetonitrile.

Since no satisfactory buffer was found, an alternative approach was indicated. For each electron removed from a neutral organic molecule in an anodic reaction there is left in solution one positively charged ion, either a hydrogen ion or a carbonium ion. The carbonium ion is in most cases unstable and may be expected to combine with other molecules in the solution to give a neutral molecule and a hydrogen ion. Ultimately, therefore, there should be a net generation of one hydrogen ion in solution for every electron which

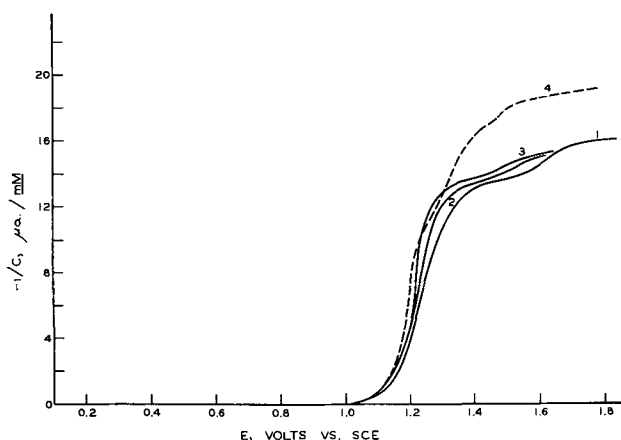


Fig. 1. Effect of hydrogen ion on the voltammetry of 2,6-DTBC

Curve No.	Conc. 2,6-DTBC, mM	Conc. H ⁺ , mM
1	0.901	0
2	0.901	0.125
3	0.897	1.36
4	0.881	11.5

is transferred at the electrode, i.e., one equivalent of hydrogen ion per faraday of electricity. This principle offered a practical way out of the buffering dilemma. While the electrolysis was being conducted, a base could be added continuously at a rate which was exactly equivalent to the current flowing.

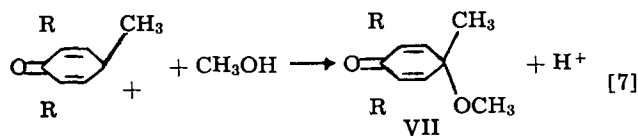
An electrolysis by this method was conducted on a $10^{-2}M$ solution of 2,6-DTBC with 0.5M sodium perchlorate as a supporting electrolyte.⁴ To minimize any overconcentration of hydrogen ion in the vicinity of the anode, the electrolysis was conducted at a constant low current density of 1 ma/cm², corresponding approximately to the current density at a concentration of 0.5 mM in the voltammetric studies.

The base added was tetraethylammonium hydroxide. The anolyte originally contained no methanol, but the rate of addition was such that at the end of the electrolysis the methanol content was 1600 mM. The anolyte was originally only 1-2 mM in water, but as the electrolysis progressed more water was formed at a rate of one equivalent per faraday so that its final concentration was approximately 40 mM.

The plot of anode potential vs. time for this electrolysis shows a small decrease in potential during the first 600 min which was expected because a shift in half-wave potential to a less positive value was observed in a solution containing water or methanol. For the next 700 min the potential remained relatively steady, and then for 700 min it rose gradually as is expected in an electrolysis at constant current. Then for a period of 500 min the anode potential varied very erratically, and some extremely low potentials (<0.4v) were observed. This behavior was significant, indicating the formation of electrolysis products which had a very low half-wave potential. The anode potential rose rather sharply during the last part of the electrolysis to a final value of 1.55v when the electrolysis was stopped. At the low current density used, the original 2,6-DTBC should have been more than 95% consumed for the potential to reach this level.

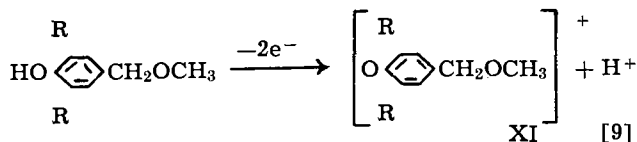
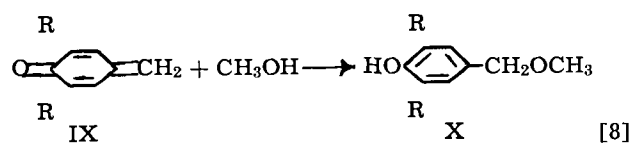
The coulometric n value for this electrolysis was 3.45. By titration the anolyte was shown to contain excess base equivalent to 3% of the total hydroxide ion added during the electrolysis. A crude product was separated from the anolyte in 103% yield based on the starting 2,6-DTBC.

2,6-Di-*tert*-butyl-4-methyl-4-methoxy-cyclohexadienone, VII, was separated from the crude product and positively identified. By quantitative gas chromatography this compound was known to represent 65.3% of the crude product. It is believed that this compound was formed by addition of methanol to the phenoxonium ion from the initial electrode reaction according to Eq. [7].



Voltammetric experiments in the presence of excess methanol or water showed that the second wave of 2,6-DTBC was completely absent, and the diffusion current constant for the first wave was reduced to a value corresponding to an n value of 2.58 over the concentration range from 0.5 to 10 mM. Since a nonintegral n value is an impossibility, it is believed that the phenoxonium ion from the initial electrode reaction was undergoing two different reactions. The first reaction with an n value of 2 led to the cyclohexadienone, VII. The second reaction was believed to involve the methylenequinone, IX, from Eq. [3]. Thus, methanol could add to give a benzyl ether, X, according to Eq. [8], and X could undergo further oxidation at the electrode surface according to Eq. [9], an over-all four-electron oxidation.

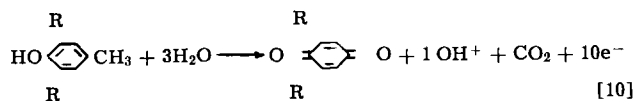
⁴ For electrolysis, 1.000g of 2,6-DTBC was dissolved in 600 ml of 0.5M sodium perchlorate in acetonitrile.



From the apparent n value of 2.58 in the voltammetric studies it is possible to calculate the percentage of 2,6-DTBC going to the cyclohexadienone, VII, assuming that the original phenoxonium ion only reacts according to Eq. [7]-[9]. This calculation indicates a 71% yield of VII, a remarkably good agreement with the yield of 65.3% in the electrolysis.

Another compound, indicated as 10.4% of the crude product of electrolysis by quantitative gas chromatography, was separated in a large enough quantity for an infrared spectrum by collection from the gas chromatograph. Its spectrum was identical with that of 2,6-di-*tert*-butyl-1,4-benzoquinone. The question arises as to the origin of this product. Cook *et al.* (17) believe that in the chemical oxidation of 2,6-DTBC it is formed via the "oxidatively induced decarboxylation of 3,5-di-*tert*-butyl-4-hydroxybenzoic acid," presumably via the corresponding free radical. The electrochemical oxidation should follow a similar path.

The phenoxonium ion, XI, could rearrange and add water or methanol to give an acetal or hemiacetal, and these by hydrolysis could give the aldehyde V (see Table III). Oxidation of the aldehyde by a two-electron process would not have been possible because this reaction occurs at a potential considerably higher than existed at the anode during the electrolysis (see Table II). It is known, however, that an excess of base was present in the anode compartment during the latter stages of the electrolysis. This would lead to ionization of some phenols in the reaction mixture. The phenoxide anion reacts via a one-electron free radical mechanism at a much lower potential than the nonionized phenol, a fact which explains the low anode potentials which were observed during the latter stage of the electrolysis. It is believed therefore that the benzoquinone, VIII, was formed by a stepwise oxidation of the paramethyl group of 2,6-DTBC via free radical mechanisms with a decarboxylation of the acid, VI, in the over-all ten-electron process of Eq. [10].



Such a mechanism would help to explain the high coulometric n value observed for this electrolysis.

The most significant result of this electrolysis is the relatively high yield of the cyclohexadienone, VII. Since, in chemical oxidations of 2,6-DTBC, this type of product results from the use of ionic reagents such as bromine or nitric acid in polar media (16, 27, 28), its occurrence as an electrolysis product is confirming evidence for the phenoxonium ion mechanism in the electrode reaction of the nonionized phenol.

Mechanism of the electrode reaction.—There are three reasons for believing that the electrode reaction of the nonionized phenol involves an initial electrophilic attack on the aromatic nucleus at a position either ortho or para to the phenolic hydroxyl. First, the cyclohexadienone, VII, isolated as a product of electrolysis is also obtained in chemical oxidations with molecular bromine, a reagent which evidently reacts

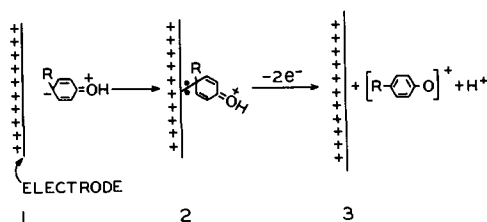


Fig. 2. Schematic representation for the electrode reaction of a phenol.

with aromatics in polar solvents through the electrophilic attack of the bromonium ion on the aromatic ring (29). Second, in the nonionized phenol the centers of electron density are in the positions ortho and para to the phenolic hydroxyl, and one should expect that the point of electrode attack should be at these electron-rich centers. Third, it has been shown (*vide infra*) that the electrode reactions of both phenols and aromatic methoxyl compounds can be correlated on the same Hammett-type plot by assuming an electrophilic attack on the aromatic nucleus.

It is known from the value of βn_β and the insensitivity of the half-wave potential to added hydrogen ion that the reaction may be classified as totally irreversible. The average value of βn_β at low levels of concentration on an oxidized electrode is about 0.5. It is impossible from the evidence at hand to separate β , the transfer coefficient, from n_β , the number of electrons transferred in the potential-determining step of the electrode process. Lund (20, 21) favors the theory that one electron is removed at a time (*i.e.*, $n_\beta = 1$). The present author by further analogy with the electrophilic attack of chemical oxidants favors the simultaneous removal of two electrons. Thus, when the bromonium ion attacks an aromatic ring and is subsequently cleaved as bromide, there has been a simultaneous removal of two electrons from the original molecule.

A schematic representation of this viewpoint for the electrode reaction of a phenol is presented in Fig. 2. In step 1 the molecule becomes polarized under the influence of the electric field. As a closer approach to the electrode surface is realized in step 2, two electrons are attracted from the molecule to the electrode surface with the transitory formation of a bond having some covalent character. These electrons are further withdrawn from the molecule until actual cleavage occurs to give the phenoxonium ion and a hydrogen ion.

Correlation of half-wave potentials.—Half-wave potentials for a totally irreversible electrode reaction at 25°C may be correlated by the Hammett equation (29) which in this case may be stated

$$E_{1/2} - E^{\circ}_{1/2} = \frac{-0.0591}{\beta n_\beta} \sigma \rho \quad [11]$$

It was found in agreement with Eq. [11] that the

hindered phenols of formula $\text{HO} \text{---} \text{C}_6\text{H}_3 \text{---} \text{R}$ where

$\text{R} = \text{CH}_3$, *t*-butyl, CHO, and COOH gave a straight line plot when $E_{1/2}$ was plotted against σ for the R group. It was found that σ rather than σ^c values fitted the correlation.⁵ This is not surprising since the postulated reaction mechanism does not involve the phenolic group directly. A similar correlation was found valid for the monosubstituted methoxyl compounds which Lund (20, 21) has studied.

A general correlation for both methoxyl and hydroxyl substituted aromatics was possible using σ^+ values for electrophilic substitution in accordance with the proposed reaction mechanism. In order to achieve

⁵ These σ values were chosen in relation to the phenolic hydroxyl.

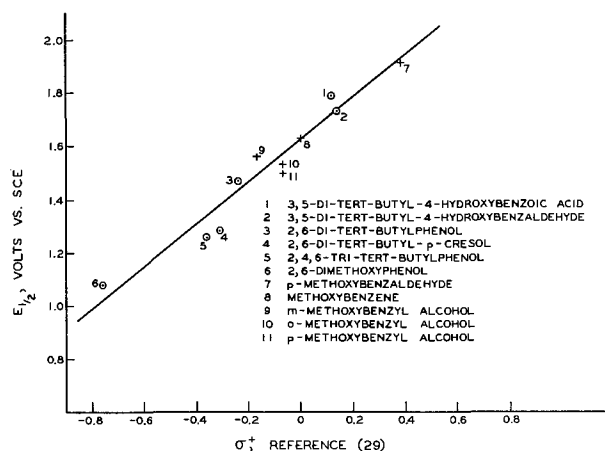


Fig. 3. Hammett σ^+ plot. O, Present study; +, data of Lund (21,22).

the correlation shown in Fig. 4, the following assumptions were necessary:

1. It was assumed that in each case the point of attack was ortho or para to the hydroxyl or methoxyl substituent, and that σ^+ for a substituent ortho to the point of attack was the same as σ^+ for a substituent para to the point of attack.

2. It was assumed that σ^+ for a substituent at the site of attack was the same as σ^+ for a substituent meta to the site of attack.

3. The half-wave potential data of Lund *vs.* the Ag/Ag⁺ electrode was converted to the SCE scale by adding a factor of 0.30v (30).

4. From Lund's discussion of his experimental method it was believed that his platinum electrodes were probably oxidized. Therefore, half-wave potentials for compounds of the present study were those for oxidized electrodes.

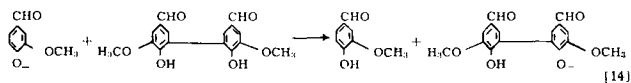
Furthermore, since no σ^+ value was available for the para or ortho hydroxyl substituent, this value as well as σ^+ for the para or ortho methoxyl substituent was taken as zero. It was expected that by using this procedure two parallel lines, one for methoxyl and one for hydroxyl compounds, would be obtained. Actually, in Fig. 3 all the points seem to scatter around the same line. Therefore, it appears that there is little difference between σ^+ for a hydroxyl and σ^+ for a methoxyl substituent. Since σ^+ for the para methoxyl group is given as -0.76 , (29), the plot of Fig. 3 is displaced by this amount.

Considering the assumptions which were made in the calculation of σ^+ values, the plot of Fig. 3 fits the observed data amazingly well. It is believed that by a systematic study of other simple aromatic compounds a more precise general correlation could be achieved.

The utility of the correlation in Fig. 3 is demonstrated by the cases of 2,6-dimethoxyphenol and vanillin. For the former compound an apparent four-electron wave is observed at 1.08v, but it is believed that the primary electrode reaction involves two electrons as do the phenols and methoxyl compounds of Fig. 3. The most negative σ^+ value for 2,6-dimethoxyphenol, and therefore the highest electron density occurs in the *meta* position to the phenolic hydroxyl. Using a σ^+ of -0.76 for the *meta* position, the half-wave potential for 2,6-dimethoxyphenol fits the correlation of Fig. 3 very well. This may be taken as an indication that the proposed primary electrode reaction is correct. For vanillin, which gives a two-electron wave at 1.43v, no σ^+ value calculated for an attack on the aromatic nucleus fits the correlation of Fig. 3 at all. This is believed to be an indication that the position of primary electrode attack for vanillin is the carbonyl oxygen.

of the acetonitrile solvent. Thus, addition of vanillin to the diphenoxide completely removes the wave for the latter, but gives new waves for the vanillinate anion and the monophenoxide. This indicates that the vanillin is ionized completely before the second ionization of dehydrodivanillin begins. When vanillin is added to a solution of the monophenoxide, however, there is no change in the voltammetric behavior. This indicates that the first ionization of dehydrodivanillin must be complete before ionization of the vanillin begins.

This behavior was important in planning an electrolysis of vanillin because it showed that, as dehydrodivanillin was formed, the vanillinate anion would be consumed in reaction [14], as well as in the electrode reaction



(Eq. [12]). If only enough hydroxyl ion were added to neutralize the original vanillin the reaction could, therefore, only be carried to 66.7% completion. An excess of hydroxyl ion, on the other hand, could not be tolerated because of the reaction of vanillin in the presence of excess hydroxyl (Fig. 4), and because of the electrode reaction of the diphenoxide of dehydrodivanillin. An electrolysis was, therefore, conducted by adding enough hydroxyl ion at the beginning to neutralize the vanillin and periodically adding more at a rate of 0.5 equivalent per faraday of electricity. The concentration of vanillin was approximately 8 mM and the supporting electrolyte was 0.5M sodium perchlorate.

The progress of this electrolysis was followed by voltammetry with the indicating electrode set directly in the anode compartment of the cell. It was noted that at this concentration level the diffusion current constant of vanillin was only $-1 \mu\text{a}/\text{mM}$ on electrode B. The reasons for this low value are twofold. First, at high concentrations, reaction [14] could be expected to decrease the current constant 33%. Second, there is probably some film formation on the electrode surface. As the electrolysis progressed, the wave for the monophenoxide of dehydrodivanillin developed. When the electrolysis was stopped at the end of 956 min, a total of 1.5 equivalents of hydroxyl ion per original equivalent of vanillin had been added. Voltammetry indicated a yield of approximately 62% dehydrodivanillin in close agreement with a recovered crude yield of 65.4%.

The calculated coulometric n value for the reaction based on the recovered dehydrodivanillin was 1.77. Since the true n value for the formation of this product should be 1.0, there must have been some side reactions which consumed additional electricity. A logical course for such a side reaction in view of the results from the electrolysis of 2,6-DTBC would be oxidation of vanillin to vanillic acid and decarboxylation of the acid to form, eventually, quinoidal structures. Such a reaction would represent a net oxidation of six electrons. A rough calculation shows that only 8% of the original vanillin would have been oxidized by such reactions to give an increase in the apparent coulometric n value from 1.00 to 1.77. In addition to this side reaction some polymerization processes may have occurred.

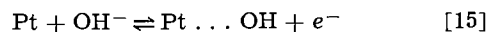
It is believed that an improved yield of dehydrodivanillin could be achieved in this electrolysis, because by paper chromatography the presence of unreacted vanillin in a fairly large amount was noted in the ether-soluble fraction of the crude product of electrolysis.

The obtaining of dehydrodivanillin as the major product of electrolysis verifies the one-electron nature of the electrode reaction as postulated from the voltammetric studies.

Mechanism of the electrode reaction.—The results obtained with the vanillinate anion in particular, and with the other phenolates which were investigated have indicated the following characteristics for the primary electrode reaction:

1. One electron is transferred.
2. The reaction is voltammetrically reversible.
3. Diffusion currents on an oxidized platinum surface are much lower than on a reduced platinum surface.

The third characteristic may be an indication that the point of electrode attack is the phenolic oxygen. The reduction in current level on an oxidized surface must mean that specific active sites on the platinum surface are necessary for the reaction of the phenolate. Since the small oxidation wave for hydroxyl ion is absent on an oxidized surface (32), it seems probable that the same surface sites are required for the oxidation of the phenoxide anions as for hydroxyl ions. The initial oxidation of hydroxyl ions evidently involves the removal of an electron from the oxygen atom with the adsorption of the resulting free radical on the platinum surface (33)⁶ according to Eq. [15]. When the platinum surface is covered with an oxide



film, reaction [15] does not occur. Since the phenoxide anions also contain an oxygen atom with a localized negative charge, the electrode reaction might well be expected to be similar to that of the hydroxyl anion.

A schematic representation of the proposed electrode reaction is given in Fig. 6. As the phenoxide anion approaches the electrode it becomes preferentially polarized so that the negative charge is localized on the phenolic oxygen atom. A temporary bond with the positive electrode surface is formed and broken with the removal of one electron. The resulting phenoxy radical is stabilized through resonant structures as it leaves the electrode surface.

Correlation of half-wave potentials.—Equation [16] predicts the variation of $E_{1/2}$ with the Hammett function for a reversible electrode reaction at 25°C. A plot for

$$E_{1/2} = E^{0_{1/2}} = -0.0591 \sigma_p \quad [16]$$

the few phenoxides investigated is given in Fig. 7. The values for orthomethoxyl, and 2,6-di-*tert*-butyl substitution for this plot were calculated from the data of Suatoni *et al.* (1).

It was found that a σ rather than a σ^c value fitted the aldehyde group of vanillin for this correlation. This is a further indication that the point of electrode attack is the phenolic oxygen.

Aqueous Buffered Solutions

From the foregoing results in acetonitrile solutions, voltammetric behavior of phenols in aqueous systems can be predicted. If the pH is low enough, the phenol should be completely nonionized and the two-electron, phenoxonium ion reaction should occur. If the pH is high enough, the phenol is totally ionized, and the one-

⁶ In the discussion of Laitinen and Enke only the reaction in acidic media is considered, hence their equations discuss the formation of the intermediate $\text{Pt} \dots \text{OH}$ from water rather than hydroxyl ion. However, in basic media the hydroxyl ion is believed to be the reacting species (34).

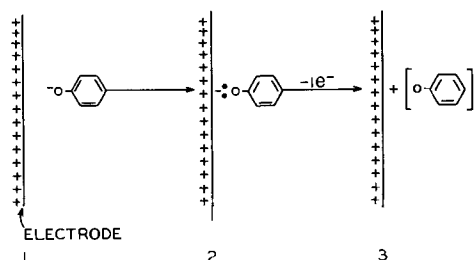


Fig. 6. Proposed reaction mechanism of phenoxide anions

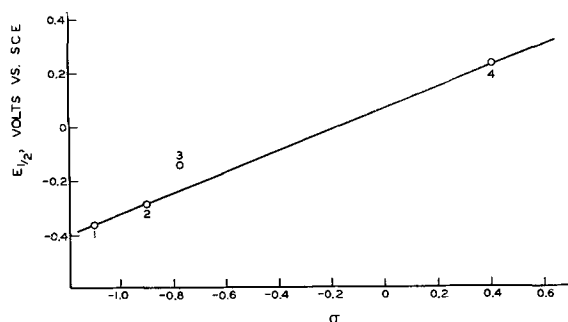


Fig. 7. Hammett plot for phenoxides. 1, 2,4,6-tri-*tert*-butylphenol; 2, 2,6-di-*tert*-butylphenol; 3, 3,5-di-*tert*-butyl-4-hydroxybenzoic acid (both carboxyl and phenol ionized); 4, vanillin.

electron, free radical reaction should occur. At intermediate levels of pH both the ionized and nonionized forms of the phenol are present. If, as proposed by Hedenberg and Freiser (2), the rate of ionization of the phenol is very fast compared to the rate of the electrode reaction, the phenoxide anion should be preferentially oxidized. In this case the observed voltammetric wave should have the same characteristics as the free radical reaction except that the wave will be pH dependent.

Some brief voltammetric studies were carried out in buffered 50% aqueous isopropanol solutions in order to confirm the general behavior predicted in the previous paragraph. Because of the problem of platinum surface oxides, the rotating carbon paste electrode was used.

It was found that 2,6-DTBC gave a pH independent wave which corresponded to the phenoxonium ion mechanism at pH levels of 1.4 and 3.7. The wave for the free radical reaction of this compound was evident at higher levels of pH, but was very drawn out and ill-defined.

Vanillin (0.12 mM) gave well-formed waves for the free radical process at all levels of pH as shown in Fig. 8. From these curves the second wave of the vanillin anion is clearly defined only at a pH level of 5.8. At lower pH it is superimposed on the first wave, and at higher pH it is blended with the decomposition wave of the background solution. It is evidently pH independent.

A plot of half-wave potential *vs.* pH for vanillin is given in Fig. 9. The limiting slope of this curve at low pH is -0.0591 . At high pH the half-wave potential is pH independent. This behavior is exactly as predicted for a fast ionization of the phenol followed by a reversible reaction of the phenoxide anion (2). From the limiting value of $E_{1/2}$ at high pH, and the intercept at zero pH, pK_D for vanillin in 50% isopropanol is calculated as 8.33. Thus, this compound conforms very closely to theoretical behavior.

Manuscript received April 8, 1964; revised manuscript received June 18, 1964. This paper is from the thesis of one of the authors (F. J. V.) prepared in partial fulfillment of the requirements of The Institute of Paper Chemistry for the Ph.D. degree from Lawrence College, Appleton, Wisconsin, June, 1963.

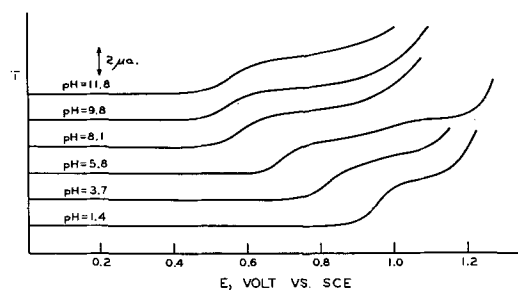


Fig. 8. Voltammetry of vanillin in 50% aqueous isopropanol; carbon paste electrode.

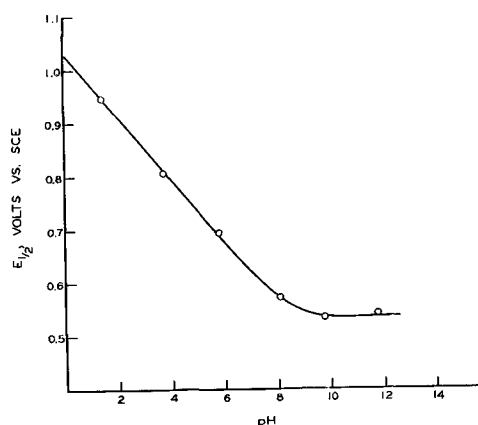


Fig. 9. Effect of pH on the half-wave potential of vanillin in 50% aqueous isopropanol.

Any discussion of this paper will appear in a Discussion Section to be published in the June 1965 JOURNAL.

SYMBOLS

C	concentration, mM
E	potential, v
$E_{1/2}$	half-wave potential, v
i	current, amp
i_D	diffusion current, amp
n	electrons transferred in electrode reaction
n_β	electrons transferred in potential-determining step of irreversible electrode reaction
β	transfer coefficient for irreversible oxidation
R	resistance, ohms
$\sigma, \sigma^c, \sigma^+$	Hammett substituent constants as defined by Gould (29)
ρ	Hammett reaction constant (29)
$E_{1/2}^0$	half-wave potential in Hammett-type correlations for compound with only hydrogen substituents (i.e., $\sigma = 0$), v

REFERENCES

- J. C. Suatoni, R. E. Snyder, and R. O. Clark, *Anal. Chem.*, **33**, 1894 (1961).
- J. F. Hedenberg and H. Freiser, *ibid.*, **25**, 1355 (1953).
- V. I. Ginzberg, *Zh. Fiz. Khim.*, **33**, 1504 (1959).
- V. F. Gaylor, P. J. Elving, and A. L. Conrad, *Anal. Chem.*, **25**, 1078 (1953).
- V. F. Gaylor, A. L. Conrad, and J. H. Lenderl, *ibid.*, **29**, 224 (1957).
- P. J. Elving and A. F. Krivis, *ibid.*, **30**, 1645 (1958).
- J. E. Morris and J. M. Schempf, *ibid.*, **31**, 286 (1959).
- R. A. Nash, D. M. Skauen, and W. C. Purdy, *J. Am. Pharm. Assoc.*, **47**, 433 (1958).
- J. J. O'Connor and I. A. Pearl, *This Journal*, **111**, 335 (1964).
- C. Olsen and R. N. Adams, *Anal. Chim. Acta*, **22**, 582 (1960).
- I. M. Kolthoff and J. F. Coetzee, *J. Am. Chem. Soc.*, **79**, 870 (1957).
- D. L. Burdick, A. V. Santoro, W. E. McEwen, and J. Kleinberg, *ibid.*, **79**, 5467 (1957).
- D. H. Geske, *J. Phys. Chem.*, **63**, 1062 (1959).
- C. D. Cook, *J. Org. Chem.*, **18**, 261 (1953).
- R. F. Moore and W. A. Waters, *J. Chem. Soc.*, **1955**, 2753.
- G. Coppinger and T. Campbell, *J. Am. Chem. Soc.*, **75**, 734 (1953).
- C. D. Cook, E. S. English, and B. J. Wilson, *J. Org. Chem.*, **23**, 755 (1958).
- G. R. Yohe, J. E. Dunbar, R. L. Pedrotti, F. M. Scheidt, F. G. Lee, and E. C. Smith, *ibid.*, **21**, 1289 (1956).
- G. R. Yohe, Illinois State Geological Survey, Urbana, Illinois.
- H. Lund, *Acta Chem. Scand.*, **11**, 491 (1957).
- H. Lund, *ibid.*, **11**, 1323 (1957).
- D. H. Geske, *J. Am. Chem. Soc.*, **81**, 4145 (1959).
- T. Fujisaki, *Nippon Kagaku Zasshi*, **77**, 727 (1956); *C.A.*, **52**, 8096.
- T. Fujisaki, *ibid.*, **77**, 731; *C.A.*, **52**, 8096.

25. T. Fujisaki, *ibid.*, **77**, 733; *C.A.*, **52**, 8097.
 26. T. Fujisaki, *ibid.*, **77**, 869; *C.A.*, **52**, 8097.
 27. M. S. Kharasch and B. S. Joshi, *J. Org. Chem.*, **22**, 1439 (1957).
 28. C. D. Cook and R. C. Woodworth, *J. Am. Chem. Soc.*, **75**, 6242 (1953).
 29. N. S. Gould, "Mechanism and Structure in Organic Chemistry," 790 p, Holt, Rinehart, and Winston, New York (1959).
 30. R. C. Larson, R. T. Iwamoto, and R. N. Adams, "Reference Electrodes for Voltammetry in Acetonitrile," A preprint supplied by Dr. R. N. Adams, 1961.
 31. I. A. Pearl, *J. Org. Chem.*, **12**, 85 (1947).
 32. I. M. Kolthoff and N. Tanaka, *Anal. Chem.*, **26**, 632 (1956).
 33. H. A. Laitinen and C. G. Enke, *This Journal*, **107**, 773 (1960).
 34. E. C. Potter, "Electrochemistry," Cleaver-Hume Press, London, Ltd. (1956).

Self-Gettering and Impurity Transfer in the Vapor Deposition of Thorium by the Carbide Iodide Process

A. F. Reid

Division of Mineral Chemistry, C.S.I.R.O., Chemical Research Laboratories, Melbourne, Australia

ABSTRACT

The reactions of carbon monoxide, oxygen, and nitrogen at micron pressures with variously solid thorium tetraiodide, thorium carbide, and thorium nitride, have been studied in the temperature range 300°-900°C, and found to display first order kinetics. Activation energies for the reaction of oxygen and carbon monoxide with thorium carbide were 6 and 11 kcal, respectively. These studies combined with thermodynamic calculations show that in the carbide-iodide process for thorium deposition, suitable degassing of the thorium carbide feed and heating of the deposition vessel (containing thorium iodide) at operating temperature before the filament is heated will remove residual oxygen, oxides of carbon, and water vapor from the feed and from the vessel volume. Nitrogen can be removed before its reaction with carbide by degassing of the latter below 700°C. It is concluded that once deposition is begun, vapors subsequently outgassed from the feed or vessel will largely react with the heated thorium metal. Filaments containing 1 ppm of nitrogen and hydrogen, 9-13 ppm oxygen, and an estimated 3-6% of carbon were prepared.

The properties of metals are often decisively modified by minute traces of impurities, in particular those derived from common gases. The advantages of the carbide-iodide development of the van Arkel-de Boer process for reducing these and other impurities in thorium to a low level have been enumerated by Scaife and Wylie (1). In this process (1-3), thorium carbide feed, prepared by heating the oxide with graphite and hydrocarbon binder to 2100°-2200°C under argon, is vacuum degassed at 800°-900°C. Thorium iodide is then formed from the carbide by reaction with iodine vapor at 300°C in a previously degassed vapor deposition bulb. After a further evacuation to remove any gases released from the surface layers of the carbide by its reaction with iodine the bulb is sealed off, brought to 460°-480°C to produce a vapor pressure of thorium iodide, and the thin tungsten or tantalum starting wire heated to 1300°-1450°C to cause deposition of thorium.

Residual vapors in the bulb, besides impeding diffusion of thorium iodide to and iodine from the filament, cause impurity transfer to it, since the heated thorium will react readily with traces of oxygen, nitrogen (4), water vapor, oxides of carbon, and hydrocarbons (6, 7). Such impurity gases can result from inadvertent exposure of the feed materials to the atmosphere, caus-

ing absorption of air gases and formation of hydrocarbons by hydrolysis, or simply from inadequate vacuum or degassing procedures.

The purpose of this paper is to report the feasibility of using the gettering reactions of thorium carbide and iodide in order to remove undesirable nonmetallic contaminants before the deposition of thorium metal commences.

Thermodynamic functions for the solid thorium compounds involved are given for the appropriate states in Table I. Iodine is taken to be in the gaseous state. With oxygen containing species, thorium carbide was assumed to give thorium oxide, after Engle (8), and thorium iodide, always present in excess, to give thorium oxyiodide, since its reaction products were immediately water soluble. Using thermodynamic data for gaseous elements and common gases from Quill (14) and the data from Table I, it can readily be concluded that the reactions of thorium iodide, thorium carbide, and thorium nitride with oxygen, water vapor, carbon monoxide, and carbon dioxide are thermodynamically favored, as are the reactions of thorium carbide with nitrogen, and of thorium nitride with iodine. Reaction of thorium iodide with hydrogen or hydrocarbons is not favored.

Carbon monoxide and oxygen were chosen for investigation as being of lesser reactivity than carbon dioxide and water vapor. At room temperature thorium carbide (8), thorium nitride (4), and particularly thorium iodide react much more rapidly with atmospheric water vapor than with oxygen, and there is no reason to suppose that this is not the case at low pressures. Carbon dioxide will almost certainly have a reactivity greater than that of carbon monoxide.

Experimental

The solid reactant was heated to reaction temperature in a silica or glass tube of 50 ml volume connecting through a greaseless diaphragm valve to a gas dosing volume of 200 ml comprising an ion gauge and a limb

Table I. Heats, entropies, and free energies of formation of solid thorium compounds from the elements in their standard states

Compound	ΔH_{298} , kcal	S_{298} , e.u.	ΔS_{298} , e.u.	$\Delta F_{750^\circ K}$, kcal
ThI ₄ (10)	-190.9	65	-72.4	-136.5
ThO ₂ (9)	-293.2	15.6	-46.2	-258.6
ThOI ₂ (10)	-252.3	40.3	-59.3	-207.8
ThC ₂ (11)	-48	—	-0.2 (13)	-48
"Th ₃ N ₄ " (9)	-310	42.7	-87	-245

* Calculated using the relationship given in ref. (9), p. 210, that $\Delta F_T = \Delta H_{298} - T\Delta S_{298}$.

which could be cooled in liquid air. This volume connected to vacuum and gas supply manifolds through greaseless valves. The system had a static leak rate of less than 10^{-5} mm/min.

Thorium iodide was prepared *in vacuo* from iodide thorium and vacuum purified iodine, and 1-2g was sublimed into place. Thorium carbide was ground to less than 20 mesh in an atmosphere of dry nitrogen and 10-20g spread along a horizontal quartz tube, 20 mm in diameter, for 8-10 cm. Thorium nitride was made by heating thorium metal turnings in dry nitrogen at 1000°C (4). Both the iodine and carbide were degassed at 5×10^{-6} mm before reaction, at temperatures of 350° and 900°C respectively.

Carbon monoxide was prepared under vacuum by the reaction of 1g of formic acid with 5 ml of concentrated sulfuric acid, and purified by two successive expansions from bulbs cooled in liquid air. Oxygen and dry oxygen-free nitrogen were admitted from cylinders to the system without purification.

Pressures were measured (intermittently if necessary) with ion gauge-grid current at 10 or 100 μa to make ion gauge pumping negligible during a run. When the valve admitting reactant gas to the sample was opened, a stop clock was started and a record made of ion gauge current *vs.* time. In reactions involving thorium iodide, the liberated iodine condensed just above the liquid air level in the cooled limb, and affected the ion gauge readings. Reaction rates were therefore estimated approximately from the rate of appearance of iodine, the size of the bands of condensed iodine obtained by moving the liquid air level up a few centimeters at regular intervals, and by closing off the thorium iodide, freezing down all iodine vapor and then measuring the residual pressure.

Results

Reaction rates.—Individual reactions are discussed below and the results summarized in Table II.

ThI₄ reactions.—The reaction surface presented was 8-10 cm². At 380°C evaporation of the iodide was slow. Several experiments were performed with each reactant gas.

Consideration of the numbers of molecules present at micron pressures, the number of collisions occurring per second with 10 cm² of thorium iodide surface, and of the fact that, for $t_{1/2} = 10$ sec, 0.16 of molecules are removed per second shows that for such a half-time 1 in 10^3 to 10^4 collisions of carbon monoxide or oxygen with thorium iodide cause reaction. Presumably a similar, if not greater, reaction probability is shown with gaseous thorium iodide.

ThC₂ reactions.—The BET surface area of approximately 20 mesh thorium carbide was found by Engle (8) to be 990 cm²/g. One micron liter of reactant gas will occupy approximately 40 cm² as a monolayer so that first order reactions are to be expected and were generally observed. Reaction rate depended to some extent on the previous history of the carbide. If more than a few micron-liters of gas had reacted, the rate fell off sharply after an initial period of first order

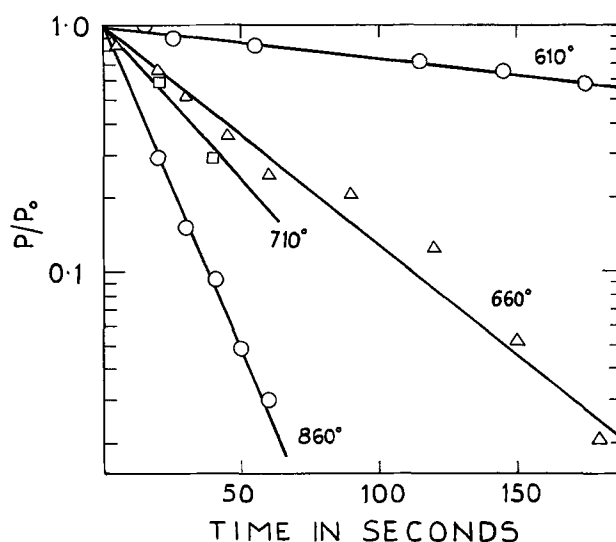


Fig. 1. Typical rate plots for the reaction of carbon monoxide with thorium carbide. Initial pressures 1-5 μ , in a gas volume of 250 cc; reaction times corrected to that for 1g of -20 mesh carbide.

reaction. Carbide samples were therefore degassed for 15 hr at 900°C after each 2 or 3 runs. Reaction rates were calculated from initial slopes when necessary. **ThC₂ with CO.**—This system showed first order removal of carbon monoxide over the pressure range 5 to 0.1 μ . Typical rate plots are shown in Fig. 1. The plot of $\log k_1$ *vs.* $1/T$ is linear above 650°C , giving an activation energy of 11 ± 3 kcal, but below 650°C the rate falls more rapidly with temperature, indicating a lower temperature process with an activation energy of 30-40 kcal.

ThC₂ with O₂.—In several cases, after prolonged heating of the carbide at 900°C in a vacuum of 5×10^{-6} mm, first order reaction was observed to 1/10 of the initial pressure. The plot of $\log k_1$ *vs.* $1/T$ although scattered, showed a low regression, giving an activation energy of 6 ± 3 kcal for ten runs in the range 300° - 900° . When approximately 0.5 mm of oxygen was introduced the reaction rate was sufficiently slowed that the temperature, raised in 100°C steps each quarter hour from 500° , was brought to 800°C before the pressure fell below 5 μ . Murbach (17) has observed somewhat similar behavior for the reaction of uranium carbide with pressures of oxygen of the order of 50 mm. For this latter reaction an activation energy based on the initial more rapid reaction was 7.1 kcal.

ThC₂ with N₂.—Below 700°C reaction was negligibly slow, with $t_{1/2} > 10^5$ sec. Engle (8) found the rate of reaction of thorium carbide with nitrogen at pressures of the order of 50 mm to be negligible at 50°C .

"Th₃N₄" reactions.—The rapid reaction between oxygen and thorium nitride was inferred from the observation that when oxygen at pressures of 2-3 μ was admitted to carbide which had already reacted with nitrogen, the measured pressure fell rapidly to approximately half its initial value, and then very slowly subsequently. This behavior was observed up to 850°C and also at temperatures (500° - 700°C) at which nitrogen was found to react with negligible speed with thorium carbide; the rates of removal of oxygen were approximately 10 times greater than with un-nitrided carbide at the same temperature. After the vessel and carbide were pumped free of liberated nitrogen, subsequent reaction with a further sample of oxygen showed normal oxygen-carbide reaction behavior.

A slow reaction between thorium nitride and iodine with liberation of nitrogen was observed at 500° - 800° . **ThC₂ with residual manifold atmosphere.**—When the closed gauge manifold volume, at 3×10^{-5} mm after pump out, was opened to 10g of carbide at 1000°C , the pressure dropped with a half-time of 10 sec to below

Table II. Thorium iodide, carbide^a, and nitride reaction rates with micron pressures of oxygen, carbon monoxide, and nitrogen

Reactants	Temp. range, $^{\circ}\text{C}$	Range of $t_{1/2}$, sec.	Pressure range followed, μ
ThI ₄ + O ₂	380	5	2-0.1
ThI ₄ + CO	380-420	30-10	5-0.1
ThC ₂ + O ₂	300-900	300-10	4-0.1
ThC ₂ + CO	500-900	10 ⁴ -10 ²	5-0.1
ThC ₂ + N ₂	700-900	10 ⁵ -10 ³	2-1
"Th ₃ N ₄ " + O ₂	500-700	30 ^b -1	3-1 ^c
ThC ₂ + residual gases	1000	100	0.03

^a ThC₂ as -20 mesh powder. Rates given are per gram of solid.

^b Observed rate for 10g of ThC₂ previously reacted with 0.3 μ liters of nitrogen, causing formation of surface nitride.

^c Residual 1 μ pressure of liberated nitrogen.

Table III. Effect of preparative and treatment procedures on thorium purity

Bulb No.	Carbide, in silica	Degassing procedure		
		Deposition bulb and contents		
		Bulb alone	Starting filament	After ThI ₄ formation
I ^a	20 hr at 3×10^{-7} mm 1000°C, 2 hr at 1100°C (After grinding under argon)	30 hr at $<10^{-7}$ mm 500°C	5 hr at $<10^{-7}$ mm 2000°C	1 hr at $<10^{-7}$ mm 300°-400°C
II & III	20 hr at 10^{-6} mm 850°C (Ground under nitrogen)	20 hr at 10^{-6} mm 500°C	1 hr at 10^{-6} mm 2000°C	0.5 hr at 10^{-6} mm 300°C
Nonmetal impurities, ppm (replicate values on 0.3-0.6g samples)				Transfer and treatment of filament
	Oxygen	Nitrogen	Hydrogen	Carbon (estimated) ^d
I	13, 8.8	1.0, (3.4) ^b	0.9 (4.0) ^b	6
II	12, 11, 17, 22;	4, 7, 3, 4;	1.1, 1.1, 1.1, 1.1	6
III	17, 20	7, 2	3.3, 2.7	20
Metal feed ^c	32	20	8	20

^a Separate section of filament grown in bulb before main filament. Tantalum starting wire.

^b Values in parentheses appear inadvertently high, especially for hydrogen, by comparison with replicates for II and III.

^c Data from Metal Hydrides Incorporated (25).

^d Calculated assuming hydrocarbons are the main carbon carriers, and carbon content is thus proportional to hydrogen content.

10^{-5} mm, showing that heated carbide continues to react with residual atmospheres at these pressures.

Residual atmosphere after deposition of thorium.—After careful growth of a filament according to the procedure described for Bulb I, Table III, an ion gauge reading equivalent to a pressure of 7×10^{-4} mm of hydrogen was obtained with a degassed Alpert-type ionization gauge connected to the bulb through a glass break seal and initially sealed off at 10^{-8} mm. That hydrogen was indeed the residual gas was shown by running the filament up to 1500°C during several minutes; no change in ion gauge pressure was observed, nor was a significant change observed on reheating the bulb, containing thorium iodide and carbide, to 450°. Any other gases would have reacted rapidly with the heated filament or with the carbide or iodide.

Bulb outgassing during growth.—Use of molecular sieve trapping (15) and ion gauge pumping after bake-out at 500° for 20 hr of an ionization gauge connected to an empty deposition bulb brought the pressure below 10^{-9} mm, when the gauge and bulb were sealed off together. Reheating the bulb at 450°C during 1 hr, the time previously taken to grow a 1-g filament, produced a pressure of 10^{-4} mm. Considering [after ref. (6)] that this pressure is made up of H₂O, CH₄, and CO in the ratios 2:1:1, the decomposition of such gases by a heated filament would produce 1×10^{-4} mm of hydrogen, considerably less than the residual pressure of 7×10^{-4} mm obtained after filament growth. Moreover, as discussed subsequently, extension of the data of Mallet and Campbell (16) shows that even at 1500°K there will be a concentration of 0.3 ppm of hydrogen in thorium metal in equilibrium with 7×10^{-4} mm of hydrogen gas pressure; this is equivalent, per gram of thorium, to approximately 700 bulb volumes at 10^{-4} mm pressure. Thus for thoroughly degassed deposition vessels outgassing during growth will introduce negligible hydrogen (or other impurities).

Thorium oxyiodide as a possible oxygen carrier.—Thorium oxyiodide is formed by the partial oxidation of thorium tetraiodide or by the action of the latter on thorium oxide. It decomposes on strong heating with an evolution of ThI₄ to give an iodine-free insoluble residue consisting solely of thorium oxide (1). In the present study thorium oxyiodide, formed in vacuum by the reaction of the tetraiodide with oxide at 500°C, was freed from excess thorium iodide by heating for 15 hr at 450°C. Heating at 500°C for 1 hr produced a slight but visible yellow film of thorium iodide on the clear silica tube emergent from the furnace. Heating for 24 hr periods at 600°C and then at 650°C caused evolution of most of the thorium iodide, and the final traces were evolved at 700°C. At each temperature the evolved

thorium iodide could be readily and completely sublimed from the emergent zone by surrounding this with a furnace held at 450°C, at which temperature the oxyiodide was observed to be completely involatile. No discernible traces of residue could be seen on the clear wall after sublimation of a total of approximately 1g of tetraiodide. It is thus evident that the oxide constituent of thorium oxyiodide is virtually nonvolatile at temperatures up to 700°C, and thorium oxyiodide should therefore be unable to function as an oxygen carrier. These conclusions are confirmed by observations (3) made on a filament grown in a bulb in which visible oxyiodide was present; room temperature and high-temperature resistivities and electron emission constants determined *in situ* agreed well with those of filaments grown in "clean" bulbs under otherwise similar conditions.

Impurity content of a filament grown with special care.—Details of the procedure are given in Table III, bulb I. The carbide was prepared and transferred entirely under argon or in vacuum, and iodine used in thorium iodide formation was vacuum sublimed through molecular sieves predried at 500°C in high vacuum (18). Deposition was begun on one leg only of the 16 cm hairpin filament, and this was then allowed to cool and growth begun on the other leg, after the manner of Veigel and Blocher (19). After growth, the bulb was taken into an argon filled dry box, the filament carefully removed to avoid contact with bulb walls, and cut into sections for analysis with clean end cutters. The samples were placed in prebaked glass tubes and sealed off under argon prior to vacuum fusion analyses for oxygen, nitrogen, and hydrogen.

The results of the analysis of this filament and two others grown under rather less stringent conditions are given in Table III. Values for metal grown from metal feed (25) are also given for comparison.

Discussion

The data of Table I combined with free energy data for common gases show that thorium carbide and thorium iodide are capable variously of reaction with oxygen-containing gases to remove oxygen and carbon, but not hydrogen. However hydrocarbons will not react with thorium iodide or with thorium carbide. Consequently there is no mechanism for hydrocarbon removal from a deposition vessel except by reaction with a part of the thorium metal itself, as described for bulb I, Table III, or with other suitable getter metals such as tantalum or molybdenum placed in the vessel. The bulb outgassing experiment shows that there is insufficient water vapor in a well degassed deposition bulb to account for the hydrogen content found in the metal, even

if water vapor was not removed by reaction with carbide or thorium iodide. The hydrogen can apparently only have come from hydrocarbons residual in the thorium carbide, as suggested by Scaife and Wylie (1).

Mallet and Campbell (16) have determined the equilibrium pressure of hydrogen over a range of Th:H compositions. Extrapolation of their data for $\text{ThH}_{0.05}$ (200 ppm hydrogen) to 1500°K gives an equilibrium pressure of 400 mm. They observe that "in the range of rapidly increasing pressure at low hydrogen concentrations, the amount of sorbed hydrogen is proportional to the square root of the equilibrium pressure." On this basis the observed residual hydrogen pressure of 7×10^{-4} mm will be in equilibrium with 0.3 ppm of hydrogen in thorium deposited at 1500°K. This value is in reasonable accord with the level of 1 ppm found in filaments grown under conditions similar to that used in the residual hydrogen pressure experiment.

Apart from carbon oxides evolved after deposition is begun, hydrocarbons, as well as being the main hydrogen carriers, should be the only significant carbon carriers.

The rate of the reactions of carbon monoxide and oxygen with thorium iodide and thorium carbide shows that these gases (and water vapor and carbon dioxide if present) will be removed from association with the feed during a suitable preliminary degassing and heating procedure. Those evolved after deposition is begun however will in large part reach the filament surface, since at thorium iodide vapor pressures of 0.1-1 mm and consequent mean free paths of 0.1-0.01 mm, the calculated reaction probability per collision, $\sim 3 \times 10^{-4}$ for $t_{1/2} = 10$ sec, is too low to allow substantial reaction in a diffusion path of centimeter dimensions.

The most stringent degassing procedure is evidently necessary to remove all traces (*i.e.*, to well below 1 ppm) of hydrocarbons from the carbide, and as high a temperature as possible should be used.

Mechanical transfer of carbon particles from the feed surface to the filament has not been disproved, but at the vapor pressures and flow rates obtained in a deposition vessel, such transfer seems most unlikely.

The origin of the 10 ppm of oxygen observed in the thorium metal is unexplained. A residual oxygen content of 100 ppm in the tungsten or tantalum starting wire after outgassing at 2000°C would introduce less than 1 ppm to the thorium samples. If the protective oxide film on thorium which has been exposed to air is 30Å thick, as on aluminum (22), then a typical analysis sample would contain only 1-2 ppm of oxygen from this source, and atmospheric contamination of samples should be small. Comparison between bulbs I and II in Table III indicates that this is probably so.

In the absence of any feasible carrier vapor, it appears likely that the oxygen is introduced from a finite source associated with the deposition procedure, and that the oxygen levels in larger deposits will be proportionally lower. The oxygen values obtained even for small filaments compare more than favorably with those for the best metal grown from metal feed, or that deoxidized with calcium (26).

Since nitrogen does not react at a significant rate with thorium carbide below 700°C, degassing somewhat below this temperature before raising the carbide temperature to 800°-900°C should allow its removal. The use of molybdenum or tantalum shielding and containing structures can assist in the removal of nitrogen, as discussed by several authors (23, 24, 28). For

thorium produced from metal feed residual nitrogen contents below 10 ppm (23) and as low as 3 ppm (27) have been reported. In the present work it is seen that nitrogen levels in gram scale filaments can be brought as low as 1 ppm; for larger filaments the level may possibly be lower.

Acknowledgment

The author is greatly indebted to Mr. G. H. Bush, Royal Armament Research and Development Establishment, England, for vacuum fusion analyses. Discussions with Dr. A. W. Wylie during the work and the preparation of this paper have been most helpful.

Manuscript received March 2, 1964.

Any discussion of this paper will appear in a Discussion Section to be published in the June 1965 JOURNAL.

REFERENCES

1. D. E. Scaife and A. W. Wylie, Proc. 2nd Internat. Conf. on Peaceful Uses of Atomic Energy, Geneva, 1958, Vol. 4, pp. 215-36.
2. D. E. Scaife and A. W. Wylie, Proc. Symposium on Atomic Energy, Sydney, June 1958, Section 1, pp. 172-181, Melbourne University Press, 1959.
3. A. F. Reid, R. E. Wilmshurst, and A. W. Wylie, *This Journal*, **110**, 429 (1963).
4. A. F. Gerds and M. W. Mallet, *ibid.*, **101**, 175 (1954).
5. L. G. Overholser and J. P. Blakely, U.S.A.E.C. Report ORNL-3102, p. 216, 1961.
6. G. Lewin, *Endeavour*, **20**, 85 (1961).
7. R. F. Rolsten, "Iodide Metals and Metal Iodides," p. 401, John Wiley & Sons, Inc., New York (1961).
8. (a) G. B. Engle, U.S.A.E.C. Report GA-2068 (1961); (b) C. P. Kempter and N. H. Krikorian, *J. Less-Common Metals*, **4**, 244 (1962).
9. O. Kubaschewski and E. LL. Evans, "Metallurgical Thermochemistry," pp. 210, Pergamon Press, London (1958).
10. D. E. Scaife and A. G. Turnbull and A. W. Wylie, To be published.
11. H. A. Eick, E. G. Rauh, and R. J. Thorn, U.S.A.E.C. Report TID-17413 (1962).
12. A. J. Darnell, U.S.A.E.C. Report NAA-SR-5045 (1960).
13. O. H. Krikorian, U.S.A.E.C. Report UCRL-2888 (1955).
14. L. L. Quill, Ed., "The Chemistry and Metallurgy of Miscellaneous Materials; Thermodynamics," McGraw-Hill Book Co., New York (1950).
15. M. A. Biondi, *Rev. Sci. Insts.*, **30**, 831 (1959).
16. M. W. Mallet and I. E. Campbell, *J. Am. Chem. Soc.*, **73**, 4851 (1951).
17. E. W. Murbach, U.S.A.E.C. Report NAA-SR-6331, 1961.
18. A. F. Reid and R. Mills, *J. Inorg. Nucl. Chem.*, **26**, 892 (1964).
19. N. D. Veigel and J. M. Blocher, *This Journal*, **109**, 647 (1962).
20. R.A.R.D.E. Chemical Services Branch Report No. 990.
21. G. A. Haas and J. T. Jensen, *J. Appl. Phys.*, **31**, 1231 (1960).
22. N. F. Mott and R. W. Gurney, "Electronic Processes in Ionic Crystals," 2nd ed, p. 267, Oxford University Press (1948).
23. R. E. McCarley and W. Tadlock, U.S.A.E.C. Report IS-193, p. 16, (1961).
24. D. S. Evans and G. V. Raynor, *J. Nuclear Materials*, **1**, 281 (1959).
25. Bulletin No. 901A, Metal Hydrides Incorporated.
26. D. T. Peterson, *Trans. Met. Soc. A.I.M.E.*, **221**, 924 (1961).
27. D. C. Wallace, *Phys. Rev.*, **120**, 84 (1959).
28. E. G. Zubler, *This Journal*, **110**, 1071 (1963).

The High Carbon Portion of the Uranium-Gadolinium-Carbon System

Terry C. Wallace, Nerses H. Krikorian, and Patrick L. Stone

Los Alamos Scientific Laboratory, University of California, Los Alamos, New Mexico

ABSTRACT

The high carbon portion of the uranium-gadolinium-carbon system was investigated using x-ray, thermal analysis, and chemical techniques. It was found that UC_2 and GdC_2 form a continuous series of solid solutions above $1525^\circ \pm 25^\circ\text{C}$ with the exception of a narrow two-phase region [tetragonal- $(\text{U,Gd})\text{C}_2$ + cubic- $(\text{U,Gd})\text{C}_2$] lying along a line connecting UC_2 at 1785°C and approximately $(\text{U}_{0.8}\text{Gd}_{0.2})\text{C}_2$ at 1510°C . The $(\text{U,Gd})\text{C}_2$ decomposition curve and the equilibrium associated with it were determined for the 1300° to 1525°C temperature range. The results at 1300°C show that the solid solution is still stable over the region from $(\text{U}_{0.12}\text{Gd}_{0.88})\text{C}_2$ to GdC_2 . A lattice parameter curve is given for the quenched tetragonal- $(\text{U,Gd})\text{C}_2$ solid solution phase that varies continuously from $a_o = 3.522\text{\AA}$, and $c_o = 5.982\text{\AA}$ at UC_2 to $a_o = 3.717\text{\AA}$ and $c_o = 6.264\text{\AA}$ at GdC_2 . The solidus temperature decreased from $2475^\circ \pm 30^\circ\text{C}$ for UC_2 to $2370^\circ \pm 30^\circ\text{C}$ for GdC_2 , whereas the eutectic temperature decreased from $2450^\circ \pm 30^\circ\text{C}$ for $\text{UC}_2 + \text{C}$ to $2310^\circ \pm 30^\circ\text{C}$ for $\text{GdC}_2 + \text{C}$. The tetragonal to cubic transformation temperature of $1785^\circ \pm 20^\circ\text{C}$ for UC_2 was found to decrease with the addition of GdC_2 ; likewise the tetragonal to cubic transformation temperature of $1275^\circ \pm 20^\circ\text{C}$ for GdC_2 was found to decrease with the addition of UC_2 . Because of the slow rate of decomposition of the solid solution compared to the time required to determine the tetragonal to cubic transformation temperature of single phased $(\text{U,Gd})\text{C}_2$ samples, it was possible to determine the total transformation curve. A minimum was found at $1155^\circ \pm 20^\circ\text{C}$ and a composition of $(\text{U}_{0.34}\text{Gd}_{0.66})\text{C}_2$. The course of the transformation curve was used to estimate the heat of transformation of tetragonal to cubic GdC_2 at 1275°C as 3.1 ± 0.5 kcal/mole and the change in the free energy of mixing in transforming from tetragonal- $(\text{U,Gd})\text{C}_2$ to cubic- $(\text{U,Gd})\text{C}_2$ solid solution as $\Delta F_{M \rightarrow c} = -x(1-x)[5,330 \pm 960 - (2.29 \pm 0.62)T]$ cal/mole, where x is the mole fraction of GdC_2 in the solid solution.

Knowledge of phase relationships in uranium-metal-carbon systems is a necessary prerequisite to intelligent engineering of uranium-fueled, graphite-moderated, high-temperature reactors. The uranium-transition metal-carbon systems have been studied (1) in some detail, but little or no work has been done in the uranium-rare earth metal-carbon systems. Although the uranium-carbon binary (1, 2) has been extensively investigated and the intermediate phases in the gadolinium-carbon binary (3) have been established, there are no data on the uranium-gadolinium-carbon system.

Experimental

Sample preparation.—The starting materials were depleted uranium metal rod, arc cast gadolinium ingot, and National Carbon spectrographic grade graphite rod. Spectrochemical analysis showed that the major metal impurities in the uranium were Fe, Mn, Mo, V, and Ni which were present in quantities of less than 70, 40, 25, 20, and 15 ppm, respectively. Major metal impurities in the gadolinium were Ce, Pr, Nd, Sm, Ta, and Pb, each of which was present in quantities of less than 0.5 w/o. Spectrochemical analysis of the carbon rod indicated that B, Mg, and Na were the major impurities, each being less than 50 ppm.

The alloys were prepared in a "gettered" helium atmosphere by arc melting the components on a water-cooled copper hearth with a carbon electrode. Samples were stored and handled in an airtight, helium-atmosphere dry box.

For annealing, the samples were contained in graphite crucibles, which had a 0.040 in. hole in the crucible lids to permit pyrometric determination of temperature. A 25 kw high-frequency induction heater with an eddy current concentrator (4) was used to heat the crucibles, which were contained in a vacuum system capable of maintaining pressures of 10^{-5} Torr or lower.

Decomposition studies.—During the determination of the decomposition curve of the $(\text{U,Gd})\text{C}_2$ solid solution it was found that very long annealing times were required to reach equilibrium. The rate at which the solid solutions decomposed into their respective equilibrium products (below 1500°C) appeared to be proportional to the annealing temperature and the mole fraction of UC_2 . For example, at 1300°C a sample near the UC_2 boundary $(\text{U}_{0.89}\text{Gd}_{0.11})\text{C}_2$ required 100 hr to reach equilibrium, while a sample of $(\text{U}_{0.5}\text{Gd}_{0.5})\text{C}_2$ required 400 hr. A sample of composition $(\text{U}_{0.89}\text{Gd}_{0.11})\text{C}_2$ had just begun to show signs of decomposition after 200 hr at 1000°C . To assure that equilibrium was reached for a given temperature and composition, x-ray samples were taken periodically, and the annealing was continued until two successive x-ray patterns showed no further changes in the sample.

Thermal analysis.—The solidus curve of the $(\text{U,Gd})\text{C}_2$ solid solution region was determined by melting cylinders of various compositions prepared by pressing 5-10g portions of powdered (-325 mesh) arc melted material in a $\frac{3}{8}$ in. steel die at 100,000 psi. A 0.040 x 0.400 in. hole was drilled in the top of each cylinder to give black-body conditions for pyrometric measurements. The cylinders were supported in the field of the eddy-current concentrator by means of a tantalum wire tripod. The temperature of the cylinder was raised rapidly to within 100° of the melting point, then slowly raised until the blackbody hole filled with liquid which ordinarily occurred over a 10° temperature interval.

The eutectic curve was determined by observing temperature *vs.* time cooling curves on samples contained in carbon crucibles. Light from a sight hole in the crucible lid was divided by a beam splitter so that one beam of the light from the sample was focused on a sensing photo-diode tube which was connected to the y-axis of a time sweep oscilloscope (5). Upon cooling

through the eutectic temperature a flat in the cooling trace was observed. A Polaroid camera was used to record the cooling trace and subsequent constant temperature traces (the temperature was determined from the other beam while the trace was being photographed). By bracketing the eutectic flat with the constant temperature traces, the eutectic temperature was determined to an accuracy of $\pm 30^\circ\text{C}$.

The cubic to tetragonal transformation curve was determined by similar observations of temperature *vs.* time cooling curves of cylinders of various compositions. Cylinders with a 0.060 in. x 0.5 in. blackbody hole were prepared by hot pressing powdered material at 1700°C in a graphite die to 80-90% of theoretical density. An advanced version of the thermal analysis apparatus was used which simultaneously displayed not only the cooling curve but also the derivative of the cooling curve (6). This latter innovation made possible more accurate determinations of the transition curve in the central region where the heat effect was quite small. Both heating and cooling curves were observed.

The Pyro Micro-Optical pyrometer and optical system were calibrated against a standard lamp that had been certified by the National Bureau of Standards.

Chemical and x-ray analysis.—The samples were chemically analyzed for uranium, gadolinium, and total carbon (7). For the x-ray analysis, the material was removed from the crucible and crushed in a "diamond" mortar. A representative sample was ground into powder (-325) for lattice parameter measurements. The x-ray samples were sealed in Lindemann glass capillaries, and the diffraction studies were carried out on a Norelco unit using a nickel-filtered copper radiation and a 114.59 mm Debye-Scherrer camera. The x-ray wavelength used in calculating the lattice parameters were: $K_{\alpha 1} = 1.54050\text{\AA}$, $K_{\alpha 2} = 1.54433\text{\AA}$ and a weighted value (for unresolved doublets) of $K_{\alpha} = 1.54178\text{\AA}$. Lattice parameters were obtained from the back-reflection lines by applying the modified least-squares extrapolation of Hess (8) using an IBM 7090 computer. Standard deviations were calculated for each lattice parameter. Generally, the deviations were less than $\pm 0.008\text{\AA}$ for a_0 and less than $\pm 0.015\text{\AA}$ for c_0 for the tetragonal-(U,Gd) C_2 phases, and less than $\pm 0.001\text{\AA}$ for a_0 for the (U,Gd) C_3 phases.

Results and Discussion

(U,Gd) C_2 solid solution region.—In this paper we use the symbol MC_2 to represent the solid solution metal dicarbide phase which appears to have a slight range of homogeneity. UC_2 has been shown to have a range of homogeneity lying between $\text{UC}_{1.89}$ and $\text{UC}_{1.94}$ (2). Likewise we have found from metallographic examination that $\text{GdC}_{1.93}$ is single phased whereas $\text{GdC}_{1.99}$ shows the presence of graphite in the grain boundaries. The samples that were prepared for this study had total carbon contents varying from $\text{MC}_{1.89}$ to $\text{MC}_{1.98}$ with the mean at $\text{MC}_{1.93}$. All of the stock arc-melted samples were single phased by x-ray examination. It is interesting to note that arc melted GdC_2 had a metallic gold color in contrast to the metallic silver color of UC_2 .

Figure 1 shows the variation of the lattice parameters of the tetragonal (U,Gd) C_2 phase with composition for samples annealed in the temperature range 1600° - 2000°C . Each point is the average of two or more samples at the given composition. The lattice parameters of the quenched eutectic samples were in agreement with the annealed samples and those for UC_2 ($a_0 = 3.522\text{\AA}$, $c_0 = 5.982\text{\AA}$) and GdC_2 ($a_0 = 3.717\text{\AA}$, $c_0 = 6.264\text{\AA}$) in good agreement with data reported by others (1, 2).

From Fig. 2 it is seen that the cubic to tetragonal transformation curve passes through areas of the stable solid solution region near the UC_2 boundary and near the GdC_2 boundary. The limited number of experiments in the required two-phase region between the cubic and tetragonal solid solution fields did not

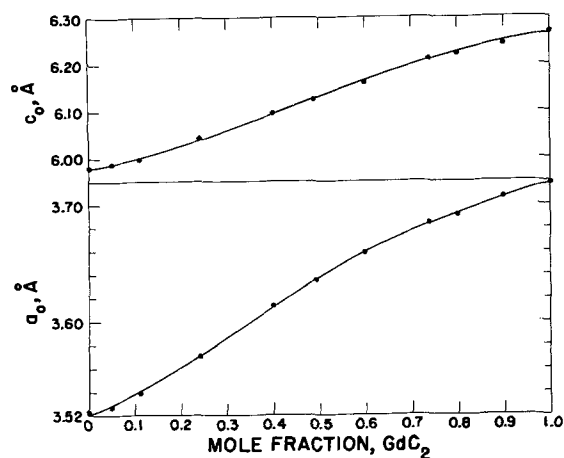


Fig. 1. Lattice parameter variation of the quenched tetragonal-(U,Gd) C_2 solid solution.

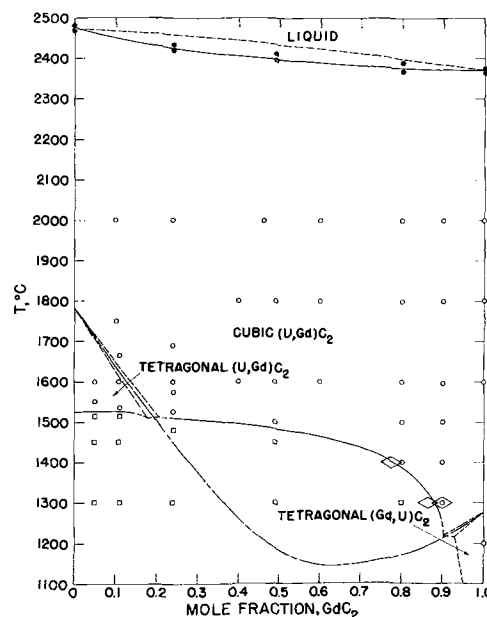


Fig. 2. The $C = 0.67$ atom fraction isoplethal section of the U-Gd-C ternary system. \bullet , solidus melting point; \circ , single-phased (U,Gd) C_2 solid solution; \square , unstable (U,Gd) C_2 solid solution; \diamond , decomposition phase boundary as determined from the three-phased field-($\text{U}_{0.91}\text{Gd}_{0.09}$) $\text{C}_3 + (\text{U,Gd})\text{C}_2 + \text{C}$; - - - tetragonal to cubic transformation curve of the (U,Gd) C_2 solid solution.

allow us to determine its width, but one can conclude that it is fairly narrow as indicated by dashed lines in Fig. 2 and 5.

Table I and Fig. 2 give the results of the determinations of the eutectic and solidus curve which are in good agreement with the limited information that is available (2).

(U,Gd) C_2 tetragonal to cubic transformation curve.—Uranium dicarbide reportedly undergoes a polymorphic cubic to tetragonal transformation upon cooling at

Table I. (U,Gd) $\text{C}_2 + \text{C}$ eutectic temperatures

Composition	Eutectic temperature, $^\circ\text{C}$
$\text{UC}_2 + \text{C}$	2450 ± 30
$(\text{U}_{0.89}\text{Gd}_{0.11})\text{C}_2 + \text{C}$	2420 ± 30
$(\text{U}_{0.76}\text{Gd}_{0.24})\text{C}_2 + \text{C}$	2400 ± 30
$(\text{U}_{0.63}\text{Gd}_{0.37})\text{C}_2 + \text{C}$	2390 ± 30
$(\text{U}_{0.51}\text{Gd}_{0.49})\text{C}_2 + \text{C}$	2385 ± 30
$(\text{U}_{0.60}\text{Gd}_{0.40})\text{C}_2 + \text{C}$	2340 ± 30
$(\text{U}_{0.26}\text{Gd}_{0.74})\text{C}_2 + \text{C}$	2355 ± 30
$(\text{U}_{0.20}\text{Gd}_{0.80})\text{C}_2 + \text{C}$	2335 ± 30
$(\text{U}_{0.10}\text{Gd}_{0.90})\text{C}_2 + \text{C}$	2320 ± 30
$\text{GdC}_2 + \text{C}$	2310 ± 30

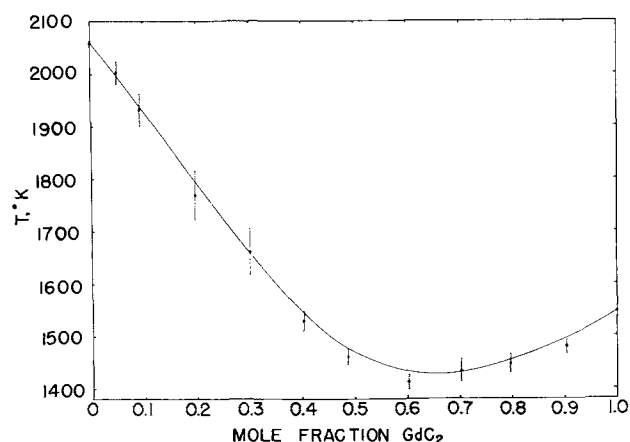


Fig. 3. Tetragonal to cubic transformation curve for the (U,Gd) C_2 solid solution. \circ , mean transformation temperature, T_o . The ends of the vertical lines through each T_o point lie at the experimentally determined transformation temperatures on heating, T_h , and cooling, T_c . — the calculated transformation curve based on Eq. [2].

1750°C (1, 2). The transformation is a diffusionless (martensitic) transformation (9) which is characterized by cooperative atom movements involving a pure lattice distortion combined with a twinning shear (over a fraction of the crystal) which does not affect the lattice structure, but produces a macroscopic change in shape (10). Hence (at least for rapid quenching) the transformation product has the same composition as the parent phase. In Fig. 3 the determined transformation temperatures occurring on cooling (T_c), heating (T_h), and the mean of the two (T_o) are shown as a function of composition of the (U,Gd) C_2 solid solution alloys.

A thermodynamic approach appears to be the best basis for interpreting the data. Each phase has a chemical free energy that varies with temperature and composition. Thus for a given alloy there is a temperature, T_o , at which the two free energies are equal, $F^{\text{cubic}} = F^{\text{tetragonal}}$. At any other temperature the difference in free energy may be expressed as $F^c - F^t = \Delta F^{t \rightarrow c}$ cal/mole (at T_o , $\Delta F^{t \rightarrow c} = 0$). Thus $\Delta F^{t \rightarrow c}$ is negative when the cubic phase is more stable than the tetragonal and positive when the tetragonal phase is more stable than the cubic phase. In their review, Kaufman and Cohen (11) note that it is generally observed that the transformation temperatures on cooling and heating are different ($T_h > T_c$) and from thermodynamic calculations that the temperature (T_o) at which $\Delta F^{\alpha \rightarrow \beta} = 0$, is very near the arithmetic mean of T_c and T_h . The differences

$$\left(T_o - T_c = T_h - T_o = \frac{T_h - T_c}{2} \right)$$

are related to the amount of driving energy needed to balance nonchemical free energy factors such as interfacial, strain, and nucleation energies. Using the above interpretation our value for the UC_2 transformation of $1785^\circ \pm 20^\circ C$ is in good agreement with that reported earlier ($1750^\circ C$) which was determined from cooling curves. Since GdC_2 forms solid solutions with both the known cubic and tetragonal forms of UC_2 , it seems reasonable to assume that it also exists in both crystal structures. Only the low-temperature (tetragonal) structure has been reported previously (3). In this work, the GdC_2 solid-state transformation temperature was found to be $1275^\circ \pm 20^\circ C$.

From Fig. 2 and 3 it is seen that the transformation curve passes into a region in which the solid solution is thermodynamically unstable. However, the kinetics of decomposition are very slow (100-500 hr) compared to the time required to make a transformation

temperature measurement (0.5 hr). The x-ray patterns of the samples used for transformation determinations were single phased after the experiment and had the same lattice parameters as the starting material. Hence, due to the slow kinetics of decomposition, one is in the interesting position of being able to observe the total martensitic transformation curve even though it passes into a region which is unstable. Further, the course of the curve is determined by the thermodynamic properties of the cubic and tetragonal solid solutions.

Using the treatment of Kaufman and Cohen (11), the T_o vs. composition curve may be expressed by the equation

$$\Delta F_{ss}^{t \rightarrow c}(x, T_o) = (1-x)\Delta F_{UC_2}^{t \rightarrow c}(T_o) + x\Delta F_{GdC_2}^{t \rightarrow c}(T_o) + \Delta F_M^{t \rightarrow c}(x, T_o) = 0 \quad [1]$$

where $\Delta F_{ss}^{t \rightarrow c}(x, T_o)$ is the change in free energy in transforming from tetragonal to cubic structure an alloy of x moles of GdC_2 , and $(1-x)$ moles of UC_2 ; and because of the diffusionless nature of the process, $\Delta F_{ss}^{t \rightarrow c}(x, T_o) = 0$. $\Delta F_{UC_2}^{t \rightarrow c}(T_o)$ and $\Delta F_{GdC_2}^{t \rightarrow c}(T_o)$ are the changes in free energy in transforming from tetragonal to cubic structure of the pure components, respectively. $\Delta F_M^{t \rightarrow c}(x, T_o)$ is the change in the free energy of mixing in transforming from the tetragonal to the cubic structure. The minimum in the T_o vs. composition curve requires that $\Delta F_M^{t \rightarrow c}(x, T_o)$ be zero at x equal 0 and 1, and that it be negative for all other values of x .

Equation [1] may thus be used to estimate some thermodynamic properties of the UC_2 - GdC_2 solid solution region. Although the calculations will not be quantitative, the values will be useful as approximations in view of the fact that there are no measured values for either the heat of transformation of GdC_2 or $\Delta F_M^{t \rightarrow c}(x, T_o)$. Four assumptions need to be made: (i) T_o , as measured, is the temperature at which $\Delta F_{ss}^{t \rightarrow c} = 0$ for a given composition; (ii) the solid solutions in the tetragonal and cubic domains are random solutions; (iii) that the specific heat corrections ($\Delta C_{UC_2}^{t \rightarrow c}$ and $\Delta C_{GdC_2}^{t \rightarrow c}$) may be neglected; and (iv) the free energy mixing term may be represented by a regular solution model. Equation [1] then becomes

$$\Delta F_{ss}^{t \rightarrow c}(x, T_o) = (1-x)\Delta H_1^{t \rightarrow c} \left(1 - \frac{T_o}{T_1} \right) + x\Delta H_2^{t \rightarrow c} \left(1 - \frac{T_o}{T_2} \right) + x(1-x)[\Delta H_M^{t \rightarrow c} - T_o\Delta S_M^{t \rightarrow c}] = 0 \quad [2]$$

where T_1 , T_2 , $\Delta H_1^{t \rightarrow c}$, and $\Delta H_2^{t \rightarrow c}$ are the transformation temperatures and heats of transformation of UC_2 and GdC_2 , respectively. Furthermore, $x(1-x)\Delta H_M^{t \rightarrow c}$ and $x(1-x)\Delta S_M^{t \rightarrow c}$ are the changes in the heat content and entropy of mixing in transforming from tetragonal to cubic solid solution at a given x and T_o . Using $\Delta F^{t \rightarrow c} = 0$ as the independent variable, the measured quantities, x and T_o , and Levinson's value of $\Delta H_{UC_2}^{t \rightarrow c} = 2900$ cal/mole (12) Eq. [2] is solved for $\Delta H_2^{t \rightarrow c}$, $\Delta H_M^{t \rightarrow c}$, and $\Delta S_M^{t \rightarrow c}$ by the method of least squares. The computation was performed on the MANIAC II computer with the results: $\Delta H_{GdC_2}^{t \rightarrow c} = 3070 \pm 440$ cal/mole, $\Delta H_M^{t \rightarrow c} = -5330 \pm 960$ cal/mole and $\Delta S_M^{t \rightarrow c} = -2.29 \pm 0.62$ e.u. Figure 3 shows the moderately good agreement between the observed x , T_o and the calculated x , T_o (Eq. [2]). For comparison purposes $\Delta S_{GdC_2}^{t \rightarrow c} = 1.98 \pm 0.28$ e.u. is in fair agreement with $\Delta S_{UC_2}^{t \rightarrow c} = 1.41$ e.u. (12) and $\Delta S_{CaC_2}^{t \rightarrow c} = 1.85$ e.u. (13).

Equilibrium along the solid solution decomposition curve.—Table II lists the equilibrium phases that are associated with the decomposition curve for various temperatures and compositions. Recent data (1, 2) show that uranium dicarbide undergoes a eutectoid decomposition to $U_2C_3 + C$ at $1500^\circ \pm 25^\circ C$. This finding is in disagreement with the phase diagrams pub-

Table II. Equilibrium data associated with the solid solution decomposition curve

Starting composition	Lattice parameters, Å	Anneal temp, °C	Anneal time, hr	Phases present by x-ray and lattice parameters, Å	Composition of phase from lattice parameters	Remarks
(U _{0.95} Gd _{0.05})C ₂	$\left\{ \begin{array}{l} a_o = 3.527 \\ c_o = 5.989 \end{array} \right\}$	1600	30	MC ₂ $\left\{ \begin{array}{l} a_o = 3.527 \\ c_o = 5.988 \end{array} \right\}$		No decomposition
(U _{0.95} Gd _{0.05})C ₂	$\left\{ \begin{array}{l} a_o = 3.527 \\ c_o = 5.989 \end{array} \right\}$	1550	45	MC ₂ $\left\{ \begin{array}{l} a_o = 3.525 \\ c_o = 5.987 \end{array} \right\}$		No decomposition
(U _{0.95} Gd _{0.05})C ₂	$\left\{ \begin{array}{l} a_o = 3.527 \\ c_o = 5.989 \end{array} \right\}$	1515	30	M ₂ C ₃ (a _o = 8.098) + C	(U _{0.95} Gd _{0.05}) ₂ C ₃	
(U _{0.95} Gd _{0.05})C ₂	$\left\{ \begin{array}{l} a_o = 3.527 \\ c_o = 5.989 \end{array} \right\}$	1450	100	M ₂ C ₃ (a _o = 8.097) + C	(U _{0.95} Gd _{0.05}) ₂ C ₃	
(U _{0.95} Gd _{0.05})C ₂	$\left\{ \begin{array}{l} a_o = 3.527 \\ c_o = 5.989 \end{array} \right\}$	1300	144	M ₂ C ₃ (a _o = 8.096) + C	(U _{0.95} Gd _{0.05}) ₂ C ₃	
(U _{0.89} Gd _{0.11})C ₂	$\left\{ \begin{array}{l} a_o = 3.539 \\ c_o = 5.990 \end{array} \right\}$	1535	42	MC ₂ $\left\{ \begin{array}{l} a_o = 3.536 \\ c_o = 6.002 \end{array} \right\}$		No decomposition
(U _{0.89} Gd _{0.11})C ₂	$\left\{ \begin{array}{l} a_o = 3.539 \\ c_o = 5.990 \end{array} \right\}$	1515	77	M ₂ C ₃ (a _o = 8.103) + C	(U _{0.91} Gd _{0.09}) ₂ C ₃	
(U _{0.89} Gd _{0.11})C ₂	$\left\{ \begin{array}{l} a_o = 3.539 \\ c_o = 5.990 \end{array} \right\}$	1450	68	M ₂ C ₃ (a _o = 8.103) + C	(U _{0.91} Gd _{0.09}) ₂ C ₃	
(U _{0.89} Gd _{0.11})C ₂	$\left\{ \begin{array}{l} a_o = 3.539 \\ c_o = 5.990 \end{array} \right\}$	1300	96	M ₂ C ₃ (a _o = 8.104) + C	(U _{0.91} Gd _{0.09}) ₂ C ₃	
(U _{0.76} Gd _{0.24})C ₂	$\left\{ \begin{array}{l} a_o = 3.570 \\ c_o = 6.038 \end{array} \right\}$	1525	161	MC ₂ $\left\{ \begin{array}{l} a_o = 3.573 \\ c_o = 6.042 \end{array} \right\}$		No decomposition
(U _{0.76} Gd _{0.24})C ₂	$\left\{ \begin{array}{l} a_o = 3.570 \\ c_o = 6.038 \end{array} \right\}$	1300	204	M ₂ C ₃ (a _o = 8.104) + MC ₂ (faint) + C	(U _{0.91} Gd _{0.09}) ₂ C ₃	MC ₂ phase was too faint to determine its lattice parameter.
(U _{0.51} Gd _{0.49})C ₂	$\left\{ \begin{array}{l} a_o = 3.642 \\ c_o = 6.132 \end{array} \right\}$	1580	216	MC ₂ $\left\{ \begin{array}{l} a_o = 3.643 \\ c_o = 6.140 \end{array} \right\}$		No decomposition
(U _{0.51} Gd _{0.49})C ₂	$\left\{ \begin{array}{l} a_o = 3.642 \\ c_o = 6.132 \end{array} \right\}$	1400	432	M ₂ C ₃ (a _o = 8.104) + MC ₂ $\left\{ \begin{array}{l} a_o = 3.689 \\ c_o = 6.227 \end{array} \right\}$ + C $\left\{ \begin{array}{l} (U_{0.91}Gd_{0.09})_2C_3 \\ (U_{0.22}Gd_{0.78})C_2 \end{array} \right\}$		
(U _{0.51} Gd _{0.49})C ₂	$\left\{ \begin{array}{l} a_o = 3.642 \\ c_o = 6.132 \end{array} \right\}$	1300	450	M ₂ C ₃ (a _o = 8.103) + MC ₂ $\left\{ \begin{array}{l} a_o = 3.702 \\ c_o = 6.248 \end{array} \right\}$ + C $\left\{ \begin{array}{l} (U_{0.91}Gd_{0.09})_2C_3 \\ (U_{0.13}Gd_{0.87})C_2 \end{array} \right\}$		
—	—	1500	192	MC ₂ $\left\{ \begin{array}{l} a_o = 3.643 \\ c_o = 6.133 \end{array} \right\}$	(U _{0.51} Gd _{0.49})C ₂	The solid solution was reformed from the sample above.
(U _{0.20} Gd _{0.80})C ₂	$\left\{ \begin{array}{l} a_o = 3.692 \\ c_o = 6.225 \end{array} \right\}$	1500	70	MC ₂ $\left\{ \begin{array}{l} a_o = 3.695 \\ c_o = 6.221 \end{array} \right\}$		No decomposition
(U _{0.20} Gd _{0.80})C ₂	$\left\{ \begin{array}{l} a_o = 3.692 \\ c_o = 6.225 \end{array} \right\}$	1400	168	MC ₂ $\left\{ \begin{array}{l} a_o = 3.699 \\ c_o = 6.228 \end{array} \right\}$		No decomposition
(U _{0.20} Gd _{0.80})C ₂	$\left\{ \begin{array}{l} a_o = 3.692 \\ c_o = 6.225 \end{array} \right\}$	1300	438	M ₂ C ₃ (faint) + MC ₂ $\left\{ \begin{array}{l} a_o = 3.708 \\ c_o = 6.242 \end{array} \right\}$ + C (U _{0.10} Gd _{0.90})C ₂		M ₂ C ₃ phase was too faint to determine its lattice parameter.
(U _{0.10} Gd _{0.90})C ₂	$\left\{ \begin{array}{l} a_o = 3.708 \\ c_o = 6.248 \end{array} \right\}$	1500	96	MC ₂ $\left\{ \begin{array}{l} a_o = 3.704 \\ c_o = 6.242 \end{array} \right\}$		No decomposition
(U _{0.10} Gd _{0.90})C ₂	$\left\{ \begin{array}{l} a_o = 3.708 \\ c_o = 6.248 \end{array} \right\}$	1400	186	MC ₂ $\left\{ \begin{array}{l} a_o = 3.708 \\ c_o = 6.240 \end{array} \right\}$		No decomposition
(U _{0.10} Gd _{0.90})C ₂	$\left\{ \begin{array}{l} a_o = 3.708 \\ c_o = 6.248 \end{array} \right\}$	1300	264	MC ₂ $\left\{ \begin{array}{l} a_o = 3.705 \\ c_o = 6.248 \end{array} \right\}$		No decomposition
GdC ₂	$\left\{ \begin{array}{l} a_o = 3.717 \\ c_o = 6.263 \end{array} \right\}$	1200	312	MC ₂ $\left\{ \begin{array}{l} a_o = 3.717 \\ c_o = 6.264 \end{array} \right\}$		No decomposition

lished by Hansen (14) showing UC₂ to be stable to room temperature. Our experimental data are in good agreement with the newer findings. We have found that (U_{0.95}Gd_{0.05})C₂ decomposes between 1515° and 1550°C and (U_{0.89}Gd_{0.11})C₂ decomposes between 1515° and 1535°C to give (U,Gd)₂C₃ and C. The remainder of the samples which had a higher GdC₂ content decomposed into three phases; (U,Gd)₂C₃ + (U,Gd)C₂ + C.

The gadolinium carbide-rich phase boundary of the (U,Gd)₂C₃ phase was determined by plotting the lattice parameter of (U,Gd)₂C₃ vs. atom fraction of Gd divided by the sum of the atom fractions of Gd and U. The a_o value for U₂C₃ was taken as 8.089Å (2). The

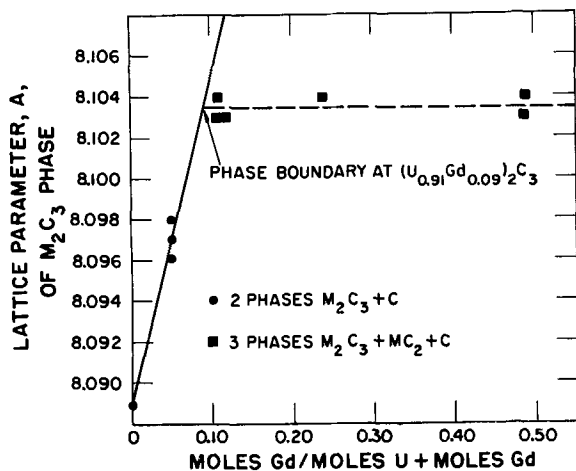


Fig. 4. Lattice parameter variation of the (U,Gd)₂C₃ phase as a function of composition. ●, two-phased points—(U,Gd)₂C₃ + C; ■, three-phased points—(U,Gd)₂C₃ + (U,Gd)C₂ + C.

results are shown in Fig. 4, and the limiting composition is determined to be (U_{0.91}Gd_{0.09})₂C₃. It is also apparent that the phase boundary is essentially constant in the temperature range 1300°–1500°C. Thus the decomposition curve from UC₂ to (U_{0.91}Gd_{0.09})C₂ is connected with the decomposition products, (U,Gd)₂C₃ + C by isothermal tie lines and is essentially horizontal at 1525°C. From (U_{0.91}Gd_{0.09})C₂ to higher atom fractions of Gd, the decomposition curve is connected with the decomposition products by isothermal tie triangles. Thus, we have the interesting case of tie triangles collapsing to a ternary tie line at (U_{0.91}Gd_{0.09})C₂ and 1525°C. The phase rule requires that the point at which these tie triangles collapse to a ternary tie line be at a temperature maximum with respect to the rest of the decomposition curve that is connected by the tie triangles (15). This maximum corresponds to point I in Fig. 5, and the limiting ternary tie line is FIT.

The superposition of the T_o vs. composition curve on Fig. 5 leads to another important structural feature of the phase diagram. As noted earlier there must be a two-phase region [tetragonal-(U,Gd)C₂ + cubic-(U,Gd)C₂] associated with the T_o curve. The decomposition curve intersects this two-phase region. On the UC₂ side of the intersection, tetragonal-(U,Gd)C₂ is in equilibrium with the decomposition products, and on the GdC₂ side one has cubic-(U,Gd)C₂ (until the T_o curve again intersects the decomposition curve) in equilibrium. The phase rule requires that tetragonal (U,Gd)C₂ undergo a ternary eutectoid decomposition to (U_{0.91}Gd_{0.09})₂C₃ + cubic (U,Gd)C₂ + C (15). At this point there is a ternary four phase equilibrium (15) which is represented by the isothermal tie triangles AEB, AEC, and CEB as shown in Fig. 5. The temperature at this intersection is approximately 1510°C and the composition is approximately (U_{0.8}Gd_{0.2})C₂. This region of the phase diagram is dotted in Fig. 3 and 5. From point B to where the decom-

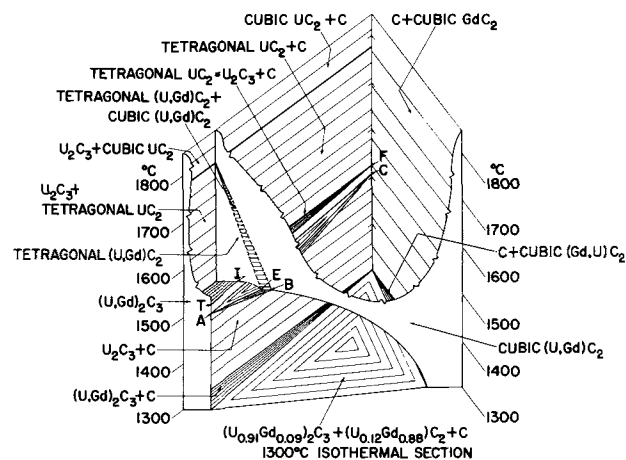


Fig. 5. Perspective drawing of the high carbon portion of the U-Gd-C ternary system.

position curve intersects the 1300°C isothermal plane (Fig. 5) the tie-triangles connect the phases $(U_{0.91}Gd_{0.09})_2C_3 + \text{cubic } (U,Gd)C_2 + C$. From Fig. 2 it is seen that the cubic $(Gd,U)C_2$ phase must also undergo a ternary eutectoid decomposition below 1300°C.

Figure 5 shows a perspective view of the equilibrium phases associated with the decomposition curve. The base represents the high carbon portion of the 1300°C isothermal section of the U-Gd-C ternary.

Conclusions

From this study it was found that UC_2 and GdC_2 form a continuous series of solid solutions above 1785°C with the solid solution solidus and carbon eutectic temperatures decreasing in a regular manner from the UC_2 boundary to the GdC_2 boundary. Along the line which lies between UC_2 (1785°C) and approximately $(U_{0.8}Gd_{0.2})C_2$ (1510°C) there is a two-phase region that connects solid solution regions of tetragonal $(U,Gd)C_2$ and cubic $(U,Gd)C_2$. Below 1525°C there is a decomposition curve below which the UC_2 - GdC_2 solid solution is unstable. The decomposition curve progresses from the UC_2 boundary (1525°C) to a composition of $(U_{0.12}Gd_{0.88})C_2$ at 1300°C.

The tetragonal to cubic transformation curve of the UC_2 - GdC_2 solid solution decreases as one moves from both boundaries indicating that $\Delta F_M^{t \rightarrow c}$ is negative. Further, the course of the T_0 curve may be used to make thermodynamic approximations on various properties of the solid solution region.

Acknowledgments

The authors gratefully acknowledge the advice and support of Dr. Melvin G. Bowman during the course of this work. Acknowledgment is also made of the work of members of Group CMB-1 of this Laboratory for the chemical analyses and Mrs. M. J. Ulery for reading the x-ray diffraction patterns. Thanks are due to Willard G. Witteman and Charles Radosevich for assistance in obtaining the transformation curves. Without the ingenuity of Mr. George N. Rupert in designing and building the thermal analysis apparatus used, the work on the transformation temperatures could not have been performed. Finally, the help of Dr. Allen L. Bowman and Mr. Paul McWilliams is acknowledged for the programming and computing of the results obtained from Eq. [2].

Manuscript received May 7, 1964. Work performed under the auspices of the United States Atomic Energy Commission.

Any discussion of this paper will appear in a Discussion Section to be published in the June 1965 JOURNAL.

REFERENCES

1. S. Langer, General Atomics Report, GA-4450, September 5, 1963.
2. W. G. Witteman and M. G. Bowman, To be published.
3. F. Spedding, K. Gschneider, and A. Daane, *J. Am. Chem. Soc.*, **80**, 4499 (1958).
4. J. M. Leitnaker, M. G. Bowman, and P. W. Gilles, *J. Chem. Phys.*, **36**, 350 (1962).
5. G. N. Rupert, *Rev. Sci. Instr.*, **34**, 1183 (1963).
6. G. N. Rupert, To be published.
7. O. H. Krieger, Los Alamos Scientific Laboratory Report LA-2306, March 1959.
8. J. B. Hess, *Acta Cryst.*, **4**, 209 (1951).
9. A. L. Bowman, W. G. Witteman, G. P. Arnold, and N. G. Nereson, To be published.
10. Roger Chang, *Acta Cryst.*, **14**, 1097 (1961).
11. Larry Kaufman and Morris Cohen, "Thermodynamics and Kinetics of Martensitic Transformations," in "Progress in Metal Physics," **7**, 167, Pergamon Press, New York (1958).
12. L. S. Levinson, *J. Chem. Phys.*, **38**, 2105 (1963).
13. K. K. Kelley, *Contribution to the data on theoretical metallurgy, XIII, High-Temperature Heat Content, Heat-Capacity, and Entropy Data for the Elements and Inorganic Compounds*, Bulletin 584 (1960).
14. Max Hansen, "Constitution of Binary Alloys," p. 387, McGraw-Hill Book Co., Inc., New York (1958).
15. F. N. Rhines, "Phase Diagrams in Metallurgy, Their Development and Applications," Chap. 14, McGraw-Hill Book Co., Inc., New York (1956).

Preparation of Metallic Calcium by Electrolysis of Calcium Oxide Dissolved in Molten Calcium Chloride

W. D. Threadgill

Department of Chemical Engineering, Vanderbilt University, Nashville, Tennessee

ABSTRACT

Metallic calcium was prepared by electrolysis of calcium oxide dissolved in molten calcium chloride in a modified moving cathode-type cell. For comparison, control electrolyses of the chloride were made. Average cell voltage with the oxide-bearing electrolyte ranged up to 23% less than that with the chloride alone. The oxide content of the electrolyte decreased due to electrolysis, and tests showed that chlorine was not released at the anode. This appears to be the first demonstration that calcium oxide can be fed to a chloride electrolyte for calcium production.

The first experiments of record with a fused electrolyte were made by Sir Humphrey Davy (1) in 1802. Subsequent to his time, the electrolysis of fused salts has been used as a method for either the discovery or

commercial preparation of many metals. The processes and equipment used show wide variation because of dependence on the specific characteristics of each metal and its electrolyte.

Of the earlier investigations (2-8) concerned with the electrolytic production of calcium, probably the greatest advancement was made in 1904. At this time Rathenau (9) described a method of drawing out the calcium metal in the form of a rod attached to the cathode. The following year Goodwin (10) described a similar apparatus. Subsequent to this time, several investigators (11-16) have made various changes and improvements in the apparatus of Goodwin and Rathenau.

The energy consumption of calcium is high compared to other products in the fused electrolyte industry. Mantell (17) gives the average energy consumption of calcium as 23 kwhr/lb as compared to 9 for aluminum, 8 for magnesium (chloride process), and 5.2 for sodium. According to Mantell (18), variation in energy consumption for any one process is due to size of the cell, details of construction and insulation of the cell, and length of time the cell is operated before changes need to be made either in the electrolyte, the cell proper, or the electrical connections.

Johnson (19) lists the factors which influence the decomposition voltage of the electrolyte as chemical composition, temperature, nature of the electrodes, and their geometrical disposition with respect to each other. Lorenz (20) and Brockman (21) summarize the conditions affecting the current yield at the cathode as temperature, distance between electrodes, current density, secondary chemical reactions at the electrodes, and formation of metallic fog.

Collection of the calcium metal produced is much more difficult than that of any other metal made commercially by fused salt electrolysis. Calcium metal floats on top of the bath, is active and soluble in the electrolyte, and cannot be protected by a film of the melt held over it by surface tension. If allowed to remain in contact with the electrolyte for any length of time, it will be converted back to the chloride or the oxide due to the circulation of the bath which carries the dispersed metal into the gas producing area around the anode, or it will burn due to atmospheric oxygen. Consequently, it is necessary to use a contact cathode, that is, one that just touches the bath surface. The cathode is raised gradually as the metal is collected and a solid stick or "carrot" obtained.

The decomposition voltage of calcium chloride is reported as 2.04-3.24v (14, 18, 22, 23) with the commonly accepted value being 3.2v. Taking the value as 3.2v, the voltage efficiency calculated from the operating voltages reported by various investigators is 10.3-20%. German industrial practice has been reported as 25v per cell (17), which represents a voltage efficiency of 12.8%.

No information was found in the literature on the decomposition voltage of a calcium chloride-calcium oxide mixture.

Investigations of calcium production by use of mixed electrolytes have generally been limited to mixtures of the chloride and the fluoride. Johnson (14) and Frary (24) both experienced difficulty with such an electrolyte due to its low melting point.

Apparatus

The modified moving cathode type cell used in this investigation is shown in Fig. 1. The container and anodes (not shown) were of graphite. The cathode consisted of a 1-in. diameter water-cooled aluminum bar with a removable 1-in. diameter iron tip. Temperature measurements were made with a bare chromel-alumel thermocouple immersed in the electrolyte. A direct-current welding generator was used as the source of current.

Cell Operation

The electrolyte was brought to approximately the desired operating temperature by external heating. The anode was immersed in the electrolyte and an arc struck between the cathode and the electrolyte in order to heat the tip momentarily above the melting

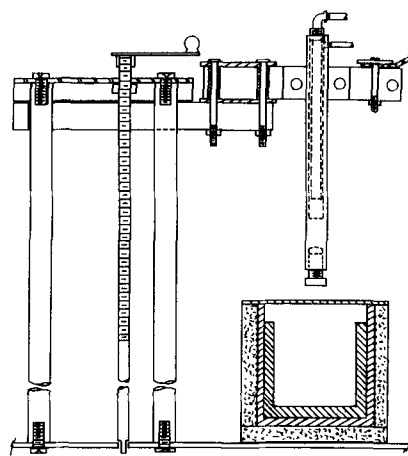


Fig. 1. Electrolytic cell (anodes not shown)

point of calcium metal. Without this heating, the metal would not wet the cathode surface except in spots. Adjustment of the cathode was then made to effect good operation.

Generally, operation was unsteady for a period of 5-10 min at the start of electrolysis. Current and voltage fluctuated, and the electrolyte temperature increased from 25° to 50°F.

During normal operation, the heating effect of the electrolyzing current was sufficient to keep the temperature fairly constant ($\pm 10^\circ\text{F}$). The cathode was at the center of an irregular bright rosette with radial markings formed by currents of hot electrolyte moving away from it. Normal operation was maintained by raising or lowering the cathode in such a manner that this rosette was kept at approximately the same size and color. The calcium metal could be observed in a molten condition just underneath the bath surface and was drawn out in good solid form covered by a thin film of frozen electrolyte.

When the electrolyte temperature around the cathode was allowed to become too low by raising the cathode too slowly, metal was deposited in a spongy form with branches of much the same appearance as moss or fern. These branches were easily dislodged by convection currents. A low bath temperature required more rapid raising of the cathode in order to control the cathode temperature, and a smaller diameter carrot resulted.

When the electrolyte temperature around the cathode was allowed to become too high as a result of too rapid raising of the cathode, the protecting film of frozen electrolyte melted and drained off. A globule of molten metal formed underneath the cathode and sometimes broke away due to the influence of convection currents. When this occurred an arc was struck between the bath surface and the remaining stick of metal thereby causing the metal to melt rapidly and to be lost or, in extreme cases, even to be ignited.

If the electrolyte contained moisture, normal operation was impossible to achieve at the start of electrolysis. No metal deposited on the cathode, and there was a continuous burning of gas at the cathode, such as burning with a yellow flame. This behavior has been explained by previous investigators as being due to electrolysis of the water contained in the electrolyte. Generally, the evolution of gas ceased after a few minutes' operation and normal operating conditions could then be effected.

If the graphite powder which formed a scum on the bath surface was not removed occasionally and was allowed to come in contact with the molten metal, flames at the cathode resulted, suggesting that possibly the graphite was reacting with the metal. Occasionally, a froth would also form depending on whether the electrolysis contained moisture.

Cathode current density seemed to be of importance only insofar as it affected the cathode temperature. In this respect, Frary (13) considered the allowable and most satisfactory cathode current density to be a constant for any particular cell and not of the process itself. Anodic current density seemed of no great importance except with an electrolyte of calcium chloride alone. In this case, occurrence of the so-called "anode effect" was promoted by higher current densities.

During electrolysis with calcium alone, there was vigorous evolution of gas at the anode. The spattering of electrolyte caused by this escaping gas was sufficient to coat the exposed portions of the cell and protect it from rapid attack by the atmosphere. A much less vigorous evolution of gas occurred with the oxide-bearing electrolyte. Anodic attack was less with the chloride electrolyte alone than with the electrolyte containing oxide. As in the aluminum industry (25), higher furnace temperatures caused more rapid consumption of the anode.

A troublesome phenomenon, known as "anode effect," caused concern among practically all persons who have prepared calcium by electrolysis. This phenomenon manifests itself in a sudden interruption of normal operation. The voltage increases markedly and the current decreases to almost zero. A gas film is formed around the anode, and the electrolyte is prevented from wetting the anode surface. This film glows with a bluish color, and the current seems to pass from the anode to the electrolyte by a series of small arcs. The anode itself soon becomes red hot. Numerous attempts (13, 20, 26, 27) have been made to explain this phenomenon.

In the course of this investigation, the anode effect occurred quite readily with calcium chloride alone. Temperature of the bath seemed to have no effect on its occurrence. The larger the anode surface exposed to the electrolyte the more difficult it was to induce the effect. The effect could be eliminated temporarily by momentary interruption of current, reduction in applied voltage, or mechanical shaking of the anode.

No difficulty was experienced with anode effect when using the electrolyte containing oxide. As long as normal operation had started, large currents would not cause the effect to appear. One reference (27) was made in the literature to the fact that calcium oxide would inhibit this effect. This was attributed to a clean anode surface since the oxygen liberated combines with the carbon and it is thus etched and a new surface is continually being formed.

Results

Table I contains the results of the electrolysis of electrolytes of calcium chloride alone and calcium oxide in calcium chloride. Runs were made at several temperatures and with various currents in two sizes of cells. Oxide concentrations from 0.26 to 2.00% by weight were used in these runs. The runs were of 20-60 min duration.

Cathode current density could not be calculated accurately because the carrot diameter did not remain uniform throughout the electrolysis period. Approximate values were in the range 200-300 amp/in.².

Numerous additional runs were made with oxide concentrations in the range of 2-12%. All these runs were unsuccessful in that the temperature around the cathode could not be controlled. The melt was so fluid that it was impossible to keep a protective film of frozen electrolyte on the metal as it emerged from the bath. Without this protection, the calcium would ignite and be lost. Flames continually burned around the cathode, and it was not possible to eliminate them.

In an attempt to eliminate the excessive burning and high convection currents around the cathode, runs of up to 2 hr in duration were made with low electrolyzing currents of 25-35 amp and maximum cooling water flow. While this reduced the intensity of the convection currents, the burning was not eliminated,

Table I. Electrolysis data

CaCl ₂ electrolyte					
Cell size	Temp. range, °C	Current range, amp	Avg cell voltage, v	Avg voltage efficiency, %	
7 1/16 in. I.D. Two 3/4 in. dia. anodes	774-899	90-130	16.6	19.26	
7 1/16 in. I.D. One 3/4 in. dia. anode	800-843	60-120	18	17.78	
4 1/2 in. I.D. One 3/4 in. dia. anode	816-857	75-110	17	18.82	
CaO-CaCl ₂ electrolyte					
Oxide conc. range, wt %	Cell size	Temp. range, °C	Current range, amp	Avg cell voltage, v	Decrease in avg cell voltage, %
0.68-1.34	7 1/16 in. I.D. One 3/4 in. dia. anode	774-828	50-60	13.7	17.46-23.9
0.67-1.90	4 1/2 in. I.D. One 3/4 in. dia. anode	800-843	40-100	14.1	15.06-17.05
0.26-2.00	4 1/2 in. I.D. One 1/2 in. dia. anode	788-843	45-85	15.3	No comparable data for CaCl ₂ alone

and only isolated particles of calcium could be collected. Cell voltage ranged from 10½ to 18v, and current ranged from 30-90 amp. Temperatures were in the range 774°-857°F. Data on a number of these unsuccessful runs may be found in ref. (28).

Next, runs were made with the cathode shielded as suggested by Kunitomi (29). Burning still persisted, and the shield resulted in a higher temperature around the cathode and an increase in cell voltage. Oxide concentrations from 2 to 10% were used.

Since it was observed that oxide concentrations in the neighborhood of 15% gave a more viscous melt, the next step in an attempt to eliminate the aforementioned difficulty was to employ an electrolyte with oxide concentrations in this range. In general, cell voltages were significantly higher than those obtained with oxide concentrations less than 2.0%. Burning around the cathode and convection currents were less severe, but only isolated branches of calcium could be obtained.

In all instances, operation was more difficult with the electrolyte containing oxide than with the chloride alone. Extreme care was necessary in cathode adjustment to control temperature around the cathode. The calcium would ignite quite readily when the film of frozen electrolyte drained away, and it was practically impossible to extinguish it and again effect normal operation. For this reason and the greater tendency toward stronger convection currents, the use of lower electrolyzing currents was necessary.

The gases evolved at the anode during electrolysis of the chloride-oxide electrolyte were tested for chlorine with starch iodide paper. After steady operation was achieved, this test was negative.

In order to verify the decrease in oxide content as a result of electrolysis, a melt of known oxide concentration was subjected to electrolysis. Samples of the melt were taken at intervals and analyzed for oxide content. In all instances, the oxide concentration decreased during electrolysis.

Calcium chloride-calcium fluoride-calcium oxide as electrolyte.—It was thought possible that addition of the fluoride to the electrolyte might overcome some of the operating difficulties experienced with the oxide-chloride electrolyte and, in particular, permit operation with high oxide concentrations by possibly decreasing the pastiness of the melt. However, preliminary runs with this electrolyte in a new apparatus were unsuccessful due to operating difficulties with the power source.

Conclusions

Carrots of metallic calcium may be obtained by electrolysis of an electrolyte of calcium oxide in calcium chloride containing up to 2% by weight of oxide. With concentrations between 2% and approximately 14% oxide, the melt was so fluid that the metal carrot could not be protected with a film of frozen electrolyte as it emerged from the melt, and severe burning resulted. Convection currents were also particularly troublesome in this concentration range.

The most favorable temperature range for electrolysis of the oxide-bearing electrolyte from the standpoint of ease of control and good carrot formation was 788°-816°C. The most favorable oxide concentration range from the same standpoint was 0.5-1%, with satisfactory operation being possible with concentrations up to 2%. Operation was more difficult with the oxide-bearing electrolyte than with chloride alone. No significant temperature effect on cell voltage was noted with either of the electrolytes. No advantage in cell voltage was noted in using oxide concentrations greater than 2% over that to be obtained with use of concentrations less than 2%.

Average cell voltage with the oxide-bearing electrolyte ranged up to 23.9% less than that with the chloride alone. The large cell and large anode surface area were advantageous in both lower average cell voltage and ease of operation and control.

Anode effect presented no problem with the oxide-bearing electrolyte. This was probably due to the fact that a clean surface is continually maintained by the etching effect caused by combination of the liberated oxygen with the anode.

This research presents the first known demonstration that calcium oxide can be fed to a calcium chloride electrolyte for calcium production. This is contrary to literature claims that calcium oxide causes the electrolyte to become pasty. Such pastiness was not in evidence except at high oxide concentrations, approximately 14% and above.

Manuscript received Nov. 5, 1963; revised manuscript received June 5, 1964.

Any discussion of this paper will appear in a Discussion Section to be published in the June 1965 JOURNAL.

REFERENCES

1. Humphrey Davy, *Phil. Trans.*, **98**, 1, 333, 343, 354 (1808).
2. Kurt Arndt, *Z. Elektrochem.*, **8**, 861 (1902).
3. Wilhelm Borchers and Lorenz Stockem, *ibid.*, **8**, 757 (1902).
4. J. H. Goodwin, *J. Am. Chem. Soc.*, **25**, 873 (1903).
5. A. Matthiessen, *J. Chem. Soc. London*, **8**, 27 (1856).
6. Henri Moissan, *J. Chem. Soc.*, **74**, Part 2, 578 (1898).
7. Henri Moissan, *ibid.*, **87**, Part 2, 483 (1904).
8. Bela von Lengyel, *ibid.*, **76**, Part 2, 218 (1899).
9. W. Rathenau, *Z. Elektrochem.*, **10**, 508 (1904).
10. J. H. Goodwin, *J. Am. Chem. Soc.*, **27**, 1403 (1905).
11. P. H. Brace, *Trans. Am. Electrochem. Soc.*, **37**, 465 (1920).
12. *Chemical Abstracts*, **3**, 1948 (1909).
13. F. C. Frary and W. L. Badger, *Trans. Am. Electrochem. Soc.*, **16**, 185 (1909).
14. A. R. Johnson, *ibid.*, **18**, 125 (1910).
15. S. A. Tucker and J. B. Whitney, *J. Am. Chem. Soc.*, **28**, 84 (1906).
16. Paul Wohler, *J. Chem. Soc.*, **88**, Part 2, 708 (1905).
17. C. L. Mantell, "Industrial Electrochemistry," 3rd ed., p. 735, McGraw-Hill Book Co., New York (1950).
18. C. L. Mantell and Charles Hardy, "Calcium Metallurgy and Technology," p. 140, Reinhold Publishing Corp., (1945).
19. A. R. Johnson, *Ind. Eng. Chem.*, **2**, 466 (1910).
20. Richard Lorenz, *Trans. Am. Electrochem. Soc.*, **6**, 160 (1904).
21. C. J. Brockman, *ibid.*, **47**, 245 (1925).
22. Paul Drossbach, "Elektrochemie Geschmolzener Salze," p. 27, Edwards Brothers, Inc., Ann Arbor (1943).
23. R. E. Kirk, Editor, "Encyclopedia of Chemical Technology," **1**, p. 459, The Interscience Encyclopedia, New York (1947).
24. F. C. Frary, H. R. Bicknell, and C. A. Tronson, *Trans. Am. Electrochem. Soc.*, **18**, 117 (1910).
25. J. D. Edwards, F. C. Frary, and Zay Jeffries, "The Aluminum Industry—Aluminum and Its Production," p. 80, McGraw-Hill Book Co., New York (1930).
26. H. H. Kellogg, *This Journal*, **97**, 133 (1950).
27. C. S. Taylor, *Trans. Am. Electrochem. Soc.*, **47**, 301 (1925).
28. W. D. Threadgill, Ph.D. Thesis, University of Missouri, 1954.
29. Minoru Kunitomi, *J. Chem. Soc. Japan, Pure Chemistry Section*, **71**, 212 (1950).

Ellipsometric Investigation of the Optical Properties of Anodic Oxide Films on Tantalum

S. Kumagai¹ and L. Young

Department of Electrical Engineering, The University of British Columbia, Vancouver, British Columbia

ABSTRACT

Tantalum surfaces were examined both immersed in the electrolyte and dry. The optical constants of the metal and of the oxide were obtained by comparing experimental and theoretical ellipsometer curves. It was found that the method of estimating the optical constants of the metal by neglecting the effects of the oxide film already present before anodization leads to serious error. The ellipsometric method gave results in agreement with those obtained using light polarized in the plane of incidence. The advantages of the method seem to lie in the investigation of films which are too thin or otherwise unsuitable for the spectrophotometric method, and for *in situ* measurements.

In the study of thin films and, in particular, of anodic oxide films (1), optical techniques are important because they give accurate and absolute estimates of the thickness. The thickness is, of course, needed to calculate such quantities as field strength and dielectric constant. Several nonoptical methods give quite sensitive measurements of the thickness of anodic oxide

films in indeterminate units, but it is very desirable to be able to determine the absolute thickness, if only to allow comparisons to be made between the oxides of different metals. Optical measurements may also be used to show whether the films are homogeneous and to detect variations with formation conditions in the nature of the film material.

A complete measurement of the optical properties of an isotropic homogeneous film would include the deter-

¹ Present address: OKI Electric Company, Tokyo, Japan.

mination as functions of the angle of incidence and wavelength of the absolute phase and amplitude changes on reflection of the components of the light with electric vector polarized in (p), and at right angles to (s), the plane of incidence. The various practical methods which have been developed differ in what is discarded, in the technique of measurement, and in the method of computation. Ellipsometry is a classical method due to Drude (published 1889) in which the relative amplitude and phase changes on reflection of p and s components are measured. It has been particularly associated with the work of Winterbottom (2) but has recently come into wider use (3-5) because of the ease with which the computations may now be dealt with. There is still, however, little accurate experimental data in the literature obtained by this method largely because of the difficulty of obtaining the film free substrate. The original development of the method was presumably due to the fact that the instrument is used to determine the settings corresponding to the extinction of the light beam. With present instrumental techniques an adjustment to a null is no longer the only sufficiently accurate mode of operation. The purpose of the present work was to investigate what special advantages the method might have in the study of anodic oxide films, and to check previous estimates obtained by other methods [Young (6), Masing, Orme, and Young (7)] of the optical constants of tantalum and its anodic oxide film, on which estimates of various quantities have been based, and which differ considerably from other published values.

Experimental Procedures

Calculations.—It is assumed that an idealized plane parallel-sided slab of homogeneous isotropic oxide of refractive index n_1 and thickness D , attached to a semi-infinite slab of metal of (complex) index of refraction $n_2 = n_2 - ik_2$ where $i = (-1)^{1/2}$ is immersed in a medium of refractive index n_0 . Thus any gradations of properties across the interfaces are neglected. For an effectively coherent beam of parallel light of wavelength λ , incident at an angle to ψ_0 to the normal to the surface, the changes in the amplitude and the phase on reflection are given by the modulus and argument of the complex quantity $R = (r_1 + r_2 e^{-2i\delta}) / (1 + r_1 r_2 e^{-2i\delta})$ where $\delta = (2\pi D n_1 \cos \psi_1) / \lambda$ and r_1 and r_2 are the Fresnel coefficients for the reflection at the outer surface of the oxide and at the oxide/metal interface, respectively. Let R_p and R_s denote the values of R for p and s light components. Ellipsometry is the determination of Ψ and Δ where $\tan \Psi \exp i\Delta = R_p/R_s$. The Fresnel coefficients are given by:

$$r_{p1} = (n_0 \cos \psi_1 - n_1 \cos \psi_0) / (n_0 \cos \psi_1 + n_1 \cos \psi_0)$$

$$r_{s1} = (n_0 \cos \psi_0 - n_1 \cos \psi_1) / (n_0 \cos \psi_0 + n_1 \cos \psi_1)$$

with $n_1 \sin \psi_1 = n_0 \sin \psi_0$, where n_0 and n_1 become complex if the media absorb light, and with similar expressions for r_{2p} and r_{2s} . Programs were written for the IBM 1620 at the Computing Centre of The University of British Columbia to calculate the required quantities. The programs were checked by recalculating data obtained in the previous work and, also, by recalculating data for silicon, kindly supplied by Archer (3). A convention exists which establishes the direction of polarization of the incident and reflected p light corresponding to zero phase change, in such a way that at normal incidence there would be a physically wrong π change of phase of p light respect to s light. According to whether or not this convention is adopted an extra π may appear in Δ .

Preparation of specimens.—The bulk tantalum specimens were prepared as in the previous work (7). For examination dry, they were anodized in a cell similar to that previously described. The dry specimens were held in a specially made holder with provision for traversing horizontally when setting up the ellipsometer. For examination *in situ* a glass cell was con-

structed with two side arms at an angle of about 140° to which optically flat glass plates were attached using epoxy resin. The specimen was supported by a glass tube through a hemispherically ground joint. A device was constructed so that the other end of the tube could be adjusted in two directions at right angles in order to bring the plane of the specimen into the vertical. The cell and the telescope of the ellipsometer were adjusted so that light entered the windows as nearly as possible at normal incidence. The specimen was then brought into the vertical and rotated about a vertical axis until the light beam was reflected in the required direction. The cell was operated with the solution saturated with hydrogen and a platinized platinum electrode was used as cathode.

The ellipsometer and its calibration.—A Gaertner Scientific Corporation L119 model was used. The instrument is merely a spectrometer table with collimator and telescope, with Glan-Thompson prisms reading to 0.01 degree as polarizer and analyzer, and with phase compensation provided either by an ordinary quarter wave plate or by a Soleil Babinet Compensator set as a quarter wave plate. The compensator was used at $\pm 45^\circ$ azimuth. The apertures of the prisms were further stopped down to about 0.25 in. in order to examine a smaller area of the specimen and to improve the perfection of the plane polarization. Gaertner filters were used to select the 4358Å or 5461Å lines from a high-pressure mercury discharge lamp. The light was chopped at 1470 cps by a mechanical chopper. A circular slit was used. The actual measurement consists of adjusting the ellipticity of light incident on the specimen so that the reflected light is plane polarized and therefore extinguishable by the analyzer prism. The detector was an R.C.A. 931 A photomultiplier with a chain of 10 kohm resistors and a 1000v power supply leading to a tuned amplifier. With the specimen removed, the sensitivity was such that the analyzer and polarizer could be crossed almost to the accuracy with which the scales could be read. With light reflected from a specimen, the minima were flatter and Archer's method (8) was adopted of averaging angles on either side of the minimum giving equal photomultiplier readings.

The alignment of the instrument is important since the errors of calibration which are likely to be found are sufficient to cause very appreciable errors in the estimates of the optical constants. The methods described by McCrackin, Passaglia, Stromberg, and Steinberg (5) were used whose work together with the papers by Archer (3) and the earlier publications of Winterbottom (2) are referred to for details of the calculation of Ψ and Δ from the settings of the instrument. The alignment procedure was briefly as follows. The analyzer and polarizer were first crossed with no specimen present, i.e., with an undeflected beam. The maker's settings of the analyzer with respect to the polarizer were essentially exact. The plane of the fast axis of the quarter wave plate was located with respect to the polarizer by rotating the quarter wave plate with

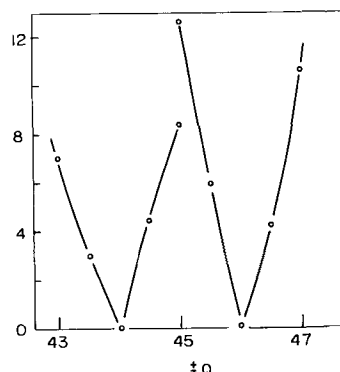


Fig. 1. Light intensity vs. azimuth setting of compensator with $A = 0^\circ$, $P = 90^\circ$.

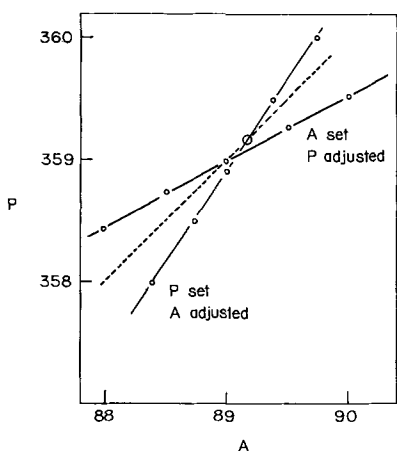


Fig. 2. Calibration of polarizer (P) and analyzer (A). Settings for minimum light transmission with A set and P adjusted, and for P set and A adjusted. Dotted line is $A = P + \pi/2$.

analyzer and polarizer crossed until extinctions were obtained as shown in Fig. 1. The absolute settings (that is, with respect to the plane of incidence) were obtained by using an aluminum mirror near its principal angle of incidence, so that the reflected light would be strongly s-type, i.e., elliptically polarized light was produced with the plane of its major axis known and this was used to locate the plane of polarization of the Glan-Thompson prisms. Figure 2 shows plots of the settings for minimum transmission obtained (i) by fixing A and adjusting P and (ii) by fixing P and adjusting A. The intersection of (i) with the line $P = A + \pi/2$ gives the correction to be applied to the readings. The settings of the compensator were made by finding the phase shift settings giving (for the selected wavelength) zero phase shift with the fast axis in the plane of P, i.e., so that extinctions occurred with polarizer and analyzer crossed. The phase was then set for $\pi/2$ by assuming linearity of the scale. Readings through a complete set of instrument settings were made with typical surfaces, and these readings were arranged in "zones" as described by McCrackin *et al.* Once this was done, it was considered necessary subsequently to measure in two zones only, these readings then being averaged. A typical set of readings, actually for "bare" tantalum, is given in Table I.

Results and Discussion

Unanodized metal and the optical constants of the metal.—The normal method of estimating the optical

Table I. Analysis into zones of a set of ellipsometer readings (using quarter wave plate). For perfect quarter wave plate $\Delta = \pi/2 + 2p$; $\Psi = a_p = a_s$. Data are for $\psi_0 = 70^\circ$, $\lambda = 5461\text{\AA}$, unanodized bulk tantalum

Zone	Compensator	Polarizer	Analyzer	p	a_p	a_s
1	$\pi/4$	$2\pi - p$	$\pi - a_p$	10.69	23.32	
		$2\pi - p$	$2\pi - a_p$	10.65	23.36	
		$\pi - p$	$2\pi - a_p$	10.72	23.34	
2	$\pi/4$	$\pi - p$	$\pi - a_p$	10.78	23.39	
		$\pi/2 - p$	$\pi + a_s$	10.85		21.93
		$\pi/2 - p$	a_s	10.85		21.91
		$3\pi/2 - p$	a_s	10.85		21.95
		$3\pi/2 - p$	$\pi + a_s$	10.83		21.94
3	$-\pi/4$	p	$a_p + \pi$	10.27	23.08	
		$\pi + p$	$a_p + \pi$	10.33	23.12	
		$\pi + p$	a_p	10.30	23.13	
		p	a_p	10.25	23.12	
4	$-\pi/4$	$3\pi/2 + p$	$\pi - a_s$	10.43		22.19
		$\pi/2 + p$	$\pi - a_s$	10.43		22.20
		$\pi/2 + p$	$2\pi - a_s$	10.42		22.19
		$3\pi/2 + p$	$2\pi - a_s$	10.42		22.17

Mean Values

Zone	p	a_p	a_s
1	10.71	23.35	
2	10.85		21.94
3	10.29	23.11	
4	10.42		22.19
All zones	10.57		22.65

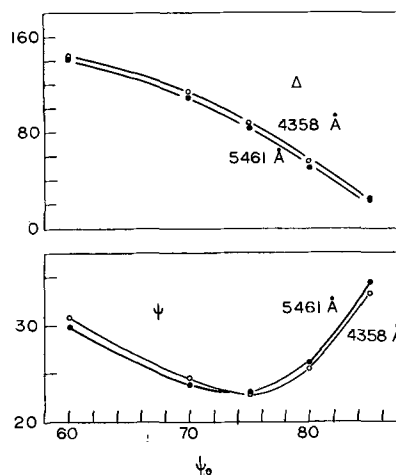


Fig. 3. Relative amplitude ($\tan \Psi$) and phase (Δ) change on reflection for unanodized tantalum as function of angle of incidence (ψ_0).

constants of metals has been to measure freshly prepared surfaces exposed to air and then to neglect any oxide film unavoidably present. With reactive metals such as tantalum, special techniques are required if an oxide film is not to be present. Actually, the change in the structure of the surface layers of metal between the situation of a clean surface exposed to vacuum and a surface covered by a film of oxide would in theory tend to make the optical constants derived from reflectivity studies on a bare surface inapplicable for substitution in equations to describe the reflectivity of oxide coated metal. It is not known how important this effect may be. The classical method was to measure the value of Ψ at the principal angle of incidence such that $\Delta = \pi/2$. The equations then take on a simple form for numerical work. This restriction to the principal angle is, of course, not needed when a computer is used to reduce the readings.

In the case of tantalum, Wartenberg (9) obtained many years ago the values $n_2 \approx 2.05$ and $k_2 \approx 2.3$ in the present region of wavelength. These are given in the handbooks. Heavens and Kelly (10) fitted curves of absolute intensity of reflection for p-light as a function of angle of incidence neglecting any oxide present. They obtained $n_2 = 2.04$ and $k_2 = 2.09$ (with reliability claimed at 1 or 2%) for evaporated films of tantalum, at 5461Å. Masing, Orme, and Young (7) used a method in which the pre-existing film was not neglected and a perfectly flat surface was not assumed. This method involved the measurement of the ratio of maximum to minimum reflectivity to p-light as the thickness of oxide was increased and the ratio between the thicknesses of oxide for the first minimum in reflectivity and the increment in thickness between successive minima. The thickness zero was obtained essentially on the very reasonable assumption that the ratio of oxide overpotential to total thickness was equal to the constant ratio of increments in these quantities at constant ionic current density during formation of the film. This method gave $n_2 = 3.5 \pm 0.1$ and $k_2 = 2.4 \pm 0.1$ at 4358Å.

Figure 3 shows typical values of Ψ and Δ as a function of angle of incidence for electropolished tantalum

Table II. Values of optical constants of tantalum obtained from Ψ and Δ by (unjustifiably) neglecting oxide present on unanodized metal (N.B. curve fitting gives $n_2 \approx 3.5$, $k_2 \approx 2.4$)

ψ_0	$\lambda = 5461\text{\AA}$		$\lambda = 4358\text{\AA}$	
	n_2	k_2	n_2	k_2
60	2.42	2.41	2.56	2.61
70	2.41	2.31	2.55	2.49
75	2.40	2.28	2.55	2.45
80	2.40	2.23	2.57	2.43
85	2.40	2.19	2.58	2.39

freshly etched in HF. Values of n_2 and k_2 found from these values of Ψ and Δ assuming $D = 0$ are given in Table II. The time dependence of Ψ and Δ under these conditions is shown in Fig. 4. The slowness of the change with time is probably due to the fact that most of the oxidation has occurred before the first measurement. [Archer's method with silicon (3) depends on the slower oxidation of silicon and on the nature of the values of n_2 and k_2 for silicon.]

The large discrepancy is in fact due to the effect of the very thin pre-existing film. Figure 5 shows what thickness of oxide would account for the observed Ψ and Δ for unanodized metal, if the optical constants of the metal were actually $n_2 = 3.5$ and $k_2 = 2.4$. Calculated contours of Δ and Ψ are plotted against axes n_2 and k_2 for conditions of zero oxide thickness. The additional line shows the values of n_2 and k_2 which would be calculated from observed Ψ and Δ values if the true values of the optical constants were $n_2 = 3.5$ and $k_2 = 2.4$, but if oxide films of various thicknesses were present and were neglected. The estimate of the pre-existing thickness obtained from this figure assuming $n_2 = 3.5$ and $k_2 = 2.4$ with experimental values of Ψ and Δ of Fig. 3 is about 70Å, which is reasonable and agrees well with the estimate which may be inferred from comparison of calculated and experimental intensity reflectivity curves for p-light vs. angle of incidence given in Fig. 15 of ref. (7). The thickness of the pre-existing film is somewhat larger than we have usually found in capacity measurements, but this could well be due to the pre-existing film's having different electrical properties from the anodic film, as is certainly the case for the pre-existing film on chemically polished tantalum (1) and to the difference between the present method of preparing the surface and that used for specimens for capacity measurements.

The calculated curve for oxide coated metal in Fig. 5 was chosen since it fits experimental Ψ , Δ plots. Thus if both the thickness of the pre-existing film and the optical constants are regarded as unknown, this curve

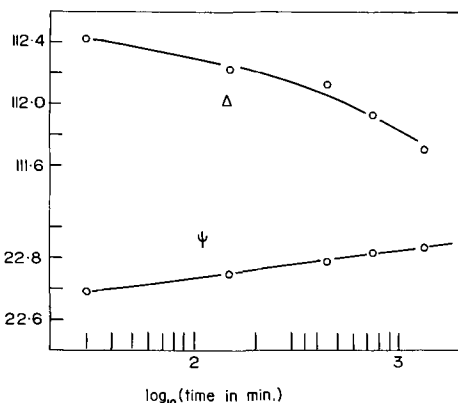


Fig. 4. Change with time after etching of Δ and Ψ for tantalum at $\psi_0 = 70^\circ$, $\lambda = 5461\text{\AA}$.

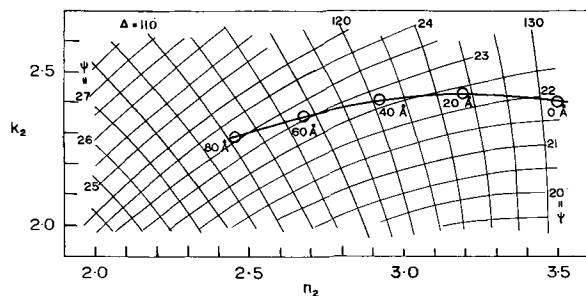


Fig. 5. The grid shows values of Ψ and Δ calculated for oxide-free metal surface with optical constants n_2 and k_2 . The line labelled with thicknesses 0, 20, 80Å shows Ψ and Δ for metal with $n_2 = 3.5$, $k_2 = 2.4$ and indicated thicknesses of oxide with $n_1 \sim 2.26$ (insensitive to n_1).

may be regarded as defining a relation between possible values of n_2 and k_2 , with a limit set by the fact that the thickness of the pre-existing film cannot be less than zero. In practice, the curve essentially fixes $k_2 \approx 2.4$ with free choice of $n_2 > 2.5$. Thus the previous value of k_2 is confirmed, but n_1 and n_2 must be obtained by the use of further data.

Anodized metal.—Figure 6 shows ellipsometry data for dry, anodized tantalum at 4358Å, $\psi_0 = 50^\circ$ and 70° . The points are experimental and the curves are calculated. Similar data for $\lambda = 5461\text{\AA}$ are given in Fig. 7, and results for specimens measured still immersed in the forming solution are given in Fig. 8 and 9 for $\psi = 67.5^\circ$ and 70° . Data for both of these angles of

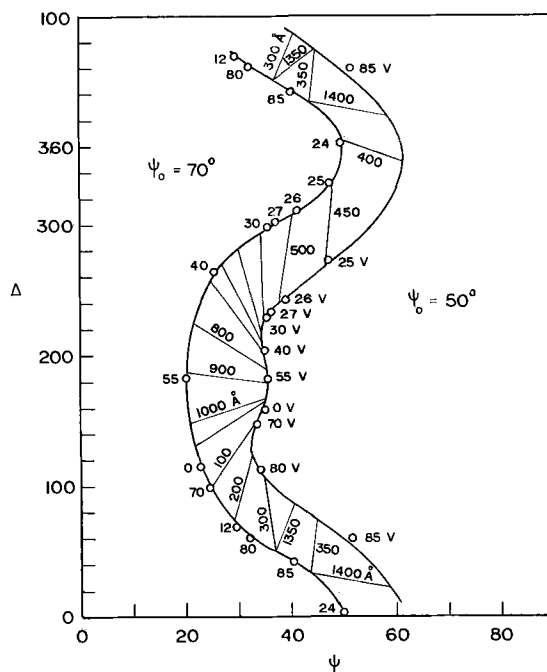


Fig. 6. Comparison of experimental data at $\lambda = 4358\text{\AA}$ for films formed to voltages shown at about $1 \text{ ma}\cdot\text{cm}^{-2}$ and 25°C in $0.2N \text{ H}_2\text{SO}_4$ at angles of incidence 50° and 70° with calculated data for $n_1 = 2.28$, $n_2 = 3.5$, $k_2 = 2.4$.

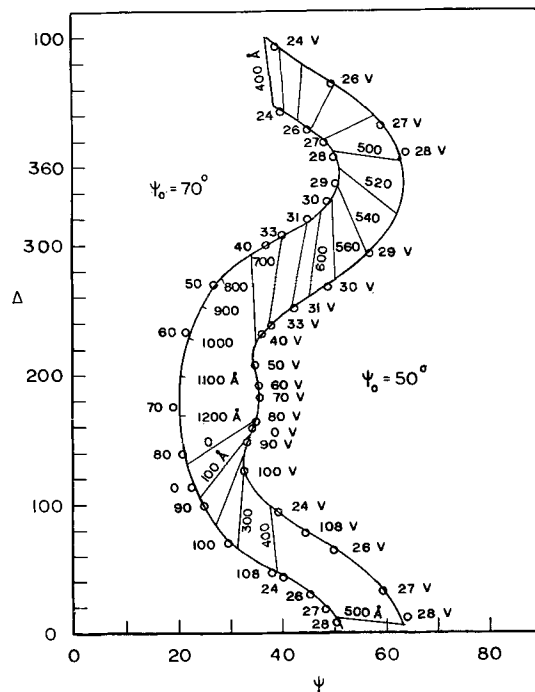


Fig. 7. Similar to Fig. 6 except $\lambda = 5461\text{\AA}$, $n_1 = 2.26$

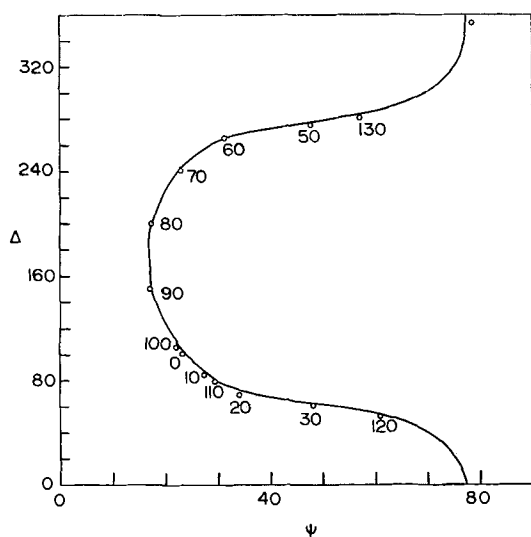


Fig. 8. Comparison of experimental data for $\lambda = 5461$, $\psi_0 = 67.5^\circ$ taken *in situ* for films formed to voltages shown at room temperature with calculated curves for $n_0 = 1.334$, $n_1 = 2.26$, $n_2 = 3.5$, $k_2 = 2.4$.

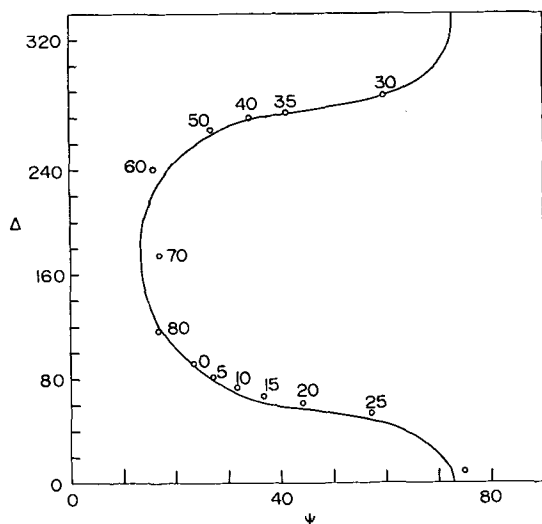


Fig. 9. Similar to Fig. 8 except $\psi_0 = 70^\circ$

incidence are included in order to demonstrate that any small error in setting up the beams perpendicular to the windows did not appear to affect the goodness of fit to calculated curves.

A first point is that Ψ and Δ trace out a closed curve (modulus 2π) as the thickness of oxide is increased (for films formed in dilute solution). This confirms that any absorption of light by the oxide may be neglected in fitting the curves. If light is absorbed the curve would trace out a unique path from the point corresponding to the bare metal to the point corresponding to infinitely thick oxide.

Analytical methods could be developed for fitting calculated curves, but in practice a trial and error approach was used. The directions and amounts of the changes in Ψ and Δ resulting from small variations in n_1 , n_2 , and k_2 from the fitted values are shown in Fig. 10 for $\lambda = 5461\text{\AA}$ and $\psi_0 = 50^\circ$ and in Fig. 11 for $\psi_0 = 70^\circ$. The sensitivity is evidently greater at $\psi_0 = 50^\circ$. The values of n_1 , n_2 , and k_2 established by this process of curve fitting agree within experimental error with those found in the previous work with p-light [see Tables 1, 2, and 3, ref. (7)]. The fact that a fit can be obtained at all indicates that the oxide material is reasonably homogeneous and independent of thickness, in contrast to (10). The few angstroms

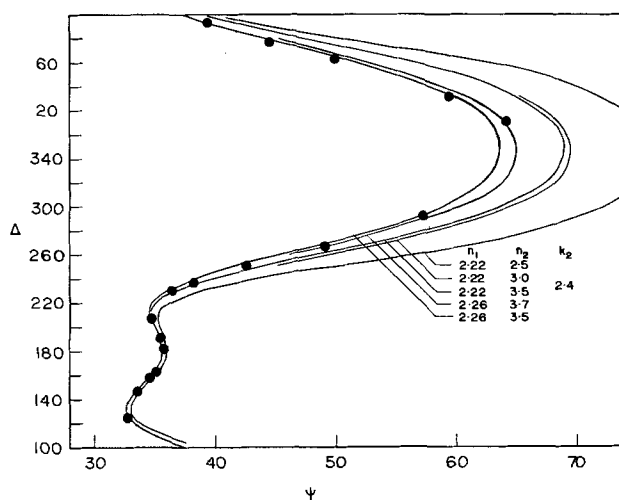


Fig. 10. Comparison of experimental points with various calculated curves for $\lambda = 5461\text{\AA}$, $\psi_0 = 50^\circ$.

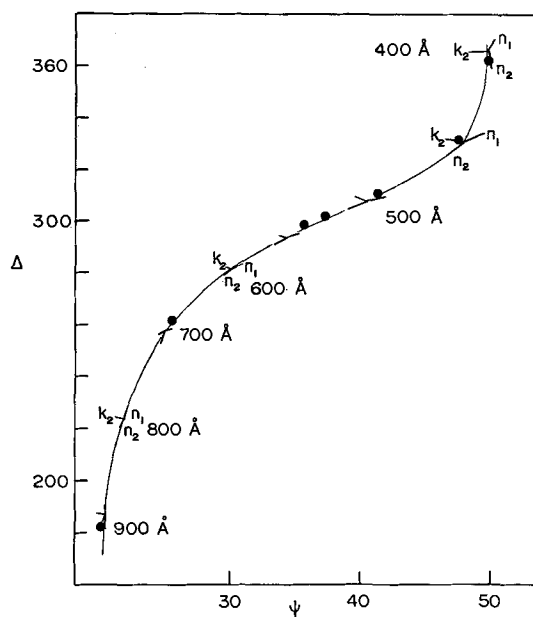


Fig. 11. Comparison of experimental data at 4358\AA , $\psi_0 = 70^\circ$ with calculated curve for $n_1 = 2.28$, $n_2 = 3.5$, $k_2 = 2.4$. Lines labeled n_1 , n_2 , and k_2 show effects of changing these quantities to 2.26, 3.3, and 2.3, respectively.

of absorbing oxide on the outer surface of the film found by the p-light method evidently did not affect the present results, but this would be expected since in the previous work the effect appeared only at the Brewster angle of the oxide.

The precision with which the refractive index of the oxide may easily be determined by the present method is less than that obtained by the modified Abelès method (7), and the present method is certainly much less convenient to apply. The agreement is within experimental error. The situation as regards n_1 is as follows. The spectrophotometric method gave $n_1(\lambda)$ in arbitrary units. An absolute value in sodium light was obtained by the Becke method with S/Se melts. This gave $n_1 = 2.14 + 0.292 (\lambda/10^3\text{\AA} - 2.305)^{-1.2}$, i.e., 2.26 and 2.21 at 4358 and 5461 \AA . The uncertainty was given as "of the order of one percent." This value was about 10% lower than most previous estimates. The Abelès method indicated some dependence on formation conditions with $2.26 < n_1 < 2.29$ at 4358 \AA for the ordinary range of formation conditions in dilute solution. The present data are consistent with 2.28 ± 0.1 at 4358 \AA and 2.25 ± 0.1 at 5461 \AA . The best estimate of the average value of $n(\lambda)$ is apparently about 1.5%

higher than given by the equation above, say $n_1 = 2.18 + 0.296 (\lambda/10^3\text{\AA} - 2.305)^{-1.2}$. No information is available on what effect surface imperfections may have on the ellipsometric method.

The ellipsometric method could detect the small dependence of n_1 on formation conditions, such as was found to exist to at least statistical significance by the modification of the Abelès method, only by working at the most sensitive ψ_0 and D . Since data based on thicknesses of anodic oxide films derived from the density of Ta_2O_5 8.735 g cm^{-3} of unknown origin given by the Handbook of Physics and Chemistry are still being published (11), it is perhaps worth noting that the thickness obtained from this density will be about 10% too small on the basis of the values of n_1 here confirmed. The fact that a good fit is obtained for $\psi_0 = 70^\circ$, and for $\psi_0 = 50^\circ$ confirms that the optical constants do not depend on the angle of incidence. The fit immersed as well as dry confirms the accuracy of n_1 and also shows that pores into which electrolyte may enter are absent. A further test is that when points of equal thickness are compared at different angles of incidence (Fig. 6, 7) experimental and theoretical results agree. The increases in thickness for one cycle of the ellipsometer plot $\lambda/2n_1 \cos \psi_1$ are consistent when the thickness is obtained from spectrophotometric data with adjustment of n_1 .

Conclusions

The chief value of the ellipsometric technique in the determination of the thickness of films would seem to lie in its application to films to which the more precise and speedy spectrophotometric location of wavelengths of minimum reflectivity (1, 6) cannot be applied either because the films are too thin ($<150\text{\AA}$

or so for tantalum) or because they must be measured still immersed in the electrolyte or because the optical constants of oxide and substrate are poorly "matched" for sharp interference minima. The method is very sensitive to the film thickness at certain thicknesses and quite insensitive at others, as may be seen by examining the figures. The measurement of intensity of reflection of p-light (7) is more precise for the determination of the optical constants of the oxide and metal.

Acknowledgments

The authors thank the Defence Research Board of Canada for supporting this work.

Manuscript received April 6, 1964.

Any discussion of this paper will appear in a Discussion Section to be published in the June 1965 JOURNAL.

REFERENCES

1. L. Young, "Anodic Oxide Films," Academic Press, London and New York (1961).
2. A. B. Winterbottom, *Det. Kgl. Norske Videnskabers Selskabs Skrifter*, No. 1, 1 (1955). (In English)
3. R. J. Archer, *J. Opt. Soc. Amer.*, **52**, 970 (1962).
4. R. C. Menard, *ibid.*, **52**, 427 (1962).
5. F. L. McCrackin, E. Passaglia, R. R. Stromberg, and H. L. Steinberg, *J. Res. NBS*, **A67**, 363 (1963).
6. H. von Wartenberg, *Ber.*, **12**, 105 (1910).
7. L. Masing, J. E. Orme, and L. Young, *This Journal*, **108**, 428 (1961).
8. R. J. Archer, *Phys. Rev.*, **110**, 354 (1958).
9. H. von Wartenberg, *Ber.*, **12**, 105 (1910).
10. O. S. Heavens and J. C. Kelly, *Proc. Phys. Soc.*, **72**, 906 (1958).
11. P. H. G. Draper and P. W. M. Jacobs, *Trans. Faraday Soc.*, **59**, 2888 (1963).

The Anodic Dissolution of Gold in Cyanide Solutions

K. J. Cathro and D. F. A. Koch

Division of Mineral Chemistry, C.S.I.R.O., Melbourne, Australia

ABSTRACT

The anodic dissolution of gold in alkaline cyanide solutions has been studied by potentiostatic and galvanostatic techniques under high-purity conditions. Measurements were made at room temperature and in the pH range 11-13, the KCN concentration varying from 0.05 to 0.50%. The results show that gold has three current maxima in the potentiostatic curve at -0.6 , $+0.1$, and 0.4 v vs. SCE . The first and last are pH dependent, but that at $+0.1\text{ v}$ is not. The rate-determining step in the active region (more cathodic than -0.6 v) is interpreted as the reaction $\text{Au} + \text{CN}^- = [\text{AuCN}]_{\text{Ads}} + e$, occurring at a low coverage of adsorbed species. The passive states at -0.6 v and $+0.1\text{ v}$ are considered to arise from basic cyanide films, while auric oxide is formed at $+0.4\text{ v}$. The change in reflectivity of the gold surface at constant potential has indicated that the three regions of passivity can be associated with surface films.

Despite its importance in the gold mining industry very few electrochemical studies of gold dissolution in cyanide solutions have been published. Polarization curves have been reported by Kudryk and Kellogg (1) and Mills (2), but their results are not in agreement. Kudryk and Kellogg claimed that the gold surface was unaffected by the reaction products while Mills showed the onset of passivity at potentials more positive than $-0.55\text{ v vs. a saturated calomel electrode (SCE)}$. The practical significance of a passive layer on the gold surface has been considered by Cathro (3) who showed that the dissolution of gold in aerated cyanide solutions would be controlled by the diffusion rate of dissolved oxygen if the surface was unaffected by the reaction products ("active surface"), but would be controlled by the anodic dissolution rate of gold if it were passive.

The anomaly in the published results could result from trace impurities in the gold or solution, as it has been shown by Mills (2) and Cathro (3) that the presence of lead, mercury, bismuth, and especially

thallium can delay or prevent the gold becoming passive. Consequently, it was decided to re-examine the anodic behavior of gold in cyanide solutions under conditions of high purity. Modern potentiostatic techniques have also been applied to provide more detailed information over the range of potential -0.8 to $+0.6\text{ v vs. SCE}$. The results in the active region ($< -0.6\text{ v}$) under these conditions will be interpreted in terms of a reaction mechanism which suggests that there is little effect of adsorbed species. A complex behavior has been observed at potentials more positive than -0.6 v with three regions of passivity. Measurements of the change of reflectivity of the surface due to etching or polishing provide further indirect evidence for the presence of surface films at potentials corresponding to passivity.

Experimental

Analytical reagent grade chemicals were twice recrystallized from water which had been doubly distilled in glass vessels (specific conductivity 10^{-6} to

2×10^{-7} mhos) under an atmosphere of purified nitrogen. Stock solutions of approximately 1M potassium cyanide, sodium sulfate, and sodium hydroxide were prepared by adding the required volume of oxygen-free double-distilled water to the recrystallized solids, and the solutions were stored under a nitrogen atmosphere at 5°C until required. Electrolytes containing 0.5M sodium sulfate, 0.0076-0.076M potassium cyanide (0.05-0.50%) and at a pH varying from 11 to 13 were made up from these solutions and transferred rapidly to the electrolysis cell through which purified nitrogen was passed. The nitrogen was purified by passing commercial "oxygen-free" grade through a train containing activated copper oxide at 500°C, soda-asbestos, and copper turnings at 550°C to remove traces of hydrocarbons, carbon dioxide, and oxygen.

The Pyrex glass electrolysis cell was similar to that described by Pentland, Bockris, and Sheldon (4). It was cleaned with a sulfuric-nitric acid mixture overnight prior to each run, rinsed with clean running tap water, and then thoroughly washed with double-distilled water. All taps in the cell were water sealed, and no greases were used as lubricants. The counter electrode of platinum gauze was separated from the anode compartment by a solvent-sealed tap. The gold electrode was made from a 3 mm diameter, 30 mm long rod of Specpure gold (Johnson Matthey) embedded in a Teflon holder which fitted tightly into a B14 socket in the electrolysis cell. Before each run the working surface of the gold (0.071 cm^2) was abraded with fine emery cloth and etched in purified 1M potassium cyanide for several hours. Potentials were measured by a Luggin capillary and a valve voltmeter, against a SCE. All potentials quoted in this paper are with respect to the SCE. The electrode potential was controlled by an electronic potentiostat similar in principle to that described by Fleishmann and Thirsk (5).

Polarization curves were obtained by measuring the current at a series of potentials between -0.8 and $+0.6 \text{ v}$. vs. SCE starting at the more negative potential. In most cases a steady current was obtained within 2 min, but at potentials near -0.5 v , when the gold was first becoming passive, up to 30 min was necessary for the current to reach a steady value. Some indication of the reproducibility is shown in Fig. 2(b) where the two curves were obtained three months apart using different preparations of electrolyte. Galvanostatic measurements were made in the potential region -0.8 to -0.6 v to obtain the Tafel plots (Fig. 5). All experiments were made at room temperature ($22^\circ \pm 3^\circ \text{C}$).

Potential-time curves for the reduction of the oxide film on gold were obtained in 0.5M sodium carbonate in a nitrogen atmosphere. A small constant current was passed between the gold and the counter electrode and the potential of the gold surface was traced on a pen recorder driven by a voltage follower which drew less than 10^{-8} amp. In this phase of the work Specpure gold, and gold deposited on a platinum substrate from cyanide solution [El Wakkad and El Din (6)] and chloride solution [Gray (7)] were used. For the latter electrodes approximately equal surface areas were obtained by producing a surface with approximately the same capacitance as measured by an a-c bridge.

Reflectance measurements were made on a 6.3 cm^2 gold electrode mounted vertically within a few millimeters of an optical silica window which formed one wall of an electrolysis cell. The cell was mounted in a light tight box and placed against the sample port of the integrating sphere of a Beckmann DK2A spectrophotometer. The total reflectance was measured at $520 \text{ m}\mu$ using a gold sheet as the reference. The potential of the electrode was controlled by an electronic potentiostat and nitrogen bubbled through the electrolyte during operation. The reflectance work was not made under high-purity conditions, but chemicals of A.R. standard were used. At this level of purity the gold did not become as passive as in the high-purity work and a current of about 0.3 ma cm^{-2} was

passed in the "passive" region. The peak potentials however were similar to the high-purity values.

Results

Polarization curves at pH 12 for four cyanide concentrations are shown in Fig. 1. These results agree qualitatively with the finding of Mills (2), the gold becoming passive at about -0.5 v with a peak current at -0.6 v . Once passive the recovery to the active state was very slow. When the electrode was open-circuited, after a steady current had been reached at -0.1 v , the potential immediately fell to -0.5 v (i.e., in the passive region) and then very slowly became more negative until it reached the potential of "active" gold at -0.8 v after about 20 hr. Polarization curves with 0.25% (0.038M) KCN for three different pH values are shown in Fig. 2.

Charging curves for gold-plated platinum electrodes in 0.5M Na_2CO_3 are shown in Fig. 3(a) and (b) where the gold was plated from cyanide and chloride solutions, respectively. The electrode was first charged anodically to a potential of oxygen evolution and then the cathodic potential-time curve measured since the cathodic curves gave better defined steps. The Specpure gold electrode gave a similar curve to the one deposited from chloride solution.

The variation in per cent reflectance with potential is shown in Fig. 4. Reflectance changed with time and the plotted values were obtained after 4 min. An arrow indicates the continued direction of change.

Discussion

The polarization curves of Fig. 1 and 2 are of a complex type and show three regions of passivity with maximum currents at -0.6 , $+0.1$, and $+0.5 \text{ v}$. For the

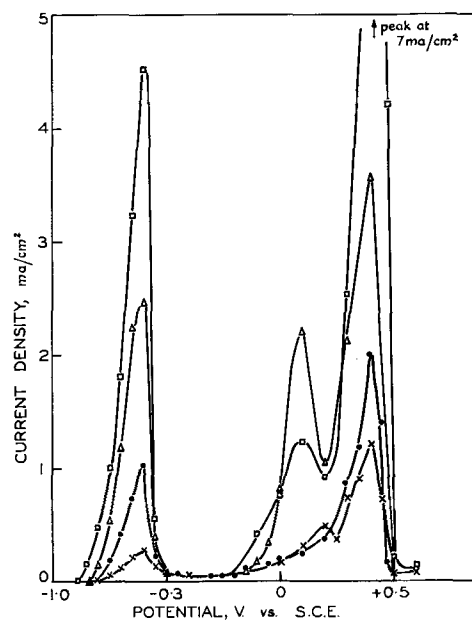


Fig. 1. Polarization curves for a gold electrode: X, 0.052% (0.0080M) KCN; O, 0.15% (0.023M) KCN; Δ, 0.25% (0.038M) KCN; □, 0.50% (0.077M) KCN; pH 12, $22^\circ \pm 3^\circ \text{C}$.

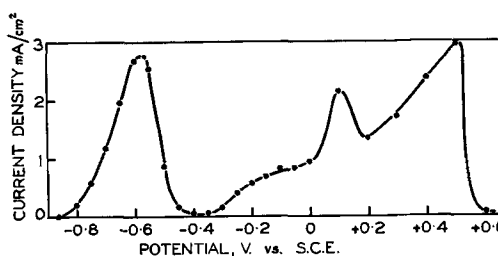


Fig. 2a. Effect of pH 11.2

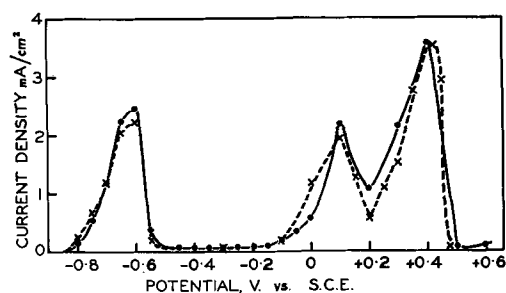


Fig. 2b. Effect of pH 12: O, April; X, July.

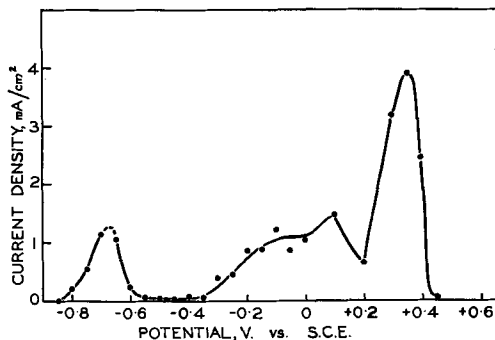
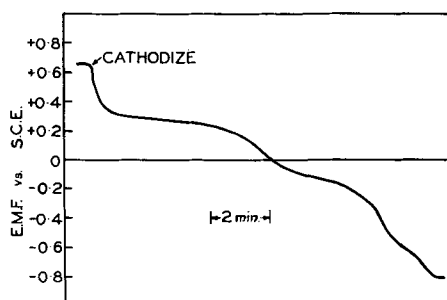
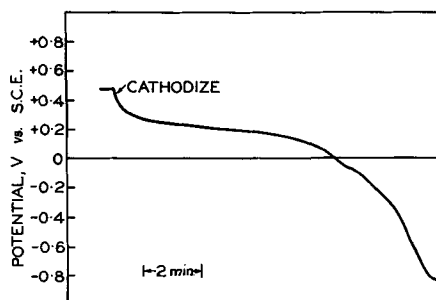


Fig. 2c. Effect of pH 12.8

Fig. 3a. Charging curve for electrode plated from cyanide solution, 0.4M Na₂CO₃, 5.2 μA current density.Fig. 3b. Charging curve for electrode plated from chloride solution 0.4M Na₂CO₃, 5.2 μA current density.

practical purpose of cyanidation of gold, the "active" region from -0.85 to -0.6 v is of interest, and a possible kinetic explanation of the results in this region will be discussed in some detail. This will be followed by a general discussion on the phenomena observed at more anodic potentials.

Potentials more cathodic than -0.6 v.—There is evidence (3) that the gold dissolution is diffusion-controlled when it is activated with thallium,¹ so that the expected currents for diffusion control can be calculated from the limiting current in the presence of

¹ A marked increase in dissolution rate was observed when low concentrations (10 ppm) of Tl⁺ were added to the cyanide solution. This increased activity was observed in the potential region in which Tl metal could be deposited on the gold surface. Details of this effect will be published at a later date.

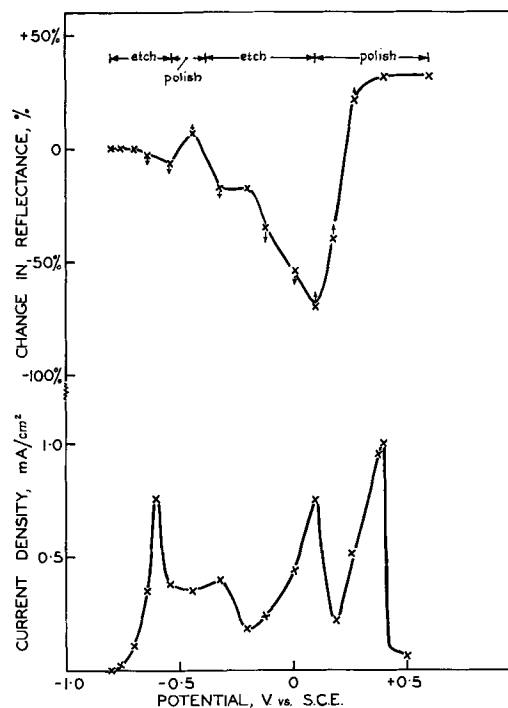


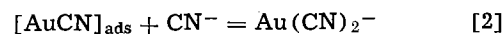
Fig. 4. Change in reflectance of gold surface, 0.25% KCN, pH 12, 20°C approximate.

thallium. The observed values are about 1/10 of that expected for diffusion control. Furthermore agitation under controlled conditions (3) has no effect on the anodic dissolution rate, and we can assume therefore that the reaction is activation controlled. Rate equations will now be developed for some possible activation controlled mechanisms.

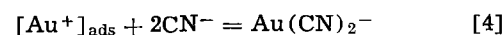
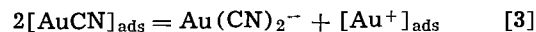
The dissolution of active gold may occur through adsorbed intermediates on the surface or by the direct attack of cyanide ions on a surface free of adsorbed species. In the first case cyanide ions will be adsorbed on the gold surface and this can be represented by



The removal of adsorbed cyanide may be achieved in two ways; either by the reaction of cyanide ion with the adsorbed species



or by a surface recombination



In the case of a direct attack (*i.e.*, the adsorption and desorption processes are rapid and the equilibrium surface coverage is low) the reaction may be simply expressed



The rate equations for these reaction mechanisms may be written as follows. If [1] is rate determining

$$i = k_1(1-\theta)a_{\text{CN}^-} \exp(\beta F \Delta\phi / RT) \quad [6]$$

where $\Delta\phi$ is the Galvani potential difference between the electrode and solution at a current density i , k_1 the rate constant for reaction [1] when $\Delta\phi = 0$, θ the fraction of surface covered with AuCN, a_{CN^-} the activity of the cyanide ion in solution, and β the symmetry factor. R , T , and F are the gas constant, temperature and Faraday, respectively. Equation [6] assumes a Langmuir adsorption isotherm which would probably apply when $\theta < 0.2$ or $\theta > 0.8$ (8).

If reaction [2] is rate determining and [1] is assumed to be rapid and at a quasi-thermodynamic equilibrium there are two cases. For $\theta \approx 1$

$$i = k_2 a_{\text{CN}^-} \quad [7]$$

and for $\theta \ll 1$

$$i = k_2 K_1 a_{\text{CN}^-}^2 \exp [F(\Delta\phi)/RT] \quad [8]$$

where k_2 is the rate constant for reaction [2] and K_1 the equilibrium constant for [1] which may be expressed

$$K_1 = \frac{\theta \exp [-F(\Delta\phi)/RT]}{(1-\theta) a_{\text{CN}^-}} \quad [9]$$

If reaction [3] is rate determining and both [1] and [4] are rapid then for $\theta \ll 1$

$$i = K_1^2 k_3 a_{\text{CN}^-}^2 \exp [2F(\Delta\phi)/RT] \quad [10]$$

For $\theta \approx 1$

$$i = k_3 \quad [11]$$

where k_3 is the rate constant for reaction [3].

It is unlikely that reaction [4] would be rate determining because of the instability of Au^+ . Furthermore it would lead to a rate equation including the fourth power of cyanide concentration which is not observed experimentally.

Finally if the reaction path is [5]

$$i = k_5 a_{\text{CN}^-}^2 \exp [\beta F(\Delta\phi)/RT] \quad [12]$$

Some numerical values for the parameters distinguishing the above steps are summarized in Table I. For the sake of conciseness the rate-determining steps [2] and [3] at $\theta \approx 1$ (represented by rate equations [7] and [11]) have been omitted since our results show that the current is dependent on potential. The numerical values in Table I are calculated on the basis of $\beta = 1/2$, and in the experimental results cyanide concentration has been used in place of activity.

The experimental results on the effect of cyanide concentration on current (last column of Table I) have been obtained at a constant potential with reference to SCE which would differ only by a constant from $\Delta\phi$. This assumes no change in $\Delta\phi$ with the tenfold change in cyanide concentration employed in this work. $\Delta\phi$ would be effected by a change in the dipole contribution, but the low concentration of adsorbed species (vide infra) in the relatively small potential range in question supports our assumption.

The data in the last row of Table I strongly point to reaction [1] as the rate-determining step. The apparent Tafel slope of less than 0.12 when the overpotential is less than 20 mv (Fig. 5) may arise if the back reaction of [1] is significant at these low overpotentials. The kinetic parameters calculated for reaction [1] assume low coverage with the adsorbed species at potential more negative than -0.6v vs. SCE , and this is supported by the differential capacitance measurements of Mills (2). A low coverage furthermore validates our assumption of a Langmuir adsorption isotherm in the derivation of the kinetic equations.

Potentials more anodic than -0.6v .—When the potential reaches -0.6v , the gold becomes passive and the potential at maximum current is independent of cyanide concentration but is dependent on pH (Fig. 1 and 2). The pH dependence of this and the subsequent peaks at $+0.1$ and $+0.4\text{v}$ are shown in Fig. 7, and it is apparent that at -0.6 and $+0.4\text{v}$ the potential-pH

Table I. Characteristic parameters for rate-determining steps

Rate-determining step	$(\partial V / \partial \log i)_{a_{\text{CN}^-}}$	$(\partial \log i / \partial \log a_{\text{CN}^-})_{\phi}$
1. $\text{Au} + \text{CN}^- = [\text{AuCN}]_{\text{Ads}} + e$	0.12	1.0
2. $[\text{AuCN}]_{\text{Ads}} + \text{CN}^- = \text{Au}(\text{CN})_2^-$	0.059	2.0
3. $2[\text{AuCN}]_{\text{Ads}} = \text{Au}(\text{CN})_2^- + [\text{Au}^+]_{\text{Ads}}$	0.029	2.0
5. $\text{Au} + 2\text{CN}^- = \text{Au}(\text{CN})_2^- + e$	0.12	2.0
Experimental parameters	0.13 (Fig. 5)	1.2 (Fig. 6)

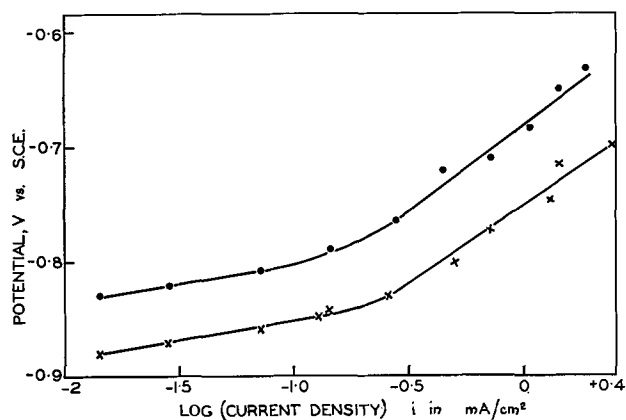


Fig. 5. Tafel plot for "active" gold: ○, 0.29% KCN, pH 12; x, 0.50% KCN, pH 12.

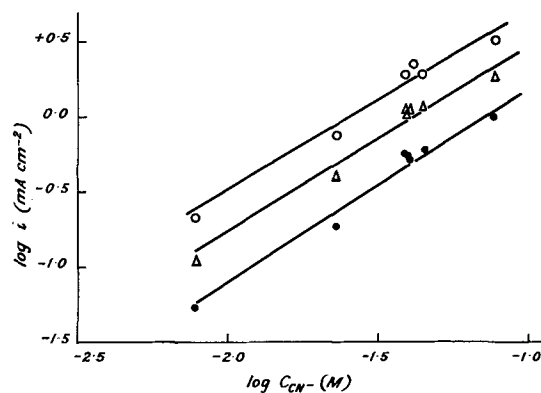


Fig. 6. Current as a function of cyanide concentration at constant potential: ○, -0.65v vs. SCE ; Δ, -0.70v vs. SCE ; ●, -0.75v vs. SCE .

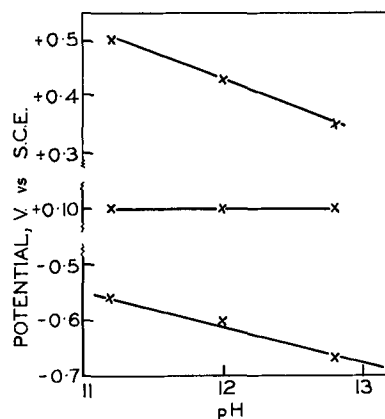


Fig. 7. Effect of pH on peak potentials

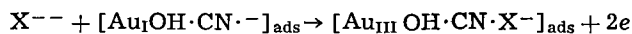
curve has a slope, but at $+0.1\text{v}$ the potential is pH independent.

The linear relationship between potential and pH at the Flade potential of gold during the formation of auric oxide in noncomplexing solutions has been reported before (9,10). At -0.6v the slope (Fig. 7) is about -0.06 and can be the result of a reaction of the type



The slope at $+0.04\text{v}$ however is -0.09 and indicates a more complex mechanism which must involve a basic salt. As shown above, the oxidation at -0.6v can result from the formation of an oxide, and a similar pH dependence could also arise for the formation of a hydroxide or basic cyanide from the metal. The pH independence of the $+0.1\text{v}$ maximum could arise from the

conversion of an Au(I) basic cyanide to an Au(III) basic cyanide and may occur according to



where X^{--} can be any anion except OH^- (e.g., in this system $2CN^-$ or SO_4^{--}). The peak current at this potential was not sufficiently reproducible to indicate whether the anion was cyanide or sulfate.

El Wakkad and El Din (6) observed arrests on charging curves for gold in 0.1M sodium carbonate solutions at -0.50 , -0.10 , and $+0.45$ v which they attributed to the three oxides of gold. However other workers (2, 9-11) have shown only one arrest on the anodic charging curve of gold at $+0.3$ to $+0.4$ which has been generally accepted as the potential at which auric oxide (Au_2O_3) is formed. One possibly significant difference in the experimental conditions of El Wakkad and El Din and the other workers was the preparation of the gold surface. The former used gold electroplated on a platinum surface from cyanide solutions while the latter all used massive gold. In order to check the significance of any difference in the gold surface, a series of charging curves was made using platinum electrodes plated with gold from either cyanide or chloride solutions. Typical charging curves in 0.1M sodium carbonate are shown in Fig. 3(a) and 3(b). The electrode plated from cyanide solution showed two well-defined arrests at $+0.30$ and -0.10 v with a third less-defined step at -0.60 v. That plated from chloride solution gave only one well-defined step at about $+0.3$ v, and a similar result was obtained with a Specpure gold sample. This is strong evidence that adsorbed or occluded cyanide was present on the gold used by El Wakkad and El Din and that the arrests were caused by a cyanide complex. Together with the effect of pH on the passivity reported above it suggests that the passive films at -0.6 and $+0.10$ v (Fig. 1 and 2) are due to basic cyanides. The peak at $+0.4$ v is most likely due to the formation of auric oxide.

Some further information on the properties of these films may be obtained by examining the change in surface roughness of the gold surface as the potential is changed. The reflectance of the gold surface as a function of potential (Fig. 4) shows that the surface becomes etched in the active region (up to -0.6 v), but

when the passive film is formed, polishing occurs. This is in agreement with the model proposed by Hoar and Mowat (12) for electrolytic polishing, and a similar change in reflectance after the formation of a film has been observed with nickel (13). These reflectance measurements were carried out in solutions of normal A.R. purity, and the gold never went completely passive as in the high-purity solutions. After the peak at -0.6 v a current of about 0.3 ma cm^{-2} flowed, and it can be seen that the surface becomes etched again at -0.35 v suggesting that there is a breakdown in the surface film with a subsequent grain boundary attack on the gold surface. This continues until the passive layer at $+0.1$ v is formed, and here the surface is continually polished up to oxygen evolution indicating that there is a smooth transition from the second passive film to auric oxide without any breakdown.

Manuscript received Dec. 24, 1963; revised manuscript received July 1, 1964.

Any discussion of this paper will appear in a Discussion Section to be published in the June 1965 JOURNAL.

REFERENCES

1. V. Kudryk and H. H. Kellogg, *J. Metals*, **6**, 541 (1954).
2. T. Mills, Ph.D. Thesis, University of Melbourne (1951).
3. K. Cathro, *Proc. Aust. Inst. Min. Met.* (1963), No. 207 in press.
4. N. Pentland, J. O'M. Bockris, and E. Sheldon, *This Journal*, **104**, 182 (1957).
5. M. Fleischmann and H. R. Thirsk, *Trans. Faraday Soc.*, **51**, 71 (1955).
6. S. El Wakkad and A. Shams El Din, *J. Chem. Soc.*, **1954**, 3098.
7. A. G. Gray, "Modern Electroplating," p. 255, John Wiley & Sons, New York (1953).
8. R. Parsons, *Trans. Faraday Soc.*, **54**, 1053 (1958).
9. A. Hickling, *ibid.*, **42**, 518 (1946).
10. K. J. Vetter and D. Berndt, *Z. Elektrochem.*, **62**, 378 (1958).
11. G. Armstrong, F. Himsworth, and J. Butler, *Proc. Roy. Soc.*, **A143**, 89 (1934).
12. T. P. Hoar and J. A. S. Mowat, *Nature*, **165**, 64 (1950).
13. D. F. A. Koch, *Austral. Corr. Eng.*, **7**, 9 (1963).

Integration of Single Sweep Oscillopolarograms

II. Comparison with Theory

J. H. Christie,¹ G. Lauer, and R. A. Osteryoung

North American Aviation Science Center, A Division of North American Aviation, Inc., Thousand Oaks, California

ABSTRACT

Relationships for the dependence of charge passed, Q , during application of a linear potential sweep to an electrode on the sweep rate, v , and the potential limits are developed. It is shown that reversible systems give linear $Q-v^{-1/2}$ plots when integration is carried out between potential limits fixed with respect to an external reference; linear $Q-v^{-1/2}$ plots are obtained for irreversible systems when integration is carried out between potential limits fixed with respect to the peak potential. These conclusions are verified experimentally.

In Part I of this work, it was shown that integration of single sweep oscillopolarograms for reversible systems was a useful method for separating charge arising from diffusing and nondiffusing sources (1). The current-potential relationship considered was (2)

$$i = n^{3/2} F^{3/2} A D^{1/2} C v^{1/2} (RT)^{-1/2} P(vt) \quad [1]$$

This equation represents the current-potential relationship observed during application of a potential

sweep to a system where both reactant and product are soluble, where mass transfer is controlled by semi-infinite linear diffusion, and the electrode reaction is "reversible." For a "reversible" system, the peak potential of the $i-E$ curve will not shift with sweep rate. $P(vt)$ is a function only of E since $E = E_i - vt$, where E_i is the initial potential and $v = dE/dt$. Integration of Eq. [1] yields

$$Q = kC/v^{1/2} \quad [2]$$

where

$$k = n^{3/2} F^{3/2} A D^{1/2} (RT)^{-1/2} \int_{E_i}^E P(E - E_i) dE \quad [3]$$

¹ Present address: Department of Chemistry and Chemical Engineering, California Institute of Technology, Pasadena, California.

The value of k depends only on the potential interval $E_i - E$ over which the integration is performed, and, since k is not dependent on v , the product of the number of coulombs passed in a given potential interval and the square root of the sweep rate is a constant for a given concentration of reactant. This conclusion was experimentally verified for Fe(III) reduction and I-oxidation (1).

The work in Part I did not specifically evaluate the integral in Eq. [3], nor did it consider the problem of integration if the electrode reaction were not reversible. The present paper considers these problems and compares the results of the theoretical work with the experimentally determined quantities.

The theory of single sweep oscillopolarography has been worked out in detail by Matsuda and Ayabe, and the equations considered below are taken from their work (3).

Theory

Reversible process.—The current is given by (3)

$$i = nFA C D_{ox}^{1/2} \left(\frac{nF}{RT} v \right)^{1/2} \Psi_r(\xi) \quad [4]$$

where

$$\Psi_r(\xi) = (1 + e^{-a}) \frac{1}{2\sqrt{\eta}} \int_0^{\sqrt{\xi+a}} \frac{d\eta}{\cosh^2 \frac{1}{2}(\xi - \eta^2)} \quad [5]$$

$$\xi = -\frac{nF}{RT} (E - E_{r_{1/2}}) \quad [6]$$

$$a = \frac{nF}{RT} (E_i - E_{r_{1/2}}) \quad [7]$$

In the above equations, η is an integration variable, $E_{r_{1/2}}$ is the reversible half-wave potential, v is the time rate of change of potential, and E_i is the initial potential. Thus, we see, $\Psi_r(\xi)$ is the function which determines the shape of the i - E curve.

Integration yields

$$Q = \int_0^t i dt = nFA C D^{1/2} \left(\frac{nFv}{RT} \right)^{1/2} \int_0^t \Psi_r(\xi) dt \quad [8]$$

Since

$$\xi = -\frac{nF}{RT} [E(t) - E_{r_{1/2}}] = \frac{nF}{RT} vt - a \quad [9]$$

$$\int_0^t \Psi_r(\xi) dt = \frac{RT}{nFv} \int_{-a}^{\xi} \Psi_r(\eta) d\eta \quad [10]$$

$$Q = nFACD^{1/2} \left(\frac{RT}{nFv} \right)^{1/2} \int_{-a}^{\xi} \Psi_r(\eta) d\eta \quad [11]$$

Since the function $\int_{-a}^{\xi} \Psi_r(\eta) d\eta$ is dependent only on potential, the Q observed between two potentials will be linearly dependent on $v^{-1/2}$ as was pointed out previously.

$\Psi_r(\xi)$ was evaluated numerically from Eq. [5] for $a = 6$, and $a = 0$; the results are shown in Fig. 1. The integral $\int_{-a}^{\xi} \Psi_r(\eta) d\eta$ was evaluated by using the trapezoidal rule with intervals of $\Delta\xi = 0.2$. The results are shown in Fig. 2.

Totally irreversible reaction.—The current is given by (3)

$$i = nFA C_{ox} D^{1/2} \left(\frac{\alpha nF}{RT} v \right)^{1/2} \Psi_{irr}(\xi^*) \quad [12]$$

where

$$\xi^* = -\frac{\alpha nF}{RT} E + \ln[k_f^0 \sqrt{D_{ox}}] - \frac{1}{2} \ln \left[\frac{\alpha nF}{RT} v \right] \quad [13]$$

k_f^0 is the formal heterogeneous rate constant at the normal hydrogen potential and E is referred to the N.H.E. Under conditions such that the sweep is initiated considerably anodic to the peak potential, i.e., the value of ξ^* at $t = 0$ is < -7 , $\Psi_{irr}(\xi^*)$ is given by (3)

$$\int_{-7}^{\xi^*} \left(\frac{\sqrt{\xi^* - \eta^*}}{\sqrt{\pi}} + e^{-\eta^*} \right) \Psi_{irr}(\eta^*) d\eta^* = \xi^* + 7 \quad [14]$$

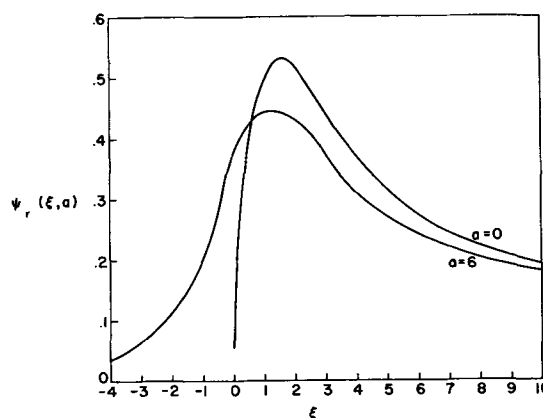


Fig. 1. $\Psi_r(\xi)$ vs. ξ (See Eq. [5])

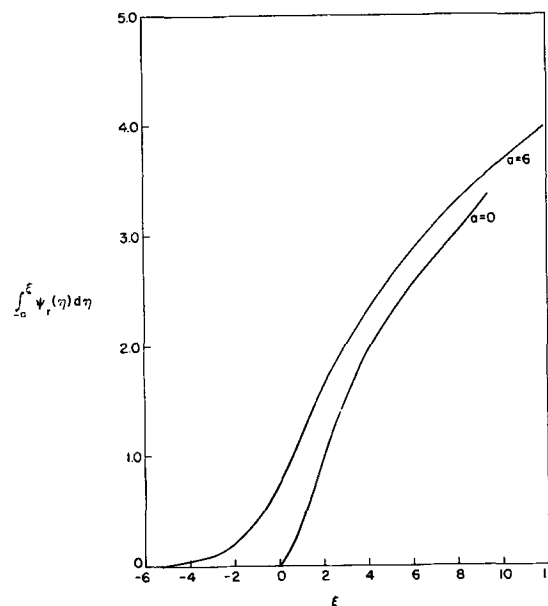


Fig. 2. $\int_{-a}^{\xi} \Psi_r(\eta) d\eta$ (See Eq. [10])

This approximation is equivalent to saying $\Psi_{irr}(\xi^*) = 0$ for $\xi^* < -7$.

$\Psi_{irr}(\xi^*)$ has a maximum value of 0.496 at $\xi^* = 0.78$. Substitution of $\xi^* = 0.78$ into Eq. [13] gives a peak potential

$$(E_p)_{irr} = \frac{RT}{\alpha nF} \left(-0.78 + \ln k_f^0 \sqrt{D_{ox}} - \left[\frac{1}{2} \ln \frac{\alpha nF}{RT} v \right] \right) \quad [15]$$

The peak current is given by

$$(i_p)_{irr} = 0.496 nFA C_{ox} D_{ox}^{1/2} \left(\frac{\alpha nF}{RT} v \right)^{1/2} \quad [16]$$

To obtain Q , integration of the $i - \xi^*$ equation is required

$$Q = \int_0^t i dt = nFAD^{1/2} C_{ox} \left(\frac{\alpha nF}{RT} v \right)^{1/2} \int_0^t \Psi_{irr}(\xi^*) dt \quad [17]$$

From Eq. [13], and since $E = E_i - vt$,

$$\frac{d\xi^*}{dt} = \left(\frac{d\xi^*}{dE} \right) \cdot \left(\frac{dE}{dt} \right) = \left(\frac{\alpha nF}{RT} \right) v \quad [18]$$

and

$$\int_0^t \Psi_{irr}(\xi^*) dt = \left(\frac{RT}{\alpha nFv} \right) \int_{-7}^{\xi^*} \Psi_{irr}(\eta^*) d\eta^* \quad [19]$$

[Since $\Psi_{irr}(\xi^*) = 0$ for $\xi^* < -7$, we need to consider the lower integration limit to be $\xi^* = -7$ regardless

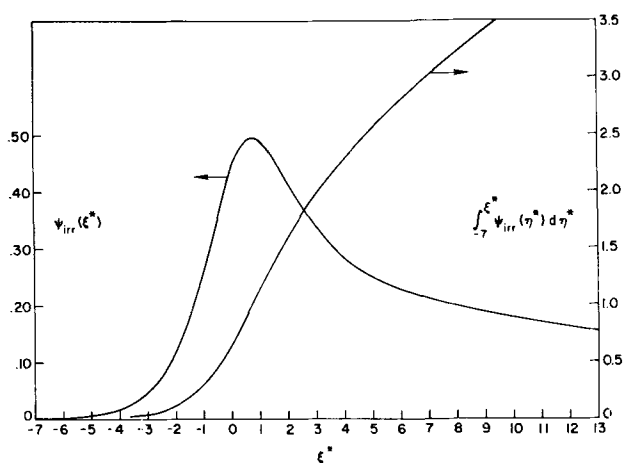


Fig. 3. $\Psi_{irr}(\xi^*)$ and $\int_{-7}^{\xi^*} \Psi_{irr}(\eta^*) d\eta^*$ vs. ξ^*

of whether this corresponds to $t = 0$ or a positive value of t .) Thus

$$Q = nFACD^{1/2} \left(\frac{RT}{\alpha nFv} \right)^{1/2} \int_{-7}^{\xi^*} \Psi_{irr}(\eta^*) d\eta^* \quad [20]$$

It is therefore obvious that Q is linearly dependent on $v^{-1/2}$ for integration to a fixed value of ξ^* , but that this value of ξ^* corresponds to different potentials, dependent on the sweep rate used. Since a Q - E curve is observed experimentally, ξ^* must be related to E .

Since, from Eq. [13],

$$d\xi^* = - \frac{\alpha nF}{RT} dE \quad [21]$$

and for $E = E_p$, $\xi = 0.78$

$$\int_{0.78}^{\xi^*} d\xi^* = - \frac{\alpha nF}{RT} \int_{E_p}^E dE \quad [22]$$

$$\xi^* = 0.78 - \frac{\alpha nF}{RT} (E - E_p) \quad [23]$$

Thus the potential limit to which integration must be carried in order for linear Q - $v^{-1/2}$ plots to be obtained is related simply to the peak potential. Since the peak potential shifts with sweep rate, linear Q - $v^{-1/2}$ plots will be obtained if integration is carried out to a potential $E_p \pm \Delta E$, when ΔE is a constant. This may be done most easily from a photograph of both Q and i as functions of E on a dual trace X-Y oscilloscope.

Figure 3 shows $\Psi_{irr}(\xi^*)$ and $\int_{-7}^{\xi^*} \Psi_{irr}(\eta^*) d\eta^*$ as functions of ξ^* . $\Psi_{irr}(\xi^*)$ was calculated by the method used by Matsuda and Ayabe using an interval of 0.2 for $\xi^* < 5$. For $\xi^* > 5$, the equation $\Psi_{irr}(\xi^*) = 1/\sqrt{\pi\xi^*}$ was used. The integral $\int_{-7}^{\xi^*} \Psi_{irr}(\eta^*) d\eta^*$ was then evaluated numerically by the trapezoidal rule, again with an interval of 0.2.

Since E_p corresponds to $\xi^* = 0.78$ and $\int_{-7}^{0.78} \Psi_{irr}(\eta^*) d\eta^* = 1.03$ (see Fig. 3)

$$Q_p = 1.03 nFAD^{1/2} C \left(\frac{RT}{\alpha nFv} \right)^{1/2} \quad [24]$$

and

$$\frac{i_p}{Q_p} = \frac{0.496}{1.03} \frac{\alpha nF}{RT} v \quad [25]$$

Thus a plot of i_p/Q_p vs. v should be linear with a slope $0.482 \alpha nF/RT$, permitting determination of α . The ratio $\{[dQ_p/dv^{-1/2}]/[di_p/dv^{1/2}]\}$ determined from the corresponding linear plots also permits determination of α .

Results and Discussion

Figure 4 shows plots of Q vs. $v^{-1/2}$ for iodide oxidation for three integration limits. The points are experimental and the lines are calculated from Eq. [11]. A value of D of 1.34×10^{-5} cm²/sec calculated from the slope of the linear i_p - $v^{1/2}$ plot was used. (The experi-

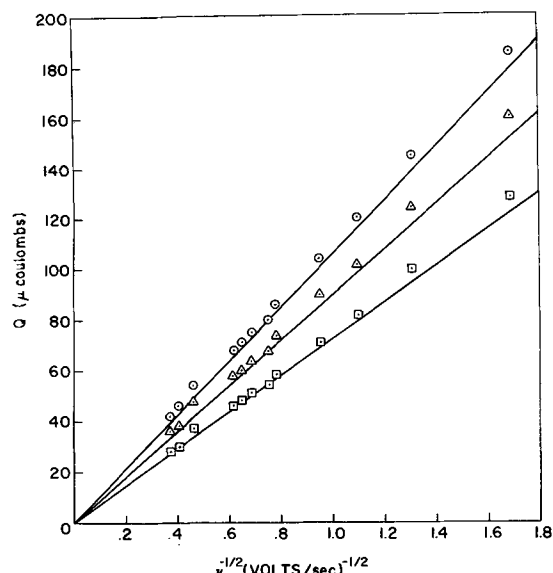


Fig. 4. Q - $v^{-1/2}$ for iodide oxidation. Points are experimental, solid line calculated using $D = 1.34 \times 10^{-5}$ cm² sec⁻¹. Potentials in figure refer to value where integral was determined. Circle with dot, $E_f = +800$ mv vs. SCE; triangle with dot, $E_f = +700$; box with dot, $E_f = +600$.

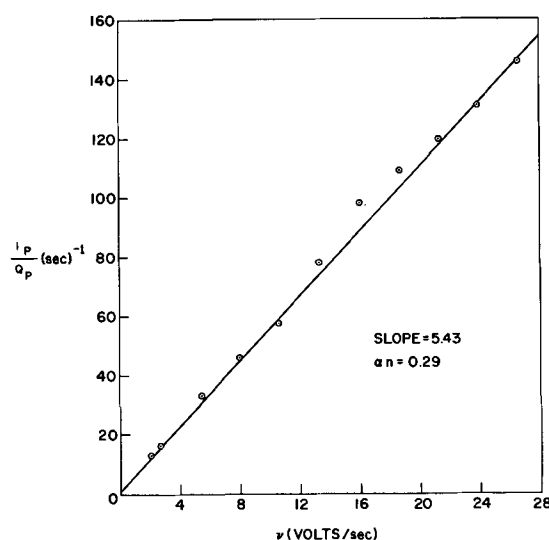


Fig. 5. i_p/Q_p vs. v (see Eq. [25]). Slope = 5.43; $\alpha n = 0.29$

mental points are fitted from Eq. [11] by a D value of 1.46×10^{-5} .)

Figure 5 shows a plot of i_p/Q_p vs. v for O₂ reduction. The value for αn calculated from the slope is 0.29, which may be compared to a value of 0.49 determined from chronopotentiometry by Delahay and Mattax (4). A value of 0.30 was calculated from the ratio of the slopes of the i_p - $v^{1/2}$ and Q_p - $v^{-1/2}$ plots, and a value of 0.28 from the slope of a plot of E_p vs. $\log v$ (see Eq. [15]).

Figure 6 shows plots of Q vs. $v^{-1/2}$ for O₂ reduction. The curves correspond to integration to potentials of E_p , E_p-100 mv, and E_p-200 mv. The peak potentials shifted approximately 150 mv for a 13-fold change in sweep rate. Since the concentration and diffusion coefficient for O₂ were not known, no detailed comparison with theory can be made. If the experimentally determined value of $\alpha n = 0.29$ is used, the potentials E_p , E_p-100 mv and E_p-200 mv correspond to values of ξ^* of 0.78, 1.91, and 3.04, respectively. The slopes of the lines in Fig. 6 should then be in the ratio 1.00:1:57:1.92 (see Eq. [20] and Fig. 3). The experimental ratios are 1.00:1.52:1.90, in very good agreement. The points

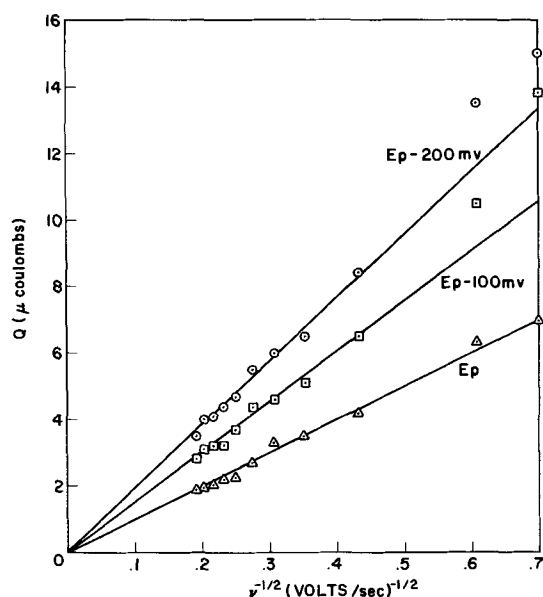


Fig. 6. Q vs. $v^{-1/2}$ for oxygen reduction. Q determined at potential fixed with respect to E_p .

corresponding to slow sweep rate, particularly those for potentials negative to the peak potential, fall off the curves, possibly due to the inclusion of coulombs from the start of the second oxygen reduction wave.

For "reversible" systems, *i.e.*, systems studied at sweep rates such that the peak potential is constant, integration of the current between potential limits fixed with respect to a reference electrode yield $Q-v^{-1/2}$ plots which are linear. For irreversible systems, linear

$Q-v^{-1/2}$ plots are obtained if integration is carried out over potential limits which are fixed with respect to the peak potential.

Presumably, studies may be carried out to determine adsorption for species undergoing an irreversible electrode reaction in a manner similar to that previously discussed (1).

Experimental

Experimental arrangements were similar to those previously reported (1). Photographs of the $i-E$ and $Q-E$ trace were obtained using a Tektronix oscilloscope. The iodide oxidation was carried out on $2 \times 10^{-3}F$ KI in $1F$ H_2SO_4 , using a Beckman platinum button electrode of area 0.2 cm^2 . E_i was $+0.014v$ vs. the S.C.E. O_2 reduction was studied in an O_2 saturated $0.5F$ acetic acid- $0.5F$ sodium acetate buffer solution at a Kemula-type hanging mercury drop electrode. E_i was $+0.12v$ vs. the S.C.E.

Acknowledgment

The authors thank Dr. E. R. Cohen for pointing out the form of $\Psi_{irr}(\xi^*)$ for $\xi^* > 5$.

Manuscript received April 27, 1964; revised manuscript received July 16, 1964.

Any discussion of this paper will appear in a Discussion Section to be published in the June 1965 JOURNAL.

REFERENCES

1. R. A. Osteryoung, G. Lauer, and F. C. Anson, *Anal. Chem.*, **34**, 1833 (1962); *This Journal*, **110**, 926 (1963).
2. P. Delahay, "New Instrumental Methods in Electrochemistry," p. 118, Interscience Publishers, Inc., New York (1954).
3. H. Matsuda and Y. Ayabe, *Z. Elektrochem.*, **59**, 494 (1955).
4. C. C. Mattax and P. Delahay, *J. Am. Chem. Soc.*, **76**, 874 (1954).

Technical Notes



Magnetic Films of Electroless Cobalt-Phosphorus with Uniaxial Anisotropy

Lloyd D. Ransom and Victor Zentner

Hughes Aircraft Company, Culver City, California

The initial object of this study was to investigate and verify the magnetic properties of electroless nickel-cobalt-phosphorus films which have been reported to exhibit low coercive forces and uniaxial anisotropy (1, 2). In the course of preliminary experimentation it was found that such films did not show any magnetic characteristics until the cobalt concentration in the solution exceeded 30% of the combined metal content.

Since the presence of nickel did not seem to influence the magnetic properties of the electroless alloy significantly, it was decided to omit it completely and restrict the investigation to the electroless cobalt-phosphorus films which in the preliminary survey exhibited interesting magnetic features.

This note, then, describes the preparation of magnetically soft cobalt-phosphorus films by chemical reduction which exhibit low coercive forces, rectangular hysteresis loops, and uniaxial anisotropy. These films

have potential applications as computer storage elements in high-speed switching devices.

The deposition of nickel, cobalt, and cobalt-nickel alloys by chemical reduction with sodium hypophosphite, also termed electroless plating by the inventors, has been described by Brenner *et al.* in 1947 (3). It has also been reported there that electroless nickel as deposited is practically nonmagnetic; this observation has been confirmed by the authors since no hysteresis loops were observed by techniques described later in this report.

Fisher and Chilton, on the other hand, have used the electroless cobalt process described by Brenner (3) to prepare high coercive force cobalt-phosphorus coatings suitable for high-density recording (4).

The phenomenon of uniaxial anisotropy in these films occurs with or without the use of an external magnetic field during deposition (1, 2). The use of the magnetic field is necessary to control the orientation

of the anisotropy field in the films with respect to the plane of the substrate material. Further studies are required to determine the actual source of anisotropy in this process.

Experimental

The solution finally adopted for the consistent production of low coercive force electroless cobalt films had the following composition in grams per liter: cobalt sulfate (heptahydrate), 24; ammonium sulfate, 40; sodium hypophosphite (monohydrate), 20; sodium citrate, 80; sodium lauryl sulfate, 0.1; ammonium hydroxide, sufficient quantity to adjust the pH to 8.5. Chemicals used in this study were of A.R. quality; distilled water was used to make up all solutions. The temperature of the plating solution was controlled at $92^{\circ}\text{C} \pm 1^{\circ}$ by a water bath.

The substrate materials used were copper, brass, and beryllium copper. After careful studies of electroless cobalt phosphorus films on these various substrates it was apparent that the nature of the base metal was not so important as the surface preparation in obtaining films with consistent and reproducible magnetic characteristics. Beryllium copper was selected and used throughout most of this study since it was the easiest to polish to a consistent final surface finish.

Initially, chemical polishing was used to finish the surface of the substrate. The roughness obtained from this type of finishing measured a rms average value of $20 \mu\text{in}$. It was essential that all pits and scratches were removed from the substrate to obtain homogeneous magnetic properties throughout the film. A super-finish surface was achieved by using standard metallographic finishing procedures (5). This technique decreased the surface roughness rms average by a factor of ten. The surface of the substrate appeared scratch free when examined at a microscope magnification of 100X.

Preparation before plating was found to be a major factor in obtaining reproducible results. The plating area, 1 cm^2 , was masked off by the Kodak Photosensitive Resist technique (6). This KPR mask was very stable in the hot, ammoniacal solution, whereas the adhesive of masking tapes initially used was attacked after a few minutes in this solution. The plating area was cleaned by (a) degreasing with trichlorethylene and methyl alcohol, respectively, (b) rinsing with distilled water, (c) using a soft material to swab lightly with a fine aluminum oxide (0.05μ) paste, (d) rinsing with distilled water, and (e) dipping into a solution of 10% HCl, followed by a thorough rinsing in distilled water. The surface of the plating area was activated by dipping the sample into a solution of palladium chloride for 10 sec. The solution contains 0.1g of palladium chloride per liter, adjusted to pH 0.9 with hydrochloric acid. The best results were obtained when the activating solution was used at 60°C . It was observed that dirt, pits, or other imperfections on the plating area resulted in an increase of gas activity in the particular area where the imperfection existed. In this case, the resultant hysteresis loops were usually distorted.

A diagram of the plating apparatus is shown in Fig. 1. Controlled uniaxial anisotropy was induced by plating in a magnetic field of approximately 450 oe. The plating vessel consisted of a three-necked flask equipped with a thermometer, a sample holder, and a reflux condenser to prevent the loss of ammonia and solution by evaporation, thereby controlling the pH and the solution composition during the plating process. The sample was supported by a Nylon clamp and submerged into 100 ml of solution per square centimeter of plating area.

Thickness and Magnetic Measurements

Film thicknesses were measured by the Tolansky method (7) of multiple beam interferometry. Figure 2 shows the interference fringes of a typical film viewed with a 100X amplification microscope. It was

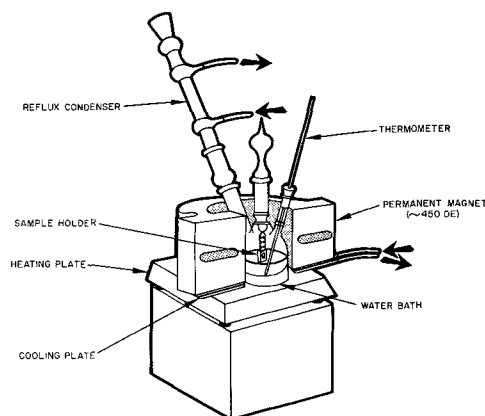


Fig. 1. Apparatus for chemical reduction of cobalt

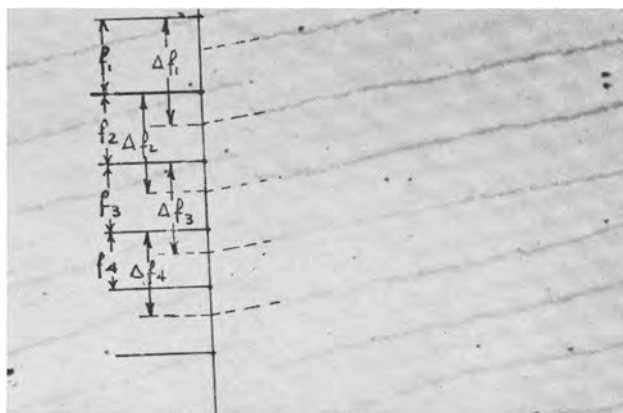


Fig. 2. Interference fringes of a typical Co-P film

essential that a smooth, flat substrate be used to obtain straight fringes and a clear image of the line shift.

The magnetic properties were measured at low frequency with a Crittenden type instrument (8) at 60 cps and checked by classical methods (9) at 2500 cps used extensively in thin film studies. The properties measured were the wall coercive force (H_c), the anisotropy field (H_k), and the remanent (B_r) and saturation (B_s) flux density. The horizontal drive field was calibrated with a Beckman Thin Film Hall Generator (Model No. 350). The anisotropy field was measured by extrapolating the transverse loop to saturation under conditions of reduced drive. The magnetic flux density was derived from a known standard of pure nickel (99.999%).

Results

The magnetic properties and thickness measurements of a series of cobalt-phosphorus films prepared from the standard solution are given in Table I. The coercive force of the films measured at two different frequencies as a function of thickness is shown in Fig. 3. The

Table I. Magnetic properties and thickness measurements

Sample No.	Thickness, Å	Coercive force, H_c , oe	Anisotropy field, H_k , oe	Saturation flux density, B_s , gauss	Square-ness $\left(\frac{B_r}{B_s}\right)$ %
55	1230	11.34	14.4	14,700	100
57	1530	12.50	18.6	11,800	100
68	2380	3.21	14.1	12,300	100
60	2730	2.38	17.5	11,100	100
53	3000	1.60	15.9	13,100	98
69	3280	1.86	17.2	11,400	95
66	3820	1.52	18.1	11,200	95
52	5050	1.10	13.6	11,600	95
62	5750	1.27	18.4	14,000	93
61	6500	1.01	15.2	14,500	93

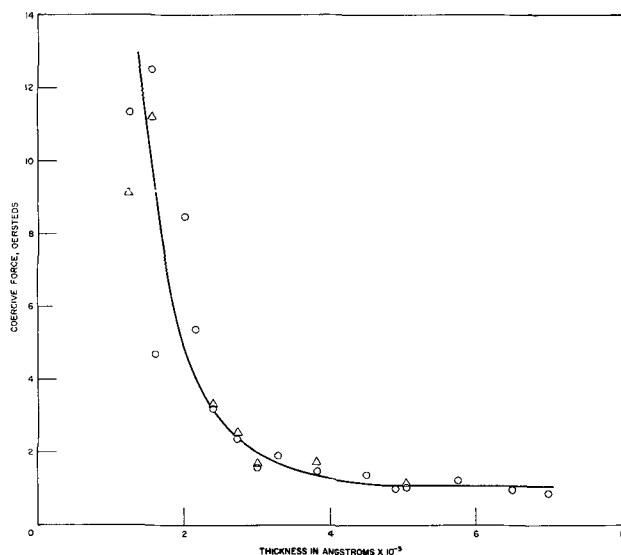


Fig. 3. Coercive force of Co-P films as a function of thickness; ○, measured at 60 cps; △, measured at 2500 cps.

film thickness is controlled by plating time at a deposition rate of approximately 300 Å/min. The minimum coercive force, averaging 1.10 oe, is between film thicknesses and 5000 and 7000Å. The anisotropy field and saturation flux density do not appear to be dependent on thickness, averaging 16.2 oe and 11,800 gauss, respectively. The squareness of the films (B_r/B_s) decreases with increasing thickness, from 100% below 3000Å to 93% between 5000 and 7000Å.

As stated previously, uniaxial anisotropy exists in these films with or without the use of an external magnetic field during chemical deposition. The easy axis of magnetization is established by aligning the magnetic lines of force parallel to the horizontal axis of the substrate. In the absence of a magnetic field, the magnetization may or may not lie parallel to this axis. In either case, the hysteresis graphs of the films are rectangular in the easy direction with closed loops in the transverse direction.

The optimum pH of the plating solution used to prepare magnetically soft films with uniaxial anisotropy is 8.5. At pH values below 8.5, the deposition rate decreases until there is practically no deposition at 7.2. The coercive force of films prepared from solutions of higher pH values (9.5-10.0) are extremely high, e.g., approximately 350 oe for a film thickness of 5000Å.

Preliminary data indicate that the films contain between 1.0 and 1.5% phosphorus, which is significantly lower than percentages reported for electroless nickel (10), cobalt (2), and nickel-cobalt (3, 4). The phosphorus content of the deposits was determined by pre-

cipitation as ammonium phosphomolybdate, dissolving the precipitate in excess of sodium hydroxide and titrating back with hydrochloric acid.

Conclusions

The results and measurements from this study show that cobalt-phosphorus films can be produced which exhibit low coercive forces, rectangular hysteresis loops, and uniaxial anisotropy.

Deviations from the standard solution and plating conditions described here usually produce films exhibiting magnetic properties different from those stated above. In most cases, when the change causes a great increase in the deposition rate, the resultant films have high coercive forces (200-500 oe), and uniaxial anisotropy is absent.

It is probable that the very low deposition rate, observed with the described bath composition and conditions of deposition, induces preferred orientation in the electroless cobalt-phosphorus film which causes the strong uniaxial anisotropy and low coercive force seen in the hysteresis curves.

Acknowledgments

The authors wish to acknowledge the assistance of the following people in the preparation of this paper: D. Menschenfreund for chemical analysis of solutions and coatings; F. Ricaud for technical support in experimental techniques; R. Jensen for generous help in measuring the magnetic properties of the films.

Manuscript received April 1, 1964; revised manuscript received July 21, 1964. This paper was presented at the Pittsburgh Meeting, April 15-18, 1963.

Any discussion of this paper will appear in a Discussion Section to be published in the June 1965 JOURNAL.

REFERENCES

1. R. J. Heritage and M. T. Walker, *J. Electronics and Control*, **1**, 543 (1959).
2. J. Bagrowski and M. Lauriente, *This Journal*, **109**, 987 (1962).
3. A. Brenner and G. Riddell, *J. Research NBS*, **39**, 385 (1947).
4. R. D. Fisher and W. H. Chilton, *This Journal*, **109**, 485 (1962).
5. Kehl, "Principles of Metallographic Laboratory Practice," McGraw-Hill Book Co., Inc., New York (1949).
6. Eastman Kodak Co., Industrial Uses of Kodak Photo Resist, No. Q-24, Rochester, New York (1959).
7. S. Tolansky, "Multiple-Beam Interferometry of Surfaces and Films," Clarendon Press, Oxford (1948).
8. E. C. Crittenden, Jr., A. A. Hudimac, and R. I. Strough, *Rev. Sci. Instr.* **22**, 872 (1951).
9. A. A. Borsei, Ph.D. Thesis, University of California, Los Angeles, August, 1962.
10. A. W. Goldenstein, W. Rostoker, R. Schossberger, and G. Gutzeit, *This Journal*, **104**, 104 (1957).

Room Temperature Chemical Polishing of Ge and GaAs

Arnold Reisman and Robert Rohr

Thomas J. Watson Research Center, International Business Machines Corporation,
Yorktown Heights, New York

A notable deficiency in surface preparation methods for Ge epitaxial substrates has been the absence of a simple low-temperature chemical polishing technique whose end result is a smooth, damage-free surface.

In studies of the effects of surface characteristics on the I.R. transmittance of Ge and Si wafers, Bogenschütz and Schütze make mention of the use of a 0.3% boiling NaOCl solution as a nonselective etch for Ge (1). The authors do not clarify the concentration parameter further and characterize the polished surface as ex-

hibiting a "cobblestone effect." Starting with mechanically polished wafers and treating them with "white etch" (5 volumes HNO₃:1 volume HF), one also obtains this "cobblestone" or "orange peel" effect so that at first impression the potential of NaOCl in providing planar surfaces does not appear promising. The etchant had also been previously employed at 40°C to form thin Ge films by floating wafers on a NaOCl solution (2). Recently, however, the authors learned that the boiling oxychloride treatment has met with some meas-

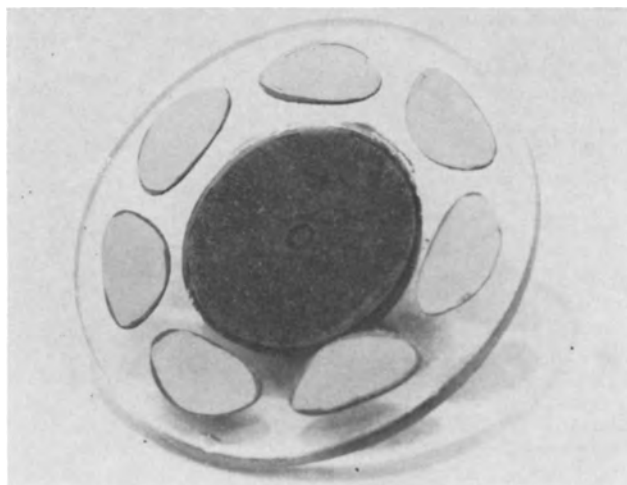


Fig. 1. Wafer plate assembly

ure of success as a chemical polish for GaAs (3), and it was decided to explore the behavior of this etchant more extensively.

The following describes the results of such a study on both Ge and GaAs lapped wafers and presents techniques for obtaining smooth damage-free surfaces on common Ge and GaAs crystallographic orientations.

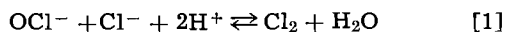
Experimental Procedure

Studies at boiling temperatures involved two approaches, one in which the sample was stationary and the solution was magnetically stirred, the second in which the sample was placed in an inclined rotating beaker.

Studies at room temperature utilized a Pellon¹ Pan W covered polishing plate rotated on a Lapmaster 12² lapping machine. Sullivan and Kolb (4) have used a rotating wheel and a different etchant in somewhat different fashion for GaAs chemical polishing. The wafers to be treated were first machine lapped to uniform thickness while affixed to a circular Pyrex or quartz disk with wax, Fig. 1. A sequence of 5 and 3 μ Al₂O₃ lapping grits were employed in this grinding operation. Following lapping, the wafers while still affixed to their holder were cleaned ultrasonically in a dilute Alconox solution³ (0.8g Alconox: 950 ml H₂O), followed by 6 ultrasonic rinses in deionized water, 3 ultrasonic rinses in transistor grade trichlorethylene, and 3 ultrasonic rinses in transistor grade methyl alcohol. The wafers were blown dry in nitrogen and the wafer-plate assembly was mounted on the Lapmaster. No pressure other than provided by the weight of the assembly was applied.

Baker and Adamson reagent grade NaOCl, 5.0% minimum assay was employed in all experiments. Analyses of a number of batches of this material for available and total chlorine content showed variations in their assays. As a consequence, dilutions were always related to a reference solution containing 62 mg available chlorine/ml of solution.

This available chlorine content is based on the following. Because of the method of preparing NaOCl, a fresh solution will contain at least one mole of NaCl for each mole of NaOCl. In highly acidified solution the complete redox relationship [1] will therefore obtain



Consequently, one mole of oxychloride anions is capable of oxidizing one mole of chloride ions to form one mole of free chlorine, hence the term available chlorine. This released chlorine is then used to liberate

I₂ from a KI solution, the I₂ being determined by conventional thiosulfate titration techniques. The total chlorine content will in general be \cong available chlorine value depending on whether the oxychloride has partially decomposed or not. In most of the solutions studied, the available and total chlorine contents were found within experimental limits to be the same. In a few instances the total chlorine content was larger than the available chlorine value indicating an excess of Cl⁻ ion was present, due either to decomposition of the oxychloride or incomplete process conversion of Cl⁻ to NaOCl. The results with both types of solutions were undistinguishable.

Results

Boiling temperature studies on Ge.—Using both of the techniques described above, NaOCl reference solution diluted 4/1, 6.5/1, 12.5/1, 27.5/1, 33/1, and 34/1 was used as a Ge polishing agent. The more dilute solutions provided surfaces of the most desirable nature, with a minimum of cobblestone character and a high polish. However, the surfaces still exhibited erratic pitting, a cobblestone appearance, and resistivity seemed to affect the final results markedly.

Room temperature studies on Ge.—At this point, the boiling temperature studies were discontinued in favor of the low temperature approach. The latter immediately provided more encouraging results, and it was found that in the dilution range 2-3H₂O/1NaOCl reference, planar, pit-free, highly polished surfaces exhibiting minimal edge rounding could be obtained. This dilution range has provided the most consistent results (removal rate \sim 0.8-1.3 mil/hr for orientations studied), and no tendency toward selective or cobblestone etching occurs even when 6 mils of Ge have been removed. Since the depth of saw and lapping damage varies markedly, depending on the equipment employed, the ability to maintain planarity through an extensive removal range is of great value. As an added feature of the polishing procedure one can, by inspection, determine when the etchant has consumed all of the damage area. Thus, as the polish becomes visible (15-30 min) scratch marks are observed. These are similar in appearance to the scratch marks observed when a mechanically polished wafer is treated briefly with white etch. As the polish becomes more enhanced, the scratch marks become more pronounced. Finally, the scratches begin to disappear and ultimately vanish. On occasion, a new level of scratch patterns develops after the first ones have been partially removed. These also disappear and ultimately a planar mirror finish wafer results. It is interesting that wafers cut 20 mils thick using an outside diameter diamond sawing technique where the blade has become old or somewhat distorted are sometimes so heavily damaged that before damage on one side can be removed the damage from the other side is encountered.⁴ In general, good O.D. cuts exhibit damage 2-3 mils deep. Inside diameter sawed wafers, on the other hand, have been found to exhibit damage rarely deeper than 1-2 mils.

In conducting the polishing operation, certain techniques and conditions other than those pertaining to the oxychloride concentration are important. For example, the oxychloride solution, when dripped onto the Pellon cloth, frequently resulted in wafers exhibiting pits and an over-all poor polish. For consistently good results we have found it advantageous to apply the solution periodically onto the cloth in bursts to wash it clean of etch products. In addition, the Pellon-liquid-wafer interfaces must not be permitted to run dry during the polishing operation or the wafers will acquire a mottled, pimply appearance. Very satisfactory results are obtained with Ge when the etchant is applied in 2-ml bursts of approximately 2-3 sec duration at intervals of 1 min, but doubtless other injection sequences would be equally satisfactory. These applications are made automatically from a solenoid-con-

⁴ Prior to using the chemical polish the wafers in question were lapped. This lapping process removed 4-5 mils.

¹ Trademark Pellon Company, Lowell, Massachusetts.

² Trademark Crane Packing Company, Chicago, Illinois.

³ Trademark Alconox, Inc., New York, N. Y.

trolled polyethylene reservoir attached to a nitrogen line.

A variety of polishing cloths were tried in addition to the Pellon Pan W material. All were either severely attacked by the etchant or did not have proper nap and pile qualities to develop equivalent polishes. The Pellon cloth which was used in the form of an adhesive backed material was specified as a "high nap" cloth. In operation, the cloth is useable for 2-hr periods after which it must be replaced. A complete Ge polishing operation based on the following procedure can be conducted without replacing the polishing pad.

Subsequent to sawing, the wafers while supported in an etching holder are etched in "white etch" twice for 30 sec in unused solutions. They are affixed to the wafer plate assembly with a hard stick wax with a softening point of ca. 50°C or greater, i.e., Apiezon Black Wax, lapped as described in the Experimental Section and then subjected to a further 30-sec white etch treatment to remove more of the damage. The first two etchings remove approximately 0.5 mil of material from each side of the wafer, and the final etching removes approximately 0.25 mil from the surface to be polished. If the white etch treatments are eliminated and the NaOCl polishing procedure is utilized directly on lapped surfaces, the final polish quality is equally good, but the total polish time required to remove damage is increased by approximately 1-1.5 hr, and two polishing pads are required in the polish operation.

To first order, the polishing procedures and resultant wafer quality appear to be independent of resistivity, type and crystallographic orientation. Thus, p- and n-type Ge ranging in resistivity from 0.01-35 ohm-cm and having $\langle 100 \rangle$, $\langle 111 \rangle$, $\langle 211 \rangle$, or $\langle 110 \rangle$ orientations behaved in a similar manner. In general, the order presented represents the relative rates of polishing in decreasing order. Using a $\langle 111 \rangle$ wafer as a reference, the $\langle 211 \rangle$ wafers polished at about the same rate, the $\langle 100 \rangle$ surfaces polished approximately 30% faster, and the $\langle 110 \rangle$ substrates approximately 50% slower. Figures 2(a)-(c) show the status of $\langle 100 \rangle$, $\langle 111 \rangle$, and $\langle 110 \rangle$ wafers polished simultaneously on one plate for 30 min. Figures 3(a) and (b) show a similar comparison between $\langle 111 \rangle$ and $\langle 211 \rangle$ substrates. Figures 4(a) and (b) show double beam interferometric comparisons between high quality mechanical polished and NaOCl polished Ge $\langle 111 \rangle$ surfaces. Figures 5(a) and (b) show interferometric results of the entire mechanically and chemically polished wafers to demonstrate the extent of rounding on chemically polished wafers after a total removal of ~3.5 mils in both the white etch and NaOCl procedures. In general, the degree of rounding depends on

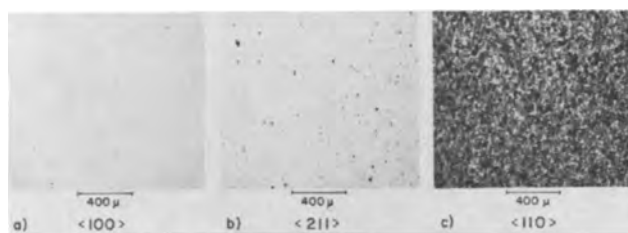


Fig. 2. Relative rates of polishing of different germanium surface orientations.

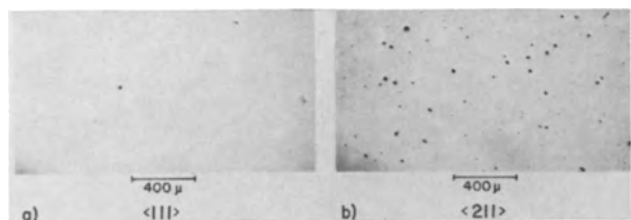


Fig. 3. Relative rates of polishing of different germanium surface orientations.

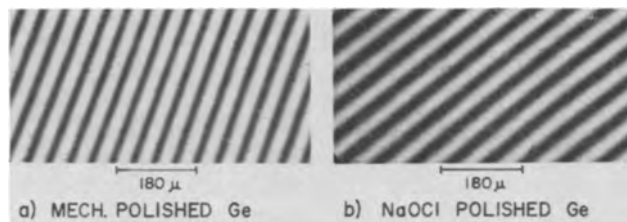


Fig. 4. Interferometric comparison between mechanically and NaOCl polished germanium $\langle 111 \rangle$ surface orientations. Fringe spacing 2730Å.

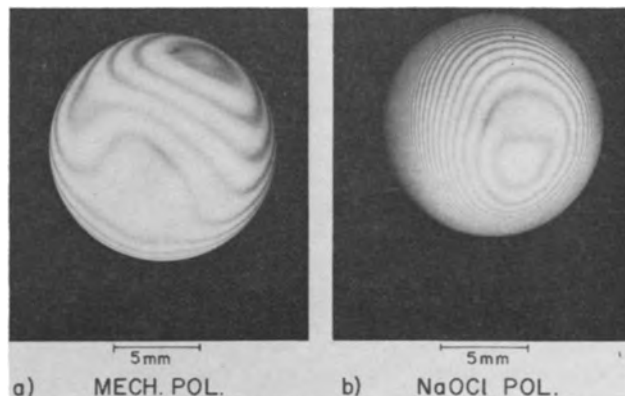


Fig. 5. Interferometric comparison between mechanically and NaOCl polished germanium $\langle 111 \rangle$ surface orientations. Fringe spacing 2730Å.

the size of the wafers chemically polished, less rounding accompanying increased diameter. Even with small wafers, however, the degree of rounding is much less than one obtains on Si using standard solution or vapor polishing techniques and after having removed similar thicknesses.

As with other polishing techniques, samples after polishing while exhibiting a clean appearance to the eye in direct lighting, evince a haze under oblique illumination (5). This is shown in Fig. 6(a) and (b) for Ge and Si. Although the nature of this haze on Ge is unknown, it being observed independently of whether the wafer is lapped with Al_2O_3 or diamond grit, it is readily removed from the Ge surfaces in a final polishing step. When the polish quality has achieved a maximum finish, a 1-1 NaOCl- H_2O solution is sprayed onto the polish pad to flood the surface, with the wheel still rotating. After 10 sec, the wheel rotation is stopped, the wafer plate assembly is removed and placed in d.i. water heated to 45°C. The resultant surfaces are free of visible haze under oblique illumination.

While rotational speeds are not critical in the polishing procedures as described above, it has been found that with a 12 in. diameter plate a range of 60-70 rpm provides the most satisfactory results. Below this value, the polishing rate becomes too slow,

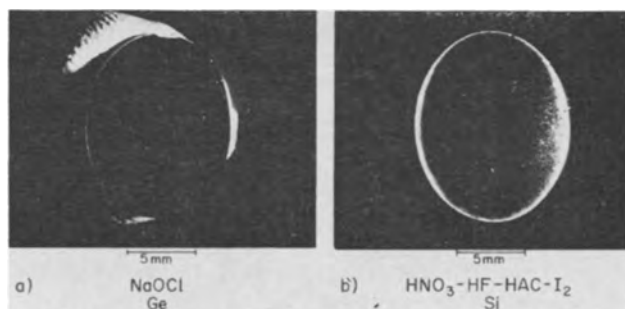


Fig. 6. Haze characteristics of chemically polished Ge and Si under dark field illumination.

while at higher speeds the etchant is centrifuged off the wheel, making it difficult to retain sufficient etchant-cloth-wafer interface thicknesses. This results in a decided deterioration of the polish quality.

Room temperature studies on GaAs.—Having obtained high quality finishes on Ge, attempts were made to apply the technique to GaAs. Using similar procedures, but employing a dilution range of 15-25/1 equally good results were obtained with the latter. The preferable etchant application rates in this dilution range are 2.5-ml bursts applied at 1-min intervals. Haze removal is accomplished by flooding the pad with d.i. water for 10 to 15 sec after the polish is complete, followed by immersion of the wafer-plate assembly into d.i. water, again at 45°C.

As with Ge the etchant solution provides equally good finishes on all common orientations including both the A and B faces of wafer surfaces oriented perpendicular to the $\langle 111 \rangle$. The range of resistivities studied was from 0.01 ohm-cm to ca. 10^8 ohm-cm without apparent differences being observed. The relative polishing rates are somewhat different than for Ge, the $\langle 111 \rangle$ B face showing a slightly faster polish rate than the other orientations. The latter are to first order indistinguishable from each other in polish rate. Removal rates with GaAs range between 1-1.4 mils/hr.

The GaAs $\langle 111 \rangle$ A surfaces sometimes show a tendency to blacken when the maximum NaOCl concentration is employed (15/1). If this occurs, a 20/1 solution will generally remove this film and be useful for the remainder of the polishing operation, although a slight decrease in polish rate will occur.

General Remarks

It has been observed that the ultimate polish quality obtained with polishing pads of different nap may vary significantly. Thus, if unnaped Pellon cloth is employed, the substrates do not polish uniformly and tend to exhibit a fine cobblestone structure. If on the other hand the unwoven cloths are highly napped so as to provide a uniform, dense pile of the order of 3-5 mils depth, the polish qualities previously discussed are readily obtained. This apparent correlation between pile density and uniformity prompted a study of the feasibility of employing nylon polishing cloths which were available in greater pile thicknesses and which would presumably offer greater chemical resistance to the etchant. While removal rates obtained with nylon cloths at a given dilution were much greater than obtainable with the Pellon material, the final finishes were never as good. At much greater dilutions than employed with Pellon (10 H₂O/1 NaOCl) the best Ge polishes were obtained with the nylon cloths, but these were still inferior to those obtained using the Pellon product. Under the best conditions for nylon it is interesting that the removal rates were approximately the same as those obtained in the preferred procedure. In order to decrease polish time it is useful to remove a few mils with a nylon backed wheel supplied with the 2/1 etchant and then achieve a final finish on a Pellon backed wheel.

The relationship between pile height and pile density can best be explained with reference to Fig. 7-10. Figure 7 shows a schematic representation of a surface to be polished by a high nap low pile cloth. When a high nap, short pile cloth is employed, the protrusions on the floating sample are subjected to maximum turbulence and consequently etchant replenishment, while depressions effectively constitute dead spaces where etchant replenishment occurs via a diffusion process (Fig. 8). Thus, protrusions etch faster until a level of smoothness is reached at which time the reaction rate of the etchant-semiconductor system becomes similar to the diffusion rate into depressions (Fig. 9). From this point on further improvement of polish quality with a given reactant cannot be achieved. In the NaOCl polishing studies it is observed that an initial polish is achieved rapidly and that improvement of the polish quality then slows down markedly.

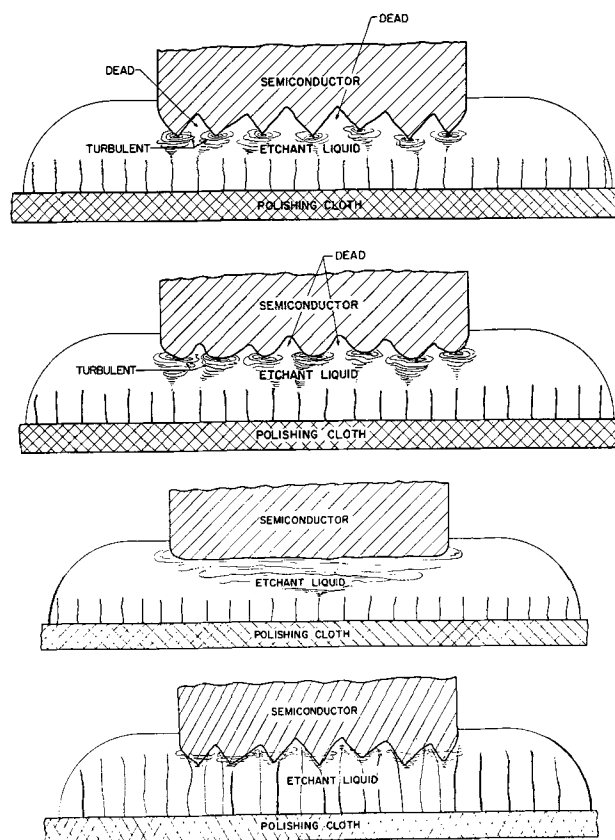


Fig. 7-10. Schematic representation of polishing conditions: Fig. 7, with a high nap, low pile cloth; Fig. 8, intermediate polishing stage with high nap, low pile cloth; Fig. 9, terminal polishing stage with high nap, low pile cloth; Fig. 10, with either a high nap, high pile or low nap, high pile cloth.

When a high nap, high pile or low nap, high pile cloth is used, the conditions depicted in Fig. 10 obtain. Here both the depressions and protrusions are subjected to turbulence, and consequently both protrusions and depressions see similar etchant replenishment rates. The net result is an effective decrease in depression dead space and less etching selectivity of protrusions. While control of the concentration parameter can be used to some extent to achieve a favorable balance between replenishment to protrusions and depressions when different cloths are employed the empirical relationships between concentration, pile height, and pile density have not been evaluated because of the unavailability of a wide enough range of cloth characteristics.

Acknowledgment

The authors wish to thank Dr. W. Reuter of the Analytical Department for his assistance in defining the standards used in these studies.

Manuscript received June 29, 1964. This work was in part supported by AFCRL AF'19(628)-2468.

Any discussion of this paper will appear in a Discussion Section to be published in the June 1965 JOURNAL.

REFERENCES

1. A. F. Bogenschütz and H. J. Schütze, *Z. angew. Phys.*, **14**, 475 (1962).
2. P. I. Holmes, "The Electrochemistry of Semiconductors," pp. 366-370, Academic Press, New York (1962).
3. G. Hellbardt, M. Michelitsch, and W. von Muenche, I.B.M., Germany, Private communication.
4. M. V. Sullivan and G. A. Kolb, *This Journal*, **110**, 585 (1963).
5. R. Lieberman, W. R. Bracht, and D. L. Klein, Abstract No. 78, Paper presented at Toronto Meeting of The Electrochemical Society, May 3-7, 1964.

Damaged Layers in Abraded Silicon Surfaces

E. N. Pugh¹ and L. E. Samuels

Defence Standards Laboratories, Australian Defence Scientific Service, Sydney, Australia

The nature of the damaged layers in abraded semiconductor surfaces is now well established. In germanium (1,2) and silicon (3) it has been shown that the damaged layers contain cracks and associated crack-like dislocation arrays of the type first reported by Allen (4); in indium antimonide (5) the damaged layers contain glide dislocations and features thought to be deformation twins in addition to the defects observed in the elemental semiconductors. However, there is little reliable data on the relative depths of damage. Various methods have been used to measure the depth of damage, but agreement between them is often poor (6,7). Consequently, to make any comparison between the depth of damage in different materials it is necessary to apply the same method to each after abrasion under the same conditions. The present authors have previously determined the depth of damage in germanium (1) and indium antimonide (5) using a metallographic taper-sectioning technique (optical microscopy). This method has now been applied to silicon. The results are presented in this note and compared with those for germanium and indium antimonide, and with the results of other workers.

Metallographic studies of the damaged layers.—Studies were carried out on {111} surfaces of silicon single crystals which were abraded unidirectionally by hand with various grades of silicon carbide particles, used both in papers and as water slurries on a glass plate. Before measuring the depth of damage it was first necessary to identify the damage features under the optical microscope. Previous work by Stickler and Booker (3), using transmission electron microscopy, indicated that the damaged layer in silicon was essentially the same as that found earlier by Pugh and Samuels (1,2) in germanium, that is, it contained cracks and crack-like dislocation arrays. The latter were identified by the way in which they change contrast when the specimens are tilted. However, Stickler and Booker were unable to identify the dislocation arrays by means of optical microscopy and hence were not able to study the morphology of the arrays and their relation to the damage cracks; the complexity and

magnification of the electron microscope images do not lend themselves to such studies.

In the present work, it was found that the dislocation arrays could be identified under the optical microscope by means of the chromic-hydrofluoric acid reagent developed by Sirtl and Adler (8) which produces pyramidal etch pits at dislocations emerging at {111} surfaces. The rate at which these pits are developed depends on the relative amounts of chromic and hydrofluoric acids; this was adjusted so that etching times of several minutes were required for the formation of detectable dislocation etch pits. A convenient method of studying the damage features consists of polishing the abraded surface with fine diamond abrasives used on a napless cloth, the operation being continued until the surface irregularities are just removed. The resulting flat surface is then polished metallographically using fine magnesium oxide abrasives. This operation removes the damage introduced by the diamond abrasives so that the final surface contains only damage produced by the abrasion treatment under investigation. Examination of such surfaces with high-aperture objectives revealed arrays of fine cracks. These were made readily visible by short etching treatments (10–20 sec) with the chromic-hydrofluoric acid reagent (Fig. 1a). The morphology of the cracks is the same as that of damage in germanium (1,2); they are generally curved, but tend to lie along the traces of {111} cleavage planes. Etching for progressively longer times caused the cracks to be widened into fissures and at the same time produced additional markings (cf. Fig. 1a and 1b). These markings, which at higher magnifications can be seen to consist of shallow grooves (Fig. 2), have the same morphology as the damage cracks and in many cases occur along the extension of cracks. On the other hand, their etching characteristics are consistent with their being arrays of closely spaced dislocations; for example, compare the width of the etch groove in Fig. 2 with the size of the etch pits at grown-in dislocations (marked D). The grooves thus have precisely the same characteristics as those which have been shown by etching techniques to correspond to Allen-type dislocation arrays in germanium (2,9). There can be little doubt that they correspond to the dislocation arrays observed by Stickler and Booker (3), using electron microscopy.

The grooves produced at the dislocation arrays by the chromic-hydrofluoric acid reagent can be readily distinguished from the fissures formed at cracks. The reason that Stickler and Booker (3) were unable to

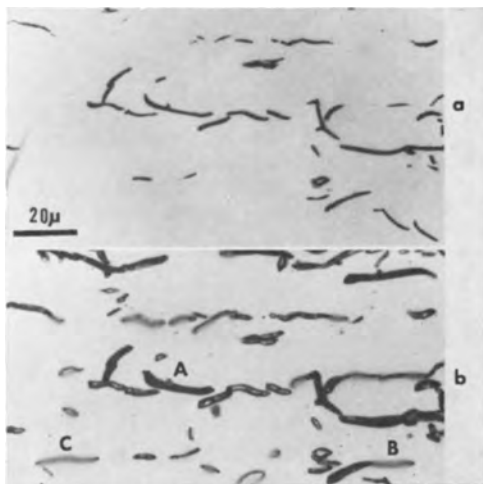


Fig. 1. The surface was originally abraded with 220 grade paper (abrasion direction horizontal) and then the surface irregularities were removed by polishing: (a) etched for 10 sec to show cracks; (b) etched 5 min to reveal dislocation arrays.

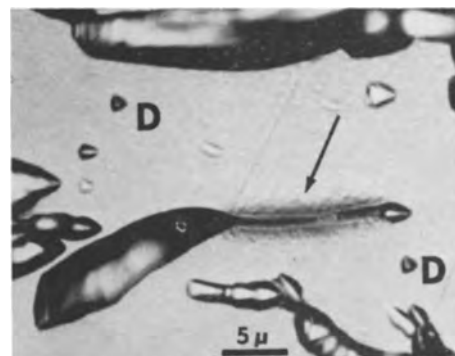


Fig. 2. Region B of Fig. 1b showing a typical groove at a dislocation array (arrowed).

¹ Present address: Research Institute for Advanced Studies (Martin Company), Baltimore, Maryland.

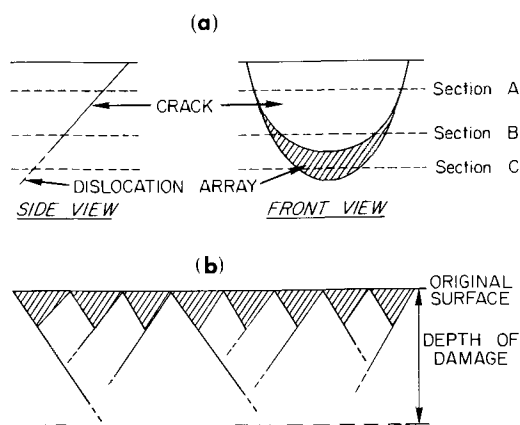


Fig. 3. Schematic representation of the damage in elemental semiconductors showing (a) an individual crack and its associated dislocation array and (b) a section of the damaged layer illustrating the irregular nature of the damage. Cracks and arrays are represented by straight lines, but it must be remembered that they are in fact curved.

distinguish between these features appears to be that they used the conventional CP4 etching reagent which was found in the present studies to be unsatisfactory for this purpose.

The relationship between the arrays and the parent cracks was determined by studying selected areas during progressive polishing treatments. These studies indicated that the cracks originated at the surface and that, as in germanium (2) and indium antimonide (5), the dislocation arrays occur as extensions to the cracks. A damage crack and its associated array is illustrated schematically in Fig. 3a. Sections parallel to the original surface at various depths may thus reveal either the trace of the crack, the crack associated with the dislocation array, or the dislocation array alone, corresponding to levels A, B, or C, respectively. It can be seen in the section shown in Fig. 1b that damage traces exist which correspond to each of stages A, B, and C (typical examples are labelled). This is due to extreme irregularity of the individual damage cracks which is also a characteristic of the damaged layers in germanium (1) and indium antimonide (5). The irregular nature of the damaged layer is illustrated in the sketch in Fig. 3b.

Depth of damaged layers.—The depth of the damaged layers produced by various abrasion processes was determined by means of a taper-sectioning technique described previously (1). In this method, the abraded surface is sectioned at a nominal angle of $5^{\circ}43'$, providing a geometrical magnification of 10:1 perpendicular to the section line. The depth of damage is taken from the outermost crests of the surface irregularities to the extremities of the deepest damage features (see Fig. 3b). Thus the values represent the maximum local depths of damage. The reproducibility of the method is about 5%. Results are given in Table I, together with those for germanium (1) and indium antimonide (5) determined by the same method and using identical abrasion conditions. It can be seen that the relative depths are $\text{InSb} > \text{Si} > \text{Ge}$ except for the coarsest grade

Table I. Depth of damage produced by abrasion of semiconductor surfaces with silicon carbide particles

Abrasion process	Present studies	Depth of damage, μ			
		Silicon			
		Faust (10)	Stickler & Booker (3)	Ge (1)	InSb (5)
220 grade papers	30	—	23	22	59
400 grade papers	15	—	15	10	18
600 grade papers	10	—	11	6½	—
220 grade slurry	65	10-14	—	85	78½
400 grade slurry	32	5-6	—	22	35½
600 grade slurry	15	3-4	—	11½	—

slurry where the value for germanium is unexpectedly large. This value has been confirmed by a variety of methods in a previous paper (7) so that this anomaly appears to be real.

The present results are contrary to the conclusion of Buck (6) that the depth of damage in silicon is one-fourth to one-half that in germanium. This view was based largely on data by Faust (10), determined by the etching-rate method. These results were obtained from specimens abraded with silicon carbide particles used as water slurries on a glass plate so that they can be compared with the present values. However, it can be seen in Table I that the etching-rate results, taken from the paper by Buck (6), are considerably lower than those obtained from the taper-sectioning method. A possible explanation for this discrepancy was suggested in the present studies. It was found that the surface layers in silicon were severely shattered, considerably more so than for germanium. The severely shattered layer constitutes about one-fourth or one-fifth of the total damaged layer. It is conceivable that the etching-rate method detected only this severely shattered layer.

The depth of damage in silicon has been investigated by several other workers. Buck and McKim (11) using the PME method, found that the depth of damage in surfaces abraded with 600 grade silicon carbide slurries was $8-10\mu$. This value is significantly lower than that obtained in the present work (*viz.*, 15μ), but this discrepancy is consistent with previous studies of germanium (1, 7). This difference in sensitivity has been discussed previously (7, 12). Stickler and Booker (3) have measured the depth of damage in surfaces abraded with silicon carbide papers by means of a progressive-sectioning technique (optical microscopy). It can be seen from Table I that excellent agreement exists between these values and the present results, particularly for the finer grades of abrasives. However this agreement may be somewhat fortuitous for several reasons. First, while Stickler and Booker also measured to the deepest detectable damage features² the datum for measurement was the original abraded surface as determined from the focussing position of the microscope. The taper-sectioning method would consequently be expected to give higher results because it measures the damage from the peaks of the surface irregularities whereas using the focussing method some average position between their peaks and roots would be taken. This difference would be expected to be appreciable; for example, in germanium the depth of the surface irregularities was about one-fourth that of the total damage (1). Second, the abrasion conditions were not the same. Specimens were abraded unidirectionally in both cases, but in the present work abrasion was carried out manually while in that of Stickler and Booker abrasion was carried out on a rotating wheel with a linear speed of about 350 cm/sec, at a pressure of 200 g/cm².

It is concluded that the relative depths of damage in abraded {111} semiconductor surfaces are in general $\text{InSb} > \text{Si} > \text{Ge}$. Analysis of this relationship clearly requires further understanding of both the mechanism of fracture in these materials and the mechanism of abrasion.

Acknowledgments

This paper is published by permission of the Chief Scientist, Department of Supply, Australia.

Manuscript received April 1, 1963; revised manuscript received July 27, 1964.

Any discussion of this paper will appear in a Discussion Section to be published in the June 1965 JOURNAL.

REFERENCES

- E. N. Pugh and L. E. Samuels, *This Journal*, **108**, 1043 (1961).
- E. N. Pugh and L. E. Samuels, *ibid.*, **109**, 1197 (1962).

² Note that while Stickler and Booker were not able to distinguish between cracks and dislocation arrays using CP4, it is likely that they did in fact detect the last traces of the damage.

3. R. Stickler and G. R. Booker, *Phil. Mag.*, **8**, 859 (1963).
4. J. W. Allen, *ibid.*, **2**, 1475 (1957).
5. E. N. Pugh and L. E. Samuels, *J. Appl. Phys.*, **35**, 1966 (1964).
6. T. M. Buck, "The Surface Chemistry of Metals and Semiconductors," H. C. Gatos, Editor, p. 107, John Wiley & Sons, Inc., New York (1960).
7. E. N. Pugh and L. E. Samuels, *This Journal*, **109**, 409 (1962).
8. E. Sirtl and A. Adler, *Z. Metallkunde*, **52**, 529 (1961).
9. E. N. Pugh and L. E. Samuels, *Phil. Mag.*, **8**, 301 (1963).
10. J. W. Faust, Jr., Am. Soc. Testing Materials, Symposium on Cleaning of Electronic Device Components and Materials, Special Tech. Publ. 246.
11. T. M. Buck and F. S. McKim, Reported by Buck, ref. (6).
12. T. M. Buck, *This Journal*, **109**, 1220 (1962).

The Effect of Oxygen and Nitrogen on the Hafnium α - β Transition

N. H. Krikorian and T. C. Wallace

Los Alamos Scientific Laboratory, University of California, Los Alamos, New Mexico

A number of divergent values for the α to β transition (determined by a variety of techniques) were reported (1-5) prior to 1954. Deardorff and Kato (6) published a $1750^\circ \pm 20^\circ\text{C}$ value in 1959. They gave a fairly complete history of previous work and explained some of the earlier discrepancies. Much of the same history, though more complete, was given by Roland in 1960 in the book edited by Thomas and Hayes (7). This book lists a slightly earlier ($1760^\circ \pm 35^\circ\text{C}$) value of Deardorff and Kato which was given limited publication in USBM-U-426 (April 1958). The value was later revised to $1750^\circ \pm 20^\circ\text{C}$ (6). Work done on the Th-Hf system at essentially the same time by Gibson, Loomis, and Carlson (8) gave a 1735°C value, so the 1750° and 1735°C values were in fair agreement. However, a preference for a 1950°C value has been expressed by Taylor, Kagle, and Doyle (12) on the basis of alloy investigations. Further acceptance of the lower value came when Deardorff and Kato disputed (9) an $1875^\circ \pm 20^\circ\text{C}$ value of Giessen, Rump, and Grant (10), and these latter authors revised their value to $1755^\circ \pm 20^\circ\text{C}$ (11). This discussion article (9, 11) gave good circumstantial evidence that oxygen and nitrogen contamination would cause the transformation temperature to raise, but gave no quantitative analytical evidence as to the effect of these impurities.

Recent experimental evidence by Rudy and Stecher (13) on the Hf-O system, Wallace on the Hf-N (14), and Avarbe *et al.* (15) on the Hf-C system confirmed the realization of earlier investigators (3, 6, 9) regarding the possible stabilization of the α -hafnium by impurities such as nitrogen and oxygen.

In the present work the effects of oxygen and nitrogen impurities in addition to zirconium impurity on the hafnium metal transition temperature were investigated using a new, highly sensitive, and very versatile high temperature thermal analysis apparatus described in detail elsewhere by Rupert (16, 17).

The induction heating technique using an eddy current concentrator has also been described by Rupert (17). Briefly, the thermal analysis system is operated by focusing the light beam from a black body hole in the hafnium cylinder on a sensing diode, and cooling through the transition temperature. In detecting and measuring the temperature of the α - β transition of hafnium the oscilloscope traces show both the thermal analysis curve and the negative of the first derivative of the thermal analysis curve. Calibration traces for temperature are made by photographing a horizontal sweep across the oscilloscope at temperature intervals observed through the pyrometer.

Table I gives the analytical data for the starting materials listing possible pertinent contaminants. Table II gives the same data after completing the α - β transformation measurements, as well as the measured and calculated transition temperatures. The low zirconium (<200 ppm) content hafnium powder was obtained from the U. S. Bureau of Mines, the hafnium powder (1% Zr) and the hafnium crystal bar (3.1%) from the Carborundum Company. The high-purity hafnium crystal bar (0.02% Zr) was available through the courtesy of Haruo Kato of the U. S. Bureau of Mines.

Measurements of the transition temperatures were made on pressed cylinders of hafnium powder or ma-

Table I. Analyses of starting material

Hafnium identification	Hf, %	Zr, %	O, ppm	N, ppm	C, ppm	Major impurities, spectrographic*
Powder (<200 ppm Zr)	98.9 \pm 0.6	<0.02	1900	240	30	Fe, 0.3%, Cr, 0.1%, Mn, Mg, Al, 0.01%
Powder (1% Zr)	98.4 \pm 0.6	1.36 \pm 0.02	6700	360	170	Fe, 0.05%, Al, Mg, Si, 0.02%
Crystal bar (3% Zr)	96.1 \pm 0.6	3.31 \pm 0.05	200	230	30	Fe, Al, Ti, 0.01%
Crystal bar (0.02% Zr)	100 \pm 0.3	190 ppm \pm 30	700	<20	30	Fe, 0.02%

* All other detected impurities <100 ppm.

Table II. Analyses after determinations

Sample No.	Hf, %	Zr, %	O, ppm	N, ppm	C, ppm	Major impurities, spectrographic*	Observed transformation, $^\circ\text{C}$	Calculated transformation, $^\circ\text{C}$
1	98.1 \pm 0.6	1.40 \pm 0.02	4500	420	35	Al, Fe, 0.01%	1820 \pm 20	1824
2	98.0 \pm 0.6	1.25 \pm 0.02	3000	420	25	Al, Fe, 0.01%	1810 \pm 20	1803
3	95.6 \pm 0.6	3.45 \pm 0.05	200	580	20	Al, Fe, 0.01%	1730 \pm 20	1726
4	96.0 \pm 0.6	3.29 \pm 0.05	200	650	35	Al, 0.01%	1730 \pm 20	1731
5	100.1 \pm 0.3	0.02	800	70	30	Al, Fe, 0.01%	1755 \pm 20	1756

* All other detected impurities <100 ppm.

chined cylinders in the case of the hafnium crystal bars. In each case holes 0.060 in. diameter and 0.50 in. deep were drilled for black body conditions in measuring the temperature. The cylinders were supported in the concentrator field by three vertical tantalum rod supports (0.060 in. diameter). The interaction of Ta with Hf was negligible.

The melting point measurement on the sample of hafnium powder (<200 ppm Zr) was made by a stepwise increase in temperature from just below the melting point. On the appearance of liquid in the sight hole, a marked shimmering and broadening of the oscilloscope trace could be observed.

The spectral emissivity at 0.65μ was determined in the range 1750°-2300°K on the machined crystal bars of hafnium (3.1% Zr) by comparison of the surface temperature and the black body hole temperature using the equation $1/T - 1/T_\beta = \ln \epsilon_\lambda/C_2$ where $\lambda = 0.65$ and $C_2 = 14350$.

Discussion

The observed transition temperatures listed in Table II for the various hafnium samples show a markedly higher value for those with higher oxygen and nitrogen content. Samples 1 and 2 were prepared from powdered (1% Zr) hafnium. The initial transition temperature (determined within 5 min of the start of the heating cycle) of both of these samples was approximately 2100°C. The initial oxygen and nitrogen contents were 6.83 and 0.42 a/o, respectively. These samples showed a dramatic lowering of the transition temperature (by 290°C) from 2100°C to a value of 1820° and 1810°C, respectively, after being annealed at 1900°C for approximately 40 hr at 2×10^{-6} Torr. In light of the work of Rudy and Stecher (13), we suspect that the initial value of 2100°C was that of the eutectic melting isotherm between melt (8 a/o O) \rightarrow β -Hf solid solution (5 a/o O) + α -Hf-solid solution (11 a/o O). Indeed oxygen was driven from the samples and the nitrogen content increased slightly as can be seen by comparing the analytical data in Tables I and II. After 30 hr of annealing the transition temperature was essentially constant, suggesting that the partial pressure of oxygen and nitrogen in the Hf solid solution was equal to the partial pressure of oxygen and nitrogen in the vacuum environment.

Thermal analyses of samples 3 and 4 were performed on crystal bar hafnium (3% Zr). The transition temperature of sample 3 was determined within 10 min of the initial heating whereas sample 4 was annealed for 5 hr, with no apparent change in transition temperature. Indeed the oxygen determinations show no change between the starting material and after the determinations. However, the nitrogen content appears to have increased slightly.

The transition temperature of sample 5, crystal bar hafnium (0.02% Zr) was determined within 5 min of the initial heating. Chemical analysis shows that the oxygen content remained the same but that the nitrogen increased.

These samples afford an opportunity to determine the effect of zirconium, oxygen, and nitrogen on the transition temperature. At the low concentrations of zirconium (0.04-6.53 a/o), oxygen (0.21-4.72 a/o), and nitrogen (0.09-0.80 a/o) studied, the available data could be correlated by an equation of the form

$$T_{\text{obs}} = T_{\text{pure}} + a_{\text{Zr}}x_{\text{Zr}} + a_{\text{O}}x_{\text{O}} + a_{\text{N}}x_{\text{N}} \quad [1]$$

where T_{obs} is the observed transition temperature; T_{pure} is the transition temperature of pure hafnium; a_{Zr} , a_{O} , and a_{N} are the transition temperature variation coefficients of zirconium, oxygen, and nitrogen, respectively. x_{Zr} , x_{O} , and x_{N} are the atom per cents of zirconium, oxygen, and nitrogen, respectively. Using the data from Table II, Eq. [1] was solved for T_{pure} , a_{Zr} , a_{O} , and a_{N} by the method of least squares (18) using the Los Alamos MANIAC II computer with the results: $T_{\text{pure}} = 1735^\circ \pm 14^\circ\text{C}$, $a_{\text{Zr}} = -11.2 \pm 11.1^\circ$ per a/o Zr, $a_{\text{O}} = 16.1 \pm 5.1^\circ\text{C}$ per a/o O, and $a_{\text{N}} = 83.6 \pm 101^\circ\text{C}$ per a/o N. The weighted variance, which is defined as

$\Sigma w\delta/M - N$, was 119. M is the number of experimental points (five), N is the number of parameters to be solved (four), δ is the difference between the observed transformation temperature and the calculated transformation temperature, and w is the weighting factor (in this case $w = 1$).

Unfortunately, the effect of carbon is indeterminate since it is present at the same concentration level in all the samples. However, the small amount present should not lower the transformation temperature of pure hafnium by more than 2°C.

The value of $a_{\text{Zr}} = -11.2^\circ\text{C}$ per a/o Zr may be compared with that determined from the work of Deardorff and Kato (6) (-7.2°C per a/o Zr). The difference can be attributed to that fact that the current work was determined from cooling curves and the other from heating curves. Since it is generally observed that there is a hysteresis associated with transition temperatures with an increase in the impurity components, one should expect different coefficients depending on whether the transition temperatures were determined by heating or cooling curve analysis.

By correcting the value of the transition temperature of Deardorff and Kato (6) for the 200 ppm of O_2 that was present, one obtains 1746°C. Kaufman and Cohen (19) note that the thermodynamic martensitic transformation temperature of a material is generally very nearly the mean of the transformation temperatures determined from heating and cooling curves. Thus using our value of 1735°C (cooling) and Deardorff and Kato's value of 1746°C (heating) the α - β thermodynamic transition temperature of hafnium is $1740^\circ \pm 20^\circ\text{C}$.

The great sensitivity of the transformation temperature to oxygen and nitrogen content emphasizes the requirement for thorough analytical chemical characterization of material. In view of the high reactivity of oxygen and nitrogen with hafnium and their effect on the transition temperature it can be assumed that the transition temperatures reported by previous workers (after correction for the Zr content) were high.

The melting point of $2230^\circ \pm 20^\circ\text{C}$ is in excellent agreement with the findings of deBoer and Fast ($2230^\circ \pm 50^\circ\text{C}$) (20), Deardorff and Hayes ($2222^\circ \pm 20^\circ\text{C}$) (21), and the work at Iowa State College ($2235^\circ \pm 50^\circ\text{C}$) (22), but somewhat higher than the value of Taylor, Kagle, and Doyle (2190°C) (12), and considerably higher than the value reported by Grigorovitch (1943°C) (23), Adenstadt (1975°C) (24), and Litton (2130°C) (25).

The spectral emissivity was found to be $\epsilon_{0.65\mu} = 0.40 \pm 0.02$ and is in good agreement with the value used by Deardorff and Kato (6).

Conclusion

The results of the hafnium α - β investigation indicate that even small amounts of oxygen and nitrogen stabilize the α -phase, and that the transition is also dependent on the zirconium content. On the basis of the current interpretation of the best available data, $1740^\circ \pm 20^\circ\text{C}$ is the most acceptable value for the α - β transition of pure hafnium.

Manuscript received Feb. 5, 1964; revised manuscript received July 12, 1964. This paper was presented at the Toronto Meeting, May 3-7, 1964. Work was performed under the auspices of the United States Atomic Energy Commission.

Any discussion of this paper will appear in a Discussion Section to be published in the June 1965 JOURNAL.

REFERENCES

1. C. Zwicker, *Physica*, **6**, 361 (1926).
2. P. Duwez, *J. Appl. Phys.*, **22**, 1174 (1951).
3. J. D. Fast, *ibid.*, **23**, 350 (1952).
4. R. K. McGeary, Westinghouse Atomic Power Div. Progress Report, WAPD-RM-92, (1952).
5. R. B. Russell, *J. Appl. Phys.*, **24**, 232 (1953).
6. D. K. Deardorff and H. Kato, *Trans. AIME*, **215**, 876 (1959).

7. D. E. Thomas and E. T. Hayes, Editors, "The Metallurgy of Hafnium," USAEC, p. 214 (1960).
8. E. D. Gibson, B. A. Loomis, and O. N. Carlson, *Trans. Am. Soc. Metals*, **50**, 348 (1958).
9. D. K. Deardorff and H. Kato, *Trans. AIME*, **227**, 264 (1963).
10. B. C. Giessen, I. Rump, and N. J. Grant, *ibid.*, **224**, 60 (1962).
11. B. C. Giessen, I. Rump, and N. J. Grant, *ibid.*, **227**, 264 (1963).
12. A. Taylor, B. J. Kagle, and N. J. Doyle, *J. Less-Common Metals*, **5**, 26 (1963).
13. E. Rudy and P. Stecher, *ibid.*, **5**, 78 (1963).
14. T. C. Wallace, Unpublished work.
15. R. G. Avarbe, A. I. Avgustinik, Yu. N. Vil'k, Yu. A. Omelchenko, and S. S. Ordanian, *Russian J. Appl. Chem.*, **35**, 1976 (1962).
16. G. N. Rupert, "Advanced Application of Derivative and Differential Techniques to High Temperature Thermal Analysis," to be published.
17. G. N. Rupert, *Rev. Sci. Instr.*, **34**, 1183 (1963).
18. R. H. Moore and R. K. Zeigler, Los Alamos Scientific Lab., Report LA-2367 (Oct. 1959).
19. L. Kaufman and M. Cohen, "Thermodynamics and Kinetics of Martensitic Transformations," *Progress in Metal Physics*, **7**, 167, Pergamon Press, New York (1958).
20. J. H. deBoer and J. D. Fast, *Z. anorg. u. allgem. Chem.*, **187**, 193 (1930).
21. D. K. Deardorff and E. T. Hayes, *Trans. AIME*, **206**, 509 (1956).
22. Quarterly Summary Research Report in Metallurgy for April, May, June, ISC-531 Iowa State College (1954).
23. V. K. Grigorovitch, *Izv. Akad. Nauk. SSSR, Otd. Tekhn. Nauk. Met. i Toplivo*, **6**, 93 (1960).
24. H. K. Adenstadt, *Trans. Am. Soc. Metals*, **44**, 949 (1952).
25. F. B. Litton, *This Journal*, **98**, 488 (1951).

Brief Communication



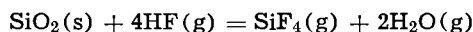
A Novel Technique for the Deposition of Silica Films

T. L. Chu, J. R. Gavaler, G. A. Gruber, and Y. C. Kao

Research Laboratories, Westinghouse Electric Corporation, Pittsburgh, Pennsylvania

Silica films are used frequently in the fabrication of semiconductor devices as masks against the diffusion of certain impurities into germanium, silicon, gallium arsenide, etc., and for surface passivation purposes. Doped silica films are useful as diffusion sources and could produce more planar and uniform junctions than the conventional techniques; the use of these films is particularly advantageous when the semiconductor is unstable at the high temperature required for diffusion. This communication describes a chemical transport technique by which pure or doped silica films can be deposited on various substrates at relatively low temperatures, 400°-600°C. The use of low temperature is advantageous for most applications.

The chemical transport technique has been widely used for material preparation and crystal growth during the past few years. When a solid substance reacts reversibly with a gaseous reagent to form volatile products and the equilibrium constant of this reaction is temperature-dependent, this substance can be transported by a temperature gradient. Silica reacts reversibly with hydrogen fluoride at room temperature and above, presumably according to the equation



The equilibrium constants of this reaction in the temperature range 500°-800°K, calculated from the thermochemical data of the species involved (1), are as follows

Temp., °K	Equilibrium const.
500	1.8×10^7
600	1.8×10^5
700	6.5×10^3
800	5.6×10^2

Thus, the equilibrium of the above reaction is shifted toward the formation of silica as the temperature is increased. In a closed system where the equilibrium conditions are approached, hydrogen fluoride is able to transport silica from a low-temperature region to regions at high temperatures. Dense silica films up to

tens of microns in thickness have been deposited on α -quartz, silicon, germanium, and gallium arsenide substrates in this manner. These depositions were carried out in sealed, evacuated fused silica reaction tubes containing the substrates and hydrofluoric acid (or anhydrous hydrogen fluoride); the reaction tubes served as the silica source. These tubes were then heated in a furnace containing two different temperature zones. The substrates were maintained at 400°-600°C while the lower temperature regions of the tube was kept at 100°-300°C. Depending on the substrate temperature, temperature gradient of the reaction tube, composition and pressure of the transport agent, diameter and length of the reaction tube, etc., the deposition rate of silica films could be varied between 0.01-1 μ /hr.

It should be pointed out that under isothermal conditions, silicon is not inert toward hydrofluoric acid at high temperatures. For example, when single crystal silicon substrates of {111} orientations were heated at 550°C in a fused silica reaction tube containing hydrogen fluoride and water at 6.5 and 7.5 atm, respectively, the substrates were found to be oxidized at a rate of higher than 15 μ /hr. This rate is many times higher than the oxidation rate of silicon in the absence of hydrogen fluoride. Thus, hydrogen fluoride catalyzes the oxidation of silicon by steam. This catalytic action is presumably similar to the action of high pressure used in the steam oxidation of silicon. In the steam oxidation of silicon (2, 3), the rate-determining step has been shown to occur at the silica-silicon interface, and the diffusion of interstitial water is responsible for the growth of silica films. Since the diffusion constant of water in silica is large, the use of high-pressure steam increases the concentration of interstitial water thus increasing the rate of oxidation. Hydrogen fluoride is a small molecule and fits interstitially into silica. It also has approximately 50% ionic character. Thus, the interactions between hydrogen fluoride and silica, and between hydrogen fluoride and water could increase the concentration of water in silica and accelerate the oxidation process. In the presence of a properly chosen temperature gradient, however, the transport of silica

to silicon was made to predominate over the oxidation of silicon.

Silica films transported onto α -quartz, germanium, silicon, and gallium arsenide substrates are transparent and are adherent to the substrates. They exhibited no structural features when examined with an optical microscope and were found to be amorphous by x-ray and transmission electron diffraction techniques. The density of the transported film was determined to be 2.23 ± 0.05 g/cc by the floating equilibrium technique. The silica films transported onto silicon substrates were studied in more detail. The chlorine etch technique (4) indicated that a 1μ film was essentially free of pinholes. When a transported film on a 30 ohm-cm n-type silicon substrate was heated at 1200°C for 16 hr, the resistivity of the substrate remained the same within the errors of the measurement, indicating that the electrically active impurities in the film are either negligible or diffuse very slowly. The transported films were found to be similar to the thermally grown silica films in their abilities to mask against the diffusion of phosphorus into silicon at 1100°C .

The commonly used dopants for silicon, such as boron, gallium, phosphorus, arsenic, antimony, etc.,

were incorporated into the silica films during the transport process. These doped films were used successfully as diffusion sources. The highest surface concentrations of these impurities in silicon obtained thus far were mostly of the order of 10^{19} cm $^{-3}$. The surface concentration and the junction depth could be controlled over a wide range by varying the doping level of the silica film or the temperature and duration of the heat treatment required for the diffusion process.

Manuscript received July 27, 1964. This work was supported in part by the United States Electronics Research and Development Laboratory, Fort Monmouth, New Jersey, under Contract No. DA 36-039 SC-90835.

Any discussion of this paper will appear in a Discussion Section to be published in the June 1965 JOURNAL.

REFERENCES

1. K. K. Kelley, Bureau of Mines Bulletin 584, U. S. Government Printing Office, Washington, 1960.
2. J. R. Ligenza, *This Journal*, **109**, 73 (1962).
3. J. R. Ligenza and W. G. Spitzer, *J. Phys. Chem. Solids*, **14**, 131 (1960).
4. E. Tannenbaum, *J. Appl. Phys.*, **31**, 940 (1960).

The Value of the Faraday

Walter J. Hamer and D. Norman Craig

National Bureau of Standards, Washington, D. C.

In 1960 Craig, Hoffman, Law, and Hamer (1) as a result of measurements of the electrolytic dissolution of silver in aqueous solutions of perchloric acid reported values of 96,516.5 and 96,490.0 coulombs (gram-equivalent) $^{-1}$ for the faraday on the physical and chemical scales, respectively. These values were based on 1.117972 mg coulomb $^{-1}$ for the electrochemical equivalent of silver and 107.9028 and 107.8731 for the atomic weight of silver on the physical and chemical scales, respectively. The physical atomic weight, 107.9028, was based on $O^{16} = 16$ and on the absolute abundance ratio of Ag^{107}/Ag^{109} as measured by Shields, Craig, and Dibeler (2). The chemical atomic weight, 107.8731, was calculated by dividing the physical atomic weight by 1.000275, the factor recommended for converting values from one scale to the other. This chemical value, 107.8731, for the atomic weight of silver is significantly lower than the value, 107.880, which was accepted at that time by the International Commission on Atomic Weights.

In 1961 a unified scale of atomic weights based on $C^{12} = 12$ was universally adopted (3). Before this scale was adopted, the International Commission had care-

fully reviewed the results of both the physical and chemical determinations for each element and recommended the value 107.870 for the atomic weight of silver for the unified scale. This value together with the above value for the electrochemical equivalent of silver gives 96,487.2 coulombs (gram-equivalent) $^{-1}$ for the faraday. The value 96,487.0 is the value recommended by the N.A.S.-N.R.C. Committee on Fundamental Constants (4). This Committee expressed the value in coulombs mole $^{-1}$ with univalent charge and the gram-mole implied.

This communication is intended to explain the change made in the value of the faraday since the publication of the original article (1).

REFERENCES

1. D. N. Craig, J. I. Hoffman, C. A. Law, and W. J. Hamer, *J. Research NBS*, **64A**, 381 (1960).
2. W. R. Shields, D. N. Craig, and V. H. Dibeler, *J. Am. Chem. Soc.*, **82**, 5033 (1960).
3. A. E. Cameron and E. Wichers, *ibid.*, **84**, 4175 (1962).
4. *Chem. and Eng. News*, **41** [46], 43 (1963); *Bur. Standards Tech. News Bull.*, **47**, 175 (1963); *Physics Today*, **17** [2], 48 (1964).

Discussion Section



This Discussion Section includes discussion of papers appearing in the *JOURNAL* of The Electrochemical Society, Vol. 110, No. 8 (August 1963) and Vol. 111, No. 1, 2, 5, and 6 (January-June 1964). Discussion not available for this issue will appear in the Discussion Section of the June 1965 *JOURNAL*.

A Technique for the Evaluation of Hydrogen Embrittlement Characteristics of Electroplating Baths

M. A. Devanathan, Z. Stachurski, and W. Beck
(pp. 886-890, Vol. 110, No. 8)

M. A. V. Devanathan¹, Z. Stachurski, and W. Beck²: Details about the experimental procedure are given in the sections concerned with principles of the procedure, electrolytic cell and electrical circuit and operation which are supplemented by Fig. 1 and 2.

As can clearly be seen from Fig. 2, the potential at the anodic side of the membrane is maintained by a potentiostat and the H ionization current recorded.

The polarizing current is in milliamps; that of the H permeation in microamps.

More details about the experimental procedure have been given in ref. (1) and presented in a paper published in the May issue of the *JOURNAL*.³

Regarding diffusion of H, reference is made to the standard work by Barrer, "Diffusion In and Through Solids." Further details were given in the just mentioned paper published in the May issue of the *JOURNAL*.

Various methods may be used for the pretreatment of the specimens which consists essentially in an H saturation of the membranes. For the 4340 steel, the thermal treatment had to be excluded because the temperature required for it exceeded by far the tempering temperature of the high strength steel.

The weight loss suffered by the membrane in the acid solution which was protected cathodically was considered negligible.

Due to excessive reduction in the size of the drawings, the initial sigmoid shape of curve 1 in Fig. 3 is not clearly discernible.

SCS stands for saturated calomel scale.

The authors of this paper appreciate the detection of a typographical error on p. 889. Instead of curve 5 in Fig. 6, it should be curve 6 in Fig. 5.

G. Dubpernell⁴: The further comments from Dr. Beck are most welcome and helpful. It appears that the method consists in maintaining a constant potential corresponding to zero hydrogen concentration, on the back side of the membrane, and that the anodic current required for this purpose is considered to be utilized for ionizing the hydrogen which has diffused through the membrane, and for no other purpose. This anodic current is assumed to be a measure of the hydrogen diffused, and is called the "permeation," or the permeation current.

However, small anodic currents like this, in the microampere range, are susceptible to side reactions, and proof would be required that there were no such side reactions before the anodic current could be accepted as a measure of the permeation of hydrogen. In ref. (1).⁵

¹ Present address: Central Electrochemical Research Institute, Karaikudi-3, Madras, India.

² Present address: Dept. of the Navy, Office of Naval Res., Branch Office, London, Navy 100, Box 39, F.P.O., New York, N. Y.

³ M. A. V. Devanathan and Z. Stachurski, *This Journal*, 111, 619 (1964).

⁴ M&T Chemicals, Inc., Detroit 20, Mich.

⁵ *Proc. Roy. Soc. A*, 270, 90 (1962).

Devanathan and Stachurski found that with large times with a palladium membrane, anodic dissolution occurred on both sides of the membrane when the cathodic current was switched off. Again, when they attempted to investigate the diffusion of gaseous hydrogen and obtained large permeation currents, the palladium showed a tendency to passivate with the formation of visible oxide films.

In spite of this, palladium is considered to be completely resistant to anodic attack, and measuring the permeation rate of corrodible metals such as iron is stated to require the use of thin coatings of palladium. Under these circumstances, the validity of the method seems open to serious question.

The pretreatments of the membranes used seem excessive, and damaging to the fine structure of the metal. Surely it is not necessary to treat steel for 6 hr at 10 ma/cm² in 0.1N H₂SO₄ to saturate it with hydrogen, since the solubility at room temperature is close to zero anyway. This cathodic treatment in acid is known to cause severe hydrogen embrittlement and damage to the structure of steel, even though as Dr. Beck has pointed out there is cathodic protection and the weight loss was considered negligible. It is noted, however, that the steel membranes were polished to a smooth finish with fine emery paper after this treatment in acid.

The remarkable effectiveness of an electrodeposited iron layer to rapidly inhibit hydrogen permeation, mentioned on p. 889, should not be considered remarkable, but rather normal, since we have here an undamaged layer of iron in which hydrogen has little or no true solubility. The anomalous lack of diffusion of hydrogen which is often observed should not be considered anomalous at all, but rather the result to be expected. More work should be done with thinner membranes handled with extreme care to avoid mechanical damage.

The assumption of atomic hydrogen diffusion at room temperature seems unjustified and its nonexistence would seem to be proven by the lack of diffusion through thin undamaged membranes such as the electrodeposited iron mentioned in the preceding paragraph. The need to assume such atomic hydrogen diffusion is often based on the extremely high pressures of hydrogen which sometimes build up within metal, and which sometimes cause blisters. An alternative physical-chemical explanation for these high pressures has been proposed⁶ which makes the assumption of atomic hydrogen unnecessary.

Pitting and Uniform Corrosion of Aluminum by pH 3.5 Citrate Buffer Solution

E. L. Koehler and S. Evans (pp. 17-21, Vol. 111, No. 1)

U. R. Evans⁷: The research provides interesting information particularly the observation, that, among identical specimens identically treated, some suffer pitting and others general attack; the facts deserve statistical study according to the probability principles largely developed by American investigators working in England.⁸

The limiting current density in Fig. 2 is regarded as equivalent to the dissolution rate of the film substance.

⁶ *Proc. Am. Electroplaters' Soc.*, 51, 110 (1964).

⁷ 19 Manor Court, Grange Road, Cambridge, England.

⁸ R. B. Mears, U. R. Evans, and P. Quenneau, *Engineering*, 136, 689 (1933); *Proc. Roy. Soc. A*, 146, 153 (1934); *Trans. Faraday Soc.*, 31, 527 (1935).

If so, it should presumably become zero if the liquid is presaturated with alumina. Has the effect of presaturation, suggested by the work of Mayne and Lorking,⁹ been studied?

Again, if the authors' interpretation is the correct one, the limiting current should tally with the dissolution rate of oxide. The published dissolution rates of the oxides of iron¹⁰ and aluminum,¹¹ carried out by Pryor and others, refer to solutions free from complexing agents, and for various reasons may not be directly comparable. It should, however, be possible to transfer alumina films to plastic and study the dissolution rates in the citrate buffer.

If it is found that the results do not support the interpretation offered, another is available. The "expected" anodic reaction at low current densities in a liquid undersaturated with alumina should be the passage of Al^{+++} ions into the liquid, since this represents the maximum energy decrease and should occur—provided that time is allowed. Only at high current densities, demanding a large supply of cations with sufficient energy to pass through, and out of, the (negative) oxygen zone of the oriented anions, will some of them stay in that zone as oxide. The matter has been discussed elsewhere.¹² The principle developed, which involves no assumption other than accepted energy concepts, explains the known facts; an iron anode in dilute sulfuric acid gives ferrous sulfate at low current densities, but oxide at high ones. The line of reasoning rather suggests that the limiting current density may represent the rate of production of ions with sufficient activation energy to pass over the energy barriers into the liquid.

Whether or not this interpretation is required, may I press the authors, and everyone else in the aluminum industry, to answer the following question: why is it so often assumed that, in the anodic treatment of aluminum in sulfuric acid (to take just one example), the primary reaction is the formation of an oxide film, and that any aluminum sulfate found in solution is due to a secondary change, the chemical dissolution of alumina in the acid? Perhaps an objective answer can be given. If not, a subjective one suggests itself. The formation of oxide is the basis of a useful, and not unprofitable, industrial process. If no oxide were formed, the anodizer would be out of a job. Is it not natural that he regards the formation of oxide as the proper behavior of right-minded aluminum, and the formation of sulfate as a delinquency? I do not suggest that he has ever expressed matters quite in that way, but if he could really analyze the line of thought which he has followed in answering that question (if indeed he has ever brought himself to ask it), I suspect that he would find the argument to have been influenced by some such considerations. If no objective answer can be given, I am afraid that we must regard the assumption as having no scientific basis.

M. J. Pryor¹³: The authors' use of anodic polarization curves to distinguish between pitting and general corrosion of aluminum is an interesting and useful contribution. However, certain aspects of their explanation of this phenomenon deserve comment and possibly additional study. Since the writer has had the advantage of being able to study, in advance, the discussion of Dr. Evans, these comments must be regarded as being essentially complementary to his.

The authors appear to feel that the dissolution rate of the surface oxide film on the 3003 aluminum alloy in a given electrolyte is potential independent within the

particular ranges studied. This conclusion appears to be questionable in the absence of real supporting data. There are many cases that can be found in published work that bear closely on the experiments reported by the authors.

As an example only, the writer¹⁴ studied the form of the potential-time curves of super purity aluminum, polarized anodically at constant impressed current density in chromate solutions. Within the range of 0 to +1.5v on the hydrogen scale, the primary anodic reaction appeared to be the formation of γ - Al_2O_3 ; the potential-time curves were linear but exhibited differing gradients, depending on the pH and applied current density. It was possible to analyze these gradients in the nearly neutral pH range and to show that their variation with applied current density at any one pH value was consistent with the anodic formation of oxide at 100% efficiency and a simultaneous "parasitic" process that was pH dependent and potential independent.

It is, of course, tempting to define this process as oxide dissolution and that was done originally. On the basis of such an interpretation, the dissolution rate of an aluminum oxide film in chromate solution at pH 7.6, at potentials between 0 and 1.5v was calculated to be 1.7×10^{-7} g/cm²/hr. Subsequent experimental determination of the actual dissolution rate by a capacitance method¹⁵ in the same solution, but at a potential of around -0.3v on the hydrogen scale yielded a value of around 10^{-6} g/cm²/hr, i.e., in substantial disagreement with the previously calculated value.

These results indicate that the measured dissolution rates of oxide films are influenced significantly by potential. Such factors as variation of local pH, and in the case of citrate solutions, of interfacial citrate ion concentration should serve to generate a potential dependence of true dissolution rate. Even the "equivalent dissolution rate" of $3.6 \mu\text{a}/\text{cm}^2$, i.e., around 2.2×10^{-6} g of $Al_2O_3/\text{cm}^2/\text{hr}$ reported by authors in the citrate buffers at pH 3.5 appears to be inconsistent with a measured dissolution rate of 10^{-6} g $Al_2O_3/\text{cm}^2/\text{hr}$ in chromate solution at pH 7.6 when it is realized that the equilibrium aluminum concentration stable in aqueous solutions at the two pH values differs by around four orders of magnitude.¹⁶

Probably a more correct interpretation of the anodic polarization phenomena is offered in the discussion by Dr. Evans, where it is assumed that both oxide formation and aluminum dissolution are competing (and potential dependent) anodic processes. Indeed, this position is reinforced by the recent work of Murphy and Michelson¹⁷ on anodic films formed on aluminum in sulfuric acid. Here it was shown quite definitely that the pore form and distribution found in such films could not be attributed uniquely to the normal "hot acid" dissolution theory. Accordingly, the writer feels that the dissolution of oxide films on aluminum during anodic polarization could benefit from additional direct study by specifically applicable techniques and that such study appears necessary before the anodic characteristics of this metal can be fully understood.

E. L. Koehler and S. Evans: We have considered running tests with solution presaturated with alumina, as suggested by Dr. Evans, but have not done so as yet. We have, however, done something which is somewhat equivalent. In this case, the corrosive medium was 0.05M sodium citrate solution and the corrosion rate was much greater. We allowed corrosion to proceed until the concentration of aluminum in solution approached saturation. At such time, the corrosion rate was reduced almost to zero, as was the limiting cur-

⁹ J. E. O. Mayne and K. F. Lorking, *J. Appl. Chem.*, **11**, 170 (1961).

¹⁰ M. J. Pryor and U. R. Evans, *J. Chem. Soc.*, **1949**, 3330.

¹¹ M. A. Heine and M. J. Pryor, *This Journal*, **110**, 1205 (1963); M. A. Heine, D. S. Keir, and M. J. Pryor, *This Journal*, In press.

¹² U. R. Evans, *1st International Cong. Met. Corrosion 1961*, p. 3 (report published by Butterworths, 1962).

¹³ Metal Research Labs., Olin Mathieson Chemical Corp., New Haven, Conn.

¹⁴ M. J. Pryor, *Z. Electrochem.*, **62**, 782 (1958).

¹⁵ M. A. Heine and M. J. Pryor, *This Journal*, **110**, 1205 (1963).

¹⁶ C. Edeleanu and U. R. Evans, *Trans. Faraday Soc.*, **47**, 1121 (1951).

¹⁷ J. F. Murphy and C. E. Michelson, *Proceedings of the Nottingham Conference on Anodizing*, p. 83, Aluminum Development Association, 1962.

rent. Lesser degrees of saturation produced intermediate values for both corrosion rate and limiting current. At points well removed from saturation, stirring the solution produced a marked effect on limiting current.

It is certainly to be agreed that the passage of aluminum into solution represents the maximum energy decrease, and from a thermodynamic standpoint this is the "expected" net anodic reaction. If this were all that need be considered, one would wonder why there should be here any oxide film on the aluminum at all since it is certain that alumina does dissolve at some appreciable rate. Dr. Evans qualifies his remarks to "a liquid under-saturated with alumina." However, there seem to be good indications that the liquid at the interface is saturated with dissolved aluminum and that the limiting current density represents a limiting diffusion current. It would appear equally correct to consider the dissolution process in terms of aluminum ions passing from the oxide into the solution where this viewpoint better suits the needs of the investigator.

Referring to work of his own on high-purity aluminum in pH 7.6 chromate solution at 25°C, Dr. Pryor points out a discrepancy between his "parasitic process" studied by polarization methods and the rate of dissolution of aluminum oxide as determined by a different method. In his results however, there does not appear to be any logical basis for the conclusion that the dissolution rates of oxide films are significantly affected by potential. He points out that the dissolution rate for the oxide film in his test is about 10^{-6} g/hr cm² while the equivalent rate in our work in pH 3.5 citrate buffer solution is about 2.2×10^{-6} g/hr cm². While it is difficult to compare data on 3003 aluminum in citrate solution at 38°C with data on high-purity aluminum in chromate solution at 25°C, it is evident that his concern is that the oxide dissolution rate under our conditions should be much higher than under his. It must be pointed out that we determined the rate of weight loss for the aluminum specimens in aerobic pH 3.5 citrate buffer solution. It is not possible for the oxide film to maintain a dissolution rate which is greater than the equivalent of the rate of specimen weight loss. On this basis, it appears that it can be said with certainty that the rate of dissolution of the oxide under the conditions existing in our work may be equal to or less than the limiting current, but not greater.

It is evident from Dr. Pryor's suggestion that he is in agreement that dissolution of oxide occurs at a significant rate in terms of the quantities we are here considering. It has been demonstrated that the rate of metal corrosion is equivalent to the limiting current and that the limiting current is independent of potential. If the rate of oxide dissolution is to account for only a part, but a significant part, of the metal corrosion rate and the rate of dissolution of the oxide should be potential dependent, we would be left with finding a good explanation as to why the sum of two processes, one of which is potential dependent, should be potential independent.

The Possible Mechanisms of Complex Reactions Involving Consecutive Steps

P. C. Milner (pp. 228-232, Vol. 111, No. 2)

P. C. Milner: In a private communication, Dr. A. Despić¹⁸ has pointed out by example that there exist systems to which certain of the general conclusions reached by the author are inapplicable. On examination, these systems prove to be characterized by a choice of I intermediate species and S possible unit steps which leads to a set of relations [1] in which the equations are not linearly independent of one another. These I equations in S unknowns express the requirement that none of the intermediates shall appear in the chemical equa-

tion for the over-all reaction; but inasmuch as the choice of intermediates and unit steps is essentially arbitrary, there is no reason that the equations should be linearly independent, although it has been the experience of the author that this is typically the case in systems where a reasonable choice of intermediates yields a wide variety of possible unit steps.

In the more general case, where $I_i \leq I$ is the number of the relations [1] that are linearly independent, the argument presented in the paper requires modification only by the substitution of I_i for I . The principal conclusions then become (a) the number of nonzero stoichiometric numbers specifying a direct path can be no more than $I_i + 1$ and (b) the maximum number of direct paths is $C(S, I_i + 1)$. The former is, if anything, more restrictive and hence more useful than the previously derived result.

Dynamic Analysis of Activation Overpotential

L. Karasyk, R. W. Law, and H. B. Linford

(pp. 237-241, Vol. 111, No. 2)

J. M. Matsen¹⁹: The computer analysis of charging curves by Karasyk, Law, and Linford injects a note of optimism to the presently tedious task of determining charging parameters. Three aspects of their paper seem subject to improvements which do not, however, alter their basic approach:

1. *Accuracy of equations.*—The computer approach fits an approximate analytic solution of the differential charging equation to experimental data. It is limited by the accuracy of the approximation. Their Eq. [7], used in the computer program, is a solution to the equation

$$\frac{d\eta}{dt} = -\frac{1}{c} [i - i_0 \exp(-ab\eta)]$$

and not a solution to the correct differential charging equation, which is

$$\frac{d\eta}{dt} = -\frac{1}{c} [i - i_0 \exp(-ab\eta) + i_0 \exp(\theta - \alpha)b\eta]$$

It can be seen that at any t their η will be less negative than the true value. The initial slope of their equation would be $-i/c(1-\rho)$ rather than the correct value of $-i/c$. Setting $\rho \leq 0.03$ would begin to give results within experimental error of the true answer, but it is felt that their restriction, $\rho \leq 0.15$, is too lenient and will allow undesirable errors to be introduced.

Their Eq. [6] is not an exact solution even for the limited case of $\alpha_c = \theta/2$, which may be verified by re-differentiating Eq. [6] and comparing it to the correct differential charging equation. Their Eq. [8] is incorrectly printed and should read

$$\eta_A(t) = \frac{1}{\theta b} \ln \left[\frac{\exp \left[-\frac{\theta b i (1 + \rho) t}{c_a} \right] + \rho}{1 + \rho} \right]$$

It should be noted that their Eq. [10] now reduces to this for the case $\alpha_c = \theta$ and is an exact solution for this case. For the sign convention used, the inequalities which qualify Eq. [7] and [10] should be reversed, so that η (Eq. [7]) $\geq \eta$ (exact) $\geq \eta$ (Eq. [10]).

Statistical approach.—The least squares calculation of parameters statistically reduces any random errors due to impreciseness in reading over-potential at a given time from a charging curve. It cannot, however, reduce errors arising from nonlinearity or poor calibration of the measuring and recording equipment. In addition it fits data to an analytic expression which is a biased approximation to the true charging curve model.

With the above reservations in mind, a least squares fit gives the best statistical estimate of the charging

¹⁸ Faculty of Technology, University of Beograd, Karnigijeva, Yugoslavia.

¹⁹ Esso Research and Engineering Co., Linden, N. J.

parameters in the face of uncertainty of experimental data. The process in which the authors average all parameter values which satisfy their Eq. 15 does not give as good an estimate as a simple least squares fit and is without basis on statistical or mechanistic grounds. Their computer program can be easily modified (simplified) to make a least squares fit.

Variable capacitance.—If the double layer capacitance is not constant during the charging process, variation of the capacitance with time or overpotential must be known independently of the charging curve being analyzed. Otherwise the problem is indeterminate. For instance, given a charging curve one could arbitrarily pick a value of α and calculate an i_0 consistent with the value of η at $t = \infty$. Then at each t a value could be found for C which would exactly satisfy the differential charging equation at that point. This could be done for any α , and hence the parameters obtained would be meaningless.

Even if a variable C can be determined at a number of points on the charging curve, caution should be exercised in reducing this to a single "average" value. The type of average should be explicitly stated, and it should not be subject to variation due to the way in which the points are selected, as a time or number average would be. The average should also be of general utility in characterizing the system and should not be merely another number that can be measured.

The real test of the method of Karasyk, Law, and Linford is, of course, how well it is able to estimate the charging parameters from a single charging curve. An earlier paper²⁰ came to the conclusion that this would be extremely difficult to do, but the present authors seem to have done so to a reasonable degree of accuracy. It would be interesting to make a more controlled test of their program. For instance an exact charging curve calculated by the method of ref. (1) might be analyzed by their method to see what agreement could be attained.

L. Karasyk²¹, R. W. Law²², and H. B. Linford: We agree that the computer fits the data to the approximate equation which is the solution to the first differential equation Matsen lists. This approximate differential equation differs from the exact differential equation (the second one listed by Matsen) only in that it omits the term for the reaction in the reverse direction. However, we wish to call attention to the fact that this omission results in negligible error in $d\eta/dt$ as η becomes more negative than -30 to -40 mv. For example, the table below lists calculated values of both of the expressions for $d\eta/dt$ for typical values of α , θ , and T of 0.57, 2.0, and 298°K, respectively.

v	Approximate expression for $d\eta/dt$	Exact expression for $d\eta/dt$
-0.010	$-\frac{1}{C} [i - 1.249 i_0]$	$-\frac{1}{C} [i - 0.678 i_0]$
-0.030	$-\frac{1}{C} [i - 1.946 i_0]$	$-\frac{1}{C} [i - 1.758 i_0]$
-0.040	$-\frac{1}{C} [i - 2.430 i_0]$	$-\frac{1}{C} [i - 2.322 i_0]$
-0.050	$-\frac{1}{C} [i - 3.034 i_0]$	$-\frac{1}{C} [i - 2.973 i_0]$
-0.070	$-\frac{1}{C} [i - 4.711 i_0]$	$-\frac{1}{C} [i - 4.691 i_0]$
-0.100	$-\frac{1}{C} [i - 9.207 i_0]$	$-\frac{1}{C} [i - 9.203 i_0]$

For $\rho = 0.15$, which means that $i_0 = 0.15 i$, at $\eta = -0.030v$, the approximate expression gives $d\eta/dt = -0.708 i/C$ compared with $-0.736 i/C$ for the exact expression. Similarly at $\eta = -0.040v$, the approximate expression gives $-0.636 i/C$ compared with $-0.652 i/C$ for the exact expression. Obviously as η becomes more

negative and ρ becomes less than 0.15 (or $i_0 \leq 0.15 i$), the approximate expression will differ from the exact expression by a much smaller (insignificant) degree. Furthermore, one would hardly hope to estimate α and i_0 from readings at the start of the charging curve. As the equations indicate, the shape of the charging curve is nearly independent of i_0 and α at values of η near 0. The best estimates of kinetic parameters are obtained from portions of the charging curve which occur after η vs. t begins to exhibit curvature. In addition it would be prudent to obtain charging curves in which η_0 is of sufficient magnitude to apply the Tafel equation. Consequently the sample points read from the charging curves would be wisely chosen at overpotentials less than $-0.040v$ (for the examples in the article η went as low as about $-0.120v$).

Equation [6] in the article is an exact solution to the correct differential equation. Obviously, since the differential equation is written in terms of η and not t explicitly, the direct differentiation of the exact solution which is written as a function of time will not be in the same form as the original equation although it is mathematically equivalent to it. However, one may obtain the exact differential equation from the solution given by Eq. [6] after several transformations have been made.

Thus if we let

$$Z = K_1 \exp[r_1 t] + K_2 \exp[r_2 t]$$

and

$$u = \exp[-ab\eta]$$

We get from Eq. [6]

$$abB \exp[-ab\eta] = abB u = \left(\frac{1}{Z}\right) \frac{dZ}{dt} = \frac{d \ln Z}{dt}$$

or

$$Z = \exp[abB \int u dt]$$

However, Z is also an exact solution to

$$\frac{d^2 Z}{dt^2} - (abA) \frac{dZ}{dt} - (abB)^2 Z = 0$$

Substituting the value of Z at $\alpha = \theta/2$ or

$$Z = \exp\left[\frac{\theta}{2} bB \int u dt\right] \text{ and } u = \exp\left[-\frac{\theta}{2} b\eta\right]$$

into this differential equation gives

$$\frac{d\eta}{dt} = -A + B \left(\exp\left[-\frac{\theta}{2} b\eta\right] - \exp\left[\frac{\theta}{2} b\eta\right] \right)$$

which is the exact differential equation at $\alpha = \theta/2$.

Equation [8] is incorrectly printed in the article and should include θ as Matsen shows. Also there is an inconsistency in the direction of the inequality signs of Eq. [7] and [10]. These signs should be reversed as Matsen indicates.

We sympathize with Matsen in his realization that errors can arise from nonlinearity or poor calibration of recording equipment. However, this is a problem which exists with any experimental measurements and is a fact of life which any researcher must live with. While the approximate equation we do fit to the experimental data is biased, the real question is how serious the bias is. As shown earlier, the bias has a negligible effect for η less than $-0.040v$.

By averaging parameters, we tend to eliminate random errors arising from reading the charging curve realizing full well that errors due to equipment will exist with any measurements made using the equipment no matter what method is used in estimating kinetic parameters.

We cannot see how Matsen could have obtained "better estimates with 'simple' least squares" since our experience indicates the reverse to be true. Furthermore his statement that "the procedure which averages all parameter values which satisfy equation [15] is without statistical basis" is erroneous. Similar methods

²⁰ J. M. Matsen, *This Journal*, 110, 222 (1963).

²¹ Present address: Socony Mobil Oil Co., New York, N. Y.

²² Present address: Esso Research & Engineering Co., Madison, N. J.

of estimating variance of least square estimates are well known, well justified, and have been used in the past with fitting data to nonlinear expressions.

Matsen's argument that a value of C which satisfies the charging equation for an α and i_0 consistent with the Tafel equation could be selected at each value of t is irrelevant here. The article clearly mentions that a set of values of i_0 , α , and C is chosen which satisfy the equation within the estimated tolerance for all 11 data points chosen. Thus while a value of C might satisfy the differential equation at only one point, it is highly unlikely that one can select any values of C which will simultaneously satisfy all 11 points for a given α and i_0 .

We disagree with Matsen's comments regarding average parameter values. It seems that average values are frequently measured and are of great utility in describing the way systems behave: heat transfer coefficients, current density, and surface roughness factor are a few examples of meaningful averages. Since we are estimating an average capacitance by a discrete number of experimental points, it is not surprising that this estimate will depend on the way in which the points are chosen. Obviously any average of a sample (11 data points) chosen from an infinite population (the entire charging curve) is only an estimate of the average of the infinite population. To reduce the difference between the estimate and the true average, we could read off a larger number of points from the charging curve or we could recognize that we were estimating the average capacitance, and that this estimate of the average had an error associated with it—as any measurement does!

We agree with Matsen in the desirability of additional testing of the methods outlined in our article against other charging curves both experimental and theoretical. However, by the same token, we cannot dismiss the encouraging results with the experimental data examined so far.

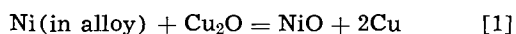
Errata: In addition to misprints in Eq. [8] and the reversal in direction of inequality signs in Eq. [7] and [10] which Matsen pointed out in his comments, Eq. [5a] and [5b] are misprinted. The first term to the right of equality sign in both equations should have a + sign instead of the — sign shown.

Furthermore, the constant b in Eq. [7a], [7b], and [7c] should be replaced by θb . When these changes are made the correct version of Eq. [8] will follow.

Effect of Vacuum Annealing of Oxide Films on Copper-Nickel Alloys

T. Yamashina and T. Nagamatsuya (pp. 249-252, Vol. 111, No. 2)

R. L. Levin²³ and J. B. Wagner, Jr.²⁴: The authors suggest that the oxidation results of Levin and Wagner²⁵ in which a 62% Cu-38% Ni alloy was oxidized in pure oxygen at 800°C, interrupted by a 4-hr anneal in argon, were not due to a displacement reaction claimed by Levin and Wagner



but rather “due to the change in the physical properties of the NiO structure with vacuum annealing, such as formation of voids or decrease of the defect density in the oxide with annealing.” The authors substantiate their suggestion by replotting the data of Levin and Wagner as $[\Delta m_1/A + \Delta m_2/A]^2 = [\Delta m_3/A]^2$ vs. time rather than $[(\Delta m_1/A)^2 + (\Delta m_2/A)^2]$ vs. time, where Δm_1 and Δm_2 are weight gains prior to and after annealing in an inert atmosphere, respectively, and A is the area of the specimen.

²³ U.S. Naval Test and Evaluation Detachment, Key West, Fla.

²⁴ Dept. of Materials Science, Northwestern University, Evanston, Ill.

²⁵ R. L. Levin and J. B. Wagner, Jr., *This Journal*, **108**, 954 (1961).

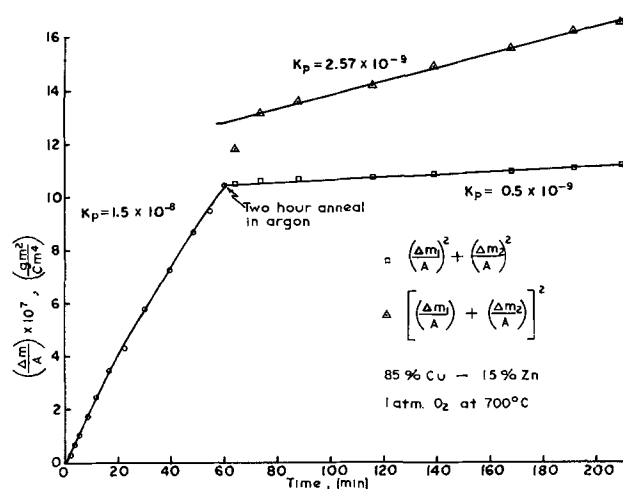


Fig. 1. Effect of annealing in an inert gas on the oxidation kinetics of an 85% Cu-15% Zn alloy. The data obtained after the 2 hr anneal in argon are plotted as $(\Delta m_1/A)^2 + (\Delta m_2/A)^2$ and as $[(\Delta m_1/A) + (\Delta m_2/A)]^2$.

Two points are at issue. The first is the role of a displacement reaction in the oxidation of alloys. The second is the validity of describing the parabolic kinetics by a plot of $[(\Delta m_1/A)^2 + (\Delta m_2/A)^2]$ vs. time.

Consider point one. Structural changes brought about by recrystallization have been studied on pure metals. On alloys a second phenomenon may also occur and for the alloys Cu-Zn and Cu-Ni in the compositions stated, Levin and Wagner presented metallographic evidence for the displacement reaction in the form of pure metallic copper present in cross sections of the oxidized samples. Levin and Wagner presented evidence for the displacement reaction being a major factor in the decreased parabolic kinetics exhibited by certain alloys after an isothermal anneal in an inert atmosphere. Yamashina and Nagamatsuya studied films an order of magnitude less thick than Levin and Wagner. Perhaps the difference in oxide thicknesses could also contribute to the apparently conflicting results.

Consider point two. Levin and Wagner treated their data by plotting $[(\Delta m_1/A)^2 + (\Delta m_2/A)^2]$ vs. time. Comparable graphs plotted both this way and as the square of the sum of the two weight gains are shown in Fig. 1. In both cases the role of the displacement reaction is clearly shown. The plot of the square of the sums of the weight gains may be preferable for theoretical reasons. The oxidation of the Cu-Ni alloy was not as clear cut as that of the Cu-Zn alloys, but the displacement reaction, Eq. [1], was shown to have occurred by means of metallographic examinations. In the oxidation of Cu-Zn alloys, the effect of a displacement reaction was a major one. In the case of the Cu-Ni alloy, the effect is admittedly not so great.

T. Yamashina and T. Nagamatsuya: In the original paper, we did not refer to the oxidation of copper-zinc alloy, but only copper-nickel alloy.

In the case of copper-zinc alloy, it may be true that a displacement reaction could occur and result in decreased parabolic kinetics as shown in Fig. 1 by Drs. Levin and Wagner.

In the oxidation of copper-nickel alloy, however, we cannot accept the possibility of occurrence of the displacement reaction, for the following reasons:

(A) No visible change in the x-ray diffraction intensity from NiO was observed after vacuum annealing (Fig. 4 in the original paper). If the displacement reaction occurred, the intensity of NiO could be increased somewhat.

(B) In the case of pure nickel oxidation, the oxidation rate was decreased by annealing, being about half the rate before annealing, which was almost the same as the case of copper-nickel alloy (Fig. 2 in the original paper).

For these reasons it can be concluded that the cause of the decrease in the oxidation rate after annealing can be due to the change in physical properties of the NiO structure.

More detailed results can be seen in our other paper.²⁶

The possibility of occurrence of the displacement reaction could be revealed by means of more quantitative analysis of oxide films, such as an electron probe microanalysis technique. Such experiments are planned.

The Oxidation Kinetics of Zirconium in the Temperature Range of 400°-600°C

R. J. Hussey and W. W. Smeltzer, (pp. 564-568, Vol. 111, No. 5)

E. A. Gulbransen²⁷: The authors show in Fig. 1 that surface preparation has a major effect on the kinetics of oxidation. This effect occurs both in the initial stage of the reaction as well as in the later stages. A chemical polished sample of zirconium shows a weight gain of 80 $\mu\text{g}/\text{cm}^2$ after 150 hr of oxidation at 400°C while an abraded and annealed specimen shows a weight gain of 220 $\mu\text{g}/\text{cm}^2$. The authors attribute this effect to the 16-20 μ of zirconium removed during chemical polishing and the elimination of gross deformations arising from the abrading process.

We think that the surface film formed during chemical polishing should also be considered to effect the kinetics of oxidation. Although the structure of this surface film is not known several facts support the existence of a very impermeable film on chemically polished zirconium surfaces. We have shown in an earlier paper²⁸ that the hydriding reaction can be used to determine the presence and the properties of this film. Chemical polished and annealed zirconium samples are much less reactive to hydrogen at 150°C than the abraded and annealed samples. A simple correlation can be made between the kinetics of hydrogen uptake and the presence or absence of air formed oxide films and films formed during chemical polishing. Engineers studying the high-temperature pressure welding in high vacua have also noted that chemically polished zirconium sections are difficult to weld. This may be related to the presence of an insoluble surface film which prevents bonding of the two zirconium sections. We have noted that the chemical polished surface film is not dissolved in the zirconium after 2 hr at 800°C in high vacua while air formed surface oxide films are easily dissolved.

The authors prefer to use the parabolic rate law treatment of the kinetic data although the cubic rate law is stated to fit the experimental data. Empirically the cubic rate law gives an excellent fit to the experimental data for abraded zirconium samples from zero time to reaction times close to breakaway oxidation conditions. The fit of the experimental oxidation rate data for chemical polished samples is also good after an initial induction period. This induction period appears to be characteristic of the oxidation process on chemically polished zirconium surfaces.

R. J. Hussey and W. W. Smeltzer: As suggested by Dr. Gulbransen, a possible reason for the variation in oxidation rates reported for abraded and chemically polished specimens is the difference in resistance properties between the two types of residual oxide films. We did not intend to imply in our paper that different surface properties of the metal accounted for the different reaction characteristics of abraded and chemically polished specimens. Both types of surface treatment removed gross deformation in the metal. Chemical

²⁶ T. Yamashina and T. Nagamatsuya, *J. Electrochem. Soc. Japan*, **31**, 118 (1963).

²⁷ Physical Chemistry Dept., Westinghouse Electric Co., Research and Development Center, Pittsburgh, Pa.

²⁸ E. A. Gulbransen and K. F. Andrew, *Proc. of Third Ann. Metallurgical Soc. Conf.—Reactive Metals*, AIME, May 1958.

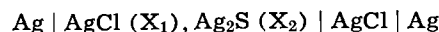
polishing was chosen for the standard method of surface preparation because excellent oxidation reproducibility was obtained.

Neither a cubic nor a parabolic rate relationship completely defines the oxidation rates found for the chemically polished specimens. Since there is at present no adequate model to explain the cubic oxidation of zirconium, we prefer representation of the experimental data at long times according to a parabolic rate equation, accounted for by lattice diffusion of oxygen in the oxide and concurrent oxygen solution in the metal. Prior to the onset of parabolic oxidation there is an initial period, during which the oxidation rate is greater than parabolic. This behavior is possibly associated with short-circuit diffusion of oxygen through the oxide film.

The Electrical Conductivity, and the Thermodynamic and Structural Properties of Molten AgCl-Ag₂S Mixtures, I. Thermodynamic and Structural Properties

M. C. Bell and S. N. Flengas (pp. 569-575, Vol. 110, No. 5)

C. T. Moynihan²⁹: The authors have misinterpreted the significance of the electromotive force of the cell



The emf of this cell^{30,31} is given correctly by the equation

$$E = \frac{RT}{F} \int_L^R \left(1 - \frac{t_{\text{SAg}}}{N_{\text{Ag}_2\text{S}}} \right) d \ln a_{\text{AgCl}}$$

where t_{SAg} is the transference number of the sulfide ion taking the silver ion as reference, $N_{\text{Ag}_2\text{S}}$ is the equivalent fraction of silver sulfide, and the integration is carried out between the composition on the left side of the cell and that on the right. Without prior knowledge of the transference numbers or relative anion mobilities in this system, activities cannot be calculated from the potential of this cell.

Junction potential is experimentally defined as the difference between the emf of a concentration cell with transference and the emf of the same cell without transference. For a binary fused salt mixture this turns out to be simply the emf of the concentration cell with transference with electrodes reversible to the common ion. Thus the emf of the above cell is ascribable entirely to what is usually thought of as a junction potential.

Junction potentials in molten salt cells may be neglected *a priori* only when the melt is very similar in composition on both sides of the junction, for example, in emf determinations where a small amount of potential-determining species is dissolved in a large excess of inert molten salt solvent. Otherwise additional information is required. Laity³² was able to neglect junction potentials in his measurements on the AgNO₃-NaNO₃ system only because of previous knowledge that the relative cation mobilities were equal over the entire composition range. Murgulescu and Sternberg³³ concluded that junction potentials were negligible in the systems they studied by comparing their results with measurements on identical concentration cells without transference. The AgCl-Ag₂S cell is an example of a system where the liquid junction potential cannot be neglected.

The authors' results are nonetheless important because of the information they impart regarding relative anion mobilities in the fused AgCl-Ag₂S system. If the

²⁹ Frick Chemical Lab., Princeton University, Princeton, N. J.

³⁰ R. W. Laity in "Reference Electrodes," D. Ives and G. Janz, Editors, Academic Press, New York, N. Y., 1961, pp. 532-543.

³¹ A. Klemm in "Molten Salt Chemistry," M. Blander, Editor, Interscience, New York, N. Y., 1964, pp. 554-559.

³² R. W. Laity, *J. Am. Chem. Soc.*, **79**, 1849 (1957).

³³ I. G. Murgulescu and S. Sternberg, *Discussion Faraday Soc.*, **32**, 107 (1961).

sulfide ion is less mobile than the chloride ion, the ratio $t_{S_{Ag}}/N_{Ag_2S}$ is less than unity, and the coefficient of the differential in the expression for E is positive. Since the measured value of E is positive in the concentration span $X_{AgCl} = 1.0$ to $X_{AgCl} = 0.94$, we can conclude that the sulfide ion is the less mobile over at least the greater portion of this range. Further, since E increases with an increase in the concentration span of the cell, the sulfide ion must remain less mobile beyond $X_{AgCl} = 0.94$. Since chloride and sulfide have approximately the same ionic radius, one would intuitively suspect that the doubly charged sulfide ion would be more strongly attracted to the silver ion and hence less mobile than the chloride ion.

By assuming the mobility ratio $U_{S_{Ag}}/U_{Cl_{Ag}}$ constant over a limited concentration span, rough estimates of this mobility ratio can be made from the authors' data. In the concentration span $X_{AgCl} = 1.0$ to $X_{AgCl} = 0.9$ $U_{S_{Ag}}/U_{Cl_{Ag}}$ is 0.6 at 550°, 0.4 at 600°, 0.2 at 650°, -0.2 at 700°, and -0.6 at 750°. If the data are of sufficient accuracy to make these figures meaningful, the implication of the negative values of $U_{S_{Ag}}/U_{Cl_{Ag}}$ is presumably that the sulfide migrates as part of a cationic complex at the higher temperatures. This brings to mind Klemm's assertion³⁴ that ionic melts eventually tend to become more associated with increasing temperature. In any event the variation in the emf of the cell with temperature definitely indicates that as the temperature increases the sulfide ion becomes increasing less mobile than the chloride ion.

M. C. Bell and S. N. Flengas: Dr. Moynihan is quite correct that neglecting the junction potential of the cell referred to is incorrect. The equation for the cell potential contains both a term for the activity of silver chloride in the mixtures containing sulfide, and anion transport terms. Dr. Moynihan chooses to assume that the activity is ideal and uses the measured cell potential to calculate relative anion mobilities. Such an assumption has some basis, as the phase diagram indicates that silver sulfide is completely dissociated and forms ideal mixtures in dilute solution in silver chloride. The relatively high-temperature dependence of the cell potential then requires the mobility of the sulfide ion to be almost as large as the chloride ion at 450°C ($U_{S_{Ag}}/U_{Cl_{Ag}} = 0.8$) and to decrease rapidly with temperature until the sulfide ion is travelling in the opposite direction to the chloride ion at high temperatures. Dr. Moynihan interprets this large temperature dependence of the mobility of the sulfide ion to be due to the formation of a cationic complex at higher temperatures, implying that the melts become more molecular at the higher temperatures. If Dr. Moynihan's interpretation were correct, one would expect a small change in electrical conductivity on the addition of silver sulfide to silver chloride at low temperatures, and would expect the temperature dependence of the conductivity to be less than that for pure silver chloride. The electrical conductivity measurements, however, show that exactly the opposite occurs. There is a large decrease in conductivity at low temperatures on the addition of silver sulfide, and the temperature dependence of the conductivity is greater than for pure silver chloride. The formation of a complex cationic sulfide species postulated by Dr. Moynihan is also not compatible with the assumption of an ideal solution. Dr. Moynihan's assumption that the activity of silver chloride is ideal may therefore not be a good approximation.

We would simply like to show that a change in the activity of silver chloride may account for some of the temperature dependence of the cell potential. The equation for the cell potential in terms of the external transport numbers may be derived as

$$F.E. = \int_L^R \left(t_{Cl} - \frac{t_S}{2} \frac{N_{Cl}}{N_S} \right) RT \ln \gamma X_{AgCl} \quad [1]$$

³⁴ A. Klemm, *J. Chim. Phys.*, **60**, 237, (1963).

where the transport numbers are referred to an external stationary reference frame, and N_S and N_{Cl} are the anion fractions of chloride and sulfide ion, respectively. On changing the frame of reference to the silver ion as the zero velocity ion, the equation given by Dr. Moynihan results. The external transport number of chloride ion in pure silver chloride has been determined by Duke *et al.*³⁵ as 0.15 ± 0.03 at 650°C to 0.17 ± 0.03 at 850°C.

Most of the current is seen to be carried by the silver ion. The sulfide ion has approximately twice the charge density of the chloride ion, and is therefore expected to have a much lower mobility. If the transport number of sulfide ion is assumed to be negligible, the activity coefficient of silver chloride in the mixtures may be calculated. Using the lower limit of the reported transport number of chloride ion in pure silver chloride, the activity coefficients and partial molar heats of mixing of silver chloride in the melts were calculated and are shown in Table I.

Table I. Thermodynamic properties of AgCl in AgCl-Ag₂S melts determined from emf measurements assuming the sulfide ion transference to be negligible

T°, C	E cell mv		Activity coefficient		$\Delta\bar{H}^M$, kcal	
	10%	20%	10%	20%	10%	20%
450	1.0	1.9	0.94	0.92	1.4	2.1
550	3.0	4.5	0.75	0.71	4.0	4.6
650	7.4	13.0	0.51	*	8.9	*

* Electronic conduction in the sulfide melts is occurring.

The liquidus for the silver chloride-silver sulfide system was carefully determined, and it is possible to compare the values of the thermodynamic properties calculated from the emf measurements with the phase diagram. The van't Hoff equation may be written

$$\ln a_{AgCl} T_F = - \frac{\Delta H_F + \bar{\Delta H}^M}{R} \left(\frac{1}{T_L} - \frac{1}{T_F} \right) \quad [2]$$

where the partial molar heat of mixing is assumed to be constant over the temperature range from T_F to T_L . Substituting the values of γ and $\bar{\Delta H}^M$ from Table I, the liquidus for the system may be calculated. The measured liquidus is only 1°C higher, and 1°C lower than that calculated at the 10 and 20 mole % sulfide compositions, respectively. It is evident that within the error of the reported external transport number, the thermodynamic properties calculated from the cell potential predict the correct liquidus for the system. The assumption that the transport number of sulfide ion was negligible may then have some validity at low temperatures where a comparison with the measured phase diagram is possible. At temperatures above 550°C, the heats of mixing are higher than expected for such a system, and the transport of the sulfide ion in the negative direction (opposite to the chloride ion) is probably significant. This is essentially the same conclusion that Dr. Moynihan makes.

We would then conclude that some of the temperature dependence of the cell potential may be accounted for by the change in activity of silver chloride with temperature, and that the transference of sulfide ion is probably small at low temperatures. The silver ion is carrying most of the current in the melts, and we would interpret the negative transport number of the sulfide at high temperatures to be due to an appreciable interaction mobility coefficient, 1_{AgS} , in an external flux equation (see, for example, Laity³⁶) which coupled with the high flux of silver ions causes a net flux of sulfide ions in the same direction as the silver ions. This

³⁵ F. R. Duke, A. L. Bowman, and E. Wolf, *Ann. N. Y. Acad. Sci.*, **79**, 1023 (1960).

³⁶ R. W. Laity, *Discussion Faraday Soc.*, **32**, 172 (1961).

interpretation of the cell potential would then be compatible with both the phase diagram and electrical conductivity measurements. A direct measurement of the transport properties, or the thermodynamic properties by calorimetric methods, would be required to make any definite conclusion as to which approximation is more correct.

Rates of Formation of Thermal Oxides of Silicon

H. C. Evitts, H. W. Cooper, and S. S. Flaschen
(pp. 688-690, Vol. 111, No. 6)

R. P. Donovan³⁷: The parabolic rate constant contained in the equation that the authors empirically fitted for

³⁷ Research Triangle Institute, P.O. Box 490, Durham, N. C.

the steam oxidation of silicon in this paper disagrees with their data for steam oxidation as plotted in Fig. 3. If the 10^9 factor in that equation is changed to 10^7 , the predicted values of oxide thickness will fit the curves of Fig. 3 and at the same time the parabolic rate constant becomes of the same order of magnitude as that previously published by Deal³⁸.

H. C. Evitts, H. W. Cooper, and S. S. Flaschen: We are in complete agreement with Mr. Donovan as to the incorrect exponent, overlooked during editing. The corrected equations should read as

$$\text{Steam: } X^2 = 1.21 \times 10^7 t \exp(-0.8 q/kT)$$

$$\text{Dry: } X^2 = 3.53 \times 10^7 t \exp(-1.33 q/kT)$$

with all terms as originally defined.

³⁸ B. E. Deal, *This Journal*, 110, 527 (1963).

Manuscripts and Abstracts for Spring 1965 Meeting

Papers are being solicited for the Spring Meeting of the Society, to be held at the Sheraton Palace in San Francisco, Calif., May 9, 10, 11, 12, and 13, 1965. Technical sessions probably will be scheduled on: Electric Insulation, Electronics (including Luminescence and Semiconductors and a Symposium on Optical Masers), Electro-Organic (including a Symposium on Industrial Organic Chemistry and a Symposium on Elucidation of Electro-Organic Electrode Processes jointly with the Theoretical Electrochemistry Division), Electrothermics and Metallurgy (including joint Symposium on Molten Salts jointly with the Theoretical Electrochemistry Division, and, also, a Symposium on Strengthening Mechanisms in Nonmetallics), Industrial Electrolytic (including a Symposium on Electrolytic Diaphragms and Battery Separators jointly with the Battery Division and, also, a Symposium on the Production of Chlorine without Caustics).

To be considered for this meeting, **triplicate copies of the usual 75-word abstract, as well as of an extended abstract of 500-1000 words** (see notice on page 274C of this issue), must be received at The Electrochemical Society, 30 East 42 St., New York, N. Y., 10017, *not later than December 15, 1964. Please indicate on 75-word abstract for which Division's symposium the paper is to be scheduled, and underline the name of the author who will present the paper.* No paper will be placed on the program unless one of the authors, or a qualified person designated by the authors, has agreed to present it in person. Clearance for presentation of a paper at the meeting should be obtained before the abstract is submitted. An author who wishes his paper considered for publication in the *JOURNAL OF ELECTROCHEMICAL TECHNOLOGY* should send triplicate copies of the manuscript to the Managing Editor of the appropriate publication 30 East 42 St., New York, N. Y., 10017. Concerning papers to be published in *JOURNAL*, see notice on per page charges on page 281C of this issue.

Presentation of a paper at a technical meeting of the Society does not guarantee publication in the *JOURNAL OF ELECTROCHEMICAL TECHNOLOGY*. However, all papers so presented become the property of The Electrochemical Society, and may not be published elsewhere, either in whole or in part, unless permission for release is requested of and granted by the Editor. Papers already published elsewhere, or submitted for publication elsewhere, are not acceptable for oral presentation except on invitation by a Divisional program Chairman.